12TH INTERNATIONAL SYMPOSIUM ON PROCESS SYSTEMS ENGINEERING AND 25TH EUROPEAN SYMPOSIUM ON COMPUTER AIDED PROCESS ENGINEERING

PART A

Edited by
KRIST V. GERNAEY
JAKOB K. HUUSOM
RAFIQUL GANI

COMPUTER-AIDED CHEMICAL ENGINEERING, 37

12TH INTERNATIONAL SYMPOSIUM ON PROCESS SYSTEMS ENGINEERING

&

25TH EUROPEAN SYMPOSIUM ON COMPUTER AIDED PROCESS ENGINEERING

This page intentionally left blank

COMPUTER-AIDED CHEMICAL ENGINEERING, 37

12TH INTERNATIONAL SYMPOSIUM ON PROCESS SYSTEMS ENGINEERING AND 25TH EUROPEAN SYMPOSIUM ON COMPUTER AIDED PROCESS ENGINEERING

PART A

Edited by

Krist V. Gernaey, Jakob K. Huusom and Rafiqul Gani

Department of Chemical and Biochemical Engineering
Technical University of Denmark
DK-2800 Lyngby, Denmark

Amsterdam – Boston – Heidelberg – London – New York – Oxford
Paris – San Diego – San Francisco – Singapore – Sydney – Tokyo

Elsevier
Radarweg 29, PO Box 211, 1000 AE Amsterdam, The Netherlands
The Boulevard, Langford Lane, Kidlington, Oxford OX5 1B, UK

British Library Cataloguing in Publication Data
A catalogue record for this book is available from the British Library

Library of Congress Cataloging-in-Publication Data
A catalog record for this book is available from the Library of Congress

ISBN (Part A): 978-0-444-63578-5
ISBN (Set): 978-0-444-63429-0
ISSN: 1570-7946

Printed and bound in Great Britain

14 15 16 17 10 9 8 7 6 5 4 3 2 1

Contents

Contributed Papers
T-1: Modelling, Numerical Analysis and Simulation

This page intentionally left blank

Preface

It is our great pleasure to present this volume of Computer-Aided Chemical Engineering for the joint event of the 12th International Symposium on Process Systems Engineering (PSE) and the 25th European Symposium on Computer Aided Process Engineering (ESCAPE) in Copenhagen, Denmark. Through this conference we would like to highlight the contributions of the process systems engineering community to the sustainability of the modern society. Through contributions from academia and industry, we aim to establish the core products of PSE/CAPE, to point out the new and changing scope of our achievements, and to define the future challenges we face. We also would like to celebrate the 25th anniversary of the ESCAPE-series, the 12th PSE conference and the 39th year of the Computers and Chemical Engineering journal.

The PSE series is a triennial conference which has been held since 1982, organized on behalf of the international PSE Executive Committee with representations from countries from the Asia-Pacific, Europe and the Americas. The annual ESCAPE series started in Elsinore, Denmark in 1992 and is organized on behalf of the CAPE working party of the European Federation of Chemical Engineering. In 2006 these two events were also combined in Garmisch-Partenkirchen, Germany.

Both symposia serve as a forum for engineers, scientists, researchers, managers and students from academia and industry to report on progress that has been made in PSE/CAPE, to discuss the current challenges that need to be addressed, and, to highlight new developments in the applications of methods, algorithms, tools to solve a wide range of problems. The PSE-2015/ESCAPE-25 joint event includes a large number of keynote lecturers from industry and academia as well as four plenary lectures covering topics on globalization, energy, environment and health from well-known experts from all over the world. In addition close to 525 papers will be presented covering the following topics: modelling, numerical analysis and simulation; mathematical programming (optimization); cyber-infrastructure, informatics and intelligent systems; process and product synthesis/design; process dynamics, control and monitoring; abnormal events management and process safety; plant operations, integration, planning/scheduling and supply chain; enterprise-wide management and technology-driven policy making. As well as the following domain applications: molecular, biological, pharmaceutical, food, energy, and environmental systems engineering.

More than 1200 abstracts were submitted and the final technical program includes around 520 presentations out of which, 425 manuscripts are included in this proceedings volume. These manuscripts have been peer-reviewed and we thank the scientific committee members for their timely and thorough reviews. We would also like to thank our volunteers (Stefano Cignitti, Seyed S. Mansouri, Amata Anantpinijwatna, Maria-Ona Bertran, Rebecca Frauzem, Thomas Bisgaard and Xavi Flores-Alsina), without whose help this proceedings volume would not have been ready on time. Finally, we thank all the authors for their high quality manuscripts and for submitting them on time. We do hope the contents of this volume will serve as valuable reference to the scientific community and practitioners of systems engineering and a permanent record of the joint PSE-2015/ESCAPE-25 conference.

Krist V. Gernaey, Jakob K. Huusom & Rafiqul Gani
7 March 2015
Department of Chemical & Biochemical Engineering
Technical University of Denmark, DK-2800 Lyngby, Denmark

PSE2012/ESCAPE-25 Committees

Symposium Chair

Rafiqul Gani, Technical University of Denmark, Denmark

International Program Committee

- G. Henning, Universidad Nacional del Litoral, Argentina
- S. Diaz, PLAPIQUI, Argentina
- M. Narodoslawsky, Graz University of Technology, Austria
- F. Logist, University of Leuven, Belgium
- C. A. O. Nascimento, University of São Paulo, Brazil
- F. L. P. Pessoa, UFRJ, Rio de Jeneiro, Brazil
- R. M. de Brito Alves, University of São Paulo, Brazil
- P. Stuart, École Polytechnique de Montréal, Canada
- L. Cisternes, Universidad de Antofagasta, Chile
- J. Wang, Sinopec, China
- J. Zhao, Tsinghua University, China
- F. Xiao, Xi'an Jiaotong University, China
- S. Zhang, IPE, Chinese Academy of Sciences, China
- S. Pierucci, Politecnico di Milano, Italy
- F. Bezzo, University of Padova, Italy
- S. Hasebe, Kyoto University, Japan
- M. Hirao, University of Tokyo, Japan
- Y. Yamashita, Tokyo University of Agriculture and Technology, Japan
- M. Kano, Kyoto University, Japan
- Y. Fukui, Mitsubishi Chemical Corporation, Japan
- I.-B. Lee, Pohang University of Science and Technology, Korea
- I. Moon, Yonsei University, Korea
- J. H. Lee, KAIST, Korea
- C. Han, Seoul National University, Korea
- D. Foo, University of Nottingham, Malaysia
- Z. A. Manan, Universiti Teknologi Malaysia, Malaysia
- J. V. Schijndel, Shell International Chemicals, The Netherlands
- A. J. B. ten Kate, AkzoNobel Chemicals B.V., The Netherlands
- M. Turkay, Koc University, Turkey
- E .N. Pistikopoulos, Imperial College London, UK
- C. C. Pantelides, PSE Enterprise, UK
- P. Piccione, Syngenta Ltd., UK
- A. Azapagic, University of Manchester, UK
- I. D. L. Bogle, University College London, UK
- G. V. Reklaitis, Purdue University, USA
- L. Biegler, Carnegie Mellon University, USA
- I. E. Grossmann, Carnegie Mellon University, USA
- V. Venkatasubramanian, Columbia University, USA
- M. Ierapetritou, Rutgers University, USA

- K. M. Ng, Hong Kong University of Science and Technology, China (H.K.)
- K. Gernaey, Technical University of Denmark, Denmark
- J. K. Huusom, Technical University of Denmark, Denmark
- J. M. Woodley, Technical University of Denmark, Denmark
- B.-G. Rong University of Southern Denmark, Denmark
- B. Sarup, Alfa Laval Copenhagen, Denmark
- P. M. Harper, Harper & Vedel Denmark
- X. Joulia, INP-ENSIACET, France
- J. M. Le Lann, INP-ENSIACET, France
- S. Engell, Technical University of Dortmund, Germany
- J. Kussi, Bayer AG, Germany
- A. Bode, BASF AG, Germany
- M. Sales-Cruz, Universidad Autónma Metropolitana-Cuajimalpa, Mexico
- A. Jimenez Instituto Tecnologico de Celaya, Mexico
- E. Perez-Cisneros, Universidad Autónoma Metropolitana, Mexico
- S. Skogestad, Norwegian University of Science and Technology, Norway
- A. Barbosa- Póvoa, Technical University of Lisbon, Portugal
- H. Matos, Universidade de Lisboa, Portugal
- N. ElBashir, Texas A&M University at Qatar, Qatar
- S. Agachi Babes-Bolyai, University, Romania
- N. Menshutina, D. Mendeleev University of Chemical Technology of Russia, Russia
- I. A. Karimi, National University of Singapore, Singapore
- Z. Kravanja, University of Maribor, Slovenia
- D. Hildebrandt, University of the Witwatersrand, South Africa
- A. Linninger, University of Illinois at Chicago, USA
- M. R. Eden, Auburn University, USA
- C. A. Floudas, Princeton University USA
- Z. Nagy, Purdue University, USA
- Y. Huang, Wayne State University, USA
- M. El-Halwagi, Texas A&M University, USA
- L. Achenie, Virginia Polytechnic Institute & State University, USA
- J. J. Siirola, Carnegie Mellon University/Purdue University, USA
- C. T. Maravelias, University of Wisconsin-Madison, USA
- N. Sahinidis, Carnegie Mellon University, USA
- M. Bassett, Dow AgroSciences LLC, USA
- B. Wayne Bequette, Rensselaer Polytechnic Institute, USA

- I. Harjunkoski, ABB, Germany
- P. Lutze, Technical University of Dortmund, Germany
- A. C. Kokossis, National Technical University of Athens, Greece
- F. Friedler, University of Pannonia, Hungary
- J. Klemes, University of Pannonia, Hungary
- S. Munawar, Indian Institute of Technology Delhi, India
- M. Bhushan, Indian Institute of Technology Bombay, India
- R. Srinivasan, Indian Institute of Technology Gandhinagar, India
- N. Mostoufi, University of Tehran, Iran
- T. Majozi, University of the Witwatersrand, South Africa
- L. Puigjaner, University Politecnica de Catalunya, Spain
- A. Espuña, Universidad Politecnica de Catalunya, Spain
- F. Marechal, École Polytechnique Fédérale de Lausanne, Swiss
- C.-L. Chen, National Taiwan University, Taiwan
- I.-L. Chien, National Taiwan University, Taiwan
- P. Kittisupakorn, Chulalongkorn University, Thailand
- A. Kammafoo, SCG Chemicals, Thailand
- R. Meier, DSM, The Netherlands
- K. C. Furman, Exxon, USA
- M. K. Burka, NSF, USA
- Fengqi You, Northwestern University, USA
- C. Gonzalez-Jimenez, GSK, USA
- S. Balakrishna, Optience, USA

This page intentionally left blank

Local Organizing Committee (Technical University of Denmark, Denmark)

Rafiqul Gani
John M. Woodley
Krist V. Gernaey
Ulrich Krühne
Jakob K. Huusom
Eva Mikkelsen
Maria-Ona Bertran
Rebecca Frauzem
Stefano Cignitti
Seyed S. Mansouri
Amata Anantpinijwatna
Thomas Bisgaard
Deenesh K. Babi
Xavi Flores-Alsina

This page intentionally left blank

Sponsors

Gold Sponsors

Silver Sponsors

Bronze sponsors

This page intentionally left blank

Krist V. Gernaey, Jakob K. Huusom and Rafiqul Gani (Eds.), 12th International Symposium on Process Systems Engineering and 25th European Symposium on Computer Aided Process Engineering.
31 May – 4 June 2015, Copenhagen, Denmark

Recent Advances in Mathematical Programming Techniques for the Optimization of Process Systems under Uncertainty

Ignacio E. Grossmann, Robert M. Apap, Bruno A. Calfa, Pablo Garcia-Herreros, Qi Zhang

Department of Chemical Engineering, Carnegie Mellon University, Pittsburgh, PA 15213, U.S.A.

Abstract

Optimization under uncertainty has been an active area of research for many years. However, its application in Process Synthesis has faced a number of important barriers that have prevented its effective application. Barriers include availability of information on the uncertainty of the data (ad-hoc or historical), determination of the nature of the uncertainties (exogenous vs. endogenous), selection of an appropriate strategy for hedging against uncertainty (robust optimization vs. stochastic programming), large computational expense (often orders of magnitude larger than deterministic models), and difficulty in the interpretation of the results by non-expert users. In this paper, we describe recent advances that have addressed some of these barriers.

Keywords: decision rule, robust optimization, stochastic programming, exogenous uncertainty, endogenous uncertainty, scenario generation.

1. Introduction

Optimization under uncertainty has been an active area of research in Process Systems Engineering (Sahinidis, 2004; Li and Ierapetritou, 2008; Grossmann et al., 2014). This area has been motivated by the fact that parameters involved in optimization models for synthesis, design, planning, scheduling and supply chain are often uncertain. Typical parameters include product demands, prices of chemicals, product yields, oil reservoir sizes, and technical parameters like kinetic constants or transfer coefficients. Yet, despite the importance of accounting for uncertainties, the impact of techniques for optimization under uncertainty at the level of applications has been limited. This has been due to a number of modeling and computational barriers. In this paper, we first provide a brief overview of the area and then describe some recent advances that are facilitating the wider deployment and application of optimization under uncertainty.

A major modeling decision in optimization under uncertainty is whether one should rely on robust optimization (Ben-Tal et al., 2009; Lin et al., 2004; Li and Ierapetritou, 2008b), or whether one should use stochastic programming (Ierapetritou and Pistikopoulos, 1994; Subrahmanyam et al., 1994; Iyer and Grossmann, 1998; Schultz, 2003; Ahmed and Garcia, 2003; Li and Ierapetritou, 2012). The basic idea in the robust optimization approach is to guarantee feasibility over a specified uncertainty set, while in stochastic programming a subset of decisions are made by anticipating that recourse actions can be taken once the uncertainties are revealed over a pre-specified scenario tree with discrete probabilities of the uncertainties. On the one hand, the robust

optimization approach tends to be more appropriate for short-term scheduling problems in which feasibility over a specified set of uncertain parameters is a major concern, and when there is not much scope for recourse decisions. The stochastic programming approach, on the other hand, tends to be more appropriate for long-term production planning and strategic design decisions, since it does not fix all the decisions at the initial point of the planning horizon as it allows recourse decisions in future times to adapt in response to how the uncertainties are revealed. It should also be noted that chance constrained optimization can be regarded as a generalization of robust optimization in which distribution functions are specified for the uncertainties with which a level of probability for meeting the constraints is specified (Li et al., 2008).

Computationally, stochastic programming problems tend to be very expensive to solve. This is particularly true if one has to deal with both exogenous and endogenous parameters, where the realization of the latter depends on the decisions taken (e.g., oilfield size), while the former are independent of decisions (e.g., demands) (Jonsbråten, 1998). Chance constrained programming is also computationally challenging, especially when the level of probability is specified for the joint constraints. Robust optimization tends to be the least computationally expensive, especially for linear problems. In all cases, however, it is of great importance to have as a basis a computationally efficient deterministic model since adding uncertainty unavoidably adds complexity to the computations. Aside from the computational issues, there is also the question of how to specify the uncertainties (e.g., an intuitive guess or through statistical analysis of historical data) and how to interpret the results that are predicted from the various models.

In this paper, we address the following specific challenges in optimization under uncertainty: (a) how to account for recourse in robust optimization, (b) how to effectively solve two- or multi-stage stochastic optimization problems, (c) how to effectively handle both exogenous and endogenous uncertainties in multi-stage stochastic programming, and (d) how to incorporate historical data in the generation of scenarios. As will be shown, significant progress has been made to address these issues.

2. Decision Rule Approach for Modeling Recourse in Robust Optimization

Robust optimization (Ben-Tal et al., 2009) is one approach for incorporating uncertainty in optimization models. The uncertainty is specified in terms of an uncertainty set in which any point is a possible realization of the uncertainty. The goal is to find a solution that is feasible for all possible realizations of the uncertainty while minimizing (or maximizing) the objective function. Since the worst case scenario is one of the possible realizations, a robust optimization model returns a solution that is optimal for this particular scenario. However, considering the worst case is often overly conservative. One can reduce the level of conservatism by appropriately adjusting the size of the uncertainty set. Bertsimas and Sim (2004) propose such an approach in which a pre-specified "budget" parameter limits the number of uncertain parameters that can change at the same time. The general formulation for linear models is as follows:

$$\min_{x}\{c^T x: A(u)x \leq b \quad \forall\, u \in U\} \tag{1}$$

where the parameter u is uncertain and defined over the corresponding uncertainty set U in which we assume the uncertainty budget is included. Eq. (1) corresponds to a semi-

infinite programming problem, but can be simplified by considering the dual of each row in the matrix A (robust counterpart), which yields a finite dimensional optimization problem. A drawback with this approach is that specifying the uncertainty set U is not trivial, not only because the uncertainty set might not be well known, but also because the user has to specify the uncertainty "budget," ranging from very conservative (all parameters vary independently) to less risk averse (e.g., limiting the number of independent variations). Another reason for over-conservatism in traditional robust optimization is the disregard of recourse (i.e., reactive actions after the realization of the uncertainty), which is a very unrealistic assumption in many cases, such as in problems involving investment and long-term contract decisions. In this section, we present a recent development in robust optimization that allows recourse to a certain extent, and demonstrate the effectiveness of this method by applying it to an industrial case study.

2.1. The Affine Decision Rule Approach

Consider the following multi-stage (T stages) optimization problem under uncertainty,

$$\min_{x}\left\{ c^T x_1 : A_1(u)x_1 + \sum_{t=2}^{T} A_t x_t(u) \le b \quad \forall\, u \in U \right\} \tag{2}$$

where x_t is the vector of the t-th-stage variables. For simplicity, we assume that the objective function only depends on x_1 and that only matrix A_1 is uncertain. While x_1 does not depend on u, x_t for $t \ge 2$ are recourse variables and depend on the realization of the uncertainty. Note that x_t only depends on the u that are realized up to stage t.

The problem given in Eq. (2) cannot be solved as such since the set of possible functions for $x_t(u)$ is infinitely large. The idea in the Decision Rule approach (Kuhn et al., 2011), also referred to as Adjustable Robust Optimization (Ben-Tal et al., 2009), is to restrict oneself to a certain type of functions for $x_t(u)$, in particular to the set of affine functions. Hence, we set $x_t(u) = \alpha_t + \mathrm{B}_t u$, and we obtain the following robust formulation by constraint-wise construction:

$$\min_{x_1,\alpha,B}\left\{ c^T x_1 : \max_{u\in U}\left\{ a_{1,i}^T(u)x_1 + \sum_{t=2}^{T} a_{ti}^T(\alpha_t + \mathrm{B}_t u)\right\} \le b_i \quad \forall\, i \right\} \tag{3}$$

which can be reformulated into a single-level problem for certain types of uncertainty sets by using techniques applying strong duality. This results in a robust counterpart formulation in which the decision variables are x_1 as well as the parameters for the affine decision rules, α and B. By applying the Decision Rule approach, the multi-stage problem is transformed into a single-stage problem to which the classic robust optimization reformulation is applied. Obviously, it is quite restrictive to only consider affine functions; however, this allows us to retain computational tractability and still account for recourse to a certain extent (for rigorous treatment of recourse see Grossmann et al. (2014)).

2.2. Industrial Case Study

In this case study, we consider the scheduling of an air separation unit (ASU) with added cryogenic energy storage (CES) capability. In an integrated ASU-CES system,

electricity recovered from the CES can be used internally to power the ASU, to sell power back to the grid during higher-price periods, or to provide operating reserve capacity which can be dispatched in case of emergency. The uncertainty lies in the reserve demand since we do not know in advance when and how much of the provided reserve capacity will be requested. However, since noncompliance results in very high penalties, reserve providers have to operate in a way such that dispatch of the committed reserve capacities can be guaranteed. For the discrete-time MILP model on which this work is based, we refer to Zhang et al. (2015). The data for this case study are provided by Praxair. In the proposed model, the first-stage decisions are the ones related to the base operation of the plant as well as how much reserve capacity to provide. The recourse variables are the amounts of liquid produced in addition to the base production after a reserve dispatch occurs. This additional liquid is then fed into the CES tank to make sure that there is sufficient inventory to also guarantee the next potential dispatch. The affine decision rules are constructed such that the recourse variables depend on the realization of the uncertainty prior to the corresponding time period. Furthermore, in order to reduce the degree of conservatism, we apply an uncertainty set which sets a limit to the number of time periods in which maximum reserve dispatch can occur.

Applying the proposed model, the scheduling problem is solved for a one-week time horizon, obtaining a 5% cost reduction compared to the worst-case solution. Figure 1 shows the flows into and out of the CES tank as well as the CES inventory profile in the particular scenario in which no reserve power is dispatched. The budget parameter is chosen such that maximum reserve dispatch can only happen once during the entire scheduling horizon. Note that the final inventory level is nonzero, and not as high as the maximum reserve capacity that is provided, which is due to the recourse actions. We should note that the resulting MILP model with approximately 53,000 constraints, 55,000 continuous variables, and 2,500 binary variables was solved in about 10 minutes to 1 % optimality gap using CPLEX 12.6.

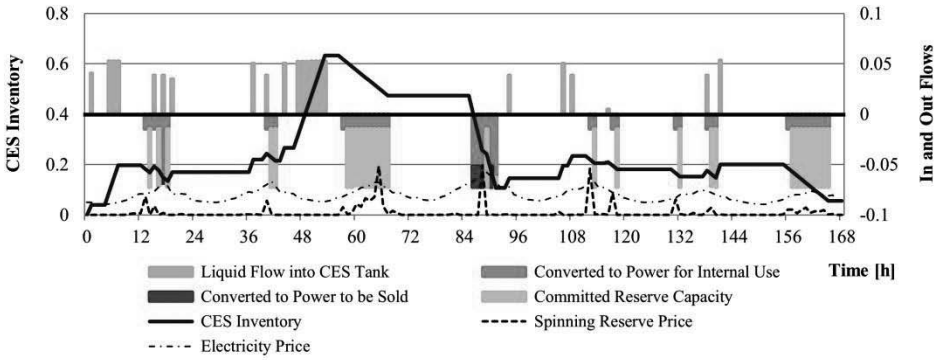

Figure 1. The CES inventory is shown for the scenario in which no reserve power is dispatched, resulting in a nonzero final CES inventory level.

3. Two-Stage and Multistage Stochastic Programming

Stochastic programming is the framework that models mathematical programs with uncertainty by optimizing the expected value over the possible realizations. In general, the expected value is computed by integrating over the set of uncertain parameters,

which might be a challenging task. In the case of discrete uncertainty sets with finite support, the realizations can be characterized with a finite number of scenarios, simplifying the calculation of the expected value. Accordingly, stochastic programming is often regarded as a scenario-based approach for optimization under uncertainty (Birge and Louveaux, 2011). The formulations can accommodate decision making at different stages according to the sequence in which uncertainty reveals. The stages imply a discrete time representation of the problem and establish the information of the uncertain parameters available at that time. The potential paths in which discrete uncertain parameters might evolve are represented in a scenario tree as shown in Figure 2. In these trees, each node is a decision-making instance with known realization of the uncertain parameters up to the current state; potential future realizations are represented with branches from the given node.

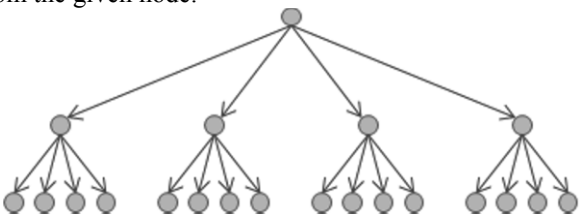

Figure 2. Tree representation of scenarios in a stochastic program with three stages.

The simplest stochastic programming formulation considers decisions that are made before uncertainty reveals. It is called single-stage stochastic programming or stochastic programming without recourse. Among the stochastic programs that consider recourse, the most widely used formulation is the Mixed-Integer Linear Program (MILP) with continuous recourse in a second stage. The two-stage stochastic programming formulation divides the decisions into two sets: here-and-now decisions that are made before uncertainty reveals, and wait-and-see decisions that are independent for each scenario. The typical formulation of a linear stochastic programming problem is presented in Eq. (4),

$$\begin{aligned} \min_{x \in X} \quad & c^T x + \mathbb{E}[Q(x,s)] \\ \text{s.t.} \quad & Q(x,s) = \min_{y_s \in Y} \; d_s^T y_s \\ & \qquad \text{s.t.} \;\; W y_s \le h_s - T_s x \end{aligned} \tag{4}$$

where x is the vector of first-stage decisions in mixed-integer polyhedral set X, y_s is the vector of second-stage (recourse) decisions in polyhedral set Y, and s is the index for scenarios. An important property of the formulation presented in Eq. (4) is that the feasible region for the first-stage variables x is a convex polyhedron (Birge and Louveaux, 2011). Based on this property and assuming that the second-stage problems ($Q(x,s)$) are bounded, an MILP reformulation that explicitly calculates the expected value can be derived by including all second-stage problems. This reformulation, the deterministic equivalent of the stochastic programming problem that is presented in Eq. (5), may lead to very large problem sizes if the number of scenarios is large.

$$\begin{aligned} \min \quad & c^T x + \sum_{s \in S} p_s (d_s^T y_s) \\ \text{s.t.} \quad & W y_s \le h_s - T_s x \qquad \forall\, s \in S \end{aligned} \tag{5}$$

$$x \in X;\ \ y_s \in Y$$

The benefits of using a stochastic programming model can be quantified by the Value of the Stochastic Solution (VSS). The VSS is the difference between the expected value of the objective functions obtained from the stochastic formulation and a deterministic formulation that substitutes the uncertain parameters with their expectation. The expected value of the deterministic formulation is calculated by solving the problem, implementing the first-stage solution, and evaluating the scenarios with their optimal recourse. The model in Eq. (4) can also be extended to a multistage stochastic programming model. The tree corresponding to a three-stage problem has the same structure as the one shown in Figure 2. The solution of multistage stochastic programming problems is considerably harder, and special care must be taken to avoid anticipating the uncertain parameters that have not been revealed. The general formulation of a three-stage stochastic programming problem is presented in Eq. (6),

$$\begin{aligned} &\min_{x\in X} \quad c^T x + \mathbb{E}[Q_2(x,s)] \\ &\text{s.t.} \quad Q_2(x,s) = \min_{y_s\in Y} \ d_s^T y_s + \mathbb{E}[Q_3(x,y_s,s)] \\ &\qquad\qquad \text{s.t.}\ W y_s \le h_s - T_s x \\ &\qquad\qquad\quad Q_3(x,y_s,s) = \min_{z_s\in Z} \ f_s^T z_s \\ &\qquad\qquad\qquad\qquad \text{s.t.} \quad V z_s \le g_s - U_s x - W y_s \end{aligned} \tag{6}$$

One way of transforming the formulation in Eq. (6) into its deterministic equivalent is to generate a set of copied variables for each path from the root node to the branches, and introduce non-anticipativity constraints (Ruszczyński, 1997). This reformulation has the advantage of being relatively easy to implement. The solution of large-scale stochastic programming problems is a challenging area of research due to the very large number of scenarios needed to model industrial problems and the rapid growth of scenarios in multistage stochastic programming. Methods frequently used to solve large stochastic programming problems leverage the scenario structure of the problems. The L-shaped method is the implementation of Benders decomposition to two-stage stochastic programming problems (Van Slyke & Wets, 1969). The method considers the first-stage variables as complicating and iterates between a relaxed master problem and subproblems that are solved by scenario. Lagrangean relaxation is also used in decomposition strategies for two-stage and multistage stochastic programming problems. The most common implementation generates sets of copied variables for each scenario and their corresponding non-anticipativity constraints. A Lagrangean relaxation of the problem is obtained by dualizing the non-anticipativity constraints, which makes the problem amenable to scenario decomposition. Other decomposition strategies are Progressive Hedging and Nested Decomposition procedures.

3.1. Example of Two-Stage Stochastic Programming

The design of a resilient supply chain with risk of disruptions is presented by Garcia-Herreros et al. (2014). The problem is formulated as a two-stage stochastic program. In the first stage, distribution centers (DCs) are selected from a set of candidate locations and their capacities are established. In the second stage, the demand assignment decisions are made according to the selected DCs and random disruptions in each scenario. The example includes: 1 production plant, 9 candidate locations for DCs, and

30 customers with demands for 2 commodities. The parameters of the instance were generated randomly. The candidate DCs have disruption probabilities between 2% and 10%. The number of scenarios in the full-space problem is $2^9 = 512$. The design is based on a time-horizon (N) of 365 days; on this time-scale, investment cost can be interpreted as annualized cost. The instance is used to illustrate the use of Benders decomposition, the benefits of strengthening the master problem, and the impact of solving a reduced subset of relevant scenarios. The selected relevant subset of scenarios includes scenarios with up to 4 simultaneous disruptions, for a total of 256 scenarios with probability equal to 99.99%. The full-space model yields a total cost of $7,225,447, while the reduced model yields a similar cost of $7,224,591. Both solutions predict the same design decisions and therefore the same investment cost. The largest difference in the results is in the expected cost of penalties. Both problems were solved to 0% optimality tolerance using the special Benders decomposition algorithm described in Garcia-Herreros et al. (2014). Both formulations involve 9 binary variables; the full-space model has 318,479 constraints and 309,263 continuous variables, while the reduced-space model has 159,247 and 154,639, respectively. The Multi-cut Benders solution times were 281 s and 151 s, respectively, while the Strengthened multi-cut Benders solution times were 176 s and 89 s, respectively. As can be seen in Figure 3, the use of the strengthened multi-cut master problem reduces the solution time because it requires fewer iterations. The solution times for the full-space and the reduced instances without any decomposition strategy, using GUROBI 5.5.0, were 3,349 s and 1,684 s, respectively. The much smaller solution times with the decomposition algorithms demonstrate that the proposed methodology is effective to solve large-scale instances of high computational complexity.

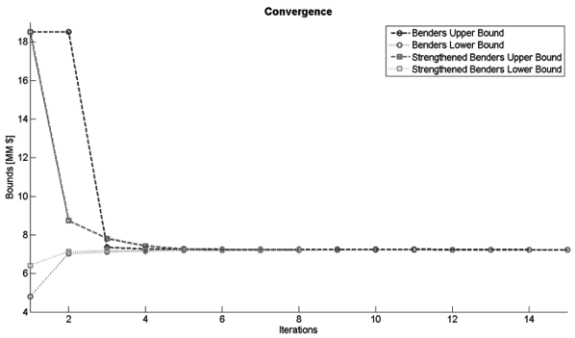

Figure 3. Convergence of Benders algorithms for the full-space instance of the large-scale example.

4. Multistage Stochastic Programming under Endogenous and Exogenous Uncertainties

Uncertain parameters can be classified into two categories depending upon the way the uncertainty is resolved: exogenous, where realizations occur independently of the decisions; and endogenous, where the realizations are affected by the decisions. In the endogenous case, the decisions may affect the timing of the realizations or their underlying probability distribution (Jonsbråten, 1998). In this section, we consider the first class of endogenous uncertainty where decisions affect the timing of realizations. In the context of process systems engineering, exogenous uncertainties often correspond to market uncertainties, such as oil prices. Endogenous uncertainties are technical

uncertainties, such as oilfield size, that are only resolved after a decision is made at a given point in time (e.g., to drill a particular oilfield). Surprisingly, although many problems contain both types of uncertainties, optimization under both types has been largely unexplored in the literature.

In the case where the uncertainty is purely exogenous, the shape of the scenario tree is known in advance, since exogenous realizations occur automatically in each time period. This is shown in Figure 4 with the standard form of the tree, as well as its alternative representation which gives each scenario a unique set of nodes.

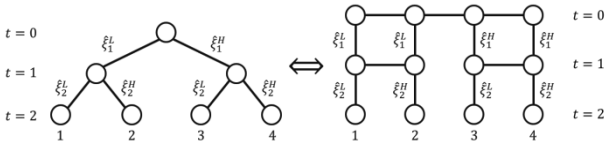

Figure 4. An exogenous scenario tree and its alternative representation.

In the case of endogenous uncertainty, however, the shape of the scenario tree is conditional, since the timing of realizations depends on the process decisions. As shown in Figure 5, we use a superstructure form of the alternative tree in order to capture all possible outcomes (Apap and Grossmann, 2015).

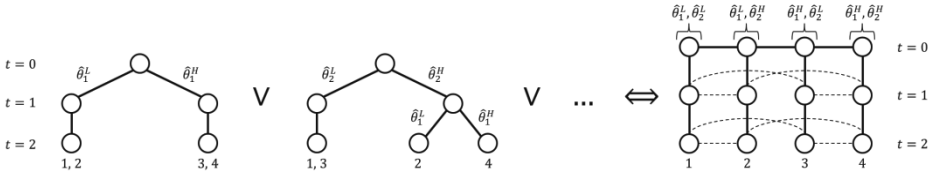

Figure 5. A superstructure representation for endogenous scenario trees.

For simplicity, we assume that the scenarios correspond to all possible combinations of realizations of the uncertain parameters. In other words, the set of scenarios in the exogenous scenario tree corresponds to a Cartesian product over the sets of realizations for the exogenous parameters (denoted by $\mathcal{R}_X$), and, similarly, the set of scenarios in the endogenous scenario tree corresponds to a Cartesian product over the sets of realizations for the endogenous parameters (denoted by $\mathcal{R}_N$). For the case of both endogenous and exogenous parameters, we generate the set of scenarios by simply taking the Cartesian product of all possible combinations of realizations of the endogenous parameters and all possible combinations of realizations of the exogenous parameters, $\mathcal{R}_N \times \mathcal{R}_X$. This is equivalent to copying the exogenous scenario tree for each possible combination of realizations of the endogenous parameters. We then link these exogenous trees by adding first-period and endogenous non-anticipativity constraints, thereby producing what we refer to as a 'composite' scenario tree as shown in Figure 6.

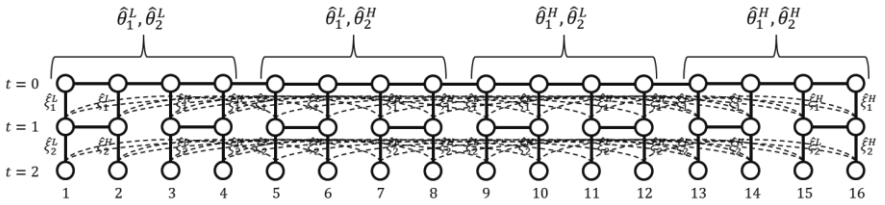

Figure 6. A 'composite' scenario tree for endogenous and exogenous realizations.

The general model for this class of problems, originally proposed by Goel and Grossmann (2006), is a mixed-integer linear disjunctive program. A simplified, compact form of the updated model (Apap and Grossmann, 2015) is given in Eq. (7)-(15).

$$\min_{x} \phi = \sum_{s \in \mathcal{S}} p^s \sum_{t \in \mathcal{T}} c_t^s x_t^s \tag{7}$$

$$\text{s.t.} \quad \sum_{\tau=1}^{t} A_{\tau,t}^s x_\tau^s \leq a_t^s \qquad \forall\, t \in \mathcal{T},\ s \in \mathcal{S} \tag{8}$$

$$x_1^s = x_1^{s'} \qquad \forall\, (s, s') \in \mathcal{SP}_F \tag{9}$$

$$x_{t+1}^s = x_{t+1}^{s'} \qquad \forall\, (t, s, s') \in \mathcal{SP}_X \tag{10}$$

$$\begin{bmatrix} Z_t^{s,s'} \\ x_{t+1}^s = x_{t+1}^{s'},\ t < T \end{bmatrix} \vee \left[\neg Z_t^{s,s'}\right] \qquad \forall\, (t, s, s') \in \mathcal{SP}_N \tag{11}$$

$$Z_t^{s,s'} \Leftrightarrow F(x_1^s, x_2^s, \ldots, x_t^s) \qquad \forall\, (t, s, s') \in \mathcal{SP}_N \tag{12}$$

$$x_{k,t}^s \in \{0,1\} \qquad \forall\, t \in \mathcal{T},\ s \in \mathcal{S},\ k \in \mathcal{K}' \tag{13}$$

$$x_{k,t}^s \in \mathbb{R} \qquad \forall\, t \in \mathcal{T},\ s \in \mathcal{S},\ k \in \mathcal{K} \backslash \mathcal{K}' \tag{14}$$

$$Z_t^{s,s'} \in \{True, False\} \qquad \forall\, (t, s, s') \in \mathcal{SP}_N \tag{15}$$

The objective function, Eq. (7), minimizes the total expected cost associated with decisions x_t^s, weighted by the probability of each scenario, p^s. Eq. (8) represents constraints that govern decisions x_t^s and link decisions across time periods. First-period non-anticipativity constraints (NACs) are given by Eq. (9), exogenous NACs are given by Eq. (10), and disjunctive constraint (11) conditionally enforces endogenous NACs based on the value of Boolean variable $Z_t^{s,s'}$. The value of $Z_t^{s,s'}$ is determined by an uncertainty resolution rule in Eq. (12).

Because the number of NACs grows exponentially as the number of time periods, uncertain parameters, or realizations increases, most problems of practical interest are too large to be solved directly with commercial MILP solvers. In order to eliminate redundant NACs, a number of theoretical properties have been proposed by Goel and Grossmann (2006), Gupta and Grossmann (2011), and Apap and Grossmann (2015) based on the concepts of symmetry, adjacency, transitivity, and scenario grouping. These properties drastically reduce the number of constraints; however, the resulting model is often still intractable, and special solution approaches are required.

One effective approach is Lagrangean decomposition (LD), in which the complicating non-anticipativity constraints are dualized in order to decompose the problem into independent scenario subproblems that can be solved in parallel. More recently, a

sequential scenario decomposition heuristic (SSD) has been proposed that involves sequentially solving endogenous MILP subproblems to determine the integer decisions, fixing these decisions to satisfy the first-period and exogenous NACs, and then solving the original problem as an LP (Apap and Grossmann, 2015).

4.1. Oilfield Planning Example

We consider a modified form of the MILP described in Gupta and Grossmann (2014) (see Case (i)) for maximizing the total expected NPV in the development planning of an offshore oilfield. There are 3 oilfields, 3 potential FPSOs, and 9 possible field-FPSO connections. A total of 30 wells can be drilled over a 5-year planning horizon. Fields 2 and 3 have a known recoverable oil volume; however, the size of field 1 has two possible realizations with equal probabilities. The oil and gas prices are also uncertain, with two possible realizations with equal probabilities in each time period. (The oil and gas prices are assumed to be correlated.) This gives rise to a total of 64 scenarios with equal probabilities. This instance of the modified oilfield problem (Apap and Grossmann, 2015) is an MILP with 333,249 constraints, 70,465 continuous variables, and 7,360 binary variables. After applying the theoretical reduction properties, there are 124,980 constraints (a 62% reduction), 70,465 continuous variables, and 7,000 binary variables. The problem was modeled in GAMS 24.3.3 and solved with CPLEX 12.6.0.1.

In the case of solving the reduced model directly, the optimality gap cannot be improved past 50% after more than 11 hours. In contrast, the sequential scenario decomposition heuristic (SSD) finds a high-quality feasible solution in only 41 seconds, and the Lagrangean decomposition (LD) algorithm finds a high-quality upper bound in only 14 seconds. This is an optimality gap of only 0.20%, obtained in under one minute. Table 1 summarizes the results for the example problem.

Table 1. Numerical results for the oilfield development planning example.

Problem Type	Total Expected NPV ($\$10^9$)		Optimality Gap	Solution Time (s)
	Lower Bound	Upper Bound		
Reduced Model	6.968	10.495	50.61%	40,562
LD	-	7.180	0.20%	14
SSD	7.166	-		41

5. Data-Driven Approaches to Scenario Generation

Before solving a robust or stochastic optimization model in practice, one has to choose a proper model of the uncertainty. This is motivated by the fact that the quality of such model directly impacts the quality of the solution of the optimization problem. In this section, we discuss methods for uncertainty modeling that use historical and forecast data for scenario-based optimization frameworks (e.g., stochastic programming).

Scenario trees are discrete representations of the probable outcomes of uncertain parameters, which are continuous random variables in most applications in process systems engineering. Also, a scenario tree is an input to a stochastic programming model. Therefore, systematically generating scenario trees that more accurately capture

the true, but generally unknown structure of the uncertainty improves the quality of the solution to the original stochastic problem (see Chapter 4 in King and Wallace, 2012). Given an initial structure of the tree (number of stages and number of branches from each node), data-driven scenario tree generation methods directly use available data to specify the probabilities of the branches and values of the outcomes.

In this section, we discuss the property-matching method of Høyland and Wallace (2001) and an extension that addresses the potential under-determination of such method. The property-matching method aims at generating scenario trees by matching statistical properties (e.g., moments and co-moments) calculated from the tree to the respective properties estimated from actual data (historical or forecast). Specifically, generating a scenario tree requires solving an optimization problem in which the objective function is an error measure (deviation of properties from the tree and data), and the decision variables are branch probabilities and node values. Consider the case of a two-stage scenario tree with N scenarios that is used to model a single uncertain parameter (see Figure 7). The scenario probabilities and node values are represented by the vectors p and x, respectively.

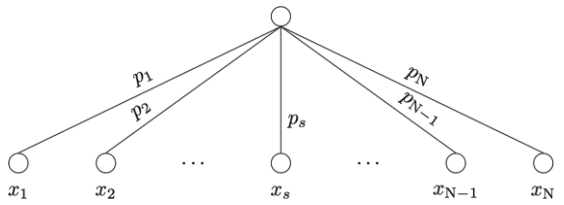

Figure 7. Two-stage scenario tree for one uncertain parameter.

The property-matching optimization model is given in Eq. (16). The set of statistical properties to be matched is denoted by J, and the target value for property j is given by Sval_j. Also, $f_j(\cdot,\cdot)$ is the mathematical expression of statistical property j calculated from the tree, and w_j is a weight vector.

$$\begin{aligned} &\min_{x,p} \sum_{j\in J} \text{w}_j \cdot \left(f_j(x,p) - \text{Sval}_j\right)^2 \\ &\text{s.t.} \quad \sum_{s=1}^{\text{N}} p_s = 1 \\ &\qquad p_s \in [0,1] \qquad\qquad \forall\, s = 1,\ldots,\text{N} \end{aligned} \tag{16}$$

The optimization model in (16) may be over- or under-determined depending on the number of branches, targets, and uncertain parameters. For instance, for one uncertain parameter and four moments as targets (Calfa et al., 2014), it can be calculated that we can only have a tree with $\text{N} = 2$ scenarios for a well-posed model. If we were to increase N to three or more, then this would result in an under-specified model. To overcome this under-specification issue and to allow more scenarios to be considered, a distribution-matching approach has been proposed and is briefly described as follows.

In addition to matching (co-)moments, points of the (empirical or estimated) marginal cumulative distribution function (CDF) are also matched, thus increasing the number of

target values and balancing the difference between the number of variables and data points. Specifically, let $j = \text{CDF}$ denote the marginal CDF property to be matched. Following the notation in Eq. (16), the functional form used in the distribution matching problem is given by Eq. (17).

$$f_{\text{CDF}}(x,p) = \widehat{CDF}(x_s) - \sum_{s'=1}^{s} p_{s'} \qquad \forall\, s = 1, \ldots, \text{N} \tag{17}$$

where $\widehat{CDF}(\cdot)$ denotes the empirical or estimated marginal CDF of random variable x. Note that we must ensure that the node values are ordered due to the cumulative information being matched, e.g., $x_s \leq x_{s+1}$, $\forall\, s = 1, \ldots, \text{N} - 1$. The approach described above can be extended for the case of multiple uncertain parameters as well as autocorrelated uncertainties (stochastic processes), such as product demand and price. In the latter case, scenario tree generation is aided by time series forecasting (see Calfa et al. (2014) and references therein).

5.1. Two-Stage Scenario Tree Generation Example

A network of three chemical plants is described in Calfa et al. (2014) (see Example 1). The yield of plant P1 is the uncertain parameter and the distribution of its historical data is given in Figure 8. The empirical CDF was obtained and approximated by a smooth function (generalized logistic function), i.e., $\widehat{CDF}(\cdot)$ in Eq. (17). In this example, $\text{N} = 5$ scenarios were considered, and the targets include the first four moments and CDF information. The scenario generation problem is a nonlinear program with 10 variables and 14 constraints. It was modeled in AIMMS 3.13 and solved with IPOPT 3.10.1 using AIMMS' multi-start module in less than one second. Figure 9 shows the profile of optimized scenario probabilities as well as node values of the generated scenario tree. Note that the profile captures the shape of the distribution of the original data, including tail effects.

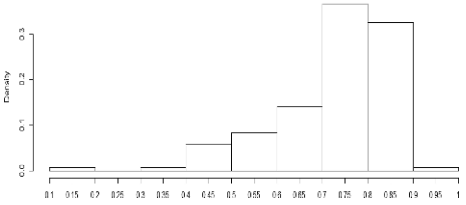

Figure 8. Distribution of the historical data for the production yield of plant P1.

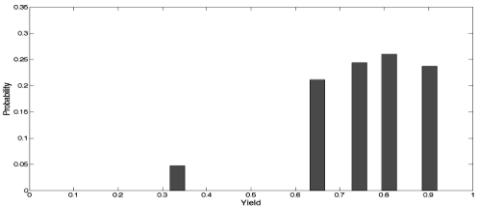

Figure 9. Profile of scenario probabilities obtained with the distribution-matching approach.

6. Conclusions

In this paper, we have addressed several major challenges in optimization under uncertainty. We have shown that recourse can be accounted for in robust optimization with linear decision rules, which has the effect of producing less conservative solutions, as was shown in the example on cryogenic energy storage. To effectively solve two-stage stochastic optimization problems, we have shown the importance of developing tailored solution strategies; e.g., by reducing the number of scenarios, tightening the MILP formulation, and applying decomposition schemes like Benders with multiple cuts. This was illustrated in the case of supply chains under disruptions. We have also

shown that both exogenous and endogenous uncertainties can be effectively handled in multi-stage stochastic programming by relying on theoretical properties to reduce the number of non-anticipativity constraints, and applying Lagrangean decomposition coupled with fast heuristics. This was illustrated in an oilfield planning problem. Finally, we have shown that to avoid assigning arbitrary probabilities and outcomes in scenario trees, historical data can be incorporated to generate these scenarios by using moment matching supplemented by matching cumulative distribution function values. This was illustrated with a production planning problem.

All of the examples in this paper have demonstrated the progress that has been made in this area, although the models have been restricted to MILP models. It is clear that major challenges remain in this area that we have not addressed in this paper. One of these challenges is the effective solution of stochastic MINLP problems (Li et al., 2011; Tarhan et al., 2013). Another one is the interpretation of results from these models, which can be aided by the addition of risk measures in the objective function and/or by the use of simulation (Applequist et al., 2000; Barbaro and Bagajewicz, 2004; You et al., 2009).

Acknowledgments. The authors would like to acknowledge financial support from NSF Grant No. 1159443, Praxair, Dow Chemical and the Center for Advanced Process Decision-making.

References

Apap, R. M., I. E. Grossmann, 2015. Models and computational strategies for multistage stochastic programming under endogenous and exogenous uncertainties. In preparation.

Applequist, GE; Pekny, JF; Reklaitis, GV, (2000). Risk and uncertainty in managing chemical manufacturing supply chains. Computers & Chemical Engineering, 24, 2211-2222

Ahmed, S., Garcia, R., 2003. Dynamic capacity acquisition and assignment under uncertainty. Ann. of Oper. Res. 124, 267–283(17).

Barbaro, A; Bagajewicz, MJ, (2004). Managing financial risk in planning under uncertainty AIChE Journal, 50, 963-989.

Ben-Tal, A., El Ghaoui, L., Nemirovski, A., 2009. Robust Optimization. New Jersey: Princeton University Press.

Bertsimas, D., Sim, M., 2004. The Price of Robustness. Operations Research 52 (1), 35-53.

Birge, J.; Louveaux, F. V. Introduction to stochastic programming (2nd Ed.); Ch. 3: Basic Properties and Theory. Springer: New York (NY), 2011.

Calfa, B. A., Agarwal, A., Grossmann, I. E., & Wassick, J. M., 2014. Data-Driven Multi-Stage Scenario Tree Generation via Statistical Property and Distribution Matching. Computers & Chemical Engineering, 68 (1), 7-23.

Garcia-Herreros, P. Wassick, J.M. & Grossmann, I.E. Design of Resilient Supply Chains with Risk of Facility Disruptions. Ind. Eng. Chem. Res., 2014, 53, 17240–17251.

Goel, V., I. E. Grossmann, 2006, A class of stochastic programs with decision dependent uncertainty, Mathematical Programming, 108 (2-3, Ser. B), 355-394.

Grossmann, I.E, B. Calfa and P. Garcia-Herreros. 2014. "Evolution of Concepts and Models for Quantifying Resiliency and Flexibility of Chemical Processes," Computers & Chemical Engineering 70, 22-34.

Gupta, V., I.E. Grossmann, 2011, Solution strategies for multistage stochastic programming with endogenous uncertainties, Computers and Chemical Engineering, 35, 2235–2247.

Gupta, V., I.E. Grossmann, 2014, A new decomposition algorithm for multistage stochastic programs with endogenous uncertainties, Computers and Chemical Engineering, 62, 62–79.

Høyland, K., & Wallace, S. W. 2001. Generating Scenario Trees for Multistage Decision Problems. Management Science. 46 (2), 295-307.

Ierapetritou, M. G., Pistikopoulos, E. N., 1994. Novel optimization approach of stochastic planning models. Industrial and Engineering Chemistry Research 33, 1930-1942.

Iyer, R. R., Grossmann, I. E., 1998. A bilevel decomposition algorithm for long-range planning of process networks. Industrial and Engineering Chemistry Research 37 (2), 474-481.

Jonsbråten, T. W. 1998, Optimization Models for Petroleum Field Exploitation, Ph.D. thesis, Norwegian School of Economics and Business Administration, Norway.

King, A. J., & Wallace, S. W. 2012. Modeling with Stochastic Programming. Springer Series in Operations Research and Financial Engineering. New York, NY. Springer Science+Business Media New York.

Kuhn, D., Wiesemann, W., Georghiou, A., 2011. Primal and dual linear decision rules in stochastic and robust optimization. Math Programming, 130, 177-209.

Lin, X., S.L. Janak, C.A. Floudas, 2004. A new robust optimization approach for scheduling under uncertaint. Computers & Chemical Engineering, 28, 1069–1085

Li, P., H Arellano-Garcia, G Wozny, 2008. Chance constrained programming approach to process optimization under uncertainty. Computers & Chemical Engineering, 32 (1-2), 25-45

Li, X., A. Tomasgard and P.I. Barton, 2011. Nonconvex Generalized Benders Decomposition for Stochastic Separable Mixed-Integer Nonlinear Programs. Journal of Optimization Theory and Applications, 151(3), 425-454.

Li, Z. and M. Ierapetritou, 2008. Process scheduling under uncertainty: Review and challenges. Computers & Chemical Engineering, 32, 715–727

Li, Z., Ierapetritou, M., 2012. Capacity expansion planning through augmented Lagrangian optimization and scenario decomposition. AIChE Journal, 58(3), 871–883.

Ruszczyński, A. 1997. Decomposition Methods in Stochastic Programming. Mathematical Programming 79(1-3):333–353.

Sahinidis, N.V. 2004. Optimization under uncertainty: state-of-the-art and opportunities. Computers & Chemical Engineering 28 (6), 971-983.

Schultz, R., 2003. Stochastic programming with integer variables. Mathematical Programming, 97 (1–2), 285–309.

Subrahmanyam, S., J.F. Pekny and G.V. Reklaitis, 1994. Design of Batch Chemical-Plants Under Market Uncertainty, Industrial & Engineering Chemistry Research, 33 (11), 2688-2701.

Tarhan, B., I.E. Grossmann and V. Goel, 2013. Computational Strategies for Non-convex Multistage MINLP Models with Decision-Dependent Uncertainty and Gradual Uncertainty Resolution, Annals of Operations Research 203, 141-166.

Van Slyke, R. M.; Wets, R. L-Shaped Linear Programs with Applications to Optimal Control and Stochastic Programming. SIAM Journal on Applied Mathematics, 1969, 17, 638.

You, F., J.M. Wassick and I.E. Grossmann, 2009. Risk Management for a Global Supply Chain Planning under Uncertainty: Models and Algorithms, AIChE J. 55, 931-946.

Zhang, Q., Heuberger, C.F., Grossmann, I.E., Sundaramoorthy, A., Pinto, J.M., 2015. Air Separation with Cryogenic Energy Storage: Optimal Scheduling Considering Electric Energy and Reserve Market Participation. To appear in AIChE Journal.

Krist V. Gernaey, Jakob K. Huusom and Rafiqul Gani (Eds.), 12th International Symposium on Process Systems Engineering and 25th European Symposium on Computer Aided Process Engineering.
31 May – 4 June 2015, Copenhagen, Denmark

A Multidisciplinary Hierarchical Framework for the Design of Consumer Centered Chemical Products

Ka M. Ng

Department of Chemical and Biomolecular Engineering, The Hong Kong University of Science and Technology, Clear Water Bay, Hong Kong
kekmng@ust.hk

Abstract

New consumer products such as personal care products, mobile phones, smart windows, LED lamps, EV batteries, thin film solar cells, printed electronics, air purifiers, and medical devices, are being introduced to the market at an increasingly rapid pace. This is driven partly by consumer demands and partly by the emergence of new molecules, nanomaterials, advanced materials, and innovative processing technologies. This presentation describes a framework for the design of chemical products in which the chemical engineer drives the product design project in collaboration with personnel in marketing, finance, business development, chemistry, physics, mechanical engineering, electronic engineering, and so on. In this framework, the many product design and development tasks are classified into management, business and marketing, research and design, manufacturing, and finance and economics. These are performed in three phases – product conceptualization, product design and prototyping, and product manufacturing and launch. The framework includes rule-based methods such as Quality Function Deployment and *RAT*^{2}*IO*, and model-based methods such as computer-aided molecular design, and transport models. It also includes databases for chemicals and equipment, and computer-aided tools for property prediction, process simulation, computational fluid dynamics, etc. Experiments are used whenever model predictions are impossible or not sufficiently accurate. This framework is illustrated with two examples – a sunscreen cream and a die attach adhesive for LED lamps.

Keywords: Multidisciplinary, hierarchical, chemical products, design.

1. Introduction

The importance of chemical product design to the development of the chemical engineering profession has long been established (Stephanopoulos, 2003; Cussler and Wei, 2003; Hill, 2004; Gani, 2004a,b, Seider and Widagdo, 2012). Many texts have appeared (Bröckel, 2007, 2013; Ng *et al*., 2007, Wesselingh *et al*., 2007; Wei, 2007; Cussler and Moggridge, 2011) which help define the scope and approach for chemical product design. Different methods of relevance to consumer centered chemical product design have also been developed in the last decade (Wibowo and Ng, 2001; Bagajewicz, 2007; Cheng *et al.*, 2009; Whitnack *et al.*, 2009; Conte *et al.*, 2011, 2012; Mettie *et al.*, 2014; Bernardo and Saraiva, 2014; among others).

There are four broad questions in product design:

- What (product) to make?
- How to make (the desired product)?
- Do we want to make the identified product (among other alternative products)?

- If the above is affirmative, how do we come up with such a product from conceptualization to product launch efficiently and profitably?

The first two questions are answered by the 4-step product design procedure proposed by Cussler and Moggridge – needs, ideas, selection and manufacture, and the many methods and tools developed in the literature. Answering the last two questions requires a broader perspective.

2. Multidisciplinary Hierarchical Framework

To this end, a multidisciplinary hierarchical framework for the design of chemical products has been developed. It is consumer centered ensuring that the consumers' wants and needs are met. It is hierarchical covering the design activities level by level with additional details at ever finer scales while keeping the overall product design project in mind. It is multidisciplinary in that skills and knowledge from various disciplines such as basic sciences, material science, chemical engineering, electronic engineering, marketing and finance are considered. It does not mean that the chemical engineers will become marketing personnel or tax lawyers. Rather, this chemical engineering centered framework call for a thorough understanding of what is offered by other disciplines so that the chemical engineer can manage a product development project effectively. We believe, because of the collaborative nature of product design, the proposed approach can enhance the chemical engineers' contribution to chemical product design in industry and to promote the teaching of product design in academia.

Figure 1 shows such an approach which covers all the tasks for product design from conceptualization to product launch. The design activities span three phases in time – product conceptualization (Phase I), detail design and prototyping (Phase II), and product manufacturing and launch (Phase III) – and can be classified by job function in terms of management, business and marketing, research and design, manufacturing, and finance and economics. The activities can also be grouped into various tasks (such as project management, market study, product design, prototyping, etc.), which may last over more than one development phase (Cheng *et al.*, 2009). For example, economic analysis includes activities in both Phase II and Phase III, and involves manufacturing as well as finance and economics. Of particular interest are those activities, italicized in Figure 1, that require the input of a chemical engineer. The rest of the issues, non-italicized, such as product launch, are normally handled by personnel from other disciplines. The personnel from different disciplines work together to come up with the final product. For example, product specifications cannot be fixed without the input from the business team on customers' preference. It is hard for the project team to evaluate the return on investment without considering the tax issues. With the rapid pace of introducing new products to the market, effective project management is crucial to launch the product on time.

While Figure 1 shows the workflow with timeline, a product design model as well as the accompanying methods, tools, databases and experiments is still needed to execute a product design project. This is discussed in the next section.

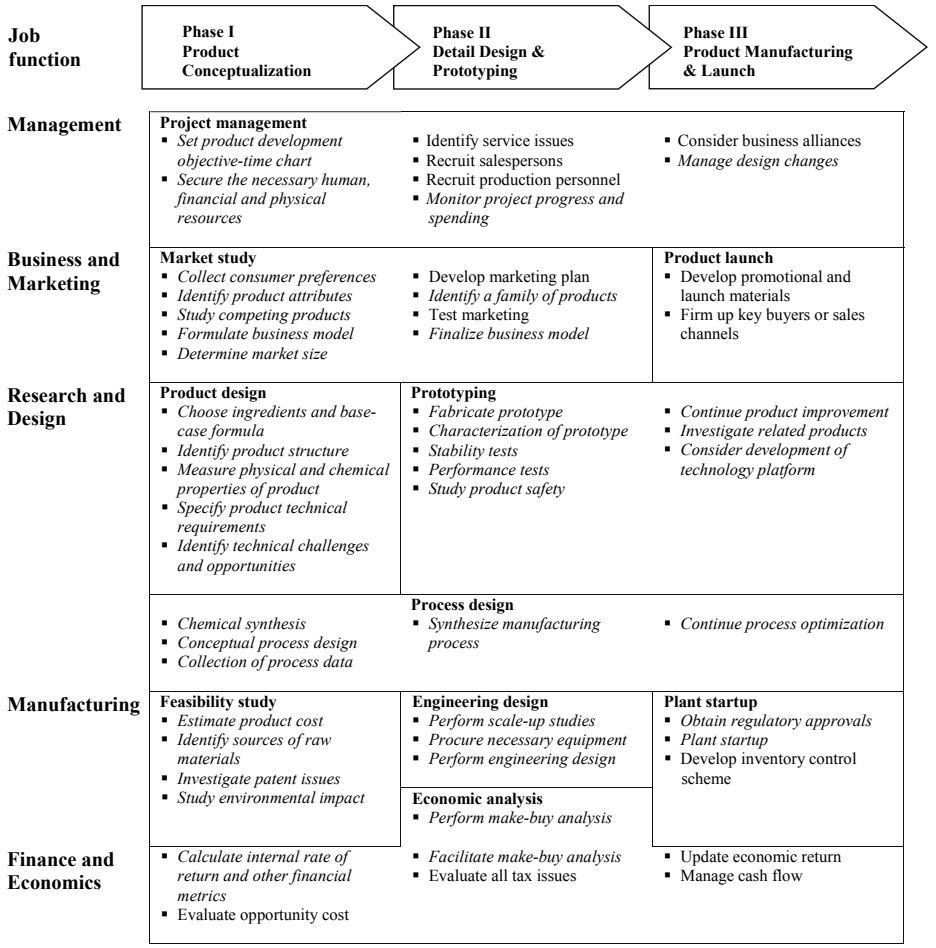

Figure 1. The phases and job functions in a multidisciplinary framework for product design.

3. Grand Product Design Model

Figure 2 captures the most important tasks in Figure 1 that are central to Chemical Engineering. Let us go down the figure from the top. The **product structure** ($\underline{s}$), either a microstructure such as the phase volume fraction or emulsion particle size of an emulsion or a macro structure such as the structure of an air purifier, depends on the **ingredients** ($\underline{x}$), and **process design** ($\underline{pd}$), which can be further broken down into process flowsheet ($\underline{pd}_{fs}$) and **operating conditions** ($\underline{pd}_{op}$). The **product structure** is obtained by the process model $\underline{s} \leftarrow T_S(\underline{x},\underline{pd})$.

The transformation symbol signifies the fact that the 'model' might involve computations, heuristics and experiments. For example, there is a wealth of qualitative information on the selection of emulsification equipment ranging from stirred tanks to colloid mills. Equations are available for calculating the viscosity of emulsions, and for calculating the emulsion droplet size as a function of the continuous phase viscosity, the applied pressure

and equipment specifications of a homogenizer. Criteria for the selection of emulsification units based on capacity and energy consumption are also available (Wibowo and Ng, 2002). However, there are no reliable equations for predicting the emulsion particle size under sonication and experiment data are required. In fact, since so much is not known or is not known as exactly as desired, it is often necessary to iterate between modeling and experiments in product design and process synthesis. Of course, if only equations are used for predicting the product structure, the transformation simply becomes a mathematical function $\underline{s}=T_s(\underline{x},\underline{pd})$.

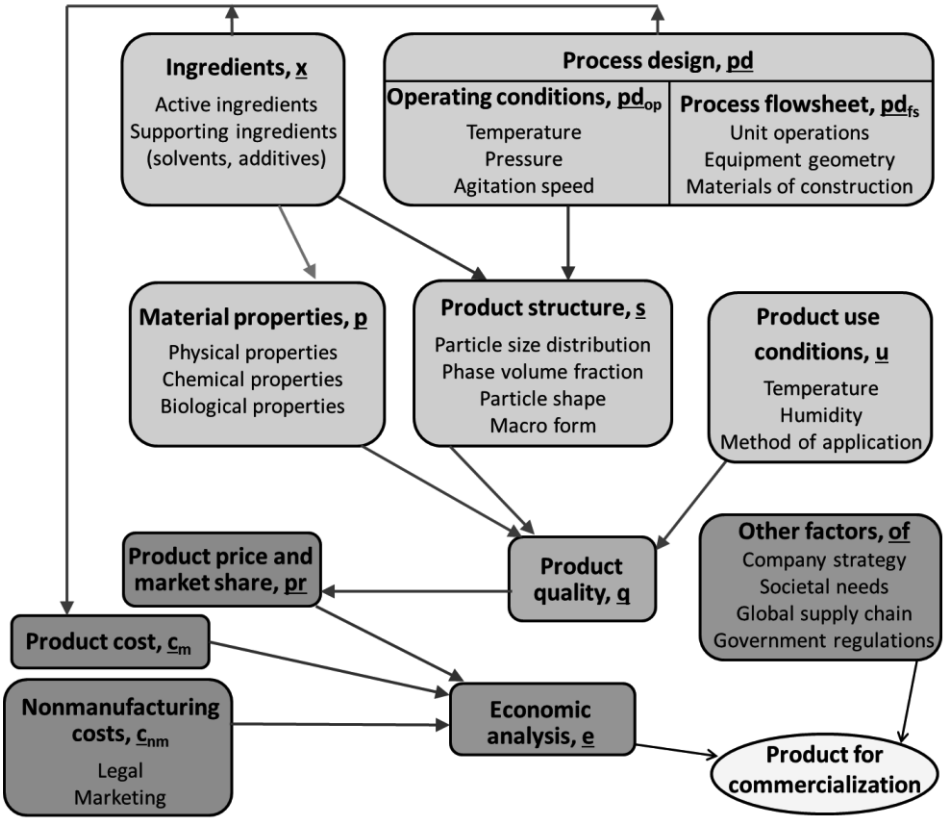

Figure 2. The Grand Product Design Model.

Material properties depend on the type of active ingredients, additives and their composition, $\underline{p}\leftarrow T_p(\underline{x})$. Software such as ICAS developed at the Technical University of Denmark can be used for property predictions. The product structure and material properties in turn determine the **product quality** ($\underline{q}$). Note that the product quality also depends on the **product use conditions** under which the product is used. Thus, we have $\underline{q}\leftarrow T_q(\underline{p},\underline{s},\underline{u})$. For example, a water-based moisturizing sun lotion is not expected to fare well at the beach although it may be an excellent day cream. The qualitative product qualities are customarily distinguished from the more quantitative product performance although they are often lumped into product quality. Setting the **product price** and the desired **market share** ($\underline{pms}$) using a suitable pricing model $\underline{P}_{pms}\leftarrow T_{pms}(\underline{q};\underline{M})$ is an

important exercise because the market size determines the amount of production and the necessary investment. The pricing model accounts for the quality, price, and market share of the competing products (as represented by $\underline{M}$). The manufacturing component of the **product cost** ($\underline{c}_m$) is determined by the materials used in the product and the production process, $\underline{c}_m \leftarrow T_{cm}(\underline{x},\underline{pd})$. The cost model should reflect the amount of production in order to account for the economies of scale. Other **non-manufacturing costs**, $\underline{c}_{nm}$, such as those related to legal issues and marketing need to be included in the total product cost. The parameters $\underline{c}_m$, $\underline{c}_{nm}$ and $\underline{P}_{pms}$ constitute the input information to the economic model $\underline{e} \leftarrow T_e(\underline{c}_m, \underline{w}_{nm}, \underline{P}_{pms})$. If $\underline{e}$ includes only financial metrics such as NPV, present value and ROI, the economic model basically represents a capital budgeting process. If other factors such as environmental considerations, sustainability issues, government policies, etc. are considered alongside the profitability analysis, the model has to be solved as a **multiobjective optimization** problem to determine the product for commercialization, $\underline{Pc}$. Here, $\underline{Pc}$, the product alternatives, are related to $\underline{x}$ and $\underline{s}$. Thus, we have the *Grand Product Design Model*:

Max [$\underline{\text{Pc}}$, $\underline{\text{of}}$]

subject to

$\underline{p} \leftarrow T_p(\underline{x})$	(Property model)
$\underline{s} \leftarrow T_s(\underline{x},\underline{pd})$	(Process model)
$\underline{q} \leftarrow T_q(\underline{p},\underline{s},\underline{u})$	(Quality model)
$\underline{P}_{pms} \leftarrow T_{pms}(\underline{q};\underline{M})$	(Pricing model)
$\underline{c}_m \leftarrow T_{cm}(\underline{x}, \underline{pd})$	(Cost model)
$\underline{e} \leftarrow T_e(\underline{c}_m, \underline{c}_{nm}, \underline{P}_{pms})$	(Economic model)
$\underline{f}(\underline{e}, \underline{of}, \underline{c}_m, \underline{c}_{nm}, \underline{P}_{pms}, \underline{x}, \underline{pd}, \underline{q}, \underline{p}, \underline{s}, \underline{u}; \underline{Y}) \le 0$	(Model parameter constraints)

There are four challenges in solving this model. One is the fact that we have to deal with an inverse problem. As can be seen in Figure 1, product design begins with a concept (i.e. a vision of the final product), which leads to product specifications. Thus, we have to work "backwards" in Figure 2 to identify the material properties and product structure. Most of the existing equations and design procedures are formulated in the "forward" direction. Another challenge is the fact that not all the transformation relations are cast in equation form. The solution method or strategy has to be sufficiently flexible to accommodate information in the form of heuristics, graphs, and output from other computer programs. Third, domain knowledge of specific market segments or classes of products is required for the product designer to be effective. For example, a designer familiar with home appliances such as air purifiers or water filters may not be as effective in designing creams and pastes. Often, experience accumulated over time may not be in written form. Fourth, there are unresolved scientific problems that have to be handled by experiments. A case in point is the process model $\underline{s} \leftarrow T_s(\underline{x},\underline{pd})$. While the emulsion droplet size in a simple emulsion can be predicted, there is no theory or model for predicting the more complex lamellar microstructures. In fact, the missing knowledge gaps identified in product design are research opportunities in chemical engineering sciences.

Currently, the grand product design model is executed by and large sequentially and iteratively in industry without taking full advantage of the advances in computations. A thorough understanding of the interplay of the different elements of the grand product design model is expected to minimize the time for product design and maximize the value of the product for market launch. To expedite the execution of the Grand Product Design

Model from a chemical engineer's perspective requires the methods, databases, tools and experiments to be discussed next.

4. Methods, Databases, Tools and Experiments

Because of the diversity of chemical product types, a wide variety of methods, databases, tools and experiments are needed to execute the *Grand Product Design Model*. They can be classified as follows:

- Methods
  - Rule-based (Objective-time chart, quality function deployment, house of quality, root cause analysis, fishbone diagram, innovation map, RAT^2IO, table of heuristics, business model canvas, etc.)
  - Model-based (*CAMD*, transport processes, experimental correlations, etc.)
  - Hybrid (Design procedures, etc.)
- Databases (Thermodynamic database, equipment database, etc.)
- Tools (*ICAS*, *CFD*, *GAMS*, etc.)
- Experiments (*VLE*, *SLE*, reaction kinetics, etc.)

Various generic methods and tools have already been developed for product design. For example, the use of the consumer preference function is a powerful technique for identifying a desirable product (Whitnack *et al.*, 2009). An objective-time chart can be used to set the objectives and sub-objectives that have to be met within a given time horizon. Resources are important to achieve an objective or sub-objective. RAT^2IO, a mnemonic acronym that stands for resources, activities, time, tools, input/output, information, and objective, can be used to help identify what is needed for the various activities in a product development project. House of quality in quality function deployment can be used to relate the desired product attributes to quantitative and measurable metrics.

While the methods, databases, tools, and experiments can be defined at a higher level, it is expected that the details would differ considerably at a lower level where specific classes of products are considered. The development of these methods, databases and tools and the formulation of the strategy to use them to solve the Grand Product Design Model will require substantial research effort. Perhaps, the best way to proceed is to perform case studies to fill in the details for the Grand Product Design Model.

5. Case Studies

Two case studies focusing on different facets of the grand product design model are discussed next. One is concerned with the development of a sunscreen cream (Cheng *et al.*, 2009). It illustrates a design procedure that uses some modelling, but primarily depends on experience and experiments. The other is concerned with a die attach adhesive for *LED* lamps, emphasizing the use of models in product design.

5.1. Sunscreen Cream

A sunscreen cream is an emulsion with many ingredients including sunblock agents, emollients, emulsifiers, stabilizers, neutralizers, humectants, film formers, thickeners, fragrances, etc. It should rub-in quickly, feel smooth, not oily or greasy, and flow well when poured from the bottle, but not appear runny. These qualitative product attributes

are translated into a shear-thinning product with a viscosity of around 0.025Pa.s when applied to the skin at a shear rate of around 1,000 s^{-1} and a viscosity of around 500Pa.s at a shear rate of 0.01s^{-1}. The selection of ingredients $\underline{x}$ is often based on a hybrid method. Natural or synthetic chemical compounds as well as their concentrations are chosen based on in-house or literature information (Table 1) while the emulsifiers are selected using the HLB method.

Table 1. A Database of Ingredients and Their Selection Criteria.

Ingredients	Examples	Suggested concentration (wt%)
Emollient [HLB value]	Synthetic oils: Caprylic/Capric triglyceride [5], C_{12}-C_{15} alkyl benzoate [13]; Natural oils: Sunflower oil [7], sweet almond oil [7], coconut oil [8]; Silicone oils: Cyclomethicone [5], dimethicone [5]	10-40
Humectant	Glycerol, propylene glycol, butylene glycol, sorbitol	1-5
Thickener	Carbomers, xanthan gum, carboxymethyl cellulose	0.1-0.5
Emulsifier [HLB value]	Steareth-2 [4.9], oleth-20 [15], glyceryl stearate [3.8], PEG-100 stearate [16], Polysorbate 20 [16.7]	1-6
Film former	PVP/ dimethylaminoethyl-methacrylate copolymer, PVP/ hexadecene copolymer, aloe vera	0.1-2.5
Stabilizer	Sodium chloride, EDTA disodium salt dihydrate	0.01-0.2
Neutralizer	Triethanolamine, citric acid	0.01-0.5
Preservative	Tocopheryl, diazolidinyl urea, iodopropynyl butylcarbamate, methylparaben, propylparaben	0.01-0.5

After fixing the composition of the cream, rheological models such as the Herschel-Bulkley model and the Oldroyd model can be used to adjust the thickener concentration. To calculate the energy intensity required to obtain the desired emulsion droplet size of 100 μm in a stirred tank (a pre-emulsification unit), mechanistic models for coalescence and breakage can be used. Figure 3 shows the region at the upper right-hand corner where breakage is feasible. For an emulsion droplet size of 100 μm, the maximum energy required for the stirred tank is around 25W/kg. Typical flowsheets for the manufacture of creams and pastes are available. In a typical flowsheet, the stirred tank is followed by a homogenizer or colloid mill to further breakup the emulsion particles to 5 μm. Design equations with adjustable parameters for these equipment units are also available.

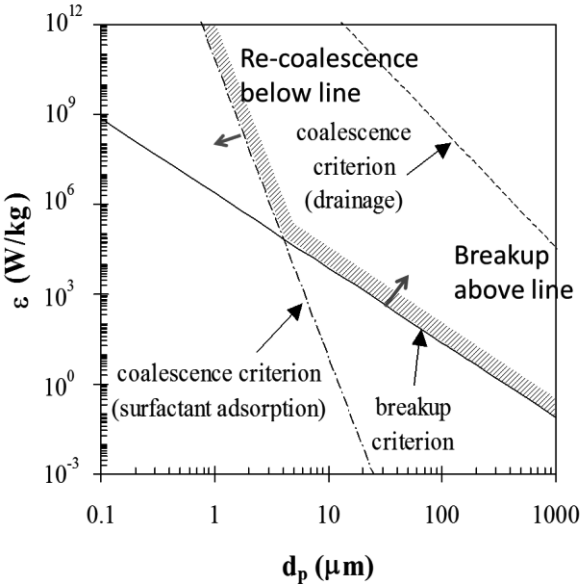

Figure 3. Depiction of coalescence and breakup criteria.

5.2. Die Attach Adhesive

The key component of an *LED* lamp is the *LED* chip, which is attached to a substrate such as alumina by a die attach adhesive (*DAA*). Despite its relatively high efficiency in converting energy to light, typically over half of the power to an *LED* is still dissipated as heat, which shortens the *LED* chip life. Hence, it is crucial that the heat generated by the chip be removed as fast as possible (a qualitative product attribute), which requires a *DAA* with high thermal conductivity (25-40 W/mK) (a quantitative technical specification). A conventional *DAA* consists of micron-sized silver particles embedded in a polymer matrix. A new product concept involves the addition of silver nanorods or silver nanoparticles in the matrix to connect the micron-sized particles. With improved connectivity, it is expected that the thermal conductivity of the *DAA* can be increased while keeping the total amount of silver at a fixed level.

The objective of product design was to maximize the economic return (NPV) in producing a die attach adhesive with the desired thermal conductivity. After an investigation of the competing products on the market, the thermal conductivity of DAA was set at 40 W/mK. For the property model $\underline{p} \leftarrow T_p(\underline{x})$, a simple model can be used to relate the thermal conductivity of a composite to the volume fraction and thermal conductivity of polymer, silver microparticles and nanoparticles.

$$\lambda_e = (\lambda_1^{0.5}\phi_1 + \lambda_2^{0.5}\phi_2 + \lambda_3^{0.5}\phi_3)^2 \quad (1)$$

Here, λ_e is the thermal conductivity of the composite, λ_1, λ_2, λ_3 (ϕ_1, ϕ_2, ϕ_3) are the thermal conductivities (volume fractions) of the polymer, silver microparticles, and silver

nanoparticles, respectively. The thermal conductivity of the polymer (λ_1) can be estimated from a database or using a *CAMD* tool,

$$\lambda_1 = f(T_c, M_w, T_b, T) \tag{2}$$

where T_c is critical temperature, M_w molecular weight, T_b boiling point, and T temperature. λ_2 is the thermal conductivity of the silver microparticle fillers; it equals 429 W/mK. λ_3 is the thermal conductivity of the silver nanoparticle fillers which is size-dependent and has to be measured. For the process model $\underline{s} \leftarrow T_s(\underline{x},\underline{pd})$, a proper mixing procedure is crucial to produce a composite with nanoparticles dispersed evenly among the microparticles. However, a basic understanding of the process let alone a model is available. In the current study, the mixing conditions were fixed after experimental optimization. For the quality model $\underline{q} \leftarrow T_q(\underline{p},\underline{s},\underline{u})$, in addition to thermal conductivity, the storage temperature, curing temperature and time, and the *DAA* viscosity prior to curing are important product attributes as well. For the pricing model $\underline{P}_{pms} \leftarrow T_{pms}(\underline{q};\underline{M})$, the following model proposed by Bagajewicz (2007) can be used to relate the product price (p_n) and sales volume (d_n) to those of the competition's.

$$p_n d_n = \left(\frac{\alpha}{\beta}\right)^{\rho} p_c \left(\frac{Y - p_n d_n}{p_c}\right)^{1-\rho} d_n^{\rho} \tag{3}$$

$$Y \geq p_n d_n + p_c d_c \tag{4}$$

Here, Y is the total market size, ρ is an adjustable parameter, α measures how much the consumer knows about the new product, and β relates the appeal of the new product in comparison to the competing product. The following equation can be used for the manufacturing product cost:

$$c_m = (w_2 c_2 + w_3 c_3) d_n + process\ cost \tag{5}$$

Here w_2, w_3 (c_2, c_3) are the weight fractions (costs) of silver microparticles and nanoparticles, respectively. The IRR can be obtained by setting NPV to be zero:

$$NPV = \sum_{j=-n}^{m} \frac{(Project\ Cash\ Flow)_j}{(1+R)^j} = 0 \tag{6}$$

Here, R is the internal rate of return. A base-case product formulation has been established (Table 2) which can be further optimized using the models above.

Table 2. Composition and component cost of the DAA product.

Ingredient	Composition (wt%)	Component Cost ($/kg DAA)
Silver flakes	79	1,185
Silver nanoparticles	10	200
Epoxy resin	5	0.25
Curing agent	5	0.15
Dispersing agent	1	0.02
Solvent	NA	0.06
Syringe dispenser (10mL)	NA	0.05
Total	100	1,385.53

6. Conclusions

Considerable research effort over the past decade has taken consumer-centered chemical product design to a point where a chemical engineer has a clearer perspective and some of the necessary methods and tools to champion the development of a superior product rapidly, efficiently and effectively. This multidisciplinary hierarchical framework is an attempt to capture what we have learned and identify what else needs to be developed. The demand for new consumer products in a rapidly changing global marketplace would help propel the research on product design forward.

References

M. J. Bagajewicz, "On the role of microeconomics, planning, and finances in product design," AIChE Journal, 53, 2007, 3155-3170.

F. P. Bernardo, P. M. Saraiva, "A conceptual model for chemical product design," AIChE Journal, DOI: onlinelibrary.wiley.com. 10.1002/aic.14681.

U. Bröckel, W. Meier, and G. Wagner (editors), 2007, *Product Design and Engineering: Basics and Best Practices* (2 Volume Set), Wiley-VCH.

U. Bröckel, W. Meier, G. Wagner (editors), 2013, *Product Design and Engineering: Formulation of Gels and Pastes*, Wiley, Somerset, NJ.

Y. S. Cheng, K. W. Lam, K. M. Ng, R. K. M. Ko, C. Wibowo, "An integrative approach to product development-a skin-care cream," Computers and Chemical Engineering," 33, 2009,1097-1113.

E. Conte, R. Gani, K. M. Ng, "Design of formulated products: a systematic methodology," AIChE Journal, 57, 2011, 2431-2449.

E. Conte, R. Gani, Y. S. Cheng, K. M. Ng, "Design of formulated products: experimental component," AIChE Journal, 58, 2012, 173-189.

E. L. Cussler, J. Wei, "Chemical product engineering," *AIChE J.*, 49, 2003, 1072-1075.

E. L. Cussler, G. D. Moggridge, 2011, *Chemical Product Design*, 2nd Edition, Cambridge University Press, Cambridge, U.K.

R. Gani, "Computer-aided methods and tools for chemical product design," *Chemical Engineering Research and Design*, 2004a, 82, 1494-1504.

R. Gani, "Chemical product design: challenges and opportunities," Computers and Chemical Engineering, 28, 2004b, 2441-2457.

M. Hill, "Product and process design for structured products," AIChE Journal, 50, 2004, 1656-1661.

M. Mattei, G. M. Kontogeorgis, R. Gani, "A comprehensive framework for surfactant selection and design for emulsion based chemical product design," Fluid Phase Equilibria, 362, 2014, 288-299

K. M. Ng, R. Gani, K. Dam-Johansen (editors), 2007, *Chemical Product Design: Toward a Perspective through Case Studies*, Computer Aided Chemical Engineering, 23.

W. D. Seider, S. Widagdo, "Teaching chemical engineering product design," *COCHE*, 1, 2012, 472-475.

G. Stephanopoulos, *Invention and Innovation in a Product-Centered Chemical Industry: General Trends and a Case Study*, AIChE Institute Lecture (2003).

K. T. Ulrich, S. D. Eppinger, 2012, *Product Design and Development*, 5th Edition, McGraw-Hill, New York.

J. Wei, 2007, *Product Engineering: Molecular Structure and Properties*, Oxford University Press, Oxford, New York, NY.

J. A. Wesselingh, S. Kiil, M. E. Vigild, 2007, *Design & Development of Biological, Chemical, Food and Pharmaceutical Products*, Wiley, Chichester, U.K.

C. Whitnack, A. Heller, M. T. Frow, S. Kerr, M. J. Bagajewicz, "Financial risk management in the design of products under uncertainty," Computers and Chemical Engineering, 33, 2009, 1056-1066.

C. Wibowo, K. M. Ng, "Product-oriented process synthesis and development: creams and pastes," AIChE Journal, 47, 2001, 2746-2767.

Krist V. Gernaey, Jakob K. Huusom and Rafiqul Gani (Eds.), 12th International Symposium on Process Systems Engineering and 25th European Symposium on Computer Aided Process Engineering.
31 May – 4 June 2015, Copenhagen, Denmark

Multi-Level Design of Process Systems for Efficient Chemicals Production and Energy Conversion

Kai Sundmacher [a,b]

[a] *Max Planck Institute for Dynamics of Complex Technical Systems, Department for Process Systems Engineering, Sandtorstr.1, D-39106 Magdeburg, Germany,*
[b] *Otto-von-Guericke- University Magdeburg, Department for Process Systems Engineering, Universitätsplatz 2, D-39106 Magdeburg, Germany, sundmacher@mpi-magdeburg.mpg.de*

Abstract

A model-based methodology is proposed which derives process design decisions at different levels of the process hierarchy under consideration of various process intensification options. The approach integrates process analysis, model identification, and process synthesis. The methodology is exemplified by designing a process for the production of a long-chain aldehyde via homogeneously catalyzed hydroformylation of 1-dodecene.

Keywords: Process Design, Multi-scale Systems, Reaction Networks, Dynamic Optimization, Chemicals Production.

1. Introduction

Optimal design of sustainable chemical process systems is of paramount importance for best utilization of raw materials and realization of energetically efficient conversion chains. A process system can be decomposed into a multi-scale structure (Freund and Sundmacher, 2011) with four hierarchical levels (Fig. 1): molecular level, phase level, process unit level, and plant level. Every scale is characterized by individual phenomena and events. Process analysis breaks a process down to convey inputs, outputs and transfer behavioral functions in order to gain a detailed understanding of the internal processes and identify accessible decision variables. Process synthesis is a bottom-up aggregation procedure that makes use of this information to derive an optimal system configuration. The final optimum depends strongly on the applied objective function (e.g., minimal costs, maximal productivity) and additional constraints the process has to fulfill (e.g., product quality, safety, operability).

The molecular level deals with all process design decisions which are linked to the structure of individual molecules, namely the choice of suitable molecular reactants to generate the desired product and the selection of auxiliary substances, in particular catalysts and solvents. E.g., Norskov et al. (2009) use quantum chemical methods to support the “in silico” design of catalysts based on molecular descriptors. Recently, Zhou et al. (2014) developed a method for the selection of reaction solvents based on the surface charge distribution of molecules.

On the phase level, one is interested in analysing and designing thermodynamic and transport properties as function of intensive state variables. Besides classical fluid property models (EoS, G^E-models), recently molecular models became an emerging tool in chemical engineering that allows the prediction of pure component and mixture properties based on molecular information (Guevara-Carrion et al., 2012).

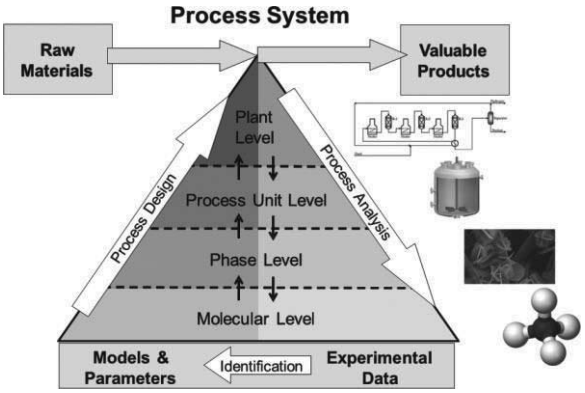

Figure 1: Efficient design of process systems requires integration of process analysis, identification and synthesis on all levels of the process hierarchy.

Process units realize the generation, contacting and separation of phases and organize the transport of mass, heat, and momentum between them. On the process unit level, models of different complexity are used for analysis and design. Short-cut models can be used to identify attainable regions in the composition space, while rigorous models are the basis for detailed optimization under consideration of decision variables such as the geometrical parameters, dosing points of reactants, extraction points of products, and heating/cooling mechanisms (Peschel et al., 2011).
Finally, the interconnection of many process units to constitute the whole process is investigated on the plant level. Variations of the topology of the process unit network can lead to dramatic performance improvements of the overall production process. While in many cases heuristic rules are still used to optimize the structure of chemical production plants (Dimian and Bildea, 2008), applied mathematics provides powerful mixed integer nonlinear programming (MINLP) algorithms for systematic optimization based on superstructures (Yeomans and Grossmann, 1999, Adjiman et al., 2000; Floudas and Lin, 2004; Gangadwala et al., 2008; Mitsos and Barton, 2009; Trespalacios and Grossmann, 2014).
In this contribution, a process design approach is proposed that tries to link the four levels of the process hierarchy, i.e., from the molecular level up to the plant level. The approach is briefly exemplified with the design of a process example, namely the synthesis of the linear aldehyde tridecanal via hydroformylation using a transition metal-organic complex as homogeneous catalyst. Tridecanal is a biodegradable chemical used as flavour compound, surfactant and plasticiser.

2. Molecular level

On the molecular level, all decisions linked to the structure of individual molecules involved in the production process are to be considered: the selection of suitable molecular reactants A and B to generate the target product molecule C, and the selection of auxiliary substances, in particular suitable catalysts and solvents.

2.1. Selection of reactants

For the choice of the main reactant A, atomic efficiency, transformation efficiency, and feedstock are key parameters to be accounted for. To achieve high atomic efficiency, one should avoid excess atoms of A not being part of the product molecule C, because such atoms yield a coupled by-product D. Single-product stoichiometry is always

preferred in the main reaction, unless the coupled by-product has an added value which improves the economic potential of the overall process. The underlying reaction mechanism should feature high transformation efficiency, i.e. the number of intermediate reaction steps at the catalyst should be as small as possible. Moreover, the feedstock for A needs to be selected under consideration of availability, price, storage capability, and sustainability. If A can be converted to C via alternative reaction schemes with different partner reactants B, one should select B such that the achievable equilibrium conversion of A is maximized, and the properties of B and C are very different to ensure simple separation and recovery of B. Of course, in selecting B not only the stoichiometry of the main reaction is important, but also the appearance of undesired by-products. Their formation is strongly controlled by the catalyst selected and – in case of liquid phase syntheses – also by the type and composition of the solvents used.

2.2. Selection of catalysts

Even if thermodynamically feasible, chemical reactions are often kinetically hindered. Hence, suitable catalysts must be selected to activate reactants, in order to enhance the rates of desired reactions and suppress undesired side reactions. Regarding catalyst selection, one has to account for catalyst activity, selectivity, stability, price, and separation from the reaction products. With regard to the last criterion, heterogeneous catalysts are advantageous. But modern homogeneous catalysts, such as metal-organic ligand systems, often offer higher selectivity. Moreover, their properties can be tuned by optimal design of the molecular catalyst structure. Screening of possible catalytic compounds today can be efficiently performed in high throughput devices (e.g. Senkan, 2001). In addition, computer-aided catalyst design receives increasing interest. In particular coupled cluster theory and density functional theory is used for the investigation of reaction pathways and/or for the estimation of rate constants of individual reaction steps (e.g. Metcalfe et al., 2010).

2.3. Selection of solvents

Another important class of auxiliary agents in chemical processes are solvents. They increase the solubility of reactants and catalysts in the liquid phase, avoid hazardous operation conditions, and support product isolation and/or catalyst recovery. Due to the fact that a solvent influences reaction rates and may deactivate the catalyst, normally solvent and catalyst should be selected simultaneously. Key criteria for the selection of reaction solvents are: separation from reaction products, low price, high stability, and non-hazardousness. Computer Aided Molecular Design (CAMD) has become a key approach for the rational derivation of optimal molecular structures of solvents (e.g. Struebing et al., 2013; Zhou et al., 2014). The design of solvents can be supported using molecular modelling/quantum chemical calculations (MM/QC), group contribution methods (GC), or data-driven approaches based on existing data banks and high-throughput screening.

2.4. Example: Molecular level decisions for tridecanal synthesis

We consider the synthesis of the target molecule C, the biodegradable linear aldehyde tridecanal (TDC), via hydroformylation. The olefin 1-dodecene is acting as the main reactant A. It can be obtained in sustainable manner via dehydration of bioethanol followed by the Shell Higher Olefin Process (SHOP) (Cornils and Herrmann, 1997). Alternatively, 1-dodecene could be produced from 1-dodecane via dehydrogenation, a route which features low carbon footprint if it is performed photocatalytically instead of thermocatalytically (Franke and Julis, 2014). The syngas components CO and H_2 are the partner reactant(s) B. No coupled by-product D is formed. The hydroformylation reaction is catalyzed by homogeneous transition metal-ligand catalyst. The transition

metal of choice is Rhodium due to its very high activity (see Figure 2). The chemo- and regio-selectivity of the catalyst is controlled by the chelating ligands. Ligand design decisions still are mainly based on heuristics, but computer-aided catalyst design is expected to become an important approach in the next years. For the hydroformylation of 1-dodecene, Schäfer et al. (2012) found in systematic batch reactor experiments that Rh-Biphephos is a highly active as well as highly selective catalyst.

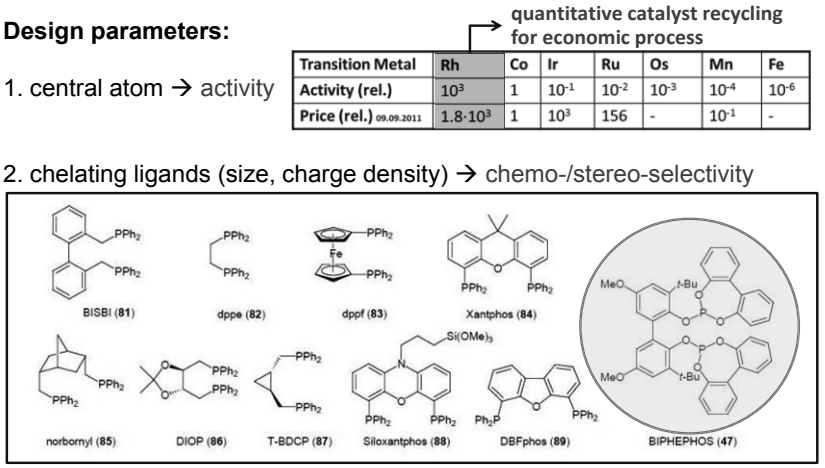

Figure 2: The hydroformylation catalyst can be designed from central atoms and ligands such that high activity, high chemo- and high stereo-selectivity are achievable.

The synthesis of tridecanal via hydroformylation of 1-dodecene features excellent atomic efficiency and transformation efficiency, and it uses a well accessible feedstock. Furthermore, a very high equilibrium conversion of A (1-dodecene) is achievable, and the pair B/C (syngas/tridecanal) can be easily separated due to their different size and physicochemical properties. The stability of Rh-Biphephos catalyst is also sufficient.

But the very high prices of both Rhodium and the ligand (Figure 2) require efficient recovery of the catalyst, i.e. separation from the product mixture. Economic input/ output calculations of the overall process show that the rest concentration of Rhodium in the product mixture must not exceed 1 ppm. For efficient catalyst recycling, Subramaniam (2010) proposed a polymer-supported ligand. The catalyst solubility can be tuned by control of the polymer molecular weight such that catalyst recycling can be achieved via precipitation followed by filtration or by membrane nanofiltration. This is a very good example how a separation function can be directly integrated into the molecular structure of a homogeneous catalyst.
Alternatively, unmodified Rh-Biphephos can be separated via liquid-liquid phase splitting inducible by suitable mass separating agents which can be selected and optimized via CAMD. By means of quantum chemical calculations (COSMO-RS), McBride and Sundmacher (2015) found dimethylformamide/n-decane as best solvent mixture to separate the Rh-Biphephos from the reaction product tridecanal at room temperature, while the same solvents form a single-phase mixture with the reactants at reaction temperature (ca. 100 °C).

3. Phase level

3.1. Determination of optimal process route

Once the main species involved in a chemical conversion process are identified on the molecular level, the optimal process route must be determined. For this purpose, the core of the conversion process, namely the underlying chemical reaction network must be inspected in detail. This requires knowledge about the reaction mechanism, based on which a thorough kinetic-thermodynamic analysis can be performed. The essential quantitative information can be harvested from optimally designed (OED) perturbation experiments in a semi-batch reactor, using suitable Process Analytical Tools (PAT) such as GC, HPLC, IR and Raman spectroscopy. Statistical analysis of perturbation experiments yields useful information from which a reaction kinetic model can be extracted. Ideally, the kinetic model should comprise thermodynamically consistent rate expressions of all essential reaction steps involved in the network. Of course, the level of detail depends on the availability of experimental data and on the constraints under which perturbation experiments are performed. In addition to experiments, today theoretical data from quantum chemical models can be very helpful for deriving suitable kinetic expressions (Karst et al., 2014).

A valid reaction kinetic model is the essential input information for the determination of the optimal process route. For this purpose, we do not consider any pre-defined reaction device, but an arbitrary well-mixed matter element moving in the thermodynamic state space (Figure 3). It is characterized by the time-dependent state vector $x(t)$, containing temperature T, pressure P, chemical composition y, and linear velocity v as observable variables. Depending on the physico-chemical situation, the state vector can be extended to describe additional states of interest, e.g. the size distribution of a particle population existing within the matter element. The state of a matter element evolves during processing time due to the action of internal and external fluxes j, namely the vector of species mass fluxes m_A, the vector of chemical reactions fluxes r_V, the heat flux q_A, the work flux w, surface forces f_A, and body forces f_V.

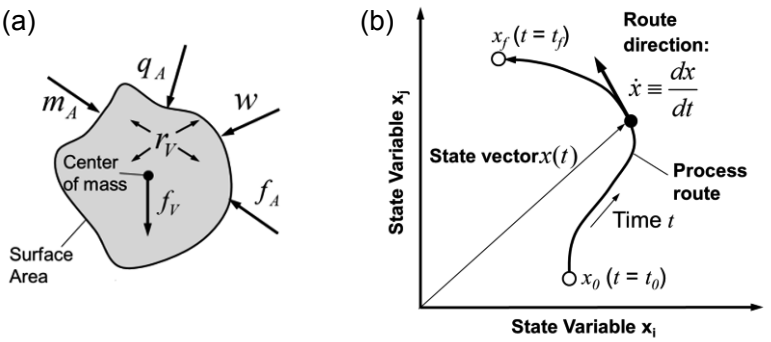

Figure 3: (a) Matter element with acting fluxes; (b) process route in state space.

In each process the state of the matter elements, $x^T = (T, P, y, v)$, is transformed from the initial point x_0 to a final point x_f (see Fig. 3). Each trajectory in state space which connects the initial and final point is called a feasible "process route". The best process route can be determined by solving the following dynamic optimization problem:

$$\min_{j(t),p}\left\{\int_{t_0}^{t_f} E(x(t),j(t),p)dt + E_0(x_0) + E_f(x_f)\right\}$$

s.t.

$C\frac{dx(t)}{dt} = Fj(t) + Nr_V$	balance equations of matter element	(1)
$r_V = r_V\big(x(t)\big)$	reaction rate expressions	
$C = C\big(x(t)\big)$	capacity matrix (from thermodyn. eqs. of state)	
$F = F(p)$	matrix of flux-weighting factors	
$x(t_0) = x_0;\ \ x\big(t_f\big) = x_f$	initial state and final state	
$h(x(t),p) \le 0$	inequality constraints	

According to Eq. (1), a generalized cost function (process cost + initial cost + final cost) is minimized via manipulation of the time-dependent fluxes $j^T = (m_A, q_A, w, f_A, f_V)$ and time-independent parameters *p*. The dynamic equality constraints are the mass, energy and momentum balance equations of the matter element. The capacity matrix *C* contains the thermodynamic system properties, e.g. density, heat capacity etc., obtainable from equations of state. *F* represents the matrix of flux-weighting factors, and *N* is the stoichiometry matrix. Eq. (1) is a generally valid formulation for matter elements in batch processes as well as in continuous processes. In the latter case *t* represents the residence time. To identify the ideal process route, i.e. the full performance potential of the reaction system, it is advisable to solve Eq. (1) for unlimited fluxes *j*. However, to obtain technically meaningful results, some inequality constraints (*h* in Eq.(2)) are to be included such as non-negativity of temperature and concentrations, as well as constraints concerning the validity range of the rate expressions and equations of state. When solving Eq.(1), we have to take into account that the initial and final state are often coupled due to recycling of unconverted reactants and products. Eq.(1) is a DAE-constrained optimization problem which the treated discretizing the control and state variables simultaneously (Biegler, 2007). The resulting NLP problem can be solved e.g. with the solver CONOPT (Drud, 1985). The optimal flux profiles $j_{opt}(t)$ represent the ideal process route which can be used for benchmarking any possible technical approximation on the next design level, namely the process unit level.

3.2. Example: Phase level decisions for tridecanal synthesis

The reaction network of the homogeneously catalyzed synthesis of tridecanal was investigated in detail by Kiedorf et al. (2014) using experimental perturbation techniques. The authors proposed a reduced model consisting of 6 reaction steps (Fig. 4b). Hentschel et al. (2014) used this network and corresponding rate expressions to determine the optimal process route of matter elements via dynamic optimization, according to Eq.(1). Thereby, the initial and final states were coupled by an ideal separation sub-system which allows recycling of any species in the network at arbitrarily high purity (Fig.4a). The chemo-selectivity w.r.t. the tridecanal (nC13al) was maximized. The results show that recycling of iso-dodecene (iC12en) is essential for achieving high chemo-selectivity (Fig.4c). This is due to the fact that iC12en can be isomerized back to 1-dodecene (n-C12en) via reaction step r_2 and converted into the desired product nC13al via step r_1 (Fig.4b). For 95 % conversion of 1-dodecene the optimal concentration profiles (Fig.4d), the corresponding mass and heat flux profiles (Fig.4e), and the resulting temperature and gas pressure profiles (Fig.4f) are shown below. The temperature profile reflects the fact that the reverse isomerisation of iC12en to nC12en is favored at higher temperature. Lower partial pressure of H_2 in the first time period (Fig.4f) suppresses the undesired hydrogenation steps r_3 and r_4. In summary, the selectivity-optimal process route requires distributed dosing of the reactants H_2, CO and

nC12en, distributed cooling due to the exothermic hydroformylation, and selective recycling of isomer iC12en, catalyst Rh-Biphephos, and solvents (n-decane/DMF).

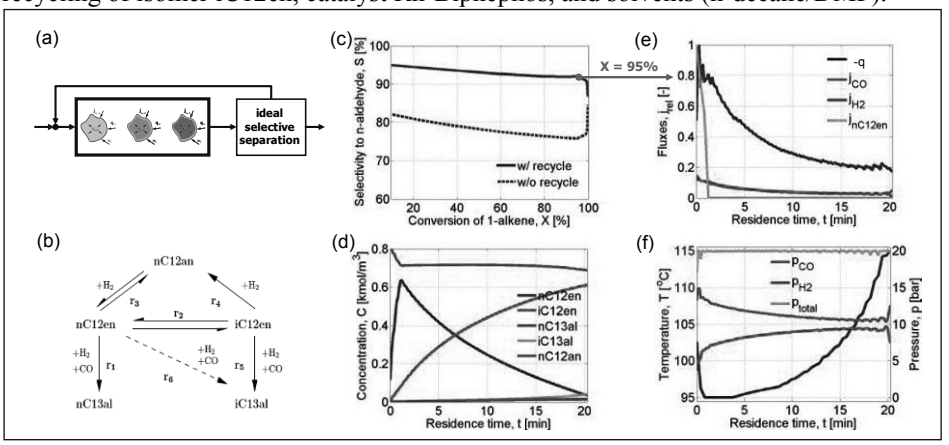

Figure 4: a) reaction-separation recycle system, b) reaction network of TDC synthesis, c) optimal selectivity-conversion curves with/without recycle, d) concentration profiles at X = 95 %, e) optimal flux profiles, f) optimal temperature and pressure profiles.

These findings set the conditions to be met by the separation system. As first separation steps after the reaction, a flash for syngas recovery and a decanter for catalyst recovery via LL-phase splitting are the methods of choice (Dimian and Bildea, 2008). The decantation yields a DMF-rich phase containing the Rh-Biphephos catalyst which is recycled to the reaction's initial state, and a n-decane-rich phase containing some unconverted reactant and all products showsn in Fig.4b. The conceptual design of the separation sequence for the n-decane phase can be derived from conventional Residue Curve Map analysis (RCM; Doherty and Malone, 2003), a methodology closely related to the process route analysis proposed in section 3.1 since both approaches essentially investigate trajectories of matter elements in the thermodynamic state space.

4. Process unit level

4.1. Technical realization of optimal process route

On the process unit level, the optimal process route is approximated by means of suitable existing or novel devices. Thereby, additional physical and technical constraints regarding the fluxes have to be accounted for. While the matter element on the phase level is optimally controlled over the time coordinate, on the unit level one has to decide whether the optimal route should be realized in a continuously operated, spatially distributed device or in a semi-batch operated, temporally distributed device. Secondly, one has to check if the interesting fluxes are directly controllable in practice or must be replaced by other variables, and if simultaneous action of fluxes is realizable. According to irreversible thermodynamics, the fluxes are driven by conjugated forces which are related to the difference between the actual state and the equilibrium state ($x - x_{eq}$). For small deviation from the equilibrium state, a quasi-linear transport law can be used:

$$j = K(x)\left(x - x_{eq}\right) \tag{2}$$

where $K(x)$ stands for the matrix of transport coefficients. According to Eq. (2), instead of the fluxes j, one can use the corresponding equilibrium states x_{eq} as control variables. This requires specification of the transport mechanisms to be applied. The choice of

mechanisms, the feasible windows of transport coefficients and geometrical parameters (volume-related surface areas, $a=A/V$) determine the technically realizable extensive fluxes, the type of devices to be selected and the size of equipment. When optimizing technically feasible process routes, one must integrate additional constraints: a) the transport laws, Eq. (2), and b) bounds of transport coefficients as well as geometrical parameters. Since these bounds often become active constraints, one should perform systematic sensitivity analysis of the optimal solution. Even if properly designed, each type of equipment will only approximate, but not directly match the ideal process route. In particular, matter elements in reality are neither perfectly mixed, nor is the residence time of matter elements traveling through a process unit uniformly distributed. Hence, we must also investigate the robustness of the obtained optimal solution with respect to non-ideal micro- and macro-mixing of matter elements.

4.2. Example: Process unit level decisions for tridecanal synthesis

From systematic dynamic optimization studies, we found that a segmented flow reactor with discrete dosing of syngas and alkene is the best technical approximation of the cost-optimal process route in a continuously operated system (Peschel et al., 2012). The gas-liquid mass transfer coefficient was identified as critical parameter for the achievable chemo-selectivity at given alkene conversion (Fig.5a). Thus, the reactor should be equipped e.g. with static mixtures in order to enhance gas-liquid mass transfer in a sufficient manner (Fig.5b).

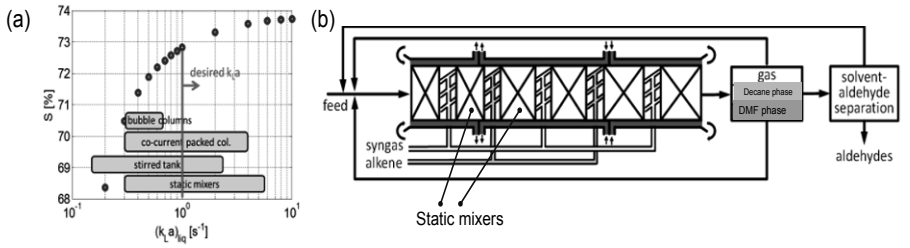

Figure 5: (a) Selectivity vs. GL-mass transfer coefficient; (b) segmented flow reactor.

5. Plant level

5.1. Process integration and operability analysis

Process design decisions on the plant level are mainly focused on material and energy integration as well as on operability aspects. As a versatile tool for evaluating many integration possibilities, superstructure based optimization is a widely used technique. Regarding energy integration, pinch analysis is a classical but still important method for determination of the best heat exchanger network (HEN). Once the optimal plant topology is identified one should investigate its operability, i.e. the controllability of steady states as well as also the start-up behavior. In order to ensure long-term stability of catalysts, experiments on the miniplant scale are an indispensable element of operability analysis on the plant scale (Zagajewski et al., 2014).

5.2. Example: Plant level decisions for tridecanal synthesis

The cost-optimal flowsheet for the production of tridecanal is sketched in Fig.6a. There, a tubular reactor featuring optimal dosing of H_2 and CO and optimal cooling along the flow direction is embedded into the process. This reactor provides 2.8 % cost savings compared to a standard stirred tank reactor (CSTR, Fig.6b). By application of selectors (Dimian and Bildea, 2008), it was decided to apply distillation for material integration, i.e. for separation of the solvent n-Decane and non-converted n/iso-C12-alkenes. For final nC13al separation, vacuum distillation must be applied to avoid thermal aldehyde

decomposition. Micovic et al. (2013) found that combining distillation with melt crystallization further reduces the energy demand for C13-isomers separation.

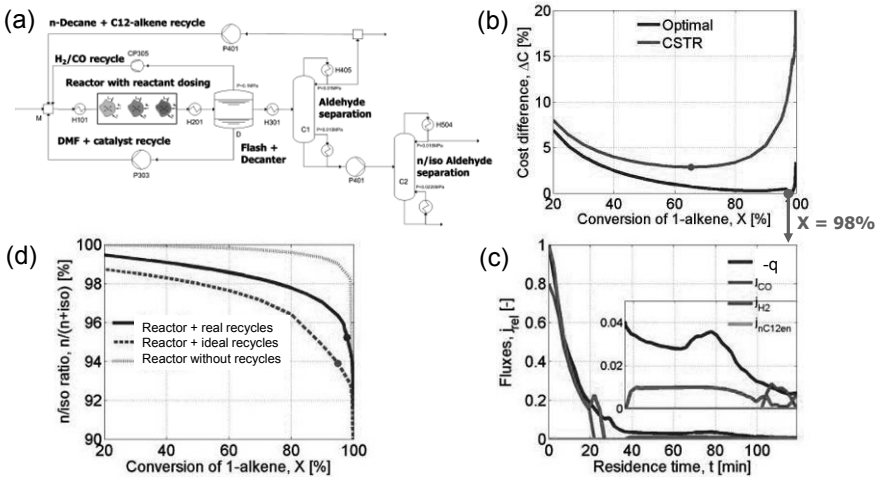

Figure 6: a) Flowsheet for n-aldehyde production using the solvent pair n-decane/DMF for catalyst separation, b) total cost vs. conversion of 1-alkene, c) optimal flux profiles at 98 % conversion, d) n/iso ratio of aldehydes vs. conversion of 1-alkene.

6. Conclusion

The presented multi-level process design approach was successfully applied to several examples of chemicals production and energy conversion (Karst et al., 2014; El Sibai et al., 2015). The core element is the detailed kinetic analysis of the underlying reaction network based on which the optimal processing route of matter elements is identified. The proposed flux-oriented methodology allows systematic comparison of various process intensification options during the design of process units.

Acknowledgement
This work was partly supported by the German Research Foundation (DFG) under the roof of the Collaborative Research Center SFB/TRR 63 “InPROMPT”.

References

C. S. Adjiman, I. P. Androulakis, C. A. Floudas, 2000, Global optimization of mixed-integer nonlinear problems, AIChE J., 46, 1769-1797.
L. Biegler, 2007, An overview of simultaneous strategies for dynamic optimization, Chem. Eng. Process., 46, 1043-1053.
B. Cornils, W. Herrmann, 2004, Aqueous-phase organometallic catalysis. Wiley, N.Y., 639.
A. C. Dimian, C. S. Bildea, 2008, Chemical process design, Wiley-VCH, Weinheim.
M.F. Doherty, M.F. Malone, 2001, Conceptual design of distillation systems, McGraw-Hill, New York.
A. Drud, 1985, CONOPT – A GRG code for large scale dynamic nonlinear optimization problems, Math. Program., 31, 153-191.
A. El Sibai, L. Rihko-Struckmann, K. Sundmacher, 2014, Synthetic methane from CO_2: Dynamic optimization of the Sabatier process for power-to-gas applications, PSE12 & ESCAPE25, 31 May - 4 June, Copenhagen, Denmark.
C. A. Floudas, X. X. Lin, 2004, Continuous-time versus discrete-time approaches for scheduling of chemical processes: a review, Comput. Chem. Eng., 28, 2109-2129.

R. Franke, J. Julis, 2014, elements 49, Evonik Industries AG, Essen, 14-18.
H. Freund, K. Sundmacher, 2011, Process Intensification, Parts 1-4, in: Ullmann's Encyclopedia of Industrial Chemistry, Wiley-VCH, Weinheim.
J. Gangadwala, U. U. Haus, M. Jach, A. Kienle, D. Michaels, R. Weismantel, 2008, Global analysis of combined reaction distillation processes, Comput. Chem. Eng., 32, 343-355.
G. Guevara-Carrion, H. Hasse, J. Vrabec, 2012, Thermodynamic properties for applications in chemical industry via classical force fields, in: Multiscale molecular methods in applied chemistry (Eds: B. Kirchner, J. Vrabec), Springer-Verlag, Berlin.
B. Hentschel, A. Peschel, H. Freund, K. Sundmacher, 2014, Simultaneous design of the optimal reaction and process concept for multiphase systems, Chem. Eng. Sci., 115, 69-87.
F. Karst, H. Freund, M. Maestri, K. Sundmacher, 2014, Multiscale chemical process design exemplified for a PEM fuel cell process, Chem. Ing. Tech., 86, 2075-2088.
G. Kiedorf, D.M. Hoang, A. Müller, A. Jörke, J. Markert, H. Arellano-Garcia, A. Seidel-Morgenstern, 2014, Kinetics of 1-dodecene hydroformylation in a thermomorphic solvent system using a rhodium-biphephos catalyst, Chem. Eng. Sci., 115, 31-48.
K. McBride, K. Sundmacher, 2015, Computer-aided design of solvents for the recovery of a homogeneous catalyst used for alkene hydroformylation, PSE12 & ESCAPE25, 31 May - 4 June, Copenhagen, Denmark.
W.K. Metcalfe, J.M. Simmie, H.J. Curran, 2010, Ab initio chemical kinetics of methyl formate decomposition: The simplest model biodiesel, J. Phys. Chem. A, 114, 5478-5484.
J. Micovic, T. Beierling, P. Lutze, G. Sadowski, A. Gorak, 2013, Design of hybrid distillation/ melt crystallisation processes for separation of close boiling mixtures, Chem. Eng. Process., 67, 16-24
A. Mitsos, P. I. Barton, 2009, Parametric mixed-integer 0-1 linear programming: The general case for a single parameter, Eur. J. Oper. Res. 194, 663-686.
J. K. Norskov, T. Bligaard, J. Rossmeisl, C. H. Christensen, 2009, Towards the computational design of solid catalysts, Nature Chemistry 1, 37-46.
A. Peschel, H. Freund, K. Sundmacher, 2010, Methodology for the design of optimal chemical reactors based on the concept of Elementary Process Functions, Ind. Eng. Chem. Res., 49, 10535–10548.
A. Peschel, F. Karst, H. Freund, K. Sundmacher, 2011, Analysis and optimal design of an ethylene oxide reactor, Chem. Eng. Sci., 66, 6453-6469.
A. Peschel, B. Hentschel, H. Freund, K. Sundmacher, 2012, Design of optimal multiphase reactors exemplified on the hydroformylation of long chain alkenes, Chem. Eng. J., 188, 126-141.
E. Schäfer, Y. Brunsch, G. Sadowski, A. Behr, 2012, Hydroformylation of 1-dodecene in the thermomorphic solvent system dimethylformamide/decane: phase behavior, reaction performance, catalyst recycling, Ind. Eng. Chem. Res., 51, 10296-10306.
S. Senkan, 2001, Combinatorial heterogeneous catalysis: A new path in an old field, Angew. Chem. Int. Ed., 40, 312-329.
H. Struebing, Z. Ganase, P.G. Karamertzanis, E. Siougkrou, P. Haycock, P.M. Piccione, A. Armstrong, A. Galindo, C.S. Adjiman, 2013, Computer-aided molecular design of solvents for accelerated reaction kinetics, Nature Chem., 5, 11, 952-957.
B. Subramaniam, 2010, Gas-expanded liquids for sustainable catalysis and novel materials: Recent advances, Coord. Chem. Rev., 254, 15-16, 1843-1853.
F. Trespalacios, I. E. Grossmann, 2014, Review of mixed-integer nonlinear and generalized disjunctive programming methods, Chem. Ing. Tech., 86, 991-1012.
H. Yeomans, I.E. Grossmann, 1999, A systematic modeling framework of superstructure optimization in process synthesis, Computers & Chemical Engineering 23, 709-731.
M. Zagajewski, A. Behr, P. Sasse, J. Wittmann, 2014, Continuously operated miniplant for the rhodium catalyzed hydroformylation of 1-dodecene in a thermomorphic multicomponent solvent system (TMS), Chem. Eng. Sci., 115, 88-94.
T. Zhou, Z. Qi, K. Sundmacher, 2014, Model-based method for the screening of solvents for chemical reactions, Chem. Eng. Sci., 115, 177-185.

Krist V. Gernaey, Jakob K. Huusom and Rafiqul Gani (Eds.), 12th International Symposium on Process Systems Engineering and 25th European Symposium on Computer Aided Process Engineering.
31 May – 4 June 2015, Copenhagen, Denmark

PSE Tools for Process Intensification

Philip Lutze

Technical University Dortmund, Dep. of Biochemical & Chemical Engineering, Laboratory of Fluid Separations, Emil-Figge-Strasse 70, D-44277 Dortmund, Germany.

Abstract

Process intensification is considered to be one important tool to meet the requirements for more efficient and sustainable processing. Even though many different intensified technologies have been developed, only some of them have been implemented in industry yet. One of the reasons is that process synthesis and design of intensified processes, benchmarking between different intensified technologies or targeted intensification beyond currently existing solution is complex and challenging. Addressing such complexity and offering systematic solution procedures is the strength of process systems engineering. Therefore, an overview of some of the recently developed methods and tools for process design and synthesis to achieve process intensification acting at different scales of the process is given.

Keywords: Conceptual process design; Optimization. Process synthesis;

1. Introduction

In recent years, Process Intensification (PI) has attracted much interest to meet the increasing demands for highly efficient and more sustainable processing. Many different definitions on scope, principle and target of PI exist. However, one particularly practical definition of PI is that PI is a tool for the targeted enhancement of involved phenomena at different scales which overcome occurring bottlenecks and limitations of the performance to achieve a targeted benefit based on a set of performance criteria (Lutze et al., 2010). The four scales are i) process & plant; ii) equipment & operation; iii) phase & transport; and iv) fundamental & molecular; (Freund and Sundmacher, 2011; Lutze et al., 2012). Examples for PI ranges from vapour recompression in distillation to reactive distillation, micro reactors all the way down to apply new kind of solvents or new kind of energy sources for the operation. Process systems engineering (PSE) offers a broad set of methods and tools for efficient problem solving for different domains. That includes modelling; product design; simulation, synthesis, design, optimization, dynamics, and control of processes; safety, knowledge management etc.
The symbiosis of PSE and PI has been stressed earlier in some of those domains (Moulijn et al., 2008). However, since then, more intensified equipment has been developed which potentially creates a large number of options to improve a process. However, to date only a limited number have achieved implementation in industry (Harmsen, 2010). A reason for this is that the identification of the best PI option is neither simple nor systematic. Until now, most PI has been selected based on case-based trial-and-error procedures, not comparing different PI options on a quantitative basis. Hence, it is believed that tools from PSE are keys to enable the implementation of PI in industry (Lutze et al., 2010). Therefore, some of the recent contributions in this area are addressed within this paper.

2. PSE tools for process synthesis/design incorporating PI

PI has always been used as a solution technique at different scales to improve process performance limiting phenomena. Hence, different PSE methods/tools on how to systematically address the identification and benchmarking of PI solutions at different scales have been developed (see Figure 1). Those include methods for process synthesis for improved integration of conventional unit operations, synthesis/design methods incorporating PI equipment but also synthesis/design methods which work apart from existing PI solutions in order to come up with predictive solutions. Additionally, solvent or reaction selection is important tools to enable PI. Within chapters 3-6, some of the recent contributions of PSE tools to achieve PI are addressed.

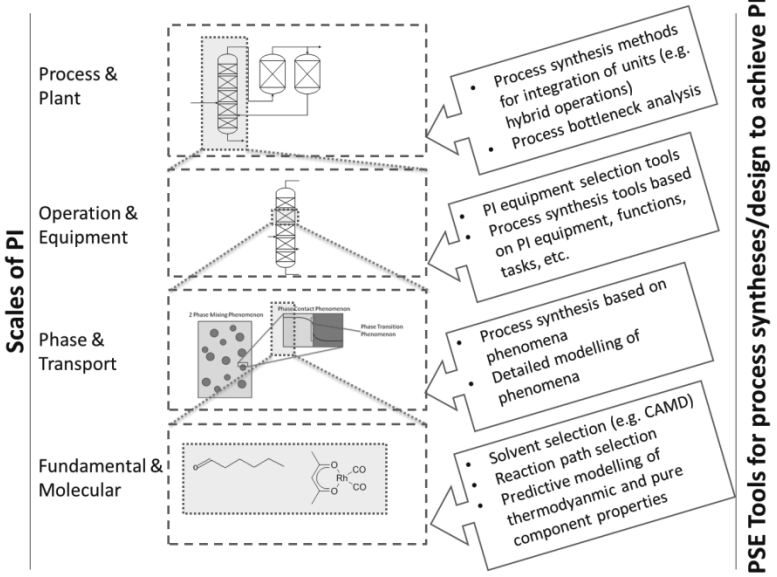

Figure 1: Illustration of PSE tools for process syntheses/design to achieve PI at different scales.

3. PSE tools at Process & Plant level

A process or a plant is producing one or more products from one or more raw materials in a desired quality and quantity. A process consists of a set of unit operations which are connected to each other in a specific way. Improved connection between or an external integration of these unit operations can be performed to intensify the process. Examples are the external integration of reactor and separator or the external integration of two different unit operations to fulfil one separation, also known as hybrid separation (Lutze and Gorak, 2013; see Fig. 2). Heat exchanger networks are not PI. But the integration of vapour recompression units to increase the energy utilization is considered to be PI at the process/plant level because the flowsheet structure itself is not changed.

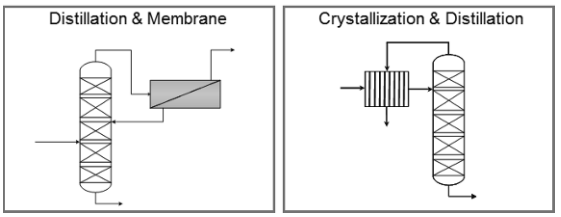

Figure 2: Exemplified scheme of two different hybrid separations.

Recently developed PSE tools for synthesis/design of hybrid separations have been summarized in an excellent review by Skiborowski et al. (2013). Recker et al. (2014) proposed a systematic and optimization-based approach to design integrated reaction-separation Processes exploiting shortcut methods to screen a set of alternative processes and rigorous optimization of the entire to identify the best. An important discussion on targeting PI at the process level is a proper selection of criteria and a sophisticated method for bottleneck analysis. Even though PI is often linked with a volume reduction due to efficiency increase, more proper criteria to benchmark PI should include intrinsic PI performance measures including costs (Criscuoli and Drioli, 2007; Lutze et al., 2010), sustainability (Carvalho et al., 2008) as well as Life-cycle-assessment (Babi et al. 2014). For bottleneck analysis systematic methods to source bottlenecks such as method of Carvalho et al. (2008) have been proposed. Their method decomposes the process into a set of process graphs. For each of these process graphs, mass and energy indicators such as material-value-added or energy and waste costs are calculated needing information about costs/prices of input and output mass/energy. Based on these indicators limitations/bottlenecks are identified for improving the sustainability of the process. Hildebrandt and Fox (2014) proposed to exploit mass, energy and entropy balances because those give not only big insights in the process in terms of a proper bottleneck analysis but also they can be directly targeted for improved process design.

4. PSE tools at Operation & Equipment level

Each process is a connection of tasks. A task can be defined as a purpose which it fulfils in the process such as conversion, separation, mixing and energy supply tasks. A task can be realized by one or multiple equipment and/or multiple tasks can be realized in single equipment. At this level, the task of the equipment is not changed by PI but rather the process space within the equipment/operation. Examples for PI at this scale are structuring or miniaturization of the apparatuses in order to support the involved phenomena without changing the task of this process step or without necessarily changing the involved transport phenomena. For example, a micro heat exchanger improves the heat addition/removal by offering a better surface area to volume ratio.

Besides, specific design methods for single PI equipment, different tools for the selection of suitable PI technologies have been developed. Kiss et al. (2012) developed a framework for the selection of energy efficient distillation technologies based on systems information. Commenge and Falk (2014) developed a methodological framework for the selection of intensified equipment and development of innovative technologies. Based on the identification of the bottleneck of the process a set of intensification strategies are selected through a connection matrix including structuring, altering operating conditions, etc.. Following, through an additional matrix, the PI equipment can be selected. Lutze et al. (2012) proposed a systematic synthesis/design method incorporating more than 100 PI equipment stored in a database. This method employs a decomposition-based solution approach in which based on an identification of the bottlenecks of an existing process, a set of intensified solutions are generated which are afterwards subsequently screened by a stepwise procedure. Even though the number of process options generated for complex case studies are large, the decomposition approach is a suitable solution strategy which reduces the number of options in case the constraints are properly selected (see Figure 3). Holtbruegge et al. (2014) developed a tool in Matlab© for the automatized generation of (reaction-) separation processes including reactive and hybrid separations based on exploiting

thermodynamic knowledge on the system. The highlighted their tool for the separation of a fermentation supernatant as well as the production of ethyl lactate.

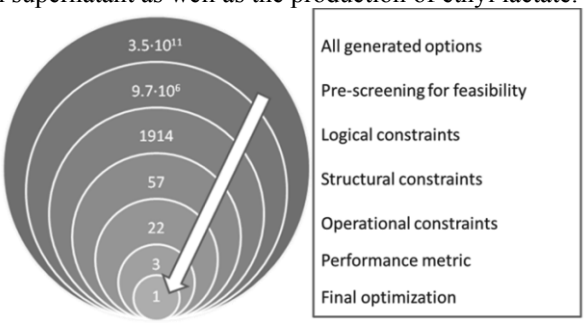

Figure 3: Generation and reduction of PI options for the production of n-acetyl-neuraminic acid by decomposition approach (Lutze et al. (2012).

A synthesis/design method going beyond existing PI solutions are the development of novel reactor networks based on elementary process functions using a three-level approach (Peschel et al., 2010). Firstly, the optimal route in the state space is identified. In the second level operational constraints based on detailed transport calculations are integrated. In the third level, different set and combinations of equipment are identified and filled with technical constraints which form the basis of the optimization of a detailed model leading to the identification of the best technical solution. The method has been illustrated for an SO_2 oxidation reactor (Peschel et al., 2010) and the production of ethylene oxide (Peschel et al., 2012). Another design/synthesis framework is proposed by Babi et al. (2014) in which the bottlenecks of a process are connected to tasks which are subsequently improved at the task level through recombination or integration with other tasks or which are directly targeted by improving the involved thermodynamic phenomena of equipment. They have tested their method on the production of methyl acetate. Their method allowed the systematic built-up a number of different conventional and intensified processes. Their best options in terms of LCA and costs were reactive distillation and integrated membrane-assisted distillation process.

5. PSE tools at Phase & Transport level

Within an equipment one or multiple phases occur in which a set of components form a phase. Within each phase mass, energy and momentum are transferred. Basic PI concepts at this scale are the integration of multiple actions in one phase or the addition of multiple phases. For example, the integration of a vapour phase and a liquid phase in which a reaction takes place will enable reactive flash or in case of countercurrent connection of many of those into a reactive distillation.

The synthesis concept from Rong et al. (2008) is based on process phenomena such as chemical reaction, materials phases, transport phenomena, phase behaviour and separation phenomena etc. Each phenomenon is influenced by materials, operating modes, flow pattern, facility medium, structure, energy sources as well as key variables, components and phases. If a key phenomenon including key variables is identified to be limiting the process, trial-and-error variations are used to enhance them which may lead to PI solutions. The concept has been briefly illustrated for the production of peracetic acid (Rong et al., 2008). Lutze et al. (2013) developed a systematic synthesis/design methodology based on elementary phenomena. Elementary phenomena include transport phenomena - which are mass transfer, energy transfer and fluid dynamics or

momentum transfer - , thermodynamics including reactions and kinetics. Transport phenomena are grounded on the conservation laws within the system and subject to driving forces based on thermodynamics as well as subject to boundaries including equipment and material-bound characteristics. Their method is capable to stepwise generate a set of phenomena-based options as well as stepwise reduce the number of options through a decomposition approach. Furthermore, their model-based method gives fully predictive solutions. They have explained each step of their method in detail for the production of isopropyl acetate in which they have generated more than 200.000 feasible solutions which they reduced stepwise to 22 by refinement of the solution. Their obtained best option was an integrated membrane-heat-exchanger flow reactor (Fig. 4)which outcompete reactive distillation as well as a conventional process.

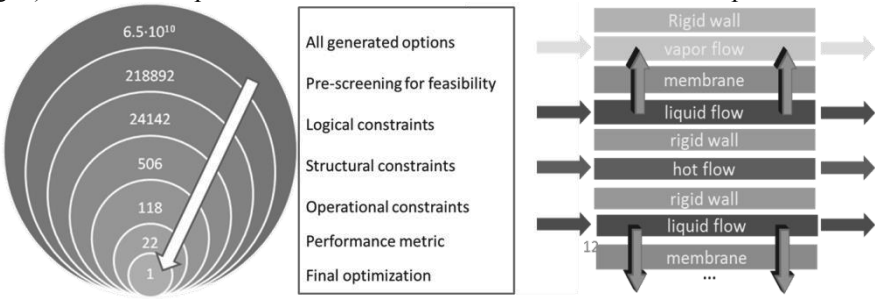

Figure 4: Generation and reduction of PI options for the production of isopropyl acetate (left) and integrated membrane-heat-exchanger flow reactor (right) (Lutze et al. (2013).

6. PSE tools at Fundamental & Molecular level

At the fundamental and molecular level the basis of the performance of molecules in pure or mixture state are set involving thermodynamics and kinetics of reactions. Here PI aims at the targeted tuning of solvents for separation systems incorporating the development of ionic liquids as tuneable solvents, reactive solvents, or the targeted enhancement of kinetics by catalyst development.

Any PSE tools at this level, either for example focussing on improved reaction pathways or identifying better solvents, for example by CAMD approaches enable more efficient processing and the potential use of PI technologies. An example is given by Roughton et al. (2011). They presented an integrated method incorporating the design of the solvent in terms of an ionic liquid and the design of the associated extractive distillation processes breaking azeotropes. Voll and Marquardt (2012) presented an approach for optimization-based evaluation of reaction pathways for biorenewables processing based on reaction network flux analysis.

7. Conclusions

Different PSE methods/tools on how to systematically address the identification and benchmarking of PI solutions at different scales have been developed (see Figure 1) and are between ready-to-be–applied and promising. Each of those has its advantages and disadvantages. Process synthesis tools at higher levels allow the potentially quick identification of a set of suitable PI equipment to improve the process but are limited to the initial search space of PI solutions. Here development of common or open databases will help to further push those developments. Process synthesis tools for PI at lower levels may allow the generation of truly predictive and innovative PI solutions but the problem to be solved is much more complex. It is believed that future development in

mathematical approaches as well as database management will increase the applicability of these concepts. Furthermore, integration of methods/tools from the fundamental/molecular level will increase further the degree of freedoms in process synthesis/design for PI, however, also the complexity of the solution identification. Finally, the development within PSE and PI separately and also together are promising to push implementation of more efficient technologies into industrial processes.

References

D. K. Babi, P. Lutze, J.M. Woodley, R. Gani, 2014, A process synthesis-intensification framework for the development of sustainable membrane-based operations, Chem Eng Process, 86, 173-195.

A. Carvalho, R. Gani, H. Matos, 2008, Design of sustainable chemical processes: Systematic retrofit analysis generation and evaluation of options, Process Saf Environ Prot, 86, 328-346.

A. Criscuoli, E. Drioli, 2007, New metrics for evaluating the performance of membrane operations in the logic of process intensification, Ind Eng Chem Res, 46, 2268-2271.

H. Freund, K. Sundmacher, 2011, Process Intensification. In Ullmann's Encyclopedia of Industrial Chemistry, Wiley-VCH Verlag GmbH & Co. KGaA, Weinheim.

J. Harmsen, 2010, Process Intensification in the petrochemicals industry: drivers and hurdles for commercial implementation, Chem Eng Process, 49, 70-73.

D. Hildebrandt, J.A. Fox, 2014, Addressing a design defect: Process targets and flowsheets, Comp Aided Chem Eng, 34, 134-143.

J. Holtbruegge, H. Kuhlmann, P. Lutze, 2014, Conceptual Design of Flowsheet Options Based on Thermodynamic Insights for (Reaction−)Separation Processes Applying Process Intensification, Ind Eng Chem Res, 53, 13412−13429.

A.A. Kiss, S.J. Flores Kandaeta, C.A. Infante Ferreira, 2012, Towards energy efficient distillation technologies – Making the right choice, Energy, 47, 531-542.

P. Lutze, D.K. Babi, J.M. Woodley, R. Gani, 2013,Phenomena based methodology for process synthesis incorporating process intensification, Ind Eng Chem Res, 52, 7127-7144.

P. Lutze, R. Gani, J.M. Woodley, 2010, Process intensification: A perspective on process synthesis, Chem Eng Process, 49, 547-558.

P. Lutze, A. Gorak, 2013, Reactive and membrane-assisted distillation: Recent developments and perspective, 2014, Chem Eng Res Des, 91, 1978-1997.

P. Lutze, A. Roman-Martinez, J.M. Woodley, R. Gani, 2012, A systematic synthesis and design methodology to achieve process intensification in (bio) chemical processes, Comp Chem Eng, 36, 189-207.

A. Peschel, H. Freund, K. Sundmacher, 2010, Methodology for the design of optimal chemical reactors based on the concept of elementary process functions, Ind Eng Chem Res, 49, 10535-10548.

A. Peschel, A. Jrke, K. Sundmacher, H. Freund, 2012, Optimal reaction concept and plant wide optimization of the ethylene oxide process, Chem Eng J, 207-208, 656-674.

J. Moulijn, A. Stankiewicz, J. Grievink, A. Gorak, 2008, Process intensification and process systems engineering: A friendly symbiosis, Comp Chem Eng, 32; 3-11.

S. Recker, M. Skiborowski, C. Redepenning, W. Marquardt, 2014, Systematic and Optimization-Based Design of Integrated Reaction-Separation Processes, Comp Aided Chem Eng, 34, 417-422.

B.G. Rong, E. Kolehmainen, I. Turunen. 2008, Methodology of conceptual process synthesis for process intensification, Comp Aided Chem Eng, 25, 283-288.

B.C. Roughton, B. Christian, J. White, K.V. Camarda, R. Gani, 2012, Simultaneous design of ionic liquid entrainers and energy efficient azeotropic separation processes, Comp Chem Eng, 42, 248-262.

M. Skiborowski, A. Harwardt, W. Marquardt, 2013, Conceptual design of distillation-based hybrid separation processes, Annu Rev Chem Bio Eng, 4, 45-68.

A. Voll, W. Marquardt, 2011, Reaction Network Flux Analysis: Optimization-Based Evaluation of Reaction Pathways for Biorenewables Processing, AIChE J, 58, 1788–1801.

Krist V. Gernaey, Jakob K. Huusom and Rafiqul Gani (Eds.), 12th International Symposium on Process Systems Engineering and 25th European Symposium on Computer Aided Process Engineering.
31 May - 4 June 2015, Copenhagen, Denmark.

Towards the integration of process design, control and scheduling: Are we getting closer?

Efstratios N. Pistikopoulos[a,b], Nikolaos A. Diangelakis[a] and Amit M. Manthanwar[a]

[a]*Department of Chemical Engineering, Imperial College London, London, United Kingdom.*
[b]*Artie McFerrin Department of Chemical Engineering, Texas A&M University, College Station TX, United States.*
e.pistikopoulos@imperial.ac.uk; stratos@tamu.edu

Abstract

The integration of design and control, control and scheduling and design, control and scheduling, all have been core PSE challenges. While significant progress has been achieved over the years, it is fair to say that at the moment there is not a generally accepted methodology and/or "protocol" for such an integration - it is also interesting to note that currently, there is not a commercially available software [or even in a prototype form] system to fully support such an activity.

Here, we present the foundations for such an integrated framework and especially a software platform that enables such integration based on research developments over the last twenty -five years. In articular, we describe PAROC, a prototype software system which allows for the representation, modelling and solution of integrated design, scheduling and control problems. Its main features include: (i) a high-fidelity dynamic model representation, also involving global sensitivity analysis, parameter estimation and mixed integer dynamic optimisation capabilities; (ii) a suite/toolbox of model approximation methods; (iii) a host of multi-parametric programming solvers for mixed continuous/integer problems; (iv) a state-space modelling representation capability for scheduling and control problems; and (v) an advanced toolkit for multi-parametric/explicit Model Predictive Control and moving horizon reactive scheduling problems. Algorithms that enable the integration capabilities of the systems for design, scheduling and control are presented on a case of a series of cogeneration units.

Keywords: multi-parametric receding horizon policies, control, design optimisation, optimal scheduling, integration

1. Introduction and Overview

Designing economically profitable plants and improving their operational performance has been a core research field in Process Systems Engineering. The need to optimise the performance of a plant includes (i) long-term decisions, (ii) mid-term decisions and (iii) short-term decisions as well as (iv) their interactions. Therefore, a variety of computational tools has been developed for advanced model development (e.g. ASPEN Plus®, gPROMS®), – including global sensitivity analysis, parameter estimation, and mixed-integer dynamic optimisation capabilities – as well as algorithms for operational scheduling procedures and advanced control methodologies.

It is generally accepted that the decisions regarding the plant design affect its operation in a most determinative manner, since they are the less likely to change while a possible change usually requires not only a considerable investment but also the permanent cease of operation; an action

that affects production profit. Operational scheduling optimises the plant performance in the mid-term while taking into account uncertainty that originates from raw material shortages, fluctuation in pricing, demand changes, equipment failure and the like. Most commonly, the operational scheduling optimisation procedures are based on the assumption that the design of the plant is given and remains fixed for the entire operational horizon and that the regulatory and supervisory control of the system work flawlessly. The control strategies of a process constitute the short-term decisions in terms of operation. A variety of procedures are implemented with regulatory (P, PI, PID) control and model predictive control to be the most notable. The main burden of the controller is to reject measured and unmeasured disturbances while trying to maintain certain operation set-points imposed by the mid-term operational optimisation. Table 1 presents a list of the most notable contributions on model predictive control.

Table 1: Model-based control - Indicative list

Authors	On-line/off-line	Remarks
Campo and Morari (1987)	on-line	min worst case ∞ norm
Mayne and Schroeder (1997)	off-line	min settling time, use invariant set
Lee and Yu (1997)	on-line	min worst case quadratic cost, use of dynamic programming for closed-loop
P. O. M. Scokaert and Mayne (1998)	on-line	min worst case quadratic, invariant set for stability.
Schwarm and Nikolaou (1999), Badgwell (1997)	on-line	min nominal objective s.t. robustness quadratic/linear constraints. Large number of combinations.
Kassmann et al. (2000)	on-line	Apply robustness constraints to steady state target calculation.
Lee and Cooley (2000)	on-line	min worst case quadratic cost s.t. quadratic constraints for stability.
Bemporad et al. (2003)	off-line	min worst case -∞ norm. use of dynamic programming, solve consecutively mp-LPs.
Christofides and El-Farra (2014)	on-line	Recent advances in economic model predictive control and economic non-linear model predictive control.

The focus of the operational performance optimisation has shifted from addressing the design, scheduling and control aspects individually into a combined, integrated approach. The common factor in these approaches is the effect of short-term decision-making into mid- or long-term decisions. Therefore, numerous works have appeared in the literature throughout the past years regarding (i) the interactions of design and control and (ii) the integrated approach to scheduling and control. An indicative list of the different techniques employed to target the design and control problem is presented in Table 2. Superstructures, MIDO formulations and combinations of online optimisation techniques with embedded model predictive control are worth noting.

On the other hand, recent contributions (from 2002 onwards) have opened the road to the integration of operational mid-term scheduling and control via a variety of methods. Among them, the MIDO approaches as well as the state-space scheduling problem representation with integrated online or offline model predictive control strategies are the most notable. Table 3 indicates the major contributions.

While significant progress has been achieved over the years in integrating design with control and control with scheduling, it is fair to say that at the moment there is not a generally accepted methodology and/or "protocol" for the integration of all three aspects - it is also interesting to note

Table 2: Interaction of design and control - Indicative list

Authors	Contributions
Lee et al. (1972)	Introduction to design and control
Narraway et al. (1991)	Steady state and dynamic economics
Luyben and Floudas (1994)	Superstructure of design alt. into MINLP
Mohideen et al. (1996)	Economically optimal design and control
Van Schijndel and Pistikopoulos (2000)	Review on process design and operability
Sakizlis et al. (2003)	Simultaneous mpMPC and online design optimisation. Case studies on binary distilation column and evaporator.
Sakizlis et al. (2004)	Review on design and control
Flores-Tlacuahuac and Biegler (2007)	MIDO transformed to MINLP
Würth et al. (2011)	Dynamic optimisation and NMPC
Yuan et al. (2012)	Review on design and control
Liu et al. (2013)	Optimal design and operation of distributed systems with focus on the trade offs between modeling acuracy and computational complexity and efficiency.
Diangelakis et al. (2014a)	Sequential design optimisation and mp-MPC. Application on a residential cogeneration systems.

that currently, there is not a commercially available software [or even in a prototype form] system to fully support such an activity. In this work we present the foundations for such an integration, based on 25 years of research. We present PAROC, a prototype software system which allows for the representation, modelling and solution of integrated design, scheduling and control problems.

2. The PAROC Framework

The PAROC (PARametric Optimisation and Control) framework (depicted in Figure 1) is the cornerstone for the development and testing of receding horizon optimisation policies for process systems. Starting with a "high-fidelity" dynamic model of the process at hand, PAROC provides the theoretical, technical and software basis for the development of multi-parametric model predictive controllers, multi-parametric moving horizon estimators, multi-parametric rolling horizon process schedules, and the like, with embedded dynamic optimisation capabilities as well as model validation techniques. A brief step-by-step description follows.

"High-fidelity" model analysis and dynamic optimisation. The "high-fidelity" model of the process at hand, implemented in gPROMS®, is the framework basis. Ranging from simple, ordinary differential equations to complex, partial differential equations and non-linear algebraic relations it provides the platform upon which analysis such as parameter estimation and global sensitivity analysis is performed. Most commonly, a "first principle" approach is followed to capture the dynamic behaviour of the process.

Model Approximation. The modelling techniques employed for the derivation of a "high-fidelity" model usually result in highly complex systems which are too computationally expensive to be handled by the standard multi-parametric optimisation programming approach. Therefore, an intermediate step that simplifies the model interpretation of the process into a linear, discrete ODE system is needed. For the model approximation, (i) the linearization capabilities of gPROMS®, (ii) the System Identification Toolbox of MATLAB® or (ii) the model reduction techniques presented in Narciso and Pistikopoulos (2008); Rivotti et al. (2012); Lambert et al. (2013) (and ref-

Table 3: Integration of scheduling and control - Inidicative list

Authors	Contributions
Shobrys and White (2002)	Interactions of planning scheduling and control and their impact to decision making in process industry operations
Mahadevan et al. (2002)	Robust control for the targeting of transition times in scheduling of polymerization operation
Chatzidoukas et al. (2003b)	Impact of control structure on process operability, product quality optimisation and time optimal grade transition
Chatzidoukas et al. (2003a)	Integration of production scheduling and optimal grade transition profiles with a MIDO approach
Nyström et al. (2005)	Production optimisation through determination of transition trajectories, operating points and manufacturing sequence
Flores-Tlacuahuac and Grossmann (2006b,a)	Simultaneous cyclic scheduling and control via reformulating an MIDO problem into an MINLP
You and Grossmann (2008)	Supply chain optimisation under uncertainty via multi-period MINLP
Harjunkoski et al. (2009)	Discussion on the problems arising from the integration of production scheduling and control and its implementation
Biegler and Zavala (2009)	Real-time optimisation and control for decision making via the formulation and efficient solution of NLP
Subramanian et al. (2013)	Distributed MPC and Cooperative MPC to integrate scheduling objectives with process operation constraints
Subramanian et al. (2012)	MI scheduling problem formulation based on state space models
Zhuge and Ierapetritou (2014)	Continuous-time event-point formulation scheduling incorporating explicit constraints derived from mpMPC to target complexity
Kopanos and Pistikopoulos (2014)	Reactive scheduling of a state space representation based system using multi-parametric programming
Baldea and Harjunkoski (2014)	A comprehensive systematic review of the integration of scheduling and control

erences therein) are utilised. The resulting state-space representation is adequately simple to be treated in a multi-parametric receding horizon basis, yet it is focused on compromising the original model accuracy as little as possible[1].

Multi-parametric programming, receding horizon policies and mpMHE. In this step, the approximate state-space model is treated in a receding horizon policy that results into the formulation of a linear or quadratic program with continuous or continuous and binary decision variables (i.e. LP, QP, MILP, MIQP problems). The optimisation problem is subjected to constraints that result from the state-space representation (equality constraints) as well as box constraints for the state variables, the input and output variables and the input rate (inequality constraints). In the most

[1]The state-space model accuracy is determined as the mismatch between the original "high-fidelity" model and the approximate model via simulation results under the same inputs and initial conditions.

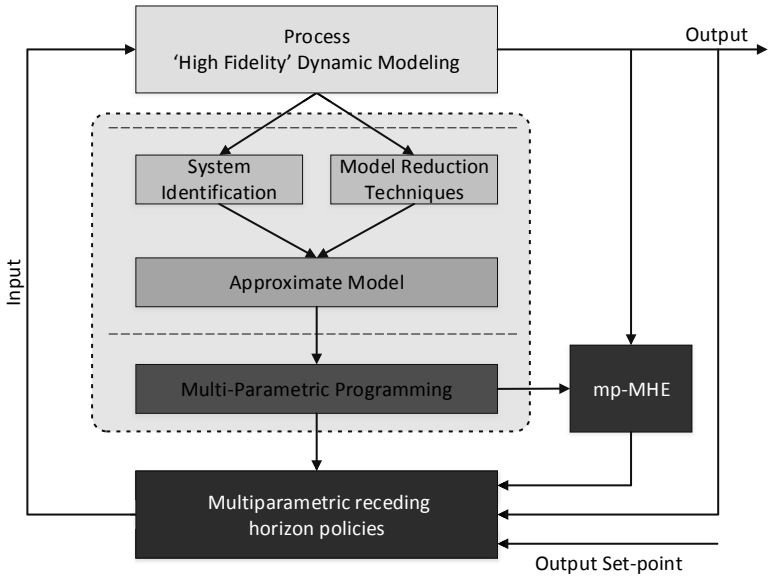

Figure 1: The PAROC Framework. Actions in the gray area happen once and offline.

generic case, treating the states as uncertain but bounded parameters and reformulating the problem statement accordingly results into multi-parametric programming problem which, based on the initial formulation, is classifed as an mpLP, mpQP, mpMILP or mpMIQP. The solution of such problems is provided once and offline by the software package POP®, thereby eliminating the need of an online optimiser to handle the receding horizon problem whether this is model predictive controller, a scheduler or a moving horizon estimator. The online solution of the receding horizon policy is therefore reduced into a piecewise affine evaluation.

Closed-Loop validation and software implementation. The closed loop validation of the receding horizon policies takes place against the original "high-fidelity" model and is enabled by the interactions between the modeling software and the solution of the multi-parametric programming problem. There are currently two approaches regarding this. The first is based on the inteconnectivity between the gPROMS® platform and MATLAB® via the use of gO:MATLAB® while the second relies on the development of a dynamic link library, which contains the solution to the receding horizon optimisation problem and is called by the simulator at every simulation step.

The next section discusses the interactions of process design and operations for a series of heat and power cogeneration (CHP) units for domestic/residential use.

3. Towards the integration of design and operational optimisation

In this section, an example for the integration of design and operational optimisation is presented. A series of CHP units based on Diangelakis et al. (2014b) is considered for domestic/residential use. The objective is to acquire the optimal operation policy, the optimal model based controller and the optimal design of the series through a single optimisation formulation, utilising the PAROC software platform. The process design aspect of this example consists mainly of the size of the prime movers, hence the ability of power and heat production of the system is affected. Fur-

thermore, an insulated tank for hot water storage is considered, the size of which is subjected to optimisation. The choice between a single or multiple units is also considered, therefore the scheduled operation and control of the units is also a matter of optimisation.

Following the principles described in section 2, a "high-fidelity" model of a CHP unit is considered, similar to the procedure described in Diangelakis et al. (2014a). In this case though, an integrated approach is followed where the model approximation procedure also takes into account the design variables of the high fidelity model, in this case the engine displacement volume as well as the volume of an insulated hot water buffer tank. After the approximation the electrical power output of the internal combustion engine is the output of a state-space model the inputs of which are the position of the butterfly in the throttle valve and the displacement volume of the internal combustion engine. Similarly the optimal action of the heat recovery subsystem is a subject to the size of the insulated tank. For the design of the mp-MPC the design variables are treated as measured uncertain parameters. The resulting control scheme, is exported in the dynamic link library format of a gPROMS® ModelBuilder foreign object as described formerly.

The scheduling problem formulation in the form of Kopanos and Pistikopoulos (2014) is taken into consideration, enhanced by dynamic control decision and dynamics feedback in a bottom-up approach as described in Baldea and Harjunkoski (2014). The use of the design-dependent mp-MPC scheme presented above coupled with a design-dependent scheduling formulation, forms the core of the operational strategies. A conceptual schematic representation of the system and the configuration is presented in Figure 2.

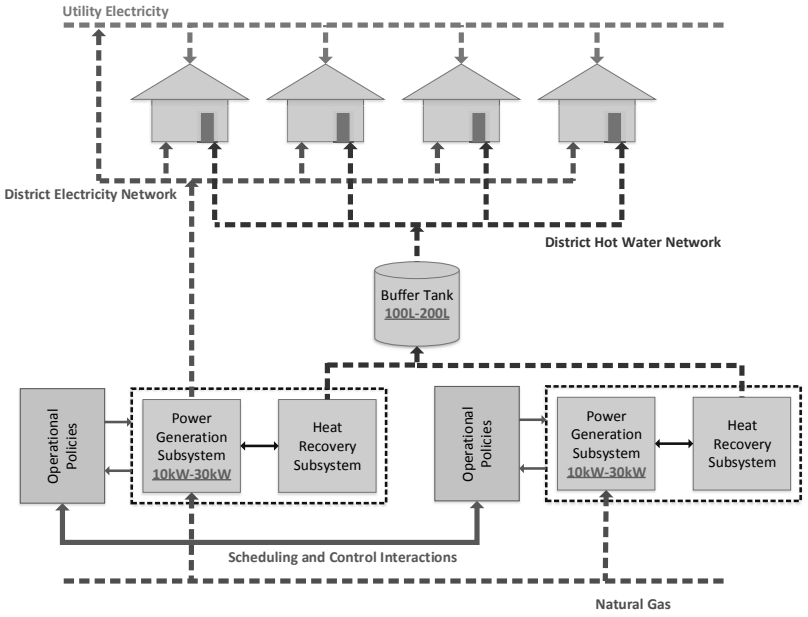

Figure 2: Simultaneous design and operational optimisation via design dependent mp-MPC. An indicative range for the design variables is denoted in red.

The realisation of the design uncertainty is subject to optimisation. More specifically, the design dependent multi-parametric controller as well as the design-dependent optimal scheduling[2] are

[2]The optimal scheduling is addressed as a receding horizon multi-parametric programming problem.

inserted in gPROMS®. Using the dynamic optimisation capabilities of the latter, the model is optimised using single vector shooting techniques. The value for the design variables as a result of the optimisation procedure acts as an uncertainty realisation for both the controller and the scheduler, therefore achieving simultaneous design and operational optimisation. This novel approach manages to determine (i) the mid-term operational strategy (ii) the short-term optimal control actions and (iii) the design of the system as a result of a single dynamic optimisation procedure. Consequently, the dependence among the control strategy, the operational policy and the design of the system is examined.

4. Concluding Remarks

In this paper we have presented the PAROC framework and the software platform for the development of receding horizon policies via multi-parametric programming. Furthermore, we showed how the framework and its software components enable the simultaneous design and operational optimisation of process systems using research conducted in the last 25 years. The example of the series of CHP units for domestic/residential use helps us demonstrate the concept of design and operational optimisation.

5. Acknowledgments

The financial support from CPSE Industrial Consortium, EPSRC (EP/I014640/1) and the European Commission (OPTICO/G.A. No. 280813) is gratefully acknowledged.

References

Badgwell, T. A., 1997. Robust model predictive control of stable linear systems. International Journal of Control 68 (4), 797–818.

Baldea, M., Harjunkoski, I., 2014. Integrated production scheduling and process control: A systematic review. Computers & Chemical Engineering 71, 377 – 390.

Bemporad, A., Borrelli, F., Morari, M., 2003. Min-max control of constrained uncertain discrete-time linear systems. Automatic Control, IEEE Transactions on 48 (9), 1600–1606.

Biegler, L., Zavala, V., 2009. Large-scale nonlinear programming using ipopt: An integrating framework for enterprise-wide dynamic optimization. Computers and Chemical Engineering 33 (3), 575–582.

Campo, P. J., Morari, M., 1987. Robust model predictive control. In: American Control Conference, 1987. pp. 1021–1026.

Chatzidoukas, C., Kiparissides, C., Perkins, J., Pistikopoulos, E., 2003a. Optimal grade transition campaign scheduling in a gas-phase polyolefin fbr using mixed integer dynamic optimization. Computer Aided Chemical Engineering 15 (C), 744–747.

Chatzidoukas, C., Perkins, J., Pistikopoulos, E., Kiparissides, C., 2003b. Optimal grade transition and selection of closed-loop controllers in a gas-phase olefin polymerization fluidized bed reactor. Chemical Engineering Science 58 (16), 3643–3658.

Christofides, P., El-Farra, N., 2014. Editorial board. Journal of Process Control 24 (8), IFC –, economic nonlinear model predictive control.

Diangelakis, N. A., Manthanwar, A. M., Pistikopoulos, E. N., 2014a. A framework for design and control optimisation: Application on a chp system. In: Proceedings of the 8th International Conference on Foundations of Computer-Aided Process Design. Vol. 34 of Computer Aided Chemical Engineering. Elsevier, pp. 765–770.

Diangelakis, N. A., Panos, C., Pistikopoulos, E. N., 2014b. Design optimization of an internal combustion engine powered chp system for residential scale application. Computational Management Science 11 (3), 237–266.

Flores-Tlacuahuac, A., Biegler, L. T., 2007. Simultaneous mixed-integer dynamic optimization for integrated design and control. Computers & Chemical Engineering 31 (5–6), 588–600.

Flores-Tlacuahuac, A., Grossmann, I., 2006a. An effective mido approach for the simultaneous cyclic scheduling and control of polymer grade transition operations. Computer Aided Chemical Engineering 21 (C), 1221–1226.

Flores-Tlacuahuac, A., Grossmann, I., 2006b. Simultaneous cyclic scheduling and control of a multiproduct cstr. Industrial and Engineering Chemistry Research 45 (20), 6698–6712.

Harjunkoski, I., Nyström, R., Horch, A., 2009. Integration of scheduling and control - theory or practice? Computers & Chemical Engineering 33 (12), 1909–1918, {FOCAPO} 2008 - Selected Papers from the Fifth International Conference on Foundations of Computer-Aided Process Operations.

Kassmann, D. E., Badgwell, T. A., Hawkins, R. B., 2000. Robust steady-state target calculation for model predictive control. AIChE Journal 46 (5), 1007–1024.

Kopanos, G. M., Pistikopoulos, E. N., 2014. Reactive scheduling by a multiparametric programming rolling horizon framework: A case of a network of combined heat and power units. Industrial & Engineering Chemistry Research 53 (11), 4366–4386.

Lambert, R. S., Rivotti, P., Pistikopoulos, E. N., 2013. A monte-carlo based model approximation technique for linear model predictive control of nonlinear systems. Computers & Chemical Engineering 54 (0), 60–67.

Lee, H., Koppel, L., Lim, H., 1972. Integrated approach to design and control of a class of countercurrent processes. Industrial and Engineering Chemistry: Process Design and Development 11 (3), 376–382.

Lee, J. H., Cooley, B. L., 2000. Min–max predictive control techniques for a linear state-space system with a bounded set of input matrices. Automatica 36 (3), 463–473.

Lee, J. H., Yu, Z., 1997. Worst-case formulations of model predictive control for systems with bounded parameters. Automatica 33 (5), 763–781.

Liu, P., Georgiadis, M. C., Pistikopoulos, E. N., 2013. An energy systems engineering approach for the design and operation of microgrids in residential applications. Chemical Engineering Research and Design 91 (10), 2054 – 2069, the 60th Anniversary of the European Federation of Chemical Engineering (EFCE).

Luyben, M. L., Floudas, C. A., 1994. Analyzing the interaction of design and control—1. a multiobjective framework and application to binary distillation synthesis. Computers & Chemical Engineering 18 (10), 933–969.

Mahadevan, R., Doyle III, F., Allcock, A., 2002. Control-relevant scheduling of polymer grade transitions. AIChE Journal 48 (8), 1754–1764.

Mayne, D. Q., Schroeder, W. R., 1997. Robust time-optimal control of constrained linear systems. Automatica 33 (12), 2103–2118.

Mohideen, M. J., Perkins, J. D., Pistikopoulos, E. N., 1996. Optimal synthesis and design of dynamic systems under uncertainty. Computers & Chemical Engineering 20, Supplement 2 (0), S895–S900.

Narciso, D. A., Pistikopoulos, E. N., 2008. A combined balanced truncation and multi-parametric programming approach for linear model predictive control. In: Bertrand Braunschweig, Xavier Joulia (Eds.), 18th European Symposium on Computer Aided Process Engineering. Vol. 25 of Computer Aided Chemical Engineering. Elsevier, pp. 405–410.

Narraway, L., Perkins, J., Barton, G., 1991. Interaction between process design and process control: economic analysis of process dynamics. Journal of Process Control 1 (5), 243–250.

Nyström, R., Franke, R., Harjunkoski, I., Kroll, A., 2005. Production campaign planning including grade transition sequencing and dynamic optimization. Computers and Chemical Engineering 29 (10), 2163–2179.

P. O. M. Scokaert, Mayne, D. Q., 1998. Min-max feedback model predictive control for constrained linear systems. IEEE Transactions on Automatic Control 43 (8), 1136–1142.

Rivotti, P., Lambert, R. S., Pistikopoulos, E. N., 2012. Combined model approximation techniques and multiparametric programming for explicit nonlinear model predictive control. Computers & Chemical Engineering 42 (0), 277–287.

Sakizlis, V., Perkins, J. D., Pistikopoulos, E. N., 2003. Parametric controllers in simultaneous process and control design optimization. Industrial & Engineering Chemistry Research 42 (20), 4545–4563.

Sakizlis, V., Perkins, J. D., Pistikopoulos, E. N., 2004. Recent advances in optimization-based simultaneous process and control design. Computers & Chemical Engineering 28 (10), 2069–2086.

Schwarm, A. T., Nikolaou, M., 1999. Chance-constrained model predictive control. AIChE Journal 45 (8), 1743–1752.

Shobrys, D., White, D., 2002. Planning, scheduling and control systems: Why cannot they work together. Computers and Chemical Engineering 26 (2), 149–160.

Subramanian, K., Maravelias, C. T., Rawlings, J. B., 2012. A state-space model for chemical production scheduling. Computers & Chemical Engineering 47 (0), 97–110.

Subramanian, K., Rawlings, J. B., Maravelias, C. T., Flores-Cerrillo, J., Megan, L., 2013. Integration of control theory and scheduling methods for supply chain management. Computers & Chemical Engineering 51, 4–20.

Van Schijndel, J., Pistikopoulos, E., 2000. Towards the integration of process design, process control and process operability - current stares and furore trends. Foundations of Computer-Aided Process Design 96, 99–112.

Würth, L., Hannemann, R., Marquardt, W., 2011. A two-layer architecture for economically optimal process control and operation. Journal of Process Control 21 (3), 311–321.

You, F., Grossmann, I., 2008. Design of responsive supply chains under demand uncertainty. Computers and Chemical Engineering 32 (12), 3090–3111.

Yuan, Z., Chen, B., Sin, G., Gani, R., 2012. State-of-the-art and progress in the optimization-based simultaneous design and control for chemical processes. AIChE Journal 58 (6), 1640–1659.

Zhuge, J., Ierapetritou, M. G., 2014. Integration of scheduling and control for batch processes using multi-parametric model predictive control. AIChE Journal 60 (9), 3169–3183.

Krist V. Gernaey, Jakob K. Huusom and Rafiqul Gani (Eds.), 12th International Symposium on Process Systems Engineering and 25th European Symposium on Computer Aided Process Engineering.
31 May – 4 June 2015, Copenhagen, Denmark

Industrially Applied PSE for Problem Solving Excellence

Antoon J.B. ten Kate

AkzoNobel, Zutphenseweg 10, 7418 AJ Deventer, the Netherlands
antoon.tenkate@akzonobel.com

Abstract

PSE, process systems engineering, is about the development and application of systematic methods for process studies by the chemical engineer. By means of software tools, the application of these methods is facilitated. Over the last about half a century, CAPE (computer aided process engineering) tools have found their way into process engineering. E.g. nowadays it is unthinkable to design a plant without a simulation in a flow sheet package. But there are many more applications of PSE in industry.

With this paper we aim to provide a taste of the meaning of PSE in our industrial R&D environment. We do not intend our overview to being complete, but we hope to give a flavour of what we perceive as the benefits of PSE during process development in our industry, and in which aspects we believe the PSE arena should be extended to render further benefits.

Keywords: PSE, CAPE, PI, industrial process & product development

1. Introduction

Traditionally PSE is concerned with the understanding and development of systematic procedures that assists the chemical engineer to design, operate and control the chemical production facilities (Gani et al., 2007). The typical engineering work stream for the chemical engineer comprises the development of (conceptual) process design, mass and energy balances, equipment selection and sizing, control strategies, techno-economic evaluations and so on. CAPE tools are applied in all of these work streams.

These are typical activities for any kind of chemical engineer, either working at the plant, in an engineering unit or in process R&D. Yet, obviously the focus in R&D is more on the ‘unknown’ than it is at the plant or in engineering, where the focus is more on debottlenecking and troubleshooting or designing a plant based on existing knowledge.

PSE offers both the methodological approach to unravelling the unknown, as well as the software tools needed in that approach. In the following sections, we will first discuss software tools, and subsequently, outline a structured approach in process R&D.

2. Providing Software to Exploration

When applying CAPE tools, our objective is to provide a (semi-)quantitative description of at least a part of the process or product of concern. A variety of CAPE modelling tools is available for R&D purposes, for different scales in dimensions and time:

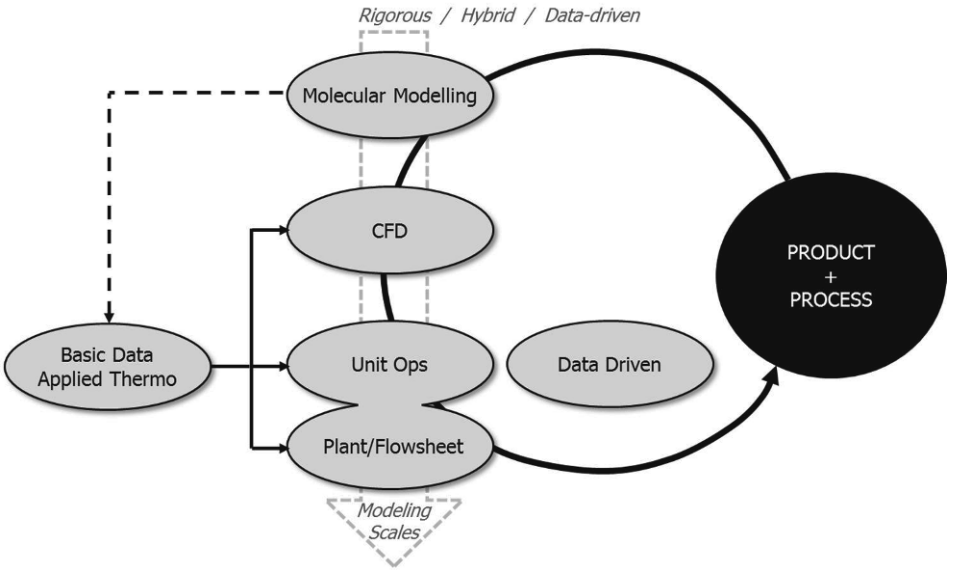

Figure 1. Chemical engineering modelling platforms at the various scales

- At the smallest scale molecular modelling tools are available. They provide an alternative approach to experiments for gaining insight into reaction mechanism, crystallization behavior, emulsion stability and so on.
- At a somewhat larger scale, CFD (computational fluid dynamics) provides insight into flow characteristics in systems that otherwise are hard to investigate, e.g. at high temperature or harsh corrosive conditions. CFD has long outgrown its infancy state of 'colors for directors' as e.g. it is capable to describe multi-phase reactive systems.
- The heart of process engineering modeling remains the simulation of single and integrated unit operations up to the entire plant. Aspen Engineering Suite, ChemCAD, Hysis, Pro/II, ProSim and gProms are software platforms that offer flow sheeting capabilities for steady state and dynamic simulation.

Larger scale models are typically more of use for manufacturing, like manufacturing execution system (MES) and enterprise resource planning (ERP). The related CAPE tools are less applicable in the R&D environment.

Basic data, comprising chemical and physical properties, are crucial for plant and unit operation models and CFD models. In general the basic data models used in unit operation and plant modeling are more sophisticated than those in CFD applications.

The time and effort for building the model is typically larger than for running the model and the interpretation of the simulation results. Likewise it takes more time and effort to set up an experiment than performing the experiment and interpreting the results:

- model: computation time << interpretation time << model synthesis time
- experiment: interpretation time << experimental time << preparation time

It typically takes a much shorter time to simulate the effect of a certain event than to perform an experiment, if the model is available. However, if not available, the model needs to first be developed and just doing an experiment may be much more efficient.

On top of that, the experiment may reveal certain aspects not covered by the model, e.g. unforeseen side reactions. A balanced choice between modelling and experimentation should be made.

The previous remarks should not be interpreted as a plea to strive for 'universal models', i.e. models that include everything. The strength of models lie in the fact that they are an abstraction of reality. The model should be fit for its purpose. In that sense, the purpose affects the shape of the model. E.g. the vapour pressure does not have to be included in the kinetic model of a liquid phase reaction. Vice versa, the user should not expect this model to represent the vapour pressure of the reaction mixture.

Hence, a pragmatic choice should be made between models and experiments or the combination of those. In our practice, we strive for the latter: where models serve as quantitative input for the hypothesis based research and where experiments serve as quantitative input for building and validating the models. This will be further exemplified in the section 4.

3. Providing Structure to Exploration

PSE provides a structured approach to problem solving. Methodologies have been and are being developed to provide this structure for (conceptual) process and product design. There are numerous methodologies: some of them make use of superstructures, others of heuristic and rule-based systems, again others of expert systems, and so on.

However, all of these methodologies have to start from somewhere, and it is our impression that typically a database forms the starting point. After the targets for the conceptual design are set, the tools start searching their database, retrieving information about the heuristic rules or parameters for the predictive evaluation. If the information is not available, the user is required to put in the specific information. We believe an open structure would be more useful allowing the user to selectively use those parts of the methodology that are of specific interest. Moreover, we believe the use of semi-predictive models would be beneficial.

Semi-predictive models require only a few data points for parameterization of the system of concern. As a physical property example, NRTL-SAC (Chen et al., 2006) and HSP (Abbott et al., 2013) require polymer solubility data in a few solvents to enable representation of the solubility of that polymer in a wide domain of solvents and solvent mixtures. It shows the strength of the intimate alignment of experiments and modelling, delivering an accurate representation with a small experimental and modelling effort.

We believe the power of the semi-predictive modelling approach is underestimated, not only for physical properties but in general. We would like to see more of these semi-predictive models. We believe these kinds of models have a better chance of providing representation at the required quality level, than extending the fully predictive methods with a higher order correction and extending their database. We believe semi-predictive models can be very powerful instrument in industrial R&D as they generate a high-precision representation but only need a few dedicated data points for parameterization. These data points should be obtained through well-designed experiments, the design of which could be based on the model.

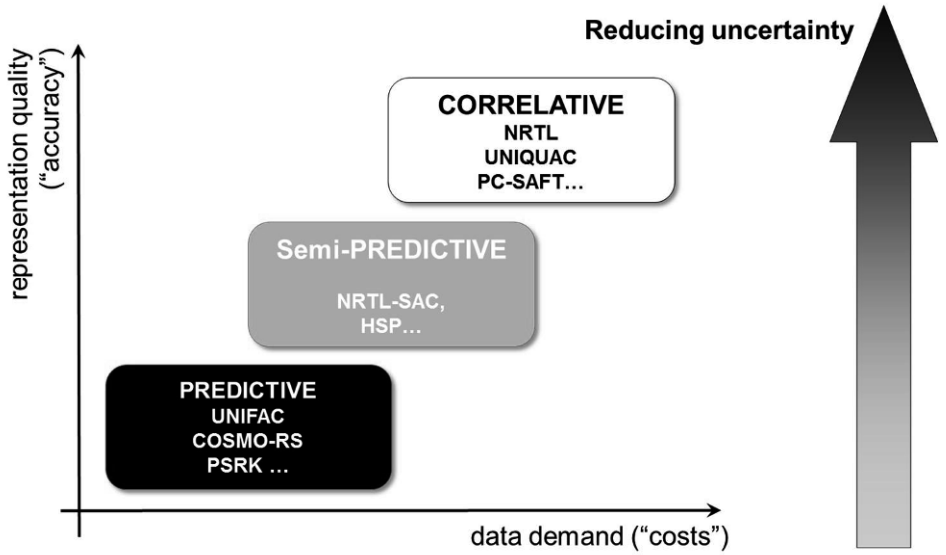

Figure 2. Different types of physical property models

Another intriguing trend in PSE is its application in product design. CAPE tools are finding their use in product design, which are derived from existing and proven methods in process design. The methods are typically based on reverse modelling: whereas in process design the properties of a mixture are calculated from the mixture composition, in product design the search is towards identifying constituents and compositions that match a desired property set (Gani et al., 2006). More and more use is made of PSE in product design and some even call it the third paradigm in process engineering (Hill, 2009). It is a very welcome trend that has the potential at least to enhance the typical trial-and-error approach in this area.

Another application area of PSE is related to PI (process intensification). It requires a different kind of approach than the methodologies based on unit operation modeling. It is encouraging to notice that methods are becoming available for this, like the function-based approach (Freund et al., 2008) that, in essence, is based on driving force analysis. Though the methods provide an excellent basis, in many cases they require very detailed and quantitative information of the process, e.g. a high precision kinetic model. However, in industrial reality the information is frequently not available at the necessary quality level, making the methods less applicable for an industrial environment. Nonetheless, the structured approach is still very interesting as it offers an excellent way for developing a PI assessment of a chemical process. In industry, we would appreciate a more open structure that does not require the very detailed information, but that can build on qualitative descriptions and reasoning.

4. Problem Solving Excellence

PSE can be applied industrially for problem solving excellence. PSE offers methods to deal with challenges like a malfunctioning process or poor control of quality, and to seize opportunities like a novel, lower cost and more environmentally friendly process for an existing product.

In process development projects we generally adopt a staged-wise approach, as schematically shown in Figure 3. In all stages, PSE methods and CAPE models play a crucial role. The integral process model is the technology backbone, giving directions to the type of experiments and integrating all information in a single place.

- In the first phase, preliminary investigations are conducted to obtain a first semi-quantitative impression of the technology. The derived preliminary techno-economic assessment provides data for the business case. As a result, already at a very early stage a picture is available of the potential benefits plus the technological challenges ahead. This translates into a time, resources and cost picture.
- The second stage deals with filling in the gaps. Experiments are conducted to collect the relevant data on which the model parameters are regressed. The operation and conditions of the experiments may be chosen differently than those of the targeted process system, aiming at simplifying the experimentation, easier interpretation of the results or a higher quality level of information. The model enables the translation from the experimental operation and conditions to those of the targeted process system. At the same time, the model provides a structure for designing the experiments. As example, reaction kinetics and vapor-liquid equilibria typically are measured separately and brought together in a process model, e.g. to evaluate the concept of reactive distillation.
- In the third stage, the developed model is validated against data from a pilot plant. It is the first time the targeted process is performed, e.g. the reactive distillation. The model serves as basis for the pilot plant design and the experimental plan. Based on the experimental outcome the model is validated.
- If needed, an additional stage is included. This might be the case if the fate of contaminants is unclear and the effect of closing the loops needs to be investigated. An alternative reason might be customer sample preparation. Quite often demo and pilot stages are combined.
- Finally, in the last stage, typically considered beyond the scope of the R&D project itself, the plant is designed, constructed, commissioned and started-up.

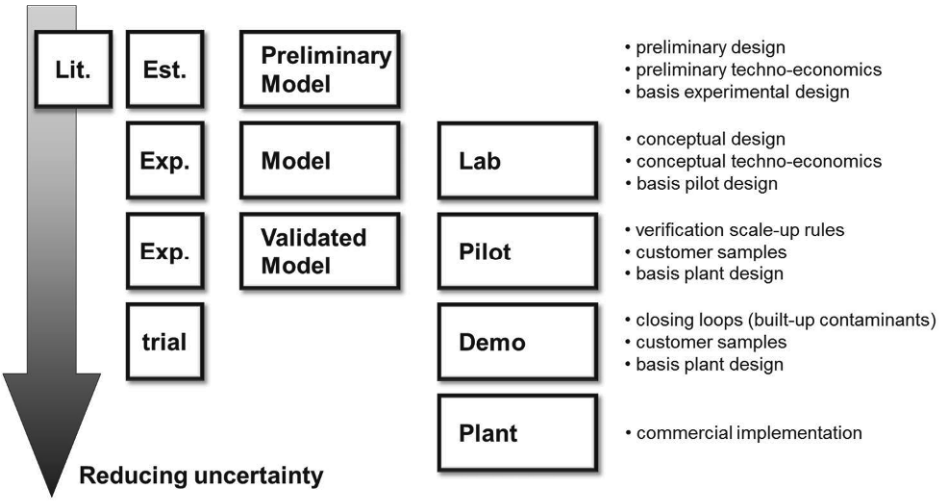

Figure 3. staged-wise approach in process development projects

In the practice of industrial R&D, there is tension between the business objectives posing constraints on time and budget, and the time and effort required for acquiring in-depth knowledge and developing quantitative models. Shortest time to market, or preferably shortest time to profit, and maximum financial benefits are key factors in the business context. So, how uncertain are we about the technology? And how does that uncertainty relate to acceptable risks and the health of the business case?

PSE offers a systematic platform assisting us in reducing the uncertainty of the technology. As a consequence it also helps us to better evaluate the business case, as it depends on the technology among others. From that point of view, our interest is not only about reducing the uncertainty but also we would like to know the level of uncertainty and its effect on the depending business risk. With respect to the latter, we would appreciate CAPE models that provide information about the reliability of the simulation outcome, preferably in a quantitative manner. Although a lot of effort is directed towards improving the chemical engineering models and process conceptual design, this area of uncertainty seems to be an area attracting less attention.

5. Conclusions

It is particularly useful to applying the basic principle of PSE in process development work. In process R&D the systematic engineering approach of PSE guides the laboratory experiments, it helps in interpreting the experimental observations and it assists in translating the results to other process configurations and conditions.

From a perspective of industrial R&D, we would like to suggest the following recommendations to the PSE community:

- extension of PSE methods in the area of PI,
- extension of PSE methods in the area of (conceptual) product design,
- development and application of semi-predictive methods,
- more attention to the subject of uncertainty in the PSE community.

PSE is more than just CAPE by offering a systematic and structured framework. Using principles of PSE, we strive for the best of both worlds integrating experimental or plant observations, and computer simulations. In this way, PSE enhances our problem solving excellence.

References

S. Abbott, C. Hansen, H. Yamamoto, 2013, Hansen Solubility Parameters in Practice, 4th ed.

C. Chen, P. Crafts, 2006, Correlation and Prediction of Drug Molecule Solubility in Mixed Solvent Systems with the Non-Random Two-Liquid Segment Activity Coefficient (NRTL-SAC) Model, Industrial & Engineering Chemistry Research, 45, 4816-4824

H. Freund, K. Sundmacher, 2008, Towards a methodology for the systematic analysis and design of efficient chemical processes; Part 1. From unit operations to elementary process functions, Chemical Engineering and Processing, 47, 2051–2060

R. Gani, C. Jiménez-González, A. ten Kate, P. Crafts, M. Jones , L. Powell, J. Atherton, J. Cordiner, 2006, A Modern Approach to Solvent Selection, Chemical Engineering, March 30-43

R. Gani, I. Grossmann, 2007, Process Systems Engineering and CAPE – What Next?, 17th European Symposium on Computer Aided Process Engineesing – ESCAPE17

M. Hill, 2009, Chemical Product Engineering - The third paradigm, Computers & Chemical Engineering, Volume 33, Issue 5, 947–953

Krist V. Gernaey, Jakob K. Huusom and Rafiqul Gani (Eds.), 12th International Symposium on Process Systems Engineering and 25th European Symposium on Computer Aided Process Engineering. 31 May – 4 June 2015, Copenhagen, Denmark

Sustainable Production of Liquid Fuels

Jonathan P. Raftery and M. N. Karim*

Texas A&M University, College Station, TX 77843, USA
nazkarim@che.tamu.edu

Abstract

Sustainable energy is the key to long term, global energy stability, which includes the need for a sustainable liquid transportation fuel. Ethanol and butanol are options to fill this energy need if they can be produced in an economical and sustainable fashion. This paper looks at various processes designed for the continuous production of ethanol and butanol via the biochemical conversion of lignocellulosic biomass. Processes designed for ethanol production include conventional separate hydrolysis and fermentation (SHF) as well as consolidated bioprocessing (CBP) with options for various biomass feedstocks and corresponding pretreatment technologies are optimized to determine the minimum breakeven selling price of the ethanol produced. The production of butanol via acetone-butanol-ethanol (ABE) fermentation and a gas stripping recovery process is also analyzed. It is found that both SHF and CBP processes give favourable economic outlooks, with SHF being favoured without energy generation and CBP being favoured when the waste is used for energy production. In addition, it has been shown that using continuous ABE fermentation with gas stripping is capable of producing a product stream with

Keywords: bioethanol, biobutanol, sustainability, consolidated bioprocessing, acetone-butanol-ethanol fermentation

1. Introduction

Though currently in the midst of the shale gas boom, the global, long term energy outlook will depend on the development of sustainable energy sources to displace the current petroleum-based energy sources. For this, many possible sustainable energy sources can be implemented, including wind, solar, geothermal and hydroelectric. While these forms of sustainable energy can displace much of the need of petroleum products, current energy needs also include liquid transportation fuels which the previously mentioned sustainable technologies cannot directly provide. However, sustainable liquid transportation fuels can be sustainably produced through the use of thermochemical or biochemical biomass conversion methods in the form of ethanol or butanol. Of these two conversion technologies, the biochemical production of ethanol from cellulosic materials produces the lowest amount of carbon dioxide emissions with the highest net energy yield and similar petroleum input (Farrell et al., 2006). A further analysis of these processes can be critical to ensuring a complete, sustainable energy future after petroleum.

Many different processes have been considered for the production of ethanol from lignocellulosic biomass. Traditional ethanol processes, termed separate hydrolysis and fermentation or SHF, involve the pretreatment of the biomass to degrade the crystalline

lignin structure, the use of enzymes to break down the cellulose and hemicellulose polymers to simple 5-carbon and 6-carbon sugars, then the fermentation of those simple sugars to ethanol (Humbird et al., 2011). Other process designs try to eliminate the use of enzymes through the use of genetically modified organisms with saccharolytic and ethanologenic capabilites, a process known as consolidated bioprocessing or CBP (Argyros et al., 2011; Ryu and Karim, 2011). Butanol is primarily produced as the main product of acetone-ethanol-butanol (ABE) fermentation using *Clostridium acetobutylicum* (Jones and Woods, 1986). These processes, while promising, are mostly batch processes that have not been implemented at the large scale, leaving doubts in their commercial feasibility.

This work examines continuous methods of ethanol and butanol production through biochemical means to determine the viability of continuous, sustainable processes to produce of liquid fuels. Focus is placed on the economic feasibility of ethanol production from both the SHF and CBP process designs. Energy generation through the use of the lignin waste products is also considered for both ethanol processes to reduce the external energy requirements of the processes. A novel process design for the biochemical production of butanol using ABE fermentation and gas stripping is also examined for overall feasibility of butanol production.

2. Methodology and Modelling

2.1. Ethanol Production

Separate hydrolysis and fermentation and consolidated processing are considered for the production of ethanol from lignocellulosic biomass. The process was designed to run for 350 days over a 10 year period, with a 5% interest added to the capital investment over that period. Each process is first considered with the use of external energy, and then the use of biological waste for energy production is considered as a way to reduce the utility and waste treatment costs of the plant. Biomass options for both processes were focused on those available in the state of Texas, USA, including sugarcane bagasse (SB), sorghum (SOR), hybrid poplar (HP), switchgrass (SW) and corn stover (CS) (State Energy Conservation Office). The total combined biomass flowrate to the process was constrained to be within 2,000 and 3,500 U.S. tons per day. Each biomass type considered has at least two pretreatment options available, based on available literature data, and include sodium hydroxide (NaOH), liquid hot water (LHW), dilute sulfuric acid (DSA) and ammonia fiber explosion (AFEX). Table 1 shows the pretreatment options considered for each biomass option and the source from which the data was taken. Due to consolidated bioprocessing only being applicable for cellulose fermentation, a separate fermentation path was required for the fermentation of the solubilized 5-carbon sugars. Ethanol recovery was done using a flash tank, distillation column and molecular sieve. Figure 1 shows the simplified process superstructure of both the SHF and CBP processes.

Mass balance, energy balance and cost models were constructed around each process unit. The objective is to minimize the selling price of the produced ethanol necessary to overcome the annualized capital, operating and labor costs of the plant. Global optima for each of the four mixed-integer nonlinear programs are found using the Couenne solver available in the GAMS modeling environment.

Table 1. Biomass and corresponding pretreatment options for the proposed bioethanol plant design.

Biomass Type	Pretreatment Available	Source
Sugarcane Bagasse	Sodium Hydroxide	Yu et al, 2013
	Liquid Hot Water	Yu et al, 2013
Sorghum	Dilute Sulfuric Acid	Banjeri et al, 2013
	Sodium Hydroxide	Wu et al, 2011
Hybrid Poplar	Dilute Sulfuric Acid	Esteghlalian et al, 1997
	Liquid Hot Water	Kim et al, 2009
Switchgrass	Ammonia Fiber Expansion	Alizadeh al, 2005
	Dilute Sulfuric Acid	Esteghlalian et al, 1997
	Sodium Hydroxide	Xu et al, 2010
Corn Stover	Ammonia Fiber Expansion	Teymouri et al, 2005
	Dilute Sulfuric Acid	Esteghlalian et al, 1997

a)

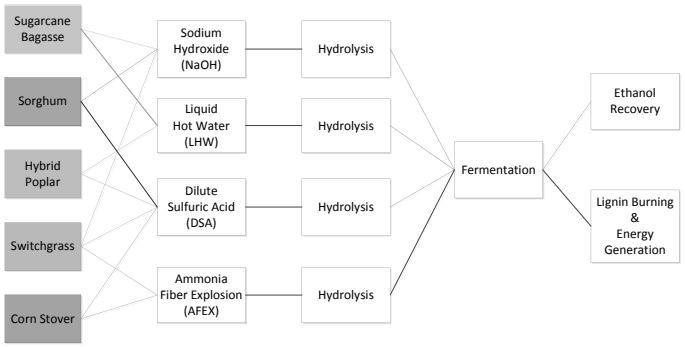

b)

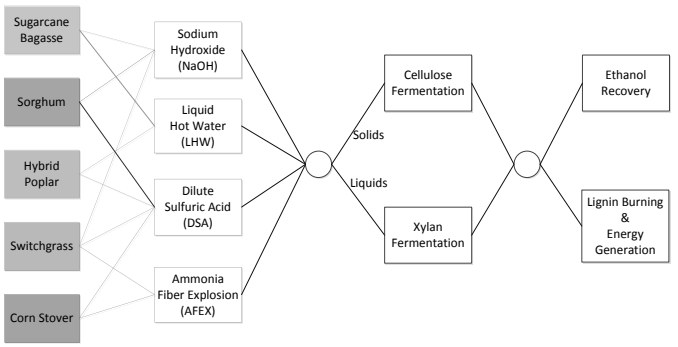

Figure 1. Simplified process flow diagrams for the proposed (a) SHF and (b) CBP processes for commercial scale, continuous ethanol production.

2.2. Butanol Production

The production of butanol via ABE fermentation of a 60 grams/L glucose solution was analyzed using Aspen Plus. The process, shown in Figure 2, consisted of an immobilized cell bioreactor utilizing *Clostridium acetobutylicum*. The flowrate of the reactor feed is 1,000 L/hr with a reactor volume of 1,000 L, a dilution rate in the reactor of 1 hr^{-1}. Reactor yields of each product were determined based on the stoichiometry of the ABE reaction, as shown in Eq. 1 (Gottschalk 1979).

$$100\ \text{Glucose} \rightarrow 22\ \text{Acetone} + 56\ \text{Butanol} + 7\ \text{Ethanol} + 14\ \text{Acetate} + 4\ \text{Butyrate} + 211\ CO_2 + 135\ H_2 + \text{Biomass} \quad (1)$$

The effluent of this reactor is sent to a gas stripping processes consisting of two consecutive absorption columns that use a continuously cycling mixture of carbon dioxide and hydrogen as a stripping agent, chosen due to their production during fermentation. The outlet gas of each absorption column is condensed for recovery of the acetone, ethanol, and butanol products. A gas purge is used to prevent byproducts of the ABE fermentation from building up in the recycled stripping gas. Operation conditions in the absorption columns and condensers and the inlet composition and flowrate of the stripping gas was allowed to vary to determine the optimal mass fraction of butanol in the product stream subject to a recovery of 90% of the produced butanol during fermentation.

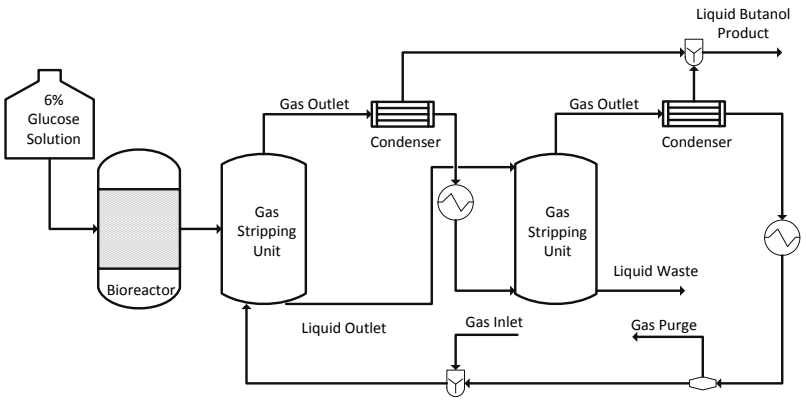

Figure 2. Butanol production through the use of ABE fermentation and gas stripping.

3. Results

3.1. Ethanol Production

Table 2 shows the optimal results for the four ethanol production facilities. Sugarcane bagasse, the cheapest of the five biomass options at $13.60 per ton, is chosen for separate hydrolysis and fermentation and is combined with a sodium hydroxide pretreatment option that provides the highest conversion its cellulose and hemicellulose to simple sugars at 96% and 86%, respectively. Consolidated bioprocessing is done most economically with a mixture of bagasse, sorghum and hybrid poplar pretreated with sodium hydroxide, dilute sulfuric acid and liquid hot water, respectively. While

sorghum with sodium hydroxide remains the primary biomass and pretreatment, the addition of sorghum with dilute sulfuric acid and hybrid poplar with liquid hot water reduced the xylan composition in the process, thereby reducing the size of reactor necessary for its processing.

From the economic results in Table 2 it can be seen that separate hydrolysis and fermentation is a more economical option for ethanol production in the absence of energy generation, due to the decreased ethanol production of the CBP process. When internal energy generation is considered, CBP becomes the a slightly more economically attractive production method due to the difference of $42 million in operating costs, attributed to the decrease in the organism, including enzymes and fermentation organisms, and utilities costs. Energy generation is based on the lignin content of the process waste, so its inclusion leads to an increase in the total biomass flowrate of the process, which also results in an increase of the amount of ethanol produced from each process.

Table 2. Optimal results for the separate hydrolysis and fermentation and consolidated bioprocessing process designs with external energy use only (SHF; CBP) and energy generation from biological waste (SHF-Energy; CBP-Energy).

	CBP	**SHF**	**SHF-Energy**	**CBP-Energy**
Ethanol Cost	$3.17	$2.97	$2.44	$2.42
Ethanol Produced (MM gal)	53.6	73.5	76.2	55.7
Biomass Flowrate (U.S. tons/day)	3,210	3,377	3,500	3,491
Sugarcane Bagasse	83%	100%	100%	81%
Sorghum	14%	-	-	15%
Hybrid Poplar	3%	-	-	4%
Pretreatment Type				
Sugarcane Bagasse	NaOH	NaOH	NaOH	NaOH
Sorghum	DSA	-	-	DSA
Hybrid Poplar	LHW	-	-	LHW
Process Costs				
Capital Cost (MM$/yr)	10.4	9.4	10.7	12.0
Operating Cost (MM$/yr)	138.0	170.8	135.1	93.6
Organism Cost	3.5	25.6	26.6	3.5
Utilities Cost	80.0	96.6	72.0	52.6
Waste Cost	20.7	21.1	8.1	0.0
Labor Cost (MM$/yr)	29.2	38.4	39.8	29.0

3.2. Butanol Production

Results for the optimized ABE recovery system are shown in Table 2. Small discrepancies in the mass balance can be attributed to minor adjustments made to the stoichiometry made in the Aspen simulation to allow for fermentation without the need for biological components. These results show that 90.3% of the butanol produced by ABE fermentation reaction can be recovered using a 2:1 ratio of carbon dioxide to hydrogen in the gas feed of the process, fed at a flowrate of 35.5 kg/hr. The recovered butanol exits the process at a flowrate of 13.5 kg/hr which consists of 13.28% of the total product stream. In addition, ethanol and acetone were also recovered with a flowrate of 1.16 kg/hr and 4.6 kg/hr, a yield of 85.14% and 75.16% respectively, and bringing the total ABE recovery to 86.6% overall. The optimal operating conditions for the process unit operations to achieve this butanol output are shown in Table 3.

Table 3. Process feed and outlet stream data for the proposed butanol recovery system using gas stripping with hydrogen and carbon dioxide.

Component	Feed Streams (kg/hr)		Outlet Streams (kg/hr)		
	Reactor Feed	Gas Feed	Gas Purge	Liquid Waste	Product Stream
Glucose	60.00	0.00	0.00	0.00	0.00
Water	956.00	0.00	2.67	875.40	78.40
Carbon Dioxide	0.00	23.50	51.74	2.29	4.65
Hydrogen	0.00	12.02	13.14	0.00	0.00
Acetone	0.00	0.00	0.27	0.87	3.46
Butanol	0.00	0.00	0.06	1.38	13.50
Ethanol	0.00	0.00	0.00	0.18	0.98
Acetate	0.00	0.00	0.02	2.47	0.54
Butyrate	0.00	0.00	0.00	1.17	0.10
Total Mass		1051.66			1053.28

Table 4. Optimal operating conditions for the various process units used for butanol stripping and recovery.

Process Unit	Manipulated Variable	Optimal Value
Stripper 1	Stage 1 Pressure	1.00 bar
Stripper 2	Stage 1 Pressure	1.00 bar
Condenser 1	Temperature	0.00 ℃
	Pressure	9.82 bar
Condenser 2	Temperature	17.97 ℃
	Pressure	0.11 bar
Heater 1	Temperature	37.00 ℃
	Pressure	2.00 bar
Heater 2	Temperature	37.00 ℃
	Pressure	1.00 bar

4. Conclusions

One of the major steps toward overcoming petroleum dependence in the area of energy is the production of a liquid transportation fuel that can be produced at commercial levels and is competitive with the economics of current gasoline and diesel production

processes. This work has shown that the continuous production of biofuels, both ethanol and butanol, is achievable. Two different biological processing platforms for the production of ethanol, separate hydrolysis and fermentation and consolidated bioprocessing, were analysed for their technoeconomic feasibility. It was shown that SHF performs better in the absence of internal energy generation, while CBP is a more viable option when energy generation is considered. In addition, the production and recovery of butanol through fermentative means was explored. By using a gas stripping process composed of two absorbers and a cycling hydrogen-carbon dioxide stripping agent it was possible to achieve a butanol recovery of 90.3% and an ABE recovery of 86.6% overall. These results are important steps toward the commercialization of biochemically based biofuels production as an alternative to petroleum-based options.

Acknowledgements

We would like to acknowledge the Texas A&M Institute for Advanced Studies (TIAS) as well as the National Science Foundation (grant number CBET-1066616) for the funding of this project.

References

Alizadeh, H., Teymouri, F., Gilbert, T.I. and Dale, B.E., 2005 Pretreatment of switchgrass by ammonia fiber explosion (AFEX). Appl Biochem Biotechnol 124, 1133–1141

Argyros, D.A., Tripathi, S.A., Barrett, T.F., Rogers, S.R., Feinberg, L.F., Olson, D.G., Foden, J.M., Miller, B.B., Lynd, L.R., Hogsett, D.A., Caiazza, N.C., 2011. High Ethanol Titers from Cellulose by Using Metabolically Engineered Thermophilic, Anaerobic Microbes. Appl. Environ. Microbiol. 77, 8288–8294.

Banerji, A., Balakrishnan, M. and Kishore, V.V.N., 2013. Low severity dilute-acid hydrolysis of sweet sorghum bagasse. Applied Energy. 104, 197–206.

Esteghlalian, A., Hashimoto, A.G., Fenske, J.J. and Penner, M.H., 1997. Modeling and optimization of the dilute-sulfuric-acid pretreatment of corn stover, poplar and switchgrass. Bioresource Technology 59, 129–136.

Farrell, A.E., Plevin, R.J., Turner, B.T., Jones, A.D., O'Hare, M., Kammen, D.M., 2006. Ethanol Can Contribute to Energy and Environmental Goals. *Science* 311, 506–508.

Gottschalk, Gerhard. 1979. Bacterial metabolism. New York: Springer-Verlag. 359 p.

Humbird, D., Davis, R., Tao, L., Kinchin, C., Aden, A., 2011. Process design and economics for biochemical conversion of lignocellulosic biomass to ethanol. Technical Report Contract No. DE-AC36-08GO28308, 1–147.

Jones, D.T., Woods, D.R., 1986. Acetone-butanol fermentation revisited. Microbiol Rev 50, 484–524.

Kim, Y., Mosier, N.S. and Ladisch, M.R., 2009. "Enzymatic digestion of liquid hot water pretreated hybrid poplar." Biotechnol Progress 25, 340–348.

Ryu, S., Karim, M.N., 2011. A whole cell biocatalyst for cellulosic ethanol production from dilute acid-pretreated corn stover hydrolyzates. Appl Microbiol Biotechnol 91, 529–542.

State Energy Conservation Office. Cellulosic Ethanol. Energy Efficiency: Texas' Newest Energy Resource. http://www.seco.cpa.state.tx.us/energysources/biomass/ethanol.php

Teymouri, F., Laureano-Perez, L., Alizadeh, H. and Dale, B.E., 2005. Optimization of the ammonia fiber explosion (AFEX) treatment parameters for enzymatic hydrolysis of corn stover. Bioresource Technology 96, 2014–2018.

Wu, L., Arakane, M., Ike, M., Wada, M., Takai, T., Gau, M., and Tokuyasu, K., 2011. Low temperature alkali pretreatment for improving enzymatic digestibility of sweet sorghum bagasse for ethanol production. Bioresource Technology. 102, 4793–4799.

Xu, J., Cheng, J.J., Sharma-Shivappa, R.R. and Burns, J.C., 2010. Sodium Hydroxide Pretreatment of Switchgrass for Ethanol Production. Energy Fuels. 24, 2113–2119.

Yu, Q., Zhuang, X., Lv, S., He, M., Zhang, Y., Yuan, Z., Qi, W., Wang, Q., Wang, W., and Tan, X., 2013. Liquid hot water pretreatment of sugarcane bagasse and its comparison with chemical pretreatment methods for the sugar recovery and structural changes. Bioresource Technology. 129, 592–598.

Krist V. Gernaey, Jakob K. Huusom and Rafiqul Gani (Eds.), 12th International Symposium on Process Systems Engineering and 25th European Symposium on Computer Aided Process Engineering.
31 May – 4 June 2015, Copenhagen, Denmark

Industrial perspectives on the deployment of scheduling solutions

Iiro Harjunkoski

ABB Corporate Research, Wallstadter Str. 59, 68526 Ladenburg, Germany
iiro.harjunkoski@de.abb.com

Abstract

A scheduling optimization solution is in many ways still a complex and "exotic" function that seldomly finds its way into the daily practice of the industrial plant floor. Scheduling is too often seen as something decoupled and theoretical that requires high-level experts for using and maintaining it. In this paper we discuss some of the hurdles for deploying scheduling solutions. Some needs for improvements are identified both in academia and industry and by addressing the main pain points it can be seen that with a common mindset the complexity of scheduling can be lowered significantly.

Keywords: scheduling deployment, communication, integration, ISA-95.

1. Introduction

Despite many significant achievements in the development of scheduling methods and solutions, one important still unresolved technical challenge and hurdle is their deployment in an industrial context. Today the most typical and successful approach to bring a theoretical solution "live" is that plant experts directly collaborate with the university experts to locally build a solution that is tailored to their needs. This often results in strongly tailored implementations that are normally not reusable, which limits a wider distribution of novel approaches. Also, as a difference to hardware solutions (e.g. sensors), the life cycle of the locally developed scheduling solution heavily depends on the availability of the key implementers and the long-term strategic interest and commitment of the company management to maintain and further enhance the tools. Many scheduling companies successfully extend their businesses mainly building on already established technologies. This means that in times where cost- and process efficiency or throughput is valued higher than ever, it is not evident how novel optimization strategies that are today developed in academia can reach their end users. In the following we discuss challenges, lessons learned and ongoing trends affecting the scheduling. The cost and time aspects of deployment are key issues to be resolved.

2. An academic challenge

In general, the industrial need for new optimization schemes is growing and this has also been addressed by earlier PSE-events (Henning, 2009; Harjunkoski, 2012), highlighting some arising challenges. New communication technologies make it possible to collect and exchange information, which creates many opportunities for including a wider scope of aspects related to production. With the ever increasing availability of data and higher level of automation and electrification, production scheduling cannot anymore be seen as an autonomous solution. Concepts such as Internet-of-Things, Smart Grids, Smart Manufacturing, Big Data, Industry 4.0 and enlarged scope on Enterprise-wide Optimization topics (EWO, Grossmann, 2012)

increase the pressure to connect and interact with neighboring solutions and systems. To define what actually makes sense, what brings additional value and is technically feasible is also a clear academic challenge. Examples of this are the increasing research on industrial demand-side management taking advantage of the fluctuating price information of electricity (e.g. Mitra et al., 2014), as well as on integration of scheduling and control. A generic overview of the latter can be found in Engell and Harjunkoski (2012) and Baldea and Harjunkoski (2014), some concrete approaches are proposed e.g. in Subramanian et al. (2012). In a similar fashion, integration to the supply chain level (e.g. Maravelias and Sung, 2009) is important in order to receive up-to-date commercial order information, including their priorities. All of the above areas of research ensure, among others, that the provided schedule is aware of the surrounding environment as well as the underlying process. Figure 1 illustrates the required flexibility and dynamics of a modern scheduling solution.

Some of the main hurdles are identified in modeling and solution of the resulting problems. Modeling is a challenge when combining different optimization domains: how to express the main decisions and limitations in a compact and balanced way such that different targets are simultaneously met? One fairly common approach is bi-level or Lagrangean decomposition if enabled by the underlying problem structure. Especially in scheduling, the represention of time is very important and for instance in industrial demand-side management the process itself may need to be planned on a minute-level, whereas the electricity consumption only needs to be accounted for every 15 or 60 minutes. To solve the resulting models is mathematically challenging: Many of the complex requirements are non-linear and non-convex, which poses a main challenge to the solution algorithms. Also, by combining or expanding the models to cover more problem aspects, the number of decisions to be optimized often increases significantly, for instance through a larger number of binary variables. To make problems solvable, smarter modeling strategies are needed besides more efficient solution algorithms.

To summarize, even if this paper mainly focuses on the industrial aspects, the collaboration and inventive contribution from the academia is crucial to tackle the practical challenges faced by the industry – today and tomorrow.

3. Industrial realities

The principal question in the industry is where should a scheduling solution in the first place be located. In most industrial environments, a scheduling solution cannot live as an “island” but must be closely connected to the production environment – for instance to a distributed control system (DCS), manufacturing execution system (MES) or collaborative production management (CPM) system – in order to be able to automatically obtain all the production and process data that is important for scheduling.

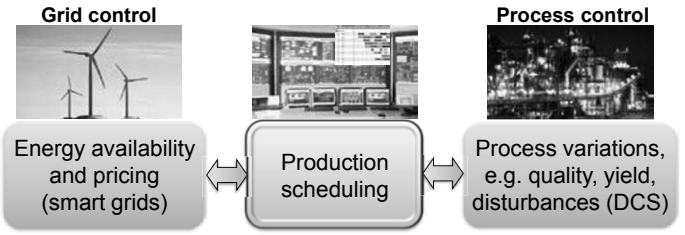

Figure 1. Scheduling dynamics – balancing between control systems

A connection to the enterprise resource planning (ERP) is also a must since the whole production is triggered by customer orders mostly entering via an ERP interface. ERP systems are further also used for procurement to ensure that all material and resources are available when needed according to the production plan. The connectivity issues is in fact one of the main differences between the academic and industrial focuses.

Another, even a more important aspect, is the cost and return of investment (ROI). For any company, an investment without clear and provable ROI is normally not approved. For this, typically the net present value (NPV) is used to account for future revenues and costs, c_n, using a discount rate, r. See Eq. (1), where N is the number of years considered. NPV however only gives a rough idea of how an investment compares to other alternatives and here the well known "garbage in – garbage out" law applies.

$$NPV = \sum_{n=0}^{N} \frac{c_n}{(1+r)^n} \quad (1)$$

Nevertheless, NPV is widely used as it is one of the few comparable metrics that can be calculated for each investment alternative. Here, a key challenge is how to reliably prove how much the improvement of deploying a new scheduling solution actually is. This is necessary also for defining the revenues (price tag), since few companies allow more than a couple of months to a year payback time on software investments. Two issues make it especially difficult to come up with hard facts or clear figures:

- A scheduling solution is a plan for the future production for which no exact reference exists – how to compare reality with a theoretical option?
- Real production is dynamic, it is often difficult to exactly follow a given schedule due to disturbances, uncertainties in processing times or involved manual decision steps

The common approach to evaluate the potential is to take a historical production schedule, extract the production orders and make a reschedule with a more "optimal" methodology to compare and prove a positive difference. This mainly works only in fully predictable environments as a future schedule cannot react to changes that are unknown by the time of the scheduling. Even if the potential improvement is significant, it is very important to be able to itemize each improvement factor in detail. Most of the current scheduling approaches do not directly support this. Both industry and academia must be involved in enabling a more reliable value proposition: Industry to provide some clear metrics to evaluate the goodness and information of the most common uncertainties and academia to build methologies that can also take these into account in the generation of production schedules, e.g. by serving multiple objectives.

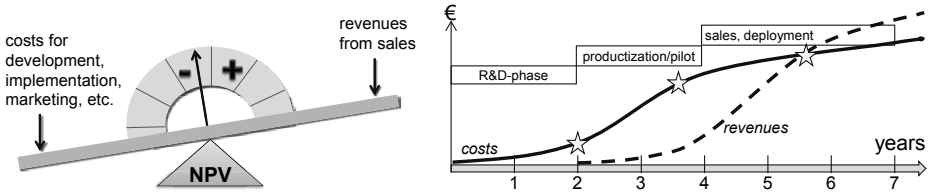

Figure 2. NVP should be positive for an investment decision, example costs/revenues on the right

In Figure 2, the NPV is simplified. On the right hand side typical cumulative costs (solid line) and revenues (dashed line) of a productization of scheduling are displayed.

A couple of remarks: The R&D phase constitutes to only a fraction of the total costs, as making a model into a maintainable product is a significant effort. Most products also imply a responsibility to deliver to promise with some responsibilities. In Figure 2, the R&D phase is assumed to be finished by year 2, productization including first pilot(s) starts at that point (leftmost star) and the market introduction of the product happens sometimes between year 3 and 4 (second star). Sales material, training, and direct deployment costs are also not to be neglected by advanced solutions such as scheduling. The revenues ramp up after the market introduction and first references but may slow down in some years as either competition has launched its products or an advanced function becomes a commodity. Therefore, in this theoretical example the payback time is around 5,5 years. This issue should nevertheless not be neglected as it may be one of the biggest hurdles for productization – how long a payback time can a company afford? Another observation is that in case a vendor wants to be profitable with a scheduling solution he needs most likely to sell more than 20 installations before reaching a profit. It is thus very important to shorten the productization time without losing the quality.

4. Communication challenge

As discussed above, new developments do not only challenge the solution algorithm developers, which are commonly from the academia when it comes to novel methods. In order to achieve faster solution response times, to tackle the modeling challenges when combining various domains into one concept and meet the expectations on solution quality, the deployment efficiency in the industries must be also significantly improved (Harjunkoski et al., 2014). Here one the key challenges is to create more modular and flexible systems that enable seamless data communication and even can combine earlier separated business models. This ensures that new opportunities can be exploited. Standards such as ISA-95 (ANSI/ISA-95.00.03-2005) can be helpful in paving the way for some of these tasks.

5. Lessons learned

It is important to acknowledge best practices and things to avoid from earlier deployment projects in order to ensure good quality and eliminate unnecessary costs. Framinan and Ruiz (2012) provide well-covered guidelines taking into account a multitude of deployment aspects. A thorough discussion on the lessons learned from practical implementations is given in Harjunkoski et al. (2014). Here we can only highlight a few facts. As already stated above, the success depends on resolving many practical issues, such as change management, deployability, ease of use, application development and maintenance. The following list highlights some of the major aspects:

- The production scheduler is finally responsible for the schedule and must also take some manual decisions, especially when there are conflicting goals between related organizations. His targets are safety, meeting customer orders and inventory targets, lower the manufacturing, inventory and logistics costs. He must feel supported by the scheduling tool in his everyday job having all critical information available to him. Also, the scheduling tool must be flexible enough to allow him to handle the disruptions in the production.
- The business opportunity in improved scheduling must be well recognized to ensure a full organizational support. This implies tracking certain metrics that depend on the quality of production scheduling, such as customer service level, sales volume, asset utilization, manufacturing costs, inventory costs, to name a few. The main challenge

here is to accurately estimate the impact of improved scheduling for establishing alignment of all stakeholders.

- Quick proof-of-concept study. At the beginning of any deployment project the following must be demonstrated: expected value of the improved scheduling process, ability to solve the problem, availability of data needed, how to integrate to existing scheduling process and information system. This should be accomplished within a few weeks.
- Effective system integration is a must since the scheduling model is only a small piece of an overall scheduling application. The software infrastructure must be capable of communicating with the ERP system as well as with spreadsheets and databases. Also, the generated schedule must be available to the scheduler in a flexible user interface.
- Effective user control also requires good graphical user interfaces (GUI). The scheduler must be able to response to dynamic changes in the production scheduling environment. Since it is practically impossible to incorporate all business considerations into a scheduling model the production scheduler must be able to manually modify some input data and adjust the resulting schedule to address unsolved business issues. Here, interactive Gantt charts and trend curves are enablers to more efficient use of the scheduling tool.
- The automated scheduling must be robust, i.e. the scheduling should always return a feasible schedule, even when the optimization would fail. The solution should also be scalable, i.e. able to solve the whole range of problem sizes in the daily business.

6. The implementation

The multitude of aspects that are discussed above require a systematic approach for the deployment. It is evident that all aspects may not apply everywhere, nor may it be difficult to fulfill all requirements and recommendations. Nevertheless, there are standards to support the integration by offering a uniform data structure. The ISA-95 standard (ANSI/ISA-95.00.03-2005) defines most of the required data fields and offers an XML-based integration that is very useful in a SW-context as it contains supporting functions such as XML-schemas. Many programming languages have built-in functions to enable easy handling of XML data. The XML implementation of the ISA-95 standard is called B2MML (business to manufacturing markup language) and a basic introduction with a simple example on how to use it for scheduling can be found in Harjunkoski and Bauer (2014). Using a standard avoids some problems in agreeing on the data design and also makes it easier to communicate between unrelated systems.

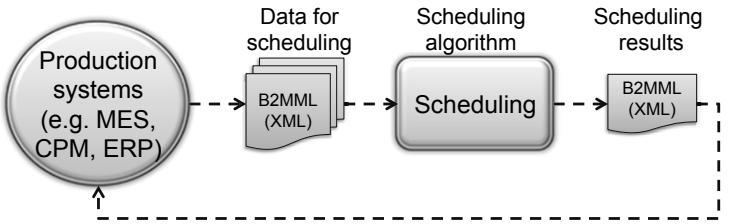

Figure 3. Scheduling as a part of a larger system

An example of the information flow between a production system and the scheduling algorithm is shown in Figure 3. Note that in Figure 3 we refer to the actual solution engine (main academic scope) – there can be a number of user interfaces including Gantt charts, planning sheets and order management embedded into the MES but those

imply mainly software programming and require normally no extensive optimization skills. The benefit of connecting to the scheduling algorithm via XML is that this makes it easy to plug it into an existing system and also enables the use of web services, i.e. where the algorithm is running on a remote server with powerful computing resources.

Another aspect is that ISA-95 is becoming the industrial standard between ERP and the manufacturing layer and there are an increasing number of trained professionals. Therefore, maintaining more generic data for instance in an ISA-95 database is much easier than collecting data that is specifically aimed for a certain scheduling model, the meaning of which is not clear to non-scheduling experts. Ideally, the B2MML data can be even used for modeling the scheduling problem in a more operator-friendly way using terminology that is closer to the operations. The most common B2MML-elements within the context of scheduling are listed in Table 1.

Table 1. B2MML-elements relevant for scheduling

Element	Description	Function
Equipment	Equipment resources to for planning	input
Material	Material relevant for scheduling	input
Personnel	Personnel required for planning purposes	input
ProcessSegment	Process structure (stages, steps)	input
OperationsDefinition	Production recipes for making a product	input
OperationsSchedule	Input: production orders, Output: schedule	input/output
OperationsCapability	Availability of resources, e.g. for shifts	input
OperationsPerformance	Feedback from the process, e.g. from MES	input

A small example of B2MML is given in Figure 4, where the beginning of scheduled order is shown. It shows the references to the recipe and resource decisions.

```
- <OperationsSchedule xmlns="http://www.wbf.org/xml/B2MML-V05">
    <ID>Factory A schedule requests</ID>
    <Description>This example shows the schedule *after* optimization</Description>
    <StartTime>2012-08-30T08:00:00</StartTime>
    <EndTime>2012-08-30T17:30:00</EndTime>
    <ScheduleState>Forecast</ScheduleState>
    <PublishedDate>2012-08-30T07:40:00</PublishedDate>
  - <OperationsRequest>
      <ID>Order1</ID>
      <StartTime>2012-08-30T08:00:00</StartTime>
      <EndTime>2012-08-31T08:00:00</EndTime>
      <Priority>1</Priority>
      <OperationsDefinitionID>Chemical1</OperationsDefinitionID>
    - <SegmentRequirement>
        <ProcessSegmentID>Mix</ProcessSegmentID>
        <EarliestStartTime>2012-08-30T08:00:00</EarliestStartTime>
        <LatestEndTime>2012-08-30T08:30:00</LatestEndTime>
        <Duration>PT0H30M</Duration>
      - <PersonnelRequirement>
          <PersonnelClassID>Mixeroperator</PersonnelClassID>
          <PersonID>Mixeroperator-2</PersonID>
        </PersonnelRequirement>
      - <EquipmentRequirement>
          <EquipmentClassID>Mixer</EquipmentClassID>
          <EquipmentID>Mixer1</EquipmentID>
```

Figure 4. B2MML example on OperationsSchedule

Regardless of the use of standards, the path from an idea to a product contains several hurdles and requires commitment throughout the project as well as a wide pool of competences. Figure 5 summarizes the main steps. Unfortunately, each of the steps cannot be discussed within the context of this paper.

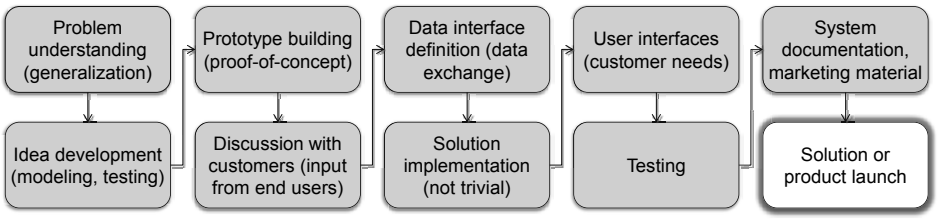

Figure 5. Generic development steps for any deployment project

7. Trends affecting scheduling

As everything else, scheduling is affected by changes in the environment and this section focuses on a few of them. The so called hypes or trends may not all be long-lived but they certainly also affect the expectations of the end users. Also, at least for researchers it is always desired to challenge the current state-of-the-art and investigate the true potential of emerging technologies. Below some of the relevant trends for scheduling are discussed.

- Internet of Things: This is the enabler for cyber-physical systems, which is the core of for instance Industrie 4.0 (Germany) and Smart Manufacturing (US) activities. What it basically means is that any device can be connected to the internet allowing both way communication across- or between plants. This makes new data available also to scheduling and supports more horizontal applications with decentralized decision making. Can scheduling benefit from this collaboration potential?
- Automation Cloud enables software applications be installed not physically in the plant but anywhere through either intra- or internet connection. This enables the use of much more powerful computing resources (e.g. parallel computing) and remote administration. Technically, it is possible to solve larger scheduling problems but there are still few algorithms fully taking advantage of this.
- Big Data technologies aim at analyzing large sets of non-structured data. This can enable new knowledge about the production identifying problems early or creating more accurate data-based models. The scheduling function can become more aware and knowledgeable about the underlying and surrounding processes.
- Smart Grids and Renewable Energy. These energy-related topics have increased the importance of energy for scheduling. It has already opened a bi-directional information flow making it possible for scheduling to adapt to changing energy availability and pricing (industrial demand-side management). Also, new processes related to energy may become part of the production planning.
- Mobility, Unmanned Sites and Remote Operations all contribute to more automated scheduling. The main idea is to increase the safety of operations, reduce costs and be able to monitor and interact with the process from anywhere at any time. Not having operators at hand puts more responsibility on the automated scheduling. This raises the global perspective possibly leading to larger problem instances.
- Service, for instance software as a service, provides a large number of opportunities, where basically the imagination is the limit. Can this be a way to make scheduling

easier deployable or provide a performance-based solution where the end-customer pays related to the quality of the resulting schedule or the computational efforts?

It is evident that fulfilling all of these aspects requires one or two decades of further developments. What it in any case shows is that the function of scheduling will have a central role also in a more automated and integrated industrial landscape.

8. Conclusions

This paper has summarized some of the main aspects and challenges of deploying scheduling solution into an industrial product, also including some ongoing and emerging trends. As scheduling is worthless as an "island" solution it is important to take the hosting environment into consideration. The natural "home" of a scheduling solution is within an operations management system. Moreover, the economic impact of scheduling should be stronger highlighted, where both academia and industry should collaborate closely. Often the deployment costs are so significant that this alone may hinder deployment projects. Thus one should be able to prove the actual value of a scheduling solution to the end customers. In order to partly reduce the implementation costs and to increase re-usability, standards should be applied.

References

ANSI/ISA-95.00.03-2005, 2005, Enterprise-Control System Integration. Part 3: Activity models of manufacturing operations management, ResearchTriangle Park,NC: ISA – The Instrumentation, Systems, and Automation Society

M. Baldea and I. Harjunkoski, 2014, Integrated production scheduling and process control: A systematic review, Computers and Chemical Engineering, 71 , pp. 377-390

S. Engell and I. Harjunkoski, 2012, Optimal Operation: Scheduling, Advanced Control and their Integration, Computers and Chemical Engineering, 47, pp. 121-133

J.M. Framinan and R. Ruiz (2012). Guidelines for the deployment and implementation of manufacturing scheduling systems, International Journal of Production Research, 50 (7), pp. 1799-1812.

I.E. Grossmann, 2012, Advances in mathematical programming models for enterprise-wide optimization, Computers and Chemical Engineering, 47, pp. 2-18

I. Harjunkoski, 2012, Planning and Scheduling as a Part of a Control System – Implementation Aspects, Proceedings of the 11th International Symposium on Process Systems Engineering – PSE 2012, pp. 1110-1114

I. Harjunkoski and R. Bauer, 2014, Sharing data for production scheduling using the ISA-95 standard, frontiers in Energy Research, 2, 44, doi: 10.3389/fenrg.2014.00044

I. Harjunkoski, C.T. Maravelias, P. Bongers, P.M. Castro, S. Engell, I.E. Grossmann, J. Hooker, C. Méndez, G. Sand and J. Wassick, 2014, Scope for industrial applications of production scheduling models and solution methods, Computers and Chemical Engineering, 62, pp. 161-193

G.P. Henning, 2009, Production Scheduling in the Process Industries: Current Trends, Emerging Challenges and Opportunities, Proceedings 10th International Symposium on Process Systems Engineering - PSE2009, pp. 23-28

C.T. Maravelias and C. Sung, 2009, Integration of production planning and scheduling: Overview, challenges and opportunities. Computers and Chemical Engineering, 33(12), pp. 1919–1930

S. Mitra, J.M. Pinto and I.E. Grossmann (2014). Optimal multi-scale capacity planning for power-intensive continuous processes under time-sensitive electricity prices and demand uncertainty. Part I: Modeling, Computers and Chemical Engineering, 65, pp. 89-101

K. Subramanian, C.T. Maravelias and J.B. Rawlings (2012). A state-space model for chemical production scheduling. Computers and Chemical Engineering, 47, pp. 97–110.

Krist V. Gernaey, Jakob K. Huusom and Rafiqul Gani (Eds.), 12th International Symposium on Process Systems Engineering and 25th European Symposium on Computer Aided Process Engineering.
31 May – 4 June 2015, Copenhagen, Denmark

Overview of Smart Factory Studies in Petrochemical Industry

Defang Li,[a] Baihua Jiang,[b] Hansheng Suo,[b☆] Ya Guo[b]

[a] *SINOPEC Information Management Department, 22 Chaoyangmen North Street Chaoyang District, Beijing 100728, China*
[b] *Petro-CyberWorks Information Technology Co., Ltd. MES Department, A 22 Dongsishitiao Dongcheng District, Beijing 100007, China*
hansheng.suo@pcitc.com

Abstract

The smart factory in petrochemical industry is operational excellence as the goal, through the operational management of the whole process, with a high degree of automation, digitization, visualization, modeling and integrated refining chemical factory, which is the future development direction of the petrochemical enterprises. This paper discusses the development process of petrochemical industry smart factory, describes its architecture and key technologies. Then based on industry background, the paper gives a smart factory model definition. It puts forward thesis in production control, equipment management, HSE management, energy management, supply chain management and decision support six business domain as the focus, information technology and standardization to support the petrochemical smart factory "6+2" model framework. Finally, the paper points out the future development trend of smart factory and further research directions.

Keywords: process system engineering; petrochemical industry; smart factory

1. Introduction

The industry of petrochemical has become the large modern industrial system after decades of development, and it has made great contributions to the development of world economy and the improvement of people's lives. In recent years, the size of the petrochemical industry has been enlarged and industrial patterns have also changed considerably (Kadambur and Kotecha, 2015), which made regions play increasing role in the petrochemical industry, like North America, the Middle East and Asia-Pacific. The whole related industry has quickened the adjustment of the industrial structure, and began to transform from the stage of scale-economy to that of quality-effectiveness-economy. Product structure is reforming remarkably, and output of highly-performed, high value-added, specific chemical increase day by day (Industrie 4.0 Working Group, 2013). The development of petrochemical industry has been more and more limited by the resources and protection of environment. Driven by the Technology Revolution, the petrochemical industry will develop rapidly with the help of the technical innovation (Khosravi et al., 2015; Ramteke and Srinivasan, 2011). And the combination of new information technology, operation technology and manufacturing technology will bring great changes in the production patterns of petrochemical industry (Sa'idi et al., 2014).

In such background, traditional industry of petrochemical has not adapted to the requirement of the customer, market and the technology development. A new production pattern needs to adjust to the new changes of shorter product life cycle (Industrie 4.0

Working Group, 2013), to cope with the rapid upgrading of many types of products in small scales, to ameliorate the effectiveness resource optimization and energy utilization, to satisfy the need of global manufacturing and sustainable development of enterprises. Therefore, smart factory seems to be the best choice.

2. The emergence and development of smart factory

In recent years, Smart factory has been widely mentioned in the business and academic circles (Lucke et al., 2008; Radziwon et al., 2014). In some papers, Yoon et al.(2011) used Ubiquitous Factory (U-Factory), Zkule (2011) used Factory- of- Things (FoT) to explain the concept of smart factory. In addition, the key factor of Smart Process Manufacturing and German Industry 4.0 (Industrie 4.0 Working Group, 2013) is also smart factory.

2.1. Ubiquitous Factory

The PARC in Xerox put forward the concept of ubiquitous computing, which allows the small, low-cost, networked devices to distribute in various places in our lives (Weiser, 1991; Zuehlke, 2010). In the model of U-computing, people can acquire and process the desired information by any method, anytime, anywhere. As the development of sensor net, RFID etc., the U-Computing has many specific forms, such as U-home (Lai et al., 2013) etc.. Yoon (2012) came with up the concept of Ubiquitous Factory. He pointed out that the frame of the U-Factory should integrate the information technology, advanced manufacturing technology and automatically complete the whole industrial process through the data acquisition and exchange of workers, resources, products and systems. The frame mainly consists of four parts: U-human, U-Resources, U-Product, and U-MES.

2.2. Factory-of-Things

MIT founded the Auto-ID Center, and Ashton (2009) put forward the concept of the Internet-of-Things (IoT), which means that all items are connected through the RFID and the Internet, can realize the intelligent identification and management. The IoT requires that items automatically acquire and process data, exchange information with other items (Maass and Varshney, 2012). The IoT is more like an uncertain and open network, in which the intelligent devices and pseudo entities are endowed enough capacities to complete the required operation independently according to the goal and circumstance (Lucke, et al., 2008). Based on the IoT, Zuehlke (2010) held the opinion that the future factory should be the Factory-of-Things (FoT). In this mode, intelligent devices interact with each other on the basis of semantic services. Devices inside of the factory can achieve specific goals through self-organization. Zuehlke (2010) explained the concept with four dimensions: technology, framework, security and human.

2.3. Smart Process Manufacturing

The research on the Smart Process Manufacturing (SPM, 2010) has been conducted by the Engineering Virtual Organization (EVO). The EVO developed the roadmap of Smart Process Manufacturing and defined the SPM as: an integrated, knowledge-enabled, model-rich enterprise in which all operating actions are determined and executed proactively applying the best possible information and a wide range of performance metrics.

2.4. Industry 4.0

Industry 4.0 is based on the Cyber Physical Systems (CPS), and realized the novel manufacturing method (Industrie 4.0 Working Group, 2013). The CPS is that the devices are connected to the Internet, which makes them have the ability of computing, communication, accurate control, remote coordination and autonomy (Håkansson and Hartung, 2014). Therefore, the CPS realized the fusion between the virtual cyber world and the real world. The core of the Industry 4.0 is that a highly flexible, personalized, digital smart manufacturing pattern which was established by the real-time web and effective communications among people, equipment and products. In this mode, the production process becomes more distributed, and scale effect is no longer the key factor of industrial production; the product becomes more specific, and the future product will be produced in the custom-made pattern; and the users will participate in the production throughout the whole process.

3. Research progress in smart factory of petrochemical industry

3.1. Modeling and Simulation

The modeling and simulation of enterprises is a very important way to research on these entities, and it can also provide strategies for the enterprises' operation and management. Since the manufacturing process of petrochemical is usually very complicated, many key technological parameters cannot be obtained directly, the producing systems are also multi-scale in time. It is an indispensable method to have a better understanding of the whole production process with the development of models and simulation systems. In the early period of the research of smart factory, Pei and Rong (2005) came up with a smart factory simulation platform based on Matlab, which is the prototype of the smart factory. Zhang and Rong (2005) put forward an enterprise logistics balance layered modeling theory according to the ISA-95 standard, which was also used to develop the decision support system of smart factory. Zhu et al. (2013)conducted the research about the information integration of smart factory and put forward an information integration solution in the multi-scale perspective. Qi et al.(2013) came up with a four-storey framework for modeling and simulation. This method was used to construct the multi-layered and modular simulation systems.

3.2. Intelligent Control

Intelligent control is derived from conventional control, which is used to deal with the complex processes that cannot be controlled by traditional methods. The intelligent control systems mainly have the following characters: learning function, adaptive function and organizing function (Sun, 2007).

Bhuvaneswari et al. (2012) used the artificial neural network to maintain the pipelines and make fault diagnosis of them. Monedero et al. (2012) developed a decision-making system based on data mining technology and kernel of neural networks, which is used to make predictions for future optimization. The test results showed that this decision system can help reduce about 7 % energy consumption. The system will be piloted in the petrochemical industry. Sa'idi et al. (2014) built a Risk-based maintenance model through fuzzy logic method, and used this model to conduct the risk assessment of failures in Abadan oil refinery, Iran. Yüzgeç et al. (2010) optimize the control operation of the short-term plan of the petroleum refining using the Model Predictive Control method.

3.3. Intelligent Optimization Algorithms

The research of optimization for petrochemical engineering is quite significant, which mainly includes global optimization methods and heuristic methods. These methods are intriguing interest for researchers at current time, especially applicable for the complicated that cannot be dealt with by tradition approaches (Yu, 2007).

Kadambur and Kotecha (2015) optimized the production plan of petrochemical industry based on Teaching-Learning-Based-Optimization algorithm. Compared with traditional methods, this approach can increase the profit about 8.16 %. Zhou et al. (2015) optimized heated oil pipeline based on Particle Swarm Optimization-Differential Evolution method, which can save 17.59 % of energy cost in the application of 2640 m^3/h oil transfer. Lavric et al. (2005) used Genetic Algorithm to optimize the conversion rate of hydrogenated waste to hydrogen. By using this algorithm, an oil refinery factory in Iran can increase 22.6 % hydrogen products and save about 1.9 million every year. Ramteke and Srinivasan (2011) solved the refinery crude oil scheduling problem by combining the Genetic Algorithm and Graph-based Representation method. Khosravi et al. (2015) optimized the parameters of shell and tube heat exchangers to maximize the thermal efficiency by using three methods: Genetic Algorithm, Firefly Algorithm, and Cuckoo Algorithm.

4. The definition and framework of smart factory in petrochemical industry

On the basis of the above study, in the context of the petrochemical industry, we believe that smart factory in petrochemical industry is operational excellence as the goal, through the operational management of the whole process, with a high degree of automation, digitization, visualization, modeling and integrated refining chemical factory, which is the direction of future development of the petrochemical enterprises. Through the revolution of technology and business, the enterprises could have the outstanding capabilities of perception, prediction, interoperability, analysis and optimization. The smart factory mainly contains six core business, four capabilities, and two supporting systems. The framework of smart factory in petrochemical industry can be shown in Figure 1.

Moreover, the factors of smart factory in petrochemical industry consist of characteristics, capabilities, key business areas, intelligent application fields and key technologies. The details are presented in Table 1.

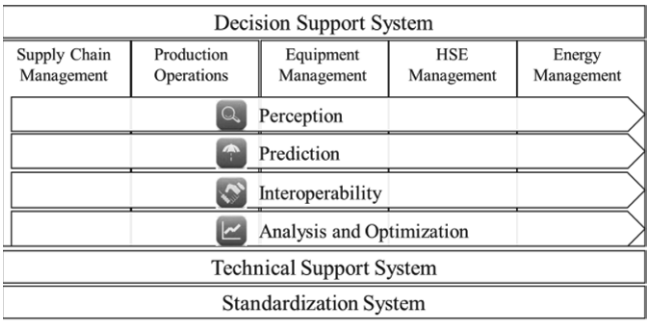

Figure 1. The framework of smart factory in petrochemical industry.

Table 1. Factors of the smart factory in petrochemical industry.

Factors	Descriptions
Characteristics	Digitization, Visualization, Modeling , Integration , Automation
Capabilities	Perception, Prediction, interoperability, Analysis and Optimization
Business Areas	Production Operations, Equipment Management, Energy Management, HSE Management, Supply Chain Management, Decision Support
Intelligent Application Fields	Business Intelligence, Manufacture Intelligence, Control Intelligence
Key Technologies	Optimization Technology, Artificial Intelligence, Control Technology, Information Technology, Petrochemical Technology

5. Conclusions and future researches

Establishing the smart factory is the important measure to handle the shortage of the gas and oil resources, the update of the oil quality, the optimization of industrial structure, the fierce competition in the global market, energy conservation and emission reduction, and environmental protection. The prospects of the smart factory are listed as below:

For equipment, traditional manufacturing units will be gradually changed to be the smart manufacturing units which have capacity of state acquisition, perception and can make intelligent predictions, optimizations and decisions; the smart control systems can optimize multi-devices, conduct self-study and -organize; the industrial robots are also used in the harsh conditions of the petrochemical production processes.

For technology, the knowledge based on analysis of the big data will be developed, which can help realize the combination of the massive information of heterogeneous perception; the technology of the combination of virtual reality and visualization will be widely applied in the petrochemical field; the modeling technology of complex systems, collaborative optimization technology etc. will make great progresses; the molecular technologies and ‘green’ system engineering will be spread in this industry.

For business, the construction of the smart factories in petrochemical industry can be divided into three process domains: production operations, petrochemical supply chain and whole lifecycle management.

References

K. Ashton, 2009, That 'Internet of Things' Thing, http://www.rfidjournal.com/articles/view?4986 .

S. Bhuvaneswari, R. Hemachandran, and R. Vignashwaran, 2012, Neural network precept diagnosis on petrochemical pipelines for quality maintenance innovative systems design and engineering, 3, 61-69.

A. Håkansson, and R. Hartung, 2014, An infrastructure for individualised and intelligent iecision-making and negotiation in Cyber-physical Systems, Procedia Computer Science, 35, 0, 822-831.

Industrie 4.0 Working Group, 2013, Recommendations for implementing the strategic initiative INDUSTRIE 4.0, http://www.acatech.de/fileadmin/user_upload/Baumstruktur_nach_Website/Acatech/root/de/Material_fuer_Sonderseiten/Industrie_4.0/Final_report__Industrie_4.0_accessible.pdf, Germany.

R. Kadambur, and P. Kotecha, 2015, Multi-level production planning in a petrochemical industry using elitist Teaching–Learning-Based-Optimization, Expert Systems with Applications, 42, 1, 628-641.

R. Khosravi, A. Khosravi, S. Nahavandi, and H. Hajabdollahi, 2015, Effectiveness of evolutionary algorithms for optimization of heat exchangers, Energy Conversion and Management, 89, 0, 281-288.

Y. X. Lai, C. F. Lai, Y.M. Huang, and H. C. Chao, 2013, Multi-appliance recognition system with hybrid SVM/GMM classifier in ubiquitous smart home, Information Sciences, 230, 0, 39-55.

V. Lavric, P. Iancu, and V. Pleşu, 2005, Genetic algorithm optimisation of water consumption and wastewater network topology, Journal of Cleaner Production, 13, 15, 1405-1415.

D. Lucke, C. Constantinescu, and E. Westkämper, 2008, Smart Factory - A Step towards the next generation of manufacturing, Manufacturing Systems and Technologies, 115-118.

W. Maass, and U. Varshney, 2012, Design and evaluation of Ubiquitous Information Systems and use in healthcare, Decision Support Systems, 54, 1, 597-609.

I. Monedero, F. Biscarri, C. León, J. I. Guerrero, R. González, and L. Pérez-Lombard, 2012, Decision system based on neural networks to optimize the energy efficiency of a petrochemical plant, Expert Systems with Applications, 39, 10, 9860-9867.

L. Pei, and G. Rong, 2005, Flow sheet simulation platform of intelligent plant in oil refinery, Control and Instruments in Chemical Industry, 32, 43-46.

R. Qi, G. Rong, Y. Feng, and Y. Hu, 2013, Configurable hierarchical modeling method for intelligent plant, CIESC Journal, 65, 4354-4365.

A. Radziwon, A. Bilberg, M. Bogers, and E. S. Madsen, 2014, The Smart Factory: Exploring adaptive and flexible manufacturing solutions, Procedia Engineering, 69, 0, 1184-1190.

M. Ramteke, and R. Srinivasan, 2011, Integrating Graph-based representation and Genetic Algorithm for large-scale optimization: refinery crude oil Scheduling, Computer Aided Chemical Engineering, 29, 567-571.

E. Sa'idi, B. Anvaripour, F. Jaderi, and N. Nabhani, 2014, Fuzzy risk modeling of process operations in the oil and gas refineries, Journal of Loss Prevention in the Process Industries, 30, 0, 63-73.

SPM, 2010, SPM roadmap technical, https://smart-process-manufacturing.ucla.edu/workshops/2010/ materials/SPMroadmaptechnical.pdf/view , LA, USA.

Y. Sun, 2007, Industrial intelligent control technology and applications, Science Press Ltd., Beijing, China.

M. Weiser, 1991, The Computer for the 21st Century, Scientific American, 265, 94 – 104.

U. Yüzgeç, A. Palazoglu, and J. A. Romagnoli, 2010, Refinery scheduling of crude oil unloading, storage and processing using a model predictive control strategy, Computers & Chemical Engineering, 34, 10, 1671-1686.

J.S. Yoon, S. J. Shin, and S. H. Suh, 2011, A conceptual framework for the ubiquitous factory, International Journal of Production Research, 50, 8, 2174-2189.

J. Yu, 2007, Information Science and Engineering, Science Press Ltd., Beijing, China.

Q. Zhang, and G. Rong, 2005, New approach to data rectification of hybrid systems, CIESC Journal, 56, 1057-1062.

M. Zhou, Y. Zhang, and S. Jin, 2015, Dynamic optimization of heated oil pipeline operation using PSO–DE algorithm, Measurement, 59, 0, 344-351.

F. Zhu, Y. Feng, and G. Rong, 2013, Information integration strategy of the petrochemical industry from the multi-scale perspective. 10th IEEE International Conference on Control and Automation (ICCA), 1284-1289.

D. Zuehlke, 2010, Smart Factory—Towards a factory-of-things, Annual Reviews in Control, 34, 1, 129-138.

Krist V. Gernaey, Jakob K. Huusom and Rafiqul Gani (Eds.), 12th International Symposium on Process Systems Engineering and 25th European Symposium on Computer Aided Process Engineering.
31 May – 4 June 2015, Copenhagen, Denmark

A PSE approach to patient-individualized physiologically-based pharmacokinetic modeling

Roberto Andrea Abbiati[a], Gaetano Lamberti[b], Anna Angela Barba[c], Mario Grassi[d], Davide Manca[a]

[a]*PSE-Lab, CMIC Department, Politecnico di Milano, P.zza L. da Vinci, 32 – 20133 Milan – ITALY*
[b]*Industrial Engineering Department, Università degli Studi di Salerno, Via Giovanni Paolo II, 132 – 84084 Fisciano Salerno – ITALY*
[c]*Pharmacy Department, Università degli Studi di Salerno, Via Giovanni Paolo II, 132 – 84084 Fisciano Salerno – ITALY*
[d]*Engineering and Architecture Department, Università di Trieste, Via Alfonso Valerio, 6/A, 34127 Trieste – ITALY*

Abstract

Pharmacokinetic modeling allows predicting the drug concentration reached in the blood as a consequence of a specific administration. When such models are based on mammalian anatomy and physiology it is possible to theoretically evaluate the drug concentration in every organ and tissue of the body. This is the case of the so-called physiologically based pharmacokinetic (PBPK) models. This paper proposes and validates a procedure to deploy PBPK models based on a simplified, although highly consistent with human anatomy and physiology, approach. The article aims at reducing the pharmacokinetic variations among subjects due to inter-individual variability, by applying a strategy to individualize some model parameters. The simulation results are validated respect to experimental data on remifentanil.

Keywords: Pharmacokinetics; Physiologically-Based modeling; Complexity reduction; Lumping; Personalization; Remifentanil.

1. Introduction

The knowledge of drug concentration reached in blood and tissues is fundamental information in the medical field. In fact, it allows understanding the drug bio-distribution extent and the related pharmacological effects. The purpose of pharmacokinetics (PK) is to evaluate how the drug administered to a patient is affected by the body activity in terms of absorption, distribution, metabolism, and excretion (*i.e.* the so-called ADME elements). Ordinary PK studies are characterized by an empirical source and require sampling of blood at various time intervals to determine a concentration-time profile. When organ and tissue concentrations are also required, this activity becomes even more critical, as the sampling of tissues is a highly invasive practice in particular in case of human patients.

PK models were originally conceived as tools to evaluate the drug concentration-time curves in blood with the target of limiting/reducing the experimental activity. Those models were formulated by defining simple mass balances for the drug respect to few controlled volumes, which resembled the schematization of continuous stirred tank reactors (CSTRs) as the ones commonly solved in chemical engineering problems. A detailed description of such models is available in Wagner (1993), while a modern application of compartmental models is reported in Laínez-Aguirre *et al.* (2014). These

models have the limitation to asses only the drug concentration in blood. More sophisticated models, designed to study drug distribution in the whole organism, are based on human/mammal anatomy and physiology.

By considering a rather high number of compartments, it is possible to reproduce a simplified mockup of the mammalian organism. This can be achieved by assigning to every compartment a correspondence to a given organ or tissue. These are the so-called physiologically based pharmacokinetic (PBPK) models, which are obtained by interconnecting the compartments according to a faithful similarity respect to mammal anatomy. Himmelstein and Lutz (1979) published an extended review of these models. A whole-body PBPK model, commonly taken as reference, is the one proposed by Jain *et al.* (1981). In that study the rat body is partitioned into 21 compartments that are mathematically described by a system of 38 ordinary differential equations (ODEs) and 98 adaptive parameters. Some of these parameters may be estimated from either experimental or literature information, but 37 require to be fitted by means of a nonlinear regression procedure. When the number of regressed parameters is so high the mathematical procedure (*i.e.* nonlinear regression) becomes risky and inaccurate, despite the detailed description of the PK in the different organs. In addition, the amount of experimental data necessary to carry out the nonlinear regression is so high and complex that the model itself becomes almost useless and too much specialized to the specific mammalian body respect to which the experimental data are measured.

Drugs can be administered via several routes (*e.g.*, enteral, parenteral, inhalation, topical). In particular, as far as the parenteral route is concerned, the body absorption is considered complete and practically instantaneous, so that the entire dose is readily available for distribution in the organism. Conversely, in case of oral (*i.e.* enteral) administration, the drug bioavailability is a function of gastrointestinal absorption. This point introduces a significant and challenging complexity in the model. Specific intestinal absorption model for drugs available in the literature feature quite complex formulations and nevertheless do not usually take into account the amount of drug released in the intestinal lumen prior to absorption. The most well-known model of this category is the compartmental absorption and transit (*i.e.* CAT) model proposed by Yu *et al.*(1996a,b), and afterwards slightly modified and finally commercialized as ACAT model (Agoram *et al.*, 2001). Recently, Pavurala and Achenie (2012, 2013) proposed a model that couples the CAT model with a drug dissolution one. By doing so, they analyzed the entire process of oral absorption. Del Cont *et al.* (2014) published a model considering the physical processes determining drugs release from an ensemble of poly-dispersed, swelling, and not eroding polymeric particles. Mošat' *et al.* (2013) implemented a PBPK model for the rat based on a program that can automatically generate an ODEs system, featuring a vascular network structure. They identified also the optimal set of parameters that describe the cyclosporin PK.

Some drugs are characterized by a peculiar phenomenon occurring as a consequence of bile recirculation during digestion that is named enterohepatic circulation (EHC). This is due to the fact that a drug fraction in the liver is excreted with the bile, which accumulates and concentrates in the gall bladder, and is finally reintroduced into the intestine. This causes a double intestinal absorption for a certain fraction of the dose, and produces the characteristic *double peak* in the PK concentration-time curves. This aspect is often neglected because of the modeling complexity introduced, but it is important as the EHC extends the drug permanence in the organism. Jain *et al.* (2011) proposed a simple PK model accounting for this feature.

Several authors focused on reducing the complexity introduced when a large number of compartments are accounted for and proposed to lump the organs and tissues that show

a similar behavior respect to drug distribution. On one hand, this practice can reduce the model complexity but on the other hand preserves the physiological consistency (*e.g.*, Gueorguieva *et al.* (2006); Nestorov *et al.* (1998)). Reduced complexity PBPK models are rather common. For instance, Di Muria *et al.* (2010) devised a simplified model based on just seven compartments, which lump together organs and tissues as a function of affinity to blood perfusion. Indeed, they assumed that a higher blood perfusion is related to a faster drug distribution. Consequently, the poorly perfused organs and tissues are lumped into a single compartment called Tissues, while the highly perfused ones are considered with the blood in the Plasma compartment. That model is characterized by a system of 7 ODEs and 22 adaptive parameters, which can be either determined from the literature or by a nonlinear regression respect to experimental data. Abbiati *et al.*(2014) adopted a similar approach but they moved the anatomical and physiological consistency a step forward by proposing a personalization of some parameters that took to the so called patient-individualized PBPK definition. This PK modeling has to face some challenging issues, first of all the inter-individual variability among patients. In fact, the PK profile is affected by a large number of aspects (*e.g.*, sex, body mass, age, health status, race) that cause the concentration to vary in a rather wide interval. To address this problem, this paper proposes a strategy to individualize the PBPK model respect to some given characteristic of the patient (*e.g.,* body mass (BM), body surface area (BSA), sex). An interesting potential of PBPK models is that they can be applied also to small/medium size mammals (*e.g.*, mice, rat, monkeys) and scaled up to humans, even if this practice is quite challenging and somehow risky in terms of consistency (Kenyon, 2012). Another field where PBPK models can play an important role is the cancer-fight, since antitumor drugs have often negative side effects that limit clinical trials. A further possible action to improve the predictive feature of PBPK models consists in supporting the pharmacokinetics with the pharmacodynamics. This coupling makes viable the evaluation of the pharmacological effect induced by the drug concentration on the action site (Meibohm and Dorendorf, 1997).

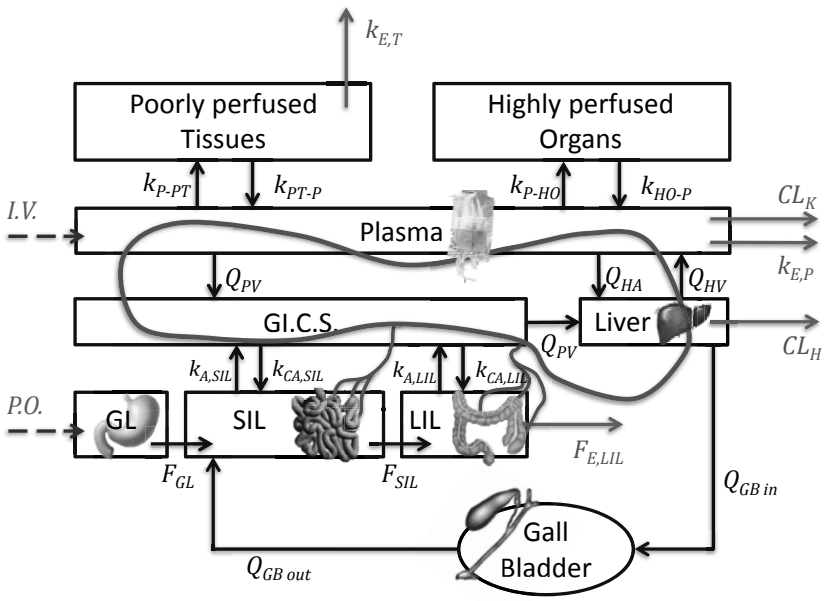

Figure 1: PBPK model structure.

2. Methods

The PBPK model proposed in in this paper draws inspiration from the work of Di Muria *et al.* (2010) but implements a new formulation of the compartmental structure and the related equations (see also Abbiati *et al.*, 2014). The model goal is to be consistent with the absorption, distribution, metabolism, and excretion (ADME) processes which characterize the presence of drug in the body. Section 2.1 analyses in depth the model, while Section 2.2 discusses how some of the model parameters can be personalized.

2.1. Model structure

Figure 1 shows how the proposed PBPK model is structurally organized. In the following, we provide a description of the model centered on its anatomical and physiological consistency. For the sake of conciseness, some details are not fully commented but can be found in Abbiati *et al.* (2014).

The model is based on nine compartments. The gastrointestinal tract features the gastric (GL), the small intestinal (SIL), and the large intestinal (LIL) lumina. If the drug is administered as an oral bolus ($P.O.$) it passes through the stomach and intestinal tracts with a fraction being finally eliminated with the faeces ($F_{E,LIL}$). The absorption from the intestine into the blood circulation system is a complex phenomenon, which is treated in a simplified fashion. We assume that the SIL is responsible for most of the absorption/diffusion into the $GI.C.S.$, as those blood vessels receive the drug from the intestine and bring it to the liver. Because of its morphology, the SIL should be considered as a longitudinal duct, *i.e.* similar to a plug flow reactor (PFR) in terms of modeling conceptualization. To avoid the solution of partial differential equations (PDE) originated by the axial and time variables, the PFR can be spatially discretized into a series of continuously stirred reactors (*i.e.* CSTRs). By doing so, the PDE is reduced to a set of ODEs, which are numerically simpler to solve. A specific mass transfer coefficient ($k_{A,SIL}$) quantifies the body absorption. However, it is worth considering also a dual phenomenon based on the so-called active expulsion mechanism that is induced by glycoprotein P. That mechanism sends back to the intestinal lumen a fraction of the absorbed drug and allows introducing in the numerical model a counterdiffusion mass transfer coefficient ($k_{CA,SIL}$) along with the typical PSE terminology. These two coefficients are different because the wall of the intestinal lumen is not isotropic and therefore diffusion and counterdiffusion phenomena are not equimolar. Finally, a similar modeling approach is adopted for the LIL, which is considered as a single compartment as its contribution to drug absorption respect to the SIL is much reduced if not minimal.

Once the drug reaches the blood circulation, it moves to the liver, which is an important metabolic site. Here a fraction of drug molecules reacts to give metabolites, the related term being the hepatic clearance (CL_H), while another fraction is excreted into the bile. Here the EHC takes place; the drug conveyed to the gall bladder is then delivered to the SIL. Again, according to the PSE terminology, the drug is recycled to the SIL compartment. The drug portion that remains unmodified in the liver reaches the systemic circulation. Here it can be either distributed in every organ and tissue of the organism or eliminated (see terms $k_{E,P}$ and CL_K). The extended PBPK structure shown in Figure 1 can be treated in a simplified version in case of endovenous administration as the gastrointestinal tract can be neglected. This takes to a reduced five-compartment model, whose numerical model is reported in Equations (1-5).

$$\frac{dC_P(t)}{dt} = -C_P(t)\cdot\left(\frac{k_{P-PT}}{R}+\frac{k_{P-HO}}{R}+\frac{Q_{HA}}{V_P}+\frac{Q_{PV}}{V_P}\right)+C_{PT}(t)\cdot k_{PT-P}\cdot\frac{V_{PT}}{V_P}+C_L(t)\cdot\frac{Q_{HV}}{V_P}+ C_{HO}(t)\cdot k_{HO-P}\cdot\frac{V_{HO}}{V_P}-C_P(t)\cdot\frac{k_{E,P}}{R}-C_P(t)\cdot\frac{CL_K}{V_P}+\frac{IV(t)}{V_P} \quad (1)$$

$$\frac{dC_{GICS}(t)}{dt} = -C_{GICS}(t) \cdot \left(\frac{Q_{PV}}{V_{GICS}} + \frac{k_{CA,SIL}}{R} + \frac{k_{CA,LIL}}{R}\right) + C_{SIL}(t) \cdot k_{A,SIL} \cdot \frac{V_{SIL}}{V_{GICS}} + C_{LIL}(t) \cdot k_{A,LIL} \cdot \frac{V_{LIL}}{V_{GICS}} + C_P(t) \cdot \frac{Q_{PV}}{V_{GICS}} \quad (2)$$

$$\frac{dC_L(t)}{dt} = -C_L(t) \cdot \left(\frac{Q_{HV}}{V_L} + \frac{CL_H}{V_L}\right) + C_P(t) \cdot \frac{Q_{HA}}{V_L} + C_{GICS}(t) \cdot \frac{Q_{PV}}{V_L} \quad (3)$$

$$\frac{dC_{PT}(t)}{dt} = -C_{PT}(t) \cdot \left(k_{PT-P} + k_{E,T}\right) + \frac{C_P(t)}{R} \cdot k_{P-PT} \cdot \frac{V_P}{V_{PT}} \quad (4)$$

$$\frac{dC_{HO}(t)}{dt} = -C_{HO}(t) \cdot k_{HO-P} + C_P(t) \cdot \frac{k_{P-HO}}{R} \cdot \frac{V_P}{V_{HO}} \quad (5)$$

2.2. Model identification

One of the challenging activities of PK modeling is the difficulty to deal with patients' variability, which depends on a number of factors as discussed in the Introduction. To account for this variability, the adaptive parameters of Equations (1-5) are subdivided into three main categories: (i) individualized, (ii) assigned, and (iii) degrees of freedom (DoF).

2.2.1. Individualized parameters

Whenever experimental or literature data about the dependency of anatomical and physiological values from patient features are available, it is possible to exploit their characteristics to evaluate the adaptive parameters. For instance, the volumes of organs and cardiac stroke volume are assessed as a function of patient's sex and body mass.

If the body surface area value is available, Cowles *et al.* (1971) propose for the human cardiac stroke volume (CO) the following formula:

$$CO = 3.5 \cdot BSA \quad (6)$$

Conversely, if the body mass value is known, Lindstedt and Schaeffer (2002) propose:

$$CO = 0.084 \cdot BM \quad (7)$$

To assess how the cardiac stroke volume is conveyed to a specific organ, Williams and Leggett (1989) list a set of coefficients that depend on the patient's sex. Similar information, but related to the volume of organs can be found in Brown *et al.* (1997).

2.2.2. Assigned parameters

Some parameters cannot be individualized, however they are available in literature as experimental data. In this case the value is assumed constant for every patient.

2.2.3. Degrees of freedom

Because of its simplified nature, the PBPK model accounts for some parameters that cannot be determined from either literature or experimental data because they do not have a real physiological meaning. For instance, this is the case of the mass transfer coefficient of the lumped organs compartment. It is then advisable to implement a fitting procedure to identify the adaptive parameters based on available PK experimental values. A nonlinear regression routine minimizes the objective function that measures the distance between the experimental concentrations and the model predicted values by modifying the adaptive parameters that play the role of DoF.

3. Model validation

Both identification and validation of Equation (1-5) model were performed by considering the PK of an analgesic drug, *i.e.* remifentanil based on two available literature studies. The former PK study (Egan *et al.*, 1993) was used to identify the DoF as discussed in Section 2.2.3; the latter PK study (Westmoreland *et al.*, 1993) was used to validate the model predictions respect to the experimental data.

For what concerns the DoF evaluation, a bounded optimization process allows identifying the optimal DoF within a suitable feasibility region. Table 1 lists the optimal DoF values and assigned bounds. Once identified, the DoF values are assumed as

known and constant for any future application of the model that was tuned for that specific drug (*i.e.* remifentanil).

Table 1: Optimal values of the DoF in the PBPK model of Equations (1-5).

Parameters	Value	Unit of measure	Lower Bounds	Upper Bounds
Eff_H	0.144	-	0.1	0.3
Eff_K	0.394	-	0.1	0.7
$k_{E,P}$	1.732	min^{-1}	0	3
$k_{E,T}$	0.063	min^{-1}	0	3
k_{HO-P}	0.044	min^{-1}	0	2
k_{P-HO}	0.662	min^{-1}	0	2
k_{P-PT}	0.479	min^{-1}	0	1
k_{PT-P}	0.279	min^{-1}	0	1

Westmoreland *et al.* (1993) studied the PK of remifentanil administered through an endovenous injection of four doses (2, 5, 15, 30 µg/kg) to an equivalent number of mixed groups of patients. Every group (composed by 6 patients) was treated as a hypothetical individual with averaged body characteristics. The knowledge of the BM of single patients allowed the personalization of some parameters, while the remaining ones were either assigned from literature values or calculated by a nonlinear regression respect to the Egan *et al.* (1993) work. Figure 2 shows a comparison between experimental values and PBPK model predictions.

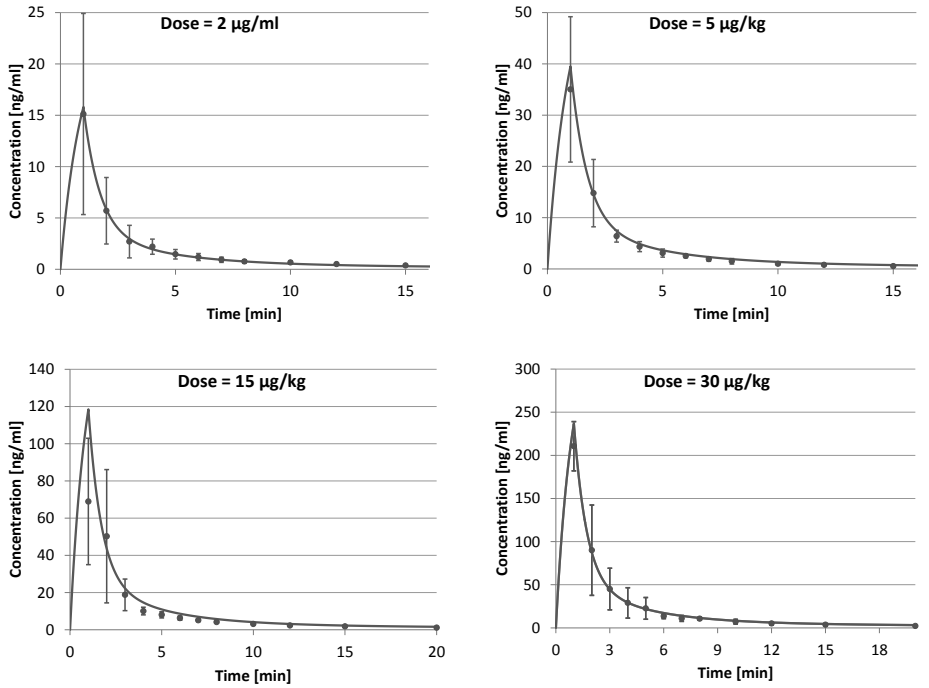

Figure 2: Comparison between model prediction (line) and experimental data (points with standard deviation) from the Westmoreland *et al.* (1993) study.

The model predictions are analyzed in terms of proximity to experimental values (see Table 2) by considering two important PK indicators (*i.e.* the area under the curve, AUC, and the blood peak concentration, C_{MAX}).

Table 2: AUC and C_{MAX} percentage distance between experimental data and model predictions.

	Group 1 [2 µg/kg]	Group 2 [5 µg/kg]	Group 3 [15 µg/kg]	Group 4 [30 µg/kg]
$\Delta\ AUC$ %	9.3	7.5	30.4	5.9
$\Delta\ C_{MAX}$ %	4.5	12.8	71.7	12.9

To assess the usability of mathematical tools in PK studies, one can refer to the specifications issued by FDA (1997) about the level-A IVIVC thresholds that recommend a percent Prediction Error, %PE = 100·[(observed value – predicted value)/observed value] lower than 10% for both C_{MAX} and AUC. Indeed, the predictions reported in Table 2 are lower than or pretty close to the 10% thresholds with the exception of Group 3. However, such values are not only badly described by the PBPK model but they are also scarcely consistent with the experimental data observed in the other groups (*i.e.* #1, #2, and #4). For instance, Figure 2 shows how the trends of peak values measured for Groups 1, 2, and 4 are much higher than the Group 3 one.

4. Conclusions

The capability to asses in a reliable and reproducible way the PK profiles of specific patients administered with different active principles is one of the main objectives of pharmaceutical researchers. This paper proposed and discussed a PSE approach to PBPK modeling. The human body was described as a system of interconnected compartments, whose mathematical behavior is assumed similar to interconnected CSTRs. The mathematical formulation of the PBPK model was tailored to the specific human subject by applying as far as possible correlations, available in literature, for the determination of the adaptive parameters (either general or individualized). The remaining unknown parameters were estimated by a nonlinear regression procedure. Simulations results are encouraging as the blood concentration-time curves, obtained with the individualized parameter set, show a rather good consistency. The AUC, which is the reference PK parameter in pharmaceutical studies, is close to the experimental one for at least three out of four predictions. In addition the single experimental data points are pretty well forecast by the model, which is not just within the standard deviation window but also close to the central value of the distribution. A possible improvement of the model would consist in further enhancing its personalization capability by having more detailed information related to single patients.

References

R.A. Abbiati, G. Lamberti, M. Grassi, F. Trotta, D. Manca, 2014, Definition and validation of a patient-individualized physiologically based pharmacokinetic model, Computers & Chemical Engineering, SUBMITTED.

B. Agoram, W. S. Woltosz, M. B. Bolger, 2001, Predicting the impact of physiological and biochemical processes on oral drug bioavailability, Advanced Drug Delivery Reviews, 50, S41-S67.

R. P. Brown, M. D. Delp, S. L. Lindstedt, L. R. Rhomberg, R. P. Beliles, 1997, Physiological parameter values for physiologically based pharmacokinetic models, Toxicology and Industrial Health, 13, 407-484.

A. L. Cowles, H. H. Borgstedt, A. J. Gillies, 1971, Tissue weights and rates of blood flow in man for the prediction of anesthetic uptake and distribution, Anesthesiology, 35, 523-526.
R. Del Cont, M. Abrami, D. Hasa, B. Perissutti, D. Voinovich, A. Barba, G. Lamberti, G. Grassi, I. Colombo, D. Manca, 2014, A physiologically-oriented mathematical model for the description of in vivo drug release and absorption, ADMET and DMPK, 2, 80-97.
M. Di Muria, G. Lamberti, G. Titomanlio, 2009, Modeling the pharmacokinetics of extended release pharmaceutical systems, Heat and mass transfer, 45, 579-589.
M. Di Muria, G. Lamberti, G. Titomanlio, 2010, Physiologically Based Pharmacokinetics: A Simple, All Purpose Model, Industrial & Engineering Chemistry Research, 49, 2969-2978.
T. D. Egan, H. J. M. Lemmens, P. Fiset, D. J. Hermann, K. T. Muir, D. R. Stanski, S. L. Shafer, 1993, The Pharmacokinetics of the New Short-acting Opioid Remifentanil (GI87084B) in Healthy Adult Male Volunteers, Anesthesiology, 79, 881-892.
FDA, 1997, Guidance for industry: extended release oral dosage forms: development, evaluation, and application of in vitro/in vivo correlations, Center for Drug Eval. and Research (CDER).
I. Gueorguieva, I. A. Nestorov, M. Rowland, 2006, Reducing whole body physiologically based pharmacokinetic models using global sensitivity analysis: diazepam case study, Journal of pharmacokinetics and pharmacodynamics, 33, 1-27.
K. J. Himmelstein, R. J. Lutz, 1979, A review of the applications of physiologically based pharmacokinetic modeling, Journal of Pharmacokinetics and Biopharmaceutics, 7, 127-145.
L. Jain, S. Woo, E. R. Gardner, W. L. Dahut, E. C. Kohn, S. Kummar, D. R. Mould, G. Giaccone, R. Yarchoan, J. Venitz, W. D. Figg, 2011, Population pharmacokinetic analysis of sorafenib in patients with solid tumours, British journal of clinical pharmacology, 72, 294-305.
R. K. Jain, L. E. Gerlowski, J. M. Weissbrod, 1981, Kinetics of uptake, distribution, and excretion of zinc in rats, Annals of Biomedical Engineering, 9, 347-361.
E. M. Kenyon, 2012, Interspecies extrapolation, Methods in Molecular Biology, 929, 501-520.
J. M. Laínez-Aguirre, G. E. Blau, G. V. Reklaitis, 2014, Postulating compartmental models using a flexible approach, Computer Aided Chemical Engineering, 33, 1171-1176.
S. L. Lindstedt, P. J. Schaeffer, 2002, Use of allometry in predicting anatomical and physiological parameters of mammals, Laboratory animals, 36, 1-19.
B. Meibohm, H. Dorendorf, 1997, Basic concepts of pharmacokinetic/pharmacodynamic (PK/PD) modelling, International Journal of Clinical Pharmacology and Therapeutics, 35, 401-413.
A. Mošat', E. Lueshen, M. Heitzig, C. Hall, A. A. Linninger, G. Sin, R. Gani, 2013, First principles pharmacokinetic modeling: A quantitative study on Cyclosporin, Computers & Chemical Engineering, 54, 97-110.
I. A. Nestorov, L. J. Aarons, P. A. Arundel, M. Rowland, 1998, Lumping of whole-body physiologically based pharmacokinetic models, Journal of Pharmacokinetics and Biopharmaceutics, 26, 21-46.
N. Pavurala, L. E. K. Achenie, 2012, An advanced model for controlled oral drug delivery, Computer Aided Chemical Engineering, 31, 1150-1154.
N. Pavurala, L. E. K. Achenie, 2013, A mechanistic approach for modeling oral drug delivery, Computers & Chemical Engineering, 57, 196-206.
J. G. Wagner, 1993, Pharmacokinetics for the Pharmaceutical Scientist. Lancaster, Pennsylvania U.S.A.: Technomic.
C. L. Westmoreland, J. F. Hoke, P. S. Sebel, C. C. J. Hug, K. T. Muir, 1993, Pharmacokinetics of Remifentanil (GI87084B) and Its Major Metabolite (GI90291) in Patients Undergoing Elective Inpatient Surgery, Anesthesiology, 79, 893-903.
L. R. Williams, R. W. Leggett, 1989, Reference values for resting blood flow to organs of man, Clinical Physics and Physiological Measurement, 10, 187-217.
L. X. Yu, J. R. Crison, G. L. Amidon, 1996a, Compartmental transit and dispersion model analysis of small intestinal transit flow in humans, International Journal of Pharmaceutics, 140, 111-118.
L. X. Yu, E. Lipka, J. R. Crison, G. L. Amidon, 1996b, Transport approaches to the biopharmaceutical design of oral drug delivery systems: Prediction of intestinal absorption, Advanced Drug Delivery Reviews, 19, 359-376.

Krist V. Gernaey, Jakob K. Huusom and Rafiqul Gani (Eds.), 12th International Symposium on Process Systems Engineering and 25th European Symposium on Computer Aided Process Engineering.
31 May – 4 June 2015, Copenhagen, Denmark

Modeling and Optimization of Continuous Pharmaceutical Manufacturing Processes

Amanda Rogers[a], Marianthi Ierapetritou[a*]

[a] *Department of Chemical and Biochemical Engineering, Rutgers, The State University of New Jersey, 98 Brett Road, Piscataway, NJ 08854, USA*
marianthi@soemail.rutgers.edu

Abstract

The increased availability of software tools for solids-based process modeling has created opportunities to enhance pharmaceutical development through the use of models. In particular, recent work in the area of integrated process modeling has demonstrated the potential of these simulations to complement experimental studies during process development. Once developed, these models also facilitate the use of other mathematical tools like process feasibility analysis and optimization. This work will emphasize recent developments in the area of flowsheet modeling for pharmaceutical processes. Methods for feasibility analysis and optimization of these complex process models will also be discussed. These tools can play an important role in pharmaceutical process development.
Keywords: flowsheet modelling, feasibility analysis, surrogate-based optimization

1. Introduction

The use of continuous processes for pharmaceutical manufacturing has been increasingly discussed as a strategy for reducing manufacturing costs and enhancing product quality. Despite the potential to realize economic and quality advantages through continuous manufacturing, adoption of this technology within the pharmaceutical industry has been slow (Plumb, 2005). This may be due in part to the new and unique challenges associated with process development for continuous, solids-based systems. Among these is the need to develop accurate and computationally efficient predictive models for particulate processes that can be used for simulation and optimization. These models can supplement experimental work during process development and suggest optimal operating conditions for product manufacturing (Gernaey et al., 2012). In addition, process models can be used to explore design space and optimize process performance (Boukouvala & Ierapetritou, 2013). This work will focus on the development of integrated process models for continuous tablet manufacturing processes and the use of these models for process design and optimization applications. The use of reduced-order modeling as a tool for flowsheet improvement and surrogate-based optimization will also be discussed.

2. Integrated flowsheet modeling

Modeling solids-based processes is challenging due to the nature of granular flows. The behavior of bulk granular materials is influenced by particle-level phenomena, which makes it difficult to develop continuum equations describing powder flows (Muir Wood, 2008). Although these particle-level phenomena can be described using discrete element method (DEM) simulations (Ketterhagen et al., 2009), the computational

expense associated with DEM renders it prohibitive for flowsheet modeling and optimization applications. Therefore it is necessary to develop lower-order, semi-empirical and empirical models for pharmaceutically relevant unit operations. This has been accomplished for a variety of processes including continuous powder blending (Boukouvala, Dubey, et al., 2012), roller compaction(Hsu et al., 2010) and wet granulation(Marshall et al., 2013). In recent years, flowsheet models that integrate these various unit operations have been developed using gPROMS^{TM} ModelBuilder. These can be used to simulate continuous tablet manufacturing processes via methods including wet granulation (Boukouvala, Chaudhury, et al., 2013), dry granulation and direct compaction (Boukouvala, Niotis, et al., 2012).

2.1. Integration of reduced-order models

While detailed process models are preferred for process simulation, these models are not always available. In these cases, reduced-order or data-based models can be implemented (Boukouvala et al., 2011). Reduced-order models can be used to bridge the gap between experimental knowledge or high-fidelity (e.g. DEM) simulations and equation-oriented process models. For instance, PCA-based reduced-order models have been shown to facilitate efficient and accurate representation of distributed parameter information from DEM simulations (Boukouvala, Gao, et al., 2013; Rogers & Ierapetritou, 2014). These reduced-order models evaluate in a matter of cpu-seconds (as compared with hours or even days for DEM) and are therefore much better suited to flowsheet modeling applications. Figure 1shows an example of a flowsheet model that incorporates particle velocity information from a discrete-element reduced-order model (DE-ROM). The flowsheet model represents a continuous feeding and blending process that consists of three loss-in-weight feeders and a single continuous blender. A reduced-order model is used to predict distributed axial velocity information within the blender as function of the agitator rotation rate. This information can be used to model the residence time distribution within the blender. The flowsheet model has been used to simulate the dynamic response of the continuous blending system to a disturbance introduced by refill of one of the loss-in-weight feeders, Feeder A. The results of this dynamic simulation are shown in the chart in Figure 1, where the black line indicates the concentration of component A entering the blender and the red line indicates the concentration of component A exiting the blender. The feeder refill occurs at t=100 seconds and immediately thereafter the concentration of component A entering the blender increases sharply. This increase in concentration is dampened due to the residence time distribution in the blender, as indicated by the broader concentration profile at the blender exit. Through the use of a reduced-order model it is thus possible to simulate the dynamic response of the continuous blending process to a transient disturbance.

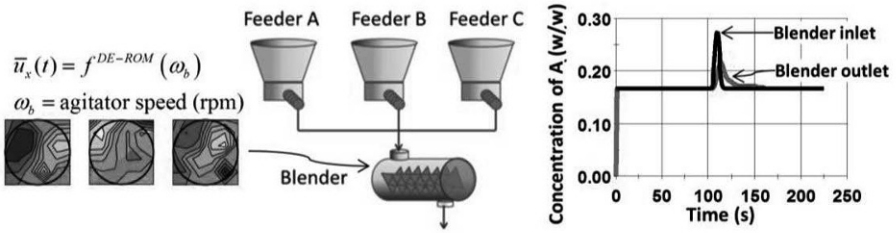

Figure 1: Flowsheet simulation for a continuous feeding and blending process. A discrete-element reduced-order model is used to obtain distributed axial velocity information in the blender.

3. Pharmaceutical process optimization

In the previous section it has been shown that flowsheet models can be developed to simulate solids-based pharmaceutical processes. While these models are useful for scenario analysis, they may not be well suited to applications requiring a large number of model evaluations. Integrated process models can incorporate tens of thousands of equations, making them difficult for deterministic optimization solvers to handle efficiently (Jones et al., 1998). In addition, the use of reduced-order models within flowsheet simulations can make it difficult to obtain gradient information. For both of the aforementioned reasons, surrogate-based optimization strategies may be needed to optimize processes that are described by integrated flowsheet models (Boukouvala & Ierapetritou, 2013).

Surrogate-based optimization, also referred to as black-box or response-surface optimization, describes the use of input-output mappings to approximate a complex process model followed by the use of this response surface for optimization purposes (Jones, 2001; Jones et al., 1998). The response surface is more computationally efficient to evaluate than the original flowsheet model and may also have other desirable properties such as smoothness. Surrogate-based strategies can be used to optimize objectives related to cost or profit for continuous pharmaceutical manufacturing processes. For instance, Boukouvala and Ierapetritou (Boukouvala & Ierapetritou, 2013) have demonstrated the use of a kriging response surface to minimize the cost of a continuous direct compression process for tablet manufacturing. Surrogate-based methods can be extended to constrained optimization problems by incorporating a black-box feasibility stage (Banerjee & Ierapetritou, 2002). In the context of pharmaceutical manufacturing, constraints can be placed on product quality and the feasibility test problem can be solved in order to identify boundaries of the process design space. Establishing design space is a particularly important aspect of process development given the current focus on quality by design (QbD) in the pharmaceutical industry(Yu, 2008).

Important considerations when implementing a surrogate-based optimization algorithm are:

- Selection of a reduced-order modeling method for surrogate development
- Balancing sample requirements with computational cost during model development
- Assurance of convergence to a global optimum

Surrogate models can be developed using a variety of methods including, but certainly not limited to, quadratic response surfaces, radial basis functions, artificial neural

networks and kriging interpolators (Jones, 2001). In the current work we will present surrogate-based strategies that employ kriging response surfaces. Kriging is selected for its ability to model highly nonlinear and dynamic processes, and due to the demonstrated efficacy of kriging in pharmaceutical process modeling (Boukouvala et al., 2010, 2011; Jia et al., 2009). In order to balance sampling requirements for surrogate-model development with the computational expense associated with large numbers model evaluations, many surrogate-based optimization algorithms include an iterative model improvement phase. The selection of additional samples during the model improvement phase can be guided by an expected improvement function, which seeks to identify samples that are likely to improve the current best value of the objective function given the accuracy, or lack thereof, of the surrogate model (Jones et al., 1998). Kriging response surfaces are well-suited to the use of an expected improvement function, as the variance of the kriging predictor can be estimated at each point on the response surface (Kleijnen, 2009). In the context of surrogate-based feasibility analysis, the modified expected improvement function introduced by Boukouvala and Ierapetritou (F. Boukouvala & M. G. Ierapetritou, 2012) can be implemented. This function guides sampling towards the boundaries of the feasible region in order to provide an accurate representation of black-box constraints with a limited number of model evaluations. Demonstrating convergence to a global solution is an ongoing challenge in the area of surrogate-based optimization. Several authors (Agarwal & Biegler, 2013; F. Boukouvala & M. Ierapetritou, 2012) have recommended the use of a surrogate-based global search coupled with a local trust-region search in the area surrounding the optimum to ensure global convergence. These methods can be applied to constrained global optimization problems, so they are appropriate for pharmaceutical applications which often involve strict constraints on product quality.

3.1. Surrogate-based feasibility analysis

For pharmaceutical applications, surrogate-based feasibility analysis is of particular interest, as it can be used to inform the selection of process design space. Feasibility analysis can be used to identify the limits within which acceptable product quality can be achieved. In general it is recommended for the design space to be well within those limits in order to ensure process robustness.(Chatterjee, 2012) Given the importance of selecting a design space conservatively relative to the boundaries of the feasible region, it may be desirable to explicitly account for surrogate model prediction error in pharmaceutical applications. When a surrogate model based on kriging is used, it is straightforward to account for model inaccuracy through the variance of the kriging predictor. This can be accomplished as shown in Figure 2, which depicts the feasible region for a roller compaction process with respect to the bulk density of the entering powder (ρin) and the inlet angle (θin), an estimated model parameter. The formulation of the feasibility test problem for this process has previously been described in the literature (F. Boukouvala & M. G. Ierapetritou, 2012; Hsu et al., 2010). In this case, the variance of the kriging predictor can be explicitly added to the feasibility function in order to ensure that the surrogate model is conservative relative to the original process model. This is shown in Figure 2, where the black line indicates the boundary of the feasible region obtained from the original process model and the boundary of the surrogate-based feasible region is shown in blue. Although the surrogate model is quite accurate, it is still possible for an infeasible point to be classified as feasible approximately 1 percent of the time, as established over a validation set of 10,000 samples. In order to avoid operating outside of the feasible region, the conservative

approximation of the feasible region is shown in red can be used. This approximation takes into account the variance of the kriging predictor and is always conservative relative to the original process model.

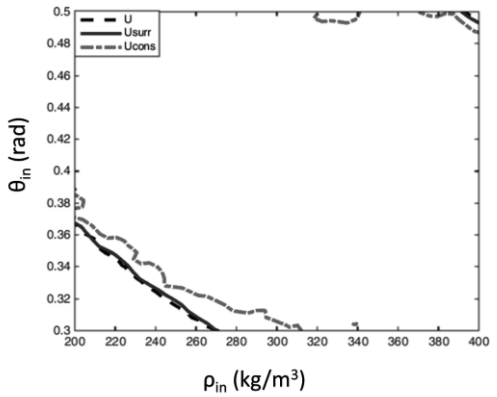

Figure 2: Surrogate-based feasibility analysis for a roller compaction process. The feasible region obtained from the original process model (U) is shown in black. The surrogate-based feasible region (Usurr) is given in blue. The conservative approximation of the feasible region (Ucons) is shown in red.

4. Conclusions and future perspectives

Recent advances in solids-based process modeling have made it possible to develop integrated process models for pharmaceutical applications. The use of reduced-order models can help to enhance the accuracy of these flowsheet simulations for pharmaceutical applications, as demonstrated by the case study in Figure 1. Flowsheet simulations have many potential industrial applications for pharmaceutical process development. Among these is the use of process models to guide design space selection. This requires the use of surrogate-based optimization methods, which can be applied to complex and computationally expensive process models.

The developments discussed in this work indicate the exciting potential for the implementation of modeling and optimization tools within the pharmaceutical industry. However there is still much work to be done in the area of pharmaceutical process modeling. For instance, models that can explicitly account for the effect of bulk material properties on the performance of solids-handling unit operations would improve the accuracy of pharmaceutical process models. Also, models that can better capture the dynamics of continuous processes, such as residence time distribution approaches, would improve the ability to model the response of continuous systems to transient disturbances. Within the area of surrogate-based optimization, there exist many ongoing challenges related to surrogate-model development and global algorithm convergence. Ongoing work to address these challenges can help to improve the solution speed and accuracy of optimization problems involving pharmaceutical flowsheet simulations.

Acknowledgements

The authors would like to acknowledge financial support from Bristol-Myers Squibb as well as from the Engineering Research Center for Structured Organic Particulate Systems at Rutgers University (NSF-0504497, NSF-ECC 0540855).

References

Agarwal, A., & Biegler, L. T. (2013). A trust-region framework for constrained optimization using reduced order modeling. Optim Eng, 14, 3-35.

Banerjee, I., & Ierapetritou, M. G. (2002). Design Optimization under Parametr Uncertainty for General Black-Box Models. Industrial & Engineering Chemistry Research, 41, 6687-6697.

Boukouvala, F., Chaudhury, A., Sen, M., Zhou, R. J., Mioduszewski, L., Ierapetritou, M. G., & Ramachandran, R. (2013). Computer-Aided Flowsheet Simulation of a Pharmaceutical Tablet Manufacturing Process Incorporating Wet Granulation. Journal of Pharmaceutical Innovation, 8, 11-27.

Boukouvala, F., Dubey, A., Vanarase, A., Ramachandran, R., Muzzio, F. J., & Ierapetritou, M. (2012). Computational Approaches for Studying the Granular Dynamics of Continuous Blending Processes, 2 – Population Balance and Data-Based Methods. Macromolecular Materials and Engineering, 297, 9-19.

Boukouvala, F., Gao, Y. J., Muzzio, F., & Ierapetritou, M. G. (2013). Reduced-order discrete element method modeling. Chemical Engineering Science, 95, 12-26.

Boukouvala, F., & Ierapetritou, M. (2012). Simulation-Based Derivative-Free Optimization for Computationally Expensive Function. In AIChE Annual Meeting. Pittsburgh, PA: AIChE.

Boukouvala, F., & Ierapetritou, M. G. (2012). Feasibility analysis of black-box processes using an adaptive sampling Kriging-based method. Computers & Chemical Engineering, 36, 358-368.

Boukouvala, F., & Ierapetritou, M. G. (2013). Surrogate-Based Optimization of Expensive Flowsheet Modeling for Continuous Pharmaceutical Manufacturing. Journal of Pharmaceutical Innovation, 8, 131-145.

Boukouvala, F., Muzzio, F. J., & Ierapetritou, M. G. (2010). Predictive Modeling of Pharmaceutical Processes with Missing and Noisy Data. AIChE Journal, 56, 2860-2872.

Boukouvala, F., Muzzio, F. J., & Ierapetritou, M. G. (2011). Dynamic Data-Driven Modeling of Pharmaceutical Processes. Industrial & Engineering Chemistry Research, 50, 6743-6754.

Boukouvala, F., Niotis, V., Ramachandran, R., Muzzio, F. J., & Ierapetritou, M. G. (2012). An integrated approach for dynamic flowsheet modeling and sensitivity analysis of a continuous tablet manufacturing process. Computers & Chemical Engineering, 42, 30-47.

Chatterjee, S. (2012). Design Space Considerations. In AAPS Annual Meeting. Chicago, Il.

Gernaey, K. V., Cervera-Padrell, A. E., & Woodley, J. M. (2012). A perspective on PSE in pharmaceutical process development and innovation. Computers & Chemical Engineering, 42, 15-29.

Hsu, S. H., Reklaitis, G. V., & Venkatasubramanian, V. (2010). Modeling and Control of Roller Compaction for Pharmaceutical Manufacturing. Part I: Process Dynamics and Control Framework. Journal of Pharmaceutical Innovation, 5, 14-23.

Jia, Z. Y., Davis, E., Muzzio, F. J., & Ierapetritou, M. G. (2009). Predictive Modeling for Pharmaceutical Processes Using Kriging and Response Surface. Journal of Pharmaceutical Innovation, 4, 174-186.

Jones, D. R. (2001). A taxonomy of global optimization methods based on response surfaces. Journal of Global Optimization, 21, 345-383.

Jones, D. R., Schonlau, M., & Welch, W. J. (1998). Efficient global optimization of expensive black-box functions. Journal of Global Optimization, 13, 455-492.

Ketterhagen, W. R., Ende, M. T. A., & Hancock, B. C. (2009). Process Modeling in the Pharmaceutical Industry using the Discrete Element Method. Journal of Pharmaceutical Sciences, 98, 442-470.

Kleijnen, J. P. C. (2009). Kriging metamodeling in simulation: A review. European Journal of Operational Research, 192, 707-716.

Marshall, C. L., Rajniak, P., & Matsoukas, T. (2013). Multi-component population balance modeling of granulation with continuous addition of binder. Powder Technology, 236, 211-220.

Muir Wood, D. (2008). Modelling granular materials: discontinuum-continuum. In J. F. Chen, J. Y. Ooi & J. G. Teng (Eds.), Structures and Granular Solids: From Scientific Principles to Engineering Applications. Leiden, The Netherlands: CRC Press/ Balkema.

Plumb, K. (2005). Continuous processing in the pharmaceutical industry - Changing the mind set. Chemical Engineering Research & Design, 83, 730-738.
Rogers, A., & Ierapetritou, M. G. (2014). Discrete element reduced-order modeling of dynamic particulate systems. AIChE Journal, 60, 3184-3194.
Yu, L. X. (2008). Pharmaceutical quality by design: product and process development, understanding, and control. Pharm Res, 25, 781-791.

Krist V. Gernaey, Jakob K. Huusom and Rafiqul Gani (Eds.), 12th International Symposium on Process Systems Engineering and 25th European Symposium on Computer Aided Process Engineering.
31 May – 4 June 2015, Copenhagen, Denmark

Process Technology Licensing: An Interface of Engineering and Business

Andreas Bode,[a*] Jose Castro-Arce,[b] Bernd Heida,[b] Carsten Henschel,[a] Achim Wechsung,[b] Justyna Wojcicka,[a]

[a]*BASF New Business GmbH, Benckiserplatz 1, 67059 Ludwigshafen, Germany*
[b]*BASF SE, Carl-Bosch-Strasse 38, 67056 Ludwigshafen, Germany*
andreas.bode@basf.com

Abstract

New technologies are developed at a high rate in many areas like in process industries. Basis for new technologies are inventions and innovations generating intellectual property rights. By licensing, permission is granted to others to use these rights under controlled circumstances. Technology licensing often includes not only patents but for example also know-how, design and trademarks.

Drivers for in- or out-licensing of process technologies are manifold. Some very important drivers include, reducing own development risks, speeding up commercialization, earning royalties or partnering with other companies, all of which are business reasons. Engineering know-how of the in-licensing party is necessary to assess the technology, the own development options, the fit within the companies' value chain, and foremost, to calculate the cost benefit using a new process technology. Relevant engineering know-how of the out-licensing party is in offering and selling the technology: engineers need to describe the advantages for licensees, design and optimize the process, or calculate potential license fees by analyzing the benefits of the technology for the licensee.

The licensing business requires continuous development of the licensed technology. Processes need to be analyzed and continuously improved. Specific and optimized designs for licensees are required based on the licensee's design or optimization targets and constraints. Examples from ongoing business will be used to describe the engineering-business-interface.

Keywords: Commercialization, Intellectual Property, optimization, process.

1. Introduction

Licensing is known to almost everyone from software licenses or from patent licensing. It is an important basis of different businesses and has become more popular and relevant within the last years: for example, royalties from patent licensing have increased in the US from US$15 billion in 1990 to more than $110 billion in 2000 (Poltorak and Lerner (2004)). Many petrochemical, chemical or pharmaceutical companies are active in the licensing business. Most universities are spending money for a technology transfer department trying to commercialize results of their employees, like chemical engineers, in different stages of technology development. Licensing as a business model is an interesting option to commercialize technologies especially if inventions are involved.

Commercialization of technology products, e.g. by licensing, is mainly relevant to engineers in Business-to-Business (B2B) relationships, where sellers and buyers are often engineers or other scientists, who mostly perceive marketing as a discipline of minor importance. But, due to the organizational realities, as well as market, technological and competitive uncertainties, the marketing concept and a modification and adaption of standard tools like the Marketing Mix are of high importance (Mohr et al (2005)), and marketing of technology products in B2B markets is a distinct discipline (Taylor (2013)). The characteristics of B2B markets are described for example by Hutt and Speh (2007), Homburg et al (2013) and Kotler and Keller (2009).
In Technology Licensing, engineers in business and technology development are working closely together forming the interface across which all relevant information is passed to achieve a successful commercialization with advantages for suppliers and customers. Characteristics of licensing and examples from the chemical industry are described.

2. What is Licensing?

A useful description is: "A license is, simply stated, permission to do something the granting party (the licensor) has the right to otherwise prohibit". (Poltorak and Lerner, 2004). In the case of intellectual property (IP), licensing is an agreement between the owner of IP and another party (the licensee) to use the licensed rights in exchange for compensation.
According to the World Intellectual Property Organisation WIPO, "Intellectual property (IP) refers to creations of the mind, such as inventions; literary and artistic works; designs; and symbols, names and images used in commerce. IP is protected in law by, for example, patents, copyright and trademarks, which enable people to earn recognition or financial benefit from what they invent or create. By striking the right balance between the interests of innovators and the wider public interest, the IP system aims to foster an environment in which creativity and innovation can flourish." (WIPO 2015)
Therefore, different forms of licensing are present in different markets, like

- Character and entertainment licensing,
- Corporate trademark and brand licensing,
- Fashion licensing - Designer fashion, names and brands,
- Sports licensing - Major sport leagues,
- Art licensing - Literary and artistic works, performances, broadcasts,
- Science & Industry - Scientific works, discoveries and any inventions in all fields of human endeavour.

The most relevant types of licensing are depicted in Figure 1: Cross-licensing – each party allows others to use its IP; Exclusive licensing – licensor provides the right to use IP only to one licensee exclusively; Non-exclusive licensing – licensor provides the right to use the same scope of IP to several licensees; Sub-licensing – is an agreement given by a licensee to a third party, under the rights of the licensee originally granted by the owner of IP to licensee.

3. Technology Licensing

Technology Licensing is a special form of IP licensing. "Technology can be defined broadly as "know-how," more specifically (with respect to a firm), as the information required to produce and/or sell a product or service." (Capon and Glazer (1987)). Often, know-how is patentable and patents can be licensed. Also, and important to technology

licensing, Know-How itself can be licensed requiring a confidentiality agreement between the supplier of know-how and the user. Technology licensing often includes a license to execute patents, use know-how received under confidentiality and use a registered trademark to sell the products.

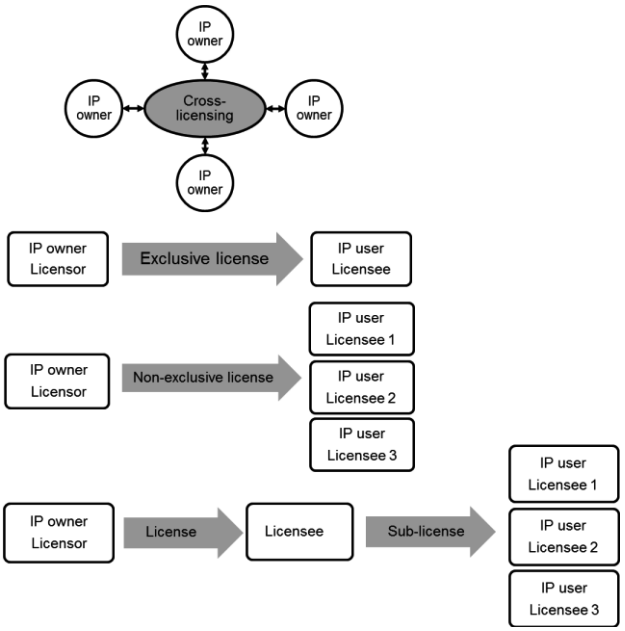

Figure 1: Types of licensing

Technology licensing is different depending on the status of technology development. Based on Megantz (1996), four stages of technology development can be described:

• **The basic-research results stage** – The technology is an early development by R&D specialists. Commercial implications are difficult to estimate.

• **The prototype-development stage** – Prototype units are generally available, but documentation is still preliminary. Market viability and manufacturability are to be proved.

• **The pilot production stage** –Technology has been proved in terms of functionality and manufacturability, but not in the market. There are sample units built and documentation is finished.

• **The industrial stage** – Last stage of the technology development, at which the technology has been successfully marketed. Several plants have been purchased and built. The economic viability and utility are proved.

In general, the more advanced the stage of technology development is, the easier it is to market it. Usually, the first stage at which a company can try to market the technology is prototype stage. However, the risk for customers is very high and not many of them decide to license technology which is only in the second stage of the development. Moreover, the more advanced technology is and the more often its performance has been proved, the higher value it has.

In the chemical industry, technology licensing has a long tradition. At the beginning of the 20th century, cross-licensing agreements between few dominating chemical companies have been used to increase market entry hurdles into the chemical market.

Technology licensing in this industry became popular after World War II, in order to make a profit from innovations. Since then the market for chemical technologies started to grow rapidly (Fosfuri (2006), Arora (1997)). Many petrochemical, chemical, pharmaceutical and engineering companies are active in licensing, some of which even with a focus on licensing. Even search engines for licensed technologies by chemical companies exist on the internet.
An overview of advantages and disadvantages of technology licensing is given Table 1.

Table 1: Advantages and disadvantages of technology licensing

	Advantages	Disadvantages
For Licensor	• Partnering/shared resources • Financial revenues from IP • No production investment • No production risk • Access to new markets • Some control of innovation and technology development	• Specialized personnel with technology and commercial skills • Less revenue than by own production • Potential competition by licensee • Commercial success depends on licensee
For Licensee	• Partnering/shared resources • Lower risk • Faster access to market • Access to new technologies for further development	• Technology not ready for commercial use • License fee as additional cost • Dependence on licensed technology

4. Examples from BASF

4.1. Hydrogen separation based on CELTEC®

BASF has a broad portfolio of research projects that ideally get transferred to prototype-development and pilot production before becoming an industrial product and solution. Due to technical and commercial challenges, only a fraction of research projects reach the pilot phase.
For more than 10 years, BASF had developed the CELTEC technology, a membrane electrode assembly (MEA) for high temperature polymer electrolyte membrane fuel cells based on a sol-gel-process for the membrane production (Seel et al (2009), Schmidt and Baurmeister (2007)). The MEA comprises of several components, namely a proton conducting membrane and two gas diffusion electrodes (Figure 2 left).
CELTEC can also be used for hydrogen separation. Hydrogen is catalytically activated at the anode and protons are transported through the membrane. The technology can increase the yield of chemical processes or recycle hydrogen in industrial processes.
After fuel cell customers qualified the product and started to order larger quantities, BASF invested in production capacities. A team of chemists and engineers set up a highly complex production process including the production of catalyst, polymer solution and membrane, coating and sintering processes, the automatized assembly of MEAs and a state-of-the art test and qualification facility (Figure 2 right).
Since market growth lagged behind expectations, BASF decided to terminate the MEA business. In order to secure the material supply for the fuel cell industry as well as for the hydrogen purification process, BASF approached potential licensees. Since no company could take over the complete production, the business was divided into three

main activities and products: membrane, gas diffusion electrode, and MEA. BASF initiated close links between the players of the value chain to promote the business success. The licensees agreed to pay a fix fee and royalties based on the quantity of the products sold. In return, they have access to the respective BASF patents, know how, and in the case of the membrane also to the production equipment.

- Membrane-license: The licensee took over the polymer solution and membrane casting line from BASF. During a technology transfer phase, the licensee was trained to run the sol-gel-process and meanwhile also produces a new generation membrane based on recent developments by BASF.
- Electrode-license: The gas diffusion electrodes (GDE) are responsible for the anode and the cathode reaction in the MEA. The production process is sensitive, and includes the production of catalyst, coating with microporous layer and with precious metal catalyst. BASF identified two licensees. One of them is the leading producer of electrodes for chlorine-alkaline electrolysis. The company acquired the former brand of the GDE and invested in coating equipment. The technology transfer covers all Standard Operating Procedures and Quality Processes, as well as practical support during coating and sintering runs. Additionally, a customer was asked to ensure the testing and qualification of the GDE.
- MEA-license: BASF found two companies to license the MEA-production technology. The licensees received all the necessary documentation, equipment specifications, quality procedures as well as a training session at the BASF MEA manual production facilities. BASF keeps the manual manufacturing lab for the time being to support licensees and to ensure the supply of large-area MEAs for hydrogen purification.

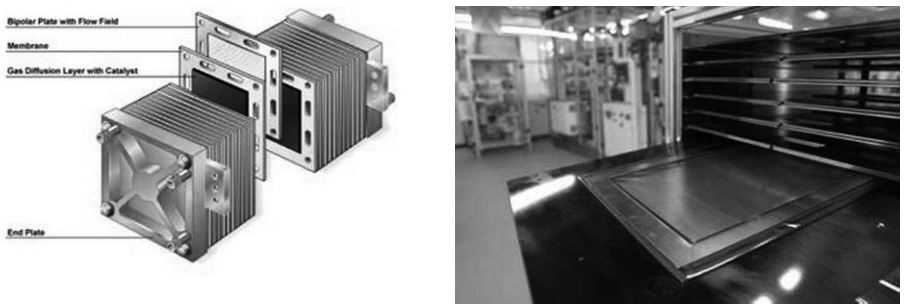

Figure 2: Left: Fuel Cell stack with MEAs (membrane, gas diffusion electrodes), separated by bipolar plates, endplates including current collector. Right: MEA production line

4.2. Selective hydrogenation SELOP®

An example of technology licensing on industrial stage is selective hydrogenation of hydrocarbon streams from steam crackers. Steam crackers are the main source of hydrocarbons for the chemical industry by cracking various hydrocarbon feedstocks to C1-C5+ streams serving as the basis for many value chains.

Depending on cracker feedstock and cracking conditions, the hydrocarbon streams are containing amounts of unwanted, for example unstable components, or compositions of isomers, that are not beneficial for downstream processing (Müller et al (1995). Catalysts have been developed during many years suitable for the different hydrocarbon chains and the specific selective hydrogenation purposes, e.g. hydrogenation of diolefins to olefins with low hydrogenation of olefins to paraffins or isomerization (Büchele et al (1996)). Selective hydrogenations have to be customized for each and every feedstock, steam cracker and site conditions based on different catalysts, reactor design and process flowsheets.
Technology licensing in the field means, to be able to select and supply the suitable catalyst and to design the optimum process flowsheet for the customer. Technology licensing in a mature industry often is not focused on patents, but more on know-how, that is only supplied to the licensee under confidentiality. A key success factor for licensing is, to provide know-how on the whole process in design, construction, start-up and operations. But, continuous development of such technology is also required to stay competitive.

4.3. Butadiene extraction

Butadiene is the raw material for many elastomers, ABS (acrylonitrile butadiene styrene polymer), in low quantities for nylon and few others. It is used in the industry since around 1930. Butadiene is mainly produced from liquid cracker's C4 fraction, but also from butane or butene dehydrogenation.
BASF is licensing a process for extractive distillation of butadiene based on the solvent N-methylpyrolidone (NMP). Other important solvents in the market are dimethylformamide and acetonitrile. The BASF process is successfully marketed for around 50 years and continuously improved to deliver economical and ecological benefits to the customer (Heida 2007). Improvements for example are made to increase capacity based on new distillation column packing (Hugo et al (2011)).
All technology licensors strive to have their technology recognised in the market as BAT (best available technology). Getting there requires a good invention or innovation, entrepreneurship and most of all a willingness to accept risk. Staying there requires to further invest in R&D over an extended period of time and to integrate key lessons learned or findings from all sources including licensees.

5. The roles of chemical engineers and process optimization in process technology licensing businesses

Some key factors for successful technology licensing businesses are, based on evaluation of several studies and own experience, market, competitor and technology evaluation, choice of partners, uniqueness of technology, unique selling proposition, customized design, service, continuous development, IP rights, marketing strategy, negotiation process and agreement conditions.
Engineers are playing a key role in process technology licensing since they are involved from the early beginning of technology development until a phase out of such technology in all of above mentioned key factors. Not only are engineers involved in classical engineering task like process R&D, process design and optimization, but also, they are involved in business tasks like identifying market need, market segmentation, set-up of business model, strategy development, and operative strategy implementation

in marketing and sales. Typical tasks in in-licensing and out-licensing as listed in Table 2 are corresponding and experience in one area greatly facilitates activities in the other. All of these tasks directly relate to the marketing and sales or purchasing of the technology license. Therefore, engineers usually are active in engineering as well as in marketing and sales to enable educated decisions to the benefit of supplier and customer.

Table 2: Typical engineering task for out- and in-licensing of process technologies

Out-licensing	In-licensing
• Offering and selling the technology: Engineers need to describe the advantages for licensees • Design and optimize the process • IP-generation • Calculate potential license fees by analyzing the benefits of the technology for the licensee	• Assess the technology • Evaluate own development options • Analyse technology fit within the companies' value chain • Calculate the cost benefit using the process technology

As described by examples in Section 4, one key factor for successful technology licensing is customization of the technology. Typically, boundary conditions and constraints for implementing the technology at customers differ in certain ranges and are given as so called battery limits. The battery limit conditions are used to design the process technology. In some cases, the realization of a technology requires equipment installation outside battery limits at the customer, creating additional investments. One important task for the engineer therefore is to optimize the technology in a way to minimize the total investment and at the same time keep production cost low so that the investment stays not only profitable but is more profitable than competitor's technology. At the same time, safety and environmental features of the technology and of the products produced with the technology have to comply with highest standards. Process design and optimization therefore are crucial elements in process technology licensing and need to take multiple objectives into account.

In recent years, process optimization underwent a strong development (Biegler (2014), Floudas and Gounaris (2009)). Methods and tools are slowly becoming implemented in industry. But currently optimization tools are still non-standard, for example due to parallel catalyst and process development or due to complex changes in battery limit conditions during the project planning phase so that the flow sheet has to be adapted quickly. But, there is implementation in industry ongoing (Asprion et al (2014), Burger et al (2014)). It can be assumed that the methods and tools will be further improved with regards to optimization of multi-objectives, flow-sheet, safety and environmental performance of process and products, but also with user friendliness.

6. Conclusions

Licensing is an interesting option to commercialize existing and new technologies, incremental and breakthrough innovations. Chemical engineers play key roles in licensing in the chemical industry in R&D, Engineering and in marketing and sales. Successful technology licensing requires specialized and dedicated marketing and direct interface of R&D, engineering and marketing with the customer.

References

Arora, A. (1997): Patents, licensing, and market structure in the chemical industry, in Research Policy, Vol. 26 (1997), No. 4 – 5, pp. 391 – 403.

Asprion, N.; Benfer, R.; Blagov, S.; Böttcher, R.; Bortz, M.; Welke, R.; Burger. J.; von Harbou, E.; Küfer, K.-H.; Hasse, H. (2014): INES-Interface between Experiments and Simulation, Proceedings of the 24th S^{ym}posium on Computer Aided Process Engineering – ESCAPE 24, June 15-18, 2014, Budapest, Hungary

Biegler, L.T. (2014): Recent Advances in Chemical Process Optimization. Chemie Ingenieur Technik, Volume 86, Issue 7, pages 943–952, July, 2014

Büchele, W.; Roos. H.; Wanjek, H.; Müller, H.-J. (1996): Catalyst research – one of the cornerstones of modern chemical production. Catalysis Today 30 (1996) 33-39

Burger. J.; Asprion, N.; Blagov, S.; Böttcher, R.; Nowak, U.; Bortz, M.; Welke, R.; Küfer, K.-H.; Hasse, H. (2014): Multi-Objective Optimization and Decision Support in Process Engineering – Implementation and Applicattion. Chemie Ingenieur Technik 2014, 86, No. 7, 1-9

Capon, N.; Glazer, R. (1987): Marketing and Technology: A Strategic Coalignment, in Journal of Marketing, Vol. 51 (1987), No. 3, pp. 1 – 14.

Fosfuri, A. (2006): The Licensing Dilemma: Understanding the Determinants of the Rate of Technology Licensing, in Strategic Management Journal, Vol. 27 (2006), No. 12, pp. 1141 – 1158.

Heida, B. (2007): Solvent swap: more capacity, greener process. The Chemical Engineer, September 2007

Hugo, R.; Heida, B.; Metzen, B.; Peschel, W. (2011): Beyond classics – new technology to boost capacity in a butadiene unit. 23rd Ethylene Producers Conference, Chicago, IL, USA, March 13-17, 2011

Homburg, C.; Kuester, S.; Krohmer, H. (2013): Marketing management: a contemporary perspective, 2nd Edition, London: McGraw-Hill Higher Education, 2013

Hutt, M. D.; Speh, T. W. (2007): Business Marketing Management: B2B, 9th Edition, Mason, Ohio: Thomson South-Western, 2007.

Kotler, P.; Keller, K. L. (2009): Marketing management, 13th Edition, New Jersey: Pearson Prentice Hall, 2009.

Megantz, R. C. (1996): How to License Technology, New York et al: John Wiley & Sons, Inc., 1996.

Mohr, J; Sengupta, S.; Slater, S. (2005): Marketing of high-technology products and innovations, 2nd Edition, New Jersey: Pearson Prentice Hall, 2005.

Müller, H.-J.; Herion, C.; Meyer, G.; Polanek, P.; Laib, H. (1995): The SELOP-process: BASF-technology for hydrogenations in the steamcracker downstream treatment. Petroleum and Coal, Vol. 37, No. 4, 34-44

Schmidt. T.J.; Baurmeister, J. (2007): Properties of high-temperature PEFC Celtec®-P1000 MEAs in start/stop operation mode. In: Journal of Power Sources 176 (2008), p. 428-434

Seel, D.C.; Benicewicz, B.C.; Xiao, L. and Schmidt, T.J. (2009): High temperature polybenzimidazole-based membranes. In Handbook of Fuel Cells – Fundamentals, Technology and Applications. Edited by Vielstich, Yokokawa, Gasteiger: Volume 5: Advances in Electrocatalysis, Materials, Diagnostids and Durability. 2009 Wiley,

Taylor, H. (2013): B2B Technology Marketing, Los Angeles: Taylor Market Intelligence, Inc., 2013.

Poltorak, A.I.; Lerner, P. J. (2004): Essentials of Licensing Intellectual Property, New Jersey: John Wiley & Sons, Inc., 2004.

World Intellectual Property Organisation http://www.wipo.int/about-ip/en/, January 2015.

Krist V. Gernaey, Jakob K. Huusom and Rafiqul Gani (Eds.), 12th International Symposium on Process Systems Engineering and 25th European Symposium on Computer Aided Process Engineering.
31 May - 4 June 2015, Copenhagen, Denmark.

Simple Rules for Economic Plantwide Control

Vladimiros Minasidis[a], Sigurd Skogestad[a*] and Nitin Kaistha[b]

[a]*Department of Chemical Engineering, Norwegian University of Science and Technology, 7491 Trondheim, Norway*
[b]*Department of Chemical Engineering, Indian Institute of Technology, 208016 Kanpur, India*
**skoge@ntnu.no*

Abstract

In this work, we consider the systematic economic plantwide control design procedure proposed by Skogestad (2004) and from this we derive practical rules that can be used to devise close-to-optimal control structures based on engineering insight. We attempt to present these rules in an easy-to-understand fashion and exemplify them on a simple but quite famous reactor-separator-recycle plant case study. We successfully demonstrate that while Skogestad's procedure requires an optimization of the plant model under various disturbances in order to be fully utilized, using its practical rules, combined with a good engineering insight of the process, can facilitate the design of a close-to-optimal control structure by suggesting what should be controlled and how.

Keywords: Self-Optimizing Control, Economic Plantwide Control, Advanced Process Control

1. Introduction

Designing a control structure for an entire chemical plant, that ensures safe and stable economic operation, is known as economic plantwide control. Energy integration, smaller in-process inventories and material recycles, all contribute to an increase of operational complexities and thus a plantwide perspective becomes crucial when designing control systems for such plants. Many different plantwide control methodologies have been proposed during the last decades, nonetheless, they can all be classified based on their approach. Vasudevan and Rangaiah (2011) suggest the following classification: mathematical, optimization-based, heuristic and mixed approaches. The first two approaches lead in many cases to an optimal control structure design but often require an optimization of rigorous process models in order to be fully utilized. Often, the entire plant model is not available and it is too time consuming to develop one. More seriously, the resulting mathematical and optimization problems are often difficult to formulate and even more difficult to solve. The alternative in such cases, is to attempt to apply the practical rules derived from heuristic/mixed procedures, that require only a good engineering insight in order to design a close-to-optimal control structure. In addition, these practical guidelines are usually easier to understand, thus easier to implement and support without requiring high expertise (Konda, 2005).

Many such practical rules that either focus on a complete plantwide control structure design or its specific parts, have been proposed in scientific literature. Just to mention a few, starting with the pioneering work of Page S. Buckley (1964), are: (Price et al., 1994), (Luyben et al., 1997), (Skogestad, 2004), (Aske et al., 2007). It should be noted that, Skogestad (2004) procedure is inspired by Luyben et al. (1997) procedure, but it clearly distinguishes between economic control for economic performance and regulatory control for stability and robustness and in order to emphasize this distinction, it is referred to as Economic Plantwide Control. For a more detailed overview of

plantwide control design methodologies we refer the reader to (Larsson and Skogestad, 2000) and (Vasudevan and Rangaiah, 2012).

When examining the suggested practical guidelines, we often find that the assumptions behind them are not stated clearly, leading to the likelihood of non-optimal control strategies. For example, the most famous of Luybens laws *"Fix a Flow in Every Recycle Loop"*, when applied to certain systems, can lead to poor economic performance and a small feasible range. The correct interpretation could be that the flow should only be fixed on a fast time scale. If it is indeed truly fixed, then it should involve moving the throughput manipulator to this location. This motivates this work's attempt to present and justify the practical rules derived from Skogestad's procedure in an easy-to-understand fashion .

In this work, we briefly present the systematic plantwide control design procedure proposed by Skogestad (2004) in a simple Q&A form. We present its practical guidelines, with emphasis on those rules that can be used based on engineering insight and propose an additional rule, that is stated as follows: "*Never try to control a cost function*". We apply the presented rules and demonstrate their effectiveness on a simple but quite famous reactor-separator-recycle case study (T. Larsson et al., 2003). We conclude that, while Skogestad's procedure requires an optimization of the plant model under various disturbances in order to be fully utilized, using its practical rules, combined with a good engineering insight of the process, can facilitate the design of a close-to-optimal control structure by suggesting what should be controlled and how.

2. Economic Plantwide Control

2.1. Preliminaries

The definitions and terms presented here are based on terminology used in (Larsson and Skogestad, 2000) and (Skogestad, 2012), unless otherwise noted. A typical hierarchical decomposition of the plantwide control structure is depicted in Figure 1a. The lowest layer, the regulatory (or stabilizing) layer, consists usually of single loop (decentralized) PID controllers and operates in a time scale of seconds. Next, the supervisory (or advanced, or economic) layer, which provides setpoints to the regulatory layer, may consist of a multivariable controller (MPC) or a mix of various decentralized "advanced" controllers, including PID controllers selectors, feedforward controllers and so on. We define some of the terms extensively used in this work, as follows:
Controlled variable (CV) is a variable with a given setpoint.
Manupulated variable (MV) is a degree of freedom used by the controller to control a CV.
Pairing is a selection of a MV to be used to control a specific CV.
Control structure design deals with the structural decisions of identification/selection of the following sets: controlled variables $\{\boldsymbol{CV}_1\boldsymbol{CV}_2\}$, physical manipulated variables $\{\boldsymbol{u_D}\}$, measurements $\{\boldsymbol{y_m}\}$, control pairings $\{\boldsymbol{H},\boldsymbol{H_2}\}$ and controller algorithms for the layers depicted in Figure 1a.
Plantwide control is a control philosophy of the overall plant with emphasis on the structural decisions and is used interchangeably with the term "control structure design".
Self-optimizing variables are controlled variables for which the optimal setpoints $\boldsymbol{CV}_{1s}$ can be kept relatively unchanged, i.e. their optimal values are insensitive to disturbances, at least on a fast time scale.
Optimal control structure is a control structure that achieves economically optimal -in addition to safe and stable- plant operation.
Rule in this work means a practical guideline, and both terms are used interchangeably.

Before describing the procedure for economic plantwide control it should be noted that, in general, it is simple to define the economic cost function J for a steady-state optimal operation of chemical processes. Since the plant has already been built and the operators are already at the site, there are no costs related to capital costs or other fixed costs. The cost function can be expressed as

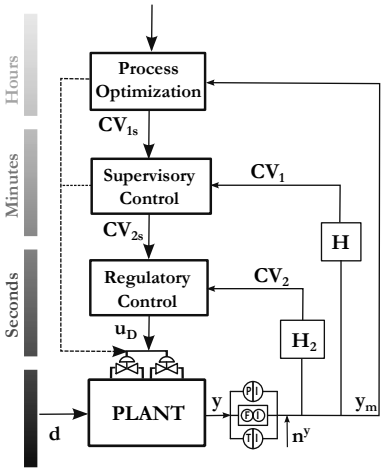

(a) Hierarchical time-scale decomposition of the control structure.

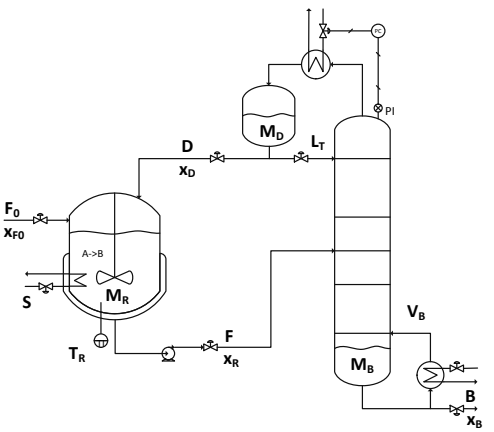

(b) Reactor-separator-recycle process flow diagram

$J = p_F F + p_Q Q - p_P P$, where: p is the corresponding price, $p_F F$ is the sum of the costs of all the feed streams, $p_Q Q$ is the cost of all utilities (including energy) and $p_P P$ is the sum of the values of all products. In this context, we can define two main operational modes: **Mode 1** (nominal operation) where the feeds are given, so the term $p_F F$ is fixed. Furthermore, because of given product specifications, this may imply that the product rates P are also fixed. So, to minimize plant operation cost, we want to minimize the utility costs $p_Q Q$. This mode often has an unconstrained optimum, since there is a tradeoff between using too much or too little energy. This is the case for our simple example in Mode 1, where the optimal operation is the same as minimizing $J = V_B$, since the energy (boilup) to the column is the only utility; **Mode 2** (maximum throughput) that has high product prices and low energy prices, so the optimal operation corresponds to maximizing the product rate P. In general, we have more active constraints in Mode 2 than in Mode 1.

2.2. Economic Plantwide Control description

Any methodology that aims to facilitate the design of an optimal control structure, based on the hierarchical decomposition depicted on Figure 1a, should, independent of the approach, at least consider the following structural decisions:

1. **Decision 1:** Select primary controlled variables $\boldsymbol{CV}_1$ for the supervisory control layer or select $\boldsymbol{H}$. The setpoints $\boldsymbol{CV}_{1s}$ link the process optimization with supervisory control layer.
2. **Decision 2:** Select secondary controlled variables $\boldsymbol{CV}_2$ for the regulatory control layer or select $\boldsymbol{H_2}$. The setpoints $\boldsymbol{CV}_{2s}$ link the supervisory and regulatory control layers.
3. **Decision 3:** Locate the throughput manipulator (TPM) location. This is an important step, since it links the top-down and the bottom-up parts of the economic plantwide control.
4. **Decision 4:** Select pairings for the stabilizing layer controlled variables $[\boldsymbol{CV}_2 \leftrightarrow \boldsymbol{u}_D]$

Furthermore, the operational goals should be defined clearly and if possible separated into: i) economic objective ii) stabilization/regulation objectives. One reason for the separation is, that it is very difficult to measure them in the same units, for example, how much is a gain margin increase from 2 to 3 worth in dollars?

Skogestad's procedure clearly distinguishes between the economic control and regulatory control and decomposes the structural decisions, into two parts: the ***Top-down*** part, which attempts to find a slow-time-scale supervisory control structure that achieves a close-to-optimal economic

operation and the ***Bottom - up*** part that aims to design a fast-time-scale regulatory control structure that is stable and robust and works under all the conditions imposed by the economic supervisory layer. A brief description of the procedure is presented in Table 1 in the form of typical structural decisions (Q) and how it attempts to address those in a systematic manner (A).

Note that, the structural decisions related to the parings (steps *S5, S5, S6*) could in theory be avoided, if we used a single multivariable controller (e.g. MPC). Furthermore, the choice of economic controlled variables $\boldsymbol{CV}_1$ (related to steps S3, S7) could also, in theory, be avoided, if we used a single dynamic real-time optimizer, which combined optimization and control. However, designing, maintaining and tuning such a controller can be too difficult and too expensive for a large plant.

Top-down part	*(mainly steady-state)*
Step S1:	**Define the operational objectives (economics) and constraints.**
Q:	*What are the overall economic objectives for operation?*
A:	*Identify a scalar cost function J and the operational constraints. Identify the dynamic degrees of freedom (DOFs)* $\boldsymbol{u_D}$*. Determine how many steady state DOFs* n_{SS} *are available. Identify the expected economic disturbances* $\boldsymbol{d}$ *and and their range.*
Step S2:	**Determine the steady-state optimal operation**
Q:	*What are the operational conditions for an optimal steady state operation?*
A:	*Determine the optimal operation and, in particular, the optimal constraints regions (regions in the disturbance space with the same active constraints) for the expected disturbance* $\boldsymbol{d}$ *ranges*
Step S3:	**Select primary (economic) controlled variables** (Decision 1)
Q:	*What should be controlled to maintain a close-to-optimal economic operation in-spite of disturbances ?*
A:	*Identify the candidate measurements* $\boldsymbol{y_m}$ *and select the primary controlled variables such as* $\boldsymbol{y_m} \supset \boldsymbol{CV}_1 = \boldsymbol{H y_m}$*, where* $\boldsymbol{H}$ *is a selection matrix. The set* $\boldsymbol{CV_1}$ *should include active constraints* $\boldsymbol{A_C}$ *and if* $\#\boldsymbol{A_C} < n_{SS}$*, a* n_{SS} *number of "self-optimizing variables"* $\boldsymbol{CV}_{soc}$ *should be identified and included in* $\boldsymbol{CV}_1$*.*
Step S4:	**Select the location of throughput manipulator (TPM)** (Decision 3)
Q:	*Where should the plant's "gas pedal" be located ?*
A:	*The location of the TPM is a dynamic issue but it may have significant economic implications and, therefore, is located in the Top-down part. For TPM location see Rules 4 and 5.*
Bottom-up part	*(mainly dynamic)*
Step S5:	**Select the control structure for the Regulatory Control layer.** (Decisions 2 and 4)
Q:	*What variables should be controlled to stabilize the operation and how ?*
A:	*Select all the "drifting" process variables* $\boldsymbol{CV}_2 = \boldsymbol{H_2 y}$ *that need to be controlled to ensure safe and stable plant operation e.g. inventories, pressures, temperatures. The inventory control structure should be designed starting from the TPM location and following the radiating rule to achieve local consistency. Usually single loop (decentralized) PID controllers are used in this layer.*
Step S6:	**Select the control structure for the Supervisory Control layer.**
Q:	*How should the economic controlled variables* $\boldsymbol{CV}_1$ *be controlled ?*
A:	*The primary economic variables* $\boldsymbol{CV}_1$ *should be controlled at this layer, using the setpoints to the regulatory layer in addition to any unused valves. Two types of controllers are usually selected for this layer: multivariable controller (e.g. MPC) or a mix of various decentralized "advanced" controllers, including PID controllers selectors, feedforward controllers and so on.*
Step S7:	**Select the control structure for the Real-Time Optimization layer.**
Q:	*How often should the optimal setpoints for the economic controlled variables* $\boldsymbol{CV}_1$ *and their pairings be updated ?*
A:	*This layer should re-optimize the setpoints for* $\boldsymbol{CV}_1$ *and track any changes in the set of active constraints, in order to update the economic control structure, if necessary. A limiting factor for the updating frequency is the requirement that the plant has to settle, before the re-optimization problem can be solved. A successful mapping of the active constraints regions for the entire range of expected disturbances, combined with set of good self-optimizing variables, may remove the need for having this layer.*

Table 1: Economic Plantwide Control design procedure. The nomenclature used here is depicted in Figure 1a. For more details we refer the reader to (Skogestad, 2012)

3. Practical rules

Here we present a set of simple rules for economic plantwide control to facilitate a close-to-optimal control structure design in cases where the optimization of the plant model is not possible. Due to space limitations, only short justifications for the rules are given and, in addition, we attempt to exemplify the rules, when possible, using the reactor-separator-recycle process (Figure 1b). Note that, the rules may be conflicting in some cases and in such cases, human reasoning is strongly advised.

Rules for Step S3: Selection of primary (economic) controlled variables, $\boldsymbol{CV}_1$

Rule 1: *Control the active constraints.*
In general, process optimization is required to determine the active constraints, but in many cases these can be identified based on a good process knowledge and engineering insight. Here is one useful rule:

Rule 1A: The purity constraint of the valuable product is always active and should be controlled.
This follows, because we want to maximize the amount of valuable product and avoid product "give away" (Jacobsen and Skogestad, 2011). Thus, we should always control the purity of the valuable product at its specification. For "cheap" products we may want to overpurify (purity constraint may not be active) because this may reduce the loss of a more valuable component.
In other cases, we must rely on our process knowledge and engineering insight. For reactors with simple kinetics, we usually find that, the reaction and conversion rates are maximized by operating at maximum temperature and maximum volume (liquid phase reactor). For gas phase reactor, high pressure may increase the reaction rate, but this must be balanced against the compression costs.

Rule 2: *(for remaining unconstrained steady-state degrees of freedom, if any): Control the "self-optimizing" variables.*
This choice is usually not obvious, as there may be several alternatives, so this rule is in itself not very helpful. The ideal self-optimizing variable, at least, if it can be measured accurately, is the gradient of the cost function J_u, which should be zero for any disturbance. Unfortunately, it is rarely possible to measure this variable directly and the "self-optimizing" variable may be viewed as an estimate of the gradient J_u. The two main properties of a good "self-optimizing" variable are: (1) its optimal value is insensitive to disturbances (such that $\boldsymbol{F} = \frac{\Delta \boldsymbol{CV}_{1,opt}}{\Delta \boldsymbol{d}}$ is small) and (2) it is sensitive to the plant inputs (so the process scaled gain $\boldsymbol{G} = \frac{\Delta \boldsymbol{CV}_1}{\Delta \boldsymbol{u}}$ is large). The following rule shows how to combine the two desired properties:
Rule 2A: Select the set $\boldsymbol{CV}_1$ such that the ratio $\boldsymbol{G}^{-1}\boldsymbol{F}$ is minimized.
This rule is often called the "maximum scaled gain rule". For proof, see (Halvorsen et al., 2003).

Rule 3: *(for remaining unconstrained steady-state degrees of freedom, if any): Never try to control the cost function J (or any other variable that reaches a maximum or minimum at the optimal operating point).*
First, the cost function J has no sensitivity to the plant inputs at the optimal point and so $\boldsymbol{G} = 0$, which violates Rule 2A. Second, if we specify J lower than its optimal value, then clearly, the operation will be infeasible, see Figure 2a. From Figure 2a, we can also see that specifying J higher than its optimal value is problematic, as we have multiplicity of solutions. As mentioned above, rather controlling the cost J, we should control its gradient, J_u.

Rules for Step S4: Location of throughput manipulator (TPM)

Rule 4: *Locate the TPM close to the process bottleneck.*

The justification for this rule is to take advantage of the large economic benefits of maximizing production in times when product prices are high relative to feed and energy costs (**Mode 2**). To maximize the production rate, one needs to achieve tight control of the active constraints, in particular, of the bottleneck, which is defined as the last constraint to become active when increasing the throughput rate. For more details, we refer the reader to (Jagtap et al., 2013).

Rule 5: *(for processes with recycle) Locate the TPM inside the recycle loop.*
The point is to avoid "overfeeding" the recycle loop which may easily occur if we operate close to the throughput where "snowballing" in the recycle loop occurs. This is a restatement of Luyben's rule *"Fix a Flow in Every Recycle Loop"* (Luyben et al., 1997). From this perspective, snowballing can be thought of as the dynamic consequence of operating close to a bottleneck which is within a recycle system. In many cases, the process bottleneck is located inside the recycle loop and Rules 4 and 5 give the same result.

Rules for Step S5: Structure of regulatory control layer.

Rule 6: *Arrange the inventory control loops (for level, pressures, etc.) around the TPM location according to the radiation rule.*
The radiation rule (Price et al., 1994), says that, the inventory loops upstream of the TPM location must be arranged opposite of flow direction. For flow downstream of TPM location it must be arranged in the same direction. This ensures "local consistency" i.e. all inventories are controlled by their local in or outflows.

Rule 7: *Select "sensitive/drifting" variables as controlled variables $\boldsymbol{CV}_2$ for regulatory control.*
This will generally include inventories (levels and pressures), plus certain other drifting (integrating) variables, for example, a reactor temperature or a sensitive temperature in a distillation column. This ensures "stable operation, as seen from an operator's point of view.

Some component inventories may also need to be controlled, especially for recycle systems. For example, according to *"Down's drill"* one must make sure that all component inventories are "self-regulated" by flows out of the system or by removal by reactions, otherwise their composition may need to be controlled (Luyben, 1999).

Rule 8: *Economically important active constraints, a subset of $\boldsymbol{A_C}$, should be selected as controlled variables $\boldsymbol{CV}_2$ in the regulatory layer.*
Economic variables $\boldsymbol{CV}_1$ are generally controlled in the supervisory layer. Moving them to the faster regulatory layer may ensure tighter control with a smaller backoff. The backoff is the difference between the actual average value (setpoint) and the optimal value (constraint).

Rule 9: *"Pair-close" rule: The pairings should be selected such that, effective delays and loop interactions are minimal.*

Rule 10: *: Avoid using MVs that may optimally saturate (at steady state) to control CVs in $\boldsymbol{CV}_2$.*
The reason is that we want to avoid re-configuring the regulatory control layer. To follow this rule, one needs to consider also other regions of operation than the nominal, for example, operating at maximum capacity (**Mode 2**) where we usually have more active constraints.

Rules for Step S6: Structure of supervisory control layer.

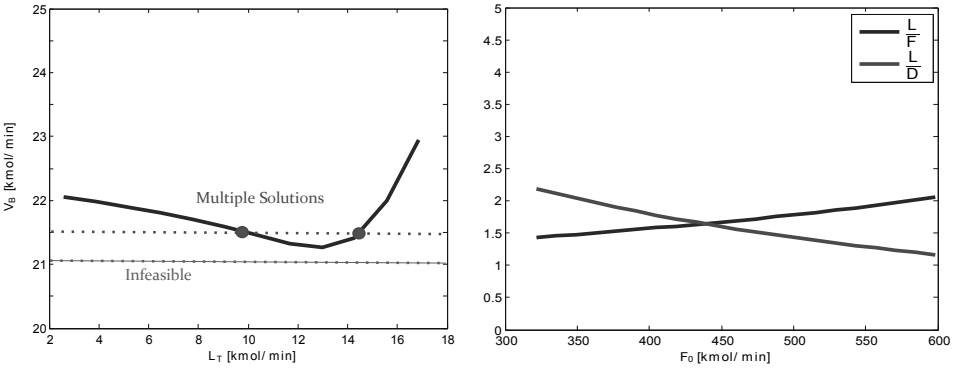

(a) Steady state boilup flow rates V_B w.r.t. reflux flow rate L_T changes while all the active constraints are kept constant

(b) Optimal steady state of suggested $\boldsymbol{CV}_{soc}$ candidates $\{\frac{L_T}{F}, \frac{L_T}{D}\}$ w.r.t. feed flow F_0 changes ± 30 percent while all the active constraints are kept constant

Rule 11: *MVs that may optimally saturate (at steady state) should be paired with the subset of* $\boldsymbol{CV}_1$ *that may be given up.*
This rule applies for cases when we use decentralized control in the supervisory layer and we want to avoid reconfiguration of loops. The rule follows because when a MV optimally saturates, then, there will be one less degree of freedom, so there will be a CV_1 which may be given up without any economic loss. The rule should be considered together with rule 10.

4. Case study

4.1. Process description

In this section we consider a quite famous example of a chemical plant that consists of a reactor, a separator and a recycle stream. For this case study, all the operational parameters have been taken from (Larsson et al., 2003). The process flow diagram of the process and all the required nomenclature are depicted in Figure 1b. An irreversible first order elementary reaction $A \rightarrow B$ takes place in continuous stirred tank reactor (CSTR). The effluent of the reactor, which consist of a solution of A and B is sent to fractional distillation column, where the products are separated and the distillate stream (mostly component A), is recycled back to the CSTR.

4.2. Applying the practical rules

S1: Assuming that the plant, depending on market conditions, will be switching between Mode 1 and 2, the objective for Mode 1 is to minimize energy consumption $J = V_B$ and for Mode 2, to maximize the production $J = -B$. The operational constraints are: $M_R \leq 2800\,kmol$, $x_B \leq 0.0105$, $V_B \leq 1500\,mol/min$, $T_R \leq 600K$. Assuming that the pressure in the column is kept constant by the condenser flow, the process has 7 DOFs: $\boldsymbol{u_D} = [L_T, V_B, D, B, F, F_0, S]$. Only two DOFs from $[L_T, V_B, D, B]$ can be set independently at a steady state, which means $n_{SS} = 5$ steady state DOFs.
S2: We assume, based on our engineering insight and *Rule 1A*, that the following constraints will be most probably be active $\boldsymbol{A_C} = [M_R, x_B, T_R]$.
S3: In addition to a DOF consumed by the TPM, all $\boldsymbol{A_C}$ need to be controlled, thus 1 DOF is left that can be used to improve the operational economics. Some candidates for $\boldsymbol{CV}_{soc}$ are $\{\frac{L_T}{F}, \frac{L_T}{D}\}$.
S4: The last constraint that becomes active in Mode 2 is V_B. In addition, there are two recycle loops in the process (one is the column itself) and V_B is inside both of the loops. According to the *Rule 4 and 5* the best candidate for TPM location is V_B.

S5: The selection of V_B as the TPM leads to the following pairings $(B \rightarrow M_B), (D \rightarrow M_D), (F_0 \rightarrow M_R), (S \rightarrow T_R)$ according to Rules 6 or 9. In order to get a tighter control of x_B and to stabilize the composition profile in the column, we can cascade the x_B control with some sensitive column temperature T_C such that $(F \rightarrow T_C \rightarrow x_B)$ according to Rule 7 and 8. The suggested pairings may remove the need to re-configure the structure when switching from one mode to another.
S6: The only available DOF for this layer is L_T, so it needs to be used to control one of the suggested $\boldsymbol{CV}_{soc} = \{\frac{L_T}{F}, \frac{L_T}{D}\}$. A preferable controller in this case would be a single loop PID.
S7: Assuming that the assumptions for the active constraints set and the "self-optimizing" controlled variable are correct, the additional benefits from having this layer would be quite limited.

5. Results and Conclusions

The validity of our practical analysis is checked using the optimization results presented in (Larsson et al., 2003). The practical choice of active constraints is in agreement with Larsson's findings. The optimal sensitivity of the $\boldsymbol{CV}_{soc}$ w.r.t to disturbances is depicted in Figure 2b, which shows that the optimal values of the suggested CVs change very little with quite large disturbances thus qualifying them as good "self-optimizing" variables. The dynamic performance of the plant control structure is omitted due to space limitations.

In conclusion, despite the fact that to fully utilize the true potential of the economic plantwide control procedure a series of plant model optimizations is required, the derived practical guidelines can be used to decide on "what to control and how" in order to improve the economics of the plant operation, even if the model is not available or optimization of the plant model is difficult.

References

Aske, E., Skogestad, S., Strand, S., 2007. Throughput maximization by improved bottleneck control. In: Dynamics and Control of Process Systems (DYCOPS), Volume 8, Part 1, IFAC Symposium. pp. 63–68.

Buckley, P. S., 1964. Techniques of process control. Wiley, New York.

Halvorsen, I. J., Skogestad, S., Morud, J. C., Alstad, V., Jul. 2003. Optimal Selection of Controlled Variables . Industrial & Engineering Chemistry Research 42 (14), 3273–3284.

Jacobsen, M. G., Skogestad, S., Oct. 2011. Active Constraint Regions for Optimal Operation of Chemical Processes. Industrial & Engineering Chemistry Research 50 (19), 11226–11236.

Jagtap, R., Kaistha, N., Skogestad, S., Jul. 2013. Economic Plantwide Control Over a Wide Throughput Range: A Systematic Design Procedure. AIChE Journal 59 (7), 2407–2426.

Konda, N. M., 2005. Plantwide control of industrial processes: An integrated framework of simulation and heuristics. Industrial & Engineering Chemistry Research, 8300–8313.

Larsson, T., Govatsmark, M. S., Skogestad, S., Yu, C. C., Mar. 2003. Control Structure Selection for Reactor, Separator, and Recycle Processes. Industrial & Engineering Chemistry Research 42 (6), 1225–1234.

Larsson, T., Skogestad, S., Jan. 2000. Plantwide control - A review and a new design procedure. Modeling, Identification and Control: A Norwegian Research Bulletin 21 (4), 209–240.

Luyben, M. L., Tyreus, B. D., Luyben, W. L., Dec. 1997. Plantwide control design procedure. AIChE Journal 43 (12), 3161–3174.

Luyben, W. L., Jun. 1999. Inherent Dynamic Problems with On-Demand Control Structures. Industrial & Engineering Chemistry Research 38 (6), 2315–2329.

Price, R. M., Lyman, P. R., Georgakis, C., May 1994. Throughput Manipulation in Plantwide Control Structures. Industrial & Engineering Chemistry Research 33 (5), 1197–1207.

Skogestad, S., Jan. 2004. Control structure design for complete chemical plants. Computers & Chemical Engineering 28 (1-2), 219–234.

Skogestad, S., 2012. Economic plantwide control. In: Rangaiah, G. P., Kariwala, V. (Eds.), Plantwide Control: Recent Developments and Applications. John Wiley & Sons, Ltd, Chichester, UK, Ch. 11.

Vasudevan, S., Rangaiah, G. P., Jul. 2011. Integrated Framework Incorporating Optimization for Plant-Wide Control of Industrial Processes. Industrial & Engineering Chemistry Research 50 (13), 8122–8137.

Vasudevan, S., Rangaiah, G. P., 2012. A Review of Plantwide Control Methodologies and Applications. In: Plantwide Control. John Wiley & Sons, Ltd, pp. 179–201.

Krist V. Gernaey, Jakob K. Huusom and Rafiqul Gani (Eds.), 12th International Symposium on Process Systems Engineering and 25th European Symposium on Computer Aided Process Engineering.
31 May – 4 June 2015, Copenhagen, Denmark

Mixed-Integer Fractional Programming: Models, Algorithms, and Applications in Process Operations, Energy Systems, and Sustainability

Fengqi You

Northwestern University, 2145 Sheridan Road, Evanston, Illinois 60208, USA
you@northwestern.edu

Abstract

A wide range of optimization problems arising in practical applications can be formulated as mixed-integer fractional programming (MIFP) problems, which combine the combinatorial difficulty of optimizing over discrete variable sets with the challenges of handling the nonconvex fractional objective function. This paper reviews recent developments of tailored global optimization algorithms for large-scale MIFP problems. These MIFP methods are illustrated through three applications: (1) function-unit-based life cycle optimization of sustainable supply chains, (2) integrated optimization of production scheduling and process dynamics of multi-product continuous processes, and (3) optimal design of algae processes for fuel and chemical production.

Keywords: MINLP, algorithm, life cycle optimization, scheduling, biorefinery.

1. Introduction

Mixed-integer fractional programming (MIFP) refers to a class of nonconvex mixed-integer nonlinear programs (MINLPs), of which the objective is the ratio of two functions (see Figure 1). MIFP finds applications in a variety of fields that include, but are certainly not limited to, biopharmaceutical manufacturing (Liu et al., 2014), capital investment (Bradley & Arntzen, 1999), hybrid energy systems (Tong et al., 2014), polymerization processes (Chu & You, 2012), marketing (Hua et al., 2011), cyclic scheduling (Pochet & Warichet, 2008), water-energy nexus (Gao & You, 2015), and environmentally conscious process operations (Capón-García et al., 2010).

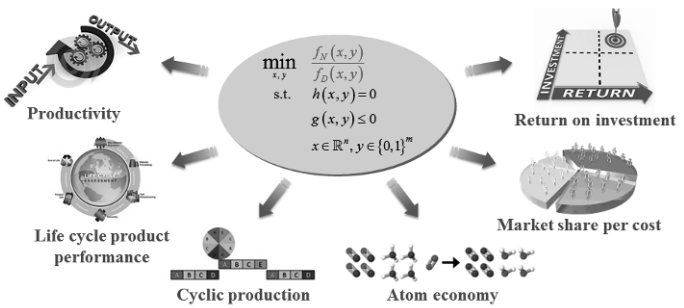

Figure 1. A general form of mixed-integer fractional programming and its applications.

Despite the wide applicability of MIFP, it is usually a challenging task to global optimize MIFP problems, especially for large-scale applications. This paper reviews recent developments of parametric algorithms for MIFP that can address some large-scale and complex problems, which are previously considered intractable by using

general-purpose MINLP and global optimization methods. These MIFP techniques are further illustrated through three recent applications.

2. Parametric algorithms for MIFP

2.1. Parametric form and its properties

For every MIFP problem with a positive denominator in the objective, i.e. $D(x, y)>0$, we can consider its parametric form with the same constraints and a parametric objective function as the difference between the numerator and the product of the denominator and a one-dimension parameter q, as shown in Figure 2.

$$\min_{(x,y)\in S} \frac{N(x,y)}{D(x,y)} \qquad F(q)=\min_{(x,y)\in S} N(x,y)-q\cdot D(x,y)$$

MIFP Problem Parametric MIP Subproblem

Figure 2. MIFP problem and its parametric MIP problem.

There is an equivalence property between the original MIFP problem and the parametric MIP problem: $(x, y)^*$ is the global optimal solution of the original MIFP problem if and only if $(x, y)^*$ is the global optimal solution of the parametric mixed-integer programming (MIP) subproblem for the parameter q^* such that $F(q^*)=0$. Thus, he global optimization of the MIFP problem is equivalent to solving $F(q^*)=0$. Due to the inner MIP problem $F(q)$ does not have a close-form analytical expression, but the equation $F(q^*)=0$ can be solved using a numerical root-finding algorithm. It has been proved that the one-dimension function $F(q)$ is concave, continuous, and monotonically decreasing (You et al., 2009). Since we only consider the cases with $D(x, y)>0$, there is a unique solution for $F(q^*)=0$. As the subgradient of $F(q)$ can be approximated with $-D(x, y)^*$, generalized Newton's method can be applied to solve a sequence of the parametric MIP subproblems for obtaining the value of q^* such that $F(q^*)=0$, as well as the global optimal solution to the MIFP problem (see Figure 3).

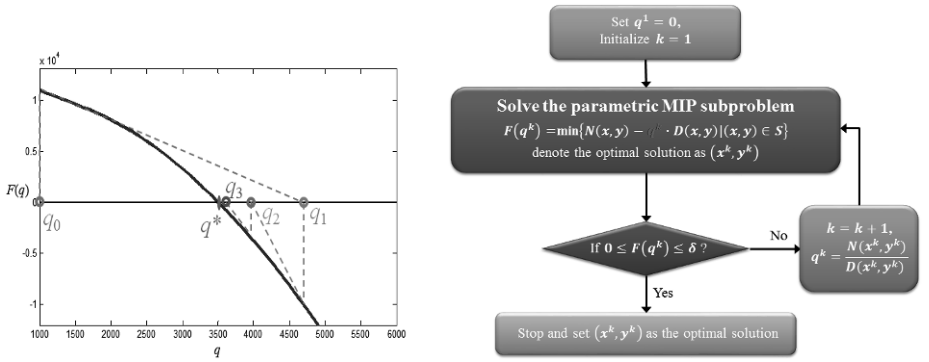

Figure 3. Generalized Newton's method for one-dimension root-finding of solving $F(q^*) = 0$ (left) and the algorithmic flowchart of the parametric approach using Newton's method (right).

2.2. Exact parametric algorithm

The flowchart of using generalized Newton's method for solving MIFP problems via the parametric approach is given on the right of Figure 3. This algorithm iteratively solves MIP subproblems by varying the value of parameter q, which is updated based on the optimal solution of the MIP subproblem in each iteration, until $F(q)$ falls into the neighbor of zero. It is important to note that all the MIP subproblems have exactly the

same number of variables and constraints. This method is called the "exact" parametric algorithm, because each MIP subproblem is expected to be solved to the global optimum, in order to provide the exact functional value for $F(q)$. The method has the same quadratic convergence rate as the generalized Newton's method.

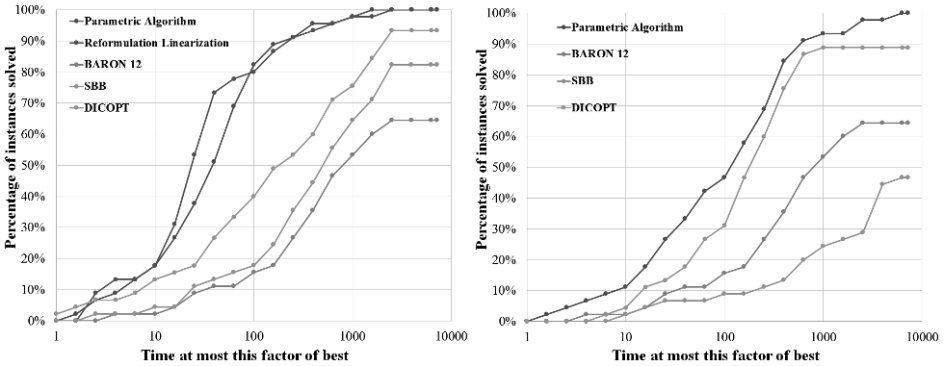

Figure 4. Performance profiles for solving general MILFP problems (left) and convex MIQFP problems (right) by comparing exact parametric algorithm with DICOPT, SBB and BARON 12.

This exact parametric algorithm based on the Newton's method was first applied to continuous linear fractional program (Isbell & Marlow, 1956) and convex nonlinear fractional program (Dinkelbach, 1967), although these continuous optimization problems can nowadays be solved more efficiently using the nonlinear programming (NLP) techniques directly. However, this exact parametric algorithm would have advantages for solving some MIFP problems, of which the corresponding parametric MIP subproblems are relatively easier to solve. For example, the MIP subproblems for mixed-integer linear fractional program (MILFP) and convex mixed-integer quadratic fractional program (MIQFP) problems are mixed-integer linear program (MILP) and convex mixed-integer quadratic program (MIQP), respectively, which can both be efficiently solved using the branch-and-cut algorithms. Figure 4 shows the performance profiles for solving randomly generated MILFP and convex MIQFP problems using this exact parametric algorithm (the corresponding MILP or MIQP subproblems were solved by CPLEX 12), and using the general-purpose MINLP solvers DICOPT and SBB, as well as the global optimizer BARON 12. We can see that the exact parametric algorithm clearly outperforms the general-purpose local and global MINLP solvers.

2.3. Inexact parametric algorithm

The efficiency of the parametric algorithm largely depends on the solution of the parametric MIP problem. It is known that MIP problems are usually NP-hard, and solving all MIP subproblems to 0% optimality gap might be very computationally challenging. Zhong and You (2014) recently theoretically proved that the convergence of the parametric algorithm shown in Figure 3 is still guaranteed if each MIP subproblem is solved to a relative optimality gap strictly less than 100%. This inexact parametric approach might require shorter computational time in each iteration to obtain a near-optimal solution of the MIP subproblem, although it has a superlinear convergence rate and may need more iterations than the exact one.

More importantly, this inexact parametric approach is applicable to general convex and nonconvex MIFP problems. It can be combined with other solution techniques to globally optimize complex nonconvex MIFP problems. An example is the following

MIFP problem, which comes from the application to be presented in Section 3.3. This MIFP problem includes a set of exponential terms, $(x_i)^{\alpha_i}$, where $1<\alpha_i<1$, in the numerator of the objective function to model the capital cost scaling functions.

$$\begin{aligned} \min \quad & \frac{A_0 + A_1 \cdot x + A_2 \cdot y + \sum_{i=1}^{n} \beta_i \cdot (x_i)^{\alpha_i}}{B_0 + B_1 \cdot x + B_2 \cdot y} \\ \text{s.t.} \quad & A + B \cdot x + C \cdot y = 0 \\ & x \in \mathbb{R}^n \quad \text{and} \quad y \in \{0,1\}^m \end{aligned} \tag{1}$$

Global optimization of the above MIFP problem could be challenging due to the multiple nonconvex terms. By applying the inexact parametric algorithm, we can consider a parametric subproblem, which is a separable concave minimization problem with the same constraints as (1) and a new objective function as follows:

$$F(q) = \min_{(x,y)\in S} \; A_0 + A_1 \cdot x + A_2 \cdot y + \sum_{i=1}^{n} \beta_i \cdot (x_i)^{\alpha_i} - q \cdot (B_0 + B_1 \cdot x + B_2 \cdot y) \tag{2}$$

Although this subproblem is still a nonconvex MINLP due to the presence of the exponential terms, it has a special structure that can be globally optimize by a successive piecewise linear approximation method (shown on the left of Figure 5). This method solves a sequence of MILP problems for the piecewise linear under-estimator to obtain the lower bound, and the upper bound is evaluated from the original functions based on the MILP solution. Thus, the tailored global optimization algorithm for solving the MIFP problem (1) includes two loops (on the right of Figure 5): The inner loop is for iteratively constructing the piecewise linear under-estimator for the parametric subproblem and the outer loop is for the inexact parametric algorithm.

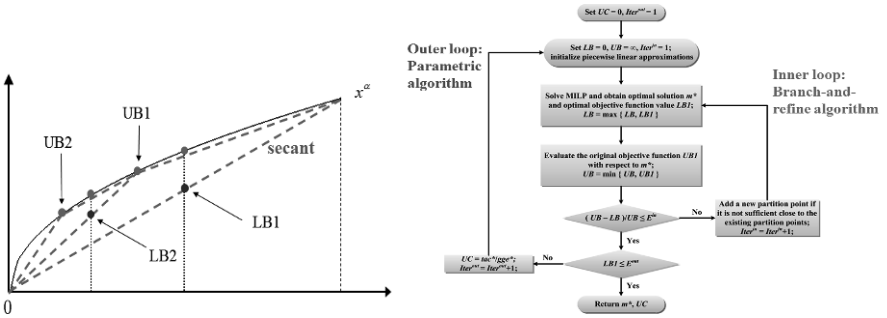

Figure 5. Successive piecewise linear approximation approach for separable concave minimization problems (left) and algorithmic flowchart for the global optimization of nonconvex MIFP problems with separable concave terms in the numerator of the objective function.

3. Applications

3.1. Functional-unit-based life cycle optimization of sustainable supply chains

Life cycle optimization, which explicitly combines life cycle analysis (LCA) with multi-objective optimization to simultaneously optimize the economic and environmental performances, is an emerging tool for sustainable supply chain optimization (Azapagic & Clift, 1999). Yet, almost all the life cycle optimization studies neglect the concept of "functional unit", which is a key element of LCA. To bridge this gap, Yue et al. (2013) proposed a functional-unit-based life cycle optimization approach for sustainable supply

chains. This framework considers a standard quantity of functional unit associated with the product systems. The functional unit provides a reference, to which the system's inputs and outputs can be related, and a logical basis for comparing the sustainability performance for different products. For example, gasoline equivalent gallon (GEG) is defined as the amount of alternative fuel it takes to equal the energy content of one liquid gallon of gasoline, which is 114,000 BTU lower heating values per gallon, so it is usually used as the functional unit to characterize different fuel products, e.g. 1 gallon of base-line gasoline is equivalent to 1 GEG and 1 gallon of biodiesel is equivalent to 1.0417 GEG. The use of functional unit in the life cycle optimization framework leads to a fractional objective function, where the denominator is the quantity of functional units involved in the product system, and the numerator is the economic/environmental sustainability indicator of the entire supply chain. Because most supply chain design models are formulated as MILP, the functional-unit-based life cycle optimization approach leads to the following multi-objective MILFP problem, which can be efficiently solved using the parametric algorithm presented in Section 2.

$$\begin{aligned} &\min \left\{ \frac{\text{total cost across life cycle}}{\text{quantity of the function unit}}, \frac{\text{total life cycle environmental impacts}}{\text{quantity of the function unit}} \right\} \\ &\text{s.t.} \quad A_k + \sum_{i \in I} B_{ik} x_i + \sum_{j \in J} C_{jk} y_j = 0, \forall k \in K \\ &\quad x_i \in \mathbb{R}^n, \forall i \in I \quad \text{and} \quad y \in \{0,1\}^m, \forall j \in J \end{aligned} \tag{3}$$

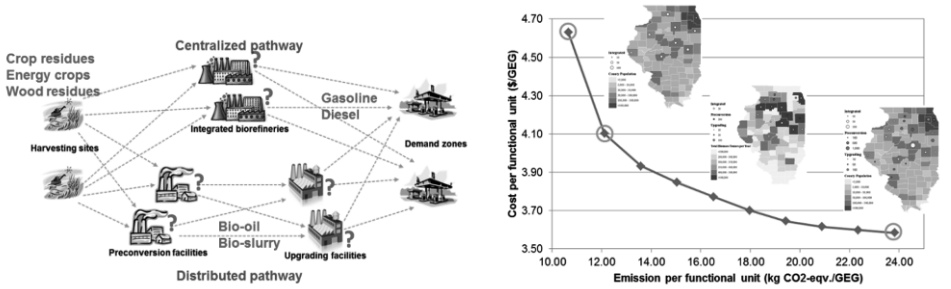

Figure 6. Superstructure (left) and Pareto optimal curve (right) of the case study on county-level biofuel supply chains in Illinois.

This framework was applied to a case study on hydrocarbon biofuels (gasoline and diesel from three cellulosic biomass sources) through a spatially-explicit model for the county-level supply chain in Illinois (see Figure 6). The problem is to optimize the number, sizes, locations, and technology selection for all the conversion facilities, as well as the profiles of the manufacturing, transportation, and storage activities, with respect to both the economic and environmental criteria. GEG was choose the functional unit. The resulting Pareto-optimal curve and the optimal design of the county-level hydrocarbon biofuel supply chain of Illinois are given in Figure 6. This case study leads to an MILFP problem with 224 discrete variables, 131,351 continuous variables, and 30,826 constraints. Neither BARON 12 nor SBB were not able to return any solution within 10% gap after 10 hours. DICOPT returned local optimal solutions within 1 hour, but their global optimality cannot be guaranteed. Yet, the parametric algorithm with CPLEX 12 can globally optimize the MILFP problems or all instances on the Pareto curve within 20 CPU seconds.

3.2. Integrated optimization of production scheduling and dynamics

Multi-product continuous processes can be operated in cyclic mode (Flores & Grossmann, 2006), in which each product is produced once per cycle and there is a transition period involving process dynamics from producing one product to another (see Figure 7). The scheduling problem determines the production sequence, and provides the initial condition and setpoint values to control the dynamic transition processes. The dynamic optimization problems provide the transition time and cost, which are input parameters for scheduling optimization. Thus, integrated optimization of scheduling and dynamics would lead to better process performance. The objective of this problem is to minimize the total cost rate, which includes the production cost, transition cost and inventory cost per unit of cycle time, by determining the production sequence, dynamic operating trajectories and the cycle time. The model formulation is given in Figure 8. Due to the triangular inventory profiles for cyclic production (lower left of Figure 8), the inventory cost is modeled by a quadratic function. Consequently, the objective function is quadratic fractional. This mixed-integer dynamic optimization (MIDO) problem can be reformulated to an MINLP using the colocation method by fully discretizing the differential equations into nonlinear systems (Biegler, 2007).

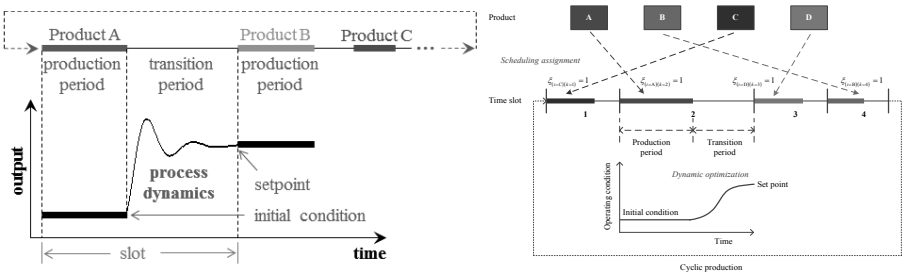

Figure 7. Integrated scheduling and dynamic optimization of multi-product continuous processes.

Because direct solution of this problem may be intractable for general-purpose MINLP solvers, Chu and You (2013) developed a solution method that combines the MIFP techniques with generalized Benders decomposition (GBD) by Geoffrion (1972). The GBD method first decomposes the full-space MINLP problem into a master problem and a set of primal problems, which are NLPs corresponding to the dynamic optimization of the transition periods (see Figure 8). The NLPs are optimized based on the solution of the master problem over every transition, iteratively constructing the Benders' cuts that are added to the master problem. The master problem has the same objective function as the MIDO problem; its constraints include the scheduling model, the linking equations, and the accumulated Benders cuts, which are mixed-integer linear inequalities. Thus, the master problem is a convex MIQFP that can be globally optimized by solving a sequence of convex MIQP problems, based on the parametric algorithm presented in Section 2. This framework was applied to a polymerization process producing 8 different grades products. The full-space MINLP has 63 binary variables, 32,156 continuous variables and 32,708 constraints. DICOPT encountered solver failure when solving this MINLP directly, and BARON 12 ran out of memory very quickly. SBB was able to solve this problem after 14,355 CPU seconds and returned a minimum cost rate of 223.0 m.u./h. Exactly the same optimal solution (minimum cost rate and optimal production schedule) was obtained by applying the GBD method combining with the parametric approach for the MIQFP master problem. Yet, this approach only requires 19.7 CPU seconds, reducing the computational time by 3 orders of magnitude and allowing online optimization.

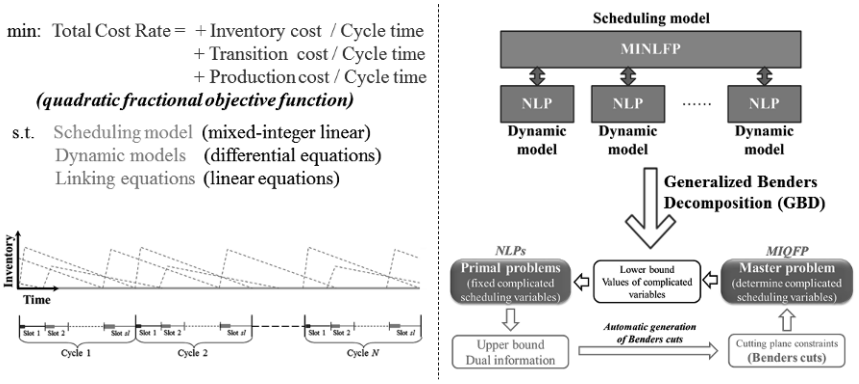

Figure 8. Integrated scheduling and dynamic optimization model and the nonlinear inventory profile (left), as well as the generalized Benders decomposition framework (right).

3.3. Optimal design of algae process making fuels and bioproducts

MIFP methods also find applications on superstructure optimization for process and energy systems design. An example is the work by You and Gong (2014) that investigates the economic and environmental implications of algae-based biorefinery for producing fuels and value-added products from *Chlorella vulgaris*. A main challenge on the design of algae-based energy systems is the diverse processing pathways and various possible products, e.g. biodiesel and renewable diesel (Rizwan et al., 2013). A process superstructure of the algae processing network was developed that includes more than 7,800 potential processing pathways. The algae process superstructure optimization involves various decisions such as the selection of technology, pathway, and processing methods, the determination of product portfolio under the given feed, the mass balance and size of each processing unit, and the energy and utility consumption. The objective is to determine the most cost-effective and environmentally sustainable design of the algae processing network. Because multiple fuel products can be produced from the processing the given algae feedstock, GGE was selected as the functional unit for optimizing the superstructure. The resulting model formulation, which follows the functional-unit-based life cycle optimization approach, is given in Figure 9.

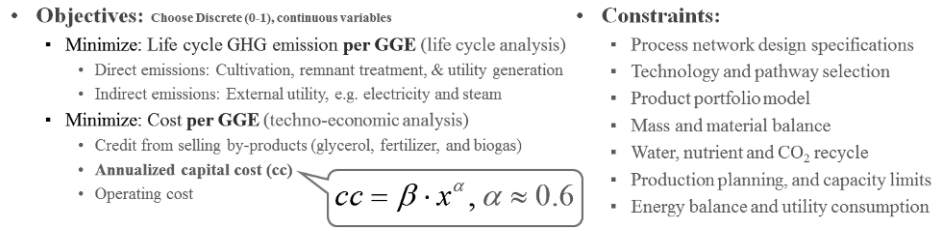

Figure 9. Nonconvex nonlinear MIFP model for superstructure optimization of algae processes.

Due to the capital cost scaling terms, this model is a nonconvex nonlinear MIFP, corresponding to Problem (1) presented in Section 2.2. The nonconvex MIFP problem for algae process superstructure optimization includes 49 binary variables, 32,958 continuous variables, and 56,274 constraints. Due to the nonconvexity, the global optimizer BARON 12 was not able to return any feasible solution after 20 hours, and the two local MINLP solvers, DICOPT and SBB, both return local infeasible within the same computational limits. However, this previously intractable MIFP problem was globally optimized to 0.01% global optimum within 10 CPU seconds (between 6 and 10

iterations for all instances) by using the solution method described in Section 2.3 that combines the branch-and-refine algorithm and the parametric approach.

4. Conclusions

This paper reviews three recent MIFP applications with increasing complexity: the first one is a linear MIFP problem for sustainable supply chain optimization, the second application involves quadratic (nonlinear) MIFP problems for process operations, and the last one handles nonconvex MIFP problems for energy systems design. These large-scale MIFP problems were all efficiently solved using the exact and inexact parametric algorithms that take advantage of MIFP properties and the powerful MILP techniques.

References

A. Azapagic, R. Clift, 1999, The application of life cycle assessment to process optimisation. Computers & Chemical Engineering, 23, 1509-1526.

L. T. Biegler, 2007, An overview of simultaneous strategies for dynamic optimization. Chemical Engineering and Processing: Process Intensification, 46, 1043-1053.

J. R. Bradley, B. C. Arntzen, 1999, The simultaneous planning of production, capacity, and inventory in seasonal demand environments. Operations Research, 47, 795-806.

E. Capón-García, A. Espuña, L. Puigjaner, 2010, Multiobjective optimization of batch plants scheduling under environmental and economic concerns. AIChE Journal, 57, 2766-2782.

Y. Chu, F. You, 2012, Integration of scheduling and control with online closed-loop implementation. Computers & Chemical Engineering, 47, 248-268.

Y. Chu, F. You, 2013, Integration of production scheduling and dynamic optimization for multi-product CSTRs: GBD coupled with MIFP. Computers & Chemical Engineering, 58, 315-333.

W. Dinkelbach, 1967, On nonlinear fractional programming. Management Science 13, 492-498.

A. Flores-Tlacuahuac, I. E. Grossmann, 2006, Simultaneous cyclic scheduling and control of a multiproduct CSTR. Industrial & engineering chemistry research, 45, 6698-6712.

J. Gao, & F. You, 2015, Optimal Design and Operations of Supply Chain Networks for Water Management in Shale Gas Production. AIChE Journal, DOI: 10.1002/aic.14705.

J. Gong, F. You, 2014, Global Optimization for Sustainable Design and Synthesis of Algae Processing Network using Life Cycle Optimization. AIChE Journal, 60, 3195-3210.

G. Hua, T.C.E. Cheng, S. Wang, 2011, The maximum capture per unit cost location problem. International Journal of Production Economics, 131, 568–574.

J. R. Isbell, W. H. Marlow, 1956, Attrition games. Naval Research logistics Quarterly 3, 71-94.

S. Liu, A. S. Simaria, S. S. Farid, L. G. Papageorgiou, 2014, Mathematical Programming Approaches for Downstream Processing Optimisation of Biopharmaceuticals. Chemical Engineering Research and Design, DOI: 10.1016/j.cherd.2014.1012.1002

Y. Pochet, F. Warichet, 2008, A tighter continuous time formulation for the cyclic scheduling of a mixed plant. Computers & Chemical Engineering, 32, 2723-2744.

M. Rizwan, J. H. Lee, R. Gani, 2013, Optimal processing pathway for the production of biodiesel from microalgal biomass. Computers & Chemical Engineering, 58, 305-314.

K. Tong, F. You, G. Rong, 2014, Robust design of hydrocarbon biofuel supply chain integrating with existing petroleum refineries considering unit cost objective. Computers & Chemical Engineering, 68, 128-139.

D. Yue, M. A. Kim, F. You, 2013, Design of Sustainable Product Systems and Supply Chains with Life Cycle Optimization Based on Functional Unit. ACS Sustainable Chemistry & Engineering, 1, 1003-1014.

F. You, P. M. Castro, I. E. Grossmann, 2009, Dinkelbach's algorithm as an efficient method to solve a class of MINLP models for large-scale cyclic scheduling problems. Computers & Chemical Engineering, 33, 1879-1889.

Z. Zhong, F. You, 2014, Globally convergent exact and inexact parametric algorithms for solving large-scale mixed-integer fractional programs and applications in process systems engineering. Computers & Chemical Engineering, 61, 90-101.

Krist V. Gernaey, Jakob K. Huusom and Rafiqul Gani (Eds.), 12th International Symposium on Process Systems Engineering and 25th European Symposium on Computer Aided Process Engineering.
31 May – 4 June 2015, Copenhagen, Denmark

Advances and Challenges in Modelling of Processing of Lipids

Bent Sarup

Alfa Laval Copenhagen A/S, Maskinvej 5, DK-2860 Søborg, Denmark,
bent.sarup@alfalaval.com

Abstract

Unlike the processing of crude and petroleum oils, the lipid processing industry has until recently not taken much advantage of the progress made in property modelling or process - product design over the last few decades. While there are some similarities in the modelling and processing of petroleum and lipids, a number of features of both lipids and their processing present new challenges. A brief introduction will be given to the processing of lipids, emphasizing the refining of edible oil. Some examples are provided on advances in both modelling of the lipids properties (pure components, phase equilibria) as well as how such property modelling enables use of standard process simulation programs for design and process optimisation. These advances have for example lead to new insights on optimum withdrawal of valuable components (micronutrients) in by-products from refining operations.

Keywords: lipids, modelling, thermodynamics, transport properties

1. Introduction

Oils of biological origin are complex hydrocarbon mixtures. Fossil oils have furthermore undergone chemical transformations that increase their complexity. Nevertheless, petroleum oils can often be modelled in sufficient accuracy for process design by a pseudocomponent and group contribution approach (Fredenslund et a., 1977; Magnusson et al., 1981), dividing the oils a suitable number of boiling point fractions and based on estimated densities of each of these fractions through correlations establish thermodynamic and physical properties. Ultimately fossil hydrocarbons will be depleted and replaced from renewable sources. One such source is lipids, being "a loosely defined term for substances of biological origin that are soluble in nonpolar solvents. They consist of saponifiable lipids, such as glycerides (fats and oils) and phospholipids, as well as nonsaponifiable lipids, principally steroids" (IUPAC, 2006). The estimated 2013/14 world production of fats and oils is 208 mill t/y, most of which arise from processing of 524 mill t/y of oilseeds, but also include oils from palm fruits, marine and animal origins (Hallam et al., 2014). Fats and oils are used mainly for edible purposes, but also may others such as biofuels, detergents, personal care and pharmaceuticals. With only a few exceptions, such as olive oil, the crude fats and oils undergo extensive processing to provide the desirable end-product characteristics. Until recent years the fats and oil processing industry has not be able to benefit much from process simulators such as PRO/II and Aspen Plus. One reason being that the lipid mixtures could not be modelled with sufficient accuracy.

2. Lipid processing and modelling requirements

Components occurring in crude fats and oils can be classified as shown in Table 1. In addition the crude oil will contain oxidized compounds (lipid peroxides and secondary oxidation products such as aldehydes), the amount of which depends on oil storage conditions. Focus here will be a brief overview of edible oil processing, for details see e.g. Hamm et al. (2013). Other important areas are biodiesel and oleochemical processes, for which the advances described below also would apply. Normal requirements for a liquid, food grade refined oil is bland taste and smell, clear appearance with a faint yellow colour and being stable during storage for months. The oil refining scheme is shown in Figure 1. Phospholipids ("gums") are removed, optionally in two steps, the first being using a water wash to extract phospholipids which can be dried to make food or feed grade lecithins. Free fatty acids can be removed either as soaps by neutralisation with caustic (chemical refining) route, or stripping with steam under vacuum (deodorization, physical refining). For both processing routes a "bleaching" section removes impurities and some coloured components contacting a solid adsorbent as slurry. Most often a bleaching clay, but silica gels and activated carbon are also used in some cases. Dewaxing and winterisation steps remove high melting point lipids that otherwise would make the refined oil unclear with precipitates. Refining ends with a high temperature steam stripping operation (deodorization) to remove volatiles.

Modelling requirements include mixture temperature dependent properties as well as phase equilibria and transition enthalpies. The phospholipids pose a special challenge, being charged organic molecules with emulsifying properties (leading to oil losses) Phase equilibria include liquid-liquid (e.g. neutralisation), liquid-solid (crystallisation, adsorption during bleaching) and vapour-liquid (deodorization step). The deacidification step in the deodorized has earlier been modelled e.g. by Ceriani and Meirelles (2006).

Table 1. Components in crude fats and oils

Components	Description	Concentration (typical) % wt
Acylglycerides	Tri-, di- and monoacylglycerides	balance
Phospholipids	Free or as calcium and magnesium salts.	0.6 – 4%
Fatty acids	Free fatty acids	0.5 - 5
Tocopherols	Tocopherols and tocotrienols	0.05 – 0.15
Sterols	Free sterols and esterified to e.g. fatty acids,	0.1 – 0.2
Waxes	Esters of long chain fatty acid and alcohols	0.03 – 0.1
Squalene and other hydrocarbons		0.005 – 0.05
Carotenoids	Colour bodies, e.g. carotene	0.001 – 0.05
Trace metals	Iron, copper	0.003 – 0.01
Moisture and impurities	Water, oil seed residues, proteins	0.1 – 0.2

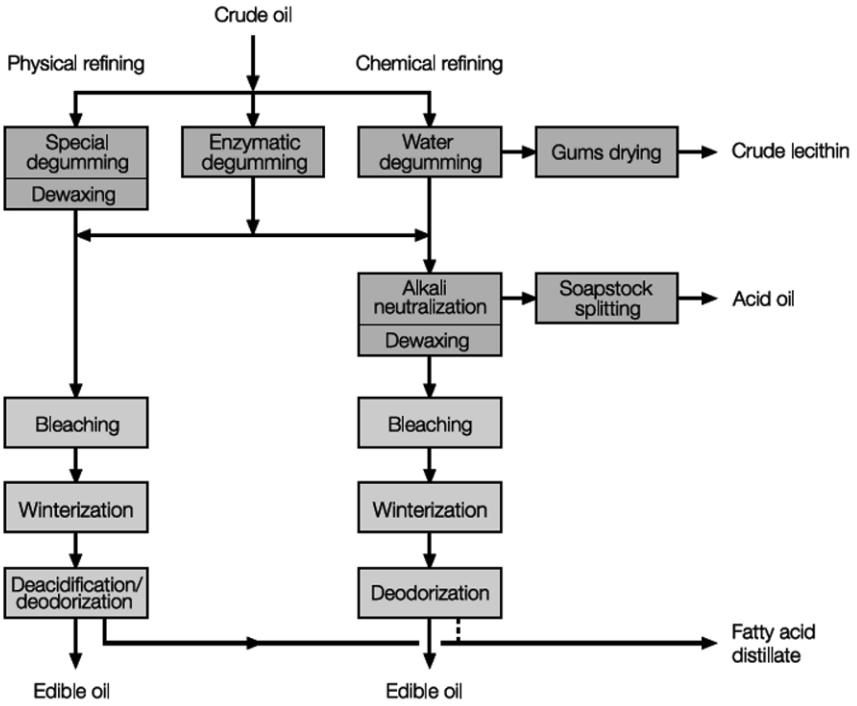

Figure 1. Refining of Fats and Oils (courtesy of Alfa Laval)

Fats used in solid form (in e.g margarines, shortenings, confectionary products) go furthermore through or more of the fat modification steps shown in Figure 2. Fractionation involves cooling the oil to crystalize out major amounts of high melting point lipids, applied extensively for palm oil. Hydrogenation saturates double bonds and increases the melting point. Interesterfication provides a random mixing of fatty acids on the glycerine backbone, and can produce lipids with sharp melting point curves. Which for example is required for confectionary fats, having to melt at mouth temperatures and not when handling by hand. Clearly SLE are of major importance in fat modification, complicated by new lipids being formed by the chemical reactions.

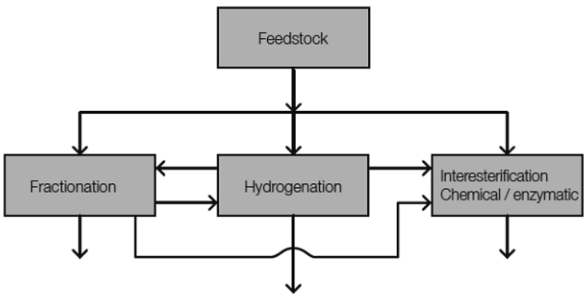

Figure 2. Fat Modification Steps (courtesy of Alfa Laval)

3. Modelling of lipid mixtures

The complexity of lipids is somewhat reduced by the fundamentals of their biological synthesis, resulting in even carbon numbers fatty acids. Most prominent are fatty acid carbon chain length 16 and 18. Fatty acids are either fully saturated, or having a few (non-conjugated) double bonds in well-defined positions. Furthermore, unsaturated fatty acids are all in cis-configuration. Even then, considerable simplification is required to make the modelling manageable, one approach being to select a sufficient number of components from each significant component class listed in Table 1.

Modelling begins with the pure compounds, moving on to single phase mixtures and finally to multiple phases. A fundamental difficulty is the lack of experimental data on lipid properties, and the time and cost associated with generating new data. However, a group contribution approach appears to quite suitable for a parametric fit to the data available and predict properties for other conditions and/or lipid compounds. See Diaz-Tovar (2011), Ceriani et al (2013) Cunico et al (2013, 2014) and references therein for details of the approach taken to build the CAPEC LIPID database. This LIPID database can then be made available to process simulators to take full advantage of the computational efficiency of such programs.

4. Deodorizer application example

Figure 3 depicts a deodorizer column. The oil enters the stripping section and flows counter-current to stripping steam in a packed column. Typical operating conditions are vacuum levels of 3 – 5 mbar and temperatures of 250 – 260 ºC. The stripped oil spends typically 30 – 45 min in a retention section to thermally break down coloured and other unwanted components. The stripping steam is scrubbed for lipid volatiles before entering the vacuum system.

Deodorizer destillates contain valuable compounds such as tocopherol and sterols; see e.g. Gunawan and Yi-Hsu Ju (2009). It is therefore of interest to recover these in yields and concentrations that makes further separation and purification processing feasible.

A number of processing schemes have been proposed to achieve this based on introducing a higher temperature intermediate scrubber. Faessler (1998) achieves this by quenching with a small amount of cold distillate and Copeland and Belcher (2001) by an additional full hot scrubber loop as shown in more detail in Figure 4.

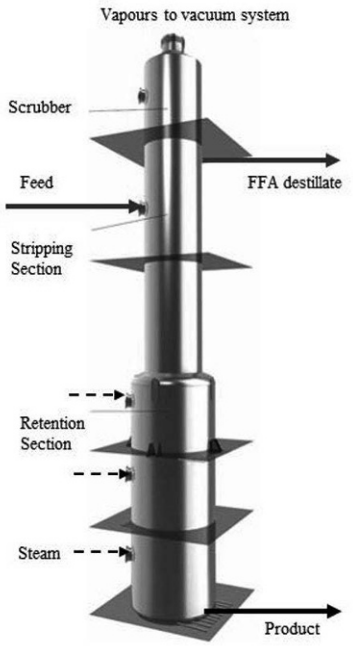

Figure 3. SoftColumn Deodorizer (courtesy of Alfa Laval)

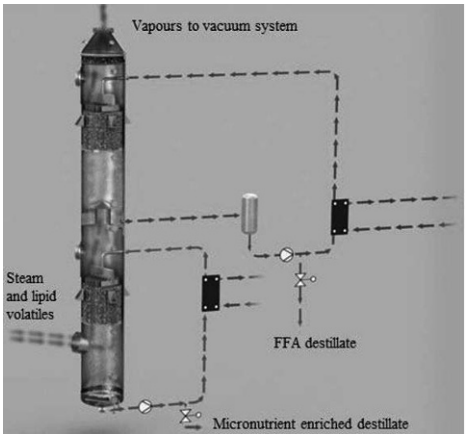

Figure 4. Double Scrubber
(courtesy of Alfa Laval)

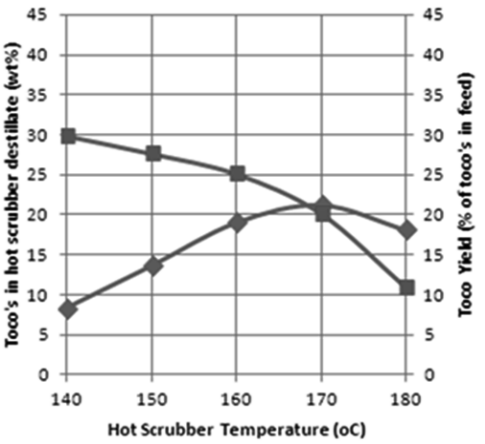

Figure 5. Double Scrubber Performance
(♦ concentration, ▪ yield)

A soybean oil deacidification column was modelled with PRO/II and based on the CAPEC LIPID database described above. The model provided insights for example as shown in Figure 5 for tocopherols in the condensate from the hot scrubber. The model quantifies the effects of more fatty acid condensing at lower hot scrubber temperature and increasing losses of tocopherol to the distillate from the cold scrubber at higher temperatures in the hot scrubber. Therefore a limitation of the double scrubber became clear, since a maximum concentration of the high valued tocopherol can only be achieved at expense of the yield of tocopherols.

The simulation framework could be used to quantify improvements with alternative processing schemes overcoming this limitation of the double scrubber system, simultaneously achieving quantitative recovery of tocopherols at high concentrations. (Marques de Lima and Sarup, 2011). Furthermore, the new scheme recovers oil that can be recycled and recovered as refined oil and the purity of the FFA distillate exceeds what is achievable in a double scrubber.

5. Conclusions

Modelling of lipids for process simulation purposes has progressed considerably within the last decade, with emphasis on fluid and thermodynamic VLE properties. However, much remains to be done, including LLE and SLE thermodynamics and charged organic molecules (phospholipids).

Validation remains a challenge as experimental data is scarce, but the combination of the fundamental work with commercial process simulators begins to prove useful for industrial design and as support for new technology development.

References

R. Ceriani, A.J.A. Meirelles, 2006, Simulation of continuous physical refiners for edible oil deacidification, J. Food Eng., Vol. 76, p. 261–271

R. Ceriani, R. Gani, Y.A. Liu, 2013, Prediction of vapor pressure and heats of vaporization of edible oil/fat compounds by group contribution, Fluid Phase Equilibria, Vol. 337, Pages 53–59

D. Copeland and M. Belcher, 2001, Methods for Treating Deodorizer Destillate, US Patent No. 6,750,359.

L. P. Cunico, R. Ceriani, B. Sarup, J. P. O'Connell, R. Gani, 2014, Data, analysis and modeling of physical properties for process design of systems involving lipids, Fluid Phase Equilibria, Vol. 362, p. 318–327

L. P. Cunico, A. S. Hukkerikar, R. Ceriani, B. Sarup, R. Gani, 2013, Molecular structure-based methods of property prediction in application to lipids: A review and refinement, Fluid Phase Equilibria, Vol. 357, p. 2–18

C. Díaz-Tovar, R. Gani, B. Sarup, 2011, Lipid technology: Property prediction and process design/analysis in the edible oil and biodiesel industries, Fluid Phase Equilibria, Vol. 302, Issues 1–2, 15 , p. 284–293

D.R. Erickson (Ed), 1990, Edible Fats and Oils Processing. Basic Principles and Modern Practices., World Conference Proceedings, AOCS

P. Faessler, 1998, Recent Developments and Improvements in Palm Oil Stripping and Fatty Acid Destillation, in Proc.World Conf. Palm Coconut Oils for the 21st Century, 15-19 Feb, Bali, Indonedia, published by American Oil Chemist Society.

A. Fredenslund, J. Gmehling, P. Rasmussen, 1977, Vapor Liquid Equilibria Using UNIFAC, Elsevier.

S. Gunawan and Yi-Hsu Ju ,2009, Vegetable Oil Deodorizer Distillate: Characterization, Utilization and Analysis, Separation & Purification Reviews, 38: 3, p. 207 — 241

D. Hallam, C. Calpe, A. Abbassian and others, 2014, FAO Food Outlook Report, Biannual Report on Global Food Markets, October issue, p. 38ff

W. Hamm, R.J. Hamilton and G. Calliauw (eds), 2013, Edible Oil Processing, Second Edition, John Wiley & Sons, Ltd, Chichester, UK

T. Magnussen T, P. Rasmussen P, A. Fredenslund A. 1981, UNIFAC parameter table for prediction of liquid-liquid equilibria. Ind Eng Chem Process Des Dev 20, p. 331-339.

D. Marques de Lima, B. Sarup, 2011, De-acidification of fats and oils, EP 2 597 142

A. D. McNaught and A. Wilkinson (editors), 2006, IUPAC, Compendium of Chemical Terminology, 2nd ed. (the "Gold Book"). Compiled by Blackwell Scientific Publications, Oxford (1997). XML on-line corrected version: http://goldbook.iupac.org (2006-) created by M. Nic, J. Jirat, B. Kosata; updates compiled by A. Jenkins

Krist V. Gernaey, Jakob K. Huusom and Rafiqul Gani (Eds.), 12th International Symposium on Process Systems Engineering and 25th European Symposium on Computer Aided Process Engineering.
31 May – 4 June 2015, Copenhagen, Denmark

A Perspective on PSE in Fermentation Process Development and Operation

Krist V. Gernaey*

CAPEC-PROCESS, Department of Chemical and Biochemical Engineering, Technical University of Denmark (DTU), DK-2800 Lyngby, Denmark
**kvg@kt.dtu.dk*

Abstract

Compared to the chemical industry, the use of PSE methods and tools is not as widespread in industrial fermentation processes. This paper gives an overview of some of the main engineering challenges in industrial fermentation processes. Furthermore, a number of mathematical models are highlighted as examples of PSE methods and tools that are used in the context of industrial fermentation technology. Finally, it is discussed what could be done to increase the future use of PSE methods and tools within the industrial fermentation technology area.

Keywords: control, fermentation, modelling, on-line sensor, optimisation

1. Introduction

Industrial fermentation processes are increasingly popular for the production of bulk and fine chemicals, pharmaceuticals etc. It is indeed remarkable that the term 'fermentation process' covers a broad range of production hosts: (1) Filamentous fungi are used for production of organic acids, where citric acid production by *Aspergillus niger* (Shu and Johnson, 1948) is a well-known example; (2) Penicillin, the first antibiotic that was discovered, is produced at large scale by fermentation of *Penicillium chrysogenum* (Moyer, 1948); (3) Recombinant proteins such as insulin are produced by fermentation with *Escherichia coli* (Johnson, 1983) and the yeast *Saccharomyces cerevisiae* (Ostergaard et al., 2000). Fermentation also plays a prominent role in 2nd generation bioethanol production processes. As a consequence, industrial fermentation processes are considered to form an important technological asset for reducing our future dependence on chemicals and products produced from fossil fuels.

However, despite their increasing popularity, fermentation processes have not yet reached the same maturity as traditional chemical production processes, particularly when it comes to using engineering tools such as mathematical models, process control algorithms and optimization techniques to support the search for improved and more efficient processes.

This perspective starts with a description of some of the most important engineering challenges within industrial fermentation technology, since a basic understanding of these challenges is an advantage when trying to understand the limitations in the current use of PSE methods and tools. Afterwards, the focus shifts towards PSE tools and their application in the fermentation area, with special focus on mathematical models. The paper ends with a number of future perspectives in this area: several potential solutions are proposed to facilitate the future use of PSE methods and tools in fermentation process development, operation and optimisation.

2. Engineering challenges within fermentation technology

An extended discussion of engineering challenges is given in Formenti et al. (2014).

2.1. Scaling up and scaling down

Most fermentations are operated as batch or fed-batch systems. Experiments in laboratory (0.5-20 L) and pilot scale (20-2000 L) have traditionally been used to screen for conditions that yield maximal volumetric productivity, since it is too expensive – due to loss of valuable production time – to do such screening in a full-scale reactor. In production of pharmaceuticals, where Good Manufacturing Practice (GMP) applies, performing experiments at large scale is usually completely out of the question.

Scaling up a fermentation process serves the purpose of transforming optimal operating conditions from laboratory/pilot scale to production scale bioreactors. The results from experiments at laboratory and pilot scale are, however, often difficult to compare to large industrial bioreactors, and scale-up is therefore still one of the major challenges in the fermentation industry. The main reason for this is that lab and pilot-scale fermenters can be considered well-mixed; in large scale, on the contrary, concentration gradients do exist, as for example documented in the study by Enfors et al. (2001), and such gradients are known to have a significant influence on the productivity of the host organism.

In practice, the scale-up to a production scale reactor is done iteratively: as soon as pilot plant experiments demonstrate a feasible business case, pilot plant results are attempted to be transferred to industrial scale. If similar performance can be demonstrated at large scale, scale-up is considered successful. If not, additional pilot plant experiments might be performed, to investigate the effect of additional process parameters on process performance.

Scaling down also poses a challenge in industrial fermentation technology. Most biotechnological processes are designed for existing equipment, since full scale bioreactors are very expensive and therefore used for several decades. As a consequence, the available process equipment ranges are known before a new process is designed, and it is important to find a setup of the small scale equipment that mimics the effect of full-scale process parameter changes on the process performance as closely as possible in order to develop new processes as efficiently as possible.

During the past decades, fermentation experiments at very small scale have become popular for gaining initial knowledge on fermentation process performance – sometimes the term ‘ultra-scale-down’ is used. This has resulted in the creation of completely new devices (microfluidic devices, microbioreactors and milliliter-scale stirred systems) that are considered suitable scale-down versions of larger bioreactors. Experience has shown that each small scale system brings benefits as well as problems during process development across scales, and it is especially important that the user is aware of this when applying such ultra-scale-down systems to a practical case. Successful scaling was reported by Isett et al. (2007), who demonstrated scalability from a 24-well plate (4-6 mL) to a laboratory scale stirred tank (20 L) using *S. cerevisiae*, while Islam et al. (2008) showed predictive scale-up from micro well plate (2 mL) to laboratory (7.5 L) and pilot (75 L) scale using *E. coli*. However, even with such positive results in mind, it is important to realize that there is still a long way if the aim is to demonstrate successful scale-up to industrial scale reactors, which can have a volume of 100 m^3 or more.

2.2. Mass transfer, morphology and rheology

Mass transfer is crucial for a fermentation process, as O_2 and nutrients have to be distributed, and possible toxic compounds, such as CO_2, have to be removed. The mass

transfer is strongly dependent on the viscosity of the fermentation broth, where the rheology of the broth is dependent on both the biomass concentration and the morphology of the production host cells (Cascaval et al., 2003). The complex relation between these variables is still not completely understood, which contributes to making scaling up/scaling down difficult. In general, stirring and aeration are a prerequisite for almost all types of cells, even for cell cultures with mammalian cells, in order to have a proper oxygen supply.

The most challenging expression systems are the filamentous microorganisms in terms of mass transfer and rheology: their morphology, both at the microscopic and macroscopic level, will have a major influence on mass transfer. At the microscopic level, the optimal morphology for a given bioprocess varies and cannot be generalized, and relies on the desired product (Gibbs et al., 2000). Dependent on the fermentation and the employed strain, pellet formation can occur. In some processes, a pellet type morphology is preferred since it allows for simplified downstream processing and yields a Newtonian fluid behavior of the medium (macroscopic level), which results in low aeration and agitation power input. However, the pelleted morphology has the disadvantage that it results in nutrient concentration gradients within the pellet. The latter is not observed in freely dispersed mycelia, although gradients can occur in such a system dependent on the mixing time of the reactor system, due to the high broth viscosity (Riley et al., 2000). Thus, freely dispersed mycelia allow enhanced growth and production. This has been attributed to the influence of morphology on the production kinetics at the microscopic level, e.g. higher enzyme secretion was observed from a more densely branched mutant of *Aspergillus oryzae* (Spohr et al., 1998).

It still remains challenging to estimate a reliable shear rate to evaluate the viscosity across scales for filamentous fungi, a problem that is usually not experienced in bacteria and yeast cultivation which exhibit a Newtonian behaviour which is attributed to the spherical shape of their morphology (Oniscu et al., 2003). This facilitates the work with these types of microorganisms considerably, and it also explains why many fermentation process optimization studies are focused on filamentous fungi.

2.3. Data handling, advanced sensors and control

The sensors in industrial bioreactors are most often limited to pH, dissolved oxygen and temperature sensors which are placed at a single location in vessels with large volumes, often with concentration gradients (Larsson et al., 1996). As a consequence, at best such standard univariate sensors display an average value for the entire process which can be correlated to the processes in the vessel, but little or no information on the spatial heterogeneity in the vessel is available.

A PID controller is the standard controller in fermentation processes to keep a controlled variable at or close to its set point or set point trajectory. However, the PID controller cannot guarantee that the fermentation is operated optimally. The set points (often time-varying trajectories in batch or fed-batch operation) only result in an optimal operation under certain nominal conditions. In most cases, a set point trajectory is the result of a time-consuming procedure where small adjustments are made to the ideal set point trajectory – the golden batch – whenever results of the last batch demonstrate an improvement. However, disturbances such as changes in substrate quality or composition take place, and ideally the set points should be modified accordingly. The latter optimization is difficult in industrial fermentations for a number of reasons: (1) Most common controlled variables, dissolved oxygen (DO) and pH, are only indirectly linked to the optimal operation of a fermenter, i.e. the operation that leads to the highest volumetric productivity. Important variables such as the biomass, substrate, product or

by-product concentration are only sporadically monitored (and less frequently controlled); (2) Models can be used to synthesize controllers that operate close to optimal conditions and to determine optimal trajectories for (fed-)batch operations. In the fermentation industry, however, sufficiently accurate models that can be used for this purpose are often lacking, as for example pointed out by Smets et al. (2004) in a review on optimal feed rate strategies.

Introduction of more advanced sensors in industrial scale fermentation could be beneficial and allow the introduction of more advanced or improved control strategies. However, this is not an easy development task. Cervera et al. (2009), in a literature review on the use of near infrared spectroscopy in fermentation and cell culture, concluded that most reported applications refer to at-line or off-line measurements. What industry really needs is a demonstration that such advanced sensors can be operated on-line to generate real-time data that can be used as input for controlling the fermentation process. Also worth mentioning is that a major limitation in the introduction of new sensors for process monitoring originates from GMP aspects, especially in the pharmaceutical biotechnology industry.

Process knowledge extraction from historical data is another area which has not been explored that much. The fermentation industry possesses large databases with historical data, but in most cases these are not used for a number of reasons: (1) Retrieval of the data is often experienced as far too time-consuming; (2) Data compression algorithms sometimes remove the most interesting dynamics from the data that are stored; (3) In many cases, especially for smaller companies, the knowledge and experience to work with large historical data sets is not available within the company. Furthermore, it is often problematic, due to proprietary reasons, to involve external partners – academia or consultants – in such a historical data interpretation task.

3. Fermentation process modelling

The main purpose of this section is to briefly illustrate the use of PSE methods and tools in the frame of fermentation projects, and this will be done by giving insight in the broad range of models that are available for studying fermentation processes.

3.1. Mechanistic models

Mechanistic models are useful for representing available process knowledge, and can therefore support process development. Reviews on mathematical models can be found in Nielsen and Villadsen (1992), Henson (2003) and Gernaey et al. (2010), among othres. The opinion article by Bailey (1998) is still highly relevant as well, and highlights both the history and the future of mathematical modelling in biochemical engineering.

Mechanistic fermentation process models are based on mass, heat and momentum balances, supplemented with an appropriate mathematical formulation of the key mechanisms (e.g. kinetic expressions to reflect process dynamics). The kinetic expressions are often empirical, thus providing a simplified and idealized view of a complex biological mechanism, with the Monod expression for microbial growth kinetics as the most well-known example. Assuming a homogeneous reactor environment, a generally accepted classification of mechanistic models of cell populations is presented in Figure 1 (Frederickson et al., 1970; Bailey, 1998). If the assumption of a homogeneous reactor environment does not hold, then a distributed model is needed (i.e. a model where not only time, but also space (1-, 2- or 3D), forms an independent variable): well-known examples are compartment models (Vrabel et al., 2000), as well as computational fluid dynamics (CFD). Unsegregated models are most

common, and rely on an average cell description. Within this category, unstructured models are the simplest – and also the most popular) models that use a single variable to describe biomass.

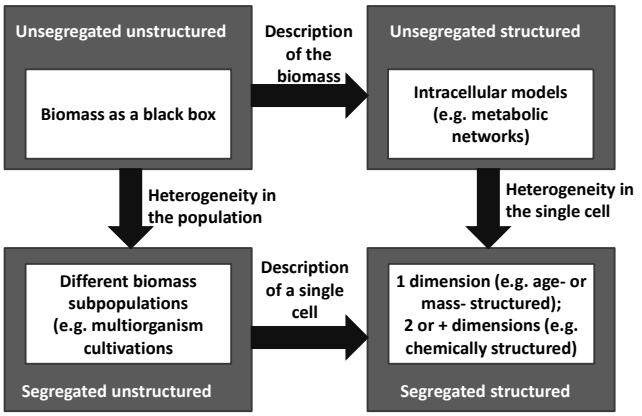

Figure 1. Schematic classification of mechanistic models for cell cultivations (Frederickson et al., 1970; Bailey, 1998; Lencastre-Fernandes et al., 2011).

Unsegregated structured models describe the biomass as consisting of several variables (such as NADH, precursors, metabolites, ATP, biomass), and have been used for modeling complex processes such as yeast intracellular metabolism (Nielsen and Villadsen 1992). Morphologically structured models (Agger et al. 1998) were specifically developed to describe growth of important production organisms, filamentous fungi,— and distinguish between different regions of the hyphal elements.
Segregated models consider individual cells, in recognition of the fact that cells in a population – a pure culture – are different, and are most often formulated as a population balance model (PBM). Lencastre Fernandes et al. (2011) provide a concise review of the status of PBM in the fermentation area. An unstructured segregated model characterizes cells by one distributed property (i.e. cell size or age of individual cells; Zamamiri et al., 2002) without considering intracellular composition. Obviously, structured segregated models are more complex, since the distribution of one or more intracellular variables is also considered. Solving the resulting multi-dimensional PBM is difficult, unless the intracellular state can be captured with just a few variables (Henson, 2003). One alternative to PBMs is cell ensemble modeling (Domach and Shuler, 1984; Henson, 2003), where the parameters of a single cell model are randomized to simulate a cell population. Apart from the cells, the PBM framework also offers the possibility to make detailed studies of other phenomena of interest, for example the behaviour of air bubbles in an aeration tank, where the bubble size will change when the gas bubbles move through the reactor as a result of the action of the impeller on the one hand, and coalescence of gas bubbles on the other hand.

3.2. Computational fluid dynamics (CFD)

Aeration and agitation design and scale-up have for a long time been performed based on empirical correlations and engineering experiences. Typical scale-up parameters that are used in practice are constant power to volume ratio, constant tip speed, constant Reynolds number and constant volumetric air flow rate. Scale up with constant power to volume ratio will result in an increased tip speed (i.e. shear) while the mixing time is decreased (Stanbury et al., 1995). However, none of these correlations includes vessel

geometry, mixing intensities, operating conditions, feed location, physical properties etc. (Leng et al., 2008).
In view of the general lack of sufficient understanding of aeration and agitation design/scale-up, there is general agreement that Computational Fluid Dynamics (CFD) is a valuable tool that can be used to support the scaling up and scaling down of bioreactors, and for studying mixing and the potential occurrence of gradients in a tank. Ideally, assuming that the kinetics of a process hold across scales, CFD can ideally be used to support transfer of research results across scales: from the first experiment in an ultra-scale-down reactor via well-mixed pilot scale experiments towards the full-scale reactor with its concentration gradients. One of the challenges in this area is the fact that many academic groups with an interest in CFD only have access to laboratory scale and pilot scale data. This is illustrated by the fact that one of the only published data sets in large scale (30 m^3) is almost 20 years old (Larsson et al., 1996).

4. Future perspectives

4.1. Industry-academia collaboration

Industrial scale data are proprietary, which forms a severe limitation. Data from process scale up studies can for example not be found as part of the scientific literature, and can thus not be used as a basis for extending the available knowledge about this important engineering task. Significant progress with respect to understanding the scaling up problem can thus only be made through a close collaboration between industry and academia: industry has equipment – large scale reactors which are not affordable for university – and knowhow about how to run a full-scale fermentation, whereas academia can contribute with expertise in for example CFD and detailed knowledge related to the cellular behavior at large scale to develop a better understanding of the major scaling up challenges. For the future, it should be considered to define a number of industrially relevant cases, using old production strains that are no longer in use or wild type strains with industrial value, which should be described in detail in order to allow people to compare results and make progress.
Another area where industry-academia collaboration is important is specifically on the transformation of historical data to useful information. Academia often lacks industrially relevant data sets of significant size that can be used to demonstrate the value of data mining tools. The main hurdle to be taken there, again, is the fact that data are proprietary, but this can often be solved by appropriate scaling of the raw data before they are transferred from industry to academia. Here as well, it could be useful to establish collaboration between several industrial partners, in order to make a number of data sets publicly available such that academic groups can test their research work on industrially relevant data, instead of solely relying on idealized toy examples with academic value which cannot be transferred to industrial practice.

4.2. Soft sensors

Introducing new, more advanced sensors is not straightforward. Therefore, one method to increase both data quality of on-line sensors and data quantity, even without violating GMP regulations, is by increased use of soft sensors. In a soft sensor, robust on-line measurements, which are not subject to time delay, are used to calculate the expected value of new variables of interest that could be useful to allow improved control of fermentation processes. A recent report by an expert group concluded that the use of soft sensors in the fermentation industry is very limited at this moment, despite the obvious potential (Luttmann et al., 2012). This is clearly a topic with a considerable unexplored potential that should be more in focus in the future.

4.3. Hybrid models

Hybrid models combine fundamental knowledge with data-driven techniques to model fundamentally unknown dependencies, and more attention should be paid to the future use of such hybrid models. It has indeed been demonstrated that the integration of knowledge from first-principles with multivariate data analysis methods, resulting into a hybrid semi-parametric modeling approach, has the potential to improve process understanding and can enable significantly increased prediction performance (von Stosch et al., 2012). The strength of hybrid models is that they can integrate different sources of knowledge in form of parametric and nonparametric structures, where the structure of the parametric models is a priori fixed on the basis of first-principles knowledge, whereas the structure of nonparametric models is identified from data.

4.4. Benchmarking of control strategies

In the wastewater treatment field, an area that is closely related to fermentation, the development of models to support benchmarking of control strategies – i.e. the objective simulation-based comparison of control strategies – has been very successful, and has resulted in the recent publication of a benchmarking report to document an effort that has lasted almost 20 years (Gernaey et al., 2014). The result of the benchmarking work is a set of validated models, a number of reference control strategies and a set of standardized evaluation criteria to compare performance of different control strategies. Such an effort should be repeated in the fermentation area as well with the aim of promoting the use of modelling and more advanced control in the fermentation area as well. The key to success in the benchmarking developments in the wastewater treatment area is the fact that validated simulation models were made available for free, such that the model user could focus on development and testing of control strategies instead of getting lost in the tedious task of writing and validating the model code.

5. Conclusions

The increased use of models and PSE tools in the fermentation area will result in improved understanding of reactor operation across scales, and can potentially support more efficient transfer of results across scales. However, for these efforts to be successful, close collaboration between industry and academia will be required.

Acknowledgements

Financial support of the following organizations is acknowledged: The Danish Council for Strategic Research, project “Towards robust fermentation processes by targeting population heterogeneity at microscale” (project number 0603-00203B). The Novo Nordisk Foundation, project “Exploring biochemical process performance limits through topology optimization.” Region Zealand, the European Regional Development Fund (ERDF), CAPNOVA, CP Kelco, DONG Energy, Novo Nordisk, and Novozymes for funding the BIOPRO project

References

Agger T., Spohr A.B., Carlsen M., Nielsen J. (1998) Growth and product formation of *Aspergillus oryzae* during submerged cultivations: verification of a morphologically structured model using fluorescent probes, Biotechnol. Bioeng., 57, 321-329.

Bailey J.E. (1998) Mathematical modeling and analysis in biochemical engineering: past accomplishments and future opportunities. Biotechnol. Progr., 14, 8-20.

Cascaval D., Oniscu C., Galaction A. (2003) Rheology of fermentation broths 2. Influence of the rheological behavior on biotechnological processes. Rev. Roum. Chim., 48, 339-356.

Cervera A.E., Petersen N., Eliasson Lantz A., Larsen A. and Gernaey K.V. (2009) Application of near-infrared spectroscopy for monitoring and control of cell culture and fermentation. Biotechnol. Progr., 25, 1561-1581.

Enfors S.O., Jahic M., Rozkov A., Xu B., et al. (2001) Physiological responses to mixing in large scale bioreactors. J. Biotechnol., 85, 175-85.

Formenti L.R., Nørregaard A., Bolic A., Quintanilla-Hernandez D., et al. (2014) Challenges in industrial fermentation technology research. Biotechnol. J., 9, 727-738.

Fredrickson A.G., Megee R.D. III, Tsuchiya H.M. (1970) Mathematical models in fermentation processes. Adv. Appl. Microbiol., 13, 419-465.

Gernaey K.V., Eliasson Lantz A., Tufvesson P., Woodley J.M., Sin G. (2010) Application of mechanistic models to fermentation and biocatalysis for next generation processes. Trends Biotechnol., 28, 346-354.

Gernaey K.V., Jeppsson U., Vanrolleghem P.A., Copp J.B. (Eds.) (2014). Benchmarking of control strategies for wastewater treatment plants. IWA Scientific and Technical Report No. 23. IWA Publishing, London, UK.

Gibbs P.A., Seviour R.J., Schmid F. (2000) Growth of filamentous fungi in submerged culture: problems and possible solutions. Crit. Rev. Biotechnol., 20, 17-48.

Henson M.A. (2003) Dynamic modeling of microbial cell populations. Curr. Opin. Biotechnol., 14, 460-467.

Isett K., George H., Herber W., Amanullah A. (2007) Twenty-four-well plate miniature bioreactor high-throughput system: Assessment for microbial cultivations. Biotechnol. Bioeng., 98, 1017-1028.

Islam R.S., Tisi D., Levy M.S., Lye G.J. (2008) Scale-up of *Escherichia coli* growth and recombinant protein expression conditions from microwell to laboratory and pilot scale based on matched k_La. Biotechnol. Bioeng., 99, 1128-1139.

Johnson I.S. (1983) Human insulin from recombinant DNA Technology. Science, 219, 632-637.

Larsson G., Törnkvist M., Wernersson E.S., Trägard C., et al. (1996) Substrate gradients in bioreactors: origin and consequences. Bioprocess. Eng., 14, 281-289.

Lencastre Fernandes R., Nierychlo M., Lundin L., Pedersen A.E., et al. (2011) Experimental methods and modeling techniques for description of cell population heterogeneity. Biotechnology Advances, 29, 575-599.

Leng D.E., Katti S.S., Atiemo-Obeng V. (2008) Industial Mixing Technology. In: Albright L.F. (Ed.) Albright's Chemical Engineering Handbook, USA. CRC Press, p. 615-707.

Luttmann R., Bracewell D.G., Cornelissen G., Gernaey K.V., et al. (2012) Soft sensors in bioprocessing - A status report and recommendations. Biotechnol. J., 7, 1040-1048.

Moyer A.J. (1948) Method for production of penicillin. US patent 2442141,.

Oniscu C., Galaction A., Cascaval D. (2003) Rheology of fermentation broths 2. Rheological behaviors and influence factors. Re. Roum. Chim., 48, 91-110.

Ostergaard S., Olsson L., Nielsen J. (2000) Metabolic engineering of *Saccharomyces cerevisiae*. Microbiol. Mol. Biol. Rev., 64, 34-50.

Nielsen, J., Villadsen, J. (1992) Modeling of microbial kinetics. Chem. Eng. Sci., 47, 4225-4270.

Riley G.L., Tucker K.G., Paul G.C., Thomas C.R. (2000) Effect of biomass concentration and mycelial morphology on fermentation broth rheology. Biotechnol. Bioeng., 68, 160-172.

Shu P., Johnson M.J. (1948) Citric acid. J. Ind. Eng. Chem., 40, 1202-1205.

Smets I., Claes J., November E., Bastin G., van Impe J. (2004) Optimal adaptive control of (bio)chemical reactors: past, present and future. J. Process Contr., 14, 795-805.

Spohr A., Dam-Mikkelsen C., Carlsen M., Nielsen J., et al. (1998) On-line study of fungal morphology during submerged growth in a small flow-through cell. Biotechnol. Bioeng., 58, 541-553.

Stanbury P.F., Whitaker A., Hall S.J. (1995) Principles of Fermentation Technology. 2nd ed. Elsevier Science Ltd.

von Stosch M., Oliveria R., Peres J., Feyo de Azevedo S. (2012) Hybrid modeling framework for process analytical technology: Application to *Bordetella pertussis* cultures. Biotechnol. Progr., 28, 284-291.

Vrabel P., van der Lans R.G.J.M., Luyben K.C.A.M., Boon L., Nienow A.W. (2000) Mixing in large-scale vessels stirred with multiple radial or radial and axial up-pumping impellers: modelling and measurements. Chem. Eng. Sci., 55, 5881-5896.

Zamamiri A.M., Zhang Y., Henson M.A., Hjortsø M.A. (2002) Dynamics analysis of an age distribution model of oscillating yeast cultures. Chem. Eng. Sci., 57, 2169-2181.

Krist V. Gernaey, Jakob K. Huusom and Rafiqul Gani (Eds.), 12th International Symposium on Process Systems Engineering and 25th European Symposium on Computer Aided Process Engineering.
31 May – 4 June 2015, Copenhagen, Denmark

Sustainable Production and Consumption: A Decision-Support Framework Integrating Environmental, Economic and Social Sustainability

Adisa Azapagic

School of Chemical Engineering and Analytical Science, The Mill, Sackville Street, The University of Manchester, Manchester M13 9PL,UK

adisa.azapagic@manchester.ac.uk

Abstract

The idea of sustainable production and consumption is becoming a widely-accepted societal goal worldwide. However, its implementation is slow and the world continues to speed down an unsustainable path. One of the difficulties is the sheer complexity of production systems that would need to be re-engineered in a more sustainable way as well as the number of sustainability constraints that have to be considered and satisfied simultaneously. This paper argues that bringing about sustainable production and consumption requires a systems approach underpinned by life cycle thinking as well as an integration of economic, environmental and social aspects. In an attempt to aid this process, a decision-support framework has been developed comprising a range of tools, including scenario analysis, life cycle assessment, life cycle costing, social sustainability assessment, system optimisation and multi-attribute analysis. An application of the framework is illustrated on a case study related to energy.

Keywords: decision-support framework, energy, life cycle thinking, sustainable production and consumption, systems approach.

1. Introduction

It is increasingly becoming apparent that the lifestyles and practices of modern society cannot be sustained indefinitely, with growing scientific evidence showing that we are exceeding the Earth's capacity with respect to resource use and emissions to the environment (IPCC, 2013; UNEP, 2012). One of the many challenges of moving towards sustainable production and consumption is to find out which options are sustainable and to balance a plethora of disparate economic, environmental and social aspects. The challenge is exacerbated by the complexity of production systems and a large number of different stakeholder groups with conflicting interests. It is also often unclear what sustainability criteria are relevant for which alternatives. An additional difficulty is related to the need to consider both quantitative and qualitative criteria, often based on imprecise or subjective information. However, probably the greatest challenge is that sustainability problems are "wicked" problems which are intractable and highly resistant to resolution (Rittel and Webber, 1973; Azapagic and Perdan, 2014). Different approaches have been proposed for dealing with "wicked" problems (e.g., Roberts, 2000; Brown et al., 2010) but this paper argues that the best way is taking a systems approach and considering all three dimensions of sustainable development – environmental, economic and social – on a life cycle basis. The main reason for that is that such an approach treats sustainability issues as complex systems, and instead of focusing just on 'cause and effect', recognises their complexity and interrelationships,

acknowledging that technological solutions must be considered in a wider social, environmental, economic, regulatory, political and ethical framework (Azapagic and Perdan, 2014).

In an attempt to facilitate the process of better understanding and solving "wicked" sustainability problems, this paper proposes a decision-support framework which is underpinned by a systems, life cycle approach that integrates all three dimensions of sustainable development. The framework is outlined in the next section, followed in Section 3 by its application to a decision problem related to identifying sustainable electricity options for the future.

2. Decision-support framework

The proposed decision-support framework is outlined in Figure 1. Engaging stakeholders and understanding their concerns is a prerequisite for sustainable production and consumption, so that stakeholder identification and involvement is the first and probably the most important step. Depending on the decision problem, stakeholders may be representatives from industry, government, non-governmental organisations (NGOs) and consumer groups. They help to identify alternative options and key decision-criteria that will be used for a sustainability assessment of the defined alternatives. The sustainability of the alternatives is evaluated on a life cycle basis considering environmental, economic and social aspects of interest to the stakeholders. Different tools can be used for these purposes, including life cycle assessment (LCA), life cycle costing (LCC) and social life cycle assessment (S-LCA). Depending on stakeholders' interests and the type of the decision problem, the sustainability assessment will result in a large number of often disparate decision criteria, usually with some alternatives being better for some sustainability aspects but worse for others. To help the stakeholders deal with this complex information, multi-criteria decision analysis (MCDA) can be used. MCDA tools used for these purposes include single and multiobjective system optimisation as well as multi-attribute analysis (for a review, see e.g. Azapagic and Perdan, 2005). At the end of this process, the stakeholders can choose the most sustainable alternative, based on their preferences for different sustainability criteria. The decision-support framework can be used in a modular and/or iterative manner to suit the type of the problem and stakeholders. A practical application of the framework is illustrated in the next section.

3. Applying the decision-support framework

3.1. Problem definition and stakeholders

The decision problem considered here is related to identifying sustainable options for future electricity supply in the UK, extending up to the year 2070. The example is based on the data reported in Stamford and Azapagic (2014). The aim is to evaluate the sustainability of a range of technological options and identify an electricity mix that would have the lowest negative economic, environmental and social impacts. The stakeholder groups relevant for this problem include the energy industry, government, NGOs and consumers. Over 30 organisations and more than 600 consumers were engaged and consulted and their input used to inform the next steps of the decision-support framework, as discussed below.

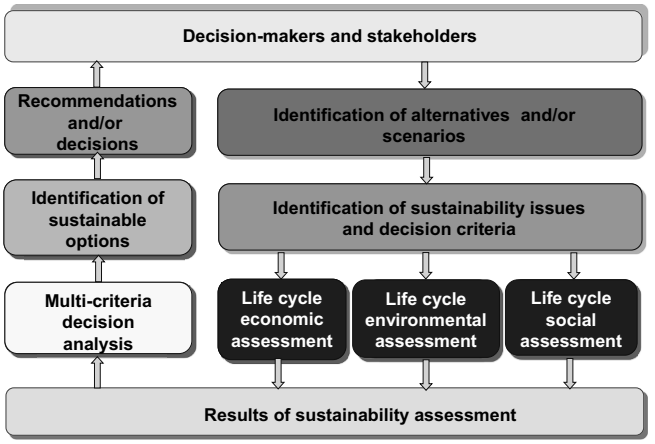

Figure 1 Decision-support framework for identifying sustainable production and consumption options

Table 1 Definition of scenarios (adapted from Stamford and Azapagic, 2014)

Scenario	Coal CCS and nuclear	Electricity mix
65%-1	Coal CCS, no new nuclear build	70% fossil and 30% renewables
65%-2	Coal CCS, new nuclear build	1/3 each of fossil, nuclear and renewables
80%	Coal CCS, new nuclear build	10% fossil, 30% nuclear and 60% renewables
100%-1	No coal CCS, no new nuclear build	100% renewables
100%-2	No coal CCS, new nuclear build	Equal proportions of nuclear and renewables

3.2. Identification of alternatives and scenarios

The following electricity generation options are considered, expected to play a major role in a future UK electricity mix (DECC, 2011): coal with and without carbon capture and storage (CCS), natural gas, nuclear, solar photovoltaics, wind and biomass. Taking a life cycle approach, all technologies are considered from 'cradle to grave', including the construction and decommissioning of power plants, extraction, processing and transport of fuels (if relevant), generation of electricity and waste management.

Five future scenarios up to 2070 have been formulated to examine the sustainability implications of different electricity mixes; the scenarios are summarised in Table 1. All scenarios are driven by the need to reduce greenhouse gas (GHG) emissions. Achieving the UK's legally-binding target of reducing the GHG emissions by 80% by 2050 on 1990 levels (DECC, 2012) will require a complete decarbonisation of the UK electricity mix (UKERC, 2009). This is considered in scenarios 100%-1 and 100%-2 (Table 1). The other three scenarios consider a case whereby the GHG targets are not achieved and the electricity mix is decarbonised by 65% or 80%. The scenarios also assume different penetration of the electricity technologies, as given in Table 1.

3.3. Identification of sustainability issues and decision criteria

Following extensive consultations with the stakeholders, 19 sustainability issues have been identified (Table 2) and translated in to 36 indicators or decision criteria (see Stamford and Azapagic, 2014). Each indicator addresses a particular sustainability issue on a life cycle basis, from 'cradle to grave'.

Table 2 Sustainability issues identified by stakeholders

Economic	Environmental	Social
Operability	Material recyclability	Provision of employment
Technological lock-in resistance	Water eco-toxicity	Human health impacts
Immediacy	Global warming	Large accident risk
Levelised cost of generation	Ozone layer depletion	Energy security
Cost variability	Acidification	Nuclear proliferation
	Eutrophication	Intergenerational equity
	Photochemical smog	
	Land use and quality	

3.4. Sustainability assessment

To assess the sustainability of different scenarios and technologies on a life cycle basis, LCA, LCC and S-LCA have been carried out. The results are shown in Figure 2 (owing to space constraints, only selective results are shown for illustration). For example, for all the scenarios the levelised costs would go up in the future relative to the present day, with scenario 100%-1 being the worst and 65%-2 and 100%-2 the least expensive options (Figure 2a). However, the sensitivity to fuel prices reduces significantly over the period for all the scenarios because of the lower contribution of fossil fuels than today (Figure 2b). Furthermore, all the scenarios would have lower life cycle environmental impacts than the current UK grid, including the global warming potential, GWP (Figure 2c). The exceptions are terrestrial eco-toxicity (Figure 2d) and land use (not shown) both of which would go up for all the scenarios. Finally, for the social impacts, some scenarios are better than today but others are worse. For instance, the employment in the supply chain would increase across the scenarios but so would the depletion of minerals and metals.

Therefore, as we can seen, the sustainability of different scenarios differs for different indicators, making it difficult to identify the most sustainable option. The next section shows how MCDA can help towards that.

3.5. Multi-criteria decision analysis and identification of sustainable options

The stakeholders were also consulted on their preferences for different sustainability issues as well as the electricity technologies. Example results are shown here for the UK public's preferences for different sustainability issues and electricity technologies (Youds, 2013). As indicated in Figure 3, water contamination is the most important and the cost of electricity least important in distinguishing between different electricity options. Solar photovoltaics, hydro and wind power are the most favourable options for the UK public while the fossil fuel options are least favoured.

To identify the most sustainable electricity scenarios, a simplified approach has been applied, assuming that all the criteria are equally important; the results are summarised in Table 3. Using a simple summed-rank method, the present and future scenarios have been ranked for each sustainability indicator and their individual ranks summed up to obtain a single score; the lower the score, the better the option (Stamford and Azapagic, 2014). Each scenario has then been ranked based on their overall summed score. The overall ranking suggests that all future scenarios are superior to the present electricity mix with the exception of 65%-1, which has the same ranking as the present mix. The best option, within the limitations of this simplified ranking approach, is 100%-2, followed by 80% (see Table 1 for scenario definitions).

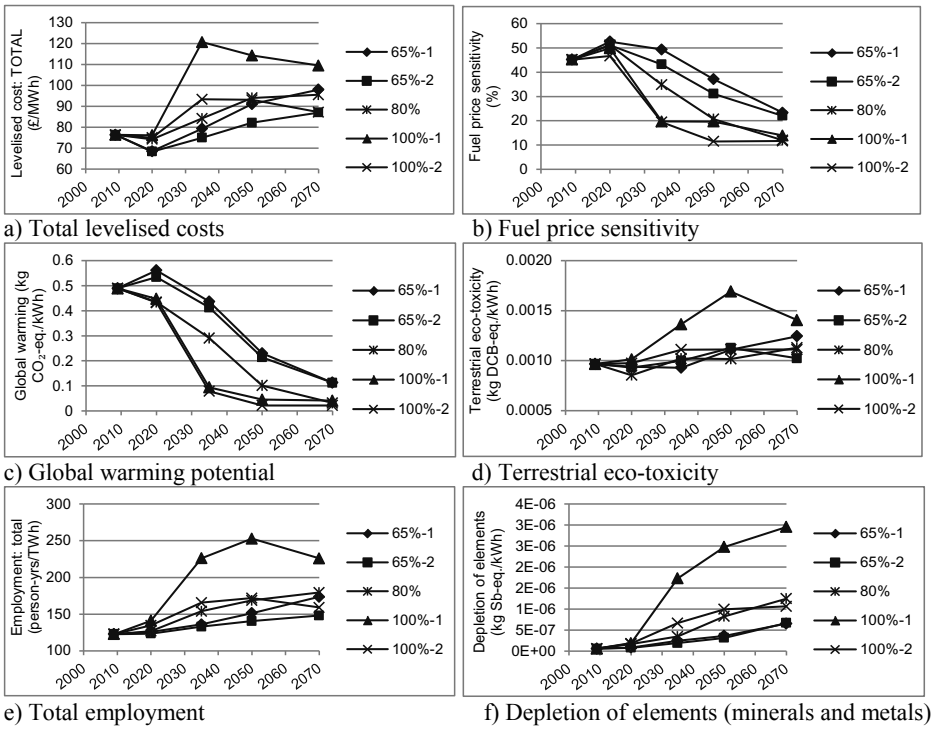

Figure 2 The results of the economic, environmental and social sustainability assessment (All indicators are on a life cycle basis. Only selective results are shown. For other indicators, see Stamford and Azapagic, 2014).

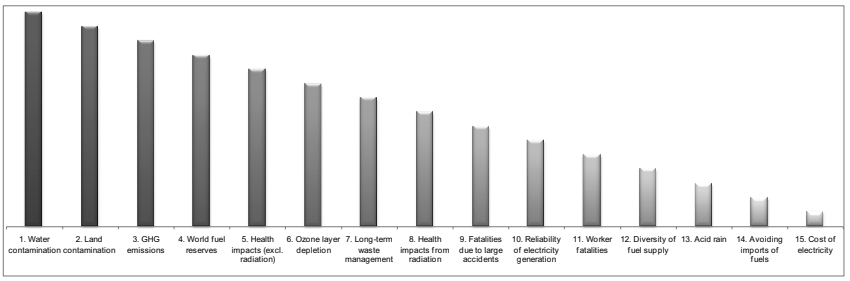

Figure 3 The importance of different sustainability issues to the UK public (Sample=625. Ranking order: 1=most important; 15=least important).

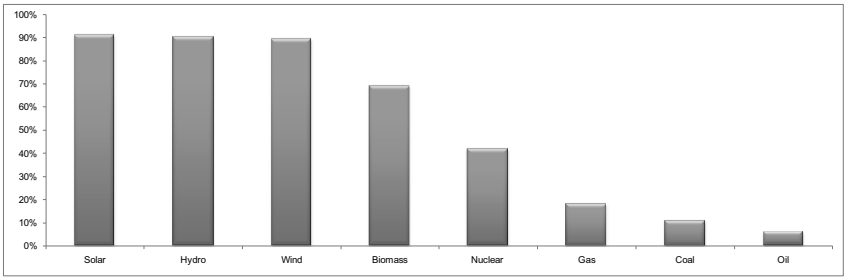

Figure 4 UK public's preferences for different electricity technologies (Sample=625. Values on the y-axis show the percentage of the respondents that favoured each electricity option).

Table 3 Ranking of scenarios

	Present UK grid	65%-1	65%-2	80%	100%-1	100%-2
Economic ranking	1	5	3	4	5	2
Environmental ranking	6	4	3	2	5	1
Social ranking	6	4	5	3	1	2
Overall ranking	5-6	5-6	3-4	2	3-4	1

However, if the scenarios are optimised, a different ranking emerges, depending on the objective function. For example, optimising on total life cycle costs favours scenarios 65% but the carbon targets are missed by a large margin; optimising on the total GWP favours the 100% scenarios but the costs are high (Bartezcko-Hibbert et al., 2014).

4. Conclusions

Unsustainable consumption drives unsustainable production and vice versa so that they cannot be tackled in isolation of each other. This calls for a systems, life cycle approach, taking into account environmental, economic and social concerns of different stakeholders. This paper has illustrated how such an approach can be incorporated within a decision-support framework to enable identification of sustainable production and consumption options. The framework facilitates engagement of different stakeholders and comprises a range of tools, including scenario analysis, life cycle assessment, life cycle costing, social sustainability assessment, system optimisation and multi-attribute analysis. The framework has been illustrated on an example related to future electricity options.

References

A. Azapagic and S. Perdan, 2005, An Integrated Sustainability Decision-Support Framework: Methods and Tools for Problem Analysis, Part II, Int. J. Sustainable Development & World Ecology, 12, 2, 112-131.

A. Azapagic and S. Perdan, 2014, Sustainable Chemical Engineering: Dealing with Wicked Sustainability Problems. AIChE J, 60, 12, 3998-4007.

C. Bartezcko-Hibbert, I. Bonis, M. Binns, C. Theodoropoulos and A. Azapagic, 2014, A Multi-Period Mixed-Integer Linear Optimisation of Future Electricity Supply Considering Life Cycle Costs and Environmental Impacts, Applied Energy, 133, 317–334.

V.A. Brown, J.A. Harris and J.Y. Russell (eds.), 2010, Tackling Wicked Problems through the Transdisciplinary Imagination, Earthscan, London, UK.

DECC, 2011, Overarching National Policy Statement for Energy (EN-1), TSO, London, UK.

DECC, 2012, UK Emissions Statistics, Department of Energy and Climate Change, London, UK.

IPCC, 2013, Climate Change 2013 – The Physical Science Basis, Working Group I Contribution to the Fifth Assessment Report of the IPCC, Cambridge University Press, Cambridge, UK.

H.W.J. Rittel and M. M. Webber, 1973, Dilemmas in a General Theory of Planning, Policy Sciences, 4, 2, 155–169.

N. Roberts, 2000, Coping with Wicked Problems, Naval Postgraduate School, Department of Strategic Management, Monterey, California, USA.

L. Stamford and A. Azapagic, 2014, Life Cycle Sustainability Assessment of UK Electricity Scenarios to 2070, Energy for Sustainable Development, 23, 194–211.

UKERC, 2009, Energy 2050 Project Report, UK Energy Research Centre, London, UK.

UNEP, 2012, GEO-5, Global Environmental Outlook – Environment for the Future We Want, United Nations Environmental Programme, Nairobi, Kenya.

L.H. Youds, 2013, Sustainability Assessment of Nuclear Power in the UK Using an Integrated Multi-Criteria Decision-Support Framework, Phd Dissertation, University of Manchester.

Krist V. Gernaey, Jakob K. Huusom and Rafiqul Gani (Eds.), 12th International Symposium on Process Systems Engineering and 25th European Symposium on Computer Aided Process Engineering.
31 May - 4 June 2015, Copenhagen, Denmark.

Control of Reaction Systems via Rate Estimation and Feedback Linearization

Diogo Rodrigues*, Julien Billeter and Dominique Bonvin

Laboratoire d'Automatique, EPFL, Lausanne, Switzerland
diogo.mateusrodrigues@epfl.ch

Abstract

The kinetic identification of chemical reaction systems often represents a time-consuming and complex task. This contribution presents an approach that uses rate estimation and feedback linearization to implement effective control without the use of a kinetic model. The reaction rates are estimated by numerical differentiation of reaction variants that are computed from measurements. The approach is illustrated in simulation through the temperature control of a continuous stirred-tank reactor.

Keywords: feedback linearization, rate estimation, numerical differentiation, reaction variants.

1. Introduction

Efficient control of reaction systems typically requires good kinetic models, whose identification however can be rather difficult and time consuming. As an alternative, one could try to infer the reaction rates directly from measurements, that is, without the help of a kinetic model, which can be done if the various rates can be decoupled (Mhamdi and Marquardt (2004)).

The concept of reaction variants and invariants has been proposed to decouple the dynamic effects in reaction systems, thereby facilitating their analysis and control (Asbjørnsen and Fjeld (1970); Asbjørnsen (1972)). A finer separation of the various dynamic effects in both homogeneous and heterogeneous open reaction systems has been proposed by Amrhein et al. (2010) and Bhatt et al. (2010), and reformulated recently as a linear transformation of the numbers of moles to so-called vessel extents by Rodrigues et al. (2015).

Although various control structures for continuous stirred-tank reactors based on reactions variants and extensive variables have been proposed throughout the years (Hammarström (1979); Georgakis (1986); Farschman et al. (1998); Dochain et al. (2009); Hoang et al. (2014)), there does not exist a systematic way of tackling the problem, in particular without the use of a kinetic model. The long-term objective of this research is the development of such a systematic control approach, which would utilize the linear transformation to vessel extents and control selected extents by adjusting the corresponding rates such as inlet flowrates or the power exchanged with the jacket.

This paper is a first step in that direction as it investigates the possibility of controlling chemical reactors without the explicit use of kinetic models. The reaction rates are estimated from concentration and temperature measurements via the concept of variants and then used via a feedback-linearization scheme to control the reactor temperature by manipulating the amount of heat that is exchanged with the environment in a continuous stirred-tank reactor.

2. System description

Let us consider an open homogeneous reactor with S species, R independent reactions, p inlet streams and one outlet stream. The mole and heat balances can be written as follows (Rodrigues et al. (2015)):

$$\underbrace{\begin{bmatrix}\dot{\mathbf{n}}(t)\\ \dot{Q}(t)\end{bmatrix}}_{\dot{\mathbf{z}}(t)} = \underbrace{\begin{bmatrix}\mathbf{N}^{\mathrm{T}}\\ (-\boldsymbol{\Delta}\mathbf{H})^{\mathrm{T}}\end{bmatrix}}_{\mathscr{A}} \mathbf{r}_v(t) + \underbrace{\begin{bmatrix}\mathbf{0}_S\\ 1\end{bmatrix}}_{\mathbf{b}} q_{ex}(t) + \underbrace{\begin{bmatrix}\mathbf{W}_{in}\\ \check{\mathbf{T}}_{in}^{\mathrm{T}}\end{bmatrix}}_{\mathscr{C}} \mathbf{u}_{in}(t) - \omega(t) \underbrace{\begin{bmatrix}\mathbf{n}(t)\\ Q(t)\end{bmatrix}}_{\mathbf{z}(t)}, \qquad \underbrace{\begin{bmatrix}\mathbf{n}(0)\\ Q(0)\end{bmatrix}}_{\mathbf{z}(0)} = \underbrace{\begin{bmatrix}\mathbf{n}_0\\ Q_0\end{bmatrix}}_{\mathbf{z}_0}, \quad (1)$$

where $\mathbf{n}$ is the S-dimensional vector of numbers of moles, $Q(t) = m(t)c_p(t)\big(T(t) - T_{ref}\big)$ the heat of the reaction mixture, $\mathbf{r}_v$ the R-dimensional vector of reaction rates, q_{ex} the heat power that is exchanged with the jacket and the environment, $\mathbf{u}_{in}$ the p-dimensional vector of inlet flowrates, $\omega(t) := \frac{u_{out}(t)}{m(t)}$ the inverse of the residence time, with u_{out} the outlet flowrate and m the mass in the reactor, $\mathbf{N}$ the $R \times S$ stoichiometric matrix, $\boldsymbol{\Delta}\mathbf{H}$ the R-dimensional vector of heats of reaction, $\mathbf{W}_{in}$ the $S \times p$ inlet-composition matrix, $\check{\mathbf{T}}_{in}$ the p-dimensional vector of inlet specific enthalpies, V the reactor volume, c_p the specific heat capacity, T the temperature and T_{ref} a reference temperature. The state vector $\mathbf{z}$ and the vector $\mathbf{b}$ are both of dimension $S+1$, while the matrix $\mathscr{A}$ has dimension $(S+1) \times R$ and the matrix $\mathscr{C}$ has dimension $(S+1) \times p$.

2.1. Transformation to reaction-variant states

If $\operatorname{rank}(\mathscr{A}) = R$, there exists a transformation matrix $\mathscr{T}$ of dimension $R \times (S+1)$ such that

$$\mathscr{T}\mathscr{A} = \mathbf{I}_R. \quad (2)$$

Applying the transformation $\mathscr{T}$ to Eq.(1) and defining $\mathbf{x}_{\mathbf{r}_v}(t) := \mathscr{T}\mathbf{z}(t)$ leads to

$$\dot{\mathbf{x}}_{\mathbf{r}_v}(t) = \mathbf{r}_v(t) + (\mathscr{T}\mathbf{b})\, q_{ex}(t) + (\mathscr{T}\mathscr{C})\, \mathbf{u}_{in}(t) - \omega(t)\mathbf{x}_{\mathbf{r}_v}(t), \qquad \mathbf{x}_{\mathbf{r}_v}(0) = \mathscr{T}\mathbf{z}_0. \quad (3)$$

The transformed states $\mathbf{x}_{\mathbf{r}_v}$ are reaction variants, with each state $x_{r_{v,i}}$ $(i = 1, \ldots, R)$ depending on the rate $r_{v,i}$, the manipulated variable q_{ex}, a combination of the inlet flowrates $\mathbf{u}_{in}$, and ω the inverse of the residence time. To be applicable, the transformation $\mathscr{T}$ requires that at least R elements of the vector $\mathbf{z}$ be measured (Rodrigues et al. (2015)). Note that transformations based on $[\mathscr{A}\ \ \mathbf{b}]$ or $[\mathscr{A}\ \ \mathbf{b}\ \ \mathbf{z}_0]$ could also be used, but they would require stricter rank conditions and thus more measured quantities, that is, $R+1$ or $R+2$ instead of R.

The proposed control scheme includes two steps, namely, the estimation of the reaction rates from the reaction-variant states $\mathbf{x}_{\mathbf{r}_v}$ and temperature control via feedback linearization.

3. Control Problem

The objective is to implement temperature control, that is, to control the heat signal $Q(t)$ to either the constant setpoint Q_s or the reference trajectory $Q_s(t)$ by manipulating the exchanged heat power $q_{ex}(t)$. The reaction rates $\mathbf{r}_v(t)$ will be estimated without the use of a kinetic model using the measured quantities $\mathbf{z}(t)$, $\mathbf{u}_{in}(t)$, $\omega(t)$ and the manipulated variable $q_{ex}(t)$.

3.1. Estimation of reaction rates

The estimation of $\mathbf{r}_v(t)$ proceeds via the differentiation of the reaction variants $\mathbf{x}_{\mathbf{r}_v}(t)$ that are obtained by transformation of $\mathbf{z}(t)$, or of subset of it (of dimension $S_a + 1 \geq R$), and the knowledge of the quantities $q_{ex}(t)$, $\mathbf{u}_{in}(t)$ and $\omega(t)$.

Reformulating Eq.(3) yields the reaction rates

$$\mathbf{r}_v(t) = \dot{\mathbf{x}}_{\mathbf{r}_v}(t) - (\mathscr{T}\mathbf{b})\, q_{ex}(t) - (\mathscr{T}\mathscr{C})\, \mathbf{u}_{in}(t) + \omega(t)\mathbf{x}_{\mathbf{r}_v}(t). \quad (4)$$

Different transformations $\mathscr{T}$ that satisfy the condition in Eq.(2) can be found. An example is the Moore-Penrose pseudo-inverse of the matrix $\mathscr{A}$. However, when only noisy measurements of the state vector $\mathbf{z}$ are available, a better alternative is to consider an estimator in the maximum-likelihood sense, for which the transformation (2) is computed as

$$\mathscr{T} = (\mathscr{A}^{\mathrm{T}}\boldsymbol{\Sigma}^{-1}\mathscr{A})^{-1}\mathscr{A}^{\mathrm{T}}\boldsymbol{\Sigma}^{-1}, \tag{5}$$

where $\boldsymbol{\Sigma}$ is the $(S+1)$-dimensional variance-covariance matrix of the measurements. Note that the weighted transformation in Eq.(5) satisfies Eq.(2). The estimates $\hat{\mathbf{r}}_v(t)$ of the reaction rates given by Eq.(4) can be computed as described in Appendix A.

3.2. Temperature control via feedback linearization

The controller forces the heat signal $Q(t)$ to converge towards its reference trajectory $Q_s(t)$ at a desired rate. Defining the new input $v(t)$ to represent the right-hand side of the heat balance in Eq.(1) results in an integral relationship between the input $v(t)$ and the controlled variable $Q(t)$,

$$\dot{Q}(t) = (-\boldsymbol{\Delta}\mathbf{H})^{\mathrm{T}}\mathbf{r}_v(t) + q_{ex}(t) + \check{\mathbf{T}}_{in}^{\mathrm{T}}\mathbf{u}_{in}(t) - \omega(t)Q(t) \stackrel{!}{=} v(t). \tag{6}$$

Such an approach builds on feedback linearization, as shown in Figure 1. Solving Eq.(6) for q_{ex} and replacing $\mathbf{r}_v$ by its estimate $\hat{\mathbf{r}}_v$ according to Eq.(12) in Appendix A gives the following expression for the manipulated variable:

$$q_{ex}(t) = v(t) - (-\boldsymbol{\Delta}\mathbf{H})^{\mathrm{T}}\hat{\mathbf{r}}_v(t) - \check{\mathbf{T}}_{in}^{\mathrm{T}}\mathbf{u}_{in}(t) + \omega(t)Q(t). \tag{7}$$

One can design a feedback controller that forces the control error $e(t) := Q_s(t) - Q(t)$ to converge exponentially to zero at the rate γ,

$$\dot{e}(t) = -\gamma e(t), \qquad e(0) = Q_s(0) - Q(0), \tag{8}$$

by using the control law

$$v(t) = \dot{Q}_s(t) + \gamma\big(Q_s(t) - Q(t)\big). \tag{9}$$

Note that this control law uses $\dot{Q}_s(t)$, which ideally requires prior knowledge of the reference signal $Q_s(t)$.

4. Simulated example

Consider the simulated example of the acetoacetylation of pyrrole in a homogeneous CSTR of constant volume with $S = 4$ species (A: pyrrole; B: diketene; C: 2-acetoacetylpyrrole; D: dehydroacetic acid), $R = 2$ reactions (A + B $\rightarrow$ C, 2B $\rightarrow$ D), $p = 2$ inlets (of A and B) and 1 outlet, the flowrate of which is adjusted to keep the volume constant (Ruppen et al. (1998)).

For this simulation, the following values are used: $\mathbf{N} = \left[\begin{smallmatrix} -1 & -1 & 1 & 0 \\ 0 & -2 & 0 & 1 \end{smallmatrix}\right]$, $\mathbf{W}_{in}^{\mathrm{T}} = \left[\begin{smallmatrix} 67.09^{-1} & 0 & 0 & 0 \\ 0 & 84.08^{-1} & 0 & 0 \end{smallmatrix}\right]$ kmol kg^{-1}, $\boldsymbol{\Delta}\mathbf{H} = \left[\begin{smallmatrix} -70 \\ -50 \end{smallmatrix}\right] \times 10^3$ kJ kmol^{-1}, $\check{\mathbf{T}}_{in} = \mathbf{0}_p$ at $T_{ref} = 298.15$ K, $r_{v,1} = Vk_1c_Ac_B$ and $r_{v,2} = Vk_2c_B^2$, where $\mathbf{c}(t) = \mathbf{n}(t)/V(t)$, $k_1 = A_1 \exp\left(-\frac{E_{a,1}}{RT}\right)$ and $k_2 = A_2 \exp\left(-\frac{E_{a,2}}{RT}\right)$. The values of A_1, A_2, $E_{a,1}$, $E_{a,2}$, densities and specific heat capacities are adapted from Maria and Dan (2011). The volume is constant at $V = 90.16$ L. Furthermore, it is assumed that the density and the specific heat capacity are constant, which results in the constant heat capacity $mc_p = 129.5$ kJ K^{-1}.

The system is initially at steady state corresponding to the inputs $\bar{q}_{ex} = -4.9 \times 10^3$ kJ min^{-1} and $\bar{\mathbf{u}}_{in} = \left[\begin{smallmatrix} \bar{u}_{in,A} \\ \bar{u}_{in,B} \end{smallmatrix}\right] = \left[\begin{smallmatrix} 40 \\ 15 \end{smallmatrix}\right]$ kg min^{-1}, which gives the initial values $\mathbf{n}_0^{\mathrm{T}} = [0.833 \;\; 0.093 \;\; 0.143 \;\; 0.028]$

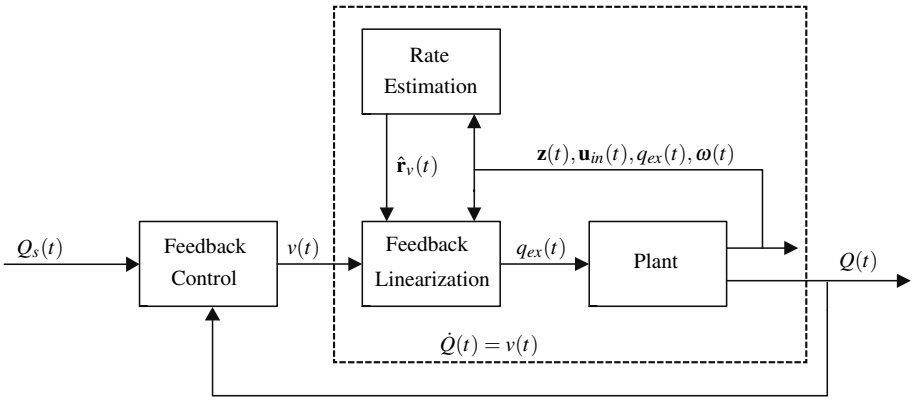

Figure 1: Temperature control based on feedback linearization and estimation of the reaction rates.

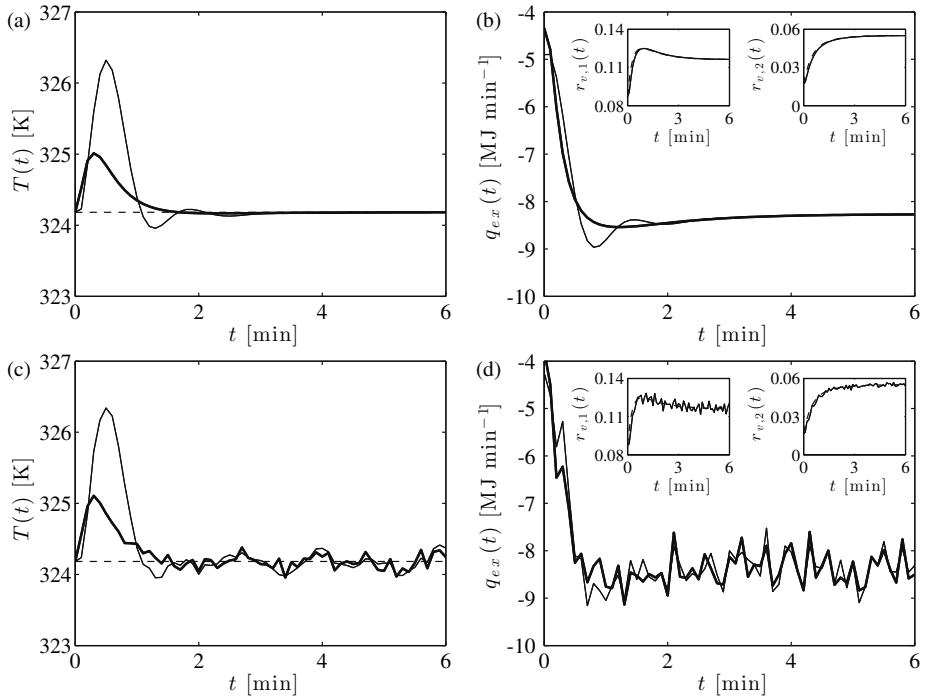

Figure 2: (a) and (c): Temperature profiles for feedback-linearization control (thick line) and PI control (thin line), with the setpoint shown by the dashed line; (b) and (d): Exchanged heat power and, insets, estimated (solid lines) and true (dashed lines) reaction rates in kmol min^{-1}. The subfigures (a) and (b) show results without measurement noise, whereas (c) and (d) show results with measurement noise.

kmol and $Q_0 = 3.37 \times 10^3$ kJ (corresponding to $T_0 = 324.2$ K). The reaction rates $\mathbf{r}_v$ are estimated from Eq.(12) in Appendix A. The control objective is to reject a 15 kg min^{-1} step disturbance in $u_{in,B}$ by manipulating $q_{ex}(t)$.

Measurements of $\mathbf{z}$, q_{ex}, $\mathbf{u}_{in}$ and ω are available at the sampling time $h_s = 0.4$ s. It is assumed that the measurement errors in q_{ex}, $\mathbf{u}_{in}$ and ω are negligible in comparison to those in $\mathbf{z}$, for which the standard deviation of the concentration measurements is 0.5% of the maximum concentration of each species and the standard deviation of the temperature measurements is 0.5 K. This results in the variance-covariance matrix $\mathbf{\Sigma} = \text{diag}\left(\left[0.004^2 \;\; 0.001^2 \;\; 0.001^2 \;\; 0.00025^2 \;\; 65^2\right]\right)$. A differentiation filter of order 1 and window size $q = 25$ is used (Savitzky and Golay (1964)).

Feedback-linearization control using the exponential convergence rate $\gamma = 5$ min^{-1} is compared to PI control with the gain $K_p = 5$ min^{-1} and the integral time constant $\tau_I = 0.2$ min. Figure 2 shows that the feedback-linearization scheme is able to reject the disturbance more quickly than the PI controller. However, if the standard deviation of the concentration measurements is larger than about 1% of the maximum concentration of each species, the estimated reaction rates become too imprecise or delayed (due to the choice of a larger window size q), and the advantage of feedback linearization over PI control is less clear (results not shown).

5. Conclusions

This paper has considered the control of the heat signal Q (or temperature T) by manipulating the exchanged heat power q_{ex} in an open homogeneous reactor. Control is implemented without the knowledge of a kinetic model. Instead, the reaction rates are (i) estimated via differentiation of reaction variants that are computed from measured states, and (ii) used in a feedback-linearization scheme that simplifies control design significantly. The parameters of the feedback-linearization controller are determined by readily available information, namely, the stoichiometry, the heats of reaction, the inlet composition and specific heat, and the inlet and outlet flow rates. Instead of linearizing the system around a given steady state, this controller implements feedback linearization that allows tracking a trajectory by forcing the control error to decay exponentially to zero. The resulting controller shows good performance for the case of frequent and precise concentration measurements of several species.

The controller requires $\text{rank}(\mathscr{A}) = R$, that is, at least as many measured quantities as there are reaction rates ($S_a + 1 \geq R$). The controller has two tunable parameters, namely, the exponential convergence rate γ and the parameter of the differentiation filter (the number of samples q in the case of the Savitzky-Golay filter) used for the rate estimation. These parameters need to be chosen to guarantee closed-loop stability. This study has shown that, at least in the case of low measurement noise, feedback linearization coupled to rate estimation can outperform PI control for the purpose of disturbance rejection.

A. Appendix

Let us approximate the derivative $\dot{\mathbf{x}}_{\mathbf{r}_v}(t)$ using a differentiation filter, such as the first-order filter proposed by Savitzky and Golay (1964), denoted as $\mathscr{D}_q(\mathbf{x}_{\mathbf{r}_v}, t)$, where q is the window size expressed in number of samples in the time interval $[t - \Delta t, t]$, with $\Delta t := (q-1)h_s$ and h_s the sampling time. It can be shown that, since $\mathbf{x}_{\mathbf{r}_v}$ is Lipschitz continuous, $\mathscr{D}_q(\mathbf{x}_{\mathbf{r}_v}, t)$ can be reformulated as

$$\mathscr{D}_q(\mathbf{x}_{\mathbf{r}_v}, t) = \sum_{k=0}^{q-2} b_{k+1} \int_k^{k+1} \dot{\mathbf{x}}_{\mathbf{r}_v}(t_\xi) d\xi \tag{10}$$

with the weighting coefficients $b_{k+1} = \frac{6(q-1-k)(k+1)}{q(q^2-1)} > 0$, such that $\sum_{k=0}^{q-2} b_{k+1} = 1$, and $t_\xi := t - \Delta t + \xi\, h_s$. Replacing $\dot{\mathbf{x}}_{\mathbf{r}_v}$ by its expression in Eq.(3) gives

$$\begin{aligned}\mathscr{D}_q(\mathbf{x}_{\mathbf{r}_v}, t) &= \sum_{k=0}^{q-2} b_{k+1} \int_k^{k+1} \left(\mathbf{r}_v(t_\xi) + (\mathscr{T}\mathbf{b})\, q_{ex}(t_\xi) + (\mathscr{T}\mathscr{C})\, \mathbf{u}_{in}(t_\xi) - \omega(t_\xi)\mathbf{x}_{\mathbf{r}_v}(t_\xi)\right) d\xi \\ &\approx \mathbf{r}_v(t) + \sum_{k=0}^{q-2} b_{k+1} \left((\mathscr{T}\mathbf{b})\, q_{ex}(t_k) + (\mathscr{T}\mathscr{C})\, \mathbf{u}_{in}(t_k) - \omega(t_k)\, \mathbf{x}_{\mathbf{r}_v}(t_k)\right), \end{aligned} \tag{11}$$

where $t_k := t - \Delta t + k\, h_s$.

The approximation in Eq.(11) is valid under the assumptions that $\mathbf{r}_v(t)$ is approximately constant in the time interval $[t - \Delta t, t]$ and the quantities $q_{ex}(t)$, $\mathbf{u}_{in}(t)$ and $\omega(t)\,\mathbf{x}_{\mathbf{r}_v}(t)$ are approximately constant in each time interval $[t_k, t_{k+1}[$.

Defining the operator $\mathscr{W}_q(f,t) := \sum_{k=0}^{q-2} b_{k+1} f(t_k)$ for any function $f(t)$, rearranging Eq.(11) for $\mathbf{r}_v(t)$ and using measured quantities, denoted as $\tilde{(\cdot)}$, yields

$$\hat{\mathbf{r}}_v(t) = \mathscr{D}_q(\tilde{\mathbf{x}}_{\mathbf{r}_v}, t) - (\mathscr{T}\mathbf{b})\, \mathscr{W}_q(\tilde{q}_{ex}, t) - (\mathscr{T}\mathscr{C})\, \mathscr{W}_q(\tilde{\mathbf{u}}_{in}, t) + \mathscr{W}_q(\tilde{\omega}\, \tilde{\mathbf{x}}_{\mathbf{r}_v}, t) \tag{12}$$

Eq.(12) approximates Eq.(4) for the case of measured quantities and can be used in Eq.(7).

References

M. Amrhein, N. Bhatt, B. Srinivasan, D. Bonvin, 2010, Extents of reaction and flow for homogeneous reaction systems with inlet and outlet streams, AIChE J., 56, 11, 2873–2886.

O. A. Asbjørnsen, 1972, Reaction invariants in the control of continuous chemical reactors, Chem. Eng. Sci., 27, 4, 709–717.

O. A. Asbjørnsen, M. Fjeld, 1970, Response modes of continuous stirred tank reactors, Chem. Eng. Sci., 25, 11, 1627–1636.

N. Bhatt, M. Amrhein, D. Bonvin, 2010, Extents of reaction, mass transfer and flow for gas–liquid reaction systems, Ind. Eng. Chem. Res., 49, 17, 7704–7717.

D. Dochain, F. Couenne, C. Jallut, 2009, Enthalpy based modelling and design of asymptotic observers for chemical reactors, Int. J. Control, 82, 8, 1389–1403.

C. A. Farschman, K. P. Viswanath, B. E. Ydstie, 1998, Process systems and inventory control, AIChE J., 44, 8, 1841–1857.

C. Georgakis, 1986, On the use of extensive variables in process dynamics and control, Chem. Eng. Sci., 41, 6, 1471–1484.

L. G. Hammarström, 1979, Control of chemical reactors in the subspace of reaction and control variants, Chem. Eng. Sci., 34, 6, 891–899.

N. H. Hoang, D. Dochain, B. E. Ydstie, 2014, Partial inventory control of the CSTR via reaction-dependent generalized inventories, 19th IFAC World Congress, Cape Town, South Africa, 9123–9128.

G. Maria, A. Dan, 2011, Derivation of optimal operating policies under safety and technological constraints for the acetoacetylation of pyrrole in a semi-batch catalytic reactor, Comp. Chem. Eng., 35, 1, 177–189.

A. Mhamdi, W. Marquardt, 2004, Estimation of reaction rates by nonlinear system inversion, ADCHEM 2003, Hong Kong, China, 171–176.

D. Rodrigues, S. Srinivasan, J. Billeter, D. Bonvin, 2015, Variant and invariant states for reaction systems, Comp. Chem. Eng., 73, 1, 23–33.

D. Ruppen, D. Bonvin, D. W. T. Rippin, 1998, Implementation of adaptive optimal operation for a semi-batch reaction system, Comp. Chem. Eng., 22, 1, 185–189.

A. Savitzky, M. Golay, 1964, Smoothing and differentiation of data by simplified least squares procedures, Anal. Chem., 36, 8, 1627–1639.

Krist V. Gernaey, Jakob K. Huusom and Rafiqul Gani (Eds.), 12th International Symposium on Process Systems Engineering and 25th European Symposium on Computer Aided Process Engineering.
31 May – 4 June 2015, Copenhagen, Denmark

Modeling the Fixed-Bed Fischer-Tropsch Reactor in Different Reaction Media

Rehan Hussain,[a] Jan H. Blank,[a] Nimir O. Elbashir [a*]

[a]*Chemical Engineering Program, Texas A&M University at Qatar, PO Box 23874, Doha, Qatar*

* Corrsponding author *nelbashir@tamu.edu*

Abstract

Reactor modeling is a very useful tool in the design and scale-up of commercial reactors, enabling prediction of the system behavior under different operating conditions without the need for expensive and time-consuming experimentation. In this paper we present our approach towards developing a comprehensive fixed-bed reactor model for Fischer-Tropsch synthesis (FTS) on a cobalt-based catalyst using a detailed mechanistic model to predict the FTS product distribution. In the current study, we developed a multi-scale approach to mode the FTS reactor whereby we combine the use of a detailed mechanistic kinetic model with a particle diffusion model to account for heat and mass transfer limitations both locally and in the whole reactor bed. Simultaneously, we have implemented a fixed-bed reactor model, also in MATLAB® that is capable of predicting the whole bed behavior taking into account the heat and mass transfer resistances in the reactor bed such as the loss in catalytic activity due to diffusion in the catalyst pores. For experimental validation of the model, a high pressure bench-scale reactor unit has been utilized. The kinetic model developed here is to be integrated into a model of the whole reactor bed, with a view towards facilitating the optimization and scale-up of novel FTS reactor bed designs for both the conventional gas phase FTS and the supercritical phase FTS.

Keywords: Gas-to-liquids, Fischer-Tropsch Synthesis, fixed-bed, reactor modelling, catalysis.

1. Introduction

The global rise in crude oil prices over the last several years, combined with the increase in production of natural gas, have meant that alternative pathways for natural gas monetization, such as Gas-to-liquids (GTL) technology (whereby natural gas is converted into easily-transportable liquid hydrocarbons and other value-added chemicals), are increasingly preferred. The key step in the GTL process is conversion of syngas (a mixture of CO and H_2 obtained from reforming methane or from coal/biomass gasification) via Fischer-Tropsch synthesis (FTS) into a range of hydrocarbon products such as paraffins, olefins and oxygenates of varying chain lengths by reaction over an active metal catalyst (typically Co, Fe, Ni, or Ru).

Despite the long history of FTS, there remained comparatively few studies (e.g. Liu et al. 1999, Wang et al. 2003) done on modeling the conventional gas-phase FTS fixed-bed reactor until recent years, wherein several significant modeling studies appeared in the literature. In many of these studies, the ‘psuedo-homogeneous’ approach, whereby the catalyst, reactants and products are treated as a single phase in the conservation

equations, remains the preferred means for modeling fixed-bed FTS reactors. Wang et al. (2003) employed a simplified pseudo-homogeneous model assuming and negligible axial or radial mass dispersion and only radial heat conduction, as well as a catalyst effectiveness factor of one; the resulting ideal plug-flow model was capable of achieving good agreement with experimental data for externally-cooled fixed-bed tubular reactors.

In the current study, we aim to model the fixed-bed FTS reactor using a multi-scale approach whereby we combine the use of a detailed mechanistic kinetic model with a particle diffusion model to account for heat and mass transfer limitations both locally and in the whole reactor bed. We attempt to validate the model under typical gas-phase FTS conditions using experimental data generated from our high-pressure FTS reactor unit. This work represents a first step towards developing a comprehensive model for FTS capable of accounting for the presence of different reaction media such as supercritical fluid (SCF) solvents, which have been shown to provide several advantages over operation in the conventional gas-phase FTS (Elbashir et al. 2010).

2. Methodology

2.1. Experimental Setup

The experimental data reported here was generated using an advanced high-pressure FTS reactor unit, a schematic of which is shown in Figure 1. The unit, which was designed in-house and custom-built by Xytel US, is capable of using supercritical fluid (SCF) solvents up to 85 bar. The analytical setup is composed of a single online custom-built Shimadzu GC setup composed of a dual oven system fitted with three TCD detectors and one FID detector for analysis of the permanent gases and low-boiling hydrocarbons up to C_{15}. This unit is capable of fully automated sampling and online analysis of permanent gases and low-boiling liquids in a single experiment, thus allowing for an accurate mass balance of reactants and products. In addition to the Shimadzu GC, an Agilent GC-MS/FID unit is available for offline analysis of the higher-boiling liquid compounds, up to C_{34}. As the data presented here is preliminary data from an ongoing study, further details regarding this unit are to be made available elsewhere.

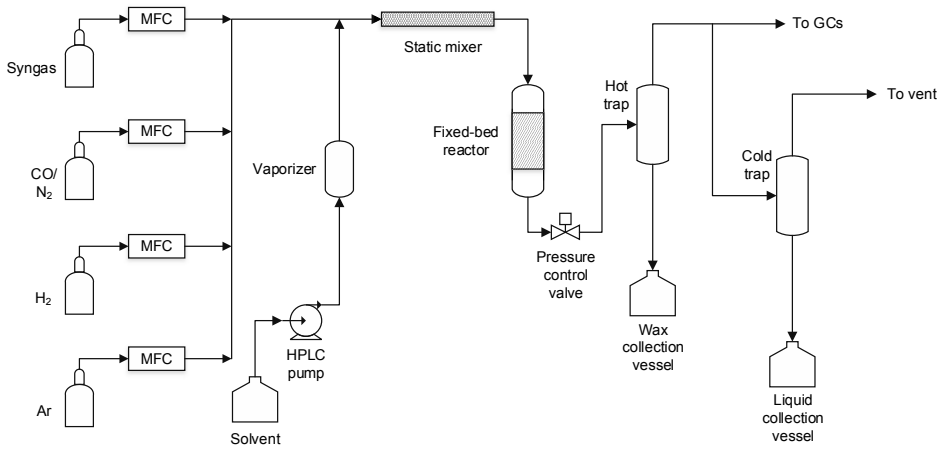

Figure 1: Schematic of the high-pressure FTS reactor unit.

The fixed-bed reactor, which consists of a single stainless steel tube of inner diameter 1.75 cm and wall thickness 0.4 cm, was loaded with a mixture of 0.5 g of 15 wt% Co/Al_2O_3 catalyst (150–250 µm particle size) and 10 g of crushed silica sand (Sigma Aldrich, 210–297 µm particle size). The catalyst and sand particles were mixed thoroughly prior to loading and the bed was loaded slowly while rotating the reactor tube in an effort to ensure a regular distribution of catalyst particles throughout the bed. The catalyst used for this study was provided by Dr Dragomir Bukur at Texas A&M Qatar. Catalyst reduction was done in-situ under a hydrogen flow of 100 sccm g_{cat}^{-1} at 350 °C for 10 hours. Subsequently, gas-phase FTS experiments were carried out on the activated catalyst at a feed temperature of 240 °C using syngas (2:1 H_2 to CO ratio) at a partial pressure of 20 bar, with Ar supplied at a constant flowrate of 10 sccm. The total pressure of the system was adjusted accordingly in order to keep the syngas partial pressure constant.

2.2. Reactor Bed Model

For the reactor simulations, a one-dimensional pseudo-homogeneous reactor model (as described in Froment et al. 2011) was used to calculate the overall CO concentration and temperature profiles in the fixed-bed FTS reactor. The model assumed plug-flow in the reactor bed and hence ignored temperature and concentration gradients in the radial direction. We justify this assumption by noting the relatively large particle-to-tube diameter ratio of ~1/70 (based on an average particle size of 250 µm, as was used in this study) and relative homogeneity of the bed packing used in experiments. The model, however, does account for diffusion limitations inside the catalyst particles through the use of the local bed effectiveness factor, η, which will be described in more detail in the following section. The steady-state conservation equations for mass (in terms of CO consumption), energy and momentum are therefore as follows:

$$-\frac{d(u_s c_{CO})}{dz} = \eta r_{CO} \rho_B \tag{1}$$

$$u_s \rho_g c_p \frac{dT}{dz} = (-\Delta H)\eta r_{CO} \rho_B - 4\frac{U}{d_t}(T - T_r) \tag{2}$$

$$-\frac{dp_t}{dz} = f\frac{\rho_g u_s^2}{d_p} \tag{3}$$

Here, u_s is the superficial gas velocity, c_{CO} is the concentration of CO, r_{CO} is the rate of consumption of CO, ρ_b is the bed density, ρ_g is the gas-phase density, c_p is the specific heat capacity of the reaction medium, ΔH is the heat of reaction for FTS, U is the overall heat transfer coefficient, T_r is the surrounding temperature, d_t is the tube diameter, p_t is the pressure across the reactor bed, and d_p is the average particle diameter. All other symbols have their usual meanings. The conservation equations were solved in MATLAB® using an ODE solver, ode45. In our model implementation, the length of the reactor bed was fixed, and the resulting CO conversion (defined as the percentage of CO consumed over the concentration of CO at the inlet), temperature and pressure profiles were obtained.

For the heat transfer in the bed, Equation (2), the coolant surrounding the reactor tube was modeled as air at a constant temperature T_r, which was set at 230 °C in order to match the furnace temperature used in experiments (as described in 2.1). The overall heat transfer coefficient U of the reactor bed was obtained experimentally as a function

of syngas flowrate at P = 20 bar and T = 513 K over a bed made from the sand particles used to dilute the catalyst (i.e. without Co/Al_2O_3 catalyst particles present). Two different temperatures were measured at a fixed distance over the bed and Equation (2) was used to calculate the corresponding U value. A straight line was fit to the data, as shown in Figure 2, with a gradient of 8.66×10^{-7} kW m^{-2} K^{-1} $sccm^{-1}$ and a y-intercept of 7.19×10^{-6} kW m^{-2} K^{-1}. As the reactor bed used in experiments was made up of a large excess of sand over catalyst (20:1 ratio by mass), it was assumed that the effect of the cobalt metal on the heat transfer properties in the catalyst bed could be neglected. The value of ΔH used in the model, -152 kJ mol^{-1}, was taken from a study by Jess and Kern (209). The c_p value of the gas-phase mixture was calculated using a weighted linear sum of the individual components of the mixture.

For the pressure drop in the bed, Equation (3), Hicks's correlation for the value of the bed friction factor f was used:

$$f = 6.8\frac{(1-\varepsilon_b)^{1.2}}{{\varepsilon_b}^3}Re^{-0.2} \tag{4}$$

The inter-particle porosity of the bed, assuming perfectly spherical particles, was calculated using the correlation of Benyahia and O'Neill (2005):

$$\varepsilon_b = 0.1504 + \frac{0.2024}{\phi_p} + \frac{1.0814}{\left(\frac{d_t}{d_p} + 0.1226\right)^2} \tag{5}$$

where ε_b is the bed porosity and ϕ_p is the sphericity ($\phi_p = 1$ in this case). The density of the diluted catalyst bed used in experiments was measured gravimetrically to be 1.60 ± 0.06 g cm^{-3}. In order to calculate the Reynolds number of the reaction mixture, its viscosity was estimated using Davidson's (1993) correlation for gas-phase mixtures.

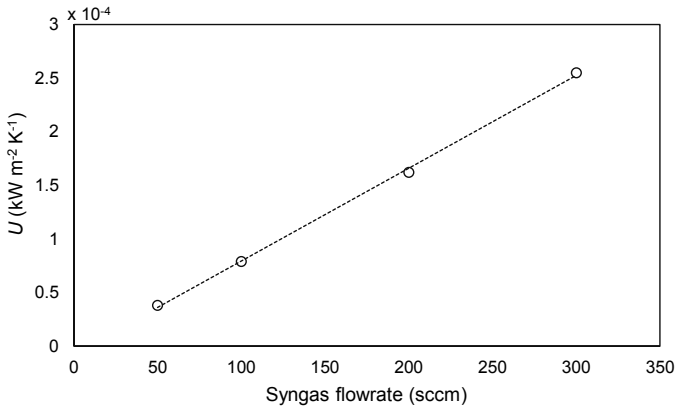

Figure 2: Overall heat transfer coefficient of a reactor tube filled with a bed of sand particles as a function of syngas flowrate at T = 513 K and P = 20 bar.

3. Results and Discussion

The experimental results for CO conversion and CH_4 selectivity obtained from the FTS reactor unit under the conditions as outlined in section 2.1 were compared with the

simulations as outlined in section 2.2. The comparison between experimental and simulation results is shown in Figure 4; as the figure shows, the CO conversion in the simulations is lower than the experiments by a factor of about 2 for all flowrates, whereas the CH_4 selectivity from simulations shows an excellent agreement with the experimental data. The discrepancy between the experimental and simulated data with regards to the CO conversion may be explained by a difference in activity between the catalyst used in Todic et al. (2013) and the current study. However, as both studies were done on a cobalt-based catalyst, it appears that the selectivity model of Todic et al. (2013), which accounts for deviations from the 'ideal' ASF product distribution, accurately captures the methane selectivity seen experimentally.

The temperature profiles obtained from the model at the different syngas flowrates are shown in Figure, and show a temperature rise ranging between 14–17.5 °C in the bed, with the higher temperature rise seen at lower flowrates, as expected. While an exact comparison cannot be made with experiments as limited temperature data was obtained experimentally, the results are consistent with data from Huang and Roberts (2003), who found a 15 °C rise in their reactor bed for gas-phase FTS on a Cobalt-based catalyst under similar conditions (T = 250 °C, P(syngas) = 20 bar, H_2/CO ratio 2:1, syngas flowrate of 50 sccm/g catalyst) as those used in the current study.

4. Conclusion

In the current study, the steady-state fixed-bed Fischer-Tropsch synthesis reactor was modeled using a one-dimensional approach, which incorporates a detailed kinetic and selectivity model taken from the literature and accounts for heat and mass transfer limitations on the performance of the catalyst through the use of a particle diffusion model. For model validation, a comparison was shown with preliminary experimental data from an ongoing study; the model showed good agreement with experimental data for methane selectivity but under-predicted CO conversion. Thus, we conclude that in order for the model to be predictive, the kinetic parameters for our experimental system need to be determined.

In future, we intend to incorporate an extended version of the PR EoS, as developed by Travalloni et al. (2014), into the model in order to account for the effect of confinement in heterogeneous porous media (such as catalyst pellets) on the thermodynamic properties of the FTS reaction mixture. Thermodynamic effects will become particularly important when modelling the effect on the FTS process of using non-ideal reaction media such as supercritical fluid solvents. Ultimately, our goal is to develop a comprehensive model to enable a direct comparison of the gas-phase and supercritical solvent-assisted FTS reactions under a variety of conditions; the current study represents an important first step towards this aim.

Acknowledgments

The authors are grateful to Dr. Dragomir Bukur for providing the catalyst used in the experiments. This paper was made possible by a NPRP award [NPRP 4-1484-2-590] from the Qatar National Research Fund (a member of the Qatar Foundation). The statements made herein are solely the responsibility of the authors.

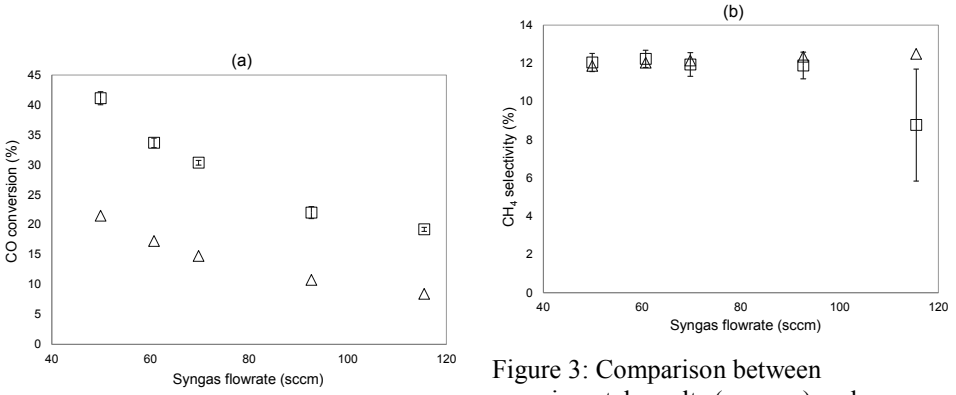

Figure 3: Comparison between experimental results (squares) and simulations (triangles) for (a) CO conversion; (b) CH_4 selectivity, as a function of syngas flowrate in the FTS fixed bed reactor at T = 513 K and P(syngas) = 20 bar.

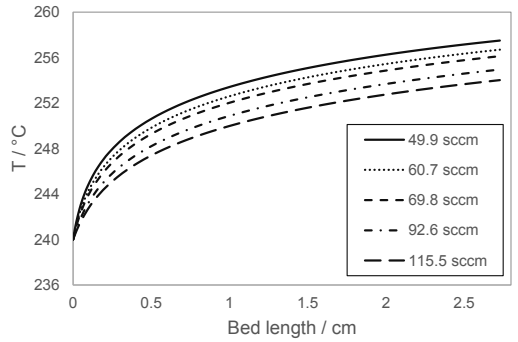

Figure 4: Simulated temperature profiles in the FTS reactor bed as a function of syngas flowrate under gas-phase conditions (T = 513 K and P(syngas) = 20 bar.

References

F. Benyahia, K. O'Neill, 2005. Enhanced voidage correlations for packed beds of various particle shapes and sizes. Particulate Sci. Technol., 23, 169–177.

T. A. Davidson, 1993. A simple and accurate method for calculating viscosity of gaseous mixtures..

N. O. Elbashir, D. B. Bukur, E. Durham, C. B. Roberts, 2010. Advancement of Fischer-Tropsch synthesis via utilization of supercritical fluid reaction media. AIChE J., 56, 997–1015.

G. Froment, K. Bischoff, J. De Wilde, 2011.Chemical reactor analysis and design, 3rd ed., John Wiley & Sons,

X. Huang, C. B. Roberts, 2003. Selective Fischer-Tropsch synthesis over an Al2O3 supported cobalt catalyst in supercritical hexane. Fuel Proc. Technol., 83, 81–99.

Q. Liu,Z. Zhang, J. Zhou, 1999. Steady-state and dynamic behavior of fixed-bed catalytic reactor for Fischer-Tropsch synthesis II. Steady-state and dynamic simulation results. J. Nat. Gas Chem. 8, 238–247.

B. Todic, T. Bhatelia, G. F. Froment, W. Ma, 2013. Kinetic Model of Fischer-Tropsch Synthesis in a Slurry Reactor on Co-Re/Al2O3 Catalyst. Ind. Eng. Chem. Res., 52, 669–679.

L. Travalloni, M. Castier, F. W. Tavares, 2014. Phase equilibrium of fluids confined in porous media from an extended Peng-Robinson equation of state. Fluid Phase Equilr. 362, 335–341.

Y. N. Wang, Y. Y. Xu, W. Y. Li, Y. L. Zhao, 2003. Heterogeneous modeling for fixed-bed Fischer-Tropsch synthesis: reactor model and its applications. Chem. Eng. Sci. 58, 867–875.

Krist V. Gernaey, Jakob K. Huusom and Rafiqul Gani (Eds.), 12th International Symposium on Process Systems Engineering and 25th European Symposium on Computer Aided Process Engineering.
31 May – 4 June 2015, Copenhagen, Denmark

Process Simulators: What Students Forget When Using Them, Their Limitations, and When Not to Use Them

Joseph A. Shaeiwitz[a*], Richard Turton[b]

[a]*Auburn University, Auburn University, Alabama, 36849-5127, USA*
[b]*West Virginia University, Morgantown, West Virginia, 26506-6102, USA*
jas0105@auburn.edu

Abstract

Steady state process simulators allow students to perform in-depth analyses of chemical process designs, including economic optimization, due to the ability to run multiple case studies rapidly. However, process simulators are not necessarily a panacea. The simulations should correspond to realistic equipment. Students often use them carelessly. Several typical examples of careless use of process simulators are presented. Process simulators also have their limitations in dealing with certain types of problems, like scale-up, scale-down, debottlenecking, and troubleshooting. Examples of situations in which simulation defaults should be changed and where problems might be more appropriately solved outside the simulation environment are presented.

Keywords: process simulators, student design, performance problems

1. Introduction

Process simulators allow students to perform in-depth analyses of chemical process designs. The ability to simulate different process configurations and to vary design parameters allows them to make decisions and move towards an optimum process based on an objective function, for example, a profitability criterion. However, students often use process simulators carelessly. It is also true that there are certain types of advanced problems for which process simulators are not well suited, including scale-up and scale-down of chemical processes. For some problems, the simulator defaults cannot be used, and in some cases, it is best not to use simulators.

That students can use simulators carelessly should come as no surprise to most instructors. Dahm, et al. (2002) discussed how students can use simulators to construct models without a full understanding of the process. Flach (1999) observed that students often resort to simulators when they are not needed and further observed the tendency of students not to evaluate critically the results of simulations.

In this paper, one example of careless use of simulators will be presented in detail. Several more are summarized briefly. The situations when simulators should not be used or must be modified from the defaults will be discussed in detail. In all of these cases, the relationship between simulation models and actual equipment behaviour is highlighted, because it is considered to be important that this relationship be appreciated by students.

2. Carless Use of Simulators

A very common example of careless use of process simulators is for heat exchangers involving phase change. In organic chemical processes, it is common for a liquid feed to be vaporized to perform a gas-phase reaction. The process feed may be subcooled and may need to be superheated before entering the reactor. An approximate *T*-*Q* diagram for this process is shown with the solid lines in Figure 1, assuming that steam is used to provide the heat, going from saturated vapour to saturated liquid.

In a process simulator, a heat transfer coefficient may be entered so the area can be calculated. However, the heat transfer coefficient is different for each zone. If only one heat transfer coefficient is entered for the whole heat exchanger, an incorrect area is be calculated. The *T*-*Q* diagram for the incorrect case is shown with the dotted line in Figure 1. The correct method for performing this simulation is to use a different heat exchanger for each zone, with an appropriate overall heat transfer coefficient for the respective zone. Alternatively, since the simulator will generate the *T*-*Q* diagram (often called a heat curve) for the heat exchanger, it may be simpler to do the area calculation outside the simulation environment.

When a correspondence to actual equipment is considered, there may not even be three zones. For example, in a kettle-type boiler, the boiling liquid acts like a stirred tank, and the subcooled liquid immediately comes to the boiling temperature. To superheat the effluent, there must be tubes that are not covered with boiling liquid. In this situation, there would only be two zones with two different heat transfer coefficients, with the heat load on the boiling zone being the sum of the desuperheating and vaporization enthalpy changes.

There are cases when the simulation can be done that will result in an impossible situation. Suppose a clever student decides to use a hot stream in the process to vaporize the feed. The *T*-*Q* diagram in Figure 2 with the solid lines shows the correct situation, and the *T*-*Q* diagram with the dotted line in Figure 2 shows the physically impossible situation that results if the different zones are not considered. With the dotted hot-stream line in Figure 2, there would be a temperature cross.

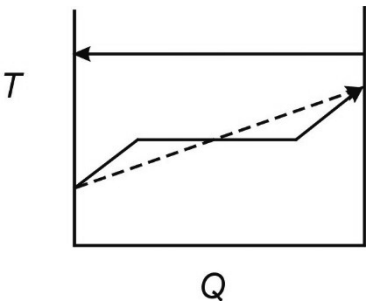

Figure 1: *T*-*Q* Diagram Requiring Analysis

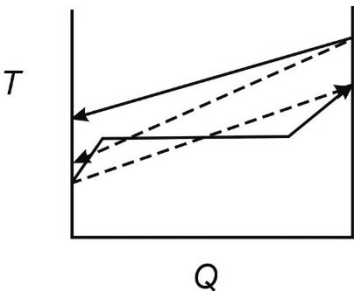

Figure 2: *T*-*Q* Diagram Resulting in Zoned Temperature Cross

Table 1: Commonly Observed Simulation Errors

Physical Situation	Error Observed	Correct Method
zoned analysis required	one heat transfer coefficient used for only one zone	simulate each zone as separate heat exchanger with separate heat transfer coefficient
LMTD correction factor required but ignored	assume standard 1-2 configuration for all heat exchangers not involving phase change	check approach temperatures to see if more shell passes are needed, often occurs if heat integration used
inappropriate reactor size	desired product rate approaches constant value or starts to decrease	examine reactor profiles to determine if reactor is oversized or if selectivity is decreasing
real vs. actual trays	column design and cost calculated for number of equilibrium trays	include tray efficiency in simulation before performing cost calculation
column pressure drop	column assumed to be at constant pressure or pressure drop chosen does not correspond to reality	include pressure drop and make sure pressure drop per tray roughly corresponds to weir height, and that weir height is not too small or not more than 50% of tray spacing
incorrect use of flash unit simulation	including flash unit with heat load	simulate as heat exchanger followed by flash unit at inlet conditions

This is just one case in which simulators have been observed to be used incorrectly. Table 1 summarizes several other situations that have been observed, and these are discussed in more detail in Shaeiwitz and Turton (2014). The observation is that students need to be taught the limitations of process simulators, where to find useful information within simulations, and to make their simulations correspond to actual process equipment.

3. Situations When Simulators Should not be Used

A class of problems that are not always appropriate for simulators is performance problems. Examples of these are debottlenecking and troubleshooting problems. In these cases, the equipment is specified; however, not always at the level of detail necessary to use a simulator. An example debottlenecking problem is to determine what part of a process limits scale-up, and an example troubleshooting problem is to determine the cause of a disturbance, which could be a flowrate disturbance.

For example, the individual heat transfer coefficients change as the stream flowrates change (for no phase change). However, in most simulators, the overall heat transfer coefficient is specified. If the simulator is used to calculate the individual heat transfer coefficients, the heat exchanger specifications must include number of tubes, tube pitch,

tube diameter, shell diameter, and baffle spacing. In general, most student designs do not include this level of detail, especially since a typical attribute for a cost estimate of a heat exchanger is the area. Outside the simulation environment, the NTU method may look attractive; however, the change in heat transfer coefficient with flowrate is not included in this method.

In order to solve this problem, the relevant heat transfer equations must be solved simultaneously for the new conditions, and the equations are the energy balance and the design equation

$$Q = \dot{m}_h C_{p,h} \Delta T_h = \dot{m}_c C_{p,c} \Delta T_c \tag{1}$$

$$Q = U_o A_o \Delta T_{lm} F \tag{2}$$

Solutions of Equations 1 and 2, which are actually three equations, require numerical methods. To make the equations easier to solve, it is recommended that ratios be used

$$\frac{Q_2}{Q_1} = \frac{\dot{m}_{h2} C_{p,h2} \Delta T_{h2}}{\dot{m}_{h1} C_{p,h1} \Delta T_{h1}} = \frac{\dot{m}_{c2} C_{p,c2} \Delta T_{c2}}{\dot{m}_{c1} C_{p,c1} \Delta T_{c1}} \tag{3}$$

$$\frac{Q_2}{Q_1} = \frac{U_{o2} A_o \Delta T_{lm2} F_2}{U_{o1} A_o \Delta T_{lm1} F_1} \tag{4}$$

where, the subscripts 1 and 2 refer to the original case and the new case, respectively. In Equation 2, the heat capacities are considered constant for small temperature changes, and in Equation 4, the area ratio is unity for the same equipment, and the ratio of the LMTD correction factors is generally assumed to be unity for small temperature changes. Therefore, the unknowns are the two outlet temperatures, the new heat duty, and perhaps the flowrate of a utility stream. The utility flowrate is often the parameter than can be varied to ensure controllability. The ratio of the heat transfer coefficients is based on the scaling of the individual heat transfer coefficients

$$h_i \propto \dot{m}^{0.8} \tag{5}$$

for turbulent flow in the tubes and

$$h_o \propto \dot{m}^{0.6} \tag{6}$$

for turbulent flow in the shell.

Examples of these problems and solution methods are presented in Turton, et al. (2012). Solution methods for situations involving phase change are also shown.

A related example involves heat removal from a reactor using a cooling loop, as illustrated in Figure 3.

In a scale-up or scale-down problem, the reactor loop must be analyzed simultaneously with the reactor. If the reactor is considered to be a heat exchanger for the purposes of this analysis, two sets of Equations 3 and 4 must be solved simultaneously. However, the problem is more complex, since the ability to scale-up, for example, also depends on the characteristic pump curve, which could be the bottleneck to scale-up. While some simulators allow pump curve information to be added, this might be a more advanced

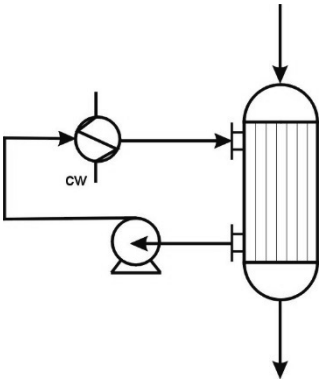

Figure 3: Reactor with Cooling Loop

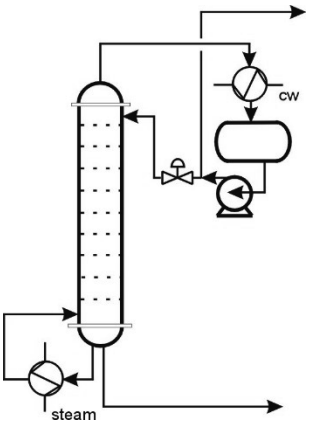

Figure 4: Distillation Column with Peripheral Equipment

simulation for a typical undergraduate. In this case, the problem is probably best solved outside the simulation environment.

Another example of the need either to modify a typical simulator default or not to use a simulator is in the simulation of a distillation column. The simulator calculates the heat load on the reboiler and condenser, and some simulators calculate the utility load if the utility is specified. However, no other calculations are done on those heat exchangers. If more detailed analysis is desired, the column should be simulated without a reboiler and condenser, and they should be added as distinct units. In this case, the reflux drum and reflux pump should also be included. Figure 4 illustrates the distillation column with all of the peripheral equipment shown.

For a performance problem such as scale-up, all of the units shown in Figure 4 must be analysed in detail. In fact, it is the condenser and reboiler that most strongly affect the ability to scale-up or scale-down the process. If a modest scale-up is required, an initial design at 75% of flooding should be able to handle the larger throughput. The relevant equations for the reboiler are

$$\frac{Q_2}{Q_1} = \frac{\dot{m}_{steam2}\lambda}{\dot{m}_{steam1}\lambda} = \frac{\dot{m}_{process2}\lambda}{\dot{m}_{process1}\lambda} = \frac{U_{o2}A_o\Delta T_2}{U_{o1}A_o\Delta T_1} \tag{7}$$

For a small temperature change, the latent heat, λ, is assumed constant. The increased process flowrate requires proportional increases in the heat load on the reboiler and on the driving force. This is illustrated on the *T*-*Q* diagram for a reboiler shown in Figure 5. It is assumed that the heat transfer coefficients for boiling and condensation are weak functions of flowrate, making the overall heat transfer coefficient approximately constant. If the steam temperature is fixed, the only way to increase the driving force is for the reboiler temperature and consequently the column pressure to decrease (dashed line). The condenser *T*-*Q* diagram is shown in Figure 6. If the column pressure drop is approximately constant, the condensation pressure and temperature both decrease, reducing the driving force in the condenser (dashed line). The driving force can only be increased by increasing the cooling water flowrate (dashed line); however, the required

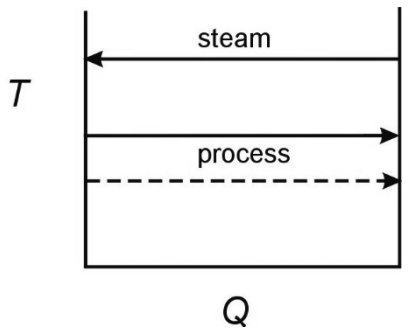

Figure 5: *T-Q* Diagram for Reboiler

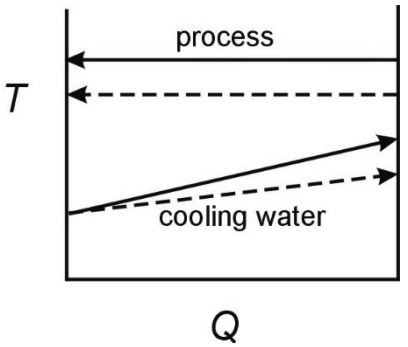

Figure 6: *T-Q* Diagram for Condenser

amount of increase is affected by the increase in the heat transfer coefficient for the cooling water. Another way to handle this problem is to have a desuperheater on the steam source in the reboiler to adjust its temperature, which can maintain the original boiling temperature and pressure. In either case, the simulator defaults do not provide a suitable method for analysing this problem. Related examples are presented in Turton, et al. (2014).

4. Conclusions

Process simulators, when used correctly, enable students to analyse and optimize a chemical process by allowing them to study different process configurations and to vary design variables. However, students must use the process simulator correctly by relating the simulation to actual equipment behaviour. Additionally, performance problems such as scale-up, scale-down, debottlenecking, and troubleshooting are not always solved correctly by the default simulation methods. At times, it is better to solve these problems in a different environment.

References

K.D. Dahm, R.P. Hesketh, and M.J. Savelski, 2002, Is Process Simulation Used Effectively in CHE Courses?, Chemical Engineering Education, 36 (3) 192-197, 203

L. Flach, 1999, Experiences with Teaching Design. Do We Blend the Old with the New?, Chemical Engineering Education, 33 (2) 158-162

J.A. Shaeiwitz and R. Turton, 2015, Are Your Students Getting the Most Out of the Process Simulator?, Proceedings of the 2015 ASEE Meeting, Seattle, WA, USA.

R. Turton, R.C. Bailie, W.B. Whiting, J.A. Shaeiwitz, and D. Bhattacharyya, 2012, Analysis, Synthesis, and Design of Chemical Processes, 4th ed, Prentice Hall, Upper Saddle River, NJ, USA, Chapters 21-22.

Krist V. Gernaey, Jakob K. Huusom and Rafiqul Gani (Eds.), 12th International Symposium on Process Systems Engineering and 25th European Symposium on Computer Aided Process Engineering.
31 May – 4 June 2015, Copenhagen, Denmark

Learning to solve mass balance problems through a web-based simulation environment

Alexandros Koulouris*, Dimitris Vardalis

Alexander Technological Education Institute, Dept. of Food Technology , Thessaloniki 57400, Greece
akoul@food.teithe.gr

Abstract

Being able to solve mass and energy balance problems on any given process is a key skill required for students in chemical, or, in general, process engineering. Yet, many students have serious problems solving such problems because the necessary equations do not come in a ready-to-use form; instead, the general and abstract balance equations must be tailored by the student to the problem and the data at hand before they can be used. To solve mass balance problems, students must first recognize the input/output structure of the system(s) around which balance equations can be written, identify the components present and, from all possible balance equations, choose those that, based on the available data, will lead to results in the fastest and more efficient way. In a typical textbook problem, there is no predefined structure in the input data (as it exists, for example, in a process simulator) and the solution process is completely data-driven.
We have developed a web-based environment that attempts to imitate the process of solving mass balances by hand. The webpage embeds a solution algorithm which identifies in a stepwise fashion the smallest subset of equations which, based on the available data, can yield results (even partial). A student will not do degrees of freedom analysis on the entire data set nor can he/she solve large sets of equations with many unknowns; the solution algorithm respects those restrictions. Two web pages embodying this problem-solving environment have been developed; one around a single continuous process with a collection of options on its input/output structure, and one around a batch process. Visual feedback is provided for the user to identify variables whose values can be calculated with the available data and the equations that can be used in the calculation. Through these web pages, users can solve their own problems or practice on predefined problems displayed at the bottom of the page in the form of multi-choice quizzes. The expectation is that such an environment of free, student-centred experimentation can provide structure and guidance on the process of formulating and solving mass balance problems.

Keywords: mass balances, process engineering, e-learning.

1. Introduction

Nowadays, e-learning tools in process or, in particular, chemical engineering abound. E-learning can be incorporated as a supplement to traditional teaching methodologies formulating what is called blended, hybrid or mixed learning, or used as a stand-alone tool to deliver teaching material in the context of synchronous or asynchronous learning (Krajnc, 2012). Web-based e-learning tools have been used to remotely operate actual labs (as in Selmer *et al.*, 2007 or Klein and Wozny, 2006), simulate virtual labs (as in Schofield and Lester, 2010), or as a means to deliver, enhance the understanding and test the student's knowledge of theoretical material, improve the collaboration between

students in team projects and in many other applications (Krajnc, 2012). In all cases, e-learning is celebrated for its ability to provide an always accessible, student-centred, self-paced environment for learning outside the confines of the traditional classroom or laboratory.

Mass and energy balances are everywhere in process engineering calculations; they formulate the basis for the development of any process model irrespectively of the nature of the process or the modelling detail. Students in chemical, food or, in general, any process engineering field should master mass and energy balance equations before they can cope with the detailed models of specific operations or integrated plants. Yet, formulating and solving mass and energy balance equations presents a difficult task to many students in process engineering. The main difficulty in coping with mass balance problems is that there are no predefined equations to use. Instead, students are taught the general form of the conservation equations and they must learn how to customize these equations to solve a problem at hand depending on the number of components involved, the number of input and output streams, the presence of reactions etc. What complicates the matter further is that the number of potential equations to form is large (if the number of components is large, as is the case in food processing) and the fact that there is great variability in the form that the problem data are given.

To efficiently solve a mass balance problem, the student must customize the general conservation equations not only to the specific problem but also to the available data of the problem and identify the (preferably small) subset of equations that lead to fast solutions. That teacher's challenge is to effectively guide and train the students in finding the fastest and most efficient solution strategy. This could be done with the help of heuristic rules such as to use balances for components with the most known data on their mass fraction or flow rate. Still, this knowledge can come only from laborious supervised practice but how feasible is it to have a teacher guiding every student in every problem?

This paper presents an approach to offer this guidance to the students through a web-based environment in the context of e-learning and as a supplement to traditional classroom teaching. The objective is to develop a generic environment where a student could interactively solve any mass balance problem with the environment providing structure and guidance in the solution process.

2. Automating the mass balance solution process

Consider a continuous steady-state process with an arbitrary number, m, of input and output streams carrying an arbitrary number, n, of components. Let us consider the case where no reactions take place into the process. The mass conservation principle suggests that the total input flow of each component must equal its total output flow. In other words, if $F_{j,i}$ is the mass flow rate of component i in stream j, then the following equation holds:

$$\sum_j F_{j,i} = 0 \quad \forall i \tag{1}$$

In Eq.(1), the flow rate is considered positive for input streams and negative for output streams. A similar equation can be written for the overall mass based on the stream flow rates F_j:

$$\sum_j F_j = 0 \tag{2}$$

The component flow rate $F_{j,i}$ is related to the component mass fraction $x_{j,i}$ and the total stream flow rates F_j through the relation:

$$F_{j,i} = x_{j,i} F_j \quad \forall i \, \forall j \tag{3}$$

Then, the component mass balance of Eq.(1) can be rewritten as:

$$\sum_j x_{j,i} F_j = 0 \quad \forall i \tag{4}$$

Component flow rates in each stream should sum up to the total stream flow rate:

$$\sum_i F_{j,i} = F_j \quad \forall j \tag{5}$$

Finally, the component mass fractions in each stream should sum to 1:

$$\sum_i x_{j,i} = 1 \quad \forall j \tag{6}$$

All above are candidate equations to use in solving a mass balance problem but, obviously, they are not independent. It is known that from the set of n+1 balance equations only n of them are independent. Considering that in each stream there exist only n independent variables (e.g. flow rate and n-1 mass fractions), there exist $m \cdot n$ variables and, therefore, (m-1)n degrees of freedom (DOF). An automated solution process (as, for example, applied in a process simulator) would first enforce that the DOF are satisfied and then solve the n independent balance equations in one shot.

Solving such a problem by hand, however, does not work like that. First, there is no 'discipline' in the way the DOF are covered with the available data as it exists in a process simulator. For example, a process simulator would typically assume that all data in input streams are given. In a student problem, known and unknown variables are spread in random ways among input and output streams; this variability in the provided data is purposely used to extend the breadth of the problems students are exposed to. Secondly, and more importantly, students do not (and are not encouraged to) think as process simulators. They do not do formal DOF analysis and cannot solve equation sets with more than 2 or, at most, 3 unknowns. Instead, from all the potential (and probably redundant) set of equations, they try to identify small solvable subsystems of equations, formulate partial solutions and repeat until the problem is solved.

We attempted to imitate this process by developing an automated algorithm that would work in the same way. The algorithm must have the following characteristics:

- All possible equations can be considered as candidate equations to use
- The solution process will have to be stepwise and recurrent
- The equation selection and solution must be data-driven.

The objective is to create an algorithm that would, as the data become available, create partial solutions by identifying the smallest solvable equation subsystem, feed the results as data back into the system and repeat until all variables are known.

The developed algorithm involves the following steps which are executed every time a single piece data becomes available (either as user-provided or as a result from a previous solution):

1. Formulate all (n+1) balance equations and incorporate the values of all known variables. In the component balance equations, each term corresponding to the flow of component i in stream j is represented as $x_{j,i}F_j$ if either $x_{j,i}$ or F_j is known; otherwise as $F_{j,i}$. In this way, unnecessary non-linearities arising from the product $x_{j,i}F_j$ are avoided and the set of equations is always linear.
2. Search for the smallest set of independent balance equations with the same common set of unknowns starting from a single equation with one unknown and gradually moving to larger sets. If found, solve the system and set the values to the variables.
3. For each stream, formulate the stream equations (Eqs. (3),(5) and (6)) and check what variables can be calculated.
4. Repeat the process if some variable has been calculated in steps 2 or 3 or if user provides new data until all stream variables in step 3 have known values.

It should be noted that, although all balance equations are considered as candidates to be used, the selected equations to use are always checked for independence. Also, as it is apparent from the description of the algorithm, the stream equations are considered and solved separately for each stream. This, however, is expected since streams do not share common variables; it is only through the balance equations that the stream variables are connected.

Solving the constraining equations for each stream requires the implementation of some rules that go beyond the typical mathematical solution process but are necessary to maintain the validity of the solution. For example, if the sum of mass fractions for any number of components in a stream is equal to 1, then the mass fractions for all remaining components (irrespectively of their number) should be set to 0 and considered known.

3. Web-page implementation

The above stepwise solution algorithm was implemented in a web-based environment where students would interactively solve mass balance problems. The iterative nature of the algorithm is exploited in the graphical implementation to help students see the solution unfold before them as data are entered. The algorithm was coded in C# and embedded in an ASP.NET webpage. For simplicity of the interface, the implementation of the algorithm was restricted to a single process with a total of at most 4 streams.

Figure 1 shows the webpage interface for a single continuous process. The user would have to first select the input/output structure of the process by clicking one of the five picture buttons at the top and, then specify, the components present in the process. The graphical display of the process in the middle shows the selected structure and, for each stream, there is a total flow rate field and a table with each component's mass fraction and rate. To use the page, the user will have to start entering whatever data are available for the problem at hand. As this process goes on, the embedded algorithm is run to identify what other variables can be calculated using the provided data.

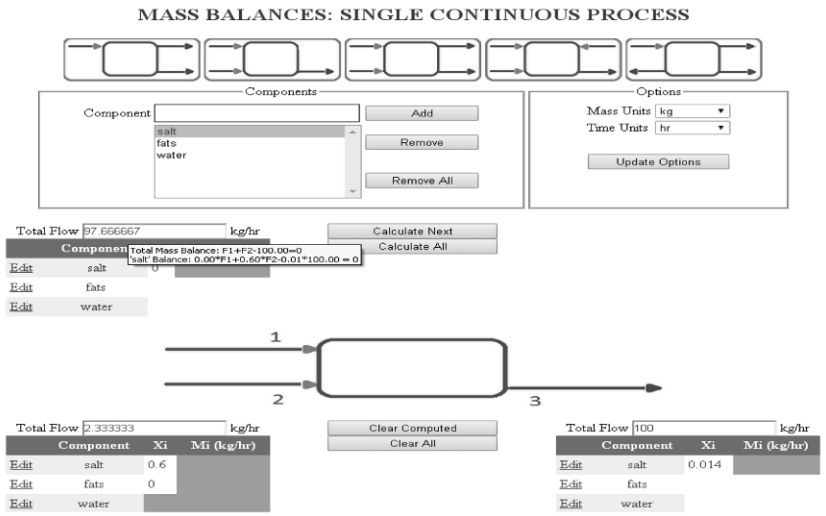

Figure 1. The Webpage Interface for Solving Continuous Mass Balance Problems

The values of the calculated variables are not immediately displayed but are blocked from user-editing. A colour-coding scheme is employed to differentiate variables set by the user, variables calculated and variables that could potentially be calculated. A grey background over a field in Figure 1 (orange in the actual webpage) indicates that the variable cannot be set because it can be calculated from the available equations. At this point, the student should wonder how it is possible to have this value calculated. By pressing the Calculate Next button the answer can be revealed both in terms of the value (the grey background is removed and the value is displayed) and in terms of what equation(s) can be used to calculate this value; the equations will show up in a flying tooltip if the user moves the mouse over the variable field.

A series of predefined problems posed as multiple-choice questions at the bottom of the page can be used by the student for practice. Alternatively, a student can use the webpage to solve their own mass balance problem. A similar in spirit, webpage was also developed for the solution of mass balances in batch processes (Figure 2). In the batch configuration, there is one (optional) input stream and one (optional) output stream along with the specifications for the initial and final state of the process. The user can edit any of the above to simulate any possible scenario (e.g. find the final state for given material addition or removal, or, find the stream flows that can result in given final state etc.) When calculations are done, the user can reset the initial state equal to the final state and continue with the implementation of a new scenario. In this way, the evolution of a stepwise batch process can be simulated.

Both web pages are available through the site www.food.teithe.gr/fepsim where a series of educational modules for basic process engineering topics are under development.

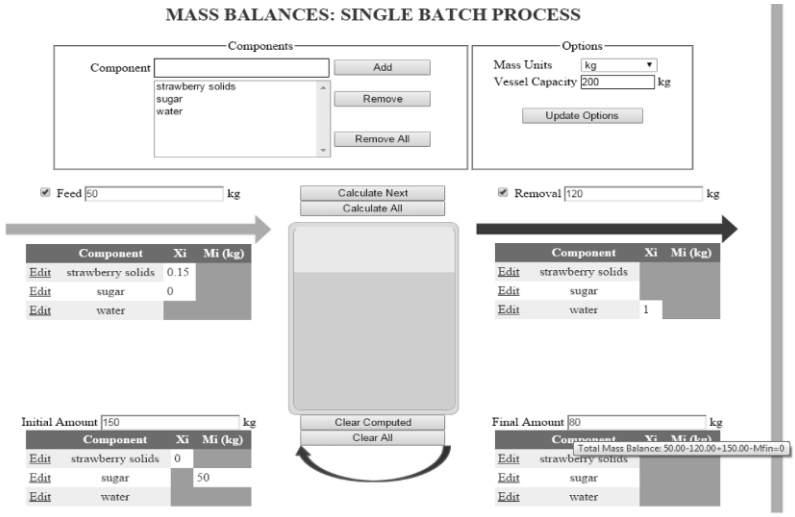

Figure 2. The Webpage Interface for Solving Batch Mass Balance Problems

4. Conclusions

The webpage presented in this paper attempts to imitate the mental process of solving a mass balance problem and is designed to provide to the novice engineer structure and discipline in the solution process. The embedded solution algorithm does not solve the problem as a process simulator would. Instead of immediately displaying the results, it tries to guide the user through the solution steps based on whatever data are available. It is hoped that the skills acquired after adequate experimentation in this webpage could be learned and transferred into solving more complicated problems by hand. This webpage can be used both for self-learning as well as an accessory to class work.

Acknowledgements

This research has been co-financed by the European Union (European Social Fund – ESF) and Greek national funds through the Operational Program "Education and Lifelong Learning" of the National Strategic Reference Framework (NSRF) - Research Funding Program: ARCHIMEDES III Investing in knowledge society through the European Social Fund.

References

A. Klein and G. Wozny, 2006, Web Based Remote Experiments for Chemical Engineering Education: the Online Distillation Column, Trans IChemE, Part D, Education for Chemical Engineers, 1, 134-138

M. Krajnc, 2012, E-Learning Usage During Chemical Engineering Courses, E-Learning – Engineering, On-Job Training and Interactive Teaching, S. Kofuji (Ed.), InTech

D. Schofield and E. Lester, 2010, Virtual Chemical Engineering: Guidelines for E-Leaning in Engineering Education, Seminar.net – International Journal of Media, Technology and Lifelong Learning, 6, 1, 76-93

A. Selmer, M. Kraft, R. Moros and C. K. Colton, 2007, Weblabs in Chemical Engineering Education, Trans IChemE, Part D, Education for Chemical Engineers, 2, 1, 38-45

Krist V. Gernaey, Jakob K. Huusom and Rafiqul Gani (Eds.), 12th International Symposium on Process Systems Engineering and 25th European Symposium on Computer Aided Process Engineering.
31 May - 4 June 2015, Copenhagen, Denmark.

Model Predictive Control of Post-Combustion CO_2 Capture Process integrated with a power plant

Evgenia D. Mehleri[a,b], Niall Mac Dowell[a,b] and Nina F. Thornhill[b]

[a]*Centre for Environmental Policy;Imperial College London,UK*
[b]*Centre for Process System Engineering;Department of Chemical Engineering; Imperial College London,UK*
e.mehleri@imperial.ac.uk

Abstract

The process of CO_2 capture and storage is a promising and effective way to control the emissions of CO_2 from large-scale power plants. One of the most used promising near-term options for large-scale deployment of CO_2 capture and storage (CCS) technologies is the post-combustion CO_2 capture. However, it is vital that the decarbonisation of power plants does not limit the ability of the plant to operate in a flexible, load following manner. Therefore, the integration of CO_2 capture process and power plants will increase the need to design advanced model-based control systems to account for the process interactions and maintain dynamic operability of power plant and CCS unit. In this work an advanced Model Predictive Control (MPC) scheme has been designed to evaluate the controllability of a post-combustion plant in the presence of disturbances associated with the dynamic operation of the power plant. The results have shown that the implementation of the MPC formulation proves to be a very good option to address such complex problems in CO_2 capture.

Keywords: Model Predictive Control(MPC), post combustion CO_2 capture, SAFT-VR, gCCS

1. Introduction

Owing to the continued use of fossil fuels in the global energy system for the foreseeable future, the International Energy Agency(IEA) suggests that CCS is an essential part of the technology portfolio needed to achieve deep reductions in global CO_2 emissions, with CCS expected to contribute around 14-20 % of total reductions in emissions by 2050. IEA. (2010)

One of the most promising near-term options for large-scale CCS deployment is post-combustion capture of with a mono-ethanol-amine (MEA) solevnt. The benefits of this process are high capacity of CO_2 capture, fast reaction kinetics, inexpensive and abundant solvent. On the other hand the main challenge with this process is the substantial decrease in the efficiency of the power plant owing to the energy required for solvent regeneration that would otherwise be used to produce electricity. Further, as the power plant ramps up and down, the variation in liquid-to-gas ratios in the absorption columns can impose an important effect on the efficiency of the capture plant. Therefore the dynamic modelling and controllability analysis of the complete capture process is quite important. Bui et al. (2014)

Most of the studies in literature implement a general control structure consisting of Proportional (P) and Proportional-Integral (PI) controllers. Lin et al. (2011) performed a plant-wide control study of the MEA-based CO_2 capture process using Aspen dynamics. A control structure is proposed in which CO_2 capture is guaranteed by manipulating the lean solvent feed rate to the top of

the absorber column. The system was tested by applying several disturbances, such as the flue gas flow, CO_2 concentration and H_2O concentration. In their work, Nittaya et al. (2014), presented a mechanistic dynamic model of post-combustion CO_2 capture plant using the MEA absorption process. They developed and tested three different control strategies based on Relative Gain Array (RGA) analysis and heuristics. Their analysis provided insight regarding the dynamic operation of a CO_2 capture plant in closed-loop and concluded that the control scheme based on heuristics which controls CO_2 removal with the lean MEA flowrate entering the absorber unit and the reboiler's temperature with the reboiler's heat duty, resulted in shorter closed-loop settling.

To our knowledge, only four studies have implemented MPC strategy for this process. Bedelbayev et al. (2008) presented a mechanistic model for the absorption process and MPC is only implemented for the standalone absorber. Arce et al. (2012), proposed and developed a multilevel model predictive control architecture for the solvent regeneration system of an amine-based CO_2 capture process. Focusing on minimising the operational cost associated with the post-combustion CO_2 capture,the two level control architecture maximises the flexibility of the solvent regeneration process whilst simultaneously ensuring cost-optimal performance and safety. Panahi et al. (2012), implemented an MPC-based control scheme which included only two control variables in their formulation, i.e. CO_2 recovery and reboiler's temperature. Sahraei et al. (2014), presented an advanced centralised multivariable model predictive control (MPC) technique to address the controllability of a post-combustion CO_2 capture process from a coal-based power plant and compared it to decentralised Proportional-Integral (PI) control schemes. The CO_2 capture model was developed on the Aspen Hysys dynamic simulator while the MPC was implemented in Matlab.The MPC performed significantly better than the PI controllers in terms of close-loop settling time, integral square error and compliance of operational and environmental constraints.

In this work we propose the use of model predictive control as the work of Sahraei et al. (2014) has shown that it provides better performance, in terms of close-loop settling time, integral square error and compliance of operational and environmental constraints than the PI control schemes when applied in a post-combustion CO_2 capture process.The purpose of this article is to explore the application of a multivariable model-based control technique to assess the controllability of a post-combustion CO_2 capture plant.

2. Process structure

2.1. Model development and controllability analysis

This section presents the CO_2 capture model used in this work. The first step of the model framework is the development of a high fidelity dynamic model of the system and the dynamic design optimisation. The quality of the model determines to a high degree the validity of the framework as it is both the cornerstone of the entire development procedure as well as the testing platform for the controller. The model was developed in gCCS a system modelling tool for support of design and operating decisions across the CCS chain. gCCS is built on PSE's gPROMS advanced process modelling platform, and inherits many of the platform's powerful capabilities. PSE (2014). The process flowsheet considered for this study is presented in Figure 1. As shown

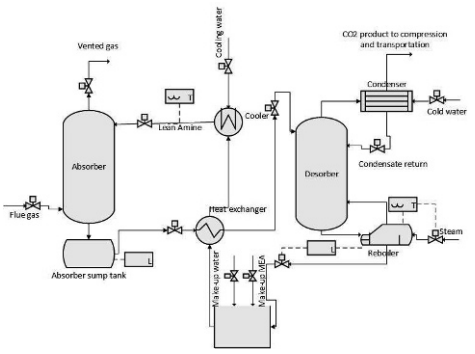

Figure 1: Base case flowsheet

in that figure, the flue gas enters the absorber at the bottom and is contacted with the counter current flow of the amine solution. The treated gas, leaves from the top of the absorber, while the rich amine solution, loaded with CO_2, leaves the absorber from the bottom and is collected in a sump tank. Then, this stream is heated in a heat exchanger by the hot lean amine solution coming from the bottom of the stripper. The heated amine solution is sent to the stripper column for the desorption process of CO_2 from the amine solution. The gas stream of CO_2 is collected at the top of the stripper while the lean amine solution is recycled back to the absorber. The two make-up streams of water and MEA are maintaining the solvent's stream concentration in the entire system. The thermophysical properties of the complex fluids used in this process are described using the statistical associating fluid theory Chapman et al. (1989), Chapman et al. (1990) for potentials of variable range Galindo et al. (1998) (SAFT-VR). SAFT-VR was also used to describe the effect of the reactions on the fluid-phase properties and phase behaviour of the MEA-H_2O-CO_2-N_2 fluid mixture in the CO_2 capture process. A detailed description of the thermodynamic modelling approach used and molecular models developed Mac Dowell et al. (2011) in addition to how the molecular models are integrated with the process models Mac Dowell et al. (2013), Mac Dowell et al. (2013) is provided in separate contributions and is not repeated here. In summary, all reactions are treated as equilibrium reactions, as is consistent with the SAFT-VR model used. This is a reasonable assumption as it is well accepted that in these systems, the mass transfer is limited by diffusion. This approximation has also been successfully used in conjunction with other dynamic, non-equilibrium models of MEA-based CO_2 capture processes. The main control objective of this plant is to maintain the CO_2 removal fixed at a specified rate and maintain a constant composition in the CO_2 product stream. Also based on the decentralised control analysis the liquid levels in the absorber sump and reboiler are controlled in order to maintain the solvent inventory within the system. Further the MEA concentration in the lean solvent stream needs to be below 30wt % to minimise corrosion in the equipment. Once the controlled variables have been identified, the next step is to identify the manipulated variables. The lean amine flowrate, condenser heat duty, absorber valve, reboiler valve and reboiler heat duty were selected similarly to the work of Nittaya et al. (2014). In keeping with the literature, the CO_2 removal rate is maintained constant at 90%. Similarly the temperature in the reboiler is held at 388K to avoid amine degradation Chi et al. (2002), Nittaya et al. (2014). Finally, the condenser temperature is kept at 325 K in order to keep the purity in the CO_2 stream at 95 mol% in line with the work of Harun et al. (2012).

2.2. Model Predictive Control

Model predictive control is a multivariable control stragety that has been successfully applied to a variety of industrial processes since the 1990s. The key advantage of MPC is that it uses an optimisation framework, which makes use of the explicit process models to predict the future behaviour of the plant, to determine the most suitable actions on the manipulated variables Camacho et al. (2004). The high fidelity dynamic model of the system described above is comprised by systems of Differential-Algebraic equations of high complexity. The DAE systems are approximated by linear discrete time models. These linear models are used to predict the behaviour of the real system and a compromise between the accuracy of these predictions and control performance should be found. The linear models are ob-

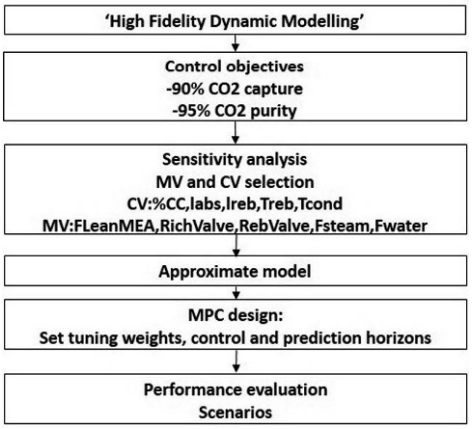

Figure 2: Controllability analysis

tained by performing a system identification
from a number of simulations of the non-linear model for a wide range of industrially relevant conditions. The evaluation has shown that these models represent in very detail the high fidelity models and can be therefore used for the development of the MPC.

The System Identification Toolbox of Matlab developed by Ljung (1995), is used to obtain linear transfer functions between each manipulated and controlled variable. The linear transfer functions obtained from the sensitivity analysis were transformed into controllable (state-space) canonical form. One Multiple Input-Multiple Output (MIMO) system of 5 inputs and 5 outputs was obtained. The MPC controller was designed in Matlab. The prediction and control horizon were 10 and 2 respectively, while the weights on the controlled and manipulated variables were set based on several case studies, as presented in the next section. Figure 2 illustrates the methodology followed to design and evaluates the MPC control structure. The last step of the framework enables the validation on the original high fidelity model, consequently determining the validity of the framework. The coupled system is put into test for different output set-points. The closed loop validation of the control system shows that the controller is able to capture the output set-points efficiently.

3. Results and discussions

The MPC controller as presented above, was evaluated under several scenarios, including changes in the flue gas flowrate that comes from the power plant and in the percentage of CO_2 captured in order to evaluate the amount of steam extracted from the thermodynamic cycle of the power plant during periods of high electricity demand.

3.1. Load changes

In this scenario we examine how the MPC control structure responds to a change in the flue gas flowrate. This is a common disturbance in the operation of power plants, e.g. changes in flue gas flow rate during plant start-up, shut-down, or during the course of the day. In this study a step increment of 20% in the flue gas flowrate with respect to its nominal operating point was introduced to the plant at the first hour of operation.

As we can observe from the results in Figure 3, the degree of CO_2 capture rate resumed to its set-point almost immediately, while the CO_2 capture did not show large deviation from its set-point. Also the CO_2 was kept above the lower limit 85%. In order to compensate for this disturbance, additional steam supply to the reboiler was required and also additional lean amine flowrate. The temperature of the reboiler reset to its set-point while the levels in the reboiler and absorber and the temperature in the condenser were not significantly affected by the disturbance.

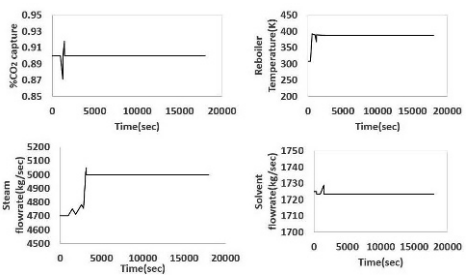

Figure 3: Results-Load change scenario

3.2. Set-point tracking

The steam supplied in the reboiler is supplied by extraction from the steam cycle of the power plant; hence an increase in the electricity demand may decrease the steam availability to the reboiler. This may result in a reduction of a plant's availability to capture CO_2 during peaks in

electricity demand. To evaluate how the plant will operate under this scenario, we consider a reduction of the CO_2 removal set-point from 90 % to 50 %. The ramp change which was introduced lasted 1h.

As we can observe from Figure 4, as soon as the change in the rate of CO_2 capture was introduced, the flowrate of the lean amine was decreased in order to keep the set-point, while the flue gas flowrate entering the absorber was kept unchanged. From this figure we can also observe the fast reduction in the steam provided to the reboiler, which shows how quickly the capture plant responds to changes, so that the amount of excess steam can used by the power plant to produce more electricity in times with high demands. Mac Dowell et al. (2014), Mac Dowell et al. (2014). Of course, it will be important to consider the trade-off in the additional cost associated with additional CO_2 emissions under this operational regime against the additional profit gained by selling the electricity for a few high-value MWh. Optimal techniques for the flexible operation of post-combustion CO_2 capture processes have been described elsewhere. The decrease in the rate of CO_2 increases the CO_2 stream coming from the top and so the water content is increased. The cooling water flowrate provided to the condenser is increased since higher duty in needed in order to maintain the temperature in a specific set-point and therefore the purity in the CO_2 stream coming from the top.

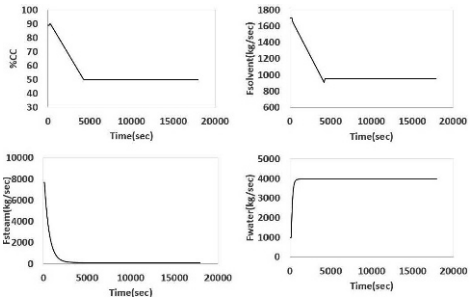

Figure 4: Results-Set-point tracking

4. Conclusions

In this paper we have presented the application of an advanced MPC approach to a dynamic model of a post-combustion CO_2 capture plant via chemical absorption using monoethanolamine (MEA) for a power plant. This model was implemented in gCCS, a tool developed as part of the gPROMS platform for the modelling of decarbonised power generation. A model predictive control strategy was implemented in Matlab in order to assess the dynamic operability of the CO_2 capture plant in the presence of changes in the power plant output (mediated through changing exhaust gas flowrates) and in the set-point tracking. In order to implement the MPC control strategy, the detailed dynamic model of the capture plant was represented by a state-space model of five inputs and five outputs. The approximation of the models was implemented by a sensitivity analysis on the high level model and the use of the System Identification toolbox in Matlab. Two scenarios were implemented: the flue gas flowrate disturbance and also the set-point tracking scenario. The results showed that the MPC control strategy can quickly adapt to any disturbance applied to the capture plant, which is essential for the profitable operation of decarbonised power plants.

5. Acknowledgements

The authors gratefully acknowledge the financial support of the ABB Chair of Process Automation of EPSRC through grant EP/J020788/1 Gas-FACTS: Gas - Future Advanced Capture Technology Options and through grant EP/M001369/1 MESMERISE-CCS: Multi-scale energy systems modelling encompassing renewable, intermittent, stored energy and carbon capture and storage.

References

Arce A., Mac Dowell N., Shah N., Vega L.F., 2012, Flexible operation of solvent regeneration systems for CO_2 capture processes using advanced control techniques: Towards operational cost minimisation , Journal of Greenhouse Gas Control, 11, 236-250.

Bedlebayev A., Greer T., Lie B., 2008, Model based control of absorption tower for CO_2 capturing, In: Proceeding for the 49th Scandinavian Conference, Norway.

Bui M., Gunawan I., Verheyen V., Feron P., Meuleman E., Adeloju S., 2014, Dynamic Modelling and optimisation of flexible operation in post-combustion CO_2 capture plants - A review, Computers & Chemical Engineering, 61, 245-265.

Camacho E., Bordons C., 2004, Model Predictive Control, second ed., Springer.

Chapman W. G., Gubbins K. E., Jackson G., Radosz M., 1989, SAFT: Equation of state solution model for associating fluids, Fluid Phase Equilibrium, 52, 3138.

Chapman W. G., Gubbins K. E., Jackson G., Radosz M., 1990, New reference equation of state for associating liquids, Industrial & Engineering Chemistry Research, 29, 1709-1721.

Chi S., Rochelle G.T., 2002, Oxidative degradation of monoethanolamine, Industrial & Engineering Chemical Research, 41, 4178-4186.

Galindo A., Davies L. A., Gil-Villegas A., Jackson G., 1998, The thermodynamics of mixtures and the corresponding mixing rules in the SAFT-VR approach for potentials of variable range, Molecular Physics, 93, 241-252.

Harun N., Nittaya T., Douglas P.L., Croiset E., Ricardez-Sandoval L.A., 2012, Dynamic simulation of MEA absorption process for CO_2 capture from power plants , International Journal of Greenhouse Gas Control, 10, 295-309.

International Energy Agency, 2010, Carbon Capture and Storage, Model Regulatory Framework.

Lin Y., Pan T., Wong D.S., Jang S., Chi Y., Yeh C., 2011, Plantwide control of CO_2 capture by absorption and stripping using monoethanolamine solution, Industrial and Engineering Chemistry Research, 50, 1338-1345.

Ljung L., 1995, System Identification Toolbox. For use with Matlab.

Mac Dowell N., Shah N., 2014, The multi-period optimisation of an amine-based CO_2 capture process integrated with a super-critical coal-fired power station for flexible operation, Computers & Chemical Engineering (Accepted).

Mac Dowell N., Shah N., 2014, Optimisation of post-combustion CO_2 capture for flexible operation, Energy Procedia (Accepted).

Mac Dowell N., Pereira F. E., Llovell F., Blas F. J., Adjiman C. S., Jackson G., Galindo A., 2011, Transferable SAFT-VR models for the calculation of the fluid phase equilibria in reactive mixtures of carbon dioxide, water and n-alkylamines in the context of carbon capture, The Journal of Physical Chemistry B, 115, 8155-8168.

Mac Dowell N., Samsatli N., Shah N., 2013, Dynamic modelling and analysis of an amine-based post-combustion CO_2 capture absorption column, International Journal of Greenhouse Gas Control, 12, 247-258.

Mac Dowell N., Shah N., 2013, Identification of the cost-optimal degree of CO_2 capture: An optimisation study using dynamic process models,International Journal of Greenhouse Gas Control, 13, 44-58.

Nittaya T., Douglas P.L., Croiset E., Ricardez-Sandoval L.A., 2014, Dynamic modelling and control of MEA absorption processes for CO_2 capture from power plants, Fuel, 116, 672-691.

Panahi M., Skogestad S., 2012, Economically efficient operation of CO_2 capturing process. Part II:Control layer, Chemical Engineering and Processing, 52, 112-124.

gCCS overview. Retrieved November, 30, 2014, from: http://www.psenterprise.com/power/ccs/gccs.html.

Sahraei M.S., Ricardez-Sandoval L.A., 2014, Controllability and optimal scheduling of a CO_2 capture plant using model predictive control, International Journal of Greenhouse Gas Control, 30, 58-71.

Krist V. Gernaey, Jakob K. Huusom and Rafiqul Gani (Eds.), 12th International Symposium on Process Systems Engineering and 25th European Symposium on Computer Aided Process Engineering.
31 May – 4 June 2015, Copenhagen, Denmark

A Framework to Structure Operational Documents for Chemical Processes

Hiroshi Osaka [a], Yuji Naka [a], Tetsuo Fuchino [a]

[a]*Tokyo Institute of Technology, 2-12-1, Oookayama, Megro-ku, Tokyo, Japan*

Abstract

It is widely recognized that inadequate and ineffective operational documents contribute substantially to the occurrence of plant downtime and often costly and dangerous industrial incidents. This is largely because the operational design for chemical processes is performed during the earlier process and plant design phase without carrying forward the key operational design information into the later operational documents. To improve the quality of operational documents for safer and more efficient operations, we propose a framework that structures operational documents so that the key operational information is retained.

Keywords: Framework, Operational Design, Operational Document, Operating Procedure, ANSI/ISA S88

1. Introduction

In the chemical process industry, it is well accepted that operational documents such as operating procedures and training manuals are often inadequate and ineffective. As a result, it is widely recognized that these inadequate and ineffective operational documents contribute substantially to the occurrence of plant downtime and often costly and dangerous industrial incidents.

The key reasons for these inadequate and ineffective documents are that the original operational requirements from plant owners are not clear, and the fundamental design intentions and design rationales by process designers are not incorporated into these operational documents. This is because the operational design for chemical processes is performed by the process designers during the earlier process and plant design phase, and, (in a largely separate and much later exercise), operational documents are created by the plant owners. This decoupling of design and operations means that these documents don't cover all the necessary operation modes and they don't support the design intentions and design rationales.

This paper presents a logical methodology and data structure whereby the key operational design output is carried forward into the operational documents producing efficient, easily understood and flexible procedural documents that will ultimately result in safer and more efficient operations.

To achieve this, first, we identify typical data elements for the operational documents by referring to generally accepted design guidelines. Next, we identify the operational design output during the process and plant design phase by utilizing a systematized business process models for plant lifecycle engineering (Fuchino *et al.*, 2011). In particular, with regard to the description of processes, operations and equipment, we apply the design philosophy of ANSI/ISA-88(ANSI/ISA-S88.01, 1995) to the methodology. (ANSI/ISA-88 is a widely accepted industry standard addressing batch process control). Finally, we integrate these techniques to construct effective, structured

operational documents. Documents structured using this methodology reflect all the underlying design intentions and design rationales and operation modes and, at the same time are easier to use and easier to maintain. We propose that this will substantially contribute to safer and more efficient operations for chemical processes.

2. Framework Overview

In this paper, we propose a framework to structure operational documents to meet the needs of chemical processes that have non-routine operations at startup and shutdown. The methodology we use to structure these operational documents is described as follows:

Step-1 We identify the required data elements for various types of operational documents.

Step-2 We identify the operational design output during the process and plant design phase by utilizing the systematized business process model for plant lifecycle engineering.

Step-3 We review the ANSI/ISA-S88 Model from the view point of the process and plant design to develop a model for the structured operational documents. Then, we apply the identified data elements and design output from Step-1 and Step-2 to the model for the structured operational documents.

Step-4 We create a database application to store the structured operational documents.

Figure 1 shows the framework used to structure operational documents. Please refer to the Framework Details in Section 3 below.

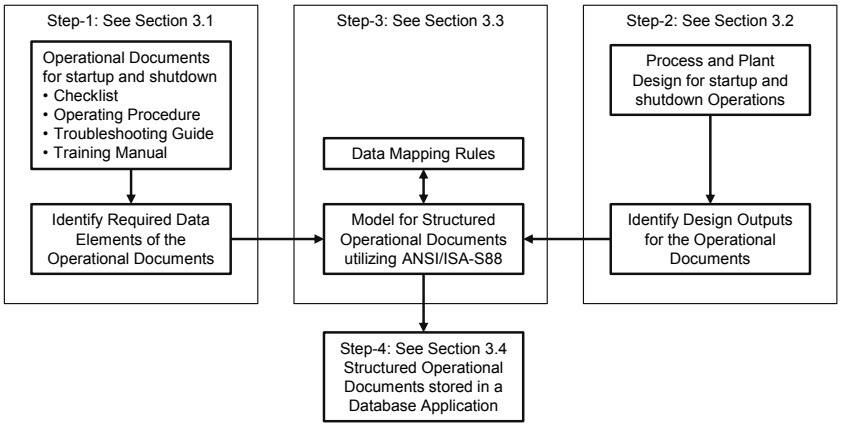

Figure 1 Framework to Structure Operational Documents

3. Framework Details

3.1. Identify the Required Data Elements for the Operating Documents

In general, operational documents are composed of various types of documents such as checklists, operating procedures, troubleshooting guides and training manuals. We identify the data elements for these operational documents using the technique described in an article of Create Effective Safety and Operating Manuals (Bridges *et al.*, 1997) and a widely-recognized guideline; Guidelines for Risk Based Process Safety published by Center of Chemical Process Safety (CCPS, 2007). The data elements for the operational documents are categorized into (i) background information and (ii) operational information about startup and shutdown. The background information

should include an overview of the process, its hazards, and its equipment and safety systems. Table 1 shows the required data elements for typical operational documents.

Table 1 Data Elements for Typical Operational Documents

Data Elements Required for Operational Documents	Typical Operational Documents (X: Applicable)			
	Checklist	Operating Procedure	Troubleshooting Guide	Training Manual
Background Information				
Process overview		X		X
Hazard overview		X		X
Description of equipment and safety systems		X		X
Operational Information about Startup and Shutdown				
Step number or index	X	X	X	X
Action step	X	X	X	X
Physical location of the equipment				X
Expected system response		X	X	X
Troubleshooting			X	X
Safe operation limits and limiting conditions		X		X
Warnings, cautions or notes	X	X		X
Other pertinent remarks				X
Theory of operation				X
Equipment description				X

3.2. Identify Design Output for Process and Plant Design for startup and shutdown Operations

The information for the operational documents should be created during the process and plant design phase. Fuchino *et al.* has developed the systematized business process model for plant lifecycle engineering that is an IDEF0 (FIPS, 1993) activity model specifying all the activities for the process and plant design. We utilize this model to identify relevant activities which create the operational information for the startup and shutdown operations. Figure 2 shows the node tree which highlights the activities related to the process and plant design for the startup and shutdown operations. Figure 3 shows the corresponding design output from the process and plant design for the startup and shutdown operations shown in Figure 2. This design output contains design intentions and design rationales that contribute to safer and more efficient operations for the chemical processes.

3.3. Model for Structured Operational Documents

i. We identify two sets of data elements for the operational documents from Step-1 and Step-2. This means we can clearly determine the required data elements for the operational documents at the process and plant design phase when these two sets of data elements are clearly interrelated. To manage these data elements properly, it is better to relate these data elements to actual processes, operations, and equipment so that users of operational documents can easily access the necessary data elements. So, we apply the design philosophy of ANSI/ISA-S88 model as a reference to represent the operational documents as shown in Figure 4.

ii. We review the ANSI/ISA-S88 model from the view point of the process and plant design. Then, we reconstruct a new model for the structured operational documents by considering the following four object models in this order: (i) process requirements, (ii) operational requirements, (iii) equipment requirements and (iv) plant structure. The general relationship among these four object models is illustrated in Figure 5. Each object model is made up of corresponding subdivisions that are combined in a hierarchical manner to accommodate the relevant data elements identified above. It is obvious that the activities related to the process and plant design for the startup and shutdown operations shown in Figure 2 correspond

to the gray area in Figure 5 and this gray area can represent the structured operational documents.

iii. To relate the identified two sets of data elements to the relevant object models shown in Figure 5, we introduce the data mapping rules as shown in Table 2.

iv. Finally, we combine the identified data elements with the model for the structured operational documents using the data mapping rules to represents the structured operational documents.

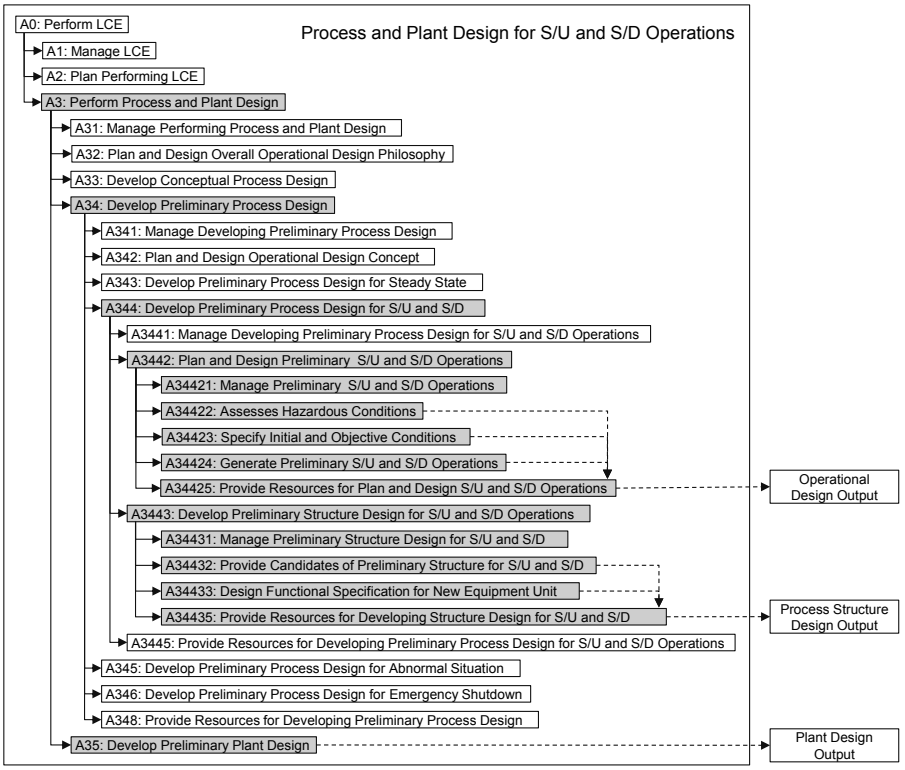

Figure 2 Systematized Business Process Model for Lifecycle Engineering

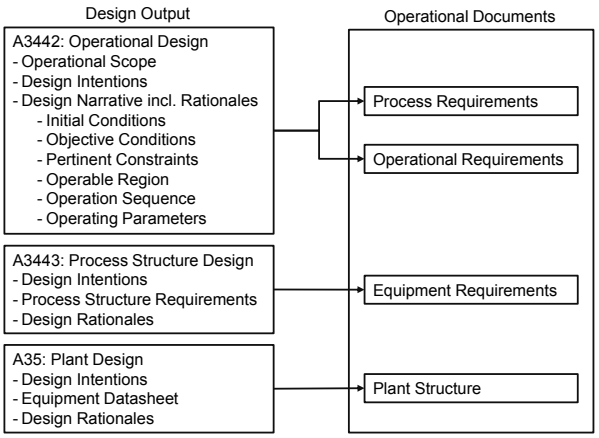

Figure 3 Process and plant design output for Startup and Shutdown Operations

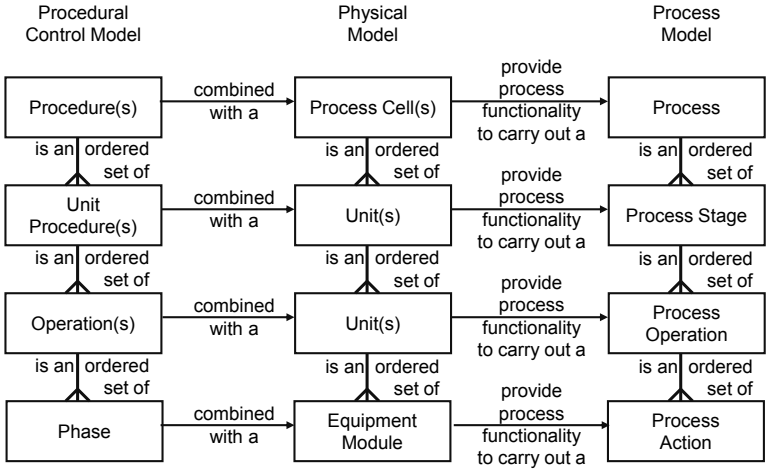

Figure 4 ANSI/ISA S88 Model

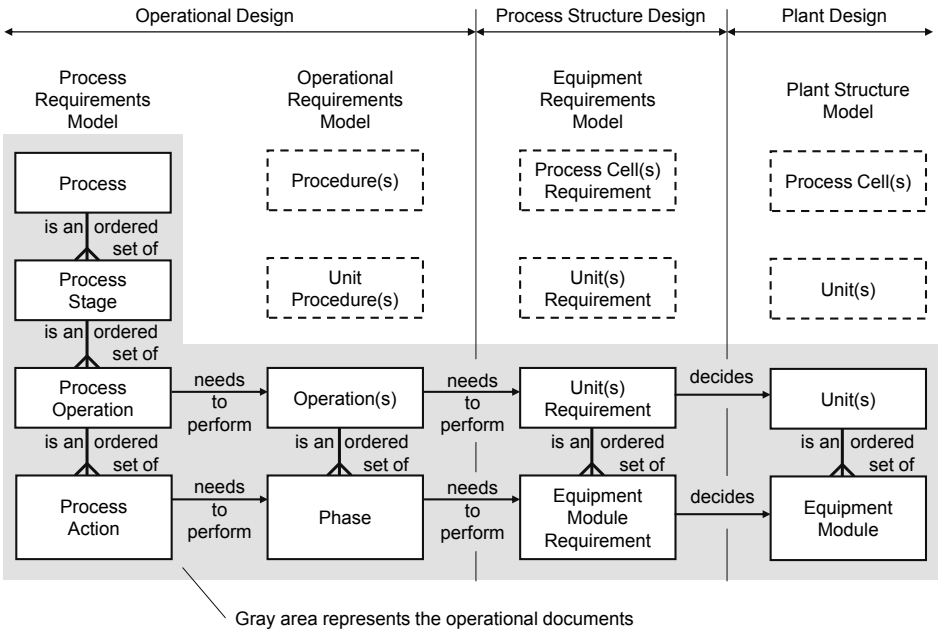

Figure 5 Model for Structured Operational Documents

v. When applying Step-3, it is important to ensure that the data elements for the operational documents from Step-2 are sufficient and comply with the required data elements from Step-1.

3.4. Structured Operational Documents stored in a Database Application

A database application can efficiently accommodate various types of operational documents into one place electronically. This is an integrated operational document environment. A user of the operational document environment can easily obtain various documents by selecting the different data elements that are listed in Table 1.

Table 2 Data Mapping Rules in the Model for Structured Operational Documents

Data Elements to be mapped to the Model for Structured Operational Documents	Object Models shown in Figure 5 (X: Applicable)			
	Process Requirements	Operation Requirements	Equipment Requirements	Plant Structure
Typical Data Elements Required for Operational Documents (See Section 3.1)				
Process overview	X			
Hazard overview	X			
Description of equipment and safety systems	X	X		X
Step number or index		X		
Action step		X		
Physical location of the equipment				X
Expected system response	X	X		
Troubleshooting	X	X		
Safe operation limits and limiting conditions for operation related to action step	X	X	X	X
Warnings, cautions or notes	X	X	X	X
Other pertinent remarks	X	X	X	X
Theory of operation	X	X		
Equipment description			X	X
Process and Plant Design Output for Startup and Shutdown Operations (See Section 3.2)				
Operation scope	X	X		
Design intentions	X	X	X	X
Design rationales	X	X	X	X
Initial conditions	X	X		
Objective conditions	X	X		
Pertinent constraints	X	X		
Operable region	X	X		
Operation sequence	X	X		
Operating parameters	X	X		
Process structure requirements			X	
Equipment datasheet				X

4. Conclusions

This paper has introduced a framework to structure operational documents for chemical processes. In contrast to conventional methodologies, documents structured using this methodology reflect the rich underlying design output including the design intentions and design rationales that are generated during the process and plant design phase.

We will apply this framework to the actual implementation of a practical database of operational documents. The proposed framework should substantially contribute to safer and more efficient operations for chemical processes.

References

T. Fuchino, Y. Shimada, T. Kitajima, K. Takeda, R. Batres, Y. Naka, 2011, A Business Process Model for Process Design that Incorporates Independent Protection Layer Considarations, Computer-Aided Chem. Eng., 29, pp.326-330

ANSI/ISA-S88.01, 1995, Batch Control, Part 1: Models and Terminology, ISA

W. G. Bridges, T. R. Williams, 1997, Create Effective Safety Procedures and Operating Manuals, Chemical Engineering Progress, American Institute of Chemical Engineers

CCPS, 2007, Guidelines for Risk Based Process Safety, American Institute of Chemical Engineers, Center for Process Safety

Federal Information Processing Standards (FIPS) Publications, 1993, Integration Definition for Function Modeling (IDEF0), http://www.itl.nist.gov/fipspubs/

Krist V. Gernaey, Jakob K. Huusom and Rafiqul Gani (Eds.), 12th International Symposium on Process Systems Engineering and 25th European Symposium on Computer Aided Process Engineering.
31 May – 4 June 2015, Copenhagen, Denmark

Teaching Sustainable Process Design Using 12 Systematic Computer-Aided Tasks

Deenesh K. Babi[a]

[a]*CAPEC-PROCESS Research Center, Department of Chemical and Bio-chemical Engineering, Technical University of Denmark, Søltofts Plads, Building 229, DK-2800, Kgs. Lyngby, Denmark*

Abstract

In this paper a task-based approach for teaching (sustainable) process design to students pursuing a degree in chemical and biochemical engineering is presented. In tasks 1-3 the student makes design decisions for product and process selection followed by simple and rigorous model simulations (tasks 4-7) and then sizing, costing and economic analysis of the designed process (tasks 8-9). This produces a base case design. In tasks 10-12, the student explores opportunities for heat and/or mass integration, followed by a sustainability analysis, in order to evaluate the base case design and set targets for further improvement. Finally, a process optimization problem is formulated and solved to obtain the more sustainable process design. The 12 tasks are explained in terms of input and output of each task and examples of application of this approach in an MSc-level course are reported.

Keywords: Education, Teaching, Sustainable Process Design, Chemical Engineering

1. Introduction

One of the fundamental courses in chemical and biochemical engineering education is a course related to chemical (and biochemical) process design. An example of such a course is the Capstone Design course taught in the USA at universities that offer undergraduate and post graduate studies in chemical and biochemical engineering.

The students taking the process design course need to gain fundamental understanding in four key areas. First, the students need to learn that process design requires the making of good design decisions, in order to generate a process flowsheet that converts some raw materials to desired products while satisfying process specifications. Second, to make appropriate design decisions, they need to have a good theoretical background and process understanding. Third, they should use process simulators only to verify/validate decisions/designs and must not use these tools to make design decisions by trial and error or blind simulations that are not based on prior analysis. Fourth, they should consider sustainability related issues (carbon footprint, toxicity, etc.) in the early stages of design when looking for more sustainable designs. It is important that students understand the scope and significance of performing sustainable process design because it is a requirement in proposing new and innovative designs for the industry that may want to hire them.

In the course, sustainable process design is introduced as the design of a process that corresponds to improved values of a set of targeted performance criteria related to economical, operational and sustainability factors (Babi et al., 2014). Therefore, matching these targets means a more sustainable design is obtained. In teaching sustainable process design, there is a need for a systematic task-based approach that

students can easily apply in order to generate, design and analyse process alternatives in their search for more sustainable solutions.
In this paper a task-based approach is presented for teaching sustainable process design. This approach is currently being used at the Technical University of Denmark (DTU), Denmark, the Sino-Danish Center for Education and Research (SDC), China and the Petroleum and Petrochemical College, Chulalongkorn University, Thailand.

2. Sustainable Process Design: Mathematical formulation

The students are first introduced to the definition of the (sustainable) design problem (Fig. 1) and then how to express it mathematically (Eq. 1 to Eq. 5)

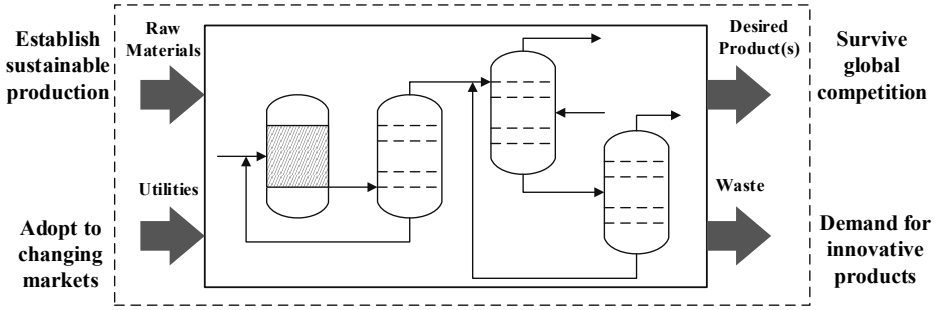

Figure 1: Graphical Definition of the (Sustainable) Design Problem

$$F_{OBJ} = \max\left\{C^T y + f(x)\right\} \quad (1)$$

$$f_1(x) = 0 \quad (2)$$

$$f_2(x, y) = 0 \quad (3)$$

$$l_1 \le g(x, y) \le u_1 \quad (4)$$

$$\underline{Y} = 0/1,\ \underline{X} \ge 0 \quad (5)$$

In Eq. 1 to Eq. 5, x represents a vector of continuous variables, for example, flowrates, design variables etc. and y represents the vector of binary integer variables, for example, unit operation identity, $f_1(x)$ and $f_2(x)$ represents equality constraints related to process specifications and process model equations, $g(x,y)$ represents a set of inequality constraints related to process design specifications and environmental impacts. The objective function, F_{OBJ} (to be maximized or minimized) consist of $f(x)$ that represents a system of linear and/or non-linear functions. From the mathematical formulation presented in Eq. 1 to Eq. 5, the process design problem is defined as a mixed integer non-linear programming problem (MINLP) because the objective function and/or constraints can be either linear and/or non-linear and binary, integer decisions are required. The solution of this generic problem, however, is decomposed into the solution of a hierarchal set of 12-tasks, where the final step is the optimization step.
In applying the task-based approach, the students solve the process design problem by first generating a base case design where constraints in Eq. 2-3 are satisfied. Then the environmental impacts and sustainability issues are considered (Eq. 4). This also leads

to an integrated process. Finally, the objective function is calculated and ordered for a feasible set of alternatives in order to determine the more sustainable design.

3. Sustainable Process Design: 12 Task approach

The sequential (hierarchal), task-based approach for teaching process design is divided into 12 tasks. Each task has required inputs and therefore, desired outputs. In order for the student to proceed from one task to another, the previous task must be completed and if necessary, they can return to a previous task and modify the required input, thereby, obtaining an updated output. It is not possible to skip a task, unless the problem allows it, because the output of a previous task is used as the input to the next task.

3.1. Task 1-2- Identify Chemical Product and Economic Viability

Task objective: To identify details about the chemical product to be produced and analyse its economic viability.

Input to the task:

- Properties of compounds

Output of the task:

- Product selection
- Chemical product uses and thermo-physical properties
- Manufacturers and yearly production rate of the chemical product
- Raw material, reaction pathway and reaction steps
- Economic potential

Action required: First, the student must select the chemical compound to be produced. This can be specified by the teacher or selected by the student. Second, details about the product is obtained, for example, why the product is needed, its uses and its thermo-physical properties. Third, using a selected reaction pathway, a yearly production rate of the chemical product and, raw material and product prices, an economic potential is calculated. It is based on an overall mass balance of the process, and stoichiometry of the selected reaction pathway. The economic potential at this stage must be sufficiently high in order to have a profitable process.

3.2. Task 3- Initial design selection and verification

Task objective: To select and verify an initial design.

Additional input to the task:

- Raw material, reaction pathway and reaction steps

Output of the task:

- Verified initial design

Action required: First, the student must select a process that utilizes the reaction pathway selected in task 2 to convert the raw material to the desired product. This selected process is referred to as the initial design. Second, the initial design is verified using the process synthesis method (Douglas, 1985). The student also has the option to generate a process using this method, taking into account the compounds present in the reactor inlet and outlet streams, recovery of the raw materials (where applicable) and recovery of the products.

3.3. Task 4- Mass balance

Task objective: To perform a mass balance on the initial design using a process simulator.

Additional input to the task:

- Raw material, reaction pathway and reaction steps
- Verified initial design

Output of the task:

- Mass balance for the initial design

Action required: First, the student, together with the reaction information, must decide on the product recoveries for all the separators present in the process flowsheet. Second, for the process flowsheet under consideration, a mass balance is performed using simple in/out mass balance models available in process simulators. Note, recycle streams are also included in this mass balance model and purge fractions must be decided.

3.4. Task 5- Identify process stream conditions

Task objective: To identify the process stream conditions.

Additional input to the task:

- Mass balance for the initial design

Output of the task:

- Stream condition

Action required: The minimum data needed to define a stream are the component flowrates, temperature, pressure and phase state (optional). Students are introduced to this concept, where the component flowrates are obtained already from task 4. Now using thermodynamic insights, they need to decide about temperature, pressure and phase state. The students are given a guideline, for selection of the appropriate thermodynamic model. This information is to be used in task 6 for the energy balance model. The design decisions here introduce also the concepts of phase equilibria.

3.5. Task 6- Mass and Energy balance

Task objective: To perform a mass and energy balance on the initial design using a process simulator.

Additional input to the task:

- Mass balance for the initial design
- Stream condition

Output of the task:

- Mass and energy balance for the initial design

Action required: First, the mass balance model is extended in order to include the energy balance. Second, the heat added or removed from each unit operation is calculated in order to verify the decision decisions made in task 5.

3.6. Task 7- Rigorous simulation

Task objective: To perform rigorous simulation by replacing simple models with rigorous models.

Additional input to the task:

- Mass and energy balance for the initial design

Output of the task:

- Rigorous simulation results

Action required: First, each simple in/out model for separation is replaced one at a time with its corresponding rigorous version, for example, a stream calculator used for representing the separation of a zeotropic multicomponent mixture is replaced with a rigorous model that use as input the results from tasks 4-6.

3.7. Task 8-9- Equipment Sizing & Costing and Economic Analysis

Task objective: To perform equipment sizing and costing and, an economic analysis on the rigorous design.

Additional input to the task:

- Rigorous simulation results

Output of the task:

- Equipment dimensions and costs
- Economic analysis

Action required: First, the results obtained from the rigorous simulation of the initial design are used to perform equipment sizing based on the power-law correlations developed by Guthrie (1969). Second, the cost (capital) associated with the initial design are calculated. Third, additional costs (direct and indirect) are calculated as factors of the equipment cost. Finally, an economic analysis is performed based on cash flow, depreciation and project lifetime in order to analyse whether the process is profitable. After performing the economic analysis, the initial design is referred to as a base case design. It is a feasible design because it satisfies all constraints but, it is not optimal.

3.8. Task 10-12- Process Integration and Optimization

Task objective: To perform a process integration and optimization.

Additional input to the task:

- Base case design

Output of the task:

- Heat and/or mass integrated design
- Environmental impact analysis
- Sustainable design

Action required: First, opportunities for heat integration are explored, that is, streams to be heated are integrated with streams to be cooled, for example, reactor inlet and outlet streams. Second, opportunities for mass integration are explored. Third, a sustainability analysis is performed on the integrated design in order to set targets for further improvement. Finally, an optimization problem is formulated and solved. Here any process alternative that improves the defined objective function is more sustainable solution.

4. Sustainable Process Design: Computer-Aided tools

The students learn to use different tools as they apply the 12 task approach. The software used in the course consist of both in-house and commercial tools. A list of the tools used in the course is given in Table 1.

Table 1: List of Computer-Aided Tools

Name	**Function**	**Notes**
ICAS	Compound database, experimental data	Model based analysis, database*
SolventPro	Solvent selection and Design	Model based analysis, database*
ProPred	Property prediction	Model based- group contribution*
ECON**	Economic analysis	Model & rule based analysis*
LCSoft**	LCA analysis	Model & rule based analysis*
SustainPro**	Sustainability analysis	Model & rule based analysis*
PROII	Process Simulation	PROII 9.3 (2015)

*Note: Part of ICAS suite (Gani et al., 1997, **Kalakul et al., 2014)

5. Sustainable Process Design: Examples of Designed Processes

The 12 task approach for achieving sustainable process design has been applied numerous times, for example, at DTU, the course is taught every spring semester, for the past 20 years, as an advanced course for the MSc degree (http://bit.ly/1G08Lk5). Table 2 lists some process designs developed by students taking the course.

Table 2: Selected Design projects

Design Project Product	**Payback period-** ***Tasks 10-12 (1-9)***	**Production target**	**Remarks**
DME	3.4 (5.4) yrs.	53000 kg/hr	Co-production of DME & methanol
Cumene	1.9 (2.3) yrs.	34247 kg/hr	Carbon footprint reduction
Styrene	2.4 (7.6) yrs.	17123 kg/hr	Reduction in environmental impacts
Phenol	2.5 (2.9) yrs.	45700 kg/hr	Novel reactor design without by-products

6. Conclusion and Future Perspectives

In this paper a task-based approach to teaching (sustainable) process design that explores different facets of theory/knowledge gained from previous courses has been presented. Process design text books such as Seider, Seader, Lewin, Widgado, Gani and Ng (2015) also employ a similar approach. In perspective, it is important that a design course is structured in such a way that research methods and tools that are currently being developed, can be incorporated into teaching, in order to provide meaningful and up to date insights to the students. This is important in the area of sustainability, for example, the use of sustainability and LCA analyses, for analysis of chemical processes. Finally students should also be given the opportunity to do a design project on ‘’product design’’, but how can this be done in a similar way?

Acknowledgement
The author would like to thank Professor Rafiqul Gani of DTU for his thorough feedback and guidance in the writing of this paper.

References

D. K. Babi, P. Lutze, J. M Woodley & R. Gani, (2014). A Process Synthesis-
Intensification Framework for the Development of Sustainable Membrane-based Operations. Chem. Eng. Process. Process Intensif., 86, 173–195.
J. M. Douglas, (1985). A hierarchical decision procedure for process synthesis. AIChE
J., 31(3), 353–362.
K. M. Guthrie, "Capital Cost Estimating," Chern. Eng., 76(6): 114
Kalakul, S., Malakul, P., Siemanond, K., & Gani, R. (2014). Integration of life cycle assessment software with tools for economic and sustainability analyses and process simulation for sustainable process design. J. Cleaner Prod. 71, 98–109
PROII Manual & Simulation software, Version 9.3, Schneider Electric, 2015.
R. Gani, G. Hytoft, C. Jaksland, & A. K. Jensen, (1997). An integrated computer aided system for integrated design of chemical processes. Comput. Chem. Eng., 10, 1135–1146
W. D. Seider, J. D. Seader, D. R. Lewin, R. Gani, K. Ng, Product and Process Design Principles: Synthesis, Analysis and Design, 4th Edition, Wiley, New York (in print)

Krist V. Gernaey, Jakob K. Huusom and Rafiqul Gani (Eds.), 12th International Symposium on Process Systems Engineering and 25th European Symposium on Computer Aided Process Engineering.
31 May – 4 June 2015, Copenhagen, Denmark

Optimization of Chemical Processes Using Surrogate Models Based on a Kriging Interpolation

Natalia Quirante,[a*] Juan Javaloyes,[a] Rubén Ruiz-Femenia,[a] José A. Caballero.[a]

[a]*Institute of Chemical Processes Engineering. University of Alicante. P.O. 99, E-03080 Alicante, Spain.*
natalia.quirante@ua.es

Abstract

Superstructure approaches are the solution to the difficult problem which involves the rigorous economic design of a distillation column. These methods require complex initialization procedures and they are hard to solve. For this reason, these methods have not been extensively used. In this work, we present a methodology for the rigorous optimization of chemical processes implemented on a commercial simulator using surrogate models based on a kriging interpolation.

Several examples were studied, but in this paper, we perform the optimization of a superstructure for a non-sharp separation to show the efficiency and effectiveness of the method. Noteworthy that it is possible to get surrogate models accurate enough with up to seven degrees of freedom.

Keywords: process optimization, design, kriging algorithm, modular simulators.

1. Introduction

Computationally efficient process models have been recently demanded in many engineering applications. When we want to optimize a model, the process model has to trade-off the model accuracy against computational efficiency. The problem is that most of those models have a modular structure to which users have limited internal access (they see a “grey box model”) and some of these models introduce numerical noise, so that its derivatives cannot be accurately estimated.

In addition, the rigorous design of distillation column sequences is a difficult problem in chemical process engineering because it includes simultaneous optimization of continuous decisions related to the operational conditions, and discrete decisions allied to the number of trays in each column section or the columns connectivity.

In this work we study the replacement of complex systems of distillation columns by surrogate models based on a kriging interpolation generated from rigorous models, including continuous and discrete variables, and use these metamodels to design the distillation columns. Thereby, we keep the rigor of simulations models, removing most of the numerical problems and increasing the reliability of the synthesis algorithms.

In this work we use simulation data to build models for individual parts of a large system. We focus on kriging metamodels because they are computationally efficient and they use relatively small sampling data. Kriging can be applied to replace a complete system or to substitute one or some of the components of the model.

2. Kriging interpolation

Kriging was developed by a South African mining engineer in his geostatistics Master Thesis (Krige, 1951). Its fitting consists of two parts: a polynomial expression and a deviation from that polynomial:

$$y(x) = f(x) + Z(x) \tag{1}$$

where $Z(x)$ is a stochastic Gaussian process that represents the uncertainty about the mean of $y(x)$ with expected value zero. The covariance for two points x_i and x_j is given by a scale factor σ^2 and by a spatial correlation function $R(x_i,x_j)$. The most common alternative for kriging models is using the extended exponential correlation (Sacks et al., 1989).

$$R(x_i, x_j) = exp\left(-\sum_{l=1}^{d} \theta_l \left(x_{i,l} - x_{j,l}\right)^{P_l}\right) \tag{2}$$

where $\theta_l \geq 0$ and $0 \leq P_l \leq 2$ are adjustable parameters. To estimate the values of the parameters, θ_l and P_l, we maximize the logarithm of the likelihood function of the obtained data y.

$$log(L) = -\frac{n}{2} ln(2\mu) - \frac{n}{2} ln(\sigma^2) - \frac{1}{2} ln(|R|) - \left(\frac{-(y - 1\mu)^T R^{-1} (y - 1\mu)}{2\sigma^2}\right) \tag{3}$$

where y is the vector of obtained responses (n x 1), $\boldsymbol{1}$ is a vector of ones (n x 1), n is the number of sampled points and σ^2 and μ are parameters.

Differentiating Eq.(3) with respect σ^2 and μ, and equating it to zero, we obtain the optimal values for σ^2 and μ.

$$\hat{\mu} = \frac{1^T R^{-1} y}{1^T R^{-1} 1} \tag{4}$$

$$\hat{\sigma}^2 = \frac{(y - 1\hat{\mu})^T R^{-1} (y - 1\hat{\mu})}{n} \tag{5}$$

To interpolate a new point x_{new}, we add the point (x_{new}, y_{new}) to the data and compute the augmented likelihood function keeping the parameters constant. The value for y_{new} will be calculated maximizing the augmented likelihood function. With the Eq.(6) is given the final predictor of the kriging method (Sasena, 2002).

$$\hat{y}(x_{new}) = \hat{\mu} + r^T R^{-1} (y - 1\hat{\mu}) \tag{6}$$

where r (n x 1) is the vector of correlations $R(x_{new},x_i)$ between the sample design points and the points to be correlated.

Kriging allow us to estimate the accuracy with the correlation of the errors, from the formula for the mean-squared error (Sacks et al., 1989).

$$s^2(x_{new}) = \hat{\sigma}^2 \left(1 - r^T R^{-1} r + \frac{(1 - r^T R^{-1} r)^2}{1^T R^{-1} 1}\right) \tag{7}$$

3. Application of the kriging algorithm in distillation columns

The kriging algorithm implementation is as follows:

a. First, N points are generated, separated enough to ensure that the noise generated by the simulator has no effect on. These points are sampled.
b. Kriging metamodel is fitted with the simulation data.
c. Validate the accuracy of the model using cross-validation (Jones et al., 1998).
d. Substitute the actual model by the kriging metamodel.
e. Perform the (MI)NLP optimization. If the accuracy of the model is good, we can finish.
f. In case that the accuracy was not good, add the optimal point to the set of sampled points, and update and re-optimize kriging. If there is no improvement in two consecutive iterations, go to step g.
g. In this case, we have to contract the feasible search region within a trust region around the solution obtained and repeat steps d to f, until we can guarantee that the error in gradient is below a given tolerance.

In this work, sampling points are generated distributed throughout the search area using a max-min approach (maximizing the minimum distance between two points). For this, we fix the bounds of all independent variables and then we distribute the rest of the points through the max-min approach.

4. Examples and results

Several examples were studied to verify the effectiveness of the method, but in this paper only an interesting example is presented. It consists of a superstructure for a non-sharp separation. We enumerate the column trays from the top to the bottom of the column. The example was solved on a computer with a 2.60 GHz Pentium® Dual-Core Processor and 4 GB of RAM under Windows 7.

4.1. Objective function

The objective function consists of minimizing the total annualized cost (*TAC*) of a chemical process. The total annualized cost is function of the capital costs of the column shells, trays and exchangers, and function of the operating cost (we have considered the cost of cooling water and vapor stream).

The objective function is determined by the Eq.(8) (Turton, 2012).

$$min\ TAC\left(\frac{\$}{year}\right) = C_{op} + F \cdot C_{cap} \tag{8}$$

where C_{op} is the operating cost per year, F is an annualization factor and C_{cap} is the capital cost. Both are updated by the global CEPCI cost index of 2013. The annualization factor is calculated by the Eq.(9) (Smith, 2005).

$$F = \frac{i(1+i)^n}{(1+i)^n - 1} \tag{9}$$

where n in the horizon time and i is the fractional interest rate per year. We have used a horizon time of 5 years and a fixed interest rate of 10 %.

4.2. Distillation sequences. Nonsharp separations.

We want to separate a multicomponent feed stream given into several desired multicomponent product streams. Figure 1 shows the superstructure that contains all possible alternatives to get the desired products (Aggarwal and Floudas, 1990). The objective is to determine the optimal sequence and number of trays of the columns to minimizing the total annualized cost (TAC) for separating an iso-molar mixture of benzene, toluene and p-xylene. This cost is composed of the operational and fixed costs of both columns. Mixer and splitters costs are neglected. Peng-Robinson equation of state has been used.

Assume that the pressure is fixed (P = 101.3 kPa). The independent variables chosen for the rigorous design of the conventional distillation columns are the number of trays in the rectifying section, number of trays in the stripping section and the recoveries of key components for each column.

The problem is formulated as an MINLP. It can be solved by reformulating the disjunctions using a Big-M approach (Grossmann and Ruiz, 2012). Disjunctions are shown in Eq.(10).

$$\begin{bmatrix} Y_1 \\ [Q_{Reb}^{C1}, Q_{Cond}^{C1}, D^{C1}] = Kr_1(N_{R1}^{C1}, N_{S1}^{C1}, f_{LK}^{C1}, f_{HK}^{C1}, F5_i) \\ TAC_1 = \Omega(Q_{Reb}^{C1}, Q_{Cond}^{C1}, D^{C1}) \end{bmatrix} \underline{\vee} \begin{bmatrix} \neg Y_1 \\ TAC_1 = 0 \\ F5_i = F6_i = F9_i = 0 \; \forall i \end{bmatrix}$$
$$\begin{bmatrix} Y_2 \\ [Q_{Reb}^{C2}, Q_{Cond}^{C2}, D^{C2}] = Kr_2(N_{R2}^{C2}, N_{S2}^{C2}, f_{LK}^{C2}, f_{HK}^{C2}, F13_i) \\ TAC_2 = \Omega(Q_{Reb}^{C2}, Q_{Cond}^{C2}, D^{C2}) \end{bmatrix} \underline{\vee} \begin{bmatrix} \neg Y_2 \\ TAC_2 = 0 \\ F13_i = F14_i = F18_i = 0 \; \forall i \end{bmatrix} \quad (10)$$

Y_1 and Y_2 are Boolean variables that take the value of True if the corresponding column is selected and False otherwise. The symbol '*f*' makes reference to the key components recoveries.

The minimum objective function (TAC = 0.3129 M$/year) is obtained with the sequence shown in Figure 2.

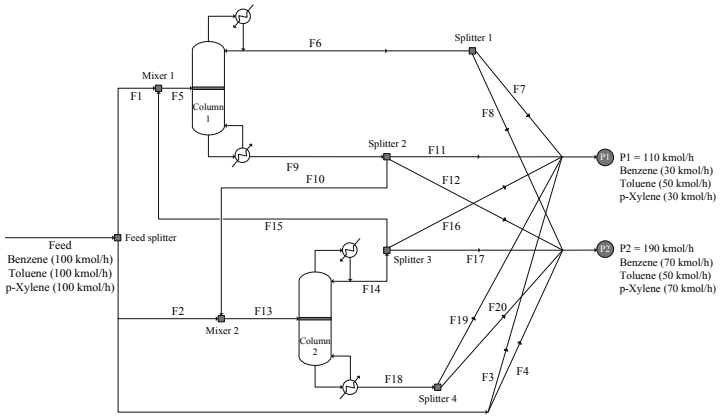

Figure 1. Superstructure for a three-component system.

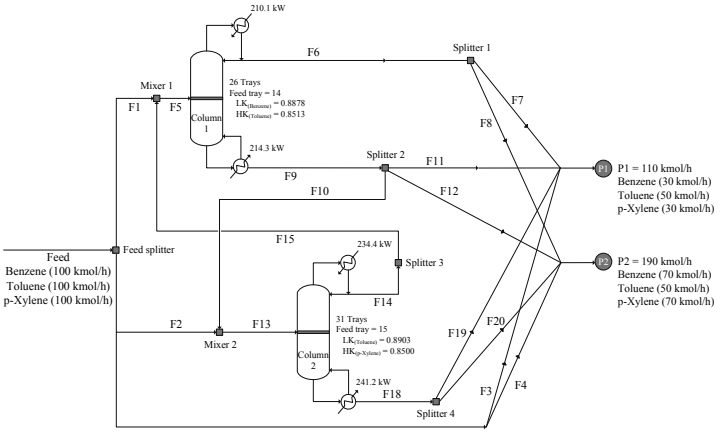

Figure 2. Optimal solution for the three-component system.

The column 1 has 26 trays and it is fed on the 14th tray. The column 2 has 31 trays and it is fed on the 15th tray.

A summary of results obtained is shown in Table 1. A contraction step around the optimal solution was performed. Then, a new resampling and kriging calibration was needed.

5. Conclusions

In this work, was presented and applied an algorithm for constrained optimization of distillation columns. This optimization includes implicit grey box functions which are substituted by a kriging metamodel.

Table 1. Summary of results obtained (optimal solution).

Optimal valued (after refining stage)			
Number of sampled points in each columns = 202 TAC = 0.3129 M$/year			
Column 1		Column 2	
$F5_{,benzene}$	13.1490	$F13_{,benzene}$	3.6504
$F5_{,toluene}$	11.2260	$F13_{,toluene}$	9.5000
$F5_{,p\text{-}Xylene}$	3.4158	$F13_{,p\text{-}Xylene}$	12.6589
Number of trays in the rectifying section	13	Number of trays in the rectifying section	14
Number of trays in the stripping section	12	Number of trays in the stripping section	16
Recovery (LK = Benzene)	0.8878	Recovery (LK = Toluene)	0.8903
Recovery (HK = Toluene)	0.8513	Recovery (HK = p-Xylene)	0.8500

The "quality" of the optimum will depend on how accurately the surrogate model represents the actual model. It is interesting remark that though the final model includes discrete variables the kriging surrogate can be generated without taking into account that fact.

The implementation presented in this work only guarantees a local optimum. However, we have checked that it is possible to get accurate global surrogate models with up to seven degrees of freedom, being necessary a high number of sampling points. The problem presented is that if the number of points is large, it will be necessary a large CPU time for calibrating the kriging. A reduced set of sampling points reduce the CPU time for calibrating the kriging and interpolation, but it is likely that we need more contraction, resampling and recalibrating stages.

The algorithm presented has proved to be robust, reliable and also allows a fast interpolation of new values.

Acknowledgements

The authors with to acknowledge the financial support by the Ministry of Economy and Competitiveness from Spain, under the project CTQ2012-37039-C02-02.

References

Aggarwal, A., Floudas, C.A., 1990. Synthesis of general distillation sequences-nonsharp separations. Computers and Chemical Engineering 14, 631-653.

Grossmann, I., Ruiz, J., 2012. Generalized Disjunctive Programming: A Framework for Formulation and Alternative Algorithms for MINLP Optimization, in: Lee, J., Leyffer, S. (Eds.), Mixed Integer Nonlinear Programming. Springer New York, pp. 93-115.

Jones, D.R., Schonlau, M., Welch, W.J., 1998. Efficient Global Optimization of Expensive Black-Box Functions. Journal of Global Optimization 13, 455-492.

Krige, D., 1951. A Statistical Approach to Some Mine Valuation and Allied Problems on the Witwatersrand., Masters Thesis, University of Witwatersrand, South Africa.

Sacks, J., Welch, W.J., Mitchell, T.J., Wynn, H.P., 1989. Design and Analysis of Computer Experiments. 409-423.

Sasena, M.J., 2002. Flexibility and efficiency enhancements for constrained global design optimization with kriging approximations. University of Michigan.

Smith, R., 2005. Chemical process design and integration. Wiley.

Turton, R., 2012. Analysis, Synthesis, and Design of Chemical Processes. Prentice Hall.

Krist V. Gernaey, Jakob K. Huusom and Rafiqul Gani (Eds.), 12th International Symposium on Process Systems Engineering and 25th European Symposium on Computer Aided Process Engineering.
31 May - 4 June 2015, Copenhagen, Denmark.

Global Sensitivity Analysis for a Model of B-Cell Chronic Lymphocytic Leukemia Disease Trajectories

Symeon Savvopoulos[a], Ruth Misener[b], Nicki Panoskaltsis[c], Efstratios N. Pistikopoulos[a,d] and Athanasios Mantalaris[a]

[a]*Department of Chemical Engineering; Imperial College London; South Kensington UK*
[b]*Department of Computing; Imperial College London; South Kensington UK*
[c]*Department of Hematology; Imperial College London; Northwick Park & St. Marks Campus UK*
[d]*Artie McFerrin Department of Chemical Engineering, Texas A&M, College Station TX*
a.mantalaris@imperial.ac.uk

Abstract

This paper implements global sensitivity analysis in the Savvopoulos et al. (2014) mathematical model of B cell chronic lymphocytic leukemia (B-CLL); this dynamic model represents a framework for modelling dynamic B-CLL trajectories. B-CLL is a heterogeneous, slowly-progressing disease where a type of white blood cell, B lymphocytes, accumulates in bone marrow, peripheral blood, lymph nodes and spleen. The Savvopoulos et al. (2014) modelling framework integrates both temporal and spatial disease aspects; delay differential equations capture latency in the cell proliferation cycle and population balance equations between disease centres represent inter-tissue B-CLL migration. This manuscript conducts global sensitivity analysis using the random sampling - high dimensional mathematical representation (RS-HDMR) method to: (1) uncover which are the most critical model parameters; (2) analyse the system of model equations; (3) provide clinically-relevant patient testing recommendations leading to effective model parametrisations.

Keywords: global sensitivity analysis, multi-compartmental model of B-CLL, cell cycle kinetics

1. Introduction

B-CLL is the most commonly-incurred leukemia or blood cancer; approximately 16,000 and 2,800 patients are diagnosed annually in the USA and UK, respectively (American Cancer Society, 2014). B-CLL is a heterogeneous disease representing with abnormally increased proliferation and reduced apoptosis (programmed cell death) of B lymphocytes. The disease progresses slowly with most cancerous cells arrested in the resting (G0) or growth (G1) phases of the cell cycle. B-CLL cells are monoclonal (*i.e.*, derived from a single cell) lymphocytes which accumulate abnormally in bone marrow (BM), peripheral blood (PB), lymph nodes (LN), and spleen (S) (Granziero et al., 2001).

Signs often include: (1) elevated lymphocyte count (lymphocytosis) with $> 5,000$ cells $/\mu$L in peripheral blood; (2) LN enlargement, (3) enlarged S (splenomegaly); (4) BM failure; (5) decreased red blood cells (anaemia, Hgb $< 11\text{g} \cdot \text{dL}^{-1}$); (6) decreased platelet count (thrombocytopenia) $< 100 \cdot 10^9$ / L (Galton, 1966), all leading to the widely-used Binet et al. (1981) system for staging (Binet Stage A – C): (A) lymphocytosis with fewer than 3 areas of enlarged lymph nodes; (B) lymphocytosis with both lymphadenopathy and splenomegaly; (C) lymphocytosis with bone marrow failure, anaemia and thrombocytopenia.

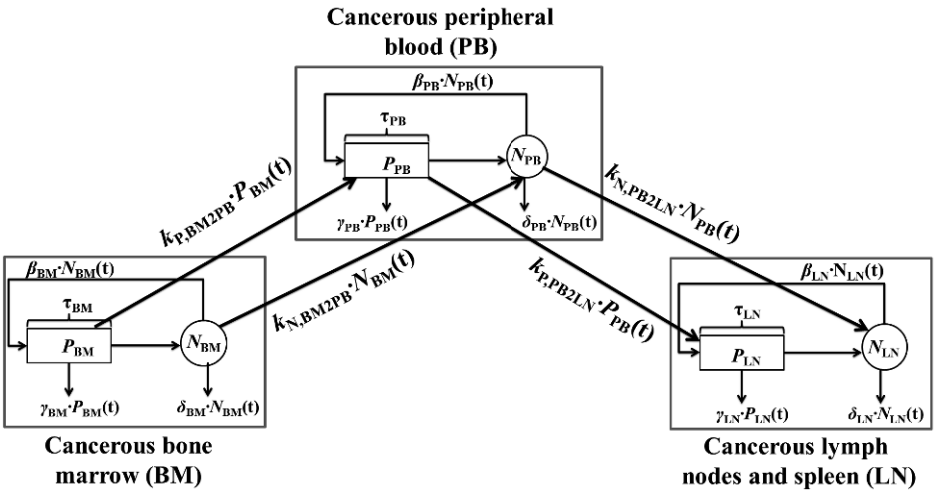

Figure 1: The compartmental analysis of B-CLL (Savvopoulos et al., 2014)

We (Savvopoulos et al., 2014) have developed a dynamic, physiologically-relevant mathematical model of B-CLL interconnecting the most affected tissues: PB, LN, BM and S. This modelling framework integrates both temporal and spatial disease aspects; delay differential equations capture latency in the cell proliferation cycle and population balance equations between disease centres represent inter-tissue B-CLL migration.

This manuscript proposes global sensitivity analysis (GSA) of the nonlinear model of B-CLL using the method that is alternatively called the Sobol method or random sampling - high dimensional model representation, RS-HDMR (Li et al., 2002). GSA has been repeatedly shown to highlight key elements of model structure such as in the works of Kiparissides et al. (2009, 2011) where they used the Sobol method in order to find the most experimentally validated parameters from nonlinear biological systems. In this paper, sensitivity indices derived from RS-HDMR are ranked according to their values; the results show which input parameters or interactions of two inputs contributes most significantly to the overall output variance (Ziehn and Tomlin, 2008).

Deducing key model parameters from global sensitivity analysis allows effective analysis of model equations and may provide clinically-relevant patient testing recommendations leading to effective model parametrisations; the goal is to provide insight into the development and subsequent personalised treatment of B-CLL. This manuscript uses as springboard the Acute Myeloid Leukemia model of Pefani et al. (2013, 2014) which similarly incorporates cell cycle analysis and compartmental models of disease centres. In this manuscript: Section 2 briefly introduces the Savvopoulos et al. (2014) model; Section 3 describes the GSA algorithm; Section 4 analyses the relevant model parameters; Section 5 discusses the results; Section 6 concludes the manuscript. This work belongs to an ongoing effort developing building blocks for modelling and optimising biomedical systems (Velliou et al., 2014).

2. Mathematical Model of B-CLL

Our model (Figure 1; Eqs (1) – (7)) integrates the most affected tissues: BM, PB, LN and S. The net flow of cancerous cells starts in BM, the site of pathogenesis, wherein CLL cells proliferate according to the time-delayed feedback function β; both non-proliferative (N_{BM}) and proliferative

(P_{BM}) cells may subsequently migrate to LN and S through PB or accumulate in BM and thereby change the bone marrow infiltration pattern. The LN microenvironment also promotes B-CLL proliferation and causes LN and S enlargement.

Bone Marrow (BM):

$$\frac{dN_{\mathrm{BM}}}{dt} = -\delta_{\mathrm{BM}}\, N_{\mathrm{BM}} - \beta_{\mathrm{BM}}(N_{\mathrm{BM}})\, N_{\mathrm{BM}}\, cc + 2\, \beta_{\mathrm{BM}}(N_{\mathrm{BM},\,\tau_{\mathrm{BM}}})\, N_{\mathrm{BM},\,\tau_{\mathrm{BM}}} \\ e^{-\gamma_{\mathrm{BM}}\,\tau_{\mathrm{BM}}}\, cc - k_{\mathrm{N,BM2PB}}\, N_{\mathrm{BM}} \tag{1}$$

$$\frac{dP_{\mathrm{BM}}}{dt} = -\gamma_{\mathrm{BM}}\, P_{\mathrm{BM}} + \beta_{\mathrm{BM}}(N_{\mathrm{BM}})\, N_{\mathrm{BM}}\, cc - \beta_{\mathrm{BM}}(N_{\mathrm{BM},\,\tau_{\mathrm{BM}}})\, N_{\mathrm{BM},\,\tau_{\mathrm{BM}}} \\ e^{-\gamma_{\mathrm{BM}}\,\tau_{\mathrm{BM}}}\, cc - k_{\mathrm{P,BM2PB}}\, P_{\mathrm{BM}} \tag{2}$$

$$cc = \frac{800 \cdot 10^9 - C_{\mathrm{NC,BM}} - N_{\mathrm{BM}} - P_{\mathrm{BM}}}{800 \cdot 10^9} \tag{3}$$

Peripheral Blood (PB):

$$\frac{dN_{\mathrm{PB}}}{dt} = -\delta_{\mathrm{PB}} \cdot N_{\mathrm{PB}} - \beta_{\mathrm{PB}}(N_{\mathrm{PB}}) \cdot N_{\mathrm{PB}} + 2 \cdot \beta_{\mathrm{PB}}(N_{\mathrm{PB},\,\tau_{\mathrm{PB}}}) \cdot N_{\mathrm{PB},\,\tau_{\mathrm{PB}}} \cdot e^{-\gamma_{\mathrm{PB}} \cdot \tau_{\mathrm{PB}}} \\ + k_{\mathrm{N,BM2PB}} \cdot N_{\mathrm{BM}} - k_{\mathrm{N,PB2LN}} \cdot N_{\mathrm{PB}} \tag{4}$$

$$\frac{dP_{\mathrm{PB}}}{dt} = -\gamma_{\mathrm{PB}} \cdot P_{\mathrm{PB}} + \beta_{\mathrm{PB}}(N_{\mathrm{PB}}) \cdot N_{\mathrm{PB}} - \beta_{\mathrm{PB}}(N_{\mathrm{PB},\,\tau_{\mathrm{PB}}}) \cdot N_{\mathrm{PB},\,\tau_{\mathrm{PB}}} \cdot e^{-\gamma_{\mathrm{PB}} \cdot \tau_{\mathrm{PB}}} \\ + k_{\mathrm{P,BM2PB}} \cdot P_{\mathrm{BM}} - k_{\mathrm{P,PB2LN}} \cdot P_{\mathrm{PB}} \tag{5}$$

Lymph Nodes and Spleen (LN):

$$\frac{dN_{\mathrm{LN}}}{dt} = -\delta_{\mathrm{LN}} \cdot N_{\mathrm{LN}} - \beta_{\mathrm{LN}}(N_{\mathrm{LN}}) \cdot N_{\mathrm{LN}} + 2 \cdot \beta_{\mathrm{LN}}(N_{\mathrm{LN},\,\tau_{\mathrm{LN}}}) \cdot N_{\mathrm{LN},\,\tau_{\mathrm{LN}}} \cdot e^{-\gamma_{\mathrm{LN}} \cdot \tau_{\mathrm{LN}}} \\ + k_{\mathrm{N,PB2LN}} \cdot N_{\mathrm{PB}} \tag{6}$$

$$\frac{dP_{\mathrm{LN}}}{dt} = -\gamma_{\mathrm{LN}} \cdot P_{\mathrm{LN}} + \beta_{\mathrm{LN}}(N_{\mathrm{LN}}) \cdot N_{\mathrm{LN}} - \beta_{\mathrm{LN}}(N_{\mathrm{LN},\,\tau_{\mathrm{LN}}}) \cdot N_{\mathrm{LN},\,\tau_{\mathrm{LN}}} \cdot e^{-\gamma_{\mathrm{LN}} \cdot \tau_{\mathrm{LN}}} \\ + k_{\mathrm{P,PB2LN}} \cdot P_{\mathrm{PB}} \tag{7}$$

Auxiliary Helper Functions (Temporal Delays & Feedback Functions):

$$N_{i,\,\tau_i} = N(t - \tau_i);\ \beta_i(N_i) = \beta_{N_i,0} \cdot \theta_i^{\mathrm{n}} / (\theta_i^{\mathrm{n}} + N_i^{\mathrm{n}});\ \theta_i = \theta_{i,1} \cdot t + \theta_{i,2}; \qquad \forall\, i \in \{\mathrm{BM, PB, LN}\}$$

where in each tissue $i \in \{\mathrm{BM, PB, LN}\}$, N_i, P_i are the number of B-CLL cells in non-proliferative and proliferative phase, δ_i, γ_i are the cell death rates in non-proliferative and proliferative phases, β_i, θ_i, n are parameters defining the time-delayed cell proliferation feedback function, $\beta_{N_i,0}$ is the maximum number of cells entering the proliferative phase, τ_i is the time spent in proliferative phase, $k_{\mathrm{N,BM2PB}}$, $k_{\mathrm{P,BM2PB}}$, $k_{\mathrm{N,PB2LN}}$, $k_{\mathrm{P,PB2LN}}$ are the B-CLL migration rates in non-proliferative phase and proliferative phase from BM to PB and from PB to LN and S, cc denotes the BM carrying capacity, $C_{\mathrm{NC,BM}}$ is the number of normal BM lymphocytes which equals $50{\cdot}10^9$ cells (Savvopoulos et al., 2014). The cell cycle formulation in each disease compartment is derived from Mackey (1978).

The delay differential equations incorporate the temporal aspect of cell division τ; Andersen and Mackey (2001) show that explicitly incorporating a time delay will, in future work, allow proper modelling of chemotherapy response. We capture the spatial elements of the disease via the migration rates k between compartments of the most affected tissues; the approach is similar to population balance modelling. Observe that this model is fundamentally a modular framework that could incorporate advanced aspects such as the interaction between B and T lymphocytes (Nanda et al., 2013); the baseline cell cycle equations taken from Mackey (1978) could be augmented if we could expect additional clinical and experimental data.

3. Global Sensitivity Analysis

In RS-HDMR, model output is decomposed into summands of first-, second- and higher-order terms (Li et al., 2002):

$$f(\mathbf{x}) = f_0 + \sum_{i=1}^{n} f_i(x_i) \quad + \sum_{i,j}^{n} f_{i,j}(x_i, x_j) + \ldots + f_{12\ldots n}(\mathbf{x})$$

where:

$f_0 = \int_{K^n} f(\mathbf{x})\mathrm{d}\mathbf{x}$; $f_i(x_i) = \int_{K^{n-1}} f(\mathbf{x})\mathrm{d}\mathbf{x}^i - f_0$; $f_{ij}(x_i,x_j) = \int_{K^{n-2}} f(\mathbf{x})\mathrm{d}\mathbf{x}^{ij} - f_i(x_i) - f_j(x_j) - f_0$; $\ldots$

and $\mathbf{x} = [x_1, x_2, \ldots, x_n]$ is the input of parameters whose values change; $\mathrm{d}\mathbf{x}^i$ represents the product $\mathrm{d}x_1\mathrm{d}x_2\ldots\mathrm{d}x_n$ without $\mathrm{d}x_i$; $\mathrm{d}\mathbf{x}^{ij}$ is the same product without $\mathrm{d}x_i$ and $\mathrm{d}x_j$.

This decomposition, also called analysis of variance (ANOVA), creates unique, orthogonal terms; first order and higher order effects to the model output are revealed via variance-based methods. The total variance D can be obtained by (Ziehn and Tomlin, 2008):

$$D = \int_{K^n} f^2(\mathbf{x})\mathrm{d}\mathbf{x} - f_0^2$$

and the partial variances $D_{\mathrm{i}_1,\ldots,\mathrm{i}_1}$ are calculated by:
$D_i = \int_0^1 f_i^2(x_i)\mathrm{d}x_i$; $D_{ij} = \int_0^1\int_0^1 f_{i,j}^2(x_i,x_j)\mathrm{d}x_i\mathrm{d}x_j$; $\ldots$
The sensitivity indices are given by: $S_{i_1,\ldots,i_s} = \frac{D_{i_1,\ldots,i_s}}{D}$, $1 \leq \mathrm{i}_1 < \ldots < \mathrm{i}_s \leq \mathrm{n}$, so that all terms add up to 1: $\sum_{i=1}^{n} S_i + \sum_{1\leq i<j\leq \mathrm{n}} S_{i,j} + \ldots + S_{1,2,\ldots,n} = 1$

The main effect of the input variable x_i on the output is showed by each first order sensitivity index S_i, the effect of x_i and x_j on the output is estimated by the second order sensitivity indices and so forth for parameter ranking.

4. Parameters of the Studied Hypothetical Cases

An algorithm developed by Savvopoulos et al. (2014) indirectly calculates cell death and migration rates using experimentally measureable data; these values change between disease phases and thereby influence trajectories from one stage to the next. The 19 parameters are given in Table 1.

We applied the RS-HDMR to the outputs N_{BM}, N_{LN}, N_{PB}, P_{BM}, P_{LN} and P_{BM} by varying the 19 input parameter values $\pm 50\%$. Figures 2 and 3 show the results for the non-proliferative (N_{BM}, N_{LN}, N_{PB}) and proliferative (P_{BM}, P_{LN}, P_{BM}) cell populations.

5. Results and Discussion

Using the cell cycle model mentioned above, RS-HDMR shows that parameters $\theta_{\mathrm{BM},1}$, $\theta_{\mathrm{BM},2}$ and $\theta_{\mathrm{LN},2}$, representing the transition from the non-proliferative to proliferative phase, are the most important parameters affecting the number of non-proliferative cells in BM and LN. Secondarily important to the number of non-proliferative cells is the apoptotic rate δ_{LN} in LN. Our final observation for the non-proliferative cells is that their population in PB is mainly affected by $k_{\mathrm{N,BM2PB}}$ and $k_{\mathrm{N,PB2LN}}$.

For the proliferative B-CLL population, the most important parameter for all outputs is τ_{BM}, followed by migration parameters $k_{\mathrm{P,BM2PB}}$ and $k_{\mathrm{P,PB2LN}}$, and feedback function parameter $\theta_{\mathrm{BM},2}$. Proliferative populations in BM are also highly affected by the apoptotic rates of proliferative cells γ_{BM} and γ_{LN}; any proliferation in PB is primarily affected by recent cellular migration $k_{\mathrm{P,PB2LN}}$.

Table 1: Cell cycle parameters of the five studies in each case

Patient No	**1**		**2**		**3**		**4**		**5**	
Transitions	Naive	A	A	B	A	B	B	C	A	C
Duration (day)	1000	2190	1800	365	365	365	365	365	365	365
γ_{BM} **(day^{-1})**	0.006		0.005		0.005		0.030		0.010	
γ_{LN} **(day^{-1})**	0.002		0.001		0.001		0.002		0.001	
γ_{PB} **(day^{-1})**	0.008		0.009		0.009		0.009		0.020	
δ_{BM} **(day^{-1})**	0.080		0.060		0.060		0.020		0.060	
δ_{LN} **(day^{-1})**	0.009		0.009		0.007		0.008		0.010	
δ_{PB} **(day^{-1})**	0.002		0.003		0.003		0.009		0.004	
$\theta_{BM,1}$ **($\cdot 10^8$ cells)**	0.000	0.050	0.050	0.500	0.020	0.850	0.900	5.000	0.003	25.000
$\theta_{BM,2}$ **($\cdot 10^8$ cells)**	116.000	125.000	220.000	330.000	300.000	330.000	420.000	750.000	130.000	130.000
$\theta_{LN,1}$ **($\cdot 10^8$ cells)**	0.100		0.040		0.090		0.000		0.000	5.000
$\theta_{LN,2}$ **($\cdot 10^8$ cells)**	20.000		200.000		200.000		800.000		500.000	500.000
$\theta_{PB,1}$ **($\cdot 10^8$ cells)**	0.000		0.000		0.000		0.000		0.000	
$\theta_{PB,2}$ **($\cdot 10^8$ cells)**	30.000		40.000		40.000		416.000		85.000	
$k_{N,BM2PB}$ **(day^{-1})**	0.007	0.038	0.005	0.010	0.015	0.020	0.100		0.020	0.020
$k_{P,BM2PB}$ **(day^{-1})**	0.007	0.020	0.005	0.008	0.010	0.010	0.100	0.100	0.020	0.020
$k_{N,PB2LN}$ **(day^{-1})**	0.006	0.045	0.006	0.009	0.015	0.015	0.011	0.020	0.003	0.050
$k_{P,PB2LN}$ **(day^{-1})**	0.060	0.450	0.040	0.060	0.150	0.150	0.150	0.275	0.041	0.610
τ_{BM} **(day)**	0.66		0.75		0.83		0.80		0.66	
τ_{LN} **(day)**	0.65		0.75		0.75		0.80		0.66	
τ_{PB} **(day)**	0.60		0.75		0.75		0.80		0.66	

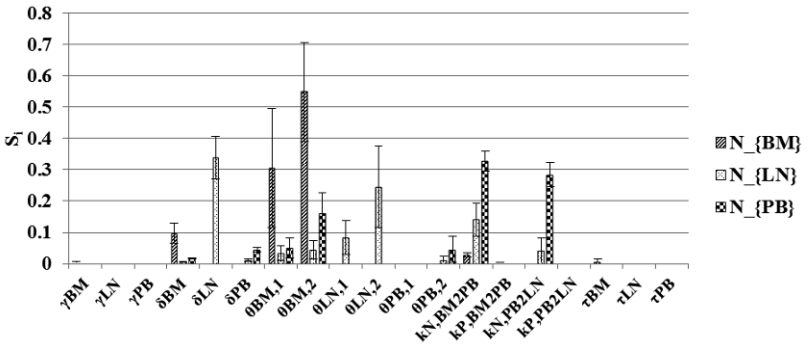

Figure 2: Average values of $S_i \pm SD$ indices in each non-proliferative output for n=10 transitions

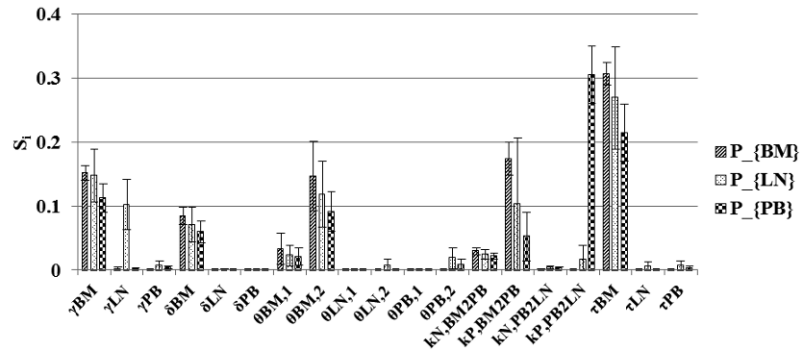

Figure 3: Average values of $S_i \pm SD$ indices in each proliferative output for n=10 transitions

6. Conclusions

RS-HDMR analysis reveals the most important parameters of the Savvopoulos et al. (2014) B-CLL model and may be useful for applying personalised treatment based on inter- and intra- patient leukemia heterogeneity. Personalised treatment for improved efficacy and reduced toxicity of chemotherapy is feasible because B-CLL is slow progressive, giving time to apply what is learned from the model. These important parameters are not simple to calculate *ex vivo* because B-CLL cells undergo apoptosis spontaneously in *in vitro* cultures, but they could be derived from experiments simulating the microenvironment (Mortera-Blanco et al., 2012) or from *in vivo* labelling studies (Messmer et al., 2005).

7. Acknowledgements

ERC-BioBlood (no. 340719), the Richard Thomas Leukemia Research Fund, the National Institute for Health Research Clinical Research (NIHR) Network: Cancer via Northwick Park Hospital R&D. R. M. is thankful for a Royal Academy of Engineering Research Fellowship.

References

American Cancer Society, 2014. CLL.
URL `www.cancer.org/cancer/leukemia-chroniclymphocyticcll/detailedguide/index`

L. K. Andersen, M. C. Mackey, 2001. Resonance in periodic chemotherapy: a case study of acute myelogenous leukemia. Journal of Theoretical Biology 209 (1), 113–130.

J.-L. Binet, D. Catovsky, P. Chandra, G. Dighiero, E. Montserrat, K. R. Rai, A. Sawitsky, 1981. Chronic Lymphocytic Leukaemia: Proposals for a Revised Prognostic Staging System. British Journal of Haematology 48 (3), 365–367.

D. Galton, 1966. The pathogenesis of chronic lymphocytic leukemia. Canadian Medical Association Journal 94 (19), 1005.

L. Granziero, P. Ghia, P. Circosta, D. Gottardi, G. Strola, M. Geuna, L. Montagna, P. Piccoli, M. Chilosi, F. Caligaris-Cappio, 2001. Survivin is expressed on CD40 stimulation and interfaces proliferation and apoptosis in B-cell chronic lymphocytic leukemia 97 (9), 2777–2783.

A. Kiparissides, M. Koutinas, C. Kontoravdi, A. Mantalaris, E. N. Pistikopoulos, 2011. 'Closing the loop' in biological systems modeling - from the in silico to the in vitro. Automatica 47, 1147–1155.

A. Kiparissides, S. S. Kucherenko, A. Mantalaris, E. N. Pistikopoulos, 2009. Global sensitivity analysis challenges in biological systems modeling. Industrial & Engineering Chemistry Research 48 (15), 7168–7180.

G. Li, S.-W. Wang, H. Rabitz, 2002. Practical approaches to construct RS-HDMR component functions. Journal of Physical Chemistry A 106 (37), 8721–8733.

M. Mackey, 1978. Unified hypothesis for the origin of aplastic anemia and periodic hematopoiesis. Blood 51 (5), 941–956.

B. T. Messmer, D. Messmer, S. L. Allen, J. E. Kolitz, P. Kudalkar, D. Cesar, E. J. Murphy, P. Koduru, M. Ferrarini, S. Zupo, G. Cutrona, R. N. Damle, T. Wasil, K. R. Rai, M. K. Hellerstein, N. Chiorazzi, 2005. *In vivo* measurements document the dynamic cellular kinetics of chronic lymphocytic leukemia B cells. Journal of Clinical Investigation 115 (3), 755–764.

T. Mortera-Blanco, M. Rende, H. Macedo, S. Farah, A. Bismarck, A. Mantalaris, N. Panoskaltsis, 2012. Ex vivo mimicry of normal and abnormal human hematopoiesis. Journal of Visualized Experiments.

S. Nanda, L. G. de Pillis, A. E. Radunskaya, 2013. B Cell Chronic Lymphocytic Leukemia-A Model with Immune Response. Discret Contin Dyn S B 18 (4), 1053 – 1076.

E. Pefani, N. Panoskaltsis, A. Mantalaris, M. Georgiadis, E. N. Pistikopoulos, 2014. Chemotherapy drug scheduling for the induction treatment of patients with acute myeloid leukemia. IEEE Transactions in Biomedical Engineering 61 (7), 2049–2056.

E. Pefani, N. Panoskaltsis, A. Mantalaris, M. C. Georgiadis, E. N. Pistikopoulos, 2013. Design of optimal patient-specific chemotherapy protocols for the treatment of acute myeloid leukemia (AML). Computers in Chemical Engineering 57, 187–195.

S. Savvopoulos, R. Misener, N. Panoskaltsis, E. N. Pistikopoulos, A. Mantalaris, 2014. A personalized framework for dynamic modelling of chronic lymphocytic leukemia disease tranjectories. (In preparation).

E. Velliou, M. Fuentes-Garí, R. Misener, E. Pefani, M. Rende, N. Panoskaltsis, E. N. Pistikopoulos, A. Mantalaris, 2014. A framework for the design, modeling and optimization of biomedical systems. In: Eden, Siirola, Towler (Eds.), FOCAPD. Computer Aided Chemical Engineering. pp. 225 – 236.

T. Ziehn, A. Tomlin, 2008. Global sensitivity analysis of a 3D street canyon modelpart I: The development of high dimensional model representations. Atmospheric Environment 42 (8), 1857–1873.

Krist V.Gernaey, Jakob K.Huusom and RafiqulGani (Eds.), 12th International Symposium on Process Systems Engineering and 25th European Symposium on Computer Aided Process Engineering.
31 May – 4 June 2015, Copenhagen, Denmark

Modeling and Simulation of Complex Nonlinear Dynamic Processes Using Data Based Models: Application to Photo-Fenton Process

Ahmed Shokry[a,1], Francesca Audino[a,1], Patricia Vicente[a,2], Gerard Escudero[b,2], Montserrat Perez Moya[a,2] , Moises Graells[a2] , and Antonio Espuña[a,1*]

[a]*Department of Chemical Engineering,* [b]*Department of Computer Science.*
[1]*ETSEIB. Av.Diagonal 647,08028,* [2]*EUETIB. Comte d'Urgell 187, 08036.*
Universitat Politècnica de Catalunya, Barcelona, Spain.
antonio.espuna@upc.edu

Abstract

This paper investigates data based modelling of complex nonlinear processes, for which a first principle model useful for process monitoring and control is not available. These empirical models may be used as soft sensors in order to monitor a reaction's progress, so reducing expensive offline sampling and analysis. Three different data modelling techniques are used, namely Ordinary Kriging, Artificial Neural Networks and Support Vector Regression. A simple case is first used to illustrate the problem, assess and validate the modelling approach, and compare the modelling techniques. Next, the methodology is applied to a photo–Fenton pilot plant to model and predict the reaction progress. The results show promising accuracy even when few training points are available, which results in huge savings of time and cost of the experimental work.

Keywords: Kriging, support vector machines, neural networks, chemical kinetics.

1. Introduction

The photo-Fenton process is a photochemical advanced oxidation process widely investigated for its efficiency in degrading emerging contaminants, especially pharmaceuticals and personal care products, through the formation of highly reactive hydroxyl radicals (•OH). Different approaches have been used to model treatment systems based on the photo-Fenton process and, among them, some First Principle Models (FPMs) have been proposed to match the degradation of very simple organic molecules (Farias et al., 2009), but the complexity and nonlinear nature of these systems hinders the development of a comprehensive FPM including all the involved reaction mechanisms in more general cases. Moreover, most of the measures available from the online sensors of pilot or industrial plants are not easy to link with the variables included in such FPMs, which complicates their application for process monitoring and control. Empirical simple regression models based on experimental results have been also used (Pérez-Moya et al., 2008). Despite their importance, these regression models tend to excessively simplify the complex nonlinear behaviour of the process, they have limited capabilities to correlate larger sets of process variables (Shokry et al. 2014) and they are usually applied as linear or lower-order models, unable to capture sophisticated nonlinear relations. Conversely, multivariate data based modelling requires more sophisticated and advanced techniques that can capture highly nonlinear system behaviours (Nagy, 2007, Shokry et al., 2014); in this line, Artificial Neural Networks (ANN), Support Vector Regression (SVR), or Ordinary Kriging (OK) have been widely used in many areas to provide efficient alternatives to construct simple and accurate

data-based models (metamodels), saving time and cost of experimental work and reducing the complexity of fitting and using FPMs simulation.

This work addresses the data-based modelling of a photo-Fenton process, using data measured and recorded from a batch pilot plant (Pérez-Moya et al., 2008). The model is aimed to predict the reaction progress as a function of other online measured variables. The SCADA system of the plant provides thousands of cheap on-line measurements of these variables along each batch run. But, on the other hand, the reaction progress is measured by expensive off-line sampling and analysis of Total Organic Carbon (TOC) at a significantly coarser time grid/resolution, which results in very few measurements during the batch time. This large difference between the number of the available online and offline data makes the modelling task problematic and challenging, since for each batch only few input/output (online/offline) sets of measures are really available.

An additional challenge is caused by the different nature of the uncertainties and errors in the online and the offline data (i.e.: relatively small errors or white noise in the online data and relatively high experimental errors in the offline measurements). The rest of the paper investigates the mentioned techniques (OK, ANN, and SVR) for the modelling of such challenging case study, describing the modelling approach adopted, and their application to an illustrative example and to the photo-Fenton pilot case.

2. Modelling techniques (data based models)

2.1. Ordinary Kriging (OK)

Given a set of training data $[x_i,y_i]$, $i=1,2,..n, x \in R^k, y \in R$ (where k is the number of input variables), the OK assumes a stochastic process in which the error in the predicted value is a function of the input variables x. The predictor $\hat{y}(x)$ is composed by a polynomial term $f(x)=\mu$, and a deviation $Z(x)$ from that polynomial. So, $\hat{y}(x)=f(x)+Z(x)$, where $Z(x)$ is a stochastic Gaussian process with expected zero value, $E(Z(x))= 0$, and a covariance between x_i, x_j as $cov(Z(x_i),Z(x_j))=\sigma^2 R(x_i,x_j)$. Being σ^2 is the process variance, and $R(x_i,x_j)$ is a correlation function $R(x_i, x_j) = exp\left(-\sum_{l=1}^{k} \theta_l \left|x_{i,l}-x_{j,l}\right|^{p_l}\right) + \delta_{i,j}\,\lambda$, being δ_{ij} the Kronecker delta, and λ the regularization constant that enables the Kriging predictor to regress noisy data and not passing through them (over-fit) (Azman et al., 2007). To estimate the μ, σ^2, θ_l, p_l, λ values, the likelihood function of the observed data $[y]_{n*1}$ is maximized (this work uses the "*fmincon"* function of the Matlab library). The Kriging predictor (Eq.(1)) is obtained by driving the augmented likelihood function of the original training data set and a new interpolating point (x_{new},y_{new}). In Eq. (1), r is the $n\times1$ vector of correlations $R(x_{new}, x_i)$ between the point to be predicted x_{new} and the training data points. The variance of the predictor is given by Eq.(2).

$$\hat{y}(x_{new}) = \mu + r^T R^{-1}(Y - 1\mu) \quad (1)$$

$$\hat{s}^2(x_{new}) = \hat{\sigma}^2(1 + \lambda - r^T R^{-1} r + (1 - r^T R^{-1} r)^2/(1^T R^{-1} 1)) \quad (2)$$

2.2. Artificial Neural Networks (ANN)

A well-known efficient method, widely used for nonlinear system modelling, is the use of ANN. Feedforward ANN are frequently used in engineering applications for system modelling and identification (Z. K. Nagy, 2007). Although they exhibit very powerful capabilities, ANN have some specific limitations as the huge effort and time consumed in selecting the ANN configuration (T. Masters, 1993), and the cruse of dimensionality (Azman et al., 2007). In this work, the Matlab ANN toolbox and the function "*feedforwardnet*" have been used to create a feed forward ANN; the number of neurons and layers (one hidden layer of eight neurons), and the training algorithm ("*trainbr"* using the Levenberg-Marquardt optimization method - Bayesian regularization) were selected to balance simplicity and accuracy.

2.3. Support Vector Regressions (SVR)

Recently, SVR are used in many applications in the area of chemical process engineering, showing promising capabilities (P. Jain et al., 2007). Given a set of *n* input-output training data *[x_i,y_i], i=1,2,..n,* $x \in R^k, y \in R$, SVR map the input data's original space into a higher dimensional feature space usually through nonlinear Gaussian kernel function $\phi(x_i, x_j) = exp(-\|x_i, x_j\|^2/2\sigma^2)$. In the feature space the problem becomes the construction of an optimal linear surface $f(x) = \mu + w^T \Phi(x)$ that fits the data, where μ is a base or bias, and $w \in R^k$ are weights. So, the flattest function *f(x)* is sought by minimizing the vector norm w^2, subjected to a set of constraints: the error in the predicted value of each of the training data should be at most equal to ε. To allow for outliers, the data that have prediction error bigger than ε is penalized using the so called ε-sensitive loss function. The constrained optimization problem is then reformulated into a dual problem form by using Lagrange multipliers α_i, α^*_i for each constraint. The Lagrange multipliers are determined by solving the problem using Quadratic Programming (QP). Once α_i, α^*_i are determined, the optimal weights *w* and the base μ can be computed, and the final predictor is given in Eq(3).

$$f(x_{new}) = \mu + \Sigma_{i=1}^{n}(\alpha_i - \alpha_i^*)\phi(x_{new}, x_i) \quad (3)$$

3. Modelling approach

The main idea is to use OK, ANN and SVR to obtain a static correlation of TOC as a function of the on-line variables in the same time instant. Assuming no control (no perturbation along the batch run) these models will predict the expensive offline variable *y(t)* as a function of the cheap online variables *x(t)*, and the initial conditions.

$$y(t) = f[\ x(t), y(t=0), x(t=0)] \quad (4)$$

4. Simulation-based case study

A mathematical example of a series of reactions $A \xrightarrow{k1} B \xrightarrow{k2} C$ is used to mimic a case study, illustrate the approach and validate and compare the different techniques. For a batch operation with no perturbations, the process depends only on the initial values. Hence, during a 30-minute batch, the concentration of product *C* is calculated at 8 specific time instants, simulating expensive offline sampling and analysis. On the contrary, the concentrations of products *A*, *B* are calculated every second, simulating online measured variables (1s sampling time). To generate the training data, 24 batches are simulated in this way, using different initial values [$C_a(t=0)$, $C_b(t=0)$, $C_c(t=0)$] generated by a Hammersley sampling procedure within the limits [14:20, 0:2, 0:2]. Small white noise $N(\mu=0,\sigma=0.07)$ is added to the simulated online values (C_a, C_b), while a higher error $N(\mu=0,\sigma=0.7)$ is also added to the simulated offline data (C_c). Figure 1(a) shows the results obtained for one batch.

The online data of the 24 batches are smoothed by using a moving average approach, with a period of 50 seconds. Then, the 8 input-output (offline-online sets) training points are collected for each one of the 24 batches, and the three metamodels (Eq.(5)) are fitted into these 192 data values.

$$C_c(t) = f[c_a(t=0), c_b(t=0), c_c(t=0), c_a(t), c_b(t)] \quad (5)$$

An extra set of 100 batches with different initial concentrations (within the same range used to generate the training set) are then simulated and used as validation set to test the predictions of the offline variable C_c obtained by each one of the trained metamodels.

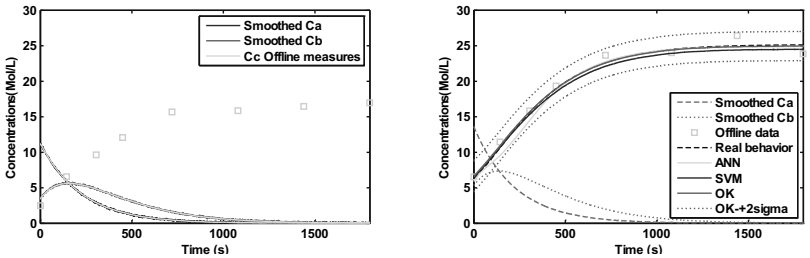

Figure 1: (a) Data of one of the 24 batches used as training set, (b) Prediction of one the 100 batches used as validation set.

Figure 1(b) shows the prediction of C_c produced by each metamodel for one of such validation batches. Table 1 shows the Average Root Mean Square Error (ARMSE), the Pearson coefficient, and the fitting and interpolation computational effort required for each one of the metamodels used. Figure 2 shows the ARMSE for each validation batch. The errors are given respect to the noisy training data and also respect to the not noisy FPM describing the system's underlying theoretical behaviour.

Table 1: ARMSE, Pearson coefficient, and fitting and interpolation times.

	ARMSE		*Pearson*		*CPU Time (s)**	
	W.R.T. Experiments	W.R.T. FP model	W.R.T. Experiments	W.R.T. FP model	Fitting	Interpolation
OK	0.367462	0.25554	0.99922	0.999986	036.0	0264.0
ANN	0.382541	0.29265	0.99916	0.999882	459.0	2019.0
SVM	0.407109	0.30128	0.99915	0.999976	000.9	0149.0

* HP-dc7900, Intel core 2-duo 3.16 GHz, RAM 6 GB.

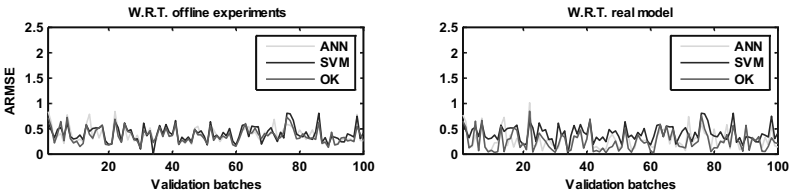

Figure 2: ARMSE for 100 validation batches.

Kriging not only provides slightly higher accuracy, but its tuning is robust and fast, since all the model parameters [θ_l, p_l, μ, σ, λ] are implicitly optimized, the modeller just makes a guess about the parameters initial values and the optimization/training procedure provides their optimal values. Conversely, significant effort and time is required to decide the ANN structure and the SVR parameters [σ, ε, C]. Additionally, OK outperforms the results obtained by the other compared methods, by providing the estimated variance (Eq.(2)) of the prediction (Figure 1(b) red dotted line) that can be used as quantitative confidence assessment when the system's real behaviour is unknown or it is hard to estimate the prediction accuracy.

These conclusions are confirmed by expanding the range of initial values to [*10:20, 0:7, 0:7*] and using 8 batches for training and 100 batches for validation.

5. Applications to the Photo-Fenton pilot plant

A real photo-Fenton batch pilot plant is used to produce experimental data. Along the batch time (90 min), the SCADA system registers two variables, Temperature (T) and

Redox potential (R), which are expected to determine the process performance. Both variables are on-line measured and recorded every second at a minimum cost (5400 measurements per batch). Instead, the reaction progress is measured by expensive off-line sampling and analysis of TOC every 15 minutes, which results in only seven input/output (online/offline) set of measurements available for each batch run.

Table 2: Set of twelve experiments used for training and validation.

BATCH	*[TOC]t=0 (mg/L)*	*[H_2O_2]t=0 (mg/L)*	*TRAINING*	*VALIDATION*
1	21	99		●
2	21	99	●	
3	21	198		●
4	42	99		●
5	42	198	●	
6	42	198	●	
7	42	395	●	
8	42	395	●	
9	84	395		●
10	84	395		●
11	84	791	●	
12	84	791	●	

Data for twelve batches (Table 2) with different initial concentration of TOC and H_2O_2 (the oxidizing agent) have been selected to train and validate the three selected metamodels. It should be noticed that the use of Redox potential as online variable, implicitly allows to take into consideration one of the most significant factors in photo-Fenton process, such as the Fenton reagent ratio with respect to the amount of contaminant ($TOC/H_2O_2/Fe^{2+}$). Figure 3 shows data of two of these batches.

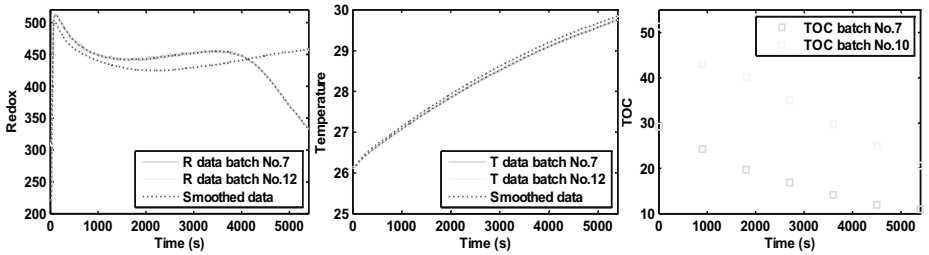

Figure 3: Online and offline data of two Fenton batches.

Table 3: ARMSE for the validation batches.

	ARMSE of each validation batch					*Total*
Batch No.	1	3	4	9	10	*ARMSE*
OK	1.093	1.146	0.738	3.662	1.753	1.6790
ANN	1.404	1.048	1.653	3.718	2.340	2.0324
SVR	1.126	1.040	0.986	3.821	1.616	1.7185

To reduce the sensor noise, the online data (T, R) are smoothed using a moving average with a 60 s period. Then, 7 input-output training points are collected from each batch of the training group, and the metamodels Eq.(6) are fitted to the 49 training points.

Figure 4 and Table 3 show how the three methods accurately predict the TOC for different batches of the validation set, as well as the confidence interval given by OK.

$$TOC(t) = f[TOC(t=0), T(t=0), R(t=0), T(t), R(t)] \quad (6)$$

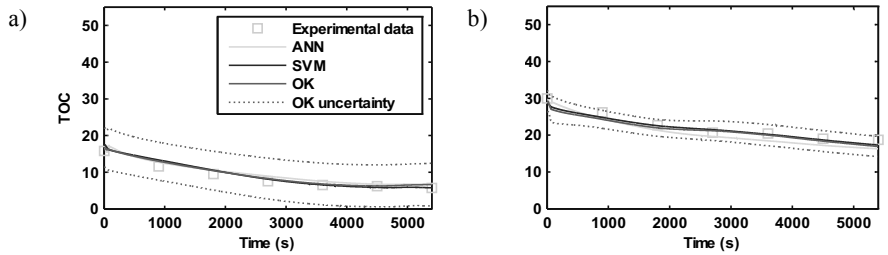

Figure 4: TOC prediction: a) batch 3, b) batch 4.

6. Conclusions

The results show how data based models can be used as soft sensors to monitor complex processes, difficult to follow through FPMs, without expensive offline sampling, saving huge costs and time. In addition, a simple static modelling approach has shown to be capable of accurately estimating a dynamic behaviour. Based on the proposed approach, three types of metamodels have been built to infer the progress of a chemical process from cheap on-line data. The results produced reveal that all methods exhibit high prediction accuracy with a significant low number of training data. Especially, OK shows a slightly higher accuracy and more importantly, higher flexibility and robustness in terms of easiness and rapidness of tuning the model parameters, while providing the modeller with a quantitative confidence interval of the prediction. An immediate extension of the presented approach would allow to use these methods for Advanced Control, by building autoregressive models to predict several steps ahead.

Acknowledgements

The authors would like to thank the financial support received from the Spanish Ministry of Economy and Competitiveness and the European Regional Development Fund (both funding the research Project SIGERA, DPI2012-37154-C02-01), and from the Generalitat de Catalunya (2014-SGR-1092-CEPEiMA).

References

A.Shokry, A. Espuña, 2014, Applying Metamodels and Sequential Sampling for Constrained Optimization of Process Operations, Lecture Notes in Computer Science, 8468, 396-407.

J. Farias, E.D. Albizzati, O.M. Alfano, 2009, Kinetic study of the photo-Fenton degradation of formic acid: Combined effects of temperature and iron concentration,Cat.Today, 144,117-123.

K. Azman, J. Kocijan, 2007, Application of Gaussian processes for black-box modelling of biosystems, ISA Transactions 46, 443–457.

M. Pérez-Moya, M. Graells, P. Buenestado, H.D. Mansilla, 2008, A comparative study on the empirical modeling of photo-Fenton treatment process performance, Appl. Catal. B: Environmental, 84, 313–323.

T. Masters,1993, Practical Neural Network Recipies in C++.

Z. K. Nagy, 2007, Model based control of a yeast fermentation bioreactor using optimally designed artificial neural networks, Chemical Engineering Journal 127, 95-109.

P. Jain, I. Rahman, B. D. Kulkarni, 2007, Development of a Soft Sensor for a Batch Distillation Column Using Support Vector Regression Techniques, Chem.Eng.Res.Des., 85, 283-287.

Krist V. Gernaey, Jakob K. Huusom and Rafiqul Gani (Eds.), 12th International Symposium on Process Systems Engineering and 25th European Symposium on Computer Aided Process Engineering.
31 May – 4 June 2015, Copenhagen, Denmark

A Meshfree Maximum Entropy Method for the Solution of the Population Balance Equation

Menwer Attarakih[a,c*], Abdelmalek Hasseine[b],Hans-Jörg Bart[c]

[a]*Department of Chemical Engineering, University of Jordan, Amman 11942, Jordan*
[b]*Department of Chemical Engineering, University of Biskra, Biskra 07000, Algeria*
[c]*Chair of Separation Science and Technology, TU Kaiserslautern, Kaiserslautern 67653, Germany*
m.attarakih@ju.edu.jo

Abstract

In this work, the number density function in the population balance equation (PBE) is approximated in terms of field nodes through a complete set of orthogonal basis functions in a semi-logarithmic space. We proposed the functional values at these field nodes to satisfy the maximum entropy solution. This hybridization of function approximation and information theories based on Shannon Maximum Entropy principle, allowed us to construct a sequence of positive continuous approximations of the PBE. The Lagrange multipliers, which result from the maximization of the Shannon entropy subject to the available average information, was estimated by solving a well-conditioned linear system of algebraic equations. As an application, this meshfree solution of the PBE is validated using an analytical solution of the microbial cell dynamics in a constant abiotic environment with simultaneous cell growth and division for which the analytical solution was derived by using the Adomian method.

Keywords: Population balances, Maximum Entropy Method, Meshfree method.

1. Introduction

Many applications in physical and engineering sciences are discrete either at the micro or macroscopic levels. The transport equation governing the evolution of such systems is a Boltzmann-like equation which is called the population balance equation (PBE) (Ramkrishna, 2000). Being an equation that describes the transport of a number density concentration function, it can be theoretically viewed as an infinite system of integro-partial differential equations which are strongly coupled through nonlinear integral source terms. Therefore, general solutions of this equation in complex flow fields is impossible due to its geometrical and functional dependencies on particle property states. This justifies the growth of interest in the numerical solution during the last decade. Attarakih (2013) and Attarakih and Bart (2014a) presented a condensed review on the available numerical solutions for the PBE including the classical finite difference schemes (CFDS), the Quadrature Method of Moments (QMOM) and the Differential Maximum Entropy Method (DMaxEntM), to name but a few. The CFDS has the advantage of tracking the full number density concentration using finite number of grid points along the particle property space with difficulties to estimate population mean properties (e.g. mean particle diameter, interfacial area concentration etc.) unless high number of grid point is used. The other extreme, is full concentration on the population moments and total relaxation on the particle size distribution using the QMOM. To have a compromise between accurate population mean properties and particle size recovery, Attarakih (2013) introduced the Cumulative QMOM. In this method, the full particle distribution is recovered using a continuous version of the QMOM. Parallel

to this work, Attarakih and Bart (2014a) introduced a novel idea for continuous approximations of the particle number density concentration using the DMaxEntM. The approximate solutions are recovered by solving a few number of transport equations, which are consistent with the first N+1 moments of the particle size distribution. Compared to the QMOM which has difficulties in dealing with bivariate PBEs (Favero et al., 2014), the DMaxEntM can be extended without running in trouble by the wrong choice of the targeted moments. In an advanced step, Attarakih and Bart (2014b) extended the DMaxEntM to a meshfree MaxEntM for particle growth in one and two dimensions by maximizing the Shannon entropy functional using pointwise sampling as filed nodes for the continuous number density concentration. In this way, the optimal Lagrange multipliers appearing in the continuous solution were estimated using these field nodes instead of solving a convex nonlinear program or transporting the Lagrange multipliers. Instead of this, the logarithm of the MaxEnt functional is expanded using a complete set of orthogonal basis functions with and imposed regularity conditions.

In this work, we extend this meshfree MaxEntM to solve the PBE in the presence of particle growth, breakage and aggregation using complete set of orthogonal functions. As a case study, the method is applied to solve the microbial cell population balance dynamics which includes cell growth and division in a constant abiotic environment. Additional assumptions are placed on the growth and division rates and daughter cell distribution function to get a dynamic analytical solution. The Adomian method is used to obtain this analytical solution (Hasseine et al., 2011) which is compared to the meshfree MaxEnt method.

2. Meshfree Maximum Entropy Solution of the PBE

The PBE in one dimensional particle property space with particle growth, breakage and aggregation is written as:

$$\frac{\partial f(x,\mathbf{r},t)}{\partial t}+\nabla\cdot\left(\langle\mathbf{v}\rangle f(x,\mathbf{r},t)\right)+\frac{\partial[G(x,S)f(x,\mathbf{r},t)]}{\partial x}=R\{f\}\quad(1)$$

$$\begin{aligned}R\{f\}&=-\Gamma f(x,\mathbf{r},t)+\int_x^\infty \upsilon(x')\Gamma(x',S)\beta(x,x')f(x',\mathbf{r},t)dx'\\&-f(x,\mathbf{r},t)\int_0^\infty \omega(x,y)f(y,\mathbf{r},t)dy+\frac{1}{2}\int_0^x \omega(x,y)f(y,\mathbf{r},t)f(x-y,\mathbf{r},t)dy\end{aligned}\quad(2)$$

In Eqs.(1) and (2) $f(x,\mathbf{r},t)$ is the number density concentration as function of particle size (x), physical space vector ($\mathbf{r}$) and time t and $\langle\mathbf{v}\rangle$ is the mean particle velocity vector in physical space which is function of particle size and other continuous environment variables. The particles are supposed to undergo relatively slow growth at a rate of $G(x,S)$, and relative instantaneous breakage at a frequency of $\Gamma(x,S)$ with daughter particle distribution $\beta(x,x')$ and mean particle number $\upsilon(x')$, while $\omega(x,y,S)$ is the aggregation frequency among particles of sizes x and y. The dependency of these functions on the continuous phase environment is taken into account through the variable S.

To solve Eq.(1) with general dependency of $\{G, \Gamma,\omega\}$ on particle size, one can use the Quadrature Method of Moments due its compactness and accuracy to avoid classical discretization methods which ends up with dozens of transport equations (Mantzaris et al., 2000). Like any other moment methods, the QMOM loses the particle density concentration (f) because of averaging of(f) over the particle property space. Unfortunately, the reconstruction of (f) in simple or complex physical space domains is

by no means trivial (Gzyl & Tagliani, 2010). This is well-known in theoretical physics literature as a classical moment problem and in particular as Hausdorff moment problem. In this regard, the attempt is to reconstruct the non-negative number density concentration from a finite set of low-order moments (m_r, r = 0, 1, …N). Difficulties face this problem are twofold: Ill-conditioning and uniqueness of the recovered number density function (Lawrence & Papanicolaou,1984). To overcome the first problem, the maximum entropy method was used to reconstruct a continuous number concentration function constrained by the available mean integral properties of the distribution. The uniqueness issue is solved by maximizing the Shannon entropy functional, which results in a distribution that is statistically most likely to occur (Baker-Jarvisa, 1989). The solution of this constrained NLP results in the following optimal functional:

$$f_N(x,\mathbf{r},t) = g(x)\exp\left(\sum_{j=0}^{N}\lambda_j(t)\pi_j(x,\mathbf{r})\right) \quad (3)$$

In Eq.(3), λ_r are the Lagrange multipliers which can be generally estimated by solving a convex potential function (Mead and Papanicolaou,1984), $\pi_j(x)$ are set of orthogonal basis functions and $g(x)$ results from the particle property space coordinate transformation. This coordinate transformation is necessary such that $f_N(0) = 0$ to satisfy the left regulatory condition. To estimate the Lagrange multipliers in Eq.(3), we applied the orthogonal collocation method in a weak-form sense to transform Eq.(1) into into a set of PDE that are exactly satisfied at the particle property field nodes x_i , i = 0, 1, ..$N \in [a,b]$ where f($\mathbf{x}$,t) is supported on [a,b]. The solution of these PDEs will produce a set of field variables f_i , i = 0, 1, ..N which reflect local information about $f(x)$ in space and time. This local information is then used to estimate the Lagrangian multipliers by solving the system of linear equations $P_N(\mathbf{x}) = \prod\boldsymbol{\lambda}$. The elements of the square matrix $\prod$ are $ln(g(x_i)) + \pi_j(x_i) = j$, i =0,1,.. N and $P_N(\mathbf{x}) = ln(f(\mathbf{x}))$. This matrix is invertible and well-conditioned since its columns are a complete set of orthogonal functions. The approximate density function $f_N(x)$ is then used to close the integrals in Eq.(2) with the desired accuracy since $f_N(x)$ does not depend on the nodal points x_i. On the other hand, the derivative of $f(x)$ in the convective term of Eq.(1), with respect to x, is found exactly by differentiating Eq.(3):

$$\frac{\partial f_N(x,\mathbf{r},t)}{\partial x} = f_N(x,\mathbf{r},t)\left[g(x)^{-1}\frac{dg(x)}{dx} + c(\mathbf{x})^T\Pi^{-1}\mathbf{P}(\mathbf{x},\mathbf{r},t)\right] \quad (4)$$

Where $c(\mathbf{x})$ is a vector of ($\pi_j(x)$, j= 0,1, .. N) derivatives with respect to x. This alleviates the discretization problem of the particle convection term using CFDS which require huge number of grid points. Note that the solution of Eq.(1) using Eq.(3) is a true meshfree solution because of the continuity of $f_N(x,\mathbf{r},t)$. The consistency of this solution with respect to the continuous PBE is guaranteed since the maximum entropy solution satisfies the given integral constraints imposed on $f(x,\mathbf{r}, t)$. The only assumptions required to derive Eq.(4) are that $f(x,\mathbf{r},t)$ and $G(x)$ should be smooth enough to allow at least the existence of their first order derivatives. Two advantages are achieved by using the meshfree MaxEntM: Firstly, the need for solving a NLP to estimate Lagrange multipliers is replaced by a solution of linear system of equations. Secondly, the field nodes used in the reconstruction of f(x,$\mathbf{r}$,t) provides rich information about the number density concentration (Attarakih and Bart, 2014b). In this work, we used the coordinate transformation function $g(x) = x^{\alpha}$, where α is estimated along with the Lagrange multipliers as described above.

3. Numerical results and discussion

3.1. Numerical Analysis

In this section, the proposed meshfree MaxEntM is tested against a known solution of the population balance equation. This is used to analyze the numerical features of the method in terms of the effect of the left regulatory condition and the numerical accuracy when solving for Lagrange multipliers ($P_N(\mathbf{x}) = \prod \boldsymbol{\lambda},$).

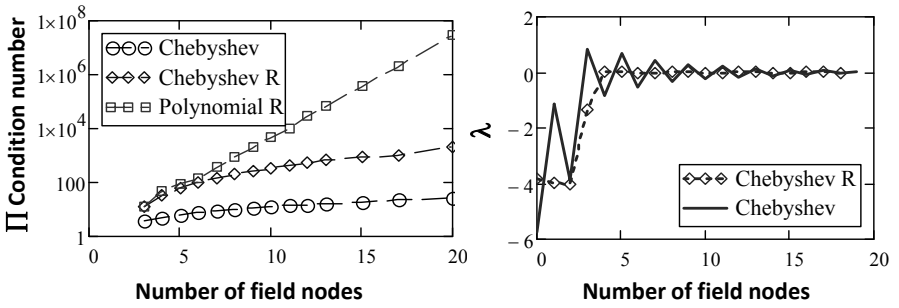

Figure (1): (Left): Effect of bases functions on ∏ matrix condition number. (Right): Variation of Lagrange multipliers (λ) as function of filed nodes with and without left regulatory condition.

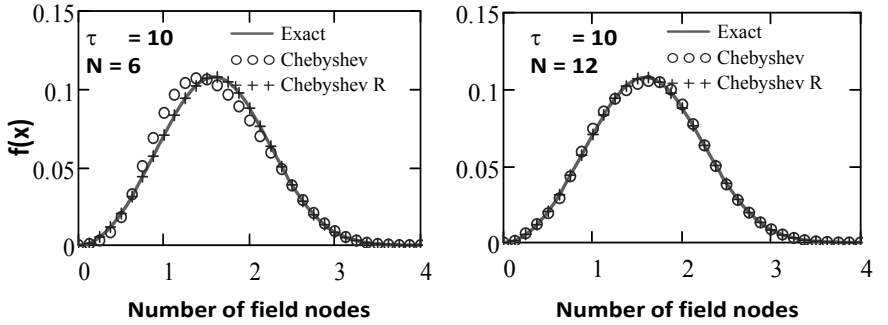

Figure (2): Constant frequency particle aggregation (Ramkrishna, 2000) in closed system reconstructed using the Meshfree MaxEntM using Chebyshev polynomials as basis functions.

Figure (1-upper panel) shows the effect of number of field nodes (transformed Chebyshev polynomial roots such that $x_i \in (a, b)$) on the condition number of the ∏ matrix using $\pi_j(x) = x^j$ (simple polynomials) and $\pi(x)$ as Chebyshev basis functions. The symbol (R) in the legend indicates that the left regulatory condition is included in Eq.(3) with $g(x) = x^{\alpha}$. The left side of the upper panel of this figure shows the remarkable reduction in the ∏ matrix condition number which is ~ 100 for Chebyshev basis functions, while it is ~ 10^8 for simple polynomial basis functions when $N = 20$. This result is not surprising since the ∏ matrix is reduced to the well-known ill-conditioned Vandermonde matrix when using the simple polynomial basis functions. On the other hand, the regulated maximum entropy solution with Chebyshev basis functions is increased to ~ 10^4 due to the introduction of the simple polynomial $g(x) = x^{\alpha}$. However, the condition number of the ∏ matrix remains bounded when using the Chebyshev polynomials and increases without bound using simple power polynomials. In the left

hand side of the upper panel of Figure (2), the estimated Lagrange multipliers are shown as function of field nodes when N = 20. It is clear that the gain of using regulated Chebyshev polynomials is remarkable by the fast non-oscillatory convergence Lagrange multipliers for these polynomials when compared to the non-regulated ones. This accuracy is reflected directly on the predicted number density function as can be seen in the lower panel of Figure (2). This is in particular at low number of filed nodes, where the prediction error decreases when N is increased from 6 to 12. This is attributed to the extra degree of freedom we imposed on the maximum entropy functional through the dynamic fitting parameter α in $g(x) = x^{\alpha}$.

3.2. Analytical validation using the Adomian method

In this section, we present a practical case study of microbial cell dynamics in abiotic environment with a constant quantity of substrate (S). This case study is modified from the work of Mantzaris et al. (2000) to allow for analytical solution of simultaneous cell growth and division.

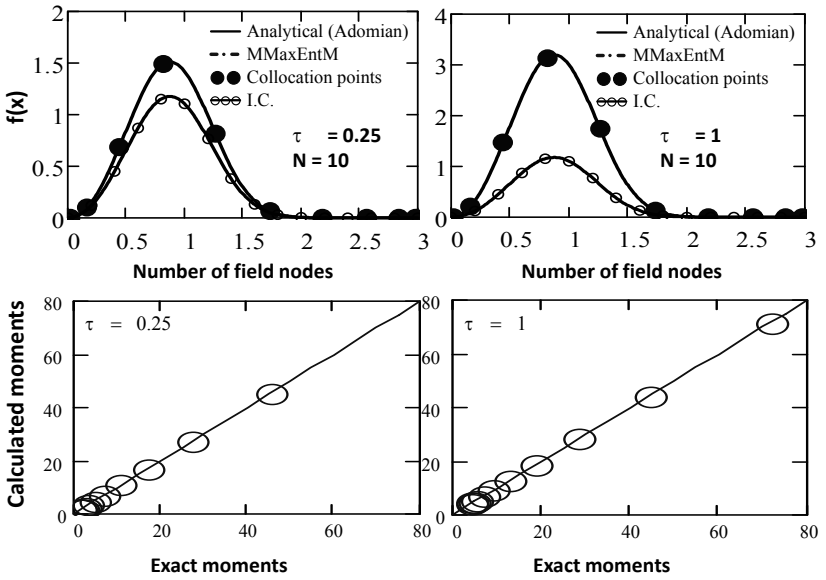

Figure (3): Prediction of microbial cell dynamics in constant abiotic environment with binary division and growth using the Meshfree MaxEntM as compared to the Adomian analytical solution. Upper panel: Evolution of f(x,τ). Lower panel: Evolution of first 10 moments.

The assumptions used here are as follows: An isothermal batch chemostat, constant abiotic environment, the single cell growth rate is proportional to its mass, and the dividing cells partition their material uniformly to the two daughter cells. These conditions can be mathematically translated into: $G(x) = (1/3)G_0x$, $\Gamma(x) = G(x)x^2$, $\beta(x,x') = 3(x^2/x'^3)$, $f(x,0) = 3x^5\exp(-x^3)$, $\tau = G_0t$ and $x = d/d_0$. The intercellular state is represented here by the cell biomass which reflects its size (x). The cell property mass is transformed into cell diameter (d) with an assumed spherical shape. These assumptions allows us to apply the Adomian decomposition method as follows (Hasseine et al., 2011):

$$f_{n+1} = \int_0^t \left(-\partial G f_n(m,t)/\partial x + \int_v^\infty \beta(m,m')\Gamma(m') f_n(m',t)\,dm' - \Gamma(m) f_n(m,t) \right) dt \qquad (5)$$

Where the index n runs from zero to infinity. The Adomian decomposition method finds the analytical solution recursively starting from the given initial condition ($f_0(m) = m\exp(-m)$). Using symbolic integration, the final solution to this case study is found to be $f(x,t) = 3x^2[x^3\exp(-x^3) + 2\exp(-x^3)[\exp(G_0 t)-1]]$. This analytical solution is compared to the meshfree MaxEntM as shown in Figure (3-upper panel) at two different dimensionless times ($\tau = 0.25$ and 1). This figure shows the dynamic evolution of the microbial cell population which undergoes simultaneous growth and division. As can be seen, the meshfree MaxEnt method captures with a high accuracy the evolution of the population dynamics using only 10 field nodes. Note that due to simultaneous cell growth and division the cell density evolution to the small size range is slower when the cell division is dominant. The lower panel of Figure (3) shows a parity plot of the evolution of the first 10 low-order moments of $f(x,\tau)$. The accuracy with which these moments were estimated could not be offered by any other explicit methods for solving the PBE thanks to the maximum entropy solution.

4. Summary and conclusions

The Shannon Maximum Entropy method and the approximation theory of functions are combined to provide a novel and effective solution method for the population balance equation. This results in a meshfree method which is consistent with particle population mean properties with an accuracy that can be controlled through the number of filed nodes. The proposed approach for estimating the coefficient of expansion (in a semi-logarithmic space) of the orthogonal functions is proved to be numerically efficient by solving a well-conditioned linear system of algebraic equations.

References

M. Attarakih and H.-J. Bart, 2014a, Solution of the population balance equation using the differential maximum entropy method (DMaxEntM): An application to liquid extraction columns. Chem. Eng. Sci, 108, 123-133.

M. Attarakih and H.-J. Bart, 2014b, A novel MaxEnt method for the solution of two-dimensional population balance equation with particle growth, Comp. Aided Chem. Eng., 33, 901-906.

M. Attarakih and H.-J. Bart, 2012, Integral formulation of the Smoluchowski coagulation equation using the cumulative quadrature method of moments (CQMOM), Comp. Aided Chem. Eng., 31, 1130-1134.

J. Baker-Jarvisa, M., Racine and J. Alameddine, 1989, Solving differential equations by a maximum entropy-minimum norm method with applications to Fokker-Planck equations. J. Math. Phys. 30, 1459-1463.

H. Gzyl and A. Tagliani (2010). Stieltjes moment problem and fractional moments, Applied Mathematics and Computation, 216, 3307–3318.

A. Hasseine, A. Bellagoun and H.-J. Bart, 2011, Analytical solution of the droplet breakup equation by the Adomian decomposition method. Applied Math. Comp., 218, 2249–2258.

L. R. Mead and N. Papanicolaou (1984). Maximum entropy in the problem of moments, J. Math. Phys. **25**, 2404- 2417.R.

N. V. Mantzaris, P. Daoutidis and F. Srienc, 2000, Numerical solution of multi-variable cell population balance models: I. Finite difference methods. Com. Chem. Eng., 25,1411–1440.

Krist V. Gernaey, Jakob K. Huusom and Rafiqul Gani (Eds.), 12th International Symposium on Process Systems Engineering and 25th European Symposium on Computer Aided Process Engineering.
31 May – 4 June 2015, Copenhagen, Denmark

Modelling the Hydrodynamics of Bubble Columns using Coupled OPOSPM-Maximum Entropy Method

Menwer Attarakih[a,b*], Ferdaous Al-Slaihat[a], Mark W. Hlawitschka[b], Hans-Jörg Bart[b]

[a]*Department of Chemical Engineering, University of Jordan, Amman 11942, Jordan*
[b]*Chair of Separation Science and Technology, TU Kaiserslautern, 67653, Kaiserslautern, Germany*
m.attarakih@ju.edu.jo

Abstract

In this contribution, we used a reduced population balance model to describe the hydrodynamics of bubble columns, which play a major role in in determining the bubble size distribution and hence the interfacial area concentration. This model consists of a set of transport equations to track the total number and total interfacial area concentrations and the gas phase volume fraction of bubbles. The model is essentially derived using the One Primary and One Secondary Particle Method (OPOSPM) and its higher extension using an Implicit Two-Equal Weight Quadrature (TwoEqWQ). This is coupled with the Shannon Maximum Entropy Method to predict the bubble size distribution along the bubble column axial direction. The model predictions show good agreement with the published experimental data in the bubbly flow regime.

Keywords: Bubble column, Population balances, Maximum Entropy Method.

1. Introduction

Bubble columns are multiphase equipment which is widely used in the chemical, petrochemical and biochemical industries (Kantarci et al., 2005). Estimation of the specific interfacial area is necessary in bubbly flows (e.g. the two-fluid model) to provide a closure for the momentum, mass and energy transport equations which are solved for each phase. The design and operation of these two-phase equipment are dependent on the adequate modelling of these transport phenomena (Jakobsen, 2008).

In such equipment, the gas phase is dispersed in a continuous environment with a population of bubbles that may undergo breakage, coalescence, expansion and growth. Modelling such a process using the mixture models, which could not take into account these instantaneous discrete events, is not sufficiently accurate to predict the hydrodynamics and mass transport. On the other hand, using the multi-fluid models which could include bubble-bubble interactions were proved to be computationally expensive when detailed column geometry is concerned. For example, typical number of groups is ~ 15-20 as used by the MUSIG model (Jakobsen, 2008). As a result, the need for a transport equation to describe the transport of the interfacial area concentration has been reflected by the interest of many researchers during the last two decades (Ishii and Hibiki, 2010). Among these is the work of Hibiki and Ishii (2000) which is of great importance. They used the population balance equation (PBE) to derive an Interfacial Area Transport Equation (IATE) for bubbly flow in vertical tubes using section averaging. As the PBE is concerned, many issues arise with respect to the

accuracy and consistency of the reduced interfacial transport equation (Drum et al., 2010). These authors developed a two-equation model that is consistent w.r.t the continuous PBE and hence its accuracy can easily be extended. This is unlike the IATE of Ishii and Hibiki (2000) that could not be further improved in terms of accuracy and consistency w.r.t. the continuous PBE.

In this work, we used a reduced population balance model to describe bubble transport, expansion, breakage and coalescence . The reduced population balance model consists of a set of transport equations to track the total number and volume concentrations, which are coupled through mean mass diameter (d_{30}), while the interfacial area concentration is calculated from the number and volume concentrations of bubbles. This model is essentially derived using the One Primary and One Secondary Particle Method (OPOSPM), which is coupled with the Shannon Maximum Entropy Method (MaxEntM) to predict the bubble size distribution along the bubble column axial direction. To increase the quadrature order for approximating source terms in the continuous PBE, an implicit TwoEqWQ is proposed, which require an additional transport equation for interfacial area concentration.

2. Bubble hydrodynamics

The present model for the bubble column hydrodynamics is derived from the population balance equation which is a special type of the Boltzmann transport equation. This equation evolves the number concentration function in space, time and the particle property space. The transported quantity, which is used to describe the population of bubbles, is the number concentration function $f(\boldsymbol{x},d,t)$. This is assumed to be continuous, satisfies regulatory conditions and describe the number density concentration of bubbles moving with velocity ($\langle v_g \rangle$) at a given time t, in a spatial space (x) and along particle size (d). The rth moment of this bubble number concentration function is written as:

$$\frac{\partial m_r}{\partial t} + \nabla \cdot \left(\langle v_g \rangle m_r \right) = \int_0^\infty \frac{\partial \psi}{\partial \zeta} \dot{\zeta} f(x,\zeta,t) d\zeta + S_r^b + S_r^c \quad (1)$$

In Eq.(1), $\langle v_g \rangle$ is the mean bubble velocity which is function of a pre-defined mean bubble diameter, $\psi = d^r$ (where r = 0, 1,2, …), $\zeta = v$ (where v is the bubble volume) and the dot over ζ denotes derivative with respect to time. The last two source terms on the right hand side S^b and S^c describes the the rth moment of particle appearance by breakage and disappearance by coalescence respectively(Attarakih and Bart, 2014).These sources terms contain unclosed integrals due to the general dependency of bubble breakage and coalescence kernels on bubble size (Hibiki and Ishii, 2000).

To close these source terms, Hibiki and Ishii (2000) and Ishii and Hibiki (2010) used two sets of bubble mean diameters: The mean volume (d_{30}) and the Sauter mean diameters (d_{32}) and derived what is called the Interfacial Area Transport Equation (IATE) followed by the simplifications of the source terms by assuming an equal-size binary bubble breakage and the bubble coalescence was allowed by only two bubbles of the same size. By following Coulaglou and Tavlarides (1977), they derived bubble breakage and coalescence kernels which were included in the source terms (S^b and S^c). Unfortunately, these kernels were merged with the numerical parameters which were used to close the integrals in the IATE. This approach has two major disadvantages: Firstly, it complicates the addition of new bubble kernels to the IACE, and secondly, it prevents increasing the numerical accuracy of the model by further increasing the order of quadrature approximation of the integrals in the source term (Drumm et al., 2010).

Due to the mixing between two types of mean droplet diameters: Sauter mean diameter (d_{32}) and volume mean diameter (d_{30}), conflicting source term for the IATE with that

derived from the PBE is observed as shown in Table (1). This is because d_{30} is a quadrature node based on OPOSPM (Drumm et al., 2010) while d_{32} is only a physical definition which is not related to a quadrature approximation of the source terms in the PBE. Therefore, using this mathematically consistent mean droplet diameter (d_{30}), the bubbly flow hydrodynamics is derived from Eq.(1) using the One Primary and One Secondary Particle Method (OPOSPM) as a reduced population balance model. OPOSPM for the bubble flow is obtained by using the zero, 2nd and 3rd moments (r =0, 2, 3) from Eq.(1) with proper transformations to obtain the total bubble number concentration $N = m_0$, interfacial area concentration $a = \pi m_2$ and volume fraction $\alpha = (\pi/6)m_3$:

$$\frac{\partial N}{\partial t} + \nabla \cdot \left(\langle v_g \rangle N \right) = \sum_{j=b,c} S_0^j \qquad (2)$$

$$\frac{\partial a}{\partial t} + \nabla \cdot \left(\langle v_g \rangle a \right) = \frac{2}{3} \left(\frac{a}{\alpha} \right) \left[\frac{\partial \alpha}{\partial t} + \nabla \cdot \left(\langle v_g \rangle \alpha \right) \right] + \left(\frac{\alpha}{a} \right)^2 \sum_{j=b,c} k_j S_0^j \qquad (3)$$

$$\frac{\partial (\alpha)}{\partial t} + \nabla . \left(\langle \mathrm{v_g} \rangle \alpha \right) = \frac{1}{3} \left[\frac{\partial \alpha}{\partial \mathrm{t}} + \nabla \cdot \left(\langle \mathrm{v_g} \rangle \alpha \right) \right] \qquad (4)$$

Where $S_0^b = \Gamma(d_{30})N$ and $S_0^c = -\frac{1}{2}\omega(d_{30}, d_{30})N^2$. The mean gas velocity for counter current flow is defined as $\langle v_g \rangle = j_f / (1-\alpha) + u_r$, where j_f is the superficial velocity of the liquid phase and u_r is the relative velocity of the bubbles which is given by (Ishii and Hibiki, 2010):

$$u_r = \sqrt{\frac{d_{30} g \Delta\rho}{3 C_D \rho_f}} \qquad (5)$$

In the above equation, C_D is the drag coefficient that is function of the mixture Reynolds number. Note that in Eqs.(3 and 4) the term in the square brackets represent bubble expansion due to pressure drop in the physical space.

It is worthwhile to mention that the interfacial area concentration could be predicted from $a = 6\alpha/d_{32}$ using the N and α transport equations. However, we proposed here Eq.(3) for consistent prediction of (a) since d_{32} could not be estimated from the N and αtransport equations (only d_{30} can be expressed in terms of N and α).

Table (1): Constants for the source term in the interfacial area concentration equation.

	OPOSPM	Ishii and Hibiki (2010)
k_b	$36\pi\left(2^{1/3}-1\right)$	$36\pi/3$
k_c	$36\pi\left(2^{2/3}-2\right)$	$36\pi/3$

According to the model numerical constants (k_b and k_c) in Table (1), the bubble breakage and coalescence kernels (Γ and ω respectively) of Hibiki and Ishii (2000) with their adjustable parameters need to be modified. This is to recover the internal consistency with respect to the continuous population balance equation, which allows the increase of the quadrature order approximation to achieve the desired accuracy in closing the integral source term.

3. The Maximum Entropy Method

The Quadrature Method of Moments (QMOM) is one of the most used solver for the PBE because of the low number of transport equations and its high accuracy. This is required to overcome the long CPU time when coupling discrete population balances with CFD codes (Drum et al.,, 2010). The QMOM solves the PBE, where a finite set of population moments is transported. Due to its inherit averaging principle, the QMOM cannot reproduce the particle size distribution, which is replaced by a few set of non-physical moving particles along the particle property space. However, in industrial particulate system applications, the particle size distribution has a significant impact on the physical, chemical and mechanical product properties (Attarakih and Bart, 2012). To preserve the advantages of the QMOM and concentrating on distribution reconstruction away from the discrete methods, the MaxEntM seems to be natural candidate for the problem at hand. The MaxEntM is used to estimate the least biased probability density function subject to the available moment information about the sought distribution. The consistency of the recovered solution is achieved by maximizing the Shannon entropy functional with the constraint that the available moments of the averaged distribution are reproduced from the reconstructed one.
Following Attarakih and Bart (2014), this constrained nonlinear program has a unique positive solution provided that the sequence of the targeted moments is completely monotone. This maximum entropy solution is function of Lagrange multipliers, which can be found by minimizing the a convex potential function or using the MaxEntM:

$$f(x,d,t) = d^{\delta} \exp\left(\sum_{j=0}^{N} \lambda_j d^j\right) \tag{6}$$

In Eq.(6) λ_j's (λ_j corresponds to m_j) are the Lagrange multipliers which guarantee the reproduction of the targeted moments and δ is a positive real number that is introduced here to satisfy the regulatory conditions ($f(0) = f(d\to\infty) = 0$). In this work, we selectively chose $\{m_0, m_2, m_3\}$ as a set of moments which are satisfied by the transport equations (Eq. (1)). In addition to this, an Implicit Two-Equal Weight Quadrature (TwoEqWQ) was derived which reproduces exactly the above targeted set of moments. This TwoEqWQ is used to close the integral source term in Eq.(1) which is given by the following set of weights and nodes $\left\{w_1 = w_2 = 0.5\mu_0, d_1 = \sqrt{z}, d_2 = \sqrt{2\hat{m}_2 - z}\right\}$ andz is a solution of $\left\{(2\hat{m}_2 - z) - (2\hat{m}_3 - z^{3/2})^{2/3} = 0\right\}$. The hat denotes normalization w.r.t. m_0. This equation has two roots, where the first onelies in the interval [0, $(\hat{m}_3)^{2/3}$].

4. Numerical results and discussion

4.1. Analytical validation

In this section, the proposed two-equal weight implicit quadrature to close the source term in Eq.(1) is validated analytically along with the MaxEntM to reconstruct the averaged distribution. The Lagrange multipliers (λ_j, j = 0, 2,3) were found by solving a convex potential function (Attarakih and Bart, 2014) using the Levenberg-Marquardt algorithm. The case study is particle aggregation with constant kernel and an exponential (w.r.t. particle volume) initial condition. The left panel of Figure (1) shows the evolution of the targeted moments $\{m_0, m_2, m_3\}$ as function of dimensionless time (τ). Due to the remarkable accuracy of of the QMOM, not only the targeted moments were produced with high accuracy, but also the interpolated moment (m_1).

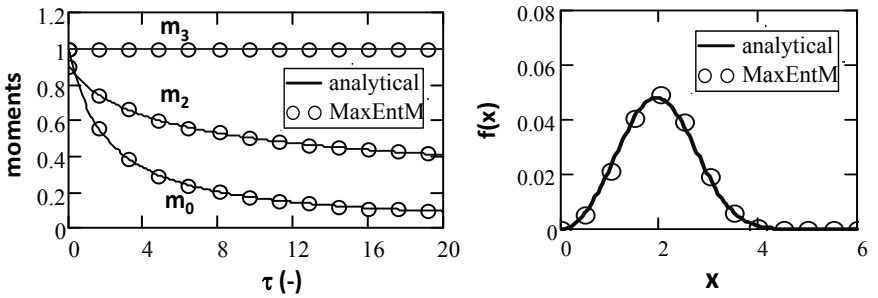

Figure (1): Validation of the MaxEntM with two implicit equal-weight quadrature for constant kernel aggregation in batch system against analytical solution (Gelbard and Seinfeld, 1978).

This moment was predicted using the implicit two-equal weight quadrature and the reconstructed MaxEnt solution (Eq.(6)) with Lagrange multipliers (λ_0 = -3.830, λ_1 = 0.090, λ_3 = -0.115) at τ = 20. The mean percentage relative error in the prediction of m_1 using the two-weight quadrature is 0.311 and that predicted from the MaxEntM is 0.519. The recovered distribution at τ = 20 is shown on the right panel of Figure (1) and compared to the analytical solution (Gelbard and Seinfeld, 1978). It is clear that the coupled implicit TwoEqWQ and the MaxEntM achieved two targets: Accurate tracking of distribution moments and accurate reproduction of the particle number concentration.

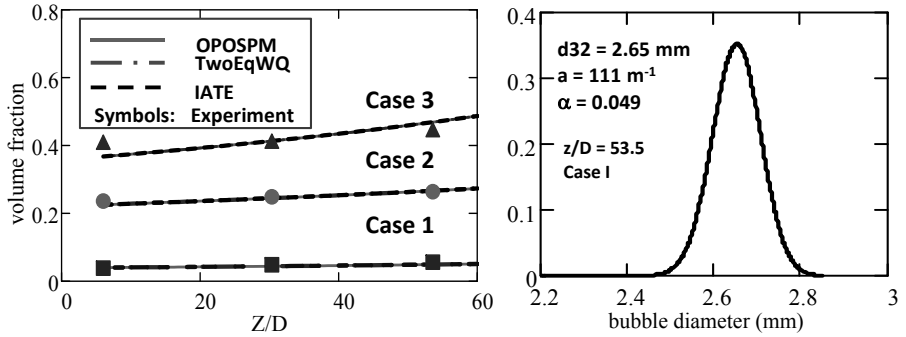

Figure (2): Experimental and numerical validation of OPOSPM, the implicit TwoEqWQ using air-water bubbly flows in a 50.8 mm diameter column (Hibiki and Ishii, 2000) . In Case 1: j_g = 0.0275 m/s , j_f =0.491 m/s, $d32^{in}$ = 2.49 mm, Case 2: j_g = 0.19 m/s, j_f = 0.491 m/s, $d32^{in}$= 3.31 mm, and Case 3: j_g = 3.90 m/s, j_f = 5.00m/s, $d32^{in}$ = 2.83.

4.2. Experimental validation

As shown in the previous section, the results show that the present model can be extended to higher-order approximations of the PBE using more secondary particles(quadrature nodes) with distribution reconstruction. This is an obvious advantage over the existing models such as that of Hibiki and Ishii (2000). As a first step of model validation, the pilot plant bubble column of Hibiki and Ishii (2000) was modeled and simulated after the necessary modifications of the adjustable parameters in the breakage and coalescence kernels to recover the mathematical consistency with the PBE. The column diameter is 50.8 mm with 3060 mm height which is operated adiabatically in the bubbly flow regime using air-water mixture in a cocurrent flow. The

investigated inlet superficial gas velocity ranges from 0.0275 to 3.90 m/s and that for the liquid phase is from 0.491 to 5.00 m/s with a void fraction in the range 0.0127-0.468. The axial measuring points (z/D) are at 6, 30.3 and 53.5 with detailed boundary conditions as described by Hibiki and Ishii (2000).

Figure (2-left) shows the variation of the gas void fraction along column height and the recovered bubble size distribution (right) as compared to the experimental data Hibiki and Ishii (2000) using three different models (OPOSPM, Implicit TwoEqWQ and IATE). The results are almost identical after adjusting the IATE model parameters to reflect the changes imposed by the new consistent formulation (see Table 1). As discussed by Hibiki and Ishii (2000),the simulated bubbly flow is dominated by bubble expansion for Case 1 due to the axial pressure drop along the column height. This is reflected by the increase in the mean size of the bubbles when compared to the mean inlet size (2.49 mm) as shown in Figure(2-right).For this case, the Lagrange multipliers used in Eq.(6) are found to be ((λ_0 = -369.825, λ_1 = 156.147, λ_3 = -39.335)).

5. Summary and conclusions

In this work, we derived the transport equations of bubble column hydrodynamics using OPOSPM and an implicit TwoEqWQ as reduced population balance models. The equations from the latter method were found consistent with the bubble number, interfacial area and volume concentrations and the Sauter mean bubble diameter. The coupling of these reduced bubble hydrodynamic models with the constrained MaxEntM allowed the reconstruction of a unique bubble number concentration by minimizing a convex potential function. A very good agreement between the predictions of the present model and those of the IATE and the Experimental data was obtained.

References

M. Attarakih and H.-J. Bart, 2014, Solution of the population balance equation using the differential maximum entropy method (DMaxEntM): An application to liquid extraction columns. Chem. Eng. Sci, 108, 123-133.

M. Attarakih and H.-J. Bart, 2012, Integral formulation of the smoluchowski coagulation equation using the cumulative quadrature method of moments (CQMOM), Computer - Aided Chem. Eng., 31, 1130-1134.

C. A. Coulaloglou and L. L. Tavlarides,1977, Description of interaction processes in agitated liquid-liquid dispersions, Chem. Eng. Sci., 32, 1289-1297.

C. Drumm, M. Attarakih, M. W. Hlawitschka and H.-J. Bart, 2010, One-group reduced population balance model for cfd simulation of a pilot-plant extraction column. Ind. Eng. Chem. Res., 49, 3442–3451.

F. Gelbard and J. H. Seinfeld, 1978, Numerical solution of the dynamic equation for particulate systems. J. Comput. Phys., 28, 357-375.

T. Hibiki and M. Ishii, 2000, One-group interfacial area transport of bubbly flows in vertical round tubes. Int. J. Heat Mass Tran., 43, 2711 - 2726.

M. Ishii and T. Hibiki, 2010, Thermo-fluid dynamics of two-phase flow, Springer New York.

H. A. Jakobsen, 2008, Chemical reactor modeling: Multiphase reactive flows, Springer-Verlag, Heidelberg.

N. Kantarci, F. Borak and K. O. Ulgen, 2005, Bubble column reactors: Review. Process Biochemistry, 40, 2263–2283.

Krist V. Gernaey, Jakob K. Huusom and Rafiqul Gani (Eds.), 12th International Symposium on Process Systems Engineering and 25th European Symposium on Computer Aided Process Engineering.
31 May – 4 June 2015, Copenhagen, Denmark

Process Simulation of a 420MW Gas-fired Power Plant using Aspen Plus

Bao-Hong Li,[a*] Nan Zhang[b], Robin Smith[b]

[a]*Department of Chemical Engineering, Dalian Nationalities University, Dalian 116600, China. libh@dlnu.edu.cn*
[b]*Center for Process Integration, School of Chemical Engineering and Analytical Science, The University of Manchester, Manchester M13 9PL, UK*

Abstract

A detailed flowsheet of natural gas fired Combined Cycle Power Plant (CCPP) is introduced and modelled by ASPEN PLUS software in this paper. The results obtained by this model were compared with the operation data of a plant in Europe whose capacity is 420 MW of electricity. The model consists of Gas Turbine (GT) and Heat Recovery Steam Generation (HRSG) sections. The simulation results are in good agreement with the operating data.

Keywords: Cogeneration; Electricity and steam; Natural gas; APEN PLUS

1. Introduction

It is believed that combustion of natural gas is the most efficient means for generating electricity from fossil fuels (Zheng and Furimsky, 2003). However, only one paper thus far is found to simulate the gas-fired power plant, and just general and some key data rather than detailed information was reported (Zheng and Furimsky, 2003). Obviously, such information is far from enough to lay a basis to carry out an effective integration of Post-Combustion Capture (PCC) to a gas-fired power plant. Under such situation, a typical 420MW gas-fired CCPP in Europe is modelled in detail. The plant is divided into three sections: (1) Feed gas preparation and gas turbine, (2) HRSG and steam turbine, (3) water recycle system. The model of first two sections was developed using Aspen Plus software of version 8.0 (Aspen Technology, 2011) while only mass balance is calculated by hand for the third section. Comparing with the operating data of the commercial plant, the simulation results are in good agreement with the operating data.
The novelties of this paper are: (1) the most complete process model of a gas-fired CCPP thus far is built and validated by operating data. The boundary of the model covers the whole range of the CCPP; (2) much more detailed and rigorous models of gas turbine and HRSG than ever before are built although some key parameters cannot be disclosed to protect the power plant.

2. Brief process description

A schematic flowsheet of the combined cycle power plant is shown in Figure 1. In this process, electricity is produced by means of the Alston gas turbine and steam turbine. The gas turbine shaft and the steam turbine shaft are coupled together to drive the generator, which produces the 420 MW output. Nature gas and excess air are feed to the gas turbine, and burned in two combustion chambers in serial under a firing temperature of 1100 ℃ and 1280 ℃ separately. The hot exit gas (mainly N_2, O_2, CO_2 and H_2O)

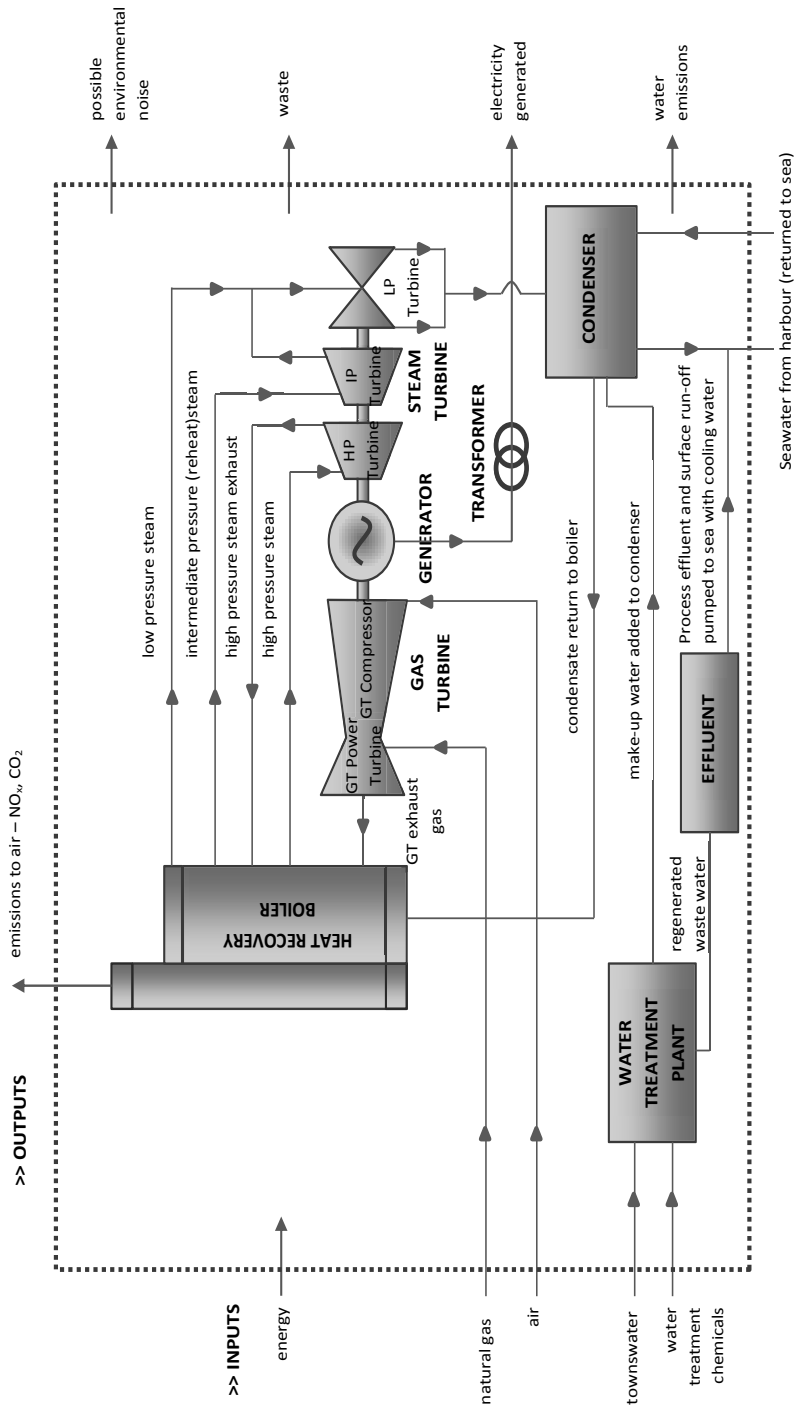

Figure 1: The CCGT power plant flowsheet

are sent to HRSG unit, from which three steam streams of HP(High Pressure, 110 bar (absolute pressure, the same rule will be followed in the rest part)), IP(Intermediate Pressure, 26 bar) and LP (Low Pressure, 4.2 bar) are generated. The steam turbine consists of a high pressure, intermediate pressure and a low pressure turbine. The HP steam produced in HRSG unit is fed to the high pressure turbine, producing an outlet stream of 27 bar. The IP stream from the HRSG is mixed with the outlet stream of HP steam turbine and reheated by HRSG and then fed to the IP steam turbine, producing an outlet stream of 5 bar. Similarly, the LP steam produced in the HRSG is mixed with the outlet stream of the IP steam turbine first, and then fed to the LP steam turbine. The exhaust steam of the LP steam turbine is condensed in the condenser by sea water and the condensate is returned to HRSG for recycle reuse. The lost water is made up by town water after pretreatment.

3. Aspen model of the CCPP

The simulation flowsheet of the power plant is divided into two sections as shown in Figure 2, the gas turbine section(Gasturb) and the heat recovery and steam generation section(HRSG). All important parameters are provided in the flowsheet. Note that the predicted output electricity power is 413 MW which is lower than 420 MW by 1.7% . The detailed description of the model is given below.

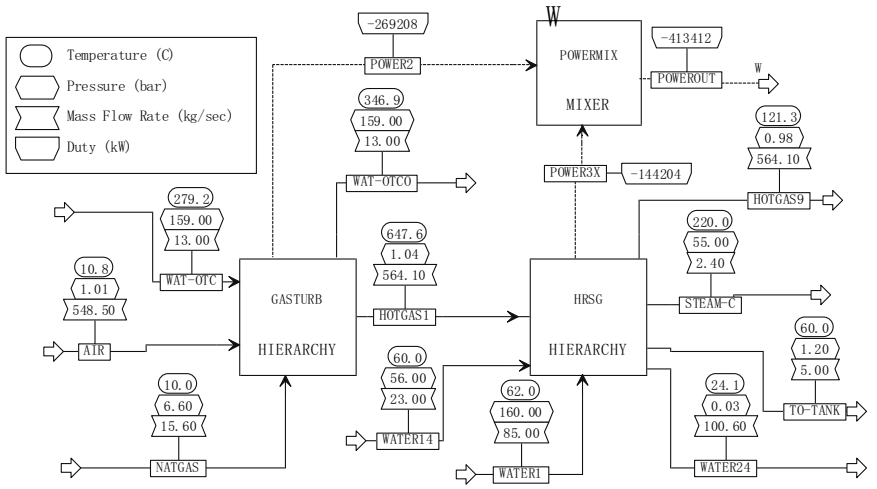

Figure 2: Simulation floweet of the power plant

3.1. Feed preparation and Gas turbine

3.1.1. Natural gas pressurization

As shown in Figure 3, the natural gas with 10 ℃ and 6.6 bar is fed to a two stage compressor and an intercooler is installed immediately after each stage to cool down the output streams to 25℃ and 50 ℃ respectively. The cooling media of these two coolers is seawater. The output pressures of the two-stage compressor are 20 bar and 48 bar separately. The output stream of the later intercooler is then equally split into two branches: One branch goes to the preheater and its temperature is raised to 150 ℃ and the hot stream of the preheater is a branch of hot water of 2.4 kg/s leaving the IP economizer in HRSG. Then, it goes to the first set of burners (EV) and an excess of air of 436.8 kg/s is sent to EV at the same time. The other branch goes to the second

combustion chamber (SEV) and burned with the output stream of EV and a new air stream of 111.7 kg/s. A High Pressure Gas Turbine (HPGT) and a Low Pressure Gas

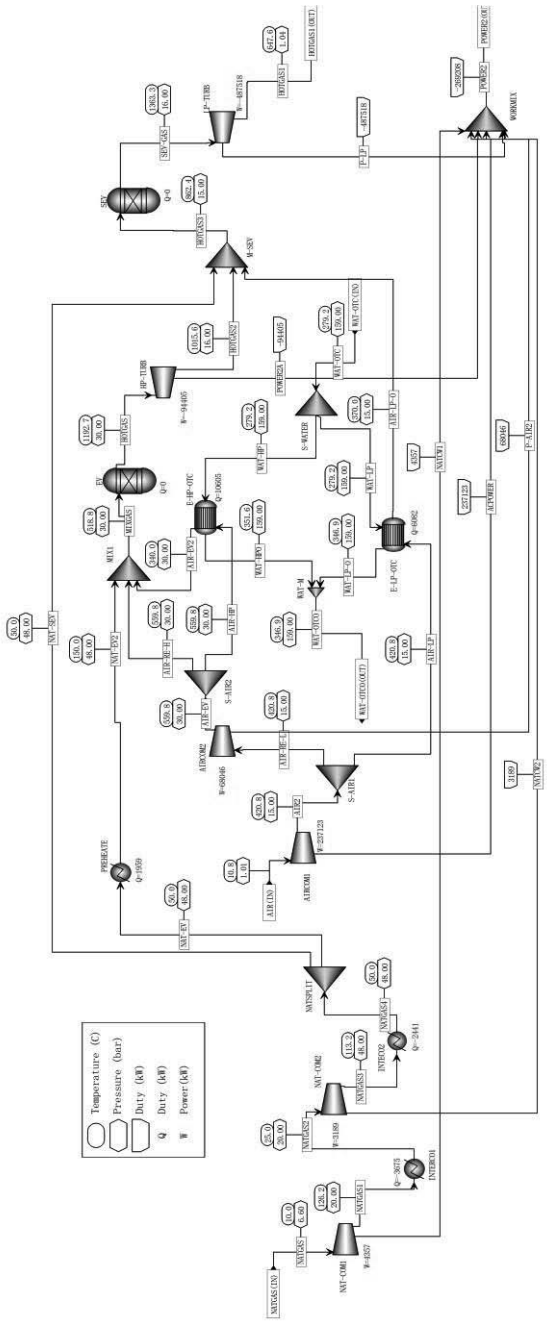

Figure 3: Flowsheet of section GASTURB

Turbine (LPGT) immediately follow the EV and SEV respectively, and the discharge pressure of the HRGT and LPGT are 16 bar and 1.04 bar separately.

3.1.2. Air pressurization

The air with flowrate of 548.3 kg/s is fed to a two-stage compressor. The first stage consists of 17 row blades while the second stage consists of 5 row blades. The discharge pressure of these two stages are 15 bar and 30 bar respectively. Two large heat exchangers named as HP Once Through Cooler (HPOTC) and LP Once Through Cooler (LPOTC) are attached to GT in order to cool the pressurized air from the GT and vaporize the water stream from the HRSG, the water flow is about 13 kg/s. A branch of the output stream of the first stage (Unit Aircom1) is fed to LPOTC and its inlet temperature is 420.8℃ and outlet temperature is 370 ℃ and returns to SEV. The remaining of the output stream of Unit Aircom1 is fed to the second stage and pressurized further to 30 bar. Similarly, a branch of the output stream of the second stage (Unit Aircom2) goes to HPOTC and its temperature is reduced from 560 ℃ to 340℃ and returns to GT at EV. After Units LPOTC and HPOTC, the water returns to the HP superheater of HRSG as steam.

3.1.3. Gas turbine

Gas turbine consists of a HP and LP gas turbine. The HP gas turbine accepts the output stream of EV as its input and drive its shaft to produce electricity, and its output pressure is 16 bar. The output pressure of the LP gas turbine is 1.04 bar. The flue gas leaving the LP gas turbine is entering HRSG as the only heat source.

3.2. HRSG and steam turbine

The HRSG system is a triple reheat system. It consists of HP steam and IP/LP steam system. Three drums and three steam turbines are involved. Details on HRSG and steam turbine is not provided here because of limit on paper length.

3.3. Water recycle system

The plant has its own on site water treatment facilities where potable water is demineralized and then used in the HRSG and water and steam cycle (WSC) system as shown in Figure 4. Specifically, WSC consists of two main water cycles, i.e., HP water cycle and IP water cycle. The pressures of HP and IP feed water are 58 bar and 170 bar respectively, which are produced by the sixth and the end stage of a ten-stage water pump. After the water pump, the feed water is split into two branches, one branch with flowrate of 85 kg/s is fed to HRSG HP steam system while the other branch of 23 kg/s is fed to HRSG IP/LP steam system. The feed water is heated and vaporized and superheated in HRSG, then, the produced HP, IP and LP steam are used to drive the shaft of steam turbine, and finally condensed in the condenser and recycled to the water feed tank.

Note thant a hot water stream of 2.4 kg/s is withdrawn from the HRSG before it entering the IP drum and used for preheating the fuel gas to 150 ℃. At the same time, a steam stream of 5 kg/s is withdrawn from the middle of the LP steam turbine and fed to the water tank feed to heating the feed water to HRSG to about 60 ℃. Seawater is only used for cooling in the main condenser to control the discharge pressure of the LPST in the HRSG to be 30 mbar.

4. Simulation result

The key results of our model is compared with plant data and provided in Table 1. It is safe to say that the obtained results are in good agreement with the operating data.

Table 1: Comparison of key results

Variable	plant data	simulation
Nat. Gas inlet flow (kg s^{-1})	15.6	15.6
GT Exhaust Flow (kg s^{-1})	564.1	564.1
Fuel to air ratio ((g/g))	0.0278	0.0284
GT Exhaust temperature (°C)	645	647.6
Net Power (MW)	420	413
GT Exhaust pressure (bar)	1.03	1.04
Condensing pressure(mbar)	30	30
Condensed water temperature (°C)	25-30	24.1

5. Conclusions

A detailed model for the gas-fired CCPP has been developed and compared with a set of data from the operation. The obtained results match well with the plant data. Based on these findings, it is concluded that the built model is suitable for CCPP simulation and can be adopted as a useful tool to predict the impact of operation parameters and explore opportunities for further integration with other plants.

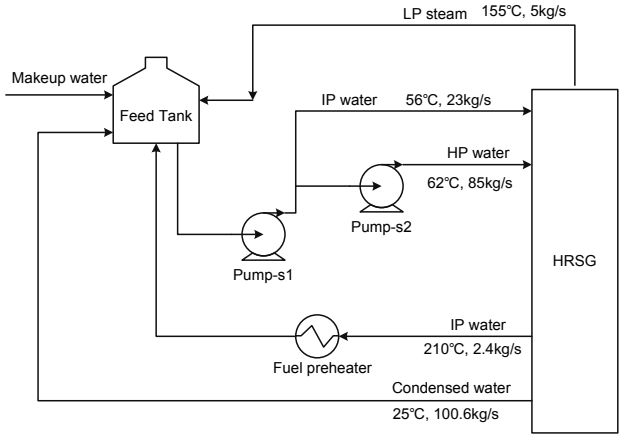

Figure 4: Water and steam cycle

6. Acknowledgements

Financial support by CAPSOL project under the Seventh Framework Programme of the European Commission and Program for Liaoning Excellent Talents in University (LNET) (under Grant No. LJQ2012113) are gratefully acknowledged.

References

L. Zheng ; E. Furimsky 2003, ASPEN simulation of cogeneration plants. Energy Conversion and Management, 44, 1845–1851.

Aspen Technology, Inc. 2011, Aspen Plus cogeneration model. Burlington, MA 01803-5501, USA

Krist V.Gernaey, Jakob K.Huusom and RafiqulGani (Eds.), 12th International Symposium on Process Systems Engineering and 25th European Symposium on Computer Aided Process Engineering.
31 May – 4 June 2015, Copenhagen, Denmark

Optimal blending study for the commercial gasoline

Cristian Patrascioiu,[a] Bogdan Doicin[a], Grigore Stamatescu[b]

[a]*Petroleum-Gas University of Ploiesti, Bd. Bucuresti 39, Ploiesti 100680, Romania*
[b] *University Politehnica of Bucharest, Splaiul Independenței 313, Bucureşti, Romania*

Abstract

Commercial ecological gasoline is being obtained by blending multiple components. Increasing a refinery's economic performance depends, among other things, on obtaining optimum blending recipes for the available components. To determine the optimum blending recipe, knowing the mathematical blending model for blending properties estimation and a linear optimization algorithm are necessary. As a blending properties estimation model, the authors used a mathematical model which can be found in the literature, validated through own laboratory experiments. Based on the Simplex algorithm developed by Jean-Pierre Moreau, the authors elaborated a software program, program that was used to study different blending recipes. The studied recipes varied from recipes that took into consideration one restrictive blending property, to recipes that took into consideration two restrictive properties and recipes that took into account one restrictive property, but a fixed proportion of bioethanol in the final blending.

Keywords: blending, modelling, linear optimization, optimization program.

1. Introduction

The commercial ecological gasoline is obtained by blending a number of components, process which is called formulation. The finished product must fulfill some quality standards, set by today's legislation. To fulfill the imposed quality standards, blending the gasoline's components using different blending recipes is necessary (Suciu, 1993). Commercial gasoline is a blending of three types of components: base components (in proportion of about 60%), correction components (about 40%) and additives (less than 1%). The blending recipes for obtaining commercial gasoline are conceived so as the finished product is suitable in terms of quality. An essential condition for a refinery to function is profitability. Because of this reason, the blending recipes must be chosen so as they bring profits to the refinery. The blending recipe that will yield the highest profit is the optimum blending recipe. To determine the optimum blending recipe, the optimization problem has a linear nature, containing an objective financial function, and a restrictions system. In literature, program packages strictly destined to linear programming and which implement the Simplex algorithm are described. Among these, the following are exemplified:

a) ASLO – represents an advanced implementation of the Simplex method, destined to solve general linear problems of large dimensions (Andrei, 2001).
b) C-WHIZ – the Simplex algorithm containing procedures regarding the problem analysis, which is used to solve problems up to 32000 restrictions (Andrei, 2001).
c) LPAKO – is a program package written in C++, which implements the Simplex method to solve the general linear programming problem (Park et al., 1998).

The purposes of this work are:

a) The elaboration of a dedicated optimization tool.

b) The synthesis of blending recipes using different scenarios.
c) The study the optimal blending properties in relation to the blending quantity.

2. Optimization problem

The optimization problem is a mathematical application which selects a solution, among many possible solutions, based on the evaluation of the objective function (Pătrăşcioiu, 2005). The objective function has a financial nature, representing the commercial gasoline cost, computed like the sum of the products between the component cost c_i and the utilized quantity, x_i

$$F_{ob} = \sum_{i=1}^{nc} c_i x_i \ . \tag{1}$$

The restrictions system has three components: a) the finished product quality, estimated by a mathematical component blending model; b) components quantities; c) variables non-negativity restrictions (Pătrăşcioiu, Nicolae, 2012).

2.1. Property Estimation Model

To estimate the gasoline properties, obtained by blending its components, a linear model, existent in the literature, was utilized (Bărbatu et al., 1970). The model taken into account was validated by Doicin (Doicin, 2014). The model contains mathematical relations for the estimation of the following properties: density, Research octane number, Motor octane number, benzene content, vapor pressure, olefin hydrocarbons content, aromatic hydrocarbons content and oxygen content.

2.2. Quality and quantity restrictions

The quality restrictions are derived from the EN228 standard and they refer to the commercial gasoline properties, obtained by its component blending. For the studied problem, the quality restrictions have the form presented in table 1.

Table 1 Gasoline quality restrictions

Restriction	UM	Restriction Type	Restriction Value
Blending density	g/cm^3	max	0.775
Research octane number	-	min	95
Motor octane number	-	min	85
Final boiling point	°C	max	210
Aromatic hydrocarbons content	%volume	max	35
Olefin hydrocarbons content	%volume	max	18
Oxygen content	%volume	max	2.7
Vapor pressure	kPa	max	90
Benzene content	%volume	max	1

The quantity restrictions refer to the total obtained quantity of the gasoline, M, and the available quantities of each component. $D_i, i = 1,\ldots,nc$.

The two restriction types have the following expressions:

$$M = \sum_{i=1}^{nc} x_i \tag{2}$$

$$x_i \le D_i, \quad i = 1,\ldots,nc \tag{3}$$

2.3. Non-negativity restrictions

To solve the optimization problem, the Simplex algorithm uses non-negativity restrictions of the x_i variables:

$$x_i \ge 0, \quad i = 1,\ldots,nc \tag{4}$$

3. Optimization program

To study the optimum blending recipes, the authors have developed a dedicated software program that allows the interactive study of the blending recipes. The authors have used the Simplex program developed by Jean-Pierre Moreau (Moreau, 2009). The program developed by the authors was written using the Embarcadero Delphi XE3 integrated development environment and it has the following characteristics:

a) A maximum of 9 properties for the determination of the optimum blending recipe can be used;
b) The possibility of selection, from the input data, of both the blending components and the properties that will be taken into account to determine the optimum blending recipe;
c) The possibility of modifying the total quantity of commercial gasoline that can be obtained.

The main window of the program is presented in figure 1. The program determines the optimum blending recipe of the commercial gasoline, being able to be used as a study tool, by modifying the following variables:

- The property or properties that form the restrictions system for the determination of the optimum recipe;
- The total quantity of the finished product that must be obtained;
- The fixed bioethanol quantity (between 0 and 5% volume).

4. Optimum blending recipe synthesis

The optimum blending recipes were studied using the following variants:

a) Recipes that take into consideration one restrictive property;
b) Recipes that take into consideration two restrictive properties;
c) Recipes that take into consideration one restrictive property with an imposed bioethanol proportion in the final blending.

4.1. Recipes that take into consideration one restrictive property

The objectives followed by this study are the following:

- Dependence of the restrictive property's value of the optimum blending with the total blending quantity that must be obtained;
- The components' distribution with the total blending quantity.

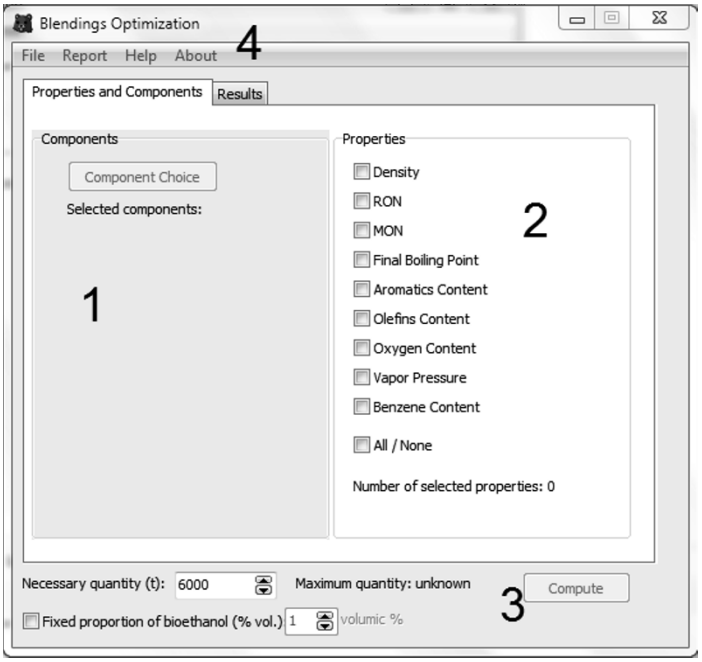

Figure 1:The main window of the optimum blending recipe determining program: 1 –component selection area; 2 –restrictions selection area; 3 –total quantity of gasoline selection zone; 4 – auxiliary menus.

The optimum recipes based on one restriction, from the 9 restrictions present in table 1, were determined. For every restriction taken into consideration, the optimum blending recipes for a total quantity of commercial gasoline varying between 4000 and 9000 t were determined. To exemplify, in figure 2 is presented the variation of the commercial gasoline density with the total quantity of gasoline that must be obtained.

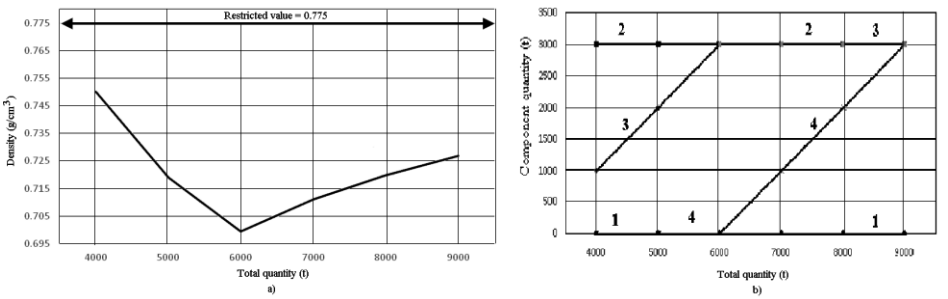

Figure 2 a) commercial gasoline density; b) commercial gasoline composition: 1 – FCC gasoline; 2 – catalytic reforming gasoline; 3 – iC_5 fraction; 4 – bioethanol.

The gasoline density obtained using the optimum recipe is under 0.775 (table 1) for the entire variation scope of the total quantity of gasoline. Figure 2b exemplifies the way in which the four components of the commercial gasoline are being used, regarding the total quantity. In the presented case, the components are used, successively: catalytic reforming gasoline (all quantity), iC_5 fraction (increasing quantity from 1000 to 3000 t);

bioethanol (increasing quantity from 0 to 3000 t). Because of its high density, the FCC component is not used in the optimum recipe.

4.2. Recipes that take into consideration two restrictive properties

The optimization program allowed the study of the dependence of the values of two restrictive properties of the optimum blending with the total blending quantity. In figure 3 the results regarding the density and Motor octane number behavior with the total quantity of gasoline are presented. The blending density constantly increases with the total increase of the quantity of commercial gasoline, this being caused by using a larger increasingly quantities of catalytic reforming gasoline and bioethanol, the components with the highest densities (figure 3a).Meanwhile, the Motor octane number decreases because of using catalytic reforming gasoline, component with lower MON(figure 3-b). From a numerical standpoint, both properties are within the admissible limits. Figure 3-csynthesizes the way in which the optimization program uses successively the four components, along with their quantities.

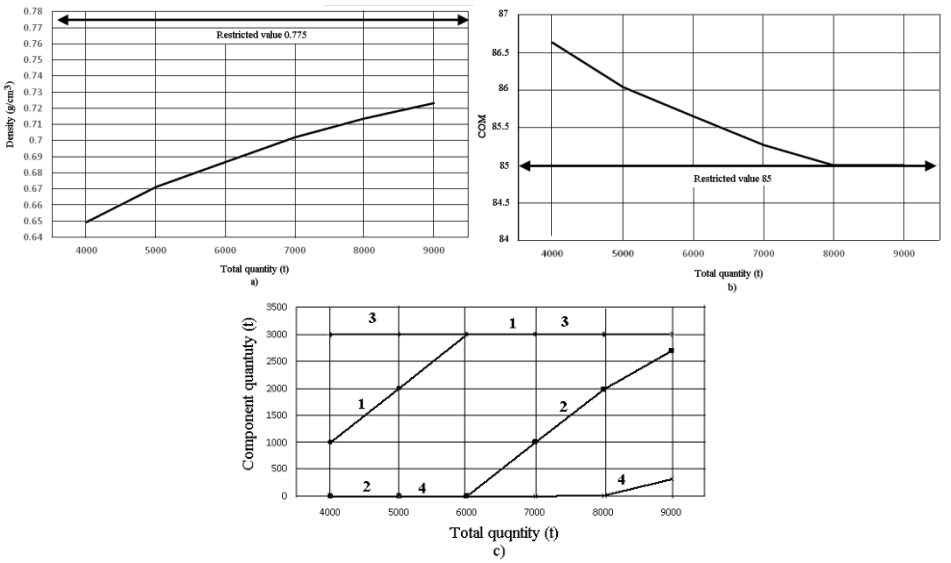

Figure 3 a) commercial gasoline density; b) Motor octane number c) commercial gasoline composition: 1 – FCC gasoline; 2 – catalytic reforming gasoline; 3 – iC5 fraction; 4 – bioethanol.

4.3. Recipes which have one imposed bioethanol proportion and one restrictive property taken into consideration

Because of the EN228 standard, the mandatory use of a fixed quantity of bioethanol in the commercial gasoline is necessary. The study of the influence of the bioethanol concentration on the commercial gasoline properties can be made using the same optimization problem. To exemplify, in figure 4 the variation of the gasoline COM with both the total quantity of gasoline and the imposed bioethanol concentration in the commercial gasoline is presented. The bioethanol concentration has varied in steps, between 0 and 5 % volume. The figures 4b and 4c present the variation of the gasoline components both the total quantity of gasoline and the imposed bioethanol concentration.

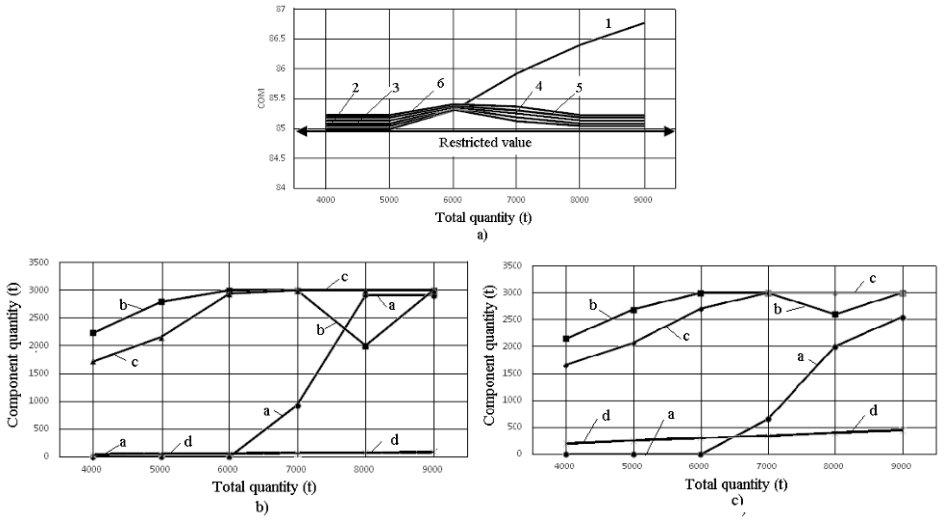

Figure 4 Optimum recipe corresponding to the bleedings with imposed bioethanol quantities: a) COM variation (1 – 0%; 2 – 1%; 3 – 2%; 4 – 3%; 5 – 4%; 6 – 5% bioethanol); b) Component quantitiesfor 1% bioethanol; c) Component quantities for 5% bioethanol (a – FCC gasoline; b – RC gasoline; c – iC5 fraction; d – bioethanol).

5. Conclusions

To study the process of obtaining commercial gasoline by optimal blending of different components, the authors have developed: a mathematical model for the estimation of the gasoline properties and an optimization software program to calculate the optimum blending. Using their own software tool, the authors studied the variation of the optimum recipe with the optimal blending quantity. A special attention has been given to study the influence of the bioethanol quantity on the optimum blending properties. The obtained results have confirmed the authors' software potential and this program can be used to quickly verify the optimum blending recipes.

References

N. Andrei, 2001, Models and Test Problems for Mathematical Programming, MatrixRom Publishing House, Bucharest, pp 124-125.

G. Bărbatu, M. Mănescu, V. Dumitru, V. Ionescu, 1970, Mathematical Programming in Petroleum Industry, Academic Romanian Publishing House,Bucharest, pp 70-74.

B. Doicin, 2014,Blending Recipe Optimization for Echological Petroleum Fuels of Type Gasoline Reformulation, Doctoral Thesis, Ploiesti, pp 49-69

J.P. Moreau, 2009, Linear Programming in Pascal, http://jean-pierre.moreau.pagesperso-orange.fr/p_linear.html.

S. Park, W-J Kim, C-K Park, S-M Lim, 1998, Software of Simplex Method for Linear Programming, Korean Management Science Review, vol. 15, issue 1, pp 49-62.

C.Pătrăşcioiu, 2005, Optimization Nummerical Techniques, MatrixRom Publishing House, Bucharest, pp 9.

C.Patrascioiu, N.Nicolae, 2012, The optimal gasoline blending into Romanian refinery, Case study, 9th International Conference on Informatics in Control, Automation and Robotics, vol 2, pp. 527-532.

G.C.Suciu, 1993, Hydrocarbon Processing Engineering, Vol. 4, Tehnical Publishing House, Bucharest, pp 429-434.

Krist V. Gernaey, Jakob K. Huusom and Rafiqul Gani (Eds.), 12th International Symposium on Process Systems Engineering and 25th European Symposium on Computer Aided Process Engineering.
31 May - 4 June 2015, Copenhagen, Denmark.

Population balance model for enzymatic depolymerization of branched starch

Christoph Kirse and Heiko Briesen

Chair of Process Systems Engineering; Technische Universität München, Freising, Germany
heiko.briesen@mytum.de

Abstract

A population balance model to describe the enzymatic depolymerization of branched starch is proposed. This model is based on the subsite theory which is established for the enzymatic depolymerization of linear polymers. Extensions of this theory to branched polymers by including hindering by branchings have been published. In this study, this model is transformed in a form suitable for usage with efficient numerical techniques for solving population balance equations, such as the Direct Quadrature Method Of Moments. Such methods are necessary to perform model based optimization and control for this process. A novel numerical method recently developed by the authors was employed. A preliminary comparison to experimental data shows that the data can be reproduced reasonably well. Possible reasons for the deviations from the experimental results are discussed and improvements to the model are suggested.

Keywords: Bivariate population balance; Depolymerization; Starch; Enzyme; Subsite theory

1. Introduction

Starch is a large (mean amount of monomer units up to 10^6) and highly branched (average of around one branching per 20 bonds) biopolymer with a broad distribution in amount of monomer units. It is one of the most abundant polymers in the world (Pérez and Bertoft, 2010). In several industrial processes (e.g., the mashing process during beer brewing (Eßlinger, 2009)) starch is depolymerized into saccharides by enzymes. The saccharides are normally used as the feedstock for a fermentation process. It might be possible to improve the performance and economic feasibility by using an optimal temperature profile. In order to perform such an optimization without having to run many experiments accurate models are needed. Like most bioproducts starch has a large variability (Pérez and Bertoft, 2010) which might necessitate an optimization for each specific batch run. Then, efficiency of the simulation technique becomes crucial. The first models proposed to describe the depolymerization of starch used very simple reaction schemes that are unable to reproduce experimental results such as the evolution of the variation in the amount of monomer units (Rollings and Thompson, 1984). Recent models were solved using Monte Carlo (MC) techniques (Besselink et al., 2008). This enabled consideration of the full complexity of reaction and substrate. However, MC techniques are computationally very expensive. A more promising approach is to develop and use a population balance model. In this work such a model is developed for α-amylase, one of the important enzymes in mashing (MacGregor, 1987).

2. Population balance model

To describe the depolymerization process using a population balance equation the same basic assumption as in Kirse and Briesen (2015) are made. It is assumed that all polymers with the

same number of monomer units k and bonds associated with branching (called branching bonds) b behave identically and deterministically. This only allows a statistical, instead of an explicit, treatment of the steric hindrance due to branchings which introduces several problems that are solved in this study. Furthermore, the polymers are assumed to be ideally dissolved.

2.1. Structure of starch

Because starch/amylopectin does not crosslink, the number of branching bonds must be less than or equal to the number of monomer units minus one. However, not every glycosidic α-(1-6) bond (called branching bond) must be the start of a newly branched chain. Accordingly, it is possible to have a dimer with a branching bond. For the purpose of this work a chain is defined as the α-(1-4) (linearly) connected monomers between the start of a chain at either the reducing end or at monomer unit with a branching bond up to either the end of the polymer or to another branching bond. Accordingly, every branched starch polymer has $2 \cdot b + 1$ chains: $b+2$ chains are end-chains and $b-1$ chains are inner chains. The average amount of monomer units per chain is $\frac{k}{2 \cdot b+1}$. A limitation of a bivariate population balance modelling is that the chain length distribution is not available. It is therefore assumed here that all chains have the average chain length which changes with time. This assumption was not necessary in the previous study (Kirse and Briesen, 2015).

2.2. Numerical solution of the population balance equation

The enzyme considered in this study only performs hydrolytic cleavage of the linear bonds (MacGregor, 1987). The population balance equation is therefore a pure binary breakage population balance equation. The algorithm developed in a previous study (Kirse and Briesen, 2015) to solve such equations is used and the notation is adopted. The algorithm divides the domain into three subdomains as shown in Figure 1. In Subdomain I the population balance equation is completely continuous and the bivariate Direct Quadrature Method of Moments (DQMOM) is used to solve the population balance equation in this subdomain. In Subdomain II the amount of monomer units is continuous but the amount of branching bonds is discrete. The resulting population balance equation is solved using monovariate DQMOM. In Subdomain III the population balance equation is completely discrete and only a system of coupled ordinary differential equations needs to be solved. The accent $\bar{}$ and $\check{}$ indicate that the variable is continuous or discrete, respectively. Furthermore, the accent $'$ shows that the variable belongs to a polymer that is cleaved into two smaller polymers. Because the action of the mechanisms $\bullet$ create polymer in the other subdomains, the algorithm discretizes the birth by conserving the amount of monomer units and branching bonds. The normalized fragment distribution functions $\gamma_\bullet$ and the hydrolysis rates $D_\bullet$ need to be determined for all the mechanisms (see Sections 2.4-2.7). For further detail about the algorithm the reader is referred to (Kirse and Briesen, 2015).

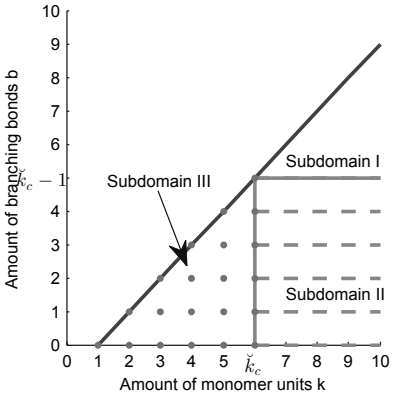

Figure 1: Division of the domain, where $\check{k}_c = 6$ for illustrative purposes.

2.3. Hydrolysis rate

Under the assumption that the product-forming reaction is much slower than the generation of the enzyme complex a competitive Michaelis-Menten kinetics is obtained for the hydrolysis rate

(Hiromi, 1970):

$$\breve{D}_{\bullet}(\breve{k}',\breve{b}') = c_{cat,\bullet}(\breve{k}',\breve{b}') \cdot N_{\text{chain},\bullet} \cdot K'_{\bullet}(\breve{k}',\breve{b}') \cdot \frac{E \cdot n(\breve{k}',\breve{b}')}{1+\sum_{\breve{k}'=1}^{\infty}\sum_{\breve{b}'=0}^{\breve{k}'-1}\frac{n(\breve{k}',\breve{b}')}{K_{m,\text{total}}(\breve{k}',\breve{b}')}}, \tag{1}$$

where $c_{cat,\bullet}$ is the catalytic constant, $N_{\text{chain},\bullet}$ is the number of chains that can be attacked by the specific mechanism, $K'_{\bullet}$ is the constant to relate the equilibrium concentration of the enzyme-polymer complex to the polymer concentration, E is the amount of enzyme, n is the polymer amount, and $K_{m,\text{total}}$ is the Michaelis-Menten constant.

There are three possible mechanisms. One is the attack of linear polymers which is completely characterized using established results from the subsite theory (see Sec. 2.4 and 2.5). The remaining two mechanisms are the attack of an end-chain (see Sec. 2.6) or an inner-chain (see Sec. 2.7) of a branched polymer. One can then show that the Michaelis-Menten parameter $K_{m,total}(k,b)$ can be obtained as follows:

$$\frac{1}{K_{m,\text{total}}(k,b)} = N_{\text{chain,inner}}(b) \cdot K'_{\text{inner}}(k,b) + N_{\text{chain,end}}(b) \cdot K'_{\text{end}}(k,b) + \frac{N_{\text{chain,linear}}(b)}{K_{m,\text{linear}}(k)}. \tag{2}$$

2.4. Subsite theory

According to the subsite theory (Hiromi, 1970) the active site of an enzyme consists of several subsites and a catalytic site. The binding of a polymer to the enzyme is a reversible binding of some monomer units of the polymer to the subsites which do not interact with each other. The subsites are numbered in direction from the reducing end to the non-reducing end. There are $\breve{z}_-$ and $\breve{z}_+$ subsites with lower and, respectively, higher numbers than the catalytic center. If the cleavage rate of the bond is much slower than the formation rate of enzyme-polymer complex, the equilibrium concentration of the enzyme-polymer complex is related to the energy of the occupied subsites. The Michealis-Menten constant can then be computed (Hiromi, 1970). A bond can only be broken if the two subsites adjacent to the catalytic center are occupied. The catalytic coefficient for a specific binding position $c_{cat,s,\breve{k}}$ of productive bindings was assumed by Allen and Thoma (1976) to be a function of the number of occupied subsites $N_{oc}(s,\breve{k})$. For an unproductive binding $c_{cat,s,\breve{k}}$ is equal to zero. The fragment distribution γ_{linear} can then also be computed:

$$c_{cat,\text{linear}}(\breve{k}) = K_{m,\breve{k},\text{linear}} \cdot \sum_{s=1}^{\breve{z}_-+\breve{z}_++\breve{k}-1} c_{cat,s,\breve{k}} \cdot K'_{s,\breve{k}} \tag{3}$$

$$\breve{\gamma}_{\text{linear}}(\breve{k},\breve{k}') = \frac{K_{m,\breve{k},\text{linear}}}{2 \cdot c_{cat,\text{linear}}(\breve{k})} \cdot \left(c_{cat,\breve{z}_{minus}+\breve{k},\breve{k}'} \cdot K'_{\breve{z}_{minus}+\breve{k},\breve{k}'} + c_{cat,\breve{z}_{minus}+\breve{k}'-\breve{k},\breve{k}'} \cdot K'_{\breve{z}_{minus}+\breve{k}'-\breve{k},\breve{k}'} \right), \tag{4}$$

where s is the index of the highest occupied subsite and $K'_{s,\breve{k}}$ is the association constant that can be computed using the subsite theory. Once a polymer is large enough to occupy all subsites, the binding specific catalytic coefficient and the association constant have a constant value K'_{int} and $c_{cat,int}$ for certain binding positions which allows a simplification of the equation for the Michaelis-Menten constant (Allen and Thoma, 1976). Furthermore, for $\breve{k}' > 2 \cdot \max(\breve{z}_-,\breve{z}_+)+2$ and $\max(\breve{z}_-,\breve{z}_+)+1 < \breve{k} < \breve{k}' - \max(\breve{z}_-,\breve{z}_+)-1$ the fragment distribution function has a constant value and in this study those monomers are called inner monomers. The enzyme performs an attack similar to random-chain scission for those monomers.

2.5. Linear polymers

For a discrete population balance equation one can directly use the results from the subsite theory. However, for large polymers this would necessitate the consideration of many products which

would be computational expensive. Therefore, all polymers larger than $\breve{k}_c$ were considered to be continuous. The summation in Equation (1) is accordingly split into a summation and an integral, the simplified equation for K_m is used, and the same arguments lead to a similar equation for $c_{cat,\text{linear}}$. The products generated by attack on non-inner monomers are still considered to consist of one discrete product and one continuous product. However, all the products generated by attack on inner monomer units are considered to be continuous. This yields the fragment distribution function for attack on a continuous polymer:

$$\begin{aligned}\bar{\gamma}_{\text{linear}} = \Big[&\breve{\gamma}_{\text{linear}}(\max(\breve{z}_-,\breve{z}_+),2\cdot\max(\breve{z}_-,\breve{z}_+))H(k-\max(\breve{z}_-,\breve{z}_+)-1)\cdot H(k'-k-\max(\breve{z}_-,\breve{z}_+)-1)\\ &\cdot\frac{k'-2\cdot\max(\breve{z}_-,\breve{z}_+)}{k'-2\cdot\max(\breve{z}_-,\breve{z}_+)-2}+\sum_{j=1}^{\max(\breve{z}_-,\breve{z}_+)}\breve{\gamma}_{\text{linear}}(j,k')\cdot\big(\delta(k-j)+\delta(k'-k-j)\big)\Big]\\ &\cdot\frac{1}{1+(k'-2\cdot\max(\breve{z}_-,\breve{z}_+))\cdot\breve{\gamma}_{\text{linear}}(\max(\breve{z}_-,\breve{z}_+),2\cdot\max(\breve{z}_-,\breve{z}_+))}\cdot\delta(b).\end{aligned} \tag{5}$$

2.6. Attack on end-chains

The attack on end-chains is similar to the attack on a linear polymer with as many monomer units as the average chain length. However, the enzyme is assumed to be unable to bind to a monomer unit with a branching bond. Together with the assumption that the polymer is always oriented with the index of the subsite increasing towards the reducing end, the association constant for the binding on an end-chain of the average chain length on the i-th monomer unit counting from the free end can be computed by taking into account which subsites are occupied. The association constant K'_{end} is obtained by summing up the binding specific association constants. The number of occupied subsites is $\min(i,\breve{z}_-+\breve{z}_+)$ and the binding is only productive if $i>\breve{z}_+$. On every attack on an end-chain scissors, one linear fragment is removed and leaves the large remaining polymer with the same amount of branching bonds. If i is larger than or equal to $\breve{z}_++\breve{z}_-$, the association constant and the catalytic constant again become a constant, and the products generated by this attack are considered to be continuous. One should note that in this study the end-chain that carries the reducing end is treated the same as all other end-chains. The fragment distribution function is not shown due to space limitations.

2.7. Attack on inner-chains

It is assumed that the enzyme can only bind to an inner chain if all subsites can be occupied. This implies that the average chain length must be greater than or equal to $\breve{z}_++\breve{z}_-$ for a binding to be possible. It follows that K'_{inner} is zero for a chain length less than $\breve{z}_-+\breve{z}_+$. According to the subsite theory the reaction constant then is $c_{cat,int}$. Under the assumption that all monomer units of a chain have the same probability of being attacked, the association constant is obtained

$$K'_{\text{end}}=\left(\frac{k'}{2\cdot b'+1}-\breve{z}_-+\breve{z}_++1\right)\cdot H\left(\frac{k'}{2\cdot b'+1}-\breve{z}_-+\breve{z}_+\right)\cdot K'_{int}. \tag{6}$$

Every hydrolysis forms two products with at least $\min(\breve{z}_-,\breve{z}_+)+1$ monomer units and at least one branching bond. The fragment distribution function is independent from the size of the product formed for all physically possible polymers but cannot be shown here due to space limitations.

2.8. Simulation parameters

Using the algorithm described by Kirse and Briesen (2015) but the much more complex model derived in this study the experiment performed by Besselink et al. (2008) is simulated. The critical amount of monomer units for discrete computation $\breve{k}_c$ was 14. Furthermore, 3 quadrature points in the continuous subdomain and 1 in the semi-discrete subdomain were used. The constant C

that converts from simulation to experimental time was found by finding the best fit between the simulated and the experimental dextrose equivalent for the first two measurement points. In this study, a value of $1.34 \cdot 10^5$ s was obtained. The binding energies, the acceleration factor, the percentage of amylose, and the initial mass concentration of starch were taken from Besselink et al. (2008). The amount of monomer units distribution was assumed to follow a Schulz-Zimm distribution where the parameters for amylopectin were taken from Rolland-Sabate et al. (2007) as waxy wheat starch and for amylose from (Hanashiro and Takeda, 1998). Amylose was assumed to be linear and the degree of branching for amylopectin was assumed to follow Equation (15) from Rolland-Sabate et al. (2007) with the parameters for waxy wheat starch.

3. Results and discussion

Figure 2 shows the experimental and simulation results by Besselink et al. (2008), which have been obtained using Monte Carlo techniques, and the simulation results from this study. One can see that the fit between the experimental data and our simulation is slightly worse than for the one obtained by Besselink et al. (2008). We postulate that this discrepancy is due to the fact that in the ad hoc inhibition due to proximity of branching introduced by (Marchal et al., 2003) and used by Besselink et al. (2008) was not used and rather a total inhibition was assumed in this study. Therefore, a different behavior of the depolymerization velocity was obtained.

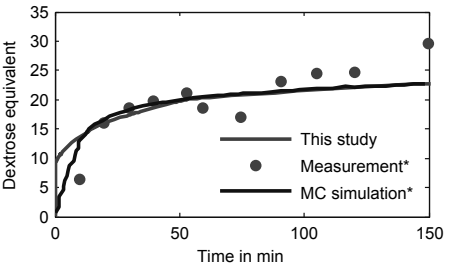

Figure 2: A comparison of the simulated and measured dextrose equivalent. *Besselink et al. (2008)

The simulated and experimental mass percentage of two linear saccharides is shown in Figure 3. The fit for the glucose concentration is very good and even better than the MC results. However, the fit for the maltotriose concentration is poor. Again this is likely due to the different inhibition model used in this study. The simulated maltotriose concentration in our study slowly decreases for larger times. This is in agreement with data measured by Steverson et al. (1984). However, the experimental data used in this study (Besselink et al., 2008) was not measured for a sufficiently long time to observe this effect.

4. Conclusion

In this study, the subsite theory for depolymerization was extended to branched polymers. For the first time this was done with a population balance equation. A decrease in computational effort is expected, but could not be shown because the computation time for the reference Monte Carlo simulation is not available. Furthermore, for the first time the subsite theory was used for polymers that have a realistic number of monomer units. The agreement with experimental data was worse than using Monte Carlo simulations but acceptable. However, in this study the inhibition by proximity to branchings was not modeled using the ad hoc model introduced by Marchal et al. (2003). The inclusion of this model is possible in a population balance framework. After inclusion of this effect the improved model should be compared to more experimental data such as data measured for longer times (Steverson et al., 1984) or the amount of longer chained saccharides (Rollings and Thompson, 1984). An additional reason for the deviation from the experimental data is that the initial condition was not measured directly but estimated from different measurements.

It was shown that the algorithm developed in a previous study (Kirse and Briesen, 2015) is able to

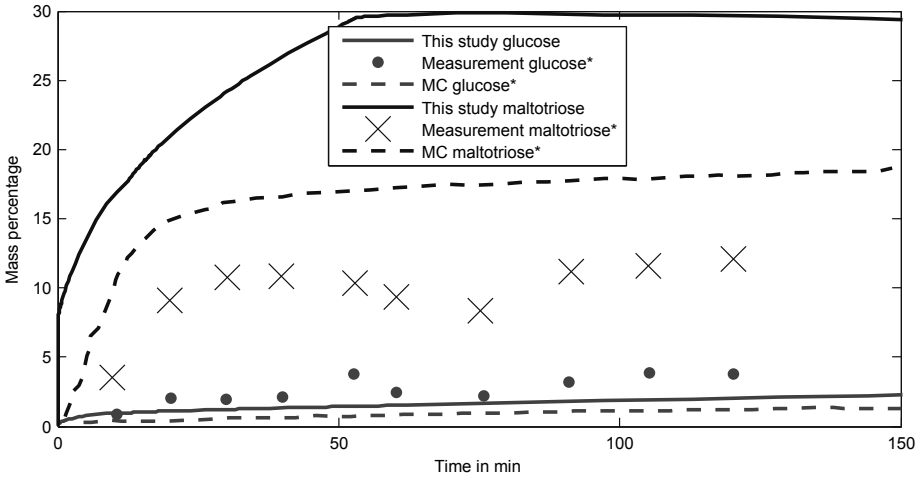

Figure 3: A comparison of the simulated and measured mass concentration of some saccharides. *Besselink et al. (2008)

deal with more complex hydrolysis rates and product distributions, but the convergence properties of this algorithm still need to be studied for such a complex case.

5. Acknowledgments

This research was supported by the German Ministry of Economics and Technology (via AiF) and the FEI (Forschungskreis der Ernährungsindustrie e.V., Bonn) Project AiF 16542 N.

References

J. Allen, J. A. Thoma, 1976. Subsite mapping of enzymes - depolymerase computer modeling. Biochem. J. 159 (1), 105–120.

T. Besselink, T. Baks, A. E. M. Janssen, R. M. Boom, 2008. A stochastic model for predicting dextrose equivalent and saccharide composition during hydrolysis of starch by alpha-amylase. Biotechnolog. Bioeng. 100 (4), 684–697.

H. M. Eßlinger (Ed.), 2009. Handbook of Brewing: Processes, Technology, Markets. Wiley, Weinheim.

I. Hanashiro, Y. Takeda, 1998. Examination of number-average degree of polymerization and molar-based distribution of amylose by fluorescent labeling with 2-aminopyridine. Carbohyd. Res. 306 (3), 421–426.

K. Hiromi, 1970. Interpretation of dependency of rate parameters on degree of polymerization of substrate in enzyme-catalyzed reactions - evaluation of subsite affinities of exo-enzyme. Biochem Biophys. Res. Commun. 40, 1–6.

C. Kirse, H. Briesen, 2015. Numerical solution of mixed continuous-discrete population balance models for depolymerization of branched polymers. Comput. Chem. Eng 73, 154 – 171.

A. W. MacGregor, 1987. α-amylase, limit dextrinase, and α-glucosidase enzymes in barley and malt. Crit. Rev. Biotechnol. 5 (2), 117–128.

L. Marchal, R. Ulijn, C. Gooijer, G. Franke, J. Tramper, 2003. Monte carlo simulation of the α-amylolysis of amylopectin potato starch. 2. α-amylolysis of amylopectin. Bioproc. Biosyst. Eng. 26, 123–132.

S. Pérez, E. Bertoft, 2010. The molecular structures of starch components and their contribution to the architecture of starch granules: A comprehensive review. Starch - Stärke 62 (8), 389–420.

A. Rolland-Sabate, P. Colonna, M. G. Mendez-Montealvo, V. Planchot, 2007. Branching features of amylopectins and glycogen determined by asymmetrical flow field flow fractionation coupled with multiangle laser light scattering. Biomacromolecules 8 (8), 2520–2532.

J. Rollings, R. Thompson, 1984. Kinetics of enzymatic starch liquefaction - simulation of the high-molecular-weight product distribution kinetics of enzymatic starch liquefaction - simulation of the high-molecular-weight product distribution. Biotechnolog. Bioeng. 26 (12), 1475–1484.

E. Steverson, R. Korus, W. Admassu, R. Heimsch, 1984. Kinetics of the amylase system of saccharomycopsis-fibuliger. Enzyme Microb. Tech. 6 (12), 549–554.

Krist V. Gernaey, Jakob K. Huusom and Rafiqul Gani (Eds.), 12th International Symposium on Process Systems Engineering and 25th European Symposium on Computer Aided Process Engineering. 31 May – 4 June 2015, Copenhagen, Denmark

Analysis of the Transfer of Radical Co-polymerisation Systems from Semi-batch to Continuous Plants

Thilo Goerke[a], Sebastian Engell[a]

[a]*Process Dynamics and Operations Group, Technische Universität Dortmund, 44227 Dortmund, Germany*
thilo.goerke@bci.tu-dortmund.de

Abstract

Continuous production in tubular reactors has the advantages of better product uniformity and better space-time yield compared to the traditional semi-batch production mode. In this work the transferability of the production of co-polymers from a discontinuous semi-batch process to a continuously operated plug flow reactor is investigated. The critical aspect of the transfer is that the continuous addition of one of the monomers in the semi-batch process is changed to an addition at discrete injection points in the continuous plant. This leads to different product properties. The feasible ranges of product properties for both plants are determined by means of optimisation. The presented method can be used to analyse whether a given polymer production can be transferred to a continuous plant or which changes in the product qualities have to be considered.

Keywords: Radical copolymerisation, batch-to-conti transfer, product properties

1. Introduction

The production of copolymers with different reaction rates of the two monomers is nowadays mostly done in discontinuous batch or semi-batch reactors. The idea of transferring such production processes to the continuous mode of operation has been investigated during the European research project F3 Fast Flexible Future Factory, that started in 2009 (Buchholz 2009). The continuous plants, which were considered for co-polymerisations of monomers with different reactivities, are modular plug-flow reactors (PFR) with side injections. By the switch to continuous production, the continuous feed of reactants is replaced by lumped feeds at the injection points. This poses the question for which copolymers it is possible to obtain the same product in the continuous mode of operation as in the semi-batch mode. If this is possible, the better heat transfer characteristic in the continuous plant enables higher production rates and better space-time yields which, together with the improved uniformity of the production, make the continuous production an interesting alternative. The transfer of a batch process to a continuous PFR plant is restricted by the minimum flow velocity needed for sufficient heat transfer, narrow residence time distributions and the possible residence time in the PFR. Additionally the question arises whether the transfer to a continuous plant enables the production of new products, which cannot be produced in discontinuously operated plants.

In this paper the transferability is investigated by analysing the product ranges that result from the two modes of operation for a broad range of combinations of two monomers. Section 2 contains the description of the considered processes and of the possible combinations of monomers, which are represented by four reactivity ratios

within a simplified terminal model. The optimization algorithm used for the investigation of the space of attainable product properties is introduced in Section 3. In Section 4 the results for an example reaction system are presented. The work is concluded in Section 5.

2. Radical Polymerisation Model and Reactivity Ratios

In this work, the radical copolymerisation of linear copolymers containing two monomers is investigated. For a concise description of the possible combination of reaction rates, four ratios of kinetic constants are introduced.

2.1. Radical Polymerisation Model

The mechanism of radical polymerisation is based on the transfer of a radical functionality from a thermally decomposed initiator to a growing chain of monomer units. A suitable model to describe the mechanism of radical polymerisation is the terminal model. The assumption of the model is that the reactivity of a polymer chain can be described by kinetic constants which depend only on the terminal monomer of a growing chain, that carries the radical functionality. Zargar et al. (2009) presented a terminal model using the method of moments to describe the evolution of the product qualities within a radical copolymerisation. As the product qualities of copolymers, produced by the radical polymerization mechanism, are determined by the statistical process of chain growth and termination, the resulting product qualities have to be described by distributions. The most important product qualities in a copolymerisation process are the chain length distribution and the sequence length distributions of both monomers. The sequence length describes the number of subsequent identical monomer units for each monomer in a copolymer chain. During this work, the distributions are described by the number average and the weight average of the chain length distribution (NACL, WACL) and of both sequence length distributions ($NASL_{M1}$, $WASL_{M1}$, $NASL_{M1}$, $WASL_{M2}$). The full set of kinetic rate constants needed to calculate the product qualities in the terminal model from Zargar et al. (2009) contains 27 parameters if an Arrhenius-type temperature dependency is considered.

Our goal is to investigate the transferability from batch to continuous production for a broad range of combinations of monomers. This necessitates the reduction of the number of independent parameters, which are used to describe the combinations of monomers. The assumptions for the simplification of the model concern the chain initiation and the termination of polymer chains. It is assumed that the reaction rates of the chain initiation are equal to the corresponding homo propagation rates, furthermore that the cross termination can be described as the mean value of the homo termination rates. In total four different ratios of reaction rates are used within this work to define the combinations of two monomers and an initiator. The decomposition kinetic of the initiator is assumed to be known. The reactivity ratios are given in Eq. (1). The parameters r_1 and r_2 describe the ratios of the homo polymerisation rate to the cross propagation rates for both monomers, while the third ratio relates the homo propagation rates of both monomers. The fourth parameter describes the ratios of the homo termination rates.

$$r_1 = \frac{k_{p,11}}{k_{p,12}} \quad r_2 = \frac{k_{p,22}}{k_{p,21}} \quad \frac{k_{p,11}}{k_{p,22}} \quad \frac{k_{t,1}}{k_{t,2}} \tag{1}$$

In most cases the polymerisation reaction is exothermic. Therefore semi-batch processes are investigated, where the feeding strategy is to prefill the slower reacting monomer to the reactor in advance and to dose the faster reacting monomer and initiator during the

reaction. Such strategies are applied to reaction systems where the cross propagation is preferred for both monomers. Thus the investigated range for r_1 and r_2 is between 10^{-4} and 10^{0}. The definition of the faster reacting monomer is implied by the ratio of the homo propagation rates being between 10^{-4} and 10^{0}. The termination ratio is not restricted, which results in an investigated range for this ratio between 10^{-4} and 10^{4}. Acrylic acid is used as the reference substance for the kinetics. It acts as the faster reacting monomer 2 during the reactions. The kinetic values were taken from Cutie et al (1997).

2.2. Modelling the Plants, Feeding Strategies and Process Windows

The plants considered in this work are on the one hand a stirred tank reactor and on the other hand a modular plug flow reactor plant with side injections. It is assumed that the discontinuous semi-batch reactor is operated isothermally. In the plug flow reactor plant the temperature of the cooling liquid is assumed to be constant. The temperature in the discontinuous reactor is assumed to be controlled perfectly via the jacket, but in the continuous plant a non-ideal temperature control is assumed. The modular plant consists of eight modules of two different diameters, equipped with static mixers and cooling jackets. As the progress of the reaction depends on the spatial coordinate, a constant reactor temperature cannot be achieved within a module by using the cooling jacket. This results in temperature profiles with hot spots due to the injection of the feed streams. We assume a fixed reactor configuration, consisting of four consecutive groups. Each group contains one injection point at the beginning followed by two modules. A larger number of feeds would facilitate the approximation of the semi-batch operation but will increase the cost of the reactor and most likely make the continuous reactor economically unattractive.

The feeding strategy that is applied to both plants is to prefill the slower reacting monomer or to add it at the first injection point into the continuous plant, while the second monomer and the initiator are fed with a constant feeding rate to the discontinuous reactor or via all injection points into the modular PFR plant.

In order to determine the possible process windows for both plants, the inputs to the plants, i.e. the feeding rates, are varied to design reaction recipes that do not violate reasonable process constraints. These constraints enforce minimal values for the conversions of both monomers, for the concentration of the initiator at the end of the reaction and for the NACL. Furthermore upper and lower limits for the composition of the copolymer chains are assumed. In the discontinuous process the volume of the reactor and the minimum temperature of the cooling jacket, to achieve an isothermal process, are restricted. Additional constraints in the continuous process are a minimum flow velocity, as required by the static mixers to achieve a sufficient mixing, and a maximum hot spot temperature difference in each module.

3. Method for the Analysis of the Transferability

The range of possible products for each reaction system is defined by the combination of the kinetics and the process constraints. An optimization based approach is applied to compute the set of feasible recipes for both reactor concepts. The optimization approach used in this work is based on an evolutionary algorithm as presented in Ashlock (2006) in combination with a local optimization. The combination of both types of algorithms was proposed in Urselmann et al (2010) and is called a memetic algorithm. Within the evolutionary algorithm, different fitness functions are applied to explore the space of feasible processes. Within the selection step, a two stage-cost function is used to first find solutions, which are feasible, and if there are feasible solutions, to maximize their distance from known solutions within the space of the input variables. The definition of

a feasible solution is that v_{viol} in Eq. (2) is zero. In Eq. (2) u_i denotes the i^{th} input and c_j represents the j^{th} constraint. The indices u and l indicate the upper and the lower bounds on the inputs/constraints.

$$v_{viol} = max\left(0,\ [u_{i,l} - u_i], [u_i - u_{i,u}], [c_{j,l} - c_j], [c_j - c_{j,u}]\right) \tag{2}$$

If a feasible solution is found, the sum of the Euclidean distances to each previously computed feasible solution is calculated according to Eq. (3). N_{feas} denotes the number of feasible solutions found during the execution of the algorithm, the index m refers to the currently investigated feasible solution.

$$D_m = \sum_{k=1}^{N_{feas}} \frac{\|u_m - u_k\|}{N_{feas}} \tag{3}$$

Hence during the selection step feasible solutions, which are located at a larger distance in space spanned by the input variables, i.e. the feed rates, to the previously found solutions are preferred. In addition to the global search by the evolutionary algorithm, a local search is applied. A combination of KNITRO and CONOPT from the TOMLAB toolbox (Holmström et al., 2003) is used to solve the local optimization problems. If no feasible solution is found, KNITRO is used to minimise (2), while CONOPT is used for the local optimization of feasible solutions. Starting from a feasible solution, the distance to the constraints is minimized and the resulting solutions are added to the population. The cost function of the local optimization is shown in Eq. (4). $D_{c,m}$ denotes the distance between the value of the constraint function for the current solution c_m and the desired constraint c.

$$D_{c,m} = \|c - c_m\| \tag{4}$$

The presented combination of global search and local optimization turned out to be efficient to explore the boundaries of the ranges of feasible processes.

Within this set, each feasible process results in another product quality. The resulting product qualities of the two processes can be analysed by projections on the 2-dimensional product parameter spaces. The six different product qualities that are used to characterize a product of a copolymerisation process are shown in three different graphs. Figure 1 shows an example of the resulting graphs. From these graphs the information which products can be transferred with the same values of two of the product quality parameters can be detected. If no overlapping areas for a group of product quality parameters exist, the transferability must be judged based upon the acceptable change in the product quality parameters, e.g. in the sequence length distributions. In addition to the changes in the product qualities, the space-time-yields of the two processes can be compared for a given product to be able to trade the change in product properties with the space time yield due to the change of the operation mode.

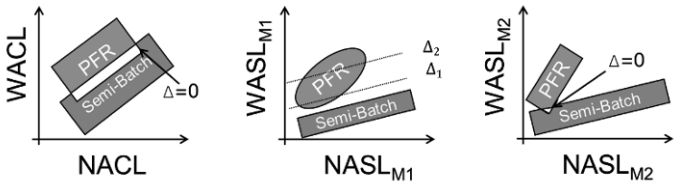

Figure 1 Representation of the resulting product ranges (conceptual representation)

4. Results

The analysis of the transferability can be performed on three different levels by applying the presented approach. On the kinetic level, the variation of the four kinetic ratios followed by the determination of feasible processes show the feasible combinations of monomers, within the assumed limitations concerning the feed strategy and the process constraints. In Figure 2, the reaction systems where feasible solutions were found are marked. For values of r_1 close to one the heat removal limits the possibility to generate the product in the pure semi-batch mode where the complete amount of monomer 1 is fed at the beginning of the batch run. In the continuous process the production is possible.

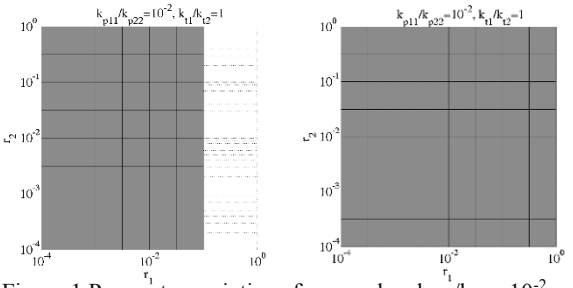

Figure 1 Parameter variations for r_1 and r_2, $k_{p11}/k_{p22}=10^{-2}$, $k_{t1}/k_{t2}=1$; feasible processes marked in green; left: discontinuous process, right: continuous process

The second level of detail is the investigation of a specific reaction system, which is described, as an example, by the four ratios $r_1=10^{-3}$, $r_2=10^{-2.5}$, $k_{p11}/k_{p22}=10^{-2}$ and $k_{t1}/k_{t2}=1$. In Figure 3 the resulting ranges of product properties are shown for both modes of operation. While the range of products of the discontinuous process is narrow, the range is broadened in the continuous process due to the change in the type of monomer addition. The narrow range is caused by the fact, that in the chosen feed strategy the slower reacting monomer is added slowly to the reactor and controls the polymerisation of the faster reacting monomer. In the continuous plant the addition takes place at fixed injection points, thus the amount of faster reacting monomer compared to the amount of slower reacting monomer is increased. This fact leads to the production of chains that contain longer sequences of the faster reacting monomer. The broadening of the range of products however is in the direction of higher poly-dispersity indices, which may not always be desirable.

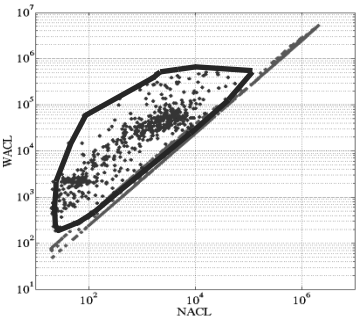

Figure 3 Resulting product ranges with respect to the chain length distribution for the example reaction system

As shown in Figure 3, overlapping regions exist for the two processes, where the transfer can be executed without a difference in the quality of the product. To investigate a possible trade-off between process intensification and differences in product qualities, a third level of detail in the analysis can be used. This level concerns the analysis for a specific recipe. For the chosen reaction system a discontinuous process is taken from the set of feasible processes, e.g. one with

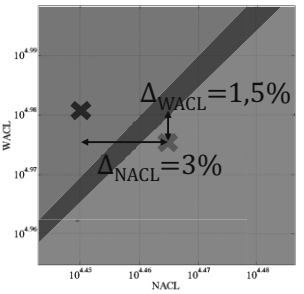

Figure 4 Changes in the product qualities shown for the chain length distribution; feasible area for discontinuous processes in the lower right corner; overlapping region marked in dark

a maximized product output. The resulting product is the reference for the transfer to a continuous plant, with the restriction of a maximum change of the product quality parameters of e.g. 5 % with respect to the discontinuously generated product. The limiting factor usually is the sequence length distribution of monomer 1. For this example, the change in the total chain length parameters is less than 3 % as shown in Figure 4. The space time yield for this specific process is increased by a factor of 150 due to the change to a continuously operated plant with side injections.

5. Summary

The analysis presented helps to explore the potential of continuous co-polymerization processes for a broad range of monomers. The transferability of existing processes and products can be investigated in terms of the resulting changes in the product quality parameters. The trade-off between process intensification and changes of the product can be evaluated, providing information, if a possible transfer to a continuously operated modular plug flow plant is worthwhile from a chemical and economical point of view.

Acknowledgement

The research leading to these results received funding from the European Community's Seventh Framework Program (FP7/2007-2013) under Grant Agreement n°228867

References

Buchholz, Sigurd (Project manager);2009, F3 Factory –fast,flexible,future; www.f3factory.com; last call: 19.01.2015

Zargar, A., Schork, F.J.; 2009, Copolymer Sequence Distributions in Controlled Radical Polymerization; Macromolecular Reaction Engineering, Vol. 3,Issue 2-3, 118-130

Cutie, S.; Smith, P.; Henton, D.; Staples, T.; Powell, C.; 1997; Acrylic Acid Polymerization Kinetics; Journal of Polymer Science Part B: Polymer Physics; Vol. 35, Issue 13; 2029-2047

Ashlock, D.;2006; Evolutionary Computation for Modeling and Optimization, XX, Springer Verlag GmbH, Heidelberg

Urselmann, M.; Barkmann, S.; Sand, G.; Engell, S.;2011; Optimization-based design of reactive destillation columns using a memetic algorithm; Computers & Chemical Engineering Vol. 35, Issue 5, 787-805

Holmström K.; Edvall, M.; Göran, A.; 2003; TOMLAB – for Large-Scale Robust Optimization; Proceedings, Nordic MATLAB Conference

Krist V. Gernaey, Jakob K. Huusom and Rafiqul Gani (Eds.), 12th International Symposium on Process Systems Engineering and 25th European Symposium on Computer Aided Process Engineering.
31 May – 4 June 2015, Copenhagen, Denmark

Thermodynamic Calculations for Systems Biocatalysis

Rohana Abu, Maria T. Gundersen, John M. Woodley*

Department of Chemical and Biochemical Engineering, Technical University of Denmark, Søltofts Plads Building 229, Kgs. Lyngby, Denmark.
**jw@kt.dtu.dk*

Abstract

'Systems Biocatalysis' is a term describing multi-enzyme processes *in vitro* for the synthesis of chemical products. Unlike *in-vivo* systems, such an artificial metabolism can be controlled in a highly efficient way in order to achieve a sufficiently favourable conversion for a given target product on the basis of kinetics. However, many of the most interesting non-natural chemical reactions which could potentially be catalysed by enzymes, are thermodynamically unfavourable and are thus limited by the equilibrium position of the reaction. A good example is the enzyme ω-transaminase, which catalyses the transamination of a pro-chiral ketone into a chiral amine (interesting in many pharmaceutical applications). Here, the products are often less energetically stable than the reactants, meaning that the reaction may be thermodynamically unfavourable. As in nature, such thermodynamically-challenged reactions can be altered by coupling with other reactions. For instance, in the case of ω-transaminase, such a coupling could be with alanine dehydrogenase. Herein, the aim of this work is to identify thermodynamic bottlenecks within a multi-enzyme process, using group contribution method to calculate the Gibbs free energy change, $\Delta G_r^{o\prime}$, of the overall cascade. The findings show that unfavourable reactions in the cascade can be improved by coupling to a favourable reaction giving more energetically stable products.

Keywords: Systems Biocatalysis, multi-enzyme, thermodynamics, group contribution

1. Introduction

Servi and co-workers (2013) recently introduced the term 'Systems Biocatalysis' to describe the science associated with multi-enzyme cascades via the use of isolated enzymes *in-vitro* for the synthesis of chemical products. To date, several promising multi-enzyme processes have been reported in the scientific literature and no doubt many more examples will be forthcoming in the future as such systems are established as a useful approach for industrial synthesis (Riva, 2014). In an example of a multi-enzyme processes (Figure 1), the primary enzyme (E1) is the main enzyme that determines the synthesis of the target product (P1) while a second enzyme (E2) is added to the system to assist the main reaction. This secondary enzyme acts in such a way as to aid the primary enzyme to achieve the desired product in a high enough yield. In this representative example, the second enzyme requires a cofactor (X) which is crucial for the functionality of the secondary enzyme. Addition of a cofactor is frequently expensive and it must therefore be re-generated *in-situ*, and thus a third enzyme (E3) is introduced to the system. In this way, the multi-enzyme system is built.

The production of methylbenzylamine from acetophenone using ω-transaminase (EC.2.6.1.18) as a catalyst provides a good example of such a scheme. In this chiral amine synthesis, the equilibrium constant of $4.03*10^{-5}$ has been determined

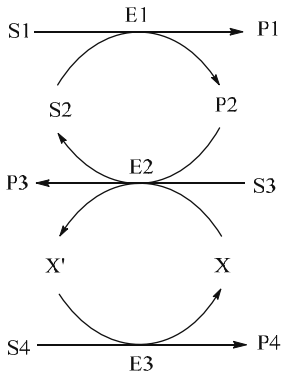

Figure 1: Representative scheme of multi-enzyme processes. E: enzyme, S: substrate, P: product, and X: cofactors.

determined experimentally where alanine was employed as the amine donor (Tufvesson et al., 2012). The value shows that the reaction alone is thermodynamically unfavourable and thus the maximum achievable conversion is only 0.63 %. Interestingly, a sufficiently favorable conversion of methylbenzylamine can be achieved, when transaminase is coupled with secondary enzymes. Using alanine as the same amine donor, the transamination achieved >70 % conversion (Truppo et al. 2009). The secondary enzymes were lactate dehydrogenase, LDH (EC 1.1.1.27) and glucose dehydrogenase, GDH (E.C.1.1.1.1). The LDH was added to remove the co-product pyruvate that hinders the formation of the target amine while GDH was used to re-generate cofactor *in situ* required by the LDH. An alternative option could be to use transaminase coupled with alanine dehydrogenase, AlaDH (EC.1.4.1.1), which was used to achieve 96 % conversion. In this system, alanine was re-generated *in situ* by recycling the pyruvate. As well as LDH, the AlaDH requires cofactors, in which the third enzyme (GDH) was also added to complete the multi-enzyme system. Even though the study claimed that the role of LDH and AlaDH was to drive the reaction to completion, there was no thermodynamic analysis to support this. Likewise, for many other multi-enzyme processes reported in the scientific literature (Simon et al., 2014), there is remarkably little thermodynamic background. Herein, this work is aimed to identify thermodynamic bottleneck in multi-enzyme processes, using the group contribution method to calculate the Gibbs free energy change $\Delta G_r^{o\prime}$. Such thermodynamic evaluation is fundamental to successfully apply systems biocatalysis.

2. Thermodynamic analysis

The thermodynamic favourability of biocatalytic reactions can be quantified by the standard Gibbs free energy change of reaction, $\Delta G_r^{o\prime}$, using Eq. 1. The data on thermodynamic properties, the standard Gibbs free energy of formation, $\Delta G_f^{o\prime}$, of reactants and products, are thus required. These data can be obtained from group contribution (GC) methods developed by Jankowski and co-workers (2008). To date, the Jankowski-GC method is established tools for estimating such properties of

biochemical molecule. It has a large training set that allows for accurate estimation of $\Delta G_f^{o\prime}$.

$$\Delta G_r^{o\prime} = \sum_j^p n_j \, \Delta G_{f,j}^{o\prime} - \sum_i^r n_i \, \Delta G_{f,i}^{o\prime} \tag{1}$$

Usually, $G^{o\prime}$ is used to denote the standard Gibbs free energy of biochemical compounds (pH 7, a temperature of 298 K, and zero ionic strength), while G^o refers to the standard state for chemical compounds. However, in practice, biocatalytic reactions are not operated at the standard state conditions. Therefore, the Eq. 2 is used to calculate the Gibbs free energy change of reaction under different conditions, which is termed as ΔG. *R* is the gas constant, *T* is the temperature, *c* is the concentration of component *i* in reactant *r* and component *j* in product *p* which obtained from experiments, and *n* is the stoichiometric coefficient of component *i* and *j*.

$$\Delta G = \Delta G_r^{o\prime} + RT \ln \frac{\prod_j^p c_j^{n_j}}{\prod_i^r c_i^{n_i}} \tag{2}$$

The sign of ΔG shows the favourability of a reaction; a minus ΔG means that the reaction will proceed towards the products, whereas, a positive ΔG means the opposite direction. When the reaction is at equilibrium, the value of ΔG is equal to zero, which in turn gives the apparent (concentration-based) equilibrium constant, K' of a reaction can be determined (Eq. 3).

$$\Delta G_r^{o\prime} = -RT \ln K' \tag{3}$$

3. Case study

In this paper, we have chosen one interesting case study from the scientific literature in order to demonstrate a suitable thermodynamic analysis for a multi-enzyme processes (Tauber et al., 2013). In this case, the artificial multi-enzyme process is constructed for the transformation of 4-phenyl-2-butanol (**a**) to a chiral amine, 4-phenyl-2-butanamine (**b**). Figure 2 illustrates the reaction scheme of the ADH/ωTA/AlaDH coupled system to produce the chiral amine. The first step is on oxidation step catalysed by an alcohol dehydrogenase (ADH), consuming cofactor (NAD+) leading to the formation of an intermediate product, 4-phenyl-2-butanone (**b**). Secondly, ω-transaminase (ωTA) catalyses the intermediate product and alanine (amine donor) to produce the desired product. In this system, alanine and the cofactor NAD+ are re-generated *in situ* through alanine dehydrogenase (ADH). The system reportedly gave 25 % conversion of the ketone (**b**) and 47 % conversion of the amine (**c**).

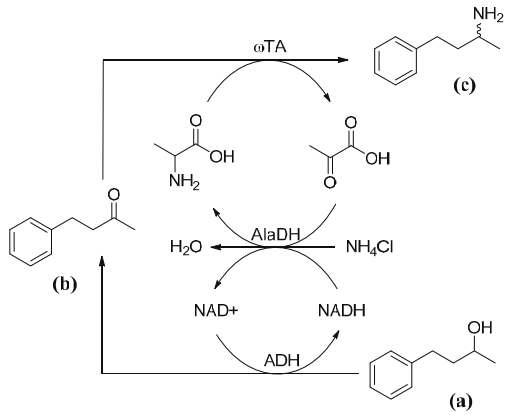

Figure 2: ADH/ωTA/AlaDH coupled system. Reaction conditions: NADH (1 mM), alanine (250 mM), NH_4Cl (200 mM) and 4-phenyl-2-butanol, (**a)** (50 mM). ADH: alcohol dehydrogenase (EC1.1.1.1), ωTA: ω-transaminase (EC2.6.1.18), and AlaDH: alanine dehydrogenase (EC1.4.1.1).

4. Results and discussion

In principle, a favourable reaction proceeds spontaneously towards the minimum energy level state (equilibrium). In the case of ADH/ωTA/AlaDH coupled system, the thermodynamic feasibility was determined and used to make the energy profile as shown in Figure 3. This diagram describes the free energy content between reactants and products (vertical axis) through the progress of reaction steps (horizontal axis) from starting material (**a**) to the final product (**c**).

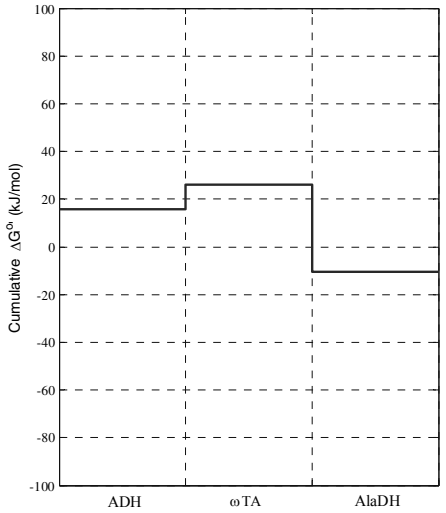

Figure 3: The energy profile represents the cumulative energy $\Delta G_r^{o'}$ at the standard state conditions for producing 4-phenyl-2-butanamine through pathways of ADH, ωTA and AlaDH. ADH: alcohol dehydrogenase, ωTA: ω-transaminase and AlaDH: alanine dehydrogenase.

In the standard state conditions, it was found that ωTA-catalyzed reaction is the thermodynamic bottleneck within the ADH/ωTA/AlaDH coupled system which is shown by the uphill reaction in the cumulative energy of $\Delta G_r^{o\prime}$. However, a positive $\Delta G_r^{o\prime}$ does not necessarily indicate a bottleneck within the system. In the ADH and ωTA reactions, both have the $\Delta G_r^{o\prime}$ constraint of positive values of 15.73 kJ/mol and 10.29 kJ/mol respectively. The values signify that the reactions are unfavourable since both products (**b** and **c**) are energetically unstable which contribute to the positive values of $\Delta G_r^{o\prime}$. The overall $\Delta G_r^{o\prime}$ for the ADH/ωTA/AlaDH coupled system is thermodynamically downhill where AlaDH is identified as a thermodynamic driving force to push the equilibrium system to completion and ending with a negative $\Delta G_r^{o\prime}$ value (-10.33 kJ/mol). At equilibrium, the apparent equilibrium constant, K' of ADH/ωTA/AlaDH system is 60.4, calculated using Eq. 3. The GC-method can be useful to determine the feasibility of the cascades when experimental thermodynamic data is not available. To date, very few data on equilibrium constants are available from experiments, in particular for multi-enzyme cascades.

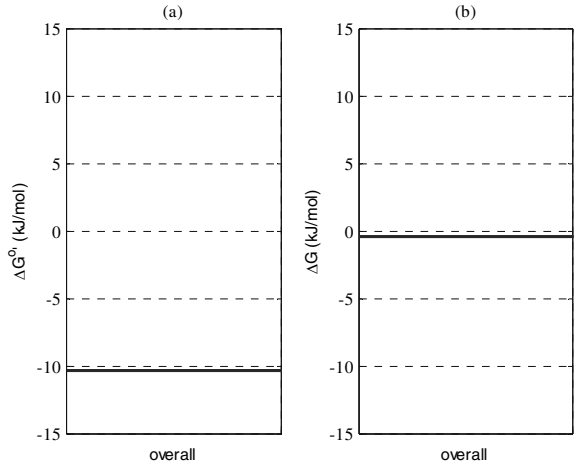

Figure 4: The free energy difference in ADH/ωTA/AlaDH coupled system. (a) $\Delta G_r^{o\prime}$ (Reaction conditions: pH 7, 298 K) and (b) ΔG (Reaction conditions: pH 7.5, 303 K, $C_{10}H_{14}O$ (37.5 mM), $C_{10}H_{15}N$ (5.9 mM), NH_4Cl (194.1 mM), and water (55.6 M)).

A system is rarely operated at standard state conditions and thus it is interesting to find the thermodynamic feasibility of ADH/ωTA/AlaDH system using the actual ΔG which calculated as a function of concentration of products and reactants (Eq. 4). From the calculation, the ΔG of the system has changed from -10.33 kJ/mol to -0.75 kJ/mol. Here, the concentration of pure water is 55.6 M and the regeneration system of NAD+ and alanine is assumed run efficiently using AlaDH. The results show that the system is thermodynamically feasible and the value of ΔG describes how far the free energy has changed from the standard state conditions. In most cases, biocatalytic reactions are controlled at pH >7. However, in this ΔG calculation, the pH value is not taken into account. Recently, Hoffmann and coworkers (2013) has found that the activity coefficient strongly correlates with pH in which the $\Delta G_r^{o\prime}$ changed accordingly. Further study on activity effect is currently carried out as more data is needed to confirm such an effect.

$$\Delta G = \Delta G_r^{o\prime} + RT \ln \frac{[C_{10}H_{15}N][H_2O]}{[NH_4^+][C_{10}H_{14}O]} \quad (4)$$

5. Conclusions

In conclusion, multi-enzyme system can be a useful approach for biocatalytic processes, but it requires fundamental knowledge of the thermodynamics. The thermodynamic bottlenecks can be identified through the energy profile of reaction steps in the overall reactions. It is, however, it is necessary to obtain values for the thermodynamic properties of Gibbs free energy of formation of a compound to draw the diagram. For an unfavourable reaction such as transaminase, it can be improved by coupling with thermodynamically favourable reactions to drive the system to completion. Such multi-enzyme processes if successfully designed can yield high conversions of unfavourable transformation. Likewise, high conversion of the multi-enzyme processes is also attractive in the downstream processes since fewer unit operations are required to remove intermediates/by-products within the reaction step. Nevertheless, more work should be done to evaluate the multi-enzyme systems in term of economics, determine whether designed cascades can reduce the downstream cost.

References

P. Hoffmann, M. Voges, C. Held, and G. Sadowski, 2013, The role of activity coefficients in bioreaction equilibria: thermodynamics of methyl ferulate hydrolysis. Biophysical Chemistry, 173-174, 21–30.

M. D. Jankowski, C. S. Henry, L. J. Broadbelt and V. Hatzimanikatis, 2008, Group contribution method for thermodynamic analysis of complex metabolic networks, Biophysical Journal, 95(3), 1487–1499.

S. Servi, R. Wohlgemuth and W. D. Fessner, 2013, CMST COST Action CM1303: Systems Biocatalysis, Retrieved August 26, 2014, from http://www.cost.eu/domains_actions/cmst/Actions/CM1303.

S. Riva, 2014, Cascade biocatalysis integrating stereoselective and environmentally friendly reactions. Wiley-Vch.

R. C. Simon, N. Richter, E. Busto and W. Kroutil, 2014, Recent developments of cascade reactions involving ω-transaminases, ACS Catalysis, 4(1), 129–143.

K. Tauber, M. Fuchs, J. H. Sattler, J. Pitzer, D. Pressnitz, D. Koszelewski, K. Faber, J. Pfeffer, T. Haas and W. Kroutil, 2013, Artificial multi-enzyme networks for the asymmetric amination of sec-alcohols. Chemistry (Weinheim an Der Bergstrasse, Germany), 19(12), 4030–4035.

M. D. Truppo, J. D. Rozzell, J.C. Moore, and N. J. Turner, 2009. Rapid screening and scale-up of transaminase catalysed reactions. Organic & Biomolecular Chemistry, 7(2), 395–398.

P. Tufvesson, J. S. Jensen, W. Kroutil, and J. M. Woodley, 2012, Experimental determination of thermodynamic equilibrium in biocatalytic transamination, Biotechnology and Bioengineering, 109(8), 2159–2162.

Krist V. Gernaey, Jakob K. Huusom and Rafiqul Gani (Eds.), 12th International Symposium on Process Systems Engineering and 25th European Symposium on Computer Aided Process Engineering.
31 May – 4 June 2015, Copenhagen, Denmark

Parallel Computation Method for Solving Large Scale Equation-oriented Models

Yannan Ma[a], Jinzu Weng[a], Zhijiang Shao[a], Xi Chen[a]*, Lingyu Zhu[b], and Yuhong Zhao[a]

[a] *State Key Laboratory of Industrial Control Technology, Department of Control Science and Engineering, Zhejiang University, Hangzhou, 310027, P.R .China*
[b] *College of Chemical Engineering, Zhejiang University of Technology, Hangzhou, 310014, P.R .China*
**E-mail: xichen@iipc.zju.edu.cn*

Abstract

Equation-oriented approach (EO) is an important method for process simulation and optimization. A large scale EO model consists of a very large number of nonlinear equations, resulting in the solving process a challenging and time-consuming task. In this project, a parallel computation method for solving EO model is proposed and discussed. During the solving process, function evaluation of residual errors at each iteration is an essential step. With the EO feature, this step can be parallelized in a natural way. By dividing the equations into several groups, the function evaluation can be conducted by using multiple threads on a parallel hardware platform simultaneously. In this paper, the theoretical analysis on speedup ratio is first discussed. The implementation of the proposed method on the NVIDIA GPU platform and multi-core processor platform is presented with a number of numerical examples. The results are compared and discussed to show that how the hardware platform can greatly affect the performance of the proposed method.

Keywords: equation-oriented model, function evaluation, parallel computing, GPU, multi-core processor.

1. Introduction

Process simulation and optimization are of great importance for the design and operation of chemical manufacturing process as they can help improve productivity, performance and product quality in a reliable and economical manner. In many cases, EO approach is the most efficient way to deal with process simulation and optimization. It assembles all the variables and equations corresponding to the process model and then solves the whole model simultaneously. Though the EO approach has the credit in computation speed and convergence efficiency, the solving for large-scale models could also be challenging and time-consuming, which requires considerable computational efforts. Parallel computation enables multiple tasks to be performed simultaneously (Almasi & Gottlieb, 1989). Several popular parallel computing platforms become available, including multi-core processor platforms, graphics processing unit (GPU) computing platforms and cloud computing platforms. In chemical manufacturing process, parallel computing has also been widely applied (Vegeais & Stadtherr, 1992; Radeke, Glasser, & Khinast, 2010; Laird, Wong, & Akesson, 2011; Chen, et al., 2013). In the current paper, a parallel computation method based on function evaluation is

proposed to accelerate the solving of EO models. A brief theoretical analysis is conducted. The proposed method is implemented on both NVIDIA graphics-processing-unit-based and Intel multi-core-processor-based parallel platforms. To demonstrate the applicability and efficiency of parallel computing, three large scale EO models are presented. Finally, further analysis and discussion is conducted to interpret the different performance of the proposed methods on the different platforms.

2. Parallel computation method based on function evaluation

A typical procedure of the EO approach in process simulation and optimization consists of several steps, including initialization, function evaluation and/or gradient evaluation, iterate updating, and termination judgment. The flowchart is presented in the left part of Figure 1. During the solving process, the function evaluation of residual errors is conducted at each iteration. It describes the infeasibility at each iterative point from the equation point of view. For a gradient-based algorithm, the gradient should be calculated at each iteration, which is also through function evaluation basically. Due to the simultaneous feature of an EO model, the function evaluation can be computed in a parallel mode.

The natural way to speed up the calculation is to implement the function evaluation step using parallel threads, as illustrated in the right part of Figure. 1. The equations to be calculated in an EO model are divided into several groups and parallelized by N_t threads, through which the function evaluations can be calculated simultaneously. After all the threads complete their task, the function evaluation of residual errors is gathered from each thread and then return to the iteration process.

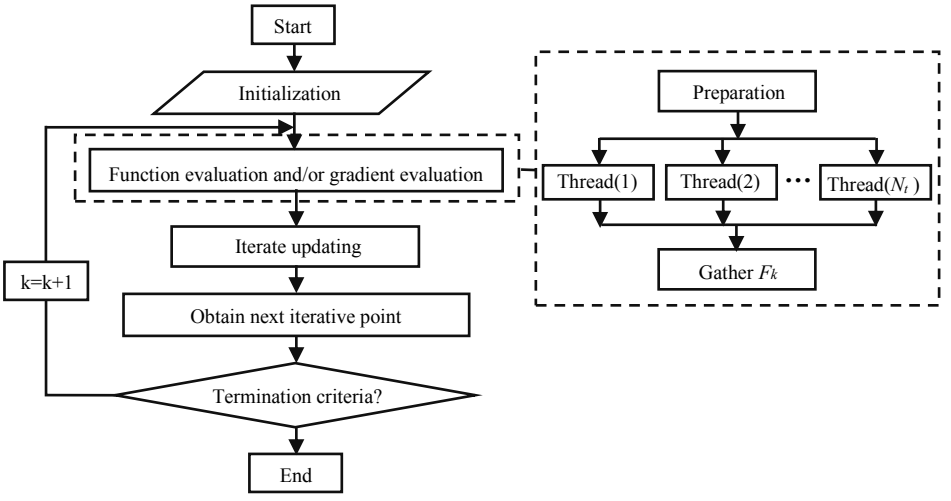

Figure 1. Schematic of the parallel computation method

The time cost of the function evaluation is a very significant component of the total time cost of the solving process. If we accelerate the function evaluation step, we can thus accelerate the whole solving process. The theoretical analysis on the parallel performance of the proposed method can be elaborated as follows.

Denote the computing time required for function evaluation in a conventional way as t_f, and the time required for the rest as t_r. In the parallel mode, we can use multiple

threads for this task. Meanwhile, the acceleration is also limited by the processor number. Denote the parallel thread number as N_t and the real hardware core number as N_{core}. The speedup ratio of the function evaluation step is bounded by $N_p = \min(N_t, N_{core})$. Thus, the theoretical speedup ratio of the whole process can be derived as $SR_i = (t_f + t_r)/(\frac{t_f}{N_p} + t_r + t_c)$, where t_c is the extra communication time caused by parallelization on different processors.

In this paper, the EO models are solved by SNOPT, which uses a sequential quadratic programming (SQP) algorithm. The function evaluation is parallelized during the solving process. It is implemented on both Intel multi-core-processor platform and NVIDIA GPU platform.

3. Numerical examples for parallel computation method

Three examples are used for the demonstration of the proposed method.

3.1. Homopolymerization model

Homopolymerization is a type of polymerization which forms a homopolymer from a single type of monomer. The model used here only involves the kinetic part with propagation and transfer to hydrogen. The total equation number is determined by the maximum chain length. Assuming that the homopolymerization in a CSTR operates at steady state with given residence time, we can derive population balances for the living and dead chains (Soares & McKenna, 2012). By solving the equations, the molecular weight distribution (MWD) of the product can be obtained.

3.2. Cubic equations model

This case studies a cubic numerical example as follows. It consists of *n* equations and variables.

$$\begin{aligned} &f_1 = x_1^3 + x_2^3 + x_3^3 - 2x_1 / x_2 - x_2 / x_3 = 0 \\ &\vdots \\ &f_{n-2} = x_{n-2}^3 + x_{n-1}^3 + x_n^3 - 2x_{n-2} / x_{n-1} - x_{n-1} / x_n = 0 \\ &f_{n-1} = x_{n-1}^3 + x_n^3 + x_1^3 - 2x_{n-1} / x_n - x_n / x_1 = 0 \\ &f_n = x_n^3 + x_1^3 + x_2^3 - 2x_n / x_1 - x_1 / x_2 = 0 \end{aligned} \tag{1}$$

3.3. Crude argon column model

Argon is a product of air separation through cryogenic distillation. This case deals with the steady state simulation of a crude argon column with 191 stages. The column is modelled using the rigorous equilibrium stage concept with thermodynamics based on the Redlich-Kwong-Soave-Boston-Mathias (RKS-BM). According to the reference (Kamath, et al., 2010), the thermodynamics can be handled with an EO approach. But to reduce the variable number and avoid complex terms, intermediate variables are introduced into the thermodynamic model. This results in a partially sequential feature for the function evaluation.

3.4. Accuracy analysis for proposed parallel method

First, tests are conducted on the above-mentioned examples to prove that the solutions are not affected by the parallel computation. Figure 2 presents the MWD results of the homopolymerization simulation using different methods. There are totally three curves,

which are obtained by the analytical, serial and parallel methods. The analytical solution was obtained by Flory methods. The serial was conducted by solving the equations using SNOPT. The parallel was conducted similarly, except that the function evaluation was implemented on a GPU platform. Obviously, these three curves overlap very well, which indicates that the numerical solutions are correct and the parallelization does not affect the results. This is also proved by the other two examples. Due to the length limitation, detailed results are skipped here. Considering that only function evaluation part is parallelized during the solving process, we will focus on the parallel performance of function evaluation in the following sections.

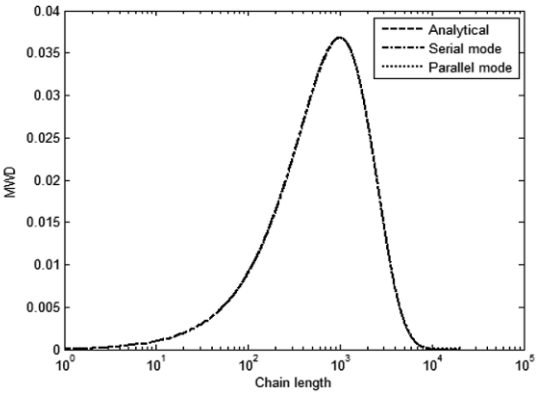

Figure 2. Flowchart for parallel computation method

4. Implementation results on GPU platform

The parallelization was first studied on a GPU platform under NVIDIA Compute Unified Device Architecture (CUDA) programming environment. The GPU mode is NVIDIA Tesla C 1060 with 240 scalar processor cores.

4.1. Implementation of homopolymerization example

The equation number of this model is determined by the maximum chain length. We can vary it to construct models with different dimensions. Each thread executes the function evaluation of one equation. Because of core restriction from the hardware, all threads would be conducted when any core is free. Table 1 compares the time costs for function evaluation in serial mode and in GPU parallel mode. The model size varies from 5000 to 20000, which results in that the number of function evaluation called by SNOPT (the last column in Table 1) also varies. As Table 1 shows, the parallel strategy applied on the homopolymerization example is less efficient than that of the serial strategy. The communication between CPU and GPU costs too much time. After analysing the model, we find that all equations are either linear or quadratic. It does not need much effort to compute. Thus, the time spent on communication exceeds the time saved by parallel computing by 240 cores.

4.2. Implementation of cubic-equation example

In this example, each thread also deals with one-function-evaluation task, which means that the parallel performance is limited by GPU cores. The results of running time for function evaluation are shown in Table 1. The model size ranges from 10000 to 30000. As the model size increases, the acceleration of the proposed methods comes out with a maximum speedup ratio as 1.33 when the model size is 30000. Compared with the previous example, this cubic model has higher computational complexity. The computation time on GPU occupies a larger proportion in the total time for function evaluation, which enables the parallel performance satisfied.

4.3. Implementation of crude argon column example

As mentioned in Section 3.3, the thermodynamic model has sequential feature. Therefore, unlike the former two cases in which the thread number can be set as many as the equation number, this case is implemented with much fewer threads. We arranged all equations of a stage to be calculated by a thread. The results are also listed in Table 1. The existence of the intermediate variables in the thermodynamics results that the equation number is triple of the variable number. This greatly reduces the ratio of the communication time over the computation time, as shown in Table 1. It may be thought the higher compute utilization would contribute to good parallel performance. However, the parallel method did not perform well in this case. Although the proportion of communication time cost is reduced relatively, the hardware resource is not fully exploited in this case as the thread number is bounded by the stage number. Thus, the proposed method did not accelerate the computation as expected.

Table 1. Performance on GPU platform

Model	Model size	CPU	GPU	GPU computation	Communication	Numbers of FE called
Homopolymerization model	5000	1.579	2.855	1.396	1.459	35036
	10000	6.004	8.386	3.817	4.569	70034
	20000	25.937	28.225	11.315	16.910	140036
Cubic-equation model	10000	15.272	15.350	7.638	7.712	120017
	20000	65.417	54.262	27.415	26.847	260017
	30000	184.687	138.762	68.697	70.065	480026
Crude argon column model	17191	21.552	34.070	30.378	3.692	92281

4.4. Summary & Discussion

In this part, three examples were implemented with the parallel method on the GPU platform. The solving process of an EO model requires communication between CPU and GPU at each iteration. This results that the communication time cannot be ignored in this work. In addition, to obtain good parallel performance, the equation size in each thread should be large, which can lead to higher compute utilization. All these factors limit the performance of the proposed method on the GPU platform.

5. Implementation on multi-core processor platform

A multi-core processor can process instructions of each core at a time. Compared with GPU, few cores are available on a CPU processor chip. But a multi-core processor has an obvious advantage on computing and communication. Since each core shares the global memory in the multi-core processor, the extra time cost for the communication under the GPU situation are avoided. Here, the equations of function evaluation are distributed evenly into several threads, which have the same number as the available core number. The *pthread* is selected as the multi-threaded programming model, and the *pthread mutex* is employed for the communication and synchronization among all threads. The examples in Section 3 are also tested on a 4-core CPU platform. The parallel performance is shown in Table 2.

The calculations in all the three examples are accelerated significantly by the proposed method on the multi-core processor platform. The speedup ratio (SR) reaches up to 3.73, which is quite close to the ideal value, 4. For each model, the speedup ratio increases with model size, which means that mass amount of computations is preferred in CPU thread. Better than GPU platform, calculation on multi-core CPU does not have

extra communication time like that between GPU and CPU. Besides, all cores in CPU have high performance in computing consistently. For the reason that in most solving process the time cost of function evaluation part takes 30-60 percentage of total time, the function-evaluation-based parallel method is quite favoured on the multi-core platform.

Table 2. Performance on multi-core processor platform

Model	Model size	CPU single-core(s)	CPU multi-core(s)	SR	Numbers of FE called
Homopolymerization model	5000	1.579	0.827	1.91	35036
	10000	6.004	2.336	2.57	70034
	20000	25.937	7.474	3.47	140036
Cubic-equation model	10000	15.272	5.051	3.02	120017
	20000	65.417	18.342	3.57	260017
	30000	184.687	49.470	3.73	480026
Crude argon column model	17191	21.552	6.709	3.21	92281

6. Conclusions

To accelerate EO model solving, this paper proposes a parallel computation method based on function evaluation. A theoretical analysis is conducted on the speedup ratio of the proposed method. Implementation on both NVIDIA GPU-based and Intel multi-core-processor-based parallel platforms are carried out. Three numerical examples are tested. Acceleration can be achieved by both platforms. But the good performance is more favoured to the multi-core processor platform than the GPU platform due to the large demand of the communication in this work.

Acknowledgements

We gratefully acknowledge the financial support of 973 Program of China (No. 2012CB720503) and National Natural Science Foundation of China (No. 61374205 & No. 21206149).

References

G. S. Almasi, & A. Gottlieb, 1989. Highly parallel computing. Redwood City, CA: Benjamin-Cummings Publishers.

Z. Chen, X. Chen, Z. Shao, Z. Yao, & L. T. Biegler, 2013. Parallel calculation methods for molecular weight distribution of batch free radical polymerization. *Computers & Chemical Engineering,* 48: 175-186.

R. S. Kamath, L. T. Biegler, & I. E. Grossmann, 2010. An equation-oriented approach for handling thermodynamics based on cubic equation of state in process optimization. *Computers & Chemical Engineering*, *34*(12), 2085-2096.

C. D. Laird, A. V. Wong, & J. Akesson, 2011. Parallel solution of large-scale dynamic optimization problems. *Computer Aided Chemical Engineering*, 29: 813–817.

C. A. Radeke, B. J. Glasser, & J. G. Khinast, 2010. Large-scale powder mixer simulations using massively parallel GPUarchitectures. *Chemical Engineering Science*, 65(24), 6435-6442.

J. B. P. Soares, & T. F. L. McKenna, 2012. Polyolefin Reaction Engineering. Weinheim:Wiley-vch Verlag GmbH & Co. KGaA.

J. A. Vegeais, & M. A. Stadtherr, 1992. Parallel processing strategies for chemical process flowsheeting. *AIChE Journal*, 38(9), 1399-1407.

Krist V. Gernaey, Jakob K. Huusom and Rafiqul Gani (Eds.), 12th International Symposium on Process Systems Engineering and 25th European Symposium on Computer Aided Process Engineering.
31 May – 4 June 2015, Copenhagen, Denmark

Dynamic investment appraisal: Economic analysis of mobile production concepts in the process industry

G.Bas,[a*] T.E. Van der Lei[a]

[a] *Faculty of Technology, Policy and Management , Delft University of Technology , Jaffalaan 5, PO Box 5015 , 2600 GA Delft, The Netherlands*
**email:g.bas@tudelft.nl*

Abstract

Due to technological developments new small-scale mobile production concepts have become available in the processing industry. These novel production concepts have mobility as an attribute and the profitability of the production concepts depends, amongst others, on how well this attribute can be exploited as an important part of the cash flows of these concepts may depend on optimal location choice in volatile markets. Current investment appraisal techniques do not take the effect of these dynamics into account and therefore typically disregard the value of mobility, which may lead to the underestimation of the novel production concepts' value and consequently prohibits their deployment. In this paper we combine an agent-based model simulation with a net present value calculation to account for these dynamics in the appraisal of these new production concepts. The agent-based model uses a q-learning algorithm to simulate an existing dynamic world scale market in which we introduce the new production concepts and let them compete with the existing industry. During the simulation, we measure the cash flows of the production concepts, which are used in the net present value calculation to appraise the concepts. We illustrate the approach with a case study in which we appraise a stationary and mobile production concept. We show that quality of investment decisions may be improved with a simulation that is able to capture the dynamics of mobile production concepts. Future work will focus on removing some of the current limitations and on introducing lead times in the simulation to enable the valuation of the new production concepts' shorter time to market.

Keywords: agent-based model, investment appraisal, market forecast, market simulation, q-learning

1. Introduction

In the last years new small-scale production concepts, based on process intensification and modularization principles, have been developed for the processing industry (e.g. the F3Factory (F3Factory, 2014)). One of the main attributes of these novel production concepts is that their small size enables relative easy relocation if new business opportunities arise (Lier, et al., 2013). However, despite flexibility being a major competitive advantage in an increasingly volatile world (Seifert, et al., 2014), to date the novel production concepts are deployed very sparsely. And if they are deployed, they are typically used to replace equipment within a traditional environment (e.g. a continuous reactor replacing a batch reactor in a world-scale plant), thereby eliminating the advantage of mobility.

One of the issues limiting the deployment of the novel production concepts is that the commonly used investment appraisal techniques have difficulties appraising the value

of mobility and thus may underestimate the value of mobile production concepts. The value of mobility is difficult to appraise because the orders and prices (and hence the cash in- and outflows) in the market are affected by a decision to relocate the production concept. Market entry effects change the balance of supply and demand at the new location. This makes exogenous forecasting of price and demand development inaccurate, because it does not take into account the changed market situation.
To support the deployment of mobile production concepts at an operational scale, this paper presents an investment appraisal approach that integrates market forecasting with the appraisal in a dynamic way. We use an agent-based market model to simulate an existing market, deploy a mobile production concept in that market, and let its cash flows emerge from its operations and interactions with the market. By comparing its cash flows to those of a stationary production concept we can determine the value of the mobility.
In section 2 we review the main investment appraisal techniques, assess their suitability to value mobility, and discuss the requirements to enable the appraisal of a mobile production concept. In section 3 we present our dynamic investment appraisal approach. We illustrate this approach in section 4, through a case study. In section 5, we end this paper with conclusions and recommendations for future work.

2. Investment appraisal

When confronted with a number of alternatives to invest in, one has to decide which investment is the most worthwhile. Investment appraisal is the process of assessing how the future benefits of an investment relate to the initial expenses, in order to compare different investment alternatives (Götze, et al., 2008). Over the years a wide range of investment appraisal techniques have been developed, that each regard an investment from a different perspective. The main investment appraisal techniques can be grouped in three categories: economic analysis methods (e.g. net present value), strategic approaches (e.g. how the investment contributes to the competitive advantage) and analytic models (e.g. scoring models) (Karsak and Tolga, 2001). An approach that is becoming increasingly popular is the real options approach, which acknowledges uncertainty in market forecasts and the possibility to make decisions after the initial investment decision (Amram and Kulatilaka, 1998).
The investment appraisal techniques differ in a.o. the target measure(s) they use as decision criterion (Götze, et al., 2008); economic analysis methods and real options only consider financial metrics, while strategic approaches and analytic models are capable of also considering other metrics, such as emissions, flexibility, etc. We set out to improve the market forecasts used for economic analysis, and therefore focus on the financial metrics. The financial metrics of the investment appraisal techniques rely on market forecasts, which specify the expected market development, i.e. order volumes and prices over a certain time horizon (Götze, et al., 2008). In the appraisal cash flows are combined in a certain target measure. The linearity of this approach makes it impossible to include effect of a relocation decision in the market forecast and therefore makes the approach unsuited to appraise the value of mobile production concepts.
To consider how the market is influenced by the relocation decisions, the market forecasting has to be integrated with the investment appraisal (as illustrated by figure 1). Instead of forecasting the market outcomes for the entire time horizon, the market outcomes for a single time period need to be determined, on basis of which a relocation

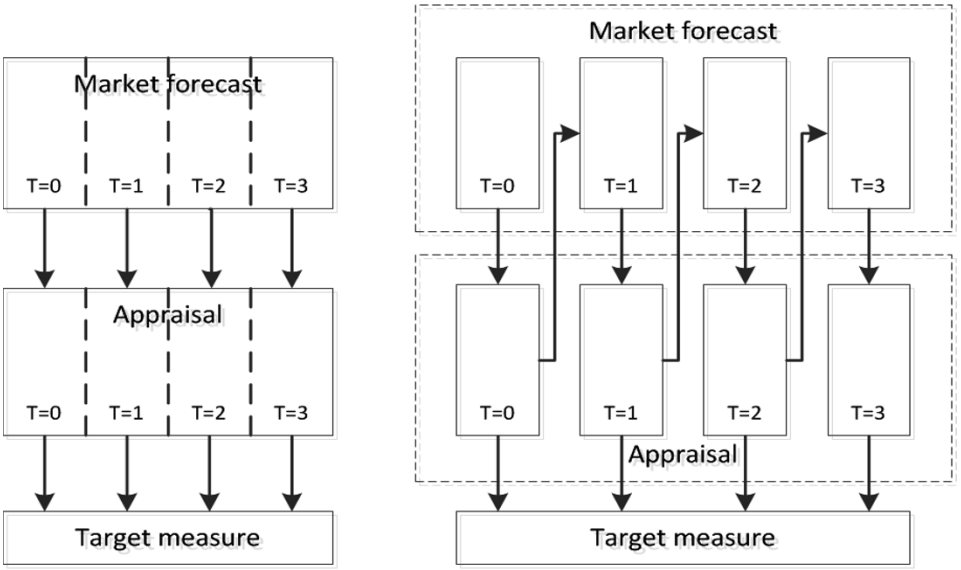

Figure 1: External market forecast (left) and integrated market forecast (right)

decision is made. This relocation changes the market situation (supply, demand, and market structure), which is used for determining the market outcomes in the followingtime period. This way the market entry effects are accounted for.

3. Integrating market forecasting with investment appraisal

We model the market from an agent-based computational economics perspective. Modeling a market as autonomous negotiating agents enables the representation of strategic behavior, bounded rationality, learning, and adaptation, which is not possible with the often applied general equilibrium market models (Farmer & Foley, 2009). The production concept is deployed in this market. The resulting cash flows are used to appraise the production concept, for which we use a net present value calculation. These cash flows influence the decision where to relocate the production concept to. If the production concept is relocated it changes the supply in the market in enters, thereby changing the price and orders of goods in that market.

3.1. Market simulation

The simulation consists of two markets: one market for feedstock and one for produced product. Following Moyaux, et al. (2010), the two markets are connected by the production concept and its competitors (i.e. the processors) buying in one market and selling in the other. Besides the processors, we also consider suppliers of feedstock and customers of product that negotiate with the processors in respectively the feedstock and product market. The conceptualization of both markets builds on the work of Dogan and Güner (2013). In each market buyers purchase from the sellers that can supply at the lowest costs and each seller applies Q-learning to learn – on basis of the received orders – a pricing strategy that maximizes its profits. The pricing strategy specifies what price is the most profitable at a given market price.

3.2. Relocation decisions

To assess the value of mobility, the mobile production concept decides every couple of time periods autonomously where it wants to be located. We assume that mobile

production concepts (represented by agents) can be located at the site of potential customers. First, the mobile agent selects the site with the highest margin between product and feedstock price, which is assumed to be public knowledge. Second, for that site the mobile agent assesses its profitability, by negotiating with suppliers and customers as if it would be situated at the new site. It compares that profitability with the profitability at its current site. A decision to relocate is made when a profitability threshold is met. This is expressed as a percentage of profitability and represents the risk aversion of the mobile production concept.

4. Case study

To illustrate our approach we use a global polymer case. Two alternatives are being appraised, a mobile plant and a stationary plant. Both plants use monomers, which are supplied by monomer suppliers, as feedstock to produce polymers, which are consumed by compounders.

In total the market consists of 16 plants, each of which is represented as an agent in the simulation. All plants are situated in either one of three regions: North-America, Europe, or Asia-Pacific. Concerning monomers we assume that they are available near all processors, i.e. the distance from a supplier to a processor (in the same region) is 100 kilometers. Table 1 shows how the plants and capacity are distributed over the regions. Due to confidentiality it is not possible to present the initial market situation in greater detail. Both the mobile and stationary plants are initially located in Europe and have a capacity that is 10% of the global market. Besides the mobility, the two alternatives are identical.

A period of 10 years is simulation in weekly intervals. Every quarter the agents renegotiate global prices and every half year the mobile agents will assess whether to relocate or not. During the simulation we consider a scenario in which the demand declines after 5 years and demand in the Asia-Pacific region increases.

To compare the mobile and stationary plants we determine the net present value of the mobile and stationary production concept. We use a discount rate of 14% to discount the cash flows and calculate the net present value. The cash flows considered are the sales revenues, the costs of feedstock, the operating expenses, and the shipping expenses. As the purpose of this case is to illustrate how a market simulation can be used to appraise the value of mobility, we focus on the cash flows that influence the value created by mobility. Consequently, the initial expenses are not considered as they do not affect the value created by mobility.

Besides comparing the mobile and the stationary production concept we also assess the effect of different risk aversion percentages, knowing 0, 10, 20, 30, 40, and 50%. The risk aversion only needs to be considered for the mobile production concept, and consequently we run 7 different experiments. To reduce the impact of stochasticity on the experiment results, each experiment is run 100 times.

4.1. Experiment results

Table 2 presents the net present values of the stationary and mobile production concepts. Depending on the risk aversion, the net present value of a mobile production concept is 7.06% to 9.72% higher than that of the stationary production concept, with an average increase of 8.46%. The ANOVA and Tukey's HSD test indicate that for each risk aversion the difference between the mobile and stationary production concept is statistically significant, which implies that the mobility a production concept increases its value.

Table 1: Distribution of global capacity over regions

	North-America		Europe		Asia-Pacific	
	Plants	Capacity	Plants	Capacity	Plants	Capacity
Suppliers	33%	42%	33%	15%	33%	42%
Processors	20%	43%	40%	29%	40%	27%
Customers	25%	43%	37%	29%	37%	27%

Table 2: Experimental results

Production concept	Risk aversion	Net present value	Difference from stationary	Relocations
Stationary	N/A	211,501,770	N/A	N/A
Mobile	0%	232,058,766	9.72%	8.26
	10%	228,610,754	8.09%	7.27
	20%	231,163,872	9.30%	6.51
	30%	226,438,525	7.06%	6.13
	40%	228,326,574	7.95%	5.02
	50%	229,853,863	8.67%	4.58

The increase of the net present value due to mobility is in line with expectations, since the mobile production concept can relocate free of charge from Europe to Asia-Pacific to follow the demand. Being able to follow the demand saves the mobile production concept, in comparison to the stationary production concept, the expenses of shipping its products from Europe to Asia-Pacific. As a consequence it has higher net cash flows and a higher net present value.

The tests also indicate that the risk aversion has no significant effect on the net present value. We expected a higher risk aversion to result in a higher net present value, as it reduces the number of erroneous relocation decisions. The prices in individual runs of the simulation are volatile and therefore the projections of a location's profitability have a high margin of error. A high risk aversion makes that a mobile production concept only relocates if the rewards are high enough for the risk of an erroneous relocation. The experimental results show that the number of relocations decreases as the risk aversion increases. However, this does not result into a higher net present value. An explanation is that a higher risk aversion not only reduces the number of erroneous relocation decisions, but also makes that profitable opportunities are missed. As these two factors cancel each other out, the net present value effectively remains the same.

5. Conclusions and recommendations

In this paper we set out to support the deployment of mobile production concepts at an operational scale, by combining an agent-based market simulation with a net present value calculation. Using this approach the market entry effect of a relocation decision can be taken into account, which is essential for appraising the value of a mobile production concept. The case study has indicated that this approach is capable of appraising the value of a mobile production concept, as it indicated that there is a significant difference in the value of a stationary and mobile production concept.

In its current form the approach requires some improvements to be made, in order to enable the actual application of the approach. First, the stochastic volatility of the price needs to be reduced as it appears to impact the relocation decisions. This may be done through simplifying the pricing strategy to just the most profitable price. This is

expected to reduce the price volatility and enables an increase in the price resolution of the pricing strategy. Second, the relocation expenses and relocation duration need to be considered in the relocation decision, to improve that decision. Third, the relocation expenses need to be included in the net present value calculation. And fourth, the initial expenses need to be included in the calculation of the net present value. The current approach assumes that for both alternatives the initial expenses are similar, but in reality mobile production concepts are usually more expensive.

Besides those essential improvements, the dynamic investment appraisal approach can be expanded in a number of ways. An expansion could be the expansion of the agents' operational behavior and the supplier selection decision. Currently, processing and shipment durations are not represented in the simulation. Nor is the lead time an issue in the supplier selection decision. As a lower time to market is one of the advantages of the novel mobile production concepts, including the durations and expanding the supplier selection decision might have a significant effect on those concepts' value. A second improvement would be to relax the assumption that, besides their mobility, the stationary and mobile production concepts are identical. In reality mobile production concepts typically have a smaller throughput and a different cost structure. To support the materialization of mobile production concepts, it is necessary that all characteristics – including the disadvantages – of those concepts are appraised, in order to present the full picture of the concepts' value. This requires that we enable more differentiation between the stationary and mobile production concepts.

References

Amram, M., & Kulatilaka, N. (1998). Real Options: Managing Strategic Investment in an Uncertain World. OUP Catalogue.

Dogan, I., & Güner, A. R. (2013). A reinforcement learning approach to competitive ordering and pricing problem. Expert Systems.

Farmer, J. D., & Foley, D. (2009). The economy needs agent-based modelling. Nature, 460(7256), 685-686.

F3Factory. (2014). Welcome to the F3Factory. Retrieved 2014-08-13, from http://f3factory.com/scripts/pages/en/home.php

Götze, U., Northcott, D., & Schuster, P. (2008). Investment appraisal. Methods and Models, Berlin, Heidelberg 2008.

Karsak, E., & Tolga, E. (2001). Fuzzy multi-criteria decision-making procedure for evaluating advanced manufacturing system investments. International journal of production economics, 69(1), 49-64.

Lier, S., Wörsdörfer, D., & Gesing, J. (2013). Business Models and Product Service Systems for Transformable, Modular Plants in the Chemical Process Industry. In Product-Service Integration for Sustainable Solutions (pp. 227-238). Springer Berlin Heidelberg.

Moyaux, T., McBurney, P., & Wooldridge, M. (2010). A supply chain as a network of auctions. Decision Support Systems, 50(1), 176-190.

Seifert, T., Lesniak, A. K., Sievers, S., Schembecker, G., & Bramsiepe, C. (2014). Capacity Flexibility of Chemical Plants. Chemical Engineering & Technology, 37(2), 332-342.

Krist V. Gernaey, Jakob K. Huusom and Rafiqul Gani (Eds.), 12th International Symposium on Process Systems Engineering and 25th European Symposium on Computer Aided Process Engineering.
31 May – 4 June 2015, Copenhagen, Denmark

Prediction of Heat Capacity of Ionic Liquids Based on COSMO-RS $S_{\sigma\text{-profile}}$

Yongsheng Zhao, Ying Huang, Xiangping Zhang*, Suojiang Zhang

Beijing Key Laboratory of Ionic Liquids Clean Process, State Key Laboratory of Multiphase Complex Systems, Institute of Process Engineering, Chinese Academy of Sciences, 100190, Beijing, China.
xpzhang@ipe.ac.cn

Abstract

Multiple linear regression (MLR) and artificial neural network (ANN) algorithms have been used to establish the quantitative structure-property relationship (QSPR) models for predicting the heat capacity of ionic liquids based on the $S_{\sigma\text{-profile}}$ descriptors calculated by COSMO-RS. To validate the two novel models, heat capacity data for 2416 experimental data points of 46 ILs was applied. The average absolute relative deviation (AARD) of test set of the MLR and ANN is 2.72 % and 0.64 %, respectively. Although the MLR and ANN can both be applied to predict the heat capacity, ANN algorithm has better performance.

Keywords: Quantitative structure-property relationship (QSPR), Ionic liquids (ILs), Heat capacity.

1. Introduction

Ionic liquids (ILs) are considered as an important family of "green" solvent which have attracted much attention for their remarkable properties, such as negligible vapor pressure, thermal and electrochemical stability, non-inflammability and tunable property (Rogers and Seddon, 2003). All these characteristics make ILs promising options for the use in the chemical processes including catalytic synthesis, extraction separation, electrochemistry, etc (Zhang et al, 2012). However, there are too many possible combinations of ions to create easily useful ILs, thus measuring the properties of various ILs under a wide range of conditions through experimental techniques is impractical and costly due to these large amount of ILs. Therefore, it was essential to develop new model to predict the properties of ILs.

The heat capacity is one of the basic thermodynamic and thermophysical properties of ILs (Gardas and Coutinho, 2008), which is generally used in the process of chemical thermodynamics, and is also the indispensable parameter in the process of design and research of petroleum and chemical industry. Due to the new or required certain compound heat capacity cannot be detected from the manual of chemical thermodynamics. In addition, the different experimental conditions and equipment are also resulted in the uncertainty of measurement (Shi et al, 2013). Thereby, it is necessary to predict the heat capacity of ILs through various accurate predictive tools.

Quantitative structure-property relationship method (QSPR) provides a solution to this problem. QSPR is an effective approach to connect physical or chemical properties to a set of molecular descriptors related to the molecular structure. After a QSPR model is developed, it is not only capable of estimating the property of one compound or

screening the compound with the desired property, but is also capable of uncovering the underlying relationship between macro-property and micro-structure (Zhao et al, 2012). $S_{\sigma\text{-profile}}$ is an a priori quantum-chemical parameter that quantitatively represents the molecule's polar surface screen charge on the polarity scale, and can be obtained from the histogram function σ-profile given by COSMO-RS computation. It has been used effectively as a parameter of QSPR models to predict the density (Palomar et al, 2007) and toxicity (Torrecilla et al, 2010) of ILs. However, to the best of our knowledge, it has not been utilized to predict the heat capacity of ILs.

In order to progress in predicting heat capacity of ILs, the first aim of this work is to collect a large amount of heat capacity data. Secondly, the multiple linear regression (MLR) and artificial neural network (ANN) algorithms are utilized to construct the linear and nonlinear QSPR models for predicting the heat capacity of ILs from the $S_{\sigma\text{-profile}}$ descriptors. In this study, the characteristic parameters that have great impact on the heat capacity of ILs were screened, and the performances of the obtained models were investigated and compared.

2. Data and methods

2.1. Heat capacity data points and $S_{\sigma\text{-profile}}$ of ILs

In the present study, all experimental data points were taken from IL Thermo Database (IL Thermo, 2010). A total of 2416 experimental heat capacity data values of 46 ILs were investigated. The collected heat capacity data points (254.0-1805.7 J mol^{-1} K^{-1}) cover a wide range of temperature (223.1-663 K). To develop a reliable model, all the selected experimental data points are divided into a training set of 1933 data points to develop the models and a test set of the remained 483 data points to verify its prediction performance. Each category (nearly 80 % of the data as training set, 20 % as test set) of the total data points is separated at random.

$S_{\sigma\text{-profile}}$ represents molecule surface area of surface screening charge density, which is a priori two-dimensional quantum-chemical parameter to characterize electronic stucture and molecular size of ILs. The deatailed introduction of the $S_{\sigma\text{-profile}}$ can be found elsewhere (Torrecilla et al, 2010). All the $S_{\sigma\text{-profile}}$ of ILs in this study are taken from the COSMO IL database, which were calculated in terms of the BP-TZVP quantum chemical level (Eckert and Klamt, 2013).

2.2. Artificial neural network (ANN) algorithm

ANN is a flexible method that can model the nonlinear behavior of properties through learning processes emulated the functioning of a human brain (Huang et al, 2014). More detailed introduction of the ANN theoretical basis can be referred in elsewhere (Gasteiger and Zupan, 1993). The ANN employed in this study is a multilayer perceptron (MLP) neural network, which usually consists of three layers (topology of ANN), including input, hidden, and output layers, respectively.

2.3. Evaluation of the model performance

Model performance can be measured by different metrics. R^2, which gives the fraction of explained variance for an analyzed set, is used to measure the model's fit performance. Average absolute relative deviation (AARD) is used to evaluate the model's predictive effectiveness, as shown by the following equation:

$$\text{AARD (\%)} = 100 \times \sum_{i=1}^{N_p} \left| \frac{y_i^{cal} - y_i^{exp}}{y_i^{exp}} \right| / N_p \qquad (1)$$

where y_i^{cal} is the desired output (experimental property), y_i^{exp} is the actual output of the models, and N_P is the number of compounds in the analyzed set.

3. Results and discussion

3.1. Results of MLR model

Based on the collected ILs heat capacity data points, the MLR Eq.(2) is established by using stepwise regression algorithm:

$$C_P = 1.454M - 3142.507S_{A\text{-}0.011} + 0.394T + 4.477S_{C\text{-}0.003} + 6.490S_{A0.016} - 7.862S_{A0.018} - 192.002 \quad (2)$$

(n=1933, R^2=0.985, AARD=2.58 %)

where C_p stands for the heat capacity of ILs, S represents molecular suface area with a specific surface screening charge density, subscript A is anion, C is cation, and the numerical value after A or C represents surface screening charge density of ILs. T and M are the temperature and molecular weight respectively. As shown in Table 1, all of the linear correlation coefficient of any two descriptors is less than 0.8, which means that there is no strong linear relation between the descriptors. It is observed that all the descriptors contained in the MLR model have physical meaning, and these descriptors can account for structural features affecting the heat capacity of the ILs studied.

Table 1. Correlation matrix of six descriptors

	M	$S_{A\text{-}0.011}$	T	$S_{C\text{-}0.003}$	$S_{A0.016}$	$S_{A0.018}$
M	1					
$S_{A\text{-}0.011}$	0.495	1				
T	0.111	0.305	1			
$S_{C\text{-}0.003}$	0.786	0.043	0.022	1		
$S_{A0.016}$	0.073	0.138	0.199	0.076	1	
$S_{A0.018}$	0.071	0.093	0.104	0.398	0.363	1

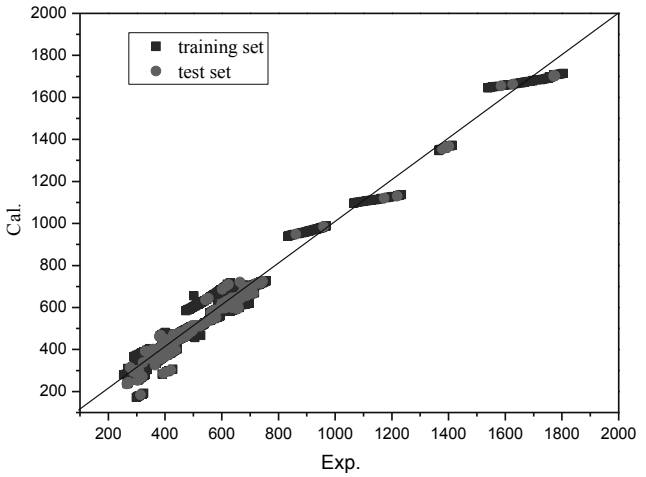

Figure 1. Calculated versus experimental heat capacity values using the MLR algorithm

In Eq.(2), positive sign in front of a parameter suggests positive correlation between the parameter and ILs heat capacity, and negative sign stands for negative correlation. The structure descriptors in Eq.(2) have been arranged in the descending order of t-test values so that the most improtant one comes firsy.
Eq.(2) with R^2=0.985, which is established by 1933 data points could be useful for predicting the heat capacity of ILs. As can be seen from Figure 1, most of the data points of heat capacity are near by diagonal line, and it can be observed from Figure 2 that relative deviation of most substances are within 20 %, and the AARD of the whole data set is 2.72 % (Table 2), so the MLR model can be used to predict the heat capacity of ILs.

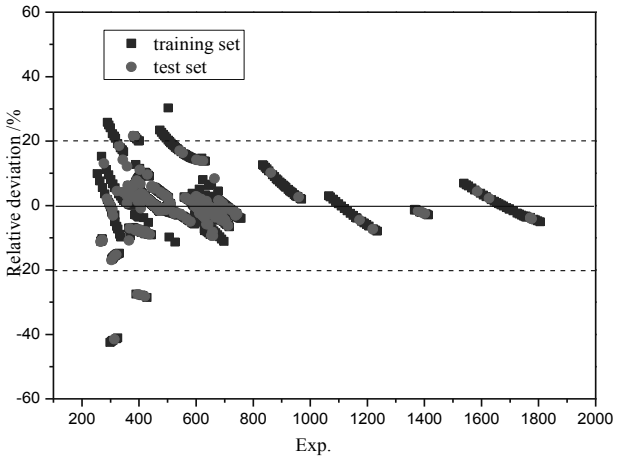

Figure 2. Relative deviation of the MLR algorithm

3.2. Results of ANN model and comparison

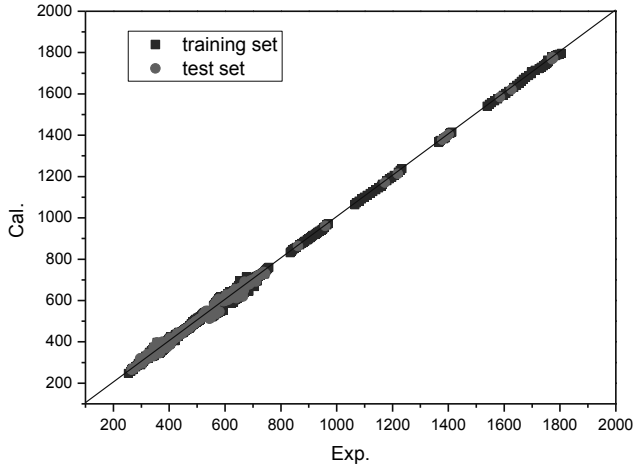

Figure 3. Calculated versus experimental heat capacity values using the ANN algorithm

The same descriptors applied by the MLR algorithm were utilized as the input parameters to develop an accurate nonlinear model by the ANN. To get the optimal model, 1933 data points are used as the training set to construct the model, 483 data

points are carried out as the test set to monitor the quality of the generalization performance of the ANN model. When the number of neurons is 10, the overall MSE is the least, and the R^2 is the largest, so we can determine that the optimized network structure is 6-10-1.The plot of predicted in comparison with experimental heat capcacity values for each data set are recorded in Figure 3. The statistical parameter R^2 for the training, test, and whole sets are 0.999, 0.998, and 0.999 respectively. Relative deviations of the predicted heat capacity values versus experimental data are depicted in Figure 4. It is seen that the relative deviation of the most of data points is within 5 %, and the overall AARD of all the data points is only 0.64, which explains that the model has good results.

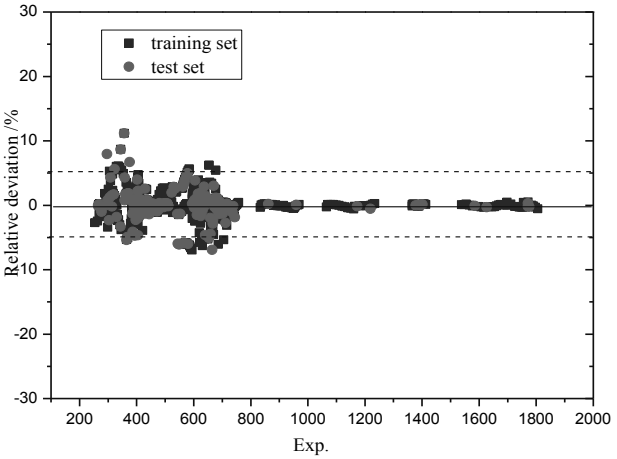

Figure 4. Relative deviation of the ANN algorithm

A summary of the performance of the MLR and ANN models for the all the data set is given in Table 2. In general, judging by R^2 and AARD, although the MLR and ANN can both be used to predict the heat capacity, ANN algorithm has better performance, for example, the R^2 of the training set, test set and the whole set of ANN model is bigger than the R^2 of the MLR model, and the AARD of the ANN model is less than the MLR model. Therefore, the ANN algorithm can be better used to predict the heat capacity of ILs.

Table 2. Comparison of the statistical parameters by MLR and ANN algorithms

Algorithms	Data set	No.	R^2	AARD %
MLR	Training	1933	0.985	2.58
	Test	483	0.984	2.88
	Total	2416	0.985	2.72
ANN	Training	1933	0.999	0.61
	Test	483	0.998	0.76
	Total	2416	0.999	0.64

4. Conclusions

In this work, two novel QSPR models for heat capacity estimation using 2416 experimental data points of 46 ILs were developed based on the $S_{\sigma\text{-profile}}$ descriptor calculated by COSMO-RS method. The AARD and R^2 of the whole data set by MLR and ANN algorithms are 2.72 %, 0.64 % and 0.985, 0.999, respectively. The results

show that both the linear (MLR) and nonlinear (ANN) models can provide acceptable results. Comparatively, the models developed by the ANN algorithm gives a higer R^2 and lower AARD, thereby the ANN model has better performance than MLR model. Furthermore, since the heat capacity is the function of $S_{\sigma\text{-profile}}$ of ILs, the presented derived models can provide some insight into what structural features are connected with the heat capacity of ILs.

Acknowledgement

We would like to acknowledge the support from the National Natural Science Foundation of China (No.21106146), the National Basic Research Program of China (973 Program) (No.2013CB733506) and the Beijing Natural Science Foundation (2141003).

References

F. Eckert, A. Klamt, 2013, COSMOtherm Version C3. 0, Release 13.01. COSMOlogic GmbH & Co. KG, Leverkusen, Germany, Available at ww w. cosmologic. de

J. Palomar, V.R. Ferro, J.S. Torrecilla, F. Rodríguez, 2007, Density and molar volume predictionsusing COSMO-RS for ionic liquids, An approach to solvent design, Industrial & Engineering Chemisty Research, 46, 6041-6048

J. Shi, L. Chen, W. Chen, 2013, Prediction of the heat capacity for compounds based on theconjugate gradient and support vector machine methods, Journal of Chemometrics, 27, 251-259

J.S. Torrecilla, J. Palomar, J. Lemus, F. Rodríguez, 2010, A quantum-chemical-based guide to analyze/quantify the cytotoxicity of ionic liquids, Green Chemistry, 12, 123-134

J. Zupan and J. Gasteiger, 1993, Neural networks for chemists: an introduction, John Wiley & Sons, Inc.

NIST Ionic Liquids Database (IL Thermo), 2010, In NIST Standard Reference Database, http://ilthermo.boulder.nist.gov/ILThermo/mainmenu.uix:

R.D. Rogers, K.R. Seddon, 2003, Ionic liquids-solvents of the future? Science, 302, 792-793

R. L. Gardas, J. A. P. Coutinho, 2008, A group contribution method for heat capacity estimation of ionic liquids, Industrial & Engineering Chemisty Research, 47, 5751-5757

X.P. Zhang, X. Zhang, H.F. Dong, Z.J. Zhao, S.J. Zhang, Y. Huang, 2012, Carbon capture with ionic liquids: overview and progress, Energy & Environmental Science, 5, 6668-6681

Y. Huang, Y.S. Zhao, S.J. Zeng, X.P. Zhang, S.J. Zhang, 2014, Density Prediction of Mixtures of Ionic Liquids and Molecular Solvents Using Two New Generalized Models, Industrial & Engineering Chemisty Research, 53, 15270-15277

Y.S. Zhao, X.P. Zhang, J.H. Zhao, H.Z. Zhang, K.X. Jing, F. Dong, 2012, Research of QSPR/QSAR for Ionic Liquids, Progress in Chemistry, 24, 1236-1244

Krist V. Gernaey, Jakob K. Huusom and Rafiqul Gani (Eds.), 12th International Symposium on Process Systems Engineering and 25th European Symposium on Computer Aided Process Engineering.
31 May – 4 June 2015, Copenhagen, Denmark

OPOSSIM: A Population Balance-SIMULINK Module for Modelling Coupled Hydrodynamics and Mass Transfer in Liquid Extraction Equipment

Menwer Attarakih[a,b*], Samer Al-Zyod[a],Mark Hlawitschke[b], Hans-Jörg Bart[b]

[a]*Department of Chemical Engineering, University of Jordan, Amman 11942, Jordan*
[b]*Chair of Separation Science and Technology, TU Kaiserslautern, Kaiserslautern 6765, Germany*
m.attarakih@ju.edu.jo

Abstract

Dynamic behaviour, control and design strategies for liquid extraction equipment are faced by the complex hydrodynamic behavior of the dispersed phase with many droplet interactions (e.g. breakage and coalescence). To take this into account, the population balance modelling framework is used by implementing the bivariate OPOSPM (One Primary and One Secondary Particle Method) with a one-dimensional finite volume method in the physical space. To narrow the gap between the steady state and dynamic design during process synthesis, OPOSPM is implemented in a MATLAB/Simulink flowsheeting environment. As an outcome of this, we present a new OPOSPM-MATLAB/Simulink module which is called OPOSSIM for modeling and simulation the coupled two-phase flow and mass transfer in a Kuhni liquid extraction column.

Keywords: Population balances, OPOSPM, OPOSSIM, Liquid-extraction.

1. Introduction

Liquid extraction columns are multiphase equipment with wide applications in the petrochemical, pharmaceutical, biochemical industries, hydrometallurgy, nuclear technology and wastewater treatment (Kislik, 2012). The key physical phenomena, which take place in such equipment including momentum, mass and energy transfer, require an accurate estimation of the interfacial area concentration. Therefore, the design and operation of these two-phase equipment are dependent on the adequate modelling of these transport phenomena (Mohanty, 2000). In liquid extraction columns, one of the phases is dispersed in a continuous environment which results in a population of droplets that may undergo breakage, coalescence, and growth (Attarakih et al., 2013). The lumped modelling approach (e.g. mixture models), which could not take into account these instantaneous discrete events, is generally not accurate from dynamic and steady state point of views, where coupled hydrodynamics and mass transfer take place. On the other hand, using the multi-fluid models based on direct discretization of the population balances to include droplet-droplet interactions were proved to be computationally expensive when detailed column geometry is concerned in CFD simulations (Drumm et al., 2010). For example, Drumm et al., (2010) used FLUENT software to simulate an RDC column DN 150 with 50 compartments, where 178 hours were needed to perform 4000 computational steps with 0.05 s step size using 1.5 GHz single core processor. Therefore, due to this computational cost and

mathematical complexity of the detailed population balance modelling, they had not been utilized in control system design and computer-aided flowsheeting. In this regard, Wachs et al (1997) developed an empirical Simulink module for controlling a Kar liquid extraction column followed by the work of Weinstein et al. (1998) who derived a nonlinear dynamic model for both Kar and Kuhni extraction columns based on the dispersed phase mean droplet diameter and neglecting droplet-droplet interactions. Mjalli (2005) derived and implemented a non-equilibrium backflow mixing cell model with no droplet interactions to control the product composition in Scheibel extraction column. Goryunov and Mikhaylov (2012) implemented a simplified non-equilibrium dynamic model and automatic control system using MATLAB/Simulink package. Therefore, the need for a an efficient population balance model is obvious and will be described in section 2. This contribution extends the work of Attarakih et al. (2013) where its implementation and validation in SIMULINK are described in detail.

2. Droplet hydrodynamics and mass transfer using OPOSPM

OPOSPM for droplet hydrodynamics is derived from the Sectional Quadrature Method Of Moments (Attarakih et al., 2013), where the whole distribution function is collapsed into one particle. This particle has four attributes: Number concentration (N), volume fraction (α_y), position (d_{30}) and concentration (C_y) along the particle property spaces (size & concentration respectively). These equations of the state variables $\{N, \alpha_y, C_y\}$ describe the evolution of the dispersed phase droplets which move with velocity ($\langle u_y \rangle$) at a given time t, in a spatial space ($\mathbf{r}$) and along droplet property space $\{d_{30}, C_y\}$. These equations are given in a vector form as follows (Attarakih et al., 2013):

$$\frac{\partial \mathbf{U}}{\partial t} + \nabla \bullet \left(\langle u_y \rangle \mathbf{U} - \langle D_y \rangle \nabla \mathbf{U} \right) = \mathbf{U}^{in} \delta(\mathbf{r} - \mathbf{r}_y) + \mathbf{S} \tag{1}$$

In Eq.(1), $\langle u_y \rangle$ is the mean droplet velocity which is function of a pre-defined mean droplet diameter and is defined as $\langle u_y \rangle = j_x / (1 - \alpha_y) + \mathbf{u}_r$, where j_x is the superficial velocity of the continuous phase and $\mathbf{u}_r$ is the relative velocity of the droplets which is given by (Attarakih et al., 2013):

$$\mathbf{u}_r = \frac{g(\rho_x - \rho_y) {d_{30}}^2}{18 \mu_x} \left(\frac{24}{C_D \, \mathrm{Re}} \right) \tag{2}$$

In the above equation, C_D is the drag coefficient that is function of the mixture Reynolds number (Re) and could be found using suitable correlation, μ and ρ are the density and viscosity of the respective phases. $\langle D_y \rangle$ is the mean axial dispersion coefficient , $\mathbf{U} = [N \; \alpha_y]$, $\delta(\mathbf{r}\text{-}\mathbf{r}_y)$ is the Dirac delta function specified at the dispersed phase inlet ($\mathbf{r}_y$), $\mathbf{U}^{in} = [u_y / \langle v_y \rangle \; u_y]^{in}$, (where $\langle v \rangle$ is the mean volume of inlet droplets, u_y is the superficial dispersed phase velocity) and the source term ($\mathbf{S}$) is given by (Attarakih et al., 2013):

$$\mathbf{S} = \begin{pmatrix} (\upsilon(d_{30}) - 1) \Gamma(d_{30}, C_y) N - \frac{1}{2} \omega(d_{30}, d_{30}, C_y) N^2 \\ G(d_{30}) N \end{pmatrix} \tag{3}$$

In Eq.(3), υ is the mean number of daughter droplets formed upon breakage at a frequency Γ, ω is the droplet coalescence frequency and G is the particle growth rate due to solute transfer which approaches zero at thermodynamic equilibrium.

The transport equations which describes the solute transport in both phases (x) and (y) are given by (Attarakih et al., 2013):

$$\frac{\partial}{\partial t}\begin{pmatrix} X \\ Y \end{pmatrix} + \nabla \bullet \begin{pmatrix} -\langle u_x \rangle X - D_x \nabla X \\ \langle u_y \rangle Y - D_y \nabla Y \end{pmatrix} = \begin{pmatrix} u_x c_x \delta(\mathbf{r} - \mathbf{r}_x) \\ u_y c_y \delta(\mathbf{r} - \mathbf{r}_y) \end{pmatrix}^{in} + \frac{6K_{oy}(d_{30}, C_y)}{d_{30}} \left(m' X - Y\right) \begin{pmatrix} +1 \\ -1 \end{pmatrix} \quad (4)$$

Where $X = \alpha_x C_x$, $Y = \alpha_y C_y$, K_{oy} is the overall mass transfer coefficient which depends on the individual film mass transfer coefficients in both phases using the two-resistance film theory (Attarakih et al, 2013). The mean droplet diameter d_{30} is related to the dispersed phase volume fraction and number concentration as $d_{30} = [(6/\pi)N/\alpha_y]^{1/3}$ and (m') is related to the distribution coefficient (m) Through $m' = \alpha_y/\alpha_x m$.

3. OPOSPM SIMULINK/MATLAB implementation

The system of Eqs.(1-4) and the other constitutive relations (droplet interaction functions, droplet rise velocity, individual mass transfer coefficients) were discretized using a first-order upwind scheme with flux vector splitting (Attarakih et al., 2013) and then converted to a set of ODEs. The size of this ODE system is equal to $4 \times n$ (n is number of numerical cells along the column height) which is classified as a stiff system. This is because each droplet has its own time scale inside the column. As a result, the diffusional mass transfer process takes longer time to reach steady state than that of droplet hydrodynamics (Attarakih et al., 2013). These different time scales call for a special ODE stiff solver to ensure numerical stability such as MATLAB/SIMULINK ode15s and ode23tb, where ode23tb could be more efficient than ode15s if high accuracy of dynamic solution is not needed. The structure of the algorithm is shown in detail in Figure (1), where the dashed boundaries represent the time loop, while the continuous ones represent the flow of information in one direction. The algorithm is self-explanatory which is implemented using SIMULINK and MATLAB GUI. This is referred to as OPOSSIM (OPOS SIMULINK) module. The OPOSSIM is shown in Fig.(2) which consists of three main sections: The input section, the implementation section, and the output section. These sections allows the user to define and model the Kuhni extraction column in terms of geometry, operating conditions, chemical system, hydrodynamic parameters and correlations and numerical inputs. OPOSSIM can be utilized at two levels: Steady state and dynamic simulation where different step changes can be introduced in inlet flow rates, concentration and rotor speed. The results are viewed using SIMULINK scopes or using standard MATLAB graphical output.

4. Numerical results and discussion

4.1. Steady state analytical and experimental validation

In this section, OPOSSIM is validated analytically using 1D CFD-PBM model which is implemented in PPBLAB software with a detailed bivariate population balances for different agitated columns including the Kuhni column (Attarakih et al., 2012). In this case study a DN32 Kuhni column (with total height of 1.53 m and 40 compartments) is simulated. The chemical system is toluene-acetone-water with total throughput 14 $m^3/m^2/h$ and 200 rpm rotor speed. More details about this case study and the used mass transfer models (oscillation droplet model) can be found in Hlawitschka (2013). The second analytical validation for the same case study is the implementation of bivariate OPOSPM in a 3D CFD OPENFOAM module to simulate the coupled hydrodynamics and mass transfer (Hlawitschka, 2013). Figure (3) shows a full comparison of the three

software predictions of the acetone concentration profiles in the Kuhni column at steady state along with the experimental data which was measured by Hlawitschka (2013).

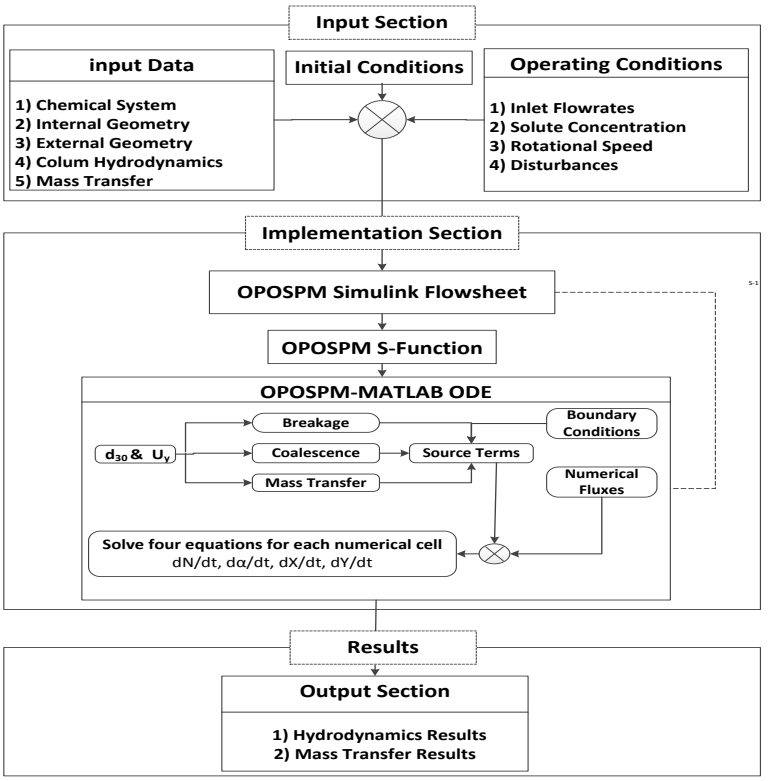

Figure (1): Algorithm structure of OPOSSIM Module for Kuhni extraction column.

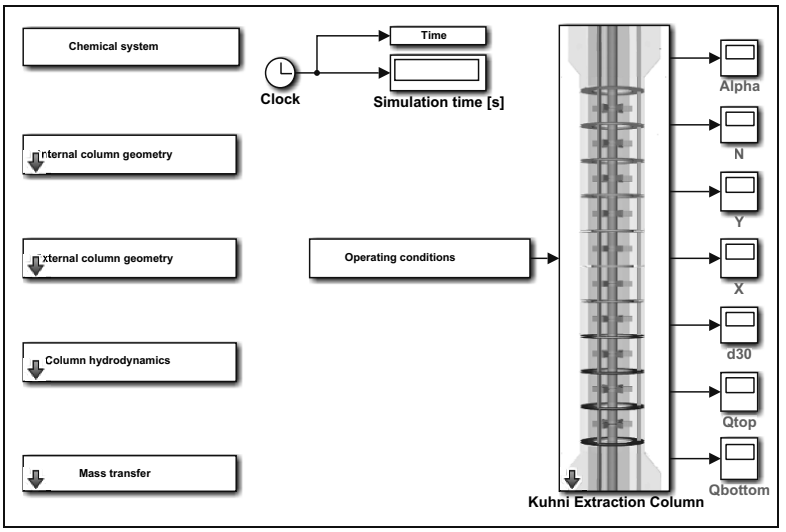

Figure (2): Structure of OPOSSIM Module which is implemented using SIMULINK/MATLAB.

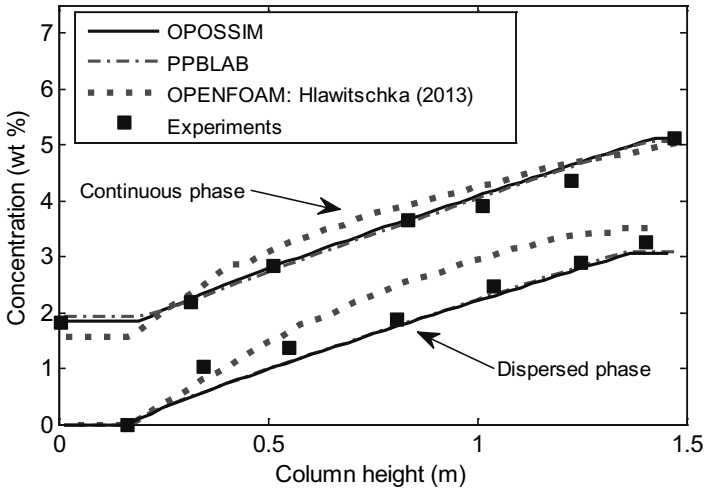

Figure (3): Comparison between the simulated acetone mass fraction profiles in both phases using three different software: OPOSSIM, PPBLAB and CFD (OPENFOAM), and experimental data (Hlawitschka, 2013) along the column height using the chemical system toluene-acetone-water with mass transfer direction is from C→D.

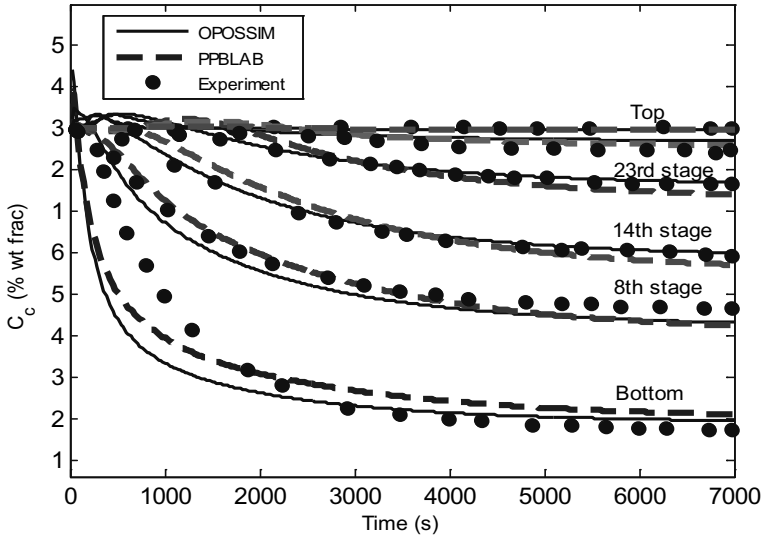

Figure (4): Comparison between the simulated solute mass fraction in the continuous phase using the OPOSSIM and PPBLAB software and the experimental data (Zamponi, 1996) due to positive step change in the dispersed phase inlet flow rate from 0 to 160 liter/h at t = 0. Q_x = 125 *l*/h, Q_y = 160 *l*/h, C_x = 4.5 % , C_y = 0, rotor speed 160 rpm direction and mass transfer C → D.

The results shown in Figure (3) are very impressive as OPOSPM (which is a reduced PBM) predicts in an excellent way the solute concentration profiles of PPBLAB software and the experimental data as well. The 3D Simulations compare well with the continuous phase solute concentration, while the deviation is relatively large when the dispersed phase is considered. The simulation times are in order of seconds using, minuets and weeks for OPOSSIM, PPBLAB and OPENFOAM respectively. Therefore, the advantages of OPOSSIM are simplicity and efficiency as a 1D CFD Model.

4.2. Dynamic analytical and experimental validation

To further validate OPOSSIM during transient simulations of extraction columns and its ability to follow column scale up, mass transfer in Kuhni extraction column of DN150 and active height of 2.52 m with 36 compartment is used (Zamponi, 1996). The chemical system is toluene-acetone-water and the individual mass transfer coefficients are those for circulating droplets. Firstly, OPOSSIM is compared to the detailed model of PPBLAB software to predict the dynamic behaviour of the acetone concentration in the continuous phase. This is due to the start-up of the column where it was initially at steady state with 4.5 percent acetone in the continuous phase which flows at 125 *l*/h and the stirrer speed is 160 rpm . At $t = 0$, the solute-free dispersed phase was introduced at the bottom of the column with a flow rate of 160 *l*/h.

As shown in Figure (4) OPOSPM follows well the dynamic behaviour of the acetone concentration where most of acetone was removed in the first 23 stages measured from the bottom. The predictions of the transient acetone concentration by the two models (OPOSSIM and PPBLAB) are comparable when compared to the experimental data of Zamponi (1996) with slight improvement in favor of PPBLAB as a detailed population balance solver.

5. Summary and conclusions

The OPOSPM as a reduced population balance model is implemented in a new SIMULINK/MATLAB module which offers steady state and dynamic simulation of Kuhni extraction column. The OPOSSIM module was found to predict both steady state and dynamic behaviour of a Kuhni extraction column in the order of second CPU time. As a conclusion, the reduction of the PBM into OPOSPM did not lose much of the information contained in the detailed model. Hence, OPOSPM has been used in SIMULINK flowsheeting environment and CFD complex geometry as well.

References

M. Attarakih, M. Abu-Khader and H.-J. Bart, 2013, Modelling and dynamic analysis of an RDC extraction column using OPOSPM. Chem. Eng. Sci., 91, 180-196.

M. Attarakih, S. Al-Zyod, M. Abu-Khader and H.-J. Bart, 2012, PPBLAB: A New Multivariate Population Balance Environment for Particulate System Modelling and Simulation. Procedia Eng. 42, 1445-62.

C. Drumm, M. Attarakih, M. W. Hlawitschka and H.-J. Bart, 2010, One-group reduced population balance model for CFD simulation of a pilot-plant extraction column. Ind. Eng. Chem. Res., 49, 3442–3451..

A. G. Goryunov, V. S. Mikhaylov, 2012, The automatic control system of a multicomponent nonequilibrium extraction process in the pulse column, J. Process Control, 22, 1034-1043.

M. W. Hlawitschka, 2013, Computational fluid dynamics-aided design of stirred Liquid-Liquid extraction columns, Dissertation, TU Kaiserslautern, Germany.

V. S. Kislik, 2012, Solvent extraction: Classical and Novel Approaches, Elsevier, Amsterdam.

F. S. Mjalli, 2005, Neural network based predictive control of liquid-liquid extraction contactors, Chem. Eng. Sci., 60, 239-253.

S. Mohanty, 2000, Modeling of liquid-liquid extraction column: A review, Rev. Chem. Eng., 16**,** 199-248.

A. Wachs, J. Benyamin, R. Semiat and D. R. Lewin, 1997, Control of a pilot-scale Karr liquid-liquid extraction column. Comp. Chem. Eng., 21**,** S601-S606.

O. Weinstein, R.Semiat and D. R. Lewin, 1998, Modeling Simulation and Control of Liquid-liquid Extraction Columns, Chem. Eng. Sci., 53, 325-339.

G. Zamponi,1996, Das dynamische Verhalten einer gerührten Solventextraktionskolonne, Shaker Verlag, Aachen.

Krist V. Gernaey, Jakob K. Huusom and Rafiqul Gani (Eds.), 12th International Symposium on Process Systems Engineering and 25th European Symposium on Computer Aided Process Engineering.
31 May – 4 June 2015, Copenhagen, Denmark

CFD-DEM simulation of a fluidized bed crystallization reactor

Kristin Kerst,[a] Luis Medeiros de Souza,[a] Antje Bartz,[b,c] Andreas Seidel-Morgenstern,[b,c] and Gábor Janiga[b]

[a]*Institute of Fluid dynamics and Thermodynamics, University of Magdeburg Otto von Guericke, Magdeburg, Germany*
[b]*Institute of Process Engineering, University of Magdeburg Otto von Guericke, Magdeburg, Germany*
[c]*Max Planck Institute for Dynamics of Complex Technical Systems, Magdeburg, Germany*

Abstract

In the present study, a fluidization process in a fluidized bed crystallizer is examined using multiphase CFD-DEM (CFD: Computational Fluid Dynamics; DEM: Discrete Element Method) simulations. The simulations were carried out using the coupled open source software CFDEMcoupling. After validating the simulation results with first experimental measurements, have been used for process understanding and improvement. In particular, regions with complex flow features but important for process outcome have been identified within the crystallizer. Moreover the simulations delivered valuable information that are difficult or even impossible to measure experimentally with sufficient accuracy.

Keywords: CFD-DEM, fluidized bed, crystallization reactor

1. Introduction

Liquid/solid fluidized beds are important in the chemical, pharmaceutical and food industry. Contrary to solid-gas fluidized beds, studies pertaining to solid-liquid fluidization are rare in the scientific literature. For this reason a fluidization process in a fluidized bed crystallizer is examined in this study.

The fluidized bed crystallizer is the main component of a complex innovative reactor concept developed for the continuous separation and crystallization of enantiomers, as examined by Lorenz and Seidel-Morgenstern (2014). Enantiomers are chemical molecules that spatially behave like mirror images of each other. A mixture of enantiomers is separated by selective crystallization in the fluidized bed crystallizer. By controlling reactor parameters, small starter crystals can be added continuously, and grown crystals (with the desired final diameter) are discharged continuously from the fluidized bed. The flow conditions in the fluidized bed crystallizer affect the fluidization process significantly. A model for the simulation of the fluidization process has been developed by Mangold et al. (2014). To investigate the flow conditions detailed, CFD-DEM simulation were used in this study.

Coupled CFD-DEM simulations (CFD: Computational Fluid Dynamics; DEM: Discrete Element Method) constitute relatively new methods, for the simulation of multiphase flows. CFD-DEM calculations are so-called four-way coupling methods, which means that 1) the particles can collide with each other and with the reactor walls, 2) the fluid (continuous phase) influences the particles, 3) particle disturbance of the fluid locally affects another particle's motion (an effect known as particle swarm), and 4) the particles have an influence on the fluid flow. The strong advantage of CFD-DEM-simulations toward other multiphase models, e.g., Discrete Phase Simulations (DPM) is that particle-particle-interactions are directly taken into account, and the flow modifications taking place in dense, which is examined by Ashraf Ali et al. (2014). In the studied fluidized bed crystallization reactor, these interactions have an impact, as the solid volume fraction is high in the examined crystallizer.

At first the employed CFD-DEM model is briefly described. Next, details of the applied simulation models are given. Thanks to the coupled simulation, areas with complex features but important for process outcome have been detected in the crystallizer. In order to validate the simulation results with experimental results, the fluidization process was performed with colored, equal-sized glass beads instead of heterogeneous crystals. Finally, CFD-DEM simulations provided valuable information for the process, such as fluidization limits, mean particle velocities and crystal pathlines. Experimental results are not in agreement with simulations. Possible reasons for this behavior are provided. Further model improvements are currently being implemented.

2. Model

In this section the computational details of the CFD-DEM simulation is briefly described. Further details can be found, e.g., in Goniva et al. (2012).

DEM - The physical particles are mathematically approximated as spheres. The particle motion is based on the Lagrangian approach, which means that each trajectory is solved explicitly. The basis for computing the translational and angular accelerations of each particle are the corresponding momentum balances. Summing up all forces acting on a particle, one obtains:

$$F_{total} = F_n + F_t + F_f + F_b \tag{1}$$

where F_n is the normal force associated to repulsion between the particles, F_t is the tangential contact force that depicts the elastic tangential deformation of the particle surfaces and the energy dissipation of the tangential contact, F_f is the force that the fluid exerts on the particles and F_b is the body force that encompasses gravity, as well as possible electrostatic and magnetic forces.

CFD-DEM - To describe the movement of an incompressible fluid with particles, the Navier-Stokes equations can be used in a modified form:

$$\frac{\partial(\varrho_f \alpha_f)}{\partial t} + \nabla \cdot (\varrho_f \alpha_f u_f) = 0 \tag{2}$$

$$\frac{\partial(\varrho_f \alpha_f u_f)}{\partial t} + \nabla \cdot (\varrho_f \alpha_f u_f) = -\alpha_f \nabla p + R_{f,p} + \nabla \cdot \partial(\varrho_f \tau_f) \tag{3}$$

where α_f represents the volume fraction occupied by the fluid, ρ_f the density, t the time, v_f the velocity, p the pressure, τ_f the stress tensor and $R_{f,p}$ the momentum exchange between fluid and particles.

In practice, where very many particles are simulated (as in the present case), a so-called non-resolved approach is used. In this case the particles are smaller than the computational grid. Consequently the particles are not resolved in the CFD simulation. Only their interaction with the fluid phase (e.g. momentum exchange and resulting porosity) is considered in the calculations.

3. Computational Details

CFD-DEM simulations with a lot of particles require a high computational effort. Therefore, the application of powerful parallel computers is absolutely necessary. In this work, a complete three-dimensional model of the fluidized bed crystallizer was simulated using an in-house Linux cluster.

CFD simulation - CFD simulations provide valuable information about the flow conditions in the crystallizer geometry. Therefore, in a first step a pure CFD simulation was carried out using the open source software OpenFOAM without considering the particles. The complete three-dimensional geometry of the fluidized bed crystallizer and the applied block-structured computational mesh are illustrated in figure 1. The fluid is considered as incompressible (water) and the flow is completely laminar, since the maximum Reynolds number is 1710, as found at the smallest cross-section, near the inlet. For the CFD simulation the transient solver pisoFoam was used. The solver uses PISO algorithm (Pressure Implicit with Splitting of Operator) and is the only CFD solver that is available in the coupled software (for DEM) so far.

Figure 1: Computational Grid

CFD-DEM simulation - The CFD-DEM simulations were performed using the coupled open source software CFDEM- coupling. The software CFDEMcoupling contains a solver that was developed by combining the C++-based open source software environments OpenFOAM (for CFD) and LIGGGHTS (for DEM). The solver carries out the fluid (CFD) and particle (DEM) calculations using two separate codes. The

interaction is realized by exchanging relevant information with a predefined time step. The simulation parameters for the CFD-DEM simulation are shown in Table 1.

Number of cells	40,000
CFD time step	10 µs
Kinematic viscosity	$1 \cdot 10^{-6} \frac{m^2}{s}$
Relative pressure at outlet	0 Pa
Inlet velocity	$0.15 \frac{m}{s}$
Velocity at wall	$0 \frac{m}{s}$
DEM time step	1 µs
Coupling interval	10 µs
Number of particles	100,000 (real: about 1,500,000
Total physical simulation time	30 s

Table1: CFD-DEM simulation parameters. The simulation was performed on a grid with 40,000 cells. Simulations on a finer grid (400,000 cells) showed no significant changes for both, the fluid and the solid phase. The time after that the fluidized bed height has reached a quasi-steady state is 30 s (end of the simulation). During the entire physical simulation time no particles are discharged from the crystallizer. The simulation of particle growth is principally possible in the DEM. However it becomes more difficult to validate the model, so that experiments and simulations are carried out without crystal growth here.

4. Results

Geometrically difficult areas of the reactor - The velocity magnitudes determined by CFD are shown in Figure 2 (a). The figure shows the crystallizer in a section plane in the center of the reactor at a physical time of 30 s (end of simulation). The highest velocities are found at the reactor inlet and outlet. The lowest flow rates are at the product outlet nozzles at the side of the reactor. The velocity distribution agrees well with the results expected from the continuity equation, stating that magnitude of velocity decreases with increasing cross-sectional area.

In order to experimentally estimate the fluidization process in the fluidized bed crystallization reactor, experiments were also performed with colored, equal-sized glass beads instead of heterogeneous crystals. A comparison between experimental data and CFD-DEM solutions first showed a noticeable difference concerning the fluidized bed height. After analyzing the computed velocity field, it was found that the product outlet nozzles are associated to complex flow features in the crystallizer.

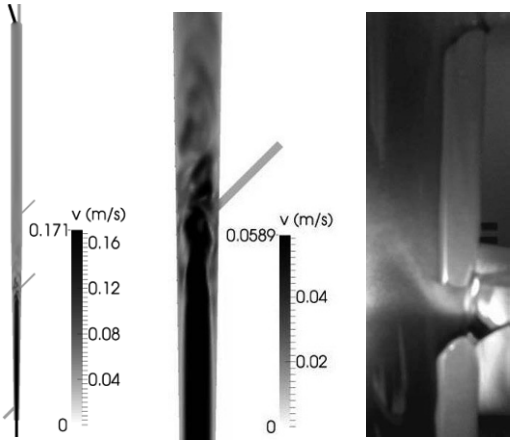

Figure 2: (a) - velocity field in a section plane in the center of the crystallizer at 30 s, (b) - velocity field of the crystallizer without product outlet nozzle (left) and with product outlet nozzle (right), (c) - experiment with fluidized glass beads.

Figure 2 (b) shows the velocity magnitudes near the lower product outlet nozzle. Figure 2 (c) shows a close-up view of an outlet nozzle during an experiment with glass beads. The product outlet nozzles are closed during the process and act as a sudden change in flow cross-section. In agreement with the continuity equation lower velocities are found at these areas. Additionally, disturbances like separation bubbles and recirculation zones are found near the nozzles. This leads to a significant change in the fluidized bed height. For further comparisons, the outlet nozzles will be sealed in such a manner that such effects are avoided, leading to a smooth evolution of flow cross-section. Nevertheless, these first comparisons have demonstrated that detailed flow simulations are a valuable tool for the identification of complex flow areas in the fluidized bed crystallizator.

CFD-DEM simulation of the fluidized bed crystallizer - The starting point of the CFD-DEM simulation in the fluidized bed crystallizer with 100,000 particles is shown in figure 3 (a). CFD-DEM simulations and experiments were performed again with glass beads. This time, glass beads with two different colors and sizes (d_{purple} = 175 µm; d_{orange} = 108 µm) were used. Figure 3 (b) shows the simulation after a physical time of 30 s. Figure 3 (c) shows the experiment for glass beads with different sizes and colors.

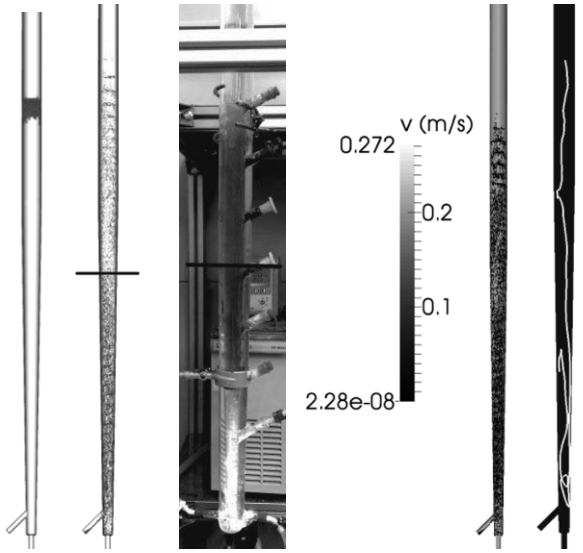

Figure 3: (a) - Initial conditions of the simulation in the fluidized bed crystallizer, (b) - CFD-DEM simulation with 100,000 particles after a physical time of 30 s, (c) - experiment with different sized and colored glass beads, (d) - section plane in the center of the crystallizer with particles colored by velocity, (e) - pathline of an arbitrarily selected particle.

A comparison between figures 3 (b) and 3 (c) shows qualitatively a good agree-ment. The separation process of large and small particles takes place in a similar manner in both figures. The 'separation line' that separates orange and purple particles is marked in both figures. Figure 3 (d) depicts the crystallizer with particles colored by velocity in a section plane in the center of the geometry. The mean particle velocity is an important information for the process. From the simulations, a mean particle velocity of 1.34 cm/s could be determined. Simultaneously, the pathlines of the particles are obtained from the CFD-DEM simulations, as exemplified in Figure 3 (e).

Comparison with experimental data - To validate further the CFD-DEM simulations, experimental measurements were carried out by means of a camera (Canon EOS 600D). The camera is focused on the crystallizer at a height of 54 cm (from the bottom of the crystallizer). By image analysis, the proportion of orange and purple pixels was

determined. In this way it is possible to compare the proportion of orange and purple particles in the crystallizer with the CFD-DEM simulation results. Table 2 compares the results. These first comparisons agree on the fact that orange particles strongly dominate at this location, but still show a noticeable difference between experiment and simulation. The proportion of purple pixels is higher in the experimental measurement. A reason might be that the particle-fluid porosity is higher in the experiment. If the flow rate is constant and more particles are found locally in the reactor, the cross-sectional area of the crystallizer is smaller and the local flow velocities increase (as a direct consequence of the continuity equation). Then the purple (heavy) particles reach higher speeds in the experiment and are located at a higher position in the reactor.

Table 2: Comparision of experiment and CFD-DEM simulation via pixel quantification.

	Experiment	CFD-DEM-Simulation
Proportion of orange pixels	93,49 %	99,31 %
Proportion of violet pixels	6,51 %	0.69 %

5. Conclusion

In this study a fluidized bed reactor was investigated using CFD-DEM simulations and companion experiments. For the computations, a high-resolution grid was generated. For the simulation of 100,000 particles in the crystallizer, 30 s of physical time were considered. First comparisons between experimental data and CFD-DEM results show that the product outlet nozzles lead to noticeable changes in the local flow structure due to sudden modifications of the flow cross-section, which must be avoided in future tests. Hence, the simulations were useful to identify critical regions in the crystallizer. Particle velocities, pathlines and particle discharge have been determined by CFD-DEM and are helpful for process analysis and improvement. Further comparisons between CFD-DEM simulations and camera measurements showed that the particles might reach even higher velocities in reality, which is perhaps a consequence of an underestimated porosity in the simulation. Such discrepancies have a direct influence on the bed height. The CFD-DEM simulations already provided interesting information for the process, and further model improvements are currently being implemented.

Acknowledgements

The financial support of the Deutsche Forschungsgemeinschaft (DFG) within the Research Program SPP 1679 ”Dynamische Simulation vernetzter Feststoffprozesse” is gratefully acknowledged.

References

Ashraf Ali, B., Börner M., Peglow M., Janiga, E., Seidel-Morgenstern, A., Thévenin, D., 2014. Numerical analysis of hydrodynamics and crystal motion in a batch crystallizer. Journal of Crystal Growth, 372, 219-229.

Goniva, C., Kloss, C., Deen, N. G., Kuipers, J. A. M., Pirkers, S., 2012. Influence of rolling friction on single spout fluidized bed simulation. Particulogy.

Lorenz, H., Seidel-Morgenstern, A., 2014. Processes to separate enantiomers. Angewandte Chemie International Edition, 53, 1218-1251.

Mangold, M., Khlopov, D., Danker, G., S. Palis, V. S., Kienle, A., 2014. Development and nonlinear analysis of dynamic plant models in ProMoT/Diana. Chemie Ingenieur Technik 86, 1107-1116.

Krist V. Gernaey, Jakob K. Huusom and Rafiqul Gani (Eds.), 12th International Symposium on Process Systems Engineering and 25th European Symposium on Computer Aided Process Engineering.
31 May - 4 June 2015, Copenhagen, Denmark.

A Modelling, Simulation, and Validation Framework for the Distributed Management of Large-scale Processing Systems

Shaghayegh Nazari[a], Christian Sonntag[a,c], Goran Stojanovski[a] and Sebastian Engell[a]

[a]*Process Dynamics and Operations Group, Department of Biochemical and Chemical Engineering, Technische Universität Dortmund, Germany*
[c]*euTeXoo GmbH, Dortmund, Germany*
shaghayegh.nazari@bci.tu-dortmund.de, goran.stojanovski@bci.tu-dortmund.de, christian@eutexoo.de, sebastian.engell@bci.tu-dortmund.de

Abstract

Petrochemical and chemical complexes are so-called Systems of Systems (SoS) that consist of many subsystems that interact by exchanging energy, material and information. The individual plants or units are managed locally, by human managers and operators or by automatic algorithms, but the efficiency of the overall site depends on the coordinated use and generation of resources and on the balancing of various resource networks, e.g. for steam on different pressure levels, hydrogen, ethylene etc. Therefore global coordination is required, but the local autonomy has to be respected. Coordination of local optimization is currently an active research area. When solutions for site-wide coordination are developed, they have to be tested in faithful system-wide simulations. In this paper we present an innovative framework for modeling, simulation, and validation of large Systems of Systems that integrates physical plant models, local control and optimization algorithms, connecting networks and site-wide coordination algorithms. The framework is described and demonstrated on a coordination problem for an integrated petrochemical site.

Keywords: Site-wide management, coordination of chemical plants, modeling and simulation framework

1. Introduction

Industrial production sites consist of many production plants that are interconnected via networks for different materials and carriers of energy to enable the efficient use of material and energy, to avoid waste streams, and to achieve a cost-efficient production. While the operation of the individual plants is managed mostly locally, the optimization of global performance indicators (such as minimal energy and material consumption, or reductions in CO2 emissions) requires a site-wide strategy for demand-supply management.

Today, companies mostly rely on infrequent planning of production and consumption of the different units and interactive management of deviations in daily meetings or by phone, which leaves a significant potential for optimization due to the existence of many dynamic interactions within a site and with its environment (e.g. changes in production volumes, disturbances, start-ups, shut-downs, product changeovers, short-term variations of the cost of electricity). Automated, optimization-based site-wide management strategies are expected to significantly improve the operational efficiency of large production sites with independently operated units. This coordination has to be performed in a distributed and hierarchical fashion, making use of local automation and

optimization functionalities and respecting the management structures of the site. Such systems with local decision power and a need for global coordination are termed Systems of Systems. Model-based engineering is indispensable to guide and to validate the design of such large complex management and automation structures and requires the composition of site-wide models from modular descriptions of the different units on different levels of details and complexity.

In this paper, a new framework is presented that is tailored towards the modelling, simulation, and validation of such large Systems of Systems with decentralized management. The framework is based on the *Modelica* language for heterogeneous modelling (see e.g. Fritzson and Bunus (2002)), and aims at reducing the effort for model creation by providing standard interfaces for the connection of physical process model components of different levels of detail (both existing and newly developed models) as well as management algorithms. The plug-and-play approach facilitates the testing and validation of different management algorithms of an industrial site, and simplifies the integration of new management architectures into an existing system.

The applicability of the framework is illustrated on an example from the petrochemical industry. Petrochemical production sites are usually organized in business units which possess partial autonomy but the plants that are operated by the business units are strongly interconnected by streams of energy and material. The business units perform their local optimization of the production processes, but global coordination is needed to balance the utilization of the shared resources. The current practice for balancing of production and consumption of shared resources in petrochemical sites is through direct negotiation of the prices of the shared resources between the management of the different business units. One reason for this is the fact that different business units use different and often not compatible tools to perform the local optimization. The business units also often do not want to share sensitive information about their operation. The presented framework provides the user with the possibility to interface optimization solutions from different platforms in order to implement a cross platform coordination in an automated fashion without sharing details about plant operation. Also, the frameworks provides standard interfaces through external C functions to the most important control and optimization software tools which enables fast and easy integration.

The remainder of this paper is structured as follows: In section 2, an overview of the modelling, simulation, and validation framework is given, followed by a description of the industrial case study in section 3. Section 4 summarizes the results of the validation of the industrial case study within the framework, and finally section 5 draws conclusions and provides an outlook on future work.

2. The Modelling, Simulation, and Validation Framework

The proposed framework is based upon a modular and structured approach towards modeling, simulation and validation of large-scale complex system of systems with many interactions. The framework is implemented in the object-oriented, equation-based *Modelica* language which is specifically designed for heterogeneous modeling. *Modelica* includes libraries for a large variety of domains such as electronics, mechanics, thermodynamics, control, etc. which matches with our goal of providing a generic framework that can be applied to as many areas as possible.

However, the users of the framework are not restricted to use *Modelica* and are free to connect black box models either using co-simulation via the *Functional Mockup Interface/FMI* or using the *Modelica* option which allows calling external functions which are not written in *Modelica* but translated into C or Fortran. The external functions can be called from *Modelica* via a Dynamic Link Library of the exported functions.

As shown in figure 1, the framework represents each subsystem by four model components: the *design model* is a possibly simplified version of the subsystem model which can be used by a *local*

management and control algorithm in cases where a model-based optimization strategy is used in order to drive the subsystem towards an optimal operation with respect to a *local (optimization) problem formulation.*

After the required number of iterations with the design models, the result of the optimization algorithms can be validated using a set of *validation models*, detailed models that precisely represent the physical SoS. The black arrows on the right most part of the figure 1 represent the physical connections between the subsystems (flows of material or energy). For the implementation of such interfaces, the standard *Modelica* interfaces are used. Similar connections are realized between the design models. An optional *global coordination algorithm* is included which interacts with the local optimizers in cases where a system-wide coordination algorithm is implemented.

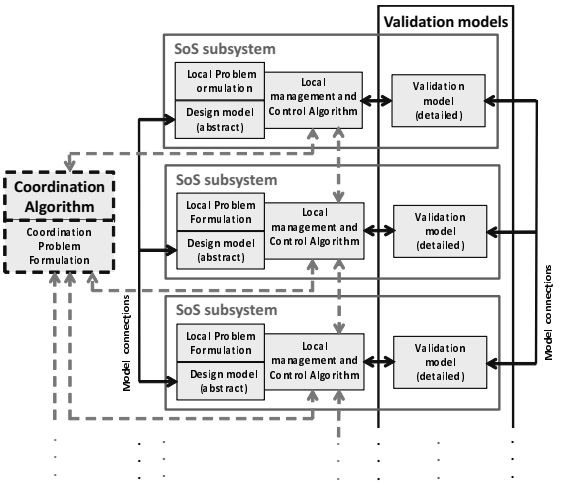

Figure 1: Structure of the modeling, simulation, and validation framework.

The framework offers generic interfaces for the implementation of interconnections between model components and validation components and optimization algorithms. All interfaces support time-discrete as well as event-driven communication. The interface between local management and optimization algorithms and validation models additionally supports time-continuous communication for situations where the local management system includes a low-level controller that is acting on the real plant.

In large-scale SoS, for which the modeling and simulation framework is designed, manual interconnection of the components requires considerable effort. Besides, full knowledge of the communicated variables is necessary. Worst of all, there is always a probability that errors are made. The framework therefore offers an automatic routine for generating the interconnections using a *Modelica* model generator. An XML configuration file which contains information on the parametrization of all the interfaces (i.e. the names, types, dimensions of the variables, the required frequency of information exchange, etc.) together with two repositories of white box and black box models are provided to the model generator. Using this information, the *Modelica* model generator verifies the structural correctness of the model components, generates the

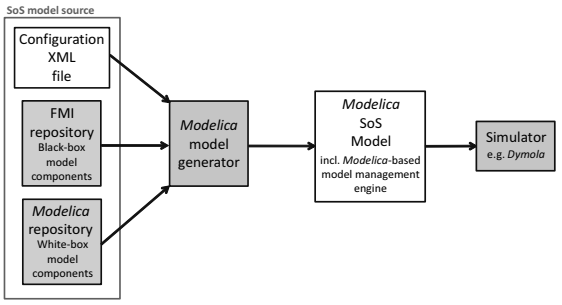

Figure 2: Workflow for the automatic generation and execution of the SoS.

required communication structure and adds the required model components. The work flow of such an automatic process is represented in figure 2.

All components must communicate via a *Modelica-based model management engine*. The model management engine requires the local management systems to define their parameters in the beginning of the simulation (i.e. either they support discrete-time or event-driven simulation, execution delays, the possibility of being triggered by other coordinators, etc.) and send data requests in order to obtain information from other management systems during the simulation. The data request contains (1) the ID of the target, (2) the ID of the requested variable, and (3) a specific index/indices of the requested variable if it is of type vector or matrix. The data request might be rejected by the model management engine in situations where triggering the operation of the target management system is not allowed according to the parameterization information which is provided to the model management engine in the beginning of the simulation. In addition, a publish/subscribe communication pattern between local and global optimizers is supported. For more details on the modeling, simulation and validation framework, please see Kampert et al. (2014).

The use of the framework is demonstrated below for the model of a petrochemical production complex where three different plants, a power plant, a cracker and an ammonia plant, are connected via networks of mass and energy.

3. Case Study: Price-based Coordination of an Integrated Petrochemical Site

We illustrate the applicability of the presented framework on a case study that was extracted from the coordination problem of a typical integrated petrochemical site. The case study comprises three plants that are interconnected by resource networks of steam of 5 and 30 bars, and hydrogen. Positive values of the utilization vector denote consumption and negative values denote production of the respective shared resource. In the example we consider four products: ethylene (*C2*) and propylene (*C3*) produced by the cracker and ammonia (*Am*) and ammonia water (*AW*) produced in the ammonia plant. A simple illustration of the case study with the shared resources streams is presented in Fig. 3.

The power plant produces electrical power, 5 and 30 bar steam and it is not connected to the hydrogen network. The manipulated variables in the power plant are the fuel gas input and the performance factor. The production of ethylene and propylene in the cracker is controlled by manipulating the naphtha feed, the severity and the 30 bar steam input. Additionally, the cracker produces hydrogen and 5 bar steam which are fed to the corresponding networks. The ammonia plant processes natural gas, hydrogen and 5 bar steam to produce ammonia, ammonia water and 30 bar steam which is fed to the network. The reader can refer to Stojanovski et al. (2015) for a detailed description of the case study.

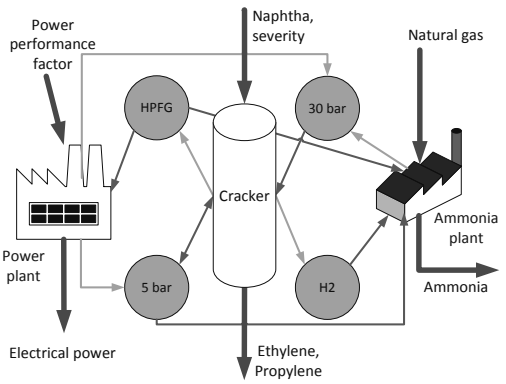

Figure 3: Example system

The coordinator initializes and updates the prices of the shared resources for all units. After the local optimizations have been performed for a given set of coordination variables (prices), the

coordinator evaluates the network balance based on the individual resource utilization vectors. If the shared resource networks are not balanced, the prices are updated by a factor proportional to the error using a weighting (gain) vector. Then, the prices are communicated to the sub-problems and the local optimization is performed again. In each iteration the prices converge towards the equilibrium prices and the difference between demand and supply decreases until the markets are cleared (Walker (1987)). The iterations are performed at each sampling time and the converged variables are then applied until the end of the next sampling interval. So the local optimizers may be queried many times at each sampling time. The formulation of the sub-problems and the price update method vary depending on the algorithm implemented, see (Stojanovski et al. (2015)).

4. Application Results

Recently, there has been much interest in the application of the coordination methods such as Alternating Direction Method of Multipliers (ADMM) on distributed problems due to their minimum communication requirements and good convergence properties (Liang (2014); Ye (2014); Kozma et al. (2014)). In this paper we use the proposed framework for the implementation of ADMM to coordinate the shared resource utilization in the integrated petrochemical site as described in Stojanovski et al. (2015). The local optimization problems for the power plant, cracker and ammonia plant are implemented in *Matlab* as stand alone optimization problems. The framework integrates the local optimization problems with the real plant simulated in *Dymola* using C-function calls through the generated DLLs and passes the necessary arguments to the coordinator. This example illustrates the ability of the framework to interface with any desired tool as long as the required dynamic/static C libraries are provided.

Figure 4 shows the changes in demands of ammonia, ethylene and propylene, the production of 5 bar and 30 bar steam, the transfer prices of the shared resources and the number of iterations needed for the coordination scheme to converge. The distributed optimization provides variable prices of the shared resources that reflect their marginal values at a given point in time due to the current product demands and prices for feedstock and energy.

A drawback of the coordination algorithms is the number of iterations needed to calculate a solution that balances the resource networks. The necessary number of iterations is strongly dependent on the tolerance, and for tight tolerances may rapidly increase. Large number of iterations require increased communication between different components in the framework which implies increased computational time. Nevertheless for this case study the computational time is sufficiently short to render a real time implementation feasible.

The proposed framework is not limited to a specific coordination approach for System of Systems and provides required interfaces and communication structure for other algorithms such as the ones presented in Ponce et al. (2014); Fele et al. (2014); Parise et al. (2015).

5. Conclusions & Outlook

The presented framework provides a plug-and-play solution to the simulation of large-scale system of systems with distributed management. The structured approach facilitates modifications of the model components which might occur due to changes in the local units, production planning, etc. Similarly, applying a new management algorithm can be done easily without having detailed knowledge about the complete SoS model. Last but not least, a less error-prone implementation of the communication structure is provided by the automatic model generation routine.

The applicability of the framework was demonstrated on a case study for price-based coordination for a subset of plants of an integrated petrochemical site. The initial results show that the proposed framework can be used to validate the incorporation of automated market mechanisms (and also

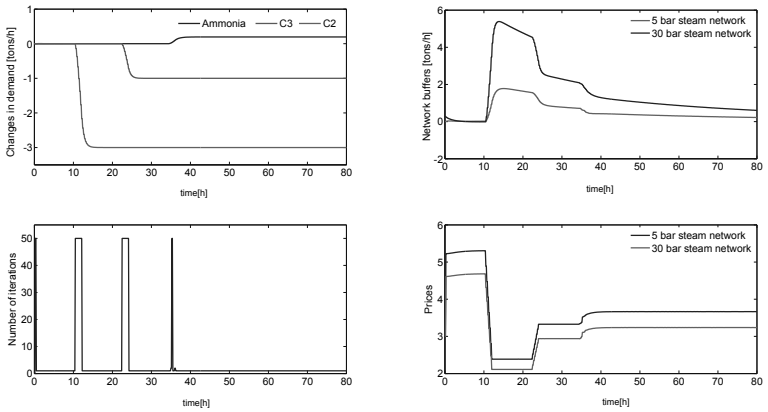

Figure 4: Changes in demands, steam network buffers, number of iterations and the transfer prices.

other coordination algorithms) in the real-time management of integrated plants. Moreover, the proposed architecture is coherent with current practice and supports the coordination of different optimization tools without revealing details of the optimization problems. The coordination algorithms can also be included as Functional Mock-up Units (FMUs) (this option is currently under development).

6. Acknowledgement

This research is supported by the project ”Dynamic Management of Physically Coupled Systems of Systems (DYMASOS)”, funded from the European Union’s 7th Framework Programme for research, technological development and demonstration under grant agreement No 611281.

References

Fele, F., Maestre, J. M., Hashemy, S. M., Muñoz de la Peña, D., Camacho, E. F., Apr. 2014. Coalitional model predictive control of an irrigation canal. Journal of Process Control 24 (4), 314–325.

Fritzson, P., Bunus, P., 2002. Modelica - a general object-oriented language for continuous and discrete-event system modeling and simulation. In: Proc. 35th Annual Simulation Symposium. pp. 365–380.

Kampert, D., Nazari, S., Sonntag, C., 2014. Dymasos project deliverable: Engineering concept specification.

Kozma, A., Conte, C., Diehl, M., May 2014. Benchmarking large-scale distributed convex quadratic programming algorithms. Optimization Methods and Software 30 (1), 191–214.

Liang, L., Aug. 2014. Separable Model Predictive Control Via Alternating Direction Method of Multipliers for Large-Scale Systems. In: Boje, E. (Ed.), Proceedings of the 19th IFAC World Congress. pp. 10499–10504.

Parise, F., Colombino, M., Grammatico, S., Lygeros, J., 2015. Mean Field Constrained Charging Policy for Large Populations of Plug-in Electric Vehicle. In: IEEE Conference on Decision and Control.

Ponce, M., Javier;, F., Maestre, J. M., Algaba Durán, E., Alamo, T., Eduardo, C. F., Aug. 2014. An Iterative Design Method for Coalitional Control Networks with Constraints on the Shapley Value. In: Edward, B. (Ed.), IFAC WC 2014. pp. 1188–1193.

Stojanovski, G., Krämer, S., Engell, S., 2015. Real-time shared resource allocation by price coordination in an integrated petrochemical site. In: European Control Conference 2015 (submited).

Walker, D. A., 1987. Walras’s Theories of Tatonnement. Journal of Political Economy 95 (4), 758–774.

Ye, P., Aug. 2014. Fast Alternating Minimization Algorithm for Model Predictive Control. In: Boje, E. (Ed.), Proceedings of the 19th IFAC World Congress. pp. 11980–11986.

Krist V. Gernaey, Jakob K. Huusom and Rafiqul Gani (Eds.), 12th International Symposium on Process Systems Engineering and 25th European Symposium on Computer Aided Process Engineering.
31 May – 4 June 2015, Copenhagen, Denmark

Performance Analysis and Optimization of the Biomass Gasification and Fischer-Tropsch Integrated Process for Green Fuel Productions

Karittha Im-orb,[a] Lida Simasatitkul,[b] Amornchai Arpornwichanop[a,]*

[a]*Computational Process Engineering Research Unit, Department of Chemical Engineering, Chulalongkorn University, Bangkok 10330, Thailand*
[b]*Department of Industrial Chemistry, Faculty of Applied Science, King Mongkut's University of Technology North Bangkok, Bangkok 10800, Thailand*
Amornchai.a@chula.ac.th

Abstract

Continuous increase in fuel prices driven by high energy demand and limited fossil fuel resources has been presently considered a major problem. Moreover, gas emissions from internal combustion engines lead to air pollution and global warming issues. Therefore, the development of clean, alternative energy is required in order to relieve the fossil fuel shortage and environmental impact. A biomass-to-liquid (BTL) process is recognized as a promising technology to convert biomass to liquid fuels. This study focused on the theoretical analysis of the BTL process consisting of a gasification unit for synthesis gas production and a Fischer-Tropsch (FT) unit as a downstream process for synthesis gas conversion to liquid fuels. Rice straw, one of the most biomass residuals found in Thailand, was considered a feedstock. The integrated model of the BTL process consisting of three major sections, i.e., the gasification based on the reaction kinetics of char gasification, the gas conditioning process including tar steam reforming and water gas shift reaction, and the FT synthesis was developed and used to investigate the influence of gasifying agents on the product distribution and the overall energy consumption. Two gasification systems using different gasifying agents, i.e., oxygen/steam and air/steam were considered and compared. The suitable conditions that provide the highest yield of a high-valued diesel product were identified.

Keywords: Gasification, Fischer-Tropsch process, Rice straw, Liquid fuel.

1. Introduction

Presently, an increase in fuel prices driven by high energy demand and limited fossil fuel resources has been considered a major problem. Moreover, gas emissions from combustion engines lead to air pollution and global warming issues. As the liquid transportation fuel plays an important role in human daily life. In the year 2012, around 28 % of the total world energy consumption was shared in the transportation sector (EIA, 2014). In Thailand, this sector represents about 35% of the total country energy consumption (DEDE, 2012). Therefore, the production of this fuel type from renewable energy sources in order to relieve the impact of fossil fuel shortage and environmental impact has been extensively attention.

Biomass is nowadays given closer attention due to its CO_2 neutral and environmental friendliness. In Thailand, rice is the second favorite agricultural product next to sugarcane, but it provides the highest amount of biomass residue (rice straw). In the

year 2010, 25.6 million tons of rice straw was approximately produced based on the rice production of 31.5 million tons (DEDE, 2012). As rice straw mainly contains carbon and hydrogen, therefore its conversion to energy is possible (Garivait et al., 2006). A biomass gasification and Fischer-Tropsch integrated process (BG-FT) is regarded as the promising technologies for producing green liquid fuels and this process is also known as a biomass to liquid (BTL) process (Omer, 2008).

Many previous studies on the gasification process have relied on a thermodynamic analysis (Sadhwani et al., 2013). However, the deviation between thermodynamic model-based prediction and actual behaviour of the gasification is generally observed due to its relatively low reaction rate. For the Fischer-Tropsch (FT) process, the Anderson-Schulz-Flory (ASF) distribution model (Hamelinck et al., 2004) is widely used for process design to predict a fraction of the FT product. In this study, the performance of the BG-FT process using rice straw as feedstock is investigated. The gasification model including tar formation and reaction kinetics of char reduction reactions and the FT synthesis model based on the ASF distribution are employed to analyze two gasification systems using different gasifying agents, i.e., oxygen/steam and air/steam. The syngas (H_2+CO) yield and H_2/CO of producer gas and the FT product distribution are considered. Optimal conditions giving the highest diesel production of the BG-FT process are identified.

2. Modelling of Biomass Gasification and Fischer-Tropsch Process

Model of the biomass gasification and Fischer-Tropsch process was developed using Aspen Custom Modeler V 7.1. It was divided into three parts, i.e., biomass gasification, synthesis gas cleaning and conditioning and Fischer-Tropsch synthesis as shown in Figure 1.

2.1 Biomass gasification

For simplification, the biomass gasification model was separated into two sections: the first one explains the combined pyrolysis and oxidation reactions and the second one involves the char reduction reactions.

The combined pyrolysis and oxidation section was assumed at the isothermal condition (T = 1228 K). As the pyrolysis and oxidation reactions are relatively fast, the thermodynamics equilibrium could be assumed. The overall reaction is shown in Eq.(1).

$$C_xH_yO_z + wH_2O + mO_2 + pH_2O + 3.76mN_2 = n_{CO}CO + n_{CO2}CO_2 + n_{H2}H_2 + n_{H2O}H_2O + n_{CH4}CH_4 + n_{C6H6}C_6H_6 + n_{char}Char + 3.76mN_2 \quad (1)$$

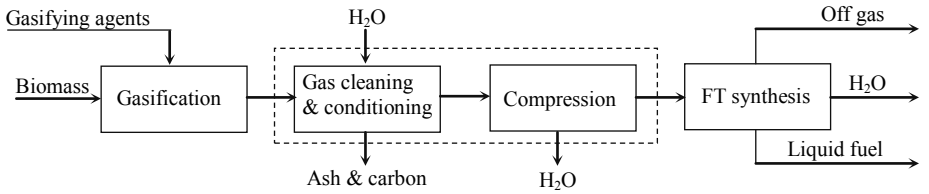

Figure 1. The schematic of the BG-FT process.

where n_{CO}, n_{CO2}, n_{H2}, n_{H2O}, n_{CH4}, n_{C6H6}, n_{Char} and n_{N2} are the number of moles of CO, CO_2, H_2, H_2O, CH_4, C_6H_6, Char and N_2, respectively, and w and m are the amount of water and oxygen per mole of biomass, respectively.

In this study, tar generated in the gasifier was represented by benzene and its concentration in the product gas was assumed to be 2 wt.% (Basu, 2010). The amount of char was obtained from the value of fixed carbon reported by the proximate analysis. Moreover, the chemical equilibrium was assumed for water gas shift and methane reactions. Eqs. (2)-(5) show the elemental balance of the reactions in this section.

Carbon balance: $x = n_{CO} + n_{CO2} + n_{CH4} + n_{C6H6}$ (2)

Hydrogen balance: $y + 2w + 2p = 2n_{H2} + 2n_{H2O} + 4n_{CH4} + 6n_{C6H6}$ (3)

Oxygen balance: $z + p + w + 2m = n_{CO} + 2n_{CO2} + n_{H2O}$ (4)

Nitrogen balance: $3.76m = n_{N2}$ (5)

The char reduction section is based on the following reactions:

R1: Boudouard reaction: $C + CO_2 = 2CO$ (6)

R2: Water gas reaction: $C + H_2O = CO + H_2$ (7)

R3: Methane reaction: $C + 2H_2 = CH_4$ (8)

R4: Methane Steam reforming reaction: $CH_4 + H_2O = CO + 3H_2$ (9)

Because the rate of the char reduction reactions is relatively low, their chemical kinetics are considered. The rate expressions of the reactions are shown in Eqs.(10)-(13).

$$r_1 = C_{RF} k_1 (x_{CO2} - \frac{x_{CO}^2}{K_{eq,1}}) \quad (10)$$

$$r_2 = C_{RF} k_2 (x_{H2O} - \frac{x_{CO} x_{H2}}{K_{eq,2}}) \quad (11)$$

$$r_3 = C_{RF} k_3 (x_{H2}^2 - \frac{x_{CH4}}{K_{eq,3}}) \quad (12)$$

$$r_4 = C_{RF} k_4 (x_{H2}^2 x_{CO} - \frac{x_{H2O} x_{CH4}}{K_{eq,4}}) \quad (13)$$

The kinetics data of such reactions were taken from Wang and Kinoshita (1993). To account for active sites on the char surface, the char reactivity factor (C_{RF}) was considered to be the constant value of 1000 (Giltrap et al., 2003). To calculate the composition of the producer gas leaving this reaction zone, the reduction section was divided into small control volumes (CV) and the mass balance of each CV was performed. The molar flow rate of species *i* leaving each CV is computed by Eq.(14)

$$n_{i,out} = n_{i,in} + V_{CV}.Rt_i \quad (14)$$

2.2 Synthesis gas cleaning and conditioning

Ash and unreacted carbon contained in the raw synthesis gas were removed in a solid separation unit. In a tar steam reforming process, benzene (tar model compound) and methane were completely converted to H_2 and CO via steam reforming reaction over Ni based catalyst at 780 ^oC, 1 atm (Basu, 2010). The chemical equilibrium was assumed for water gas shift, methane and benzene steam reforming reactions.

2.3 Compression

The clean syngas with a desired H_2/CO ratio was compressed to the FT operating pressure of 20 bar. The efficiency of compressor was assumed to be 75% (Kaneko et al., 2006).

2.4 FT reactor

The FT hydrocarbon products were assumed to be linear paraffins (Eq.(15)). The operating temperature and pressure were 220 °C and 20 bar, respectively. The product distribution was assumed to follow the ASF distribution, as shown in Eq.(16), and the chain growth probability (α) could be determined from Eqs.(17)-(18).

$$\mathrm{nCO} + (2\mathrm{n}+1)\mathrm{H}_2 \rightarrow \mathrm{C_nH_{2n+2}} + \mathrm{nH_2O} \quad (15)$$

$$M_n = \alpha^{n-1}(1-\alpha) \quad (16)$$

$$\alpha = 0.75 - 0.373\sqrt{-\log(S_{C5+})} + 0.25S_{C5+} \quad (17)$$

$$S_{C5+} = 1.7 - 0.0024T - 0.088\frac{[H_2]}{[CO]} + 0.18([H_2] + [CO]) + 0.0079P_{Total} \quad (18)$$

where S_{C5+} is the selectivity of hydrocarbon with a chain length longer than 5, $[H_2]$ and [CO] are the molar concentration of H_2 and CO in the feed gas, T and P_{Total} are the operating temperature (K) and pressure (bar), respectively.

The reaction rate used to determine the conversion of carbon monoxide during the FT synthesis was derived from the kinetic study of Yates and Satterfield (1991), as shown in Eq. (19).

$$-R_{\mathrm{CO}} = \frac{aP_{\mathrm{CO}}P_{\mathrm{H2}}}{(1+bP_{\mathrm{CO}})^2} \quad (19)$$

where R_{CO} is the CO consumption rate (mol/s $\mathrm{kg_{cat}}$), $\underline{P}_{\mathrm{CO}}$ and P_{H2} are the partial pressure of CO and H_2 (bar), and a and b are the kinetic parameters which are calculated from the correlation developed by Krishna and Sie (2000). The vapour liquid equilibrium was calculated using Raoult's law, as shown in Eq. (20).

$$y_n P_{Total} = x_n P_{vap,n} \quad (20)$$

2.5 Energy balance

The overall energy balances for each unit can be calculated by Eqs. (21)-(23).

$$H_{reactant} + Q_{in} = H_{product} + Q_{out} \quad (21)$$

$$H_{reactant} = \sum_{reactants} n_i h_{fi}^0 \quad (22)$$

$$H_{product} = \sum_{products} n_i [h_{fi}^0 + \Delta h_{Ti}] \quad (23)$$

where, h_{fi}^0 is the enthalpy of formation in kJ/kmol at the reference state (298 K, 1 atm) and Δh_{Ti} is the enthalpy difference a given state and the reference state.

3. Results and Discussions

3.1 Effect of gasifying agents (oxygen and steam) on the BG-FT process

It is found from Figure 2 that as oxygen feed rate increases; more steam is required to maintain the thermal self-sufficient condition in the gasifier. Figure 2 (a) shows that H_2/CO ratio of the produced syngas increases with oxygen content and the syngas yield shows the same effect as oxygen increases in the oxygen to biomass ratio range of 0.12 to 0.14 due to the domination of water gas shift reaction; however, the inverse effect is found as O_2 to biomass ratio is over 0.15 because the combustion reaction dominates the system. Figure 2 (b) shows the increase of diesel production with oxygen feed rate at H_2/CO ratio around 2 due to the increase in syngas production rate in gasifier. However, the diesel production sharply decreases to zero as oxygen feed rate increases since syngas feed rate dramatically decreases. The maximum diesel production is found at the oxygen and steam to biomass ratio equal to 0.14 and 0.58, respectively.

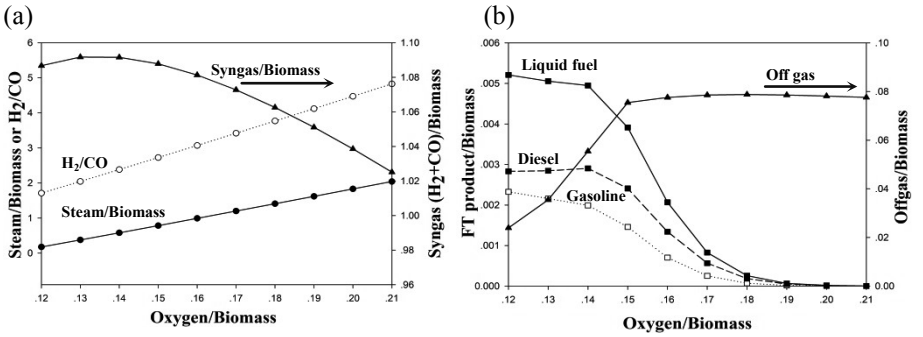

Figure 2. Effect of gasifying agents (oxygen and steam) on: (a) syngas (H_2+CO) yield and H_2/CO ratio and (b) FT product distribution.

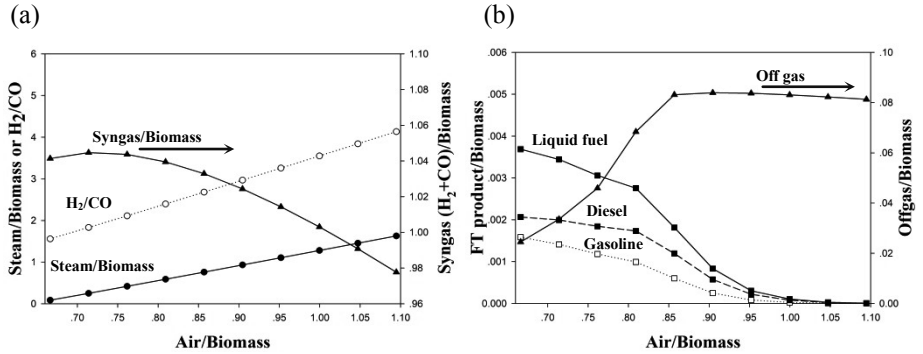

Figure 3. Effect of gasifying agents (air and steam) on: (a) syngas (H_2+CO) yield and H_2/CO ration and (b) FT product distribution.

3.2 Effect of gasifying agents (Air and steam) on the BG-FT process

The effect of air and steam feed rate on performance of BG-FT process where the gasifier is operated under thermal self-sufficient condition shows a similar trend as the system using oxygen and steam. However, a higher amount of air feed rate is required, whereas a smaller amount of syngas and diesel products are obtained due to the effect of nitrogen dilution. Figure 3 (a) shows the increase of syngas yield with air feed rate increases in the air to biomass ratio range of 0.67 to 0.70; however, the inverse effect is found as the air to biomass ratio becomes over 0.75. Figure 3 (b) shows that the relative high of diesel production is found at the H_2/CO ratio around 2 due to the increase in syngas production rate in the gasifier. However, the diesel production sharply decreases to zero as air feed rate increases because syngas feed rate dramatically decreases. The maximum diesel production is found at the air and steam to biomass ratio equal to 0.67 and 0.85, respectively.

3.3 Effect of gasifying agents on overall energy consumption of the BG-FT process

The effect of gasifying agents on overall energy consumption of the BG-FT process which the thermal self-sufficient condition is considered at gasifier is shown in Figure 4. The rate of heat release significantly increases when oxygen and air to biomass ratios are in the ranges of 0.12-0.15 and 0.67-0.85, respectively. Nevertheless, the decrease in increasing rate of heat release is observed as the oxygen and air to biomass ratios became higher than the above ranges. The released heat from air-steam system is always higher than that of the other.

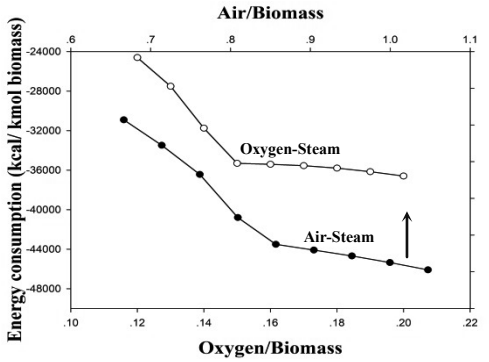

Figure 4. Effect of gasifying agents on overall energy consumption of BG-FT process.

4. Conclusions

The biomass gasification and Fischer-Tropsch (BG-FT) integrated process using rice straw as feedstock was studied. Modelling of the integrated process was performed using Aspen Custom Modeler V 7.1. Two gasification systems operated under thermal self-sufficient condition with different gasifying agents, i.e., oxygen/steam and air/steam were considered. The yield and H_2/CO ratio of the producer gas derived from the two systems as well as the diesel production show a similar trend. However, the gasifier with air/steam required a higher amount of air feed rate to achieve the thermal self-sufficient condition and the smaller amount of derived syngas and diesel products were achieved due to the effect of nitrogen dilution, whereas the higher amount of heat was released. Finally, it could be concluded that the type and amount of gasifying agent played an important role in the production of liquid fuel from rice straw using the BG-FT process. The optimum value of diesel production and overall energy consumption could be achieved via the suitable adjustment of a gasifying agent to biomass ratio.

Acknowledgements

Support from the 90th anniversary of Chulalongkorn University Fund and the Ratchadaphiseksomphot Endowment Fund is gratefully acknowledged.

References

A.M. Omer (2008). Renewable & Sustainable Energy Reviews 12, 1789-1821.
C.N. Hamelinck, A.P.C. Faaij, H. Den Uil, H.Boerrigter (2004). Energy 92, 1743-1771.
D.L. Giltrap, R. McKibbin, G.R.G. Barnes (2003). Solar Energy 74, 85– 91.
DEDE (cited 24 Nov. 2014). Available from: http://biomass.dede.go.th/Symfony/web/map /district?year=2552.
EIA (cited 24 Nov. 2014). Available from: www.eia.gov/forecasts/aeo/pdf/0383(2012).pdf.
I.C. Yates, T. Lee (2007). Journal of Natural Gas Chemistry 16, 329-341.
N. Sadhwani, Z. Liu, M.R. Eden, S. Adhikari (2013). In A. Kraslawski, I. Turunen (eds). Proc. 23th European Symposium on Computer Aided Process Engineering, 421-426.
P. Basu (2010). Biomass gasification and pyrolysis: practical design and theory. Acadamic press, Burlington.
R. Krishna, S.T. Sie (2000). Fuel Processing Technology 64, 73-105.
S. Garivait, U. Chaiyo, S. Patumsawad, J. Deakhuntod (2006). 2nd Joint International Conference on Sustainable Energy and Environment, Bangkok, Thailand.
T. Kaneko, J. Brouwer, G.S. Samuelsen (2006). Power Sources 160(1), 316-325.
Y. Wang, C.N. Satterfield (1991). Energy & Fuels 5, 168-173.

Krist V. Gernaey, Jakob K. Huusom and Rafiqul Gani (Eds.), 12th International Symposium on Process Systems Engineering and 25th European Symposium on Computer Aided Process Engineering.
31 May – 4 June 2015, Copenhagen, Denmark

Dynamic behavior adjustment of 1, 3-propanediol fermentation process

Hao Jiang, Nan Zhang, Jinsong Zhao, Tong Qiu, Bingzhen Chen*

Department of Chemical Engineering, Tsinghua University, Beijing 100084, China
dcecbz@mail.tsinghua.edu.cn

Abstract

Multiple steady-state solutions typically exist for nonlinear chemical processes and the stability of various solutions may be different. Stability is a key component of chemical process operability and represents the tolerance for small perturbations in the process, which is related to process benefits and safety. As one of the multiple steady-state solutions, the optimal operating point may be located in the unstable branch. 1, 3-propanediol is an important chemical material, however, the optimal operating point with the highest product concentration is unstable. This paper introduced the washout filter-aided controller which was originally used for electric power system and aircraft to adjust the dynamic behavior of the anaerobic fermentation process. By selecting appropriate controller parameters, eigenvalues of an unstable point near the optimal operating point are reassigned to stabilize the high product concentration parts of the equilibrium manifold including the optimal operating point without affecting the shape of the equilibrium manifold. Finally, simulations of the closed-loop system were used to verify the effectiveness of the proposed method of adjusting dynamic behavior.

Keywords: propanediol, washout filters, stability, adjustment

1. Introduction

1, 3-propanediol is an important chemical material, mainly used in the production of polyester, e.g., polytrimethylene terephthalate (PTT), as well as the synthesis of pharmaceutical intermediates. The microbial anaerobic fermentation is an efficient and environmentally friendly process as opposed to the traditional ethylene oxidation and acrolein hydrolysis. However, the open-loop system is unstable at the optimal operating point. To overcome this problem, the method of adjusting the stability of 1, 3-propanediol fermentation process with washout filter-aided controller is studied.

Washout filter-aided controller is a kind of dynamic feedback controller with washout filters that washout(reject) steady state inputs, while passing transient inputs (Hassouneh et al., 2004). Washout filters are used commonly in control systems for power systems and aircraft (Lee and Abed, 1991). In addition, Wang and Abed (1995) studied bifurcation control of a chaotic system with washout filter, Ding and Hou (2010) studied the stabilizing control of Hopf bifurcation in the Hodgkin-Huxley model via washout filter.

The dynamics of the simplest washout filter can be written as (Lee, 1991)

$$\dot{z} = x_k - d_t z \tag{1}$$

where x_k is the kth element of the state vector, d_t is the reciprocal of the filter time constant. The output equation is

$$y = x_k - d_t z \tag{2}$$

The control law is a function of y, usually has the following form

$$\mathbf{u} = \mathbf{h}(y) = \mathbf{w}y + y^T \mathbf{Q_u} y + \mathbf{C_u}(y, y, y) \tag{3}$$

where $\mathbf{w}$ is a vector, $\mathbf{Q_u}$ is a real symmetric $n \times n$ matrix, and $\mathbf{C_u}$ is a cubic form, corresponding to linear, quadratic and cubic terms, respectively. In this paper, only the linear term is applied.

The paper is organized as follows. In Section 2, the model of 1, 3-propanediol anaerobic fermentation is presented. In Section 3, the washout filter-aided controller is introduced and implemented to stabilize the optimal operating point. In Section 4, the advantages and limitations of washout filter-aided controller are discussed. The conclusions are presented in Section 5.

2. Propanediol Anaerobic Fermentation

The mathematical model of 1,3-propanediol fermentation is as follows (Xiu et al., 1998).

$$\begin{aligned}
\frac{dx_1}{d\tau} &= x_1(p - d) \\
\frac{dx_2}{d\tau} &= d(y_0 - x_2) - x_1\varphi_1\left(\beta_1 + \gamma_1 p + \frac{x_2}{x_2 + \alpha_1}\right) \\
\frac{dx_3}{d\tau} &= x_1\varphi_2\left(\beta_2 + \gamma_2 p + \frac{x_2}{x_2 + \alpha_2}\right) - x_3 d \\
p &= \frac{x_2}{x_2 + \alpha_3}(1 - x_2)(1 - x_3)
\end{aligned} \tag{4}$$

The state variables are x_1, x_2, and x_3, which mean dimensionless biomass concentration, dimensionless substrate concentration, and dimensionless product concentration, respectively. The operating variables are dimensionless dilution rate d, dimensionless feed substrate concentration y_0 and dimensionless parameter α_3. The values of the parameters are listed in Table 1.

Table 1. Parameters of 1, 3-propanediol fermentation

Parameters	Parameters
α_1=0.01	γ_1=2.3929
α_2=0.025	γ_2=0.5583
β_1=0.0286	φ_1=0.1306
β_2=0.0083	φ_2=0.8955

The operating point is optimized to get the highest product concentration, where d=0.3, y_0=0.2744, and α_3=0.00014. Correspondingly, the optimal dimensionless product

concentration x_3 is 0.6928. The bifurcation diagram of dimensionless product concentration x_3 versus dimensionless substrate concentration is depicted in Figure 1(a), showing that the optimal operating point is unstable. The same result is also reported by Wang et al (2013). Since the optimal operating point is unstable, the steady state will drop to the lower stable point, leading to economic losses and safety problems. Therefore, a control system must be implemented. In this paper, the washout filter-aided controller is introduced to stabilize the unstable operating point.

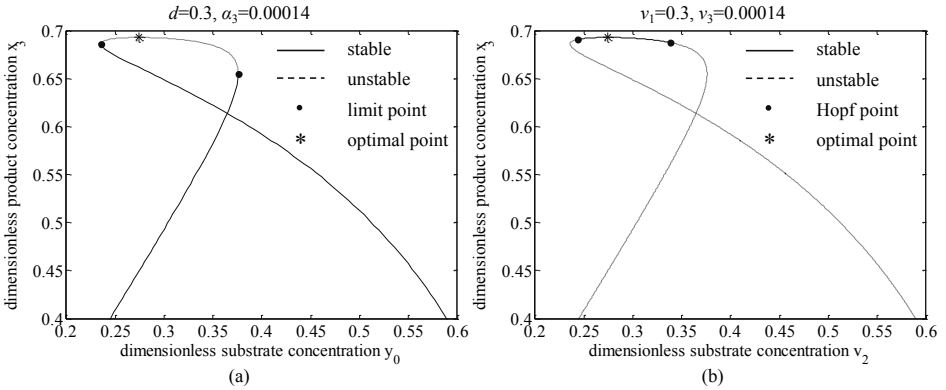

Figure 1. Bifurcation diagram of x_3 versus y_0: (a) open-loop, (b) closed-loop

3. Implementation of Washout Filter-aided Controller

Mönnigmann (2002) proposed a method to deliberately introduce Hopf bifurcations to stabilize parts of the equilibrium manifold of an ODE process model without affecting the equilibrium manifold.

Eq.(4) can be described by

$$\dot{\mathbf{x}} = \mathbf{f}(\mathbf{x}, \mathbf{u}) \tag{5}$$

where $\mathbf{x} \in \mathbf{R}^3$ is the state vector (x_1, x_2, x_3) and $\mathbf{u} \in \mathbf{R}^3$ is the input vector (d, y_0, α_3). Apply washout filter to the third state variable x_3, and only the linear term is used in the control law $\mathbf{u}=\mathbf{h}(y)$. The augmented system can be written by

$$\begin{aligned} \dot{\mathbf{x}} &= \mathbf{f}(\mathbf{x}, \mathbf{u}) \\ \dot{z} &= x_3 - d_t z \\ y &= x_3 - d_t z \\ \mathbf{u} &= \mathbf{v} + \mathbf{w} y \end{aligned} \tag{6}$$

where z is the state variable of the dynamic equation of washout filters, d_t and $\mathbf{w}$ are controller parameters, $\mathbf{v}$ is the reference input vector, corresponding to the original input vector (d, y_0, α_3) in the open-loop system. The control structure is shown in Figure 2, where G_w is the transfer function of the washout filter (Hassouneh et al., 2004).

$$G_w(s) = \frac{y(s)}{x_k(s)} = \frac{s}{s + d_t} \tag{7}$$

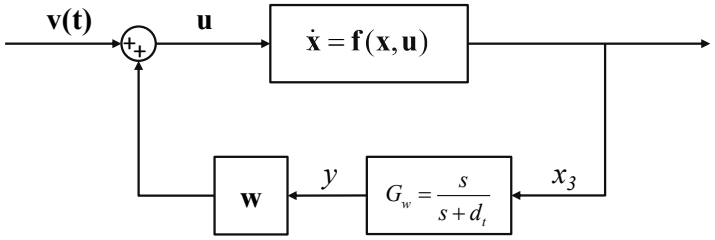

Figure 2. Control structure of washout filter-aided controller

If there is only one positive real eigenvalue at the unstable point, the positive real eigenvalue can be replaced by two arbitrarily given eigenvalues with appropriate controller parameters. Here, the key points are which point should be selected and what new eigenvalues should be assigned to make the optimal operating point locate in the stabilized parts, meanwhile, the stabilized parts should be as large as possible. Therefore, a lot of cases are evaluated and some of them are listed in Table 2.

Table 2. Some evaluated cases

Selected points	Assigned eigenvalues	Stable regions
(0.3, 0.27, 0.00014)	-0.5, -0.5	$0.2594<y_0<0.3072$
(0.3, 0.27, 0.00014)	-0.1, -0.1	$0.2620<y_0<0.3760$
(0.3, 0.25, 0.00014)	-0.5, -0.5	$0.2440<y_0<0.2676$
(0.3, 0.25, 0.00014)	-0.1, -0.1	$0.2435<y_0<0.3383$

The chosen point is

$$(d, y_0, \alpha_3) = (0.3, 0.25, 0.00014) \tag{8}$$

At the chosen point, the eigenvalues of the open-loop system is

$$(\lambda_1, \lambda_2, \lambda_3) = (-1.1083, -0.4311, 0.2349) \tag{9}$$

The single positive eigenvalue can be replaced by two given eigenvalues -0.1 and -0.1. Therefore, the eigenvalues of the augmented system become

$$(\lambda_1, \lambda_2, \lambda_3, \lambda_4) = (-1.1083, -0.4311, -0.1, -0.1) \tag{10}$$

with the following controller parameters obtained by the method proposed by Mönnigmann (2002).

$$d_t = -0.0426, w = (1.7403, -0.4586, -0.2596)^T \tag{11}$$

The bifurcation diagram of dimensionless product concentration x_3 versus the second reference input v_2 is depicted in Figure 1(b), showing that parts of the unstable equilibrium manifold is stabilized without changing the shape of the equilibrium manifold. Even though the rest of the equilibrium manifold becomes unstable, the optimal operating point is stabilized.

To verify the effectiveness of the designed washout filter-aided controller, the set-point tracking curves of the open-loop and close-loop systems are illustrated in Figure 3.

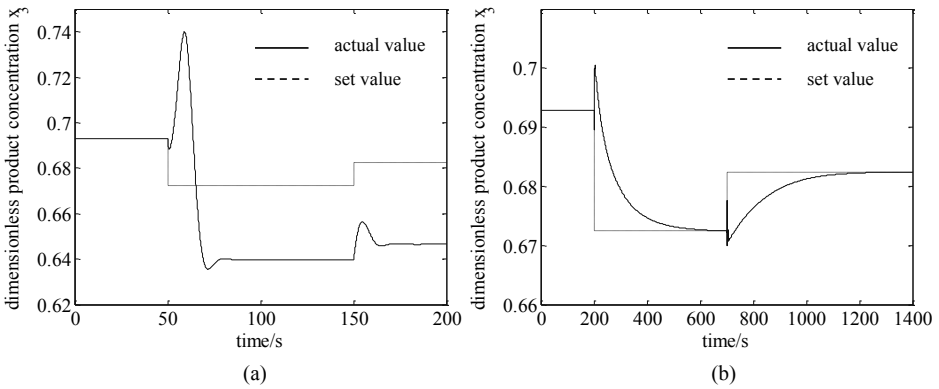

Figure 3. Set-point tracking curve. (a) open-loop, (b) closed-loop

The dashed lines mean the set values which are the same in Figure 3(a) and Figure 3(b). As shown in Figure 3(a), in the open-loop system, the steady state solution converges to the lower stable point instead of the desired higher unstable point when the operating variables vary. On the contrary, in the closed-loop system, the steady state solution converges to the stabilized optimal operating point when the operating variables vary.

4. Advantages and Limitations of Washout Filter-aided Controller

The main advantage of washout filter-aided controller is the ability to preserve all the equilibrium points of the open-loop system. In addition, washout filter-aided controller has the character of automatic equilibrium following.

Assuming that $\mathbf{x}_e$ is the steady state solution of the open-loop system in Eq.(5) when $\mathbf{u}$ is equal to $\mathbf{u}_e$. Hence

$$\mathbf{f}(\mathbf{x}_e, \mathbf{u}_e) = \mathbf{0} \tag{12}$$

Consider the closed-loop system in Eq.(6), the output y is equal to 0 when steady state is reached. Therefore, the following equation holds

$$\mathbf{u} = \mathbf{v} \tag{13}$$

The steady state solution of the closed-loop system should satisfy

$$\mathbf{f}(\mathbf{x}, \mathbf{v}) = \mathbf{0} \tag{14}$$

When $\mathbf{v}$ is equal to $\mathbf{u}_e$, $\mathbf{x}_e$ is also the solution of Eq.(14), meaning that the open-loop and closed-loop systems have the same steady state solutions. Therefore, the equilibrium manifold is preserved.

In contrast to a traditional control structure designed for a certain operating point, the washout filter-aided controller can operate in a wide range of operating conditions (Lee, 1991). In a typical direct state feedback, the control law is

$$\mathbf{u} = \mathbf{h}(\mathbf{x} - \mathbf{x}_e) \tag{15}$$

From the above control law it can be seen that the new steady state $\mathbf{x}_e$ must be computed when operating condition is changed. However, the output of washout filters can be written as Eq.(2), $\mathbf{x}_e$ is not involved in, so there is no need to do any on-line computation and adjustment.

Although the advantages of washout filter-aided controller are very attractive, there are two limitations to achieve the goal of stabilizing arbitrary unstable point without affecting the equilibrium manifold. Firstly, only one positive real eigenvalue is allowed at the unstable point we want to stabilize. Secondly, the dimension of the operating variables should be the same with the state variables. How to overcome these limitations is the future work.

5. Conclusions

In order to operate at the unstable optimal operating point, a new control structure named washout filter-aided controller is designed for the 1, 3-propanediol fermentation process. By selecting appropriate controller parameters, eigenvalues of an unstable point near the optimal operating point are reassigned to stabilize the high product concentration parts of the equilibrium manifold including the optimal operating point without affecting the shape of the equilibrium manifold, meaning that the dynamic behavior of the 1, 3-propanedoil fermentation process is adjusted.

Acknowledgement

The authors gratefully acknowledge support from the National Basic Research Program (No. 2012CB720500) and the National Natural Science Foundation of China (No. 21306100).

References

L. Ding, C. Hou, 2010, Stabilizing control of Hopf bifurcation in the Hodgkin–Huxley model via washout filter with linear control term, Nonlinear Dynam., 60, 131-139.

M. A. Hassouneh, H. C. Lee, E. H. Abed, 2004, Washout filters in feedback control: Benefits, limitations and extensions, Proceedings Of the 2004 American Control Conference, 3950-3955.

H. C. Lee, 1991. Robust control of bifurcating nonlinear systems with applications, Ph.D dissertation, University of Maryland, College Park, USA.

H. C. Lee, E. H. Abed, 1991. Washout filters in the bifurcation control of high alpha flight dynamics, American Control Conference, 206-211.

M. Mönnigmann, W. Marquardt, 2002, Bifurcation placement of Hopf points for stabilization of equilibria, Proceedings of the 15th IFAC World.

H. O. Wang, E. H. Abed, 1995, Bifurcation control of a chaotic system, Automatica, 31, 9, 1213-1226.

H. Z. Wang, N. Zhang, T. Qiu, J. S. Zhao, X. R. He, B. Z. Chen, 2013, A process design framework for considering the stability of steady state operating points and Hopf singularity points in chemical processes, Chem. Eng. Sci., 99, 252-264.

Z. L. Xiu, A. P. Zeng, W. D. Deckwer, 1998, Multiplicity and stability analysis of microorganisms in continuous culture: effects of metabolic overflow and growth inhibition, Biotechnol. Bioeng., 57, 3, 251-261.

Krist V. Gernaey, Jakob K. Huusom and Rafiqul Gani (Eds.), 12th International Symposium on Process Systems Engineering and 25th European Symposium on Computer Aided Process Engineering.
31 May – 4 June 2015, Copenhagen, Denmark

Modelling and Simulation of Pressure Swing Adsorption (PSA) Processes for post-combustion Carbon Dioxide (CO_2) capture from flue gas

George N. Nikolaidis,[a,c] Eustathios S. Kikkinides,[b,c] Michael C. Georgiadis[a,c*]

[a]*Aristotle University of Thessaloniki, Department of Chemical Engineering, 54124, Thessaloniki, Greece*
[b]*University of Western Macedonia, Department of Mechanical Engineering, Bakola & Sialvera Str., 50100 Kozani, Greece*
[c]*Chemical Process and Energy Resources Institute (CPERI), Centre for Research and Technology Hellas (CERTH), PO box 60361, 57001 Thessaloniki, Greece*
mgeorg@auth.gr

Abstract

A modelling framework for the separation of gas mixtures using multibed Pressure Swing Adsorption (PSA) and Vacuum Swing Adsorption (VSA) flowsheets has been developed. The core of the modelling framework represents a detailed multi-scale adsorbent bed model relying on a coupled set of mixed algebraic and partial differential equations for mass, heat and momentum balance at both bulk gas and particle level, equilibrium isotherm equations and boundary conditions according to the operating steps. The proposed modelling equations have been implemented in the gPROMS™ modelling environment. The modelling framework has been applied on the capture of post-combustion carbon dioxide (CO_2) from dry flue gas by PSA/VSA process in order to validate its predictive power against experimental and simulation data available from the literature. The simulation results in terms of process performance indicators are in good agreement with data available from the literature. The results of sensitivity analysis illustrate the typical trade-offs between process performance indicators.

Keywords: pressure swing adsorption (PSA), modelling, simulation, CO_2 capture

1. Introduction

A considerable increase in the applications of adsorptive gas separation technologies, such as pressure swing adsorption (PSA), have been reported during the last few decades. A pressure swing adsorption (PSA) process is a widely used industrial unit operation process for separating gas mixtures where one or more gases are preferentially adsorbed at high pressure and then desorbed at a lower pressure. The regeneration of the adsorbent is performed by reducing the total pressure of the system, the process is termed Pressure Swing Adsorption (PSA) and the total pressure of the system changes (swings) between high pressure in feed and low pressure in regeneration. PSA like all adsorption separation processes requires the use of a fixed bed packed with a microporous-mesoporous adsorbent material that selectively adsorbs one component (or a group of related components) from a gas mixture. The effluent stream during the adsorption step that no-longer contains the preferentially adsorbed species is called the light product or “raffinate”, while the effluent stream during the desorption step that contains the strongly adsorbed species in larger proportions compared to the feed stream, is often called the heavy product or “extract”.

2. Mathematical model formulation

2.1. Problem description

Depending on the general assumptions describing the adsorbent (porous solid) – adsorbate (gas mixture) system one can employ a broad variety of mathematical models and equations to describe the PSA/VSA process. Kikkinides et al. (2011) and Nikolic et al. (2008) presented the development of a generic modelling framework for efficient simulation and optimization strategies of PSA/VSA processes with detailed adsorption and transport models. The modelling framework is coupled with a novel state transition network (STN) approach adopted from the work of Nikolic et al. (2009) to identify which state transitions are feasible and under which conditions a particular state (operating step) change occurs under a given current state in multibed PSA systems.

The following basic assumptions have been adopted in the derivation of the model equations in this study:

- An axially dispersed plug flow model is used to represent the bulk fluid flow.
- No concentration, temperature, and pressure gradients exist in the radial direction.
- The adsorbent is represented by uniform micro-porous spheres
- Thermal equilibrium between the gas and solid phase (adsorbent) is established instantaneously.
- The gas phase is described by the ideal gas law.
- Competitive adsorption behaviors are described by the dual-site Langmuir isotherm for the gas mixture.
- The mass transfer rate between adsorbent (porous solid) and adsorbate (gas mixture) is described by the linear driving force (LDF) model.
- The physical properties of the adsorbent and adsorption column void are uniform across the column and independent of the temperature.
- Pressure drop along the adsorption column is calculated by the Ergun equation.
- During the pressure-change step the interstitial velocity profile is exponential along the adsorption column and affected by the gas valve equation.

2.2. Mathematical model

The mass balance equation which describes the mass transfer in the bulk gas flow is:

$$\varepsilon_{bed}\frac{\partial(uC_i)}{\partial z}+\varepsilon_{bed}\frac{\partial C_i}{\partial t}+(1-\varepsilon_{bed})N_{g,i}=\varepsilon_{bed}\frac{\partial}{\partial z}\left(D_{z,i}\frac{\partial C_i}{\partial z}\right),\forall z\in(0,L),i=1,\dots,N_{comp} \quad (1)$$

where ε_{bed} is the porosity of the bed, u is the interstitial velocity, C_i is the molar concentration of component i in the bulk gas, $D_{z,i}$ is the mass axial dispersion coefficient and the term $N_{g,i}$ is the generation term given per unit volume of adsorbent which quantifies the mass transfer occurring between bulk flow and particles. The actual expression for the generation term $N_{g,i}$ depends on the nature of the resistances to the mass transfer and for linear driving force (LDF) mechanism is provided by the following equation (2):

$$N_{g,i}=\rho^p\frac{\partial Q_i}{\partial t},\qquad \forall z\in(0,L),i=1,\dots,N_{comp} \quad (2)$$

where Q_i is the adsorbed amount per unit mass of adsorbent and ρ^p is the density of the particle.

The heat balance equation which describes the heat transfer in the bulk gas flow is:

$$\varepsilon_{bed}\frac{\partial(\rho c_p T u)}{\partial z}+\varepsilon_{bed}\frac{\partial(\rho c_p T)}{\partial t}+(1-\varepsilon_{bed})q_g+\frac{3k_{h,wall}}{R_{bed}}(T-T_{wall})=\varepsilon_{bed}\frac{\partial}{\partial z}\left(\lambda_z\frac{\partial T}{\partial z}\right),\quad \forall z\in(0,L) \tag{3}$$

where ρ is the density of bulk gas, c_p is the specific heat capacity of bulk gas, T is the temperature of bulk gas, λ_z is the heat axial dispersion coefficient, $k_{h,wall}$ is the heat transfer coefficient between the bulk flow and the column wall, T_{wall} is the temperature of the column wall and R_{bed} is the bed radius and q_g is the generation term given per unit volume of adsorbent, which quantifies the heat transfer occurring between bulk flow and particles. The actual expression for the generation term q_g depends on the nature of the resistances to the heat transfer and for linear driving force (LDF) mechanism is provided by the following equation (4):

$$q_g=\frac{\partial(\rho^p c_p^p T)}{\partial t}+\rho^p\sum_{i=1}^{N_{comp}}\Delta H_{ads,i}\frac{\partial Q_i}{\partial t},\qquad \forall z\in(0,L) \tag{4}$$

where $\Delta H_{ads,i}$ is the isosteric heat of adsorption and c_p^p is the specific heat capacity of the particle.

The pressure drop is an important variable in the modelling of fixed adsorption columns having a high impact on the separation quality and operating cost. The hydrodynamics of flow through porous media is the most commonly described by using the following Ergun equation (non-linear, turbulent flow) for pressure drop:

$$-\frac{\partial P}{\partial z}=150\left(\frac{1-\varepsilon_{bed}}{\varepsilon_{bed}}\right)^2\frac{\mu u}{(2R_p)^2}+1.75\left(\frac{1-\varepsilon_{bed}}{\varepsilon_{bed}}\right)\frac{\rho u|u|}{2R_p},\qquad \forall z\in(0,L) \tag{5}$$

where P is the total pressure, μ is the viscosity of bulk gas and R_p is the particle radius.

An equation of state is necessary to link concentration with temperature and pressure in the gas mixture. The ideal gas law is provided by the following equation:

$$P=\sum_{i=1}^{N_{comp}}C_i RT,\qquad \forall z\in[0,L] \tag{6}$$

where R is the universal gas constant.

Physical properties (density, viscosity, thermal conductivity, specific heat capacity) of the gas mixture can be assumed constant or calculated using some of the available correlations or thermo-physical packages. In any case, physical properties are functions of temperature, pressure and composition, presented in the following general form:

$$\rho,\mu,\lambda,c_p=f\left(T,P,C_1,C_2,\dots,C_{Ncomp}\right),\qquad \forall z\in[0,L] \tag{7}$$

The mass axial dispersion coefficient $D_{z,i}$ and the heat axial dispersion coefficient λ_z can be calculated by using Wakao correlations:

$$D_{z,i}=\frac{D_{m,i}}{\varepsilon_{bed}}(20+0.5ScRe),\qquad \forall z\in[0,L], i=1,\dots,N_{comp} \tag{8}$$

$$\lambda_z=\lambda(7+0.5PrRe),\qquad \forall z\in[0,L] \tag{9}$$

where $D_{m,i}$ is the molecular diffusivity, λ is the thermal conductivity of bulk gas, Sc is the Schmidt number, Re is the Reynolds number and Pr is the Prandl number.

In linear driving force (LDF) mechanism the overall uptake rate in a particle is expressed as a function of the bulk gas flow concentration:

$$\frac{\partial Q_i}{\partial t} = \frac{15 D_{e,i}}{R_p^2}(Q_i^* - Q_i), \qquad \forall z \in [0, L], i = 1, \dots, N_{comp} \tag{10}$$

where Q_i is the adsorbed amount per unit mass of adsorbent, Q_i^* is adsorbed amount in equilibrium with the gas phase and $D_{e,i}$ is the effective diffusivity. The effective diffusivity $D_{e,i}$ can be calculated by using Bosanquet equation:

$$D_{e,i} = \frac{\varepsilon_p}{\tau_p}\frac{D_{m,i} D_{k,i}}{D_{m,i} + D_{k,i}}, \qquad \forall r \in [0, R_p], i = 1, \dots, N_{comp} \tag{11}$$

where ε_p is the porosity of the particle, τ_p is the tortuosity factor of the particle, $D_{k,i}$ is the Knudsen diffusivity and $D_{m,i}$ is the molecular diffusivity.
The Knudsen diffusivity $D_{k,i}$ can be calculated by using Kauzmann correlation:

$$D_{k,i} = 97 R_{pore}\sqrt{\frac{T^p}{MW_i}}, \qquad \forall r \in [0, R_p], i = 1, \dots, N_{comp} \tag{12}$$

where R_{pore} is the radius of the pore, T^p is the temperature of the particle and MW_i is the molecular weight of component i.
The molecular diffusivity $D_{m,i}$ is independent of the composition and for a binary mixture can be calculated by using Chapman-Enskog equation:

$$D_{m,i} = 1.8583 * 10^{-7}\frac{\sqrt{T^3\left(\frac{1}{MW_1} + \frac{1}{MW_2}\right)}}{P\sigma_{12}^2 \Omega_{12}}, \qquad \forall r \in [0, R_p], i = 1,2 \tag{13}$$

where σ_{12} is the collision diameter from the Lennard-Jones potential and Ω_{12} is the collision integral.
The following dual-site Langmuir isotherm describes the adsorption equilibrium:

$$Q_i^* = \frac{q_{mi(1)} b_{i(1)} P_i}{1 + \sum_{i=1}^{N_{comp}} b_{i(1)} P_i} + \frac{q_{mi(2)} b_{i(2)} P_i}{1 + \sum_{i=1}^{N_{comp}} b_{i(2)} P_i} \tag{14}$$

where $q_{mi(j)}$ and $b_{i(j)}$ are the isotherm parameters and P_i is the partial pressure which is a function of the molar fraction in gas phase y_i given by the following equation:

$$P_i = y_i \mathrm{P} \tag{15}$$

3. Case study

The proposed modelling framework has been applied in a PSA/VSA process concerning the separation of CO_2 from dry flue gas (15 % CO_2, 85 % N_2) using zeolite 13X as an adsorbent. The parameters of adsorption column model and the parameters of the dual-site Langmuir adsorption isotherm have been adopted from the works of Ko et al. (2004) and Ko et al. (2005).
The sequence of the operating steps for the one-adsorption column configuration is: Pressurization with the feed stream co-currently (FP), Adsorption (F), Co-current depressurization or Blowdown (CoD) to intermediate pressure and Counter-current depressurization or Evacuation (CnD) to low pressure. A 4-step PSA/VSA process with the pressure profiles adopted from the work of Haghpanah et al. (2013) is illustrated in Figure 1.

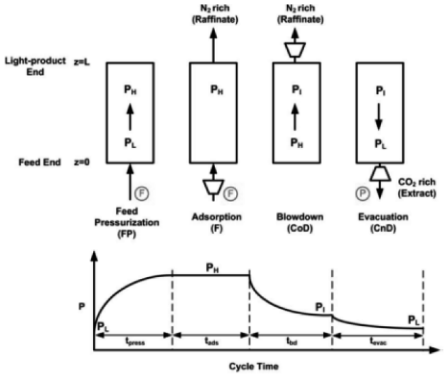

Figure 1. A 4-step PSA/VSA process with the pressure profiles.

4. Results

The modelling framework has been validated against analytical PSA models, full adsorption numerical simulations, and experiments. The simulation results in terms of process performance indicators with absolute deviations from the results of works of Ko et al. (2004) and Ko et al. (2005) are summarized in Table 1.

Furthermore, a systematic parametric analysis provides significant insight into the most critical design and operating parameters, and their effect on the process performance indicators. The parametric studies performed in this work have been carried out only in cases when it was necessary to clarify the effect of certain parameter on the process performance. Thus, once the base case parameters have been selected, only one variable at the time has been varied, and its effect analyzed. We have conducted a sensitivity study to determine which properties are most important in order to improve process performance. The results of sensitivity analysis illustrate the typical trade-offs between process performance indicators. The effect of feed pressure (P_{feed}), feed flowrate (F_{feed}), blowdown pressure (P_{blow}) and adsorption step duration (t_{ads}) on the PSA/VSA process performance indicators are presented in Figures 2,3,4,5 respectively.

Table 1. Simulation results in terms of process performance indicators with absolute deviations from the results of works of Ko et al. (2004) and Ko et al. (2005).

						Ko et al	Ko et al	this work	this work		
Reference	Pfeed (bar)	Tfeed (K)	L/D	Number of cycles (CSS)	Discretization method	Purity CO_2	Recovery CO_2	Purity CO_2	Recovery CO_2	Deviation Purity CO_2	Deviation Recovery CO_2
Ko et al. (2005)	6.52	370.00	11.36	100	CFDM,2,40	88.94	96.90	84.82	97.93	-4.63	1.06
Ko et al. (2004)	6.94	365.32	11.36	100	CFDM,2,40	95.46	15.00	92.12	14.35	-3.50	-4.33
Ko et al. (2004)	8.69	364.42	17.64	100	CFDM,2,40	92.29	80.00	97.19	79.20	5.31	-1.00

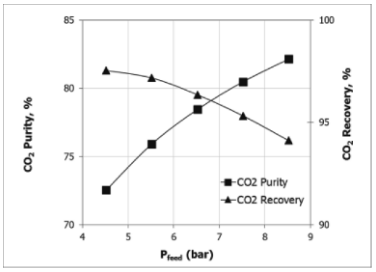

Figure 2. Effect of feed pressure.

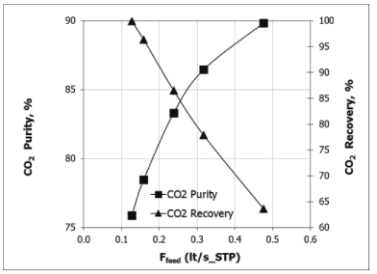

Figure 3. Effect of feed flowrate.

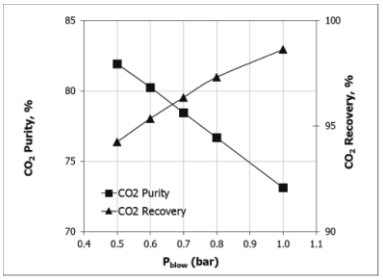

Figure 4. Effect of blowdown pressure.

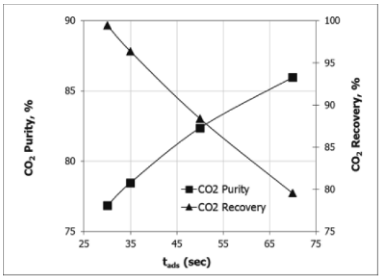

Figure 5. Effect of adsorption step duration.

5. Conclusions

The core of the modelling framework represents a detailed adsorption column model relying on a coupled set of mixed partial differential and algebraic equations (PDAEs) for mass, heat and momentum balance at both bulk gas and particle level, equilibrium isotherm equations, transport and thermo-physical properties of the gas mixture and boundary conditions according to the operating steps. The modelling framework is coupled with a novel state transition network (STN) approach developed in our previous work to account for all feasible adsorption column interconnections. The modelling framework provides a comprehensive qualitative and quantitative insight into the key phenomena taking place in the process.

The proposed modelling equations have been implemented in the gPROMS™ modelling environment. The simulation results of the proposed modelling framework in terms of process performance indicators (CO_2 purity and CO_2 recovery) are in good agreement with data available from the literature. The results of sensitivity analysis illustrate the typical trade-offs between process performance indicators.

6. Acknowledgement

Financial support from: (i) the co- Financed by the European Union and the Greek State program FENCO-NET: Project MOFCCS (Contract No.13FENCO-13-940) and (ii) the EFENIS FP7 project (Contract No. ENER/FP7/296003) are gratefully acknowledged.

References

R. Haghpanah, A. Majumder, R. Nilam, A. Rajendran, S. Farooq, I. A. Karimi, M. Amanullah, 2013, Multiobjective optimization of a four-step adsorption process for postcombustion CO_2 capture via finite volume simulation, Industrial and Engineering Chemistry Research, 52, 11, 4249-4265.

E. S.Kikkinides, D. Nikolic, M.C. Georgiadis, 2011, Modeling of Pressure Swing Adsorption Processes, In: Engineering PS, ed. Dynamic Process Modeling, 7,137-172.

D. Ko, R. Siriwardane, L.T. Biegler, 2004, Optimization of pressure swing adsorption and fractionated vacuum pressure swing adsorption processes for CO_2 sequestration, AIChE Annual Meeting, Unpublished manuscript.

D. Ko, R. Siriwardane, L.T. Biegler, 2005, Optimization of pressure swing adsorption and fractionated vacuum pressure swing adsorption processes for CO_2 capture, Industrial and Engineering Chemistry Research, 44, 21, 8084-8094.

D. Nikolic, A. Giovanoglou, M.C. Georgiadis, E.S. Kikkinides, 2008, Generic modeling framework for gas separations using multibed pressure swing adsorption processes, Industrial and Engineering Chemistry Research, 47, 9, 3156-3169.

D. Nikolic, E.S. Kikkinides, M.C. Georgiadis, 2009, Optimization of multibed pressure swing adsorption processes, Industrial and Engineering Chemistry Research, 48, 11, 5388-5398.

Krist V. Gernaey, Jakob K. Huusom and Rafiqul Gani (Eds.), 12th International Symposium on Process Systems Engineering and 25th European Symposium on Computer Aided Process Engineering.
31 May – 4 June 2015, Copenhagen, Denmark

Validation of a functional model for integration of safety into process system design

Wu, J.,[a,c*] Lind, M.,[b] Zhang, X., [b] Jørgensen, S. B.,[c] Sin, G.[c]

[a]*Beijing Waterworks Group Co.,Ltd.,Beijing, China,100031*
[b] *Department of Electrical Engineering, Technical University of Denmark, Building 326, 2800 Lyngby, Denmark*
[c]*CAPEC-PROCESS, Department of Chemical and Biochemical Engineering, Technical University of Denmark, Building 229,2800 Lyngby, Denmark*
wj87811@126.com

Abstract

Qualitative modeling paradigm offers process systems engineering a potential for developing effective tools for handling issues related to Process Safety. A qualitative functional modeling environment can accommodate different levels of abstraction for capturing knowledge associated with the process system functionalities as required for the intended safety applications. To provide the scientific rigor and facilitate the acceptance of qualitative modelling, this contribution focuses on developing a scientifically based validation method for functional models. The Multilevel Flow Modeling (MFM) methodology is adopted in the paper as a formalized qualitative functional modeling methodology for dynamic process systems. A functional model validation procedure is proposed to assess whether the intended modeling purpose indeed represents a relevant proposal and whether the model represents the system behavior sufficiently well. With the reasoning capability provided by the MFM syntax and semantics, the validation procedure is illustrated on a three-phase separator system of an MFM model. The MFM model reasoning results successfully compares against analysis results from API RP. 14-C.

Keywords: Functional Model; Multilevel Flow Modeling; Model Validation; Process Safety

1. Introduction

A lack of general acceptance of a qualitative modeling paradigm for process systems has limited process system engineers in developing effective tools for handling issues related to Process Safety(Stephanopoulos, Reklaitis, 2011). The most effective and economical way of dealing with hazards and risks is to address them in Conceptual and Design Steps in a design process (Manuele, 2013). However, the demands for safety through design provided by available guidelines and procedures are far beyond the existing supporting design approaches. Therefore there is a need to explicitly represent system safety features in a model-based design framework. The top-down procedure from design goals to components through functions is regarded to be of great importance in a conceptual design. A qualitative functional modeling environment can accommodate different levels of abstraction for capturing knowledge associated with the process system functionalities as required for the intended application. The intended use of the model indeed determines the necessary degree of sophistication and complexity of the model. Hence, it is necessary to check the consistency and usefulness

of a model against its end use before a model is applied. For example, a model intended for design is required to describe steady-state mass/energy balances of a system. Hence for model validation purposes, validation of a design model would require steady-state type experiments under different design/operation conditions.

In quantitative modelling, model validation concept is well established using statistical frameworks (a body of literature exists on parameter estimation, hypothesis testing via goodness of fit test, F-test, etc) that compares model predictions against experimental observations (Belia et al., 2009). However this is not the case for the field of qualitative modelling, which is the subject of this study.

The Multilevel Flow Modeling (MFM) methodology (Lind, 2013) has been shown to be applicable for the steps of goal decomposition, listing up design conditions and constraints and function assignment. MFM is selected for demonstrating the model validation of process simulation due to its powerful expression ability and a set of reference rules (Zhang et al., 2013; Lind, 2012). With the reasoning capability provided by the MFM syntax and semantics, the proposed validation procedure is illustrated on a three-phase separator system of an MFM model with the external modeling purpose of addressing the safety requirements early in the system design.

2. A scientific basis for a functional model validation

The MFM methodology builds upon a teleological-oriented view of the function to represent process plants. The elements of an MFM model constitute representation of the intentions, the process functionality and their causal relations. The use of means-end relations (Lind, 2013) is a core concept. In MFM modeling, means-end relations link the goals with a structure of flow functions. There are two validation aspects of a means-end relation, namely, a causal aspect and a teleological aspect (Lind, 2014). The causal aspect relates to the designer's experience that the means can produce or prevent the end depending upon the purpose. The teleological aspect implies that the means should be used to achieve the goals. Dealing with functional models then truth cannot be established or tested alone by physical experiments. In order to test the validity of objectives and purposes we need to test these against the consensus among a group of experts (e.g. designers and operators). In this paper, because the experiment results compare with the API standard which is agreed upon within experts of the designed system purpose, in this sense, the validity of objectives and purposes is performed.

A model validation in reality can only be carried out as a model in-validation, i.e. to determine within which range of applications a model represents the process and its functions with the required accuracy for the intended purpose, i.e. application. As claimed by Popper (1934), a theory can only be falsified.

3. Validation procedure for an MFM model

Validation of an MFM model of an artifact (the process) is here proposed as a task of performing a number of experiments using the model and testing, whether the experimental results are in agreement with knowledge, as depicted in Figure 1. The first step is to specify the modeling purpose, i.e. the intended use of the model. Therefore, the modeling is divided into two categories: internal modeling, i.e. of internal system behavior and external modeling, i.e. of system purpose. To validate external modeling is to ascertain whether the intended purpose indeed represents a relevant proposal. To

validate the internal model behavior amounts to ascertain whether the model represents the system behavior sufficiently well for the intended modeling purpose. There are a number of sources available for validation of an external model: Interviews, procedures and guidelines. To verify the internal model representation of the conceptual description of the real system, the internal MFM model behavior is investigated as the second step. It is assumed that the verification of the model implementation is handled by the MFM syntax, i.e. the modeling environment. For the internal model validation there is a realization of the system or a quantitative simulator which has been validated for some specific conditions within the operating window. Because a functional model is a conceptual model and explicitly aims at representing the tacit knowledge behind the model usage; the scope of a functional model is broader than that of a quantitative mathematical model. Thus in some cases, a validated quantitative simulator constitutes an insufficient source to validate an MFM model. Therefore, interviews, procedures and guidelines also may be important sources to complement a validated quantitative simulator for validating the internal model behavior, because these two sources implicitly contain some of the tacit knowledge. For internal model validation, a number of validation experiments should be designed to validate each of the above discussed elements of MFM model. The experiments are implemented by iteratively for i less than or equal to N(i for one design/operation condition, N for all possible design/operation conditions). If a validated quantitative simulator is chosen to be used as a source to validate an MFM model and the qualitative results derived from the MFM model include the quantitative simulation results, then the experiments are valid within the investigated range of the quantitative model; if the qualitative results are entirely consistent with the quantitative results, then the validation procedure directly proceeds to the next iteration. However if the qualitative analysis results contain more assumptions, then additional reasoning rules can be created based on either the behavior of the real system, the interviews or the quantitative simulation results. If the qualitative results derived from the MFM model follows the behavior of real system the interviews or the quantitative simulation results until i=N, then the MFM model is not invalidated which means the validation procedure ends. However, if a qualitative analysis results do not include a result derived from the behavior of real system the interviews or the quantitative simulation experiments, then that aspect of the MFM model is invalidated. Consequently that aspect of the MFM model behavior has to be further analyzed.

In this paper, because the application purpose of an MFM model is intended for the early design phase with respect to safety, quantitative model of the studied system is considered not available. Therefore, the guidelines and procedures are selected as a validation source. However, after the detailed design phase, where the quantitative information is known, and if a validated quantitative simulator is chosen to be used as a source to validate an MFM model, then the criteria for accepted discrepancy between behaviors of an MFM model and a validated quantitative simulator is related to two considerations: the difference in granularity and differences in suitable application range between a qualitative and a quantitative model. When designing validation experiments it is important to consider the difference in granularity between a qualitative and a quantitative model. The disturbance to be applied has to be sufficiently large to inflict a discernible change in the qualitative model behavior. Such a change can appear rather large in the quantitative model. On the other hand, a quantitative model has limited range of application. When the designed experiment is out of the applicable range, it is unsuitable to carry out such experiment in a quantitative simulator. Therefore validation of a functional model depends both on validation of the reasoning capability of the

functional model for "small" changes in a quantitative simulator and on determining the validity range for these predictions as indicated by the limits determined from large(-r) disturbances in the quantitative simulator.

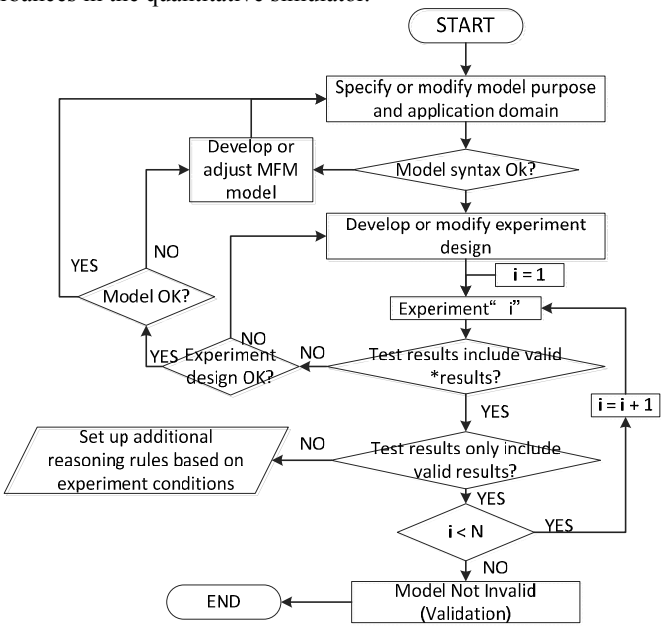

Figure 1. Validation procedure for an MFM model

(*Experimental result is consistent with qualitative functional model reasoning)

4. Case study

In the petroleum industry, a 3-phase separator is necessary equipment for the oil and gas production and transportation process. An MFM model of a three phase separator is shown in Figure 2. The model is built based on the goal decomposition, and functional requirements of the 3-phase separator and its control system. The mass flow structure mfs3 represents the mass flow of the heating system inside the separator. The tra 10 heating inlet mass flow mediates (me 1) the energy exchange between mixed oil, gas, water inlet flow and heating mass flow to achieve proper mixed oil, gas, water inlet temperature(obj6)as a condition for the separator to separate (sep1) the gas and water-oil liquid in desired velocity. The separated water-oil liquid produces the source (sou2) in the settling chamber of the separator separating (sep2) the oil (sto2) and the water (sto1) based on their gravity difference. The barrier (bar 1) is the function of the weir plate between the settling chamber and oil chamber. The control structures for modelling the functions of the control of the separating temperature (cfs4), the pressure control (cfs3), oil level control (cfs2), and the water level control (cfs1) are modeled.

To validate the internal modelling, the following experiments considering undesirable events for each flow structure are executed to identify causes: (1)overpressure(sto1 high), (2)underpressure(sto1 low), (3)liquid overflow(sto2 high or sto3 high), (4) gas blowby(sto2 low), (5) leak(sto1 low and sto2 low) and (6)excess temperature(tra 16 high).

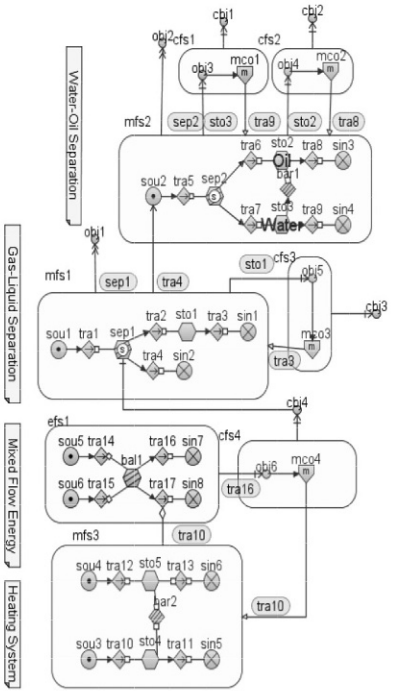

Figure 2. An MFM model of a 3-phase separator

Figure 3. Reasoning results to be compared to validation results

Table 1. Comparison experiment results with API RP 14C

Experiment No.	Causes in API RP 14C	Causes produced from the MFM model
1. Overpressure (sto1 high)	Blocked or restricted outlet	sin 1 high volume
	Inflow exceeds outflow	tra 3 low flow, tra 2 high flow
	Gas blowby(upstream component)	tra 1 high flow
	Thermal expansion	sep1 fill
	Excess heat input	obj6 fail
2. Underpressure(sto1 low)	Withdrawals exceed inflow	tra 2 low flow
	Thermal contraction	sep1 leak
	Open outlet	tra 3 high flow
	Pressure control system failure	cbj3 fails
3. Liquid overflow (sto3 high)	Inflow exceeds outflow	tra 9 low flow, tra7 high flow
	Liquid slug flow	tra 6 low flow
	Blocked or restricted liquid outlet	sin 4 high voloume
	Level control system failure	cbj 1 fail
4. Gas blowby (sto2 low)	Liquid withdrawal exceed inflow	tra 6 low flow, tra 8 high flow
	Open liquid outlet	tra 8 high flow
5. Leak (sto1 low and sto2 low)	Deterioration	
	Erosion	
	Corrosion	sep1 leak
	Impact damage	
	Vibration	
6.Excess temperature(tra 16 high)	Temperature control system failure	cbj 4 fail
	High inlet temperature	sou 5 high volume

The experimental results for each undesirable event identifying the causes are shown in Figure 3. The underlined causes are all possible root causes(">"means because of). By comparison of the results with Table A.4.1-Safety Analysis Table (SAT) Pressure

Vessels in API RP. 14-C (1998) (shown in Table 1), we find that the experiments results are in accordance with Table A 4.1. With these comparative analysis, MFM model is considered not falsified hence can be utilized as external modeling tool for safety-based design and analysis. In this way, different design of safety systems can be generated to provide primary and secondary levels of protection to prevent or minimize the effects of the failure causes identified by the MFM model.

5. Conclusions

Qualitative process knowledge is inherently used in certain PSE tasks, i.e., design and analysis of safety systems in the early project development phase using HAZID/HAZOP type structured brainstorming sessions. To facilitate the development and use of qualitative models for such ends, assessment of the validity and the validity range for qualitative models represents an important scientific challenge. Based upon the functional modeling paradigm a two layered procedure for validating functional models is proposed. The key principles of the validation procedure are demonstrated on a three phase separator system which is modeled using MFM. The causal reasoning system behind MFM is shown to be essential for demonstrating the validation procedure.

6. Acknowledgement

The first author thanks to the support from the research groups at Department of Electrical Engineering and Department of Chemical and Biochemical Engineering at DTU. This work is also supported by National Natural Science Foundation of China (Grant No. 51104168); Program for New Century Excellent Talents in University （NCET-12-0972）; Beijing Natural Science Foundation （Grant No.3132027）.

References

API, RP.14-C, 1998, Recommended Practice for Analysis, Design, Installation, and Testing of Basic Surface Safety Systems for Offshore Production Platforms, API Recommended Practice 14C, American Petroleum Institute/01-Mar-2001.

E. Belia, Y. Amerlinck, L. Benedetti, B. Johnson, G. Sin, P.A. Vanrolleghem, K.V. Gernaey, S. Gillot, M.B. Neumann, L. Rieger, A. Shaw and K. Villez, 2009, Wastewater Treatment Modelling: Dealing With Uncertainties, Water Science Technology, 60(8), 1929-1941.

M. Lind, 2012, Reasoning About Causes and Consequences in Multilevel Flow Models. In: Advances in Safety, Reliability and Risk Management - Proceedings of the European Safety and Reliability Conference, ESREL 2011, European Safety and Reliability Association, 2359-2367.

M. Lind, 2013, An Overview of Multilevel Flow Modeling, Nuclear Safety and Simulation, 4, 186-191.

M. Lind, 2014, Applying Functional Modeling for Accident Management of Nuclear Power Plant. In Proceedings of ISOFIC/ISSNP, Jeju, Korea.

F.A. Manuele, 2013, On the Practice of Safety, John Wiley & Sons.

K.R. Popper, 1934, Logik der Forschung. Wien. Springer, 308, 34-50..

G. Stephanopoulos, G.V. Reklaitis, 2011, Process Systems Engineering: From Solvay to Modern Bio-and Nanotechnology.: A History of Development, Successes and Prospects for the Future. Chemical Engineering Science, 66(19), 4272-4306.

X. Zhang, M. Lind, O. Ravn, 2013, Consequence Reasoning in Multilevel Flow Modelling. In Proceedings of the 12th IFAC/IFIP/IFORS/IEA Symposium on Analysis, Design, and Evaluation of Human - Machine Systems,12(1),187-194.

Krist V. Gernaey, Jakob K. Huusom and Rafiqul Gani (Eds.), 12th International Symposium on Process Systems Engineering and 25th European Symposium on Computer Aided Process Engineering.
31 May - 4 June 2015, Copenhagen, Denmark.

A Dynamic Method for Computing Thermodynamic Equilibria in Process Simulation

Alexander Zinser[a,b], Kongmeng Ye[a], Liisa Rihko-Struckmann[a] and Kai Sundmacher[a,b,*]

[a]*Max Planck Insitute for Dynamics of Complex Technical Systems, D-39106 Magdeburg, Germany*
[b]*Otto-von-Guericke University, Process Systems Engineering, D-39106 Magdeburg, Germany*
**sundmacher@mpi-magdeburg.mpg.de*

Abstract

A generalized approach for the calculation of complex chemical and phase equilibria is presented which is based on the simulation of the dynamic evolution of a mixture from arbitrary nonequilibrium initial composition towards the final equilibrium composition. The proposed method is able to deal with pure chemical or pure phase equilibria as well as with simultaneous chemical/phase equilibria. The unique advantage of our approach, compared to conventional equilibrium calculations, is the fact that the simulation algorithm always converges towards the thermodynamic equilibrium state regardless which initial composition is chosen.

Keywords: Process Simulation, Chemical Equilibria, Phase Equilibria

1. Introduction

In process simulation, a large variety of thermodynamic equilibria, such as reaction equilibria and phase equilibria between two or more phases, have to be solved in the different process units. It is common, that for different types of equilibria, different mathematical approaches are applied. For reaction equilibria, the most common approach is the direct Gibbs energy minimization which formulates the equilibrium condition in terms of an optimization problem (Gmehling et al., 2012). In the case of phase equilibria, such as vapour-liquid equilibria (VLE) or liquid-liquid equilibria (LLE), a set of algorithms is available, that solve the necessary conditions to be fulfilled at the equilibrium state, namely the equality of the chemical potentials of all species in the coexisting phases at constant pressure and temperature (Gmehling et al., 2012; Steyer et al., 2005).

In the next section, we describe the proposed method for computing thermodynamic equilibria. After that, two different types of equilibria calculations are solved.

2. Method formulation

We define a set of species $\mathscr{S}$ and a set of phases $\mathscr{P}$ that can coexist in the considered closed thermodynamic system. E. g. $\mathscr{P} = \{\mathrm{V}, \mathrm{L1}, \mathrm{L2}\}$ denotes a VLL-system, were V refer to the vapor phase and L1 and L2 refers to the two liquid phases. Without loss of generality, the presented method can also be applied to systems containing other phases like a solid phase or a third liquid phase.

In order to compute the thermodynamic phase equilibrium of a p-phase system with s species, one needs $sp(p-1)/2$ rate expressions $r_{\sigma}^{\pi,\pi'}$ that describe the mass fluxes of all species $\sigma \in \mathscr{S}$ between the phases π and π' with $\pi, \pi' \in \mathscr{P}$ and $\pi \neq \pi'$. Additionally, in each phase $\pi \in \mathscr{P}$ may occur a set of chemical reactions $\rho \in \mathscr{R}^{\pi}$.

The proposed methodological approach for solving chemical as well as phase equilibria is formulated as a set of evolution equations in the form of a set of ordinary differential equations (ODE):

$$\frac{\mathrm{d}\mathbf{n}}{\mathrm{d}\tau} = \mathbf{A}\mathbf{r} \qquad \mathbf{n}(0) = \mathbf{n}_0 \tag{1}$$

that describes the dynamics of the molar composition in all phases

$$\mathbf{n} = [\mathbf{n}^\pi]_{\pi\in\mathscr{P}} \qquad \text{with } \mathbf{n}^\pi = [n_\sigma^\pi]_{\sigma\in\mathscr{S}} \tag{2}$$

w. r. t. time τ, a stoichiometric matrix $\mathbf{A}$ and a vector of rate expressions $\mathbf{r}$ that describes the fluxes between the phases as well as the mass fluxes due to chemical reactions. The stoichiometric matrix $\mathbf{A} = \begin{bmatrix}\mathbf{A}_\mathrm{p} & \mathbf{A}_\mathrm{r}\end{bmatrix}$ can be partitioned into the sub-matrix $\mathbf{A}_\mathrm{p}$ that models the connections between the phases, and a sub-matrix $\mathbf{A}_\mathrm{r}$ that models the stoichiometry of the reactions. Correspondingly, the vector of rate expressions $\mathbf{r} = \begin{bmatrix}\mathbf{r}_\mathrm{p}^\mathrm{T} & \mathbf{r}_\mathrm{r}^\mathrm{T}\end{bmatrix}^\mathrm{T}$ consists of two sub-vectors $\mathbf{r}_\mathrm{p}$ and $\mathbf{r}_\mathrm{r}$.

All those rate expressions are to be formulated in a thermodynamically consistent way, such that (i) the steady state of the ODE system, Eq. (1), is identical to the molar composition of the system in thermodynamic equilibrium, and such that (ii) the second law is not violated, i. e. the system's entropy production must not become negative at any time along its evolution towards the final equilibrium state.

2.1. Rate expressions for the mass transfer between phases

The rate expressions for the mass transfer between coexisting phases π and π'

$$\mathbf{r}_\mathrm{p} = \left[\mathbf{r}^{\pi,\pi'}\right]_{\substack{\pi,\pi'\in\mathscr{P}\\ \pi\neq\pi'}} \qquad \text{with } \mathbf{r}^{\pi,\pi'} = \left[r_\sigma^{\pi,\pi'}\right]_{\sigma\in\mathscr{S}} \tag{3}$$

are directly derivated from the thermodynamic equilibrium condition between the two phases π and π' (using the same reference state in all phases)

$$f_\sigma^\pi = f_\sigma^{\pi'}\,. \tag{4}$$

Any derivation from the equilibrium Eq. (4), gives rise to the mass transfer from one phase to the other. The rate of mass transfer can be expressed as follows:

$$r_\sigma^{\pi,\pi'} = k_\sigma^{\pi,\pi'}\left(f_\sigma^\pi - f_\sigma^{\pi'}\right). \tag{5}$$

At thermodynamic equilibrium, the rate becomes $r_\sigma^{\pi,\pi'} = 0$. $k_\sigma^{\pi,\pi'}$ stands for the rate constant of mass transfer. Due to the fact, that we are only interested in the steady state of the ODE system (1), this constant can be set to an arbitrary positive value, to be chosen such that the stiffness of the ODE system, Eq. (1), is small, e. g. $k_\sigma^{\pi,\pi'} = 1$.

2.2. Rate expressions for chemical reactions

The rate expressions for chemical reactions

$$\mathbf{r}_\mathrm{r} = [\mathbf{r}^\pi]_{\pi\in\mathscr{P}} \qquad \text{with } \mathbf{r}^\pi = \left[r_\rho^\pi\right]_{\rho\in\mathscr{R}^\pi} \tag{6}$$

are formulated as thermodynamically consistent mass action kinetics. Starting at the equilibrium condition for a single reaction ρ (Gmehling et al., 2012, p. 532)

$$K_{\mathrm{eq},\rho}^\pi = \prod_{\sigma\in\mathscr{S}}\left(\frac{f_\sigma^\pi}{f_\sigma^{\circ\pi}}\right)^{\nu_{\sigma\rho}^\pi} = \frac{\prod_{\substack{\sigma\in\mathscr{S}\\ \nu_{\sigma\rho}^\pi>0}}\left(\frac{f_\sigma^\pi}{f_\sigma^{\circ\pi}}\right)^{\nu_{\sigma\rho}^\pi}}{\prod_{\substack{\sigma\in\mathscr{S}\\ \nu_{\sigma\rho}^\pi<0}}\left(\frac{f_\sigma^\pi}{f_\sigma^{\circ\pi}}\right)^{|\nu_{\sigma\rho}^\pi|}} \tag{7}$$

the following rate law is proposed:

$$r_\rho^\pi = k_\rho^\pi \times \left[\prod_{\substack{\sigma\in\mathscr{S} \\ \nu_{\sigma\rho}^\pi<0}} \left(\frac{f_\sigma^\pi}{f_\sigma^{\circ\pi}}\right)^{|\nu_{\sigma\rho}^\pi|} - \frac{1}{K_{\mathrm{eq},\rho}^\pi} \prod_{\substack{\sigma\in\mathscr{S} \\ \nu_{\sigma\rho}^\pi>0}} \left(\frac{f_\sigma^\pi}{f_\sigma^{\circ\pi}}\right)^{\nu_{\sigma\rho}^\pi} \right] \tag{8}$$

which becomes $r_\rho^\pi = 0$ if the chemical equilibrium is attained. k_ρ^π stands for the reaction rate constant. Again, due to the fact that we want to determine the final steady state, also this constant can be set to an arbitrary value, e. g. $k_\rho^\pi = 1$.

3. Examples

For illustration, the here proposed nonequilibrium apporach to equilibrium calculations is applied to two examples in the context of the Fischer-Tropsch (FT) synthesis which is a key process for converting syngas into liquid fuels. As first example the chemical equilibria of the synthesis of alkanes is computed. It is common, that the product spectrum can be described by a Flory-type distribution $x_{\mathrm{C}i} = (1-\alpha)\alpha^{i-1}$ (Flory, 1936), where α is the chain growth probability and i the number of carbon atoms. The subscript Ci refers to the alkane $\mathrm{C}_i\mathrm{H}_{2i+2}$. As second example, a vapour-liquid-liquid separation of the product spectrum of the Fischer-Tropsch reactor is performed.

In both examples, the resulting ODE systems were implemented in MATLAB and solved by use of the `ode15s`-solver (Shampine and Reichelt, 1997).

3.1. Fischer-Tropsch reactions

In the first example, we consider a reactive gas-phase system in which syngas is converted into n-alkanes up to C8 according to the following main FT reactions:

$$\mathrm{CO} + 3\,\mathrm{H_2} \longleftrightarrow \mathrm{CH_4} + \mathrm{H_2O}\,, \tag{9a}$$

$$\mathrm{CO} + 2\,\mathrm{H_2} + \mathrm{C}_{n-1}\mathrm{H}_{2n} \longleftrightarrow \mathrm{C}_n\mathrm{H}_{2n+2} + \mathrm{H_2O} \qquad \forall n = 2\ldots 8\,. \tag{9b}$$

In this system, we have 11 species

$$\mathscr{S} = \{\mathrm{CO}, \mathrm{H_2}, \mathrm{H_2O}, \mathrm{C}_n\mathrm{H}_{2n+2} \forall n = 1\ldots 8\}\,, \tag{10}$$

one phase $\mathscr{P} = \{\mathrm{V}\}$ and 8 chemical reactions, Eq. (9). The stoichiometric matrix $\mathbf{A}$ of this system is given by

$$\mathbf{A} = \mathbf{A}_\mathrm{r} = \begin{bmatrix} -1 & -3 & 1 & 1 & & & 0 \\ -1 & -2 & 1 & -1 & 1 & & \\ \vdots & \vdots & \vdots & & \ddots & \ddots & \\ -1 & -2 & 1 & 0 & & -1 & 1 \end{bmatrix}^\mathrm{T} \in \mathbb{R}^{11\times 8}. \tag{11}$$

Due to the fact, that we have only one phase, $\pi \equiv \mathrm{V}$, the superscript π that refers to the phase is omitted in the following equations for better readability. Expressing the species fugacity in terms of the fugacity coefficient φ_σ and the mole fraction x_σ, $f_\sigma = x_\sigma\varphi_\sigma P = (x\varphi)_\sigma P$, and setting $P^\circ = 101325\,\mathrm{Pa}$, the rate expressions applied in this case are:

$$r_1 = k_1 \times \left[(x\varphi)_\mathrm{CO}\,(x\varphi)_\mathrm{H2}^3 \left(\frac{P}{P^\circ}\right)^4 - \frac{(x\varphi)_\mathrm{C1}(x\varphi)_\mathrm{H2O}}{K_{\mathrm{eq},1}} \left(\frac{P}{P^\circ}\right)^2 \right], \tag{12a}$$

$$r_i = k_i \times \left[(x\varphi)_\mathrm{CO}\,(x\varphi)_\mathrm{H2}^2\,(x\varphi)_{\mathrm{C}(i-1)} \left(\frac{P}{P^\circ}\right)^4 - \frac{(x\varphi)_{\mathrm{C}i}(x\varphi)_\mathrm{H2O}}{K_{\mathrm{eq},i}} \left(\frac{P}{P^\circ}\right)^2 \right] \quad \forall i = 2\ldots 8\,. \tag{12b}$$

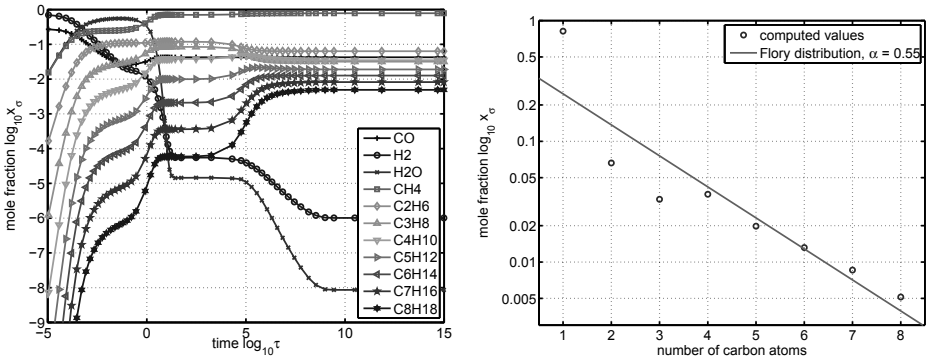

Figure 1: Evolution of the mole fractions x_σ and distribution of the alkanes at equilibrium which corresponds to the Flory distribution with $\alpha = 0.55$ (right).

Table 1: Feed composition n^0_σ and product composition n_σ of the Fischer-Tropsch reactor.

species	σ	CO	H_2	H_2O	CH_4	C_2H_6	
feed	n^0_σ/mol	1.0	2.6				
product	n_σ/mol	0.0425	0.0000	0.0000	0.7828	0.0633	
species	σ	C_3H_8	C_4H_{10}	C_5H_{12}	C_6H_{14}	C_7H_{16}	C_8H_{18}
product	n_σ/mol	0.0317	0.0349	0.0190	0.0126	0.0082	0.0049

The fugacity coefficients φ_σ are obtained from the predictive Soave-Redlich-Kwong (PSRK) Equation of State (EoS) (Holderbaum and Gmehling, 1991; Fischer and Gmehling, 1996; Soave, 1972). The rate constants k_n are used here to normalize the rate expressions by setting $k_\rho = \sqrt{K_{\mathrm{eq},\rho}}$. The equilibrium constants $K_{\mathrm{eq},\rho} = \exp(-\Delta_R g/RT)$ are defined by the Gibbs energy of reaction ρ.

The ODE system, Eq. (1), for this example was solved at $T = 530\,\mathrm{K}$ and $P = 1.5\,\mathrm{MPa}$ with a feed of $n_{\mathrm{CO}}(0) = 1\,\mathrm{mol}$ and $n_{\mathrm{H2}}(0) = 2.6\,\mathrm{mol}$. This leads to a very small yield of longer alkanes, $\alpha \approx 10^{-3}$. Therefore, a sink term for the side product H_2O was added to the ODE system

$$\frac{\mathrm{d}n_{\mathrm{H2O}}}{\mathrm{d}\tau} = \cdots - \begin{cases} (n_{\mathrm{H2O}} - n^{\mathrm{lim}}_{\mathrm{H2O}}) & : n_{\mathrm{H2O}} > n^{\mathrm{lim}}_{\mathrm{H2O}} \\ 0 & : \text{else} \end{cases} \tag{13}$$

with $n^{\mathrm{lim}}_{\mathrm{H2O}} = 10^{-5}\,\mathrm{mol}$ to shift the equilibrium to the longer alkanes. A technical approximation of this water removal can be achieved by intermediate cooling and condensation of the water or by a condensation of the water directly in the reactor at high operating pressure. This leads approximately to a Flory distribution with $\alpha = 0.55$, see Fig. 1 (right), which is in good agreement with published experimental data on this process (Stenger and Askonas, 1986). The dynamic evolution of the mole fractions x_σ in the reactor is shown in Fig. 1 (left). The feed and product compositions are also given in Tab. 1.

3.2. Separation of the Fischer-Tropsch products

In the second example, we apply our method to a phase equilibrium problem, i. e. we compute the vapour-liquid-liquid equilibrium (VLLE) of the product composition of the Fischer-Tropsch reactor as given in Table 1 at $T = 288.15\,\mathrm{K}$ and $P = 2\,\mathrm{MPa}$. In order to demonstrate the suitability

of our method for a system that forms two liquid phases, the water which was already removed in the reactor in the first example, was added to the feed of the VLL separation.

In this case, the set $\mathscr{S}$ is the same as in the first example, Eq. (10), and the set of considered phases is $\mathscr{P} = \{\mathrm{V}, \mathrm{L1}, \mathrm{L2}\}$. In this system, we have to formulate driving forces for each species across each interface. The rate expressions of the V-L mass fluxes are formulated using the φ-φ-approach for the fugacities.

$$r_\sigma^{\mathrm{V},\mathrm{L}i} = k_\sigma^{\mathrm{V},\mathrm{L}i} P \left(x_\sigma^{\mathrm{V}} \varphi_\sigma^{\mathrm{V}} - x_\sigma^{\mathrm{L}i} \varphi_\sigma^{\mathrm{L}i} \right), \qquad i \in \{1,2\} \tag{14a}$$

and the mass fluxes between the two liquid phases is described using the γ-γ-approach

$$r_\sigma^{\mathrm{L1},\mathrm{L2}} = k_\sigma^{\mathrm{L1},\mathrm{L2}} P^\circ \left(x_\sigma^{\mathrm{L1}} \gamma_\sigma^{\mathrm{L1}} - x_\sigma^{\mathrm{L2}} \gamma_\sigma^{\mathrm{L2}} \right) \tag{14b}$$

with $k_\sigma^{\pi,\pi'} = 1$. The fucacity coefficients φ_σ^π are obtained from the PSRK EoS and the activity coefficients γ_σ^π are computed from a modified UNIFAC activity coefficient model (Horstmann et al., 2005; Holderbaum and Gmehling, 1991; Fredenslund et al., 1975). The stoichiometric matrix which connects the mass balances of the species in each phase is given by

$$\mathbf{A} = \mathbf{A}_\mathrm{p} = \begin{bmatrix} -\mathbf{I} & -\mathbf{I} & \mathbf{0} \\ \mathbf{I} & \mathbf{0} & -\mathbf{I} \\ \mathbf{0} & \mathbf{I} & \mathbf{I} \end{bmatrix} \tag{15}$$

where $\mathbf{I}$ denotes the 11×11 identity matrix and $\mathbf{0}$ is a 11×11 null matrix.

The ODE system, Eq. (1), of this system was solved at $T = 288.15\,\mathrm{K}$ and $P = 2\,\mathrm{MPa}$. In order to solve systems containing more than one phase, the feed composition has to be distributed among the phases that may occur. In this example, we have chosen a random distribution of all species between the three phases as initial condition for Eq. (1). The evolution of the composition in all phases is shown in Fig. 2, as well as the final compositions at equilibrium, see also Tab. 2. As it can seen, the nonconverted carbon monoxide as well as the light alkanes (C1–C3) are dominating the vapour phase. Additionally, we get two liquid phases, one organic phase which is dominated by the heavier alkanes (C4–C8) and one aqueous phase which consists only of water that is formed as coupled by-product of the reactions.

Table 2: Molar compositions x_σ^π at equilibrium.

phase	V	L1	L2
CO	0.045	0.002	0
H_2	0	0	0
H_2O	0.001	0.003	0.999
CH_4	0.825	0.091	0.001
C_2H_6	0.064	0.040	0
C_3H_8	0.029	0.064	0
C_4H_{10}	0.025	0.193	0
C_5H_{12}	0.008	0.204	0
C_6H_{14}	0.002	0.185	0
C_7H_{16}	0	0.135	0
C_8H_{18}	0	0.084	0

4. Conclusion

We showed that our proposed method is able to reliably compute complex chemical as well as phase equilibria. In a future work, we will apply our method also to combined phase and chemical equilibria computations. Furthermore, we will demonstrate how to perform dynamic equilibrium calculations within chemical process simulations.

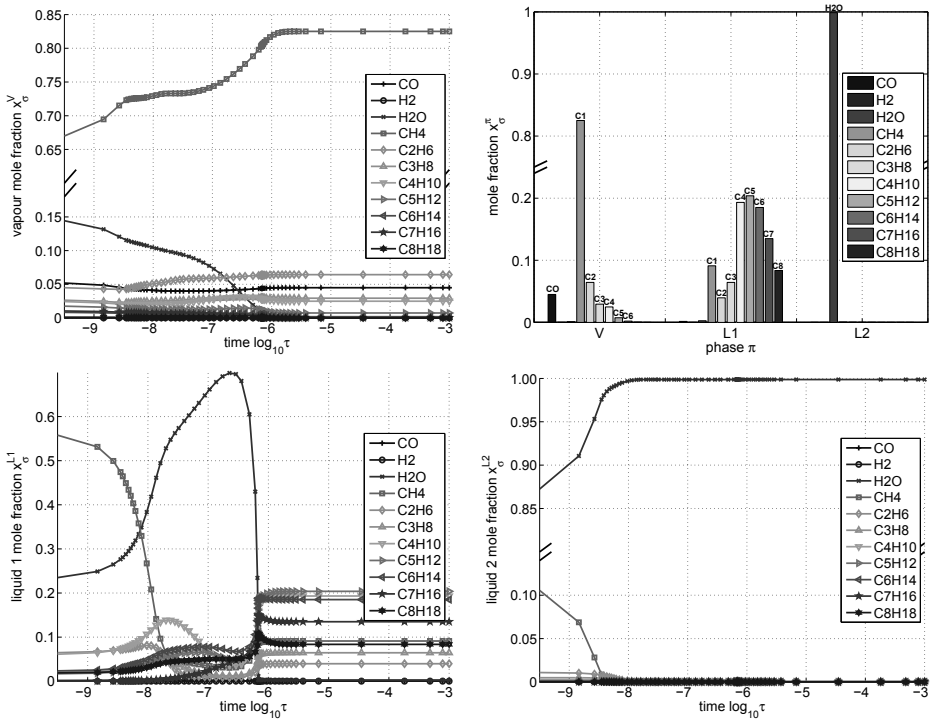

Figure 2: Evolution of the composition in the vapour phase x_σ^{V} (upper left), the evolution of the composition in the organic liquid phase x_σ^{L1} (lower left) and the evolution of the composition in the aqueous liquid phase x_σ^{L2} (lower right) w. r. t. time τ, as well as the final equilibrium composition of all phases (upper right).

References

K. Fischer, J. Gmehling, 1996. Further Development, Status and Results of the PSRK Method for the Prediction of Vapor-Liquid Equilibria and Gas Solubilities. Fluid Phase Equilib. 121, 185–206.

P. J. Flory, 1936. Molecular Size Distribution in Linear Condensation Polymers. J. Am. Chem. Soc. 58 (10), 1877–1885.

A. Fredenslund, R. L. Jones, J. M. Prausnitz, 1975. Group-Contribution Estimation of Activity Coefficients in Nonideal Liquid Mixtures. AIChE J. 21 (6), 1086–1099.

J. Gmehling, B. Kolbe, M. Kleiber, J. Rarey, 2012. Chemical Thermodynamics for Process Simulation. Wiley.

T. Holderbaum, J. Gmehling, 1991. PSRK: A Group Contribution Equation of State Based on UNIFAC. Fluid Phase Equilib. 70, 251–265.

S. Horstmann, A. Jabłoniec, J. Krafczyk, K. Fischer, J. Gmehling, 2005. PSRK Group Contribution Equation of State: Comprehensive Revision and Extension IV, Including Critical Constants and α-Function Parameters for 1000 Components. Fluid Phase Equilib. 227 (2), 157–164.

L. F. Shampine, M. W. Reichelt, 1997. The MATLAB ODE Suite. SIAM Journal on Scientific Computing 18, 1–22.

G. Soave, 1972. Equilibrium Constants from a Modified Redlich-Kwong Equation of State. Chem. Eng. Sci. 27 (6), 1197–1203.

H. G. Stenger, C. F. Askonas, 1986. Thermodynamic Product Distribution for the Fischer-Tropsch Synthesis. Ind. Eng. Chem. Fundam. 25, 410–413.

F. Steyer, D. Flockerzi, K. Sundmacher, 2005. Equilibrium and Rate-Based Approaches to Liquid-Liquid Phase Splitting Calculations. Comput. Chem. Eng. 30 (2), 277–284.

Krist V. Gernaey, Jakob K. Huusom and Rafiqul Gani (Eds.), 12th International Symposium on Process Systems Engineering and 25th European Symposium on Computer Aided Process Engineering.
31 May – 4 June 2015, Copenhagen, Denmark

Dynamics and operation analysis of the PHB (polyhydroxybutyrate) fermentation

Moises González-Contreras,[a] Omar Anaya-Reza,[b] Mauricio Sales-Cruz,[c] Teresa Lopez-Arenas [c]*

[a]*Posgrado en Ciencias Naturales e Ingeniería, Universidad Autónoma Metropolitana-Cuajimalpa, Vasco de Quiroga 4871, 05300 Mexico, D.F., Mexico*
[b]*Posgrado en Energía y Medio Ambiente, Universidad Autónoma Metropolitana-Iztapalapa, San Rafael Atlixco 186, 09430 Mexico, D.F., Mexico*
[c]*Departamento de Procesos y Tecnología, Universidad Autónoma Metropolitana-Cuajimalpa, Vasco de Quiroga 4871, 05300 Mexico, D.F., Mexico*
mtlopez@correo.cua.uam.mx

Abstract

PHB (polyhydroxybutyrate) is a biodegradable polymer that is gaining importance worldwide due to their applications. In this study, the PHB fermentation process is studied using sucrose as substrate and *Azohydromonas australica* as strain. A dynamic model of the isothermal reactor fermentation is used to calculate mainly product yield and productivity. Employing modelling and simulation tools, first a sensitivity analysis is performed to determine the parameter model dependence, then the model is used to analyse the dynamic effect of operation mode (batch or fed-batch). Results show a better performance for a fed-batch reactor and will be used in the short term for economic and environmental analyses of the production process.

Keywords: fermentation, modelling, simulation.

1. Introduction

Biorefineries are mostly known for the production of energy, but the production of some biomolecules of interest and other biomaterials are also integrated. They require complex production process engineering tools for design, analysis and optimization, in order to include important factors such as low production costs, high yields and a process that is environmentally friendly. A variety of organic chemicals can be obtained from sustainably use of renewable raw materials. For instance the production of PHB (polyhydroxybutyrate), which belongs to the group of PHA (polyhydroxyalkanoate) that is a biodegradable polymer belonging to the polyesters class. This biotech product is gaining importance worldwide due to their applications such as packaging material, fibber and foam materials, medical implants, carriers for drug delivery among others.

In general, the production of PHA granules is promoted due to unfavourable conditions for the growth of bacteria. These biopolymers are produced and accumulated inside the cell as energy reserve when the bacterial cells are under stress (as limitation of phosphorus, nitrogen, oxygen, or in a non-optimal pH) and an excess of carbon source. It has been reported that it can be reached in bacteria up to 80% of its dry weight in PHA molecules (Peña et al., 2014). Currently the main problem, which limits the widespread use of PHB, is its relatively high cost compared with polypropylene. The

fermentation process, substrates and product recovery are the major cost (Madison and Huisman, 1999). Several studies have tackled this problem using different approaches, focusing mainly on the kind of microorganisms and substrates, as well as on the process configuration design and optimization. The process analysis efforts are primarily focused on the reactor because of the high value of raw materials and products, but also because of its high sensitivity to operating conditions, and risk. Hence, it is necessary to submit the process to an initial screening design prior to optimization and control.

In this study, the PHB fermentation process is studied using sucrose as substrate and *Azohydromonas australica* as strain. A dynamic model for an isothermal fermentation reactor is used to obtain mainly product yield and productivity. Employing modelling and simulation tools, first a sensitivity analysis is performed to determine the parameter model dependence, then the model is used to analyse the dynamic effect of operation mode (batch or fed-batch). The results can help the process designer to understand the fermentation process, as well as to focus experimental efforts on the parameter estimation and the determination of operating conditions with greater relevance.

2. Fermentation model

The PHB fermentation takes place in a stirred tank bioreactor. The cell growth process and PHB synthesis that is an intracellular product are shown in the Figure 1, where residual biomass (R) is the difference between total cell dry mass (X) and product PHB (P), $R = X - P$ (Dunn et al., 2008). The assumptions to develop a mathematical model are: the substrate (S_1) and nitrogen (S_2) are the only limiting substrates, the reactor contents are perfectly mixed, physicochemical properties of the mixture are constant, the level of oxygen saturation is considered constant, and the reaction is isothermal. The reactor can be either batch or fed-batch, in this latter a feed flow (F) containing substrate (S_{F1}) and nitrogen source (S_{F2}). The feed strategy is shown in Figure 2.

For the case study, the batch kinetic data were taken from Gahlawat and Srivastava (2013) for the PHB production using sucrose as substrate and *A. Australica* as strain. So that the specific growth rate (μ) of the microorganism can be expressed as a function of two limiting nutrients (S_1 and S_2), including inhibition:

$$\mu = \mu_{max}\left(\frac{S_1}{S_1 + K_{s1}}\right)\left(\frac{S_2^n}{S_2^n + K_{S2}^n}\right)\left(\frac{K_{In}}{K_{In} + S_1}\right)\left(1 - \frac{S_2^a}{S_m^a}\right) \tag{1}$$

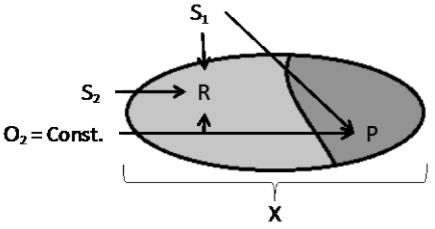

Figure 1. Cell growth and PHB synthesis.

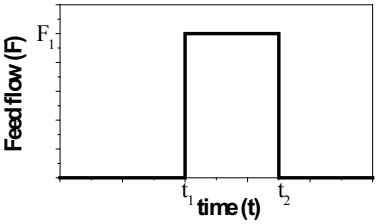

Figure 2. Feed flow for a fed-batch reactor.

The mathematical model of the PHB fermentation reactor is given by:

$$\frac{dR}{dt} = \mu R - \frac{F}{V}R, \qquad X = R + P, \qquad R(0) = R_0 \tag{2}$$

$$\frac{dS_1}{dt} = -q_{S1} R + \frac{F}{V}(S_{1F} - S_1), \qquad q_{S1} = -\left(\frac{\mu}{Y_{R/S_1}} + m_{S1}\right), \qquad S_1(0) = S_{10} \tag{3}$$

$$\frac{dS_2}{dt} = -q_{S2} R + \frac{F}{V}(S_{2F} - S_2), \qquad q_{S2} = -\left(\frac{\mu}{Y_{R/S_2}} + m_{S2}\right), \qquad S_2(0) = S_{20} \tag{4}$$

$$\frac{dP}{dt} = q_P R - \frac{F}{V}P, \qquad q_P = K_1 \cdot \mu, \qquad P(0) = 0 \tag{5}$$

$$\frac{dV}{dt} = F, \qquad V(0) = V_0 \qquad (F = 0 \text{ for a batch reactor}) \tag{6}$$

The product yield ($Y_{P/S}$) and productivity (i.e. space-time yield, Pr) are given by

$$Y_{P/S} = \frac{P \cdot V}{S_{10}V_0 + S_{1F}(V - V_0)}, \qquad Pr = \frac{P}{t} \tag{7}$$

3. Parameter sensitivity analysis

The kinetic parameters for the fermentation model (Eqs. 1-7) were adjusted from Gahlawat and Srivastava (2013) and are given in Table 1. Next a sensitivity analysis is performed for several reasons, such as the need to determine which parameters require further experimental research to enhance understanding of the process, which parameters are insignificant and can be eliminated from the model, which parameters are most highly correlated with the output; and once the model is in production use, what consequence results from changing a given input parameter (Hamby, 1994).

Table 1. Model parameters for PHB fermentation

Parameter	Value	Unit	notation
μ_{max}	0.41	h^{-1}	maximum specific growth rate
K_{s1}	10.31	g/L	sucrose affinity constant
K_{s2}	0.39	g/L	nitrogen affinity constant
K_1	3.80	g/g	growth associated product constant.
K_{In}	90.0	g/L	sucrose inhibition constant
$Y_{R/S1}$	0.099	g/g	biomass yield on sucrose
$Y_{R/S2}$	5.263	g/g	biomass yield on nitrogen
m_{S1}	0.062	g/(g.h)	maintenance coefficient respect to sucrose
m_{S2}	0.004	g/(g.h)	maintenance coefficient respect to nitrogen
S_m	13.0	g/L	critical nitrogen concentration
a	1.102	-	exponent for nitrogen inhibition
n	1.260	-	exponent for the sigmoidal relationship

A sensitivity ranking was obtained by increasing each parameter by a given percentage while leaving all others constant, and quantifying the change in model output. This sensitivity analysis was performed using the ICAS-MoT tool (Heitzig et al., 2011). Figures 3 and 4 show the corresponding results for the two main outputs (i.e. product and biomass concentrations) when varying one input parameter from its reference value of Table 1. According to these results the parameters K_1, $Y_{R/S2}$, μ_{max}, $Y_{R/S1}$ are those with more relevance (i.e. with more than 5% output difference), and they should be studied and estimated experimentally with more accurately to guaranty a satisfactory model prediction. In fact the parameters K_1, $Y_{R/S2}$, $Y_{R/S1}$ are directly related to the product and biomass yields, which depend strongly of the fermentation microorganism; while μ_{max} from the Monod Kinetics affects more the specific growth rate than K_{s1}.

4. Fermentation strategies

Batch fermentation is a popular process due to its flexibility and low operation costs, but the disadvantage is that the yield and productivity are usually low. Then, a fed-batch operation is employed to achieve high cell densities and a high concentration (Peña et al., 2014). Here both operating modes are compared by simulation to analyse their effect on the dynamics, and to achieve higher product yields and productivities.

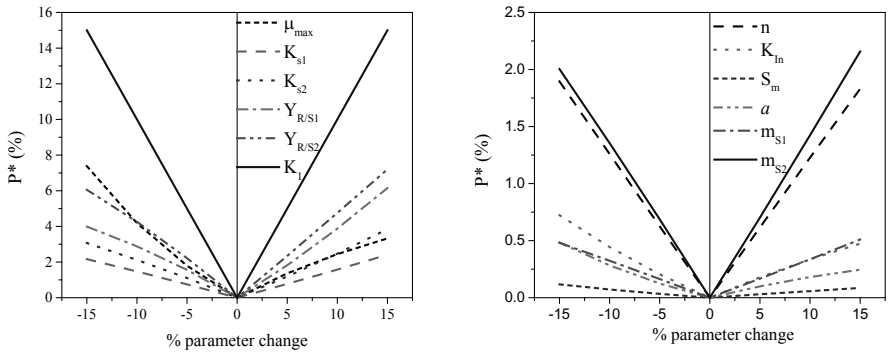

Figure 3. Parameter sensitivity analysis: product concentration difference (P^*).

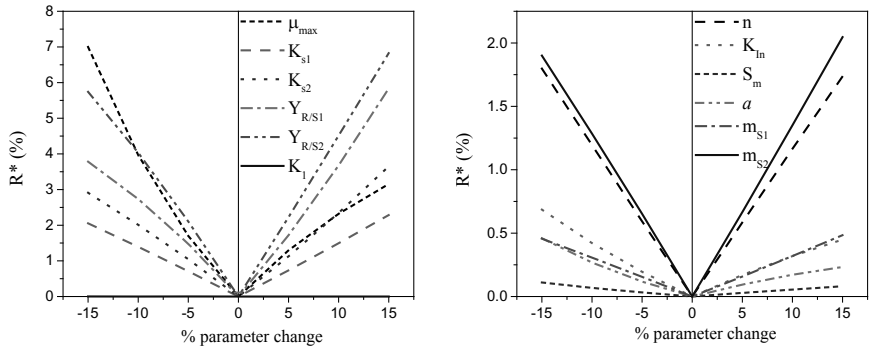

Figure 4. Parameter sensitivity analysis: residual biomass concentration difference (R^*).

All simulations consider an initial sucrose concentration of 25 g/L, as the culture growth with *A. Australica* has shown to have the maximum specific growth rate at this point; while the initial nitrogen concentration should be around 0.63 g/L to achieve the maximum specific growth rate and away from values greater than 13 g/L that corresponds to the total inhibition (Gahlawat and Srivastava, 2013). Thus, two different initial operating conditions are used for the nitrogen source to analyse its effect on the dynamic response: (a) S_{20} = 0.63 g/L, (b) S_{20} = 1.2 g/L. Simulations were performed using the ICAS-MoT tool (Heitzig et al., 2011).

4.1. Batch operation

Figure 5 shows the dynamic performance for the two different values of initial nitrogen concentration. It can be observed that the higher the nitrogen concentration almost the same product and biomass concentrations are achieved, but in shorter reaction time. The reaction time, final PHB concentration, product yield and productivity for each case are: (a) θ = 40 h, P = 8.2 g/L, $Y_{P/S}$ = 0.33 g/g, Pr = 0.21 g/(L·h); and (b) θ = 23 h, P = 8.75 g/L, $Y_{P/S}$ = 0.35 g/g, Pr = 0.35 g/(L·h). This means that the yield is not significantly improved with a slight increase in the nitrogen concentration, but productivity is increased. So that PHB production rate in multiple batches could be benefited with this finding.

4.2. Fed-batch operation

The operating conditions used for the feed strategy were: F_1 = 0.1 L/h ($16 \le t \le 31$), S_{1F} = 125 g/L and S_{2F} = 2.8 g/L. The corresponding dynamic performances are shown in Figure 6. The reaction time, final PHB concentration, product yield and productivity for each case are: (a) θ = 38 h, P = 23.4 g/L, $Y_{P/S}$ = 0.35 g/g, Pr = 0.62 g/(L·h); and (b) θ = 33 h, P = 24.0 g/L, $Y_{P/S}$ = 0.73 g/g, Pr = 0.35 g/(L·h). Comparing fed-batch reactor versus batch reactor, it can be concluded that effectively product concentrations and biomass are increased significantly in a fed-batch mode. Comparing the fed-batch reactors, it can be seen that a slight increase of the initial nitrogen concentration does not increase the PHB production, but the reaction time is reduced significantly again and thus higher productivity. Therefore, the best case found with this study corresponds to a fed-batch reactor with initial nitrogen concentration of 1.2 g/L.

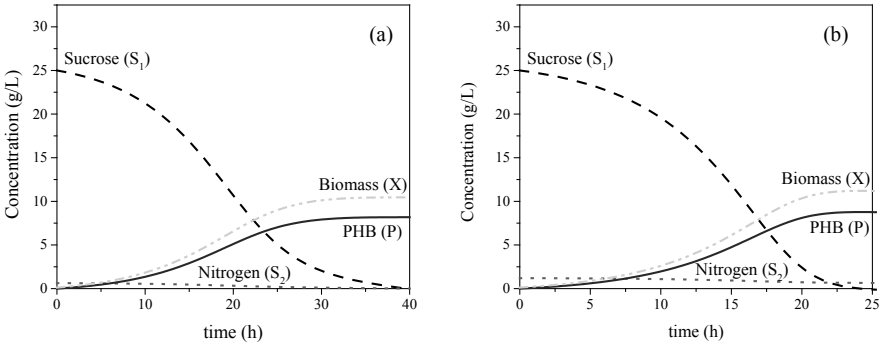

Figure 5. Dynamic response for a batch reactor: (a) S_{20} = 0.63 g/L, (b) S_{20} = 1.2 g/L.

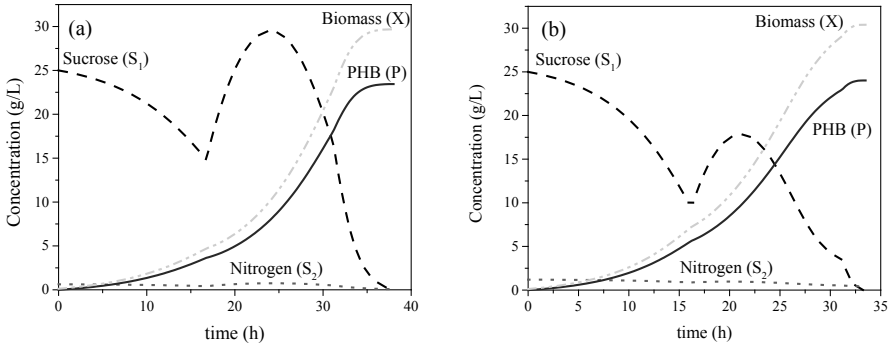

Figure 6. Dynamic response for a fed-batch reactor: (a) S_{20} = 0.63 g/L, (b) S_{20} = 1.2 g/L.

5. Conclusions

In this work, the PHB fermentation process using sucrose as substrate and *Azohydromonas australica* as strain was studied, through modelling and simulation tools. Sensitivity analysis showed that the parameters with major relevance in the fermentation model are the product and biomass yields (K_1, $Y_{R/S2}$, $Y_{R/S1}$), as well as the maximum specific growth rate (μ_{max}) used in the Monod equation. This result could help to reduce the model for control and monitoring purposes. In the other hand, relevant findings were obtained from the analysis done for the reactor operating mode. Results will be used in the short term to do optimization studies, as well as economic and environmental impact analyses, but in addition they can help the process designer to understand the process at different scales, to implement online process monitor and control, and so on.

Acknowledgements

The authors would like to thank Prof. Rafiqul Gani for discussions, comments and ideas to improve this project.

References

I.J. Dunn, E. Heinzle, J. Ingham, J.E. Prenosil, 2008, Biological Reaction Engineering, Wiley-VCH.

G. Gahlawat, A.K. Srivastava, 2013, Development of a mathematical model for the growth associated Polyhydroxybutyrate fermentation by *Azohydromonas australica* and its use for the design of fed-batch cultivation strategies. Bioresour Technol, 137, 98-105.

D. M. Hamby, 1994, A review of techniques for parameter sensitivity analysis of environmental models, Environm. Monit. and Assessm. 32, 135-154.

L. L. Madison, G. W. Huisman, 1999, Metabolic Engineering of Poly(3-hydroxyalkanoates): From DNA to Plastic, Microbiol. Mol. Biol. Rev. 63(1), 21-53.

C. Peña, T. Castillo, A. García, M. Millán, D. Segura, 2014, Biotechnological strategies to improve production of microbial poly-(3-hydroxybutyrate): a review of recent research work, Microb. Biotech. 7(4), 278–293.

M. Heitzig, G. Sin, M. Sales-Cruz, P. Glarborg, R. Gani, 2011, Computer-Aided Modeling Framework fro Efficient Model Development, Analysis, and Identification, Ind. Eng. Chem. Res. 50 (9) 5253-5265.

Krist V. Gernaey, Jakob K. Huusom and Rafiqul Gani (Eds.), 12th International Symposium on Process Systems Engineering and 25th European Symposium on Computer Aided Process Engineering.
31 May – 4 June 2015, Copenhagen, Denmark

Retrofitting of Concentration Plants Using Global Sensitivity Analysis

Freddy Lucay[a,b], Luis A. Cisternas[b,a], Edelmira D. Gálvez[c,a,*]

[a]*Centro de Investigación Científico Tecnológico para la Minería, Antofagasta, Chile*
[b]*Depto. de Ing. Química y Procesos de Minerales, Universidad de Antofagasta, Chile*
[c]*Depto. de Ing. Metalurgia y Minas, Universidad Católica del Norte, Chile.*
egalvez@ucn.cl

Abstract

This work presents the use of global sensitivity analysis to retrofit mineral concentration plants. The ore that is fed to a concentration plant is heterogeneous, and it changes over time as the mine is operated. Moreover, the costs and the selling price of the concentrate can undergo significant changes. This situation forces readjustment of mineral concentration plants to new conditions. The methodology consists of three steps: 1) process modeling, 2) global sensitivity analysis to identify key variables, and 3) economic optimization of the plant. Sobol's method is used to identify the variables that most significantly affect the recovery of the species and the grade of the final concentrate. The methodology is applied to a copper and molybdenum concentrator plant of three concentration stages. The species present in the mineral correspond to chalcopyrite, chalcocite, covellite, molybdenite, pyrite, and quartz. The results show that the methodology could be helpful to improve the revenue of a flotation plant by making targeted changes to it.

Keywords: plant retrofit, global sensitivity analysis, flotation, copper, molybdenum.

1. Introduction

Flotation is a process of the physical-chemical separation of valuable species from gangue (waste material) that makes use of surface properties. The process is carried out in aerated tanks (cells or flotation columns) where the mineral particles are mixed with water and reagents that make the surface of the valuable mineral hydrophobic. When air enters the tank, the hydrophobic particles adhere to the air bubbles and form a froth, which overflows the top of the tank forming the valuable mineral concentrate. Generally, the cells are arranged in series to increase their efficiency, forming a bank of cells. To predict the metallurgical performance of a bank of cells or flotation column, a mathematical model is needed. This model should be able to relate the main operating conditions to the recovery of minerals to assist engineers in the design, monitoring and scaling of flotation devices. Many authors have proposed different models to describe the process of continuous flotation (Ek, 1992; Yianatos, 2007). Considering that the ore fed to the plant is heterogeneous and constantly changing and the costs and selling prices of the concentrate may experience significant changes, it is necessary to determine the key variables of the model, which is not easy because of the large number of equations, variables and operational aspects involved. The present work proposes a methodology for improvements in concentration plants based on the modification of key variables of the process.

2. Retrofit methodology

The retrofit methodology consists of three steps: 1) modeling of the flotation plant, 2) identification of key variables, and 3) optimization of the concentrator.

2.1 Modeling the flotation plant.

In the literature, there are several models to describe the process of flotation. The general rate equation for this type of process (Polat and Chander, 2000) involves distribution functions for the residence time and the flotation kinetics constant. The distribution function of the flotation kinetics may be rectangular, normal, or gamma, among others (Yianatos et al., 2005; Ferreira and Loveday, 2000). For residence time there are two extreme conditions, plug flow and perfect mixing (Yianatos et al., 1994). With such models, it is possible to model flotation stages that use either flotation cell banks or flotation columns.

2.2 Sensitivity analysis to identify key variables

Global sensitivity analysis (GSA) can be defined as "the study of how the uncertainty in the outcome of a model can be distributed to different sources of uncertainty in the input model" (Saltelli et al., 2008). GSA methods can be categorized into three groups (Confalonieri et al., 2010): screening methods, regression-based methods, and variance-based methods. In the last methods, the variance of the model output is expressed in terms of increasing dimensions, called partial variations, which represent the contribution of the inputs to the overall uncertainty of the model results. These methods allow the simultaneous exploration of the data space with uncertainty, which is usually performed via Monte Carlo sampling. Statistical estimators quantify the sensitivity of all input factors and groups of inputs via multidimensional integrals. The computational cost in terms of simulation models to estimate the sensitivity of higher-order interactions between the inputs can be very high. To prevent a high computational cost, Homma and Saltelli (1996) introduced the concept of a total sensitivity index. The total sensitivity index indicates the overall effect of a given input, considering all possible interactions of the corresponding entry with all other entries. It should be noted that when the value of the total sensitivity of an input variable is zero, this variable will have no influence on the model output. Examples of techniques of this group include analysis of variance (ANOVA), Fourier amplitude sensitivity test (FAST), its evolution extended FAST (S-FAST), Sobol's method (1993), and high-dimensional model representation (HDMR).

Sepulveda et al., (2013) applied global sensitivity analysis to analyze separation circuits. They concluded that Sobol's method works well in the analysis of flotation circuits. In this work, Sobol's method was used to perform the GSA. The model output was the grade and recovery of valuable metals generated by the plant. The distribution function used to represent the uncertainty of the input factors was the uniform distribution function. The software used to perform the GSA was RStudio.

2.3 Economic optimization

After identifying the key input factors, the most influential variables on the grade and recovery of concentrate, it is necessary to optimize the concentration plant from an economic point of view through revenue maximization. This optimization is performed by fixing the input factors with a sensitivity index close to zero and freeing the other input factors. Revenues will be obtained from equation (1), (Cisternas et al., 2004)

$$Revenue = \sum_k CF_k \ [p_k(g_k - \mu_k)(q_k - Rfc_k) - Trc_k]H \quad (1)$$

where k is Cu and Mo, p_k is the fraction of metal paid, g_k is the concentrate grade, Trc_k is the treatment charges, μ_k is the grade deduction, q_k is the price of metal per ton, Rfc_k is the concentrated refining charges, and H is the number of hours per year of plant operation.

3. Application: El Salvador concentration plant

3.1 Modelling of the plant

Consider the concentrator plant shown in Figure 1 (Codelco Division El Salvador, Chile), which consists of rougher, cleaner, and cleaner-scavenger stages. This plant processes 1,458.3 t/h of ore with 0.6 % Cu and 0.021 % Mo. The existing species and their feed mass flow rates are 12.64 t/h of chalcopyrite, 4.38 t/h of chalcocite, 1.32 t/h of covellite, 0.51 t/h of molybdenite, 1,223.56 t/h of pyrite, and 215.92 t/h of quartz. To model the concentrator mass balances, Eqs. (2) to (5) were used (Yianatos et al., 2005, and Yianatos and Henriquez, 2006).

$$R = R_{max}\left[1 - \frac{(1 - (1 + k_{max}\tau)^{1-N})}{(N-1)k_{max}\tau}\right] \quad (2)$$

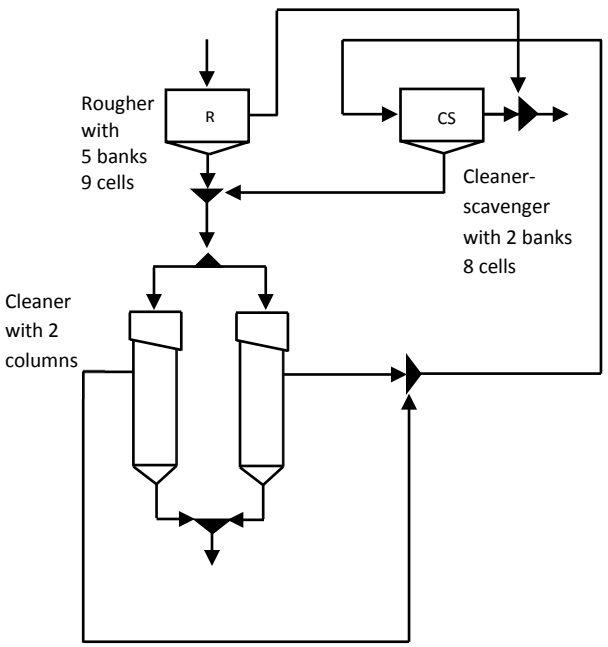

Figure 1: El Salvador (Chile) concentration plant.

$$R_C = R_{max}\left[1 - \frac{4}{3k_{max}\tau}\left(\frac{12}{k_{max}\tau + 12} - 1 + \frac{10}{9}\ln\left(\frac{10k_{max}\tau + 12}{k_{max}\tau + 12}\right)\right)\right] \quad (3)$$

$$R_F = 95exp^{\left(-0.0144\frac{H_F(1+3J_w)}{J_g^3}\right)} \quad (4)$$

$$R_G = \frac{R_C R_F}{1 - R_C + R_C R_F} \quad (5)$$

Specifically, Eq. (2) was implemented to model cell banks, and Eq. (3-5) were used to model the columns. R_{max} is the maximum recovery at infinite time, k_{max} is the maximum rate constant of the rectangular distribution function, τ is the residence time of one cell, and N is the number of cells in the bank. The maximum kinetic constants (min^{-1}) and maximum recovery included in the model are shown in Table 1.

For column flotation modelling, Eq. (5), distinguishes the collection zone recovery (R_C) and the froth zone recovery (R_F) to calculate the overall recovery R_G. The other constants involved in Equation (2-5) take the following values: 1.8 cm/s for the superficial air rate (J_g), 0.25 cm/s for superficial water rate (J_w), 100 cm for froth depth (H_F), 13.2 min for column residence time (τ_C), 3.5 min for cell rougher residence time(τ_R), and 4.8 min for cell CS residence time (τ_{CS}). The solids concentration in the R, C, and CS stages were 0.35, 0.195, and 0.22, respectively. The mathematical model used to assess the El Salvador plant gives the recoveries and grades shown in Table 2. The equipment sizes were 41 m^3 for R cells, 43 m^3 for CS cells, and 157 m^3 for columns in the C stage. The following values were used to evaluate the revenues in Eq. (1): p_k, 97 % and 98 % for Cu and Mo; Trc_k, 0.25 MUS $/t Cu and 0.1 MUS $/ t Mo; μ_k, 1.5 % and 0 % for Cu and Mo; q_k, 7 MUS $ /t Cu and 29 MUS $/t Mo; Rfc_k, 0.3 MUS $/t Cu and 0.9 MUS $/ t Mo; and H 7200 h/y. With these values, the plant revenue reaches 233 million US $/ y.

3.2. Sensitivity analysis to identify key variables

The objective of the flotation circuit used by the mining concentration plant in El Salvador is to obtain a concentrate rich in Cu and Mo. The influence of the input factors on the variability of the grade and recovery of Cu and Mo in the final concentrate is analyzed. The input factors to consider are the kinetic constants of each species in each stage, maximum recoveries of each species in each stage, residence time of the pulp in each stage, number of cells in the R and RS stages, solids concentration in each stage, froth depth height on the columns, and superficial air and water rates in the column. In total, there are 47 input factors, and uncertainty ranges were taken from Yianatos et al. (2005) and Yianatos and Henriquez (2006). Based on the current operating conditions of the El Salvador plant, variations of ∓ 15% and ∓3% for kinetic constants and maximum recoveries, respectively, were considered. In the case of the solids concentration and the froth depth, variations of ∓10% were considered. In the case of superficial air and water rates, variations of ∓11% and ∓ 12%, respectively, were considered. The variation in the number of cells in R and CS were 7-9 and 8-10, respectively. The variation of the residence time in the R and CS stages was ∓ 10%. Finally, the residence time in C varied by ∓ 7%.

Table 1. Maximum flotation kinetic constants (min^{-1}) and maximum recovery

	Chalcopyrite		Chalcocite		Covelline		Molybdenite		Pyrite		Quartz	
	R_{max}	k_{max}	R_{max}	k_{max}	R_{max}	k_{max}	R_{max}	k_{max}	R_{max}	k_{max}	R_{max}	k_{max}
R	0.85	0.65	0.82	0.54	0.82	0.45	0.81	0.47	0.19	0.17	0.13	0.10
C	0.90	0.35	0.86	0.34	0.86	0.34	0.86	0.32	0.17	0.07	0.10	0.04
CS	0.85	0.65	0.82	0.55	0.82	0.45	0.80	0.45	0.20	0.17	0.15	0.10

Table 2. Copper and Molybdenum grade and recovery, before and after plant retrofit. (chalcopyrite $CuFeS_2$, chalcocite Cu_2S, covellite CuS, molybdenite MoS_2, pyrite FeS_2, quartz SiO_2)

	Grade, %		Recovery, %		Species recovery, %					
	Cu	Mo	Cu	Mo	$CuFeS_2$	Cu_2S	CuS	MoS_2	FeS_2	SiO_2
Before	28.3	0.89	63.7	57.0	67.2	60.5	59.1	57.0	0.59	0.13
After	28.5	0.95	66.1	62.7	70.5	61.9	60.5	62.7	0.59	0.14

Figure 2 shows that input factors 10 (k_{max} molybdenite in C), 11 (k_{max} of pyrite in C), 25 (surface flow), 27 (R_{max} chalcopyrite in R), 30 (R_{max} molybdenite in R), and 42 (R_{max} molybdenite in CS) are the main sources of variability of Cu and Mo recoveries and grades. Input factor 10 affects the Mo grade and recovery, input factor 11 affects the Mo and Cu grades, input factor 25 affects both the Cu and Mo grades and recoveries, input factor 27 affects the Cu recovery, and input factors 30 and 42 affect the Mo grade and recovery. From these results, it is clear that six of the 47 input factors are the key variables for the Cu-Mo grade and recovery.

3.3. Optimization of concentrator

To optimize the plant economically, the six key variables were left free in their ranges of uncertainty, while other variables were kept fixed. The optimization was performed with the computer program using BARON-GAMS. The results indicate that the new values for the six key variables are 0.368 min^{-1} for k_{max} of molybdenite in the cleaner stage; 0.0595 min^{-1} for k_{max} of pyrite in the cleaner; 1.998 cm/s for superficial air rate; R_{max} 0.876 and 0.834 for chalcopyrite and molybdenite in R, respectively; and 0.824 for molybdenite in CS. The new metallurgical parameters for the plant are provided in Table 2.

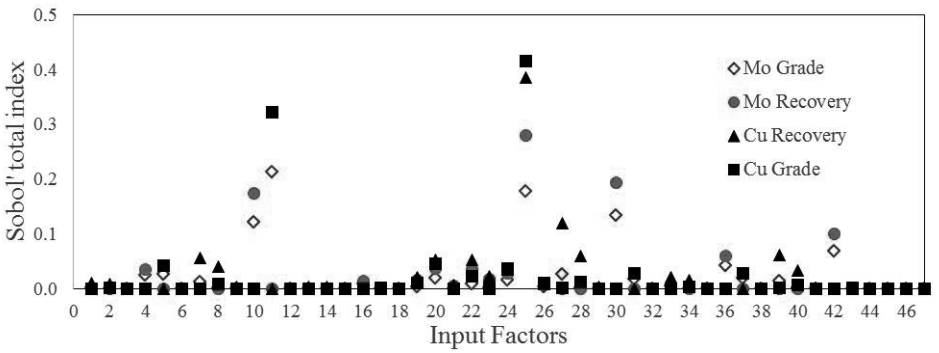

Figure 2. Sobol´s total sensitivity index.

The Cu and Mo recoveries increase from 63.7 to 66.6 % and 57.0 to 62.7 %, respectively. Moreover, the Cu and Mo grades increase from 28.3 to 28.54 % and 0.89 to 0.95 %, respectively. The revenues obtained are 244.6 million US$/y, an annual revenue increase of 11.6 million US$ with respect to the current operating conditions.

4. Conclusions

A methodology was developed for improvements in concentration plants. The methodology consists of three steps: 1) modeling of the concentrator; 2) identification of key variables, and 3) economic optimization of the plant. The contribution of this methodology is the use of Sobol's method for global sensitivity analysis to determine the variables that generate more variability on the metallurgical parameters of the concentrator. The methodology was applied to the El Salvador (Chile) concentration plant. The results indicate that GSA can significantly reduce the number of variables on which to focus when economically optimizing the plant because of the 47 input factors involved in the grade and recovery of Cu and Mo, only six factors are the most influential on these metallurgical parameters. The values obtained allowed economic optimization to increase annual revenues by almost 11.6 million US $.

Acknowledgments
Financial support from CONICYT (Fondecyt 1120794), CICITEM (R10C1004) and the Antofagasta Regional Government is gratefully acknowledged.

References

R. Confalonieri, Bellocchi G., Bregaglio S., Donatelli M., Acutis M., 2010. Comparison of sensitivity analysis techniques: a case study with the rice model WARM, Ecological Modelling, 221, 1897-1906.

L.A. Cisternas, Gálvez E. D.,Zavala M. F., Magna J., 2004. A milp model for the design of mineral flotation circuits. Int. J. Miner. Process. 74, 121-131.

C. Ek, 1992. Flotation kinetics in innovations in flotation technology. In: Mavros P., Matis K. A. (Eds). NATO ASIS series, vol. 208. Pp. 183-210.

J.P. Ferreira, Loveday B. K., 2000. An improved model for simulation of flotation circuits. Mineral Engineering, Vol. 13 N° 14-15, pp 1441-1453.

T. Homma, Saltelli A., 1996. Importance measures in global sensitivity analysis of nonlinear models. Reliability Engineering & System Safety, 52 1-17.

M. Polat, Chander S., 2000. First-order flotation kinetics models ans methos for estimation of the true distribution of flotation rate constants. Int. J. Miner. Process 58, 145-166.

A. Saltelli, Ratto M. Andres T., Campolongo F, Cariboni J., Gatelli D., Saisana M., Tarantola S., 2008. Global sensitivity: The primer, john Wiley & Sons Ltd.

I.M. Sobol's, 1993. Sensitivity analysis for no-linear mathematical models. Methematical Modelling and Computational Experiment. 1, 407-414.

F.D. Sepulveda, L.A. Cisternas, E.D. Gálvez, 2013, Global sensitivity analysis of a mineral processing flowsheet, Computer Aided Chemical Engineering, 32, 913-918.

J.B. Yianatos, Henríquez F. D., 2006. Short-cut method for flotation rates modelling of industrial flotation Banks. Mineral Engineering 19, 1336-1340.

J.B. Yianatos, Bucarey R., Larenas J., Henríquez F., Torres L., 2005. Collection zone kinetic model for industrial flotation columns. Mineral Engineering 18, 1373-1377

J.B. Yianatos, Bergh, L, G., Duran O. U., Díaz F. J. and Heresi N. M., 1994. Measurement of residence time distribution of the gas phase in flotation columns. Minerals Engineering, Vol. 7, Nos 2/3, 333-344.

J.B. Yianatos, 2007. Fluid flow and kinetic modelling in flotation related processes: columns and mechanically agitated cells - A review. Chemical Engineering Research and design, Vol. 85, p 1591-1603.

Krist V. Gernaey, Jakob K. Huusom and Rafiqul Gani (Eds.), 12th International Symposium on Process Systems Engineering and 25th European Symposium on Computer Aided Process Engineering.
31 May - 4 June 2015, Copenhagen, Denmark.

Differential-Algebraic Approach to Solve Steady-State Two-Phase Flow Drift-Flux Model with Phase Change

Rodrigo G. D. Teixeira[a], Argimiro R. Secchi[b] and Evaristo C. Biscaia Jr.[b]

[a]*PETROBRAS; Rio de Janeiro, Brazil*
[b]*Programa de Engenharia Química; COPPE/UFRJ; Rio de Janeiro, Brazil*
rodrigogdt@petrobras.com.br

Abstract

Two-phase flow in pipes occurs frequently in petroleum refineries. Simulation and design calculations for their processing units require methods for predicting void fractions and axial pressure drops, thus making it essential that precise models of the relevant thermo-fluid dynamics be combined with efficient numerical techniques. In this work, the two-phase flow with phase change problem of a refinery multicomponent naphtha (C5-C8) was modeled through the steady-state one-dimensional mixture model, which comprises continuity, momentum and energy differential equations for the mixture, in addition to an extra continuity equation for the vapor phase. Relative motions between the phases are accounted for by a constitutive expression for the one-dimensional drift velocity. Evaporation and condensation are considered via vapor-liquid equilibrium calculations, and suitable thermodynamic methods are also applied in the evaluation of physical properties. It is proposed in this work that this rigorous formulation fits in the scope of Differential-Algebraic Equations (DAE) systems and is preferably solved by proper established numerical methods rather than the customary iterative segregated semi-implicit algorithms based on finite volume approaches. Efficiency and accuracy gains are demonstrated as a result of the proposed numerical strategy, which yields higher-order numerical solutions in much less CPU time. Specific regularization functions were also developed in order to eliminate expected numerical issues of convergence failure due to discontinuities in the drift-flux parameters at flow-regime transitions.

Keywords: Two-phase flow, Drift-Flux Model, Differential-Algebraic Equations

1. Introduction

Modeling and simulation of liquid-vapor two-phase flows through pipes have motivated intense scientific research for quite a few decades now, partly due to the common occurrence of this scenario in several industrial applications. Two-phase flow plays, for instance, an important role in the thermal-hydraulics of nuclear power reactors. In the petroleum industry specifically, it can be encountered in oil and gas wells and in distillation units and boilers of petrochemical plants and refineries, as well as in pipelines for long-distance transportation of natural gas. Optimum design calculations rely on mathematical models and numerical methods for accurately predicting two-phase flow behavior in order to improve profitability and ensure that safety requirements are met.

2. Mathematical Modeling

Two-phase flow is analogous to single-phase flow in that its local instant values of densities, velocities, pressure and other field properties all exhibit random fluctuations induced by turbulence and irregular movements of liquid-vapor interfaces. Detailed predictions capturing such sudden microscopic motions would fall in the scope of *Direct Numerical Simulations* (DNS). In practice, important as though DNS may be as a research tool, its inapplicability in tackling complex engineering problems with today's available computational resources is well known. Hence, engineers resort to macroscopic formulations based on proper averaging techniques in which turbulent and interfacial fluctuations are smoothed out, with their effects being statistically accounted for. Solving these averaged equations also bears the advantage of calculating directly the mean values of most key variables, which would be the primary concern even if local instant results could be obtained (Prosperetti and Tryggvason, 2007; Yeoh and Tu, 2010).

Averaged conservation equations can be obtained for each phase or for the mixture as a whole. The latter approach lends itself more naturally than the former to the solution of many engineering problems, as they often require the response of the total mixture and not of each constituent phase. Thus, the Mixture Model is composed of four field equations, namely: the mixture continuity, momentum and energy equations, together with the vapor continuity equation (Ishii and Hibiki, 2011). A one-dimensional steady-state formulation of the model was considered in this study, as follows:

$$\frac{d\left[\rho_m v_m\right]}{dx} = 0 \tag{1}$$

$$\frac{d\left[\rho_m v_m^2\right]}{dx} = -\frac{dP}{dx} - \rho_m \frac{f_m}{2d} |v_m| v_m - \rho_m g \sin(\theta) - \frac{d}{dx}\left[\frac{\alpha_v \rho_v \rho_l}{\alpha_l \rho_m} \widehat{v}_v^{\mathrm{des}\,2}\right] \tag{2}$$

$$\frac{d\left[\rho_m v_m h_m\right]}{dx} = \frac{S\dot{Q}_w}{A} - \frac{d}{dx}\left[\frac{\alpha_v \rho_v \rho_l}{\rho_m}(h_v - h_l)\widehat{v}_v^{\mathrm{des}}\right] + \left[v_m + \frac{\alpha_v(\rho_l - \rho_v)}{\rho_m}\widehat{v}_v^{\mathrm{des}}\right]\frac{dP}{dx} \tag{3}$$

$$\frac{d\left[\alpha_v \rho_v v_m\right]}{dx} = \Gamma_v - \frac{d}{dx}\left[\frac{\alpha_v \rho_v \rho_l}{\rho_m}\widehat{v}_v^{\mathrm{des}}\right] \tag{4}$$

Talebi et al. (2012) obtained satisfactory agreement between predicted void fractions α_v and available experimental data upon solving the above model. It can be shown that these equations correspond to the Mixture Model deduced by Ishii and Hibiki (2011) when specific common assumptions are applied to the latter. These include neglecting viscous stresses, axial heat conduction, surface tension effects and covariance terms arising from area averaging.

In addition to physical properties and heat transfer, constitutive equations for the volumetric mass transfer rate Γ_v and the one-dimensional drift velocity $\widehat{v}_v^{\mathrm{des}}$ must also be provided to take into account the energy differences between phases and their relative motion, respectively. For simplicity, this study considered only the mass transfer at the wall due to the external heat transfer flux $\dot{Q}_w$ in calculating the former.

Ishii and Hibiki (2011) refer to their Mixture Model as the *Drift-Flux Model* in order to emphasize that the relative motions between both phases are taken into account by the *drift velocity* $\widehat{v}_v^{\mathrm{des}}$. The following *kinematic constitutive equation* relates this variable to the distribution parameter C_0 and the weighed mean local drift velocity $\left\langle v_v^{\mathrm{des}}\right\rangle_\alpha$:

$$\widehat{v}_v^{\mathrm{des}} = \frac{\rho_m\left[\left\langle v_v^{\mathrm{des}}\right\rangle_\alpha + (C_0 - 1)\, v_m\right]}{\rho_m - (C_0 - 1)(\rho_l - \rho_v)\,\alpha_v} \tag{5}$$

Both C_0 and $\left\langle v_v^{\mathrm{des}}\right\rangle_\alpha$ (and also the friction factor f_m) are flow-regime dependent, hence the need to establish expected flow patterns prior to selecting suitable correlations. In this study, flow regimes were predicted when necessary by means of the flow-pattern map of Mandhane et al. (1974).

3. Numerical Solution

3.1. Finite Volume Method

Standard finite volume discretization techniques have been extended to solve the general averaged equations of two-phase flows in conjunction with semi-implicit segregated algorithms such as SIMPLE and its variants. Common concepts and practices are thus retained, such as the need for staggered grids, the use of the upwind method in discretizing the advective terms or the conversion of the continuity equation into a linear system for the pressure corrections (Prosperetti and Tryggvason, 2007; Yeoh and Tu, 2010). In particular, the discretization of one-dimensional governing equations typically yields tri-diagonal algebraic systems, which Talebi et al. (2012) solved in every iteration by means of the widely used *Tri-Diagonal Matrix Algorithm* (TDMA).

Regarding the present study, a literature survey found no discussions concerning alternative numerical possibilities which exploit the model's steady one-dimensional character. Instead, predictably enough, such equations have been currently solved in the finite volume method framework as well.

3.2. Proposed Numerical Strategy

The Drift-Flux Model presents itself as an Initial-Value Problem when its equations are supplemented with known upstream conditions (at $x = 0$). Furthermore, it should be pointed out that only four of these equations are differential in x, whereas the rest are algebraic constraints comprising constitutive equations for the drift velocity and physical properties. This brief description matches the definition of *Differential-Algebraic Equations* (DAE) systems, the numerical solution of which is preferably pursued in other fields of study by available general purpose codes such as DASSL (Brenan et al., 1996). The model at hand can be readily rearranged into the most general form of DAE systems, which reads:

$$F\left[x; y(x); \frac{dy}{dx}\right] = 0 \tag{6}$$

in which y is the state vector of dependent variables and F includes both differential and algebraic equations. Many of the aforementioned general purpose integrators employ the backward differentiation formulas (BDF) with Newton's method at each integration step (Brenan et al., 1996).

There are important efficiency gains to expect from choosing this DAE approach over the Finite Volume Method in the solution of the one-dimensional steady-state Drift-Flux Model. Its capability of solving all involved equations (differential and algebraic) in a simultaneous fashion stands out next to the segregated algorithms whose iterations consist of several sub-procedures, some of which are iterative as well. Among the latter are the thermodynamic stage of updating physical properties and the successive substitution method suggested by Patankar (1980) when a tri-diagonal system is actually non-linear and thus cannot be handled by the TDMA alone. Further on, the BDF method's multistep (higher order of accuracy) nature and the adaptive (variable step-size) capability of modern computer codes also enable the latter to use very small steps only where they are really needed, thus enhancing efficiency and accuracy. Finite-volume-based solutions, on the other hand, are often based on less accurate discretization techniques. They also require testing for grid independence with successive mesh refinement between simulations until certain key results do not change above a specified tolerance (Versteeg and Malalasekera, 2007). DAE integrator codes, in turn, are capable of delivering such converged results after one simulation by estimating the truncation error and accordingly adjusting the step size throughout the solution process.

3.3. Proposed Treatment of Discontinuities

Two-phase flow models are generally known to bear numerical discontinuities which stem from switching equations at flow-regime transition boundaries. This is expected in the present study

regarding constitutive models for C_0, $\langle v_v^{\text{des}} \rangle_\alpha$ and f_m. Though this switching can be easily coded by combining IF-ELSE statements with the possible predictions of a flow-pattern map, such approach is highly inadvisable in the integration of DAE systems, for the discontinuities that are introduced in the derivatives of F (Equation 6) will cause serious problems in Newton iteration, error estimates and stepsize selection algorithms which may even lead to integration failure (Brenan et al., 1996). Proper treatment of the discontinuities is thus essential to this DAE proposal.

The standard procedure in addressing the above issue is to restart the integration after discontinuities. The present study proposes instead that the more convenient *regularization function* approach successfully used by Teixeira et al. (2014) be applied to the Drift-Flux Model. In that reference, discontinuities generically given by:

$$z(X) = \begin{cases} z_1(X), & p(X) \geq p_{max} \\ z_2(X), & p(X) < p_{max} \end{cases} \tag{7}$$

were replaced by a single continuous algebraic equation:

$$z(X) = \eta(p(X) - p_{max}; \varepsilon) z_1(X) + [1 - \eta(p(X) - p_{max}; \varepsilon)] z_2(X) \tag{8}$$

in which $\eta(arg; \varepsilon)$ is a *continuous* regularization function evaluated at scalar argument *arg* and parameter ε. In order for Equation 8 to closely reproduce 7, η was chosen as follows:

$$\eta(arg; \varepsilon) = \frac{1 + \tanh(arg/\varepsilon)}{2} = \begin{cases} 1, & arg > +\xi \\ 0, & arg < -\xi \end{cases} \tag{9}$$

in which $0 < \xi << 1$. ξ is a function of user-supplied parameter ε, which must be adjusted to each particular application so that the interval $[-\xi, \xi]$ is small enough that deviations between Equations 7 and 8 can be neglected.

In the present context, it was sought to smooth the expected discontinuities at the flow-regime boundaries of Mandhane et al. (1974). Every switch of equations in the FORTRAN code provided in that reference was continuously reproduced upon applying regularization functions exactly as discussed. This ultimately resulted in continuous functions named *elongatedBubble*, *Slug*, etc. which vary sharply but continuously between 1 and 0 as the given set of variables enter or leave the corresponding regions in the flow-pattern map. The selections of constitutive equations for C_0, $\langle v_v^{\text{des}} \rangle_\alpha$ and f_m then become three simple weighted sums of regime-specific correlations with the devised flow-pattern functions employed as weighting factors.

4. Parameters and Methods

All reported calculations considered the two-phase flow of 115000 kg/h of naphtha through a horizontal, 12-meter long carbon steel pipe segment with inner and outer diameters of 7.981 in and 8.625 in. Thermophysical and transport properties (phasic enthalpies, densities, viscosities and surface tension) were predicted through the compositional approach with constitutive methods presented by Daubert and Danner (1997) and Riazi (2005) for petroleum fractions of defined composition. Calculations of residual enthalpies and vapor-liquid equilibrium (flash) were based on the Peng-Robinson equation of state. The assumed naphtha's molar composition is very similar to that of the gas chromatography example presented by Riazi (2005).

The DAE strategy's implementation employed DASSL's extended version DASSLC, which features all desirable numerical aspects previously discussed. It minimally requires from the user an initial conditions vector and a residuals subroutine for F in Equation 6 (Secchi, 2012). Absolute and relative tolerances used were 10^{-9} and 10^{-6}. Subsequently, a finite-volume discretization of the Drift-Flux Model on a staggered grid was also carried out so as to allow a thorough assessment of the proposal's advantages. Mostly used approximations were the upwind method and the

"stepwise profile" so nicknamed by Patankar (1980). The discretized equations were sequentially and iteratively solved by the TDMA and SIMPLER algorithms. The latter, which does not require pressure underrelaxation, has been shown to be more efficient than SIMPLE and possibly as efficient as SIMPLEC or PISO (Versteeg and Malalasekera, 2007).

5. Results and Discussion

5.1. Computer Effort Assessment

The DAE strategy was first compared with the finite-volume segregated method in terms of computing times programatically measured in an average computer (2.20 GHz i7 with 8 GB of RAM). The fictional case study was a pipe exposed to 27° C and 36 km/h wind. The outer convection resistance between the pipe and its surroundings was accounted for by the forced-convection Nusselt correlation of Churchill and Bernstein (1977). Inlet conditions were 4.95 kgf/cm^2 and 163.95° C. Such values were initally chosen so that the *Elongated Bubble* flow regime prevailed through the entire range of x, and hence no discontinuity issues arose. In this flow pattern, the friction factors f_m were predicted from a single-phase correlation with the mixture's void-fraction-weighted physical properties (Hasan and Kabir, 1988). As for the drift-flux variables, the following suitable constitutive equations were used (Ishii and Hibiki, 2011; Levy, 1999):

$$C_0 = 1.2 - 0.2\sqrt{\frac{\rho_v}{\rho_l}} \tag{10}$$

$$\left\langle v_v^{\text{des}} \right\rangle_\alpha = 1.53 \left[\frac{\sigma_l g \left(\rho_l - \rho_v\right)}{\rho_l^2} \right]^{1/4} \tag{11}$$

It took DASSLC only 1.03 seconds to solve the illustrative problem, whereas the SIMPLER algorithm required 9.58 s with a 25 control-volume mesh ($NV = 25$). These measured times differ by a factor of nearly 10, which clearly demonstrates the anticipated advantages of the DAE approach regarding the one-dimensional model. A grid-independence study was also performed, with NV successively doubled up to a value of 200. After each simulation, relative errors were calculated based on DASSLC's solution, which was deemed appropriate given the latter's tight reported tolerances. Figure 1, which presents these results for the void fraction profiles, shows that only with $NV = 200$ did all relative errors fall below 0.10%. Also, the errors are shown to decrease by half when NV is doubled, which implies only first-order accuracy and thus explains the need for small steps in satisfying a given tolerance. The measured times with 50, 100 and 200 cells (27.15 s, 56.75 s and 439.0 s) also greatly exceed that required by DASSLC.

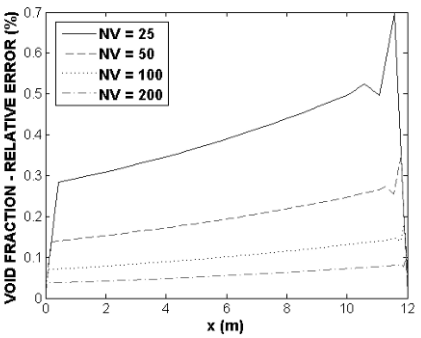

Figure 1: Vapor void fraction relative errors.

5.2. Integration of Discontinuous Equations

The effects of discontinuities on the proposed approach were investigated by replacing the assigned atmospheric conditions with a skin temperature of 215° C. Integration with DASSLC then failed at first, but succeeded when the regularization functions were applied to the flow-regime boundaries with $\varepsilon = 10^{-3}$. Figure 2 indeed shows a -6.5% discontinuity in the drift-velocity profile at $x \approx 0.78$ m, where the flow pattern was found to change from Elongated Bubble to Slug.

Calculations for the Slug regime assumed $\rho_m \approx \rho_l (1-\alpha_v)$ in predictions of f_m and also considered $C_0 = 1.2$ and $\left\langle v_v^{\text{des}} \right\rangle_\alpha = 0$ (Hasan and Kabir, 1988). Assigning $\varepsilon = 10^{-3}$ in regularization function 9 yields $\xi \approx 0.02$, which was verified to be less than 0.4% of liquid and vapor superficial velocities in the transition region and also much smaller than their variations from inlet to outlet. This successfully confined interpolations such as Equation 8 to the very vicinities of regime-transition boundaries. One side effect of such sharp variations is their need for much smaller steps, which explains the increase to 6.33 s in the measured DASSLC integration time. It seems therefore advisable to also consider a lower limit when tuning ε so as to not render the calculations too ineficient. Nevertheless, this increased time is still considerably smaller than those reported for the finite-volume method, and the regularization approach is thus shown to be an effective alternative to restarting integrations at every discontinuity.

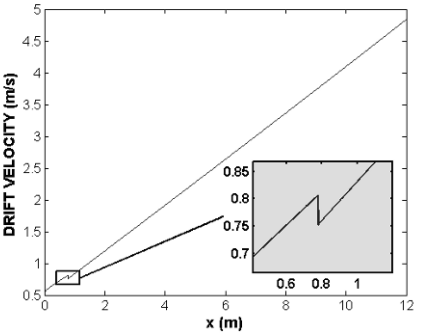

Figure 2: Discontinuous drift-velocity profile.

6. Summary and Conclusions

Modern DAE integrators have been successfully shown to be more efficient than finite-volume based iterative algorithms in numerically solving the one-dimensional steady-state equations of the Drift-Flux Model. Potential problems with the proposed strategy due to expected typical discontinuities in flow-regime boundaries were also successfully and conveniently handled by means of so-called regularization functions.

References

Brenan, K. E., Campbell, S. L., Petzold, L. R., 1996. Numerical Solution of Initial-Value Problems in Differential-Algebraic Equations, 1st Edition. Society for Industrial and Applied Mathematics, Philadelphia.

Churchill, S. W., Bernstein, M., May 1977. A correlating equation for forced convection from gases and liquids to a circular cylinder in crossflow. Journal of Heat Transfer 99, 300–306.

Daubert, T. E., Danner, R. P., 1997. API Technical Data Book - Petroleum Refining, 6th Edition. American Petroleum Institute, Washington, DC.

Hasan, A. R., Kabir, C. S., Nov. 1988. Predicting multiphase flow behavior in a deviated well. SPE Production Engineering 3 (4), 474–482.

Ishii, M., Hibiki, T., 2011. Thermo-Fluid Dynamics of Two-Phase Flow, 2nd Edition. Springer, New York.

Levy, S., 1999. Two-Phase Flow in Complex Systems, 1st Edition. John Wiley & Sons, New York.

Mandhane, J. M., Gregory, G. A., Aziz, K., Oct. 1974. A flow pattern map for gas-liquid flow in horizontal pipes. International Journal of Multiphase Flow 1, 537–553.

Patankar, S. V., 1980. Numerical Heat Transfer and Fluid Flow, 1st Edition. McGraw-Hill, New York.

Prosperetti, A., Tryggvason, G., 2007. Computational Methods for Multiphase Flows, 1st Edition. Cambridge University Press, Cambridge.

Riazi, M. R., 2005. Characterization and Properties of Petroleum Fractions, 1st Edition. American Society for Testing and Materials, West Conshohocken.

Secchi, A. R., 2012. Differential-algebraic system solver in c. http://www.enq.ufrgs.br/enqlib/numeric, Universidade Federal do Rio Grande do Sul.

Talebi, S., Kazeminejad, H., Davilu, H., Jan. 2012. A numerical technique for analysis of transient two-phase flow in a vertical tube using the drift flux model. Nuclear Engineering and Design 242, 316–322.

Teixeira, R. G. D., Secchi, A. R., Biscaia Jr, E. C., Apr. 2014. Two-phase flow in pipes: Numerical improvements and qualitative analysis for a refining process. Oil & Gas Science and Technology.

Versteeg, H. K., Malalasekera, W., 2007. An Introduction to Computational Fluid Dynamics, 2nd Edition. Pearson Education, Harlow.

Yeoh, G. H., Tu, J., 2010. Computational Techniques for Multi-Phase Flows, 1st Edition. Elsevier, Oxford.

Krist V. Gernaey, Jakob K. Huusom and Rafiqul Gani (Eds.), 12th International Symposium on Process Systems Engineering and 25th European Symposium on Computer Aided Process Engineering.
31 May – 4 June 2015, Copenhagen, Denmark

Model-based design of experiments for the identification of kinetic models in microreactor platforms

Federico Galvanin, Enhong Cao, Noor Al-Rifai, Asterios Gavriilidis, Vivek Dua*

Department of Chemical Engineering, University College London, Torrington Place, London WC1E 7JE, United Kingdom, v.dua@ucl.ac.uk

Abstract

Microreactor platforms represent advanced tools in reaction engineering for the quick development of reliable kinetic models. Experiments can be performed with a better reaction temperature control, enhanced heat and mass transfer and mixing of reactants. However, the effectiveness of the model identification procedure is strictly related to the execution of properly designed experiments, allowing elucidation of the reaction mechanisms and providing a precise estimation of the kinetic parameters. In this paper a model-based design of experiments (MBDoE) approach is proposed where experiments are designed for both discriminating among competing models and for improving the estimation of kinetic parameters. The procedure is tested on a real case study related to the identification of kinetic models of methanol oxidation on silver catalyst.

Keywords: design of experiments, model discrimination, microreactor technology.

1. Introduction

Microreactor platforms represent the ideal system for the study and determination of intrinsic reaction kinetics for strongly exothermic, endothermic, and fast catalytic reactions. These systems allow these reactions to be performed isothermally and in the absence of mass transfer limitations, ensuring the rapid manipulation of reaction conditions and the precise control of the hydrodynamic environment (Al-Rifai et al., 2013). However, the quantity, quality, and speed of information generated by these systems, due to the exploitation of small volumes and fast dynamics, are particularly affected by the experimental conditions realised during the trials. Model-based design of experiments (MBDoE) techniques (Franceschini and Macchietto, 2008) have been proposed for the purpose of designing a set of experiments yielding the most informative data to be used for model identification. Experiments can be designed for discriminating between candidate kinetic models (Schwaab et al., 2006) or, if a suitable model structure is available, to improve the precision in parameter estimation (Reizman and Jensen, 2012). Whilst the first objective is achieved based on the maximisation of the discriminating power, the second is based on the maximisation of the expected information given as a measurement function of the Fisher information matrix (FIM).

In this paper, a novel MBDoE formulation is proposed where the trade-off between Fisher information and discriminating power is computed using a *multi-objective* approach, allowing for the optimisation of the information which can be obtained from experiments in microreactor platforms. The MBDoE sequential procedure is articulated into three main steps: *i*) given a set of candidate kinetic models, a ranking of experiments is realised in order to detect both the experimental regions yielding the

maximum amount of Fisher information and the ones providing the maximum discriminating power; *ii*) information maps are detected and used for the optimal design of experiments; *iii*) the optimally designed experimental conditions are implemented in the microreactor system, providing new experimental data to be used for model identification. The iteration of steps *i*) to *iii*) lead to the detection of the best model structure representing the system, elucidating the most plausible kinetic mechanism for a given catalyst, ensuring a precise estimation of the kinetic parameters. Steps *i*)-*iii*) of the proposed procedure are tested on a real case study concerning the identification of kinetic models for the oxidative dehydrogenation of methanol to formaldehyde on silver catalyst (Andreasen et al., 2005). Experiments are carried out on a specifically designed silicon-glass microreactor fabricated by photolithography and deep reacting ion etching, and where the silver catalyst is deposited on the channel wall by sputtering (Cao and Gavriilidis, 2005). The temperature, pressure and volumetric flow rate are controlled and continuously monitored; concentrations are analyzed online at the inlet and outlet of the microreactor using gas chromatography.

2. Optimal design of experiments in microreactor platforms

As a first approximation, a microstructured reactor is modelled as a dynamic plug flow reactor (PFR) in the form:

$$\frac{\partial c_i}{\partial t} - u_z \frac{\partial c_i}{dz} = \sum_{j=1}^{N^{reaz}} \nu_{ij} r_j \tag{1}$$

where c_i is the species concentration, r_j and ν_{ij} are the reaction rate and the stoichiometric coefficient of the i-th species in the j-th reaction respectively, z is the axial coordinate, u_z is the speed of fluid flow in the z-direction and t the integration time. Equations (1), together with the reaction rate expressions, represent a system of differential and algebraic equations (DAEs) which can be written in the general form as:

$$\mathbf{f}\left(\dot{\mathbf{x}}(z,t), \mathbf{x}(z,t), \mathbf{u}(z,t), \boldsymbol{\theta}, t\right) = 0 \qquad \hat{\mathbf{y}}(z,t) = \mathbf{g}\left(\mathbf{x}(z,t)\right) \tag{2,3}$$

with the set of initial conditions $\mathbf{x}(0,0) = \mathbf{x}_0$, where $\mathbf{x}(z,t)$ is the N_x-dimensional vector of state variables (i.e. the concentrations c_i in (1)), $\mathbf{u}(z,t)$ is the N_u-dimensional vector of manipulated input variables (i.e. flow rate, temperature, pressure of the system) and $\boldsymbol{\theta}$ is the N_θ-dimensional set of unknown kinetic model parameters to be estimated. The symbol ^ is used to indicate the estimate of a variable (or of a set of variables): thus, $\mathbf{y}(z,t)$ is the vector of measured values of the outputs, while $\hat{\mathbf{y}}(z,t)$ is the vector of the corresponding values estimated by the model. Note that, in general, state variables and input variables can be characterised in both time and space.

MBDoE techniques for improving parameter estimation aim at decreasing the parameter uncertainty region predicted by model through the solution of the optimisation problem:

$$\boldsymbol{\varphi}^{\mathrm{PE}} = \arg\min_{\boldsymbol{\varphi}\in D}\left\{\psi\left[\mathbf{V}_\theta(\boldsymbol{\theta},\boldsymbol{\varphi})\right]\right\} = \arg\min_{\boldsymbol{\varphi}\in D}\left\{\psi\left[\mathbf{H}_\theta^{-1}(\boldsymbol{\theta},\boldsymbol{\varphi})\right]\right\} \tag{4}$$

The design optimisation (4) is carried out by computing the n_φ-dimensional experiment design vector $\boldsymbol{\varphi} = [\mathbf{y}_0, \mathbf{u}, \mathbf{t}^{sp}, \tau]^{\mathrm{T}}$, which includes the N_y-dimensional set of initial conditions $\mathbf{y}_0$ (subset of $\mathbf{x}_0$) on the measured variables, the set of manipulated inputs $\mathbf{u}$, the set of time instants at which the output variables are sampled ($\mathbf{t}^{sp}$) and (possibly) the experiment duration τ. Equation (4) is subject to (2,3) and to a n_φ-dimensional set of constraints on design variables, defining the design space D (i.e. the operating range of

experimental decision variables). In (4) $\mathbf{V}_\theta$ and $\mathbf{H}_\theta$ are the variance-covariance matrix of model parameters and the FIM, respectively. $\mathbf{H}_\theta$ is defined by

$$\mathbf{H}_\theta(\boldsymbol{\theta},\boldsymbol{\varphi}) = \mathbf{H}_\theta^0 + \sum_{k=1}^{n_{sp}} \sum_{i=1}^{N_y} \sum_{j=1}^{N_y} s_{ij} \left[\frac{\partial \hat{y}_i(z_k,t_k)}{\partial \theta_l} \frac{\partial \hat{y}_j(z_k,t_k)}{\partial \theta_m}^T \right]_{l,m=1\ldots N_\theta} . \quad (5)$$

In (5) s_{ij} is the *ij*-th element of the $N_y \times N_y$ inverse matrix of measurements error and $\mathbf{H}_\theta^0$ is the prior dynamic information matrix, taking into account preliminary statistical information about the parametric system before each trial is carried out. According to (4), the experiment is designed so as to minimise a measurement function ψ of $\mathbf{V}_\theta$, representing the design criterion. The most common design criteria are the A-, D-, E-optimal criteria, minimising the trace, the determinant and the maximum eigenvalue of $\mathbf{V}_\theta$ respectively (Pukelsheim, 1993), or its singular values (Galvanin et al., 2007).

2.1 MBDoE for model discrimination: multi-objective formulation

In order to evaluate the relative amount of information which can be obtained for the estimation of the *j*-th model parameters from the *i*-th experiment the following Relative Fisher Information (RFI) index can be computed:

$$RFI_{ij} = \frac{\left\|\mathbf{H}_{ij}\right\|}{\sum_{i=1}^{N_{exp}} \left\|\mathbf{H}_{ij}\right\|} = \frac{\left\|\mathbf{H}_{ij}\right\|}{\left\|\mathbf{H}_j\right\|} \quad (6)$$

where $\left\|\mathbf{H}_{ij}\right\|$ is the FIM related to the *i*-th experiment for the *j*-th competitive model evaluated from (5) and $\left\|\mathbf{H}_j\right\|$ is the global information obtained from the N_{exp} experiments for the identification of the *j*-th model according to a norm $\| \cdot \|$. In this study, the trace has been used as a suitable matrix norm. The utility of (6) is that it allows for a ranking of the available experiments, underlining the most informative regions of the design space *D* to be exploited for parameter identification.

A multi-objective MBDoE is formulated with the purpose of discriminating between N_M competing models ensuring at the same time the best possible estimation of kinetic parameters:

$$\boldsymbol{\varphi}^{\mathrm{MD}} = \arg\max_{\boldsymbol{\varphi}\in D} \left\{ \psi^{\mathrm{MD}} \right\} = \arg\max_{\boldsymbol{\varphi}\in D} \left\{ \sum_{M,N=1}^{N_M} P_M P_N \left[\sum_{i=1}^{N_y} \frac{\left(\hat{y}_{M,i} - \hat{y}_{N,i}\right)^2}{\sigma_{y,i}^2} \right]_{M,N} \right\} \quad (7)$$

$$\text{s.t.} \qquad \psi^{\mathrm{PE}} = \sum_{j=1}^{N_M} \left\|\mathbf{H}_j\right\| / N_M \le \varepsilon \qquad \varepsilon^{MIN} \le \varepsilon \le \varepsilon^{MAX} \quad (8)$$

In (7) ψ^{MD} is the discriminating power, ψ^{PE} is the design optimality criterion, $\hat{y}_{M,i}$ and $\hat{y}_{N,i}$ are the *i*-th predicted responses of model *M* and *N*, while P_i is the relative probability of the i-th model to be the "true" model computed after parameter estimation (Schwaab et al., 2006). The optimisation (7-8) is carried out for a number of values of ε, ranging from the minimum value ($\varepsilon = \varepsilon^{\mathrm{MIN}}$, MBDoE for model discrimination) to the maximum value ($\varepsilon = \varepsilon^{\mathrm{MAX}}$, MBDoE for improving parameter estimation).

3. Case study: methanol oxidation on silver catalyst

3.1 Reaction mechanisms

In the identification study the simplified model proposed by Andreasen et al. (2005) was used as a reference model (Model 1). According to Model 1, the following reactions constitute the base (global) mechanism:

$$CH_3OH + 1/4\ O_2 \rightleftharpoons CH_2O + 1/2\ O_2 + 1/2\ H_2O \quad (9)$$

$$CH_2O + 1/2\ O_2 \rightleftharpoons H_2 + CO_2 \quad . \quad (10)$$

Two additional simplified kinetic models of increasing level of complexity were considered:

1. Model 2: including the following combustion reactions for both CH_3OH and CH_2O:

$$CH_3OH + 3/2\ O_2 \rightarrow 2H_2O + CO_2 \quad (11)$$

$$CH_2O + O_2 \rightarrow H_2O + CO_2; \quad (12)$$

2. Model 3: including combustion reactions (11,12) for CH_3OH and CH_2O; the global methanol oxidation reaction (9) was split into a dehydrogenation reaction ($CH_3OH \rightleftharpoons CH_2O + H_2$) and a selective oxidation reaction ($CH_3OH + 1/2O_2 \rightleftharpoons CH_2O + H_2O$).

The hydrogen oxidation reaction ($H_2 + 1/2O_2 \rightarrow H_2O$) has also been included in each reaction mechanism. Although this reaction is known to occur only at higher temperatures (Schubert et al., 1998), it has been considered to account for the low hydrogen concentrations observed in the experiments. The reaction rate expressions for (9,10) are the ones proposed by Andreasen et al. (2005), while power law kinetic expressions have been used for the other reactions in the proposed mechanisms.

3.2 Model discrimination and ranking of experiments

In this case study the elements of the design vector $\boldsymbol{\varphi}$ which can be optimised are:

1. Composition of reactants in terms of molar fractions: methanol (0.07-0.14), oxygen (0.03-0.10) and water (0.02-0.22) modelled as initial conditions $\mathbf{y}_0$;
2. Temperature T (725 K < T < 826 K) modelled as input $\mathbf{u}$;
3. Pressure P (1.6-1.7 atm) modelled as input $\mathbf{u}$;
4. Flow rate F (25-27 mL/min) modelled as input $\mathbf{u}$.

The ranges of operability shown in parenthesis in the above represent the investigated design space D, where P and F have been basically kept constant during the trials. Concentration measurements are available as molar fractions of CH_3OH, O_2, CH_2O, H_2, H_2O and CO_2 at the inlet ($z = 0$) and outlet ($z = l$, where l is the reaction channel length [mm]) of the reactor and they are assumed corrupted by Gaussian noise with zero mean and a standard deviation of 1% on the reading. Preliminary data from N_{exp}= 21 experiments from the microreactor system were available in order to discriminate among the rival models (Model 1-3) where the effect of temperature (T) and feed composition (CH_3OH, O_2 and H_2O molar fraction, $\mathbf{y}_0 = [y_{CH3OH}\ y_{O2}\ y_{H2O}]^T$) on final products ($CH_3OH$, O_2, H_2O, CH_2O, H_2, CO_2) was investigated:

1. Experiments E1-5: T varied from 725 to 826 K (y_{CH3OH}=0.10, y_{O2}=0.04, y_{H2O}=0.07);
2. Experiments E6-9: T varied from 725 to 826 K (y_{CH3OH}=0.15, y_{O2}=0.06, y_{H2O}=0.11);
3. Experiments E10-21: T kept at 733 K, variable y_{CH3OH} (range 0.07-0.14, E10-E14), y_{O2} (range 0.03-0.10, E15-E17) and y_{H2O} (range 0.02-0.21, E18-E21).

In all these performed experiments He was used as an inert, the volumetric flow rate was kept at F = 26.5 mL/min and the pressure at P = 1.6 atm. The reaction channel length containing the catalyst was 12.5 mm long, 0.12 mm high and 0.6 mm wide. A

model discrimination was carried out from experimental data by assessing for each proposed model: *i*) the lack-of-fit in terms of χ^2 obtained after parameter estimation is carried out; *ii*) the Akaike information criterion (AIC) investigating the trade-off between fitting capability and model complexity (i.e. N_θ); *iii*) the probability P_i. Results after model discrimination are shown in Figure 1. Model 3 provides the most satisfactory results in terms of lack-of-fit, underlined by the lower χ^2, and turns out to be the most probable "true" model (P_3 = 39%). However, it also represents the most complex model in terms of number of model parameters, as clearly indicated by the relatively high AIC value, which tends to promote the use of Model 1.

	Model		
	Model 1	*Model 2*	*Model 3*
χ^2	9762	7721	6874
N_θ	6	10	12
AIC	-6.4	2.1	6.3
P_i	27%	34%	39%

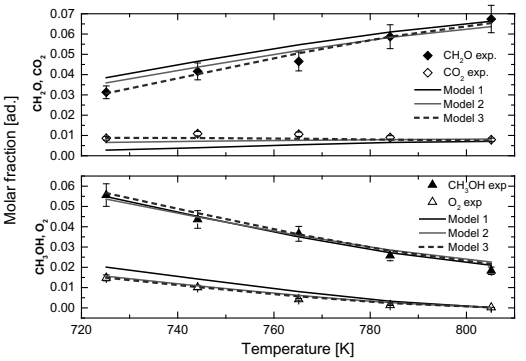

Figure 1. Relative performance of candidate kinetic models after model identification in terms of molar fractions as a function of temperature for selected species. Model discrimination results are given in the table on the left hand side.

Model 1 (solid line) is ineffective in representing oxygen, formaldehyde and CO_2 molar fractions, while methanol profiles are always represented in a satisfactory way by all the proposed models. Interestingly, the representation of oxygen and methanol concentration as a function of the investigated temperature was significantly improved by including the combustion reactions in the model formulation (Model 2 and 3) as compared to the original model formulation (Model 1). Furthermore, a better representation of both CO_2 and CH_2O can be realised if competitive dehydrogenation and selective oxidation steps are included (Model 3). The model availability allows the definition of the best experimental conditions in order to estimate the model parameters with the greatest precision. Figure 2a shows the RFI evaluated from (6) for a ranking of experiments E1-E21. Each proposed model shows a different RFI response to a change in experimental conditions. In particular: *i*) an increment in temperature *T* would be beneficial for Model 2, but would be unhelpful for the estimation of Model 1 and Model 3 kinetic parameters; *ii*) an increment on oxygen concentration in the feed is beneficial for the identification of all the proposed models; *iii*) higher methanol concentration in the feed is beneficial for the identification of Model 2 and 3, while a maximum in the information level is realised for Model 1; *iv*) water concentration increases the information for Model 1 and 2, while does not particularly affect Model 3 identification.

3.2 Multi-objective design of experiments for model discrimination

Results in terms of solutions of the multiobjective problem (7-8) are given in Figure 2b. Points 1-4 in the figure represent the solutions of the optimization problem (7-8) in terms of trade-off between discriminating power (ψ^{MD}) and design optimality (ψ^{PE}). Interestingly, the temperature *T* turns out to be the most influential design variable to be considered. In fact, points 1-4 in the plot are all identified by $\mathbf{y}_0 = [y_{CH3OH}\ y_{O2}\ y_{H2O}]^T$ = [0.14 0.10 0.22] ^{T}, F = 26.0 mL/min, P = 1.6 atm (same inlet conditions) but totally

different reaction temperatures (T^1 = 826 K , T^2 = 796 K, T^3 = 765 K, T^4 = 732 K). Low temperatures are beneficial for the precise estimation of the model parameters, while high temperatures allow for a higher difference between the model responses.

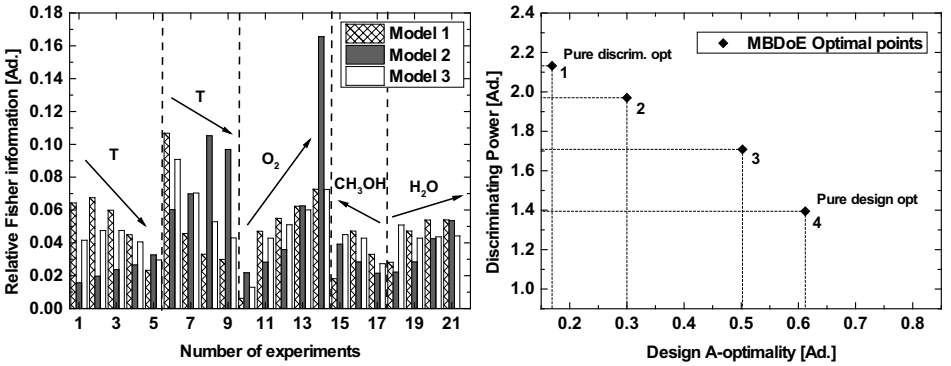

(a) (b)

Figure 2. (a) Ranking of experiments based on Relative Fisher Information (RFI). (b) Multi-objective MBDoE solution points as results of optimisation (7-8).

4. Conclusions

A new MBDoE approach has been proposed and applied for a ranking of the experiments in microreactor platforms showing the best experimental conditions to be used for a precise estimation of the set of kinetic parameters of candidate kinetic models. A discrimination of simplified kinetic models of methanol oxidation on silver has been carried out, underlining a better representation of experimental results when dehydrogenation and a selective oxidation step are included in the model formulation, paving the way to new (possible) model formulations. Furthermore, a multi-objective MBDoE underlined the important role of temperature in the model discrimination task.

5. Acknowledgements

Funding from EPSRC grant (EP/J017833/1) is gratefully acknowledged.

References

N. Al-Rifai, E. Cao, V. Dua, A. Gavriilidis, 2013, Microreactor technology aided catalytic process design, Curr. Opin. Chem. Eng., 2, 1-8
G. Franceschini, S. Macchietto, 2008, Model-based design of experiments for parameter precision: state of the art, Chem. Eng. Sci., 63, 4846-4872
M. Schwaab, F. M. Silva, C. A. Queipo, A. G. Barreto Jr., M, J. C. Pinto, 2006, A new approach for sequential experimental design for model discrimination, Chem. Eng. Sci., 61, 5791-5806
B. J. Reizman, K. F. Jensen, 2012, An automated continuous-flow platform for the estimation of multistep reaction kinetics, Org. Process Des. Dev., 16, 1770-1782
A. Andreasen, H. Lynggaard, C. Stagelman, P. Stolze, 2005, A simplified kinetic model of methanol oxidation on silver, Applied Cat, 189, 267-275
E. Cao, A. Gavriilidis, 2005, Oxidative dehydrogenation of methanol in a microstructured reactor, Catal. Today, 110, 154-163
F. Pukelsheim, 1993, Optimal design of experiments, J Wiley & Sons, New York (U.S.A.)
F. Galvanin, F. Bezzo, S. Macchietto, 2007, Model-based design of parallel experiments, Ind. Eng. Chem. Res., 46, 871-877
H. Schubert, U. Tegtmeyer, R. Schlögl, 1998, On the mechanism of the selective oxidation of methanol over elemental silver, Catal. Lett., 28, 383-390

Krist V. Gernaey, Jakob K. Huusom and Rafiqul Gani (Eds.), 12th International Symposium on Process Systems Engineering and 25th European Symposium on Computer Aided Process Engineering.
31 May – 4 June 2015, Copenhagen, Denmark

Application of Derivative - Free Estimator for Semi Batch Autocatalytic Esterification Reactor: Comparison Study of Unscented Kalman Filter, Divided Difference Kalman Filter and Cubature Kalman Filter

F.S. Rohman, S. Abdul Sata and N. Aziz*

School of Chemical Engineering, Universiti Sains Malaysia, Engineering Campus 14300 Nibong Tebal, Seberang Perai Selatan, Penang, Malaysia
**Corresponding Author's Phone: +604-5996457; Fax: +604-6941013; E-mail: chnaziz@usm.my*

Abstract

The online or real time optimization system required an on-line monitoring for important state variables and parameters in order to provide feedback to the algorithm implemented. The unmeasured states and unknown parameters can be determined by estimator. The estimator used must be feasible and has several functionalities such as bias-free parameter and state estimates, high speed of convergence from initialization errors, perfect tracking and short computational time. To address those issues, the derivative free stochastic observer is applied in this work. Different derivative-free techniques implemented which are based on the Gaussian approximation are scaled Unscented Kalman Filter technique (sUKF), Divided Difference Kalman filter (DDKF) and Cubature Kalman filter (CKF). Here, an autocatalytic esterification of Propionic Anhydride with 2-Butanol is considered as a case study. The performance of estimator which is indicated by the accuracy, speed convergence and robustness, is represented by the root mean squared error (RMSE). While, the efficiency of the estimator's computation are evaluated by CPU time consumed. The derivative free-estimators are then evaluated within two case studies which are normal condition and effect of uncertainty of initialization parameter. The results of overall state and parameter estimator study show that the CKF outperform the sUKF and DDKF for both cases. Moreover, computational load consumed for the CKF is feasible for online practice However, in term of CPU time DDKF results to the shortest among all techniques implemented.

Keywords: Nonlinear estimation, sUKF, DDKF, CKF, semi batch processes, auto catalytic esterification.

1 Introduction

Online optimization and control strategy which are based on the key state variables cannot be implemented unless those required variables can be measured on-line. Despite the advent of process analytical technology in the recent years, online measurement of all process variables is not often viable due to various technological and economical limitations. Thus, there is an urgent need to provide the estimator for estimating those

state variables from other state variables which are relatively simple and easy to measure (Hartikainen et al., 2011).

The best estimator must have several functionalities such as bias-free state estimates, high speed of convergence from initialization errors, perfect tracking and short computation time. The most common way of applying the estimator to a nonlinear batch system is in the form of the extended Kalman filter (EKF). Nevertheless, EKF contains several flaws that may seriously affect its performance. One of the flaws is the computation of the state transition matrix which calls for calculation of the Jacobian matrix and its matrix exponential, which, in turn, requires linearization of the system model (van der Merwe, 2004).

In this work the derivative free stochastic estimator is applied. The different derivative-free techniques which is based on the Gaussian approximation namely; scaled Unscented Kalman Filter technique (sUKF), Divided Difference Kalman filter (DDKF) and Cubature Kalman filter (CKF) (Hartikainen et al., 2011) are implemented. To the best authors' knowledge, there is no work reported in application of CKF on batch chemical processes. Therefore a comparison study between CKF and other derivative-free estimators (sUKF and DDKF) is required in order to select the best estimator applied in this study. The process considered is Catalyzed Esterification of Propionic Anhydride with 2-Butanol in semi batch reactor. The derivative free- estimators are then evaluated based on two case studies which are normal condition and effect of uncertainty of initialization parameter.

2. Modeling of autocatalytic esterification process

Esterification of propionic anhydride with 2-butanol is producing sec-butyl propionate and propionic acid. It exhibits a kind of autocatalytic behaviour when sulphuric acid is introduced. The reaction kinetics of this esterification has been investigated and the data of parameters is depicted from Zaldivar et al. (1993) and the parameter involved in heat transfer is depicted from Ubrich (2000). The semi batch reactor model which the mass and energy balances are represented by following equations, are considered as the process plant.

$$\frac{dC_B}{dt} = -((k_1 + k_2 C_{cat1}) C_A C_B + k_3 C_{cat2} C_B) + \frac{F_o}{V}(C_{B0} - C_B) \tag{1}$$

$$\frac{dC_C}{dt} = \frac{dC_D}{dt} = ((k_1 + k_2 C_{cat1}) C_A C_B + k_3 C_{cat2} C_B) - \frac{F_0 C_C}{V} \tag{2}$$

$$\frac{dC_{cat1}}{dt} = -\frac{dC_{cat2}}{dt} = -(k_4 10^{-H} C_{cat1} C_A) - \frac{F_0 C_{cat1}}{V} \tag{3}$$

$$\frac{dT}{dt} = \frac{-\Delta Hr_{total}}{\rho C_p} + \frac{UA}{\rho C_p V}(T_j - T) + \frac{F_O}{V}(T_{feed} - T) \tag{4}$$

$$\frac{dT_j}{dt} = \frac{F_j}{V_j}(T_{jin} - T_j) + \frac{UA}{\rho_j V_j C_j}(T - T_j) \tag{5}$$

$$\frac{dV}{dt} = F_o \tag{6}$$

where C_A, C_B,C_C, C_{Cat1}, and C_{cat2} are concentration of 2-butanol, propionic anhydride; propionic acid, sulphuric acid and mono-butyl sulphuric acid, respectively. F_o, V are the feed rate and the volume of solution within reactor. F_j is the jacket flowrate, T_j is the jacket temperature; T_{jin} is the inlet jacket temperature; T_{feed} is the feed temperature; A is the heat exchange area; V_j is volume of the jacket; U is the heat exchange coefficient; C_p, C_j is heat capacity of solution in the reactor and the jacket, respectively; H is the acidity function; ΔHr is the heat of reaction; ρ is density of solution in the reactor; ρ_j is density of the jacket solution. The initial value of C_A, C_B, C_C, C_D, C_{cat1}, C_{cat2}, V, T and T_j is 3.4M, 0M, 0M, 0M, 1.02x 10^{-2}M, 0M, 1L, 303K, and 303K, respectively.

3. Estimation method

The estimator problem is concerned with the estimation of the state vector of a dynamic system which is governed by the non-linear stochastic differential equations approximated in discrete time as:

$$x_k = f(x_{k-1}, k-1) + q_{k-1}$$
$$y_k = h(x_k, k) + r_k \quad (7)$$

where $x_k \in R^n$ is the state on the step time k, **f** is the dynamic model function, $q_{k-1} \sim N(0, Q_{k-1})$ is the process noise on the step time k−1, Q is process noise covariance. The prior distribution for the state is $x_0 \sim N(m_0, P_0)$, where parameters m_0 and P_0 are initial mean and covariance of the states which are set using the known information from the system under consideration. $y_k \in R^m$ is the measurement on the step time k, **h** is the measurement model function, $r_k \sim N(0, R_k)$ is the measurement noise of step time k, R is the measurement noise covariance (van der Merwe, 2004). In this study, the sUKF, DDKF and CKF have been used to develop nonlinear state observers for the esterification process.

Scaled Unscented Kalman Filter (sUKF) uses deterministically chosen sigma points to approximate the nonlinearities. The unscented transformation (UT) is a method for calculating the statistics of a random variable which undergoes a nonlinear transformation and builds on the principle that it is easier to approximate a probability distribution than an arbitrary nonlinear function (van der Merwe, 2004). The computer code *KalmTool* was used for sUKF which was developed by Nørgaard et al. (2003).

Divided Difference Kalman filter (DDKF) uses Sterling's polynomial interpolation to approximate the distribution (Nørgaard et al., 2000). The divided difference filters (DDFs) are similar to the extended Kalman filter (EKF). At the propagation step, the DDKF also involve a local expansion of a nonlinear function, not via a Taylor series expansion as in the EKF, but through Stirling's interpolation formula. The computer code *KalmTool* was also used for DDKF which was developed by Nørgaard et al. (2003).

Cubature Kalman filter (CKF) uses a third-degree cubature approximation to solve the Gaussian integrals (Arasaratnam and Haykin, 2009). Specifically, a third- degree spherical-radial cubature rule provides a set of cubature points scaling linearly with the state-vector dimension. The CKF may therefore provide a systematic solution for high-dimensional nonlinear filtering problems. CKF method was implemented using package code developed by Hartikainen et al (2011).

4 Simulation of the derivative-free estimators

The derivative free-estimators were evaluated based on two case studies which were normal condition and effect of uncertainty of state initialization. The normal condition case evaluates the accuracy of the estimators where there were no noises, disturbance and uncertainties. The estimators were also performed to check of their nominal character included the efficiency of estimator. The efficiency of the estimator's computation is determined by CPU time consumed. The uncertainty of state initialization case examines the speed convergence of the estimators. They were initialized with the initial estimates which are varied far from the true values i.e. different initial value of concentration of 2-butanol, +30% of C_{A0}.

The states x and measurements y of the autocatalytic esterification semi batch reactor considered were:

$$x = [C_A \; C_B \; C_c \; C_D \; C_{cat1} \; C_{cat2} \; T \; T_j]; y = [C_A \; T \; T_j]$$

The initial condition of the state estimation which is the same as the initial model is:

$x_0 = [3.4\text{M } 0\ 0\ 0\ 1.02\text{x } 10^{-2}\text{M } 1\ 303\text{ K } 303\text{ K}]$

Measurement noise has been considered on concentration of 2-butanol, the reactor and jacket temperatures. State noise was added to the system dynamic equations. The noises involved in the cases was maintained at low level where their values set as process noise covariance (Q matrix) = diag [0 2.4 x 10^{-14} 2.4 x 10^{-10} 1x 10^{-12} 1 x 10^{-14} 1x 10^{-14} 0 0] and measurement noise covariance (R matrix) = diag [5x 10^{-1} 5 x 10^{-1} 5x 10^{-1}] (Ramkhelawan, 2000).

5 Results and discussion

All the cases were simulated in MATLAB environment and were conducted by using IntelRCoreTM i3 CPU 530 with 2.93GHz and 3.17GB of RAM. In this simulation, the process time considered is 100 min which is the time required to achieve more than 90% conversion as reported by Zaldivar et al. (1993).

5.1 Estimator performance in a normal condition.

The RMSE results and CPU time for all estimators obtained are tabulated in Table 1. From the table, for under the normal condition, it can be seen that all the estimators provide a good estimation of ester (sec- butyl propionate) with very small RMSE. Among those three estimators, CKF has the highest accuracy due to the lowest RMSE obtained, followed by sUKF's and DDKF. The DDKF suffers to the lowest accuracy because the posterior mean and covariance obtained is only covered accurately to the first order with all higher order moments truncated (Nørgaard et al., 2000, van der Merwe, 2004). Meanwhile, the sUKF is able to encompass the posterior mean and covariance accurately to the 2nd order for any nonlinearity choosing by the weights and sigma-point locations such that the first and second order terms matched exactly. Under this scheme, errors are only introduced in the 3rd and higher orders (Luo, 2009). Therefore, sUKF has a higher accuracy than DDKF. On the other hand, CKF produced highest accuracy since it considers the third-degree spherical-radial rule which is accurate for polynomials of all odd degrees even beyond three (Arasaratnam and Haykin, 2009). Meanwhile, the computation time requested to complete a single run by DDKF is the shortest, followed by CKF and sUKF. The CPU time of estimators is depending on the numerical complexity as indicated by the number of points inherited for function evaluations.

Table.1: RMSE of sec- butyl propionate under normal condition and CPU obtained

Case study	sUKF	DDKF	CKF
1. Normal condition:			
- RMSE $x10^{-2}$	0.83	0.94	0.61
- CPU time (s)	3.26s	1.16s	1.33 s
2 Uncertain initial condition			
- RMSE $x10^{-2}$	166	162	173

The DDKF was the fastest among filters due to the simplest algorithm constructed which requires a single point and 2n+1 sample in the probabilistic state space to propagate the mean and covariance, respectively (Wu *et al.*, 2006). Meanwhile, the cubature rule in CKF entails 2n cubature points to calculate both mean and covariance (Arasaratnam and Haykin, 2009). In contrast, the sUKF needs 2n+1 point to capture correctly both mean and covariance which can be considered as the most complex algorithm and thus the longest computation time is consumed (Wu *et al.*, 2006).

5.2 Effect of initial condition uncertainty

In this study, the deviation in C_{A0} was considered as initial state uncertainty, which effected directly on concentration C_A behavior. Figure 1 show the profile of C_A when +30% uncertainty in C_{A0} is introduced. From the Figure, it can be observed that all the estimators are still able to converge to the true states. It is also indicate that the convergence speed of the state estimators from initialization deviation is quite fast. It can be found that both DDKF and sUKF have almost the same speed convergence. Meanwhile, the CKF is converged to true state slower than both DDKF and sUKF.

From Table 1, it can be observed that the amount of RMSE can be link to the speed of convergences. Higher error the estimates signify slower convergence to the correct state. The RMSE of CKF is found to be the highest among the others since it is the slowest to converge. It was assumed that the error obtained in CKF incurred in computing the integral of nonlinear function with respect to a Gaussian weight function. The information loss in some integration points for capturing the true evolving posterior density is afforded from the cubature rule which some of its points outside the integration region. This occurrence yields round off errors and then degrades covariance accuracy (Wu *et al*., 2006, Arasaratnam and Haykin, 2009).

6. Conclusion

The performance of CKF, UKF and DDKF on normal condition and uncertain initial state condition that is occurred in semi batch autocatalytic esterification reactor has been evaluated. In the normal condition, CKF produced highest accuracy and comparable CPU time. Meanwhile, DDKF suffered worst accuracy but had the shortest CPU time. In the presence of uncertain initial of C_{A0}, the DDKF showed the fastest speed convergence. Meanwhile, the CKF obtained the slowest one. To conclude, CKF outperformed the sUKF and DDKF for both cases. Therefore, CKF is preferred to be implemented in online system since the RMSE obtained from CKF, sUKF and DDKF is almost similar in the two case studies. In order to determine the best performance of estimators, the performance evaluation in the presence disturbance and uncertainty is required which will be considered as future study.

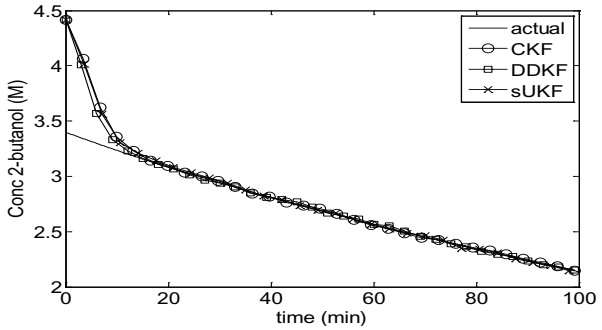

Figure 1: Concentration of 2- butanol in the presence of +30% error in $C_{A0:}$

Acknowledgement

The financial support from Ministry of Science, Technology and Innovation (MOSTI), Malaysia through Sciencefund grant and Universiti Sains Malaysia through RU grant is greatly acknowledged.

References

Arasaratnam, I. and Haykin, S. (2009). Cubature Kalman filters. *IEEE Transactions on Automatic Control,*54(6):1254–1269.

Hartikainen, J, Solin, A and Särkkä, S (2011) Optimal Filtering with Kalman Filters and Smoothers: a Manual for the Matlab toolbox, Department of Biomedical Engineering and Computational Science, Aalto University School of Science, Finland

Luo, X (2009) Recursive Bayesian Filters for Data Assimilation, Dissertation, University College, University of Oxford

Nørgaard, M., Poulsen, N., and Ravn, O. (2003) Kalmtool for use with matlab, in 13th IFAC Symposium on System Identification, SYSID03, Rotterdam.Rotterdam: IFAC, 2003, pp. 1490–1495

Nørgaard, M., Poulsen, N., and Ravn, O. (2000).New developments in state estimation for nonlinear systems.*Automatica*, 36(11):1627–1638.

van der Merwe, R. (2004) Sigma-Point Kalman Filters for Probabilistic Inference in Dynamic State-Space Models, PhD Dissertation, OGI School of Science & Engineering at Oregon Health & Science University

Ramkhelawan, P (2000) Modelling and Estimation of PolycondensationProcesse, Thesis, University of Toronto

Ubrich, O (2000) Improving Safety andProductivity of isothermal semi batch reactorbymodulating feed rate, PhD thesis, Écolepolytechniquefédérale de Lausanne

Wu, Y, Hu,D , Wu,M and Hu , X (2006) A Numerical-Integration Perspective on Gaussian Filters, *IEEE Transactions on Signal Processing* 54:2910-2921

Zaldivar, J. M., Hernandez, H., Molga, E., Galvan, I. M., &Panetsos, F. (1993).The use of neural networks for the identification of kinetic functions of complex reactions. In Proceedings of the third European symposium on computer aided process engineering, ESCAPE 3.

Krist V. Gernaey, Jakob K. Huusom and Rafiqul Gani (Eds.), 12th International Symposium on Process Systems Engineering and 25th European Symposium on Computer Aided Process Engineering.
31 May - 4 June 2015, Copenhagen, Denmark.

Modeling and parameter estimation of coke combustion kinetics in a glycerol catalytic conversion reactor

Minghai Lei[a], François Lesage[a], M. Abderrazak Latifi[a] and Serge Tretjak[b]

[a]*Laboratoire Réactions et Génie des Procédés, University of Lorraine, Nancy, France*
[b]*Centre de Recherche et Développement de l'Est, Arkema, Carling, France*
Francois.Lesage@univ-lorraine.fr

Abstract

A two dimensional, heterogeneous model was developed for the simulation of a coked catalyst regeneration fixed-bed reactor in a green acrylics process. A kinetic model which consists of combustion of coke containing carbon, hydrogen and oxygen was derived. The unknown parameters (including the kinetic parameters, initial composition and concentration of coke, heat transfer parameters and catalyst pore diameter) were identified using the results of regeneration experiments with the coke formed in a glycerol dehydration process. Good agreements between the model predictions and experimental results were obtained.

Keywords: Fixed-bed reactor modeling; Catalyst regeneration; Coke combustion kinetics; Parameter identification

1. Introduction

Chemistry as it is perceived today has largely developed from oil, natural gas and coal, i.e. non-renewable fossil resources. This is particularly the case of acrylic acid production that uses propylene as the raw material. However, the expected exhaustion of oil and current environmental requirements lead chemical industries to seek new raw materials from biomass to meet the needs of the population. An interesting alternative resource to propylene in acrylic acid industry is glycerol (Katryniok et al., 2010) that is renewable, sustainable, available and abundant, particularly as a major by-product in the biodiesel production process. However, during the selective catalytic dehydration of glycerol to acrolein, coke (or heavy products) is formed and thus deactivates the catalyst. Substantial coke formation means that the catalyst regeneration step is an essential part of the industrial process that is normally carried out by combustion of the coke with a small amount of oxygen in an inert gas stream. As the reaction is highly exothermic, either thermal runaway or catalyst sintering may happen. In order to investigate the influence of different process parameters, to identify the conditions leading to runaway, and finally to develop a method to maximize the effectiveness of the oxidation of coke while maintaining a moderate level of temperature in the bed, a predictive model of the process is necessary. The aim of this work is to develop the most predictive possible model (including reactor and kinetic model) for a coked catalyst regeneration process. The needed experimental measurements for the model identification and validation were carried out and provided by Arkema Company.

2. Experimental rig and measurements

The process considered here is a gas-solid fixed-bed tubular reactor which is schematically presented on figure 1. This figure shows the location of temperature probes, which are actually placed

in a thermowell of radius R_{in} at the center of the reactor. Catalyst particles fit in the annular space left between the thermowell and the inner wall of the reactor. A coolant fluid is used to remove the heat generated by the reactions. A set of five experiments where either the coolant temperature

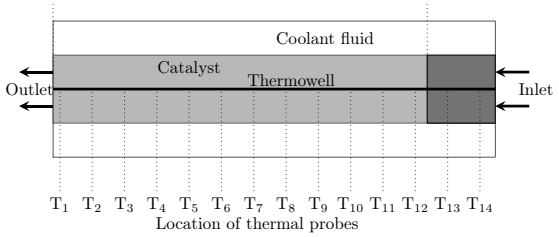

Figure 1: Experimental rig

or inlet gas composition were varied is available. Experimental measurements consist mainly of temperatures along the thermowell, inlet and outlet pressure, inlet oxygen flow rate, outlet gas flow rate and its composition in terms of CO, CO_2 and O_2. It is noteworthy that other components are present in the outlet gas stream, but their concentration was not measured. These measurements will be used for the development of the kinetic and reactor models in the next section.

3. Reactor and kinetic modelling

In order to develop a comprehensive reactor model, the knowledge of kinetics of the coke combustion is required. These kinetics are widely investigated in literature (Kanervo et al., 2001; Sierra et al., 2010), but most of the studies ignore the reaction of hydrogen contained in the coke. Indeed, the oxygen mass balance in the reactor is not satisfied and this is clearly shown on figure 2. This figure compares the equivalent oxygen flow rate at outlet computed by considering its presence in all measured components to its inlet flow rate. The lack of oxygen for times below 0.5 advocates for the creation of an oxygenated product that is not measured at outlet. With the possible presence of hydrogen in the coke, this product is considered to be water only.

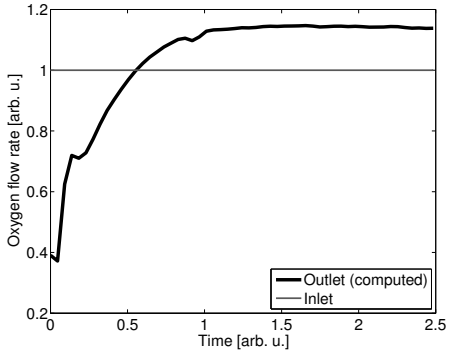

Figure 2: Oxygen flow rate in feed, and calculated from O2, CO2 and CO measurements at outlet

However, after t=0.5 and even with the additional consumption due to water formation, the oxygen balance shows a generation of oxygen in the system. This oxygen is assumed to be present in the coke. This is coherent with experimental studies (Suprun et al., 2009) which have shown that coke is formed through condensation of oxygenated compounds such as aldehydes.

We can now state that coke is made of carbon, hydrogen and oxygen in unknown proportions, i.e. CH_xO_y. Taking into account this information, the initial composition of the coke will then be identified from experimental measurements through a reactor model. To our knowledge, the determination of coke composition through measurements of temperature profiles and gas composition has not been investigated so far in literature.

The kinetic scheme used to model the coke combustion should take into account its specific composition. In particular, it has been postulated that a carbon atom bonded to an oxygen has different reactivity than one which is not. We thus considered two kinds of carbon atoms in the coke, one noted [C] which is not bonded to oxygen, and the other noted [CO], which represents both carbon and oxygen atoms. These two carbons can be oxidized to CO_2, whereas [C] can also be oxidized into CO. This leads to the following kinetic scheme:

$$\begin{array}{lcl} [C]+\frac{1}{2}O_2 & \longrightarrow & CO \\ [C]+O_2 & \longrightarrow & CO_2 \\ [CO]+\frac{1}{2}O_2 & \longrightarrow & CO_2 \\ [H]+\frac{1}{4}O_2 & \longrightarrow & H_2O \end{array} \tag{1}$$

The reaction rates are assumed to be of first order with respect to coke (Keskitalo et al., 2006; Sierra et al., 2010) and an unknown order with respect to oxygen. The unknown orders for the four reactions should thus be identified.

3.1. Coke spatial profile

From the evolution of the temperature profiles measured during the regeneration step (not represented, temperature peaks move slowly near the entrance and faster close to the exit) and the measurement of the coke concentrations in a laboratory scale reactor (figure 3), we assumed that the initial concentration of the coke is not uniform along the reactor and is modelled by the following linear expression where C_1 and C_2 are constants :

$$(\mathrm{CH}_x\mathrm{O}_y)_0 = C_1 - C_2 z \tag{2}$$

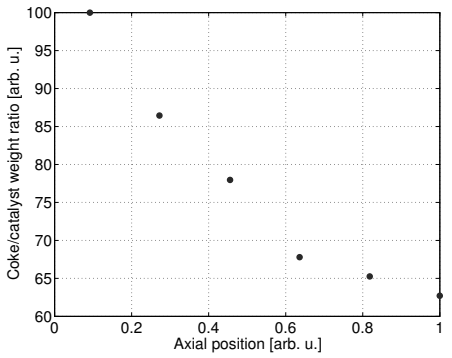

Figure 3: Coke concentration profile in a laboratory reactor (arbitrary units)

As the coked catalyst for each regeneration experiment was not obtained with exactly the same operating conditions, its initial concentrations and compositions might be different. The initial concentration (i.e. C_1 and C_2) of coke and its composition (i.e. x and y) will thus be identified for each experiment.

Now, the kinetic model as well as initial profile of coke composition will be included in a reactor model developed in the next section.

3.2. Reactor model

The catalyst regeneration step involves both chemical reactions and transport of reactants and products. Some studies (e.g. Müller et al. (2010)) show that the diffusion resistance of oxygen into the pores strongly influences the actual speed of coke combustion . In addition, the concentration profile of the coke in a catalyst particle during the combustion may be non-uniform (Tang et al. (2004)). This leads to the use of a two-phase model, where the mass balance is considered in the catalyst and in the surrounding gas phase. The process model developed is also based on the following additional assumptions: (i) the ideal gas law can be used, (ii) the internal temperature gradients in the catalyst particles are neglected owing to high thermal conductivity of the catalyst material, (iii) the heat and mass transfer resistances between solid and gas are neglected.

Based on the above assumptions, and taking into account the possible presence of intraparticle diffusion resistance, and as the radial temperature gradient in the reactor is not negligible (according to the Mears criterion (Mears, 1971)), a two-dimensional heterogeneous model was thus considered. The model equations include mass balances on both solid and gas phases for each component, heat balance on a pseudo-homogeneous phase and momentum balance on gas phase. As the pore diameters are small, the effective mass diffusion coefficient in the catalyst is given as :

$$D_e = \frac{\varepsilon_p}{\tau_p} \frac{1}{\frac{1}{D_k} + \frac{1}{D_m}} \tag{3}$$

where $\varepsilon_p = 0.571$ and $\tau_p = 2.5$ are respectively the catalyst porosity and tortuosity, $D_m = 1.114 \times 10^{-9} T^{1.726}$ is the molecular diffusion and Knudsen diffusivity D_k is given by the relation:

$$D_k = \frac{1}{3} d_{\text{pore}} \sqrt{\frac{8RT}{\pi M}} \tag{4}$$

The mass balance of component i in the solid phase (noted with subscript s) is derived as:

$$N_{s,T}\varepsilon_p \frac{\partial x_{s,i}}{\partial r_p} + c_{T,s}\varepsilon_p \frac{\partial x_{s,i}}{\partial t} = \varepsilon_p \frac{1}{r_p^2} \frac{\partial}{\partial r_p} \left(D_e c_{T,s} r_p^2 \frac{\partial x_{s,i}}{\partial r_p} \right) + \rho_s \sum_{j=1}^{NR} \left[R_j \left(\nu_{ij} - x_{s,i} \sum_{i=1}^{NC} \nu_{ij} \right) \right] \tag{5}$$

where r_p is the radial coordinate in pellet, ρ_s the catalyst density, c_T the overall gas concentration, N_T is the total mole flux, R_j the rate of reaction j, ν_{ij} the stoichiometric coefficient of component i in reaction j, and x_i the component i mole fraction.

In the reactor, the mass balance per component is:

$$uc_T \frac{\partial x_i}{\partial z} + vc_T \frac{\partial x_i}{\partial r} + c_T \varepsilon \frac{\partial x_i}{\partial t} = \nabla (D_e c_T \nabla x_i) + \varepsilon_p (1-\varepsilon) a_v \left(N_i|_{r_p=R_p} - x_i N_T|_{r_p=R_p} \right) \tag{6}$$

where r and z are the radial and axial coordinates, u the gas superficial velocity, ε the porous bed void fraction, a_v the specific area of catalyst pellet and N_i the mole flux of component i.

The overall mass balance can be deduced by summing the previous equations :

$$\frac{\partial (uc_T)}{\partial z} + \frac{\partial (vc_T)}{\partial r} + \varepsilon \frac{\partial c_T}{\partial t} = \varepsilon_p (1-\varepsilon) a_v N_T|_{r_p=R_p} \tag{7}$$

The heat balance equation can be written as:

$$\begin{aligned} c_T \sum_{i=1}^{NC} \left(u x_i C_{p,i} \frac{\partial T}{\partial z} \right) + \left[\varepsilon c_T \sum_{i=1}^{NC} (x_i C_{p,i}) + (1-\varepsilon) \rho_s C_{p,s} \right] \frac{\partial T}{\partial t} \\ = \nabla (\lambda_{\text{bed}} \nabla T) - \varepsilon_p (1-\varepsilon) a_v \sum_{i=1}^{NC} \left[\left(\Delta_f H_i^0 + H_i - H_i^0 \right) N_i|_{r_p=R_p} \right] \end{aligned} \tag{8}$$

where $C_{p,i}$ and $C_{p,s}$ are the heat capacity of component i and solid respectively, λ_{bed} the heat conductivity of homogeneous phase, H_i the enthalpy of component i (exponent ^{0} denotes standard conditions) and $\Delta_f H_i$ the standard enthalpy of formation of coke.

Finally, the pressure drop is computed using Ergun equation as:

$$\frac{dP}{dz} = \alpha u + \beta u^2 \tag{9}$$

The coefficients α and β are assumed to be unknown, mainly since the wall effect are by far not negligible in our case, and will be identified from experimental measurements.

For all these equations, initial and boundary conditions are classical and are not be presented here, except for the heat balance. Heat transfer at the wall depends on an overall coefficient h_t, given by correlations (Green and Perry, 2008). The resulting conditions are given in equation 10.

4. Results and discussion

The model equations were implemented within gProms software (Process Systems Enterprise, 2012), which uses the Method of Lines to solve the PDEs. These PDEs were discretized using a centered finite difference scheme. The modelling software does not allow different discretization schemes for advective and diffusive terms. In order to avoid a bias in second order terms, a centered scheme was chosen. This required a grid Péclet number lower than 2, and thus a large number (100) of discretization intervals on axial coordinate. On radial coordinates (both in the reactor and particles), a non uniform grid was used and the number of intervals was chosen to ensure an acceptable precision.

It is important to mention that an index problem was encountered during the simulations. In order to cope with this issue, a time derivative had to be added to both sides of the boundary conditions on temperature, that is:

$$\left.\frac{\partial T}{\partial r}\right|_{r=R_{in}} + \frac{\partial T}{\partial t} = \frac{\partial T}{\partial t} \quad \text{and} \quad -\lambda \left.\frac{\partial T}{\partial r}\right|_{r=R} + \frac{\partial T}{\partial t} = h_t \left(T_{cool} - T|_{r=R}\right) + \frac{\partial T}{\partial t} \tag{10}$$

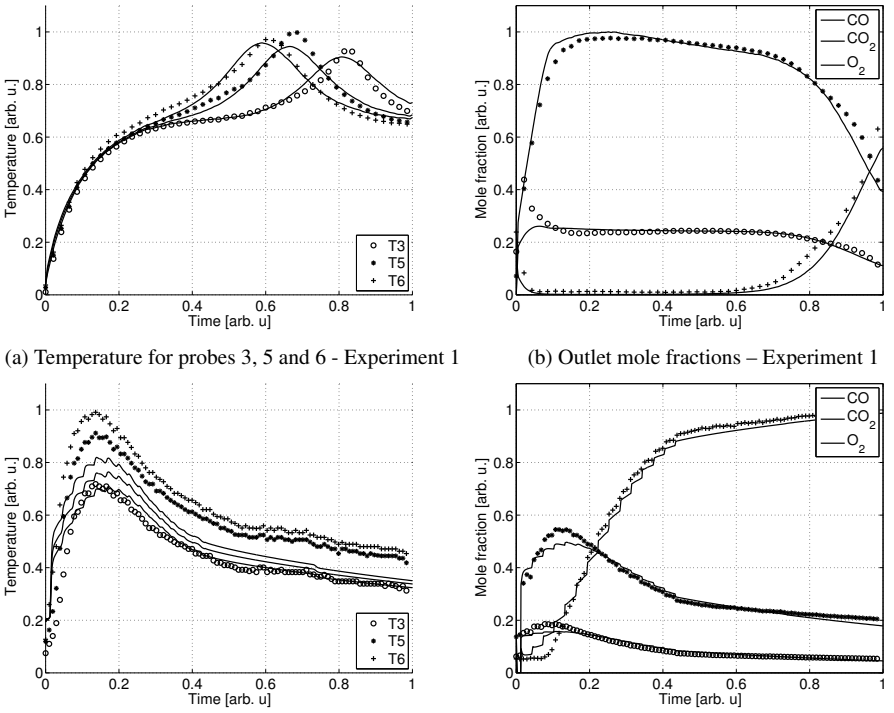

(a) Temperature for probes 3, 5 and 6 - Experiment 1

(b) Outlet mole fractions – Experiment 1

(c) Temperature for probes 3, 5 and 6 - Experiment 3

(d) Outlet mole fractions – Experiment 3

Figure 4: Comparison of experimental results (dots) and model prediction (lines)

Finally, the resulting number of parameters to be identified is 19. They include pressure drop equation coefficients α and β, pre-exponential factor, activation energy and oxygen reaction order per reaction, catalyst pore diameter d_p, coke composition in terms of hydrogen (x) and oxygen (y) for each experiment and coke distribution coefficients C_1 and C_2 for each experiment.

The parameter identification is carried out using the maximum-likelihood method, implemented within the Parameter estimation tool of gProms. One very interesting result of this identification is related to the values of hydrogen and oxygen fraction in the coke, which are different from one experiment to another but have an average value of 0.47 and 0.43 respectively. This shows that the coke cannot be considered to be consituted of carbon only, and can give hints on the kinetic scheme of coke formation.

Simulations are then carried out using the identified model, which is common to all experiments, and the coke composition and distribution, which is calculated for each experiment. Some results are presented in figure 4, for two types of operating conditions: either the oxygen feed is constant and coolant temperature increases with time (figure 4a and 4b) or its flow rate increases with time for a constant coolant temperature (figure 4c and 4d). In both cases, the predictions are quite accurate. The mole fractions of measured products are in very good agreement with the predictions. This is a major difference with the results obtained when the coke initial profile was considered uniform, as shown by Lei (2014): in this case, the model highly underestimated the CO_2 fraction. In terms of temperature, although a difference in temperature value might exist (figure 4c), the peak positions are always well predicted.

5. Conclusions

A predictive model for coke combustion in a glycerol dehydration reactor is proposed. The unknown parameters were identified using several experiments, and the simulated results showed that the model is reliable. Identification also allowed to determine the coke composition and spatial distribution. More specifically, it was shown that hydrogen and oxygen are present in the coke in substantial amounts (average ratio to carbon of respectively 0.47 and 0.43). These data will be useful for the study of glycerol dehydration kinetics. The resulting model is considered accurate enough to be used for process design and optimization.

References

Green, D. W., Perry, R. H., 2008. Perry's Chemical Engineers' Handbook, 8th Edition. McGraw-Hill Publishing.

Kanervo, J. M., Krause, A. O. I., Aittamaa, J. R., Hagelberg, P. H., Lipiäinen, K. J. T., Eilos, I. H., Hiltunen, J. S., Niemi, V. M., 2001. Kinetics of the regeneration of a cracking catalyst derived from TPO measurements. Chem. Eng. Sci. 56, 1221–1227.

Katryniok, B., Paul, S., Belliere-Baca, V., Rey, P., Dumeignil, F., 2010. Glycerol dehydration to acrolein in the context of new uses of glycerol. Green Chem. 12, 2079–2098.

Keskitalo, T. J., Lipiäinen, K. J. T., Krause, A. O. I., 2006. Modelling of carbon and hydrogen oxidation kinetics of a coked ferrierite catalyst. Chem. Eng. J. 120, 63–71.

Lei, M., 2014. Modélisation, simulation et optimisation des réacteurs de production d'acroléine à partir du propylène ou du glycérol. Ph.D. thesis, Université de Lorraine, Nancy, France.

Mears, D., 1971. The role of axial dispersion in trickle-flow laboratory reactors. Chemical Engineering Science 26, 1361–1366.

Müller, N., Kern, C., Moos, R., Jess, A., 2010. Direct detection of coking and regeneration of single particles and fixed bed reactors by electrical sensors. Applied Catalysis A: General 382, 254262.

Process Systems Enterprise, 2012. gProms Manual. www.psenterprise.com/gproms, London.

Sierra, I., Erea, J., Aguayo, A. T., Arandes, J. M., Bilbao, J., 2010. Regeneration of CuO-ZnO-Al_2O_3/γ-Al_2O_3 catalyst in the direct synthesis of dimethyl ether. Applied Catalysis B: Environmental 94, 108–116.

Suprun, W., Lutecki, M., Haber, T., Papp, H., 2009. Acidic catalysts for the dehydration of glycerol: Activity and deactivation. Journal of Molecular Catalysis A: Chemical 309, 71–78.

Tang, D., Kern, C., Jess, A., 2004. Influence of chemical reaction rate, diffusion and pore structure on the regeneration of a coked Al_2O_3-catalyst. Applied Catalysis A: General 272, 187–199.

Krist V. Gernaey, Jakob K. Huusom and Rafiqul Gani (Eds.), 12th International Symposium on Process Systems Engineering and 25th European Symposium on Computer Aided Process Engineering.
31 May – 4 June 2015, Copenhagen, Denmark

Behavior of heavy metals during gasification of phytoextraction plants: thermochemical modelling

Marwa SAID,[a,b,c] Laurent CASSAYRE,[b,c] Jean-Louis DIRION,[a] Ange NZIHOU,[a] Xavier JOULIA,[b,c]

[a] *Université de Toulouse, Mines Albi, CNRS, Centre RAPSODEE, Campus Jarlard, F-81013 Albi cedex 09, France*
[b] *Université de Toulouse; INPT, UPS; Laboratoire de Génie Chimique; 4, Allée Emile Monso, F-31030 Toulouse, France*
[c] *CNRS; Laboratoire de Génie Chimique; UMR 5503, F-31030 Toulouse, France*

Abstract

Waste such as contaminated biomass, which contain potentially high level of heavy metals, are widely available resources. One of the drawbacks of using this biomass in gasification processes is that some heavy metals might be transferred in the produced syngas, and requires then specific further cleaning steps. Thermodynamic equilibrium calculations are a relevant tool to estimate the behavior of those heavy metals to manage the syngas treatment. The calculations were made with the commercial software FactSage. Due to the several thousands of produced compounds, a specific methodology was set up to choose the stable compounds of the database for the simulations. As an illustrative example, the results of the thermodynamic equilibrium calculations of lead are presented in this paper.

Keywords: Biomass, Heavy metals, Thermodynamic equilibrium, Simulation, Gasification.

1. Introduction

Biomass is considered to be the only natural and renewable carbon resource that can effectively be a substitute to fossil fuels. This is why current researches focus on the development of the use of this alternative renewable fuel in many processes in order to produce energy. Gasification has recently been receiving increasing attention thanks to the success of the first plants for the production of electricity from biomass. In fact, gasification is the partial oxidation of biomass, which transforms the organic matter into energy carrier gas. The synthesis gas (CO and H_2) allows a wide range of application: power production or biofuel. Most of research works in literature are focused on process using clean biomass as opposed to contaminated biomass which is available in significant quantities. However it is used to a much smaller extent as a source of energy due to their potentially high level of heavy metals.

An example of such biomass is phytoextraction plants which are used to extract contaminants from polluted soils. Heavy metals are then accumulated inside the roots, stems and leaves of these plants (Gupta and Sinha 2007). Following the thermochemical process of biomass gasification, these metals are found in the ash, gas and tar products which make them difficult to use and may increase risks to human health and the environment (Nzihou and Stanmore, 2013). Recent works have shown that heavy metals can have a significant influence on reaction kinetics and on thermodynamics equilibrium. The aim of this work is to contribute in understanding the behavior of heavy metals during the gasification process of contaminated biomass by modeling the

thermodynamic equilibrium. This study aims at predicting the partitioning of heavy metals in the gasification products (gas, tar or ash fractions) (Al Chami et al. 2014). This is an important scientific challenge for optimizing the thermochemical conversion processes applied to the contaminated biomass.

2. Materials and method

2.1. Biomass characterization

The biomass considered in this study is willow, which is the most used plant in phytoextraction thanks to its high absorption capacity of heavy metals. Willow is composed of 55% cellulose, 28% hemicellulose and 17% lignin (Phyllis Database, 2012). The elementary composition of willow is indicated in Table1 (Phyllis Database, 2012).

Table 1

Elementary composition of dry contaminated willow.

Element	mol/kg	Element	mol/kg	Element	mol/kg
C	41.25	S	0.012	Pb	$6.51\ 10^{-4}$
H	58.40	F	$5.30\ 10^{-3}$	Ti	$1.87\ 10^{-4}$
O	27.56	Na	$5.20\ 10^{-3}$	Sr	$1.59\ 10^{-4}$
N	0.300	Al	$3.70\ 10^{-3}$	Mn	$1.46\ 10^{-4}$
Ca	0.090	Fe	$1.97\ 10^{-3}$	Cu	$1.10\ 10^{-4}$
Si	0.060	Ni	$1.32\ 10^{-3}$	Ba	$2.91\ 10^{-5}$
K	0.050	Zn	$9.48\ 10^{-4}$	Cd	$1.51\ 10^{-5}$
P	0.020	Cr	$8.65\ 10^{-4}$	V	$3.92\ 10^{-6}$
Mg	0.014	B	$8.18\ 10^{-4}$	Sn	2.5210^{-6}

2.2. Calculations methodology

The aim of the thermodynamic modeling is to determine the nature, the state (gas, liquid or solid), speciation the amount of gasification products in given operating conditions considering that all chemical reactions reach their equilibrium. Thermodynamic models can be developed using two approaches (Basu, 2010):

- Stoichiometric Equilibrium Models, based on equilibrium constants of each reaction.
- Non-Stoichiometric Equilibrium Models, where the only inputs needed are the elemental compositions of the feeds.

The non-stoichiometric method which is often referred to as “Gibbs free energy minimization approach” is the usual approach since no chemical reaction needs to be assumed (Basu, 2010). It may be calculated using modern software provided the thermodynamic data for all compounds (reactants and products) under consideration exist. In a reacting system, a stable equilibrium condition is reached when the Gibbs free energy of the system is at the minimum. Since the thermodynamic properties of the willow components are unconventional in most software, willow has to be split into its constituent elements/molecules as input data to the software. The operating conditions chosen as initial data for the calculations are:

- initial quantity of biomass: 7 mol (biomass chemical formulae: $C_6H_9O_4$),
- reactor pressure: 1 or 10 bar,
- reactor temperature: from 500 to 1000 °C (step value: 25 °C),
- gasification agent: 41 mol of H_2O (Froment et al. 2013).

Calculations were performed with FactSage 6.3 commercial software (Bale C.W. et al. 2009), which has already found applications in the field of biomass gasification modelling (Fraissler et al. 2009) (Froment et al. 2013) and includes a large database on heavy metals. FactSage uses the Gibbs free energy minimization method. For each compound, the structure of the database is as follow: available thermochemical data (standard enthalpy of formation ΔH° at 298 K, absolute entropy S° at 298 K) and heat capacity polynomial dependence on temperature Cp(T)) are provided for a given state (solid, liquid and gas) and a given temperature range.

As thousands of compounds and phases exist in the multicomponent system consisting of contaminated willow, a preliminary selection of the compounds which might form in gasification conditions was required: software limitations and computing time impose to take into account a maximum of 1500 compounds, while the commercial SGPS database includes more than 256 liquids, 813 solids and 894 gases. The selection procedure, based on the systematic calculation of predominance diagrams for gaseous compounds, leads to the definition of a new specific database containing a few hundreds compounds. The following methodology was applied:

1. Selection of the major elementary compounds of the main organic components of wood: C, H, N, O and S.
2. Removal of gas, liquid and solid C_nH_m compounds with n > 3.
3. Selection of all gaseous compounds existing in the contaminated willow system.
4. Removal of unstable gaseous compounds, based on predominance diagram calculations (this step is developed below).
5. Removal of gaseous compounds whose Cp(T) range validity is outside the range [500 °C-1000 °C].

Predominance diagrams were computed in order to identify the most stable compounds over specific partial pressure ranges of gaseous master species: O_2, S_2, F_2, C_2 and H_2. By combination with a metal element, these master species allow to account for the formation of oxides, sulfides, fluorides, carbides, hydrides and their combinations (e.g. hydroxydes, oxyfluorides, etc.). The predominance diagrams are plotted for a given fixed temperature and a total pressure. In this work, two extreme conditions of gasification process were taken into account: 500 °C/1 bar and 1000 °C/10 bar. For compounds involving O, S, H and C, all compounds shown stable on the predominance diagram were selected. Fig. 1 shows as illustrative example, the Cr-H-O predominance diagram at 500 °C and 1 bar. All those compounds were selected.

Furthermore, due to the high number of existing fluoride compounds, it has been decided to eliminate the compounds that are unlikely to form in gasification conditions

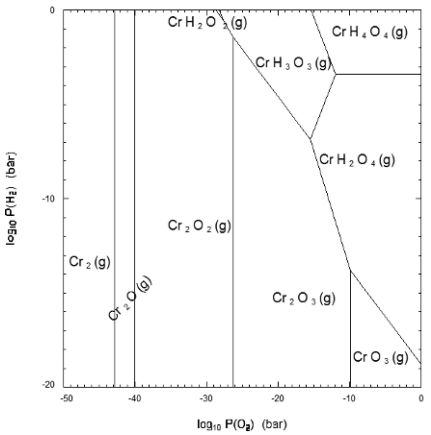

Figure 1. Cr-H-O predominance diagram (500 °C - 1 bar).

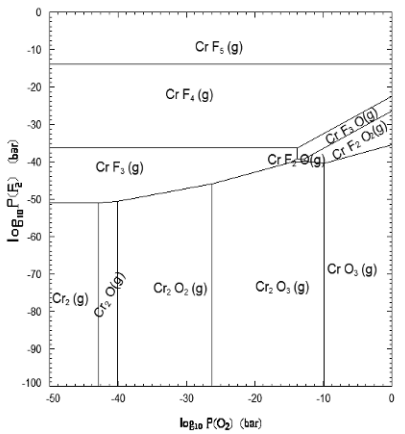

Figure 2. Cr-F-O predominance diagram (500 °C - 1 bar).

due to the low partial pressure of F_2(g).
Preliminary calculations using a simplified biomass mixture showed that at 500 °C and 1 bar the fluoride partial pressure $P(F_2)$ is below 10^{-39} bar and below 10^{-21} bar at 1000 °C and 10 bar. So all stable compounds which appeared in the predominance diagrams at a $P(F_2)$ above those two values were eliminated from the database. For instance, CrF_5(g) and CrF_4(g) which are present in the Cr-F-O diagram (Fig.2) were not selected in the database.

3. Results

After the calculation and examination of 163 predominance diagrams for 20 elements (Al, B, P, Na, K, Mg, Ca, Ti, V, Mn, Cr, Fe, Ni, Cu, Zn, Cd, Pb, Si, Sr et Sn), 271 gaseous compounds were selected amongst 894 and grouped in a specific user database. Hence, the thermodynamic equilibrium calculations were performed, with the elemental composition of willow (Table 1), with the user database for the gases and the SGPS database for the liquid and solid compounds.

3.1. Partial Pressure of gaseous master species and total volume of gas

The equilibrium calculations allow determining the total gas volume and the partial pressure of all the gaseous compounds. Fig. 3 shows the variation of partial pressure of gaseous master species (O_2, S_2, F_2, H_2) at two total pressures 1 and 10 bar. These pressures are related to the predominance diagrams so we can exactly determine the stable compounds and their fate at the real partial pressure of this system. The calculations confirm that the fluoride partial pressure at 500 °C/1 bar is less than 10^{-39} bar and 10^{-21} bar at 1000 °C/10 bar. Hence, the hypothesis regarding the selection of fluoride compounds is validated. Hence, the hypothesis regarding the selection of fluoride compounds is validated. And as expected from thermodynamic point of view, the total volume of gas increases with the temperature and the total pressure (Fig. 4).

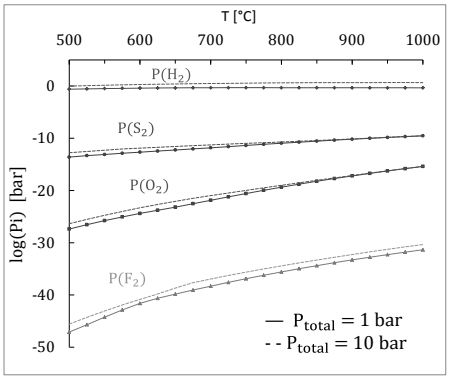

Figure 3. Partial pressure of gaseous master species at 1 and 10 bar.

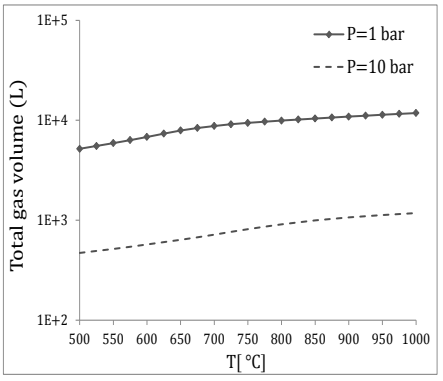

Figure 4. Total volume gas variation at 1 and 10 bar.

3.2. Speciation of Pb species

As an example of heavy metals, the behavior of lead is discussed in this work, because of its high volatility.

The thermodynamic calculations are used to identify the speciation of all biomass elements. Fig. 5 presents the speciation of the lead at a total pressure of 1 bar. Above 700 °C, liquid Pb vaporizes to form mainly Pb(g) and PbS(g), as well as small quantities of PbO(g). The calculations also show that, even if the PbO(g) amount notably increases at high temperature, this compound remains a minor component of the gas phase in the whole temperature range.

3.3. Pressure effect

The total pressure effect from 1 to 10 bar is reported in Fig. 6. As expected from thermodynamic stand point, increasing the total pressure delays volatilization of most Pb species. At 1 bar the whole amount of lead volatizes at 700 °C, while for a total pressure of 10 bar it volatizes at 800 °C. A comparison of the speciation of lead at 1bar and 10 bar (Fig. 5 and Fig. 6), evidences the presence of PbS in the condensed phase at high pressure and low temperature.

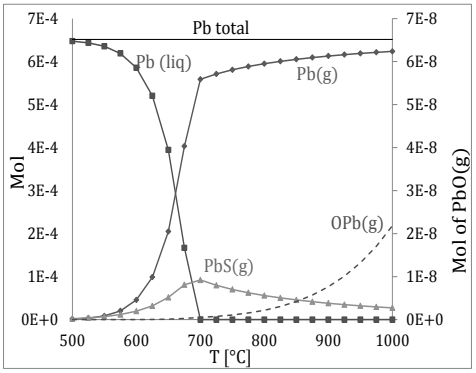

Figure 5. Speciation of Pb calculated at 1 bar.

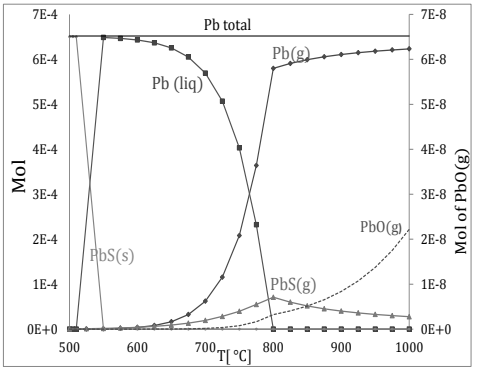

Figure 6. Speciation of Pb calculated at 10 bar.

3.4. Concentration effect

As willow is a plant which has a high potential to accumulate heavy metals, the concentration of Pb can vary for a plant to other depending in the soil contamination. The initial lead concentration in the willow used in this work is 135 $mg.kg^{-1}$. Nzihou et al. (2013) summarized the different limits concentration of heavy metals in phytoextraction plants: the concentration of Pb can vary between 55 and 300 $mg.kg^{-1}$.

Fig. 7 shows that doubling the initial concentration of Pb increases the temperature at which the whole amount of Pb volatilizes by 30 °C. Conversely, a speciation of inorganics during wood gasification realized by Froment et al. (2013) using a lower lead concentration (1 ppm) shows that the whole amount of Pb volatilizes at 500 °C. This is linked with the increase of the total volume of gas with temperature (Fig. 4): a higher volume of gas is required to evaporate a higher amount of Pb. No other concentration effect was evidenced.

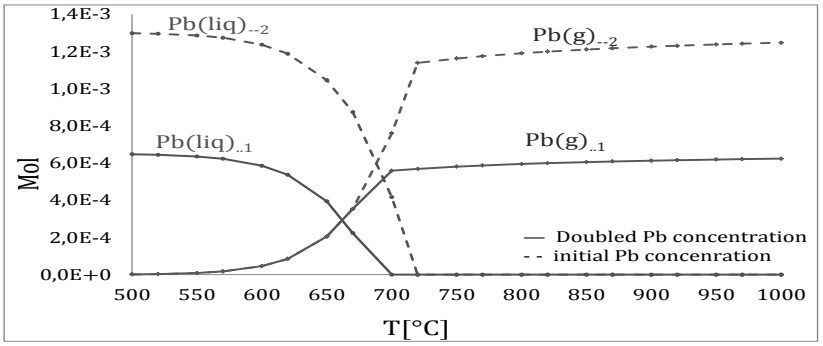

Figure 7. Effect of lead concentration (135 and 270 mg.kg^{-1})

4. Conclusions

Equilibrium calculations using a compound thermodynamic database were carried out to simulate contaminated biomass gasification. Due to the high number of compounds related to biomass composition, a selective methodology was applied in order to focus on the most relevant gaseous compounds.

An example dealing with the behavior of lead during gasification is provided. It shows that, at concentration of about 135 mg/kg in a contaminated willow biomass, lead is mostly found in the gaseous phase under its metal form, and in smaller quantity as sulfur and oxide.

Ongoing work is considering the behavior of other metal species (Transitions metals, Alkali and alkaline earth metals).

References

Al Chami Z., Amer N., Smets K., Yperman J., Carleer R., Dumontet S., and Vangronsveld J. 2014. “Evaluation of Flash and Slow Pyrolysis Applied on Heavy Metal Contaminated Sorghum Bicolor Shoots Resulting from Phytoremediation.” Biomass and Bioenergy 63 (April): 268–279.

Bale C.W., Bélisle E., Chartrand P., Decterov S.A, Eriksson .G, Hack K., Jung I.H, et al. 2009. “FactSage Thermochemical Software and Databases — Recent Developments.” Calphad 33 (2) (June): 295–311.

Basu Prabir. 2010. Biomass Gasification and Pyrolysis: Practical Design and Theory, Elsevier.

Fraissler G., Jöller M., Mattenberger H., Brunner T., and Obernberger I.. 2009. “Thermodynamic Equilibrium Calculations Concerning the Removal of Heavy Metals from Sewage Sludge Ash by Chlorination.” Chemical Engineering and Processing: Process Intensification 48 (1) (January): 152–164.

Froment K., Defoort F., Bertrand C., Seiler J.M., Berjonneau J., and Poirier J.. 2013. “Thermodynamic Equilibrium Calculations of the Volatilization and Condensation of Inorganics during Wood Gasification.” Fuel 107 (May): 269–281.

Gupta A.K, and Sinha S.. 2007. “Phytoextraction Capacity of the Plants Growing on Tannery Sludge Dumping Sites.” Bioresource Technology 98 (9) (July): 1788–94.

Nzihou A., and Stanmore B.. 2013. “The Fate of Heavy Metals during Combustion and Gasification of Contaminated Biomass-a Brief Review.” Journal of Hazardous Materials 256-257 (July 15): 56–66.

Phyllis Database. 2012. “ECN Phyllis Classification.” Energy Research Center of Netherlands.

Krist V. Gernaey, Jakob K. Huusom and Rafiqul Gani (Eds.), 12th International Symposium on Process Systems Engineering and 25th European Symposium on Computer Aided Process Engineering. 31 May – 4 June 2015, Copenhagen, Denmark

Multi-objective optimization for the production of fructose in a simulated moving bed reactor

Edwin Zondervan,[a], Bram van Duin,[a], Nikola Nikacevic,[b], Jan Meuldijk, [a]

[a]*Eindhoven University of Technology, Eindhoven, the Netherlands*
[b]*Belgrade University, Belgrade, Serbia*

Abstract

In this work we develop a simulated moving bed reactor model for the parallel isomerization and separation of fructose and glucose. The model consists of component balances and equilibrium relations. The appropriate computation of the cyclic steady state forms the core of the model. The resulting partial differential equation system is discretized and solved using a continuous prediction method. After testing the model, an optimization strategy is implemented that can be used to optimize the performance of the simulated moving bed reactor. First single objectives are optimized; the purity and the throughput. Secondly we use a multi-objective optimization approach to optimize for both systems parallel, the result is a pareto-front.

Keywords:

1. Introduction

The isomerization of glucose into fructose is an important reaction for the food industry. Fructose based syrups compete with sucrose (from cane sugar) in many food applications as sweetener. Fructose is 2-3 times sweeter than sucrose - which means basically that less raw material is required to give taste to for example soft drinks and that makes the production cheaper. As a result the change in world prices of cane sugar dropped and basically crippled sugar economies.

However, more recently the isomerization reaction of glucose into fructose was also proposed as a new means towards the bio based economy. Fructose is the starting material for the synthesis of furanic precursors which can be used to produce non-petroleum derived polymers. In addition, glucose is a monomer unit of the abundantly available polysaccharide cellulose. Glucose has the potential to become the most important organic raw material for a society depending on biomass recourses.

The big challenge exists in the separation of the formed product from the reaction mixture. The separation of isomers and other similar components is generally performed in a chromatographic/adsorption separation system.

These systems are operated in a non-continuous fashion. The isomerization reaction can be combined with the adsorption reaction into a simulated moving bed reactor. The introduction of the simulated moving bed reactor makes it possible to perform reactions and chromatographic separations quasi-continuously.

Moreover, since the reaction is reversible, the combination of reaction and separation intensifies the process by shifting the equilibrium. It is, however, difficult to optimize the design and operation of a simulated moving bed reactor due to the many variables and the cyclic nature of the process. A schematic representation of a simulated moving bed system is depicted in Figure 1.

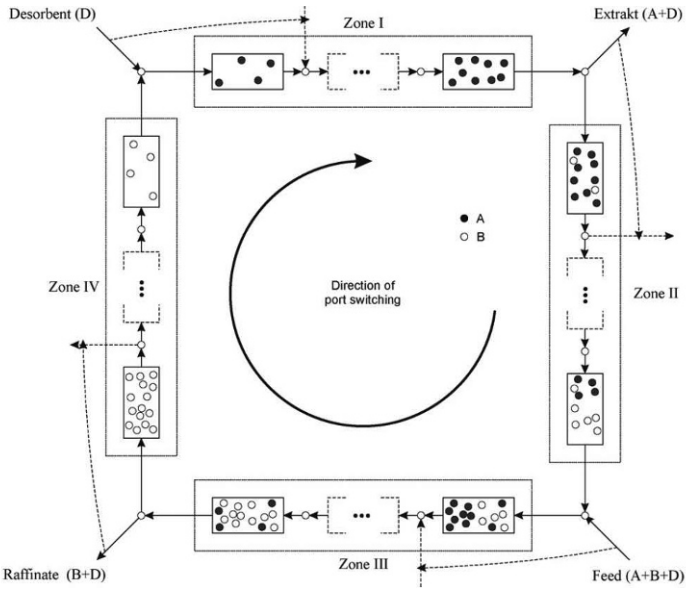

Figure 1: Principle of a Simulated Moving Bed system (Toumi *et al.* 2007)

2. Model development

In earlier work (Zondervan *et al.* 2012) we have endeavoured to develop a mathematical model in GProms for the SMBR. The resulting partial differential algebraic equation system was complex and gave computational issues when we build an optimization shell around it. We now propose a new model that neglects diffusion and we implement the model in MATLAB. The overall performance seems much better.

Given the zone velocities and the concentration of glucose and fructose in the inlet streams, our model will predict the concentration of both components as a function of time and space. It is assumed that no radial concentration distribution is present in the system and that the axial dispersion of the components is negligible. Typical liquid velocities for SMB systems are around 5 $m.h^{-1}$ (Menacho *et al.* 2013). For velocities of this magnitude, the Peclet number is in the range of 10^3, indicating that the influence of the diffusion terms are minimal. For this reason the diffusion term is not implemented in the model. We further assume that thermal and pressure effects on the separation are very small.

We now define the component balance in the liquid phase:

$$\varepsilon_b \frac{\partial C_{n,i}(x,t)}{\partial t} + (1-\varepsilon_b)\frac{\partial q_{n,i}(x,t)}{\partial t} + u_m(t)\frac{\partial C_{n,i}(x,t)}{\partial x} = 0 \qquad (1)$$

The component balance over the adsorbent:

$$\frac{\partial q_{n,i}(x,t)}{\partial t} = K_{abs,i} k_{eff,i} (q^*_{n,i} - q_{n,i}) \quad (2)$$

For the isomerization reaction rate a simple relation is used:

$$\frac{\partial C_{n,i}(x,t)}{\partial t} = K_i C_{n,i} \quad (3)$$

For this system (Eq. 1-3), the following boundary conditions hold:

$$C_{n,i}(0,t) = C^{in}_{n,i}(t) \quad (4)$$

$C_{n,i}(x,t)$ is the concentration of component i (i = fructose, glucose) in the liquid phase of column n (n=1,…,N). $q_{n,i}(x,t)$ is the concentration in the solid phase. $C^{in}{}_{,n,i}(t)$ is the inlet concentration to the n^{th} column, $u_m(t)$ is the superficial liquid velocity in zone m (m = I,II,III,IV) $q^*_{n,i}$ is the equilibrium concentration in the solid phase, $K_{abs,i}$ is the component mass-transfer coefficient and $k_{eff,i}$ denotes the component adsorption coefficient.

In addition, we have mass balances over the entrance- and exit nodes of each column. We follow an approach similar as in (Strube *et al*., 1998) We define a desorbent node (or eluent node) as:

$$C^{in}_{i,I} Q_I = C^{out}_{i,IV} Q_{IV} + C_{i,D} Q_D \;\; ; \;\; Q_I = Q_{IV} + Q_D \quad (5)$$

We define the extract draw-off node balance as:

$$C_{i,E} Q_E + C^{in}_{i,II} Q_{II} = C^{out}_{i,I} Q_I \;\; ; \;\; Q_{II} = Q_I + Q_E \quad (6)$$

The feed node:

$$C^{in}_{i,III} Q_{III} = C^{out}_{i,II} Q_{II} + C_{i,F} Q_F \;\; ; \;\; Q_{III} = Q_{II} + Q_F \quad (7)$$

The raffinate draw-off node:

$$C_{i,R} Q_R + C^{in}_{i,IV} Q_{IV} = C^{out}_{i,III} Q_{III} \;\; ; \;\; Q_{IV} = Q_{III} + Q_R \quad (8)$$

Where Q_D, Q_E, Q_F and Q_R are the flow velocities (flow rate divided by cross sectional area) of the desorbent, extract, feed and raffinate respectively.

Since the SMBR repeats the same operation for the number of columns, the profiles at the beginning of a step are identical to those of the downstream adjacent column at the end of each step. To ensure this the following equations are introduced:

$$C_{n,i}(x,0) = C_{n+1,i}(x, t_{step}) \quad (9)$$

$$q_{n,i}(x,0) = q_{n+1,i}(x, t_{step}) \quad (10)$$

$$C_{N,i}(x,0) = C_{I,i}(x,t_{step}) \quad (11)$$

$$q_{N,i}(x,0) = q_{I,i}(x,t_{step}) \quad (12)$$

With n = 1,..,N-1. The model parameters used in the model are listed in Table 1. To reach the CSS fast a continuous prediction (CPM) method is used. The method used in this work is described by Yao *et al*. (Yao *et al*. 2010) and Lubke *et al*.(Lubke *et al*. 2007) and does not depend on a good initial estimation for the CSS operation parameters. This calculation scheme computes new initial values for the next cycle based on the end state of the last switch.

Parameter	Value	Glucose	Fructose
ε_b (-)	0.389	-	-
L (cm)	52.07	-	-
$q^*_{n,i}$ (g/l)	-	$0.32C_{gluc} + 0.000457C_{fruc}C_{gluc}$	$0.675C_{fruc}$
$K_{eff,}i$ (1/min)	-	0.90	0.72
$k_{abs,i}$ (1/s)	-	$6.84.10^{-3}$	$6.84.10^{-3}$
K_i (1/h)	-	0.743	0.518
$C^{in}_{n,i}$ (g/l)	-	322	363

Table 1: Parameters for the glucose/fructose isomerization and separation

The partial differential equations were discretized and the MATLAB ODE solvers were used to compute the concentration profiles for fructose and glucose over the column lengths and time. As an illustration a typical concentration profile is shown in Figure 2.

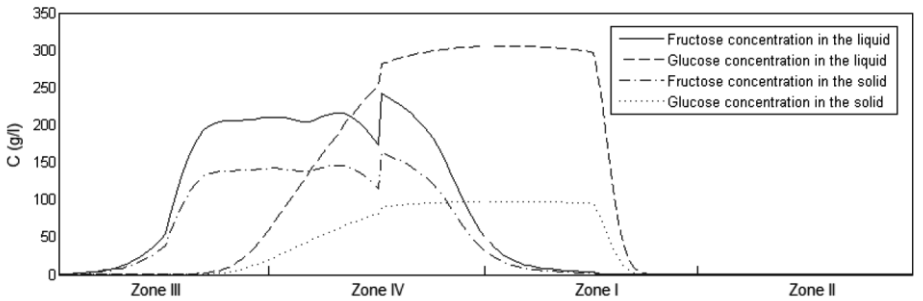

Figure 2: Concentration profiles for the isomerization and separation of fructose and glucose for an 8 column system, operated over 4 zones.

3. Optimization

Given the SMBR model as described under Eq. 1-12, the objective is to find the entrance- and exit node velocities that maximize the throughput while the purity requirements for the product in the extract and raffinate are satisfied. This problem translates into a nonlinear programming (NLP) problem that is solved with a gradient based solver in MATLAB (the built-in *fmincon* function). Mathematically the objective function of the optimization problem can be expressed as followed:

$$\max \bar{u}_F = \sum_n^N u_F^n \quad (12)$$

This objective is subject to the model equation proposed in Eq. 1-12. Furthermore the following constraints for the extract purity (EP) and raffinate purity (RP) hold:

$$EP = \frac{\int_0^{t_{step}} u_E(t) C_{E,k}(t) dt}{\sum_i^N \int_0^{t_{step}} u_E(t) C_{E,i}(t) dt} \geq EP^{min} \quad (13)$$

$$RP = \frac{\int_0^{t_{step}} u_R(t) C_{R,k}(t) dt}{\sum_i^N \int_0^{t_{step}} u_R(t) C_{R,i}(t) dt} \geq RP^{min} \quad (14)$$

the index k refers to the desired product. In this work we will use the same specifications for the minimum extract- and raffinate purities, i.e. $EP^{min} = RP^{min}$. In addition, there are limits on the zone velocities:

$$u_L \leq u_m(t) \leq u_U \quad (15)$$

We have solved the optimization model for different target purities. Table 2 shows the purity requirements versus the maximized throughput and the optimized values for the velocities and the step times.

PUR (%)	50	60	70	80	90	100
u_F(m/h)	11,91	10,62	9,69	8,58	7,71	5,62
u_{II} (m/h)	11,85	9,37	7,5	6,79	5,27	2,9
u_{III} (m/h)	18,57	19,42	18,57	19,94	20,34	22,23
u_{IV} (m/h)	7,89	7,78	7,63	8,33	8,33	9,1
t_{step}	4740	4740	4740	4740	4800	4740
PUR FRUCT (%)	81,3	86,9	96,4	92,9	96,5	99,4
PUR GLUC (%)	50	60	70	80	90	97,9
THROUGHPUT FRUC (g/h)	3570	3340	2840	2480	2100	1350
THROUGHPUT GLUC (g/h)	2460	2750	2660	2780	2340	1060

Table 2: Optimal solutions for the isomerization and separation with various purity requirements

If we now compare the maximized throughputs with the targeted purity we obtain a pareto-front as shown in Figure 3.

Figure 3 shows that for fructose as well as glucose the throughput decreases as product purity increases. We can obtain a maximum purity of fructose and glucose of 99.4% and 97.9%, respectively. At these purities the throughputs are 1350 g/h for fructose and 1060 g/h for glucose. If we maximize for throughput we obtain maximum throughput of fructose at 3570 g/h At this throughput the purity requirements are 81.3% for fructose and 50% for glucose. If we maximize for glucose, we obtain a value of 2780 g/h where the purity requirements are 92.9% and 80% for fructose and glucose respectively.

Each of the solutions on the front are pareto optimal. utopian point analysis can be used to select one of the outcomes as best trade-off. In utopian point analysis an utopian point is identified; the maximum throughput and the maximum product purity. Subsequently the point on the pareto front that has the shortest measurable distance to the utopian point is selected as the best trade-off. In this case the utopian point is located

at a fructose purity of 92.9%, a glucose purity of 80%, a fructose throughput of 2480 g/h and a glucose throughput of 2780 g/h.

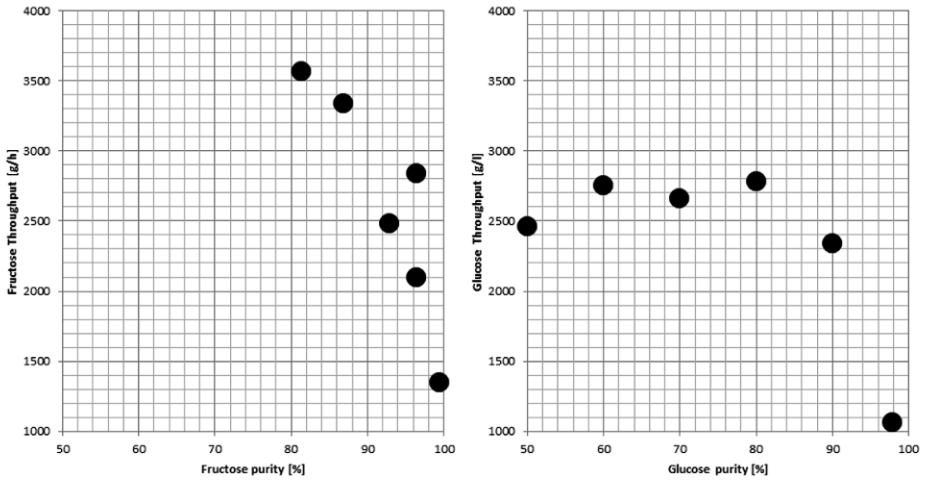

Figure 3: Fructose (left) and glucose (right) purity versus throughput.

4. Conclusions

In this work we have developed a model that can be used to compute the concentration of fructose and glucose over time and column length in a simulated moving bed reactor. The model contains component balances and equilibrium relation. The resulting partial differential equation is discretized and solved in MATLAB with a continuous prediction method. Next we use the model to optimize the entrance- and exit velocities of each of the columns in such way that the overall throughput is maximized. We then balance the throughput with the product purity by determining the pareto front and measuring the solution that is closest to the utopian point.

References

R. Lubke, A. Seidel-Morgenstern, and L. Tobiska, 2007, Numerical method for accelerated calculation of cyclic steady state of modicon-smb-processes, *Computers and Chemical Engineering* 31, pp. 258-267.

J. Menacho, O. Pou, X. Tomas, E. Serra, R. Nomen and J. Sempere, 2013, *Efficient simulation of a separation column with axial diffusion and mass transfer resistance*, Computers and Chemical Engineering 53, pp. 143-152.

J. Strube and H. Schmidt-Traub, 1998, *Dynamic simulation of simulated moving bed chromatographic processes*, Computers and Chemical Engineering, 22, pp. 1309-1317.

A. Toumi, S. Engell, M. Diehl, H.G. Bock and J. Schloder, 2007, Efficient optimization of simulated moving bed processes, Chemical Engineering and processing 46, pp. 1067-1084.

H.M. Yao, M.O. Tada, and Y-C Tian, 2010, *Accelerated computation of cyclic steady state for simulated moving bed processes*, Chemical Engineering Science, 65, pp. 1694-1704.

E. Zondervan, N. Nikacevic, H. Khajuria, E.N. Pistikopoulos, A.B. de Haan, 2012, *Integration operation and design of a simulated moving bed reactor*, Computer Aided Chemical Engineering, 30, pp. 642-646.

Krist V. Gernaey, Jakob K. Huusom and Rafiqul Gani (Eds.), 12th International Symposium on Process Systems Engineering and 25th European Symposium on Computer Aided Process Engineering.
31 May – 4 June 2015, Copenhagen, Denmark

A Modeling Framework for Optimal Design of Renewable Energy Processes Under Market Uncertainty

Aryan Geraili, Jose A. Romagnoli*

Department of Chemical Engineering, Louisiana State University, Baton Rouge, LA, USA, 70803
Jose@lsu.edu

Abstract

A distributed optimization strategy for development of a reliable framework to address optimal design of renewable energy systems under uncertainty is presented. A structural approach is utilized for production capacity design, simulation of the process in detail, and optimizing the operating condition of the plant. To demonstrate the effectiveness of the proposed approach, a hypothetical multiproduct lignocellulosic biorefinery is considered as a case study. The results prove the efficiency of the proposed approach, and provide a quantitative analysis to determine the optimal design in the face of uncertainty.

Keywords: Decision support framework; Integrated biorefinery; Stochastic programming; Risk management.

1. Introduction

In recent years there has been a marked surge in the search for alternative sources of energy that wean the world off of dependence on fossil fuels and reduce the carbon foot-print. As the world has recognized the importance of diversifying its energy resource portfolio away from fossil resources and more towards renewable resources such as biomass, there arises a need for developing strategies which can design renewable sustainable value chains that can be scaled up efficiently and provide tangible net environmental benefits from energy utilization. Second generation biofuels are examples of such fuels that are extremely attractive owing to the fact that the raw materials can be composed completely of “left-over” wastes of food crops and forest harvests that don't interfere with the human food chain and the natural ecosystem. It also can provide new income and employment opportunities in rural areas.

Several contributions have appeared over the last few years in order to manage the complexity of decision making process for designing profitable renewable energy production systems. Many of the proposed studies in the literature use deterministic modeling approaches which assume that all the parameters are known in advance. However, common to early stages of process design is the lack of certain information that will introduce variability into the decision-making problem.

In this study we present the development and implementation of a multi-layered decision support tool for the optimal design of renewable energy systems under the presence of uncertainties. We apply a distributed, systematic approach which is composed of different layers including strategic, tactical, and operational tasks. Market

uncertainty is incorporated to the decision support framework through stochastic programming in strategic model. To demonstrate the effectiveness of the proposed methodology, a multiproduct lignocellulosic biorefinery is considered as a case study.

2. Optimization framework

A major component of any decision support system is a forecasting module which estimates the future parameters that will impact the enterprise performance. In our study, product supplies, demands, and prices are considered as uncertain parameters. Once the requisite parameters are forecasted over desired time scales, these parameters are inputted into the decision analysis framework. The process is formulated as a stochastic mixed integer linear programming (MILP) model which incorporates a stepwise capacity expansion strategy by defining binary variables for capacity increments at each time period in the planning horizon instead of establishing the whole capacity during the first planning year. These mass and energy balances that dictate core technologies in the energy production system are integrated with cost and revenue functions through a techno-economic model. The output of the model includes optimal design of production capacity of the plant for the planning horizon by maximizing the expected net present value (NPV).

To overcome the mismatch between nonlinear process mechanisms and LP-based strategic optimization, a decomposition strategy is proposed that combines net present value (NPV) optimization for long term planning with rigorous non-linear process simulation and process-level optimization. The second stage, which optimizes the operating conditions of the plant, consists of two main steps including simulation of the process in the simulation software (nonlinear modeling), and employing stochastic optimization methodologies to optimize the operating condition of the plant. Process simulation and optimization will be performed iteratively until the convergence criteria are met. A general schematic structure of the proposed iterative hybrid optimization framework is presented in Figure 1. Each component of the proposed algorithm (Figure 1) is described in more detail in section 4.

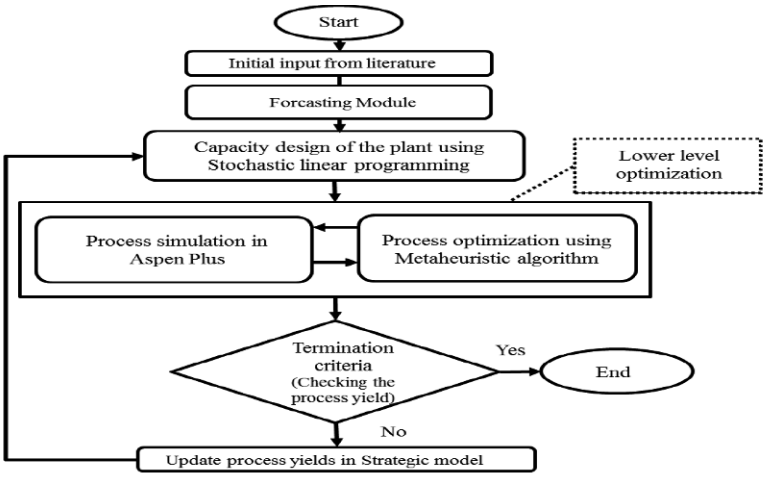

Figure 1. Proposed hybrid optimization framework

3. Process description

The lignocellulosic biorefinery, used in this study to demonstrate the capabilities of the proposed decision support framework, is a multiproduct plant that uses a fermentation-based sugar conversion platform, with 3 products: cellulosic ethanol, biosuccinic acid, and bioelectricity. Switchgrass serves as the selected feedstock for the biorefining process. The production chain comprises of 6 major systems: feedstock pretreatment, sugar hydrolysis, sugar fermentation, product purification, heat and power generation, and wastewater treatment. The systems superstructure is shown in Figure 2.

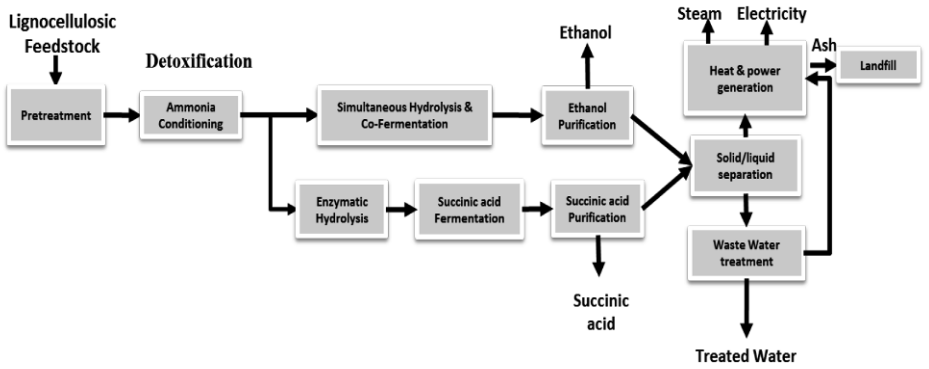

Figure 2. Block diagram for the multiproduct biorefinery plant

Technological configurations along with capital and operational cost, yield, and energy data for bioethanol production are obtained from Humbird et al. (2011) and Kazi et al. (2010). For succinic acid production, operational and economic data are obtained from Vlysidis et al. (2011); these are used as starting estimates to begin the iterative optimization process.

4. Framework details

In this section each component of the proposed framework (Figure 1) is described in some detail. While the description of the framework is based on the design of the case study presented in Section 3, each component, and the framework, can readily be adapted to other energy value chains. Due to space limitations, all model equations used for optimization cannot be listed. A description of model constraints is provided for each layer of the proposed optimization model.

4.1. Strategic layer

In the first layer, strategic planning is formulated as a mixed integer based linear program (MILP) with a 14-year planning horizon and bi-annual time steps. The mathematical formulation is broken into sub-models for ease of description which include a production model, financial model and risk management model. In production model, all major process systems are represented as linear black boxes. Major equations include linearly approximated mass and energy balances for each node in the value chain.

Financial model is broken into 2 salient aspects including market model and calculation of capital costs, operating expenses and revenues. In market model, price and demand evolution of bioproducts are described by considering that crude oil is represented as a stochastic input following Geometric Brownian Motion (GBM) and assuming that

market of bioproducts are impacted primarily by the price of crude oil. Binomial lattice generation approach is utilized to discretize the continuous stochastic model of oil price yielding Markov chain decision tree. Each node in the decision tree is represented as a price scenario for crude oil (and consequently for bioproduct markets). Calculation of the price and the demand of products (ethanol and succinic acid) is derived from the hypothetical market model proposed in the previously published journal paper Sharma et al. (2013). Additionally, to reflect and control the variability of performances associated with each specific scenario, a risk metric based on the downside risk management approach is utilized.

4.2. Operational layer

Then results from strategic layer (optimal capacity plan) are utilized to simulate the technological configuration in Aspen Plus. By simulating the entire model in Aspen Plus, the implicit correlations between upstream and downstream stages of the process are taken into consideration. One of the characteristics of our approach is the incorporation of the complex kinetics of bio-reactions in the simulation model. An iterative dynamic data exchange between process simulation model in Aspen Plus and developed kinetic models in Matlab is embedded as part of the process simulation (Geraili et al., 2014b). Developed mathematical formulations for the kinetics are based on the validated models by (Kadam et al., 2004; Morales-Rodriguez et al., 2011; Song et al., 2008). Differential evolution (DE) algorithm, which is a metaheuristic approach, was selected as an efficient optimization method for biorefinery processes in the previously published paper (Geraili et al., 2014a). This algorithm is utilized here to optimize operating conditions of the plant. Enzyme loading, pretreated biomass allocation between ethanol and succinic acid production, and hydrolysis temperature are selected as operating conditions to be optimized to maximize the annual cash flow.

5. Results and discussion

In this section, the results for the optimal design of the multiproduct biorefinery are discussed. The decision variables considered in the framework are composed of the optimal capacity plan for long term production in biorefinery, optimal temperature for enzymatic hydrolysis, optimal enzyme amount utilized in hydrolysis reaction and optimal allocation of pretreated biomass for production of final products. Plant life time considered in this study is 14 years with an annual discount rate of 10%.

Base on the results of the MILP model for the strategic optimization which is implemented in the modeling system GAMS and solved with a CPLEX linear solver, the distribution of the NPVs for two different scenarios are calculated as shown in Figure 3. First layer (strategic planning model) is solved in one scenario by utilizing stochastic approach and for the other scenario strategic model is reformulated by incorporating risk management model (multiobjective model) to demonstrate the effectiveness of controlling the variability of parameters. The optimal expected NPV of the enterprise for the first scenario (single objective model) is 62.8 $MM which indicates that value is created through the corporate activities and it is a profitable project investment. Figure 3 shows a wide range of values for calculated NPVs which represent the influence of market variability in the optimization model. In the calculation of the downside risk, the target level π is set to 51 $MM. The optimal expected NPV for this scenario (multiobjective model) is 60.0 $MM and we can see that the risk of occurrence of NPV in low cost area has been reduced (from 10% to 3%). Therefore, results show that reduction of the risk of occurrence of unfavorable scenarios

can be attained in the expense of a reduction in the expected value of the economic objective. It is also shown in the Figure how the risk management approach reconstructed the NPV distribution to reduce the risk of occurrence of unfavorable scenarios while maintaining acceptable expected revenue.

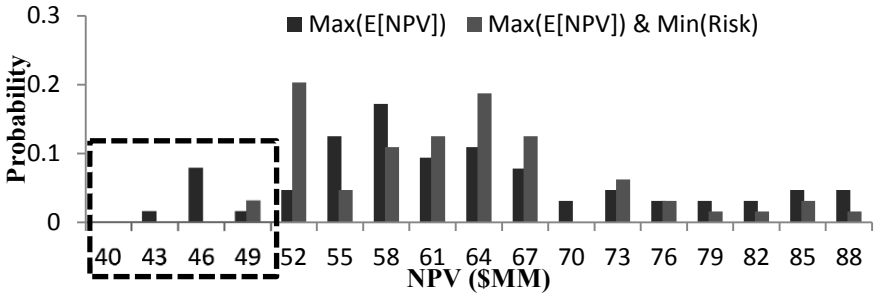

Figure 3. Block diagram for the multiproduct biorefinery plant

Iterative results of the hybrid optimization methodology are presented in Table 1 which shows that in two iterations the model is converged. Initial process yields are obtained from literature (step1); then these yields are utilized in strategic model to calculate the production capacity plan (step2); the optimal values for the capacity are passed to the process level simulation and optimization to find the optimal process conditions and calculate the process yields based on the results of simulation (step3). These calculated yields are compared with the initial values used in the strategic model to check the convergence. Since the difference between calculated yields and initial yields is greater than the threshold, this hybrid optimization needs to be carried out again based on the new yield values. Optimal values of the decision are shown in Table 2.

Table 1: Iteration results in hybrid optimization strategy

Parameters and Variables		Iteration1			Iteration2	
		Step 1	Step 2	Step 3	Step 1	Step 2
Capacity Constraints	Feedstock (1000 ton/yr)	--	222.2	--	218.0	--
	Ethanol (MM gal/yr)	--	15.3	--	11.4	--
	Succinic Acid (1000 ton/yr)	--	6.0	--	5.9	--
Yield Parameters	Sugar (kg / kg)	0.87	--	0.65	--	0.65
	Ethanol Fermentation	0.85	--	0.98	--	0.98
	Succinic Acid Fermentation	0.25	--	0.45	--	0.45
	Ethanol Purification	0.99	--	0.98	--	0.98
	Succinic Acid Purification	0.78	--	0.78	--	0.78

Table 2: Optimal values for decision variables and objective function

Temperature	33.55 °C
Sugar allocation	0.62 (ethanol), 0.38 (succinic acid)
Enzyme loading ratio	34.8 (g enzyme/ Kg Cellulose)
Cash flow	$71 million per year

6. Conclusions

In this paper a procedure was proposed to develop optimal design of renewable energy systems by utilizing a hybrid optimization algorithm. The proposed approach has the advantage of integrating long term planning with operational level decisions in the face of uncertainty. The analysis of the results reveals that considering uncertainty will provide an optimal design that reflects the variation of market parameters. In the second layer of the optimization model, results show a deviation from the values obtained from literature. This is attributed to the nonlinear modeling of our proposed framework to impart a greater degree of realism to the actual representation of the value chain.

References

A. Geraili, P. Sharma, & J. A. Romagnoli, (2014a). A modeling framework for design of nonlinear renewable energy systems through integrated simulation modeling and metaheuristic optimization: Applications to biorefineries. Computers & Chemical Engineering, 61, 102-117.

A. Geraili, P. Sharma, & J. A. Romagnoli, (2014b). Technology analysis of integrated biorefineries through process simulation and hybrid optimization. Energy, 73, 145-159.

D. Humbird, R. Davis, L. Tao, C. Kinchin, D. Hsu, & A. Aden, (2011). Process Design and Economics for Biochemical Conversion of Lignocellulosic Biomass to Ethanol. National Renewable Energy Laboratory, Technical Report NREL/TP-5100-47764, Golden Colorado.

K. L. Kadam, E. C. Rydholm, & J. D. McMillan, (2004). Development and validation of a kinetic model for enzymatic saccharification of lignocellulosic biomass. Biotechnology Progress, 20, 698-705.

F. K. Kazi, J. Fortman, & R. Anex, (2010). Techno-Economic Analysis of Biochemical Scenarios for Production of Cellulosic Ethanol. National Renewable Energy Laboratory, Technical Report, NREL/TP-6A2-46588

R. Morales-Rodriguez, K. V. Gernaey, A. S. Meyer, & G. Sin, (2011). A Mathematical Model for Simultaneous Saccharification and Co-fermentation (SSCF) of C6 and C5 Sugars. Chinese Journal of Chemical Engineering, 19, 185-191.

P. Sharma, j. A. Romagnoli, & R. Vlosky, (2013). Options analysis for long-term capacity design and operation of a lignocellulosic biomass refinery. Computers & Chemical Engineering, 58, 178-202.

H. Song, S. H. Jang, J. M. Park, & S. Y. Lee, (2008). Modeling of batch fermentation kinetics for succinic acid production by Mannheimia succiniciproducens. Biochemical Engineering Journal, 40, 107-115.

S. Vlysidis, M. Binns, C. Webb, & C. Theodoropoulos, (2011). A techno-economic analysis of biodiesel biorefineries: Assessment of integrated designs for the co-production of fuels and chemicals. Energy, 36, 4671-4683.

Krist V. Gernaey, Jakob K. Huusom and Rafiqul Gani (Eds.), 12th International Symposium on Process Systems Engineering and 25th European Symposium on Computer Aided Process Engineering.
31 May - 4 June 2015, Copenhagen, Denmark.

A molecular reconstruction feed characterization and CAPE OPEN implementation strategy to develop a tool for modeling HDT reactors for light petroleum cuts

César G. Pernalete[a], Jasper van Baten[b], Juan C. Urbina[a] and José F. Arévalo[a]

[a]*Refining Management, PDVSA Intevep, Los Teques, Venezuela*
[b]*AmsterCHEM, Cuevas del Almanzora, Almería, Spain*
pernaletec@pdvsa.com

Abstract

A light petroleum cuts hydrotreating model was developed comprising a molecular reconstruction approach based on the entropy maximization criteria to characterize the feed and to develop a kinetic mechanisms as follow: Langmuir-Hinshelwood, direct first order power law and reversible first order power law approaches to hydrodesulfurization, hydrodenitrogenation and aromatic hydrogenation reactions, respectively, on a trickled bed reactor. Only liquid phase reactions were considered, assuming a complete wetting of the catalyst surface. Rigorous phase equilibrium calculations were used in order to calculate the component concentrations in the gas-liquid interphase along the reactor length. The model was tuned using data generated under pilot plant test conditions for different temperatures at constant pressure, LHSV and hydrogen/feed. In addition, it was implemented as an interoperable software component based on the CAPE-OPEN standard, where a dedicated thermodynamic package was used to calculate the properties and phase equilibria required for the reactor model calculations. Results for the reconstruction step and model prediction were found in good agreement with experimental data.

Keywords: Molecular reconstruction, hydrotreatment, trickle bed reactor, CAPE-OPEN

1. Introduction

Hydrotreating is a process widely used in the petroleum industry for producing high quality fuels and as part of a scheme for upgrading heavy crude oil by reducing sulfur, nitrogen and/or metal content (Chen et al., 2011). Frequently, detailed studies are required in order to operate at optimal conditions and/or to design new plants, where a rigorous steady state reactor model becomes an imperative tool to face these process engineering tasks (Korsten and Hoffmann, 1996; Chen et al., 2011; Murali et al., 2007).

In the case of refinery reactors such as light-medium cuts hydrotreating reactors, since the feed is a mixture of hundreds (or even thousand) of compounds, not all compounds can be considered explicitly. Instead, pseudo or hypothetical compounds are defined, which are taken as a basis to represent the feed. A feed characterization step is required to obtain a representative feed composition in terms of these pseudo-components.

A traditional approach to face this task is by defining a set of pseudo-compounds generated from a true boiling point distillation curve as described in (Kaes, 2000). Another approach used by many

authors, is the "lumping" of species, where different species are grouped by families (Chen et al., 2011; Korsten and Hoffmann, 1996).

Since hydrotreating of light-medium petroleum cuts is based on three phase heterogeneous catalysis, the model must consider a proper way to formulate the kinetics that govern the reactions with the re-characterization as a starting point, then estimation kinetic parameters with data generated at bench or pilot plant scale, and finally scaling up for cases of commercial units performance predictions (Kaes, 2000; Korsten and Hoffmann, 1996; Muñoz et al., 2007; Murali et al., 2007). A drawback that could arise when using "pseudo-compounds" or "lumps" with the purpose of refinery reactor modeling is that new compounds, in terms of their properties, are generated for each new feed, which prevents from formulating a fixed reaction set.

In order to overcome this problem, many proposals have been made in the last years to have a detailed representation of hydrocarbon mixtures starting from the feedstock properties, where the molecular reconstruction technique has given adequate results (Alvarez et al., 2014; Pyl et al., 2010; Hudebine et al., 2011).

With the purpose of developing a tool for modeling hydrotreating reactors for light to medium petroleum cuts, this work used the molecular reconstruction approach to have a molecular representation of the feedstock as explained in Section 2. In Section 3 the reactor model formulation is explained, the kinetics of which are based on elementary reaction steps derived from the feedstock re-characterization. Finally, Section 4 explains the software architecture used for this model in order to assure its availability in different simulation platforms.

2. Feed characterization

2.1. Molecular reconstruction approach

The "Shannon entropy" is a concept introduced by Shannon (1948), where a measure of the uncertainty of occurrence of certain event, given partial information about the system, is proposed.

In the context of molecular reconstruction, the Shannon entropy is defined as $\mathscr{H} = -\sum_{i=1}^{n} x_i \cdot \log x_i$, and solving the reconstruction is posed as an optimization problem,

$$\max(\mathscr{H}) = \max(-\sum_{i=1}^{n} x_i \cdot \log x_i) \qquad \text{subject to} \qquad \sum_{i=1}^{n} x_i = 1 \tag{1}$$

where x_i is the mass fraction for each compound that constitute the mixture (Hudebine et al., 2011). In this work, a fixed selection of compounds, whose presence in light to medium hydrocarbon mixtures is well described in literature (Hudebine et al., 2011), is taken as the set of compounds for all cases studied.

2.2. Properties estimation

The solution of the equation 1 gives as a result the same mass fraction for each compound, where the function $\mathscr{H}$ is maximized. According to the conceptual meaning of the Shannon entropy, this results would be interpreted as, if there is no more information available about the system, there is an equal probability of each compound to be present. The reconstruction is fully defined when adding restrictions of the form $p_k = f_k(x)$, and equation 1 becomes,

$$\max(\mathscr{H}) = \max(-\sum_{i=1}^{n} x_i \cdot \log x_i) \qquad \text{subject to} \qquad \sum_{i=1}^{n} x_i = 1, \quad |p_k - f_k(x)| \leq \varepsilon \tag{2}$$

where p_k is the k^{th} experimental property available of the sample, f_k is the k^{th} function that estimates the property p_k as a function of the composition vector x and ε is the uncertainty of the experimental value.

Properties (p_k) considered in this study are shown in the column *Properties* of Table 1 and are essentially bulk properties that provide information about the molecular nature of feeds and products. The column *Estimation Function* shows the functions used to estimate each property p as a function of x. In Table 1, for each compound i sg_i is specific gravity, mw_i molecular weight, $^{\circ}S_i$ and $^{\circ}N_i$ the number of sulfur and nitrogen atoms respectively while mw_i^S and mw_i^N are the atomic mass for a nitrogen and sulfur atom.

Properties, p	**Estimation function,** $f(x)$
API Gravity (°API)	$141.5 \cdot \sum_{i=1}^{n} \frac{x_i}{sg_i} - 131.5$
TBP (K)	*see text*
Saturates (sT) (%wt)	$\sum_{i=1}^{n} x_i \; \forall \; i \in \{sT\}$
mono-Aromatics (mA) (%wt)	$\sum_{i=1}^{n} x_i \; \forall \; i \in \{mA\}$
di-Aromatics (dA) (%wt)	$\sum_{i=1}^{n} x_i \; \forall \; i \in \{tA\}$
tri-Aromatics (tA) (%wt)	$\sum_{i=1}^{n} x_i \; \forall \; i \in \{dA\}$
Sulfur (ppm)	$\sum_{i=1}^{n} \frac{x_i \cdot {}^{\circ}S_i \cdot mw_S}{mw_i} \cdot 10^6$
Nitrogen (ppm)	$\sum_{i=1}^{n} \frac{x_i \cdot {}^{\circ}N_i \cdot mw_N}{mw_i} \cdot 10^6$

Table 1: Properties considered as restrictions in the reconstruction formulation

The calculated TBP curve is composed by normal boiling points for each compound $\mathrm{nbp_i}$, sorted in ascending, in combination with the accumulative mass fraction, so an assumption of a perfect compound separation in the TBP distillation is made. In addition, a regression function is required in order to estimate TBP temperature at standard points for this curve such as 10%wt or 90%wt.

2.3. Composition estimation

Once equation 2 is set, the reconstruction problem is ready to be solved where the weight fraction of each compound is estimated. In this work, a general non-linear optimization method with an augmented Lagrange multiplier method was used, available as an open source package *"RSolnp"* in R (R core team, 2013).

3. Reactor model

3.1. Reaction network

Different reactions including hydrodesulphurization (HDS), hydrodenitrogenation (HDN), aromatic hydrogenation (HDA), olefins hydrogenation (HDO) and hydrocracking (HCK) occur during hydrotreatment. In the studied cases, because of the low olefin content and low severity process conditions HDO and HCK reactions were not taken into account, as shown in Figure 1.

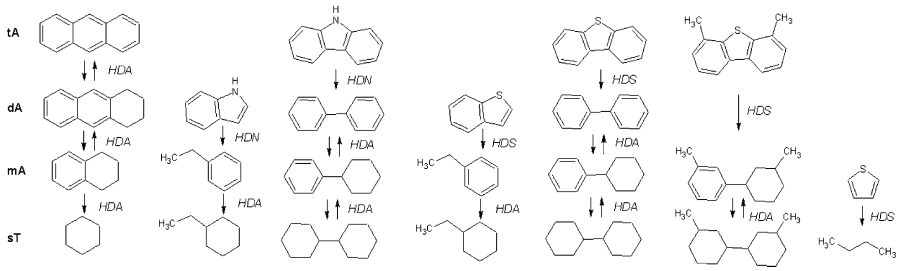

Figure 1: Reaction network

3.2. Assumptions and mathematical formulation

The following assumptions were made in order to pose the mathematical formulation of the reactor model: ideal plug flow reactor (Eq. 3), no mass transfer limitations, total catalyst wetting, liquid-vapor equilibrium (LVE) along the reactor lenght, isothermal temperature, Langmuir-Hinshelwood mechanism for hydrodesulphurization (HDS) (Eq. 4), direct reaction for nitrogenated compounds (HDN) (Eq. 5) and kinetic reversible reaction for aromatic (de)hydrogenation (HDA) (Eq. 6).

The reactor was modeled using equations 3, 4, 5 and 6, where F is molar flux, V is volume, r is the reaction rate, k_0 is the preexponential factor, E_a is the activation energy, C is the concentration in the liquid phase and K is the adsortion factor. Concentrations were taken from phase equilibrium calculations at each reaction step, values for K were taken from literature (Macías and Ancheyta, 2004) while E_a and k_0 where determined by error minimization of experimental and calculated data, using the BFGS algorithm. R is the universal gas constant and T is the absolute temperature.

$$\frac{dF}{dV} = -r_i \tag{3}$$

$$r_{HDS} = \frac{k_0^S \exp(-\frac{E_a^S}{RT}) C_s C_{H_2}^m}{(1 + K_{H_2S} C_{H_2S})^2} \tag{4}$$

$$r_{HDN} = k_0^N \exp(-\frac{E_a^N}{RT}) C_N C_{H_2}^m \tag{5}$$

$$r_{HDA} = k_0^A \exp(-\frac{E_a^A}{RT}) C_A C_{H_2}^m - k_0^{HA} \exp(-\frac{E_a^{HA}}{RT}) C_{HA} \tag{6}$$

4. Implementation architecture

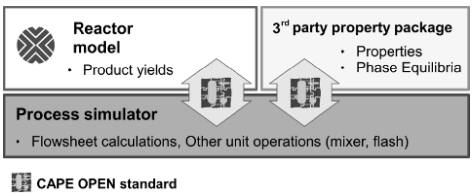

Figure 2: Conceptual approach

Most process simulators offer flexibility to model different kinds of unit operations. However, models that require experimental data to be set up, such as refinery reactor models, are typically developed as "in-house" software. In this work, the 1.1 version of the CAPE OPEN standard was used as the basis of the architecture. Since we envision use the combination of thermodynamics and unit operation in other process simulators, CAPE-OPEN has been used as the implementation platform.

Figure 2 shows the conceptual integration of the model developed, a third party property package and the process simulator, using the CAPE-OPEN standard. While the reactor model calculates the product yield of each compound, the property package performs thermophysical property calculations and phase equilibrium calculations and the simulator defined stream objects store calculation conditions and thermophysical property values. The reactor model requests thermophysical property calculations and phase equilibrium calculations from the simulator, that are performed by the third party property package. All this information is communicated through the process simulator using CAPE-OPEN. Major commercial and non-commercial process simulators allow for using external unit operations and property packages via CAPE OPEN which ensure the possibility of using the developed model in a wide range of simulators (Van Baten and Pons, 2014). It is important to remark that the using of a dedicated property package ensures the availability of the compounds used for the reconstruction step in any simulator selected.

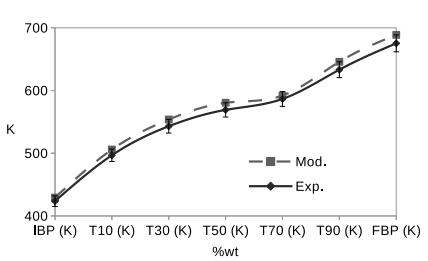

(a) TBP curve.

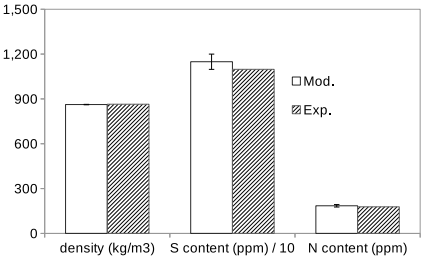

(b) Density, sulfur and nitrogen content in the feed.

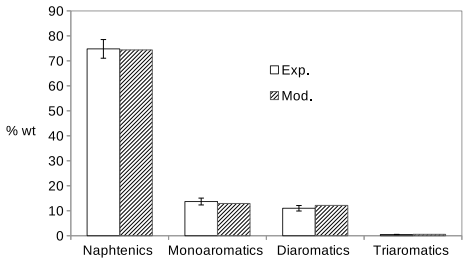

(c) Naphtenics and aromatics distribution in the feed.

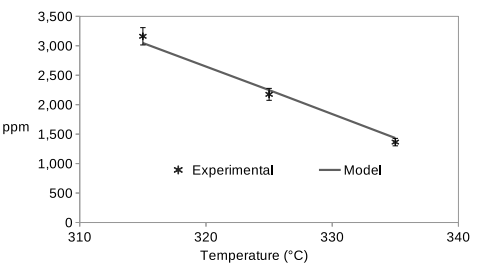

(d) Sulfur content in the liquid product.

Figure 3: Case A, P = 476 *psig*, LHSV = 2.9 h^{-1} and H2/oil = 99 Nm^3/m^3.

5. Results

The model was adjusted with experimental data generated in pilot plant conditions. Case A shows a process with low conversion for sulfur compounds while Case B is about a process where an ultra-low sulfur product is produced. With the aim of testing the extrapolative capability of the model, in both cases the two lower temperatures where used for kinetic parameter optimization and a prediction was made for the higher one. . Results for the molecular reconstruction step and reactor HDS model performance for both cases are shown in Figures 3 and 4.

Figures 3 and 4 shows a succesful reconstruction of the feed in terms of the reproduction of the properties within the uncertainty limits for the experimental properties values. The sulfur content prediction for the product in both cases followed the experimental trend with an accuraccy into the experimental value uncertainty.

6. Conclusions

A molecular reconstruction strategy was succesfully applied for two light petroleum cuts, where TBP distillation, density, sulfur content, nitrogen content, naphtenic content and aromatic distribution were taken as the variables to be reproduced by the reconstructed feed.

Since the molecular reconstruction was based on a fixed set of compounds, it served as a basis to propose a fixed reaction network and a kinetic formulation with the aim of modeling the hydrotreating process for each of the feeds.

The adoption of CAPE-OPEN as the basis architecture will allow running along the model, with the required thermodynamics server, in a variety of process simulators, without modifying the reactor model or the thermodynamic server. Due to the choice of a fixed reaction set, no refinery-reactor specific requirements were present on the used CAPE-OPEN interfaces.

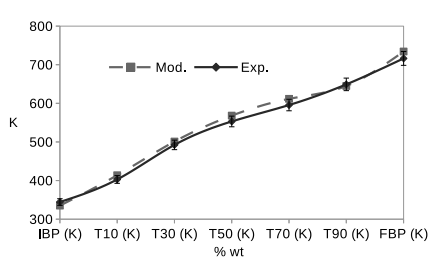

(a) TBP curve in the feed.

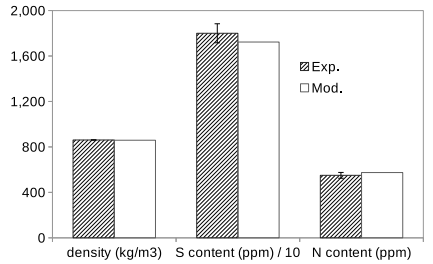

(b) Density, sulfur and nitrogen content in the feed.

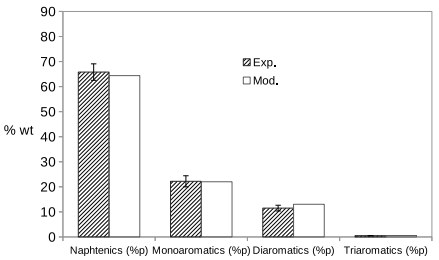

(c) Naphtenics and aromatics distribution in the feed.

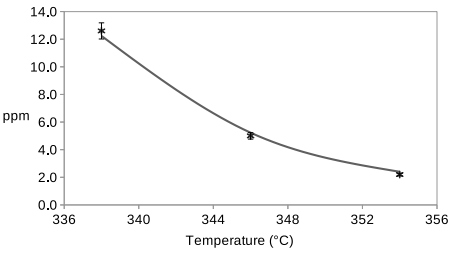

(d) Sulfur content in the liquid product.

Figure 4: Case B, P = 1598 *psig*, LHSV = 0.81 h^{-1} and H2/oil = 1472 Nm^3/m^3.

Finally, in the cases studied the developed model reproduces adequately the trend of the sulfur content in the liquid product at different reactor temperatures and is able to extrapolate for a higher temperature.

References

Alvarez, A., Castañeda, L. C., Ancheyta, J., 2014. On the application of petroleum feedstock modeling techniques for developing molecule-based models of hydrocarbon. Catalysis Today 220-222, 198–207.

Chen, J., Mulgundmath, V., Wang, N., 2011. Accounting for Vapor-Liquid Equilibrium in the Modeling and Simulation of a Commercial Hydrotreating Reactor. Ind. Eng. Chem. Res 50, 1571–1579.

Hudebine, D., Verstraete, J., Chapus, T., 2011. Statistical Reconstruction of Gas Oil Cuts. Oil & Gas Science and Technology 66 (3), 461–477.

Kaes, G. L., 2000. Refinery process modeling. A practical guide to steady state modeling of petroleum processes, first edition Edition. The Athens printing company.

Korsten, H., Hoffmann, U., 1996. Three-phase reactor model for hydrotreating in pilot trickle-bed reactors. AIChE Journal 42 (5).

Macías, M., Ancheyta, J., 2004. Simulation of an isothermal hydrodesulfurization small reactor with different catalyst particle shapes. Catalysys today 98, 243–252.

Muñoz, J., Elizalde, I., Ancheyta, J., 2007. Scale-up of experimental data from an isothermal bench-scale hydrotreatment plant to adiabatic reactors. Fuel 86, 1270–1277.

Murali, C., Voolapalli, R. K., Ravichander, N., Gokak, D. T., Choudary, N. V., 2007. Trickle bed reactor model to simulate the performance of commercial diesel hydrotreating unit. Fuel 86, 1176–1184.

Pyl, S., van Geem, K., Reyniers, M., Marin, G., 2010. Molecular reconstruction of complex hydrocarbon mixtures: An application of principal component analysis. AIChE Journal 56 (12), 3174–3188.

R core team, 2013. R: A Language and Environment for Statistical Computing. R Foundation for Statistical Computing, Vienna, Austria.

Shannon, C. E., 1948. A mathematical theory of comunication. The Bell System Technical Journal 27, 379–423, 623–656.

Van Baten, J., Pons, M., 2014. CAPE-OPEN: Interoperability in Industrial Flowsheet Simulation Software. Chem. Ing. Tech. 86 (7), 1052–1064.

Krist V. Gernaey, Jakob K. Huusom and Rafiqul Gani (Eds.), 12th International Symposium on Process Systems Engineering and 25th European Symposium on Computer Aided Process Engineering.
31 May - 4 June 2015, Copenhagen, Denmark.

Techno-economic analysis of ethanol-selective membranes for corn ethanol-water separation

Adam Kelloway[a], Michael Tsapatsis[a] and Prodromos Daoutidis[a]

[a]*Department of Chemical Engineering and Materials Science, University of Minnesota, Minneapolis, Minnesota, U.S.A.*
daout001@umn.edu

Abstract

The economic and technical feasibility of a hybrid distillation-membrane system applied to the separation of ethanol from water in traditional dry-grind corn ethanol facilities was studied. The current distillation technology was modeled in Aspen Plus and the proposed membrane unit in gPROMS. A system with the membrane placed after the distillation column with the membrane retentate recycled to the column feed was determined to be the most suitable for the separation requirements of this industry. Sensitivity analyses were performed to assess the effect of key membrane performance parameters such as flux, selectivity and cost on the economic feasibility of this system. These allowed for appropriate technical and economic performance targets for the membrane to be determined.

Keywords: Hybrid Separation Systems, Membranes, Techno-Economic Analysis

1. Introduction

The separation of ethanol from water is a crucial, energy intensive, step in the refining of corn ethanol. This separation step is particularly energy intensive because of the azeotrope formed between ethanol and water. Membrane technologies are not limited by this azeotropic behaviour and have been shown to be a promising alternative to traditional distillation technologies (O'Brien et al. (2000); Vane and Alvarez (2008)). The objective of this work is to investigate the technical and economic feasibility of one such technology based on an ethanol selective membrane and to ultimately develop a target set of membrane performance criteria which would render the system technically and economically feasible.

A simulation study of the current technology, which is based on a three distillation column configuration, is first performed to establish performance benchmarks that the membrane technology must meet or exceed in order to be considered technically and economically attractive. A hybrid configuration with a membrane system replacing two of the distillation columns is proposed that can achieve the desired separation targets.

The economics of this configuration are then studied. Performance targets for membrane parameters such as flux, selectivity and cost are established to ensure the economic feasibility of the proposed hybrid system.

2. Base Case: Distillation Modelling Results

The current state of the art technology used to separate ethanol produced by fermentation of corn sugars from water is a series of three distillation columns whose configuration is shown in fig-

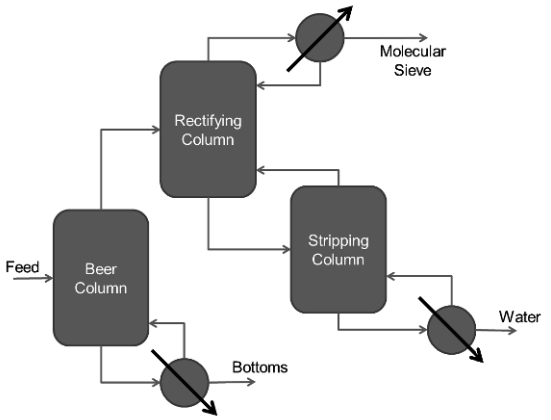

Figure 1: Process Flowsheet for Ethanol Distillation Base Case

ure 1 (Kwiatkowski et al. (2006)).

The first column, known as the beer column, has 22 trays, a reboiler but no condenser. The column produces a vapour top product that contains the feed ethanol and approximately equal amount of water. The reboiler steam flowrate is chosen such that almost all the ethanol is recovered in the top product. The bottom product contains all the fermentation solids (corn kernels, yeast cells and corn oils) and water which, once dried, are sold as dry distillers grains with solubles (DDGS) to be used as animal feed. The revenues from DDGS contribute significantly towards the total revenue of these facilities.

The second column, the rectifying column, has 22 trays, a condenser but no reboiler. This column produces a top liquid product at the azeotropic ethanol concentration of 95wt%. The bottom liquid effluent is fed to the third column, the stripping column.

The stripping column has 35 trays, a reboiler but no condenser. It produces a top vapour product which is fed to the bottom of the rectifying column. Again, the reboiler steam flowrate is chosen to recover almost all the ethanol in the top product.

The three columns have been simulated in Aspen Plus. The overall recovery achieved is 99% and the top product purity is 95wt% ethanol. The reboiler energy costs are the largest operating expenses of these columns and far outweigh the capital costs (Kwiatkowski et al. (2006)). The Aspen Plus results show that the beer column uses 9.50MW and the stripping column uses 4.20MW of steam which costs $1.66MM and $0.74MM, respectively, assuming natural gas boilers operating at 80% efficiency and $5.00/MMBTU natural gas price.

This base case is capable of recovering 99% of the ethanol produced during fermentation and produces a 95wt% product. These two values become the performance targets that a membrane system must meet or exceed in order to outperform the existing technology.

3. Membrane Modelling

The membrane unit considered was modeled as a plug-flow counter-current hollow-fiber membrane module where the feed enters the hollow fibers (retentate side), ethanol permeates through the membrane and leaves in the product stream exiting the shell side (permeate side). Nitrogen is used as a sweep gas on the permeate side and assumed not to permeate through the membrane. The system of equations was solved in gPROMS v3.6 by discretization of the length of the membrane. The key parameters of the membrane system are the total membrane area, nominal flux and

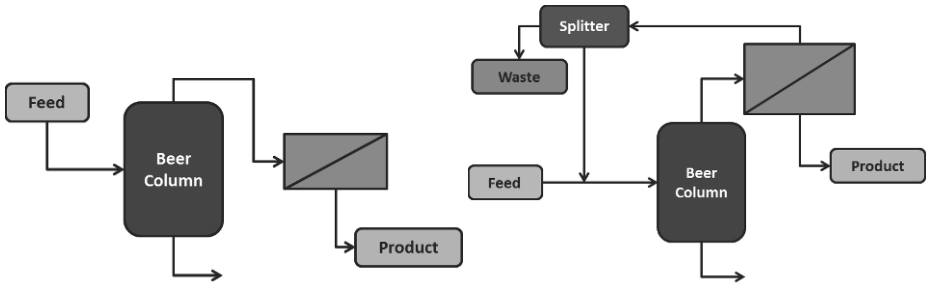

(a) Single Pass (b) Recycle Scheme

Figure 2: Process Schematic for Single Pass and Recycle Schemes

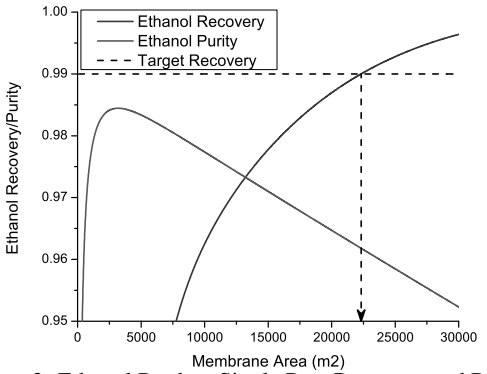

Figure 3: Ethanol Product Single Pass Recovery and Purity vs Membrane Area for Selectivity 250

selectivity. The selectivity is defined as the ratio of ethanol to water permeability. The nominal flux is defined in units of kg/hr.m^2 assuming a fixed driving force of 1atm. This reported nominal flux is not the same as the modelled flux of ethanol or water through the membrane which will vary according to the partial pressure difference across the membrane.

4. Results and Discussion

Three possible configurations were studied: a membrane system in place of all distillation columns, a membrane placed before the distillation series, and a membrane placed after the beer distillation column. Based on an energy analysis, the latter is the most attractive option and will be analyzed further in the rest of the paper.

We begin with the configuration shown in figure 2a which must achieve the required separation in a single pass. As an example of the type of results that we have generated, we present figure 3 which shows the ethanol purity and recovery as a function of membrane area for a fixed flux of 6kg/hr.m^2 and a selectivity of 250. We see that purity initially increases as more ethanol is permeated through the membrane and dilutes the nitrogen sweep gas. At approximately 4,000m^2, the trend is reversed as increasing amounts of water permeates through the membrane and dilutes the ethanol product stream. The required membrane area is chosen as the area required to meet the 99% recovery target as shown by the black arrow in the figure. Once the required membrane area is found, the corresponding product purity can be read from the graph which in this case is just above 95%.

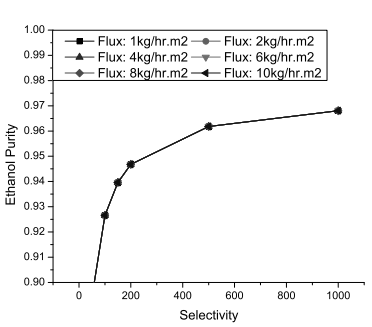

(a) Ethanol Product Purity vs Membrane Selectivity for Different Values of Flux

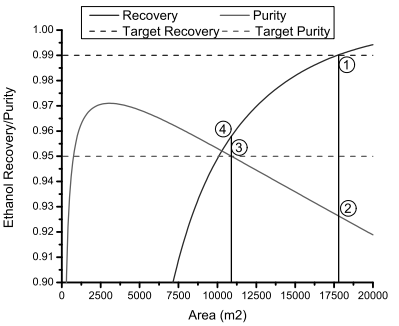

(b) Ethanol Product Purity and Recovery vs Membrane Area - Selectivity: 100, Flux: 6kg/hr.m^2

Figure 4: Membrane Simulation Results

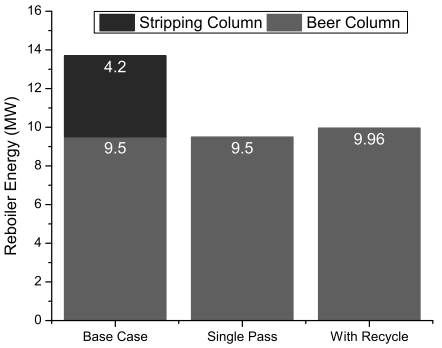

Figure 5: Column Energy Requirements for Three Scenarios

We can repeat the analysis for a range of fluxes and selectivities and produce figure 4a which shows the final ethanol product purity achieved at the 99% recovery target for different values of flux. The figure shows that the achieved product purity is a very weak function of flux and that in order to achieve the desired 95wt% purity target a membrane with selectivity of at least 250 is required. Since such a value can be considered unrealistic given the current state of membrane technology (Zhang et al. (2013)) a more reasonable upper bound of 100 should be used, however, as shown in figure 4a the required purity and recovery cannot both be met in a single-pass membrane configuration with this selectivity.

Figure 4b shows ethanol product purity and recovery as a function of membrane area for a membrane with selectivity 100 and a flux of 6kg/hr.m^2. The single pass membrane configuration must be operated at point 1 (17,800m^2) for the required recovery to be achieved; however, this means that the achieved product purity (point 2, $\sim$93wt%) does not meet the 95wt% target. A smaller membrane can be used which achieves the required product purity at point 3 (10,900m^2) but does not achieve the required recovery at point 4 ($\sim$96%).

In order to increase the overall recovery, we introduce a recycle loop as shown in figure 2b with a purge stream to avoid material accumulation. In this configuration both the target purity and target recovery can be achieved with a membrane with selectivity 100.

The split fraction between the purge and recycled streams is set such that exactly 1% of the feed

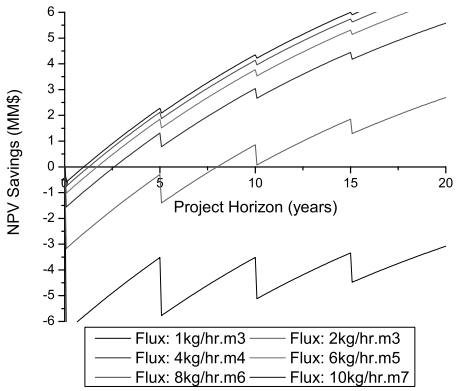

Figure 6: NPV Savings Projections for Different Flux Values - Membrane Cost: $100/m2

ethanol is in the purge stream and therefore the overall recovery target of 99% is achieved. As expected the recycle stream will cause the beer column feed stream to increase in flow rate and decrease in ethanol concentration, and this is expected to increase the energy required in the beer column reboiler. The column(s) is modeled for the three scenarios considered in Aspen Plus and the energy requirements are shown in figure 5. The results show that as expected the beer column in the recycle scenario uses slightly more energy than in the single pass case, however, significant energy is saved compared to the base case. It was found that 3.77MW are saved which corresponds to a savings of $656,000/year.

5. Membrane Economics

The Net Present Value (NPV) savings that can be achieved over the current best practice are calculated assuming a discount rate of 7%. The NPV savings projections over the course of an assumed 20 year project lifetime for a membrane cost of $100/m^2 are shown in figure 6 for the same set of fluxes studied above. In the figure, we see that each set of points follows a similar pattern. The initial investment in the membrane unit results in a negative NPV. The total energy cost savings of $656,000/year is in place for the next four years. The membrane tubes are assumed to have a lifetime of five years and cost half the initial investment to replace. This pattern is repeated for the next 15 years. Overall, we see that as the flux increases, the system's economics improve because the required membrane area decreases.

Obviously, the results in figure 6 will change according to the assumed membrane cost. The process economics will improve with decreasing membrane costs. In order to understand the trade-offs between increasing flux or decreasing costs, we plot the breakeven time, defined as the time in years needed to reach an NPV of zero, against membrane costs for a set of fluxes. These results are shown in figure 7a. To further improve the clarity and usefulness of our results we suggest a new parameter termed "flow cost" which is calculated as the membrane cost ($/m^2) divided by the membrane flux (kg/hr.m^2) and therefore has units of $/kg/hr. The flow cost can be thought of as the cost of ethanol flow rate through the membrane.

When the results shown in figure 7a are recast using this new parameter, the results shown in figure 7b are obtained. In this figure, all the points lie on a single line as long as the breakeven time is less than the lifetime of the membrane (assumed to be 5 years here). Results with a breakeven times higher than 5 years correspond to scenarios that require at least one membrane replacement thus increasing the slope of the breakeven time vs flow cost curve. The five year

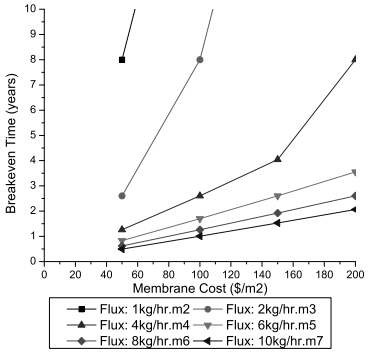

(a) Breakeven Time vs Membrane Cost for Different Flux Values

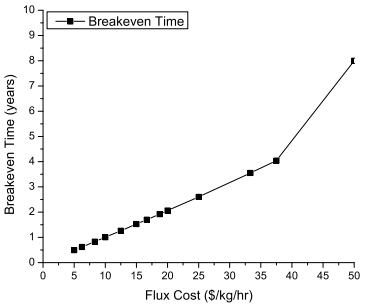

(b) Breakeven Time vs Flow Cost

Figure 7: Breakeven Time Graphs

membrane lifetime assumption provides a reasonable upper bound on the required breakeven time. This breakeven upper bound, therefore, sets a limit on the flow cost of $42/kg/hr. Any membrane with a combination of membrane flux and cost that achieves this upper flow cost limit will be economically attractive given the assumptions used.

6. Conclusions

We have designed a novel hybrid system that combines a distillation column with a membrane unit to be used to separate corn ethanol from water. The distillation column is fed the fermentation effluent stream and produces a vapour product with an ethanol concentration of 56wt%. This is fed to a membrane unit with enriches the ethanol to the required 95wt% purity target. The overall ethanol recovery target of 99% is achieved by the use of a recycle stream. The required membrane performance targets are a selectivity of 100 and a flow cost less than $42/kg/hr. An energy savings of approximately 3.74MW is achievable which corresponds to 24.6% of the total energy currently used in corn ethanol water distillation.

7. Acknowledgments

The authors would like to acknowledge funding from the ARPA-E Award No. DE-AR0000338. The authors would also like to acknowledge Luca Zullo for his insightful comments and suggestions.

References

Kwiatkowski, J. R., McAloon, A. J., Taylor, F., Johnston, D. B., 2006. Modeling the process and costs of fuel ethanol production by the corn dry-grind process. Industrial Crops and Products 23, 288–296.

O'Brien, D. J., Roth, L. H., McAloon, A. J., 2000. Ethanol production by continuous fermentation-pervaporation: a preliminary economic analysis. Journal of Membrane Science 166, 105–111.

Vane, L., Alvarez, F., 2008. Membrane assisted vapor stripping: energy efficient hybrid distillation: Vapor permeation process for alcohol-water separation. Journal of Chemical Technology & Biotechnology 1287, 1275–1287.

Zhang, K., Lively, R., Zhang, C., Koros, W., Chance, R., 2013. Investigating the intrinsic ethanol/water separation capability of zif-8: an adsorption and diffusion study. The Journal of Physical Chemistry C 117, 7214–7225.

Krist V. Gernaey, Jakob K. Huusom and Rafiqul Gani (Eds.), 12th International Symposium on Process Systems Engineering and 25th European Symposium on Computer Aided Process Engineering.
31 May – 4 June 2015, Copenhagen, Denmark

Equation-oriented Modeling of Multi-stream Heat Exchanger in Air Separation Units

Liuzhen Jiang[a], Kai Zhou[b], Lingyu Zhu[a*]

[a] *College of Chemical Engineering, Zhejiang University of Technology, Hangzhou, 310014, China*
[b] *State Key Laboratory of Industrial Control Technology, Department of Control Science and Engineering, Zhejiang University, Hangzhou, 310027, China*
zhuly@zjut.edu.cn

Abstract

Multi-stream heat exchanger (MHEX) is an important equipment to recover cold energy in air separation units (ASU). Multiple streams are designed to exchange heat simultaneously in this equipment. Modelling and simulation of MHEX is an essential step for operational optimization for an air separation process. In the MHEX of an ASU, some streams are designed to enter or leave from a certain layer in the middle section, which increases the complexity of modeling the MHEX. In this paper, an equation oriented (EO) modelling method for complex MHEX is proposed. By considering the structural feature, the complex MHEX is decomposed into several bundles. In each bundle, all streams leave and enter from two ends. A regression model is used to describe the relation among the flowrates, inlet temperatures, and outlet temperatures of the stream in a bundle. The overall model can be solved in an EO mode by lumping the multi-bundle models together. The proposed modelling method is demonstrated with a large number of plant data from a commercial 20000Nm^3/h internal compressed ASU. The results show that the developed model can well predict the operation of the MHEX without knowing the detailed information of the internal structure.

Keywords: equation-oriented model, multi-stream heat exchanger, air separation unit.

1. Introduction

MHEX is a single process unit in which multiple hot and cold streams exchange heat simultaneously with high flexibility and efficiency(Wang et al., 2001; Boehme et al., 2003). It has been widely used in cryogenic systems to recover the huge amount of cold energy at very small temperature approach such as 1-3 K(Hasan et al., 2009). Therefore, the performance of the MHEXs plays an important role in the control and optimization of load change process of an ASU (Zhu et al., 2009; Xu et al., 2011). It is necessary to establish a robust and efficient MHEX model under various operation points. However, first principle model of an industrial MHEX is difficult to be established due to the complex structure of the proprietary(Khan et al., 2012). Moreover, some streams enter or leave an MHEX from a certain layer in the middle section with phase changing. In this project, a model for complex MHEX of ASU is developed based on data regression. The proposed method decomposed the complex MHEX into several bundles to prevent streams from entering or leaving a bundle in the middle layer. A regression model is used to correlate the outlet temperatures with the inlet temperatures and flowrates for each bundle and then lumped into the whole MHEX model. The regression model for the whole unit is no longer an explicit function of input variables due to the existence of variables at the intermediate layers. Both the parameter estimation and process

simulation require solving simultaneously in an EO mode. The performance of the proposed method will be demonstrated with real plant data obtained from a commercial 20000Nm^3/h internal compressed ASU.

2. Multiple Bundle EO Model of MHEX

The schematic of an MHEX is illustrated in Fig. 1. It is a typical MHEX equipment designed for a commercial 20000Nm^3/h internal compressed ASU. In this equipment, three hot streams (H1 to H3) and four cold streams (C1 to C4) exchange heat together. Among the streams, H1 and C3 leave the equipment from middle layers while H3 enters at another layer. Flowmeters and temperature transducers are mounted on each stream to obtain the flowrate and inlet/outlet temperatures.

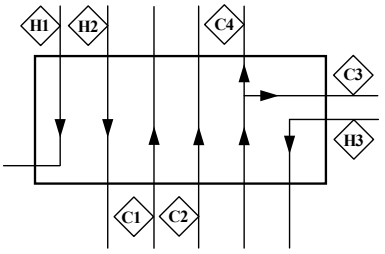

Figure 1. Schematic of an ASU MHEX

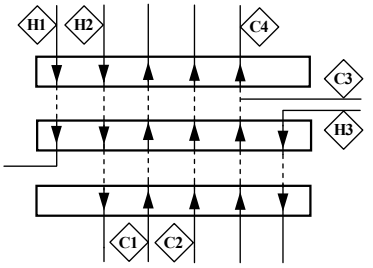

Figure 2. Multiple Bundle Structure of the Model

Instead of treating the regression as a pure black-box model, a multiple bundle structure is proposed as illustrated in Fig. 2. The MHEX is decomposed at every intermediate inlet and outlet section. A three bundle structure is then developed for the original MHEX in Fig. 1. In each bundle, streams are no longer entering or leaving the bundle in the middle layer but from the two ends of the bundle. To further simplify the modelling work for each bundle, the following assumptions are made.

(1) Ignore the heat loss from streams to equipment, and from equipment to environment;
(2) Fouling and other thermal resistance are negligible;
(3) Ignore the impact on heat transfer from small pressure drop;
(4) No heat transfer between hot streams or cold streams.

For each bundle, an explicit polynomial model can be built by choosing flowrates and inlet temperatures as input and outlet temperatures as output. To depict the nonlinear feature, a quadratic regression is the simplest approach:

$$y = \beta_0 + \sum_{p=1}^{n} \beta_p x_p + \sum_{p=1}^{n} \sum_{q>p}^{n} \beta_{pq} x_p x_q + \sum_{p=1}^{n} \beta_{pp} x_p^2 + \varepsilon \quad (1)$$

where x denotes the input variables, y denotes the output variables, β denotes the parameters to be estimated, and ε is the residual error. It consists of constant, linear, interactive, and pure-quadratic terms. With enough data, the least square regression can be used to obtain the parameters. However, even with a medium scale like in the case, the total number of the parameters to be estimated in a full quadratic regression is very large, which in turn requires a large number of data under different operating conditions for a proper regression. Therefore, rules based on process analysis are concluded to reduce the polynomial terms and the estimated parameters.

For a traditional heat exchanger with only one hot stream and one cold stream, the outlet temperature of a stream can be correlated as a function of the flowrates and inlet temperatures of both streams as:

$$T_{out,s}=f\ (F_i, F_j, T_{in,i}, T_{in,j})\ s \in i \cap j \tag{2}$$

where *i* and *j* represent the indexes of the hot stream and cold stream, respectively. The analysis of the heat transfer equation and the heat balance equation for a heat exchanger shows that the flowrate and temperature of a stream always appears in a pair as a product term. Therefore, rather than building a relation for outlet temperature, we choose the product of the flowrate and temperature of a stream as the output. Still keeping the description form in Eq. (2), the regressed model for the hot and cold streams are changed to the following formulations by multiplying the flowrate to both the input and output variables in Eq. (2).

$$F_i T_{out,i}=f(F_i^2, F_i F_j, F_i T_{in,i}, F_i T_{in,j}) \tag{3}$$

$$F_j T_{out,j}=f(F_i F_j, F_j^2, F_j T_{in,i}, F_j T_{in,j}) \tag{4}$$

By extending the description to a multi-stream case and unify the input variables for prediction of both the hot and cold streams in one formulation, the following description is eventually determined for a bundle section of the MHEX:

$$\begin{aligned} F_s T_{out,s} = f(&F_{H,1}^2,..,F_{H,N_I}^2,F_{C,1}^2,...,F_{C,N_J}^2,\\ &F_{H,1}F_{C,1},...,F_{H,1}F_{C,N_J}F_{H,2}F_{C,1},...,F_{H,N_I}F_{C,N_J},\\ &F_{H,1}T_{in,H,1},...,F_{H,N_I}T_{in,H,N_I},F_{C,1}T_{in,C,1},...,F_{C,N_J}T_{in,C,N_J},\\ &F_{H,1}T_{in,C,1},...,F_{H,1}T_{in,C,N_J},F_{H,2}T_{in,C,1},...,F_{H,N_I}T_{in,C,N_J},\\ &F_{C,1}T_{in,H,1},...,F_{C,1}T_{in,H,N_I},F_{C,2}T_{in,H,N_I},...,F_{C,N_J}T_{in,H,N_I})\quad s \in S = I \cap J \end{aligned} \tag{5}$$

where *I* represents the index set of the hot streams, *J* represents the index set of the cold streams, and *S* represents the union of two stream sets, N_I represents the total number of hot streams, N_J represents the total number of cold streams. Function *f* is chosen as a quadratic expression as shown in Eq. (1). Therefore, the coefficients of each term consist of the parameter set to be estimated. As a summary, the eventual description is composed by (a) constant term; (b) the square term of the flowrate of the hot stream *i*; (c) the square term of the flowrate of the cold stream *j*; (d) the interactive flowrate term between hot stream *i* and cold stream *j*; (e) the product term of flowrate and inlet temperature of hot stream *i*; (f) the product term of flowrate and inlet temperature of cold stream *j*; (g) interactive product term of flowrate of hot stream *i* multiplied by inlet temperature of cold stream *j*; (h) interactive product term of flowrate of cold stream *j* multiplied by inlet temperature of hot stream *i*. By following this description, the total term number is greatly reduced from $\sum_1^{2(N_I+N_J)} n + 2(N_I+N_J)$ of the full quadratic regression to $2(N_I+N_J)+3N_I N_J$. For this specific case, it is reduced from 119 to 50. As the measurement of the plant data is only available for variables at the inlet and outlet of the MHEX and no measurement is available for the variables at middle layers, the parameter estimation of this multi-bundle model cannot be formulated as a linear least-squares problem. Instead, by lumping the three-bundle models together, the modelling work can be converted to a nonlinear programing as described below.

$$Min \sum (T_{out,s,b}^{predict} - T_{out,s,b}^{measure})^2 + \delta \sum (T_{intermediate,s,b}^{predict} - T_{intermediate,s,b}^{measure})^2 \tag{6a}$$

$$s.t.\ F_{s,b} T_{out,s,b}^{predict} = f(F_{s,b}^{measure}, T_{in,s,b}^{measure}, T_{in,s,b}^{predict}, \beta) \quad \forall b \in 1,2,3 \tag{6b}$$

$$T_{out,i,b}^{predict} = T_{in,i,b+1}^{predict} \tag{6c}$$

$$T_{out,j,b+1}^{predict} = T_{in,j,b}^{predict} \tag{6d}$$

$$T_{out,i,b}^{predict} \geq T_{in,j,b}^{predict} + 1 \tag{6e}$$

$$T_{in,i,b}^{predict} \geq T_{out,j,b}^{predict} + 1 \tag{6f}$$

$$\frac{\partial f(F_{s,b}^{measure}, T_{in,s,b}^{measure}, T_{in,s,b}^{predict}, \beta)}{\partial F_{i,b}^{measure}} > 0 \tag{6g}$$

Eq. (6a) is the objective function which contains two terms. The first term denotes the error between prediction and measurement, which relates to the variables at the two ends of the equipment. The second term relates to temperature approach at intermediate layers, where only the stream leaving or enter the equipment there has the measurement. An optimal structure should not only predict as close as the measurement but also ensures that the intermediate temperature not vary far from the side stream. To constrain the temperatures of the streams, the temperature approaches at these points are also anticipated as described by the second term. Eq. (6b) represents the regression model of each bundle b, where β represents the parameter set to be estimated. Function f follows the description in Eq. (5). Eqs. (6c) & (6d) are connection equations for outlet stream and inlet stream at two bundle junction. Eqs. (6e) & (6f) constrain that hot stream should always be hotter than the cold streams at least 1K at the same level, which assumes the minimum temperature difference constraint is 1K according to the design. At last, Eq. (6g) states that the structural coefficients should satisfy certain physical law, e.g., if the flowrate of a hot stream increases, the outlet temperature should also increase.

3. Results and discussion

Applying the aforementioned modeling method, a three-bundle regression model is developed to capture the structural nature of the process. Real operational data is collected from the DCS system from the ASU plant. The operational data include flowrate, inlet temperature, outlet temperature of each stream. Note that the raw data contains measurement noise. In addition, the cyclic switch of the molecular sieves is a large disturbance for the operation which causes the large fluctuation in temperatures and flowrates. Therefore the raw operational data is pre-processed by averaging data for every 15 min and eliminating invalid data that is outside the normal range. After the pre-processing, 2500 data points are collected as the full data set. The first 1500 points are used for training and the other 1000 points are selected for validation. Figs. 3a & 3b plot the flowrate and inlet temperature in time sequence, respectively. The vertical dotted line in the figures represents the division of the training and checking samples. As shown in Fig. 3a, we can see that all flowrates change collectively. When one flow rate increases, other flowrates will also increase. This is mainly because the load change of ASU affects all the flowrates of the MHEX in the same direction. Fig. 3b plots all the inlet temperatures. To better illustrate them under the large temperature range of the streams, two vertical axes are used. Hot streams in Fig. 3b correspond to the vertical axis on the left and cold streams correspond to the vertical axis on the right. We can observe the cyclic feature with sudden changes for every 200 to 300 points. It is due to the cyclic operation for switching the molecular sieves as mentioned earlier. Basically, the flowrate and temperature varies within a certain range in all time. This means that a regression model based on part of these data should also apply to the other part.

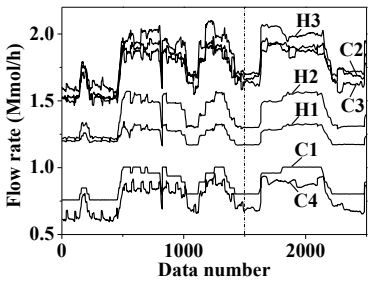

Figure 3a. Variation of flowrate

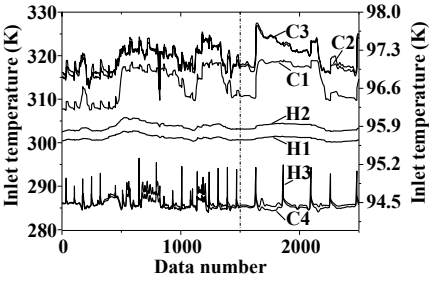

Figure 3b. Variation of inlet temperature

We build our MHEX model on the General Algebraic Modeling System (GAMS). The regression problem is constructed as a quadratic optimization problem which tries to find the optimal structural coefficients that minimize the error between the predicted temperature and real measurement. The final regression model includes 39,423 and 100,501 constraints (including 37,500 equality constraints). CONOPT solver is applied to solve the model which takes about 253 minutes to obtain the optimal solution. Fig. 4 shows the prediction error of the regressed model with both the training and checking data. The curves at the upper part of the figure denote the error of the outlet temperature and the curve at the bottom is the inlet temperature of stream H3 (denoted as TMinH3), which corresponds to the right vertical axis. From Fig. 4, the maximum error of outlet stream temperature of the training data is within 3K. The error distributes along the zero horizon line, indicating that the regression model is well trained. Also we can find out through the dotted curve of TMinH3 that relatively large error happens when the inlet temperature of stream H3 changes abruptly. This may be either due to the model mismatch when the temperature deviates from the normal operating condition or dynamic features of the MHEX system that is not taken account in our model.

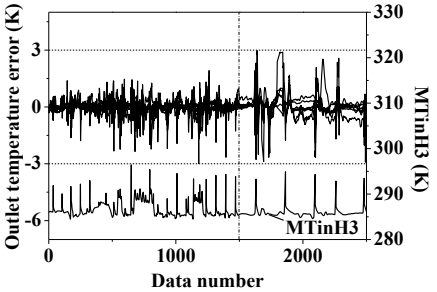

Figure 4. Outlet temperature error for simulation data

For the checking data, the optimal structural coefficients are imported to the simulation model to test the error between the predicted and real outlet temperature. As the structural coefficients are fixed in the validation model, the validation problem degenerates to a linear simulation problem with zero degree of freedom. CPLEX is used to solve this problem in a few seconds. The detailed information of the model accuracy in terms of the mean and max absolute errors is listed in Table 1. The mean errors for both the training and checking data are quite small. The max errors of the checking data are also within 3K. The comparison with the bottom curve of TMinH3 shows that the relatively large error occurs around the cyclic changes of the inlet temperature, corresponding to the cyclic switch operation. Apart from these points, the model predicts accurately. This indicates that the regression model is able to perform well

under most cases. Therefore the multi-bundle model can be used for outlet temperature prediction.

Table 1 Error of training and testing data of the multiple bundle model

		H1	H2	H3	C1	C2	C3	C4
Training data	Mean*	0.291	0.090	0.133	0.135	0.147	0.368	0.135
	Max*	1.922	0.548	0.723	0.946	0.936	2.985	1.199
Checking data	Mean	0.499	0.155	0.218	0.145	0.141	0.587	0.172
	Max	2.525	0.528	0.633	1.147	0.918	2.972	1.502

* In table 1, "Mean" refers to mean absolute error, "Max" refers to max absolute error.

4. Conclusions

An EO model of a complex MHEX is built by considering the equipment structure. Industrial plant data are collected to regress the multiple bundle model through EO optimization. Without using detailed structure information of the MHEX, the regressed model can correlate the equipment operation in good performance. This model is applicable for simulation of MHEX and air separation process.

Acknowledgments

We gratefully acknowledge the financial support of National Natural Science Foundation of China (No. 21206149).

References

R. Boehme, J. A. R. Parise, & R. P. Marques, 2003. Simulation of multistream plate–fin heat exchangers of an air separation unit. *Cryogenics*, 43(6), 25-334.

M. M. F. Hasan, I. A. Karimi, H. E. Alfadala, & H. Grootjans, 2009. Operational modeling of multistream heat exchangers with phase changes. *AIChE Journal*, 55(1), 150-171.

M. S. Khan, Y. A. Husnil, & M. Getu, 2012. Modeling and simulation of multi-stream heat exchanger using artificial neural network. 11th International Symposium on Process Systems Engineering(PSE), *Computer-Aided Chemical Engineering*, 31, 1196-1200.

L. K. Wang, & B. Sunden, 2001. Design methodology for multistream plate-fin heat exchangers in heat exchanger networks. *Heat Transfer Engineering*, 22(6), 3-11.

Z. Xu, J. Zhao, X. Chen, & Z. Shao, 2011. Automatic load change system of cryogenic air separation process. *Separation and Purification Technology*, 81, 451–465.

L. Zhu, Z. Chen, X. Chen, & Z. Shao, 2009. Simulation and optimization of cryogenic air separation units using a homotopy-based backtracking method, *Separation and Purification Technology*, 67(3), 262-270.

Krist V. Gernaey, Jakob K. Huusom and Rafiqul Gani (Eds.), 12th International Symposium on Process Systems Engineering and 25th European Symposium on Computer Aided Process Engineering.
31 May – 4 June 2015, Copenhagen, Denmark 2015 Published by Elsevier B.V.

Proposal of a New Pathway for Microalgal Oil Production and its Comparison with Conventional Method

Sofia Chaudry[a], Parisa A. Bahri[a*], Navid R. Moheimani[c]

[a]*School of Engineering and Information Technology, Murdoch University, 90 South Street, Murdoch, 6150, Western Australia*
[b]*Algae R & D Centre, School of Veterinary and Life Sciences, Murdoch University, 90 South Street, Murdoch, 6150, Western Australia*
P.Bahri@murdoch.edu.au

Abstract

The use of fertilizers for microalgae growth is one of the major constraints for energetically feasible and sustainable production of fuel from microalgae at commercial scale. In a recent biological study, a distinct species of microalgae, *Botryococcus braunii*, which can produce long chain hydrocarbons and excrete them outside of the cell wall, has been tested for repetitive extraction of its hydrocarbons - termed as milking. The determination of the ability of the *Botryococcus braunii* to produce the hydrocarbons repeatedly without any extra supply of nutrients is expected to be an important step towards the sustainable production of fuels and chemicals from microalgae. In this study, the newly proposed method has been compared with the conventional method for the growth of microalgae to produce similar amount of microalgal oil. The mathematical models consisting of mass balance equations were developed using Aspen Custom Modeler for both the conventional microalgal growth system and the process of repetitive production of hydrocarbons from *Botryococcus braunii*. The results show that compared to the conventional system, the fertilizer requirement, water consumption and energy inputs in the milking process can be decreased by 90 %, 30 % and 70 %, respectively. This shows that the milking system has the potential to reduce the overall energy input to the process of production of fuel from microalgae. Also, high heating value of hydrocarbon contents of *Botryococcus braunii* gives the higher energy output resulting in higher output to input energy ratio of the process, making it energetically more feasible than the conventional system.

Keywords: Energy, Fuel, Microalgae, Repetitive Hydrocarbon Production, Milking

1. Introduction

High use of fossil resources due to increase in energy demand is causing the climate change and depletion of fossil resources. Renewable energy sources other than biomass are the alternate for fossil resources for electricity generation. Biomass is the only alternate of fossil fuels for liquid fuel and fossil derived industrial chemicals production. Microalgae are the source having tremendous potential for contributing to the energy crisis and greenhouse gas emissions solutions. Microalgae are the single cell organisms living in colonies or individually. They utilize sunlight, carbon dioxide, water and fertilizers (nitrogen and phosphorus) to produce organic compounds by photosynthesis. The major compounds present in microalgae are proteins, carbohydrates, nucleic acids and lipids. Microalgal oil (lipids) has high heating value of average 38 MJ/Kg

(Williams and Laurens 2010) which is very close to the heating value of petroleum crude oil (45 MJ/Kg).

Algal fuel production pathway follows the cultivation (growth), harvesting (dewatering), extraction of oil and upgradation steps (Pragya et al. 2013). The process of algal fuel production is not commercial yet. The main constraints are high energy consumption and high cost of the process. The cultivation of microalgae on commercial scale for the production of fuel or fuel based chemicals needs large amount of CO_2, water, nitrogen and phosphorus fertilizers and energy associated with them (Borowitzka and Moheimani 2013). Nitrogen and phosphorus fertilizers are used as the nutrient source for the growth of microalgae. Production of nitrogen fertilizers consumes vast amount of energy from fossil resources and generates greenhouse gas emissions. Phosphorus is obtained from finite natural phosphorus rocks. The use of these fertilizers is one of the major energy consuming and cost contributing factors and sustainability constraints for microalgal fuel production (Borowitzka and Moheimani 2013). Furthermore, the supply of nitrogen and phosphorus fertilizers for microalgal growth for commercial scale fuel production will affect the supply of these fertilizers for the agriculture sector (Chisti 2013).

In a recent biological study, a distinct species of microalgae, *Botryococcus braunii*, has been tested for non-destructive repetitive extraction of its hydrocarbons - termed as milking. *Botryococcus braunii* has two unique properties: a) produces long chain hydrocarbons and b) stores most of the hydrocarbons in extracellular matrix, outside of the cell walls (Weiss et al. 2012). This is in contrast to all other microalgal species which produce lipids instead of hydrocarbons and store them inside the cells (Hirose et al. 2013). Based on the produced hydrocarbons, *Botryococcus braunii* is divided to four races A, B, L and S. Race A produces straight odd numbered from C23 to C33 alkadienes and alkatrienes, race B produces triterpenoids from C30 to C37 also called botryococcenes and race L produces tetraterpenoids (Metzger and Largeau 2005). Race S produces n-alkanes and epoxy n-alkanes ranging from C18 to C20 (Kawachi et al. 2012). *Botryococcus braunii* has high oil contents ranging from 25 % to 75 % of dry weight biomass, most of which are the hydrocarbons (Mata et al. 2010). The energy contents of *Botryococcus braunii* hydrocarbons (49 MJ/Kg) (Dote et al. 1994) are higher than average energy contents of lipids of other microalgal species. These hydrocarbons can be hydrocracked to produce gasoline, aviation fuels and diesel (Hillen et al. 1982). But *Botryococcus braunii* is not considered suitable for conventional microalgal fuel production process due to its very low productivity (biomass growth rate).

In milking, some biocompatible solvents (usually alkanes) are used to extract the lipids from microalgae without damaging it (Frenz et al. 1989). In two recent studies (Moheimani et al. 2013, Moheimani et al. 2013), it was found that the same biomass of *Botryococcus braunii* after milking, produces similar amount of hydrocarbons again without any extra nutrients supply and extraction can be repeated many times. *Botryococcus braunii* BOT-22 (Race B) can be milked after every 5 days up to 15 times with 1 % CO_2 aeration to the culture, without extra supply of nutrients (Moheimani et al. 2013). This repetitive hydrocarbon production process omits the requirement of growing the new algal biomass for each extraction as in the case of conventional process. After extracting hydrocarbons, the algal biomass is recycled back to the ponds and kept under the same growth conditions (sunlight, water, CO_2) to let it reproduce the

hydrocarbons between two consecutive extractions. The repetitive extraction will not only decrease the fertilizer requirement but it will also decrease the water losses in the downstream process. Both of these parameters will affect the energy requirements of the process. In this study, the growth ponds have been modeled for the repetitive production of hydrocarbons from the same microalgae culture to determine the material and energy requirements of the growth phase. The conventional system (new microalgae growth for each extraction) has also been modeled to compare the two systems.

2. Methodology

Open ponds were considered for the growth of algae in both systems and for the phase of repetitive production of hydrocarbons by microalgae in milking system. The mathematical models consisting of mass balance equations were developed using Aspen Custom Modeler for both systems. The amount of microalgal oil/hydrocarbons to be produced was taken as the basis. The biological parameters such as productivity and oil contents of microalgae, concentration of algal biomass in culture media, number of days required for repeated production of hydrocarbons and number of repetitions up to which *Botryococcus braunii* is able to produce the hydrocarbons are the inputs to the model. Nitrogen and phosphorus fertilizer, water and CO_2 requirements have been calculated for both the conventional and repetitive hydrocarbon production systems. The area of open ponds required for the growth of algae in both systems has also been calculated using the model. Using the outputs from material balance equations together with the assumptions taken from literature for energy consumption, the direct and indirect energy requirements for the paddle wheel mixing, the fresh water pumping, the culture pumping to and from the ponds, the CO_2 supply and the indirect energy associated with the fertilizer production have also been calculated. Important growth phase assumptions and energy input assumptions for base case scenarios are shown in Table 1. Sensitivity analysis was performed to quantify the effect of important input assumptions for the range of their values reported in the literature on the ratio of the energy requirements of the two processes.

Table 1: Productivity, lipid contents and energy input assumptions for base case analysis

Parameter	Value	Reference
Biomass productivity (conventional)	20 g/m^2 day	(Borowitzka and Moheimani 2013)
Lipid contents (conventional)	40 %	(Borowitzka and Moheimani 2013)
Biomass productivity (milking)	9 g/m^2 day	(Zhang 2014)
Hydrocarbon contents (milking)	40 %	(Banerjee et al. 2002)
Fresh water supply energy	0.443 MJ/m^3	(Davis et al. 2011)
Harvest and recycle pump energy	0.09 MJ/m^3	(Davis et al. 2011)
Paddle wheel mixing energy	173 MJ/ha day	(Frank et al. 2011)
CO_2 transfer to ponds energy	0.076 MJ/Kg	(Frank et al. 2011)
Nitrogen fertilizer energy	35 MJ/Kg N	(Jonker and Faaij 2013)
Phosphorus fertilizer energy	17 MJ/Kg P	(Jonker and Faaij 2013)
Heat rate for electricity	32%	(EIA 2014)

3. Results and Discussion

The results of the material balance analysis for the conventional system and the repetitive hydrocarbon production system with different no. of repetitions (n) for hydrocarbon production are shown in Table 2. The results show that both nitrogen and phosphorus fertilizer consumption was reduced by 80 %, 90 % and 94 % for 5, 10 and 15 repetitions, respectively when repetitive hydrocarbon production system was considered. CO_2 consumption was the same in all cases as we considered the same CO_2 aeration for the recycled culture for repetitive production of hydrocarbons. Water consumption was reduced to 8 giga litres per year in the repetitive production system in contrast to 26 giga litres per year in the conventional system showing 70 % reduction. This is because the whole culture is recycled back in milking which reduces the downstream water losses. The open pond area required to grow the microalgae and reproduce the hydrocarbons in the repetitive hydrocarbon production system is 11 % higher than the open pond area required in the conventional system. It is because the productivity of the *Botryococcus braunii* is very low as compared to the average productivity of other microalgal species used in conventional system, increasing the growth pond area.

Table 2: Material consumption and area requirements for open ponds for microalgae cultivation in conventional system and in milking system with 5, 10 and 15 repetitions for hydrocarbon production from same *Botryococcus braunii* culture to produce 100,000 bbl of oil per year

Parameter	Conventional	Milking (n=5)	Milking (n=10)	Milking (n=15)
Nitrogen consumption (t/y)	2,253	450	225	150
Phosphorus consumption (t/y)	312	62	31	20
CO_2 consumption (t/y)	84,600	84,600	84,600	84,600
Water consumption (GL/y)	26	8	8	8
Open pond area (ha)	490	544	544	544

The total energy (onsite and indirect) requirements of the process are shown in Figure 1. The energy required for the paddle wheel mixing in open ponds and the energy required for pumping culture to the downstream harvesting unit and then back to the ponds is higher for the repetitive production system. On the other hand, the energy required for pumping fresh water to the ponds and the indirect energy associated with the production and transport of fertilizer are lower for the repetitive production system. Overall, the repetitive production system consumes 10 %, 30 % and 37 % less energy than the conventional system for 5, 10 and 15 repetitions, respectively.

For the sensitivity analysis (Figure 2), the ratio of the energy requirements of the two systems (energy requirement of the repetitive hydrocarbon production system/energy requirement of the conventional system) was defined as the parameter to compare the two systems. 10 repetitions for the hydrocarbon production system give an energy ratio of 0.7 indicating 30 % reduction in the energy consumption. This was considered as the base case for sensitivity analysis. The results of the sensitivity analysis show that energy ratio of the two systems is less than unity in all cases except one indicating less energy consumption in the repetitive production system. The hydrocarbon contents for the repetitive production system and the lipid contents in the conventional system are the

most influencing parameters for the energy consumption. 50 % decrease in hydrocarbon contents relative to the base case value in the repetitive hydrocarbon production system makes this system relatively more energy consuming.

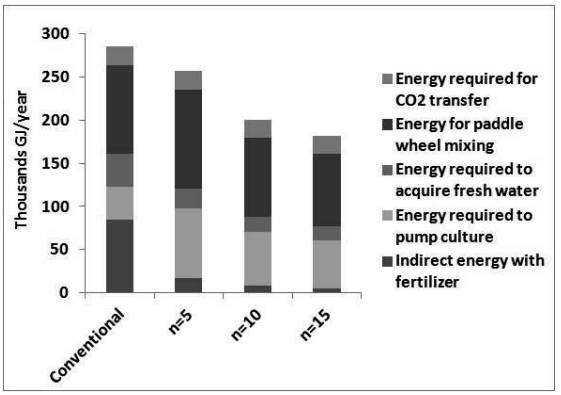

Figure 1: Energy consumption of conventional and repetitive hydrocarbon production systems with 5, 10 and 15 repetitions

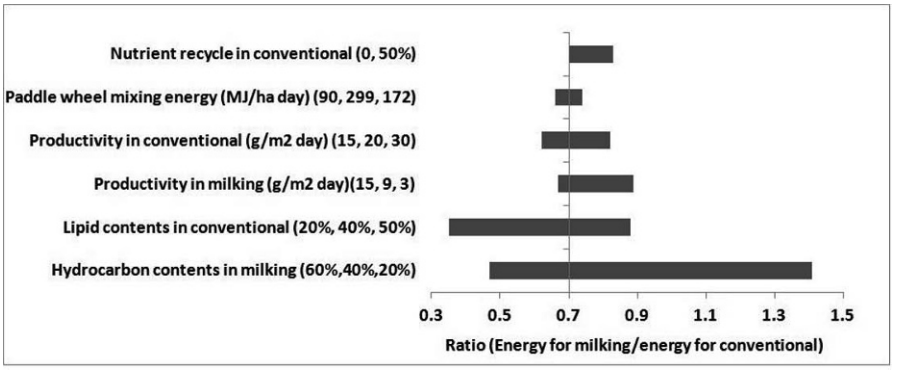

Figure 2: Sensitivity analysis on the ratio of energy requirements of the repetitive hydrocarbon production and the conventional systems. The ratio was found to be 0.7 for base case scenarios indicating that milking has 30 % less energy requirements.

4. Future Work

The next step in this project is the techno economic analysis of the fuel production using milking process in order to determine the energetic and economic feasibility of the process.

5. Conclusions

The production of fuel from microalgae is a highly energy consuming process. *Botryococcus braunii* is a hydrocarbon producing alga but the extraction of hydrocarbons from it by the conventional pathway is not feasible. The newly proposed milking process has the potential of reducing the energy requirements of extracting the hydrocarbons from *Botryococcus braunii* by decreasing the fertilizer consumption, water consumption and energy requirements. Lower energy consumption for hydrocarbon production and higher energy contents of the hydrocarbon produced from *Botryococcus braunii* will result in higher energy output/input ratio of the repetitive

hydrocarbon production process compared to the conventional process of microalgal oil production from other species.

References

A. Banerjee, R. Sharma, Y. Chisti and U. C. Banerjee, 2002, Botryococcus braunii: a renewable source of hydrocarbons and other chemicals, Crit Rev Biotechnol, 22, 3, 245-279

M. Borowitzka and N. Moheimani, 2013, Sustainable biofuels from algae, Mitigation and Adaptation Strategies for Global Change, 18, 1, 13-25

Y. Chisti, 2013, Constraints to commercialization of algal fuels, J Biotechnol, 167, 3, 201-214

R. Davis, A. Aden and P. T. Pienkos, 2011, Techno-economic analysis of autotrophic microalgae for fuel production, Applied Energy, 88, 3524-3531

Y. Dote, S. Sawayama, S. Inoue, T. Minowa and S.-y. Yokoyama, 1994, Recovery of liquid fuel from hydrocarbon-rich microalgae by thermochemical liquefaction, Fuel, 73, 12, 1855-1857

U. S. EIA, 2014, Monthly Energy Review, September 2014, U.S. Energy Information Administration, U.S. Department of Energy, Washington, DC

E. D. Frank, J. Han, I. Palou-Rivera, A. Elgowainy and M. Q. Wang, 2011, Life-Cycle Analysis of Algal Lipid Fuels with the GREET Model, Energy Systems Division, Argonne National Laboratory, U.S. Department of Energy, U.S.

J. Frenz, C. Largeau and E. Casadevall, 1989, Hydrocarbon recovery by extraction with a biocompatible solvent from free and immobilized cultures of Botryococcus braunii, Enzyme and Microbial Technology, 11, 11, 717-724

L. W. Hillen, G. Pollard, L. V. Wake and N. White, 1982, Hydrocracking of the oils of Botryococcus braunii to transport fuels, Biotechnol Bioeng, 24, 1, 193-205

M. Hirose, F. Mukaida, S. Okada and T. Noguchi, 2013, Active hydrocarbon biosynthesis and accumulation in a green alga, Botryococcus braunii (race A), Eukaryot Cell, 12, 8, 1132-1141

J. G. G. Jonker and A. P. C. Faaij, 2013, Techno-economic assessment of micro-algae as feedstock for renewable bio-energy production, Applied Energy, 102, 0, 461-475

M. Kawachi, T. Tanoi, M. Demura, K. Kaya and M. M. Watanabe, 2012, Relationship between hydrocarbons and molecular phylogeny of Botryococcus braunii, Algal Research, 1, 2, 114-119

T. M. Mata, A. A. Martins and N. S. Caetano, 2010, Microalgae for biodiesel production and other applications: A review, Renewable and Sustainable Energy Reviews, 14, 1, 217-232

P. Metzger and C. Largeau, 2005, Botryococcus braunii: a rich source for hydrocarbons and related ether lipids, Appl Microbiol Biotechnol, 66, 5, 486-496

N. Moheimani, R. Cord-Ruwisch, E. Raes and M. Borowitzka, 2013, Non-destructive oil extraction from Botryococcus braunii (Chlorophyta), Journal of Applied Phycology, 25, 1653-1661

N. Moheimani, H. Matsuura, M. Watanabe and M. Borowitzka, 2013, Non-destructive hydrocarbon extraction from Botryococcus braunii BOT-22 (race B), Journal of Applied Phycology, 1-11

N. Pragya, K. K. Pandey and P. K. Sahoo, 2013, A review on harvesting, oil extraction and biofuels production technologies from microalgae, Renewable and Sustainable Energy Reviews, 24, 0, 159-171

R. Razeghifard, 2013, Algal biofuels, Photosynthesis Research, 117, 1-3, 207-219

T. L. Weiss, R. Roth, C. Goodson, S. Vitha, I. Black, P. Azadi, J. Rusch, A. Holzenburg, T. P. Devarenne and U. Goodenough, 2012, Colony Organization in the Green Alga Botryococcus braunii (Race B) Is Specified by a Complex Extracellular Matrix, Eukaryot Cell, 11, 12, 1424-1440

P. J. l. B. Williams and L. M. L. Laurens, 2010, Microalgae as biodiesel & biomass feedstocks: Review & analysis of the biochemistry, energetics & economics, Energy & Environmental Science, 3, 5, 554-590

J. Zhang, 2014, Culture of Botryococcus braunii, Honours Study, Under review, Murdoch University, Australia

Krist V. Gernaey, Jakob K. Huusom and Rafiqul Gani (Eds.), 12th International Symposium on Process Systems Engineering and 25th European Symposium on Computer Aided Process Engineering.
31 May – 4 June 2015, Copenhagen, Denmark 2015 Published by Elsevier B.V.

Superstructure Development, Simulation and Optimization of Desalination Systems using Aspen Custom Modeler

Sidra N. Malik, Parisa A. Bahri*, Linh T. T. Vu

School of Engineering and Information Technology, Murdoch University, 90 South St., Murdoch, WA 6150, Australia
**p.bahri@murdoch.edu.au*

Abstract

In this paper, Multistage Flash (MSF), Reverse Osmosis (RO) and hybrid MSF/ RO systems are modelled and simulated in Aspen Custom Modeler (ACM) V.8.4. Both steady state models include material balances; but RO focusses more on pressure differences, while MSF relies on energy balances. The model of a hybrid superstructure is developed by combining individual models of MSF and RO systems. The hybrid superstructure is developed in an optimization framework to analyse and optimize various process configurations. Operating conditions such as temperatures, pressures and process design variables such as the number of membrane elements in a pressure vessel and the number of stages in an MSF system are used as optimization variables to minimise the economic objective function. Primary results show that the hybrid MSF/ RO systems sharing common intake-outfall facilities have lower annual intake cost and can be considered in the areas where high overall product recovery and high product quality is required.

Keywords: hybrid MSF/RO, superstructure, simulation, optimization, minimum energy

1. Introduction

The overtaking demand of freshwater all around the world can be fulfilled by innovative and adaptive technologies such as desalination. Multistage Flash desalination (MSF) system is based on thermal technologies. Despite the high cost it is the first choice of the consumer because of its proven reliability and large production capacity especially in the areas where fuel prices are low (El-Dessouky and Ettouney, 2002). On the other hand, Reverse Osmosis (RO) is a pressure driven membrane process. Its low energy consumption, simple automation and control, easy scale up and high product recovery and quality makes it the second choice of the consumer (El-Dessouky andEttouney, 2002). A lot of efforts have been made in the past three decades to reduce the cost of MSF plant. Considering the advantages of RO plant, it is believed that one possible way to reduce the cost of MSF plant is to hybridize MSF and RO systems (Helal et al., 2003). Another significant advantage of using MSF/RO hybrid plant is that the fresh water produced from both systems is mixed and the concentration of the final product is the average between the concentrations of both systems. In this manner the RO plant can work for lower product quality requirements.

The research work around modelling and optimization of hybrid MSF/RO plant is limited. Al-Sofi et al. (1984) performed an optimization study to maximize overall plant

recovery. Helal et al. (2003) reported an optimization study based on minimum water cost to compare the configurations suggested by Al Sofi et al. (1984) along with two additional hybrid plant configurations. All of these efforts were based on individual flow sheets for different configurations and simple models were developed by using average values of the physical properties. Moreover the model of the RO plant does not consider design parameters. Helal et al. (2003) suggested in the results of their study that among all configurations RO plant and MSF plant operating individually and sharing the same intake-outfall facilities is worth consideration for future desalination plants.Considering the efforts of researchers and the gap analysis in hybrid desalination system modelling and optimization, this work presents an optimization study based on minimum energy cost of MF/RO hybrid systems with common intake-outfall facilities. For this purpose a superstructure is developed using Aspen Custom Modeler (ACM) V.8.4. The superstructure provides a flexible way of analyzing various configurations using one flow sheet.

2. Process Model

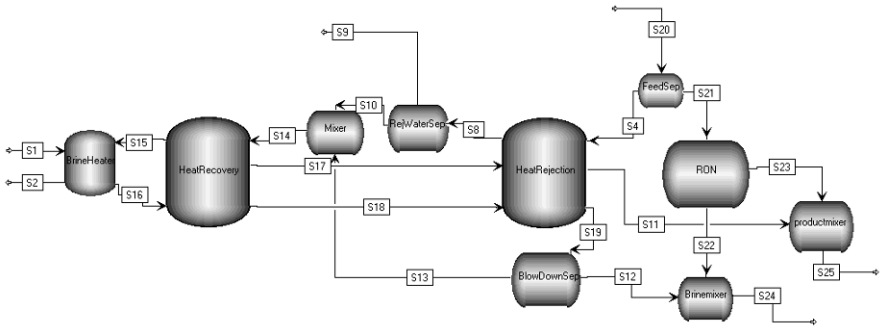

Figure.1 Schematic diagram of superstructure

The schematic diagram of the superstructure is presented in Figure. 1. The process model developed for MSF plant is based on the mass balance, enthalpy balance and heat transfer models. The thermo-physical properties functions used for water, steam and brine solutions are taken from Rosso et al. (1997). These functions contribute to the non-linearity and complexity of the equations. The RO process model is developed for a single stage RO module with spiral wound membrane by combining the widely accepted and most commonly used solution-diffusion transport model (Sassi and. Mujtaba, 2013) with the film theory approach (Wijmans, 2007) and with the hydraulic design model(Lu et al., 2007). Film theory approach is used to predict the wall concentration and the hydraulic design model takes into account the pressure drop and the concentration changes in the membrane channel (Lu et al., 2007).In this manner a detailed description of the MSF and RO processes is achieved by characterizing all process streams in a good manner. The development time for the model is reduced because the solution algorithm is specified in ACM instead of writing it. The developed model can be used to perform multiple simulation and optimization studies by just changing the input specifications.

MSF Process Model

The model for the MSF plant is based on the following assumptions:

- The distillate produced is salt free.

- Heat of mixing for brine solutions is negligible.
- There is no subcooling of condensate produced in the brine heater.

RO Process Model

The model for the RO plant is developed according to the following assumptions:

- The feed concentration varies linearly along the feed side channel.
- The feed channels of spiral wound membrane are flat.
- The pressure drop along the permeate channel is neglected.

The model equations for the MSF and RO systems are presented in Figure. 2 and Figure. 3.

Overall balance: $Fm = D + BD$; Overall salt balance: $Fm.CF = BD.CBN$; Brine heater balance: $W = BO$; Brine heater salt balance: $CR = CBO$; Mixer balance: $W = R + Fm$; Mixer salt balance: $W.CR = R.CBN + FmCF$; Blow down splitter balance: $BD = BN - R$; Reject water splitter balance: $CW = Fsea - Fm$; Balance for any stage:$B_{j_{-1}} + D_{j_{-1}} = B_j + D_j$; Salt balance for any stage: $B_{j_{-1}}.C_{B,j-1} = B_j.C_{B,j}$; Equilibrium equation: $TD_j = TB_j - (BPE_j + NEA_j + \Delta_j)$; Brine heater enthalpy balance: $Ws.\lambda s = W.S_{bh}.(TBO - TF1)$; Brine heater heat transfer model: $Ubh.Abh = \frac{Ws.\lambda s}{(LMTD)bh}$; Mixer enthalpy balance: $W.hw = R.hR + Fm.hm$; Overall enthalpy balance for any stage:

$W.Src_j.(TF_j - TF_{j+1}) = D_{j-1}.SD_{j-1}.(TD_{j-1} - Tref) + B_{j-1}.SB_{j-1}.(TB_{j-1} - Tref) - D_j.SD_j.(TD_j - Tref - Bj.SBj.(TBj - Tref)$; Bottom enthalpy equation: $Bj - 1.hj - 1 = Bj.hj + Bj - 1 - Bj.hvj$; Heat Transfer Model at the condenser for heat recovery section: $W.Sr_j.(TF_j - TF_{j+1}) = U_j.Ar_j.(LMTD)_j$; Note: For heat rejection section $W = Fsea$

Figure.2 MSF Process Model

Flow Balance: $Qf = Qp + Qr$; Salt Balance: $Qf.Cf = Qp.Cp + Qr.Cr$; Bulk flow rate: $Qb = \frac{Qf+Qr}{2}$; Average velocity in feed side: $V = \frac{Qb}{w.hsp.\varepsilon}$; Pressure drop: $\Delta P = Pf - \Delta\frac{Pf}{2} - Pp$; Pressure drop on the feed side: $\Delta Pf = \frac{0.0033.Qb.3600bLpv.\mu}{w.d^3}$; Osmotic pressure: $\pi = \frac{0.2641.C.1000.(T+273)}{10^6-(C.1000)}$; Water flux: $Jw = Aw.(\Delta P - \Delta\pi.1000$; Salt flux: $Js = As.(Cw - Cp)$; Concentration polarization: $Cw - CpCb - Cp = ep.kJw$; Mass transfer coefficient: $k = 0.04.Re.0.75.Sc^{0.33}.\frac{Ds}{df}$; Salt Rejection: $SR = 1 - \frac{Cp}{Cf}$; Length of the pressure vessel: $Lpv = m.Lm$; Membrane width: $w = \frac{Amem}{Lm.N1}$; Reynolds number: $Re = \frac{\rho.df.V}{\mu}$; Schmidt number: $Sc = \frac{\mu}{\rho.Ds}$

Figure. 3 RO Process Model

3. Optimization Problem formulation

The performance of the MSF plant is highly dependent on the evaporation range. The evaporation range can be elongated by using high top brine temperature which requires significant amount of energy. Similarly, the RO process performance is based on mass transfer driving force. The performance of the RO process can be maximized by managing the temperature and pressure of the feed stream which also needs notable amount of energy. Thus appropriate optimization approaches should be used to determine optimum values of design and operating conditions of both MSF and RO plants while managing the cost of energy. The optimization problem incorporates process models of the MSF, RO and any additional equipment (separator, mixer) for the hybrid system. Operating variables (steam temperature, steam flow rate, feed pressure, feed flow per membrane element) and design variables (number of stages, number of elements in a pressure vessel) are optimized to minimize the economic objective

function. The energy cost per kg of feed is minimized based on 1 hour of operation. The cost of steam in MSF process and the energy cost of high pressure pump in RO process are considered as these are the major contributors to the total energy cost. The cost functions used to evaluate energy cost are taken from (Helal et al., 2003) for MSF plant and from (Marcovecchio et al., 2005) for RO plant and are presented in Figure. 4. For comparison basis, overall plant recovery, annual intake cost and product quality of MSF, RO and hybrid plants are also evaluated. The cost functions for the intake cost are taken from Helal et al., (2003). The optimization strategy employed in this research work which looks at both design and operating parameters is presented in Figure. 4.

MSF optimization formulation:
Given: Feed water conditions, condenser and stage design specifications
Determine: Optimal steam flow rate, steam temperature, no of recovery stages
Objective Function: Minimize energy cost per unit of feed
Subject to: Equality constraints: Process model, product demand and specification
Inequality constraints: Linear bounds on optimization variables and other parameters
RO optimization formulation:
Given: Feed water conditions, membrane properties and specifications
Determine: The optimal feed pressure, feed flow per membrane, number of elements in a pressure vessel
Objective Function: Minimize energy cost per unit of feed
Subject to: Equality constraints: Process model, product demand and specification
Inequality constraints: Linear bounds on process and design variables
Steam cost for MSF: $8000.Ws.\frac{T_s-40}{85}.0.00415$, Energy Cost for RO: $\frac{Pf.\ Qf}{\eta_{pump}}.D_{energy}.f_c$, Energy charge rate, D_{energy} = 0.08 $/kWh (Lu et al., 2007)
Where Ts is steam temperature, η_{pump} is pump efficiency and f_c is plant load factor

Figure. 4 Optimization formulation

4. Case Study

The process models for the MSF, RO and hybrid systems are simulated using Aspen Custom Modeler V.8.4. The hybrid system consists of independent MSF and RO systems with common intake-outfall facilities. The MSF plant considered in this work has fixed number of stages (3 stages) in the heat rejection section for the independent MSF plant and the MSF plant section in the hybrid plant. For both plants the number of stages in the heat recovery section can vary from 13 to 16. Single stage RO system with spiral wound RO membrane element SW30XLE-400 is considered for the independent RO plant and the RO section in the hybrid plant. The number of elements per pressure vessel varies from 2 to 8 for both plants. The input data used to solve the models is taken from Wahab et al., (2012) and Lu et al., (2007). The three processes are compared on the basis of the same plant capacity. For this purpose the ratio of MSF plant capacity to RO plant capacity in hybrid plant is taken equal to 1:2. To achieve this capacity in the independent MSF plant, three MSF plants operating in parallel are considered with common intake-outfall facilities.

5. Results and Conclusions

The optimum design of a hybrid MSF/ RO system with common intake-outfall facilities was studied in this work. Detailed process models for MSF and RO plant based on thermo-physical properties functions, solution-diffusion model and hydraulic design model were developed in ACM. The optimization variables consist of steam temperature, steam flow rate, number of recovery stages, feed pressure and number of membrane elements in a pressure vessel. The proposed design was compared with conventional MSF and RO systems on the basis of energy cost per kg of feed, annual intake cost, product quality and overall plant recovery. The design and optimization results are presented in Table 1. The minimum energy cost per kg of feed, annual intake cost, overall plant recovery and plant capacity are presented in Table 2.
Note: The design and operating variables for the independent MSF plant belong to one of the three identical MSF plants.

Table 1 Optimal design characteristics of MSF, RO and hybrid plant

MSF plant section:	Independent MSF plant	Hybrid MSF/RO
Number of recovery stages	13	13
Steam Temperature, °C	105	105
Steam flow rate, kg/ h	23724	23724
RO plant section:	Independent RO plant	Hybrid MSF/RO
Feed Pressure, kPa	7000	7000
Feed flow per module, kg/h	14688	11016
Number of elements per pressure vessel	7	7
Number of pressure vessels	90	66
Product concentration, g/L	0.12	0.07

Table 2 Minimum energy cost, annual intake cost, overall plant recovery and plant capacity of the optimal designs

MSF plant	RO plant	Hybrid plant	
Energy cost, $/kg	0.18	0.000162	0.04
Annual intake cost, $	5500000	5400000	3700000
Overall plant recovery	13%	45%	24%
Plant capacity, m^3/d	89394	89394	89394

The results show that the hybrid MSF/RO has higher overall system recovery than MSF system, higher product quality than RO system, low annual intake cost compared to MSF and RO systems and 77% decrease in energy cost per kg of feed compared to independent MSF plant. This suggests that while having higher energy cost per kg of feed compared to independent RO plant such systems should be used in the areas where high overall system recovery and high product quality is required. The number of stages touched the lower bound for both independent MSF and hybrid MSF section. This shows that the defined decision variables have no pronounced effect on heat recovery section. In the future work, the superstructure will be used for multiple optimization studies and will also be extended to perform sensitivity analysis and control studies of the hybrid systems.

Nomenclature

Ws, Fm, D, BD, W, BO, R, BN, CW, Fsea, B_j, B_{j-1}, D_j and D_{j-1} are flow rates of steam, makeup seawater, distillate, brine blow down, cooling brine in heat recovery section, flashing brine entering first stage, recycle brine, flashing brine leaving last stage, reject

seawater, feed seawater, flashing brine leaving stage j, flashing brine entering stage j, distillate leaving stage j and distillate entering stage j respectively, CF, CBN, CR, CBO, $C_{B,j}$ and $C_{B,j-1}$ are salt concentrations of feed, flashing brine leaving last stage, recycle brine, flashing brine entering first stage, flashing brine leaving stage j and flashing brine entering stage j respectively, TB_j, TB_{j-1}, TBO, TF1, TF_j, TF_{j+1}, TD_j and TD_{j-1} are temperatures of flashing brine leaving stage j, flashing brine entering stage j, flashing brine leaving brine heater, cooling brine leaving stage 1, cooling brine leaving stage j, respectively, λs is the latent heat of vaporization of water in brine heater, Ubh and U_j are overall heat transfer coefficients at the brine heater and at stage j respectively, Abh and Arj are total heat transfer areas of brine heater and stage j respectively, $(LMTD)bh$ and $(LMTD)_j$ are log mean temperature differences for brine heater and stage j respectively, BPEj, NEAj and Δj are boiling point elevation, non-equilibrium allowance in temperature for flashing brine and temperature drop in demister in stage j, Tref is reference temperature, Qf, Qp and Qr are the feed, permeate and reject flow rates respectively, Cf, Cp, Cr, Cw and Cb are the feed, permeate, reject, wall and bulk concentrations respectively, Pf and Pp are the feed and permeate pressures respectively, μ is brine viscosity, d is diameter of element, C is concentration, T is temperature, Aw is water permeability, Δπ is osmotic pressure drop, As is salt permeability constant, ρ is brine density, Ds is solute diffusivity, df is feed spacer thickness, m is no of membrane element in a pressure vessel, Lm is length of membrane element, Amem is area of membrane, N1 is number of leaves in a membrane element, hsp is height of spacer channel, ε is feed spacer void fraction

References

A.M. Helal, A.M. El-Nashar, E. Al-Katheeri and S. Al-Malek. (2003), Optimal design of hybrid RO/MSF desalination plants Part I: Modeling and algorithms, Desalination, 154, 43-66.

El-Dessouky H and Ettouney H. (2002), Fundamentals of salt water desalination. Amsterdam: Elsevier.

Kamal M. Sassi and Iqbal M. Mujtaba. (2013), Optimal operation of RO system with daily variation of freshwater demand and seawater temperature, Computers and Chemical Engineering, 59, 101– 110.

M. Rosso, A. Beltramini, M. Mazzotti and M. Morbidelli. (1997), Desalination, 108, 365.

M. A. Al-Sofi and A. B. Khan. (1984), Application of MSF/RO hybrid concept, WSIA 12th Annual Conference, Technical Proc.

M.G. Marcovecchio, P.A. Aguirre and N.J. Scenna. (2005), Global optimal design of reverse osmosis .networks for seawater desalination: modeling and algorithm, Desalination, 184, 259–271.

Sabah A. Abdul-Wahab, K. V. Reddy, Mohammed A. Al-Weshahi, Salim Al-Hatmi and Yasir M. Tajeldin. (2012), Development of a steady state mathematical model for multistage flash (MSF) desalination plant, Int J. Energy Res, 36, 710-723.

Wijmans, H. (2007), Concentration polarization, In Encyclopedia of Separation Science ; Wilson, I. D. , Ed.; Elsevier Science Ltd. : London , 1682 – 1687.

Yan-Yue Lu, Yang-Dong Hu, Xiu-Ling Zhang , Lian-Ying Wu and Qing-Zhi Liu, 2007, Optimum design of reverse osmosis system under different feed concentration and product specification, Journal of Membrane Science, 287, 219–229.

Krist V. Gernaey, Jakob K. Huusom and Rafiqul Gani (Eds.), 12th International Symposium on Process Systems Engineering and 25th European Symposium on Computer Aided Process Engineering.
31 May – 4 June 2015, Copenhagen, Denmark

Microalgae growth determination using modified breakage equation model

Ergys Pahija,[a] Yu Zhang,[a] Maojian Wang,[a,b] Yi Zhu,[a] Chi Wai Hui[a]

[a]*Chemical and Biomolecular Engineering Department, The Hong Kong University of Science and Technology, Clear Water Bay, Hong Kong*
[b]*Department of Chemical Engineering, Xi'an Jiao Tong University, Xi'an, China*

Abstract

Simulation of growth rate and cells size distribution is important in order to predict and improve productions from microalgae. Aim of this paper is to use a modified breakage equation model to calculate the growth rate, the "breakage rate" and the particle size distribution of microalgae, which are changing over the time. Differently from previous mathematical models, various stages of the life cycle of Chlorella Vulgaris have been considered. According to the experimental data, the proposed method is able to predict the growth and, similarly, it can be extended to other kind of microalgae. This wants to be a new starting point for future development of microalgae growth kinetic.

Keywords: microalgae, growth model, breakage equation, size distribution.

1. Introduction

Global warming is a topic of great concern in many countries and this situation led to the development of new international emissions regulations. For that reason, investments on renewable energy production have gained great importance in the past few years. For instance, microalgae can be a very good choice and give a double benefit: CO_2 emission reduction and biofuel production. For example, Van den Hende et al. (2010) illustrated that these microorganisms can subtract carbon dioxide and other pollutants directly from the flue gas emitted by power plants. On the other hand, since there is a continuous increment in energy demand, electricity generation and biofuels production from microalgae have been studied by numerous research groups around the world in the past years (Mata et al., 2010). Also, deserves to be noted that the production of fine chemicals for pharmaceutical and cosmetic industries and proteins for human and animal consumption has been taken under consideration in a number of life cycle assessment studies (Williams and Laurens, 2010) (Slade and Bauen, 2013).

In order to increase the production of useful chemicals, the conditions must be set in order to improve the microalgae productivity. Indeed, microalgae growth is influenced by several factors: temperature, pH, light intensity, CO_2 and nutrients concentrations. Most of the studies, trying to reproduce the growth using mathematical models, do not consider all of the mentioned factors; for example Mayo (1997) has considered in his paper temperature and pH, while in other works (Goldman and Carpenter, 1974) the model is temperature-nutrients based. Moreover, seems that the life cycle of cells has been generally neglected by many authors even though the concentration of useful substances inside the cells do vary depending on its size (Morimura, 1959). The size and contents of microalgae are varied by the growing conditions (de-Bashan et al.

2002). Microalgae with the same size may carry different contents. As discussed, size distribution and population growth provide us additional information such as breakage, growth and even death rates. Knowing these information may help us to improve the cultivation as well as the harvesting system.

The model we are going to propose has many analogies with the breakage equation (Vanni, 1999) used for calculating the number/mass of particles in various processes, such as crushing, grinding and for modelling crystallizers performance. Main purpose and contribution of this work is to build a correlation between the total number of microalgae and its PSD (population size distribution). The model depends strongly on the growing conditions and, as it will be explained, the parameters are functions of the environmental factors.

2. Model

Before going to present our model, it is good to provide some information related to the traditional breakage equation. The number-based breakage equation (Hill and Ng, 1995) can be written as shown in Eq. (1).

$$\frac{dn(v)}{dt} = \int_v^\infty b(v,w)S(w)n(w)dw - S(v)n(v) \tag{1}$$

where $n(v)$ is the number of particles between volume v and $v+dv$. $S(w)$, which is commonly called specific rate of breakage, is the fraction of particles at size w that will break into smaller sizes. Finally, $b(v,w)$ is the breakage function and it represents the fraction of particles at size w that break into the $[v, v+dv]$. The integral is expressed from v to ∞ because any particle bigger than v might be broken into v. After discretization, Eq. (1) can be rewritten as Eq. (2).

$$\frac{d}{dt}N_i(t) = \sum_{j=i+1}^{\infty} b_{ij}S_jN_j(t) - S_iN_i(t) \tag{2}$$

where $N_i(t)$ is the number of particles in interval i, between volumes v_{i-1} and v_i. Similarly, as described in Eq. (1), particles included into a generic interval j (with $j > i$) break into smaller particles and, some, will end up into interval i.

It can be interesting to see that a good discretization plays a very important role in the solution of the problem. Indeed, as shown in an example presented by Hill and Ng (1995), a particle situated inside interval j can break into two particles of smaller intervals; anyway there is the possibility for one of the particles to remain inside interval j itself.

The modified breakage equation we would like to suggest for the determination of microalgae growth works similarly. Anyway, there are several differences between them! In primis, a microalgae can't be considered as a solid particle, such as those we use for grinding problems, and, even more important, in microorganisms the growth factor shall be taken under consideration. This actually means that the cells can break into smaller parts, but they can also grow in size inside the same interval or they might "jump" on an interval which contains larger particles.

Equation (3) below introduced a new breakage function *B(v,w)* that represents the breakage and/or growth from size *w* to size *v*. The discretization form of equation (3) is written as Equation (4).

$$\frac{dn(v)}{dt} = \int_{v_{min}}^{v_{max}} B(v,w)n(w)\,dw \tag{3}$$

$$\frac{d}{dt}N_i(t) = \sum_{v_{min}}^{v_{max}} B_{ij}N_j(t) \tag{4}$$

The total growth and breakage are represented by the B_{ij} (i and j have the same meaning of the traditional model) in Eq. (3) and Eq. (4). In other words, the B_{ij} includes b_{ij} and S present in the traditional breakage equation. Another difference that can be noticed with the previous model is that in this case, *j* can be any interval included between the minimum and maximum volume since both growth and breakage may occur. v_{min} and v_{max} are the minimum and maximum volume that microalgae can achieve (note that in Eq. (4) v_{min} and v_{max} are intervals).

Since microalgae grow in a cycle, unlike equation (2), *w* can be either larger or smaller or even equal to *v*. For instance, if the size is divided from 1 (smallest) to 10 (largest) intervals, the smallest microalgae (i.e. size 1) may grow into larger intervals (e.g. 3, 4 or 5) without breaking during a measurement period. In this case, the summation of *B(v,'1')* or B_{v1} equals to one. At the largest intervals (i.e.10), it may likely break into small intervals (e.g. 1, 2 or 3). In this case, the summation of *B(v,'10')* or B_{v10} can be any number smaller than b_{max} (the maximum possible breakage). For Chlorella Vulgaris, b_{max} is around 4. With these consideration, equation (5) below limits the summation of breakage (B_{ij}).

$$\sum_{v_{min}}^{v_{max}} B_{ij} \leq \sum_{j}^{v_{max}} B_{ij} + \left[1 - \sum_{j}^{v_{max}} B_{ij}\right] b_{max} \tag{5}$$

The first term on the right hand side of equation (5) is the number of microalgae that grow without breaking. The second term on the right hand side is the number microalgae that grow and break into smaller sizes. In this model, we assume that the time interval between two measurements is shorter than a growing cycle of microalgae. Although the model is not limited by this but if the measurement interval is too long, the number of b_{max} can be a number larger than the number of the physical breakage of a matured cell.

3. Results

3.1. Experiment

The model was verified on Chlorella Vulgaris UTEX 2714 which was used in the experiment. Microalgae were grown inside a 2-liter transparent plastic bottle and the experiment was run for 15 days. Light intensity was maintained constant at about 1.1 klux and temperature and pH were kept at 26 C and 7.8 respectively. For counting microalgae, a drop of solution positioned on a hemocytometer was observed at the

microscope. The particle size distribution was measured using a particle size analyser. Main objective of the experiment was to prove the possibility to use this model.

Figure 1 shows the size distribution at day 1 and 15. Data from day 1 are used as initial conditions in the model.

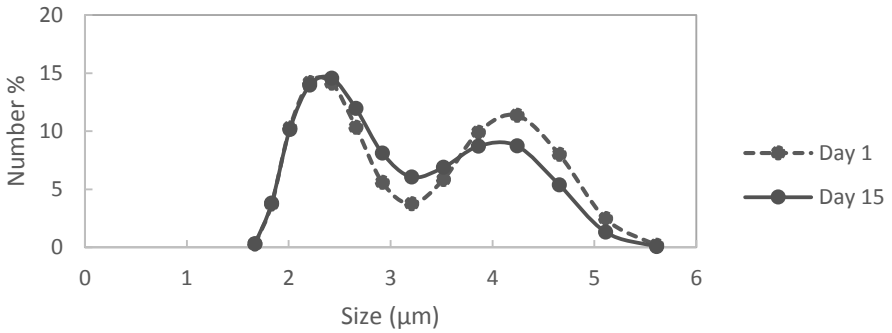

Figure 1 Size distribution of microalgae - day 1 and day 15.

3.2. Simulation

The model was developed using Microsoft® Excel 2013. The cells were divided into 14 intervals (same number of intervals get from the particle size analyser) and the following results will show how the model can be used to fit the experimental data. In Figure 2 and Figure 3 are illustrated the good similarity between the model and the experimental data. In particular, Figure 2 shows the total number of cells over the time, while Figure 3 shows the particle size distribution after 15 days (the initial distribution is not illustrated since it is an initial condition). To be noticed is the stiffness of the problem. Indeed when we try to minimize the gap between the experiment and the simulation, it is possible to note that there are different orders of magnitude (overall population number >> fraction number); therefore some weight factor were necessary in order to balance the objective functions for curve fitting.

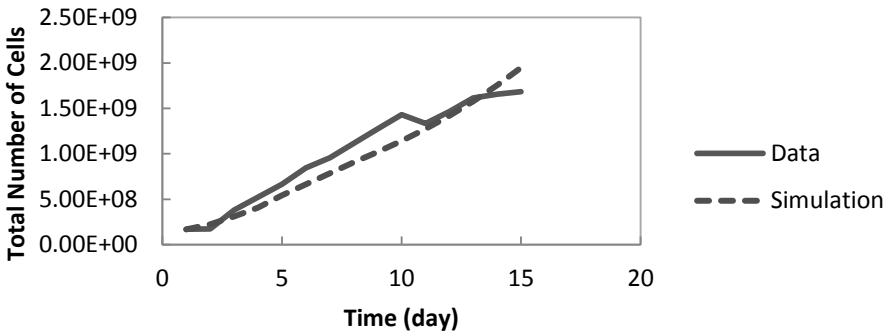

Figure 2 Comparison between experimental data and breakage equation model.

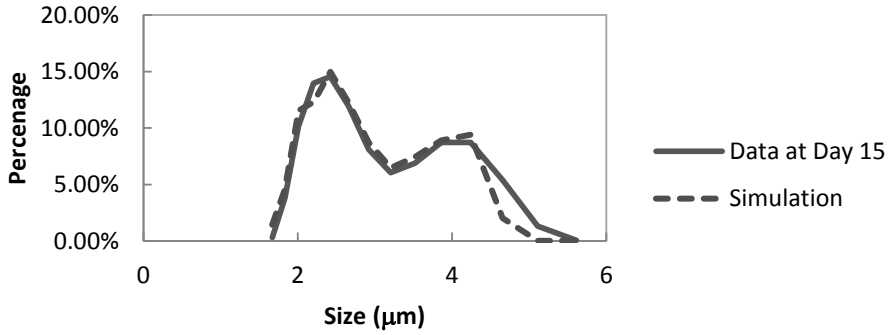

Figure 3 Comparison between size distribution in experimental data and the model.

An example of the parameters B_{ij} present in the model are shown in Table 1. Notice that the sizes (1.669, 1.832, …, 5.611) are all expressed in μm. Also consider that the growth/breakage happens from *j* to *i* and not vice versa.

Table 1 B_{ij} parameters.

j \ i	1.669	1.832	2.01	2.207	2.423	2.66	2.92	3.206	3.519	3.862	4.241	4.656	5.111	5.611
1.669	1.05E-02	1.59E-04	3.81E-03	9.26E-04	5.44E-03	3.49E-03	4.53E-03	5.50E-04	5.66E-03	9.61E-01	4.11E-03	9.78E-05	5.17E-05	1.02E-05
1.832	3.61E-05	1.95E-05	4.47E-05	1.65E-04	9.90E-01	4.00E-04	8.97E-04	1.11E-05	3.74E-03	2.89E-04	4.08E-03	5.73E-05	7.07E-05	2.46E-05
2.01	1.33E-01	9.61E-04	1.72E-05	1.43E-05	1.63E-04	9.66E-01	1.85E-04	1.56E-04	2.01E-04	2.55E-05	0	1.94E-05	1.71E-05	2.64E-05
2.207	9.90E-05	4.04E-01	1.04E+00	4.56E-01	1.50E-04	2.98E-04	1.48E-04	1.63E-04	1.22E-04	1.73E-04	1.24E-04	1.81E-01	1.16E-05	7.75E-05
2.423	2.03E-04	3.95E-04	9.43E-05	5.15E-05	1.41E-03	1.85E-04	3.71E-05	5.63E-05	1.21E-03	1.69E-04	6.92E-01	1.09E-05	1.54E-05	0
2.66	1.27E-04	1.27E-03	4.42E-04	2.16E-05	9.76E-01	3.13E-04	1.02E-03	5.86E-01	1.18E-03	1.66E-01	5.54E-04	2.47E-05	1.58E-05	1.56E-05
2.92	1.52E-05	0	0	6.27E-05	7.89E-03	1.07E-03	1.10E-04	1.24E-04	9.32E-01	6.37E-04	2.06E-03	1.80E-05	2.64E-05	1.99E-05
3.206	5.01E-03	2.07E-03	8.10E-05	4.39E-05	7.19E-03	1.86E-05	3.08E-03	1.38E-05	1.27E-03	9.94E-01	6.22E-04	2.16E-05	2.17E-05	2.30E-05
3.519	2.85E-06	7.63E-04	2.06E-05	1.88E-05	3.94E-04	1.87E-04	5.17E-04	7.31E-05	2.89E-03	2.36E-05	3.56E-03	4.00E-05	1.74E-05	1.09E-05
3.862	4.67E-05	8.27E-04	1.37E-04	2.96E-05	5.34E-03	1.11E-05	1.08E+00	6.20E-04	6.06E-03	2.13E-03	2.08E-05	2.35E-05	1.75E-05	1.58E-05
4.241	2.19E-04	4.86E-04	4.65E-05	9.88E-05	5.52E-04	2.59E-01	4.22E-04	1.90E-04	9.18E-04	3.01E-04	7.91E-04	3.18E-05	3.41E-05	2.25E-05
4.656	1.58E-04	3.83E-04	4.35E-04	4.00E+00	0	2.84E-05	4.25E-04	5.80E-04	1.17E-04	0	0	3.35E-04	1.12E-04	5.59E-05
5.111	8.23E-04	8.27E-04	2.36E-05	3.95E-04	3.64E-04	1.48E-05	1.30E-04	1.01E-03	5.19E-04	4.16E-04	9.47E-04	4.41E-05	9.05E-04	9.98E-01
5.611	5.97E-04	2.83E-03	1.68E-04	3.99E+00	5.35E-04	6.46E-04	6.71E-04	6.24E-04	3.57E-04	2.76E-03	5.93E-04	4.80E-05	1.36E-05	4.42E-05

As mentioned already, the parameters shown in Table 1 are related to both growth and breakage. To read the table, consider that the particles can break into the same interval. If we consider the first column, the first cell is the *B* value of cells breaking into the same interval; going down we will find the cells breaking from second to first interval and so on. Moving on the second column, the first cell (top) is the one representing the growth from the first interval while the rest represent the breakage from bigger particles. The diagonal represent the parameter of the particles remaining in the same interval. Practically there is growth over it and breakage below.

Looking at the values above it is not easy to find a physical meaning for these values. Indeed, all these parameters are related to the environmental conditions: light intensity, pH, temperature, CO_2 and nutrients concentrations. To understand the kind of correlation additional experimental data will be necessary in future.

4. Conclusions

A new microalgae growth model has been derived from breakage equation and, according to the results, the model works and can be applied for the designed experiment. The model takes into account the growth cycle of microalgae, its growth rate and its breakage from microalgae of size *j* to microalgae of size *i*. Since just one case study has been developed so far, the proposed model can be applied only for the proposed environmental conditions and, very important, for Chlorella Vulgaris. Further studies and additional experiments (in different conditions) would lead to better understand the physical meaning of the parameters, obtained adapting the proposed model.

References

L. E. de-Bashan, Y. Bashan, M. Moreno, V. K. Lebsky and J. J. Bustillos, 2002, Increased pigment and lipid content, lipid variety, and cell and population size of the microalgae Chlorella spp. when co-immobilized in alginate beads with the microalgae-growth-promoting bacterium Azospirillum brasilense, Canadian Journal of Microbiology, 48(6), 514-521.

J. C. Goldman and E. J. Carpenter, 1974, A kinetic approach to the effect of temperature on algal growth, Limnology and Oceanography, 19(5), 756-766.

P. J. Hill and K. M. Ng, 1995, New discretization procedure for the breakage equation. AIChE Journal, 41(5), 1204-1216.

T. M. Mata, A. A. Martins and N. S. Caetano, 2010, Microalgae for biodiesel production and other applications: A review, Renewable and Sustainable Energy Reviews, Volume 14, Issue 1, Pages 217-232.

A. W. Mayo, 1997, Effects of temperature and pH on the kinetic growth of unialga Chlorella vulgaris cultures containing bacteria, Water Environment Research, 64-72.

Y. Morimura, 1959, Synchronous culture of Chlorella I. Kinetic analysis of the life cycle of Chlorella ellipsoidea as affected by changes of temperature and light intensity, Plant and Cell Physiology, 1(1), 49-62.

R. Slade and A. Bauen, 2013, Micro-algae cultivation for biofuels: cost, energy balance, environmental impacts and future prospects, Biomass and Bioenergy, 53, 29-38.

S. Van Den Hende, H. Vervaeren, N. Boon, 2012, Flue gas compounds and microalgae: (Bio-)chemical interactions leading to biotechnological opportunities, Biotechnology Advances, Volume 30, Issue 6, Pages 1405-1424.

M. Vanni, 1999, Discretization procedure for the breakage equation, AIChE journal, 45(4), 916-919.

P. J. L. B. Williams and L. M. L. Laurens, 2010, Microalgae as biodiesel & biomass feedstocks: review & analysis of the biochemistry, energetics & economics, Energy & Environmental Science 3(5), 554-590.

Krist V. Gernaey, Jakob K. Huusom and Rafiqul Gani (Eds.), 12th International Symposium on Process Systems Engineering and 25th European Symposium on Computer Aided Process Engineering.
31 May – 4 June 2015, Copenhagen, Denmark

A New Strategy for the Simulation of Gas Pipeline Network Based on System Topology Identification

Zengzhi Du, Chunxi Li, Wei Sun, Jianhong Wang*

College of Chemical Engineering, Beijing University of Chemical Technology, Beijing 100029, China
wjhmaster@263.net

Abstract

Pipeline network plays a very important role in chemical plant, refinery, oil and gas gathering. Design, optimization and scheduling of pipeline network are based on the simulation of pipeline network. With the increase of the number of pipe segments, pipeline network model becomes more difficult to be solved. Traditionally, nonlinear equations of pipeline network need to be calculated by equation oriented method. However, this method has large computational complexity and it highly depends on initial values. When there are more unknown variables, it is harder to assign appropriate initial values and also harder to get convergence. In this work, a new strategy for the simulation of gas pipeline network is introduced. A pipeline network model suitable for compressible gas is built. Pipeline network is identified and simplified by adjacent matrix searching. After adjacent matrix searching, the number of equations is reduced and pipeline network model becomes easier to solve. This solution is applied to a case study for verifying the proposed model and strategy.

Keywords: pipeline network, adjacent matrix, nonlinear equations

1. Introduction

Gas pipeline network is widely presented in chemical plants and natural gas gathering. Design and optimization of gas pipeline network are usually based on the simulation of gas pipeline network. Flow and pressure for each pipe segment need to be calculated first in simulation. Gas pipeline network has been studied by many workers. Kiuchi (1994) analyzed unsteady gas networks at isothermal conditions by an implicit method. Ke and Ti (1999) studied isothermal transient gas flow by using electrical models. Behbahani-Nejad and Bagheri (2010) proposed and developed a MATLAB-Simulink library for the transient flow simulation of gas pipeline network. Alamian et al. (2012) proposed a transient flow simulation for gas pipeline network based on the state space equations. Gonzales et al. (2009) simulated a gas distribution pipeline network by MATLAB-Simulink component library, which is built based on S-functions philosophy. Nonlinear equations are usually calculated by equation oriented method in steady state simulation. But this method has large computational complexity and it highly depends on initial values. In this paper, a gas pipe segment model is proposed together with a new strategy for the simulation of gas pipeline network, in order to reduce the computational complexity.

2. Mathematical model

2.1. Pipe segment model

In pipeline network, one pipe with fixed length, diameter and material is defined as one pipe segment. Pipeline network can be considered as an assembly of pipe segments. The gas flows in a pipe segment, as shown in Fig. 1, can be described by Bernoulli's equation. The following equations describe pipe segment model.

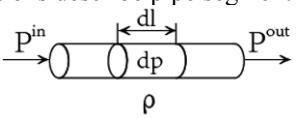

Figure 1. A pipe segment

$$g\Delta z + \Delta\frac{u^2}{2} + \frac{\Delta P}{\rho} = w_e - h_f \tag{1}$$

where h_f is flow resistance loss, can be calculated as $h_f = \lambda \cdot \frac{l}{d} \cdot \frac{u^2}{2} = \lambda \cdot \frac{l}{d} \cdot \frac{(FM/\rho A)^2}{2} = \lambda \cdot \frac{l}{d} \cdot \frac{(FM/\rho(\pi d^2/4))^2}{2}$; g is the acceleration of gravity; Δz is height difference; u is velocity; ΔP is pressure drop; ρ is gas density; w_e is external work; λ is Fanning factor; l is pipe length; d is pipe diameter; F is molar flow rate; and M is the molecular weight of gas in the pipe.

2.2. Model simplification

In order to study pipeline network topology conveniently, it is possible to simplify model calculation by assuming (1) the height difference of pipe segments are negligible, then $g\Delta z=0$; (2) gas is in steady flow state, then $\Delta u2/2=0$; (3) there is no external work in pipe segment, i.e., $w_e=0$; (4) gas flow under isothermal condition; (5) gas physical properties can be described by ideal gas state equation, i.e., $\rho=PM/RT$. According to above assumptions, pipe segment equation can be derived as following:

$$\Delta P = \frac{8}{\pi^2} \cdot \lambda \cdot \frac{l}{d^5} \cdot \frac{M^2}{\rho} \cdot F^2 \tag{2}$$

$$dP = \frac{8}{\pi^2} \cdot \lambda \cdot \frac{dl}{d^5} \cdot \frac{MRT}{P} \cdot F^2 \tag{3}$$

$$\Delta P = P^{in} - P^{out} = \frac{8}{\pi^2} \cdot \lambda \cdot \frac{l}{d^5} \cdot \frac{MRT}{(P^{in} + P^{out})/2} \cdot F^2 \tag{4}$$

$$\Delta P = rF^2 \tag{5}$$

For liquid pipe segment, density is constant, but gas density is not. In Fig. 1, when pipe segment length is dl and pressure drop is dP, gas density can be considered as constant. Thus, Eq.(2) can be rewritten as Eq.(3). Integrating Eq.(3) obtains Eq.(4), which is the model equation for a pipe segment. As it can be seen in Eq.(4), λ, l, d are pipe segment parameters. M and T are gas physical properties. $(P^{in}+P^{out})/2$ is average pressure of pipe segment. For a given pipe segment and gas, these parameters will remain constants. So a pipe segment resistance coefficient r can be designated to replace these parameters. Eq.(4) is rewritten as Eq.(5).

3. Pipeline network topology identification

Pipeline network topology is described by adjacent matrix *A*. *A* is an n-dimensional matrix, where *n* is pipe segment number. When the element of row *i*, column *j* is equal to 1 in the adjacent matrix, i.e. A_{ij}=1, there is a path from pipe segment *i* to *j*; when A_{ij}=0, no path from pipe segment *i* to *j*. There are many similar sub-networks in a pipeline network. Typical sub-networks can be roughly classified as series and parallel structures.

3.1. Series sub-network and its identification

Series sub-network is defined as two pipe segments connected one after the other. Series sub-network topology and adjacent matrix are shown in Fig. 2a.

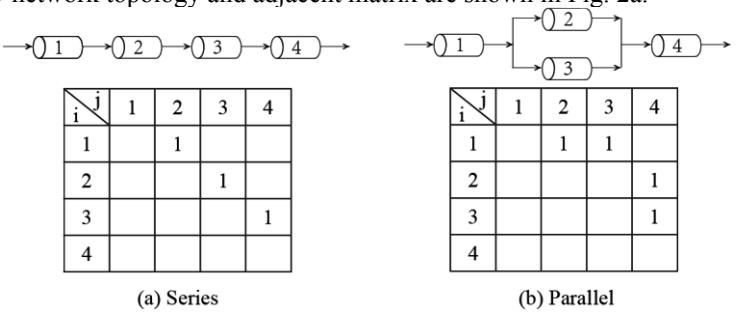

i \ j	1	2	3	4
1		1		
2			1	
3				1
4				

i \ j	1	2	3	4
1		1	1	
2				1
3				1
4				

Figure 2. Series and parallel sub-network topology and corresponding adjacent matrixes

It can be seen in Fig. 2a, $A_{23} = \sum_{j=1}^{4} A_{2j} = \sum_{i=1}^{4} A_{i3} = 1$. It means pipe segment 2 connects to pipe segment 3. Thus, if pipe segment *k* connects pipe segment *l* in the adjacent matrix, it can be identified by Eq.(6).

$$A_{kl} = \sum_{j=1}^{n} A_{kj} = \sum_{i=1}^{n} A_{il} = 1 \tag{6}$$

3.2. Parallel sub-network and its identification

Two pipe segments are defined as a parallel sub-network, when they share the same upstream pipe segment and downstream pipe segment. Parallel sub-network topology and its adjacent matrix are shown in Fig. 2b. When $A_{12} = A_{13} = 1$ and $A_{24} = A_{34} = 1$, it means pipe segment 2 parallels with pipe 3. Thus, if pipe segment *k* is parallel with pipe segment *l* in the adjacent matrix, it can be identified by Eq.(7).

$$\begin{cases} A_{ik} = A_{il} = 1 \\ A_{kj} = A_{lj} = 1 \end{cases} \tag{7}$$

4. Pipeline network topology simplification

Pipeline network model includes a large number of equations. The simultaneous solution of equations is challenging. So pipeline network topology needs to be simplified. Series sub-network and parallel sub-network can be simplified as equivalent pipe segments.

4.1. Series sub-network simplification

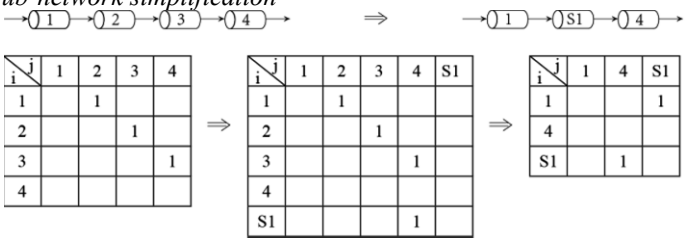

Figure 3. Simplification of series sub-network

In Fig. 3, Eq.(6) is employed to identify series sub-network (pipe segment 2 and 3). Adjacent matrix A needs to be added row S1 and column S1. Let $A_{i,S1} = A_{i2}(i = 1 \cdots 4)$, $A_{S1,j} = A_{3j}(j = 1 \cdots 4)$, $A_{S1,S1} = 0$. Delete row 2, 3 and column 2, 3. The new adjacent matrix is shown in Fig. 3. Pipe segment S1 can be represented by Eq.(8). It is known that the resistance coefficient of pipe segment S1 is equal to the sum of the resistance coefficient of pipe segment 2 and 3 shown in Eq.(9). When n pipe segments are in series, $r_s = \sum_{i=1}^{n} r_i$. The relationship between series sub-network and its equivalent pipe segment is described by Eq. (10).

$$\Delta P_S = P_2^{in} - P_3^{out} = r_S F_S^2 \tag{8}$$

$$r_S = r_2 + r_3 \tag{9}$$

$$\begin{cases} \Delta P_2 = P_2^{in} - P_2^{out} = \dfrac{r_2}{r_S}\Delta P_S \\ \Delta P_3 = P_3^{in} - P_3^{out} = \dfrac{r_3}{r_S}\Delta P_S \\ F_S = F_2 = F_3 \end{cases} \tag{10}$$

4.2. Parallel sub- network simplification

In Fig. 4, pipe segment 2 is parallel with pipe segment 3. Equivalent pipe segment P1 is used to represent parallel sub-network. Pipe segment P1 is described by Eq.(11). The resistance coefficient of pipe segment P1 can be calculated by Eq.(12). When n pipe segments are in parallel, $\sqrt{\dfrac{1}{r_P}} = \sum_{i=1}^{n} \sqrt{\dfrac{1}{r_i}}$. The relationship between parallel sub-network and its equivalent pipe segment is described by Eq. (13).

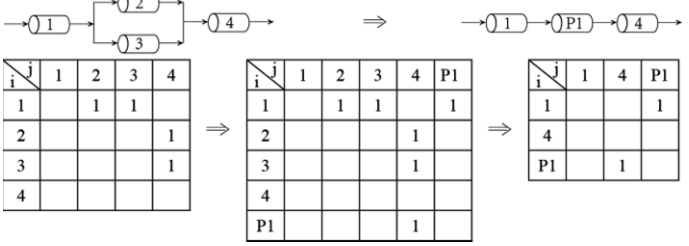

Figure 4. Simplification of parallel sub-network

$$\Delta P_P = P_2^{in} - P_2^{out} = r_P F_P^2 \text{ or } \Delta P_P = P_3^{in} - P_3^{out} = r_P F_P^2 \tag{11}$$

$$\sqrt{\frac{1}{r_P}} = \sqrt{\frac{1}{r_2}} + \sqrt{\frac{1}{r_3}} \tag{12}$$

$$\begin{cases} F_2^2 = \dfrac{r_P}{r_2} F_P^2 \\ F_3^2 = \dfrac{r_P}{r_3} F_P^2 \\ F_P = F_2 + F_3 \end{cases} \tag{13}$$

5. Case study

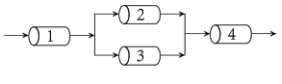

i \ j	1	2	3	4
1		1	1	
2				1
3				1
4				

(a) Original pipeline network

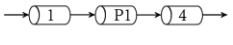

i \ j	1	4	P1
1			1
4			
P1		1	

(b) Simplification of parallel sub-network

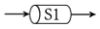

i \ j	S1
S1	

(c) Simplification of series sub-network

Figure 5. Pipeline network topology and adjacent matrix

$$\begin{cases} \Delta P_i = P_i^{in} - P_i^{out} = r_i F_i^2 (i = 1 \cdots 4) \\ P_1^{out} = P_2^{in} \\ P_1^{out} = P_3^{in} \\ P_2^{out} = P_4^{in} \\ P_3^{out} = P_4^{in} \\ F_1 = F_2 + F_3 \\ F_2 + F_3 = F_4 \end{cases} \tag{14}$$

$$\Delta P_{S1} = P_1^{in} - P_4^{out} = r_{S1} F_{S1}^2 \tag{15}$$

A pipeline network topology is shown in Fig. 5a. It includes a series sub-network and a parallel sub-network. There are 4 pipe segments, and each pipe segment is described by 4 variables. Initially, boundary values are given before simulation. Inlet pressure of pipe segment 1 is 300,000Pa; outlet pressure of pipe segment 4 is 100,000Pa. In order to facilitate calculation, all resistance coefficients are $10Pa \cdot s^2 \cdot kmol^{-2}$. Parallel sub-network is simplified in Fig. 5b and Series sub-network is simplified in Fig. 5c. Pipeline network

model is described by Eq.(14). After identification and simplification, original pipeline network becomes an equivalent network shown in Fig. 5c. In the equivalent network, there are 1 pipe segment and 4 variables. Equivalent network model is described by Eq.(15). Compared with Eq.(14), it is easier to calculate Eq.(15) obviously.

6. Results and discussion

After simplification, resistance coefficients of equivalent pipe segments are calculated by Eq.(9) and Eq.(12). Before simplification, the pressure and flow of original pipeline network are calculated by Eq.(10) and Eq.(13). The calculated results, which are simulated by this new strategy, are listed in Table 1. Eq.(14) is also solved by equation oriented method using MATLAB. The results agree with that in Table 1. When initial values are 1, it converges at iteration 68. When initial values and calculated results are at the same order of magnitude, the number of iterations converged is 21. By using adjacent matrix searching strategy proposed in this paper, computational complexity is significantly reduced.

Table 1. Calculated results for pressure and flow

Pipe segment No.	Boundary of inlet pressure, Pa	Boundary of outlet pressure, Pa	Inlet pressure of pipe segment, Pa	Outlet pressure of pipe segment, Pa	Flow rate, kmol/s
1	300,000	-	300,000	211,111.11	94.28
2	-	-	211,111.11	188,888.89	47.14
3	-	-	211,111.11	188,888.89	47.14
4	-	100,000	188,888.89	100,000	94.28

7. Conclusions

In this work, a new strategy for the simulation of gas pipeline network has been presented. By adjacent matrix operations, a complex pipeline network is simplified hierarchically. In fact, adjacent matrix simplification is equation simplification. After identification and simplification, the numbers of equations and variables are significantly reduced. The simulation of pipeline network becomes easier. The results of case study prove that the proposed strategy is effective in the simulation of gas pipeline network.

References

A.H. Gonzales, J.M. De La Cruz, B.D. Andres-Toro, J.L. Risco-Martin, 2009, Modeling and simulation of a gas distribution pipeline network, Applied Mathematical Modelling, 33, 3, 1584–1600

M. Behbahani-Nejad, A. Bagheri, 2010, The accuracy and efficiency of a MATLAB-Simulink library for transient flow simulation of gas pipelines and networks, Journal of Petroleum Science and Engineering, 70, 3-4, 256–265

R. Alamian, M. Behbahani-Nejad, A. Ghanbarzadeh, 2012, A state space model for transient flow simulation in natural gas pipelines, Journal of Natural Gas Science and Engineering, 9, 51-59

S.L. Ke, H.C. Ti, 1999, Transient analysis of isothermal gas flow in pipeline network, Chemical Engineering Journal, 76, 2, 169-177

T. Kiuchi, 1994, An implicit method for transient gas flow in pipe networks, International Journal of Heat and Fluid Flow 15, 5, 378-383

Krist V. Gernaey, Jakob K. Huusom and Rafiqul Gani (Eds.), 12th International Symposium on Process Systems Engineering and 25th European Symposium on Computer Aided Process Engineering.
31 May – 4 June 2015, Copenhagen, Denmark

Modelling and optimization of a heat integrated gasification process

Yi Zhu, Adetoyese Olajire Oyedun, Maojian Wang, Ergys Pahija, Chi Wai Hui

Department of Chemical and Biomolecular Engineering, The Hong Kong University of Science and Technology, Clear Water Bay, Kowloon, Hong Kong

Abstract

In this study, an iteration optimization is performed based on the Gibbs free energy minimization approach. Further, simultaneous optimization of a heat integrated gasification process is presented. The study shows how heat integration can improve the overall efficiency of a gasification process. We formulated a mathematical model which simultaneously optimizes the operating parameters and its interaction via heat integration among the hot syngas, steam generation and the feed preheat. This allows the model to simultaneously maximize the cold gas efficiency and also minimize the Gibbs free energy. The model also combined gasification model with an energy targeting model that is able to handle processes with variable stream temperatures and flow rates.

Keywords: gasification, heat integration, simultaneous optimization.

1. Introduction

The threats of global warming and energy crises urge the need of cleaner conversion technologies for fossil fuels such as coal. Due to the ability to mitigate the pollutions to the environment and greenhouse gas emissions, gasification becomes a promising conversion technology and receives increasing attention worldwide (Clayton et al., 2007). The production of syngas from gasification, however, is a complex process that is strongly affected by the composition of feedstock, the gasification temperature and pressure, the amount of gasification feed water (GFW) and oxygen, etc. (Abuadala et al., 2010).

To evaluate how these parameters would influence the gasification performance, several equilibrium models based on Gibbs free energy have been developed to effectively study the process in measurement of cold gas efficiency (CGE). However, most of efforts are placed on the parametric studies through control variant methods rather than find the optimum operating condition considering feed flow rates along with gasification temperature. Additionally, in gasification, quite a lot of feedstock is fully or partly oxidized to provide heat for raising the reaction temperature to a very high level, often over one thousand degree Celsius. The recovery of the sensible heat from the hot syngas plays a key factor in the overall energy efficiency and has seldom been taken into account in previous studies.

In this work, the iteration algorithm is first utilized to identify the operating condition of a gasification process corresponding to the highest CGE. Further, a heat integrated gasification model is developed that maximizes CGE of a gasification process with considerations of the amount of feed as well as heat integration simultaneously. A heat integration model is established to ensure the feasibility of heat exchange among the hot

syngas, feed streams and steam boiler. The model will be illustrated through case studies of carbon gasification.

2. Equilibrium modelling

The gasification modelling approach is based on the theory that chemical equilibrium is achieved when the total Gibbs free energy for a set of considered gasification products is minimized. The total Gibbs free energy is calculated as:

$$G_{sys} = \sum_{i=prod}^{N} n_i \Delta G_{f,i}^{0} + \sum_{i=prod}^{N} n_i RT \ ln \ P + \sum_{i=prod}^{N} n_i RT \ ln \ y_i \quad (1)$$

Besides, the function, G_{sys}, also needs to satisfy the elemental and heat balance. The energy balance for the gasification process is calculated using Eq. (9).

$$nH_{f,fuel} + H_p(T_{in}) + \sum_{i=react}^{N} n_i H_{f,i}(T_0) = \sum_{i=prod}^{N} n_i H_{fa,i}\,(T_{out}) \quad (2)$$

As suggested by de Souza-Santos, the enthalpy of formation for the solid fuel reactant can be calculated as shown in Eq. (10) (de Souza-Santos, 2004).

$$H_{f,fuel} = LHV + \sum_{i=prod}^{N} H_{f,i}\,(T_0) \quad (3)$$

where LHV is the lower heat value in kJ/kmol and $H_{f,i}$ is the enthalpy of formation of *i*th gas under complete combustion of the solid fuel. In the calculation, the outlet temperature of syngas is taken as the gasification temperature. The initial temperature of reactants (T_0) is assumed to be 298.15 K. Thus, preheating heat represents the enthalpy change from 298.15 K of all reactants.

In addition, the minimization of Gibbs free energy is subject to elemental balance by:

$$\sum_{k=react}^{N} n_k \, a_k = \sum_{k=prod}^{N} n_k \, a_k \quad (4)$$

The constrain now is to find a set of n_i and a gasification temperature (T) in Eq. (1) which can minimize the total Gibbs free energy of the system while satisfying heat balance (Eq. (2)) and elemental balance (Eq. (4)). The direct minimization is accomplished by generalized reduced gradient nonlinear method. The reaction pressure is pre-specified. Providing initial values, the minimization of Gibbs free energy generates a set of n_i and determines the reaction temperature simultaneously.

3. Optimization through iteration

Based on the developed equilibrium model based on Gibbs free energy minimization, the iteration algorithm is utilized to identify the optimum operating condition. The details of calculation procedure are illustrated in Figure 1.

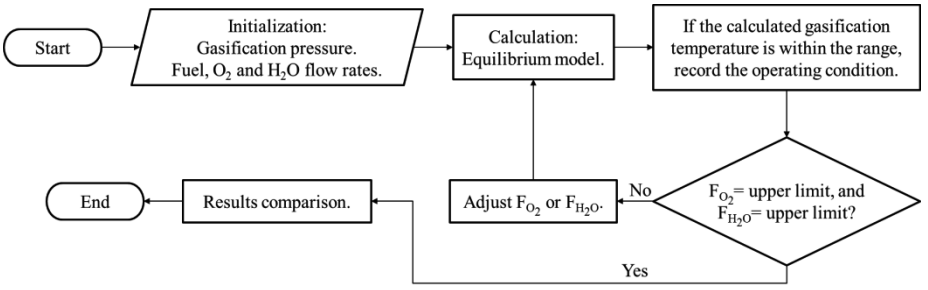

Figure 1. Calculation procedure of iteration

The upper limit of O_2 feed can be set as the stoichiometric amount for complete combustion. The value of O_{H2O}/C at 1 is considered as the upper limit for GFW feed. Although the approach is direct, we should also notice that the iteration process will be exponentially increased if the heat integration is also included or the high fidelity is required.

4. Simultaneous optimization of a heat integrated gasification process

To improve the optimization process, an approximation model which can consider the heat integration along with the gasification process parameters is developed.

Assuming that coal contains only carbon, gasification of coal consists of several major reactions (Li et al., 2001): partial and complete combustion, carbon-steam, boudouard, methanation and water-gas shift reactions.

Table 1. The major reactions and equilibrium constants at different temperatures

	1,000 K	1,200 K	1,400 K	1,600 K
$C + 0.5O_2 = CO$	2.89E+10	3.04E+09	5.94E+08	1.72E+08
$CO + 0.5O_2 = CO_2$	1.65E+10	57,535,774	1,023,261	50,350
$C + H_2O = CO + H_2$	2.52	38.43	267.56	1,141.03
$C + CO_2 = 2CO$	1.75	52.75	580.46	3,423.81
$C + 2H_2 = CH_4$	0.10	0.02	0.00	0.00
$CO + H_2O = CO_2 + H_2$	1.44	0.73	0.46	0.33

As shown in Table 1, the calculated equilibrium constants indicate that:

(1) Gasification is in favour of high temperature to promote complete conversion of carbon. High temperature facilitates the production of H_2 and CO instead of CO_2.
(2) With sufficient supply of oxygen, the reactions tend to produce more CO than CO_2. The CO_2 formation is only subject to the energy balance.
(3) At reaction temperature above 1,200K, CH_4 production can be eliminated.

Based on the above analysis, the question is whether the Gibbs free energy of the product gas can be simultaneously minimized while maximizing CGE. In order to ascertain this, Eq. (1) is removed from the developed equilibrium model to form a "simultaneous model". The simultaneous model is used to maximize CGE at a specific reaction temperature between 1,000K to 1,800K by varying oxygen and steam feed at 1 bar pressure. The reaction pressure is fixed since it should not have a strong influence to the product yield or composition. The elevated pressure in commercial gasifiers was mainly for reducing equipment size (Phillips, 2006).

At each reaction temperature, the optimized feed rates from the simultaneous model are used as inputs to the equilibrium model that minimizes Gibbs free energy. Reaction temperature is recalculated from the equilibrium model and compared to that from the simultaneous model. As shown in Figure 2, results (reaction temperature) from both models are identical when reaction temperature above 1,400K. These results are verified by Aspen Plus Gibbs reaction model.

The tests indicate that when the reaction temperature is above 1,400K, maximizing CGE will simultaneously minimize the Gibbs free energy of the product gas. This observation greatly simplifys the solution procedure. Having the reaction temperature at above

1,400K also coincide with the latest commercial entrained-flow coal gasifiers that are operated at 1,473 K-1,873 K (Collot, 2006).

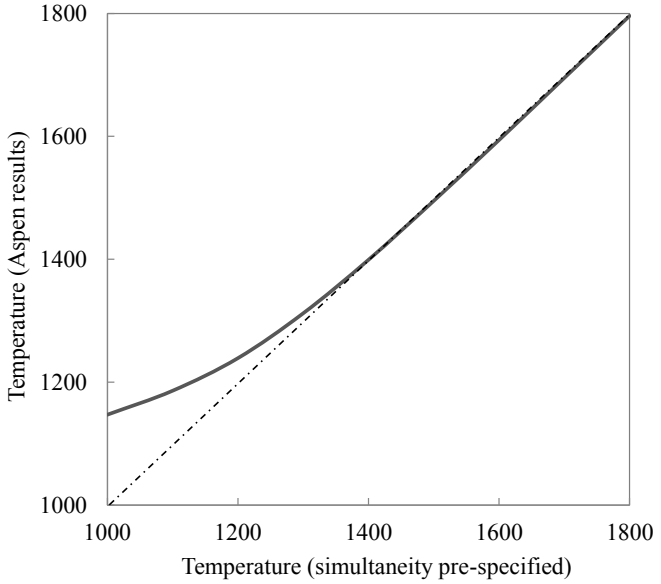

Figure 2. Temperature profile of simultaneous model and equilibrium model.

On the other hand, sensible heat utilization is evaluated between feed preheating and steam generation. Ensuring feasible heat integration imposed new constraints to the problem. The model of heat integration ensures the feasibility of heat transfer. In this work, the simultaneous optimization model proposed by Duran and Grossmann (Duran and Grossmann, 1986) is applied to simultaneously optimize the gasification process and the amount of energy recovery. The model is modified to accommodate process streams with phase change.

5. Case study

The feeding rate of coal (with 100% carbon) is fixed at 10,000 kg/h and reacts with oxygen and GFW at 1 bar. HP steam is produced at (832 K, 125 bar) for export and the cooled syngas is utilized for electricity generation in combined cycle. Minimum approach temperature of heat exchange is set at 10K. Two cases are presented in the following sections. Case 1 shows the approach to identify optimum feed flow rates and reaction temperature by iteration. In Case 2, flow rates as well as stream temperatures are optimized simultaneously with consideration of heat integration. The heat integration model is considered in Case 2 to ensure the feasible heat recovery.

5.1. Case 1

In this case, the optimization is conducted with gasification temperature ranging from 1,273 K to 1,873 K. An iterative approach is applied to maximize CGE by varying the feed flow rates while Gibbs free energy is minimized. Reaction temperature is converged at 1,273 K with feeding 3,909 kg/h GFW and 10,009 kg/h O_2. The highest CGE reaches 87.11%. Since require iteration, the solution process is slow and easily trapped at local optimum.

To further study the gasification, O_{H2O}/C vs CGE in two typical temperatures are plotted in the Figure 3. As shown in it, the highest CGE for each operating temperature appears at the carbon conversion turning point where the carbon happens to be completely converted. Before or after it, CGE has a lower value due to the negative effects brought by the wasted carbon residue or the excessive GFW respectively. Because in the equilibrium model, the higher operating temperature means the more energy is wasted on raising the temperature. Therefore, the optimizations converged at the allowed lowest temperature, 1,273 K, which saves the most heat.

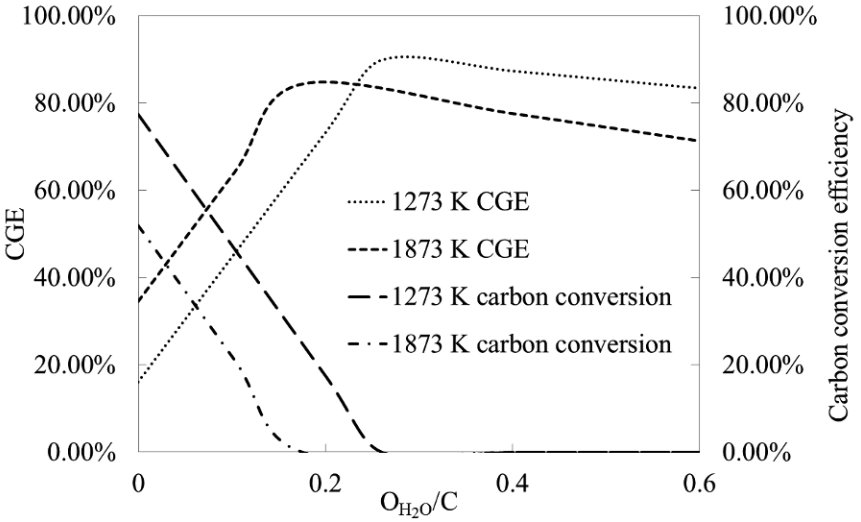

Figure 3. CGE and carbon conversion efficiency at 1,273 K and 1,873 K

5.2. Case 2

The flow rates of gasification process are optimized directly through simultaneous model while the sensible heat recovery through feed preheating as well as HP steam generation is also considered. The gasification temperature is allowed to be varied between 1,673 K and 1,873 K. Considering reasonable endurance of heat exchanger (Gupta et al., 1999), we set the related temperature limits as shown in Table 2.

Table 2. Parameters of the heat integrated gasification process.

Parameters	Lower temperature limit (K)	Upper temperature limit (K)
O_2	298	700
GFW	298	700
Gasification temperature	1673	1873

Optimum solution of Case 2 is shown in Figure 4 where 9,863.73 kg/h O_2 and 3,903.29 kg/h GFW are fed and preheated to 700 K. Reaction temperature is converged to 1,673 K with CGE reaches 87.95%. The difference comes from the higher feed temperatures which are both optimized at 700 K. As a result, O_2 supply is reduced dramatically to 9,863.73 kg/h. Meanwhile, due to the lower oxygen feed, more GFW is fed that resulted in more H_2.

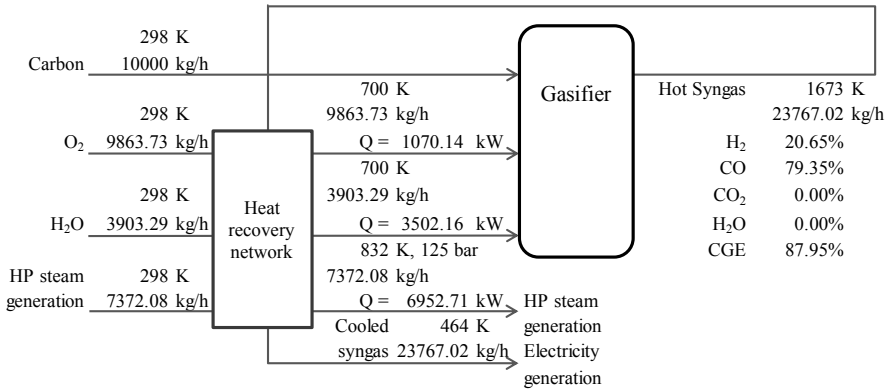

Figure 4. Process flowsheet of Case 2.

6. Conclusion

Effectively utilize the sensible heat from the syngas for feed preheating or steam generation can reduce oxygen demand and improve the overall gasification performance. In this study, a novel model is formulated to simultaneously optimize the gasification conditions, flow rates and preheating levels of the feeds and the utilization of the hot syngas. When reaction is at temperatures above 1,400K, maximizing CGE automatically results gas products with minimum Gibbs free energy. This observation reduces the complexity in solving the bi-level optimization problem and reduces the chances of being trapped at local optimum. The gasification model is integrated with a heat integration model that guarantee feasible reaction on one hand and optimize the feed flow rates and preheating levels on the other. Case studies have demonstrated the effectiveness of the integrated model.

Acknowledgements

The authors gratefully acknowledge the support from Hong Kong RGC -GRF grant (613513) and the UGC-Infra-Structure grant (FSGRF13EG03).

References

A. Abuadala, I. Dincer, G. Naterer, 2010, Exergy analysis of hydrogen production from biomass gasification, International Journal of Hydrogen Energy, 35, 10, 4981-4990.
A. G. Collot, 2006, Matching gasification technologies to coal properties, International Journal of Coal Geology, 65, 3-4, 191-212.
A. Gupta, S. Bolz, T. Hasegawa, 1999, Effect of air preheat temperature and oxygen concentration on flame structure and emission, Journal of energy resources technology, 121, 3, 209-216.
J. Phillips, 2006, Different types of gasifiers and their integration with gas turbines, The gas turbine handbook.
M.A. Duran, I.E. Grossmann, 1986, Simultaneous optimization and heat integration of chemical processes, AIChE Journal, 32 , 1, 123-138.
M.L. de Souza-Santos, 2004, Solid fuels combustion and gasification: modeling, simulation, and equipment operations, CRC Press.
S. Clayton, J. Childress, G. J. Stiegel, 2007, Gasification World Database 2007: Current Industry Status, National Energy Technology Laboratory.
X. Li, J. Grace, A. Watkinson, C. Lim, A. Ergüdenler, 2001, Equilibrium modeling of gasification: a free energy minimization approach and its application to a circulating fluidized bed coal gasifier, Fuel, 80, 2, 195-207.

Krist V. Gernaey, Jakob K. Huusom and Rafiqul Gani (Eds.), 12th International Symposium on Process Systems Engineering and 25th European Symposium on Computer Aided Process Engineering.
31 May – 4 June 2015, Copenhagen, Denmark

Analyzing and Modeling Ethylene Cracking Process with Complex Networks Approach

Zhou Fang, Tong Qiu*, Bingzhen Chen

Department of Chemical Engineering, Tsinghua University, Beijing, China
** Corresponding author: Tong Qiu. qiutong@tsinghua.edu.cn.*

Abstract

This paper focus on understanding the ethylene cracking reaction (ECR) networks with complex networks approach to polish up the accuracy of the product prediction. Though the radical reaction model (Ranzi, 2005) has been widely used in industrial simulations of pyrolysis process by SPYRO for years, analysis of the reaction scheme is still one of the important subjects the scholars concerned. According to the radical kinetic scheme, a simulation system of the ethylene cracking process has been developed include the feedstock reconstruction model, detailed kinetic schemes generator, and the reactor simulation model. As the complex networks research has grown steadily for its potential to represent, characterize and model a wide range of intricate natural systems and phenomena, a modified PageRank algorithm is applied to represent the topological structure and dynamic system characteristic of ECR networks. As a result, the hubs and authorities in reaction networks are illustrated by the algorithm and correction coefficients derived from these hubs is applied in detailed kinetic schemes generator. The product yield the adjusted model predicted is verified in an industrial case of naphtha pyrolysis process which shows a reasonable match with the industrial data. Furthermore, the simplification of kinetic scheme by PageRank algorithm has also shown in this case.

Keywords: Complex network, Reaction model, PageRank algorithm, Naphtha pyrolysis

1. Introduction

The accurate mathematic model applied in simulation of ethylene cracking process is appreciated in the industry. Though the molecular reaction model (Kumar, 1985) and lumped reaction model are introduced for the petrochemical industry, these crude models can't afford the description of the real kinetic mechanism. Recently, the radical reaction model (Dente et al., 2007) has made great progress in the pyrolysis reaction simulation and the SPYRO software adopting the reaction network generated by the radical model is applied in practical industrial process. Unfortunately, the complexity and scale of the reaction scheme built by detailed reaction mechanism still impede the calculate speed of the whole simulation with different reactor geometry and the operating condition. The lumping procedures and the automatic generation (Dente et al., 2010) are used in the radical kinetic schemes created by the SPYRO. Apart from the lumping methods derived from the chemical mechanism, the mathematic analysis methods such as the sensitivity analysis, principal component analysis (PCA), asymptotic theories, and computational singular perturbation (CSP) are applied in reaction scheme simplification. To sum up, the major difficulties in kinetic schemes generation not only lie in the large amount of reactions and parameters it contained but also in the complexity of the corresponding dynamic system. The main focus of this paper is to analyse the characteristics of the detailed kinetic schemes by transforming

the reaction networks into visualized graph and apply the graph algorithm to assist the generation and simplification of the detailed kinetic schemes. Besides the analysis, a whole simulation model of the naphtha pyrolysis with three function modules is also developed in this work.

2. Simulation Model

To establish the simulation model of the pyrolysis process, this paper builds the feedstock reconstruction model, detailed kinetic schemes generator with both reaction networks and corresponding kinetic parameters, and the reactor simulation model. The flow chart of the whole simulate model is shown in Figure 1.

2.1. Feedstock reconstruction model

The feedstock reconstruction approach discussed in this work uses the probability distribution function (Steven P. Pyl et al, 2011) to model the composition of the complex oil fractions. The molecular composition of petroleum fractions is calculated by Shannon entropy optimization with the bulk property of the feedstock including average molecular weight, H/C ratio, density, true boiling point distillation curve, and PINA group number as Figure 1 shows.

2.2. Detailed kinetic schemes generator

The radical reaction mechanism plays the most important role in the thermal degradation of the hydrocarbon. For pyrolysis process, radical chain propagation mechanism can be classified as 5 types of reaction: Initiation, H-Abstraction, Isomerization, Beta-scission, and Termination reactions. Therefore, the reaction kinetic parameters used in this paper are referenced from the literature (Dente 2007, Ranzi 2005). As the manual generation of the whole set of reactions becomes intractable, especially when the hydrocarbon molecular weight is increased, an automatic generator of the reaction scheme is introduced in structuring the radical reaction networks with the estimated kinetic parameters.

2.3. Reactor simulation model

Considering the geometry of tubular cracking furnace, the one-dimension reactor model is established to simulate transfer and reaction process. Then the ordinary differential equations (ODEs) is solved by GEAR Methods. In addition, the zone method (Vercammen, 1980) combined with the Monte-Carlo Integral method is utilized in calculating the radiative transfer heat of the tubular reactor furnace. This set of ordinary differential equations (ODEs) are given by

$$\frac{dN_m}{dL} = \frac{S}{V}\sum_i v_{im} r_i = f_N\left(T, P, N_m\right) \tag{1}$$

$$\frac{dT}{dL} = \frac{Q - \sum_m \Delta H^0_{fm} \frac{dN_m}{dL}}{\sum_m C_{pm} N_m + C_{pH_2O} N_{H_2O}} = f_T\left(Q, P, N_m\right) \tag{2}$$

$$\frac{dP}{dL} = f \frac{W_g G^2 \times 10^{-4}}{19.62 \times D_i \rho} = f_P\left(T, P, N_m\right) \tag{3}$$

Where L is the length of the reaction tube; N_m is the concentration of substance m in reaction tube; S is the flow area of reaction tube; V is the volume flow rate of the gas in reaction tube; v_{im} is the stoichiometric coefficient of substance m in reaction i; r_i is the

reaction rate of reaction i; T is the temperature in the reaction tube; Q is heat transfer by the furnaces; ΔH^0_{fm} is the standard enthalpy of formation of substance m; C_{pm} is the heat capacity at constant pressure; P is the pressure in reaction tube; f is the frictional factor; W_g is the equivalent length of reaction tube; G is the mass flow rate of the gas in reaction tube; D_i is the inner diameter of reaction tube; ρ is the density of the gas in reaction tube.

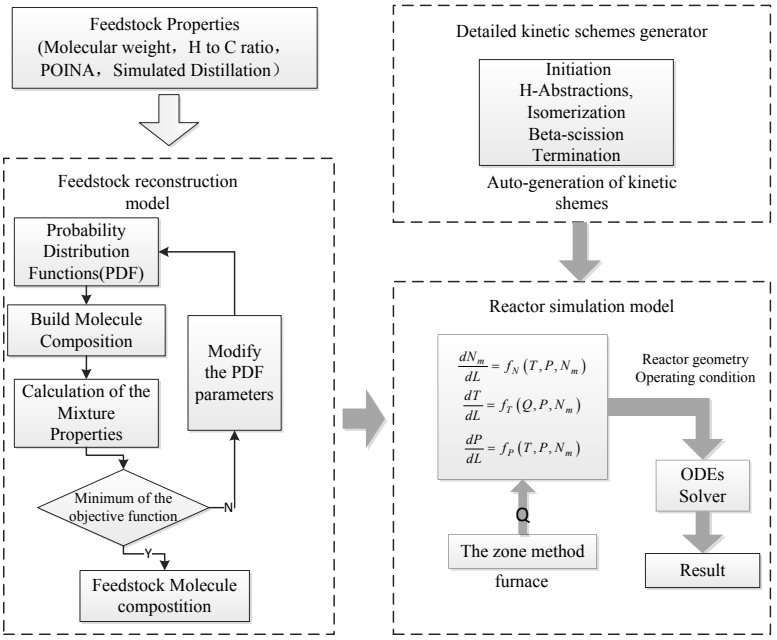

Figure 1 Flow chart of cracking process simulation

3. Reactions Networks Analysis

Most goals of reaction network analysis (both mathematic and chemical approaches) are to clarify the nature of intermediates and correlative reactivity principle. However within a kinetic schemes (reaction networks), the topological and chemical components are logically interrelated and can't be considered separately. Therefore, it is necessary that graph theory takes a view of the chemical mechanism as a graph-like structure.

First, the reaction networks are transformed into the petri-net which links the places (the set of substances) with the transitions (the set of reactions).With the petri-net model, the kinetic schemes can be written as a graph matrix as well. The kinetic parameters are calculated into the weight of the edge as the element in the matrix (Figure 2).

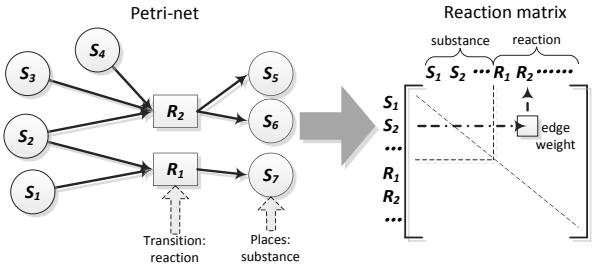

Figure 2 Petri-net model and the reaction matrix

Recently, facing the intricacy of the complex networks, most algorithms are focus on the topology of the undirected graph which can't express the dynamic system feature. The PageRank algorithm (L. Page, 1998) is widely used in the analysis of the direct graph and PageRank works by counting the number and quality of links to a nodes to determine an estimate of how important the nodes is. The nodes with high PageRank (PR) value could be the hubs or authorities in the graph. The core idea in PageRank is present the probability distribution of a random walk on the graph. Intuitively, this can be thought of as modeling the behaviour of a "random surfer". Because of the directed driving force in the ethylene cracking dynamic system is different from "random surfer", we improve the PageRank algorithm by adding the Markov process of reaction rate into the edge weight of graph and calculates the transfer matrix of PageRank with the edge weight. Moreover, for the reactions begin with the feedstock, the initial values of PR vector should correspond to the feedstock fractions. To sum up, the modified PageRank may be computed as follows:

S1: Set the initial value of the Page Rank vector $\bar{P}_0$:

$$\bar{P}_0(S_i) = \frac{C(S_i)}{\sum_{S_i} C(S_i)} \tag{4}$$

Where S_i is the composition of the feedstock; $C(S_i)$ is concentration of S_i;

Loop:

S2: Calculate the transfer Matrix A of the reaction system:

$$A(reactant, reaction) = r_{reactant} \cdot V_{reaction} \tag{5}$$

$$A(reaction, resultant) = r_{resultant} \cdot V_{reaction} \tag{6}$$

$$V_{reaction} = \frac{\sum_i rate_{\Delta L_i} \cdot \Delta L_i}{\sum_i \Delta L_i} \tag{7}$$

Where $r_{reactant}$ is the stoichiometric number of the reactant; $r_{resultant}$ is the stoichiometric number of the resultant; $V_{reaction}$ is reaction rate of the reaction, calculated by Eq.(7); $rate_{\Delta Li}$ is reaction rate in the infinitesimal section ΔL_i of reactor;

S3: Calculate the PageRank vector $\bar{P}_{k+1}$:

$$\bar{P}_{k+1} = \alpha A \cdot \bar{P}_k + \frac{1-\alpha}{N} \tag{8}$$

S4: Calculate the error δ

$$\delta = \left\| \bar{P}_{k+1} - \bar{P}_k \right\|_1 \tag{9}$$

While: $\delta > \varepsilon$

After every simulate process, the PR value is calculated to state the importance of the nodes including both reactions and substances. Though the PR values has already revealed the character of the reaction networks and information of the simulate process, these values can be applied to adjust the kinetic networks as well. In the yield data the model simulated, some errors will inescapably occur compared with the data from the industry. To fix these errors, the algorithm establishes a reaction queue for each product.

Within the queue, the reactions related to the product are chosen and sorts the queue by the PR value. Two type of the reactions can be in the queue as Figure 3 shows:
1-degree reaction: the reactions link to the object product.
2-degree reaction: the reactions link to the resultant or reactant of the 1-degree reaction
The corrected coefficients $\bar{A}_i$ of the reaction i is calculate with the error between the industrial data and the simulate result following the queue to adjust the kinetic schemes.

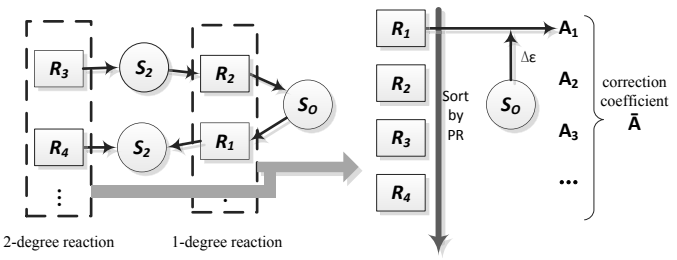

Figure 3 Calculation of correction coefficient $\bar{A}_i$

4. Case result

An industrial cases of naphtha pyrolysis from a petrochemical plant is used to testify this model. The generator establishes the original kinetic schemes with 4694 reactions and 142 substances. Then, these substances and reactions in the networks has been sorted by the modified PageRank algorithm as Figure 4 shows. The radical molecule and the cracking product are chosen as the vital nodes of the networks by the algorithm and the reactions contain these the hubs are considered positive in the react process.

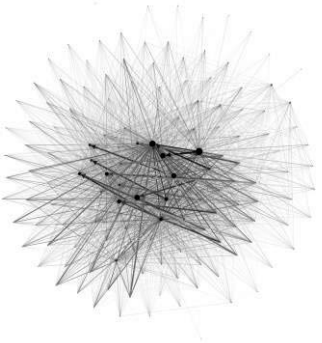

Reactions:

1*C_2H_5·+1*C_2H_4>1.0*C_2H_3·+1.0*C_2H_6 (0.0364)
1*H_2O+1*H·+1*C_2H_4>1.0*H_2O+1.0*C_2H_5·(0.0259)
1*C_3H_6>1.0*H2+1.0*AC_3H_4 (0.0144)
1*H_2+1*SC_4H_7·>1.0*H·+1.0*NC_4H_8 (0.0137)
1*CH_2CHCH_2·+1*C_2H_6>1.0*C_2H_5·+1.0*C_3H_6 (0.0120)
1*H·+1*C_2H_6>1.0*H_2+1.0*C_2H_5· (0.0112）
1*NC_4H_9P·+1*C_2H_4>1.0*NC_3H_7·+1.0*C_3H_6 （0.0109)
1*CH_4+1*CH_2CHCH_2·>1.0*CH_3·+1.0*C_3H_6 (0.0103)

Substances:

C_2H_4(0.0507) C_2H_5·(0.0374) CH_3·(0.0317)
CH_4(0.0310) H·(0.0292) H_2(0.0278)
C_2H_6(0.0273) C_3H_6(0.0213) C_2H_3·(0.0188)

Figure 4 The PageRank value graph and the PR values

The correction coefficients derived from model are applied in the kinetic scheme generation which polishes up the accuracy of the product prediction. The product yields of the adjusted kinetic scheme obtained by reactor simulation model are shown in Table 1. To test the reduced function of the algorithm, a kinetic scheme with 4622 reactions is also simulated in the industrial process. The reduced scheme is simplified by picking off the reactions with lower PageRank value on the basis of the adjusted scheme. The product yields are also shown in Table 1. Furthermore, the average relative error of the product yield of adjusted kinetic and the reduced scheme is 6.05%. The error is acceptable considering the scale of the original networks which has been reduced by pseudo steady state assumption (PSSA).

Table 1 Product yields with the different reaction kinetic

product yield	original kinetic scheme	adjusted kinetic scheme	reduced kinetic scheme	industrial data
H_2	1.68	1.39	1.3612	1.04
CH_4	13.02	15.42	14.3669	16.22
C_2H_4	27.10	30.48	30.1434	30.22
C_2H_6	3.51	3.82	3.6171	3.76
C_3H_6	17.80	15.60	15.3924	16.26
C_4H_6	5.70	5.97	5.334	5.94
n-C_4H_8	2.36	1.76	1.6143	1.46
i-C_4H_8	4.69	3.19	3.1095	2.69
i-C_4H_{10}	0.30	1.08	0.9948	1.01

5. Conclusions

In this paper, the simulate model for pyrolysis process was established, including feedstock composition reconstruction model, detailed kinetic schemes generator and reactor simulation model. As the literature referenced kinetic schemes is inappropriate in some specific cases, the modified PageRank algorithm has been applied to adjust the kinetic scheme. The result of this algorithm demonstrates that the hubs and authorities in the networks contribute significantly to the simplification of the reaction networks. To modify the networks, these hubs and authorities are treated preferentially and the kinetic scheme with corrected coefficients has more accurate prediction of product yield compared with industrial data. The method to adjust model could be expected to be applied in future simulation of industrial ethylene cracking furnace. In addition, the simplification of the kinetic scheme could be assist by the algorithm as well.

References

E. Ranzi, A. Frassoldati, S. Granata, and T. Faravelli, 2005, Wide-Range Kinetic Modeling Study of the Pyrolysis , Partial Oxidation , and Combustion of Heavy n-Alkanes, Ind. Eng. Chem. Res., 44, 14: 5170-5183.

M. Dente, G. Bozzano, T. Faravelli, A. Marongiu, S. Pierucci, E. Ranzi, 2007, Kinetic Modeling of Pyrolysis Processes in Gas and Condensed Phase, Advances in Chemical Engineering, 32: 51-166.

P. Kumar, D. Kunzru, 1985, Modeling of Naphtha Pyrolysis, Ind. Eng. Chem. Process Des., 24, 3: 774-782

Dente Mario, Ranzi Eliseo, Bozzano Giulia, Kleinendorst Sauro Pieruccia Florian I., van Goethem, Marco W.M., 2010, Pyrolysis of naphtha feedstocks: Automatic generation of detailed kinetics and lumping procedures. Computer Aided Chemical Engineering, 28:823-828

Steven P. Pyl, Zhen Hou, Kevin M. Van Geem, Marie-Franc-oise Reyniers, Guy B. Marin, Michael T. Klein, 2011, Modeling the Composition of Crude Oil Fractions Using Constrained Homologous Series, Ind. Eng. Chem. Res., 50:10850-10858

Vercammen, H.A.J. and G.F. Froment, 1980,An improved zone method using Monte-Carlo technigues for the simulation of radiation in industrial furnaces. International Journal of Heat and Mass Transfer,.23, 3: 329-337.

L. Page, S. Brin, R. Motwani, and T. Winograd, The pagerank citation ranking: Bringing order to the Web, Technical Report; Stanford University, 1998.

Krist V. Gernaey, Jakob K. Huusom and Rafiqul Gani (Eds.), 12th International Symposium on Process Systems Engineering and 25th European Symposium on Computer Aided Process Engineering.
31 May – 4 June 2015, Copenhagen, Denmark

Optimization and Economic Evaluation of Bioethanol Recovery and Purification Processes involving Extractive Distillation and Pressure Swing Adsorption

Y.Y. Loy[a, b], X.L. Lee[a], G. P. Rangaiah[a*]

[a]*National University of Singapore, Department of Chemical & Biomolecular Engineering, 4 Engineering Drive 4, Singapore 117585*
[b]*Lloyd's Register Global Technology Centre Pte. Ltd., 1 Bukit Batok Street 22, #03-03B Singapore 659592*
chegpr@nus.edu.sg

Abstract

Biofuels are an attractive source of renewable energy as they can easily replace liquid fuels used in transportation and other machinery. The present study considers typical feed of ethanol-water-CO_2 from which ethanol is recovered and purified using two popular techniques: pressure swing adsorption with molecular sieves and extractive distillation using ethylene glycol. Heat integration in both processes is performed to ensure a fair basis for evaluation. Optimal separation cost is found to be US$0.1394/kg and US$0.1185/kg for the extractive distillation and pressure swing adsorption process, respectively. Hence, fuel-grade ethanol production via pressure swing adsorption with 15% lower separation cost is better than extractive distillation using ethylene glycol.

Keywords: Bioethanol; Cost of manufacture; Extractive distillation; Optimization; Pressure swing adsorption

1. Introduction

Fossil fuel reservoirs are depleting rapidly and are unsustainable in the long run. Rising environmental concerns have also motivated the search for cleaner fuel alternatives. Among the different types of renewable energies, bioenergy is interesting since biofuels can directly substitute liquid fuels used in transportation and other machinery (Sunggyu, 2006). Production of bioethanol in the world, with more than half of it in US and Brazil (Chum et al., 2013), still relies on 1st generation biofuel crops since technologies to produce from 2nd and 3rd generation crops are relatively immature and difficult to control (McAloon et al., 2000).

Bioethanol concentration in the fermentation broth is about 10 wt% whereas fuel grade ethanol can be up to 99.8 wt% pure. Atmospheric distillation is used for preliminary recovery of bioethanol to various degrees of concentration depending on the process design. Ethanol and water form an azeotrope mixture of 95.6 wt% of ethanol at 1atm and 78.15°C. Hence, to further purify bioethanol, the industry employs either of the common techniques: pressure swing adsorption (PSA) using molecular sieves and extractive distillation (ED) using ethylene glycol (EG). Publications in the last decade have focused mainly on evaluating the amount of energy consumed for recovery and separation of ethanol without regards to economic feasibility. Recently, Kiss and Ignat

(2012) studied and optimized ED and extractive dividing-wall column (E-DWC) processes by minimizing the total heat duty of the distillation sequence. For this, they have simulated the processes using a binary feed of ethanol-water, which does not accurately reflect separation cost of a multi-component feed. Roth et al. (2013) made an economic evaluation of hybrid processes involving distillation, molecular sieve adsorption and membrane separation, but their work focused on purification starting from ethanol concentration of 45, 80 and 92 wt%, without optimization.

In this paper, ED and PSA processes are designed and compared, on a consistent basis, for recovery and purification of bioethanol from a typical mixture of ethanol-water-CO2 from the fermenter. Unit separation cost derived from the cost of manufacture (COM) is used as the objective function, to determine the competitive process. Heat integration is taken into account through feed pre-heating and use of mechanical vapor recompression (MVR), if applicable.

2. Literature Review

After pre-concentration of bioethanol by distillation, further purification can be achieved through adsorption using molecular sieves of pore diameter 3Å (3A zeolites) since water molecules are roughly 2.5Å in diameter (Kumar et al., 2010). Molecular sieve properties from ZEOCHEM are used for modelling in this study. Strength of adsorption of target molecules in molecular sieves depend strongly on temperature and pressure; water molecules are adsorbed at high pressures and low temperatures, and regenerated at low pressures and high temperatures (Sowerby and Crittenden, 1988). Alternatively, ED can be used for purification after pre-concentration. A relatively non-volatile liquid solvent is fed into the column to alter the volatility of one of the components in order to improve separation and overcome azeotrope point. The solvent, which accumulates in the column bottoms, is recovered and recycled using an additional column. Among the commonly used liquid solvents as extractive agents for ethanol-water system are EG, diethyl ether, toluene and furfural (Kumar et al., 2010). ED using EG has favorable features such as high product quality, suitability for large scale production and relatively low volatilization amount. However, large amount of solvent is required to achieve the purity requirement of fuel-grade ethanol, resulting in high energy consumption for the recovery process (Kumar et al., 2010).

3. Process Specifications and Simulation Methodology

More than 15 components are present in the bioethanol-water solution produced by sugar fermentation. Many of these components exist in very small quantities, and can be neglected as they would not have substantial impact on distillation/separation. For simplicity, only 3 major components are considered in the feed for this simulation: CO_2, ethanol and water. According to Moncada et al. (2013), “beer” formed in a sugarcane biorefinery contains 7-10 wt% ethanol. After considering future improvements to fermentation, feed composition used in this work is 10 wt% ethanol, 0.1 wt% CO_2 and 89.9 wt% water. Assuming overall recovery of at least 0.99 of ethanol in the feed and plant operation of 8,250 hours/year, the required feed mass flow rate can be calculated.

For bioethanol to be used as fuel, its moisture content is subjected to a maximum limit to prevent corrosion of the machinery interior. The maximum allowable water is 0.2 vol% in Europe (CSN EN 15376, 2011), 2.0 vol% in Brazil (Resolucao ANP No. 7, 2011) and 1.0 vol% in USA (ASTM D4806-11, 2011). Considering these standards,

purity of ethanol is taken to be 99 wt%. At the same time, CO_2 concentration in the product is reduced to less than or equal to 100 ppm. Production capacity is based on the sizes of bioethanol plants that can be found in the industry. In the 2012 industry outlook report, the Renewable Fuels Association (RFA, 2012) listed the production capacities of all fuel ethanol plants in USA; these data show that annual production volumes are concentrated around 2 values: 50 (medium scale) or 100 (large scale) million gallons (equivalent to 189,270m^3 and 378,541m^3). Rounding up, the production volume used in this work is 200,000 m^3. The final product is depressurized to 1 atm and cooled to 40^{o}C.

In this study, Aspen HYSYS v8.2 is used for simulating and optimizing the two separation processes. Aspen Properties NRTL-RK model is chosen to describe ethanol-water-CO_2 system since it gives better estimates for important intensive properties of the components involved. For ED, presence of EG requires additional validation of this model, and it is checked against the recently published experimental isobaric VLE data of the ternary system. The binary interaction parameters (BIPs) have been refitted with values as correlated by Pla-Franco et al. (2013). The form of equation used to describe the temperature-dependency of dimensionless asymmetric interaction parameter, τ_{ij} in Aspen Properties is different from the form used by Pla-Franco et al. (2013).

Form of equation used by Pla-Franco et al.: $\tau_{ij} = \frac{A_{ij}+B_{ij}T}{RT}$ (1)

Form of equation used by Aspen Properties: $\tau_{ij} = a_{ij} + \frac{b_{ij}}{T}$ (2)

In Eq.(1), R is the gas constant (= 8.314J/mol-K), and A_{ij} has units of J/mol while B_{ij} has units of J/mol-K. In Eq.(2), a_{ij} is dimensionless, while b_{ij} has unit of K. By comparing Equations 1 and 2, $a_{ij} = \frac{B_{ij}}{R}$ while $b_{ij} = \frac{A_{ij}}{R}$. The adjusted values closely agree with the experimental data with very low average absolute deviation for both vapor mole fractions and temperature.

Although many unit operations are readily available in HYSYS, PSA module is not one of them because this simulator does not normally deal with pseudo-continuous processes. However, it is possible to treat PSA separation as a fully continuous process by using a component splitter for PSA unit in the simulation model. The component splitter allows the user to define pressure and temperature of each outlet, thus it is possible to simulate column pressure drop, vacuum conditions needed to regenerate the molecular sieves, as well as temperature changes due to heat of adsorption. As recommended by ZEOCHEM, a 2-bed PSA system is used in this study. Each bed has a 16 min cycle split equally for adsorption and regeneration. The adsorption and desorption pressures and temperatures are decision variables for optimization. Using Excel and defining constraints in the optimizer, the simulator interacts with the spreadsheet containing molecular sieve isotherm data, allowing the PSA system to be fully defined. An excess of molecular sieves is used to provide processing margin, considering the mass transfer zone (breakthrough curve) in the PSA column.

4. Results and Discussion

The objective function is to minimize the separation cost per unit of fuel ethanol produced, subject to the product purity constraint. It is dependent on decision variables such as pre-concentrator feed temperature, CO_2 concentration level after pre-concentration, feed/recycle/side-draw stages, number of trays, and distillate and bottoms

purity of each distillation column. Feasible boundaries are defined for each variable to avoid non-convergence of simulation and lengthy computational time. The choice between the use of a vapour or liquid side draw is also investigated to understand its impact on separation cost. The in-built optimizer of Aspen HYSYS v8.2 is used to optimize the separation process, using sequential quadratic programming method as the solver since it can handle both equality and inequality constraints.

The model layouts for each system simulated are shown in Figures 1 and 2. Preliminary analysis indicated having only one pre-concentrator column (PDC) is better for EG process; followed by an extractive distillation column (EDC) and solvent recovery column (SRC). On the other hand, PSA process requires two columns (DC1 and DC2) for concentration; this is related to the choice of liquid or vapour side-draw from column, which affects overall energy demand. All equipment in each of the processes is sized according to established design practices, simulation data and results. COM can be determined using Eq.(3) after estimating the following costs: fixed capital investment (FCI), cost of operating labor (C_{OL}), cost of utilities (C_{UT}), cost of waste treatment (C_{WT}) and cost of raw materials (C_{RM}) (Turton et al., 2013).

$$\text{COM (US\$/year)} = 0.280\ \text{FCI} + 2.73\ C_{OL} + 1.23\ (C_{UT} + C_{WT} + C_{RM}) \quad (3)$$

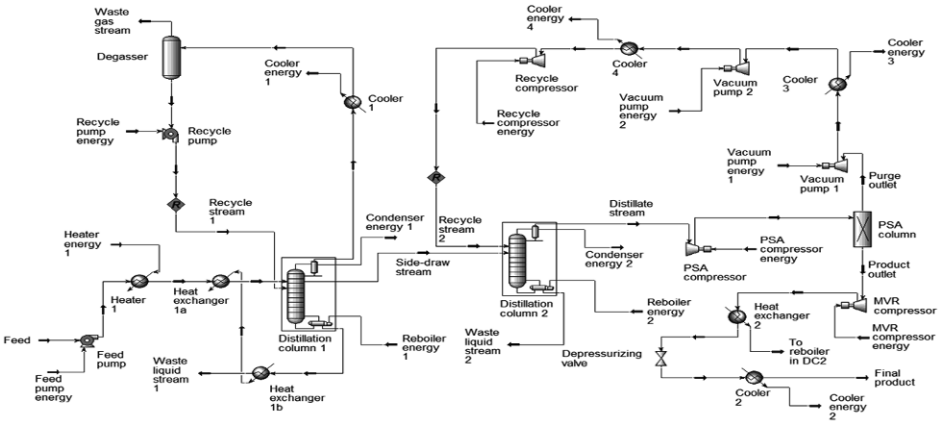

Figure 1: Aspen HYSYS model layout for PSA process

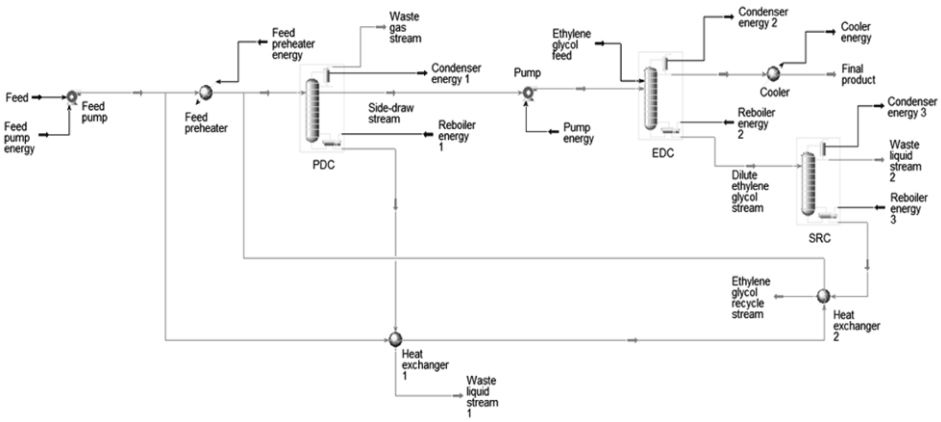

Figure 2: Aspen HYSYS model layout for ED using EG process

Here, depreciation allowance of 0.10 FCI is taken into account but waste treatment and raw materials costs are not considered in this work. Unit separation cost is calculated by dividing COM by ethanol produced (kg/year), for minimization. Optimal separation cost obtained for PSA process is US$0.11854 with ethanol recovery rate of 99.7%, whereas that for E*D using EG process is US$0.13938* with ethanol recovery rate of 99.6%. Clearly, recovery and purification using the PSA proc*ess is more advantageous at 15*% lower cost and slightly higher recovery rate. This is *more* significant *at higher production capacities; that which is considered in this work is* of a medium-size fuel ethanol plant, and so the difference in unit separation cost is likely to increase for large plants. Optimal values of parameters of both processes are shown in Table 1.

Table 1: Optimal values of process parameters of PSE and ED processes

Process parameters	**PSA**		**ED using EG**		
	DC1	**DC2**	**PDC**	**EDC**	**SRC**
Number of stages	35	38	50	57	23
Feed stage	4	16	18	32	6
Recycle stage	1	15	-	-	-
Side-draw stage	7	-	2	-	-
Distillate purity (wt%)	54.7	92.6	90.9	99.8	0.14
Bottoms purity (wt%)	0.01	0.01	0.02	0.02	0.00
Feed temperature (^oC)	90.0	-	98.71	-	-
CO_2 concentration (ppm)	-	100	-	50	-
Heat energy demand (GJ/h)	106	17	111	34	17

4.1. Cost Savings from Lower Energy Demand and MVR

Thermal energy demand for the PSA process is 122.7 GJ/h, which is 24.3% lower than that for the ED using EG process which requires 162.1 GJ/h. One reason for this is the lower distillate purity required in the PSA process since it is cheaper to use molecular sieves for purification from 92.6 wt% to 99 wt%. In addition, ED process requires energy to recover EG. Another factor that lowered the separation cost of the PSA process is the use of MVR for additional heat integration. As shown in Table 2, although capital cost has risen by US$1 million because of the additional compressor, operating cost has dropped by US$1.2 million/y. Annualizing capital cost over 10 years (10% depreciation), net cost savings from MVR is US$1.1 million/y or 2.4% of COM. However, cost savings from MVR depends on the relative cost of steam and electricity; locations with high electricity cost will not reap any benefits. Further, compressor operation is challenging in most plants. Nevertheless, even without MVR, separation cost using PSA process is 12.6% lower than that for ED using EG.

Table 2: Summary of cost savings from MVR

Capital cost			
Additional equipment		**Removed equipment**	
MVR compressor	US$2,050,700	**Heat exchangers**	US$1,041,300
Total increase in capital cost		US$1,009,400	
Operating cost			
	LP steam	**Cooling water**	**Electricity**
Cost per unit (Turton et al., 2013)	US$29.29/1000 kg	US$14.80/1000 m^3	US$0.06/kWh
Quantity required	-	-	921.8 kWh
Quantity reduced	6,855 kg	89.8 m^3	-
Total reduction in operating costs		US$1,211,100/yr	

5. Conclusions

In this paper, separation cost to produce fuel-grade ethanol by two common industrial processes is studied and compared on a consistent basis. It is found that, for a ternary system of ethanol-water-CO_2, it is less costly to produce fuel-grade ethanol with PSA rather than ED using EG. The optimal separation cost of fuel-grade ethanol is 15% lower at US$0.11854/kg for the PSA process. This is because the PSA process requires 24.3% lower energy demand, partly due to the additional energy required to recover EG in the ED process. Furthermore, the integration of MVR in the PSA process contributed to additional savings of about 2.4% of COM. Therefore, in order for ED to become competitive against PSA, the use of a dividing-wall column can be considered for reducing energy demand in the overall process.

References

Agencia Nacional de Petroleo, 2011, DE 9.2.2011 – DOU 10.2.2011 – Retificada dou 14.4.2011, Gas Natural e Biocombustiveis, Resolucao ANP No. 7.

ASTM International, 2011, Standard specification for denatured fuel ethanol for blending with gasolines for use as automotive spark-ignition engine fuel, ASTM D4806-11.

H. L. Chum, E. Warner, J. E. Seabra, I. C. Macedo, 2013, A comparison of commercial ethanol production systems from Brazilian sugercane and US corn, Biofuels, Bioprod. & Bioref, 8, 205.

European Standards, 2011, Automotive fuels – Ethanol as a blending component of petrol – Requirements and test method, CSN EN 15376.

A. A. Kiss, R. M. Ingat, 2012, Innovative single step bioethanol dehydration in an extractive dividing-wall coulmn, Separation and Purification Technology, 98, 290.

S. Kumar, N. Singh, R. Prasad, 2010, Anhydrous ethanol: A renewable source of energy, Renewables and Sustainable Energy Reviews, 14, 1830.

A. McAloon, F. Taylor, W. Yee, K. Ibsen, R. Wooley, 2000, Determining the cost of producing ethanol from corn starch and lignocellulosic feedstocks, National Renewable Energy Laboratory, NREL/TP-580-28893. Retrieved from www.nrel.gov/docs/fy01osti/28893.pdf

J. Moncada, M. M. El-Halwagi, C. A. Cardona, 2013, Techno-economic analysis for a sugercane boiorefinery: Comlombian case, Bioresource Technology, 135, 533.

J. Pla-Franco, E. Lladosa, S. Loras, J. Monton, 2013, Phase equilibria for the ternary systems ethanol, water + ethylene glycol or + glycerol at 101.3kPa, Fluid Phase Equilibria, 341, 54.

RFA, 2012, 2012 ethanol industry outlook, Renewable Fuels Association. Retrieved from http://ethanolrfa.3cdn.net/d4ad995ffb7ae8fbfe_1vm62ypzd.pdf

T. Roth, P. Kreis, A. Gorak, 2013, Process analysis and optimization of hybrid processes for the dehydration of ethanol, Chemical Engineering Research and Design, 91, 1171.

B. Sowerby, B. D. Crittenden, 1988, An experimental comparison of type A molecular sieves for drying the ethanol-water azeotrope, Gas Separation & Purification, 2, 77.

L. Sunggyu, 2006, Encyclopedia of chemical processing, 1, 1st edition, Taylor & Francis.

R. Turton, R. Bailie, W. Whiting, J. Shaeiwitz, D. Bhattacharyya, 2013, Analysis, synthesis, and design of chemical processes, 4th edition, Pearson Education International.

Krist V. Gernaey, Jakob K. Huusom and Rafiqul Gani (Eds.), 12th International Symposium on Process Systems Engineering and 25th European Symposium on Computer Aided Process Engineering.
31 May - 4 June 2015, Copenhagen, Denmark.

Data Reconciliation in Reaction Systems using the Concept of Extents

Sriniketh Srinivasan[a], Julien Billeter[a], Shankar Narasimhan[b] and Dominique Bonvin[a]

[a]*Laboratoire d'Automatique, EPFL, Lausanne, Switzerland*
[b]*Department of Chemical Engineering, IIT Madras, Chennai, India*
sriniketh.srinivasan@epfl.ch

Abstract

Concentrations measured during the course of a chemical reaction are corrupted with noise, which reduces the quality of information. When these measurements are used for identifying kinetic models, the noise impairs the ability to identify accurate models. The noise in concentration measurements can be reduced using data reconciliation, exploiting for example the material balances as constraints. However, additional constraints can be obtained via the transformation of concentrations into extents and invariants. This paper uses the transformation to extents and invariants and formulates the data reconciliation problem accordingly. This formulation has the advantage that non-negativity and monotonicity constraints can be imposed on selected extents. A simulated example is used to demonstrate that reconciled measurements lead to the identification of more accurate kinetic models.

Keywords: Kinetic identification, Data reconciliation, Model discrimination, Vessel extents

1. Introduction

Chemical reactions are used in the chemical, biotechnological and pharmaceutical industries to convert feed materials into manufactured products. Measurements of concentrations made during the course of the reaction are vital for efficient reactor operation. Process monitoring, control and optimization can be carried out using measurements by either building first-principles (kinetic) models or using data-driven models, or by combining these two approaches.

Kinetic modeling of chemical reaction systems is generally performed via simultaneous identification, Bardow and Marquardt (2004). This identification path suffers from combinatorial complexity and is therefore computationally intensive. As an alternative, the extent-based incremental identification introduced by Amrhein et al. (2010) can be used to build first-principles kinetic models incrementally. The procedure involves a transformation of the measured numbers of moles to extents. This transformation decouples the modeling task into a set of sub-problems, thereby reducing the combinatorial complexity when there are several candidate models for each reaction. Since measurements are corrupted by noise, the performance of the modeling/identification task, and thus also of the subsequent monitoring, control and optimization steps, depends highly on the accuracy of the measurements.

To reduce noise and improve the accuracy of the measured information, data reconciliation (DR) techniques are often used as a pre-processing step, see Narasimhan and Jordache (1999). Data reconciliation exploits process constraints derived from conservation equations to reconcile measurements, that is, to correct the measured data so as to satisfy constraints that are valid at all times. This paper describes a reconciliation approach that is based on extents instead of concentrations. This novel problem formulation allows using additional constraints such as the non-negativity and

monotonicity of extents, which improves significantly the accuracy of the reconciled concentrations and of the identified kinetic models, as illustrated through a simulated example.

2. Preliminaries

2.1. Mole Balance Equations

The mole balance equations for an homogeneous reaction system involving S species, R independent reactions, p inlet streams, and one outlet stream can be written as follows:

$$\dot{\mathbf{n}}(t) = \mathbf{N}^{\mathrm{T}}\mathbf{r}_v(t) + \mathbf{W}_{in}\,\mathbf{u}_{in}(t) - \omega(t)\mathbf{n}(t), \qquad \mathbf{n}(0) = \mathbf{n}_0, \tag{1}$$

where $\mathbf{n}$ is the S-dimensional vector of the numbers of moles, $\mathbf{r}_v := V\,\mathbf{r}$ with V the volume and $\mathbf{r}$ the R-dimensional vector of reaction rates, $\mathbf{u}_{in}$ the p-dimensional vector of inlet mass flowrates, $\omega := \frac{u_{out}}{m}$ the inverse of the residence time with m the mass of the reaction mixture and u_{out} the outlet mass flowrate, $\mathbf{N}$ the $R \times S$ stoichiometric matrix, $\mathbf{W}_{in} = \mathbf{M}_w^{-1}\check{\mathbf{W}}_{in}$ the $S \times p$ matrix of inlet compositions, $\mathbf{M}_w$ the S-dimensional diagonal matrix of molecular weights, $\check{\mathbf{W}}_{in} = [\check{\mathbf{w}}_{in}^1 \cdots \check{\mathbf{w}}_{in}^p]$ with $\check{\mathbf{w}}_{in}^j$ being the S-dimensional vector of weight fractions of the jth inlet flow, and $\mathbf{n}_0$ the S-dimensional vector of initial numbers of moles. If needed, the concentration are computed from the numbers of moles as $\mathbf{c}(t) = \frac{\mathbf{n}(t)}{V(t)}$.

2.2. Conservation Equations

The S dynamic equations (1) are often redundant, as the variability in the system is determined by the number of independent reactions and inlet/outlet streams, and not by the number of chemical species. These redundancies can usually be expressed in terms of algebraic constraints. The number and nature of these constraints depend on the operating mode of the reactor. Table 1 lists the number of constraints q and the procedure for deriving them from structural elements of (1), in particular $\mathbf{N}$, $\mathbf{W}_{in}$ and $\mathbf{n}_0$, for three different operating modes. The matrix $\mathbf{P}$ represents the null space of the corresponding structural matrix.

Table 1: Algebraic constraints under different operating modes.

Operation	# constraints	Constraint derivation	Constraints
Batch	$q = S - R$	$\mathbf{P}^{\mathrm{T}}[\mathbf{N}^{\mathrm{T}}] = \mathbf{0}_{q\times R}$	$\mathbf{P}^{\mathrm{T}}\mathbf{n}(t) = \mathbf{P}^{\mathrm{T}}\mathbf{n}_0$
Fed-batch	$q = S - R - p$	$\mathbf{P}^{\mathrm{T}}[\mathbf{N}^{\mathrm{T}}\ \mathbf{W}_{in}] = \mathbf{0}_{q\times(R+p)}$	$\mathbf{P}^{\mathrm{T}}\mathbf{n}(t) = \mathbf{P}^{\mathrm{T}}\mathbf{n}_0$
Open	$q = S - R - p - 1$	$\mathbf{P}^{\mathrm{T}}[\mathbf{N}^{\mathrm{T}}\ \mathbf{W}_{in}\ \mathbf{n}_0] = \mathbf{0}_{q\times(R+p+1)}$	$\mathbf{P}^{\mathrm{T}}\mathbf{n}(t) = \mathbf{0}_q$

2.3. From numbers of moles to vessel extents

Amrhein et al. (2010) and Rodrigues et al. (2015) have developed a linear transformation for open reaction systems that transforms the numbers of moles $\mathbf{n}$ into four contributions, namely, the R extents of reaction $\mathbf{x}_r$, the p extents of inlet $\mathbf{x}_{in}$, a dimensionless extent of initial conditions x_{ic}, and the $q = S - R - p - 1$ invariants $\mathbf{x}_{iv}$ that are identically zero. The linear transformation $\mathscr{T}$ reads:

$$\begin{bmatrix} \mathbf{x}_r(t) \\ \mathbf{x}_{in}(t) \\ x_{ic}(t) \\ \mathbf{x}_{iv}(t) \end{bmatrix} = \mathscr{T}\,\mathbf{n}(t) := \begin{bmatrix} \mathbf{R} \\ \mathbf{F} \\ \mathbf{i}^{\mathrm{T}} \\ \mathbf{Q} \end{bmatrix} \mathbf{n}(t), \tag{2}$$

The transformation matrix $\mathscr{T}$ is given by $\left[\mathbf{N}^{\mathrm{T}}\ \mathbf{W}_{in}\ \mathbf{n}_0\ \mathbf{P}\right]^{-1}$, where $\mathbf{P}$ represents the null space of $\left[\mathbf{N}^{\mathrm{T}}\ \mathbf{W}_{in}\ \mathbf{n}_0\right]$, and brings the dynamic model (1) to the following decoupled form:

$$\dot{\mathbf{x}}_r(t) = \mathbf{r}_v(t) - \omega(t)\,\mathbf{x}_r(t) \qquad \mathbf{x}_r(0) = \mathbf{0}_R \tag{3a}$$

$$\dot{\mathbf{x}}_{in}(t) = \mathbf{u}_{in}(t) - \omega(t)\,\mathbf{x}_{in}(t) \qquad \mathbf{x}_{in}(0) = \mathbf{0}_p \tag{3b}$$

$$\dot{x}_{ic}(t) = -\omega(t)\,x_{ic}(t) \qquad x_{ic}(0) = 1 \tag{3c}$$

$$\mathbf{x}_{iv}(t) = \mathbf{0}_q\,, \tag{3d}$$

where $\mathbf{R}$, $\mathbf{F}$ and $\mathbf{Q} = \mathbf{P}^+$ are matrices of dimensions $R \times S$, $p \times S$ and $q \times S$, respectively, and $\mathbf{i}$ is a S-dimensional vector. Each individual extent $x_{r,i}$ or $x_{in,j}$ defined in (3) is in fact a vessel extent expressing the amount of material (due to a reaction or an inlet) that is still in the reactor, the negative terms on the right-hand side accounting for what has left the reactor. Similarly, the extent $x_{ic}(t)$ in (3c) indicates the fraction of the initial conditions that is still in the reactor at time t.

The vector of numbers of moles $\mathbf{n}(t)$ can be reconstructed from the various extents by pre-multipliying (2) by $\mathscr{T}^{-1} = \begin{bmatrix}\mathbf{N}^{\mathrm{T}} & \mathbf{W}_{in} & \mathbf{n}_0 & \mathbf{P}\end{bmatrix}$ and considering that $\mathbf{x}_{iv} = \mathbf{0}_q$, which yields:

$$\mathbf{n}(t) = \mathbf{N}^{\mathrm{T}}\mathbf{x}_r(t) + \mathbf{W}_{in}\mathbf{x}_{in}(t) + \mathbf{n}_0 x_{ic}(t). \tag{4}$$

Remark 1 (Fed-batch reactor)
For fed-batch reactors, the transformation (2) *transforms the* $\mathbf{n}$ *into the* R *extents of reactions* $\mathbf{x}_r$*, the* p *extents of inlets* $\mathbf{x}_{in}$ *and the* $q = S - R - p$ *invariants* $\mathbf{x}_{iv}$*.*

Remark 2 (Batch reactor)
For batch reactors, the transformation (2) *transforms* $\mathbf{n}$ *into the* R *extents of reactions* $\mathbf{x}_r$ *and the* $q = S - R$ *invariants* $\mathbf{x}_{iv}$*.*

Proposition 1 (Monotonicity of x_{ic})
The extent $x_{ic}(t)$ *is strictly positive and monotonically decreasing over time in an open reactor.*

Proof: The solution to (3c) is $x_{ic}(t) = e^{-\int_0^t \omega(\tau)d\tau}$ with $\omega(t) = \frac{u_{out}(t)}{m(t)}$. Since $\omega(t) \geq 0$, $x_{ic}(t)$ varies as a negative exponential function and hence is monotonically decreasing.

Proposition 2 (Monotonicity of $\mathbf{x}_r$ and $\mathbf{x}_{in}$ in batch and fed-batch modes)
The extents $\mathbf{x}_r$ *for reactions with net positive rates and the extents* $\mathbf{x}_{in}$ *are strictly increasing in batch and semi-batch modes.*

Proof: In absence of outlet, that is for $u_{out} = 0$, (3a) reduces to $\dot{\mathbf{x}}_r(t) = \mathbf{r}_v(t)$ and (3b) to $\dot{\mathbf{x}}_{in}(t) = \mathbf{u}_{in}(t)$. It follows from $\mathbf{r}_v(t) \geq \mathbf{0}_R$ and $\mathbf{u}_{in}(t) \geq \mathbf{0}_p$ that both extents are strictly positive and increasing.

3. Data Reconciliation

Data reconciliation applied to reaction systems uses redundancy expressed as algebraic constraints, such as those provided in Table 1, to improve the accuracy of measured concentrations. The following assumptions are made in this study:

A1. the concentrations of all S species are measured and available,

A2. the volume is measured accurately without noise, and

A3. the initial conditions are known perfectly.

Let $\tilde{\mathbf{c}}(t_h) = \mathbf{c}(t_h) + \boldsymbol{\varepsilon}_c$ denote the S-dimensional vector of noisy concentrations measured at H time instants, $t_h \in [t_1, t_H]$ with $t_1 = 0$, where $\boldsymbol{\varepsilon}_c$ is an S-dimensional vector of zero-mean Gaussian noise with the constant variance-covariance matrix $\boldsymbol{\Sigma}_c$. The noise in the numbers of moles $\tilde{\mathbf{n}}(t_h) = V(t_h)\tilde{\mathbf{c}}(t_h)$ also follows a zero-mean normal distribution with the time-varying variance-covariance matrix $\boldsymbol{\Sigma}_n(t_h) = V(t_h)^2\boldsymbol{\Sigma}_c$.

3.1. Data reconciliation in terms of numbers of moles

For all operating modes, the reconciliation of the measured numbers of moles $\tilde{\mathbf{n}}$ can be formulated as an optimization problem constrained by algebraic relationships:

$$\begin{aligned} \min_{\hat{\mathbf{n}}(t_i)} \quad & \left(\tilde{\mathbf{n}}(t_i)-\hat{\mathbf{n}}(t_i)\right)^{\mathrm{T}} \mathbf{W}(t_i) \left(\tilde{\mathbf{n}}(t_i)-\hat{\mathbf{n}}(t_i)\right) \\ \text{s.t.} \quad & \mathbf{P}^{\mathrm{T}}\hat{\mathbf{n}}(t_i)=\mathbf{0}_q, \quad \hat{\mathbf{n}}(t_i)\geq \mathbf{0}_S \end{aligned} \tag{5}$$

where $\hat{\mathbf{n}}$ is the vector of reconciled numbers of moles and $\mathbf{W}(t_i)=\boldsymbol{\Sigma}_n^{-1}(t_i)$ is the weighting matrix. Note that, due to the presence of inequality constraints, Problem (5) does not have an analytical solution and hence must be solved numerically. In this formulation, the DR problem for different time instants are decoupled, that is, the reconciled number of moles can be estimated independently at each time instant.

3.2. Data reconciliation in terms of extents

An alternative consists in defining the DR problem directly in terms of extents. The formulation of this problem depends on whether the reactor has an outlet (open reactors) or not (batch and fed-batch reactors). In this formulation, the reconciliation in terms of extents at instant t_i involves reconciling all the previous measurements as well.

3.2.1. Open reactors

In the presence of an outlet, there is a monotonicity constraint only for x_{ic}. The reconciliation problem for reactions with net positive rates reads:

$$\begin{aligned} \min_{\substack{\hat{\mathbf{x}}_r(t_1),\ldots,\hat{\mathbf{x}}_r(t_H)\\ \hat{\mathbf{x}}_{in}(t_1),\ldots,\hat{\mathbf{x}}_{in}(t_H)\\ \hat{x}_{ic}(t_1),\ldots,\hat{x}_{ic}(t_H)}} \quad & \sum_{i=1}^{t_H} \left(\tilde{\mathbf{n}}(t_i)-\hat{\mathbf{n}}(t_i)\right)^{\mathrm{T}} \mathbf{W}(t_i) \left(\tilde{\mathbf{n}}(t_i)-\hat{\mathbf{n}}(t_i)\right) \\ \text{s.t.} \quad & \hat{x}_{ic}(t_i)-\hat{x}_{ic}(t_{i-1})\leq 0 \quad \forall i>1, \\ & \hat{\mathbf{n}}(t_i)\geq 0, \quad \hat{\mathbf{x}}_r(t_i)\geq 0, \quad \hat{\mathbf{x}}_{in}(t_i)\geq 0, \quad \hat{x}_{ic}(t_i)\geq 0 \end{aligned} \tag{6}$$

with $\hat{\mathbf{n}}(t_i)=\mathbf{N}\hat{\mathbf{x}}_r(t_i)+\mathbf{W}_{in}\hat{\mathbf{x}}_{in}(t_i)+\mathbf{n}_0\hat{x}_{ic}(t_i)$ from (4).

3.2.2. Batch and fed-batch reactors

In the absence of outlet, monotonicity constraints can be imposed on $\mathbf{x}_r$ in batch mode, and on $\mathbf{x}_r$ and $\mathbf{x}_{in}$ in fed-batch mode. For a fed-batch reactor, the reconciliation problem for reactions with net positive rates then reads:

$$\begin{aligned} \min_{\substack{\hat{\mathbf{x}}_r(t_1),\ldots,\hat{\mathbf{x}}_r(t_H)\\ \hat{\mathbf{x}}_{in}(t_1),\ldots,\hat{\mathbf{x}}_{in}(t_H)}} \quad & \sum_{i=1}^{t_H} \left(\tilde{\mathbf{n}}(t_i)-\hat{\mathbf{n}}(t_i)\right)^{\mathrm{T}} \mathbf{W}(t_i) \left(\tilde{\mathbf{n}}(t_i)-\hat{\mathbf{n}}(t_i)\right) \\ \text{s.t.} \quad & \hat{\mathbf{x}}_r(t_i)-\hat{\mathbf{x}}_r(t_{i-1})\geq \mathbf{0}_R \quad \forall i>1, \qquad \hat{\mathbf{x}}_{in}(t_i)-\hat{\mathbf{x}}_{in}(t_{i-1})\geq \mathbf{0}_p \quad \forall i>1, \\ & \hat{\mathbf{n}}(t_i)\geq 0, \qquad \hat{\mathbf{x}}_r(t_i)\geq \mathbf{0}_R, \qquad \hat{\mathbf{x}}_{in}(t_i)\geq \mathbf{0}_p \end{aligned} \tag{7}$$

with $\hat{\mathbf{n}}(t_i)=\mathbf{N}\hat{\mathbf{x}}_r(t_i)+\mathbf{W}_{in}\hat{\mathbf{x}}_{in}(t_i)+\mathbf{n}_0$ from (4) with $x_{ic}(t_i)=1$. The constraint $\mathbf{P}^{\mathrm{T}}\hat{\mathbf{n}}(t_i)=\mathbf{0}_q$ is implicitly satisfied in (6) and (7) since the invariants $\mathbf{x}_{iv}$ are zero.

4. Application to Model Identification

The different formulations of the reconciliation problem are compared via a simulated example. The chosen reaction system is the catalyzed acetoacetylation of pyrrole, which consists of $R = 4$ reactions and $S = 6$ species (plus the catalyst), Ruppen et al. (1998). The reaction scheme and the kinetic models used to generate the data are:

$$\begin{array}{llllll} \text{R1:} & \text{A} + \text{B} & \rightarrow & \text{C} & r_1 = k_1 c_A c_B c_K \\ \text{R2:} & \text{B} + \text{B} & \rightarrow & \text{D} & r_2 = k_2 c_B^2 c_K \\ \text{R3:} & \text{B} & \rightarrow & \text{E} & r_3 = k_3 c_B \\ \text{R4:} & \text{C} + \text{B} & \rightarrow & \text{F} & r_4 = k_4 c_C c_B c_K \end{array}$$

This reaction system is simulated in an isothermal batch reactor. The values of the rate constants are $k_1 = 0.0530$, $k_2 = 0.1280$, $k_3 = 0.0280$ s^{-1} and $k_4 = 0.003$ L^2 mol^{-2} s^{-1}. The initial volume is 1 L with the concentrations $\mathbf{c}_0 = \begin{bmatrix} 1.25 & 1 & 0 & 0 & 0 & 0 \end{bmatrix}^{\mathrm{T}}$ mol L^{-1} and $c_{K0} = 0.5$ mol L^{-1} for the catalyst K. Since the density is assumed constant, the volume is also constant.

According to Table 1, this batch reaction system has $q = S - R = 2$ invariant relationships:

$$\begin{aligned} -2c_A(t) + c_B(t) - c_C(t) + 2c_D(t) + c_E(t) &= -2c_{A,0} + c_{B,0} - c_{C,0} + 2c_{D,0} + c_{E,0} \\ c_A(t) + c_C(t) + c_F(t) &= c_{A,0} + c_{C,0} + c_{F,0}. \end{aligned} \tag{8}$$

Each concentration is corrupted with additive independent zero-mean Gaussian noise of standard deviation corresponding to 10% of its maximum concentration. Catalyst K and species F are assumed to be noise free. The variance-covariance matrix $\mathbf{\Sigma}_n$ is constant (batch conditions) and is assumed to be known. Measurements are taken every 0.5 min for 30 min.

The measured numbers of moles $\tilde{\mathbf{n}}$ are reconciled in two ways. First, in terms of numbers of moles, according to the problem formulation (5) using constraints given by the invariant relationships (8). Second, in terms of extents, according to the formulation (7) (with $\hat{\mathbf{x}}_{in} = \mathbf{0}$) with constraints on the positivity and monotonicity of the extents of reaction $\hat{\mathbf{x}}_r$. The performance of the different approaches is assessed using the residual sum of squares (RSS) calculated as the difference between the *true* simulated data and the measured/reconciled data. Table 2 shows that the formulation (7) improves significantly the accuracy of the reconciled data compared to the unreconciled (original) measurements and the data reconciled according to the formulation (5). Figure 1 shows the simulated, measured and extent-based reconciled concentrations of species A to E.

Table 2: Residual sum of squares between the *true* simulated numbers of moles and the numbers of moles obtained without reconciliation ($\tilde{\mathbf{n}}$) and with reconciliation according to (5) and (7).

Species	Measurements	Data reconciliation	
	via $\tilde{\mathbf{n}}$	via $\hat{\mathbf{n}}$ (5)	via $\hat{\mathbf{x}}$ (7)
A	0.9164	0.0332	0.0108
B	0.4615	0.1317	0.0355
C	0.0316	0.0332	0.0109
D	0.0392	0.0268	0.0062
E	0.0162	0.0155	0.0115

Note that incremental model identification can be performed independently for each reaction, as discussed in Srinivasan et al. (2012) and Billeter et al. (2013). For each rate law, kinetic identification is performed using the measured data ($\tilde{\mathbf{n}}$) and the data reconciled according to (5) and (7). For each set of data (measurements, reconciled estimates via $\hat{\mathbf{n}}$ and reconciled estimates via $\hat{\mathbf{x}}$), the capability of discriminating between correct and incorrect kinetic laws is assessed by comparing the RSS of each candidate rate law to that of the correct law. Table 3 shows drastic improvement when measurements are reconciled with (7), that is, using constraints on extents. In all cases, the least RSS is obtained for the correct kinetic model, which implies that the correct model is identified. However, the use of the raw measurements (without reconciliation) makes it difficult to discriminate between models 1 and 3 for R1 and models 1 and 4 for R2. In contrast, the use of reconciled estimates based on the formulation (7) enables unambiguous identification of the correct kinetic model.

Table 3: Ratios of RSS (with respect to the correct model, thus giving 1 for the correct model) for different kinetic models for reactions R1 and R2 using the measured numbers of moles $\tilde{\mathbf{n}}$ and the numbers of moles reconciled according to 5 ($\hat{\mathbf{n}}$) and 7 ($\hat{\mathbf{x}}$).

R1	Measurements via $\tilde{\mathbf{n}}$	Reconciled estimates via $\hat{\mathbf{n}}$ (5)	Reconciled estimates via $\hat{\mathbf{x}}$ (7)	R2	Measurements via $\tilde{\mathbf{n}}$	Reconciled estimates via $\hat{\mathbf{n}}$ (5)	Reconciled estimates via $\hat{\mathbf{x}}$ (7)
$r_1 = k_1 c_A c_B c_K$	1	1	1	$r_2 = k_2 c_B^2 c_K$	1	1	1
$r_1 = k_1 c_A$	1.1761	3.3886	10.1717	$r_2 = k_2 c_B$	1.518	695	8.1858
$r_1 = k_1 c_A^2 c_B$	1.0017	1.0365	1.2355	$r_2 = k_2$	3.9516	12.6008	42.5469
$r_1 = k_1 c_A c_B^2$	1.1201	2.1703	6.7232	$r_2 = k_2 c_B^3$	1.0593	1.4487	2.4062

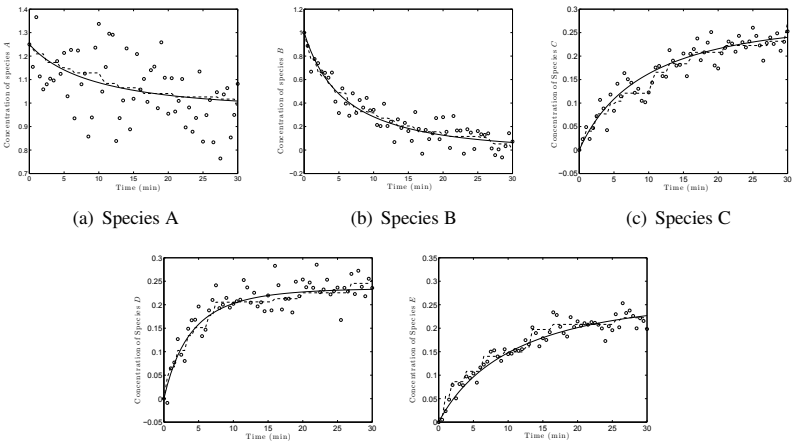

(a) Species A (b) Species B (c) Species C

(d) Species D (e) Species E

Figure 1: Simulated (continuous line), measured (dots) and extent-based reconciled (dashed line) concentrations of the species A to E.

5. Conclusion

This paper has shown that data reconciliation using invariant relationships helps reduce the effect of measurement noise. Furthermore, formulating the reconciliation problem in terms of extents allows exploiting additional monotonicity constraints. It has also been shown through a simulated example that the use of reconciled estimates together with the extent-based incremental approach leads to improved model discrimination. Future work will focus on developing monotonicity constraints for the extents of reaction and mass transfer in the context of open heterogeneous reaction systems.

References

M. Amrhein, N. Bhatt, B. Srinivasan, D. Bonvin, 2010, Extents of reaction and flow for homogeneous reaction systems with inlet and outlet streams, AIChE J., 56, 2873–2886.

A. Bardow, W. Marquardt, 2004, Incremental and simultaneous identification of reaction kinetics: Methods and comparison, Chem. Eng. Sci., 59, 13, 2673–2684.

J. Billeter, S. Srinivasan, D. Bonvin, 2013, Extent-based kinetic identification using spectroscopic measurements and multivariate calibration, Anal. Chim. Acta, 767, 21–34.

S. Narasimhan, C. Jordache, 1999. Data Reconciliation and Gross Error Detection. Elsevier.

D. Rodrigues, S. Srinivasan, J. Billeter, D. Bonvin, 2015, Variant and invariant states for reaction systems, Comp. Chem. Eng., 73, 1, 23–33.

D. Ruppen, D. Bonvin, D. Rippin, 1998, Implementation of adaptive optimal operation for a semi-batch reaction system, Comp. Chem. Eng., 22, 185 – 199.

S. Srinivasan, J. Billeter, D. Bonvin, 2012, Extent-based incremental identification of reaction systems using concentration and calorimetric measurements, Chem. Eng. J, 207-208, 785 – 793.

Krist V. Gernaey, Jakob K. Huusom and Rafiqul Gani (Eds.), 12th International Symposium on Process Systems Engineering and 25th European Symposium on Computer Aided Process Engineering.
31 May - 4 June 2015, Copenhagen, Denmark.

Development of a Generic Model of a Ruthenium Reactor

Norbertin Nkoghe Eyeghe[a], Carl Sandrock[b] and Carel Van Dam[b]

[a]*Department of Chemical Engineering; University of Pretoria; Pretoria, South Africa*
[b]*Department of Chemical Engineering; University of Pretoria; Pretoria, South Africa*
carl.sandrock@up.ac.za

Abstract

A mathematical first-principle model (FPM) of a ruthenium reactor was developed, implemented and successfully validated against a set of measurements of the real reactor of a precious metal refinery (PMR). The model describes the dynamic behavior of a process involving two exothermic reactions, occurring simultaneously in a semi-batch reactor equipped with a jacket. The reactions describe the dissolution of solid ruthenium (Ru) to produce liquid ruthenium trichloride ($RuCl_3$), which is then evaporated into ruthenium tetroxide gas (RuO_4). This paper presents a lumped model of the process whose main objective was to achieve satisfactory tracking of temperature and pressure data sets of the real reactor. The model was written as an explicit system of ordinary differential equations (ODEs), and has demonstrated satisfactory predictions of temperature and pressure dynamics. However, more work aiming at achieving better validation of the model is still in progress. This involves using nonlinear optimization techniques to find optimum parameter estimates of reaction kinetics constants, together with some heat and mass transfer coefficients, only obtained by trial-and-error at this point.

Keywords: FPM, ODE, Estimation, Semi-batch Reactors, Model Validation.

1. Introduction

Mathematical models can be built to describe various dynamic behaviors taking place in systems of continuous, batch or semi-batch processes. A ruthenium semi-batch reactor is such a system for which a mathematical model can be developed. Ruthenium is a precious metal, an element of the platinum group metals (PGMs). It is regarded as a specialty product and often processed in batch or semi-batch reactors, operating sequentially through the phases of heating, reaction, cooling and filtering. Modeling the ruthenium reactor involves capturing such reaction dynamics that are descriptive of the operation of a semi-batch reactor.
Two types of models are commonly developed and used. They are empirical models (EM) and first-principles models (FPM). The former are generated by fitting a polynomial algorithm to a set of data, using model identification techniques provided by commercial software packages. The latter are developed by capturing dynamic behaviors describing their systems. This is done by applying the principles of conservation laws of mass and energy balances in the mathematical formulations of either ODEs or DAEs. Those models are built and solved in numerical platforms, their formulation, development and numerical integration can become more difficult with large and complex systems (Pantelides and Renfro (2013)).

Although first-principles modeling of batch and semi-batch reactors have been well addressed in the scientific literature, there is still little work that has been published on PGMs related processes. However, all dynamic FPMs of batch and semi-batch reactors are based on the same mathematical principles regardless of the process recipe. Nyström (2007) has reported that processes are mod-

eled using DAEs or ODEs, consisting of differential equations that describe the dynamic behavior of the system, as mass and energy balances, and algebraic equations that ensure physical and thermodynamic relations. The same mathematical principles have been reported on by Prokopová and Prokop (2009). FPMs have been developed and validated to predict temperature behaviour of an industrial, semi-batch, emulsion polymerization reactor (Hvala and Kukanja (2013), Hvala et al. (2011)).

2. System Description

The system is a jacketed semi-batch reactor (see Figure 1), in which two exothermic reactions take place simultaneously, according to the following chemical equations of reactions.

$$Ru(s) + Cl_2(g) \rightarrow 2RuCl_3(l) \quad (1)$$

$$2H_2O(l) + 2RuCl_3(l) + 2NaClO_3(l) \rightarrow 4HCl(l) + 2RuO_4(g) + Cl2(g) + 2NaCl(l) \quad (2)$$

Steam and cooling water are the hot and cold utilities used to regulate the temperature conditions of the reactor during the process. The first reaction (Eq.1), describes the dissolution of solid ruthenium (Ru) in the presence of chlorine ($Cl_{2(g)}$) to produce ruthenium tri-chloride ($RuCl_{3(l)}$). The second reaction (Eq.2) describes the evaporation of $RuCl_{3(l)}$ in the presence of sodium chlorate ($NaClO_{3(l)}$), used as the oxidizing agent, to produce ruthenium tetroxide ($RuO_{4(g)}$) as the main product, sodium chloride ($NaCl_{(l)}$) and Hydrochloric acid ($HCl_{(l)}$) as by-products.

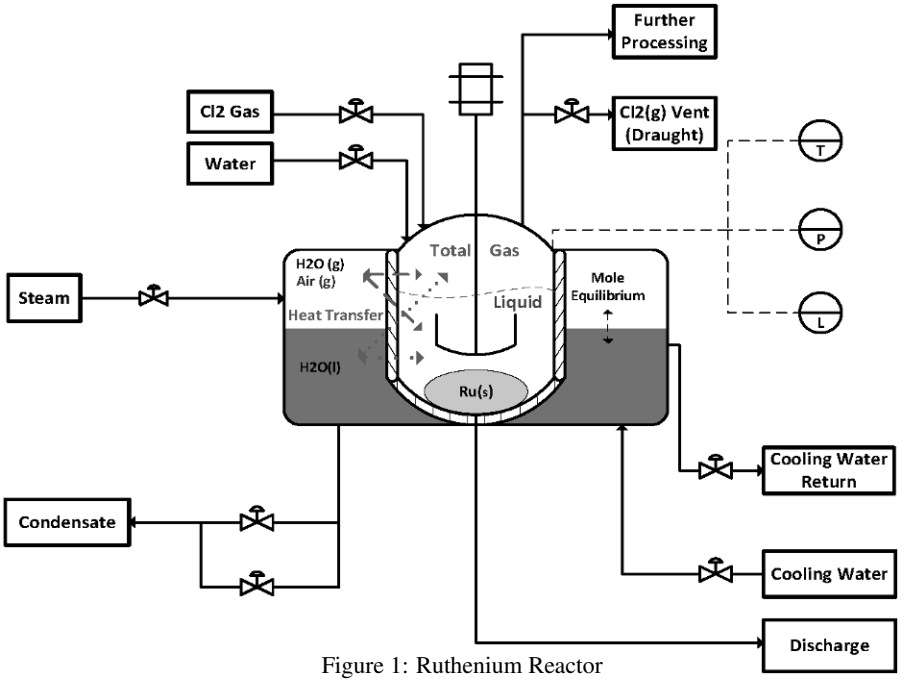

Figure 1: Ruthenium Reactor

The process takes place in five phases. The first phase involves loading the reactor with $H_2O_{(l)}$, $Ru_{(s)}$ and catalyst $NaClO_{3(l)}$. The second phase involves heating the reactor up to a temperature of about 40 $^{\circ}C$ by introducing steam into the jacket. The third phase is the chlorination, where $Cl_{2(g)}$ is added into the reactor and dissolves into water to react with $Ru_{(s)}$. $Cl_{2(g)}$ is also used to maintain the reaction pressure condition to the required operational level of $\pm$ 400 kPa. At this point the reaction phase starts, steam is cut off and the exothermic reactions proceeds. The last phase involves cooling the reactor by pumping cooling water into the jacket at the end of the batch. The phases of heating, cooling and chlorination take place simultaneously with the reaction phase. Utilities are pumped alternately into the jacket to regulate the reaction temperature such that there be no temperature runaways, leading to potentially dangerous situations.

3. Model Development

The mathematical model of the reactor was developed with respect to the chemical reactions of Eq.1 and Eq.2. Those reactions were modeled primarily to lump the reaction heat to be handled and the transport dynamics between the jacket and reactor compartments. In the system, temperature and pressure are the most important variables for the initial control situation.The model was developed and implemented in the "Matlab" computational environment.

3.1. Explicit ODE Model

The equations were written as an explicit system of ODEs, with a total of 115 equations describing the system, of which, 18 are differential equations and 97 algebraic equations. They were written for the solid, liquid, and gas phases. Ru is the solid specie. H_2O, Cl_2, $RuCl_3$, HCl, $NaClO_3$ and NaCl are in the liquid phase, and H_2O, Cl_2, RuO_4 are in the gas phase. Matlab solver "Ode15s" was used for numerical integration.The model was subject to the following assumptions:

- The reactor solution is perfectly mixed.
- There is negligible heat loss to the surroundings.
- The solutions are ideal (i.e molar concentrations considered instead of activity coefficients).
- Ionic species do not contribute to volume but do contribute to density.
- There is a mixed phase (liquid and gas) into the jacket compartment at all times.
- The dynamics of the reactor wall are neglected, to enhance direct heat transfer.

The model parameters of heat and mass transfers coefficients, as well as reaction kinetic constants were estimated by trial-and-error, as no experimental values of those were available, and no generic method of tuning them has been developed at this point.

3.2. Model Differential Equations

Due to the size of the model, with 115 equations, which cannot all be presented in this document, the equations are mostly presented in the liquid phase, and give the general formulation used to derive the model dynamics, in both compartments, for all species and phases involved.

Moles in Reactor:

$$\frac{dN_{Ru_{(s)}}}{dt} = F^{In}_{Ru_{(s)}} - F^{Out}_{Ru_{(s)}} - r_1 V_{rx_{(g)}} \tag{3}$$

$$\frac{dN_{i_{(l)}}}{dt} = F^{In}_{i_{(l)}} - F^{Out}_{i_{(l)}} \pm F_{i_{(l-g)}} \pm x^{r1}_i \cdot r_1 V_{rx_{(g)}} \pm x^{r2}_i \cdot r_2 V_{rx_{(l)}} \tag{4}$$

Temperatures in Reactor:

$$\frac{dT_{rx_{(l)}}}{dt} = \frac{1}{Cp^{rx}_l \cdot N^{tot}_{rx_{(l)}}} \times \left(\sum_{Reaction,\, i} \left((-r_1 V_{rx_{(g)}} + r_2 V_{rx_{(l)}}) \times Cp^{i_{(l)}} \Big|_{T_{rx_{(l)}}} \dots \right. \right. \tag{5}$$

$$\left. \left. \times (T_{rx_{(l)}} - T_{ref}) \right) + H_{rx_{(l-l)}} + H_{rx_{(g-l)}} \right)$$

$$\frac{dT_{rx_{(g)}}}{dt} = \frac{1}{Cp^{rx}_g \cdot N^{tot}_{rx_{(g)}}} \times \left(F^{In}_{Cl_{2(g)}} \cdot Cp^{Cl_{2(g)}} \Big|_{T^{In}_{rx_{(g)}}} \times (T^{In}_{rx_{(g)}} - T_{ref}) \dots \right. \tag{6}$$

$$\left. - \sum_{\substack{Outlet \\ streams,\, i}} \left(F^{Out}_{i_{(g)}} \cdot Cp^{i_{(g)}} \Big|_{T_{rx_{(g)}}} \times (T_{rx_{(g)}} - T_{ref}) \right) + H_{rx_{(g-g)}} + H_{rx_{(l-g)}} \right)$$

Moles in Jacket:

$$\frac{dN_{H_2O_{(l)}}}{dt} = F^{In}_{CW} - F^{Out}_{CW} - F_{H_2O_{(l-g)}} \tag{7}$$

$$\frac{dN_{H_2O_{(g)}}}{dt} = F^{In}_{Steam} - F^{Out}_{Steam} + F_{H_2O_{(l-g)}} \tag{8}$$

Temperatures in Jacket:

$$\frac{dT_{hx_{(l)}}}{dt} = \frac{1}{Cp_l^{hx} \cdot N_{hx_{(l)}}^{tot}} \times \Bigg((F_{CW}^{In} + F_{Steam}^{In}) \cdot Cp^{H_2O_{(l)}} (T_{hx_{(utility)}}^{In}) \times \ \ldots \tag{9}$$

$$(T_{hx_{(utility)}}^{In} - T_{ref}) - (F_{CW}^{Out} + F_{Steam}^{Out}) \cdot Cp_l^{hx} \times (T_{hx_{(l)}} - T_{ref}) \ \ldots$$

$$+ F_{H_2O_{(l-g)}} \cdot H_v^{H_2O}(T_{hx_{(l)}}) - H_{rx_{(l-l)}} \Bigg)$$

3.3. Model Algebraic Equations

A total of 97 algebraic equations were solved simultaneously with the 18 differential equations. The general formulation of the key algebraic equations are presented for the reactor compartment of the system only. The corresponding equations, in the jacket, were derived similarly.

3.3.1. Reactor Side

Total Moles:

$$N_{rx_{(l)}}^{tot} = \sum_{Species,\, i} N_{i_{(l)}} \tag{10}$$

Volumes:

$$V_{rx_{(l)}}^{tot} = \sum_{Species,\, i} \frac{N_{i_{(l)}}}{\rho_{i_{(l)}}\big|_{T_{rx_{(l)}}}} \tag{11}$$

Pressures:

$$P_{rx_{(g)}}^{tot} = \frac{N_{rx_{(g)}}^{tot} \times R \times T_{rx_{(g)}}}{V_{rx_{(g)}}^{tot}} \tag{12}$$

$$P_{rx_{(l)}}^{tot} = \rho_{rx_{(l)}} \times \mathrm{g} \times h_{rx_{(l)}}^{eq} + P_{rx_{(g)}}^{tot} \tag{13}$$

Flow rates of Phase Changes in H_2O & Cl_2: (14)

$$F_{i_{(l-g)}} = k_i \times (P_{i_{(l)}} - P_{i_{(g)}}) \tag{15}$$

Rates of Reactions:

$$r_1 = k_{r1} \times C_{Cl_{2(g)}} \tag{16}$$

$$r_2 = k_{r2} \times C_{RuCl_{3(l)}} \times C_{NaClO_{3(l)}} \tag{17}$$

Heat Transfers from Liquid in Jacket to Liquid in Reactor:

$$H_{rx_{(l-l)}} = (h_{rx_{(s)}} + h_{rx_{(l)}}) \times (2 \cdot \pi) \times (r_{rx} + w_{rx}) \times U_{l-l} \times (T_{hx_{(l)}} - T_{rx_{(l)}}) \tag{18}$$

A total of four additional relations, similar to Equation 18, are calculated to account for the cross-phase heat transfer between the two compartments. From liquid in jacket to solid and gas in reactor, then from gas in jacket to liquid and gas in reactor.

4. Results and Discussion

Simulating the model, the generated responses of temperature and pressure showed some good tracking of the batch data set they were compared to (see Figure 2). The model parameters were tuned by trial-and-error with a single batch run. A total of 28 different batches were simulated with those same parameters as the estimation could not be repeated for all batches.

4.1. Explicit Model Simulations

Figure 2a shows the model temperatures responses against the temperature data of a selected batch. In this simulation, steam and cooling water were supplied at the temperatures of 115 $^{\circ}C$ and 27 $^{\circ}C$, respectively. The reactor model was set at a steady state temperature of 30 $^{\circ}C$. The first subplot (top graph), shows the molar flow rates of the utilities pumped into the jacket. The second and third subplots (counting from top), demonstrate good tracking of batch data by the simulated temperatures responses. The bottom figure shows the dynamics of temperatures in the jacket of the reactor model, when subjected to the utility inputs.

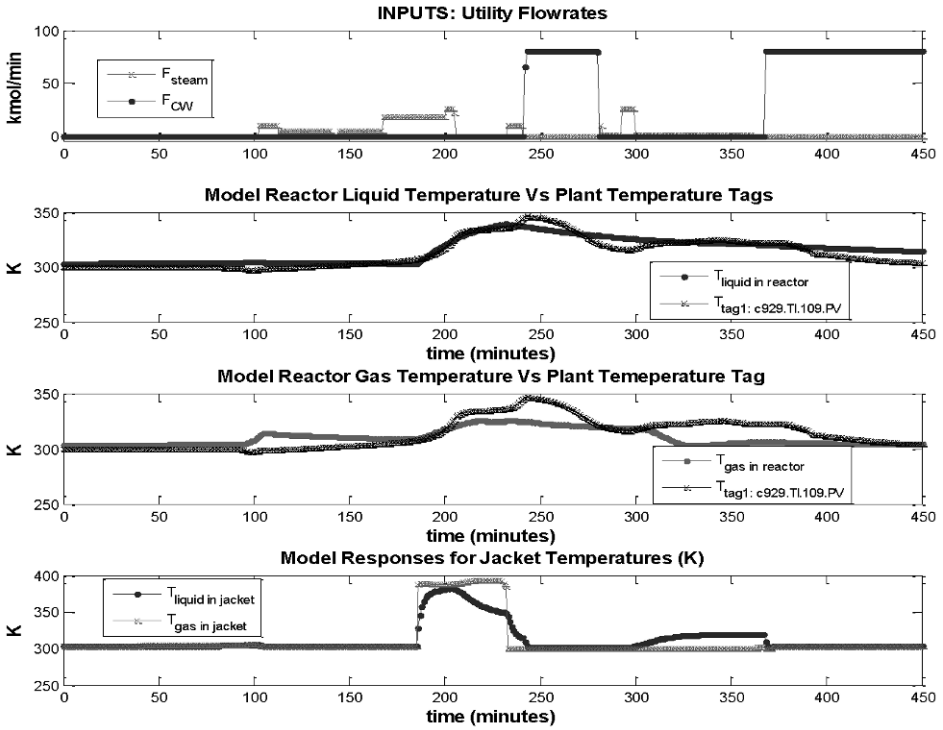

(a) Model Temperatures against Temperature Data

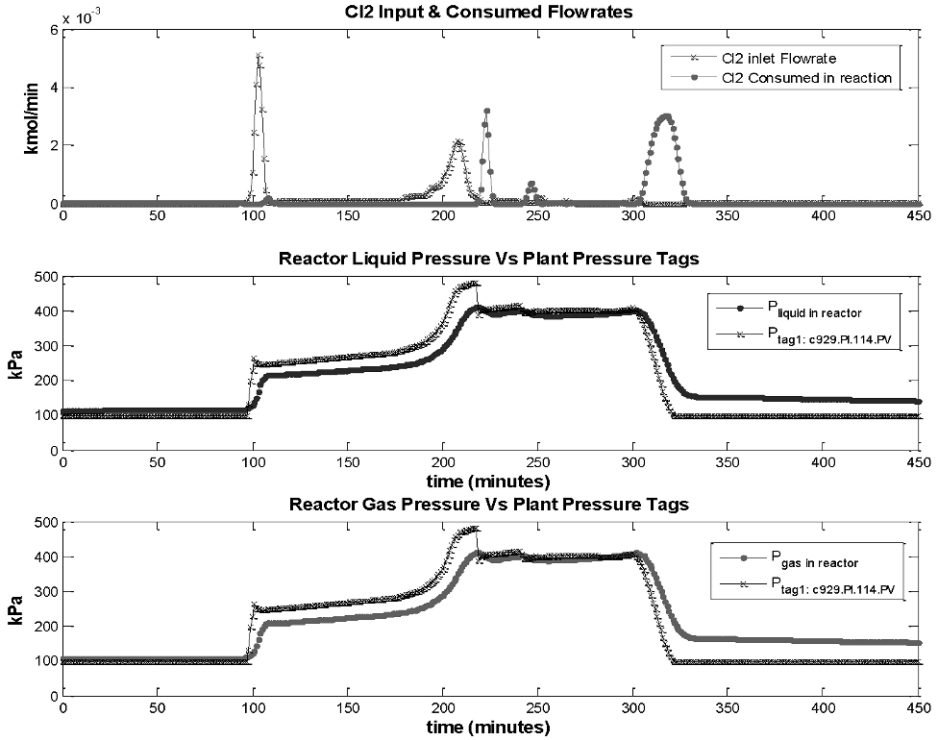

(b) Model Pressures against Pressure data

Figure 2: Temperature and Pressure responses

Figure 2b shows the model pressure responses against the pressure data of the same batch. During the reaction, the required pressure condition inside the reactor is achieved and maintained by pumping Cl_2 gas into the reactor, at variable time intervals. The top graph of Figure 2b shows the Cl_2 (g) flow rate into to the reactor model and the amount of Cl_2 (g) consumed as the reaction proceeds. The second and third graphs, from the top, show the liquid and gas pressures of the reactor model, respectively. The model responses show a similar trend to that of the pressure data set ($P_{tag1:\ c929.PI.114.PV}$), although the pressure simulated responses do not track the pressure data very closely as some offset can be seen between the two.

5. Conclusions

We have developed a first-principle mathematical model of a ruthenium reactor. The aim of this work was to develop a model that could achieve good predictions of temperature and pressure dynamics of the real reactor. The parameters of heat and mass transfer coefficients, together with the reaction kinetic constants were estimated by trial-and-error. However, a more systematic method of parameterization is being developed, such that optimum parameters could be computed repeatedly as the model is run with various batches. The validation work, for better responses, is still in progress.

Nomenclature

C = Molar concentration
C_p = Specific heat capacity at constant pressure
CW = Cooling Water
H = Enthalpy
H_v = Heat of vaporization
hx = Jacket compartment
h_{rx} = Height of reactor vessel
i = A given specie
k_i = Mass transfer coefficient of a given specie
k_{r1} = Kinetic constants of reaction 1
$N_{Ru_{(s)}}$ = Moles of ruthenium solid
$N_{i_{(l)}}$ = Moles of specie in liquid phase
r1 = Reaction 1
r_1 = Rate of reaction1
rx = Reactor compartment
r_{rx} = Radius of reactor vessel
T_{ref} = Reference temperature
U = Heat transfer coefficient
w_{rx} = Thickness of reactor wall
x_i^{r1} = Stoichiometric constant of specie (i) in reaction 1

References

Hvala, N., Aller, F., Miteva, T., Kukanja, D., Oct. 2011. Modelling, simulation and control of an industrial, semi-batch, emulsion-polymerization reactor. Computers & Chemical Engineering 35 (10), 2066–2080.
URL http://linkinghub.elsevier.com/retrieve/pii/S0098135411001876

Hvala, N., Kukanja, D., Apr. 2013. Modelling and simulation of semi-batch polymerisation reactor for improved reactants dosing control. Simulation Modelling Practice and Theory 33, 102–114.
URL http://linkinghub.elsevier.com/retrieve/pii/S1569190X12001360

Nyström, A., 2007. Modeling and simulation of a multi phase semi-batch reactor. SIMS 2007, 173–182.
URL http://www.ep.liu.se/ecp/027/021/ecp072721.pdf

Pantelides, C., Renfro, J., Apr. 2013. The online use of first-principles models in process operations: Review, current status and future needs. Computers & Chemical Engineering 51, 136–148.
URL http://linkinghub.elsevier.com/retrieve/pii/S0098135412002360

Prokopová, Z., Prokop, R., 2009. Modelling And Simulation Of Chemical Industrial Reactors. ECMS (1).
URL http://www.scs-europe.net/conf/ecms2009/ecms2009 CD/ecms2009 accepted papers/ind_0044_24232ee3.pdf

Krist V. Gernaey, Jakob K. Huusom and Rafiqul Gani (Eds.), 12th International Symposium on Process Systems Engineering and 25th European Symposium on Computer Aided Process Engineering.
31 May – 4 June 2015, Copenhagen, Denmark

Dynamic Modelling and Experimental Validation of a Pilot-Scale Tubular Continuous Reactor for the Autohydrolysis of Lignocellulosic Materials

C. González-Figueredo[a], A. Sánchez[b*], G. Díaz[b], F. Rodríguez[b], R. Flores[b], M. A. Ceballos[b], R. Puente[a], H. A. Ruiz[c].

[a] *Instituto Tecnológico y de Estudios Superiores de Occidente, Departamento de Procesos Tecnológicos e Industriales, Tlaquepaque, Jalisco 45604, México. figueredo@iteso.mx*

[b] *Centro de Investigación y Estudios Avanzados, Unidad de Ingeniería Avanzada, Zapopan, Jalisco 45010, México arturo@gdl.cinvestav.mx*

[c] *Biorefinery Group, Food Research Department, School of Chemistry, Autonomous University of Coahuila, 25280, Saltillo, Coahuila, Mexico.*

Abstract

This work focuses on the dynamic modelling of a Pilot-scale Tubular Reactor (PTR) for the pre-treatment of lignocellulosic materials (LCM), with three main process stages: extrusion, autohydrolysis and steam explosion. The reactor was modelled as an arrangement of Continuous Stirred Tank Reactors (CSTR), in order to have the residence time (τ) as an explicit variable, to be used as input variable in the associated control scheme. This dynamic model also takes into account the production of intermediate oligosaccharides as well as of acetyl-compounds in the reaction rates. The model performance was validated with experimental data, consisting of concentration profiles of hemicellulose, cellulose, glucose and xylose in the PTR outlet stream, as well as temperature and acidity profiles. The proposed model is able to describe the dynamic behaviour of the PTR at 160 ºC and 75 psig, within reasonable tolerances.

Keywords: lignocellulosic material, autohydrolysis, pilot-scale reactor.

1. Introduction

The production of ethanol and other products from lignocellulosic materials (LCMs) is attracting great interest due to their low cost and vast availability. These raw materials represent an attractive source of fermentable sugars; nonetheless, their complex chemical structure makes it difficult to extract them from the lignocellulosic matrix. Traditionally, the ethanol production process from LCMs using biochemical platforms consists of four stages; pretreatment, enzymatic hydrolysis, fermentation and separation. The overall performance of this process depends highly on the pretreatment stage, due to its effect on the cellulose and hemicellulose accessibility in the LCM matrix for the enzymatic hydrolysis. This accessibility directly impacts on the process yields and costs (Mosier, et al., 2005).

There are several LCMs pretreatment alternatives consisting on physical, chemical and biological treatments aiming to improve the performance of the enzymatic hydrolysis stage of the ethanol production process. Physical treatment includes size reduction techniques and extrusion, which have been studied in order to improve the carbohydrates release from the biomass (Karunanithy, et al., 2008). Chemical treatments

consist mainly on the addition of alkalis or acids that perform a partial LCM hydrolysis. However, fermentation inhibiting products may be formed, and reactor corrosion may be a serious issue in the case of acid treatment (Saha, et al., 2005). Another physico-chemical treatment that greatly improves the process overall performances is the steam explosion. In steam explosion, LCM undergoes a treatment with high pressure steam, followed by a violent depressurization. The high temperatures promote acetic acid formation, which partially hydrolyses the biomass, and the depressurization process manages to separate its fibres (Pan, et al., 2005). Aiming to optimize the LCM pre-treatment performance without adding acids or alkalis under a continuos operation strategy, a pilot-scale tubular reactor for continuous wheat straw pre-treating was constructed.. The reactor design involves the sequential use of the extrusion, thermal hydrolysis and steam explosion techniques.

LCM hydrolysis models have been developed for batch reactors, but most of these models are not fully scalable because heat and mass transport phenomena, which are important in larger-than-bench scales, are usually not considered. Hence, the necessity of extending them for continuous reactor schemes. These kinetic studies involve first order pseudo-homogeneous kinetics (Mittal, et al., 2009), with Arrhenius temperature dependence, (Zhuang, et al., 2009). Other models make use of a severity factor R_0 (Overend, et al., 1987) to take into account the empiric measured effects, but fail to adequately describe the rise in saccharides concentrations caused by temperature changes (Kabel, et al., 2007). Other effects that are also considered in these kinetic models are the formation of acetic acid from acetyl groups, and its role in LCM autohydrolysis (Sidiras, et al., 2011).

This work focuses on the analysis and characterization of the continuous PTR for LCM pre-treatment, in which a sequence of extrusion, thermal hydrolysis and steam explosion processes takes place. As a first attempt at process modelling, thePTR was modelled as an arrangement of Continuous Stirred Tank Reactors (CSTR), in order to have the residence time (τ) as an explicit variable to be used as input variable in the design of the associated controller law. Model validation was performed with experimental data consisting on cellulose, hemicellulose, xylose and glucose concentration profiles in the reactor outlet stream, as well as its temperature and pH. This model is a first modelling attempt, aiming to define the role of each type of pre-treatment that takes place in the reactor, to define whether a more complex model is needed or not.

2. Pretreatment reactor modelling

2.1. Experimental reactor

Wheat straw pretreatment was performed in the PTR (3 meters long, 10 cm. diameter) at 160 ºC and 90 psig steam pressure. LCM with a particle size of 1.19 mm is fed to the PTR by an arrangement of hydraulic pistons that form a compact “wheat straw plug”, managing to maintain the inner pressure, and performing the extrusion pretreatment. After this, the wheat straw goes into the main reactor body, where it is heated with saturated steam at 160 ºC, and is transported through it by a screw conveyor. Finally, at the end of the tubular reactor, the LCM enters a chamber, where a set of automatic valves perform the steam explosion, while the main reactor body remains pressurized. The residence time inside the reactor can be manipulated between 50 to 10 minutes by

controlling the screw conveyor motor speed. In order to capture the dynamic behaviour of the reactor, experiments were performed applying step changes to the residence time.

2.2. Kinetic model

The tubular reactor kinetic characterization is based on the kinetic model presented by Sidiras, et al., (2011). This model considers the cellulose and hemicellulose hydrolysis to oligosaccharides, and then to glucose and xylose respectively. Acid activity is considered to change, mainly by the formation of acetic acid, produced from the acetyl groups in the LCM. This kinetic model is based on the following set of stoichiometric reactions:

$$RRH \xrightarrow{k_{H1}} WSOH \xrightarrow{k_{H3}} xylose \xrightarrow{k_{H4}} furfural \quad (1)$$

$$ERH \xrightarrow{k_{H2}} WSOH \xrightarrow{k_{H3}} xylose \xrightarrow{k_{H4}} furfural \quad (2)$$

$$CC \xrightarrow{k_{C1}} WSOC \xrightarrow{k_{C3}} glucose \xrightarrow{k_{C4}} HMF \quad (3)$$

$$AC \xrightarrow{k_{C2}} WSOC \xrightarrow{k_{C3}} glucose \xrightarrow{k_{C4}} HMF \quad (4)$$

$$AG \xrightarrow{k_A} AA \quad (5)$$

Where *RRH* stands for reaction resistant hemicellulose, *WSOH* for water soluble oligosaccharides from hemicellulose, *ERH* for easy reaction hemicellulose, *CC* for crystalline cellulose, *WSOC* for water soluble oligosaccharides from cellulose, *HMF* for hydroxymethyl furfural, *AC* for amorphous cellulose, *AG* for acetyl groups and *AA* for acetic acid.

First order kinetics are considered for the autohydrolysis of cellulose, hemicellulose and oligosaccharides, while the acidity kinetics are a first order function of acidity and the acidity at $t \to \infty$. Equations 6 through 12 describe the kinetic behaviour of the LCM autohydrolysis, where $i = C$ for cellulose hydrolysis, $i = H$ for hemicelluloses hydrolysis, $j = 1, 2, 3$ or 4; p_{ij} and E_{ij} are the pre-exponential factor (min^{-1}) and the activation energy (kJ/mol), respectively; a is the activity of the acids produced during the autohydrolysis, while a_∞ is the value for a for $t \to \infty$; A is the subscript for activity. All concentration values C_{ij} in this model are expressed in w/w units, based on the initial quantity of dry components in the reacting system. The rate constants k_{ij} were expressed in min^{-1}, the reaction time in minutes, and the temperature T in K. Table 1 contains the kinetic parameter values of this model.

$$r_{i1} = dC_{i1}/dt = -k_{i1}\, C_{i1} \quad (6)$$

$$r_{i2} = dC_{i2}/dt = -k_{i2}\, C_{i2} \quad (7)$$

$$r_{i3} = dC_{i3}/dt = k_{i1}\, C_{i1} + k_{i2}\, C_{i2} - k_{i3}\, C_{i3} \quad (8)$$

$$r_{i4} = dC_{i4}/dt = k_{i3}\, C_{i3} - k_{i4}\, C_{i4} \quad (9)$$

$$r_A = da/dt = k_A\, (a_\infty - a) \quad (10)$$

$$k_{ij} = p_{ij}\, a\, e^{-E_{ij}/RT} \quad (11)$$

$$k_A = p_A\, e^{-E_A/RT} \quad (12)$$

Table 1. Kinetic parameter for the lignocellulosic material (LCM) autohydrolysis

Kinetic parameters			
Component	ij	Frequency factor p_{ij} (min^{-1})	Activation Energy E_{ij} (kJ/mol)
Crystalline cellulose	C1	7.82×10^{14}	116.4
Amorphous cellulose	C2	5.22×10^{15}	116.4
WSOC	C3	1.40×10^{17}	125.0
Glucose	C4	1.23×10^{20}	164.0
RRH	H1	1.93×10^{15}	104.0
ERH	H2	1.40×10^{16}	104.0
WSOH	H3	4.30×10^{21}	156.5
Xylose	H4	4.50×10^{29}	232.5
pH	A	1.89×10^{4}	58.0

2.3. PTR model

Regardless that the reactor can be described by a traditional plug flow reactor (PFR) model, assuming that the reaction takes place in the main body of the reactor (substracting the spaces occupied by the screw conveyor and all the empty spaces on the porous LCM matrix), a simpler approach is herein proposed. A model based on a series of continuous stirred tank reactors (CSTR) was developed, in order to have the residence time (τ) as an explicit variable to be manipulated in the design of the associated control scheme. This model takes into account the kinetic model described in the previous section. The extrusion and steam explosion stages are not considered in this approach, due to the inherent difficulties in their modelling. Equation 13 describes the dynamic behaviour of the concentration of the species involves in each of the CSTR's.

$$\frac{dC_{ij,k}}{dt} = \frac{1}{\tau_k}\left(C_{ij,k-1} - C_{ij,k}\right) + r_{ij.k} \tag{13}$$

where τ_k is the residence time in each of the CSTR's, and is a result of dividing the overall process residence time by the total number or CSTRs n; k is the number of each reactor in the sequence, where $k = 0$ correspond to the different concentrations in the inlet stream.

2.4. Experimental set up

First, the wheat straw size was reduced to 1.19 mm, and then it was fed into the reactor at a continuous rate of 325 g/h, during 310 minutes. The LCM at the outlet stream was sampled every 10 minutes, and the solids were separated from the extract. *pH* measurements in the extract were performed with a ORION STAR A211 *pH* meter. Glucose and xylose concentration were measured with a biochemistry analyzer YSI 2700D Select. In the case of oligosaccharides, a second hydrolysis of the extract was carried out, now with sulfuric acid (4% v/v) at 121 °C for 1h.The hydrolizates were

analyzed with the YSI; the initial oligosaccharides concentration on the extract is subtracted to this reading. Finally, the extract was subject of one last acid hydrolysis stage, now with sulfuric acid (72% v/v), for 30 minutes at 30 °C, and then the monosaccharides concentration was measured; stoichiometric relations were used to calculate the hemicellulose concentration.

Table 2. Composition of Wheat Straw

Component	% w/w [a]	Component	% w/w [a]
Cellulose	32.7	Acid - insoluble lignin	16.8
Hemicelluloses	24.5	Ashes	4.7
Xylose	19.3	Extractives	6.2
Arabinose	2.7	Acid – soluble components	15.1
Acetyl groups	2.5	Cellulose degree of crystallinity	79.5
Reaction - resisting hemicelluloses	32.6		

[a] (% dry weight)

3. Results and Discussion

The composition of the wheat straw was taken from Sidiras (2011), shown in Table 2. These concentrations were used as the inlet composition in the autohydrolysis model (Eq. 6-13), and simulations were made under non-isothermal reaction conditions. First, simulation runs were performed varying the number of total CSTR's, in order to determine the number of tanks that can describe the tubular reactor behaviour within reasonable tolerance. Experiments were carried out with residence time set to a fixed value, until the steady state was reached; then a step perturbation was induced to the screw conveyor motor speed, in order to increase (or decrease) the residence time, and reach another steady state. Since discrete temperature and *pH* measurements were performed, interpolated profiles of these two variables were used on the respective simulations. Even when the experimental concentration profiles were somewhat irregular, the 4 CSTR's model was able to reproduce the tubular reactor dynamics within reasonable tolerances, as shown on Fig. 2. The irregular flow of the wheat straw inside the tubular reactor leaves empty spaces in the LCM bed, due to the screw conveyor speed. These irregularities on the tubular reactor flow, and some temperature fluctuations may cause the oscillations on the concentration profiles.

4. Conclusions

A first attempt to obtain a dynamic model for lignocellosic material (LCM) pretreatment in a pilot-scale tubular reactor was developed. This model is based on a kinetic model for wheat straw autohydrolysis with steam at 160 °C, and the approximation of a tubular reactor behaviour by an arrangement of continuous stirred tank reactors in series. This approximation describes, within reasonable tolerances, the dynamic behaviour of an experimental pilot scale reactor. The empty spaces inside the reactor body, may cause irregularities on the mass flow, which partially explains the differences between the experimental concentration profiles and the models dynamic response.. At these low

temperatures, the extrusion and steam explosion stages present low, if no contribution to the pre-treatment process, so it is not necessary to develop more complex models. It is expected that at higher temperatures, the contribution of these two pretreatment steps, play a greater role, and a more complex model is therefore needed.

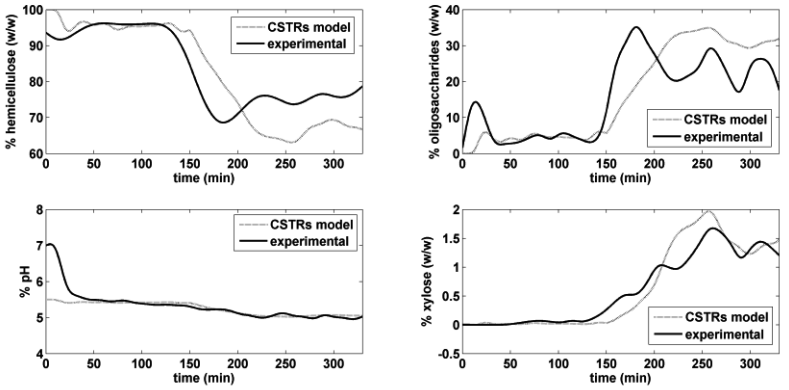

Figure 1. Experimental vs model concentration profiles: hemicellulose (top-left), oligosaccharides (top-right), pH (bottom-left) and xylose (bottom-right).

5. References

Kabel, M. A., et.al. , 2007, Effect of pretreatmen severity on xylan solubility and ezymatic breakdown of the remaining cellulose from wheat straw, Bioresource Technology, Vol. 98, Issue 10, pp. 2034-2042.

Karunanithy, C., Muthukumarappan, K. & Julson, J., 2008, Influence of high shear bioreactor parameters on carbohydrate release from different biomasses, ASABE Paper, Issue 84109.

Mittal, A., Chatterjee, S. G., Scott, G. M. & Amidon, T., 2009,Modeling xylan solubilization during autohydrolysis of sugar maple and aspen wood chips: Reaction kinetics and mass transfer, Chemical Engineering Science, Vol. 64, Issue13, pp. 3031-30141.

Mosier, N. et al., 2005, Features of promising technologies for pretreatment of lignocellulosic biomass, Bioresource Tecnology, Vol. 96, Issue 6, pp. 673-686.

Overend, R., Chornet, E. & Gascoigne, J., 1987, Fractionation of lignocellulosics by steam-aqueous pretreatments, Philosophical Transactions of the Royal Society of London. Series A, Mathematical and Physical Sciences, Vol. 321, Issue1561, pp. 523-536.

Pan, X. y otros, 2005, Strategies to enhance the enzymatic hydrolisis of pretreated softwood with high residual lignin content, Springer, pp. 1069-1079.

Saha, B., Iten, L., Cotta, M. A. & Wu, Y. V., 2005, Dilute acid pretreatment, ezymatic saccarification and fermentation of wheat sraw to ethanol, Process Biochemistry, Vol, 40, 12, pp. 3693-3700.

Sidiras, D., Batzias, F., Ranjan, R. & Tsapatsis, M., 2011,Simulation and optimization of batch autohydrolyisis of wheat straw to monosaccharides and oligosaccharides, Bioresource Technology, Vol. 102, Isuue22, pp. 10486-10492.

Zhuang, X. y otros, 2009, Kinetic study of hydrolysis of xylan and agricultural wastes with hot liquid water, Biotechnology Advances,Vol. 27, Isuue 5, pp. 578-582.

Krist V. Gernaey, Jakob K. Huusom and Rafiqul Gani (Eds.), 12th International Symposium on Process Systems Engineering and 25th European Symposium on Computer Aided Process Engineering.
31 May – 4 June 2015, Copenhagen, Denmark

First-Principles Model Diagnosis in Batch Systems by Multivariate Statistical Modeling

Natascia Meneghetti[a], Pierantonio Facco[a], Sean Bermingham[b],David Slade[b],Fabrizio Bezzo[a], Massimiliano Barolo[a,*]

[a]*CAPE-Lab – Computer-Aided Process Engineering Laboratory, Department of Industrial Engineering, University of Padova, via Marzolo 9, 35131 Padova PD (Italy)*
[b]*PSE – Process Systems Enterprise Ltd, 26-28 Hammersmith Grove, London W6 7HA (United Kingdom)*
max.barolo@unipd.it

Abstract

Process/model mismatch may arise when a first-principles model is challenged against historical experimental data. In this study, a methodology recently proposed to diagnose the root cause of the mismatch in continuous processes is extended to batch systems, taking a batch drying process as a case study to test the proposed methodology. The likely sources of the mismatch are identified using a multivariate statistical model and analyzing the model residuals as well as the scores shifts. Two simulated examples demonstrate the effectiveness of the proposed methodology.

Keywords: process/model mismatch, PCA, batch processes, latent variable models

1. Introduction

When a first principles (FP) model is challenged against a historical dataset, the model outputs may not match the historical evidence with the desired accuracy, and process/model mismatch (PMM) occurs. Recently, a methodology has been proposed to diagnose the root causes of PMM (Meneghetti et al., 2014) by exploiting the available historical dataset and a simulated dataset, generated by the FP model using the same inputs as those of the historical dataset. A data-based (DB) model (namely, a multivariate statistical model) is used to analyze the correlation structure of the historical and simulated datasets, and information about from where the PMM originates is obtained using diagnostic indices and engineering judgment. The methodology was developed for continuous processes. However, for batch processes the diagnosis of an observed PMM is more difficult because of the time-varying nature of the measurements, which imply data auto-correlation and cross-correlation, as well as a more strongly nonlinear behavior that may be difficult to capture using a linear multivariate model.

In this study, the PMM diagnosis methodology is extended to batch system, using a simulated semi-batch solids drying process as a test bed. Multi-way principal component analysis (MPCA; Nomikos and MacGregor, 1994) is employed as a DB model, enhancing it with an orthogonal rotation (VARIMAX rotation) of the principal directions (Magnus and Neudecker, 1999; Wang et al., 2005). Two examples are analyzed to discuss the ability of the proposed methodology to point to the FP model sections needing improvement.

2. Case study and available data

A simulated lab-scale drying process is considered, in which hot dry air flows through a bed of wet solid alumina granules, partially evaporating the water contained in the particles. The model equations derive from the work of Burgschweiger and Tsostas (2002), and are solved in the gSOLIDS® modeling environment (gSOLIDS®, 2014). The particle size distribution is discretized in 10 bins and no shrinkage of particles is considered. The global massand energy balances for the particulate phase and vapor phase (indicated by subscripts *p* and *vap*, respectively)are:

$$\frac{dM_{i,p}}{dt} = F_p^{in} x_{i,p}^{in} - F_p^{out} x_{i,p}^{out} - R_{drying,i,p} \;,\; \frac{dH_p}{dt} = F_p^{in} h_p^{in} - F_p^{out} h_p^{out} - \Delta H_{drying,p} \quad (1)$$

$$\frac{dM_{i,vap}}{dt} = F_{vap}^{in} x_{i,vap}^{in} - F_{vap}^{out} x_{i,vap}^{out} + R_{drying,i,p} \;,\; \frac{dH_{vap}}{dt} = F_{vap}^{in} h_{vap}^{in} - F_{vap}^{out} h_{vap}^{out} + \Delta H_{drying,p} \quad (2)$$

Where F is the mass flowrate, h is the specific enthalpy,x_i is the mass fraction of species i in the solid phase (alumina or water) or in the vapor phase (dry air or water), and superscripts *in* and *out* refer to the bed inlet and outlet, respectively. The drying rate $R_{drying,i,p}$ is given by:

$$R_{drying,i,p} = A_p \nu_i \rho_i k_{c,i} \left(Y_{eq,i} - Y_{bulk,i} \right), \quad (3)$$

And $\Delta H_{drying,p}$ is the enthalpy change rate due to drying. In (3), A_p is the particle surface area available for drying, ρ_i is the density of the gas phase, k_c is the mass transfer coefficient, and $Y_{eq,i}$ and $Y_{bulk,i}$ are respectively the equilibrium and actual dry-basis moisture content of the water in the gas phase. Finally, v_i is the normalized single-particle drying rate, which can be estimated from the experimental drying curve. The latter is a function of the normalized moisture content η_i, which is in turn calculated from the dry basis moisture content X_i, the equilibrium dry-basis moisture content $X_{eq,I}$ (which is a function of the relative humidity ϕ_i), and the critical dry basis moisture content $X_{cr,i}$. Details on the values of model parameters are reported in the original work of Burgschweiger and Tsostas (2002). This FP model will be referred to as "the process" in the following.

A set of $N = 25$ batches, representing the historical dataset, are simulated using different combinations of the following measurable inputs: inlet solid mass flowrate (F_p^{in}), initial moisture content (X^{in}), inlet mass flowrate (F_{vap}^{in}), and air temperature (T_{vap}^{in}). It is assumed that four measurable outputs exist: moisture content in the granules (X_i), granules temperature (T_p^{out}), outlet air temperature (T_{vap}^{out}), and outlet air relative humidity (ϕ_i). The batch length is 1420 s and the measurement interval is 30 s; hence, T=48 samples are available for each measured variable in each batch.

The PMM diagnosis methodology is tested by considering two process models that use the same set of equations as described above, but where two different parametric mismatches are purposely introduced. These sets of equations and (wrong) parameters will be referred to as "the model" in the following.

3. Proposed methodology

In order to diagnose the root-cause of an observed PMM, the framework proposed by Meneghetti et al. (2014)is applied. However, appropriate adjustments are introduced to deal with batch data. According to the proposed rationale, a DB model (namely, a latent variable model) is first developed to model the correlation structure of appropriate combinations of the simulated process variables, these combinations being suggested by the FP model structure. Then, it is assessed whether the combinations of the same variables, but calculated from the historical measurements, conform to this correlation structure. Finally, from the analysis of some model diagnostic indices, engineering knowledge is used pinpoint the FP model sections that are mostly responsible for the observed PMM. In detail, the following steps are followed (subscripts Π and M refer to the process and to the model, respectively).

1. Auxiliary data designation. A set of $C = 9$ auxiliary variables is defined considering the modele quation terms that, according to engineering judgment, are expected to be possibly related to the observed PMM:

$$\begin{aligned} u_1(n,t) &= A_P & u_4(n,t) &= \eta_i & u_7(n,t) &= T^{vap} \\ u_2(n,t) &= v_i & u_5(n,t) &= k_{c,i} & u_8(n,t) &= X_i \\ u_3(n,t) &= X_{eq} & u_6(n,t) &= \alpha_i & u_9(n,t) &= \phi_i \end{aligned} \tag{4}$$

   Where element (n, t) of the $[N\times T]$ matrix $\mathbf{U}_c$ is indicated by $u_c(n,t)$ and represents the c-th auxiliary variable evaluated at time t for batch n.In (4), i refers to water and α is the heat transfer coefficient involved in the calculation of the energy balances. The simulated and historical datasets are separately used to estimate the values of the auxiliary variables. The values taken by the auxiliary variables throughout the whole batches are arranged in the $[N\times C\times T]$ arrays $\underline{\mathbf{U}}_{\mathrm{M}}$ and $\underline{\mathbf{U}}_{\Pi}$, which are the model matrix and the process matrix, respectively.
   Note that the values taken by some auxiliary variables (u_1, u_2, u_4, u_5 and u_6) are bin-dependent. However, only the bin including the largest number of particles is considered for their calculation. Also note that variables T^{vap}, X_i and ϕ_I(which can be measured) are purposely included in the auxiliary variable set (u_7, u_8 and u_9) to make the available measurements directly affect the correlation structures of $\underline{\mathbf{U}}_{\mathrm{M}}$ and $\underline{\mathbf{U}}_{\Pi}$.
2. Data-based model development. An MPCA model (Nomikos and MacGregor, 1994) is built from $\underline{\mathbf{U}}_{\mathrm{M}}$. MPCA is equivalent to performing PCA (Jackson, 1991) on the $[N\times(C\cdot T)]$ matrix$\mathbf{U}_{\mathrm{M}}$obtained by unfolding $\underline{\mathbf{U}}_{\mathrm{M}}$ batch-wise. Also $\underline{\mathbf{U}}_{\Pi}$ is unfolded (to $\mathbf{U}_{\Pi}$), and both $\mathbf{U}_{\mathrm{M}}$ and $\mathbf{U}_{\Pi}$ are autoscaled on the mean and standard deviation of $\mathbf{U}_{\mathrm{M}}$. PCA decomposes $\mathbf{U}_{\mathrm{M}}$ as the sum of A scores $\mathbf{t}_i$ and A loadings $\mathbf{p}_i$, where A is the number of principal components (PCs) that describe an adequate percentage of the dataset variability:

$$\mathbf{U}_{\mathrm{M}} = \mathbf{t}_{1,\mathrm{M}}\mathbf{p}_{1,\mathrm{M}} + \mathbf{t}_{2,\mathrm{M}}\mathbf{p}_{2,\mathrm{M}} + \cdots + \mathbf{t}_{A,\mathrm{M}}\mathbf{p}_{A,\mathrm{M}} + \mathbf{E}_{\mathrm{M}} = \mathbf{T}_{\mathrm{M}}\mathbf{P}_{\mathrm{M}}{}^{\mathrm{T}} + \mathbf{E}_{\mathrm{M}}, \tag{5}$$

   where $\mathbf{T}_{\mathrm{M}}$ $[N\times A]$ is the scores matrix and $\mathbf{P}_{\mathrm{M}}$ $[(C\cdot T)\times A]$ is the loadings matrix.
   In both examples,4 PCs are selected. Note however that the selected number of PCs can affect the ability of the methodology to effectively diagnose an observed PMM. How to provide a general guideline for the selection of A is still under investigation.
   In this challenging case study, most of the auxiliary variables are very strongly correlated and provide similar contributions along all latent directions, thus

confounding the analysis. In order to amplify the contribution of each auxiliary variable on one latent direction only, the VARIMAX rotation is applied (Magnus and Neudecker 1999; Wang et al., 2005). This technique uses an orthogonal rotation to transform the MPCA model space so that only a subset of the auxiliary variables show high weight values along each PC. Upon VARIMAX application, the residuals matrix $\mathbf{E}_M$ is not modified, but can be calculated also from:

$$\mathbf{U}_M - \mathbf{T}_{var,M}\mathbf{P}_{var,M}^T = \mathbf{E}_M \,, \tag{6}$$

where $\mathbf{T}_{var,M}$ and $\mathbf{P}_{var,M}$ are (respectively) the scores and loadings matrices obtained by application of the VARIMAX rotation.

3. Process matrix projection. $\mathbf{U}_\Pi$ is projected onto the rotated MPCA model space and the residuals matrix $\mathbf{E}_\Pi$ is calculated as:

$$\mathbf{T}_{var,\Pi} = \mathbf{U}_\Pi \mathbf{P}_{var,M}\,, \quad \mathbf{U}_\Pi - \mathbf{T}_{var,\Pi}\mathbf{P}_{var,M}^T = \mathbf{E}_\Pi \tag{7}$$

4. Mismatch diagnosis. The mismatch may appear in the MPCA model as a large residual value or as a shift in the scores space (or both). For this reason, a mismatch analysis should evaluate both these aspects.
   The residuals analysis is performed by comparing $\mathbf{E}_M$ and $\mathbf{E}_\Pi$ to identify the auxiliary variables that are most responsible for the inconsistency in the correlation structures of $\mathbf{U}_M$ and $\mathbf{U}_\Pi$. These auxiliary variables, together with engineering judgment, are used to pinpoint which model sections are likely the cause of the observed PMM. In order to reduce the residuals contribution due to the fraction of data variability not described by the MPCA model, the results of residuals analysis are expressed using the mean residuals-to-limit ratio(MRLR), i.e. the mean of the ratios between the residuals of each column of $\mathbf{E}_\Pi$ and the corresponding 95 % confidence limit, calculated considering a normal distribution of the residuals for each variable (Choi and Lee, 2005;Meneghetti et al.,2014).
   An analysis of the scores shift can be performed by jointly analyzing $\mathbf{T}_{var,M}$, $\mathbf{T}_{var,\Pi}$ and $\mathbf{P}_{var,M}$. For each PC, the scores shift is calculated as $(\mathbf{t}_{a,M,var} - \mathbf{t}_{a,\Pi,var})$, i.e., as the difference between the model matrix scores and the process matrix scores. The rationale beyond this approach is to identify the auxiliary variables that most affect the scores shift. These variables are identified by analyzing the MPCA model loadings along the direction that most contributes to the shift.To this purpose, the use of the VARIMAX rotation is particularly effective, as it allows one to emphasize the contribution of a single auxiliary variable (or very few of them) along each PC.The information obtained by this analysis may reveal particularly useful when a small-dimension historical dataset is available.

4. Results for Example 1

The mismatch is forced by altering the value of the critical moisture content (which is involved in the calculation of η_i) and results in a relative error of 1.6-17 % in the simulated final dry-basis particle moisture content. Hence, to correctly diagnose the PMM, the proposed methodology should point to auxiliary variable $\mathbf{U}_4$.
The residuals analysis (not reported for the sake of conciseness) cannot clearly point to the root cause of the mismatch, since all auxiliary variables have similar and low values of MRLR (high residuals are actually seen in $\mathbf{U}_3$ and $\mathbf{U}_9$, but this happens at the very beginning of the batch only). The scores shift analysis is more effective, instead. Figure 1a reports the scores shifts for each batch together with the mean shifts through

all batches along each PC. By far the largest shifts are seen along PC2; hence, the auxiliary variables having a significant weight along this direction are possibly related to the observed PMM. The $[1\times(C\cdot T)]$ loadings $\mathbf{p}_{a,\mathrm{M,var}}$ are shown as black bars in Figure 1b. It can be seen that PC2 mainly captures the variability due to model terms $\mathbf{U}_2$ and $\mathbf{U}_3$, as well as that due to outputs $\mathbf{U}_7$ and $\mathbf{U}_9$. Hence, further investigation on the FP model should focus on the $\mathbf{U}_2$ and$\mathbf{U}_3$ terms. Model inspection suggests that their values are strongly and directly correlated to $\mathbf{U}_4$. Therefore, according to these considerations, to improve the FP model further investigation on model sections $\mathbf{U}_2$, $\mathbf{U}_3$ and $\mathbf{U}_4$ should be done. The other model sections (including those representing heat and mass transfer phenomena) are not likely sources of the observed PMM.

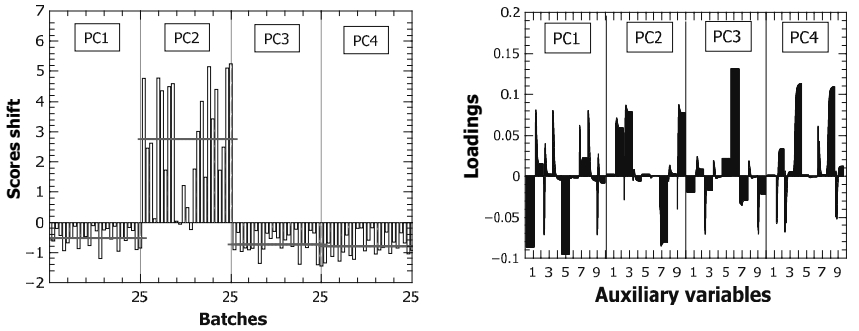

(*a*) (*b*)

Figure 1.Example 1. (a) Shift of $\mathbf{t}_{a,\mathrm{M,var}}$ from $\mathbf{t}_{a,\Pi,\mathrm{var}}$ for each batch(bars) and mean value of these differences (lines) for each PC. (b) Loadings for each PC obtained by applying the VARIMAX rotation to the MPCA model built on $\mathbf{U}_\mathrm{M}$.

5. Results for Example 2

The mismatch is forced by changing the mass transfer coefficient k_c, and results in a 1.3-37 % error in the simulated final dry-basis particle moisture content. Hence, to correctly diagnose the PMM, the proposed methodology should point to auxiliary variable $\mathbf{U}_5$.

Figure 2a reports the results obtained by the residuals analysis. Although, at the very beginning of the batches, MRLR peaks for auxiliary variables $\mathbf{U}_3$ and $\mathbf{U}_9$,consistently high MRLR values along the entire batch lengths are seen only on $\mathbf{U}_1$, $\mathbf{U}_5$ and $\mathbf{U}_6$. These latter auxiliary variables are therefore regarded as the most responsible ones for the observed PMM. As $\mathbf{U}_1$, $\mathbf{U}_5$ and $\mathbf{U}_6$ refer to the contact area and to the mass and heat transfer coefficients, their values are strongly correlated, so that it is difficult to furtherdiscriminate their contribution to the PMM.

Figure 2b reports the scores shift for each PC. Although the main direction of the scores shift is along PC1, this is clearly not dominant, because significant shifts occur also along the other principal directions. We conclude that several auxiliary variables concur to the shift occurrence, and the scores shift analysis does not effectively identify a likely PMM source.

Summarizing, according to proposed methodology the observed mismatch is not related to model sections $\mathbf{U}_2$, $\mathbf{U}_3$ or $\mathbf{U}_4$. Conversely, model sections $\mathbf{U}_1$, $\mathbf{U}_5$ and $\mathbf{U}_6$ should be investigated to improve the FP model performance.

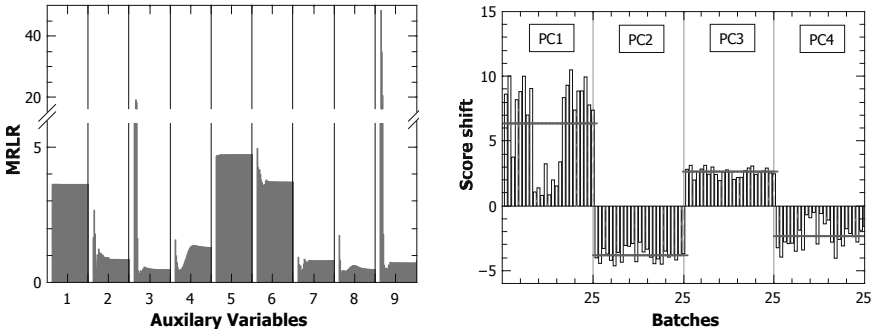

Figure 2. Example 2.(a) MRLR values for each auxiliary variable. (b) Shift of $\mathbf{t}_{a,\mathrm{M,var}}$ from $\mathbf{t}_{a,\Pi,\mathrm{var}}$ for each batch (bars) and mean value of these differences (lines) for each PC.

6. Conclusions

In this study,a recently proposed methodology to diagnose process/model mismatch has been extended to batch systems using a realistic model of a batch drying process as a test bed. The methodology exploits a set of historical data and a simulated dataset, generated by the first-principles model using the same inputs as those of the historical data set. Auxiliary variables were defined as appropriate nonlinear combinations of the model variables and parameters, as well as of process measurements. A multiway principal component analysis model was used to analyze the correlation structure of the historical and simulated data sets. Information on the root cause of the PMM was obtained by the combined analysis of two diagnostic indices: the data-based model residuals and the data-based model scores shifts. With respect to the scores shifts, an orthogonal rotation of the principal axes was carried out in order to magnify the contribution of the most significant auxiliary variables to the shifts.Two examples have been presented showing that the proposed methodology is able to direct the first-principles model improvement efforts towards the model sections that are truly affected by modeling errors.

Acknowledgments
Financial support from ‘‘Fondazione Ing. Aldo Gini’’ is gratefully acknowledged.

References

J. Burgschweiger, E. Tsotsas, 2002, Experimental investigation and modelling of continuous fluidized bed drying under steady-state and dynamic conditions, Chem. Eng. Sci., 57, 5021–5038.
S. W. Choi and I. B. Lee, 2005, Multiblock PLS-based localized process diagnosis, J.Process Control, 15, 295-306.
gSOLIDS®, 2014, (version 4.0), Process Systems Enterprise Ltd., London, UK.
J.E. Jackson, 1991, A User’s Guide to Principal Components, John Wiley & Sons, New York, NJ.
J.R. Magnus and H. Neudecker, 1999, Matrix Differential Calculus with Applications in Statistics and Econometrics, Revised Ed., pp 373-376.
N. Meneghetti,P. Facco, F. Bezzo, M. Barolo, 2014, A methodology to diagnose process/model mismatch in first-principles models, Ind. Eng. Chem. Res, 53, 14002-14013.
P. Nomikos,J.F.MacGregor, 1994, Monitoring Batch Processes Using Multiway Principal Component Analysis, AIChE J. 40, 1361–1375.
H. Wang, Liu, Q., Tu, Y., 2005,Interpretation of partial least-squares regression models with VARIMAX rotation,Comput. Stat. Data Anal., 48, 207-219.

Krist V. Gernaey, Jakob K. Huusom and Rafiqul Gani (Eds.), 12th International Symposium on Process Systems Engineering and 25th European Symposium on Computer Aided Process Engineering.
31 May – 4 June 2015, Copenhagen, Denmark

Integrated Analysis of an Evaporation and Distillation Bioethanol Industrial System Using Direct and Indirect Heating

Rodrigo O. Silva,[a*] Vandré C. Tiski,[a] Rafael O. Defendi,[a] Lucas B. Rocha, [a] Oswaldo C. M. Lima,[a] Laureano Jiménez, [b] Luiz Mario M. Jorge, [a]

[a]*Department of Chemical Engineering, State University of Maringa, 5790 Colombo Avenue, Maringa 87020-900 , Brazil, orgeda@hotmail.com*
[b]*Department of Chemical Engineering, University Rovira i Virgilli, 26 Paisos Catalans Avenue, Tarragona, 43007, Spain.*

Abstract

In this work we simulate and integrate the systems of evaporation, fermentation and distillation with direct heating. In addition, we propose a new scenario using indirect heating in order to decrease the quantity of stillage, and consequently, minimize environmental and economic impacts associated. In this sense, a reboiler using the steam produced in the evaporators is included in the distillation column to analyse the effect of such revamping. Sensitivity analyses were performed to detect some key operational variables with effect on the process. Results show that the replacement of direct steam injection by use of reboilers decreases significantly the quantity of stillage, consequently, minimizing the problems generated by it. Moreover, once there are no changes in flegma and ethanol mass flows, and the bleeding heat flow is suitable to exchange heat with reboilers, it means the replacement may be done without modify the industrial productivity.

Keywords: simulation, stillage, distillation columns, sugarcane, Aspen Hysys.

1. Introduction

Sugarcane processing is one of the most important and strategic sectors in the Brazilian economy. This important segment has steadily increased its activity in the last decades, propelling all sugarcane-related activities. It is expected that the 2013/2014 crop reaches 652 million tons, what in turn will suppose 27.17 billion liters processed in the ethanol distillation plants, a 15% increase compared to 2012/2013 (CONAB, 2013).

The success of Brazilian distilleries depends on how they overcome the new scientific challenges faced. The traditional sugarcane industry still presents a huge field to be explored, mainly regarding the optimization of process, energy integration, cogeneration, and sustainability (Amorim et al., 2011).

One of the scientific challenges to be faced is related to reduce the volume of sugarcane stillage (called vinasse). This final by-product of the biomass distillation is rich in minerals and is commonly used to irrigate sugarcane plantation (called fertirrigation); however, if it is produced in excess, may bring environment and economic problems. The direct application of stillage in the soil may cause salinization, leaching of metals present in the soil to groundwater (it may kill animals and aquatic plants), changes in

soil quality due to unbalance of nutrients, mainly manganese, alkalinity reduction, crop losses, increase of phytotoxicity and unpleasant odor (Santana and Machado, 2008). Moreover, vinasse may be a significant source of greenhouse gas emission to the atmosphere. Emissions may result from aerobic and anaerobic decomposition of the organic matter in vinasse that occurs during transportation, temporary storage or even after application to soil (Oliveira et al., 2013). In Brazil, the fertirrigation frequently becomes an economic problem once there is no enough area to apply it. This can happen when the plantation belongs to the suppliers or it is placed far away from the plant, making it impossible to transport (Christofoleti et al., 2013; Laime et al., 2011).

The rapid growth experienced by sugarcane industry in Brazil necessitates the design and installation of few new facilities, expansion, and optimization of the existing ones. Process analysis using a properly validated process simulator is essential to reduce production costs in each of these steps as well. Among the commercial process simulator, Hysys stands out due to its ease of use and quality databank even though it requires corroborating or adapting for applicability in sugarcane sector (Jorge et al., 2010).

The process simulator Aspen Hysys has been used in several technical and economic analysis of process. Modeling, simulation, validation, and analysis were successful performed by Jorge et al. (2010), using Hysys, for a sugarcane juice industrial evaporation system composed of a falling film evaporator followed by three short vertical-tube evaporators arranged in parallel. Ruhul et al. (2013) simulated the production of ethanol by fermentation of molasses using software Aspen Hysys 7.1 in order to investigate the effect of few important parameters like fermentation temperature or pressure, that affect the production of ethanol and to optimize those parameters. Sensitivity analysis is very useful to determine the impact of a particular variable or parameter on the process outcome.

In this work, simulation and analysis of a full-scale industrial evaporation system of an alcohol distillery (COCAFÉ) are performed using Aspen Hysys 8.4 process simulator. The research started using the validated industrial evaporation system made by Jorge et al. (2010) and integrated to the fermentation and distillation systems. The distillery of the Cooperativa Agrícola de Astorga Ltda (COCAFÉ), which is located in the northwest of Paraná State, Southern Brazil, processes around 180 tons/h of sugarcane juice, producing approximately 380m³/day of hydrated ethanol.

2. Methodology

The COCAFE process is simulated in Aspen Hysys 8.4. It offers a comprehensive thermodynamics foundation for accurate determination of physical properties, and phase behaviour. Aspen Hysys can be used to determine outlet process conditions if the inlet conditions are specified. The NRTL model was chosen because Marquini et al. (2007) compared the results obtained from simulations in ethanol distillation columns using the thermodynamic models and have found the NRTL model is the one that leads to the best results.

2.1. Process Description

The whole process of producing ethanol from sugarcane is shown in a block diagram in Figure 1.

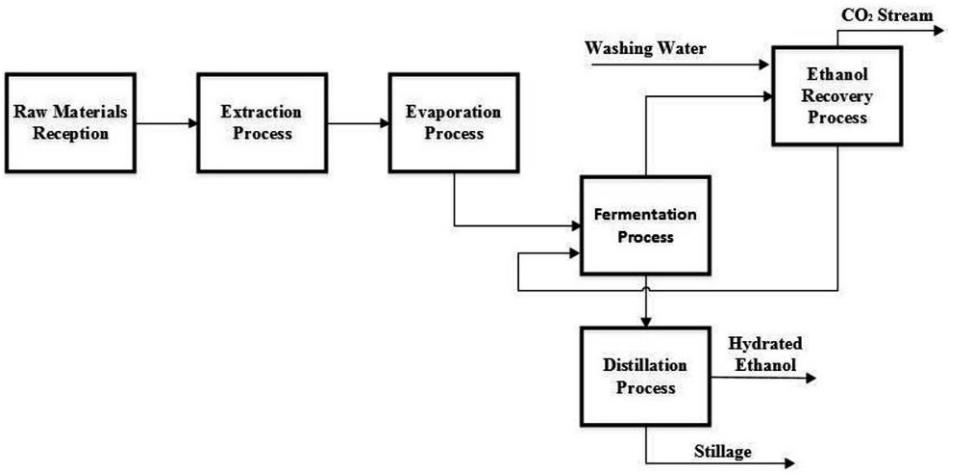

Figure 1. Process block diagram of COCAFÉ ethanol production from sugarcane.

2.2. Sugarcane Industry Hysys Model

The evaporation system was made based on Foust et al. (1982) who described an evaporator as basically consisting of a heat exchanger capable of raising the solution temperature up to the boiling point and a device for separating the vapour phase from the boiling liquid. Using this concept, Jorge et al. (2010) successfully simulated the COCAFÉ evaporation system using Aspen Hysys; each of the four evaporators was represented by the combination of a multitubular heat exchanger and a flash vessel (separator). In this work the evaporation system is composed by four combinations of heat exchanger and flash tank in order to represent four evaporators. The first combination represents the evaporation first effect which produces the Bleeding and the First Effect Stream that goes to the other three combinations of heat exchanger and flash tank representing the evaporation second effect. There is also a heater (E-100) between the first and second effect that simulates the necessity of high pressurized steam that happens when the first effect energy is not enough to heat the second effect. The input and output of the evaporation system are clarified juice, which contains 15,69% of sucrose and 84,31 of water in mass fraction, and concentrated juice, with 17,72% of sucrose and 82,28% of water in mass fraction.

The concentrated juice goes to the fermentation system which is composed by a fermentation column and an absorption column. The conversion was based on Ruhul et al. (2013) who specified the conversion of sucrose in the fermenter in 90%; glucose and fructose are converted into ethanol and carbon-dioxide, where conversion rate is defined as 95%. In this work the reaction involved is a global one (Equation 1) with 85,5% of conversion, which is the product of the two reactions cited.

$$C_{12}H_{22}O_{11} + H_2O = 4C_2H_5OH + 4CO_2 \quad (1)$$

As CO_2 gas leaving the fermenter carries away some ethanol with it, this gaseous stream is sent to absorption column. Here ethanol is absorbed by wash water. The gaseous stream leaving the absorber contains negligible amount of ethanol and this stream is vented in atmosphere. The liquid stream is recycled to the fermenter.

The liquid stream leaving the fermenter (Beer) is a very dilute ethanol solution (6,71% of ethanol and 93,29% of water in mass fraction). This stream is sent to the first distillation column (A-A1), operating with 26 equilibrium stages and total reflux in the condenser. The bottom product of this column is stillage and the middle product is called Flegma, which is a stream rich in ethanol (between 30 and 40% in volume fraction) that enters in the second distillation column (B-B1), also operated with total reflux in the condenser. The bottom product of the second column is Flegmass, also a by-product. Finally, the ethanol is withdrawn in the middle of the second distillation column with 93,2 ±0,6% of mass fraction. All the heating of the distillation columns is provided by direct steam injection in the bottom of A-A1 and B-B1 columns. In this model, the exclusive heating by direct steam injection is ensured by setting the reboilers heat flow of the streams Energy2 and Energy4 to 0 $kJ.h^{-1}$, and using the adjusts ADJ-1 and ADJ-2.

2.3. Comparative Study Between the Use of Reboilers and Direct Steam Injection

A comparative study is made removing the adjusts ADJ-1 and ADJ-2. Thus, it is analysed the heat flow offered by the Bleeding and the heat flow required by the reboilers of the first distillation columns in order to verify if Bleeding is capable to exchange heat with the reboiler. Furthermore, it is estimated the quantity of stillage decreased when the direct heating is replaced by indirect heating.

2.4. Sensitivity Analysis

After setting the process variables and with the simulation active it is possible to execute the sensitivity analysis increasing and decreasing our input variables in 5%. The input variables are the composition and the temperature of the clarified juice and the global conversion of the fermenter. The output variables are the ethanol and stillage mass flow for all cases. The quantity of steam injected in the distillation columns is fixed in order to not change the energy required.

3. Results and Discussion

The Table 1 presents the comparative study between direct steam injection and use of reboilers, which is the aim of the work. The Figure 2 shows the industrial system Hysys model including evaporation, fermentation and distillation process.

Table 1. Comparative study between the direct steam injection and the use of reboilers.

Mass Flow ($Kg.h^{-1}$)	Direct steam injection	Use of reboilers	Percentage variance (%)
Stillage	188600	161200	-14,53
Flegma	31790	31880	+0,28
Ethanol	15320	15330	+0,06

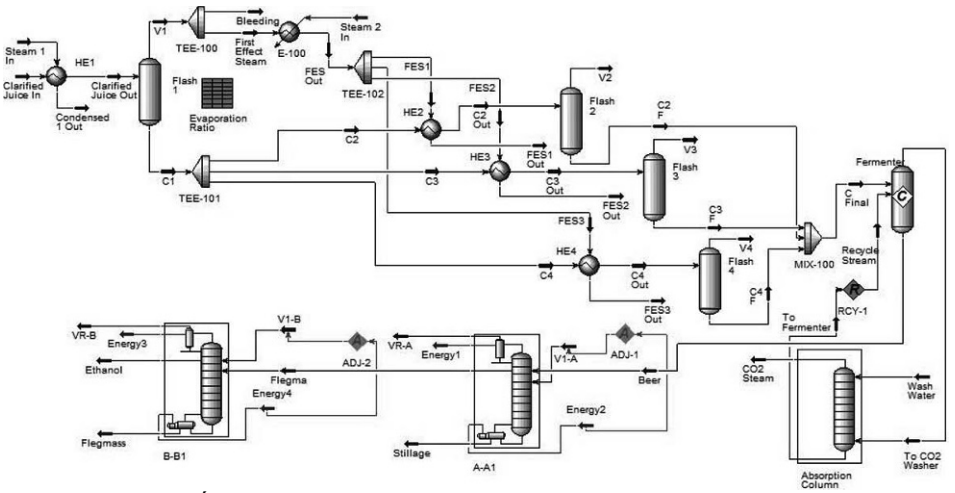

Figure 2. COCAFÉ Industrial system Hysys model.

There is a significant decrease of 14,53% of the stillage quantity produced. Decrease the amount of this by-product means to minimize the environmental and economic problems that it generates. In addition, the mass flows of flegma and ethanol have a very low variation; it shows the industry is able to do the replacement proposed without change the productivity. Figure 3 presents the results of the sensitivity analysis.

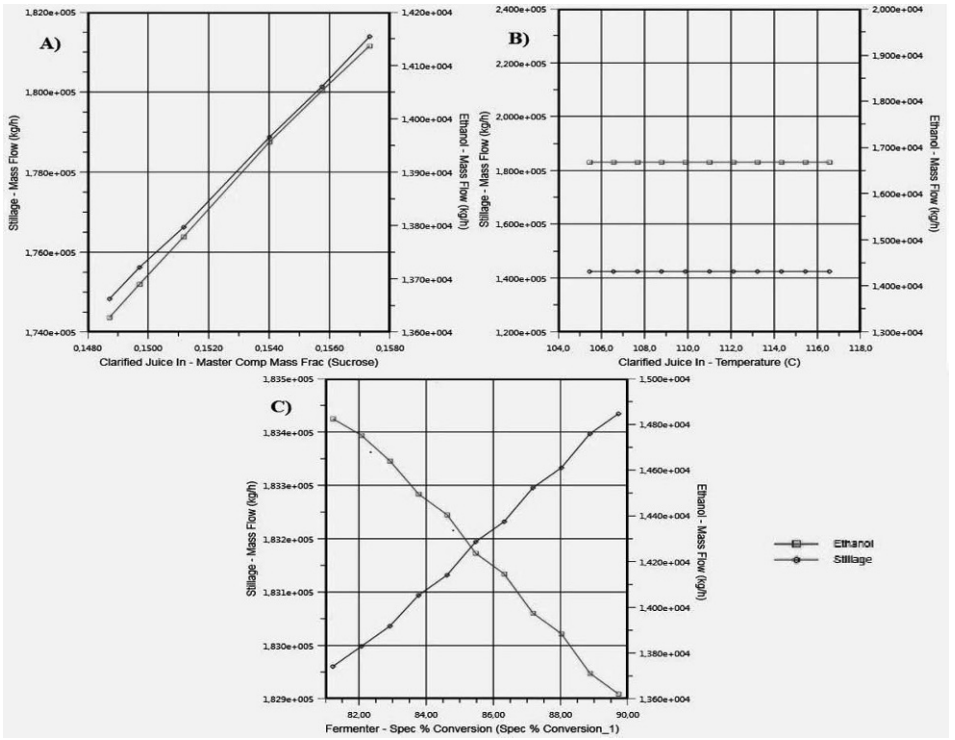

Figure 3. A) Sensitivity analysis of clarified juice composition B) Sensitivity analysis of clarified juice temperature C) Sensitivity analysis of fermenter conversion.

Figure 3 shows there is a direct proportionality between clarified juice sucrose composition and the outputs mass flow of stillage and mass flow of ethanol. On the other hand, these same outputs are not affected when clarified juice temperature is modified. The last sensitivity analysis indicates a direct proportionality between the fermenter global conversion and the mass flow of ethanol, but in inverse proportion to the mass flow of stillage.

Finally, when the adjusts ADJ-1 and ADJ-2 are removed, the stream Bleeding offers a heat flow of 1,674E08 $kJ.h^{-1}$ and the reboiler of the A-A1 column requires a heat flow of 7,378E07 $kJ.h^{-1}$. It may demonstrate that Bleeding is able to heat properly the reboiler proposed.

4. Conclusions

The adapted evaporation process was successfully integrated into the distillation process, inserting the fermentation and ethanol recovery process in Aspen Hysys V8.4. The sensitivity analysis indicated an increase in the flow of ethanol and stillage by increasing the sucrose in the clarified juice and its invariance with temperature. The variation of the fermenter global conversion is directly proportional to the flow of ethanol and inversely proportional to the mass flow of stillage.

The comparative study between direct steam injection and use of reboilers in the distillation process showed a reduction of 14.53% for stillage but a very low variation on ethanol and flegma mass flows; thus minimizing the environmental and economic impacts caused by vinasse and maintaining the standard of quality and productivity of the plant. Once the steam used in the indirect heating goes back to boiler, it shows it may optimize the heat integration of the process as well as reducing the operating cost of the plant when eliminating steam injection. Moreover, less vinasse means less cost to treat it before its application to soil. Finally, the simulated system without direct steam injection in distillation columns shows that the steam produced in the first effect evaporator has a suitable heat load to exchange heat with the proposed reboiler.

References

H.V. Amorim, M.L. Lopes, J.V.C.O. Oliveira, M.S. Buckeridge, G.H. Goldman, 2011, Scientific challenges of bioethanol production in Brazil, Applied Microbiology and Bioetechnology, 91(5), 1267-1275.

CONAB. Acompanhamento de safra brasileira : cana-de-açúcar, segundo levantamento, agosto/2013 - Companhia Nacional de Abastecimento. – Brasília : Conab 2013., p. 10. <http://www.conab.gov.br/conteudos.php?a=1253&t=2> (acessed 23.06.14).

C.A. Christofoletti, J.P. Escher, J.E. Correia, J.F.U. Marinho, C.S. Fontanetti, 2013, Sugarcane vinasse: environmental implications of its use, Waste Management, 33, 2752-2761.

L.M.M. Jorge, A.R. Righetto, P.A. Polli, O.A.A. Santos, R. Maciel Filho, 2010, Simulation and analysis of a sugarcane juice evaporation system, Journal of Food Engineering, 99, 351-359.

E.M.O. Laime, P.D. Fernandes, D.C.S. Oliveira, E.A. Freire, 2011, Possibilidades tecnológicas para a destinação da vinhaça: uma revisão, Revista Trópica, 5(3), 16-29.

M.F. Marquini, D.C. Mariani, A.J.A. Meirelles, O.A.A.S. Santos, L.M.M. Jorge, 2007, Análise de um sistema industrial de colunas de destilação, Acta Science Technology, 29(1), 23-28.

B.G. Oliveira, J.L.N. Carvalho, C.E.P. Cerri, C.C. Cerri, B.J. Feigl, 2013, Soil greenhouse gas fluxes from vinasse application in Brazilian sugarcane areas, Goderma, 77-84.

A.M. Ruhul, H.M. Saquib, M. Sarker, 2013, Simulation of ethanol production by fermentation of molasses, Journal of Engineering, 1(4), 69-73.

V.S. Santana, N.R.C.F. Machado, 2008, Photocatalytic degradation of the vinasse under solar radiation, Catalysis Today, 133, 606-610.

Krist V. Gernaey, Jakob K. Huusom and Rafiqul Gani (Eds.), 12th International Symposium on Process Systems Engineering and 25th European Symposium on Computer Aided Process Engineering.
31 May - 4 June 2015, Copenhagen, Denmark.

Reformulating The Minimum Eigenvalue Maximization In Optimal Experiment Design Of Nonlinear Dynamic Biosystems

Dries Telen[a], Nick Van Riet[a], Filip Logist[a] and Jan Van Impe[a]

[a]*KU Leuven; Department of Chemical Engineering; BioTeC+ & OPTEC; Willem de Croylaan 46; 3001 Leuven, Belgium*
jan.vanimpe@cit.kuleuven.be

Abstract

Experiments that yield as much information as possible are desired for estimating parameters in nonlinear dynamic bioprocesses. Techniques for optimal experiment design ensure the systematic design of such informative experiments. A possible objective function in optimal experiment design is the E-criterion which corresponds to the maximization of the smallest eigenvalue of the Fisher information matrix. However, a potential problem with the minimal eigenvalue function is that it can be nondifferentiable. In addition, a closed form expression does not exist for the computation of eigenvalues of a matrix larger than a 4 by 4 one. A reformulation strategy from the field of convex optimization is presented in this paper to circumvent the aforementioned difficulties. It requires the inclusion of a matrix inequality constraint involving positive semidefiniteness. The positive semidefiniteness constraint is imposed via Sylverster's criterion. By applying the suggested reformulation, the maximization of the minimum eigenvalue function can be implemented in standard optimal control solvers through the addition of nonlinear constraints.

Keywords: Dynamic optimization, Minimum eigenvalue optimization, Nonlinear matrix inequality, Sylvester's criterion, Predictive microbiology

1. Introduction

Dynamic bioprocess models play a valuable role to analyze, control and optimize bioprocesses in the biochemical industry. Identifying parameters in biosystems is, however, not trivial as these systems often exhibit a strong nonlinear nature. Especially, for cost intensive applications, it can be beneficial to design a dynamic control input such that an experiment is as informative as possible. An overview of the state of the art has been presented in, e.g., Franceschini and Macchietto (2008).

The uncertainty in the parameters can be quantified by the Fisher information matrix (FIM) (Walter and Pronzato (1997)). If the Fisher information matrix is used in an optimization routine, a specific scalar function has to be used as an objective function. Several functions have been proposed in the literature during the past decades, e.g., minimizing the trace of the inverse of the FIM (A-criterion), maximizing the determinant of the FIM (D-criterion) or maximizing the minimum eigenvalue of the FIM (E-criterion) (Franceschini and Macchietto (2008); Walter and Pronzato (1997); Telen et al. (2012); Houska et al. (2015)).

When gradient based optimization routines are applied, the E-criterion can pose numerical challenges. The main advantage of gradient based schemes is that they are fast and can tackle a

problem with a large number of decision variables. By construction is the FIM symmetric and positive semidefinite. So, all eigenvalues are nonnegative real numbers but the minimum eigenvalue function can be nondifferentiable. Furthermore, no closed expression exists for eigenvalues of a matrix larger than a 4 by 4 matrix. A reformulation of the problem can be used (Vandenberghe and Boyd (1996)) to overcome these problems. This reformulation involves a constraint requiring positive semidefiniteness. In the current paper this constraint is addressed by using Sylvester's criterion (Wicaksono and Marquardt (2013)) in order to enable the use of classic optimal control tools for solving the resulting large scale optimization problems.

The paper is structured as follows. Dynamic systems and the mathematical formulation of optimal experiment design are presented in Section 2. Section 3 discusses the suggested reformulation strategy and how positive semidefiniteness can be enforced using Sylvester's criterion. Section 4 introduces a case study from the field of predictive microbiology. The numerical simulation and optimization results are described in Section 5. Finally, the paper concludes with Section 6.

2. Mathematical formulation

This section discusses first the mathematical description of dynamic systems. In the second part, the formulation of optimal experiment design is presented.

2.1. Dynamic systems

Consider a system that is described by the following set of ordinary differential equations in the interval $t \in [0,\, t_\mathrm{f}]$:

$$\begin{aligned} \dot{x}(t) &= f(x(t), p, u(t))\,, && (1)\\ 0 &= b_\mathrm{c}(x(0))\,, && (2)\\ z(t) &= h(x(t))\,. && (3) \end{aligned}$$

Here, $x(t) \in \mathbb{R}^{n_\mathrm{x}}$ denotes the state vector, $p \in \mathbb{R}^{n_\mathrm{p}}$ a time-invariant parameter vector and $u(t) \in \mathbb{R}^{n_\mathrm{u}}$ is the vector of the control inputs. All these variables enter the right hand side function f in a possibly nonlinear way. The vector function b_c denotes the initial conditions of the system. The function $h(x(t))$ denotes the measurement function of the system which can be nonlinear but which is usually a subset of the states $x(t)$. The vector $z(t)$ is the measured output. If there are any path or terminal constraints present, these can be formulated as:

$$\begin{aligned} 0 &\geq c_\mathrm{p}(x(t), p, u(t))\,, && (4)\\ 0 &\geq c_\mathrm{t}(x(t_\mathrm{f}), p)\,. && (5) \end{aligned}$$

The measurement error, $\varepsilon(t)$ is assumed to be additive to $h(x(t))$ and normally distributed with zero mean, and variance-covariance matrix $Q(t)$.

2.2. Optimal experiment design

In this paper *optimal experiment design for parameter estimation* (OED/PE) is considered. The information content in the experiment is quantified by a suitable measure of the Fisher information matrix. This matrix is defined as:

$$F(t_\mathrm{f}) = \int_0^{t_\mathrm{f}} \frac{\partial x}{\partial p}(t)^\top C(t)^\top Q(t)^{-1} C(t) \frac{\partial x}{\partial p}(t) dt\,. \qquad (6)$$

As the true values for p are not exactly known, the Fisher information matrix is evaluated at the current best guess. The expression $C(t) = \frac{\partial h(x(t))}{\partial x}$ denotes the derivative of the measurement function $h(x(t))$ with respect to the states, x. So, the Fisher information matrix combines information about the variance-covariance matrix of the output error measurements, $Q(t)^{-1}$ and the sensitivities of the states with respect to small variations in the model parameters, $\frac{\partial x}{\partial p}(t)$. These sensitivities are computed as the solutions of the following additional differential equations:

$$\frac{d}{dt}\frac{\partial x}{\partial p}(t) \quad = \quad \frac{\partial f}{\partial x}\frac{\partial x}{\partial p}(t) + \frac{\partial f}{\partial p} \quad \text{with} \quad \frac{\partial x}{\partial p}(0) = \frac{\partial}{\partial p} b_{\mathrm{c}}(x(0)) = 0. \tag{7}$$

Several scalar maps of the Fisher information matrix have been proposed in the literature for the design of informative experiments (Walter and Pronzato (1997)), e.g., A-criterion (minimizing the trace of the inverse of the Fisher information matrix), D-criterion (maximizing the determinant of the Fisher information matrix). In the current paper the focus is on the E-criterion, maximizing the smallest eigenvalue of the Fisher information matrix:

$$\max \lambda_{\min}\left(F(t_{\mathrm{f}})\right). \tag{8}$$

This design criterion aims at minimizing the largest parameter error and corresponds to minimizing the length of the largest uncertainty axis of the joint confidence region. For the E-criterion, there is, however, a problem with the use of the minimum eigenvalue function in the derivative-based optimization routines.

It is possible that the derivative does not exist. Consider the following tutorial example, with a parametrized matrix A:

$$A = \begin{pmatrix} 1 & 0 \\ 0 & k \end{pmatrix}. \tag{9}$$

The evolution of the minimum eigenvalue function as function of the parameter k is depicted in Figure 1. It illustrates that the minimum eigenvalue function of the matrix A is continuous everywhere but that it is not differentiable for $k = 1$. How this problem can be avoided, is discussed in the following section.

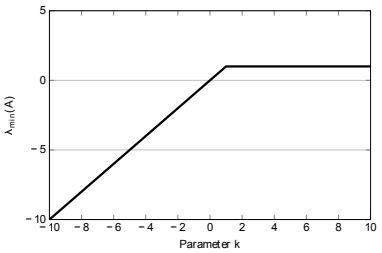

Figure 1: Illustration of the minimum eigenvalue function of the matrix A.

3. Reformulation strategy

Using a well-known reformulation strategy from the field of convex optimization, the minimum eigenvalue optimization is reformulated. An additional parameter τ is introduced which is to be maximized. To relate τ with the minimum eigenvalue, a new constraint is added, see Equation (16). The latter equation ensures that τ is bounded by the minimum eigenvalue of the Fisher information matrix. The reformulated problem is described as (Vandenberghe and Boyd (1996)):

$$\max_{u(\cdot),x(\cdot),\frac{\partial x}{\partial p}(\cdot),F(\cdot),\tau} \quad \tau \tag{10}$$

subject to:

$$\frac{dx}{dt}(t) = f(x(t), p, u(t)) \text{ with } 0 = b_{\mathrm{c}}(x(0)), \tag{11}$$

$$\frac{d}{dt}\frac{\partial x}{\partial p}(t) = \frac{\partial f}{\partial x}\frac{\partial x}{\partial p}(t) + \frac{\partial f}{\partial p} \quad \text{with} \quad \frac{\partial x}{\partial p}(0) = \frac{\partial}{\partial p} b_{\mathrm{c}}(x(0)) = 0, \tag{12}$$

$$\frac{d}{dt}F(t) = \frac{\partial x}{\partial p}(t)^{\top} C(t)^{\top} Q(t)^{-1} C(t) \frac{\partial x}{\partial p}(t) \quad \text{with} \quad F(0) = 0, \tag{13}$$

$$0 \geq c_{\mathrm{p}}(x(t), p, u(t)), \tag{14}$$

$$0 \geq c_{\mathrm{t}}(x(t_{\mathrm{f}}), p)\ , \tag{15}$$

$$F(t_{\mathrm{f}}) - \tau I \succeq 0\ . \tag{16}$$

In this dynamic optimization formulation, the last equation, $F(t_{\mathrm{f}}) - \tau I \succeq 0$ denotes that $F(t_{\mathrm{f}}) - \tau I$ is required to be positive semidefinite, i.e., $\forall z \in \mathbb{R}^{n_{\mathrm{p}}} :\ z^{\top}(F(t_{\mathrm{f}}) - \tau I) z \geq 0$. Equation (16) is a nonlinear matrix inequality as the Fisher information matrix is nonlinearly dependent on the decision variables. This optimization problem can be solved by linearization such that a *linear matrix inequality* is obtained. This formulation allows the use of a semidefinite program solver (e.g., SeDuMi (Sturm, 1999)) such that the whole dynamic optimization problem can be solved by sequential semidefinite programming (Telen et al. (2014)). The problem, however, is that standard optimal control tools do not have such dedicated semidefinite program solvers.

Positive semidefiniteness can also be guaranteed using a result from linear algebra. The Sylvester criterion states that *a matrix A is positive definite if the determinant of all its principal minors is positive* (Wicaksono and Marquardt (2013)) or mathematically expressed:

$$\det(A[(1:i) \times (1:i)]) > 0 \quad \text{with} \quad i = 1, \ldots, n_{\mathrm{p}}. \tag{17}$$

This reformulation allows the nonlinear matrix inequality (16) to be rewritten in n_{p} additional inequality constraints. This leads to the following problem formulation:

$$\max_{u(\cdot), x(\cdot), \frac{\partial x}{\partial p}(\cdot), F(\cdot), \tau} \tau \tag{18}$$

subject to:

$$\frac{dx}{dt}(t) = f(x(t), p, u(t)) \quad \text{with} \quad 0 = b_{\mathrm{c}}(x(0)), \tag{19}$$

$$\frac{d}{dt}\frac{\partial x}{\partial p}(t) = \frac{\partial f}{\partial x}\frac{\partial x}{\partial p}(t) + \frac{\partial f}{\partial p} \quad \text{with} \quad \frac{\partial x}{\partial p}(0) = \frac{\partial}{\partial p} b_{\mathrm{c}}(x(0)) = 0, \tag{20}$$

$$\frac{d}{dt}F(t) = \frac{\partial x}{\partial p}(t)^{\top} C(t)^{\top} Q(t)^{-1} C(t) \frac{\partial x}{\partial p}(t) \quad \text{with} \quad F(0) = 0, \tag{21}$$

$$0 \geq c_{\mathrm{p}}(x(t), p, u(t)), \tag{22}$$

$$0 \geq c_{\mathrm{t}}(x(t_{\mathrm{f}}), p)\ , \tag{23}$$

$$0 < \det\left((F(t_{\mathrm{f}}) - \tau I)\,[(1:i) \times (1:i)]\right) \quad \text{with} \quad i = 1, \ldots, n_{\mathrm{p}}. \tag{24}$$

The above formulation allows the incorporation of the maximization of the minimum eigenvalue in standard optimal control tools. Problems with the nondifferentiability of the objective function are avoided and positive semidefiniteness is ensured through the addition of n_{p} nonlinear constraints.

Remark. The information is quantified using the classic Fisher information matrix approach. The reformulation of Equations (18) - (24) can also be used if a different computational method for the approximation of the parameter variance-covariance is used, e.g., the unscented transformation (Heine et al. (2008)).

4. Case study

The case study considered in this paper originates from the field of predictive microbiology. In this field (dynamic) models are constructed to describe the growth, survival and inactivation of micro-organisms in food products. The model concerns the *Cardinal Temperature Model with Inflection point* (CTMI) (Rosso et al. (1993)). This is an adaptation of the Baranyi and Roberts model which describes microbial growth (Baranyi and Roberts (1994)). The dynamic model equations are:

$$\frac{dn(t)}{dt} = \frac{Q(t)}{Q(t)+1}\mu_{\max}(T)[1-\exp(n(t)-n_{\max})]\,, \tag{25}$$

$$\frac{dQ(t)}{dt} = \mu_{\max}(T)Q(t)\,. \tag{26}$$

In this set of equations $n(t)$ [ln(CFU/ml)] expresses the logarithm of the cell density. The factor containing $Q(t)$ is a black-box factor which is introduced to describe the experimentally observed lag phase. $Q(t)$ is assumed to represent a physiological state of the cell population during the lag or adaptation phase. The CTMI model describes the temperature dependency of the maximal growth rate, i.e., $\mu_{\max}(T)$ (Rosso et al. (1993)). If the temperature is below the minimum temperature for growth $T_{\min}$ or above the maximum temperature for growth $T_{\max}$, the maximum specific growth $\mu_{\max}$ is set to 0. The mathematical expression of the CTMI is:

$$\begin{cases} \mu_{\max}(T) = \mu_{\text{opt}}\gamma(T), & \forall T \in [T_{\min}, T_{\max}]\,, \\ \gamma(T) = \frac{(T-T_{\min})^2(T-T_{\max})}{(T_{\text{opt}}-T_{\min})((T_{\text{opt}}-T_{\min})(T-T_{\text{opt}})-(T_{\text{opt}}-T_{\max})(T_{\text{opt}}+T_{\min}-2T))}\,, & \\ \mu_{\max}(T) = 0, & \forall T \notin [T_{\min}, T_{\max}]\,. \end{cases} \tag{27}$$

The computation is performed with the optimal control package ACADO (Houska et al., 2011). A single shooting approach (Telen et al., 2014) is employed and all simulations are performed on a 64 bit Ubuntu 12.04 system with an Intell Core 2 Quad CPU 3.00 Hhz and 4.00 GB RAM.

5. Simulation results

The obtained E-optimal temperature profile and the corresponding predicted cell density $n(t)$ are illustrated in Figure 2 and 3. The maximum value of the smallest eigenvalue that is obtained is 1.887. For a single optimization is the computational time below 120 s when a feasible initialization is provided. The temperature profile in Figure 3 starts at the maximum allowed temperature of

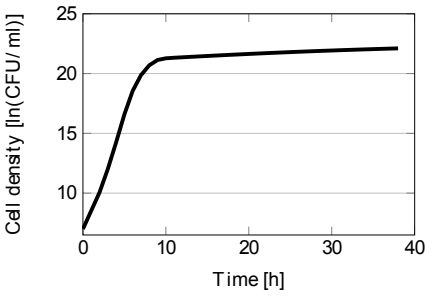

Figure 2: Cell density $n(t)$ resulting from the optimized control profile.

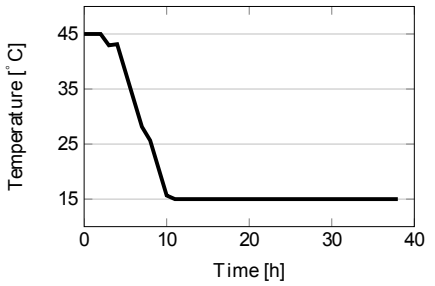

Figure 3: Optimized control profile with 38 degrees of freedom.

45°C and remains at this temperature for 2 hours after which there is a small decrease to 43°C. After 6 hours, there is a steady decrease in temperature until the lowest possible temperature value of

15°C is reached for the remainder of the experiment. The temperature profile is the result from an optimization procedure allowing for a piecewise linear approach in 38 intervals. The temperature profile results in a minimum eigenvalue of 1.89. This illustrates that small temperature changes in the complex profile are indeed contributing significantly to the information content as measured with the minimum eigenvalue of the Fisher information matrix. The effect of the temperature profile is also visible in the expected cell density profile in Figure 2. The optimized temperature profile results in a larger cell density growth. This is the result from the temperature profile evolution between 2 and 4 hours in the experiment. The designed temperature is in this interval closer to the optimal growth temperature profile T_{opt} and thus results in a larger increase of the cell density. In the next 6 hours there is a rapid increase in the cell density concentration due to the temperature being closer in the range of the optimal growth temperature. Subsequently, after 10 hours the growth decreases as the temperature remains constant at 15°C for the remainder of the experiment.

6. Conclusions

A reformulation strategy for minimum eigenvalue maximization in optimal experiment design has been presented in this work. This function can be nondifferentiable and no explicit expression exists for matrices larger than a 4 by 4 matrix. In this paper a reformulation from the field of convex optimization has been employed for designing optimal dynamic experiments. This introduces a matrix inequality requiring positive semidefiniteness. Positive semidefiniteness can be enforced using Sylvester's criterion. This approach allows the maximization of the minimum eigenvalue in standard optimal control solvers by the addition of several nonlinear constraints. Consequently, accurate derivatives can be obtained and numerical problems are avoided.

Acknowledgments: DT has a PhD grant of the IWT-Vlaanderen. JVI holds the chair Safety Engineering sponsored by essenscia. The research was supported by: PFV/10/002 (OPTEC), FWO KAN2013 1.5.189.13, FWO-G.0930.13 and BelSPO: IAP VII/19 (DYSCO).

References

J. Baranyi, T. Roberts, 1994. A dynamic approach to predicting bacterial growth in food. International Journal of Food Microbiology 23, 277–294.

G. Franceschini, S. Macchietto, 2008. Model-based design of experiments for parameter precision: State of the art. Chemical Engineering Science 63, 4846–4872.

T. Heine, M. Kawohl, R. King, 2008. Derivative-free optimal experimental design. Chemical Engineering Science 63, 4873–4880.

B. Houska, H. Ferreau, and M. Diehl, 2011. ACADO Toolkit - an open-source framework for automatic control and dynamic optimization. Optimal Control Applications and Methods, 32, 298–312.

B. Houska, D. Telen, F. Logist, M. Diehl, J. Van Impe, 2015. An economic objective for optimal experiment design of nonlinear dynamic processes. Automatica, 51, 98–103.

L. Rosso, J., Lobry, J., Flandrois, 1993. An unexpected correlation between cardinal temperatures of microbial growth highlighted by a new model. Journal of Theoretical Biology 162, 447–463.

R. Schenkendorf, A. Kremling, M. Mangold, 2009. Optimal experimental design with the sigma point method. IET Systems Biology 3, 10–23.

J. Sturm, 1999. Using SeDuMi 1.02, a MATLAB toolbox for optimization over symmetric cones. Optimization Methods and Software 11–12, 625–653, version 1.05 available from `http://fewcal.kub.nl/sturm`.

D. Telen, F. Logist, E. Vanderlinden, and J. Van Impe, 2012. Optimal experiment design for dynamic bioprocesses: a multi-objective approach. Chemical Engineering Science, 78, 82–97.

D. Telen, F. Logist, R. Quirynen, B. Houska, M. Diehl, J. Van Impe, 2014. Optimal experiment design for nonlinear dynamic (bio)chemical systems using sequential semidefinite programming. AIChE Journal 60, 1728–1739.

L. Vandenberghe, S. Boyd, 1996. Semidefinite programming. Society for Industrial and Applied Mathematics Review 38, 49–95.

E. Walter, L. Pronzato, 1997. Identification of Parametric Models from Experimental Data. Springer, Paris.

D. Wicaksono, W. Marquardt, 2013. Reformulation strategies for eigenvalue optimization using Sylvester's criterion and Cholesky decomposition. In: Proceedings of the 23rd European Symposium on Computer Aided Process Engineering (ESCAPE23). pp. 487–492.

Krist V. Gernaey, Jakob K. Huusom and Rafiqul Gani (Eds.), 12th International Symposium on Process Systems Engineering and 25th European Symposium on Computer Aided Process Engineering.
31 May - 4 June 2015, Copenhagen, Denmark.

A Framework for Modular Modeling of the Diesel Engine Exhaust Gas Cleaning System

Andreas Åberg[a], Thomas K. Hansen[a], Kasper Linde[a], Anders K. Nielsen[a], Rune Damborg[a], Anders Widd[b], Jens Abildskov[a], Anker D. Jensen[a] and Jakob K. Huusom[a*]

[a]*Department of Chemical and Biochemical Engineering, Technical University of Denmark, Søltofts Plads, Building 229, DK-2800 Kgs. Lyngby, Denmark*
[b]*Haldor Topsøe A/S, Nymøllevej 55, DK-2800 Kgs. Lyngby, Denmark*
[*]*jkh@kt.dtu.dk*

Abstract

Pollutants from diesel engines have a negative effect on urban air quality. Because of this and new legislation restricting the emission level, it is necessary to develop exhaust gas treatment systems for diesel engines that can reduce the amount of pollutants. A modular model capable of simulating the whole catalytic exhaust system would be beneficial towards this goal. A methodology for developing a modular model capable of simulating a system consisting of several sub systems is presented. The methodology describes the steps the user should take to go from problem formulation to the final modular model. Four different models in the automotive diesel exhaust gas cleaning system are presented briefly. Based on the presented methodology, it is discussed which changes are needed to the models to create a modular model of the whole catalytic system.

Keywords: Modeling, Automotive flue gas treatment, Simulation

1. Introduction

Diesel engine exhaust gases contain several harmful substances. The main pollutants are carbon monoxide (CO), hydrocarbons (HC), particulate matter (PM), and nitrous gases such as nitrogen monoxide (NO) and nitrogen dioxide (NO_2) (together abbreviated NOx). Reducing the amount of these substances is of great importance due to new legislation, and because of the effect they have on urban air quality (A. Fritz and V. Pitchon, 1997; R. M. Heck and R. J. Farrauto, 2001). In a modern EU VI exhaust gas cleaning system the flue gases are typically handled with four different catalysts: a Diesel Oxidation Catalyst (DOC) which oxidizes HC and CO, and NO into NO_2, a Diesel Particulate Filter (DPF) which filters PM, a Selective Catalytic Reduction (SCR) catalyst where ammonia (NH_3) is added to remove NO, and NO_2, and an Ammonia Slip Catalyst (ASC) which removes excess NH_3 before the gases are released to the atmosphere. A representation of the system can be seen in Fig. 1. To be able to fully understand and optimize the system without using too many resources, it is beneficial to be able to simulate the complete system under different scenarios. A modular model consisting of different blocks representing the different catalysts would be able to simulate almost all configurations of diesel flue gas cleaning systems. The main advantage with a modular structure is that it allows for changes in a single or several blocks. For example, the model structure or the catalyst formulation in one of the catalysts can be changed with minimal effort. Volumes of the catalysts, parameter values, etc. can be changed

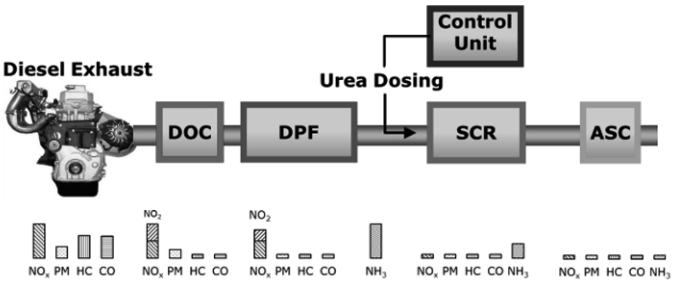

Figure 1: A typical EU VI diesel engine exhaust gas cleaning system. The column charts show the relative concentration, and the effect each catalyst has on the composition.

to investigate the effect the changes will have on the overall system performance. It would be possible to go between different catalyst setups, for example EU V and EU VI. It would also be possible to simulate combinational dynamic effects, for example how changing one catalyst will affect the dynamics of the whole system. The experimental effort can be reduced substantially if the model accurately can describe the system. To achieve this, models of the catalysts have to be developed or collected from literature and modified in a way so that they can work together.

Modeling of the different catalysts independently is a well studied area. The DOC has been modeled by for example (Y.-D. Kim and W.-S. Kim, 2009), early DPF modeling was done by (E. J. Bissett, 1984), and more recently for example by (C. Depcik et al., 2013). The SCR has been modeled by (D. Chatterjee et al., 2005) and (X. Song et al., 2013), and the ASC by (M. Colombo et al., 2012). To the authors knowledge, no effort has been done to develop a methodology to combine independently developed models to create a modular model combining all the catalyst in the system, that is aimed at simulating the complete exhaust system during transient operation. Some software exists that are able to simulate the whole system, for example AVL Boost (2014) and Exothermia SA (2014). Commercial software is however limited with regards to programming language, model structure, and interface, while the presented methodology allows the user to use his or her favourite. This paper will briefly present four different models that have been independently developed at DTU Chemical Engineering. It will present a methodology of the steps needed to make a modular model based on independently developed models. The methodology will be used to investigate the necessary steps to combine the models in the automotive exhaust gas after treatment system into a modular model for the whole catalytic system.

2. Methodology

This section will present a suggested methodology of necessary steps to make a modular model that is able to handle transient simulation. Step 1 through 7 below are the suggested steps.

1. Problem formulation.
2. Model collection and understanding.
3. Data collection.
4. Modification into dynamic formulation.
5. Equalization of the inputs and outputs for the models.
6. Implementation of the models in compatible software.
7. Model validation.

Step 1 involves a proper formulation of the problem: what is the application and how many underlying models are necessary to describe the system. This step will also clearly define if the

presented methodology is the correct one to use, since the user should realise if a modular model is needed. Based on the requirements formulated in 1, the relevant models will be collected in step 2. This involves both physical models and kinetic models if the system is chemical. It also concerns understanding the system to such a degree that it can be concluded if a fully dynamic model is necessary, or if the dynamics are so fast that a pseudo-steady state model is enough to handle a transient input. Step 3 involves collection of data for the models. If the models are collected from literature, some physical constants and kinetic constants that are required might be unavailable. Based on the analysis in step 2 and the current configuration of the collected models, step 4 requires the user to modify the models into a dynamic formulation. For the models to be able to work together, the inputs and outputs must be matched in all the underlying models, which is done in step 5 of the methodology. To be able to simulate the models together, step 6 tells the user to implement the models in compatible software. When the modular model is working, a recommended step is to validate the model. Since the nature of the model is modular, it will require much experimental effort to validate all configurations, thus it is preferable to use well validated models from the start.

3. Case Study: Automotive Diesel Exhaust Gas Cleaning System

3.1. Models

This section will present an overview of independently developed models and the physics of the catalysts. The specific information about the presented models comes from models developed at DTU, but the methodology can be used with models found in literature as well.

For the DOC, SCR and ASC, the catalyst is made up from several small channels, with two phases in each channel: a bulk phase and a washcoat phase. The channel walls are made from washcoat, which contain the active catalytic material.

3.1.1. Diesel Oxidation Catalyst Model

A single monolith channel for the DOC can be represented as in Fig. 2, which was the basis for the model development. A one dimensional heterogeneous plug-flow reactor (PFR) model was used to model the energy and mass equations for both bulk and washcoat phases. The two phases were coupled through the transport coefficients for convective heat and mass transfer. The developed model is fully dynamic and can handle transient simulations. The model is able to calculate the concentration of CO, O_2, NO, HC, CO_2, H_2O, and NO_2, as well as the gas temperature. The inputs and outputs to and from the catalyst are the gas velocity, the gas composition (CO, O_2, NO, HC, CO_2, H_2O, and NO_2), and the gas temperature. The reaction kinetics were based on the work by (S. E. Voltz et al., 1973), and the kinetic constants were also taken from literature.

3.1.2. Diesel Particulate Filter Model

The wall-flow DPF has the geometry of a catalytic converter, but with plugged opposite ends of adjacent channels. Unfiltered exhaust gases enter the inlet channels and pass through the porous substrate layer orthogonal to the inlet flow direction, before it exits through the outlet channel. During DPF operation, a deposit layer of soot will build up on the substrate layer, leading to an increasing pressure drop over time. The model was developed around a single inlet/outlet channel and involves quasi-steady state equations of mass, momentum, and energy for the exhaust gases along with dynamic equations for particle mass and temperature for the filter substrate. A schematic view of a single inlet/outlet channel can be seen in Fig. 3a. The model tracks the changes in concentration of NO, NO_2, O_2, CO, and CO_2, and uses the filter substrate temperature

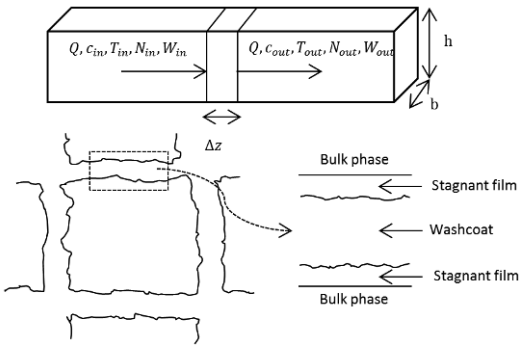

Figure 2: Schematic view of a single channel in a DOC and SCR catalyst.

to compute reaction speed for the kinetics. The kinetics are based on the work of (A. Messerer et al., 2006). The inputs and outputs to and from the model are: exhaust mass flow rate, inlet gas composition (NO, NO_2, O_2, CO, and CO_2), gas temperature, and outlet pressure.

3.1.3. Selective Catalytic Reduction Catalyst Model

The physics of the monolith channels were described with a plug-flow reactor model, as in the DOC model. The model is dynamic and can handle transient inputs. A complicating factor in the SCR kinetics is that adsorbed NH_3 on the catalyst surface is involved in all the relevant reactions. The NH_3 is supplied to the catalyst by injecting aqueous urea before the catalyst, which decomposes into NH_3. The kinetic model used was a modification of the work done by (L. Olsson et al., 2008), and the kinetic parameters were calibrated using stationary isothermal data from a bench-scale monolith. The model was validated using transient data from a full-scale monolith and a real engine. The inputs and outputs to and from the model are the gas velocity, the gas composition (NH_3, NO, NO_2, and N_2O), and the gas temperature.

3.1.4. Ammonia Slip Catalyst Model

The washcoat of the ASC has a different configuration from the other catalysts. The washcoat phase consists of two different layers. At the top there is an SCR layer and at the bottom an NH_3-oxidation layer, as illustrated in Fig. 3b. The excess NH_3 from the SCR catalyst will enter the

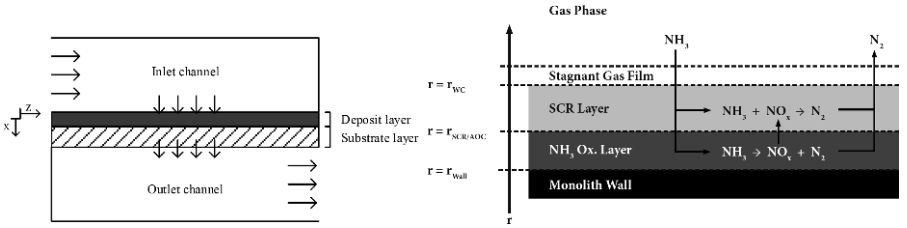

(a) Schematic view of a single inlet/outlet channel in a DPF.

(b) Schematic view of the phases in the modeled ASC.

Figure 3: Schematic views of the washcoat construction in the DPF and ASC.

ASC and transport from the bulk phase to the washcoat, diffuse into the washcoat where some of it will adsorb onto the SCR surface. Some NH_3 will diffuse further into the oxidation layer. The NH_3-oxidation is not selective towards N_2, but instead produces mostly NOx. This is unwanted since the exhaust gases have already been cleaned of NOx. This is the reason for placing an SCR layer at the top of the washcoat. The produced NOx will be reduced to N_2 when its diffuses back into the bulk phase. This catalyst design requires that a model has resolution into the washcoat. To model the catalyst a steady-state tanks-in-series approach was used to describe the bulk phase, and a steady-state reactive diffusion equation was used to describe the washcoat phase. The kinetic model and the kinetic parameters for the SCR layer were taken from the work of (D. Chatterjee et al., 2007) and the NH_3-oxidation kinetic parameters were estimated with experimental data. The inputs and outputs to and from the catalyst are the volumetric flowrate, and the gas composition (NH_3, NOx, and N_2O). The model does not contain any energy equations, and therefore does not give any output temperature.

3.2. Results

This section will apply the methodology to the presented models by discussing the changes needed to make them work together.

Step 1: The requirement is a model that can simulate the whole automotive exhaust gas cleaning system, from the gases exits the engine until they are released to the atmosphere. The model should be able to be used to investigate how changes in specific catalysts will affect the performance of the exhaust system, and also make simulations on the standard EU VI system to reduce experimental effort. Based on these requirements it becomes clear that a modular model is needed, and the methodology should be used.

Step 2: The models presented in Sec. 3.1 are the ones the author would like to use. Due to the washcoat diffusion occuring in the washcoat in the DOC, SCR and ASC, it is likely that a fully dynamic model is required and a pseudo-steady state approach is not enough. Some of the DPF dynamics are fast enough to allow that some of the equations in the DPF model are pseudo-steady state.

Step 3: Physical parameters and kinetic parameters are supplied with the models, thus no additional work is needed to collect more parameters.

Step 4: The models for the DOC and SCR are already fully dynamic and no work is required for modification. As previously explained the DPF model is a combination of equations that assume pseudo-steady state and dynamic ones. The time-scale of the dynamics of the phenomena described by pseudo-steady state assumptions are however so short that they are still able to handle transient behaviour. The time-scale of the dynamics in the ASC are in the same range as the SCR dynamics. Since the equations only consider steady state, they will have to be modified into a dynamic formulation. This can be done without much effort, since the model is a tanks-in-series model.

Step 5: The different models are not consistent in their inputs and outputs regarding chemical species. Two options are available: add components missing from some sub models and state that the catalyst has no effect on the composition of these species. An example of this is to add PM, which is needed in the DPF model, to the other models. The other option is to critically examine if all species are needed. Two examples of this are CO_2 and H_2O in the DOC model. These appear in much higher concentration than the other species, so the concentration will be practically unaffected by the reactions occuring. The suggested action for this system is to add PM, N_2O, HC, CO and NH_3 to all the models, and remove the variation in CO_2, O_2, and H_2O in all the models, and say that the concentration of these species is constant. All the sub models except the ASC have heat models calculating the output temperature. This is a required input to all models and a heat model for the ASC therefore has to be developed. All the models require

a quantity related to the flow, such as velocity or volumetric flow. This can easily be changed through density and cross sectional area.

Step 6: All the models have been implemented in Matlab, and can therefore be used together in for example Simulink.

Step 7: The models have been validated separately either with data from literature or with experimental data. A useful validation test for the finished modular model would be to simulate the standard EU VI exhaust treatment system and compare with data.

4. Conclusions

The proposed methodology to develop a transient modular model based on independently developed models was used on the automotive diesel exhaust gas cleaning system by discussing the required steps needed in order to get the models to work with each other in a modular model. The methodology included problem formulation, model collection, and modifying the model inputs, outputs, and formulation so they can work together. It also included implementation in compatible software and model validation. From the case study it was concluded that the ASC model needs to be modified into a dynamic formulation, and a heat equation added. It was also concluded that N_2O, HC, CO and NH_3 should be added, and that CO_2, O_2, and H_2O should be removed from all models.

5. Acknowledgment

The financial support from Innovation Fund Denmark under Grant number 103-2012-3 is gratefully acknowledged.

References

A. Fritz, V. Pitchon, 1997. The current state of research on automotive lean NOx catalysts. Appl. Catal. B 13, 1–25.

A. Messerer, R. Niessner, U. Poschl, 2006. Comprehensive kinetic characterization of the oxidation and gasification of model and real diesel soot by nitrogen oxides and oxygen under engine exhaust conditions: Measurement, langmuir-hinshelwood, and arrhenius parameters. Carbon 44, 307–324.

AVL Boost, 2014.
URL https://www.avl.com/sv/boost

C. Depcik, J. C. Ragone, O. Haralampous, G. Koltsakis, 2013. Catalyzed diesel particulate filter modeling. Rev. Chem. Eng. 29, 1–61.

D. Chatterjee, T. Burkhardt, B. Bandl-Konrad, T. Braun, E. Tronconi, I. Nova, C. Ciardelli, 2005. Numerical Simulation of Ammonia SCR-Catalytic Converters: Model Development and Application. SAE Paper, doi: 10.4271/2005-01-0965.

D. Chatterjee, T. Burkhardt, M. Weibel, I. Nova, A. Grossale, E. Tronconi, 2007. Numerical simulation of zeolite- and V-based SCR catalytic converters. SAE paper, doi: 10.4271/2007-01-1136.

E. J. Bissett, 1984. Mathematical model of the thermal regeneration of a wall-flow monolith diesel particulate filter. Chem. Eng. Sci 39, 1233–1244.

Exothermia SA, 2014.
URL http://www.exothermia.com/home/index.php

L. Olsson, H. Sjövall, R. J. Blint, 2008. A kinetic model for ammonia selective catalytic reduction over Cu-ZSM-5. Appl. Catal. B 81, 203–217.

M. Colombo, I. Nova, E. Tronconi, 2012. A simplified approach to modeling of dual-layer ammonia slip catalysts. Chem. Eng. Sci 75, 75–83.

R. M. Heck, R. J. Farrauto, 2001. Automobile exhaust catalysis. Appl. Catal., A 221, 443–457.

S. E. Voltz, C. R. Morgan, D. Liederman, S. M. Jacob, 1973. Kinetic study of carbon monoxide and propylene oxidation on platinum catalysts. Ind. Eng. Chem. Prod. Res. Dev. 12, 294–301.

X. Song, G. Parker, J. H. Johnson, J. Naber, J. Pihl, 2013. A Modeling Study of SCR Reaction Kinetics from Reactor Experiments. SAE Paper, doi: 10.4271/2013-01-1576.

Y.-D. Kim, W.-S. Kim, 2009. Re-evaluation and Modeling of a Commercial Diesel Oxidation Catalyst. Ind. Eng. Chem. Res. 48, 6579–6590.

Krist V. Gernaey, Jakob K. Huusom and Rafiqul Gani (Eds.), 12th International Symposium on Process Systems Engineering and 25th European Symposium on Computer Aided Process Engineering.
31 May – 4 June 2015, Copenhagen, Denmark

An Approximate Modelling Method for Industrial L-lysine Fermentation Process

Hangzhou Wang[a], Faisal Khan[a], Bo Chen[b], Zongmei Lu[c],

[a] *Safety and Risk Engineering Group, Faculty of Engineering and Applied Science, Memorial University, St. John's, NL A1B 3X5, Canada, fikhan@mun.ca*
[b]*COFCO Nutrition and Health Research Institute, Beijing, 102209, China*
[c]*COFCO Biochemical (AnHui) Co., Ltd., Bengbu, Anhui, 233010, China*

Abstract

L-lysine is an important chemical, usually produced by fed-batch fermentation process. Usually, feed stock compositions, reactant or product concentrations, and operating conditions vary with different fed-batches in this process. It is difficult to establish a kinetics-based model for an industrial fed-batch fermentation process. In this paper, we proposed a data-based approximate graphical modelling method to model this process. Variables values are treated as correlated Gaussian process. The methodology comprises of two important steps: i) the missing-data imputation within records, and ii) the dynamic Bayesian network learning, including structure learning, using the low order conditional independence method, and parameters learning, using the multivariate auto regressive method. The L-lysine fed-batch fermentation process is studied to demonstrate the effectiveness of this approximate modelling method.
Keywords: L-lysine, fed-batch fermentation, Gaussian approximate, missing-data imputation, dynamic Bayesian network

1. Introduction

L-Lysine is one of the most important amino acids, which is used as food and feed supplements, human medicine, pharmaceuticals, cosmetics, polymer materials, and agricultural chemicals. More than 2 million tons of L-lysine are annually produced by microbial fermentation (Anastassiadis, 2007; Brautaset et al., 2007). L-lysine is mainly produced by fermentation, using strains of coryneform bacteria. Corynebacterium glutamicum is commonly used. This is a multi-step process including fermentation, cell separation by centrifugation or ultrafiltration, product separation and purification by crystallization, evaporation and drying (Anastassiadis, 2007; Claes and Bathe, 2014). To get better performance (yield, productivity, and titer) than batch and continuous culture, fed-batch cultures are used in this fermentation process. There are some advantages of fed-batch culture, such as prevention of substrate inhibition, high cell density cultivation, cultivation of auxotrophic mutants, etc. (Kiss and Stephanopoulos, 1991; Zuo and Wu, 2000). However, fed-batch culture is more complicated to operate than batch or continuous cultures. Because concentrated sugar solution, ammonium sulphate solution, and liquid ammonia are continuously fed into the culture medium at speeds that frequently change during the fermentation process, to maintain concentrations of glucose, ammoniacal nitrogen and pH value, and this operation increases the complexity of non-linearity and time varying characteristics which is already very complex in batch or continuous fermentation. High cell density increases the L-lysine productivity, while costing more carbon sources and reducing the yield of L-lysine on glucose. Precise control of the feeding speeds and the fermentation conditions is essential for balancing the trade-off of obtaining high concentration and

high yield of L-lysine product with low operation cost. An accurate model is needed for optimization and controlling. However, fermentation processes are complicated for modelling, because they involve complex transport phenomena, diverse biochemical reactions, and dynamic intracellular interactions (Valente et al., 2009). Furthermore, experiences of workers also play an important role in processes operating. As a result, it is complicated to establish an accurate and kinetic-based model of fed-batch fermentation processes for bulk chemicals, such as L-lysine. Additionally, in the industrial production environments the following problems are observed: i) the compositions of energy and nutrient sources (carbon, nitrogen, mineral etc.) are complicated and may vary from batch to batch due to the demand for low-cost raw materials, ii) the lack of robust online or *in situ* continuous monitoring instruments for important fermentation process parameters in industrial fermenters (Beutel and Henkel, 2011) causes the lack of continuous recorded data for kinetic modelling, such as concentrations of substrates, products and by-products in the fermentation culture, iii) a defined feeding strategy which is the base for many kinetic modelling, such as constant feeding strategy, is usually not the optimal strategy (Salehmin et al., 2013) in industrial fermentation practices, iv) the inconsistency of workers' operation and equipment increase the inconsistency between batches. Fortunately, there are plenty of accumulated records from DCS, quality testing and regular sampling during process operating. Methods that do not rely on a kinetic model but large quantity of data sets, such as artificial neural networks, etc., have been explored in modelling and optimizing the fed-batch (Valente et al., 2009). Here we introduce our trials of applying a dynamic Bayesian network based probability graphical modelling method for modelling the fed-batch fermentation process of L-lysine with data records from the L-lysine factory of COFCO.

2. Methodology

The schematic of approximate graphical modelling methodology is shown in Figure 1. The methodology comprises of two important steps: i) the missing-data imputation, and ii) dynamic Bayesian network learning (including structure learning and parameter learning).

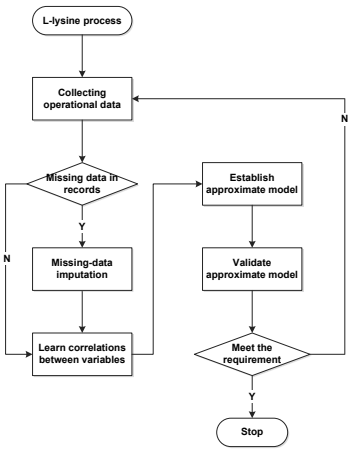

Figure 1. Approximate modelling methodology

2.1. Missing-data imputation

Operating data records are incomplete sometimes; only key variable values or broths in key stages are analyzed and recorded. Methods for treating missing data includes

discarding data, parameter estimation and imputation (Batista and Monard, 2002). Imputation methods replace missing values with estimated ones based on information available in the data set itself. There are two types of imputation methods: i)single imputation (e.g. mean/mode imputation, mean imputation, conditional mean imputation), ii) multiple imputation (e.g. hot decking, hot decking by covariate pattern, hot decking by observation, hot decking including outcome, multiple imputation by chained equations and k-nearest neighbor imputation) (Ambler et al., 2007). The mean/mode imputation is one of the most frequently used methods. This method replaces the missing data for a given attribute by the mean. In this paper, the mean/mode method is used to impute the missing data.

2.2. Dynamic Bayesian network

Bayesian networks have been applied to different areas including medical diagnosis, gene modelling, cancer classification, sensor validation, risk management, and reliability analysis (Yu and Rashid, 2013). However, there are limited literature reports on the use of Bayesian networks for approximate modelling of complex processes. Here we try to use dynamic Bayesian network (DBN) to establish the approximate fermentation process model. Dynamic Bayesian network is a type of graphical models for conducting time-varying probabilistic inference and causal analysis under system uncertainty (Yu and Rashid, 2013). Up to now, various dynamic Bayesian network representations based on different probabilistic models have been proposed: i) discrete models (Ong et al., 2002; Zou and Conzen, 2005), ii) multivariate autoregressive process (Opgen-Rhein and Strimmer, 2007) , iii) State Space or Hidden Markov Models (Beal et al., 2005; Perrin et al., 2003; Rangel et al., 2004; Wu et al., 2004), iv) nonparametric additive regression model (Imoto et al., 2001; Kim et al., 2004; Kim et al., 2003; Sugimoto and Iba, 2004), v) low order independence model (Lèbre, 2009). Dynamic Bayesian network can deal with continuous variables state (Murphy and Mian, 1999), with condition probability distribution $P(\mathbf{X}_t = \mathbf{x}_t \mid \mathbf{X}_{t-1} = \mathbf{x}_{t-1}) = N(\mathbf{x}_t; \boldsymbol{\mu} + \mathbf{W}\mathbf{x}_{t-1}, \boldsymbol{\Sigma})$ between two neighbored time slices, and the distribution is the normal distribution at $\mathbf{x}_t$. Dynamic Bayesian network can deal with cycled correlation in networks, this is an advantage compare to static Bayesian networks. Consequently, we could represent and study the multivariate time series fermentation data in an approximate graphical model. In this paper we use the low order conditional independence method (Lèbre, 2009) to learn the structure of the dynamic Bayesian network, and multivariate autoregressive process method (Opgen-Rhein and Strimmer, 2007) to learn the parameters.

3. Case study

3.1. *Operational data*

Usually, L-lysine is fermented in fed-batch culture, the variables at certain time slice, between different batches, can be treated as a normal distribution. Here, key variables, accumulated amount of sugar and $(NH_4)_2SO_4$ fed in to the fermenter, Optical Density ("OD"), pressure of the fermenter ("pressure"), dissolved oxygen ("DO"), Air flux and L-lysine concentration ("L-lysine") change with time in different fed-batch operations. These variables values are presented in Figure 2, together with means and 90% credible intervals as a Gaussian process.

3.2. *Approximate model*

We established the dynamic Bayesian network as a probability graphical model for this process. The correlations between seven recorded key variables are illustrated in the digraph network in Figure 3. Every node in the network is a Gaussian process, and the edges describe the influences between these variables.

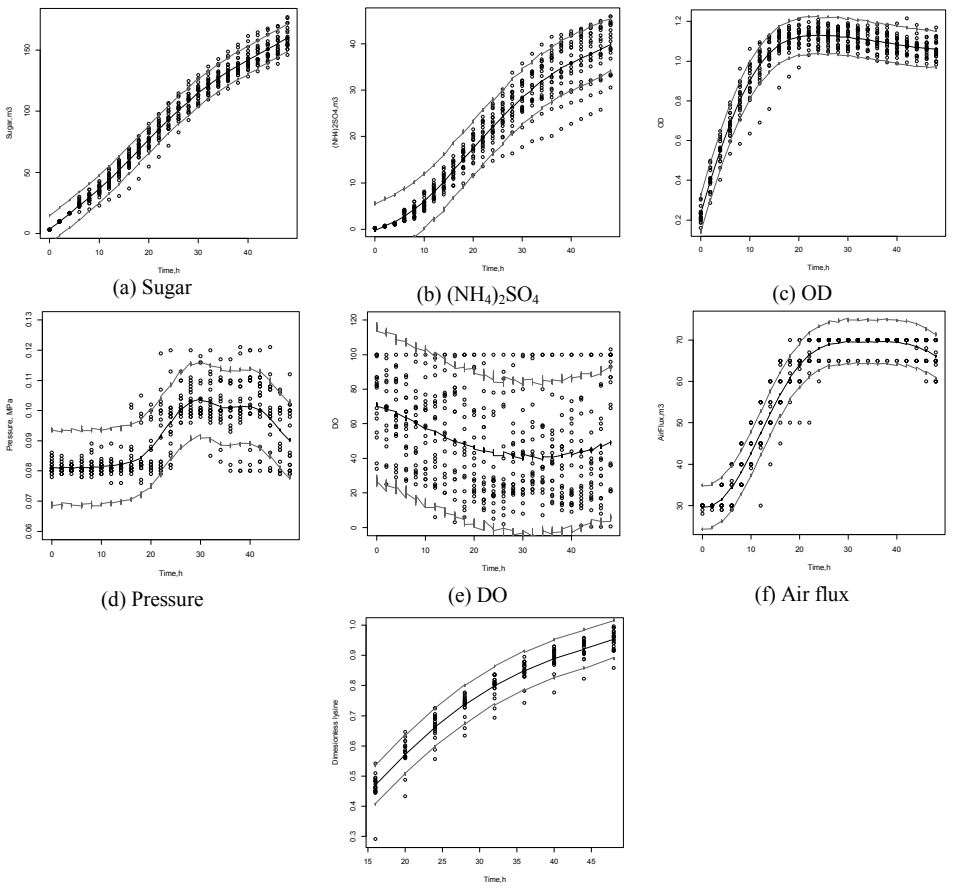

Figure 2. Sugar, $(NH_4)_2SO_4$, OD, Pressure, DO, Air flux and L-lysine change with time in different fed-batches operations, with means and 90% credible intervals as Gaussian process

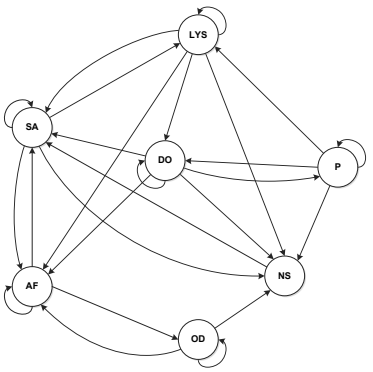

Figure 3. Approximate probability graphical model, SA: sugar, NS: (NH4)2SO4, OD: Optical Density, P: pressure; DO: dissolved oxygen, AF: Air flux and LYS: L-lysine concentration

3.3. Model validation

After learning the parameters, we get the approximate graphical model. With this result, we can validate the model with predicted variable values. Such as, we can validate the

variable change through a certain fed-batch process. Compare between predicts and experiments are shown in Figure 4.

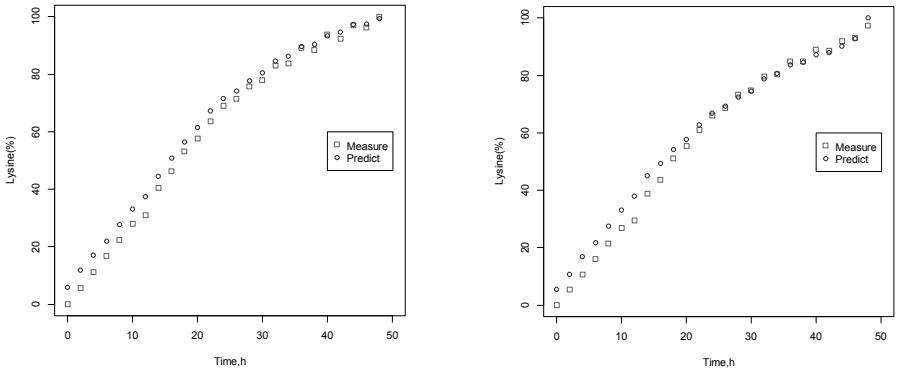

(a) No. 28 (b) No. 40

Figure 4. Measure and predict values in different fed-batches

From Figure 4, we can see the approximate graphical model can well represent the fed-batch fermentation process of L-lysine.

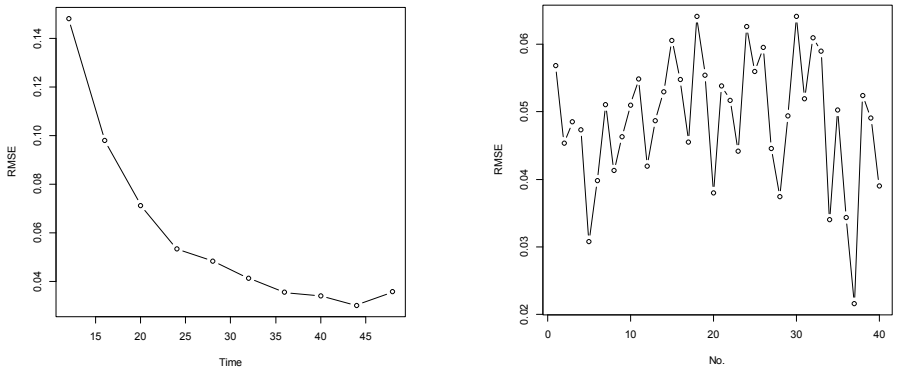

(a) Time slices (b) Batches

Figure 5. The RMSE between predictions values and experiments data

Figure 5 summaries the root mean square error (RMSE) between predicted product concentrations of L-lysine and experiments data. All these L-lysine concentration values are dimensionless, the concentrations varied from 0 to 1. The values of RMSE indicate that predicted values agree well with experiment data.

4. Conclusions

L-lysine is an important chemical, and it is mainly produced by fed-batch fermentation processes. In this process, the feed stock, operation conditions, and reactant/product vary all the time, also changes between different batches. It is difficult to formulate a kinetics-based model. With plenty of data records, we proposed a data-based approximate probability graphical modelling methodology to represents this L-lysine fed-batch fermentation process. Variables values in this process can be treated as a Gaussian process. First, we impute the missing-data within records, and then, the structure and parameters of dynamic Bayesian network are learned to get the graphical model. This model could be helpful in: i) identify the key state variables, ii) learn quantitative relationships between variables, and iii) improve the performance of L-lysine fed-batch fermentation process.

References

G. Ambler, R.Z. Omar, P. Royston, 2007. A comparison of imputation techniques for handling missing predictor values in a risk model with a binary outcome. Statistical methods in medical research 16, 277-298.
S. Anastassiadis, 2007. L-Lysine Fermentation. Recent Patents on Biotechnology 1, 11-24.
G.E. Batista, M.C. Monard, 2002. A Study of K-Nearest Neighbour as an Imputation Method. HIS 87, 251-260.
M.J. Beal, F. Falciani, Z. Ghahramani, C. Rangel, D.L. Wild, 2005. A Bayesian approach to reconstructing genetic regulatory networks with hidden factors. Bioinformatics 21, 349-356.
S. Beutel, S. Henkel, 2011. In situ sensor techniques in modern bioprocess monitoring. Applied Microbiology and Biotechnology 91, 1493-1505.
T. Brautaset, Ø. Jakobsen, K. Josefsen, M. Flickinger, T. Ellingsen, 2007. Bacillus methanolicus: a candidate for industrial production of amino acids from methanol at 50°C. Applied Microbiology and Biotechnology 74, 22-34.
W. Claes, B. Bathe, 2014. Process for the production of L-lysine. Google Patents.
S. Imoto, T. Goto, S. Miyano, 2001. Estimation of genetic networks and functional structures between genes by using Bayesian networks and nonparametric regression.
S. Kim, S. Imoto, S. Miyano, 2004. Dynamic Bayesian network and nonparametric regression for nonlinear modeling of gene networks from time series gene expression data. Biosystems 75, 57-65.
S.Y. Kim, S. Imoto, S. Miyano, 2003. Inferring gene networks from time series microarray data using dynamic Bayesian networks. Briefings in bioinformatics 4, 228-235.
R.D. Kiss, G. Stephanopoulos, 1991. Metabolic Activity Control of the L-Lysine Fermentation by Restrained Growth Fed-Batch Strategies. Biotechnology Progress 7, 501-509.
S. Lèbre, 2009. Inferring dynamic genetic networks with low order independencies. Statistical applications in genetics and molecular biology 8, 1-38.
K. Murphy, S. Mian, 1999. Modelling gene expression data using dynamic Bayesian networks. Technical report, Computer Science Division, University of California, Berkeley, CA.
I.M. Ong, J.D. Glasner, D. Page, 2002. Modelling regulatory pathways in E. coli from time series expression profiles. Bioinformatics 18, S241-S248.
R. Opgen-Rhein, K. Strimmer, 2007. Learning causal networks from systems biology time course data: an effective model selection procedure for the vector autoregressive process. BMC Bioinformatics 8, 1-8.
B.-E. Perrin, L. Ralaivola, A. Mazurie, S. Bottani, J. Mallet, F. d'Alché–Buc, 2003. Gene networks inference using dynamic Bayesian networks. Bioinformatics 19, ii138-ii148.
C. Rangel, J. Angus, Z. Ghahramani, M. Lioumi, E. Sotheran, A. Gaiba, D.L. Wild, F. Falciani, 2004. Modeling T-cell activation using gene expression profiling and state-space models. Bioinformatics 20, 1361-1372.
M.N.I. Salehmin, M.S.M. Annuar, Y. Chisti, 2013. High cell density fed-batch fermentations for lipase production: feeding strategies and oxygen transfer. Bioprocess and Biosystems Engineering 36, 1527-1543.
N. Sugimoto, H. Iba, 2004. Inference of gene regulatory networks by means of dynamic differential Bayesian networks and nonparametric regression. Genome informatics. International Conference on Genome Informatics 15, 121-130.
E. Valente, I. Rocha, M. Rocha, 2009. Modelling Fed-Batch Fermentation Processes: An Approach Based on Artificial Neural Networks, in: Corchado, J., De Paz, J., Rocha, M., Fernández Riverola, F. (Eds.), 2nd International Workshop on Practical Applications of Computational Biology and Bioinformatics (IWPACBB 2008). Springer Berlin Heidelberg, pp. 30-39.
F.X. Wu, W.J. Zhang, A.J. Kusalik, 2004. Modeling gene expression from microarray expression data with state-space equations. Pacific Symposium on Biocomputing. Pacific Symposium on Biocomputing, 581-592.
J. Yu, M.M. Rashid, 2013. A novel dynamic bayesian network-based networked process monitoring approach for fault detection, propagation identification, and root cause diagnosis. Aiche Journal 59, 2348-2365.
M. Zou, S.D. Conzen, 2005. A new dynamic Bayesian network (DBN) approach for identifying gene regulatory networks from time course microarray data. Bioinformatics 21, 71-79.
K. Zuo, W.T. Wu, 2000. Semi-realtime optimization and control of a fed-batch fermentation system. Computers & Chemical Engineering 24, 1105-1109.

Krist V. Gernaey, Jakob K. Huusom and Rafiqul Gani (Eds.), 12th International Symposium on Process Systems Engineering and 25th European Symposium on Computer Aided Process Engineering.
31 May – 4 June 2015, Copenhagen, Denmark

Model-based prediction and experimental validation of viscosities of soap emulsions

Daniel M. Macías-Pelayo[a,b], Pedro A. Alonso-Dávila[a], Alfonso Martínez-Villalobos[b] and Alicia Román-Martínez[a*]

[a] *Facultad de Ciencias Químicas, Universidad Autónoma de San Luis Potosí, Dr. Manuel Nava No. 6 Zona Universitaria San Luis Potosí, 78210, México (alicia.romanm@uaslp.mx)*

[b] *Jabonera Potosina S.A de C.V, Juan Álvarez No. 100 Industrial Mexicana, San Luis Potosí,78300, México*

Abstract

Soap is a very common end-consumer product which is used worldwide, with ten billion pounds produced per year. In Mexico, for example, the annual soap production industry is valuated 200 million dollars, making the soap production profitable. During the continuous saponification process, the emulsion viscosity is an essential variable which influences the conversion due to mass transfer limitations. Viscosity also impacts the operation of the downstream processing steps, such as the extrusion and the soap compression, to achieve the final product quality. Laundry soap emulsion viscosity prediction is complex due to the heterogeneous and variable composition: moisture, free sodium hydroxide, sodium chloride, sodium sulphate and fatty acids concentrations. Therefore, in this contribution the objective is to obtain a mathematical model via response surface methodology, to predict the emulsion viscosity for the system under study, which is the production of laundry soap in a facility located in Mexico: *Jabonera Potosina*. The methodology to develop such a model is the following: 1. Definition of the response property (viscosity). 2. Analysis of the variables that influence the viscosity: compounds concentrations, fat saponification value (FSV) and fatty acid value (FAV). 3. Determination of the ranges of the variables. 4. Creation of a response surface via a central composite design. 5. Performance of the experiments. 6. Analysis of the results, and 7.Model development. The obtained equation relates all the variables mentioned previously with the emulsion viscosity. This equation will be useful to identify the operational adjustments in the process for different scenarios, such as the change of product from laundry soap to toilet soap.

Keywords: soap, viscosity, emulsion, experimental design.

1. Introduction

Soap is a widely used commodity product, but despite being produced since antiquity, the manufacturing has been more an art than a science. For example, large kettle tanks were used for centuries, manipulating a soap mass around and through various phases with cryptic names such as nigre, middle soap, neat soap, kettle wax, and curd. From the emergence of transport phenomena knowledge, it has been possible to elucidate a rational understanding of structure and phase behaviour (Paul *et al.*, 2013). As results, better production processes have been developed, such as the continuous saponification process, which consists of a stirred tank to increase the phase contact to favour the mass transfer. In the continuous saponification process the emulsion viscosity in the reactive

mixture is a property that has effect not only in the downstream process to ensure that the equipment can handle the emulsion, but also it has wide importance in the reaction process due to mass transfer limitations. For example, the conversion depends on the capacity of the reactor to ensure contact between phases, and the stirring system can only handle certain range of viscosities (Hvala *et al.*, 2011). Saponification reaction consists of a fatty acids alkaline hydrolysis. It can be carried on either neutralizing carboxylic acids with an alkali, or by the alkaline hydrolysis of triglycerides**.** There are many quality variations in fat and oils used due to the market fluctuations depending on harvesting seasons**.** In addition, the production of biodiesel, which utilize the same raw materials, is increasing. Therefore, the competition for the raw materials and its price is highly variable. Nowadays, the soap manufacturing companies are using all kinds of fats and oils, meaning that it is necessary to pre-treat the raw materials to ensure the quality for the process. For these reason *Jabonera Potosina* aims to ensure the quality of the finished soap bar by using any kind of fat just adjusting controllable variables: a) sodium hydroxide content, b) sodium chloride content, c) sodium sulphate content, d) saponification number, e) moisture and f) acid value. All these variables have been observed to have influence in the soap paste viscosity, and they have a specific function in soap formulations. In this work the objective is to verify the empirical observations that the operators and supervisor have done to control the emulsion viscosity and to build a mathematical model which includes all the variations produced by the variables involved, in order to predict the viscosity under certain conditions and then to apply corrective actions by adjusting the controllable variables. In addition, this model can be used to formulate other products such as toilet soap.

2. Materials and Methods

2.1. Materials

Industrial grade fats (palm fat and tallow) and oils (palm kernel and coconut oil) were used and provided by *Jabonera Potosina.* The saponification number and the acid value were adjusted by mixing fats with oils. The caustic soda solution used was 27% w/w in water. Sodium chloride and sodium sulphate were at industrial grade. The water content adjustment was done with tap water.

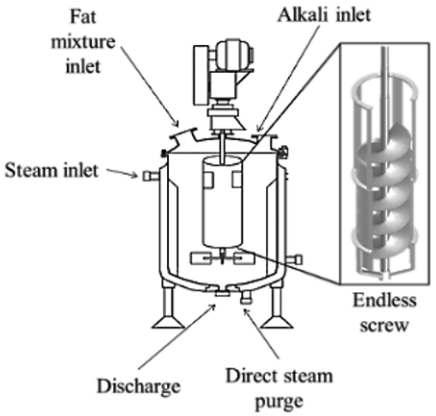

Figure 1. Pilot-scale saponification reactor.

2.2 Equipment

A pilot-scale reactor was used for the experiments. It consists of a stainless steel stirred tank with a capacity of 35 kilograms. It has a heating jacket to preheat the mixture.

Steam can be fed to the reactive mixture from the bottom of the reactor. The raw materials are fed from the top. The stirring velocity was 60 rpm. In order to measure the temperature a needle thermometer was attached. Inside the reactor, to enhance the mass transfer and to ensure a homogeneous mixture, there is an endless screw to transport the mixture from the bottom to the top. With this, the sodium hydroxide concentration can be the same in all the reactor volume. A schematic representation of the pilot-scale reactor is shown in Fig. 1.

2.2. Design of experiments

In order to correlate all the variables having impact on the viscosity, a response surface was created. A central composite design was done to minimize the number of experiments. The design was specifically structured with a minimal resolution V by the software Design Expert 7.0.0., to avoid aliasing effects in the ANOVA. (Rozet *et al.*, 2013)

2.2.1. Variables and range values

All variables that empirically demonstrated to have impact on the emulsion viscosity can be divided in operational and characteristic variables. The effect of the operational variables (e.g. flowrates, temperatures, pressure, stirring velocity, batch time) was discarded by standardizing the experimental procedure. Only the characteristic variables (compounds concentrations) were studied. Only 6 variables could be controlled and measured by the lab. The selected variables were: 1) water percent, 2) sodium chloride percent, 3) sodium sulphate percent, 4) sodium hydroxide percent, 5) saponification value and 6) acid value. The first four variables maximum values are regulated by Mexican official norms for laundry soap bars (NMX-Q-010-CNCP-2013). The minimum value was fixed with at the operational values of the subsequent steps in the process. The last two variables are raw material characteristics and can be adjusted by mixing the fat with the oils. The high and low values for these were selected considering process stability and raw material variations. The acid value provides information of the final glycerol percent in the emulsion. Therefore, this variable was regulated adding the necessary glycerol to reach the value from the design of experiments. Forty experiments were performed in total. Table 1 shows the experimental design low and high variable values.

Table 1. Range values for the design of experiments.

Name	***Units***	***Low***	***High***	***Mean***	***Std. Dev.***
Sap. Value	g-KOH/g-fat	208.72	211.28	210	1.05
% NaCl	%	0.25	0.40	0.325	0.07
% Na_2SO_4	%	0.13	0.17	0.15	0.02
% H_2O	%	30.73	31.57	31.15	0.34
% NaOH	%	0.21	0.26	0.235	0.02
% Glycerol	%	1.8	2.0	1.9	0.1

2.3. Experimental procedure

The experimental procedure begins with the melting and heating of the fats (tallow and palm fat) at 60°C. 5% of the total charge is tallow, which is added first with an excess of sodium hydroxide which is twice the saponification number measured, for example if the saponification number of tallow is 142.9 mg NaOH/gr of tallow, then 285.8 mg of NaOH are added. The next step consist of adding the necessary palm fat to neutralize

the emulsion due to the sodium hydroxide excess, followed by further addition of seven batches of palm fat and sodium hydroxide in a stoichiometric ratio of 1:1 to complete the full charge. Then, the sodium chloride and sodium sulphate are dissolved in water and added to the reactive mixture. A sample of this is carried to the lab to be analysed. Sodium hydroxide is measured by dissolution of the emulsion in alcohol and then it is filtered under vacuum. The product is titrated with sulphuric acid. Sodium chloride is measured by titration with silver nitrate after adding magnesium nitrate to separate the chlorides from the rest of the solution. Water is measured by weight difference with a heating lamp. If necessary, an adjustment is done before the viscosity measurement, to reach the variable values from experimental design. Finally the viscosity is measured at 80°C (operational process temperature) with a DV2TLVTJ0 Brookfield viscometer with a needle 64, at 10 rpm. A thermal bath was used to maintain the temperature and avoid product solidification (Maddah *et al*, 2013).

3. Results

Table 2 shows the ANOVA of the experiments. The factors that have effect in the response variables are highlighted with grey. Linear variables (despite they do not have effect) were added by hierarchy due to their quadratic effect in the ANOVA. The most important result is that binary interactions (%NaCl-%NaOH, SV-%NaOH) have effect in the model.

Table 2. Analysis of Variance (90% probability)

Source of Variation	***Sum of Squares***	***Freedom Degrees***	***Mean Square***	***F Value***	***Prob > F***
Model	2.63E-18	11	2.39E-19	3.99	0.0015
Sap. Value	5.40E-20	1	5.40E-20	0.90	0.3511
% NaCl	2.23E-20	1	2.23E-20	0.37	0.5470
% Na_2SO_4	9.84E-21	1	9.84E-21	0.16	0.6887
% H2O	7.76E-19	1	7.76E-19	12.92	0.0012
% NaOH	5.24E-21	1	5.24E-21	0.09	0.7699
SV * % NaOH	4.19E-19	1	4.19E-19	6.98	0.0134
%NaCl *% NaOH	2.15E-19	1	2.15E-19	3.58	0.0689
$(\%\ NaCl)^2$	4.87E-19	1	4.87E-19	8.12	0.0081
$(\%\ Na_2SO_4)^2$	4.49E-19	1	4.49E-19	7.47	0.0107
$(\%\ H_2O)^2$	2.04E-19	1	2.04E-19	3.39	0.0761
$(\%\ NaOH)^2$	2.23E-19	1	2.23E-19	3.72	0.0640
Residual	1.68E-18	28	6.00E-20		
Lack of Fit	1.36E-18	23	5.93E-20	0.93	0.5988
Pure Error	3.18E-19	5	6.36E-20		
Total	4.31E-18	39			

The resulting model equation is the following:

$$\mu = [\beta_o + (\beta_1 \cdot SV) + (\beta_2 \cdot \%NaCl) + (\beta_3 \cdot \%Na_2SO_4) + (\beta_4 \cdot \%H_2O) + (\beta_5 \cdot \%NaOH) + (\beta_6 \cdot SV.\%NaOH) + (\beta_7 \cdot \%NaOH \cdot \%NaCl) + (\beta_8 \cdot \%NaCl^2) + (\beta_9 \cdot \%Na_2SO_4{}^2) + (\beta_{10} \cdot \%H_2O^2) + (\beta_{11} \cdot \%NaOH^2)]^{2.66} \quad (1)$$

Where the values of the constants are: $\beta_0 = -1.13080 \times 10^{-8}$, $\beta_1 = 1.54994 \times 10^{-11}$, $\beta_2 = -4.13240 \times 10^{-10}$, $\beta_3 = -1.59939 \times 10^{-9}$, $\beta_4 = 5.14840 \times 10^{-10}$, $\beta_5 = 1.47619 \times 10^{-8}$, $\beta_6 = -6.40753 \times 10^{-11}$, $\beta_8 = 7.35720 \times 10^{-10}$, $\beta_9 = 5.28462 \times 10^{-9}$, $\beta_{10} = -8.18148 \times 10^{-12}$, $\beta_{11} = -3.30304 \times 10^{-9}$.

To validate the model, viscosities of normal production soap emulsions were measured and compared with the model predicted values. Results are listed in Table 3.

Table 3. Comparison between predicted and measured viscosity values

N	*Sap. Value (mg/g)*	*NaOH (%)*	*NaCl (%)*	*Na_2SO_4 (%)*	*H_2O (%)*	*Exp. (cp)*	*Mod.(cp)*	*%Error*
1	205.5	0.21	0.33	0.2	31.8	13800	13372	-3.201
2	207.5	0.22	0.31	0.2	31.7	10400	10740	3.163
3	209.5	0.25	0.27	0.21	31.6	10040	9838	-2.049
4	209.5	0.22	0.35	0.2	31.4	9940	10117	1.753
5	210	0.23	0.33	0.22	32.4	9520	9134	-4.228

Fig. 2 shows that there is no induced tendency and there is a normal dispersion for all measurements. For adjusting the model a power transformation to the response (Hou *et al.*, 2011) was necessary. Interactions behaviour was plotted in Fig. 3, where a saddle point in the sodium chloride and sodium hydroxide interaction effect can be observed.

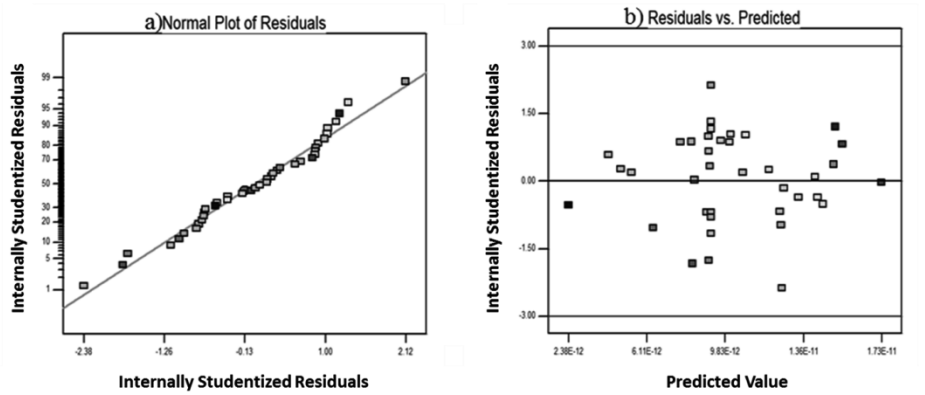

Figure 2. a) Normal plot of residuals; b) Residuals vs Predicted comparison.

4. Analysis and Discussion

From the ANOVA, only 5 variables that have effect in the viscosity were identified. The glycerol percent does not affect the response, contrary to the plant personnel empirical observations. This effect may have been covered by the fact that the range of the variable is too narrow to observe it. Water percent is the only variable that has both effects (linear and nonlinear) in the response according to Table 2. The interaction of the percent of sodium hydroxide and sodium chloride can be associated to the presence of emulsion electrolytes with a common dissociated ion. This interaction could not occur with sodium sulphate due to it hygroscopic nature instead of dissociating nature. The interaction between the saponification value and the sodium hydroxide could be related with the soap chain length and the emulsion alkalinity. Thermodynamic studies

in order to describe both interactions nature are recommended to be done. Sodium hydroxide, sodium chloride and sodium sulphate have a quadratic effect in the response, reaching a maximum or a minimum, making possible a further optimization. This behaviour is also reported in other publications with the presented regression methodology (Liu *et al., 2011).* Box-Cox analysis in Design Expert software suggested a power transformation for the response. Fig. 2 shows that the values are properly adjusted with such transformation. A mass balance model development would be the logical next step to validate the variable effect presented in the emulsion viscosity.

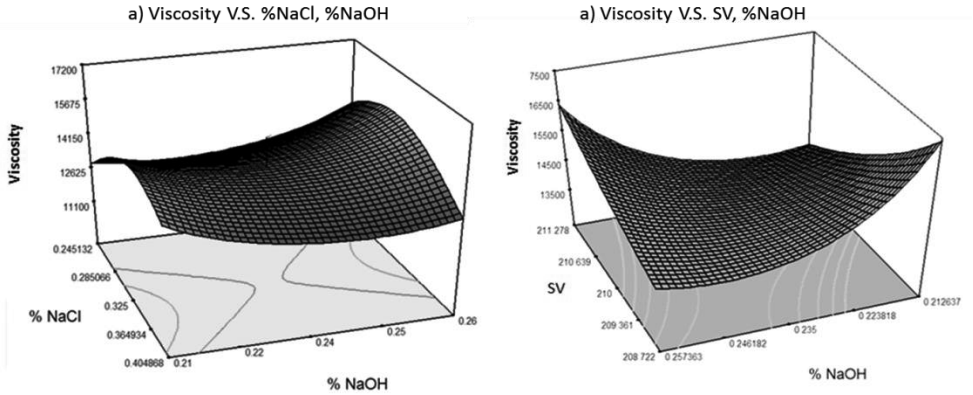

Figure 3. Interaction 3D plots

5. Conclusions

A viscosity prediction model was obtained with the response surface methodology. It was proven that it can predict accurately the soap emulsion viscosity. The model equation shows dependence from electrolytic compounds percent, water percent, interaction of saponification value-sodium hydroxide percent, and interaction of sodium hydroxide-sodium chloride percent. The model has immediate application in the company to formulate different products such as toilet soap, which can be developed without investment of new equipment. As a result the product portfolio can be diversified.

6. References

Q. Hou, J. D. Mahnken, B. J. Gajewski, N. Dunton, 2011, The Box-Cox power transformation on nursing sensitive indicators, BMC Medical Research Methodology , 11, 118.

N. Hvalaa, F. Aller, T. Miteva, D. Kukanja, 2011, Modelling, simulation and control of an industrial, semi-batch, emulsion-polymerization reactor, Computers & Chemical Engineering, 35,10, 2066-2080.

H. Liu, H. Li, X. Huang, H. Chen, A. Ren, Y. Zhao, 2011, Optimization of gel electrolyte using dual quadratic rotary regression orthogonal design, Chinese Journal of Power Source, 6.

H. Maddah, M. Rezazadeh, M. Maghsoudi, S NasiriKokhdan, 2013, The effect of silver and aluminum oxide nanoparticles on thermophysical properties of nanofluids, Journal of Nanostructure in Chemistry, 3, 28-33

N. Paul, P. Schrader, S. Enders, M. Kraume, 2013, Effects of phase behaviour on mass transfer in micellar liquid/liquid systems, Chemical Engineering Science, volume 115, pp 148–156.

E. Rozet, P. Lebrun, B. Debrus, B. Boulanger, P. Hubert, 2013, Design Spaces for analytical methods, Trends in Analytical Chemistry, 42, 157-167.

Krist V. Gernaey, Jakob K. Huusom and Rafiqul Gani (Eds.), 12th International Symposium on Process Systems Engineering and 25th European Symposium on Computer Aided Process Engineering.
31 May - 4 June 2015, Copenhagen, Denmark.

A Novel Quantisation-based Integration Method for ODEs

Vassilios S. Vassiliadis[a], Fabio Fiorelli[a] and Harvey Arellano-Garcia[b]

[a]*Department of Chemical Engineering and Biotechnology; University of Cambridge; Cambridge, United Kingdom*
[b]*School of Engineering and Informatics; University of Bradford, Bradford, United Kingdom*
vsv20@cam.ac.uk

Abstract

Integration of Ordinary Differential Equations (ODE's) plays a paramount role in the dynamic simulation of a wide spectrum of processes in Chemical Engineering. This paper presents a novel approach within our discipline, namely the Quantised State Integration technique (QSI) (also known as Quantised State Simulation, QSS) which was introduced in its raw form several decades ago within Electrical Engineering for the simulation of electrical and electronic circuits in dynamic operation. While traditionally integration of ODE's considers time to be the coordinating parameter and it is discretised to allow the calculation of the state variables evolution, in QSS methods the states are discretised and time is calculated at points states go state events (changes by an amount equal to the discretisation level for each of them)–this allows effectively the decoupling of the state integration within accuracy tolerances. In the current work, we present significant theoretical and implementational extensions to the method, rendering it capable of handling large- to huge-scale applications involving stiff systems, state discontinuities (discrete events in hybrid systems) as well as the efficient calculation of sensitivity equations–all aspects that have previously been impossible to incorporate in the QSS suite of techniques presented over the years. Overall, all theoretical and preliminary computational demonstrations show it to be a very promising and powerful integration technique with a strong potential for future evolution and contributions. A mutlitude of areas that can benefit from this technique are identified in the paper.

1. Introduction and literature survey

Integration of Ordinary Differential Equations (ODE's) plays a paramount role in the dynamic simulation of a wide spectrum of processes in Chemical Engineering. Traditionally the time is treated as the free parameter, coordinating the integration of the state variables and is thus discretised. In the techniques presented here (Quantised State Integration, QSI, or Quantised State Simulation, QSS–names used equivalently) the state variables are discretised by a given (or variable) step size ('quantum') and the time at which they change becomes the calculated variable. This allows the decoupling of the integration of the state differential equations, and can be a very effective method to deal with difficult systems of very large dimensionality. Additionally the methods are matrix-free which renders them very efficient computationally.

Although equivalent to an explicit integration scheme, through our work we are able to show that they exhibit stability during integration and to a certain extent, with a specially modified limited Newton procedure per involved differential equations subject to a single changing state variable, stiff systems can be integrated adequately with good precision.

The initial concepts related to QSS can be traced to 1976 and in the most recent edition of Zeigler et al. (2000), the clear inception of this idea can be said to start with Zeigler and Lee (1998) and

the DEVS representation (Zeigler et al., 2000). DEVS or Discrete Event System Specification, is a formalism that allows modelling of system where events happen at discrete times, or hybrid systems. It found a certain popularity in Signal Processing, some types of Simulation, Electrical and Electronic Engineering; a search on Web of Knowledge turns up almost 750 articles and proceedings. **?** takes up the idea and expands it in the context of using DEVS representation in simulation environments. His group better defines the idea of trajectories approximated as piecewise polynomials, a fundamental feature of State Discretisation as we describe.

Kofman and his group started working on QSS from 2001 onward (Kofman et al., 2001). A first order "explicit" method is developed, the Quantized State Solver (QSS1) (Kofman and Junco, 2001), with quantized variables as stand-ins for the state variables. The latter are updated asynchronously only after the former have been manipulated and the conditions are verified. Among its theoretical properties the authors show that not only the state variables have continuous piecewise linear trajectories as Giambiasi did, but their derivatives as well follow piecewise constant trajectories like the quantized variables. More importantly, they show the first proofs that the method can be stable and convergent at the same time provided that the system matrix is a Hurwitz matrix (all eigenvalues negative, whatever the size), although the error is still a first order error, contained by the size of the quantum.

A second order version called QSS2 was developed (Kofman, 2002) following that, with the same properties and a better performance, though equally problematic with non-linear and stiff systems as the authors themselves note. However the limits of the system are much better defined, and the idea of defining the quantum so that those properties are respected is introduced, though it remains impossible to calculate it without effectively solving the system before the simulation. Kofman's doctoral thesis (Kofman, 2003) cleanly collects the theory developed up to that point, making the application to process control much more evident.

Nutaro is another worker in this field, although his research did not continue into more recent times. In his thesis (Nutaro, 2003) he worked on, among other things, the investigation of Adam-Bashford type linear Multi-Step methods, which he further developed up to second order in a pair of successive papers (Nutaro, 2005, 2007), with point interpolation to create virtual past time-steps that are usable. This particular form of the methods was not studied further, even though an improvement in the order of the global error was obtained. Of particular interest is the stability analysis in his papers. He concluded that QSI methods have very interesting stability properties and that they are mostly self-correcting in this regard: if the initial assumptions are respected these integrators will produce time steps that will make them remain always stable, with error cleanly bounded by the state quanta and the magnitude of the functions themselves.

In the meantime the applications of this type of solver to hybrid systems became apparent (Kofman, 2004). Being discrete, these methods handle discontinuity naturally and can easily handle state discontinuities. State discontinuities can be easily found through root-finding for the equations describing their transition conditions, in a one-variable-at-a-time fashion.

2. Advances in Quantised State Integration

Due to space limitations only the general principle of the QSS methods will be presented in this section. The method presented is equivalent to an explicit Euler scheme, but the discretised variables here are the states and not time. In any interval k we know that the next interval $k+1$ starts at a distance h_t from the beginning of the current one as in

$$t_{k+1} = t_k + h_t \,\forall\, k \in \{1,2,\ldots,N_{Intervals}\}$$

Knowing this in a regular ODE solver we can then approximate the value of the state variables at

that future time, as seen in the basic Euler method

$$x_{k+1} = x_k + \dot{x}_k h_t \tag{1}$$

In the case of state discretised solvers the perspective is turned around: we know the value that the state variables are going to have in the future. This is because we establish at the beginning of the simulation a discrete step h_x or quantum for every state variable $\{x_i \,|\, i = 1,2 \ldots N_{Variables}\}$, by which they can either increase or decrease, depending on the sign of the associated rate equation. The parameter h_x is also liable to change in some variants of the methods, such as the one presented here. What we wish to find is the future time t_{k+1} at which an absolute change by the quantum is effected. So in a system with only one state variable we know that

$$x_{k+1} = x_k \pm h_x \tag{2}$$

hence the next time step will start only when the following condition holds true

$$|x_{k+1} - x_k| = h_x \tag{3}$$

Note the absolute value, as the direction of change is not specified here. In a simple first order method the above condition is followed by first approximating a derivative at any point k as

$$f_x(x,t) = \frac{dx}{dt} \approx \dot{x}_k \tag{4}$$

implying that

$$\int_{x_k}^{x_{k+1}} dx = \int_{t_k}^{t_{k+1}} \dot{x}_k dt \Rightarrow \pm h_x = (t_{k+1} - t_k)\dot{x}_k \tag{5}$$

hence if we bring to the left hand side the current time we obtain

$$t_{k+1} = t_k + \frac{h_x}{|\dot{x}_k|} \tag{6}$$

Pictorially the integration by discretising states versus that of discretising time is shown in Figure 1.

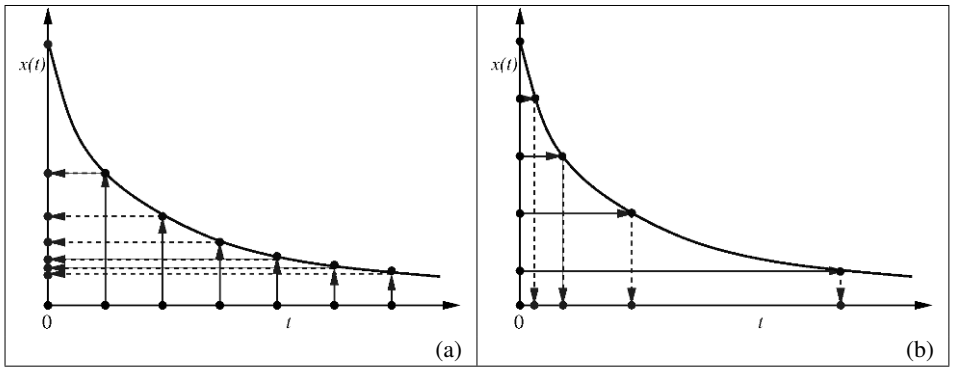

Figure 1: Time discretisation versus state discretisation integration schemes. (a) presents the time discretisation scheme with states being calculated, while (b) presents the state discretisation scheme with time calculated instead.

In our implementation many advances have been made over the state-of-the-art in QSS methods, which significantly suffer in the handling of stiff systems and in not having been extended for sensitivity equation integration. These aspects are the major ones presented next in this paper. Stiffness has been observed to cause instability in QSS methods (Migoni et al. (2013)). Kofman and coworkers presented there many methods and approaches. The shortcoming of all these presented approaches is that they handle effectively diagonally implicit systems, or at least ones that the dominant coupling is along the diagonal of the state Jacobian of the ODE systems. All these approaches are totally inadequate to handle a general stiff system reliably without depending on special properties it may possess. We generalised the approach to any stiff system of ODE's by observing that the instability in QSS methods due to stiffness results in crosses of the rate around zero, thus a root finding procedure subject to a state change over all involved rates is applied to lock to the zero location of the involved quantum for the changing state. This removes the instability observed and stiff systems can be integrated without problems, although still in a semi-explicit fashion.

The second major contribution of our work is the integration of sensitivity equations in tandem with the quantised state integration scheme. This is achieved by considering the following general ODE system

$$\begin{aligned} \frac{d}{dt}\boldsymbol{x}(t) &= \boldsymbol{f}(\boldsymbol{x}(t),\boldsymbol{p}) \\ \boldsymbol{x}(t_0) &= \boldsymbol{x}_0(\boldsymbol{p}) \end{aligned} \tag{7}$$

$$t_0 \leq t \leq t_f$$

The state vector is represented by variables $\boldsymbol{x} = (x_1, x_2, \ldots, x_{NX})^T$ and the parameter vector by variables $\boldsymbol{p} = (p_1, p_2, \ldots, p_{NP})^T$. Differentation of equation (7) w.r.t. $\boldsymbol{p}$ yields the first order sensitivity equations

$$\begin{aligned} \frac{d}{dt}\boldsymbol{x}_p(t) &= \frac{\partial \boldsymbol{f}}{\partial \boldsymbol{x}}(\boldsymbol{x}(t),\boldsymbol{p}) \cdot \boldsymbol{x}_p + \frac{\partial \boldsymbol{f}}{\partial \boldsymbol{p}}(\boldsymbol{x}(t),\boldsymbol{p}) \\ \boldsymbol{x}_p(t_0) &= \frac{\partial \boldsymbol{x}_{0,\boldsymbol{p}}}{\partial \boldsymbol{p}}(\boldsymbol{p}) \end{aligned} \tag{8}$$

$$t_0 \leq t \leq t_f$$

where $\boldsymbol{x}_p = \frac{\partial \boldsymbol{x}}{\partial \boldsymbol{p}} = \left[\frac{\partial x_i}{\partial p_j}\right]_{i=1,2,\ldots,NX,\ j=1,2,\ldots,NP}$. Taking a slice at a time of the sensitivity matrix $\boldsymbol{x}_{p_j},\ j = 1,2,\ldots,NP$, and assigning to it a copy of the system in equation (7) can be solved independently taking care of the coupling of the state variables into the right hand side of the parametric sensitivities. This scheme is readily parallelisable as is obvious, leading to potentially highly efficient implementations.

3. Illustrative case study

The system under investigation is a system presented in Migoni et al. (2013), integrate with state quantum equal to 1.0. Without the special Newton procedure the QSS method produces oscillations in the solution as shown in Figure 2a. This illustrates clearly a 'chattering' behaviour in the state output, a result of crossing a zero value of the rate as a result of not being able to modify the stepsize of the state to lock onto the zeros of the rate function.

With the Newton procedure discussed, our implementation produces a stable integration trajectory as in Figure 2b. The procedure simply locates within numerical tolerances a root of the right hand side of the differential equations, whenever they are found to be changing sign subject to a state updating event, for any of the states involved in the system and for all rates. It shows a remarkable difference between the standard QSS method which is effectively a totally explicit integration scheme.

In terms of events produced, without the stabilising Newton procedure there are 16,911 events (integration steps) in the integration horizon, while with the Newton procedure the number of events drops dramatically to 42. It should be noted that the stepsize used is also relatively high, covering a range of amplitudes in the profiles from 0.0 to 20.0 in steps of 1.0.

Further case studies have confirmed the stable behaviour of our proposed approach, but space limitations do not permit the exposition of many more case studies in this present paper.

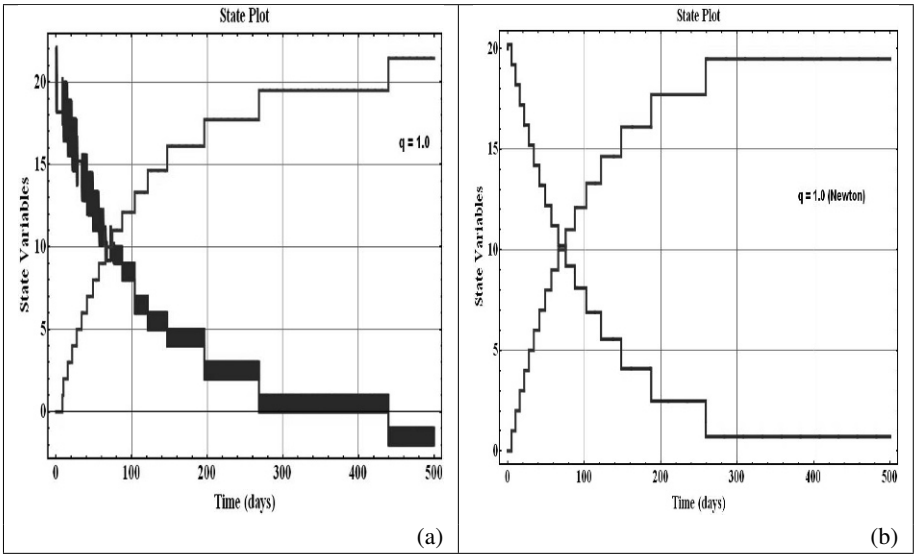

Figure 2: Integration of a stiff system: (a) presents the traditional QSS method solution, while (b) presents the solution implementing our Newton stabilisation scheme.

4. Discussion and future work

Overall, with our work we have been extending steadily the theoretical and implementational capabilities of the QSS methods so as to be able to tackle the most general and difficult huge-scale problems in Chemical Engineering dynamic process simulation. A summary of the current state-of-the-art and our contributions is given in Table 1. All the details outlined in the previously mentioned Table will be presented in a forthcoming extensive publication under preparation.

Item	Current state of published results on QSS	Our work
Stiffness	Very limited results published, specific to only "diagonally implicit-dominant" ODE systems	Generalised approach through a simple Newton procedure (single equation, single variable at a time basis)
Parametric sensitivities	No research published whatsoever	Easy to extend, no more costly than traditional methods, and additionally fully parallelisable
Discrete event location	Fully developed	Must be integrated correctly with Newton procedure and sensitivities
Error control and stepsize control	In terms of error control nothing to speak of. Some "scaling-based" work published for automatic stepsize choice, but very poorly done.	Preliminary implementation in our current prototype.
Higher order integration schemes	Some attempts published, but in a very unclear and non-general way.	Higher order multistep schemes to be implemented as a next step in our work.

Table 1: Work on QSS methods

5. Acknowledgement

Author Fabio Fiorelli wishes to thank his family for their unfailing moral and material support.

References

Kofman, E., Feb. 2002. A Second-Order Approximation for DEVS Simulation of Continuous Systems. Simulation 78 (2), 76–89.

Kofman, E., 2003. Discrete event based simulation and Control of Continuous Director. Ph.D. thesis, Universidad Nacional de Rosario.

Kofman, E., 2004. Discrete event simulation of hybrid systems. SIAM Journal on Scientific Computing 25 (5), 1771–1797.

Kofman, E., Junco, S., 2001. Quantized-state systems: a DEVS Approach for continuous system simulation. Transactions of the Society for Modeling and Simulation International 18 (3), 123–132.

Kofman, E., Lee, J., Zeigler, B. P., 2001. DEVS Representation of Differential Equation Systems. Review of Recent Advances. Proceedings of ESS'01.

Migoni, G., Bortolotto, M., Kofman, E., Cellier, F. E., Jun. 2013. Linearly implicit quantization-based integration methods for stiff ordinary differential equations. Simulation Modelling Practice and Theory 35, 118–136.

Nutaro, J., 2003. Parallele Discrete Event Simulation with application to continuous systems. Ph.D. thesis, Arizona.

Nutaro, J., 2005. Constructing Multi-point Discrete Event Integration Schemes. In: Proceedings of the Winter Simulation Conference, 2005. Vol. 1. IEEE, pp. 267–273.

Nutaro, J., Jun. 2007. A Second Order Accurate Adams-Bashforth Type Discrete Event Integration Scheme. 21st International Workshop on Principles of Advanced and Distributed Simulation (PADS'07) (1), 25–31.

Zeigler, B. P., Lee, J., 1998. Theory of quantized systems: formal basis for DEVS/HLA distributed simulation environment. SPIE Proceedings 3369 (April), 49–58.

Zeigler, B. P., Praehofer, H., Kim, T. G., 2000. Theory of modeling and simulation, 2nd Edition. Elsevier Science.

Krist V. Gernaey, Jakob K. Huusom and Rafiqul Gani (Eds.), 12th International Symposium on Process Systems Engineering and 25th European Symposium on Computer Aided Process Engineering.
31 May – 4 June 2015, Copenhagen, Denmark

Modelling and Parameter Estimation of Enzymatic Biodiesel Synthesis

Priscila S. Sabaini,[a,b] Thais Fabiana C. Salum,[b] Rossano Gambetta,[b] Fabricio Machado[a,*]

[a]*Institute of Chemistry, University of Brasília, Campus Universitário Darcy Ribeiro, CP04478, CEP: 70910-900 Brasília, DF, Brazil, fmachado@unb.br.*
[b]*Embrapa Agroenergy, Parque Estação Biológica, PqEB s/n°, W3 Norte, CEP: 70770-901, Brasília, DF, Brazil.*

Abstract

The current work addresses the modelling and parameter estimation of the biodiesel synthesis using supported lipases as catalysts. A kinetic reaction model was proposed in order to describe the enzymatic (trans)esterification reaction of vegetable oils and the set of kinetic parameters were numerically estimated with help of the direct search Complex algorithms. The proposed model was evaluated for different experimental conditions, leading to a very suitable prediction of the process data. In summary, the general proposed model is able to predict very well the reaction behavior of biodiesel (BD). Based on the algebraic-differential model performance, the proposed strategy can be successfully used to describe and optimize the biodiesel production through enzymatic reactions performed in batch and semibatch operating mode.

Keywords: Modelling, parameter estimation, biodiesel, enzymatic catalysis.

1. Introduction

The development of renewable sources of energy has been determined by two major issues: energy security and global warming. Biodiesel has attracted considerable attention as an alternative fuel for diesel engines, due to its remarkable characteristics of being renewable, biodegradable, less toxic and polluting than diesel. Traditionally, biodiesel is produced by chemical-catalyzed transesterification of vegetable oils carried out in homogeneous reaction medium. Although homogeneous catalysis is widely used for biodiesel production, there are several problems inherent in this process, such as difficult in the glycerol recovery, undesirable saponification reactions (when raw materials containing high contents of free fatty acids are employed), and high production cost associated to the mandatory removal of the alkali-soluble catalyst from the product, which results in effluent generation. Biodiesel produced by enzymatic route is a technology with a great potential to solve some of the problems that commonly observed in chemical-catalyzed alkaline processes. Despite this, in order to be considered economically viable, issues like high cost and inhibition of the enzyme should be resolved (Guldhe et al., 2015, Christopher et al., 2014; Gog et al., 2012).
Mathematical modelling is an important tool that allows for a better understanding of the process and therefore may assist in solving these mentioned problems. As a useful tool, process modelling based on the kinetic mechanism can successfully be used for understanding the mechanism and process behavior involved in the production of biodiesel through enzymatic route.

Process modelling can usually be performed following two main strategies: phenomenological or empirical models. Phenomenological models are more interesting for the study of new production processes as they are based on both the physical and the chemical phenomena involved in this process. However, empirical models may be successfully used to optimize the process parameters (Fedosov et al., 2013; Schwaab et al., 2008, Schwaab et al., 2006).

For the particular case of biodiesel production, independent of the adopted modelling strategy, classical process variables such as, temperature, alcohol/oil ratio, substrates flow rate, enzyme and water amounts must be considered. Additionally, mass transfer mechanism should also be taking into account when immobilized enzymes are used as heterogeneous catalysts (Yucel, 2012, Fedosov et al., 2013, Liu et al., 2014, Meunier et al., 2014). The current work objective is the modelling and parameter estimation of the enzymatic biodiesel synthesis using supported lipases as catalysts.

2. Modelling

2.1. Kinetic Mechanism and Process Model

The kinetic mechanism used to describe the enzymatic biodiesel synthesis is represented by the following reaction steps:

$$\begin{aligned}
&TG + E \underset{k_2}{\overset{k_1}{\rightleftarrows}} E \cdot TG \\
&E \cdot TG + ROH \xrightarrow{k_3} BD + DG + E \\
&E + DG \underset{k_5}{\overset{k4}{\rightleftarrows}} E \cdot DG \\
&E \cdot DG + ROH \xrightarrow{k_6} BD + MG + E \\
&E + MG \underset{k_8}{\overset{k_7}{\rightleftarrows}} E \cdot MG \\
&E \cdot MG + ROH \xrightarrow{k_9} BD + GL + E
\end{aligned} \tag{1}$$

where, *TG*, *DG*, *MG*, *GL*, *ROH*, *E* and *BD* are the concentration of triglyceride, diglyceride, monoglyceride, glycerol, alcohol, enzyme and biodiesel, respectively. Assuming that the quasi-steady-state hypotheses for the enzyme-substrate complexes are valid, Eqs.(2)-(4) can be expressed as follows:

$$\frac{d[E \cdot TG]}{dt} = \frac{d[E \cdot DG]}{dt} = \frac{d[E \cdot MG]}{dt} = 0 \tag{2}$$

$$[E]_E^T = [E] + [E \cdot TG] + [E \cdot DG] + [E \cdot MG] \tag{3}$$

$$[E]_E^T = \left(1 + \frac{k_1[TG]}{k_2 + k_3[ROH]} + \frac{k_4[DG]}{k_5 + k_6[ROH]} + \frac{k_7[MG]}{k_8 + k_9[ROH]}\right)[E] \tag{4}$$

According to the proposed kinetic mechanism for the species involved in biodiesel production, the following set of differential equation can be written:

$$\frac{d[TG]}{dt} = \left(\frac{k_2 k_1}{k_2 + k_3[ROH]} - k_1\right)[E][TG] \tag{5}$$

$$\frac{d[DG]}{dt} = \left(\frac{k_3 k_1}{k_2 + k_3[ROH]}[TG][ROH] - k_4[DG] + \frac{k_5 k_4}{k_5 + k_6[ROH]}[DG]\right)[E] \tag{6}$$

$$\frac{d[MG]}{dt} = \left(\frac{k_6 k_4}{k_5 + k_6[ROH]}[DG][ROH] - k_7[MG] + \frac{k_8 k_7}{k_8 + k_9[ROH]}[MG]\right)[E] \tag{7}$$

$$\frac{d[GL]}{dt} = \frac{k_9 k_7}{k_8 + k_9[ROH]}[E][MG][ROH] \tag{8}$$

$$\frac{d[BD]}{dt} = \left(\frac{k_3 k_1}{k_2 + k_3[ROH]}[TG] + \frac{k_6 k_4}{k_5 + k_6[ROH]}[DG] + \frac{k_9 k_7}{k_8 + k_9[ROH]}[MG] \right)[E][ROH] \tag{9}$$

$$\frac{d[ROH]}{dt} = -\frac{d[BD]}{dt} \tag{10}$$

2.2. Parameter Estimation

For the parameter estimation task, it is required that a set of ordinary differential equations be solved iteratively as a dynamic optimization problem (Machado et al., 2010, Soares et al., 2011). In this scenario, direct search methods (N.B. according to this procedure, the candidate optimum solutions of the estimation problem are generated at random inside the search region) can be regarded as an interesting tool because they do not need the computation of derivatives, the inversion of matrices nor the process constraints. According to Machado and co-authors (2010), the use of the Complex optimization technique is strongly recommended when the optimization task is carried out using a large system of differential equations. Figure 1 shows the parameter estimation procedure adopted here based on a standard sequential optimization procedure (Machado et al., 2010, Soares et al., 2011), which is responsible for the determination of an optimum solution that has to satisfy the process model represented by Eqs. (3)-(10).

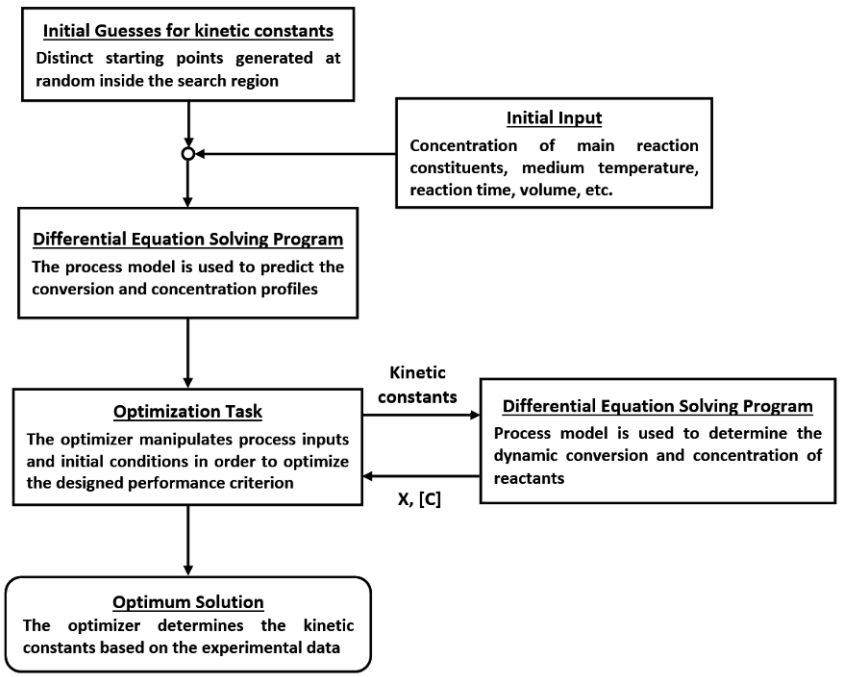

Figure 1. Proposed numerical scheme for the parameter estimation. X and [C] are the conversion and the concentration of reactants, respectively.

3. Results and Discussion

The experimental data used in this work were obtained from Salum et al. (2010), whose study was focused on the synthesis of biodiesel through the transesterification of soybean oil with ethanol in shake flasks. According to the adopted experimental conditions, 30 mmol soybean oil (871.34 g/mol), 1.5 g of fermented solid with immobilized lipase activity of 24 U/g were employed. The reactions were conducted at different alcohol:oil molar ratios (3:1, 6:1, 9:1 and 12:1) and at different water fractions (m/m) (0%, 0.5%, 1%, 5% and 10%).

Differential model equations [Eqs. (5)-(10)] were implemented in FORTRAN and solved numerically with the integration package IVPAG, whereas the parameter estimation task was performed with help of the direct search Complex algorithm. The standard numerical procedures IVAPG and BCPOL (employed for kinetic constant estimation), obtained from the IMSL^{TM} library (IMSL, 1991), were used for implementation of the computer code. Calculations were conducted on a laptop computer, equipped with an Intel® Core™ i7 processor, with CPU clock of 2.20 GHz and 8.00 Go memory RAM. The CPU computer times required to complete the estimation task were in the order of seconds, lying in the interval from 0.40 s to 1.00 s.

Based on the estimation task (Figure 1), different experimental conditions for alcohol/oil molar ratio were evaluated. Figure 2 shows the comparison between estimated and experimental data. There is a very good agreement between model and experimental data for the different experimental conditions studied. According to Figure 2, the highest conversion was obtained with a stoichiometric alcohol:oil molar ratio (3:1) and the reaction rate decreased with increase in alcohol:oil molar ratio up to 12:1. This experimental behaviour is in accordance with the works developed by Liu et al. (2014) and Yucel (2012), where it was also observed similar effect of alcohol/oil ratio on the biodiesel reaction performance.

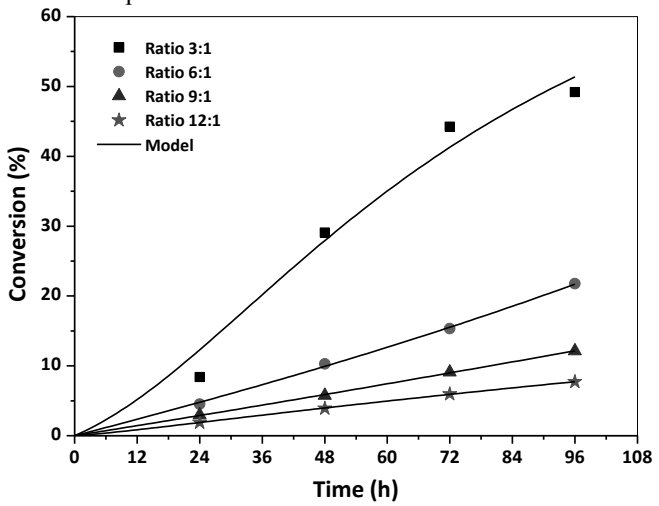

Figure 2. Influence of alcohol:oil molar ratio on the biodiesel production carried out at 37 °C and with 1 wt% of water.

The effect of water content was also explored. There is an optimal amount of water (0.5 wt% or 1.0 wt%) where biodiesel conversion is higher. Very small or very high water amount reduces conversion. Figure 3 also illustrates the process model performance against experimental data for the different conditions, illustrating that the proposed

model is able to predict very well the experimental behavior, indicating once more that the parameter estimation strategy leads to an excellent prediction of experimental data.

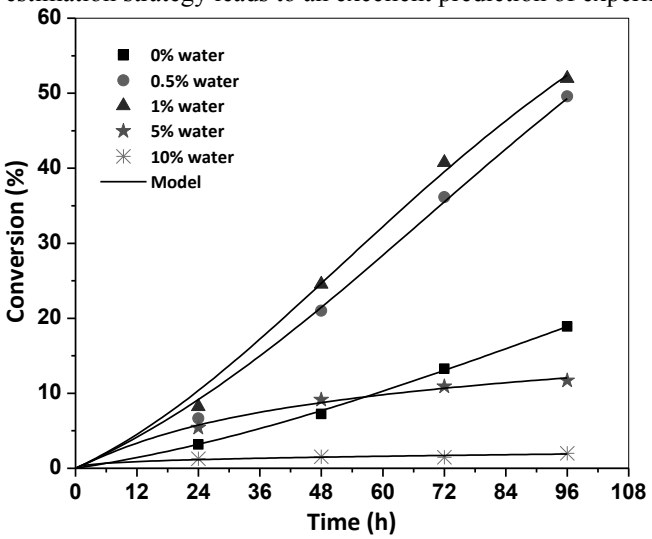

Figure 3. Influence of the water content on biodiesel synthesis performed at 37 °C and alcohol:oil molar ratio of 3:1.

Figure 4 shows for the concentration profiles for triglyceride, diglyceride, monoglyceride, glycerol, alcohol and biodiesel when the reactions is carried out with an alcohol:oil ratio of 9:1 and 1 wt% of water. The estimated kinetic constant for this experimental condition were k_1 = 0.5132 L·mol^{-1}·h^{-1}, k_2 = 3.6833 h^{-1}, k_3 = 3.6921 L·mol^{-1}·h^{-1}, k_4 = 1.4235 L·mol^{-1}·h^{-1}, k_5 = 3.6122 h^{-1}, k_6 = 1.0537 L·mol^{-1}·h^{-1}, k_7 = 2.0014 L·mol^{-1}·h^{-1}, k_8 = 0.2907 h^{-1} and k_9 = 2.3083 L·mol^{-1}·h^{-1}. As depicted in Figure 4, the model was able to describe the experimental data and it can be ultimately used to predict the concentration profiles of the main constituents in the reaction medium.

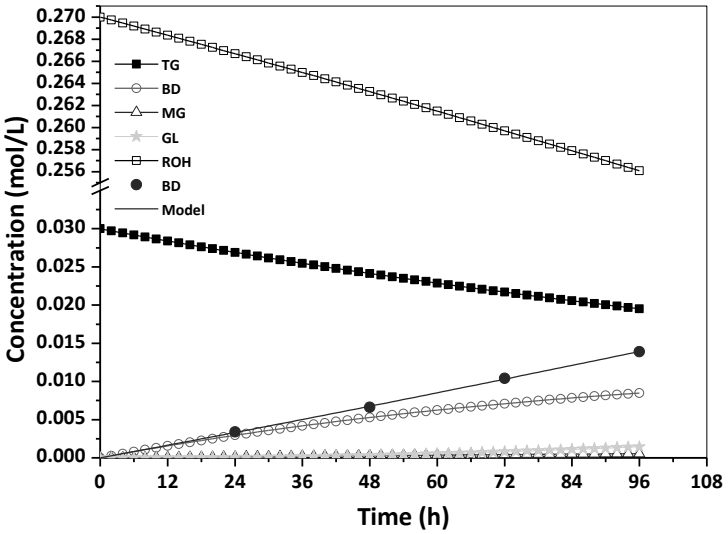

Figure 4. Estimated concentration profiles for triglyceride, diglyceride, monoglyceride, glycerol, alcohol and biodiesel when the reaction is carried out with an alcohol:oil ratio of 9:1 and 1 wt% of water.

4. Conclusion

The general proposed model is able to predict very well the reaction behavior of biodiesel production in several different experimental conditions. Based on the algebraic-differential model performance, the proposed strategy can be successfully used to describe and optimize the biodiesel production through enzymatic reactions performed in batch and semibatch operating mode.

References

A. Gog, M. Roman, M. Tos, C. Paizs, F. D. Irimie, 2012, Biodiesel production using enzymatic transesterification – Current state and perspectives, Renewable Energy, 39, 10-16.

A. Guldhe, B. Singh, T. Mutanda, K. Permaul, F. Bux, 2015, Advances in synthesis of biodiesel via enzyme catalysis: Novel and sustainable approaches, Renewable and Sustainable Energy Reviews, 41, 1447-1464.

F. Machado, E. L. Lima, J. C. Pinto, 2010, Dynamic optimization of semibatch vinyl acetate/acrylic acid suspension copolymerizations, Polymer Engineering and Science, 50(4), 697-708.

IMSL STAT/LIBRARY User's Manual, 1991, Version 2.0, IMSL, Houston.

L. Christopher, H. Kumar, V. P. Zambare, 2014, Enzymatic biodiesel: Challenges and opportunities, Applied Energy, 119, 497-520.

M. Soares, F.Machado, A. Guimarães, M. M. Amaral, J. C. Pinto, 2011, Real-time monitoring and parameter estimation of the emulsion polymerization of carboxylated styrene/butadiene latexes, Polymer Engineering and Science, 51, 1919-1932.

M. Schwaab, E. C. Biscaia, Jr., J. L. Monteiro, J. C. Pinto, 2008, Nonlinear parameter estimation through particle swarm optimization, Chemical Engineering Science 63, 1542-1552.

M. Schwaab, F. Machado, C. A. Queipo, A. G. Barreto Jr., M. Nele, J. C. Pinto, 2006, A new approach for sequential experimental design for model discrimination, Chemical Engineering Science, 61(17), 5791-5806.

S. M. Meunier, A. R. Rajabzadeh, R. L. Legge, Biochemical Engineering Journal, 2014, 85, 63-70.

S. Fedosov, J. Brask, A. K. Pedersen, M. Nordblad, J. M. Woodley, X. Xu, 2013, Journal of Molecular Catalysis B: Enzymatic, Kinetic model of biodiesel production using immobilized lipase Candida antarctica lipase B, 85-86, 156-168.

T. Salum, P. Villeneuve, B. Barea, C.Yamamoto, L.Côcco, D. Mitchell, N. Krieger, 2010, Synthesis of biodiesel in column fixed-bed bioreactor using the fermented solid produced by Burkholderia cepacia LTEB11, Process Biochemistry, 45, 1348-1354.

Y. Liu, C. Li, S. Wanga, W. Chen, 2014, Solid-supported microorganism of Burkholderia cenocepacia cultured via solid state fermentation for biodiesel production: Optimization and kinetics, Applied Energy, 113, 713-721.

Y. Yucel, 2012, Optimization of biocatalytic biodiesel production from pomace oil using response surface methodology, Fuel Processing Technology, 99, 97-102.

Krist V. Gernaey, Jakob K. Huusom and Rafiqul Gani (Eds.), 12th International Symposium on Process Systems Engineering and 25th European Symposium on Computer Aided Process Engineering.
31 May – 4 June 2015, Copenhagen, Denmark

Analysis of two Alternatives to Produce Ethylene from Shale Gas

Andrea P. Ortiz-Espinoza,[a] Mahmoud M. El-Halwagi,[b] Arturo Jiménez-Gutiérrez[a*]

[a]*Departamento de Ingeniería Química, Instituto Tecnológico de Celaya, Av. Tecnológico S/N, Celaya, Gto, 38010, México*
[b]*Chemical Engineering Department, Texas A&M University, College Station, Texas 77843, U.S.*

Abstract

The recent discoveries of shale gas have caused a decrease in the price of natural gas, which has opened a window of opportunities for its use not only as a source of energy but also as a feedstock for the production of chemical products. In this work, the use of shale gas for the production of ethylene is analysed. Two methods, the Oxidative Coupling of Methane (OCM) and the Methanol to Olefins (MTO) process are considered. The OCM is a direct-conversion process in which methane is converted to ethylene using a catalytic reactor. The MTO is a process with several steps where methane has to be first converted to syngas and then to methanol. The product, crude methanol, is finally converted to ethylene. Based on process simulations, an assessment of economic, energy and environmental considerations for each process was carried out. The results show that the MTO process provides a better alternative for the production of ethylene using shale gas. A sensitivity analysis shows that the OCM process can only be profitable under low prices of shale gas and high prices of ethylene.

Keywords: Ethylene, Shale gas, OCM process, MTO process, Techno-Economic Analysis.

1. Introduction

The availability of natural gas has increased within the last decade due to the implementation of new extraction techniques such as horizontal drilling and hydraulic fracturing, which have made possible the extraction of the denominated Shale gas, trapped in low permeability rock formations. The new abundance of natural gas has lowered the price of natural gas, encouraging its use not only as an energy source but also as a feedstock for the production of valuable chemicals (Wang et al., 2014). Although the production of some chemicals such as methanol have already been analysed, there is a need for the analysis of other production processes that could be part of the supply chain. One of the main building blocks for many products such as plastics, resins and fibers is ethylene. Although ethylene is typically produced by thermal cracking of ethane and propylene from natural gas, alternative processes for its production using methane as feedstock have been gaining significance over the past few years. Among the alternative processes for the production of ethylene, the Oxidative Coupling of Methane (OCM) and a Methanol to Olefins (MTO) technology have raised particular interest (Sundaram et al., 2010). The OCM is a direct process in which methane is converted to ethylene using a catalytic reactor (Godini et al., 2013), while the production of ethylene via methanol involves several steps (Vora et al., 1997).
The aim of this work is to evaluate the profitability of these two processes under a shale gas scenario and perform an environmental assessment, in order to find the

compromises between economics and the environmental considerations, as well as to perform a sensitivity analysis to show the impact of changes in the price of ethylene and shale gas on the profitability of the processes.

2. Description of the processes

The analysis is based on a plant capacity of 500,000 tpy for ethylene production. As the source of shale gas, the Barnet Shale Play, located in the state of Texas in the U.S. was selected. This play has been largely operated and much of the technology used for extraction of gas has been developed there (Bullin and Krouskop, 2009). The average composition of the different wells in the play shown in Table 1 was used in this work.

Table 1. Average composition for the Barnett Shale play*

Component	Composition (%)
Methane	86.8
Ethane	6.7
Propane	2.0
Carbon Dioxide	1.7
Nitrogen	2.9

*Source: Bullin and Krouskop (2009)

Before the shale gas can be sent through the pipelines to the production process, a purification process is needed. It usually consists of an acid gas removal unit, a dehydration unit, the removal of nitrogen and a series of distillation columns to remove natural gas liquids (Bullin and Krouskop, 2009). Once purified, the gas is sent to the production process that can be one of the following alternatives.

Oxidative Coupling of Methane (OCM)

In this process, methane is directly converted to ethylene through a catalytic reactor using pure oxygen provided by an air separation unit. This reactor operates at a temperature of 825 °C and a pressure of 1.1 bar. The reactions that take place in the reactor are as follows:

$$CH_4 + 2O_2 \longrightarrow CO_2 + 2H_2O \qquad C_2H_6 \longrightarrow C_2H_4 + H_2$$
$$2CH_4 + 0.5\,O_2 \longrightarrow C_2H_6 + H_2O \qquad CO + H_2O \longrightarrow CO_2 + H_2$$
$$CH_4 + O_2 \longrightarrow CO + H_2O + H_2 \qquad CO_2 + H_2 \longrightarrow CO + H_2O$$

The outlet stream from the reactor is sent to a multi-stage compressor where water is removed. Then, a cooler is used to lower the temperature before the gas stream is sent to an amine absorber, which uses MEA, to remove the CO_2. After CO_2 has been removed, the remaining stream is sent through a series of cryogenic distillation columns were unreacted methane is recovered for recycling and ethane and ethylene are separated. This process is limited due to the medium conversion of methane (less than 50%) and the poor selectivity to ethylene, leading to the production of high amounts of CO_2 and water (Godini et al., 2013). Despite this factor, the process is worth of analysis as an alternative for the production of ethylene from shale gas given its simple flowsheet. In this work yields for the reported catalysts are used.

Methanol to Olefins (MTO)

The production of ethylene via methanol involves several steps. The first step is a natural gas reforming process, where natural gas is converted into synthesis gas, which

consists of CO and H_2. For the reforming stage, different process are available (Julián-Durán et al., 2014). In this work, steam methane reforming was chosen due to its endothermic nature, which together with the high exothermic OCM process offers a possible option for integrating both processes, as suggested in other works (Godini et al., 2013). The second stage of the process is the methanol production; here the synthesis gas is sent to a catalytic reactor to obtain crude methanol. Since methanol is to be used as a feedstock, no purification process is needed. The final stages consist in the Methanol-to-Olefins process. Crude methanol is sent through a catalytic reactor, where the catalyst SAPO-34 provides a high selectivity to small linear olefins. The reactions that take place in the reactor are:

$$CO_2 + 3H_2 \longrightarrow CH_3OH + H_2O$$
$$CO_2 + H_2 \longrightarrow CO + H_2O$$

The reactor product is sent to a quenching tower, then CO_2 and water are removed by an absorber and dryer, and finally the different products are separated with a series of distillation columns (Chen et al., 2005). In addition to the production of ethylene, a significant amount of propylene is produced, which can be sold for a profit.

3. Results

Both processes were modelled in Aspen Plus using data from the literature. The consumption of raw materials is reported in Table 2, while Table 3 shows the energy requirements per kg of ethylene for each process. With the recycling of unreacted methane, the consumption of fresh natural gas for the OCM was reduced to almost half of the original amount. The energy consumption for the MTO process is slightly higher for heating and cooling, but the electricity needed for the OCM process is considerably higher than that for the MTO, which affects the process economics.

Table 2. Raw Material Consumption (kg/kg ethylene).

	OCM	MTO
Natural Gas	3.52	4.09
Oxygen	7.53	
Steam		12.28

Table 3. Energy requirements per kg of ethylene produced

		OCM	MTO
Heating	(MMBtu)	0.0350	0.0478
Cooling	(MMBtu)	0.0726	0.0838
Electricity	(kW-h)	7.1881	1.3071

Economic evaluation

For the economic analysis, an operating period of 330 days per year and a tax rate of 30% were assumed. Also, a 10-year linear depreciation with a salvage value of 10% was used. The working capital investment (WCI) was taken as 15% of the total capital investment (TCI), with the rest belonging to the fixed capital investment (FCI) (El-Halwagi, 2012). The estimations for the FCI of each process are shown in Table 4, which were based on reported data and using the six-tenths rule for capacity adjustment. For the MTO process, the value for the methanol plant and the methanol-to-olefins plant were estimated separately. In order to compare the two processes, return on investment (ROI) values were estimated (El-Halwagi, 2012),

$$ROI = \frac{(Annual\ sales - Annual\ Fixed\ Cost - Annual\ Operating\ Cost)(1 - tax\ rate) + Annual\ Fixed\ Cost}{TCI} \quad (1)$$

Table 4. FCI and TCI estimated values for ethylene production processes.

	FCI (MM$)	TCI (MM$)	References
OCM	$677.00	$796.47	Godini et al. (2013)
MTO	$1,466.00	$1,724.71	Julián-Durán et al. (2014) Wu (2013) Vora et al. (2013) Chen et al. (2004)

The ethylene price was assumed as $0.65/lb, and for the MTO process the price for propylene was set at $0.75/lb. The cost of shale gas, oxygen, and water for steam were assumed as $3.5/kscf, $0.05/lb, and $0.74/$m^3$ respectively (El-Halwagi, 2012). Table 5 summarizes the major economic results. Although the MTO plant has a higher FCI, its ROI seems attractive, while the OCM process is not profitable under the scenario considered here.

Table 5. Key Economic information for the ethylene production processes.

	MTO	OCM
Annual Income (MM$)	$1,251.90	$716.49
Annual Operating Costs (MM$)	$578.28	$1,044.38
Depreciation (MM$/yr)	$131.95	$60.93
Tax Rate	0.3	0.3
ROI (%)	29.63	-26.52

Energy Integration

The operating cost of each process can be reduced through energy integration. In order to identify the minimum cooling and heating utilities, a thermal pinch analysis was carried out. Figure 1 shows the grand composite curves for each production alternative. A minimum driving force of 10 K was used. It can be observed that the heating utilities can be reduced to zero in both cases, while the cooling utilities can be lowered to 2233 MMBtu/h for the MTO process and 1335 MMBtu/h for the OCM process. If cogeneration is considered, the cooling utilities can be further reduced to 0 for the MTO and 535 MMBtu/h for the OCM process, with the generation of 64 MW and 21 MW respectively. Details of the cogeneration method can be found in El-Halwagi (2012). Considering the energy integration and the cogeneration implementation, the ROI of the processes increases to 37.66% for the MTO and to -14.23% for the OCM.

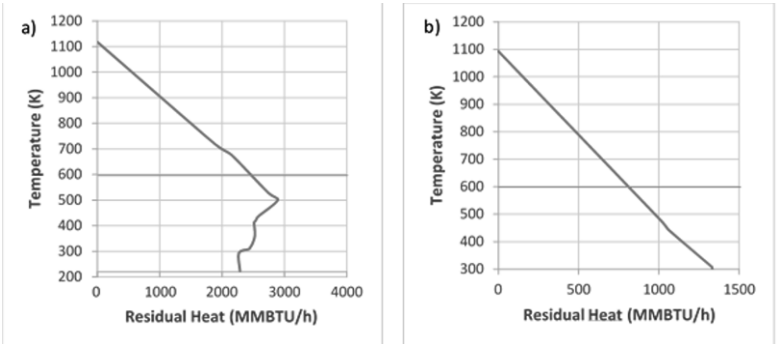

Figure 1. Grand composite curves for the MTO (a) and the OCM (b) processes.

Sensitivity analysis

A sensitivity analysis was carried out to evaluate the impact on the process profitability due to changes in products and feedstock prices. Figure 2 shows the ROI for ethylene prices ranging from \$0.5 to \$0.9 per pound and shale gas prices (pipeline quality) from \$2/kSCF to \$6/kSCF. It can be seen that the OCM process can only make a profit at high prices of ethylene and very low prices of shale gas.

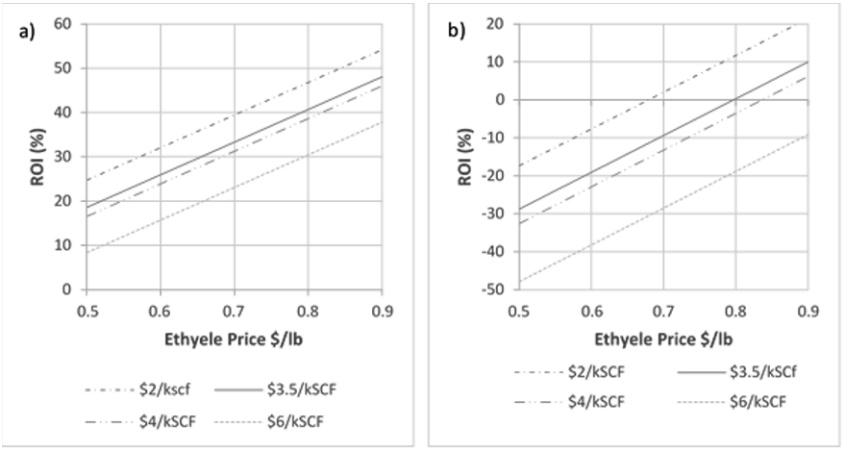

Figure 2. Sensitivity analysis for the MTO (a) and OCM (b) process at different prices of ethylene and shale gas.

Environmental Assessment

To estimate the environmental impact, CO_2 emissions were calculated for each process. CO_2 equivalents for outlet streams were obtained from Aspen Plus simulations. The emissions due to the use of the utilities were estimated with the EPA method for stationary combustion sources (EPA, 2008), and the CO_2 emissions related to the use of electricity were assessed using a factor of 0.73 MT of CO_2/MWh (EIA, 2014). The total amount of CO_2 emissions for each process is shown in Table 6. The MTO shows a higher impact due to purge streams that contain syngas, as this is translated into high CO_2 equivalents.

Table 6. CO_2 emissions, Mt/y

	MTO	OCM
Streams	19.80	12.60
Burning Fuels	1.26	0.93
Electricity	0.48	2.62
Total	21.55	16.15

4. Conclusions

The development of flowsheets for two processes to produce ethylene from shale gas and the results from their simulations using the ASPEN Plus® process simulator have been presented. From an economic basis, the MTO process showed the best profitability, with a high ROI, while the OCM process showed a suitable profitability only at low shale gas prices and high ethylene prices. Such unfavourable economics of the OCM process could be overcome with the design of new catalysts that provide

better reaction performance with respect to the information collected for the development of this work. The starting of a demonstration facility for the production of ethylene with this technology has recently been announced (Greenwood, 2014). The information about the catalyst details, however, is not available.
On energy and environmental aspects, the estimation of energy integration targets showed that both processes could be self sufficient in terms of their heating duties. From an environmental viewpoint, the MTO process showed higher CO_2 emissions than the OCM process, although this issue could be resolved by reducing purge streams or using them for another process.

References

K.A. Bullin, P.E. Krouskop, 2009, Compositional variety complicates processing plans for US Shale Gas, Oil & Gas J., 107, 50-55.

J.Q. Chen, B.V. Vora, P.R. Pujadó, Å. Grønvold, B. Fuglerud, 2004, Most recent developments in ethylene and propylene production from natural gas using the UOP/Hydro MTO process, Studies in surface and catalysis, 147, 1-6

J.Q. Chen, A. Bozzano, B. Glover, T. Fluglerud, S. Kvisle, 2005, Recent advancements in ethylene and propylene production using the UOP/Hydro MTO process, Catalysis Today, 106, 103-107.

M.M. El-Halwagi, 2012, Sustainable design through process integration: fundamentals and applications to industrial pollution prevention, resource conservation, and profitability enhancement, Butterworth-Heinemann: Oxford.

V.M. Ehlinger, K.J. Gabriel, M.M.B Noureldin, M.M. El-Halwagi, 2014, Process Design and Integration of Sahle gas to Methanol, ACS Sustainable Chem. Eng., 2, 30-37.

EIA, Electricity Emission Factors, Voluntary Reporting of Greenhouse Gases Program. http://www.eia.gov/survey/form/eia_1605/emission_factors.html (accessed September 20, 2014).

EPA, EPA430-K- 08-003, Direct Emissions from Stationary Combustion Sources; U.S. Environmental Protection Agency: Washington, DC, May 2008.

H.R. Godini, S. Xiao, S. Jašo, S. Stünkel, D. Salerno, N.X. Son, S. Song, G. Wozny, 2013, Techno-economic analysis of integrating the methane oxidative coupling and methane reforming processes, Fuel Processing Technology, 106, 684-694.

A. Greenwood, 2014. Silura to build methane-to-C_2 plant on Braskem US site. http:www.icis.com/resources/news/2014/01/15/9744050/silurat-to-build-methane-to-c2-plnat-on-braskem-us-site.html [accessed Septembre 18, 2014].

L.M. Julián-Durán, A.P. Ortiz-Espinoza, M.M. El-Halwagi, A. Jiménez-Gutiérrez, 2014, Techno-economic assessment and environmental impact of shale gas alternatives to metanol, ACS Sustainable Chem. Eng., 2, 2338−2344.

K. Sundaram, M. Shreehan, E. Olszewski, 2010, Ethylene, Kirk-Othmer Encyclopedia of Chemical Technology, John Wiley & Sons, 1-37.

B.V. Vora, T.L. Marker, P.T. Barger, H.R. Nilsen, S. Kvisle, T. Fuglerud, 1997, Economic route for natural gas conversion to Ethylene and Propylene, Studies in surface science and catalysis, 107, 87-98.

B.V. Vora, M. Turowicz, M. Cleveland, J. Gregor, 2013, Utilization of Coal in India: Opportunities for Petrochemicals, Chemical Processing, http://chemtech-online.com/CP/binpin_jan13.html (accessed June 19, 2014).

Q. Wang, X. Chen, A.N. Jha, H. Rogers, 2014, Natural gas from shale formation – The Evolution, evidences and challenges of shale gas revolution in United States. Renewable and sustainable energy reviews, 30, 1-28.

D. Wu, 2013, China's Sinopec to build Methanol-To-Olefins project at Huainan, ICIS, http://www.icis.com/resources/news/2010/12/20/9420679/china-s-sinopec-to-build-methanol-to-olefins-project-at-huainan/ accessed June 20, 2014.

Krist V. Gernaey, Jakob K. Huusom and Rafiqul Gani (Eds.), 12th International Symposium on Process Systems Engineering and 25th European Symposium on Computer Aided Process Engineering.
31 May – 4 June 2015, Copenhagen, Denmark

A Crude Oil Economic Model for PSE applications

Davide Manca[a], Valentina Depetri[a], Clément Boisard[a,b]

[a] *PSE-Lab, CMIC Department, Politecnico di Milano, 20133 Milan – ITALY*
[b] *Process and Informatics Engineering Dep., ENSIACET – 31030 Toulouse – FRANCE*

Abstract

The paper proposes a revised economic model to forecast the price of crude oil over medium- and long-term horizons so to take into account recent variations in both Brent and WTI quotations. This model uses as sampling interval the quarters, which cover most of Conceptual Design problems such as feasibility studies, economic assessments, and production/allocation planning. The elements of volatility and market fluctuations for supply-and-demand terms are taken into account by introducing the contributions of both producers (OPEC) and consumers (OECD).

Keywords: Crude oil; Economic model; Feasibility studies; Market uncertainty.

1. Introduction

Crude oil (CO) is one of the most basic and globally used raw materials in refineries and petrochemical plants. Fluctuations of CO prices can produce significant impacts on international economies. Indeed, CO prices are tracked very closely not only by investors worldwide, but also by process designers because CO is a reference component for both Oil&Gas and petrochemical supply chains. CO quotations are either directly (*i.e.* distillates) or indirectly (*i.e.* derived commodities) taken into account for the economic assessment and feasibility study of PSE problems (Manca, 2013). Depending on the specific problem under study, the time horizon considered in the economic assessment can be a short-, medium-, or long-term interval. On one hand, short- and medium-term horizon models are involved in scheduling and planning and require covering and therefore forecasting daily/weekly/monthly intervals. On the other hand, long-term horizon models are involved in Conceptual Design and are even more challenging as they need to estimate variables such as supply, demand, production, and capacity storage for quite long periods (*i.e.* quarters/years). Manca (2013) showed how CO economics influences at a great extent the quotations of commodities and utilities, which play a major role in the assessment of OPEX (operative expenditures) terms. Furthermore, Mazzetto *et al.* (2013) used CO as the reference component for econometric models of bioprocesses and showed a functional dependency of both raw biomaterials and final bio-products from the CO market. Due to high degrees of volatility, the real price of CO is difficult to model. Both CO and distillate prices are affected by exogenous elements, which have the potential to disrupt the flow of oil and products to market (Zhang *et al.*, 2008). This paper proposes an economic model of CO prices for forecasting purposes and discusses a possible geographical localization of CO quotations. The most important global CO benchmarks are West Texas Intermediate (WTI) for the Americas and Brent for Europe and middle Asia (Rasello and Manca, 2014). From 2011 on, WTI and Brent indexes lost their mutual consistency. The reason for the coming apart of their trends consists in a number of distinct but correlated reasons. Shale gas, shale oil, international crises, embargos, available infrastructures, industrial and transport accidents, natural calamities, and weather variability are

examples of the exogenous terms that played a major role in the quotation fluctuations even over short periods with a further influence from complex geopolitical backgrounds (Manca and Rasello, 2014). According to Liu *et al.* (2014), the recent sudden abundance of shale oil in the USA since 2011 has produced a substantial discount of WTI respect to Brent quotations. Since 2005, production of conventional CO has not grown concurrently with the growth of demand, so the oil markets have undergone a so-called *phase transition*. Indeed, current manufacturing is *inelastic*, which means that it is unable to follow the demand growth. This point pushes prices to fluctuate significantly because the resources of other fossil fuels do not seem to be able to fill that gap in the supply chain. In addition, the curves of CO production and net imports are close to a cross point in the United States. As in recent years US production of shale oil has boomed, North America imports of CO have essentially halved. The roots of the last 2014 quarter price crash lie on different factors: the massive reduction of import growth in China, the stagnation of oil demand in western world and Japan, the oversupply due to the US fracking boom and growth of oil sands in Canada, the imbalance of price ratios between oil and natural gas, the role of speculative investors, and a stronger USD respect to other currencies. All these factors were responsible for the 40% drop of CO prices from May to December 2014. Technical floors of 70 and 54 USD/bbl for the CO quotations, dating back to 2010 and 2006 respectively, showed to be inconsistent as they were repeatedly broken down in last 2014 quarter (Davis and Fleming, 2014). This points out that no real support level exists for the current oil marketplace.

2. Methods

The scientific literature (Ye *et al.*, 2009) showed a significant attention to forecast *variations* (technically speaking: *shocks*) of CO quotations. Most of literature papers on economics of petroleum prices are based on a financial background that focuses on the forecasting capability to trade CO by means of futures, selling/buying options, and other financial operations that have a time horizon which is much shorter than the one typically required by PSE applications (Manca, 2013). Price fluctuations cannot be modeled simply by a trend-line (Manca, 2013). Conversely, high volatility and bull-and-bear periods put both the investors and process managers in a difficult position to track the price trend of CO and finalize feasibility studies based on sound economic assumptions. Among forecasting models, one can distinguish two major classes: economic and econometric models. Economic models involve purely economic variables and simulate fluctuations of either *spot* or *futures* markets subject to the supply-and-demand law. This is the case of OPEC model (Cooper, 2003; Kaufmann *et al.*, 2004; Dees *et al.*, 2007). Econometric models do not try to understand the forces that cause price fluctuations, but are only focused on time series, trends followed by prices, and possible future extrapolations. The use of economic models on long-term horizons is challenging as they are based on forecasts of supply-and-demand levels, and capacity storage. The inability to predict all the variables that affect the dynamics of prices, such as technical advances in exploration and production of hydrocarbons, the political dynamics or changes in collective behaviors and both national and international legislations, make the implementation of economic models rather challenging. For the sake of space, the paper focuses only on economic models. Further details on econometric models can be found in Manca (2013) and Rasello and Manca (2014).

2.1. Economic models

According to Dees *et al.* (2007), oil prices are defined by a rule based on changes in market conditions and OPEC (Organization of Petroleum Exporting Countries)

behavior. OPEC decisions about quota and capacity utilization have a significant and immediate impact on oil price and some models are developed to comply with these hypotheses. Oil markets are characterized by the presence of both OPEC cartel and independent producers. The supply-and-demand terms can be identified respectively by CO producers and consumers. For the sake of simplicity, these can be assumed to be clustered in OPEC and OECD (Organization for Economic Cooperation and Development). Some papers studied the behavior of OPEC and its decisions (Cooper, 2003; Kaufmann *et al.*, 2004; Dees *et al.*, 2007). The pivotal work of Kaufmann *et al.*, (2004) provides a model of real oil prices that includes variables representing market conditions, such as OECD stocks for CO, capacity utilization by OPEC, OPEC announced quotas, and the degree to which OPEC production adheres to those quotas. Kaufmann's model comprises also a boolean variable for the Persian Gulf War, and three boolean variables for the first three quarters of the year that are taken as initial condition for a one-step forward forecast. The last three boolean variables cannot be extended to multi-step forecasts that work on long-term horizons as the effect of the initial quarter vanishes rapidly after few predictions (*i.e.* after few quarters). Dvir and Rogoff (2014) presented evidence of significant interactions among four factors of CO international markets: production, demand, stocks, and price. The involved variables are not easy to model because they are function of the economic activities run by both producing and consuming countries. This paper draws inspiration from the work of Kaufmann *et al.*, (2004) and proposes the following adapted model to take into account the recent disturbances that influenced and changed significantly the CO markets:

$$P_t = \alpha_0 + \alpha_1 Days_t + \alpha_2 Quotas_t + \alpha_3 Cheat_t + \alpha_4 Caputil_t + \alpha_5 Q_1 \quad (1)$$

where P_t is the CO quarterly price at time t [USD/bbl]; $Days$ is the number of days of forward consumption of OECD CO stocks (it is calculated by dividing OECD CO stocks by OECD CO demand); $Quotas$ is the OPEC production quota [Mbbl/d]; $Cheat$ is the difference between OPEC CO production and OPEC quotas [Mbbl/d]; $Caputil$ is the capacity utilization by OPEC (calculated by dividing OPEC production [Mbbl/d] by OPEC production capacity [Mbbl/d]); Q_1 is a boolean variable that takes into account the level of oversupply of OPEC respect to US production. Eq. (1) is linear in the adaptive parameters α_i whose values are reported in Table 1.

Table 1: Adaptive parameters in Eq. (1) for the models of WTI and Brent quotations.

Coefficient	WTI	Brent
α_0	868.70	780.09
α_1	-10.39	-11.33
α_2	-11.22	-9.60
α_3	-11.68	-8.45
α_4	184.33	294.80
α_5	-25.42	-30.20
R	0.8160	0.8105

The last term of Eq. (1) accounts for the recent decrease between OPEC and US productions which fell under 22 Mbbl/d. The sign of the estimated adaptive parameters are in part consistent with previous results described by Dees *et al.* (2007) as per the variables $Days_t$, $Cheat_t$, $Quotas_t$, and $Caputil_t$ for WTI prices. At the same time, it is worth observing the different values of Brent parameters respect to WTI ones. This is

mainly due to the dissimilar evolution of Brent and WTI quotations subject to separate dynamics produced by the abovementioned events occurred in recent years. It is worth observing that Eq. (1) cannot forecast the unpredictable conflicts, tenses, and events that may occur all over the world and influence CO markets. For instance, the first-month events of 2011 such as the conflict in Libya and the tsunami in Japan, combined with the Fukushima nuclear accident, increased significantly the CO prices. Similar comments can also be made for the political situation of Iraq that recently impacted on the CO quotations.

Eq. (1) calls for suitable forecasting models of the input variables: OECD demand, OECD inventories, OPEC production, and OPEC production capacity. The time interval chosen to identify these models is Q1-2012 to Q4-2014 and is a compromise between being as close as possible to current situation and preserving the generality accuracy. The model of OECD demand is a modified version of Cooper's model (Cooper, 2003):

$$Demand_{t+1}^{OECD} = \alpha_0 GGDP_{t+1} + \alpha_1 P_t + \alpha_2 Q_1 + \alpha_3 Q_2 + \alpha_4 Q_3 + \alpha_5 Q_4 \quad (2)$$

where *GGDP* is the Global Gross Domestic Product of the corresponding quarter whose growth (*GGGDP*) seems to be stable at around 2% (in terms of annual variations) and Q_1, Q_2, Q_3, Q_4 are boolean variables respectively referred to first, second, third, and fourth quarters. Just for the demand term the contribution played by quarters should not be neglected as it allows improving significantly the forecast capability of the whole economic model. The effect of *GGGDP* is interesting as it can create different scenarios according to the degree of economic activity in a country, region, and the world. Although oil demand conditions respect the periodic trend in OECD countries, the supply modeling is extremely difficult to model as oil markets reflect the complex background of production conditions and OPEC behavior (Dees *et al.*, 2007). OECD inventory is the result of the difference between the OECD demand and the OPEC supply. At our knowledge, the literature does not report any forecasting models for OPEC inventories, production, and capacity utilization to be fruitfully applied to PSE problems. Our research efforts on the OECD inventories showed that they are correlated with OECD demand and OPEC production capacity:

$$Inventory_{t+1}^{OECD} = \alpha_0 + \alpha_1 Capacity_t^{OPEC} + \alpha_2 Demand_{t+1}^{OECD} \quad (3)$$

The OPEC production depends on several ambiguous and unpredictable parameters, such as local political situations in the different countries of the cartel, even if OPEC itself tries to regulate the production by means of compensations in case of an unintended production decrease or increase by a country member. For the sake of clarity, the model proposed in this paper depends on current OECD inventories and on the previous price of CO:

$$Production_{t+1}^{OPEC} = \alpha_0 + \alpha_1 Inventory_{t+1}^{OECD} + \alpha_2 P_t \quad (4)$$

OPEC tries to produce less than its capacities allow so to be able to intervene in case of sudden variations in CO demand and produce a price impact. A very basic model representing the OPEC competitive behavior assumes that:

$$Production^{OPEC} = 0.95 \cdot Capacity^{OPEC} \quad (5)$$

As American CO production started a new growth in 2008, a dedicated rather simple model for recent trend of the American production assumes that:

$$Production_{t+1}^{USA} = \alpha_0 + \alpha_1 \cdot Production_t^{USA} \quad (6)$$

Eq. (6) is used to trigger the boolean variable Q_1 in Eq. (1) so to account for the offer

surplus originated by the shale-oil revolution. Eventually, as far as OECD inventories are concerned, the proposed model is:

$$Capacity_{t+1}^{OPEC} = \alpha_0 + \alpha_1 Inventory_{t+1}^{OECD} \quad (7)$$

Since our economic model was designed to reproduce as faithfully as possible the future trends of CO quotations, which depend on different geopolitical and economic scenarios (*e.g.*, wars, tensions, local crisis) then the standard deviation of petroleum prices ought to be taken into account when shaping the model stochastic features. In particular, by analyzing the CO trend, it is possible to quantify that the standard deviation (σ) of WTI CO price in the last five years was 9.5%. Major increases of the price ($+3\sigma$) were due to major variations (*e.g.*, wars, attacks, crashes) and were characterized by a 10-year period. Minor increases of the price ($+1.5\sigma$) were due to minor variations (*e.g.*, tensions and growth in China) and were characterized by a 3-year period. Minor decreases of the price (-1.5σ) were due to minor variations (*e.g.*, economic or social issues, technical defects) and had a frequency of about 7 years. Finally, major price reductions (-3σ) were due to major economic/financial instabilities and were rather rare having a return frequency of about 10 years. Other critical elements are given by OPEC decisions about quota and capacity utilization, which have a significant and immediate impact on oil quotation and act as a control term on prices even if the cartel does not have the same power as the one it had in the past (*i.e.* in the 70's of last century) when OPEC could set almost independently the CO prices. In the 70-80's, OPEC strategy of pushing up prices by restricting supply was responsible for the development of competing oil resources and deep-water technology.

Nowadays, the economic background has changed and is more complex than just 5-10 years ago as OPEC and OECD do not include the so-called BRIC countries (*i.e.* Brazil, Russia, India, and China) and other emerging countries such as Indonesia. Furthermore, the increasing concern about tar sands in both USA and Canada has given a new power to the American economy that could become independent of OPEC decisions about quotas and production in the short future.

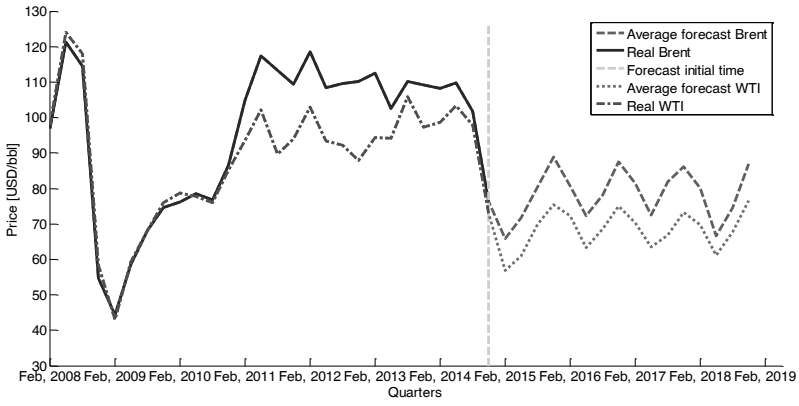

Figure 1: Brent and WTI forecast prices start from the vertical dashed green line (Nov, 2014).

In front of these emerging scenarios, Middle East producers decided not to cut their quotas at the end of 2014 to maintain their production competitive with the global crude oil spot market. The highest authorities of Saudi Arabia declared acceptable that prices remained low for long periods if that would reduce investments in shale oil and rebalance global markets. The recent highly-variable trend of CO prices made oil

companies and some traditional producers (*i.e.* Iran, Venezuela, and Russia) afraid about breaking their own neutrality threshold between incomes and outcomes (*i.e.* their breakeven point). Figure 1 shows on the left of the vertical dashed line the real past quotations of Brent and WTI, and on the right the corresponding forecast average prices resulting from 50 stochastic scenarios based on Eq. (1) under the hypothesis of bullish trend of the *GGGDP* (*i.e.* 2% annual constant increase). It is worth observing that according to the very drastic changes measured at the end of 2014, the expected *GGGDP* ratings were decreased. To confirm this, EIA expects WTI monthly average prices fluctuating in 2015 between 34 and 76 USD/bbl with a 95% confidence interval.

3. Conclusions

Starting from the qualitative classification of economic and econometric models, the paper proposed a new economic model to forecast the evolution of CO quotations over long-term horizons. Eq. (1) summarized the proposed economic model to be supplemented by Eqs. (2-7) that describe the future dynamics of input variables. These equations can simulate different reference scenarios based on a set of stochastic trends. The call for creating distinct scenarios comes from the necessity to identify possible distributions of economic trends to answer the typical question of PSE applications about the feasibility of products and processes. It is advisable to update Eq. (1) rather often because of the ever-changing events that can influence market quotations. Today, more than ever, CO markets are seeing the emergence of new countries, the economic development of other ones, and the revival of interest and investment in nonconventional petroleum reservoirs (*e.g.*, shale oil, tar sands). The power of the proposed economic model consists in its capacity to account for the stochastic nature of CO prices that are globally influenced by the abovementioned events and factors. Similarly, the model accounts for both CO producers and consumers to influence and determine the price dynamics.

References

Cooper, J.C.B., 2003. Price elasticity of demand for crude oil: estimates for 23 countries. Organization of the Petroleum Exporting Countries, Glasgow, Scotland.

Davis, N., Fleming, N., 2014. The oil price crash and what it means for the petrochemical industry. ICIS Report. http://www.icis.com/contact/oil-price-crash-impact-on-petrochemicals

Dees, S., Karadeloglou, P., Kaufmann, R., Sanchez, M., 2007. Modelling the world oil market: Assessment of a quarterly econometric model. Energy Policy, 35(1), 178-191.

Dvir, E., Rogoff, K., 2014. Demand effects and speculation in oil markets: theory and evidence. Journal of International Money and Finance, 42, 113-128.

Kaufmann, R.K., Ullman, B., 2009. Oil prices, speculation, and fundamentals: interpreting causal relations among spot and futures prices. Energy Economics, 31, 550-558.

Liu, W.M., Schultz, E., Swieringa, J., 2014. Price dynamics in global crude oil markets. The Journal of Futures Markets, 0, 1-15.

Manca, D., 2013. Modelling the commodity fluctuations of OPEX terms. Computers and Chemical Engineering, 57, 3-9.

Mazzetto, F., Ortiz-Gutiérrez, R.A., Manca, D., Bezzo, F., 2013. Strategic design of bioethanol supply chains including commodity market dynamics. I&ECR, 52, 10305-10316.

Rasello, R., Manca, D., 2014. Stochastic price/cost models for supply chain management of refineries. Computer aided Chemical Engineering, 33, 433-438.

Ye, M., Zyren, J., Blumberg, C.J., Shore, J., 2009. A short-run crude oil forecast model with Ratchet effect. Atlantic Economic Journal 37, 37-50.

Zhang, X., Lai, K.K., Wang, S.Y., 2008. A new approach for crude oil price analysis based on empirical mode decomposition. Energy Economics, 30(3), 905-918.

Krist V. Gernaey, Jakob K. Huusom and Rafiqul Gani (Eds.), 12th International Symposium on Process Systems Engineering and 25th European Symposium on Computer Aided Process Engineering.
31 May – 4 June 2015, Copenhagen, Denmark

Simulation Study of Temperature Distribution in the Thermal Drying Oven for a Lacquer Coating Process

Paisan Kittisupakorn,[a*] Patsarawan Lipikanjanakul[a]

[a]*Chulalongkorn University, Pathum Wan, Bangkok 10330, Thailand*

Abstract

Metal sheets have to be coated with food grade lacquer and dried at thermal drying oven for metal can making process. At the thermal drying oven, exhaust gas is delivered out by the blower to eliminate the solvent. This leads to the temperature decreasing at the drying zone of the thermal drying oven, especially to unloading. To handle this, an inverter has been implemented to provide saving of electricity bill. In this work, temperature distribution and flow pattern of gas mixture between air and solvent have been studied. A three-dimensional model of the transient heat transfer has been developed and validated against the real data. Comparison of the temperature distribution and flow pattern between the conventional system or full speed and the new system with the inverter by changing speed of outflow has been made. Simulation results show that the system with the inverter obtains low temperature of the exhaust gas released out to the incinerator leading to heat loss decreasing of 10.4%. It is applicable to energy saving for the thermal drying oven.

Keywords:thermal drying oven, temperature distribution, flow pattern, gas mixture.

1. Introduction

In a metal can making process for food products, the metal sheets have to be coated with coating solution in order to protect any corrosion caused by chemical reaction between products and metal containers. Basically, a coating process can be divided into three steps; varnishing, drying, and curing. In the varnishing step, lacquer is transferred to metal sheets by roller coating. After that, the metal sheets are passed to a thermal drying oven in which either drying or curing is operated. In a drying zone, solvent medium in lacquer on the metal sheets are removed. The parameters leading to the oven's performance are air velocity, relative humidity, temperature, time, and nature of the coating solution (Blotta et al., 2011). The temperature must be kept at 453 K to completely dry all the solvent off. Moreover, to reduce the solvent accumulation, a blower operating at full speed has been employed to remove the exhaust gas in the oven. In spite of unloading, the blower still drives with full speed. This leads to heat losses, the decrease in the oven's temperature, and insufficient consumption in electricity and fuel. Consequently, an inverter, adjustable-speed drive used to control AC motor speed and torque by varying motor input frequency and voltage, has been implemented to control the operation of the blower by adjusting the rotating speed corresponding to a desired loading condition. Therefore, the implementation of the inverter can save electricity cost and increase thermal performance.

[*]Corresponding author: Paisan.k@chula.ac.th (P. Kittisupakorn)

The simulation study for the thermal system has been reported in several studies. The simulation must be analyzed under turbulence flow. Therefore, Reynolds-averaged Navier–Stokes (RANS) equations including heat transfer are frequently applied to study for temperature distribution. Simulation studies using the RANS equations are, for examples, the continuous bread-breaking oven (Khatir et al., 2012), the newly designed economizer (Niamsuwan et al., 2013) and the heating oven (Smolka et al., 2013).

The objective of this work is to study temperature distribution and flow pattern of gas mixtures between air and the solvent in the thermal drying oven. A mathematical model has been developed and validated with real data. The temperature distribution and the flow patter are presented in two cases: the conventional system or full speed and the new system with the inverter by changing speed of outflow.

2. Oven geometry and parameter

Geometry of the oven has been formulated in a three-dimensional model as shown in Figure 1. The oven is 5.1 m long, 2.095 m high and 1.2975 m wide. The width is considered as half width of real scale due to symmetry surface (a). Surface (b) is an inlet duct with cross section of 0.292 m × 5.1 m and surface (c) is an interface between drying zone and curing zone. Semi-circle in surface (d) is represented an outlet chimney of the oven with diameter of 0.502 m. It is located at 1.435 m from the oven entrance which is presented by surface (e) and surface (f), (g), and (h) are walls of the oven.

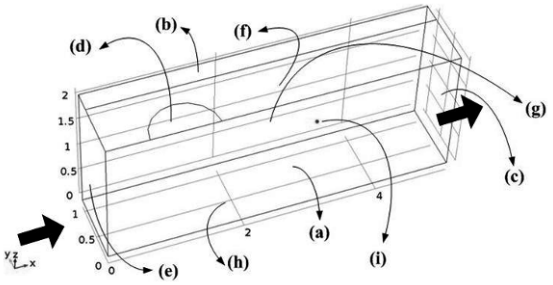

Figure 1 Geometry of the oven

In this study, fluid domain is specified as the gas mixture between air and solvent vapour. Normally, the solvent used is Butyl Cellosolve ($C_6H_{14}O_2$) for food grade lacquer. The gas mixture is considered as incompressible and Newtonian fluid and its properties are based on data in the Aspen plus software; the heat capacity, density, viscosity, and thermal conductivity are 1,135.81 J/kg-K, 0.408271 kg/m^3, 3.8348× 10^{-5} Pa·s, and 6.1103× 10^{-5} kW/m-K, respectively.

3. Mathematical model

A mathematical model of an air flow characteristic in a turbulent condition has been developed. The turbulent Reynolds Averaged Navier-Stokes standard model (RANS) is applied to provide the temperature distribution and flow pattern by Cartesian coordinate. It contains three governing equations: the mass, momentum, and energy conservation.

The equation of mass conservation (Continuity equation)

$$\frac{\partial \rho}{\partial t} + \frac{\partial}{\partial x_x}\rho u_x + \frac{\partial}{\partial x_y}\rho u_y + \frac{\partial}{\partial x_z}\rho u_z = 0 \tag{1}$$

The equation of momentum conservation (Navier-Stokes equation)

$$\rho\left(\frac{\partial u_i}{\partial t} + u_x\frac{\partial u_i}{\partial x_x} + u_y\frac{\partial u_i}{\partial x_y} + u_z\frac{\partial u_i}{\partial x_z}\right) = -\frac{\partial p}{\partial x} - \left(\frac{\partial u}{\partial x_x}\tau_{xi} + \frac{\partial u}{\partial x_y}\tau_{yi} + \frac{\partial u}{\partial x_z}\tau_{zi}\right) + \rho g_i \tag{2}$$

The equation of energy conservation

$$\rho C_p\left(\frac{\partial T}{\partial t} + u_x\frac{\partial T}{\partial x_x} + u_y\frac{\partial T}{\partial x_y} + u_z\frac{\partial T}{\partial x_z}\right) = k'\left(\frac{\partial^2 T}{\partial x_x^{\,2}} + \frac{\partial^2 T}{\partial x_y^{\,2}} + \frac{\partial^2 T}{\partial x_z^{\,2}}\right) + Q \tag{3}$$

ρ is the density. x is Cartesian coordinate in the subscript is coordinate direction (x, y, z). u is the velocity component in the subscript is coordinate direction (x, y, z). The subscript i is an index of Cartesian components. p is pressure. τ is viscous stress tensor. g is gravity force in coordinate axis. C_p is the specific heat capacity at constant pressure. T is the absolute temperature. k′ is the thermal conductivity. Q is a heat source.

In the turbulence term, the standard k-ε model incorporated with the turbulence kinetic energy is used to give convection and diffusion transport. This model consists of two model equations: turbulence kinetic energy (k) and viscous dissipation (ε).

Equation of turbulence kinetic energy

$$\frac{\partial(\rho k)}{\partial t} + \rho(u\cdot\nabla)k = \nabla\cdot\left[\left(\mu + \frac{\mu_T}{\sigma_k}\right)\nabla k\right] + P_k - \rho\varepsilon \tag{4}$$

Equation of viscous dissipation

$$\frac{\partial(\rho\varepsilon)}{\partial t} + \rho(u\cdot\nabla)\varepsilon = \nabla\cdot\left[\left(\mu + \frac{\mu_T}{\sigma_\varepsilon}\right)\nabla k\right] + C_{\varepsilon 1}\frac{\varepsilon}{k}P_k - C_{\varepsilon 2}\rho\frac{\varepsilon^2}{k} \tag{5}$$

In eq.(4) and eq.(5), μ_T is eddy viscosity. The five adjustable constants: C_μ, σ_k, σ_ε, $C_{\varepsilon 1}$, and $C_{\varepsilon 2}$ are 0.09, 1.00, 1.30, 1.44, and 1.92, respectively (Versteeg and Malalasekera, 2007).

A completely mathematical model with boundary and initial conditions is formulated and solved. The boundary and initial conditions are given in Table 1. The velocity is constant over the inlet surface. At outlet surface, there is no viscous stress. The surface (a) is set as symmetry condition in heat and flow simulation. At the external wall of the geometry, heat at the surface losses to the surrounding. Therefore, it is considered as the convective heat flux with external natural force.

Table 1 Boundary condition

Boundary	Surface*	Convectional	New system	Unit
Initial temperature		453.1500		K
Mass flow rate		1.6667	1.5000	m^3/s
Normal velocity inlet	(b)	0.1584	0.1584	m/s
Normal velocity inlet	(c)	0.6223	0.5498	m/s
Normal velocity outlet	(d)	4.2104	3.7893	m/s
Temperature inlet	(b)	473.1500		K
Temperature inlet	(c)	453.1500		K
Temperature inlet	(e)	303.1500		K
Pressure	(e)	101,314.9978		bar
Outlet velocity	(e)			
Outflow temperature	(d)			
Symmetry heat and flow	(a)			
Convectional heat flux	(f), (g), (h)			

* Surface boundary shown in Figure 1

The model is solved by a numerical method on the commercial software (COMSOL multiphysics version 4.3b). The mesh geometry is generated by fine element size in free tetrahedral. The numbers of generated meshes are 149,475 domain elements, 12,967 boundary elements, and 518 edge elements.

4. Computational validation and result

4.1. Validation with measurement values

To validate the temperature prediction, the calculated data based on the model is plotted against observed data. A type K thermocouple is used to give measured temperature data. It has been installed at a center of the oven for width, 0.5 m height from the top of the oven, and 3 m length from the entrance. The measurement position is displayed at the point (i) in Figure 1. The measurement has been observed in unloading period for 10 minutes with every 15 seconds. The temperature is kept at the operating condition for loading period at around 453±1 K before changing to unloading period. The simulated and measured temperatures are compared as shown in Figure 2. It can be seen that the model gives a good agreement of the temperature with an error of ±1.1 K.

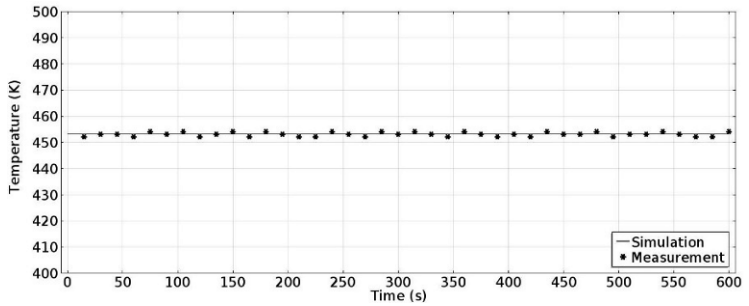

Figure 2 Temperature comparison between the simulation and measurement

4.2. Case 1: The conventional system or full speed

In this case, the blower operates at full speed in order to remove the exhaust gas of 1.6667 m^3/s. Simulation results show temperature distribution and flow pattern for the gas mixture at the drying zone. The temperature distribution at time of 5 min is presented in Figure 3(A). Near the entrance, the gas mixture temperature is initially at

295 K because heat is lost to the surrounding. Then, the gas mixture temperature rapidly goes to a desired temperature of 453.15 K after moving into 1.5 m from the entrance.

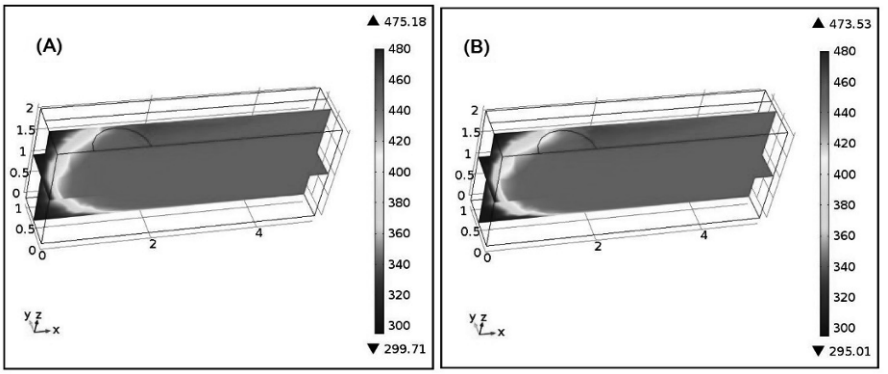

Figure 3 Temperature distribution (K) at time = 5 min: (A) Case 1 and (B) Case 2

In addition, the flow pattern at time of 5 min is illustrated in Figure 4(A). It can be seen that most gas mixture is moved from the interface to discharge at the chimney. Some gas mixture leaks out at the entrance. Figure 4(B) shows the profile of average velocity over x-y surface throughout the distance of drying zone at time of 2 min. As shown in solid line, the maximum velocity occurs at 1.5 m from the entrance owing to driving force by the blower.

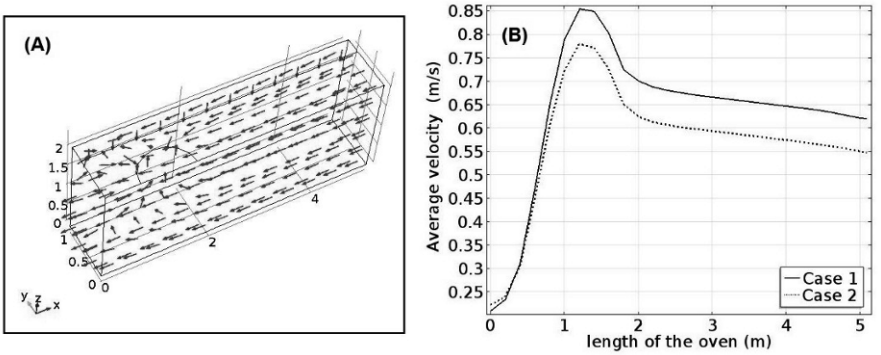

Figure 4 Velocity in the oven: (A) Flow pattern and (B) Velocity change by length of the oven

4.3. Case 2: The new system with the inverter to provide a change of outflow speed

In case of the new system, the inverter controls the blower's speed to operate at 1.5 m^3/s flow rate corresponding to unloading condition. Regarding to Figure 3(B), decrease of the blower's speed directly causes to the different temperature distribution around the outlet. Meanwhile, the similar profile is presented at other zones. According to Figure 4(B), the profile in dash line presents the analogous profile with low velocity. This is because of the decrease of the blower's speed leading to lower movement of the gas mixture compared to case 1.

Comparison of the temperature profiles of the exhaust gas released out to the incinerator for both systems has been made. As shown in Figure 5, the temperature profiles for full speed (case 1) and optimum speed (case 2) are represented by solid line and dot line,

respectively. It was found that the difference of average temperature between case 1 and case 2 is about 2 K. With Eq. (6), the calculated decrease in the heat loss (Q′) of about 10.4% is obtained.

$$Q' = \int_t m_1 c_p T_1(t)dt - \int_t m_2 c_p T_2(t)dt \tag{6}$$

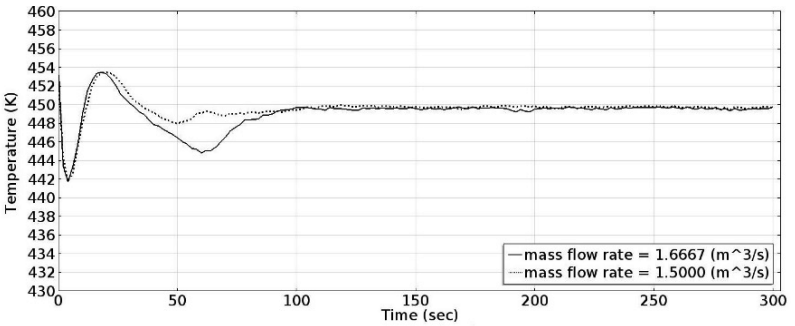

Figure 5 Temperature profiles at outlet surface

5. Conclusions

This work presents the simulation study for the temperature distribution in the drying zone of the thermal drying oven. The three-dimensional model of the transient heat transfer has been developed and validated with real data. The temperature distribution and flow pattern have been studied in two cases: full blower's speed and optimum blower's speed. The simulation results show that both cases give the similar profiles for temperature distribution and flow pattern. However, with the inverter installed, less blower's speed gives lower temperature of the exhaust gas released out to the incinerator leading to the decrease in the heat loss of 10.4%.

Acknowledgement

The financial support to this work under The Institutional Research Grant (The Thailand Research Fund), IRG 5780014, and Chulalongkorn University, Contract No. RES_57_411_21_076

References

E. Blotta, W.E. Stewart, E.N. Lightfoot, 2011, Evaluation of speckle-interferometry descriptors to measuring drying-of-coatings. Signal Processing, 91, 2395–2403.

Z. Khatir, J. Paton, H. Thompson, N. Kapur, V. Toropov, M. Lawes,D. Kirk, 2012, Computational fluid dynamics (CFD) investigation of air flow and temperature distribution in a small scale bread-baking oven. Applied Energy, 89, 89–96.

S. Niamsuwan, P. Kittisupakorn, I. M. Mujtuba, 2013, A newly designed economizer to improve waste heat recovery: A case study in a pasteurized milk plant.Applied Thermal Engineering, 60, 188-199.

J. Smolka, Z. Bulinski, A.J. Nowak,2013, The experimental validation of a CFD model for a heating oven with natural air circulation. Applied Thermal Engineering, 54, 387-398.

H.K. Versteeg, W. Malalasekera, 2007, An introduction to computational fluid dynamics , 2 ed. Englant: Pearson prentice hall.

Krist V. Gernaey, Jakob K. Huusom and Rafiqul Gani (Eds.), 12th International Symposium on Process Systems Engineering and 25th European Symposium on Computer Aided Process Engineering.
31 May – 4 June 2015, Copenhagen, Denmark

Outlier treatment for improving parameter estimation of group contribution based models for upper flammability limit

Jérôme Frutiger, Jens Abildskov, Gürkan Sin*

Department of Chemical and Biochemical Engineering, Technical University of Denmark (DTU), Building 229, DK-2800 Lyngby, Denmark
gsi@kt.dtu.dk

Abstract

Flammability data is needed to assess the risk of fire and explosions. This study presents a new group contribution (GC) model to predict the upper flammability limit UFL of organic chemicals. Furthermore, it provides a systematic method for outlier treatment in order to improve the parameter estimation of the GC model. The new method identifies and removes outliers based on the empirical cumulative distribution plot. It is compared to outlier detection based on Cook's distance and normal cumulative distribution.

Keywords: Outlier treatment, Flammability limit, Group contribution

1. Introduction

Flammability data provide important information in order to quantify the risk of fire and explosion in process safety studies and assessments. The upper flammability limit (UFL) is defined as the highest possible concentration of a substance in air at which a flammable mixture is formed (Crowl and Louvar, 2013). Experimental data on UFL are not always available due to cost and time constraints in particular at the early stage of process development where alternative concepts are evaluated and ranked before proceeding for more detailed analysis. Property prediction models can in this case be used to estimate the desired flammability data.

Group contribution (GC) based prediction methods use structurally dependent parameters in order to determine the property of pure components. The aim of the parameter estimation is to find the best possible set of model parameters that fits the experimental data.

However, outliers from the model set can strongly influence the parameter estimation, such that the property prediction can be inaccurate in the end. Therefore, it is necessary to identify possible outliers and remove them from the experimental data set. The outlier detection should be simple, following the structure of the model and mathematically consistent.

The Cook's distance (Cook, 1977) measures, how large the degree of influence of a data point is on the parameter set. A large Cook's distance indicates an outlier.

The approach suggested by Furguson, (1961) considers residuals between the experimental and the predicted values as observations coming from a hypothetical distribution, i.e. the normal distribution. The latter can be used in order to determine the outliers of the model.

In this study a methodology for outlier identification based on empirical cumulative distribution function (empirical CDF) is suggested and compared to the outlier treatments using normal probability and Cook's distance.

2. Methodology

2.1 Property model structure according to Marrero and Gani group contribution method

The Marrero Gani (MG) method considers the group contribution in three levels: The contributions from a specific functional group (1st order parameters), from polyfunctional (2nd order parameters) as well as from structural groups (3rd order parameters). Eq. (1) shows its general form.

$$f_i(\mathrm{X}) = \sum_j N_j C_j + \sum_k M_k D_k + \sum_l E_l O_l \qquad f(\mathrm{X}) = T \cdot \theta \tag{1}$$

In Eq. (1) C_j is the contribution of the 1st order group of type-*j* that occurs N_j times whereas D_k is the contribution of the 2nd order group of type-*k* that occurs M_k times in the molecular structure of a pure component. E_l is the contribution of the 3rd order group of type l that has O_l occurrences. The function $f(X)$ is specific for a certain property X (Marrero and Gani, 2001). The parameters can be summarized into the vector θ and the occurrences of the groups can be depicted in the matrix T. As examples, the different GC-factors of Adiponitrile and Methacrylonitrile are visualized in figure 1.

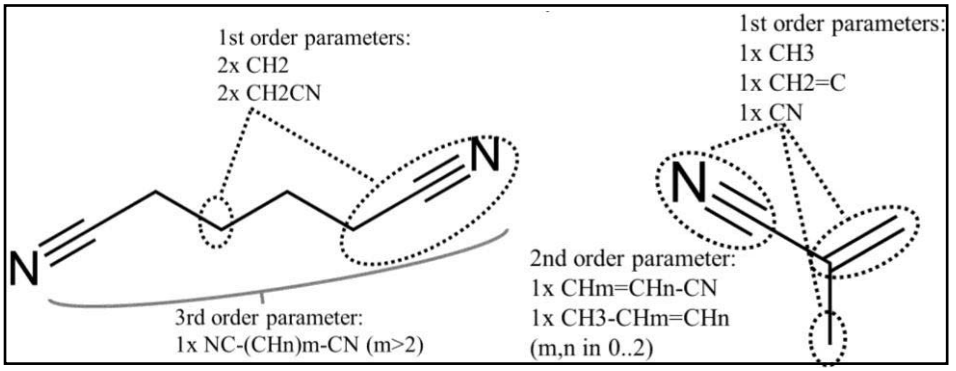

Figure 1. Example of GC-factors of Adiponitrile (left) and Methacrylonitrile (right).

The underlying assumption of group contribution principles is that a certain function of the property is linearly dependent on the contributions of the functional groups. Plots of various classes of pure components versus their increasing carbon number suggest that the appropriate form of the model function is logarithmic as specified in Eq. (2), where UFL_{const} is a universal constant. A selection of classes of compounds is showed in figure 2.

$$f_i(UFL) = \log\left(\frac{UFL_i}{UFL_{const}}\right) \tag{2}$$

2.2 Flammability limit data

Experimental data for UFL of 371 compounds, which includes alkanes, alkenes, alkynes, alcohols, aldehydes, halogenated substances, esters, aromatics and nitrogen compounds, are used from AIChE DIPPR 801 Database (AIChE, 2014). Flammability limits of each compound are provided in percentage volume in air at 298 K.

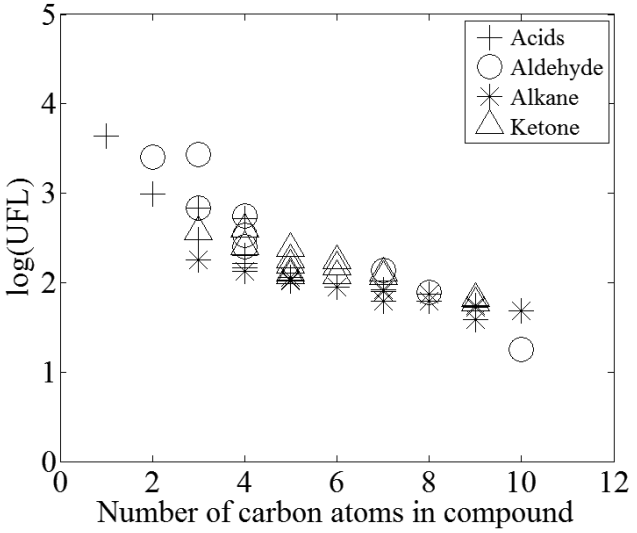

Figure 2. UFL of a selection of pure components versus their increasing carbon number.

2.3 Initialization and sequential parameter estimation

A first guess for the a priori unknown universal constants and MC-GC factors is provided by an approximation using linear algebra according to equation (3).

$$\hat{\theta} = (T^T T)^{-1} \cdot T^T \cdot f(UFL) \tag{3}$$

A value for the constant UFL_{const} is assumed in order to calculate the first guess for the parameters $\hat{\theta}$ from UFL data and the occurrence matrix *T*.

Afterwards the universal constants as well as the 1st, 2nd and 3rd order parameters are estimated separately applying ordinary non-linear regression according to Eq. (4).

$$\theta^* = \arg\min \sum_i (y_i^{\exp} - y_i^{pred})^2 \tag{4}$$

where θ^* corresponds to the estimated parameters and y_i^{exp} to the measurement and y_i^{pred} to the predicted value of compound *i*.

2.4 Simultaneous parameter estimation

The result of the sequential estimation serves as initial guess for the simultaneous parameter estimation algorithm, where all the parameters are estimated together for the ordinary non-linear regression problem.

2.5. Outlier treatment

Three ways of outlier treatment are applied separately to identify the corresponding outliers. The latter are then excluded and the parameter estimation is performed again. The three outlier treatments are compared and evaluated.

2.5.1 Outlier treatment using Cook's distance

Cook's distance measures the influence of a particular data point on the parameter estimation. A particular Cook´s distance D_i can be assigned to every value *i* according

to Eq. (5) (Cook, 1977). By definition compounds having a Cook´s distance larger than 4 divided by the number of data *n* is considered as an outlier (Hardin and Hilbe, 2007).

$$D_i = \frac{\sum_{k=1}^{n}(y_k^{pred} - y_{k(i)}^{pred})^2}{p \cdot MSE} \qquad D_i > \frac{4}{n} \tag{5}$$

In Eq.(5) y_k^{pred} is the prediction from the full regression for compound *k*, whereas $y_{k(i)}^{pred}$ is the prediction for compound *k* from a refitted regression where observation *i* is excluded. *MSE* is the mean square error and *p* is the number of parameters.

2.6.2 Outlier treatment using normal distribution

The underlying assumption is that the residuals between the predicted and experimental values are normally distributed and centred around zero (Ferguson, 1961). 95% of the data lie within two times the standard deviation σ of the residuals $y_j^{pred} - y_j^{pred}$. Residuals that fall outside this range of values that could reasonably be expected to occur, i.e. plus and minus 2 times the standard deviation σ, can be considered as outliers. The criterion is formulated in Eq. (6) for the data point *j* to be an outlier.

$$r_j = \left| y_j^{pred} - y_j^{pred} \right| > 2\sigma \tag{6}$$

2.6.2 Outlier treatment using empirical cumulative distribution

In this study we suggest a methodology where the residuals are not assumed to be normally distributed. The empirical cumulative distribution function (empirical CDF) tries instead to estimate the true underlying CDF. For the current data the empirical is depicted in figure 3.

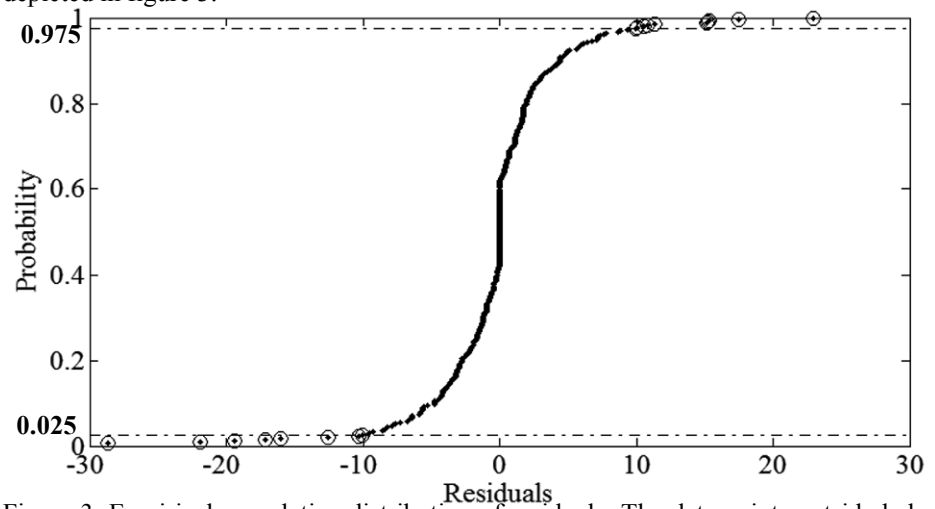

Figure 3. Empirical cumulative distribution of residuals. The data points outside below 0.025 and above the 0. 975 probability levels are considered as outliers.

The emperical CDF is a step function that increases by *1/n* in every data point.

Data points that are not reasonably likely expected to occur according to the empirical CDF can be considered as outliers, i.e. data points that lie below the 2.5% or above the 97.5% probability levels (see figure 3).

3. Results and discussion

The performance statistics of the regression before and after outlier exclusion is depicted in table 1. R^2 is the squared Pearson correlation coefficient between the experimental and the predicted values, N_{out} is the number of outliers removed, *SD* is the standard deviation, *ARE* is the average relative error between the predicted and the experimental values, *SSE* is the sum of squared errors, P_{rc} represents the percentage of the experimental data-points found within ± 25% relative error range respectively (Hukkerikar et al. 2012). In figure 4 the identified outliers are compared by depicting the prediction versus the experimental value. The equality line indicates a perfect fit.

Table 1. Model performance statistics

	R^2	N_{out}	*SD*	*AAD*	*ARE*	*SSE*	P_{rc} *25%*
Before outlier exclusion	0.72	0	6.2	3.0	24	14,398	66
After exclusion of Cook´s outliers	0.81	18	3	1.7	16	3,106	77
After exclusion of normal probability outliers	0.93	18	2.5	1.7	16	2,284	78
After exclusion of empirical CDF outliers	0.93	20	2.5	1.7	16	2,247	78

All three outlier treatments improve the regression performance. The outlier treatment using empirical cumulative distribution improves the regression similar to outlier detection using normal probability.

Considering figure 4, there are large value data points that are identified as outliers according to Cook's distance even though these compounds match the model. They influence the regression strongly and are assigned a large Cook's distance. Hence, large data points are removed from the data set, even though their prediction matches the experimental value and therefore should not be deemed as outliers. Although removing Cook's distance outliers improves the performance statistics, this outlier treatment is not recommended, because it also removes data points which are clearly in perfect agreement with the model prediction trends.

However, for the outlier treatment using normal CDF and empirical CDF approach of outlier identification, the potential outliers are those that differ a lot from the equality-line. The advantage of empirical CDF is that it does not a priori assume the property to be normally distributed, but tries to reveal the real underlining CDF. In cases where residuals follow a normal distribution, the difference between our approach that uses empirical distribution function and the Ferguson's method will indeed be negligible as is the case in this contribution. In that case, the empirical CDF will approximate a normal CDF distribution hence verifying the validity of the Ferguson's approach. However, in cases where residuals do not confirm to normal distribution and in particular the residual distribution displays long tails – as can be observed in several property model fittings in Hukkerikar et al. (2012), the empirical CDF approach is expected to guide better outlier detection hence model fitting. A potential caveat of using empirical CDF is that the number of data points (i.e. the size of sample used to

construct the cumulative probability function is expected to be representative of residuals distribution) will influence the outcome hence it is recommended to use the empirical CDF approach for relatively large size of data samples as often the case in building GC models.

Table 2 shows an example of the prediction of UFL for Methacrylonitrile, which is depicted in figure 1, using model Eq. (1) and (2).

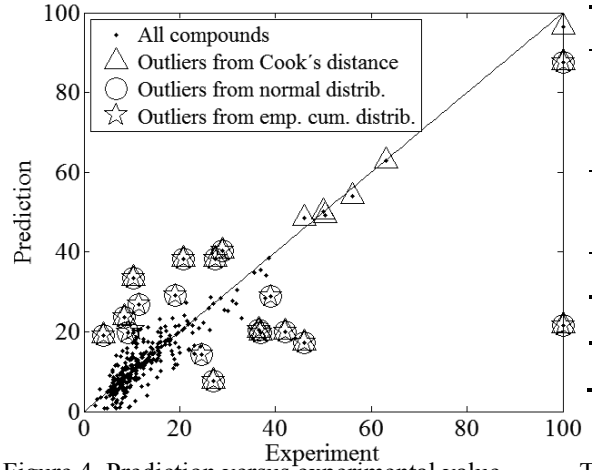

Figure 4. Prediction versus experimental value with identified outliers.

UFL_{const}		123.29
1st	CH3	-1.11
	CH2=C	0.52
	CN	-0.69
2nd	CH3-CHm=CHn	-0.53
	CHm=CHn-CN	-0.61
3rd	none	-
Predicted	*UFL*	10.96
Experim.	*UFL*	11.00

Table 2. Example of prediction of UFL for Methacrylonitrile

4. Conclusion

The study shows a novel prediction model for UFL using the MR-GC method. In this scope an outlier treatment methodology based on the empirical CDF is suggested. The performance statistics of the regression improves similarly to the use of normal CDF. However, the usage of empirical CDF is not restricted by the assumption that residuals should follow a normal distribution and hence have a wider application range. The usage of Cook's distance as an outlier detection method is found unreliable with high number of false detection of data points. This is not surprising since Cook's distance is in fact just a measure of data influence on the regression. High data influence is necessary but not sufficient condition of an outlier since data points in good agreement with regression line may also have a high influence on the regression.

References

Cook, Dennis R. 1977. "Detection of Influential Observation in Linear Regression." *Technometrics* 19 (1): 15–18.

Crowl, Daniel A., and Joseph F. Louvar. 2013. "Chemical Process Safety." In , 2nd ed., 253–56. New Jersey: Prentice Hall International Series in the Physical and Chemical Engineering Sciences.

Ferguson, T S. 1961. "On the Rejection of Outliers." *Proceedings of the Berkeley Symposium on Mathematical Statistics and Probability* 1 (1): 253.

Hardin, James William, and Joseph Hilbe. 2007. *Generalized Linear Models and Extensions*. 2nd ed. State Press.

Hukkerikar, Amol Shivajirao, Bent Sarup, Antoon Ten Kate, Jens Abildskov, Gürkan Sin, and Rafiqul Gani. 2012. "Group-Contribution+ (GC+) Based Estimation of Properties of Pure Components: Improved Property Estimation and Uncertainty Analysis." *Fluid Phase Equilibria* 321 25–43.

Marrero, Jorge, and Rafiqul Gani. 2001. "Group-Contribution Based Estimation of Pure Component Properties." *Fluid Phase Equilibria* 183-184: 183–208.

Project 801, 2014, Evaluated Process Design Data, Public Release Documentation, Design Institute for Physical Properties (DIPPR), American Institute of Chemical Engineers (AIChE).

Krist V. Gernaey, Jakob K. Huusom and Rafiqul Gani (Eds.), 12th International Symposium on Process Systems Engineering and 25th European Symposium on Computer Aided Process Engineering.
31 May – 4 June 2015, Copenhagen, Denmark

Integration and optimization of an air separation unit (ASU) in an IGCC plant

Maojian Wang [a,b], Adetoyese Olajire Oyedun[b], Ergys Pahija[b], Yi Zhu[b], Guilian Liu [a], Chi Wai Hui[b]

[a]*Department of Chemical Engineering, Xi'an Jiao Tong University, Xi'an, China.*
[b]*Department of Chemical and Biomolecular Engineering, The Hong Kong University of Science and Technology, Clear Water Bay, Kowloon, Hong Kong.*

Abstract

The integrated gasification combined cycle (IGCC) is a promising and efficient electrical power generation technology with less environmental effects than conventional coal power plant. However, improvement of its efficiency is an important task needs to be achieved. In this paper, a mathematical model of an IGCC plant is built, which includes a gasification unit, an air separation unit (ASU) and a combined cycle unit with energy and mass conversion. Gibbs free energy minimization method is used for predicting the composition of the syngas. Isentropic process calculation with efficiencies are taken into account for modelling the combined cycle. ASU is simulated mainly using bubble point method which can give rigorous prediction of the double distillation columns. Some contributions have been done to give the better strategy for supplying initial value to converge and to achieve the integration. The overall efficiency of 39.8 % can be reached considered as a base case, and simulated using Microsoft® Excel 2013. An additional case with not standard ASU is followed. The comparison between two cases shows that the Standard ASU may not the best choice of each IGCC plant. Some adjustments may be needed to fit the ASU with the whole plant to improve the overall efficiency.

Keywords: ASU, Heat integration, IGCC, optimization.

1. Introduction

As one of the promising green technologies, IGCC offers an efficient way to generate electricity from coal, biomass or any other suitable solid or liquid fuels with lower impact to the environment. The biggest challenge of making IGCC to become a viable technology is its high energy production cost. This creates a barrier for this green technology to enter into the stage of a highly competitive electricity market. In another aspect, the target of developing the IGCC technology should be increase the efficiency of the power plant.

Among the IGCC power plant, ASU is considered as most energy intensive part, which still using the traditional cryogenic technology (Nakaiwa, 2003). So heat integration is considered to play a very important role in ASU optimization. Pinch Analysis, which was introduced by Linnhoff and Flower (1978), is used to analyze ASU in order to create constrains for achieving minimize cold utility usage.

Previous researches are mostly aimed at optimization of the ASU with fixing the ASU product streams are nearly pure oxygen or nitrogen (Cornelissen, 1998). When it comes to the IGCC, one product stream of ASU is used as the oxidation agent instead of reactant. So oxygen purity from ASU product stream can be not only 99 %, but also lower like 96

%. So far, it is rarely discussed in literature. This paper is focused on the influence of this change for the plant efficiency by doing case study.

2. Process description

The process flow diagram given in Figure 1 describes the simulated IGCC power plant. The coal (Illinois #6), is crushed and mixed with water and is pumped into the gasifier with oxygen produced by ASU. The crude syngas is mainly composed of H_2, CO, CO_2 and H_2O. Sensible heat is used to generate steam for recovery. After cooling and cleaning, the clean syngas drives a gas turbine after combustion with additional air and injected nitrogen. The heat of fuel gases from gas turbine is used to generate superheated steam in the heat recovery steam generator (HRSG). A steam turbine is drove by that steam to product additional power.

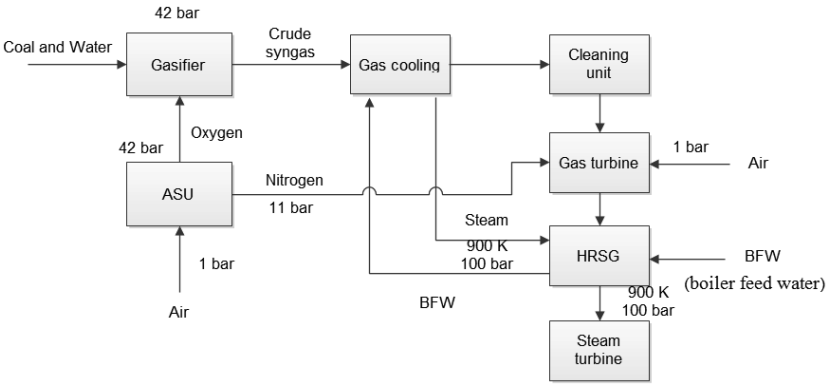

Figure 1. Schematic diagram of the process.

3. Modelling methods

The overall efficiency of the IGCC plant, η_{all}, is defined to measure the performance :

$$\eta_{all} = \left(\frac{P_{out} - W_{asu}}{\sum HHV}\right) * 100\% \quad (1)$$

Where P_{out} is the net produced electricity, W_{asu} is energy consumption of ASU and HHV is the higher heating value of coal which injects into the power plant.In the thermodynamics aspect, all the components in the IGCC plant are assumed as ideal. So the properties can be calculated according to the conditions, such as enthalpy and entropy values of the gases can be identified as below:

$$H^o - H^o_{298.15} = At + B\,t^2/_2 + C\,t^3/_3 + D\,t^4/_4 - E/_t - H \quad (2)$$

$$S^o = Aln(t) + Bt + C\,t^2/_2 + D\,t^3/_3 - E/(2t^2) + G \quad (3)$$

Where H^o is standard enthalpy (kJ/mole) and S^o is standard entropy (J/mole*K). A, B, C, D, E, H, G are constant values that can be found from NIST chemistry database. t equals physical temperature divided by 1000 K. The simulation of the ASU unit and IGCC plant is built as a Macro in Excel 2013 cooperating with Standard GRG Non-linear Solver and Water 97 add-in, which is property database using the industrial standard IAPWS-IF97 (Spang, 2002).

3.1. Modelling of the Gasifier

Gasification is completed in the gasifier, including a series of reactions which can convert the solid fuel to combustible gases, such as carbon monoxide and hydrogen, by supplying gasifying agent like oxygen (Minchener, 2005). Considering the complexity of the gasification, equilibrium models have been developed to simulate the gasifier which can directly calculate the outcome compositions based on the feed stock and operation conditions without taking any reaction details into consideration.

The crude syngas is assumed as a mixture of CH_4, H_2, CO, CO_2, H_2S, COS, NH_3, NO_2, SO_2, N_2O, SO_3. The composition is calculated simultaneously with the equilibrium temperature in adiabatic statement. At the equilibrium state, the total Gibbs free energy of the system is minimized. The total Gibbs free energy of a system, G_{system}, is defined:

$$G_{system} = \sum_{i=1}^{N} n_i (G_{f,i}^0 + RT \ln \frac{\hat{f}_i}{f_i^0}) \tag{4}$$

Where $G_{f,i}^0$ is the standard Gibbs free energy of formation (kJ/mole), n_i (mole) is amount of component i of the system. T (K) is system temperature and R is gas constant. With ideal gas assumption, $\hat{f}_i$ is related with system mole composition y_i and pressure P (Pa):

$$\hat{f}_i = y_i P \tag{5}$$

When at low pressures, f_i^0 is taken as the standard state pressure. $G_{f,i}^0$, is the calculated based on the concept using equation (6) which is presented as:

$$G_{f,i}^0(T) = \Delta H_{f,i}^0(T) - T\Delta S_i^0(T) \tag{6}$$

The enthalpy and entropy changes from standard state to system state at T (K), $\Delta H_{f,i}^0(T)$ and $\Delta S_i^0(T)$, are calculate based on the equation (2) and (3). Heat balance and mass balance are also achieved for the gasifier as a whole.

3.2. Modelling of the combined cycle

The combined cycle is referred to the combination of gas turbine, steam turbine and HRSG. Simplified mathematical model of the gas turbine is consist of three key units: a compressor, a combustor and a turbine. In another hand, the process of steam turbine is proposed including a turbine and a pump. Those two sections are connected by HRSG to recover fuel gas sensible heat. The principle of modelling the combined cycle unit is idealizing the process then adding the efficiency. Isentropic process is assumed as the ideal process for the compressor, turbine and pump in the combined cycle unit. For steam turbine and HRSG, the isentropic process is calculated based on the concept using Water97 database. Those differences are due to the ideal gas, then the entropy equation is not related with the pressure. So the isentropic relation for an ideal gas assumption in gas turbine expresses as below:

$$(T_2/T_1) = (p_2/p_1)^{(\gamma-1)/\gamma} \tag{7}$$

Where through the isentropic process, gas temperature T_1 (K) will be changed to T_2 (K), and the gas pressure will simultaneously changes from p_1 (Pa) to p_2 (Pa). γ , for an ideal gas, is the heat capacity ratio which is calculated. When it comes to the efficiencies, The HRSG feed water pumps are assumed to operate at 90 % isentropic efficiency, η_{pump}, defined by equation (8).

$$\eta_{pump} = \frac{(H_{out,s} - H_{in})}{(H_{out} - H_{in})} \times 100\% \quad (8)$$

Where $H_{out,s}$ is enthalpy of the outlet stream of the pump by isentropic process. H_{out} is the actual enthalpy of the stream from the pump. Two turbines in combined cycle are assumed to operate at 80 % isentropic efficiency. And the compressor is assumed to operate at 90 % isentropic efficiency. The definitions of those efficiencies are similar as η_{pump} in equation (8).

The combustor in the gas turbine is treated as an adiabatic reactor. The output compositions and the operating temperature can be decided by energy and mass conservation principles. The efficiency of HRSG is defined as the ratio of output enthalpy and input enthalpy, which is fixed as 90 %.

The total power output, P_{out} (MW), for the combined cycle of the IGCC power plant can be calculated by equation (9). W (MW) stands for the overall power output of the two turbines and W_{ax} (MW) stands for all of the auxiliary work:

$$P_{out} = W - W_{ax} \quad (9)$$

3.3. Modelling of the ASU

The process of cryogenic ASU is shown in Figure 2, which is consist of a feed compression section, two multi-phase heat exchangers (MHEX), a distillation section (low-pressure (LP) column and high-pressure (HP) column) and a product compression section. The air is compressed and cooled down to 298 K and split into two stream. Those streams are respectively injected into LP column and HP column after heat exchange with products of LP column in MHEX1 and pressure controlling pretreatment. Two product streams firstly go through the valve to control the pressure and cool down in MHEX2 by cooling the top product from LP column. High-purity nitrogen and oxygen streams from MHEX1 are compressed in order to inject into the combustor and gasifier.

The models of the compressors and expanders are built similar as the ones in combined cycled. MHEX is assumed as the general heat exchanger with the temperature constraints and satisfying the energy balance.

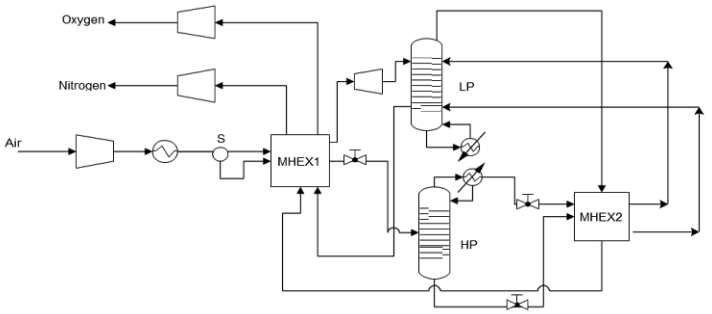

Figure 2. Schematic diagram of the ASU.

The models of LP and HP columns are based on the Mass balance equations (M), Equilibrium relations (E), Sum (or conservation) equation(S) and Enthalpy balance relations (H), which are call MESH equations together. Bubble point method (Wang, 1966) is used by solving those equations in the formation of triple diagonal matrix. A strategy to create initial values is added before the bubble method. The prediction of initial value is either calculated based on the constant molar flow hypothesis or get from

previous calculation experiences. LP column has zero bottom rate with only reboiler and HP column has only a total condenser.

Because integration inside the ASU is quite critical, Pinch analysis is used to measure the performance of ASU, which proves nonexistence of hot utility. In the model, constrains about relationships among the condenser duty, reboiler duty and MHEX heat duty are used to minimized cold utility. What's more, air feedstock is only consist of ideal gas: O_2 and N_2, which the mole ratio 1:4. The total energy consumption of ASU, W_{asu} (MW) , is the difference of total compressor consumption $W_{compressor}$ (MW) and total expander consumption $W_{expanders}$ (MW), which represents as:

$$W_{asu} = \sum W_{compressor} - \sum W_{expanders} \quad (10)$$

4. Results and discussions

One base case with standard ASU, which can produce 99 % purity oxygen and 99 % purity nitrogen, is built. And one additional case with non-standard ASU, which supply 96 % purity oxygen and same level nitrogen is followed. The detail parameters and results of both IGCC plants are shown in Table 1.

Table 1 Simulation Results of IGCC Plant

Parameter	Case 1(base case)	Case 2
Reference fuel type	Illinois No.6 coal	Illinois No.6 coal
Coal feed flow rate	17 kg/s	17 kg/s
Gasifier pressure	42 bar	42 bar
Gasification temperature	1550 K	1475 K
Air flow rate	8000 kmol/h	8000 kmol/h
Injected Nitrogen flow rate	100000 kmol/h	100000 kmol/h
GT Combustor Temperature	1120 K	1120 K
Steam Temperature (Gas Cooling)	900 K	900 K
Steam Pressure (Gas Cooling)	100 bar	100 bar
Steam Temperature (HRSG)	900 K	900 K
Steam Pressure (HRSG)	100 bar	100 bar
Net Power Output of GT	152.8 MW	152.8 MW
Net Power Output of ST	88.1 MW	87.8 MW
Work consumption of ASU	34.7 MW	30.7 MW
Net Power Output of Plant	206.2 MW	209.9 MW
Total HHV Input	518.6 MW	518.6 MW
Overall efficiency	0.398	0.405

With comparison, using non-standard ASU causes slightly negative effects for the other parts of IGCC. The Gasifier Temperature decreases because some nitrogen are inject into the gasifier. The dilution effect not only decrease the amount of steam generate in Gas Cooling unit, but also have slight negative effect the total net power output. The interesting part is that the overall efficiency increase about 1 % instead of going down. The decrement of energy consumption of ASU contributes a lot as shown in Table 1. But for further discussion, the detail ASU operation conditions are needed which are listed in Table 2. Based on that, the decrement is the combined influence of increasing the main air compressor energy consumption and decreasing the energy consumption of product compressors. For two cases, the suitable non-standard ASU can save about 10 % energy of the standard configuration in case 1.

Table 2 Simulation Results of ASU Unit

Parameter	Case 1(base case)	Case 2
Air compressor discharge pressure	7 bar	10.2 bar
Split ratio	0.95	0.95
No. of stage in LP column	100	100
LP column Pressure	1.2 bar	3 bar
No. of stage in HP column	45	45
HP column Pressure	6.8 bar	10 bar
Oxygen product purity	0.99	0.96
Nitrogen product purity	0.99	0.99
Oxygen product pressure	42 bar	42 bar
Nitrogen product pressure	11 bar	11 bar
Air compressor work	14883 kW	18935 kW
Oxygen compressor work	6638 kW	4717 kW
Nitrogen compressor work	13293 kW	7110 kW
Expander work	116 kW	89 kW
Total energy consumption of ASU	34698 kW	30673 kW

The comparison between two cases shows that the Standard ASU may not the best choice of each IGCC plant. Some adjustments may be needed to fit the ASU with the whole plant to improve the overall efficiency.

5. Conclusions

In this paper, a mathematical model of an IGCC plant is built, which includes a gasifier, an ASU and a combined cycle unit with energy and mass conversion. The overall efficiency of 39.8 % can be reached in base case which simulated using Microsoft® Excel 2013. An additional case with non-standard ASU is followed, which performs slightly better in efficiency aspect. The comparison between two cases shows that the Standard ASU may not the best choice of each IGCC plant. Some adjustments may be needed to fit the ASU with the whole plant to improve the overall efficiency. It gives a suggestion and a starting point to integrate and optimize the IGCC plant in the future.

Acknowledgement

The authors would acknowledge the financial support from the Hong Kong RGC-GRF grant (613513) and the UGC-Infra-Structure Grt. (FSGRF13EG03).

References

R. L. Cornelissen, G. G. Hirs, 1998, Exergy analysis of cryogenic air separation, Energy Conversion and Management, 39(16), 1821-1826.

B. Linnhoff, J.R. Flower, 1978, Synthesis of heat exchanger networks: I, Systematic generation of energy optimal networks, AIChE Journal, 24, 633-642.

A. J. Minchener, 2005, Coal gasification for advanced power generation, Fuel, 84(17), 2222-2235.

M. Nakaiwa, K. Huang, A. Endo, T. Ohmori, T. Akiya, T. Takamatsu, 2003, Internally heat-integrated distillation columns: a review, Chemical Engineering Research and Design, 81(1), 162-177.

B. Spang, 2002, Water97_v13.xla – Excel Add-In for Properties of Water and Steam in SI-Units, Hamburg, Germany.

J. C. Wang, G. E. Henke, 1966, Tridiagonal matrix for distillation, Hydrocarbon Processing, 45(8), 155.

Krist V. Gernaey, Jakob K. Huusom and Rafiqul Gani (Eds.), 12th International Symposium on Process Systems Engineering and 25th European Symposium on Computer Aided Process Engineering.
31 May – 4 June 2015, Copenhagen, Denmark

Mathematical Modeling of an Industrial Delayed Coking Unit

Cláudio N. Borges[a,b], Maria Anita Mendes[a], Rita M. B. Alves[a,*]

[a]*Department of Chemical Engineering, Polytechnic School - University of São Paulo, Av. Prof. Luciano Gualberto, n. 380, trav. 3, 05508-900, São Paulo - SP, Brazil.*
[b]*Presidente Bernardes Refinery – RPBC, PETROBRAS, Av. Nove de Abril, 777, Jardim das Indústrias, Cubatão, 11505-000, Brazil.*
rmbalves@usp.br

Abstract

This paper describes the mathematical modeling of the physical-chemical phenomena in the coking furnace and coke drum in a steady-state delayed coking unit based in a lumped kinetic scheme and vapor-liquid equilibrium conditions. Feedstock and products composition, and molecular structure are also required. For better understanding of the coking process and effect of the feedstock physical-chemical properties on yield and quality parameter of the products, especially the petroleum coke, molecular characterization of crude oil and heavy fraction was carried out by MALDI TOF mass spectrometry. Mathematical algorithm has been developed based on experimental data and operating conditions from an industrial delayed coking unit. A good prediction capability of the model and an accurate industrial unit representation of the industrial unit is expected. The developed model will be used for monitoring the industrial process and implementing real time optimization (RTO). Meanwhile, the acquired knowledge obtained during the model development has already improved the quality of green coke produced and the operational procedure of industrial plant.

Keywords: Delayed Coking, Mathematical Modeling, Lumps.

1. Introduction

The increasing competitive market, the frequent changes in prices, higher demand for oil and petroleum availability, restrictions on product specifications and operational bottlenecks require quick responses. The delayed coking is a semi continuous thermal cracking process used in petroleum refineries to upgrade and convert vacuum residue into liquid and gas products leaving behind a solid concentrated carbon material, known as petroleum coke (Ellis et. al.,, 1998). However, the delayed coking unit is one of the most difficult process to operate and control. That is so, because the furnace supplies thermal energy demanded by the thermal cracking of the hydrocarbon molecules, while the coke drum provides the residence time for chemical reactions to continue and accumulation coke formed. Being highly endothermic, the coking reactions rate drops dramatically as coke drum temperature decreases. The residue compositions are much more complicated that of heavy gas oil fractions. They are much larger and heteroatoms compounds with sulfur, nitrogen and oxygen groups (Zhou et. al., 2007). The basic idea of this work is to develop a mathematical model of the reaction kinetics and conditions of vapor-liquid equilibrium using an industrial plant as base to determine the parameters of the model in question.

2. Mathematical Modeling

2.1 Mass Balance Data to Reconciliation

Measured process data inevitably contain some inaccurate information, since measurements are obtained with uncertainties. The problem consists in obtaining more accurate estimates for process variable measurements, satisfying the mass and energy conservation laws, according to the least square objective function:

$$min. \quad F.O. = \left(\underline{X} - \underline{\hat{X}}\right)^T \cdot \underline{\underline{W}}^{-1} \cdot \left(\underline{X} - \underline{\hat{X}}\right) \tag{1}$$

Subject to the constraints:

$$X_1 = X_2 + X_3 + X_4 + X_5 + X_6 \qquad \left(\underline{X} \geq 0\right) \tag{2}$$

where $\underline{X}$ is a vector of measurements for n process variables, $\underline{\hat{X}}$ is a vector of estimates for the n process variables and $\underline{\underline{W}}$ is a weight matrix of the measurements.

2.2 Effluent Coke Drum Characterization

The methodology to determine the coke drum effluent characteristics is based on extrapolation of the true boiling point distillation curve, given the mass and energy balance and the dew point temperature in the overhead coke drum (Figure 1).

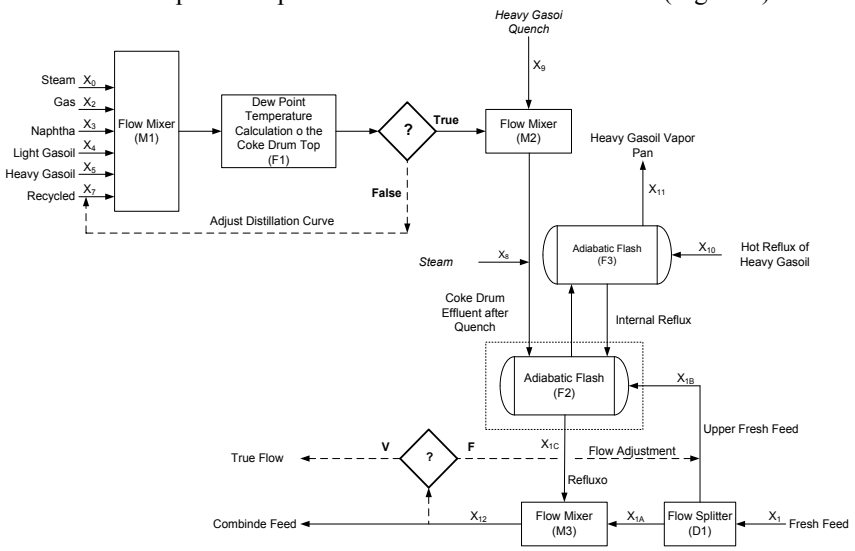

Figure 1. Strategy to determine the recycled charactheristics.

The coke drum effluent is divided into 22 pure components and 74 pseudo-components, which properties are calculated by different methods and correlations available in literature (Riazi, 2005). Liquid-vapor equilibrium calculations are carried out by Peng-Robinson equation of state.

2.3 Mass and Energy Balance of the System Furnace-Coke Drum

The components obtained in the coke drum are used in the mass and energy balances and vapor-liquid equilibrium calculations. In the kinetic thermal cracking model was assumed six discrete lumps: gas, naphtha, light gasoil, heavy gasoil, coke and residue. These lumps were selected based on the five main streams from the coking process (Figure 2).

As the vacuum residue and reaction products are complex mixtures of hydrocarbons, it is difficult to develop a mechanistic approach for each molecule to explain the true kinetics and their behavior. Thus, the pseudo-components are obtained by group composition based on their physic-chemical properties such as boiling point and density.

Following are the main related mass and energy balance equations for the system:

Boundary N. 1:

$$X_1 + S = X_0 + X_2 + X_3 + X_4 + X_5 + X_6 \tag{3}$$

Boundary N. 2:

$$X_1 + X_7 + S = Y_0 + Y_1 + Y_2 + Y_3 + Y_4 + Y_5 + Y_6 + Y_7 \tag{4}$$

Outlet Coil:

$$Y_i = \alpha_i \cdot X_i \tag{5}$$

Boundary N. 3:

$$\Delta X_i = (1 - \alpha_i) \cdot X_i \tag{6}$$

Boundary N. 1 and N. 2:

$$(\Delta H)_{IN} + Q_0 = (\Delta H)_{OUT} + (\Delta H)_{REACTION} + Q_1 \tag{7}$$

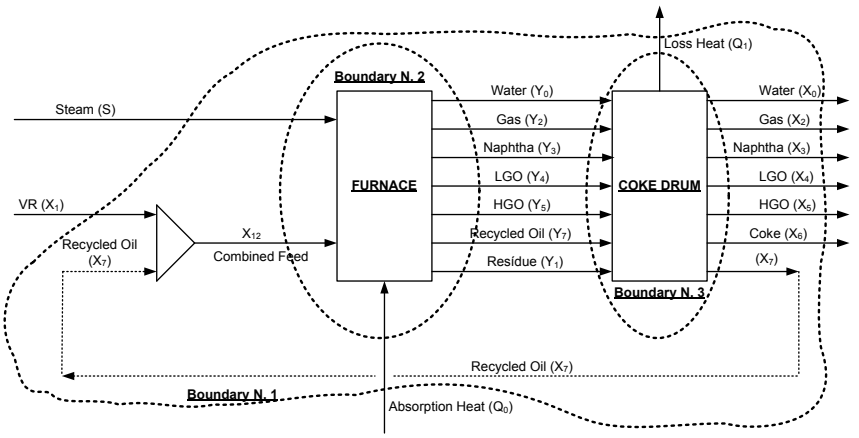

Figure 2. Boundaries for mass and energy balances.

2.4 Coking Furnace

After the establishment of the product distribution coefficient at the exit of the coking furnace (α_i), the composition profile is determined through the coil to the different lumps from the heat flow based on the flue gas, wall tubes temperature, and fluid pressure and temperature profiles.

The furnace are divided into two sections: pre-heating and reaction. The furnace reaction section can be considered as a tubular reactor in steady state with two-phase flow. The result of simultaneous solution of the set of equations of mass and energy balances, heat transfer and liquid-vapor equilibrium predicts the lumps composition through the coil. As the fluid moves through the furnace coil, the chemical reaction takes place, producing larger amounts of light components and changes in the conditions physical-chemical.

The fluid temperature profile inside the furnace coil is directly measured from the industrial plant by thermocouples located in different positions. As a result, it is possible to determine the fluid physical properties at any coil location and the heat absorbed in both pre-heating and reaction sections.

The kinetic model proposed for the thermal cracking furnace is constituted by five lumps (Figure 3). The first lump represents the total amount of cracked oil from vacuum residue (VR). The other four lumps represent products, which are progressively vaporized inside the coil. The coke formation rate was considered negligible.

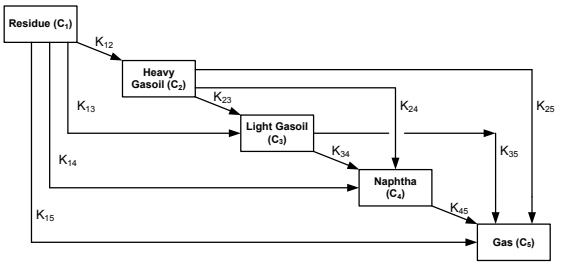

Figure 3. Proposed five lumped kinetic models with 10 rate parameters.

Given the lumps composition from mass and energy balances, it is possible to predict the furnace coil kinetics. From Figure 3 the following reaction rate expressions for the five groups can be written by assuming first order irreversible approach:

$$\left(\frac{d[C_1]}{dt}\right) = -(K_{12} + K_{13} + K_{14} + K_{15}) \cdot [C_1] \tag{8}$$

$$\left(\frac{d[C_2]}{dt}\right) = K_{12} \cdot [C_1] - (K_{23} + K_{24} + K_{25}) \cdot [C_2] \tag{9}$$

$$\left(\frac{d[C_3]}{dt}\right) = K_{13} \cdot [C_1] + K_{23} \cdot [C_2] - (K_{34} + K_{35}) \cdot [C_3] \tag{10}$$

$$\left(\frac{d[C_4]}{dt}\right) = K_{14} \cdot [C_1] + K_{24} \cdot [C_2] + K_{34} \cdot [C_3] - K_{45} \cdot [C_4] \tag{11}$$

$$\left(\frac{d[C_5]}{dt}\right) = K_{15} \cdot [C_1] + K_{25} \cdot [C_2] + K_{35} \cdot [C_3] + K_{45} \cdot [C_4] \tag{12}$$

The kinetic constants of the Arrhenius equations are calculated as a function of the feed physical-chemical properties.

$$\ln(K_{ij}) = \ln(A_{ij}) - \frac{E_{ij}}{R \cdot T} \tag{13}$$

The compositions of the five lumps through the furnace coil, together with the temperature profile will allow determining the kinetic constants (A_{ij} and E_{ij}) of the model by the least squares method.

2.5 Coke Drum

The coke drum is considered a perfect continuous stirred tank reactor in pseudo-steady state, which can be represented by the equation (14).

$$\frac{V}{(F_i)_0} = \frac{[(f_i)_{OUT} - (f_i)_{IN}]}{\left(\pm r_i^*\right)_F} \tag{14}$$

Based on operational experience of the thermal cracking process Eureka (Takatsuba et al., 1996), the minimum residence time required to start the coke formation is about four hours. The kinetic model proposed for the thermal cracking coke drum was divided in three phases: vapor, liquid and solid (Figure 4 and 5).

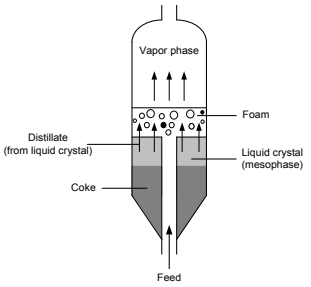

Figure 4. The coke drum filling system.

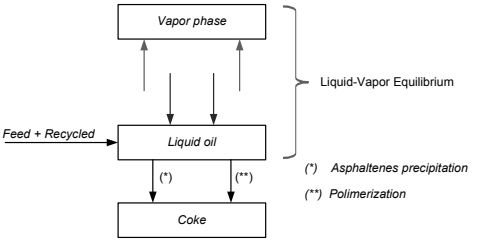

Figure 5. The coke drum modeling strategy.

The coke formed from the precipitation of asphaltenes tends to be amorphous and it is a poor quality sponge coke, while the coke derived from the reactions of polymerization and polycondensation tends to be more crystalline. This coke formed contains a small amount of liquid hydrocarbons trapped in the pores, known as volatile combustible material (VCM).

3. Vacuum Residue Characterization

The vacuum residue is classified in four fractions: saturates, aromatics, resins and asphaltenes. Being the asphaltenes was characterized by Mass Spectrometry Matrix-Assisted Laser Desorption/Ionization (MALDI TOF). Results can be found elsewhere (Borges et al., 2012).

4. Results and Discussion

To solve the problem of mass balance reconciliation was using the LCONF subprogram in IMSL Fortran library to minimize the objective function for linear equality and inequality constraints. A summary of data reconciliation results is presented in Table 1.

Table 1. Data reconciliation results.

Run Number	Yields, weight %				
	Gas	Naphtha	Light Gasoil	Heavy Gasoil	Coke
10	8.43	15.96	17.75	35.86	23.50
33	9.75	23.75	26.75	26.92	27.62

Figure 5 shows the true boiling point curve as a result from the mass and energy balance in the main fractionator bottom section and the coke drum overhead according to the strategy in Figure 1. Based on Figure 5, the yields are estimated according to Table 2.
The reported lumped kinetic models are used due to the complexity of coker feed and products, which makes it extremely difficult to characterize and describe its kinetics at a molecular level.

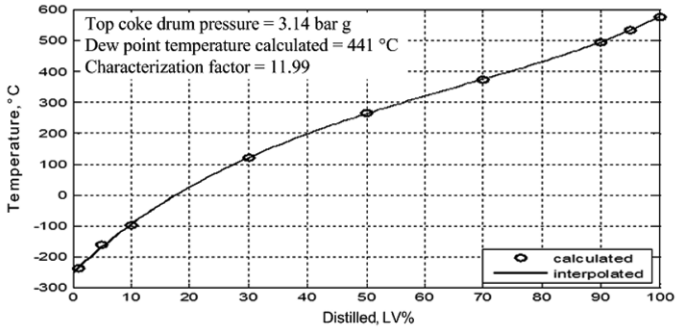

Figure 5. Effluent true boiling point distillation curve from the coke drum.

Table 2. Lumps yields form effluent coke drum.

Lump	Range	Yield, LV %
Gas	$^{-}C_4$	17.42
Naphtha	C_5 – 200°C	23.22
Light Gasoil	200 – 370°C	28.26
Heavy Gasoil	370 – 540°C	27.27
Residue	> 540°C	3.82

5. Conclusion

The strategy to characterize the feedstock and the products using the molecular information with the phenomena observed in the actual industrial unit provided a rigorous mathematical modeling in delayed coking process. Besides, to be capable to simulate the effects of the feedstock in the coking process, it is necessary to include the coke drum and the bottom section main fractionator in the model. The simultaneous solution of mass and energy balances involving the furnace and coke drum is the key element to determine the conversion among them. The results obtained so far from coke drum effluent indicate that it is capable to predict the recycle characteristics, as well as lumps yields.

Acknowledgements

Authors would like to acknowledge PETROBRAS for technical support.

References

C. N. Borges, R. M. B. Alves, M. A. Mendes, R. R. Ramos, G. C. Ungar, Study of Vacuum Residue Characterization for Development of Mathematical Model for Delayed Coking Unit: Using Molecular Information, 2012, in ACS 244th National Meeting, Philadelphia, PA, USA.

P. J. Ellis and C. A. Paul, 1998, Tutorial: Delayed Coking Fundamentals, In Proceedings of 1998 AIChE Spring Meeting, News Orleans, LA, 1 - 20.

M. R. Riazi, 2005, Characterization and Properties Petroleum Fractions, ASTM Manual Series: MNL50, West Conshohocken, 1st ed, 407.

T. Takatsuba, R. Watari and H. Hayakawa, 1996, Renewed Attention to the Eureka Process: Thermal Cracking Process and Related Technologies for Residual Oil Upgrading, Studies in Surface Science and Catalysis, 100, 293 - 301.

X. L. Zhou, S. Z. Chen and C. L. Li, 2007, A predictive kinetic model for delayed coking, Petroleum Science and Technology, 25(12), 1539 - 1548.

Krist V. Gernaey, Jakob K. Huusom and Rafiqul Gani (Eds.), 12th International Symposium on Process Systems Engineering and 25th European Symposium on Computer Aided Process Engineering.
31 May – 4 June 2015, Copenhagen, Denmark

Post-Combustion CO_2 Capture with Sulfolane Based Activated Alkanolamine Solvent

Sukanta K. Dash[a], Bikash K. Mondal[b], Amar N. Samanta[b], Syamalendu S. Bandyopadhyay[c,*]

[(a)]*Department of Chemical Engineering, Pandit Deendayal Petroleum University, Gandhinagar-382007, Gujarat, India.*
[(b)]*Chemical Engineering Department, IIT Kharagpur, Kharagpur-721302, India*
[(c)]*Cryogenic Engineering Centre, IIT Kharagpur, Kharagpur-721302, India.*
Email: ssbandyo@hijli.iitkgp.ernet.in

Abstract

In this work, new experimental data on vapour-liquid equilibrium (VLE) of CO_2 in piperazine (PZ) activated aqueous solutions of n-methyldiethylamine (MDEA) and hybrid solvents containing sulfolane as physical solvent along with aqueous (MDEA+PZ) have been reported over the temperature range of (313-333) K and CO_2 partial pressure range of (1-1400) kPa. PZ is used as a rate activator with a concentration range of 2 to 8 mass% and the total amine concentration in the aqueous solution of (MDEA+PZ) has been kept within 50 mass%, while the concentration of physical solvent sulfolane has been maintained at 10 mass%. Electrolyte non random two-liquid (ENRTL) theory has been used to model the VLE. A simulation work has been carried out using Aspen Plus (V7.1) to evaluate the energy requirements on % CO_2 removal. The hybrid solvent showed higher % CO_2 removal when compared with those of PZ-activated aqueous MDEA.

Keywords: CO_2 capture, VLE, activated solvent, modelling and simulation.

1. Introduction

Carbon dioxide (CO_2) removal from flue gas stream of fossil fuel power plants has received much attention because of the environmental need for reducing CO_2 emission to the atmosphere. There are many processes for removal of CO_2 from power plant flue gas. The emphasis in the present work is post-combustion CO_2 absorption involving (MDEA + PZ + sulfolane) based solvent. The main objective of this work is to investigate the efficiency of the hybrid solvent in achieving higher %CO_2 removal from low CO_2 partial pressure flue gas streams. Although sulfolane has been used in the hybrid solvents sulfinol-D and sulfinol-M of Shell Oil Company along with DIPA and MDEA, resprctively, no work has been reported so far using sulfolane with PZ activated aqueous MDEA solvent for CO_2 capture. In a regenerative chemical absorption process, the amount of solvent which needs to be circulated in the process between absorber and stripper depends on the amine concentration in the aqueous solution, the required CO_2 capture and the difference in CO_2 loading between the rich and the lean solution. A higher total amine concentration in the selected solvents has been chosen in order to increase the cyclic loading capacity of the solvent in the CO_2 removal process. The increased cyclic loading reduces the solvent circulation rate and higher amine concentration reduces the regeneration heat requirement. Methyldiethylamine (MDEA) has a stable structure and does not degrade readily, so it does not cause corrosion

problems for carbon steel (Bishnoi and Rochelle, 2002). Because of chemical reactions in the liquid phase and the strong deviation from ideality, the thermodynamic description of aqueous systems containing (CO_2+MDEA+PZ+sulfolane) is a difficult task (Dash et al., 2011). Reliable experimental data for the solubility of CO_2 in these solvents are required to develop and test thermodynamic models used to describe VLE of this systems. However, reliable data on these systems are scarce in the open literature. In this work, the solubility of CO_2 in aqueous solutions containing MDEA, sulfolane, and PZ for a wide range of concentrations and temperatures was measured and modeled. To explore further industrial benefits of the (MDEA+PZ+sulfolane) based solvent, a modeling and simulation study of CO_2 capture process using a commercial simulator is essential. Hence simulation of CO_2 separation process using this solvent has been carried our using Aspen Plus.

2. Experimental

MDEA, PZ and solfolane (> 95 % pure) was supplied by Sigma Aldrich, USA and was used without further purification. CO_2 gas (> 99.9 % pure) was obtained from Chemtron Science Pvt. Ltd., India. Double distilled degassed water was used to prepare aqueous amine solutions.

The VLE measurements were conducted in a high pressure stainless steel stirred equilibrium cell which was connected to a high pressure stainless steel gas buffer vessel. A detail description of the experimental set up, procedure and validation of experimental procedure is presented in Dash et al. (2011a). VLE of CO_2 in the activated and hybrid solvents are calculated in terms of CO_2 loading (mole of CO_2 absorbed per mole of total amine) as shown in equation (1). In calculating CO_2 loading non-ideality of the gas phase is accounted for by considering Peng-Robinson equation of state.

$$\alpha_{CO_2} = \left((n_{CO_2} - n^g_{CO_2}) / n_{(MDEA+PZ)} \right) \quad (1)$$

where $(n_{CO_2} - n^g_{CO_2})$ is the no of moles of CO_2 present in amine solution and $n_{(MDEA+PZ)}$ is the total moles of amine (MDEA + PZ) present in the liquid phase.

3. Modeling

3.1 Phase and chemical equilibrium

Model development of the chemical and phase equilibria of the system (CO_2 + PZ + H_2O) has been discussed by Dash et al. (2011). The models for (CO_2 + MDEA + PZ+ H_2O) and (CO_2 + MDEA + PZ + sulfolane+H_2O) are developed by considering the following reactions in aqueous phase.

$$2H_2O \overset{K_1}{\rightleftharpoons} H_3O^+ + OH^- \quad (R1)$$

$$CO_2 + 2H_2O \overset{K_2}{\rightleftharpoons} H_3O^+ + HCO_3^- \quad (R2)$$

$$HCO_3^- + H_2O \overset{K_3}{\rightleftharpoons} H_3O^+ + CO_3^{2-} \quad (R3)$$

$$PZH^+ + H_2O \overset{K_4}{\rightleftharpoons} PZ + H_3O^+ \quad (R4)$$

$$PZ + CO_2 + H_2O \overset{K_5}{\rightleftharpoons} PZCOO^- + H_3O^+ \quad (R5)$$

$$H^+PZCOO^- + H_2O \overset{K_6}{\rightleftharpoons} PZCOO^- + H_3O^+ \quad (R6)$$

$$PZCOO^- + CO_2 + H_2O \overset{K_7}{\rightleftharpoons} PZ(COO^-)_2 + H_3O^+ \quad (R7)$$

$$MDEA + H_2O \overset{K_8}{\rightleftharpoons} MDEAH^+ + OH^- \quad (R8)$$

Sulfolane does not undergo any reaction in carbonated aqueous medium. Each of the above chemical equilibria is characterized by the thermodynamic equilibrium constant, K_j , defined in terms of mole fraction, x_i , and activity coefficient, γ_i, of the i th component as,

$$K_j = \prod_i (x_i \gamma_i)^{v_{ij}} \tag{2}$$

where ϑ_{ij} is the reaction stoichiometric coefficient of component *i* in j^{th} reaction.
Equilibrium constant for the reactions are taken form Aspen data bank (2008). In this work water, MDEA, sulfolane and PZ are considered as solvents leading to a mixed solvent system. The standard state associated with each solvent is the pure liquid at the system temperature and pressure. The chosen reference state for ionic solutes and the molecular solute (CO_2) is the ideal, infinitely dilute aqueous solution at the system temperature and pressure. Vapour phase model has been described by equation (3) and (4) for CO_2 and amines respectively according to the activity coefficient approach.

$$\phi_i^v y_i P = x_i \gamma_i^* H_i \exp\left(\frac{v_i^\infty (P - P_{solv}^0)}{RT}\right) \tag{3}$$

$$\phi_i^v y_i P = x_i \gamma_i P_i^0 \exp\left(\frac{v_i (P - P_i^0)}{RT}\right) \tag{4}$$

where y_i and x_i are concentration of species in vapour and liquid phase, v_i^∞, partial molar volume of CO_2 at infinite dilution, can be calculated from the Brelvi-O' Connell method. H_i is the Henry's law constant, P^0 is the Vapour pressure. Henry's constant of CO_2 is adjusted in this work for the mixed solvent system.

3.2 Electrolyte NRTL activity coefficient model
The ENRTL equation (Austgen et al., 1989) which is based on excess Gibbs energy, have been used in this work to model VLE data. In this model excess Gibbs energy is calculated using the following equation.

$$\frac{G^{*E}}{RT} = \frac{G_{PDH}^E}{RT} + \frac{G_{BORN}^E}{RT} + \frac{G_{NRTL}^E}{RT} \tag{5}$$

Where G^{*E} is excess Gibbs energy of mixed solvent electrolyte system, G_{PDH}^E is excess Gibbs energy calculated by Pitzer-Debye-Huckel formula, G_{BORN}^E is excess Gibbs energy calculated by Born expression and G_{NRTL}^E is excess Gibbs energy calculated by non random two-liquid hypothesis. The first two terms of the equation account for the long range interactions and the third term account for the local interaction contribution. The interaction parameters are expressed in temperature dependent form as given below.

$$\tau_{ij} = a_{ij} + \frac{b_{ij}}{T} \tag{6}$$

The activity coefficient for any species (ionic or molecular, solute or solvent) is calculated from the partial derivative of the excess Gibbs energy with respect to mole number.

$$\ln \gamma_i = \frac{1}{RT}\left[\frac{\partial\left(n_i G^{*E}\right)}{\partial n_i}\right]_{T,P,n_{j\neq i}} \tag{7}$$

The interaction parameters of ENRTL equation are regressed from VLE data using data regression system in Aspen Plus (V7.1) software.

3.3. Simulation of absorption-regeneration

Process simulation software Aspen Plus® (V7.1) has been used to estimate the percentage CO_2 capture from the flue gas of coal based power plant by absorption at steady state conditions using aqueous MDEA, PZ activated aqueous MDEA and the hybrid solvents. The CO_2 capture process used in this study is shown in Fig. 1. The flue gas enters the bottom of the absorber with the lean amine solvent introduced at the top of the absorber. The lean amine enters with a loading of 0.1- 0.12 and leaves with a loading close to 0.45-0.55. The rich stream from the lean-rich heat exchanger is fed to the regenerator. The regenerator is a packed column with a kettle reboiler. The regenerator typically operates at slightly elevated pressures (~0.18-0.2 Mpa). The rich amine enters the second stage of the regenerator and flows down the column. The vapour from the reboiler flows counter currently to the liquid. The stream from the top of the column is taken to a condenser in order to condense the water and lower the temperature and then flashed in order to separate CO_2 from water.

A part of the liquid reflux is returned to the first stage of the regenerator column. The first stage in the regenerator acts as a water wash stage to return any entrained amine in the vapor to the reboilor. In the reboiler of the regenerator, steam from the power plant is used to furnish the required heat duty. Typical values of the CO_2 partial pressure are 4-6 kPa for gas-fired power plants and 10-14 kPa for coal-fired power plants. This study has been performed considering a CO_2 partial pressure of 13 kPa.

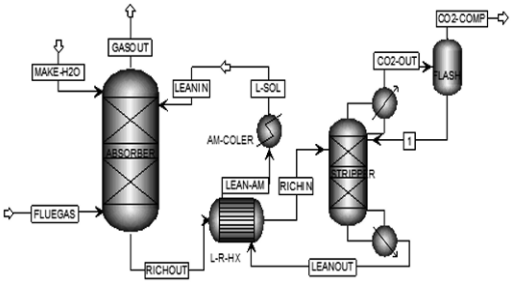

Figure 1: Process flow diagram of CO_2 capture

The diameter of the column has been determined based on flooding approach. A design factor of 80% approach to flooding has been chosen since this also allows for some safety factors in case the operating conditions change suddenly. There is also a limit set on the pressure drop of the column and this translates into a constraint on the calculation of the diameter of the column. As the CO_2 capture rate depends on process parameters such as L/G ratio, lean loading etc., the desired extent of capture has been achieved by varying the amount of amine flow rate and lean loading. The appropriate lean loading is achieved by suitably choosing the reboiler duty in the regenerator in an iterative process during each simulation run.

4. Results and Discussion

ENRTL theory has been used to model the VLE of CO_2 in all the solvents used. The model predicted CO_2 partial pressures have been plotted against experimental results of this work and from literature in Figure 2 and 3. Figure 2 shows the comparison of experimental CO_2 solubility data over aqueous MDEA from literature with our eNRTL model. Figure 3 shows the comparison of experimental CO_2 solubility data over aqueous (MDEA+PZ) from literature with our ENRTL model.

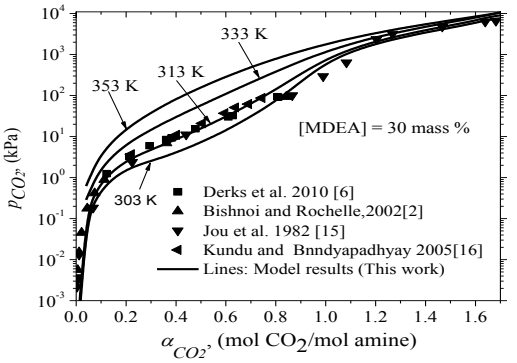

Figure 2: Comparison of model predicted equilibrium partial pressure of CO_2 above aqueous 30 mass% MDEA at various temperatures with the experimental data from literature.

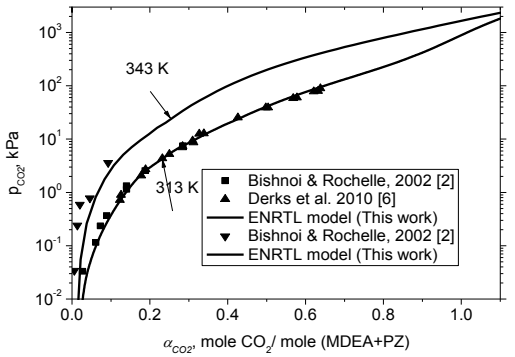

Figure 3: Comparison of model predicted VLE of CO_2 over aqueous (MDEA+PZ) with the experimental data from literature.

From the results presented in Figure 2-3, it is clear that there is a good agreement between the model predicted results and experimental results.
It has also been observed that the solvent capacity increases with the PZ concentration and decreases with the increasing in lean loading. The solvent circulation rate decreases with the increases in PZ concentration and increases with increase in the lean loading. It has also been observed that the solvent capacity increases with the PZ concentration and decreases with the increasing in lean loading. The solvent circulation rate decreases with the increases in PZ concentration and increases with increase in the lean loading. From the simulation study it is observed that the $\%CO_2$ removal is higher with all hybrid solvent formulations compared to that with PZ activated aqueous MDEA solvents. At an L/G ratio of 3 the hybrid solvent (42 mass% MDEA+8 mass% PZ+10 mass% sulfolane + 40 mass% H_2O) achieved 85% CO_2 capture at 40 ^oC. All hybrid solvents have been found to have about 35-40% higher solvent capacity compared to that of the corresponding activated amine solvents.

The reboiler heat duty represents the largest fraction of the overall cost in a PCC plant. The reboiler heat duty is therefore an important quantity which needs to be considered carefully. The energy requirement for solvent regeneration have three components viz.,

energy to be supplied (i) for providing the desorption enthalpy of CO_2, (ii) to generate additional stripping steam, and (iii) for heating up the solvent and provide the condensate reflux. Estimation of all these quantities requires an energy balance around the regenerator. The overall mass-specific heat duty, Q_{reb}, which is supplied in the reboiler of the regenerator column, can be expressed as the sum of three terms:

$$Q_{reb} = Q_{sensible}(\text{sensible heat}) + Q_{Vapour.H_2O}(\text{stripping steam}) + Q_{absorption,CO_2}(\text{heat of desorption}) \quad (8)$$

where, $Q_{sensible}$ is the sensible heat to raise the temperature of the solution and reflux water at the regenerator inlet to the conditions in the reboiler. $Q_{vapour, H2O}$ is the heat of vaporisation required to generate the stripping steam in the regenerator, $Q_{absorption,CO2}$ is the heat of desorption required to strip the CO_2 from the solution. Out of this three quantities, the heat of desorption is the most important contribution to the total energy requirement and can be estimated by utilizing an energy balance around the regenerator. The split of energy requirement estimated by simulation study is represented by Figure 4.

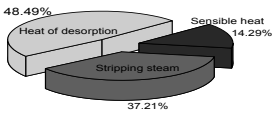

Figure 4: Split of reboiler duty (kJ/kg CO_2) for CO_2 capture at a constant lean loading and a ΔT of 5K at the lean-rich heat exchanger

5. Conclusions:

In this work the CO_2 capture performance of a new hybrid solvent system (MDEA + PZ + Sulfolane + H_2O) has been studied and compared with that of the corresponding PZ activated aqueous MDEA solvent. The hybrid solvent has been found to achieve much better performance than the PZ activated aqueous MDEA solvent with respect to solvent capacity, regeneration energy requirement and %CO_2 capture even at low L/G ratio and higher temperatures.

6. References

Aspen Technology Inc., 2008, Aspen Physical Property System. V-7.0 Cambridge.

D.M. Austgen, G.T.,Rochelle, X. Peng, C.C Chen, 1989. Model of vapor-liquidequilibria for aqueous acid gas-alkanolamine systems using the electrolyte-NRTL equation. Industrial & Engineering Chemistry Research 28, 1060–1073.

S. Bishnoi, G.T. Rochelle, 2002, Thermodynamics of piperazine/ methyldiethanolamine / water / carbon dioxide, Ind. Eng. Chem. Res., 41, 604−612.

S. K. Dash, A. Samanta, A. N. Samanta, S. S. Bandyopadhyay, 2011, Vapor liquid equilibria of carbon dioxide in dilute and concentrated aqueous solutions of piperazine at low to high pressure, Fluid Phase Equilib, 300, 145–154.

Krist V. Gernaey, Jakob K. Huusom and Rafiqul Gani (Eds.), 12th International Symposium on Process Systems Engineering and 25th European Symposium on Computer Aided Process Engineering.
31 May – 4 June 2015, Copenhagen, Denmark

Modeling and Sensitivity Analysis of a Medium-Temperature Gas Cleaning Process of Biogenous Synthesis Gas

Michaela Fraubaum*, Heimo Walter

Vienna University of Technology, Institute for Energy Systems and Thermodynamics, Getreidemarkt 9, 1060 Vienna, Austria
michaela.fraubaum@tuwien.ac.at

Abstract

Tar removal is the major technical obstacle in the implementation of the gasification technology. This paper deals with the modelling, simulation and design of a small scale production process of biogenous synthetic natural gas (SNG) using a novel catalytic gas cleaning process which operates in a considerably lower temperature range than catalytic hot gas cleaning methods. Mathematical models for the different gas cleaning steps are developed and implemented into an already existing model library of the commercial simulation software IPSEpro. A special focus lies on the tar reforming reactor, which is modelled by applying mass and energy balances, reaction kinetics and chemical equilibrium equations. Energy savings of the individual process steps are identified and the overall process, which is based on an allothermal gasifier, is integrated in the software. Additionally, a sensitivity analysis is performed to show the influence of various operating parameters on the single elements and the whole system. Their effects on the overall process efficiencies as well as on important process factors are evaluated and discussed in this paper. The analysis described in this paper shows that a promising total efficiency for the overall process (with district heating) of approximately 90% can be reached.

Keywords: biomass gasification, tar conversion, methanation, process modelling

1. Introduction

In addition to the main components CO, CO_2, CH_4, H_2 and H_2O, synthetic natural gas (SNG), which is produced by gasification of biomass, contains considerable amounts of particulate matter, inorganic impurities and organic impurities. Especially high molecular weight polyaromatic hydrocarbons (tars) pose a serious threat to downstream equipment due to condensation or polymerization. Depending on the type of gasifier and the operating conditions, biomass gasifiers produce a gas with tar content levels between 0.01 and 150 g/ Nm^3 (Hasler and Nussbaumer, 1999). The so-called Heatpipe Reformer, which is considered in this work, shows a total tar concentration in the dry product gas between 1 and 8 g/Nm^3 (Gallmetzer et al., 2012). Since the gas quality requirements are considerably lower, under 100 mg/ Nm^3 for internal combustion engines and as low as 0.1 mg/Nm^3 for methanol synthesis (Laurence and Ashenafi, 2012), tar removal is essential in SNG production.

The current state-of-the-art tar removal technologies can be broadly divided into five groups: physical methods like cyclones, filters, and scrubbers; self-modification of the gasifier; Catalytic Cracking; Thermal Cracking and Plasma methods (Han and Kim, 2008). Industrial CHP-Plants in Oberwart, Güssing (Austria), Ulm/Senden (Germany) and Götenborg (Sweden) clean the gas in a wet scrubber, using organic liquids.

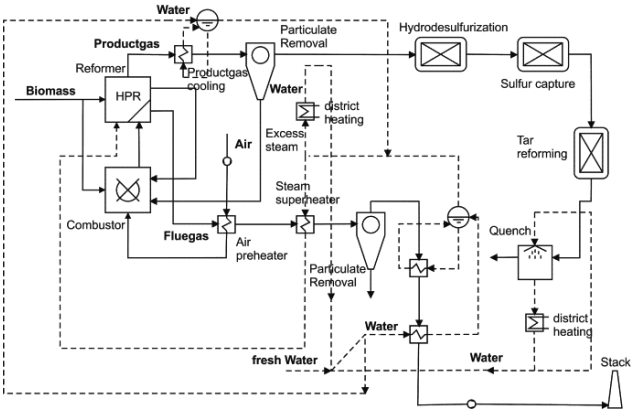

Figure 1: Detailed flow sheet of the SNG process

A promising prospective alternative is catalytic hydrocarbon reforming. Great advantage of this method is the high degree of gas purity combined with an increased fuel heat value.
A process modelling and design of a small-scale production of Raw-SNG with an innovative catalytic tar removal process, operating at a considerably lower temperature than conventional catalytic hot gas cleaning methods is presented in this contribution.

2. Process description and modelling methodology

The overall process, as illustrated in Figure 1, is integrated into the commercial simulation software IPSEpro, using thermodynamic models of the individual process steps.
IPSEpro is a steady state, equation oriented software environment for simulating and analyzing processes in energy- and chemical engineering and related areas. New user defined component models can be prepared and already existing models can be modified with IPSEpro's Model Development Kit (MDK). The IPSEpro Pyrolysis and Gasification Process Library (PGP-Library) is used as a basic library (Proell and Hofbauer, 2008). Mathematical models for different desulfurization steps, for scrubbing as well as for tar removal and methanation of SNG are developed by applying mass and energy balances and reaction kinetics and chemical equilibrium equations. Missing kinetic data and property data in IPSEpro were adopted from an Aspen Plus model of the process, created on the basis of experimental data which was measured with the test plant described in (Zuber et al., 2014). The additional model of the gas cleaning process in Aspen Plus allows analysing aspects not considered in the IPSEpro models like coke formation in the tar reforming reactor and solubility of components in the scrubber.
The process uses an allothermal gasifier, the so-called Heatpipe Reformer. Groebl et al. (2012) describes the mathematical models and the main design parameter for the gasification. After the gasifier the synthesis gas (SNG) is cooled to 300°C before passing a particle filter. To avoid catalyst deactivation in the tar reforming reactor, the sulphur is captured by chemical adsorption on a zinc-oxide sorbent. The removal of H_2S using a metal oxide can be described by following thermodynamic equilibrium equation.

$$MeO + H_2S \leftrightarrow MeS + H_2S \quad (1)$$

The steam reforming of tars occurs simultaneously with the methanisation reaction in the following fixed bed reactor. The exothermic gas reactions lead to the necessary temperature rise to approximately 550 °C for the tar reforming reaction. As an essential

step in the gas cleaning process, the model for the catalytic tar reforming reactor is described in Section 2.1. To cool the gas to the outlet temperature of 70 °C, the SNG passes a spray tower.
Partially modified standard models from the PGP-Library (heat exchangers, pumps...) are used for the remaining process units.

2.1. Tar reforming

The tar reforming occurs simultaneously with exothermic gas reactions in one fixed bed reactor. The following gas reactions are considered in the model. To calculate the outlet gas stream thermodynamic equilibrium of reactions (2) – (4) is assumed or the outlet composition of the corresponding components is defined.

$$CO + H_2O \leftrightarrow CO_2 + H_2 \quad (2)$$

$$CH_4 + H_2O \leftrightarrow CO + 3H_2 \quad (3)$$

$$C_2H_4 + 2\ H_2O \leftrightarrow 2CO + 4H_2 \quad (4)$$

To distinguish different tar components, the tar loading of the inlet gas stream is split into two organic pseudo components. The differentiation is based on the commonly accepted ECN classification system (Rabou et al., 2009), heterocyclic tars (Tar class 2) and polyaromatic tars (Tar class 4 and 5). The weight distribution of the model components is based on experimental data.
Tar and water steam are converted into CO and H_2 according to reaction (5). Optionally the tar removal rate can be defined by the user or calculated as a kinetic reaction first order.

$$C_xH_yO + (x\text{-}z)H_2O \leftrightarrow xCO + (y/2+x\text{-}z)H_2 \quad (5)$$

If fast methanation is assumed, equilibrium temperature can be presumed over the whole length of the catalytic bed and the tar conversion will be calculated using the equilibrium temperature, the overall residence time t and kinetic data provided by the user.
For more precise results, the tar reforming reactor is modelled as two separate zones, before and after the equilibrium of the methanation reaction is reached. The time to reach equilibrium Δt_1 is calculated according to (6), using the generated CH_4 amount ΔC_{CH4}, the volume flow $\dot{V}$, the reaction rate of (3) r_{CH4} and the catalyst density ρ_{Cat}.

$$\Delta t_1 = \frac{\Delta C_{CH4} / \dot{V}}{r_{CH4} * \rho_{Cat}} \quad (6)$$

Based on experimental data and due to the logarithmic temperature profile in the reactor a medium temperature T_m, which only varies slightly over time, can be calculated in the reactor part before equilibrium is reached. Using user provided kinetic data and T_m, the tar conversion rate can be calculated for the time Δt_1 and the time $t\text{-}\Delta t_1$. This approach further allows the implementation of catalyst deactivation.
In addition an energy balance, elementary mass balances and equations of mass conservation for the components which are not affected by reactions (2) – (5) are implemented in the model. The pressure loss in the packed bed Δp is calculated according to the Ergun equation (Wirth, 2010) considering bed length L, porosity ψ, dynamic viscosity η, superficial fluid velocity ν, fluid density ρ_f and Sauter diameter d_p.

$$\frac{\Delta p}{L} = 150\frac{(1-\psi)^2}{\psi^3}\frac{\eta \nu}{\bar{d}_p^2} + 1.75\frac{(1-\psi)^2}{\psi^3}\frac{\rho_f \nu^2}{\bar{d}_p^2} \quad (7)$$

3. Results and discussion

The individual models are combined in the IPSEpro Process Simulation Environment (PSE) to build up a complete model from biomass to raw-SNG. A flowsheet of the complete process can be seen in Figure 1 including the optimal thermal integration.
The high temperature waste heat of the fluegas and the productgas is used for air preheating as well as for production and superheating of process steam. The produced excess steam and the low temperature heat generated in the spray quench tower can be delivered to a district heat system. This polygeneration approach improves the overall efficiency substantially.
To show the influence of different operating parameters on the process a sensitivity analysis was performed. In this contribution the influence of steam excess ratio, gasification pressure and the temperature of the SNG after the productgas cooling will be evaluated. Table 1 shows the limits in which the parameters were varied and gives the chosen design parameter.

Table 1: parameter of the sensitivity analyse

Parameter	Lower limit	Upper limit	Design value	Unit
Steam excess ratio	2	6	4	-
Outlet temp. of SNG cooling	300	500	300	°C
Gasification pressure	1.5	5	5	bar_{abs}

In this work the parameters cold gas efficiency η_{chem} (ratio of the chemical energy content of the SNG $\dot{m}_{SNG}LHV_{SNG}$ compared to the chemical energy in the fuel $\dot{m}_{F}LHV_{F}$) and the overall thermal utilization rate η_{tot} (ratio of the chemical energy content of the SNG minus the electric power consumption $\sum P_{el}$ plus the district heat P_{DH} compared to the chemical energy in the fuel) are used to evaluate the performance of the whole process. To assess the influence of the parameters on the catalyst amount in the reactor a dimensionless factor was developed. It is defined as the minimum catalyst mass for complete tar reforming without considering catalyst deactivation in relation to the value at design conditions. The definition of the evaluated values is given in Table 2.

Table 2: evaluated process values

Parameter	Definition
Cold gas efficiency	$\eta_{chem} = \frac{\dot{m}_{SNG}LHV_{SNG}}{\dot{m}_{F}LHV_{F}}$ %
Overall thermal utilization rate	$\eta_{tot} = \frac{\dot{m}_{SNG}LHV_{SNG} + P_{DH} - \sum P_{el}}{\dot{m}_{F}LHV_{F}}$ %
Catalyst mass	$\frac{m_{Cat,min}}{m_{Cat,min\ at\ design\ parameters}}$ %

3.1. Influence of steam excess ratio σ

The steam excess ratio is an important operational parameter for the gasification as well as for the downstream gas cleaning processes. Steam is used as a gasification and fluidization agent in the gasifier. It impacts the composition and heating value of the productgas of the gasification. Further the productgas composition influences the sulphur capture and especially the methanation and tar reforming. Figure 2 and 3 show that the cold gas efficiency and the overall thermal efficiency are decreasing while the necessary catalyst mass is increasing with increasing σ. Although a lower σ benefits the

process, it cannot be chosen arbitrarily low. Considering process requirements like the necessary fluidization in the gasifier and the prevention of coke formation in the tar reforming reactor, an optimum steam excess ratio of 4 was chosen.

Influence of outlet temperature of SNG cooling

Figure 4 shows that a high SNG temperature after productgas cooling has a positive effect on the cold gas efficiency due to a lower H_2O content in the SNG. Since more steam is needed in the gasifier, the amount of excess steam, which can be used for district heating, decreases. This leads to a decreasing overall efficiency with rising gas temperature. Although the influence is less distinct than with gasification pressure and steam excess ratio, the necessary catalyst amount reduces with higher temperatures (Figure 5). Since a lower SNG temperature leads to a better sulphur capture by ZnO which is necessary to avoid catalyst deactivation, a design value of 300°C was chosen.

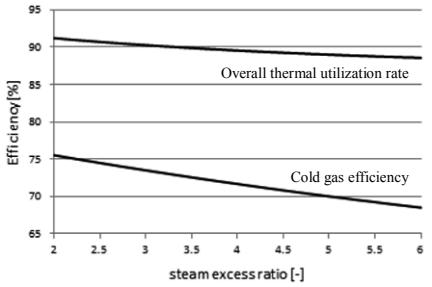

Figure 2: steam excess ratio vs. efficiency

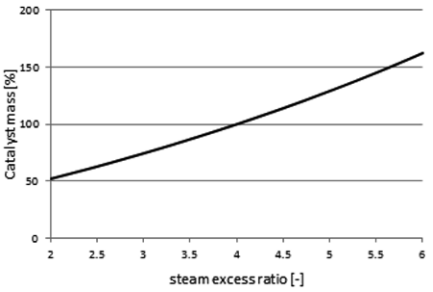

Figure 3: steam excess ratio vs. catalyst mass

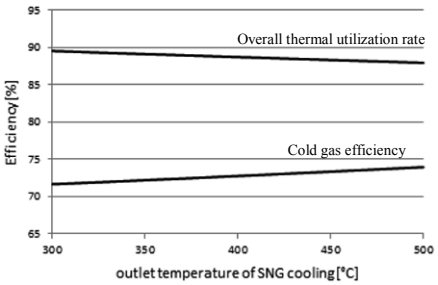

Figure 4: outlet temperature of SNG cooling vs. efficiency

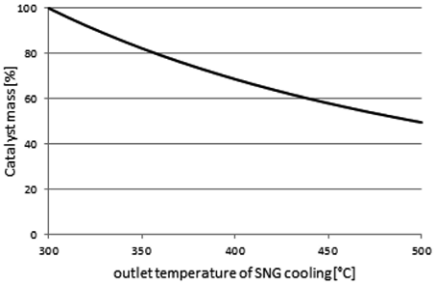

Figure 5: outlet temperature of SNG cooling vs. catalyst mass

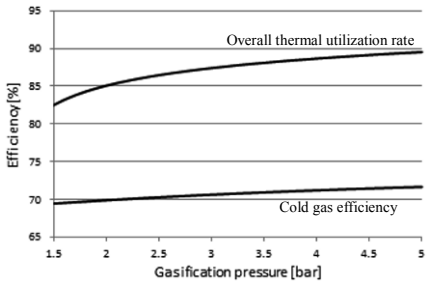

Figure 6: gasification pressure vs. efficiency

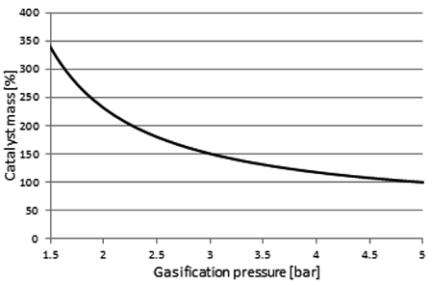

Figure 7: gasification pressure vs. catalyst mass

3.2. Influence of gasification pressure

In contrast to most conventional gasifiers, the Heatpipe Reformer can operate under pressure. Figure 6 shows that the cold gas efficiency and the overall thermal utilization rate, benefit from higher gasifier pressure. This correlation can be explained by a higher CH_4 content in the productgas after the gasifier and in the SNG after the tar reforming reactor. In addition, the heat extracted from the quench water cycle rises substantially with high process pressures due to the higher amount of condensate from the SNG. An increasing gasification pressure lowers the necessary catalyst mass in the tar reformer significantly (Figure 7). This correlation could be explained by the higher reaction rate of reaction (5). Due to the positive influence of a high gasifier pressure on the overall process and based on practical experience of the project partner Agnion a design pressure of 5 bar_{abs} was chosen.

4. Conclusions

Process modelling and simulation are useful tools for primary process design and the evaluation of process parameters. Using mathematical models for the individual steps the overall process was analysed and optimized. The analysis shows that under optimized process conditions a cold gas efficiency of over 70% can be achieved. By using the waste heat, the total efficiency for the overall process can be increased to approximately 90%. Moreover the necessary amount of consumables like catalyst can be reduced considerably by working under optimized operating parameters.

All of the most relevant issues regarding the design of the process are implemented in the model. On the basis of the simulated data and practical experience a basic engineering of the overall system will be performed, which facilitates the technical and economic analysis and comparison with other gas cleaning processes.

Acknowledgments

The authors thank the Austrian Research Promotion Agency FFG for funding the project “InnoGasClean” (FFG 838730) and the project partner Agnion (www.agnion.de) for the pleasant and constructive working relationship.

References

G. Gallmetzer, P. Ackermann, A. Schweiger, T. Kienberger, T. Groebl, H. Walter, M. Zankl, and M. Kroener, 2012, The agnion heatpipe-reformer operating experiences and evaluation of fuel conversion and syngas composition, Biomass Conversion and Biorefinery, 2, 3, 207–215

T. Groebl, H. Walter, and M. Haider, 2012, Biomass steam gasification for production of SNG: Process design and sensitivity analysis, Applied Energy, 97, 0, 451–461

J. Han, and H. Kim, 2008, The reduction and control technology of tar during biomass gasification/pyrolysis: An overview, Renewable and Sustainable Energy Reviews, 12, 2, 397–416

P. Hasler and T. Nussbaumer, 1999, Gas cleaning for IC engine applications from fixed bed biomass gasification, Biomass and Bioenergy, 16, 6, 385–395

L. Laurence, and D. Ashenafi, 2012, Syngas treatment unit for small scale gasification - application to IC engine gas quality requirement, Journal of Applied Fluid Mechanics, 5, 1, 95–103

T. Proell, and H. Hofbauer, 2008, Development and application of a simulation tool for biomass gasification based processes, International Journal of Chemical Reactor Engineering, 6

L.P.L.M. Rabou, R.W.R Zwart, B.J. Vreugdenhil, and L. Bos, 2009, Tar in biomass producer gas, the energy research centre of the Netherlands (ECN) experience: An enduring challenge, Energy Fuels, 23, 12, 6189–6198

K.E. Wirth, 2010, L1.6 pressure drop in fixed beds. VDI Heat Atlas, 1106–1110

C. Zuber, C. Hochenauer and T. Kienberger, 2014, Test of a hydrodesulfurization catalyst in a biomass tar removal process with catalytic steam reforming. Applied Catalysis B: Environmental, 156-157, 62–71

Krist V. Gernaey, Jakob K. Huusom and Rafiqul Gani (Eds.), 12th International Symposium on Process Systems Engineering and 25th European Symposium on Computer Aided Process Engineering.
31 May – 4 June 2015, Copenhagen, Denmark

Exergy Analysis of Monoethylene Glycol (MEG) Recovery Systems

Alexandre M. Teixeira[a], José Luiz de Medeiros[a], Ofélia Q. F. Araújo[a]

[a]*Escola de Química, Federal University of Rio de Janeiro (UFRJ), Av. Athos da Silveira Ramos, 149, Rio de Janeiro, 21941-909, Brazil*
alexandremtxr@gmail.com

Abstract

Hydrates are ice-like compounds comprised of water and light hydrocarbons whose formation in natural gas pipelines can lead to several problems such as pipeline blockage. To avoid these problems, the injection of Thermodynamic Hydrate Inhibitors (THI) in well-heads is widely employed. There are several options of THIs. In the present work, Monoethylene Glycol (MEG) was chosen due to its comparative advantages. As MEG can be reused, it must be re-concentrated and stripped of salts before recirculation through subsea pipelines. MEG Recovery Units (MRU) can be divided into three types: Traditional Process (TP), Full-Stream Process (FS) and Slip-Stream Process (SS). TP, FS and SS were discussed and compared via Energy and Exergy Analyses. The Exergy Analysis was based on two different approaches: firstly allocating the Reference Environmental Reservoir (RER) as the atmosphere at sea level; secondly allocating the RER as sea level atmospheric air saturated with water in equilibrium with liquid water containing MEG at infinite dilution. Those two approaches led to different results, but, in both cases TP shows the highest exergy efficiency and lowest energy consumption, while FS exhibits the lowest exergy efficiency and highest energy consumption. SS occupied an intermediate position.

Keywords: exergy; energy; monoethylene glycol; hydrate.

1. Introduction

The recent advent of deep-water offshore exploration of oil & gas entailed the arrival of stringent challenges. Concerning deep-water natural gas (NG) production, a main challenge is to avoid the formation of methane hydrates, which may cause clogging and even stopping NG flow. Formation of CH_4 hydrates is propelled by three factors (Gupta and Singh, 2012): (i) coexistence of water with NG; (ii) high pressure flow; (iii) external temperature close to 0^oC. Therefore prevention of hydrate formation is required. One approach that has been widely used is the injection of a Thermodynamic Hydrate Inhibitor (THI) in well-heads (Chandragupthan, 2011). MEG has been successfully used as THI due to its advantages compared to other inhibitors. In this study only applications of MEG as THI are considered. MEG is injected in well-heads and returns to the platform along with the production fluids. This stream is separated into three phases: (i) bottom aqueous phase with MEG and salts; (ii) hydrocarbon condensate; and (iii) NG phase. The MEG-H_2O-Salts stream is pre-treated to remove hydrocarbons and sent to the MEG Recovery Unit (MRU). This stream is the Rich MEG feed which is processed by the MRU to regenerate MEG to be returned to the NG wells as Lean MEG; i.e. regeneration means water and salt removal. Salt accumulation in the MEG loop is an issue because it causes fouling at saturation.

MRU falls into three categories: Traditional Process (TP), Full-Stream Process (FS) and Slip-Stream Process (SS). In offshore platforms, where space and resources are limited, it is of great importance to determine the energy requirements of each process, as well as to perform a thermodynamic analysis to assess degradation of energy quality. This last approach can be done via Exergy Analysis (ExA). ExA quantifies and compares the percentage of exergy destroyed via process irreversibilities. ExA also assesses the sinks of exergy destruction or inefficiencies (BoroumandJazi et al., 2013).

2. Objectives and Methodology

Three steady-state MRU processes (TP, FS, SS) were compared in terms of energy consumption (EC) and exergy efficiency. TP, FS and SS were installed in a process simulator for solving mass/energy balances, providing values of EC and thermodynamic properties of streams for ExA. The expression of exergy flow was developed by applying conservation laws and the First and Second Laws of Thermodynamics. The Reference Environment Reservoir (RER) was defined using two different criteria for the reference atmosphere and the reference state of MEG. Exergy flows were calculated for the relevant streams via spreadsheets with properties extracted from simulations.

3. MRU Implementation in Process Simulator

3.1. Premises

Typical flow rates and conditions reported in the literature of real MRUs were used for TP, FS and SS (Nazzer and Keogh, 2006). Operating pressure of MEG boiling systems was set at 0.2 bar abs (boiling points $\leq 140^{o}C$) to avoid thermal degradation of MEG above $162^{o}C$. NaCl is the main ionic species, representing 1-3% w/w of Rich MEG, whereas other salts – $CaCl_2$, etc – reach only hundreds of ppm and are irrelevant in terms of thermal effects. Even so, NaCl was not included in the simulation for two reasons: (i) NaCl only settles in the flash-evaporator after vaporization of MEG and H_2O, which are responsible for the main energy effects associated with phase changes – to confirm this, MRU was simulated with/without NaCl and the differences in terms of heat duties were always found below 1-2% (Teixeira, 2014); (ii) Aqueous solution models are not reliable with strong electrolytes at saturation, leading to inaccurate thermodynamic properties and ExA. Thus, after discarding NaCl, Rich MEG stream was defined as: 100t/d, 55%w/w H_2O + 45%w/w MEG at $25^{o}C$, 1 bar. The Slip Fraction in SS was chosen as 50%. Temperature and pressure of Rich and Lean MEG have same values for TP, FS, SS. Thermodynamic calculations used the simulator Glycol Package.

3.2. Traditional Process (TP)

TP simply distillates water from Rich MEG via an atmospheric distillation column (ADC) with Lean MEG as bottoms. TP works well without formation water. However, with formation water there is accumulation of salts and dissolved minerals in the MEG loop overtime, leading to saturation and precipitations on exchangers, thermally degrading MEG. Figure 1 depicts the simulation implementation of TP.

3.3. Full-Stream Process (FS)

FS treats Rich MEG with three serial steps: (i) Atmospheric Distillation Column (ADC) for a first removal of water below 140°C; (ii) Flash-Evaporator (FLS) at 0.2 bar, wherein the feed instantaneously vaporizes after mixing with the recycled hot liquor, precipitating salt; and (iii) vapor from FLS goes to Sub-atmospheric Distillation Column (SDC) at 0.2 bar giving pure H_2O distillate and Lean MEG as bottoms. Figure 2 illustrates the simulation implementation of FS.

3.4. Slip-Stream Process (SS)

SS combines TP with a smaller FLS-SDC train to treat the Slip Fraction of the effluent from TP section. An advantage of SS is the reuse of inhibitors and pH stabilizers, which are lost in the FS within the FLS solids. SS is suitable for low to intermediate water loads (Brustad et al., 2005). Figure 3 shows the implementation of SS.

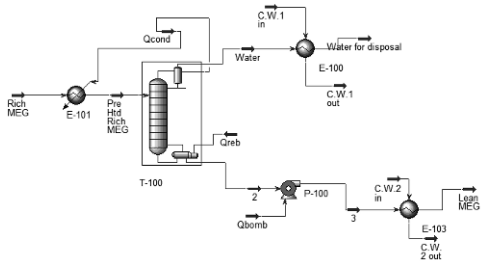

Figure 1. TP Implementation

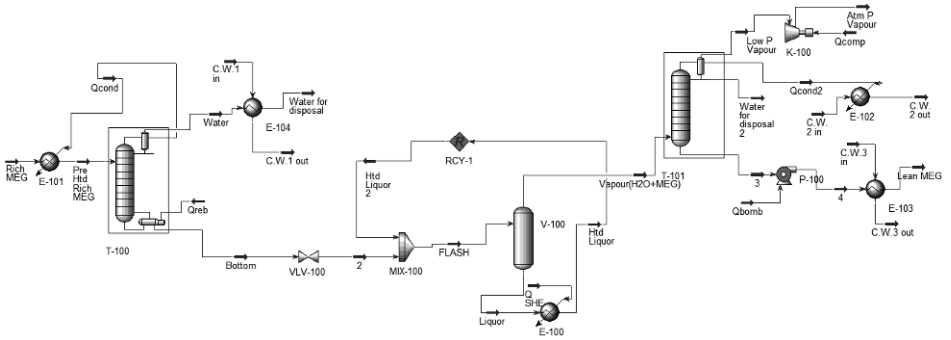

Figure 2. FS Implementation

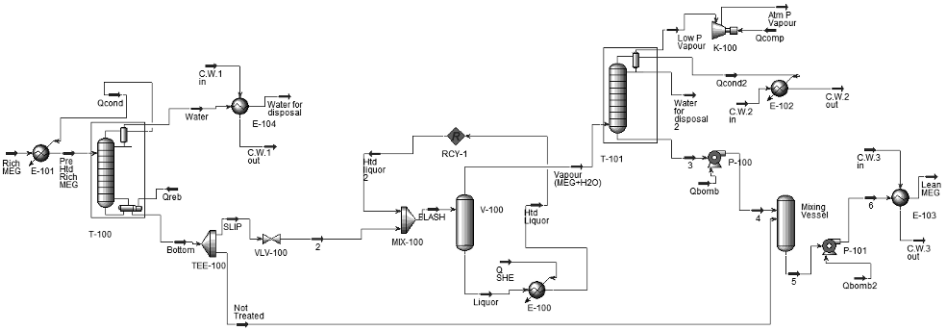

Figure 3. SS Implementation

3.5. Energy Consumption (EC)

EC was found for TP, FS and SS in Table 1, which also shows the respective Lean MEG composition. All heating duties represent direct electricity consumptions as usual in offshore rigs (Myhre, 2001). TP has the lowest EC, as it is the simplest process with only one separation. On the other hand, FS has the highest EC. SS is the second as only part of the Rich MEG is evaporated.

Table 1. Electric Energy Consumptions (EC) and Lean MEG Compositions for MRU Processes

Process	%w/w MEG of Lean MEG	EC (kW)
TP	89.46	1685.73
FS	91.36	2330.38
SS	86.77	1894.50

4. Exergy Analysis (ExA)

4.1. Exergy Definition

The exergy flow of a stream is the maximum rate of work obtainable when it is brought to equilibrium with the environment. Exergy is destroyed due to irreversibilities in real processes. ExA evaluates the exergy efficiency by calculating the % of destroyed exergy. From the First and Second Laws of Thermodynamics for a multi-stream, steady-state, open system, the rate of maximum work obtainable is the difference between the input and output flows of exergy in Eqs. (1) and (2) (Teixeira, 2014; De Medeiros, 2011):

$$\dot{B}_{in} + \dot{B}_{in}^{W} = \sum_{j}^{nfs} F_j \left(\overline{H}_{F_j} + P_0 \overline{V}_{F_j} - T_0 \overline{S}_{F_j} - \sum_{k=1}^{nc} \mu_k^0 Y_{kF_j} \right) + \sum_{j=1}^{nwi} \left| \dot{W}_j^{imported} \right| \tag{1}$$

$$\dot{B}_{out} + \dot{B}_{out}^{W} = \sum_{j}^{nps} K_j \left(\overline{H}_{K_j} + P_0 \overline{V}_{K_j} - T_0 \overline{S}_{K_j} - \sum_{k=1}^{nc} \mu_k^0 Y_{kK_j} \right) + \sum_{k=1}^{nwe} \left| \dot{W}_k^{exported} \right| \tag{2}$$

Where $\dot{B}_{in}$, $\dot{B}_{out}$ are the exergy flows of input and output streams; $\dot{B}_{in}^{W}$, $\dot{B}_{out}^{W}$ are the exergy flows assigned to input/output streams of pure electric energy; F_j is the mol flow rate of inlet stream *j*; K_j is the mol flow rate of outlet stream *j*; *nfs* and *nps* refer to the numbers of feed and product streams; μ^0_k is the chemical potential of *k* species in the Reference Environment Reservoir (RER); $\overline{H}, \overline{S}, \overline{V}$ refer to molar enthalpy, entropy and volume; P_0 and T_0 are the pressure and temperature of RER; *W* represents a rate of work imported/exported by the system; and Y_k refers to the mol fraction of *k*. All properties are obtained from simulations, except μ^0_k, which belongs to RER. In this regard, two approaches are used for RER: (i) RER Approach#1: usual in the literature with atmospheric air at T_0=298.15 K and P_0=1 atm, Y^0_{N2}=0.7652, Y^0_{O2}=0.2053, Y^0_{Ar}=0.0092, Y^0_{H2O}=0.02, Y^0_{CO2}=0.0004, where MEG is at Chemical Equilibrium (ChE) with RER species via a combustion reaction; (ii) RER Approach#2: Air at T_0=298.15 K and P_0=1 atm, with the same dry basis composition as before, but now saturated with H_2O in Vapor-Liquid Equilibrium (VLE) with liquid H_2O containing MEG at infinite dilution.

4.2. RER Approach #1

RER is an ideal gas with chemical potentials of species by Eq. (3), where the first term in the right side is found via process simulator with pure low pressure gas. Since MEG is absent in atmospheric air, μ^0_{MEG} comes via ChE with other RER species as in Eq. (4).

$$\mu_i^0 = \mu_i^{f,0}(T_0, P_0) + RT_0 \ln Y_i^0 \tag{3}$$

$$\mu_{MEG}^0 = 2\mu_{CO2}^0 + 3\mu_{H_2O}^0 - 2.5\mu_{O2}^0 \tag{4}$$

4.3. RER Approach #2

Chemical potentials of N_2, O_2, Ar, CO_2 and H_2O are also given by Eq. (3) assuming VLE of H_2O. For MEG, its RER chemical potential is calculated at infinite dilution in liquid H_2O at (T_0, P_0) with Eq. (5), where X is the mol fraction of MEG (Smith et al., 2007). The derivative term is obtained via numerical differentiation on the curve $\overline{G} = \overline{H}(X, T_0, P_0) - T_0\overline{S}(X, T_0, P_0)$ generated by several composition definitions of H_2O+MEG liquid streams at (T_0, P_0) in the process simulator.

$$\mu_{MEG}^{\infty,H2O} = \overline{G}\Big|_{X=0} + \frac{d\overline{G}}{dX}\Big|_{X=0} \tag{5}$$

5. Results and Discussion

Exergy efficiency is a ratio between output and input flows of exergy, respectively from Eqs. (2) and (1). Table 2 shows the ExA performances of TP, FS and SS for both RER approaches.

Table 2. Exergy Efficiencies (%) of MRU Configurations for RER Approaches #1 and #2

Process	RER Approach #1	RER Approach #2
TP	91.49	18.83
FS	90.19	14.97
SS	91.02	17.14

TP had always the highest efficiency, while FS had the lowest. TP is a brute technology with only one primary sink of exergy destruction (ADC) with low exergy losses. FS performs a huge effort of separation (ADC, FLS, SDC) vaporizing all MEG and H_2O from Rich MEG producing the best Lean MEG with the highest EC and exergy destruction rate, and lowest exergy efficiency. SS is intermediate. Table 2 also shows why RER Approach#2 is better than Approach#1. Both calculate the same rate of lost exergy, but Approach#1 achieves very high efficiencies (≈90%). The reason is that in Approach#1 μ^0_{MEG} is obtained via ChE with a very negative value (-1.71.10^6 J/mol), giving MEG streams with very high positive exergy flows (≈11500 kW) much greater than typical EC (≈1700 kW). As the MRU does not destroy MEG, the input and output flows of exergy are very high positive numbers, with only ≈1600kW of lost exergy. Thus the total flow of exergy has a small relative fall, entailing exergy efficiencies close

to 90%. On the other hand, Approach#2 assign the RER condition of MEG closer to the MRU state of MEG, entailing much lower positive values of exergy flows of streams (≈280 kW). Since the same rate of exergy is lost in both approaches, much lower (but more meaningful) exergy efficiencies are obtained in Approach#2. These more realistic efficiencies are closer to what is expected for distillation trains.

6. Conclusions

Exergy Analysis was conducted for MRU processes in offshore NG production. Exergy efficiencies result from the exergy flows entering/leaving processes. Since exergy depends both on the state of streams and on the RER, two RER approaches were used: (i) Usual RER Approach#1, allocating MEG in ChE with atmospheric species; and (ii) RER Approach#2 where the atmosphere is in VLE with liquid H_2O containing MEG at infinite dilution. Both approaches calculated the same rate of lost exergy for the same MRU. But Approach#1 seems inappropriate because exergy flows of streams are too high, masking results. On the other hand, Approach#2 defines the RER condition of MEG as a liquid in water, thus exergy flows of streams are much lower, with better discrimination of exergy efficiencies.

7. Acknowledgments

Financial support from PETROBRAS S.A., FINEP-Brazil and ANP-Brazil (PRH-ANP / MCT via PRH-13 of Escola de Química/UFRJ) is gratefully acknowledged.

References

G. BoroumandJazi, B. Rismanchi and R. Saidur, 2013. A Review on Exergy Analysis of Industrial Sector. Renewable and Sustainable Energy Reviews, Volume 27, p. 198-203.

S. Brustad, K.-P. Løken and J. G. Waalmann, 2005. Hydrate Prevention using MEG instead of MeOH: Impact of experience from major Norwegian developments on technology selection for injection and recovery of MEG. Offshore Technology Conference. OTC 17355.

B. Chandragupthan, 2011. An Insight to Inhibitors. PetroMin Pipeliner. July-Sept, p. 50-57.

J. L. De Medeiros, 2011. Exergy Analysis of Chemical Processes. PSE-Worshop, Lecture Notes.

G. Gupta and S.K. Singh, 2012. Hydrate Inhibition – Optimization in Deep Water Field. SPE Oil and Gas India Conference and Exhibition. SPE 153504.

J. Myhre, 2001. Electrical Power Supply to Offshore Oil Installations by High Voltage Direct Current Transmission. Doctoral Thesis. Norwegian University of Science and Technology.

C.A. Nazzer and J. Keogh, 2006. Advances in Glycol Reclamation Technology. Offshore Technology Conference. OTC 18010.

J. M. Smith, H. C. Van Ness and M. M. Abbott, 2001. Introduction to Chemical Engineering Thermodynamics. 6th ed., McGraw-Hill, p. 359-361.

A. M. Teixeira, 2014. Análise Exergética de Processos de Recuperação de Monoetileno Glicol (MEG) em Plataformas Offshore. M. Sc. Dissertation. TPQBq, UFRJ (Brazil).

Krist V. Gernaey, Jakob K. Huusom and Rafiqul Gani (Eds.), 12th International Symposium on Process Systems Engineering and 25th European Symposium on Computer Aided Process Engineering.
31 May – 4 June 2015, Copenhagen, Denmark

Production of Biodiesel via Enzymatic Palm Oil Ethanolysis: Kinetic Study

Shayane P. Magalhães,[a*] Fernando L.P. Pessoa,[b] Tito L. M. Alves[a]

[a] *PEQ/COPPE– Federal University of Rio de Janeiro, Av. Athos da Silveira Ramos, 149, Centro de Tecnologia, Bl. G, Cidade Universitária, Ilha do Fundão, Rio de Janeiro – RJ, CEP 21941-909, Brazil*
[b] *DEQ - Department of Chemical Engineering, Chemistry School – Federal University of Rio de Janeiro, Av. Athos da Silveira Ramos, 149, Centro de Tecnologia, Bl. E, s. 201, Cidade Universitária, Ilha do Fundão, CEP 21941-909, Rio de Janeiro – RJ, Brazil*
shayane@peq.coppe.ufrj.br

Abstract

Biodiesel is an alternative fuel that has become attractive due to its environmental benefits compared to conventional diesel. Over the years an initial reaction rate based on the Ping Pong Bi Bi enzyme mechanism has been adopted to represent the kinetics of the enzymatic transesterification in several references in the open literature. However, in this work, a two parameters model taking into account the inhibitory effects due to the concentration of both product species was proposed and the experimental oil conversion data were fitted to the model. The kinetic study of the palm oil ethanolysis reaction catalyzed by immobilized lipase Novozyme 435 (from *Candida antarctica*) has been made in a temperature of 42 °C at atmospheric pressure. A maximum conversion of 70% of oil was obtained after 7 hours of reaction. The model proposed was successful in predicting the experimental data behavior (mean absolute deviation <5%) with the reactor operating in batch. The confidence interval of the parameters was small, and the parameters did not show a high dependency between each other with a correlation coefficient between them equal to 0.855, ratifying the excellent fit of the rate equation proposed.
Keywords: biodiesel, transesterification, lipase, palm oil, Ping Pong Bi Bi model.

1. Introduction

By definition, biodiesel is a mixture of fatty acid alkyl esters (FAAE) derived from renewable sources. It can be synthesized through the reaction of edible/non-edible oils or animal fats with an alcohol. The oils and fats consist of a mixture of triglycerides which can be transformed to FAAE through a chemical reaction with a short chain alcohol known as transesterification (or alcoholysis).

The general scheme of the ethanolysis reaction can be seen in Figure 1; a triglyceride molecule reacts with three alcohol molecules producing three molecules of alkyl esters, named as biodiesel, and one glycerol molecule as the main by-product. In fact, the reaction consists of three consecutive steps in which first the triglyceride is converted into diglyceride; the second step is the conversion of the diglyceride into monoglyceride which is converted into glycerol at the final step (Shahid and Jamal, 2011). Furthermore, due to its reversibility, an excess of alcohol is usually required to perform the transesterication reaction.

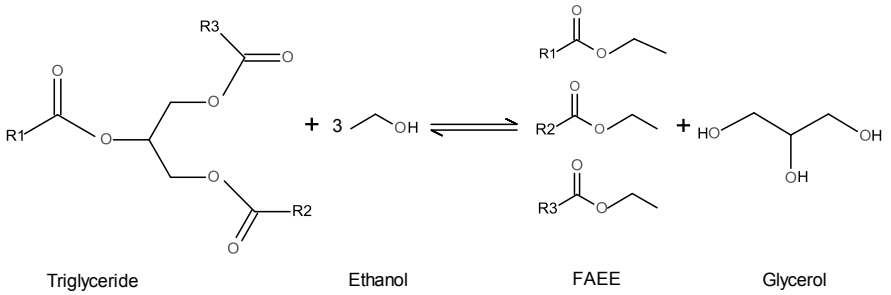

Figure 1: Transesterification reaction of triglycerides with ethanol. R1, R2, and R3 represent the fatty acid chains; FAEE is the fatty acid ethyl esters.

Different types of oils can be used as feedstock to produce biodiesel; soybean, palm, sunflower, canola, rapeseed, and cotton are among the most common vegetable oils employed. Palm oil is the major feedstock for biodiesel production in Malaysia and is also commonly used in others countries like Brazil and Indonesia. Up to date, palm is the most effective oilseed due to the large quantity of oil produced with a minimum land demand (Lam and Lee, 2011).

Although methanol is mainly obtained from fossil sources, it is currently the primary alcohol used to synthesize the biodiesel fuel; however, ethanol has been frequently employed due to its advantages such as a higher dissolving power and lower toxicity in comparison to the previous one (Stamenkovic et al., 2011). In Brazil, bioethanol derived from sugarcane is widely available. Thus, its use as a reactant is advantageous since the biodiesel produced can be considered as 100% renewable based (Gui et al., 2009).

The catalyst is needed to increase the speed of the reaction and it can be alkaline, acid, or an enzyme. Concerning to the biocatalysts, the lipases are enzymes able to catalyze reactions of the triglycerides by acting on their ester bond (Pessoa et al., 2010). In spite of the drawbacks of the enzymatic transesterification such as the deactivation of enzymes by the presence of the alcohol and their high cost, this technology is widely studied once the problems characteristics of the reactions with alkaline and acid catalysts, like the difficulties during some downstream processes (glycerol recovery, catalyst removal and purification steps) are not found in lipase catalyzed alcoholysis.

Different studies related to the ethanolysis of vegetable oils via enzymatic catalysis to produce biodiesel can be found in the open literature (Wang et al., 2011, Ribeiro et al., 2012). Despite that, works that deal with a kinetic modeling are rarely found. Therefore, the objective of this work is study the kinetic of the ethanolysis of palm oil with the commercial lipase Novozyme 435 as the catalyst. Experimental oil conversion data versus reaction time was obtained and these values were used to fit an empirical model proposed and the results were compared with the Ping Pong Bi Bi with alcohol inhibition model.

2. Materials and methods

2.1. Materials

Absolute ethanol was supplied by Vetec Química Fina with a mass fraction purity of 0.998; refined palm oil was kindly donated by Agropalma S/A, Brazil. According to the company, the free fatty acid contained in the oil is <0.5% and its composition (% mass) is: 37.6% triolein, 46.8% tripalmitin, 10.5% trilinolein, 3.8% triestearin, 1.2% trimyristin, 0.1% trilaurin. Based on this composition, the oil molecular weight is 843.46 g/gmol. Novozyme 435 (lipase from *C. antarctica* immobilized on acrylic resin) was purchased from Sigma-Aldrich, USA. Standard fatty acid ethyl esters were acquired from Sigma-Aldrich, USA. All other reagents were of chromatographic grade and were also purchased from Sigma-Aldrich.

2.2. Enzymatic ethanolysis

The batch reactions were carried out in 50 mL closed glass flasks. The commercial lipase (0.4% of reactants mass) was added to flasks containing palm oil (12 g) and 4 g of ethanol (6:1 alcohol:oil initial molar ratio). The mixture was incubated at 42 °C with constant shaking at 170 rpm. The reactions were carried out in triplicate and allowed to proceed for 7 h. Samples were periodically taken and analyzed. The aliquots (100 μL) were diluted with n-heptane (800 μL) and mixed with the internal standard (IS) ethyl heptadecanoate (100 μL) and analyzed by gas chromatography (CG).

2.3. Gas-chromatography analysis

The ethyl esters were analyzed on an Agilent (Palo Alto, CA) gas chromatograph model 7890A with a mass spectrometer (MS) detector and a DB-WAX column (30 m x 0.25 mm x 0.25 μm). The injector temperature was 250 °C and helium was used as the carrier gas (1mL/min). The temperature program was as follows: the column temperature started at 60 °C for 2 min and then heated to 200 °C at 10 °C/min and then raised to 240 °C at 5 °C/min and held for 7 min.

3. Kinetic modeling

The reactions involving materials derived from natural products, such as in the enzymatic transesterification of vegetable oils, can be described by a two-step mechanism where the products of each step are released between additions of the substrates (Pessoa et al., 2009). As reported by several authors (Dossat et al., 2002; Al-Zuhair et al., 2006; and Fjerbaek et al., 2009), the lipase alcoholysis of triglycerides are in accordance with the Ping Pong Bi Bi mechanism and an initial reaction rate equation (called here, model 1) can be expressed by Eq. (1), including the influence of the alcohol on the deactivation of the enzyme.

$$(-r_{oil,model\ 1}) = \frac{V_{max}}{\frac{Km_1}{[oil]} + Km_2 \cdot [alc]/[oil] + 1} \quad (1)$$

where ($-r_{oil}$) denotes the initial rate of oil consumption; [oil] and [alc] represent the initial molar concentrations of oil and alcohol, respectively; V_{max} is the maximum initial rate for the reaction; $Km_1 = Km_{oil} + Km_{alc}/\theta$ and $Km_2 = Km_{oil}/K_i$ with θ representing the initial alcohol:oil molar ratio, Km_{oil} and Km_{alc} representing the apparent Michaelis constants for the oil and alcohol, respectively, and K_i is the apparent inhibition constant of the alcohol.

Different authors (Dossat et al., 2002; Shimada et al, 2002; Fjerbaek et al., 2009; Ko et al., 2012), however, have reported that the glycerol obtained during the transesterification reduces the catalytic activity of the lipase by forming a film layer around the support of the immobilized enzyme which affects the internal mass transfer resistance within the solid support. This effect is not accounted in model 1 once it is an initial reaction rate expression. Hence, an empirical model (called model 2) was proposed in this work to consider it. The model rate expression is given by Eq. (2). Due to the possibility of internal diffusion limitations when using immobilized lipases, the kinetic parameters from models 1 and 2 may be considered as apparent values. In addition to considering the presence of the products, another advantage of the proposed model is that it has only two adjustable parameters.

$$(-r_{oil,model\ 2}) = \frac{K_1 \cdot \{[oil] \cdot [alc] - 3 \cdot [oil]^2 \cdot X_{oil}^2\}}{\left(1 + \frac{3 \cdot [oil]^2 \cdot X_{oil}^2}{K_2}\right) \cdot [oil] \cdot [alc]} \quad (2)$$

where X_{oil} is the conversion of oil; K_1 and K_2 are the apparent kinetic constants.

Thereby, combining the reaction velocity expression (model 1 or model 2) with the mass balance for a batch reactor, the kinetic parameters of each model were fitted to the experimental data for the ethanolysis of palm oil catalyzed by enzyme Novozyme 435 according to the Eq. (3). The parameters were determined by nonlinear regression using the software Mathcad to perform the particle swarm optimization (PSO) and the gradient-conjugated methods. The ordinary differential equation was solved using the fixed-step fourth-order Runge-Kutta method.

$$\frac{dX_{oil}}{dt} = \frac{V}{n_0^{oil}} \cdot (-r_{oil}) \quad (3)$$

where t is the time of reaction; V is the reaction volume; n_0^{oil} represents the initial mol of oil.

4. Results and Discussion

Regarding to the kinetic modeling showed above, the comparison between the experimental and predicted conversions for the palm oil transesterification is illustrated in Figure 2. It can be observed that, qualitatively, the model proposed in this work (model 2) and the model 1 were able to describe the experimental data. However, the model predicted the experimental data with an absolute mean deviation of 8% for model 1 and 4% for model 2. Hence, according to these values, it can be notice that the model 2 showed a better fit of the data than the modified Ping Pong Bi Bi model (model 1).

In order to make a better selection of the most suitable model do fit the experimental data, the standard deviation of best-fit parameters and the correlation coefficient between the parameters were calculated. The results are shown in Table 1.

The confidence interval identifies how tightly the determination of the parameters values was. From the values on Table 1 is possible to see that for model 1 the confidence interval (with 95% of confidence level) is very wide, starting from negatives values, which has no physical meaning. Therefore, the data do not define the parameters well and the model cannot be consider appropriate. On the other hand, the confidence

interval for model 2 is small meaning that the experimental data define well the best-fit curve of this model.

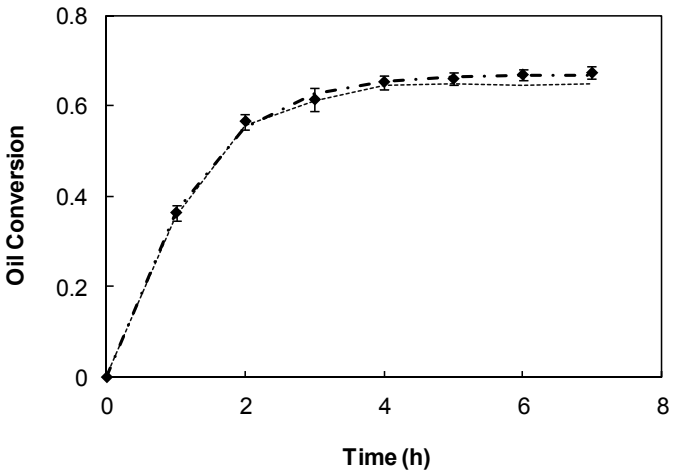

Figure 2: Palm oil conversion for a batch reactor. (■) Experimental data; (- - -) Model 1; (— · -) Model 2. Conditions: 42 ºC, 12g palm oil, ethanol:oil molar ratio=6:1, 4 % w/w enzyme.

Table 1: Kinetic parameters, standard deviation and confidence level of parameters for model 1 and model 2.

Model	Parameter	Estimated Value	Standard deviation	Lower limit (95% confidence level)	Upper limit (95% confidence level)
Model 1	V_{max} (mol/L·h)	11.11	145.25	-344.30	366.52
	Km_1 (mol/L)	3.21	96.56	-233.06	239.48
	Km_2	0.42	23.46	-56.98	57.81
Model 2					
	K_1(mol/L)	0.33	0.025	0.27	0.39
	K_2 $(mol/L)^2$	0.50	0.029	0.44	0.57
Correlation coefficients between the parameters					
	$\rho_{Vmax, Km1}$, $\rho_{Vmax, Km2}$, $\rho_{Km1, Km2}$		1.000		
	$\rho_{K1, K2}$		-0.855		

Notwithstanding, the correlation coefficient between parameters V_{max} and Km_1, V_{max} and Km_2, Km_1 and Km_2 from model 1 are equal to one suggesting that the parameters are redundant, i.e., a change made in the value of one parameter, changes the value of the other. On the opposite, the absolute value of correlation coefficient between parameters K_1 and K_2 from model 2 (i.e, $|\rho_{K1, K2}| = 0.855$) do not show a high dependency between them. These results confirm the model 2 as the best choice to describe the data obtained.

5. Conclusion

In this study the palm oil was used to successfully produce biodiesel through the lipase-catalyzed transesterification with ethanol. Under 42 °C and atmospheric pressure, a maximum oil conversion of 70% was obtained after 7 hours of reaction. Moreover, the experimental data were used to fit two different kinetic models and their apparent kinetic parameters were estimated. Considering the results obtained, the rate expression proposed in this work (Model 2) proved to be a better choice to fit the experimental data than the model based on the Ping Pong Bi Bi mechanism (Model 1), considering the fact that Model 2 accounts for the presence of the products. The parameters from Model 2 are not intertwined ($\rho_{K1, K2} = -0.855$) and have a small confidence interval suggesting that the data define the parameters very well. The high correlation coefficient values found for Model 1 indicate an over-parameterization of the model.

References

S. Al-Zuhair, K.V. Jayaraman, S. Krishnan, W. Hoong Chan, 2006, The Effect of Acid Concentration and Water Content on the Production of Biodiesel by Lipase, Biochemical Engineering Journal, 30, 212-217.

V. Dossat, D. Combes, A. Marty, 2002, Lipase-Catalysed Tranesterfication of High Oleic Sunflower Oil, Enzyme and Microbial technology, 30, 90-94.

L. Fjerback, K.V. Christensen, B. Norddahl, 2009, A Review of the Current State of Biodiesel Production Using Enzymatic Transesterification, Biottechnology and Bioengineering, 102, 5, 1298-1314.

M. Gui, K.T. Lee, S. Bhatia, 2009, Supercritical ethanol technology for the production of biodiesel: process optimization studie, The Journal of Supercritical Fluids, 49, 286-292.

M.J. Ko, H.J. Park, S.Y. Hong, Y.J. Yoo, 2012, Continuous biodiesel production using in situ glycerol separation by membrane bioreactor system, 35, Bioprocess Biosyst. Eng., 35, 69-75.

M.K. Lam, K.T. Lee, 2011, Biofuels: Alternative Feedstocks and conversion Processes, ed. Elsevier Inc., 15, 353-373.

F.L.P Pessoa, S.P. Magalhães, P.W. Falcão, 2009, Kinetic Study of Biodiesel Production by Enzymatic Transesterification of Vegetable Oils, Computer Aided Chemical Engineering, 27, 1809-1814.

F.L.P Pessoa, S.P. Magalhães, P.W. Falcão, 2010, Production of Biodiesel via Enzymatic Ethanolysis of the Sunflower and Soybean Oils: Modeling, Appl., Biochem. Biotechnol, 161, 238-244.

L.M.O. Ribeiro, B.C.S. Santos, R.M.R.G. Almeida, 2012, Studies on reaction parameters influence on ethanolic production of coconut oil biodiesel using immobilized lipase as a catalyst, Biomass and Bioenergy, 47, 498-503.

E.M Sahid, Y. Jamal, 2011, Production of biodiesel: A technical review, Renewable and Sustainable Energy Reviews, 15, 4732-4745.

Y. Shimada, Y. Watanabe, A. Sugihara, Y. Tominaga, 2002, Enzymatic Alcoholysis for Biodiesel Fuel Production and Application of the Reaction to Oil Processing, Journal of Molecular Catalysis B: Enzymatic, 17, 133-142.

L.F. Sotoft, B-G. Rong, K.V. Christensen, B. Norddahl, 2010, Systematic approach for sythesis of biodiesel production processes, Computer Aided Chemical Engineering, 28, 1099-1104.

O.S. Stamenkovic, A. V. Velickovic, V. B. Beljkovic, 2011, The production of biodiesel from vegetable oils ethanolysis: Current state and perpectives, Fuel, 90, 3141-3155.

Y-N. Wang, M-H. Chen, C-H. Ko, P-j. Lu, J-M. Chern, C-H. Wu, F-C. Chang, 2011, Lipase catalyzed transeterification of tung and palm oil for biodiesel, World Renewable Energy Congress, Sweden, 87-92.

Krist V. Gernaey, Jakob K. Huusom and Rafiqul Gani (Eds.), 12th International Symposium on Process Systems Engineering and 25th European Symposium on Computer Aided Process Engineering.
31 May – 4 June 2015, Copenhagen, Denmark

Integration of Retrofitted Coal-fired Power Plant with CCS: Power De-rate Minimization

Jinjoo An,[a] Ung Lee,[b] Jaeheum Jung,[a] Chonghun Han, [a]

[a]*School of Chemical and Biological Engineering, Seoul National University, Gwanak-ro 599, Gwanak-gu, Seoul, 151-744, Republic of Korea*
[b]*Engineering Research Institute, Seoul National University, Gwanak-ro 599, Gwanak-gu, Seoul, 151-744, Republic of Korea*
chhan@snu.ac.kr

Abstract

Post-combustion carbon dioxide (CO_2) capture using aqueous monoethanolamine (MEA) has been the most widely implicated method utilizing existing coal-fired power plants. However, the heat and energy requirement of the solvent regeneration and CO_2 liquefaction results in a 30% decrease in net power output, which is called "power de-rate". In this study, optimum operating conditions of the integrated CCS process are proposed by simulation-based parametric optimization to reduce the power de-rate. Post-combustion CO_2 capture with aqueous MEA and CO_2 liquefaction integrated with a 550 MWe supercritical coal-fired power plant was simulated base on the data of a 0.1 MW pilot plant in South Korea. The stripper operating pressure and liquid to gas ratio were chosen as the manipulated variables based on the variable evaluation. The power de-rate was reduced to 17.4% when operating at optimum conditions.

Keywords: power de-rate, variable evaluation, parametric optimization, CCS

1. Introduction

The International Panel on Climate Change (IPCC) reported that the energy sector is the largest greenhouse gas (GHG) source, and coal is accounted for 40.58% of electricity generation in 2010 (IPCC, 2014). Owing to the abundance of coal, it is highly possible that energy generation will continue to depend on coal-related power generation for a while. Therefore, technology is needed that allows coal to be utilized for power generation while mitigating climate change, which is carbon capture and storage (CCS).
Unfortunately, the power de-rate is a significant issue when introducing the CCS process into an existing steam power plant. In the post-combustion capture process, CO_2 is captured through a chemical reaction with a solvent. The heat requirement for regenerating the solvent is often met using steam extracted from a power plant. Steam extraction for solvent regeneration causes a decrease in net power output. Furthermore, the compression energy during the liquefaction process also increases the power de-rate. Therefore, reducing the power de-rate is the one of keys to CCS implementation.
The process and heat integration have been studied to reduce the power de-rate. Hanak et al. (2014) investigated several new heat exchanger network (HEN) designs for a high ash coal-fired power plant with CCS and proposed to use flue gas for heating the feedwater. Liew et al. (2014) analyzed capture module design options for the heat and process integration, cooling, and using waste heat by HEN design and process modification. However, considerable modification of the existing system is required in order to introduce HEN designs into it. Since the optimization of operating variables, on

the other hand, achieves the reduction of power de-rate with less modification, it can be more practical way of minimizing power de-rate with the existing CCS plants.
The evaluation of the power de-rate based on the different operating scenarios also has been conducted by many researchers. Dave et al. (2011) performed case studies on the plant efficiencies of existing coal-fired power plants and new coal-fired power plants by evaluating the CO_2 capture demand and cooling options. Liang et al. (2011) conducted an optimization of some important process parameters, including the operating stripper pressure, CO_2 capture efficiency, and steam extraction location. However, many of previous studies have focused on finding the optimum operating conditions for the unit CCS processes, not for the integrated CCS system. Also, the influences of operating variables lack quantitative evaluation in terms of the power de-rate.
In this study, the power de-rate of an integrated retrofitted coal-fired power plant with CCS was minimized by parametric optimization. To validate the simulation model, the simulation model of a 550 MWe steam cycle integrated with CO_2 capture and liquefaction processes was rigorously developed based on the data obtained from a 0.1 MW CO_2 capture pilot plant in South Korea. All of possibly influential variables in the power de-rate were quantitatively evaluated. Steam extraction unit options with different locations and depressurizers are also taken into account for the reduction of the power de-rate. In addition, the nonlinearity between the selected influential variables and the power de-rate are discussed to achieve much insight on the overall process.

2. Process description

2.1. The steam cycle

A 550 MWe air-based supercritical steam cycle was developed based on a DOE/NERL report (Ciferno, 2008). STEAMNBS was used for the property method. Superheated steam that is generated in a coal-fired boiler is expanded through two high pressure, two intermediate pressure, five low pressure turbines connected to an electrical generator, and finally condensed. Part of the turbine energy is converted into mechanical energy. At the same time, a small amount of steam is extracted from the inlet stream of each turbine in order to regenerate the feedwater so that the irreversibility of steam generation is reduced. In seven feedwater heaters, the temperature of the condensed feedwater is increased through the heat exchange with the extracted steam.

2.2. CO_2 capture model using aqueous MEA solvent

A typical post-combustion CO_2 capture process with an absorber, a stripper and a lean-rich solvent heat exchanger was used. The model specifications were obtained from the data of a 0.1 MW CO_2 capture pilot plant in Boryeong, Republic of Korea. The capture efficiency of the plant is 90% CO_2 removal when 30 wt% aqueous MEA is used as the solvent. To properly validate the model, mass transfer coefficient and interfacial area methods were used for the absorber and the stripper as 0.7 and 0.5, respectively. The Henley IMTP model was used to predict the temperature profile in the columns, and the Electrolyte-NRTL model was used as the property method to estimate the MEA–H_2O–CO_2 system with a kinetic model suggested by Hikita et al. (1977).
Flue gas from a power plant is contacted with the cold lean solvent in the absorber column, and the solvent absorbs CO_2 exothermically. The cold rich solvent drained out from the absorber is fed to the stripper column after exchanging heat with the hot lean solvent drained out from the stripper. The hot rich solvent desorbs CO_2 endothermically at high temperature. Captured CO_2 is sent to the liquefaction process while the hot lean solvent is sent back to the heat exchanger to increase the temperature of the cold rich solvent.

2.3. CO_2 liquefaction model

The simulation model for the liquefaction process was built based on the report of Lee et al. (2012). Soave-Redlich-Kwong (SRK) was used as the property method with a modified binary interaction parameter (k_{ij}) of 0.193 in the van der Waals mixing rule (Heggum et al., 2005). Captured CO_2 is compressed up to 54.4 bar through four stage compressors, and expanded through three stage valves. Between the compression stages, the stream is cooled by cold gaseous CO_2 that is generated in the expansion by passing through the two process heat exchangers. Cold liquefied CO_2 is obtained at the target conditions of 6.5 bar and -52 °C.

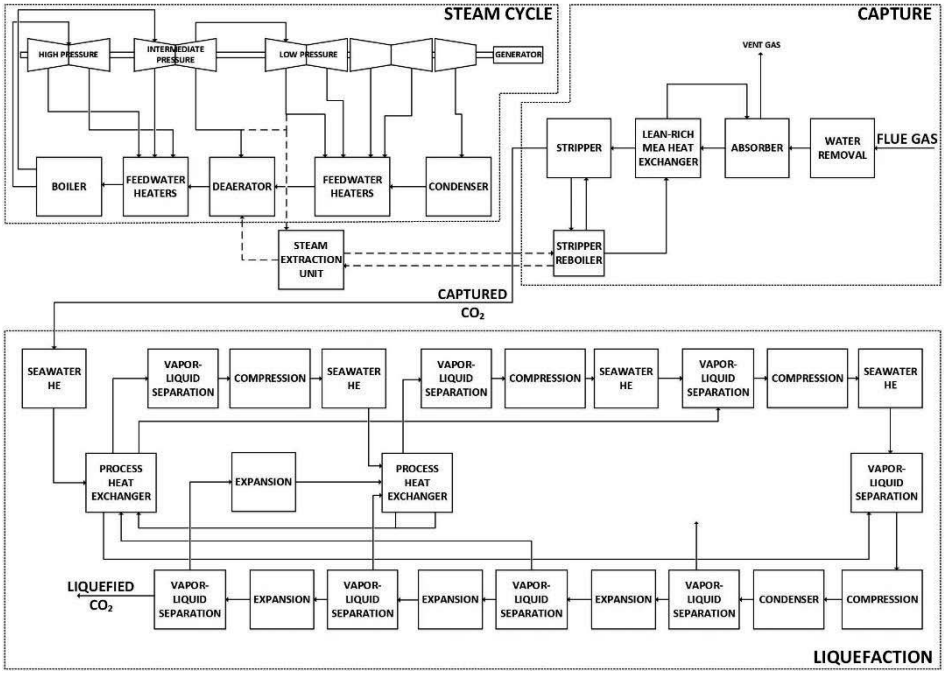

Figure 1. Block diagram of the integrated CCS process

3. Integration of steam cycle with CO_2 capture and liquefaction processes

3.1. Definition of power de-rate

To introduce CCS processes into existing steam cycles, a heat source should be supplied to a reboiler of the stripper for solvent regeneration. The steam cycle is a suitable option owing to the abundance in low quality steam. However, the steam extraction decreases the steam flowrate, thus decrease in the net plant power is inevitable. The compression energy in the liquefaction process also decreases the net plant power. This plant efficiency penalty is called "power de-rate" (D) as calculated following Eq.(1).

$$D = 1 - \frac{W_{power\ plant\ w/\ ccs} + W_{depressurizer} - W_{compressor}}{W_{power\ plant\ w/o\ CCS}} \quad (1)$$

As increase in the power de-rate means a power plant generates less energy than the original power plant with the same amount of coal, the power de-rate can be an indicator of operational economics.

3.2. Steam extraction from an existing power plant

To extract steam from the steam cycle, finding optimum extraction locations is important to avoid extracting steam with unnecessarily high temperature and pressure. Figure 1 shows a flow diagram of the integrated CCS process with the two possible steam extraction locations, which are intermediate pressure-low pressure (IP-LP) crossover steam and the first LP turbine steam.

A steam extraction unit is necessary for steam to obtain suitable conditions for the reboiler. Steam extraction units consist of three pieces of equipment: depressurizer (valve and turbine), desuperheater, and saturated water pump. The depressurizer and desuperheater vary the pressure and temperature of the extracted steam to be suitable for a reboiler. The saturated water pump delivers saturated feedwater drained out from the stripper reboiler into the deaerator of the steam cycle.

3.3. Variable selection

The following variables (x_i) possibly influence the power de-rate (D).

- CO_2 capture process: temperature of flue gas (T_{fg}), liquid to gas ratio (L/G), stripper operating pressure (P_{str}), temperature of lean solvent (T_{lean}), temperatures of condensers of absorber and stripper (T_c)
- CO_2 liquefaction process: pressure ratio of compressors (C_R)

Parameter evaluation was performed to investigate the influence of each parameter and to decide which parameters should be included in the analysis as the following Eq.(2).

$$J = \frac{\partial D}{\partial x_i} \cong \lim_{\Delta x \to 0} \left| \frac{D_{x+\Delta x} - D_x}{\frac{x_{i,x+\Delta x} - x_{i,x}}{\Delta x}} \right|_{x_j} \tag{2}$$

If $\partial D / \partial x_i$ is close to zero, variable i has little impact on the power de-rate within a chosen range. The results of the variable evaluation showed that J values of P_{str} and L/G were 7.5 %/bar and 7.3 %/(L/m^3) respectively, whereas the J value of the rest variables were near zero.

4. Results and discussion

4.1. CO_2 capture process

4.1.1. Effect of stripper operating pressure

The operating pressure of the stripper is a sole variable that affects not only the solvent regeneration energy but also the compression energy of the liquefaction process. The operating range was set from 1 to 2 bar based on the reboiler temperature. In the CO_2 capture process, an increased operating pressure tends to decrease the solvent regeneration energy and elevate the temperature at the reboiler of the stripper as shown in Figure 2. The regeneration energy is 5.03 GJ/tonCO_2 at 1 bar, sharply decreased to 3.84 GJ/tonCO_2 for a pressure of 1.25 bar, and then stabilizes at about 3.3 GJ/tonCO_2 as the stripper operating pressure is further increased.

4.1.2. Effect of liquid to gas ratio

The L/G in the capture process is the amount of lean amine solvent supplied compared with the amount of incoming flue gas to the absorber; this variable is solely influential in the capture process. When L/G is manipulated at fixed stripper operating pressure, the regeneration energy has its optimum value where the slope of the curve is near zero. As the stripper pressure increased, the optimum L/G was observed at lower values.

4.2. Liquefaction process for shipping

The compressors are the major energy consumer in the liquefaction. The compression energy is mainly determined by the compression ratio (P_2/P_1) and flowrate ($\dot{m}$). The incoming flowrate increases owing to having the target amount of CO_2 with the different pressures. However, the compression ratio greatly decreases as the stripper pressure increases. Therefore, the compression energy decreases from 39 MW to 31 MW as the stripper pressure increases from 1 to 2 bar.

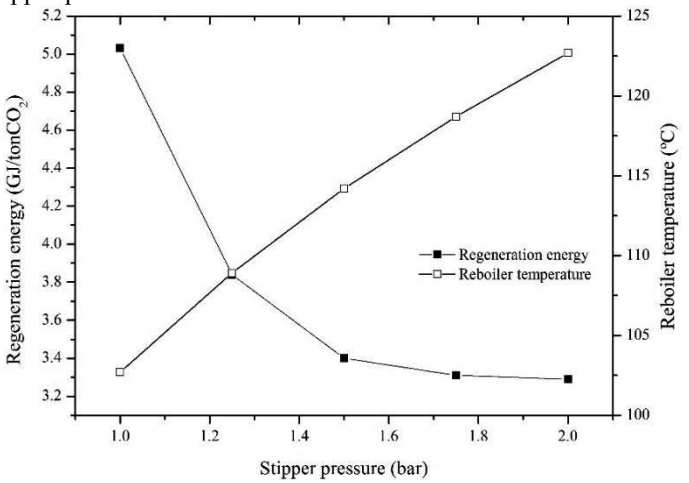

Figure 2. Simulation results for the effect of the stripper pressure on the stripper temperature and the regeneration energy

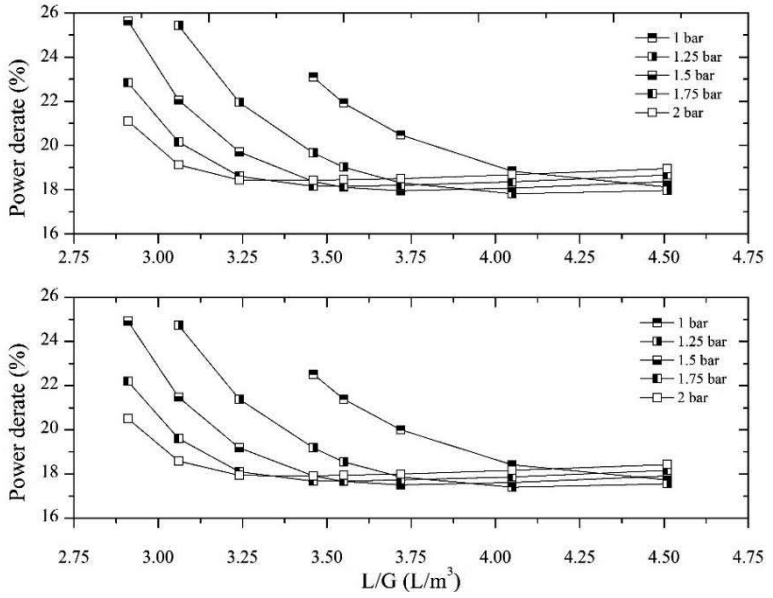

Figure 3. Effect of stripper pressure and L/G on the power de-rate from the steam extraction locations of LP steam (top) and IP-LP crossover pipe steam (bottom)

4.3. Power de-rate minimization

The power de-rate was derived from the simulation result for the integrated process. Figure 3 shows a power de-rate graph by manipulating the stripper pressure and L/G.

Higher power de-rate are generally observed at lower pressure with lower L/G, whereas high operating pressure shows less power de-rate regardless of L/G. However, the lowest power de-rate occurs at a lower pressure with an intermediate L/G of 1.25 bar and 4.05 L/m^3, respectively. The result is significantly different from previous research that proposed higher operating pressures for optimum operating conditions. This means that the optimum operating conditions of the integrated process are different from those of the unit process owing to the steam extraction unit. Higher operating pressure requires less amount of steam extracted allowing less power de-rate to the steam cycle. However, the increased reboiler temperature decreases the expansion ratio of the auxiliary turbine from 6.2 to 3.2, recovering less energy from the auxiliary turbine per unit flowrate of extracted steam.

5. Conclusion

Although CCS is considered a realistic near-term technology to decelerate global warming, the power de-rate caused by the heat required for solvent regeneration and compression energy blocks CCS implementation. In this study, simulation based parametric optimization was performed to reduce the power de-rate. A 550 MWe supercritical coal-fired power plant integrated with a post-combustion capture and liquefaction process was developed based on the data for a 0.1 MW CO_2 capture pilot plant. The stripper operating pressure and L/G were the manipulated variables. The results show that the optimum operating condition was 1.25 bar of the stripper pressure and 4.05 L/m^3 of L/G, and the minimum power de-rate was 17.3 %. This indicates that the optimum conditions for the integrated CCS process are different from those for the unit processes. Also, it is predictable that the achievable minimum power de-rate that could be obtained by including all the possible variables would be at a similar level to the suggested value.

Reference

J. Ciferno, 2008, Pulverized Coal Oxycombustion Power Plants, DOE/NETL report

N. Dave, T. Do, D. Palfreyman, P. H. M. Feron, 2011, Impact of liquid absorption process development on the costs of post-combustion capture in Australian coal-fired power stations, Chem. Eng. Res. Des., 89, 1625-1638

D. P. Hanak, C. Biliyok, H. Yeung, R. Białecki, 2014, Heat integration and exergy analysis for a supercritical high-ash coal-fired power plant integrated with a post-combustion carbon capture process, Fuel, 134, 126-139

G. Heggum, T. Weydahl, R. Mo, M. Mølnvik, A. Austegaard, 2005, CO_2 conditioning and transportation, Carbon Dioxide Capture for Storage in Deep Geologic Formations, 2, 925-936

H. Hikita, S. Asai, H. Ishikawa, M. Honda, 1977, The kinetics of reactions of carbon dioxide with monoethanolamine, diethanolamine and triethanolamine by a rapid mixing method, Chem. Eng. J., 13, 7-12

IPCC, 2014, Climate Change 2014: Mitigation of Climate Change

U. Lee, S. Yang, Y. S. Jeong, Y. Lim, C. S. Lee, C. Han, 2012, Carbon dioxide liquefaction process for ship transportation, Ind. Eng. Chem. Res., 51, 15122-15131

H. Liang, Z. Xu, F. Si, 2011, Economic analysis of amine based carbon dioxide capture system with bi-pressure stripper in supercritical coal-fired power plant, Int. J. Greenhouse Gas Control, 5, 702-709

P. Y. Liew, J. J. Klemeša, A. Doukelis, N. Zhang, P. Seferlis, 2014, Identification of process integration options for CO_2 capture in Greek lignite-fired power plant, Chem. Eng. Trans., 39, 1447-1452

Krist V. Gernaey, Jakob K. Huusom and Rafiqul Gani (Eds.), 12th International Symposium on Process Systems Engineering and 25th European Symposium on Computer Aided Process Engineering.
31 May - 4 June 2015, Copenhagen, Denmark.

CUDA-optimized cellular automata for diffusion limited processes

Andrey Kolnoochenko[a] and Natalia Menshutina[a]

[a]*Department of Computer Aided Process Engineering; MUCTR; Moscow, Russia*
andrey@kolnoochenko.ru

Abstract

In this work diffusion-limited processes are considered in terms of cellular automata (CA) approach. This method allows to simulate processes in different size scales and levels of accuracy. The transition rules allows to take into account main mass transfer processes that drive system to thermodynamic equilibrium: diffusion, adsorption/desorption and directed flow. CA simulations even in small scales show good similarity with real world systems.

Proposed model can be used for simulations in different processes, such as adsorption in porous media and chromatography.

Use of parallel computing (process level parallelism and GPU-based CUDA technology) in all stages gave from 5x to 100x speed up in comparison with standard sequential realization.

Keywords: diffusion, CUDA, GPGPU, cellular automata

1. Introduction

A lot of chemical technology processes in porous media are limited mainly by diffusion mass transfer. Adsorption, drying and chromatography are good examples of such processes. After certain time the process depends only by molecular diffusion in disordered porous media and energy interactions between moving particles in mobile phase and stationary solid body. Modeling of this processes demand for taking into account transport properties including tortuosity, permeability and local characteristics of the internal structure. Especially all those properties are hard to estimate for high porous disordered media.

The main object of research is a process of supercritical fluid chromatography (SFC) with carbon dioxide as an eluent. This process have several advantages over HPLC and gas chromatography:

- It faster than HPLC thanks to lower viscosity of eluent and higher diffusion coefficient of analyte.
- Solvating power of mobile phase is higher than it in gas chromatography.
- Lower pressure gradient in column.
- Use same chromatography columns as in HPLC.

In this work aerogels were chosen for modeling. Aerogels — are very perspective materials with unique properties such as low density, high internal surface area, low thermal an electric conductivity and with diameter of pores in only about few nanometers. The stochastic model of aerogel structure was developed for further simulations.

Cellular automata as well as many modern techniques for numerical simulations are hardly possible without high performance computing (HPC) units and methods. In this work multi-CPU parallelism and also CUDA technology (Compute Unified Device Architecture) by nVidia was used for different steps of modeling.

2. Cellular automata for diffusion

Cellular automata are the computational systems with discrete space and time. They allow to describe local interactions using uniform transition rules for each selected point of space (*cell*). Each cell can be in one of the states from *state alphabet* (Toffoli and Margolus, 1990). In each "time" step (it's better to call it iteration) algorithm should:

- select either all or some part of cells;
- determine the *neighborhood* cells to each selected cell;
- return a new state of cell, based on current cell state and the state of neighborhood cells.

For our purposes developed model should simulate main steps of chromatography process:

- diffusion, as a random walk of molecules;
- adsorption, as a continuous movement to local thermodynamic equilibrium;
- convection, as a directed flow of molecules.

The main difference of adsorption process is the lack of last step due to main role of diffusion and adsorption steps.

As the backbone of developed model the CA with Margolus neighborhood was chosen to simulate the diffusion of particles. In its original version (Toffoli and Margolus, 1987) it allows to simulate random walk of molecules in space with constant diffusion coefficient. The simple illustration of CA is shown in Figure 1. On each iteration the lattice of cells divided down into blocks 2×2 (for 2D case) and each block rotated in random direction: clockwise or counterclockwise. In this case blocks became cells in terms of CA for time of half-iteration. The state alphabet of block consists of alphabets of all contained cells.

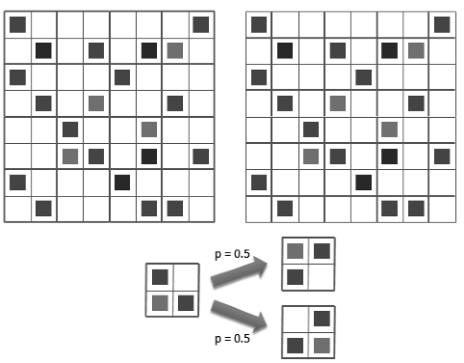

Figure 1: Diffusion simulation in CA. Division of cells by blocks in two ways. Probability on rotations distributed equaly.

Diffusion coefficient can be hardly calculated analytically, but computational experiments allow to estimate the limit value $D = 1$. It can be stated using, for instance, infinite lattice with independent moving particles. Dynamic of such systems can be described by Einstein relation:

$$D = \frac{< z^2 >}{4t} \tag{1}$$

Where $< z^2 >$ is a mean square displacement of particles in current moment t.

The results of such simulations gives a straight line in coordinates $< \bar{z}^2 >= f(t)$, what means good agreement with theoretical analysis of CA.

To generalize Margolus model, there are several changes were taken:

1. besides clockwise (cw) and counterclockwise (ccw) rotations, a block is allowed to remain unmoved (um);
2. all components of the system had been divided to three classes: a) solid, stationary phase; b) solute, a mixture of different substances, moving through the column and interacting with solid; c) solvent or carrier cells acts like an free space. In such system solvent particles are not prevent solute movement and solid particles are always preserve their positions;
3. interaction energies between solute and solid phase was taken into account.

To describe thermodynamic considerations, the probabilities of block rotations were derived from the local equilibrium assumption. To take into account both energetic and entropic effects, the energy of interaction between neighbor cells represented as:

$$f_{jk} = \varepsilon_{jk} - T s_{jk} \tag{2}$$

In that case full energy of the block after rotation $r \in R$ is

$$F_r = \sum_{j=1}^{4} \sum_{k \in N} f_{jk} \tag{3}$$

Where N are all neighbors of cell, j is the index of cell in the block. R is a set of all possible rotations for current block. Not all kinds of rotations could be available inside the block, due to possible collisions of solute and solid cells.

The partition function Z is determine probabilities of rotations:

$$Z = \sum_{r} \exp\left\{ -\frac{F_r}{kT} \right\} \tag{4}$$

$$p(r) = \frac{1}{Z} \exp\left\{ -\frac{F_r}{kT} \right\} \tag{5}$$

Where k is the Boltzmann constant and T is the thermodynamic temperature.

Finally, to describe directed flow it was represented as an additional negative free energy for preferred rotations. If after rotation r solute moved to the direction of the flow, when its F_r was changed to the flow rate intencity:

$$F'_r = F_r + \varepsilon_{mov} \tag{6}$$

Altogether these changes allows to simulate more complicated behavior than classical CA with Margolus neighborhood, preserve its synchronous work and locality of transition rules which is essential for use of HPC with maximum throughput.

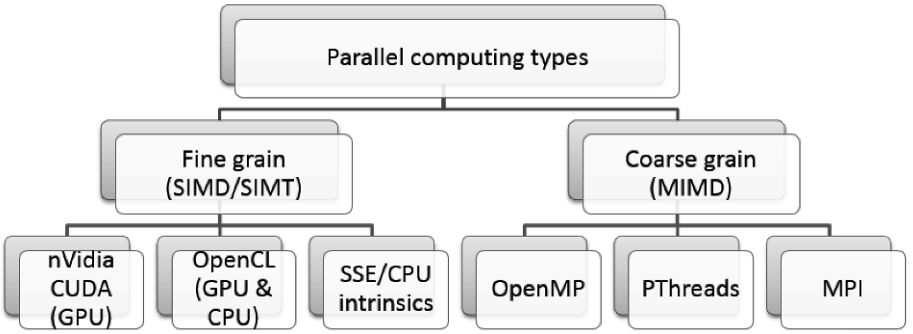

Figure 2: Main parallel computing types and technologies

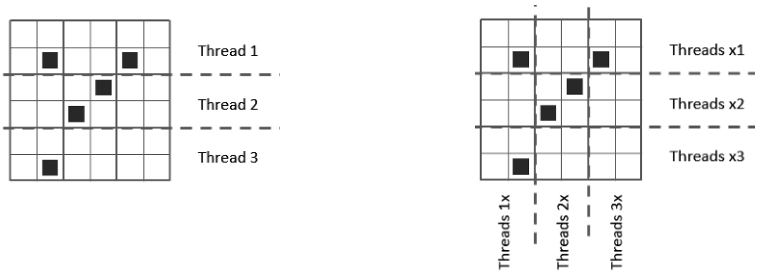

(a) MIMD approach (b) SIMD approach

Figure 3: Examples of lattice division by threads in different types of parallelism

3. Parallel computing techniques

The main types of parallel computing techniques and most widely used standard libraries are shown on Figure 2. Every technology have its own best practices and suitability.

Coarse grain parallelism is widely used in numerous applications due to universality, good support in hardware (multicore systems), operating systems (using of simultaneous multithreading), programming languages and standart libraries. In this approach every execution thread compute its current instruction independent from other threads (multiple instruction/multiple data or MIMD). Threads can also have or have no shared memory, in last case the computations can be effectively distributed between multiple units. The main advantage of coarse grain parallelism is applicability even for sequential algorithms with complicated internal logic running on demand in separated processes with different starting points. Support of multiple execution threads result in big overhead of resources. Due high cost of context switching, for CPU-intensive tasks number of threads less or equal to number of CPUs in system. For input/output intensive tasks number of threads can be higher than number of CPUs to hide the IO-latency.

Fine grain parallelism allows to create a large number of very lightweight threads with minimum context switching time. Threads are usually group together and each thread in group compute the same instruction using different input data (single instruction/multiple data or SIMD). Also additional internal processing unit logic is reduced: threads shares memory, registers, caches, constants, etc, so units became more compact and energy effective (in terms of FLOPS/W).

In case of CA simulations main points of division problem between threads are different for coarse

grain and fine grain approaches. In MIMD systems usually different init states of lattice are used, which allows to observe an evolution of system in different conditions. The main tools for such programms are message-passing libraries and frameworks: MPI, Hadoop, etc. This approach is the only one that can be used in distributed systems and compute clusters with low-speed shared memory access. Also for multicore systems with fast shared memory MIMD parallelism can be used by division of cellular automata lattice to smaller "slices" (Figure 3a). Unfortunately in that case big overhead in threads synchronization between iterations leads to low throughput, but this technique can be reasonable in systems with complicated transition rules with a lot of execution branches.

In SIMD systems the main path of optimization is not to decrease synchronization time, but rather minimize non-consecutive memory access and remove branching from execution flow. In most cases synchronous CA are work naturally in fine grained environment, thanks to simple, local and uniform rules. In SIMD approach the number of created threads should be significantly higher than number of streaming processing units to hide memory access latency. While one group of threads suspended and waiting response from memory, scheduler switch context and run another group. Division of lattice to threads for developed CA is shown on Figure 3b. So in each sub-iteration entire block is considered as one cell with widened state alphabet.

4. Results

Developed cellular automaton show good agreement with analytic solutions of test problems and simulations of real-world experiments.

4.1. Test case: steady state diffusion in pore

Let's consider the system of pore and the substance that moves along it with boundary conditions:

$$\begin{cases} c(x=0,t)=1 \\ c(x=L,t)=0 \end{cases} \tag{7}$$

Pore with length L, and radiuses $r(x=0)=a$ and $r(x=L)=b$. For some shapes of the pore the analytical solutions of Fick law could be found:

$$\frac{\partial c}{\partial t} = \frac{1}{S}\frac{\partial}{\partial x}\left(DS\frac{\partial c}{\partial x}\right) \tag{8}$$

$$\text{for conical pore: } c(x) = \frac{\ln(a+\beta x)-\ln b}{\ln a-\ln b},\ \beta = \frac{b-a}{L} \tag{9}$$

$$\text{for parabolic pore: } c(x) = 1-\frac{\tan^{-1}\sqrt{\frac{\gamma}{a}}x}{\tan^{-1}\sqrt{\frac{b-a}{a}}},\ \gamma = \frac{b-a}{L^2} \tag{10}$$

Where $c(x,t)$ — concentration, $S(x)$ is a cross-section of pore, $D(x)$ — diffusion coefficient. CA shows perfect agreement with analytical solutions. More complicated shapes of pore leads to changes of initial lattice in CA (rearrangement of solid cells) and haven't affect computational complexity.

4.2. Test case: adsorption within a disordered porous media

Study of the adsorption was aimed to show that not only dynamic character of diffusion, but also reaching of thermodynamic equilibrium which correspond monolayer adsorption can be reached by this model. Non-zero energy ε_{MS} and entropy s_{MS} correspond to the adsorptive interaction between movable cells (adsorbate) and solid porous structure (adsorbent).

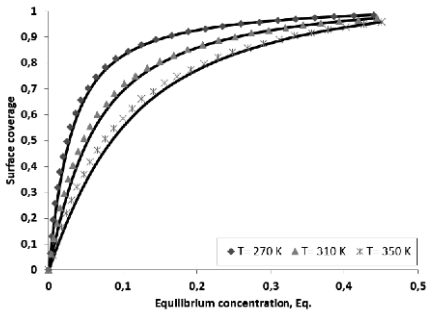

Figure 4: Comparison between computed (points) and Langmuir isotherms (solid lines) at three different temperatures

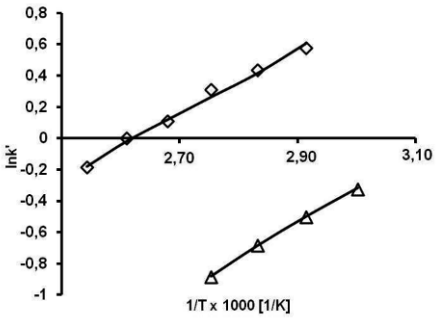

Figure 5: Comparison between retention factor in experiment of SFC (dots) and CA modeling (lines) at different fluid densities

For these energies Langmuir isotherms were found and particles are treated as the ideal gas with excluded volume, since they are not allowed to overlap. Results of comparison are shown in Fig. 4.

4.3. Test case: chromatography

Chromatography is the most complex test of representation of real-world phenomena in model. As the model of solid porous media an algorithm of slightly overlapped spheres was used (see details in Gurikov et al. (2009) and Gavalda et al. (2001)). For generation of larger size structures, it was accelerated using CUDA technology. That affect not only the generation itself, but also the step of measure the parameters of final structure: specific surface area and pore size distribution.

In the initial state of CA left side of lattice (the input of column) was filled by movable cells, solid porous media was generated to correspond experimental aerogel structure. In the right side of lattice boundary condition $c(x = L,t) = 0$ had been applied. Each movable cell at $x = L$ was counted and transformed to solvent state. It allows to get plots similar to chromatograms, and work with them in the same way as the experimental data. For example, retention factor was calculated: $k' = (t_R - t_0)/t_0$, as a ratio of time an analyte is retained in the stationary phase to the time it is retained in the mobile phase. As it shown in Figure 5 model with same energies of interactions shows the same behavior as the experimental system.

5. Acknowledgment

The authors gratefully acknowledge financial support from DFG (projects SM 82/8-1 and SM 82/8-2) and RFBR (project 12-08-91330).

References

Gavalda, S., Kaneko, K., Thomson, K. T., Gubbins, K. E., 2001. Molecular modeling of carbon aerogels. Colloids and surfaces A: Physicochemical and engineering aspects 187, 531–538.
URL http://www.sciencedirect.com/science/article/pii/S0927775701006410

Gurikov, P. A., Kolnoochenko, A. V., Menshutina, N. V., 2009. 3d reversible cellular automata for simulation of the drug release from aerogel-drug formulations. In: Jacek Jeowski and Jan Thullie (Ed.), Computer Aided Chemical Engineering. Vol. Volume 26 of 19th European Symposium on Computer Aided Process Engineering. Elsevier, pp. 943–947.
URL http://www.sciencedirect.com/science/article/pii/S1570794609701579

Toffoli, T., Margolus, N., 1987. Cellular Automata Machines: A New Environment for Modeling. MIT Press.

Toffoli, T., Margolus, N. H., Sep. 1990. Invertible cellular automata: A review. Physica D: Nonlinear Phenomena 45 (1-3), 229–253.
URL http://linkinghub.elsevier.com/retrieve/pii/016727899090185R

Krist V. Gernaey, Jakob K. Huusom and Rafiqul Gani (Eds.), 12th International Symposium on Process Systems Engineering and 25th European Symposium on Computer Aided Process Engineering.
31 May – 4 June 2015, Copenhagen, Denmark

Effect of Ship Motion on Amine Absorber with Structured-Packing for CO_2 Removal from Natural Gas: An Approach based on Porous Medium CFD Model

Dung A. Pham,[a] Young-Il Lim,[a*] Hyunwoo Jee,[b] Euisub Ahn,[b] Youngwon Jung[b]

[a]*Department of Chemical Engineering, Hankyong National University, 456-749 Anseong, Korea*
limyi@hknu.ac.kr
[b]*GS E&C, Gran Seoul, 33 Jonro Jongno-gu, Seoul 110-121 Korea*

Abstract

Acid gases (H_2S and CO_2) must be removed from the crude natural gas. The process performance may be deteriorated because of ship movement on FPSO (Floating production, storage and offloading). This research aims to investigate the effects of ship motion on acid gas removal performance in the amine absorber with Mellapak 500.X structured packing.

A simple cylindrical column (packed zone: 0.1 m diameter × 2.205 m high) was used as the domain for the calculations. A porous media CFD (computational fluid dynamics) model was developed in the framework of Eulerian two-fluid flows with user-defined functions (UDF) taking into account liquid dispersion, mass-transfer and chemical reaction in the packed zone. The effective interfacial area, CO_2 concentration profile and mal-distribution factor were compared for two cases of vertical standing and ship motion.

Keywords: FPSO (Floating production, storage and offloading), Natural gas, Amine absorber, Structured-packing, Ship motion, CFD.

1. Introduction

A floating production, storage and offloading (FPSO) unit is a floating vessel used by the offshore oil and gas industry for the processing of hydrocarbons and for the storage of oil or natural gas. FLNG (Floating Liquid Natural Gas) is a new type of floating LNG (Liquid Natural Gas) platform that consists of a ship-type FPSO hull equipped with LNG storage tanks and liquefaction plants (Zhao et al., 2011).

The crude natural gas is treated to remove acid gases (H_2S and CO_2) on FPSO, where the process performance can be deteriorated because of ship motion. This research aims to investigate the effects of ship motion on acid gas removal performance in the amine absorber with structured packing. The computational fluid dynamics (CFD) has been considered as a good alternative to identify the motion effect. Table 1 shows the literature survey on CFD studies with simplified geometry of structured-packing (Aroonwilas et al., 2003; Fourati et al., 2013; Haroun et al., 2012; Shilkin et al., 2006).

Table 1 - Literature survey on simplified geometry models of structured-packing.

Classification	Authors	Remarks
2D one vertical channel model	Haroun et al. (2012)	2 phases VOF model, mass transfer & chemical reactions
2D tubular channel model	Shilkin et al. (2006)	2 phases CFD model & no mass transfer
Pseudo 3D model	Aroonwilas et al. (2003)	Steady-state 2 phases pseudo 3D hydrodynamics, & mass transfer
Porous media model	Fourati et al. (2013)	Unsteady-state 2 phases porous medium 3D model, liquid dispersion & momentum transfer

An Eulerian multiphase isotropic porous media model is used to simulate the structured-packing for gas (G) and liquid (L) contact. The effective interfacial areas are compared in two cases of vertical standing (case 1) and ship motion (case 2) of the absorber. The mal-distribution coefficient of the liquid defined by the standard deviation per mean velocity is also compared for the two cases. The CO_2 concentration profile of vertical standing case is compared to experiments in order to validate the model.

2. Eulerian multiphase porous media model

Local liquid hold-up which directly relates to the effective area is studied by using the porous media model. In the present study, incompressible and isothermal flows are considered. The governing equations of the CFD model deal with average quantities that are volume-averaged over a representative averaging porous volume as shown in Figure. 1 (Fourati et al., 2013). For a continuous phase, the governing equation contains continuity equation, momentum conservation equation, and species transport equation.

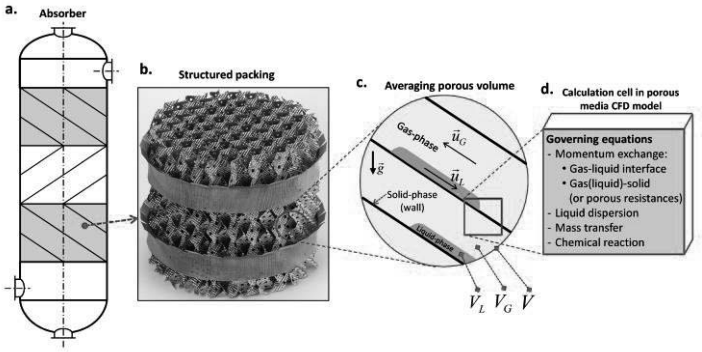

Figure. 1. Porous media CFD model for structured-packing.

2.1 Mass conservation equation

The incompressible gas-liquid system is expressed as in the porous medium:

$$\frac{\partial}{\partial t}(\alpha_q \rho_q) = -\nabla \cdot \left(\alpha_q \rho_q \vec{u}_q\right) + \dot{m} + \alpha_q R_q, \quad q = G,\ L \tag{1}$$

where $\alpha_q = \varepsilon \times V_q / \left(V - V_s\right)$ means the volume fraction of q phase, $\dot{m}$ [kg/m^3-s] is the mass transfer rate and R_q is the homogeneous chemical reaction rate. Here, V is the total volume, V_s is the solid volume and ε is the porosity.

2.2 Momentum conservation equation

The Eulerian two-phases porous media model adds source terms ($\vec{S}$) into the original Navier-Stokes equation:

$$\rho_q \frac{\partial}{\partial t}\left(\alpha_q \vec{u}_q\right) + \rho_q \vec{\nabla}\cdot\left(\alpha_q \vec{u}_q \vec{u}_q\right) = -\alpha_q \vec{\nabla} P + \vec{\nabla}\cdot\left(\alpha_q \tau_q\right) + \alpha_q \rho_q \vec{g} + \vec{S}_q \tag{2}$$

where *P* is the pressure, $\vec{g}$ is the gravity, τ *i*s the viscous stress tensor, and the source terms $(\vec{S})$ include the isotropic porous resistances ($\vec{F}_{porous}$), gas-liquid momentum exchanges ($\vec{F}_{exch}$), and liquid dispersion ($\vec{F}_{disp}$) terms (Fourati et al., 2013).

$$\begin{aligned}\vec{S}_q &= -\frac{\alpha_q}{\varepsilon}\vec{F}_{porous,q} + \varepsilon\vec{F}_{exch,q} + \vec{F}_{disp,q} \\ &= -\frac{\alpha_q}{\varepsilon}\left(\mu_q R_{vis,q}\vec{u}_q + \frac{1}{2}\rho_q R_{in,q}\left|\vec{u}_q\right|\vec{u}_q\right) + \varepsilon\left(K_{exch}\cdot\vec{U}_{Slip}\right) + \left(K_{qS}\cdot\vec{U}_{Drift,q}\right)\end{aligned} \tag{3}$$

Here, $\vec{u}$ is the interstitial volume-averaged velocity, and $\vec{R}_{vis,q}$ and $\vec{R}_{in,q}$ are a kind of tensor implying the viscous loss resistance and the inertial loss resistance, respectively.

2.3 Species transport equation

The interphase species transport equations are solved along with the mass and momentum equations. Assuming that mass transfer between the gas and liquid phases occurs for only CO_2, the transport equation of species *i* in *q* phase is:

$$\rho_q \frac{\partial}{\partial t}\left(\alpha_q Y_q^i\right) + \rho_q \vec{\nabla}\cdot\left(\alpha_q \vec{u}_q Y_q^i\right) = -\rho_q D_q \vec{\nabla}\cdot\left(\alpha_q \vec{\nabla} Y_q^i\right) + \dot{m}^i + \alpha_q R_q^i \tag{4}$$

where Y_q^i is the local mass fraction of species *i* in *q* phase, D is the diffusivity (m^2/s).

The volumetric rate of species mass transfer is a function of mass concentration gradient.

$$\dot{m}^i = K_L a_e\left(\rho_{L,equilibrium}^i - \rho_L^i\right) \tag{5}$$

The overall liquid mass transfer coefficient (K_L) can be derived from the two film theory (McCabe et al., 2005):

$$1/K_L = 1/k_L + 1/\left(H_{CO_2-MEA}\cdot k_G\right) \tag{6}$$

For the CO_2-MEA system, the reaction rate may be expressed by the 2^{nd} -order kinetics (Hikita et al., 1977):

$$\begin{aligned}&CO_2(l) + 2HORNH_2 \leftrightarrow HORNH_3^+ + HORNHCOO^- \\ &R_L^{CO_2} = d\left(\rho_L^{CO_2}\right)/dt = -k_c \rho_L^{CO_2}\rho_L^{MEA}, \quad k_c = k_0 e^{-E_a/(RT)}\end{aligned} \tag{7}$$

3. Geometry and mesh of amine absorber

The three dimensional (3D) geometry of the amine absorber is illustrated in Figure. 2a, 2b and 2c. The amine absorber consists of nine elements (element height of 24.5 cm), a liquid distributor in the top, and a bottom side for the uniform gas inlet. The monoethanolamine (MEA) solution is injected through the liquid distributor.

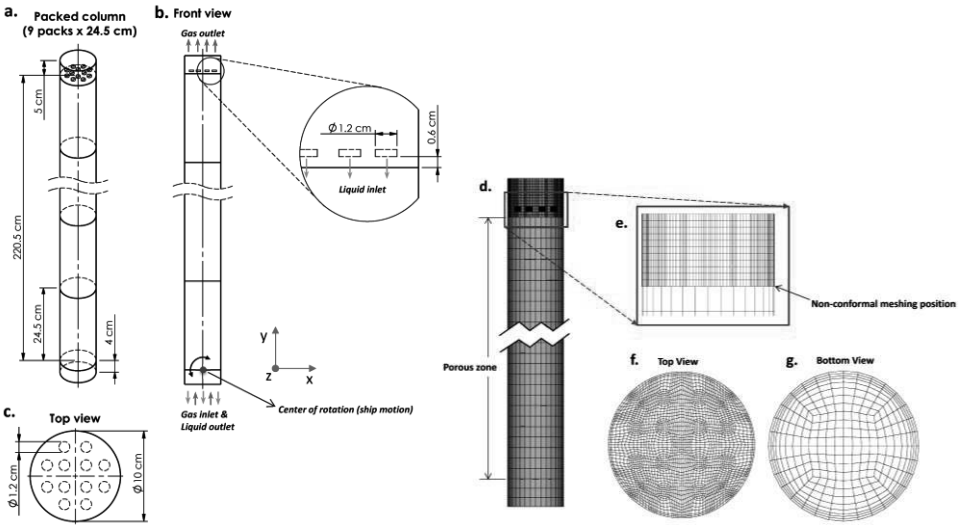

Figure. 2. Geometry and mesh of amine absorber for CFD calculation domain.

The mesh structure of the amine absorber is shown in Figure. 2d-g. The top of the column has a fine hexahedral mesh structure to represent the twelve holes in the liquid distributor. For the ship motion case. The absorber has a harmonic oscillation with the angular amplitude of 1.57^{o} and the period is equal to 12 seconds.

4. Simulation setup

The continuity equation, momentum and mass conservation equations were solved by using a commercial code ANSYS Fluent (ANSYS Inc., USA). Table 2 and Table 3 show simulation parameters.

Table 2 - Model parameters of mass-transfer and chemical reaction.

Maximum effective interfacial area (m^2/m^3) ,a_e	225 (Aroonwilas et al., 2003)
Overall mass-transfer coefficient (m/s), K_x	0.00293
Operating pressure (atm), P	1.0
Operating temperature (K), T	304 (isothermal)
Henry's constant ($Pa \cdot m^3/mol$), $H_{CO2\text{-}MEA}$	3690
Pre-exponential factor ($m^3/kmol/s$), k_0	5.928×10^4
Activation energy (cal/gmol), E_a	4.274×10^3
Diffusivities of gas and liquid (m^2/s), D	2.8×10^{-7}, 2.88×10^{-9}

Table 3 - Boundary condition (BC) and simulation parameters.

Parameters	Value
Mesh number (N_{cell})	About 60,000 cells
Eulerian multiphase model	Un-steady state, sequential, and implicit solver
Bottom-side BC	Incompressible ideal gas inlet (back flow), liquid (pressure-outlet), gas load (natural gas) = 38.5 kmol/m^2/h, and gas mole composition: CH_4 = 0.85, CO_2 = 0.15.
Top-side BC	Gas (mass flow outlet)
Liquid distributor BC	Liquid (mass flow inlet), liquid load = 22.9 m^3/m^2/h, and liquid mass composition: MEA = 0.317, H_2O = 0.683.
Maximum number of iterations	100
Convergence tolerance	1×10^{-3}
Total operation time (s)	43

5. Results and discussion

In Fig. 3a, the contour of the CO_2 mole fraction (y_{CO_2}) is shown for the whole column.

The radially-averaged mole fraction along the height is compared to experimental data in Fig. 3b. A decline of the CO_2 capturing performance can be seen in Fig. 3c.

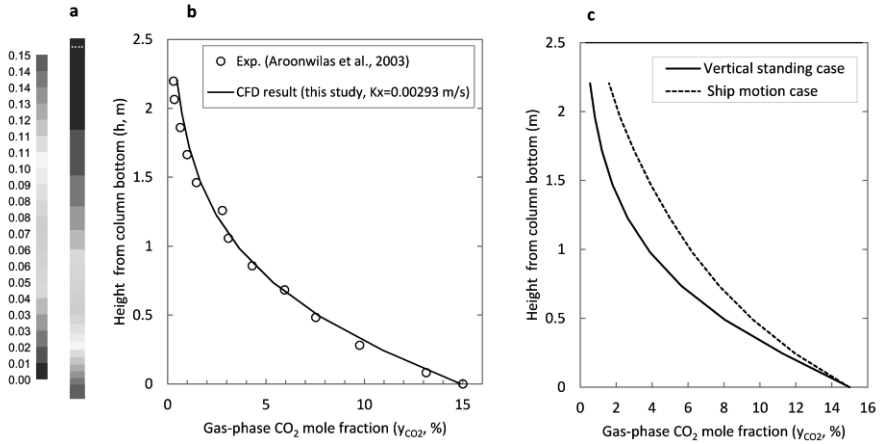

Figure. 3. CO_2 mole fraction (y_{CO2}, %) along column height (h, m). a/CFD results in whole column in case (1); b/comparison between CFD results and experimental data in case (1); c/comparison CFD results between case (1) and case (2).

Fig. 4 compares the contour of liquid hold-up in the porous zone for the two cases. The radical liquid distribution was affected significantly by the ship motion. This is attributed by the fact that the tangential and inertial forces influences the liquid phase, when the column rolls. A reduction of local liquid hold-up may lead to the reduction of the effective interfacial area. Thus, in order to obtain a good liquid distribution, it is necessary to design or arrange appropriately liquid collectors and distributors inside an absorption column.

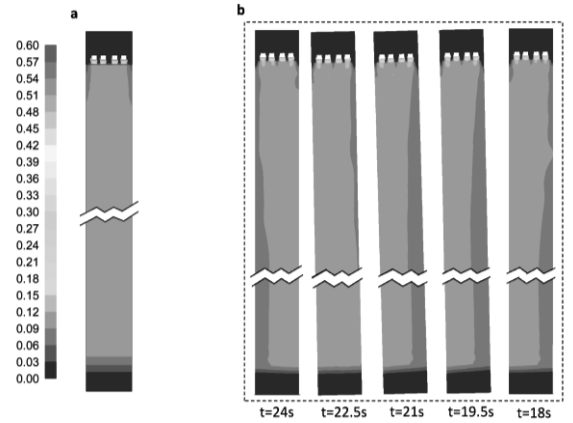

Figure. 4. Contour of liquid hold-up in CO_2-MEA Eulerian CFD simulation. a/Case 1; b/Case 2 (a half period, flow time is from right hand side)

Table 4 indicates the effective interfacial area between two phases (a_e), the standard deviation of velocity (σ), the means velocity (μ), and the coefficient of variation (C_v). The ship motion affects significantly a_e and C_v.

Table 4. Comparison of vertical standing and ship motion on mal-distribution factors.

	a_e (m^2/m^3)	μ (m/s)	σ (m/s)	C_v
Case 1	225	0.146	0.001	0.007
Case 2	196 (mean value)	0.147	0.006	0.042

6. Conclusions

A porous medium Eulerian multiphase model was used for the simulation of corrugated structured-packing in CO_2-amine absorber. The effect of ship motion was significant on the effective interfacial area and the mal-distribution of velocity. Anisotropic porous resistance would be useful for more realistic simulation of structured-packing. More complex ship motions (sway, heave, etc) will also be considered in the future.

References

A. Aroonwilas, A. Chakma, P. Tontiwachwuthikul, A. Veawab, 2003. Mathematical modelling of mass-transfer and hydrodynamics in CO_2 absorbers packed with structured packings. Chem. Eng. Sci. 58, 4037-4053.

M. Fourati, V. Roig, L. Raynal, 2013. Liquid dispersion in packed columns: Experiments and numerical modeling. Chem. Eng. Sci. 100, 266-278.

Y. Haroun, L. Raynal, D. Legendre, 2012. Mass transfer and liquid hold-up determination in structured packing by CFD. Chem. Eng. Sci. 75, 342-348.

H. Hikita, S. Asai, H. Ishikawa, M. Honda, 1977. The kinetics of reactions of carbon dioxide with monoethanolamine, diethanolamine and triethanolamine by a rapid mixing method. Chem. Eng. J. 13, 7-12.

W.L. McCabe, J.C. Smith, P. Harriott, 2005. Unit operations of chemical engineering, 7th ed. McGraw-Hill, Boston.

A. Shilkin, E.Y. Kenig, Z. Olujic, 2006. Hydrodynamic-analogy-based model for efficiency of structured packing columns. AlChE J. 52, 3055-3066.

W.H. Zhao, J.M. Yang, Z.Q. Hu, Y.F. Wei, 2011. Recent developments on the hydrodynamics of floating liquid natural gas (FLNG). Ocean. Eng. 38, 1555-1567.

Krist V. Gernaey, Jakob K. Huusom and Rafiqul Gani (Eds.), 12th International Symposium on Process Systems Engineering and 25th European Symposium on Computer Aided Process Engineering.
31 May – 4 June 2015, Copenhagen, Denmark

Model-Based Analysis and Efficient Operation of a Glucose Isomerization Reactor Plant

Emmanouil Papadakis[1], Ulrich Madsen[2], Sven Pedersen[2], Krist V. Gernaey[1], John M. Woodley[1], Rafiqul Gani[1]*

[1]*CAPEC-PROCESS, Department of Chemical and Biochemical Engineering, Technical University of Denmark, Søltofts Plads, Building 229, DK-2800 Kgs. Lyngby, Denmark.*
[2]*Novozymes A/S, Krogshøjvej 36, DK-2880 Bagsvaerd, Denmark*
**rag@kt.dtu.dk*

Abstract

The application of computer-aided model based methods within an integrated systematic framework is illustrated with the objective to assist the multi-purpose pharmaceutical/biochemical industry to systematically solve the complex problems that are experienced when aiming at improving the process efficiency. The objective of this study is the application of the developed framework on an industrial case study of a glucose isomerization (GI) reactor plant that is part of a corn refinery, with the objective to improve the productivity of the process. Therefore, a multi-scale reactor model is developedfor use as a building block for the GI reactor plant simulation. An optimal operation strategy is proposed on the basis of the simulation results.

Keywords: Systematic Model-Based Analysis, Glucose Isomerization, Reactor Plant Modelling, Operation.

1. Introduction

Model-based computer aided methods and tools can play an important role in the development and improvement of pharma/biochemical processes. The mathematical models however, need to be developed first and require detailed understanding and analysis of the phenomena that govern the operation of these processes. When validated against experimental data, mathematical models are useful tools to predict the behavior of a system subject to different scenarios. In this way, the models can in general be used to supplement the available knowledge with new data and to reduce the cost and the time related to performing expensive experiments (Gernaey and Gani, 2010, Marquardt et al., 2009). Mathematical models can be used in optimization studies, to improve the operation of the system or to predict the behavior of the system in different scenarios such that process operability and design can be studied.

In this study, the use of model-based methods within a systematic framework is developed by integrating parts of other studies (Cervera et al. 2012; Jaksland et al. 1995), and illustrated through a glucose isomerization (GI) reactor case study. The objective of this study is the use of a multi-scale reactor model which includes the reaction kinetics and the enzyme activity decay as a function of temperature with and without the diffusion term, to simulate the reactor and to investigate opportunities for improving the productivity of the reactor.

2. Methodology

The systematic framework (Figure 1) is developed to obtain enhanced process understanding and to exploit potential opportunities for improvements of the pharma/biochemical processes. In this work, only the relevant parts of the methodology (Section A, B and D) are used to achieve the final objective of the case study. The overall effectiveness and detailed description of the complete framework will be presented in a future paper. The framework (Figure 1) starts with the problem definition where the objectives of the study are defined. The subsequent reaction pathway identification section (Section A) aims at identifying the reaction pathway producing a pharma/bio-product of interest. Section B is the reaction analysis, and aims at the efficient reaction development, reactor design and separation objectives definition. Section C (Separation Synthesis and Design) is performed in case separation of a specific compound is needed. Section C aims at generating separation process alternatives based on feasible separation techniques (Jaksland et al., 1995) and based on the driving force principles (Bek-Pedersen and Gani, 2004). Once a flowsheet (or the state-task network) has been obtained, a process simulation (Section D) needs to be performed in order to evaluate the process and identify the process hotspots. Based on the process evaluation, process optimization and process operation can be performed.

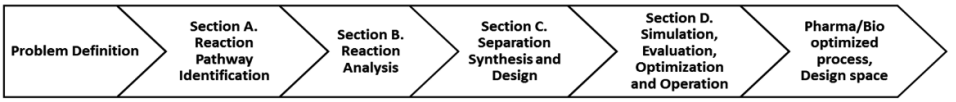

Figure 1. The Integrated Systematic Methodology for pharma/biochemical processes.

3. Case Study: Glucose Isomerization

Problem Definition: The aim of the study is the development of a multi-scale reactor model for the glucose isomerization which includes the enzyme activity decay with and without diffusion limitation as function of the temperature. The reactor model is used to simulate a typical reactor plant (Figure 2, 20-30 reactors in parallel) in order to improve the operation and increase the productivity.

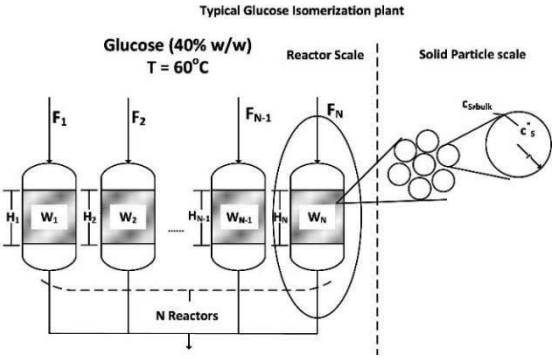

Figure 2. Typical Glucose Isomerization plant with N reactors.

Section A. Reaction Pathway: The reaction pathway is presented in Eq. (1):

$$E + S \leftrightarrow SE \leftrightarrow P + E \tag{1}$$

Section B. Reaction Analysis: Glucose (S) syrup (40% w/w) reacts with the immobilized Sweetzyme® to produce fructose. The glucose isomerization is a reversible reaction given by Eq. (1) and it has been proven to follow the reversible modified Michaelis-Menten

kinetics. The reaction is equilibrium limited and it takes place in a continuous fixed bed reactor where the enzyme is immobilized. The reactor model needs to be developed and evaluated, and used as a tool for investigating more efficient operation of a typical GI reactor plant. The development of the multi-scale reactor model is illustrated through a modelling framework developed by Heitzig (2011). The multi-scale reactor plant (Figure 2) requires a model describing the reaction kinetics, the enzyme activity decay and the internal diffusion as a function of temperature. The framework consists of five phases (Heitzig, 2011): Phase I: Modelling objective/System Information, Phase II: Model construction, Phase III: Model Identification/ Discrimination, Phase IV: Model Evaluation/Validation and Phase V: Application.

Phase I: Modelling objective/System Information: The modelling objective has been defined in the *Problem Definition* section.

Phase II: Model Construction: To achieve the objectives, models for the reaction kinetics, the fixed bed reactor, the diffusion in the reaction pellet and the enzyme activity decay need to be developed and combined in one multi-scale reactor model.

Reaction Kinetics (Dehkordi et al., 2008, 2009):

$$R_s = -\frac{\rho_p V_m c_{S,0}\ \left(y_S^* - y_{S,eq}\right)}{K_m + c_{S,0}\ \left(y_S^* - y_{S,eq}\right)} \tag{2}$$

$$V_m = \left[1 + \frac{1}{K_e}\right]\frac{k_{mr} v_{mr}}{k_{mr} - k_{mf}} \tag{3}$$

$$K_m = \left[1 + \left(\frac{1}{k_{mf}} + \frac{K_e}{k_{mr}} c_{S,eq}\right)\right]\frac{k_{mr} k_{mf}}{k_{mr} - k_{mf}} \tag{4}$$

Fixed Bed Reactor (Papathanasiou et al., 1988; Asif et al, 1998):

$$\begin{aligned} &\frac{\partial y_s}{\partial \tau} = \frac{1}{Pe}\frac{\partial^2 y_s}{\partial z^2} - \frac{\partial y_s}{\partial z} - a\ \left(y_s - y_s^*\right) \\ &IC: y_s = 0\ \ for\ \tau = 0,\ z \geq 0 \\ &BC1: -\frac{1}{Pe}\frac{\partial y_s}{\partial z} + y_s = 1,\ \ for\ \ \tau > 0,\ z = 0 \\ &BC2: \frac{\partial y_s}{\partial z} = 0,\ \ for\ \ \tau > 0,\ z = 1 \end{aligned} \tag{5}$$

Solid Particle (Papathanasiou et al., 1988; Asif et al., 1998):

$$\begin{aligned} &\frac{\partial y_s^*}{\partial \tau} = Q_2\left(\frac{\partial^2 y_s^*}{\partial \lambda^2} + \frac{2}{\lambda}\frac{\partial y_s^*}{\partial \lambda}\right) - Q_1 y_E \frac{y_s^* - y_{s,eq}}{1 + \left(y_s - y_{s,eq}\right)\ Q_3} \\ &IC: y_s^* = 0\ \ for\ \tau = 0,\ \xi \geq 0 \\ &BC1: \left.\frac{dy_s^*}{d\lambda}\right|_{\lambda=0} = 0,\ \ for\ \ \tau > 0,\ \xi = 0 \\ &BC2: \left.y_s^*\right|_{\lambda=1} = y_{S,bulk}\ \ for\ \ \tau > 0,\ \xi = 1 \end{aligned} \tag{6}$$

Enzyme Activity Decay (Verhoff et al., 1982; Houng et al., 1992):

$$\begin{aligned} &\frac{dy_E}{d\tau} = -k_d y_E \\ &IC: y_E = 1,\ \tau = 0 \end{aligned} \tag{7}$$

Activity decay(Jørgensen et al., 1988):

$$A[\text{IGU/ gr enzyme}] = 0.926\frac{F}{w}\cdot DP\cdot DS\cdot \ln\left(\frac{X_{eq}}{X_{eq}-X}\right) \quad (8)$$

*Productivity (*Houng et al., 1992):

$$P = \frac{\int Fc_{S,0}dt}{w} \quad (9)$$

Model Analysis: The model consists of different types of equations, ODEs (1), PDEs (2) and AEs (29), 32 in total. The total number of variables (system variables, model parameters, and known variables, dependent and algebraic variables) is 59. A degree of freedom analysis showed that 27 variables (system variables, model parameters, and known variables) need to be specified and 32 variables need to be predicted from the model (dependent and algebraic variables).

Phase III: Model Identification: The kinetic parameters have been identified from the literature (Dehkordi et al., 2008, 2009). They have been evaluated against experimental data, and they produce results which are consistent with these data.

Phase IV. Model Evaluation/Validation: In that phase different scenarios are tested to evaluate the developed multi-scale model for the reactor. Figure 3 shows the glucose concentration profile in the reactor (with (a) and without (b) diffusion) with respect to dimensionless time τ for different locations z in the reactor (where z is the dimensionless length of the reactor). The glucose concentration profiles show the glucose conversion through the rector length, where the decrease of glucose conversion is due to enzyme deactivation during the operation.

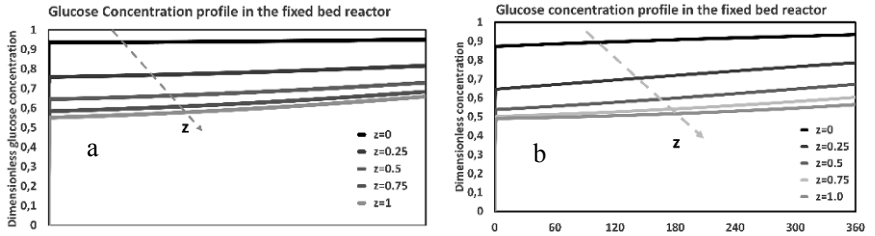

Figure 3. Glucose concentration profile in the reactor (a) with diffusion limitation; and, (b) without diffusion limitation,where z is the dimensionless length of the reactor.

The Figure 4a illustrates the glucose conversion at the outlet of the reactor with respect to Reynolds number, which decreases as the Re number increases. The Figure 4b presents the conversion with respect to the dimensionless time which also decreases with time.

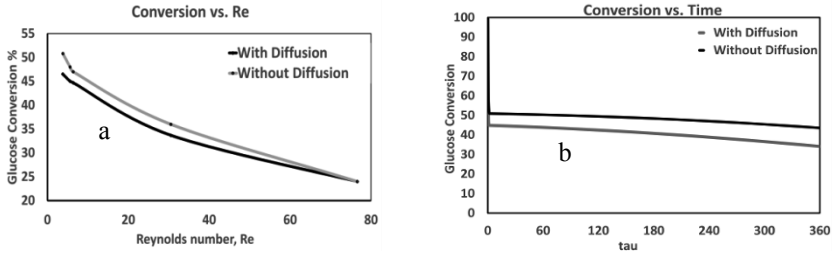

Figure 4. Glucose conversion in the reactor for different Reynolds number (a) and with respect to operation time (b).

The Figure 5a shows the enzyme deactivation due to decay with respect to dimensionless time, with and without considering the diffusion term. Figure 5b, shows

the specific activity of the enzyme in IGU/g enzyme, where IGU is the amount of enzyme that converts glucose to fructose at an initial rate of 1 μmol min^{-1}.

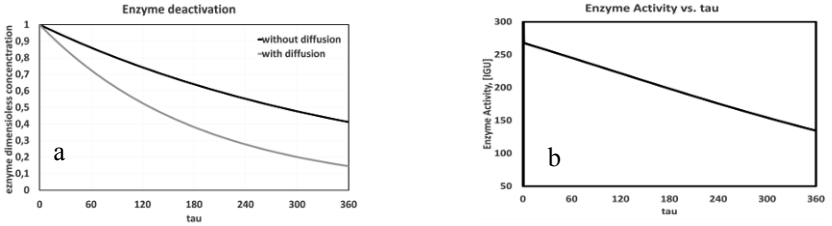

Figure 5. (a) Enzyme deactivation with respect to time, (b) enzyme activity decay vs. time.

*Section C. Separation Synthesis and Design:*The separation of the reaction mixture is fixed and separation is not included in the objectives of the problem.
Section D. Simulation, Evaluation, Optimization and Operation: Once the multi-scale reactor model has been evaluated. The GI reactor plant can be simulated. The operation conditions and the values of the physical variables are presented in Table 1.

Table 1. Process Variables for the reactor operation and physical variables for the enzyme.

Reactor Variables		
Variable	Value	Units
Temperature	55-60	^oC
Flow rate	3.6	$m^3 h^{-1}$
Catalyst weight	560	kg enzyme/reactor
Bed Height	3.3	m
Diameter	0.8	m

Physical Variables		
Variable	Value	Units
Density	3300	kg m^{-3}
Porosity, ε	0.36	-
Particle Diameter	0.2	cm
Effective Diffusivity	$6.9x10^{-6}$	m sec^{-1}

The GI reactor plant consists of 10 parallel reactors. The operation of the GI reactor plant is based on constant glucose conversion (~45%) which can be maintained either by recycling the enzyme to keep its activity constant or by decreasing the inlet glucose flowrate during the operation. In this case, fixed bed reactors are used and the conversion is maintained constant by decreasing the flowrate. Once the residual enzyme activity is 10% compared to the initial one, the temperature in the reactor is increased and then the reactor is shut down. The relative flowrate is presented in Figure 6a and it is based on the enzyme activity decay for temperatures 55^{o}C and 60^{o}C. The Figure 6b illustrates the productivity (kg glucose/kg enzyme) of the reactor for constant flow rate and constant glucose conversion at 55^{o}C and 60^{o}C. The results in the Figure 6 (a and b) strongly depend on the enzyme deactivation parameter k_d. The inlet concentration also plays an important role in the improvement of the reactor efficiency because it affects the viscosity of the inlet syrup and the pressure drop in the reactor.

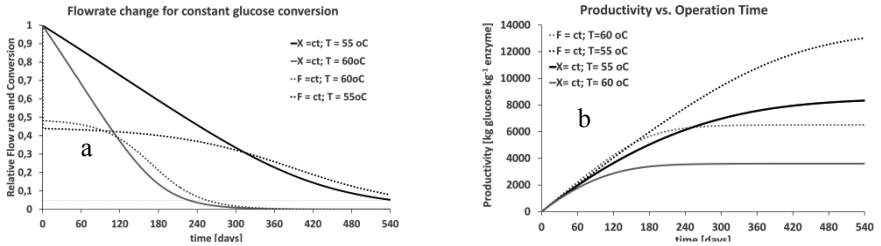

Figure 6. (a) The inlet flowrate change to maintain constant glucose conversion (X= 45%) and conversion for constant flowrate; (b) The productivity for the cases in Figure 6a.

4. Conclusions

In this study, the application of model-based computer aided methods as a tool within an integrated framework to enhance the pharma/biochemical process operation is illustrated. The framework was applied to a GI case study with the objective to analyse and improve the operation of a GI reactor plant. Mathematical models to describe phenomena at different scales were used in order to simulate the GI reactor plant. The analysis has shown that the enzyme deactivation is an important parameter for the reactor plant efficiency improvement. Moreover, the productivity of the plant can also be enhanced by selecting the proper inlet glucose concentration. To conclude, the analysis has shown the importance of computer-aided model based methods and tools in the evaluation, analysis and improvement of pharma/biochemical processes, and especially the usefulness of these tools in supporting the decision making process during the early stage design and during the industrial operation.

References

M. Asif, & A.E. Abasaeed, 1998, Modeling of glucose isomerization in a fluidized bed immobilized enzyme bioreactor, Bioresource Technol., 64, 229–235.

E. Bek-Pedersen, & R. Gani, 2004, Design and Synthesis of Distillation Systems using a Driving-Force-Based Approach, Chem. Eng. Process, 43, 3, 251-262.

A. E. Cervera-Padrell, T. Skovby, S. Kiil, R. Gani, & K. V. Gernaey, 2012, Active pharmaceutical ingredient (API) production involving continuous processes - a process system engineering (PSE)-assisted design framework, Eur. J. Pharm. Biopharm., 82, 2, 437–456.

A. M. Dehkordi, I. Safari, & M. M. Karima, 2008,Experimental and Modeling Study of Catalytic Reaction of Glucose Isomerization: Kinetics and Packed-Bed Dynamic Modeling, AIChE J., 54, 5, 1333–1343.

A. M. Dehkordi, M.S. Tehrany, & I. Safari, 2009, Kinetics of Glucose Isomerization to Fructose by Immobilized Glucose Isomerase (Sweetzyme IT), Ind. Eng. Chem. Res., 48, 3271-3278.

K. V. Gernaey, & R. Gani, 2010. A model-based systems approach to pharmaceutical product-process design and analysis, Chem. Eng. Sc., 65, 5757–5769.

M. Heitzig, 2011, Computer-aided modelling for efficient and innovative product-process engineering Computer-aided modelling for efficient and innovative product-process, Technical University of Denmark.

J. Y. Houng, H. Y. Yu, K. C. Chen, & C. Tiu, 1993, Analysis of substrate protection of an immobilized glucose isomerase reactor, Biotechnol. Bioeng., 41, 451–458

O. B. Jørgensen, L.G. Karlsen, N. B. Nielsen, S. Pedersen, & S. Rugh, 1988, A new immobilized glucose isomerase with high productivity produced by a Strain of Streptomyces murinus, Starch, 40, 8, 307-313.

C. Jaksland, R. Gani & K. M. Lien, 1995, Separation process design and synthesis based on thermodynamics insights, Chem. Eng. Sci., 50, 3, 511-530.

K. U. Klatt, & W. Marquardt, 2009, Perspectives for process systems engineering—Personal views from academia and industry, Comput. Chem. Eng., 33, 536–550.

D. Vasic-Racki, N. Pavlovic, S. Cizmek, M. Drazic, & B. Husadzic, 1991, Development of reactor model for glucose isomerization catalyzed by whole-cell immobilized glucose isomerase, Bioprocess Eng., 7, 183–187.

F. H. Verhoff, & W. E. Goldstein, 1982, Diffusion resistance and enzyme activity decay in a pellet, Biotechnol. and Bioeng., 24, 703–723.

Krist V. Gernaey, Jakob K. Huusom and Rafiqul Gani (Eds.), 12th International Symposium on Process Systems Engineering and 25th European Symposium on Computer Aided Process Engineering.
31 May - 4 June 2015, Copenhagen, Denmark.

pyIDEAS: an Open Source Python Package for Model Analysis

Timothy Van Daele[a], Stijn Van Hoey[a] and Ingmar Nopens[a,*]

[a]*BIOMATH, Dept. of Mathematical Modeling, Statistics and Bioinformatics, Faculty of Bioscience Engineering, Ghent University, 9000 Ghent, Belgium*
Ingmar.Nopens@ugent.be

Abstract

Mathematical models are used in many scientific areas such as enzyme kinetics and process engineering. They can be used for process analysis and optimization. However, a model is always a simplified representation of the real process and predictions always come with uncertainty. Therefore, the model building process should be performed thoroughly addressing calibration and validation procedures. Specific modeling tools (e.g. sensitivity analysis, optimization algorithms, experimental design techniques,...) to derive additional information (e.g. importance of parameters, estimate parameter uncertainty,...) are at hand and available in existing software. First, implementing these algorithms is time-consuming and often suboptimal in efficiency. Second, existing software is in many cases closed-source and not flexible in use. In both cases this results in the unavailability of the programmed algorithms in the corresponding articles making use of them. Therefore it is hard to validate the published findings and in some cases even impossible to reproduce the presented results. To address this problem the scientific community needs a certain critical mass of 'off-the-shelf' algorithms to perform model analyses which are available to the modeling community. To improve overall quality and reliability, such kind of code library should be open source and well documented.
We hereby present pyIDEAS, an open source Python package to thoroughly but swiftly analyze systems represented by a set of (possibly mixed) differential and algebraic equations. The pyIDEAS package allows performing a model analysis in a straightforward and fast way. pyIDEAS provides a well-structured and logic framework which allows non-programmers to perform some model analysis and more advanced users to extend or adapt current functionality to their own requirements.

Keywords: model analysis, optimal experimental design, open source, Python

1. Introduction

Nowadays, model analysis and optimization is performed by many people and for these objectives specific tools such as sensitivity analysis and experimental design techniques are used. These algorithms are at hand in existing software packages, but in many cases the software is closed-source and not flexible in use. For academics this poses the extra burden that the source cannot be adapted and poses philosophical questions too (Heron et al., 2013). Moreover, only publishing the algorithm descriptions and code diagrams is most of the time not sufficient, because there are always implementation subtleties that make it difficult for others to recreate the software and reproduce the presented results (Heron et al., 2013). Therefore, all code implementations should be available and ultimately lead to the so-called 'open science'. This way of publishing research is being supported by an increasing number of people and journals (Nature Editorial, 2014). An open source

initiative could provide the sufficient toolset to perform model analyses for most people and even allow them to go a step further than they did before. The flexibility of the package allows more experienced users to extend and optimize current functionalities. To achieve these goals, the open source package needs to be well documented, because most developers over-estimate the computer literacy of novice users (Knight and Jefsioutine, 2002).
We hereby present an open source Python package which tries to address the issues mentioned above. The aim of the package is to provide an integrated environment to perform basic actions like model definition and calibration, but also provide easy access to more advanced tools such as the estimation of parameter confidence and optimal experimental design. In this way these techniques can be applied by less experienced modellers in a reliable way without requiring advanced modelling knowledge and costly, non-flexible closed-source software. The use of this package will not only allow people to calibrate models, but also to estimate the parameter confidence. The availability of optimal experimental design tools creates an extra value which is not yet available in other open source packages. By providing a well-documented and structured package with illustrative examples, the aim is to convince both novice and experienced users that they can benefit from such an open source framework and maybe even contribute. Such an approach also helps to guard the principles of good modelling practice by making the tools needed for this explicitly available.

The core abilities of the presented package will be discussed based on a real-life model building process applied to the Michaelis-Menten model of Johnson and Goody (2011).

2. Methods

2.1. Michaelis-Menten Model

The reaction used in this paper is the conversion of sucrose to fructose and glucose catalysed by the enzyme invertase (Johnson and Goody, 2011):

$$E + S \underset{k_r}{\overset{k_f}{\rightleftharpoons}} ES \xrightarrow{k_{cat}} E + F + G$$

with enzyme E, sucrose S, enzyme-substrate complex ES, fructose F and glucose G. The rate constants are represented by k_f $[mM^{-1} \cdot s^{-1}]$, k_r $[s^{-1}]$ and k_{cat} $[s^{-1}]$. This diagram can be used to set up a system of ordinary differential equations (ODEs) from which the widely used Michaelis-Menten equation (Equation 1) can be derived by using the quasi steady-state assumption.

$$v = \frac{V_{max}[S]}{K_S + [S]} \tag{1}$$

with V_{max} $[mM \cdot s^{-1}]$ the maximum rate of the enzyme, which is equal to $k_{cat} \cdot (E + ES)$. K_S $[mM]$ is the substrate concentration at which half V_{max} is reached, which is equal to $(k_r + k_{cat}) \cdot k_f^{-1}$.

2.2. Package core capabilities

The implemented package makes use of widely used Python packages like Pandas (McKinney, 2010), Scipy (Jones et al., 2001), Sympy (SymPy Development Team, 2014) and matplotlib (Hunter, 2007). These packages are well-established in the Python community and provide many functionalities which are used in pyIDEAS. The core abilities of pyIDEAS will be presented by using the procedure shown in Figure 1. The presented procedure is based on real-life experience and illustrates the power of an integrated framework.

2.2.1. Model definition

The first step is to create the model under consideration $\hat{y}(x, \theta, args)$, so that it can be used to perform model simulations. The aim of the package is to minimise the user effort to implement,

run and analyse a model. The model is defined by using the built-in Python dictionaries. Currently, models consisting of ordinary differential equations (ODEs) and/or algebraic equations can be used as input, possible dependencies between the different equations are automatically taken care of in the underlying algorithms. So the order of defining equations is not important. Parameters also need to be defined when initiating the model instance. Subsequently, the model initialisation is executed to perform a symbolic model integrity check and to generate the underlying functions to run the model simulations. To define the Michaelis-Menten model (Equation 1) and the corresponding parameters, following Python dictionaries have to be constructed:

```
parameters = {'Vmax': 0.76, # mM/s
              'Ks': 16.7}   # mM
model = {'v':'Vmax*S/(Ks + S)'}
```

These two dictionaries and a string containing the model name are the only inputs required for generating the model instance.

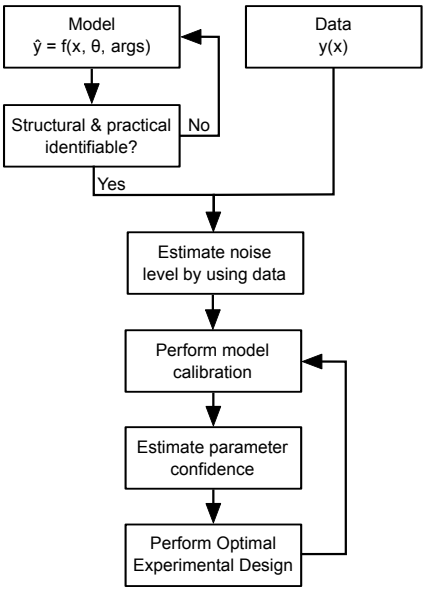

Figure 1: The presented model analysis requires a model $\hat{y}(x, \theta, args)$ and data $y(x)$ to perform the model calibration. Afterwards the parameter confidence intervals can be estimated and if necessary additional experiments can be developed using optimal experimental design.

2.2.2. Identifiability analysis

After the model definition it should be verified whether the model is (at least locally) identifiable, i.e. only one unique parameter set should be able to predict the observed input-output behaviour. If this is not the case the model should be adapted. A collinearity analysis based on the local sensitivities is implemented to verify whether (local) identifiability problems occur. Moreover, the pyIDEAS package provides a framework to implement more advanced identifiability methods in the future.

2.2.3. Model calibration

In many cases the model has to be calibrated by use of experimental data $y(x)$. Before starting the actual model calibration, it is necessary to estimate the measurement error characterics. This can be done based on the available data and/or based on expert knowledge. One should try to determine which error characterics are most realistic: is the noise level the same for every data point (e.g. absolute noise) or is the noise dependent on the y value (e.g. relative noise)? These questions have to be answered before starting the model calibration, because this has an impact on the shape of the objective function and consequently also on the retrieved estimates of the different parameters. The objective function available in the package is the weighted sum of squared errors (WSSE) and is typically used for performing parameter estimations (Equation 2).

$$WSSE(\theta) = \sum_{i=0}^{n_m} \sum_{j=0}^{n_{sp_i}} w_{i,j} \left(y_i(x_j) - \hat{y}_i(x_j, \theta)\right)^2 \tag{2}$$

with y_i the data for measurable output i, $\hat{y}_i$ the model output for measurable i, $w_{i,j}$ the weight of sample j of measurable i, n_m the total number of measurable outputs and n_{sp_i} the total number of samples for each specific measurable output (Donckels, 2009).

To perform the model calibration, local and global minimisation methods are available by using the 'minimize' function of the Scipy package. More advanced global optimisation methods (e.g. particle swarm optimisation) are also available by coupling the package with the Inspyred package (Garrett, 2012).

2.2.4. Estimate parameter confidence

After finishing the model calibration it is important to assess whether the parameter estimates can be regarded as reliable. For this the Fisher Information Matrix (FIM) can be used (Donckels et al., 2009). Under the conditions of uncorrelated and white measurement noise, the inverse of the FIM gives a lower bound of the variance-covariance matrix and contains information about parameter confidence intervals and correlations (Donckels, 2009). The calculation of the FIM can be challenging, which makes the technique less accessible for less experienced modellers. However, by providing well-documented access to these kind of functionalities it will be possible for anyone to verify the quality of the parameter estimations without the need to know how to implement the technique. The function not only returns the confidence interval for each parameter, but also verifies whether the parameter estimates can be regarded as reliable using the Student's t-test (Donckels, 2009).

2.2.5. Optimal Experimental Design for parameter estimation

Assume a model structure and some preliminary data is available for the system under study. Then it would be possible to calibrate the model parameters using the model calibration function discussed above. However, the amount of available data is limited and noise-corrupted, thereby reducing overall confidence levels of the parameters. To reduce this uncertainty, more experiments have to be carried out. Instead of randomly choosing new experiments, one could use the preliminary data to design new experiments. By using logical sense, one would select new measuring points for which the parameters show a high sensitivity and low correlation, but also conditions at which the noise is low. All this 'logic' is combined in one matrix: the FIM. To optimise the information of the FIM, different optimality criteria exist (A, modA, D, E and modE), which are all available in the software package. In this paper only the D-optimality design criterion will be used. For this criterion the idea is to maximise the determinant of the FIM. The FIM is inversely proportional to the volume of the confidence region of the parameter estimates, and this volume is minimised by maximising the FIM (Donckels et al., 2009). By maximising the FIM, future experiments can be designed which are highly informative. After performing these optimal experiments, it is important to perform the model calibration and estimate the confidence intervals of the different parameters (see Figure 1). The OED loop which consist of designing experiments, calibrating the model and estimating the parameter confidence intervals, should be repeated until the required confidence levels are met. This allows one to achieve the required confidence levels while keeping the experimental effort to a minimum.

3. Results

The Michaelis-Menten equation (see Equation 1) will be used to illustrate the different core functionalities of the package by following the stepwise approach of Figure 1. The following results were achieved by using only 25 lines of code from model definition until OED (ignoring loading of packages and comments), this illustrates the power and accessibility of the package. This limited number of lines gives the user access to advanced functionalities. In the following part only the results and figures of the different steps are shown, the code will be made publicly available prior to the conference. A (local) identifiability analysis was performed by using collinearity analysis, and showed no identifiability problems.

3.1. Model calibration

First the parameters V_{max} and K_S of the Michaelis-Menten reaction have to be estimated by use of some data. Six data points were generated in silico, using the parameter values of the paper published by Johnson and Goody (2011). For each of these data points relative noise was added, what means that higher model output values of v can have a higher absolute noise compared to low values of v. This noise was randomly sampled from a normal distribution with mean zero and a standard deviation of 0.05. The six data points were taken at substrate concentrations S of 5, 10, 20, 30, 75 and 100 mM. By using a WSSE with relative weights more weight/certainty was given to low v values. This resulted in the fit shown in Figure 2. The estimated parameter values were slightly different from the real parameter values (a V_{max} value of 0.746 mM/min and a K_S value of 17.55 mM). This is due to the normal noise that was added. To assure that the objective function is not prone to local minima, it is considered good practice to repeat a parameter estimation multiple times with different starting points to assure that the same values are always retrieved. If this is not the case, one should use global minimisation methods (e.g. particle swarm optimisation) or verify whether the model is (practical) identifiable.

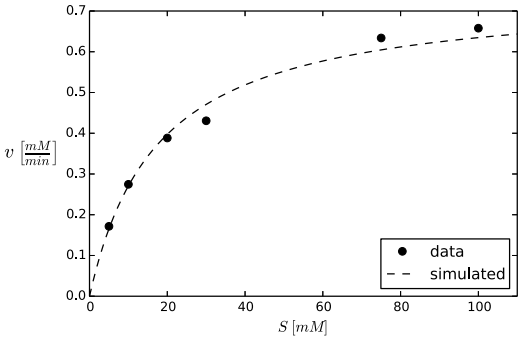

Figure 2: The in silico data with noise was used to estimate the parameters V_{max} and K_S of the Michaelis-Menten model (Equation 1). The minimisation of the objective function yielded a V_{max} value of 0.746 mM/min and a K_S value of 17.55 mM. These results are slightly different from the real parameter values, because of the normal noise which was added.

3.2. Estimate parameter confidence

After finishing the parameter estimation the confidence levels for the different parameters can be calculated using the FIM. Using the built-in function 'get_parameter_confidence', the different parameter and corresponding 95 % confidence intervals are retrieved: $V_{max} = 0.746 \pm 0.094$ mM/min and $K_S = 17.55 \pm 4.55$ mM and were both considered as reliable based on the Student's t-test.

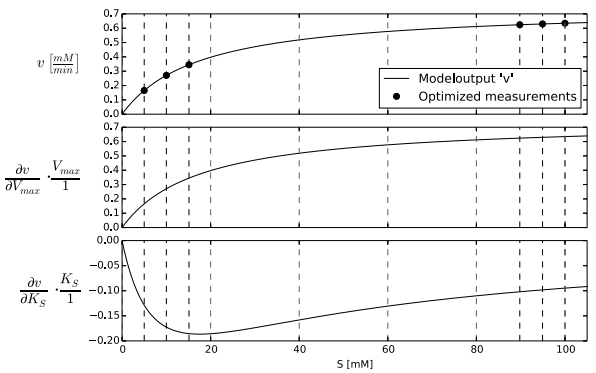

Figure 3: By using optimal experimental design and the D-optimality criterion, the experiments are optimised and the confidence intervals are decreased for both parameters. In the two lower figures, the local parameter relative sensitivity is showed for both V_{max} and K_S.

3.3. Optimal Experimental Design for parameter estimation

Instead of ignoring available knowledge reported in the paper of Johnson and Goody (2011), it is possible to take this knowl-

edge into account when designing experiments. The total number of experiments is still equal to six and the only experimental degree of freedom is the sucrose concentration S, which can be varied between 5 and 100 mM. The minimum sucrose concentration was set to 5 mM to assure sufficiently high reaction rates. An extra optimisation constraint was added, i.e. the difference in sucrose concentration between two experiments should be at least 5 mM. This allows to make the design less dependent on the actual parameter values. This optimisation led to lower confidence intervals for both parameters. For V_{max} the optimised experimental design led to a 95 % confidence interval of only 0.070, a decrease of 25.5 %. For K_S the 95 % confidence interval decreased to 3.73, which is 18.0 % lower compared the the original experimental setup. This illustrates that OED is a powerful technique which can improve the confidence levels of the models without requiring an additional experimental effort.

4. Conclusions

The pyIDEAS package allows novice and experienced modellers to execute basic and more advanced techniques by executing just a few lines of code. pyIDEAS will be open source and well-documented so that everybody is able to use it and has the ability of extending or adding functionalities. Such an integrated and flexible modelling package, providing access to optimal experimental design techniques, is not yet available to our knowledge and could improve overall access to these kind of tools and, hence, the quality of many modelling studies which often ignore this. Moreover, it allows modelling experts to verify current implementations and to debug them, something which is not possible for closed-software packages. We believe that an integrated package such as pyIDEAS can speed up research and innovation.

5. Acknowledgements

Financial support by the European Union FP7 Project BIOINTENSE - Mastering Bioprocess Integration and Intensification across Scales (Grant Agreement Number 312148) is gratefully acknowledged. The Python implementation with the different modelling steps in the paper will be made publicly available at http://users.ugent.be/~timvdael.

References

Donckels, B. M., 2009. Optimal Experimental Design to discriminate among rival dynamic mathematical models. Ph.D. thesis, Ghent University.

Donckels, B. M. R., De Pauw, D. J. W., Vanrolleghem, P. A., De Baets, B., 2009. A kernel-based method to determine optimal sampling times for the simultaneous estimation of the parameters of rival mathematical models. Journal of computational chemistry 30 (13), 2064–2077.

Garrett, A., 2012. Inspyred: Bio-inspired Algorithms in Python.

Heron, M. J., Hanson, V. L., Ricketts, I., 2013. Open Source and Accessibility: Advantages and Limitations. Journal of Interaction Science 1 (1), 2.

Hunter, J. D., 2007. Matplotlib: A 2D Graphics Environment. IEEE Comput. Sci. Eng. 9 (3), 90–95.

Johnson, K. A., Goody, R. S., 2011. The original Michaelis constant: translation of the 1913 Michaelis-Menten paper. Biochemistry 50 (39), 8264–9.

Jones, E., Oliphant, T., Peterson, P., Others, 2001. SciPy: Open source scientific tools for Python.

Knight, J., Jefsioutine, M., 2002. Relating usability to design practice. In: Proceedings of the 1st European UPA Conference on European Usability Professionals Association Conference - Volume 3. British Computer Society, Swinton, UK, pp. 2–12.

McKinney, W., 2010. Data Structures for Statistical Computing in Python. In: Proceedings of the 9th Python in Science Conference. pp. 51–56.

Nature Editorial, 2014. Code share. Nature 514 (7524), 536.

SymPy Development Team, 2014. SymPy: Python library for symbolic mathematics.

Krist V. Gernaey, Jakob K. Huusom and Rafiqul Gani (Eds.), 12th International Symposium on Process Systems Engineering and 25th European Symposium on Computer Aided Process Engineering.
31 May - 4 June 2015, Copenhagen, Denmark.

A Numerical Procedure for Model Identifiability Analysis Applied to Enzyme Kinetics

Timothy Van Daele[a], Stijn Van Hoey[a], Krist V. Gernaey[b], Ulrich Krühne[b] and Ingmar Nopens[a,*]

[a]*BIOMATH, Dept. of Mathematical Modeling, Statistics and Bioinformatics, Faculty of Bioscience Engineering, Ghent University, 9000 Ghent, Belgium*
[b]*CAPEC-PROCESS, Dept. of Chemical and Biochemical Engineering, Technical University of Denmark, 2800 Kongens Lyngby, Denmark*
Ingmar.Nopens@ugent.be

Abstract

The proper calibration of models describing enzyme kinetics can be quite challenging. In the literature, different procedures are available to calibrate these enzymatic models in an efficient way. However, in most cases the model structure is already decided on prior to the actual calibration exercise, thereby bypassing the challenging task of model structure determination and identification. Parameter identification problems can thus lead to ill-calibrated models with low predictive power and large model uncertainty. Every calibration exercise should therefore be preceded by a proper model structure evaluation by assessing the local identifiability characteristics of the parameters. Moreover, such a procedure should be generic to make sure it can be applied independent from the structure of the model.
We hereby apply a numerical identifiability approach which is based on the work of Walter and Pronzato (1997) and which can be easily set up for any type of model. In this paper the proposed approach is applied to the forward reaction rate of the enzyme kinetics proposed by Shin and Kim (1998). Structural identifiability analysis showed that no local structural model problems were occurring. In contrast, the practical identifiability analysis revealed that high values of the forward rate parameter V_f led to identifiability problems. These problems were even more pronounced at higher substrate concentrations, which illustrates the importance of a proper experimental design to avoid (practical) identifiability problems. By using the presented approach it is possible to detect potential identifiability problems and avoid pointless calibration (and experimental!) effort.

Keywords: model analysis, structural identifiability, practical identifiability, enzyme kinetics

1. Introduction

Nowadays, mathematical models are often used to describe enzymatic reactions, because in that way it is possible to gain information about the underlying kinetics (i.e. parameter values) and optimize overall performance of these reactions. By improving the performance, enzymatic reactions can become competitive with the chemical synthesis and yield a greener process. This is also the case for the production of chiral amines, for which transaminases can provide an interesting alternative for current chemical production (Tufvesson et al., 2011). Shin and Kim (1998) and Al-Haque et al. (2012) presented ping-pong bi-bi models to describe the observed behaviour, but the parameter identifiability was not investigated in these articles. Identifiability is an important model characteristic and can be defined as the existence of a unique combination of parameter values describing the system's behaviour. However two types of identifiability problems exist:

structural and practical identifiability problems. In a structural identifiability problem, multiple parameter sets result in the same input/output behaviour because of the model structure. Practical identifiability also includes the quality and availability of data. The latter gives an answer to the question: is the available data informative enough to allow finding this unique parameter set? A parameter which is practically identifiable is per definition also structurally identifiable but not vice versa. Therefore it is also important to assess the practical identifiability of parameters (Dochain et al., 1995; De Pauw et al., 2008).

For the assessment of the structural identifiability of non-linear models different techniques are available. The techniques which are used most often are the Taylor Series Approach (TSA), Generating Series Approach (GSA) and Differential Algebra Approach (DAA) (Chis et al., 2011). All techniques require significant computational resources and the question whether the model is identifiable or not, may even remain unanswered. TSA and GSA rely on the fact that one should take a certain (in most cases a priori unknown) number of derivatives and check whether the combination of all these derivatives yield a unique solution. An additional burden for the structural identifiability analysis for enzymatic models is the presence of (large) expressions in the denumerators, which drastically reduce the applicability of methods relying on mathematical differentation. In order to use DAA, it is necessary to have a model which has a polynomial form and is generally controllable. This adds an extra burden and reduces the attractiveness of the method. In order to counter these problems an identifiability tool is required which is model independent and is also able to take into account noise, hence allowing to use the same tool for both structural and practical identifiability analyses.

We hereby present an identifiability procedure which is based on the numerical local approach of Walter and Pronzato (1997). The original technique consists of two steps: first some nominal value for the parameters is selected and the model under investigation is used to generate a lot of high quality, but fictitious data y^f. Second, the aim is to estimate the parameters from y^f by minimizing an objective function. The minimization is started at the nominal parameter values, so if the parameter set remains stable the solution is structurally locally identifiable, otherwise it is structurally unidentifiable. This procedure needs to be repeated for different nominal values before drawing conclusions about the model identifiability (Walter and Pronzato, 1997). The extended identifiability procedure we present in this paper is developed to cope with both structural and practical identifiability issues. The forward reaction rate of the ping-pong bi-bi kinetic model of Shin and Kim (1998) is used to show the advantages of the proposed technique.

2. Methods

2.1. Kinetic model of ω-transaminase

The reaction under study is the conversion of isopropylamine (IPA) and benzylacetone (BA) to 1-methyl-3-phenylpropylamine (MPPA) and acetone (ACE) by the ω-transaminase (Figure 1). The enzyme requires the cofactor pyridoxal phosphate (PLP) to act as a shuttle to transfer the amine moiety between the molecules. The ω-transamination reaction obeys the ping-pong bi-bi kinetics for which the quasi steady-state reaction equation was proposed by Shin and Kim (1998). Based on the robust methodology of Al-Haque et al. (2012), the model is split to submodels and the identifiability procedure is performed for the initial forward reaction rate.

The initial forward reaction rate v (without considering inhibition) is shown in Equation 1.

$$v = \frac{V_f[IPA][BA]}{K_m[BA] + K_p[IPA] + [IPA][BA]} \tag{1}$$

with $[IPA]$ and $[BA]$ the concentrations of respectively isopropylamine and benzylacetone in mM. V_f is the maximum forward rate $[mM/min]$ and K_m $[mM]$ and K_p $[mM]$ are Michaelis-Menten constants.

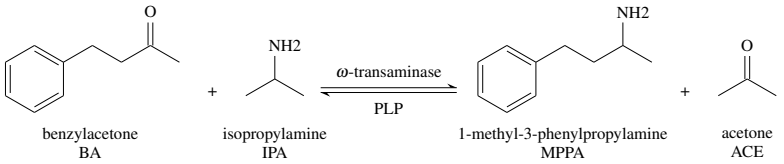

Figure 1: Transamination of isopropylamine (IPA) and benzylacetone (BA) to 1-methyl-3-phenylpropylamine (MPPA) and acetone (ACE) catalysed by the ω-transaminase enzyme in presence of the required cofactor pyridoxal phosphate (PLP).

2.2. Extended numerical identifiability analysis approach

To assess whether a model is both structurally and practically (locally) identifiable, the structural numerical local approach of Walter and Pronzato (1997) was adapted on two major points. First, instead of starting the identifiability procedure at the real parameter values, the procedure is started at a random point in the parameter space P. Second, in case of practical identifiability, noise is added to the model output to mimic the behaviour of real-life experimental data.

The developed numerical identifiability procedure can be divided in three parts: 1) preparative part, 2) actual identifiability part and 3) postprocessing part.

2.2.1. Part 1: Preprocessing

The first step in the preprocessing part is to select a model to perform the numerical identifiability analysis on. However, one needs to keep in mind that the model complexity should always be related with the available data. Second, the initial parameter values need to be chosen based on preliminary data or on expert knowledge. The final preprocessing step is to calculate the noise-free model output and select those outputs which can be measured. For each of the measurable outputs a certain number of datapoints must be selected. For assessing structural local identifiability, the number of datapoints can be almost infinite. When assessing practical (local) identifiability, the actual experimental facilities and the type and number of experiments should reflect what is feasible in practice.

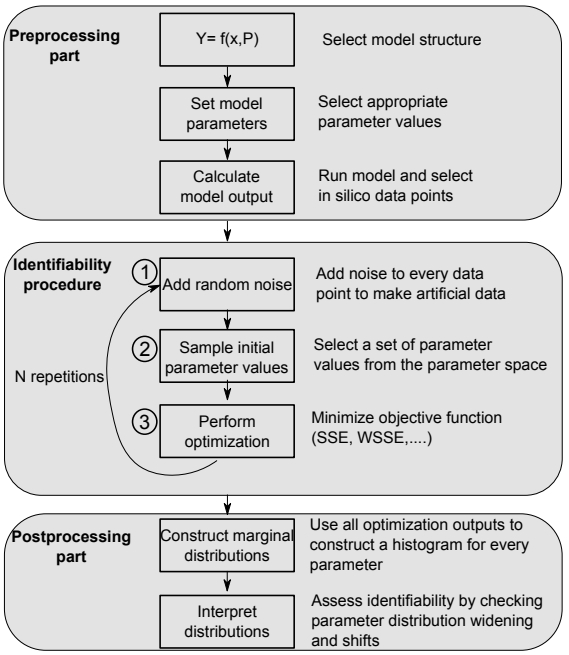

Figure 2: Schematic overview of the proposed numberical procedure for assessing structural and practical identifiability of (simple) models.

2.2.2. Part 2: Identifiability procedure

Now the actual identifiability procedure, which consists of three steps, can be started. When structural identifiability is the aim, the first step (①) may be ignored. For assessing practical identifiability, add random noise to each datapoint (①). The noise level and distribution can be chosen freely however, in most cases the normal distribution (white noise) is most logical to choose. The noise level or variance can be chosen accordingly, however the higher the noise levels the less likely it will be that the model will be practically identifiable. Noise levels should therefore be chosen wisely and if possible based on prior experiments or knowledge. Second (②), one should sample an initial parameter set from the parameter space P according to the underlying marginal distribution of every parameter. The final step (③) in the identification procedure is to perform the optimization, thus minimizing the objective function based on the difference between the model and the in silico data. The identifiability procedure is repeated N times to cover the entire parameter space. N should be sufficiently large to obey the a priori assumption of random white noise and be based on the dimensionality of the problem.

2.2.3. Part 3: Postprocessing

The postprocessing part consist of two steps: First from the N repetitions of the identifiability procedure, one gets N optimized parameter sets. For each individual parameter a histogram can be constructed. The second step is to interpret these distributions and detect whether identifiability problems are occurring or not.

2.3. Implementations

The approach described above was implemented using the IPython Notebook environment (Pérez and Granger, 2007). This environment was selected because of the availability of the so-called magic functions, which drastically reduced the effort to use multiple cores at the calculation cluster. In order to perform the optimizations the optimization module of the Scipy package was used and gave access to the minimize function (Jones et al., 2001). This function gives access to different local (and global) minimization approaches. The plotting of the histograms was done by using the hist function in matplotlib.pyplot (Hunter, 2007).

3. Results and Discussion

In this section the presented methodology is applied to the forward reaction rate of the ping-pong bi-bi kinetics to examine whether the model structure of the forward rate equation (Equation 1) is at least locally identifiable. Preliminary data was available, from which three plausible parameter sets were derived (Table 1). For each of the parameter sets both structural local identifiability (i.e. sufficient and noise free data) and practical local identifiability (i.e. experimental limited and noisy data) were investigated. In both cases, the chosen objective function was the sum of squared errors (SSE).

Table 1: Three plausible parameter sets were selected from the relationships derived from the preliminary data.

Parameter	$V_f[mM \cdot min^{-1}]$	$K_m[mM]$	$K_p[mM]$
low set	0.1	174.41	3.59
moderate set	1.0	1744.19	125.93
high set	10.0	17441.97	1349.27

3.1. Structural local identifiability

For each of the three parameter sets in Table 1, 10000 repetitions (N) of the identifiability procedure were executed by using sufficient and noise free data. This resulted in the marginal distributions of Figure 3. For each of the parameter sets, the optimization retrieved the original values. Therefore it could be concluded that, the model is (at least locally) structurally identifiable. It is important to assess this characteristic, because deviations of the real value can point out that the model is under/overparametrized or the model structure is inappropriate (De Pauw et al., 2008). In the case of a model overparametrization, one needs to reduce or simplify the current model or generate additional data to solve this issue.

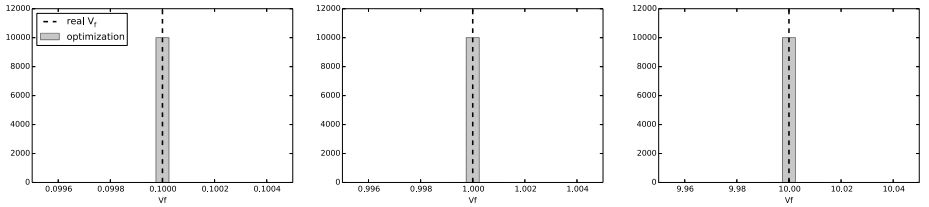

(a) $V_f = 0.1\,mM \cdot min^{-1}$ (b) $V_f = 1\,mM \cdot min^{-1}$ (c) $V_f = 10\,mM \cdot min^{-1}$

Figure 3: Histogram for each of the parameter sets in Table 1, 10000 initial parameter samples were optimized with the in silico data. Each optimization ended at the real parameter values which shows that the model is structurally identifiable. For visibility reasons the gray optimization bar is made much wider.

3.2. Practical local identifiability

After checking the structural local identifiability, a practical identifiability analysis was performed for each of the parameter sets in Table 1. This procedure was done for each of the parameter sets for 3 different noise levels: a relative white noise with a standard deviation of 5 %, 10 % and 20 %. In that way higher values of v can have a larger absolute noise compared to lower v values. For each combination of parameter sets and noise levels 10000 repetitions were performed, resulting in marginal distributions showed in Figure 4. The identifiability procedure was also conducted for absolute noise levels (constant for all datapoints), however this did not result in significant output changes and is therefore not shown.

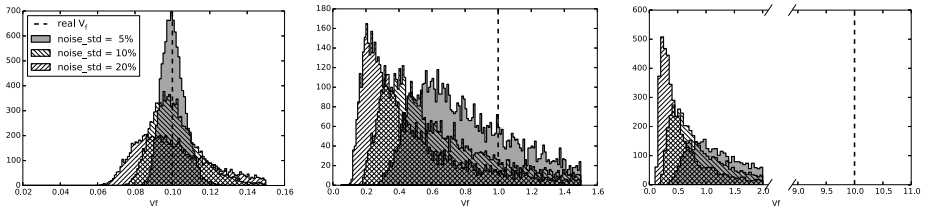

(a) $V_f = 0.1\,mM \cdot min^{-1}$ (b) $V_f = 1\,mM \cdot min^{-1}$ (c) $V_f = 10\,mM \cdot min^{-1}$

Figure 4: Histogram for each parameter set in Table 1. The practical identifiability procedure was done for 3 different noise levels (standard deviations of 5, 10 and 20 %). At higher values of V_f (1.0 and 10.0 mM) a clear shift of the distribution can be observed, indicating practical identifiability problems. As could be expected, this effect even gets worse at higher noise levels. Therefore it can be concluded that the model is only practically identifiable at low V_f levels and for low levels of noise.

From Figure 4, it can be concluded that the model is practically locally unidentifiable at high V_f values, even if the noise levels are low (5 % standard deviation). This has a huge impact on the reliability of the calibration and validation of the model under study. A calibrated V_f value of 0.5, would be unreliable based on Figure 4. Maybe V_f is truly 0.5 but it is also possible that V_f was 1.0 or even 10.0. The conclusion would be that a V_f parameter value of 0.5 (given the selected noise levels and data) can never be regarded as a reliable estimate. One should bear in mind that the conclusions drawn from Figure 4 are only valid for the data which is provided. For other data sets, which may be more informative or less noisy, no conclusions can be drawn about the practical identifiability. In this case different data sets were tried, but it seemed that varying isopropylamine between 0 and 800 mM at a constant benzylacetone concentration (5 and 10 mM) resulted in slightly lower uncertainties compared to the variation of benzylacetone at a constant isopropylamine concentration. This information is useful for deciding which experiments yield less uncertainty and might be used as a basic method for optimal experimental design.

4. Conclusions

A conceptually simple yet powerful technique to assess the structural and practical local identifiability was presented. This technique allows the model user who wants to perform modelling and calibration to verify whether the model under study is (at least locally) identifiable. The technique requires the use of a considerable amount of computational power, however this requirement depends on the desired accuracy and the complexity of the model. For simple models one can obtain high accuracy at a reasonable cost. The choice of which kind of data will be used to check the identifiability of a model is of major importance for this technique. The dependence of the technique on the provided data, makes it suitable for designing experiments.

5. Acknowledgements

Financial support by the European Union FP7 Project BIOINTENSE - Mastering Bioprocess Integration and Intensification across Scales (Grant Agreement Number 312148) is gratefully acknowledged.

References

Al-Haque, N., Santacoloma, P. A., Neto, W., Tufvesson, P., Gani, R., Woodley, J. M., 2012. A robust methodology for kinetic model parameter estimation for biocatalytic reactions. Biotechnol. Prog. 28 (5), 1186–1196.

Chis, O.-T., Banga, J. R., Balsa-Canto, E., 2011. Structural identifiability of systems biology models: a critical comparison of methods. PloS one 6 (11), e27755.

De Pauw, D. J. W., Steppe, K., De Baets, B., 2008. Identifiability analysis and improvement of a tree water flow and storage model. Math. Biosci. 211 (2), 314–332.

Dochain, D., Vanrolleghem, P., Van Daele, M., 1995. Structural identifiability of biokinetic models of activated sludge respiration. Water Res. 29 (11), 2571–2578.

Hunter, J. D., 2007. Matplotlib: A 2D Graphics Environment. IEEE Comput. Sci. Eng. 9 (3), 90–95.

Jones, E., Oliphant, T., Peterson, P., Others, 2001. SciPy: Open source scientific tools for Python.

Pérez, F., Granger, B. E., 2007. IPython: A System for Interactive Scientific Computing. IEEE Comput. Sci. Eng. 9 (3), 21–29.

Shin, J. S., Kim, B. G., 1998. Kinetic modeling of omega-transamination for enzymatic kinetic resolution of alpha-methylbenzylamine. Biotechnol. Bioeng. 60 (5), 534–40.

Tufvesson, P., Lima-Ramos, J., Jensen, J. S., Al-Haque, N., Neto, W., Woodley, J. M., 2011. Process considerations for the asymmetric synthesis of chiral amines using transaminases. Biotechnol. Bioeng. 108 (7), 1479–1493.

Walter, E., Pronzato, L., 1997. Identification of parametric models from experimental data., xviii Edition. Springer-Verlag, Heidelberg.

Krist V. Gernaey, Jakob K. Huusom and Rafiqul Gani (Eds.), 12th International Symposium on Process Systems Engineering and 25th European Symposium on Computer Aided Process Engineering.
31 May – 4 June 2015, Copenhagen, Denmark

Integrated Simulation Platform of Chemical Processes Based on Virtual Reality and Dynamic Model

Na Luo, Xiaoqiang Wang, Feng Van, Zhen-Cheng Ye, Feng Qian*

Key Laboratory of Advanced Control and Optimization for Chemical Processes (East China University of Science and Technology), Ministry of Education, Shanghai, 200237, China

Abstract

Due to the upcoming shortages of plant operators, more and more simulation platforms are widely developed for training. However, the conventional simulation environment is not intuitive for the beginners. In this study, a new integrated simulation platform based on virtual reality and dynamic model was proposed. Realistic 3D model of the chemical plant was developed which interacts with the dynamic model and the companied control system. Also the scene on site was integrated for monitoring the real process conditions. With the OPC interface, the dynamic model could run simultaneously with the actual plant. As a case study, the integrated simulation platform of ethylene process was illustrated. The simulation results showed that the integrated platform is more friendly and accurate to be used for training operators.

Keywords: simulation platform, dynamic modeling, virtual reality, chemical process.

1. Introduction

As an important production process, chemical processes are dynamic systems in which states of material change according to various physical and chemical changes. Generally, the role of the operator have to monitor a sophisticated system and make decisions about the health of the process and the performance of the system based upon trends and meta-information. Nowadays, the reliable system and process avoid upset conditions in industry, so the operators often have no chance to deal with critical situations, which may cause the operators to quickly lose the skills. On the other hand, though modern, field-based automation systems have great reliability and performance, the risk introduced by human engineering still remains. Especially when advanced control strategies are used in process, the system cannot be trusted because of error or incompletion. From this point of view, virtual plant provides an important platform in automated process plant.

In the last two decades, virtual factory theories and concepts are developing rapidly, significantly improving the efficiency of design, planning and reconfiguration in the manufacturing system. Nowadays, many manufacturing enterprises are facing challenges such as faster product design changes, shortened planning and delivery time or more flexible production schedule [1]. Jain et al.[2] classify virtual factory definitions into four categories: a) representation of all major aspects of a factory; b) a virtual organization; c) the virtual reality representation of a factory and d) an emulation facility for production activity in a factory. In the definitions, more studies were developed in every aspect of the relevant technology. With the development of virtual reality, virtual plant is not only a dynamic process simulator integrated with a control

system simulator. Virtual reality technology is used widely in industrial applications, especially in early planning stages of manufacturing system, e.g. the assembly design; machining process simulation; evaluation and visualization of planned facility or training employees parallel to the running production. With more virtual reality approach, the user and the information support elements are put in direct relation with the operation of the system in a realistic environment. Based on a virtual reality approach, Manesh[3] developed a real industrial plant, a medium sized die-casting factory. Though virtual factory is been applied successfully to hundreds if not thousands of scenarios, only a single research group worked specifically on the application of virtual reality to chemical engineering is aware. Bell[4; 5] Presented their work to apply virtual reality to engineering education, in three broad project areas: Virtual chemical plants, virtual laboratory accidents, and a virtual UIC campus. Quan[6] proposed a three-dimensional interactive virtual chemical laboratory framework based on constructivist learning theory, three-dimensional modeling and scene interactive technology of VRML. Also they developed a real experimental environment and implement the complex human-machine interaction in chemistry to make the learners get the senses of realism and immersion. Chen[7] built a distributed interactive chemical process simulation system with the abilities of chemical process training, monitoring, testing and replaying.

In this study, a virtual factory is developed which simulate the chemical process. A 3-D visualization platform provided through a virtual reality based simulation tool allows system users to create any kind of common manufacturing operations. The underlying control architecture is built upon the real control system in the process. The bottom is the dynamic simulation of the process which provides operation data for the above control system. The overall methodology has been implemented as an easy-to-use tool for manufacturing systems education and operation training.

2. Framework of the virtual factory

A brief diagram for virtual factory is shown in Figure 1, which includes three layers. The bottom layer is the dynamic model which represents the units, pipes, sensors and control valve in the factory. Upper is the control system layer, developed using the factory commonly-used control platform, such as IFIX. On the top, actual industrial scene is portrayed in 3D virtual environment in real time.

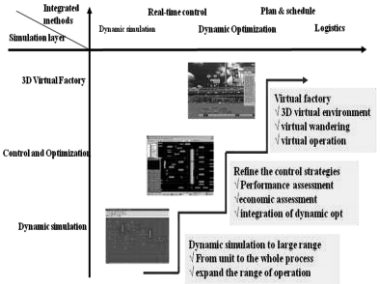

Figure 1. Diagram for virtual factory

In the bottom layer, dynamic simulations are from unit to the whole process. Also the simulated model expands the range of operations. The generated data are provided to the upper layer for control and optimization. In the platform of the control strategies, performance assessment, economic assessment is made. In addition, dynamic optimization to the process is integrated. These operations are represented using the

virtual reality in 3-D environment. Also the virtual wandering, virtual operations can be realized in the platform.

2.1. Virtual reality

Virtual Reality (VR) is a comprehensive and widely developed concept. It is usually understood as computer technologies to create virtual environments consisting of realistic 3D models and their interrelationships. To facilitate the operation process in manufacturing system, the simulation results are implemented in virtual reality.

Virtual reality can attract and affect the operators mostly. The key area is the navigation and orientation. There are three modes in our work: randomly automatic walking, role operation and orientation location. The directional cues are related with the location of the unit in the control system. Teleports are used to move from one unit to another.

The information of units is shown in the 3D environment to make the greener to be familiar with the process. In addition, operational conditions, such as stream flow, valve location are also illustrated in the scene.

2.2. Control system

A virtual control system is selected according to the real control system running in the real plant. The control strategies duplicate the real ones in the process. This allows testing of the identical control strategies running in the actual process controllers with a virtual I/O system. It allows operator training on graphics, alarms and controls that are identical to the actual plant HMI.

In addition, a virtual process and I/O dynamic simulation system is used. The system is complementary to the virtual control system, providing real-time I/O and model updates so that the virtual control system appears to control the real process. The dynamic simulation allows the user to develop process models to the level of complexity or fidelity required by the task at hand. The system needs to be easy to use and change so that modeling changes can be made quickly and efficiently.

2.3. Dynamic model

The simulation system is built to support both control system testing and operator training, so that it can provide the greatest benefit to the system user. Ideally, the virtual plant will be available for plant operations as a strategic asset to improve the quality of control system enhancements and increase the effectiveness of plant operators.

Dynamic simulation interact real-time changes with the environment. Layouts for models are changed, dynamic simulation is update. Also simulation signals can be transferred to a physical models and these physical models' signal can be transferred to virtual units, which will enable us to perform an integrated simulations with a whole virtual/physical model.

2.4. communications between three layers

Based on Microsoft's OLE, Component Object Model (COM) and Distributed Component Object Model (DCOM) technologies, OPC consists of standard interfaces, properties and methods for the use in process control and manufacturing-automation applications. One of the valuable features of OPC is that it provides a common interface for communicating with diverse process control devices, regardless of the controlling software or protocols used in the process. Before OPC became available, application developers had to create specific communications drivers for each control system with which they wanted to connect. With OPC, application vendors no longer need separate drivers for each new processor or protocol. Instead, the manufacturers create a single optimized OPC driver for their product.

3. An illustrative Example

In the following section a real industrial plant, a full-scale sized ethylene factory is analyzed. This example is a model of a plant located in China. The factory comprises of several cracking furnaces and dozens of columns, accompanied by lots of bumps, heat-exchanges, valves and so on.

The production process begins with the arrival of naphtha to react in cracking furnace. In the furnace, the naphtha is cracked to ethylene, propylene, butane and other raw materials. In next units, different materials are purified.

3.1. VR model

The VR model of ethylene factory is shown in Fig. 2. In it, units, pipes, bumps and buildings are all illustrated. The operators can have a role of worker who is male or female. Then the role can do some routine work in the virtual plant such as monitoring the unit, checking the location of the liquid level and so on. Also the role can adjust the valve location and change the operation of the process. For the beginner, the role needs to be familiar with the process. The automatic walking mode will direct the role to visit the virtual plant and show the information of the important equipment.

The VR model is developed in 3D max environment and animated using the software named VRP. The scene of the virtual plant is vivid and the integration is easy. For complex process, the development work is enlarged and the reusing of the unit model is a difficult problem to be solved.

Figure 2. Snapshot of the VR model

3.2. Control system

Most industrial SCADA (Supervisory Control And Data Acquisition) systems like iFix (General Electric), WinCC (Siemens) or RSView (Rockwell Automation) can be used for process visualization as well because they naturally directly operate with the OPC data. In this study, iFix is used as the control system. The system emulates the SCADA system in the industrial plant which is shown in Fig. 3.

3.3. dynamic simulation

HYSYS dynamics has been recently used in real industry, served as a simulation platform to experiment with new control technologies for similar units. Steady-state and dynamic simulation for ethylene process is done using Aspen HYSYS. The

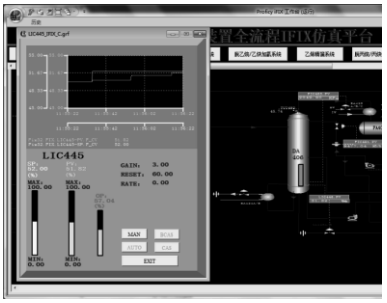

Figure 3. Snapshot of SCADA system

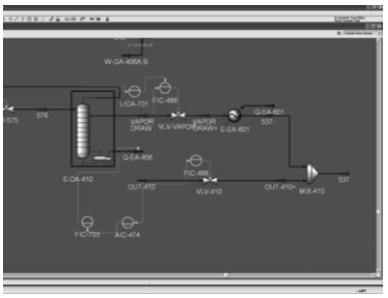

Figure 4. Snapshot of dynamic system

control loops are implemented, together with the corresponding manipulator, with is shown in Fig. 4.

4. Conclusion

This study proposed a dynamic modeling environment based on virtual reality. Realistic 3D model of the plant was developed and interacted with the dynamic modeling and the companied control system. With the OPC interface, the dynamic modeling environment ran simultaneously with the actual plant. A case study of ethylene virtual plant was illustrated as a case study. Other virtual plants could be also developed using this method. As the web has grown in popularity and utility, the transplant to the web is the direction of the virtual plant.

References

X. Yang, E. Deines, C. Lauer, & J. C. Aurich, 2011, A human-centered virtual factory. In, Harbin, China: IEEE Computer Society, 1138-1142.

S. Jain, N. F. Choong, K. M. Aye, & M. Luo. 2001, Virtual factory: an integrated approach to manufacturing systems modeling, International Journal of Operations & Production Management*,* 21,5/6, 594-608.

H. Farahani Manesh, D. Schaefer, & M. Hashemipour. 2010, Information requirements analysis for holonic manufacturing systems in a virtual environment, International Journal of Advanced Manufacturing Technology*,* 53,1-4, 385-398.

J. T. Bell, & H. S. Fogler. 1996, The Status and Prospects of Virtual Reality in Chemical Engineering,AIChE 1996 National Meeting, Chicago, IL, Pages.

J. T. Bell, & H. S. Fogler, 2004, The application of virtual reality to (chemical engineering) education. In IEEE Virtual Reality 2004, Proceedings, New York: IEEE, 217-218.

L. Quan, G. Zhao, Y. Pan, T. Ming, & M. Gao, 2008, Three-dimensional virtual chemical laboratory based on virtual reality modeling language. In 2008 IEEE International Symposium on IT in Medicine and Education (ITME), 491-496496.

C.-j. Chen, F.-s. Liu, & N. Li. 2010, Research on Chemical Process Simulation System Using Distributed Virtual Reality, Proceedings of the Third International Conference on Information and Computing Science (ICIC 2010)133-136136.

Krist V. Gernaey, Jakob K. Huusom and Rafiqul Gani (Eds.), 12th International Symposium on Process Systems Engineering and 25th European Symposium on Computer Aided Process Engineering.
31 May – 4 June 2015, Copenhagen, Denmark

OsmoseLua – An Integrated Approach to Energy Systems Integration with LCIA and GIS

Min-Jung Yoo[a], Lindsay Lessard[a, b], Maziar Kermani[a], François Maréchal[a]

[a]*EPFL-STI-IGM-IPESE, Station9, Lausanne CH-1015, Switzerland*
[b]*Quantis Intl, EPFL Innovation Park, Bât. D, 1015 Lausanne, Switzerland*

Abstract

In this paper, we present our recent work on the implementation of an Energy Systems Integration platform allowing the modeling of Energy Systems integrating LCI (Life Cycle Inventory), LCIA (Life Cycle Impact Assessment) and GIS (Geographical Information Systems) data as modeling parameters and variables included in an industrial process model.
Based on our previous experience in methodologies and models of Energy Systems Integrations, we developed a new generation of the platform using the script language Lua. The main motivation for choosing Lua was to radically improve the performance of the system, which was the main drawback of the existing Matlab-based system, while proposing a more convenient way of describing the modeling elements and their combination.
The second objective of our work was to integrate LCI and LCIA aspects as a generic part of the Energy Systems modeling methodology. We are currently working on the process data mapping algorithm in order to match the appropriate Unit process and Elementary flows identifiers used in the ecoinvent v3 database.
Thirdly, by having the possibility of importing GIS databases (in csv format), some coordination data, such as longitude and latitude, can be directly included as Energy System elements' location parameters. This possibility improves the efficiency in modeling the energy integration of urban systems.

Keywords: process system engineering, energy integration, LCA, Lua, OSMOSE

1. Introduction

Many different modeling environments (e.g. MATLAB®, GAMS®, AMPL®, gPROMS®, BELSIM®) and commercial solvers (e.g. GLPK®, CPLEX®) exist for process system engineering (Martin, 2015). One of the biggest challenges is to handle the communication among them, while performing design and optimization of the overall system. With this in mind, the OSMOSE® platform was designed in the Laboratory of Industrial Energy Systems (LENI software, 2005) at EPFL as a flexible and robust tool for the design of complex integrated energy systems in a Matlab environment.

Figure 1 illustrates the methodology implemented in OSMOSE® for the design and optimization of energy systems. Energy systems are generally Mixed-Integer Non Linear Programming (MINLP) models with multiple conflicting objectives (e.g. economic, thermodynamic and environmental indicators). Following a two-stage decomposition strategy the problem is divided into a master problem and a slave sub-problem (Gerber et al. 2013, Weber, 2008). The master problem is solved using a

Queueing Multi-Objective Optimization (QMOO) technique (Leyland 2002). QMOO is a robust evolutionary algorithm designed at EPFL to find the global optimum together with many local sub-optimal solutions. This is important as it provides the decision maker with many possibilities. The slave sub-problem is a Mixed-Integer Linear Programming (MILP) model solved by using a branch-and-bound algorithm. In the Matlab-based platform, the LCA database was based on ecoinvent version 2.2.

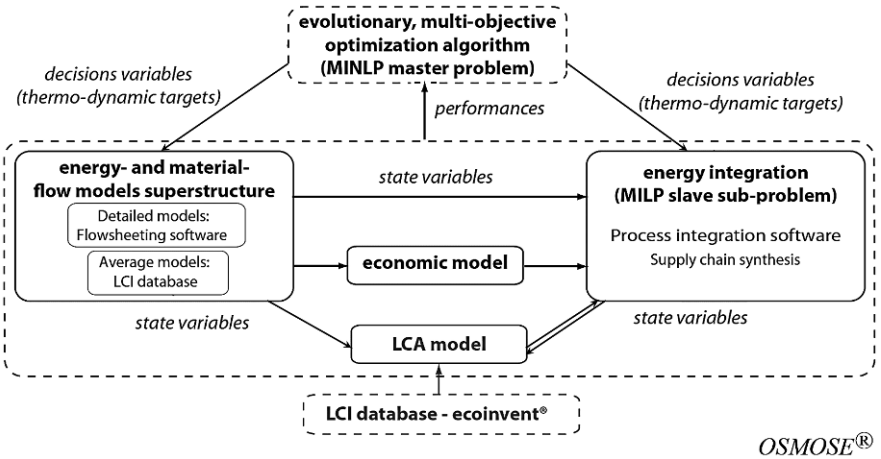

Figure 1. OSMOSE computational framework for energy system optimization. Adapted from (Gerber et al., 2013)

2. OSMOSE Generation II - OsmoseLua

Based on our previous experience with the OSMOSE methodology, we developed a new approach using the script language Lua (Ierusalimschy, 2013). As a first step, the slave sub-problem of OSMOSE was handled while integrating GLPK and Belsim-Vali for solving MILP problems. We are continuing to complement the multi-objective optimization algorithm in Lua. The main motivation for choosing Lua was to radically improve the performance of the system, which was the main drawback of the existing Matlab-based system, while proposing a more convenient way of describing the modeling elements and their combination.

Another important feature of the Lua version of OSMOSE is its extensibility and ease of integration (Figure 2). This was taken into consideration while designing the core architecture. The interface part depicted as GenericFrontend and GUI in Figure 2 is the user interfacing API either on the users' stationary computing environment or on portable devices. Due to the Lua language's portability and small footprint, the integration on mobile devices for model search and results consultation is strongly encouraged as our future development plan.

Finally, while implementing the OSMOSE core part in Lua, we redesigned the LCI and LCIA parts as pluggable and extensible generic SW modules rather than integrating the LCA database as part of the energy and material structures as depicted in Figure 1. Consequently, in the currently available OsmoseLua architecture we provide two types of library elements: on the one hand the Energy process model ((1) in Figure 1); and on the other hand the associated LCA dataset model ((2) in Figure 1) where both are generic and reusable. The main advantage of such improvement is twofold: i) firstly, modelers can achieve a more detailed analysis while including LCI material flows

and/or life cycle impact assessment separately or jointly. ii) secondly, the evolution of both model parts can be dealt with independently by modifying the process model without changing the LCA aspects, or inversely by updating only the LCA database.
In the following section we discuss LCI and LCIA principles in more detail.

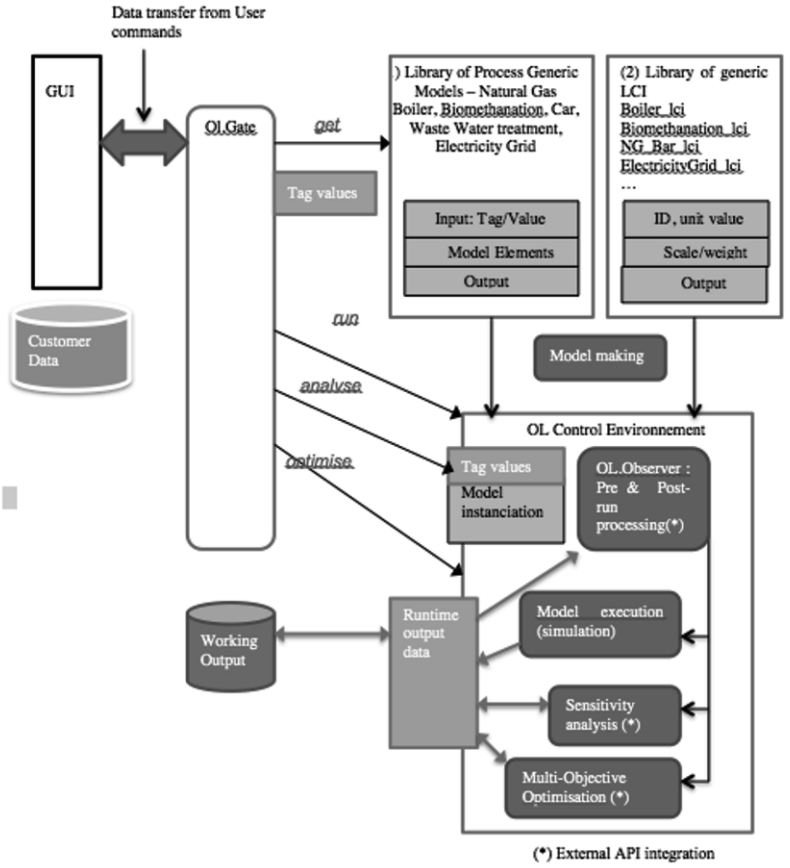

Figure 2. Global overview of OsmoseLua architecture

3. LCI and LCIA with ecoinvent version 3.1

Life cycle assessment (LCA) is the evaluation of environmental impacts over the life cycle of a product, process or activity, from the extraction of raw materials to the end-of-life. LCA can be used to identify opportunities to reduce environmental impacts of a product, to inform decision makers in order to aid in strategic planning and design, to select relevant indicators based on environmental performance and/or for marketing purposes (ISO 2006).
In our work, one of the objectives is to integrate life cycle inventory (LCI) and life cycle impact assessment (LCIA) into the energy systems modeling methodology. The database ecoinvent version 3.1 was used for the integration of energy modeling variables accessible for the optimization modeling (Weidema et al. 2013). As done by Gerber et al. (2013), energy flows such as fuel or electricity consumption are modeled by associating with each flow a corresponding LCI ecoinvent unit process. Likewise,

material flows and flows are modeled in this manner. Direct emissions are modeled by associating with each flow a corresponding elementary flow, again from the ecoinvent database. A general representation of the above methodology is shown in Figure 3. Care is taken to avoid double counting of emissions; if an emission is already included in the unit process, then the same emission is not modeled with an elementary flow.

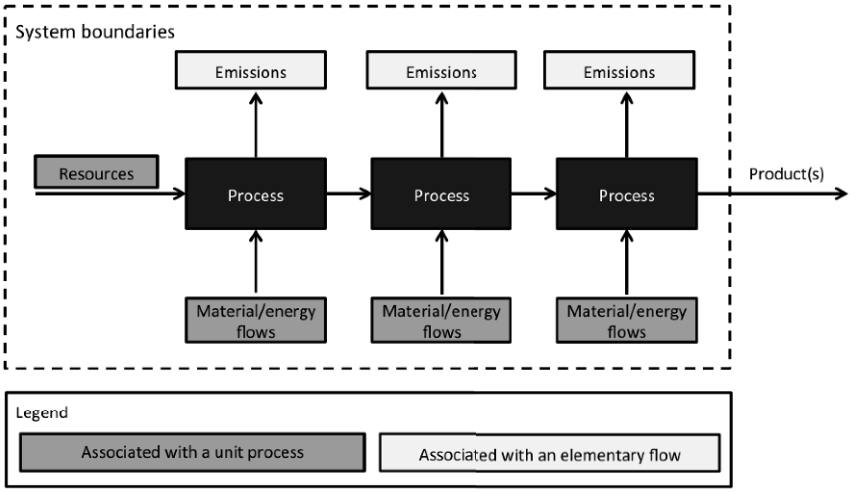

Figure 3. General representation for association of material/energy flows and resources with unit processes and emissions with elementary flows.

Different LCA methods (e.g. IMPACT 2002+) and indicators can be used for the impact assessment, to be included in the energy optimization. LCIA results are obtained by multiplying life cycle inventory flows with the appropriate characterization factor for each inventory flow. This results in environmental impacts for different midpoint categories such as, Global warming, Aquatic eutrophication, Respiratory effects, etc. One or more environmental indicator(s) may be considered as an objective function in the optimization.

In the following section, OsmoseLua application architecture is presented which includes a discussion of LCIA pluggable architecture.

4. OsmoseLua generic architecture

4.1. LCA plug-in model

We modeled the LCA dataset as a distinguishable part of the process model definition while cutting off the tight-coupling relationship in the previous approach (Figure1). The separated LCA dataset was then modeled as Lua module definitions for data construction and necessary functions for scaling and weighting factor setting.

One of the advantages of a loosely coupled LCA model is that, if the modeler has no detailed information of its energy process model, the modeler can reference existing LCA elements from the LCA libraries which provide a set of generic databases while selecting a similar energy process model. The OsmoseLua plug-in then provides methods for further specialization of dataset elements. The scaling and weight factors are implemented as LCA dataset parameters which can be customized according to the target model.

When applying impact assessment methods, two types of identifiers were taken considered: Unit process IDs, based on ecoinvent v2.2 and Activity IDs based on ecoinvent v3. This requirement is for recovering all the available Energy Processing Models and previously defined LCA datasets declared within each Model element. As we are in the transition phase from ecoinvent v2.2 to ecoinvent v3, this method will allow us to reuse our existing LCA database of models. Such cross-referencing is possible now with our OsmoseLua LCA plugins.

4.2. Integration of GIS information

One evolving aspect with OsmoseLua is its way of handling GIS data from a standard file format and recovering values as state information of energy model superstructure. By having the possibility of importing GIS databases (in csv format as a first trial), data such as longitude and latitude can be directly included as Energy System elements' location parameters. This improves the efficiency of modeling urban systems energy integration, where building locations or heights are often necessary as a constituent of the modeling units.

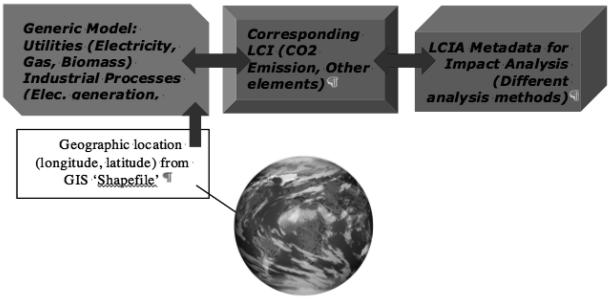

Figure 4. Overall relationship between GIS data handling and LCI-LCIA plug-in in OsmoseLua .

4.3. Validation

In the context of the project PFE3 (PFE3), two case studies are studied among project partners for the purpose of validating the modeling approach and the technical feasibility. One case study considers a hypothetical system with a population of 450'000 inhabitants including four categories of energy services: space heating, domestic hot water production, electricity and transport. Waste treatment includes municipal solid waste, organic waste and wastewater. Four industries are studied: a sawmill, a greenhouse producing vegetables, an industrial laundry service and a bio-refinery. A baseline model of the mentioned case study was implemented and analyzed in the Matlab version of. Afterward, the same conceptual model was re-written, as a proof-of-concept example, in the OsmoseLua environment and similar energy integration results were obtained. The life cycle impact assessment was analyzed with the IMPACT 2002+ method.

5. Conclusions

Throughout the implementation phase in Lua, we recognized that Lua made it easy to achieve the implementation of new sub-systems, such as a GIS data handler, LCA dataset integration and LCIA meta tables. It is due to the Lua language feature which is suitable for rapid prototyping and developing high level domain specific languages (DSL).

Currently, other partners of the project are working on a Java-based User interface layer for the purpose of customizing and integrating visualized GIS integration.
A future objective is to include the customization of the Generic Frontend layer on a mobile application environment. Lua is a popular language for many types of application developments on portable devices and game development. The Lua community provides a rich set of specialized IDE tools almost all of which are freely available.
It would be of interest to use and integrate a specialized tool such as OpenLCA into OsmoseLua. In this case, it might become more efficient to construct a new LCA dataset starting from process system specifications to be studied. An important benefit of such a tool is the possibility of composing a new process model and life cycle impact matrix with the capability of exporting/importing standard data formats such as XML, csv or database files. With OpenLca, such kind of process composition and data exportation is possible using executable system libraries. In this case, the exported dataset from OpenLCA under the XML format, for example, would be directly interpreted by the Lua LCA data handler and can be used in combination with other parts of our Lua LCA plug-in.

Acknowledgements

This work is partially funded by the program SEED 2012 from the French National Agency for Research ANR in the frame of the Plate-Form(E)3 project. Our thanks go to all the project partners for their collaboration and helpful supports.

References

L. Gerber, S. Fazlollahi, F. Maréchal, 2013. A systematic methodology for the environomic design and synthesis of energy systems combining process integration, Life Cycle Assessment and industrial ecology. Comput Chem Eng. 59: 2–16.
R. Ierusalimschy, 2013, Programming in Lua, Lua.org
ISO, 2006, Environmnental management – Life cycle assessment – Requirements and guidelines. International Standard, ISO 14044
LENI software, 2005, Introducing OSMOSE. Retrieved November 28, 2014 from LENI: http://leni.epfl.ch/files/content/sites/leni/files/pdf/osmose.pdf
G. B. Leyland, 2002. *Multi-Objective Optimization Applied to Industrial Energy Problems.* Lausanne: EPFL.
M. M. Martin, (Ed.), 2015, *Introduction to Software for Chemical Engineers.* NW: CRC Press - Taylor & Francis Group
OpenLCA, http://www.openlca.org
Plate-Form(E)3 project, program SEED, 2012, from the French National Agency for Research ANR
C. Weber, 2008, *Multi-objective design and optimization of district energy systems including polygeneration energy conversion technologies.* Lausanne: EPFL
B. P. Weidema, C. H. Bauer, R. Hischier, C. H. Mutel, T. Nemecek, J. Reinhard, C. O. Vadenbo, G. Wernet, 2013, The ecoinvent database: Overview and methodology, Data quality guidelines for the ecoinvent database version 3, www.ecoinvent.org

Krist V. Gernaey, Jakob K. Huusom and Rafiqul Gani (Eds.), 12th International Symposium on Process Systems Engineering and 25th European Symposium on Computer Aided Process Engineering.
31 May - 4 June 2015, Copenhagen, Denmark.

Incremental Kinetic Identification based on Experimental data From Steady-state Plug Flow Reactors

Nirav Bhatt[a] and Srividhya Visvanathan[a]

[a]*Systems & Control Group; Department of Chemical Engineering; IIT Madras, Chennai, India*
niravbhatt@iitm.ac.in

Abstract

This work develops an incremental model identification approach for analyzing concentrations from non-isothermal steady-state plug flow reactors (SPFR) with tubular geometry. A model of non-isothermal SPFRs consists of the material and energy balance equations of SPFR in form of a set of differential equations. Since SPFRs often are used for studying gas phase reactions, the pressure drop equation will also be included. Two scenarios of reactor operations for collecting concentration measurements are distinguished: (S1) Concentrations of species are measured along the length of reactors, and (S2) concentrations of species in the outlet stream are measured for the given inlet concentration condition at various volumetric flowrates. For Scenarios S1 and S2, the incremental identification is extended to identify reaction kinetics from experimental data. Scenario S1 is corroborated with a simulated example of pyrolysis of dimethylformamide in an isothermal tubular reactor.

Keywords: Reaction kinetics, Incremental identification, Plug flow reactor, Non-isothermal

1. Introduction

The distributed reactors such as plug flow reactor, axial flow reactor are often used in chemical process industries. Thermal cracking, catalytic gas phase reactions etc., are some examples where these reactors are employed in industries. Plug flow reactors (PFR) are often used to identify reaction kinetics for these reactions in the laboratory. These experiments of kinetic identification are performed at steady-state operation of the reactor where concentrations at inlet and outlet of the reactor or along the length of reactors are often measured. Then, these data can be analyzed using the simultaneous kinetic identification approach (Thaore and Gaikar, 2013; Marquardt, 2005).

Recently, the incremental approaches have been proposed to identify reaction and mass-transfer rates based on experimental data from tank reactors (Marquardt, 2005). The incremental model identification (IMI) approaches decompose task of identification into a sequence of subtask such as the identification of stoichiometry and rate expressions. Hence, the number of model candidates can be kept small in each subtask, and the information available from one task can be used in the subsequent steps. The incremental kinetic identification approaches can be classified as: (i) Rate-based methods, and (ii) extent-based methods (Bhatt et al., 2011, 2012). A comparison of these approaches has been given in Bhatt et al. (2012). The best of our knowledge, these approaches have not been developed to analyze experimental data from plug flow reactors. The objective of this paper is to extend the framework of IMI to analyze the experimental data obtained from steady-state PFR.

The paper is organized as follows. The second section sets up the material balance and energy balance equations for a steady-state non-isothermal PFR. Further, the pressure-drop equation is

also written. Then, the linear transformation of the concentrations (or the molar flux) is extended for computing the contribution of each reaction.

2. Model Equations

2.1. Mole balance equations

The mole balance equations for a homogeneous reaction system involving S species, and R independent reaction in steady-state plug flow reactor (SPFR) can be written generically as follows:

$$\frac{d\mathbf{F}}{dV_r} = \mathbf{N}^{\mathrm{T}}\mathbf{r}, \quad \mathbf{F}(0) = \mathbf{F}_0 \tag{1}$$

where $\mathbf{F}$ is an S-dimensional vector of molar flow-rate exiting the control volume V_r, $\mathbf{N}$ is the $R \times S$ stoichiometric matrix, and $\mathbf{r}$ is the R dimensional reaction-rate vector. The molar flow-rate $\mathbf{F}$ can be expressed as: $\mathbf{F} = q\,\mathbf{c}$ where $\mathbf{c}$ is an S-dimensional vector of concentrations, and q is the volumetric flow-rate. The symbols $\bar{u}$, L, and A are defined as the fluid velocity, the length and the cross-section area of the reactor. It is also assumed that they are constant during the operation of the reactor. Then, Eq. (1) can be written in terms of the molar flux, and concentration as:

$$\frac{d\mathbf{F}_r}{dz} = \mathbf{N}^{\mathrm{T}}\mathbf{r}, \quad \mathbf{F}_r(0) = \mathbf{F}_{r,in} \tag{2}$$

$$\frac{d\mathbf{c}}{d\tau} = \mathbf{N}^{\mathrm{T}}\mathbf{r}, \quad \mathbf{c}(0) = \mathbf{c}_{in} \tag{3}$$

where $\mathbf{F}_r$ is the S-dimensional vector of molar flux, and $\mathbf{c}$ is the S-dimensional vector of concentrations of the S species spending the space-time (mean residence time, $\tau = \frac{z}{\bar{u}}$) in the reactor. τ can be interpreted in terms of batch time t. Under the assumption of plug behaviour (no mixing), suppose that a plug of material enters SPFR at $\tau = 0$ and leaves it τ time. Then, the concentrations $\mathbf{c}$ at the outlet of SPFR can be interpreted as the concentrations of species as if they have been processed in a batch reactor for t time. In SPFR, the concentrations of species vary along the length of reactor while in batch reactor, the concentrations vary with the batch time. This analogy will be useful for extending the IMI approach to SPFR.

2.2. Energy balance equation

The steady-state energy balance along the length of the reactor can be written as follows (Rawlings and Ekertdt, 2002):

$$\frac{d\left(q\sum_{i=1}^{S} c_i H_i\right)}{dV_r} = UA_{ext}(T_{ext} - T), \tag{4}$$

where H_i is the enthalpy of the ith component; U is the heat-transfer coefficient expressed; A_{ext} is the external surface area per unit volume. Using material balance and Gibbs-Duhem equation, Eq. (4) can be written in terms of reactor temperature as follows:

$$q\rho\hat{C}_p\frac{dT}{dV_r} = -\Delta\mathbf{H_R}\mathbf{r} + UA_{ext}(T_{ext} - T) - q(1 - \alpha T)\frac{dP}{dV_r}, \tag{5}$$

where ρ is the reacting mixture density, $\hat{C}_p$ the mass heat capacity of the reacting mixture, $\Delta\mathbf{H}_R$ is an R-dimensional reaction rate vector, α is the compressibility factor, P is pressure. Under the

assumption an ideal gas ($\alpha T = 1$), Eq. (5) reduces to:

$$q\rho\hat{C}_p\frac{dT}{dV_r} = -\Delta\mathbf{H_R}\mathbf{r} + UA_{ext}(T_{ext} - T), \quad T(0) = T_{in}. \tag{6}$$

For the constant cross-section area, Eq. (6) can be written as follows:

$$\frac{dT}{d\tau} = -\Delta\mathbf{H_R}\mathbf{r}/\rho\hat{C}_p + UA_{ext}(T_{ext} - T)/\rho\hat{C}_p, \quad T(0) = T_{in}. \tag{7}$$

2.3. Pressure drop equation

For liquid flow and gas phase with average density, the pressure drop across the tube is modeled as:

$$-\frac{dP}{dz} = \frac{2\rho\bar{u}^2 f}{d_i}, \quad P(0) = P_{in} \tag{8}$$

where $f = \frac{16}{N_{Re}}$ is the frictional factor for a tube with the Reynolds number $N_{Re} = \frac{d_i\bar{u}\rho}{\mu}$. For gas phase, the velocity can be computed using the total flux using the ideal gas law as follows:

$$u(z) = \frac{\sum_{i=1}^{S} F_{r,i}(z)RT(z)}{P(z)}. \tag{9}$$

The residence time can be computed using the velocity at particular length ($u(z)$) and the dimension of the reactor z.

3. Computation of Contribution of Each Reaction

This section extends a linear transformation of computing the contribution of each reaction using the concept of reaction variants and invariants (Amrhein et al., 2010). It will be shown that the S dimensional space in which the concentrations (or molar fluxes) evolve can be split into an R dimensional reaction space and an $(S-R)$-dimensional reaction invariant space.

Reaction Variants: Any set of R linearly independent variables that evolve in the reaction space constitutes a reaction variant set.

Reaction invariants: Any set of $(S-R)$ linearly independent variables that evolve in space orthogonal to the reaction space constitutes a reaction invariant set.

Using Eq. (3), a linear transformation of the concentration vector into the reaction variants and invariant can be given by

$$\mathbf{c}(\tau) \longrightarrow \begin{bmatrix} \mathbf{x}_r \\ \mathbf{x}_{iv} \end{bmatrix} = \begin{bmatrix} \mathbf{N}^{\mathrm{T}+} \\ \mathbf{P}^{\mathrm{T}} \end{bmatrix} (\mathbf{c}(\tau) - \mathbf{c}_{in}) \tag{10}$$

with

$$\begin{aligned} \dot{x}_{r,i} &= r_i(\mathbf{c}), \qquad x_{r,i}(0) = 0, \forall\, i = 1,\ldots,R, \\ \dot{x}_{iv,j} &= 0, \qquad x_{iv,j}(0) = 0, \forall\, j = 1,\ldots,(S-R). \end{aligned} \tag{11}$$

The concentrations can be reconstructed from $\mathbf{x}_r$ and $\mathbf{x}_{iv}$:

$$\mathbf{c}(\tau) = \mathbf{N}^T\mathbf{x}_r + \mathbf{c}_{in} \tag{12}$$

where "+" indicates the Moore-Penrose pseudo inverse of a matrix, $\mathbf{x}_r$ is the R-dimensional vector of reaction variants, $\mathbf{x}_{iv}$ is the $(S-R)$-dimensional vector of reaction invariants. $\mathbf{P}$ is an $S \times (S-R)$ matrix describing the null space of $\mathbf{N}$, i.e $\mathbf{NP} = \mathbf{0}_{R\times(S-R)}$. Note $x_{r,i}$ describes the progress of the ith reaction after spending the space-time τ in the reactor. Note that $x_{r,i}$ cannot be interpreted as the extent of reaction. The linear transformation can be also be applied to $\mathbf{F}_r(\tau)$, and Eq. (12) can also be used for the reconstruction.

4. Extension of Incremental Identification Approach to SPFR

This section extends the idea of incremental identification method to SPFR. The IMI approach can be implemented as follows: (i) compute the extent of each reaction, and (ii) identify the rate expressions and corresponding parameters. For sake of demonstration, we will assume that the volumetric flowrate does not vary considerably along the length of the reactor, i.e. $\bar{q} = q(z) = \bar{u}A$. Often, the volumetric flowrate will be varied in different experiments and the concentrations at the inlet and outlet of the reactor can be measured. Then, the mean residence time (τ_h) at the length z_h with $h = 0, 1, \ldots, l$ can be computed using $\bar{u}$. Further, if pressure drop between two points in the reactor is measured, then $\bar{u}$ can be computed using Eq. (8) for the liquid or the gas phase with average density.

We consider two scenarios of experimental data in SPFR as follows: (S1) Concentrations of species are measured along the length of reactors, and (S2) concentrations of species in the outlet stream are measured for the given inlet concentration at various volumetric flowrates.

4.1. Scenario 1

Let $\mathbf{c}(\tau_h)$ be the S-dimensional vector of the concentration measurements spending τ_h space-time in the reactor. Note that $\tau_0 = 0$ (at the inlet of PFR) and $\tau_l = L$ (at the outlet of PFR). The following corollary states the conditions required to compute the extents of the ith reaction $x_{r,i}, \forall\, i = 1, \ldots, R$ from $\mathbf{c}(\tau_h)$.

Corollary 1 *If (i) the matrix* $\mathbf{N}$ *is known, (ii)* $\mathbf{c}(\tau_h)$ *and* $\mathbf{c}_{in}$ *are measured, and (iii)* $\text{rank}([\mathbf{N}, \mathbf{c}_{in}]) = R + 1$*, then the contribution of each reaction* $x_{r,i}(\tau_h), i = 1, \ldots, R$ *at the space-time* τ_h *can be computed as:*

$$x_{r,i}(\tau_h) = (\mathbf{N}^{\mathrm{T}})^{+}(\mathbf{c}(\tau_h) - \mathbf{c}_{in}). \tag{13}$$

(Proof follows from Theorem 2 of Amrhein at al Amrhein et al. (2010))

4.2. Scenario 2

In Scenario 2, multiple experiments are performed at different volumetric flowrates, and consequently, the velocity will be different in each experiment. In this scenario, the concentrations are measured at the outlet of the reactor ($z_l = L$), and the corresponding time can be computed from q. Let assume that the inlet concentration ($\mathbf{c}_{in}$) is fixed,and the experiments are conducted at various flowrates. In other words, the experimental data are collected under the identical conditions except varying flowrates. The values of the volumetric flowrates in different experiments can be arranged in ascending order as: $q_1 < q_2 <, \ldots, < q_n$. The corresponding space-time can also be arranged $\tau_1 > \tau_2 >, \ldots, > \tau_n$. The corresponding concentrations can also be tabulated. Since the inlet concentration is identical in each experiment, this arrangement can be visualized as the reactor with the larger length with $\mathbf{c}(\tau_1)$, $\mathbf{c}(\tau_2), \ldots, \mathbf{c}(\tau_n)$ being concentrations along the length. Then, we can apply Corollary 1 to the experimental data obtained in Scenario 2 after the arrangement. Further, the larger space-time allows further the progress of the reactions, $\mathbf{x}_r$, and thus,

the computed contribution of each reaction for different space-time at the outlet can be arranged as: $x_{r,i}(\tau_1) > x_{r,i}(\tau_2) >, \ldots, > x_{r,i}(\tau_n)$. The contribution of each reaction can be used to identify reaction rates as described in the next sectioin.

4.3. Identification of Reaction Kinetics

For the ith reaction, let $\hat{\mathbf{x}}_{r,i}(\tau)$ and $\mathbf{x}_{r,i}(\tau)$ denote the H-dimensional vectors of computed (according to Corollary 1) and simulated (according to a postulated rate law involving the parameters $\theta_{r,i}$) contribution of reaction H space-time instants. The following parameter estimation problem can be formulated:

$$\begin{aligned} &\min_{\theta_{r,i}} f_i = (\hat{\mathbf{x}}_{r,i} - \mathbf{x}_{r,i}(\theta_{r,i}))^{\mathrm{T}} (\hat{\mathbf{x}}_{r,i} - \mathbf{x}_{r,i}(\theta_{r,i})) \\ &\text{s.t.} \quad \dot{x}_{r,i}(\tau_h, \theta_{r,i}) = r_i(\mathbf{c}_l(t_h), \theta_{r,i}), \quad x_{r,i}(0) = 0, \\ &\qquad \theta_{r,i}^L \leq \theta_{r,i} \leq \theta_{r,i}^U, \end{aligned} \tag{14}$$

where J_i is the cost to be minimized, r_i is the rate of the ith reaction, which is a known function of the measured molar concentrations $\mathbf{c}_l$ and the l-dimensional unknown parameter vector $\theta_{r,i}$ that can vary between the bounds $\theta_{r,i}^L$ and $\theta_{r,i}^U$.

5. Simulation studies

The pyrolysis of Dimethylformamide (DMA) in an isothermal tubular reactor is studied for the simulation studies (Thaore and Gaikar, 2013). The following four reactions are considered for this study:

$$\begin{array}{lccccccccc} \text{R1:} & (CH_3)_2NCOH & + & H_2O & \xrightarrow{k_1} & (CH_3)_2NH & + & HCOOH \\ \text{R2:} & & & HCOOH & \xrightarrow{k_2} & HCHO & + & 0.5O_2 \\ \text{R3:} & & & HCHO & \xrightarrow{k_3} & CO & + & H_2 \\ \text{R4:} & 2CO & + & O_2 & \xrightarrow{k_4} & 2CO_2, & & \end{array}$$

from which one can write the stoichiometric matrix $\mathbf{N}$:

$$\mathbf{N} = \begin{bmatrix} -1 & -1 & 1 & 1 & 0 & 0 & 0 & 0 & 0 \\ 0 & 0 & 0 & -1 & 1 & 0.5 & 0 & 0 & 0 \\ 0 & 0 & 0 & 0 & -1 & 0 & 1 & 1 & 0 \\ 0 & 0 & 0 & 0 & 0 & -1 & -2 & 0 & 2 \end{bmatrix}. \tag{15}$$

It is assumed that the all reactions are elementary reactions. The inlet concentration vector $\mathbf{F}_{r,in} = [1, 4.3, 0, 0, 0, 0, 0, 0, 0]^{\mathrm{T}}$. The temperature is maintained at 775 degK. The length of reactor is taken to be 0.25 m. The data are collected along the length of the reactor (Scenario 1). It is assumed that the noisy concentrations along the length of reactor and the pressure drop are measured. Using Eq. (8), the velocity are computed under the assumption of the constant density and viscosity properties. Corollary 1 is applied to compute the contribution of each reaction. The computed extents are shown in Figure 1. The computed extent of each reaction is used to estimate the parameters (k_1, k_2, k_3, and k_4) in the rate expressions using Eq. (14). The estimated parameters along with the confidence intervals are shown in Table 1. The IMI approach provides a good estimates of the parameters. However, it has introduced a bias in the rate constants k_1 and k_4.

6. Conclusions

In this paper, we have extended the IMI approach to non-isothermal varying pressure SPFR. Two experimental scenarios of data collection in steady-state PFR have been considered. For Scenario 1, it has shown that the contribution of each reaction can be computed from the data collected

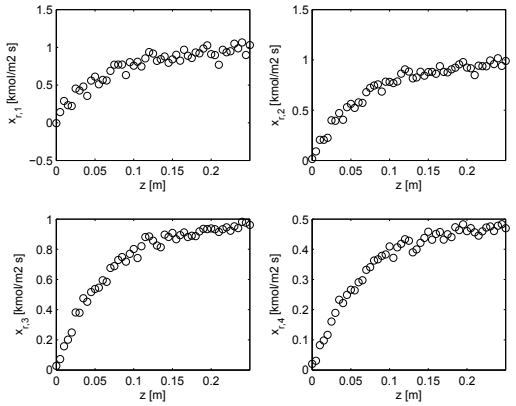

Figure 1: The computed contribution of each reaction along the reactor length

Table 1: True, initial and estimated values of the four kinetic parameters along with the 95% confidence interval for the estimated parameters.

Parameter	True value	Initial value	Estimated value	Confidence interval
k_1 [m^3 mol^{-2} s^{-1}]	0.5551	0.8000	0.5252	[0.5247, 0.5256]
k_2 [s^{-1}]	155.47	0.8000	160.3	[153.1842, 167.4060]
k_3 [s^{-1}]	843.46	0.8000	863.6451	[841.36, 885.9302]
k_4 [m^3 mol^{-1} s^{-1}]	1.665×10^5	8000	1.678×10^5	$[1.667 \times 10^5, 1.686 \times 10^5]$

along the reactor length. For Scenario 2, the multiple experiments need to rearrange such that the results of Scenario 1 can be applied compute the contribution of each reaction from data. Then, the computed contribution of each reaction has been used to estimate parameters. The method has been demonstrated on an pyrolysis of DMA in an varying pressure steady-state PFR for Scenario 1. Note that the method can be applied to non-isothermal and varying pressure SPFR. Future work will extend the IMI approach to axial flow reactors.

References

Amrhein, M., Bhatt, N., Srinivasan, B., Bonvin, D., 2010. Extents of reaction and flow for homogeneous reaction systems with inlet and outlet streams. AIChE J. 56, 2873–2886.

Bhatt, N., Amrhein, M., Bonvin, D., 2011. Incremental identification of kinetic and transport phenomena using the concept of extents. Industrial & Engineering Chemistry Research 50, 12960–12974.

Bhatt, N., Kerimoglu, N., Amrhein, M., Marquardt, W., Bonvin, D., 2012. Incremental model identification for reaction systems – a comparison of rate-based and extent-based approaches. Chemical Engineering Science 83, 24–38.

Marquardt, W., 2005. Mode-based experimental analysis of kinetic phenomena in multi-phase reactive systems. Chem. Eng. Res. Des. 83(A6), 561–573.

Rawlings, J. B., Ekertdt, J. G., 2002. Chemical Reactor Analysis and Design Fundamentals, 1st Edition. Nob Hill Publishing, Madison, USA.

Thaore, V. B., Gaikar, V. G., 2013. Kinetic model development for steam pyrolysis of dimethylformamide in a tubular reactor. Industrial & Engineering Chemistry Research 53, 10601–10608.

Krist V. Gernaey, Jakob K. Huusom and Rafiqul Gani (Eds.), 12th International Symposium on Process Systems Engineering and 25th European Symposium on Computer Aided Process Engineering.
31 May – 4 June 2015, Copenhagen, Denmark

Nonlinear Fuzzy Identification of Batch Polymerization Processes

Nádson N. M. Lima,[a] Lamia Zuniga Linan,[a] Delba N. C. Melo,[a] Flavio Manenti,[b] Rubens Maciel Filho,[a] Marcelo Embiruçu,[c] Maria R. Wolf Maciel[a]

[a]*University of Campinas (UNICAMP), Department of Processes and Products Development, 13083-852, Campinas/SP, Brazil*
[b]*Politecnico di Milano, CMIC Dept. "Giulio Natta", Piazza Leonardo da Vinci 32, 20133, Milano, Italy*
[c]*Federal University of Bahia (UFBA), Polytechnic Institute, 40210-630, Salvador/BA, Brazil*

Abstract

First-principles modelling of polymer systems is usually complex and time-consuming, often leading to correlations of restricted range of applicability with unavailable parameters. Thus, the optimal control of polymerization processes using such models is a demanding task, especially when tracked batch reactors in which the systems have typical transient behaviour. In this paper, the fuzzy logic is applied to model discontinuous polymerization reactors. The proposed fuzzy methodology allows the formulation of a global nonlinear long-range prediction model from the conjunction of a number of local linear fuzzy dynamic models. The pilot-plant-scale synthesis of poly(lactic acid) (PLA) and nylon-6 were adopted for performance evaluation of proposed method. Satisfactory results were achieved. Therefore, the proposed technique can be useful to obtain appropriate representations of systems of complex modelling.

Keywords: fuzzy modelling; nonlinear system identification; batch reactor; polymerization.

1. Introduction

It is well-known that batch systems are very important in chemical engineering. Batch reactors comprise an essential operation unit of laboratory pilot-plants scale, since they are suitable for small-scale operation, for testing new processes that have not been fully developed, for the manufacture of expensive products and for processes that are difficult to convert to continuous operations (Lima et al, 2014). According to Aziz and Mujtaba (2002), batch processes are particularly suitable for products such as pharmaceuticals, polymers, biotechnological or other fine chemicals products for which total requirement can be manufactured in a few days or a few batches in an existing plant. Nevertheless, the control of batch reactors is rather complex due to intrinsic dynamic nature of the system that either moves from one steady-state condition to others or never reaches a steady-state at all during the overall batch operation. Therefore, the physical and chemical properties of the compounds in the bulk, such as viscosity, heat transfer coefficient, heat capacity, and reaction rate vary, sometimes significantly, with time. Additionally, the dynamic of polymerization processes is highly complex. These systems have inherent strong nonlinearities and multivariable nature with significant interactions and constraints. Thus, both modelling and consequently control of batch

polymerization reactors is still a cumbersome and open issue for the community and a challenging task.

Although nonlinear classic modelling approaches have still been commonly used, new learning technologies in process engineering that allow better, simpler, and more accurate behaviour predictions have recently been introduced. However, according to Mehran (2008), for many chemical processes, building an accurate mathematical model is very difficult and time consuming and only the input-output data yielded from running the process are generally accessible for an estimation. The use of fuzzy systems is interesting from this perspective since they allow to develop a global nonlinear long-term prediction model using some pieces of information and composing a number of local linear sub-models which are straightforward, understandable, and responsible for respective sub-domains.

This paper describes the application of the fuzzy logic to model batch polymerization reactors. The proposed fuzzy methodology is quite effective to handle modelling and control issues typical of processes with nonlinear and time-varying behaviours and complex dynamics (such as the ones here considered). The selection of an appropriate model structure for a future design of advanced controllers is also broached. For dynamic analysis, each generated fuzzy output must be fed back to the fuzzy structure to calculate the current output through one or more time-delay units. The production processes of Poly(Lactic Acid) (PLA) and nylon-6 were adopted for performance evaluation of proposed method. The reactions were carried out in a laboratory pilot-plant scale. A rigorous phenomenological model is available for such a system. The mathematical model for the PLA process is solved using a Runge-Kutta type algorithm implemented in C++ programming language and, for the production of nylon-6, the equations system was implemented in Aspen Plus process simulator. Therefore, the two resulting computational programs were experimentally validated and they are considered as virtual plants for obtaining of identification dynamic data. Additionally, data sets from experimental measurements were used. Then, appropriate techniques for fuzzy models identification were used and the formulations were built in Fortran 90 and Matlab programming languages. Satisfactory results were achieved from the pilot-plant and this is confirming that the proposed method can be useful to obtain appropriate mathematical representations of complex modelling systems and it can be applied in several ways, as on the tracking of processes as well as on optimization techniques and advanced control.

2. Experimental campaign

Figure 1 provides the schematic diagram of the batch polymerization system used in this work. The jacketed stainless-steel reactor has a capacity of 15 L and it is equipped with a pitched-turbine stirrer for mixing the reactants. An inverter is adopted to maintain the stirring speed at 360 rpm. The reactor temperature may be controlled by manipulating the electrical power of the thermal oil heater (serpentine) and by manipulating the electrical power supplied to the six resistances that act on the water stream in the jacket. The collar type resistances connected in parallel to the tube of the jacket inflow can vary in the range of 0.0 – 581.0 W. A HP personal computer (s5520br) and a PLC are employed for data acquisition and polymer process control. A flow rate of 0.04 L/min of gaseous nitrogen (grade 5.0 Praxair-White Martins) is bubbled through the reacting

medium to keep oxygen out of the reactor. Samples of each polymeric mixture were taken time to time (30 to 30 minutes) to determine the respective properties.

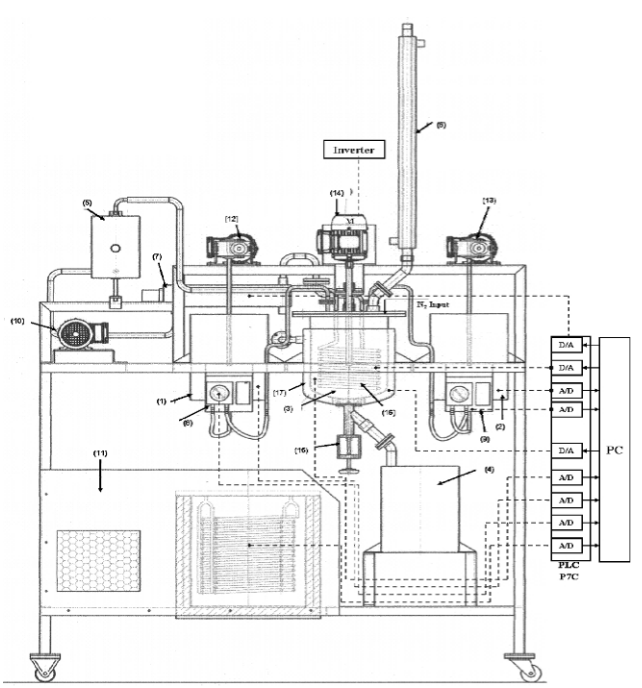

(1) monomer storage tank
(2) initiator and/or chain terminator and /or solvent storage tank
(3) batch polymerization reactor
(4) product storage tank
(5) thermal oil storage tank
(6) reflux condenser
(7) thermal oil heater
(8) monomer pump
(9) initiator and/or chain terminator and /or solvent pump
(10) thermal oil pump
(11) cooling bath
(12) monomer stirring motor
(13) initiator and/or chain terminator and /or solvent stirring motor
(14) reactor motor
(15) product outlet solenoid valve
(16) helical coil (serpentine)
(17) jacket

Figure 1. Experimental reaction system.

3. Working equations and processes simulation

3.1. Synthesis of PLA

The polymerization mechanism that represents the reaction kinetics and a phenomenological mathematical model are obtained from Yu et al. (2011). In addition, based on the peculiar design of the laboratory pilot-plant scale, such rigorous model was adjusted. Each kinetic rate constant is computed by Arrhenius expression and the kinetic parameters were estimated using the *BzzMath* Library (Refinetti et al, 2014; Buzzi-Ferraris and Manenti, 2012). The mathematical model is solved by a Runge-Kutta type algorithm implemented in C++ programming language.

3.2. Synthesis of nylon-6

The polymerization kinetic and a model equations system have been already described in Seavey et al. (2003) and Arai et al. (1981). In addition, based on the particular design of the laboratory pilot-plant scale, the phenomenological model was adjusted and the Arrhenius expression is used to calculate each kinetic rate constant. The kinetic parameters have been obtained by Funai et al. (2012). Subsequently, the process was implemented in Aspen Plus simulator (by Aspen Technology).

These mathematical models are in good agreement with the behaviour of the laboratory pilot-plant and reused as virtual plants for the purposes of this work.

4. Fuzzy modelling

Fuzzy set theory was introduced by Zadeh (1965) and it is an extension of the classical crisp logic into a multivariate form. Fuzzy approaches have several advantages over crisp ones: the main one being that they have more flexible decision boundaries, and thus are characterized by their higher ability to adjust to a specific domain of application and more accurately reflect its particularities (Tsipouras et al., 2008). Such models are expressed by a set of linguistic fuzzy rules, which are derived from the experience of skilled operators, or by a set of fuzzy implications that locally represents the input–output relationship in the process.

The first point to be considered in the procedure of fuzzy modelling is the definition of the model structure that makes up the system rule base. The structure considered in this work was originally proposed by Takagi-Sugeno (1985). In this approach, fuzzy IF-THEN rules represent local input-output relations of a nonlinear system. Thus, a fuzzy model can be regarded as a collection of several linear models applied locally in the fuzzy regions defined by the rule premises where the overall model is represented as the interpolation of these linear models. According to Lima et al. (2010), it has a conveniently dynamic structure so that well-established linear systems theory can easily apply to the theoretical analysis and design of the overall closed-loop system. After, the identification data for the fuzzy models are generated. Thus, the training and test data set are obtained and the models parameters are evaluated.

Here, the formulation of the functional fuzzy models was realized in two steps: first, the techniques for fuzzy models identification were tested on Matlab platform; second, the appropriate methodologies were used to build a fuzzy modeling algorithm in Fortran 90 programming language. The resulting program was reached by using subtractive clustering and least-squares methods (Lima et al., 2010). The results of model validation are illustrated through figures and quantified as follows by average quadratic error:

$$Error = \sqrt{\frac{\sum_{k=1}^{m} (\bar{y}_k - y_k)^2}{m}} \tag{1}$$

where k = time, m = number of considered discrete instants, $\bar{y}_k$ = predicted output by the fuzzy model, and y_k = output of the process (from phenomenological model).

5. Results and discussion

For the PLA production, a total simulation time equal to 2 h and a sampling rate of 0.001 h were adopted. A data set with 2,000 points was used as for training as for validation of the fuzzy model. A Takagi-Sugeno fuzzy model was formulated for the real-time identification of the weight average molecular weight (*Mw*). The temperature of the water stream in the jacket (*Tj*) is used as manipulated variable. Three inputs are considered for the model: *Tj* at the *k*th sampling time, *Tj* at the (*k* - 1)th sampling time, and *Mw* at the (*k* - 1)th sampling time. Five rules were generated for the fuzzy model. Average quadratic errors lower than 1 % were obtained. The results of validation are illustrated in Figure 2, which shows a very good prediction for the output variable since fuzzy and phenomenological models are practically overlapped. In addition, the long-

range predictions are quite accurate and can be reliable to apply on a future development of optimal control policies.

In the synthesis of nylon-6, a total simulation of 6 h was considered. In this case, the simulation occurs in steady state (no dynamics in the simulation and only the final value is considered). A data set from 9 different operating conditions was used as for training as for validation of the fuzzy model. Thus, a Takagi-Sugeno fuzzy model was formulated for the steady identification of the number average molecular weight (*Mn*). Three control variables were adopted: the reactor temperature, the reactor pressure, and the initial mass of acetic acid, which is used as chain terminator. Two rules were generated for the fuzzy model. Average quadratic errors of about 9 % were obtained, indicating the need for more identification data. However, good results of validation were achieved and these are illustrated in Figure 3, which shows a very good prediction for the output variable as fuzzy and phenomenological data are very close.

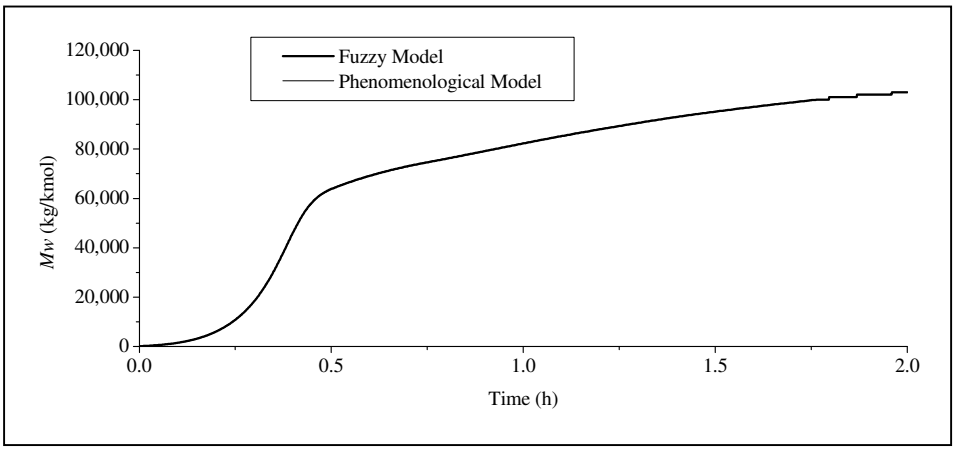

Figure 2. Validation of the fuzzy model for the PLA production.

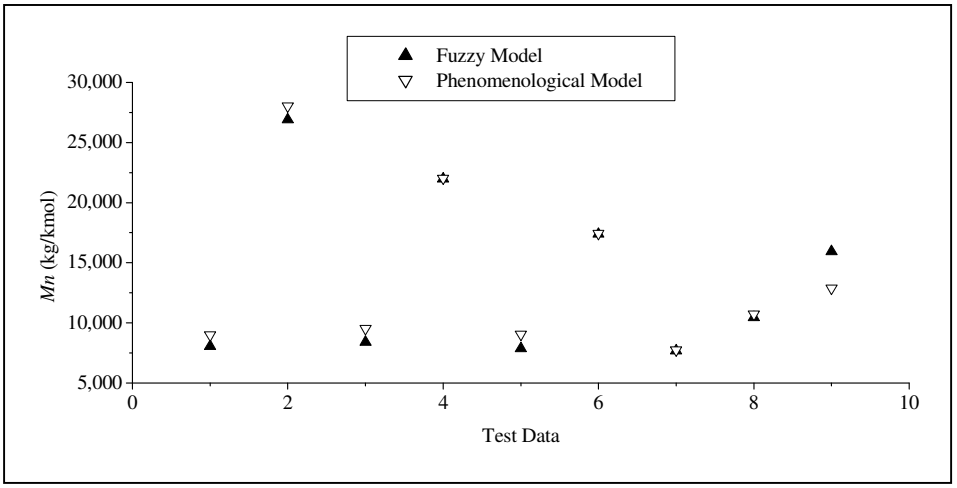

Figure 3. Validation of the fuzzy model for the synthesis of nylon-6.

6. Conclusions

Fuzzy models were developed in this work for two batch polymerization processes. The analysis of results has demonstrated that the Takagi-Sugeno fuzzy models represent the systems in a very satisfactory way for the respective average molecular weights. In fact, the use of functional fuzzy models is a good and promising alternative to model complex chemical reaction processes such as the polymerization systems. The main advantage of such a model approach is the use of an input/output data set together with qualitative information. As described, discontinuous polymerization reactors are usually tricky and they are represented by complicated differential equations, particularly hard to solve. On the other hand, a fuzzy model is simpler to construct, identify, and solve and, therefore, presents an efficient way to model a system for control and real-time optimization purposes, among others.

Acknowledgements

The authors acknowledge the financial support of FAPESP (Fundação de Amparo à Pesquisa do Estado de São Paulo), CAPES (Coordenação de Aperfeiçoamento de Pessoal de Nível Superior), CNPq (Conselho Nacional de Desenvolvimento Científico e Tecnológico) and INCT-BIOFABRIS (National Institute of Science and Technology in Biomanufacturing).

References

Y. Arai, K. Tai, H. Teranishi, T. Tagawa, 1981, Kinetics of Hydrolytic Polymerization of ε-Caprolactam: 3. Formation of Cyclic Dimer, Polymer, 22, 273-277.

N. Aziz, I. Mujtaba, 2002, Optimal Operation Policies in Batch Reactors, Chemical Engineering Journal, 85, 313-325.

G. Buzzi-Ferraris, F. Manenti, 2012, BzzMath: Library Overview and Recent Advances in Numerical Methods, 22 European Symposium on Computer Aided Process Engineering, 30, 1312-1316.

V. Funai, D. Melo, N.M.N. Lima, R. Maciel Filho, 2012, Simulation and Application of Response Surface Methodology to a Nylon-6 Hydrolytic Polymerization in a Semibatch Reactor, Journal of Applied Polymer Science, 127, 2910-2921.

N.M.N. Lima, L. Zuniga, F. Farias Júnior, F. Manenti, R. Maciel Filho, M. Embiruçu, M. Wolf Maciel, 2014, Optimal Fuzzy Control of Batch Polymerization Reactors: Application to PMMA Production for Biomedical Purposes, Computer Aided Chemical Engineering, 33, 799-804.

N.M.N. Lima, L. Zuniga, R. Maciel Filho, M. Wolf Maciel, M. Embiruçu, F. Grácio, 2010, Modeling and Predictive Control using Fuzzy Logic: Application for a Polymeraztion System, AIChE Journal, 56, 965-978.

K. Mehran, 2008, Takagi-Sugeno Fuzzy Modeling for Process Control, Industrial Automation, Robotics and Artificial Intelligence (EEE8005).

D. Refinetti, A. Sonzogni, F. Manenti, N. Lima, L. Zuniga, R. Maciel Filho, 2014, Modeling and Simulation of Poly(L-Lactide) Polymerization in Batch Reactor, Chemical Engineering Transactions, 37, 691-696.

K. Seavey, N. Khare, Y. Liu, T. Williams, C. Chen, 2003, A New Phase-Equilibrium Model for Simulating Industrial Nylon-6 Production Trains, Industrial & Engineering Chemistry Research, 42, 3900-3913.

T. Takagi, M. Sugeno, 1985, Fuzzy Identification of Systems and its Applications to Modeling and Control, IEEE Transactions on Systems, Man, and Cybernetics, 15, 116-132.

M. Tsipouras, T. Exarchos, D. Fotiadis, 2008, A Methodology for Automated Fuzzy Model Generation, Fuzzy Sets and Systems, 159, 3201-3220.

Y. Yu, G. Storti, M. Morbidelli, 2011, Kinetics of Ring-Opening Polymerization of L,L-Lactide, , Industrial & Engineering Chemistry Research, 50, 7927-7940.

L. Zadeh, 1965, Fuzzy Sets Information and Control, 8, 338-353.

Krist V. Gernaey, Jakob K. Huusom and Rafiqul Gani (Eds.), 12th International Symposium on Process Systems Engineering and 25th European Symposium on Computer Aided Process Engineering.
31 May – 4 June 2015, Copenhagen, Denmark

Modeling dissolution of solids based on cellular automata with changing sizes of cells

Sviatoslav I. Ivanov, Irina A. Tiptsova, Natalia V. Menshutina,

D. Mendeleev University of Chemical Technology of Russia (MUCTR), Miusskaya sq.9, Moscow, 125047, Russia
chemcom@muctr.ru

Abstract

Nowadays the actual task for science and industry development (aerospace, pharmaceutics, construction and etc.) is obtaining of new materials with desired properties. To obtain new materials it is necessary to carry out a lot of experiments and as a result, it demands much labor and energy costs. This work presents the mathematical model of cellular automata with variable cells size. The comparison of the developed mathematical model with the previous one has been done.

Keywords: mathematical modeling, cellular automata, modeling of dissolution

1. Introduction

During the search of new materials composition with a certain structure and certain physicochemical properties, the important task is to develop mathematical and computer models and their realization using high-performance parallel computing in order to significantly reduce the number of experimental researches. The modern generation of computers allows to carry out the mathematical modeling of various processes at different nano-, micro- and meso-levels. Mathematical and computer modeling allow to determine the search area for the developed compounds that could significantly accelerate the developing process and reduces its cost.
This paper presents the new mathematical model based on cellular automata with variable cells sizes.

2. Model of solid dissolution based on cellular automata

Currently there are several models describing the process of solid dissolution (J. Siepmann and F. Siepmann, 2013). The most widely used models are based on cellular automata (Laaksonen et al., 2009). At all previously known dissolution models based on cellular automata the cells had the fixed size that impose the certain restrictions on the model (Kimber et al., 2011). The proposed model for the solid dissolution based on cellular automata with variable cells sizes avoids the disadvantages of the previous ones.
The following assumptions have been accepted in the mathematical model:
1) the system is a set of cells;
2) the field has open borders; the substance is removed from the cells at the borders on each iteration;
3) each cell has three characteristics: the type of substance, the amount of substance (concentration) and aggregate state (solid, liquid);
4) the calculation is carried out iteratively (on each iteration dissolution and diffusion processes are occurred at the same time).
The model of dissolution is described by the Eq.(1):

$$\frac{dc}{dt} = D * F * (C_i - C_j) \quad (1)$$

where D is diffusion coefficient, F is surface of contact area while cells interaction, C_i, C_j are concentrations respectively in the i-th and j-th cells.

Next four figures present the possible states of the cells in the cellular automata. The initial state of the cell (relative to which it is considered by cellular automata) is shown on the left, the changed state of the cell is on the right.

In all cell «liquid – solid» pairs the border is shifted to direction of cell with solid, and it is accompanied by transfer of substance from solid to liquid state. It means that in cell with solid state the amount of substance is decreased, and in cells with liquid state the amount of dissolving substance is increased. The figure 1 presents a cell with solid surrounded by cells with liquid on four sides. Hence, the cell with «liquid-solid» borders is displaced with all sides and this cell is reduced in size.

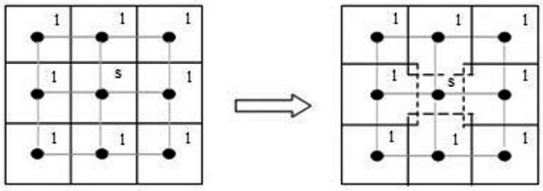

Fig.1. Cell with solid surrounded by cells with liquid

The figure 2 presents a cell with solid surrounded by three cells with liquid and one cell with solid, therefore, and only three sides of the «liquid-solid» cell border will be displaced.

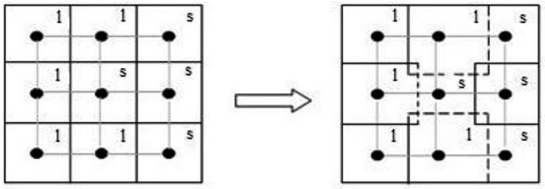

Fig.2. Cell with solid surrounded by three cells with liquid.

The figure 3 presents the cell with solid borders with two cells with liquid, so the shifting of the «liquid – solid» cell borders are only from two sides.

The figure 4 presents the case when the cell with solid has the left boundary with the cell with liquid, so the shifting of the «liquid – solid» cells borders are only between these cells.

While the calculation of dissolution the input data are linear size of the field - N cells and the maximum amount of each substance in the cell volume.

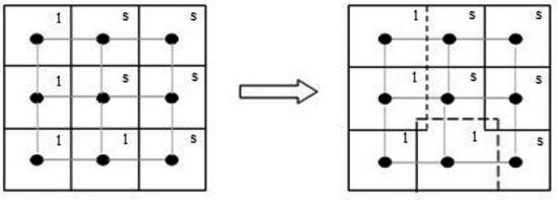

Fig.3. Cell with solid surrounded on two sides by cells with liquid

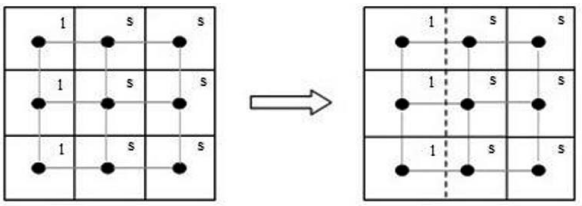

Fig.4. Cell with solid surrounded on one side by cells with liquid.

During dissolution the substance from cells with solid transfers to the cells with liquid, consequently, the substance amount in the cells is changed. On this basis one may assume that the distance between cells are changed too. In all pairs of the «liquid – solid» cells their boundaries are shifted toward cells with solid.
The values for all distances between the cells are stored in the linked matrix presented in the table 1.

Table 1. Linked matrix.

№ i-th cell	№ j-th cell	Distance i-j	Distance j-i
1	2	dl12	dl21
1	3	dl13	dl31
…	…	…	…

The symbols in the Table 1:
dl12 - distance from the cell 1 center to the border of cell 1 and cell 2;
dl21 - distance from the cell 2 center to the border of cell 1 and cell 2;
dl13 - distance from the cell 1center to the border of cell 1 and cell 3;
dl31 - distance from the cell 3 center to the border of cell 1 and cell 3.
The linked matrix contains the values of the distances between eight neighboring cells that allow to resize cells, or even to remove the cells (during substance transfer from solid to liquid state).
The figure 5 presents the interaction between two neighboring cells. In case a) it is seen the change of distance between the cells and the shifting of cell borders towards the cell with solid. In case b) there is a "shift of the center" when the substance from cell 2 transfers to cell 1, thus the volume of cell 2 is reduced (volume of cell 1 is increased respectively). The calculated distance dl2 becomes negative. In order to avoid this, the center of cell 2 is shifted and the distance dl2` becomes positive. If the "shift of the center" is not possible due to lack of substance in the cell, such cell is removed.

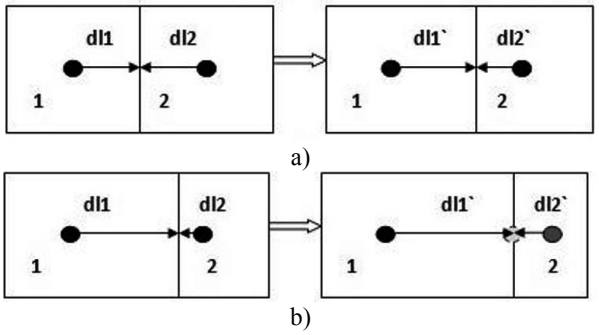

Fig. 5. Interaction of the neighboring cells: 1-liquid 2-solid;

a) change of distance between the cells during the dissolution;

b) "shift of the center".

The figure 6 presents the graphics of the density for the substance distribution from the selected iterations. As it is seen from the graphics in the iteration №1 the system has only two types of cells: the substance concentration is equal 0, and the maximum substance concentration (it is given in advance) is equal 255. In iteration №100 the number of cells with concentration 0 are decreased approximately by 4 times. On the graphics it is seen that while increasing of iterations, the cells concentration are gradually aligned.

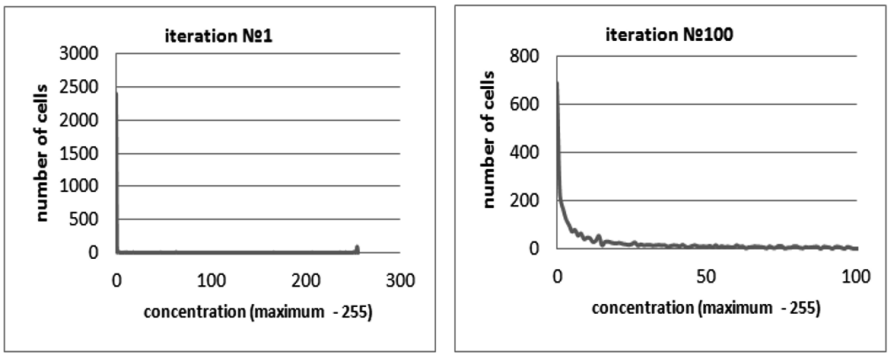

Fig.6. Graphics of the density of substance distribution

3. Discussion

The comparison of the proposed model by cellular automata presenting a set of cubic fields with linear size N cells with the solubility model developed before has been done (Ivanov et al., 2013).

The graphic illustration of the cellular automata is shown in figure 7.

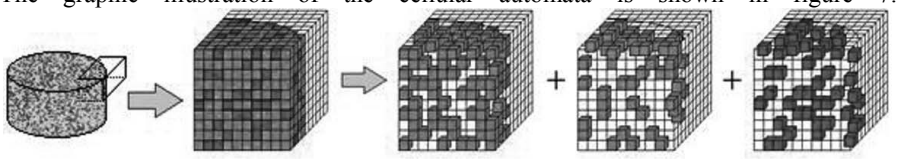

Fig.7. The graphic illustration of the cellular automata

Each iteration consists of three stages:

• calculation of dissolution (the transfer from solid to liquid state);
• calculation of diffusion (substance exchange in liquid state);
• calculation of substance transfer due to external factors.

During the calculation of dissolution the linear sizes of one cell and cellular automata fields are given as input data. The maximal possible amount of substance inside one cell depending on cell volume is determined.

After that, the substance amount corresponding to this substance-saturated solution is determined too for the one cell volume. Then the following assumption has been done: if the substance concentration in the cell is between the saturated solution concentration in one cell volume and possible maximal substance amount then the substance aggregate state is adopted as "solid". If the substance concentration is between zero and the saturated solution concentration in one cell volume, then the substance aggregate state is accepted as "liquid."

After input of initial data the iterative calculation process for substance dissolution takes place. The dissolution is calculated in all cells having the aggregate state "solid" to all neighboring cells and it is inversely to the concentration of the dissolved substances therein. The calculation of the substance amount transferred to the dissolved state is as

the following. The cell mass change where the substance is dissolved it can be calculated by the Eq.(2):

$$\frac{dM}{d\tau} = -kF(\mathrm{C}^* - \mathrm{C}) \tag{2}$$

where M is mass of solid, k is dissolution coefficient, F is dissolution surface, C^* is the saturated solution concentration, C is the current concentration in the solution. The expression for the dissolution coefficient (k) calculation in the stirred reactors has been obtained on the assumption that the decisive role in external mass transfer plays the destruction of the boundary layer by small-scale turbulent fluctuations:

$$k = e^{1/4} Sc^{-3/4} \tag{3}$$

$$e = \frac{N}{G} \tag{4}$$

$$Sc = \frac{\omega}{D} \tag{5}$$

e is the specific dissipation of mechanical energy; Sc is Schmidt criterion; N is power consumed for mixing; G - stirred volume mass.

New cell aggregate state is determined after the dissolution calculation in all possible cells that is based on new values of substance amount in the cells taking into account the rules mentioned above.

The diffusion calculation is based on Fick's equation. The substance diffusion coefficient in solution has been founded by molecular dynamics method using software NAMD, which allows to takes into account the interactions between the molecules of solvent and dissolved substance depending on the dissolution conditions.

Only cells having the aggregate state "liquid" are involved to diffusion calculation. For each cell with dissolved substance and its new neighbors new values of the cell substance amount are calculated based on previous ones.

The last part of the cellular automata iteration is the calculation of substance transfer due to the external factors impact.

The figure 8 shows the comparison of the calculated data on two computer models and the experimental researches.

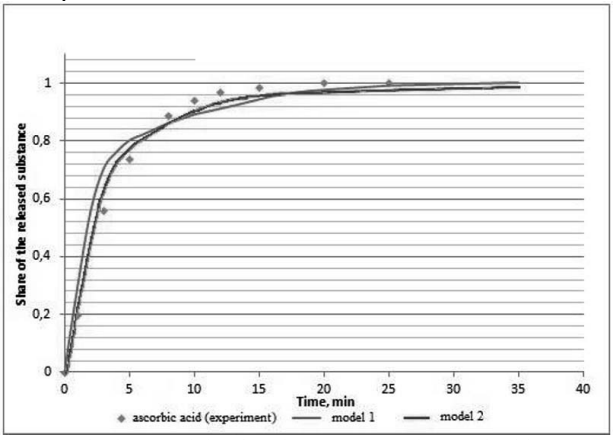

Fig.8. Calculation of the dissolution of ascorbic acid tablet. Comparison of the values calculated using the model with experimental data: model 1 - the cellular automata model for solubility made before; model 2 - the proposed model.

The comparison showed that the calculation accuracy for the proposed model is on 10-15% higher. This model based on cellular automata with variable cell size has several advantages:
• give the possibility of qualitative image of geometric shapes;
• the gradual reduction of the cells with solid reduces the number of the cellular automata elements that accelerate the calculating;
• allows to take into account the swelling process;
• give the possibility to calculate any body undergoing deformation as well as flexible body too.
The developed algorithm is enough resource-intensive in terms of time, but the removal of cells from solid during dissolution allows to accelerate the calculation process. However, the calculation productivity increasing is the priority task. Therefore, the apparent prospect is the use of parallel computing by means of CUDA technology.

4. Conclusions

In the future, it is planned to develop this mathematical model and to test it during the simulation of complex systems including a number of factors:
• substance dissolution;
• components swelling;
• solvent diffusion through the surface.
The study was supported by the Ministry of Education and Science of Russian Federation within the contract № 14.574.21.0111 «Creation of software and computer systems for the computer modeling of nanostructured sorbents based on organic and inorganic aerogels, including with embedded carbon nanotubes, and adsorption processes in its" 2014 .
In addition, during the model development in future it is planned to take into account the capturing film layer and polarization effects, in particular, the mutual influence of the soluble components.
In future the development of models based on cellular automata and their methodology will allow to transfer to more accurate and computing performance by using parallel computing. These mathematical and computer models can be used in such areas as pharmaceutics, agriculture, development of new materials and designs of its. The research is supported by the Ministry of Higher Education and Science within the framework of project component of the State Assignment №2.429.2014/K.

References

S. Ivanov, D. Lovskaya, N. Menshutina, 2013. Cellular automata modeling of dissolution of solid-dosage forms. Computer Aided Chemical Engineering, 883-888.
J. Kimber, S. Kazarian, F. Stepanek, 2011. Microstructure-based mathematical modelling and spectroscopic imaging of tablet dissolution. Computers and Chemical Engineering 35.
T. Laaksonen, H. Laaksonen, J. Hirvone, L. Murtomaki, 2009. Cellular automata model for drug release from binary matrix and reservoir polymeric devices. Biomaterials 30.
J. Siepmann, F. Siepmann, 2013. Mathematical modeling of drug dissolution. International Journal of Pharmaceutics.

Krist V. Gernaey, Jakob K. Huusom and Rafiqul Gani (Eds.), 12th International Symposium on Process Systems Engineering and 25th European Symposium on Computer Aided Process Engineering.
31 May – 4 June 2015, Copenhagen, Denmark

Data Analysis and Modelling of a Fluid Catalytic Cracking Unit (FCCU) for an Implementation of Real Time Optimization

Juan D. Reyes*, Adriana L. Rodríguez, Carlos A.M. Riascos

Universidad Nacional de Colombia, Chemical and Environmental Department,Group of Process Systm Engineering, Avenida Carrera 30, 45-03, Bogotá 111321, Colombia.
jdreyesf@unal.edu.co

Abstract

In the Fluid Catalytic Cracking Units (FCCU) large hydrocarbon molecules are cracked into smaller molecules, generating high value products such as diesel, gasoline and useful petrochemical olefins. The control of these units is fundamental to maintain a satisfactory operation. Hence, the Real Time Optimization has proved an interesting strategy. A dynamic simulation of a FCCU was developed using a phenomenological industrial validated model. A Dynamic Neural Network (DNN) was trained with data from the FCCU model and gross and systematic errors were added to employ this system as a virtual plant. Data from this virtual plant were used to study strategies of online data processing, considering steady state identification (SSI) and gross error detection (GED), in order to eliminate measurement noise, as the initial steps into an RTO implementation.

Keywords: Fluid Catalytic Cracking Unit, Real Time Optimization, Data analysis, Virtual plant.

1. Introduction

The fluidized catalytic cracking unit (FCCU) is still a core operation in the modern fuel oriented refineries. In this unit, large hydrocarbon molecules are cracked into light high value products. Several studies have been performed on the modelling of a FCCU, such as the mechanistic model presented by Fernandes et al. (2005): a dynamic state model based on fundamental balance equations that include the riser, the stripper and the regenerator. Due to the satisfactory results, the mechanistic modelling has been extensively developed and reported.

Real Time Optimization is an operational strategy that tries to maintain the process close to the optimal operating conditions by means of adjusting a set point continuously. In that way, RTO requires measurements from the process to estimate its performance, an optimization procedure to estimate the optimal condition and a process control system to implement them. A special characteristic is that measurements from real plants are contaminated with errors; therefore, a denoising procedure is required.

In the present work, a dynamic simulation of a FCCU was developed using a phenomenological industrial validated model. A set of perturbations was applied to the model to obtain a large quantity of dynamic data. A parametric study of the input variables was developed in order to establish the most important ones for the system performance. Then, the selected variables were chosen as the inputs to design, train and test a Dynamic Neural Network (DNN) that will be considered as the virtual plant of

FCCU. Due to measurements in real systems are often corrupted with random noise, gross error and systematic errors; Gaussian error and gross error were added on simulated data from DNN. Finally, data from the virtual plant were employed to study strategies for the online data processing, considering steady state identification (SSI) and gross error detection (GED). For SSI, the wavelets method was the selected one, while for GED a strategy based on robust maximum likelihood estimator was employed. The advantage of using data from a virtual plant to study the strategies for online processing is that, due to real values are perfectly known, the performances of the strategies can be quantified without uncertainties. The developed virtual plant will be employed, in a next work, for studying Real Time Optimization (RTO) strategies.

2. Methodology

Considering that a DNN will be employed as the virtual plant of FCCU, a great quantity of data is necessary for training the network generated using a phenomenological industrial validated model. To define the input variables for the DNN a sensitivity analysis was developed and errors were added for simulating real plant data. The virtual plant data were employed to assess strategies for the data online processing.

2.1. FCCU base model and data generation

A dynamic simulation of the FCCU was developed using the industrial validated model proposed by Arbel et al. (1995). The FCCU model considers a quasi-steady state riser, a two phase regenerator and a stripper. In this model the dynamic behaviour is controlled by the residence time in the regenerator and it considers a detailed description of the cracking kinetics that occurs in the riser.

A set of modifications on the conditions was applied in the model for obtaining a large quantity of dynamic data that allows studying the system. These were systematically performed by using the control and disturbance variables, presented in the Table 1.

The oil composition bounds were in concordance with the range of stock compositions used in the model parameters in the fitting of the riser cracking kinetics, described by Arbel et al. (1995). For control variables a step type change was imposed. This is also true for the atmospheric and oil feed temperatures. The composition was changed by using a ramp type of blending between a pair of assays with a 0.05 blend fraction per minute.

Table 1. Control and disturbance variables for the FCCU dynamic model.

Variable name	Variable type	Lower bound	Upper Bound
Oil feed flow rate (kg/s), F_{of}	Control	29.7	89.1
Steam flow rate to the stripper (kg/s), F_{ss}	Control	1.6	4.8
Catalyst circulation rate (kg/s), F_{cat}	Control	178.3	534.8
Air flow rate to regenerator (kmol/s), F_{air}	Control	23.8	118.8
Atmospheric temperature (K), T_{atm}	Disturbance	302.2	330.2
Oil feed temperature (K), T_{feed}	Disturbance	338.6	505.2
Weight fraction of lumps in the oil feed (wt %)			
1) Heavy paraffins, Ph		2.45	14.79
2) Heavy naphtenes, Nh		4.05	19.61
3) Heavy aromatics substitution groups, Ah		1.74	12.83
4) Heavy carbons among aromatic rings, Rh	Disturbance	1.60	6.70
5) Light paraffins, Pl		6.15	37.11
6) Light naphtenes, Nl		10.15	49.19
7) Light aromatics substitution groups, Al		4.36	32.18
8) Light carbons among aromatic rings, Rl		4.00	16.80

2.2. Sensitivity Analysis

A sensitivity study on the input variables was developed for the FCCU in order to define the most important ones in the system performance. These variables were the input to design, train and test the Dynamic Neural Network (DNN). The analysis was performed by using the control and disturbances variables defined in the Table 1, keeping them within the upper and lower bounds of the analysis spectra.

The methodology of global sensitivity approach presented by Sobol (2001) was used to identify and calculate the effect of the coupled parameters in the performance of the gasoline yield (G), riser outlet temperature (T_{ris}), dense phase regenerator temperature (T_{rgn}) and CO/CO2 ratio.

2.3. Development of the Dynamic Neural Network (DNN)

The neural network was developed implementing the nonlinear autoregressive network with an exogenous inputs model (NARX), using the Levenberg-Marquadt training algorithm. A schematic representation of the DNN model is presented in the Figure 1 where, the inputs are consistent with the classification presented in the Table 1, and the outputs are the required measurements for RTO processing and assessing.

2.4. Error Addition

For simulating the behaviour of a real FCCU Gaussian error was added to outputs from Neural Networks with a Signal Noise Ratio of 40 (SNR=40). This ratio characterizes the detection quality of the signal of a measurement system. It compares the level of a desired signal to the level of background noise. Furthermore, a set of 20% of the overall output signal data was contaminated with randomly gross error at a magnitude from 0 to 5 % of the maxima values.

2.5. Wavelets de-noising

For denoising the output signals, the Short Time Fourier Transform (STFT) and Wavelets strategies were tested. Other strategies as the linear filter were discarded because their application is only in stationary signals. In the wavelet method, the signal is decomposed into low and high frequency components. The denoising was developed following the soft thresholding methodology that requires three steps which are decomposition of the signal, thresholding and reconstruction of the signal. The first one was carried out through wavelet transform, the second one by the universal thresholding or "sqtwolog" method proposed by Donoho (1995). The inverse wavelet transform and the retained coefficients were used for reconstructing the signal. Thresholding values are very important because they determine how much noise is removed from the signal. If the noise amount quantity is very small, some important features from the signal can be lost, and if it is very large, the noise will not be removed properly.

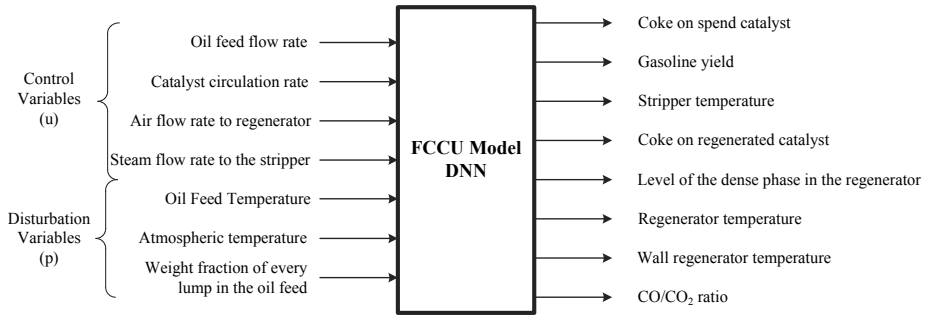

Figure 1. Input and output variables for the DNN model of the FCCU.

2.6. Steady state detection and gross error elimination

Steady State Detection (SSD) was carried out using the wavelet method proposed by Jiang (2003). The changes of an output signal of the system can be represented by means of the first order wavelet Wf(t). Then, when Wf(t)=0 the system is at steady state, but the zero crossing points through second order wavelet (WWf(t)), as proposed by Donoho(1995), are necessary to be considered.

Steady state is detected from the first and second wavelet transform with a steady state index β which is restricted between 0 and 1. β=0 indicates that an unsteady state is identified and β=1indicates that steady state is achieved. Jiang (2003) describes different conditions and restrictions associated to work out β value.

Gross error detection was done by minimizing the generalized maximum likelihood objective function with Hampel's redescending M-estimator which is a robust objective function that reduces the weight of data with higher difference against the estimation (Özyurt and Pike, 2004).

2.7. Methods efficiency estimation

For quantifying the ability of gross error detection into the steady state (SS) intervals, 24 SS (8000 data each) were evaluated. The criteria used for the evaluation were the ones reported by Özyurt Pike (2004) where, Overall Power (OP), Average number of Type I errors (AVTI) and Median Total Error Reductions (Mean TER) were employed. OP estimates the number of gross error correctly identified; while, AVTI measures the wrong gross error detection.

3. Results and discussion

The variables used as targets in this work are related to the main performance of the FCCU, such as the gasoline yield (G), riser outlet temperature (T_{ris}), dense phase regenerator temperature (T_{rgn}) and CO/CO2 ratio. The sensitivity analysis performed on the FCCU indicates that the control variables defined in the Table 1 have a high response factor for the targets, as shown in Table 2.

The global sensitivity indexes show that the rates of feed oil flow (F_{of}), catalyst circulation (F_{cat}) and air flow (F_{air}) have the highest sensitivities in relation to the targets. These values can be associated with high performance in the controllability since their changes will generate important gains.

Table 2. Global sensitivity indexes for the Input variable-target of the FCCU

Input Variable	Target			
	G	T_{ris}	T_{rgn}	CO/CO_2 ratio
F_{of}	0.859	0.740	0.414	0.385
F_{ss}	0.316	0.230	0.121	0.114
F_{cat}	0.810	0.690	0.510	0.501
F_{air}	0.780	0.124	0.890	0.910
T_{atm}	0.213	0.280	0.316	0.284
T_{feed}	0.529	0.750	0.521	0.312
Ph	0.560	0.310	0.425	0.389
Nh	0.682	0.412	0.589	0.403
Ah	0.520	0.254	0.412	0.321
Rh	0.280	0.678	0.789	0.704
Pl	0.551	0.241	0.469	0.341
Nl	0.740	0.128	0.236	0.209
Al	0.210	0.651	0.783	0.635
Rl	0.810	0.103	0.214	0.142

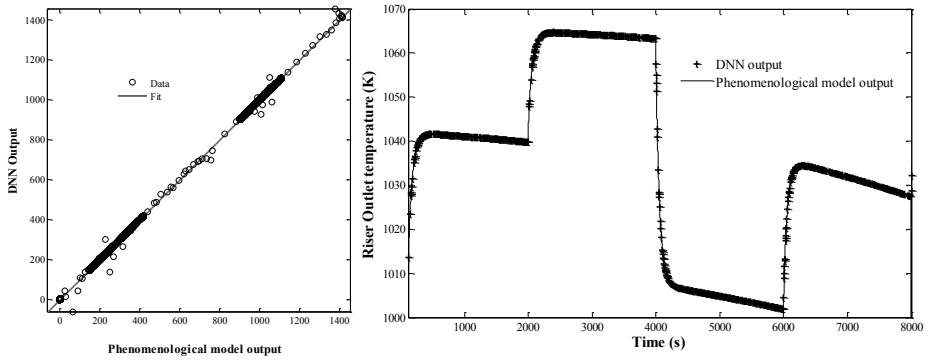

Figure 2. Regression and performance plots for the DNN

The DNN was developed using the NARX model, obtaining a network with 1 hidden layer, 17 hidden neurons, 14 input neurons and 8 output neurons. The performance of the DNN to correlate the behaviour of the phenomenological model is presented in the regression plots, Figure 2. The correlation coefficients (R^2 = 0.999 for the combination of all system outputs) and the visual comparison between DNN predictions and profiles from phenomenological model allows to affirm that the DNN achieves a good prediction of the FCCU behaviour.

For denoising and steady state identification wavelets generated satisfactory results and, based on their performance, it was selected. The DNN values are employed as the true value and the wavelets outputs will feed the next RTO steps. The comparison between them indicates that an efficient elimination of Gaussian error, still in presence of gross error, is attained when choosing the mother wavelet properly, Figure 3. In this case the most accurate wavelet family was Daubechies.

The indexes OP, AVTI and Mean TER are presented in Table 3. Mean TER value indicates that is possible to reach up to 69.8% total error reduction from a variable, and Figure 3 shows that the wavelets method proposed by Jiang (2003) is efficient for steady state detection. Due to slowly variations in signals, detection of SS based only on composition profiles, results non-presented in this work show an important quantity of type II error generating wrong steady state detections. The effect of error can be reduced by adjusting the λ_2 parameter defined by Jiang (2003).

Table 3. Parameters for gross error detection assess.

Parameter	Variable							
	C_{sc}	G	T_{sc}	C_{rgc}	L_{rgn}	T_{rgn}	T_{wall}	CO/CO_2 ratio
OP	0.847	0.856	0.721	0.845	0.789	0.701	0.711	0.804
AVTI	6.541	7.251	1.253	5.142	2.351	0.986	1.254	5.896
Mean TER	0.548	0.458	0.689	0.578	0.683	0.549	0.698	0.423

4. Conclusions

Considering that the fitted prediction of the steady states, trasient periods, and a minumium delay on calculations are fundamental characteristics for online analysis, the DNN trained with data from a validated phenomenological model is a good option to built a virtual plant for the RTO studies.

The denoising and steady state detection using the wavelets method were efficiently developed. Although the presence of type II error in signals with large time characteristic constant (τ)".

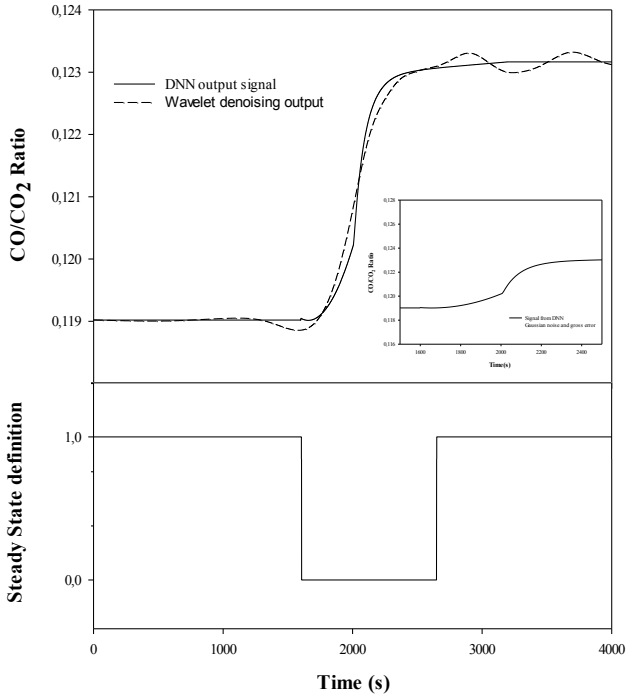

Figure 3. Denoising and steady state identification

Acknowledgments

The authors are grateful for the financial support granted by the program "Jóvenes Investigadores" from Colciencias and Universidad Nacional de Colombia.

References

A.A. Alaradi, S. Rohani, 2002, Identification and control of a riser-type FCC unit using neural networks, Computers & Chemical Engineering, v. 26, n. 3, p. 401-42.

A. Arbel, Z. Huang, I.H. Rinard, R. Shinnar, A.V. Sapre, 1995, Dynamic and Control of Fluidized Catalytic Crackers. 1. Modeling of the Current Generation of FCC´s. Industrial & Engineering Chemistry Research, v. 34, n. 4, p. 1228–1243.

D.L. Donoho, 1995, De-noising by soft-thresholding, IEEE Transactions on Information Theory, v. 41, n. 3, 613-627.

J. Fernandes, J.J. Verstraete, C.C. Pinheiro, N. Oliveira, F. R. Ribeiro, 2005, Mechanistic Dynamic Modelling of an Industrial FCC Unit, Computer Aided Chemical Engineering, v. 20, 589-594.

T. Jiang, B. Chen, X. He, P. Stuart, 2003, Application of steady-state detection method based on wavelet transform, Computers & Chemical Engineering, v. 27, p. 569–578.

D.B. Özyurt, R.W. Pike, 2004, Theory and practice of simultaneous data reconciliation and gross error detection for chemical processes, Computers & Chemical Engineering, v. 28, n. 3, p. 381–402.

I. Sobol, 2001, Global sensitivity indices for nonlinear mathematical models and their Monte Carlo estimates, Mathematics and Computers in Simulation, v. 55, n. 1-3, p. 271–280.

Krist V. Gernaey, Jakob K. Huusom and Rafiqul Gani (Eds.), 12th International Symposium on Process Systems Engineering and 25th European Symposium on Computer Aided Process Engineering.
31 May - 4 June 2015, Copenhagen, Denmark.

A Hybrid Discrete/Continuous Dynamic Model of Trayed Tower Hydraulics

David Pinilla-García and Santos Galán

Universidad Politécnica de Madrid, Department of Chemical Engineering (ETSII).
C/José Gutiérrez Abascal, 2. 28006 Madrid, Spain
santos.galan@upm.es

Abstract

A hydraulic model for trayed towers is presented that can reproduce the detailed behavior of the column in a wide range of operating conditions, including abnormal situations, while being simple, compact and flexible. As a subset of a complete one incorporating energy and material balances, it is designed to be implemented in modern dynamic simulation platforms using hybrid discrete/continuous formalisms.

Keywords: modeling, hybrid, dynamic, distillation, column, tray, hydraulics

1. Introduction

Modeling always implies a compromise between complexity and required detail. In distillation towers, hydraulics determines most of the important dynamic characteristics. Commercial dynamic simulators usually include tray and column modules conceived for the quite limited region of normal operation conditions, that can deal with regulatory control but, as Luyben (2012) points out, are inadequate for safety-related applications. Some cases in safety analysis as well as startup/shutdown simulation can be represented by the so-called high-fidelity models, such as those used in Operator Training Systems (OTS). A third class of models would be those that can reproduce abnormal situations for post-mortem and safety analysis, usually made on an *ad hoc* basis as in the BP Texas City refinery accident (Mogford, 2005). Computational fluid dynamics (CFD) models can go one step beyond, but they are still impractical (though possibly not for long). Increasing model complexity is paralleled by a lack of publicly available descriptions.

The main reference for high fidelity models is a not-so-recent paper by Gani et al. (1986). The model presented is compact and flexible, allowing the simulation of different types of towers and situations, including startup. It considers separate tray and downcomer dynamics, but it disregards vapor phase dynamics. Although it does consider some abnormal phenomena such as downcomer vapor blowing, it neglects others like downcomer liquid reverse flow. The paper also pays attention to the numerical solution, a key issue usually disregarded. More recent publications provide simpler hydraulic approaches. Some do not consider separate tray and downcomer holdups (and the important phenomena that derive from them) (Staak et al., 2011), others disregard vapor phase dynamics (Mahdipoor, 2006; Mahdipoor et al., 2007) and most neglect both (Cab et al., 2002; Chang et al., 1998). Taylor (2007) provides a comprehensive review of distillation modeling, focusing almost entirely on the development of rate-based models and, surprisingly, not discussing tray dynamics. Wittgens and Skögestad (2000) stress the importance (and the lack) of realistic and accurate hydraulic models, which have been pointed out by Kister (1997) as one of the main culprits for the increase in primary design malfunctions. The building and simulation of a compact first-principles hydraulic model that can handle abnormal situations is the aim of the present work.

2. Hydraulic model

The tower model is defined as a modular structure made of a succession of generic and special stages. The latter encompass feed and extraction trays and overhead and bottom sections and are modeled as variations of the generic stage. The former refers to the rest of conventional trays. Index j refers to the stage number for generic stages, counting from the top. Index T refers to the top stage and B to the bottom. This modular structure results in a highly flexible model that can easily reproduce different tower configurations with special features such as side strippers or pumparound refluxes.

Each stage is divided into three compartments: liquid in the tray, liquid in the descending downcomer and vapor (figure 1a). They account for the mass holdups and act as control volumes for the material balances. They are defined by the clear liquid heights, and some of them may even disappear if certain conditions are met. The model is built for generic one pass sieve trays with straight downcomer aprons. Complete mixing for both liquid and vapor phases and froth regime are assumed. Downcomer foaming, hydraulic gradient phenomena and mass-transfer derived fluxes (between different phases) are not considered.

Pressure difference across compartments drive the material fluxes. Most of the hydraulic correlations have been chosen following the recommendations of Kister (1992) and Perry and Green (2008). Other factors such as range of application and ease of implementation have also been taken into consideration. Feed and extraction stages are identical to a generic stage with the addition of the input or output streams to the corresponding mass balances. Overhead stage is similar to a generic stage. It consists of a generic tray and downcomer plus a larger vapor volume, the overhead vapor output and a liquid input, which is fed directly to the tray. Liquid entrained with the exiting vapor is not considered. Bottom stage consists of the bottom liquid and vapor holdups plus the liquid holdup on the last stage downcomer seal, the bottoms liquid output and a vapor input. It is assumed that no weeping falls into the downcomer seal. Liquid entrainment to the last stage is disregarded. Bottom liquid holdup is modeled assuming a flat bottoms geometry (measuring from the tangent line). Liquid flux to it from the downcomer seal is modeled through the standard weir correlation. Streams entering and exiting the tower depend on the characteristics of auxiliary equipment, and are thereby considered to be known variables. This hydraulic model is actually a subset of a more complete one where energy and material balances are incorporated under equilibrium or rated-based schemes.

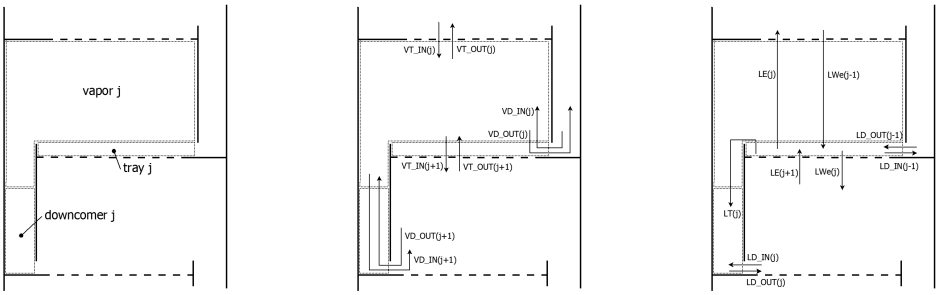

(a) Stage compartments (b) Vapor fluxes (c) Liquid fluxes

Figure 1: Generic stage material fluxes

2.1. Vapor and liquid fluxes

The vapor streams considered are shown in figure 1b. They are defined as positive variables. Although the mass balance could be done allowing negative values, this would complicate the

addition of component and energy balances. V_D is the vapor blown through the downcomers when they are not sealed. The downcomer is considered to be sealed whenever downcomer or tray liquid height exceeds apron clearance: $\max\{h_{D,j}, h_{L,j+1}\} \geq H_a$. It is modeled using Kister's correlation 1979, including the change in space under the apron due to the presence of liquid. If the pressure difference is inverted, it can change direction and go from the downcomer to the tray. As an example, the resulting set of equations are provided below:

$$V_{D,j} = \begin{cases} 0 & \text{if } \max\{h_{L,j}, h_{D,j-1}\} \geq H_a \\ |P_j - P_{j-1}| = \frac{0.4977}{\rho_{V,j}} \left[\frac{V_{D,j}}{A_{dc}}\right]^2 \left[0.7 \frac{A_{dc}}{l_w(H_a - MAX\{h_{L,j}, h_{D,j-1}\}(j))} + 1.2\right] & \text{else} \end{cases} \quad (1)$$

$$V_{D_{OUT},j} = \begin{cases} V_{D,j} & \text{if } P_j >= P_{j-1} \\ 0 & \text{else} \end{cases} \quad (2)$$

$$V_{D_{IN},j} = \begin{cases} 0 & \text{if } P_j >= P_{j-1} \\ V_{D,j} & \text{else} \end{cases} \quad (3)$$

V_T, equal to the vapor load in regular operation conditions, is derived from the standard variation on the orifice equation for sieve trays. If pressure is higher on the tray above and there is no liquid in it, this vapor flux will go downwards. The mass balance is expressed as follows:

$$\frac{dM_{V,j}}{dt} = V_{T_{IN},j} + V_{T_{OUT},j+1} + V_{D_{IN},j} + V_{D_{OUT},j+1} - V_{T_{OUT},j} - V_{T_{IN},j+1} - V_{D_{OUT},j} - V_{D_{IN},j+1} \quad (4)$$

The liquid streams considered are shown in figure 1c. Liquid flow over the downcomer weir (L_T) follows the correlation of Bennett et al. (1997). Stream L_D is derived from the conventional correlation for head loss under the downcomer apron. It has been modified for the cases in which there is no liquid seal, according to the criteria explained above for stream V_D. This flow can either enter or leave the downcomer compartment, depending on the sign of the pressure difference. Weep rate is modeled through the Hsieh and McNulty (1993) correlation. Although it specifies that clear liquid height should be calculated according to Colwell's method, Bennett's has been used instead. Entrainment is generally negligible in the froth regime. However, L_E has been modeled using the Bennett et al. (1997) correlation. Separate mass balances are derived for the tray and the downcomer:

$$\frac{dM_{LT,j}}{dt} = L_{D_{OUT}j-1} + L_{We,j-1} + L_{E,j+1} - L_{D_{IN},j-1} - L_{E,j} - L_{T,j} - L_{We,j} \quad (5)$$

$$\frac{dM_{LD,j}}{dt} = L_{D_{IN},j} + L_{T,j} - L_{D_{OUT},j} \quad (6)$$

3. Simulation

The model presented above has been implemented and solved using Jacobian (RES Group, Inc.) simulation software, but it can be easily translated to other popular platforms such as gPROMS or Aspen Custom Modeler. Issues that arose during simulations (numerical singularities) called for modifications to be introduced in the implementation of the model equations. As an example, the code for flux V_D is provided below:

```
IF (P-P_s) >=1 THEN
        dP=SQRT(P-P_s);
ELSE
        IF (P-P_s) >=-1 THEN
                dP=(P-P_s);
        ELSE
                dP=-SQRT(P_s-P);
        END
END
```

```
K_VD^2=lw*ABS((Ha-MAX(h_L, h_D_s)))/(0.7*Adc+1.2*lw*ABS((Ha-MAX(h_L, h_D_s))));
IF h_L<Ha AND h_D_s<Ha THEN
    CASE traydown_head OF
        WHEN ZERO :
            trdow_head=0;
            VD_S_OUT=0;
            VD_S_IN=0;
            SWITCH TO NEGATIVE IF (P-P_s)<0;
            SWITCH TO POSITIVE IF (P-P_s)>0;
        WHEN POSITIVE :
            trdow_head=1;
            VD_S_OUT=Adc*dP*ABS(K_VD)*SQRT(rhoV/0.4977);
            VD_S_IN=0;
            SWITCH TO NEGATIVE IF (P-P_s)<0;
        WHEN NEGATIVE :
            trdow_head=-1;
            VD_S_OUT=0;
            VD_S_IN=-Adc*dP*ABS(K_VD)*SQRT(rhoV*K_VD/0.4977);
            SWITCH TO POSITIVE IF (P-P_s)>0;
        END #CASE
ELSE
        trdow_head=0;
        VD_S_OUT=0;
        VD_S_IN=0;
END #IF
```

This flux is modeled using the square root of a pressure difference. This is problematic because it results in a numerical singularity when the radicand turns zero. Although this can be avoided explicitly, Newton iterations around this point still result problematic if the square root is maintained due to the change in the system of equations and the discontinuities in the derivative. The adopted solution, consisting in linearizing the flux for small absolute values of the pressure difference (1 Pa), has provided satisfactory results. The head loss constant, K_{VD}, is calculated in a separate equation to simplify its solving. Similar modifications have been introduced for all other equations. Linearization has been done for fluxes L_D, V_T, V_D and overhead vapor product. Reverse V_T flow is set to zero if clear liquid height is higher than 3 mm. Weep and entrainment rates are set to zero for tray liquid heights lower than 0.1 and 0.01 mm respectively.

4. Example: startup of a stripping tower

The following example reproduces tray behavior during the startup procedure, focusing on tray and downcomer sealing. Physical properties are those of the air/water system and vapor phase PVT relationships follow the ideal gas model. A constant temperature profile has been assumed. The tower has 4 trays with 21 in spacing and is 6 ft diameter. It has 0.5 in holes, 13.4% downcomer area, 10% hole/active area ratio, 2 in weir height and 1.5 in apron clearance. The simulated startup procedure is as follows: The tower is initially empty of liquid and with a constant pressure profile. Liquid is introduced in the overhead tray at a constant rate. Bottom Liquid output is set to zero until bottom liquid level reaches a height of 0.8 m. When liquid level reaches 1 m vapor is introduced into the bottom stage at a constant rate.

The following results have been obtained for the tower operating at 1 bar with a liquid rate of 25 kg/s and a vapor rate of 7.1 kg/s, which results in a flooding factor of about 0.84 (calculated using the Lygeros and Magoulas correlation). Figure 2a shows clear liquid (h_L) and froth (h_F) heights in trays. Opposite to what can be expected, rise to their steady state is not uniform, comprising an initial decrease and a strong overshoot. References to this have not been found in the published literature. When vapor is introduced the trays become completely sealed (figure 2b). The seal is temporarily lost later on (t=153s) and a ”pulse” of liquid weeps from above, starting to fill the tray. At this point liquid begins to flow from the tray to the downcomer of the stage above. This continues after the weeping has stopped, accounting for the small decrease in h_L. Shortly afterwards liquid flow under the downcomer acquires it’s normal sense and the tray steadily fills with liquid. When the froth reaches the outlet weir, liquid starts to fall into the downcomer. At the

same time a "pulse" of liquid weeps to the tray below.

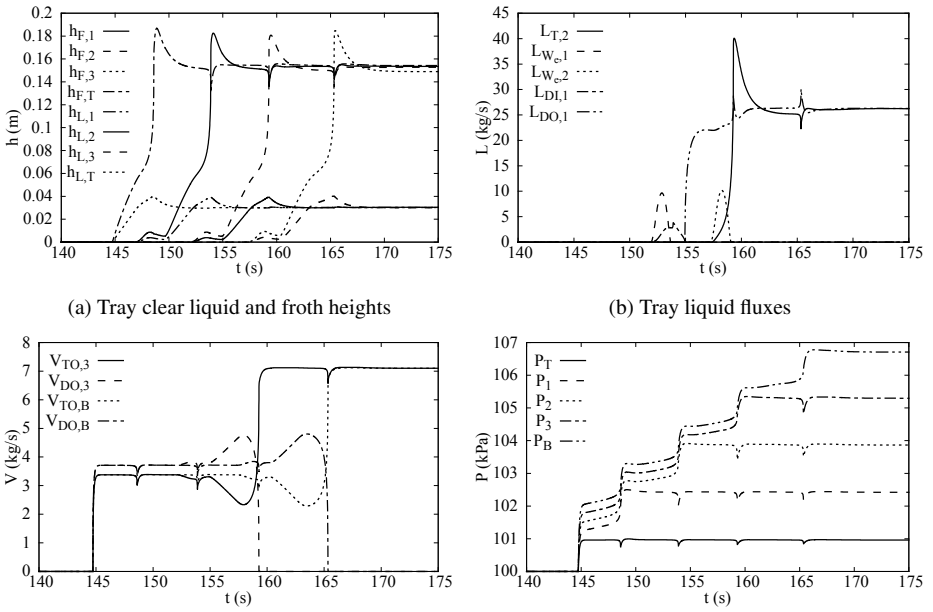

(a) Tray clear liquid and froth heights

(b) Tray liquid fluxes

(c) Vapor fluxes exiting the two bottom stages

(d) Stage pressure

Figure 2: Tray behavior during startup (f=0.84)

Flow under the downcomer V_D (figure 2c) is initially higher than flow through perforations V_T. This difference increases initially as V_T decreases due to liquid beginning to accumulate on the tray above. This temporary decrease accounts for the weeping "pulses". As the liquid level on the tray increases the downcomer seals, causing a rapid fall in V_D until it reaches zero (and the seal is achieved) and an opposite increase in V_T towards it's steady-state value. As the downcomer seals pressure builds up in the stage and in those below (figure 2d). Pressure in the stages above initially decreases due to the decrease in V_D but it subsequently increases. This accounts for the observed anomalous peaks.

Even when a formal experimental validation with an industrial partner is still lacking, the model reproduces the expected behavior of a trayed column. Compared with the results presented in Gani et al. (1986) a reasonable agreement is observed. As an example, in figures 3a and 3b vapor through downcomers and liquid over weirs at startup are shown for both models. It can be seen that, for similar shapes of the trajectories, a more complex behavior is obtained in the proposed model due to the sealing pulses and other effects caused by the inclusion of vapor dynamics. This concordance is not surprising since, to some extent, the proposed model can be considered an upgrade for modern hybrid discrete/continuous dynamic simulators of Gani's model. At lower vapor rates an unexpected phenomenon is predicted by the new model. When the liquid rate is kept the same (25 kg/s) but the vapor rate is lowered to 6.4 kg/s (flooding factor of 0.77), vapor rate is not high enough for the bottom stage froth to reach the weir height and L_T flux never appears. Weeping from the bottom tray does not fall into the bottom downcomer seal pan, so V_D never decreases and V_T does not get high enough. Consequently, it appears that the last downcomer remains unsealed while the last tray remains in a situation of excessive weeping. Although it has not been explicitly reported in the literature and has to be confirmed experimentally, this situation

could be one of the common startup sealing problems mentioned by Kister (1990).

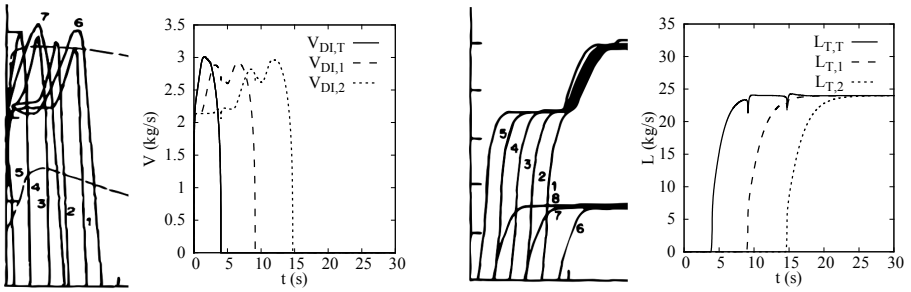

(a) Vapor blown through downcomers (b) Liquid flowrate over weir

Figure 3: Results from Gani et al. (1986) (left) and the proposed model (right) at startup

5. Conclusions

A compact and simple hydraulic model that is able to represent abnormal operating conditions in trayed towers has been built and tested. Based in common correlations, key issues for performance are the appropriate definition of the flows and the adequate treatment of numerical singularities.

6. Acknowledgements

This work was supported by Fundación Repsol - ETSII/UPM.

References

Bennett, D. L., Watson, D. N., Wiescinski, M. A., 1997. New correlation for sieve-tray point efficiency, entrainment, and section efficiency. AIChE J. 43 (6), 1611–1626.

Cab, U., Jimoh, M., Steinbach, J., Wozny, G., 2002. Simulation and experimental analysis of operational failures in a distillation column. Sep. Purif. Technol. 29, 163–170.

Chang, B., Lee, S., Kwon, H., Moon, I., 1998. Rigorous industrial dynamic simulation of a crude distillation unit considered valve tray rating parameters. Comput. Chem. Eng. 22, 863–866.

Gani, R., Ruiz, C., Cameron, I., 1986. A generalized model for distillation columns - I. model description and applications. Comput. Chem. Eng. 10 (3), 181–198.

Hsieh, C.-L., McNulty, K. J., July 1993. Predict weeping of sieve and valve trays. Chem. Eng. Prog. 89 (7), 71–77.

Kister, H. Z., February 1979. When tower startup has problems. Hydrocarbon Proc. 58 (2), 89–94.

Kister, H. Z., 1990. Distillation Operation. McGraw-Hill.

Kister, H. Z., 1992. Distillation Design. McGraw-Hill.

Kister, H. Z., 1997. Are column malfunctions becoming extinctor will they persist in the 21st century? Chem. Eng. Res. Des. 75 (6), 563–589.

Luyben, W. L., 2012. Rigorous dynamic models for distillation safety analysis. Comput. Chem. Eng. 40, 110 – 116.

Mahdipoor, H. R., 2006. Effect of liquid flow regimes on dynamic simulation of tray columns. Ind. Eng. Chem. Res. 45 (14), 5172 – 5178.

Mahdipoor, H. R., Shirvani, M., Nasr, M. R. J., Shakiba, S., 2007. Rigorous dynamic simulation of an industrial tray column, considered liquid flow regime and efficiency of trays. Chem. Eng. Res. Des. 85 (8), 1101 – 1111.

Mogford, J., December 2005. Isomerization unit explosion final report. Fatal accident investigation report, BP, Texas City, Texas.

Perry, R. H., Green, D. W. (Eds.), 2008. Perry's Chemical Engineer's Handbook, 8th Edition. McGraw-Hill.

Staak, D., Morillo, A., Schiffmann, P., Repke, J.-U., Wozny, G., 2011. Safety assessment on distillation columns: from shortcut methods and heuristics to dynamic simulation. AIChE J. 57 (2), 548–472.

Taylor, R., 2007. (Di)Still modelling after all these years: A view of the state of the art. Ind. Eng. Chem. Res. 46 (13), 4349–4357.

Wittgens, B., Skögestad, S., 2000. Evaluation of dynamic models of distillation columns with emphasis on the initial response. Model. Ident. Control 21 (2), 83–103.

Krist V. Gernaey, Jakob K. Huusom and Rafiqul Gani (Eds.), 12th International Symposium on Process Systems Engineering and 25th European Symposium on Computer Aided Process Engineering.
31 May – 4 June 2015, Copenhagen, Denmark

Application of the Lagrangian CFD Approach to Modelling of Crystallization in Stirred Batch Reactors Using the Smoothed Particle Hydrodynamics Method

Dragan D. Nikolic, Brian P. de Souza, Patrick J. Frawley

Synthesis and Solid State Pharmaceutical Centre, University of Limerick, Ireland
dragan.nikolic@ul.ie, patrick.frawley@ul.ie

Abstract

Crystallization phenomena in stirred reactors are influenced by local hydrodynamic conditions and these must be taken into account for successful process scale-up and optimization. In this work, the available state of the art grid-based CFD methods and advantages and disadvantages of their application to mathematical modelling of batch crystallization processes were analyzed. The benefits of the Langrangian meshfree methods were discussed and the Smoothed Particle Hydrodynamics method proposed as an efficient method for a rapid prediction of the global mean flow in stirred reactors. Various aspects of the simulation results were assessed: quality of the fluid prediction, computational requirements, existence of numerical problems and availability of crystal size distribution. The developed Smoothed Particle Hydrodynamics CFD model was successfully coupled with discretised population balance equations to model a cooling batch crystallization process. It has been shown that 200 additional transport equations resulting from the discretisation of the population balance leads to only 50% decrease in computational performance while the same problem is still almost intractable from the computational point of view using the grid-based CFD methods.

Keywords: Crystallization, CFD, SPH, Population Balance.

1. Introduction

The population balance (PB) framework has been adopted as the most fundamental approach for modelling particulate multiphase systems (Ramkrishna, 2000). The population balance modelling framework provides a deterministic description of the dynamic evolution of the crystal size distribution (CSD) by forming a balance to calculate the number of crystals in the crystalliser. In order to take into account local hydrodynamics conditions in a stirred reactor a common approach is to couple the population balance equations with turbulent computational fluid dynamics (CFD) modelling to predict the key process performance indicators such as CSD, yield, recovery and reactor productivity (Barett et al., 2011). Although use of CFD for simulating particulate systems is becoming a standard approach, a number of issues still need to be addressed. One major problem is the computational expense of coupling a standard discretised population balance with a grid-based CFD code, as this approach requires a solution of an intractably large number of transport equations. Another, more feasible approach is to use a method of moments (Ramkrishna, 2000). However, even the methods of moments coupled with CFD do not provide a computationally efficient approach for scale-up and optimization due to a large difference in time resolution: a

time frame of a typical crystallisation process is several hours compared to a time step necessary to achieve reasonable accuracy of only few microseconds. CFD simulations cause the major problems requiring almost one day of simulation time for one second of real process on a standard desktop PC (Ali et al., 2015). The other common problem encountered with the method of moments is that the CSD is lost and needs to be reconstructed from its distribution moments. Several reconstruction techniques were developed, however, no unified technique for reconstruction of a complete distribution from a finite number of moments is available (John et al., 2007). There is also a number of problems that need to be addressed from the numerical perspective. So far CFD models of industrial crystallizers were exclusively implemented in Eulerian reference frame using grid-based methods (Rane et al., 2014). Those methods suffer from many problems: convective transport should be simulated and can influence the integration time step and cause numerical problems (LeVeque, 2002), cumbersome numerical mapping is required to handle complex geometries, determination of free or moving boundaries and material interfaces is rather difficult and causes various numerical problems (Hartmann et al., 2004), the computational requirements poorly scale with the size of the system and the numerical methods required to solve large systems of equations are typically not capable to fully take advantage of the modern parallelisation hardware and software systems. As a consequence, optimisation studies are computationally very expensive and, at the moment, not feasible in most cases.

2. Lagrangian meshfree methods

In this work the above-mentioned issues were addressed using the Lagrangian frame meshfree Smoothed Particle Hydrodynamics (SPH) method (Lucy 1977, Gingold and Monaghan 1977). The key idea of the meshfree methods is to provide accurate and stable numerical solutions for systems of partial differential equations with a set of arbitrarily distributed nodes (or particles) without using any mesh that provides the connectivity of these nodes or particles. SPH method offers a number of attractive features. The first is that pure advection is treated exactly. The advection term disappears from the Navier-Stokes equations and velocity partial derivative becomes an ordinary time derivative allowing the momentum dominated flows to be easily handled. For example, if the particles are given a colour, and the velocity is specified, the transport of colour by the particle system is exact (Liu and Liu 2003). The mass continuity equation is not necessary anymore since the mass balance is explicitly enforced using particles of a specified mass. Linear and angular momentum are explicitly conserved using the specially derived expressions for forces acting on particles (such as pressure, shear stress and surface tension). Population balance equations can now be applied to a smaller control volume (that is at a particle level) making the CSD available explicitly without reconstruction. Representation of multi-phase systems, free and moving surfaces is easy and not bound to the prescribed spatial grid like in grid-based methods. The fact that a fluid and crystals are represented by particles can be utilised to explicitly model phenomena relating to the solid phase such as secondary nucleation and breakage. Here, the local hydrodynamic conditions, particle size and velocity, and an angle of impact can be directly used to estimate the rate of secondary nucleation, with a direct linkage to experimental particle-wall collision measurements using the shadow imaging technique. The computational power required to integrate equations in time scales linearly with the size of the system (that is with the number of particles). Integration in time is typically performed using the explicit methods avoiding numerical problems common in grid-based methods. Grid-based

numerical methods such as finite element or finite volume methods always require a solution of a large system of (non)linear equations which is not relevant in SPH. Moreover, the use of weighted contributions rather than a linear system of equations allows for massive parallelisation, taking advantage of recent developments in CUDA GPU technology to significantly reduce simulation times. In a typical crystallisation model, the Navier-Stokes equations are coupled with a number of scalar transport equations such as temperature, concentration and the population balance equations (either moment equations or discretised number density function). In grid-based methods the additional transport equations lead to a significant increase in size of the numerical system and matrix storage while in SPH only to a marginal increase in memory and computational requirements. Large numerical systems typically solved on symmetric multiprocessor systems or computer clusters require some sort of communication and synchronization mechanisms. The only synchronisation technique used in SPH is primitive atomic operations used during calculation of forces between a pair of particles. Particle based SPH also offers much higher model reduction capabilities making lengthy optimization studies computationally feasible. Basically, the number of particles used to describe a system can be decreased having the superposition effect on execution speed: use of larger particles decrease the total number of particles and larger particles are allowed to move a larger distance in space during every time step, both effects causing the simulation speed-up.

3. Smoothed Particle Hydrodynamics

The essential formulation of SPH is that any field quantity can be determined through a weighted interpolation of surrounding field values (Gingold and Monaghan, 1977). This weighting is characterized by the smoothing length, h, it decays with distance and it is given by the following integral equation:

$$A(\mathbf{r}) = \int_{\Omega} A(\mathbf{r}')W(\mathbf{r}-\mathbf{r}', h)d\mathbf{r}' \tag{1}$$

where $A(r)$ is a field function at point r in space Ω, r is any point in Ω, and W is a smoothing kernel with h as its width. The numerical equivalent to Eq. 1 is obtained by approximating the integral interpolant by a summation interpolant:

$$A(\mathbf{r}) = \sum_j A_j \frac{m_j}{\rho_j} W(\mathbf{r}-\mathbf{r}_j, h) \tag{2}$$

where m_j is the mass of the particle j, r_j the position and A_j is the value of any quantity A at r_j. Basically, this equation states that any quantity can be represented by summation of quantities at nearby points multiplied by a weighting function, also known as a smoothing kernel. The gradient and the Laplacian of field functions can be obtained in a similar fashion (Lucy, 1977).

3.1. Navier-Stokes equations

The basic physical quantities of an isothermal, viscous fluid are velocity u, mass-density ρ, and pressure p and they are considered as continuous fields in the fluid. The classical formulation of the motion for incompressible fluid flow over time t is governed by the Navier-Stokes equations coupled with the mass continuity equation:

$$\rho\left(\frac{\partial \mathbf{u}}{\partial t} + \mathbf{u}\cdot\nabla\mathbf{u}\right) = -\nabla p + \mu\nabla\cdot(\nabla\mathbf{u}) + \rho g + \mathbf{f}$$
$$\nabla\cdot\mathbf{u} = 0 \tag{3}$$

where μ is the viscosity of the fluid and f is the sum of internal and external force-densities acting on the fluid such as buoyancy, surface tension and collisions with rigid bodies. In the Lagrangian formulation, particles completely define a fluid which implies that the particles move with the fluid. Compared to the Eulerian view this means that any field quantity now depends on time only. The particles carry mass, position and velocity, and will hold smoothed quantity approximations obtained from SPH. Thus, acceleration for the Lagrangian fluid particle becomes an ordinary time derivative of its velocity and the advection term in Eq. 3 disappears. Since the mass balance is explicitly enforced using particles of the specified mass the continuity equation is not necessary anymore. The basic Lagrangian formulation of the Navier-Stokes equations for an incompressible, isothermal fluid is therefore given by (Liu and Liu, 2003):

$$\rho\frac{d\mathbf{u}}{dt} = -\nabla p + \mu\nabla^2\mathbf{u} + \rho g + \mathbf{f} \tag{4}$$

More details about the smoothing kernels and expressions for the fluid density, pressure gradient, shear stress and surface tension forces can be found in Nikolic et al. (2014).

3.2. Implementation details

The model used in this work is based on the SPH model developed by Nikolic et al. (2014) and implemented in c++ using Fluidix software (MacDonald, 2014). Fluidix is NVidia CUDA-based parallel particle simulation platform which can be applied to practically any particle-based model and allows fully customized particle interactions with searches such as “each particle”, “each pair of nearby particles”, or “each particle colliding with a mesh”.

4. Applications

In the previous work (Nikolic et al., 2014) it has been shown that the SPH method can produce a very good prediction of the global mean flow in the reactor and that there is a trade-off between the number of particles used to represent the volume of the fluid in the reactor and the computational requirements. It has been presented that by decreasing the number of particles a satisfactory quality of the fluid flow description can be maintained while dramatically reducing the computational requirements for more than 30 times. In this work, the effect of the number of elements used to discretise the population balance on computational requirements was investigated.

4.1. Case study: coupling SPH with Population Balance

CFD model developed using the SPH method can easily be extended with additional transport equations by applying a similar methodology like one previously described. Three new scalar transport equations were added: heat balance, mass balance (concentration of dissolved crystals) and a set equations resulting from discretisation of the number density function (Discretised Population Balance method, DPB). In this study, the developed model was applied to growth-only cooling crystallisation of paracetamol from ethanol solution using the lab reactor and kinetics data from Mitchell et al. (2011). The initial supersaturation was set to 1.5667 and the initial temperature to 20^0C. The reactor is then cooled down to 0^0C through the reactor jacket. The population balance equation was discretised using the van Leer k-interpolation (with k=1/3) high resolution upwind scheme with Koren flux limiter (Qamar et al., 2006) using 100 intervals. The performance of the fine volume discretisation scheme was analysed using the seed with sharp discontinuities in its CSD as shown in Figure 1a. Since the process is growth-only the analytical solution for the ideal-mixing case is simply the initial CSD translated right by a distance $G{\cdot}t$ (growth rate multiplied by the time elapsed). The

simulation results after 600 seconds for the case where the DPB was coupled with the ideal mixing model and with the SPH model are presented in Figure 1b.

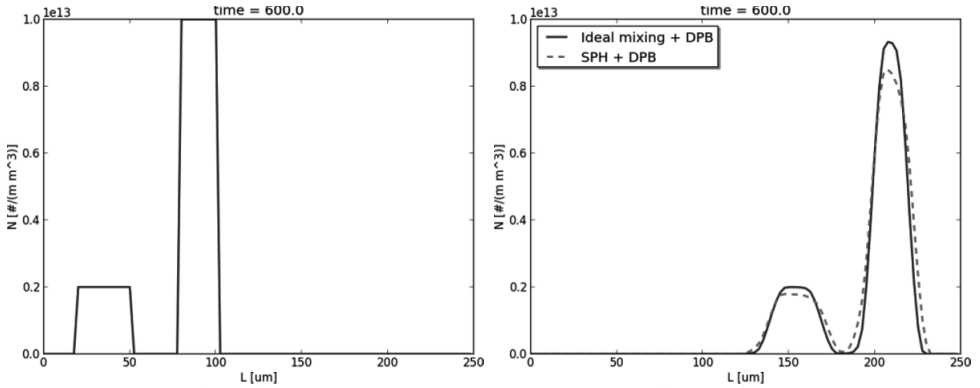

a) Inital CSD *b) CSD after 600s*

Figure 1. Simulation of the growth-only crystallisation using Discretised Population Balance method and van Leer high resolution finite volume scheme with flux limiter

The solid blue line in Figure 1b shows the performance of van Leer discretization scheme in an ideal mixing case. The scheme successfully suppressed oscillations in the solution and decreased the amount of the numerical diffusion present in all upwind schemes, although not completely. The dashed red line shows the CSD from the SPH model. Obviously, the nonidealities in the reactor cause that some fluid particles are well mixed while some other are located in poorly mixed zones (i.e. trapped in the zones around baffles or located in a poorly mixed top part of the volume) and contribute to the dispersion of the CSD. It can be observed that 100 elements are not enough to completely eliminate the numerical diffusion which is an indicator that a higher number of elements must be used. To determine the computational costs for different number of elements the same growth-only crystallisation problem was used again. Now the SPH model was coupled with the standard method of moments (SPH+MoM) keeping the first 6 moments only, and with the DPB equations (SPH+DPB) using a range of numbers of elements from 25 to 250. The simulation times were compared to the pure SPH simulations with the same number of particles. The simulation slowdown for all cases given in percents is presented in Figure 2.

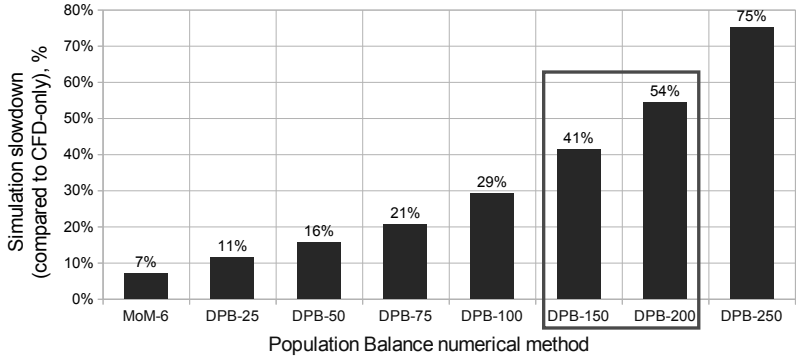

Figure 2. Computational requirements of coupled SPH and SMoM/DPB

5. Conclusions

The CFD model for a rapid prediction of the global mean flow in stirred tanks has been implemented using the Lagrangian meshfree Smoothed Particle Hydrodynamics method and its advantages for modelling of coupled hydrodynamics and crystallisation phenomena presented. The model offers an exact model of a convective transport, extreme parallelisation and model reduction capabilities, potential to directly utilize local hydrodynamics conditions for prediction of the secondary nucleation kinetics with a direct link to experimental particle-wall collision measurements using the shadow imaging technique, and the explicitly available CSD. Solution of the coupled system of Navier-Stokes and discretised population balance equations that is still almost intractable using the classical grid-based CFD methods can be efficiently solved now with only a marginal drop in performance (50% for 200 bins) compared to pure SPH simulations.

Acknowledgments: This research has been conducted as part of the Synthesis and Solid State Pharmaceutical Centre (SSPC) and funded by Science Foundation Ireland (SFI).

References

B.A. Ali, M. Börner, M. Peglow, G. Janiga, A. Seidel-Morgenstern, D. Thévenin, 2015, Coupled Computational Fluid Dynamics–Discrete Element Method Simulations of a Pilot-Scale Batch Crystallizer, Cryst. Growth Des., 15 (1), 145–155.

M. Barrett M., D. O'Grady, E. Casey, B. Glennon, 2011, The role of meso-mixing in anti-solvent crystallization processes, Chem. Eng. Sci. 66, 2523–2534.

R. Gingold, J. Monaghan, 1977, Smoothed particle hydrodynamics - theory and application to non-spherical stars, Mon. Not. R. Astron. Soc. 181, 37.

H. Hartmann, J.J. Derksen, C. Montavon, J. Pearson, I.S. Hamill, H.E.A. van den Akker, 2004, Assessment of large eddy and RANS stirred tank simulations by means of LDA", Chem. Eng. Sci. 59, 2419–2432.

V. John, I. Angelov, A.A. Öncül, D. Thévenin, 2007, Towards the optimal reconstruction of a distribution from its moments, Chem. Engi. Sci. 62, 2890-2904.

R.J. LeVeque, 2002, Finite Volume Methods for Hyperbolic Problems, Cambridge University Press, UK, ISBN-13: 978-0521009249.

G.R. Liu , M.B. Liu M.B, 2003, Smoothed Particle Hydrodynamics – a meshfree particle method, World Scientific Publishing Co. Pte. Ltd., ISBN: 981-2384561.

L.B. Lucy, 1977, A numerical approach to the testing of the fission hypothesis, Astron. J. 82 (12), 1013.

A. MacDonald, 2014, Fluidix v1.0.3, OneZero Software (http://www.onezero.ca).

N.A. Mitchell, C.T. Ó'Ciardhá, P.J. Frawley 2011, Estimation of the growth kinetics for the cooling crystallisation of paracetamol and ethanol solutions, J. Crystal Growth 328, 1, 39-49.

D.D. Nikolic, B.P. De Souza, P.J. Frawley, 2014, Simulation of Stirred Tank Hydrodynamics Using Mesh and Meshless Methods, AIChE Annual Meeting, Atlanta, USA.

S. Qamar, M.P. Elsner, I.A. Angelov, G. Warnecke, A. Seidel-Morgenstern , 2006, A comparative study of high resolution schemes for solving population balances in crystallization, Comp. Chem. Eng. 30, 6–7, 1119-1131.

D. Ramkrishna, 2000, Population Balances: Theory and Applications to Particulate Systems in Engineering, Academic Press, New York.

V.C. Rane, A.A. Ganguli, E. Kalekudithi, R.N. Patil, J.B. Joshi, D. Ramkrishna, 2014, CFD simulation and comparison of industrial crystallizers, Can. J. Chem. Eng. 92, 12, 2138–2156.

Krist V. Gernaey, Jakob K. Huusom and Rafiqul Gani (Eds.), 12th International Symposium on Process Systems Engineering and 25th European Symposium on Computer Aided Process Engineering.
31 May - 4 June 2015, Copenhagen, Denmark.

Model Reduction in Visual Modelling

Heinz A Preisig

Department of Chemical Engineering; NTNU; Trondheim, Norway
Heinz.Preisig@chemeng.ntnu.no

Abstract

Visual modelling redirects the users focus from writing model equations to the analysis if the structure and dynamics of the process model. This is enabled by having a highly structured approach to generating network models building an ontology for physical-chemical -biological processes. Visual modelling facilitates the generation of process model structures, their splitting into substructures based on time-scale assumptions and more generally model reduction. The operations can be done graphically, whilst the reduction algorithm provide the reduced models using an algorithm operating on the network representation extracted from the ontology.

Keywords: computer-aided modelling, code generation, design, control

1. Background

The main objective of the visual modelling project is to give the user a tool, which puts the focus on defining the structure of the model instead of coding the model equations. The user should be able to quickly implement his view of the process in terms of its dynamic behaviour and what is happening inside of the process, thus the reactions and phase changes, to mention the main ones. It should also enable to implement a set of consecutive simplifying assumptions making it possible to derive a group of simplified models that are tailored to specific model-based computational engineering problems that arise in the course of designing, realising and operating the plant. It is in this way, we put the model into the center of all the computational modelling tasks, thereby providing a maximum of compatibility and enable comparison of results on equal foots.

The graphical approach is simple and provides a visualisation of the initial assumptions made when generating the model in the first place. The mathematical representation is handled in the background by extracting them from an ontology that captures the behaviour of physical-chemical-biological systems comprehensively. The use of a systematically constructed ontology provides the security of structurally proper process models that are in the sequel compiled into code, thereby eliminating any transcript and interfacing errors. Implementing automatic model reduction methods on the generated mathematical models provides the means to implement the desired simplifying methods in the form of algorithms.

Visual modelling thus replaces mathematical model writing and manipulations with graphical manipulations that are easy to comprehend and provide a high-level of information concentration that provides an excellent platform for discussing the process model structure and the underlying assumptions. The whole process builds on a systematic representation of processes in the form of networks utilising basic graph-theoretical concepts and fundamental physics concepts.

2. Basice concept

The foundation is the ontology, which assumes that processes exist, operate and are represented in the frame of time and space. The process thus occupies a piece of the physical space and changes with time. The process is seen as an iteratively detailed hierarchical network of subprocesses thereby comprehending multi-scale process modelling (Preisig, 2010). Every model is thus first representing the process and its environment as hierarchical tree of volumes with the leaves of the tree being the most detailed, most granular representation of the modelled universe. This tree represents the physical containment in two sets: the process as a set of dynamic subprocesses and the environment as a static set of reservoirs. These subprocesses for an interacting network.

The defined subprocesses contain tokens that ”live” in them or make them up. In physical processes the behaviour of these tokens are described by the conservation principles, namely the conservation of mass, energy, linear and rotational momentum, and charges to mention the main ones. The tokens in the containment give raise to the definition of the state. If the tokens are continuous then the model is continuous whilst if they represent particles, the model will be discrete and is represented by population models. In both cases, the exchange of tokens is driven by differences in the potential fields associated with the different parts of the system. It is the intensive properties that are conjugates to the potentials that generate the driving forces, namely differences in the temperature, pressure, chemical potential that drive the process. Whilst these conjugates play a central role in the transport of the tokens, surprisingly the thermodynamic literature lacks a good term that comprehend these conjugates. It is the Bond-graph theory (Breedveld et al., 1991) that defines it as ”effort” variable, which appropriately characterises them as a group and it is the gradient in the effort variables that represents the driving force for the token transport. The tokens are transferred over the common boundary of adjacent systems, where the term ”system” is here used to represent a token-containing piece of the space, also simply called a capacity. The process-embedding environment consists of a set of infinitely large capacities, which provide and accept tokens.

The moving of tokens is the direct consequence of the capacities not being balanced with respect to the potentials. The process moves tokens between reservoirs driven by the reservoirs' imbalance of potentials, the process transports tokens due to an imbalance of the constituent subprocesses and the boarder subprocesses with the environment's reservoirs. It is thus the imbalances in universe that drive the processes.

Tokens may undergo transpositions inside the process, in fact this usually is the source of the term ”process”; change of phase and chemical/biological.

3. Mathematical framework

When modelling a process, the ”modeller” will make a first key assumption, namely a split of the universe into two parts: the process and its environment (Preisig, 2014). The split is intrinsically combined with a time scale assumption, namely that the most outer ring of the environment is formed by infinitely large capacities that exhibit constant intensive properties. This is a first underlying time-scale assumption.

The core element is the description of an individual capacity. Limiting ourself to continuous processes it is the conservation of extensive quantity Φ that represents the dynamic behaviour of the capacity.

$$\text{accumulation} \quad : \quad \dot{\Phi} = \int_0^S \hat{\phi}\, dS = \sum_{\forall i} \int_0^{S_i} \hat{\phi}_i dS_i \quad : \quad \text{sum of flows} \tag{1}$$

The common boundaries are characterised by a continuity condition for the effort variables π and a flux condition for the exchanged extensive quantity. Thus $\pi_{-\varepsilon} = \pi_{+\varepsilon}$ and $\hat{\phi}_{-\varepsilon} = \hat{\phi}_{+\varepsilon}$.

Connected capacities will thus form a network that can be described by a directed graph with the direction providing the reference co-ordinate for the respective connection: what is going out of one system is entering the other, according to the conservation principle. The global model of the process can be written as:

$$\underline{\dot{\hat{\Phi}}} = \underline{\underline{F}}\,\underline{\hat{\Phi}} \quad \text{where} \quad \underline{\hat{\Phi}} := \left[\hat{\Phi}_i\right]_{\forall i} \quad \text{and} \quad \hat{\Phi}_i := \int_0^{S_i} \hat{\phi}_i dS_i \tag{2}$$

3.1. Reactive systems

For reactive systems, the species are not conserved but species are transmuted into other species. So for species we can write the balance equations:

$$\underline{\dot{n}} = \underline{\underline{F}} \otimes \underline{\underline{S}}\,\underline{\hat{n}} + \underline{\tilde{\lambda}} \quad \text{with} \quad \underline{\tilde{\lambda}} := \underline{\underline{N}}^T V \underline{\xi}(\underline{c}) \tag{3}$$

and the $\underline{\xi}$ :: the extent of reaction vector, $\underline{\underline{N}}$ :: the stoichiometric matrix and V :: the volume, $\underline{c}$ :: the concentration vector. For the explanation of the $\otimes$ product and the matrix $\underline{\underline{S}}$ see Preisig (2010). If we multiply this equation with the vector of mole masses ($\underline{\lambda}$) the product with the transposition term becomes zero and we recuperate the total mass balance.

4. Model reductions

The core of the approach is in all cases the same: a complex part of the model is replace by a simpler surrogate model. Simplifications invariably remove information, thus the surrogate models are always going to contain less information than the original model. The process of generating surrogate models takes many different forms. Below we will discuss a common set of such replacement operations.

The most common operations are associated with time-scale assumptions in that parts of the model are either assumed to be constant or to be infinitely fast, thus are event-dynamic.

Approximating infinite-dimensional systems, namely distributed systems by finite-dimensional surrogate models is also a very common.

4.1. Event-dynamic assumptions

Any system can be assumed to be event dynamic. The mathematical method for handling event-dynamic assumption of any system is singular perturbation. Depending on the system, the singular perturbation parameter varies.

4.1.1. From distributed transfer to simple transfer

Applying the event-dynamic assumption to a individual distributed capacity the singular perturbation parameter is the token conductivity. As an example we take a one-dimensional heat transfer system. The dynamic description is based on the differential energy balance in the form of an enthalpy balance:

$$\dot{H} = -\frac{\partial}{\partial \underline{r}^T}\,\hat{q} \quad \text{assume one dimensional} \quad = -\frac{\partial}{\partial r_x{}^T}\,\hat{q} = k^q \frac{\partial}{\partial r_x{}^T}\,\frac{\partial}{\partial r_x{}^T}\,T \tag{4}$$

with k^q the heat conductivity, which serves as the singular perturbation parameter:

$$\lim_{k^q \to \infty} \frac{1}{k^q}\dot{H} = \frac{\partial}{\partial r_x{}^T}\,\frac{\partial}{\partial r_x{}^T}\,T = 0 \tag{5}$$

The temperature inside the system is thus a linear function defined by the temperatures at the two boundaries. The graphical operation is shown in Figure 1.

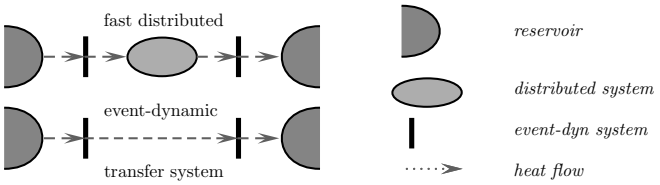

Figure 1: Simplifying a distributed transport system to a simple transfer

4.1.2. Small and large capacities

Often we design systems in which small and large capacities are combined. A sensor measuring the temperature in a fluid is such an example. The ideal design would make the sensor to have zero capacity. This is not possible, but one can aim at a very small sensor. This suggest to make a event-dynamic assumption about the temperature sensor, with the singular perturbation parameter being the capacity of the sensor.

$$\dot{H} = \hat{q} \quad \text{singularly perturbed} \quad \lim_{C_p \to 0} C_p \dot{T} = \hat{q} \quad = 0 \tag{6}$$

The time constant of the temperature sensor is inversely dependent on the heat capacity and direct dependent on the thermal conductivity. Thus we have a second possible reduction possibility, namely by choosing the thermal conductivity as the parameter for the singular perturbation.

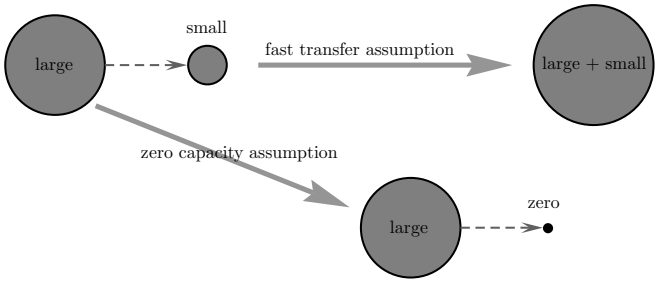

Figure 2: Approximating small capacities connected to a large capacity

$$\dot{H}_S = \hat{q} = -k^q(T_S - T_{fluid}) \quad \text{takes the form} \quad \lim_{k^q \to \infty} \dot{H}_S = -(T_S - T_{fluid}) = 0 \tag{7}$$

4.1.3. From distributed to low-order transfer

Distributed systems are infinite dimensional. Many different approximation methods are known and well documented. The one that is closest to our network approach is the finite volume approach in which the distributed spatial domain is split into a set of finite volumes for which the basic balances are applied. Key is the computation of the flows. One of the simplest methods assumed uniform conditions in each volume with the flows across the different boundary pieces being driven by the difference in the effort variables between the connected lumped systems. If we take the same heat transfer system as above, the simplification is shown in Figure 3.

The distributed system is replace by a network of lumped systems of the form Equation 2.

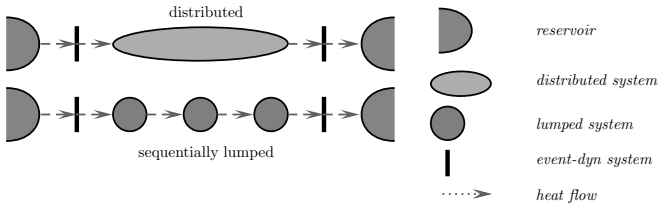

Figure 3: Distributed transfer to sequentially lumped transfer system

4.2. Reducing recycle networks

It is not uncommon to have a network in which a large amount of extensive quantity is moved in internal cycles. This is certainly the case in a stirred environment. With out any limitations, we analyse a model that consists of a generic dynamic part connected to a part that is forming a single cycle. The mathematical description for a generic extensive quantity Φ is given by:

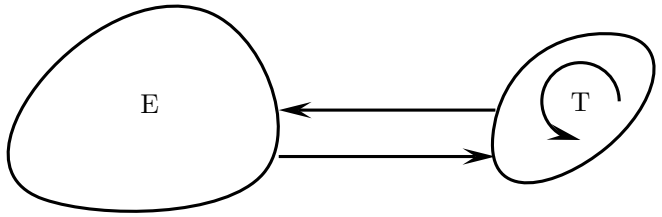

Figure 4: A cyclic network connected to a generic network

$$\dot{\underline{\mathbf{\Phi}}}_E = \underline{\underline{\boldsymbol{F}}}_{EE}\hat{\underline{\mathbf{\Phi}}}_{EE} - \underline{\underline{\boldsymbol{F}}}_{ET}\hat{\underline{\mathbf{\Phi}}}_{ET} \quad \text{and} \quad \dot{\underline{\mathbf{\Phi}}}_T = \underline{\underline{\boldsymbol{F}}}_{ET}\hat{\underline{\mathbf{\Phi}}}_{ET} + \underline{\underline{\boldsymbol{F}}}_{TT}\hat{\underline{\mathbf{\Phi}}}_{TT} \tag{8}$$

We focus on the second equation and formulate for the transfer[1] $\hat{\Phi}_m := \xi_m \hat{V}_m$ with $m \in \{ET, TT\}$. Without introducing a limitation, we assume that the cyclic process has only one cycle. We now make the order of magnitude assumption that the volumetric flow in the cycle is much larger than the flows connecting to the environment, thus $\hat{V}_{ET} << \hat{V}_{TT}$. If the process occupies a constant volume, then the volumetric flow rate is constant in the cycle. Using the large flow rate as the inverse of the singular perturbation parameter we get:

$$\lim_{\hat{V}_{TT}\to\infty} \frac{1}{\hat{V}_{TT}} \left(\dot{\underline{\mathbf{\Phi}}}_T = \underline{\underline{\boldsymbol{F}}}_{ET}\hat{\underline{\mathbf{\Phi}}}_{ET} + \underline{\underline{\boldsymbol{F}}}_{TT}\underline{\underline{\mathbf{\Psi}}}_{TT}\hat{V}_{TT} \right) \quad \text{yielding} \quad 0 = \underline{\underline{\boldsymbol{F}}}_{TT}\underline{\underline{\mathbf{\Psi}}}_{TT} \tag{9}$$

with $\underline{\underline{\mathbf{\Psi}}}_{TT} :: \mathbf{D}\left(\underline{\boldsymbol{\xi}}\right)$ the diagonal matrix of the intensive properties vector. With the process being a cycle, the properties of the inflow to each lump is equal to the outflow of the lump, thus all ξ_T are equivalent and thus the network behaves like a single lumped system with a network connection to the environment. Graphically this reflects into Figure 5.

5. Implementation issues

The implementation of the graphical editor consist of several components: a graph editor that supports the hierarchical structuring of the model. This primarily serves the purpose of administrating

[1] We use the notation *AB* for a reference co-ordenate pointing from *A* to *B*

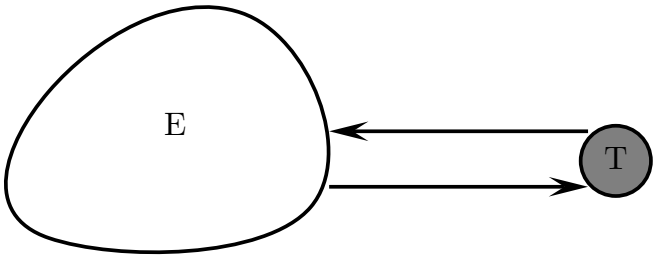

Figure 5: A cyclic network connected to a generic network

the model. The actual model is located at the leave nodes of the hierarchical decomposition tree, where also the connections are being implemented.

The graph editor has currently three inserts, one is plugging in two automata, one that defines the behaviour of the keyboard, the other define the graphical elements and the third makes the ontology with the list of model equations available. The ontology is also used to generate the automata and the graphics so as to have all elements consistent. Those operations are implemented as separate editors.

The model reduction methods, as described in this paper, are implemented over the ontology and so are the model reduction methods. One can also view the procedures as being a replacement of a complex model with a simplified surrogate model.

6. Conclusions

The algorithms for model reduction applying order-of-magnitude assumptions to individual model components, specifically distributed systems, have been presented. Large recycling rates yield a model reduction assuming very high recycling rates compared to other interactions. The order-of-magnitude assumptions are in essence all time-scale assumptions: fast vs low transfer rates, high vs small flow rates lead to short vs long residence times and thus enable a time-scale separation.

Singular perturbation theory in its basic form can be used to split the time domain and provide simplified models, of which the outer solutions - the larger time-sale solutions, are of particular interest.

The result is algorithmic and can be implemented to happen in the background automatically without the need of interference by the user. This provides a set of tools that enables the derivation of simplified models from a mother model, thus providing the desired feature of having consistent models within the context defined by the ontology.

Consecutive automatic code generation and splicing to match the target solver's code environment completes the integration of the model into the modelling suite.

References

Breedveld, P. C., Rosenberg, R. C., Zhou, T., 1991. Bibliography of bond graph theory and application. Journal of the Franklin Institute 328 (5/6), 1067–1109.

Preisig, H. A., 2010. Constructing and maintaining proper process models. Comp & Chem Eng 34(9), 1543–1555.

Preisig, H. A., 2014. Visual modelling. FOCAPD 8 (Foundation of Computer-Aided Process Design), 730–734.

Krist V. Gernaey, Jakob K. Huusom and Rafiqul Gani (Eds.), 12th International Symposium on Process Systems Engineering and 25th European Symposium on Computer Aided Process Engineering. 31 May – 4 June 2015, Copenhagen, Denmark

Automatic Reconstruction and Generation of Structured Hexahedral Mesh for Non-planar Bifurcations in Vascular Networks

Mahsa Ghaffari,[a] Chih-Yang Hsu,[a] Andreas A. Linninger,[a*]
[a] *Department of Bioengineering, University of Illinois at Chicago, 851 S. Morgan St., 218 SEO, M/C 063, Chicago, IL 60607, USA*
linninge@uic.edu

Abstract

Unstructured meshes are widely used to delineate the complex geometry of blood vessels in computational fluid dynamics simulation. However, structured parametric meshes can better represent complex geometries with lower grid density thus enabling faster and more precise computations. Current mesh generation methods require user interaction and cannot be used for automatic generation of parametric mesh representations of vascular networks. Our aim is to present a fully automatic algorithm for parametric mesh representation of vascular networks from subject-specific medical images. The methodology requires no user interaction, can create volumetric meshes for non-planar bifurcations and offers full control over the local mesh resolution at the surface and the lumen of the blood vessels. We demonstrate the reliability of our algorithm in terms of mesh quality by evaluating scaled Jacobian and equiangular skewness. The novel method was applied in case studies to reconstruct real image data for the cerebral angioarchitecture. Accurate subject-specific representations of vascular trees are necessary to perform organ-wide hemodynamics for personalized surgical planning of vascular disease.

Keywords: Parametric mesh, vascular network, non-planar bifurcation, hexahedral elements, micro-circulation structure.

1. Introduction

Unstructured grids have been widely used to mesh complex geometric domains as they are readily available with many software packages (Somayaji et al 2008, Sweetman et al. 2011, Ghaffari et al 2014). Linear unstructured mesh tends to be stiffer and can be susceptible to shear-lock (Abaqus, 2008). In contrary, linear parametric meshes are more accurate in nonlinear or impact contact analysis and even more efficient than second order unstructured meshes (Songbai at al., 2011). Parametric meshes offer more accurate computational results even with lower-density grids thus accelerating speed. For the same number of elements, parametric meshes enhance the fidelity of geometrical reconstruction and numerical solutions. However, current methods for mesh generation have still required manual operations, which are time consuming and prohibit the fully automatic reconstruction of large vascular trees from subject-specific medical images.

In last decade, several research groups employed different methods to generate structured meshes for bifurcations and vascular trees. Antiga and Steinman (2002) applied the Cooper algorithm for hexahedral meshing to a single branch of bifurcation. Verma et al. (2005) produced natural coordinates from the Laplace's equation to create structured meshes for bifurcations. This methodology requires the numerical solution of three additional heat

conduction problems. Santis et al. (2011) proposed the manual construction of block structures inside and outside the vessel, whose projections on the lumen surface allows the generation of hexahedral meshes. Clearly, this manual technique is inadequate for large vascular networks. Our aim is to generate a fully automatic parametric mesh allows for better representation and a more computationally efficient patient-specific simulation of hemodynamic of the large vascular networks.

2. Methods

Microcirculation data were obtained as described by Linninger et al. (2013). For cerebral arterial trees, MR angiograms were acquired under Institute Review Board approval with a 3D Time of Flight pulse sequence from a 28 year old volunteer. An in-house image filter was applied to suppress signals from other tissues and enhance the vessels. The filtered image was imported into VMTK software Antiga et al. (2008) to acquire radius and connectivity information.

Parametric meshes of the entire vascular trees were generated using the five steps procedure shown in Fig. 1a, the creation of a parametric structured grid for bifurcations is discussed as follows.

In step 1, centreline point locations, radii, and connectivity information are extracted from VMTK. Cubic Bezier parameterization is applied to capture the curvature of the vessels as demonstrated in Fig. 1a. A cubic Bezier curve is a vector function in terms of the scalar parameter t with end points P_0 and P_1 and control points C_0 and C_1 as defined in Eq.(1). The endpoints bracket the space curve; the control points dictate the shape of the curve. Least square method is used to approximate the Bezier curve. Between two sequences of curves G^1 continuity is enforced as shown Fig. 1d.

In step 2, the Bezier network is categorized into bifurcations, outlet, and connecting segments. The initial decomposition is carried out by dividing the Bezier network into branches. That is, a branch is defined as an array of Bezier curves. Then, bifurcation regions are automatically detected and segmented as shown in Fig. 1c. In each bifurcation point, the branches were segmented where the arch length of branch is equal to twice the local radius.

In step 3, a separation plane and two Control Points (CPs) calculated to define bifurcation topology as shown in Fig. 1d. Firstly, bifurcation branches are indexed as i, j, k. Then, SP_{ij}, SP_{jk}, SP_{ki} are calculated between the branches of ij, jk, ki respectively by Eq.(2). The separation plane is defined by three separation points using Eq.(2). To complete the geometry of separation region, the length of the normal vector of the separation plane was extended by a magnitude equal to the mean radius.

In step 4, separation region with two CPs and three SPs was divided into 6 parts connecting each CP to a SP. Parametric radii are determined by Eq.(3). Then, a parametric curve equation has been developed to calculate surface nodes by using Eq.(4).

$$\vec{B}(t) = (1-t)^3 \cdot P_0 + 3t(1-t)^2 \cdot C_0 + 3t^2(1-t) \cdot C_1 + t^3 \cdot P_1 \quad (1)$$

$$SP_{ij} = (R_i \vec{V_j} + R_j \vec{V_i}) \cdot \sqrt{R_i{}^2 + R_j{}^2 + 2R_i R_j \cos \alpha_{ij}} \quad (2)$$

$$r(t) = t \cdot \|CP - BP\| + (1-t) \cdot \|SP - BP\| \ , t \in [0,1] \quad (3)$$

$$f(t,) = r(t)\cos() \ \vec{T} + r(t)\sin() \ \left|\vec{T} \times \vec{U}\right| + BP \quad (4)$$

Where ||.|| denotes the Euclidean norm and *BP* is bifurcation point. $\vec{U}$ is a unit vector from control point to bifurcation point; $\vec{T}$ denotes a unit normal vector to the plane of CP, SP and bifurcation point. α_{ij} is the angle between *i* and *j* branches.

Step 5 serves the generation of the interior volumetric mesh. First, the surface mesh points are sorted longitudinally within each cross-sectional group. Three integers a, b and c are employed to control the topology of butterfly grid generation and cross-sectional mesh resolution along radial axis, shown in Fig. 1e.

To increase the computational accuracy near the wall, where higher velocity gradients are expected, finer elements closed to arterial wall are recommended. To provide more realistic anatomical context computational meshes may be created with vessel walls, which can easily be created by extending the parametric lumen surface.

We can also control the mesh density in longitudinal direction. By increasing the number of longitudinal divisions in each segment, finer longitudinal mesh resolution can be achieved. The number of longitudinal divisions can also be correlated to segment radius thereby producing finer meshes for thinner vessels.

In step 6, we took advantage of regular surface mesh to create an optimal automatic algorithm to index mesh nodes and element to write a structured mesh in .msh format. Finally, mesh quality is assessed using ANSYS-ICEM CFD 15.

3. Results

This section presents the result of fully-automated parametric mesh generation to real world vasculature constructed from medical imaging data. We will apply our methodology to the parametric mesh generation for microcirculation and reconstruction of the entire arterial trees in mesh domain.

Fig. 2a-c show a result meshed of arteriolar tree of the microcirculation in the human cortex. Magnified views of its penetrating arterioles merging seamlessly into the capillary bed are displayed. The entire structure has 68,816 surface elements and 246,080 cells.

Fig. 2d illustrates parametric mesh for Circle of Willis with nine bifurcations with 9,456 surface element (Quad-4) and 35520 cells (Hexa-8). A magnified view of its outlet is also shown in Fig. 2e. Fig. 2f-g show a parametric mesh of a complete human cerebral vasculature from medical images. The parametric meshes for the entire arterial tree consist of 21,224 points, 21,471 connections, and 1,280 bifurcation segments. The full mesh of the brain vasculature contains of 8,838,816 hexahedral elements which is equally parameterized along local axial and radial coordinates.

The mesh quality was evaluated using scaled Jacobian and Equiangular skewness as shown in Table 1. A hexahedral cell is optimal if the skew is less than 0.4 and the scaled Jacobian is on average of 0.8. Mesh elements are increases from 14,836 to 150,580, categorized in coarse, medium and fine mesh size. The scaled Jacobian of the computational elements is about 0.86 on average with the minimum of 0.41, indicating that the shape quality of the elements is adequate for computations.

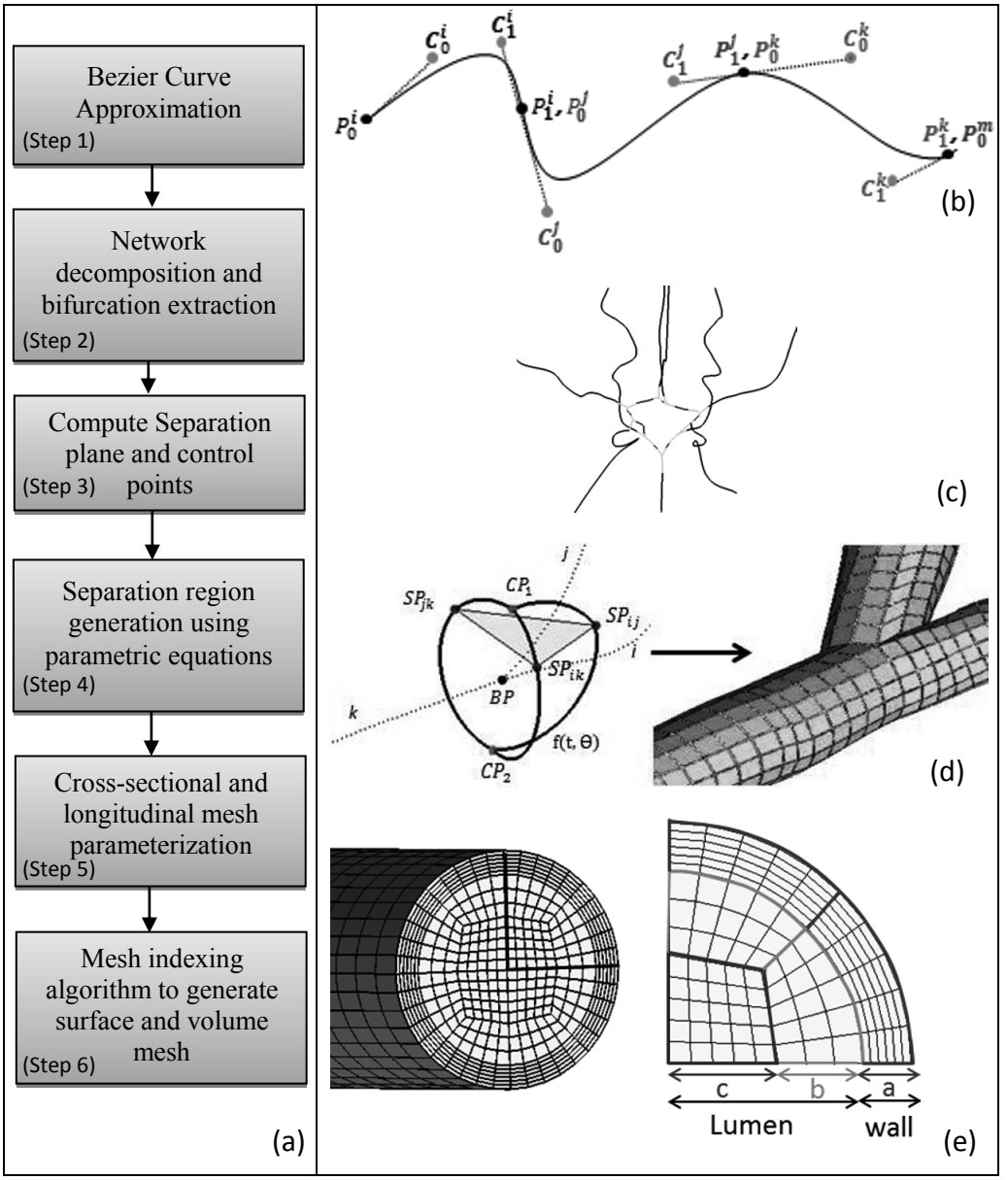

Figure 1. (a) A block diagram of stepwise generation of parametric mesh for bifurcations, (b) Bezier curve approximation, least square with cubic Bezier approximation has been used to represent tortuosity of vessel morphology. (c) Bifurcations is extracted in a position where the arch length of branch is quall to twice the relative radius, shown in green (or light grey) in Loop. (d) Separation plane is defined by SP_{ij}, SP_{jk}, SP_{ki}. Normal vector of the separation plane extends to find CPs. (e) Cross sectional mesh parameterization using butterfly grid. Parameter "a" describes the number of cells in vessel wall and "b, c" defines the mesh density in lumen area.

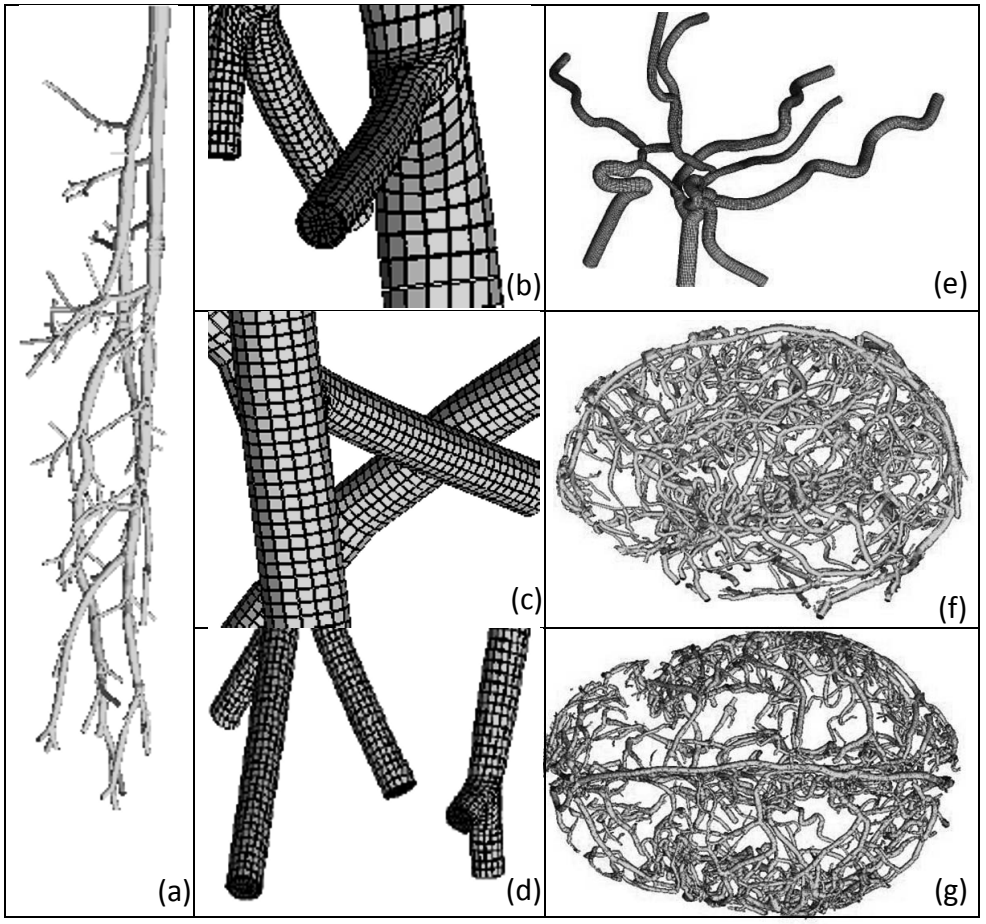

Figure 2. Result of the parametric mesh generation. (a) Schematic of micro-vessels in microcirculation structure (penetrating arteries). (b-c) Magnified view of the shrunken elements (%10) of micro-vessels. (d) Grid element generation of Circle of Willis as a local model of cerebral trees. (e) An outlet of Circle of Willis in magnified view (f-g) Full brain vasculature network.

Table 1. The mesh quality of the Loop with different resolutions is evaluated. The mesh resolution is determined by the longitudinal and cross sectional parameters.

Loop	Mesh resolution parameters (a, b, c, L)	#Elements, #nodes	Equiangular skewness (min, mean, max)	Scaled Jacobian (min, mean, max)
Coarse	3, 3, 4, 2	14836, 13898	0, 0.8, 0.79	0.41, 0.81, 1
Medium	3, 4, 8, 4	71938, 68297	0, 0.6, 0.8	0.5, 0.89, 1
Fine	4, 6, 10, 5	150580, 144804	0, 0.15, 0.8	0.61, 0.89, 1

4. Conclusion

Our novel method allows a robust and fully automatic generation of parametric meshes suitable for large vascular trees. The method does not require user input and can handle non-planar bifurcations. In our methodology all elements are oriented along the blood flow direction, thus allowing the alignment of the gridlines with the physiological velocity direction in the vessels. Such alignment will reduce numerical diffusion error occurring during the integration of the flow equation, thereby providing higher accuracy of the results, Vinchurkar et al. (2008).

3D geometric vascular models have important applications in diagnosis and investigation vascular malformations, such as aneurism, stenosis and atherosclerosis. Moreover, subject specific meshes with physiological boundaries can be used in personalized surgical planning for subject-specific hemodynamic simulations of the entire cerebral circulation.

Acknowledgments

The authors would like to gratefully acknowledge partial support of this project by NSF grants CBET-0756154 and CBET-1301198. No conflicts of interest were posed in the conduct of this research.

References

ABAQUS, 2008, Analysis User's Manual, Version 6.8. USA, Hibbitt, Karlsson and Sorensen.

L. Antiga, B. E. Iordache, L. Caverni, G. P. Cornalba. A. Remuzzi, 2002, A Geometric reconstruction for computational mesh generation of arterial bifurcations from CT angiography. Computerized Medical Imaging and Graphics, 26, 4, 227–235.

L. Antiga, M.Piccinelli, L. Botti, B. Ene-Iordache, A. Remuzzi, D. A. Steinman, 2008, An image-based modeling framework for patient specific computationla hemodynamics. Medical and Biological Engineering and computering, 46, 1097-1112.

G. De Santis, M. De Beule, P. Segers, P. Verdonck, B. Verhegghe, 2011, Patient specific computational haemodynamics: generation of structured and conformal hexahedral meshes from triangulated surfaces of vascular bifurcations. Computer Methods in Biomechanics and Biomedical Engineering 14, 9, 797–802.

G. De Santis, M. De Beule, K. Van Canneyt, P. Segers, P. Verdonck, B. Verhegghe, 2011, Full-hexahedral structured meshing for image-based computationa vascular modeling. Medical Engineering & Physics 33, 10, 1318–1325.

M. Ghaffari, M. Zoghi, , M. RostamI, N. Abolfathi, 2014, Fluid structure interaction of traumatic brain injury: effect of material properties on SAS trabeculae, Journal of Modern Engineering, 14, 2, 54-61.

S. Ji , J. C. Ford, R. M. Greenwald, J. G Beckwith, K. D. Paulsen, L.A. Flasman, T. W. McAllister, 2011, subject-specific, hexahedral mesh generation via image registration, 47, 10, 1178-1185.

A. A. Linninger, I. Gould, T. Marinnan, C. Y. Hsu, M. Chojecki, A. Alaraj, 2013, Cerebral microcirculation and oxygen tension in the human secondary cortex, Annals of Biomedical Engineering, 44, 11, 2264-2284.

M. R. Somayaji, M. Xenos, L. Zhang, M. Mekarski, A. A Linninger, 2008, Systematic design of drug delivery therapies, Computers & Chemical Engineering 32, 1, 89-98.

B. Sweetman, M. Xenos, L. Zitella, A. A. Linninger, 2011, Three-dimensional computational prediction of cerebrospinal fluid flow in the human brain, Computers in Biology and Medicine 41, 2, 67-75.

C. S. Verma, P. F Fischer, S. E Lee, F. Loth, 2005, An all-hex meshing strategy for bifurcation geometries in vascular flow simulation. Proceedings of the 14th International Meshing Roundtable, 363–375.

S. Vinchurkar and P. W. Longest, 2007, Evaluation of hexahedral, prismatic and hybrid mesh styles for simulating respiratory aerosol dynamics. Computers & Fluids, 37, 317-331.

Krist V. Gernaey, Jakob K. Huusom and Rafiqul Gani (Eds.), 12th International Symposium on Process Systems Engineering and 25th European Symposium on Computer Aided Process Engineering.
31 May - 4 June 2015, Copenhagen, Denmark.

Developing Surrogate Models via Computer Based Experiments

Mandar N. Thombre[a,b], Heinz A. Preisig[a] and Misganaw B. Addis[a]

[a]*Department of Chemical Engineering; NTNU; Trondheim, Norway*
[b]*Department of Chemical Engineering; BITS Pilani, Pilani, India*
Heinz.Preisig@chemeng.ntnu.no

Abstract

In recent years, advances in mathematical modeling techniques, algorithms for solving mathematical equations and computational power have all combined to make the study of complex phenomenon with large number of inputs possible, which could otherwise have been unattainable with physical experiments. Particularly excellent computational tools for models on the small scale have opened a new avenue for replacing physical experiments by computational experiments. Often, it is physical/chemical properties that are the target, because they are used in a multitude of models. But since the computational experiments are often of very large scale and high complexity, they require significant computational resources, not least of which is time. Hence, a direct coupling of the codes is not feasible and one has to take refuge in simpler models that are approximating the behaviour of the complex model, called the surrogate models. Naturally the objective is to generate surrogate models that approximate the complex behaviour as well as possible within a given domain. But since computational experiments are not contaminated with stochastic noise, classical design of experiment methods like blocking, randomization and replication are irrelevant (Fang et al., 2005) - the gap is all due to lack of fit. So the maximum acceptable gap in a given domain is usually the essential measure that the application of the surrogate model defines. The goal is clear, one aims at computationally cheap approximations that are sufficiently good as defined by the application. Surrogate models are commonly used in multiscale simulations for bridging the gap between the finer and the coarser scales. We discuss the approach on an illustrative example where the Redlich-Kwong equation of state is approximated by linear surrogate models.

Keywords: surrogate models, design of experiments, multiscale modeling

1. Introduction

Surrogate models are simple analytical models that mimic the input/output behaviour of complex systems. Developing such models requires performing computationally expensive simulations at a set of carefully selected sample points. These models approximate the behaviour of the underlying complex simulations to a reasonable precision while also being computationally cheaper to evaluate. Surrogate models can thus be seen as a simple representation of a complex system with relaxed accuracy in a given domain. The trade-off between the accuracy and the computational time is an important consideration during the construction of these models.

Surrogate models are constructed with the use of computer experiments where the design parameters cover a carefully chosen range of values within the design space. These values are selected according to certain specifications or patterns using a technique known as the design of experiments (see sec. 2.1) The computationally expensive simulation is carried out at these selected

points and the responses are recorded. Using this input/output data, the behaviour of the complex simulation is then approximated by simple functional relations, which we call the surrogate models. The exact nature of the complex simulation thus becomes irrelevant and only the surrogate model that approximates the behaviour of the complex simulation becomes important. These surrogate models can be based, for example, on equations where higher order terms are neglected, or on assumptions of lumped systems instead of distributed ones (Koziel et al., 2011).

The use of surrogate models is most evident in multi-scale modeling. The conventional view of modeling has been to focus on a particular scale of a system. The effects of the other scales in the system are usually neglected by making assumptions about their behaviour or by using constitutive relations. On the other hand, multi-scale modeling involves simultaneous consideration of the different scales of a system, as well as the combination of these scales into an overall model for the system. The objective is to achieve the efficiency of a higher scale and the accuracy of a lower scale. In this context, the interactions between different scales play a significant role in determining the quality of the overall model.

Suppose that in a system, a model A on a particular scale of the system requires some data from some model B on the same or a different scale. To provide this information to model A, model B might itself require some data from some model C in the system. Furthermore, simulations at the lower scale are generally more complex than those at the higher scale. In such multi-scale systems, the propagation of data from one model to another might be computationally very expensive and hence infeasible. This is where surrogate models come into the picture. They provide a computationally cheap and efficient way of linking the different models in a multi-scale system. For example, when a higher scale model calls for some data from a lower scale complex simulation, the required data can be computed using a surrogate model instead of the complex simulation. Moreover, surrogate models easily integrate with computer codes even when they are written in different programming languages, which is often the case in multi-scale modelling. In the subsequent sections, we describe the framework for constructing surrogate models, followed by an illustrative example (Giunta et al., 2003).

2. Framework of Constructing Surrogate Models

2.1. Design of Experiments

Design of experiments (DOE) constitutes the different techniques of determining the locations of the sample points in a design space (see Fig.1). The samples chosen through the DOE should give a good representation of the entire design space so that the surrogate model that is constructed from these sample points can provide a good prediction of the responses from the complex simulation. In addition to that, the number of samples chosen through the DOE should be relatively small compared to the actual design space. In general, a DOE method should be able to provide maximum information about the design space with minimum possible samples. The DOE method to be used depends on various factors like the dimensionality of the problem, the structure of the surrogate model to be used, the error tolerance criteria for the construction of the surrogate model and the existence of random error in the complex model.

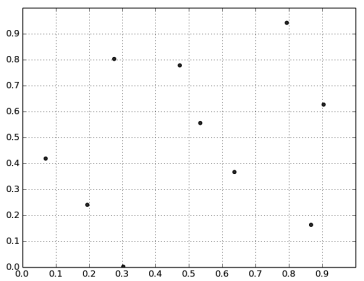

Figure 1: Latin hypercube sampling for 10 points in the design space $[0,1]^2$

The DOE methods can be broadly classified into two categories: classical and modern. In case

of laboratory experiments where the random error exists, i.e. each new run of the experiment results in a different error, the classical DOE methods are preferred. The classical methods tend to generate sample points at the extremes of the design space in order to adequately represent the design space even in the presence of this random error. Examples of the classical DOE methods are the Box-Behnken design, the Central Composite design, etc. On the other hand, in case of deterministic computer simulations, the modern DOE methods are used. The underlying assumption in case of these computer simulations is that each run of the simulation results in exactly the same responses. Examples of the modern DOE methods include the Monte-Carlo sampling, Latin-Hypercube sampling and the Orthogonal Array sampling

It might happen that the design space is extremely large and that a single surrogate model cannot sufficiently represent the complex simulation over the entire design space. In such cases, dividing the design space into smaller divisions might be feasible. The DOE is performed separately on each of these divisions and separate models are fit to each of the sampled data. In other words, local approximations for the complex simulation are found over the design space. However, if in these cases the continuity over the entire design space is a necessity, then appropriate boundary conditions have to be applied at the boundaries of the divisions.

2.2. Forward Mapping

The basic idea of forward mapping is to use the input-output data from an unknown black box function $y = f(x)$ to make the best guess $\hat{y} = \hat{f}(x)$ for this unknown function. Thus, if $y = f(x)$ represents a complex simulation, $\hat{y} = \hat{f}(x)$ represents the corresponding surrogate model. The objective is to minimize the gap between y and $\hat{y}$. The general way to do this is to define a measure for this error, and then to minimize this measure of error so that y and $\hat{y}$ are 'close enough'. There are various ways in which surrogate models can be predicted, like the response surface methodologies, kriging, etc. We present a brief overview of one common technique for constructing polynomial response surface models (Han and Zhang, 2012).

The polynomial model is constructed using least-squares regression. Suppose we have an n-dimensional design space in which the complex simulation is performed at m different points (selected using the design of experiments), leading to the generation of m sampled points. This method is demonstrated for the case of quadratic polynomials, but it can very well be used for linear models or higher order polynomials. The quadratic model, in comparison with the complex simulation, can be represented as:

$$f(x) = \hat{f}(x) + \varepsilon, x \in \mathbb{R}^n, \tag{1}$$

where $\hat{f}(x)$ is the quadratic model and ε is the random error assumed to be normally distributed with zero mean. The error at each point is assumed to be independent and identically distributed. The quadratic model $\hat{f}(x)$ for an n dimensional design space can be represented as:

$$\hat{f}(x) = \beta_0 + \sum_{i=1}^{n} \beta_i x_i + \sum_{i=1}^{n} \beta_{ii} {x_i}^2 + \sum_{i=1}^{n} \sum_{j=1}^{n} \beta_{ij} x_i x_j, \tag{2}$$

where β_0, β_i, β_{ii} and β_{ij} are unknown coefficients to be determined. In the above equation there are a total of $p = \dfrac{(n+1)(n+2)}{2}$ unknown coefficients to be determined. Thus we need at least p equations and thus p sample points to construct a quadratic model for an n-dimensional problem. Suppose that $\beta \in \mathbb{R}^p$ is the vector that contains these p unknown coefficients, the least-squares estimator of β is given by:

$$\beta = (U^T U)^{-1} U^T f_S, \tag{3}$$

where:

$$U = \begin{pmatrix} 1 & {x_1}^{(1)} & \cdots & {x_n}^{(1)} & {x_1}^{(1)}{x_2}^{(1)} & \cdots & {x_{n-1}}^{(1)}{x_n}^{(1)} & \left({x_1}^{(1)}\right)^2 & \cdots & \left({x_n}^{(1)}\right)^2 \\ \vdots & \vdots & \ddots & \vdots & \vdots & \ddots & \vdots & \vdots & \ddots & \vdots \\ 1 & {x_1}^{(m)} & \cdots & {x_n}^{(m)} & {x_1}^{(m)}{x_2}^{(m)} & \cdots & {x_{n-1}}^{(m)}{x_n}^{(m)} & \left({x_1}^{(m)}\right)^2 & \cdots & \left({x_n}^{(m)}\right)^2 \end{pmatrix} \in \mathbb{R}^{m \times p} \tag{4}$$

The unknown coefficients in β are determined using eq. 3 and eq. 4. Then, using eq. 2, which will be the resultant surrogate model, the approximate response $\hat{f}$ at any point in the design space can be calculated.

2.3. Backward Mapping

The sensitivity analysis of the surrogate model obtained from the forward mapping is performed in the backward mapping. Based on the results of the analysis, it is decided whether or not to update the surrogate model. If the surrogate model needs to be updated, the DOE is performed once again, followed by the forward mapping. This process is repeated till an acceptable surrogate model is obtained. The backward mapping thus introduces a loop in the overall framework. It is also worth noting that the backward mapping procedure is computationally less expensive than the forward mapping procedure.

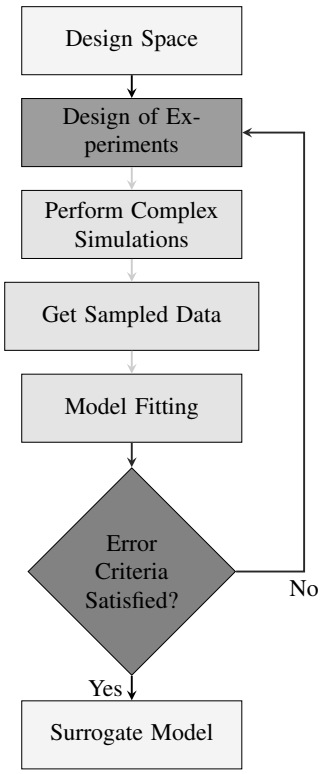

Figure 2: Overall framework for developing a surrogate model.

The traditional way of performing the sensitivity analysis of a surrogate model is with the use of the Fisher information matrix. The inverse of the Fisher information matrix is the covariance matrix. Depending on the uncertainties present in the experiment, the Fisher information matrix can be used to find the limits on the variances of the surrogate model parameters (Atkinson et al., 2014). Since in contrast to physical experiments, computational experiments are not contaminated by noise, the Fisher information provides solely a measure of the 'lack of fit' of the surrogate model. The traditional interpretation of the measure for the variance associated with the estimate is not applicable. Hence, in deterministic systems, it becomes necessary to perform the sensitivity analysis using measures that quantify the error between the outputs of the complex simulation and the surrogate models at the sampled points. An error tolerance criteria is thus defined and the algorithm is iterated till this criteria is met (see Fig.2).

In the context of multi-scale modeling, the selection of the error tolerance criteria depends not only on the model of interest but also on its interaction with other models, on same or different

scales in the system. Even a small error at one scale of a system can propagate and result in large errors at some other scale. Hence, it is important that the error tolerance criteria be defined by the model that is ultimately going to use results obtained from some other model in the system. For example, if model A requires some data from a complex model B and the surrogate model is approximating the complex model B, then the error tolerance criteria used in the construction of this surrogate model should be be defined by model A.

3. An Illustrative Example

To demonstrate the overall framework for constructing surrogate models, we consider a multi-scale system where a macroscopic model requires pressure of one mole of ammonia as an input. The macroscopic model asks for this pressure data from a lower scale model, which we consider to be the Redlich-Kwong equation of state for one mole of ammonia, $P = \dfrac{RT}{(V-b)} - \dfrac{a}{\sqrt{T}V(V+b)}$, where P is the pressure in atm. Our objective is to find local linear approximations (surrogate models) for the Redlich-Kwong equation. Each of the linear models should be of the form $\hat{P} = \beta_0 + \beta_1 T + \beta_2 V$, where β_0, β_1 and β_2 are the unknown coefficients to be determined.

Table 1: Ammonia information used in the simulation

Constant/Variable	Value/Range	Units
T	(420, 600)	K
V	(0.25, 1.00)	$L\ mol^{-1}$
R	0.082	$L\ atm\ mol^{-1}\ K^{-1}$
a	85	$atm\ K^{1/2}\ L^2\ mol^{-2}$
b	0.025	$L\ mol^{-1}$

We thus have a 2-dimensional design space with the design variables being temperature and volume (the inputs to the Redlich-Kwong equation). The ranges of temperature and volume are arbitrarily chosen above their respective critical values for ammonia. Note that we do not include very low values of volume in our demonstration because a linear surface is a very poor approximation of the Redlich-Kwong equation at very low values of volume. The values and ranges of the constants and the variables used in our simulation are shown in Table 1. The design space is divided into 5 subintervals each along the temperature and the volume axes. This results in 25 equally sized subregions in the design space. Then the Latin hypercube sampling (DOE) is performed for 20 points in each of the subregions. For a particular subregion, the pressure at each of the 20 selected points is calculated using the complex model (Redlich-Kwong equation) to get the input/output data. Then, the linear surrogate model is fit to this input/output data using the least squares regression method of the response surface methodology as described in sec. 2.2. The same procedure is applied for all the 25

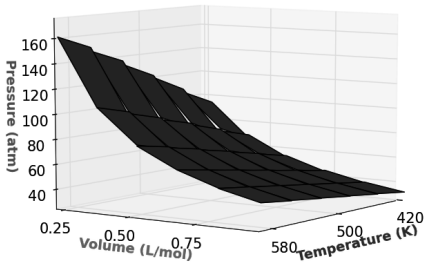

Figure 3: The linear surrogate model surfaces in the 25 subregions.

subregions to obtain a linear surrogate model for each. The maximum error between the complex and the surrogate model at the selected points in the subregion is chosen to be the measure for error. We assume that the macroscopic model's error tolerance criteria corresponds to a maximum error tolerance of 3 atm in the surrogate model. Thus, the simulation (beginning at the DOE) is run until the maximum error does not exceed 3 atm in any of the subregions. Furthermore, to rectify the discrepancies in the results at the borders of these subregions, an average value of the result obtained from the models in the bordering subregions is considered. The surface plot of the surrogate models resulting from one such simulation are shown in Fig.3. As can be seen from Fig.3, the surface profile of the surrogate model is a reasonably good approximation of the PVT surface profile of the Redlich-Kwong equation. In this particular simulation run, it took 10 iterations in the framework before the error tolerance criteria was satisfied. The values of the surrogate model coefficients for 5 random subregions are shown in Table 2.

Table 2: Surrogate model coefficients for 5 subregions.

Coefficients	β_0	β_1	β_2
Subregion 1	28.308	0.215	-125.941
Subregion 2	49.295	0.189	-143.373
Subregion 3	53.621	0.195	-159.288
Subregion 4	32.671	0.152	-79.299
Subregion 5	40.356	0.147	-87.522

4. Conclusion

The computational cost of applications involving complex simulations can be greatly reduced with the help of surrogate models. They also provide an efficient way for handling scale interactions in a multi-scale system. Usually, local surrogate models provide better approximations rather than a single surrogate model spanning the entire design space. In deterministic computer experiments without any stochastic noise, the surrogate models are better validated by defining a tolerance criteria for the gap between the responses of the complex and the surrogate model. The common variance-based arguments are only giving a measure for the lack of fit and the standard statistical arguments do not apply, so the computations are deterministic and free of stochastic contaminations. The tolerance criteria should be defined by the application using the surrogate model so as to avoid the large errors caused by error propagation from the model to the application. In the illustrative example considered, the local linear surrogate models provide a good approximation of the Redlich-Kwong equation (the exceptions being at very low values of volume). When dealing with divided design spaces, the issue of discrepancies in the results at the borders of the subregions can be addressed by using statistical techniques like averaging or interpolating.

References

Atkinson, A. C., Fedorov, V. V., Herzberg, A. M., Zhang, R., 2014. Elemental information matrices and optimal experimental design for generalized regression models. Journal of Statistical Planning and Inference 144, 81–91.

Fang, K.-T., Li, R., Sudjianto, A., 2005. Design and Modeling for Computer Experiments. Chapman and Hall/CRC.

Giunta, A. A., Jr., S. F. W., Eldred, M. S., 2003. Overview of modern design of experiments methods for computational simulations. In: 41st AIAA aerospace sciences meeting and exhibit.

Han, Z.-H., Zhang, K.-S., 2012. Surrogate-based optimization. In: Real-World Applications of Genetic Algorithms. InTech.

Koziel, S., Ciaurri, D. E., Leifsson, L., 2011. Surrogate-based methods. In: Computational Optimizations, Methods and Algorithms. Springer.

Krist V. Gernaey, Jakob K. Huusom and Rafiqul Gani (Eds.), 12th International Symposium on Process Systems Engineering and 25th European Symposium on Computer Aided Process Engineering.
31 May - 4 June 2015, Copenhagen, Denmark.

Systematic Development of Kinetic Models for Systems Described by Linear Reaction Schemes

Carolina S. Vertis, Nuno M.C. Oliveira and Fernando P.M. Bernardo

CIEPQPF; Dep. Chemical Engineering; University of Coimbra; Coimbra, Portugal
nuno@eq.uc.pt

Abstract

A phased approach for generation of linear reaction schemes, i.e., schemes where each reaction has only one reactant and one product as principal species, is proposed in this work. Exhaustive generation of all stoichiometric consistent chemical reactions and enumeration of all possible reaction schemes (based on mass flux analysis), is considered. A graph approach is used for representation of the reaction schemes, and a network model used to elucidate the structure of alternative models at a given level of complexity. After the selection of plausible model structures, determination of possible model parameters is performed in a later step, through regression of the experimental data available. We consider the application to a relevant case study, capable of evidencing the gains and advantages resulting from this systematic analysis.

Keywords: reaction schemes, identification, kinetic model development, discrete optimization.

1. Introduction

Kinetic models of chemical reaction systems provide fundamental information for chemical process design and optimization. The traditional approach to develop these models is to postulate a reaction scheme (network of chemical reactions) based on observed species, their concentrations and eventually some theoretical or heuristic considerations on plausible reaction pathways. On top of this reaction scheme, kinetic laws for each reaction step are established, and regression of experimental data is used to determine the corresponding kinetic parameters. If reasonable statistical adjustment is achieved, the overall kinetic model, comprising the initially postulated reaction scheme and the estimated kinetic parameters, is accepted. If not, modifications are introduced, either in the kinetic models and/or in the reaction scheme used to describe the system. Due to the nonlinear nature of the regression problems, the required modifications are often not prominent (or unique), and tend to be dependent on the expectations of the modeler relative to the behavior of the system. Clearly, this is not a systematic procedure and, as such, it does not guarantee that the most plausible schemes are examined. This is especially true when the number of species and consequently the total number of possible reaction schemes is high. In these cases, a successful approach for kinetic model development requires a substantial integration between different phases such as thorough enumeration of alternatives structures, discrimination between competing models and planning of new experiments, identification of the reaction network structure, selection of the kinetic laws that describe each individual step, regression of kinetic parameters, and finally the validation of the overall results.

The identification of reaction schemes is a topic addressed in the literature under different contexts, such as the analysis of biological metabolic networks and chemical systems with catalytic and non-catalytic reactions. A recent review of existent methods for reaction-pathway identification

separates these in two major groups: methods based on linear algebraic analysis and others based on graph theory (Bertók and Fan, 2013). All of these techniques consider a steady state approach, starting from an overall reaction (formed only by terminals species), and considering elementary steps that can be incrementally combined to produce the desired global reaction. These methods usually address the generation of direct (cycle-free) mechanisms, which are composed by a set of linearly independent reactions. Sellers (1984) proposed a combinatorial method to identify chemical mechanisms using linear algebraic analysis, describing a chemical system by an integer matrix which express the incidence relations between all chemical species and all elementary reactions in the system. The graph theoretic approach provides a different approach, following a list of axioms of feasible reaction pathways and feasible reaction networks to identify mechanisms at steady state, starting from a global reaction. It relies on a graph representation with several types of graphs, including bipartite graphs (P-graphs) (Seo et al., 2001; Fan et al., 2002).

Despite these contributions, a systematic and well-structured kinetic model development approach is still missing, in particular one that fully incorporates experimental data when examining alternative reaction schemes. This paper proposes a methodology that addresses these needs, organized in sequential steps, which include: (i) the exhaustive search of the space of possible reaction schemes, in order of increasing complexity, (ii) the selection of the most plausible reaction schemes in face of the available experimental data, and (iii) detailed kinetic modelling of each reaction step. In the present work, only linear reaction schemes are considered, i.e., reaction schemes where each reaction has only one reactant and one product (Temkin et al., 1996). Nevertheless, the structure of the methodology can be adapted to more general situations. Compared with the more traditional approach, an important advantage of the proposed method is the separation of the tasks of elucidation of the reaction scheme from the determination of the kinetic laws for each reaction scheme. This avoids the use of nonlinear regression in the initial development phases, eliminating their associated numerical problems, e.g., the presence of multiple local optima, which often complicate the model development task.

2. Description of the methodology

The main structure of the proposed methodology is described in Figure 1. In the first step (s1), the list of possible chemical reactions between the species present in the system is identified. In the present case only linear chemical reactions are considered; moreover, the list of possible reactions is generated solely based on stoichiometric considerations. Other useful criteria for this step include thermodynamic and energetic issues (Fishtik et al., 1999; Fishtik and Datta, 2000). The generation algorithm is based on a MILP (mixed integer linear programming) formulation and exhaustive enumeration of feasible solutions (corresponding to possible reactions), using integer cuts. The set of solutions found in this step forms a *superstructure* for the individual reaction schemes considered in the next steps.

The second step (s2) corresponds to the generation of reaction schemes through combination of reactions enumerated in step 1. Since only linear reactions were considered, the schemes generated are also linear. Each reaction scheme is represented by a graph, where nodes correspond to principal chemical species and arcs to chemical reactions. The generation methodology is presented in more detail in Section 3 and is based on a structural flux analysis, ensuring that only connected schemes are generated. The mathematical formulation corresponds to a MILP problem, whose solutions represent candidate reaction schemes.

In the third step (s3), the available experimental data is considered; it is assumed that this corresponds to concentration profiles obtained in non-stationary conditions. Continuous approximations of these profiles are obtained through orthogonal collocation on finite elements, obeying appropriate global mass conservation constraints, e.g., for closed systems. The coefficients of the approximating polynomials are calculated as the solution of a quadratic optimization problem, in-

cluding regularization constraints as needed, to avoid undesired oscillations in the approximated profiles. The smoothed profiles thus obtained are used to calculate reliable estimates of the derivatives dC/dt, for calculation of the reaction rates in the next step.

The fourth step (s4) involves the use of the time derivatives of the concentration profiles to establish a detailed flux analysis for each reaction network considered. This enables a first selection of the plausible reaction schemes from the entire list of possible schemes generated in step 2, as the ones where positive or null (net) reaction rates are observed, for each reaction. The actual analysis performed on this phase depends on the *redundancy index* (IR) of the network considered. This is defined as the number of additional pathways (chemical reactions) in the network compared with the minimum number of pathways ($\mathtt{nrx}_{\mathtt{min}}$) that allow a network to remain fully connected, with a fixed number of nodes, where $\mathtt{IR} \geq 0$. The minimum number of pathways among species that ensure a connected network is equal to the number of species minus one (Meyer, 2000; Marin and Yablonsky, 2011). For schemes with $\mathtt{IR} = 0$, the calculation of the instantaneous reaction rates can be done through the solution of a linear system of equations $Ar(t) = dC(t)/dt$, where A is the incidence matrix, and $r(t)$ the vector of reaction rates at time t. For schemes with $\mathtt{IR} > 0$ the calculation of the instantaneous reaction rates cannot be performed as in the previous case, since the above linear system is underdetermined; in this case the flux analysis requires the use of additional data sets and the correlation between fluxes in consecutive time intervals. However, even in this situation, a max-min methodology can be used to eliminate clearly infeasible reaction schemes. Due to space limitations, the complete analysis of this case is outside the scope of the present paper, where the application example considered has only $\mathtt{IR} = 0$.

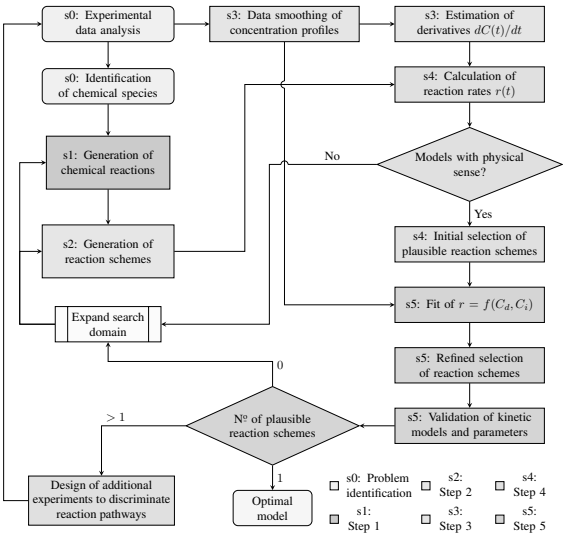

Figure 1: Structure of the methodology for development of kinetic models.

The fifth and last step (s5) of the methodology allows a finer selection of reaction schemes, now based on the regression analysis of the individual reaction rates calculated in step 4 with the concentrations of each reactant and reaction product. This task is now much simplified, since the structure of each candidate reaction network can now be considered fixed. If a good correlation between each reaction rate and the corresponding species reactant and product species is found, the scheme is considered a good plausible candidate to explain the kinetic data. If either steps 4 or 5 result in an empty set, this means that neither of the considered reaction schemes is a reasonable model for the observed data. Therefore, one should go back to steps 1 or 2 and expand the search space, considering other chemical reactions and/or more complex schemes. If, on the other hand, too many alternative schemes are equally good and remain at the end of step 5, then further experimental studies are recommended, to discriminate between competing reaction schemes, or properly identify still unclear partial pathways. In this analysis, the uncertainties inherent to the experimental data used can also be considered.

3. Generation of linear reaction schemes

The starting point for the generation step of reaction schemes is the superstructure that represents the reaction scheme with maximum complexity, by incorporating all possible reactions identified in step 1 (Figure 2). Alternative schemes contained in this superstructure are generated through a structural flux analysis with mass balances for each node. The structure has nodes corresponding to each participating species, plus two additional (fictitious) nodes: a *supersource* node, that injects the quantity X into the network, and the *supersink* node, that receives quantities Y, Z, V and W from each of the nodes. These quantities are determined depending on the desired complexity (IR) for the reaction scheme, and are such that only connected graphs are generated, thus avoiding isolated subgraphs.

The following sets are defined: c — chemical species (nodes), rx— chemical reactions (arcs), c1 and p1— subsets of c that contain the principal components and product species; p1 has the same species as c1 except the initial reactant(s). The auxiliary sets exd and exi are conditional sets used to denote that a given reaction occurs in the direct or reverse form in the scheme considered. In the superstructure of Figure 2 the supersource node is only connected to components initially present in the reacting mixture, and injects the amounts $\mathtt{ss}_i$:

$$\mathtt{ss}_i = \begin{cases} \mathtt{IR} + \mathtt{nrx}_{\mathtt{min}}, & \forall i \in \mathtt{c1} \backslash \mathtt{p1} \\ 0 & \forall i \in \mathtt{p1} \end{cases}$$

The supersink node is connected to all node species in the network, and absorbs the amount $\mathtt{ni}_i$ from each node, where $\mathtt{ni}_i$ represents the number of incident arcs in the respective node, i.e., the number of pathways that have that node as a product. Binary variables $\mathtt{ycpr}_{i,j}$ are used to represent the fact that chemical species $i \in \mathtt{c1}$ is a product in the reaction $j \in \mathtt{rx}$ (or not). In this case:

$$\mathtt{ni}_i = \sum_{j \in \mathtt{rx}} \mathtt{ycpr}_{i,j}, \qquad \forall i \in \mathtt{c1}$$

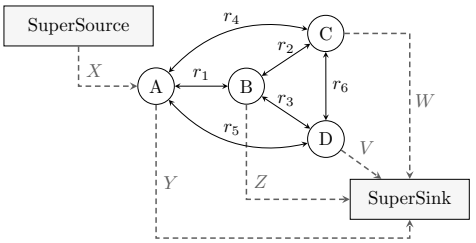

Figure 2: Reaction network superstructure representation.

A generic mass balance for each node can be written as equation (2), where $F_{i,i'}$ corresponds to the flux between the specie i to i', and am is the adjacency matrix which identifies the connections between species, with $\mathtt{am} \equiv [\mathtt{am}_{i,i'}], \forall i, i' \in \mathtt{c1}$. The formulation uses binary variables to choose the direction of the pathways, according to the reaction pathways in the corresponding network; in this case $\mathtt{yrxd}_j$ represents a direct pathway and $\mathtt{yrxi}_j$ a reverse one. Each of the reactions can be considered only in a given direction for the purpose of generation of the reaction scheme, as given by equation (3), since reversible reactions occur predominantly in a given direction, until equilibrium is reached. Additional constraints ensure that if a reaction exists in the scheme, the structural flux cannot be zero, while other constrains establish upper limits in this flux — equations (4).

The stoichiometric coefficients calculated in step 1 are stored in parameters $\mathtt{nsre}_{i,j}$ and $\mathtt{nspr}_{i,j}$, with $i \in \mathtt{c1}$, $j \in \mathtt{rx}$. These parameters are used to define equations (5–7), linking variables $\mathtt{ycpr}_{i,j}$, $\mathtt{yrxd}_j$ and $\mathtt{yrxi}_j$. Enforcing network connectivity, all products have to be generated at least once, up to a limit of $\mathtt{II}_{max}$ times, where $\mathtt{II}_{max} = \mathtt{IR} + 1$, as given by equation (8). Finally, a constant objective function is adopted, equal to the number of chemical reactions in the network (equation 1). Each feasible reaction scheme is sequentially generated through the solution of the optimization problem (1–9), corresponding to a MILP network problem with integer coefficients. The complete enumeration of all possible reaction schemes can be achieved either through incremental addition of integer cuts to the formulation (and resolving it) or, more efficiently, through the use of a MILP

solver that allows the direct enumeration of all feasible solutions at once.

$$\min_{\substack{F,\mathtt{yrxd},\\ \mathtt{yrxi},\ \mathtt{ycpr}}} \quad n_{\mathtt{rx}} = \sum_{j\in\mathtt{rx}} \mathtt{yrxd}_j + \mathtt{yrxi}_j \tag{1}$$

$$\text{s.t.} \quad \mathtt{ss}_i + \sum_{i'\in\mathtt{c1}} F_{i',i}\,\mathtt{am}_{i',i} - \sum_{i'\in\mathtt{c1}} F_{i,i'}\,\mathtt{am}_{i,i'} - \sum_{j\in\mathtt{rx}} \mathtt{ycpr}_{i,j} = 0, \quad \forall i \in \mathtt{c1} \tag{2}$$

$$\mathtt{yrxd}_j + \mathtt{yrxi}_j \le 1, \quad \forall j \in \mathtt{rx} \tag{3}$$

$$\begin{aligned} &F_{i,i'} \ge \mathtt{yrxd}_j, \quad \forall (i,i',j) \in \mathtt{exd} \qquad F_{i,i'} \ge \mathtt{yrxi}_j, \qquad \forall (i,i',j) \in \mathtt{exi} \\ &F_{i,i'} \le \mathtt{yrxd}_j N, \quad \forall (i,i',j) \in \mathtt{exd} \qquad F_{i,i'} \le \mathtt{yrxi}_j N, \qquad \forall (i,i',j) \in \mathtt{exi} \end{aligned} \tag{4}$$

$$\mathtt{yrxd}_j = \mathtt{ycpr}_{i,j}, \quad \forall i \in \mathtt{c},\ j \in \mathtt{rx}, \qquad \text{if } \mathtt{nspr}_{i,j} \ne 0 \tag{5}$$

$$\mathtt{yrxi}_j = \mathtt{ycpr}_{i,j}, \quad \forall i \in \mathtt{c},\ j \in \mathtt{rx}, \qquad \text{if } \mathtt{nsre}_{i,j} \ne 0 \tag{6}$$

$$\mathtt{ycpr}_{i,j} = 0, \quad \forall i \in \mathtt{c},\ j \in \mathtt{rx}, \qquad \text{if } \mathtt{nsre}_{i,j} = 0 \wedge \mathtt{nspr}_{i,j} = 0 \tag{7}$$

$$\sum_{j\in\mathtt{rx}} \mathtt{ycpr}_{i,j} \ge 1, \quad \forall i \in \mathtt{p1}, \qquad \sum_{j\in\mathtt{rx}} \mathtt{ycpr}_{i,j} \le \mathtt{II}_{max}, \quad \forall i \in \mathtt{c1} \tag{8}$$

$$F_{i,i'} \in \mathbb{N}_0^+, \quad \forall (i,i') \in \mathtt{c1}, \quad \mathtt{yrxd}_j,\ \mathtt{yrxi}_j,\ \mathtt{ycpr}_{i,j} \in \{0,1\}, \quad \forall i \in \mathtt{c},\ j \in \mathtt{rx} \tag{9}$$

4. α-pinene case study

This methodology is illustrated by the application to the thermal isomerization of α-pinene (Fuguitt and Hawkins, 1945; Stewart and Sørensen, 1981). This system comprises 5 chemical species: α-pinene (AP), limonene (LIM), allo-ocimene (AO), β-pironene (BP) and a dimer (D). We fixed the chemical reaction $r_9 : 2\,\mathrm{AO} \longrightarrow \mathrm{D}$ in all generated schemes, since its presence is known previously. Two data sets from isothermal batch experiments at different temperatures are used (T1 and T2). In this case 50 reaction schemes were generated, and 31 (and 34) schemes were selected as plausible in step 4, for data sets T1 and T2, respectively. In step 5 of the methodology, regression of the corresponding reaction rates considering simple homogeneous kinetics for each reaction rate in each plausible reaction scheme were considered, and used to discard most of the candidates. Figure 4 and Table 1 present the structure and numeric values of the parameters found for the best candidate, after the termination of the selection procedure. Significant differences in the regression results relative to the additional alternatives were found; together with the fact that the same solution was found for each data set considered individually, this provides additional confidence that the reaction scheme depicted in Figure 4 is the most adequate to describe the experimental data available, at this level of model complexity ($\mathtt{IR} = 0$).

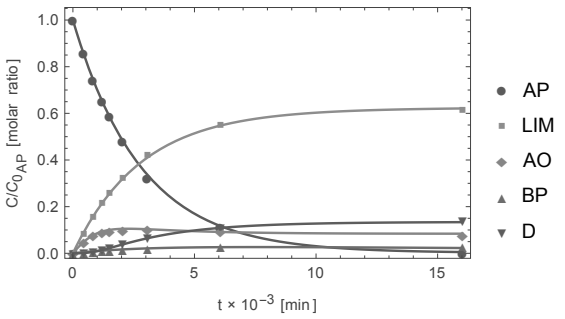

Figure 3: Experimental isothermal data T2 and simulation with the fitted kinetic parameters.

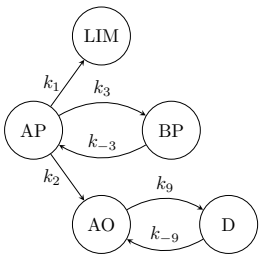

Figure 4: Reaction scheme proposed in this work for the thermal isomerization of α-pinene.

Table 2 compares the results of this model with the equivalent results provided by the model identified by Stewart and Sørensen (1981). The underlying reaction schemes are significantly

different, and the later model uses a larger number of chemical reactions. However, given the experimental data available, the proposed model is able to provide a lower sum of squared errors (SSE). This illustrates the importance of systematic evaluation of model alternatives, and the need of extra experimental or theoretical information to justify more complex model structures.

Table 1: Reaction rates and kinetic parameters, in min^{-1} for first order reactions and $\text{min}^{-1}\,\text{C}^{-1}$ for second order reactions (data set T2).

rx	Model	$k_d \times 10^3$	$k_i \times 10^3$
r_1	$k_d C_{AP}$	0.220	–
r_2	$k_d C_{AP}$	0.124	–
r_3	$k_d C_{AP} - k_i C_{BP}$	0.012	0.030
r_9	$k_d C_{AO}^2 - k_i C_D$	3.167	0.165

Table 2: Comparative results of objective function value for data sets T1 and T2.

Model	T1	T2
Stewart and Sørensen (1981)	0.00710	0.01337
This work	0.00288	0.00075

5. Conclusions

A sequential methodology for the development of chemical reaction kinetic models, which explores the space of possible reaction schemes and gradually selects the simplest schemes able to satisfactorily explain the available experimental data, is proposed. The determination of kinetic parameters through nonlinear regression is left to the final stage of the methodology where only the most plausible schemes arrive. Therefore, the confidence in the estimated kinetic parameters is likely to be higher than the one obtained using the traditional approach to kinetic modeling (based on a postulated reaction scheme with no guarantees that others may better explain the observed data). The methodology was applied to one case study, illustrating that even for relatively simple systems the number of plausible reaction schemes may be high, and that alternative reaction schemes could be found. Moreover, the methodology also illustrates that in some cases the available data is not enough to completely identify a reaction scheme; in such cases this model development should be complemented with directed additional experiments, to elucidate specific uncertain pathways.

Acknowledgments: Financial support from CNPq — Conselho Nacional de Desenvolvimento Científico e Tecnológico, Brasil (scholarship 203592/2014-0), is gratefully acknowledged.

References

Bertók, B., Fan, L. T., 2013. Review of methods for catalytic reaction-pathway identification at steady state. Current Opinion in Chemical Engineering 2 (4), 487 – 494.

Fan, L., Bertók, B., Friedler, F., 2002. A graph-theoretic method to identify candidate mechanisms for deriving the rate law of a catalytic reaction. Computers & Chemistry 26 (3), 265 – 292.

Fishtik, I., Alexander, A., Datta, R., 1999. Enumeration and discrimination of mechanisms in heterogeneous catalysis based on response reactions and unity bond index–quadratic exponential potential (UBI–QEP) method. Surface Science 430 (1â€“3), 1 – 17.

Fishtik, I., Datta, R., 2000. A thermodynamic approach to the systematic elucidation of unique reaction routes in catalytic reactions. Chemical Engineering Science 55 (19), 4029 – 4043.

Fuguitt, R. E., Hawkins, J. E., 1945. The liquid phase thermal isomerization of alpha-pinene. Journal of the American Chemical Society 67 (2), 242–245.

Marin, G., Yablonsky, G., 2011. Kinetics of Chemical Reactions. Wiley.

Meyer, C., 2000. Matrix Analysis and Applied Linear Algebra:. Society for Industrial and Applied Mathematics.

Sellers, P., 1984. Combinatorial classification of chemical mechanisms. SIAM Journal on Applied Mathematics 44 (4), 784–792.

Seo, H., Lee, D.-Y., Park, S., Fan, L., Shafie, S., Bertók, B., Friedler, F., 2001. Graph-theoretical identification of pathways for biochemical reactions. Biotechnology Letters 23 (19), 1551–1557.

Stewart, W. E., Sørensen, J. P., 1981. Bayesian estimation of common parameters from multiresponse data with missing observations. Technometrics 23 (2), pp. 131–141.

Temkin, O., Zeigarnik, A., Bonchev, D., 1996. Chemical Reaction Networks: A Graph-Theoretical Approach. Taylor & Francis.

Krist V. Gernaey, Jakob K. Huusom and Rafiqul Gani (Eds.), 12th International Symposium on Process Systems Engineering and 25th European Symposium on Computer Aided Process Engineering.
31 May - 4 June 2015, Copenhagen, Denmark.

Rigorous Modeling, Simulation and Optimization of a Dividing Wall Batch Reactive Distillation Column: a comparative study

Edna Soraya Lopez-Saucedo[a], Juan Gabriel Segovia-Hernandez[a], Ignacio E. Grossmann[b] and Salvador Hernandez-Castro[a]

[a]*Department of Chemical Engineering; Universidad de Guanajuato; Guanajuato, Mexico*
[b]*Department of Chemical Engineering; CMU, Pittsburgh, USA*
elopez@andrew.cmu.edu

Abstract

A model and solution strategies are investigated for the optimization of a Dividing Wall Batch Reactive Distillation Column (DWBRC). In order to accomplish this objective, we describe a dynamic model that involves tray-by-tray calculations for the time varying column profiles. In order to compare the simultaneous solution of the system of differential and algebraic equations, two different approaches are used: equation oriented based on orthogonal collocation implemented in GAMS, and control vector parameterization (CVP) as implemented in gPROMS.

Keywords: Reactive batch distillation, dynamic optimization, Dividing Wall Columns

1. Introduction

Reactive Batch Distillation Columns (RBC) have been studied as a promising technology due to its dual functionality: separation and reaction. Modeling, simulation, and optimization of batch distillation processes rely on dynamic models. A number of different solution approaches for this kind of systems, described by a set of differential and algebraic equations (DAEs) have been proposed in the literature. One of these approaches has been developed by Biegler (1984), in which the dynamic optimal control problem is approximated by a finite dimensional nonlinear program (NLP) through the discretization of all variables using finite elements with orthogonal collocation points. This equation oriented approach can then be solved with GAMS (General Algebraic Modeling System 24.2.2) as an NLP problem to simultaneously perform the optimization while converging the DAEs. The other solution method is the Control Vector Parametization (CVP) proposed by Vassiliadis et al. (1994) which relies on the iterative solution of DAEs in the space of the control variables in order to perform the optimization with a Successive Quadratic Programming (SQP) method.

In this study we propose the optimal design and operation of a Dividing Wall Batch Reactive Distillation Column (DWBRC). We propose an esterification reaction for the production of ethyl acetate (as the distillate product). This study investigates with the two solution approaches how the parameters such as vapor flow rate (V, $kmol/hr$) and optimal control variable reflux ratio ($RR = R/V$) are to be adjusted to maximize the productivity in the column for a given product specification. First, we provide the problem statement followed by the proposed mathematical model in section 3. The model was solved using two different approaches presented in section 4 for the production of ethyl acetate. The column configuration and operational conditions are

presented in section 5. The results are shown in section 6 followed by the conclusions in section 7.

2. Problem statement

In a general form the problem can be stated as follows:

≪ Given a feed consisting of a mixture of NC components, the column configuration, and product purity specification for a key distillate component. The goal is to maximize an objective function by manipulating the column reflux ratio RR(t) and vapor flowrate V to purify a given mixture until an NC pure component is obtained (inside some pre-specified tolerance). ≫

The specific dynamic optimization problem can then be described as:

Given:	Column configuration, feed mixture, vapor flow rate, product purity and batch time.
Determine:	Optimal reflux ratio.
To maximize:	The amount of distillate product.
Subject to:	Equality and inequality constraints.

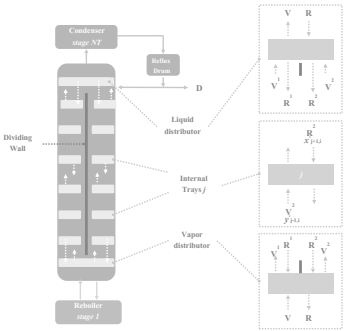

Figure 1: Batch Reactive Distillation Column (BRC)

The reflux ratio $RR(t)$ is considered the control variable in the optimization problem. A general profit function P that combines the minimum time and the maximum distillate problem is given by Mujtaba (2004) and is used in this study:

$$P = \frac{C_1 D - C_2 M_{B_0}}{t_B + t_S} - C_3 \tag{1}$$

where P is the profit ($\$/hr$), D is the amount of distillate product ($kmol$), C_1 is the sales value of the distillate product ($\$/kmol$), M_{B_0} is the initial raw material charge ($kmol$), C_2 is the cost of raw material ($\$/kmol$), C_3 is the fixed operating cost (energy, wages, depreciation, etc., $\$/hr$), t_B is the batch time (hrs) and t_S is the set up time (charging and cleaning time between batches, hrs). In mathematical terms, the optimization problem can be represented as:

$\mathbf{max}_{RR(t)}$	**D**	
s.t.	Dynamic process equations	(equality constraints)
	$x_{product}(t) \geq x_{desired}$	(inequality constraint)
	Bounds on Q_{REB} *and* $D_{product}$	(inequality constraint)

3. Dynamic Process Equations

In order to solve the optimization problem shown in the previous section, it is necessary to develop a rigorous model to successfully predict the behavior of the variables with respect to time. Two basic assumptions are applied in the formulation of the model:

1. The vapor phase holdup is assumed to be negligible compared to the liquid phase holdup on each plate.
2. Chemical reactions in the vapor phase are neglected.

The proposed set of differential and algebraic equations (DAEs), can be decomposed into different equations: mass balances, energy balances, equilibrium equations (chemical, physical and thermodynamic) and other equations such as reaction rate, summation of compositions, etc. The set of equations that constitutes the proposed model is presented in the set of Equations 2-19, which are derived from the distillation column on Figure 1. The heat of reaction in the energy balance equations is omitted because heat of formation at the standard conditions is used as a base for enthalpy calculations. The notation for the variables is given in Figure 2. The stages are numbered from bottoms to top of the batch column, stage 1 being the reboiler and condenser the stage 10. More details about the column are given in Section 5.

Total mass balances

Reboiler: $j = 1\text{n}$

$$\frac{dM_B}{dt} = -D + \Delta n_1 M_B \tag{2}$$

Distributors: $j = NT - 1$ and Tray 2

$$\frac{dM_j}{dt} = R^1_{j+1} + R^2_j - R_j + V_{j+1} - V_j + \Delta n_j M_j \tag{3}$$

Internal Trays: $j = 2$ and $NT - 2$

$$\frac{dM^1_j}{dt} = R^1_{j+1} - R^1_j + V^1_{j-1} - V^1_j + \Delta n^1_j M^1_j \tag{4}$$

Component mass balances

Reboiler: $j = 1$

$$M_B \frac{dx_{B,i}}{dt} = R_2 x_{2,i} - R_B x_{B,i} - V_B(x_{B,i} - y_{B,i}) + r_{B,i} M_B - \Delta n_i M_B \tag{5}$$

Distributors: $j = 2 and j = NT - 1$

$$\frac{d(M_j x_{j,i})}{dt} = R^1_{j+1} x^1_{j+1,i} + R^2_{j+1} x^2_{j+1,i} - R_j x_{j,i} + V_{j-1} y_{j-1,i} - V_j y_{j,i} + r_{ji} M_j \tag{6}$$

Internal Trays (section 1 and 2): $j = Distributor + 1, ..., NT - 2$

$$\frac{d(M^1_j x^1_{j,i})}{dt} = R^1_{j+1} x^1_{j+1,i} - R^1_j x^1_{j,i} + V^1_{j-1,i} y_{j-1,i} - V^1_j y^1_{j,i} + r^1_{ji} M^1_j \tag{7}$$

$$\frac{d(M^2_j x^2_{j,i})}{dt} = R^2_{j+1} x^2_{j+1,i} - R^2_j x^2_{j,i} + V^2_{j-1,i} y_{j-1,i} - V^2_j y^2_{j,i} + r^2_{ji} M^2_j \tag{8}$$

Condenser: $j = NT$

$$\frac{d(M_{NT} x_{NT,i})}{dt} = V_{NT-1} y_{NT-1,i} - (V_j + \Delta n_{NT} M_{NT}) x_{NT,i} + r_{NT,i} M_{NT} \tag{9}$$

Energy balance

Reboiler: $j = 1$

$$0 = Q_{REB} + R_2 h^L_2 - R_B h^L_B + V_B(h^L_B - h^V_B) \tag{10}$$

Distributors: $j = NT - 1$ and Tray 2

$$R^1_{j+1} h^{L_1}_{j+1} - R^2_{j+1} h^{L_2}_{j+1} - R_j h^L_j + V_{j-1} h^V_{j-1} - V_j h^V_j = 0 \tag{11}$$

Internal Trays: $j = Distributor + 1, ..., NT - 2$

$$R^1_{j+1} h^{L_1}_{j+1} - R^1_j h^{L_1}_j + V^1_{j-1} h^{V_1}_{j-1} - V^1_j h^{V_1}_j = 0 \tag{12}$$

Condenser: $j = NT$

$$Q_{COND} - V_{NT-1} h^V_{NT-1} + (V_{NT-1} + \Delta n_{NT} M_{NT}) h^L_{NT} = 0 \tag{13}$$

Equilibrium relationship and vapor and liquid summations

$$y_{j,i} = K_{j,i} x_{j,i} \quad and \quad y_{j,i}^{1,2} = K_{j,i} x_{j,i}^{1,2} \qquad , \qquad \Sigma y_{j,i} = 1 \quad and \quad x_{j,i} = 1 \tag{14}$$

Vapor-Liquid Equilibrium constant

$$K_{j,i} = K_{j,i}(x_{j,i}, T_j, P_j) \quad and \quad K_{j,i}^{1,2} = K_{j,i}^{1,2}(x_{j,i}^{1,2}, T_j^{1,2}, P_j) \tag{15}$$

Enthalpy

$$h_{j,i}^{L} = h_{j,i}^{L}(x_{j,i}, T_j, P_j) \quad and \quad h_{j,i}^{L_{1,2}} = h_{j,i}^{L_{1,2}}(x_{j,i}^{1,2}, T_j^{1,2}, P_j) \tag{16}$$

$$h_{j,i}^{V} = h_{j,i}^{V}(y_{j,i}, T_j, P_j) \quad and \quad h_{j,i}^{V_{1,2}} = h_{j,i}^{V_{1,2}}(y_{j,i}^{1,2}, T_j^{1,2}, P_j) \tag{17}$$

Reaction and Reaction Terms

$$\underset{(acetic\,acid)}{AcOH} + \underset{\text{(ethanol)}}{EtOH} \leftrightarrow \underset{\text{(ethyl acetate)}}{EtOAc} + \underset{\text{(water)}}{H_2O} \tag{18}$$

$$\Delta n_j = \Sigma r_{j,i} \quad when \quad r_{j,i} = r_{j,i}(k_{j,i}, x_{j,i}) \tag{19}$$

j and i are the number of trays and components, respectively
$x_{j,i}$ is the liquid mole fraction for tray j and component i
$y_{j,i}$ is the vapor mole fraction for tray j and component i
D is the distillate flowrate
R_j is the liquid flowrate in tray j
V_j is the vapor flowrate in tray j
M_B and M_{NT} are the reboiler and distillate holdup, respectively
Q_{REB} is the energy consumed in the reboiler
Q_{COND} is the energy consumed in the condenser
h_j^L is the liquid enthalpy in tray j
h_j^V is the vapor enthalpy in tray j
superscript 1 and 2 represent left side (*section* 1) and right side (*section* 2) of the dividing wall batch column, respectively

Figure 2: Notation used on the dynamic model

4. Solution approaches

In order to determine the optimal solution of the dynamic model presented in the previous section, we summarize below some of the issues that arise in the two approaches used in this study.

4.1. Solving the optimization problem by an Equation Oriented Approach

In this approach the set of DAEs (Equations 2 - 19) is discretized into a set of algebraic equations by applying finite elements and the orthogonal collocation method developed by Cuthrell and Biegler (1987). These equations are then used in a large-scale NLP model. The use of finite elements and collocation points provides more flexibility but the error in the discretization cannot be easily controlled. The proposed DAE system involves a complex set of equations that leads to an index 2 problem. To be solved, the index should be reduced to 1 by differentiating the equation $\sum_{i=1}^{NC} x_{j,i} = 1$. This leads to a new algebraic equation that substitutes the internal trays mass balances given in Equation 7 for one component.

4.2. Solving the optimization problem by Control Vector Parameterization Approach

To formulate the optimal control problem as a reduced NLP problem, the control variable RR(t) is approximated by a finite dimensionally equation. The time interval is divided into a finite number of subintervals, each involving a finite number of parameters for the control variables to be optimized. This new problem is subjected to the constraints of the model and can be solved using a Succesive Quadratic Programming (SQP) algorithm. This approach has the advantage of providing a direct control of the discretization error by adjusting the size and order of the integration steps using integration techniques.

5. Case study

The reaction-separation is carried out using a 10 tray Dividing Wall Batch Reactive Column (DWBRC). The operational conditions are given in Table 1. An amount of 100 kmol is fed into the reboiler at the start of the operation with the next composition in mole fraction: 0.45 acetic acid, 0.45 ethanol and 0.10 water. The distillate product must achieve a purity of at least 0.70 in mole fraction of ethyl acetate in the distillate with a fixed batch time of 1 hour. The performance is modeled assuming a constant molar holdup for each tray (a total column holdup of 4% of the initial feed where 50% is taken as the condenser hold up and the rest is equally divided in the plates). Constant relative volatilities, calculated using NRTL are used for the various components for modeling the phase equilibrium. The initial values for the system variables are calculated at total reflux in the steady state. The reaction zone extends from tray 1 to 9. The production of ethyl acetate by the esterification of acetic acid with ethanol is accomplished by the stoichiometric equation 18.

Table 1: Operational conditions for the batch reactive column: acetic acid esterification

Number of Trays	
(including reboiler and condenser)	10
Feed, M_{B_0}, kmol	100
Vapor, V, kmol/h	Variable
Vapor and Liquid Distributors	$\beta_1 = 0.70$
	$F_1 = 0.70$
Composition Feed, x_i^0, mole fraction	
Acetic Acid	0.45
Ethanol	0.45
Ethyl Acetate	0
Water	0.10
Activity coefficients (NRTL), α_i	
Acetic Acid	0.98
Ethanol	0.99
Ethyl Acetate	2.3
Water	2.5
Column Holdup, M_j, kmol	
Condenser	0.283
Internal trays	0.071
Column Pressure, P, bar	
Condenser	1.05
Internal Trays	1.12-1.08
Reboiler	1.2
Reaction equations given in Mujtaba (2004)	
r = $k_1C_1C_2$ - $k_2C_3C_4$	
$k_1 = 4.76x10^{-4}$	
$k_1 = 1.63x10^{-4}$	

6. Results

The optimization problem is solved by discretizing the differential equations using the two approaches presented in section 4 with the next specifications: the CVP approach implemented in gPROMS and the equation oriented approach with 10 finite elements and 3 collocation points implemented in GAMS (24.2.2) using CONOPT as the NLP solver. The objective is to maximize the productivity by converting the maximum profit problem in a maximum productivity problem when $C_1 = 1$ and $C_2 = C_3 = t_S = 0$ in Equation 1. The reflux ratio is used as the control variable. Five different cases with different vapor flowrates were studied. All examples were solved on a Workstation with 8 GB RAM memory and Intel®CoreTM i7 CPU (2.20 GHz).

The CVP approach results in a system of 530 equations and 600 variables. The optimization problem is solved in 40 seconds. From the results presented in Table 2(a). The fixed batch time is 1.0 *hour*, while the optimal reflux ratio is piecewise as shown in Figure 3(c) for all vapor flowrates. It is clear that the maximum amount of distillate product $D_{ethylacetate}$ $(kmol)$ is achieved for the maximum vapor flowrate $V = 90\ kmol/hr$. The equation oriented approach results in a system of 532 equations and 698 variables. The optimization problem is solved in 318 seconds. The results are presented in Table 2(b). As in the CVP approach, the batch time is 1.0 *hour*. The maximum amount of distillate product $D_{ethylacetate}$ $(kmol)$ is achieved for the maximum vapor flowrate $V = 80$ $kmol/hr$. In both approaches, the amount of distillate and the energy consumption were directly proportional to increases in vapor flowrate. Therefore, any higher purity would require higher energy consumption. A comparison between the calculated reboiler energy shows that the EOA needs a better initial point for the temperatures in the trays. The accumulated distillate composition profiles for the maximum distillate product for the two approaches are shown in Figures 3(a) and 3(b).

Table 2: Results for the productivity maximization

(a) Results for the CVP approach

Vapor (kmol/hr)	Q_{REB} (kJ)	D_{EtOAc} (kmol)
50	47.40	10.00
60	56.88	12.32
70	66.48	14.16
80	76.13	15.83
90	86.13	16.85

(b) Results for the EOA approach

Vapor (kmol/hr)	Q_{REB} (kJ)	D_{EtOAc} (kmol)
50	78.43	10.32
60	94.14	12.09
70	109.78	13.27
80	125.18	12.33

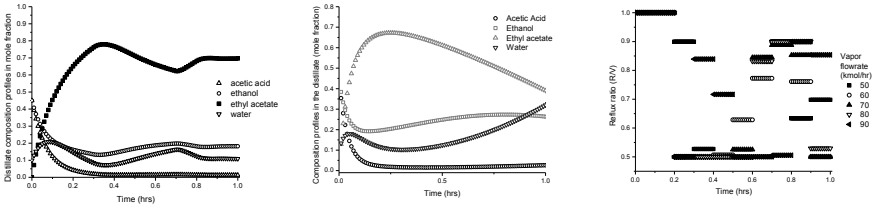

(a) CVP approach

(b) EOA

(c) Optimal reflux ratio for the CVP approach

Figure 3: Distillate composition profiles for the production of ethyl acetate in a Dividing Wall Batch Reactive Distillation Column for the CVP and EOA approaches and optimal piecewise reflux ratio for the production of ethyl acetate in a Dividing Wall Batch Reactive Distillation Column for the CVP approach

7. Conclusion

In this work, a model for the optimization of a dividing wall batch reactive distillation column when the esterification of ethanol using acetic acid to produce ethyl acetate is studied. A maximum productivity optimization problem is solved under fixed distillate product purity (ethyl acetate concentration higher than 0.70 in mole fraction). The results show that the problem is solved using the two different approaches: the finite elements with collocation points implemented in GAMS (24.2.2), and the control vector parametization implemented in gPROMS (2004) with no major differences on the calculated variables values. These differences are due to the discretization error carried out during the discretization. Also, the results show that significantly more CPU time is required with the EOA approach.

References

Biegler, L. T., 1984. Solution of dynamic optimization problems by succesive quadratic programming and orthogonal collocation. Comput. Chem. Eng. 8, 243–248.

Cuthrell, J. E., Biegler, L. T., 1987. On the optimization of differential-algebraic process systems. AIChE J 33, 257.

Mujtaba, I. M., 2004. Batch Distillation Design and Operation. Series on Chemical Engineering Vol. 3, University of Bradford, UK.

Vassiliadis, V. S., Sargent, R. W. H., Pantelides, C. C., 1994. Solution of a class of multistage dynamic optimization problems. part i-algorithmic framework. Ind. Eng. Chem. Res. 33, 2115–2123.

Krist V. Gernaey, Jakob K. Huusom and Rafiqul Gani (Eds.), 12th International Symposium on Process Systems Engineering and 25th European Symposium on Computer Aided Process Engineering.
31 May – 4 June 2015, Copenhagen, Denmark

Theoretical Modeling Of (Non)Reactive Residue Curve Maps For TAME Synthesis System Using MATLAB – SIMULIS Thermodynamics Communication Facility's

M.M. Ceauşescu[a*], Jordi Bonet-Ruiz[b], V. Pleşu[a], P. Iancu[a], A.E. Bonet-Ruiz[a]

[a]*Centre for Technology Transfer for the Process Industries Department of Chemical Engineering, University POLITEHNICA of Bucharest, 1, Gh. POLIZU Street, Building A, Room A056, RO-011061 Bucharest România, Phone : +40-21-4023916, Fax : +40-21-3185900. E-mail: escape25@chim.upb.ro*

[b]*Department of Chemical Engineering, University of Barcelona, Marti i Franques 1, floor 6, E-08028 Barcelona, Spain*

**Corresponding author*

Abstract

The representation and graphical visualization of the chemical components in the composition space is a powerful tool for the analysis and interpretation of process systems behaviour. Reactive distillation is a relatively new technique combining reaction and separation by distillation. Numerous applications are reported in literature, giving details on process design. However, no commercial software is providing tools for representation of reactive residual curve maps. Reasonable explanation can be provided by complex reaction kinetics which is not easy to implement in software. In this study, liquid vapour equilibrium in (non)reactive systems is calculated to build (non) reactive residual curve maps, using SIMULIS® Thermodynamics (from ProSim, France) as database and server for with different thermodynamic models and MATLAB to solve the mathematical model aimed to build (non)reactive residual curve maps. The communication between those software applications is ensured by a MATLAB toolbox provided by ProSim. Graphical facilities of MATLAB allow making suggestive representations. The work consists in setting up the methodology and the mathematical models for (non)reactive residue curve maps for non-reactive and kinetically controlled scenarios.

Keywords: reactive distillation, residual curve maps, feasibility analysis

1. Introduction

The main objective of this work is to theoretically simulate Reactive Curve Maps for the production on TAME (tert-amyl-methyl-ether), in order to check the feasibility of the reactive distillation process. Two theoretical models are used for this process: a non – reactive process where the RCM's are created for the Isopentane – Methanol – TAME system and a kinetically controlled process for the Isoamylenes – Methanol – TAME system.

In this respect MATLAB® – SIMULIS® Thermodynamics communication facility is used to calculate liquid vapor equilibrium in (non) reactive systems. In this way,

MATLAB powerful calculating tools are used to integrate the high complexity thermodynamic models implemented in SIMULIS® Thermodynamics.

2. Case study

The increased interest for using tertiary ethers as additives intensified the research to study thermodynamic and kinetic aspects of the chemical reactions involved in their synthesis. Most of the models published so far to characterize the process for tertiary ethers synthesis were focused only on the main reaction. The prime process involves three simultaneous reversible reactions, two etherification reactions of isoamylenes with methanol (MeOH) and the isomerization between 2M1B (2-Methyl-1-Butene) and 2M2B (2-Methyl-2-Butene), over an acidic ion-exchange resin. The networks for the reactions are presented in equations 1-3. in which the reaction pairs shown establish the reaction equilibria.

$$MeOH + 2M1B \underset{k-1}{\overset{k+1}{\Longleftrightarrow}} TAME \tag{1}$$

$$MeOH + 2M2B \underset{k-2}{\overset{k+2}{\Longleftrightarrow}} TAME \tag{2}$$

$$2M1B \underset{k-3}{\overset{k+3}{\Longleftrightarrow}} 2M2B \tag{3}$$

These are the main reactions used in most of the studies of modelling the kinetics of the reaction (Kirivanta –Paakkonen, 1998) and the chemical reactor (Su and Chang, 2000).
Mathematically, the residue curves can be calculated for any number of chemical compounds. Unfortunately, only three components can be represented in a bi-dimensional surface using a Gibbs diagram. For calculating the reactive residual curves, the isoamylenes are lumped in order to have three components in the system (Isoamylenes, Methanol and TAME). This method was proposed by Thiel et al. (1997). This is possible because the two isoamylenes components which are part of TAME synthesis – 2 methyl 1 butene and 2 methyl 2 butene – are chemically and thermodynamically similar and usually are fed in equilibrium in the column. Equations (1) and (2) are therefore lumped together and are treated as one component *IA* (isoamylene):

$$MeOH + IA \underset{k-1,2}{\overset{k+1,2}{\Longleftrightarrow}} TAME \tag{4}$$

For the three reactions taking place simultaneously, thre coupled chemical equilibrium constants are considered. Rihko et al. (1994) is proposed the following equilibrium expressions (T in K):

- TAME synthesis from 2M1B: $K_{a,1} = 1.057 \cdot 10^{-4} \exp(4273.5/T)$
- TAME synthesis from 2M2B: $K_{a,2} = 1.629 \cdot 10^{-4} \exp(3374.5/T)$
- Isoamylenes isomerization: $K_{a,3} = K_{a,1}/K_{a,2}$

The kinetic model of the global reaction is formulated according to Oost and Hoffman (1996):

$$r_{1,2} = r_1 + r_2 = k_{f,12} \cdot \left(\frac{a_{2M1B}}{a_{MeOH}} - \frac{1}{K_{a,3}} \cdot \frac{a_{TAME}}{a_{MeOH}^2} \right) \tag{5}$$

Using the following reaction rate constant:

$$k_{f,12} = \left(1 + K_{a,3}(T)\right) \cdot 2.576 \cdot exp\left[-10.764 \cdot 10^3 \left(\frac{1}{T} - \frac{1}{331.15}\right)\right] [\frac{mol}{s}] \tag{6}$$

3. Methodology

The equations systems described for the non-reactive (7) and reactive (8) residue curve models are nonlinear algebraic and differential equations. The residue curves can be obtained by integrating the models forward and backwards from an initial liquid composition. As solver, ode45 implemented in MATLAB is used in this work. The function gives a numerical solution to DAE system based on variable step size Runge – Kutta integration routines. The backward integration is performed transforming the DAE system into its inverse.

$$\begin{aligned} &\frac{dx_i}{d\tau} = x_i - y_i && i \in [1, n-1] \\ &y_i = f(P, T, xi), && i \in [1, n] \\ &\sum_{i=1}^{n} x_i = \sum_{i=1}^{n} y_i = 1 \end{aligned} \tag{7}$$

$$\begin{aligned} \frac{dx_i}{d\tau} = x_i - y_i + Da \frac{1}{k_{ref}} \Bigg[& \sum_{k=1}^{n_{rx}} \nu_{i,k}\, r_k \\ & - \left(\sum_{k=1}^{n_{rx}} \nu_{total,k}\, r_k \right) X_i \Bigg] \end{aligned} \qquad \begin{aligned} &i \in [1, n-1], \\ &k \in [1, n_{rx}] \end{aligned}$$

$$\begin{aligned} &y_i = f(P, T, x_i, x_{i+1}, \dots, x_{n-1}) && i \in [1, n] \\ &r_k = f\left(k, K_{eq}, a_i, a_{i+1}, \dots, a_{n-1}\right) && k \in [1, n_{rx}] \\ &\sum_{i=1}^{n} x_i = \sum_{i=1}^{n} y_i = 1 \end{aligned} \tag{8}$$

MATLAB 2010b and SIMULIS® Thermodynamics are used together to solve the equations (7) and (8). To call SIMULIS in MATLAB, a SIMULIS Calculator is created, using the function: *stCALCreate*. Next different functions are used to calculate system VLE characteristics: *stCALFlashWP* (Figure 1)- liquid-vapor flash at given pressure and vaporization ratio, *stCALDewTemperature* – calculation of the dew temperature, *stCALBubbleTemperature* – calculation of the bubble temperature.

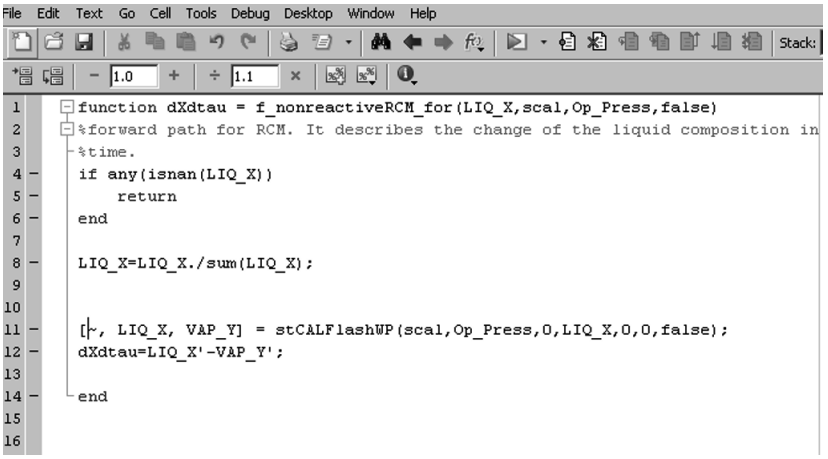

Figure 1. Generating residual curves in MATLAB using SIMULIS functions

4. Results

In Figure 2 it can be observed the trajectories of non-reactive mixture of IA / MeOH / TAME Calculations were made using *UNIFAC - Dortmund* activity model with the method presented in Chapter 2. Two azeotropes exist for the studied pressure: between IA and MeOH, an unstable node, and between TAME and MeOH, a saddle point. These points are linked by a distillation boundary. Two stable nodes are found on pure MeOH and TAME.

In the diagrams presented in Figures 3 and 4 the trajectories of the reactive IA / MeOH / TAME mixture are plotted. Four singular points are observed, as for the non-reactive mixture. The Damkohler number *Da* is enhanced starting with the value 10^{-4} until 10^{-1}. It can be observed that the TAME stable point is enriched by MeOH and by olefins for higher values of *Da*. The binary saddle point (MeOH/TAME) gets enriched with MeOH at small *Da* numbers. Increasing *Da* 10^{-1} leads to ternary saddle points.

The unstable node is leaving the physically relevant composition space by the influence of the chemical reaction at higher values of *Da*.

Bonet-Ruiz (2012), obtained different profiles for the RCMs for Da = 0.1. In the work presented by Bonet-Ruiz (2012) at 4 bar a different topology is obtained. In this case, the ternary stable node is not present. Because of this, the saddle point and the corresponding boundary lines are also not present. Thiel et al. (1997) report the same behaviour for Da = 1 and 1 bar, where the stable node disappears and every trajectory runs into the collecting trajectory which is the only remaining separatrix in the composition space. The difference between the reported values can be explained by the

different interaction parameters used by SIMULIS Thermodynamic which are used in this study.

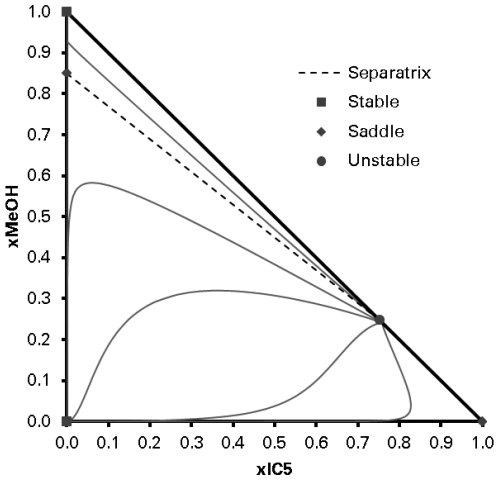

Figure 2. RCM – iC5-MeOH-TAME- P = 4 Bar Da = 0

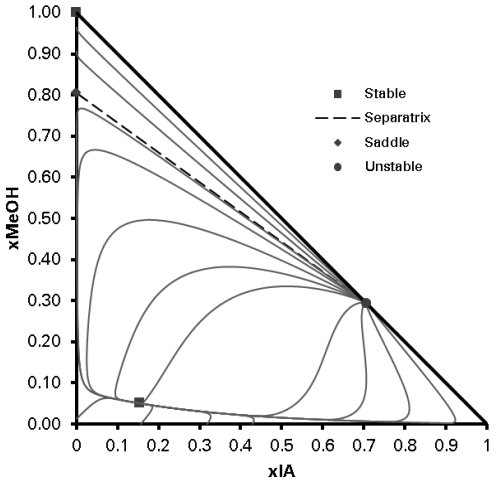

Figure 3. RCM – IA-MeOH-TAME- P = 4 Bar Da = 0.0001

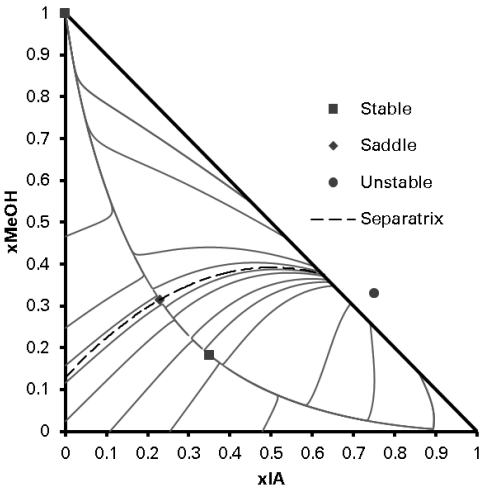

Figure 4. RCM – IA-MeOH-TAME - P = 4 bar Da = 0.1

5. Conclusions

In this work, the implementation of SIMULIS® Thermodynamics communication facility with MATLAB® is successfully done, calculating liquid vapor equilibrium with different thermodynamic models. Based on these thermodynamic properties, (non) reactive residue curve maps are generated for TAME synthesis system which involve the following components: *2 – methyl-1-butene, 2-methyl-2-butene, Isopentane, Methanol, TAME*.

For building the residual curve maps, a kinetic model where the two isoamylenes are lumped together is used, in order to have a three components system (*Isoamylenes, Methanol and TAME).*

Different topologies for the reactive residual curves are obtained compared to similar studies. This can be explained due to different interaction parameters used by SIMULIS® Thermodynamics UNIFAC Dortmund model used here.

References

Bonet-Ruiz, A., 2012. Modelling and Simulating of Continous Catalytic Distillation Processes. Department of Chemical Engineering, University Politehnica of Bucharest, Bucharest, [http://romdoc.upb.ro/record/623/files/ - Retrieved 10 October 2013].

Kirivanta –Paakkonen, P., Struckmann, L., Krause, A.O.I., 1998. Comparison of the Various Kinetic Models of TAME Formation by Simulation and Parameter Estimation. Chem Eng & Technol 21(4), pp 321-326.

Rihko, L.K., Linnekoski, J.A., Krause, A.O.I., 1994. Reaction equilibria in the synthesis of 2-methoxy-2-methylbutane and 2-ethoxy-2-methylbutane in the liquid phase. J Chem Eng Data 39(4), 700-704.

Oost, C., Hoffman, U., 1996. The synthesis of tertiary amyl methyl ether (TAME): microkinetics of the reactions. Chem Eng Sci 51(12), 329-340.

Su, W. B., Chang, J. R., 2000. Modeling and Simulation of Tubular Reactor in the tert-Amyl Methyl Ether Synthesis Process. Ind Eng Chem Res 39(11), 4140 – 4147.

Thiel, C., Sundmacher, U., Hoffmann, U., 1997. Residue curve maps for heterogeneously catalysed reactive distillation of fuel ethers MTBE and TAME. Chem Eng Sci 52(5), 993-1005.

Krist V. Gernaey, Jakob K. Huusom and Rafiqul Gani (Eds.), 12th International Symposium on Process Systems Engineering and 25th European Symposium on Computer Aided Process Engineering.
31 May – 4 June 2015, Copenhagen, Denmark

Alternative Prediction Models for Data Scarce Environment

Ali Al-shanini,[a,b] Arshad Ahmad,[a,b] Faisal Khan,[c] Olagoke Oladokun,[a,b] Shadia Husna Mohd Nor[a,b]

[a]*Institute of Hydrogen Economy, Universiti Teknologi Malaysia, 81310 Johor Bahru, Malaysia,*
[b]*Faculty of Chemical Engineering, Universiti Teknologi Malaysia, 81310 Johor Bahru, Malaysia*
[c]*Faculty of Engineering and Applied Science, Memorial University of Newfoundland, St. John's, NL, Canada, A1B 3X5*

arshad@cheme.utm.my

Abstract

Effective accident prediction is needed in the chemical process industries to facilitate risk management during plant operations. This is however hampered by the unavailability of data needed for accident modelling purposes, and models that are based on distribution theory are used as they require the least amount of data. This article discusses the application of grey modelling approach and its combination with Bayesian network. The models are applied to two case studies, i.e. a process vessel and an LNG facility. The results obtained are compared to that of Poisson model. Results show that the hybrid first-order grey model with Bayesian network BG(1,1) is most accurate, followed by the grey models G(1,1) and G(2,1), with the Poisson model trailing behind. The results illustrated the potentials of grey modelling approach in dealing with scarce data conditions.

Keywords: CPI accident prediction, Poisson–Gamma model, grey model, Bayesian network, hybrid model.

1. Introduction

One promising strategy to facilitate risk reduction efforts is by using information obtained from accident modelling. Using a few of the available techniques, accidents are predicted in terms of their likelihood to happen, the location at which they are likely to occur and the anticipated failures of relevant components. An example of this methodology is the SHIPP model (Rathnayaka *et al.*, 2011), which has the ability to identify the location of an expected failure source and predict the likelihood of an accident. Because accident data are difficult to gather, accident prediction techniques that require the least amount of data are favoured. A stochastic model has become a preferred option as it requires only one data point and a prior distribution function that represents the system's behaviour. For this reason, stochastic approach such as the Poisson model has received considerable applications in accident modelling in the CPI (e.g., Meel *et al.*, 2007; Al-shanini *et al.*, 2014b). However, this model has the tendency to underestimate and is lacking in sensitivity (Rathnayaka *et al.*, 2012; Al-shanini *et al.*, 2014a).

This paper explores an alternative strategy by adopting grey modelling approach, which has found more applications in other industries including agricultural, environmental, and

electronics due to its simplicity and capability of reasonably forecasting events using as few as four data points (Tseng *et al.*, 2001; Hsu, 2003; Lin and Yang, 2003; Deng, 1989; Chang and Tseng, 1999). The performances of this model, along with an improved version configured by combining it with Bayesian network are compared to the Poisson model.

2. Prediction Models for a Data-Scarce Environment

2.1. Stochastic Poisson-Gamma Model

Poisson-gamma model belongs to stochastic forecasting approach that is often used to predict the number of unwanted consequences in the CPI. The model offers good predictions when the mean and the variance of the data are in close proximity. A conjugate pair of distribution functions of gamma (as prior function) and Poisson (as likelihood function) is used. Once data is observed, the likelihood function updates the prior distribution to its posterior. The mean value of the probability mass function represents the number of the predicted events as shown in Figure 1. Details on Poisson model can be found in (Al-shanini *et al.*, 2014b).

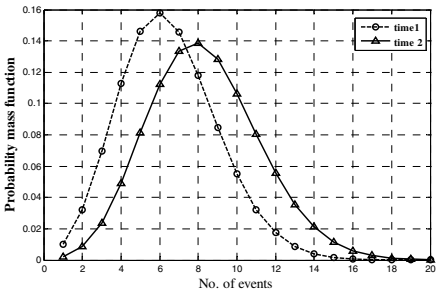

Figure 1: Poisson predictive probability mass function change for two time intervals

2.2. Time Series Grey Models

The grey model of M-order partial differential equation of N variables belongs to a time series forecasting family, referred to as G(M,N) is first introduced by Ju-Long (1982). The term "grey" represents the fact that the model contains both white and black parts. The white part has theoretical supports, while the black part depends on empirical data. Grey modelling approach assumes that the process can be represented by certain generic partial differential equation according to the order of the process. Then using accident data, the model parameters are estimated. This modelling strategy requires only four data points to predict the future event. The ratios σ = [σ(2), σ(3),…, σ(n)], where $\sigma(k) = x^{(0)}(k-1) \,/\, x^{(0)}(k)$ for $k = 2,3,\ldots,n$ and x(0) is the original data points, have to fall within the range 0.1345–7.389. Two grey models of a single variable are the most applied in literature which are the first and second orders G(1,1) and G(2,1). Table 1 briefly discusses their implementation steps.

2.3. Improving Parameters Estimation Using Bayesian Network

Another alternative is also proposed by adopting Bayesian network (BN) to improve parameters estimation in G(1,1). In this case, BN is used as a regression method of the new sequence data produced from AGO to determine model coefficients instead of OLS method normally used in the grey model. The combination of enlargement of original data provides an advantage to model's predictability especially with data containing outliers (Hsu and Wang (2007)). Bayesian analysis is used to build a statistical model that relates prior knowledge (y) and observables (x), and then estimates the conditional posterior probability p(y\x). In BN, the observed data are assumed to follow a normal distribution as shown in the following Eq. 1:

Y[i] ~ normal(mu[i],tau) (1)

where, $mu[i] = -u + a \times x[i]$, (a) and (u) are normal distributions with means and precisions in the range (0, 1.0E-6), and (tau) is a non-informative beta distribution with shaping distribution parameters of (0.01, 0.01). Other systems may require another distribution functions that better fits the observed data. Once models' coefficients are estimated, they are substituted in the partial differential equation to predict the future events.

Markov Chain Monte Carlo (MCMC) simulation software (WinBUGS), that uses the Gibbs Sampling technique, is used to compute the BN for estimating the coefficients. This is done by setting a joint posterior distribution using MCMC as the target distribution, and simulates the parameters to converge to the targeted values.

3. Case studies

Two case studies data sets are used. The first is a process vessel adopted from Kalantarnia *et al.* (2009) and the second is an LNG liquefaction and exporting facility. The data sets are summarised in table 2.

Table 2: Historical real time data of the case studies

Time interval	System 1 Vessel precursor data	System 2 LNG facility precursor data
1	7	7
2	7	6
3	8	12
4	8	11
5	5	11
6	12	13
7	14	12
8	16	-

4. Result and discussion

Four models, i.e., Poisson, G(1,1), G(2,1) and BG(1,1) are applied to the case studies, and results that are shown in table 3 and 4 are obtained. For the BG(1,1), the BN model is tested with 1000 burn samples followed by 1000 iterations for each chain. For grey models, iterative population increase configuration is applied to the case studies data in which the first four data points are used to estimate models' coefficients and predict the fifth one. Next, one more data is considered and so on.

The results show that the BG(1,1) provides the best accuracy with average absolute mean percentage error (AMPE) for the two case studies of 18.24, followed by G(1,1) with average AMPE of 21.9, G(2,1) with 21.95, and Poisson with 26.36. Figure 2 shows the validation of the four prediction models. Note that in this case the first order grey model performed better that the second order. This is probably due to the process dynamics and requires further investigations.

Table 1: G(1,1) and G(2,1) implementation steps

Sequence	G(1,1)	G(2,1)
Generation of new sequence from the original data	$X^{(1)}=\{x^{(1)}(1),x^{(1)}(2),\ldots,x^{(1)}(n)\}$, where $X^{(1)}(1)=X^{(0)}(1)$, and $X^{(1)}(k)=\sum_{i=1}^{k}x^{(0)}(i)$ for $k=2,3,\ldots,n$. the sequence mean generated of consecutive neighbours $X^{(0)}(k)=-aZ^{(1)}(k)+u,\ k=2,3,\ldots,n$, where a is the developing coefficient, u is the grey input, and $z^{(1)}(k)=\alpha X^{(1)}(k)+[1-\alpha]X^{(1)}(k-1)$, for $i=2,3,\ldots,n$.	$X^{(1)}=\{x^{(1)}(1),x^{(1)}(2),\ldots,x^{(1)}(n)\}$, where $X^{(1)}(1)=X^{(0)}(1)$, and $X^{(1)}(k)=\sum_{i=1}^{k}x^{(0)}(i)$ for $k=2,3,\ldots,n$. With inverse accumulated generator operator IAGO sequence $\alpha X^{(0)}$ of $X^{(0)}$ as $\alpha^{(1)}X^{(1)}=\{\alpha^{(1)}x^{(0)}(1),\alpha^{(1)}x^{(0)}(2),\ldots,\alpha^{(1)}x^{(0)}(n)\}$ where $\alpha^{(1)}x^{(0)}(k)=x^{(0)}(k)-x^{(0)}(k-1)$ the sequence mean generated of consecutive neighbours of X(1) is $Z^{(1)}=\{z^{(1)}(1),z^{(1)}(2),\ldots,z^{(1)}(n)\}$ where $z^{(1)}(k)=\frac{1}{2}\left[x^{(1)}(k)+x^{(1)}(k-1)\right]$
grey differential equation	$\frac{dX^{(1)}(k)}{dt}+aX^{(1)}(k)=u$	$\frac{d^2x^{(1)}}{dt}+a_1\frac{dx^{(1)}}{dt}+a_2x^{(1)}=u$
estimate grey model coefficient -s using least square method	Xn=Bâ, where $B=\begin{bmatrix}-Z^{(1)}(2) & 1\\ -Z^{(1)}(2) & 1\\ \vdots & \vdots\\ -Z^{(1)}(n) & 1\end{bmatrix}$, $X_n=[x^{(0)}(2),x^{(0)}(3),\ldots,x^{(0)}(n)]^T$, and â=[a, u]^T[B^{T}B]$^{-1}$B^{T}X	$B=\begin{bmatrix}-x^{(0)}(2) & -z^{(1)}(2) & 1\\ -x^{(0)}(3) & -z^{(1)}(2) & 1\\ \vdots & \vdots & \vdots\\ -x^{(0)}(n) & -z^{(1)}(n) & 1\end{bmatrix}$, $Y=\begin{bmatrix}\alpha^{(1)}x^{(0)}(2)\\ \alpha^{(1)}x^{(0)}(3)\\ \vdots\\ \alpha^{(1)}x^{(0)}(n)\end{bmatrix}$, and â=[$a_1$, a_2, u]^T , to estimate coefficients â=[a_1, a_2, u]=[B^{T}B]$^{-1}$B^{T}Y
The prediction formula	The estimated coefficients substituted into the partial differential equation solution $\hat{X}^{(0)}(k)=\left[x^{(0)}(1)-\frac{u}{a}\right]\left(1-e^{a}\right)e^{-a(k-1)},k=2,3,\ldots,n$	The estimated coefficients substituted into the second-order partial differential equation solution that has three probably forms depending on characteristic equation ($r^2+a_1r+a_2=0$) which are : real solutions r1 and r2 that the solution will be as $C_1e^{r_1t}+C_2e^{r_2t}$ a real solution r of multiplicity 2 that the solution will be as $e^{rt}(C_1+C_2t)$ Two complex conjugate solutions that the solution will be as $e^{\alpha t}(C_1\cos\beta t+C_2\sin\beta t)$

Table 3: Predictive models' outputs and errors of vessel tank process with population increase of data

Interval	Actual no.	Poisson model		G(1,1)		G(2,1)		BG(1,1)	
		Model value	Abs. err %	Model value	Abs. err %	Model value	Abs. err %	Model value	Abs. err%
1	7	-	-	-	-	-	-	-	-
2	7	7	0	7	0	7	0	7	0
3	8	7	12.5	8	0	7	12.5	8	0
4	8	7	12.5	8	0	8	0	8	0
5	5	7	40	9	80	8	60	8	60
6	12	6	50	6	50	8	33.3	6	58.3
7	14	8	42.9	11	21.5	7	50	11	42.9
8	16	9	43.8	15	6.3	9	43.8	15	6.3
MAPE		-	28.8	-	22.5		28.5	-	19.7

Table 4: Predictive models' outputs and errors of LNG facility with population increase of data

Interval	Actual no.	Poisson model		G(1,1)		G(2,1)		BG(1,1)	
		Model value	Absolute err %	Model value	Abs. err %	Model value	Abs. err %	Model value	Abs. err%
1	7	-	-	-	-	-	-	-	-
2	6	7	16.7	8	33.3	7	16.7	8	33.3
3	12	7	41.7	10	16.7	8	33.3	10	16.7
4	11	8	27.3	12	9.1	9	18.2	11	0
5	11	9	18.2	15	36.4	12	9.1	13	18.2
6	13	10	23.1	14	7.7	11	15.4	14	7.7
7	12	10	16.7	15	25	12	16.7	15	25
MAPE (%)		-	23.9	-	21.3		15.4	-	16.8

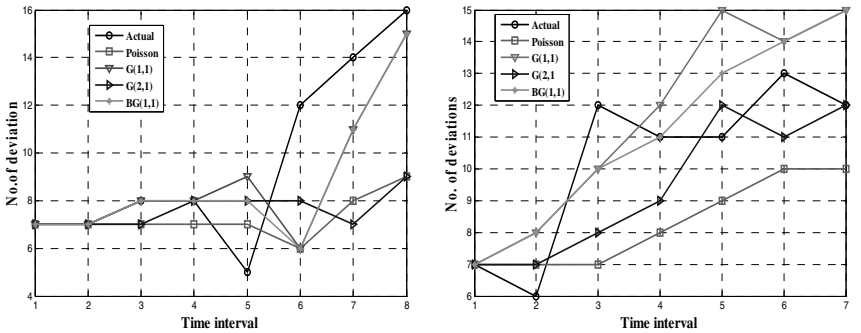

(a) Vessel processing **(b) LNG facility**

Figure 2: Validation of prediction models for case studies with iterative population increase configuration

Conclusion

The study on scarce data prediction models based on two case studies has demonstrated the capability of the grey model in surpassing Poisson-gamma model in predicting accidents in the CPI. The results show that BG(1,1), which is the hybrid of BN and G(1,1) has the highest prediction accuracy, followed by other grey models and the Poisson. However, grey models and their hybrids require at least four observed data points, while the Poisson-gamma model needs only one data point to predict the next event. The results from this work also support previous findings on the prediction based on Poisson-gamma model that are reported to underestimate the actual data. In conclusion, this study has proved the potentials of the grey-based modelling in providing prediction capability in data-scarce environment. It is anticipated, with further enhancement, this modelling strategy would be able to effectively support risk-based decisions in plant operation and maintenance.

References

Al-Shanini, A., Ahmad, A. and Khan, F. (2014a). Accident Modelling and Analysis in Process Industries. Journal of Loss Prevention in the Process Industries, 32(0), 319-334.

Al-Shanini, A., Ahmad, A. and Khan, F. (2014b). Accident Modelling and Safety Measure Design of a Hydrogen Station. International Journal of Hydrogen Energy, 39(35), 20362-20370.

Chang, N.-B. and Tseng, C. (1999). Optimal Evaluation of Expansion Alternatives for Existing Air Quality Monitoring Network by Grey Compromise Programing. Journal of environmental management, 56(1), 61-77.

Deng, J.-L. (1989). Introduction to Grey System Theory. The Journal of grey system, 1(1), 1-24.

Hsu, L.-C. (2003). Applying the Grey Prediction Model to the Global Integrated Circuit Industry. Technological Forecasting and Social Change, 70(6), 563-574.

Hsu, L.-C. and Wang, C.-H. (2007). Forecasting the Output of Integrated Circuit Industry Using a Grey Model Improved by the Bayesian Analysis. Technological Forecasting and Social Change, 74(6), 843-853.

Ju-Long, D. (1982). Control Problems of Grey Systems. Systems & Control Letters, 1(5), 288-294.

Kalantarnia, M., Khan, F. and Hawboldt, K. (2009). Dynamic Risk Assessment Using Failure Assessment and Bayesian Theory. Journal of Loss Prevention in the Process Industries, 22(5), 600-606.

Lin, C.-T. and Yang, S.-Y. (2003). Forecast of the Output Value of Taiwan's Opto-Electronics Industry Using the Grey Forecasting Model. Technological Forecasting and Social Change, 70(2), 177-186.

Meel, A., O'neill, L. M., Levin, J. H., Seider, W. D., Oktem, U. and Keren, N. (2007). Operational Risk Assessment of Chemical Industries by Exploiting Accident Databases. Journal of Loss Prevention in the Process Industries, 20(2), 113-127.

Rathnayaka, S., Khan, F. and Amyotte, P. (2011). Shipp Methodology: Predictive Accident Modeling Approach. Part I: Methodology and Model Description. Process Safety and Environmental Protection, 89(3), 151-164.

Rathnayaka, S., Khan, F. and Amyotte, P. (2012). Accident Modeling Approach for Safety Assessment in an LNG Processing Facility. Journal of Loss Prevention in the Process Industries, 25(2), 414-423.

Tseng, F.-M., Yu, H.-C. and Tzeng, G.-H. (2001). Applied Hybrid Grey Model to Forecast Seasonal Time Series. Technological Forecasting and Social Change, 67(2), 291-302.

Krist V. Gernaey, Jakob K. Huusom and Rafiqul Gani (Eds.), 12th International Symposium on Process Systems Engineering and 25th European Symposium on Computer Aided Process Engineering.
31 May – 4 June 2015, Copenhagen, Denmark

Multi-objective Optimisation of Atmospheric Crude Distillation System Operations Based on Bootstrap Aggregated Neural Network Models

Funmilayo N. Osuolale*, Jie Zhang

School of Chemical Engineering and Advanced Materials, NewcastleUniversity, Newcastle upon Tyne, NE1 7RU, UK
f.n.osuolale@newcastle.ac.uk ; fnosuolale@lautech.edu.ng

Abstract

This paper presents a new methodology for optimising the energy efficiency of a crude distillation unit without trading off the product quality and process throughput. It incorporates the second law of thermodynamics which indicates how well a system is performing compared to the optimum possible performance and hence gives a good indication of the actual energy use of a process. Bootstrap aggregated neural networks are used for enhanced model accuracy and reliability. In addition to the process operation objectives, minimising the model prediction confidence bound is incorporated in multi-objective optimisation to improve the reliability of the optimisation results. The economic analysis of the recoverable energy (sum of internal and external exergy losses) reveals the energy saving potential of the method. The proposed method will aid the design and operation of energy efficient crude distillation columns.

Keywords: crude distillation, exergy, optimisation, neural networks.

1. Introduction

Distillation process has always attracted the interest of researchers and quite a number of work in the literatures are focused on improving its energy efficiency either for binary systems (Osuolale and Zhang, 2014) or multi component systems (Ochoa-Estopier et al., 2012). In recent years optimisation of crude distillation system has received considerable research interest. This is because major cost of operation second only to the cost of crude in a refinery is energy and 35% of these is consumed in the crude distillation unit. Rather than large scale expansion, most industries will maximise available resources for maximum profitability.

Thermodynamic analysis of a crude distillation unit gives insight into its second law efficiency. Past work on the second law analysis reveals low efficiency of the system with an efficiency of 0.27-0.43 for the ADU (Al-Muslim and Dincer, 2005). This could imply that improvement of the efficiency of the column will be better off when it is based on the second law. The challenge therefore is to develop optimization procedures based on second law analysis aimed at minimising the inefficiencies without compromising the quality of the product.

In this regard, determining the thermodynamic conditions of the inlet and outlet streams for every considered possibility is of paramount importance. Rigorous, empirical and simplified models of crude distillation systems are widely publicised in the literatures. Rigorous models are however computationally demanding and might not be feasible for

real time optimisation. Also, the complexity of rigorous models often limits networking the crude distillation system with other heat integrated systems. Simplified model was implemented in the optimisation of a distillation system in a related work (Valleriote et al., 2012). Though simplified models are more robust than rigorous models, they are however sensitive to initial guesses. To overcome these problems, data driven models such as artificial neural network (ANN) models can be utilised. The computation time in ANN model evaluation is very short making them ideal for real-time optimisation. Bootstrap aggregated neural networks are used in this study for enhanced model accuracy and reliability. Neural network models for exergy efficiency and product quality are developed from simulated process operation data and are used to maximise exergy efficiency while satisfying product quality constraints.

2. Methods of Analysis

2.1. Description of Systems

The atmospheric distillation system considered in this study is presented in Fig. 1. The crude to be processed was Venezuela Tia Juana light crude (Watkins 1973). The crude was characterised using experimental assay that includes the bulk crude properties, light end volume percent, ASTM distillation, API gravity and TBP distillation. The assay data was fed into the data bank of the simulator software HYSYS. The result of the characterisation is a set of pseudo-components and a detailed chemical composition of the identified light ends components. The column processes 100,000 barrel/day of crude at 25psia and 690 ^{o}F into 6 products: light naphtha, heavy naphtha (HN), kerosene, diesel, atmospheric gas oil (AGO) and residue.

2.2. Exergy analysis

For an open system, the mass, energy and exergy balance equations are

$$\sum M_{in} = \sum M_{out} \tag{1}$$

$$\sum E_{in} + Q = \sum E_{out} + W \tag{2}$$

$$\sum Ex_{in} + \sum_{j=1}^{n}(1 - \frac{T_0}{T_j})Q = \sum Ex_{out} + W + I \tag{3}$$

where M_{in} and M_{out} are mass flow rate in and out of the system respectively, E_{in} and E_{out} are inlet and outlet energy rates respectively, Q is heat transfer rate, W is the work rate, Ex_{in} and Ex_{out} are exergy rates in and out of the system respectively and I is the irreversibility rate of the system.

The total exergy of a stream is given as

$$Ex = Ex_{phy} + Ex_{chem} + Ex_{mixing} \tag{4}$$

$$Ex_{phy} = m[h - h_0 - T_0(s - s_0)] \tag{5}$$

where m is the mass flow rate, h and s are the enthalpy and entropy at stream conditions respectively, h_0 and s_0 are, respectively, enthalpy and entropy at reference conditions of $T_0 = 298.15\ K$ and $P_0 = 101.3\ kPa$. For the crude stream considered, standard molar chemical exergy Ex_{chem} is calculated from the standard molar chemical exergies of all identified components and pseudo-components as

$$Ex_{chem} = m\left[\sum b_{qi} + \sum b_{chi} + RT_0 \sum lna_i\right] \tag{6}$$

where b_{chi} is the chemical exergy for component, b_{qi} is the chemical exergy for pseudo component, and a_i is the activity coefficient of component i. The standard chemical exergy for pseudo-compoentns can be determined from heuristic empirical expression as a function of the elementary composition and their heating values (Szargut et al., 1988).

$$B_{qi} = \varphi_i C_i \tag{7}$$

where φ_i is the regression equation to express the ratios H/C, N/C, O/C and S/C for pseudo-component i, C_i is the net calorific heating value of the pseudo-component i. The exergy efficiency and the irreversibility rate definitions are given by Eq(8) and Eq(9) respectively:

$$\varphi = \sum Ex_{out} / \sum Ex_{in} \tag{8}$$

$$I = \sum Ex_{in} - \sum Ex_{out} \tag{9}$$

2.3. Economic Analysis

Basically the economic analysis is based on the operating profit of the column and expressed mathematically as

$$Profit = \sum_{j=1}^{n} M_j C_j - [M_{crude} C_{crude} + M_{steam} C_{steam} + \sum_{x=1}^{n} Q_x C_x] \tag{10}$$

where M_j and C_j are the flow rate and cost of product *j* respectively, M_{steam} and C_{steam} are the flow rate and cost of steam respectively, Q_x and C_x are the heat requirement and the cost of utility respectively. The calculation is based on the assumption of 8600 h per year. Table 1 gives the prices of the feed, products and utility (Energy information administration, 2014).

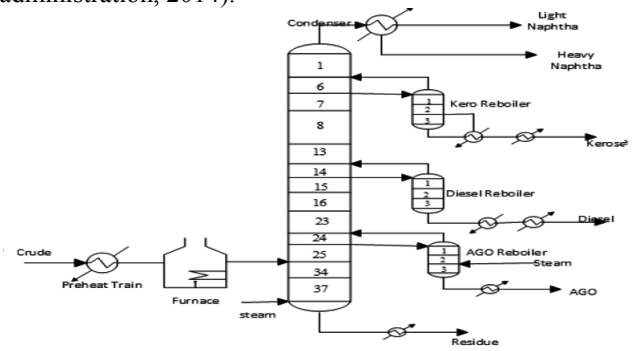

Figure 1. Schematic diagram of an atmospheric distillation unit

3. Multi-Objective Optimisation Using Bootstrap Aggregated Neural Network Models

3.1. Bootstrap aggregated neural network

In order to improve the generalisation capability of neural netwroks, several networks are developed on bootstrap resampling replication of the training data and combined. A bootstrap aggregated neural network (BANN) can be represented mathematically as

$$f(X) = \sum_{i=1}^{n} w_i f_i(X) \tag{11}$$

where $f(X)$ is the aggregated neural network predictor, $f_i(X)$ is the *i*th neural network, w_i is the aggregating weight for combining the *i*th predicted neural network, n is the number of neural networks, and X is a vector of neural network inputs. BANN can also give model prediction confidence bounds from individual network predictions (Zhang 2004). The standard error of the *i*th predicted value is calculated as

$$\sigma_e = \left\{\frac{1}{n-1}\sum_{b=1}^{n}[y(x_i;W^b) - y(x_i;)]^2\right\}^{\frac{1}{2}} \quad (12)$$

where $y(x_i) = \sum_{b=1}^{n} y(x_i;W^b)/n$ and n is the number of neural networks. The 95% prediction confidence bounds can be calculated as $y(x_i;) \pm 1.96\sigma_e$.

Table 1. Feed, products, and utility prices

Item	Crude	LN	HN	Kero	Diesel	AGO	Res	Heat duty	Cooling water	steam
Price	80	44.3	136	122.7	121.75	95.29	89.71	150	5.25	0.14
Unit	$/bbl	$/bbl	$/bbl	$/bbl	$/bbl	$/bbl	$/bbl	$/kJ	$/kJ	$/kmol

3.2. Modelling of the atmospheric distillation unit

In this study, simulated process operational data were generated from HYSYS and were divided into training (50%), testing (30%), and unseen validation (20%) data sets. A BANN containing 30 neural networks was developed to model exergy efficiency and product quality using product flow rates as inputs. The network giving the lowest mean squared errors (MSE) on the testing data is considered as having the appropriate number of hidden neurons.The Levenberg-Marquardt trainning algorithm was used to train the network. Fig. 2 shows the BANN model performance on the unseen validation data.

Fig. 3 shows the MSE of the individual networks and BANN containing different number of networks on the training and unseen validation data sets. It can be seen that individual networks give inconsistent performance on the training and unseen validation data indicating the non-robust nature of single networks. BANNs give consistent and more accurate prediction performance on the training and unseen validation data sets.

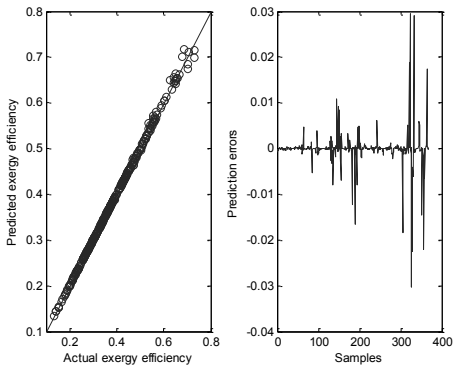

Figure 2. BANN predicted vs. actual exergy efficiency (left) and prediction errors (right)

3.3. Multi-objective optimisation

The objective of the optimisation is to maximise the exergy efficiency of the distillation unit while satisfying product quality constraints. To improve the reliability of the optimum, an additional objective of minimising the standard error of individual network

predictions was introduced and formulated using the goal attainment multi-objective optimization procedure as

$$J = \begin{bmatrix} -y \\ \sigma \end{bmatrix} \qquad (13)$$

$$min_{x,\delta}\ \delta$$

s.t. $J(y) - W_i\delta \leq F$

$[y, m] = U(x)$

$m_{lb,k} \ll m_k \ll m_{ub,k} \qquad k = 1, 2, \ldots, 5$

where J is the objective function, y is the exergy efficiency, U is the BANN model of the ADU, $x = [x_1, x_2, \ldots x_8]$ is a vector of decision variables containing 5 product flow rates and 3 pump around flow rates shown in Table 3, m is a vector of the product oil quality, σ is standard prediction error, F is the desired goal, and W is a vector of weighting parameters which controls the degree of goal achievement and introduces a measure of flexibility that allows for trade off the conflicts among objectives. A narrow confidence bounds indicate the reliability of the prediction and gives a measure of assurance of the process attaining the predicted exergy efficiency. The relative error of the multi-objective optimisation and simulation results for minimizing the confidence bounds are given in Table 2. The effect of incorporating the confidence bounds in the multi-objective optimization can be revealed in that the exergy efficiency of the HYSYS validated process is close to that predicted by the model.

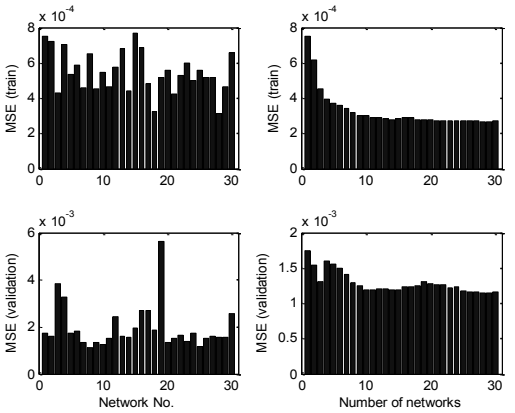

Figure 3. MSE of individual networks (left) and BANN (right) for the crude distillation unit

Table 2. Optimisation and simulation results

Hysys validated	Optimum 1 (Eff)	Optimum 2 (cb)	Goal 1 (Eff)	Goal 2 (cb)	Weight 1 (Eff)	Weight 2 (cb)	Relative error
73.86	79.62	0.3883	0.8	0.01	0.01	1	0.07798
71.90	78.12	0.1982	0.8	0.01	0.1	1	0.08650
71.68	75.34	0.0566	0.8	0.01	1	1	0.05106
61.62	65.56	0.0244	0.8	0.01	1	0.1	0.06394
50.84	53.18	0.0127	0.8	0.01	1	0.01	0.0458

Table 3 shows the base case and the optimum results of the decision variables. The products qualities are within the expected bound range. Table 4 shows the corresponding thermodynamic and economic analysis. The optimisation results in 29.6% increment of the exergy efficiency. This translates to 68% decrease in

irreversibility loss and 46.5% reduction in energy costs of the column with reference to their initial values. Every real process has an element of irreversibility which often degrades the engineering performance. With the methodology proffered from this study ways of considerably decreasing the irreversibility of the system as well as determining the efficiency of the process is made easy.

The total profit is increased by $\$38\times10^6$/year through optimally adjusting product flow rates. The increment is mainly due to the optimum operating conditions from the exergy based analysis of the column. The reduction in the cost of energy contributed to about 10% in the total profit. The results show that considerable economic benefit of the column can be achieved at no additional cost of equipments.

Table 3. Optimisation results (decision variables)

	HN	Kerosene	Diesel	AGO	Residue	PA1	PA2	PA3
Base case	517	508	952	267	1296	943	1132	943
Optimum	511	511	1000	267	1348	946	1127	940

Table 4. Optimisation results (efficiency and profit)

	Exergy (%)	Irreversibility (kJ/hr)	Energy cost ($/yr)	Profit ($/yr)
Base case	42.10	1.913×10^8	7.655×10^6	2.360×10^9
Optimum	71.68		4.095×10^6	2.398×10^9

4. Conclusions

Multi-objective optimisation for improving the exergy efficiency of a crude distillation system using bootstrap aggregated neural network model is presented. By incorporating model prediction confidence as additional optimisation objective, the reliability of optimisation is enhanced. Application to a simulated crude distillation unit shows that the proposed technique can significantly improve the second law efficiency of the system leading to an additional economic advantage. The method can aid in the operation and design of energy efficient distillation columns.

Acknowledgement

The work is supported by the Commonwealth Scholarship (Ref: NGCA-2011-50) and the EU FP7 (Ref: PIRSES-GA-2013-612230).

References

H. Al-muslim, I. Dincer, 2005, Thermodynamic analysis of crude oil distillation systems, International Journal of Energy Research, 29, 637-655.

Energy information Administration, http://www.eia.gov/dnav/pet/pet_pri_refoth_dcu_nus_m.htm

L. M. Estopier, M. Jobson, R. Smith, 2012, Operational optimisation of crude oil distillation systems using artificial neural networks, Computer aided chemical engineering, 30, 982-986.

F. N. Osuolale, J. Zhang, 2014, Energy efficient control and optimisation of distillation column using artificial neural network, Chemical Engineering Transactions, 39, 37-42.

J. Szargut, D. R. Morris, F. R. Steward,1988, Exergy analysis of thermal, chemical and metallurgical processes, New York, Hemisphere Publishing Corporation

A. Valleriote, L. Dorigo, A. R. Secchi, E. C. Biscaia Jr., 2012, Reduced rigorous models for efficient dynamic simulation and optimisation of distillation columns, Computer aided chemical engineering, 30,1262-1266.

R. N. Watkins, 1973, Petroleum refinery distillation, Texas:Gulf Publishing Company.

J. Zhang, 2004, A reliable neural network model based optimal control strategy for a batch polymerisation reactor, Ind. Eng. Chem. Res., 43, 1030-1038.

Krist V. Gernaey, Jakob K. Huusom and Rafiqul Gani (Eds.), 12th International Symposium on Process Systems Engineering and 25th European Symposium on Computer Aided Process Engineering.
31 May – 4 June 2015, Copenhagen, Denmark

Optimization Studies through Simulation of a Methanol/Water/Glycerol Distillation Column

José Palmeira[a*], João M. Silva[a,b], Henrique A. Matos[c]

[a]*ISEL-Instituto Superior de Engenharia de Lisboa, ADEQ, R. Cons. Emídio Navarro, 1959-007 Lisbon, Portugal*
[b]*CQE, Instituto Superior Técnico, Av. Rovisco Pais, 1049-001 Lisbon, Portugal*
[c]*CERENA, DEQ, Instituto Superior Técnico, Av. Rovisco Pais, 1049-001 Lisbon, Portugal*
vpalmeira@deq.isel.pt

Abstract

This paper presents an optimization study of a distillation column for methanol and aqueous glycerol separation in a biodiesel production plant. Considering the available physical data of the column configuration, a steady state model was built for the column using Aspen-HYSYS as process simulator. Several sensitivity analysis were performed in order to better understand the relation between the variables of the distillation process. With the information obtained by the simulator, it is possible to define the best range for some operational variables that maintain composition of the desired product under specifications and choose operational conditions to minimize energy consumptions.

Keywords: Simulation, optimization, distillation, biodiesel process

1. Introduction

Many industrial companies struggle to survive in a competitive market and are looking for additional strategies to increase processes efficiency. Some companies have been operating for many years with the pre-established conditions provided by the process's licensor. However, since processes first startup, changes may have occurred which would require a new tuning of the control variables not only to achieve process specifications but also to run it with energy minimization cost. Testing different conditions in running processes may not be acceptable due to restrict timetables for goal production quantities to be achieved, and to avoid products out of specification. The growing use of process simulators by research groups has allowed a greater deepening of process knowledge without disturbing the usual operation (Seider et al., 2009).

Optimization studies for efficiency increase can be performed to the whole process, or on large energy-consuming units which is the case of distillation columns (Jobson, 2014). Creating distillation columns' models in process simulators allows performing optimization without disturbing the process, which is a good tool to improve energy efficiency. In the existing columns several former design variables may not be susceptible to be modified. Some examples are the number and type of stages, feed location and pressure drop along stages. Others remain available for optimization such as reflux ratio, supplied heat in the reboiler and feed stream temperature.

This work addresses the study of the operating conditions of an existing distillation column for methanol/water/glycerol separation, operating in a biodiesel production process. The objectives of the study were to establish a better relation between the

distillation process variables, to accomplish a more energy efficient operation. The distillation column is responsible for 35 % of total thermal energy consumption of the process (Palmeira et al., 2010), which results that any energy saving will have a significant economic impact in the operating costs.
A comprehensive Aspen-HYSYS model based on thermodynamic and physical data of the distillation column was developed. The relation between column temperatures and composition specification in outlet streams were studied. The optimal reflux ratios for different reboiler's temperature and the influence of feed temperature in the column energy consumption were also investigated.

2. Methods

Based on physical dimensions of the distillation column and packing characteristics, a steady state model was developed in Aspen-HYSYS software. The rectification section of the distillation column is composed by 26 plates and the stripping section by particle packing. The column was simulated with pressures of 1.1 atm in column bottoms and 1 atm at the top. The feed stream to the column is composed by 21 % methanol, 51 % water and 28 % glycerol at 75 °C. The composition limits in outlet streams are 1000 ppm methanol in aqueous glycerin in the bottom and 300 ppm of water in distillate. NRTL thermodynamic model was used for properties estimates.
Two degrees of freedom were found in the model using all physical characteristics of the column. In the real column, the two degrees of freedom correspond to variables that can be controlled, which are reflux ratio and supplied heat in the reboiler. In the simulation model, input data could correspond to numerical values for these two real control variables. However, the simulator allows choosing desired values for other two variables (always respecting the two available freedom degrees) and will iteratively search for the correspondent solution. Depending on the studies performed, the input specifications were: water composition in distillate, methanol composition in bottoms, reflux ratio, reboiler and feed temperature.

3. Sensitivity Analysis

Several sensitivity analysis between the column variables were performed, to provide a better understanding to control the distillation process in a more effective way.

3.1. Vapor Liquid equilibrium of Methanol/Water mixture

One of the distillation specifications is the maximum of 300 ppm of water present in the distillate. Since there isn't any direct measure of water content in the real column, the water content control is obtained by indirectly measuring of the column temperatures. For that, the rectification section of the column is equipped with four temperature sensors in 1st, 5th, 8th and 13th stages (referred as T1, T2, T3 and T4, respectively). Assuming that the glycerol content in distillate is negligible, it is considered that this stream is composed exclusively by methanol and a small fraction of water. As a result, the water composition of the 1st stage vapor phase can be obtain from the dew curve in the methanol/water VLE phase diagram, when the temperature in that stage is known. Because, the vapor phase of the 1st stage and distillate compositions are effectively the same, the precise temperature measure in the 1st stage could be considered the most important because it allows precise water content determination in distillate.
VLE data extracted from the simulation model (Figure 1) shows that temperature in 1st stage has low sensitivity with water content variation. For example, when considering a temperature variation of only 0.1 °C above 64.5 °C (corresponding to 300 ppm), we obtain 64.6 °C that corresponds to 2000 ppm which is way out the allowed limit.

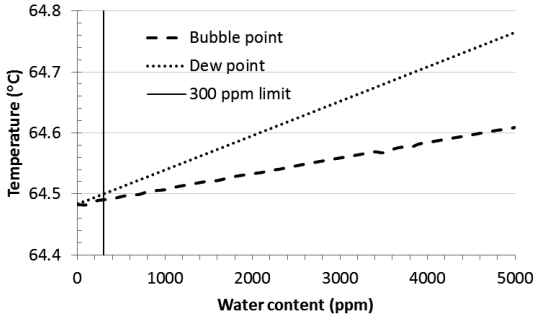

Figure 1 - VLE for methanol/water mixture for 0-5000 ppm of water for P=1 atm.

Due to intrinsic measuring error of temperature sensors which is of this magnitude order, any water content reading based exclusively in this parameter will be far from being accurate. Nevertheless, accurate and high precision temperature sensors should be used in these measures.

3.2. Column temperature profile for different water content in distillate

Due to lack of precision in water content determination based exclusively in 1st stage temperature, additional points of temperature measure in other column stages are taken in consideration. The measured temperature in each stage can be dependent not only from the distillate composition but also from feed composition and temperature, and reflux and reboiler temperatures. Assuming constant values for the latest referred variables, the temperature dependence of stages with distillate composition was investigated. Figure 2 shows the expected temperature profile for different water contents at distillate, considering the reboiler at 105.4 °C. It can be observed that there is an increase sensitivity of stage temperature to water content when descending in the column. This information is highly precious when controlling the column because water content in distillate can be estimated based in the set of stages temperatures.

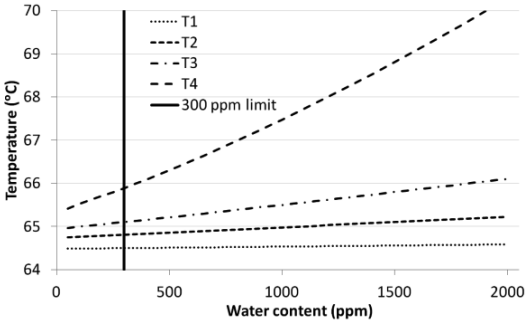

Figure 2 – Stage temperatures dependence with water content (for $T_{reboiler}$=105.4 °C).

3.3. Reflux ratio influence on distillate composition

The influence of reflux ratio and reboiler temperature in distillate water content can be observed in Figure 3. The results show that water content is reduced dramatically to values around 300-500 ppm with an increase of reflux ratio to values around 1.5. From this point forward, reflux ratio increase will have a lower impact in water content reduction. These results indicate that column control is quite sensitive when operating with reflux ratios near the optimal point, because a small decrease in this value will result in a sharp increase of water content in distillate. This will be easily detected by an

increase in temperature profile in stages, as seen in previous section. This study also shows that lower reboiler temperatures favour water content reduction in distillate, however this will increase methanol presence in bottoms, which in undesirable.

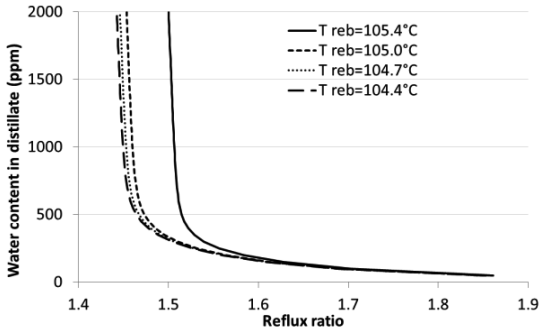

Figure 3 – Water content in distillate dependence with reflux ratio and reboiler temperature.

3.4. Methanol content in column bottoms with stripping section temperatures

In addition to water content limitation in distillate, there is also a methanol maximum of 1000 ppm in column bottom. As in the previous case, there is no direct measurement of this component composition in outlet stream so control is currently based on temperature measures in reboiler and middle of stripping section (referred as T6). As it can be observed in Figure 4, there is a correlation between reboiler temperature and methanol content that is almost independent of the reflux ratios used.

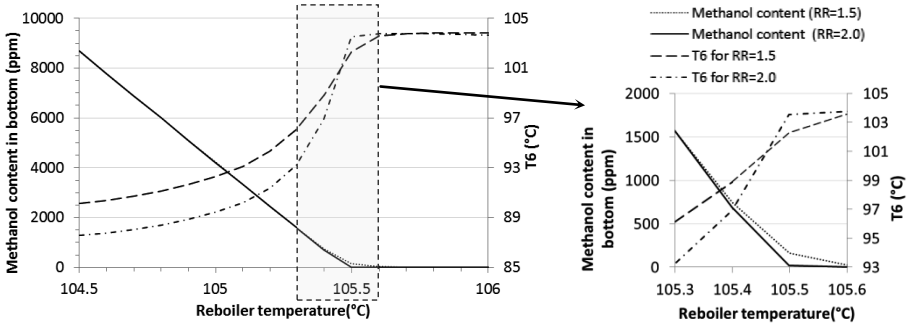

Figure 4 – Methanol content in bottom for different stripping section temperature profiles (reboiler and middle section T6) considering reflux ratios of 1.5 and 2.0.

There is a threshold temperature value of about 105.35 ºC. Below this value it is not possible to obtain aqueous glycerine with methanol content within specification limit. Temperature in middle section (T6) is highly sensitivity to methanol composition, however its absolute value depends on reflux ratio. Higher reflux ratios will decrease T6 temperature for the same methanol content. Because reboiler temperature has low sensitivity to methanol content, T6 is an important parameter to determine if the composition limitation is accomplished.

3.5. Variables control range where composition limits are observed

The real distillation column is controlled exclusively by the reboiler temperature (using a PID control loop that changes vapor rate fed to reboiler) and reflux rate (which when related to distillate rate give us reflux ratio). In section 3.3, it was established a relation between water content in distillate and reflux ratio and reboiler temperature. In

section 3.4, the same relation was made between methanol content in column bottom and the same variables. Assembling these two relations we can establish in which values range of the control variables, both composition specifications will be respected. The region in Figure 5 between the lines showed corresponds to the feasible solutions.

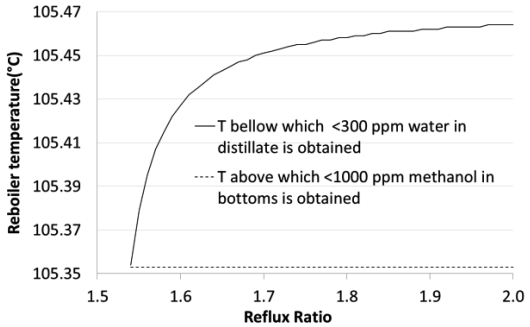

Figure 5 – Reboiler temperature and reflux ratio ranges where composition limits are respected.

It is also possible to observe that even for a higher reflux ratio of 2, the column will only be working with compositions under control if the reboiler temperature is kept between about 105.35 °C and 105.46 °C, which is a very low operational range. For this reason, the knowledge of the temperature in the middle of stripping section is of great importance as a complement of reboiler temperature. A similar study to the previously presented can be observed in Figure 6, where temperature T6 range is obtained for specifications fulfilment. This is information is of great help because the T6 range is much greater than temperature measure error of sensors.

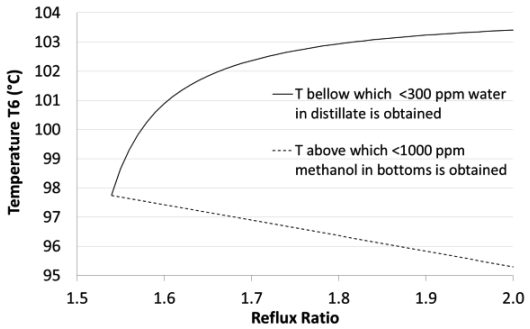

Figure 6 – T6 and reflux ratio ranges where both composition limits are observed.

The optimal operational conditions would be the contact point between the two lines at Reflux Ratio=1.54 and $T_{reboiler}$=105.35 °C, because this is where reflux ratio have lowest value corresponding to the lowest power removed in condenser. When the column is operating with higher reflux ratios, this allows a more comfortable distillation control because there is wider range of reboiler and T6 temperatures where the process is still within specifications boundary. However this advantage is achieved with greater energy expenses in condenser and reboiler.

3.6. Feed temperature influence in power consumption

Before entering in the column, the feed stream is heated from 66 °C to 75 °C in a heat exchanger that uses steam as utility. From simulation results (Figure 7a) it is observed that considering exclusively the column energy optimization, higher feed temperatures

favour the reduction of energy consumed in the reboiler and will result in higher energy consumption in condenser as a result of optimal reflux ratio increase. When the feed temperature increase is obtained at expenses of hot utility, this energy should also be accounted when searching optimal feed temperature. Observing Figure 7b, where heat power includes the power consumed in the external heat exchanger and in the reboiler, we can conclude that from energetic point of view, higher feed temperature is undesirable. Suppressing the actual feed heating with utility will result in a 1.3 % reduction in heat energy consumption and 1.5 % reduction in cooling energy. A reduction of the feed temperature to 66 °C represents an increase of the supplied thermal power into the reboiler of about 4 %. This issue must be taken in consideration since heat transfer rate capability in the reboiler is limited.

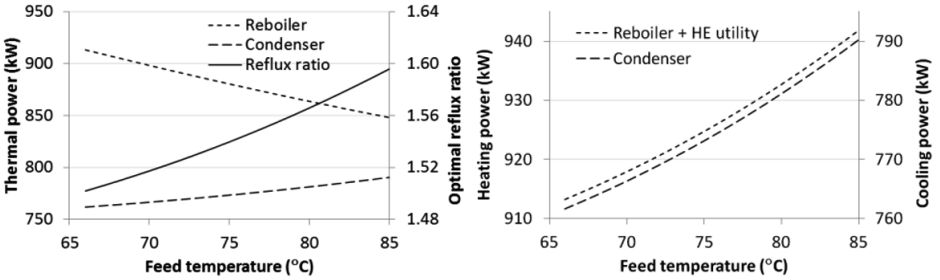

Figure 7 – Feed temperature influence in heat and cold thermal power consumption a) considering only column energy streams, b) accounting with supplied external heat.

4. Conclusions

This paper showed studies using an Aspen-HYSYS model simulation of a real industrial distillation column. After careful parameterization of the model, important information was retrieved without performing any testing in the real process. Because the mentioned methanol/water/glycerol distillation column doesn't have online composition analysis, the obtained results from these studies are of great importance in order to establish the operation conditions that correspond to the minimum thermal energy consumption subject to the composition restrictions.

In this case it was concluded that, the knowledge of temperatures measured in other stages of the column are crucial to maintain the outlet compositions within limits. The performed simulation studies showed how these temperature variables are related with outlet compositions and what are the admissible ranges.

The feed temperature study showed that the actual feed heating that uses steam utility should be suppressed since it increases total heat and cold energy supply to the process. A dynamic model of the distillation column should be the next step analysis to simulate some other perturbations in the process and determine the correction steps to maintain the process running in optimal conditions.

5. References

M. Jobson, 2014, Chapter 6 - Energy Considerations in Distillation, In Distillation, edited by A.G. Sorensen, Academic Press, pages 225-270.

J.V.N. Palmeira, J.M. Silva, H.A.S. Matos, 2012, Industry Energy Optimization: A Case Study in a Biodiesel Production Site, Chem. Eng. Trans., 29, 919-924.

W.D. Seider, J. D. Seader, D.R. Lewin, S. Widagdo, 2009, Product and Process Design Principles: Synthesis, Analysis and Design, 3rd Ed., Wiley.

Krist V. Gernaey, Jakob K. Huusom and Rafiqul Gani (Eds.), 12th International Symposium on Process Systems Engineering and 25th European Symposium on Computer Aided Process Engineering.
31 May – 4 June 2015, Copenhagen, Denmark

Simulation of a 3D Bioprinted Human Vascular Segment

Nogueira JA.[a], Lara VF.[a], Marques TS.[a,b], Oliveira DS.[a,b], Mironov V.[a], da Silva JV.[a], Rezende RA.[a*]

[a] *Division of 3D Technologies, Center for Information Technology Renato Archer, Campinas, SP, BRAZIL*
[b] *Center of Rapid and Sustainable Product Development (CDRSP), Marinha Grande, PORTUGAL*
**corresponding author: rrezende@cti.gov.br*

Abstract

The ultimate goal of bioprinting is the production of living and functional tissue and organs for transplantation in a reasonable time scale. To achieve this goal, the best process would be organ printing. It enables creation of tissue with a high level of cell density; can solve the problem of vascularization in thick tissues; organ printing can be done *in situ*.
Organ printing is a computer-aided 3D tissue engineering of living organs with layer-by-layer deposition of tissue spheroids compounded by pre-sorted cells and hydrogel with principles of self-assembly. This process can be divided in 3 technological steps: i) Development of the design files (blueprint) for the organs; ii) Actual printing; iii) Post processing or organ conditioning and accelerated tissue and organ maturation.
This work presents an initial study about the post-processing concerning the maturation phase. It was adopted a clinical image of computer tomography (CT) of a human heart. A branch of this heart was selected and handled. This image was converted into a 3D virtual mesh able to be used in the simulations. Two conditions were considered: a 3D branch formed by spheres analogously to the tissue spheroids representing a fresh organ bioprinted and the second one taking into account the surface of the branches representing a more maturated structure.
Some analysis were executed to verify the fusion process among the tissue spheroids when the spheres are under fusion to each other and the distance between them decreased at long the time. Velocity and pressure were analyzed through four selected sections in the vascular branch where there is fluid flow through the spheres that form threedimensionally the structure as a fresh organ bioprinted by a 3D bioprinter.

Keywords: 3D Bioprinting, modeling, computer simulation, vascular segment.

1. Introduction

Organ printing is a computer-aided robotic layer by layer additive biofabrication of 3D human tissues and organs constructs using tissue spheroids as building blocks (Mironov et al., 2003; Mironov et al., 2009; Mironov et al., 2011). Tissue spheroids closely placed layer by layer in supporting hydrogel can fuse in horizontal and vertical directions and form 3D tissue and organ constructs.

Tissue fusion is a natural ubiquitous process occurring during embryonic development of tissues and organs (Pérez-Pomares and Foty, 2006). In organ printing technology, tissue fusion is a fundamental biological process which enables biofabrication of 3D tissue and organ constructs. Mathematical modeling and computer simulation methods have been successfully used for predictive modeling of postprinted tissue fusion process (Yang et al. 2012; Sun et al., 2014; McCune et al., 2014).

Bioprinted 3D tissue and organ constructs must be vascularized in order to maintain their viability (Visconti et al., 2010). It has been demonstrated that bioprinting of build in intraorgan branched vascular system could be accomplished using solid and lumenized vascular tissue spheroids (Kasyanov et al., 2011; Gentile et al., 2008) which also undergo process of tissue fusion. The branched vascular tree is suitable for intravascular perfusion. It is crucial to study the fluid behavior during the tissue maturation of the cells, so the simulations help to understand which range of parameters values should be used to ensure the optimal condition for cell maturation.

For this propose, the aim is to quantify the stresses caused by the passing fluid, and it is also important to quantify the fluid velocity between the tissue spheroids.
These two parameters are important for the study because it is necessary to ensure the structural integrity of the printed organ and it is necessary to ensure a perfect cell metabolism. Several steps were executed for each fusion stage.

2. Modeling of the scenario

This part was started by reconstructing a random vain ramification located near to the hearth. This ramification came from a Computed Tomography (CT) scan. Software InVesalius originally created in the Renato Archer Information Technology Center (CTI) is able to import CT images (and also Magnetic Resonance MRI) and generate a 3D digital model. So, CT from a human heart (Figure 1 left) was imported into InVesalius.

The aim is to get a part of the 3D model – whole structure analyses requests much computer efforts and it was not the goal of this work – to segment it (treat it), generate a 3D mesh in such way the mesh could be take into a computational fluid dynamics simulation software. In order to be possible simulating the mesh, it was needed to modulate the surfaces for assembling the 3D model as presented in Figure 1 (right). Only some segments of the heart were selected and a modulation of the surfaces was performed on the reconstruction of the model.

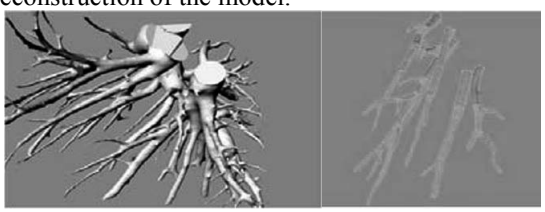

Figure 1 – Processed CT with InVesalius (left) and Surface modeling of the vascular segments (right).

After the reconstruction of the model, a little part of the vain which had a section of around 3mm was cut off. A zone with a bifurcation (Fig. 2) was selected, i.e., a zone

that had a fork-like geometry. This zone was selected because of being a branch and possibly present a higher stress area segment.

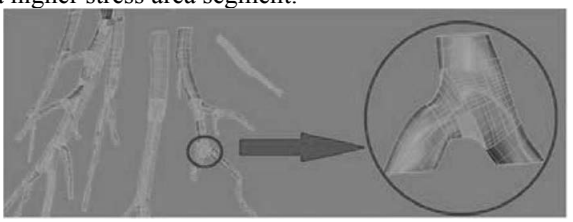

Figure 2 –Selected vascular branch for the simulation.

After selecting the zone, the structure was modeled using spheres as an analogy to tissue spheroids. Basically, a tissue spheroid is a microtissue composed by cell aggregates that will be enveloped by some type of hydrogel. Tissue spheroids contain high density of cells (Rezende et al., 2013) and undergo a natural process of fusion by surface tension when the 3D printer dispenses them onto a platform. Therefore, tissue spheroids have been considered as a special type of material. Thus, the vascular branch was 3D modeled using layers of small spheres (Fig. 3).

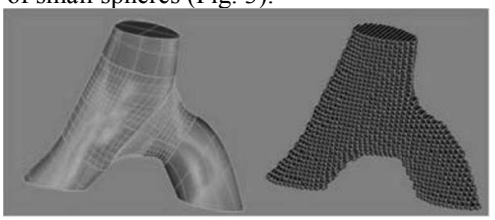

Figure 3 – Representation of printed tissue spheroids.

With the vain section of 3mm, the spheres of 2µm diameter were modeled. Two different stages of fusion were analyzed: 1% and 20% (Fig. 4).

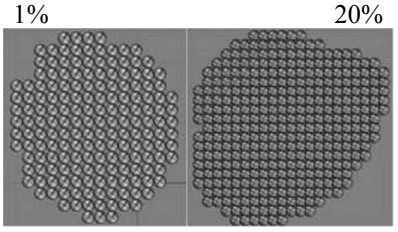

Figure 4 – Design of different tissue spheroids fusion stages.

Computational Fluid Dynamics (CFD) software developed by ANSYS CFX (version R15.0) has been used in our simulations. Each spheroid represented in the simulation was considered as a sphere of alginate. In this work, it was chosen an alginate concentration of 3%, where k = 6 Pa.s and n = 0.84 with density equals to 1.4 g/cm^3 and a shear rate range from 0.01 to 100 s^{-1} and an average viscosity in the range of 2.8 to 12.5 Pa.s (Rezende et al., 2009).

3. Results and discussions

After the mesh has been built, CFD simulations were initiated. To simplify the results and to get more concise information, four different sections (Fig. 5) specifically located on the model were created to get a term of comparison between all configurations.
A flow of fluid passing among the spheres was considered entering at the top before S1 of the structure and leaving after S4. Two different fusion stages (1% and 20%) and two different flow velocities (40 cm/s and 100 cm/s) simulations are presented in this paper. Moreover, it was set an outlet pressure of zero Pascal and temperature equals to 37˚C.

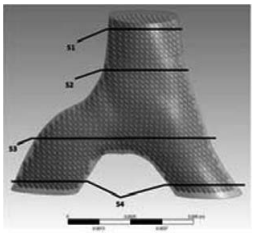

Figure 5 – Locations of the 4 sections analyzed.

Figure 6 shows the profile of velocity and pressure values at sections S1 and S4.

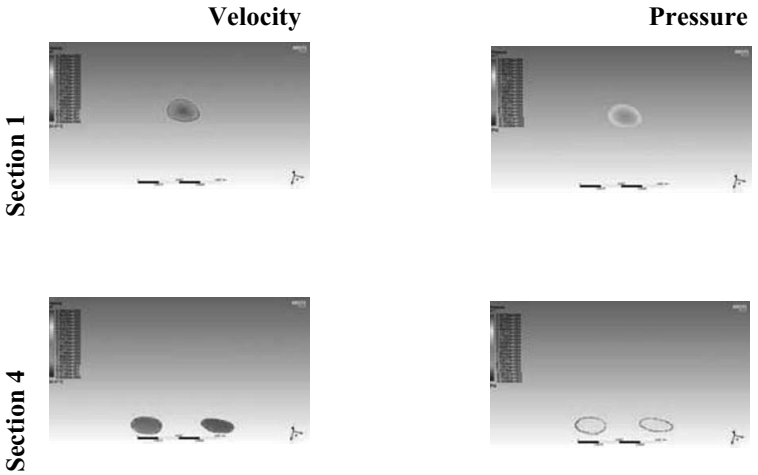

Figure 6 – Profile (color distribution) of velocity and pressure for 1% fusion and input velocity 40cm/s.

Analysing the impact of the velocity variation on the model, both velocities were compared and the following conclusions were pointed as presented in Table 1. For 1% fusion and both inlet velocities, it was observed that the velocity has a logarithmic behavior, which tends to zero. One finding is that both simulations are directly proportional each other. The fact that the velocity is high in the inlet and it's almost zero in the outlet shows that the pressure will be much higher in the inlet which can be a problem to the spheroids.

In the simulations of the 20% fusion (Table 1) with inlet velocity of 40 cm/s, the velocity was constant trough the model. For 100 cm/s, the same results were observed however with a little higher velocity trough the model. This allows having a better control in the spheroids environment guaranteeing that the spheroids have the same conditions.

Table 1 shows the relation between the velocities inside the geometry with both fusions 1 and 20%. The inlet velocities were 40 and 100 cm/s:

Table 1 – Velocities at each section.

Inlet Velocity		40 cm/s		100 cm/s	
Fusion		1%	20%	1%	20%
Section1	Min.	112,6	0	142,8	0
	Max.	140,8	33,1	285	148,1
Section 2	Min.	56,3	0	71,39	0
	Max.	84,47	33,1	142,8	148,1
Section 3	Min.	0	0	0	0
	Max.	28,16	33,1	142,8	148,1
Section 4	Min.	0	0	0	0
	Max.	28,16	33,1	142,8	148,1

Concerning the pressures, on the fusion stage of 1%, it could be verified that the pressure on the lower velocity is lower relatively to the pressure on the model with higher velocity. On both models the pressure is higher in the inlet and it tends to zero until it reaches the outlet, so this translates in a high pressure gradient. The only difference between the models with different velocities is that on the model with higher velocity the pressure will be higher on the entire model when compared to the model with the lower velocity. Table 2 presents the relation of pressure between the fusion stages with inlet velocities of 40 and 100 cm/s:

Table 2 – Pressures at each section.

Inlet Velocity		40 cm/s		100 cm/s
Fusion		1%	20%	1%
Section1	Min.	10,92	44,91	49,6
	Max.	12,52	55,85	56,81
Section 2	Min.	7,77	30,5	35,3
	Max.	9,33	34,12	42,5
Section 3	Min.	2,96	12,4	6,6
	Max.	6,14	23,26	20,95
Section 4	Min.	0,226	1,53	-0,6
	Max.	1,37	8,78	6,6

4. Conclusions

A 3D structure representing a fresh human organ obtained from a 3D bioprinter has been studied *in silico*. Computer simulations have been done to study the behaviour of fluids through tissue spheroids under fusion process. Many parameters have been analyzed. In this work, two ones were verified: velocity and pressure. Four different sections were traced in a vascular branch modeled from a computer tomography image which was imported by software InVesalius and then a 3D model and mesh were generated. The model was carried out into computational fluid dynamics simulation

software to analyze the two parameters – velocity and pressure – which demonstrated to be very critical to the fresh organ if not very well controlled.

5. Acknowledgments

Thanks to the National Council for Scientific and Technological Development (CNPq), FAPESP and the Brazilian Institute of Biofabrication (INCT-BIOFABRIS).

References

C. Gentile, P.A. Fleming, V. Mironov, K.M. Argraves, W.S. Argraves, C.J. Drake, 2008, VEGF-mediated fusion in the generation of uniluminal vascular spheroids. Dev Dyn., 237(10):2918-25.

V. Kasyanov, K. Brakke, T. Vilbrandt, R. Moreno-Rodriguez, A. Nagy-Mehesz, R. Visconti, R. Markwald, I. Ozolanta, R.A. Rezende, A.L. Lizandrão Filho, P. Inforçati Neto, F.D.A.S Pereira, D.T. Kemmoku, J.V.L. Da Silva, V. Mironov, 2011, Toward organ printing: Design characteristics, virtual modelling and physical prototyping vascular segments of kidney arterial tree, Virtual and Physical Prototyping, 6:4, 197-213.

M. McCune, A. Shafiee, G. Forgacs, I. Kosztin, 2014, Predictive modeling of post bioprinting structure formation. Soft Matter, 10,11: 1790-1800.

V. Mironov, T. Boland, T. Trusk, G. Forgacs and R.R. Markwald, 2003, Organ printing: computer-aided jet-based 3D tissue engineering. Trends Biotechnol, 21, pp. 157–161.

V. Mironov, R.P. Visconti, V. Kasyanov, G. Forgacs, C.J. Drake and R.R. Markwald, 2009, Organ printing: tissue spheroids as building blocks. Biomaterials, 30, pp. 2164–2174.

V. Mironov, V. Kasyanov, R. Markwald, 2011. Organ printing: from bioprinter to organ biofabrication line. Current Opinion in Biotechnology, 22:1–7.

J.M. Pérez-Pomares, R.A. Foty, 2006, Tissue fusion and cell sorting in embryonic development and disease: biomedical implications. Bioessays. 28(8):809-21.

R.A. Rezende, P.J. Bártolo, A. Mendes, R. Maciel Filho, 2009, Rheological Behaviour of Alginate Solutions for Biomanufacturing. Journal of Applied Polymer Science (Online), v. 113, p. 3866-3871.

R.A. Rezende, F.D.A.S. Pereira, V. Kasyanov, D. Kemmoku, I. Maia, J.V.L. da Silva, V. Mironov, 2013, Scalable Biofabrication of Tissue Spheroids for Organ Printing. Procedia CIRP, v. 5, p. 276-281.

Sun Y, Yang X, Wang Q., 2014, In-silico analysis on biofabricating vascular networks using kinetic Monte Carlo simulations. Biofabrication. 6(1):015008.

R.P. Visconti, V. Kasyanov, C. Gentile, J. Zhang, R.R. Markwald and V. Mironov, 2010, Towards organ printing: engineering an intra-organ branched vascular tree. Expert Opin Biol Ther, 10, pp. 409–420.

X. Yang, V. Mironov, Q. Wang, 2012, Modeling fusion of cellular aggregates in biofabrication using phase field theories. J Theor Biol. 21;303:110-8.

Krist V. Gernaey, Jakob K. Huusom and Rafiqul Gani (Eds.), 12th International Symposium on Process Systems Engineering and 25th European Symposium on Computer Aided Process Engineering.
31 May – 4 June 2015, Copenhagen, Denmark

Modeling Fixed-bed Multicomponent Adsorption as a step to achieve Ultra-Low Sulfur Diesel

Tristán Esparza-Isunza[a], Felipe López-Isunza[a] *

[a]*Departamento de Ingeniería de Procesos e Hidráulica. Universidad Autónoma Metropolitana-Iztapalapa, Av. San Rafael Atlixco 186, Col. Vicentina. CP 09340 D.F. MÉXICO.*
felipe@xanum.uam.mx

Abstract

The elimination by selective adsorption of nitrogen-heterocyclic compounds (NHC) in diesel may be considered as a strategic step prior to hydrodesulphurization (HDS), to achieve ultra-low sulfur diesel (ULSD). NHC compete favorably with sulfur-heterocyclic molecules (SHC) for sites in $CoMo/Al_2O_3$ and $NiMo/Al_2O$ catalysts at typical HDS operating conditions. It is also known that NHC and SHC adsorb favorably on various solids supports at mild conditions. These encourage the design of a process for the adsorption of both NHC and SHC contained in diesel prior to HDS to achieve ULSD. To this goal, a detailed process model has been developed for the simulation of the transient non-isothermal operation of a pilot-scale fixed-bed for the continuous adsorption and desorption stages treating a diesel with 500 ppm of a mixture of NHC and SHC. Model simulations of a continuous three-stage adsorption-desorption operation shows that the process can be successful, if an adequate combination of adsorbent, solvent and temperature is found, and best performance is achieved when using small microporous particles with large pore diameters.

Keywords: ultra-low sulfur diesel, multicomponent adsorption, process modeling.

1. Introduction

The elimination of nitrogen and sulfur heterocyclic compounds in diesel is one of the most important issues that refineries face to meet the existing stringent environmental regulations against NOx and SOx emissions. Current deep hydrodesulphurization (HDS) at high temperatures and pressures may not be able to reduce sulfur content by less than 15 ppm (ULSD), not only because of the known difficulties to remove alkyl derivatives of dibenzothiophene compounds, but also because nitrogen-heterocyclic compounds (NHC) in HDS compete favorably with sulfur-heterocyclic molecules (SHC) for sites in $CoMo/Al_2O_3$ and $NiMo/Al_2O$ catalysts (Lesermann, et al. 2007; Wen, et al. 2010).

On the other hand, it is known that not only NHC can adsorb on various solids supports, but also SHC adsorb on the same type of supports (Aude, 1979; Kim, 2006; Wen, 2010), which has resulted in the development of a process for the selective removal, by adsorption, of NHC and SHC in diesel prior to HDS (Lesermann, et al. 2007). Moreover, the selective adsorption of NHC and SHC can be performed at mild conditions in temperature and pressure, and with no use of Hydrogen. However, to

achieve the above, the right combination of solid adsorbents, and solvent mixtures and temperatures for desorption and regeneration stages should exist.

The aim of this work is to show that the adsorption process could be successful if three conditions are met, although only the first two are considered here. The first condition is related to the existence of solid sorbents to perform the adsorption, which according to the published literature they already exist. The second one is the availability of the right combination of solvent mixtures that make desorption to be effective to cope with diesel production in the refinery. The third and perhaps the determining condition is solvent regeneration. Additional considerations to the success of this process are to seek for the best sorbents physical and chemical characteristics like particle and pore dimensions, and the right amount and strength of active sites, to which this work is mainly focused. It is clear that a battery of packed-beds is required to satisfy the continuous production of diesel in a refinery, so that this process could be implemented accordingly.

2. The adsorption-desorption process

Typical solid adsorbents for NHC and SHC are zeolites (Audeh, 1970), Ni/SiO2-Al2O3 (Kim, et al. 2006), activated carbon (Wen, et al. 2010), and alumina and silica xerogels containing Zr, Ti; preferably with large amounts of acid sites (Ns), in pores with diameters ranging from 2-10 nm, and particle sizes between 0.6-1.5 mm, and specific surface areas (Sg) in the range 150-750 m^2/gr (Lesemmann, et al. 2007). Typical NHC molecules are Carbazole, Quinoline and Indole, whereas for SHC the alkyl derivatives of dibenzothiophene (4,6-dimetil, C2-, C3-, C4-DBT) are the target. Desorption could be accomplish using mixed solvents containing alcohols, ethers and ketones (Lesemmann, et al. 2007), and solvent regeneration seems to be the key for an economically successful process.

3. The process model

Packed-bed multicomponent adsorption is described at two levels. At the inter-particle fluid level mass and heat balances are given by convective and dispersive terms. At the intra-particle level diffusion is assumed to be Fickean at the (cylindrical) pores of the solid adsorbent, and multicomponent adsorption and desorption are assumed to follow Langmuir kinetics under no-equilibrium conditions, using a wide range of kinetic parameter values to characterize the multicomponent mixture, and to evaluate the robustness of the model.

At the inter-particle level in the fluid-phase, mass and heat balances are:

$$\varepsilon\left[\frac{\partial Cn}{\partial t}+\langle u\rangle\frac{\partial Cn}{\partial z}\right]-D_A\frac{\partial^2 Cn}{\partial z^2}-D_R\left(\frac{\partial^2 Cn}{\partial r^2}+\frac{1}{r}\frac{\partial Cn}{\partial r}\right)=\varepsilon k_L a_V\left(Cns-Cn\right) \tag{1}$$

$$\varepsilon\rho c_P\left[\frac{\partial T}{\partial t}+\langle u\rangle\frac{\partial T}{\partial z}\right]-k_{tA}\frac{\partial^2 T}{\partial z^2}-k_{tR}\left(\frac{\partial^2 T}{\partial r^2}+\frac{1}{r}\frac{\partial T}{\partial r}\right)=\varepsilon h a_V\left(Ts-T\right) \tag{2}$$

With boundary conditions:

At r=0: $\frac{\partial Cn}{\partial r} = \frac{\partial T}{\partial r} = 0$; at r=Rt: $\frac{\partial Cn}{\partial r} = 0$; $-k_{effR}\frac{\partial T}{\partial r} = h_W\left(T - T_W\right)$ (3)

At z=0: $\varepsilon\langle u\rangle Cn\big|_{O-} = \varepsilon\langle u\rangle Cn\big|_{O+} - D_A\frac{\partial Cn}{\partial z}\Big|_{O+}$; at z=Lt: $\frac{\partial Cn}{\partial z}\Big|_{Lt} = 0$ (4)

At z=0: $\varepsilon\rho c_P\langle u\rangle T\big|_{O-} = \varepsilon\rho c_P\langle u\rangle T\big|_{O+} - k_{tA}\frac{\partial T}{\partial z}\Big|_{O+}$; at z=Lt: $\frac{\partial T}{\partial z}\Big|_{Lt} = 0$ (5)

The Darcy equation is used to account for the flow velocity in the fixed-bed

$$\langle u\rangle = \frac{K_b}{\mu}\frac{\Delta P}{L_t} \tag{6}$$

Mass balances at the intra-particle level are, for the liquid in pores:

$$\varepsilon_P\frac{\partial Cns}{\partial t} = D_{eff}\left(\frac{\partial^2 Cns}{\partial\lambda^2} + \frac{\partial^2 Cns}{\partial\sigma^2} + \frac{1}{\sigma}\frac{\partial Cns}{\partial\sigma}\right) \tag{7}$$

With boundary conditions at the pore radius (σ), and pore length which is equal to the radius of the particle (λ):

At $\sigma = 0$: $\frac{\partial Cns}{\partial\sigma} = 0$; at $\sigma = R_P$: $-\varepsilon_P D_{eff}\frac{\partial Cns}{\partial\sigma} = \left(1-\varepsilon_P\right)\rho_P R_n$ (8)

At $\lambda = 0$: $\frac{\partial Cns}{\partial\lambda} = 0$ at $\lambda = L_P$: $-\varepsilon_P D_{eff}\frac{\partial Cns}{\partial\lambda} = \varepsilon k_L\left(Cns - Cn\right)$ (9)

The heat balance assumes that the solid temperature Ts remains uniform in the whole particle, and the heat of adsorption is assumed to be negligible.

$$\left(1-\varepsilon_P\right)\frac{\partial Ts}{\partial t} = \varepsilon h a_V\left(T - Ts\right) + Q_{ads} \tag{10}$$

The net rate of adsorption Rn (moles/g cat-s) for the species nis given in terms of the specific surface area (Sg- m^2/g) and the concentration of active sites (Ns- sites/m^2)

$$R_n = k_n S_g N_S\left[Cns\left(1 - \sum_{m=1}^{NComp}\theta_m\right) - \frac{\theta_n}{K_n}\right] \tag{11}$$

The adsorbed species θ*n* followsa the Langmuir expression and it is free to move by surface diffusion.

$$\frac{\partial \theta_n}{\partial t} = D_{surf} \frac{\partial^2 \theta_n}{\partial \lambda^2} + \frac{\rho_P R_n}{N_S} \tag{12}$$

However, boundary conditions state that:

At λ =0 and λ=Lp $$\frac{\partial \theta_n}{\partial \lambda} = 0 \tag{13}$$

Desorption kinetics in the presence of the mixture of solvents is assumed to be first order with respect to the adsorbed species, in which desorption dominates, and it is given as follows:

$$R_{nDes} = k_{ndes} S_g N_S \theta_n \tag{14}$$

Similar expressions of this model have been used previously to describe the isothermal adsorption of multicomponent mixtures (Kaczmarski, et al. 1997), however not with the same detail, and in none of them diffusion and adsorption in the solid adsorbent are given in terms of the (cylindrical) pore in the particle (average pore length Lp and diameter Rp). The model is used to assess the key importance of using small microporous particles (Lp) with large pore diameters (Rp),and the roles of the specific surface area (Sg) and the concentration of active sites (Ns).

Numerical Solution: The model is solved numerically using the method of orthogonal collocation on finite elements for both, the inter-particle fluid phase (axially using 20 elements of equal size with 4 interior points, and radially with one internal collocation point), and the intra-particle solid phase where diffusion and adsorption take place inside the cylindrical pore (3 elements axially, using 4 interior points with elements of different size, and one internal collocation point radially) (Villadsen and Michelsen, 1977). Other used methods are the tri-diagonal matrix, and a 4th order Runge-Kutta.

4. Results and Discussion

To analyze process feasibility for the multicomponent selective adsorption of NHC and SHC, the model is used to simulate the transient non-isothermal operation for the continuous three-stage adsorption-desorption of a pilot-scale fixed-bed (Length=3 m; Diameter=0.30 m; liquid flow rate=0.36 m^3/h), for the treatment of a diesel containing 500 ppm of a mixture of NHC and SHC species, at 333 K and 2.3 bar (adsorption), 373 K and 1.25 bar (desorption). For this, it is assumed that the right solvent exists, and we seek for the best characteristics of the solid adsorbent like: concentration of acid sites (Ns), specific surface area (Sg), average particle radius (Lp) (equivalent to the pore length), and average pore radius (Rp), which are key parameters for the success of the process. The selection of a continuous three-stage adsorption-desorption operation was chosen to show the operability of this process in terms of an efficient elimination of adsorbed species between stages. Figures 1 and 2 show respectively the sequential stages of adsorption and desorption during 50 h of continuous operation. The time-on-stream used for each of the 3-stage operation in other simulations is 10 h per each adsorption and desorption stage.

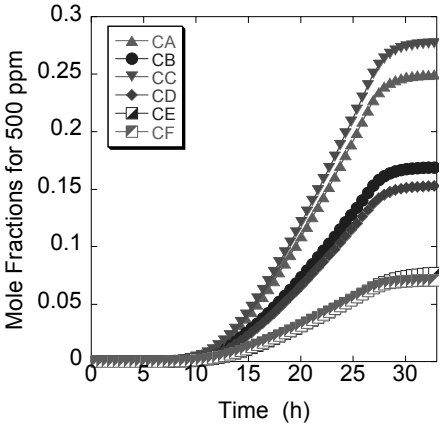

Figure 1. Breakthrough curves during bed adsorption of 500 ppm (particle radius Lp= 0.25 cm, with pore radius Rp = 9 nm) at 333 K. Sg=250 m^2/g; Ns=1.0x10^{-12} sites/cm^2.

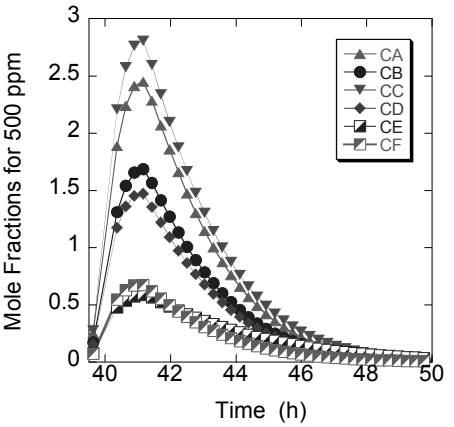

Figure 2. Desorption stage (starting at t=40 h) of NHC and SHC (particle radius Lp= 0.25 cm, with pore radius Rp = 9 nm) at 373 K.Sg=250 m^2/g; Ns=1.0x10^{-12} sites/cm^2.

4.1. Role of particle size specific surface area and active sites concentration

Figure 3 shows the base case at same conditions of Figure 1 for a continuous three-stage adsorption-desorption process of 500 ppm of NHC and SHC species in diesel.Figures 3 and 4 show thatprocess performance is enhanced when using smaller microporous particles with same porous radius (Rp), as bed dispersion of mass is smaller for the smaller particle radius. Figures 5 and 6 show the corresponding responses for larger values of specific surface areas (Sg) and concentration of active sites (Ns), showing again that for both cases a better performance is achieved as compared to that shown in Figure 3.

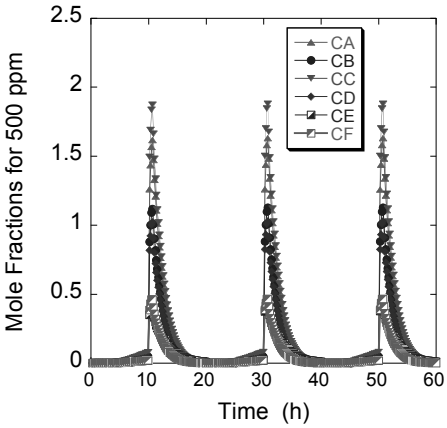

Figure 3. Particle radius Lp= 0.25 cm.

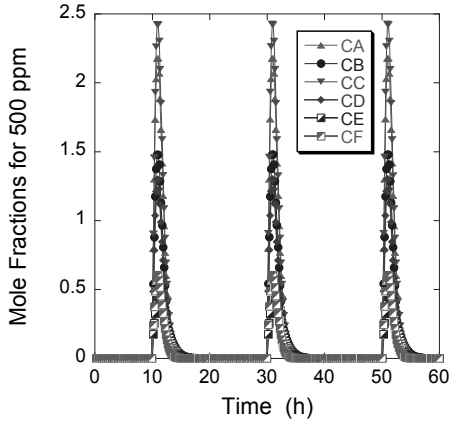

Figure 4. Particle radius Lp= 0.125 cm.

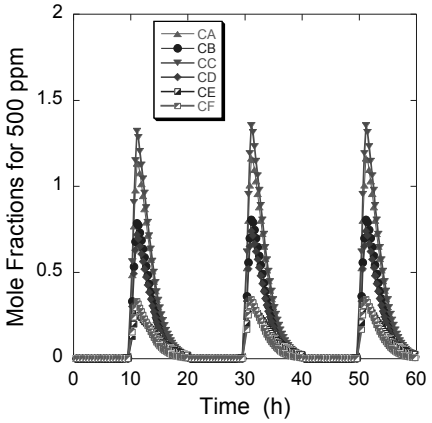

Figure 5. Continuous three-stage using Sg=400 m^2/g; Lp= 0.25 cm.

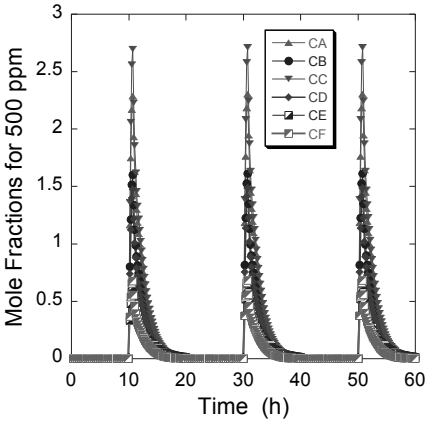

Figure 6. Continuous three-stage using Ns=2.50x10^{-12}sites/cm^2; Lp= 0.25 cm.

5. Conclusions

Multicomponent adsorption of Nitrogen and Sulphur heterocyclic compounds in diesel prior to hydrodesulphurization for ultra-low sulfur diesel can be successfully accomplished by the proper selection of adsorbents (definitely zeolites), solvents and operating conditions. Best performance is obtained when using small microporous particles with large pore diameters, but not very large specific surface areas or large concentration of active sites; these two properties should be optimized. Finally, the regeneration and solvent recovery (not treated in this work) is very important, since large volumes of solvent may be required together with a large demand of energy, making this stage the key for an economically successful process.

References

C.A. Audeh, 1979, Process for the removal of nitrogen compounds from various organic media,US Patent, No. 4,137,154.

J.H. Kim, X. Ma, A. Zhou, Ch. Song, 2006, Ultra-deep desulfurization and denitrogenation of diesel fuel by selective adsorption over three different adsorbents: A study on adsorptive selectivity and mechanism, Catalysis Today, 111, 74-83.

K. Kaczmarski, M. Mazzotti, G. Storti, M Morbidelli, 1997, Modeling fixed-bed adsorption columns through orthogonal collocations on moving finite elements, Computers & Chemical Engineering 21, 641-660.

M.M.F. Lesemann, C. Setzer, 2007, Process for removal of nitrogen containing contaminants from gasoil feed streams, US Patent, No. 7,160,438 B2.

X. Ma, M. Sprague, Ch. Song, 2005, Deep desulfurization of gasoline by selective adsorption over Nickel-based adsorbent for fuel cell applications, Industrial & Engineering Chemistry Research, 44, 5768-5775.

J. Villadsen, M. Michelsen, 1978, Solution of Differential Equation Models by Polynomial Approximation, Prentice-Hall, Englewood Cliffs, New Jersey, USA.

J. Wen, X. Han, H. Lin, Y. Zheng, W. Chu, 2010, A critical study on the adsorption of heterocyclic sulfur and nitrogen compounds by activated carbon: equilibrium, kinetics and thermodynamics, Chemical Engineering Journal 164, 29-36.

Krist V. Gernaey, Jakob K. Huusom and Rafiqul Gani (Eds.), 12th International Symposium on Process Systems Engineering and 25th European Symposium on Computer Aided Process Engineering.
31 May – 4 June 2015, Copenhagen, Denmark

Experimental and CFD Simulation Studies of Circulating Fluidized Bed Riser in the Fast Fluidization Regime

Mukesh Upadhyay,[a,b] Myung Won Seo,[a,c] Nam Sun Nho,[d] Jong-Ho Park[a,b*]

[a]*Department of Advanced Energy Technology, Korea University of Science & Technology, 217 Gajeong-ro, Yuseong-gu, Daejeon 305-350, Republic of Korea*
[b]*Petroleum and Gas Laboratory, Korea Institute of Energy Research, 152 Gajeong-ro, Yuseong-gu, Daejeon 305-343, Republic of Korea*
[c]*Clean Fuel Laboratory, Korea Institute of Energy Research, 152 Gajeong-ro, Yuseong-gu, Daejeon 305-343, Republic of Korea*
[d]*Biomass and Waste Energy Laboratory, Korea Institute of Energy Research, 152 Gajeong-ro, Yuseong-gu, Daejeon 305-343, Republic of Korea*
jongho@kier.re.kr

Abstract

Hydrodynamics of gas-solid in the fast fluidization regime were investigated by a combination of experiment and computational fluid dynamics (CFD) simulations. A two-dimensional (2D) numerical simulation of gas-solids flow in a circulating fluidized bed riser was performed based on the two-fluid model (TFM). The effect of some essential parameters, namely, specularity coefficient (φ), and particle-particle restitution coefficient (e_{ss}), was examined for one set of operating condition. A range of specularity coefficients from 0.1 to 0.0001 were investigated. When specularity coefficient is set to values of 0.001 and above gives axial solid holdup profiles that reasonably agree with the experimental data. It was found that the specularity coefficient has substantial effect on bulk flow. Moreover, the effect of the elasticity of particle collisions showed that the high particle-particle restitution coefficients gave good quantitative agreement. Further extensive validations were carried out to investigate the validity of screened model parameters for different solid circulation rate and gas velocity. Simulation results for different operating condition were able to predict the qualitative trend. Although the model under-predicted the solid holdup at a high solid circulation rate, but was able to capture axial heterogeneity. The 2D results presented in this work will provide a useful basis for the future 3D simulation work of a current CFB system.

Keywords: Kinetic theory of granular flow, circulating fluidized bed riser, Two-fluid model

1. Introduction

Circulating fluidized bed (CFB) reactors are widely applied in many industrial-scale operations because of several advantages, such as improved contact between gas and solid particles, good turndown capability and operation flexibility (Berruti et al., 1995; Grace and Bi, 1997). In general, CFB can be operated under different fluidization regimes; the most common is Fast Fluidization (FF) and present studies were carried out on this regime. In recent years, computational fluid dynamic (CFD) has become a useful tool to study and predict the hydrodynamics of multiphase flows. The approaches that

are used in the simulation of multiphase flows are the two-fluid model (TFM) and discrete element method (DEM). To model large industrial riser systems, Eulerian-Eulerian (TFM) method with the kinetic theory of granular flow (KTGF) framework are more suitable (Jiradilok et al., 2006). Despite several previous studies, the selection of proper wall boundary condition (BC) and appropriate closure model for given flow condition remains inconclusive (van Wachem et al., 2001). For the CFD simulation of a CFB riser, free-slip, partial-slip and no-slip wall boundary condition has been adopted in the literature. The partial-slip boundary condition was used by Jiradilok et al. (2006), the no-slip boundary condition was used by Lu et al. (2009) and Benyahia et al. (2005) suggested free-slip BC in the simulation of a dilute pipe. Researcher found that choosing the correct value of specularity coefficient is critical for most validation. In contrast, the varying particle-wall restitution coefficient (e_w), doesn't affect the characteristic trends (Neri and Gidaspow, 2000). Hence, an assessment of the appropriate specularity coefficient is important for accurate prediction. Further, the particle-particle restitution coefficient (e_{ss}) also plays an important role in gas-solid flow. The particle-particle restitution coefficient value represents the elasticity of particle collisions between two particles; its value ranges from zero for perfectly plastic to one for a perfectly elastic collision. It has served as a tuning parameter for matching experimental results (Cloete et al. 2011), therefore in the current work three different values of the coefficient of restitution i.e. e_{ss}–0.99, 0.9, 0.8 were examined. Among the works in the literature, most of the researchers have investigated the model parameter at one operating condition. Whereas in the current work, we evaluate the validity of these model parameters for different solid circulation rate and gas velocity in the fast fluidization regime.

2. Experimental Setup

Experiments were carried out in a cold-mode dual circulating fluidized bed (CFB) reactor, as shown in Figure 1a. The CFB system is made of plexiglas and composed of 7 m long riser, 75 mm in diameter and with a L-shape exit configuration. The riser and the downcomer are equipped with several pressure transducers for measuring the pressure profile. Solid circulation rate (G_s) was measured once the system has reached steady state using a ball valve in the downcomer. Silica sand was used as a bed material, with an averaged diameter of 249 µm and density of 2353 kg/m^3. In the present experimental work four sets of operating conditions were considered in the fast fluidization regime. With increasing solids mass flux, at constant superficial gas velocity (U_g = 3 m/s and G_s = 19, 48.9 kg/m^{2}s) and increase in superficial gas velocity, at constant solids mass flux (U_g = 3.0, 4.0 m/s and G_s = 43.7 kg/m^{2}s).

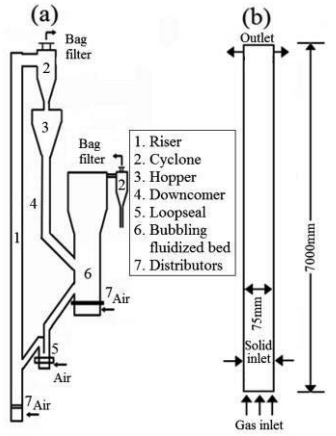

Figure 1: (a) Schematic diagram of the cold-mode CFB, (1-Riser, 2-Cyclone (b) 2D Computational riser geometry

3. Model description and implementation

3.1. Numerical Model

The governing equations were solved using the finite volume approach in FLUENT. Two-fluid model was used for simulating the flow behavior in the CFB riser. A dispersed k-ε turbulence model with standard wall function was adopted to account for the gas phase turbulence effect. The interphase momentum exchange between the two phases was provided through the drag coefficient. For the present case, the Gidaspow drag model (Gidaspow, 1994) was employed. For solving solid phase, kinetic theory of granular flow was employed to compute shear stress. Kinetic energy associate with particle velocity fluctuation is represented by a "granular temperature (Θ)".

3.2. Simulation Setup

Three-dimensional (3D) geometry consumes high simulation time, two-dimensional (2D) riser simulation were performed to keep the computational workload at a reasonable level. The schematic geometry of the 2D riser used in the simulation study is shown in Figure 1b. At the bottom inlet, only the gas velocity is specified; the inlets for solid phase are located at the two sides of the riser at the height 0.6 m; at the top outlet, atmospheric pressure is prescribed.

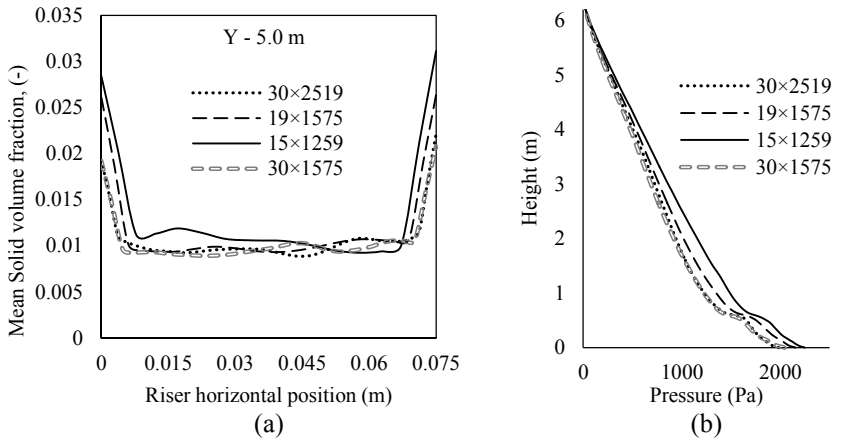

Figure 2: Effect of different grid resolutions (a) Time-averaged radial solid volume fraction (b) Time-averaged axial pressure (U_g = 3.0 m/s, G_s = 43.7 kg/m^{2}s)

To achieve an acceptable grid independent solution four different grid resolutions of 30×2519, 19×1575, 15×1259 and 30×1575 were applied to this simplified geometry. The radial profiles of mean solid volume fraction at the height of 5.0 m were presented in Figure 2a. For the 19×1575, 15×1259 grid resolution, solid volume fraction transition from wall to core quite sharp and the profile predicted by the 30×2519 and 30×1575 computational cells were similar. The effect of grid size on the axial solid holdup was also tested in the simulation, as shown in Figure 2b. Grid resolutions of 30×2519 and 30×1575 predict similar pressure along the height of a riser. However, the simulation with 19×1575, 15×1259 grid resolution predicts somewhat higher pressure than with the other two simulations. Therefore the grid resolution of 30×1575 was selected to conduct further simulation. Transient CFD simulations were carried out using a time step size of 0.0003 s with 100 iterations per time step. Transient behavior of solid mass flux was

monitored dynamically at the outlet of riser to ensure a pseudo-steady-state has achieved before any data analysis.

4. Results and Discussion

In the Johnson and Jackson, (1987) wall boundary condition theory, the specularity coefficient (φ) represents the frictional contact between the solid phase and wall, and the particle-wall restitution coefficient (e_w) quantify the dissipation of solid phase kinetic energy by collision with the wall. As discussed above, the specularity coefficient is an important parameter, in contrast, the varying particle-wall restitution coefficient has no significant effects. Therefore, in the present work, a wide range of the specularity coefficients from 0.1 to 0.0001 were investigated.

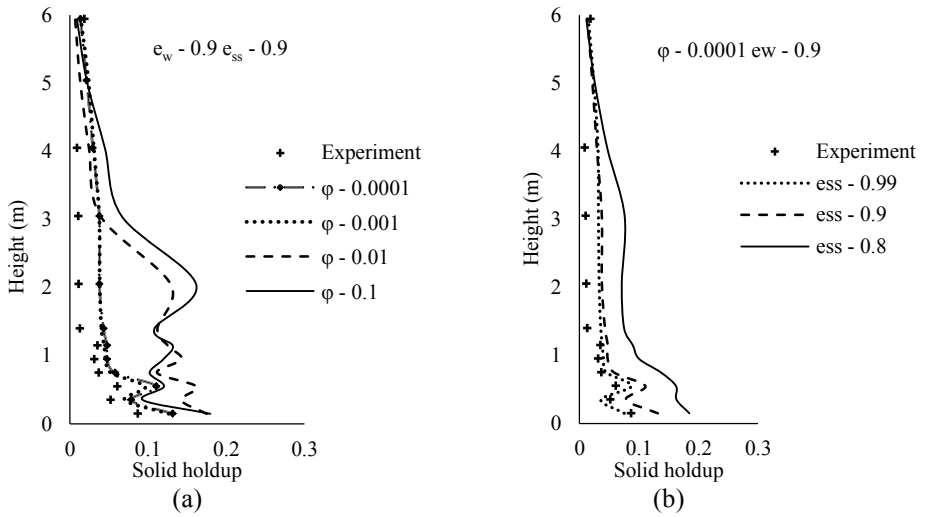

Figure 3: Effect of (a) Specularity coefficients, (b) Particle-particle restitution coefficients on the axial solid holdup profile (U_g = 3.0m/s, G_s = 43.7 kg/m^{2}s)

Figure 3a demonstrates the effect of the specularity coefficient on the axial solid holdup profile. The specularity coefficient of 0.1 predicts significantly high values of the solid holdup then the experimental data in the mid and bottom section of riser, whereas for same specularity coefficient value results in low solid holdup along 5–6 m of riser height. For the specularity coefficient of 0.01, the solid holdup for a height of 0 and 3 m is also considerably high than the experimental value, but after 3 m, the predicted values reasonably agree with the experimental data. The high value of specularity coefficient results in higher flow resistance for particles moving in an upward and downward direction result in a high solid holdup. For specularity coefficient value of 0.001 and above gives reasonably qualitative agreement with experimental data throughout the height of the riser. Thus, the lowest specularity coefficient value (φ–0.0001) will be used for remainder of the study.

As discussed in the earlier section three different values of the coefficient (e_{ss}–0.8, 0.9 and 0.99) were examined. From Figure 3b it can be clearly seen that for e_{ss}–0.8 model over predict the solid holdup in most axial locations. The computed results show a significant improvement in the axial solid holdup as the coefficient of restitution

increased from 0.8. The simulation results using particle-particle restitution coefficients of 0.99 were successfully able to predict typical flow characteristics. Comparatively at 0.9 particle-particle restitution, over predicts the solids holdup at the bottom section of a riser. A higher coefficient of restitution means no dissipation of kinetic energy resulting in more particles leaving the riser. Therefore, the solid holdup distribution in the riser declined.

Validity of above screened model parameters were further evaluated at various solid mass fluxes and superficial gas velocities. From Figure 4a it can be clearly seen that the best agreement with the experimental data observed for low solid mass flux (19.2 kg/m^{2}s). However, for increased solid flux bottom dense regions were under-predicted. One possible reason for this discrepancy is that the conventional Gidaspow drag model cannot account for the reduction in drag due to formation of clusters in the gas-solid riser flow (Shah et al. 2011). To overcome the short comings of the conventional drag correlation multiscale approaches such as the sub-grid scale (SGS) and the energy minimization multiscale (EMMS) models are expected to lead better predictions (Shah et al. 2015). Similarly, for high gas velocity (U_g = 4m/s) the model was unable to predict quantitatively, but show reasonable qualitative agreement. These discrepancies could be due to 2D simplification of the solids inlet and outlet configurations. Recent work by Li et al. (2014) has shown that the 2D simulation can only be used as an effective tool for qualitative studies and 3D simulation is required to accurately capture the quantitative flow behavior in CFB risers. The 2D results presented in this work will provide a useful basis for the future 3D simulation work of a current CFB system.

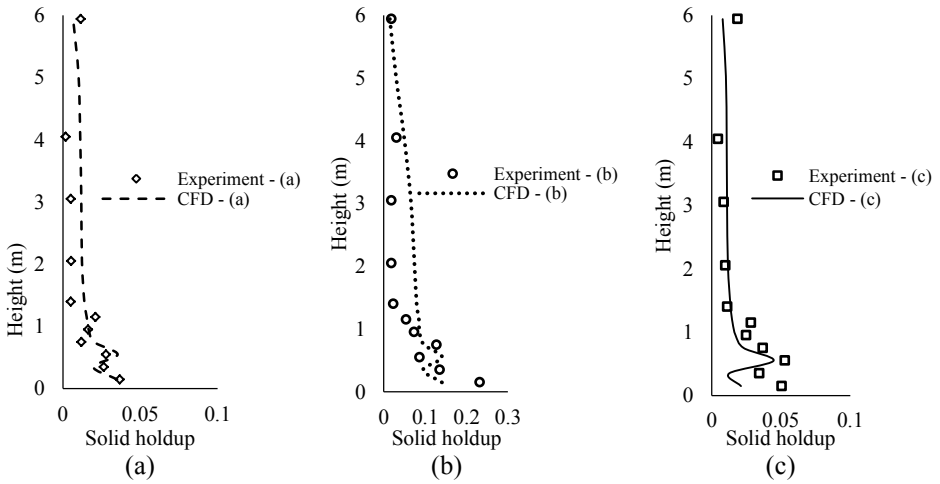

Figure 4: Model prediction at various operating conditions (φ–0.0001 e_w–0.9 e_{ss}–0.99) (a) U_g = 3.0 m/s, G_s = 19.2 kg/m^{2}s, (b) U_g = 3.0 m/s, G_s = 48.9 kg/m^{2}s, (c) U_g = 4.0 m/s, G_s = 43.7 kg/m^{2}s

5. Conclusion

In this work, the hydrodynamics of CFB riser were investigated using two-fluid model (TFM) coupling with the kinetic theory of granular flow. A lower specularity coefficient (0.001 and above) and high particle-particle restitution coefficients (e_{ss}–0.99) gives a reasonable agreement between the predicted axial solid holdup profiles and

experimental data. In the present study, specularity coefficient values significantly affects the riser bulk flow. Particle-particle restitution coefficients express the amount of the energy dissipation by collisions and were used as a tuning parameter in the present study. Particle-particle restitution coefficient (e_{ss}) was tuned to fit the overall experimental profile of axial solid holdup. With the evidence of results it was observed that the model prediction improves as the coefficient of restitution increases. Finally, the validity of screened model parameters were further evaluated for different operating conditions. The model was capable of predicting the main features of the complex gas-solids flow operated in the fast fluidization regime. However, the model showed some discrepancy in predicting the bottom dense regions particularly operating at high solid circulation rate. This study reveals that the one setup of model parameter and boundary condition can be used to predict system operating at the same flow regime. The 2D results presented in this work will provide a useful basis for the future 3D simulation work of a current CFB system.

Acknowledgement

This work was conducted under the framework of Research and Development Program of Korea Institute of Energy Research (KIER) (B4-2433-02).

References

S. Benyahia, M. Syamlal, T.J. O'Brien, 2005, Evaluation of boundary conditions used to model dilute, turbulent gas/solids flows in a pipe, Powder Technology, 156, 2-3, 62-72

F. Berruti, T.S. Pugsley, L. Godfroy, J. Chaouki, G.S. Patience, 1995, Hydrodynamics of circulating fluidized bed risers: A review, The Canadian Journal of Chemical Engineering, 73, 5, 579–602

S. Cloete, S. Amini, S.T. Johansen, 2011, A fine resolution parametric study on the numerical simulation of gas–solid flows in a periodic riser section, Powder Technol., 205, 103–111

D. Gidaspow, 1994, Multiphase Flow and Fluidization: Continuum and Kinetic Theory Description, Academic Press, San Diego, USA

J.R. Grace, H.T. Bi, 1997, Introduction to Circulating Fluidized Beds, Circulating Fluidized Beds, Chapman & Hall , London, 1–20

V. Jiradilok, D. Gidaspow, S. Damronglerd, W.J. Koves, R. Mostofi, 2006, Kinetic theory based CFD simulation of turbulent fluidization of FCC particles in a riser, Chemical Engineering Science, 61, 17, 5544–5559

P.C. Johnson, R. Jackson, 1987, Frictional–collisional constitutive relations for granular materials, with application to plane shearing, Journal of Fluid Mechanics, 176, 67–93

T. Li, S. Pannala, M. Shahnam, 2014, CFD simulations of circulating fluidized bed risers, part II, evaluation of differences between 2D and 3D simulations, Powder Technology, 254, 170–180

B. Lu, W. Wang, J. Li, 2009, Searching for a mesh-independent sub-grid model for CFD simulation of gas–solid riser flows, Chemical Engineering Science, 64, 15, 3437–3447

A. Neri, D. Gidaspow, 2000, Riser hydrodynamics: simulation using kinetic theory, AIChE Journal, 46, 1, 52–67

M.T. Shah, R.P. Utikar, M.O. Tade, V.K. Pareek, 2011, Hydrodynamics of an FCC riser using energy minimization multiscale drag model, Chemical Engineering Journal, 168, 2, 812–821

M.T. Shah, R.P. Utikar, V.K. Pareek, M.O. Tade, G.M. Evans, 2015, Effect of closure models on Eulerian–Eulerian gas–solid flow predictions in riser, Powder Technology, 269, 2015, 247–258

B.G.M. van Wachem, J.C. Schouten, R. Krishna, C.M. van den Bleek, J.L. Sinclair, 2001, Comparative analysis of CFD models of dense gas–solid systems, AIChE Journal, 47, 5, 1035–1051

Krist V. Gernaey, Jakob K. Huusom and Rafiqul Gani (Eds.), 12th International Symposium on Process Systems Engineering and 25th European Symposium on Computer Aided Process Engineering.
31 May – 4 June 2015, Copenhagen, Denmark

Application of New Electrolyte Model to Phase Transfer Catalyst (PTC) Systems

Sun Hyung Kim [a,b], Amata Anantpinijwatna [a], Jeong Won Kang [b], Mauricio Sales-Cruz [c], Rafiqul Gani[a]*

[a]*CAPEC-PROCESS, Department of Chemical and Biochemical Engineering, Technical University of Denmark, Søltofts Plads, Building 229, DK-2800 kgs. Lyngby, Denmark*
[b]*Department of Chemical and Biological Engineering, Korea University, 5 Ga Anam-Dong, Seongbuk-Gu, Seoul 136-713, South Korea*
[c]*Departamento de Procesos y Tecnología, Universidad Autónoma Metropolitana – Cuajimalpa, México D.F. 05300, Mexico*
rag@kt.dtu.dk

Abstract

Phase transfer catalyst (PTC) is used to transfer the desirable active form of an anion from the aqueous phase to organic phase where the reaction occurs. One of major challenges for process design of the PTC system is to establish a reliable thermodynamic model capable of describing phase behaviours of all components including water, organic solvents, inorganic salts, and the PTC. In this work, a new electrolyte model based on the KT-UNIFAC group contribution approach has been developed by adding the Debye-Hückel theory and a second virial coefficient-type term into the KT-UNIFAC model. The temperature-dependent parameters of the new model are introduced to improve the description of phase equilibria in temperature ranges between 273.15 and 373.15 K. The proposed model has been successfully applied to the predictions of phase behaviours of alkali halide aqueous solutions that are usually found in PTC systems, thereby, extending the application range of the PTC-system model. The solubility of PTC in organic solvents, which is a key factor for strategy of PTC and solvent selection, has been calculated using the e-NRTL-SAC model.

Keywords: phase transfer catalyst, PTC, electrolyte model, UNIFAC

1. Introduction

1.1. PTC system

Since Basolo et al. (1973) introduced the concept, biphasic reaction systems have been increasingly considered as promising organic synthesis options due to possibilities of identifying novel synthesis routes that are flexible, easier to operate and give higher production yields. Phase transfer catalyst (PTC) as an application of the biphasic system is employed to obtain higher yields and substitute hazardous or expensive solvents.

As shown in Figure 1, active anion (Y^-) is transferred via PTC cation (Q^+) from aqueous phase into organic phase where the reaction occurs with organic raw material (R-X) to produce a desirable product (R-Y). Inactive form of the PTC (QX) dissolved in aqueous phase from organic phase reacts with active inorganic salt (M^+Y^-) to complete the cycle. Mathematical models on the PTC systems, including physical and chemical equilibrium, reaction mechanism and unit operation, have been generated in our previous works (Anantpinijwatna et al., 2014; Piccolo et al., 2012) and are further developed in this work to analyse the PTC-based process.

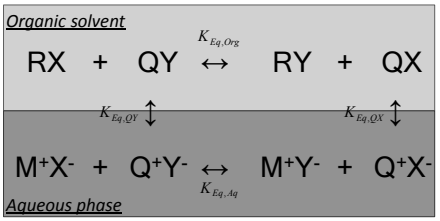

Figure 1: Reaction mechanism for a generic PTC system.

1.2. Thermodynamic model

The key information for the successful design of a PTC-based process is the solubility of active and inactive forms of the organic catalytic cations in aqueous or organic phases and the partitions between these two phases, which are calculated from the activity coefficients of the PTC as a function of compositions of all species for each phase and the system temperature. Therefore, reliable thermodynamic models capable of describing the phase behaviours of all the species presented in the PTC system are required. Due to lack of available measured data for a reactive system, predictive models based on molecular structural parameters, like UNIFAC or segments like eNRTL-SAC (Chen and Song, 2005) are preferred. With respect to thermodynamic modelling, the PTC system can be decomposed into four subsystems (A – D) consisting of:

Subsystem A (organic solvent – water): describes the mutual solubilities between organic solvent and water using NRTL or KT-UNIFAC models

Subsystem B (inorganic salt – water): describes the behaviour of inorganic salt (M^+X^- and M^+Y^-) in aqueous phase using e-NRTL, e-NRTL-SAC, or **e-KT-UNIFAC** models

Subsystem C (organic solvent – PTC): describes the behaviour of PTC (QX and QY) in organic solvent using NRTL, **e-NRTL-SAC**, or UNIFAC-IL thermodynamic models

Subsystem D (water – PTC): describes the behaviour of PTC (Q^+X^- and Q^+Y^-) in aqueous phase using e-NRTL, e-NRTL-SAC, or e-UNIQUAC models

Thermodynamic descriptions of subsystem A are well-established with existing models, whereas the models needed for subsystem D was presented in our previous work (Anantpinijwatna et al., 2014). In this work, a new electrolyte model (e-KT-UNIFAC) is developed and initially applied to the subsystem B, where some representative alkali halide salts can be used as a donor of reacting anions or an acceptor of inactive anions. Solubilities of various PTC species in various organic solvents for subsystem C are determined using the eNRTL-SAC model, reporting new parameters of the PTCs fitted to experimental data. The calculated results are compared with literature data.

2. Model and Parameters

2.1. Reactor model

The framework for the modelling of biphasic reaction systems was proposed and applied to the PTC system with a biphasic reactor model (Anantpinijwatna et al., 2014). The model is composed of 8 balance equations (Eqs. 1-8) and 4 equilibrium conditions (Eqs. 9-12) as shown below.

$$N_{X^-,Aq} = N^0_{X^+} + \xi_{Aq} \quad (1)$$

$$N_{Y^-,Aq} = N^0_{Y^-} - \xi_{Aq} \quad (2)$$

$$N_{RX,Org} = N^0_{RX} - \xi_{Org} \quad (3)$$

$$N_{RY,Org} = N^0_{RY} + \xi_{Org} \quad (4)$$

$$N^T_{QX} = N^0_{QX,Aq} + N^0_{QX,Org} - \xi_{Aq} + \xi_{Org} \quad (5)$$

$$N_{QX,Org} = N^T_{QX} + N_{QX,Aq} \quad (6)$$

$$N^T_{QY} = N^0_{QY,Aq} + N^0_{QY,Org} + \xi_{Aq} - \xi_{Org} \quad (7)$$

$$N_{QY,Org} = N^T_{QY} + N_{QY,Aq} \quad (8)$$

$$0 = X_{RY,Org}X_{QX,Org} - K_{Eq,Org}X_{QY,Org}X_{RX,Org} \quad (9)$$

$$0 = X_{X^-,Aq}X_{QY,Aq} - K_{Eq,Aq}X_{Y^-,Aq}X_{QX,Aq} \quad (10)$$

$$0 = X_{QX,Org} - K_{Eq,QX}X_{QX,Aq} \quad (11)$$

$$0 = X_{QY,Org} - K_{Eq,QY}X_{QY,Aq} \quad (12)$$

where N_i and X_i are mole number and mole fraction of component *i*, respectively, and ξ are extent of reaction. $K_{Eq,Org}$ and $K_{Eq,Aq}$ are equilibrium variables in organic and aqueous phases, while $K_{Eq,QY}$ and $K_{Eq,QX}$ are partition variables of active and inactive PTC, which are calculated by appropriate thermodynamic models.

2.2. e-KT-UNIFAC

In the proposed model the activity coefficient (γ_i) of group *i* is calculated by a sum of three different terms, a long-range (LR) for direct effects of charge interactions, a middle-range (MR) term for indirect effects of charge interactions, and a short-range (SR) term for contribution of noncharge interactions.

$$\ln \gamma_i = \ln \gamma_i^{LR} + \ln \gamma_i^{MR} + \ln \gamma_i^{SR} \quad (13)$$

The long-range term is derived from Debye-Hückel theory (Debye and Hückel, 1923) and given by Macedo et al. (1990). For the middle-range a second virial coefficient-type term from the Pitzer model (Pitzer, 1973) is added to give better description at high salt concentrations up to their solubilities. Working equations are given in Mohs and Gmehling (2013) but, in this work, the middle-range interactions between water and ions were assumed to be negligible and additional temperature-dependent coefficients were introduced for application in a wide range of temperatures. The middle-range interaction parameters (B_{ij}) between cation and anion are expressed as

$$B_{ij} = \left[b_{ij,1} + b_{ij,2}(T - T_0)\right] + \left[c_{ij,1} + c_{ij,2}(T - T_0)\right]\exp\left(-\sqrt{I} + 0.125I\right) \quad (14)$$

where T_0 is reference temperature of 298.15 K and *I* is molal ionic strength (mol/kg). The short-range contributions are calculated using KT-UNIFAC (Kang et al., 2002) composed of combinatorial and residual parts. Group volume and surface area parameters, R_i and Q_i, of ions needed for KT-UNIFAC were estimated from ionic radius with new standard segment radius for physically correct representation of the combinatorial part, $Q_i/R_i \leq 1$ (Cheng, 2003). Temperature dependence of group-interaction parameters (a_{ij}) are represented in the residual part of KT-UNIFAC.

$$a_{ij} = a_{ij,1} + a_{ij,2}(T - T_0) \quad (15)$$

All parameters for binary interactions of water-ion and ion-ion were fitted to experimental data such as mean ionic activity coefficients, osmotic coefficients, vapour-liquid equilibria, and solid-liquid equilibria and the values are listed in Table 1.

Table 1: Model parameters for middle-range and short-range interactions

i	R_i	Q_i
H_2O	0.92	1.40
Na^+	1.0612	1.0404
Cl^-	5.9298	3.2761
Br^-	7.5296	3.8416

i	j	$a_{ij,1}$ [K]	$a_{ij,2}$	$a_{ji,1}$ [K]	$a_{ji,2}$	$b_{ij,1}$	$b_{ij,2}\times10^3$ [K^{-1}]	$c_{ij,1}$	$c_{ij,2}\times10^2$ [K^{-1}]
H_2O	Na^+	-1102.1	-0.4275	1411.1	0.2492				
H_2O	Cl^-	-1096.7	1.1021	-529.37	-1.6143				
H_2O	Br^-	-1222.5	0.7635	-523.24	-1.7233				
Na^+	Cl^-	-2113.2	0.5433	-1802.3	-0.2990	0.2262	0.6458	0.2608	-1.8372
Na^+	Br^-	-2192.3	-0.6022	-163.68	-8.0123	0.3156	0.1174	-0.9607	-0.7956

2.3. e-NRTL-SAC

The e-NTRL-SAC model (Chen and Song, 2005) is based on the segment contribution concept where each molecule can be characterized by four conceptual segments (X, Y-, Y+, and Z). The working equations are given in the original paper and the parameters of water and organic solvents are obtained from published papers (Chen et al., 2001; Song and Chen, 2009). The conceptual segment numbers for eleven PTCs are newly determined from solubility data in twelve organic solvents. The parameter values are reported in Table 2 with their corresponding average deviations.

Table 2: Segment numbers of PTC for NRTL-SAC model

PTC	No. of Exp.	X	Y-	Y+	Z	σ*
Me_4NBr	1	0.074	0.003	0.106	0.057	0.00
Me_4NCl	2	2.908	3.863	0	2.787	0.00
Me_4NI	9	0	0	0	2.506	0.66
Et_4NBr	2	0.924	1.344	0	1.17	0.01
Et_4NCl	2	1.113	0.039	0	0.189	0.00
Et_4NI	9	0	1.287	1.862	2.101	0.81
Pr_4NBr	2	0.028	2.07	0	0.01	0.00
Pr_4NI	6	0.496	2.088	0	0.513	0.06
Bu_4NBr	19	2.346	0	0	0.981	0.33
Bu_4NCl	17	0.046	2.915	0	0.547	0.41
Bu_4NI	1	0.074	0.003	0.106	0.057	0.00

$$\sigma^* = \sum_i^N \left[\left(\frac{X_{Sat}^{Exp} - X_{Sat}^{Cal}}{X_{Sat}^{Exp}} \right)^2 \Big/ N \right]^{1/2}$$

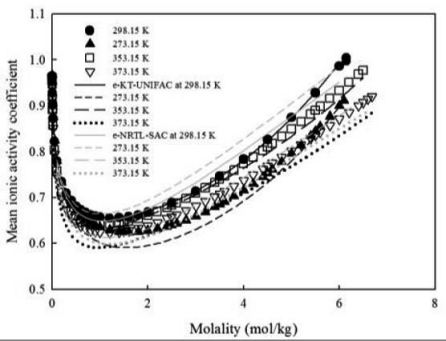

Figure 2: Comparisons of calculated mean ionic activity coefficients of NaCl with data (Hamer & Wu, 1972; Clarke & Glew, 1985)

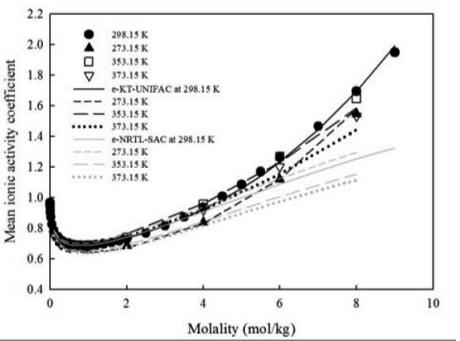

Figure 3: Comparisons of calculated mean ionic activity coefficients of NaBr with data (Hamer & Wu, 1972; Archer, 1991)

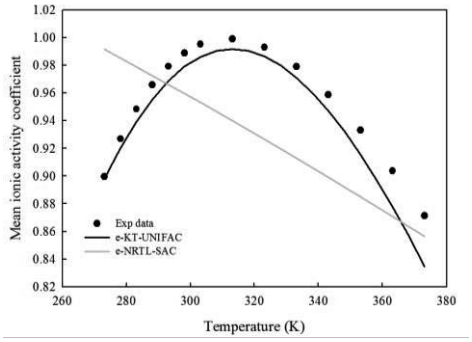

Figure 4: Comparisons of calculated mean ionic activity coefficients of NaCl with data (Clarke & Glew, 1985) at 6 molality

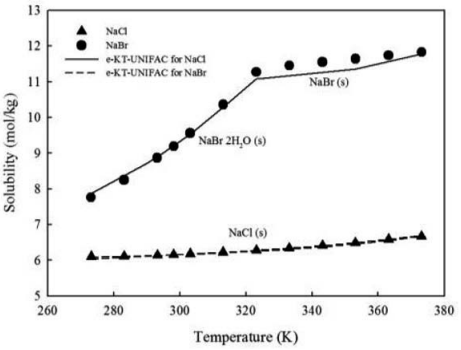

Figure 5: Comparisons of calculated solubility of NaCl and NaBr with data (Haynes et al., 2015)

3. Results and Discussions

3.1. e-KT-UNIFAC with subsystem B

Calculated mean ionic activity coefficients are compared with literature data and eNRTL-SAC model results (Chen and Song, 2005) for NaCl and NaBr in Figures 2 and 3, respectively. These calculations are found in good agreement with the experimental data and more accurate than those of eNRTL-SAC in the temperature range between 273.15 and 373.15 K. With increasing temperatures at a fixed molality, the mean ionic activity coefficients increase, reach a maximum, and decrease again as shown in the Figure 4 for NaCl. The model successfully describes the behaviour, whereas the eNRTL-SAC model shows a continuous decrease with the temperature. The model gives better description of the PTC process, where reactions may take place at temperature other than 298.15 K.

In addition, salt solubilities in water were calculated using the new model. The salt solubility is determined at a given temperature, where the equilibrium constant calculated using activity coefficients is equal to the value calculated using standard thermodynamic properties. As shown in Figure 5, the results show good agreement with the data.

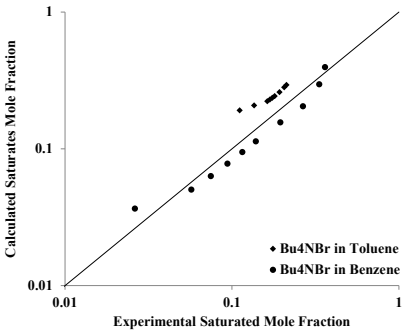

Figure 6: Comparisons of calculated solubility of Bu4NBr PTC by e-NRTL-SAC model with experimental data; ▲ in benzene; ● in toluene. (Abraham, 1970)

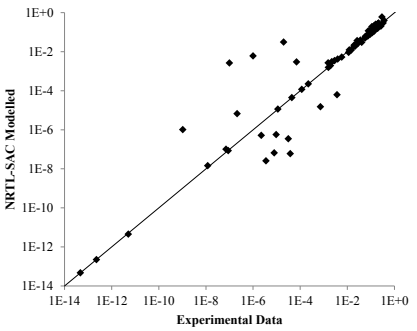

Figure 7: Comparisons of calculated solubility of 11 PTCs in 12 solvents by e-NRTL-SAC model with experimental data. (Abraham, 1970, 1972, 1971)

3.2. e-NRTL-SAC with subsystem C

The e-NRTL-SAC model (Chen and Song, 2005) has available parameters for the interactions of water and PTCs; this is subsystem D (Anantpinijwatna et al., 2014). Here the model is applied to calculate activity coefficients and the solubility of eleven PTCs in organic phases listed in Table 2. The results show an acceptable agreement between the measured experimental data and model predictions as shown in Figure 6 and 7. The modelling results on subsystems C and D are employed to calculate partitions of the PTC between aqueous and organic solvents.

Conclusions

For accurate design of the PTC-based process, complex phase behaviours need to be analysed using the thermodynamic model for systems of water, organic solvents, inorganic salts, and PTC. New electrolyte model based on KT-UNIFAC was established and applied to the PTC system. As initial step the model was found to successfully describe various thermodynamic properties of alkali halide aqueous solutions. The systematic model framework provides possibilities of extension to other systems involving the PTC. The e-NRTL-SAC model has also been used to model the PTC system. In this work solubilities of various PTCs in organic solvents were calculated using this model with good agreement. The results give a good fundamental basis for study of PTC system and the developed model can be fundamentally used to determine systematic strategies for selection of the PTC and the organic solvent.

As future works the model will be extended to other subsystems and employed for the simulation of the overall PTC-based process.

References

M. H. Abraham, 1970, Tetrahedron Letters, 11, 5233-5236.
M. H. Abraham, 1971, Journal of the Chemical Society B: Physical Organic, 299-308.
M. H. Abraham, 1972, Journal of the Chemical Society, Perkin Transactions 2, 1343-1357.
A. Anantpinijwatna, G. Sin, J. P. O'Connell, R. Gani, 2014, Computer Aided Chemical Engineering, 34, 249-254.
D. G. Archer, 1991, Journal of Physical and Chemical Reference Data, 20, 509.
F. Basolo, 1973, Catalysis. Progress in research, Burwell,(Eds.), Plenum press.
C. –C. Chen, C. P. Bokis, P. Mathias, 2001, AIChE Journal, 47, 2593.
C. –C. Chen, Y. Song, 2005, Industrial and Engineering Chemistry Research, 44, 8909.
H. Cheng, 2003, Thermodynamic modelling of surfactant solutions, PhD. Thesis, DTU.
E. C. W. Clarke, D. N. Glew, 1985, Journal of Physical and Chemical Reference Data, 14, 489.
P. Debye, E. Hückel, 1923, Physikalische Zeitschrift, 9, 185.
W. J. Hamer, Y. C. Wu, 1972, Journal of Physical and Chemical Reference Data, 1, 1047.
W. M. Haynes, 2015, CRC Handbook of Chemistry and Physics, 95th Edition, CRC Press.
J. W. Kang, J. Abildskov, R. Gani, J. Cobas, Industrial and Engineering Chemistry Research, 41, 3260.
E. A. Macedo, P. Skovborg, P. Rasmussen, 1990, Chemical Engineering Science, 45, 875.
A. Mohs, J. Gmehling, 2013, Fluid Phase Equilibria, 337, 311.
C. Piccolo, A. Shaw, G. Hodges, P. M. Piccione, J. P. O'Connell, R. Gani, 2012, The 22nd ESCAPE, 757–761.
K. S. Pitzer, 1973, The Journal of Physical Chemistry, 77, 268.
Y. Song, C. –C. Chen, 2009, Industrial Engineering Chemistry Research, 48, 5522.

Krist V. Gernaey, Jakob K. Huusom and Rafiqul Gani (Eds.), 12th International Symposium on Process Systems Engineering and 25th European Symposium on Computer Aided Process Engineering.
31 May - 4 June 2015, Copenhagen, Denmark.

A Novel Rigorous Mathematical Programming Approach to Construct Phenomenological Models

Vassilios S. Vassiliadis[a], Yian Wang[a], Harvey Arellano-Garcia[b] and Ye Yuan[c]

[a]*Process Systems Engineering (PSE) Research Group, Department of Chemical Engineering and Biotechnology, University of Cambridge, Pembroke Street, Cambridge CB2 3RA, UK*
[b]*School of Engineering, Design and Technology, University of Bradford, Bradford, West Yorkshire, BD7 1DP, UK*
[c]*Department of Engineering, University of Cambridge, Trumpington Street, Cambridge CB2 1PX, UK*
vsv20@cam.ac.uk

Abstract

The automated construction of physical laws from raw experimental measurements poses a great challenge in modern modelling and remains an open question. The work here presents a novel generalized Mixed-Integer Nonlinear Programming (MINLP) approach, which constitutes a rigorous theoretical formulation that best fits the given data. The proposal is based on the use of generic representation of analytical functions as binary evaluation trees which are Directed Acyclic Graphs (DAG) utilized to allow the construction of a superstructure out of which the optimal fitting model can be identified by solving the resulting (non-convex) MINLP problems. The trees are constructed in a way that their nodes are comprised of a linear combination of basic atomic functions, either arithmetic or unary, weighted by binary decision variables. Both single-input single-output (SISO) and multiple-input multiple-output systems are considered, as well as more complex models comprised of differential equations or even described by series summation of algebraic terms. The aim and contribution proposed methodology in this paper is to present the most general theoretical formulatioon of how models are constructed for systems quantification via analytical function forms, irrespective of the source of data. The constructed formulation is shown to contain all formulations thus far presented in the open literature, comprising a starting point either for direct fitting or for the derivation of simplified approaches.

Keywords: Directed Acyclic Graph; Function Evaluation Tree; Model Automated Construction; Mixed-Integer Nonlinear Programming;

1. Introduction

Mathematical modelling constitutes a fundamental aspect of all applied sciences and engineering, and is usually based in theoretical knowledge of underlying mechanisms to be effected. The automation of such model construction in analytical form is a highly-desirable aim, which to this date has not had a general theory behind it. In the past few decades, different approaches, such as Kriging (Oliver and Webster, 1990), Gaussian Processes (Williams and Barber, 1998), Artificial Neural Networks (Nandi and Azzouz, 1998) and Sub-model regression (Gatu et al., 2007) have been developed towards this goal. Recently, a paper claiming a similar approach has appeared in the open literature (Schmidt and Lipson, 2009). The approach in the latter article follows the lines of a customized construction technique, presented more along the context of algorithm design and relying heavily on heuristic optimization procedures ("Genetic Algorithms"). While an

interesting approach, it lacks the mathematically rigorous understanding presented in this paper, which generalizes completely the approach by setting it as a proper Mixed-Integer Mathematical Programming problem. Recently, Cozad et al. (2014) proposed automated learning of algebraic models for optimization (ALAMO) by summing algebraic terms to fit the models.

Unlike other approaches, our proposal is based on the use of a generic representation of analytical functions as binary evaluation trees (Directed Acyclic Graphs, DAG) . The trees are constructed in such a way that their nodes are comprised of a linear combination of basic atomic functions, either arithmetic or unary, which are weighted by binary decision variables. Allowing only one of the nodal binary variables to attain the value of one forces the construction of a standard representation of any analytical function. It is theoretically demonstrated that as the tree expands, it is possible to encapsulate any analytical form a noiseless function may have, and given enough measurements to establish a unique fitting. For noisy data, as for example with measurements from experiments, suitable tolerance constraints can be included to ensure adequacy and reliability of the models extracted. The approach is generalized to capture the cases of dynamic models, *e.g.* models described by ODE right hand sides, as well as models that are described by series summations of terms. The premise to guarantee the solutions obtained is that deterministic global optimization methods be used, otherwise with local optimization techniques it is only possible to guarantee a sufficiently good fitting but not the absolutely best functional structure, nor the best model parameter values, corresponding to the given data.

2. Analytical function representation as binary trees

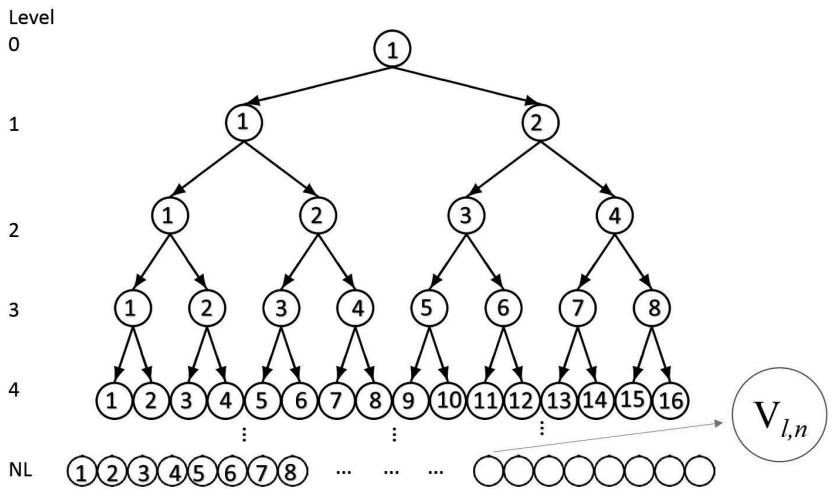

Figure 1: DAG tree representation of analytical functions

The Directed Acyclic Graph (DAG) description of analytical algebraic functions will be used throughout this work. A *superstructure* balanced binary tree is proposed to be constructed for the representation of any function. The superstructure is a term implying the inclusion of more elements in a decision making process than a final solution will contain, and their presence is to be decided automatically via the optimization process. In this way, all the possible combinations allowed in a design can be considered and the optimal one to be identified. The structure and number of nodes in a 4-level balanced binary tree is shown in Figure 1.The formulation presented

in the next sections uses the following index sets are: (a) number of layers in the superstructure tree: $l \in \{0,1,2,\ldots,NL\}$, (b) bivariate and univariate functions $f_k(\cdot)$ considered: $k = \{1,\ldots,NF\}$, and (c) the top layer of the tree is layer 0 which contains exactly 1 node (the root of the function tree). All layers have n_l nodes given by $n_l = 2^l, \quad l = 0,1,2,\ldots,NL$.

2.1. Bivariate operations

The bivariate operations correspond to arithmetic operators and are summarized in Table 1 below. These are sufficient for the description of a DAG representing the evaluation of an analytical function by assigning appropriately what the left offspring, $V_{l+1,2n-1}$, and right offspring, $V_{l+1,2n}$, are for each node, respectively. It is noted that the division and power operations have to be safeguarded against evaluations outside their domain of definition. It is also noted that the first to operations are simply assignment of either the left or right node value to the current node, thus bypassing this node without any function description.

Table 1: Arithmetic bivariate tree operations

#	$f_k(\cdot)$	#	$f_k(\cdot)$
1	$V_{l+1,2n-1}$	5	$V_{l+1,2n-1} \times V_{l+1,2n}$
2	$V_{l+1,2n}$	6	$V_{l+1,2n-1} \div V_{l+1,2n}$
3	$V_{l+1,2n-1} + V_{l+1,2n}$	7	$V_{l+1,2n-1} \hat{} V_{l+1,2n}$
4	$V_{l+1,2n-1} - V_{l+1,2n}$		

The nodal value can be represented by the inclusion of bivariate operations weighted by binary parameters, by the combination of both the left offspring $V_{l+1,2n-1}$ and right offspring $V_{l+1,2n}$ as input:

$$V_{l,n} = \sum_{k=1}^{NF} \delta_{l,n,k} f_k(V_{l+1,2n-1}, V_{l+1,2n}) \tag{1}$$

This equation will be the same as the one presented generally in the next section, with the latter being the more general description.

2.2. Univariate functions

Each node may also carry a function within it and its choice again is to be made by a suitable binary decision variable to be chosen optimally. Functions $f_k(\cdot)$ can be: $\log(\cdot)$, $\exp(\cdot)$, $\sin(\cdot)$, $\cos(\cdot)$, $\tan(\cdot)$, $\sqrt{(\cdot)}$, *etc.* It is noted that if these are to be included they have to be safeguarded against evaluations outside their domain of definition, if applicable. The nodal value can be expanded thus by the inclusion of univariate function operations weighted by additional binary decision variables, by considering only the right offspring nodal value $V_{l+1,2n}$ as input:

$$V_{l,n} = \sum_{k=1}^{NF} \delta_{l,n,k} f_k(V_{l+1,2n-1}, V_{l+1,2n}) \tag{2a}$$

$$\sum_{k=1}^{NF} \delta_{l,n,k} = 1, \quad \delta_{l,n,k} \in \{0,1\} \tag{2b}$$

$$k = 1,2,\ldots,NF; \quad n = 1,2,\ldots,2^l; \quad l = 0,1,2,\ldots,NL-1 \tag{2c}$$

2.3. Enriching the basis set of nodal functions

It is clear by the way the nodal value is represented that it comprises a linear summation of either univariate or bivariate elementary operations or functions. Unlike other approaches which use extensive sets of functions as a basis, the proposed approach requires comparatively very few terms per node. To increase the applicability and compactness of the tree representations it is thus advantageous and highly desirable to include a richer set of functions, particularly if the approach is to be used to fit or predict physical laws from data using standard forms. The extended functions may be either available in the computer system (or programming platform) used, or they will have to be input as direct approximations in the nodal value constructs.

3. Optimization problem

3.1. Formulation of the fitting optimization problem

The presented nodal expressions so far allow the construction of a general binary tree representation of any analytical function, and for any number of variables via an appropriate Mathematical Programming (MP) formulation. The fitting problem results in a Mixed-Integer Nonlinear Programing problem (MINLP) which will be hard to solve in general, being generally expected to be non-convex. Nonetheless, it is clear that the formulation presented in this work is the most rigorous representation of any analytical functional form.

Node per level equations:

The equations defining how the information (values) propagate from one level to the next is presented here going downwards in the tree from level 0 to level $NL-1$. Level NL, the final level in the tree, is handled in a different way as explained later. Some reordering and restructuring of the node value parameters is carried out to have uniformity in the presentation.

Level 0 to NL − 1 equations:

$$\begin{aligned} V_{l,n} \;=\;& \delta_{l,n,1}V_{l+1,2n-1}+\delta_{l,n,2}V_{l+1,2n}+\delta_{l,n,3}(V_{l+1,2n-1}+V_{l+1,2n})+\delta_{l,n,4}(V_{l+1,2n-1}-V_{l+1,2n}) \\ & +\delta_{l,n,5}V_{l+1,2n-1}\cdot V_{l+1,2n}+\delta_{l,n,6}\frac{V_{l+1,2n-1}}{V_{l+1,2n}}+\delta_{l,n,7}\left(V_{l+1,2n-1}\right)^{V_{l+1,2n}} \\ & +\ldots+\delta_{l,n,NF}f_{NF}(V_{l+1,2n-1},V_{l+1,2n}) \qquad (3a) \\ & \sum_{k=1}^{NF}\delta_{l,n,k}=1;\quad \delta_{l,n,k}\in\{0,1\} \qquad (3b) \\ & k=1,2,\ldots,NF;\quad n=1,2,\ldots,2^l;\quad l=0,1,2,\ldots,NL-1; \qquad (3c) \end{aligned}$$

There is a total of $2^{NL}-1$ nonlinear constraints and $2^{NL}-1$ linear constraints introduced by the equations above, and there are $NF\times(2^{NL}-1)$ binary variables in total.

Level *NL* equations

The assignment of values to the last layer of the binary tree which is comprised only of leaf nodes follows a special logic. This assigns values from the variable set of the system being modelled as well as a tunable parameter set with parameters $\boldsymbol{p}=[p_j]$, $j=1,2,\ldots,NP$, which are continuous decision variables. We assume that we have input variables $\boldsymbol{x}=[x_i]$, $i=1,2,\ldots,NX$ in the system. For a single realization (measurement point) of these variables we wish to assign them via an optimization constraint formulation that will automatically allocate them in all possible ways to the leaves of the binary tree.

$$V_{NL,n} = \sum_{i=1}^{NX} \zeta_{n,i} x_i + \sum_{j=1}^{NP} \xi_{n,j} p_j \tag{3d}$$

$$\sum_{i=1}^{NX} \zeta_{n,i} + \sum_{j=1}^{NP} \xi_{n,j} \leq 1 \tag{3e}$$

$$\zeta_{n,i} \in \{0,1\}; \quad \xi_{n,j} \in \{0,1\}; \quad p_j^L \leq p_j \leq p_j^U \tag{3f}$$

$$n = 0,1,2,\ldots,2^{NL}; \quad i = 1,2,\ldots,NX; \quad j = 1,2,\ldots,NP; \tag{3g}$$

The constraints are chosen as above, as the purpose of parameters $\zeta_{n,i}$ and $\xi_{n,j}$ is to include or cancel the presence of a single associated variable x_i or parameter p_j in a leaf of the tree, while the continuous parameters p_j are bounded below and above by fixed bounds p_j^L and p_j^U, respectively. This introduces two 2^{NL} vectors of decision variables $\zeta_{n,i}$ and $\xi_{n,j}$ respectively. The above equations introduce 2^{NL} linear constraints and 2^{NL} linear constraints. It is noted that the constraints above allow the inclusion of either a parameter or a variable at the leaf nodes.

3.2. Objective function choice

The choice of objective function beyond the simple direct fitting using least squares, is desired to be such that it minimizes the number of nonzero coefficients in the resulting evaluation tree formulation. This is in accord to the idea of the automatic derivation/identification of "physical laws" directly from data. A physical law is in effect a data-compression method, in that with a very limited number of parameters and initial conditions one is able to predict entire series of data.

Based on the idea of compression of information, and that this is in effect what a good model or "physical law" is intended to do, then it is natural that one should consider information-theoretic criteria to measure how good a model is in terms of not only fitting the data, but also in compressing information. This is simplistically done by LASSO-like approaches (Tibshirani, 2011), which aim to minimize also the number of nonzero parameters used (or in terms of linear regression, to minimize the number of regressors). Information theoretic criteria for fitting are numerous and their diversity is a result of the philosophy of how information content is measured and encapsulated mathematically. Generally, the underlying principle in all these is the Minimum Description Length (MDL) for example string length when compressing data, or algorithm steps required to compute a given calculation task, *etc.* (Foster and Stine, 1999). Some of these criteria, like the Akaike Information Criteria (Hurvich and Tsai, 1993) and Bayesian Information Criteria (Burnham and Anderson, 2004), when applied to data regression contain measures of the variance of fitting the full model. This might be acceptable in the case that there is always more data than parameters, however one has to be careful with such measures of information content in the case where the potential number of regressors is much larger (*e.g.* basis functions used in linear regression) than the data available. These criteria are very much more useful in the sense that they do not require a multiobjective approach nor do they require penalty schemes. However, they are highly nonlinear and potentially nonconvex functions which would make direct minimization even harder.

4. Conclusions and future directions

The proposed theory in this work outlines a generic representation of any analytical function form constructed by DAG, which can be used for model identification within the scheme of minimizing the number of nonzero parameters, and hence general nonlinear terms that can arise as operations in the definition of a mathematical model. The formulation presented in this paper can be seen

to be the most general one that captures and explains all previous attempts/formulations and approaches for this problem. It is thus therefore worth exploring the proposed methodology as well as committing effort to make it work – even if for limited applications to begin with. The major task is that the problem as formulated is a global optimization MINLP in order to guarantee the solutions obtained (best possible model construction and fitting to available data). Future work will be the solution of the resulting MINLP problem to global optimality, and consideration of relaxations. For impact, one should explore innovative and surprising applications in areas that would give credence to our proposed methodology and theory. The applications of this approach are envisaged to have significant impact in many diverse areas of interest: aside from physicochemical and biological systems, where for example one would be seeking to discover new interactions as well as their kinetic functional forms, it is possible to use this methodology in systems whose nature is not mechanistic, such as social and financial systems, and offer quantification via novel model construction. We believe that our approach to construct phenomenological models, even for partially defined or understood systems, will lead to a significant advancement both in modelling approaches as well as revealing interactions that otherwise could not be discovered by heuristic trial-and-error, or mere observation of these systems. Relevant applications will demonstrate the potential of the proposed approach.

5. Acknowledgment

Author Y. Wang would like to thank family members very much for their financial support.

References

Burnham, K., Anderson, D., 2004. Multimodel inference: Understanding aic and bic in model selection. Sociological Methods and Research 33 (2), 261–304.

Cozad, A., Sahinidis, N., Miller, D., 2014. Learning surrogate models for simulation-based optimization. AIChE Journal 60 (6), 2211–2227.

Foster, D., Stine, R., 1999. Local asymptotic coding and the minimum description length. IEEE Transactions on Information Theory 45 (4), 1289–1293.

Gatu, C., Yanev, P., Kontoghiorghes, E., 2007. A graph approach to generate all possible regression submodels. Computational Statistics and Data Analysis 52 (2), 799–815.

Hurvich, C. M., Tsai, C.-L., 1993. A corrected akaike information criterion for vector autoregressive model selection. Journal of Time Series Analysis 14 (3), 271–279.

Nandi, A. K., Azzouz, E. E., 1998. Algorithms for automatic modulation recognition of communication signals. IEEE Transactions on Communications 46 (4), 431–436.

Oliver, M. A., Webster, R., 1990. Kriging: a method of interpolation for geographical information systems. International Journal of Geographical Information Systems 4 (3), 313–332.

Schmidt, M., Lipson, H., 2009. Distilling free-form natural laws from experimental data. Science 324 (5923), 81–85.

Tibshirani, R., 2011. Regression shrinkage and selection via the lasso: A retrospective. Journal of the Royal Statistical Society. Series B: Statistical Methodology 73 (3), 273–282.

Williams, C. K., Barber, D., 1998. Bayesian classification with gaussian processes. IEEE Transactions on Pattern Analysis and Machine Intelligence 20 (12), 1342–1351.

Krist V. Gernaey, Jakob K. Huusom and Rafiqul Gani (Eds.), 12th International Symposium on Process Systems Engineering and 25th European Symposium on Computer Aided Process Engineering.
31 May – 4 June 2015, Copenhagen, Denmark

Dynamic Simulation of a Batch Aqueous Two-Phase Extraction Process for α-Amylase

Nehal Patel,[a,b] Daniel Bracewell,[a] Eva Sorensen[b]

[a]*Department of Biochemical Engineering, UCL, London, WC1E 6BT, United Kingdom*
[b]*Department of Chemical Engineering, UCL, London, WC1E 7JE, United Kingdom*

Abstract

Aqueous two-phase systems (ATPSs) are a promising downstream separation technology in the production of biopharmaceuticals. Understanding the fundamentals of protein separation is challenging due to the large experimental space that must be explored. To tackle this, experimental liquid-liquid equilibria and protein partitioning data is combined with a process model to explore the dynamic operation of a semi-batch aqueous two-phase extraction process for the separation of enzyme α-amylase in a PEG 4000 – phosphate ATPS containing NaCl. The semi-batch system can be readily implemented into existing biopharmaceutical production processes. Interaction parameters for chemical potential equations are estimated from tie-line data. Running multiple extraction cycles, where the bottom phase is replaced with fresh phosphate rich, protein free material, increases the purity of α-amylase while reducing the yield. The influence of the phase ratio on α-amylase purity and yield is also investigated.

Keywords: aqueous two-phase extraction, modelling, amylase, semi-batch

1. Introduction

The market for therapeutic proteins is currently increasing at a remarkable pace. In many cases, therapeutic proteins, such as monoclonal antibodies, must be administered in relatively large dosages. This large dosage requirement (> 100 mg dose^{-1}) (Shire et al., 2004), coupled with the high demand for these drugs, has resulted in an increased pressure on pharmaceutical companies to deliver high quality drugs at sufficient quantities. As a result, there has been an increasing amount of research & development (R&D) aimed at improving upstream efficiency, which has resulted in increased cell titres during the cell culture/fermentation stage of protein production. To date, improvements in upstream technology have, however, not been matched by improvements in downstream technology. Consequently, expensive chromatography columns must be scaled accordingly to cope with the increasing amounts of material generated, which is proving to be a process bottleneck due to the limitations in their capacity, but also their cost, and has highlighted the need for a re-evaluation of downstream separation methodologies.

Aqueous two-phase extraction has been shown to be a promising alternative downstream separation technology for biopharmaceutical separations (Rito-Palomares, 2004). Its method of action is the differential partitioning of proteins and other components between two established aqueous phases. Understanding the fundamental characteristics of protein separation in ATPSs is of paramount importance as the process design is to a large extent determined by the partitioning of material between the two phases of the system. Factors such as charge, hydrophobicity, solute affinity, polymer molecular weight and concentration, all play an important role in partitioning in

aqueous two phase extractions (Asenjo and Andrews, 2011). In addition, there are many different possible process configurations to explore such as batch, co-current and counter-current operations. Exploring all of the above factors and configurations manually is very resource intensive. To date, process modelling of ATPSs has been limited and focuses on continuous-operations (Mistry et al., 1996, Ahmed Samatou, 2012, Ahmed Samatou et al., 2007).To tackle this issue, we present an approach that integrates already available experimental liquid-liquid equilibria data with dynamic process models that describe aqueous two-phase extractions. The approach permits a fast, yet systematic, investigation of both process design and operation. In this work, the approach is demonstrated by considering a semi-batch extraction system operated in cycles. The semi-batch system can be readily implemented into existing biopharmaceutical production facilities.

2. Process modelling framework

2.1. Liquid-liquid equilibria modelling

There are many thermodynamic models that describe the liquid-liquid equilibria of ATPSs (Cabezas, 1996). In this work, a simple thermodynamic model based on osmotic virial expansions is used to calculate the chemical potential of the polymer (component 1), salt (component 2) and water (component 3) in terms of molality of polymer and salt (Edmond and Ogston, 1968, Zafarani-Moattar and Sadeghi, 2001):

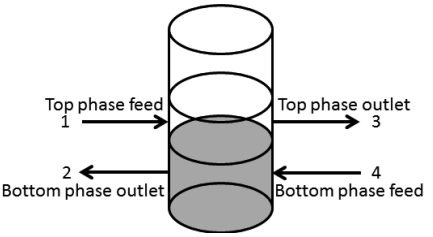

Figure 1: A single separation stage

$$\mu_1 = \mu_1^0 + RT(\ln(m_1) + \beta_{1,1}m_1 + \beta_{1,2}m_2) \quad (1)$$

$$\mu_2 = \mu_2^0 + RT(\ln(m_2) + \beta_{2,2}m_2 + \beta_{1,2}m_1) \quad (2)$$

$$\mu_3 = \mu_3^0 - RTV_3(m_1 + m_2 + \frac{\beta_{1,1}}{2}m_1^2 + \frac{\beta_{2,2}}{2}m_2^2 + \beta_{1,2}m_1m_2) \quad (3)$$

At equilibrium, the chemical potential of each component in each phase is the same:

$$\mu_i^{Top} = \mu_i^{Bottom} \qquad for\ i = 1 \ldots 3 \quad (4)$$

2.2. Estimation of interaction parameters

Interaction parameters for Eq.(1)-(3) were estimated using experimental tie-line data for a polyethylene glycol (PEG) 4,000 – phosphate ATPS at different NaCl concentrations obtained from Mistry et al. (1996).

2.3. Partition coefficient correlations

In this work, the partition coefficient of α-amylase and impurities was empirically correlated to NaCl mass fraction using experimental data obtained from Mistry et al. (1996), and the correlations obtained are similar to those already presented by the same authors:

$$ln(K_{alpha-amylase}) = 0.04874(100 \times x_{NaCl})^2 + 0.3043 \times 100 \times x_{NaCl} - 2.731 \quad (5)$$

$$ln(K_{Impurities}) = 0.01412 \times 100 \times x_{NaCl} - 0.01341 \quad (6)$$

2.4. *Process model*

A simple first principles tank model with two inlets and two outlets was used to model a batch process, i.e. a single stage (See Figure 1). Stages can also be linked together to

form a counter-current train. The relative amount of top and bottom phase is determined by integrating the equilibrium equations with the following tank model describing protein partitioning in a polymer-salt ATPS:

$$\frac{dM_p}{dt} = F_{1V}C_{1,p} - F_{2V}C_{2,p} - F_{3V}C_{3,p} + F_{4V}C_{4,p} \qquad for\ p = 1 \dots \#\ proteins \tag{7}$$

$$M_p = C_{Top,p}V_{Top} + C_{Bottom,p}V_{Bottom} \qquad for\ p = 1 \dots \#\ proteins \tag{8}$$

$$C_{Top,p} = K_p C_{Bottom,p} \qquad for\ p = 1 \dots \#\ proteins \tag{9}$$

$$C_{3,p} = C_{Top,p} \qquad for\ p = 1 \dots \#\ proteins \tag{10}$$

$$C_{2,p} = C_{Bottom,p} \qquad for\ p = 1 \dots \#\ proteins \tag{11}$$

$$M_p = initial\ value \qquad for\ p = 1 \dots \#\ proteins\ at\ t = 0 \tag{12}$$

The following mass balances were conducted for phase forming components (polymer (component 1), salt (component 2) and water (component 3)):

$$\frac{dM_i}{dt} = F_1 x_{1,i} - F_2 x_{2,i} - F_3 x_{3,i} + F_4 x_{4,i} \qquad for\ i = 1 \dots 3 \tag{13}$$

$$M_{i,O} = M_{i,Top} + M_{i,Bottom} \qquad for\ i = 1 \dots 3 \tag{14}$$

$$x_{3,i} = x_{Top,i} \qquad for\ i = 1 \dots 3 \tag{15}$$

$$x_{2,i} = x_{Bottom,i} \qquad for\ i = 1 \dots 3 \tag{16}$$

$$x_{Top,i} \times \sum M_{Top,i} = M_{Top,i} \qquad for\ i = 1 \dots 3 \tag{17}$$

$$x_{Bottom,i} \times \sum M_{Bottom,i} = M_{Bottom,i} \qquad for\ i = 1 \dots 3 \tag{18}$$

$$x_{O,i} \times \sum M_{O,i} = M_{O,i} \qquad for\ i = 1 \dots 3 \tag{19}$$

$$M_i = initial\ value \qquad for\ i = 1 \dots 3\ at\ t = 0 \tag{20}$$

It was assumed that after mixing and settling the composition of top and bottom phases is equal to the outlet concentrations as shown in equations Eq.(10), (11), (15) and (16).

2.5. Software

All process simulations and parameter estimation tasks are conducted using gPROMS ModelBuilder 3.5.3 (Process Systems Enterprise, 2014). Tie-line data was obtained by digitising phase diagrams in OriginPro 8.6 (OriginLab, Northampton, MA).

3. Interaction parameter estimation

Using gPROMS, the model parameters were estimated based on published experimental data, taking into account uncertainties in experimental measurements (see Table 1). As actual experimental error was unknown, a conservative standard deviation of 0.02 was assumed for experimental phase composition data obtained from Mistry et al. (1996) allowing for standard deviations in parameter values to be obtained.

Table 1: Estimated interaction parameters for Eq.(1), (2) and (3).

$\beta_{i,j}\ (kg\ mole^{-3})$	PEG 4,000		Phosphate	
	Value	Standard Deviation	Value	Standard Deviation
PEG 4,000	-21.131	14.35	6.2	2.343
Phosphate	-		-1.327	0.1734

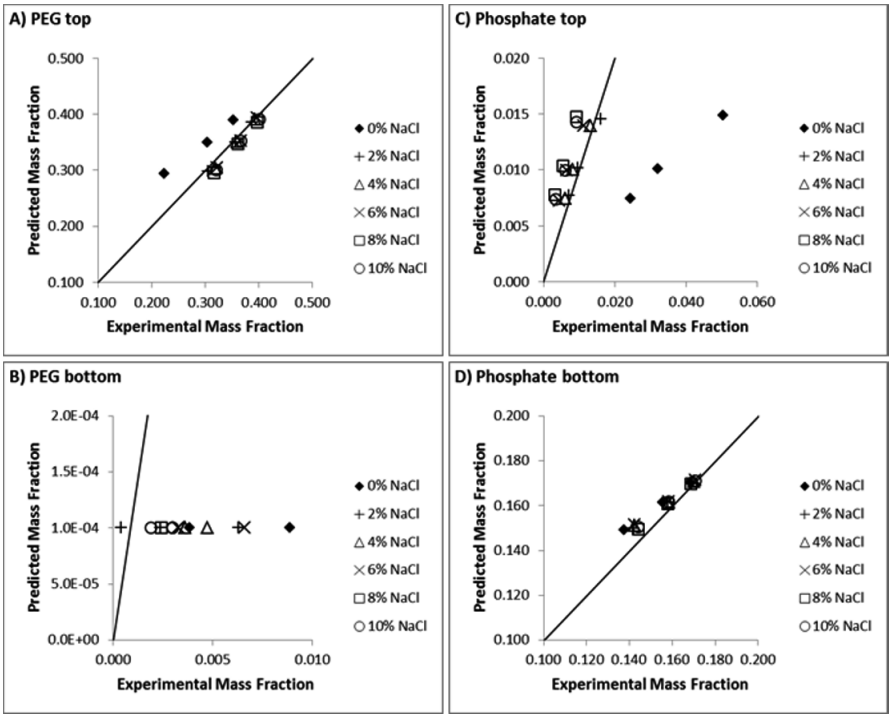

Figure 2: Parity plots comparing model predictions (y-axis) with experimental data (x-axis) from Mistry et al. (1996).

The chemical potential equations (Eq. (1), (2) and (3)) used do not take into account the presence of NaCl which influences phase equilibria. The presence of 2 wt% NaCl shifts the phase equilibria significantly; this is most noticeable in parity plots A and C in Figure 2.

For PEG 4,000 – phosphate ATPSs containing NaCl concentrations above 2 wt%, the phase equilibria predictions are sufficient for process simulations as the experimental phase diagrams for these systems are very similar. The PEG 4,000 mass fraction in the bottom phase is usually very small, therefore a constant mass fraction of 0.001 was assumed in the simulations, this also increased the robustness of the simulations. The presence of NaCl can be taken into account by extending the chemical potential equations to a 4 component system; however, this would require more parameters to be estimated.

4. Process simulations

Dynamic batch simulations were conducted as most biopharmaceutical operations are either batch or semi-batch. The streams profiles are shown in Table 2 and are based on Figure 1. The influence of the phase ratio (mass of top phase to mass of bottom phase) on yield and purity was also investigated by varying the mass flow rate of stream 4 during initial loading.

Streams 1 and 4 feed the PEG rich top phase and phosphate rich bottom phase, respectively. The following operating protocol was used (streams numbers correspond to Figure 1):

Table 2: Stream conditions.

Stream #	Operating flow rate (kg s^{-1})	Amylase concentration (kg m^{-3})	Impurity concentration (kg m^{-3})	PEG (wt%)	Phosphate (wt%)
1	1.00	1.00	1.00	57.37	0.08
2	1.00	N/A	N/A	0.10	22.94
3	N/A	N/A	N/A	N/A	N/A
4	1 to 4.00	N/A	N/A	N/A	N/A

1. Streams 1 & 4 are turned on until the mass in the tank is greater than 300 kg. (Stream 1 contains the protein).
2. Allow 10 minutes for mixing and 15 minutes for settling. (Mixing and settling is not modelled).
3. Drain the bottom phase (containing protein) via stream 2 until the mass in the bottom phase is less than 5 kg.
4. Fill with fresh phosphate rich bottom phase via stream 4 until the mass in the tank is greater than 300 kg. Go to step 2.
5. Repeat steps 2 to 4 for multiple extraction cycles.

The steps in Figure 3 at 30 minute intervals correspond to the extraction cycles outlined in the operating protocol.

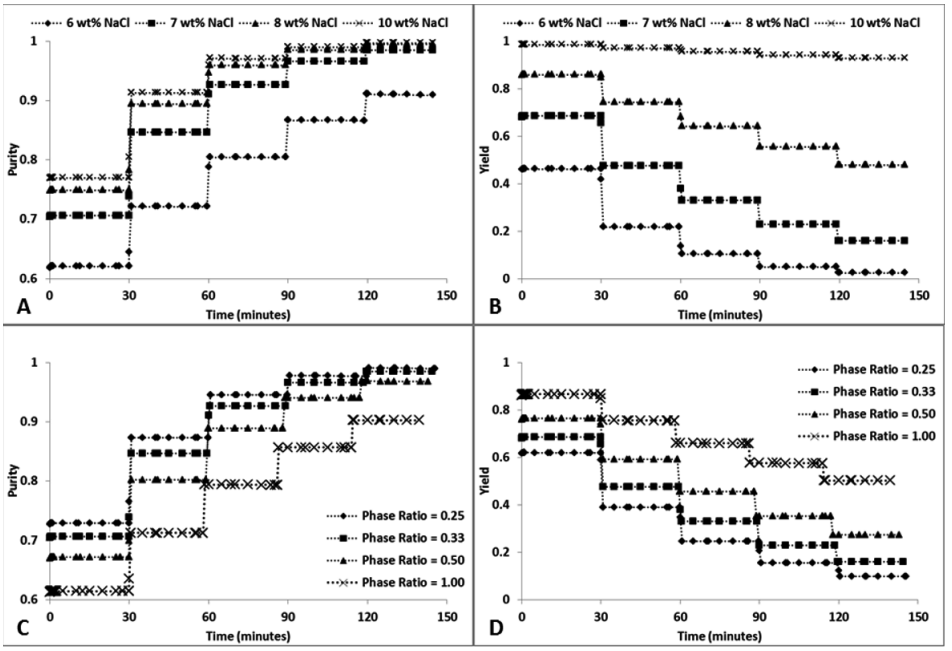

Figure 3: α-amylase yield and purity plots. A & B) influence of NaCl concentration (phase ratio = 0.33). C & D) influence of phase ratio (7 wt% NaCl).

Increasing the number of extraction cycles results in higher purity, however, the yield of α-amylase is reduced. Figure 3 shows that increasing the NaCl concentration from 6 wt% to 10 wt% will cause the purity and yield to increase. This is because the partition coefficient of α-amylase is increased almost 90-fold while the partition coefficient of the impurities is relatively constant. Operating using 10 wt% NaCl would see a purity and yield of 0.91 and 0.97 after two extraction cycles, respectively. At low NaCl

concentrations, the α-amylase partition coefficient is less than 1, meaning that the operating protocol could be adapted to replace the top phase instead of the bottom phase.

Figure 3 shows how the phase ratio can be manipulated to alter purity and yield. A smaller phase ratio (C & D) results in higher purity because, relative to α-amylase, more impurities partition into the bottom phase. Unfortunately, the amount of α-amylase in the bottom phase is also increased when the phase ratio is decreased, hence resulting in a lower yield.

5. Conclusions

Interaction parameters for chemical potential equations were estimated from experimental phase equilibria data. Phase equilibria model predictions were found to be sufficient for ATPSs containing more than 2 wt% NaCl, although future work would include extending phase equilibria models to take into account the presence of electrolytes. Phase equilibria models were then integrated with first principle mass balance models to describe the dynamic operation of a semi-batch aqueous two-phase extraction process to purify enzyme α-amylase. Multiple extraction cycles improved the purity of α-amylase but reduced yield. Although 5 extraction cycles were simulated, at a NaCl concentration of 10 wt%, a purity and yield of 0.91 and 0.97, respectively, was achieved with only two extraction cycles. It was also found that changing the phase ratio greatly influenced purity and yield. A lower phase ratio, corresponding to a larger bottom phase, resulted in a higher purity, but a lower yield.

6. Nomenclature

M_p	Mass of protein p in tank (kg)	$C_{k,p}$	Conc. of protein p in stream k (kg m^{-3})
$x_{k,i}$	Mass fraction of component i in steam k (-)	F_{kV}	Volumetric flow rate of stream k (m^3 s^{-1})
$\beta_{i,j}$	Interaction parameter between components i and j, respectively (kg $mole^{-3}$)	V_3	Molar volume of water (m^3 $mole^{-1}$)
μ_i	Chem. potential of component i (J $mole^{-1}$)	m_i	Molality of component i (mole kg_{water}^{-1})
T	Temperature (K)	K_p	Partition coefficient of protein p (-)
F_k	Mass flow rate of stream k (m^3 s^{-1})	$M_{i,O}$	Total mass of component i in tank (kg)
$M_{i,}$	Mass of component i in top or bottom phase (kg)	$x_{O,i}$	Overall mass fraction of component i in tank (-)

References

Ahmed Samatou, J. 2012. Modelling and Simulation of Antibody Purification by Aqueous Two-Phase Extraction. Technischen Universität Dortmund.

Ahmed Samatou, J., Engbert Wentink, A., Alexandra J Rosa, P., Margarida Azevedo, A., Raquel Aires-Barros, M., Bäcker, W. & Górak, A. 2007. Computer Aided Chemical Engineering, 24, 935-940.

Asenjo, J. A. & Andrews, B. A. 2011. Journal of Chromatography A, 1218, 8826-8835.
Cabezas, H. 1996. Journal of Chromatography B-Biomedical Applications, 680, 3-30.

Edmond, E. & Ogston, A. 1968. Biochem J, 109, 569-576.

Mistry, S. L., Kaul, A., Merchuk, J. C. & Asenjo, J. A. 1996. Journal of Chromatography A, 741, 151-163.

Process Systems Enterprise 2014. gPROMS manual.

Rito-Palomares, M. 2004. Journal of Chromatography B-Analytical Technologies in the Biomedical and Life Sciences, 807, 3-11.

Shire, S. J., Shahrokh, Z. & Liu, J. 2004. Journal of Pharmaceutical Sciences, 93, 1390-1402.
Zafarani-Moattar, M. T. & Sadeghi, R. 2001. Fluid Phase Equilibria, 181, 95-112.

Krist V. Gernaey, Jakob K. Huusom and Rafiqul Gani (Eds.), 12th International Symposium on Process Systems Engineering and 25th European Symposium on Computer Aided Process Engineering.
31 May – 4 June 2015, Copenhagen, Denmark

A framework for hybrid multi-parametric model-predictive control with application to intravenous anaesthesia

Ioana Naşcu[a], Richard Oberdieck[a], Efstratios N. Pistikopoulos[a,b*]

[a]*Dept. of Chemical Engineering, Centre for Process Systems Engineering (CPSE), Imperial College London SW7 2AZ, Lodnon, U.K*
[b]*Artie McFerrin Department of Chemical Engineering, Texas A&M, College Station TX*
*e.pistikopoulos@imperial.ac.uk/stratos@tamu.edu

Abstract

In this paper we present a framework for the development of hybrid multi-parametric model predictive controllers applied to intravenous anaesthesia. A step-by-step procedure is described featuring a piece-wise model for anaesthesia describing the induction and maintenance phase, a recently developed multi-parametric mixed-integer quadratic programming solver and a novel hybrid control strategy tested for a set of 12 patients.

Keywords: multi-parametric/explicit model predictive control, multi-parametric mixed-integer quadratic programming, hybrid systems

1. Introduction

In most biomedical systems the mathematical model contains pharmacodynamic models which usually include strong nonlinearities. In particular the Hill curve representation is often used as an approximation for the description of such nonlinearities. This is a common feature that can be also found in other branches of science (Demetriou, 2012), economy (Porter, 1985) and engineering (Lindley, 1985, Gonzalez and Wintz, 1987). For the case of infusion of anaesthetic agents, the nonlinear Hill curve approximation has been used in both volatile (Krieger et al., 2014) and intravenous (Nascu et al., 2012, Nascu et al., 2014) anaesthesia and it describes the relation between the concentration of the drug and the effect observed on the patient.

In this paper we first generate a piece-wise linearization of the Hill curve. The main advantage of this procedure is that the parameter space is linearized and that the uncertainty in some key parameters of the Hill curve is compensated for. As a result of the linearization, the anaesthesia model is described by a piece-wise affine system, the control of which results in a hybrid model predictive control (hMPC) problem (Bemporad and Morari, 1999) and thus a mixed-integer quadratic programming (MIQP) problem formulation. However, the online implementation of hMPC involves the online solution of the MIQP problem, which introduces a high computational burden. Thus in this paper, we present a step-by-step procedure for the development of explicit hMPC controllers via a multi-parametric MIQP algorithm. This development is part of PAROC, a comprehensive framework and software solution for the general design, operational optimization and control of process systems (Pistikopoulos et al., 2014). The framework includes a high-fidelity model of the system which is approximated using discrete time models in state space form via model order reduction techniques.

The reduced model is then used to formulate an optimization problem subject to the state space model and constraints. The resulting multi-parametric programming problem is solved with state-of-the-art techniques. In the last step, the solution is validated against the original high fidelity model, thus closing the loop.

2. Framework Description

2.1 Intravenous Anaesthesia Mathematical Model

For the automatic regulation of depth of anaesthesia (DOA) the anaesthetic agent, in our case Propofol, is the input and the Bispectral Index (BIS) the output of the system. Because of its pharmacological profile, Propofol is applicable for both induction and maintenance of hypnosis during anaesthesia and intensive care sedation.(Ionescu et al.). The BIS is a signal that is derived from the electro-encephalogram (EEG) used to assess the level of consciousness during anaesthesia. A BIS value of 0 equals EEG silence, while a BIS value of 100 is the expected value of a fully awake and conscious adult, 60-70 and 40-60 range represents light and moderate hypnotic condition, respectively. The target value during surgery is 50, providing a gap between 40 and 60 to guarantee adequate sedation (Bailey and Haddad, 2005, Absalom et al., 2011).

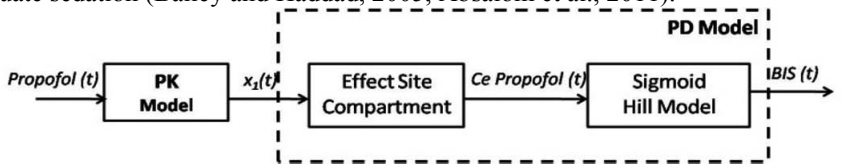

Figure. 1. Schematic representation of the NONLINEAR SISO patient model

In Figure 1 the pharmacokinetic (PK) – pharmacodynamic (PD) blocks denote compartmental models used to represent the distribution of drugs in the body, i.e. the mass balance. The pharmacokinetic model represents the relation between the drug administration and the drug concentration in the body, whereas the pharmacodynamic model represents the relation between the concentration of the drug and the effect.
The PK-PD models most commonly used for Propofol are the 4th order compartmental model described by (Schnider et al., 1999) and (Minto et al., 1997), respectively and are presented in Table 1.

Table 1. Mathematical model for intravenous anaesthesia

Intravenous Anaesthesia	
PK model	$\dot{x}_1(t) = -[k_{10} + k_{12} + k_{13}] \cdot x_1(t) + k_{21} \cdot x_2(t) + k_{31} \cdot x_3(t) + u(t)/V_1$ $\dot{x}_2(t) = k_{12} \cdot x_1(t) - k_{21} \cdot x_2(t)$ $\dot{x}_3(t) = k_{13} \cdot x_1(t) - k_{31} \cdot x_3(t)$ $\dot{x}_e(t) = -k_{e0} \cdot x_e(t) + k_{1e} \cdot x_1(t)$
Effect site compartment	$\dot{C}_e(t) = k_{e0} \cdot (C_e(t) - C_p(t))$
PD model (Hill curve)	$BIS(t) = E_0 - E_{\max} \cdot \frac{C_e(t)^\gamma}{C_e(t)^\gamma + EC_{50}^\gamma}$

In the PK model x_1 represents the drug concentration in the central compartment [mg/l]. The peripheral compartments 2 (muscle) and 3 (fat) model the drug exchange of the blood with well and poorly diffused body tissues. The concentrations of drug in the fast and slow equilibrating peripheral compartments are denoted by x_2 and x_3

respectively. The parameters k_{ij} for $i \neq j$, denote the drug transfer frequency from the i^{th} to the j^{th} compartment and $u(t)$ [mg/min] is the infusion rate of the anaesthetic or analgesic drug into the central compartment. The parameters k_{ij} of the PK models depend on age, weight, height and gender and can be calculated for Propofol. Notice that in the model used in this paper $C_e = x_e$, E_0 denotes the baseline value (awake state - without drug), which by convention is typically assigned a value of 100, E_{max} denotes the maximum effect achieved by the drug infusion, EC_{50} is the drug concentration at 50% of the maximal effect and represents the patient sensitivity to the drug, and γ determines the steepness of the curve.

2.2 Piecewise linearization

Due to the nonlinearity of the Hill curve, we propose a piecewise affine representation which divides the BIS into three partitions, where each partition i is associated with a different linear function $BIS = C_i C_e + e_i$ (see Figure 2).

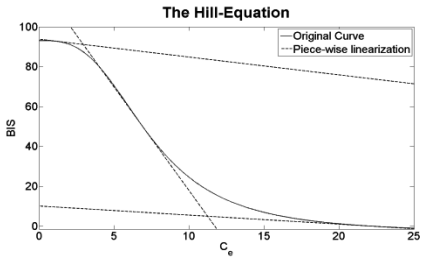

$$BIS = \begin{bmatrix} \delta_1 \\ \delta_2 \\ \delta_3 \end{bmatrix} \left(\begin{bmatrix} C_1 & C_2 & C_3 \end{bmatrix} C_e + \begin{bmatrix} e_1 \\ e_2 \\ e_3 \end{bmatrix} \right)$$

$$\delta \in [0,1]^3$$

Figure 2. Schematic of hybrid mp-MPC control

The binary variables δ thereby denote whether a certain partition is active. As a result, this system belongs to the class of hybrid systems, i.e. systems which are described by continuous as well as discrete dynamics and/or logical constraints. Thus, the problem of designing a hybrid model-predictive controller can be reformulated as a mixed-integer quadratic programming (MIQP) problem (Bemporad and Morari, 1999), i.e.

$$\begin{aligned} \min_{x,y,u} J = {} & x'_N P x_N + \sum_{k=1}^{N-1} x_k Q_k x_k + \sum_{k=1}^{N-1} (y_k - y_k^R)' Q R_k (y_k - y_k^R) + \\ & + \sum_{k=0}^{N_u-1} (u_k - u^R)' R_k (u_k - u^R) + \sum_{k=0}^{N_u-1} \Delta u_k R1_k \Delta u_k \\ s.t. \; & \mathrm{x}_{t+1} = A x_t + B u_t \\ & \mathrm{y}_t = C x_t \\ & \mathrm{BIS}_{\min} \le y \le BIS_{\max} \\ & \Delta \mathrm{u}_{\min} \le \Delta u \le \Delta u_{\max} \end{aligned} \tag{1}$$

$$x_t \in X \subseteq \Re^p, u_t \in U \subseteq \Re^s$$

where x are states, y outputs and u controls, all (discrete) time dependent vectors. The subsets of output variables that get tracked have time-dependent set points y^R. Finally Δu are changes in control variables, $\Delta u(k) = u(k) - u(k\text{-}1)$. The prediction horizon is denoted by N and control horizon by N_u. X, U are the sets of the state and input

constraints that contain the origin in their interior. Both $Q>0$, the objective coefficient for the states and $P>0$, the terminal weight matrix for the states, are symmetric semi-positive definite matrices. The quadratic matrix for manipulated variables $R>0$ is a symmetric positive matrix, QR is the quadratic matrix for tracked outputs and $R1$ is a weight matrix for the control action changes Δu. Thus, if a certain combination of integer variables is fixed, problem (1) results in a convex QP.
In classical MPC, problem (1) is solved as soon as the nominal value of the initial state x_0 is available. In case of hybrid systems, this requires the online solution of a MIQP problem, which might be computationally prohibitive. One way to overcome this computational burden is multi-parametric programming, where the initial states are treated as parameters and the optimization problem is solved as a function thereof (Pistikopoulos, 2009). For the case of problem (1) this requires the solution of a multi-parametric mixed-integer quadratic programming (mp-MIQP) problem, for which recently novel solution procedures have been described (Oberdieck and Pistikopoulos, 2014).

2.3 Multi-parametric Model Predictive Control

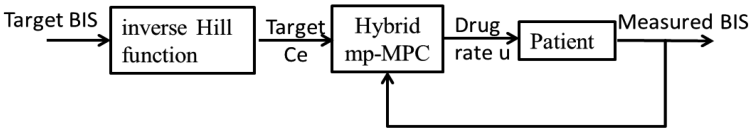

Figure 3. Schematic of hybrid mp-MPC control

The Patient block is composed of the pharmacokinetic part (linear) and the pharamacodynamic part, the Hill curve which introduces the nonlinearity in the system. Dealing with this nonlinearity and the inter- and intra- patient variability is one of the main challenges in the anaesthesia process. Due to the characteristic S-shape of the Hill curve a linearization around three points was performed.
For the implementation of mp-MPC, the problem is reformulated as a MIQP problem. The structure of the control scheme is presented in Figure 3.

3. Results

The closed loop control tests are performed on a set of 12 virtually generated realistic patients (Ionescu et al., 2008). Their performances are tested by means of the BIS index and the corresponding Propofol infusion rates. The Propofol infusion rates are limited to 10 mg/s due to pump restrictions.

3.1. Induction phase

The induction of the patient should be performed as fast as possible, such that little time is lost before the surgeon can start operating. It is therefore desirable that the patient reaches the BIS = 50 target and remains within the target value without much undershoot or overshoot.
Figure 4 shows the simulation results of the controllers for the BIS index and the corresponding control action, i.e. the Propofol infusion rates. Note that the states of the patients are considered as parameters. The controller shows good performances, with no significant undershoot and fast settling time of approximately 4 minutes. In common practice the operation procedure does not start until the patient reaches an adequate DOA, usually taking up to 15 min. Thus, a rise time between 5 min and 7 min gives good performance.

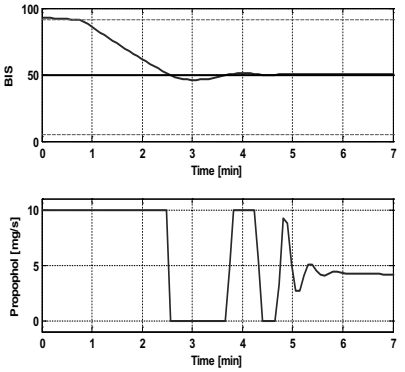

Figure 4. BIS output and corresponding infusion rates for the induction phase (the dashed lines denote the points of transition between the linearized sections of the Hill curve)

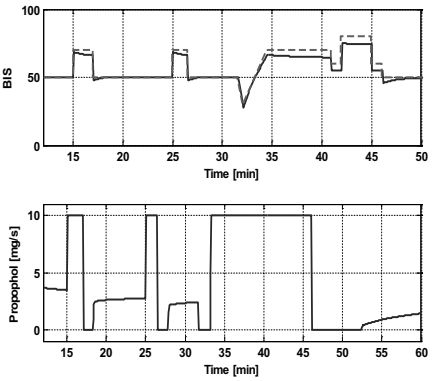

Figure 5. BIS output and corresponding infusion rates for the maintenance phase

3.2. Maintenance phase

During the maintenance phase, it is important that the controller rejects the disturbances occurred during surgery as fast as possible and bring the patient to the BIS target value. In this phase, typical disturbances can be applied additively to the output of the process in order to check the controller's ability to reject them (Dumont et al., 2009). The standard stimulus profile used for simulation is presented in Figure 5 and each interval denotes a specific event in the operation theatre (Yelneedi et al., 2009). Figure 5 also shows the performance of disturbance rejection of the hybrid controller and the corresponding infusion rates. This aspect presents the most challenging part of the disturbance rejection tests, and we can observe that the controller is able to achieve good performances even when subject to strong disturbance signal and restriction of the pump.

4. Conclusions

In this paper we present a framework for the design of hybrid multi-parametric model predictive controllers. The framework is applied to the intravenous process of anaesthesia for the induction and maintenance phase. The anaesthesia process is described by a piece-affine system via a linearized version of the Hill function. For the maintenance phase, a realistic disturbance signal was considered and applied. A simulation study is performed on a set of 12 virtually generated patients.

The results show good performances with a fast settling time and no significant overshoot or undershoot, a high-efficiency, optimal dosage and robustness of the model predictive control algorithm to induce and maintain the desired Bispectral Index reference while rejecting typical disturbances from surgery. The controller is also able to deal with the high inter- and intra- patient variability.

Some of the most important challenges in the control of anaesthesia is inter- and intra-patient variability and significant disturbances during the maintenance phase. In order to deal with these problems, future work will focus on extending the developed algorithm to simultaneous multi-parametric hybrid moving horizon estimators and model predictive control.

5. Acknowledgements

Financial support from EPSRC (EP/G059071/1, EP/I014640), the European Research Council (MOBILE, ERC Advanced Grant, No: 226462) and the European Commission (OPTICO/G.A. No.280813) is gratefully acknowledged.

References

A. R. Ablasom, R. DE Keyser&M. Struys, 2011. Closed loop anaesthesia: are we getting close to finding the Holy Grail? *Anesth Analg,* 112**,** 516-518.

J. M. Bailey&W. M. Haddad, 2005. Drug dosing control in clinical pharmacology. *IEEE Control System Magazine,* 25**,** 35-31.

A. Bemporad&M. Morari, 1999. Control of systems integrating logic, dynamics, and constraints. *Automatica,* 35**,** 407-427.

I. C.Demetriou, 2012. Applications of the Discrete Least Squares 3-Convex Fit To Sigmoid Data. *Proceedings of the World Congress on Engineering 2012, London, U. K.,* I.

G. A. Dumont, A. Martinez&J. M. Ansermino, 2009. Robust control of depth of anesthesia. *International Journal of Adaptive Control and Signal Processing,* 23**,** 435-454.

R. C. Gonzalez&P. Wintz, 1987. Digital Image Processing. *Addison Wesley Publishing Company*.

C. M. Ionescu, J. Y. Machado, R. DE Keyser,J. Decruyenaere & M. M. R. F Struys, Nonlinear dynamics of the patient's response to drug effect during general anesthesia. *Communications in Nonlinear Science and Numerical Simulation*.

C. M. Ionescu, R. DE Keyser, B. C. Torrico, T. DE Smet, M. M. R. F Struys&J. E. Normey-Rico, 2008. Robust predictive control strategy applied for propofol dosing using BIS as a controlled variable during anesthesia. *IEEE Transactions on Biomedical Engineering,* 55**,** 2161-2170.

A. Krieger, N. Panoskaltsis, A. Mantalaris, M. C. Georgiadis&E. N. Pistikopoulos, 2014. Modeling and analysis of individualized pharmacokinetics and pharmacodynamics for volatile anesthesia. *IEEE Transactions on Biomedical Engineering,* 61**,** 25-34.

D. V. Lindley, 1985. Making decisions. *Wiley and Sons*.

MINTO, C. F., SCHNIDER, T. W. & SHAFER, S. L. 1997. Pharmacokinetics and pharmacodynamics of remifentanil. II. Model application. *Anesthesiology,* 86**,** 24-33.

I. Nascu, A. Krieger, C.M. Ionescu. &E.N. Pistikopoulos, E. 2014. Advanced Model Based Control Studies for the Induction and Maintenance of Intravenous Anaesthesia. *IEEE Transactions on Biomedical Engineering* 01-10.

I. Nascu, I. Nascu. Adaptive EPSAC predictive control of the hypnotic component in anesthesia. 2012. 103-108.

R. Oberdieks, E. N. Pistikopoulod, Explicit hybrid model-predictive control: The exact solution. *Automatica,* submitted.

E. N. Pistikopoulos, N. Diangelakis, R. Oberdieck, M. M. Papathanasiou,I. Nascu&M. Sun, 2014. PAROC - an Integrated Framework and Software Platform for the Design, Operational Optimization and Advanced Model-Based Control of Process Systems. *Chemical Engineering Science,* submitted.

E. N. Pistikopoulos, 2009. Perspectives in multiparametric programming and explicit model predictive control. *AIChE Journal,* 55**,** 1918-1925.

M. E. Porter, 1985. Competitive Advantage, Creating and Sustaining Superior Performance. *The Free Press, Collier Macmillan Publishers*.

T. W. Schnider, C. F. Minto, S. L. Shafer, P. L. Ganmbus, C. Andersen, D. B. Goodale&E. J. Youngs, 1999. The influence of age on propofol pharmacodynamics. *Anesthesiology,* 90**,** 1502-1516.

S. Yelneedi, L. Samavedham&G. P. Rangaiah, 2009. Advanced Control Strategies for the Regulation of Hypnosis with Propofol. *Industrial & Engineering Chemistry Research,* 48**,** 3880-3897.

Krist V. Gernaey, Jakob K. Huusom and Rafiqul Gani (Eds.), 12th International Symposium on Process Systems Engineering and 25th European Symposium on Computer Aided Process Engineering.
31 May - 4 June 2015, Copenhagen, Denmark.

Dynamic Chance-Constrained Optimization under Uncertainty on Reduced Parameter Sets

David Müller[a], Erik Esche[a], Sebastian Werk[a] and Günter Wozny[a]

[a]*Department of Process Dynamics and Operation, Technische Universität Berlin, Str. des 17. Juni 135, D-10623 Berlin*
david.mueller@tu-berlin.de

Abstract

Uncertainty is a crucial topic for the decision making process in almost every scientific field. Therefore, the correct implementation into optimization problems is vital. Herein, the chance-constrained optimization approach is applied and compared with a standard Monte Carlo optimization on a CSTR model. The two approaches are expanded by limiting the number of uncertain parameters in the system with according subset selection strategies from parameter estimation studies. The idea here is that a high number of uncertain parameters does not add to a better description of a system. The uncertainty can be represented by a subset of uncertain parameters, which suffice to describe the system behavior. In this contribution, it is shown that the results, both for the chance constrained and Monte Carlo optimization approaches, are improved regarding result stability and control action indication. Additionally, it is discussed how the chance-constrained approach yields even better results regarding the objective function of the optimization problem and it is shown that the solution time is drastically reduced.

Keywords: Chance Constraints, Optimization under Uncertainty, Subset Selection

1. Motivation and Introduction

The consideration, proper handling, as well as the correct implementation of uncertainty are still some of the most challenging issues in process optimization today. On an industrial level, conservative measures are often applied to compensate for uncertainty, which of course lead to losses of potential profit. To minimize these, different approaches in stochastic process optimization exist. Of interest in this contribution is the chance-constrained optimization approach. Herein, a deterministic result for a stochastic optimization problem is obtained, while process constraints are adhered to with a certain probability. Independent of the way that uncertainties are implemented into an optimization problem, it can generally be said that with a higher number of uncertain parameters, the computational complexity for solving the optimization problem for certain approaches increases. Additionally, poorly estimated parameters can add unrealistic behavior to the system.

Nevertheless, it is possible to support engineers in selecting the most relevant uncertain parameters for optimization under uncertainty using a strategy proposed in (Müller et al., 2014). Core features of the algorithm presented therein are an identifiability analysis of parameters and respective subset selection as well as a sensitivity analysis of parameters towards all states and a user-defined objective function. The remaining uncertain parameters are those that are relevant for optimization under uncertainty. Therefore, the novelty in this contribution is the combination of subset selection strategies for the selection of relevant uncertain parameters with two stochastic optimization approaches: Monte-Carlo-Optimization (MCO) and chance-constrained optimization (CCO).

2. Chance-Constrained Optimization

The chance-constrained approach has intensively been studied by Charnes and Cooper (1959), Wendt et al. (2002), Li et al. (2008), Arellano-Garcia and Wozny (2009), and Werk et al. (2012). The concept is briefly revisited in the following.

2.1. Optimization Problem Formulation

The objective function of the stochastic optimization problem is formulated as shown in Eq. (1). Hereby f is the objective function. The minimization is to be achieved by manipulating the controls u. The states are the vector x and the uncertain parameters the vector ξ. For the purpose of this contribution, a multivariate normal distribution of ξ is assumed. Hereby, μ is its expected value and Σ the covariance matrix. In order to cope with the uncertain factors, the vector of inequality constraints h of the optimization problem is written as shown in Eq. (2).

$$\min_{u} \; E\,[f(x,u,\xi)] \qquad \xi = \mathcal{N}(\mu,\Sigma) \tag{1}$$

$$s.t.\; Pr\{h(\dot{x},x,u,\xi) \geq 0\} \geq \alpha \tag{2}$$

The probability of adhering to a certain constraint with a certain percentage α is of relevance. Thus, a relaxation of the inequality constraint is performed.

2.2. Optimization Problem Implementation

The optimization problem is implemented as shown in Fig. 1 and is solved in six steps. In **Step 1**,

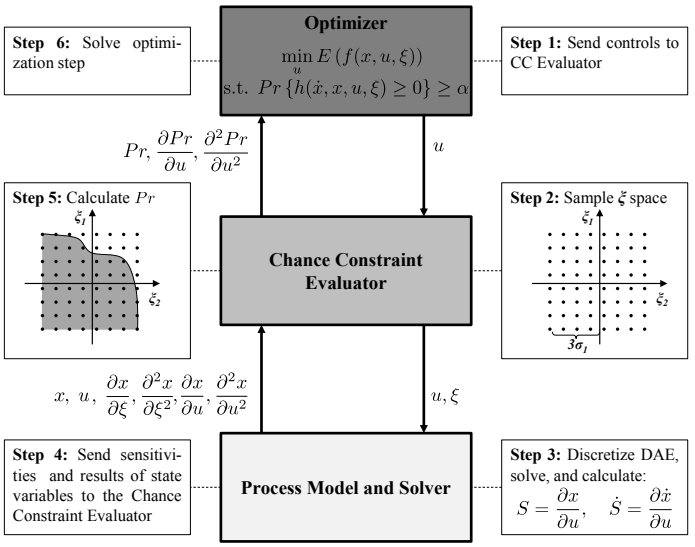

Figure 1: Complete framework for solving the chance-constrained optimization problem.

the controls u are sent to the chance constraint evaluator. In our case, this is the dynamically optimized chance constraint evaluator (DoCCE). In **Step 2**, the DoCCE performs a sparse sampling of the uncertain parameters ξ. The user has the possibility to set the grid width (e.g. 3σ), the grid resolution (number of samples within the width), as well as the grid depth of the sample. In **Step 3**, the samples of ξ and the controls u are passed down to the process model and solver. The solver discretizes the DAE into an AE and solves the model with given controls and parameters.

Hereby, the sensitivity matrix of the states regarding the controls is determined. In **Step 4**, based on the implicit function theorem, the sensitivity of the states regarding the parameters and regarding the controls is sent back to the DoCCE. Afterwards, in **Step 5**, an integration to calculate the probability *Pr* of adhering to the constraints is carried out. For this purpose, a root-finding problem is solved and the course of the constraints h is determined. Finally, the optimizer obtains the probability (1), the sensitivity of the probability regarding the controls (2), as well as its second derivative of the sensitivity regarding the controls (3). For our case, the optimization problem is implemented in Python using a framework for the chance constraint calculation presented in Werk et al. (2012) and Wendt et al. (2002). Ipopt is used as an NLP solver for the optimization problem. For the simulation part of the framework, a sparse DAE solver with automatic sensitivity generation (sDACl, developed by Barz et al. (2011)) is used in combination with an NLE solver (NLEQ1s, developed by Nowak and Weimann (1991)).

3. Case Study

The case study by (Müller et al., 2014) of a continuously stirred tank reactor (CSTR) with several reactions is further explored by comparing the results of four different optimizations under uncertainty: The first being a basic Monte Carlo-based stochastic optimization as well as a Chance-Constrained optimization on all initially uncertain parameters of the CSTR model, the third being a Monte Carlo-based stochastic optimization on a reduced set of uncertain parameters, and the fourth a chance-constrained optimization using the same subset. The calculations are performed on an intel 7 - 3770 CPU @ 3,50 GHz x 8 with 16 GB RAM running on Ubuntu 14.04 (64 Bit).

3.1. Task Description and Optimization Problem Formulation

The CSTR has one entering and exiting mole flow $\dot{F}$. The inlet stream has two relevant concentrations c_{A0} and c_{B0} at a temperature of T_0. In the CSTR, two reactions take place: A is reacted to product C and B is reacted to A. The reactor is heatable or coolable via the jacket with the heating temperature T_j. The CSTR and its reactions can be described with Eq. (3) to (5). The flow leaves the reactor at temperature T with concentrations c_A and c_B. The objective is to minimize the concentration of c_A leaving the reactor.

$$\frac{dc_A}{dt} = \frac{\dot{F}}{V} \cdot (c_{Ao} - c_A) - k_{Ao} \cdot c_A \cdot e^{\frac{-E_A}{R \cdot T}} + k_{Bo} \cdot c_B \cdot e^{\frac{-E_B}{R \cdot T}} \tag{3}$$

$$\frac{dc_B}{dt} = \frac{\dot{F}}{V} \cdot (c_{Bo} - c_B) - k_{Bo} \cdot c_B \cdot e^{\frac{-E_B}{R \cdot T}} \tag{4}$$

$$\begin{aligned} \frac{dT}{dt} = &\frac{\dot{F}}{V} \cdot (T_o - T) - \frac{U \cdot A}{\rho \cdot c_p \cdot V} \cdot (T_j - T) + \frac{-\Delta H_A}{\rho \cdot c_p} \cdot k_{Ao} \cdot c_A \cdot e^{\frac{-E_A}{R \cdot T}} \\ &+ \frac{-\Delta H_B}{\rho \cdot c_p} \cdot k_{Bo} \cdot c_B \cdot e^{\frac{-E_B}{R \cdot T}} \end{aligned} \tag{5}$$

The constants in the process are the volume of the reactor V = 1 m^3, the heat of reaction ΔH_A = $4.5 \cdot 10^4$ J/mol and ΔH_B = $-5.5 \cdot 10^4$ J/mol for reaction A and B respectively, and the incoming stream $\dot{F}$ = $6.5 \cdot 10^{-4}$ m^3/s. The applied expected values and variances of the parameters for the three optimizations are obtained from (Müller et al., 2014) and are displayed in Tab. 1 and Tab. 2.

3.2. Results and Discussion

Four cases are analyzed in greater detail, to analyze the effect of optimization under uncertainty using reduced parameter subsets. The objective is displayed in Eq. (6).

$$\min_u E\ [f(x,u,\xi)] = -c_A \text{ with } \xi \sim N(\mu, \Sigma) \tag{6}$$

$$s.t.\ g(x,u,\xi) = 0 \text{ and } h(x,u,\xi) = T \leq 340K \tag{7}$$

Table 1: Expected parameter values for uncertain parameters from (Müller et al., 2014).

	E_A [J/(molK)]	E_B [J/(molK)]	k_{Ao} [1/s]	k_{Bo} [1/s]	ρ [kg/m]	c_p [J/(kgK)]	U·A [W/K]
Real val.	$6.90 \cdot 10^4$	$7.20 \cdot 10^4$	$5.0 \cdot 10^6$	$1.0 \cdot 10^7$	$8.00 \cdot 10^2$	3.5	1.40
Full set	$6.94 \cdot 10^4$	$7.62 \cdot 10^4$	$6.1 \cdot 10^6$	$4.0 \cdot 10^7$	$5.50 \cdot 10^2$	5.0	1.37
Subset	$6.94 \cdot 10^4$	$7.62 \cdot 10^4$	$6.1 \cdot 10^6$	$4.0 \cdot 10^7$	$5.54 \cdot 10^2$	5.0	1.38

Table 2: Parameter variances for the full set and subset from (Müller et al., 2014).

	E_A	E_B	k_{Ao}	k_{Bo}	ρ	c_p	U·A
Full set	$4.0 \cdot 10^3$	$3.3 \cdot 10^3$	$7.8 \cdot 10^6$	$4.2 \cdot 10^7$	$3.2 \cdot 10^3$	$3.0 \cdot 10^1$	$1.0 \cdot 10^{-1}$
Subset	$8.4 \cdot 10^1$	$7.9 \cdot 10^1$	0	0	0	0	$1.2 \cdot 10^1$

Monte Carlo Optimization - Full Set: The first case of interest is a MCO using the whole set of estimated parameters including their determined variances. 10,000 MCOs are performed to obtain a reliable result. The differential algebraic equation system describing the CSTR is stiff and shows a tight feasible area for control and parameter combinations. Fig. 2 displays the determined control actions. The MCO shows an erratic behavior and gives no clear indication on how to operate the controllable reactor. Whilst the feed of c_{A0} reaches its lower bound (7 mol/m^3), the results for T_0 and T_j are widely spread and the feed c_{B0} jumps to both bounds. For an operator, this result is not desirable.

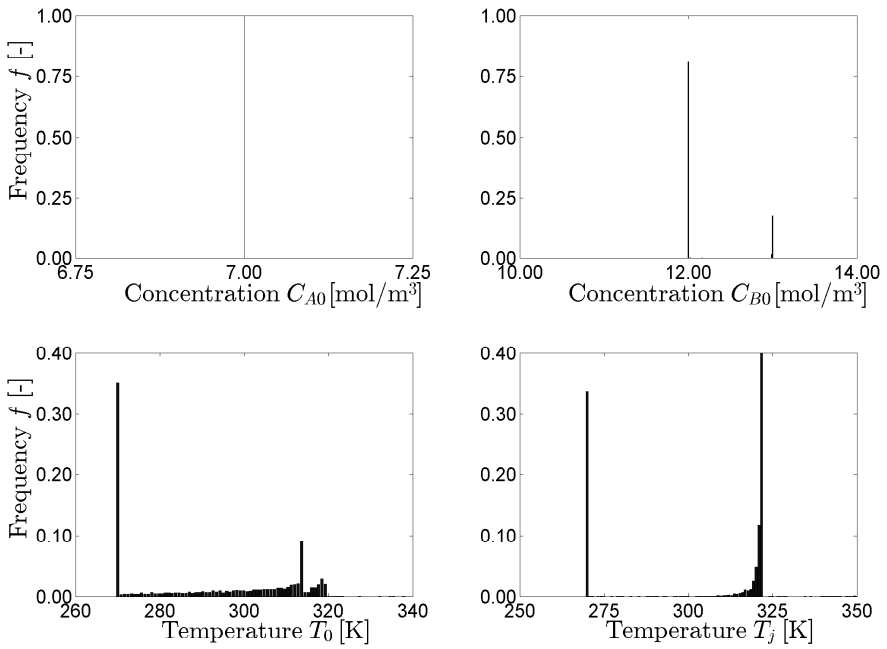

Figure 2: MCO result for the control actions using the full set of uncertain parameters.

Chance-Constrained Optimization - Full Set: The same optimization problem is then solved using chance-constrained optimization. As for the chance-constraints, a probability of $\alpha = 98\%$ is required for the upper bound on the reaction temperature. The optimization problem shown above

is expanded to Eq. (8).

$$s.t.\ g(\dot{x},x,u,\xi) = 0 \text{ and } Pr\{h(\dot{x},x,u,\xi) = T \leq 340K\} \geq \alpha \tag{8}$$

For this case, no result could be obtained within any reasonable amount of time compared to the MCO (2 days). This result strengthens the statement that if this approach is used for optimization, the uncertainty in a model must be focused on a smaller set of uncertain parameters.

Monte Carlo Optimization - Subset: The second MCO, using the reduced parameter set, shows a less erratic behavior with more than 92% of all 10,000 Monte Carlo samples leading to an optimal solution. The used subset of uncertain parameters is shown in Tab. 2. The parameters with a variance of 0 are the fixed parameters, while the others are the uncertain parameters. In all MCO cases, the value of the objective function is almost the same proving the controllability of the process. The objective function value lies at 6.6 mol/m^3. Furthermore, the range of valid control actions is not as wide as in the case of the first MCO with the full set of uncertain parameters. The control actions are displayed in Fig. 3. The result for the final temperature is shown in comparison to the result of the chance-constrained optimization result in Fig. 4. Here it is obvious, that the optimization results in control actions keeping the final temperature far away from the temperature bound of 340K. This of course means a loss of profit.

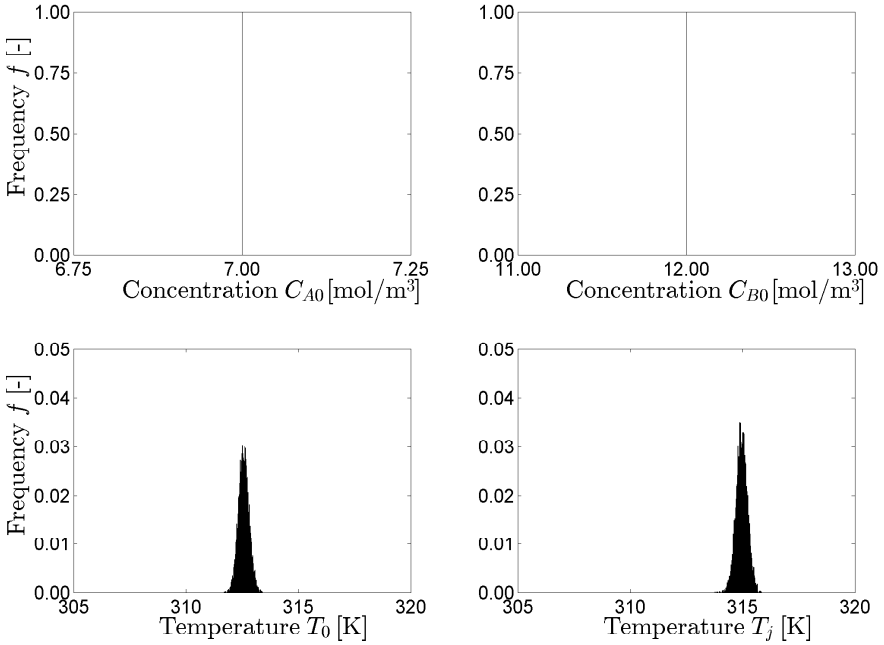

Figure 3: MCO result for the controls using the subset of estimated parameters.

Chance-Constrained Optimization - Subset: Finally, a chance-constrained optimization is carried out for the reduced subset with the same probability bound for the reaction temperature. A solution to the optimization problem can be found in less than 120 seconds as opposed to over 6 hours for the Monte Carlo optimization. A further Monte Carlo analysis of the thus found result with respect to the parameter uncertainty shows a desirable stability. The expected value of the objective function lies at 6.58 mol/m^3. Thus, a clear indication for an operator is obtained, on how the reactor should be operated and a slightly higher objective function value is achieved.

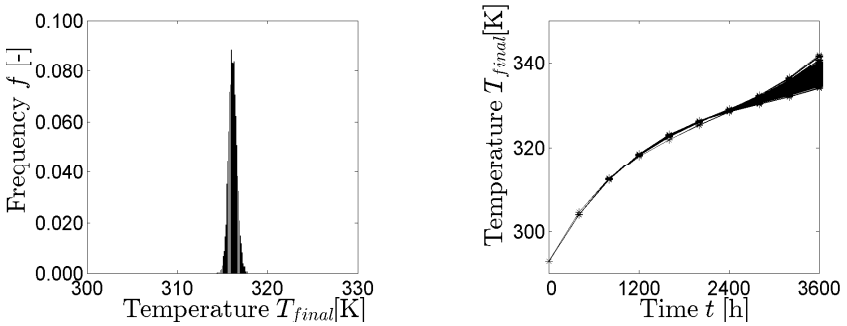

Figure 4: MCO result (left) and CCO result (right) for the subset of estimated parameters.

4. Conclusions and Outlook

Among other things, the results indicate, that implementing too much uncertainty into a process model, no sensible result for a Monte Carlo optimization as well as for the chance-constrained optimization is obtained. Secondly, the described method of using the parameter reduction algorithm combined with chance-constrained optimization is a suitable path towards comprehensive process optimization under uncertainty. This is the case both for Monte Carlo and chance constrained optimization. Thirdly, the latter yields clear, easily interpretable, and implementable optimization results as only one deterministic result is obtained. Additionally, the objective function value of the CC result is higher, as a minor constraint violation is allowed. As an outlook, the chance-constraint optimization approach will be implemented into the open source modeling environment MOSAIC (Kuntsche et al., 2011). Thus, the acceptance of the approach can be improved.

5. Acknowledgements

The authors acknowledge the support from the Cluster of Excellence “Unifying Concepts in Catalysis” and the Collaborative Research Center SFB/TRR 63 InPROMPT “Integrated Chemical Processes in Liquid Multiphase Systems” both coordinated by the Technische Universitt Berlin and funded by the German Research Foundation (Deutsche Forschungsgemeinschaft “DFG”). Grant no.: DFG EXC 314 and DFG TRR 63

References

Arellano-Garcia, H., Wozny, G., 2009. Chance constrained optimization of process systems under uncertainty: I. strict monotonicity. Computers & Chemical Engineering 33 (10), 1568 – 1583.

Barz, T., Kuntsche, S., Wozny, G., Arellano-Garcia, H., 2011. An efficient sparse approach to sensitivity generation for large-scale dynamic optimization. Computers & Chemical Engineering 35 (10), 2053 – 2065.

Charnes, A., Cooper, W. W., 1959. Chance-constrained programming. Management Science 5, 73.

Kuntsche, S., Barz, T., Kraus, R., Arellano-Garcia, H., Wozny, G., 2011. Mosaic a web-based modeling environment for code generation. Computers & Chemical Engineering 35 (11), 2257 – 2273.

Li, P., Arellano-Garcia, H., Wozny, G., 2008. Chance constrained programming approach to process optimization under uncertainty. Computers & Chemical Engineering 32, 25 – 45.

Müller, D., Esche, E., Lopez-C., D. C., Wozny, G., 2014. An algorithm for the identification and estimation of relevant parameters for optimization under uncertainty. Computers & Chemical Engineering 71 (0), 94 – 103.

Nowak, U., Weimann, L., 1991. A family of newton codes for systems of highly nonlinear equations. Tech. rep., Konrad-Zuse-Zentrum fr Informationstechnik Berlin.

Wendt, M., Li, P., Wozny, G., 2002. Nonlinear chance-constrained process optimization under uncertainty. Industrial & Engineering Chemistry Research 41, 3621 – 3629.

Werk, S., Barz, T., Wozny, G., Arellano-Garcia, H., 2012. Performance analysis of shooting algorithms in chance-constrained optimization. In: Proceedings of the 11th International Symposium on Process Systems Engineering (PSE2012). pp. 1512 – 1516.

Krist V. Gernaey, Jakob K. Huusom and Rafiqul Gani (Eds.), 12th International Symposium on Process Systems Engineering and 25th European Symposium on Computer Aided Process Engineering.
31 May – 4 June 2015, Copenhagen, Denmark

Optimal Design of Thermal Membrane Distillation Networks

Ramón González-Bravo,[a] Fabricio Nápoles-Rivera,[a] José María Ponce-Ortega,[a*] Medardo Serna-González,[a] Mahamoud M. El-Halwagi,[b,c]

[a]*Chemical Engineering Department, Universidad Michoacana de San Nicolás de Hidalgo, Morelia, Michoacán, 58060, México*
[b]*Chemical Engineering Department, Texas A&M University, College Station TX, 77843, USA*
[c]*Adjunct Faculty at the Chemical and Materials Engineering Department, King Abdulaziz University, Jeddah, Saudi Arabia*

Abstract

Thermal membrane distillation (TMD) is a promising separation technology which involves simultaneous heat and mass transfer through a hydrophobic semi-permeable membrane. Studies of this technology have focused on the performance of individual modules. However, due tospecific purity and recovery requirements in some processes, multiple TMD modules have to be used in different configurations such as series, parallel, and combinations, which might require to reroute streams from one module to another or to recycle a stream to the same unit. This paper presents a systematic approach to synthesize an optimal TMD network. All the potential configurations are embedded within a structural representation of the problem which is then formulated as an MINLP optimization model, in which the objective function is the minimization of the total cost of the system.The advantages of the presented approach over conventional design procedures is shown through a case study dealing with the desalination of water (i.e,. integrated TMD modules yield better results with respect to usual configurations).

Keywords: Process Synthesis; Membrane Distillation; Separation Networks; Seawater Desalination; Optimization.

1. Introduction

Thermal membrane distillation (TMD) is becoming an attractive alternative as a separation method owing to several compelling features such as high rejection of ions, macromolecules, colloids and cells, along with low energy requirements (Khayet and Matsuura, 2011) due to mild operation conditions (i.e., relatively low pressure and low temperature). The driving force for the mass transfer in this technology is the partial vapor pressure difference across a microporous hydrophobic membrane. This vapor pressure difference is usually a function of the temperature difference (Kim, 2013). Despite the fact that TMD units can reach high separation levels, seldom single stage modules are not enough to satisfy these requirements (either in quality or quantity). In these cases staging of permeate and/or retentate might be required in diverse configurations such as series, parallel or combinations (it should be noted that this issue has not been addressed in the literature, and this is the main contribution of the present work), Nevertheless,several works have focused on the synthesis of other desalination systems, for example in RONs (Reverse Osmosis Networks). Karuppiah et al. (2012)

presented an optimization approach for synthesizing water treatment systems accounting for RO units. Abejón et al. (2012) proposed the use of RO units for ultra-purification of chemicals. Alnouri and Linke (2012; 2013) proposed a systematic process synthesis and optimization approach that takes into consideration multiple water quality parameters for the design of RO desalination networks. Du et al. (2014) proposed a multi-objective optimization approach for synthesizing RO networks for seawater desalination. Almansoori and Saif(2014) presented an optimal integrated RO system and a pressure retarded osmosis (PRO) for seawater desalination and power generation. Saif et al. (2014) presented an approach for the optimal design of RO networks considering variations in the streamproperties. Dahdah and Mitsos(2014) introduced a methodology to identify improved thermal-based desalination structures, the model considers either a multi-effect distillation system (MED) or a stage in a multi-stage flash system (MSF) to determine the best configuration. However there have not been works about the synthesis of integrated TMD networks. Thus, in this work a novel approach for the systematic designof a TMDN based on a new superstructure and a mathematical programming formulation is presented.

2. Design approach

The network configuration was represented through a source-sink approach (El-Halwagi et al., 1996). A source is a process stream that is rich in the constituent(s) that has to be removed in the separation task. Here, it is assumed that each TMD module represents a building block. The feed is preheated in the TMD module. Enough heat should be provided to induce the evaporation at a moderate temperature. The amount of heat and the inlet temperature of the stream fed to the TMD unit are optimization variables. Water vapor passes across the membrane and is condensed on the permeate side using a recirculating permeate-sweeping liquid which is colder than the feed. The size of each element is an optimization variable (including a zero size, which indicates that the element does not exist). Each TMD unit produces two streams (permeate and reject). Either one or both may be rerouted back to the network to be assigned to new sinks.The feed may be split into several fractions and assigned to the different TMD units. The proposed superstructure for the design of an integrated TMDN is shown in **Figure 1**. The problem consists in determining the optimum network configuration, unit sizes, stream allocation, and operating conditions.

3. Mathematical model

First the indices used in this model are defined: i represents the number of TMD units connected in parallel arrangement, k indicates the number of units connected in series, and i' is used to indicate a subsequent line of TMD modules. The model is constituted by mass, solute and energy balances in the mixers and splitters in the network and additional equations to calculate the permeate flux passing through the membrane, temperature polarization coefficient and membrane area.The heating for each TMD unit is provided by external utilities and this is equal to the feed flow rate ($w_{i,k}^{TMD}$) times the heat capacity for this stream ($\mathrm{Cp}_{\mathrm{i,k}}^{\mathrm{TMD}}$) and the temperature difference ($t_{i,k}^{TMD} - t_{i,k}^{mix}$). Only a fraction of this heat is used in vaporizing the permeate. The fraction is given by the efficiency factor ($\eta_{i,k}$). Hence, the heat balance for the TMD unit is given by:

$$\eta_{i,k} w_{i,k}^{TMD} \mathrm{Cp}_{\mathrm{i,k}}^{TMD} (t_{i,k}^{TMD} - t_{i,k}^{mix}) = w_{i,k}^{perm} \Delta h_{vw_{i,k}}, \quad \forall i \in I, \forall k \in K \tag{1}$$

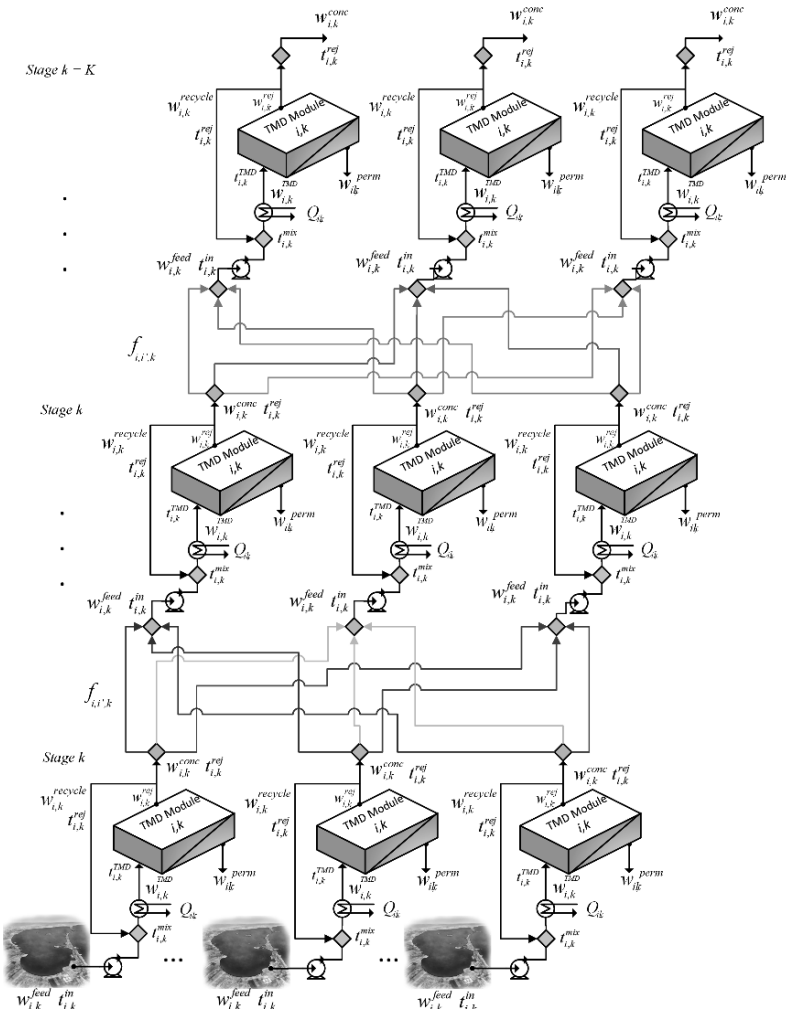

Figure 1. Superstructure for synthesizing a TMDN.

The permeate flux passing through the membrane ($j_{w_{i,k}}$) is calculated with equation (2)

$$j_{w_{i,k}} = b_{w_{i,k}} \left(p^{vap}_{wfeed_{i,k}} \gamma_{wfeed_{i,k}} x_{wfeed_{i,k}} - p^{vap}_{wperm_{i,k}} \right), \quad \forall i \in I, \forall k \in K \tag{2}$$

Where $x_{wfeed_{i,k}}$ is the mole fraction of water in the feed, $p^{vap}_{wfeed_{i,k}}$ is the vapor pressure in the feed side and $p^{vap}_{wperm_{i,k}}$ is the vapor pressure in the permeate side of the membrane, $b_{w_{i,k}}$ is a parameter for the molecular diffusion of water in air and $\gamma_{wfeed_{i,k}}$ is the activity coefficient.

A set of logical relationships are required to determine the components of the network required in the optimal solution. This depends on several factors such as the amount of recovered water, final concentration of permeate, and the impact of the total cost (capital and operating). Therefore, binary variables are used to indicate the existence or absence of such units ($y_{i,k} = Unit\ existance, \{0,1\}$).

$$\mathrm{W}^{\min} \cdot y_{i,k} \le w_{i,k}^{feed} \le \mathrm{W}^{\max} \cdot y_{i,k}, \qquad \forall i \in I, \forall k \in K \tag{3}$$

Where $\mathrm{W}^{\max}$ and $\mathrm{W}^{\min}$ are upper and lower limits for the flow rate of the feed that can be used in a TMD unit. When the inlet flow rate to the unit *i* in the stage *k* ($w_{i,k}^{feed}$) is greater than zero, then the associated binary variable ($y_{i,k}$) must be one. On the other hand, when the binary variable $y_{i,k}$ is zero (i.e., the associated TMD unit does not exist), the treated flow rate ($w_{i,k}^{feed}$) must be zero.

The total annual cost for the TMDN takes into account the fixed cost for the TMD units as a function of the membrane area ($\mathrm{C}_{\mathrm{F1}}^{\mathrm{TMD}}$) for TMD modules and as a function of the flow rate of the stream to be fed ($\mathrm{C}_{\mathrm{F2}}^{\mathrm{TMD}}$) for non-membrane elements, the installation costs of the TMD unit ($\mathrm{C}_{\mathrm{inst}}^{\mathrm{TMD}}$), and the operating cost for the TMD units ($\mathrm{C}_{\mathrm{Op1}}^{\mathrm{TMD}}$; $\mathrm{C}_{\mathrm{Op2}}^{\mathrm{TMD}}$; $\mathrm{C}_{\mathrm{Op3}}^{\mathrm{TMD}}$). In equation (4), the exponent $\beta_{\mathrm{k}}^{\mathrm{TMD}}$ is a factor used to account for the economies of scale. The heating and cooling utilities are also accounted in the terms $\mathrm{Cost}^{\mathrm{Heating}}$ and $\mathrm{Cost}^{\mathrm{Cooling}}$. Furthermore, the investment is annualized through the factor k_{F}, and H_{Y} is the operating time per year of the process. Notice that the fixed charge for the units is only added when the units exist through the use of the binary variables ($y_{i,k}$). Thus, total annual cost is stated as follows:

$$TAC = \left[\begin{array}{c} \mathrm{k_F} \sum_i \sum_k \left[\left(\mathrm{C}_{\mathrm{inst}}^{\mathrm{TMD}} \cdot y_{i,k} \right) + \left(\mathrm{C}_{\mathrm{F1}}^{\mathrm{TMD}} \cdot A_{m_{i,k}} \right)^{\beta_2} + \left(\mathrm{C}_{\mathrm{F2}}^{\mathrm{TMD}} \cdot w_{i,k}^{TMD} \right)^{\beta_3} \right] \\ + \mathrm{H_Y} \sum_i \sum_k \left[\mathrm{C}_{\mathrm{Op1}}^{\mathrm{TMD}} \cdot y_{i,k} + \mathrm{C}_{\mathrm{Op2}}^{\mathrm{TMD}} \cdot \left(1 - \xi_{\mathrm{i,k}} \right) w_{i,k}^{feed} + \mathrm{C}_{\mathrm{Op3}}^{\mathrm{TMD}} \cdot w_{i,k}^{TMD} \right] \\ + \mathrm{H_Y} \sum_i \sum_k \left[\mathrm{Cost}^{\mathrm{Heating}} \cdot Q_{i,k}^{Heating} \right] \end{array} \right] \tag{4}$$

It is worth notice that the nonlinearities and nonconvexities are included in the solute balances and energy balances for the mixers, energy balances in the heaters, in the equations for the TMD modules(i.e., solute balance, energy balance, the equation to calculate the permeate flux through the membrane, the temperature profile and the membrane area), as well as the equation of the total annual cost.

4. Results

A seawater desalination process is presented to show the applicability of the proposed approach for designing TMDN. The problem was coded using the software GAMS (Brooke et al., 2014). Where the solver DICOPT was used to solve the associated mixed-integer nonlinear programing (it should be noted that DICOPT does not guarantee to get the global optimal solution). To solve the problem, a computer with an Intel® Core TM i7-4700MQ processor at 2.40GHz and 8 GB of RAM was used.

4.1. Case Study. Seawater desalination process.

A brackish water desalination process in the coast of Saudi Arabia is considered. For this process, a feed of 3456kg/h with a concentration of 0.1% (1,000 ppm) of dissolved NaCl is processed. The maximum allowable membrane area for each module is 100 m^2/module. The objective consists in maximizing the annual gross profit obtained from the sales of permeate minus the total annualized cost of the system. The optimal

solution is shown in **Figure 2**. It involves two units in series. A total recovery of 95.90% of water as permeate was obtained. The feed temperature for the first unit (1,1) is 300 K and the feed temperature for the second unit (1,2) is 359 K. The first unit has a membrane area of 92.4 m^2 which represents 83.2% of the total required area of membrane and produces a permeate flow rate of 2,764 kg/h which is 83.4% of the total permeate of the TMDN. The total permeate is 3,316 kg/h, which yields an annual revenue of $212,340/y. The total annual cost is $170,347/y and the annual gross profit for the optimal solution is $41,993/y.Furthermore, six additional configurations were analyzed (either parallel or series arrangements) to show the advantages of the proposed approach. In scenario 3, were only a single unit is presented, the annual gross profit reaches $40,306/y which is 4% lower than the optimal solution. Scenarios 3 and 4 present parallel arrangements in which the total permeate is 16.5% lower than the optimal solution, also the total cost is affected by the installation cost of each unit in both cases. In scenario 5, although the total permeate is 2.1% greater than the optimal solution, the total annual profit is affected by the installation of 3 units in series. Scenarios 6 and 7 have similar permeate flow rates to the optimal solution, however, the total annual cost increased because of the multiple modules. **Table 1** shows the main economic results for the optimal configuration and for other analyzed scenarios.

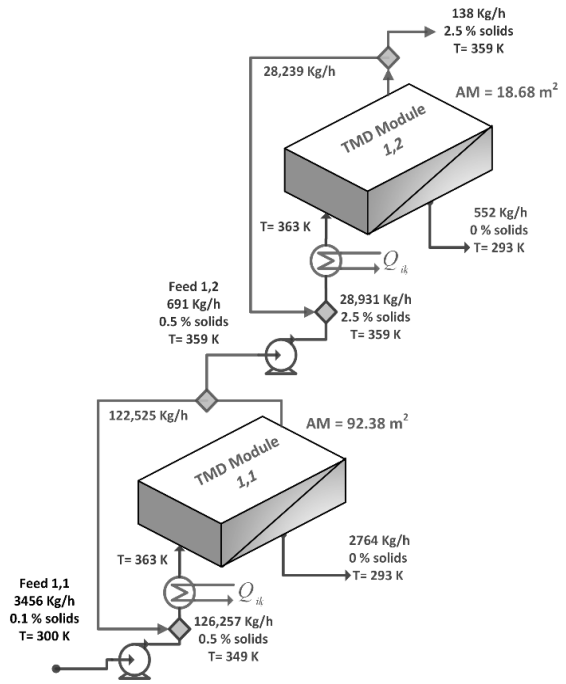

Figure 2. Optimal TMDN for the Case Study.

5. Conclusions

An optimization model for the synthesis of TMDN has been presented. The model is based on a superstructure that embeds all the possible configurations for the network. The proposed model incorporates modelling equations as well as technical and design constraints used to determine the optimal configuration and operating conditions of the process.A case study from Saudi Arabia was solved, in which the results show that two TMD modules in series arrangement yield better results than single, parallel and hybrid

configurations, based on the total permeate flow rates, total annual cost and annual profit. The on-going and future research should focus on the integration with various desalination processes in order to satisfy various water qualities that reduce the cost of desalination, also it is essential to incorporate clean energy technologies which will have a significant benefit in the desalination cost.

Table 1. Optimal results for the Case Study and comparison with six other scenarios.

		Scenario						
Concept	Unit	Optimal	2	3	4	5	6	7
Total membrane area	m^2	111.06	92.38	92.38	92.37	115.09	111.03	111.02
Number of TMD units	--	2	1	2	3	3	3	4
Thermal efficiency	--	0.9	0.902	0.902	0.902	0.89	0.9	0.9
Total permeate	kg/h	3,316	2,764	2,764	2,763	3,426	3,316	3,315
Total feed water	kg/h	3,456	3,456	3,456	3,456	3,456	3,456	3,456
Total recovery	%	95.9	80	79.97	79.94	98	96	95.92
Total heating cost	$/y	37,633	31,355	31,360	31,344	38,875	37,632	37,616
Total annual cost	$/y	170,347	136,644	142,330	146,742	180,665	173,780	178,192
Permeate value	$/y	212,340	176,950	176,948	176,948	219,400	212,275	212,275
Annual profit	$/y	41,993	40,306	34,617	30,205	38,735	38,495	34,083
Arrangement	--	Series	Single	Parallel	Parallel	Series	Hybrid	Hybrid

6. References

A. S. Kim, 2013, A two-interface transport model with pore-size distribution for predicting the performance of direct contact membrane distillation (DCMD), Journal of Membrane Science, 428, 410-424.

M. Khayet, T. Matsuura, 2011, Membrane distillation: principles and applications (1st edition), Oxford: Elsevier, Inc.

R. Karuppiah, S. J. Bury, A. Vazquez, G. Poppe, 2012, Optimal design of reverse osmosis-based water treatment systems, AIChE Journal, 58, 9, 2758-2769.

R. Abejón, A. Garea, A. Irabien, 2012, Optimum design of reverse osmosis systems for hydrogen peroxide ultrapurification, AIChE Journal, 58, 12, 3718-3730.

S. Y. Alnouri, P. Linke, 2013, Optimal SWRO desalination network synthesis using multiple water quality parameters, Journal of Membrane Science, 444, 493-512.

S. Y. Alnouri, P. Linke, 2012, A systematic approach to optimal membrane network synthesis for seawater desalination, Journal of Membrane Science, 417-418, 96-112.

Y. Du, L. Xie, J. Liub, Y. Wang, Y. Xu, S. Wang, 2014, Multi-objective optimization of reverse osmosis networks by lexicographic optimization and augmented epsilon constraint method, Desalination, 333, 66-81.

A. Almansoori, Y. Saif, 2014, Structural optimization of osmosis processes for water and power production in desalination applications, Desalination, 344, 12-27.

Y. Saif, A. Almansoori, A. Elkamel, 2014, Optimal design of split partial second pass reverse osmosis network for desalination applications, AIChE Journal, 60, 2, 520-532.

T. H. Dahdah, A. Mitsos, 2014, Structural optimization of seawater desalination: I. A flexible superstructure and novel MED–MSF configurations, Desalination, 344, 352-265.

M. M. El-Halwagi, A. A. Hamad, G. W. Garrison GW, Synthesis of waste interception and allocation networks, AIChE Journal, 42, 11, 3087-3101.

A. Brooke, D. Kendrick, A. Meeruas, R. Raman, 2014, GAMS-language guide, Washington DC: GAMS Development Corporation.

Krist V. Gernaey, Jakob K. Huusom and Rafiqul Gani (Eds.), 12th International Symposium on Process Systems Engineering and 25th European Symposium on Computer Aided Process Engineering.
31 May - 4 June 2015, Copenhagen, Denmark.

Multicolumn-multicut cross decomposition for stochastic mixed-integer linear programming

Emmanuel Ogbe[a] and Xiang Li[a]

[a]*Department of Chemical Engineering; Queen's University; Kingston, ON, Canada*
xiang.li@queensu.ca

Abstract

This paper proposes a multicolumn-multicut cross decomposition method for stochastic mixed-integer linear programming problems. In this method, multiple columns or multiple cuts are added to the Dantzig-Wolfe restricted master problem or the Benders relaxed master problem, in one iteration. We demonstrate the advantage of the proposed method in comparison with single cut and multicut Benders decomposition methods and a single column single cut cross decomposition method, through the case study of a bio-product supply chain problem.

Keywords: Stochastic programming; Mixed-integer linear programming; cross decomposition.

1. Introduction

Mixed-integer linear programming (MILP) paradigm has been applied to a host of problems in process systems engineering literature. Typical applications include supply chain optimization, process network design and operation, production planning and scheduling, etc. These applications often involve factors that are usually not known with certainty before some decisions are made, which result in uncertain parameters in the MILP model. Using the classical scenario approach, the stochastic MILP problem can be formulated into a two-stage stochastic programming problem (Birge and Louveaux (2010)) as follows:

$$\begin{aligned} \min_{\substack{x_0,\\ x_1,\ldots,x_s}} \; & c_0^{\mathrm{T}} x_0 + \sum_{\omega\in\Omega} c_\omega^{\mathrm{T}} x_\omega \\ \text{s.t. } & A_{0,\omega} x_0 + A_\omega x_\omega \le b_{0,\omega}, \quad \forall \omega \in \Omega, \\ & x_\omega \in X_\omega, \quad \forall \omega \in \Omega, \\ & x_0 \in X_0, \end{aligned} \tag{P}$$

where $x_0 \in X_0 = \{x_0 = (x_{0,b}, x_{0,c}) \in \{0,1\}^{n_{x_{0,b}}} \times \mathbb{R}^{n_{x_{0,c}}} : B_0 x_0 \le d_0\}$ denotes the first-stage decisions, $x_\omega \in X_\omega = \{x_\omega \in \mathbb{R}^{n_x} : B_\omega x_\omega \le d_\omega\}$ denotes the second-stage decisions, and the subscript $\omega \in \Omega = \{1,2,\ldots,s\}$ indexes each scenario. We assume that sets X_0 and x_ω are nonempty and bounded.

Problem (P) is computationally challenging when the number of scenarios involved is large, but its structure can be exploited by a decomposition strategy for efficient solution. Classical decomposition methods for Problem (P) include Dantzig-Wolfe decomposition (DWD) (Dantzig and Wolfe (1960)), Benders decomposition (BD) (Benders (1962)), Lagrangian decomposition (LD) (Carøe and Schultz (1999)), and cross decomposition (CD) (Van Roy (1983)) (Mitra et al. (2014)).

Recently, a new CD method has been developed through the integration of the classical DWD and BD methods, which has significant advantages over the classical DWD and BD methods for

solving Problem (P) (Ogbe and Li (2014)). In this CD method, only a single column or a single cut is added to the DWD or Benders master problem in one iteration. This paper proposes a variant of the new CD that adds multiple columns or cuts in one iteration to achieve an improved convergence rate, as it is well-known that the multicolumn and multicut strategies can accelerate the convergence of classical DWD and BD (Lasdon (1970))

The remaining part of the article is organized as follows. In section 2, we briefly introduce the new CD method. Then in section 3, the multicolumn-multicut CD is presented together with its convergence property. Case study results for a bio-product supply chain problem is presented in section 4 to demonstrate computational advantage of the proposed method. The article ends with conclusions in section 5.

2. The cross decomposition method

The CD method recently developed by the authors synergizes DWD and BD by solving the subproblems from each decomposition method in a unified framework (Ogbe and Li (2014)). On the one hand, two subproblems from DWD, called **DWD restricted master problem** and **DWD pricing problem** in this paper, are solved in the CD. They are constructed through vertex representations of bounded polyhedral sets. Specifically, set $X = \prod_{\omega\in\Omega} X_\omega$ in Problem (P) can be represented as:

$$X = \{x = (x_1,...,x_s) \in \mathbb{R}^{s\cdot n_x} : x_\omega = \sum_{j\in J} \theta^j x^j_\omega, \omega \in \Omega, \sum_{j\in J} \theta^j = 1, \theta^j \geq 0, \forall j \in J\}, \tag{1}$$

where set J includes indexes for all extreme points of X and possibly other points in X as well (Ogbe and Li (2014)). Each point used for defining X is called a *column*. The following set, used in the lth DWD iteration in the CD method, is a subset of X,

$$X^l = \{x = (x_1,...,x_s) \in \mathbb{R}^{s\cdot n_x} : x_\omega = \sum_{j\in J^l} \theta^j x^j_\omega, \omega \in \Omega, \sum_{j\in J^l} \theta^j = 1, \theta^j \geq 0, \forall j \in J^l\}, \tag{2}$$

where $J^l \subset J$. When using X^l instead of X, Problem (P) is restricted into the DWD restricted master problem, which can be written in the following form:

$$\begin{aligned} obj_{DWRMP^l} = \min_{x_0,\theta^j} \; & c_0^{\mathrm{T}} x_0 + \sum_{\omega\in\Omega} c_\omega^{\mathrm{T}} \left(\sum_{j\in J^l} \theta^j x^j_\omega \right) \\ \text{s.t. } & A_{0,\omega} x_0 + A_\omega \left(\sum_{j\in J^l} \theta^j x^j_\omega \right) \leq b_{0,\omega}, \quad \forall \omega \in \Omega, \\ & \sum_{j\in J^l} \theta^j = 1, \quad \theta^j \geq 0, \quad \forall j \in J^l, \\ & x_0 \in X_0. \end{aligned} \tag{DWRMP^l}$$

As a result, Problem (DWRMP^l) provides an upper bound for Problem (P). Let π^l_ω be Lagrangian multipliers for the first group of constraints in Problem (DWRMP^l), then a DWD pricing problem can be solved to generate an extra point for set X^l. This problem can be decomposed over the scenarios; for scenario ω, the subproblem is:

$$\begin{aligned} obj_{DWPP^l_\omega} = \min_{x_\omega} \; & (c_\omega^{\mathrm{T}} + \left(\pi^l_\omega\right)^{\mathrm{T}} A_\omega) x_\omega \\ & x_\omega \in X_\omega. \end{aligned} \tag{DWPP$^l_\omega$}$$

On the other hand, two subproblems from BD, called **BD primal problem** and **BD relaxed master problem** in this paper, are also solved in CD. The BD primal problem is constructed at the kth BD iteration by fixing $x_0 = x_0^k$. The resulting problem provides an upper bound for Problem (P), and it can be decomposed over the scenarios. For scenario ω, the subproblem can be written as:

$$\begin{aligned} obj_{\mathrm{PP}_\omega^k} = \min_{x_\omega}\ & c_0^{\mathrm{T}} x_0^k + c_\omega^{\mathrm{T}} x_\omega \\ \text{s.t. } & A_{0,\omega} x_0^k + A_\omega x_\omega \le b_{0,\omega}, \\ & x_\omega \in X_\omega. \end{aligned} \tag{BPP$_\omega^k$}$$

Using the principles of projection and dualization (Geoffrion (1972)), Problem (P) can be equivalently formulated into a master problem that includes a finite number of duality-based constraints called *cuts*. When including a subset of the cuts, the problem becomes the following BD relaxed master problem:

$$\begin{aligned} \min_{x_0,\eta}\ & \eta \\ \text{s.t. } & \eta \ge \sum_{\omega\in\Omega} obj_{BPP_\omega^j} + \sum_{\omega\in\Omega} \left(c_0^{\mathrm{T}} + (\lambda_\omega^j)^{\mathrm{T}} A_{0,\omega}\right)\left(x_0 - x_0^j\right), \quad \forall j \in T^k, \\ & \eta \ge \sum_{\omega\in\Omega} obj_{DWPP_\omega^j} + \sum_{\omega\in\Omega} \left(c_0^{\mathrm{T}} + \left(\pi_\omega^j\right)^{\mathrm{T}} A_{0,\omega}\right) x_0 - \left(\pi_\omega^j\right)^{\mathrm{T}} b_{0,\omega}, \quad \forall j \in U^l, \\ & x_0 \in X_0, \end{aligned} \tag{BRMP^k}$$

where T^k includes indexes of Lagrangian multipliers generated from previously solved Problem (BPP$_\omega^k$) before the kth BD iteration, and U^l includes indexes of Lagrangian multipliers generated from previously solved Problem (DWPP$_\omega^l$).

The CD method solves the above four subproblems iteratively to yield a sequence of upper bounds and lower bounds of Problem (P), and the algorithm can converge in a finite number of iterations to an optimal solution. Figure 1 illustrates the algorithmic framework. More details about the CD algorithm can be found in Ogbe and Li (2014).

Remark 1. *The CD method is advantageous over the classical BD method, because it generates better upper and lower bounds via using (a) the better one of the upper bounds provided by DWD and BD upper bounding problems and (b) the better one of the lower bounds from DWD and BB lower bounding problems. Note that in Problem (BRMP^k), the cuts generated by DWD subproblems do not necessarily dominate the Benders cuts, and vice versa.*

3. The multicolumn-multicut cross decomposition method

In the multicolumn-multicut (MCMC) CD, a multicolumn DW restricted master problem instead of Problem (DWRMP^l), and a multicut BD relaxed master problem instead of Problem (BRMP^k), are solved. The multicolumn DW restricted master problem restricts set X using the following set X_{MC}^l instead of X^l:

$$X_{MC}^l = \{x = (x_1, ..., x_s) \in \mathbb{R}^{s \cdot n_x} : x_\omega = \sum_{j\in J^l} \theta_\omega^j x_\omega^j, \sum_{j\in J^l} \theta_\omega^j = 1, \theta_\omega^j \ge 0, \forall j \in J^l, \forall \omega \in \Omega\}. \tag{3}$$

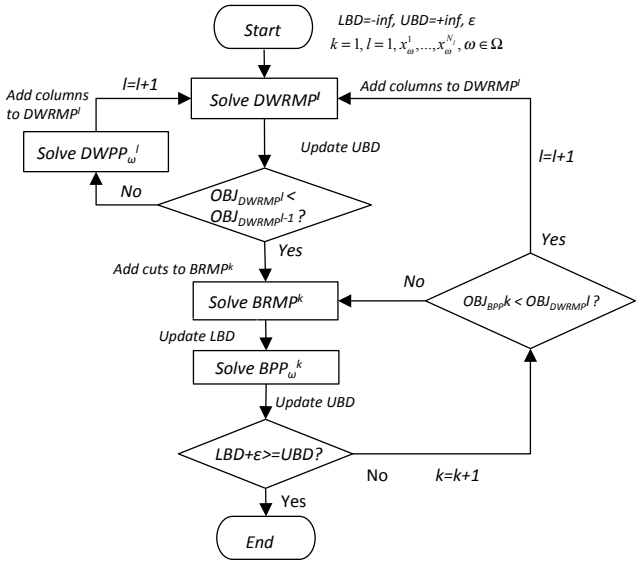

Figure 1: The cross decomposition algorithm flowchart

As a result, the problem can be written as:

$$
\begin{aligned}
obj_{DWRMP-MC^l} = \min_{x_0,\theta_\omega^j}\ & c_0^{\mathrm{T}}x_0 + \sum_{\omega\in\Omega} c_\omega^{\mathrm{T}}\left(\sum_{j\in J^l}\theta_\omega^{\mathrm{j}}x_\omega^{\mathrm{j}}\right)\\
\text{s.t. } & A_{0,\omega}x_0 + A_\omega\left(\sum_{j\in J^l}\theta_\omega^{\mathrm{j}}x_\omega^{\mathrm{j}}\right) \le b_{0,\omega}, \quad \forall\omega\in\Omega, \qquad \text{(DWRMP-MC}^l\text{)}\\
& \sum_{j\in J^l}\theta_\omega^{\mathrm{j}} = 1,\ \theta_\omega^j \ge 0, \quad \forall\omega\in\Omega,\ \forall j\in J^l,\\
& x_0\in X_0.
\end{aligned}
$$

The multicut BD relaxed master problem for the CD can be written as:

$$
\begin{aligned}
\min_{x_0,\eta_1,\ldots,\eta_s}\ & \sum_{\omega\in\Omega}\eta_\omega\\
\text{s.t. } & \eta_\omega \ge obj_{\mathrm{BPP}_\omega}(x_0^j) + \left(c_0^{\mathrm{T}} + (\lambda_\omega^j)^{\mathrm{T}}A_{0,\omega}\right)\left(x_0 - x_0^j\right), \quad \forall j\in T^k,\ \forall\omega\in\Omega,\\
& \eta_\omega \ge obj_{DWPP_\omega^j} + \left(c_0^{\mathrm{T}} + \left(\pi_\omega^j\right)^{\mathrm{T}}A_{0,\omega}\right)x_0 - \left(\pi_\omega^j\right)^{\mathrm{T}}b_{0,\omega}, \quad \forall j\in U^l,\ \forall\omega\in\Omega,\\
& x_0\in X_0.
\end{aligned}
\qquad \text{(BRMP-MC}^k\text{)}
$$

Proposition 1. *(DWRMP-MC^l) is a better restriction of Problem (P) compared to (DWRMP^l).*

Proof. $\forall x = (x_1,\ldots,x_s)\in X_{MC}^l$, consider x_ω in this vector ($\forall\omega\in\Omega$). As x_ω is a convex combination of points in the convex set X_ω (according to Eq. (1)), $x_\omega\in X_\omega$. So $x\in\prod_{\omega\in\Omega}X_\omega = X$. Therefore, $X_{MC}^l\subset X$, and Problem (DWRMP-MC^l) is a restriction of Problem (P).

On the other hand, $\forall x = (x_1, \ldots, x_s) \in X^l$, according to Eq. (2), $\exists \theta^j \geq 0$, x_ω^j ($j \in J^l$, $\omega \in \Omega$) such that $\sum_{j \in J^l} \theta^j = 1$, $x_\omega = \sum_{j \in J^l} \theta^j x_\omega^j$. According to Eq. (3) this implies that $x \in X_{MC}^l$. So $X^l \subset X_{MC}^l$, which means that the feasible set of Problem (DWRMP-MC^l) is closer to the feasible set of Problem (P) and therefore Problem (DWRMP-MC^l) is a better restriction of Problem (P). □

Proposition 2. *(BRMP-MC^k) is a better relaxation of Problem (P) compared to (BRMP^k).*

Proof. This has been proved (in the context of multicut Benders decomposition) in the literature (Birge and Louveaux (1988)). □

Theorem 1. *if Problem (P) is feasible, and all the subproblems can be solved to ε-optimality in a finite number of steps, the MCMC CD algorithm terminates in a finite number of steps with an ε-optimal solution of Problem (P).*

Proof. The CD algorithm in proved to be finitely convergent in Ogbe and Li (2014). Propositions 1 and 2 show that the multicolumn and the multicut reformulations of the master problems even improves the upper and lower bounds generated at each iteration, so the MCMC CD method is finitely convergent. □

4. Case Study

4.1. Case Study Problem and Implementation

We compare BD, multicut BD (MC BD), CD and MCMC CD through a bio-product supply chain optimization problem. This problem was originally presented in Čuček et al. (2010), and later modified into a two-stage stochastic MILP formulation by McLean and Li (2013). The stochastic MILP model contains 18 binary variables and 1876*s* continuous variables, where s is the number of scenarios.

The case study was implemented on a virtual machine running Linux with 3.2GHz CPU and 6 GB memory installed on a Windows host system. MATLAB 2013 was used to program all algorithms. All subproblems were modeled in GAMS 24.1.1 and interfaced with MATLAB using the interface GDXMRW provided by GAMS. CPLEX 12.5 was used as the LP and MILP solver for all implementations.

4.2. Results and Discussion

Figure 2 summarizes the times used to solve the case study problem with different numbers of scenarios using the four approaches. It can be seen that BD is the slowest among the four, and with the multicut formulation, the performance of BD is significantly improved. The multicolumn-multicut formulation also significantly improves the efficiency of CD, and the MCMC CD method achieves the best performance.

Why MCMC CD is the fastest algorithm among the four can be explained with Figure 3. This figure illustrates how the bounds obtained by the four algorithms change during the solution procedure. It can be seen that the bounds generated by MCMC CD converge the fastest, which is because MCMC CD not only updates the bounds using subproblems from both DWD and BD, but also uses better restricted and relaxed subproblems (through multicolumn and multicut formulations). The number of iterations for MCMC CD to converge is about half of that for MCMC BD, less than a third of that for CD, and less than a fourth of that for BD. The fact that MCMC CD is faster than MCMC BD may be due to two reasons. One is that in MCMC CD, the upper bound is the better one of the upper bounds yielded from BD and DWD upper bounding problems. The other is that the solutions of DWD pricing problems provide extra cuts for the Benders relaxed master problem, some of which can be better than the Benders cuts.

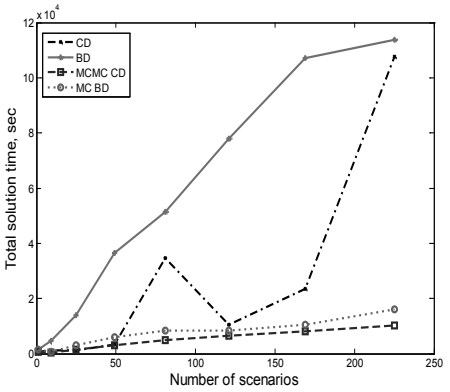

Figure 2: Summary of computational times

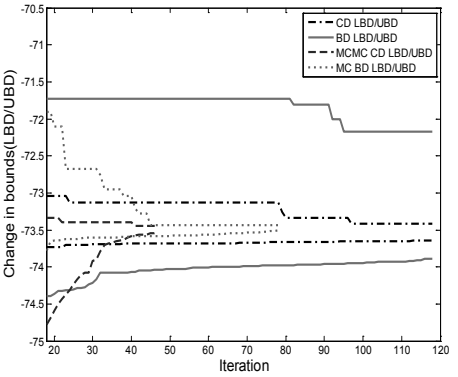

Figure 3: Bound evolution (for 9 scenarios)

5. Conclusions

A MCMC CD algorithm is developed solve stochastic MILPs in form of Problem (P). Tighter upper and lower bounds are derived for the MCMC CD through the multicolumn and multicut reformulation and the reformulation does not hurt the finite convergence of the algorithm. Case study results show that, the MCMC CD is faster than the classical BD method by an order of magnitude when the number of scenarios is large, and it is also significantly faster than CD and MC BD for all cases.

Acknowledgements

The authors are grateful to the financial support from National Sciences and Engineering Research Council of Canada (RGPIN 418411-13).

References

Benders, J., 1962. Partitioning procedures for solving mixed-variables programming problems. Numerische Mathematik 4, 238–252.

Birge, J., Louveaux, F., 2010. Introduction to Stochastic Programming. Springer, New York.

Birge, J., Louveaux, F. V., 1988. A multicut algorithm for two-stage stochastic linear programs. European Journal of Operational Research 34 (3), 384 – 392.

Carøe, C., Schultz, R., 1999. Dual decomposition in stochastic integer programming. Operation Research Letters 24, 37–45.

Čuček, L., Lam, H., Klemeš, J., Varbanov, P., Kravanja, Z., 2010. Synthesis of regional networks for the supply of energy and bioproducts. Clean. Technol. Environ. Policy 12, 635–645.

Dantzig, G., Wolfe, P., 1960. The decomposition principle for linear programs. Operations Research 8, 101–111.

Geoffrion, A. M., 1972. Generalized Benders decomposition. Journal of Optimization Theory and Applications 10 (4), 237–260.

Lasdon, L., 1970. Optimization Theory for Large Systems, 1st Edition. Macmillian, Toronto, Ontario.

McLean, K., Li, X., 2013. Robust scenario formulations for strategic supply chain optimization under uncertainty. Industrial and Engineering Chemistry Research 52, 5721–5734.

Mitra, S., Garcia-Herreros, P., Groassmann, I., 2014. A novel cross-decomposition multi-cut scheme for two-stage stochastic programming. Computer Aided Chemical Engineering 22, 241–246.

Ogbe, E., Li, X., 2014. A new cross decomposition method for stochastic mixed-integer linear programming, to be submitted.

Van Roy, T. J., 1983. Cross decomposition for mixed integer programming. Mathematical programming 25 (1), 46–63.

Krist V. Gernaey, Jakob K. Huusom and Rafiqul Gani (Eds.), 12th International Symposium on Process Systems Engineering and 25th European Symposium on Computer Aided Process Engineering.
31 May – 4 June 2015, Copenhagen, Denmark

Efficient ant colony optimization (EACO) for solvent selection using computer aided molecular design

Berhane H. Gebreslassie and Urmila M. Diwekar*

Center for Uncertain Systems, Tools for Optimization and Management (CUSTOM):Vishwamitra Research Institute,Crystal Lake, IL 60012 – USA
berhane@vri-custom.org

Abstract

Efficient ant colony optimization (EACO) is a new metaheuristic optimization algorithm for tackling linear, nonlinear and mixed integer nonlinear(MINLP) programming problems. In this work, a solvent selection optimization problem modeled based on a novel computer-aided molecular design (CAMD) methodology is optimized using an EACO algorithm. The molecular design problem is formulated as an MINLP model where a solvent solute distribution coefficient is maximized subject to structural feasibility, property and process constraints. The capability of the proposed methodology is illustrated through a case study of an extraction of acetic acid from waste process stream by liquid-liquid extraction. Environmentally benign new solvents with better targeted properties are proposed.

Keywords: Efficient Ant Colony Optimization, Group contribution method, CAMD, Hammersley Sequence Sampling, Solvent selection.

1. Introduction

Solvents are extensively used as process materials, extracting agents and process fluids in the process, pharmaceutical and solvent based industries. Environmental awareness, strict legislation and the need of high performance solvents have lead in the search for environmentally benign and high performing solvents. In many cases, the search for solvents is done through experiments, and database searches. These methods are usually expensive and time-consuming. Computer aided molecular design (CAMD), which is the reverse method of the group contribution method, is a systematic tool that generates solvents of high performance, economical, and with better environmental performance. The existence of a combinatorial search space in molecular design poses a challenge for traditional deterministic optimization methods. In this work, we propose a new approach to solvent design problem by implementing anefficient ant colony optimization (EACO) algorithm. By combining the CAMD and EACO algorithm, large numbers of solvent molecules are generated from a small set of building blocks (given in Table 1.) that satisfy target solvent properties. In the forward problem, the proposed EACO algorithm generates solvent molecules that satisfy the model constraints and the group contribution method predicts properties from the molecular structure and facilitates the solution of the CAMD problem.

ACO is a metaheuristic class of optimization algorithm inspired by the foraging behavior of real ants (DorigoandStutzle, 2004). Natural ants randomly search food by

exploring the area around their nest. If an ant locates a food source, while returning back to the nest, it lay down a chemical pheromone trail that marks its path. This pheromone trail will indirectly communicate with other members of the ant colony to follow the path. Over time, the pheromone will start to evaporate and therefore reduce the attraction of the path. The routes that are used frequently will have higher concentration of the pheromone trial and remain attractive. Thus, the shorter the route between the nest and food source imply short cycle time for the ants and these routes will have higher concentration of pheromone than the longer routes. Consequently, more ants are attracted by the shorter paths. Finally, the shortest path will be discovered by the ant colony. In ACO algorithms, artificial ants are stochastic candidate solution construction procedures that exploit a pheromone model and possibly available heuristic information of the mathematical model. The artificial pheromone trails are the sole means of communication among the artificial ants. Pheromone decay allows the artificial ants to forget the past history and focus on new promising search directions. The pheromone values are updated according to the information learned and the algorithmic procedure leads to very good and hopefully, a global optimal solution. It was originally introduced to solve combinatorial optimization problems, in which decision variables are characterized by a finite set of components. However, in recent years, its adaptation to solve continuous and mixed variable Socha(2004) programming problems has received an increasing attention.

In recent years, there has been a significant research interest in developing and implementing for different applications, however, to the authors knowledge, there is no work in the literature that implement ACO algorithm to solve the MINLP CAMD problems. The proposed algorithm combines CAMD and EACO algorithm proposed by (Gebreslassie & Diwekar, 2015a) as shown in Figure 1. The algorithm parameters, the UNIFAC building block groups and their properties such as the volume and surface area parameters, and the interaction parameters between building blocks are first introduced. These UNIFAC groups are uniquely designed to generate all possible molecules by exploring all possible combinations. For example, as shown in the algorithm, ethanol (CH_3CH_2OH) is generated from the CH_3, CH_2, and OH groups. The number of combinations can be reduced by introducing constraints from physical and chemical properties, structural feasibility as well as those from regulatory restrictions. Once molecules are generated, the properties of the molecules are predicted based on the properties of their building blocks using the UNIFAC model.

Table 1.Set of discrete decision variables

i	N_2^i	i	N_2^i	i	N_2^i	i	N_2^i
1	CH_3-	7	CH_2=C<	13	CH_3CO-	19	CH_3O-
2	-CH_2-	8	-CH=C<	14	-CH_2CO-	20	-CH_2O-
3	-CH<	9	>C=C<	15	-CHO	21	>CHAO-
4	>C<	10	-OH	16	CH3COO-	22	-COOH
5	CH_2=CH-	11	CH_3OH	17	-CH2COO-	23	HCOOH
6	-CH=CH-	12	H_2O	18	HCOO-	24	-COO-

2. Solvent Selection Model Formulation (Case Study)

Acetic acid is commonly used as a process solvent and it is produced as a byproduct. Because acetic acid can be a pollutant as well as a valuable solvent, it is important to minimize or possibly avoid the discharge of acetic acid to the environment. To recycle or remove acetic acid from waste process streams, liquid-liquid extraction is commonly

used. For absorption process, one can either use high-boiling solvents or low-boiling solvents depending on the process considered. Ethyl acetate, isoamylacetate, and isopropyl acetate are widely used in industries to extract acetic acid. Ethyl acetate, which is one of the common solvents for acetic acid extraction, has high solute distribution coefficient (m=0.3156), unfortunately it also has high solvent loss (S_L =0.0560). The high solvent loss property indicates the need alternative environmentally benign solvents. The molecular design problem is formulated as an MINLP model Eq. 1in which a solute distribution coefficient is maximized subject to structural feasibility,

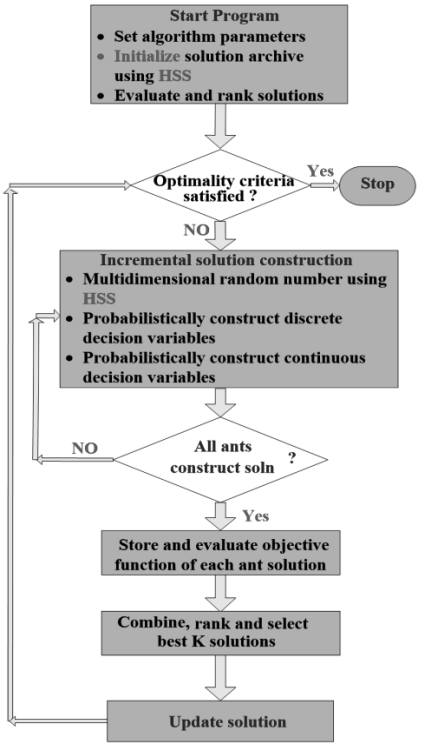

Figure 1.A basic algorithm for solvent selection using EACO.

$$
\begin{aligned}
&\min_{N_1 N_2^i} -m \\
&s.t \quad \beta \geq \beta^{\min} \\
&\quad S_L \leq S_L^{\max} \\
&\quad T_{bp}^{\min} \leq T_{bp} \leq T_{bp}^{\max} \qquad (1) \\
&\quad \mathrm{T_{bp}} = \sum_{i=1}^{N_1} \mathrm{ta(N_2^i)} + \mathrm{t_b} \\
&\quad \sum_{i=1}^{N_1} \mathrm{b_i} = 2(\mathrm{N_1}+1) \\
&\quad 1 \leq N_1 \leq 10 \\
&\quad 1 \leq N_2^i \leq 24 \qquad \forall i \in N_1
\end{aligned}
$$

property, and process constraints. The UNIFAC, the solute distribution coefficient, the solvent selectivity and the solvent loss models can be viewed in (Gebreslassie and Diwekar 2015b)

The bounds on the constraints are taken from the properties of the commonly practiced solvent for acetic acid extraction (Kim & Diwekar, 2002).Normal boiling point (T_{bp}) is estimated using the linear prediction model. $b_i$is the number of free attachments in a group index *i*. In this problem, the discrete decision variables are the number of groups N_1 involved in a solvent molecule and the building block index N_2^i; $i \in \{1, ..., N_1\}$of that molecule. From these groups a unique solvent molecule that has high solute distribution coefficient and the model constraints are generated. As shown in Table 1, the total numbers of groups used in this work are *24* and a maximum of *10* groups per molecule are allowed, therefore, the total combinatorial space is composed of $24^{10}(6.34 \times 10^{13})$ combinations. The three UNIFAC parameters, surface area, volume, and interaction parameters, as well as boiling point parameters, group free attachments and the molecular weights can be viewed in (Gebreslassie & Diwekar, 2015b).

3. Efficient Ant Colony Optimization (EACO) Algorithm

One of the simplest and most widely used methods for sampling is the Monte Carlo method which is based on the pseudorandom number generator. The pseudorandom number generator produces samples that may be clustered in certain regions of the population and does not produce uniform samples. Therefore, in order to reach high accuracy, larger sample sizes are needed, which adversely affects the computational efficiency (Diwekar & Kalagnanam, 1997). (Gebreslassie & Diwekar, 2015a) proposed EACO algorithm that improves the performance of the conventional ACO algorithm for combinatorial, continuous and mixed variable optimization problems by introducing the Hamersley sequence sampling (HSS). The initial solution archive diversity for continuous and mixed-variable optimization problems plays an important role in the performance of ACO algorithm. The uniformity property of the HSS technique is exploited to avoid clustering of the initial solution archive in a small region of the potential solution space. Moreover, ACO algorithm is a probabilistic method, several random probability functions are involved in the algorithm procedure. For example, in combinatorial ACO algorithm, the random number for the transition probability test and for continuous and mixed-variable optimization problems, the random number to test the probability of choosing ant guide from the solution archive. The distribution of these random numbers affects the performance of the ACO algorithm. At this stage, the multidimensional uniformity property of HSS is introduced to improve the computational efficiency of the ACO algorithm. The algorithm proposed in this work combines CAMD and EACO algorithm and it is given in Figure 1.

4. Results and Discussions

The algorithm terminates when it reaches maximum number of iterations (MaxIter), or if the tolerance (eps) that is the relative difference between solutions found in two consecutive iterations is lower or equal to a parameter *eps*for a set of consecutive number of iterations (*ICON)*. The parameters used for the EACO algorithm are archive sizes *K=1500*,number of antsnAnts = 30, *q=1E-3* and *eps=1E-6*, evaporation parameter ρ*=0.75*.

An attractive solvent has a high solute distribution coefficient, selectivity and low solvent loss. The EACO algorithm generated more than 30 solvents with higher m value than Ethyl acetate, which is one of the common practice of solvent for acetic acid extraction (m = 0.3156). The first top 5 solvents for high and low boiling temperature solvents are summarized in Tables 2&3, respectively. As shown in the tables, most of

the high ranked solvent molecules are ethers, alcohols and aldehydes. A high value of m reduces the size of extraction equipment and the amount of recycling solvent. In other words, these high m solvents will reduce the investment cost and the operational cost related to the energy consumption for solvent recovery. From Tables 2&3, it can be concluded that the EACO algorithm generate a set of candidate solvents with better solute distribution coefficient and low solvent loss properties.

Table 2. High boiling point temperature candidate solvents

Rank	Solvent	m	β	S_L	T_{bp}
1	$2CH_2$,C,CH_2=CH,CH=CH,CH_3OH,CH_3O	0.691	8.85	0.010	517.7
2	CH_2,CH,C,$2CH_2$=CH,CH_3OH,CH_3O	0.683	8.66	0.009	509.7
3	CH_3,CH,CH_2-CH,CH_2=C,C=C,CH_3OH,CH_3O	0.628	8.06	0.006	539.6
4	$2CH_3$,$3CH_2$,CH=C,OH	0.615	11.39	0.008	455.9
5	$2CH_3$,CH_2,CH=CH,CH=C,OH	0.613	7.76	0.009	460.1

Table 3. Low boiling point temperature candidate solvents

Rank	Solvent	m	β	S_L	T_{bp}
1	CH_2=CH,CH_2=C, CH_3O, CH_2O	0.751	7.79	0.033	374.9
2	CH_2=CH,CH=CH, CH_3O	0.709	9.25	0.019	337.2
3	CH_3, CH_2=CH,$2CH_2O$	0.666	7.58	0.044	355.4
4	CH_3,CH2=C, CH_3CO	0.612	14.59	0.052	364.4
5	CH_3, CH=CH, CH_3CO	0.610	16.10	0.048	372.0

Comparing the results from EACO algorithm shown in Tables 2&3 and the results reported by Diwekar and co-workers (Kim & Diwekar, 2002b) obtained using Efficient Simulated Annealing (ESA), the best solvent molecule found by EACO algorithm with configuration (*$2CH_2$,C,CH_2 =CH,CH= CH,CH_3OH,CH_3O*) has values of m =0.691, which exceeds the optimal solvent (*CH_3, $6CH_2$,OH*) found by ESA with m = 0.6074. Moreover, the EACO algorithm has also found a set of candidate solvent molecules with better solute distribution coefficients than the first ranked solvent molecule found by ESA. There are two reasons for this phenomenon: (1) the EACO algorithm finds a set of solutions equal to the number of ants used by the algorithm instead of one as in the simulated annealing, and this property enables EACO algorithm the ability to cover the search space easily and gives a better chance to find the global optimum; and (2) in simulated annealing, an infeasible solution is accepted or discarded randomly according to the Metropolis criterion. The disadvantage of this constraint violation handling strategy is that there is no standard for accepting or discarding solutions. Therefore, some infeasible solutions that have more chances to reach the optimum may be discarded and, consequently, some good patterns are lost in the process. In EACO algorithm the selection of q parameter is carefully chosen in such a way to focus initially at exploration and when the quality of the solution is improved to focus on exploitation.

Table 4.Results compared with decomposition methods.

Method	Solvent	m	β	S_L	T_{bp}
Karunanithi et. al. (2005)	1CH3,3CH2,1CH3CO	0.491	11.0	0.0038	404.1

Karunanithiet. al. (2005) proposed a new CAMD methodology where the general molecule/mixture design problem was decomposed into an ordered set of sub-problems such that the solution of the decomposed set of sub-problems is equivalent to that of the

original MINLP problem. In this approach, sub-problem is solved and a large portion of the infeasible part of the search space is deleted, thereby leading to a final sub-problem that is significantly manageable MINLP or NLP problem. Because all the sub-problems except the final sub-problem are constraint satisfaction, global optimality can be guaranteed. The proposed candidate solvent from Karunanithiet. al. (2005) is shown in Table 4. The candidate solvents from EACO algorithm have better solute distribution coefficient for both high (Table 2.) and low (Table 3.) boiling temperature solvents. However, the authors want to mention that the work by Karunanithiet. al. (2005) considers 15 building blocks while we consider 24 building blocks.

5. Conclusions

We propose a new solution strategy based on EACO algorithm for solving solvent selection CAMD problem. The proposed methodology involves formulating the solvent selection molecular design problem as an MINLP model and solution method for identifying candidate solvents.The capability of the proposed approach is illustrated through a case study of solvent selection for acetic acid extraction from waste process stream. The UNIFAC model is used to estimate the mixture properties and the EACO algorithm generateenvironmental benign new solvents with better targeted properties. The EACO algorithm has found a set of candidate solvent molecules with better solute distribution than the first ranked solvent molecules proposed using ESA optimization strategies

References

M. Dorigo and T. Stutzle, (2004). Ant colony optimization theory. A Brand ford Book, The MIT Press, Cambridge, Massachusetts.

K. Socha, (2004). ACO for continuous and mixed-variable optimization. Lecture Notes in Computer Science (including subseries Lecture Notes in Artificial Intelligence and Lecture Notes in Bioinformatics), 3172 LNCS, 25–36.

U.M. Diwekar and J.R. Kalagnanam, (1997).Efficient sampling technique for optimization under uncertainty.AIChE Journal, 43, 440–7.

K. Kim and U. Diwekar, (2002). Hammersley stochastic annealing: Efficiency improvement for combinatorial optimization under uncertainty. IIE Transactions Institute of Industrial Engineers, 34, 761–77.

B. H. Gebreslassie and U. M. Diwekar , (2015a). Efficient ant colony optimization (EACO) algorithm for deterministic optimization. European Journal of Operational Research, (Under revision).

B. H. Gebreslassie and U. M. Diwekar, (2015b).Solvent selection using computer aided molecular design and efficient ant colony optimization. Computers and Chemical Engineering, (Under revision).

A. T. Karunanithi and L. E. K. Achenie and R. Gani.A New Decomposition-Based Computer-Aided Molecular/Mixture Design Methodology for the Design of Optimal Solvents and Solvent Mixtures. Ind. Eng. Chem. Res. 2005, 44, 4785-4797.

Krist V. Gernaey, Jakob K. Huusom and Rafiqul Gani (Eds.), 12th International Symposium on Process Systems Engineering and 25th European Symposium on Computer Aided Process Engineering.
31 May – 4 June 2015, Copenhagen, Denmark

Optimisation of Process Parameters with Simultaneous Consideration of Energy Efficiency Measures

Timo Bohnenstaedt,[a] Kristina Zimmermann,[a] Georg Fieg[a]

[a]*Institute of Process and Plant Engineering, Hamburg University of Technology, Schwarzenbergstraße 95, D-21071 Hamburg, Germany*

Abstract

Sustainable process design and energy efficiency evaluation are major topics for recent process engineering. Process integration by the means of heat recovery is a powerful approach to reduce the need for additional heating or cooling. Usually a heat exchanger network is applied to utilize waste heat within a process directly, while a super ordinated utility system is applied for indirect heat transfer between different processes. The aim of this work is to point out the possibilities of multi-objective optimisation in order to implement the design of heat recovery measures at an early stage of process design. Similar to the well-known pinch technology this new combined optimisation procedure can be best described as an advanced targeting step. Pareto-optimal solutions are generated using a genetic algorithm. The mathematical background will be described within this work.

Keywords: Multi-objective optimisation, Process design, Energy efficiency

1. Introduction

The general concept of the incorporation of heat recovery analysis into the optimisation procedure of process design is outlined by Figure 1.

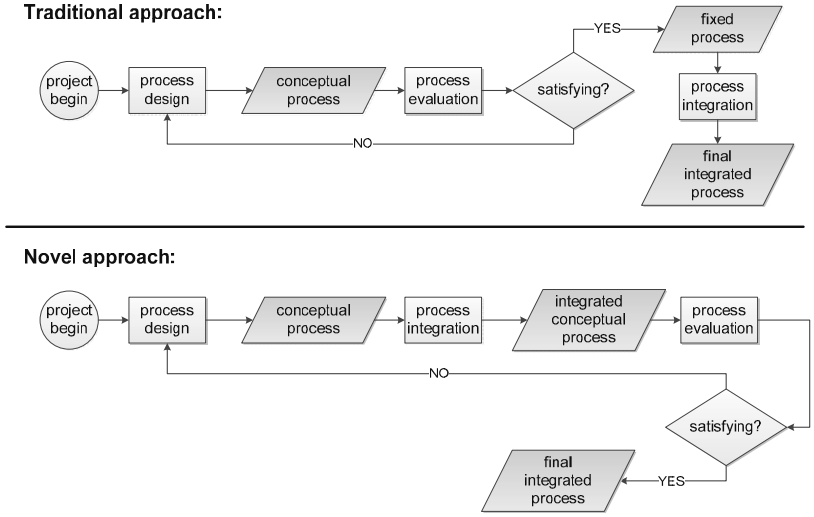

Figure 1: New optimisation approach

The concept is based on two scientific advancements: pinch analysis and multi-objective optimisation. Pinch analysis may be considered as a standard among modern analysis approaches. The development goes back to Linnhoff and Vredeveld (1984). Especially the graphical analysis approach based on the Composite Curves is an essential part of almost all recent analysis approaches. The concept of pinch analysis was extended to the level of site-wide energy analysis by Dhole and Linnhoff (1993), as well as Raissi (1994) and Klemeš et al. (1997) for the graphical methodology. The most recent developments in heat integration techniques are focusing on a wide-spread field of possible secondary objectives for the targeting and design of heat exchanger networks. Escobar et al. for example is investigating flexibility and controllability considerations (2013). Nam Sun et al. is proposing a new optimisation approach for the case of different types of utilities and heat exchanger designs (2013). Another objective of current research is the implementation of systems with heat losses or heat gains investigated by Wan Alwi et al. (2013).

Common for these state-of-the-art advancements in heat recovery methodologies is a fixed and already parameterised process layout defining the desired target temperatures, heat duties and heat capacity flow rates. Traditionally, this is following the idea of a hierarchical, sequential process design approach described by Douglas and Stephanopoulos (1995). Nevertheless does the chosen complexity of heat integration affect investment as well as operating costs just as the determination of process apparatuses or recycle streams do. Taking this reason into account it is very promising to include heat integration into the earlier steps of process design via a multi-objective evaluation.

2. Background foundation for optimisation

As already mentioned in the introduction the chosen approach for the incorporation of heat recovery measures into the procedure of process design is done by the analysis of investment and operating costs. In order to do so a typical multi-objective optimisation problem with constraints is mathematically formulated according to Equations 1 to 4.

$$f_o(\boldsymbol{x}) \qquad o = 1, 2, \dots, O \tag{1}$$

$$g_j(\boldsymbol{x}) \geq 0 \qquad j = 1, 2, \dots, J \tag{2}$$

$$h_k(\boldsymbol{x}) = 0 \qquad k = 1, 2, \dots, K \tag{3}$$

$$x_l^{LB} \leq x_l \leq x_l^{UB} \qquad l = 1, 2, \dots, L \tag{4}$$

A solution to this multi-objective optimisation is given by a vector of decision variables $\boldsymbol{x} = (x_1,\ x_2, \dots, x_L)^T$ that minimizes the dimensions o of the objective function $f_o(\boldsymbol{x})$. The solutions have to be subject to each inequality constraint $g_j(\boldsymbol{x})$ and each equality constraint $h_k(\boldsymbol{x})$. The solution space for each decision variable x_l is restricted to values within its lower bound x_l^{LB} and upper bound x_l^{UB}.

For the approach described by this work $f_1(\boldsymbol{x})$ would be a representation of the investment costs and $f_2(\boldsymbol{x})$ would be a representation of the operating costs. Both objective functions are dependent on the process parameterisation $\boldsymbol{x}$. In accordance to the aim of heat integration the vector of decision variables has to consist of all process variables that affect process temperatures, heat duties or heat capacity flow rates. Both objective functions have to be minimized for optimal solutions as shown in Figure 2.

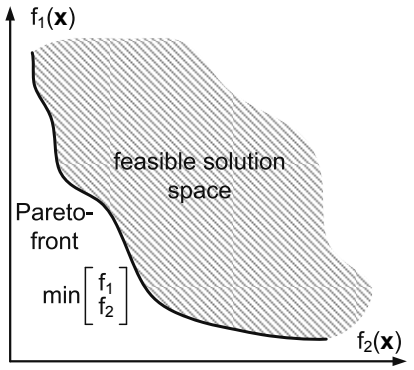

Figure 2: Illustration of a Pareto-front

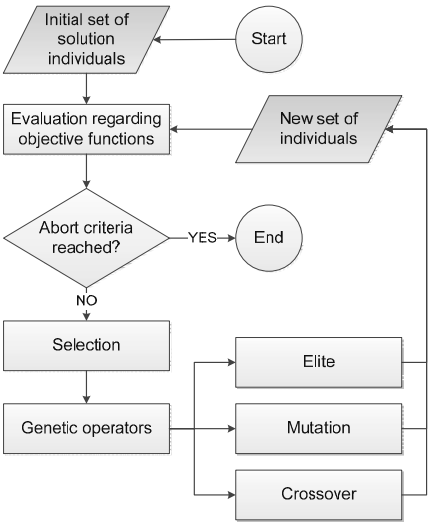

Figure 3: Flow chart for a genetic algorithm

3. Scientific implementation

The optimisation approach stated in Chapter 2 leads to a non-linear mixed integer problem type. It is obvious that rather than a single solution, multiple process design have to be evaluated for generating a Pareto-front consisting of the best solutions found. Proven methods for solving such kind of task are population-based stochastic algorithms. For the terms of this work a genetic algorithm was developed. A basic scheme for the method of operation is illustrated by Figure 3. Each solution candidate of the genetic algorithm is represented by a set of decision variables $\boldsymbol{x}$. A set of decision variables is directly related to a corresponding set of input variables of a computer aided flowsheet. The flowsheet calculation of each individual is used to complete the necessary data for the evaluation regarding the objective functions. A simplified example for a single reactor system is given by Figure 4.

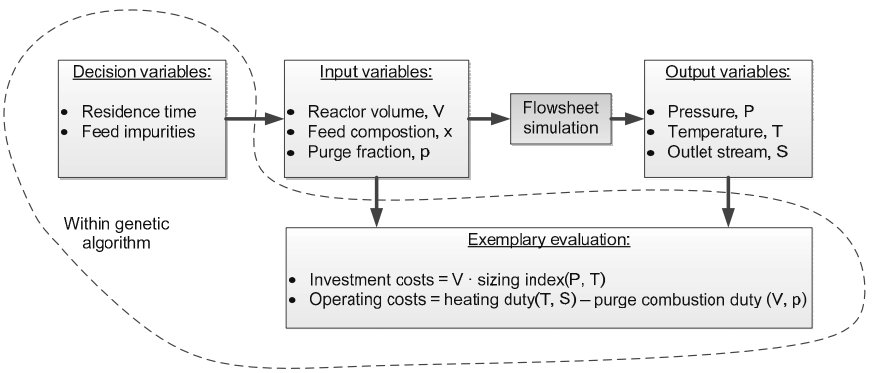

Figure 4: Relation between decision/input/output variables

4. Embedded targeting procedure

As far as the explanation from previous chapters go the investment costs as well as the operating costs are directly derived from the parameterisation of all process apparatuses. Taking direct heat recovery into account is a difficult task since the optimal heat exchanger network could be structurally different for each individual throughout the optimisation procedure. A possible solution would be the implementation of a heat exchanger superstructure to each flowsheet but the amount of decision variables would be rather large. This would result in a bad convergence behaviour.

In order to address this problem a pinch targeting step, novel in the case of multi-objective optimisation, is supposed. Heat exchangers for the purpose of direct heat integration between process streams or process units are completely removed from each individual flowsheet. Heating or cooling for process requirements is done solely by the use of utilities. The analysis of investment costs due to the acquirement of heat exchangers for direct heat integration as well as the analysis of operating costs due to the reduced utility consumption are uncoupled from the flowsheet and calculated separately. In terms of the notation introduced in Chapter 2 the mathematical background for the objective functions $f_1(\boldsymbol{x})$ and $f_2(\boldsymbol{x})$ is the following.

Investment costs:
$$f_1(\boldsymbol{x}) = \left(\sum_{i=1}^{I} f_{1,i}(\boldsymbol{x})\right) + t_1(\boldsymbol{x}) \tag{5}$$

Operating costs:
$$f_2(\boldsymbol{x}) = \left(\sum_{i=1}^{I} f_{2,i}(\boldsymbol{x})\right) + t_2(\boldsymbol{x}) \tag{6}$$

It can be seen that each objective function consists of a sum of the particular objective function values $f_{o,i}(\boldsymbol{x})$ for each apparatus i calculated with the help of the flowsheet simulation. In addition to this, an expression $t_1(\boldsymbol{x})$ for the investment costs and $t_2(\boldsymbol{x})$ for the operating costs calculated by the pinch targeting is added. An illustration is given by Figure 5. For the presented example the calculation of the pinch targeting for a set of composite curves provides the information about seven theoretical heat exchangers for the purpose of internal heat integration and as well as three units to satisfy the utility demand.

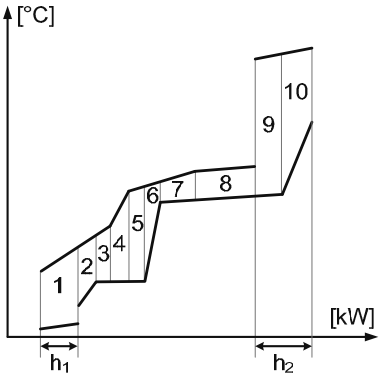

Figure 5: Pinch targeting at composite curves

$$t_1(\boldsymbol{x}) = \sum_{i=1}^{10} (a + b \cdot A_i^c) \tag{7}$$

$$t_2(\boldsymbol{x}) = d \cdot h_1 + e \cdot h_2 \tag{8}$$

With the help of the Equations 7 and 8 the addition to each objective function could be calculated. The investment costs are dependent on the area A_i of each theoretical heat exchanger modified by the costing parameters a, b and c. The operating costs are exclusively dependent on the required utility duty h_1 and h_2 modified by costing parameters d and e for hot or cold utility requirements. At this point it has to be said that the use of more complex economic models would also fit to the presented concept. The use of multiple utilities or other mathematical relations for different heat exchanger types may come to mind.

5. Technical implementation

In order to give a more complete description of the so far presented procedure a brief summary of the technical realisation will be given in this chapter. The genetic algorithm as well as the algorithm for composite curve calculation and targeting has been designed within the Matlab™ environment from MathWorks™. AspenPlus™ from AspenTech™ is used for the flowsheet simulation. The interface between those two is established by using an OLE (object linking and embedding) server. The server follows COM standard (component object model technology, Microsoft™) and is based on an DLL (dynamic link library) that is provided by AspenTech™. While the genetic algorithm could be designed using a different programming language, the full access on all simulation variables via a provided interface is crucial and not available for every commercial flowsheet simulator.

6. Conclusion

The fact that computational calculation speed doubles every two years is stated by the well-known Moore's law. This progress enables more and more advanced optimisation and design methodologies in the engineering sector. The design of a whole chemical process with overlaid multi-objective optimisation as it is presented within this document profits from this development due to the large calculation effort. Furthermore, the right choice of decision variables as well as the right setup of objective functions is crucial for comprehensive results. Apart from these drawbacks the presented concept can be easily extended by any kind of advanced targeting methodologies. Even for the presented targeting procedure it can be shown that a more detailed analysis of a process design is possible. The impact of applying this new procedure is presented by first analysis results in Figure 6 and Figure 7.

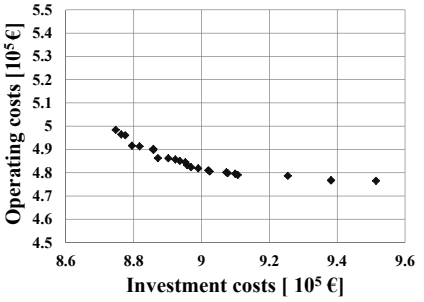

Figure 6: Results for novel approach

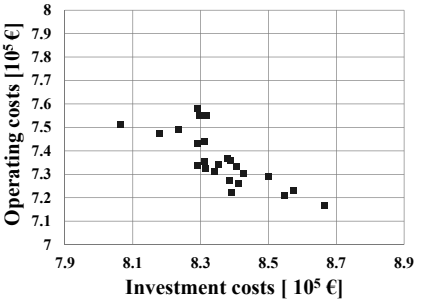

Figure 7: Corresponding results without targeting

The above presented results correspond to a process describing the dehydration of isopropanol to acetone (seven unit operations). Major decision variables have been the amount of separation stages, feed-stage and pressure of the distillation columns as well as the pressure, outlet temperature, length and amount of tubes for the tubular reactor. Figure 6 presents a front of Pareto optimal solutions for the last generation that has been calculated using the novel approach. Figure 7 presents the same individual solutions recalculated without the embedded targeting procedure of this work. It can be clearly identified that the new optimisation approach promotes solutions that otherwise would not participate in the final Pareto-front. It can be stated that the consideration of energy efficiency measures has an impact on the convergence behaviour of the genetic algorithm. Applying the new approach offers a more detailed insight while maintaining a wide variety of process alternatives to choose from.

References

V. R. Dhole, B. Linnhoff, 1993, Total site targets for fuel, co-generation, emissions, and cooling, Computers and Chemical Engineering, 17, S101-S109

J. M. Douglas, G. Stephanopoulos, 1995, Hierarchical Approaches in Conceptual Process Design: Framework and Computer Aided Implementation, L. T. Biegler (Ed.), & M. F. Doherty (Ed.), 4th International Conference on Foundations of Computer Aided Process Design – AIChE Symposium Series, 304, 183–197, American Institute of Chemical Engineers.

M. Escobar, J. O. Trierweiler, I. E. Grossmann, 2013, Simultaneous synthesis of heat exchanger networks with operability considerations: Flexibility and controllability, Computers and Chemical Engineering, 55, 158-180

J. J. Klemeš, V. R. Dhole, K. Raissi, S. J. Perry, L. Puigjaner, 1997, Targeting and design methodology for reduction of fuel, power and CO2 on total sites, Applied Thermal Engineering, 17, 993-1003.

B. Linnhoff, D. R. Vredeveld, 1984, Pinch technology has come of age, Chemical Engineering Progress, 80, 33-40.

K. Nam Sun, S. R. Wan Alwi, Z. A. Manan, 2013, Heat exchanger network cost optimization considering multiple utilities and different types of heat exchangers, Computers and Chemical Engineering, 49, 194-204

K. Raissi, 1994, Total site integration. PhD Thesis, UMIST, Manchester

S. R. Wan Alwi, C. K. Mun Lee, K. Yau Lee, Z. A. Manan, D. M. Fraser, 2013, Targeting the maximum of heat recovery for systems with heat losses and heat gains, Energy Conversion and Management, 87, 1089-1106

Krist V. Gernaey, Jakob K. Huusom and Rafiqul Gani (Eds.), 12th International Symposium on Process Systems Engineering and 25th European Symposium on Computer Aided Process Engineering.
31 May – 4 June 2015, Copenhagen, Denmark

Optimization of split fractions and cleaning schedule management in heat exchanger networks

Jian Du,[a] Jie Fan,[a] Linlin Liu,[a,b] Jilong Li,[a] Yu Zhuang,[a] Qingwei Meng[c]

[a]*Institute of Chemical Process Systems Engineering, Dalian University of Technology, Dalian 116024, Liaoning, China*
[b]*Key Laboratory of Industrial Ecology and Environmental Engineering(MOE), School of Environmental Science and Technology, Dalian University of Technology, Dalian 116024, Liaoning, China*
[c]*Key Laboratory of Fine Chemical Engineering, School of Environmental Science and Technology, Dalian University of Technology, Dalian 116024, Liaoning, China*

Abstract

Fouling is a non-negligible problem to heat exchange operation, because it will cause sustained reduction to the overall heat transfer coefficient due to the growth of deposit over heat transfer surface of heat exchange equipments. Implementing regular (routine) cleaning is a recommendable means to remove fouling. As heat load distribution of parallel branches is related to split fractions, this paper presents an approach to arrange the cleaning schedule with having split fractions optimized concurrently. To avoid the numerous integer decision variables produced in time discretization method, the maximum allowable fouling resistance of a heat exchanger is taken as the optimization variable in this study. Then the proposed method is formulated into a Mixed Integer Nonlinear Programming (MINLP) model, to aim for the minimum operating cost of an existing HEN. At last of the study, an example from literature is studied, and the effectiveness of the method has been demonstrated by the proper results.

Keywords:heat exchanger network,optimization,fouling,cleaning schedule,split fraction

1. Introduction

The gradual accumulation of deposits over the surface of heat exchanger decreases heat transfer efficiency and generates fluctuation of the outlet temperatures of hot and cold streams. This phenomenon implies an increase in the extra utility consumption in the heat exchanger network(HEN). In the past two decades, scholars paid much attention on the fouling problem. Many measures were taken to mitigate the effect of fouling(Azad et al., 2011; Pan et al., 2013). Nevertheless, only periodic cleaning can effectively remove deposits and restore thermal performance of the equipment. Therefore determining the cleaning schedule of the heat exchanger network becomes a hot spot of researchers. Smaili et al.(1999) proposed the first formulation about cleaning management for an existing HEN aiming at the minimum steam consumption. Although improved algorithms(Smaili et al., 2002) were introduced subsequently, based on the

approach of time discretization , large amount of binary variables still formulated a mixed integer nonlinear programming (MINLP) model, resulting in the difficulty to solve the problem.

Until in the design of single heat exchanger, a maximum allowable fouling resistance was proposed in the optimization of the equipment design and cleaning policy(Caputo et al., 2011), which effectively reduced the number of decision variables. In HEN composed by multiple parallel branches, stream split fractions was demonstrated to affect the distribution of heat load in each branch. According to different fouling status of the existent heat exchangers, Oliveira Filho et al.(2009) investigated an alternative operating policy based on the optimization of stream splits aiming to the minimum operating cost. While the dynamic change of fouling wasn't considered. Taking the growth of fouling into account, this paper proposed an approach combined the optimization of split fractions with the optimal cleaning schedule aiming at the minimum operating cost in a existing HEN. In order to reduce complexity of the problem, the maximum allowable fouling resistance based on the literature was applied.

2. Problem description

Here the network configuration is fixed. A set of hot and cold streams with their heat capacity flow rates, inlet and outlet temperatures passing through the units are given and the initial split fractions of parallel branches are known. Assuming that all the heat exchangers are clean at the beginning, then an universal asymptotic fouling model was adopted to describe the deposits profile in the equipments.

The problem comprises two sets of decision variables. One is the maximum allowable fouling resistances, representing cleaning schedule, which will be expounded in the following part. The other is the split fractions, redistributing the flow rates of the hot and cold streams in each branch of the heat exchanger. They are both continuous variables, along with the state variables of the equipments, defining the optimization as a mixed integer nonlinear programming(MINLP) problem. The solution is found by using Genetic/Simulated Annealing(GA/SA) algorithm(Xiao et al., 2010).

3. NLP formulation for the optimization of split fractions and cleaning schedule

3.1. The maximum allowable fouling resistance

As most of the deposits involved in the petrochemical production grow asymptotically over time, an universal asymptotic fouling formation model is adopted to describe the growth of fouling represented with Eq. (1).

$$R(t) = R_f^{\infty}\left(1 - e^{-t^*/\tau}\right) \tag{1}$$

where R_f^{∞} and τ are empirical parameters obtained by experiments. t^* is the time elapsed since the exchanger was in the clean condition.

As shown in Figure. 1, heavy line represents no cleaning condition, thin lines represent periodic cleaning condition. By setting a maximum allowable fouling resistance, R_{all}, to define the threshold level, that is, when the fouling thermal resistance reach this value, the heat exchanger should be cleaned right now, below this value, the unit runs. As the fouling model is strictly monotonic function, each maximum allowable fouling resistance corresponds to a timing of the cleaning actions, T_{cy}.

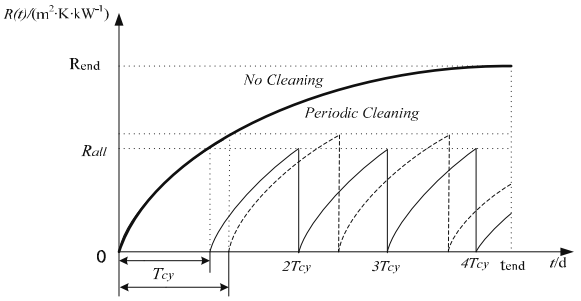

Figure 1. Scheme of a maximum allowable fouling resistance.

The following sets of indices are used to describe the network:
t is the number of days (1, . . . , T_{opr})
n is the unit number (1, . . . , NE)
where T_{opr} is the number of days that the HEN is operating and NE is the number of units. The total cleaning number of a unit, N_{cl}, can be calculated with Eq. (2).

$$N_{cl,n} = T_{opr} / T_{cy,n} \tag{2}$$

The selection of R_{all} is the key to solve the problem of cleaning schedule, referring to Figure. 1(thin and solid lines: smaller R_{all} ; thin and dashed line: larger one), the smaller is the R_{all}, the more cleaning actions should be taken, which will decrease the utility consumption yet produce more cleaning cost. There is a trade-off in the determination of R_{all} value.

3.2. Running state variables of heat exchangers

Each unit n over each day t is defined by a binary variable $Z_{t,n}$ where

$$Z_{t,n} = \begin{cases} 1 & \text{if unit n is on-line over day t} \\ 0 & \text{otherwise} \end{cases} \tag{3}$$

It can be inferred that all the $Z_{t,n}$ equal to 1 except when the fouling thermal resistance reaches $R_{all,n}$, in other words, when the unit runs to $t = NT_{cy,n}$ (N=1,2,...,Ncl,n), it should be taken off-line or pass through other units if there are ones by a standby pass for cleaning. At that moment, $Z_{t,n}$ will change to 0.

3.3. Simulation of heat exchangers

The ε-NTU method is used to simulate heat exchangers suffering from different degrees of fouling. The method is based on three dimensionless parameters: CR, NTU, and ε.

Assuming the hot stream has lower heat capacity flow rate than the cold one, then the three parameters are defined as follows:

$$CR = \frac{FCp_h}{FCp_c} \tag{4}$$

$$NTU = U \cdot A / FCp_h \tag{5}$$

$$\varepsilon = \frac{1 - \exp\left[-NTU\left(1 - CR\right)\right]}{1 - CR\exp\left[-NTU\left(1 - CR\right)\right]} \tag{6}$$

In which, the overall heat transfer coefficient is related to that in the clean state by

$$U = 1/\left[1/U_{cl} + R(t)\right] \tag{7}$$

The outlet temperatures of hot and cold streams are expressed respectively as:

$$T_{h,out} = Z_{t,n} \cdot \varepsilon \cdot T_{c,in} + \left[1 - Z_{t,n} + Z_{t,n} \cdot \left(1 - \varepsilon\right)\right] \cdot T_{h,in} \tag{8}$$

$$T_{c,out} = Z_{t,n} \cdot CR \cdot \varepsilon \cdot T_{h,in} + \left[1 - Z_{t,n} + Z_{t,n} \cdot \left(1 - CR \cdot \varepsilon\right)\right] \cdot T_{c,in} \tag{9}$$

3.4. Modeling of parallel heat exchangers

As it is shown in Figure. 2, the hot and cold streams are separated into two branches, the heat capacity flow rate of each branch flowing through the No.1 heat exchanger is given by Eq. (10) and (11):

$$Fcp_{h,1} = x_h \cdot Fcp_h \tag{10}$$

$$Fcp_{c,1} = x_c \cdot Fcp_c \tag{11}$$

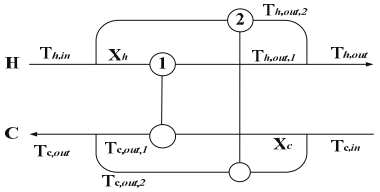

Figure 2. Schematic of parallel heat exchangers

in which x_h and x_c are the split fractions of hot and cold streams. The simulation of each heat exchanger is the same as above. It is worth mentioning that after flowing through the parallel units, each branch of hot or cold stream will be mixed,

$$T_{h,out} = x_h \cdot T_{h,out,1} + \left(1 - x_h\right) \cdot T_{h,out,2} \tag{12}$$

$$T_{c,out} = x_c \cdot T_{c,out,1} + \left(1 - x_c\right) \cdot T_{c,out,2} \tag{13}$$

But when one of parallel units is cleaned, it is advised to merge the stream which should be bypassed into the other one on-line instead. It is indicated that if $Z_{t,1}=0$, then $FCp_{c,2}=FCp_c$, $FCp_{h,2}=FCp_h$, $T_{c,out}=T_{c,out,2}$,$T_{h,out}=T_{h,out,2}$; similarly if $Z_{t,2}=0$.

3.5. Objective Function

The objective function to be minimized is the total operating cost over the time interval 0 to t_{end}, including extra energy required due to fouling, provided by heating and cooling utilities, C_E, and cleaning cost, C_{cl}.

$$obj = \min(C_E + C_{cl}) = \min[C_U \cdot \int_0^{t_{end}} (Q_{nofouling} - Q_{fouling\&cleaning}(t))dt + \sum_{n=1}^{NE} N_{cl,n} \cdot C_{cl,n}] \quad (14)$$

4. Case study

The optimization of split fractions and cleaning schedule using the above MINLP formulation will be demonstrated using an example from Oliveira Filho(2009). The optimal procedure was implemented in C++ Language.

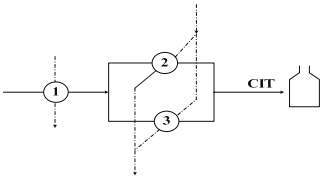

Figure 3. HEN for case study . solid line: cold streams; dotted lines: hot streams.

The parameters for case study is presented in Table 1. The HEN operates over 18 months starting from the clean state and the two splits of hot and cold stream passing through HEX 2 set to 0.5. The cost of furnace utility is taken as 0.01£/kWh. The each time cleaning cost $C_{cl,n}$ is 4000 £/unit.

Table 1. Parameters for Case Study

HEX	$T_{h,in}$/K	$T_{c,in}$/K	FCp_h /kW·K^{-1}	FCp_c /kW·K^{-1}	A/m^2	U_{cl} /kW·m^{-2}·K^{-1}	R_f^{∞} /(m^2·K·kW^{-1})	τ/d
1	523	373	49.84	100.08	800	0.2	4.68	120
2	623	439[a]	24.92	50.04	800	0.2	4.68	120
3	623	439[a]	24.92	50.04	800	0.2	9.35	120

[a]At the beginning/initial state

Table 2. Comparison of different optimization results

	Base Case	Case 1	Case 2
Operating Cost/£	192048	184858	172493
Utility Cost/£	192048	184858	164493
Cleaning Cost/£	—	—	8000
Split fraction	0.5 (H), 0.5 (C)	0.585 (H), 0.586 (C)	0.596 (H), 0.593 (C)
R_{all}/(m^2·K·kW^{-1})	Uncleaned	Uncleaned	4.00 (HEX 2)
Tcy/d			232 (HEX 2)

The results are displayed in Table 2. The extra energy consumption cost of the base case is 192048£ without cleaning. At first, only the split fraction is optimized(Case 1) while the fouling still grows, the optimal split fractions of hot and cold stream are 0.585 and 0.586, respectively. The extra utility caused by fouling is 184858£, which is 3.74% less compared with the base case. Then the split fractions and cleaning schedule are optimized simultaneously(Case 2), the optimal split fractions of hot and cold stream are

0.596 and 0.593, the total operating cost is 173944£. Besides the fuel consumption of furnace, the HEX 2 needs to be cleaned twice during the 18 months operation, which brings 6.69% less than the Case1.

5. Conclusions

This paper presents an approach that combined the optimization of split fractions with the optimal cleaning schedule. The maximum allowable fouling resistances were taken as the optimization instead of integer variables, effectively reducing the number of decision variables. The adjustment of split fractions made the allocation of heat load in the parallel units more reasonable, thus decreasing the total utility consumption of the heat exchanger networks to some extent. Cleaning actions could restore the heat transfer performance of equipments, further reducing the utility consumption.

Acknowledgements

The authors gratefully acknowledge the financial support from Natural Science Foundat ion of China (No. 21406026). Funding from China Postdoctoral Science Foundation (20 14M551091) and Natural Science Foundation of Chinese Liaoning (No. 214020007) are deeply appreciated.

References

M. Pan, I. Bulatov, R. Smit, 2013, Exploiting tube inserts to intensify heat transfer for the retrofit of heat exchanger networks considering fouling mitigation, Industrial & Engineering Chemistry Research, 52, 8, 2925-2943

A V. Azad, H. Ghaebi, M. Amidpour, 2011, Novel graphical approach as fouling pinch for increasing fouling formation period in heat exchanger network(HEN) state of the art, Energy Conversion and Management, 52, 1, 117-124

F. Smaili, D K. Angadi, C M. Hatch,1999, Optimization of scheduling of cleaning in heat exchanger networks subject to fouling: sugar industry case study, Food and Bioproducts Processing, 77, 2, 159-164

F. Smaili, V S. Vassiliadis, D I. Wilson, 2002, Long-term scheduling of cleaning of heat exchanger networks - comparison of outer approximation-based solutions with a backtracking threshold accepting algorithm, Chemical Engineering Research Design, 80, 6, 561-578

A C. Caputo, P M. Pelagagge, P. Salini, 2011, Joint economic optimization of heat exchanger design and maintenance policy, Applied Thermal Engineering, 31, 8, 1381-1392

L O. Oliveira Filho, F S. Liporace, E M. Queiroz, A L.H. Costa, 2009, Investigation of an alternative operating procedure for fouling management in refinery crude preheat trains, Applied Thermal Engineering, 29, 3073-3080

F. Xiao, J. Du, L. Liu, 2010, Simultaneous optimization of synthesis and scheduling of cleaning in flexible heat exchanger networks, Chinese Journal of Chemical Engineering, 18, 3, 402-411

Krist V. Gernaey, Jakob K. Huusom and Rafiqul Gani (Eds.), 12th International Symposium on Process Systems Engineering and 25th European Symposium on Computer Aided Process Engineering.
31 May – 4 June 2015, Copenhagen, Denmark

A cost targeting method for studying investment on heat exchanger networks for collection of industrial excess heat

Matteo Morandin[a], Lina Eriksson[b]

[a]*Industrial Energy Systems and Technologies, Chalmers University of Technology, Gothenburg, Sweden*
[b]*Energy Technology, SP Technical Research Institute of Sweden, Gothenburg, Sweden*

Abstract

This paper discusses the design of water based heat collection system for recovery of industrial excess heat. The focus in on the problem of finding the optimal combinations of excess heat sources minimizing heat exchanger network capital costs for different amounts of total recovered heat. A cost targeting approach based on vertical heat transfer between hot process streams and the heat collection medium in Pinch Analysis diagrams is used. The set of process streams where heat shall be recovered is found by solving an optimization problem where heat recovery is maximized while minimizing the capital costs simultaneously. A genetic algorithm based optimization tool is used. The analysis is conducted for three plants belonging to a chemical cluster. The results are compared with results from previous investigations in which the process excess heat sources were chosen based on their incremental heat contribution. The new approach presented in this work allows identifying a much larger set of solutions as well as considerably lower capital costs for similar amount of recovered heat in cases when process streams largely differ in terms of temperature levels and heat transfer properties.

Keywords: heat exchanger network, excess heat, pinch analysis, optimization.

1. Introduction

Large amount of heat at medium and low temperatures is often dispersed from oil-refineries and petrochemical plants to the environment by means of water or air cooling. This heat can be to large extent recovered for different purposes such as for reducing on-site fuel demand by heat exchange with cold process streams (Hackl et al., 2011), for exporting heat to nearby urban areas by district heating networks (Morandin et al., 2014), or for producing electricity by means of organic Rankine cycles (Campana et al., 2013).

A practical way to reduce the complexity of new installations, to avoid extensive process retrofit, and to avoid potential hazard of process leaks, is to use heat collection systems based on water or oil loops. Water (or oil) is used to cool hot process streams and, once heated, to provide heat to cold process streams, to a district heating network, to a centralized power plant, etc.

Feasibility studies were recently conducted on heat recovery and excess heat export from a chemical cluster in the Swedish West Coast (Morandin et al., 2014). About 230 MW of heat can be potentially recovered from the chemical cluster which could be for instance delivered to a regional district heating network. However, this could represent a prohibitive investment in infrastructures both for the industries and for the municipal

utility companies. It is therefore interesting to consider a large range of possible heat recovery capacities, and not only the maximum amount of cluster excess heat. In addition, since revenues from excess heat utilization depend on the application, it is convenient to study the profitability of excess heat utilization by separating the capital costs estimation procedure from the actual profitability analysis.
In this work we tackle the problem of finding the optimal combinations of excess heat sources from three industrial plants of the aforementioned chemical cluster that minimize heat exchanger network capital costs for different amounts of total recovered heat. This implies to generate multiple heat exchanger network solutions to cover the large range of heat recovery capacity.
This study can be considered a particular case of heat exchanger network synthesis where only one cold stream (the cold side of the heat collection system) appears. Heat exchanger network synthesis is a rather old problem and a variety of methods were proposed in the past. While heuristic methods appears of easier implementation (Sun & Luo, 2011), more elegant problem formulations were proposed based on mathematical programming based on sequential (Anantharaman et al., 2010) or simultaneous (Laukkanen & Fogelholm, 2011) approaches.
Here we opted for a capital cost targeting method based on Pinch Analysis diagrams (Kemp, 2007) and avoided the rigorous syntheses of multiple heat exchanger networks. Still, we need to establish a priori the set of process streams where heat shall be recovered.
In a previous study where the district heating application was considered, a procedure was developed to organize the excess heat sources according to their maximum incremental contribution to district heating delivery capacity, based on the idea that the number of process streams should be minimized to minimize the complexity and therefore the total capital costs (Morandin et al., 2014). We are aware that these combinations of process heat sources might only represent suboptimal subset of solutions. Here, we take a step further in our methodology by introducing a two-objective discrete optimization problem where the excess heat sources are assigned binary variables and a genetic algorithm is used to sort out the front of optimal arrays of excess heat sources that maximize the amount of recovered heat by minimizing the investment simultaneously.
The analysis is conducted for three plants belonging to the chemical cluster with more than twenty excess heat sources each and where the maximum theoretical level of heat that can be recovered is of the same order of magnitude (between 50 and 70 MW).

2. Methodology

Pinch Analysis was used in this work for estimating the amount of heat that can be recovered from process excess heat sources by water based heat collection system. The heat contributions of the process streams that are today cooled by cold water or air are aggregated in a hot composite curve. The heat recovery target is estimated considering counter-current heat transfer with the cold side of the heat collection system. Note that the send and return temperatures of the heat collection system affect the heat recovery potential as well as the type and profitability of excess heat utilization and therefore should be regarded as design variables. However, we decided to leave this aspect to future investigations and these temperatures are here kept at constant values decided with the help of industrial partners (send:54 °C, return:84 °C). For a given array of process excess heat sources, the heat recovery potential is estimated by the condition in which the water thermal profile is at a minimum temperature difference (here 10 °C)

from hot composite curve (pinch point). In practice this was calculated by solving a linear programming problem where the heat transfer feasibility is formulated with a set of linear inequality constraints (Morandin, 2013).

Following the so-called area targeting method (Kemp, 2007), the heat exchanger network capital cost is estimated considering vertical heat transfer between the excess heat sources and the water thermal profile as it appears in the composite curve diagram. In particular, the diagram is divided in enthalpy intervals where the hot composite has constant slope. Since the cold side of the heat collection system is the only cold stream, in each enthalpy interval the number of required heat exchangers is equal to the number of excess heat sources involved.

The investment costs on the heat collection system I_{HCS} for a given array of process heat sources are estimated as in Eq. (1), according to costing methodology in common chemical engineering reference books (Turton et al., 2008). It consists in a sum of heat exchanger purchase cost calculated for each stream *h* belonging to each enthalpy interval *e* of the composite curve diagram where heat recovery occurs $(e \in HCS)$. Heat exchanger cost is a function of the heat transfer surface and ultimately of the stream heat capacity c_h, its mass flow rate $\dot{m}_h$, its inlet and outlet temperature in the enthalpy interval $T_{h,e}^{1}$ and $T_{h,e}^{2}$, the water inlet and outlet temperatures in the enthalpy interval $T_{HCS,e}^{1}$ and $T_{HCS,e}^{2}$, the stream specific global heat transfer coefficient U_h, as well as the type and material of heat exchangers. This sum is then multiplied with the *Lang* factor to account for other installation costs including piping and instrumentation. The reader is referred to a previous publication for the complete formulation of investment cost calculations (Morandin et al., 2014).

$$I_{HCS} = Lang \cdot \sum_{e \in HCS} \sum_{h} f(c_h, \dot{m}_h, T_{h,e}^{1}, T_{h,e}^{2}, T_{HCS,e}^{1}, T_{HCS,e}^{2}, U_h) \tag{1}$$

The above procedure for heat and cost targeting applies for a given array of process excess heat sources. The ultimate question we try to address here is which streams should be involved in the heat recovery. The number of combinations of excess process streams is 2^n with n the number of available process excess heat sources, so the comparison of the complete set is not feasible and not that interesting.

Based on the assumption that the cost of a heat exchanger network is highly determined by the number of streams involved, in a previous work (Morandin et al., 2014) it was decided to investigate a particular subset of excess heat sources that, in a suggested order, allow maximum heat recovery. The order in which the process excess heat sources should be picked up was established by a sorting algorithm where at the *h*-th step (n-*h*) composite curve diagrams are built by combining the already sorted (*h*-1) streams with each of the remaining streams and the resulting heat recovery targets are compared to find the *h*-th stream allowing the maximum increment. Note that this procedure converges after n(n-1)/2 steps and therefore significantly reduces the combinatorial complexity of the analysis.

However, since the process heat sinks have different temperature levels and heat transfer characteristics, a stream may introduce a large heat contribution at the expenses of a very large heat transfer area. In addition, since the *h*-th stream array includes the (*h*-1)-th array, early suboptimal solutions compromise subsequent solutions.

To study such issues and to possibly overcome them in the future while still retaining the Pinch Analysis cost targeting procedure, a two-objective discrete optimization

procedure is introduced in this work. Each stream is assigned a binary variable i_h and, when i_h is equal to 1, is included in a candidate stream array for which the investment costs are calculated. A genetic algorithm is used to find the Pareto front of stream arrays simultaneously maximizing the amount of recovered heat and minimizing the capital costs as symbolically shown in Eq.(2), where Q_{rec} is the heat recovery target estimated by means of composite curve diagrams as described in (Morandin et al., 2014), I is the total investment which consists of heat collection system capital costs I_{HCS}, calculated for the active streams ($i_h = 1$) and the extra investment in coolers for those candidate streams which heat cannot be fully recovered by the heat collection system ($e \notin HCS$) due to too low temperature levels.

$$\begin{aligned} &\max Q_{rec} = g(i_1, i_2, \ldots, i_h, \ldots, i_n) \\ &\min I = I_{\mathrm{HCS}} + \sum_{\substack{h, i_h = 1 \\ e \notin HCS}} I_h^{cooler} \end{aligned} \tag{2}$$

Note that it is necessary to include this second argument in order for the investment objective to be sensitive to the activation of those streams which do not contribute to the heat recovery (first objective) although this does not represent a real capital cost since coolers are already available at the process site. If this argument is omitted, streams arrays requiring extra cooling than what provided by the heat collection system (e.g. because one or more stream appear at too low temperature levels) are retained during the genetic algorithm based optimization thus leading to a Pareto front with a big share of uninteresting solutions.

The Matlab based GA optimization was carried out with generations of 1000 individuals, 80 % created by crossover, of which 350 are retained in the Pareto front. A stopping criterion of no more than 3 generation with a change in Pareto spread less than 10^{-6} tolerance was used.

3. Results

An optimization problem was solved for each of the three plants under investigation. Depending on the plat under investigation, the total number of stream arrays evaluated varied between 20,000 and 70,000 and the computing time varied between around 2 to 5 hours in a 2.7 GHz Intel Core PC. The results are shown in Figure 1 to 6.

The Pareto fronts showing the solutions maximizing the amount of heat recovery while minimizing the investment costs in the heat collection system are shown in Figure 1, 3, 5 for the three plants respectively. In the same figures the solutions obtained with previously developed approach where the excess heat sources are sorted in descending order according to their maximum incremental contribution to the heat recovery are also shown. 30 % error bars are also added to the latter solutions to discuss the actual improvement obtained with the discrete optimization method compared to this previously developed method. This appears the maximum accuracy of heat exchanger network cost estimation in reference books (Turton et al., 2008) and applies also to the solutions on the Pareto front although error bars are omitted for sake of clarity. It should also be added that the Pinch Analysis area and unit targeting approach may introduce an additional bias in our estimation compared to other more rigorous heat exchanger network design approaches.

Figures 2, 4, and 6 show the number of excess heat sources involved for different amount of recovered heat for the three plants respectively and provide further insights about how solutions involving fewer streams but with large heat transfer areas compete with those involving more streams but with smaller heat transfer areas.

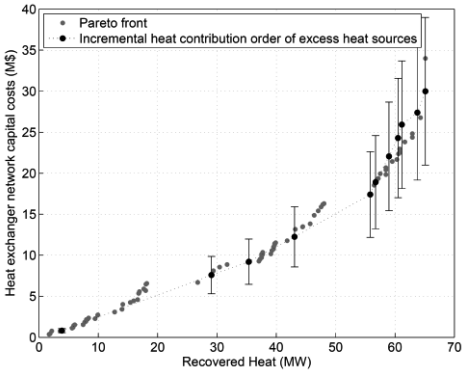

Figure 1: Capital costs, plant A.

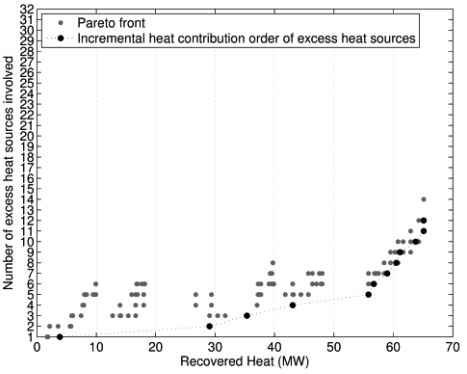

Figure 2: Excess heat sources involved, plant A.

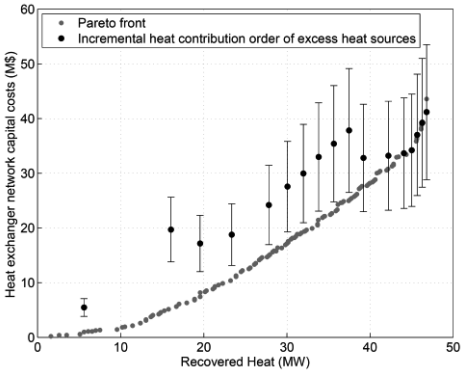

Figure 3: Capital costs, plant B.

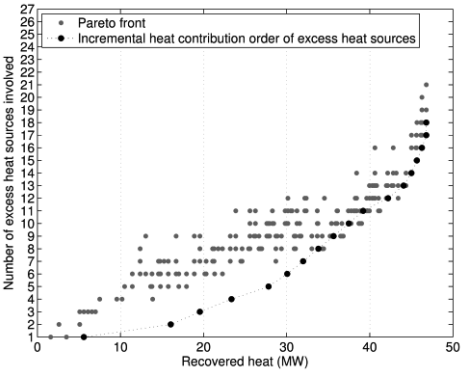

Figure 4: Excess heat sources involved, plant B.

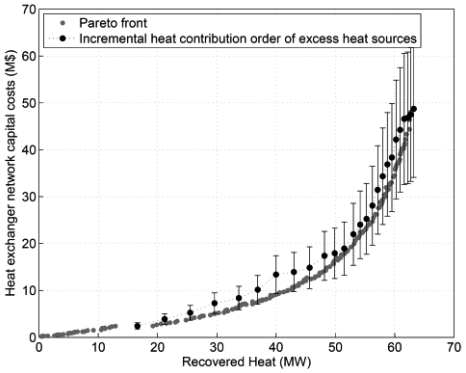

Figure 5: Capital costs, plant C.

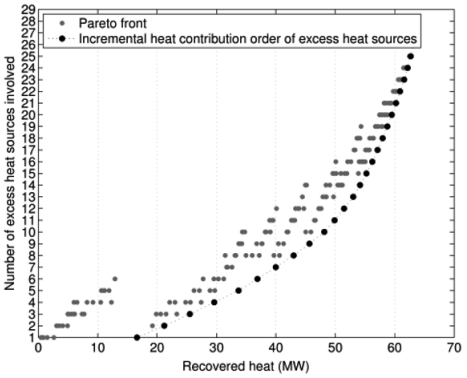

Figure 6: Excess heat sources involved, plant C.

The stream selection criterion based on the maximum incremental heat contribution order gives close to optimal solutions for plant A and plant C but substantially fails in the case of plant B. In this plant few process streams with very large heat contribution have poor heat transfer properties and are at low temperature levels and therefore compromise the selection of optimal arrays at even larger total amount of recovered heat if the old selection criterion is used. This is better shown in Figure 4 where the Pareto front solutions are based on considerably larger number of excess heat sources than the minimum baseline found with the previous approach.
With the discrete optimization based approach the whole optimal front of combinations of excess heat sources is mapped. This allows not only to pinpoint specific solutions which can be further refined in future investigations but also to highlight significant discontinuities in the optimal solution front such as in Figure 1 (plant A). These discontinuities can be in fact responsible for interesting leaps in profitability since much larger heat recovery can be obtained for very little increase in capital costs.

4. Conclusions

A discrete optimization procedure for selection of optimal arrays of process excess heat sources maximizing the amount of recovered heat while minimizing the capital costs of the heat collection system was developed and applied to the analysis of three plants belonging to a Swedish chemical cluster. The optimization results were compared with a previously developed short cut method for the selection of excess heat sources and showed that the understanding of the capital cost factors such as number of heat exchangers and total heat transfer surface can be significantly improved but is case dependent. In the best case, capital costs on heat collection system could be minimized by more than 30 % with respect to the solutions found with the previous method.

References

R. Anantharaman, I. Nastad, B. Nygreen & T. Gundersen, 2010, The sequential framework for heat exchanger network synthesis -The minimum number of units sub-problem, Computers & Chemical Engineering, 34, 1822-1830.
F. Campana, M. Bianchi, L. Branchini, A. De Pascale, A. Peretto, M. Baresi, A. Fermi, N. Rossetti & R. Vescovo, 2013, ORC waste heat recovery in European energy intensive industries: Energy and GHG savings, Energy Conversion and Management, 76, 244-252.
R. Hackl, E. Andersson & S. Harvey, 2011, Targeting for energy efficiency and improved energy collaboration between different companies using total site analysis (TSA), Energy, 36, 4609-4615.
I.C. Kemp, 2007, Pinch analysis and process integration: a user guide on process integration for the efficient use of energy: Butterworth Heinemann.
T. Laukkanen & C.-J. Fogelholm, 2011, A bilevel optimization method for simultaneous synthesis of medium-scale heat exchanger networks based on grouping of process streams, Computers & Chemical Engineering, 35, 2389-2400.
M. Morandin, 2013, A generalized approach to handle heat exchange restrictions in energy targeting, In P. Varbanov, J. Klemes, P. Seferilis, A.I. Papadopoulos & S.S. Voutetakis (Eds.), Chemical Engineering Transactions, Proceeding of 16th Conference on Process Integration, Modelling and Optimization for Energy Savings and Pollution Reduction, Rhodes (GR), 35, 157-162.
M. Morandin, R. Hackl & S. Harvey, 2014, Economic feasibility of district heating delivery from industrial excess heat: A case study of a Swedish petrochemical cluster, Energy, 65, 209-220.
L. Sun & X. Luo, 2011, Synthesis of multipass heat exchanger networks based on pinch technology, Computers & Chemical Engineering, 35, 1257-1264.
R. Turton, R.C. Bailie, W.B. Whiting & J.A. Shaeiwitz, 2008, Analysis, synthesis and design of chemical processes: Prentice Hall.

Krist V. Gernaey, Jakob K. Huusom and Rafiqul Gani (Eds.), 12th International Symposium on Process Systems Engineering and 25th European Symposium on Computer Aided Process Engineering.
31 May - 4 June 2015, Copenhagen, Denmark.

Ellipsoidal Arithmetic for Multivariate Systems

M. E. Villanueva[a], J. Rajyaguru[a], B. Houska[b] and B. Chachuat[a]

[a]*Centre for Process Systems Engineering, Imperial College London, SW7 2AZ, UK.*
[b]*School of Information Science & Technology, ShanghaiTech University, Shanghai 200031, China.*

Abstract

The ability to determine enclosures for the image set of nonlinear functions is pivotal to many applications in engineering. This paper presents a method for the systematic construction of ellipsoidal extensions of factorable functions. It proceeds by lifting the ellipsoid to a higher dimensional space for every atom operation in the function's directed acyclic graph, thereby accounting for dependencies. We present theoretical results regarding the quadratic Hausdorff convergence of the computed enclosures. Moreover, we propose an efficient implementation, whereby the shape matrix of the lifted ellipsoid is stored in sparse format, and every atom operation corresponds to a sparse update in that matrix. We illustrate these developments with two numerical examples.

Keywords: Ellipsoids, Function Bounding, Interval Arithmetic

1. Introduction

The ability to compute tight enclosures of the image set of nonlinear functions is pivotal to many methods in global and robust optimization (Tawarmalani and Sahinidis, 2004; Stuber and Barton, 2011), reachability analysis (Althoff et al., 2008), uncertainty analysis (Rao and Berke, 1997), guaranteed parameter estimation (Jaulin and Walter, 1993), etc. For real-valued, factorable functions, interval arithmetic (Moore et al., 2009) provides a natural way of computing such enclosures, since the image set of any continuous function is itself an interval. In practice, an interval enclosure can be obtained by traversing a directed acyclic graph (DAG) of the function in order to bound its atom operations recursively and as tightly as possible (Schichl and Neumaier, 2005). Although simple, this approach suffers two main limitations, namely the dependency problem and the wrapping effect. The former happens when multiple occurrences of the same variable, e.g. in a complicated function expression, are treated as if they were independent from each other. The latter is due to the fact that the image of an interval vector under a vector-valued function, even a linear linear function, is generally not an interval vector itself, thus leading to overestimation in enclosing that image set with an interval vector (Lohner, 2001).

This paper presents a method for the systematic construction of ellipsoidal extensions of factorable functions. The algorithm starts with an ellipsoid containing the uncertainty host set and proceeds by adding an extra dimension (lifting) for every atom operation in the DAG. This is similar in essence to the construction of polyhedral relaxations using a decomposition-linearization approach (Tawarmalani and Sahinidis, 2004), with the added benefit of a well-developed ellipsoidal calculus (Kurzhanski and Vályi, 2004). We also analyze how fast the computed enclosures converge to the exact image as the uncertainty set is reduced, using the concept of Hausdorff convergence order (Bompadre and Mitsos, 2012), and we develop an efficient implementation as part of the software package MC++ (`https://projects.coin-or.org/MCpp`).

The remainder of the paper is organized as follows. After defining the problem in Sect. 2, we describe the construction of ellipsoidal extensions of factorable functions in Sect. 3. Theoretical

results regarding the Hausdorff convergence of the computed enclosures are presented in Sect. 4. Then, we discuss important implementation details in Sect. 5, and illustrate mitigation of both the dependency and wrapping effects with numerical examples. Finally, Sect. 6 concludes the paper.

Notation. Besides standard mathematical notation, the diameter of a compact set $Z \subseteq \mathbb{R}^n$ is defined by $\mathrm{diam}(Z) = \max_{z1,z2\in Z} \|z_1 - z_2\|$. The Minkowski sum of two compact sets Z, W is $W \oplus Z := \{w+z \,|\, w \in W, z \in Z\}$. If $W \subseteq Z$ the Hausdorff metric between these sets is given by $d_{\mathrm{H}}(W,Z) := \max_{z\in Z} \min_{w\in W} \|w-z\|$. An n-dimensional ellipsoid is defined as:

$$\mathscr{E}(q,Q) \;:=\; \left\{ q + Q^{\frac{1}{2}} v \;\middle|\; \forall v \in \mathbb{R}^n,\; v^{\mathsf{T}} v \leq 1 \right\} \;\in\; \mathbb{E}^n \,,$$

where $\mathbb{E}^n$ denotes the class of n-dimensional ellipsoids, the vector $q \in \mathbb{R}^n$ and the positive semidefinite matrix $Q \in \mathbb{S}^n_+$ are respectively the center and the shape matrix of the ellipsoid.

2. Problem Formulation

Consider a function $f : \mathbb{R}^{n_x} \to \mathbb{R}^{n_f}$, with its argument $x \in \mathbb{R}^{n_x}$ contained in the ellipsoid $\mathscr{E}(q_x, Q_x) \in \mathbb{E}^{n_x}$. The exact image of $\mathscr{E}(q_x, Q_x)$ under the function f is defined as

$$f(\mathscr{E}(q_x,Q_x)) \;:=\; \{f(x) \,|\, x \in \mathscr{E}(q_x,Q_x)\}\,. \tag{1}$$

The main focus of this paper is on computing an enclosure of the image set of f in the form of an ellipsoid $\mathscr{E}(q_f, Q_f)$; that is, $\mathscr{E}(q_f,Q_f) \supseteq f(\mathscr{E}(q_x,Q_x))$ with $(q_f,Q_f) \in \mathbb{R}^{n_f} \times \mathbb{S}^{n_f}_+$.

The main assumption we make to enable this construction is that the function f must be factorable, i.e. it can be decomposed into a finite number N of atom operations a_i from a finite library, such as binary addition, binary product, and outer composition with a univariate function. In particular, factorable functions can be evaluated by setting $u^0(x) = x$ and applying the recursive rule

$$\forall i \in \{1,\ldots,N\}, \quad u^i(x) \;=\; g_i(u^{i-1}(x)) \;:=\; \begin{pmatrix} u^{i-1}(x) \\ a_i(u^{i-1}(x)) \end{pmatrix}, \tag{2}$$

so that $f(x) = P u^N(x) = P[g_N \circ g_{N-1} \circ \ldots \circ g_1](x)$, where $P \in \mathbb{R}^{n_f \times (n_x+N)}$ is a projection matrix selecting the appropriate components. The j-th component of $u^i(x)$ is denoted as $u^i_j(x)$ subsequently.

The main problem addressed in this paper is the development of a constructive approach for an ellipsoidal extension $f^{\mathbb{E}} : \mathbb{E}^{n_x} \to \mathbb{E}^{n_f}$ of the factorable function f, whose image $f^{\mathbb{E}}(q_x,Q_x)$ yields the ellipsoidal enclosure, $\mathbb{E}(q_f,Q_f) := f^{\mathbb{E}}(q_x,Q_x) \supseteq f(\mathscr{E}(q_x,Q_x))$.

3. Ellipsoidal Arithmetic for Factorable Functions

The proposed algorithm proceeds by lifting the ellipsoid to a higher dimensional space for every atom operation in the function's DAG upon application of an ellipsoidal arithmetic. Starting with an ellipsoid $\mathscr{E}(q^0,Q^0) \in \mathbb{E}^{n_x}$ with $q^0 := q_x$ and $Q^0 := Q_x$, an ellipsoidal extension of each factor g_i, $i = 1,\ldots,N$ is obtained such that $g_i^{\mathbb{E}}(\mathscr{E}(q^{i-1},Q^{i-1})) = \mathscr{E}(q^i,Q^i)$, with

$$q^i := \begin{pmatrix} q^{i-1} \\ \lambda^i \end{pmatrix} \quad \text{and} \quad Q^i := \begin{pmatrix} I_{i-1} \\ \Lambda^i \end{pmatrix} Q^{i-1} \begin{pmatrix} I_{i-1} \\ \Lambda^i \end{pmatrix}^{\mathsf{T}}. \tag{3}$$

Here, $I_{i-1} \in \mathbb{R}^{(n_x+i-1)\times(n_x+i-1)}$ denotes the identity matrix; and the lifting parameters $\lambda^i \in \mathbb{R}$ and $\Lambda^i \in \mathbb{R}^{n_x+i-1}$ (row vector) depend on the functional form of the corresponding atom operation a_i. When the initial host set is not an ellipsoid but an interval box, the algorithm can be initialized by enclosing it within an ellipsoid. This adds the benefits of quadratic convergence and wrapping mitigation from ellipsoids at the cost of some initial overestimation.

At the end, the ellipsoidal extension $f^{\mathbb{E}}$ of f is retrieved by projecting the lifted ellipsoid $\mathscr{E}(q^N, Q^N) \in \mathbb{E}^{n_x+N}$ onto $\mathbb{R}^{n_f}$, giving

$$f^{\mathbb{E}}(q_x, Q_x) \;:=\; \mathscr{E}(q_f, Q_f) \;=\; P \times \mathscr{E}(q^N, Q^N)\,.$$

The following two subsections describe ways that such lifting parameters can be constructed for both linear and nonlinear atom operations.

3.1. Affine Atom Operations

Consider those operations $u^i(x) := g_i(u^{i-1}(x))$, where the atom operation a_i is an affine function of at most two factors $u_k^{i-1}(x)$, $u_m^{i-1}(x)$ with $k,m \leq i-1$. This corresponds to the case of addition, subtraction, scaling and shifting.

Addition and Subtraction Operations, $u_k^{i-1}(x) \pm u_m^{i-1}(x)$. The lifting parameters are given by:

$$\lambda^i := q_k^{i-1} \pm q_m^{i-1} \quad \text{and} \quad \Lambda_j^i := \begin{cases} 1 & \text{if } j = k, \\ \pm 1 & \text{if } j = m, \\ 0 & \text{otherwise.} \end{cases} \tag{4}$$

Scaling Operation, $\alpha u_k^{i-1}(x)$ for some $\alpha \in \mathbb{R}$. The lifting parameters are given by:

$$\lambda^i := q_k^{i-1} \quad \text{and} \quad \Lambda_j^i := \begin{cases} \alpha & \text{if } j = k, \\ 0 & \text{otherwise.} \end{cases} \tag{5}$$

Shifting Operation, $u_k^{i-1}(x) + \beta$ for some $\beta \in \mathbb{R}$. The lifting parameters are given by:

$$\lambda^i := q_k^{i-1} + \beta \quad \text{and} \quad \Lambda_j^i := \begin{cases} 1 & \text{if } j = k, \\ 0 & \text{otherwise.} \end{cases} \tag{6}$$

3.2. Nonlinear Atom Operations

Consider the operation $u^i(x) = g_i(u^{i-1}(x))$, where the atom operation a_i is a possible nonlinear function of the sole factor $u_k^{i-1}(x)$ with $k \leq i-1$ first. Note that the domain $D_i \subseteq \mathbb{R}$ of a_i is given by the projection of the ellipsoid $\mathscr{E}(q^{i-1}, Q^{i-1})$ onto its k-th component, given by $D_i := q_k^{i-1} + \sqrt{Q_{k,k}^{i-1}}\,[-1,1]$. In particular, we make the assumptions that: (i) D_i is included within the domain of definition of a_i throughout—this is relevant, for instance, for the univariate functions $z \mapsto \log(z)$, $z \mapsto 1/z$, $z \mapsto \sqrt{z}$, etc; and (ii) the function a_i is Lipschitz continuous.

One way of handling the nonlinear factor g_i involves constructing a linear estimator such that

$$\forall v \in \mathscr{E}(q^{i-1}, Q^{i-1}), \quad g_i(v) \;:=\; \begin{pmatrix} v \\ a_i(v) \end{pmatrix} \;\in\; \left\{ \begin{pmatrix} 0_{i-1} \\ \gamma_0^i \end{pmatrix} + \begin{pmatrix} I_{i-1} \\ \gamma_1^i e_k^\mathsf{T} \end{pmatrix} v \right\} \oplus \begin{pmatrix} \{0_{i-1}\} \\ [-\delta^i, \delta^i] \end{pmatrix}, \tag{7}$$

whereby the scalars γ_0^i, γ_1^i and δ^i can be derived, for instance, from a Taylor model or, better, a Chebyshev model of order $q \geq 1$ of the atom operation a_i on D_i (Neumaier, 2003; Rajyaguru et al., 2014); the latter is more advantageous in that it can be applied to nonsmooth atom operations, too. In (7), e_k stands for the kth basis vector and 0_{i-1} is a zero vector of size $i-1$.

The lifting operation proceeds in two steps. In the first step, the linear part of (7) is absorbed into the a lifted ellipsoid $\mathscr{E}(q^i, \tilde{Q}^i)$ in a procedure that is similar to the one used for shifting and scaling in (5)-(6), here with the lifting parameters

$$\lambda^i := \gamma_0^i \quad \text{and} \quad \Lambda_j^i := \begin{cases} \gamma_1^i / \operatorname{rad}(D_i) & \text{if } j = k, \\ 0 & \text{otherwise.} \end{cases} \tag{8}$$

In the second step the interval $[-\delta^i, \delta^i]$ enclosing the nonlinearity is added to the ith component of the lifted ellipsoid, in the Minkowski sense. Since the set of n-dimensional ellipsoids is not closed under Minkowski addition, we use an ellipsoidal extension of the Minkowski sum so that $\mathscr{E}(q^i, Q^i) := \mathscr{E}(q^i, \tilde{Q}^i) \oplus^{\mathbb{E}} \mathscr{E}(\Delta^i)$, with $\Delta^i := (\delta^i)^2 (e_i e_i^{\mathsf{T}}) \in \mathbb{S}^{n_x+i}$. We compute the shape matrix Q^i as:

$$Q^i := \frac{1}{\mu_0}\tilde{Q}^i + \frac{1}{\mu_1}\Delta^i \quad \text{with} \quad \mu_0 = 1 - \mu_1 = \frac{\sqrt{\mathrm{Tr}\left(\tilde{Q}^{i-1}\right) + \varepsilon}}{\sqrt{\mathrm{Tr}\left(\tilde{Q}^{i-1}\right) + \varepsilon} + \sqrt{\mathrm{Tr}\left(\Delta^i\right) + \varepsilon}}. \tag{9}$$

It is important to note that, since the Minkowski sum between two ellipsoids always introduces some overestimation, a nonlinear operation cannot be approximated exactly as with intervals.

Finally, in the case of binary product operations, the atom operation a_i is a bilinear term between two factors $u_k^{i-1}(x), u_m^{i-1}(x)$ with $k, m \leq i-1$. We use a simple DC-decomposition approach to yield an ellipsoidal enclosure of the bilinear terms. Rewriting them in the form

$$u_k^{i-1}(x) \times u_m^{i-1}(x) = \frac{1}{4}\left[(u_k^{i-1}(x) + u_m^{i-1}(x))^2 - (u_k^{i-1}(x) - u_m^{i-1}(x))^2\right], \tag{10}$$

we can apply recursively the rules of binary addition/subtraction and univariate composition for the square function $z \mapsto z^2$, as explained earlier. As an alternative, and potentially tighter, approach, one can envisage the use of semi-definite programming (SDP) to handle bilinear terms.

4. Convergence Analysis

We now turn our attention to analyzing the theoretical convergence properties of the ellipsoidal arithmetic presented in the previous section. An ellipsoidal extension $f^{\mathbb{E}}$ of f is said to have Hausdorff convergence order $q \geq 1$ on $\mathbb{E}^{n_x}$ if

$$d_{\mathrm{H}}\left(f^{\mathbb{E}}(\mathscr{E}(q_x, Q_x)), f(\mathscr{E}(q_x, Q_x)))\right) \leq \mathbf{O}(\mathrm{diam}(\mathscr{E}(q_x, Q_x))^q), \tag{11}$$

for every domain $\mathscr{E}(q_x, Q_x) \in \mathbb{E}^{n_x}$ with sufficiently small diameter where $f^{\mathbb{E}}$ is defined. The following result relates the convergence order of a factorable function to that of its atom operations.

Theorem 1. *If all the atom operations a_i in the DAG of a factorable function f are Lipschitz continuous and their ellipsoidal extensions have image Hausdorff convergence order q, then the ellipsoidal extension of f itself has image Hausdorff convergence q.*

Proof. The result follows by finite induction over the atom operations, using the triangle inequality for the Hausdorff metric d_{H} and the Lipschitz continuity of each atom operation a_i. □

We now present the main result of this section.

Theorem 2. *Let all the atom operations a_i in the DAG of a factorable function f be twice-continuously differentiable, and consider the ellipsoidal extension $f^{\mathbb{E}}$ of f as constructed from the lifting procedure in Sect. 3. Then, $f^{\mathbb{E}}$ has quadratic Hausdorff convergence on $\mathbb{E}^{n_x}$.*

Proof. We show that the ellipsoidal extension of each atom operation have quadratic Hausdorff convergence, so the result follows from Theorem 1 with $q = 2$. Since the class of ellipsoids is closed under affine transformations, all the extensions for affine atom operations in Sect. 3.1 are exact, and hence have infinite Hausdorff convergence order. Since binary product operations are handled by a combination of affine operations and univariate nonlinear operations, the Hausdorff convergence order of the extension $f^{\mathbb{E}}$ is completely determined by the Hausdorff convergence order of the latter. Consider the operation $g_i(u^{i-1}(x))$ where the atom operation a_i is a nonlinear

function of the sole factor $u_k^{i-1}(x)$ with $k \leq i-1$, and assume without loss of generality that $\mathscr{E}(q^{i-1}, Q^{i-1})$ is centered at zero (mainly for notation simplicity). By construction of $g_i^{\mathbb{E}}$ and invariance of ellipsoids under affine transformations, the ellipsoidal approximation $\mathscr{E}(\tilde{Q}^i)$ matches the exact image of the linear part in (7). The exact image of the corresponding residual term is

$$\Gamma := \left\{ g_i(v) - \begin{pmatrix} 0_{i-1} \\ \gamma_0^i \end{pmatrix} + \begin{pmatrix} I_{i-1} \\ \gamma_1^i e_k^\mathsf{T} \end{pmatrix} v \;\middle|\; v \in \mathbb{E}(Q^{i-1}) \right\}.$$

Then, we have:

$$\begin{aligned} d_\mathrm{H}\left(\mathscr{E}(Q^i), g_i(\mathscr{E}(Q^{i-1}))\right) &= d_\mathrm{H}\left(\mathscr{E}(\tilde{Q}^i) \oplus^{\mathbb{E}} \mathscr{E}(\Delta^i), \mathscr{E}(\tilde{Q}^i) \oplus \Gamma\right) \\ &\leq d_\mathrm{H}\left(\mathscr{E}(\tilde{Q}^i) \oplus^{\mathbb{E}} \mathscr{E}(\Delta^i), \mathscr{E}(\tilde{Q}^i)\right) + d_\mathrm{H}\left(\mathscr{E}(\tilde{Q}^i), \mathscr{E}(\tilde{Q}^i) \oplus \Gamma)\right) \\ &\leq d_\mathrm{H}\left(\mathscr{E}(\tilde{Q}^i) \oplus^{\mathbb{E}} \mathscr{E}(\Delta^i), \mathscr{E}(\tilde{Q}^i)\right) + \mathbf{O}\left(\operatorname{diam}(\Gamma)\right) \\ &\leq \mathbf{O}\left(\operatorname{diam}\left(\mathscr{E}(\Delta^i)\right)\right) + \mathbf{O}\left(\operatorname{diam}(\Gamma)\right), \end{aligned}$$

where the last inequality follows from the definition of the ellipsoidal extension of the Minkowski sum in (9). The result is obtained by noting that

$$\operatorname{diam}(\Gamma) \leq \mathbf{O}\left(\operatorname{diam}(\mathscr{E}(Q^{i-1}))^2\right) \quad \text{and} \quad \operatorname{diam}\left(\mathscr{E}(\Delta^i)\right) \leq \mathbf{O}\left(\operatorname{diam}(\mathscr{E}(Q^{i-1}))^2\right),$$

by the assumption that g_i is twice-continuously differentiable and by the Lipschitz-continuity of natural interval extensions, respectively. □

5. Numerical Implementation and Numerical Examples

Although simple, the algorithm describe in Sect. 3 is not the most effective way to implement the ellipsoidal arithmetic. Firstly, the number of atom operations N in the DAG of a factorable function is known a priori, which allows preallocation of the center vector and shape matrix. The second observation is that the lifting operation defined in (3) corresponds to an update in the ith row of the shape matrix; for instance, for an addition or subtraction operation $u_k^{i-1}(x) \pm u_m^{i-1}(x)$:

$$\forall j \in \{0, \ldots, i\}, \quad Q_{i,j}^i = \begin{cases} Q_{k,k}^i \pm 2Q_{k,m}^i + Q_{m,m}^i & \text{if } j = 1, \\ Q_{k,j}^i \pm Q_{m,j}^i & \text{otherwise.} \end{cases}$$

Therefore, an efficient implementation is possible, whereby the (symmetric) shape matrix of the lifted ellipsoid is stored in sparse format and every atom operation corresponds to a sparse update of the shape matrix. Such an implementation of the ellipsoidal arithmetic is available as part of the software package MC++ (`https://projects.coin-or.org/MCpp`).

We illustrate the benefits of ellipsoidal arithmetic compared with traditional interval arithmetic for two problems. The left plot in Fig. 1 considers the following factorable function with $n_x = n_f = 2$,

$$f_1(x_1, x_2) = \sqrt{x_1 + x_2} + x_1 x_2 \qquad f_2(x_1, x_2) = (x_1 - x_2)^2 + 3x_2.$$

The comparison between the actual image set and the corresponding interval and ellipsoidal extensions, here for a variable host set $\mathscr{E}(q_x, Q_x)$ with $q_x = \begin{pmatrix} 3 \\ 4 \end{pmatrix}$ and $Q_x = \begin{pmatrix} 2 & 1 \\ 1 & 2 \end{pmatrix}$, illustrates the potential of ellipsoidal arithmetic to mitigate the dependency problem. The right plot of Fig. 1 shows the solution set of the parametric linear ODE (harmonic oscillator)

$$\dot{x}_1(t) = x_2(t) + p, \qquad \dot{x}_2(t) = -x_1(t) + p,$$

with joint ellipsoidal host set $\mathscr{E}(q_{x,p}, Q_{x,p})$ for the initial states $x_1(0), x_2(0)$ and the parameter p given by $q_{x,p} = (1 \;\; 0 \;\; 0)^\mathsf{T}$ and $Q_{x,p} = 0.01 I_3$. The unconditional stability of the reach tube illustrates the ability of ellipsoidal arithmetic to mitigate the wrapping effect, which is due to the property of invariance under affine transformations of ellipsoids.

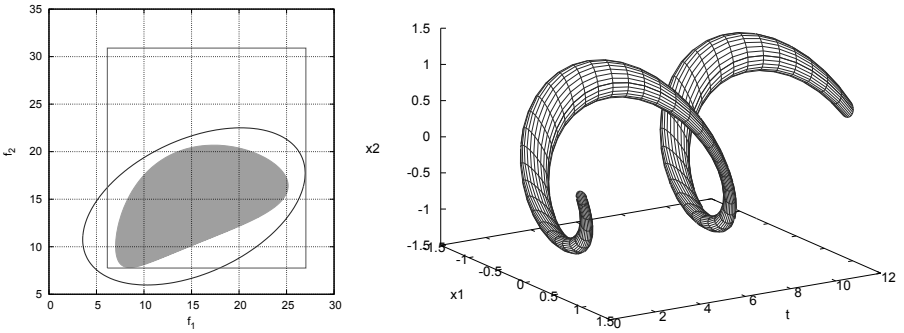

Figure 1: Left plot: Mitigation of the dependency problem using ellipsoidal arithmetic compared with interval arithmetic for a factorable function; Right plot: Mitigation of the wrapping effect by the property of invariance under affine transformation of ellipsoids for a parametric ODE.

6. Conclusion

This paper was concerned with the construction of ellipsoidal enclosures for the image set of factorable functions. Our approach provides such enclosures by traversing a DAG of the function, and it applies an ellipsoidal arithmetic that lifts the ellipsoid to a higher dimensional space for every atom operation. We have shown that this arithmetic yields quadratically convergent ellipsoidal extensions under mild assumptions, and that it can be implemented efficiently on account of sparsity. In practice, quadratic Hausdorff convergence is a very desirable property in branch-and-bound search for global optimization in order to reduce the cluster effect, as well as in the design of validated integrators for asymptotically stable systems. Further research is needed in order to extend existing interval-based algorithms to ellipsoidal techniques nonetheless.

Acknowledgments. Financial support from Marie Curie under grant PCIG09-GA-2011-293953 is gratefully acknowledged. JR thanks EPSRC and the Department of Chemical Engineering at Imperial College for doctoral training award. MEV thanks CONACYT for doctoral scholarship.

References

M. Althoff, O. Stursberg, M. Buss, 2008. Reachability analysis of nonlinear systems with uncertain parameters using conservative linearization. In: 47th IEEE Conference on Decision and Control, pp. 4042–4048.

A. Bompadre, A. Mitsos, 2012. Convergence rate of McCormick relaxations. Journal of Global Optimization 52 (1), 1–28.

L. Jaulin, E. Walter, 1993. Guaranteed nonlinear parameter estimation from bounded-error data via interval analysis. Mathematics and Computers in Simulation 35 (2), 123–137.

A. B. Kurzhanski, I. Vályi, 1994. Ellipsoidal Calculus for Estimation and Control. Birkhäuser, Boston.

R. J. Lohner, 2001. On the ubiquity of the wrapping effect in the computation of error bounds. In: Kulisch, P. D. U., Lohner, P. D. R., Facius, D. A. (Eds.), Perspectives on Enclosure Methods. Springer Vienna, pp. 201–216.

R. E. Moore, R. B. Kearfott, M. J. Cloud, 2009. Introduction to Interval Analysis. SIAM.

A. Neumaier, 2003. Taylor Forms—Use and limits. Reliable Computing 9 (1), 43–79.

J. Rajyaguru, M. E. Villanueva, B. Houska, B. Chachuat, 2014. Higher-Order Inclusions of Nonlinear Systems By Chebyshev Models. In: AIChE Annual Meeting 2014, paper 566f.

S. S. Rao, L. Berke, 1997. Analysis of uncertain structural systems using interval analysis. AIAA Journal 35 (4), 727–735.

H. Schichl, A. Neumaier, 2005. Interval analysis on directed acyclic graphs for global optimization. Journal of Global Optimization 33 (4), 541–562.

M. D. Stuber, P. I Barton, 2011. Robust simulation and design using semi-infinite programs with implicit functions. International Journal of Reliability and Safety 5 (3), 378–397.

M. Tawarmalani, N. V. Sahinidis, 2004. Global optimization of mixed-integer nonlinear programs: A theoretical and computational study. Mathematical Programming 99 (3), 563–591.

Krist V. Gernaey, Jakob K. Huusom and Rafiqul Gani (Eds.), 12th International Symposium on Process Systems Engineering and 25th European Symposium on Computer Aided Process Engineering.
31 May - 4 June 2015, Copenhagen, Denmark.

Reduced model trust region methods for embedding complex simulations in optimization problems

John P. Eason and Lorenz T. Biegler

Department of Chemical Engineering; Carnegie Mellon University, Pittsburgh, USA
jeason@andrew.cmu.edu

Abstract

As advanced simulation technologies mature, it is desirable to utilize their predictive power in process design and optimization. However, these models present unique challenges for traditional optimization frameworks. Simulations can be very computationally expensive and derivative information may be unavailable. A common approach is to construct reduced order models (RMs) that approximate the behavior of the simulation with a simple algebraic form. By substituting a RM in place of the simulation, one may simultaneously optimize the entire flowsheet with traditional, derivative-based techniques. Using trust region concepts from nonlinear programming, we systematically construct a series of local RMs to help ensure convergence of the overall problem with the complex simulation. We compare two methods of handling the constraints: a penalty method capable of handling inequality constraints, and a novel approach using a filter method that is capable of handling both inequality and equality constraints. The advantage of the filter method is demonstrated and this method is applied to two flowsheet optimization examples: the Williams-Otto process and the ammonia synthesis process.

Keywords: reduced order models, nonlinear programming, simulation optimization

1. Introduction

Nonlinear programming can be a powerful tool for chemical process optimization. However, existing methods are not suitable for problems where some parts of the system are described by computationally expensive constraints (Biegler, 2010). Models in computational fluid dynamics, molecular modeling, and other complex simulations are emerging as important tools in engineering practice. However, these simulations are computationally expensive and do not provide derivatives. Therefore, to utilize these models in an optimization work process, a common approach is to represent the behavior of the complex simulation, or original detailed model (ODM), with a simpler algebraic form, or reduced order model (RM) (Biegler et al., 2014). The general form of the problem under consideration is given in Eq. (1), where the objective function $f : \mathbb{R}^n \to \mathbb{R}$, equality constraints $c : \mathbb{R}^n \to \mathbb{R}^m$, and inequality constraints $g : \mathbb{R}^n \to \mathbb{R}^p$ are all twice continuously differentiable. The ODM $d(x)$ embedded within the model is assumed to have continuous derivatives but the values may be unknown. The solution techniques that we consider will replace the ODM $d(x)$ by a RM $r(x)$ whose derivatives are known.

$$\min_x \quad f(x, d(x)) \tag{1a}$$

$$s.t. \quad c(x, d(x)) = 0 \tag{1b}$$

$$g(x, d(x)) \leq 0 \tag{1c}$$

In the chemical engineering literature, the most popular choice of data-driven RMs are artificial neural networks and Kriging interpolation. A sampling of works include Caballero and Grossmann (2008), Davis and Ierapetritou (2009), Eason and Cremaschi (2014), Henao and Maravelias (2011), and Biegler et al. (2014). A common approach for RM-based optimization is to sample the ODM, construct a RM, then solve problem (1) with $r(x)$ in place of $d(x)$. Experience has shown that this often terminates at a point of poor accuracy for the ODM, i.e. the optimizer exploits inaccuracy in the RM to artificially improve the objective. The RM can then be refined to increase accuracy in that region. However, such a method offers no guarantee of converging to the optimum of the original problem (1), as shown by Biegler et al. (1985). In that work, the authors even give an example where such an approach converges to a local maximum rather than minimum.

To overcome this difficulty, we note the connection between the RM-based optimization and derivative free optimization algorithms. There is a clear parallel between reduced order models and the so-called model function of certain derivative free optimization techniques. "Model based" derivative free optimization algorithms (for unconstrained problems) generate a sequence of steps based on a sequence of local model functions. The model functions are built in a region around the current iterate known as the trust region. Then, the step is also restricted to fall within this space so as not to extrapolate from the model. To guarantee convergence, the model function must satisfy the "fully linear property" (Conn et al., 2009). In essence, this property says that an upper bound on the error of the function value and gradient of the RM must be directly related to the size of the trust region, i.e. smaller trust regions yield more accurate models. The outline of the basic trust region algorithm is as follows: generate a simple model problem in the trust region, solve the model problem to generate a step, judge the quality of the proposed step according to some quality measure to either accept or reject the step, and adjust the trust region radius Δ_k according to that quality measure.

2. Penalty-based methods

Some attention must be given to the difference between an unconstrained derivative free problem and a constrained NLP with an embedded RM. The simplest way to incorporate constraints is through a penalty function. The penalty function combines objective function decrease and feasibility to a single quality measure to judge whether or not to accept a step. By adding a weighted term to the objective that penalizes constraint violation, it is possible to reach a local optimum (Conn et al., 2000). However, penalty methods have two main drawbacks. First, the correct value for the penalty parameter to ensure convergence to a feasible point is unknown. If the penalty parameter is too small, the optimization path will venture too far into infeasibility. If the penalty parameter is very high, the step size will be prohibitively small (Nocedal and Wright, 1999).

The first method that we present for solving flowsheet optimization problem via a trust region RM method uses penalty functions to recast the problem as an unconstrained problem as proposed by Biegler et al. (2014). The aforementioned issues with the penalty method become especially problematic for equality constraints because lack of derivatives from the ODM leads to a less accurate search direction. Therefore, equality constraints should be avoided. One may eliminate equality constraints by using system knowledge to identify the independent variables x^I with respect to the equality constraints. For a set value of these independent variables, $c(x) = 0$ can be solved uniquely for the remaining dependent variables x^D. Inequality constraints $g(x) \leq 0$ are handled with the penalty formulation. The optimization problem (1) is re-written as

$$\min_{x^I} \quad \psi(x^I) = f(x^I, x^D, d(x^I, x^D)) + \rho \|g_+(x^I, x^D, d(x^I, x^D))\| \tag{2a}$$

$$s.t. \quad c(x^I, x^D, d(x^I, x^D)) = 0 \tag{2b}$$

where $g_+(x^I, x^D, d(x^I, x^D))$ represents the violation of the inequality constraints and ρ is the penalty parameter. A step is generated in the independent variables x^I, then (2b) is used to solve for x^D.

Depending on the structure of the problem, this may require many evaluations of the ODM due to $d(x^I, x^D)$'s dependence on changing x^D. From a process engineering perspective, the process of solving for the dependent variables is equivalent to converging the flowsheet. If a process unit described by a complex simulation is included in a recycle loop, that simulation must be run several times to converge the recycle.

The full penalty algorithm is given as Algorithm II by Biegler et al. (2014). Under assumptions on smoothness and sufficient decrease of the trial step, Theorem 10.13 in Conn et al. (2009) leads to the following convergence result: $\lim_{k\to\infty} \|\nabla\psi(x_k^I)\| = 0$. This guarantees that the algorithm will find a stationary point of the penalized objective. However, two problems prohibit the tractability for penalty-based approaches. First, it is impossible to know an appropriate penalty parameter a priori. Second, and most importantly, the elimination of equality constraints can be very expensive. Therefore, a method to handle equality constraints and dependent variables directly in the optimization process is desired. For flowsheet optimization, this means that we seek a method that optimizes and converges the flowsheet simultaneously.

3. Filter methods

Filter methods emerged with Fletcher and Leyffer (2002) as an alternative to penalty functions. Instead of using a combined metric for objective improvement and feasibility, filter methods consider these criteria somewhat independently. A step is acceptable to the filter if it satisfies either an appropriate decrease in the objective function *or* a sufficient decrease in some infeasibility measure θ. The filter conditions are presented in equation (4) of section 3.1. We propose an adaptation of the trust region filter method for RM based optimization as presented by Agarwal and Biegler (2013). First, introduce variables y and constraint (3d) to match them to the ODM. For typical filter methods, θ is the norm of all constraint violation, from eqns. (3b), (3c), and (3d). However, with the introduction of variables y, we propose to enforce feasibility for (3b) and (3c) at all iterations, and only measure infeasibility as $\theta(z) = \|d(x) - y\|$ where we have introduced $z^T = [x^T, y^T]$.

$$\min_{x,y} \quad f(x,y) \tag{3a}$$

$$s.t. \quad c(x,y) = 0 \tag{3b}$$

$$g(x,y) \leq 0 \tag{3c}$$

$$y = d(x) \tag{3d}$$

The filter method handles constraints directly, so both the objective and feasibility have to be considered when generating a step. After constructing a RM $r(x)$ and substituting for $d(x)$ in (3d), the step generation is decomposed into two subproblems in the spirit of the method introduced by Omojokun (1990). First, the *normal subproblem* is taken to minimize $\theta^R(z) = \|r(x) - y\|$ subject to (3b), (3c) and within a fixed fraction of the current trust region radius, thus yielding θ^R_{min}. This provides some estimate of the achievable level of reduction in θ^R within the trust region. The *tangential subproblem* then minimizes the objective function subject to (3b), (3c), and $\theta^R(z) \leq \theta^R_{min}$, while keeping the total step within the trust region.

3.1. Trust region filter method for RM optimization

1. Initialization: Choose $0 < \gamma_c < 1 < \gamma_E$, γ_f, $\gamma_\theta \in (0,1)$, $\kappa_\theta \in (0,1)$, $\gamma_s > \frac{1}{2}$, an initial trust-region radius Δ_0, minimum radius Δ_{min}, termination tolerance ε_x, feasibility tolerance ε_θ, maximum infeasibility θ_{max}, and an initial iterate z_0. Initialize the filter $\mathscr{F} = \emptyset$. Evaluate $d(x_0)$. Construct a ROM $r(x)$ for the initial trust region. Set $k = 0$.
2. If $\theta(z_k) \leq \varepsilon_\theta$ and $\Delta_k \leq \Delta_{min}$, STOP.

3. If $\theta(z_k) \geq \theta_{max}$, or if $\Delta_k \leq \Delta_{min}$, add (θ_k, f_k) to the filter and go to the restoration phase and attempt to find a feasible point. If restoration succeeds, set z_k and Δ_k as indicated by the restoration procedure and go to Step 4.
4. Generate a ROM $r(x)$ approximating $d(x)$ within the trust region. Compute a step s_k from the normal and tangential subproblems with RMs (described above).
5. If $\|s_k\| \leq \varepsilon_x \Delta_k$, set $z_{k+1} = z_k$, $\Delta_{k+1} = \gamma_C \Delta_k$, and $k = k+1$. Go to Step 2.
6. Filter: Evaluate $\theta(z_k + s_k) = \|d(x_k + s_{x,k}) - (y_k + s_{y,k})\|$. If, for all $(\theta_j, f_j) \in \mathscr{F} \cup (\theta_k, f_k)$,

$$\theta(z_k + s_k) \leq (1 - \gamma_\theta)\theta_j \quad \text{or} \quad f(z_k + s_k) \leq f_j - \gamma_f \theta_j \tag{4}$$

   then the step is acceptable to the filter. If the step is acceptable to the filter, go to step 8. Else, continue to step 7.
7. *Trial step unacceptable to filter* - set $z_{k+1} = z_k$ and contract trust region $\Delta_{k+1} = \gamma_c \Delta_k$. Set $k = k+1$ and go to Step 3.
8. Evaluate the switching condition:

$$f_k(z_k) - f_k(z_k + s_k) \geq \kappa_\theta \theta(z_k)^{\gamma_s} \tag{5}$$

   If true, go to step 9. Else, go to step 10.
9. *f-type step* - Accept trial step $z_{k+1} = z_k + s_k$ and expand trust region $\Delta_{k+1} = \gamma_E \Delta_k$. Set $k = k+1$ and go to Step 2.
10. *θ-type step* - Add (θ_k, f_k) to the filter. Accept trial step $z_{k+1} = z_k + s_k$ and keep trust region radius $\Delta_{k+1} = \Delta_k$. Set $k = k+1$ and go to Step 2.

4. Williams-Otto process

The Williams-Otto problem is a simple flowsheet that provides a good example process for testing algorithms. A diagram of the process and the full optimization formulation is presented in Biegler (2010). The process consists of a reactor, heat exchanger, and two separation units described by component split ratios. To benchmark the trust region RM methods, the reactor is considered to be a complex simulation. In actuality, the reactor is described as a CSTR with three sequential second order reactions. When developing reduced order models, it is helpful to use the smallest possible sets of input and output variables to describe the complex behavior. In this case, extent of reaction is modeled as a function of temperature, volume, and inlet concentrations.

4.1. Results for Williams-Otto process with penalty function algorithm

The results of this optimization are shown in the first column of Table 1. A Kriging model was used as the RM. A good introduction to Kriging may be found in Sasena (2002) and the proof that Kriging functions can satisfy the fully linear property is shown in Wild (2009). The penalty-based optimization reaches the correct solution in 53 iterations. At each iteration the ODM is sampled to construct the RM. During these 53 iterations, 573 samples were obtained. A sample in this case is an evaluation of $\psi(z)$, including solving the system of equations (2b). Because solving the system of equations involves multiple evaluations of the ODM, the actual number of ODM calls is 11,622. For a realistic problem in which ODM evaluations may take minutes or even hours, this approach is clearly intractable.

4.2. Results for Williams-Otto process with filter algorithm

The results of the trust region filter method are shown in Table 1. Three variants of the method were tested, using three choices for RM. First, Kriging models were used to represent the extents

of reaction as a function of reactor conditions. Compared to the use of Kriging in the penalty formulation, more iterations were required to reach the optimum. However, the clear advantage of the filter method emerges when comparing the number of ODM evaluations. The filter method required only 1,621 evaluations, merely 14% of the 11,622 evaluations for the penalty approach.

	Penalty	Filter		
RM:	Kriging	Kriging	linear	linear
note:	x^I only	ODM inputs	interpolation	finite diff
Objective:	-1.2111	-1.2110	-1.2111	-1.2111
Iterations:	53	148	302	7
Sample points:	573	1621	2114	49
ODM calls	11622	1621	2114	49

Table 1: Results for Williams Otto problem for 4 algorithms

The next case that was studied examined the use of finite difference derivative estimates and fitting of a linear RM for reaction kinetics. The results are in the final column of Table 1. The algorithm terminated after only 7 iterations. Because each finite difference estimate required $n+1$ samples from the ODM where n is the number of inputs to $d(x)$, only 49 ODM evaluations were needed in total to reach the optimum. These samples are small perturbations from x_k.

To explain this remarkable performance, consider two reasons based on the properties of the RM. First, the finite difference approach focuses on accuracy at the center of the trust region, at the expense of accuracy elsewhere. Second, the linear RM is a much simpler functional form than the highly nonlinear Kriging models, which could result in artificial local minima in the subproblems. To test the validity of these reasons, a third RM was used. This third approach maintained the simple, linear functional form from the finite difference approach. But this time, the data to which the the linear surface was fit was generated with perturbation sizes equal to $\Delta_k/2$. Therefore, the derivative at the center of the trust region is only accurate for small trust region radii. As with Kriging, finite difference models satisfy the fully linear property described in Section 1.

The results in the third column of Table 1 show that this RM required more iterations and more ODM evaluations than Kriging. Therefore, it is doubtful that the simpler functional form of the RM has much effect on the overall convergence of the outer trust region filter method. Kriging models satisfy an interpolation condition at every data point used to construct them, and therefore in general will have more accurate function values throughout the trust region than the linear fit. However, these results suggest that the most important factor for fast convergence is a very good derivative estimate at the center of the trust region.

5. Ammonia synthesis process

The ammonia synthesis process provides a larger case study for the performance of the trust region filter method. A detailed reactor model consisting of a system of differential algebraic equations was proposed by Murase et al. (1970) and used as an ODM in the synthesis flowsheet. This model considers specific kinetic information for the ammonia synthesis reaction. The heat transfer equations and rate equation were discretized with Radau IIa collocation (Ascher and Petzold, 1998). The resulting system of equations was solved in IPOPT (Wächter and Biegler, 2006).

The rest of the ammonia synthesis process, consisting of three compressors, four heat exchangers, and two flash units, is modeled with cubic equation of state thermodynamics in the equation oriented process optimization framework presented in Dowling and Biegler (2015). The objective was to maximize revenue from product sales minus utility costs. The largest utility cost comes from refrigeration between the reactor exit and flash sequence. The detailed reactor model captures a complex trade-off between temperature, pressure, composition, and the conversion. These

relations are compounded with the task of achieving separation to specifications, either through the cheap flash separations or expensive refrigeration. There is clear potential for optimization to help balance these trade-offs.

A linear surface with finite difference derivatives is used as the RM based on the Williams-Otto results. The filter algorithm converged to a local optimum in 22 iterations. However, the initial point was obtained by optimizing the process with a fixed 30% conversion of nitrogen to ammonia. When these reactor conditions were tested with the ODM, the conversion was actually much lower. The first near-feasible iterate had an objective value of only \$1,744/hr. The trust region filter algorithm closes this gap during the optimization process. The objective at the optimal solution is \$2,868/hr, an increase in profit of \$8.9 million each year.

6. Conclusions

In this work we use trust regions to systematically use reduced order models in a way that can converge to the true optimum. A new filter-based method is introduced and compared to a previous penalty-based method. The filter method's ability to handle equality constraints directly allowed it to outperform the penalty approach. Additionally, it was shown that linear RMs based on finite difference derivative approximations outperform more nonlienar Kriging models. This suggests that using the best derivative estimate available in conjunction with the trust region filter algorithm can exploit the cheap derivatives in the known constraints to minimize the number of ODM evaluations required to reach the optimum.

References

Agarwal, A., Biegler, L. T., 2013. A trust-region framework for constrained optimization using reduced order modeling. Optimization and Engineering 14 (1), 3–35.

Ascher, U. M., Petzold, L. R., 1998. Computer methods for ordinary differential equations and differential-algebraic equations. SIAM.

Biegler, L. T., 2010. Nonlinear programming: concepts, algorithms, and applications to chemical processes. SIAM.

Biegler, L. T., Grossmann, I. E., Westerberg, A. W., 1985. A note on approximation techniques used for process optimization. Comp & Chem Eng 9 (2), 201–206.

Biegler, L. T., Lang, Y.-d., Lin, W., 2014. Multi-scale optimization for process systems engineering. Comp & Chem Eng 60, 17–30.

Caballero, J. A., Grossmann, I. E., 2008. An algorithm for the use of surrogate models in modular flowsheet optimization. AIChE Journal 54 (10), 2633–2650.

Conn, A. R., Gould, N. I., Toint, P. L., 2000. Trust region methods. SIAM.

Conn, A. R., Scheinberg, K., Vicente, L. N., 2009. Introduction to derivative-free optimization. SIAM.

Davis, E., Ierapetritou, M., 2009. A kriging based method for the solution of mixed-integer nonlinear programs containing black-box functions. Journal of Global Optimization 43 (2-3), 191–205.

Dowling, A. W., Biegler, L. T., 2015. A framework for efficient large scale equation-oriented flowsheet optimization. Comp & Chem Eng 72, 3–20.

Eason, J., Cremaschi, S., 2014. Adaptive sequential sampling for surrogate model generation with artificial neural networks. Comp & Chem Eng.

Fletcher, R., Leyffer, S., 2002. Nonlinear programming without a penalty function. Math Prog 91 (2), 239–269.

Henao, C. A., Maravelias, C. T., 2011. Surrogate-based superstructure optimization framework. AIChE Journal 57 (5), 1216–1232.

Murase, A., Roberts, H. L., Converse, A. O., 1970. Optimal thermal design of an autothermal ammonia synthesis reactor. Industrial & Engineering Chemistry Process Design and Development 9 (4), 503–513.

Nocedal, J., Wright, S., 1999. Numerical optimization, 2nd Edition. Springer New York.

Omojokun, E. O., 1990. Trust region algorithms for optimization with nonlinear equality and inequality constraints.

Sasena, M. J., 2002. Flexibility and efficiency enhancements for constrained global design optimization with kriging approximations. Ph.D. thesis, University of Michigan.

Wächter, A., Biegler, L. T., 2006. On the implementation of an interior-point filter line-search algorithm for large-scale nonlinear programming. Math Prog 106 (1), 25–57.

Wild, S. M., 2009. Derivative-free optimization algorithms for computationally expensive functions. Ph.D. thesis, Cornell University.

Krist V. Gernaey, Jakob K. Huusom and Rafiqul Gani (Eds.), 12th International Symposium on Process Systems Engineering and 25th European Symposium on Computer Aided Process Engineering.
31 May – 4 June 2015, Copenhagen, Denmark

Optimization of LNG Supply Chain

Alice Bittante[a]*, Raine Jokinen[a], Frank Pettersson[b], Henrik Saxén[a]

[a]*Thermal and Flow Engineering Laboratory, Åbo Akademi University, Biskopsgatan 8, FI-20500 Åbo, Finland*
[b] *Process Design and Systems Engineering, Åbo Akademi University, Biskopsgatan 8, FI-20500 Åbo, Finland.*
alice.bittante@abo.fi

Abstract

Natural gas is traditionally transported from gas fields to consumer sites with pipelines, but the total cost of pipeline transportation is unfeasible for long distances. The best way to introduce natural gas to new, scattered areas is by transporting it as liquefied natural gas (LNG). This paper presents a mathematical model to aid decision making in the LNG supply chain design, with the focus on inter-terminal transportation. The model, which considers distribution of LNG to consumers from multiple supply terminals through multiple satellite terminals by a heterogeneous fleet of ships, utilizes mixed integer linear programming for finding a supply chain structure that minimizes costs associated with fuel procurement. The model has been tested in a case study inspired by a potential real-life LNG supply chain in the Caribbean islands. The results show that the model works consistently and the computation time is relatively short. The proposed MILP model results in a flexible framework that can be easily implemented in other optimization-based applications.

Keywords: Optimization, MILP, Supply chain, Routing

1. Introduction

In the last decade, natural gas has seen a substantial increase in popularity among the fossil energy sources. The increasing world energy consumption, and the growing attention to environmental aspects connected to it, has put natural gas in a privileged position. Its low carbon-hydrogen ratio and its large remaining reserves make it a satisfactory alternative (among the other fossil fuels) to fulfil the energy demand.
The common way of transporting natural gas from the gas field to the consumers is through pipelines in gaseous state. When distances are very long or geographical restrictions make the pipeline solution unfeasible, it is more economical to transport it as liquefied natural gas (LNG). Natural gas is transformed into LNG by refrigeration processes which cool down the gas below −162°C and reduce its volume 600 times. Transportation can then take place by trucks or ships, with the latter being preferable for long distances and large amounts. Maritime transportation of LNG is performed through specially designed insulated vessels, which can keep the fuel in liquid state. From the liquefaction plants LNG is loaded into the ships which then depart towards the receiving ports, where LNG is unloaded in storages and usually vaporized and fed into the local pipeline. This LNG supply chain is often a large-scale one with vessels of average capacity of about 145,000 m^3. In this paper we study a small to medium-scale LNG supply chain where demands are smaller and sparsely distributed, as it could be the case for consumers located on islands. Maritime routing and optimization of supply chain have been studied long and there is a rich literature on these topics. Vehicle routing has

a long history, with the first papers being published in the seventies (Golden et al., 1977). Review papers on vehicle and maritime routing have also been published (Eksioglu et al., 2009). Christiansen et al. (2007) presented an ample overview on maritime transportation with a comprehensive survey on mathematical models for ship routing and scheduling. Song and Furman (2013) developed a general framework for maritime inventory routing problems. They also proposed an optimization based on heuristics. Large-scale LNG ship routing and scheduling have been studied by Halvorsen-Weare and Fagerholt (2013). They proposed a solution method by decomposition in subproblems, where routing and scheduling are treated separately. Agra et al. (2013) studied the short sea inventory routing problem for distribution of different oil products in the archipelago of Cape Verde, proposing both a discrete time and a continuous time arc-load-flow formulation. In a second paper (Agra et al., 2014) the authors also presented a heuristic-based method to treat realistic routing problems. In the present paper, we present a model as a general framework for ship routing within a given time horizon. The purpose of the model is to identify optimal routes, supply-receiving port connections, and ship sizes to solve the small-scale supply chain problem.

2. Problem Description

The problem studied can be classified as a strategic maritime transportation problem. We consider the regional supply of LNG from a set of potential supply ports to a set of receiving terminals. Demands at the receiving terminals are given and must be fulfilled within the given horizon. The ships delivering the fuel to the receiving ports can be selected from a heterogeneous fleet of vessels. Each type of vessel has a given capacity, cruising speed, and fuel consumption. Some vessels can be restricted from visiting certain receiving terminals due to their incompatibility with the port specifications (i.e., port depth). Limitations on the maximum amount of LNG available at the supply ports can be included. Different supply ports may have different price of the LNG. Every port can be visited more than once and some type of vessels can visit more than one port in the same voyage, i.e., allow for load splitting. Distances between all the ports are known. The aim of the model is to select the optimal fleet and routing scheme to fulfil the demand during the planned horizon at minimum cost.

3. MILP model

The problem formulation considers a set of receiving ports $(i,j) \in \mathcal{R}$ that need to be supplied with LNG from a set of supply ports $s \in \mathcal{S}$; with $\mathcal{R}$ and $\mathcal{S}$ being subsets of $(l,m) \in \mathcal{L}$, the set of all the locations. A set of different ship types $k \in \mathcal{K}$ is considered for the transportation. The routing of the ships and the transport costs are modelled using linear equations and constraints, creating a mixed-integer linear programming (MILP) problem to be solved.

3.1. Variables

The routing requires two sets of variables, a set of integer variables, $Y_{l,m,k}$, which represent the number of times a ship of type *k* traverses between the ports *m* and *l* and a set of continuous variables, $X_{l,i,k}$, which represent how much LNG is transported from port *l* to *i*. Additionally, the model includes a set of integer variables to determine the number of each type of ships needed, N_k.

3.2. The model

The objective of the task is to fulfil the demand at the receiving ports with minimum total combined costs. Parameters c_k^{fuel} and c_k^{rent} respectively represent propulsion and renting cost of ship type *k*. Capacity of the ship is given by C_k, and the vessel's speed by v_k. The ship's load limit factor f indicates the minimum load allowed for ships with splitting restriction, while S_i represents the size limit of the terminal. Distances between ports are given by $d_{l,m}$, demands at the receiving terminals by D_i, and docking times by t_l. The parameter a denotes the availability, in days, of the ship in the given time horizon. The LNG price and maximum amount of LNG available at the supply ports are given by P_s and S_s^{max}, respectively. The objective function and constraints are as follows:

$$\min c^{tot} = \sum_{l,m,k} c_k^{fuel} \cdot d_{l,m} \cdot Y_{l,m,k} + \sum_k c_k^{rent} \cdot N_k + \sum_{s,i,k} P_s \cdot C_k \cdot X_{s,i,k} \tag{1}$$

s.t.

$$\sum_{l,k} C_k \cdot X_{l,i,k} - \sum_{j,k} C_k \cdot X_{i,j,k} \geq D_i \quad \forall i \tag{2}$$

$$Y_{l,i,k} \geq X_{l,i,k} \quad \forall l, i, k \tag{3}$$

$$\sum_l X_{l,i,k} \geq \sum_l X_{i,l,k} \quad \forall i, k \tag{4}$$

$$\sum_m Y_{m,l,k} = \sum_m Y_{l,m,k} \quad \forall l, k \tag{5}$$

$$a \cdot N_k \geq \frac{1}{v_k} \cdot \sum_{l,m} d_{l,m} \cdot Y_{l,m,k} + \sum_l t_l \cdot \sum_m Y_{l,m,k} \quad \forall k \tag{6}$$

$$Y_{l,i,k} \cdot C_k \leq Y_{l,i,k} \cdot S_i \quad \forall l, i, k \tag{7}$$

$$\sum_{i,k} X_{s,i,k} \cdot C_k \leq S_s^{max} \quad \forall s \tag{8}$$

The objective function, Eq. (1), comprises three parts: shipping costs, rental costs and the cost of LNG. The first set of constraints, Eq. (2), determines the *X* variables so that the demands at the receiving ports are satisfied and the second set of constraints, Eq. (3), defines the integer *Y* variables based on the continuous *X* variables. Constraints (4) forbid intermediate loading at the receiving terminals. Equations (5) ensure route continuity and the fifth set of constraints, Eq. (6), define the number of ships based on time usage. Equations (7) and (8) ensure that terminal restrictions are complied with.

In the above form, the model allows for load splitting for all types of ships. In reality, there are some restrictions concerning load splitting in LNG transportation, especially with larger ships. Therefore, the following set of constraints may be used to apply a no-load-splitting condition on a specified subset of ship types, $\mathcal{K}^{spec}$:

$$\sum_{i,j} X_{i,j,k} = 0 \quad \forall k \in \mathcal{K}^{spec} \tag{9}$$

$$X_{s,i,k} \geq f \cdot Y_{s,i,k} \quad \forall s, i, k \in \mathcal{K}^{spec} \tag{10}$$

4. Case Study

In the case study the model was utilized to optimize the maritime routing of a small to medium-scale LNG supply chain in the area of the Caribbean islands. In this region there are a few LNG terminals in operation and more may be built in near future. The power production in the Caribbean islands is mainly oil and coal based. Lately, renewable sources (solar and wind) have been introduced and attention has been given to natural gas as well. With its economic, cleaner, reliable, and more environmental-friendly aspects, natural gas seems to be the natural bridge energy source between the oil sources and renewables. In the case study we assumed that power plants would be the main consumers of the natural gas imported at the receiving terminal, so LNG storages were taken to exist at the receiving terminals. Demands for the time horizon are taken to be smaller than the storage capacity. This is a reasonable assumption considering the comparatively small demands in the area. As set of possible supply ports we selected three ports geographically located to surround the receiving terminals. One of these is an existing LNG export terminal located in Trinidad and Tobago (Point Fortin), while the other two are at the stage of planning and proposal; they are located in Texas (Pass Sabine) and in Florida (Jacksonville). The receiving terminals are taken to be five and are located in different countries. Two are existing terminals, in Dominican Republic (AES Andres LNG Terminal) and in Puerto Rico (Punta Guayailla), while the other three have been selected according to some proposals found in news articles: they are in Haiti (Port-au-Prince), Jamaica (Port Esquivel), and The Bahamas (Ocean Cay). The demands used for the receiving terminals are approximations based on the overall energy demand of the country. Dominican Republic is the major consumer, followed by Puerto Rico with a demand which is one third less, and Haiti and Jamaica, the demands of which are similar and about one fifth of Puerto Rico's demand. Finally, The Bahamas has a demand half of that of Haiti or Jamaica. Ships of capacity 7,500 m^3, 15,000 m^3, 30,000 m^3, 60,000 m^3, and 120,000 m^3 were given as possible options. These sizes are based on data from the Norwegian small-scale LNG supply chain (TGE Marine Gas Engineering GmbH , 2009). The biggest vessel has a capacity falling between the two higher demands. Ship parameters (such as fuel consumption, cruising speed and renting cost) have also been taken from the above mentioned case. The time horizon was chosen to be 30 days. The distances among the locations vary in the range 150-2,000 nautical miles, which correspond to voyages of 0.5-4.5 days with the smallest ship.

The MILP model was implemented in AIMMS 4.1 using the IBM ILOG CPLEX Optimizer. The case study problem results in 285 integer and 206 continuous variables. The solution time was below 5 seconds on a computer with an Intel Core i7-2600K processor.

4.1. Results

The test case has been solved firstly allowing for load splitting for all types of ships (Case 1), i.e., without constraints expressed in equations (9) and (10). Later we solved the same case including the limitations on the load splitting (Case 2). In a later set of optimization runs, we modify the LNG price at the different supply ports, which was

previously set equal for the three ports, to investigate the threshold values related to this parameter (Case 3a-b). All the runs had the same parameters and limitations on availability of LNG at the supply ports and ship-port compatibility was not restricted.
The results from the optimization of Case 1 shows that only one ship of the biggest type is needed to fulfil the demand. The time the ship will be in use is 20.4 days and the routes are shown by arrows in Figure 1a. Note that the arrows only display the route from port-to-port and not the real maritime route, and that the figure does not show how many times the same route is travelled. In the specific case each route is covered only once and the ship performs sequential load splitting in Haiti, Jamaica, Dominican Republic, and The Bahamas before returning to the supply port in Florida. In Case 2 (Figure 1b), when load splitting is banned for ships with capacity $\geq$ 60,000 m^3, the optimal fleet suggested by the model includes one ship of 60,000 m^3 and one of 15,000 m^3. The ships are used for 23.6 and 26.1 days, respectively. The bigger ship delivers LNG to the bigger consumers while the smaller ship supplies the ports with minor demands. One voyage departing from Florida includes load splitting in Jamaica and Haiti. The total combined cost of the objective function increases by 0.4 % from Case 1 to Case 2.

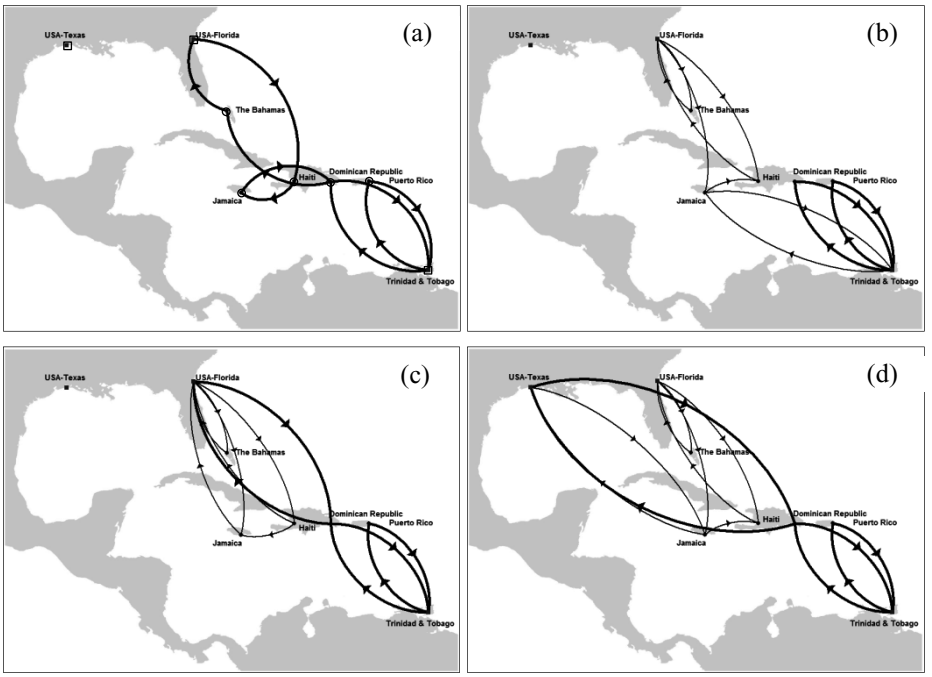

Figure 1. Optimal routes for Case 1 (a), Case 2 (b), and Case 3 (c-d). Squares in subfigure (a) denote supply port and circles demands ports. The thickness of the arrows is proportional to the capacity of the ship travelling the route.

When the LNG price at the supply ports was gradually changed (Case 3), the optimal routing was found to be sensitive to this parameter (Figure 1c-d). This is reasonable since the LNG price represents the major contribution to the total objective function. Increasing the price of LNG at Trinidad and Tobago by about 1 % makes Florida the only supply port used. In Figure 1c we show the solution for an intermediate state, where the LNG is 0.6 % more expensive in Trinidad and Tobago. The solution has changed slightly with respect to routes, but the optimal fleet configuration remains the

same as in Case 2. The main consumer (Dominican Republic) is now served by both supply ports, so we may conclude that the optimal solutions evolve in a logical way. The total cost increases by about 0.5 %. When the LNG price of the supply ports in Trinidad and Tobago and in Florida is increased by 1.8 % and 1.2 %, respectively, the terminal in Texas becomes the optimum supply port to fulfil the entire demand of the islands. Figure 1d displays an intermediate configuration where the LNG price in Trinidad and Tobago and in Florida is 1.2 % and 0.6 % more expensive. Some routes are seen to change while others remain the same as in Case 2 (Figure 1b). It is interesting to note that the same fleet can solve the problem optimally. However, more time is required due to the longer voyages, but the ship utilization is still a couple of days below the time horizon.

5. Conclusions

This paper has studied a small and medium-scale strategic maritime transportation problem. A MILP model that minimizes the costs related to fuel procurement has been presented. A case study illustrates that the model solves the problem efficiently and coherently when key parameters are perturbed. The proposed model is general enough to be easily implemented for tackling larger supply chain optimization problems. The idea is that this mathematically simple and computationally attractive model will serve as a "routing tool" within more complex applications. Future work will therefore be directed to optimization of larger energy chains and supply networks, with more realistic constraints. An analysis will also be performed to study the sensitivity of the results to uncertainty in the model parameters. This will be investigated by introducing stochastic perturbations of key parameters, such as LNG price and demands, solving the optimization problem on a large set of scenarios.

Acknowledgments

This work is part of the Efficient Energy Use (EFEU) research program under CLEEN Ltd. with funding from Tekes and participating companies. The financial support is gratefully acknowledged.

References

A. Agra, M. Christiansen and A. Delgado, 2013, Discrete time and continuous time formulations for a short sea inventory routing problem, [Online], Available at: http://hdl.handle.net/10773/10561, [Accessed 20 November 2014].

A. Agra, M. Christiansen, A. Delgado and L. Simonetti, 2014, Hybrid heuristics for a short sea inventory routing problem, European Journal of Operational Research, 236, 3, 924-935.

M. Christiansen, K. Fagerholt, B. Nygreen and D. Ronen, 2007, Maritime Transportation, Handbooks in operations research & management science, Amsterdam: Elsevier, 189-284.

B. Eksioglu, A. V. Vural and A. 0Reisman, 2009, The vehicle routing problem: A taxonomic review, Computers & Industrial Engineering, 57, 4, 1472-1483.

B. L. Golden, T. L. Magnanti and H. Q. Nguyen, 1977, Implementing vehicle routing algorithms. Networks, 7, 2, 113-148.

E. E. Halvorsen-Weare and K. Fagerholt, 2013, Routing and scheduling in a liquefied natural gas shipping problem with inventory and berth constraints, Annals of Operations Research, 203, 1, 167-186.

J-H Song and K. C. Furman, 2013, A maritime inventory routing problem: Practical approach, Computers & Operations Researce, 40, 3, 657-665.

TGE Marine Gas Engineering GmbH , 2009a, Coral Methane, [Online], Available at: http://www.tge-marine.com/37-0-Small-Scale-LNG.html, [Accessed 20 November 2014].

Krist V. Gernaey, Jakob K. Huusom and Rafiqul Gani (Eds.), 12th International Symposium on Process Systems Engineering and 25th European Symposium on Computer Aided Process Engineering.
31 May – 4 June 2015, Copenhagen, Denmark

Metaheuristic Techniques for the Optimal Design of NGL Pipelining

Paola P. Oteiza[a, c], Martín C. De Meio Reggiani[a,b,c], Diego A. Rodriguez[a,b,d], Valentina Viego[b], Nélida B. Brignole[a,c, *]

[a]*Laboratorio de Investigación y Desarrollo en Computación Científica (LIDeCC). Universidad Nacional del Sur (DCIC-UNS, Avda. Alem 1253, Bahía Blanca (B8000CPB), Argentina*
[b] *Departamento de Economía, UNS Av. Alem 1253 - Bahía Blanca (B8000CPB), Argentina*
[c] *Planta Piloto de Ingeniera Química (UNS - CONICET) Cno La Carringanda Km.7 Bahía Blanca(B8000CPB), Argentina*
[d] *Facultad de Ciencias Exactas, Universidad Nacional de Salta (UNSa), Av. Bolivia 5150, Salta (A4400), Argentina*
dybrigno@criba.edu.ar

Abstract

We have considered the problem of designing a convenient piping layout in order to transport NGL (Natural-Gas Liquids) through a country subjected to an unstable economy. In this paper we provide a preliminary design of an optimization model by applying metaheuristic algorithms to a set of networks corresponding to a real-world case study. Experimental results for Simulated Annealing and Genetic Algorithms are presented and these techniques are compared.

Keywords: Metaheuristic, NLG, Pipeline Design, GARCH

1. Introduction

A current challenge in the oil industry is the optimization of transport from the extraction areas to the processing locations. The varying price of fuels and the associated increasing haulage costs boost research in the exploration of strategies that aim at exploiting and delivering dormant energy sources. For example, particularly in Argentina, which is the second place in the world in shale gas reserves, in the future it is expected to exploit gas fields that contain about 802 trillion cubic feet of natural gas (EIA, 2013).

Concomitantly, the extraction of natural gas implies the availability of natural gas liquids (NGL), which are convenient to process. Therefore, in view of this scenario, cost-effective solutions are required. Transport is a major consideration in predicting economic benefits. Pipelines are the primary mode of transportation for crude oil, petroleum products and natural gas in producer countries since it is safer and more reliable than roads or rails, apart from providing a substantial cost advantage. (Furchtgott-Roth, 2013). The distinctive features of the model formulation presented in this paper are the incorporation of both economic uncertainty over time and the geographical distribution of the production in order to achieve reliable optimizations.

We have also focused specially with search metaheuristics as general strategies for the design of heuristic procedures with high performance for the solution of optimisation problems related to pipelining. Several successful state-of-the-art metaheuristics have

lately been developed for varied purposes. Abd-El-Barr (2009) considered a variety of techniques for the problem of topological optimization of communication networks subjected to a number of computational design constraints. Osiadacz and Góreki (1995) made a reasonably comprehensive survey of the optimization of both water and gas distribution networks by means of heuristic methods, exact procedures that consider the availability of continuous diameters, and discrete optimization methods. In turn, Marcoulaki et al. (2012) presented an optimisation framework based on stochastic optimisation for the routing and equipment design of main pipelines to be employed for fluid transmission. In fact, stochastic optimization is the research field metaheuristics belong to. Sahinidis (2004) provided a short overview of stochastic optimization, discussing and contrasting various relevant modeling philosophies, like robust stochastic programming, probabilistic programming, and stochastic dynamic programming. Lately, André et al. (2013) solved the problem of the optimal design of a hydrogen transmission network by means of a local- search method and compared their procedure with a Tabu-search heuristics.

In this paper, the analysis was applied to the design of a real-world pipeline network. NGL coming from gas fields located in Santa Cruz province (Argentina) are sent to the processing plant, which is desired to be placed at Río Gallegos. Thanks to the employment of metaheuristics, an adequate pipeline network layout could be achieved.

2. Mathematical Formulation

The increasing cost of transporting fuels has stimulated our research in the problem statement. The formulation of the objective function should be posed to make the optimization results realistic. In this perspective, the Net Present Value (NPV) of a project (Eq.(1)) is obtained from revenue flows and all kinds of construction and operating costs. By comparing alternative pipeline layouts, the most valuable one is selected so as to maximize overall benefits.

$$\begin{aligned} NPV = & \sum_{t=1}^{o} \frac{P_t \, x \, Q_t}{(1+r)^{t+m+n}} - \sum_{t=1}^{n} \sum_{i=1}^{f+q} \sum_{j=1}^{q+p} \frac{CC_{ijt}}{(1+r)^{t-1}} FP_{IJ} - \sum_{t'=1}^{\frac{m+o}{l}} \sum_{i=1}^{f+q} \sum_{j=1}^{q+p} \frac{PC_{t'} \, x \, NP_{ij}}{(1+r')^{t'-1}(1+r)^{n}} FP_{IJ} \\ & - \sum_{t=1}^{m} \sum_{k=1}^{q} \frac{\beta_{kt}}{(1+r)^{t+n-1}} \; CN_k - \sum_{t=1}^{o} \sum_{i=1}^{f+q} \sum_{j=1}^{q+p} \frac{PW_{ijt}}{(1+r)^{t+m+n-1}} FP_{IJ} \\ & - \sum_{t=1}^{o} \sum_{i=1}^{f+q} \sum_{j=1}^{q+p} \frac{MC_{ijt}}{(1+r)^{t+m+n-1}} FP_{IJ} - \sum_{t=1}^{o} \frac{LC_t}{(1+r)^{t+m+n}} \end{aligned} \tag{1}$$

As pipeline layouts ensue diverse expenditures along the project lifetime, considering a discount rate proves to be essential in order to arrange alternative developments adequately. Moreover, a discount rate that contemplates uncertainty risks is a suitable way to estimate long-term cash flows that require this kind of investment in volatile economies.

In this sense, an interest rate series that reflects a similar level of risk for comparable projects was modelled by means of an Auto-Regressive Integrated Moving Average (ARIMA) regression analysis. As a variety of unknown events sooner or later arise, even more frequently in developing markets, the error term contained in the media

equation for an interest rate usually exhibits a non-constant variance. In other words, unsystematic shocks in the economy affect the estimation of model parameters and their efficiency. Those sudden variations can be taken into account with GARCH (Generalized Autoregressive Conditional Heteroskedasticity). By applying this econometric method, or its alternative specification "in Media" (GARCH-M), confidence intervals can be defined so that the decision-maker can adjust the discount rate according to different risk-aversion profiles (Enders, 2009).
As to the problem formulation, it was based on the following assumptions:

- A control system has been implemented in order to guarantee that a continuous NGL supply will be provided. The storage tanks, which are located at the "concentrating nodes", serve to balance the flowrate, acting as contingency reservoirs. By preventing unexpected variations over time in this way, the production transported through the pipelines is regarded as constant.

- The construction costs CC_{ijt} are based on both the pipe diameter and the covered distance. Land permissions, material and construction labour costs are included.

- The installation costs β_{kt} of the concentrating nodes are obtained by evaluating the corresponding equipment costs related to their dimensions.

- The number of pumps (NP_{ij}) and the required energy (PW_{ijt}) depend on the flow rate, the pipe diameter and the covered distance (Echarte, 2010).

- The maintenance cost MC_{ijt} varies by considering the entire structural value.

- The transport tariff P_t can be taken from the market in order to determine if the project is economically viable. Another approach consists in setting the price to zero so as to know the lowest profitable limit. The metaheuristic methods employed in this paper are flexible enough to allow both solutions.

3. Metaheuristics for Pipeline Design

The formulation described in the previous section constitutes an NP-complete combinatorial optimization problem (Cook, 1971). Hence, the difficulty to find an optimal solution increases exponentially with problem size. Therefore, instead of choosing exact methods, metaheuristic techniques become more attractive because they are able to find satisfactory solutions in reasonable times.
Our framework was conceived as a Decision Support System to accommodate more specific design criteria. With the decision-maker's intervention and his acceptance of the proposed network, our stochastic optimizer guides a subordinate heuristics by cleverly combining various concepts in order to explore and exploit adequately the search space. Metaheuristic techniques founded on trajectories, such as Simulated Annealing (SA) (Kirkpatrick et al., 1983) were considered together with population-based methods, like Genetic Algorithms (GA) (Whitley, 1994). We have tested the most important metaheuristics according to the classification that categorizes them into trajectory methods and population-based methods because this division allows a clearer distinction of the algorithmic strengths.
The search strategies of different metaheuristics are highly dependent on the philosophy of the metaheuristic itself. The trajectory methods evaluate several neighborhood

structures imposed on the search space. In contrast, population-based methods deal in every iteration of the algorithm with a set of solutions (called a population) rather than with a single solution. In this way, population-based algorithms supply a natural, intrinsic mechanism for the exploration of the search space (Alba, 2005). At each iteration some operators are applied to the individuals of the current population so as to generate the individuals of the population for the next generation (i.e., iteration).
Both algorithms were implemented in JAVA language an executed in an Intel Core i5-3330 PC with 8 GB RAM. The solutions were represented with sparse binary matrices, whose rows are the oil fields and their columns are either the concentrating nodes or a processing plant. Then, an element equal to 1 denotes a connection. Although the algorithms can determine the most convenient number of concentrating nodes by themselves, it is also possible for the decision-maker to pre-establish that amount. In the latter case, the search space is restricted and therefore, the best result is obtained fastly.
The following algorithmic parameters were chosen after several executions:

- For GA: population size = 50; number of generations = 250; crossover probability = 0.7; mutation probability = 0.1.

- For SA: number of iterations with different temperatures = 500; number of iterations with the same temperature = 3; initial temperature = 0.99

As to the behaviour of both algorithms in finding networks for the case mentioned in the last paragraph of the introduction, Fig. 1 shows the evolution of the fitness function (NPV) obtained for 30 independent executions, whose results are represented by various curves. Since algorithmic progress can be measured with different search-tracking indicators for each metaheuristics, the x axis for SA and GA correspond to the number of iterations and generations, respectively. In both cases, the fitness values decrease sharply during the first half of the evolution. Then, this representative behaviour exhibits the satisfactory robustness of SA and GA when solving this problem.
The average execution times of these algorithms have been compared. For GA the total CPU time required was 383 ms. In contrast, for SA the total CPU time required was only 138 ms, which represents 36 % of GA's algorithmic time.
The results shown in Table 1 reveal that after 30 independent executions, both algorithms performed satisfactorily and always yielded the best solution. In the third column, the efficacy reports the number of times the optimum is reached.

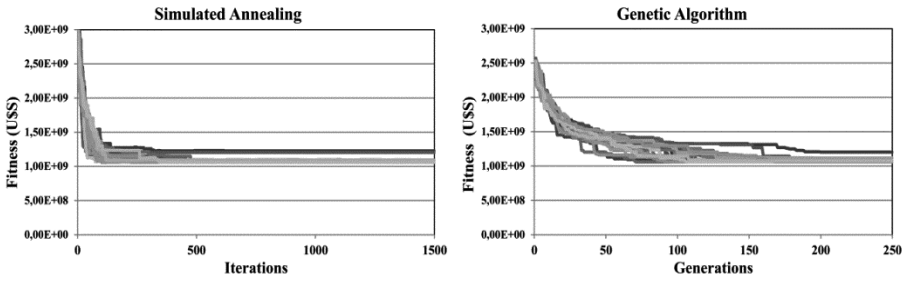

Figure 1: Contrasting the performance of SA and GA metaheuristics.

Table 1: Statistics for the final optimised networks

Algorithm	Best Solution (U$S)	Efficacy (%)	Computing Time (ms)	Number of Evaluations
GA	$1.057E^{+09}$	80	383	24038
SA	$1.057E^{+09}$	70	138	1500

GA proved to be more efficacious at the expense of CPU time, which is required because a great amount of evaluations is necessary for a population-based technique. It should be kept in mind that in our SA implementation preparing a neighbour solution takes more time than performing the crossover in our GA. For this reason, unlike SA, GA's time does not grow proportionally with the number of evaluations.

4. Conclusions

In this work a preliminary design of an optimization model is presented. In order to improve the design quality of the pipe network, a detailed economic optimization model for the fluid transportation pipe network throughout a country with an unstable economy was established, wherein the minimum investment was taken as the objective function.

The computational strategy consists in using metaheuristic algorithms in order to find the most convenient piping layout to transport NGL. The solution strategies of Genetic Algorithms and Simulated Annealing algorithms worked out in practice. Both SA and GA succeeded in finding the solution with excellent computing times. When comparing the results obtained using the GA and the SA algorithm, SA outperforms GA with better values and demanding less CPU time (36 %).

Based on this article and the expected industrial needs, we identify the following opportunities about further research for the continuation of this work:

I. As the hydrocarbon fields are getting older and oil prices are changing, economic models and transportation become more and more important. Therefore, more detail should be incorporated in the analysis.

II. Other application domains can be explored. For instance, substantial contributions can also be made by the rigorous simulation of offshore fields with enhanced objective functions.

III. It is vital to improve optimization results so that they can accommodate industrial concerns regarding techno-economical aspects, especially for unstable economies. This is often the reality where non- exploited fields are located. In those cases, uncertainties should also be contemplated.

IV. As to computational design, parallel computing with SA metaheuristics running in threads can be incorporated in order to generate more rigorous and efficient algorithms.

Nomenclature

CC_{ijt}: construction cost from the *i*-th to the *j*-th point, in the *t*-th period
CN_k: for the *k*-th concentrating node: CN_k=1 if active, otherwise CN_k=0
f: number of oil fields
FP_{ij}: feasible path from the *i*-th to the *j*-th point

l: pump's lifetime
LC_t: operating labor cost in the *t*-th period
m: total number of time periods related to the construction of pumps and concentrating nodes
MC_{ijt}: maintenance cost of the structure from the *i*-th to the *j*-th point, in the *t*-th period
n: total number of pipeline construction time periods
NP_{ij}: number of pumps from the *i*-th to the *j*-th point
o: project lifetime
p: number of plants
PC_t: pump installation cost in the *t*-th period
P_t: transport tariff in the *t*-th period
PW_{ijt}: pumping energy cost from the *i*-th to the *j*-th point, in the t-th period
q: number of concentrating nodes
Q_t: amount of NGL transported in the *t*-th period
r: discount rate
r': discount rate adjusted to the pump's lifetime
β_{kt}: installation cost of the *k*-th concentrating node in the *t*-th period

References

M. Abd-El-Barr, 2009, Topological Network Design: A Survey, Journal of Network and Computer Applications, 32, 501–509.
E. Alba, 2005, Parallel Metaheuristics. A New Class of Algorithms, 1st ed., Hoboken, New Jersey: John Wiley & Sons.
J. André, S. Auray, J. Brac, D. De Wolf , G. Maisonnier, M.M. Ould-Sidi, A. Simonnet, 2013, Design and Dimensioning of Hydrogen Transmission Pipeline Networks, European Journal of Operational Res., 229, 239–25.
S. A. Cook, 1971, The Complexity of Theorem-Proving Procedures, Proceedings of the third Annual ACM Symposium on Theory of Computing, 5, 151-158, ACM.
R. Echarte, 2010, Equipos para Procesos Químicos, EdiUNS.
EIA: Energy Information Administration, 2013, Technically Recoverable Shale Oil and Shale Gas Resources: An Assessment of 137 Shale Formations in 41 Countries Outside the United States.
W. Enders, 2009, Applied Econometric Time Series, 3rd Edition, Wiley.
D. Furchtgott-Roth, 2013, Pipelines Are Safest for Transportation of Oil and Gas, 23, 6, http://www.manhattan-institute.org/html/ib_23.htm#.VGlQSiOG-E4.
S. Kirkpatrick, C.D. Gelatt, M. P. Vecchi, 1983, Optimization by Simulated Annealing. Science, 220, 4598, 671-680.
E. C. Marcoulaki, I. A. Papazoglou, N. Pixopoulou, 2012, Integrated Framework for the Design of Pipeline Systems using Stochastic Optimisation and GIS Tools, Chem. Eng. Res. and Des. 90, 2209–2222.
A. J. Osiadacz, M. Góreck, 1995, Optimization of Pipe Sizes for Distribution Gas Network Design, http://www.psig.org/papers/1987/9511.pdf
N. V. Sahinidis, 2004, Optimization under Uncertainty: State-of-the-art and Opportunities Comp. and Chem. Eng., 28, 971–983.
D. Whitley, 1994, A Genetic Algorithm Tutorial. Statistics and Computing, 4, 2, 65-85.

Krist V. Gernaey, Jakob K. Huusom and Rafiqul Gani (Eds.), 12th International Symposium on Process Systems Engineering and 25th European Symposium on Computer Aided Process Engineering.
31 May - 4 June 2015, Copenhagen, Denmark.

Deterministic Global Dynamic Optimisation using Interval Analysis

Carlos Perez-Galvan[a] and I. David L. Bogle[a]

[a]*Centre for Process Systems Engineering; Department of Chemical Engineering; University College London; London, United Kingdom*
d.bogle@ucl.ac.uk

Abstract

There is an interest in obtaining the global optimum for dynamic optimisation problems, i.e., the absolutely best solution since it often offers substantial improvement compared to locally optimal solutions. Furthermore, in safety critical applications it is important to ensure that the behaviour of the process is within (possibly prescribed) safe limits. Currently, the main bottleneck in the deterministic solution of global dynamic optimisation problems is the computation of tight bounds guaranteed to contain all the solutions of the ordinary differential equations (ODE) system.The methods available rely on sequential approaches in which a verified ODE solver and a spatial branch and bound framework are used. In this work, the dynamic set of constraints (ODEs) is solved using an interval Taylor series method with interval contractors (Perez-Galvan and Bogle, 2014) and a spatial branch and bound framework is used as the optimisation routine in a sequential approach. The results demonstrated that when the method described is used uncertainty ($\pm$1-2 %) can be introduced in the system parameters of the two-state case study besides using the Newton contractor took 50-60 % less CPU time than the Krawczyk contractor.

Keywords: Global Optimisation, Interval Analysis, Interval Contractors

1. Introduction

In chemical engineering a vast number of systems of interest can be modelled by ordinary differential equations (ODE) and for these systems it is often necessary to obtain the optimal performance. Among the dynamic optimisation applications that arise in this field are the determination of optimal operating profiles, the formulation of process control strategies, the parameter estimation for model development, etc.

Two main approaches are used to solve these kinds of problems; they are the simulaneous and the sequential approach. In the first, both the state variables and control variables are discretised and in the second one only the control variables are discretised. In this paper only the sequential approach is considered.

Finding the global optima is not an easy task since these problems are typically nonconvex and therefore exhibit multimple local minima. Several researchers have devoted their efforts to solve the deterministic global optimisation problem for dynamic systems and most of these research works implement an extensive search NLP such as a branch-and-bound framework and a verified ODE solver in a sequential approach. For example, a branch-and-bound framework was used with the αBB method (Adjiman et al. 1996) in a sequential approach and applied to four different optimal control problems and to parameter estimation problems (Esposito and Floudas, 2000). In

principle, this method provides a guaranteed global optimum, however, hard to obtain rigorous underestimators are needed for which only sampling approaches were proposed. Another sequential approach was used with a convex underestimating procedure (Papamichail and Adjiman, 2002). Some years later, a method was devised where McCormick relaxations and constant and affine bounds were applied (Papamichail and Adjiman, 2004). The approach used by Papamichail and Adjiman (2002, 2004) is computationally expensive in constructing tight affine underestimators and overestimators. A sequential approach was used for problems with an integral objective function (Singer and Barton, 2006) it implements McCormick relaxations to construct the convex relaxations . The dynamic optimisation problem has also been addressed with focus on the tightness of the ODEs state bounds by means of a Taylor models method with interval remainder term (Lin and Stadtherr, 2006). Later, they applied the same method but this time with a branch and reduce approach using a domain reduction technique (Lin and Stadtherr, 2007). Moreover, the latter method was extended to account for inequality path constraints in a rigorous way (Zhao and Stadtherr, 2011).

Nonetheless, tighter and more efficient bounds are required in dynamic optimisation applications. Because of this a number of ways to deal with this problem have been developed e.g. convex and concave relaxations (McCormick relaxations) have been incorporated along with interval bounds (Sahlodin and Chachuat 2011b). These relaxations have been used in the Taylor Model method in the remainder term in addition to the interval bounds (Sahlodin and Chachuat 2011a). Also for this purpose McCormick relaxations have been applied in a method to derive an auxiliary system of ODEs that uses interval bounds (Scott and Barton, 2013). A kind of Taylor model with ellipsoidal remainder term has also been devised with promising results (Villanueva et al., 2013).

The work presented here provides a new approach for the deterministic global optimisation that uses an algorithm based on an interval Taylor series method that makes use of interval contractors (Krawczyk and Newton contractors) for the reduction of the overestimation. The remainder of this paper is organised as follows: in section 2 the formulation of the problem to solve and the preliminaries are given, in section 3 the verified method for ODEs and the contraction techniques are described, in section 4 the application of the method to a case study in which uncertainty has been introduced is presented and in section 5 conclusions on the results obtained are provided.

2. Preliminaries

In this section the problem we are aiming to solve is formulated. We assume that the problem can be described by the ODE model $\dot{\mathbf{z}} = \mathbf{f}(\mathbf{z}, \boldsymbol{\theta})$, with $\mathbf{z}$, the vector of state variables and $\boldsymbol{\theta}$, the vector of system parameters. In this article the bold type notation is adopted to indicate vector-valued quantities and capital case to indicate interval-valued quantities unless otherwise specified. The formulaton of the dynamic optimisation problem can be stated as

$$\begin{aligned} &\min_{\boldsymbol{\theta}} \ \phi(\mathbf{z}(t_i, \boldsymbol{\theta}), \boldsymbol{\theta}; i = 1, \ldots, ns) \\ &s.t. \quad \dot{\mathbf{z}} = \mathbf{f}(\mathbf{z}, \boldsymbol{\theta}) \\ &\mathbf{z}(t_0, \boldsymbol{\theta}) = \mathbf{z}_0(\boldsymbol{\theta}) \\ &\qquad t \in [t_0, t_f] \\ &\qquad \boldsymbol{\theta} \in \boldsymbol{\Theta} \end{aligned} \tag{1}$$

where ϕ is the objective function, $\boldsymbol{\Theta}$ is an interval vector and $\mathbf{f}$ is assumed to be continuously differentiable with respect to $\mathbf{z}$ and $\boldsymbol{\theta}$. When a sequential approach is used a verified ODE method is applied to the dynamic part of the optimisation problem leaving a problem only constrained by the system parameters $\boldsymbol{\theta}$.

3. Verified ODE method, contraction techniques and branch-and-bound

The mathematical formulation of the systems of ODEs with parameter dependence is stated as before $\dot{\mathbf{z}} = \mathbf{f}(\mathbf{z}, \boldsymbol{\theta})$, $\mathbf{z}(t_0, \boldsymbol{\theta}) = \mathbf{z}_0(\boldsymbol{\theta})$, $t \in [t_0, t_f]$. An interval Taylor series method with High Order Enclosure (Nedialkov et al., 2001) has been used. This method consists of two main steps: validating existence and uniqueness, and computing a tighter enclosure. The first stage of this method satisfies

$$\tilde{\mathbf{Y}}_j = \mathbf{Y}_j + \sum_{i=1}^{k-1} [0, h_j]^i \mathbf{f}^{[i]}(\mathbf{Y}_j, \boldsymbol{\Theta}) + [0, h_j]^k \mathbf{f}^{[k]}(\tilde{\mathbf{Y}}_j^0, \boldsymbol{\Theta}) \subseteq \tilde{\mathbf{Y}}_j^0 \tag{2}$$

where k is the order of the Taylor series expansion, $\mathbf{Y}_j$ is the vector of tight enclosures of the solutions with ranges in $\tilde{\mathbf{Y}}_j^0$, $\boldsymbol{\Theta}$ is the vector of system parameters and $\mathbf{f}^{[i]}$ are the Taylor coefficients defined according to $\mathbf{f}^{[0]}(\mathbf{y}, \boldsymbol{\theta}) = \mathbf{y}_j$, $\mathbf{f}^{[i]}(\mathbf{y}, \boldsymbol{\theta}) = \frac{1}{i}\left(\partial \mathbf{f}^{[i-1]} / \partial_{\mathbf{y}} \mathbf{f}\right)(\mathbf{y}, \boldsymbol{\theta})$ for $i \geq 1$. These Taylor coefficients can be calculated using automatic differentiation.
The second stage involves the computation of a tight enclosure $\mathbf{Y}_{j+1} \supseteq \mathbf{y}(t_{j+1}; \boldsymbol{\Theta})$ given interval bounds $\mathbf{Y}_j$ at t_j. The second stage refines the a priori enclosure $\tilde{\mathbf{Y}}_j$ on $t \in [t_j, t_{j+1}]$ provided in the first stage. It satisfies the next equation (3)

$$\begin{aligned} \mathbf{Y}_{j+1} = & \overbrace{\hat{\mathbf{y}}_j + \sum_{i=1}^{k-1} h_j^i \mathbf{f}^{[i]}(\hat{\mathbf{y}}_j, \hat{\boldsymbol{\theta}})}^{u_{j+1}} + \overbrace{\left\{ I + \sum_{i=1}^{k-1} h_j^i \frac{\partial \mathbf{f}^{[i]}}{\partial \mathbf{y}}(\mathbf{Y}_j, \boldsymbol{\Theta}) \right\}}^{S_{j+1}^y} (\mathbf{Y}_j - \hat{\mathbf{y}}_j) \\ & + \underbrace{\left\{ \sum_{i=0}^{k-1} h_j^i \frac{\partial \mathbf{f}^{[i]}}{\partial \boldsymbol{\theta}}(\mathbf{Y}_j, \boldsymbol{\Theta}) \right\}}_{S_{j+1}^\theta} (\boldsymbol{\Theta} - \hat{\boldsymbol{\theta}}) + \underbrace{h_j^k \mathbf{f}^{[k]}(\tilde{\mathbf{Y}}_j, \Theta)}_{Z_{j+1}} \end{aligned} \tag{3}$$

For the sake of simplicity we rewrite equation (3) as

$$\mathbf{Y}_{j+1} = u_{j+1} + S_{j+1}^y (\mathbf{Y}_j - \tilde{\mathbf{y}}_j) + S_{j+1}^\theta (\boldsymbol{\Theta} - \tilde{\boldsymbol{\theta}}) + Z_{j+1} \tag{4}$$

In this method the interval matrix-vector product $S_{j+1}^y (\mathbf{Y}_j - \tilde{\mathbf{y}}_j)$ in equation (4) is known to be one of the main contributors of the wrapping effect (Jackson, 1975). Because of this, a number of methods have been developed to try to avoid direct evaluations of this matrix-vector product (Nedialkov et al., 1999). In this paper the QR factorization technique devised by Lohner (1992) is used in the interval Taylor series method.
The QR factorization technique consists on the substitution of the term $S_{j+1}^y (\mathbf{Y}_j - \tilde{\mathbf{y}}_j)$ by another term containing a matrix that induces an orthogonal coordinate system that often provides a better enclosure than in the original coordinate system.

$$\mathbf{Y}_{j+1} = u_{j+1} + (S_{j+1}^y) \Gamma_j + S_{j+1}^\theta (\boldsymbol{\Theta} - \tilde{\boldsymbol{\theta}}) + Z_{j+1} \tag{5}$$

where,

$$\Gamma_{j+1} = A_{j+1}^{-1} (Z_{j+1} - \hat{z}_{j+1}) + A_{j+1}^{-1} (S_{j+1}^y A_j) \Gamma_j + (A_{j+1}^{-1} S_{j+1}^\theta)(\boldsymbol{\Theta} - \tilde{\boldsymbol{\theta}}) \tag{6}$$

Here $\Gamma_0 = \mathbf{Y}_0 - \hat{\mathbf{y}}_0$, $A_0 = I$ and A_{j+1} is chosen as the midpoint of $S_{j+1}^y A_j$, the parallelepiped enclosure of Γ_{j+1}.

3.1. Interval contraction techniques

When a real valued function is evaluated using interval arithmetic usually some overestimation is present in the range of the function. Interval contractors offer the possibility to contract the

estimated range in an interval evaluated function. Some of these contractors are counterparts of the real arithmetic techniques and are able to contract nonlinear functions such as the Krawczyk contractor and the Newton contractor. Assume we have n_y variables linked by n_f relations of the form

$$f_q(y_1, y_2, ..., y_n) = 0,\ q \in 1, 2, ..., n \tag{7}$$

Each variable $\mathbf{y}_j$ belongs to a domain $\mathbf{Y}_j$, an interval. Equation (7) can be written in a vector form and a constraint satisfaction problem (CSP) can be formulated as in equation (8).

$$\mathbf{f}(\mathbf{y}) = 0,\ \mathbf{y} \in \mathbf{Y}_j \tag{8}$$

The solution set $\mathbf{B}$ of (8) is defined as

$$\mathbf{B} = \mathbf{y} \in \mathbf{Y}_j | \mathbf{f}(\mathbf{y}) = 0 \tag{9}$$

Contracting the CSP in (8) means replacing $\mathbf{Y}_j$ by a smaller domain $\mathbf{Y}'_j$ such that the solution set remains unchanged, i.e. $\mathbf{B} \subset \mathbf{Y}' \subset \mathbf{Y}$.

The contractors considered in this work are interval counterparts of classical point algorithms such as Gauss-Seidel and Newton algorithms. For more details see (Jaulin et al., 2001) and for application examples in deterministic global optimisation refer to (Balendra and Bogle, 2009). In this work two non-linear contractors have been used, namely the Krawczyk and Newton contractor.

Krawczyk contractor. The Krawczyk contractor considers a CSP as in (8) where the number of variables is the same as the number of relations and $\mathbf{f}$ is assumed to be differentiable. The function $\boldsymbol{\psi}(\mathbf{y}) = \mathbf{y} - M\mathbf{f}(\mathbf{y})$ is a fixed-point subsolver for (8) where M is any invertible matrix. And its centred inclusion function is

$$\boldsymbol{\Psi}(\mathbf{Y}_j) = \boldsymbol{\psi}(\hat{\mathbf{y}}_j) + J_\psi(\mathbf{Y}_j)(\mathbf{Y}_j - \hat{\mathbf{y}}_j) \tag{10}$$

where J_ψ is an inclusion function for the Jacobian matrix of $\boldsymbol{\psi}$ with $\hat{\mathbf{y}}_j$ as the midpoint of $\mathbf{Y}_j$. The intersection between the original domain and the one obtained with (10) results in the fixed-point contractor as in equation (11).

$$\mathbf{Y}_j \leftarrow \mathbf{Y}_j \cap \boldsymbol{\psi}(\hat{\mathbf{y}}_j) + \{I - MJ_f(\mathbf{Y}_j)\}(\mathbf{Y}_j - \hat{\mathbf{y}}_j) \tag{11}$$

Newton contractor. We consider again a CSP as in (8) and apply the mean value theorem to obtain

$$(\mathbf{f}(\hat{\mathbf{y}}_j) + J_f(\boldsymbol{\xi})(\mathbf{y}_j - \hat{\mathbf{y}}_j) = 0,\ \mathbf{y}_j \in \mathbf{Y}_j,\ \boldsymbol{\xi} \in \mathbf{Y}_j) \tag{12}$$

The CSP in (12) can be arranged as

$$(A\mathbf{p} + \mathbf{f}(\hat{\mathbf{y}}_j) = 0,\ \mathbf{p} = (\mathbf{y}_j - \hat{\mathbf{y}}_j),\ A = J_f(\boldsymbol{\xi}),\ \mathbf{b} = -\mathbf{f}(\hat{\mathbf{y}}_j),\ \mathbf{y}_j \in \mathbf{Y}_j,\ \boldsymbol{\xi} \in \mathbf{Y}_j) \tag{13}$$

In this way, a linear contractor can be used such as the Gauss-Seidel contractor. The Gauss-Seidel contractor is able to contract domains of linear systems of the form $A\mathbf{p} - \mathbf{b} = 0$. If A is square it can be decomposed as the sum of a diagonal matrix and a matrix with zeroes in its diagonal (extdiag):

$$diag(A)\mathbf{p} + extdiag(A)\mathbf{p} = \mathbf{b} \tag{14}$$

Also if A is invertible then (14) can be rewritten as

$$\mathbf{p} = (diag(A))^{-1}(\mathbf{b} - extdiag(A)\mathbf{p}) \tag{15}$$

Hence, the solution of the Gauss-Seidel contractor is defined as the intersection of the original domain $\mathbf{p}$ and the new $\mathbf{p}$ calculated with (15). This results in:

$$\mathbf{p} \leftarrow \mathbf{p} \cap (diag(A))^{-1}(\mathbf{b} - extdiag(A)\mathbf{p}) \tag{16}$$

Finally, the Gauss-Seidel contractor solution in (16) is used to update $\mathbf{Y}_j$ and the intersection $\mathbf{Y}_j \leftarrow \mathbf{Y}_j \cap (\mathbf{p} + \hat{\mathbf{y}}_j)$ is obtained to finish with the Newton procedure.

3.2. Implementation

In order to apply the interval contractors in the verified method with the aim of reducing the overestimation this work considers an implicit form of equation (4). Making this considaration it is possible to look at the new implicit equation as a CSP problem in the form of (8). The resulting implicit equation is

$$\mathbf{g}(\mathbf{y}) = u_{j+1} + (S^{y}_{j+1})\Gamma_j + S^{\theta}_{j+1}(\boldsymbol{\Theta} - \tilde{\boldsymbol{\theta}}) + Z_{j+1} - \mathbf{Y}_{j+1} = 0 \text{ or } \mathbf{g}(\mathbf{y}) = 0, \mathbf{y} \in \mathbf{Y}_j \tag{17}$$

In this way an interval contractor such as Krawczyk or Newton can be applied in equation (17) at each time step.

An implementation of a branch-and-bound procedure has been used in this article. In the branch-and-bound tree the node on which to branch was the one with the least lower bound. At each node, the variable with the greatest diameter (distance between its upper and lower bound) was selected for branching. The program was written in C++ and the libraries FADBAD++ (Stauning and Bendtsen, 2003) and Profil/Bias (Knuppel, 1994) were used for the computation of the Taylor coefficients and the interval arithmetic operations, respectively.

4. Case study

Oil Shale Pyrolysis model: The problem considers the calculation of the optimal temperature profile in a PFR. The reactions involved and the model of the problem are shown in (18). In the model only components A_1 and A_2 are included and the objective is to maximise the production of A_2. Here u is the adjustable parameter and is taken as a piecewise constant profile. Figure 1 shows one of the states of the dynamic part of the optimisation problem with two uncertain amounts: $x_1(0) = [0.99, 1.01]$ and $u = [0.22, 0.24]$. These were obtained with a verified method based on interval Taylor series that employs the Krawczyk or Newton interval contractor. The contractors used clearly reduce the overestimation in the dynamic simulation. After obtaining the information on the profiles, the gradient information can also be obtained (sensitivity equations). This in turn represents the input for the branch-and-bound algorithm.

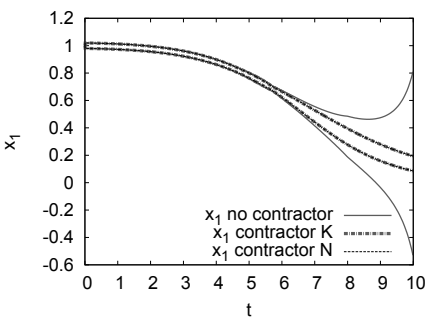

Figure 1: Simulation of x_1 with and without contraction techniques

$$\begin{aligned}
& & \min_u \ \phi &= -x_2(t_f) \\
A_1 \xrightarrow{k_1} A_2 & & s.t.\ \dot{x}_1 &= -k_1 x_1 - (k_3 + k_4 + 5) x_1 x_2 \\
A_2 \xrightarrow{k_2} A_3 & & \dot{x}_2 &= k_1 x_1 - k_2 x_2 + k_3 x_1 x_2 \\
A_1 + A_2 \xrightarrow{k_3} 2A_2 & & k_i &= a_i e^{\left(\frac{-b_i/R}{698.15+50u}\right)},\ i = 1,\ldots,5 \\
A_1 + A_2 \xrightarrow{k_4} A_3 + A_2 & & \mathbf{x}_0 &= ([0.99, 1.01], 0)^T \\
A_1 + A_2 \xrightarrow{k_5} A_4 + A_2 & & t &\in [t_0, t_f] = [0, 10] \\
& & u &\in [0, 1]
\end{aligned} \tag{18}$$

The dynamic optimisation problem has been solved to global optimality using an uncertain value of $x_1(0) = [0.99, 1.01]$ and $x_1(0) = [0.98, 1.02]$ in a second experiment. In the real application this means that the concentration of A_1 can be as uncertain as $\pm$1-2 %. The CPU time taken to obtain this solution using the Newton contractor was 606.8 seconds and 1475.6 seconds using the Krawczyk contractor and three iterations of the contractors were used in the integration stage. Since an uncertain value was used the problem was solved within an absolute tolerance of 20^{-2}. The CPU times are for an Intel^{TM} Core^{TM} i5 with 8Gb RAM, running Red Hat 6.6 and gcc 4.4.7.

5. Conclusions

The results proved that the method is able to address an small amount of uncertainty in one of the system parameters (1-2 %). Two interval contractors were used in the method presented and the Newton contractor demonstrated to take between 50 % and 60 % less CPU time compared to the Krawczyk contractor. The method behaves similarly when compared to experiments of case studies of up to six state variables (not reported here). Therefore, interval contractors are useful in the reduction of the overestimation in the solution of dynamic global optimisation problems.

6. Acknowledgements

Financial support from CONACYT, UCL and DGRI from SEP is gratefully acknowledged.

References

Balendra, S., Bogle, I. D. L., Feb. 2009. Modular global optimisation in chemical engineering. Journal of Global Optimization 45 (1), 169–185.

Esposito, W. R., Floudas, C. A., May 2000. Global optimization for the parameter estimation of differential-algebraic systems. Industrial & Engineering Chemistry Research 39 (5), 1291–1310.

Jackson, L., 1975. Interval arithmetic error-bounding algorithms. SIAM Journal on Numerical Analysis 12 (2), 223–238.

Jaulin, L., Kieffer, M., Didrit, O., Walter, E., 2001. Applied Interval Analysis. Springer, London.

Knuppel, O., 1994. PROFIL/BIAS-A Fast Interval Library. Computing 53, 277–287.

Lin, Y., Stadtherr, M. A., 2006. Deterministic global optimization for parameter estimation of dynamic systems. Industrial & Engineering Chemistry Research 45 (25), 8438–8448.

Lin, Y., Stadtherr, M. A., 2007. Deterministic global optimization of nonlinear dynamic systems. AIChE Journal 53 (4), 866–875.

Lohner, R. J., 1992. Computation of guaranteed enclosures for the solutions of ordinary initial and boundary value problems. In: Cash, J. R., Gladwell, I. (Eds.), Computational Ordinary Differential Equations. Clarendon Press, Oxford, pp. 425–435.

Nedialkov, N. S., Jackson, K. R., Corliss, G. F., 1999. Validated solutions of initial value problems for ordinary differential equations. Applied Mathematics and Computation 105, 21–68.

Nedialkov, N. S., Jackson, K. R., Pryce, J. D., 2001. An effective high-order interval method for validating the existence and uniqueness of the solution of an IVP for an ODE. Reliable Computing 7 (6), 449–465.

Papamichail, I., Adjiman, C. S., 2002. A rigorous global optimization algorithm for problems with ordinary differential equations. Journal of Global Optimization (24), 1–33.

Papamichail, I., Adjiman, C. S., Mar. 2004. Global optimization of dynamic systems. Computers & Chemical Engineering 28 (3), 403–415.

Perez-Galvan, C., Bogle, I. D. L., 2014. Comparison between interval methods to solve initial value problems in chemical process design. In: Kleme, J. J., Varbanov, P. S., Liew, P. Y. (Eds.), 24th European Symposium on Computer Aided Process Engineering. No. 33. Elsevier, pp. 1405–1410.

Scott, J. K., Barton, P. I., 2013. Bounds on the reachable sets of nonlinear control systems. Automatica 49 (1), 93–100.

Singer, A. B., Barton, P. I., Feb. 2006. Global optimization with nonlinear ordinary differential equations. Journal of Global Optimization 34 (2), 159–190.

Stauning, O., Bendtsen, C., 2003. FADBAD++ web page.
URL `http://www.fadbad.com/fadbad.html`

Villanueva, M. E., Houska, B., Chachuat, B., 2013. Unified framework for the propagation of continuous-time enclosures for parametric nonlinear odes. Journal of Global Optimization, 1–39.

Zhao, Y., Stadtherr, M. A., Nov. 2011. Rigorous global optimization for dynamic systems subject to inequality path constraints. Industrial & Engineering Chemistry Research 50 (22), 12678–12693.

Krist V. Gernaey, Jakob K. Huusom and Rafiqul Gani (Eds.), 12th International Symposium on Process Systems Engineering and 25th European Symposium on Computer Aided Process Engineering.
31 May – 4 June 2015, Copenhagen, Denmark

Separation Process Optimization under Uncertainty by Chance Constraint Programming with Recourse

Li Sun [a]*, Huajie Zhang[b]

[a]*Centre for Process Integration, University of Manchester, Manchester, M13 9PL, UK*
[b]*Department of Chemical Engineering, Dalian University of Technology, Dalian, 116023, China,*
li.sun@manchester.ac.uk

Abstract

In this paper, the methodology of chance constraints programming with resource is proposed for the separation process optimization under uncertainty. In this approach, uncertain factors are classified into two types: the first type of uncertainties is compensated for by introducing a penalty term to the optimization objective, and the other uncertainties are expressed by chance constraints at certain confidence levels in the optimization model. The solution strategy is developed by a sequence transform hybrid algorithm involving both Monte Carlo integration and improved Benders decomposition strategies with sequential quadratic programming. 1-hexene separation process is optimized as a case study to illustrate the feasibility of the proposed strategy.

Keywords: Stochastic programming, uncertainty, chance constraint, recourse.

1. Introduction

Deterministic approaches have been widely used in separation process optimization. However, there are many uncertain variables in the process design and optimization, such as raw material prices, product demands, operation pressures and temperatures, etc. The estimation of these uncertainties with their expected values might lead to a conservative design with excessively high operating costs.

Researches considering optimization under uncertainty have attracted much interest in many fields (Sahinidis, 2004), and some uncertainty-based optimization methodologies and algorithms have been developed to account for different uncertain factors (Hukkerikar et al., 2012). Stochastic programming with recourse and chance constraint programming are two important stochastic programming strategies (Requiao et, al., 2012). However, there are limits associated of these two methods.

Stochastic programming with recourse (SPR) partitions the design problem into two stages: in the first stage the design decisions are made before the realization of any uncertainty in the variables. In the second stage the operational or recourse decisions are made following the first-stage plan and after the realization of the uncertainties. The aim of SPR is to choose the first-stage decision variables in a way that the sum of the first-stage objective and the expected value of the random second-stage objective are optimal. The presence of uncertainty is translated into a stochastic nature of the

recourse, and the penalize shortfall or corrective measures are compensated for by introducing a penalty term to the objective function accounting for any infeasibility.

SPR is a relatively strict and reliable method. But, sometimes, there can be difficulties setting up penalty terms accounting for the implementation of uncertain variables. For the SPR model solution, the calculation grows exponentially with the number of uncertain factors (Higle & Sen, 1991).

Chance constraint programming (CCP) is also known as a probabilistic programming (Li et, al., 2006). CCP allows the decision to be made to satisfy feasibility requirements while some constraints are violated with a certain probability no less than a confidence level (Rockafellar & Uryasev, 2000). The confidence level can quantify the reliability of the optimization objectives and constraints. The CCP is fairly simple and direct; however, the restriction reflexion might cause some risks.

2. Chance constraint programming with recourse

For the separation process design, the uncertain factors include the feed composition, the feed rate, steam/electricity/product prices, product demands, etc. They are divided into two types:

The fluctuation of the first type of uncertainties such as product demands, material and steam prices would cause the variations in the process costs. The compensation resulting from the implementation of these uncertainties are added to the economic objective based on the SPR.

For the second uncertain variables, the compensating measures require more complex calculations, but their impacts on the optimization objective and constraints are negligible up to a certain level, so the CCP would be optional to formulate the optimization model. In the distillation process optimization, the fluctuation of separation results due to the variations of the feed composition and the feed rate is acceptable in certain extent. Thus, the CCP is utilized to account for these uncertainties on the optimization model.

2.1. Stochastic optimization model

The separation process optimization aims to achieve the minimum process cost. The following strategy of chance constraint programming with recourse is proposed by combining the CCP with the SPR, formulating the optimization model as follows:

$$
\begin{aligned}
\text{Min}\quad & O = g(x,\theta) + E_{\theta_j \in \Omega}(Q(y,\theta_j)) \\
\text{s.t.}\quad & F(x,y,\theta) = 0 \\
& \mathrm{G}(x,\mathrm{y},\theta) \le 0 \\
& P\{h(x,y,\theta_i) \ge 0\} \ge \alpha \\
& \theta \in \{\theta_i, \theta_j\};\ i = 1,2\ldots,m;\ j = 1,2,\ldots n \\
& 0 < \alpha \le 1
\end{aligned}
\tag{1}
$$

With

$$Q(y,\theta_j) = \min \quad f(\theta_j)^T y, \quad j = 1,2,...,n$$
$$\text{s.t} \quad \mathrm{D}(\theta_j) y \geq H(\theta_j) - T(\theta_j) x \tag{2}$$

Where, the optimization object O is the minimum of the process profit; g is the first-stage objective function, and Q is the penalty term. x is the state variable, and y is operation variable. θ_i and θ_j are the first and second type of uncertain variables respectively. Ω is the domain of θ_j. E is the expectation of penalty function Q; F represents equality constraints and G implies inequality constraints, including mass balance, energy balance, available raw material constraints, safety consideration, equipment size constraints, equipment operating performance, etc. $P\{h(x, y, \theta_i)\geq 0\}\geq\alpha$ implies the probability of the constraint realization $h(x,\theta_i)\geq 0$ must be no less than a confidence level α; $f(\theta_j)$ is the coefficient matrix of y; D; H and T are the constraint matrixes in the compensation term.

2.2. Sequence transform hybrid algorithm

There are uncertain variables existing in both the objective and the constraints. In this work, a sequence transform hybrid algorithm both involving Monte Carlo integration and improved Benders decomposition strategies with sequential quadratic programming (SQP) is proposed to solve a large sized sampling problem with constraints. The uncertain variables in the constraint $P\{h(x, y, \theta_i)\geq 0\}\geq\alpha$ are converted into deterministic constraints. This conversation normally requires multiple integrals. The uncertain variables in the penalty term $E_{\theta\in\Omega}(Q(y, \theta_j)$ are translated into deterministic expression. are used to solve The deterministic model with extensive constraints resulting from the uncertain variables is solved by improved Benders decomposition strategies.

3. Case study

1-hexene separation process is optimized utilizing the proposed methodology. 1-hexene is produced through ethylene oligomerication catalytic reaction. The concentration of the product 1-hesene is required to be no less than 99%. Also, the by-products are recovered containing 1-hexene less than 10%. Ethylene and cyclohexane are required to be recycled back to the system. Table1 presents the feed mixture data.

3.1. Flowsheet analysis

Since there are gaps between the boiling points of the components in the feed mixture, the feed mixture would be separated by flash distillation and rectification. By the analysis on the separation units, separation sequence, and process energy integration, three flow scenarios are generated.

Scenario 1 (S1) is shown in Figure 1. The feed mixture is initially flashed to recover ethylene. The liquid mixture after the 2-stage flash is then separated passing through three rectification columns. 1-hexene is extracted from the top of T-A. Cyclohexane is recovered from the top of T-B. The by-product is obtained from the top of T-C. Other heavy components from the bottom of T-C would be combusted for emission. There is heat integration between the top steam of T-B and the residue from T-A, not shown in Figure 1.

Table 1: The feed stream date

Concentration wt%									Rate kg·h^{-1}	T °C	P MPa
Ethylene	1-hexene	cyclohexane	C_{10}	n-hexene	1-Octanol	ethane	methane	Butane	1785.5	120	5.0
0.125	0.358	0.477	0.0297	2.90 E-3	2.78 E-3	2.43E-3	1.18E-3	8.91E-5			

Figure 2 presents the flow chart of scenario 2 (S2). Eethylene is separated completely from the mixture by rectification in T-D instead of the flashing operation used in S1.

Scenario 3 (S3) shown in Figure 3 has different rectification separation sequence compared with both S1 and S2. Ethylene is recovered from the top of T-A. A side stream drawn from T-A is purified in T-B to give separated 1-hexene and the solvent. The heavy components recovered from the bottom of T-A are then separated in T-C. This scenario allows the separation to be performed with one less flash vessel or one less rectification column compared with S1 and S2. There is no heat integration in this scenario.

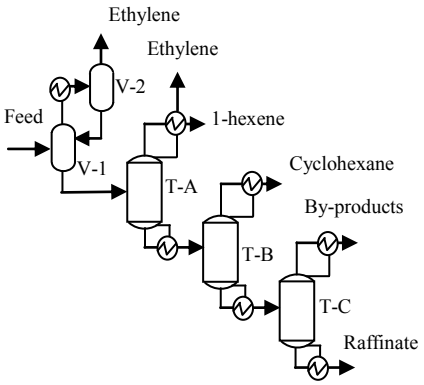

Figure 1 Scenario 1 flow chart

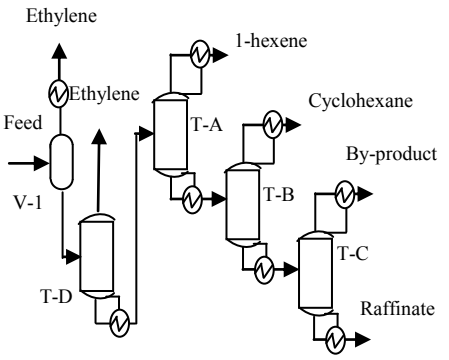

Figure 2 Scenario 2 flow chart

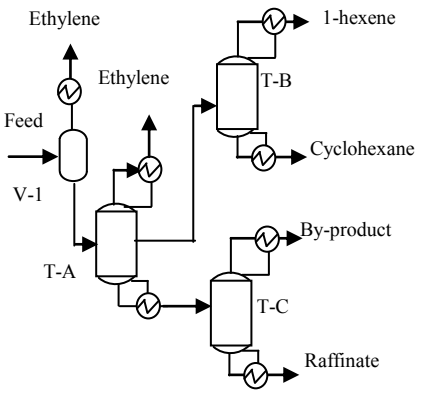

Figure 3 Scenario 3 flow chart

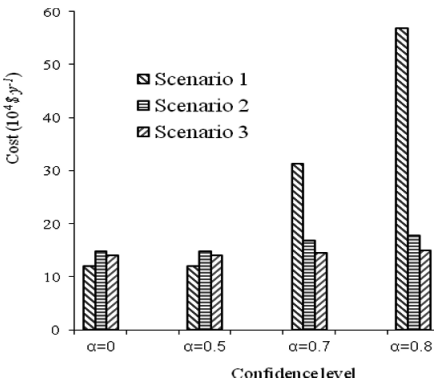

Figure 4 Costs at different confidence levels

Table 2 Uncertain variables

Uncertain variable	Expectation	Standard deviation
x_F(wt %)	0.4	0.016
C_1 ($/t)	16.3	0.65
C_2 ($/t)	19.6	0.78

Table 3 Capital costs (10^4 $\$\cdot y^{-1}$)

Scenario	T-A	T-B	T-C	T-D
S1		3.27	1.96	
S2		3.27	1.96	3.27
S3	2.45		1.96	

Table 4 The comparison between deterministic optimization and uncertain optimization

Variable	Deterministic Optimization			Confidence level								
				α=0.5			α=0.7			α=0.8		
	S1	S2	S3	S1	S2	S3	S1	S2	S3	S1	S2	S3
N_T	64	60	60	63	60	60	90	60	60	90	60	60
$R_{T\text{-}A}$	4	6.4	8.0	4.0	6.4	8.0	14.6	7.8	8.0	28.1	8.7	8.0
$R_{T\text{-}B}$	1.5	1.2	5.8	1.5	1.2	5.7	1.5	1.2	6.2	1.5	1.2	6.6
O ($10^4\$\cdot y^{-1}$)	12.0	14.9	14.0	12.1	14.8	14.0	31.4	16.9	14.5	56.9	17.8	15.0

3.2. Optimal results

The optimization for this separation process is to reach the minimum process costs, including the capital costs and operating costs. The capital cost is mainly the function of the numbers of trays and the diameters of rectification columns. In this work, the column diameters are fixed, and the tray numbers are considered as the main capital variables. The principle factors affecting the operating costs are the steam utilization by the reboilers. At the condition of the fixed product outputs, the steam demands are the function of distillation reflux ratio.

From the process analysis, it is known that the rectification column T-A in S1, column T-A in S2, and column T-B in S3 are key equipment for this process separation. The state decision variable considered in each scenario is the tray number $N_{T\text{-}A}$ in S1, $N_{T\text{-}A}$ in S2, and $N_{T\text{-}B}$ in S3. The other capital costs are assumed to be fixed in the optimization. The operation decision variables are the rectification reflux ratios $R_{T\text{-}A}$ and $R_{T\text{-}B}$ in all these three schedules.

The concentration of 1-hexene in the feed mixture x_F, LP steam price $C1$, and MP steam price $C2$ are uncertain variables with probabilities following the normal distribution. Table 2 presents uncertain variables in this case. Table 3 lists main deterministic capital costs.

Equality constraints in the optimal model are mainly MESH equations. Inequality constraints are applied to limit the range of reflux ratios, the numbers of column trays, the separation requirements, the steam demands by the reboilers.

The influence on operating costs caused by C_1 and C_2 would be compensated for through changing the reflux ratio or through additional steam heating in the reboilers. The SPR is selected in this model setting. The variation of x_F would cause a change in the purity of the product 1-hexene. It is feasible to model this variation based on CCP.

The process is optimized by the proposed strategy of chance constraint programming with recourse under three confidence levels: α=0.5, α=0.7, and α=0.8. The optimization

results are listed in Table 4. The results comparisons with those using conventional deterministic methods are presented in Table 4 as well.

As shown in Figure 4, S1 is better from the economic view point while ignoring the uncertain factors. The design would be different while considering the fluctuations of steam prices and feed compositions. At different confidence levels, S3 spent lower costs at confidence levels at α=0.7 and α=0.8. When the confidence level α is set to be 0.5, the configuration S1 is found to be the optimal case with the minimum process cost.

The confidence level indicates how well the constraints are satisfied and the how higher the confidence level is, the stricter constraints being kept, the more reliable the optimization result will be achieved. The confidence level set at a low value means the constraints are easier to be satisfied, however, the optimization result is less reliable.

In reality, the steam price varies unavoidable. The development of the catalyst, the variation of the up-stream feed and the operation would change the feed concentration. So the optimization under uncertainty is more reliable in reality and practical.

4. Conclusions

The methodology of chance constraints programming with resource is proposed to overcome the shortcomings in model formation and model solution by using chance constraint programming and stochastic programming with recourse separately. A case study involving optimization of the 1-hexene separation process demonstrates the potential of the proposed methodology. It is clear from the optimal results that consideration of uncertainty may generate more reliable and practical results.

Acknowledges

The support of EC Project EFENIS (contract ENER /FP7 /296003 /EFENIS) is sincerely acknowledged.

References

A. Hukkerikar, M. Jones, B. Sarup, J. Abildskov, G. Sin, G. Gani, 2012, Sensitivity of process design due to uncertainties in property estimates, Computer Aided Chemical Engineering, 31, 200-205

J. L. Higle, S. Sen, 1991, Stochastic decomposition: An algorithem for two-stage stochastic linear programs with recourse, Mathematics of operations Research, 16, 650-669

N.V. Sahinidis, 2004, Optimization under uncertainty: state-of-the-art and opportunities Optimization under uncertainty: state-of-the-art and opportunities, Computers & Chemical Engineering, 28, 971-983

P. Li, H. Arellano-Garcia, G. Wozny, 2008, Chance Constrained Programming Approach to Process Optimization under Uncertainty, Computers & Chemical Engineering, 32, 25-45

R.T. Rockafellar, S. Uryasev, 2000, Optimization on conditional value-at-risk, Journal of Risk, 2, 21-41

R. Requiao, M.A.F Martins, R.A. Kalid, R.P. Soares, 2012, Uncertainty evaluation for multicariate industrial process, Computer Aided Chemical Engineering, 31, 365-310

Krist V. Gernaey, Jakob K. Huusom and Rafiqul Gani (Eds.), 12th International Symposium on Process Systems Engineering and 25th European Symposium on Computer Aided Process Engineering.
31 May – 4 June 2015, Copenhagen, Denmark

Optimal operating policies for synthesizing tailor made gradient copolymers

Cecilia Fortunatti*, Bruno Mato, Adriana Brandolin, Claudia Sarmoria, Mariano Asteasuain.

PLAPIQUI, Camino La Carrindanga km 7, Bahía Blanca (8000), Argentina
cfortunatti@plapiqui.edu.ar

Abstract

In this work, a detailed mathematical model of the TEMPO mediated copolymerization of S and MMA is used to analyze the most common experimental strategies employed to produce gradient copolymers as applied to these monomers. The model is able to predict average molecular properties as well as the full bivariate molecular weight distribution (MWD) of the copolymer. Typical experimental policies reported in the literature are simulated in order to determine the exact composition profile that results from them. Optimal operating policies necessary to produce different specific gradient structures are also obtained by solving optimization problems. The results show that comprehensive mathematical modeling can aid in finding appropriate operating policies. In this way, the simulation can be regarded as a valuable tool in the design of novel materials with pre-specified characteristics.

Keywords: probability generating function, MWD, CRP, copolymerization, optimization.

1. Introduction

The discovery of the controlled polymerization of styrene in the presence of 2,2,6,6-tetramethyl-1-piperidynyl-N-oxy (TEMPO) ushered the research of the promising controlled radical syntheses. Since then, TEMPO has been extensively studied and applied due to its low cost, commercial availability and lack of environmental issues (Braunecker and Matyjaszewski, 2007). Even though the operating temperature needs to be relatively high (> 100ºC) and the control over molecular structure is not as precise as with other controlled polymerization techniques, the advantages of TEMPO mediated polymerization still make it an appealing method for obtaining high value materials in an simple, economic and environmentally friendly way.

Controlled polymerization may be used to produce copolymers, and in particular gradient copolymers, where the composition distribution varies continuously from one end of the copolymer chain to the other. Several different gradient profiles could be desirable, such as linear, hyperbolic, or blocky gradient, which may lead to different final properties (Beginn, 2008; Sun et al., 2008). However, the majority of the reported experimental policies for synthesizing gradient copolymers have been developed by trial and error (Vidts et al., 2006; Min et al., 2007). In this way, it is very difficult to achieve a precise gradient profile. The most widely used operating policy consists on feeding the total amount of one of the comonomers at the start, and adding the second comonomer at a constant rate, regardless of the comonomer pair being used (Jakubowski et al.,

2008; Karaky et al., 2007). However, this feeding policy may lead to copolymer chains with portions of nearly constant composition, particularly close to the chain ends. A piecewise constant feeding policy, on the other hand, may be designed to obtain a steadier (e.g. linear) composition change along the chain backbone (Min et al., 2007).

It is clear that minor changes in operating conditions may lead to gradient copolymers with diverse composition profile shapes. However, manufacturing a material for a pre-specified application requires a precise knowledge of the formed structure. In this context, comprehensive mathematical models are valuable tools to determine the produced molecular architecture and find optimal operating policies to obtain tailor-made materials. Taking this into consideration, Wang and Broadbelt (2011) developed a Monte Carlo based algorithm to determine feeding policies conducive to the synthesis of copolymers with a pre-designed gradient profile. On the other hand, both Sun et al. (2007) and Zhao et al. (2009) manufactured gradient copolymers with pre-specified composition profiles with the help of a computer-controlled metering pump. In these works, the comonomer feeding rate profiles were dictated by mathematical models based on the methods of moments.

Mathematical models able to calculate the characteristics of the copolymer being produced are extremely helpful. These tools not only allow minimizing expenditure of resources thanks to better experimental planning, but also facilitate finding useful relationships between operating conditions and end-use properties. For this purpose, it is necessary to predict not only average properties but the full MWD as well. In previous works we developed a mathematical model for the copolymerization of styrene (S) and methyl methacrylate (MMA) mediated by TEMPO that predicts average properties together with the full MWD in an accurate and efficient way, using probability generating functions (pgf) (Fortunatti et al., 2014). In the present work this model is used to analyze the copolymer structure resulting from usual techniques employed to prepare gradient copolymers, and to design optimal operating policies for synthesizing gradient copolymers with pre-specified composition molecular characteristics.

2. Methods

2.1. Copolymerization Process and Mathematical Modeling

The kinetic mechanism considers the copolymerization of S and MMA mediated by TEMPO using AIBN as initiator. The synthesis was considered to be isothermal at 130ºC, and to be carried out in bulk in a semibatch reactor.

Average properties such as molecular weights, composition and conversion, were modeled using the well-known method of double index moments. The bivariate MWD was obtained using the 2D probability generating functions (pgf) technique. Details on these techniques and their mathematical implementation may be found elsewhere (Asteasuain and Brandolin, 2010; Brandolin and Asteasuain, 2013; Fortunatti et al., 2014).

2.2. Simulation of Typical Operating Policies

The most widely used operating policy for obtaining gradient copolymers consists on an initial charge of one of the comonomers and a subsequent feeding of the second monomer at a constant rate. Here this methodology is simulated for the S-MMA

copolymerization and the molecular structure of the resulting polymer is analyzed in detail.

2.3. Optimization of Operating Policies

Linear gradient structures were sought with a pre-specified global copolymer composition. For this to be fulfilled, the average number fraction of S in the copolymer should reach a specified value at the end of the reaction time. Three different final compositions were specified: 50% S, 60% S, and 70% S.

The optimization aimed to find an operating policy that would allow obtaining a linear gradient copolymer with a pre-specified global composition, as detailed above, and a target chain length ($\overline{L_{n,\text{target}}}$) of 125 units. The initial charge of S was fixed at 624 g while the gradient profile was meant to be controlled by continuous addition of MMA. The operating variables included in the optimization runs were: initial charge of AIBN (I) and TEMPO (Te) ($m_{i,0}$, i = I, Te) and MMA feeding policy ($f_{\text{MMA}}(t)$). A piecewise linear profile was selected for $f_{\text{MMA}}(t)$ since it would be easily achievable with a programmed metering pump. The polydispersity (PDI) should be less than 1.3 to obtain a uniform material. At the same time, the fraction of dormant molecules should be greater than 0.9 to maintain the "living" feature of the reaction. As a productivity constraint, a minimum of 10% conversion was required while reaction time could not exceed 24 hours.

The optimization problem was posed as follows:

$$\min_{m_{i,0},\,a_j,b_j,t_j} FO = \int_0^{t_f} \left(Inst\_comp_S(t) - \left(1 - p\overline{L_n}(t)\right)\right)^2 dt \tag{8}$$

s.t.

Process model

$$t_f = \sum_{j=1}^{5} t_j \tag{8.1}$$

$$f_{\text{MMA}}(t) = a_j t + b_j \quad \text{when} \quad \sum_{k=1}^{j-1} t_j < t \le \sum_{k=1}^{j} t_j \tag{8.2}$$

$$Conv\left(t_f\right) \ge 10\% \tag{8.3}$$

$$\overline{L_{n,\text{target}}} - 3 \le \overline{L_n}\left(t_f\right) \le \overline{L_{n,\text{target}}} + 3 \tag{8.4}$$

$$y_{\text{Dormant}}\left(t_f\right) \ge 0.9 \tag{8.5}$$

$$\text{PDI}\left(t_f\right) \le 1.3 \tag{8.6}$$

$$30 \text{ min} \le t_f \le 1440 \text{ min} \tag{8.7}$$

$$1 \text{ min} \le t_j \le 200 \text{ min} \tag{8.8}$$

$$0 \le m_{\text{I},0} \le 50 \text{ g} \tag{8.9}$$

$$0 \le m_{\text{Te},0} \le 50 \text{ g} \tag{8.10}$$

$$0 \le f_{MMA}(t) \le 10 \text{ g} \cdot \text{min}^{-1} \tag{8.11}$$

The objective function shown in Eq. (8) aims at obtaining an average instantaneous composition of S in the copolymer ($Inst\_comp_{\text{S}}$ (t)) that varies linearly along the

polymer chains. The slope p of this line is related to the final average global composition of S in the copolymer ($Glob\_comp_S$ (t_f)) by

$$p = \frac{2\left(Glob\_comp_S(t_f) - 1\right)}{\overline{L_n}_{,\text{target}}} \tag{9}$$

The simulations and optimization problems were formulated and solved in gPROMS v3.5.3 (Process Systems Enterprise, Ltd.) in a standard PC.

3. Results and Discussion

Firstly, the typical constant rate feeding policy of the comonomer was simulated. Styrene must be present in the reaction medium in order for TEMPO to act as an effective mediator. Therefore, the initial charge of S was fixed at 624 g while an equimolar mass of 600 g of MMA was fed at constant rate. Three different feeding rates were considered: 1.5 g min^{-1}for 400 min, 3 g min^{-1} for 200 min, and 4.5 g min^{-1} for 133 min. The composition profiles along the copolymer chain for the three cases can be observed in Figure 1. It can be seen that the variation in the instantaneous composition along the chain is quite steady for the three cases. An approximately linear profile is obtained for the slowest feeding rate, while the other ones exhibit a concave shape. As expected, as the MMA feeding rate increases a steeper slope of the instantaneous composition is obtained, because the MMA concentration in the reaction mixture is higher. At the same time, conversion is lower due to the shorter reaction time, which results in a shorter average chain length. The final global composition is the same for the three cases. It should be noted that, without the aid of a modeling tool, a time-consuming trial an error procedure would be needed in order to find the precise operating conditions for achieving specific molecular properties, such as average chain length, global composition and composition profile along the chains. Besides, a tuned feeding scheme would be needed for tailoring the composition profile shape (e.g. a linear gradient copolymer).

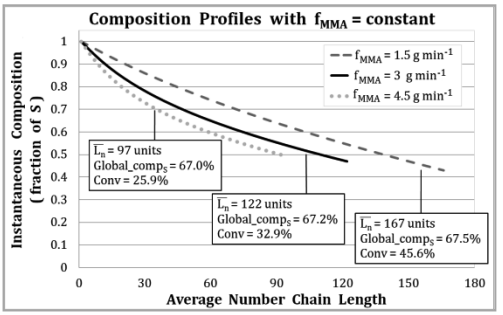

Figure 1. Composition profiles for constant feed rate policies ($m_{I,0}$ = 6.13 g, $m_{Te,0}$ = 4.9 g).

Secondly, the operating policy was optimized as described before. Figure 2 shows the optimum linear gradient profiles of the copolymers for the desired global average compositions. The optimization could take from 300 to 1400 seconds to be solved depending on how good the initial point was. To overcome the difficulties associated with the stiffness of the system of equations, the convergence tolerance of the DAE solver used in gPROMS was changed from the default value of 10^{-5} to 10^{-10} while for the re-initialization solver was set to 10^{-6}.

Perfectly linear gradients are obtained when it is required to obtain a copolymer with 60% and 70 % of S. Such perfect linear gradients are not possible when a 50% S content is sought. This is due to the reactivity ratios of S and MMA, which would require very low concentrations of S in the reaction mixture in order to achieve a 100 % composition of MMA close to the chain end. Even so, the discrepancies with respect to the linear gradient are within expected experimental errors. Figure 3 shows the optimal MMA feed rate profiles for each of the desired global average compositions.

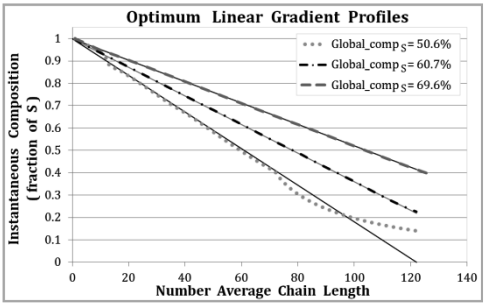

Figure 2. Optimum linear gradient composition profiles. Lines: desired composition profile – Symbols: actual composition profile.

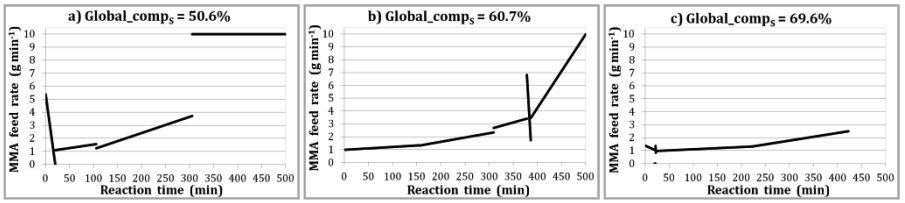

Figure 3. MMA feed rate policies for obtaining linear gradient copolymers with different average composition

Finally, in Figure 4 the MWD for the operating policy with a constant feed rate f_{MMA} = 3 g min^{-1} is presented next to the MWD for the linear gradient composition profile with a global composition of 69.6% S. It can be observed that even though similar composition profiles and average global composition are obtained, the molecular weight distributions differ, which could cause a variation in the material performance.

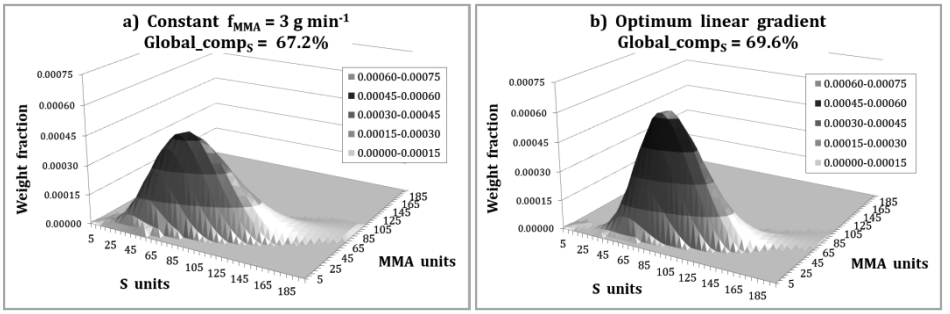

Figure 4. MWD for different composition profiles with similar global composition of S.

4. Conclusions

The effect of typical operating policies used to produce gradient copolymers was analyzed for the S-MMA copolymerization system. Besides, optimal operating policies for synthesizing polymers with pre-specified properties were computed. It was found that the composition profiles of S-MMA copolymers using constant feed rates can be different from linear profiles. Moreover, it was shown that the operating policy required for obtaining a pre-specified profile can be very difficult to find without the aid of modeling tools. Finally, the results showed that the full bivariate MWD can provide extra information about the copolymer molecular structure that could help to determine variations in the material performance.

References

M Asteasuain, A Brandolin, 2010, Mathematical modeling of bivariate polymer property distributions using 2D probability generating functions, 1 - Numerical inversion methods, Macromolecular Theory and Simulations; 19, 6, pp. 342-359.

U Beginn, 2008, Gradient copolymers, Colloid and Polymer Science; 286, 13, pp. 1465-1474.

A Brandolin, M Asteasuain, 2013, Mathematical modeling of bivariate distributions of polymer properties using 2D probability generating functions. part II: Transformation of population mass balances of polymer processes, Macromolecular Theory and Simulations; 22, 5, pp. 273-308.

W A Braunecker, K Matyjaszewski, 2007, Controlled/living radical polymerization: Features, developments, and perspectives, Progress in Polymer Science (Oxford); 32, 1, pp. 93-146.

C Fortunatti, C Sarmoria, A Brandolin, M Asteasuain, 2014, Theoretical Analysis of Nitroxide-Mediated Copolymerization of Styrene and α-Methyl-Styrene under Different Operating Policies and Reactor Designs, Macromolecular Reaction Engineering; 8, 4, pp. 260-281.

W Jakubowski, A Juhari, A Best, K Koynov, T Pakula, K Matyjaszewski, 2008, Comparison of thermomechanical properties of statistical, gradient and block copolymers of isobornyl acrylate and n-butyl acrylate with various acrylate homopolymers, Polymer; 49, 6, pp. 1567-1578.

K Karaky, L Billon, C Pouchan, J Desbrières, 2007, Amphiphilic gradient copolymers shape composition influence on the surface/bulk properties, Macromolecules; 40, 3, pp. 458-464.

K Min, J K Oh, K Matyjaszewski, 2007, Preparation of gradient copolymers via ATRP in miniemulsion. II. Forced gradient, Journal of Polymer Science, Part A: Polymer Chemistry; 45, 8, pp. 1413-1423.

X Sun, Y Luo, R Wang, B G Li, B Liu, S Zhu, 2007, Programmed synthesis of copolymer with controlled chain composition distribution via semibatch RAFT copolymerization, Macromolecules; 40, 4, pp. 849-859.

X Sun, Y Luo, R Wang, B G Li, S Zhu, 2008, Semibatch RAFT polymerization for producing ST/BA copolymers with controlled gradient composition profiles, AIChE Journal; 54, 4, pp. 1073-1087.

K R M Vidts, B Dervaux, F E Du Prez, 2006, Block, blocky gradient and random copolymers of 2-ethylhexyl acrylate and acrylic acid by atom transfer radical polymerization, Polymer; 47, 17, pp. 6028-6037.

L Wang, L J Broadbelt, 2011, Model-based design for preparing styrene/methyl methacrylate structural gradient copolymers, Macromolecular Theory and Simulations; 20, 3, pp. 191-204.

Y Zhao, Y W Luo, C Ye, B G Li, S Zhu, 2009, Model-based design and synthesis of gradient MMA/tBMA copolymers by computer-programmed semibatch atom transfer radical copolymerization, Journal of Polymer Science, Part A: Polymer Chemistry; 47, 1, pp. 69-79.

Krist V. Gernaey, Jakob K. Huusom and Rafiqul Gani (Eds.), 12th International Symposium on Process Systems Engineering and 25th European Symposium on Computer Aided Process Engineering.
31 May - 4 June 2015, Copenhagen, Denmark.

Degeneracy Hunter: An Algorithm for Determining Irreducible Sets of Degenerate Constraints in Mathematical Programs

Alexander W. Dowling[a] and Lorenz T. Biegler[a]

[a]*Department of Chemical Engineering, Carnegie Mellon University, Pittsburgh, PA, United States*
biegler@cmu.edu

Abstract

Degenerate constraints, i.e. constraints that violate the Linearly Independent Constraint Qualification (LICQ), are prevalent in many process optimization problems. These result from poor model formulations (typically human error) and overspecifications, zero flowrates and disappearing units, and recycle loops. Because degenerate constraints lead to singular Karush-Kuhn-Tucker (KKT) systems and significant challenges for numeric solvers, these constraints complicate the solution procedure for nonlinear programs (NLPs, i.e. nonlinear optimization problems). Although most modern NLP solvers implement counter-measures to detect and eliminate degeneracies, increased computational effort and convergence failures may still result. Instead, the best approach is to reformulate the original NLP model. Unfortunately, this is difficult for complex models with thousands of equations. This work describes the *Degeneracy Hunter*, an algorithm that systematically analyzes any iteration from a continuous mathematical program solver and determines irreducible sets of degenerate constraints. This tool allows the expert modeler to focus on only a handful of equations, instead of the thousands that make up a typical process optimization problem. The algorithm has been prototyped in MATLAB and analyzes derivative information exported from GAMS. Calculation of irreducible sets of degenerate equations is formulated as a mixed integer linear program. The algorithm has been applied to a non-convex, highly nonlinear Air Separation Unit (ASU) design problem with 15,000+ variables and constraints, which identified three sources of degenerate equations. Straightforward revisions of the model to remove these degenerate constraints resulted in a 16% decrease in average CPU time and less frequent termination at infeasible points. Identification of these degeneracies would have been virtually impossible without a systematic approach.

Keywords: degenerate constraints, linearly dependent constraints, nonlinear programming

1. Introduction and Motivating Examples

We consider two classes of degenerate constraints: local and global. Local (or point) degeneracies occur only at specific values for variables in the mathematical program. For example, mass balance equations, shown in (1), become degenerate when flowrates go to zero ($F = L = V = 0$). The Jacobian of the equations is shown in (2), with F and z fixed. At the zero flowrate point, pivoting on the first two columns in (2b) shows that the Jacobian matrix is rank deficient.

In contrast, global degeneracies always lead to rank deficient Jacobians, regardless of the value of the variables. These most commonly are a consequence of overspecifications. For example, if $\sum_i y_i = 1$ and $y_i = K_i x_i \ \forall i$ are added to (1), the systems is always overspecified ($2 + 2n$ variables

and $3+2n$ equations when F, z and K are specified) and the Jacobian is rank deficient.

$$F = V + L \tag{1a}$$

$$Fz_i = x_i L + y_i V, \quad \forall i \in \{Comps\} \tag{1b}$$

$$\sum_{i \in \{Comps\}} (x_i - y_i) = 0 \tag{1c}$$

$$A = \begin{array}{c} \\ \text{Overall MB} \\ \text{MB } \ i=1 \\ \vdots \\ \text{MB } \ i=n \\ \sum \end{array} \begin{array}{c} \begin{array}{cccccccc} L & V & x_1 & \cdots & x_n & y_1 & \cdots & y_n \end{array} \\ \begin{pmatrix} -1 & -1 & 0 & \cdots & 0 & 0 & \cdots & 0 \\ -x_1 & -y_1 & -L & \cdots & 0 & -V & \cdots & 0 \\ \vdots & \vdots & \vdots & \ddots & \vdots & \vdots & \ddots & \vdots \\ -x_n & -y_n & 0 & \cdots & -L & 0 & \cdots & -V \\ 0 & 0 & 1 & \cdots & 1 & -1 & \cdots & -1 \end{pmatrix} \end{array} \tag{2a}$$

$$A(F = L = V = 0) = \begin{pmatrix} -1 & -1 & 0 & \cdots & 0 & 0 & \cdots & 0 \\ -x_1 & -y_1 & 0 & \cdots & 0 & 0 & \cdots & 0 \\ \vdots & \vdots & \vdots & \ddots & \vdots & \vdots & \ddots & \vdots \\ -x_n & -y_n & 0 & \cdots & 0 & 0 & \cdots & 0 \\ 0 & 0 & 1 & \cdots & 1 & -1 & \cdots & -1 \end{pmatrix} \tag{2b}$$

As another example, consider the system shown in Figure 1, comprising two vessels, a splitter and seven streams. Stream 1 is fed into the first vessel, which has two outlets: streams 2 and 3. Without loss of generality, let streams 2 and 3 represent two different phases in equilibrium. These streams are fed into the second vessel, producing effluent streams 4 and 5. Stream 5 is split into streams 6 and 7, and the latter is recycled into the first vessel. Pressure relationships for these streams are shown in (3). The equations are derived from a two simple rules: streams leaving a vessel are in pressure equilibrium, and pressure cannot increase across vessels and is constant across a splitter. This constraint system is overspecified (and degenerate), as there are seven constraints and seven variables, but there should be one degree of freedom (e.g. P_1 should be free).

$$P_2 = P_3 \tag{3a}$$

$$P_4 = P_5 \tag{3b}$$

$$P_6 = P_7 \tag{3c}$$

$$P_5 = P_7 \tag{3d}$$

$$P_1 \geq P_3 \tag{3e}$$

$$P_2 \geq P_5 \tag{3f}$$

$$P_7 \geq P_3 \tag{3g}$$

Many nonlinear programming (NLP) solvers implement safeguards to mitigate degenerate constraints. For example, CONOPT (Drud, 1994), a large-scale active-set generalized reduced gradient (GRG) optimization solver, removes degenerate constraints from the active set, effectively ignoring these constraints. However, determining the active set for inequality (and degenerate constraints) is an NP-hard task. On the other hand, interior point methods avoid the computational complexity of active set determination by penalizing inequality constraints with a barrier term. As a consequence, degenerate constraints cannot easily be removed from the active set. In IPOPT (Wächter and Biegler, 2006), a large-scale interior point method, degenerate constraints are instead dealt with using regularization techniques (Wang et al., 2013; Chiang and Zavala, 2014). However, neither of these strategies are fully effective, as shown in the case study (Section 3).

With global degeneracies, the best option is model reformulation. For example, consider the system in Figure 1. Either the recycle pressure constraint, (3g), should be removed and all of the inequality constraints converted to equality constraints, or a pump should be added to the recycle loop. Identifying the cause of degenerate constraints such as these, however, is difficult in large problems with thousands of constraints.

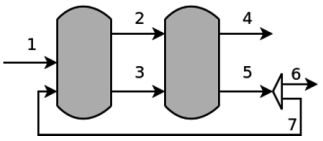

Figure 1: Pressure recycle degeneracy example

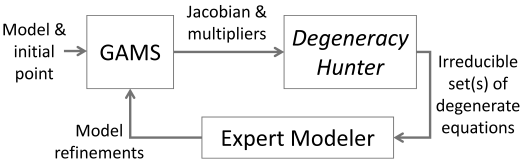

Figure 2: Recommend workflow with *Degeneracy Hunter*

Although factorization of the active Jacobian is sufficient for the identification of individual degenerate equations, it is still difficult to debug large models. Furthermore, blindly removing degenerate equation permanently from a model may be dangerous. For example, this could violate mass conservation when applied to (1). Instead *Degeneracy Hunter* aims to help expert modelers uncover the cause of degeneracies by finding the smallest sets of degenerate equations, i.e. **irreducible degenerate sets**. This allows the modeler to focus on a handful of equations instead of thousands (in large problems). Thus, the algorithms in *Degeneracy Hunter* are intended for post optimization analysis and not realtime use embedded in a NLP solver. The envisioned workflow with *Degeneracy Hunter* is shown in Figure 2.

2. The *Degeneracy Hunger* Algorithm

The *Degeneracy Hunter* algorithm is divided into four steps, and is summarized in Algorithm 1. First, in the **processing step**, the Jacobian and KKT (Karush-Kuhn-Tucker) multipliers are extracted from GAMS (or a similar environment), and the constraints are classified into four categories: equality, inactive inequality, strongly active inequality (non-zero multipliers) and weakly active inequality (zero multipliers). The *active Jacobian* (A_{dh}) is then assembled. It contains only the equality, strongly active inequality and optionally weakly active inequality constraints.

Next, in the **factorization step**, non-pivot rows of the active Jacobian are identified using either sparse or dense QR factorization. These rows are candidate degenerate equations. If the active Jacobian is not degenerate, there are no candidates and the algorithm terminates in this step.

In the **analysis step**, irreducible degenerate sets are calculated by solving a sequence of mixed integer linear programs (MILP), shown in (4), in order to minimize the number of non-zero elements in the adjoint vector λ. Integer variables y are used to count the number of non-zero elements. In order to avoid the trivial solution, $\|\lambda\| = 0$, the problem is resolved repeatedly with $\lambda_j = 1$ where $j = 1, \ldots n_{cand}$ are the indices of the n_{cand} candidate degenerate equations. Thus, this procedure may identify several irreducible degenerate sets instead of simply the smallest set. This is desirable, as there may be several independent sources of degeneracies in a large problem. Furthermore, because (4) is an MILP, its solution has the lowest possible cardinality. Through careful integration with mixed integer programming solvers, it would be possible to recover several irreducible degenerate sets containing candidate j with equal cardinality. Alternatively, it is also common for (4) to be infeasible. This indicates that candidate equation j does not significantly contribute to any degenerate set. Its original identification may have resulted from numerical noise in the factorization step. In the current implementation, the MILP is solved in GAMS with CPLEX or a

similar solver. For the test problems, including the case study with 15,000+ variables, the MILPs solve in (typically far) less than 1 CPU minute each. This is due both to the efficiency of commercial MILP solvers and the sparsity of the Jacobian for many chemical engineering problems.

$$\min \quad \sum_{i=1}^{n_{rows}} y_i \tag{4a}$$

$$\text{s.t.} \quad A_{dh}^T \lambda = 0 \tag{4b}$$

$$-My_i \leq \lambda_i \leq My_i \,, \quad \forall i = 1,...,n_{rows} \tag{4c}$$

$$\lambda_j = 1 \tag{4d}$$

Finally, in the **display step**, each irreducible degenerate set is reported (with the equation names from GAMS) along with the adjoint vector elements, λ, for these equations. This information allows the modeler to understand how a small number of equations interact to form degeneracies.

Data: Jacobian A, KKT multipliers m, constraint values c
Step 1: Assemble active Jacobian A_{dh} using A, m, c and user specified options ;
Step 2: Factorize A_{dh} and identify set of candidate degenerate equations $\{S\}$;
foreach $j \in \{S\}$ **do**
  Step 3: Solve (4) ;
  if *(4) is feasible* **then**
    Step 4: Display non-zero elements of λ (i.e. $y_i = 1$) and associated equation names ;
  else
    Step 4: Display equation j's name and "is not part of a degenerate set"
  end
end

Algorithm 1: Pseudo-code for *Degeneracy Hunter*

3. Case Study: Air Separation Unit Design and Optimization

The authors previously developed an equation-based framework for flowsheet optimization in GAMS, and applied it to design air separation units for oxy-fired advanced power systems (Dowling and Biegler, 2015). The framework includes four key features: [1] embedded cubic equation of state thermodynamic calculations with vanishing and reappearing phases; [2] a novel equilibrium based distillation model with tray bypasses instead of integer variables; [3] simultaneous heat integration and process optimization; and [4] a trust region optimization algorithm to incorporate complex reactor models (e.g. computational fluid dynamics) without exact derivatives. Complementarity constraints are used throughout the framework to model switches, such as (dis)appearing phases and equipment being (in)active. The framework also includes a sophisticated initialization and multi-start procedure. In summary, a sequence of NLPs is solved in the framework. First the flowsheet is optimized with ideal thermodynamics and shortcut distillation models. These results are used to initialize more complex models, including cubic equation of state thermodynamics and the MESH with bypass distillation model. Applied to the ASU design problems, this ultimately yields a nonlinear program 15,000+ variables and constraints and ≈500 degrees of freedom.

Degeneracy Hunter has been applied to this model, and identified three sources of degenerate equations, which are a consequence of modeler (human) error.

3.1. Overspecifications

In the final stage of the optimization workflow for the equation-based framework, each half side of a heat exchange unit (condensers, reboilers, heat exchangers) is decomposed into a specified number of subunits. This is done to refine the constant heat capacity assumption used in the heat

integration model; with subunits, the heat capacity is now represented by a piecewise linear function. The subunits are spaced with equal temperature changes. For example, if a heat exchanger changes the temperature of a stream by 25 K, and it is decomposed into 5 subunits in series, each subunit would have a temperature difference of 5 K.

Unfortunately in this subunit model, there were two instances of overspecification. For the temperature differences, the following equations were originally used:

$$T_u^{in} - T_u^{out} = \Delta T, \quad \forall u \in \{\text{Heat Exchange Units}\} \tag{5a}$$

$$T_s^{in} - T_s^{out} = \Delta T/n, \quad \forall s(u) \in \{\text{Heat Exchange Subunits}\}(u) \tag{5b}$$

where n is the number of subunits (specified constant). Clearly, (5a) can be identified as degenerate and removed. (5b) is sufficient on its own to enforce the equal temperature spacing.

The second source of degenerate equations (overspecifications) comes from inequality constraints. Each subunit is defined by either heating or cooling, and the sign of the heat duty for each unit is restricted accordingly, as shown in (6a) & (6b). Furthermore, to assist with optimization inlet and outlet temperatures are also constrained (e.g. temperature may not decrease in a heating unit), as shown in (6c) & (6d). These additional equations are also redundant. When $Q > 0$, the extra equations are inactive, and when $Q = 0$, the equations create a local degeneracy.

$$Q^i n_h \geq 0, \; Q_h^{out} = 0, \quad \forall h \in \{\text{Heating Subunits}\} \tag{6a}$$

$$Q^i n_c = 0, \; Q_c^{out} \geq 0, \quad \forall c \in \{\text{Cooling Subunits}\} \tag{6b}$$

$$T_h^{in} \leq T_h^{out}, \; \forall h \in \{\text{Heating Subunits}\} \tag{6c}$$

$$T_c^{in} \geq T_c^{out}, \; \forall c \in \{\text{Cooling Subunits}\} \tag{6d}$$

Finally, there is also a third source of degenerate equations with a pressure recycle between the distillation cascades and reboiler, similar to Figure 1.

All three of these sources of degeneracy were identified using *Degeneracy Hunter*. Although these modeling mistakes seem trivial, they easily go undetected within an equation-based framework that has several modules spread over more than ten thousand of lines of GAMS code. Without a systematical debugging tool, it is difficult to diagnose poor optimizer performances as either inadequate initialization or the presence of degenerate equations.

3.2. Computational Results

The ASU design optimization problem from our previous study was solved for the same 288 initial points, with several different configurations for the degenerate equations (Dowling and Biegler, 2015). For all of these computational studies, a desktop computer, running Ubuntu Linux and GAMS 24.3.1 with a quad-core 2.8 GHz Intel i7 processor, was used. In order to quantify variations in timings due to background jobs, GAMS overhead, disk access, etc., several of the trials were repeated. The timings are consistent within a few seconds. The average CPU time for all 288 instances of the optimization problem are reported in Table 1 for each trial. These CPU times include the entire initialization procedure described by Dowling and Biegler (2015).

The best performance was obtained with all three sources of degeneracy removed (753.9 s) and the worst performance occurred with all three sources of degeneracies remaining in the optimization formulation (896.4 s). Thus with this case study, removing the degenerate equations decreased CPU time by 16%. Furthermore, the presence of degenerate constraints also impacted the termination status with CONOPT. The last two columns of Table 1 show the number optimal and only feasible solution points, as classified by CONOPT, for each trial. “High quality” solutions

Table 1: Comparison of CPU times for the ASU design optimization problem with various degenerate constraints removed.

Trial	Pressure recycle removed?	(5a) removed?	(6c) & (6d) removed?	Average CPU time	"High Quality" Optimal	"High Quality" Only Feasible
1	No	No	No	896.4 s	210	14
2	No	Yes	Yes	863.6 s	204	17
3a	Yes	No	No	791.2 s	215	20
3b	Yes	No	No	788.7 s	215	20
4a	Yes	Yes	No	817.5 s	205	13
4b	Yes	Yes	No	818.4 s	205	13
5a	Yes	No	Yes	858.0 s	204	23
5b	Yes	No	Yes	859.8 s	204	23
6a	Yes	Yes	Yes	753.3 s	214	18
6b	Yes	Yes	Yes	754.1 s	214	18
6c	Yes	Yes	Yes	754.4 s	214	18

are defined as completely heat integrated with no complementarity violations. CONOPT terminated at locally optimal points 214 times in trial six (all degeneracies removed). In contrast, with some degeneracies present in trial five, CONOPT terminated at locally optimal only 204 times. This performance difference is expected, as the KKT multipliers are not unique in the presence of degeneracies. For the feasible only points, the active-set strategy may have not removed all of the degenerate constraints. Furthermore, in trial four (218), CONOPT terminated at 17 more infeasible and/or not high quality points than trial three (235). This speaks to the complexity of NLP solution techniques and the initialization procedure used in the framework. It is likely the presence of degeneracies (especially the pressure recycle loop) causes the NLP solver, CONOPT, to take different convergence paths early in the initialization procedure. This can result in very different solutions for each initial point considered.

4. Conclusions

In summary, we develop and describe the *Degeneracy Hunter*, an algorithm for determining irreducible degenerate sets of equations. Calculation of these sets is formulated as a mixed integer linear program. This contribution is especially important for debugging complex nonlinear programs with thousands of constraints. As demonstrated in a process design case study, the presence of a few degenerate equations may have a dramatic impact on solution time with active set methods, such as CONOPT. With interior point methods, such as IPOPT, degenerate equations can be even more serious, and could cause the solver to terminate at infeasible points. *Degeneracy Hunter* is a model debugging tool that helps expert modelers to identify degenerate constraints, reformulate their problems, and improve the performance of the large-scale optimization strategy. We recommend using *Degeneracy Hunter* to diagnose poor performance in NLP solvers, especially due to cycling and termination at non-optimal feasible points as a result of small step sizes.

References

Chiang, N., Zavala, V. M., 2014. An inertia-free filter line-search algorithm for large-scale nonlinear programming, preprint ANL/MCS-P5197-0914. URL `http://www.mcs.anl.gov/papers/P5197-0914.pdf`

Dowling, A. W., Biegler, L. T., 2015. A framework for efficient large scale equation-oriented flowsheet optimization. Computers & Chemical Engineering 72, 3 – 20.

Drud, A. S., 1994. CONOPT – A large-scale GRG code. ORSA Journal on Computing 6 (2), 207–216.

Wächter, A., Biegler, L. T., 2006. On the implementation of an interior-point filter line-search algorithm for large-scale nonlinear programming. Mathematical programming 106 (1), 25–57.

Wang, K., Shao, Z., Lang, Y., Qian, J., Biegler, L. T., 2013. Barrier nlp methods with structured regularization for optimization of degenerate optimization problems. Computers & Chemical Engineering 57, 24–29.

Krist V. Gernaey, Jakob K. Huusom and Rafiqul Gani (Eds.), 12th International Symposium on Process Systems Engineering and 25th European Symposium on Computer Aided Process Engineering.
31 May - 4 June 2015, Copenhagen, Denmark.

Dynamic Multi-Objective Optimization of Batch Chromatographic Separation Processes

A. Holmqvist[a,*], F. Magnusson[b] and B. Nilsson[a]

[a]*Department of Chemical Engineering, Lund University, P.O. Box 124, SE-221 00 Lund, Sweden*
[b]*Department of Automatic Control, Lund University, P.O. Box 118, SE-221 00 Lund, Sweden*
Anders.Holmqvist@chemeng.lth.se

Abstract

This contribution presents a novel offline dynamic multi-objective optimization framework for high-pressure liquid chromatographic (HPLC) processes in batch elution mode. The framework allows for optimization of general elution trajectories parametrized with piecewise constant control signals. It is based on a simultaneous method where both the control and state variables are fully discretized in the temporal domain, using orthogonal collocations on finite elements, and the state variables are discretized in the spatial domain, using a finite volume weighted essentially non-oscillatory (WENO) scheme. The resulting finite dimensional nonlinear program (NLP) is solved using a primal-dual interior point method and automatic differentiation techniques. The advantages of this open-loop optimal control methodology are highlighted through the solution of a challenging ternary complex mixture separation problem for a hydrophobic interaction chromatography (HIC) system. For a bi-objective optimization of the target component productivity and yield, subject to a purity constraint, the set of Pareto solutions generated with general elution trajectories showed considerable improvement in the productivity objective when compared to the Pareto set obtained using conventional linear elution trajectories.

Keywords: Batch chromatography, Dynamic multi-objective optimization, Collocation

1. Introduction

Isolation of a high purity target component from a multicomponent mixture is of significant importance in the pharmaceutical and biochemical industries. Reproducible selectivity in chromatographic separation of closely related product impurities requires optimized elution mode and fractionation or cut-times (Sreedhar et al., 2013). The current state-of-the-art methodology for optimization of HPLC separation has been limited to linear, concave/convex and step elution trajectories (Damtew et al., 2009). The main purpose of the present study is to demonstrate a novel methodology for simultaneous optimization of general elution trajectories, target component pooling decisions, column loading, and batch cycle time. The realistic multi-component system dynamics required for analysis were generated by numerical solution of the *reaction–dispersive model* (Schmidt-Traub et al., 2012). This model is governed by a set of mass-balance partial differential equations (PDEs), with a modified Langmuir isotherm and experimentally validated kinetics. Hence, the proposed methodology implies formulating and solving a large-scale dynamic optimization problem (DOP) constrained by PDEs (Biegler, 2010). However, in chromatographic separation processes, there are several incommensurable objectives which require a trade-off to ensure a satisfactory design. For the purpose of this study, a set of Pareto solutions were generated for bi-objective scenarios, with target component productivity and yield, by means of a weighted sum (WS) scalarization method.

2. Modeling of HPLC Processes

The governing one-dimensional equations in the *reaction–dispersive model* (Schmidt-Traub et al., 2012) of the mobile and stationary phase, derived under the assumptions of infinitely fast diffusion into the particles and rate-limiting adsorption kinetics, defined in the spatial, $z \in [z_0, z_f]$, and temporal, $t \in [t_0, t_f]$, domains are:

$$\frac{\partial c_\alpha}{\partial t} = -\frac{\partial}{\partial z}\left(c_\alpha v_{\text{int}} - \mathscr{D}_{\text{app},\alpha}\frac{\partial c_\alpha}{\partial z}\right) - \frac{(1-\varepsilon_c)}{\varepsilon_c + (1-\varepsilon_c)\varepsilon_p}\frac{\partial q_\alpha}{\partial t}, \tag{1}$$

$$\frac{\partial q_\alpha}{\partial t} = k_{\text{kin},\alpha}\left(H_{0,\alpha}c_\alpha e^{c_S\gamma_\alpha}\left[1 + 2K_{\text{eq},\alpha}c_\alpha e^{c_S\gamma_\alpha}\right]\left[1 - \sum_{\beta\in\{A,B,C\}}\frac{q_\beta}{q_{\max,\beta}}\right]^{\nu_\alpha} - q_\alpha\right), \tag{2}$$

where c_α and q_α are the mobile and stationary phase concentration of component $\alpha \in \{A,B,C,S\}$, v_{int} denotes the interstitial velocity of the fluid, $\mathscr{D}_{\text{app},\alpha}$ the apparent dispersion coefficient, and ε_c and ε_p the column and particle void fractions. The hydrophobic interaction isotherm described in Eq. (2) is based on the Langmuir mobile phase modulator (Melander et al., 1989). Here, c_S denotes the concentration of the non-absorbing modifier (i.e. $\partial q_S/\partial t := 0$), $k_{\text{kin},\alpha}$ the kinetic rate constant, $H_{0,\alpha}$ the Henry's constant, γ_α the solvophobicity parameter, ν_α the binding charge ratio, $q_{\max,\alpha}$ the maximum concentration of adsorbed components, and $K_{\text{eq},\alpha}$ the equilibrium constant. Eq. (1) is complemented with Danckwerts boundary conditions:

$$c_\alpha(t,z_0)v_{\text{int}} - \mathscr{D}_{\text{app},\alpha}\frac{\partial c_\alpha}{\partial z}(t,z_0) = \begin{cases} c_{\text{load},\alpha}v_{\text{int}}\Pi(t,t_0,\Delta t_{\text{load}}) & \text{if } \alpha \in \{A,B,C\}, \\ c_{\text{mix},S}v_{\text{int}} & \text{if } \alpha = S, \end{cases} \tag{3}$$

$$\frac{\partial c_\alpha}{\partial z}(t,z_f) = 0, \tag{4}$$

where $c_{\text{load},\alpha}$ is the injected load concentration and $\Pi(t,t_0,\Delta t_{\text{load}}) \in [0,1]$ a smooth rectangular function in the temporal horizon $[t_0, \Delta t_{\text{load}}]$. The dynamics of the modifier concentration in the upstream mixing tank, $c_{\text{mix},S}$, is governed by:

$$\frac{\mathrm{d}c_{\text{mix},S}}{\mathrm{d}t} = \frac{1}{\tau_{\text{mix}}}\left(u(t) - c_{\text{mix},S}\right), \tag{5}$$

where u is the elution trajectory and τ_{mix} the residence time. Finally, the PDE system was approximated using the method-of-lines and an adaptive, high-order finite volume WENO scheme (Shu, 1998) on a uniform mesh where $z_j = j\Delta z$ is the discretized spatial coordinate and $j \in [1..N_j]$.

3. Dynamic Multi-Objective Optimization

The elution trajectories at the column outlet, $c_\alpha(t,z_f)$ and $\alpha \in \{A,B,C\}$, form the basis for evaluating the incommensurable objective functions of yield, Y_α, and productivity, P_α, with the intermediately eluting component B as target. The objective functions of the αth component collected in the pooling horizon $[t_c, t_f]$ are defined as:

$$\delta_{\text{load},\alpha}\frac{\mathrm{d}Y_\alpha}{\mathrm{d}t} = c_\alpha(t,z_f)v_{\text{int}}A_c\Pi(t,t_c,t_f), \tag{6}$$

$$\frac{\mathrm{d}P_\alpha}{\mathrm{d}t} = \frac{1}{V_c}\frac{1}{(t_f+t_r)}\delta_{\text{load},\alpha}\frac{\mathrm{d}Y_\alpha}{\mathrm{d}t}, \tag{7}$$

where $\delta_{\text{load},\alpha} = c_{\text{load},\alpha}v_{\text{int}}A_c\Delta t_{\text{load}}$ is the total injected sample amount, A_c and V_c the column cross-sectional area and volume, and $t_r = 2z_f v_{\text{int}}^{-1}$ the assigned regeneration and re-equilibration time (Schmidt-Traub et al., 2012) in column volumes (CV). Hence, the aim is to derive an optimal

elution trajectory, u, load duration, Δt_{load}, and pooling horizon, $[t_c, t_f]$ that maximize $Y_\alpha(t_f)$ and $P_\alpha(t_f)$ while fulfilling the constraint imposed on purity of the target component fractionization:

$$X_\alpha(t_f) = \delta_{\text{load},\alpha} Y_\alpha(t_f) \left(\sum_{\beta \in \{A,B,C\}} \delta_{\text{load},\beta} Y_\beta(t_f) \right)^{-1}, \tag{8}$$

where the numerator of the right hand side represents the captured amount of the target component in $[t_c, t_f]$ and the denominator represents the total amount captured. Hence, $X_\alpha(t_f)$ is incorporated in the DOP as a terminal inequality constraint, $X_{L,\alpha} - X_\alpha(t_f) \leq 0$, with an assigned lower purity requirement $X_{L,\alpha}$.

3.1. Dynamic Multi-Objective Optimization Problem Formulation

The WS scalarization method was used to combine the objectives in Eqs. (6 and 7) into a single performance index with a weight $\omega \in [0,1]$ and the resulting optimization problem can be cast in the frame for *min–min optimal control*:

$$\text{min.} \quad -\left(\omega \int_{t_0}^{t_f} \frac{\mathrm{d}P_B}{\mathrm{d}t} \mathrm{d}t + (1-\omega) \int_{t_0}^{t_f} \frac{\mathrm{d}Y_B}{\mathrm{d}t} \mathrm{d}t \right) + \mathcal{U} \sum_{i=2}^{N_u} \Delta u_i^2, \tag{9a}$$

$$\text{w.r.t.} \quad \left(\Delta t_{\text{load}}, t_f\right) \in \mathbb{R}^2,$$

$$\text{s.t.} \quad \Delta t_{\text{load},L} \leq \Delta t_{\text{load}} \leq \Delta t_{\text{load},U}, \quad t_{f,L} \leq t_f \leq t_{f,U}, \tag{9b}$$

$$(\boldsymbol{x}, u, t_c) = \arg\,\text{min.} \quad -\left(\omega \int_{t_0}^{t_f} \frac{\mathrm{d}P_B}{\mathrm{d}t} \mathrm{d}t + (1-\omega) \int_{t_0}^{t_f} \frac{\mathrm{d}Y_B}{\mathrm{d}t} \mathrm{d}t \right) + \mathcal{U} \sum_{i=2}^{N_u} \Delta u_i^2, \tag{9c}$$

$$\text{w.r.t.} \quad \boldsymbol{x} : [t_0, t_f] \to \mathbb{R}^{n_x},$$

$$t_c \in \mathbb{R}, \qquad u \in \mathbb{R}^{N_u},$$

$$\text{s.t.} \quad \boldsymbol{F}\left(t, \dot{\boldsymbol{x}}(t), \boldsymbol{x}(t), u(t), \Delta t_{\text{load}}, t_f, t_c\right) = \boldsymbol{0}, \quad \boldsymbol{x}(t_0) = \boldsymbol{x}_0, \tag{9d}$$

$$X_{B,L} - X_B(t_f) \leq 0, \tag{9e}$$

$$\boldsymbol{x}_L \leq \boldsymbol{x}(t), \qquad t_{c,L} \leq t_c \leq t_{c,U}, \tag{9f}$$

$$u_L \leq u \leq u_U, \qquad |\Delta u| \leq \Delta u_U, \tag{9g}$$

$$\forall t \in [t_0, t_f], \forall i \in [1..N_i], \qquad \forall z \in [z_0, z_f], \forall j \in [1..N_j].$$

Eqs. (9a and 9c) have a typical optimal control Lagrange term together with a quadratic penalty on the differences of the piecewise constant controls, Δu, in the temporal domain, which is discretized with N_i finite elements. This will influence the smoothness of u, and $\mathcal{U}$ is a weight. The optimization variables are the free operating parameters—the discrete control signal u and free time-invariant parameters $(\Delta t_{\text{load}}, t_f, t_c)$—and the state variables $\boldsymbol{x}(t) = (c_\alpha(t, z_j), c_S(t, z_j), c_{\text{mix},S}(t), q_\alpha(t, z_j), P_B(t), Y_\alpha(t), X_B(t))$ where $\alpha \in \{A, B, C\}$. The trajectories $\boldsymbol{x}$ are determined by the free operating parameters via the implicit differential algebraic equations (DAE) system of index one in Eq. (9d). Time-invariant bounds on variables are introduced in Eq. (9f) and bounds on u and Δu are introduced in Eq. (9g).

In this study, a decomposition strategy is adopted to transform the DOP into two levels: (i) the upper-level static optimization problem (Eqs. (9a–9b)) with respect to $(\Delta t_{\text{load}}, t_f)$ which is solved using a Nelder–Mead Simplex algorithm, and (ii) the lower-level DOP (Eqs. (9c–9g) constrained by the DAE system dynamics is transcribed into a NLP using direct collocation, as described in Section 4, and solved using IPOPT (Wächter and Biegler, 2006). By these means, the lower-level DOP is solved for a fixed temporal horizon $[t_0, t_f]$ which considerably reduces the NLP complexity and hence leads to an efficient computation.

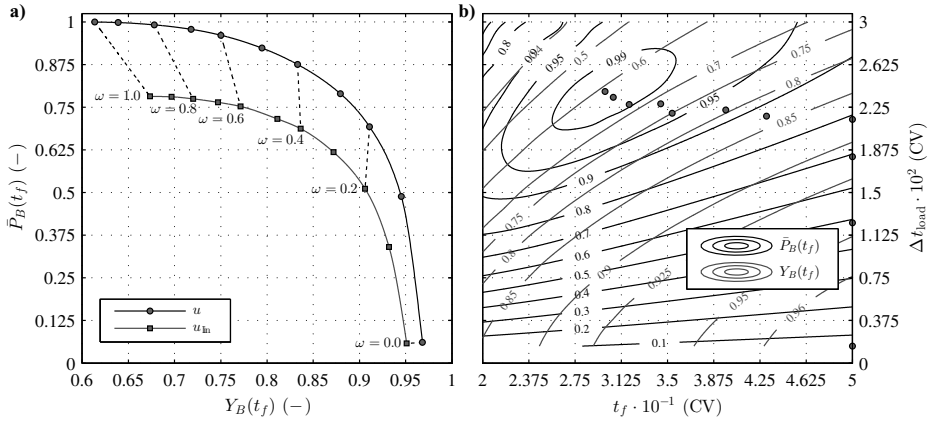

Figure 1: a) Pareto optimal solutions for $\omega \in [0.0, 1.0]$ and $X_{L,B}(t_f) = 9.9 \cdot 10^{-1}$. b) Interpolated sampled contours of $Y_B(t_f)$ and normalized $\bar{P}_B(t_f)$ generated for u as a function of $\Delta t_{\text{load}} \in [0.15, 3.0] \cdot 10^{-2}$ (CV) and $t_f \in [2.0, 5.0] \cdot 10^1$ (CV). Markers indicate the Pareto optimal time-invariant optimization variables of the upper-level static optimization problem (Eq. (9a–9b)).

4. Modeling and Optimization Environment

Modelica (The Modelica Association, 2012) was used as the description language for the HPLC process model presented in Section 2. The open-source platform JModelica.org (Åkesson et al., 2010) was used for simulation and optimization of the Modelica model. In the context of simulation, JModelica.org was used to compile the Modelica model into a functional mock-up unit (FMU) (Blochwitz et al., 2011), thus transforming it from a DAE form into an ordinary differential equation (ODE) form. JModelica.org's interface to SUNDIALS (Hindmarsh et al., 2005) was subsequently used to simulate the model.

The formulation of the DOP (Eq. (9c–9g) was made using the Modelica extension Optimica (Åkesson et al., 2010). The algorithm used in the work described in this paper to solve the DOP uses a direct and local collocation method (Biegler, 2010) on finite elements, using Radau points and Lagrange interpolation polynomials (Magnusson and Åkesson, 2012). The algorithm has been implemented in Python in the JModelica.org framework, using the computer algebra system with automatic differentiation (CasADi) optimization package (Andersson et al., 2012). By using CasADi's symbolic syntax, the DOP was transcribed into a finite dimensional NLP. The NLP was subsequently solved using the primal-dual interior point method IPOPT v.3.11.8 (Wächter and Biegler, 2006) and the linear solver MA57 from HSL (HSL, 2013).

5. Results and Discussion

The temporal horizon was discretized with $N_i = 1 \cdot 10^2$ finite elements with two Radau collocations points in each element and a piecewise constant control discretization with $N_u = 5 \cdot 10^1$ pieces was adopted. The spatial domain was discretized with $N_j = 2 \cdot 10^1$ finite volume elements with a 4th order WENO scheme and the resulting NLP has approximately $1 \cdot 10^5$ variables. In order to assess the performance of the general elution trajectories, these were benchmarked with conventional linear trajectories governed by:

$$u_{\text{lin}}(t) = u_{\text{lin}}(t_{\text{lin},0}) + \left[u_{\text{lin}}(t_f) - u_{\text{lin}}(t_{\text{lin},0})\right] \left(\frac{t - t_{\text{lin},0}}{t_f}\right), \tag{10}$$

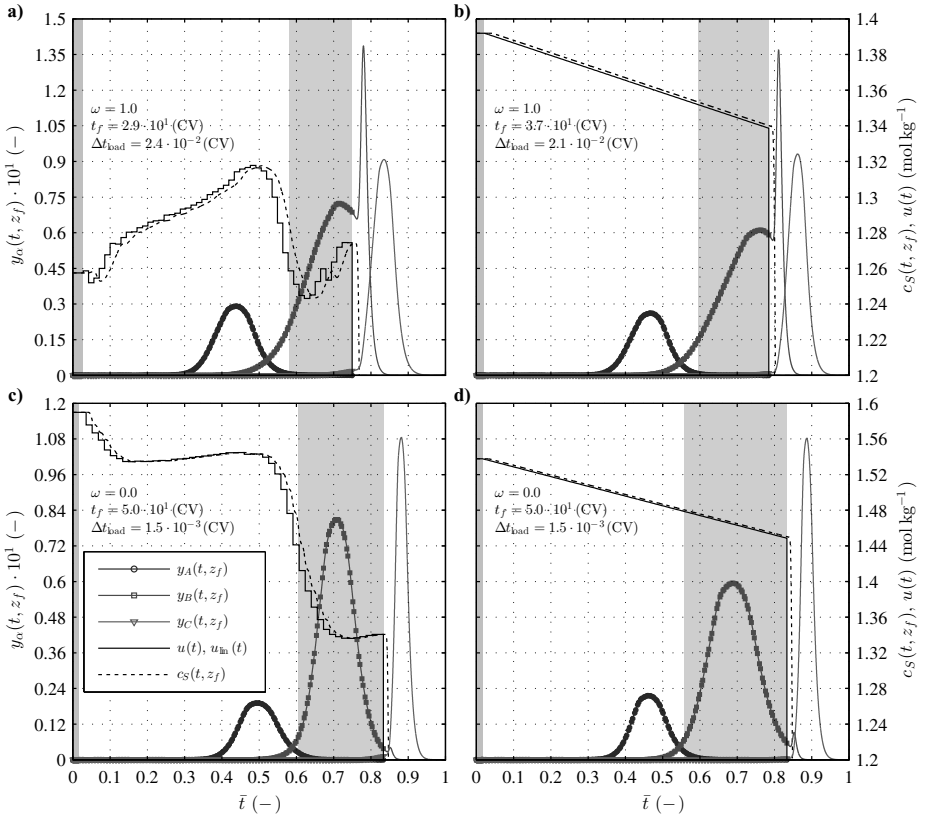

Figure 2: Optimal elution trajectories, where $y_\alpha(t,z_f) = c_\alpha(t,z_f)v_{\text{int}}(A_c^{-1}\sum_{\beta\in\{A,B,C\}}\delta_{\text{load},\beta})^{-1}$ is the normalized flux at $z = z_f$, as a function of normalized time $\bar{t} = t(t_f + t_r)^{-1}$. Markers indicate the solution at the Radau collocation points and solid and dashed lines the simulated response. The shaded areas indicate the pooling interval endpoints, $[t_c, t_f]$, and those of the initial load and wash, $[t_0, t_0 + \Delta t_{\text{load}} + \Delta t_{\text{wash}}]$.

where $t_{\text{lin},0} = t_0 + \Delta t_{\text{load}} + \Delta t_{\text{wash}}$ defines the onset of the elution mode and $(u_{\text{lin}}(t_{\text{lin},0}), u_{\text{lin}}(t_f))$ are the optimization variables. It is evident from analyzing the Pareto optimal fronts for $X_{L,B}(t_f) = 9.9 \cdot 10^{-1}$ depicted in Fig. 1a that the general elution trajectories, u, outperform the linear trajectories, u_{lin}, in terms of both objectives. Especially, for $\omega = 1.0$ the maximum productivity obtained with u is approximately 28% higher than that for u_{lin}. In addition, the dependency of $P_B(t_f)$ and $Y_B(t_f)$ on the time-invariant optimization variables $(\Delta t_{\text{load}}, t_f)$ associated with u depicted in Fig. 1b shows that $Y_B(t_f)$ is strictly decreasing as $\Delta t_{\text{load}} \to \Delta t_{\text{load},U}$ and $t_f \to t_{f,L}$ whereas $P_B(t_f)$ exhibits a convex behavior. The contours in Fig. 1b were generated by interpolating the solution to the lower-level DOP (Eq. (9c–9g) on a dense rectangular grid of $(\Delta t_{\text{load}}, t_f)$.

The associated elution profiles for $\omega = (0.0, 1.0)$ illustrated in Fig. 2 show a clear distinction in the system response generated with u and u_{lin}, respectively. As governed by Eq. (10), u_{lin} and hence the optimal modifier concentration is strictly decreasing in $[t_{\text{lin},0}, t_f]$ in order to increase hydrophobicity and to elute the components $\alpha \in \{A, B, C\}$. Contrarily, the modifier concentration

is freely controlled with the parametrized elution trajectories which ultimately promotes $P_B(t_f)$ through increasing Δt_{load} and reducing t_f while fulfilling the purity constraint (Figs. 2a and 2b). However, maximizing $Y_B(t_f)$ (which is time-invariant) implies injecting a minimal column load, and hence, $(\Delta t_{\text{load}}, t_f)$ are constrained by their lower and upper boundaries, and the gain in $Y_B(t_f)$ for u is therefore only moderate (Figs. 2c and 2d). Finally, it is noteworthy that the DOP (Eq. (9c–9g)) is solved for the temporal horizon $[t_0, t_f]$, and the control signal is prescribed a constant value of $5.0 \cdot 10^{-1}$ $(\text{mol}\,\text{kg}^{-1})$ for $t > t_f$, i.e. the column regeneration and re-equilibration.

6. Concluding Remarks

A novel methodology for rendering large-scale offline dynamic multi-objective optimization problems for HPLC processes in batch elution mode was developed in this paper. The assessment of the set of Pareto solutions generated with general elution trajectories, parametrized with a piecewise constant control signal, showed considerable improvement in the productivity objective when benchmarked with the Pareto set obtained using conventional linear elution trajectories.

Acknowledgement

The authors acknowledge the support of the strategic innovation program Process Industrial IT and Automation (SIO–PiiA) and the LCCC Linnaeus Center and the eLLIIT Excellence Center at Lund University.

References

Åkesson, J., Årzén, K.-E., Gäfvert, M., Bergdahl, T., Tummescheit, H., 2010. Modeling and optimization with Optimica and JModelica.org—Languages and tools for solving large-scale dynamic optimization problems. Computers & Chemical Engineering 34 (11), 1737–1749.

Andersson, J., Åkesson, J., Diehl, M., 2012. CasADi: A Symbolic Package for Automatic Differentiation and Optimal Control. In: Forth, S., Hovland, P., Phipps, E., Utke, J., Walther, A. (Eds.), Recent Advances in Algorithmic Differentiation. Vol. 87 of Lecture Notes in Computational Science and Engineering. Springer Berlin Heidelberg, pp. 297–307.

Biegler, L. T., 2010. Nonlinear Programming: Concepts, Algorithms, and Applications to Chemical Processes. MOS-SIAM Series on Optimization, Mathematical Optimization Society and the Society for Industrial and Applied Mathematics, PA, USA.

Blochwitz, T., Otter, M., Arnold, M., Bausch, C., Clau, C., Elmqvist, H., Junghanns, A., Mauss, J., Monteiro, M., Neidhold, T., Neumerkel, D., Olsson, H., Peetz, J.-V., Wolf, S., March 2011. The Functional Mockup Interface for tool independent exchange of simulation models. In: Proceedings of the 8th International Modelica Conference. Dresden, Germany.

Damtew, A., Sreedhar, B., Seidel-Morgenstern, A., 2009. Evaluation of the potential of nonlinear gradients for separating a ternary mixture. Journal of Chromatography A 1216 (28), 5355–5364.

Hindmarsh, A. C., Brown, P. N., Grant, K. E., Lee, S. L., Serban, R., Shumaker, D. E., et al., 2005. SUNDIALS: Suite of nonlinear and differential/algebraic equation solvers. ACM Transactions on Mathematical Software 31 (3), 363–396.

HSL, 2013. A collection of fortran codes for large scale scientific computation. URL: `http://www.hsl.rl.ac.uk`.

Magnusson, F., Åkesson, J., Sep 2012. Collocation methods for optimization in a Modelica environment. In: 9th International Modelica Conference. Munich, Germany.

Melander, W. R., El Rassi, Z., Horváth, C., 1989. Interplay of hydrophobic and electrostatic interactions in biopolymer chromatography: Effect of salts on the retention of proteins. Journal of Chromatography A 469, 3–27.

Schmidt-Traub, H., Schulte, M., Seidel-Morgenstern, A., 2012. Preparative Chromatography, 2nd Edition. Wiley-VCH, Weinheim.

Shu, C.-W., 1998. Essentially non-oscillatory and weighted essentially non-oscillatory schemes for hyperbolic conservation laws. In: Quarteroni, A. (Ed.), Advanced Numerical Approximation of Nonlinear Hyperbolic Equations. Vol. 1697 of Lecture Notes in Mathematics. Springer Berlin Heidelberg, pp. 325–432.

Sreedhar, B., Wagler, A., Kaspereit, M., Seidel-Morgenstern, A., 2013. Optimal cut-times finding strategies for collecting a target component from overloaded elution chromatograms. Computers & Chemical Engineering 49, 158–169.

The Modelica Association, 2012. The Modelica Association Home Page. URL: `http://www.modelica.org`.

Wächter, A., Biegler, L. T., 2006. On the implementation of an interior-point filter line-search algorithm for large-scale nonlinear programming. Mathematical Programming 106 (1), 25–57.

Krist V. Gernaey, Jakob K. Huusom and Rafiqul Gani (Eds.), 12th International Symposium on Process Systems Engineering and 25th European Symposium on Computer Aided Process Engineering.
31 May – 4 June 2015, Copenhagen, Denmark

An Adaptive Multi-Objective Differential Evolution Algorithm for Solving Chemical Dynamic Optimization Problems

Xu Chen, Wenli Du*, Feng Qian

Key Laboratory of Advanced Control and Optimization for Chemical Processes, Ministry of Education, East China University of Science and Technology, Shanghai, 200237, China
wldu@ecust.edu.cn

Abstract

The dynamic optimization problems appear frequently in chemical industry, and these problems are quite challenging because they often involve multiple and conflicting objectives. In this paper, a new adaptive multi-objective differential evolution algorithm named EPSMODE is proposed, which can be used to solve the multi-objective dynamic optimization problems. To solve a specific multi-objective problem, the performance of differential evolution depends on the choice of the control parameters and mutation strategies. Therefore, aiming to improve the robustness of multi-objective differential evolution, the EPSMODE approach employs an ensemble of parameter values and mutation strategies, and these parameter values and mutation strategies compete to produce offspring based on Pareto domination mechanisms. The performance of EPSMODE is first compared with powerful multi-objective algorithms on benchmark multi-objective problems; then, by combining with the control vector parameterization approach, EPSMODE is applied to solve a multi-objective dynamic optimization problem with constraints. The computational results reveal the effectiveness and efficiency of the proposed approach.

Keywords: multi-objective optimization, dynamic optimization, differential evolution, ensemble strategy.

1. Introduction

Dynamic optimization problems (i.e., optimal control problems) are encountered in a large number of chemical engineering applications. In practical chemical dynamic optimization problems, multiple and conflicting objectives are often present. The multi-objective optimization problems (MOPs) give rise to a set of Pareto optimal solutions instead of one single solution. The designer will then select one solution from this Pareto optimal set.

Solution methods for generating the Pareto front can be divided into in two categories: scalarization and vectorization methods. The scalarization methods transform the multi-objective problems into a series of single objective optimization problems by classic convex weighted sum, or novel methods as normal boundary intersection, normalized normal constraint (Logist et al. 2008). The vectorization methods involve population-based multi-objective evolutionary algorithms (MOEAs), such as elitist nondominated sorting genetic algorithm (NSGA-II) (Deb et al. 2002), multi-objective particle swarm optimization (MOPSO) (Coello et al. 2004). Compared with the scalarization methods,

MOEAs have the following advantages: (i) they can find the entire Pareto optimal front in one single run; (ii) they can be useful when the gradient information is unavailable; (iii) they can avoid falling into the local Pareto optimal front. Because of these advantages, the use of MOEAs to solve MDOPs has drawn continuing attention from researchers (Sarkar and Modak 2005, Jia et al. 2012, Chen et al.2014).

Multi-objective Differential evolution (MODE) is a new population-based evolutionary algorithm. The computational results reported in published articles show that MODE has a better convergence speed than NSGA-II and a better diversity maintenance than MOPSO (Wang and Tang, 2014). However, to solve a specific multi-objective problem, the performance of differential evolution depends on the choice of the control parameters and mutation strategies. Therefore, to improve the robustness of MODE, we develop a new multi-parameters and multi-strategies adaptive MODE algorithm, called multi-objective differential evolution with ensemble of parameters and mutation strategies (EPSMODE). In the proposed approach, a pool of mutation strategies along with a pool of values for each control parameter coexists throughout the evolution process, and competes to produce offspring based on Pareto domination mechanisms. The computational results on benchmark multi-objective problems and a multi-objective dynamic optimization problem (MDOP) reveal the effectiveness and efficiency of the proposed approach.

2. Proposed approach

The DE algorithm is a stochastic, population-based algorithm designed for optimization problems in continuous search space (Storn and Price,1997), working through three operations: mutation, crossover, and selection. However, the effectiveness of DE in solving an optimization problem depends on the selected mutation strategy and its associated parameter values. Mallipeddi et al. (2011) introduced an ensemble strategy with adaptation of all parameters and mutation strategies to DE, and proposed a DE variant called EPSDE for single optimization problem. Motivated by the promising results obtained by EPSDE, we extend the idea of ensemble strategy to multi-objective optimization, and an adaptive MODE algorithm called EPSMODE is presented in this paper. In EPSMODE, a pool of mutation strategies along with a pool of values corresponding to each associated parameter competes to produce successful offspring based on Pareto domination mechanisms. In the following, EPSMODE is described in detail.

2.1. Selection of pools of strategies and control parameters

EPSMODE firstly initializes a population of NP individuals X_i, i=1,….,NP and evaluates these individuals. After initialization, a pool of mutation strategies and a pool of values for two crucial parameters, the scale factor F and crossover probability CR, are generated. The pool of mutation strategies contains DE/rand/1, DE/rand/2, and DE/current-to-rand/1. The pool of F values is taken in the range 0.4–0.9 in steps of 0.1, i.e. the set {0.4, 0.5, 0.6, 0.7, 0.8, 0.9}, and the pool of CR values is taken in the range 0.1–0.9 in steps of 0.1, i.e. the set {0.1, 0.2, 0.3, 0.4, 0.5, 0.6, 0.7, 0.8, 0.9}. In EPSMODE, each individual X_i is randomly assigned with one of the mutation strategy MS_i and the associated parameter values (F_i and CR_i) from the pools. The ensemble strategy in EPSMODE is illustrated in Figure 1(a).

2.2. Generate offspring with DE operators

EPSMODE performs mutation and crossover using the mutation strategy MS_i and the associated parameter (F_i and CR_i) corresponding to each individuals X_i. After the crossover operator, NP offspring U_i, i=1,…,NP are produced. EPSMODE combines the parents and offspring, and the total size of the population after combination becomes 2NP. Then, it sorts the population based on fast nondominated sorting and crowding distance. The NP better solutions are selected to enter into the next generation. The details implementations of nondominated sorting and crowding distance calculation can refer to NSGA-II.(Deb et al. 2002).

2.3. Update the mutation strategies and control parameter values

After selection operator, EPSMODE updates the mutation strategies and control parameters for each individual X_i using the following criteria:

(i) If the offspring U_i survives into the next generation, the corresponding mutation strategy MS_i and parameter values (F_i and CR_i) are retained in the next generation; meanwhile, the mutation strategies and parameter values are added to a successful list.

(ii) If the offspring U_i fails surviving into the next generation, randomly select a new mutation strategy and parameter values from the pools or the store successful list with equal probability.

The two criteria lead to an increased probability of production of offspring by the better combination of mutation strategy and the associated control parameters in the future generations.

2.4. Constraint-handling method

Usually, most of practical engineering optimization problems have multiple constraints. So it is essential to handle the constraints to solve these problems. To handle these constraints, we use Deb's constrained-domination principle in EPSMODE (Deb et al. 2002). For two solutions X_1 and X_2, X_1 is said to constrained-dominate X_2 if any of the following three conditions is met: (i) both solutions are feasible, and X_1 dominates X_2; (ii) solution X_1 is feasible, but solution X_2 is infeasible; and (iii) both solutions are infeasible, and the constraint violation of X_1 is smaller than that of X_2. Based on subsection 2.1–2.4, the flowchart of the EPSMODE approach is given in Figure 1(b).

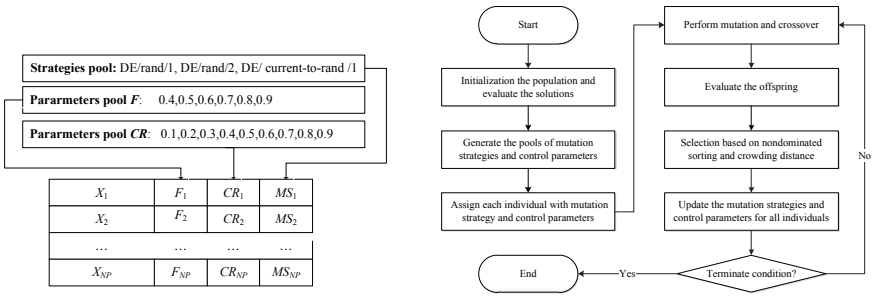

(a) (b)

Figure 1: EPSMODE (a) ensemble strategy of parameters and mutation strategies. (b) flowchart of EPSMODE.

3. Case Study

3.1. Case Study I: Benchmark Multi-objective Optimization Problems

To test the performance of the proposed EPSMODE, it is used to solve eleven constrained benchmark MOPs (Deb, 2001), and compared with two MOEAs: NSGA-II (Deb et al. 2002) and GDE3 (Kukkonen and Lampinen, 2005). The performance metric inverted generational distance (IGD) (Li and Zhang, 2009) which measures both convergence and diversity is used to evaluate the attained approximation Pareto front of an algorithm. All algorithms are conducted with population size *NP*=100, and maximum number of generations *Maxgen*=250. The results based on 30 runs are presented in Table 1.

Table 1 . Comparison of the IGD Metric between EPSMODE and Other Algorithms

	EPSMODE		NSGAII			GDE3		
IGD	mean	SD	mean	SD		mean	SD	
TNK	**1.31E-04**	**1.63E-05**	1.57E-04	1.40E-05	+	2.92E-04	1.11E-04	+
SRN	2.23E-02	1.30E-03	2.35E-02	1.76E-03	+	**1.81E-02**	**1.18E-03**	-
CONSTR	**6.48E-04**	**2.26E-05**	7.85E-04	4.47E-05	+	1.20E-03	4.51E-04	+
OSY	**8.43E-02**	**1.89E-02**	2.70E-01	3.99E-01	+	4.22E-01	1.43E-01	+
CTP1	**7.92E-05**	**3.79E-06**	2.60E-03	9.63E-04	+	2.68E-04	1.16E-04	+
CTP2	**1.16E-04**	**1.21E-05**	5.70E-03	5.90E-03	+	3.69E-04	3.11E-04	+
CTP3	**5.30E-03**	**5.34E-04**	6.07E-02	7.16E-02	+	1.14E-02	4.50E-03	+
CTP4	**2.41E-02**	**3.40E-03**	1.08E-01	6.12E-02	+	4.10E-02	1.09E-02	+
CTP5	**2.99E-04**	**8.07E-05**	3.10E-03	2.60E-03	+	5.16E-04	1.67E-04	+
CTP6	5.18E-04	1.92E-04	5.98E-04	4.50E-04	=	2.50E-03	1.80E-03	+
CTP7	**2.49E-05**	**1.10E-06**	6.55E-04	6.02E-04	+	1.66E-04	1.82E-04	+
+/=/-			10/1/0			10/0/1		

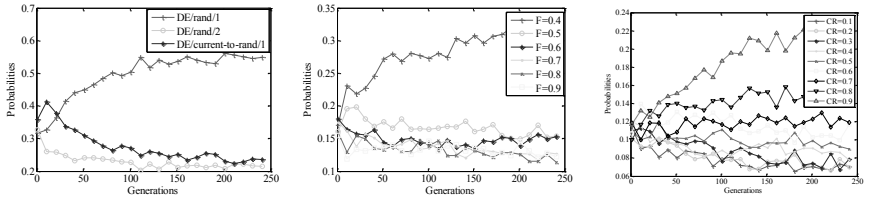

(a) (b) (c)

Figure 2: Adaptiveness of EPSMODE on problem TNK (a) Probability of an offspring production by a mutation strategy versus generations. (b) Probability of an offspring production by a particular *F* value versus generations. (c) Probability of an offspring production by a particular *CR* value versus Generation

From Table 1, it appears that our EPSMODE obtains the best IGD values on ten of eleven MOPs among the three algorithms. It means the EPSMODE achieves approximation Pareto fronts with best convergence and diversity on these problems. EPSMODE and NSGA-II get similar results on CTP6. GDE3 performs better than EPSMODE only on one problem SRN. Based on the above results, we can say that the proposed EPSMODE is a high competitive algorithm. To investigate the adaptiveness of EPSMODE, figure 2 show the probability of an offspring being produced by a particular mutation strategy or a particular parameter value versus generation on problem TNK. From the figure, all mutation strategies and parameter values in respective pools have equal probability to produce an offspring. However, as the evolution progresses, the inefficient mutation strategies and parameters are replaced with new mutation strategies and parameters, leading to an increase in the probability of producing an offspring by a suited mutation strategy and parameters.

3.2. Case Study II: Multi-objective Dynamic Optimization Problems.

By combining the control vector parameterization (CVP) approach (Balsa Canto et al. 2002), the EPSMODE is used to solve a MDOP: optimal operation for a batch reactor with cooling jacket. The problem formulates a first-order consecutive exothermic reaction, $A \rightarrow P \rightarrow S$, occurring in a batch reactor with a cooling jacket. The system dynamic equations are given in the literature (Sun et al, 2008). There are six state variables x_1 -x_6, where x_1, x_2, and x_3 denote the concentration of A, P, and S; x_4, x_5, and x_6 represent the temperatures (in Kelvin) of the contents in the reactor, the reactor wall, and the coolant, respectively. The control variable u is the coolant flow rate (expressed in units of m^3/h), which is bounded by $0 \le u(t) \le 9$ .The aim is to maximize the concentration of product P $x_2(t_f)$ and minimize the concentration of by-product S $x_3(t_f)$ at $t_f = 3.5h$. In addition, there are two constraints posed on the reactor temperature: one path constraint $x_4(t) \le 370K$ and one terminal constraint $x_4(t_f) \le 320K$.

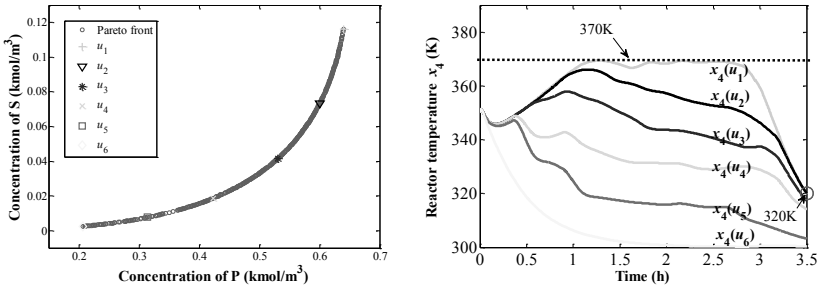

(a) (b)

Figure 3: Computational results (a) Pareto optimal front obtained by EPSMODE. (b) Pareto optimal reactor temperature corresponding to u_1-u_6.

When using EPSMODE to solve this problem, the time interval is divided in to N=20 stages in CVP approach, and the parameters settings for EPSMODE are: population size NP=400, maximal number of generation $Maxgen$=1000. The Pareto front obtained by EPSMODE is shown in Figure 3(a). Clearly, there is a tradeoff between maximizing the concentration of product P and minimizing the concentration of by-product S. We mark six Pareto optimal solutions u_1-u_6 in the Pareto front, including two extreme solutions and four intermediate solutions. The concentration of product P ranges between 0.20570 and 0.63987 kmol/m^3, and the concentration of by-product S varies 0.00247 and 0.11619and kmol/m^3. Sun et al. (2008) considered the single objective problem to maximize the concentration of product P, their best value is 0.64469. Our result in extreme solution u_1 is 0.63987, which is within 0.1% of the reported best value. When we only consider minimizing the concentration of by-product S, our result in extreme solution u_6 is 0.00247. Other four intermediate solutions u_2-u_5 are presented with equal distribution. Which solution is selected in practice is decided by the preference of the decision maker and other factor such as the cost of the separation of the product and by-product.

Pareto optimal reactor temperatures $x_4(t)$ corresponding to u_1-u_6 are shown in Figure 3(b). Obviously, the path constraint $x_4(t) \le 370K$ and terminal constraint $x_4(t_f) \le 320K$ in all six solutions are satisfied. For u_1, the path constraint is active in

the middle of the time interval (about 1h to 3h) and the terminal constraint is active. For u_2, only the terminal constraint is active. For other solutions u_3-u_6, both the path constraint and the terminal constraint are non-active.

4. Conclusions

This paper has described a new adaptive MODE algorithm EPSMODE, which can be used to solve MDOPs in chemical processes. EPSMODE employs an ensemble strategy with adaptation of all parameters and mutation strategies to improve the robustness of MODE. The computational results on benchmark MOPs and a MDOP demonstrate the effectiveness and efficiency of the proposed approach.

Acknowledgements

We gratefully acknowledge funding by the National Basic Research Program of China (No. 2012CB720500), National Natural Science Foundation of China (U1162202, 21276078), National Science Fund for Outstanding Young Scholars (61222303).

References

E. Balsa Canto, J.R. Banga, A.A. Alonso, S.V. Vassilios, 2002 Restricted second order information for the solution of optimal control problems using control vector parameterization, J. Process Contr. ,12,2,243-255.

X. Chen, W. Du, F. Qian, 2014, Multi-Objective Differential Evolution with Ranking-Based Mutation Operator and Its Application in Chemical Process Optimization. Chemometr. Intell. Lab.,136, 85–96.

C.A.C. Coello, G.T. Pulido, M.S. Lechuga, 2004, Handling multiple objectives with particle swarm optimization, IEEE T. Evolut. Comput., 8,3, 256-279.

K. Deb, 2001, Multi-objective optimization using evolutionary algorithms. Wiley, New York, 349-360.

K. Deb, A. Pratap, S. Agarwal, T.A. M. T. Meyarivan, 2002, A fast and elitist multiobjective genetic algorithm: NSGA-II, IEEE T. Evolut. Comput., 6,2, 182-197.

S. Kukkonen, J. Lampinen, 2005, GDE3: The third evolution step of generalized differential evolutio, IEEE Congress on Evolutionary Computation., 1,443-450.

H. Li, Q. Zhang, 2009, Multiobjective optimization problems with complicated Pareto sets, MOEA/D and NSGA-II. IEEE T. Evolut. Comput., 13,2, 284-302.

F. Logist, P.M.M. Van Erdeghem, J.F. Van Impe, 2009, Efficient deterministic multiple objective optimal control of (bio) chemical processes, Chem. Eng. Sci., 64,11, 2527-2538.

L. Jia, D. Cheng, M.S. Chiu, 2012, Pareto-optimal solutions based multi-objective particle swarm optimization control for batch processes. Neural Comput. Appl., 21, 6,1107-1116.

R. Mallipeddi, P.N. Suganthan, Q.K. Pan, M.F. Tasgetiren, 2011, Differential evolution algorithm with ensemble of parameters and mutation strategies, Appl. Soft. Comput., 11,2,1679-1696.

D. Sarkar, J.M. Modak, 2005, Pareto-optimal solutions for multi-objective optimization of fed-batch bioreactors using nondominated sorting genetic algorithm, Chem. Eng. Sci., 60,2,481-492.

R. Storn, K. Price, 1997, Differential evolution–a simple and efficient heuristic for global optimization over continuous spaces. J. Global. Optim., 11,4, 341-359.

D.Y. Sun, P.M. Lin, S.. Lin, 2008, Integrating controlled random search into the line-up competition algorithm to solve unsteady operation problems. Ind. Eng. Chem. Res. 47,22, 2008,8869-8887.

X. Wang, L. Tang, 2013, Multiobjective Operation Optimization of Naphtha Pyrolysis Process Using Parallel Differential Evolution. Ind. Eng. Chem. Res., 52,40,14415-14428.

Krist V. Gernaey, Jakob K. Huusom and Rafiqul Gani (Eds.), 12th International Symposium on Process Systems Engineering and 25th European Symposium on Computer Aided Process Engineering.
31 May – 4 June 2015, Copenhagen, Denmark

Optimal operation of a pyrolysis reactor

Aysar T. Jarullah[a], Shemaa A. Hameed[a], Zina A. Hameed[a], and I.M. Mujtaba[b]*

[a]*Chemical Engineering Department, College of Engineering, Tikrit University, IRAQ*
[b]**School of Engineering, Design and Technology, University of Bradford, Bradford BD7 1DP, UK, E-mail: I.M.Mujtaba@brad.ac.uk*

Abstract

In the present study, the problem of optimization of thermal cracker (pyrolysis) operation is discussed. The main objective in thermal cracker optimization is the estimation of the optimal flow rates of different feeds (such as, Gas-oil, Propane, Ethane and Debutanized natural gasoline) to the cracking furnace under the restriction on ethylene and propylene production. Thousands of combinations of feeds are possible. Hence the optimization needs an efficient strategy in searching for the global minimum. The optimization problem consists of maximizing the economic profit subject to a number of equality and inequality constraints. Modelling, simulation and optimal operation via optimization of the thermal cracking reactor has been carried out by gPROMS (**g**eneral **PRO**cess **M**odelling **S**ystem) software. The optimization problem is posed as a Non-Linear Programming problem and using a Successive Quadratic Programming (SQP) method for solving constrained nonlinear optimization problem with high accuracy within gPROMS software. New results have been obtained for the control variables and optimal cost of the cracker in comparison with previous studies.
Keywords: Thermal Cracking, Mathematical Modeling, Olefins Pyrolysis, SQP.

1. Introduction

Hydrocarbon thermal cracking is the most significant operation in the production of olefins. Recently, the worldwide olefins production (mainly ethylene) increases rapidly (around 180 billion lb/yr), and is regarded one of the most important issues for chemical industries where improving its production operation can bring several benefits. Thus, the market demand for olefins production has accelerated the improvement of a more rigorous and reliable thermal cracking model of such process. Its annual industrial production depends on the thermal cracking (pyrolysis) of oil hydrocarbons, where the heart of the process with a massive economic effect is the reactor of the cracking process. Cracking of heavier fuel oils is done to produce mainly high quality (octane number) petrol, olefins (feed for petrochemical industry), coke (by coking) and to reduce the viscosity of fuel oil by visbreaking (Masoumi et al., 2006a, Babu and Angira, 2001). The main parameter of the optimal design of such reactor is the accurate prediction of yield and reactor performance. Each reactant is known to produce a certain distribution of products. When multiple reactants are employed, it is desirable to optimize the amounts of each reactant so that the products satisfy flow and demand constraints. Control systems are designed for achieving several goals, involving product quality, safety, and minimum cost (Masoumi et al., 2006b, Edgar and Himmelblau, 2001). The feed of a thermal cracking furnace can be a variety of components (such as ethane, propane, butane, isobutane, naphtha, and gas oil) and the main factor influencing the product is the feed composition (Lee and Aitani, 1990). The optimal design and operation strategy and purchase decisions for raw materials have become

main issues in the olefin industries (Joo and Park, 2001). It is extremely difficult to obtain the detailed operation factors in the reactor from direct measurements owing to the limitation of current techniques. Thus, mathematical simulation, as an alternative, has become a powerful tool for predicting control variable distributions and olefin yields. The thermal cracking reactor is the key parameters affecting the economics of the process and the olefin yields (Lan et al., 2007). The main focus in this study is to find the optimal design of pyrolysis reactor (thermal cracker) and objective function of the process (which is the estimation of optimal flow rates of different feeds to the cracking furnace) subject to a number of equality and inequality constraints using an alternative approach to describe the reactor operating conditions as accurately as possible. The optimization problem is posed as a Non-Linear Programming problem and is solved by employing a Successive Quadratic Programming (SQP) method (which is considered to be one of the most promising approaches for solving constrained nonlinear optimization problem in addition to its successful application to many engineering optimization problems) with high accuracy within gPROMS (**g**eneral **PRO**cess **M**odelling **S**ystem) software.

2. Problem Description

The problem presented by Edgar and Himmelblau, (2001) is to obtain the maximum profit of the process, while operating within the reactor and down stream process equipment constraints. Figure 1 shows various feeds and corresponding product distribution for a thermal cracker that produces olefins. The variables to be optimized are the amounts of the four feeds (mainly, Gas-oil, Propane, Ethane and Debutanized natural gasoline (DNG)). This problem will be solved utilizing SQP method within gPROMS package.

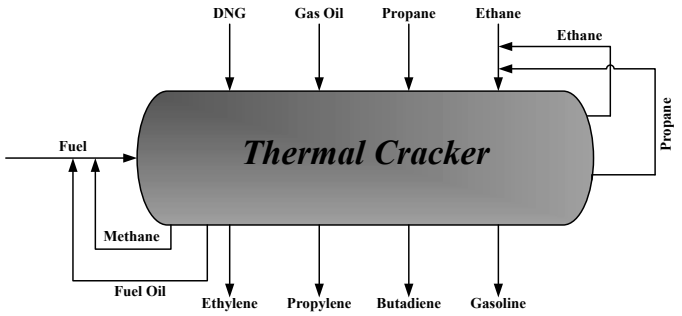

Figure 1: Pyrolysis Reactor

3. Mathematical Model of the Pyrolysis Reactor

Table 1 shows various feeds and the corresponding product distribution for a Pyrolysis reactor that produces olefins (Edgar and Himmelblau, 2001). The possible feeds include ethane, propane, debutanized natural gasoline (DNG), and gas oil, some of which may be fed simultaneously. Based on plant data, eight products are produced in varying proportions according to the following matrix. The capacity to run gas feeds through the cracker is 200,000 Ib/stream hour (total flow based on an average mixture). Ethane uses the equivalent of 1.1 Ib of capacity per pound of ethane; propane 0.9 Ib; gas oil 0.9 Ib/Ib; and DNG 1.0. Downstream processing limits exist of 50,000 Ib/stream hour on the ethylene and 20,000 Ib/ stream hour on the propylene. The fuel requirements to run the cracking system for each feedstock type are listed in Table 2. Methane and fuel oil

produced by the cracker are recycled as fuel. All the ethane and propane produced is recycled as feed. Heating values are shown in Table 3 (Geddes and Kubera, 2000).

Table 1: Yield Structure (wt. fraction)

	Feed			
Product	**Ethane**	**Propane**	**Gas oil**	**DNG**
Methane	0.07	0.25	0.10	0.15
Ethane	0.40	0.06	0.04	0.05
Ethylene	0.50	0.35	0.20	0.25
Propane	-	0.10	0.01	0.01
Propylene	0.01	0.15	0.15	0.18
Butadiene	0.01	0.02	0.04	0.05
Gasoline	0.01	0.07	0.25	0.30
Fuel oil	-	-	0.21	0.01

Table 2: Fuel Requirement

Feedstock type	**Fuel requirement (Btu/Ib)**
Ethane	8364
Propane	5016
Gas oil	3900
DNG	4553

Table 3: Heating Values

Recycled feed	**Heat produced (Btu/Ib)**
Natural gas	21,520
Methane	21,520
Fuel oil	18,000

Because of heat losses and the energy requirements for pyrolysis, the fixed fuel requirement is 20.0×10^6 Btu/stream hour and the energy (fuel) cost of $\$2.50/10^6$ Btu. The price structure on the feeds and products and fuel costs is presented in Table 4 (Edgar and Himmelblau, 2001).

Table 4: Feeds and Products Prices

Feeds	**Price($/Ib)**	**Products**	**Price($/Ib)**
Ethane	0.0655	**Methane**	0.0538 (fuel value)
Propane	0.0973	**Ethane**	0.1775
Gas oil	0.1205	**Propylene**	0.1379
DNG	0.1014	**Butadiene**	0.2664
		Gasoline	0.0993
		Fuel oil	0.0450 (fuel value)

The following variables for the flow rates (input and output) of the reactor (in Ib/h) can be defined as: C_1 = fresh ethane feed, C_2 = fresh propane feed, C_3 = gas oil feed, C_4 = DNG feed, C_5 = ethane recycle, C_6 = propane recycle, C_7 = fuel added.

Objective function (profit). The objective function is the economic profit depending upon the difference between the value of the product and the value of feed and energy cost and all costs are calculated in cents/h. In other words, the profit f is written as:

f = Product value – Feed cost – Energy cost

Product value:

Ethylene: $17.75(0.5C_1 + 0.5C_5 + 0.35C_2 + 0.35C_6 + 0.20C_3 + 0.25C_4)$ (1)

Propylene: $13.79(0.01C_1 + 0.01C_5 + 0.15C_2 + 0.15C_6 + 0.15C_3 + 0.18C_4)$ (2)

Butadiene: $26.64(0.01C_1 + 0.01C_5 + 0.02C_2 + 0.02C_6 + 0.04C_3 + 0.05C_4)$ (3)

Gasoline: $9.93(0.01C_1 + 0.01C_5 + 0.07C_2 + 0.07C_6 + 0.25C_3 + 0.30C_4)$ (4)

Total product sales $= 9.39C_1 + 9.51C_2 + 9.17C_3 + 11.23C_4 + 9.39C_5 + 9.51C_6$ (5)

Feed cost:

Feed cost (cents/h) $= 6.55C_1 + 9.73C_2 + 12.50C_3 + 10.14C_4$ (6)

Energy cost: The fixed heat loss of 20×10^6 Btu/h can be expressed in terms of methane cost using a heating value of 21,520 Btu/Ib for methane. The fixed heat loss represents a constant cost that is independent of the variables C_i, hence in optimization this factor can be ignored, but in evaluating the final costs this term must be taken into account.

The value for C_7 depends on the amount of fuel oil and methane produced in the cracker (C_7 provides for any deficit in products recycled as fuel). Equation (5) and (6) is combined to get the objective function, which is

$$f = 2.84C_1 - 0.22C_2 - 3.33C_3 + 1.09C_4 + 9.39C_5 + 9.51C_6 \quad (7)$$

Process limitations:

1- Cracker capacity of 200,000 Ib/h

$$Crc = 1.1C_1 + 0.9C_2 + 0.9C_3 + 1.0C_4 + 1.1C_5 + 0.9C_6 \leq 200{,}000 \quad (8)$$

2- Ethylene processing limitation of 50,000 Ib/h

$$Eth = 0.5C_1 + 0.35C_2 + 0.25C_3 + 0.25C_4 + 0.5C_5 + 0.35C_6 \leq 50{,}000 \quad (9)$$

3- Propylene processing limitation of 20,000 Ib/h

$$Pro = 0.01C_1 + 0.15C_2 + 0.15C_3 + 0.18C_4 + 0.01C_5 + 0.15C_6 \leq 20{,}000 \quad (10)$$

4- Ethane recycle

$$Ethr = C_5 = 0.4C_1 + 0.4C_5 + 0.06C_2 + 0.06C_6 + 0.04C_3 + 0.05C_4 \quad (11)$$

By rearranging equation (11), we get

$$Ethr = 0.4C_1 + 0.06C_2 + 0.04C_3 + 0.05C_4 - 0.6C_5 + 0.06C_6 = 0 \quad (12)$$

5- Propane recycle

$$Pror = 0.1C_2 + 0.01C_3 + 0.01C_4 - 0.9C_6 = 0 \quad (13)$$

6- Heat constraint. The total fuel heating value (THV) in (Btu/h) is given by

$$THV = \underset{\text{fuel}}{21{,}520C_7} + \underset{\text{methane from cracker}}{21{,}520(0.07C_1 + 0.25C_2 + 0.10C_3 + 0.15C_4 - 0.07C_5 + 0.25C_6)} + \underset{\text{fuel oil from cracker}}{18{,}000(0.21C_3 + 0.01C_4)} = 1506.4C_1 + 5380C_2 + 5932C_3 + 3408C_4 + 1506.4C_5 + 5380C_6 + 21{,}520C_7 \quad (14)$$

The required fuel for cracking (Btu/h) is

$$\underset{\text{ethane}}{8364(C_1 + C_5)} + \underset{\text{propane}}{5016(C_2 + C_6)} + \underset{\text{gas oil}}{3900C_3} + \underset{\text{DNG}}{4553C_4} = 8364C_1 + 5016C_2 + 3900C_3 + 4553C_4 + 8364C_5 + 5016C_6 \quad (15)$$

Thus the sum of eq. (15) + 20,000,000 Btu/h is equal to the THV from eq. (14), which gives the constraint

$$HC = -6857.6C_1 + 364C_2 + 2032C_3 - 1145C_4 - 6857.6C_5 + 364C_6 + 21{,}520C_7 = 20{,}000{,}000 \quad (16)$$

3.1. Optimization Problem Formulation

The optimal design problem is to obtain the optimal flow rate of different feeds giving maximum economic profits from the reactor operation corresponding to different constraints. Mathematically, the optimization problem can be stated as:

$$\begin{aligned} &Max && f \\ &C_i\,(i=1-7) \\ &s.t && y(x, u, q) = 0, && \text{(model, equality constraints)} \\ & && Ci^L \leq Ci \leq Ci^U, Crc \leq Crc^*, Eth \leq Eth^* && \text{(inequality constraints)} \\ & && Pro \leq Pro^*, Ethr = Ethr^*, Pror = Pror^*, Hc = Hc^* && \text{(inequality constraints)} \end{aligned}$$

The model equations can be written in compact form as: $y(x, u, q) = 0$, where x gives the set of all algebraic variables, u is the control variables, and q represents the design variables and the function y is assumed to be continuously differentiable with respect to all its arguments (Jarullah et al., 2011, Jarullah et al., 2012). L and U are the lower and upper bounds, respectively. The optimization solution method utilized by gPROMS is a two-steps method known as feasible path approach. The first step performs the simulation to converge all the equality constraints and to satisfy the inequality constraints. The second step performs the optimization (updates the values of the optimization parameters).

4. Results and Discussion

The purpose of this study is to obtain the optimal design of thermal cracking reactor via optimal flow rates of different hydrocarbons feeds (namely, Gas-oil, Propane, Ethane and Debutanized natural gasoline) to get maximum profit. The modelling, simulation and optimization process has been carried out by using gPROMS software and the

optimization problem based on a Non-Linear Programming (NLP) problem, which is solved using Successive Quadratic Programming (SQP) method. The optimal parameters obtained for two cases: case1 at maximum ethylene production of 50000 lb/hr and 100000 lb/hr for case2, are shown in Table 5. As noticed from the results presented in this Table that the maximum possible amount of ethylene is produced for both cases. Where, the optimal feed flow rate in lb/hr of ethane, ethane recycle and the fuel that should be added is 60000, 40000 and 32795.5 for case 1 and 109091, 72727.3 and 58867.9 for case 2, respectively with no feed of propane, gas oil, DNG and propane recycle for both cases. This means that the process depends mainly on the ethane (fresh feed as well as ethane recycle) in addition to the fuel. The maximum objective function (economic profit) is 5460 $/h for case 1 and 9927.28 $/h for case2 with satisfying all the inequality constraints. It has also been observed as the ethylene production constraint is relaxed, the objective function value increases. Once the constraint is raised above 90909.15 lb/hr, the objective function remains constant for whole process.

Table 5: Optimization Results for Pyrolysis Reactor

Control Variables	**Optimized value (lb/hr)**		**Process Constraints**	**Values (lb/hr)**	
	Case 1	**Case 2**		**Case 1**	**Case 2**
C_1 (Fresh Ethane Feed)	60000	109091	*Crc*	110000	200000
C_2 (Fresh Propane Feed)	0.0	0.0	*Eth*	50000	90909.15
C_3 (Gas Oil Feed)	0.0	0.0	*Pro*	1000	1818.183
C_4 (DNG Feed)	0.0	0.0	*Ethr*	0.0	0.0
C_5 (Ethane Recycle)	40000	72727.3	*Pror*	0.0	0.0
C_6 (Propane Recycle)	0.0	0.0	*Hc*	2×10^7	2×10^7
C_7 (Fuel Added)	32795.5	58867.9			
Objective function($/h)	*5460.0*	*9927.28*			

In order to describe the performance of the pyrolysis reactor, the simulation of such reactor is necessary. The simulation results for the products obtained by thermal cracking reactor for both cases are presented in Table 6. It is noted from this table that the highest favourable product (the main target), which is ethylene is achieved at 50000 lb/h for case 1 and 90909.15 lb/h for case 2 (whole process) among all products.

Table 6: Simulation Results for Stream Pyrolysis Reactor

Simulation Results		
Product (lb/hr)	**Case 1**	**Case 2**
Ethylene	50000	90909.15
Propylene	1000	1818.183
Butadiene	1000	1818.183
Gasoline	1000	1818.183
Methane	7000	12727.28
Fuel Oil	0.0	0.0

Table 7 shows the comparison results obtained from this study and those obtained by last studies. It is clearly observed from this Table that the new approach (SQP) used in this work to maximize the process profit related to thermal cracking reactor is better than the methods used with all previous works (that used different solution methods for maximizing the objective function to get the optimal design of pyrolysis reactor in this field). Where, the economic profit of the process is increased by 47% for both cases and the CPU-time was reduced by 86% for case 1 compared with last studies. This new result obtained can be attributed to the SQP approach employed in the present work (has high accuracy in evaluating the control variables of the process) within gPROMS package. Furthermore, this approach is a highly trusted method for solution of such mathematical models.

Table 7: Comparison results between this work and last studies

Authors	Solution method	CPU-time (sec) – Case1	Objective function ($/h)	
			Case 1	Case 2
Edgar &Himmelblau (2001)	LP	-----	3695.6	-----
Babu & Angira (2007)	LP Simplex	-----	3695.6	6760.18
Babu & Angira (2007)	DE with GA	0.113	3695.6	6760.18
This work (2015)	SQP	0.015625	5460.0	9927.28

5. Conclusions

In this paper, an optimal design of thermal cracking (pyrolysis) reactor is studied. The optimization framework has been presented to tackle the optimal design and operation problem of pyrolysis reactor. The optimization problem formulation has been presented to give maximum economic index of such process. It has been carried out using a new alternative approach (the optimization problem was posed as a Non-linear programming (NLP) problem and was solved using a SQP method within gPROMS software). Based on the results obtained from this study using two cases (based upon ethylene production), it can be concluded that the operation depends mainly on the ethane and the fuel under process restriction to get maximum profit and maximum yield. As well as, the accurate process model of such reactor is namely depends on the solution methods in evaluating the control variables of the process so that the model can be effectively used for simulation, optimization and control. SQP is the most efficient in terms of function evaluations in dealing with process constraint problems. Finally, SQP method has been demonstrated to be able to give accurate results of feed flow rates with corresponding economic profit of 9927.28 $/h for whole process and gave highest profit (increased by 47%) and lowest CPU-time (reduced by 86%) in comparison with those obtained by previous studies.

References

B.V. Babu, R. Angira, 2001, *In Proceeding of International Symposium & 54th Annual Section of IICHE, Chennai*.

T.F. Edgar, D.M. Himmelblau, 2001, *Optimization of Chemical Processes*, McGraw-Hill Science.

D. Geddes, T. Kubera, 2000, Integration of planning and real-time optimization in olefins production, *Comput. Chem. Eng.,* 2-7, 24, 1645-1649.

A.T. Jarullah, I.M. Mujtaba, A.S. Wood, 2011, Kinetic Model Development and Simulation of Simultaneous Hydrodenitrogenation and Hydrodemetallization of Crude Oil in a Trickle-Bed Reactor, *Fuel*, 90, 2165-2181.

A.T. Jarullah, I.M. Mujtaba, A.S. Wood, 2012, Improving Fuel Quality by Whole Crude Oil Hydrotreating:A Kinetic Model for Hydrodeasphaltenization in a Trickle Bed Reactor, *Applied Energy*, 94, 182-191.

E. Joo, S. Park, M. Lee, 2001, Pyrolysis Reaction Mechanism for Industrial Naphtha Cracking Furnaces, *Ind. Eng. Chem. Res*., 40, 11, 2409-2415.

X. Lan, J. Gao, C. Xu, H. Zhang, 2007, Numerical simulation of transfer and reaction process in ethylene furnaces, *Trans. IChemE*, 85, A12, 1565-1579.

A.K.K. Lee, A.M. Aitani, 1990, Saudi ethylene plants move toward more feed flexibility, *Oil & Gas J.* 88, 60-63.

M. Masoumi, M. Shahrokhi, M. Sadrameli, J. Towfighi, 2006a, Modeling and Control of a naphtha Thermal Cracking Pilot Plant, *Ind. Eng. Chem. Res*., 45, 10, 3574-3582.

M. Masoumi, S.M. Sadrameli, J. Towfighi, A. Niaei, 2006b, Simulation, Optimization and Control of Thermal Cracking Pilot Plant Furnace, *Energy*, 31, 4, 516-527.

Krist V. Gernaey, Jakob K. Huusom and Rafiqul Gani (Eds.), 12th International Symposium on Process Systems Engineering and 25th European Symposium on Computer Aided Process Engineering.
31 May - 4 June 2015, Copenhagen, Denmark.

Representation of the Convex Envelope of Bilinear Terms in a Reformulation Framework for Global Optimization

Andreas Lundell[a] and Tapio Westerlund[a]

[a]*Optimization and Systems Engineering; Åbo Akademi University; Turku, Finland*
andreas.lundell@abo.fi

Abstract

Branch-and-bound in combination with convex underestimators constitute the basis for many algorithms in global nonconvex mixed-integer nonlinear programming (MINLP). Another option is to rely on reformulation-based techniques such as the α signomial global optimization (αSGO) algorithm, where power and exponential transformations for signomial or polynomial function and the α reformulation (αR) technique for general nonconvex twice-differentiable functions are used to reformulate the nonconvex problem. The transformations are approximated using piecewise linear functions (PLFs), resulting in a convex relaxation of the original nonconvex problem in an extended variable space. The solution to this reformulated problem provides a lower bound to the global minimum (of a minimization problem), and by iteratively refining the PLFs, the ε-global solution can be obtained. A drawback with many reformulation-based techniques is that known convex envelopes cannot directly be utilized. However, in this paper, a formulation for expressing the convex envelope of bilinear terms in the αSGO framework is described, and it is shown that this improves the tightness of the lower bound.

Keywords: Nonconvex global optimization, MINLP, reformulation framework, bilinear terms, signomial functions, convex envelope, αSGO algorithm, αR technique

1. Introduction

The αSGO algorithm as described in Lundell et al. (2013) can solve MINLP problems containing nonconvex constraints of signomial or general twice-differential type to ε-global optimality. The general formulation of applicable problem type is

$$\begin{aligned} &\text{minimize} && f(\mathbf{x}), \\ &\text{subject to} && \forall k \in K: \quad q_k(\mathbf{x}) + s_k(\mathbf{x}) + g_k(\mathbf{x}) \leq 0, \qquad s_k(\mathbf{x}) = \sum_{j \in J_k} c_j \prod_{i \in I} x_i^{p_{ji}}, \\ &&& \forall i \in I: \quad \underline{x}_i \leq x_i \leq \bar{x}_i, \end{aligned} \tag{1}$$

where the functions f and q are convex functions, s are nonconvex signomial functions and g are nonconvex twice-differentiable functions. A signomial function is a sum of positive or negative signomial terms, each made up by a product of power functions, *i.e.,* the c's and p's are real coefficients and powers respectively. This class of functions include also bilinear terms and in this paper these will be handled separately as described in Section 2. The variables $\mathbf{x} = [x_1, \ldots, x_I]$ can be integers or reals, so in the general form problem (1) is a MINLP problem. The variables in the signomial terms are assumed to be strictly positive, otherwise translations or other reformulations

are necessary, *cf.* Pörn et al. (1999). By using a simple reformulation, a problem with a nonlinear objective function f can also be rewritten in the form of problem (1) by including the constraint $f(\mathbf{x}) - \mu \leq 0$, with the variable μ being the new objective function of the reformulated problem. Nonlinear equality constraints $q_k(\mathbf{x}) + s_k(\mathbf{x}) + h_k(\mathbf{x}) = 0$ can be replaced by two inequality constraints with different signs.

In the αSGO algorithm, single-variable power and exponential transformations are used to obtain convex underestimators for nonconvex signomial functions and the transformations (represented as nonlinear equalities) are approximated by PLFs. The transformations are applied term-wise, so convex terms do not need to be convexified. For nonconvex twice-differentiable functions, quadratic convex spline functions overpowering all nonconvexities are added and linearizations through PLFs are subtracted. The result is a reformulated convex problem in an extended variable-space consisting of the original variables, transformation variables, and variables needed for the PLFs. The new problem is solved using a convex MINLP method such as Lundell et al. (2014), with the solution obtained being a lower bound to the nonconvex problem. By iteratively tightening the PLFs and resolving, the lower bound increases until all nonconvex constraints are fulfilled (to an ε-tolerance) and the global solution is found. No upper bound is needed in the algorithm.

1.1. Convex underestimation of signomial functions

Rules for the convexity of signomial terms have been presented in *e.g.,* Lundell (2009). For a positive signomial term, there are two separate cases: *(i)* all powers in the signomial term are negative, or *(ii)* all powers in the signomial term are negative except for one and the sum of the powers is greater than or equal to one. For a negative signomial term to be convex, all powers should be positive and their sum less than or equal to one. Based on these rules, it is possible to deduce the positive power transformation (PPT) and the mixed power and exponential transformation (MPET) for positive terms and the power transformation (PT) for negative terms. For more details see, *e.g.,* Lundell and Westerlund (2012).

1.2. Convexifying twice-differentiable constraints

In Lundell et al. (2013) the αR technique was described. In this method, the spline αBB convex underestimator from Meyer and Floudas (2005) is included in the SGO algorithm from Lundell and Westerlund (2012) for handling nonconvex twice-differentiable functions. A convex underestimator for a nonconvex function $g(\mathbf{x})$ is obtained by first adding a sum of convex quadratic spline functions S_i for each variable x_i and then subtracting a linearization W_i by the means of a PLF from the convexified function. Thus, the resulting reformulated constraint will be

$$g(\mathbf{x}) + \sum_{i \in I} S_i(x_i) - \widehat{S} \leq 0, \qquad \text{where} \qquad \widehat{S} = \sum_{i \in I} \text{PLF}\, S_i(x_i).$$

For fulfilling the convexity requirement, the coefficients of the quadratic terms in the splines must be positive and large enough so that the Hessian is positive semidefinite.

2. Including the McCormick underestimator in the reformulation framework

Instead of utilizing the signomial transformation strategies or the αR for reformulating bilinear terms, it is in this section described how the convex envelope for bilinear terms McCormick (1976) can be used in the αSGO framework. There are also other possible formulations available, see Wicaksono and Karimi (2008) for some variants, however the presented formulation utilizes the linearizations already available in the αSGO framework.

The convex envelope for a bilinear term $x_m x_n$ is given by the linear constraints

$$\begin{cases} w_{mn} \geq \underline{x}_m x_n + \underline{x}_n x_m - \underline{x}_m \underline{x}_n & (2) \\ w_{mn} \geq \overline{x}_m x_n + \overline{x}_n x_m - \overline{x}_m \overline{x}_n & (3) \end{cases} \qquad \begin{cases} w_{mn} \leq \overline{x}_m x_n + \underline{x}_n x_m - \overline{x}_m \underline{x}_n & (4) \\ w_{mn} \leq \underline{x}_m x_n + \overline{x}_n x_m - \underline{x}_m \overline{x}_n & (5) \end{cases}$$

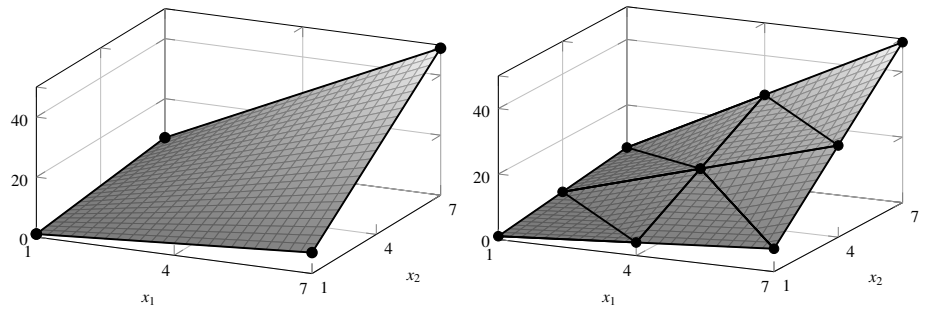

Figure 1: An illustration of the nonconvex term x_1x_2 on the interval $[1,7]\times[1,7]$ (*left*) and the piecewise convex envelope (underestimator) on the four regions $[1,4]\times[1,4]$, $[4,7]\times[1,4]$, $[1,4]\times[4,7]$ and $[4,7]\times[4,7]$ (*right*). The envelope in each region consists of the maximum of two planes.

on the box domain $[\underline{x}_m,\overline{x}_m]\times[\underline{x}_n,\overline{x}_n]$. For a positive term, the expressions (2) and (3) provide the lower bound and expressions (4) and (5) the upper bound, while the opposite is true for a negative bilinear term. Since all variables in bilinear terms are assumed to be positive in problem (1) no change of signs for the terms occur. An illustration of the underestimator is given in Figure 1.

To illustrate the difference in tightness of the convex underestimators mentioned earlier when applied to the bilinear term x_1x_2, the underestimation error of the MPET with exponential transformations only, the PPT (with transformation powers $Q_1=2$, $Q_2=-1$), the αR and the McCormick (MC) underestimator are shown in Figure 2 for two refinement levels of the PLFs. It is clear that including the McCormick underestimator for bilinear terms would render a tighter convex underestimator in the considered domain, and therefore we want to utilize this type of underestimator in the αSGO framework. In the framework, only the convex underestimator is required, so equations (2) and (3) or (4) and (5) are needed in the case of a positive or negative bilinear term respectively.

To partition the domain, some additional variables and expressions are required. The variables x_i and x_j are assumed to be partitioned in the intervals $[\omega_{m,1},\omega_{m,2}],[\omega_{m,2},\omega_{m,3}],\ldots,[\omega_{m,K_m-1},\omega_{m,K_m}]$, where $\omega_{m,1}=\underline{x}_m$, $\omega_{m,K_m}=\overline{x}_m$, and $[\omega_{n,1},\omega_{n,2}],[\omega_{n,2},\omega_{n,3}],\ldots,[\omega_{n,K_n-1},\omega_{n,K_n}]$, where $\omega_{n,1}=\underline{x}_n$, and $\omega_{n,K_n}=\overline{x}_n$, respectively. In other words, the variable x_m has the set of breakpoints $\{\omega_{m,1},\omega_{m,2},\ldots,\omega_{m,K_m}\}$ and x_n the set of breakpoints $\{\omega_{n,1},\omega_{n,2},\ldots,\omega_{n,K_n}\}$. With each of the breakpoint intervals a binary variable $b_{m,k}$ or $b_{n,k}$ and a real variable $s_{m,k}$ or $s_{n,k}$ are associated; these variables are zero if we are not in the corresponding interval. For the variable x_m (and equivalently for x_n) this can be expressed as

$$x_m=\sum_{k=1}^{K_m-1}\omega_{m,k}+\left(\omega_{m,k+1}-\omega_{m,k}\right)s_{m,k},\qquad \sum_{k=1}^{K_m-1}b_{m,k}=1, \tag{6}$$

$$\forall k=1,\ldots,K_m:\ 0\le s_{m,k}\le b_{m,k}. \tag{7}$$

These expressions can be reused for all bilinear terms containing x_m or other signomial transformations or αRs in the reformulated problem, *i.e.,* only one set of binaries $\{b_{m,k}\}_{k=1}^{K_m}$ and continuous variables $\{s_{m,k}\}_{k=1}^{K_m}$ are needed for each variable x_m involved in transformations in the problem.

For a positive term $w_{mn}=x_mx_n$, the piecewise McCormick underestimator should be defined by equation (2) in the unshaded regions in the left part of Figure 3, and by equation (3) in the shaded regions. For a negative bilinear term $w_{mn}=-x_mx_n$ equation (4) in the unshaded regions of the right part of Figure 3 and equation (5) in the shaded regions should be used instead. This requires the addition of a binary variable γ_{mn} for each unordered combination (m,n) in a bilinear term indicating if we are in the shaded domains or not. The expression (8) sets the values of γ_{mn} for a

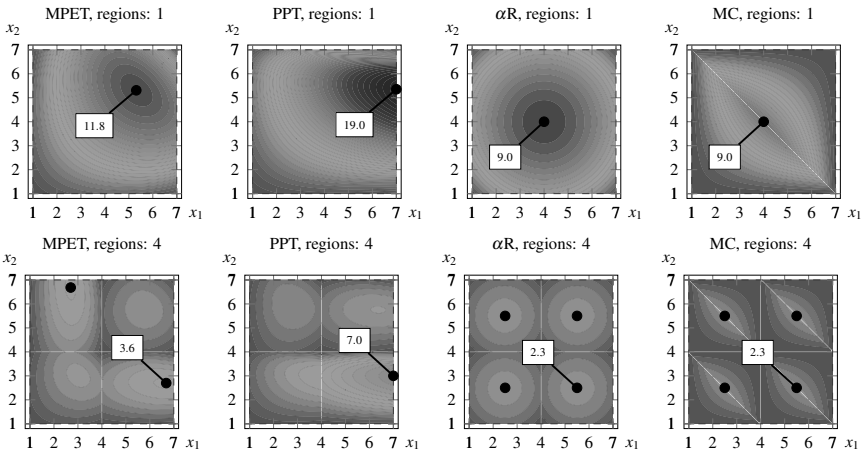

Figure 2: The underestimation error when underestimating the bilinear term x_1x_2 on the region $[1,7]\times[1,7]$ without extra partitioning (above) and with an extra breakpoint in the midpoint, *i.e.,* considering the regions $[1,4]\times[1,4]$, $[4,7]\times[1,4]$, $[1,4]\times[4,7]$ and $[4,7]\times[4,7]$ (below).

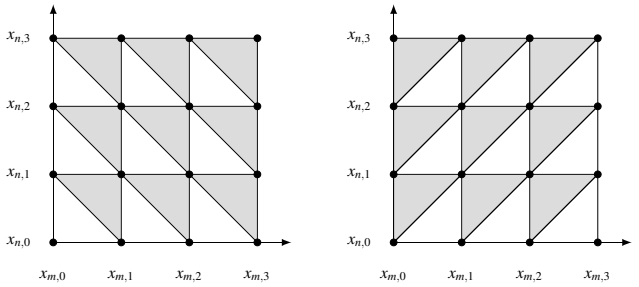

Figure 3: The shaded area indicates where the binary variable $\gamma_{mn}=1$ for a positive *(left)* or negative bilinear term *(right)*.

positive term $w_{mn}=x_mx_n$ and the expression (9) for a negative bilinear term $w_{mn}=-x_mx_n$:

$$s_{m,k_m}+s_{n,k_n}+b_{m,k_m}+b_{n,k_n}-3\leq\gamma_{mn}\leq s_{m,k_m}+s_{n,k_n}-b_{m,k_m}-b_{n,k_n}+2, \tag{8}$$
$$-s_{m,k_m}+s_{n,k_n}+b_{m,k_m}+b_{n,k_n}-2\leq\gamma_{mn}\leq+s_{m,k_m}+s_{n,k_n}-b_{m,k_m}-b_{n,k_n}+3. \tag{9}$$

Then, the underestimator for a positive term can be written $\forall k_m=1,\ldots,K_n-1\wedge k_n=1,\ldots,K_n-1$:

$$W_{mn}\geq\omega_{m,k_m}x_j+\omega_{n,k_n}x_i-\omega_{m,k_m}\omega_{n,k_n}+M_1\left(b_{m,k_m}+b_{n,k_n}-2\right)-M_1\gamma_{mn} \tag{10}$$
$$W_{mn}\leq\omega_{m,k_m}x_j+\omega_{n,k_n}x_i-\omega_{m,k_m}\omega_{n,k_n}-M_1\left(b_{m,k_m}+b_{n,k_n}-2\right)+M_1\gamma_{mn} \tag{11}$$
$$W_{mn}\geq\omega_{m,k_m+1}x_j+\omega_{n,k_n+1}x_i-\omega_{m,k_m+1}\omega_{n,k_n+1}+M_1\left(b_{m,k_m}+b_{n,k_n}-2\right)-M_1\left(1-\gamma_{mn}\right) \tag{12}$$
$$W_{mn}\leq\omega_{m,k_m+1}x_j+\omega_{n,k_n+1}x_i-\omega_{m,k_m+1}\omega_{n,k_n+1}-M_1\left(b_{m,k_m}+b_{n,k_n}-2\right)+M_1\left(1-\gamma_{mn}\right) \tag{13}$$
$$W_{mn}\leq M_2b_{m,k_m} \tag{14}$$

$$W_{mn} \leq M_2 b_{n,k_n} \tag{15}$$
$$0 \leq W_{mn} \leq M_2 \tag{16}$$
$$M_1 = \max\left\{\omega_{m,k_m}\omega_{n,k_n+1} + \omega_{n,k_n}\omega_{m,k_m+1} - \omega_{m,k_m}\omega_{n,k_n}, \omega_{m,k_m+1}\omega_{n,k_n+1}\right\} \tag{17}$$
$$M_2 = \omega_{m,k_m+1}\omega_{n,k_n+1}. \tag{18}$$

Here M_1 and M_2 are calculated parameters. The expressions (10) and (11) give the correct value for the underestimator if $\gamma_{mn} = 0$, *i.e.,* if we are in the lower left part of the box $[\omega_{m,k_m}, \omega_{m,k_{m+1}}] \times [\omega_{n,k_n}, \omega_{n,k_{n+1}}]$. If $\gamma_{mn} = 1$, *i.e.,* if we are in the upper right part of the same box expressions (12) and (13) are active. Expressions (14) and (15) make sure that the variable W_{mn} is zero if we are in another region, *i.e.,* if not both b_{m,k_m} and b_{n,k_n} are equal to one.

The corresponding expressions for a negative term are $\forall k_m = 1,\ldots,K_m - 1 \wedge k_n = 1,\ldots,K_n - 1$:

$$W_{mn} \geq \omega_{m,k_m+1}x_j + \omega_{n,k_n}x_i - \omega_{m,k_m+1}\omega_{n,k_n} + M_1\left(b_{m,k_m} + b_{n,k_n} - 2\right) - M_2\gamma_{mn} \tag{19}$$
$$W_{mn} \leq \omega_{m,k_m+1}x_j + \omega_{n,k_n}x_i - \omega_{m,k_m+1}\omega_{n,k_n} - M_1\left(b_{m,k_m} + b_{n,k_n} - 2\right) + M_2\gamma_{mn} \tag{20}$$
$$W_{mn} \geq \omega_{m,k_m}x_j + \omega_{n,k_n+1}x_i - \omega_{m,k_m}\omega_{n,k_n+1} + M_1\left(b_{m,k_m} + b_{n,k_n} - 2\right) - M_2\left(1 - \gamma_{mn}\right) \tag{21}$$
$$W_{mn} \leq \omega_{m,k_m}x_j + \omega_{n,k_n+1}x_i - \omega_{m,k_m}\omega_{n,k_n+1} - M_1\left(b_{m,k_m} + b_{n,k_n} - 2\right) + M_2\left(1 - \gamma_{mn}\right) \tag{22}$$
$$W_{mn} \leq M_2 b_{m,k_m} \tag{23}$$
$$W_{mn} \leq M_2 b_{n,k_n} \tag{24}$$
$$0 \leq w_{mn} \leq M_2. \tag{25}$$

The parameters M_1 and M_2 are the same as in the positive case. Expressions (19) and (20) gives the correct value for the underestimator if $\gamma_{mn} = 0$, *i.e.,* if we are in the lower right part of the box $[\omega_{m,k_m}, \omega_{m,k_{m+1}}] \times [\omega_{n,k_n}, \omega_{n,k_{n+1}}]$. If $\gamma_{mn} = 1$, *i.e.,* if we are in the upper left part of the same box, expressions (21) and (22) are active. Expressions (23) and (24) make sure that the variable W_{mn} is zero if we are in another region, *i.e.,* if not both b_{m,k_m} and b_{n,k_n} are equal to one.

Replacing a bilinear term $c \cdot x_m x_n$ ($c \in \mathbb{R}$) in the nonconvex function with $c \cdot W_{mn}$ and including expressions (8) and (10–16) if the term is positive or the expressions (9) and (19–25) if the term is negative as well as expressions (6) and (7) will render a reformulated convex problem whose solution is a lower bound to the global solution. The same expressions can be reused if the bilinear variable occurs in several constraints. The same is true for expressions (6) and (7) if the variables in the bilinear term are transformed using either signomial transformation strategies or αRs.

3. Computational comparisons

In Table 3, a comparison on the lower bounds of some reformulated and convexified problems from Floudas and Pardalos (1999) containing signomial and bilinear terms is given. When the formulation for bilinear terms in Section 2 is not used for the bilinear terms, the MPET with exponential transformations only is used to convexify all positive signomial terms including the bilinear ones. The PT transformation is used for negative signomial terms. The results are also compared to using the αR for reformulating all terms (including the signomial and bilinear terms) and αR for signomials only with the MC formulation for bilinear terms. Also the global solution is presented to illustrate the tightness of the convex underestimators. The reformulated problems were solved using the convex MINLP solver αECP available in GAMS. Obviously, the MC formulation gives a tighter or equally tight convex underestimation as the other underestimation methods. However, since bilinear terms are not present solely in the objective function of the test problems, the impact of the tightness of the convex underestimation may vary from problem to problem. The results also indicate (especially in the last two problems) that the αR may give a very bad underestimator compared to the signomial transformation strategies when applied to signomials.

Table 1: The obtained initial lower bounds of some problems from Floudas and Pardalos (1999) containing signomial and bilinear terms. The bold values indicate the tightest underestimator of the compared ones.

Problem	MPET + PT	MPET + PT + MC	αR	αR + MC	Global solution
7.2.1	1057.4	**1094.4**	1070.3	1090.7	1227.2
7.2.2	-0.9093	**-0.7028**	-1.0000	**-0.7028**	-0.3888
7.2.4	0.6376	**1.1774**	-9.7655	-9.7655	3.9511
7.2.5	9546.8	**9687.7**	9578.7	9669.3	10122
7.2.6	-96.073	**-95.962**	-99.845	-99.845	-83.254
7.2.7	-8.2734	**-7.5827**	-80.649	-80.649	-5.7398
7.2.8	-9.8008	**-9.4017**	-8741.3	-8741.3	-6.0482

4. Conclusions

In this paper it was shown how a convex envelope for bilinear terms can be included in the αSGO reformulation framework for signomial problems. This further extends the available set of transformations that can be utilized for reformulating nonconvex problems in the αSGO algorithm. Being tighter than the signomial transformations, the McCormick underestimators will give a higher, and thus better, lower bound, as was illustrated by solving some test problems. It is also possible to include convex envelopes and special convex underestimators for other types of functions, *e.g.,* trilinear terms, but this needs to be investigated further.

5. Acknowledgment

Support from the Foundation of Åbo Akademi University, as part of the grant for the Center of Excellence in Optimization and Systems Engineering, is gratefully acknowledged. The first author also acknowledges the financial support received from the Ruth och Nils-Erik Stenbäck foundation.

References

Floudas, C. A., Pardalos, P. M., 1999. Handbook of Test Problems in Local and Global Optimization. Vol. 33 of Nonconvex Optimization and Its Applications. Kluwer Academic Publishers.

Lundell, A., 2009. Transformation techniques for signomial functions in global optimization. Ph.D. thesis, Åbo Akademi University.

Lundell, A., Kronqvist, J., Westerlund, T., 2014. An extended supporting hyperplane algorithm for convex MINLP problems. In: XII Global Optimization Workshop. pp. 21–24.

Lundell, A., Skjäl, A., Westerlund, T., 2013. A reformulation framework for global optimization. Journal of Global Optimization 57 (1), 115–141.

Lundell, A., Westerlund, T., 2012. Global optimization of mixed-integer signomial programming problems. In: Lee, J., Leyffer, S. (Eds.), Mixed Integer Nonlinear Programming. Vol. 154 of The IMA Volumes in Mathematics and its Applications. Springer New York, pp. 349–369.

McCormick, G. P., 1976. Mathematical programming computability of global solutions to factorable nonconvex programs: Part i – convex underestimating problems. Mathematical Programming 10, 147–175.

Meyer, C. A., Floudas, C. A., 2005. Convex underestimation of twice continuously differentiable functions by piecewise quadratic perturbation: Spline αBB underestimators. Journal of Global Optimization 32 (2), 221–258.

Pörn, R., Harjunkoski, I., Westerlund, T., 1999. Convexification of different classes of non-convex MINLP problems. Computers and Chemical Engineering 23, 439–448.

Wicaksono, D. S., Karimi, I. A., 2008. Piecewise MILP under- and overestimators for global optimization of bilinear programs. AIChE Journal 54 (4), 991–1008.

Krist V. Gernaey, Jakob K. Huusom and Rafiqul Gani (Eds.), 12th International Symposium on Process Systems Engineering and 25th European Symposium on Computer Aided Process Engineering.
31 May - 4 June 2015, Copenhagen, Denmark.

Interactive Multi-Objective Decision-Support for the Optimization of Nonlinear Dynamic (Bio)Chemical Processes with Uncertainty

Mattia Vallerio[a], Jan Hufkens[a], Jan Van Impe[a] and Filip Logist[a]

[a]*KU Leuven, Department of Chemical Engineering, BioTeC+ & OPTEC, Leuven, Belgium*
Filip.Logist@cit.kuleuven.be

Abstract

The manufacturing industry is faced with the challenge to constantly improve its processes under more and more stringent conditions, e.g., due to more strict environmental policies, lower profit margins and increased societal awareness. These three aspects are considered as the pillars of *sustainable development* and typically give rise to multiple and conflicting objectives. Hence, any decision taken will require trade-offs to be evaluated and compromises to be made. To support decision making, in this work an interactive multi-objective software framework is presented to systematically optimize nonlinear dynamic systems based on mathematical models. In particular, a numerically efficient strategy to account for parametric uncertainty, based on the Sigma Point method, is introduced allowing directly minimizing the operational risk. Consequently, the proposed software can provide sound decision-support for dynamic process optimization under uncertainty. The framework is tested on a three-objective case study of a fed-batch reactor.

Keywords: dynamic nonlinear optimization, uncertainty quantification, interactive multi-objective optimization

1. Introduction

The increased awareness towards societal (e.g., increase safety, maintain occupational level) and environmental aspects (e.g., reduce energy consumption and emissions) of public institutions has put great pressure on the manufacturing industry. Mathematical process models and model based optimization methods have over the years improved the economic sustainability (e.g., maximize profit or production). However, dedicated instruments: (i) to systematically include the societal and environmental impact in optimization studies, (ii) to quantify the *trade-offs* between conflicting objectives, (iii) to propose several alternatives for improvement and (iv) to make sound decisions for operating industrial processes under uncertainty, are scarce. However, model based methods are always afflicted by model related and also by external uncertainties (e.g., Sahinidis (2004)). When dealing with inherent uncertainty in dynamic processes and models, mainly two different strategies are used: (i) a *probabilistic approach* with the formulation of expected values and chance constraints (e.g., Wendt et al. (2002); Recker et al. (2012); Li et al. (2008)) or, (ii) a *worst case scenario approach* with the formulation of min-max optimization problems (e.g., Nagy and Braatz (2004); Houska and Diehl (2009); Houska et al. (2012)).

By directly accounting for uncertainty in optimization problems, an increased level of robustness is achieved. Unfortunately, this increased robustness is usually accompanied by a loss of performance (Datskov et al. (2006)). Hence, a trade-off between robustness and performance is introduced. This aspect can be studied via multi-objective optimization (Miettinen (1999)) as suggested

in Logist et al. (2011). However, robustness was not directly considered as one of the objective functions. Moreover, apart from the uncertainty and the multi-objective aspect, it has to be noted that optimizing the dynamic process operation already leads to dynamic optimization problems, which after discretization result in large-scale Nonlinear Programmming Problems (NLPs).

In this paper, a novel interactive adaptation of scalarization based multi-objective optimization algorithms (Marler and Arora (2004); Das and Dennis (1998); Sanchis et al. (2008)) is proposed along with a Graphical User Interface (GUI) for the systematic evaluation of the trade-offs arising between multiple and conflicting objectives in nonlinear dynamic optimization problems under uncertainty. The uncertainty is tackled in a computationally tractable way via the *Sigma Point* method (Julier and Uhlmann (1996)). Several contributions are combined in the novel tool *Pareto Browser*: (i) development of an interactive algorithm for high dimensional multi-objective optimization problems, (ii) development of a tailored GUI for the interactive solution and visualization of dynamic optimization problems under uncertainty, (iii) formulation of dynamic optimization problems under uncertainty to consider robustness as an objective function and (iv) efficient solution of the resulting large-scale optimization problems. The article is structured as follows: Section 2 introduces a generic problem formulation, gives a brief introduction to the Sigma Point method and defines the proposed reformulation. Then, Section 3 introduces the framework *Pareto Browser* and the GUI via the solution of a three-objective dynamic optimization problem under uncertainty.

2. Mathematical formulation

Generally, a multi-objective dynamic optimization problem with uncertainty can be formulated as:

$$\min_{\mathbf{x}(\xi),\mathbf{u}(\xi),\xi_\mathrm{f}} \{J_1, J_2, \ldots J_\mathrm{m}\}, \tag{1}$$

$$\text{subject to: } \frac{d\mathbf{x}}{d\xi} = \mathbf{f}(\mathbf{x}(\xi),\mathbf{u}(\xi),\xi,\mathbf{p},\lambda), \tag{2}$$

$$\mathbf{0} = \mathbf{b}_\mathrm{c}(\mathbf{x}(0),\mathbf{p},\lambda), \tag{3}$$

$$\mathbf{0} \geq \mathbf{c}_\mathrm{p}(\mathbf{x}(\xi),\mathbf{u}(\xi),\xi,\mathbf{p},\lambda), \tag{4}$$

$$\mathbf{0} \geq \mathbf{c}_\mathrm{t}(\mathbf{x}(\xi_\mathrm{f}),\xi_\mathrm{f},\mathbf{p},\lambda). \tag{5}$$

Here, $\mathbf{x}$ are the state variables, while $\mathbf{u}$ and $\mathbf{p}$ denote the time-varying and time-constant control variables. Moreover, λ represents the vector of uncertain parameters. The vector $\mathbf{f}$ represents the dynamic system equations (on the interval $\xi \in [0,\xi_\mathrm{f}]$) with initial conditions given by the vector $\mathbf{b}_\mathrm{c}$. In particular $\mathbf{f}$ comprises Ordinary Differential Equations (ODE) but extensions to Differential Algebraic Equations (DAE) and Partial Differential Equations (PDE) are possible. The vectors $\mathbf{c}_\mathrm{p}$ and $\mathbf{c}_\mathrm{t}$ indicate path and terminal inequality constraints on the states and controls.

This work introduces a low computational methodology and gives the possibility to directly consider robustness as an objective function. The uncertainty is quantified via the Sigma Point method (Julier and Uhlmann (1996)). The Sigma Point method allows to efficiently approximate probability distributions through any nonlinear transformation. The method is centred on the intuitive notion of approximating the resulting distribution via the propagation of a fixed number of selected samples from the parameter distribution, i.e., the *sigma points* π_i, rather than approximate an arbitrary nonlinear function. In this case, the sigma points are the nominal parameter values for the uncertain parameters (i.e., $\lambda = \pi_0$) and $2n_\lambda$ deviations (i.e., $\lambda = \pi_i$ for $i = 1,\ldots,2n_\lambda$ where n_λ is the number of uncertain parameters) which are calculated as in Julier and Uhlmann (1996). These Sigma Points are propagated through the nonlinear dynamic system and give rise to an equivalent number of outputs. The outputs are then used to compute the *expected value* and *variance-covariance* matrix of the state variables, constraints and objective functions.

The introduction of the *expected value* for the considered objective functions $\bar{J}_\mathrm{i}$ and the more critical constraints $\bar{\mathbf{c}}_{\mathrm{p,j}}$ and $\bar{\mathbf{c}}_{\mathrm{t,j}}$ allows to reformulate the multi-objective dynamic optimization problem under uncertainty as follows:

$$\min_{\mathbf{x}_\mathrm{i}(\xi),\mathbf{u}(\xi),\xi_\mathrm{f}} \left\{\bar{J}_1,\bar{J}_2,\ldots\bar{J}_\mathrm{m},-\alpha_{\mathrm{c_p}},-\alpha_{\mathrm{c_t}}\right\}, \tag{6}$$

$$\text{subject to: } \frac{d\mathbf{x}_\mathrm{i}}{d\xi} = \mathbf{f}(\mathbf{x}_\mathrm{i}(\xi),\mathbf{u}(\xi),\xi,\mathbf{p},\pi_\mathrm{i})\ \xi\in[0,\xi_\mathrm{f}], \tag{7}$$

$$\mathbf{0} = \mathbf{b}_\mathrm{c}(\mathbf{x}_\mathrm{i}(0),\mathbf{p},\pi_\mathrm{i}),\ \text{with i} = 0,\ldots,2\mathrm{n}_\lambda, \tag{8}$$

$$\mathbf{0} \geq \bar{\mathbf{c}}_{\mathrm{p,j}} + \alpha_{\mathrm{c_p}}\sqrt{\mathbf{P}_{\mathrm{c_p,jj}}},\quad \text{for j} = 1,\ldots,\mathrm{n}_{\mathrm{c_p}}, \tag{9}$$

$$\mathbf{0} \geq \bar{\mathbf{c}}_{\mathrm{t,j}} + \alpha_{\mathrm{c_t}}\sqrt{\mathbf{P}_{\mathrm{c_t,jj}}},\quad \text{for j} = 1,\ldots,\mathrm{n}_{\mathrm{c_t}}. \tag{10}$$

where $\mathbf{P}_{\mathrm{c_p,jj}}$ and $\mathbf{P}_{\mathrm{c_t,jj}}$ represent the diagonal element of the *variance-covariance* matrix of the constraints $\bar{\mathbf{c}}_{\mathrm{p,j}}$ and $\bar{\mathbf{c}}_{\mathrm{t,j}}$. Moreover, Eqs. (9)-(10) are formulated as *single chance* constraints. These constraints are approximately described by the Probability Density Function (PDF):

$$\Pr\left(\bar{\mathbf{c}}_{\mathrm{p,j}} + \alpha_{\mathrm{c_p}}\sqrt{\mathbf{P}_{\mathrm{c_p,jj}}} \geq \mathbf{0}\right) \leq A, \tag{11}$$

which defines the probability associated with the non-violation of the *single chance* constraints in Eqs. (9)-(10). $\alpha_{\mathrm{c_p}}$ and $\alpha_{\mathrm{c_t}}$ are *back-off* parameters and define the level of robustness of the *single chance* constraint by modifying the confidence level A. Moreover, if the PDF of the constraints is assumed to be normal then the parameters $\alpha_{\mathrm{c_p}}$ and $\alpha_{\mathrm{c_t}}$ can be interpreted as the quantiles of the Gaussian distribution. Hence, if, e.g., $\alpha_{\mathrm{c_p}} = 1.96$ then $A = 95\%$ in Eq. (11). The assumption of normality on the PDF of the constraints can be checked, e.g., via Monte Carlo simulations. In this work the parameters $\alpha_{\mathrm{c_p}}$ and $\alpha_{\mathrm{c_t}}$ will be taken as objective functions. This allows directly quantifying the trade-offs between increasing robustness of the solution and the other objectives.

3. Interactive multi-objective dynamic optimization under uncertainties

Scalarization methods reformulate the existing multi-objective optimization problem into a parametric single-objective optimization problem. By consistently varying the scalarization parameters (often called *weights* $\mathbf{w}$) an approximation of the Pareto set is obtained. However, the computation of the entire set could become expensive especially for nonlinear large-scale systems as typically occur in the (bio)chemical industry. Moreover, as the decision-maker is often only interested in a specific part of the Pareto front, an interactive algorithm for the progressive exploration of the Pareto set is introduced along with a dedicated Graphical User Interface (GUI).

3.1. Developed framework: The Pareto Browser

The proposed framework is developed within the programming language Python. Fig. 1 reports the framework schematically. As multi-objective optimization methods, the weighted sum (WS), normal boundary intersection (NBI) and enhanced normalized normal constraint (ENNC) methods are adopted. The scalarization parameter values or weights are initially generated automatically to enable a first coarse exploration of the criterion space, while afterwards they are adapted interactively. The exact features and GUI will be illustrated in the next

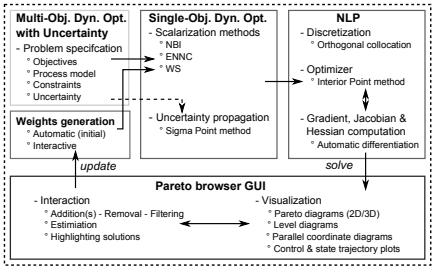

Figure 1: *Pareto Browser*'s schematic overview.

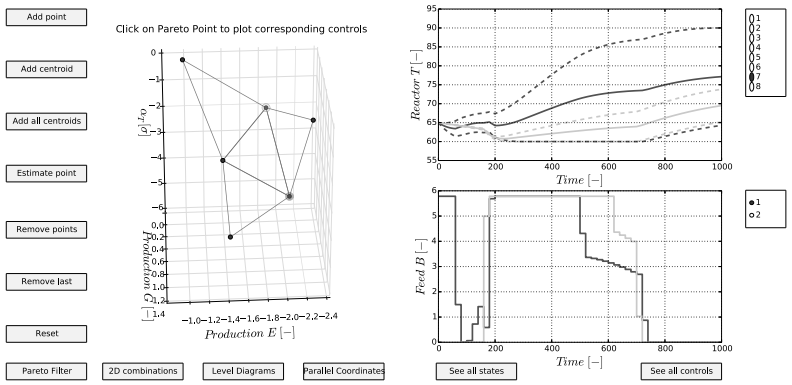

Figure 2: *Pareto Browser* applied to a three-objective case. Two points on the Pareto front (left) are highlighted and corresponding state (top right) and control (bottom right) profiles are plotted.

section based on a case study. To enable a computationally tractable uncertainty propagation through the optimization problem the Sigma Point method is exploited. To tackle the dynamic optimization problem an orthogonal collocation approach is employed delivering a large-scale NLP that is solved using the interior point optimizer IPOPT (Wächter and Biegler (2006)). Exact derivative information (i.e., gradients, Jacobians and Hessians) is provided through efficient automatic differentiation techniques (Andersson et al. (2012)). It has to be stressed that any model based optimization problem with multiple objectives can be tackled with the proposed framework, as long as it can be described as an NLP.

3.2. Case study: a fed-batch reactor with uncertain parameters

The Williams-Otto fed-batch reactor is considered. The following reaction scheme takes place in the reactor: $A+B \rightarrow C$, $C+B \rightarrow P+E$ and $P+C \rightarrow G$. A is initially present in the reactor and B is fed. The compounds P and E are useful products, whereas G is an undesired by-product. The jacket temperature can be manipulated. For the sake of brevity, the reader is referred to Logist et al. (2012) for the detailed model. The problem is formulated with the introduction of a *single chance* constraint (Eq. (12)) on the reactor temperature to account for the uncertainty on two parameters (with standard deviation of 10% from their nominal value) the feed temperature T_{F} and the heat transfer coefficient l_1 between the reactor and the cooling jacket. The *single chance* constraint is formulated via the Sigma Point method:

$$60\ ^{\circ}\mathrm{C} \leqslant \bar{T} - \alpha_{\mathrm{T}}\sqrt{\mathbf{P}_{\mathrm{T}}}, \quad \bar{T} + \alpha_{\mathrm{T}}\sqrt{\mathbf{P}_{\mathrm{T}}} \leqslant 90\ ^{\circ}\mathrm{C}. \tag{12}$$

Three objectives are defined in Eq. (13): (i) the maximization of product E, (ii) the minimization of waste product G, and (iii) the minimization of operational risks, i.e., the maximization of α_{T}.

$$J_1 = -x_E(t_{\mathrm{f}})V(t_{\mathrm{f}}), \qquad J_2 = x_G(t_{\mathrm{f}})V(t_{\mathrm{f}}), \qquad J_3 = -\alpha_{\mathrm{T}}. \tag{13}$$

The presented multi-objective dynamic optimization problem under uncertainty constitutes of 50 ODEs. The problem is subsequently reformulated into an NLP via orthogonal collocation with 50 piecewise constant intervals for the controls. The resulting NLP presents 8100 decision variables, 8000 equality and 300 inequality constraints. The solution of one NLP corresponds to a Pareto point and it is achieved in less than 10 s enabling real-time decision-making. Fig. 2 depicts the screenshot that appears when a multi-objective dynamic optimization problem under uncertainty is solved with the *Pareto Browser*. The decision-maker can click on interesting points in the left part.

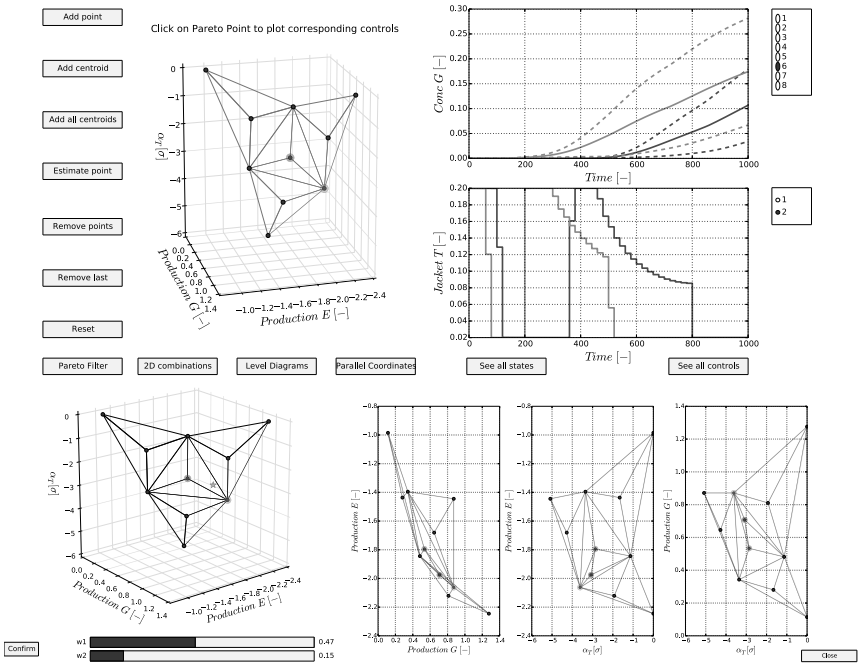

Figure 3: The centroids of all displayed simplices are added (top). Decision-support window for adding a point (bottom left). 2D plots with the three possible non-ordered combinations of two objective functions (bottom right).

These points will then be highlighted in the Pareto front while the corresponding state and control profiles will be depicted with matching colors in the right part (see Fig. 2). The confidence region associated with the value of the *back-off* parameter α_T is plotted with a dashed line for each of the state profiles as can be seen in the right part of Fig. 2. The different robustness levels adopted for the two points induce a difference in the reactor temperature profile T. In fact, the confidence region related to the solution highlighted in dark gray is much larger than the one corresponding to the Pareto point identified with a light gray color. Hence, a lower operational risk is achieved when the batch reactor is run according to the Pareto point highlighted in dark gray. The *radio buttons* on the right allow visualizing different states and controls. The amount of *radio buttons* is given by structure of the investigated case study, i.e., for this case eight states and two controls. Additionally, the Pareto set is divided into simplices. The collection of simplices is updated when a new solution is added or removed. This is achieved by clicking on one of the buttons on the left side of the left graph in Fig. 2. The simplicial discretization allows for a better understanding of the relation between different solutions and to add points in a systematic way, e.g., by adding the centroids of all displayed simplices (see top graph in Fig. 3). Dedicated decision-support windows are deployed to decide the desired location of the point to be added (see bottom left plot in Fig. 3). By moving the sliders, the position of the new point (orange star), changes. When the position is satisfactory to the decision-maker an optimization problem is solved by clicking on the *Confirm* button. Several visualization strategies are available (see bottom right plot in Fig. 3) and can be exploited to gain further insight in the achieved solution. Finally, it is possible to simultaneously visualize all states and controls in one single plot to verify that all the preferences of the decision-maker are correctly satisfied.

4. Conclusion

This work introduces the *Pareto Browser*, a novel interactive decision-support system for multi-objective optimization of nonlinear (dynamic) processes with uncertainty. The tool features: (i) an interactive algorithm for multi-objective optimization problems, (ii) a tailored GUI that allows to seamlessly exploit the algorithm's features, (iii) the use of interactive visualization strategies to enhance the understanding of the solutions, and (iv) a computationally efficient formulation for multi-objective (dynamic) optimization problems under uncertainty. The proposed formulation exploits the Sigma Point method to systematically account for parametric model uncertainty in the optimization problem. Hence, it increases the robustness of the solution by reducing the operational risk. The operational risk can be considered as an additional objective function enabling a direct *trade-off* evaluation between reducing operational risk and, e.g., productivity and/or energy consumption. Finally, the *Pareto Browser* is tested on a fed-batch dynamic optimization problem with two uncertain parameters and three objective functions. The *trade-offs* between the considered objective functions were correctly quantified while no additional computational time was spent in uninteresting parts of the Pareto set.

Acknowledgments:
MV has a PhD grant of the IWT-Flanders. JVI holds the chair Safety Engineering sponsored by essenscia. The research was supported by KU Leuven: PFV/10/002 (OPTEC), the Research Foundation Flanders (FWO): FWO KAN2013 1.5.189.13 & FWO-G.0930.13; and the BelSPO: IAP VII/19 (DYSCO).

References

Andersson, J., Åkesson, J., Diehl, M., 2012. CasADi – A symbolic package for automatic differentiation and optimal control. In: Recent Advances in Algorithmic Differentiation. Vol. 87 of Lecture Notes in Computational Science and Engineering. Springer Berlin Heidelberg, pp. 297–307.

Das, I., Dennis, J., 1998. Normal-Boundary Intersection: A new method for generating the Pareto surface in nonlinear multicriteria optimization problems. SIAM Journal on Optimization 8, 631–657.

Datskov, I., Ostrovsky, G., Achenie, L., Volin, Y., 2006. An approach to multicriteria optimization under uncertainty. Chemical Engineering Science 61, 2379 – 2393.

Houska, B., Diehl, M., 2009. Robust nonlinear optimal control of dynamic systems with affine uncertainties. In: Proceedings of the 48th IEEE Conference on Decision and Control (CDC09). Shanghai (China), pp. 2274–2279.

Houska, B., Logist, F., Van Impe, J., Diehl, M., 2012. Robust optimization of nonlinear dynamic systems with application to a jacketed tubular reactor. Journal of Process Control 22, 1152–1160.

Julier, S., Uhlmann, J., 1996. A general method for approximating nonlinear transformations of probability distributions. Tech. rep., Robotics Research Group, Department of Engineering Science, University of Oxford.

Li, P., Arellano-Garcia, H., Wozny, G., 2008. Chance constrained programming approach to process optimization under uncertainty. Computers and Chemical Engineering 32, 25 – 45.

Logist, F., Houska, B., Diehl, M., Van Impe, J., 2011. Robust multi-objective optimal control of uncertain (bio)chemical processes. Chemical Engineering Science 66, 4670 – 4682.

Logist, F., Vallerio, M., Houska, B., Diehl, M., Van Impe, J., 2012. Multi-objective optimal control of chemical processes using ACADO toolkit. Computers and Chemical Engineering 37, 191–199.

Marler, R., Arora, J., 2004. Survey of multi-objective optimization methods for engineering. Structural and Multidisciplinary Optimization 26, 369–395.

Miettinen, K., 1999. Nonlinear multiobjective optimization. Kluwer Academic Publishers, Boston.

Nagy, Z., Braatz, R., 2004. Open-loop and closed-loop robust optimal control of batch processes using distributional and worst-case analysis. Journal of Process Control 14, 411–422.

Recker, S., Kühl, P., Diehl, M., Bock, H., 2012. Sigmapoint approach for robust optimization of nonlinear dynamic systems. In: Proceeding of SIMULTECH 2012. pp. 199–207.

Sahinidis, N., 2004. Optimization under uncertainty: state-of-the-art and opportunities. Computers and Chemical Engineering 28, 971–983.

Sanchis, J., Martinez, M., Blasco, X., Salcedo, J., 2008. A new perspective on multiobjective optimization by enhanced normalized normal constraint method. Structural and Multidisciplinary Optimization 36, 537–546.

Wächter, A., Biegler, L., 2006. On the implementation of a primal-dual interior point filter line search algorithm for large-scale nonlinear programming. Mathematical Programming 106, 25–27.

Wendt, M., Li, P., Wozny, G., 2002. Nonlinear chance-constrained process optimization under uncertainty. Industrial and Engineering Chemistry Research 41, 3621–3629.

Krist V. Gernaey, Jakob K. Huusom and Rafiqul Gani (Eds.), 12th International Symposium on Process Systems Engineering and 25th European Symposium on Computer Aided Process Engineering.
31 May – 4 June 2015, Copenhagen, Denmark

Superstructure Optimisation of a WaterMinimisation Network with an Embedded Multi-Contaminant Electrodialysis Model

Chiedza D. Nezungai, Thokozani Majozi*

School of Chemical and Metallurgical Engineering, University of the Witwatersrand, 1 Jan Smuts Ave, Johannesburg, 2001, South Africa
thokozani.majozi@wits.ac.za

Abstract

The water-energy nexus considers the relationship between water and energy resources. The increase in environmental regulations and social pressures has made it necessary to develop processes that are conservative with respect to both these resources. This work outlines the development of an optimisation model of a water network comprised of water sources, water sinks and an electrodialysis unit for the partial purification of contaminated water. The optimisation model is based on a superstructure framework, where the objective is to minimise freshwater consumption, wastewater production, energy consumption and the operating and capital costs involved in the process integration. A comparison was done between the developed model and the more common black box model, which simplifies regeneration units to linear expressions. The results show that the black box approach can lead to inaccuracies of up to 85% in the costing of regeneration units. Furthermore, it is shown that there are significant environmental and financial benefits in the simultaneous minimisation of water and energy in water networks.

Keywords: Water-energy nexus, water minimisation, mathematical modelling

1. Introduction

In the realm of process integration, water minimisation involves the interaction of process units in a system with the goal of reducing the amount of freshwater consumed and/or the amount of wastewater produced by the individual units and the entire system. This can be achieved by either reusing or recycling effluent produced, in conjunction with partial treatment or regeneration of contaminated water. Partial purification can be achieved by membrane processes, such as electrodialysis, reverse osmosis, and ultrafiltration, as well as non-membrane processes, such as stream stripping or using ion exchange resins. The choice of which minimisation approach to adopt must be informed by the nature of the processes involved and the cost of regeneration.

Water purification is an energy intensive process. As such, it is necessary to minimise the amount of energy required to treat effluent in a water network. The treatment process considered in this work is electrodialysis (ED). The process of ED, depicted in Figure 1, involves electromigration of ionic species across selectively permeable and alternately charged membranes. This results in the formation of a highly concentrated concentrate stream, and a diluate stream with a low contaminant concentration.

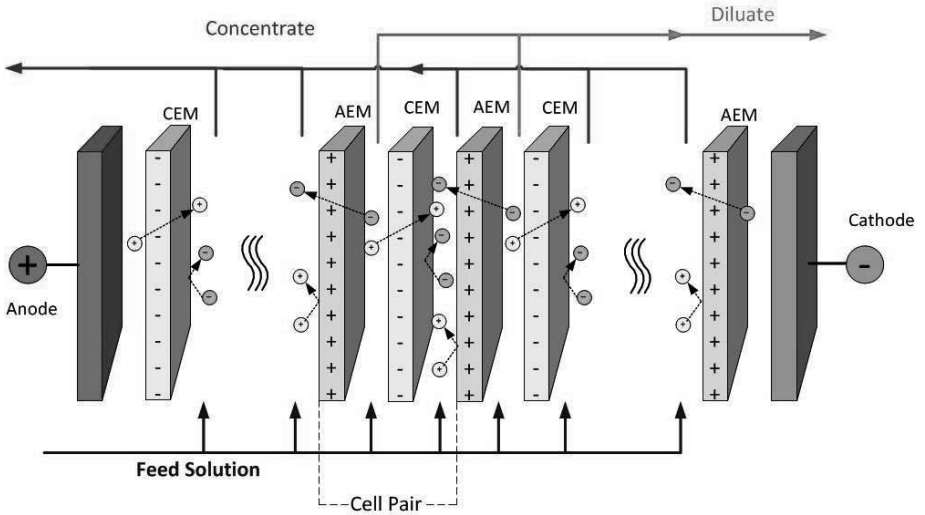

Figure 1: Schematic diagram of a single stage electrodialysis unit comprised of multiple cell pairs

Different approaches to ED modelling exist, including the convective-diffusion model, and the fixed flowrate design model. The latter was adopted in this work, owing to its simplicity and ease of integration. An ED design model was developed by Lee et al (2002) for single contaminant systems, to determine the area, current and voltage involved in desalination. This model was applied by Tsiakis and Papageorgiou (2005), to optimise the capital cost and energy consumption. It was also validated against experimental work by Brauns et al., (2009). In this work, a reformulation that allows the optimisation of multi-contaminant systemsis proposed. This involves the introduction of expressions for equivalent concentration and equivalent conductivity, taking into account the complex nature of ionic mixtures.

There are two major approaches adopted in water minimisation, namely, graphical and mathematical optimisation techniques. In this case, the mathematical optimisation approach was adopted, using the superstructure method. This approach allows the processing of complex systems containing multiple contaminants, as well as the capability to conveniently integrate the water network model with a regenerator model.(Khor et al., 2011).

In many of the water network superstructure models to date, regeneration units are represented by a simplified linear expression of the unit performance. The disadvantage of this approach is that it does not provide an accurate representation of the cost of the water network. In most instances, the cost of purification is not considered, or a generic linear cost function is applied. This results in an offset between the actual costs of regeneration and the costs factored into the regeneration model. This work aims to highlight the adverse impact if this simplification on achieving an optimum performance index.

2. Problem statement

A fixed flowrate approach was taken in the model development, i.e. a stream is described by the total flowrate of fluid and the concentration of each of the

contaminants in the stream. According to this assumption,a water source is a unit that produces water or effluent while a water sink is a unit that consumes water.

In short, the problem statement can be stated as follows. Given :

- A set of water sources, J, with known flowrates, F_j, and known contaminant concentrations, $C_{j,o}$
- A set of water sinks, I, with known flowrates, F_i ,and known maximum allowable concentrations, $C_{i,o}^{U}$
- A set of regenerators ,R, i.e. electrodialyisis unit, with some design parameters
- A freshwater source, with a variable flowrate, and known contaminant concentrations
- A wastewater sink, with a variable flowrate and known maximum allowable contaminant concentrations

It is required to synthesise the water network that minimises the amount of freshwater consumed, wastewater produced, the energy consumed in the regeneration unit and the overall cost of the water network. In addition, it is necessary to determine the optimum operating and design conditions of the electrodialysis unit (e.g. area, number of cell pairs, current and voltage).

3. Mathematical model

Material balances are established on the source-regenerator-sink basis.For the units involving mixing of streams, i.e. the regenerator and the sinks, a contaminant balance was conducted for each contaminant. The performance of the regeneration unit was described by the contaminant-specific removal ratio, *RR*, Eq. (1). This expression is often used in isolation when developing a black box model. It expresses the contaminant load in the concentrate stream, as a fraction of the contaminant load in the feed to the regenerator.

$$RR_{r,o} = \frac{C_{r,o}^{con} \sum_{i} F_{r,i}^{con}}{\sum_{j} C_{j,o} F_{j,r}} \qquad \forall\, r \in R,\ \forall\, o \in O \tag{1}$$

A comprehensive electrodialysis energy minimisation model is developed and included in the water network.The driving force for electrodialysis is the electric current, I, flowing across the unit. The current is determined using a modified expression of Faraday's law, given by Eq.(2), where z_o and $v_o$represent the valence and stoichiometric coefficient of either the cation or the anion of any contaminant, o. $Q^d$is the flowrate of the diluate stream, N, is the number of cell pairs in the ED unit, F, is the Faraday constant and ζ is the current efficiency.

$$I = \frac{F Q^d C^{\Delta}}{\xi N} \sum_{o} |z_o| v_o \tag{2}$$

In order to account for the multi-contaminant nature of the ED feed, C^{Δ},the concentration flux over the unit, is given in terms of the equivalent concentration of the

solution. For any given solution of salts with concentrations C_o, the solution equivalent concentration, C_{eq} is defined according to Eq. (3).

$$C_{eq} = \sum_{o} |z_o| v_o C_o \tag{3}$$

Based on the driving force, it is then possible to determine physical characteristics of the required unit, such as the membrane area, the length and the throughput. In addition, one is able to determine the amount of energy required for desalination and for pumping purposes, and subsequently, the capital and operating costs associated with regeneration.

The combination of the water network and ED model culminates in an objective function that takes into account freshwater consumption, wastewater production, and accurate capital and operating costs of ED units and necessary piping interconnections.

4. Illustrative Example

The above model is applied to a pulp mill and bleached paper plant adapted from Chew et al., (2008).In the original scenario, shown in Figure 2, four separate freshwater feeds are used, with a total consumption of 8 500 tonnes per day, and 4 separate effluent streams are produced, totalling 10 500 tonnes per day.

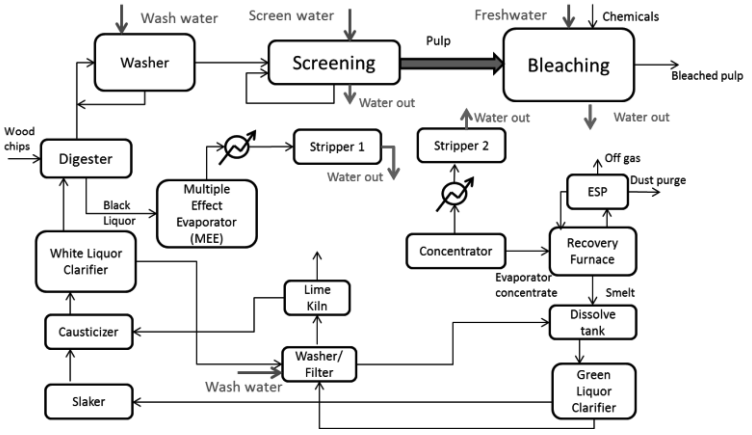

Figure 2: Simplified PDF of Pulp mill and bleached paper plant

Two alternate process integration scenarios were compared. Firstly, the case in which a black box model is used and the costing of the actual required ED unit is performed separately; i.e. water minimisation only.The second case involves simultaneous minimisation of water and energy, using the developed model. Two contaminants were identified,namely,NaCl and $MgCl_2$. The flowrates and contaminant concentrations of the sources and sinks are detailed in Table 1.

Table 1: Given data for water network

Sources				Sinks			
		Contaminant Concentration (Kmol/cm^3)				Maximum contaminant Concentration (Kmol/cm^3)	
Source	Flowrate (cm^3/s)	NaCl	$MgCl_2$	Sink	Flowrate (cm^3/s)	NaCl	$MgCl_2$
Stripper 1	2.07	0	0	Washer	3.26	0.0046	0.0004
Screening	0.34	0.046	0.035	Screening	0.34	0.0125	0.0007
Stripper 2	0.24	0	0	Washer/filter	1.34	0	0
Bleaching	7.22	0.026	0.0002	Bleaching	7.22	0.0002	0.00003
Freshwater	Variable	-	-	Wastewater	Variable	0.01	0.01

The results obtained from the optimisation are given in Table 2. In the first scenario,application of process integration results in a 36% saving in freshwater and 60% reduction of wastewater produced, in comparison with the original plant.The water minimisation black box model employs a linear cost function to determine the cost of regeneration. Such a function, however, is inaccurate as it does not account for the energy penalty associated with regenerating highly concentrated effluent. The deviation of the cost function from the actual cost of regeneration is 85%. The required ED unit has a total area of 438 m^2 and requires 353 cell pairs.

In the second scenario, the simultaneous minimisation of both energy and water within the water network results in a further reduction in freshwater consumption, wastewater production and cost of regeneration, as indicated in Table 2. By applying a penalty to the energy consumption, a more modest ED unit, with only 230 cell pairs and 144 m^{2}area, is required. Subsequently there is a 53% reduction in the total cost of the water network. The modified flowsheet after energy and water minimisation is given in Figure 3.

Table 2: Summary of costs in the 2 cases considered, values are given in $1000/annum

		Scenario 1		**Scenario 2**
	Original	Water minimisation - estimated ED cost	Water minimisation - true ED cost	Water and energy minimisation
Freshwater	2 814.86	1 776.00	1 776.00	1 736.70
Wastewater	3 468.12	1 122.80	1 122.80	1 083.50
Energy*	-	3.90	26.08	5.25
Piping	-	92.40	92.40	86.62
Total	6 282.98	2 995.10	3 017.28	2 912.07

*Energy associated with regeneration

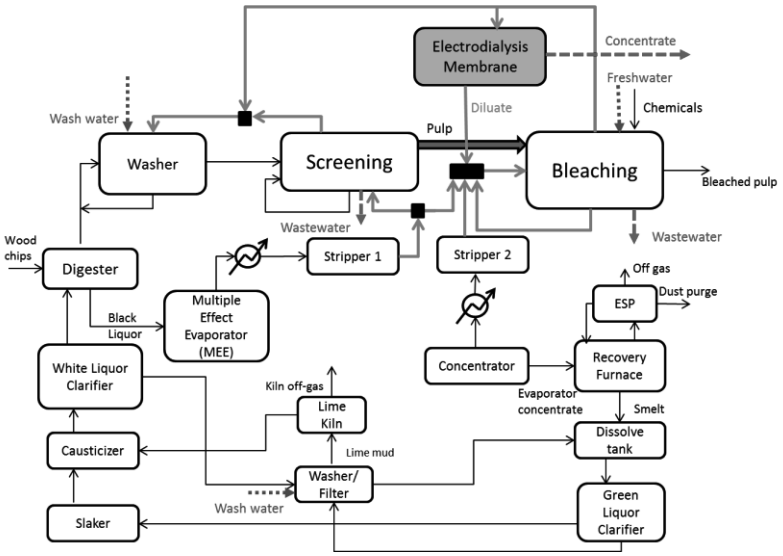

Figure 3: Process flowsheet after integration with the electrodialysis unit

5. Conclusion

This work explores the shortcomings of the black box model in water network optimisation by adopting an accurate representation of regeneration units. It is shown that by simultaneous minimisation of water and energy in the network, there is a significant reduction in freshwater consumption and wastewater production as well as an overall reduction in the cost of the water network. This approach also results in an 80% reduction in energy consumption in the regeneration units. Furthermore, the simultaneous approach results in more favourable design parameters for the regeneration units.

6. References

E.Brauns, W. De Wilde, B. Van de Bosch, P. Lens, L. Pinoy, M.Empsten, 2009, On the experimental verification of an electrodialysis simulation model for optimal stack configuration design through solver software. Desalination, 249, 1030-1038

I.M.L. Chew, R. Tan, D.K.S. Ng, D.C.Y. Foo, T. Majozi, J. Gouws, 2008, Synthesis of Direct and Indirect Interplant Water Network. Ind. Eng. Chem. Res. 47, 9485–9496.

H.J Lee, F. Sarfert, H. Strathmann, S.H.Moon, 2002, Designing of an electrodialysis desalination plant. Desalination 142, 267–286.

P. Tsiakis, L.G.Papageorgiou, 2005, Optimal design of an electrodialysis brackish water desalination plant. Desalination 173, 173–186.

S.C. Khor, D.C.Y. Foo, M. El-Halwagi, R. Tan, N. Shah, 2011, A Superstructure Optimization Approach for Membrane Separation-Based Water Regeneration Network Synthesis with Detailed Nonlinear Mechanistic Reverse Osmosis Model. Ind. Eng. Chem. Res. 50, 13444–13456.

Krist V. Gernaey, Jakob K. Huusom and Rafiqul Gani (Eds.), 12th International Symposium on Process Systems Engineering and 25th European Symposium on Computer Aided Process Engineering.
31 May - 4 June 2015, Copenhagen, Denmark.

Deterministic Global Optimization and Transition States

Dimitrios Nerantzis and Claire S. Adjiman

Department of Chemical Engineering; Centre for Process Systems Engineering; Imperial College London; London SW7 2AZ; United Kingdom
dimitrios.nerantzis10@imperial.ac.uk; c.adjiman@imperial.ac.uk

Abstract

Transition states (index-1 saddle points) play a crucial role in determining the rates of chemical transformations but their reliable identification remains challenging in many applications. In the current literature deterministic global optimization methods have been employed for the location of transition states (TSs) by initially finding all stationary points and then identifying the TSs among the set of solutions. Aiming to focus the computational effort on the location of TSs of general nonlinear, three times continuously differentiable functions, we introduce regional tests for the identification of hyper-rectangular areas that do not contain any TS or that may contain a unique TS. These tests can be used within the framework of global optimization methods with the potential of reducing the computational time for TS location. We present the theory behind the tests and results on a simple benchmark function.

Keywords: global optimization, transition states, interval matrix, eigenvalue bounding

1. Introduction

We consider the following problem: Given a function $f : B \subseteq \mathbb{R}^n \to \mathbb{R}$, $f \in C^3$ we want to find all the critical points, $x^* \in B : \nabla f(x^*) = 0$, of f for which the Hessian matrix $\nabla^2 f(x^*)$ has eigenvalues $\lambda_n < 0 < \lambda_{n-1} \leq ... \leq \lambda_1$. Such points are called **Transition States** (TSs) or **index-1** saddle points. TSs play a crucial role in determining the rates of chemical transformations (Wales, 2003) and are also of interest in robotics and economics (Ellabaan et al., 2009). A number of local methods have been proposed in the literature for the identification of transition states. For example, in the Rational Function Optimization (RFO) method (Banerjee et al., 1985) a local search for a single TS is performed while in the Nudged Elastic Band method (Henkelman and Jónsson, 2000) an approximation of the minimum energy path between two minima is built. The point with the maximum energy on the path is a TS. Stochastic methods such as simulated annealing (Chaudhury and Bhattacharyya, 1998) and genetic algorithms (Ellabaan et al., 2009) have also been employed for locating TSs. While more computationally expensive, such methods do not require any starting points to locate a TS and may find multiple TSs.

Our focus in this paper is on deterministic global methods, that can guarantee the identification of all TSs within a specified domain. In the existing literature, the use of such methods for TS location includes the work of Westerberg and Floudas (1999) using the αBB algorithm (Androulakis et al., 1995; Adjiman et al., 1998) and the work of Lin and Stadtherr (2004) using the interval Newton method (Hansen and Walster, 2003). In (Westerberg and Floudas, 1999) and (Lin and Stadtherr, 2004) the authors locate all critical points of a potential energy function and then identify each type of solution based on the eigenvalues of the corresponding Hessian matrix. The drawback of this approach is that computational time is spent for the location of critical points with index > 1 (i.e., with a number of negative eigenvalues > 1).

Because of the computational cost associated with deterministic global optimization, it may be beneficial to focus the search on regions that contain TSs only. In this paper, we propose several regional tests that allow the elimination of certain regions and we apply this approach to a test function. We explore the trade-off between the cost of the tests and the number of iterations and CPU time required to identify all TSs.

The paper is organized as follows: In section 2, we introduce the general approach briefly. In section 3, the regional tests are discussed. The algorithm is applied to an example in Section 4 and conclusions are drawn in Section 5.

2. Proposed approach

We use the αBB algorithm and the formulation proposed in (Westerberg and Floudas, 1999) in order to search for critical points. However, aiming to focus the computational effort on the location of TSs, we introduce a number of tests which can be used to bound the number of negative and positive eigenvalues of an interval matrix. Since αBB is a branch & bound optimization algorithm, at any given iteration, it proceeds by calculating valid lower and upper bounds over hyper-rectangular subsets R of the initial domain B and then dividing each subset area to obtain better lower and upper bounds. Whenever the lower bound of a given area is found to be greater than the best upper bound so far, the area is fathomed. We modify the approach by applying, prior to each bounding step, a test on the interval Hessian matrix, $[\nabla^2 f(R)]$, calculated over R by the natural interval extension (Hansen and Walster, 2003) of the second derivatives $\partial^2 f/\partial x_i \partial x_j$. The interval Hessian can be seen as a superset of $\{\nabla^2 f(x) : x \in R\}$. If the test reveals that every matrix in $[\nabla^2 f(R)]$ has index > 1 then we fathom the area R. If the test reveals that every matrix in $[\nabla^2 f(R)]$ is index-1 then we perform a local search, since it can be shown that this implies that there can be at most one TS in R and: if we find a TS we fathom the area. Otherwise the test is inconclusive and so we proceed with the next step of the modified αBB algorithm.

3. Regional tests

In this section, we introduce three tests to assess whether a given region may contain a TS.

3.1. Recursive inertia test

Based on Haynsworth's theorem (Carlson et al., 1974) we can construct algorithms for obtaining bounds on the number of negative and positive eigenvalues of interval matrices. First we give the following definition:

Definition 3.1 (Inertia of a symmetric scalar matrix) *Given a symmetric matrix A, the inertia of A, In(A), is the triplet $(\pi(A), \nu(A), \delta(A))$ of the numbers of positive, negative and zero eigenvalues of A respectively.*

Theorem 3.2 (Haynsworth) *Given a symmetric matrix M partitioned in the form*

$$M = \begin{bmatrix} A & B \\ B^T & C \end{bmatrix} \text{ and assuming } A \text{ is non-singular, then } In(M) = In(A) + In(C - B^T A^{-1} B).$$

We can make use of Haynsworth's theorem recursively, as shown in Cottle (1974). Cottle considers scalar matrices and chooses A to be a single non-zero entry in the diagonal. By interchanging corresponding rows and columns simultaneously, thus not affecting the eigenvalues, we bring the selected entry A to the top right position of the matrix. We note the sign of A, we then calculate

$C - B^T A^{-1} B$ (this is the Schur complement of A in M) and we repeat. If all the elements in the diagonal are zero we are either left with a zero matrix or we can choose A to be of the form $\begin{bmatrix} 0 & a \\ a & 0 \end{bmatrix}$. This way we can always calculate the complete inertia of a scalar matrix.

A straightforward adaptation of this recursive scheme for interval matrices and for our purposes is simply to scan the diagonal for intervals that do not contain zero, calculate the interval Schur complement $[C] - [B]^T [A]^{-1} [B]$ and repeat. We should give priority to negative intervals. If at any point all the diagonal interval elements contain zero then we cannot proceed further with the analysis and stop. Note that in the interval case, each time we find a negative (resp. positive) interval in the diagonal of a subsequent Schur complement, this means that all the scalar matrices contained in the initial interval matrix have a further negative (resp. positive) eigenvalue. In a similar manner Meyer and Swartz (1998) used Schur's formula, $det(M) = det(A) det(C - B^T A^{-1} B)$, for a convexity test applied to interval matrices (such a test was mentioned in Cottle (1974) for scalar matrices) along with a branch-and-bound method. In algorithm 1 we give a pseudocode for the proposed recursive inertia algorithm, RecIn.

Algorithm 1 Pseudocode for RecIn algorithm: $O(n^3)$

Set $n = \dim([M])$. Initialize neg=0, pos=0 (number of negative and positive (interval) eigenvalues).
Search for a diagonal interval $[m_{aa}]$ with $0 \notin [m_{aa}]$. Give priority to negative intervals
if none found **then**
  Stop, test is inconclusive.
else
  $pos = pos + 1$, if $[m_{aa}] > 0$ or $neg = neg + 1$, if $[m_{aa}] < 0$
  if $neg > 1$ or $pos == n$ **then**
    Fathom area.
  else if $neg == 1$ and $pos == n - 1$. **then**
    Optional: Local search.
  else if $\dim([M]) > 1$ **then**
    Calculate the interval Schur complement of $A = [m_{aa}]$ in $[M]$, set $[M]$ to the Schur complement and repeat from step 2.
  else
    Test is inconclusive.
  end if
end if

3.2. 2×2 *Inertia test*

Another possible way to make use of theorem 3.2 for our purpose is to choose $[A]$, in $[M] = \begin{bmatrix} [A] & [B] \\ [B]^T & [C] \end{bmatrix}$, to be any of the 2×2 diagonal sub-matrices of $[M]$, $[A_{ij}] = \begin{bmatrix} [m_{ii}] & [m_{ij}] \\ [m_{ji}] & [m_{jj}] \end{bmatrix}$. The maximum eigenvalue, $\overline{\lambda_{ij}} = \max_{A_{ij} \in [A_{ij}]} \lambda_1(A_{ij})$, of each of these matrices is

$$\overline{\lambda_{ij}} = \frac{\overline{m_{ii}} + \overline{m_{jj}} + \sqrt{(\overline{m_{ii}} - \overline{m_{jj}})^2 + 4 \max\{\underline{m_{ij}}^2, \overline{m_{ij}}^2\}}}{2}, \tag{1}$$

where $\underline{m_{ij}}$ and $\overline{m_{ij}}$ are the lower and upper bounds of the interval entry $[m_{ij}]$ of $[M]$. If $\overline{\lambda_{ij}} < 0$ for any of the sub-matrices then by theorem 3.2 we know that every $M \in [M]$ has at least two negative eigenvalues and thus we can fathom the corresponding area. In algorithm 2 we give a pseudocode of this test to which we will refer as the 2×2 inertia test.

Algorithm 2 Pseudocode for the 2×2 inertia test: $O(n^2)$

```
Set n = dim([M]).
for i=1:n do
    for j>i:n do
        λ̄ = ((m̄_ii + m̄_jj + sqrt((m̄_ii − m̄_jj)^2 + 4 max{m_ij^2, m̄_ij^2})) / 2
        if λ̄ < 0 then
            Fathom area. Exit test.
        end if
    end for
end for
```

Note that the 2×2 inertia test does not remove minima and TSs and that it might be inconclusive even for a scalar matrix. However it is computationally cheap and easy to implement, and is thus worth investigating.

3.3. Rohn test

A third test is based on Rohn's method (Hladk et al., 2010) which is derived from the interval extension of Weyl's inequality (Golub and Van Loan, 1996).

Theorem 3.3 (Weyl) *Given symmetric (scalar) matrices C and E then*

$$\lambda_k(C) + \lambda_n(E) \;\leq\; \lambda_k(C+E) \;\leq\; \lambda_k(C) + \lambda_1(E).$$

Any given interval matrix $[M]$ can be written as $C+[E]$ where $c_{ij} = (\overline{m_{ij}} + \underline{m_{ij}})/2$ and $[e_{ij}] = [c_{ij} - \underline{m_{ij}}, \overline{m_{ij}} - c_{ij}]$. By calculating lower and upper bounds, $\underline{\lambda_n}$ and $\overline{\lambda_1}$, for $\lambda_n([E]) = \{\lambda_n(E) : E \in [E]\}$ and $\lambda_1([E]) = \{\lambda_1(E) : E \in [E]\}$ respectively then we would have,

Theorem 3.4 (Rohn) *Given a symmetric interval matrix* $[M] = C + [E]$ *then*

$$\lambda_k(C) + \underline{\lambda_n} \;\leq\; \lambda_k(C+[E]) \;\leq\; \lambda_k(C) + \overline{\lambda_1}.$$

Note that $\underline{\lambda_n} = -\overline{\lambda_1}$ and also that the widths of the intervals $\lambda_k([M])$ are all the same. We can calculate $\underline{\lambda_n}$ (and $\overline{\lambda_1}$) using a number of methods (Adjiman et al., 1998), the simplest being the interval extension of Gerschgorin's theorem ($O(n^2)$) and the most expensive being the Hertz-Rohn method ($O(2^{n-1})$). The Rohn test is summarized in algorithm 3.

Algorithm 3 Pseudocode for Rohn's test: $O(n^2)$ - $O(2^{n-1})$

```
Set n = dim([M]).
Calculate [λ_n] and [λ_{n−1}] for [M] using Theorem 3.4 and an eigenvalue bounding method.
if λ_n ≥ 0 then
    Fathom area (convex area).
else if λ̄_n < 0 and λ_{n−1} > 0 then
    Optional: Local search.
else if λ̄_{n−1} ≤ 0 then
    Fathom area.
else
    Test is inconclusive.
end if
```

4. Application to a benchmark problem.

The proposed tests have been implemented in the αBB algorithm (Adjiman et al., 1998). We investigate the performance the proposed tests on a small example, Ackley's function in three dimensions. The form and domain are given below.

$$f(x) = -20\exp(-0.2\sqrt{\tfrac{1}{n}\textstyle\sum_{i=1}^{n} x_i^2}) - \exp\left(\tfrac{1}{n}\textstyle\sum_{i=1}^{n}\cos(2\pi x_i)\right) + 20 + e,\ x \in [0.5,3]^3,\ n = 3. \quad (2)$$

We perform six runs, one run without any regional tests, one run with the 2×2 inertia test, two runs with the Rohn test (with and without the local search step) and two runs with the RecIn test. For bounding the eigenvalues in Rohn's test we use the interval extension of Gerschgorin's theorem (Adjiman et al., 1998). The CPU time and number of solutions of each type (minima, TSs, higher-index critical points) found are reported in table 1. The number of unfathomed nodes at each iteration for each run is shown in figure 1. The computations were performed on a 3060 MHz computer using an absolute convergence tolerance of 10^{-6} and a minimum box size of 10^{-6}. All 81 TSs are identified in all cases, and significant decreases in the CPU time can be observed, with all tests performing well. The local search is found to reduce the number of iterations and to lead to a further decrease in CPU time. This is likely to be critical when dealing with larger problems.

Table 1: CPU times without local search / with local search and number of solutions of each type found for each run for the Ackley function.

Test	**CPU Time**	**#Mins**	**#TSs**	**#index $>$ 1**
No test	65 sec	27	81	84
2x2 Inertia	33 sec	27	81	0
Rohn	30/21 sec	0	81	0
RecIn	28/19 sec	0	81	0

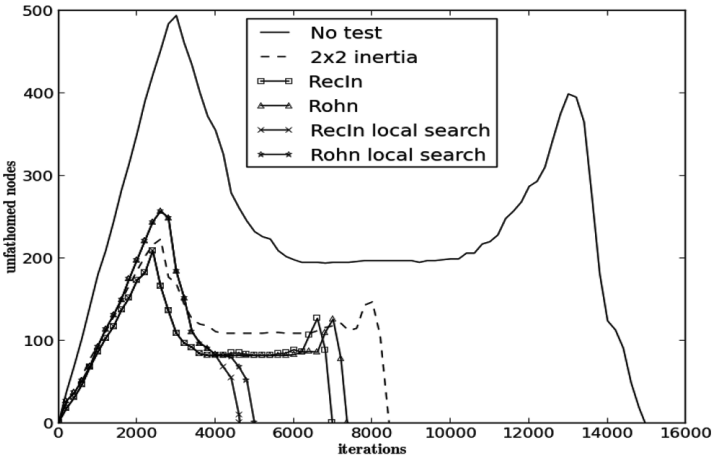

Figure 1: Number of unfathomed nodes at each iteration for each run.

5. Conclusions

In this paper we considered the problem of locating all transition states (TSs) of general nonlinear functions, in C^3, using global deterministic methods. In particular we used the αBB optimization method and we introduced a number of tests which we applied prior to the bounding step of the αBB algorithm. These tests help to identify areas of the search space which do not contain any TSs or may contain at most one. In the first case we fathom/remove the area while in the second we perform a local search and if a solution is found we fathom the area. Without the tests the algorithm simply locates all critical points while with the tests we aim to focus the computational effort on the location of TSs. We have presented the successful application of the proposed tests to a benchmark function. The results indicate that the addition of the tests can reduce the computational time significantly. Finally we note that the proposed tests can be used within any branch and bound algorithm or within the interval Newton method and that they can be altered in order to locate any index-k critical point, with the exception of the 2×2 inertia test.

6. Acknowledgements

Financial support from the Engineering and Physical Sciences Research Council (EPSRC) of the UK, via a Leadership Fellowship (EP/J003840/1), is gratefully acknowledged.

References

Adjiman, C. S., Dallwig, S., Floudas, C. A., Neumaier, A., 1998. A global optimization method, αBB, for general twice-differentiable constrained NLPs I. Theoretical advances. Comp & Chem Eng 22, 1137 – 1158.

Androulakis, I. P., Maranas, C. D., Floudas, C. A., 1995. αBB: A global optimization method for general constrained nonconvex problems. J Global Optim 7 (4), 337–363.

Banerjee, A., Adams, N., Simons, J., Shepard, R., 1985. Search for stationary points on surfaces. J Phys Chem 89 (1), 52–57.

Carlson, D., Haynsworth, E., Markham, T., 1974. A generalization of the Schur complement by means of the moorepenrose inverse. SIAM J Appl Math 26, 169–175.

Chaudhury, P., Bhattacharyya, S., 1998. A simulated annealing based technique for locating first-order saddle points on multidimensional surfaces and constructing reaction paths: several model studies. J. Mol. Struct. (Theochem) 429, 175 – 186.

Cottle, R. W., 1974. Manifestations of the Schur complement. Lin Alg Appl 8, 189 – 211.

Ellabaan, M., Ong, Y. S., Lim, M. H., Kuo, J. L., 2009. Finding multiple first order saddle points using a valley adaptive clearing genetic algorithm. In: IEEE CIRA. pp. 457–462.

Golub, G. H., Van Loan, C. F., 1996. Matrix Computations (Johns Hopkins Studies in Mathematical Sciences)(3rd Edition). The Johns Hopkins University Press.

Hansen, E., Walster, G., 2003. Global optimization using interval analysis. Pure and applied mathematics. M. Dekker, New York.

Henkelman, G., Jónsson, H., 2000. Improved tangent estimate in the nudged elastic band method for finding minimum energy paths and saddle points. J Chem Phys 113 (22), 9978–9985.

Hladk, M., Daney, D., Tsigaridas, E. P., 2010. Bounds on real eigenvalues and singular values of interval matrices. SIAM J Matrix Anal Appl 31 (4), 2116–2129.

Lin, Y., Stadtherr, M. A., 2004. Locating stationary points of sorbate-zeolite potential energy surfaces using interval analysis. J Chem Phys 121 (20), 10159–10166.

Meyer, C. A., Swartz, C. L. E., 1998. A regional convexity test for global optimization: Application to the phase equilibrium problem. Comp and Chem Eng 22, 1407 – 1418.

Wales, D., 2003. Energy Landscapes: Applications to Clusters, Biomolecules and Glasses. Cambridge University Press.

Westerberg, K. M., Floudas, C. A., 1999. Locating all transition states and studying the reaction pathways of potential energy surfaces. J Chem Phys 110 (18), 9259–9295.

Krist V. Gernaey, Jakob K. Huusom and Rafiqul Gani (Eds.), 12th International Symposium on Process Systems Engineering and 25th European Symposium on Computer Aided Process Engineering.
31 May - 4 June 2015, Copenhagen, Denmark.

A Metaheuristic for Solving Large-Scale Two-Stage Stochastic Mixed 0-1 Programs with the Time Stochastic Dominance Risk Averse Strategy

Susana Baptista*[a], Ana Paula Barbosa-Póvoa[b], Laureano Escudero[c], Maria Isabel Gomes[a] and Celeste Pizarro[c]

[a]*Centro de Matemática e Aplicações; FCT, Universidade Nova de Lisboa; Caparica, Portugal*
[b]*CEG-IST; Instituto Superior Técnico, Universidade de Lisboa; Lisboa, Portugal*
[c]*Estadística e Investigacíon Operativa; Universidad Rey Juan Carlos; Madrid, Spain*
**sbb@fct.unl.pt*

Abstract

Supply Chain Design problems often result into multiperiod stochastic mixed integer problems that are hard to solve. In this paper we propose a metaheuristic algorithm as a specialization for two-stage problems of the so-named Fix-and-Relax Algorithm presented previously for solving large-scale multiperiod stochastic mixed 0-1 optimization problems under a time stochastic dominance risk averse strategy, so-named TSD. Some computational experience is presented.

Keywords: Two-stage stochastic mixed 0-1 optimization, metaheuristic, Fix and Relax, time stochastic dominance

1. Introduction

Given the large dimensions of the real-life problems under uncertainty and of supply chains systems in particular, algorithms seeking for the optimal solution are today unaffordable. By contrary, inexact decomposition algorithms are more appropriate assuming that a methodology for goodness assessment of the solution is provided. In this work a metaheuristic decomposition algorithm is proposed as a specialization for two-stage problems of the so-named Fix-and-Relax Algorithm (FRA) for solving large-scale multiperiod stochastic mixed 0-1 optimization problems that is presented in Escudero et al. (2014). The time stochastic dominance strategy, so-named TSD Escudero et al. (2014), is used for risk reduction of the negative impact in the objective function of non-wanted scenarios (i.e., the so-named swan scenarios).

In order to assess the solution procedure applicability, computational tests were performed on multi-period and multi-commodity closed loop supply chains randomly generated from a deterministic reference case previously addressed in Salema et al. (2010), that being a large scale case, its stochastic counterpart is a very large one Baptista et al. (2014).

2. Two-stage stochastic mixed 0-1 problems under strategy TSD

Without loss of generality, let the following compact representation of the two-stage stochastic mixed 0-1 model for maximizing the expected objective function value (say, profit) over the set of

scenarios along a time horizon by only considering the risk neutral (RN) strategy,

$$
\begin{array}{lll}
z_{RN} = & \max\{a_1 x_1 + b_1 y_1 + \sum\limits_{\omega\in\Omega} w^{\omega} \sum\limits_{t\in\mathscr{T}^-} (a_t^{\omega} x_t^{\omega} + b_t^{\omega} y_t^{\omega})\} & \\
\text{s.t.} & A_1 x_1 + B_1 y_1 = h_1 & \\
& A_1^{t\omega} x_1 + B_1^{t\omega} y_1 + \sum\limits_{t'\in\mathscr{T}^-:t'\le t} (A_{t'}^{t\omega} x_{t'}^{\omega} + B_{t'}^{t\omega} y_{t'}^{\omega}) = h_t^{\omega} & \forall t \in \mathscr{T}^-, \omega \in \Omega \\
& x_1 \in \{0,1\}^{nx(1)}, y_1 \in I\!R^{ny(1)} & \\
& x_t^{\omega} \in \{0,1\}^{nx(t)}, y_t^{\omega} \in I\!R^{ny(t)} & \forall t \in \mathscr{T}^-, \omega \in \Omega,
\end{array} \tag{1}
$$

where w^{ω} is the modeler-driven weight or likelihood of scenario ω for, the first stage 0-1 and continuous variables, respectively; a_1 and b_1 are the objective function coefficient vectors for the variables in the first stage vectors x_1 and y_1, respectively; A_1 and B_1 are the first stage constraint matrices for the variables in the vectors x_1 and y_1, respectively; x_t^{ω} and y_t^{ω} are the vectors of the second stage 0-1 and continuous variables, respectively, at time period t for scenario ω, for $t \in \mathscr{T}^-$, where $\mathscr{T}^- \equiv \mathscr{T}\backslash\{1\}$ and $\omega \in \Omega$, where Ω is the set of scenarios under consideration; a_t^{ω} and b_t^{ω} are the vectors of the objective function coefficients for the variables in the second stage vectors x_t^{ω} and y_t^{ω}, respectively; $A_1^{t\omega}$ and $B_1^{t\omega}$ are the second stage constraint matrices for the variables in the vectors x_1 and y_1; $A_{t'}^{t\omega}$ and $B_{t'}^{t\omega}$ are the second stage constraint matrices for the variables in the vectors $x_{t'}^{\omega}$ and $y_{t'}^{\omega}$, respectively; h_t^{ω} is the rhs; $nx(1)$ and $ny(1)$ are the number of the first stage 0-1 and continuous variables, respectively; and $nx(t)$ and $ny(t)$ are the number of the second stage 0-1 and continuous variables, respectively. Notice that the Non-Anticipativity Constraints (NAC) are satisfied for the first stage.

The main criticism that can be made to strategy RN is that it ignores the variability of the objective function value over the scenarios and, in particular in our case, the "left" tail of the non-wanted scenarios. Alternatively, there are some other approaches that also deal with risk management by providing hedging solutions against the occurrence of some non-desired scenarios considering risk averse strategies, see a survey in Alonso-Ayuso et al. (2014). Some of these strategies consider semi-deviations, excess probabilities, conditional value-at-risk, expect shortfall on reaching given thresholds as risk measure-based functions to optimize as well as the two recent new risk averse measures, namely, the first- and second-order Stochastic Dominance Constraint strategies, say FSD (Gollmer et al. (2008)) and SDD (Gollmer et al. (2011)), respectively.

In this paper we consider the specialization of strategy TSD for solving multistage problems introduced in Escudero et al. (2014) to the two-stage environment. That strategy is a time-based mixture of strategies FSD and SSD, such that each modeler-driven so-named profile for each selected period along the time horizon is included by an objective function threshold and the targets on given bounds on the probability of failure of reaching the threshold and the related expected shortfall on reaching and the scenario shortfall itself. So, strategy TSD requires a set of profiles $\{p\}$, say $\mathscr{P}_t \, \forall t \in \tilde{\mathscr{T}}$, given by the tupla $(\phi^p, S^p, \bar{s}^p \, \bar{v}^p)$, where ϕ^p is the objective function threshold to be satisfied up to time period t, $\tilde{\mathscr{T}} \subseteq \mathscr{T} - 1$ is the period set where the TSD policy is considered, S^p is the maximum *target* for the shortfall that is allowed on reaching the threshold up to time period t, $\bar{s}^p$ is the upper bound *target* of the expected shortfall on reaching the threshold over the scenarios with shortfall, and $\bar{v}^p$ is the shortfall probability bound *target*.

Let $s^{\omega p}$ denote the shortfall (continuous) variable that, obviously, is equal to the difference (if it is positive) between threshold ϕ^p and the profit up to time period t for $p \in \mathscr{P}_t, t \in \tilde{\mathscr{T}}$ for scenario $\omega \in \Omega$. And let $v^{\omega p}$ denote a 0-1 variable such that its value is 1 if the profit up to time period t is smaller than threshold ϕ^p and otherwise, 0. In order to model the expected shortfall over the scenarios with shortfall, say set $\{\omega \in \Omega : v^{\omega p} = 1\}$, besides the constraint $s^{\omega p} \le S^p v^{\omega p}$ that force the 0-1 variable $v^{\omega p} = 1$ for $s^{\omega p} > 0$, the constraint $v^{\omega p} \le s^{\omega p}$ is required. Although we exclude fractional 0-1 values for the latter (continuous) variable, this fact has very minor influence on the value of the expected shortfall given the usual magnitude of the objective function

value for profile p. Finally, the weight w^ω should be replaced with the weight, say $w^\omega_{v^{\omega p}}$, of the scenario ω in the subset of scenarios with shortfall for profile p; it can be represented as follows: $w^\omega_{v^{\omega p}} = \dfrac{w^\omega}{\sum_{\omega' \in \Omega: v^{\omega' p}=1} w^{\omega'}}$. The nonlinearity in the expression can be equivalently replaced with the expressions given in model (2).

$$z_{TSD} = \max\{a_1 x_1 + b_1 y_1 + \sum_{\omega\in\Omega} w^\omega \sum_{t\in\mathscr{T}^-} (a_t^\omega x_t^\omega + b_t^\omega y_t^\omega) - \sum_{t\in\tilde{\mathscr{T}}} \sum_{p\in\mathscr{P}_t} (M_S^p \varepsilon_S^p + M_{\bar{s}}^p \varepsilon_{\bar{s}}^p + M_{\bar{v}}^p \varepsilon_{\bar{v}}^p)\}$$

$$\begin{array}{lll}
\text{s.t.} & A_1 x_1 + B_1 y_1 = h_1 & \\
& A_1^{t\omega} x_1 + B_1^{t\omega} y_1 + \sum\limits_{t'\in\mathscr{T}^-: t'\le t} (A_{t'}^{t\omega} x_{t'}^\omega + B_{t'}^{t\omega} y_{t'}^\omega) = h_t^\omega & \forall t \in \mathscr{T}^-,\ \omega\in\Omega \\
& x_1 \in \{0,1\}^{nx(1)},\ y_1 \in I\!R^{ny(1)} & \\
& x_t^\omega \in \{0,1\}^{nx(t)},\ y_t^\omega \in I\!R^{ny(t)} & \forall t \in \mathscr{T}^-,\ \omega\in\Omega \\
& a_1 x_1 + b_1 y_1 + \sum\limits_{t'\in\mathscr{T}^-: t'\le t} (a_{t'}^\omega x_{t'}^\omega + b_{t'}^\omega y_{t'}^\omega) + s^{\omega p} \ge \phi^p & \forall p\in\mathscr{P}_t,\ t\in\tilde{\mathscr{T}},\ \omega\in\Omega \\
& 0 \le s^{\omega p} \le S^p v^{\omega p} + \varepsilon_S^p,\ v^{\omega p} \le s^{\omega p},\ v^{\omega p} \in \{0,1\} & \forall p\in\mathscr{P}_t,\ t\in\tilde{\mathscr{T}},\ \omega\in\Omega \\
& \sum\limits_{\omega\in\Omega} w^\omega s^{\omega p} \le \bar{s}^p (\sum\limits_{\omega\in\Omega} w^\omega v^{\omega p}) + \varepsilon_{\bar{s}}^p & \forall p\in\mathscr{P}_t,\ t\in\tilde{\mathscr{T}} \\
& \sum\limits_{\omega\in\Omega} w^\omega v^{\omega p} \le \bar{v}^p + \varepsilon_{\bar{v}}^p & \forall p\in\mathscr{P}_t,\ t\in\tilde{\mathscr{T}} \\
& \varepsilon_S^p \in I\!R^+,\ \varepsilon_{\bar{s}}^p \in I\!R^+,\ \varepsilon_{\bar{v}}^p \in I\!R^+ & \forall p\in\mathscr{P}_t,\ t\in\tilde{\mathscr{T}},
\end{array} \tag{2}$$

where ε_S^p, $\varepsilon_{\bar{s}}^p$ and $\varepsilon_{\bar{v}}^p$ are the non-negative slack variables that take the violations of the S^p-, $\bar{s}^p$- and $\bar{v}^p$-bounds, respectively, being M_S^p, $M_{\bar{s}}^p$ and $M_{\bar{v}}^p$ the related big enough M-parameters for the penalization of those slack variables in the objective function. Observe that the TSD model object consists of controlling the objective function value at modeler-driven periods, instead of only performing it at the end of the time horizon. It is very useful for applications with long horizons.

3. FRA2: a Fix and Relax Coordination algorithm for two-stage stochastic mixed 0-1 problems under TSD strategy

The main characteristic of the inexact approach that is proposed consists of considering levels along the time horizon defined by disjoint sets of consecutive periods. At each level a partial scenario mixed 0-1 model is solved by fixing the 0-1 variables of ancestor levels to the value obtained at the optimization of their related models and relaxing the integrality of the 0-1 variables related to successor levels as well as the cross scenario TSD system for those other levels, such that a backstep to the immediate ancestor level is performed in case of the infeasibility of the level's model.

Let $\mathscr{L}$ denote the set of levels, such that t_e^ℓ is the last period in level ℓ (and, then, $t_e^{\ell-1}+1$ is its first one) for $\ell\in\mathscr{L}$. For easying purposes, let $t_e^0 = 0$. At a given level ℓ, let M^ω denote the scenario model for $\omega\in\Omega$ from the original RN model (1) where the NAC have been relaxed, being z^ω its solution value, and M_{TSD}^ℓ denote the TSD model (2), being z_{TSD}^ℓ its solution value. The models $M^\omega\,\forall\omega\in\Omega$ and M_{TSD}^ℓ are to be alternatively solved for level $\ell\in\mathscr{L}$ at FRA2, such that $x_1 = \hat{x}_1$, $y_1 = \hat{y}_1$ and $x_t^\omega = \hat{x}_t^\omega$, $y_t^\omega = \hat{y}_t^\omega\ \forall\omega\in\Omega$ and period t for $t\in\mathscr{T} : t \le t \le t_e^{\ell-1}$. Notice that in order to satisfy the TSD system, the model M_{TSD}^ℓ will be used provided that $\exists t\in\tilde{\mathscr{T}} : t_e^{\ell-1}+1 \le t \le t_e^\ell$; else, the models $M^\omega\,\forall\omega\in\Omega$ are solved.

The main steps of FRA2 are as follows:

Step 0: (**Initialization**). Parameter *mback* (maximum number of allowed backsteps).

Step 1: (**Solution for first level**).
Solve model M^1_{TSD}. If it is infeasible then the original problem (2) is infeasible as well, STOP.
Set $nback := 0$ and level $\ell := 2$.

Step 2: (**Forward step**)
If $\nexists t \in \tilde{\mathscr{T}} : t_e^{\ell-1} + 1 \leq t \leq t_e^{\ell}$ then solve the scenario models $M^{\omega}\, \forall \omega \in \Omega$;
else solve model M^{ℓ}_{TSD}.

Step 3: (**Detecting infeasibility**)
If any model $M^{\omega}\, \omega \in \Omega$ or model M^{ℓ}_{TSD} is infeasible, whenever it has just been solved, then: If $nback = mback$ or $\ell = 1$ then STOP: "Original problem status: unknown"; else go to Step 4. If $\ell = |\mathscr{L}|$ then STOP: "A (hopefully, good) feasible solution has been obtained for the original problem".
Update $\ell := \ell + 1$.Go to Step 2.

Step 4: (**Backward step**)
Redefine the partition structure: $t_e^i := t_e^{i+1}\, \forall i = \ell - 1, ..., |\mathscr{L}| - 1$, $|\mathscr{L}| := |\mathscr{L}| - 1$.
Update $nback := nback + 1$ and $\ell := \ell - 1$. Go to Step 2.

4. Computational experience

In this section the results of a computational testing are reported for the multi-period and multi-commodity closed loop supply chains randomly generated from a deterministic reference case presented in Salema et al. (2010) and extended in Baptista et al. (2014) to its stochastic and risk averse version. Further this extension, now considers that returned products may be sold to a secondary market, sent back to the plant to be remanufactured or just disposed.

The Fix-and-Relax algorithm FRA2 considered in this work has been implemented in C++ code, being CPLEX v12.6 as the MIP optimization engine. The computational experiments were conducted on a laptop with a 2.4 GHz Core i5 processor and **4**GB of RAM.

As testbed, two networks (N1 and N2) were randomly generated considering $|\Omega| = 12$ scenarios, $T = 15$ periods and $|\mathscr{L}| = 4$ levels whose last periods are $t_e^1 = 1, t_e^2 = 6, t_e^3 = 11$ and $t_e^4 = 15$. For the last period of each level, there is a single profil, so $|\mathscr{P}_t| = 1$, $|\tilde{\mathscr{T}}| = 1$ being $t_e^{\ell} \in \tilde{\mathscr{T}}$. Notice that in all instances, the TSD bounds $S^1, \bar{s}^1, \overline{v}^1$ may be tight enough to require that the corresponding related slack variables $\varepsilon_S^1, \varepsilon_{\bar{s}}^1, \varepsilon_{\overline{v}}^1$ to be greater than zero for the 3 last levels.

The contents of the tesbed are as follows: Network N1 is defined by 3 plants, 3 warehouses, 18 customers and 3 disassembly centers; Network N2 is defined by 4, 9, 18 and 9 respective entities. Two random instances were created for N1 (N1V1 and N1V2) and a single instance (N2V1) was created for network N2. In each network 3 products are considered in the flow plants-warehouses, 6 for the flow warehouses-customers and 1 for the flow customers-disassembly. In disassembly centers, products are graded according to their quality (G1, G2 and G3) so that 2 different products graded G1 are the outflow to the market, 1 product flow graded G3 is the outflow to disposal and, finally, 2 flows' products graded G2 are the closing loop flows. 12 random scenarios were generated, defining each of the random parameters such as transportation costs, demand, sell prices in primary and secondary markets, products' return rate, product's quality rates G1 and G2, annual amortization costs and residual values and annual available budget. Finally, table 1 gives the models' dimensions. Its headings read as follows: *m*, *n*01, *nc*, *nel*, number of constraints, 0-1 variables, continuous variables and non-zero elements in constraint matrix; and *den*, constraint matrix density. Observe the large dimensions of the instances in the testbed. Note: Our better results in our limited experience been obtained by re-running the algorithm while imposing a reduction of one in the number of plants that have been selected in the solution of the other run.

Table 1: Models dimensions

	m	$n01$	nc	nel	den (%)
N1	200735	195	91215	784596	0.004
N2	627203	504	293496	2548833	0.014

4.1. Small CLSC network

The goal in this set of experiments consists of comparing the performance of CPLEX versus FRA2 in the solution value and elapsed time for solving TSD model (2). Therefore each instance of the network N1 was solved using the two different sets of scenario's probabilities (P1 and P2) given in Table 2. Notice that the scenarios are ranked according to their outcome so that Scenario 1 is the most optimistic and Scenario 12 is the most pessimistic of the 12 scenarios.

Table 2: Scenarios' probabilities

	Sc1	Sc2	Sc3	Sc4	Sc5	Sc6	Sc7	Sc8	Sc9	Sc10	Sc11	Sc12
P1	0.01	0.01	0.03	0.10	0.10	0.10	0.15	0.25	0.15	0.05	0.04	0.01
P2	0.01	0.01	0.01	0.02	0.05	0.10	0.05	0.15	0.10	0.18	0.12	0.20

Table 3 reports the results obtained in this experimentation. Its headings read as follows: z_{TSD}^{FRA2}, algorithm solution value; z_{TSD}^{CPLX}, best solution value obtained using plain use of CPLEX within the time limit of 8h (non optimal solutions are superscripted by *); GAP_z, respective gap, computed when the optimal solution is available ; y_{TSD}^{FRA2}, algorithm expected profit value; y_{TSD}^{CPLX}, optimal solution expected profit value obtained using plain use of CPLEX within the time limit of 8h; GAP_y, respective gap, computed when the optimal solution is available ; t^{FRA2} and t^{CPLX}, elapsed times (secs.) for obtaining z_{TSD}^{FRA2} and z_{TSD}^{CPLX}, respectively.

Table 3: Small network computational results

	z_{TSD}^{FRA2}	z_{TSD}^{CPLX}	$GAP_z(\%)$	y_{TSD}^{FRA2}	y_{TSD}^{CPLX}	$GAP_y(\%)$	t^{FRA2}	t^{CPLX}
N1V1P1	-65105.8	-115443.6^*	-43.59	20894.2	-	-	1890	43200
N1V1P2	-84891.5	-115183.6^*	-26.29	13108.4	-	-	1928	43200
N1V2P1	-281641	-281483.5	0.06	15359.3	15516.5	1.01	2979	30949
N1V2P2	-290181	-290103.7	0.03	6819.2	6896.0	1.10	3830	49488

Observe that the negative value of $GAP_z(\%)$ for the first two instances is very favorable for FRA2. Since CPLEX cannot prove the solution's optimality due to reaching the allowed time limit (8h.), we did not gather its related profit. However, CPLEX did prove the solution's optimality for the last two instances such that, since the values of $GAP_z(\%)$ are very small, it is worthy to point out that the CPLEX solution gives a slightly higher profit than FRA2. However, it pays a higher price in the violation of the TSD risk reduction bounds on the scenario shortfall, expected shortfall and fraction of scenarios with shortfall.

Regarding the results reported for these not so very large networks, two major facts should be additionally pointed out. First, the metaheuristic algorithm presents a remarkable computing time reduction with respect to plain use of CPLEX ranging from 93 up to 97%. Second, in all instances, the solution values obtained with the P2 probabilities present stronger penalty costs due to the heavier weight of worse scenarios.

4.2. Larger CLSC network

The goal in this set of experiments consists of comparing the performance of algorithm FRA2 for solving RN model (1) and TSD model (2), evaluating the deterioration of the expected profit in

the later model while considering the risk reduction for not reaching the modeler-driven profiles' thresholds of the profiles for the 4 levels in the RN solution. A single instance (N2V1) of network N2 was solved using the set of scenario's probabilities P2 given in Table 2.

This experiment with the RN model (1) shows an expected profit of 85515.48 but it has one scenario (probability 1%) out of 12 with a heavy loss at the end of the time horizon (i.e., end of level 4), in fact, the amount 82843.3. It proves the add-value of the risk averse strategy TSD in the context of very risky scenarios and very small feasible regions. It is assumed that the modeler-driven risk reduction (to be obtained by the TSD model (2)) allows one scenario with a loss but with a probability not higher than 1% and an amount not greater than 61738.6. The solution offered by the TSD model presents an expected profit over the 12 scenarios of an amount of 85665.04 (since it is an heuristic) and the loss of that scenario has been reduced to 63738.6, so, below the loss computed in the RN solutions.

5. Conclusions

In this work we studied the strategies Risk Neutral and risk averse Time Stochastic Dominance for general two-stage stochastic mixed 0-1 problems, where the uncertainty appears anywhere. A metaheuristic algorithm (FRA2) was proposed as a specialization for two-stage problems of the so named Fix-and-Relax Algorithm. Computational tests for multi-period and multi-commodity closed loop supply chains showed the algorithm applicability and the add-value of risk averse strategies as an alternative for plain use of even MIP state-of-the-art solvers.

6. Acknowledgement

This work was partially supported by CMA/FCT/UNL under project PEst OE/MAT/UI0297/2011, the Spanish Ministry of Economy and Competitiveness under project PCDASO MTM2012-31514 and the European Commission under the COST action TD1207.

References

Alonso-Ayuso A., Carvallo F., Escudero L.F., Guignard-Spielberg M., Pi J., Puranmalka R. and Weinteraub A., 2014. Medium range optimization of copper extraction planning under uncertainty in future copper prices. European Journal of Operational Research, 233, 711-726.

Baptista S., Barbosa-Póvoa A.P., Escudero L.F., Gomes M.I. and Pizarro C., 2015. On risk management for a two-stage stochastic mixed 0-1 model for the design and operation planning of a closed-loop supply chain. In preparation.

Escudero L.F., Garín A., Pizarro C. and Unzueta A., 2014. FRCA, a metaheuristic algorithm for solving multistage stochastic mixed 0-1 problems with the time stochastic dominance risk averse strategy. In preparation.

Escudero L.F., Garín M.A., Merino M. and Pérez G., 2014. On time stochastic dominance induced by mixed integer-linear recourse in multistage stochastic programs. Submitted for publication.

Gollmer R., Gotzes U. and Schultz R., 2011. A note on second-order stochastic dominance constraints induced by mixed-integer linear recourse. Mathematical Programming, Ser. A, 126, 179-190.

Gollmer R., Neise F. and Schultz R., 2008. Stochastic programs with first-order stochastic dominance constraints induced by mixed-integer linear recourse. SIAM Journal on Optimization, 19, 552-571.

Salema M.I.G., Barbosa-Póvoa A and Novais A., 2010. Simultaneous design and planning of supply chains with reverse flows: A generic modeling framework. European Journal of Operational Research, 203, 336-349.

Krist V. Gernaey, Jakob K. Huusom and Rafiqul Gani (Eds.), 12th International Symposium on Process Systems Engineering and 25th European Symposium on Computer Aided Process Engineering.
31 May – 4 June 2015, Copenhagen, Denmark

Optimized Production of Multilayered Monodisperse Polymer Nanoparticles.

Brahim Benyahia,[a*] M. A. Latifi,[b] C. Fonteix,[b] F. Pla[b]

[a]*Department of Chemical Engineering, Loughborough University, Loughborough, Leicestershire LE11 3TU, United Kingdom*
[b]*Laboratoire Réactions et Génie des Procédés, CNRS-ENSIC, Université de Lorraine, BP-20451, 1 rue Grandville, 54001 Nancy Cedex, France*
b.benyahia@lboro.ac.uk

Abstract

A dynamic optimization frame work is used to produce in a controlled way multilayered latex nanoparticles. The key feature of the method is to track a glass transition temperature profile, which is designed to produce polymer layers with the targeted properties. Several constraints are considered to achieve better control and produce nanoparticles with a specified particle diameter and layers' thicknesses.To enhance the control of the different layers,two separate monomer feeds are considered under starving conditions throughout the fed-batch stages. The emulsion copolymerization of styrene and butyl acrylate in the presence of n-C12 mercaptan, as chain transfer agent (CTA), is illustrated here as a case study. The optimal feed profiles of the pre-emulsioned monomers are obtained using a genetic algorithm.

Keywords:Multilayered nanoparticles, Dynamic optimization, Fed-batch emulsion copolymerization.

1. Introduction

One of the most important and difficult tasks for researchers and engineers in the field of nanotechnology is to produce nanoparticulate materials with perfectly tailored end-use properties at industrial scales. This requires an effective control of the physical, chemical, and morphological characteristics, such as particle size distribution (PSD), particles morphology, glass transition temperature (T_g), besides the molecular weight distribution (MWD) and polymer microstructure in the particular case of polymeric nanoparticles.Multilayered nanoparticles have drawn particular interest in the area of drug and gene delivery, biosensors and the development of miniaturized optical, electronic, optoelectronic, information-storage materials and devices (Ediriwickrema et al., 2014; Shevchuk et al., 2007). Different technics have been used to synthesize this class of nanoparticles, particularly self-assembly and layer-by-layer deposition.

It was shown recently that the optimization tools can be used to tailorthe end-use properties of latex particles at the nanoscale. First, a multiobjective dynamic optimization approach was used to determine the set of the best operating alternatives (i.e. Pareto set), among which, one operating alternative was selected using a multicriteria decision aiding approach (Benyahia et al., 2012). The best solution obtained was experimentally implemented with success. As an alternative to the

multiobjective optimization, a dynamic single objective optimization approach was adopted using a weighted sum of several objective functions (Paulen et al., 2014). In this paper, a single objective optimization approach is used to determine the optimal feeding profiles for the production of multilayered polymer nanoparticles. The objective function describes the tracking of a piece-wise constant gel transition temperature (T_g) profile. The emulsion copolymerization of styrene and butyl acrylate in the presence of n-C12 mercaptan, as chain transfer agent (CTA), is used here as a case study. The key feature of the method is to optimally control the polymerization reaction at the different stages of the process (i.e. different layers) using the feed profiles of two monomers, whose homopolymers have different T_g values. The approach presented here is the extension of the results obtained in the case of core-shell nanoparticles. Nevertheless, a significant modification is brought to improve the optimization procedure by using two separate feeds for the two monomers, while implementing a different set of constraints.

This paper is organized as follows: after the formulation of the optimization problem, the main simulation results are presented and discussed followed by the conclusions.

2. Formulation of the problem

The glass transition temperature (T_g) of a polymer has a major impact on the physical and mechanical properties of the final productat a given temperature (i.e. hard or rubber-like material). The T_g, in turn,depends strongly on the microstructure of the macromolecules, which if controlled will lead to controlled properties. Recently, the instantaneous glass transition temperature profile was proven to be an effective tool to tailor and produce core-shell nanoparticles with specific end-use properties(Benyahia et al., 2012; Paulen et al., 2014). Here, the idea is extended to the case of multilayered nanoparticles. The key feature of the method is to copolymerize two monomers, in a dynamically controlled way (i.e. tracking),in order to achieve a targeted glass transition temperature profile and therefore, specific end-use properties.

The process considered is an emulsion copolymerization of styrene and butyl acrylate in the presence of n-C12 mercaptan as a chain transfer agent (CTA). The homopolymers, poly(butyl acrylate) and polystyrene, have significantly different glass transition temperatures (-54 °C and 100 °C respectively). This key characteristic makes it possible to produce copolymers with T_g values between -50 and 100 °C. The process model was developed and validated elsewhere (Benyahia et al., 2010; Benyahia et al., 2012).The mathematical model is a hybrid differential algebraic system,which entails 18 ordinary differential equations and several algebraic equations.For more flexibility, two pre-emulsions feeds are considered (one for each monomer).

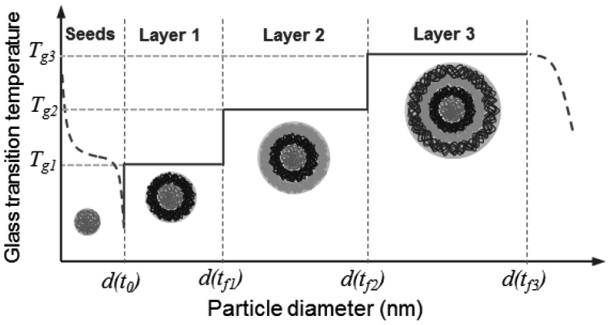

Figure 1: Instantaneous glass transition temperature (T_{gi}) profile of the multilayered particles.

The objective is to produce multilayered nanoparticles with specific final diameter, layer thicknesses and glass transition temperature profile,using optimal feed rate profiles of pre-emulsioned styrene and butyl acrylate.The resulting dynamic optimization problem is described by equations 1-13. The objective function describes the minimization of the error between the actual instantaneous glass transition temperature profile and the reference profile or trajectory (Fig. 1).

$$
\begin{cases}
\underset{Q_{Mi,i},\Delta t_i}{Min}\ f = \dfrac{1}{t_{f1}-t_0}\int_{t_0}^{t_{f1}}\left|T_g - T_{g1}\right| dt + \dfrac{1}{t_{f2}-t_{f1}}\int_{t_{f1}}^{t_{f2}}\left|T_g - T_{g2}\right| dt \\
\qquad + \dfrac{1}{t_{f3}-t_{f2}}\int_{t_{f1}}^{t_{f3}}\left|T_g - T_{g3}\right| dt & (1) \\
s.t.\quad \dot{\boldsymbol{x}} = \boldsymbol{f}(\boldsymbol{x}(t),\boldsymbol{u}(t),\boldsymbol{p},t)\ ;\ x(t=0) = x_0 & (2) \\
X(t_0) = 0.90 & (3) \\
\dfrac{1}{t_{f1}-t_0}\int_{t_0}^{t_{f3}}\left(0.9 - X(t)\right)^2 dt \le \varepsilon^2 & (4) \\
d_p(t_{f1}) = 60\ nm & (5) \\
d_p(t_{f2}) = 70\ nm & (6) \\
d_p(t_{f3}) = 80\ nm & (7) \\
X(t_f) = 0.99 & (8) \\
\bar{M}_n(t_f) \le 4\times10^4 & (9) \\
\bar{M}_w(t_f) \le 1.5\times10^5 & (10) \\
0 \le \Delta t_j \le 3600\ s & (11) \\
0 \le Q_{Mi,j}(t) \le \boldsymbol{8}.33\times10^{-7}\ m^3\cdot s^{-1} & (12) \\
\sum_{j=1}^{n} Q_{Mi,j}(t)\Delta t_j \le M_{Mi,em} & (13) \\
\boldsymbol{u}^T = \left[\Delta t_1, \Delta t_2, \ldots, \Delta t_n, Q_{M1,1}, Q_{M1,2}, \ldots, Q_{M1,n}, Q_{M2,2}, \ldots, Q_{M2,n}\right] &
\end{cases}
$$

where T_g is the time dependent glass transition temperature T_{g1}, T_{g2}, $T_{g3}$the desired glass transition temperatures for the different layers (T_{g1}= 3 °C, T_{g2} = 10 °C, T_{g3} = 17 °C), t_{f1}, t_{f2},$t_{f3}$the time required to complete the different layers, X the overall conversion, $\boldsymbol{u}$ the control vector (feed rates and time periods). $\bar{M}_n$, $\bar{M}_w$the number and weight average molecular weights, $Q_{Mi,j}$the feed rate of the pre-emulsioned it hmonomer at the jth time period, and $M_{Mi,em}$ the total mass of the pre-emulsioned ith monomer.

At the first stage of the process, the primary particles are produced under batch conditions. This stage ends when the overall conversion reaches the value of 0.9 (Eq. 4). The reactor is then fed optimally and separately with the pre-emulsioned monomers to achieve a glass transition temperature of 3°C(T_{g1}). To improve the control of the three different layers,the polymerization is conducted as close as possible to the starving

conditions (no droplets are produced and the feed rates are equal to the polymerization rates). This is described by Eq. 3. The second stage (first layer) ends when the particle diameter is equal to 60 nm as described by the constraint in Eq. 5.The third and fourth stages (second and third layer) are conducted in a similar way under starving conditions. The objective is to achieve the targeted glass transition temperatures of 10 °C and 17 °C respectively. These stages end when the particle diameter is equal to 70 then 80 nm (Eq. 6-7). The final stage is operating under batch conditions. At this stage, the objective is to achieve a higher overall conversion to consume the residual monomers as described by Eq. 8. In addition, two constraints, inherent to the polymer properties, are imposed on the number and weight molecular weights (Eq. 9-10).

3. Result and discussion

The dynamic optimization problem described by Eq.1-13 is solved using an elitist genetic algorithm developed to solve both multiobjective and single objective optimization problems (Benyahia, 2009). The formulation used for the initial charge and pre-emulsioned monomers feeds are depicted in Table 1. The number of the control variables is 27 (i.e. 9 time periods and 9 feed rates for each monomer).

For the sake of brevity, only the key simulation results are presented in Fig. 2.Additional simulation results, such as residual mass fractions, number and weight average molecular weights,are not presented here.

First, the optimal feed rate profiles are depicted in Fig.2a. It is shown that more styrene than butyl acrylate is required at the beginning of the second stage (i.e. first layer). Indeed, the reactor contains more butyl acetate, at the end of the seeding stage, which presents a lower reactivity compared styrene. As a consequence, butyl acetate is consumed more slowly than styrene leading, at the end the batch stage, to a decreasing T_g profile (Fig.2b).A very good fit is achieved between the resulting and targeted piece-wise constant profiles. This result showed an enhanced control of the T_g profile over our previous optimization problem in which only the first layer is conducted under starting conditions (Benyahia et al., 2012; Paulen et al., 2014). However, due to the slow process induced by imposing this constraint throughout the production of the different layers, the overall time required (t_f) is much larger. The overall conversion profile, depicted in Fig. 2c, gives a good indication on the conversion trajectory, which fits in well with the specified constant profile (X=0.9) inherent to the specified starving condition. In addition, as specified by the constraints (Eq. 8), the process ends when the overall conversion reaches 0.99.

Table 1:Summary of the formulation used.

Species	Initial charge (g)	Feed charge 1 (g)	Feed charge 2 (g)
Butyl acrylate	12	48	0
Styrene	12	0	48
Initiator, $(NH_4)_2S_2O_8$	1.0	0	0
REWOPOL SBFA 50	3	6	6
Water	114	228	228
n-C12 mercaptan (CTA)	0.12	0.24	0.24
Temperature (◦C)	70	25	25

At last, fig.2d shows the dynamic profile of the particle diameter. First and foremost, the final diameter drifts less dramatically from the specified diameter, at the end of the last layer, compared to our previous optimization approaches (Benyahia et al., 2012; Paulen et al., 2014). This advantage is mainly due to the separated monomers feeds as well as to the extension of the starving condition to all polymer layers. In addition, it is proven that the diameter of the particles at the end of each stage, complies perfectly with the specified constraints.

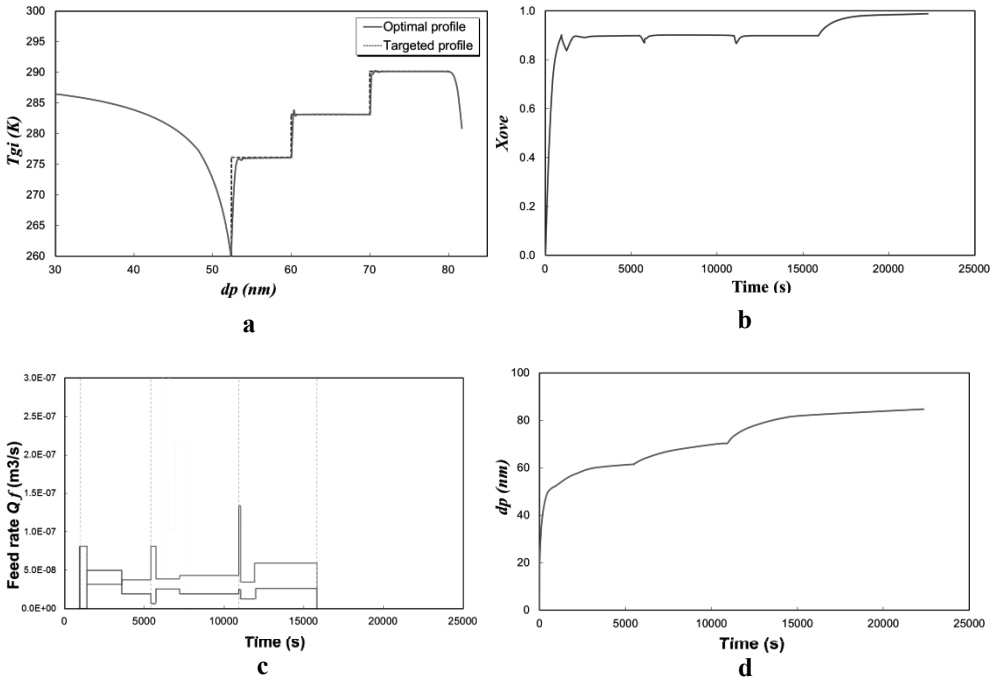

Figure 2: a-feed profile of the best solution, b- instantaneous glass transition temperature profile, c- overall conversion, d- average diameter.

4. Conclusions

A dynamic optimization framework is used to tailor the morphology of multilayer nanoparticles. A piece-wise constant T_g profile is used as a reference trajectory in the optimal tracking problem. To enhance the flexibilityof the optimization procedure, the pre-emulsioned monomers are fed separately. As a result, 27 control variables are used (9 time periods and 9 feed rates for each monomer). In addition, the starving condition is extended to all fed-batch stages. Although the process requires longer time, compared to the previous published approaches, a much better control of the T_g profile, and consequently to the resulting morphology, is achieved. In addition, a better control of the particle size is achieved as the final particle size doesn't drift away significantly. This key result is mainly due the constraint inherent to the starving condition thanks to whichthe final batch stage contains less residual monomers.

References

B. Benyahia, 2009, Modélisation, expérimentation et optimisation multicritère d'un procédé de copolymérisation en émulsion en présence d'un agent de transfert de chaîne, Ph.D. thesis, France: National Polytechnic Institute of Lorraine, Nancy-University.

B. Benyahia, M.A. Latifi, C. Fonteix, F. Pla, S. Nacef, 2010, Emulsion copolymerization of styrene and butyl acrylate in the presence of a chain transfer agent. Part 1: Modeling and experimentation of batch and fed-batch processes, Chemical Engineering Science, 65, 850-869.

B. Benyahia, M.A. Latifi, C. Fonteix, F. Pla, 2011, Multicriteria dynamic optimization of an emulsion copolymerization reactor, Computers & Chemical Engineering, 35, 2886-2895.

B. Benyahia, M.A. Latifi, C. Fonteix, F. Pla, 2012, Emulsion copolymerization of styrene and butyl acrylate in the presence of a chain transfer agent. Part 2: Parameters estimability and confidence regions, Chemical Engineering Science, 90, 110-118.

A. Ediriwickrema, J. Zhou, Y. Deng, W. M. Saltzman, 2014, Multi-layered nanoparticles for combination gene and drug delivery to tumors, Biomaterials 35, 9343-9354.

R. Paulen, B. Benyahia, M.A. Latifi, M. Fikar, 2014, Analysis of optimal operation of a fed-batch emulsion copolymerization reactor used for production of particles with core-shell morphology, Computers & Chemical Engineering 66, 233-243.

O. Shevchuk, V. Tokarev, N. Bukartyk, S. Voronov, 2007, Formation of hollow polymeric microspheres with functionalized surface on the basis of latex particles with multilayered structure, Macromolecular Symposia , 254, 260-266.

Krist V. Gernaey, Jakob K. Huusom and Rafiqul Gani (Eds.), 12th International Symposium on Process Systems Engineering and 25th European Symposium on Computer Aided Process Engineering.
31 May – 4 June 2015, Copenhagen, Denmark

Systematic Design of Chemical Reactors with Multiple Stages via Multi-Objective Optimization Approach

Mohd Nazri Mohd Fuad,[a] and Mohd Azlan Hussain[b]

[a]*Chemical and Petroleum Engineering, Faculty of Engineering, Technology and Built Environment, UCSI University (North Wing), 56000, Kuala Lumpur, Malaysia*
[b]*Chemical Engineering Department, Faculty of Engineering, University of Malaya, 50603, Kuala Lumpur, Malaysia*

Abstract

The purpose of this study is to extend the approach that was introduced by Hillestad (2010) to handle chemical reactor design problem with multiple stages. Specifically, multi-objective optimization method will be used to generate Pareto optimal solutions that characterize the non-inferior solutions set for the problem. Following the identification of path-dependent design variables, several (possibly conflicting) design objectives will be selected and solutions of the corresponding problem will be generated from multi-objective optimization algorithm. This approach is investigated for two industrially important reactor systems: ethylene oxide and phthalic anhydride synthesis. By using reference-point based multi-objective evolutionary algorithm (R-NSGA-II), Pareto-optimal solutions are successfully generated within the region of user-specified reference points, thus facilitating in the selection of final optimal designs. Apart from the extensive selection of optimal candidate reactor designs, this approach also enables further insights to be obtained regarding the optimal arrangement of the path-dependent design variables along the reactor length.

Keywords: systematic staging; chemical reactor design; multi-objective optimization; R-NSGA-II; ethylene oxide; phthalic anhydride.

1. Introduction

Chemical reactors have always been considered as the heart of chemical processes. Improved reactor design and operation will usually translate into significant cost savings and revenue potentials for the chemical plants. Various analytical methods and design strategies have been introduced to handle the complexity nature of these problems. Among such methods are attainable region, phenomena vectors, and superstructure optimization. Recently, Hillestad, (2010) has proposed a chemical reactor design that is based on a systematic staging concept along the reactor path. In this concept, the reactor path is divided into stages where each stage is designed so as to optimize a single objective function. Additional path-dependent design functions can be introduced for this purpose, for example, fluid mixing profile, distribution of extra feed points, coolant temperature profile, catalyst dilution, and many more. In this approach, the design problem is converted into an optimal control problem where the optimal path designs become the additional degree-of-freedom for optimization. This approach has the potential to derive novel reactor design that can improve further the performance of the process.

There are many trade-offs that must be considered carefully when designing a chemical reactor. Among these trade-offs are balancing the reactor size with reactant conversion, balancing reactant conversion with selectivity, or balancing heat transfer area with hot spot temperature. Suitable reactor design parameters must be selected so that these trade-offs can be balanced in an appropriate way. The multi-objective nature of this problem can be handled systematically if multi-objective optimization algorithm is adopted. In this approach, these trade-offs will become the objective functions to be optimized simultaneously while the algorithm will be used to generate non-inferior solutions along the Pareto-optimal front of these objective functions. The application of this approach for reactor design problem has been investigated for several important industrial reactor systems in the past. Some of these examples are styrene reactor system (Yee et al., 2003), steam reformer (Rajesh et al., 2000), and ethylene reactor (Tarafder et al., 2005).

The purpose of this study is to apply multi-objective optimization approach to derive optimal reactor design that employs systematic staging along the reactor path. Two industrial reactor systems are adopted to illustrate this method, i.e. ethylene oxide and phthalic anhydride synthesis. The corresponding reactors resemble a multi-tubular fixed-bed reactor with constant coolant/wall temperature. It will be shown that systematic staging concept that is coupled with multi-objective optimization algorithm will enable derivation of novel reactor design that can improve further the performance of the process in various aspects.

2. Mathematical modelling and optimization formulation

2.1. Plug-flow model

All the reactors in this study are treated as a plug-flow system to simplify the mathematical representation for optimization purpose. As the optimization step that is adopted in this work is a time-consuming process, the choice of this simpler representation will be justified front the point of view of minimizing the complexity of mathematical model solution. If required, the results can be further validated by simulating the reactor system with more complicated mathematical model later. However, the effort is being made also to validate the approach by comparing the obtained solutions with industrial reactor design that is simulated by the same mathematical model that is used for optimization. The following mathematical models are adopted to represent the corresponding reactor systems in this study:

Ethylene oxide synthesis reactor (Peschel et al., 2011):

$$\frac{dn_i}{dz} = L_t A_c \alpha \rho_b \sum_{j=1}^{N_R} \nu_{i,j} r_j \tag{1}$$

$$\frac{dT}{dz} = L_t A_c \frac{-\alpha \rho_b \sum_{j=1}^{N_R} r_j (-\Delta H_j) - \frac{4}{d_i} U (T - T_{cool})}{\sum_{i=1}^{N_I} n_i C_{pi}} \tag{2}$$

$$\frac{dP}{dz} = -L_t \left[150 \frac{\mu u_0 (1-\varepsilon)^2}{d_p^2 \varepsilon^3} + 1.75 \frac{\rho_f u_0^2 (1-\varepsilon)}{d_p \varepsilon^3} \right] 10^{-5} \tag{3}$$

with initial conditions $z = 0 \rightarrow n_i = n_{i0}$, $T = T_0$, and $P = P_0$.

Phthalic anhydride synthesis reactor (Orozco et al., 2010):

$$u_s \frac{dP_a}{dz} + L_t \left(\frac{\rho_b M_m P_t}{\rho_g}\right) r_a = 0 \quad (4)$$

$$u_s \rho_g C_p \frac{dT}{dz} - L_t \left[(-\Delta H)\rho_b r_a + \frac{4U}{d_t}(T - T_w)\right] = 0 \quad (5)$$

with initial conditions $z = 0 \rightarrow P_a = P_{a0}$ and $T = T_0$.

The kinetics expressions for the corresponding reactions are taken from the respective literatures: ethylene oxide synthesis (Al-Saleh et al., 1988) and phthalic anhydride synthesis (Anastasov, 2003).

2.2. Path-dependent design variables

A path is a line along the reactor where the reactions take place (Hillestad, 2010). Along this path, additional design variables can be introduced that act as the forcing function to modify the characteristics of the reaction process taking place. The path-dependent design variables for the respective reactor systems are summarized in Table 1. The corresponding variables are parameterized by piecewise constant profiles. This method divides the reactor path into several stages, N_z where the length and design variable for each stage is optimized.

Table 1. Path-dependent design variables for the respective reactor systems

Reactor system	Path-dependent variables	Number of stages
Ethylene oxide synthesis	Catalyst dilution	2
Phthalic anhydride synthesis	Catalyst types – low productive catalyst (Catalyst I) versus high productive catalysts (Catalyst II and Catalyst III)	3

2.3. Objective functions

The multiple objective criteria that are selected for each reactor designs are summarized in Table 2. These criteria are selected based on the profitability, safety, and cost minimization aspect of the reactor design. It can be seen that these criteria are conflicting with each other, thus requiring necessary trade-off in the final reactor design.

Table 2. Design objectives for the respective reactor systems

Reactor system	Design objectives	Target
Ethylene oxide synthesis	Ethylene oxide productivity	Maximize
	Heat transfer area	Minimize
	Active catalyst mass	Minimize
Phthalic anhydride synthesis	Phthalic anhydride composition	Maximize
	Mass of high productive catalysts	Minimize
	Total reactor volume	Minimize

2.4. Multi-objective optimization formulation

The multi-objective optimization problem for the reactor designs can be represented generally by the following mathematical statement:

$$optimize\left(f_1(x), f_2(x), \ldots, f_n(x)\right) \quad \text{objective functions vector} \quad (6)$$

s.t.

$$g_i(x) \leq 0 \quad i = 1, 2, \ldots, n_i \quad \text{inequality constraints} \quad (7)$$

$$h_i(x) = 0 \quad i = 1, 2, \ldots, n_i \quad \text{equality constraints} \quad (8)$$

$$x_l \leq x \leq x_u \quad \text{decision variables bound} \quad (9)$$

where n is the number of objective functions to be optimized simultaneously, x is the vector of m decision variables (continuous and/or discontinuous) with lower (x_l) and upper (x_u) bounds, n_i and n_e are the number of inequality (g) and equality (h) constraints, respectively. The lists of decision variables and constraints for the respective reactor systems are presented in Table 3.

Apart from the path-dependent design variables, the following reactor design parameters (i.e. tube length, tube diameter, and number of tubes) are also included as additional decision variables for the optimization. Tube diameters and number of tubes are specified by discrete variables so as to follow precisely the allowable range of variation for the corresponding reactor design parameters. The inequality constraint for the minimum exit pressure is also specified to ensure that allowable pressure drop is maintained throughout the reactor length.

Table 3. Decision variables and constraints for the reactor design optimization

Reactor system	Decision variables	Constraints
Ethylene oxide synthesis	α_k, L_k	$0.5 \leq \alpha_k \leq 1$ $\sum_k^{N_z} L_k = L_t$ $T_{max} < 553.15$
Phthalic anhydride synthesis	γ_k, L_k	$\gamma_k \in \{Cat_I, Cat_{II}, Cat_{III}\}$ $\sum_k^{N_z} L_k = L_t$ $T_{max} < 703.15$

2.5. Solution by using R-NSGA-II

As opposed to single-objective optimization that only gives single optimal solution, solutions of multi-objective optimization problems give rise to Pareto-optimal solutions that characterize the non-inferior solutions set for these problems. These solutions have the property such that when one moves from one solution to another in the corresponding set, one objective function improves while the other worsens. In this work, reference- point based multi-objective evolutionary algorithm method (R-NSGA-II) (Deb et al., 2006), a modification of the well-known and popular multi-objective genetic algorithm method (i.e. NSGA-II) is adopted to solve the corresponding reactor design problems. The modification of the original NSGA-II algorithm allows the generation of Pareto-optimal solutions near the region of user-specified reference points, thus facilitating the selection of final optimal solutions. More information regarding the algorithm implementations can be found from their original literatures (Deb et al., 2002; Deb et al., 2006).

3. Results and discussion

Pareto-optimal solutions obtained from R-NSGA-II runs are shown in Fig. 1 for each reactor system considered. The corresponding Pareto solutions are obtained after 200 generations with population size 50, crossover probability 0.7, and mutation rate 0.3. The ε parameter that controls the spread of solutions near the chosen reference points for R-NSGA-II strategy is set at 0.01. The corresponding reference points and the representative industrial reactor designs are also shown in the same figures for comparison purpose. These Pareto solutions offer extensive selections of candidate reactor designs that can be found within the region of user-specified reference points. These solutions also offer insights into the optimal arrangement of the path-dependent

design variables along the reactor length. For ethylene oxide reactor design case, the analysis of the selected Pareto solution clearly indicates that the location of catalyst dilution zone should be near the reactor inlet (see Table 4). The benefits of this configuration are that total heat transfer area can be reduced without increasing the hot spot temperature beyond acceptable limit while at the same time the productivity of ethylene oxide can be further increased. For phthalic anhydride reactor design case, the examination of the selected Pareto solution clearly indicates that the optimum staging of catalyst types can improve further the phthalic anhydride (PA) exit composition if compared with the industrial reactor designs where only one type of catalyst is employed throughout the reactor (see Table 5).

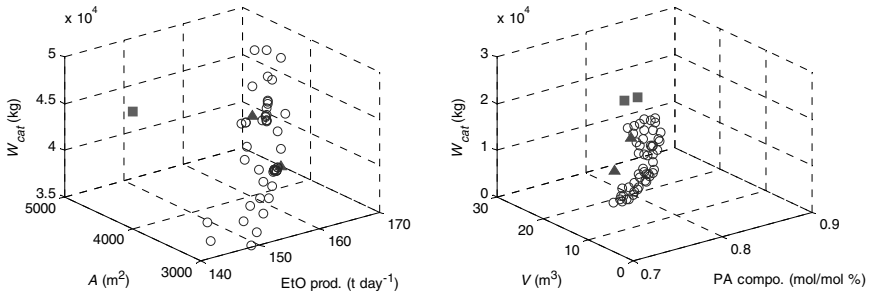

Fig. 1. Pareto optimal solutions for multi-objective optimization of ethylene oxide and phthalic anhydride reactor designs. Pareto solutions (circles), reference points (triangles), and industrial reactors (squares)

Table 4. Comparison of selected Pareto solution with industrial reactor (ethylene oxide reactor design case)

Reactor parameters	Industrial	2-stage configuration
Design parameters:		
Tube length (m)	8	6.19
Tube diameter (mm)	$d_o = 38.1$, $d_i = 31.3$	$d_o = 44.5$, $d_i = 42.7$
Number of tubes	5160	4068
Catalyst per reactor (kg)	42484	41823
Total heat transfer area (m^2)	4941	3519
Path-dependent design variables:		
α_k		$\alpha_1 = 0.5$, $\alpha_2 = 1$
L_k (m)		$L_1 = 1.64$, $L_2 = 4.55$
Operating parameters:		
Ethylene productivity (t d^{-1})	150.87	159.49
Hot spot temperature (K)	555.69	552.97

4. Conclusion

Systematic staging of chemical reactor design via multi-objective optimization approach has been investigated in this study. By demonstrating the application on two industrially important reactor systems (i.e. ethylene oxide and phthalic anhydride synthesis), it can be shown that optimal reactor designs can be obtained that utilized optimally the path-dependent design variables along the reactor length. These results show promising improvement to the reactor design and operation. Moreover, the analysis of the multi-objective optimization results also offers valuable insights into the optimal arrangement of the selected path-dependent design variables that can improve further the

performance of the reaction system. This multi-objective optimization approach is applicable to design other industrial fixed-bed reactors operated under non-isothermal condition.

Table 5. Comparison of selected Pareto solution with industrial reactor (phthalic anhydride reactor design case)

Reactor parameters	Industrial			3-stage configuration
Design parameters:				
Tube length (m)		2.8		2.84
Tube inner diameter (mm)		26		35.5
Number of tubes		10550		5579
Catalyst per reactor (kg)		23525		23486 (Cat. I = 45.2 %, Cat. II = 4.46 %, Cat. III = 50.34 %)
Total heat transfer area (m^2)		2654		1893
Total reactor volume (m^3)		15.68		15.66
Path-dependent design variables:				
γ_k				γ_1 = Cat. III, γ_2 = Cat. I, γ_3 = Cat. II
L_k (m)				$L_1 = 1.43$, $L_2 = 1.28$, $L_3 = 0.13$
Operating parameters:	Cat. I	Cat. II	Cat. III	
PA composition (mol mol^{-1} %)	0.733	0.785	0.771	0.81
Hot spot temperature (K)	727.10	703.19	688.09	701.43

References

M. A. Al-Saleh, M. S. Al-Ahmadi and M. A. Shalabi, 1988, Kinetic study of ethylene oxidation in a Berty reactor, Chemical Engineering Journal, 37, 35-41.

A. I. Anastasov, 2003, An investigation of the kinetic parameters of the o-xylene oxidation process carried out in a fixed bed of high-productive vanadia-titania catalyst, Chemical Engineering Science, 58, 89-98.

K. Deb, A. Pratap, S. Agarwal and T. Meyarivan, 2002, A Fast and Elitist Multiobjective Genetic Algorithm: NSGA-II, IEEE Transactions on Evolutionary Computation, 6, 182-197.

K. Deb, J. Sundar, U. B. Rao N. and S. Chaudhuri, 2006, Reference Point Based Multi-Objective Optimization Using Evolutionary Algorithms, International Journal of Computational Intelligence Research, 2, 3, 273-286.

M. Hillestad, 2010, Systematic staging in chemical reactor design, Chemical Engineering Science, 65, 3301-3312.

G. A. Orozco, J. R. Gomez, O. F. Sanchez, I. D. Gil and A. Duran, 2010, Effect of kinetic models on hot spot temperature prediction for phthalic anhydride production in a multitubular packed bed reactor, The Canadian Journal of Chemical Engineering, 88, 224-231.

A. Peschel, F. Karst, H. Freund and K. Sundmacher, 2011, Analysis and optimal design of an ethylene oxide reactor, Chemical Engineering Science, 66, 6453-6469.

J. K. Rajesh, S. K. Gupta, G. P. Rangaiah and A. K. Ray, 2000, Multiobjective optimization of steam reformer performance using genetic algorithm, Industrial and Engineering Chemistry Research, 39, 706-717.

A. Tarafder, B. C. S. Lee, A. K. Ray and G. P. Rangaiah, 2005, Multiobjective optimization of an industrial ethylene reactor using a nondominated sorting genetic algorithm, Industrial and Engineering Chemistry Research, 44, 124-141.

A. K. Y. Yee, A. K. Ray and G. P. Rangaiah, 2003, Multiobjective optimization of an industrial styrene reactor, Computers and Chemical Engineering, 27, 111-130.

Krist V. Gernaey, Jakob K. Huusom and Rafiqul Gani (Eds.), 12th International Symposium on Process Systems Engineering and 25th European Symposium on Computer Aided Process Engineering.
31 May – 4 June 2015, Copenhagen, Denmark

Synthesis and Design of Integrated Process and Water Networks

Zainatul B. Handani, Alberto Quaglia, Rafiqul Gani*

CAPEC-PROCESS, Department of Chemical and Biochemical Engineering, Technical University of Denmark, 2800 Kgs. Lyngby, Denmark
rag@kt.dtu.dk

Abstract

This work presents the development of a systematic framework for a simultaneous synthesis and design of process and water networks using the superstructure-based optimization approach. In this framework, a new superstructure combining both networks is developed by attempting to consider all possible options with respect to the topology of the process and water networks, leading to Mixed Integer Non Linear Programming (MINLP) problem. A solution strategy to solve the multi-network problem accounts explicitly the interactions between the networks by selecting suitable technologies in order to transform raw materials into products and produce clean water to be reused in the process at the early stage of design. Since the connection between the process network and the wastewater treatment network is not a straight forward connection, a new converter interval is introduced in order to convert the values of contaminants in the wastewater stream into wastewater characterizations. The systematic approach is used to manage the complexity of the problem by solving simultaneously process synthesis and water synthesis network problems with respect to environment, economics and sustainability. The applicability of the systematic approach is demonstrated using a conceptual case study to test the features of the solution approach under different scenarios depending on the design-synthesis problem.

Keywords: synthesis and design; simultaneous approach; process and water networks; superstructure; decision-making

1. Introduction

Currently, significant efforts are being made to reduce fresh water consumption and wastewater generation in process industries due to the escalation of fresh water and effluent treatment costs and stringent regulations. One of the more efficient ways to reduce fresh water consumption in the process is by reusing wastewater that is generated by the process after being treated in the wastewater treatment plant to acceptable limits. This can done by considering various treatment technologies and exploring numbers of alternatives. In addition, different process technologies and design alternatives are also being considered in the processing network to transform raw materials into products while reducing fresh water consumption and wastewater generation. One of the techniques used to represent the design space and identify best technology network is superstructure-based optimization techniques (Yeomans and Grossmann, 1999; Quaglia et al., 2012).

Process synthesis provides an attractive framework for tackling numerous design problems through a systemic approach either by using a sequential approach or a

simultaneous optimization approach. In a sequential approach, the subsystem, i.e., water network and heat exchanger network are solved or dealt after an optimal flowsheet is identified. As a contrast to the sequential approach, the simultaneous approach has advantages where all interactions and economical trade-offs are taken into account explicitly (Duran and Grossmann, 1986; Yee et al., 1990; Yang and Grossmann, 2013). However, it is important to note that the simultaneous optimization approach can become complex and difficult task since it involves many decision-making at the early stage of design where many alternatives are considered, involving the selection of raw materials, process and wastewater treatment technologies and product portfolio for the process network. Hence, in this contribution, we expand the framework developed by (Quaglia et al., 2012) by integrating the process and wastewater networks. A simultaneous optimization approach mathematically combines the problem of multi-network involving process and wastewater treatment networks into a single step (so called as *a network within a network*). The application of the solution approach is highlighted through a conceptual example.

2. Framework of Integrated Process and Wastewater Networks

The systematic framework for processing networks developed by Quaglia et al. is extended and the superstructure-based optimization approach is used to simultaneously synthesize and design a chemical process and its related water treatment network in order to find an optimal process flowsheet and the wastewater treatment processing path. The framework is supplemented by a software infrastructure based on EXCEL for gathering required input data and GAMS (GAMS Development Corporation, 2013) for the solution of the formulated optimization problem.

Step 1: Problem definition

The first step comprises the definition of the goal and problem scope, the selection of a suitable objective function and the description of optimization scenarios with respect to economics, resource consumption and sustainability. The selection of the objective function is based on the main goal of the synthesis and design problem.

Step 2: Superstructure representation and data collection

In this step, various alternatives for the process and wastewater treatment networks are specified with respect to raw materials, technologies and products which create the search space for the design problem. A combined superstructure is proposed for systematically addressing the simultaneous synthesis of the integrated process and water networks, and exploring the interactions between process network and water network. The superstructure is arranged as a sequence of process steps in order to transform raw materials into products/byproducts/wastewater by considering numerous technologies for each process and wastewater treatment step contained in the networks. The treated wastewater in the treatment tasks can be either discharged into the environment and/or it can be recycled for use in the same processes or in neighboring processes. A new feature of this superstructure is the connection between the process network and the wastewater treatment network through a converter interval. The purpose of this converter interval is to transform the values of contaminants in the wastewater stream into wastewater characterizations. In the superstructure, bypass intervals are considered in the process network and wastewater treatment network in order to allow the possibility of bypassing a certain type of process or treatment step. All data and information essential for the design problem formulation are collected. The data consist

of the parameters required to represent the activity of each process alternative and wastewater treatment alternative including mixing, reaction, waste splitting and product separation. If parameters used in the general process interval are not available, for instance, the complete stoichiometry of the reaction in converter interval, it can be estimated from available information about mass inlet and outlet streams of the interval using Eq. (1).

$$\gamma_{i,kk,rr} = \frac{-(mass_{(i,kk,rr)out} - mass_{(i,kk,rr)in})/MW_i}{(mass_{(react,kk,rr)out} - (mass_{(react,kk,rr)in})/MW_{react}} \quad (1)$$

Step 3: Model development

The next task is the development of generic models describing each of the elements of the superstructure as well as of models required for the calculation of the objective function and other performance indicators. All the necessary equations and constraints relevant to each process and wastewater treatment technology are also formulated in this step prior to be solved as MI(N)LP problems in optimization software i.e. GAMS.

Step 4: Formulate and solve MI(N)LP problem

The models represent the mass input-output model for each process interval in the superstructure, process constraints, structural constraints, effluent limit constraints, performance indicators and cost models together with the objective function are formulated as a MI(N)LP problem and solved in this step. The objective function is indicated based on the main goal of synthesis and design problem as defined previously in Step 1 (e.g. maximize product yield, maximize gross operating income, minimize total annual cost etc.).

2.1 Generic Interval Model

Each process interval in the superstructure is modeled in a generic way, which has been adapted from a previous study on a soybean processing network (Quaglia et al., 2012). The process interval incorporates generic models to represent alternatives in the process and wastewater treatment steps. A process interval combines different process tasks in one block. It can be described by a simple process flowsheet of different arrangements or represented as a series of unit operations depending on the identified process technology, which comprises of flow mixing (Eq. (2)), utility dosage (Eq. (3)), reaction (Eq. (4)), waste separation (Eq. (5)), product separation (Eq. (6)). It is noteworthy that the process task could be inhibited along with the relevant variables and equations if one or more of the process tasks are not available in the specific process interval. The generic interval model is given in Eq. (2-6).

$$ff_{i,kk} = fin_{i,kk} + \alpha_{i,kk} R_{i,kk} \quad (2)$$

$$R_{i,kk} = \sum_{ii} (\mu_{i,ii,kk} \cdot fin_{ii,kk}) \quad (3)$$

$$ffbar_{i,kk} = ff_{i,kk} + \sum_{rr,react} (\gamma_{i,kk,rr} \cdot \theta_{react,kk,rr} \cdot ff_{react,kk}) \quad (4)$$

$$ffdbar_{i,kk} = ffbar_{i,kk} \cdot (1 - SW_{i,kk}) \quad (5)$$

$$Fout1_{i,kk} = ffdbar_{i,kk} \cdot SPr_{i,kk} \quad (6)$$

3. Application Example: Conceptual Case Study

A conceptual case study is considered in order to show the application of the proposed framework. In the process, feed 1 contains of 95% of component A with 5% impurity E (unreactive component) while feed 2 contains of component B and it is desired to produce product C. The main chemical reaction in the process is given by:

$$A + B \rightarrow C + D$$

which is accompanied by the side reaction:

$$2C \rightarrow G + B$$

There are several alternatives to produce product C from reactant A and B. In this process, water is used as raw material and solvent. Threfore, wastewater produced from the process contains contaminants and need to be treated in a wastewater treatment facility. The objective of the conceptual case study is to synthesis and design the process and the wastewater treatment network that minimize the total annualized cost (TAC). In this scenario, effluent discharge and recycle water to be reused in the process as raw material is considered as the final products of the wastewater treatment. The aim of the problem is to determine the optimal processing route and water treatment configuration in order to satisfy product-process specification, environment limitation and water-using process requirement.

3.1 Superstructure representation and data collection

As can be seen in Figure 1, the combined process and water network superstructure are composed of 2 raw materials, 15 process intervals structured in 9 processing steps, 1 converter interval, 11 treatment intervals organized in 4 treatment steps, and 6 possible products and byproducts. Also, 16 components and 10 utilities are considered in this problem. The recycled water stream is included in the superstructure to further reduce fresh water intake. The selection of a wastewater treatment process depends on the characteristics of the wastewater. Since most of the compounds involved in the process plant are organic compounds, thus the wastewater can be characterized in terms of chemical oxygen demand (COD), biological oxygen demand (BOD) and total suspended solids (TSS). A correlation exists between the biodegradable part of the COD and the BOD but the relation between these two is usually determined experimentally and is highly dependent on the type of wastewater considered (Tchobanoglous et al., 2004). The COD values of the wastewater stream are determined by calculating the theoretical oxygen demand based on the oxygen equivalent,which is determined from the chemical formula of the organic matter. In order to simplify the calculations, BOD and TSS are assumed to be 0.6 and 0.1 of the total COD for a typical chemical industry (Smith, 2005). Since the stoichiometry reaction for the converter interval is not available, it can be estimated using Eq. (1)). A pseudo-reaction represents the conversion of the compounds in the wastewater stream generated by the process.

On the other hand, following the systematic data collection procedure, all the necessary data for the process interval models have been collected. An example is provided here

to illustrate a process model for the upflow anaerobic sludge blanket (UASB) treatment interval. The key reactant here is selected and removed with a conversion efficiency of ($\theta_{react,\ kk,\ RR}$) 90%. Although being removed from the system, it consumes nutrient (NH_3), and produces carbon dioxide (CO_2) and methane (CH_4) together with biomass. All the removal, consumption and production are defined related to the key reactant by the reaction stoichiometry given in $\gamma_{i,kk,rr}$ matrix. The required ammonia consumption is calculated to be 445.4 kg/day and this amount is added to the system via $R_{i,kk}$ and totally mixed ($\alpha_{i,kk}=1$) with the incoming flow $Fin_{i,k,kk}$. On the other hand, all of generated sludge and 30% removal efficiency of the rest solids are removed as waste. The gas produced (CO_2 and CH_4) during treatment process are 100% recovered in the secondary outlet stream.

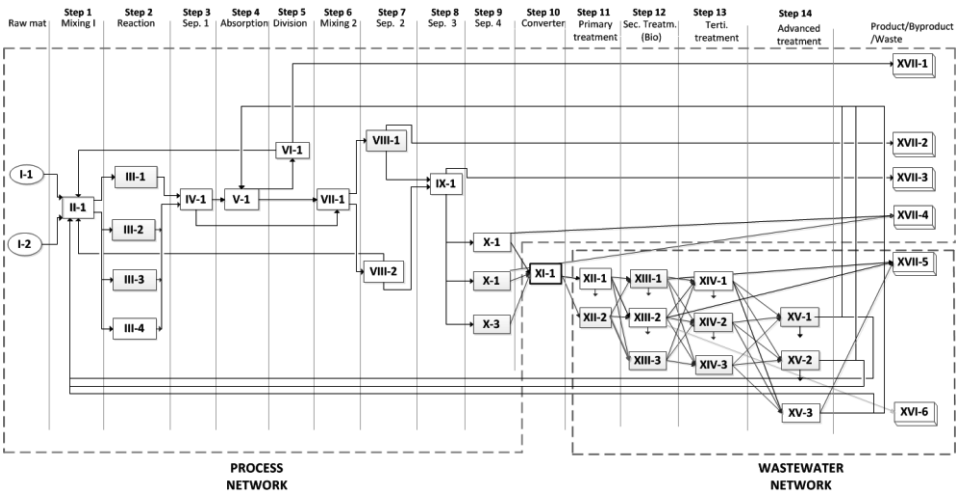

Figure 1: Process and wastewater network superstructure for conceptual case study.

3.2 Results and discussion

The problem is formulated as MINLP and solved using GAMS/BARON to identify the optimal process and water networks. The case study was performed using a standard computer, equipped with 3.60 GHz Intel (R) Xeon (R) E-51620. The superstructure of the combined process and water network features 148,120 continuous variables, 143,493 equations and 20 binary variables. In this scenario, one possible recycled water alternative is considered to reduce fresh water consumption in the process. It should be noted that the effluent discharge of partially treated wastewater to the environment is one of the options. The results in Table 1 present the comparison of optimal process and wastewater treatment path for the problem with and without considering recycled water. It is important to note that by considering recycled water opportunity to be used in the process as raw material resulted in savings of up to 51.1% fresh water consumption. On the other hand, the synthesis problem with recycled water option gives higher TAC since one of tertiary treatment has been selected in order to produce higher quality of treated wastewater to be recycled to the process as a raw material.

Table 1: Comparison of different objective functions for base case scenario. In bold the process intervals which are different from the ones selected for both scenarios

	Optimal Network				Obj. function (Min TAC)
	Raw material	Process steps	Water Treatment steps	Product/Byproducts/Effluent	
Without recycle option	I-1 I-2	II-1 III-4 IV-1 V-1 VI-1 VII-1 VIII-2 IX-1 X-1	XII-1 XIII-2 **XIV-3 (BP)** XV-3 (BP)	XVI-1 XVI-3 XVI-4 XVI-5 XVI-6	M$ 65.2 /y
With recycle option	I-1 I-2	II-1 III-4 IV-1 V-1 VI-1 VII-1 VIII-2 IX-1 X-1	XII-1 XIII-2 **XIV-1** XV-3 (BP)	XVI-1 XVI-3 XVI-4 XVI-5 XVI-6	M$ 73.2 /y

4. Conclusion and Future Work

A systematic approach is used to manage the complexity and solving simultaneously process synthesis and water synthesis network problem with respect to economics, resources consumption and sustainability. In order to achieve this task optimally and efficiently, a new superstructure is proposed and formulated for the simultaneous synthesis of the process and water network. The superstructure-based optimization methodology has been shown to be a useful decision support tool for early stage synthesis and design networks by screening a large number of design alternatives. In addition, the interaction between two networks is visualized via selection appropriate raw materials, technologies and alternatives for process and water treatment as well as products. Future work will focus on the application of the framework on different case studies involving various types of chemical processes and optimization scenarios in order to develop a flexible and versatile methodology.

References

A. Quaglia, B. Sarup, G. Sin, R. Gani, 2012, Integrated business and engineering framework for synthesis and design of enterprise-wide processing networks, Computers & Chemical Engineering, 38, 213-223.

G. Tchobanoglous, F. L. Burton, H. D. Stensel, 2003, Wastewater engineering: Treatment and Reuse, McGraw-Hill, NY, U.S.A.

GAMS Development Corporation, 2013, GAMS: General Algebraic Modeling System Washington DC, USA.

H. Yeomans, I.E. Grossmann, 1999, A systematic modeling framework of superstructure optimization in process synthesis, Computers & Chemical Engineering, 23(6), 709-731.

L. Yang, I.E. Grossmann, 2013, Water Targeting Models for Simultaneous Flowsheet Optimization, Industrial & Engineering Chemistry Research, 52(9), 3209-3224.

M.A. Duran, I.E. Grossmann, 1986, Simultaneous optimization and heat integration of chemical processes, AIChE Journal, 32, 123-138.

R. Smith, 2005, Chemical process design and integration, John Wiley & Sons, Ltd, England.

T.F. Yee, I.E. Grosmann, Z. Kravanja, 1990, Simultaneous optimization models for heat integration-III. Process and heat exchanger network optimization. Computers & Chemical Engineering, 14(11), 1185-1200.

Krist V. Gernaey, Jakob K. Huusom and Rafiqul Gani (Eds.), 12th International Symposium on Process Systems Engineering and 25th European Symposium on Computer Aided Process Engineering.
31 May – 4 June 2015, Copenhagen, Denmark

Optimization of High-Density Polyethylene Process Based on Molecular Weight Distribution and Chemical Composition Distribution under Uncertainty

Jiayuan Kang[a], Xi Chen[a], Zhijiang Shao[a*]

[a] *State Key Laboratory of Industrial Control Technology, Department of Control Science and Engineering, Zhejiang University, Hangzhou, Zhejiang, 310027, *zjshao@iipc.zju.edu.cn*

Abstract

High-density polyethylene (HDPE) is widely used as the main material in the film, pipe, and container industries. Currently, introduction of copolymer into the HDPE polymerization process can significantly improve the performance of the product due to the balance of microstructures. Microstructures of copolymers such as molecular weight distribution (MWD) and chemical composition distribution (CCD) are thus of great importance for evaluating quality of HDPE products. However, due to technical restrictions, current measurement methods bring uncertainty in the determination of polymer microstructures. This paper addresses the optimization of HDPE product with expected MWD and CCD under these uncertainties. The formulation of the optimization problem includes uncertainty metric of target MWD and CCD and productivity optimization of the HDPE process. A decomposition strategy is adopted to evaluate the uncertainty at upper level and optimize the process rigorous model at lower level. Linear Taylor expansion of the target profiles at design point is used to characterize the "worst case" adopting deterministic approach. An industrial HDPE process is discussed and the results show the effectiveness of the approach.

Keywords: copolymerization**,** MWD, CCD, uncertainty formulation, process optimization

1. Introduction

HDPE is one of the most consumed commodity polymers due to the low production cost and versatility in mechanical and rheological properties. Currently, introduction of copolymer into the HDPE polymerization process can significantly improve the performance of the product. The end-use properties such as polydispersity indices (PDI), number average molecular weights (Mn), and comonomer average molar fraction $\overline{F_A}$ are determined by the MWD and CCD profiles. However, rheological based MWD and CCD measurement methods give rise to quite uncertainty to the true profiles. Symmetric deviation of the GPC/SEC trace leads to a broaden MWD, while TREF or CRYSTAF profiles can only provide apparent values of CCD (Soares et al, 2012). These uncertainties give rise to discrepancy of HDPE product determination. This kind of uncertainty can be modelled as a symmetric and bounded random uncertainty set (Ben-Tal and Nemirovski, 2000). The uncertainties in MWD and CCD profiles involve a large number of uncertain parameters that are not suitable to be chosen as design

parameters directly. The MWD and CCD deconvolution approaches determine the best fit of the profile parameters (Alghyamah and Soares, 2009).
In this paper, the MWD and CCD uncertainty metric is proposed. By using linear Taylor expansion at the nominal profile parameters, the maximum effect of target uncertainty is characterized. A sensitivity-based uncertainty decomposition approach is proposed to evaluate the uncertainty of the target profiles in the first step and optimize the operation conditions in the second step. In the present project, an equation-oriented (EO) model is developed for an industrial HDPE process. The problem formulation and solving approach that optimizes the productivity at given MWD and CCD under uncertainty are then presented.

2. Model Development

Figure 1 illustrates the flowsheet of an industrial HDPE slurry process with two CSTRs in series under study. A five-site Ziegler-Natta catalyst with $TiCl_4$ as the primary catalyst and $Al(C_2H_5)_3$ as the co-catalyst is used. 1-Butene is introduced as the comonomer of HDPE product. A complete EO model is established for the process. The modeling work consists of thermodynamics, copolymerization kinetics, MWD and CCD calculation. Thermodynamic properties are surrogated by Kriging method based on streams, which was described in our previous work (Zhang et al, 2013).

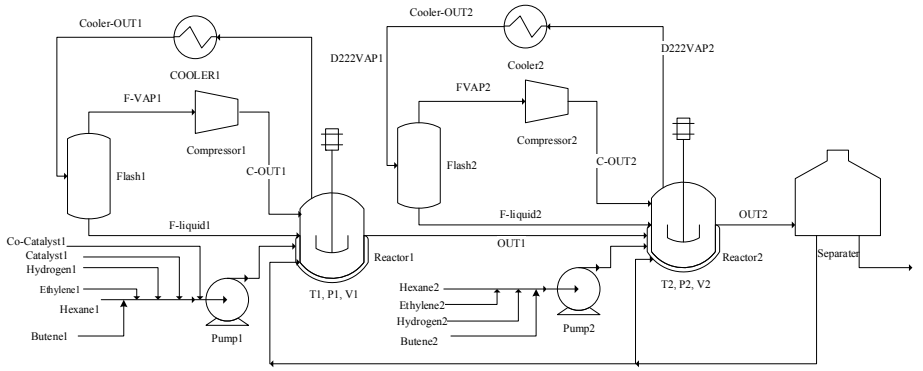

Figure 1. Flow chart of HDPE process

2.1 Copolymerization Kinetics and Moment Model

The copolymerization kinetics consist of catalyst activation, initiation, propagation, transfer to hydrogen, transfer to monomers, transfer to co-catalyst, transfer β-hydride, and deactivation. The terminal model (first-order Markov model) of binary copolymers, involving four propagation rate constants is used for the copolymerization mechanism. Population balances and the method of moments are adopted to describe the mass conservation of the polymer components. Zeroth and first order moment for both living and dead polymers are calculated for MWD and CCD models.

2.2 MWD and CCD Calculation

Instantaneous distribution method can be applied to steady state HDPE reactors (Zhang et al, 2013). The chain length distribution (CLD) made at site *j* is described by Flory distribution with a single parameter τ_j defined by pseudokinetic constants.

$$w_j(n) = n\,\tau_j^2/(1+\tau_j)^2 \tag{1}$$

The comonomer molar fraction distribution, called chemical composition distribution for binary copolymers is given by the Stockmayer bivariate distribution:

$$w_{\gamma j} = 3\tau_j^2\beta_j^2/(2\beta_j\tau_j+\gamma^2)^{5/2}, \quad \beta_j = \overline{F_{Aj}}(1-\overline{F_{Aj}})\sqrt{1-4\overline{F_{Aj}}(1-\overline{F_{Aj}})(1-r_{Aj}r_{Bj})} \tag{2}$$

where γ is the difference between the molar fraction of monomer A in a copolymer chain, F_{Aj}, and the average molar fraction of monomer A in the whole copolymer sample, $\overline{F_{Aj}}$; r_{Aj} and r_{Bj} are the reactivity ratios.

The entire distribution for a single reactor is represented as a weighted superposition of the Flory or Stockmayer distribution from each site type, respectively:

$$w(n)=\sum_{j=1}^{m} mf_j w_j(n) \quad , \quad w_\gamma=\sum_{j=1}^{m} mf_j w_{j\gamma} \tag{3}$$

where mf_j is the mass fraction of copolymer made on site type *j*.

Similarly, the CLD or CCD of the final product is also a weighted superposition of the two instantaneous distributions in each reactor, respectively:

$$w(n)=\frac{m_1 w1(n)+m_2 w2(n)}{m_1+m_2} \quad , \quad w_\gamma=\frac{m_1 w1_\gamma+m_2 w2_\gamma}{m_1+m_2} \tag{4}$$

where m_1 and m_2 are the copolymer masses made in the first and second reactors, respectively, which can be derived from the moment models.

3. Problem Formulation and Uncertainty Decomposition Approach

3.1 Problem Formulation and Uncertainty Metric of MWD and CCD

Generally, the HDPE productivity maximization problem can be formulated as a multi-object optimization problem, which maximizes the productivity and minimizes the quality deviation simultaneously. An alternative formulation is to add the quality tolerance constraint in the productivity maximization problem.

$$\begin{aligned} &\max_u F_{HDPE} \\ &s.t. \quad \left\|MWD_{cal}-MWD_{tar}\right\|\le\varepsilon_1 \quad , \quad \left\|CCD_{cal}-CCD_{tar}\right\|\le\varepsilon_2 \\ &f(z,u)\le 0 \, , \; g(MWD_{cal},z,u)=0 \, , \; h(CCD_{cal},z,u)=0 \end{aligned} \tag{5}$$

where F_{HDPE} is the flow rate of the final HDPE product, MWD_{cal} and CCD_{cal} are the calculated profile from the model, while MWD_{tar} and CCD_{tar} are the target profiles sampled from GPC and TREF data set, u and z are decision and state variables, respectively. The MWD and CCD deviation tolerance are set as ε_1 and ε_2, respectively. Considering the error of the GPC and TREF measurement may be as large as 20%, the tolerance cannot be too small, and is set all by experience.

In this paper, a symmetric and bounded random uncertainty set is used to characterize the potential behaviour of data uncertainty (Ben-Tal and Nemirovski, 2000). Associated with the uncertain target profile, denote a random variable θ, which obeys an unknown but symmetric probability distribution, and takes values in $[-\delta,\delta]$, where δ is the bound of the uncertainty set, i.e. the maximum error of GPC and TREF measurement. The uncertain data model is given by $y_{obs}=y_{nom}(1+\theta)$, where y_{obs} is the observed data set and y_{nom} is the unknown nominal profile. At given upper and lower bounds of the nominal profile y_{nom}, a relaxed deterministic description of the uncertainty set is

$$y_{obs}/(1+\delta)\le y_{nom}\le y_{obs}/(1-\delta) \tag{6}$$

To determine the source of uncertainty in distribution profile y_{nom} derived from y_{obs}, some prior knowledge is needed. The expression of Flory distribution and Stockmayer distribution consists of three parameters under determined as mf_j, τ_j, and β_j. Luckily, we have the prior estimate of mf_{prior}. Under the same catalyst system, the mass fractions

of copolymer made on different site are determined by the configured kinetic constants: $mf_{prior} = k_{pAA}(j) / \sum k_{pAA}(j)$ (Zhang et al, 2014). This estimate will not be affected by the uncertainty. Thus the nominal profile y_{nom} can be modelled as $y_{nom}(\tau_{nom} + \Delta_\tau)$, where τ_{nom} is the MWD or CCD parameter under determined, and Δ_τ is the perturbation caused by uncertainty θ. Hence the data uncertainty model (6) is modified by

$$y_{obs} / (1+\delta) \le y_{nom}(\tau_{nom} + \Delta_\tau) \le y_{obs} / (1-\delta) \tag{7}$$

Considering the inequality constraints, the effect of uncertainty Δ_τ on y_{nom} at the design point can be approximated by linear Taylor expansion as

$$y_{nom}(\tau_{nom} + \Delta_\tau) = y_{nom}(\tau_{nom}) + \sum_j \frac{\partial y_{nom}}{\partial \tau_{nom}} \Delta_{\tau j} + o(\Delta_\tau{}^2) \tag{8}$$

Neglecting high-order terms and substitute $y_{nom}(\tau_{nom} + \Delta_\tau)$ into (7), the nominal design point τ_{nom} will surely fulfill (7) if it fulfills the worst case (Beyer and Sendhoff, 2007):

$$y_{obs} / (1+\delta) \le y_{nom}(\tau_{nom}) - \sum_j \left| \frac{\partial y_{nom}}{\partial \tau_{nom}} \Delta_{\tau j} \right| \;,\; y_{nom}(\tau_{nom}) + \sum_j \left| \frac{\partial y_{nom}}{\partial \tau_{nom}} \Delta_{\tau j} \right| \le y_{obs} / (1-\delta) \tag{9}$$

The uncertainty metric of y_{nom} is given by $\max_{\tau_{nom}} \|\Delta_\tau\|$, which determines the maximum effect of uncertainty on the nominal design point τ_{nom}.

3.2 Sensitivity-based Uncertainty Decomposition Approach

The optimization problem (5) in Section 3.1 is hard to solve. The MWD and CCD constraints contribute to a large scale and ill-conditioned problem. Moreover, since the MWD and CCD calculation and the process model are not strongly coupled, it is reasonable to separate them into two parts. The first step is to estimate the profile parameters as mf_j, τ_j, and β_j, then the operation conditions are optimized. The most common approach is to minimize the scaled deviation of calculated distribution profiles to the target profiles:

$\min_{\tau_j, \beta_j, mf_j} \|(MWD_{cal} - MWD_{tar}) / MWD_{tar}\| + \|(CCD_{cal} - CCD_{tar}) / CCD_{tar}\|$ (Formulation I)

Formulation I provides the best fit of target MWD and CCD profiles. However, without modelling of uncertainty of the target profiles, these parameters are deterministic values, which contribute to tight bounds and solving difficulty for the process optimization in the second step.

The sensitivity based uncertainty decomposition approach evaluates the uncertainty of the target MWD and CCD profiles by solving a series of subproblems.

Step I: Evaluation of uncertainty metric

$\max_{\tau_{nom}} \|\Delta_\tau\|$ (Formulation II)

$$s.t. \quad MWD_{tar} / (1+\delta) \le MWD_{nom}(\tau_{nom}) - \sum_j \left| \frac{\partial MWD_{nom}}{\partial \tau_{nom}} \Delta_{\tau j} \right|$$

$$MWD_{nom}(\tau_{nom}) + \sum_j \left| \frac{\partial MWD_{nom}}{\partial \tau_{nom}} \Delta_{\tau j} \right| \le MWD_{cal} / (1-\delta) \;,\quad -\varepsilon \le mf_{nom} - mf_{prior} \le \varepsilon$$

Formulation II evaluates the uncertainty metric of MWD parameters, and contributes to robust intervals of MWD parameters, i.e. $[\tau_{nom} - |\Delta_\tau|, \tau_{nom} + |\Delta_\tau|]$, for the subsequent steps.

Next the same procedure is done for CCD to evaluate the uncertainty of β_j.

Step II: Process optimization

$\max_u F_{HDPE}$ (Formulation III)

$$s.t. \;\; \tau_{nom} - |\Delta_\tau| \le \tau_{cal} \le \tau_{nom} + |\Delta_\tau| \;,\; \beta_{nom} - |\Delta_\beta| \le \beta_{cal} \le \beta_{nom} + |\Delta_\beta| \;,\; -\varepsilon \le mf_{cal} - mf_{prior} \le \varepsilon$$

$f(z,u) \le 0$, $g_1(\tau_{cal}, z, u) = 0$, $g_2(\beta_{cal}, z, u) = 0$, $g_2(mf_{cal}, z, u) = 0$

Step II optimizes the operation conditions at the robust interval of nominal MWD and CCD parameters.

4. Results and Discussions

A simple case is analyzed to demonstrate the uncertainty metric evaluation procedure first. Considering single site MWD uncertainty metric evaluation, the real nominal parameters of the six experiments are shown in the first column of Table 1. The suffix (a) and (b) represent the uncertainty level of MWD_{tar}, i.e. δ in Formulation II, respectively. Here a=0.1, b=0.2, and corresponding Gaussian noises are imported to simulate the 100 MWD_{tar} values sampled from GPC with 10% and 20% error, respectively. Formulation I and II are adopted to estimate the MWD parameter τ. The estimated value of τ is shown in the second and third column. It should be pointed out that Formulation II provides the estimated nominal values and the uncertainty metric of τ. The sum of square deviations from the estimated MWD_{cal} or MWD_{nom} to the observed target MWD_{tar} is marked as D_{obs}, which is shown in the fourth and fifth column. D_{real} represents the sum of square deviations from the estimated MWD_{cal} or MWD_{nom} to the real MWD profile as shown in the sixth and seventh column.

Table 1. Comparison of Formulation I and II in uncertainty evaluation

Nominal	τ ($\times 10^{-6}$)		D_{obs} ($\times 10^{-6}$)		D_{real} ($\times 10^{-6}$)	
	I	II	I	II	I	II
0.001(a)	997.6	998.6 ± 4.7	6916	6922	37	13
0.002(a)	2003.2	1999.4 ± 8.5	5855	5877	16	0.6
0.003(a)	3004.1	2998.6 ± 14.8	4229	4251	12	1.5
0.001(b)	995.3	995.8 ± 9.2	27666	27668	147	117
0.002(b)	2006.5	1998.8 ± 14.8	23418	23509	66	2.3
0.003(b)	3008.2	2995.1 ± 28.3	16914	17039	48	18

From the fourth and fifth column in Table 1, we can see that D_{obs} calculated by Formulation I are always smaller than that of Formulation II. This can be explained that Formulation I minimizes the deviations from estimated nominal values to the observed values. Note that most of the deviations are contributed by the uncertainties. From the sixth and seventh column of Table 1, we can see that D_{real} calculated by Formulation II are always smaller than that of Formulation I, which means Formulation II can reduce the effect of MWD uncertainty, giving more accurate nominal estimate. Moreover, Formulation II provides the robust interval of the nominal estimate, as well as the MWD uncertainty metric, which is helpful for the subsequent process optimization steps.

The above case illustrates the effectiveness of Formulation II to uncertainty metric and reduction. An industrial HDPE case is analysed adopting the uncertainty decomposition approach proposed in Section 3.2. The uncertainty metric of target MWD and CCD are evaluated first according to Step I. The uncertainty level of MWD_{tar} and CCD_{tar} are set as $\delta_{MWD} = 0.2$ and $\delta_{CCD} = 0.3$ according to the prior information of GPC and TREF error level. Then the process optimization is performed adopting simultaneous approach, using interior point optimizer (IPOPT) as NLP solver. Comparisons of the final bimodal MWDs and CCDs are illustrated in Figure 2 and Figure 3. The unimodal MWDs in Figure 2 are the MWDs generated in each reactor. The MWD and CCD are consistent with the targets while the effect of uncertainty keeps a low level. The maximum scaled uncertainty metric of MWD is 0.0721, which is much larger than that of single site case. This means that multi-site of MWD or CCD under uncertainty contributes to more

uncertainty of design parameters. And the optimal operation conditions are presented in Table 2.

Table 2. Optimal operation conditions

	T(K)	P(atm)	Hydrogen(kmol/h)	Ethylene(kmol/h)	Butene(kmol/h)	Hexane(kmol/h)
Reactor1	358.15	7.93	4.05	125.89	0.30	14.43
Reactor2	345.20	4.18	0.22	128.26	1.87	12.30

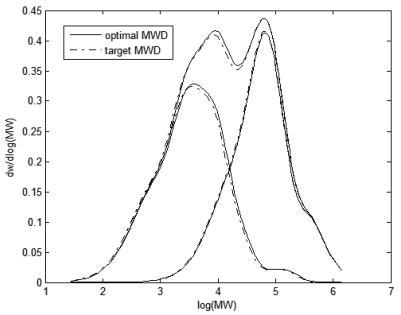

Figure 2 Comparison of MWD profiles

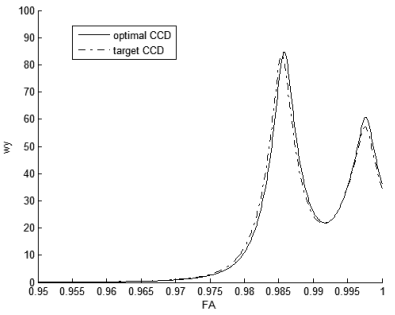

Figure 3 Comparison of CCD profiles

5. Conclusions

This study presents the optimization approach of HDPE process considering uncertainty in target MWD and CCD profiles. The uncertainty metric of MWD and CCD is proposed to evaluate the effect of uncertainty on design parameters. As has been shown, the uncertainty metric provides the nominal estimate and the robust interval of design parameters. On this basis, the proposed sensitivity-based uncertainty decomposition approach evaluates the uncertainty by solving a series of subproblems. The results show that this approach can reduce the uncertainty of MWD and CCD on the product, providing potential applications in product design.

Acknowledgement

We gratefully acknowledge the financial support of 973 Program of China (No.2012 CB720503) and National Natural Science Foundation of China (No. 61374205 and 61374167).

References

A. Alghyamah, J. B. P. Soares, 2009, Simultaneous Deconvolution of the Molecular Weight and Chemical Composition Distribution of Polyolefins Made with Ziegler-Natta Catalysts, Macromolecular Rapid Communications, 30, 4-5: 384-393.

A. Ben-Tal, A. Nemirovski, 2000, Robust solutions of linear programming problems contaminated with uncertain data, Math. Programming, 88: 411–424.

H. Beyer, B. Sendhoff, 2007, Robust optimization – A comprehensive survey, Computer methods in applied mechanics and engineering, 196: 3190-3218.

J. B. P. Soares, T. F. L. McKenna, 2012, Polyolefin Reaction Engineering, Weinheim: Wiley-vch Verlag GmbH & Co. KGaA.

C. Zhang, Z. Zhan, Z. Shao, Y. Zhao, X. Chen, X. Gu, Z. Yao, L. Feng, L.T. Biegler, 2013, Equation-oriented optimization on an industrial high-density polyethylene slurry process with target molecular weight distribution, Ind Eng Chem Res, 52:7240–7251.

C. Zhang, Z. Shao, X. Chen, Z. Yao, X. Gu, L.T. Biegler, 2014, Kinetic Parameter Estimation of HDPE Slurry Process from Molecular Weight Distribution: Estimability Analysis and Multistep Methodology, AICHE J, 60: 3442-3459.

Krist V. Gernaey, Jakob K. Huusom and Rafiqul Gani (Eds.), 12th International Symposium on Process Systems Engineering and 25th European Symposium on Computer Aided Process Engineering.
31 May – 4 June 2015, Copenhagen, Denmark

A Systematic Approach for Targeting Zero Liquid Discharge in Industrial Parks

Zakarya A. Othman[a], Patrick Linke[a], Mahmoud El-Halwagi[b]

[a]*Department of Chemical Engineering, Texas A&M University at Qatar, P.O Box 23874, Education City, Doha, Qatar*
[b]*The Artie McFerrin Department of Chemical Engineering, Texas A&M University, College Station, Texas, U.S.A.*

Abstract

The increasing environmental pressures to minimize wastewater discharge from industrial plants to the environment have led to the emergence of policies and regulations that promote Zero-Liquid Discharge (ZLD) solutions. These systems are typically associated with high capital and operating cost and pose a significant economic burden to implementing industries. ZLD solutions are explored as End-of-Pipe treatment options to eliminate liquid discharges. Instead, ZLD options should be explored in the context of overall water integration of industrial facilities to achieve desired reductions in water footprints through efficient reuse together whilst achieving ZLD. In this work, we propose a systematic approach to screen sustainable and low cost strategies that will assist in targeting water integration for Zero Liquid Discharge (ZLD) in industrial parks. The optimization model represents a decision support tool that can help the designer in quickly evaluate potential reuse and recycle scenarios with ZLD. The default objective is to achieve ZLD at minimum total annual cost. A case study of an industrial park with three plants has been solved and analysed in a number of scenarios to illustrate the usefulness of the proposed model.

Keywords: Zero Liquid Discharge, Eco-industrial parks, Water recycle/reuse, Cost minimization.

1. Introduction

Significant quantities of desalinated and surface water are used by the industrial sector for their process operations, municipal needs and other uses. The water usage together with water production in processes results in substantial wastewater discharge requirements. The conventional wastewater disposal options include discharge to the sea, surface water, deep well injection, or evaporation ponds (Mickley, 2006). In view of water scarcity in many parts of the world, there is increasing pressure to reduce water footprints of industrial facilities. This can be achieved through water integration through reuse and recycle (El-Halwagi, 2012). Eliminating waste water altogether and thereby achieving Zero-liquid Discharge (ZLD) for such industrial parks requires the consideration of high recovery treatment, ZLD processing systems and other ZLD options. This work constitutes a first approach to address ZLD options in the course of water integration for industrial parks (Mickley, 2006).

2. Previous Work

Numerous process integration techniques have been proposed to optimize water usage in the process industries. The work on water integration started first for single plant where El-Halwagi and Manousiouthak (1989) have developed a pinch analysis tool for cost effective mass exchange networks with single and multicomponent targets. Wang and Smith (1994) have presented two graphical design methods to identify targets for wastewater minimization for single and multiple contaminant. On the contributions addressing water integration across plants, Olesen and Polley (1996) have applied the water minimization targeting technique given by Wang and Smith with considering geographical constraints. Lovelady and El-Halwagi (2009) proposed a cost optimization formulation for water integration in eco industrial parks. Rubio-Castro et al. (2011) developed a MINLP model that takes into account reuse and recycle across plants for multiple contaminants. Alnouri et al. (2014, 2015) developed a spatially representation that targets shortest connections between sources and sinks in industrial facilities. Bishnu et al. (2014) developed a multi-period planning model for inter plant water integration.

ZLD is described by maximization of the reuse and recycle of water to avoid the strict environment requirements that wastewater discharge might entail. Koppol et al. (2004) presented a model to study the feasibility of achieving ZLD for various industries through enabling water reuse and recycle to minimize liquid discharge. Deng et al. (2008) presented a graphical method to estimate the targets for ZLD for fixed mass loads with single pollutant. Faria and Bagajewicz (2011) presented a planning model that takes into consideration the variation of contaminants load and number of water using units over time with considering ZLD. So far, ZLD systems have not been explored in the context of inter-plant water network synthesis for industrial parks to achieve desired reductions in water footprints through efficient reuse together whilst achieving ZLD.

3. Problem statement

Given is an industrial complex that consists of a set of plants, in which each plant consists of a set of process sources and process sinks (Rubio-Castro et al., 2011). Further information is also given about fresh water source, candidate decentralized treatment options, decentralized ZLD systems and beneficial uses sinks in term of their flow rates, water quality, cost, treatment performances, treatment recovery percentages and constraints as well as distances between all possible options. The goal is to determine the cost optimal network in terms of connections and flowrates to achieve ZLD to sea and to explore ZLD scenarios.

4. Model Formulation

The approach expands an Eco-Industrial Park (EIP) representation for water integration (Rubio-Castro et al., 2011) to include different possible ZLD options. The model has been formulated as a Mixed-Integer Non-Linear Program (MINLP) based on the superstructure presented in Figure 1, to act as a decision making tool to obtain a cost effective water allocation for an industrial complex to achieve ZLD of process water to the environment. The model is formulated to allow streams to be reused internally and externally in each plant, recycled in a shared decentralized treatment and in ZLD

systems, and utilized for a number of options that can constitute ZLD including beneficial usage and/or ZLD processing.

The objective function in this work is to Minimize Total Annual Cost (TAC) which consist of fresh water annual cost, decentralized treatment annual cost, decentralized ZLD system annual cost and piping annual cost.

Source streams from each of the process units and treatment options can segregate and directed to different sinks based on their water flow and quality requirements. The freshwater source stream can split to feed a number of sinks as needed. An if-binary function (zero or 1) has been used to determine the existence of pipe connection between the sources and sinks.

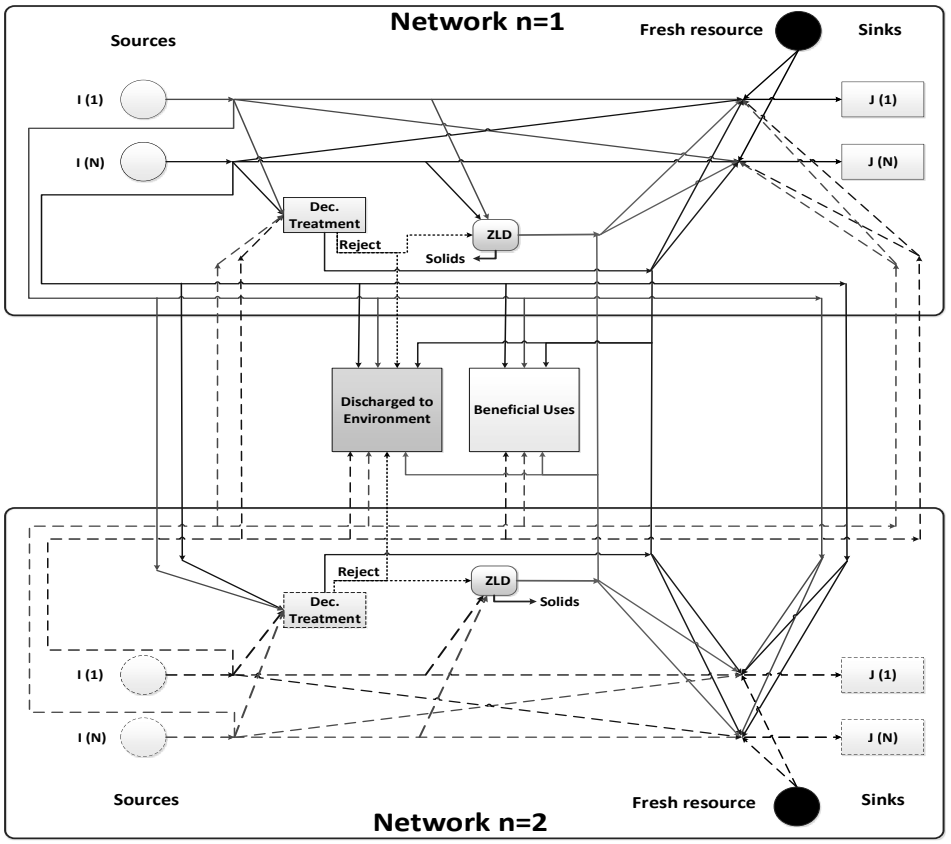

Figure 1: Proposed Superstructure for water integration to target ZLD

5. Case study

An artificial case study presented in Table 1 has been used to illustrate the effectiveness of the proposed model to target ZLD to environment and to explore various scenarios. The case study simulate an industrial complex with three plants, each plant has two process sources and two process sinks as shown in Table 1. Single contaminant has been considered in this work. Table 2 list the costing parameters, recovery percentage

and treatment performances for the decentralized treatment and ZLD systems. It has been assumed that the first decentralized treatment stage already exists in all of the plants and therefore no capital costs were considered. The operating costs have been set to be based on inlet flow size to treatment for the first treatment stage, and based on mass of contaminant removed for second treatment stage. Furthermore, the decentralized ZLD systems which are a combination of brine concentrator followed by crystallizer were considered in this work to treat highly contaminated process streams as well as to treat the treatment rejected concentrated streams. For simplicity, distance between all possible points within the same plant were assumed to be 100 meters and across the plants to be 500 meters. The fresh water cost is (0.13 US$/ton)(Rubio-Castro et al., 2011) and is available at 2 ppm contamination level. Water quality constrains for beneficial usage and wastewater discharge to environment are 100 ppm and 300 ppm respectively. In addition, no cost were considered for the utilization of the surplus quantities of treated water generated from the industrial complex and sent to beneficial usage sinks, as it has been assumed that it is the responsibility of the end user.

Table 1: Industrial complex case study data

	Sources				Sinks		
Plant	Number	Flowrate (ton/h)	Contaminants concentration (ppm)	Plant	Number	Flowrate (ton/h)	Contaminants concentration (ppm)
1	1	50	600	1	1	50	150
	2	70	300		2	70	200
2	3	80	500	2	3	80	40
	4	60	800		4	60	300
3	5	40	400	3	5	40	100
	6	55	1000		6	55	400

Table 2: Treatment and ZLD systems costing parameters

Treatment stages	Recovery (%)	Capital unit cost per flow size (US$/ton/h)	Operating unit cost per flow size (US$/ton)	Operating unit cost for mass of contaminant removed (US$/kg)	Inlet Con. Constraint (ppm)	Outlet Con. (ppm)
Stage 1 (Existing EOPT)	100	0	-	0.25	1000<C<300	200
Stage 2	95	20000	0.1	-	500<C<50	50
ZLD system	95	74500	1.1	-	40000<C<5	5

6. Results and discussion

The case study has been solved in two scenarios in addition to the original case, referenced by scenario zero, which does not involve any sort of water integration. The first scenario considers solving the case study with applying inter-plant water integration, while the second scenario considers applying Inter-plant Water Integration

with ZLD. The optimization model was solved using What'sBest!12.0.1.5 LINDO Global Solver for a 32-bit operating system.

It is clearly shown from the obtained results (Figure 2), that the total annual cost will reduce considerably after applying inter-plant water integration. This is because of the achieved reductions in water footprints through efficient water reuse and water recycle inside and across plants. However, by achieving ZLD to environment (scenario 2), the total annual cost will peak again. This is because of the higher utilization of the decentralized treatment and the involvement of the expensive ZLD systems to treat the wastewater to higher quality standers to be reused in process sinks and beneficial usage sinks rather than discharge to environment at lower water quality.

The consumed quantities of fresh water and the wastewater discharge to environment dropped from 355 (ton/h) to 97 (ton/h) after implementing inter plant water integration. In addition, after achieving ZLD (scenario 2), the 97 (ton/h) discharged to environment was recovered and utilized in process sinks and beneficial usage sinks.

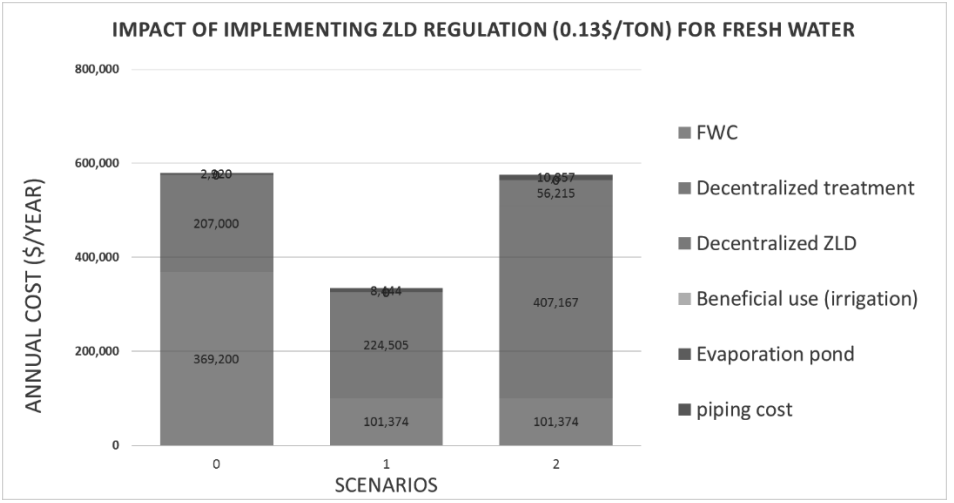

Figure 2:Impact of targeting water integration and ZLD

7. Conclusions

A method for inter-plant water integration to achieve zero liquid discharge has been developed. The developed model will support decision-making with respect to the selection of cost effective networks and flowrates. The main motivation has been to accentuate that ZLD options should be explored in the context of overall water integration to achieve desired reductions in water footprints together whilst achieving ZLD. This has been illustrated in the studied case through utilizing ZLD systems alongside with treatment.

8. Acknowledgement

This publication was made possible by NPRP grant no. 4-1191-2-468 from the Qatar National Research Fund (a member of Qatar Foundation). The statements made herein are solely the responsibility of the authors.

References

Bishnu, S. K., Linke, P., Alnouri, S. Y., & El-Halwagi, M. M. (2014). Multiperiod Planning of Optimal Industrial City Direct Water Reuse Networks. *Industrial & Engineering Chemistry Research, 53*(21), 8844-8865.

Deng, C., Feng, X., & Bai, J. (2008). Graphically based analysis of water system with zero liquid discharge. *Chemical Engineering Research and Design, 86*(2), 165-171.

El-Halwagi, M. M. (2012). Sustainable Design through Process Integration - Fundamentals and Applications to Industrial Pollution Prevention, Resource Conservation, and Profitability Enhancement: Elsevier.

El-Halwagi, M. M., & Manousiouthakis, V. (1989). Synthesis of Mass Exchange Networks. *AIChE Journal, 35*(8).

Faria, D. b. C., & Bagajewicz, M. J. (2011). Planning Model for the Design and/or Retrofit of Industrial Water Systems. *Industrial & Engineering Chemistry Research, 50*(7), 3788-3797.

Koppol, A. P. R., Bagajewicz, M. J., Dericks, B. J., & Savelski, M. J. (2004). On zero water discharge solutions in the process industry. *Advances in Environmental Research, 8*(2), 151-171.

Lovelady, E. M., & El-Halwagi, M. M. (2009). Design and integration of eco-industrial parks for managing water resources. *Environmental Progress & Sustainable Energy, 28*(2), 265-272.

Michael C. Mickley, P. E. (2006). Membrane Concentrate Disposal: Practices and Regulation (Second Edition) *Mickley & Associates*.

Olesen, S. G., & Polley, G. T. (1996). Dealing with Plant Geography and Piping Constraints in Water Network Design. *Process Safety and Environmental Protection, 74*(4), 273-276.

Rubio-Castro, E., Ponce-Ortega, J. M., Serna-González, M., Jiménez-Gutiérrez, A., & El-Halwagi, M. M. (2011). A global optimal formulation for the water integration in eco-industrial parks considering multiple pollutants. *Computers & Chemical Engineering, 35*(8), 1558-1574.

Alnouri, S., Linke, P., & El-Halwagi, M. M. (2014). Water integration in industrial zones: a spatial representation with direct recycle applications. *Clean Technologies and Environmental Policy, 16*(8), 1637-1659.

Alnouri, S. Y., Linke, P., & El-Halwagi, M. M. (2015). On the Development of Optimal Water Management Strategies for Industrial Cities through Regeneration and Reuse. *Journal of Cleaner Production, 89*, 231-250.

Wang, Y. P., & Smith, R. (1994a). Wastewater minimisation. *Chemical Engineering Science, 49*(7), 981-1006.

Krist V. Gernaey, Jakob K. Huusom and Rafiqul Gani (Eds.), 12th International Symposium on Process Systems Engineering and 25th European Symposium on Computer Aided Process Engineering.
31 May – 4 June 2015, Copenhagen, Denmark

Decomposition Techniques for the Real-time Optimization of a Propylene Production Unit

A.M. Acevedo P.[a], J.E.A. Graciano[a], Fabio D.S. Liporace,[b] A.S. Vianna Jr.[a], Galo A.C. Le Roux[a]

[a]*Department of Chemical Engineering, University of São Paulo, Av. Luciano Gualberto, Trav. 3, 380, São Paulo-SP, Brazil*
[b]*CENPES/PETROBRAS S.A, Av. Horácio Macedo, 950, Rio de Janeiro-RJ, Brazil*

Abstract

In this work an application of decomposition techniques on a propylene production unit from REPLAN refinery by Petrobras S.A. is presented. It is shown that the classic Lagrangian Relaxation (LR) technique and the alternative technique called "Pricing Interprocess Streams Using Slack Auctions" (PISUSA) do not converge for the case study presented. The issues involved in each decomposition approach are identified and discussed; then a modification of the Lagrangean Relaxation algorithm is proposed using a new constraint-updating rule. This modified algorithm is able to overcome the issues and solve the decomposed problem properly.

Keywords: real-time optimization, process optimization, decomposition techniques.

1. Introduction

Chemical process industry has a high demand for methods and tools to perform process optimization in order to enhance profitability. An alternative to increase the profitability of continuous processes is to implement the Real Time Optimization technique (RTO), which the main objective is to drive the plant at each instant of time, as close as possible to the optimal operating conditions (Sequeira et al., 2002). The classic RTO framework includes the following sequential steps: steady state detection, treatment of gross errors, data reconciliation, parameter estimation and economic optimization (White, 1997).

The problem of economic optimization encompasses the whole refinery. In 1995, Naysmith and Douglas presented two possibilities to implement the economical optimization in large refinery problem. The first method considers a centralized structure (a unique model for the whole plant), which is highly complex and then it can be more practical to solve simpler optimizations problems (models for each division) than to optimize the entire refinery considering only one model (Friedman, 1995; Rinaldo and Ungar, 2000). The second approach, distributed structure, decomposes the centralized problem into some less complex smaller optimization problems, which require the use of decomposition technique to specify, adequately, the prices for intermediate streams, allowing each division of the unit to be independently optimized.

For this purpose, two decomposition techniques (LR and PISUSA) are applied and tested in a real refinery problem. The results show that these techniques present a number of difficulties, which inspired the proposition of an alternative approach, allowing the effective decomposition of the case study.

2. Decomposition techniques for process optimization

The main concepts of the two literature decomposition techniques (LR and PISUSA) are given in this section. A detailed explanation of each method can be found in the original works.

2.1. Lagrangean Relaxation decomposition

LR decomposition is based on an iterative algorithm, which relaxes the complicating constraints (intermediary streams, e.g. eq.5 and 6) of the original optimization, generating sub-problems coordinated by a master problem. Lagrange multipliers (λ) are used in the relaxation and represent the shadow price of intermediate products; as a consequence, each division of the plant could be optimized individually, aiming to obtain the best profit for the entire unit (Conejo et al., 2006; Guignard, 2003).

2.2. Pricing Interprocess Stream Using Slack Auctions

In this technique, the complicating constraints are rewritten as resource constraints (inequality constraints) to be used as a criterion for the algorithm convergence. A negative term is added to the maximization economic objective function of each sub-problem, which is composed of a weight parameter (*p*) multiplied by the absolute value of the complicating constraints, enforcing their difference to decrease at each iteration. For economic purposes, *p* represents the price of the intermediate streams that is updated at each iteration (Rinaldo and Ungar, 2000).

3. Case study: propylene production unit

The flowsheet shown in Figure 1 illustrates the main features of the propylene production unit that is composed by three divisions: Depropanizer (D_1), De-ethanizer (D_2) and C3 splitter (D_3). The process is fed by a GLP stream, supposed in our model, to contain 10 components (mainly, propylene 37% and propane 13%). The most relevant conditions of the columns are presented in Table 1.

Table 1. Operating conditions of the propylene operating unit

Column	# of trays	Product Specification		Column Capacity	
		Bottom	Top	Max	Min
T-1	51	< 1% molar light comp.	< 0.1% molar heavy comp.	23,804	17,312
T-2	61	< 120 ppm of ethane	< 35% molar of propylene	10,865	4,939
T-3	197	< 5% molar of propylene	> 95% molar of propylene	10,061	4,573

The entire unit comprises: 3 distillation columns (T-i=1,..,3), 6 valves ($V_{i=1,...,6}$), 4 condensers ($HX_{i=1,...,4}$), 3 reboilers ($RB_{i=1,...,3}$),4 pumps ($B_{i=1,...,4}$), 8 splitters ($SB_{i=1,...3}$; SP_1; $SR_{i=1,...,3}$;SC_1), 2 mixers ($M_{i=1,2}$), 1 reflux tank (TA_1) and 1 compressor (C_1). The propylene production unit was modeled, simulated and optimized using the equation-oriented environment EMSO (Environment for Modeling, Simulation and Optimization, Soares and Secchi, 2003). The model was based on Mendoza et al. (2013), where the same assumptions were done. The optimization problem for this process has the following structure:

$$\max \quad P_1*F_9 + P_2*F_{10} - P*F_1 + P_3*F_{14} + P_4*F_{29} + P_5*F_{26} - OCD\_1 - OCD\_2 - OCD\_3 \quad (1)$$

$$\text{s.t.} \quad \text{Model and operational constraints D\_1} \quad (2)$$

$$\text{Model and operational constraints D\_2} \quad (3)$$

$$\text{Model and operational constraints D\_3} \quad (4)$$

$$5D\_1 = 5D\_2 \quad (5)$$

$$17D\_2 = 17D\_3 \quad (6)$$

where P, P_1, P_2, P_3, P_4 e P_5 are the product market prices of F_1, F_9, F_{10}, F_{14}, F_{29}, e F_{26}, respectively; OCD_1, OCD_2 and OCD_3 are operating costs of each division D_1, D_2 and D_3. Equation (5) and (6) are the so called complicating constraints.

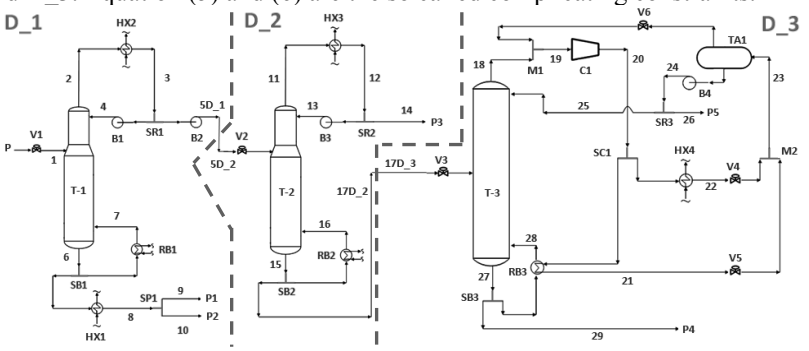

Figure 1. Simplified diagram of the propylene production unit

Solving the centralized structure, the gross operating profit (GOP) was increased by 4% from the operational condition. This new optimum operational point is the target for the decomposition techniques, applied in the next section.

4. Application of LR and PISUSA techniques

Based on Conejo et al. (2006), the resolution algorithm for LR is composed by the follows steps: at step 0, initial guesses for all the λ's are specified, this information is used at step 1, where all the optimization sub-problems are solved independently. At step 2, the λ's are updated using the classic subgradient approach; finally, at step 3 the convergence criterion is checked. Figure 2 shows the λ's obtained at each iteration. The results obtained in this case study demonstrate that there is no λ_1 and λ_2 (shadows prices of streams 5D_1; 5D_2 and 17D_2; 17D_3 respectively) able to converge the algorithm. This is due to two main causes identified by Rinaldo and Ungar (2000):

Issue 1, Indifferent divisions: In this case, there is no linear dependence between the gradients of the complicating constraints and the gradient of objective function, unless the complicating constrains variables are equal to zero (e.g. 5D_1=0 and 5D_2=0) or λ's are zero. For this reason, these results are useless for the decomposition approach, because those assumptions do not have physical or economical mean.

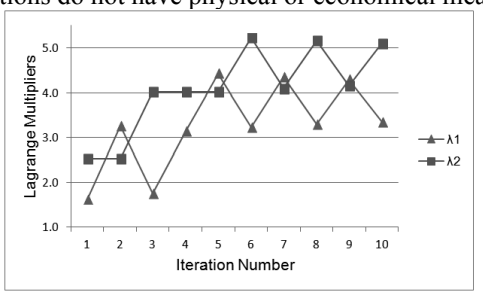

Figure 2. Convergence problem of the LR technique

Issue 2, Divisions with linear objectives: In this case, the divisions D_1, D_2 and D_3 always propose the maximum or the minimum value for the intermediate streams, depending on the value of λ_1 and λ_2. In short, for this algorithm there is no λ's values

that can guarantee the constraints 5D_1 = 5D_2 and 17D_2 = 17D_3 satisfaction (see Figure 3).

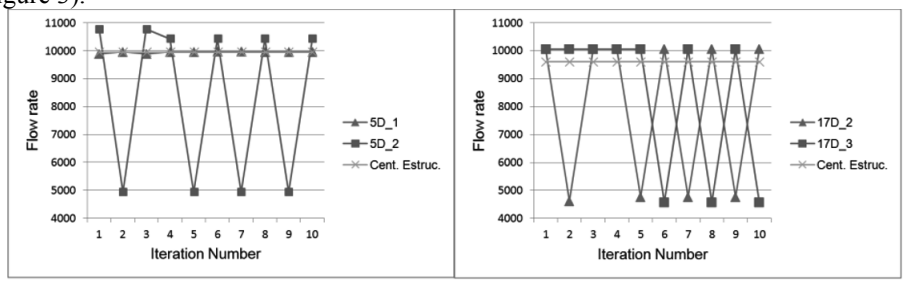

Figure 3. Flow rates of the intermediate streams obtained by centralized and LR approaches

Considering that the feed flow rate (D_1) is fixed at 21,456 kg/h, it can be observed that the intermediate product flow rate (5D_1, ▲ mark) does not swicht between the upper and lower bounds, due to the purity specification of the top product of T_1.

The second technique, based on Rinaldo and Ungar (2000), starts at step 0, in which the initial values of *p* and complicating constrains variables are set. At step 1, the sub-problems are solved independently. Then at step 2, the algorithm convergence is checked. If the convergence is not reached the algorithm continues. At step 3, the reference values for the complicating constraints variables and the price value (*p)* are adjusted in accordance to the previous results and go back to step 1.

The values obtained for the intermediate products (5D_2 and 17D_3) are p_1 = 7 \$/kg and p_2 = 9.7 \$/kg, respectively (an arbitrary scale is assumed for confidentiality reasons). Those prices for the intermediate streams are larger than the market prices of the final products in each division, which are 1.6; 2.4; 2.7; 6.27 and 1.6 \$/kg for the streams F_9, F_{10}, F_{14}, F_{26} and F_{27}, respectively. Also in this case, the algorithm is unable to converge, because the slack term included in the objective function of each sub-problem always tries to maximize the product that has a price defined by the market. Once the intermediate stream has a negative weight, price multiplied by a negative signal in the objective function, the only way this approach can converge is by setting high prices values (*p*). However, when this setting is implemented the price (*p*) loses all its economical meaning, seeing that the intermediate product price is higher than the market price of the final products. Finally, this method is not effective for the studied problem (joint production).

5. Modified Lagrangean Relaxation algorithm (proposed approach)

In this section the classic LR algorithm is modified to overcome the convergence problem observed in the previous section. For this reason, a new variable called availability of intermediate product (AIP) is now considered. The modifications of the classic LR algorithm (see Section 2.1) is introduced as follows: at step 0, initial guesses for all λ's are specified and the AIP variables are initialized as the maximum feed flow rate that can be processed in each division; at step 1, the resource constraints are added to the feed stream of each division, then all sub-problems are solved independently. For example, in our case study, the optimization problem is decomposed in three sub-problems, and the resource constraints are given by $5D\_2^{(v)} \leq AIP_1^{(v)}$ for division D_2 and $17D\_3^{(v)} \leq AIP_2^{(v)}$ for division D_3, where (v) is the iteration number. The resource constraint is not considered in D_1, because the feed stream F_1 is fixed.

D_1	Max $P_1*F_9 + P_2*F_{10} - P*F_1 + \lambda_1*5D\_1 - OCD\_1$	(7)
	s.t. Model and operational constraints D_1	(8)
D_2	Max $P_3*F_{14} - \lambda_1*5D\_2 + \lambda_2*17D\_2 - OCD\_2$	(9)
	s.t. Model and operational constraints D_2	(10)
	$5D\_2^{(v)} \leq AIP_1^{(v)}$	(11)
D_3	Max $P_4*F_{29} + P_5*F_{26} - \lambda_2*17D\_2 - OCD\_3$	(12)
	s.t. Model and operational constraints D_3	(13)
	$17D\_3^{(v)} \leq AIP_2^{(v)}$	(14)

At step 2, Lagrange multipliers are updated by the subgradient method, while the API's variables take the values of intermediary output flow rate from a previous division, resulting from the independent optimization problems. In our case study this is: $AIP_1^{(v+1)} \leftarrow 5D\_1^{(v)}$ and $AIP_2^{(v+1)} \leftarrow 17D\_2^{(v)}$. This ensures that in the next iteration the feed flow rate of each division is physically available. At step 3, the convergence criterion is checked, then, if the difference between the λ's of two consecutive iterations is less than an arbitrary tolerance (ε) the solution was found, otherwise return to step 1.

Figure 4 depicts the results obtained by the new approach. Note that after 9 iterations the algorithm converges, and the shadow prices for the intermediate streams are properly determined. In other words, the shadow prices are coherent to the market price of final products (1.85 $/kg for 5D_1 and 5D_2 streams; 2.8 $ for 17D_2 and 17D_3 streams).

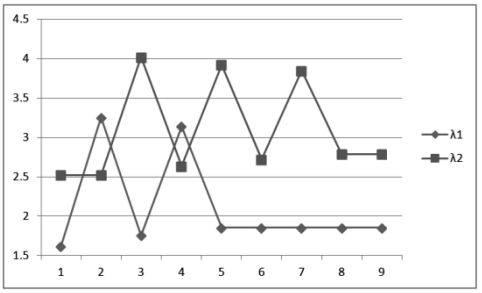

Figure 4. Convergence of the Lagrange multipliers for the proposed algorithm

Figure 5 shows a comparison of the new decomposition algorithm with the centralized approach. It can be observed that the flow rates of the intermediate streams are similar, which means that the proposed algorithm optimizes the whole plant to an operational point close to the centralized approach.

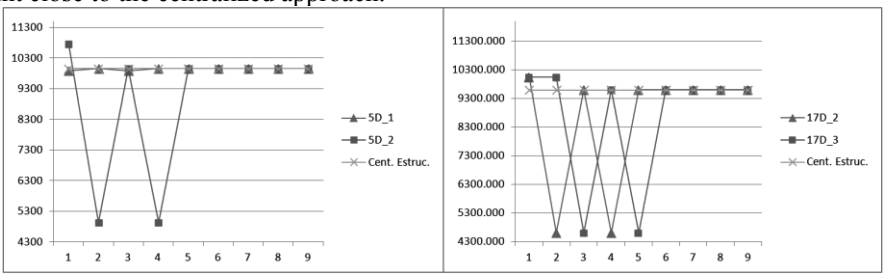

Figure 5. Flow rate values obtained by the proposed algorithm and the centralized approach

Table 2 presents some relevant information about the optimization problems of each approach disscused in the present paper. It can be observed that the distributed approaches reduces the problem complexity, since it decrease the number of variable of

each subproblem. Furthermore, each sub-problem generated by the decomposition thecniques can be optimzated in parallel, using different processors to reduce the total amount of time expended by the whole process optimization (Darby and White, 1988).

Table 2. Relevant information used in each approach

Optimization Structure	Centralized	LR			PISUSA			Proposed approach		
		D_1	D_2	D_3	D_1	D_2	D_3	D_1	D_2	D_3
# Variables	13,640	2,393	2,746	8,510	2,393	2,746	8,510	2,393	2,746	8,510
# Equations	13,634	2,391	2,743	8,507	2,391	2,743	8,507	2,391	2,743	8,507
# Inequalities	22	6	10	10	6	10	10	6	11	11
GOP ($/h)	71,622.92	---			---			71,754.71		

The distributed approch obtained a GOP 0.184% greater than the centrlized approach. This difference is due to non-linearity of the optimization problem studied, which results in different local optimum solutions.

6. Conclusions

In the present paper, the economic optimization problem of large process plants is addressed, with a case study of a propylene unit at REPLAN refinery (Petrobras S.A.). First of all, the whole unit was optimized as a centralized structure. Then, two selected literature decomposition techniques were applied. The results show that these techniques were not able to converge to feasible solutions, due to different issues. Those problems inspired the proposition of a modified LR algorithm, adding a new variable called AIP, the novel algorithm guarantees a feasible solution for the distributed structure of this case study, presenting slight better results than the local optimum obtained by the centralized problem. This proposed approach is promising to be studied and tested in other processes with similar characteristics to be generalized.

References

A. J. Conejo, E. Castillo, R. Minguez, R. Garcia-Bertrand, 2006, Decomposition Techniques in Mathematical Programming, Springer-Verlag Berlin Heidelberg, Germany.

Y. Z. Friedman, 1995, What's Wrong with Unit Closed Loop Optimization?, Hydrocarbon Processing-Section 1, 74, 10, 107-116.

M. Guignard, 2003, Lagrangean Relaxation, Sociedad de Estadística e Investigación Operativa Top, 11, 2, 151–228.

M.L. Darby, D.C. White, 1988, On-Line Optimization of Complex Process Units, Chemical Engineering Progress, 84, 10, 51-59.

D.F.M. Muñoz, L.M.P. Garcia, J.E.A. Graciano, C.A.R. Martinez, A.S. Vianna, G.A.C. Le Roux, 2013, Real-Time Optimization of an Industrial-Scale Vapor Recompression Distillation Process. Model Validation and Analysis, Industrial & Engineering Chemistry Research, 52, 16, 5735-5746.

M. R. Naysmith, P. L. Douglas, 1995, Review of Real Time Optimization in the Chemical Process Industries, Developments in Chemical Engineering and Mineral Processing, 3, 2, 67-87.

J. A. Rinaldo, L. H. Ungar, 2000, Pricing Interprocess Streams Using Slack Auctions. AIChE Journal, 46, 3, 575–587.

S. E. Sequeira, M. Graells, L. Puigjaner, 2002, Real Time Evolution for On-line Optimization of Continuous Processes, Industrial & Engineering Chemestry Research, 41, 7, 1815-1825.

R.D.P. Soares, A.R. Secchi, 2003, EMSO: A new Environment for Modeling, Simulation and Optimization. Computer Aided Chemical Engineering, 14, 947-952.

D.C. White. 1997, Online optimization: what, where and estimating ROI: Process control and Instrumentation, Hydrocarbon Processing, 76, 6, 43–51.

Krist V.Gernaey, Jakob K.Huusom and RafiqulGani (Eds.), 12th International Symposium on Process Systems Engineering and 25th European Symposium on Computer Aided Process Engineering.
31 May – 4 June 2015, Copenhagen, Denmark

An Approach to Deal with Non-Convex Models in Real-Time Optimization with Modifier Adaptation

Maximiliano García,[a],Juan Pablo Ruiz,[b]Marta Basualdo[a,c]*

[a]*Computer Aided for Process Engineering Group (CAPEG). French-Argentine International Center for Information and Systems Sciences(CIFASIS-CONICET-UNR-UPCAM). 27 de Febrero 210 bis, S2000EZP, Rosario,Argentina*
[b]*University of Texas at Austin, Austin TX 78758, USA*
[c]*Universidad Tecnológica Nacional (UTN). Facultad Regional Rosario (FRRo), Rosario, Argentina*
basualdo@cifasis-conicet.gov.ar

Abstract

Real Time Optimization (RTO) uses a model of the process to calculate the optimal operating conditions of the plant. In order to deal with plant-model mismatches, measurement-based adaptation strategies are used. The modifier-adaptation method performs corrections in the cost and constraint functions in the model of the optimization problem to match the necessary optimality conditions for the plant. By doing this, an operating point that satisfies the KKT optimality conditions of the actual process is obtained. This methodology ensures convergence to the (local) optimum of the plant. However, complex processes usually correspond to models with a large number of non-linearities and non-convexities, often leading to multiple local solutions. Typical algorithms that are used to solve these problems cannot guarantee the global optimum; hence, non-convex models are not properly exploited. This paper aims at dealing with this situation by incorporating a global optimization methodology within the modifier-adaption framework. In order to implement this composite structure we used GAMS to handle the global optimization problem and Matlab to handle the modifier-adaptation scheme. The advantage of this new technique is shown through an illustrative case study.

Keywords: Real-Time Optimization, Modifier Adaptation, Global Optimization.

1. Introduction

Process optimization aims at improving the performance of a given plant. Real-time optimization (RTO) is a subject of growing importance in industry and in the academic community (Darby et al., 2011). The main reason for this trend is that the implementation of an RTO system often generates significant returns on investment. In a high-capacity chemical plant, a small percentage improvement may mean significant annual earnings. One of the main challenges in RTO systems arises from the fact that the models are simplified representations of reality and therefore are subject to uncertainty, which is often present in the form of plant-model mismatches and unmeasured disturbances. A classical RTO scheme typically proceeds by a two-step approach, a parameter estimation step followed by an optimization step. With the availability of online data, it is possible to update the model in order to obtain a better prediction of process variables.

In contrast, in the modifier-adaptation approach, measurements are used to adapt the model via first-order correction terms, including correction modifiers for constraint values, as well as for constraints and cost gradients. This requires the use of some experimental data to estimate process gradients. A comparison of different methods for gradient estimation can be found in (Srinivasan et al., 2011). The optimal values of inputs that are obtained by the algorithm are applied directly to the plant. However, the modifier adaptation does not ensure feasibility of the steady state operation upon convergence. In order to handle such situations, the modifier adaptation approach is integrated with a model-based predictive control, where both layers use the same decision variables. Equality constraints and active inequalities are controlled by their optimal values, and the remaining degrees of freedom are controlled in their optimal values over the selected input direction, so new gradient modifiers are defined that correct the projected gradients in the tangent space of the equality constraints as proposed in (Marchetti et al., 2011).

2. Problem statement

A model-based RTO must be able to accurately predict the plant in its current operating point for the entire range of operating conditions. However, models are simplified representations of reality and therefore are subject to uncertainty. If the constraints are not well predicted by the model, the solution may be infeasible or sub-optimal. With the availability of operating data, the process model can be updated to provide a better prediction of the behavior of the plant. Often, a parameter estimation scheme is used to update the parameters of the models. However, it is known that in most of the chemical processes, physicochemical and thermodynamic relations that are part of these models are non-linear and this often leads to non-convex models (Ruiz and Grossmann, 2011). Given the non-linearities and non-convexities of the model, the implementation of a parameter estimation scheme within a RTO framework where this update is done frequently is often prohibitive. With this in mind, to avoid solving a complex optimization problem frequently the modifier-adaptation approach has been proposed.

The main idea behind this method is to use measurements with a simplified plant model and iteratively modify the model so, upon convergence, the necessary (local) optimality conditions of the modified optimization problem match those of the plant. This is possible with the use of modifiers that, at each iteration, adjust the simplified model based on the differences between predicted and measured values of the constraints, and the predicted and measured gradients of the cost function and constraints. In the k^{th} iteration, optimal inputs computed using the modified model is applied to the plant, and the resulting values of the constraints of the plant and the gradients of the cost function and constraints are compared with model predictions. Then the following optimization problem is solved to determine the next u_{k+1}:

$$\begin{aligned} \min_{u} \quad & J_m(u) = J(u) + (\lambda_k^J)^T u \\ s.t. \quad & H_m(u) = H(u) + \varepsilon_k^H + (\lambda_k^H)^T (u - u_k) = H_0 \\ & G_m(u) = G(u) + \varepsilon_k^G + (\lambda_k^G)^T (u - u_k) \le G_0 \\ & u_L \le u \le u_U \end{aligned} \tag{1}$$

where modifier values are calculated as:

$$\varepsilon_k^H = H_p(u_k) - H(u_k) \qquad (\lambda_k^H)^T = \frac{\partial H_p}{\partial u}(u_k) - \frac{\partial H}{\partial u}(u_k)$$
$$\varepsilon_k^G = G_p(u_k) - G(u_k) \qquad (\lambda_k^G)^T = \frac{\partial G_p}{\partial u}(u_k) - \frac{\partial G}{\partial u}(u_k) \qquad (2)$$
$$(\lambda_k^J)^T = \frac{\partial J_p}{\partial u}(u_k) - \frac{\partial J}{\partial u}(u_k)$$

The notation $()_m$ is related to modified model variables, $()_p$ to plant variables and no subscript to model variables; H are the equality constraints with H_0 values, G are the inequality constraints with G_0 upper values, ε are equality and inequality constraint value modifier and λ are equality and inequality constraint gradient modifiers.
It can be proved that the modifier-adaptation method guarantees that the point that is found upon convergence satisfies the KKT conditions (i.e. (local) optimum of the plant), even with structural plant-model mismatches (Chachuat et al., 2009).
However, in the presence of multiple local optima due to non-linearities and non-convexities of the process, the modifier adaptation approach may fail to find the global optimum since the data that is used to estimate plant gradients and plant constraint values belongs to the neighborhood of local solutions. Therefore, when the modified optimization problem is solved, the process will converge to a sub-optimal solution instead of the true optimum. A procedure that overcomes this issue is presented in this work.

3. Proposed technique

In order to avoid falling in local optimal solutions while still taking advantage of the benefits of the modifier-adaptation technique, we propose to add a global optimization layer that will handle the inherent non-convexities of the plant. Note that the proposed model is supposed to be detailed enough to represent most relevant non-convexities. This can be achieved by using a first-principle model.

The general procedure can be summarized as follows:

(1) The method starts by solving a first-principle model to global optimality by means of a non-linear global optimization solver. The solution obtained is defined as u_{MOD}.
(2) At the current steady state, u_{INI}, the process control set-points are set to u_{MOD}, so the process can get closer to the neighborhood were the true optimum lies.
(3) A convex approximation is performed to the detailed model around u_{MOD} to be used by the modifier-adaptation scheme.
(4) At this new process state, the modifier-adaptation approach is activated, so the modified optimization problem is iteratively solved until convergence to the optimal solution (u_{SOL}).

Under the assumption of having a detailed model, it is expected that u_{MOD} is at least in the domain of attraction of the global solution of the process, and therefore the method will converge to the true optimal solution. Considering that the step (1) in the method is computationally expensive, one major question that arises is whether we need to use it at each iteration. As long as no major changes are incurred in the plant, a significant change in the domain of attraction of the optimal solution is not expected. Hence, step (1-3) could be skipped. Having this in mind it is important to detect when the difference between the detailed model and the plant is large enough. We propose to do this by calculating the norm of the differences between predicted and measured outputs and comparing it with a preset threshold. Additionally, the distance between the solution

that was obtained with the modifier-adaptation (u_{SOL}) and model (u_{MOD}) as well as significant changes in bounds of major variables could be taken into consideration. Finding the right threshold in any of these strategies is not trivial and will be the subject of analysis in a future work.

4. Illustrative case study

4.1. Problem description

In this work, a modified version of the plant that is described in (Marchetti et al., 2012) is used as a case study. In this problem we aim at applying the proposed RTO framework to a continuous-time state-space non-linear system which consists of two state variables $x=[x_A\ x_B]^T$, three input variables $u=[u_1\ u_2\ u_3]^T$, and two measured output variables, h and y, where the output y measurement is only available at steady-state intervals. The dynamic non-linear plant equations are the following:

$$\begin{aligned} \dot{x}_A &= (-17x_A + u_3 - 1)/30 \\ \dot{x}_B &= (u_1 - 9)^2 + (u_2 - 11)^2 - x_A x_B \\ h &= (1.3 + x_A)^4 + (1/25)x_A x_B \\ y &= x_A x_B - 204x_A \end{aligned} \tag{3}$$

The steady-state plant equations are:

$$\begin{aligned} x_A &= (u_3 - 1)/17 \\ x_A x_B &= (u_1 - 9)^2 + (u_2 - 11)^2 \\ H_p(u) &= (1.3 + (u_3 - 1)/17)^4 + ((u_1 - 9)^2 + (u_2 - 11)^2)/25 \\ Y_p(u) &= (u_1 - 9)^2 + (u_2 - 11)^2 - 204(u_3 - 1)/17 \end{aligned} \tag{4}$$

The linear discrete state-space model that is used in the MPC problem is obtained by linearizing the system at the steady state operating point u_{LIN} (i.e. $H_p(u_{LIN})=10$). The MPC parameters such as discretization sample time, prediction horizon (p), control horizon is (m), and input bounds are given in Table 1.

The optimization problem for the plant is defined as:

$$\begin{aligned} \min_u \quad & J_p(u) \\ s.t. \quad & H_p(u) = 10 \\ & 1 \le u_1, u_2 \le 10, 1 \le u_3 \le 8 \end{aligned} \tag{5}$$

Where the original objective function Φ_p is modified as follows:

$$\begin{aligned} J_p(u) = \Phi_p(u) &+ 0.098u_1^4 - 1.95u_1^3 + 11.27u_1^2 - 8.42u_1 \\ &+ 5u_2 - 0.9u_3^2 + 11.4u_3 + \frac{u_1 u_2}{4} - \frac{u_2 u_3}{2} \\ \Phi_p(u) &= u_1 + 5u_2 + u_3^2 + Y_p(u) \end{aligned} \tag{6}$$

The plant-model mismatch is stated as the parametric uncertainty in the objective function J with parameters Θ_1 and Θ_2, in the equality constraint H with parameters Θ_3 and Θ_4 and in the lower bound of u_1 with parameter Θ_5. Such parameters are given in Table 2. The steady-state model equations are:

$$\begin{aligned} \min_{u} \quad & J(u) = \Phi_p(u) + +0.098u_1^4 - 1.95u_1^3 + 11.27u_1^2 - 8.42u_1 \\ & +(2\theta_3 - 17)u_2 - 0.9u_3^2 + (2\theta_4 - 17)u_3 + \frac{u_1 u_2}{4} - \frac{u_2 u_3}{2} \\ s.t. \quad & H(u) = \left(1.3 + \frac{(u_3 - \theta_1)}{17}\right)^4 + \frac{(u_1 - \theta_2)^2 + (u_2 - 11)^2}{25} = 10 \\ & \theta_5 \le u_1, u_2 \le 10, 1 \le u_3 \le 8 \end{aligned} \tag{7}$$

4.2. Results

In this illustrative example we aim at showing the benefits of the proposed method by comparing its behavior with a traditional modifier-adaptation approach. The modifier-adaptation step was implemented in the MATLAB environment, while the global optimization step was implemented in GAMS and then linked together by a MATLAB-GAMS interface. In Figure 1 (left) we show the case in which the system starts at a point P_{01}, which lies in the domain of attraction of the plant global optimum. As it is expected both algorithms converge to the plant global optimum P_{G1} from the initial point P_{01}. Note that the proposed technique achieves this after a first iteration to the global optimum of the detailed model M_{G1}. In Figure 1 (right) we show the case in which a modification on the lower bound of u_1 occurs (Θ_5 = 3) moving the domain of attraction of the plant global optimum. If we apply the traditional modifier-adaptation technique the algorithm will converge to the point P_{L2} from the initial point P_{02}, which is a local solution of the process. If, on the other hand, we apply the proposed technique, an iteration to the new global solution of the model M_{G2} is first performed. Then, within the convergence zone, the modifier-adaptation leads the process to a neighborhood of P_{G2}, which is the true global optimum. The initial points (P_{0k}), the model local and global solutions (M_{Lk}, M_{Gk}) and the plant local and global solutions (P_{Lk}, P_{Gk}), where k=1,2 as well as the cost function values are given in Table 3.

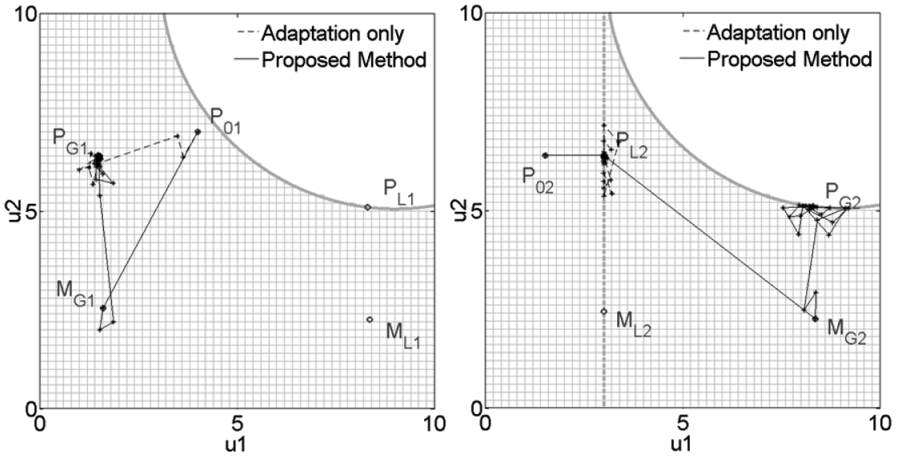

Figure 1. RTO iterations of the proposed technique on surface $H_p(u)$=10.

Table1. MPC parameters.

Parameter	Value		
T_s	1		
p	15		
m	5		
Q	10		
	u_1	u_2	u_3
u_{LIN}	5	5	7.4187
u_L	0	0	1
u_U	10	10	8
Δu	±1	±1	±1
diag(R)	10	10	10

Table 2. Model parameters.

Parameter	Value
Θ_1	2
Θ_2	6
Θ_3	2
Θ_4	10
Θ_5	1

Table 3. Initial and solution points.

	u_1	u_2	u_3	J_p
P_{01}	4	7	7.8068	-
P_{L1}/P_{G2}	8.3081	5.0942	8	-15.261
P_{G1}/P_{02}	1.5202	6.3854	6.4628	-19.94
M_{L1}/M_{G2}	8.3613	2.2542	7.3854	-0.80415
M_{G1}	1.6016	2.541	4.4037	-5.6386
M_{L2}	3	2.4431	5.4611	1.4137
P_{L2}	3	6.3681	7.2203	-13.418

5. Conclusions

An RTO technique to deal with the presence of multiple local optima has been presented and applied in an illustrative case study. We showed that a modifier-adaptation technique may fail to find the global optimum if the initial point is not within its neighborhood. This is the case because the information that is used by the modifier-adaptation technique to build the optimization problem that is solved at each iteration is only local. With this in mind we proposed a framework that adds an upper layer to the traditional modifier-adaptation approach that brings the process near a neighborhood of the true optimum of the plant. We showed how this upper layer is very important to avoid local sub-optimal solutions. Hence, leading the process to the true global optimum.

References

B. Chachuat, B. Srinivasan. and D. Bonvin, 2009, Adaptation strategies for real-time optimization, Computers and Chemical Engineering, 33, 1557-1567.

M. L. Darby, M. Nikolaou, J. Jones, and D. Nicholson, 2011, RTO: An overview and assessment of current practice, Journal of Process Control, 21, 874-884.

A. Marchetti, M. García and M. Basualdo, 2012, Model Adequacy Analysis for Real-Time Optimization via Modifier Adaptation, AADECA 2012.

A. Marchetti, P. Luppi and M. Basualdo, 2011, Real-time optimization via modifier adaptation integrated with model predictive control, 18th IFAC World Congress, Volume 18, 9856-9861.

J. P. Ruiz and I. E. Grossmann, 2011, Using redundancy to strengthen the relaxation for the global optimization of MINLP, Computers and Chemical Engineering, 35, 2729-2740.

B. Srinivasan, G. François and D. Bonvin, 2011, Comparison of Gradient Estimation Methods for Real-Time Optimization, Computer Aided Chemical Engineering, 29, 607-611.

Krist V. Gernaey, Jakob K. Huusom and Rafiqul Gani (Eds.), 12th International Symposium on Process Systems Engineering and 25th European Symposium on Computer Aided Process Engineering.
31 May - 4 June 2015, Copenhagen, Denmark.

A Robust Minimax Semidefinite Programming Formulation for Optimal Design of Experiments for Model Parametrization

Belmiro P.M. Duarte[a,b], Guillaume Sagnol[c] and Nuno M.C. Oliveira[b]

[a]*IPC; ISEC, DEQB; Rua Pedro Nunes, Quinta da Nora, 3030-199 Coimbra, Portugal.*
[b]*CIEPQPF, Dep. of Chemical Engineering; University of Coimbra; Coimbra, Portugal.*
[c]*Zuse Institut Berlin; Berlin; Germany.*
bduarte@isec.pt

Abstract

Model-based optimal design of experiments (M-bODE) is a crucial step in model parametrization since it encloses a framework that maximizes the amount of information extracted from a battery of lab experiments. We address the design of M-bODE for dynamic models considering a continuous representation of the design. We use Semidefinite Programming (SDP) to derive robust minmax formulations for nonlinear models, and extend the formulations to other criteria. The approaches are demonstrated for a CSTR where a two-step reaction occurs.

Keywords: Design of experiments, Model parametrization, Semidefinite Programming, Robust design

1. Introduction

M-bODE is a classic problem with substantial interest nowadays, particularly in pharmacokinetics, pharmacodynamics, drugs trials design, and on general model parametrization, a challenge shared by various disciplines such as Chem. Eng. (Goos and Jones, 2011). Kiefer (1959) proposed to relax the original combinatorial experiment design problem to obtain a tractable convex optimization representation. This alternative is designated as *the approximate optimal design problem*, and consists in determining a probability measure over the design space (rather than the exact number of trials for each point of the design space). Many authors have proposed algorithms to compute optimal designs in a systematic way, starting with the exchange-based method of Wynn (1972) for local designs (see also Chaloner and Larntz (1989) for Bayesian optimal designs). Within the same framework Duarte and Wong (2014b) proposed a systematic algorithm for finding minmax optimal designs employing a reformulation to convert the original problem into a semi-infinite program. The criterion to maximize is a concave operator of the Fisher Information Matrix (FIM), which in turn is linear with respect to the design measure. Convex analysis can thus be used to establish the optimality conditions of a design, also known as *equivalence theorems*, see Pukelsheim (1993). This theoretical framework enabled to derive convex programming formulations for the M-bODE problem, although the regressor domain needs to be discretized (see Atkinson et al. (2007, Chap. 12) for discretized designs). Exploiting this route, among others Vandenberghe and Boyd (1999) proposed SDP formulations for $D-$, $A-$, and $E-$optimal designs for linear models, Sagnol (2011) derived Second Order Conic Programming formulations, and recently Duarte and Wong (2014a) extended the SDP formulations to nonlinear models employing the Bayesian paradigm. Here we derive SDP formulations for robust minmax optimal designs for nonlinear models in the spirit of

Wong (1992) employing discretization techniques to convert the original semi-infinite program into a convex optimization problem.

2. Mathematical formulation

2.1. Preliminaries

We consider dynamic models represented by Differential-Algebraic Equations of the following form, the regressor being $t \in T \equiv [0, t^{\max}]$

$$\frac{\mathrm{d}\mathbf{x}}{\mathrm{d}t} = f(\mathbf{x}, \boldsymbol{\theta}), \quad \mathbf{x}(0) = \mathbf{x}_0 \tag{1a}$$

$$\mathbf{y} = g(\mathbf{x}), \tag{1b}$$

where f and g are continuously differentiable functions, the process states are $\mathbf{x}(t) \in \mathbb{X} \subset \mathbb{R}^{\mathrm{m}}$, measurements at time t are $\mathbf{y}(t) \in \mathbb{Y} \subset \mathbb{R}^{\mathrm{n}}$, and $\boldsymbol{\theta} \in \Theta \subset \mathbb{R}^{\mathrm{p}}$ is an unknown parameter. The domain Θ is a cartesian box $\times_{j=1}^{\mathrm{p}} [\theta_j^{\mathrm{LO}}, \theta_j^{\mathrm{UP}}]$. For the sake of simplicity we consider $\mathrm{n} = 1$, so measurements are scalar, but it is straightforward to extend our approach to larger values of n. The goal of the M-bODE problem is to find a *design* –i.e., a selection of measurements– that enables to estimate $\boldsymbol{\theta}$ with the best possible accuracy.

The time domain is discretized into s points, denoted by $\mathbb{T} = \{t_1, \ldots, t_s\}$, and $[s] = \{1, \cdots, s\}$. A design ξ with support points in $\mathbb{T}$ can be represented using the notation $\xi = \begin{pmatrix} t_1 & \cdots & t_s \\ w_1 & \cdots & w_s \end{pmatrix}$, where $\mathbf{w} \in [0,1]^s$ is a vector of weights satisfying $\sum_{i=1}^{s} w_i = 1$, and w_i represents the fraction of the total number of measurements N to perform at time t_i. The quantity Nw_i should be constrained to take integer values for all i, but this constraint is dropped for approximate designs, and in practical applications of M-bODE we may require to round the optimal approximate design. The set of all design measures supported by $\mathbb{T}$ is denoted by Ξ.

The FIM of a single "observational unit" t_i at $\boldsymbol{\theta} = \boldsymbol{\theta}_0$ is $M(t_i, \boldsymbol{\theta}_0) = \boldsymbol{\eta}(t_i, \boldsymbol{\theta}_0)\boldsymbol{\eta}(t_i, \boldsymbol{\theta}_0)^{\mathrm{T}}$, where $\boldsymbol{\eta}(t_i, \boldsymbol{\theta}_0) = \left.\frac{\partial g(\mathbf{x}(t_i, \boldsymbol{\theta}))}{\partial \boldsymbol{\theta}}\right|_{\boldsymbol{\theta}=\boldsymbol{\theta}_0}$ is the sensitivity of the measurement at t_i with respect to $\boldsymbol{\theta}$. The FIM of an approximate design ξ is obtained by summing the FIM over the individual design points

$$\mathscr{M}(\xi, \boldsymbol{\theta}_0) = \int_T M(t_i, \boldsymbol{\theta}_0)\, \mathrm{d}(\xi) = \sum_{i \in [s]} w_i M(t_i, \boldsymbol{\theta}_0) \succeq 0, \tag{2}$$

where $A \succeq 0$ means that A belongs to the space of symmetric positive semidefinite matrices $\mathbf{S}_+^{\mathrm{p}}$. Note that for $\boldsymbol{\theta}_0 \in \Theta$, $\mathscr{M}(\xi, \boldsymbol{\theta}_0)$ depends only on the weights w_i of the design, and so we also denote it by $\mathscr{M}(\boldsymbol{w}, \boldsymbol{\theta}_0)$. The quality of a design is measured by a criterion Φ, such as the $D-$optimality, $\Phi_D(M) = (\det\, M)^{1/p}$, $A-$optimality, $\Phi_A(M) = (\mathrm{trace}\ M^{-1})^{-1}$, or $E-$optimality, $\Phi_E(M) = \lambda_{\min}(M)$. We refer to Pukelsheim (1993) for more details on optimality criteria.

The representation of $\mathscr{M}(\xi, \boldsymbol{\theta})$ for nonlinear models depends on the unknown parameters that we wish to estimate, which is a challenging cyclic problem. In practice there are three approaches to handle it: *i.* sequential designs which rely on a sequence of local designs, computed at the current best estimate $\hat{\boldsymbol{\theta}}$ of $\boldsymbol{\theta}$; *ii.* Bayesian designs which are derived to optimize the expectation over Θ of an optimality criterion assuming that a prior distribution for parameters is available; *iii.* minimax designs which are derived so that we maximize the design efficiency for the worst combination of parameters in Θ. Such a framework is used in this paper, that is, we want to find a design ξ solving the following saddle point optimization problem:

$$\max_{\xi \in \Xi} \min_{\boldsymbol{\theta} \in \Theta} \Phi(\mathscr{M}(\xi, \boldsymbol{\theta})). \tag{3}$$

2.2. Construction of the FIM

The sensitivity of the measurements with respect to $\boldsymbol{\theta}$ at $\boldsymbol{\theta}_0$ is determined by solving the sensitivity equations (4) simultaneously with Model (1) employing a DAE solver. The sensitivity of state x_i with respect to parameter θ_j is denoted by $\sigma_{i,j}$, yielding:

$$\frac{\mathrm{d}\sigma_{i,j}}{\mathrm{d}t} = \sum_{k=1}^{\mathrm{m}} \frac{\partial f_i(\mathbf{x},\boldsymbol{\theta}_0)}{\partial x_k}\,\sigma_{k,j} + \frac{\partial f_i(\mathbf{x},\boldsymbol{\theta}_0)}{\partial \theta_j}, \qquad i\in[m],\ j\in[p], \tag{4a}$$

$$\boldsymbol{\eta}(t_i,\boldsymbol{\theta}_0) = \sum_{k=1}^{\mathrm{m}} \frac{\partial g(\mathbf{x})}{\partial x_k}\,\sigma_{k,j}(t,\boldsymbol{\theta}_0), \qquad j\in[p]. \tag{4b}$$

2.3. Robust minmax SDP formulation

We recall that a concave function $f:\mathbb{R}^{n_1}\to\mathbb{R}$ is called semidefinite representable (SDr) if and only if inequalities of the form $u\le f(\boldsymbol{x})$ are equivalent to a linear matrix inequality (LMI). More precisely, f is SDr if and only if there exists some symmetric matrices $M_0,\ldots,M_{n_1+n_2}$ such that

$$u\le f(\boldsymbol{x}) \Longleftrightarrow \exists \boldsymbol{y}\in\mathbb{R}^{n_2}:\ uM_0+\sum_{i=1}^{n_1} x_iM_i+\sum_{j=1}^{n_2} y_jM_{n_1+j}\succeq 0.$$

The criterions of $A-$, $E-$, and $D-$optimality are known to be SDr (Ben-Tal and Nemirovskiĭ, 2001, Chap. 2-3), which gave rise to SDP formulations for the computation of local optimal designs (Boyd and Vandenberghe, 2004, Sec. 7.3). We also point out that Kiefer's Φ_p-criterion is SDr for all rational values of $p\in(-\infty,1]$ (Sagnol, 2013). Due to space limitations, we give a semidefinite representation for the $D-$criterion only. The inequality $\tau\le(\det[\mathscr{M}(\xi,\boldsymbol{\theta})])^{1/\mathrm{p}}$ holds if and only if there exists a $p\times p-$lower triangular matrix $\mathscr{C}$ such that

$$\begin{bmatrix}\mathscr{M}(\xi,\theta) & \mathscr{C}^{\mathrm{T}}\\ \mathscr{C} & \mathrm{Diag}(\mathscr{C})\end{bmatrix}\succeq 0 \quad\text{and}\quad \tau\le\left(\prod_{j=1}^{\mathrm{p}}\mathscr{C}_{j,j}\right)^{1/\mathrm{p}},$$

where $\mathrm{Diag}(\mathscr{C})$ is the diagonal matrix with same diagonal entries as those of $\mathscr{C}$. The inequality involving the geometric mean of the $\mathscr{C}_{j,j}$ can, in turn, be expressed by a series of 2×2 LMIs, see Ben-Tal and Nemirovskiĭ (2001). It is also straightforward to show that when the concave functions $f_1,\ldots,f_q$ are SDr, then their pointwise minimum $f:\boldsymbol{x}\mapsto\min(f_1(\boldsymbol{x}),\ldots,f_q(\boldsymbol{x}))$ is also concave and SDr. There exists user-friendly interfaces, such as `cvx` (Grant et al., 2012) or PICOS (Sagnol, 2012), which automatically transforms constraints of the form $\tau\le\Phi[\mathscr{M}(\xi,\boldsymbol{\theta})]$ as a series of LMIs, and pass them to SDP solvers such as SeDuMi (Sturm, 1999) or Mosek (Andersen et al., 2009).

In this paper, we consider a sampling mechanism $\mathscr{S}(q)$ that extracts a finite number q of values in Θ, denoted by $\boldsymbol{\theta}_j\in\Theta,\ j\in[q]:=\{1,\ldots,q\}$ and we define $\mathbb{P}:=\{\boldsymbol{\theta}_1,\ldots,\boldsymbol{\theta}_q\}$. Then, we replace $\min_{\boldsymbol{\theta}\in\Theta}\ \Phi[\mathscr{M}(\xi,\boldsymbol{\theta})]$ by a minimum of finitely many terms, $\min_{j\in[q]}\ \Phi[\mathscr{M}(\xi,\boldsymbol{\theta}_j)]$. As a result, we obtain a SDP formulation that approximates the minmax optimal design problem (3):

$$\max_{\xi\in\Xi}\ \min_{\boldsymbol{\theta}\in\mathbb{P}}\ \Phi[\mathscr{M}(\xi,\boldsymbol{\theta})] = \max_{\tau\in\mathbb{R},\boldsymbol{w}\in\mathbb{R}^s}\ \tau \tag{5a}$$

$$s.t. \qquad \forall j\in[q],\quad \tau\le\Phi[\mathscr{M}(\boldsymbol{w},\boldsymbol{\theta}_j)] \tag{5b}$$

$$\forall i\in[s],\quad w_i\ge 0 \tag{5c}$$

$$\sum_{i=1}^{s} w_i = 1, \tag{5d}$$

where –as mentioned above– the constraints (5b) can be rewritten as LMIs if Φ is SDr; however we used this compact formulation for the sake of generality, and because constraints (5b) are accepted *as is* by high-level interfaces.

2.4. Algorithm

To prevent sub-optimal solutions for problem (3), which can be due to the insufficient variability of the sample of parameter combinations $\mathbb{P}$, we use an iterative procedure. Let $\tau^*, \boldsymbol{w}^*$ be a solution returned after solving Problem (5). Then, it is clear that the design associated with the weights $\boldsymbol{w}^*$ solves Problem (3) if and only if τ^* is equal to the optimal value of

$$\min_{\boldsymbol{\theta}\in\Theta} \Phi[\mathscr{M}(\boldsymbol{w}^*, \boldsymbol{\theta})]. \tag{6}$$

This justifies the following procedure: at each iteration, we seek a parameter combination $\boldsymbol{\theta}^*$ that solves Problem (6). The procedure stops if $\tau^* \leq \Phi[\mathscr{M}(\boldsymbol{w}^*, \boldsymbol{\theta}^*)] + \varepsilon_r$, where ε_r is a small tolerance parameter. Otherwise, $\boldsymbol{\theta}^*$ is added in the sample $\mathbb{P}$ and we go to the next iteration. After the convergence is achieved a pruning step deletes support points with $w_i < \varepsilon^p$. This procedure is summarized in Algorithm 1.

In practice, the nonlinear optimization problem (6) might be hard to solve. However, since Θ is usually a cathesian box of relatively small dimension, the optimum can be found by using local optimization procedures and multiple restarts. Of course, it is also possible to add several local optima of (6) in the sample $\mathbb{P}$. However, note that (approximate-)optimality of a design can only be assessed when the $\boldsymbol{\theta}^*$ used in the algorithm is a global optimum of (6), which would theoretically require the use of a global NLP solver.

Algorithm 1 Algorithm to find a robust minmax design with support on $\mathbb{T}$

procedure FINDDESIGN($\mathbb{T}, \Theta, \mathscr{S}, q, \varepsilon^r, \varepsilon^p$)
  Discretize T ▷ Find the grid $\mathbb{T}$
  Generate the initial sample $\mathbb{P} = \mathscr{S}(q)$ ▷ Sample Θ
  $\ell^* \leftarrow -\infty, \tau^* \leftarrow +\infty$
  while $\tau^* > \ell^* + \varepsilon_r$ **do**
    Compute $\boldsymbol{\eta}(t_i, \theta_{\mathbf{j}})$ and $M(t_i, \theta_{\mathbf{j}})$ for all $(i, j) \in [s] \times [q]$ ▷ Single point FIMs
    Get a solution $(\tau^*, \boldsymbol{w}^*)$ of the SDP (5) ▷ Get upper bound τ^*
    Get a solution $\boldsymbol{\theta}^*$ of Problem (6), $\ell^* \leftarrow \Phi[\mathscr{M}(\boldsymbol{w}^*, \boldsymbol{\theta}^*)]$ ▷ Get lower bound ℓ^*
    $\ell^* \leftarrow \Phi[\mathscr{M}(\boldsymbol{w}^*, \boldsymbol{\theta}^*)]$, $\mathbb{P} \leftarrow \mathbb{P} \cup \{\boldsymbol{\theta}^*\}$, $q \leftarrow q + 1$ ▷ Update the sample
  end while
  Prune ξ
end procedure

2.5. Extension to find the optimal support points over T

When the criterion Φ is differentiable, it is known that a design ξ is minmax optimal if and only if there exists a probability measure γ supported by $V_\Theta(\xi) := \arg\min_{\boldsymbol{\theta}\in\Theta} \Phi[\mathscr{M}(\xi, \boldsymbol{\theta})]$ such that

$$\forall t \in T, \quad h_\gamma(t) := \int_{\boldsymbol{\theta}\in V_\Theta(\xi)} \psi(\xi, \boldsymbol{\theta}, t)\, \gamma(\mathrm{d}\boldsymbol{\theta}) \leq 0, \tag{7}$$

with equality attained only at support points of ξ, where $\psi(\xi, \boldsymbol{\theta}, t)$ denotes the directional derivative of Φ at $\mathscr{M}(\xi, \boldsymbol{\theta})$ in the direction of $(M(t, \boldsymbol{\theta}) - \mathscr{M}(\xi, \boldsymbol{\theta}))$, see e.g. Fedorov and Leonov (2013, Theorem 2.5). Let ξ be a solution of Problem (5) and assume without loss of generality that $V_\mathbb{P}(\xi) = \{\boldsymbol{\theta}_1, \ldots, \boldsymbol{\theta}_k\}$. By construction, ξ is minmax optimal over the discretized sets $\mathbb{T}$ and $\mathbb{P}$, so there must exist a discrete probability measure $\boldsymbol{\gamma}$ such that Equation (7) holds if we replace T by $\mathbb{T}$ and Θ by $\mathbb{P}$. This measure can be found easily by solving the following linear program (LP):

$$\min_{\boldsymbol{\gamma}\in\mathbb{R}^k_+,\, U\geq 0} \; U \qquad \text{s.t.} \qquad \sum_{j=1}^{k} \gamma_j = 1, \qquad \forall i \in [s],\; h_{\boldsymbol{\gamma}}(t_i) := \sum_{j=1}^{k} \gamma_j\, \psi(\xi, \boldsymbol{\theta}_j, t_i) \leq U.$$

Table 1: Robust minmax designs obtained for $T=[0,20]$, $\mathbb{T}=\{0,0.2,\ldots,20\}$, and $\Theta\equiv[0.5,1.0]\times[0.1,0.5]\times[1.0,2.0]\times[1.0,2.0]$. Designs are given using the notation $\xi=\left(\begin{smallmatrix} t_1 & \cdots & t_s \\ w_1 & \cdots & w_s \end{smallmatrix}\right)$.

support	criterion	Optimal design	CPU (s)	iterations
fixed	Φ_D	$\left(\begin{smallmatrix} 0.4 & 1.6 & 1.8 & 4.4 & 4.6 & 10.8 & 11 \\ 0.2493 & 0.1517 & 0.0994 & 0.1436 & 0.1057 & 0.0330 & 0.2158 \end{smallmatrix}\right)$	11.0	1
support over $\mathbb{T}$	Φ_A	$\left(\begin{smallmatrix} 0.2 & 1.6 & 4.6 & 10.8 & 20 \\ 0.3881 & 0.2266 & 0.1595 & 0.1392 & 0.0862 \end{smallmatrix}\right)$	7.94	1
	Φ_E	$\left(\begin{smallmatrix} 0.2 & 1.6 & 4.6 & 10.8 & 20 \\ 0.3889 & 0.2278 & 0.1565 & 0.1341 & 0.0917 \end{smallmatrix}\right)$	11.93	1
optimal	Φ_D	$\left(\begin{smallmatrix} 0.44 & 1.66 & 1.7 & 4.0 & 4.49 & 10.77 & 10.8 \\ 0.2498 & 0.0846 & 0.1654 & 0.2448 & 0.0048 & 0.1151 & 0.1338 \end{smallmatrix}\right)$	39.19	5
support over T	Φ_A	$\left(\begin{smallmatrix} 0.27 & 1.61 & 4.61 & 4.63 & 10.50 & 19.0 \\ 0.3463 & 0.2527 & 0.0670 & 0.1061 & 0.1415 & 0.0851 \end{smallmatrix}\right)$	27.46	6

Then, natural candidate support points for the minmax optimal design arise as local maxima of the function $h_{\boldsymbol{\gamma}}(t)$ over T. More precisely, we propose to change the stopping condition of the main loop as "**while** ($\tau^* > \ell^* + \varepsilon_r$ and $\max_{t\in T} h_{\boldsymbol{\gamma}}(t) > \varepsilon_r$) **do**", and to add the following statements at the end of the **while** loop in Algorithm 1:

$$\text{Compute the dual weights } \boldsymbol{\gamma}\in\mathbb{R}^k, \quad \mathbb{T}\leftarrow\mathbb{T}\cup\arg\max_{t\in T} h_{\boldsymbol{\gamma}}(t), \quad s\leftarrow\text{card}(T).$$

3. Application and results

To test the algorithm presented in Section 2 we use the example of Atkinson et al. (2007, pag. 270), referring to the model for two consecutive reactions $\mathrm{A}\xrightarrow{\pi_1}\mathrm{B}\xrightarrow{\pi_2}\mathrm{C}$ occurring in a constant volume CSTR, where the concentration C_B of product B is observed, cf. the model in Equations (8).

The measurements must be selected so as to estimate the vector of parameters $\boldsymbol{\theta}=(\pi_1,\pi_2,\lambda_1,\lambda_2)$ for $\Theta\equiv[0.5,1.0]\times[0.1,0.5]\times[1.0,2.0]\times[1.0,2.0]$. We considered $T=[0,20]$, discretized as $\mathbb{T}=\{0,0.2,0.4,\ldots,20\}$ (i.e., $s=101$). The sampling mechanism $\mathscr{S}$ selects the $2^4=16$ corners of Θ, plus 34 vectors drawn from a uniform distribution over Θ (i.e., $q=50$). We used $\varepsilon^p=\varepsilon^r=10^{-3}$, and solved the SDPs with Mosek interfaced by PICOS (Grant et al., 2012; Sagnol, 2012).

Table 1 compares the optimal designs, obtained for D-, A- and E-criteria, for both the case of fixed support points (Section 2.4) and optimal support points over T (Section 2.5). We observe that the D-optimal design is in good agreement with the local designs presented by Atkinson et al. (2007, pag. 270). The local designs were determined for a singleton Θ employing an exchange algorithm which does not require the discretization of the time domain, and are consistently based on 4 support points. Our designs are based on 7, and 6 support points, respectively, which is consistent with the trend observed by several authors, that minmax and Bayesian designs tend to have more support points than local designs (Chaloner and Larntz, 1989). The increase of the number of support points occurs to handle the larger uncertainty caused by broadening the parameters domain. The sampling instants are similar for all designs, and the $D-$optimality criterion produces a design without the point $t=t^{\max}$ which has low weight for $A-$ and $E-$optimal designs. For the case of fixed support points, the optimal design was found after a single iteration for all three criteria. The reason is that the function $\boldsymbol{\theta}\to\Phi[\mathscr{M}(\boldsymbol{w}^*,\boldsymbol{\theta})]$ seems to exhibit a concave behaviour, so that its minima are at the corners of the region Θ. For example, the *answering set* for minmax $D-$optimality over $\mathbb{T}$ is $V_\Theta(\xi^*)=\{(\frac{1}{2},\frac{1}{10},2,2),(\frac{1}{2},\frac{1}{2},2,1),(\frac{1}{2},\frac{1}{2},2,2)\}$.

Figure 1 displays the evolution of the function $h_{\boldsymbol{\gamma}}(t)$ with the iterations of the modified version of Algorithm 1. We see that as support points are added, the upper bound of h_γ is pushed toward 0. Our algorithm was also tested with the logistic model — a nonlinear algebraic model commonly used for benchmark testing — and the results were in agreement with those obtained with other algorithms.

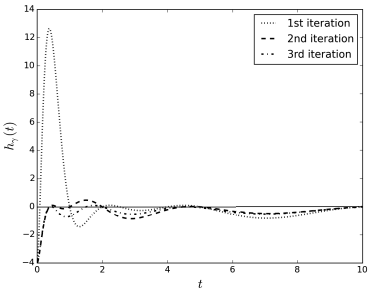

$$\frac{\mathrm{d}C_A}{\mathrm{d}t} = -\pi_1\, C_A^{\lambda_1}, \qquad C_A(0) = 1.0 \quad (8a)$$

$$\frac{\mathrm{d}C_B}{\mathrm{d}t} = \pi_1\, C_A^{\lambda_1} - \pi_2\, C_B^{\lambda_2}, \qquad C_B(0) = 0.0 \quad (8b)$$

$$\frac{\mathrm{d}C_C}{\mathrm{d}t} = \pi_2\, C_B^{\lambda_2}, \qquad C_C(0) = 0.0 \quad (8c)$$

$$y(t) = C_B(t) \quad (8d)$$

Figure 1: Evolution of $h_{\boldsymbol{\gamma}}(t)$ for $D-$optimality.

4. Conclusions

We propose a robust minmax SDP formulation for finding the optimal design of experiments for dynamic models. Our approach relies on the discretization of time domain, and subsequent construction of generalized FIM for a sample of parameter combinations. The minmax optimal design problem is solved employing convex optimization techniques. To prevent suboptimal solutions due to the small size of the sample, we iterate to add the worst parameter combinations in the sample, until a convergence condition is satisfied. A small modification of the algorithm allows one to identify the optimal support points of the minmax design. The algorithm is tested for a dynamic model for two consecutive reactions, and the results compare well with earlier references.

References

Andersen, E., Jensen, B., Jensen, J., Sandvik, R., Worsøe, U., 2009. Mosek version 6. Tech. rep., Technical Report TR–2009–3, MOSEK.

Atkinson, A., Donev, A., Tobias, R., 2007. Optimum experimental designs, with SAS. Oxford University Press.

Ben-Tal, A., Nemirovskiĭ, A., 2001. Lectures on Modern Convex Optimization: Analysis, Algorithms, and Engineering Applications. Society for Industrial and Applied Mathematics, Philadelphia.

Boyd, S., Vandenberghe, L., 2004. Convex Optimization. University Press, Cambridge.

Chaloner, K., Larntz, K., 1989. Optimal Bayesian design applied to logistic regression experiments. Journal of Statistical Planning and Inference 59, 191–208.

Duarte, B. P. M., Wong, W. K., 2014a. Finding Bayesian optimal designs for nonlinear models: A semidefinite programming-based approach. International Statistical Review, forthcomming.

Duarte, B. P. M., Wong, W. K., 2014b. A semi-infinite programming based algorithm for finding minimax optimal designs for nonlinear models. Statistics and Computing 24 (6), 1063–1080.

Fedorov, V., Leonov, S., 2013. Optimal design for nonlinear response models. CRC Press.

Goos, P., Jones, B., 2011. Optimal Design of Experiments: A Case Study Approach. Wiley.

Grant, M., Boyd, S., Ye, Y., 2012. `cvx` Users Guide for `cvx` version 1.22. 1104 Claire Ave., Austin, TX 78703-2502.

Kiefer, J. C., 1959. Optimum experimental designs. Journal of the Royal Statistical Society, Series B 21, 272–319.

Pukelsheim, F., 1993. Optimal Design of Experiments. SIAM, Philadelphia.

Sagnol, G., 2011. Computing optimal designs of multiresponse experiments reduces to second-order cone programming. Journal of Statistical Planning and Inference 141 (5), 1684–1708.

Sagnol, G., 2012. Picos, a python interface to conic optimization solvers. Tech. Rep. 12-48, ZIB, `http://picos.zib.de`.

Sagnol, G., 2013. On the semidefinite representation of real functions applied to symmetric matrices. Linear Algebra and its Applications 439 (10), 2829–2843.

Sturm, J., 1999. Using `sedumi` 1.02, a Matlab toolbox for optimization oversymmetric cones. Optimization Methods and Software 11, 625–653.

Vandenberghe, L., Boyd, S., 1999. Applications of semidefinite programming. Applied Numerical Mathematics 29, 283–299.

Wong, W., 1992. A unified approach to the construction of minimax designs. Biometrika 79, 611–620.

Wynn, H. P., 1972. Results in the theory and construction of D-optimum experimental designs. Journal of Royal Statistics Soc. - Ser. B 34, 133–147.

Krist V. Gernaey, Jakob K. Huusom and Rafiqul Gani (Eds.), 12th International Symposium on Process Systems Engineering and 25th European Symposium on Computer Aided Process Engineering.
31 May – 4 June 2015, Copenhagen, Denmark

Design of a Multi-Contaminant Water Allocation Network using Multi-Objective Optimization

Sofía De-León Almaraz*, Marianne Boix, Catherine Azzaro-Pantel, Ludovic Montastruc, Serge Domenech

[a] *Université de Toulouse, Laboratoire de Génie Chimique U.M.R. 5503 CNRS/INP/UPS 4 allée Emile Monso, 31432 Toulouse, France. sofia.deleonalmaraz@ensiacet.fr*

Abstract

The core of this study is the design of Water Allocation Networks (WAN) defined by a superstructure integrating different processes, regeneration units and contaminants. In this work, different optimization frameworks are compared to identify the main elements and criteria to be considered as well as the more robust methodology to solve problems involving multiple contaminants and several regeneration units from a multi-objective perspective. A case study previously analysed by (Feng et al., 2008) and (Boix et al., 2011) and formulated as a Nonlinear Programming (NLP) and Mixed Integer Non-Linear Programming (MINLP) problem, respectively, is treated by minimizing objective functions such as fresh water consumption, the number of network connections and the regenerated water flow rate. The comparison of the obtained results show that the use of binary variables in the MINLP approach leads to a better WAN with less connections thus eliminating low flow rates among the processes although the computation time is longer.

Keywords: Water networks (WAN), multi-contaminant, multi-objective optimization, MINLP, ε-constraint.

1. Introduction

The declining supply and higher cost of raw water is forcing industry to implement recycling technologies in an increasingly competitive market and stringent regulations and standards. During the last decades, the scientific community has been largely involved in the topic of the design of optimal water networks while minimizing both economic and environmental objectives. The design of Water Allocation Networks (WANs) is a complex task, especially when multiple contaminants are treated in the same plant with particular emphasis on the decision about the use of many regeneration units. This problem has been identified in previous works (e.g. Boix et al., 2011; Feng et al., 2008; Gunaratnam et al., 2005) and formulated as a generic framework considering one or several objective functions. The analysis of the dedicated literature shows that a robust approach that can take into account large problems is far from being straightforward and that the definition of constraints or assumptions must be specified and adapted to a case study, thus hampering the development of a generic approach. Depending of the nature of these constraints, the model can be expressed with either a Non Linear Programming (NLP) or a Mixed Integer Non Linear Programming (MINLP) formulation. In this work, the first objective is to identify a robust methodology to deal with large problems for the WAN design through multi-objective optimization. The second goal consists in defining the main criteria to be taken into

account. For this purpose, the comparison of different solution strategies will be analysed. The remainder of this paper is organised as follows: section 2 is devoted to the WAN formulation. The mathematical model and criteria are presented in section 3. Section 4 is dedicated to the development of the solution strategy. The definition of the case study and the obtained results are presented in section 5. Finally, conclusions and perspectives are given.

2. Formulation of the Water Allocation Network (WAN)

A general superstructure for WAN modelling is presented in Figure 1. From a given number of regeneration units and processes, all the possible connections between them may exist, except regeneration recycling to the same regeneration unit or from a process to the same one. Each process admits fixed maximal input and output concentrations, and in the same way, regeneration units have a given processing capacity. For each water-flow rate using a process, the water input may be freshwater, used water coming from other processes and/or recycled water; the water output for such a process may be directly discharged, distributed to other processes and/or to regeneration units. Similarly, for a regeneration unit, the input water may come from processes or other regeneration units. Regenerated water may be reused in the processes or directed to other regeneration units. For each process, input or output contaminant mass fractions (ppm) are imposed by the user, and constitute bounds for the optimization problem. Each task performed by a given process contaminates its input water up to a given mass fraction. The amount of pollutant *i* generated by a process *j* is noted $M_{i,j}$ and is expressed in mass flow rate (g h^{-1}) in order to have consistent units with the water flow rate (t h^{-1}) and the contaminant mass fraction (ppm). The regeneration units are represented by the indices *l* and *m*.

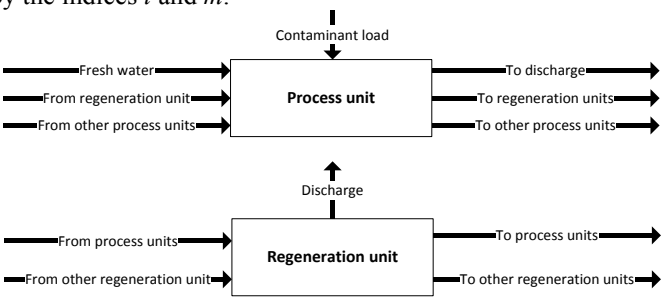

Figure1. Generic elements of the superstructure (Boix et al., 2011)

3. Mathematical model for the multi-contaminant problem

A multi-contaminant WAN can be generally stated in terms of concentrations and total mass flows involving water balances on processes and regeneration units, contaminant and mass balances on inlet processes and regeneration units and finally, the overall mass balances of contaminants on discharge considering the environmental limits for each contaminant. For reasons of brevity, not all the equations are presented here but they can be found in (Feng et al., 2008) with different constraint features (i.e. equality, inequality or bounded). Several criteria can be optimized. Let us recall that multi-objective optimization is relevant to antagonist objective functions. Several objective functions presented in the works of (Boix et al., 2011; Feng et al., 2008) can be used to solve a multi-contaminant problem with several regeneration units. The first criterion is the total flow rate of fresh water in the network (F1) (see Eq. (1)) where F1 represents the sum of freshwater flow rates at the entrance of each water-using process *j* (W_j^1):

$$F1 = \sum_j W_j^1 \quad (1)$$

The second function (F2) presented here was firstly proposed by (Feng et al. 2008). Eq. (2) minimizes the regenerated water flow considering a weighting coefficient for each of them. The water flow rate going from the process *j* (W^{PR}) and from the regeneration unit *m* to regeneration unit *l* (W^R, in t h^{-1}) is multiplied by the weighting coefficient for the treatment unit *l*(λ^{reg}: without considering directly the cost associated to the treatment units but a weight):

$$F2 = \sum_l \left[\left(\sum_j W_{\overrightarrow{j,l}}^{PR} + \sum_m W_{\overrightarrow{m,l}}^{R} \right) \times \lambda_l^{reg} \right] \quad (2)$$

A third criterion (F3) also proposed by (Feng et al. 2008) refers to the contaminant regeneration load and was also considered in this study. The water flow rates going from the regeneration unit *l* to the process *j* and the regeneration unit *m* (W^{RP} and W^R, in t h^{-1}) are multiplied by the difference inlet/outlet concentration of contaminant *i* for the regeneration unit *l* ($Cr^{In/out}$, in ppm) by the weighting coefficient for the three contaminants in the treatment unit *l* (λ^{cont}), this last value is assumed by the user.

$$F3 = \sum_l \left\{ \left(\sum_j W_{\overrightarrow{l,j}}^{RP} + \sum_m W_{\overrightarrow{l,m}}^{R} \right) \times \left[\left(\sum_i Cr_{i,l}^{In} - \sum_i Cr_{i,l}^{Out} \right) \times \lambda_l^{cont} \right] \right\} \quad (3)$$

Feng et al. (2008) used criteria [F1-F3] to solve the case study presented by (Gunaratnam et al. 2005) with the use of continuous variables in a nonlinear framework. This NLP model was solved using sequential optimization to find the optimal WAN. In a different approach, (Boix et al., 2011) minimized F1 and highlighted the complexity of the network by the use of interconnection between processes and regeneration units. The criterion of interconnections (F4) is presented in Eq. (4) where the number of connections is given by the sum of the binary variables *Y* among the processes *j*.

$$F4 = \sum_j Y_j \quad (4)$$

The inlet water flow-rate to the regeneration unit (F5) simply expressed as the sum of the water flow rates going from a process to a regeneration unit and from a regeneration unit to another is also minimized (Eq. 5). This criterion is directly related to an economic basis because if the amount of regenerated water increases, the cost will increase for the user, conversely**.**

$$F5 = \sum_l \left(\sum_m W_{\overrightarrow{m,l}}^{R} + \sum_j W_{\overrightarrow{j,l}}^{PR} \right) \quad (5)$$

The approach NLP presented by (Feng et al., 2008) does not consider the addition of binary variables to minimize the interconnections but apply sequential optimization to find the optimized WAN where the weighting coefficients for each contaminant and treatment unit (λ_l^{cont} *and* λ_l^{reg}) are difficult to set. To overcome this limitation, the approach MINLP presented by (Boix et al., 2011) [min F1, F4 and F5] is also assessed.

4. Optimization strategy

The multi-objective problem is solved by lexicographic and ε-constraint methods where all but one objective are converted into constraints by setting an upper or lower bound to each of them, and only one objective is to be optimised. By varying the numerical values of the upper bounds, a Pareto front can be obtained. Finally, a Multi-Criteria Aid Decision Making (MCDM) tool based on the so-called M-TOPSIS method (Ren et al., 2007) (Modified Technique for Order of Preference by Similarity to Ideal Solution) is selected to choose the best compromise solution. In this work, we first validate (Feng et

al., 2008) values by using GAMS instead LINGO. The second step involves the minimization of the fresh water flow rate for each contaminant to find the limiting pollutant. Then, the multi-objective optimization is applied. Finally, instead of evaluating the cost network, the so-called global equivalent cost (GEC) is used (Boix et al., 2011) expressed in equivalent of water flow rate which allows expressing the overall cost of the network in amount of fresh water. In GEC calculation, the fresh water flow rate and amounts of regenerated and discharged flow rates weighted by their contributions relative to the fresh water one (equal to 1) are considered. Consequently, three criteria are merged into only one according to the following relation:

$$GEC = F1 + \alpha \times F5 + \beta \times FD \quad (6)$$

F5 refers to the regenerated water and FD is waste flow rate to discharge. In Eq.(6), α and β are cost elements respectively related to the regenerated water cost and post-treatment cost for water sent to the discharge; α depends on the type of regeneration unit (see Table 1) and β is equal to 5.625 according to (Bagajewicz and Faria, 2009).

Table 1. Values of α according to types of regeneration units

Regeneration type	Treatment unit weight (Feng et al., 2008)	α (calculated based on (Bagajewicz and Faria, 2009)
I	49 %	3.13
II	37 %	2.34
III	14 %	0.89

5. Results for the case study

5.1. Case study

A case study for a simplified petroleum refinery (Gunaratnam et al. 2005) is treated and analysed from a multi-objective viewpoint. The problem consists of 5 water processes and 3 treatment units with three contaminants (i.e. hydrocarbon (HC), hydrogen sulfide (H_2S), and suspended solids (SS)). The regeneration units are defined by their given efficiency depending on the pollutant under treatment. The regeneration units treat wastewater up to a fixed post-regeneration concentration for each contaminant.

5.2. Solving the WAN problem through NLP

In the NLP model, freshwater consumption, regenerated water flow rate and contaminant regeneration load are minimized using sequential optimization to design an economic water network for this system. The results obtained under (Feng et al. 2008) conditions have also been found again by the use of IPOPT solver, thus validating the proposed approach (see Figure 2). It must be highlighted that the use IPOPT does not guarantee global optimality but a very good solution is found that satisfies all constraints. The quality of the solutions is good enough for industrial uses.

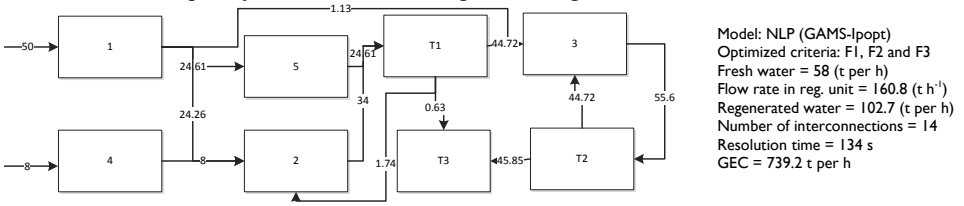

Figure 2. Solution network for the NLP formulation

The chosen point is a non-dominated solution obtained by lexicographic optimization. In this case, the number of interconnections is not minimized (a total of 14 is obtained). The GEC is also calculated to serve as a basis (739 t h^{-1}). The minimal fresh water flow rate is 58 t h^{-1} and the inlet flow rate in the regeneration unit is 160.8 t h^{-1}.

5.3. Mono-contaminant versus multi-contaminant impact

Once the NLP problem is validated, it is possible to identify the limiting contaminant. A study based on the key contaminant is valid in the aim of finding the minimum freshwater target but cannot be implemented for designing an optimal water network regarding several objectives. Figure 3 displays the results of bi-objective optimization (fixing the fresh water flow rate and minimizing the regenerated water) for the three mono-pollutant water networks compared to the multi-contaminant network. The first observation is that Pareto fronts are not straight lines for each network. The three mono-contaminant networks involve lower flow rates than the multi-contaminant one, which is relevant because the problem is more constrained with more components. It is highlighted that the addition of single points of the three contaminants given by freshwater flow rate is higher than the one obtained by the multi-contaminant problem. The key contaminant is related to the highest amount of regenerated water. In this example, the key contaminant is the second one because its curve is above the two others. The dotted line in Figure 3 shows the changing point to discontinuous pace of the mono and multi-contaminant curves. These preliminary results reinforce the interest of implementation of a multi-objective MINLP procedure because the key component method cannot be used for determining the regenerated water flow rate and also the interconnections.

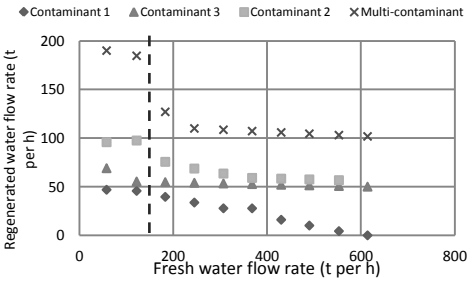

Figure 3. NLP results for the multi-contaminant water network

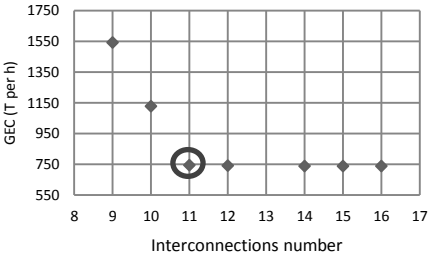

Figure 4. Minimum GEC for each value of connections

5.4. Multi-objective optimization for the MINLP formulation

The MINLP model involves 234 continuous variables, 77 discrete and 455 equations. The optimization runs were implemented with an Intel (R) Core (TM) 17-3540 CPU @3.00 GHz processor machine. The pay-off table of mono and multi-objective optimization is presented in Table 2. In the first section, results concerning mono-objective optimization are displayed where the lower and upper bounds are identified by bold characters.

Table 2. Pay-off table for mono- and multi-objective optimization approaches

Pay-off table obtained by:	*mono-objective optimization*			*lexicographic optimization*		
Resulted value/Minimize:	Fresh water (t per h)	Connect.	Reg. water (t per h)	Fresh water (t per h)	Connect	Reg. water (t per h)
Fresh water (t h^{-1})	58	597	610	**58**	613	600
Number of connections	44	9	11	10	**9**	10
Regenerated water flow-rate	1380.10	964	102.5	157.20	104	**102.50**
Resolution time (s)	6	1000	13	1000	1918	188

By using the abovementioned bounds, the 3 objective optimizations are run following the lexicographic method. This methodology allows finding non-dominated solutions for each criterion. For example, in a mono-objective optimization of fresh water, we identified the minimal value of 58 t h^{-1} with 44 connections and 1380 t h^{-1} of water flow rate in the regeneration unit (CPU time of 6 s): this is a dominated solution with respect

to the lexicographic optimization results: 58 t h^{-1}, 10 connections and 157 t h^{-1} of water flow-rate in the regeneration unit (CPU time of 1000 s).

5.5. Global equivalent cost minimization

Finally, a bi-objective optimization parameterized by the interconnection number is carried out in the range [9, 16]. Starting from the lowest bound for F4, all the possible values for GEC are tested. According to Figure 4, with an increasing interconnection number, the GEC decreases but above 14 interconnections, the GEC remains as 739 T h^{-1} because the number of connections does not have an impact on the cost. If both the GEC and interconnection numbers are considered, the most preferred network includes 11 connections by using 58 T h^{-1} and 164 T h^{-1} of freshwater and regenerated water, respectively according to the TOPSIS analysis. The GEC of this network solution is 744 T h^{-1} and is shown in Figure 5. It is highlighted that the main advantage of this network is the use of less interconnections where low flow rates are discarded.

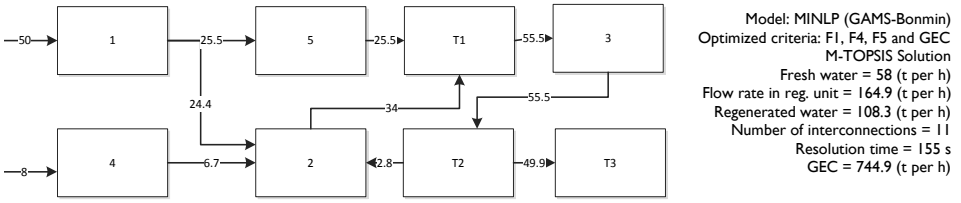

Figure 5. Solution network for the MINLP formulation

6. Conclusions

In this paper the WAN design for a multi-contaminant network considering several regeneration units has been evaluated from different perspectives. A robust methodology for WAN problems has been identified to deal with large problems through multi-objective optimization by the comparison of different solution strategies. First, an NLP model has been solved by sequential optimization following the methodology proposed by (Feng et al., 2008). In this strategy, a network with relatively good performances is obtained but suffers from the need to use arbitrary weight coefficient for each contaminant in the objective function involving the regenerated water flow. In a second time, the MINLP problem was solved using lexicographic and ε-constraints methods. The number of interconnections and the global equivalent cost (GEC) are minimized as well as flow rates. A network with less interconnections resulted from this approach with a low impact in the GEC. The calculation time is higher due to the introduction of binary variables. This second approach is based on the minimization of flow rates and of the number of interconnections. The formulation is generic enough so that new constraints could be added to the WAN problem to integrate the Heat Exchange Networks (HEN) so that a water/energy nexus could be tackled.

References

M.J. Bagajewicz and D.C. Faria, 2009. On the appropriate architecture of the water/wastewater allocation problem in process plants, Computer Aided Chemical Engineering, 19th ESCAPE. Elsevier, pp. 1–20.

M. Boix et al., 2011. A multiobjective optimization framework for multicontaminant industrial water network design. J. Environmental Management (92), 1802–1808.

X. Feng et al., 2008. Grass-roots design of regeneration recycling water networks. Comput. Chem. Eng. (32), 1892–1907.

M. Gunaratnam et al., 2005. Automated Design of Total Water Systems. I&EC (44), 588–599.

L. Ren et al., 2007. Comparative Analysis of a Novel M-TOPSIS Method and TOPSIS. Appl. Math. Res. EXpress Vol. 2007, 10 pages. doi:doi:10.1093/amrx/abm005

Krist V. Gernaey, Jakob K. Huusom and Rafiqul Gani (Eds.), 12th International Symposium on Process Systems Engineering and 25th European Symposium on Computer Aided Process Engineering.
31 May - 4 June 2015, Copenhagen, Denmark.

Simulation and Optimization of the Ethane Cracking Process to Produce Ethylene

Daison Y. Caballero[a,b], Lorenz T. Biegler[b] and Reginaldo Guirardello[a]

[a]*Department of Chemical Engineering, University of Campinas, Campinas–SP, Brazil*
[b]*Department of Chemical Engineering, Carnegie Mellon University, Pittsburgh–PA, United States*
daisonyancy@gmail.com

Abstract

One of the most important processes in the petrochemical industry is the cracking of light hydrocarbons to produce commercially more important products such as light olefins and aromatics, which are considered key components of the chemical industry. This process is carried out at high temperatures in a tubular reactor located in large gas–fired furnaces that supplies heat. The topic of this work is to apply process optimization to the operation of thermal cracking of ethane in order to maximize the production of ethylene. The cracking reactor was modeled as a one–dimensional tubular reactor, and the kinetic mechanism used here is a detailed free–radical scheme that was carefully selected from literature. This application is a challenging problem because of the presence of a free–radical mechanism that coupled with material, energy, and momentum balances of the reactant–product flow along the reactor leads to stiff differential equations that are difficult to solve. In this work, these differential–algebraic equations are discretized using orthogonal collocation on finite elements, and the collocation equations are used as equality constraints in the non–linear optimization problem. GAMS optimization–modeling platform is used to implement this optimization problem. A comparison between model results and experimental data shows that the used approach is a good alternative for dealing with this type of optimization problem.

Keywords: Reactor optimization; Thermal cracking; Ethylene

1. Introduction

Ethylene is utilized to produce a wide variety of more high value–added industrial products, e.g., polymers, co–polymers, ethylene oxide and ethylbenzene. For that reason, this is a valuable intermediate feedstock in petrochemical industry. Ethylene is commercially produced by thermal cracking of feedstocks derived from hydrocarbons such as ethane, propane, butane, naphtha, heavy gas–oil and kerosene. The thermal cracking for olefins production is carried out in long coils (tubular reactors) suspended in large gas–fired furnaces operating in very high temperatures (900–1,200 K). An typical coil is composed by several straight tubes connected by bends, and an industrial furnace may contain several such coils, heated by burners to provide the necessary heat for the endothermic cracking reactions (Froment et al., 2010). Steam is added as a diluent to the process in order to reduce the partial pressure of hydrocarbons and limit undesirable side reactions, typically a dilution rate between 0.2 to 1 kg steam/kg hydrocarbons is used (Sadrameli, 2015). Thermal cracking furnaces are divided into three sections; radiation section or firebox, convection section, and cooling section or transfer line exchangers. A simplified sketch of a steam cracking furnace is depicted in Figure 1. In the convection section the feedstock is mixed with steam and preheated to around 773–923 K. The cracking process occurs in the radiant section, this section is composed by burners and cracking tubular reactors (coils) where the pyrolysis reactions take place. Finally, the

highly reactive cracked gas leaves the radiant coils of the furnace at temperatures between 1,050–1,160 K, and must be quickly cooled down in order to prevent other side reactions and to provide the highest yield. This rapid cooling takes place in the transfer line exchangers (Sadrameli, 2015).

On the other hand, modelling, simulation and optimization are very important tools to get a better understanding of chemical processes and achieve higher performance. In this manner, many studies in this field have been reported in literature for the thermal cracking, endeavoring to investigate the influence of the operating parameters on the process in order to find an optimal operating strategy and to increase profitability. Additionally, while rigorous models that capture the behavior of the physical and chemical phenomena that occur in the reactor are preferred, thermal cracking is commonly modelled as a plug flow reactor where radial and axial dispersion are negligible, which leads to the simplification of the model. Currently, one dimensional models are accepted, and several studies indicate that these are enough to produce a reasonable level of accuracy and to have a correctly understanding of the thermal cracking (Froment et al., 2010). Reactor models consist generally of a set of mass, energy and momentum balance equations, which have to be coupled with the reaction network and some constitutive equations to predict the mixture properties. These models form a set of differential–algebraic equations (DAEs) that must be solved numerically. When the reaction network in the thermal cracking process is formulated by a free-radical mechanism, which is the most detailed and accurate way to represent this complex reaction network, the resulting model leads to a stiff non–linear DAE system due to the large differences in concentration gradient between molecular and radical species (Froment et al., 2010). In this way, the goal of the present paper is to find an optimal profile for the heat flux added along the coil length of an industrial ethane steam cracking reactor to maximize the production of ethylene. To overcome the stiffness problem in the system of equations the orthogonal collocation on finite elements method (OCFE) was incorporated in the optimization procedure.

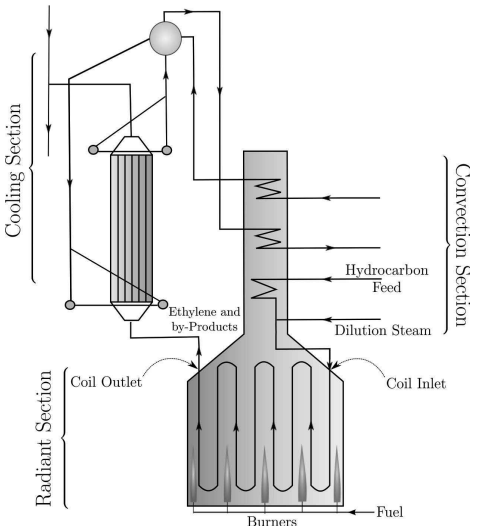

Figure 1: Sketch of a typical furnace for the steam cracking of hydrocarbons

2. Mathematical modeling

The well known one–dimensional plug flow model in steady state is considered in this study to represent the reactor. Thus, the set of differential equations consisting of mass balance for each specie is simultaneously solved with the energy and momentum balances and the kinetic model. The kinetic model used in this work describes ethane cracking with 49 reactions including 11 molecular components and 9 radical species. The rigorous reaction model has been reported in detail by Sundaram and Froment (1978). It's worth mentioning that more accurate results have been reported by using this free radical model than with other molecular kinetic models. The reactor equations are as follows:

• Mass balance for each component:

$$\frac{dF_i}{dz} = R_i \cdot A_t \tag{1}$$

with F_i the molar flow rate of component i; R_i the net production rate of component i and A_t the cross sectional surface area.

• Energy balance:

$$\sum_i F_i \cdot C_{p,i} \cdot \frac{dT}{dz} = Q(z) \cdot \pi \cdot d_t + A_t \cdot \sum_j (-\triangle H_j) \cdot r_j \tag{2}$$

with T the temperature of the reactor; $Q(z)$ the heat flux at length z of the reactor; $C_{p,i}$ the heat capacity of component i at temperature T; d_t the coil tube diameter; $\triangle H_j$ the enthalpy of reaction j and r_j the reaction rate of reaction j.

• Momentum balance:

$$-\frac{dP}{dz} = \alpha \cdot F_r + \rho \cdot u^2 + \alpha \cdot \rho \cdot u \cdot \frac{du}{dz} \tag{3}$$

with P the total pressure of the reactor; α a conversion factor for pressure; F_r the friction factor; ρ the density of the gas mixture and u the gas velocity. The momentum equation accounts the friction losses in the straight part of the coil according to the Fanning equation and an additional loss in the bends. A detailed description of the applied model can be found in Froment et al. (2010). In order to carry out a cracking reactor simulation, it is necessary to know the heat flux along the reactor $Q(z)$, so before solving the DAEs system referred above the heat flux or tube skin temperature profile should first be calculated, which is used as boundary condition in the model. Otherwise the system has a certain degree of freedom. This heat flux is commonly predicted by either independent or coupled simulations of the furnace and the coil, which are solved with iterative processes. Algorithms of such procedures are well described elsewhere in (Heynderickx and Froment, 1996). Recently, furnace CFD simulations are coupled with PFR simulations to predict accurately the heat flux (Hu et al., 2012). It is important to highlight that such prediction of heat flux was not necessary in this work because the problem was formulated as an optimization problem (Non–Linear Programming, NLP), and the heat flux was considered as decision variable.

3. Optimization Methodology

The goal of this optimization problem is to find an optimal profile for the heat flux that maximizes the production of ethylene. Hence, the most suitable objective function to be chosen from a practical standpoint of the reaction system is the ethylene yield, which can be written as the product of the ethane conversion ($X_{C_2H_6}$) and ethylene selectivity ($S_{C_2H_4}$). The equality constraints of this optimization problem are the non–linear differential–algebraic equations distributed in space presented in the previous section, which lead to an DAE–constrained optimization problem. An effective way of dealing with this kind of optimization problem is carrying out a full discretization of the DAE system and incorporating the discretized DAEs into an NLP formulation. A robust method of discretization is, therefore, necessary to deal with the stiffness caused by the kinetic model used. In this fashion, the orthogonal collocation on finite elements method is chosen in this work, along with Radau collocation points because of their compatibility with the NLP formulations and desirable stability properties (Biegler, 2010). Finally, the applied methodology leads to a large set of nonlinear algebraic equations (large scale NLP problems), and these usually require efficient solution strategies. For that reason, a robust and efficient NLP solver must be chosen for solving the optimization problem. In consequence, IPOPT solver, which is an solver based on interior–point methods, was implemented, and the problem was formulated within GAMS optimization–modeling platform. More details on the background of this methodology can be found in Biegler (2010). Inequality constraints were also included in the optimization. These

Table 1: Specifications of the simulated industrial reactor (Froment et al., 1976)

Parameter	Value
Length of the straights tubes [m]	8.85
Length of the bends [m]	0.55
Number of straights tubes	10
Number of bends	10
Total reactor length [m]	95
Tubes diameter [m]	0.108
Bend radius [m]	0.178
Inlet mass flux $\left[\frac{kg}{m^2 \cdot s}\right]$	68.68
Inlet temperature [K]	950
Inlet pressure [kPa]	303
Steam–to–ethane mass ratio	0.4

Table 2: Comparison between simulated data and industrial data

Parameter		Exp.[a]	Sim.[b]	Sim.[c]
Outlet temp. [K]		1108	1121	1121.3
Outlet pres. [kPa]		131.7	132.3	133.2
Conversion [%]		59.87	61.8	62.3
Yields (wt %)	CH_4	3.35	3.25	3.41
	C_2H_2	0.2	—	0.05
	C_2H_4	48.68	48.44	49.31
	C_2H_6	39.27	36.64	36.95
	C_3H_6	1.07	0.90	0.95
	C_3H_8	0.21	—	0.005
	C_4H_6	1.12	—	1.64
	C_4H_8	0.21	—	0.004
	C_4H_{10}	0.3	—	0.12
	C_{5+}	1.6	—	2.78
	H_2	3.71	—	3.78

[a]Froment et al. (1976) ; [b]Tarafder et al. (2005) ; [c]This work

were formulated in accordance with the industrial practice (Tarafder et al., 2005; Van-Goethem et al., 2010). The only decision variable considered in this study was the heat flux along of the reactor length, however, other decision variables like inlet feed conditions (temperature, pressure, dilution factor and molar flows of reactants) and design conditions (number of tubes and tube diameter) can also be considered.

4. Results and Discussion

Before solving the optimization problem, some preliminary simulations of the reactor were required in order to provide an appropriate number of finite elements and collocation points in the discretization method used. Another reason of implementing such simulations was to provide suitable initial guesses for states in order to initialize the optimization problem in the full discretization approach and solve it more efficiently. Specifications of the industrial cracking reactor simulated here are presented in Table 1. These were taken from Froment et al. (1976). This industrial reactor has been used several times in the literature for validation purposes. Table 2 provides a comparison between simulation results in this study and experimental results reported by Froment et al. (1976), as well as a comparison with simulation data reported in Tarafder et al. (2005). It can be seen that the simulated results obtained in this work are in good agreement with the industrial data and previous simulations of the same reactor. The ethane conversion, coil outlet temperature and pressure as well as the yields of the main components of the reactions (methane, ethane, ethylene and hydrogen), which constitute more than 95 wt % of the final gas mixture, are predicted within 6 % of the experimental data. The reactor pressure, gas temperature and conversion profiles resulted from the simulation are illustrated in Figure 2. It is important to highlight that the quadratic expression used by Tarafder et al. (2005) for representing the heat flux profile was imposed in the simulation. This simulation was implemented in GAMS with a dummy objective function and without any degrees of freedom. Moreover, 15, 20 and 30 finite elements with 3 Radau collocation points were tested to carry out the simulation, but the obtained results showed no significant differences. Accordingly, the OCFE method can be successfully applied to simulate an industrial cracker by employing only 15 finite elements and 3 collocation points. Also, the stiffness of the system is handled satisfactorily with relatively few finite elements. The solution tooks 7 CPUs (4GB and 2.2GHz HP laptop) using IPOPT.

After the solution of the simulation was obtained, these results were then used as initial guesses

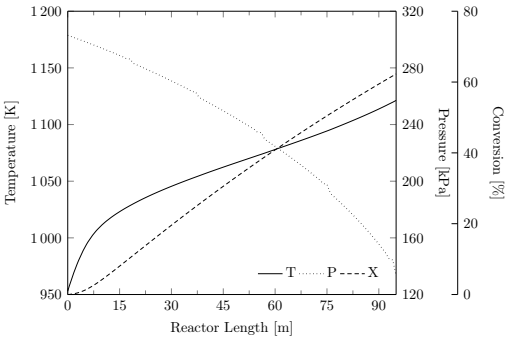

Figure 2: Temperature, pressure and conversion profiles for simulation case

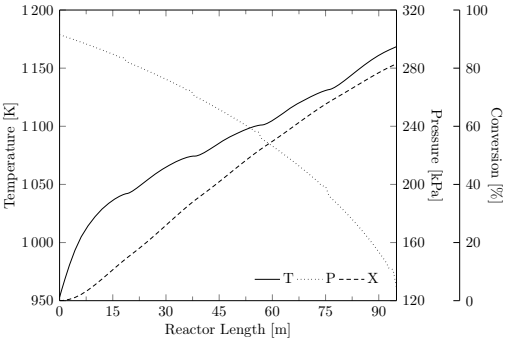

Figure 3: Optimal temperature, pressure and conversion profiles

of states and given to the optimization problem. In this way the optimization problem was solved applying the full discretization approach to the DAE model with 3 Radau collocation points and 15 finite elements, which leads to an NLP with 13,164 variables and 13,119 equality constraints, resulting in an optimization problem with 45 degrees of freedom. Using GAMS, the optimal solution was obtained in 85 CPUs (4GB and 2.2GHz HP laptop) with 17 iterations of IPOPT solver. As can be seen in Figure 3 the optimal profiles appear to follow the same trend as the simulation case, with a significant increase in the conversion and the temperature profiles. These increases are consequence of the optimal heat flux profile obtained along the reactor length. This heat flux profile is shown in Figure 4, and presents similar trend to the heat flux reported in other works using those iterative procedures referred in mathematical modeling section. The peaks in Figure 4 correspond to the bottom bends of the coils and the valleys to the top ones. The strong non–uniformity is explained as follows: At the top of the furnace the heat flux is much lower than at the bottom, where there are sharp peaks, since there are no burners in the top section of the furnace, and the heat flux decreases as the reactor length is higher because the temperature of the gas mixture increases and, therefore, the temperature gradient between the furnace and the coil becomes smaller (Sabbe et al., 2011; Hernández, 2012).

The optimal molar flow profiles for ethane and ethylene are shown in Figure 5. The maximum ethylene yield obtained was 60 wt % which corresponds to an ethane conversion of 81.5 % and an ethylene selectivity of 78.9 %. This maximum ethylene yield was obtained for a coil outlet temperature of 1,168.6 K, this is in agreement with the currently applied reaction conditions in industrial crackers that lead to a coil outlet temperature around 1,000–1,200 K (Sadrameli, 2015). However, typical conversions and maximum ethylene yields achieved in industrial ethane cracking reactors (70 % and 55 wt % respectively (Van-Goethem et al., 2010)) are lower than those obtained in this work. Similar results were reported by Van-Goethem et al. (2010) (maximum allowed temperature of 1,145 K, ethane conversion of 92 % and ethylene yield of 66.8 wt %), an ethylene yield higher than that achieved here. Nonetheless, in this work the only decision variable was the heat flux, and the ethylene yield could increase if more degrees of freedom are incorporated in the optimization study.

5. Conclusions

From the successful optimization of an industrial ethane cracking reactor carried out, it can be concluded that the methodology developed and applied in this work is able to provide reliable results when compared with industrial data, although with the kinetic scheme used it was not possible to predict accurately the yield of the minor species. In this way, other large kinetic schemes like the industrially proven kinetic scheme in SPYRO can be incorpored for a better

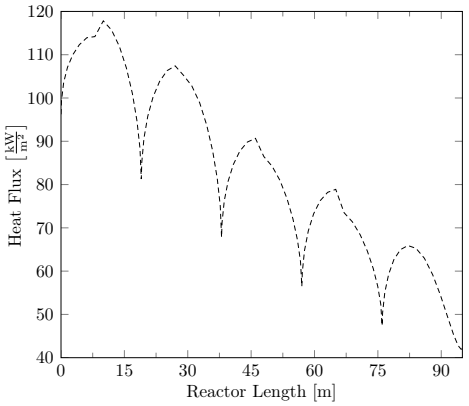

Figure 4: Optimal heat flux profile for thermal cracking of ethane

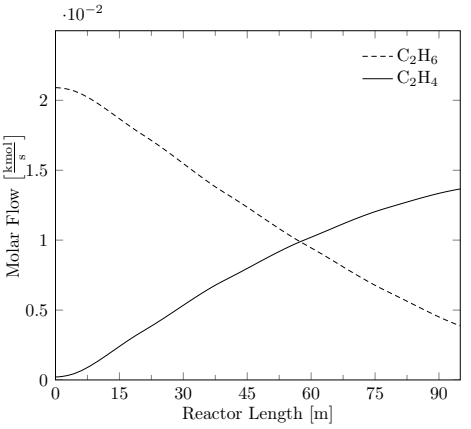

Figure 5: Optimal mass flow profiles of ethane and ethylene

prediction of these minor species. With the OCFE method implemented no stiffness problem was found either in simulations nor in the optimization. Therefore, this is a computationally efficient discretization method that can be successfully applied to theoretical studies about thermal cracking of hydrocarbons in order to improve existing industrial processes. In relation to the optimal values obtained, it can be suggested that the current ethane cracking technologies can be improved in terms of productivity. Consequently further optimization studies are required in this area and should be conducted in the future.

6. Acknowledgments

The authors would like to acknowledge the financial support from FAPESP – *Fundação de amparo à pesquisa de estado de São Paulo* under processes 2011/22800-3 and 2013/14896-6, and CNPq – *Conselho Nacional de Desenvolvimento Científico e Tecnológico, Brazil.*

References

Biegler, L., 2010. Nonlinear Programming: Concepts, Algorithms, and Applications to Chemical Processes. MOS-SIAM Series on Optimization. Society for Industrial and Applied Mathematics.

Froment, G., Bischoff, K., De Wilde, J., 2010. Chemical Reactor Analysis and Design, 3rd Edition. John Wiley & Sons.

Froment, G. F., Van de Steene, B. O., Van Damme, P. S., Narayanan, S., Goossens, A. G., 1976. Thermal cracking of ethane and ethane-propane mixtures. Ind. Eng. Chem. Prod. Res. Dev. 15 (4), 495–504.

Hernández, A. Y. R., 2012. A model for the prediction of olefin production thermal cracking of light hydrocarbons and coke deposition during. Master's thesis, National University of Colombia, School of Process and Energy, Medellín, Colombia.

Heynderickx, G. J., Froment, G. F., 1996. A pyrolysis furnace with reactor tubes of elliptical cross section. Ind. Eng. Chem. Res. 35 (7), 2183–2189.

Hu, G., Wang, H., Qian, F., Geem, K. M. V., Schietekat, C. M., Marin, G. B., 2012. Coupled simulation of an industrial naphtha cracking furnace equipped with long-flame and radiation burners. Comput. Chem. Eng. 38 (0), 24 – 34.

Sabbe, M. K., Van Geem, K. M., Reyniers, M.-F., Marin, G. B., 2011. First principle-based simulation of ethane steam cracking. AIChE J. 57 (2), 482–496.

Sadrameli, S., 2015. Thermal/catalytic cracking of hydrocarbons for the production of olefins: A state-of-the-art review i: Thermal cracking review. Fuel 140 (0), 102 – 115.

Sundaram, K. M., Froment, G. F., 1978. Modeling of thermal cracking kinetics. 3. radical mechanisms for the pyrolysis of simple paraffins, olefins, and their mixtures. Ind. Eng. Chem. Fundam. 17 (3), 174–182.

Tarafder, A., Lee, B. C. S., Ray, A. K., Rangaiah, G. P., 2005. Multiobjective optimization of an industrial ethylene reactor using a nondominated sorting genetic algorithm. Ind. Eng. Chem. Res. 44 (1), 124–141.

Van-Goethem, M. W., Barendregt, S., Grievink, J., Moulijn, J. A., Verheijen, P. J., 2010. Model-based, thermo-physical optimisation for high olefin yield in steam cracking reactors. Chem. Eng. Res. Des. 88 (10), 1305 – 1319.

Krist V. Gernaey, Jakob K. Huusom and Rafiqul Gani (Eds.), 12th International Symposium on Process Systems Engineering and 25th European Symposium on Computer Aided Process Engineering.
31 May – 4 June 2015, Copenhagen, Denmark

Study of Performance of a Novel Stochastic Algorithm based on Boltzmann Distribution (BUMDA) coupled with self-adaptive handling constraints technique to optimize Chemical Engineering process

R. Murrieta-Dueñas[a,c,*], J. Cortez-González[a,c], A. Hernández-Aguirre[b], R. Gutiérrez-Guerra[a], S. Hernandez[a], J. G. Segovia-Hernández[a]

[a]*Universidad de Guanajuato, Campus Guanajuato, Departamento de Ingeniería Química, Noria Alta s/n, 36050, Guanajuato, Gto., Mexico.*
[b]*Centro de Investigacion en Matematicas A.C., Departamento de Ciencias Computacionales, Callejón de Jalisco s/n, 36240, Mineral de Valenciana, Guanajuato, Gto., México.*
[c]*Instituto Tecnológico Superior de Guanajuato, Departamento de Computo Evolutivo Aplicado, Carretera Guanajuato-Puentecillas km 10.5, 36262, Guanajuato, Gto., Mexico.*
Correspondig author: rmurrieta@itesg.edu.mx

Abstract

The optimal design of distillation systems is a highly non-linear, multivariable and multimodal problem. The rigorous model of distillation columns is represented by mass, equilibrium, sum and heat equations called MESH equations and phase equilibrium calculations (Thermodynamic model). Furthermore, it has several local optimums and is subject to several kind constraints such as, design and topology scheme constraints, and achieves targets of purity and recovery for each split component. In this paper, we propose the employment of a novel stochastic algorithm called Boltzmann Univariate Marginal Distribution Algorithm (BUMDA, Valdez, S. I. et al., 2013) coupled with self-adaptive handling constraints technique to optimize a well-known distillation process scheme. The optimization problem consists in minimizing the total reboiler duty in a distillation train to split a mixture made of four components. The BUMDA's performance is compared with Differential Evolution (DE) due to the fact that this last algorithm is used frequently in the optimization of distillation columns. The results show that the BUMDA algorithm is better than the DE algorithm regarding effort computing, quality solution, and time used to find solution. The BUMDA algorithm is efficient, trusted, easy to use and of general applicability in any chemical engineering process.

Keywords: Optimization, BUMDA, Stochastic Algorithms, Distillation train, EDA's.

1. Introduction

The optimization of a distillation system is considered a computer problem of large proportion with a significant number of strongly nonlinear equations that cause serious numerical difficulties when solving the model. Nowadays, this optimization problem is tackled with deterministic and stochastic approaches. Deterministic strategies tackle the problem considering the sequence as superstructures which can be solved with mixed-

integer linear programming and non-linear programming approaches; other authors consider reduced models. On the other hand, the stochastic algorithms can deal with multi-modal and non-convex problems in an effective way and without the mentioned limitations. They are a suitable alternative to the design and optimization of complex separation schemes. In chemical engineering processes, distillation is a widely used separation process and a very large consumer of energy. A great amount of research has been carried out to improve the energy efficiency of distillation systems, in terms of either the design of optimal distillation schemes or improving internal column efficiency. Nowadays, the optimal design of multicomponent distillation systems remains one of the most challenging problems in processes engineering.

In this work, BUMDA algorithm performance is compared with Differential Evolution algorithm (DE) due to the fact that it is one of the most used evolutionary algorithms for solving global optimization problems in chemical engineering processes (R. Vakili et. al., 2011; Cabrera-Ruiz et. al., 2011). Both algorithms were coupled with self-adaptive handling constraints technique and were employed to optimize a distillation train that split a four components mixture.

2. Case study

In chemical engineering processes MESH equations and thermodynamic equilibrium equations have high levels of nonlinearities and nonconvexities and also present convergence difficulties. This leads to high computational times and the requirement of good initial guesses and bounds on the variables to achieve convergence.

Following case of study is described. The objective of a distillation train is to separate a multicomponent mixture using only single columns. Each column receives a feed-in and carries out the distillation of two adjacent components (adjacent volatility), and delivers two products: one at the top and the other at the bottom. In order to separate a mixture of *N* components, it is necessary to use *N-1* single columns. The order in which the components are separated is based on their relative volatility (Figure 1).

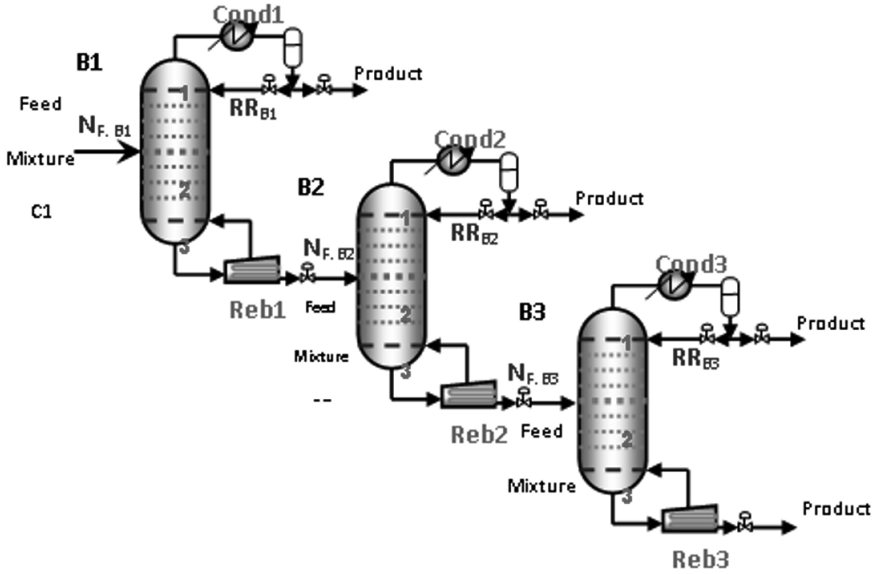

Figure 1. Flowsheet of distillation train to split a mixture of four components.

The basic design of each distillation column requires finding the best values of: the total number of stages *NT*, feed stage *NF* and reflux ratio *RR,* which is the relationship between the liquid flow *L* that returns to the column and the vapor flow *V* that rises in the column.This takes places on the upper part of the column. With this set of variables, the main goal of design is to obtain the minimum total heat duty possible to achieve the separation of the mixture. In mathematical terms, the problem statement optimization is described as following:

Find vector

$$Z = (NT_{B1}, NF_{B1}, NT_{B2}, NF_{B2}, NT_{B3}, NF_{B3}, RR_{B1}, RR_{B2}, RR_{B3})$$

To minimize fitness function

$$Q = f(Z)$$

Subject to constraint function

$$g_{1,j}(Z) = x^{\text{pur}}_{\text{target}} \qquad j = 1,...,M_{\text{constraints}}$$

$$g_{2,j}(Z) = x^{\text{rec}}_{\text{target}} \qquad j = 1,...,M_{\text{constraints}}$$

And subject to boundary constraints

$$z_i^{(L)} \le z_i \le z_i^U \qquad i = 1,...,D$$

$$2 < NF_{Bl} \le NT_{Bl} \qquad l = 1,...,B_{columns}$$

Where for each column *B*, *NT* is the total number of stages and *NF* is the number of feed stage. These dimensions are discrete variables and *RR* is the reflux ratio. These are continuous variables; in total we have nine dimensions, of which six are discrete and three are continuous. The fitness function is to minimize the total heat reboiler duty *Q* that is a function of vector *Z*. Regarding the design constraint, we have two types: one is referred to as purity, and other one as recovery; these exist for each component. Also it is important to consider the boundary constraints, because *NF* should always be less than *NT* and each dimension, *Zi* is between lower and upper boundaries.

3. Optimization strategy

In this research, we chose two stochastic algorithms: Differential Evolution (Viswanathan, J. and Grossmann, I. E., 1993). Which generates new points that are perturbations of existing points, and Boltzmann Univariate Marginal Distribution Algorithm BUMDA (Valdez, S. I. et al., 2013), that uses a normal distribution to approximate the Boltzmann Distribution, using the mean and variance of the population. These algorithms are coupled with self-adaptive handling constraints that allow use to find feasible solutions that achieve all design and specification constraints throughout distillation column optimization. Furthermore, it is important to mention that the optimization approach has been developed using an interface which links the optimizer algorithms with the modular simulator through databases. Following the characteristics of the algorithms, technique of handling constraints and optimization approach are briefly described.

3.1. Boltzmann Univariate Distribution Algorithm (BUMDA)

EDA's use a probability distribution, called the search distribution, to sample new candidate solutions. Hence, the search strategy in EDA's is to increment the probability of sampling the optimum from the search distribution. The advantage of the BUMDA algorithm is the preservation of the desired characteristics of the Boltzmann distribution,

while maintaining a low computational cost in the estimation and sampling steps. It also focuses on sampling as many promising solutions as possible, avoiding sampling promising and non-promising solutions and then rejecting some of them. The BUMDA algorithm starting with a population is initialized between the bounds of the search space and the fitness function calculated. 30% of the best individuals are stored in the selected set, and used to compute the mean and variance parameters of the Normal distribution. Then new individuals are simulated from a Normal distribution with such parameters to populate the next generation.

3.2. Differential Evolution (DE)

Differential evolution is proposed by Storn and Price (Storn, R. and Price, K., 1995). DE is a stochastic direct search method using population or multiple search points. DE has been successfully applied to the optimization problems including non-linear, non-differentiable, non-convex and multi-modal functions. It has been shown that DE is fast and robust when applied to these functions. In DE, initial individuals are randomly generated within the search space and form an initial population. Each individual i contains D genes as decision variables or a decision vector Zi. At each generation or iteration G, all individuals $Npob$ are selected as parents. Each parent is processed as follows: the mutation process begins by choosing three individuals from the parents except for the parent in the processing. The first individual is a base vector. Subsequent individuals are paired to create difference vectors. The difference vectors are scaled by the scaling factor F and added to the base vector. The resulting vector is then mated or recombined with the parent. The probability of recombination at an element is controlled by the crossover factor CR. This crossover process produces a trial vector. Finally, for survivor selection, the trial vector is accepted for the next generation if the trial vector is better than the parent.

3.3. Optimization Process

For the optimization approach implemented in this work, we have developed an interface which links the optimizer BUMDA or DE (Master, coded in MatLab) with the modular simulator Aspen Plus (Fitness Function Evaluator) through the Excel (Database). In this interface the stochastic algorithm needs one individual physically feasible of beginning the optimization process. Here, physically feasible implies that for a distillation column, the feed stage must be smaller than the total number of stages, and the reflux ratio is greater than zero. The stochastic algorithm generates individuals with the proper dimensionality, which is sent to Aspen Plus, one by one, in order to simulate the distillation scheme and get the values of the fitness function evaluated with constraints.

4. Discussion and Results

In this paper, a comparative analysis of performance ED and BUMDA stochastic algorithms is presented. Many authors have used ED algorithm to optimize chemical engineering problems while the BUMDA algorithm has been used only once. Both algorithms are tested to optimize two well-known problems in chemical engineering. The problem is to purify a four aliphatic hydrocarbons mixture in a distillation train. We carried out tuning of parameters in two algorithms. The total number of evaluation is the stop criterion and the fitness function is the total heat duty minimization. The simulations were carried out with a PC computer with an i5 processor core, clock frequency at 2.8 GHz, and 8 GB of RAM. In this case we study a mixture made of four lineal aliphatic hydrocarbons fed at a flow-rate of 100 kmol/h; which is introduced in the first column as saturated liquid. The characteristics and constraints of the mixture

are presented in Table 1. The proportion of each component is shown in mol fraction. Each component must be delivered with the specified purity and recovery. The design pressure for the separation was chosen to ensure that cooling water was used in the condensers. The phase equilibrium for liquid of this mixture is calculated with the Chao-Seader model, because it is usually recommended for hydrocarbon mixtures operating at low or medium pressure.

Table 1. Characteristics of the case study.

Characteristics of the mixture			Constraints	
ID	Component	Feed, mol fraction	Purity, x_i^{pur}	Recovery, x_i^{rec}
A	n- butane	0.05	0.987	0.98
B	n- pentane	0.45	0.98	0.98
C	n-hexane	0.45	0.98	0.98
D	n-heptane	0.05	0.986	0.98

4.1. Analysis performance of DE and BUMDA stochastic algorithms

The main aim of this paper is analyze the performance of two algorithms, DE inspired in natural phenomena and BUMDA based in estimation of Boltzmann distribution. The comparative parameters are effort of computation, time that found solution, quality of solution and behavior along optimization process. In Table 2 we analyze three comparative parameters. The first comparison is effort of computation; i.e. maximum number of function evaluations that each algorithm requires to find the best solution. It is clear that the BUMDA algorithm only needs *15 %* of *NEFmax* of what the DE algorithm requires. The time find a solution, is in direct relation with *NEFmax*, so that the BUMDA is faster than the DE algorithm. The BUMDA only requires 8% of the time that DE algorithm requires.

Table 2. Comparative analysis of best individuals obtained by DE and BUMDA algorithms

Parameter	DE Algorithm	BUMDA Algorithm
Effort of computation $\left(NEF^{\max}\right)$	20,000	3,000
Time of solution $\left(\theta, hours\right)$	100	8
Quality solution $\left(Q, BTU/h\right)$	9425750.75	7153129.14
Quality solution $\left(NT^{total}\right)$	84	71

In Figure 2 there are two sets of point: blue points that represent the best solutions given by the DE algorithm and pink points that are the feasible solutions obtained with the BUMDA algorithm. In this graph, the total number of stages is the axis "x" versus total heat duty shown in the "y" axis. Both variables are the most important in the design of distillation columns, since they show the compromise between size column and its energy consumption. It's clear that the pink points are better than blue points, both in *NT* as *Q*. If we compare the best solution only in terms of energy, the best pink point requires around 2,300,000 BTU/h less of the energy consumption than the best blue point; this behavior is similar in total number of stages. Based on these results, the best

solution obtained by the BUMDA algorithm provides the better compromise to design the distillation train.

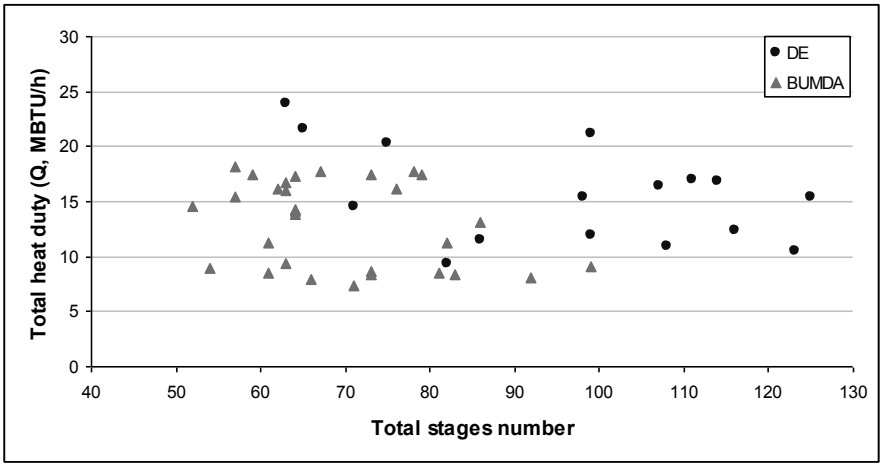

Figure 2. Comparative of the best individuals obtained by DE and BUMDA algorithms.

Finally, based on the results obtained with both algorithms in this case study, the novel stochastic algorithm based on Boltzmann distribution, the BUMDA algorithm implemented by us, is better than the DE algorithm, due to the fact that offers better solutions in less time and requires low computation effort. In addition the performance in optimization process of the BUMDA algorithm presents a high convergence in the best feasible zone and is identified clearly in an intensification zone, which leads to an improvement in the quality of solutions. This study verifies that the approach presented in this paper, BUMDA algorithm with self-adaptive handling constraints technique, is a powerful and robust tool capable of optimizing processes in chemical engineering and is potentially useful in other areas of engineering.

5. Conclusions

In this paper, a comparative study of the general performance of stochastic algorithms to optimize a distillation train is presented. We used two stochastic algorithms: Differential Evolution (ED) and Boltzmann Univariate Marginal Distribution Algorithm (BUMDA). The best solution was found by the BUMDA algorithm. The BUMDA algorithm is better than the DE algorithm because BUMDA is capable of finding the best design with little numeric effort, short computing time and a good success rate.

References

Storn, R., & Price, K. (1995). Differential Evolution—A Simple and Efficient Adaptive Scheme for Global Optimization Over Continuous Spaces, International Computer Science Institute, Berkeley. Berkeley, CA.

Valdez, S. I., Hernández, A., & Botello, S. (2013). A Boltzmann based estimation of distribution algorithm. Information Sciences, 236, 126-137.

Cabrera-Ruiz, J., Miranda-Galindo, E., Segovia-Hernandez, J. G., Hernandez, S., & Bonilla-Petriciolet, A. (2011). Evaluation of stochastic global optimization methods in the design of complex distillation configurations.

R. Vakili, P. Setoodeh, E. Pourazad, D. Iranshahi, M.R. Rahimpour, (2011). Utilizing differential evolution (DE) technique to optimize operating conditions of an integrated thermally coupled direct DME synthesis reactor, Chemical Engineering Journal 168 321–332.

Krist V. Gernaey, Jakob K. Huusom and Rafiqul Gani (Eds.), 12th International Symposium on Process Systems Engineering and 25th European Symposium on Computer Aided Process Engineering.
31 May – 4 June 2015, Copenhagen, Denmark

Dynamic Modelling and Optimal Design of the Solid-Phase Reactive Chromatographic Separation System for Biomass Saccharification via Acid Hydrolysis

Pakkapol Kanchanalai, Matthew J Realff, Yoshiaki Kawajiri*

School of Chemical & Biomolecular Engineering, Georgia Institute of Technology
311 Ferst Drive, Atlanta, GA 30332-0100

Abstract

A dynamic model of the progressing batch reactor as part of the solid-phase reactive chromatographic separation system is presented. The biomass filling and emptying steps in reactor system for two designs are proposed where each operating step is divided into two sub-steps including the transfer period and production period. The operating parameters for the progressing batch reactor with these sub-steps can be estimated from the countercurrent reactor model. The performance of the progressing batch reactor can be predicted from that of the countercurrent reactor model. A minor difference in the sugar yield was found due to the dynamics which cannot be accounted for in the countercurrent model. The proposed filling and emptying steps with the estimated operating parameters from countercurrent reactor can be used as an approximation to optimize the overall solid-phase reactive chromatographic separation system.
Keywords: Biomass hydrolysis, chromatography, reactive separation

1. Introduction

Biomass is a renewable and largely available low-cost source of sugars which can be hydrolyzed and fermented to produce bioethanol or converted to other value-added chemicals. The hydrolysis reaction of biomass using strong acid is one of the common processes; however, the main drawbacks are the cost of acid recovery and the sugar degradation with byproduct formation such as hydroxymethylfurfural (HMF) and furfural which not only reduce the sugar yield but also strongly inhibit the subsequent fermentation process to produce bioethanol.

Solid-Phase Reactive Separation System (SPRSS) has been proposed in our previous work (Kanchanalai et al, 2014) which can potentially improve sugar yield and less byproduct formation from biomass saccharification process via acid hydrolysis. This process integrates the progressing batch reactor (PBR) proposed by Wright et al (1988) and simulated moving bed chromatography (SMB) which has been applied for sugar-acid separation (Xie et al, 2005). Both processes have similar principles of the switching of all liquid inlet and outlet ports to imitate the solid phase movement. SPRSS could also be applied to other system that involves solid reactants.

This work presents dynamic modelling of the PBR system as part of the full PBR-SMB process. Unlike SMB chromatography models which have been developed and validated with numerous operating schemes in past studies, dynamic modelling of the PBR operation is not well-established. Several steps in cyclic operations for PBR such as emptying and loading the solid biomass require several assumptions that need to be

carefully analyzed. We demonstrate that the countercurrent model can represent the dynamic operation of PBR with sufficient accuracy.

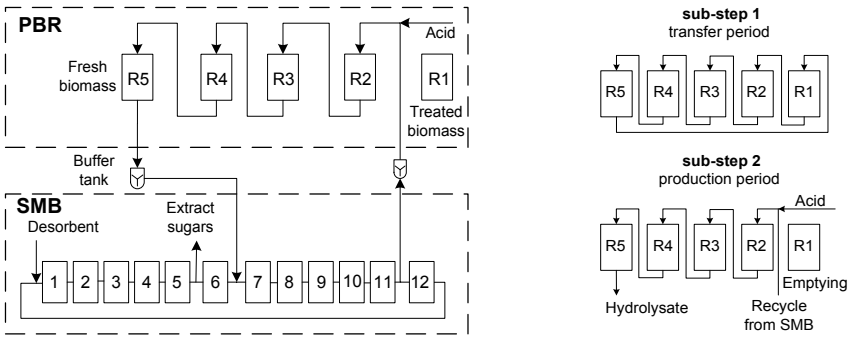

Figure 1. (a) Sequential design of PBR and SMB, (b) PBR operation in sequential design.

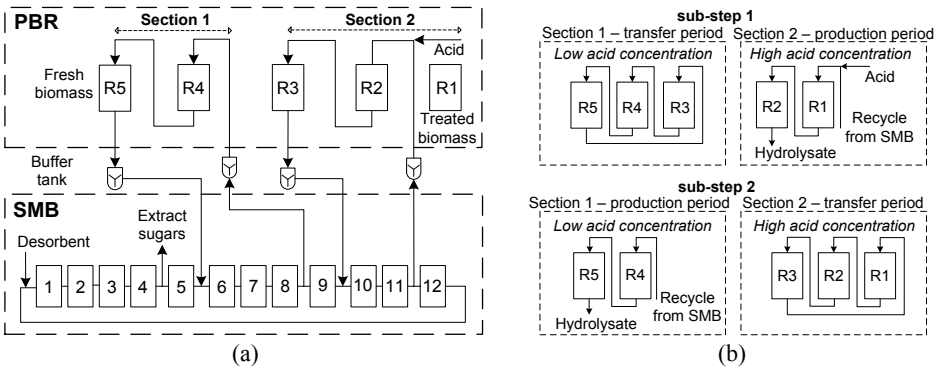

Figure 2. (a) Optimal SPRSS design found from superstructure in our previous study (Kanchanalai et al. 2014), (b) PBR operation in optimal SPRSS design.

2. Solid-Phase Reactive Chromatographic Separation System (SPRSS)

The integration of PBR and SMB for biomass saccharification via sulfuric acid hydrolysis for two alternative designs are shown in Figures 1 and 2. The PBR and SMB is connected in series without interconnecting stream in the sequential design (Figure 1a) while there are interconnecting streams between PBR and SMB in the SPRSS design (Figure 2a), which was found as the optimal solution from a superstructure based on a countercurrent approximation of the dynamic model. Our previous work shows that the SPRSS design shows the potential of improving sugar yield and selectivity over the sequential design due to the higher flexibility in varying the acid concentration (Kanchanalai et al, 2014). In Figure 1a and Figure 2a, both designs consist of five PBRs and twelve SMB columns where we assume that the system has small buffer tanks to connect all streams between these two processes and no reaction occurs in this tank due to the sufficiently small residence time. These tanks are to ensure that the component concentration of the feed streams from the PBR to SMB and that of the recycle streams from the SMB to PBR are constant.

In this study, we validate the countercurrent approximation for the SPRSS model. The dynamic model of SMB chromatography has been well established where the operating parameters can be estimated from that of true moving bed model with proper conversion. A good comparison of the concentration profile between the SMB and true moving bed model have been previously demonstrated (Schmidt-Traub et al, 2013). For the reactor system, on the other hand, such a study cannot be found, while the principles of the process operation is similar to SMB. Several assumptions must be made for the PBR operations such as the biomass filling and emptying steps, which are not captured in the steady state countercurrent reactor model. In this work, we propose two biomass filling and dumping operation corresponding to the two PBR-SMB designs illustrated in Figures 1b and 2b where the operating parameters from the steady state countercurrent reactor model can be used to estimate that of PBR. The dynamic modelling of the PBR including biomass filling and emptying steps is presented in the next section.

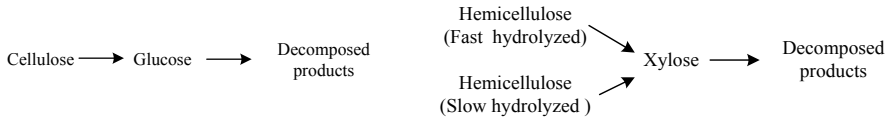

Figure 3. The biomass hydrolysis reaction scheme for cellulose (a) and biphasic hemicellulose (b)

2.1. Dynamic Modelling of the Progressing Batch Reactor

In this work, the biomass is assumed to contain both cellulose and biphasic hemicellulose where the hydrolysis reaction mechanism is shown in Figure 3, and the kinetic model proposed by Saeman (1945) is implemented for all reaction paths which depends on temperature and acid concentration.The mathematical model of a single percolation reactor has been present by Kim et al (1994). In this work, the PBR contain a series of percolation reactors where the mass balances of each component in the solid and liquid phase shown in Eq. (1-2) are applied.

$$\frac{\partial B(x,t)}{\partial t} = r \tag{1}$$

$$\frac{\partial C(x,t)}{\partial t} + u^{PBR}\frac{\partial C(x,t)}{\partial x} = D_{ax}\frac{\partial^2 C(x,t)}{\partial x^2} + r \tag{2}$$

where r is the reaction rate, u^{PBR} is the liquid flow rate in the PBR, and B and C are the solid and liquid component concentration, respectively. It should be noted that the countercurrent reactor approximation can be obtained by replacing $dt = dx/v$ in Eq.(1) where v is the solid velocity, and setting the time derivative term in Eq.(2) to be zero. The above model given in Eq. (1-2) also considers the axial dispersion in the liquid phase with Danckwerts boundary conditions (Schmidt-Traub et al, 2013) where the axial dispersion coefficient D_{ax} is set to 1.4×10^{-4} $\mathrm{m^2/s}$ for all components. In this work, an identical operation shown in Figure 1b or Figure 2b is repeated while performing the liquid port switching in the downstream direction, resulting in a symmetric and cyclic operation. In such an operation, the concentration profiles at the end of each step are identical to those at the beginning of the same step where the entire profiles are shifted in the downstream direction for the length of a one reactor chamber (Kawajiri &

Biegler, 2008). We assume that at $t = 0$, the fresh biomass is loaded at a given initial biomass concentration and is filled with fresh water, and thus the initial liquid concentration of all components are zero.

2.2. Biomass Filling and Emptying

The operations of the biomass filling and emptying steps could significantly affect the sugar concentration and yield from the hydrolysis reaction. In this study, we include the biomass filling and empting step by dividing the PBR operation in each step into two sub-steps consisting of the production period and the transfer period. The PBR in the sequential design (Figure 1b) has the same liquid residence time inside all reactors since there is no interconnecting stream. On the other hand, for the PBR in the SPRSS design (Figure 2b), the process is divided into two sections which have two and three percolation reactors. By having the interconnecting streams between PBR and SMB, the reactor system can have different liquid residence time as well as acid concentration in each section. At the beginning of a step in these two designs, the fresh biomass is filled in R5, which is filled with fresh water while the treated biomass stays inside R1.

The first sub-step of the PBR operation in the sequential design illustrated in Figure 1b corresponds to the transfer period where the acid in R4 flows to hydrolyze the fresh biomass in R5, while the water in R5 goes to R1 which contains the treated biomass. The second sub-step corresponds to the production period where the external fresh acid and the recycle stream from SMB is fed to R2 and the hydrolysate is produced at R5. The treated biomass filled with water inside R1 is also dumped at this step.

For the PBR system in the SPRSS design which has two sections shown in Figure 2b, the transfer and production period occurs simultaneously at different section. In the first sub-step, the transfer process occurs in section 1 (R3-R4-R5) while production process happens in section 2 (R1-R2). In section 1, the liquid with low acid concentration is transferred to hydrolyze the fresh biomass in R5 while the water in R5 goes to the R3. Meanwhile, in section 2, the liquid with higher acid concentration from the fresh acid stream and the recycle stream from SMB are fed to R1 to hydrolyze the treated biomass and the hydrolysate is produced at R2. In the second sub-step, the transfer process is switched to occur in section 2 (R1-R2-R3), while the production process takes place in section 1 (R4-R5). In section 1, the recycle stream from SMB is fed to R4 and the hydrolysate is produced at R5. For section 2, the water in R3 is moved to the R1 before being dumped with the treated biomass. It can be seen that a different number of reactor chamber is allocated in each section. In this operation, the hydrolysis condition of the partially treated biomass in R3 is switched from a low to a high acid concentration and is exposed to a different liquid residence time.

In this proposed filling and dumping the biomass, the operating parameters from the steady state countercurrent reactor model including the liquid interstitial velocity (u_{CCR}) and the biomass interstitial velocity (v_b) can be directly converted to the operating parameters of PBR including the overall switching time (t_{swt}), transfer period (t_{prod}), production period (t_{tran}), and the interstitial velocity of liquid phase (u_{PBR}) from the following equations:

$$t_{swt} = \frac{L_R}{v_b} \tag{3}$$

$$u^{PBR} = u^{CCR} + v_b \tag{4}$$

$$t_{prod} u^{PBR} = t_{swt} u^{CCR} \tag{5}$$

$$t_{tran} + t_{prod} = t_{swt} \tag{6}$$

In the case of SPRSS design when there are two sections inside PBR process, we assume that $t_{tran\text{-}substep1} = t_{prod\text{-}substep2}$, where $t_{tran\text{-}substep1}$ and $t_{prod\text{-}substep2}$ are the duration of the sub-steps shown in Figure 2b.

3. Problem Formulations and Numerical Approaches

This work focuses only on the PBR subsystem for two designs shown in Figures 1b and 2b where the reactor performance is compared with that of the steady state countercurrent reactor. The dynamic models of the PBR with the biomass filling and emptying sub-step for both designs are formulated in the GAMS modeling environment discretizing the time domain with six finite elements by the Radau collocation, and spatial domain with 60 elements by the centered finite difference method. The simulation problems of these two designs are solved where the flow rates and the concentration of all feed streams including the fresh acid and the recycle streams from SMB are fixed at the values in the optimal solutions obtained from the steady state countercurrent reactor and true moving bed chromatography model. The relationship in Eq. (3-6) are used to estimate all operating parameters of the PBR. All values of the model parameters can be found in our previous study (Kanchanalai et al. 2014).

4. Results

The comparison of the reactor system in the sequential and SPRSS designs between the countercurrent reactor and PBR are shown in Table 1. From the table, the conversion of the biomass in both designs between the countercurrent reactor and PBR are very close to each other. However, the sugar yield at the outlets of the PBR is lower than that from the countercurrent reactor. This is mainly because there is some amount of sugar lost during the biomass emptying step.

Figure 4 shows the concentration profile of the liquid phase for SPRSS design at the $t = t_{swt}$ before emptying the biomass in R1. From the figure, it can be seen that there are some amount of sugars and other components remaining inside R1 which are lost when emptying the biomass. Our investigation shows that these losses are caused by the axial dispersion. During the transfer periods of SPRSS (see Figure 2b) where the fresh water is transferred from R5 to R3 in sub-step 1 and then from R3 to R1 in sub-step 2, the sugars and other components diffuse into this portion of water. Consequently, the loss of these components during dumping the treated biomass with the liquid in R1 is inevitable. This phenomenon is not captured in the countercurrent reactor model. The sugar lost during biomass emptying can be recovered later by the SMB system or another separation process. By assuming these sugars can be fully recovered, the total reaction sugar yield (see Table 1) for both designs are higher than that predicted from the countercurrent reactor. The reason for this is that there is a dynamic variation in acid

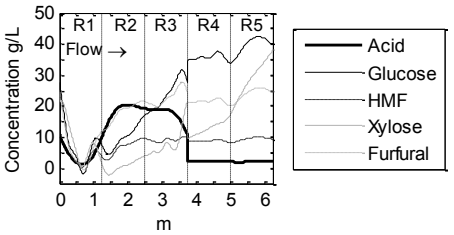

Figure 4. PBR concentration profile in the SPRSS design at $t = t_{swt}$ before biomass emptying.

Table 1. Performance comparisons between the countercurrent reactor and PBR

	Sequential Design		SPRSS Design	
	Countercurrent	PBR	Countercurrent	PBR
Biomass Conversion	85.3 %	84.1 %	94.5 %	94.2 %
Sugar Yield at Outlet	60.7 %	57.8 %	67.9 %	61.5 %
Sugar Lost in Emptying Step	-	10.9 %	-	17.3 %
Total Reaction Sugar Yield	60.7 %	64.9 %	67.9 %	74.3 %

concentration resulting from the axial dispersion in PBR which causes different reaction kinetics compared to that in countercurrent reactor. From the results, the byproduct formation in PBR is observed to be lower than that in countercurrent reactor. The performance of PBR with the proposed biomass filling and emptying steps can be partially predicted using the countercurrent reactor model.

5. Conclusions

The dynamic model of PBR in SPRSS is formulated and the biomass filling and emptying processes are proposed. The operating parameters of the PBR with the proposed configuration can be obtained from the proper conversion of the countercurrent reactor operating parameters. The results shows that the performance of the PBR process can be partially predicted from that of countercurrent reactor where the difference comes from the dynamics that are not accounted for in the countercurrent model. In future work, the full dynamic model of SPRSS with PBR and SMB will be optimized to find the optimal process configurations where the performance results from the proposed biomass filling and emptying steps can be used as an initial guess for the optimization problem.

References

Kanchanalai, P., Realff, M. J., Kawajiri, Y., 2014, Solid-Phase Reactive Chromatographic Separation System: Optimization-Based Design and Its Potential Application to Biomass Saccharification via Acid Hydrolysis. Industrial & Engineering Chemistry Research, 53, 41, p15946-15961.

Kawajiri, Y., Biegler, L. T., 2008, Large scale optimization strategies for zone configuration of simulated moving beds. Computers & Chemical Engineering, 32, 1-2, p135-144.

Kim, B. J., Lee, Y. Y., Torget, R., 1994, Modified Percolation Process in Dilute-Acid Hydrolysis of Biphasic Hemicellulose. Applied Biochemistry and Biotechnology, 45, 6, p113-129.

Saeman, J. F., 1945, Kinetics of Wood Saccharification-Hydrolysis of Cellulose and Decomposition of Sugars in Dilute Acid at High Temperature. Industrail & Engineering Chemistry Research, 37, 1, p43-52.

Schmidt-Traub, H., Schulte, M., Seidel-Morgenstern, A., 2013, Prepartive Chromatography, 2nd, Wiley-VCH, Germany.

Wright, J. D., Bergeron, P. W.,Werdene, P. J., 1987, Progressing Batch Hydrolysis Reactor. Industrial & Engineering Chemistry Research, 26, 4, p699-705.

Xie, Y., Chin, C. Y., Phelps, D. S. C., Lee, C. H., Lee, K. B., Mun, S., Wang, N. H. L., 2005, A five-zone simulated moving bed for the isolation of six sugars from biomass hydrolyzate. Industrail & Engineering Chemistry Research, 44, 26, p9904-9920.

12TH INTERNATIONAL SYMPOSIUM ON PROCESS SYSTEMS ENGINEERING AND 25TH EUROPEAN SYMPOSIUM ON COMPUTER AIDED PROCESS ENGINEERING

PART B

Edited by
KRIST V. GERNAEY, JAKOB K. HUUSOM AND RAFIQUL GANI

COMPUTER-AIDED CHEMICAL ENGINEERING, 37

12TH INTERNATIONAL SYMPOSIUM ON PROCESS SYSTEMS ENGINEERING

&

25TH EUROPEAN SYMPOSIUM ON COMPUTER AIDED PROCESS ENGINEERING

This page intentionally left blank

COMPUTER-AIDED CHEMICAL ENGINEERING, 37

12TH INTERNATIONAL SYMPOSIUM ON PROCESS SYSTEMS ENGINEERING AND 25TH EUROPEAN SYMPOSIUM ON COMPUTER AIDED PROCESS ENGINEERING

PART B

Edited by

Krist V. Gernaey, Jakob K. Huusom and Rafiqul Gani

Department of Chemical and Biochemical Engineering
Technical University of Denmark
DK-2800 Lyngby, Denmark

Amsterdam – Boston – Heidelberg – London – New York – Oxford
Paris – San Diego – San Francisco – Singapore – Sydney – Tokyo

Elsevier
Radarweg 29, PO Box 211, 1000 AE Amsterdam, The Netherlands
The Boulevard, Langford Lane, Kidlington, Oxford OX5 1B, UK

British Library Cataloguing in Publication Data
A catalogue record for this book is available from the British Library

Library of Congress Cataloging-in-Publication Data
A catalog record for this book is available from the Library of Congress

ISBN (Part B): 978-0-444-63577-8
ISBN (Set): 978-0-444-63429-0
ISSN: 1570-7946

Printed and bound in Great Britain

14 15 16 17 10 9 8 7 6 5 4 3 2 1

Contents

Contributed Papers
T-3: Cyber-Infrastructure, Informatics and Intelligent Systems

Contributed Papers
T-5: Process Dynamics, Control and Monitoring

This page intentionally left blank

Krist V. Gernaey, Jakob K. Huusom and Rafiqul Gani (Eds.), 12th International Symposium on Process Systems Engineering and 25th European Symposium on Computer Aided Process Engineering.
31 May – 4 June 2015, Copenhagen, Denmark

Life Cycle Simulation for a Process Plant based on a Two-Dimensional Co-Simulation Approach

Mathias Oppelt[a*], Gerrit Wolf[a], Leon Urbas[b]

[a]*Siemens AG, Oestliche Rheinbrueckenstr. 50, 76187 Karlsruhe, Germany, oppelt.mathias@siemens.com*
[b]*University of Technology Dresden, 01062 Dresden, Germany*

Abstract

Simulation plays an important role at multiple stages within the life cycle of a process plant. We expect that in the future, simulation will be integrated into the plant life cycle and will form the backbone of a more integrated engineering process. Engineering creates a virtual plant capable of simulating different aspects and domains. As each specific domain usually requires certain simulation capabilities, multiple specialized simulation tools are used along the life cycle. The ability to reuse existing simulation models throughout the life cycle would be very beneficial. This paper investigates the existing standards for model reuse and co-simulation and describes a basic implementation for co-simulation based on OPC, shared memory and .NET technology.

Keywords: Process Simulation, Virtual Commissioning, Operator Training, Co-Simulation, Model Integration, Process Automation

1. Motivation

The complexity of modern process plants is constantly increasing, and with it the challenges facing the engineering and operation of such plants. The use of simulations can be beneficial to investigate engineering and operational questions without the availability of an actual plant. Today, simulation is already utilized at particular stage swithin the life cycle of a process plant, for instance during the design phase (Bausa and Dünnebier, 2006). At a later stage,it is used for virtual commissioning to test the automation system (Oppelt and Urbas, 2014) and for operator training (Cox et al., 2006). In the operation phase, simulations can be used as assistance systems. Even though the benefits of time, and cost savings, increased quality and improved safety are promising, the use of simulation as an integrated part of the plant life cycle is not standard procedure. Reasons for this include in particular the effort involved in developing simulation models and the fact that the decision to use simulation is not taken from a life cycle perspective (Oppelt et al., 2013; Klatt and Marquardt, 2009). In view of these issues,the reuse of simulation models across the life cycle (horizontally) would be beneficial in bringing about more integrated use of simulation.

Furthermore, different simulation models can represent various parts of the plant. An automated process plant typically includes components such as the distributed control system (DCS), the signals and bus systems, the actuators and sensors and the process. To createa complete virtual plant, these levels must all be available within a simulation model. Consequently,the integration of different simulation models across these levels (vertically) is essential. For further work on the comparison of different model abstraction levels, please refer to (Oppelt and Urbas, 2014).

As simulation models can be realized in different tools, the availability of co-simulation approaches to support a vertical and horizontal coupling of simulation models implemented in different tools is also investigated. This evaluation is based on the requirements for co-simulation such as execution control, data exchange, configuration and management of simulations. The paper compares the ability of the Functional-Mock-Up-Interface (FMI; Modelisar, 2010), Cape-Open (CO; Peshev and Livingston, 2013), IEEE High-Level Architecture (HLA; IEEE, 2010) and Open-Service-Gateway-Initiative (OSGI; McAffer et al., 2010)to fulfill co-simulation needs. In addition, a minimum implementation for a co-simulation setup is described.

The paper investigates the gap between design simulations focused on process modeling (Bausa and Dünnebier, 2006) and simulations for virtual commissioning and operator training(Oppelt and Urbas, 2014). The availability of a suitable co-simulation approach for all simulation use cases along the plant life cycle would enable the greatest possible reuse of existing work and so maximize the return.

2. Aspects of model exchange and co-simulation

2.1. Co-simulation concepts

There are basically three different implementation concepts for model exchange and co-simulation. One solution is to describe the model behavior in a *common mathematical language* (e.g. differential equations). A simulation tool then interprets and solves the equations. This concept of model exchange is realized by exporting and importing models. The work of Schopfer et al. (2004) is an example of this approach.

Co-simulation can be defined as *tool coupling*. In this case at least two independent simulation tools work in parallel and simulate a combined model. The exchange of data and synchronization between the tools are the responsibility of a simulation master. This is either one of the involved tools or a separate application. This principle is used, for instance,by the HLA framework which is described in section 3.2. In contrast to model exchange, this concept includes the connection of the model interfaces but also an interface for control of the simulation tools. The simulation master is responsible for the consistency and the timing of the simulated data within the model. It therefore monitorsthe status of the machines and tools, and also starts, stops and synchronizes the separate processes. Usually this concept is based on proprietary interfaces, but allows all the domain-specific strengths of the involved tools to be used.

A third concept results from a synthesis of both techniques. This is used, for instance, by the FMI (see section 3.1). This is a kind of a *hybrid solution*, where a simulation unit including model and solver is integrated into another simulation tool.

2.2. Co-simulation use cases

The most prominent co-simulation use case involves coupling different simulation tools to simulate certain parts of the plant in one tool and other parts in different tool (see figure 1). As the real plant consists of many different components and processes, so does the virtual plant. For different aspects of the virtual plant, different simulation tools are utilized which need to be combined to realize a complete virtual plant model. This entails the need for a central control, which should also be capable of providing a snapshot of all coupled simulations. A snapshot preserves a certain state of the simulation and enables the user to recreate this state at a later point in time. Advanced

co-simulationis capable of coupling tools dynamically during runtime and also exchanging models during runtime (Oppelt et al., 2013).
A complex aspect of co-simulation is that models can be realized on different levels of abstraction (Oppelt and Urbas, 2014), but need to be combined. The co-simulation environment therefore needs to support data exchange across all abstraction levels. On the detailed finite level, for instance, simulators would also need to exchange data about chemical media. Co-simulation requirements can be differentiated according to three different aspects: (1) simulation execution control, (2) simulation data exchange and (3) configuration of the co-simulation environment.

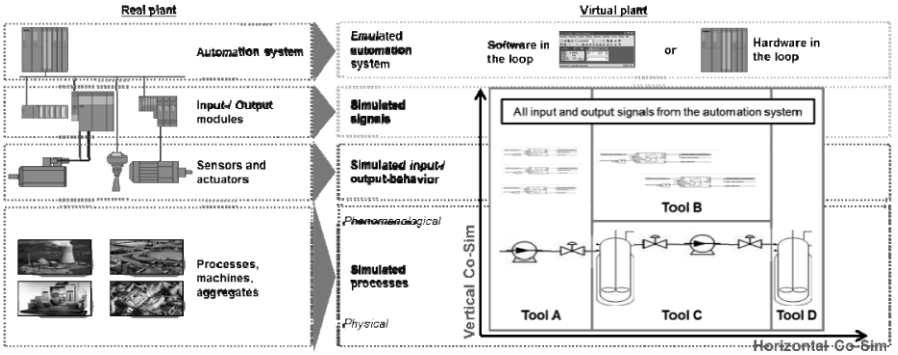

Figure 1: Co-simulation scenario showing vertical and horizontal tool coupling

2.3. Simulation execution control

Co-simulation provides benefit of bringing together a large number of simulation models of different origins. On the system level this "capability comes with the cost and complexity of coordinating all of the computing platforms for the startup, execution, shutdown and artifact collection of the simulation execution." (Snively et al., 2013) On a more detailed level, execution control is concerned with the step-by-step coordination of partial models, to ensure synchronized calculation of the different models.

2.4. Simulation data exchange

The coupled simulation systems need to exchange data during runtime within discrete time steps. This entails exchanging a predefined set of tags or values through standard interfaces. For pure data exchange standards such as OPC DA or shared memory,the technology already exists.

2.5. Configuration of the co-simulation environment

Configuration of the co-simulation environment should be as effortless as possible. Ideally, the standard supports a plug-and-play methodology to connect different simulation systems. The configuration and management tasks include selecting the required resources for the simulation scenario, organizing the resources to build the execution system, and collecting the simulation data.

3. Existing work on co-simulation approaches

There is wide-ranging literature available on co-simulation, including for instance (Yang et al., 2013; Oppelt et al., 2013; Schopfer et al., 2004). In most cases, the existing literature describes a specific implementation and its challenges. This section will compare approaches to co-simulation. The approaches compared were selected on the

basis that the standard can be found in multiple publications and is already used in industrial applications.

3.1. Functional mock up interface (FMI)

The Functional Mock-up Interface (FMI) is designed to be a tool-independent standard to support model exchange and the co-simulation of dynamic models (Modelisar, 2010). The FMI 1.0 standard was first published in 2010. The primary goal was the standardization of model exchange between different simulation tool vendors. A new version 2.0 was published in July 2014. The focus of this version shifts to unit exchange. The concepts of FMI can also be implemented around existing tools similar to a wrapper function.FMI 1.0 mainly addresses the concepts for model and unit exchange. Nevertheless, it is also possible to implement tool coupling with the FMI standard. The specification of FMI focuses on input/output behavior and allows for black box modeling, allowing it to be easily used for simulation on the system and network level. However, it does not support complex and detailed simulation on the finite element level, which is necessary for chemical reaction simulation.

3.2. High Level Architecture (HLA)

High Level Architecture (HLA) is an IEEE standard for modeling and simulation (IEEE 1516). It describes a framework for distributed modeling and simulation by defining connections and interactions between systems (Fujimoto, 2010; IEEE, 2010).

First developed by the American Defense Modeling and Simulation Office, HLA is mainly used for military simulation systems. An HLA system, which is called a federation, consists of one Runtime Infrastructure (RTI) and several connected simulation units, called federates.The HLA specification defines the communication behavior between the components and the RTI. The concept therefore equates to a tool coupling concept in which the RTI is the master of the simulation partners. HLA is an event-based architecture in which the RTI controls and synchronizes all communication between the federates.

3.3. Cape-Open

The Cape-Open (CO) standard was developed for process simulation, both stationary and dynamic (Braunschweig and Gani, 2002). CO provides open, multi-platform interfaces for process unit operations, physical properties, reaction kinetics and numerical solvers. They are maintained by the user-driven organization CAPE-OPEN Laboratories Network (www.colan.org). Major process modeling environments for the process industries have implemented CO interfaces.

3.4. OSGI framework for simulation

The OSGI framework (Open Service Gateway Initiative) was originally designed for component-based software development. It is based on the Java programming language and represents a modular and component-based software standard whose services (bundles) are offered by a dynamic runtime system (McAffer et al., 2010).The bundles of an OSGI framework can be dynamically loaded, unloaded, updated or exchanged during runtime without shutting down the OSGI framework. In the context of a distributed simulation environment, the framework offers remote service plug-ins for communication between different OSGI framework instances on a local computer or on different computers in a network. To enable the OSGI framework as a dynamic and distributed co-simulation framework, a software architecture needs to be developed. Simulator couplers are required to connect simulators. A simulator coupler implements the interface of the simulator for data exchange, synchronization and control flow during co-simulation. For an implementation example, refer to Oppelt et al. (2013).

3.5. Comparison of co-simulation approaches

Table 1 provides a detailed comparison of these four approaches. The results show that no approach currently fulfills all requirements for complete horizontal and vertical coupling of simulation models. The FMI standard is mainly used in discrete applications using Modelica as specific modeling language. HLA focuses its application within the defense industry. CO is used within process industries,where it is deployed for coupling process simulations. CO covers a wide range of interfaces necessary for co-simulation on a network and finite level. The emphasis is clearly on simulation for process design, real-time aspects are not addressed. In comparison, FMI and HLA focus on the co-simulation of models on the system and network level, missing the opportunity to couple finite process models. However, FMI and HLA also support real-time aspects.

Table 1: Comparison of co-simulation approaches

Criteria	Compared standards			
	FMI	HLA	CapeOpen	OSGI
Simulation execution control				
Central start, stop, pause execution control	x	x	PME	x
Virtual time (fast-, slow mode)	p	p	p	p
Real-Time Capabilities	x	x		p
Synchronization	x	x	x	x
Error handling	p	p	x	x
Dynamic model exchange at runtime		p		p
Snapshots (save, load)	x (2.0)	p	PME	p
Simulation data exchange				
Open standards (e.g. OPC)	x		x	x
Shared memory	p			p
TCP / UDP		x	.NET/CORBA	x
Configuration and management				
Simulation project management	p	p	PME	p
Distritution among network	x	x	x	x
Configuration files/tools for automatic setup	p	a	p	p
Know-how protection	x	x	x	p
Model abstraction levels				
Signal level	x	x		x
System level	x	x		x
Network level	x	x	x	x
Finite level			x	x
Standard independence				
Use across industries	Discrete	Military	Process	x
Driven by indepentend organization	Modelica	IEEE	COLAN	OSGI Alliance
Multiple operation system support	x	a	x	x

x: adressed by standard - out of the box use; p: possible by manual implementation; a: third party add on; PME: Process Modelling Environment

Usability is another important aspect. OSGI as a Java framework would not be usable off the shelf without adaptions. Because the effort involved in implementing a federation within HLA is quite complex, HLA has a very high entry threshold and expects any industry application to use the same RTI, which limits flexibility.

Regarding simulation execution control and data exchange, all standards provide good functionality. FMI and OSGI provide the highest functionality on these levels. HLA is limited as regards data exchange, as it only supports TCP/UDP.

4. Minimum implementation of a co-simulation approach

A minimum implementation for a dynamic simulation control system is described in the following. The data exchange between different simulation tools is realized by using either an OPC DA or a shared memory interface. The simulation tool Simit (www.siemens.com/simit) is used as the basis for the implementation. As the data exchange options can be seen as standard technology, the focus will be on the remote control interface usable for dynamic simulation control (Siemens, 2014).The remote control interface (RCI) was developed using .NET technology and is based on the Windows Communication Foundation (WCF). Within the RCI, a handshake protocol was implemented with two different operating modes: synchronous and asynchronous. The interface provides parameters of the control system (e.g. speed) for interface

configuration, and also a set of feedback parameters (e.g. error codes). In addition,information parameters such as the system state, time or the sync mode are provided. Service calls are used to establish or terminate connections between different simulation systems. A live beat supplies information to all the involved tools about the status of the overall system. The interface implementation provides simulation control functions to open or close a project, to open, close, reset, initialize, start or stop a simulation as well as to set the simulation time or calculate only a single step.In addition, interface commands to create or load snapshots are available. For a detailed description of a minimum implementation see (Siemens, 2014).

5. Conclusion and outlook

The paper investigated the current work on co-simulation and illustrates that no real industry wide co-simulation standard currently exists. The availability of co-simulation approaches is limited to specific industries or to specific tools. The paper also looks at closing the gap between design simulations focused on process modeling and simulations for virtual commissioning and operator training. A co-simulation standard would therefore allow theintegrated use of simulation along the plant life cycle with the maximum reuse of existing work. In respect of modular plants and package unit integration, this standard could also form the basis for simulation model integration which is as simple as the integration of a module into the real plant.

References

J. Bausa,G. Dünnebier,2006, Life Cycle Modelling in the chemical industries: Is there any reuse of models in automation and control?, 16th ESCAPE / 9th PSE, pp. 3–8

B.L.Braunschweig, R. Gani,2002, Software Architectures and Tools for Computer Aided Process Engineering, Elsevier Science

R.K.Cox, J.F. Smith, Y. Dimitratos, 2006, Can simulation technology enable a paradigm shift in process control? Modeling for the rest of us, Comp. Chem. Eng., Vol. 30

R.M. Fujimoto, 2000, Parallel and Distributed Simulation Systems, John Wiley & Sons, Inc.

IEEE Std 1516.1, 2010, IEEE Standard for Modeling and Simulation (M&S) High Level Architecture (HLA) - Federate Interface Specification

K.-U.Klatt, W. Marquardt, 2009, Perspectives for process systems engineering: Personal views from academia and industry, Comp. Chem. Eng., Vol. 33

J.McAffer, P. VanderLei, S. Archer, 2010, OSGI and Equinox: Creating Highly Modular Java Systems, Addison-Wesley Professional

Modelisar, 2010, Functional Mock-up Interface for Co-Simulation, MODELISAR (07006), 1.0, MODELISAR consortium

M.Oppelt, O. Drumm, B. Lutz, G. Wolf, 2013, Approach for integrated Simulation based on Plant Engineering Data, 18th IEEE ETFA

M.Oppelt, L. Urbas, 2014, Integrated Virtual Commissioning as Part of the Automation Engineering Process, 40th IEEE IECON

D. Peshev, A.G. Livingston, 2013, OSN Designer, a tool for predicting organic solvent nanofiltration technology performance using AspenOne, MATLAB and CAPEOPEN, Chemical Engineering Science, Vol. 104, pp. 975–987

G. Schopfer, A. Yang, L.von Wedel, W. Marquardt, 2004, CHEOPS: A tool-integration platform for chemical process modelling and simulation, Int. J. Software Tools Technology Transfer,Vol. 6, pp. 186–202

Siemens AG, 2014, SIMIT – Remote Control Interface, Function Manual

K. Snively, R. Leslie, C. Gaughan, 2013, Runtime execution management of distributed simulations, 2013 Winter Simulation Conference, pp. 2878-2888

C.H.Yang, G. Zhabelova, C.W. Yang, V. Vyatkin, 2013, Co-Simulation Environment for Distributed Controls of SmartGrid,IEEE Trans. on Industrial Informatics

Krist V. Gernaey, Jakob K. Huusom and Rafiqul Gani (Eds.), 12th International Symposium on Process Systems Engineering and 25th European Symposium on Computer Aided Process Engineering.
31 May – 4 June 2015, Copenhagen, Denmark

On the Process of Building a Process Systems Engineering Ontology Using a Semi-Automatic Construction Approach

Canan Dombayci[a], Javier Farreres[b], Horacio Rodríguez[b], Edrisi Muñoz[c], Elisabet Capón-García[d], Antonio Espuña[a], Moisès Graells[e]

[a]*Chemical Engineering Department, ETSEIB, Universitat Politècnica de Catalunya, 647 Diagonal Avenue, 08028 Barcelona, Spain*
[b]*Software Department, CEIB, Universitat Politècnica de Catalunya, 187 Comte D'Urgell, 08036 Barcelona, Spain*
[c] *Centro de Investigación en Matemáticas A.C., Jalisco S/N, Mineral y Valenciana, 36240 Guanajuato, México*
[d] *Department of Chemistry and Applied Biosciences, ETH Zürich, Vladimir-Prelog-Weg 1, 8093 Zürich, Switzerland*
[e] *Chemical Engineering Department, EUETIB, Universitat Politècnica de Catalunya, Comte d'Urgell 187, 08028 Barcelona, Spain*
moises.graells@upc.edu

Abstract

This work presents a novel systematic approach for the construction of domain ontologies. The suggested approach uses a semi-automatic construction methodology. For this study, parent-child concept pairs are taken from a previous work. Novel contributions include building and completing branches, introducing new relations, and resolving inconsistencies and contradictions. For the process systems engineering (PSE) domain the ISA88 Standard is chosen as a promising starting point for automatic text processing. Finally, this work concludes with a discussion of the ISA88 Standard based on the conclusions that can be obtained from the application of this semi-automatic construction methodology.

Keywords: Domain Ontology, Automatic Ontology Construction, Ontology Construction Methodology, ISA88, Standards.

1. Introduction

There has been a growing interest in the field of PSE for using ontologies as knowledge models (Muñoz, 2011), intelligent data analysis of databases (Roda and Musulin, 2014), intelligent software applications (Morbach et al., 2010) and many other applications, each one using different ontology models. The use of a general domain PSE ontology based on already existing and accepted standards would not only facilitate the development of these and other applications, but also their integration and coordination. Departing from the parent-child concept pairs resulting from a previous work (Farreres et al., 2014), this work describes the systematic procedures used to refine the relationships to be modelled in the core of the ontology. Particularly, an ontology can be defined as "an explicit specification of a conceptualization" (Gruber, 1993). In the field of Computer Engineering, large ontologies for common knowledge have been developed together with tools based on internet databases, reference books and many documents from the Internet

(Vivaldi and Rodríguez, 2002). This is expected to lead to semi-automatic procedures to help experts to develop domain ontologies, although a great effort is still required to filter the noise obtained from extensive indiscriminate searches.

In parallel, expert teams have devoted a commendable effort to produce standards. Using language analysis tools, and in order to combine efforts for creating domain ontologies, the texts defining standards seem very well suited to be taken as a source to synthesize manual and automatic approaches in the most efficient way. Thus, the aim of this work is to investigate the semi-automatic development of domain ontologies in general, and to validate the hypothesis that a document defining a standard is an efficient starting point from which the ontology may be later extended and enriched.

The ISA88 Standard for batch control is a document that is assumed suitable for creating a domain ontology because it is a technical document clearly defining models and terminology, including the explanation of processes, data structures and language guidelines. The assumption is that intelligent selection of texts will reduce noise and allow fast and straight identification of concepts and relations.

In a previous work (Farreres et al., 2014), the ISA88 document was processed using a number of tools, and a set of concept pairs were extracted and manually revised. Each pair was a proposed relation, either between a parent concept and its children, or between a concept and its parts. This study is a continuation of such preliminary work for building a domain ontology. This building process is explained in a systematic way describing the suggested methodology and the quality of the resulting ontology is assessed.

2. Methodology

Common strategies for identifying concepts for a domain ontology manage concepts from the most specific ones to the most general ones (also reverse) or from the most important concepts to the most specific and most general ones (López, 1999 and Corcho et al. 2003). Conversely, this work identifies the concepts from a technical standard that is considered the basis for the domain. As a result, the proposed construction methodology is significantly different from the other strategies, and the ontology is built from these identified concepts by using a semi-automatic construction methodology. The following sections present a brief description of the steps of the methodology.

2.1. Phase-1: Building branches by composing parent-child concept pairs

A core ontology is built using parent-child concept pairs from Farreres et al. (2014). In the case of ISA88 Standard 266 concepts are added with 188 ‘is a’ relations. The ontology is enriched with the meronymy (‘partOf’) relations and 81 doubtful cases are left apart.

2.2. Phase-2: Doubtful cases, introducing ‘partOf‘ relationship and information from the figures in the standard

First, doubtful parent-child concept pairs (e.g. concepts with ‘and’ and ‘or’) are identified and solved manually. Next, graphical information is extracted by a human expert and the newly detected relations and concepts are introduced to further enrich the ontology. The ISA88 Standard contains figures that cannot be processed via automatic pattern matching owing to the fact that figures cannot be processed by the computers. This is revealed as a

difficulty for the automation of the process and it is solved manually processing the standard by a human expert.

2.3. Phase-3: Adding commonsense and ontology pruning

Until Phase-3 knowledge introduced in the ontology was all from the text and graphics of the supporting Standard. However, this may include neither commonsense nor the knowledge shared within a domain that must not be conveyed in a text because of its obviousness. After Phase-1 and Phase-2, conceptual gaps occur as consequence of the lack of explicit commonsense knowledge in the text.

Some simple and straightforward cases of commonsense knowledge are then addressed using a set of pre-established rules for introducing implicit information that can be understood without any explanation. A particular case is identified and solved following the rules 1 and 2. Thus, the UnitRecipe concept, composed of two nouns (1), would be moved as a child of Recipe; and RegulatoryControl, composed of an adjective and a noun (2), would be moved as a child of Control. 141 concepts were refined in this way and additional 'is a' relations are added to the ontology.

$$\text{Noun}_A + \text{Noun}_B \xrightarrow{\text{'is a'}} \text{Noun}_B \quad (1)$$

$$\text{Adjective}_A + \text{Noun}_C \xrightarrow{\text{'is a'}} \text{Noun}_C \quad (2)$$

Another particular case led to the creation of additional 'partOf' relations. Container, Combination, and similar concepts are often extracted as parent concepts from 'is a' relations. However, these concepts indicate the aggregation of further concepts. In this case the actual relation that correctly represents the model is not an 'is a' relation, but a 'partOf' relation. In the case of the ISA88 based PSE ontology, 20 concepts were refined concluding with adding 34 new 'partOf' relations and 22 new concepts.

Another case of commonsense rule will lead to the identification (Zhu et al., 2009) and elimination of redundant relations already presented by other relations.

3. Example of methodology (GeneralRecipe segment)

Figure 1 shows the 'is-a' segment originating in GeneralRecipe after Phase-1 and Phase-2. It is next used as an example to discuss the methodology steps detailed as follows:

i). Container, Collection and Combination concepts: Figure 1 shows GeneralRecipe as a subconcept of Container. As explained in Section 2.3, Container is better modelled by a 'partOf' relation. Figure 2 shows the new added 'partOf' relations.

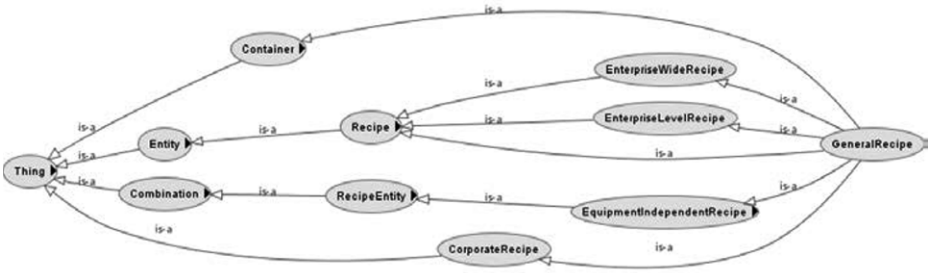

Figure 1. GeneralRecipe segment after Phase-1 and Phase-2

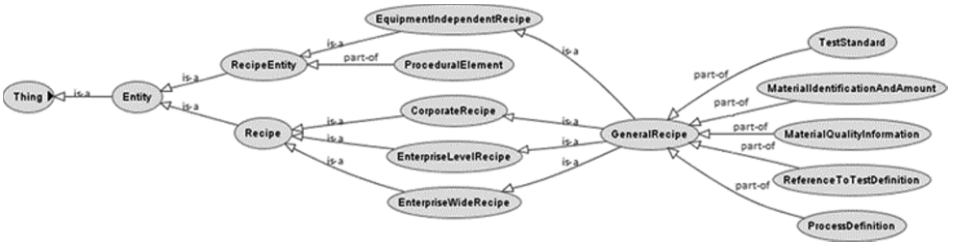

Figure 2. GeneralRecipe segment after Phase-3 (Only 'is a' and 'partOf' relations related with GeneralRecipe segment are represented, in case of clarity)

ii). Introducing commonsense knowledge: In addition, concepts given by compound nouns need reviewing (Section 2.3). For instance, it is apparent that the EnterpriseWideRecipe concept should be moved as a child concept of Recipe as shown in Figure 3a as before. Figure 3b shows the result.

iii). Removing redundant relations: Since there are two ways to reach Recipe from GeneralRecipe, the relation between GeneralRecipe and Recipe can be removed. This redundant relation is shown in Figure 3b.

Finally, Figure 2 shows the final diagram after implementing the proposed methodology.

4. Quality measure results

The direct pattern matching of the raw text after Phase-1 and Phase-2 results in a flat ontology (Figure 4a), lacking commonsense. Although there are no standard metrics for the quality of ontologies, some topological information have been used for measuring. One topological aspect taken into account is the width and depth of the ontology. Figure 4b shows a partial snapshot of the ontology after Phase-2 and Phase-3. It is clear that the first ontology is flat while the second one is deeper and tree-like, which has been considered as a sign of quality and improvement.

Additionally, Figure 5 shows the differences in the number of concepts per level after each Phase. Phase 1 generates an ontology that has most of its concepts at depth 2. After Phase-2 the number of concepts increases but there are few concepts below depth 2. After adding commonsense, the distribution is more reasonable, with a spread number of concepts between level 1 and 4, and a significant queue arriving to depth 6.

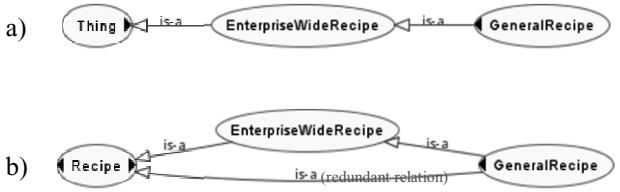

Figure 3. Redundant relations. a) Before introducing commonsense knowledge b) After introducing commonsense knowledge with redundant relation

a)

b)

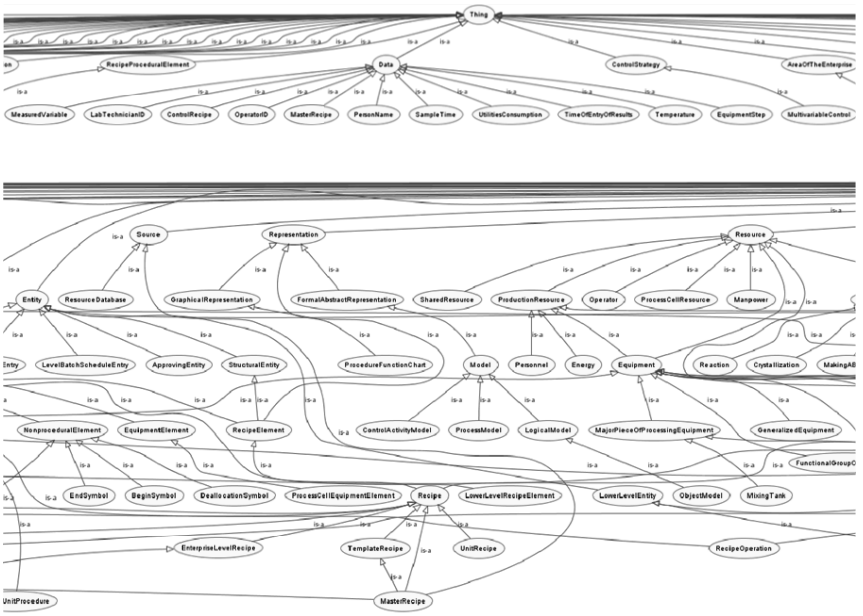

Figure 4. Depth of the ontology. a) After Phase-2. b) After Phase-3

Finally, the improvement obtained by using a text defining a standard (regarding the reduction of noise) is an assumption that can be hardly validated in a quantitative and systematic way. However, the use of another text could provide an illustrative reference. Towards this end, the same methodology was used to process a play of Shakespeare (1611) and nothing was produced: no pattern for the 'is a' or the 'part of' rules is found in the text.

5. Conclusions and future research

This paper proposes a semi-automatic methodology for building ontologies, presents most of the concepts of batch control in PSE by using the ISA88 Standard, and introduces commonsense knowledge to the ontology. The use of technical standards for building domain ontologies has been assumed. Another significant outcome raised in this study is the human expert introduction to the automatic ontology construction. An additional interesting result is that other relations ('input' and 'output') have been detected in addition to the 'is a' and 'partOf' relations for the enrichment process of ontology.

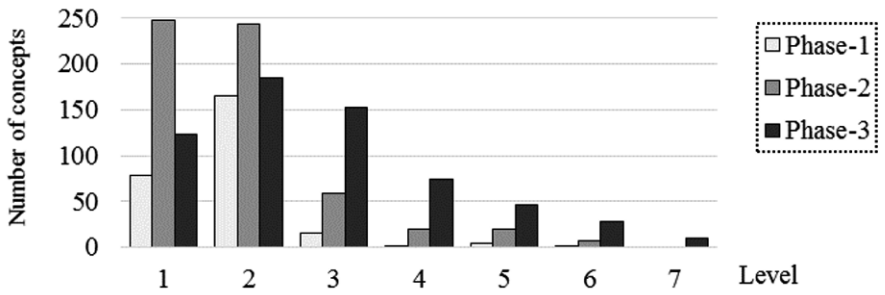

Figure 5. Number of concepts per level

Moreover, the ISA88 Standard consistency could be assessed from the point of view and formalisms of ontology development, and conclusions and guidelines for producing technical standards have been obtained. This includes ambiguous figures, undefined concepts, extended use of synonymy, and use of adjectives in the document which have been identified as problems, not only for the implication of automatic processes, but also for human readers. This contributes an analysis and suggestions for developing technical standards. On the other hand, the ISA88 Standard should be considered as a first case study for a research line, and the learning outcomes from this work are expected to be of practical interest to further ontology developments from other documents (e.g. ISA95).

Further work in this research line includes the enrichment of the ontology by extending the present semi-automatic development of domain ontologies for PSE using other technical documents and automatically searching the Internet to get implicit knowledge. The outcome of this systematic procedure could afterwards be compared to already existing ontologies of the same domain developed manually (Muñoz et al., 2011). Using some similarity metrics in order to validate their completeness. Hence, relevant feedback could be retrieved in order to further improve the systematic approach presented. Furthermore, the findings of this study provide information for developing the methodology as well as improving quality of resulting ontology from ISA88 Standard.

Acknowledgements

Financial support received from the Spanish "Ministerio de Economía y Competitividad", the “Agència de Gestió d'Ajuts Universitaris i de Recerca-AGAUR” and the European Regional Development Fund, funding the research Projects EHMAN (DPI2009-09386), SIGERA (DPI2012-37154-C02-01), SKATER (TIN2012-38584-C06-01) and the Research Group CEPEiMA (2014SGR1092), is fully appreciated.

References

O. Corcho, M. F. López, A.G. Perez, 2003, Methodologies, tools and languages for building ontologies. Where is their meeting point?, Data & Knowledge Engineering, 46, 41–64.

J. Farreres, M. Graells, H. Rodríguez, A. Espuña, 2014, Towards Automatic Construction of Domain Ontologies : Application to ISA88. Proceedings of the 24th European Symposium on Computer Aided Process Engineering, Budapest, Hungary.

T.R. Gruber, 1993, A Translation Approach to Portable Ontology Specifications, Knowledge Acquisition, 5, 2, 199–220.

ISA, 2000, Enterprise-Control System Integration Part 1: Models and Terminology, ANSI/ISA–95.00.01–2000, Technical report, ISA Standard.

ISA, 2006, Batch control, Part 1 (2006), Part 2 (2001), Part 3 (2003), Part 4 (2006), (ISA-88.01-1995 (R2006)), Technical report, ISA Standard.

M. F. López, 1999, Overview of Methodologies For Building Ontologies, Laboratorio de Inteligencia Artificial, Facultad de Informática, Universidad Politécnica de Madrid.

J. Morbach, W. Marquardt, A. Wiesner, A. Yang, 2010, Onto CAPE - A Re-Usable Ontology for Chemical Process Engineering, Springer.

E. Muñoz, 2011, Knowledge management technology for integrated decision support systems in process industries, Ph.D. Thesis, Univesitat Politècnica de Catalunya, Spain.

F. Roda, E. Musulin, 2014, An ontology-based framework to support intelligent data analysis of sensor measurements, Expert Systems with Applications, 41, 7914–7926.

W. Shakespeare, 1611, Macbeth <http://shakespeare.mit.edu>, Accessed on 20/09/2014.

J. Vivaldi, H. Rodríguez, 2002, Medical Term Extraction using the EWN ontology, Terminology and Knowledge Engineering, 137-142.

J. Zhu, J. Wang, B. Li, 2009, A formal method for integrating distributed ontologies and reducing the redundant relations, Kybernetes, 38, 1870-1879.

Krist V. Gernaey, Jakob K. Huusom and Rafiqul Gani (Eds.), 12th International Symposium on Process Systems Engineering and 25th European Symposium on Computer Aided Process Engineering.
31 May – 4 June 2015, Copenhagen, Denmark

Graphical Processing Unit (GPU) Accelerated Solution of Multi-Dimensional Population Balances Using High Resolution Finite Volume Algorithm

Botond Szilagyi[a], Zoltan K. Nagy[b,c]

[a]*Department of Chemical Engineering, Babes Bolyai University, Arany Janos Street 1, Cluj Napoca 400028, Romania*
[b]*Department of Chemical Engineering, Loughborough University,Leichestershire, Loughborough Le11 3TU, United Kingdom*
[c]*School of Chemical Engineering, Purdue University, West Lafayette 47907-2100, USA*

Abstract

Population balance modeling is a widely used approach to describe, crystallization processes, taking into accountnot only the primary phenomena like nucleation and growth, as well asparticle agglomeration and breakage which can be extended to multivariate cases where more internal coordinates i.e. particle properties can be used. The solution of the generated partial differential equation is not trivial due to its hyperbolic nature which causes numerical dispersion and diffusion. The high resolution finite volume algorithms are able to solve multidimensional population balance equations avoiding these unwanted phenomena. Unfortunately, the computational time is significantly larger, compared to e.g. moments based solutions. More recently there is an increased interest to apply parallel computations using GPU-s due to its massively parallel hardware architecture. The current study presents two accelerating possibilities for finite volume solution of population balance equations: compiled C++ code executed on CPU and CUDA C++ code running on the GPU. The case studies demonstrate that the code running on the GPU was between 6-35 times faster than the compiled C++ code and 4-6 times faster than the standard MatLab function. This significant improvement in computational time enablesthe application of model-based control approaches in real time even in case of multidimensional population balance models.

Keywords: population balance modelling, simulation, finite volume algorithm, GPU

1. Introduction

The population balance (PB) modelling approach was introduced by Hulburt and Katz (1964) to describe the population dynamics and thence it have been used in numerous fields of science as meteorology, biology, physics, chemistry and engineering. In crystallization, is the general modelling approach enabling the description of particulate properties such as particle size and shape, a variety of theoretical and experimental works appeared discussing its different aspects. For a process engineer, in order to allow on-line process optimization and control, it is crucial to have an accurate model which is solved with orders of magnitude faster than the real process time. In modern particulate sciences it is essential to control the particulate properties like particle size distribution

(PSD) and particle shape as it can affect significantly the product quality and downstream operations.

From mathematical point of view, the PB is a partial differential equation which may involve integral terms if secondary processes like breakage and agglomeration are also included. A variety of solution methods were proposed, each having its advantages and disadvantages. The high resolution finite volume methods (HR-FVM), introduced by Gunawan et al. (2004) are able tosolve numerically PB-seven with agglomeration and breakage moreovercomputes the PSD without numerical diffusion and dispersion. Thus, from modelling point of view the HR-FVM is perfectly suitable for optimization and control purposes, unfortunately the computational costs may become extremely large.The FVM solution stands on PSD discretization, as presented by Figure 1. For more for details about these methods, see the work of Qamar et al. (2006).

A several attempts were made to improve the computational efficiency of the HR-FVM: Qamar et al. (2007) presented an adaptive mesh strategy making possible to reduce the mesh size, Gunawan et al. (2008) proposed the parallel solution using a master/slave structured CPU cluster. Majumder et al. (2010) developed the Fast HR-FVM method which uses a coordinate transformation to speed up the simulation by maintaining its accuracy but Prakash et al. (2013) exploited the Matlab Parallel Computing Toolbox and Distributed Computing Server capabilities to parallelize the HR-FVM codes on CPU-s. In the above presented methods significant speedup was achieved, however, the increased price of the used supercomputers is a major disadvantage. The massive compute capabilities are generally used in different fields of science, Shane Cook (2012), GPU-s were not used to accelerate the PB equations (PBE) solution. Thus, the aim of this work is to apply GPU acceleration for HR-FVMPBE solution.

2. Methods

Here, the method described by Gunawan et al. (2004) is applied using the same Van Leer flux limiter function in three implementations: (i) in the form of Matlab function (ii) C++ code as compiled .mex function called from the Matlab and (iii) parallel CUDA C++ code in form of compiled .ptx running GPU handled by the Matlab's Parallel Computing Toolbox.It should be noted that when developing the implementations, the Matlab embedding capability was a key factor as is the generally used environment in process engineering.The most important properties of the machine are listed in Table 1: low cost devices are used with optimizing compilers which boosts up the performance of compiled codes. In the following parts, the three implementation methods will be discussed shortly.

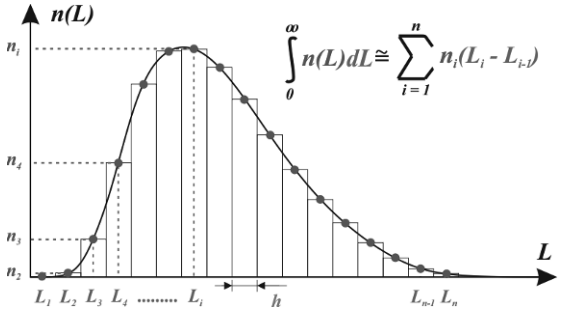

Figure 1. Representation of the finite volume discretisation of PSD

Table 1. Machine specifications

Property	CPU	GPU
Name	AMD Phenom II X4 965	Gigabyte nVidia GT 640
No. of processors / freq.	4; 3400 MHz	384; 1046 MHz
Memory specifications	16 GB DDR3; 1333 MHz	1 GB DDR5; 5000 MHz
Price	~ 100 USD	~ 100 USD
Compiler	MS. Visual Studio 2010 P.	nVidia CUDA Toolkit 6.5

2.1. Implementing in Matlab function

As the MatLab language, due to its flexibility and a variety of engineering applications like Simulink, Optimization Toolbox and Control System Toolbox etc. is widely used in engineering practice, it seems feasible to write the code directly in MatLab language. However, the computational performance compared to the high level programming languages is reduced whichit makes a poor environment for running HR-FVM codes.

2.2. Implementing in C++ code

The C++ language is known as extremely fast high level programming language thus it may be a good environment to implement the HR-FVM. In order to simultaneously profit from the flexibility of MatLab and improved speed of C++, the HR-FVM algorithm is written in C++ code and compiled to.*mex* function, what, in essence, is a special .*dll*which can be called directly from MatLab. The *Gateway function* of the .mex program makes the connection between the MatLab and the crude C++ code. In this case the memory management is handled by the programmer providing extra flexibility when optimizing the program. The operations are still executed serially which, especially for finer meshes can significantly slow down the solution. Parallelizing the code would overload the CPUthus may freeze the machine.

2.3. Implementing in CUDA C++ code

More recently there is an increased interest to apply parallel computing and computations using GPUs, which typically has a hardware architecture consisting of multiple parallel computing units. As the HR-FVM algorithm, from programming point of view is parallelizable, the natural questions rises if the GPU could accelerate the simulation? The Matlab's Parallel Computing Toolbox offers three implementation

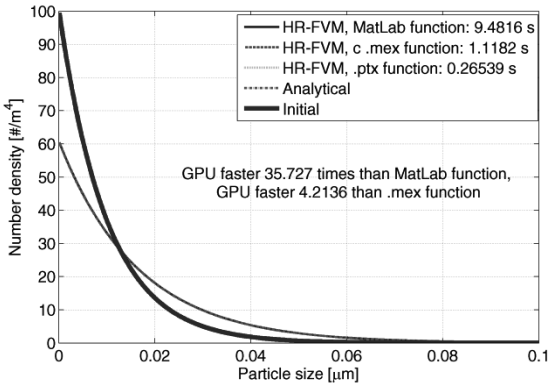

Figure 2. Results of HR-FVM implementations for a constant growth rate problem

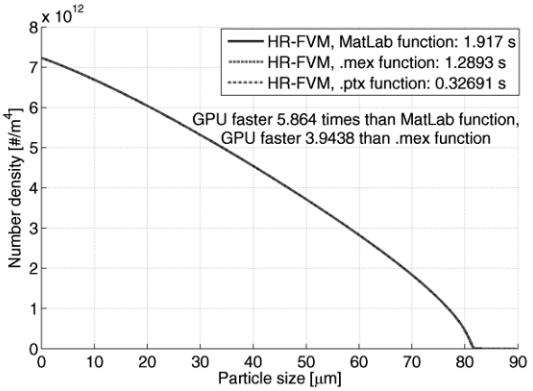

Figure 3. Results of HR-FVM implementations for monodimensional population balance with mass balance, nucleation and size dependent growth

ways to run code on GPU:(i) run built-in MatLab function, (ii) run element-wise MatLab code and(iii) run PTX code as parallel CUDA Kernel object. The PTX code offers the highest flexibility and computing performance which enables for the programmer maximal control of data flow in level of CUDA cores thus here this solution was used. As being the part of Parallel Computing Toolbox, writing a CUDA Kernel object is a comfortable solution for the engineers as the memory management is handled by the MatLab. Consequently, it highly reduces the programming efforts and crude code writing. The parallel code is written by taking into account the specific problems of parallel programming as race conditions and thread synchronization issues.

3. Results and Discussions

The upper discussed three implementations are applied to solve three benchmark cases.These are presented are presented and discussed in the following parts of this article.

3.1. Mono dimensional pure (constant) growth PBE

Let us consider a mono dimensional volume form PB Eq.(1)with growth only:

$$\frac{\partial n(v,t)}{\partial t} + \frac{\partial G(v) n(v,t)}{\partial v} = 0 \tag{1}$$

With$n_0(v) = N_0/v_0 \cdot exp(-v/v_0)$ initial distribution, $G(v)=G_0 v$ linear size dependent growth rate and $n_0(v) = N_0/v_0 \cdot exp[-v/v_0 exp(-G_0 t) - G_0 t]$ analytical solution. Here the parameters given by Gunawan et al. (2004) are used. The results and performance comparison is presented on Fig. 2: the solution curves of numerical solutions practically overlap with

Table 2. Results of HR-FVMimplementations in case solving bi PBE

quantity	MatLab f.	.mex function	.ptx function
μ_{00}[#/m^3]	$2.489 \cdot 10^{20}$	$2.489 \cdot 10^{20}$	$2.488 \cdot 10^{20}$
μ_{10}[μm/m^3]	$7.609 \cdot 10^{21}$	$7.608 \cdot 10^{21}$	$7.605 \cdot 10^{21}$
μ_{02}[μm^2/m^3]	$4.770 \cdot 10^{21}$	$4.770 \cdot 10^{21}$	$4.769 \cdot 10^{21}$
μ_{12}[μm^3/m^3]	$3.523 \cdot 10^{22}$	$3.522 \cdot 10^{22}$	$3.520 \cdot 10^{22}$
Run time (s)	5.1445	0.9954	0.1944

analytical solution. It seems that the C++ code is much faster compared to MatLab function but 4.2times slower than the GPU which can be explained by the fact that all operations are parallelizable which favors for the GPU.

3.2. Mono dimensional PBE with nucleation and growth

A PB with nucleation and growth written for linear particle size take the form Eq.(2):

$$\frac{\partial n(L,t)}{\partial t} + \frac{\partial G(S,L)n(L,t)}{\partial L} = B(S)\delta(L - L_n) \tag{2}$$

This with the corresponding mass balance and temperature profile is a batch crystallization model.In simulations, $n_0(L)=0$ initial distribution, the growth rate is $G(S,L)=0.18\cdot(S-1)^{0.6}(1+0.005\cdot L)$μm/s and$B = 2.64\cdot10^{12}(S-1)^{1.58}$#/m^{3}s nucleation rate is used where S denotes the supersaturation ratio. The temperature dependent solubility is described with $c_s=0.1286-5.88\cdot10^{-3}T+1.72\cdot10^{-4}T^2$equationand the solution is cooled from 32 to 18°C with is 1 °C/min rate.Adaptive time stepping is used to ensure the numerical stability of the algorithm. The results are presented on Figure 3. and can be observed that the computed distribution curves practically overlaps. Unfortunately, here the advantage of GPU is smaller. This can be explained with the presence of serial calculations like temperature and supersaturation calculation, mass balance and time step adaptation. As the GPU cores works on lower frequency (Table 1.), in serial calculations are less effective. However, the 3.9 times acceleration compared to the C++ code still could be beneficial for on-line application purposes.

3.3. Bi dimensional PBE with nucleation and growths

The bi-dimensional PBE with nucleation and growths generate the Eq.(3)

$$\frac{\partial n(L_1,L_2,t)}{\partial t} + \frac{\partial G_1(S,L_1)n(L_1,L_2,t)}{\partial L_1} + \frac{\partial G_2(S,L_2)n(L_1,L_2,t)}{\partial L_2} = B(S)\delta(L_1 - L_{n1})\delta(L_2 - L_{n2}) \tag{3}$$

This is together with the corresponding mass balance and temperature profile is a batch crystallization model. In simulations, a log-normal initial distribution with parameters $L_1 = 5$, $L_2 = 3$, $m_1 = 2$, $m_2 = 1$, $G_1(S, L_1)=0.208\cdot(S-1)^{1.05}(1+0.0001\cdot L_1)$μm/s and $G_2(S, L_2)=0.168\cdot(S-1)^{0.95}(1+0.00011\cdot L_2)$μm/s growth rates of the two characteristic crystal facets and $B = 2.64\cdot10^{-4}(S-1)^{1.38}V_p$#/μm^{3}s nucleation where Vp denotes the total volume of particles - secondary nucleation mechanism is considered - with $c_s=0.1286-9.88\cdot10^{-4}T+6.21\cdot10^{-5}T^2$temperature dependent solubility and the solution is cooled from 32 to 27°C with is 1 °C/min rate. Adaptive time stepping is used to ensure the numerical stability. As the graphical representation of a bivariate PSD is a surface that is not a successful way of result comparison, the moments of the distributions are computed and compared to the standard method of moment (SMOM) solution, introduced by Randolph and Larson (1971). Table 2. contains the comparison of results: all methods are highly accurate and a significant speedup, MatLab function : .mex function : .ptx function = 26 : 5.1 : 1 is achievedas, next to the mentioned serial calculations, moreparallelizableoperationsexist in the algorithm as the growth rates in both directions, respectively, the flux limiter function calculations.

4. Conclusions

In the current work three different implementations of the high resolution finite volume algorithm, namely as a MatLab function, compiled C++ .mex file and compiled parallel

.ptx file (executed on GPU), were studied and presented for solving mono and bivariate PBEs. The performance of different applications is strongly related to the nature of problem: the advantage of compiled .mex file is the faster serial calculation but GPU has a massive parallel architecture which makes it advantageous to perform parallel calculations. For the pure growth one dimensional population balance involving only parallelizable calculations the GPU was with 35 times faster than the Matlab function. The serial calculations are drastically the GPU speedup, for the one dimensional case with mass balance, nucleation and growth the MatLab : .mex : .ptx run time ratio is 5.8 : 3.9 : 1. In bi dimensional case, despite of the presence of serial calculations, the algorithm includes a massive parallelizable part thus the advantage of GPU becomes significant again, with a MatLab : .mex : .ptx run time ratio of 26 : 5.1 : 1. In the current study a low-cost GPU device is used and significant speedup is achieved which makes the method more attractive in application of real time model-based control approaches.

5. Acknowledgments

This paper is a result of a doctoral research made possible by the financial support of the Sectorial Operational Programme for Human Resources Development 2007-2013, co-financed by the European Social Fund, under the project POSDRU/159/1.5/S/132400 - "Young successful researchers – professional development in an international and interdisciplinary environment". Funding is acknowledged from the European Research Council under the European Union's Seventh Framework Programme (FP7/2007-2013)/ERC grant agreement No. [280106-CrySys].

References

A. Majumder, V. Kariwala, S. Ansumali, A. Rajendran, 2010, Fast High-Resolution Method for Solving Multidimensional Population Balances in Crystallization, Industrial & Engineering Chemistry Research 49, 3862-3872

A. Randolph, M. Larson, 1988, Theory of Particulate Processes. Academic Press, Salt Lake City

A.V. Prakash, A. Chaudhury, D. Barrasso, R. Ramachandran, 2013, Simulation of Population Balance Model Based Particulate Processes via Parallel and Distributed Computing, Chemical Engineering Research and Design 91-7, 2159-1271

H.M. Hulburt, S. Katz, 1964, Some Problems in Particle Technology. A statistical Mechanical Formulation, Chemical Engineering Science 19, 555-574

R. Gunawan, I. Fusman, R.D. Braatz, 2004, High Resolution Algorithms for Multidimensional Population Balance Equations, AIChE Journal 50-14, 2738 – 2749

R. Gunawan, I. Fusman, R.D. Braatz, 2008, Parallel High Resolution Simulation of Particulate Processes, AIChE Journal, DOI: 10.1002/aic.11484

S. Cook, 2012, CUDA Programming, Morgan Kaufman, USA

S. Qamar, A. Ashfaq, G. Warnecke, I. Angelov, M.P. Elsner, A. Seider-Morgestern, 2007, Adaptive High-Resolution Schemes for Multidimensional Population Balances in Crystallization Processes, Computers & Chemical Engineering 31-10, 1296-1311

S. Qamar, M.P. Elsner, I. Angelov , G. Warnecke, A. Seider-Morgestern, 2006, A Comparative Study of High Resolution Schemes for Solving Population Balances in Crystallization, Computers & Chemical Engineering 30-6/7, 1119-1131

Krist V. Gernaey, Jakob K. Huusom and Rafiqul Gani (Eds.), 12th International Symposium on Process Systems Engineering and 25th European Symposium on Computer Aided Process Engineering.
31 May – 4 June 2015, Copenhagen, Denmark

Development of Computer Aided Modelling Templates for Model Re-use in Chemical and Biochemical Process and Product Design: Import and export of models

Marina Fedorova[a], Gregor Tolksdorf[b], Sandra Fillinger[b], Günter Wozny[b], Mauricio Sales-Cruz[*c], Gürkan Sin[a], Rafiqul Gani[a]

[a]*CAPEC-PROCESS, Department of Chemical and Biochemical Engineering, Technical University of Denmark , DK- 2800 Lyngby, Denmark*
[b]*Chair of Process Dynamics and Operation, Berlin Institute of Technology, D-10623 Berlin, Germany*
[c]*Departamento de Procesos y Tecnología, Universidad Autónoma Metropolitana-Cuajimalpa, 05300, Mexico*
asales@correo.cua.uam.mx

Abstract

This paper focuses on the challenges in model development related to model reuse and compatibility and integration of different tools that are used in modelling. A link between two modelling tools, the computer-aided modelling framework of the ICAS system and the modelling environment, MOSAIC, has been established, in order to provide a wider range of modelling capabilities. Through this link, developed models can be exported/imported to/from other modelling-simulation software environments to allow model reusability in chemical and biochemical product and process design. The use of this link is illustrated through a case study.

Keywords: computer-aided modelling framework, model import/export, model reusability, model transfer, modelling environment.

1. Introduction

Computer aided modelling frameworks are gaining increasing attention in model-based studies of chemical and bio-chemical process-product design, as they can contribute by reducing the time and resources needed for model development and model-based applications. However, often a single modelling framework is unable to provide all the needed features, therefore, integration of modelling tools is an option worth considering. Through this integration, process models consisting of complex subsystems that cannot be modelled and simulated in a single general-purpose modelling tool can be handled. Also, the necessary support for model re-use can be provided (Schopfer et al, 2004), as well as offering new capabilities for users to write mathematical models in different formats and formalisms in addition to providing options for model transfer to other modelling-simulation software environments. One of the most time consuming activities for model developers is the exchange of the information between software systems and tools (Kraus et al, 2014). Since process modelling tools usually need different implementations for different modelling objectives, model re-usability

becomes very important. The models provided by a computer aided modelling tool should, therefore, be accessible via a programming interface to other tools (Bogusch et al, 2001). This can be achieved through a computer aided modelling tool that provides a component interface following certain standards, such as, CAPE-OPEN, COM-object, XML, DLL or TXT. This would allow user to exchange and work with a wide variety of models, increasing thereby models reuse. This integration and transfer of models between different tools will allow the use and analysis of models in the most efficient way, depending on the goal of modelling (i.e. model identification, parameter estimation, process design, system representation/understanding, process control, etc.).
The objective of this contribution is to present a general modelling framework of the ICAS system for systematic modelling building through modelling templates, which supports the reuse of existing models via its new model import and export capabilities. This new feature has been developed by establishing a connection with the MOSAIC modelling environment. A brief overview of the new modelling framework with emphasis on the above mentioned capabilities is given below, followed by an application example highlighting the modelling-simulation aspects of a batch reactor and a batch distillation process.

2. Modelling tools

2.1. ICAS modelling framework: template

The purpose of the computer aided template-based modelling framework is to enable the modeller to create a general model for a given system, to be used later to generate problem-specific models. To achieve this, the modeller is systematically guided through the steps of template-based modelling workflows and, at each step, the framework identifies and integrates the required tasks, tools, and database with model library connections (Fedorova et al, 2014; Fedorova et al, 2015). Depending on the modelling needs and goals, the modeller has the possibility to create a new model when the needed problem specific model is not available in the library. The modeller has also the possibility to identify, validate and solve the new models or use existing models from the template library. Furthermore, model templates enable the idea of model reuse as the user can employ the template as a base to build different problem-specific models for different applications. The objective here is to provide structured domain-specific knowledge, to speed-up the model development/derivation process and to improve the model quality. As the template library includes validated models, the creation of a new template-based model will reduce the modelling time and increase efficiency in the subsequent steps of model analysis, model verification and solution (Fedorova et al, 2015).
Figure 1 shows the modelling framework, which involves five main elements: 1) a modelling tool, that includes the modelling template library together with algorithms for model generation (ModDev, Jensen and Gani, 1999); 2) a model library, which provides building blocks for the templates (generic models previously developed); 3) computer aided methods and tools, that include procedures to perform model translation, model analysis, model verification/validation, model solution and model documentation (MoT, Heitzig et al, 2014); 4) model transfer – export/import to/from other application for further extension and application; 5) a user interface that provides the work-flow and data-flow to guide the user through the different modelling tasks.

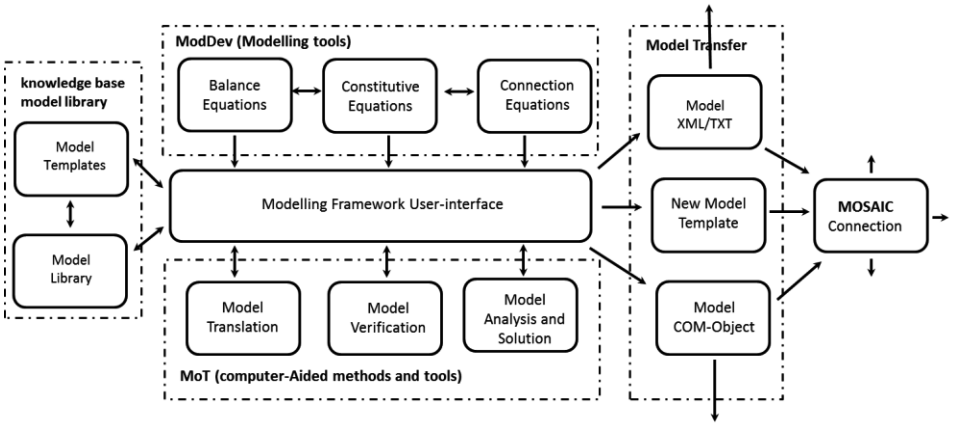

Figure 1. Schematic modelling framework implementation including transfer capabilities.

2.2. MOSAIC modelling environment

MOSAIC is a non-commercial, web based modelling, simulation, optimization, and code generation tool developed at TU Berlin, Germany (Zerry et al., 2004). The MOSAIC models are stored in a platform independent way by using XML/MathML standards and SQL-Databases. All elements of a model (e.g. notations, equations) are exchangeable and reusable. Detailed descriptions of additional features of MOSAIC have been published, focusing on experimental design (Hoang et al. 2013), data management aspects (Kraus et al. 2014) and model integration activities (Merchan et al. 2014). The general structure of MOSAIC is shown in Figure 2.

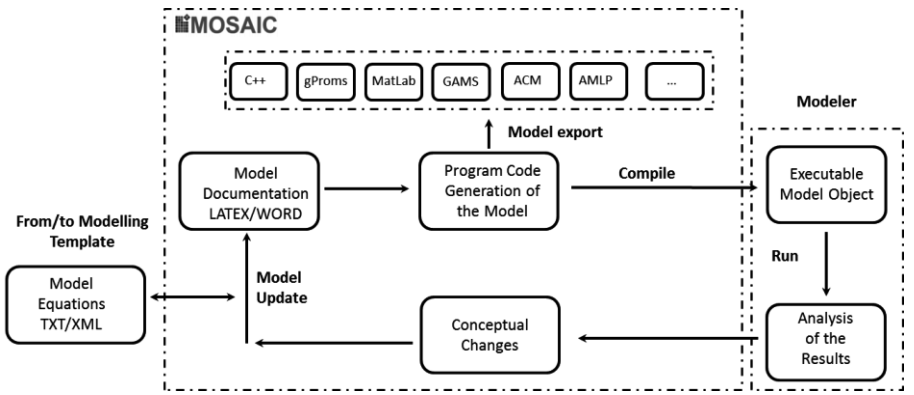

Figure 2. Model transfer interface and general structure of MOSAIC.

2.3. Implementation of the extended features through integration

The objective here is to allow the use of a wide range of programming languages (such as Fortran, C++ etc.), tools based on generic modelling languages (e.g. GAMS, gPROMS®, Matlab®) and domain-oriented tools (e.g. Aspen Plus, Pro II, ModDev) for various modelling needs..

The starting point is mathematical model created in a text editor program and then saved as a text file. The model is then pre-screened and pre-translated to make sure that it is valid, confirming that all model equations are consistent and syntactically correct. The

model transfer capabilities are schematically shown in Figure 1. Several types of formats, such as XML-format and COM-objects, are incorporated to allow the export and import of mathematical models. After the model is imported, it is stored in the modelling template library for further (re)use.
The link between the ICAS modelling framework and the MOSAIC modelling environment is established through a XML schema, which contains a formal description of the structure and elements in the XML files representing the model. This XML schema has been implemented in both ICAS modelling framework and MOSAIC, allowing translation of the model information to the transfer file in XML-format and exchange of these files between tools. Through this link it is possible to translate models into various languages, such as C++, gPROMS®, GAMS, Aspen Custom Modeler® and Matlab® together with a full model documentation. More details on the connection implementation can be found in Tolksdorf et al. (2015).

3. Case study

The application of the ICAS modelling framework and its model transfer capabilities are highlighted through a case study involving the modelling of a batch reactor followed by a batch distillation operation. The model describes the reaction and separation operations in the production of methyl acetate from acetic acid and methanol (Fig. 3). This model is obtained from the library of the ICAS modelling framework and solved using MoT (Fig. 4).

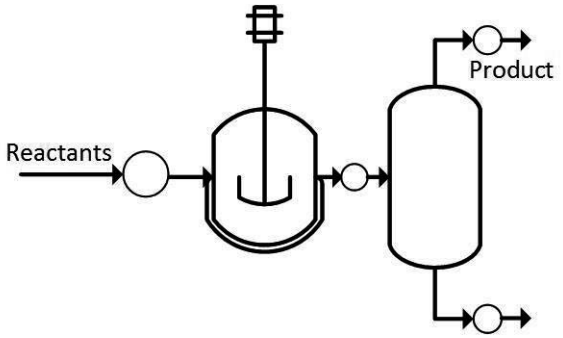

Figure 3. State-task network for batch reactor and batch distillation.

Furthermore, the model is transferred to MOSAIC via XML translation. This translation is done without additional effort from the user. All equations, variables and relations among them, as well as documentation that has been provided, are automatically transferred and implemented.
In MOSAIC, the model can be further translated into various modelling languages, as described in section 2.2.
Figure 5 shows schematic implementation of the transfer process starting from obtaining model from the template library of the ICAS modelling framework, then translating it to MOSAIC modelling environment, where code representation of the model for gPROMS® and Matlab® takes place. Results obtained from external tools are identical to the ones found by ICAS-MoT (see plots in Fig. 4 and 6) and this confirms the successful transfer and use of the new feature.

4. Conclusions

In this contribution a general modelling framework for systematic model development through modelling templates, which supports both, the derivation of models from scratch, and the reuse and further modification/extension of an existing model via its import and export model capabilities have been presented.

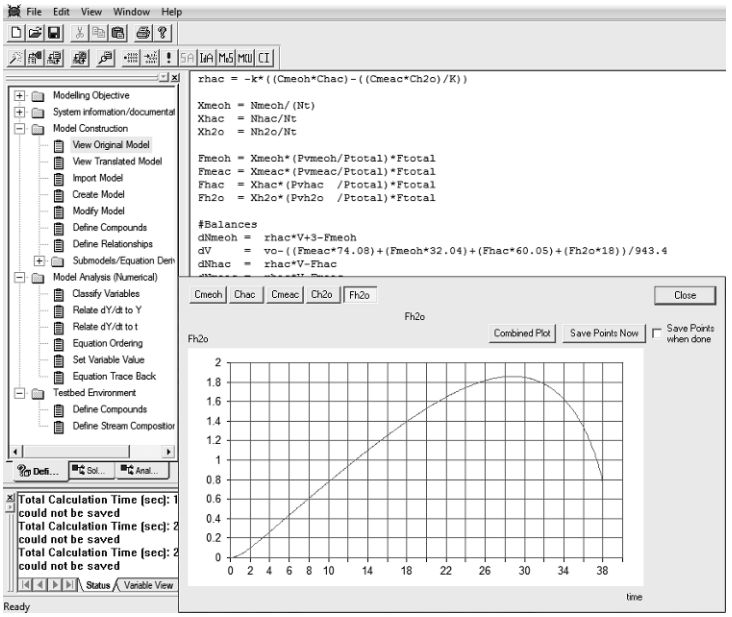

Figure 4. Model implementation in MoT

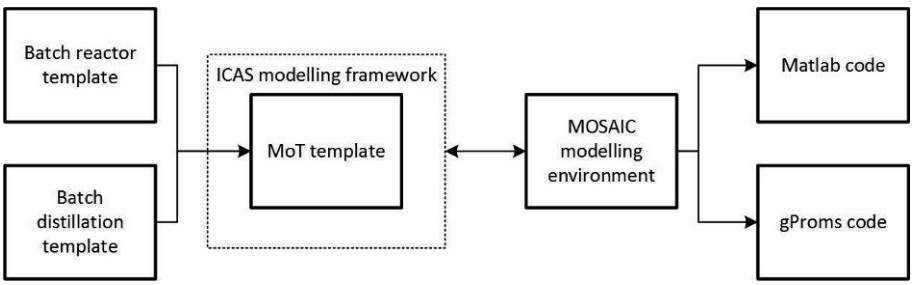

Figure 5. Schematic architecture of model implementation in ICAS modelling framework and its translation to external tools.

In industrial process modelling practice, the average number of modelling and simulation tools used by a work group is approximately five (Kraus et al, 2014). Although the diversity of tools should potentially increase the probability of finding a solution in an efficient manner, it can also lead to difficulties when the models need to be re-used by or shared within different work groups. For this reason an important feature of the tools integration is the capability to import and export the generated mathematical models from/to different modelling tools.

The possibility to translate the model, created in one modelling environment, to a variety of other languages in order to use it in the different modelling tools gives the flexibility to the model development and application process. This allows the model to be shared among modellers, who may be using different tools. Thus, a range of tools can be used for diverse purposes (e.g. model identification, analysis, control strategy etc.) without the need for rewriting the model. Also, by using another tool, a better solution strategy could be employed.

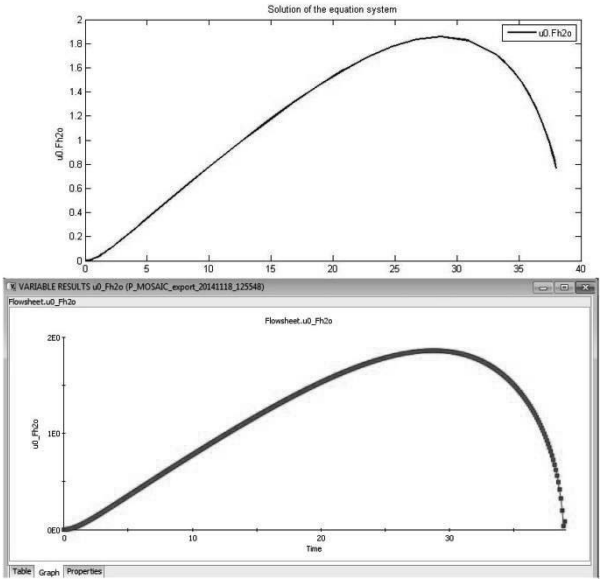

Figure 6. Resulting plots in Matlab and gProms, showing water flowrate after distillation unit.

References

JensenA.K., GaniR., 1999, A Computer Aided Modeling System, Computers and Chemical Engineering, 23, 673-678.

Bogusch, R., Lohmann,B., Marquardt, W., 2001, Computer-aided process modeling with MODKIT, Computers and Chemical Engineering 25,963–995

Fedorova M. , Sin G., Gani R., 2014, Computer-Aided Template for Model Reuse Development and Maintenance, Computer Aided Chemical Engineering, 33, 817-822.

Fedorova M. , Sin G., Gani R., 2015, Computer aided modelling template: concept and application, Computers and Chemical Engineering, SI:ESCAPE24 (submitted).

Kraus, R., Fillinger, S., Tolksdorf, G., Minh, Duc H., Merchan-Restrepo, Victor A. and Wozny, G. 2014, Improving Model and Data Integration Using MOSAIC as Central Data Management Platform, Chemie Ingenieur Technik, doi: 10.1002/cite.201400007

Heitzig M., Linninger, A., Sin G., Gani R., 2014, A computer-aided framework for development, identification and management of physiologically-based pharmacokinetic models, Computers and Chemical Engineering, 10.1016/j.compchemeng.2014.07.016.

Schopfer G., Yang A., von Wedel L., Marquardt W.: 2004, Cheops: A tool-integration platform for chemical process modelling and simulation, Int J Software Tools Transfer 6, 186–202.

D. M. Hoang, T. Barz, V. A. Merchan, L. Biegler, H. Arellano-Garcia, 2013, Simultaneous solution approach to model-based experimental design, AIChE Journal, doi: 10.1002/aic.14145

V. A. Merchan, G. Tolksdorf, R. Kraus, G. Wozny, 2014, Extending Documentation-Based Models towards an Efficient Integration into Commercial Process Simulators, Chem. Ing. Tech., doi: 10.1002/cite.201400014

Tolksdorf G., Fillinger S., Kraus R., Wozny G., Manenti F., Rossi F., Buzzi-Ferraris G., Pierucci S., Fedorova M., Gani R, 2015, A Posteriori Integration of University CAPE Software Developments, Chemical Engineering Transactions, 43 (submitted).

Zerry R., Gauss B., Urbas L., Wozny G., 2004, Web-based object oriented modelling and simulation using MathML, 2004, Comput. Aided Chem. Eng., 18, 1171-1176, DOI: 10.1016/S1570-7946(04)80261-X

Krist V. Gernaey, Jakob K. Huusom and Rafiqul Gani (Eds.), 12th International Symposium on Process Systems Engineering and 25th European Symposium on Computer Aided Process Engineering.
31 May – 4 June 2015, Copenhagen, Denmark

BiOnto: An Ontology for Biomass and Biorefining Technologies

Nikolaos Trokanas[a], Madeleine Bussemaker[a], Eirini Velliou[a], Hella Tokos[a], Franjo Cecelja[a]

[a]*PRISE Group, University of Surrey,Guildford, GU2 7XH, UK*

Abstract

This paper presents design and implementation of the BiOnto ontology in the domain of biorefining. The ontology models both biomass types and composition and biorefining processing technologies. The designed ontology is verified by a case study in the domain of Industrial Symbiosis.

Keywords: Ontological Engineering, Biomass, Biorefining Technologies, Ontology, Semantic Modelling

1. Introduction

In process engineering ontologies are commonly used for knowledge representation. Historically, their potential has been recognised in many different domains such as the biomedical (Musen et al. 2012), legal (Casellas et al. 2005, Lame 2005, Corcho et al. 2005), financial (Alonso et al. 2005), agricultural (Soergel et al. 2006) and chemical and process engineering (CPE).

This paper presents the *BiOnto* ontology, which expands on already developed and implemented processing technology ontology eSymbiosis (Raafat et al. 2013) and represents knowledge on biomass types and composition, as well as on biorefining technologies. To this end, the *BiOnto* ontology provides a reference model interpretable both by humans and computers by classifying biomass in 5 different ways: i) processing characteristics, ii) chemical composition, iii) physical properties, iv) existing standards (such as CEN/TC 335), and v) waste and residue based classification. More specifically, functionality of the *BiOnto* ontology selected by different practical scenarios, which include screening of processing technologies for particular type of biomass, screening the alternative technologies to target material or energy output or production pathway, selecting the best technology to satisfy set economic, environmental and/or social targets, and screening biomass types to supplement another one.. In addition, the *BiOnto* ontology has been demonstrated useful for searching and indexing of biomass information, enabling interoperability between applications, data integration and enabling and enhancing decision making in relation to biomass and biomass processing.

2. Ontologies and Knowledge Modelling

Ontologies are knowledge representation tools that have evolved through the years and are currently researched in the domain of Chemical and Process Systems engineering.

Previous efforts of ontology development in the domain of Chemical and Process Systems Engineering (CPE) have focused on process and process systems design (Zhang, Yin 2008, Bock et al. 2010, Fernandes et al. 2011), supply chain modelling (Muñoz, Espuña & Puigjaner 2010, Muñoz et al. 2012) and industrial symbiosis and environmental decision-making (Trokanas et al. 2013, Trokanas, Cecelja & Raafat

2014, Raafat et al. 2013) among other fields (Morbach, Wiesner & Marquardt 2009, Abanda, Tah & Duce 2013, Panetto, Dassisti & Tursi 2012). This ever increasing use of ontologies is due to their important role in formalising the diverse and volatile information and concomitant opportunity to analyse and understand the knowledge of a domain and respective sharing and reuse of the domain knowledge.

3. The BiOnto Ontology Structure

The BiOnto ontology (Figure 1) structured around two distinct streams/ontologies biorefining domain including biomass types and biorefining technologies. Both ontologies have been modelled in a number of ways forming separate sub-modules which in turn increase its spectrum of use and make the ontology application independent. Figure 1 presents an excerpt of the biorefining technologies module. The expanded sub-module (*ByType*) models processing technologies based on the type of the conversion. The other sub-modules are not presented for the sake of simplicity and presentation.

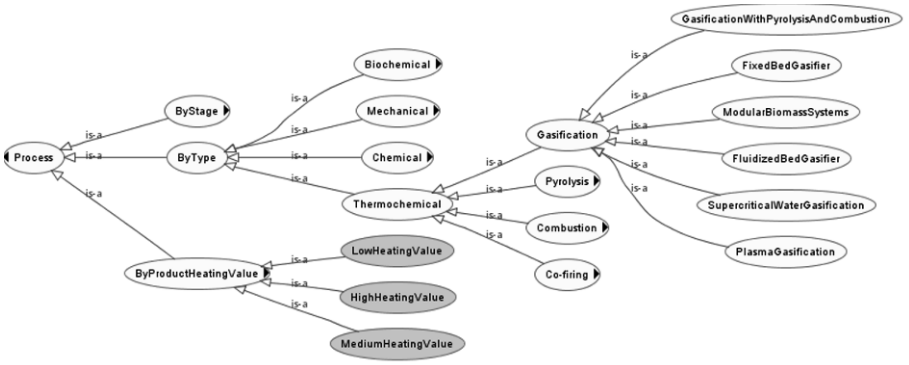

Figure 1 Excerpt of BiOnto Ontology

The BiOnto ontology consists of two main modules: i) Biomass and ii) Biorefining technologies.

3.1. Biomass Module

Biomass is modelled more generally as materials (Figure 2) and includes five identifiable sub-modules. Figure 2 presents the high level of *Materials* (biomass) module and its five sub-modules.

Products sub-module classifies energy and material products such as biofuels, electricity and biochemicals. Concepts under this sub-module are dominantly used used to describe inputs and outputs of biorefining technologies.

PlatformMaterial sub-module classifies platform materials such as syngas, lignin and H_2. These are the intermediate products that can act either as a work-in-progress or as products in cases where biochemical production is the aim.

MaterialByPhysicalForm sub-module classifies all materials of the ontology based on their physical form. This sub-module can be considered as an index.

FeedstockMaterials sub-module classifies biomass as input for the biorefining processes such as animal biomass, herbaceous biomass and aqueous biomass.

OtherMaterials module, classifies all other types of biomass or materials that are not classified. This sub-module is subject to auditing by a knowledge engineer so that *OtherMaterials* are classified in one of the other modules.

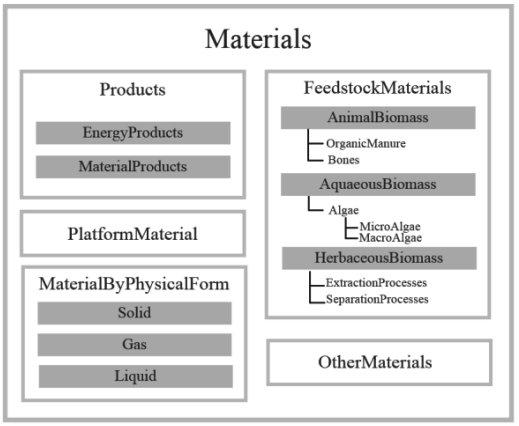

Figure 2 Biomass (Materials) Module

3.2. Biorefining Processing Technologies Module

Biorefining technologies consist of 3 sub-modules (Figure 3): i) ByProcessType, ii) ByProcessStage and iii) ByProductHeatingValue.

ByProcessType sub-module classifies technologies based on the type of conversion which takes place, such as chemical, biochemical, mechanical, thermochemical. This is an intuitive classification and a lot of information is available in literature making this classification the natural starting point.

ByProcessStage sub-module classifies processing technologies based on the stage they occur. Pre-processing technologies include pre-treatment processes such as *Chipping* and *Milling*. Main processing technologies include main conversion technologies such as *Pyrolysis* and *Gasification*. Post-processing technologies include processed such as *SteamReforming* and *WaterGasShift*.

ByProductHeatingValue sub-module classifies processing technologies based on the heating value of their product. The three ranges of heating values are defined as low (>=3, <=10), medium (>10, <=20) and high (>20, <=35). Heating value is modelled in MJ/kg.

Figure 3 presents the high level of the biorefining technologies module and its 3 main sub-modules.

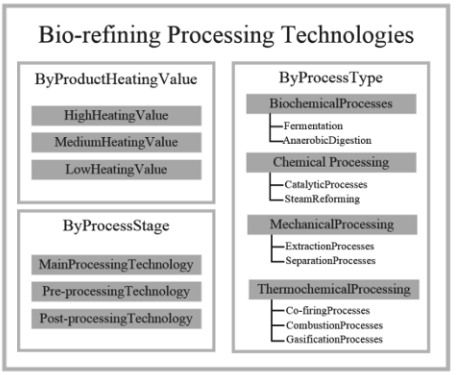

Figure 3 Biorefining Processing Technologies Module

All processing technologies have been classified based on their type during the modelling process and are consequently reclassified under different sub-modules. Reclassification of classes is enabled by the inference capabilities that ontologies offer. Reclassification of processing technologies is demonstrated in Figure 1and Figure 4. To explain, reclassification is apparent for gasification technologies such as *FixedBedGasifier* and *PlasmaGasificication* which have been reclassified as *LowHeatingValue* technologies. This inference is triggered by the specified values of product heating value for each technology.

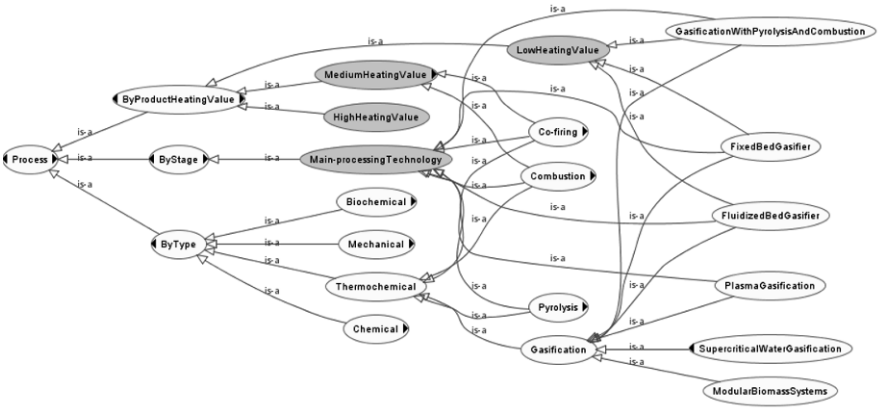

Figure 4 Inferred Ontology Excerpt

Biorefining technologies have been modelled in detail, in an effort to widen the scope of potential applications. Each biorefining technology in BiOnto, has been modelled in terms of feedstock materials, output products and by-products. Operational characteristics have also been modelled for each technology. These include conversion rate, required moisture content, operating temperature and product heating value. This information has been modelled using restrictions on properties. The example of a fixed bed gasifier is presented in Figure 5. The restrictions in Figure 5, describe *FixedBedGasifier* technologies, which is defined having a conversion rate between 60-80%. The same technology has a defined range of product heating value (<=5) that leads to the reclassification of this technology as a low heating value technology.

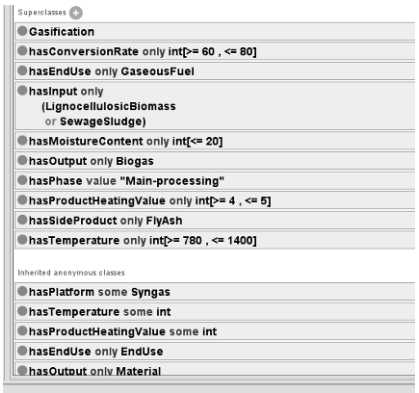

Figure 5 Fixed-bed Gasifier Restrictions

3.3. Properties

The properties used in BiOnto (both object and data type) focus on the operational characteristics of technologies and the compositional (chemical) characteristics of biomass. To name a few, technologies are characterised by their conversion rate (*hasConversionRate*), output (*hasOutput*), input (*hasInput*) and moisture content they can handle (*hasMoistureContent*). Biomass is characterised by its heating content (*hasHeatingValue*), moisture content (*hasMoistureContent*) and composition (*hasLignin*, *hasCelluloce*, *hasHemicelluloce*). Some of the properties are presented in the restrictions of the fixed-bed gasifier in Figure 5.

4. Case study

BiOnto ontology has the potential to be used in many applications such as data integration, semantic search and matching. To validate the presented ontology, we have implemented it in an Industrial Symbiosis platform, previously presented in (Raafat et al. 2013, Trokanas et al. 2012).

In more detail, the ontology was implemented in the Industrial Symbiosis portal and used for registration and matching of resources (in this case biomass) and biorefining processing technologies.

The matching process was initiated by the registration of an anaerobic digestion technology which was matched against a number of biomass types previously registered using BiOnto. The results for the feedstocks matching as inputs of anaerobic digestion technology are presented in Table 1.

Table 1 Matching Results

Resource	Relevance		Name	Quantity	Unit of measure	Valid From	Valid to
Manures	92%		Manure	62,00	Tonnes	01/05/2014	31/08/2015
Corn Stover	85%		Corn Stover	62,00	Tonnes	28/07/2014	27/08/2015
Rice Husk	83%		Rice Husk	135,00	Tonnes	01/01/2015	20/04/2016
Round Timber	79%		Round Timber	240,00	Tonnes	03/06/2014	04/03/2015

Obtained results have been compared and verified with results produced from the established eSymbiosis platform.

5. Conclusions

The presented ontology models biomass and biorefining technologies in detail, allowing the ontology to be used in a range of applications. Validation was performed through a case study in Industrial Symbiosis domain where the ontology was used to collect information from the users and identify symbiotic matches between available feedstocks and technologies. However, BiOnto is open to other applications as well. Future plans include the use of BiOnto to enable model and data integration in biorefining domain and incorporation of the ontology in the decision making process of value chain modelling for biorefineries.

References

F.H. Abanda, J.H.M Tah, & D. Duce (2013), "PV-TONS: A photovoltaic technology ontology system for the design of PV-systems", *Engineering Applications of Artificial Intelligence,* vol. 26, no. 4, pp. 1399-1412.

L. Alonso, L. Bas, S. Bellido, J. Contreras, R. Benjamins & M. Gomez (2005), "WP10: Case Study eBanking D10. 7 Financial Ontology", *Data, Information and Process Integration with Semantic Web Services, FP6-507483,* .

C. Bock, X. Zha, H. Suh & J. Lee (2010), "Ontological product modeling for collaborative design", *Advanced Engineering Informatics,* vol. 24, no. 4, pp. 510-524.

N. Casellas, M. Blázquez, A. Kiryakov, P. Casanovas, M. Poblet & R. Benjamins, (2005), "OPJK into PROTON: Legal domain ontology integration into an upper-level ontology", *On the Move to Meaningful Internet Systems 2005: OTM 2005 Workshops*Springer, , pp. 846.

O. Corcho, M. Fernández-López, A. Gómez-Pérez & A. López-Cima (2005), "Building legal ontologies with METHONTOLOGY and WebODE" in *Law and the semantic web* Springer, , pp. 142-157.

R.P. Fernandes, I.R. Grosse, S. Krishnamurty, P. Witherell & J.C. Wileden (2011), "Semantic methods supporting engineering design innovation", *Advanced Engineering Informatics,* vol. 25, no. 2, pp. 185-192.

G. Lame (2005), "Using NLP techniques to identify legal ontology components: concepts and relations" in *Law and the Semantic Web* Springer, , pp. 169-184.

J. Morbach, A. Wiesner & W. Marquardt (2009), "OntoCAPE—A (re) usable ontology for computer-aided process engineering", *Computers & Chemical Engineering,* vol. 33, no. 10, pp. 1546-1556.

E. Muñoz, A. Espuña & L. Puigjaner (2010), "Towards an ontological infrastructure for chemical batch process management", *Computers & Chemical Engineering,* vol. 34, no. 5, pp. 668-682.

E. Muñoz, E. Capón-García, A. Espuña & L. Puigjaner (2012), "Ontological framework for enterprise-wide integrated decision-making at operational level", *Computers & Chemical Engineering,* vol. 42, no. 0, pp. 217-234.

M.A. Musen, N.F. Noy, N.H Shah, P.L Whetzel, C.G. Chute, M.A. Story, B. Smith & NCBO team 2012, "The National Center for Biomedical Ontology", *Journal of the American Medical Informatics Association : JAMIA,* vol. 19, no. 2, pp. 190-195.

H. Panetto, M. Dassisti & A. Tursi (2012), "ONTO-PDM: Product-driven ONTOlogy for Product Data Management interoperability within manufacturing process environment", *Advanced Engineering Informatics,* vol. 26, no. 2, pp. 334-348.

T. Raafat, N. Trokanas, F. Cecelja & X. Bimi (2013), "An ontological approach towards enabling processing technologies participation in industrial symbiosis", *Computers & Chemical Engineering,* vol. 59, no. 0, pp. 33-46.

D. Soergel, B. Lauser, A. Liang, F. Fisseha, J. Keizer & S. Katz (2006), "Reengineering thesauri for new applications: the AGROVOC example", *Journal of digital information,* vol. 4.

N. Trokanas, T. Raafat, F. Cecelja & A. Kokossis (2013), "OFIS - Ontological Framework for Industrial Symbiosis", *Computer Aided Chemical Engineering,* vol. 32, no. 23rd European Symposium on Computer Aided Process Engineering, pp. 523-528.

N. Trokanas, T. Raafat, F. Cecelja, A. Kokossis & A. Yang (2012), "Semantic Formalism for Waste and Processing Technology Classifications Using Ontology Models", *Computer-Aided Chemical Engineering,* vol. 30, pp. 167-171.

N. Trokanas, F. Cecelja & T. Raafat (2014), "Semantic input/output matching for waste processing in industrial symbiosis", *Computers & Chemical Engineering,* vol. 66, pp. 259-268.

W. Zhang & J. Yin (2008), "Exploring Semantic Web technologies for ontology-based modeling in collaborative engineering design", *The International Journal of Advanced Manufacturing Technology,* vol. 36, no. 9-10, pp. 833-843.

Krist V. Gernaey, Jakob K. Huusom and Rafiqul Gani (Eds.), 12th International Symposium on Process Systems Engineering and 25th European Symposium on Computer Aided Process Engineering.
31 May – 4 June 2015, Copenhagen, Denmark

Linking process, electrical and logical connectivity for supported fault diagnosis

David Dorantes Romero [a,b,*], Tone-Grete Graven [a], Nina F. Thornhill [b]

[a]*ABB Oil and Gas, Ole Deviks vei 10, Oslo, Norway, david.romero@no.abb.com*
[b]*Department of Chemical Engineering, Imperial College London, London SW7 2AZ*

Abstract

Many engineering activities depend on the analysis of the plant connectivity. In particular, process operation requires a thorough understanding of the interconnections between units to be able to evaluate diverse operation scenarios. While some of the relationships between elements are obvious from process descriptions, some others (recycle flows, utility systems, and electrical interactions) are not so easy to spot. The hypothesis is that information regarding these non-explicit connections is already available inside the diagrams and technical documentation of the process. This paper suggests a method for integrating electrical and logical connectivity with process connectivity extracted from "smart P&IDs". Moreover, a prototype tool (Topoviz™) which can be used to integrate, visualise, and analyse plant connectivity is introduced.

Keywords: plant connectivity, graph networks, visualisation, XML, "smart P&IDs"

1. Introduction

Large scale petrochemical facilities are complex systems composed of interconnected processes. The increasing level of automation poses new challenges in the industry as it becomes difficult to extract valuable information when the number of variables in the process grows. Particular challenges are data visualisation, the computational limitations from current tools, and the understanding of complex dependencies amongst process units, especially when these involve different domains. Currently, engineers need to combine information from disparate sources to make inferences about how units, variables and events are related. This procedure has been performed manually, and it typically relies on experience and domain knowledge. Earlier analysis of the engineering workflows and technical documentation for oil and gas production facilities indicates that the understanding of the process connectivity is a valuable resource for activities such as troubleshooting and maintenance planning (Romero and Graven, 2013). The term plant connectivity is used here in its meaning as the physical structure of a network, encompassing the process, electrical and logical links between units inside the network.

A specific problem in troubleshooting activities is related to the analysis of plant connectivity where both electrical and process equipment are involved. As pointed out by Cecilio et al., (2014), it would be meaningful to consider the utilities that service the process for troubleshooting and diagnosis activities. The reason for this claim is that these subsystems also interact with the process through energy and information signals, and therefore disturbances can also propagate via electrical and logical paths. Similar research focusing on the integration of data from different engineering domains has been carried out before. Mordinyi et al., (2012) applied this knowledge to engineering process and lifecycle information. Cui et al., (2010) presented a customized data acquisition method for SmartPlant® P&ID for the integration of process topology with HAZOP.

The physical and material links between process units are contained in the P&IDs, or piping and instrumentation diagrams. P&IDs are "smart" if they are stored in XML files. The extraction of connectivity information from them is a solved problem, as several algorithms have been developed in order to parse information stored in them by under industrial specific standards such as AutomationML (https://www.automationml.org) and ISO 15926 (www.15926.org). On the other hand, electrical diagrams show connections between electrical components, which are usually made by wires. As far as the authors are concerned, there is no evidence of an industrial standard for data integration that can be used in the same way as the ones developed for "smart P&IDs"; hence the extraction of electrical connectivity becomes more difficult and the possibility to automatically extract connectivity information from wiring diagrams is still an open question. Logical connectivity is referred here as the information links between units (signals/interlocks).

In order to offer appropriate support to plant operations and maintenance it is necessary to define a new tool for the visualisation of interconnections between equipment from different subsystems. Figure 1 offers an overview of the different sources of technical documentation that are commonly used in the industry. The example shows how a single item FT-301 (flow transmitter with tag number 301) can be viewed from the different domains and systems, which presents a problem because of the distributed nature of the knowledge. Relevant contextual information readily available by looking at the diagrams and linking them together, is not available in the DCS or other systems used for troubleshooting and maintenance planning. Therefore, a first challenge to be solved is to define an efficient way to integrate and store connectivity information extracted from several places. Commentators suggest that some uses for an integrated connectivity model are: automated fault diagnosis, HAZOP, and maintenance planning (Yang et al., 2014).

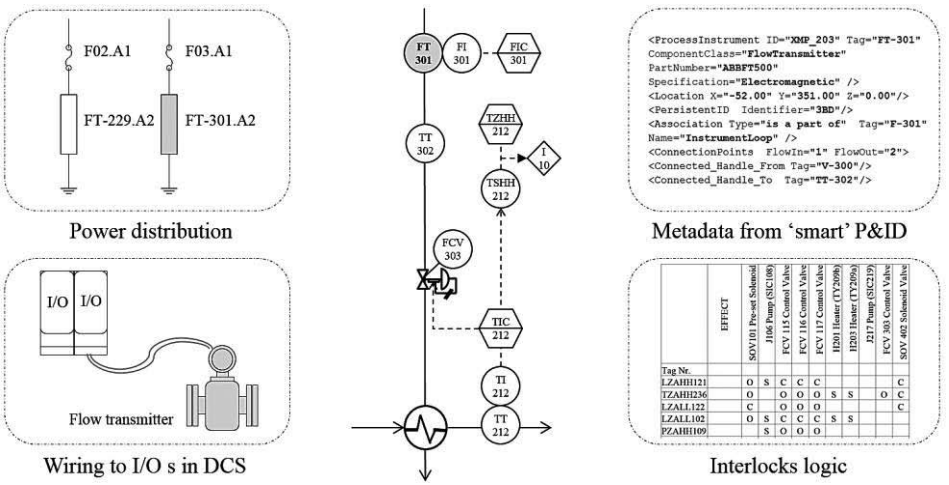

Figure 1. Example data sources, P&ID in the middle was extracted from case study.

The document is laid out as follows: Section 1 has outlined the problem statement and introduced the area of research. Section 2 covers the analysis of relevant literature. Section 3 defines the industrial context and outlines some of the challenges in the petrochemical industry behind the research question. Section 4 describes the methods integrating information about process and electrical connections from different sources. Section 5 presents the tool and the visualisation of a case study, discussing the results of using the proposed methodology.

2. Literature review

Several authors have evidenced that process connectivity extracted from structural models can enhance the isolation and diagnosis of the root-cause in plant-wide disturbances (Maurya et al., 2003; Yang et al., 2014). A number of works have focused on integrating process knowledge with other sources of information. Di Geronimo Gil et al., (2011), for instance, merged first-principles models with process connectivity. Birk et al., (2010) proposed the tool ProMoVis capable of modelling and visualising interdependencies in the control system. A proposal for the integration of P&ID and HAZOP expert systems was carried out by Cui et al., (2010), with the restraint that their customized ontology and middleware not based on any industrial standard. Extending the concept would result in a vast effort to create data acquisition and normalization modules to each data source. Schleburg et al., (2013), more recently devised an algorithm to apply process connectivity from P&IDs for alarm reduction. Nevertheless, all the examples mentioned above look only at process connectivity (material flows), and it is a fact that interconnections can happen via material, information, and electrical flow. Consequently, a problem identified in the literature is that fault propagation analysis must include not only of the process side, but also its auxiliary systems (electrical system, utility and safety). This has been recently addressed by Cecilio et al., (2014) looking at time-series.

The proposed approach is to use the concept of *property-graph* to integrate disparate data sources into a network that is navigable and supports queries. This is achieved by a series of algorithms that are used to parse, integrate and visualise plant connectivity information as a graph network. The methodology reports several advances compared with the previous work on visualisation of connectivity models, including the generation of a novel graph structure that presents several advantages over adjacency matrices, signed digraphs and other object-oriented modelling methods. Furthermore, the algorithms extract connectivity information from electrical diagrams as well as from the P&IDs. The integration of electrical diagrams with process diagrams has never been accomplished before. Thus, the expectation is that the methods proposed here can be combined with data-driven methods and greatly enhance the capabilities of the analysis, for instance, when causes of disturbance originate or are propagated through the electrical system.

3. Industrial context

A concurrent problem linked to the increase in the level of automation is the amount of data available from all the different systems used for automated fault diagnosis. These systems include the process monitoring system, process control and safety systems, as well as a number of proprietary tools and databases available for a particular units. The consequences of abnormal process conditions such as plant-wide disturbances are significant; in the petrochemical industry they are estimated to costs billions of USD dollars (at least 20 as reported by Bullemer in 1994). Surveys confirm that around 80% of these situations are avoidable, and human error causes 40% of them. Manual analysis of the interconnections between units from different systems can be time-consuming and prone to errors, and therefore there is a motivation for the automatic extraction and integration of process and electrical connectivity. A key factor to consider is that the degree of automation achieved depends heavily on the availability of process and electrical diagrams in a computer-readable form. Due to the heterogeneity of engineering documents, e.g. wiring diagrams, equipment layout plans, process flow diagrams and cause-and-effect tables, synchronisation between disciplines may also require a big collaboration effort between discipline experts.

4. Integration of plant connectivity from different domains

The main objective is to be able to enable collaboration across domains, so that experts performing plant-wide diagnosis have access to information about interconnections between process and electrical subsystems. Figure 2 describes the proposed methodology where (1) data is generated by different computer aided engineering tools and then exported to standardized formats, (2) connectivity information is extracted by parsers as node-link relationships, (3) connectivity information from the different subsystems is stored in a graph database, (4) a set of rules is used for querying and searching for propagation paths or connections between items, and (5) a visualisation layer presents the results to the user. As introduced before, the graph database uses the concept of a property-graph, which is essentially a directed graph with properties associated to its nodes and edges.

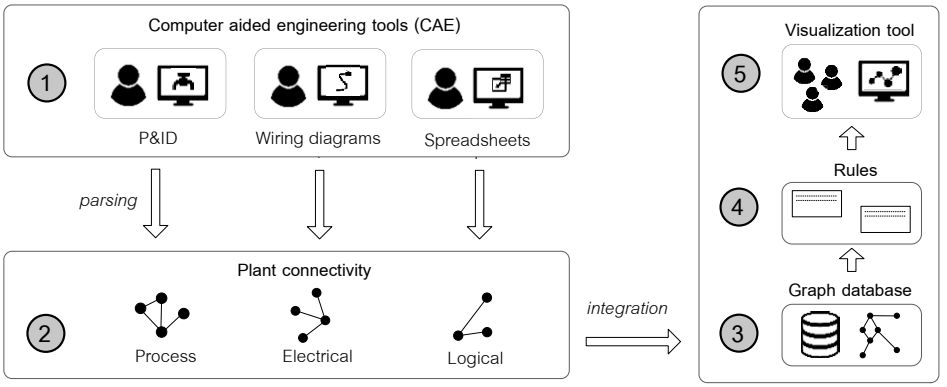

Figure 2. Proposed methodology for integrating and visualising plant connectivity information

Graph databases present an advantage against relational databases (based on tables) because they fit better for exploring data structured as a node-link or tree diagram when relations between elements are significant, and methods for searching and queries require less computational effort. Figure 3 shows an example of the information that can be contained as properties of every node in the network, as well as the source where this information is originated. A property-graph visualisation has the advantage that it can show more information than the tag-number (for example the type of element, location, or subsystem) as well as providing weights and properties in the links between units. Moreover, the graph can be traversed based on the properties attached to nodes and edges.

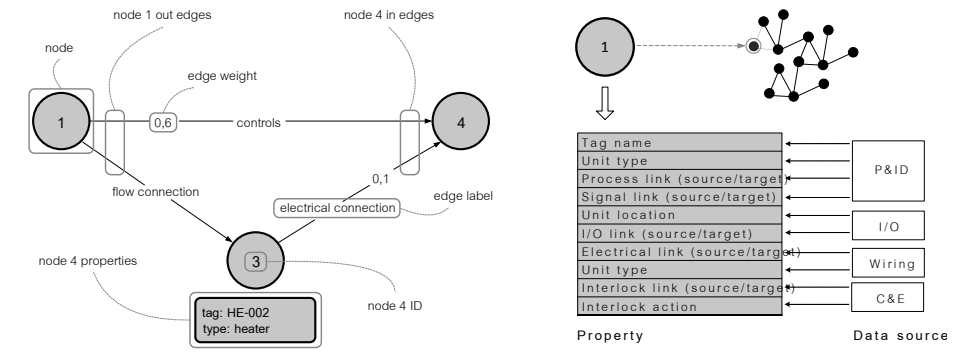

Figure 3. (Right) Main elements of a property-graph. (Left) Example properties from a node.

A ranked shortest path algorithm is use to find feasible propagation paths exploring the graph structure. The aim is to find all paths from element to element along physical, electrical and information flows. The reason for computing multiple propagation paths is because, when dealing with large networks, it is likely that more than one path between two nodes is found, and it is crucial to have them compared in the event of additional constrains. The *K*-shortest path is a generalisation of the shortest path algorithm and was proposed by Hoffman and Pavley (Hoffman and Pavley, 1959). This algorithm not only delivers the shortest path, but also *K* other paths sorted by cost. The use of the Hoffman-Pavley algorithm helps to fulfil the goals by providing all feasible propagation paths that meet the user defined criteria, and the results are sorted as well. Based on that, the engineer can compare that with other indicators (measurements, maintenance history, notifications, work order, to mention some of them) and be supported in fault diagnosis.

5. Prototype, case study, and discussion

The graphical user interface (GUI) from Topoviz™ is shown in Figure 4. As visible, the tool is built as a ribbon window with tab navigation to switch between different visualisations and use modes. A top ribbon (*File* | *Topology builder* | *Troubleshooting* | *Connectivity tools* | *Help*) is used for selecting the module to be used between three: (1) builder, (2) troubleshooting mode, and (3) operations mode. In this example, modules one and two are used in order to generate a network visualisation of the integrated plant connectivity (process + electrical + logical). The case study used is a laborary-scaled process rig from Imperial College London. All diagrams were created by following industrial standards. Autodesk Electrical was used for the single-line and cabinet diagrams, and AVEVA P&ID for the "smart P&ID". Likewise, the methodology can be applied using other P&ID design tools able to export of ISO 15926 and AutomationML compliant drawings. Results in Figure 4 present the successful integration of electrical and process connectivity. This represents an important step for plant-wide disturbance analysis when faults originate or are propagated through the electrical system, or when there is a correlation between elements connected to the same I/O unit in the control system. The nodes visible in the graph visualisation represent units parsed from the P&ID and electrical diagrams. Each of these nodes contains properties which are added as other sources of technical documentation are incorporated to the *Topology builder*. Example properties are unit location, type and parent-child relations with other units. The user gets added information about each node by hovering over it. Properties connected to the nodes or edges can be presented in a tooltip (see Figure 4). Furthermore, the user can search and highlight possible propagation paths in the diagram by using the algorithms mentioned in the previous section. The search bar and selectors on the right side of the interface are used to select elements as "from" and "to" nodes in the graph and then calculate the *k*-shortest paths. The nature of property-graphs allows the system to filter and classify the connections by type (pipe/wire/signal) and to achieve navigation between connectivy informtation from different domains. Finally, the proposed integrated graph stores relevant information into the nodes in the graph, which lowers the computational effor required when performing searches. The concept can be expanded by adding process knowledge and data coming from results of data-driven methods.

Acknowledgements

The authors would like to thank the financial support from the Marie Curie FP7-ITN project 'Energy savings from smart operation of electrical, process and mechanical equipment– ENERGY-SMARTOPS', Contract No: PITN-GA-2010-264940.

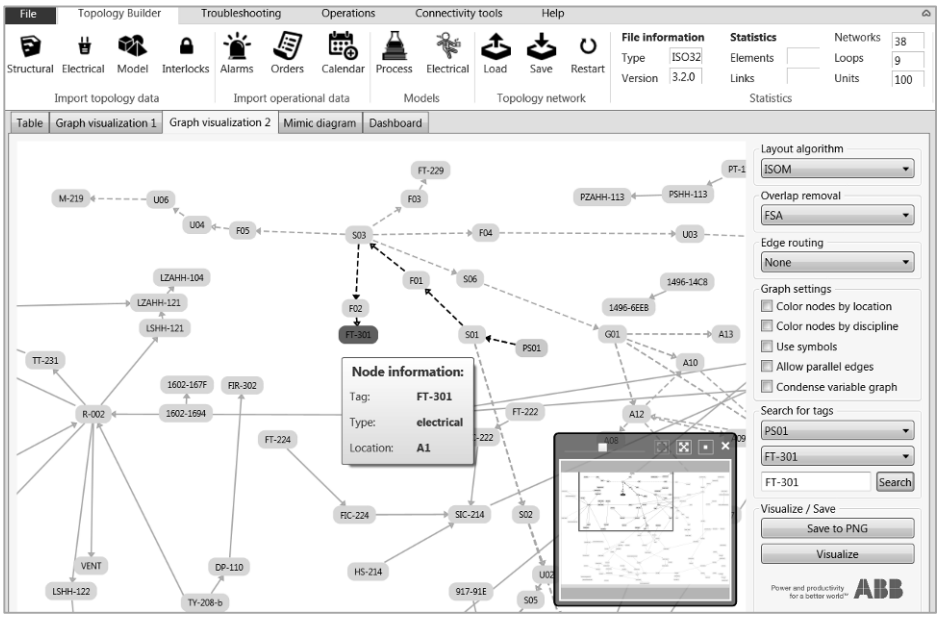

Figure 4. Topoviz™ interface showing a graph visualisation of the integrated plant connectivity

References

W. Birk, A. Johansson, M. Castano, 2010. Interactive modeling and visualisation of complex processes in pulp and paper making, in: Control Systems. Stockholm, 15-17 September 2010.

P.T. Bullemer, I. Nimmo, 1994. Understanding and supporting abnormal situation management in industrial process control environments: a new approach to training, in: Systems, Man, and Cybernetics, 1994. Humans, Information and Technology., 1994 IEEE International Conference on. pp. 391–396 vol.1.

I.M. Cecilio, J.R. Ottewill, J. Pretlove, N.F. Thornhill, 2014. Nearest neighbors method for detecting transient disturbances in process and electromechanical systems. J. Process Control 24, 1382–1393.

L. Cui, J. Zhao, R. Zhang, 2010. The integration of HAZOP expert system and piping and instrumentation diagrams. Process Saf. Environ. Prot. 88, 327–334.

G.J. Di Geronimo Gil, D.B. Alabi, O.E. Iyun, N.F. Thornhill, 2011. Merging process models and plant topology, in: 4th International Symposium on Advanced Control of Industrial Processes. Hangzhou,China, 23-26 May 2011.

W. Hoffman, R. Pavley, 1959. A method for the solution of the nth best path problem. J. ACM 6, 506–514.

M.R. Maurya, R. Rengaswamy, V. Venkatasubramanian, 2003. A systematic framework for the development and analysis of signed digraphs for chemical processes: 1. Algorithms and analysis. Ind. Eng. Chem. Res. 42, 4789–4810.

R. Mordinyi, T. Moser, D. Winkler, S. Biffl, 2012. Navigating between tools in heterogeneous automation systems engineering landscapes. IECON 2012 - 38th Annu. Conf. IEEE Ind. Electron. Soc. 6178–6184.

D.D. Romero, T.G. Graven, 2013. Visual representation of connectivity information for efficient system understanding, in: Proceedings of the Human Factors and Ergonomics Society Annual Meeting. San Diego, USA.

M. Schleburg, L. Christiansen, N.F. Thornhill, A. Fay, 2013. A combined analysis of plant connectivity and alarm logs to reduce the number of alerts in an automation system. J. Process Control 23, 839–851.

F. Yang, P. Duan, S.L. Shah, T. Chen, 2014. Capturing connectivity and causality in complex industrial processes. Springer.

Krist V. Gernaey, Jakob K. Huusom and Rafiqul Gani (Eds.), 12th International Symposium on Process Systems Engineering and 25th European Symposium on Computer Aided Process Engineering.
31 May – 4 June 2015, Copenhagen, Denmark

An Interactive Framework for Building and Analysing Models of Urban Energy Systems

K. Kuriyan[a]*

[a]*Department of Chemical Engineering, Imperial College, London SW7 2AZ, UK*
k.kuriyan@imperial.ac.uk

Abstract

This paper describes a software framework for building and analysing models of urban energy systems. The framework consists of a technology database and components for model assembly and networking coupled with a graphical user interface. The technology database, which is implemented as a Protégé ontology, describes the available energy conversion, storage and transportation processes. The spatial framework for the model is defined by a cityspace object. Distributed energy demands are specified within this cityspace, and it also identifies potential locations for energy conversion processes and links for resource flows across infrastructure networks. The user interface instantiates and assembles framework objects into an overall object model of the system. The assembled object model can be used to define optimization scenarios for the design of urban energy systems with specific goals and constraints such as minimising investment costs while meeting emission targets. These scenarios can be submitted across a network to a solver on a remote host to obtain an optimal design of the urban energy system. The results are displayed by the user interface at two levels: an aggregate level with key performance indicators and graphical analysis for the city as a whole, and a detailed level showing information about individual cells and flows between cells. The interface also provides charts and summaries for comparing alternative scenarios with variations in emission targets, cost parameters and available technologies.

Keywords: urban energy systems, modelling framework, user interface, optimization.

1. Introduction

UN population estimates show that 54% of the world's population now lives in urban areas and the urbanisation of the world population is projected to rise to 66% by 2050 (UN DESA, 2014). Global energy assessments show that between 56-78% of final energy usage is urban (GEA, 2012). An understanding of urban energy systems is critical to meeting energy sustainability challenges. For the purpose of this paper an urban energy system is defined as 'a formal system that represents the combined processes of acquiring and using energy to satisfy the energy service demands of a given urban area' (Keirstead et al., 2012). The system envelope may include both ex-urban processes for resource extraction, energy generation and transportation, with the associated costs and greenhouse gas emissions, and also potential processes for in-city energy generation and conversion. Models can improve our understanding of urban energy use, and can be used to analyse policy initiatives and infrastructure investments (Morlet and Keirstead, 2013). This paper describes a modelling framework and interactive tool that can be used to build and analyse such models.

2. Modelling framework

2.1. Integrated model

Modelling urban systems involves the analysis of the interactions between several sub-systems. Decomposition of the model into sub-systems is used to make the analysis of the overall system tractable, and also to allow the use of modelling formalisms suited to particular sub-systems. Gray et al. (2012) identify potential "axes of decomposition" for complex systems: functional decomposition along discipline boundaries (e.g. economics, engineering and sociology), control decomposition reflecting boundaries in organizational control (e.g. independent energy production companies, energy consumers and network operators), decomposition in time and space, and decomposition by modelling formalism (e.g. agent models and system dynamics models). Prototype models for land use, activity analysis and resource flow optimization have been developed. The models can be used independently to model specific sub-systems or connected together to form an integrated model of the urban energy system.

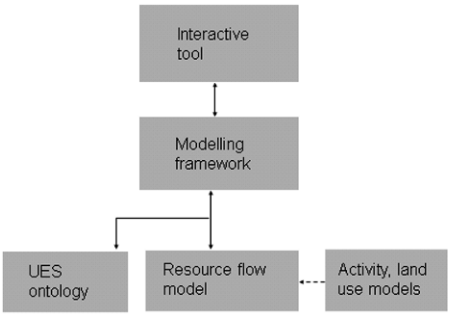

Figure 1 Architecture for modelling framework and tool.

The first component is a land use model which determines an energy efficient spatial layout of the city. The model is posed as an optimization problem to determine the locations of buildings and spaces in which activities are performed and the transportation networks that connect them. Mathematical models for this type of optimization problem are described by Keirstead and Shah (2011). The second component models the behavior of citizens and businesses to determine a spatially distributed pattern of energy demands. Agent-based micro-simulation models for this purpose are described by Keirstead and Sivakumar (2012). The third component is a "resource flow" model which gives the optimal energy strategy for a given pattern of demands calculated from the agent activity model and the set of available conversion and transportation processes. A model based on a hierarchical non-uniform discretization of time can be formulated as a mixed integer optimization problem that is solved to determine an optimal (low cost or low emissions) network of resource conversion, storage and transportation processes which can meet the specified demands while satisfying additional constraints such as carbon emission targets (Samsatli and Jennings, 2013). A simplified model, suitable for cases where a single temporal level is sufficient (e.g. Morlet and Keirstead, 2013), is used in this paper.

Analysis and synthesis of complex systems require an architecture that spans different "views" of the system (Rouse, 2003) exemplified by the three component models. The modelling framework defines abstract model classes that can be extended to implement specific model types. Figure 2 shows how a resource flow model can be implemented as

an extension of an abstract optimization model. A prototype application integrating the use of all three components is described by Keirstead et al., 2009. This paper describes current work on an interactive tool that incorporates a standalone resource flow model.

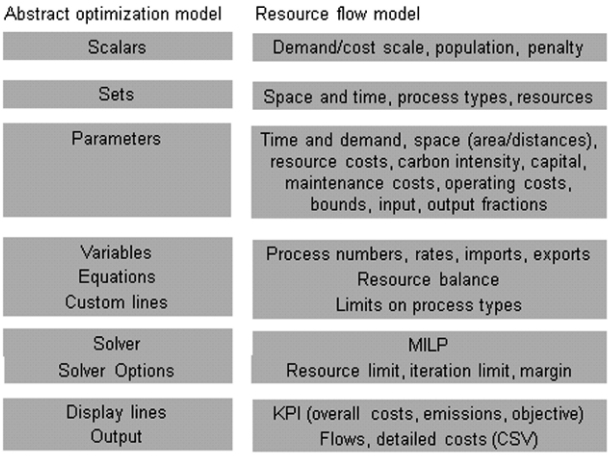

Figure 2 Structure of abstract optimization model and resource flow model objects.

2.2. Urban energy systems ontology.

At the core of the modelling framework is an ontology for urban energy systems (Keirstead and van Dam, 2010). Ontologies can be used to share a common understanding of the structure of information in a domain, to make assumptions explicit and to enable reuse of domain knowledge (Noy and McGuiness, 2001). The urban energy systems ontology is implemented within Protégé Frames (SCBIR, 2009) and fills several roles in the modelling framework. The first is to act as a database for storing the technological and cost parameters of urban energy system objects. The second is to provide consistent class definitions that can be used to transfer information from one model to another. The third is to provide a classification scheme for differentiating between storage, transportation and conversion processes, and also to define sub-classes of these primary classes. This classification is used while specifying attributes of modelling framework objects (e.g. a transportation process requires the use of an infrastructure network) and also in defining menus for technology selection within the user interface.

2.3. Technological framework

The main classes within the ontology are resources, infrastructure and processes. Resources represent both primary resources, such as natural gas, and final resources, such as electricity and heat, that can be used to satisfy the energy demands within a city. Infrastructure classes represent the physical infrastructure of the city such as buildings, roads and energy transport networks including gas pipelines, electricity supply lines and district heating networks. Processes can convert one resource into another, transport a resource from one location to another, provide temporary storage for a resource, or simply act as a sink for disposal of waste resources (e.g. CO_2 or waste heat). This framework is compatible with the construction of State Task Network representations of resource flows in urban energy systems. Resources can be represented as states, while the different types of processes are represented as tasks (Samsatli and Jennings, 2013).

As an example, a CHP unit can consume natural gas to generate district heating and electricity resources which are transported to other locations. The district heating resource can be used to satisfy heat demands in a building by passing it through heat exchangers. The electricity resource can be used to satisfy the electrical demands of households and businesses.

2.4. Spatial and temporal framework

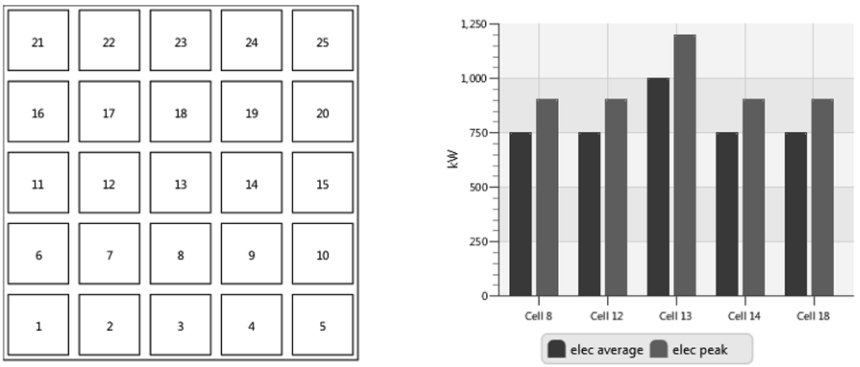

Figure 3 Cityspace with uniform grid and spatially and temporally discretized demands.

Models of urban energy systems require a spatial and temporal framework that reflects the characteristics of urban systems. The modelling framework employs a cityspace object which divides the city into a discrete grid representing possible locations for energy conversion technologies. Edges between neighboring cells represent potential network links for transporting resources. Energy demands are discretised across the cityspace and a set of demand periods representing temporal variations in energy requirements. The demands are specified with a flexible discretization at a single temporal scale consisting of one or more weighted periods (e.g. peak and average daily demands). The weights represent the relative lengths of demand periods, and are used to calculate performance metrics based on annual resource production and usage. Figure 3 shows a cityspace with a uniform grid and the corresponding peak and average electricity demands for the central cells as they appear within the user interface. In general, the cityspace grid cells can be given non-uniform locations and sizes, corresponding, for example, to administrative divisions within a city.

3. Interactive scenario construction and analysis

Typical usage of an urban energy system model involves comparison of scenarios with variations in optimization targets and cost parameters reflecting policy goals and incentives (e.g. Morlet and Keirstead, 2013). A base scenario may be constructed using technologies currently installed within the city for comparison with a future scenario with an emission target that requires the use of a mix of renewables. The interactive tool provides a graphical interface for the construction, execution and analysis of optimization model scenarios. The default costs and technological parameters (e.g. operating rates and resource requirements) for technologies selected by the user are retrieved from the ontology and displayed within the user interface. The parameters can be customized to construct a scenario that reflects local factors and incentives. The

cityspace grid and energy demands are defined in user supplied data files. An overall object model of the city is built by combining the information from the ontology with the scenario parameters and cityspace definition. An algebraic representation of the resource flow model is then assembled and optimized on a remote host on which an appropriate solver has been installed. After an optimized solution has been found the model results are written in output files which are retrieved and stored locally.

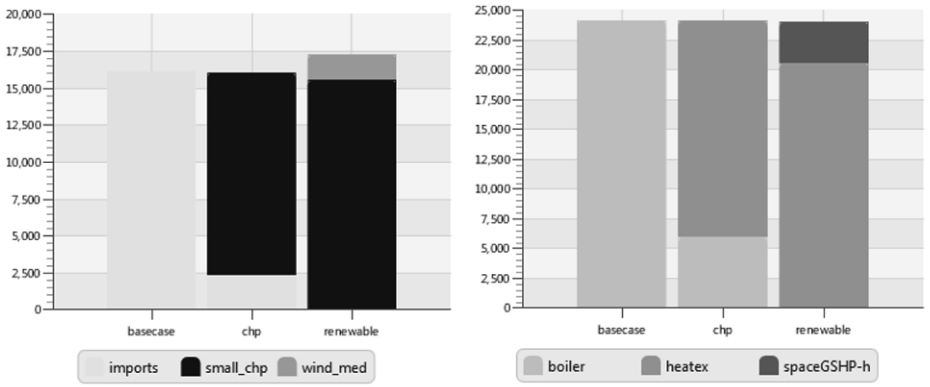

Figure 4 Sources for supply of peak electricity and heat demands (kW).

As an example, three scenarios (basecase, chp, renewable) are constructed for the urban system shown in Figure 3. The objective is cost minimization in all three cases. The basecase scenario does not consider in-city generation of heat and electricity. The chp scenario allows the use of combined heat and power (CHP) generation units to provide district heating and electricity within the city. The renewable scenario imposes an emissions target, includes wind power and solar photovoltaic panels for electricity generation, and ground source heat pumps for heating.

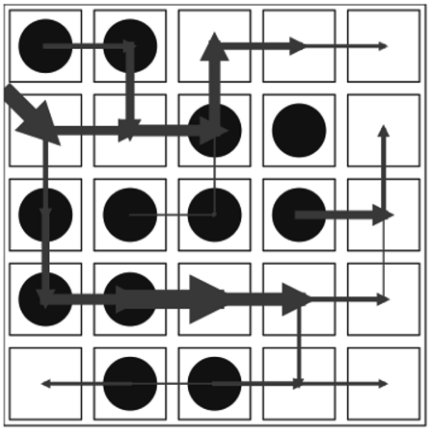

Figure 5 Peak electricity imports, flows and process locations for chp scenario.

Resource supply charts in the user interface show the sources used to satisfy energy demands in the optimized solutions to the three scenarios (Figure 4). In the basecase scenario electricity demands are satisfied entirely by imports, whereas in the chp scenario electricity imports are used only in the peak demand period with CHP units

supplying the rest of the electricity demand. In the renewable scenario, the emissions target is met by eliminating electricity imports and reducing gas consumption through a combination of wind power and ground source heat pumps. The interface has similar charts for resource usage by different technologies, capital cost breakdowns for conversion and transportation processes, costs and emissions associated with resource imports. Detailed results showing process locations, resource imports and flows are drawn as overlays on the cityspace grid (Figure 5).

4. Conclusions

This paper describes a framework of software components for data access, model assembly and remote job submission combined with a graphical user interface. The modelling framework and interactive tool can be used to build optimization scenarios for urban energy systems. The scenarios can be refined by the specification of custom constraints and technology selections. The scenarios can then be solved to determine the optimal energy system design to achieve policy objectives such as carbon emission targets.

References

GEA, 2012, Urban Energy Systems, in Global Energy Assessment: Towards a Sustainable Future, International Institute for Applied Systems Analysis, Laxenburg, Austria and Cambridge University Press, Cambridge, UK.

G. A. Gray, W. E. Hart, P. D. Hough, H. K.H. Lee, O. D. Parekh, C. A. Phillips, J. D. Siirola, L. P. Swiler, J.-P. Watson, D. L. Woodruff, 2012, Optimization of Large-Scale Heterogeneous System-of-Systems Models, Sandia National Laboratories, Albuquerque, New Mexico.

J. Keirstead, N. Samsatli, N. Shah, 2009. SynCity: An Integrated Tool Kit for Urban Energy Systems Modelling, in Proceedings of the 5th Urban Research Symposium, Marseille.

J. Keirstead, N. Shah, 2011, Calculating Minimum Energy Urban Layouts with Mathematical Programming and Monte Carlo Analysis Techniques, Computers, Environment and Urban Systems, 35, 368-377.

J. Keirstead, A. Sivakumar, 2012, Using Activity Based Modeling to Simulate Urban Resource Demands at High Spatial and Temporal Resolutions, Journal of Industrial Ecology, 16, 6, 889-900.

J. Keirstead, M. Jennings, A. Sivakumar, 2012, A Review of Urban Energy System Models: Approaches, Challenges and Opportunities, Renewable and Sustainable Energy Reviews, 16, 6, 3847–3866

J. Keirstead, K. H. van Dam, 2010, A Comparison of Two Ontologies for Agent-Based Modelling of Energy Systems, in Proceedings of the First International Workshop on Agent Technologies for Energy Systems (ATES 2010), 21-28.

C. Morlet, J. Keirstead, 2013, A Comparative Analysis of Urban Energy Governance in Four European Cities, Energy Policy, 61, 852-863.

N. F. Noy, D. L. McGuinness, 2001, Ontology Development 101: A Guide to Creating Your First Ontology, Stanford Knowledge Systems Laboratory Technical Report KSL-01-05 and Stanford Medical Informatics Technical Report SMI-2001-0880, Stanford, California.

W. B. Rouse, 2003, Engineering Complex Systems: Implications for Research in Systems Engineering, IEEE Transactions on Systems, Man, and Cybernetics, Part C: Applications and Reviews, 33, 2, 154-156.

N. Samsatli, M. G. Jennings, 2013, Optimisation and Systems Integration, in J. Keirstead, N. Shah (eds.), Urban Energy Systems – An Integrated Approach, Routledge, Oxford, UK.

SCBIR, 2009, Protégé Frames, http://protege.stanford.edu, Stanford Center for Biomedical Informatics Research, Stanford, California.

UN DESA, 2014, World Urbanization Prospects: The 2014 Revision Highlights, United Nations Department of Economic and Social Affairs, New York.

Krist V. Gernaey, Jakob K. Huusom and Rafiqul Gani (Eds.), 12th International Symposium on Process Systems Engineering and 25th European Symposium on Computer Aided Process Engineering. 31 May – 4 June 2015, Copenhagen, Denmark

Model-based Analysis of Waste Management Systems through a Natural Language Approach

Vassilis Magioglou,[a] Elisabet Capon Garcia,[b] Sara Badr,[b] Antonis Kokossis[a]

[a]*Department of Chemical Engineering, National Technical University of Athens, Athens, Greece*
[b]*Department of Chemistry and Applied Biosciences, ETH Zürich, 8093 Zürich, Switzerland*

Abstract

Waste management systems are complex interactive networks of data, knowledge and models comprising multiple parameters. In these systems the technologies and their models interact with each other in order to fully describe the problem. Inputs and outputs of the models intersect depending on the various parameters. These parameters, such as composition, pH, temperature etc., need to be computed simultaneously in order to select the appropriate processing path prior to model development. Therefore, the the selected path and the waste stream characteristics determine the context of the model. Waste management systems involve non-experts in decisions that require expertise from many disciplines. The need to synthesize the multidisciplinary domains of waste, integrate the knowledge and express them with common natural language terms is outlined by this work. The work builds on recent technology that was produced to synthesize superstructures for integrated biorefineries (Magioglou et al. 2014), which now extends to decision-making and allocation problems for waste management systems. The approach employs ontologies, Java language, OpenBabel library and suggests a natural language framework. Illustrations include an industrial wastewater treatment system of the chemical sector which evaluates the environmental impacts. The framework successfully synthesizes the network and allocates the waste, technologies, streams and auxiliaries along with their parameters.

Keywords: Waste management, ontologies, modelling, automation, waste water,

1. Introduction

Over 4 billion tonnes of waste are generated each year in the 34 countries members of OECD. The environmentally sound and economically efficient management of this waste has to be ensured (OECD, 2013). Waste management systems are complex systems that require multi-objective decision analysis in order to provide a complete and exploitable result. The multi-disciplinary knowledge required to design a management system keeps experts from focusing on integrated models development. These systems involve allocation and planning problems. Experts develop models focused on specific processes, ignoring their broader role in the system and the interaction with other technologies. The study of a single model is not sufficient in a holistic systems analysis. The integration of the relationships between materials, processes and models is examined in this work.

In a waste management system several technologies are involved, thus different levels of decision-making. The technologies are not isolated and interact with each other. The experts develop models individually for each technology. Streams come in and out of the technologies selectively. Each waste stream is required to follow a different treatment and processing path depending on the various parameters values. After each processing step, the output has altered characteristics, which require further analysis to determine the following step (e.g. following model). The interaction of the models in a waste management system is required to provide a complete and accurate overview of the systems functionality and operation.

This work proposes a systematic framework that could be managed by the use of vocabularies and semantic references. Ontologies and Java are employed to establish the models input-output relationships and to further contribute to decision-making based on various quantitative and qualitative criteria. Natural language processing of models is established to facilitate handling and decision-making (Magioglou et al. 2014). Libraries, namely OpenBabel, are applied to further automate various procedures involved in the systems analysis. Promoting waste management systems to automated intelligent systems through ontologies shows great potential in the usability and efficiency. Illustrations of the current approach include an industrial wastewater treatment system of the chemical sector which evaluates the environmental impacts (Koehler et al. 2007). The models describing the system calculate life-cycle inventory parameters as a function of the wastewater composition and the applied technologies. A framework has been designed to develop, visualize the system and enable its semantic use.

2. Methodology

The approach employs system steps to automate the path selection and model development in a waste management system. The methodology is laid out in 4 steps: (1) synthesis stage, (2) nodes development and analysis, (3) semantic models and (4) numerical models development.

2.1. Synthesis and classification

A waste management system is an interactive network of wastes, streams, technologies, pre-treatments, auxiliaries and emissions. These blocks build connections to each other selectively to synthesize the network. The main blocks synthesizing the waste management system are organized and the appropriate connections are established based on their nature and attributes. The main blocks are:

• Waste: waste is the initial stream derived from production facilities and has a defined composition. The characteristics of the waste determine the waste management system to be invoked to provide the desired outcome of the user.

• Streams: the waste streams are input and output of (i) processes, (ii) pre-treatments and (iii) mixing points. Input streams are defined as the streams entering a process, pre-treatment or mixing point. Therefore, output streams are the outcome of a process and have altered characteristics compared to the corresponding input streams. The changes in the stream influence the targeting block to follow, as well as the system itself. Each stream is described by various parameters which determine the potential input.

• Processes: streams head to processes to produce streams with different attributes. The processes operate under certain conditions, with certain wastes within a specific parameters range. A stream is valid to enter the process if the criteria (qualitative and quantitative parameters) defined by the process are satisfied.

• Pre-treatments: pre-treatments are similar to processes. They come before processes and their operation is optional. Depending on the stream characteristics a pre-treatment (e.g. pH adjustment) might be required to make the stream valid for further processing.

The categorized blocks establish connections to each other through the blocks of processes/pre-treatments. The combination of the possible connections results in a complete superstructure representing the waste management system. Secondary blocks (Energy, Emissions, Auxiliaries) are also deployed in the system. The main blocks and connections are demonstrated in Figure 1. The system is not considered as a block itself but it is indirectly related to the process itself.

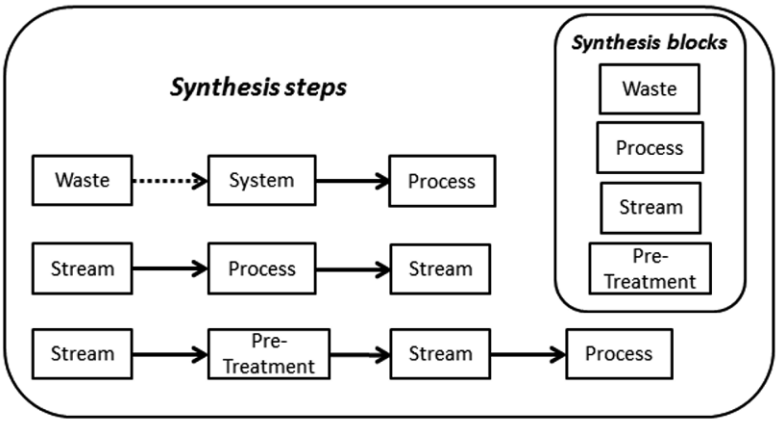

Figure 1. Synthesis procedure for waste management systems

2.2. Nodes development and analysis

Besides one-to-one connections established blocks might develop more complex connections. One-to-many, many-to-one, many-to-many relationships are common in complex networks such as waste management systems. These relationships create decision-making nodes in the network which determine the processing paths of the waste. The nodes increase the number of possible destinations and scenarios in a network. They can either be limited (all outputs of the node must exist) or conditional (not all possible outputs are required in the system). The challenge lies in conditional nodes, where the outputs are not static and logical processing is required. The different types of nodes in a waste management system are shown in Figure 2. The nodes outcome is influenced by quantitative (e.g. pH, waste composition, temperature, cost, water proportion, emissions etc.) and qualitative parameters (e.g. availability of technology, connections, auxiliaries, waste nature and acidity etc.). The selection of the viable but also optimal path depends on multiple interacting parameters. The user may not have adequate knowledge of the required parameters. Therefore, automation is required based on natural language to facilitate and increase the efficiency of the path selection. To establish automation the waste management system needs to be analysed, nodes identified and the respective parameters registered. The conditional nodes define decision-making steps of the system. The data describing the input block of the node will define the output. Hence, the data require an organised flexible structure, which will handle all the possibilities of a node.

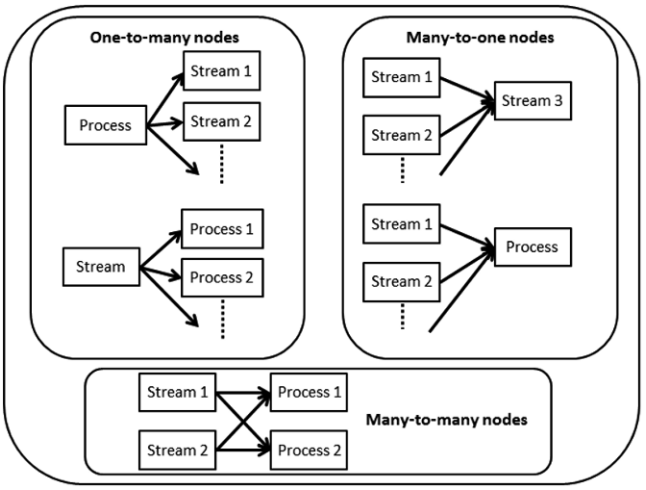

Figure 2. Nodes in waste management systems

2.3. Ontology Engineering

Ontologies are employed to (i) organise the blocks, (ii) establish the connections, (iii) automate path selection and determine the output of nodes, (iv) identify pre-treatments necessity. The blocks synthesizing the system are organised in ontology classes (Waste, Streams, Processes, Auxiliaries, Energy, Emissions, Pretreatments). The connections between blocks are represented by object-type properties. Simple "in" and "out" properties express the inputs and outputs among the blocks of Waste, Streams, Processes and Pretreatments. The class Streams incorporates the different streams coming in and out of processes/pre-treatments and the respective parameters. The classes Auxiliaries and Energy are used to represent the requirements of processes and pre-treatments, whereas Emissions state the emissions type and impact in each process. In addition, data-type properties are assigned, defining values, range of values for different parameters and qualitative statements (e.g. auxiliaries requirements, pH range, acidity, adjustment necessity, composition, units etc.). For example, a process might only be able (or more efficient) to accept acid waste streams with water composition below 40%. The data-type properties are then queried and compared to the conditions of the problem declared by the end-user to provide an accurate and logical output. The connections between the blocks/classes are filtered by the data-type properties leading to different superstructures, thus altered representations of the management system. Additionally, the data-type properties assigned to each of the connected concepts are queried and compared to the input data, to determine whether pre-treatment is required prior to a process, as well as the type and amount of respective auxiliaries. The ontology schema to describe the waste management system is illustrated in Figure 3. The concepts of the ontology have values and qualitative data attached. The data serve as comparing criteria for the nodes and path selection. When the system analysis reaches a node, the ontology is invoked to figure out the optimal processing path the waste stream should follow next. The data-type properties determine the necessity of a pre-treament by checking the boolean property if available ("requirespretreat" or "adjustment"). In case qualitative estimation is not possible, default values or ranges assigned in the ontology are compared to the input of the problem. The data-type properties shown in Figure 3 can vary depending on the decision-making criteria, the availability of data and needs of the examined system.

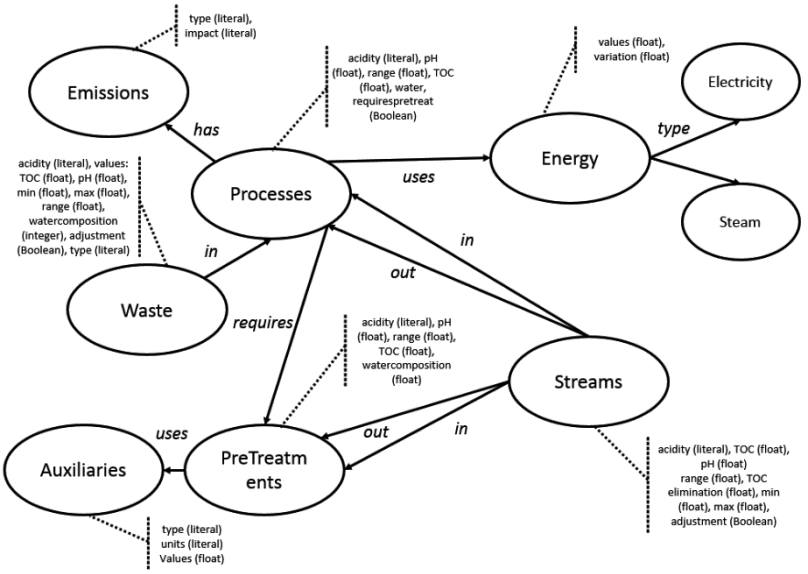

Figure 3. Ontology representation of a waste management system. Arrows show object-type arrows. Dashed lines show data-type properties and their range.

2.4. Models development and deployment

Each process in a waste management system is described by a numerical model for optimization or simulation. Models consist of a core matrix and a case dependent part, where the former is defined by the type of the application, whereas the second depends on the particular case study. Also in a system, the various processes interact with each other, therefore the models are not independent. The output of a specific model could serve as input for the linked process and respective model. For a waste management system in order to be accurate and holistic, the process and model interaction requires integration. The approach relates the problem description to ontology concepts, and then to model concepts. Models input-output relationships and context are deterermined by the ontology resulting in the automation of the models development. This is achieved with the aid of Java language to invoke and link models as well as to handle the transfer of data between ontology and models. SPARQL querying algorithms run at each conditional node to compare the data entered by user and the ontology concepts to determine the optimal problem solution. A different algorithm is also invoked for input stream of a process to compare the stream characteristics with the processing parameters (data-type properties) to determine whether a pre-treatment is required and the respective amounts of auxiliaries. Simultaneously, when interaction between technology models is required the established framework builds models based on prototypes and formats and transfers the data needed. This is achieved by interfering with the models APIs and the deployment of various matching, parsing, writing functions of Java.

3. Illustration

The methodology presented is applied to a wastewater treatment system. The models calculate life-cycle inventory parameters as a function of the waste-water composition and the technologies applied. The established framework develops the system with automated bespoken path selection depending on the composition, water proportion, TOC (Total Organic Carbon), TOC elimination, pH of the initial waste stream. In the

specific waste system analysis, the models require modifications when pH adjustment is needed prior to a process. The framework identifies the acidity of the stream, the technologies that require adjustment and executes the computations to retrieve the type and quantities of the related auxiliaries. MATLAB models that assess environmental impact are invoked and edited accordingly in an automated way. OpenBabel library is used to calculate the atomic composition from the molecules in the waste (SMILES format). Other factors such as density or flowrate are requested to satisfy the specific models needs. In Figure 4 a simple interface for the designed system and a solution of an example for some random values are illustrated.

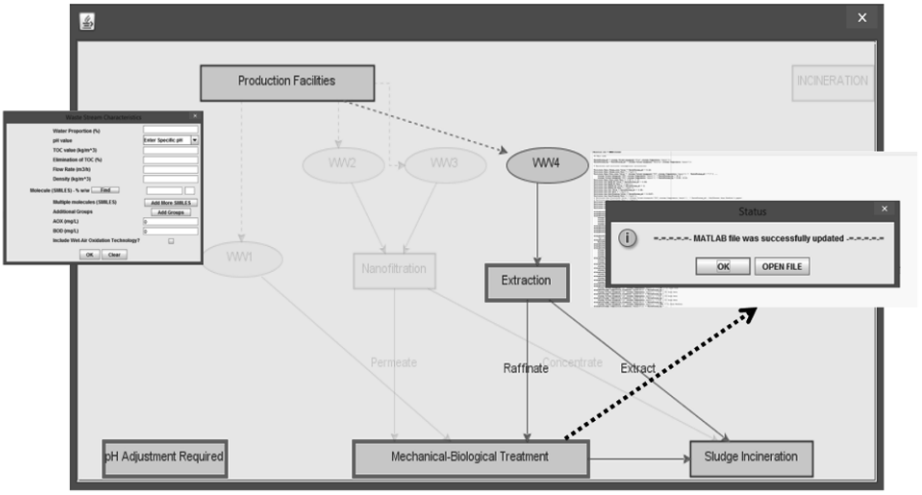

Figure 4. Interface developed for the waste water treatment system

4. Conclusions

The complexity of waste management systems requires a holistic approach that integrates data and models. The paper introduces the use of ontologies to build an intelligent waste management system to handle the multi-objective analysis. Automation through natural language is applied for wider and easier access among the experts. Examination and analysis of the system at a bigger scale provides more explicit and exploitable solutions. The importance of integrating the models interaction in the system is also outlined. Future challenges lie in increasing the involved parameters and complexity of the system, and the inclusion of additional treatment systems.

References

OECD, 2013, The Organization for Economic Co-operation and Development, Work on Sustainable Materials & Waste Management, 1.

V. Magioglou, M. Tsakalova, A. Kokossis, 2014, Natural Language Modelling in Process Synthesis and Optimization, Comput. Aided Chem. Eng., 33, 877–882.

A. Köhler, E. Recan, S. Hellweg, and K. Hungerbühler, 2007, Input-Dependent Life-Cycle Inventory Model of Industrial Wastewater-Treatment Processes in the Chemical Sector, Environ. Sci. and Technol., 41,15, 5515–5522.

R. Marshall, K. Farahbakhsh, 2013, Systems approaches to integrated solid waste management in developing countries, Waste Manage., 33, 4, 988–1003.

G. Beydoun, G. Low, F. García-Sánchez, R. Valencia-García, R. Martínez-Béjar, 2014, Identification of ontologies to support information systems development, Inform. Syst., 46, 45–60.

Krist V. Gernaey, Jakob K. Huusom and Rafiqul Gani (Eds.), 12th International Symposium on Process Systems Engineering and 25th European Symposium on Computer Aided Process Engineering.
31 May – 4 June 2015, Copenhagen, Denmark

Enterprise-Wide Scheduling Framework Supported by Knowledge Management

Elisabet Capón-García[a], Edrisi Muñoz[b], José M. Laínez-Aguirre[c], Antonio Espuña[d], Luis Puigjaner[d]

[a] *Department of Chemistry and Applied Biosciences, ETH Zürich, 8093 Zürich, Switzerland*
[b] *Centro de Investigación en Matemáticas A.C., Jalisco S/N, Mineral y Valenciana 36240, Guanajuato, Mexico*
[c] *Department of Industrial and Systems Engineering, University at Buffalo, Amherst, NY 14260*
[d] *Department of Chemical Engineering, Universitat Politècnica de Catalunya, Av. Diagonal, 647, E08028 Barcelona, Spain*

Abstract

The scheduling function determines the amount of each product to produce, the allocation of equipment and resources to tasks, as well as the sequencing and timing of such tasks, in order to fulfill plan production objectives. A knowledge-based model has been created relying on rigorous analysis of existing process scheduling models. Likewise, a reasoning tool has been developed for matching the system and scheduling task features to previously existing mathematical models. As a result, a model selection can be obtained based on features matching.

Keywords: Scheduling Models; Mathematical Modeling; Knowledge Management.

1. Introduction

The short-term scheduling problem consists of organizing the available human and technological resources in the process plant in order to optimally satisfy customer's demands. Scheduling typically involves decisions on the amount of products to be produced, equipment and resources allocation, production sequence and operations timing, on a weekly or daily basis. A significant amount of models have been proposed in the literature in order to adequately formulate scheduling problems (Floudas & Lin, 2004; Harjunkoski et al, 2014). However, each modeling option can only cope with a subset of the features, and the choice of the mathematical model has an important impact on computational performance. As a result, the model selection and corresponding problem formulation is a formidable task.

From a descriptive perspective, computer science provides with tools for representing the scheduling problem from an abstract conception. For example, artificial intelligence and semantic models, such as ontologies, offer the alternative to represent and share the knowledge of the process and engineering domains. Ontologies are increasingly seen as a key semantic technology for addressing and mitigating the effects of heterogeneities and for enabling semantics-driven knowledge processing. Ontologies are formal structures enabling acquiring, maintaining, accessing, sharing and reusing information (Fensel, 2003).

The goal of this work is to provide a knowledge-based framework capable of determining the best available mathematical models for specific scheduling requirements based on the problem description. Specifically, this work aims to exploit the knowledge found in Operations Research Ontology (Muñoz et al. 2014), by the integration of a decision application and a mathematical scheduling models database. Hence, models capabilities and limitations must be carefully considered for each scheduling problem based on its features and the expected computational performance.
The framework consists of a semantic model based on rigorous analysis of existing process scheduling models. In order to relate the problem features of the real scheduling system to the available mathematical models, a reasoning tool consisting of a decision tree analysis is developed. As a result, the model selection can be automated according to the features matching. Next, the semantic model features and the reasoning tool are described.

2. Scheduling semantic model

The intrinsic complexity of scheduling decision-making has brought forth the development of a wide variety of problem models and solution algorithms. The selection and adoption of a given approach depends on the process plant features and the problem definition and size, among other features. In fact, there is not a unique optimal approach to solve all scheduling problems, and it is highly unlikely to find a universal one at all. Therefore, the main aim of this section is to describe the current scheduling modeling and the developed semantic model.
The starting point when posing a scheduling model consists of defining the problem features, namely the objectives pursued by the scheduling function, the decisions to be made, and finally the elements which represent the system and describe its behavior. Scheduling is the process of arranging, controlling and optimizing work and workloads in a production process. Production scheduling aims to maximize the efficiency of the operation and reduce costs, and backward and forward scheduling are applied to allocate plant and machinery resources, plan human resources, plan production processes and purchase materials.
Scheduling objectives. The objective function measures the quality of the decisions to be made. The objectives traditionally considered in scheduling problems are time related, such as the total completion time or makespan, lateness, tardiness and earliness. However, decisions in chemical industry are usually driven by profitability criteria. Hence, it is necessary to adequately quantify economic criteria in order to reach a high quality decision from an integrative perspective. Therefore, global metrics such as profit, cost or profitability itself should be considered.
Scheduling decisions. The decisions involved in the scheduling function vary according to the plant management needs and depend on the problem features. Anyways, such decisions are highly connected to each other, and to other decision levels, for instance to planning for demand issues or to control for actual processing times. In general, decisions within the scheduling level can be broadly classified in four types:

- Batching. It consists of deciding on the number and size of the lots of products that are to be produced. Therefore, these decisions are directly related to the mass balances and storage management, and so to the planning level.
- Allocation. It involves the assignment along time of tasks to equipment units and other plant resources, such as manpower, electricity and water, according to their availability. Resources are usually finite and product specific, and they may be reusable or not.

- Sequencing. It determines the order in which batches of the different products are to be produced in the different equipment units along the process plant.
- Timing. It concludes the initial and final times at which batches are to be performed. Such decisions highly depend on the process features. Therefore, according to existing intermediate storage policies and the relationship between tasks, production timing may be differently performed inside the whole production time horizon. A key point in batch scheduling consists of the time representation, which depends on whether actions may take place at any time or at some predefined time points. Since actual processing times depend on process conditions, which may be influenced by external disturbances, actual timing decisions may be highly changed from the initial estimation.

Scheduling constraints. Production process features and process plant environment determine the formulation of the scheduling problem. The most fundamental element describing the production process is the product recipe, which contains the information about the amount of raw materials as well as the processing steps with their conditions, such as temperature or pressure, and the times over which they take place. Even though product recipes are usually determined and fixed in the design step, they can potentially introduce flexibility in the scheduling problem, if variable process conditions are allowed.

Depending on the equipment configuration of the plant, the number of batches that can be processed simultaneously varies. In multiproduct batch plants, the final products have an identical recipe structure. Therefore, all products require all steps in the process and follow the same sequence of operations. In contrast, in multipurpose batch plants, the production steps are not the same for all products. Such plants are more flexible and effective for a large number of products produced in small volumes, since equipment items can be fully utilized and vessels cleaned easily.

According to the perishable features of the intermediate products, alternative storage policies can be adopted, namely a zero-wait transfer, a no intermediate storage (if intermediates can be hold up in the equipment), a finite intermediate storage, which may be shared or exclusive, or an unlimited intermediate storage policy. Thus, equipment cleaning and material transfer are two practical issues that may have a significant effect in the scheduling results because they may cause a reduction in the overall equipment utilization.

2.1. Scheduling problem features

From a global perspective, batch production scheduling aims at optimizing the resource utilization of batch manufacturing facilities in order to fulfill customer orders within a specific time horizon. The building block of batch process scheduling is the process recipe, which contains the whole information required to produce the product, as well as the set of processing tasks, i.e. the process flow. The recipe is usually obtained in a design stage prior to the scheduling stage, and the process conditions to perform the product are optimized and fixed for all production batches of a given product. In addition, such information must be complemented with the production facility data regarding equipment and resources, such as manpower, inventory or general services availability; production planning information regarding sales, time horizon, order due dates or prices; and actual plant state. The complexity and variety of the scheduling problems requires effective organization of the aforementioned information in order to improve communication and process efficiency. Next, the most relevant characteristics of the scheduling problem are: (i) material routing, (ii) operation modes, (iii) equipment

assignment and connectivity, (iv) storage policies, (v) material transfer, (vi) changeovers and set-up operations, (vii) batch size and processing time, (viii) demand pattern, (ix) resource constraints, and (x) time constraints.

2.2. Scheduling models classification

The mathematical models which are more widely applied in the literature are presented in Table 1, which contains the summary of the general characteristics of such models along with the critical problem features. For the sake of brevity, the comparison between the formulations is restricted to the aforementioned table.

3. Classification mechanism of the scheduling semantic model

The semantic model classifies the scheduling domain, according to the features described in the previous section for generally characterizing the system. This characterization defines the elements which determine the behavior of the production system. These features (Figure 1) refer to: (i) product, describes whether there is a single final product or multiple final products with different families; (ii) production capacity, refers to the quantity of product; (iii) the size of the company, characterizes the company in terms of single production site or multiple production sites, human resources and economic flow; (iv) supply features, define the raw material availability and reliability; (v) demand features, describe the volume and variability of the demand; (vi) market competition, characterizes whether there is a high or low number of competitors to satisfy the customers; and (vii) environmental regulations, includes the

Table 1. Classification of scheduling models in the literature

Event representation	Time representation		Type of processes		Critical modelling issues	Critical problem features
	Discrete	Continuous	Network	Sequential		
Global time intervals	✔		✔		Time interval duration; scheduling period	Variable processing times; sequence dependent changeovers
Global time points		✔	✔		Number of time points	Intermediate due dates; raw material supply
Unit specific events		✔	✔		Number of time events	Intermediate due dates; raw material supply
Time slots		✔	✔		Number of time slots	Resource limitations
Unit specific immediate precedence		✔		✔	Number of batch tasks sharing units and resources	Resource limitations and inventory
Immediate precedence		✔		✔	Number of batch tasks sharing units and resources	Resource limitations and inventory
General precedence		✔		✔	Number of batch tasks sharing resources	Inventory

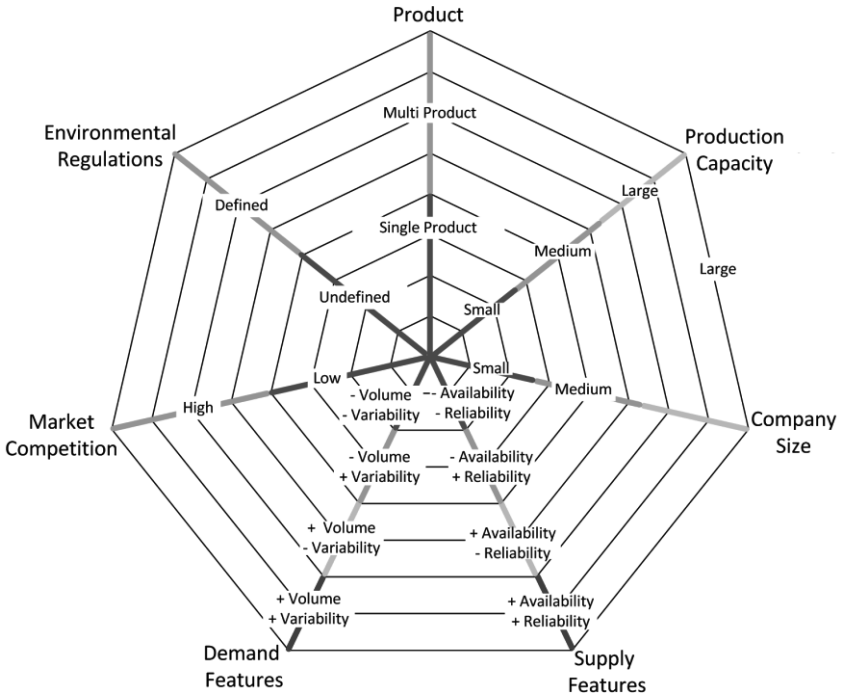

Figure 1. System characterization in terms of the general features

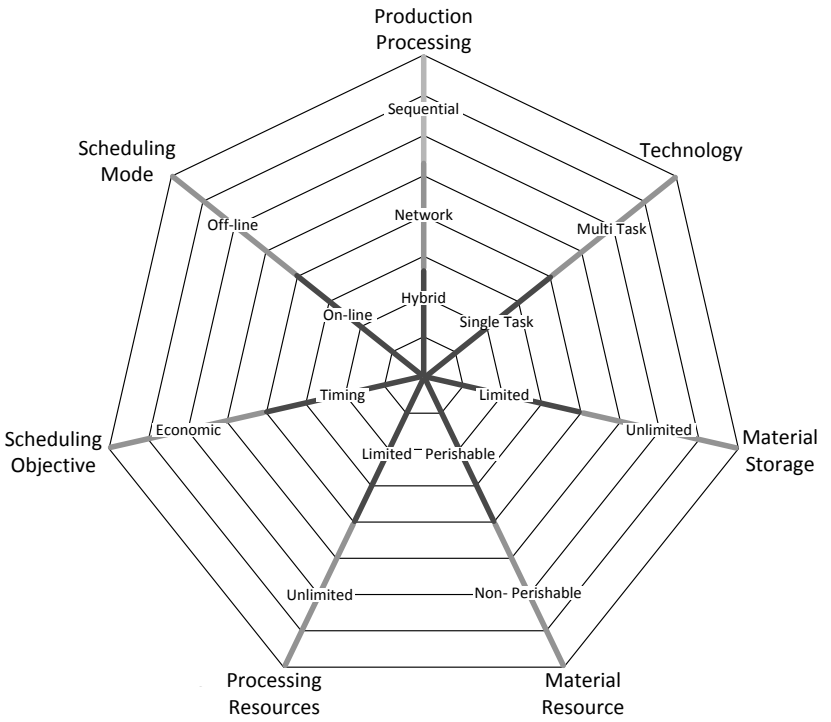

Figure 2. System characterization in terms of the tactical features

limitations or lack of limitations in terms of environmental issues. The tactical features of the scheduling environment are also characterized in the semantic model in terms of the following models (Figure 2): (i) production processing, includes the characterization of the production environment and refers to sequential (single stage, multiple stage, multipurpose), or network (STN, RTN), or hybrid environment; (ii) technology, characterizes the processing units; (iii) material storage, determines the storage (initial, intermediate, final) limitations; (iv) material resource, characterizes whether the resources are constrained in the storage task; (v) processing resources, whether there is a limitation in the resources such as energetic, human, etc.; (vi) scheduling objective, describes the strategy of the scheduling function; (vii), scheduling mode, defines whether the offline mode, that is design, or the online, production plant, mode are pursued. Likewise, the mathematical models have been thoroughly studied and decomposed in terms of their features for understanding which elements take part in the equation models and which features have been included with such models. After this formalization, each model can be characterized from the tactical features to the general features. In order to classify the scheduling problem, we can characterize the system by using the general and tactical features. The reverse path consisting of classifying the process mathematical model can be also addressed from tactical to general features. This matching allows the selection of which model or part of the mathematical model can be reused for formulating a particular production scheduling problem.

4. Conclusions

The developed approach deals with the semantic representation of the process scheduling function. This semantic model relates the problem features with the best mathematical modeling structure given a reasoning stream, consisting of the amount of each product to produce, the allocation of equipment and resources to tasks, as well as the sequencing and timing of such tasks, in order to fulfill certain objectives

In this sense, it has been necessary to develop a reasoning tool for matching the scheduling problem features to the available mathematical models. As a result, a model selection can be obtained based on features matching.

Acknowledgements

Financial support received from the Spanish "Ministerio de Economía y Competitividad", the “Agència de Gestió d'Ajuts Universitaris i de Recerca-AGAUR” and the European Regional Development Fund, funding the research Projects EHMAN (DPI2009-09386) and SIGERA (DPI2012-37154-C02-01) is fully appreciated.

References

D. Fensel, 2003, Ontologies: A Silver Bullet for Knowledge Management and Electronic Commerce, Springer, New York, NJ, USA.

C. A. Floudas, X. Lin, 2004, Continuous-time versus discrete-time approaches for scheduling of chemical processes: a review, Comput. Chem. Eng., 28, 11, 2109–2129.

I. Harjunkoski, C.T. Maravelias, P. Bongers, P.M. Castro, S. Engell, I.E. Grossmann, J. Hooker, C. Méndez, G. Sand, J. Wassick, 2014, Scope for industrial applications of production scheduling models and solution methods, Comput. Chem. Eng., 62, 5, 161–193.

E. Muñoz, E. Capón-García, J.M. Laínez, A. Espuña, L. Puigjaner, 2014, Integration of Methods for Optimization in a Knowledge Management Framework, Comput. Aided Chem. Eng. 33, 859–864.

Krist V. Gernaey, Jakob K. Huusom and Rafiqul Gani (Eds.), 12th International Symposium on Process Systems Engineering and 25th European Symposium on Computer Aided Process Engineering.
31 May – 4 June 2015, Copenhagen, Denmark

Knowledge Management to Support the Integration of Scheduling and Supply Chain Planning using Lagrangean Decomposition

Edrisi Muñoz[a], Elisabet Capón-García[b], José M. Laínez-Aguirre[c], Antonio Espuña[d], Luis Puigjaner[d]

[a] *Centro de Investigación en Matemáticas A.C., Jalisco S/N, Mineral y Valenciana 36240, Guanajuato, Mexico*
[b] *Department of Chemistry and Applied Biosciences, ETH Zürich, 8093 Zürich, Switzerland*
[c] *Department of Industrial and Systems Engineering, University at Buffalo, Amherst, NY 14260*
[d] *Department of Chemical Engineering, Universitat Politècnica de Catalunya, Av. Diagonal, 647, E08028 Barcelona, Spain*

Abstract

The complexity of integrated planning and scheduling models can be tackled with decomposition techniques based on duality and information flows between a master and a set of subproblems. Hence, the information sharing and communication of information from the industrial environments requires flexible structures, facilitating the use of analytic tools and providing higher flexibility for model building in industrial environments. In this work, an ontological framework is proposed to allow the virtualization of systems and processes and to implement a novel Lagrangean decomposition scheme based on hierarchical level decomposition. Indeed, the scheduling and planning sub-problems are created for each facility/supply chain entity and their dual solution information is shared by means of the ontological framework. Two case studies based on a STN supply chain planning and scheduling models are presented to emphasize the advantages and limitations of the proposed approach.

Keywords: Lagrangean Decomposition; Integration; Planning; Scheduling; Knowledge Management.

1. Introduction

In the integrated supply chain (SC) planning problem, several dimensions may be identified, namely geographical distribution, hierarchical levels, and business functionalities (Stephanopoulos, 2011). The performance of SCs results from the synchronization of the material, financial and information flows, based on mass balances, SC capacity and technological constraints, budget limitations, suppliers' capacity, market demand and competition, and customer satisfaction requirements among others, so as to achieve corporate goals efficiently.

The functional decision levels have different space and time scales, but they are intrinsically related to each other since the decisions made at one level directly affect others. In the chemical process industry, two key methodological components of SC management are scheduling and planning technologies. The latter function focuses on

the creation of the production, distribution, sales and inventory plans based on customer and market information while observing all relevant process constraints. In particular, operational plans are aimed to structure future production, distribution and other related activities to reach the business objectives (Kallrath, 2005). According to Kallrath (2002), most of planning problems in the process industry lead to mixed integer linear programming (MILP) or mixed integer non linear programming (MINLP) models and contain the following building blocks: tracing the states of plants, modeling production, balance equations for material flows, transportation terms, consumption of utilities, cost terms and special model features. In fact, the planning model is a simplified representation that is used to predict production targets and material flows over several months or years. At this level, effects of changeovers and daily inventories are usually neglected. This simplification tends to produce optimistic estimates that cannot be realized at the scheduling level (Grossmann et al., 2008). On the other hand, the short-term scheduling function is directly related to: i) the company's planning function which determines the production targets; ii) the process control function which implements and monitors the processes' outputs, and iii) the production process itself by means of the product recipe, which is based on the process stages. Therefore, the integration of process scheduling with other functions is a broad area which poses a number of important challenges. As discussed by Kallrath (2002), the borderlines between scheduling and planning are diffuse and there are strong overlaps between them. Furthermore, the integration between scheduling and planning is increasingly demanded so that facilities can respond quickly to demand fluctuations and better utilize existing resources close to their capacity and actual needs. The economic incentives for the integration of the planning and the scheduling levels are substantial (Grossmann et al., 2008). The goal of the SC planning and plant scheduling problem consists in determining the optimal manufacturing and network distribution policies for the entire SC of a company in order to fulfill a pre-established economic objective.

Lagrangean decomposition strategy has lately received increasing attention for solving the planning problem and its integration with scheduling. This decomposition scheme of the integrated formulation exploits the structure of the full-scale model using mathematical methods. In this work, we address the integrated multi-site planning and scheduling problems using a Lagrangean relaxation approach. Specifically, the decomposition relies on the quantities to be produced at each production site within the SC (hierarchical decomposition), in contrast to other approaches which consider the flows among the SC elements (spatial decomposition), or the flows along time intervals (temporal decomposition).

The Lagrangean decomposition strategy is supported by an ontological framework. The ontological framework manages the information exchange between the master and slave problems required by the decomposition approach. As presented in previous works Muñoz et al. (2013a, 2013b), the ontology also supports streamlining information and data integration along the different hierarchical decision levels which allows the automatic instantiation of analytical systems by gathering and processing data from transactional systems. The aim of the ontology application in this work is to provide a straightforward manner of building, instantiating and solving large scale models by taking advantage of ontologies functionalities. Overall, this work presents a hierarchical-based decomposition strategy based on the functional levels and provides a systematic ontology-based framework for information tracking and transfer, which has not been presented so far in the literature for the integrated planning and scheduling problem.

Next, the integration problem of scheduling and planning is defined as considered in this work. In the methodology section, the mathematical formulation for the planning and scheduling problems, the proposed Lagrangean strategy and the information management environment are presented. Finally, a case study illustrates the algorithm and operation of the knowledge management framework.

2. Problem statement

This work is concerned with the multiperiod and multisite supply chain planning and scheduling problem of multipurpose batch plant facilities. The planning horizon comprises a time span of years. Production plants operate under cyclic scheduling conditions during each year.

The problem assumes a fixed supply chain design.It is assumed that a set of suppliers with unlimited capacity provide raw materials to the different production plants. These production plants and several distribution centers are located in specific geographical sites and deliver final products to the markets. Each production plant produces certain amounts of final products using equipment technologies which have an installed capacity and minimum utilization rate. Production routes are defined in the product recipes, which comprise mass balance coefficients and the utilizationof production resources. The final products may be stored in the distribution centers before being sent to the markets. Each market has a nominal demand of final products, and unfulfilled demand cannot derive in back orders. The price of every product in each market is defined along the time horizon. The available transportation links among the different elements of the supply chain are also provided.

Therefore, the aim of this problem consists of determining: (i) the assignment of manufacturing and distribution tasks to the network nodes; (ii) the amount of final products to be sold; (iii) the amount of material shipped among facilities; and (iv) the detailed batching, sequencing and timing of tasks in each production plant. These decisions are driven by (i) direct cost parameters, such as production, handling, shipping, storage, and raw materials, (ii) indirect expenses, associated with the capacity utilization, and (iii) prices of the final products. The overall goal consists in maximizing the economic performance of the whole supply chain structure. The exchange of information required to build the models and to solve the problem is supported by the ontological framework.

3. Methodology

The multiperiod and multisite deterministic planning model, which provides a framework based on the state-task-network (STN) concept for the planning and scheduling of SCs, is based on the work by Laínez et al. (2009). A cyclic scheduling model (Wuand Ierapetritou, 2004) is applied at each production site. The assumption of cyclic scheduling allows to estimate the production schedule considering uniform demand along the time horizon and availability of the raw materials; which is a reasonable approximation to schedule the yearly operation of a plant. The model adopted in this work relies on the continuous time STN formulation which has been extended to consider cyclic scheduling. Then, the Lagrangean decomposition strategy, which decouples the planning and scheduling decision levels is presented in Figure 1.

Finally, an ontological framework is introduced for the adoption of the solution strategy between the different hierarchical levels to facilitate the problem representation and communication.

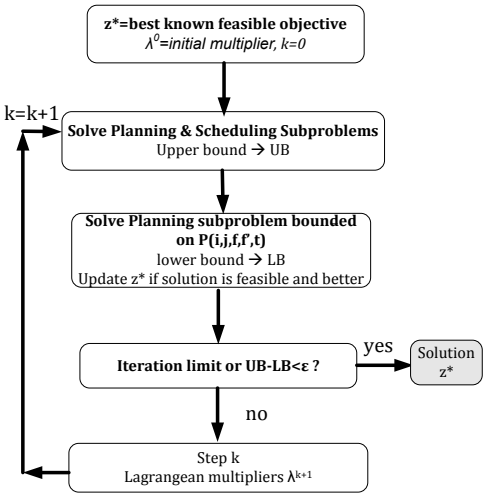

Figure 1. Interaction between the knowledge management framework and the integration strategy considering the Lagrangean decomposition

3.1. Knowledge Management strategy

The ontology is intended to promote transversal process-oriented management enabling interaction among the different functionalities. As a result, databases can be well located and their data are easily available and can be transformed into valuable information. This work uses an ontology-based framework for integrating the planning and the scheduling functions by sharing and communicating the results of the mathematical models in an iterative procedure. The objective is to use such an informationin the Lagrangean decomposition technique. Therefore, this framework allows the communication and management of multiple models and the data flow required for their efficient solution so as to provide support to decision makers in a timely fashion. One key aspect in the decision-making process is information extraction, which should ultimately result in information quality. Information quality refers to the precision of information in terms of the time, content and clarity required for a specific task. Specifically, optimization techniques require accurate information for reaching meaningful results for decision-making. Indeed, the interoperability and exchange of information from different systems and hierarchical levels is one of the most critical aspects in the daily operation of many organizations. This activity can be drastically improved by combining knowledge and expertise management approaches. The workflow of the knowledge management approach adopted in this work is presented in Figure 2. Firstly, the problem is modeled within the ontological structure and the mathematical parameters related to the Lagrangean decomposition are instantiated within the ontology. Next, Lagrangeansubproblems related to the planning and scheduling functions are solved with mathematical programming techniques according to the data contained in the ontological framework. The results from these problems are fed back to the ontological structure, which is updated with the new values. Next, the original planning problem is solved with the upper bounds to the production values obtained in the scheduling Lagrangeansubproblem, and a feasible lower bound to the integrated problem is obtained. The results of the feasible solution are updated in the ontological framework, ant the termination criteria are checked. If these criteria are not fulfilled, the new Lagrangean multipliers are computed and updated in the mathematical parameters of the ontological framework. Therefore, the new planning and scheduling

subproblems are fed with the updated values of the problem, contained in the ontology. This procedure is repeated until one of the termination criteria is met.
The ontological model is managed by means of a high level informatic program; which allows the capabilities for mining data as a decision support system tool by providing information quality at every decision level. In order to provide the optimization models with the input data, Java has been used as a high-level programming language for extracting the data managed by the ontological model.

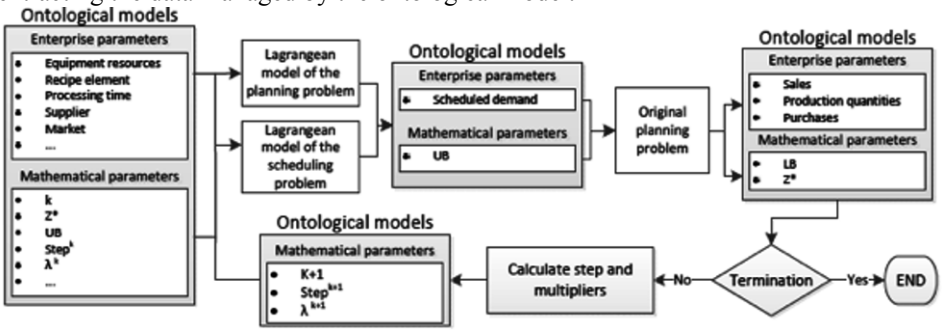

Figure 2. Interaction between the knowledge management framework and the integration strategy considering the Lagrangean decomposition

Therefore, the resulting input files stand for information quality. The code has been built using the platform NetBeans IDE 7.0, and the OWL API has been adopted to access the ontology model from Java.

4. Case study

This case study is based on a supply chain network design-planning problem presented by Laínez et al. (2009). It consists of three suppliers and two installed locations for the processing sites and the distribution centers in a planning horizon of five annual periods. The production process should fulfill the demand of two final products which are sold in six different market locations. Each production plant contains a production process consisting of four equipment technologies, five production tasks and nine states/materials. Two intermediate scheduling storage policies are proposed, unlimited intermediate storage policy (UIS) and zero wait (ZW). The results for the different iterations of the Lagrangean strategy are presented in Figure 3.

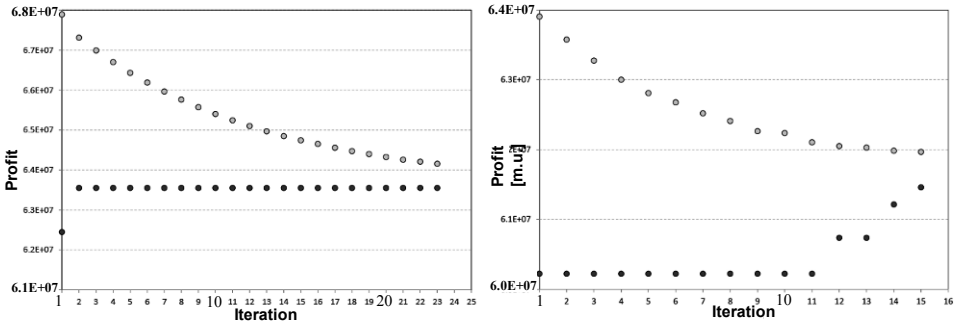

Figure 3.Results of the Lagrangeanstrategy for UIS policy (left), and ZW storage (right).

In the case of UIS, the problem converges after 23 iterations of the Lagrangean algorithm and a total computational time of $2.64 \cdot 10^3$CPU s. The optimal solution (which is represented as the lower bound), increases from the initial iteration. Therefore, the decomposition strategy enables to reach global optimal solutions from the planning perspective, considering the complete detail of the scheduling model. The maximum profit for the SC is $6.33 \cdot 10^7$m.u. In the case of ZW, the problem converges after 15 iterations and a total computational time of $4.33 \cdot 10^3$CPU s. Both the upper and lower bounds change along the iterations, and the decomposition strategy enables to reach global optimal profit value of $6.15 \cdot 10^7$m.u.

5. Conclusions

The developed approach deals with decentralized SC decision-making schemes by using a hierarchical level decomposition.This is of great interest given that the current global economy, in which outsourcing and partnering are the normal mode and SCs with varying degrees of decentralization exist, is the reality that must be addressed. By using a Lagrangean relaxation based approach for decentralized decision making, there is no need of explicit knowledge of sensitive/private information such as production cost functions and operation constraints of every supply chain member, since minimal information (i.e., dual variables and primal variables for the complicating constraints) is interchanged as feedback among SC partners instead. This interchange could be carried out using a technological infrastructure based on the proposed ontological framework.

Acknowledgements

Financial support received from the Spanish "Ministerio de Economía y Competitividad", the “Agència de Gestió d'Ajuts Universitaris i de Recerca-AGAUR” and the European Regional Development Fund, funding the research Projects EHMAN (DPI2009-09386) and SIGERA (DPI2012-37154-C02-01) is fully appreciated.

References

I. Grossmann, M. Erdirik-Dogan, R. Karuppiah, 2008,Overview of planning and scheduling for enterprise-wide optimization of process industries,Automatisierungstechnik, 56, 2, 64-79.

J. Kallrath, 2002,Planning and scheduling in the process industry, ORSpectrum, 24, 3, 219-250.

J. Kallrath, 2005,Solving planning and design problems in the process industry using mixed integer and global optimization,Ann. Oper. Res., 140, 1, 339-373.

J.M. Laínez, G. Kopanos, A. Espuña, L. Puigjaner, 2009,Flexible design-planning of supply chain networks, AIChE J., 55, 7, 1736-1753.

E. Muñoz, E. Capon-García, J.M. Laínez, A. Espuña, L. Puigjaner, 2013a,Considering environmental assessment in an ontological framework for enterprise sustainability,J.Clean. Prod., 47, 149-164.

E. Muñoz, E. Capon-García, J.M. Laínez, A. Espuña, L. Puigjaner,2013b. Integration of enterprise levels based on an ontological framework,Chem. Eng. Res.Des., 91, 8, 1542-1556.

D. E. Shobrys, D. C. White, 2002,Planning, scheduling and control systems:why cannot they work together. Comput.Chem.Eng.,26, 2,149-160.

G. Stephanopoulos, G.V.Reklaitis, 2011,Process systems engineering: Fromsolvay to modern bio- and nanotechnology. a history of development, successesand prospects for the future, Chem. Eng. Sci., 66, 19, 4272-4306.

D. Wu, M. Ierapetritou, 2004,Cyclic short-term scheduling of multiproduct batch plants using continuous-time representation. Comput. Chem.Eng.,28, 11, 2271-2286.

Krist V. Gernaey, Jakob K. Huusom and Rafiqul Gani (Eds.), 12th International Symposium on Process Systems Engineering and 25th European Symposium on Computer Aided Process Engineering.
31 May – 4 June 2015, Copenhagen, Denmark

An Ontological Approach to Integration of Planning and Scheduling Activities in Batch Process Industries

Marcela Vegetti [a], Gabriela Henning[b*]

[a]*INGAR(CONICET/UTN), Avellaneda 3657, Santa Fe 3000, Argentina*
mvegetti@santafe-conicet.gov.ar
[b]*INTEC (CONICET,UNL), Ruta Nacional 16, km 461,5, Santa Fe 3000, Argentina*
ghenning@intec.unl.edu.ar

Abstract

In the last decades, the integration of informatic applications supporting planning, scheduling and control has been a serious concern of the industrial community. Many standards have been developed to tackle this issue by addressing the exchange of data between the scheduling function and its immediate lower and upper levels in the planning pyramid. However, a more comprehensive approach is required to tackle integration problems, since this matter entails much more than data exchange. So, this article presents an ontological framework that provides the foundations to reach an effective interoperability among the various applications linked to scheduling activities.

Keywords: ISA-88, ISA-95, ontologies, scheduling

1. Introduction

Despite over twenty years of research in batch scheduling, advanced scheduling support systems are not very common in the chemical industry yet. In addition, most of the available commercial systems are not based on the solution methodologies that academia has developed. One of the reasons why academic approaches are not adopted in industry is the fact that decision support tools do not integrate with the enterprise and manufacturing applications because they rely upon quite different knowledge representations. In the last decades, the integration of informatic applications supporting planning, scheduling and control has been a serious concern of the industrial community. The ISA-88 (ANSI/ISA, 2010) and ISA-95 (ANSI/ISA, 2000) standards have been developed to tackle this issue by addressing the exchange of data between the scheduling function and its immediate lower and upper levels in the planning pyramid. However, a more comprehensive approach is required to address integration problems, since this matter entails much more than data exchange. In last decade, ontologies have been considered an effective solution to interoperability problems in many domains. Therefore, this article presents an ontological framework that provides the foundations to reach an effective interoperability among the various applications linked to scheduling activities.

The paper is organized as follows. Section 2 points out some of the problems of dealing with multiple knowledge representations in the scheduling domain. Section 3 introduces the ontological approach that is proposed to address integration problems. By means of example, Section 4 describes the ontology that was developed to formalize the ISA-88 standard, which is one of the components of the ontology network that is proposed in this contribution. Finally, section 5 presents some concluding remarks.

2. Different knowledge representations in the scheduling field

Many academic approaches addressing scheduling problems resort to intermediate representations, like the state-task (STN) or resource-task (RTN) networks (See Figs. 1 and 2 of Giménez et al., 2009), before developing the mathematical model that indeed solves the problem. However, this representation does not have a direct mapping to the master data that is usually employed in industry. Thus, the human scheduler has to manually create the STN/RTN graphical models from data that is spread in different tables of the enterprise databases.

On the other hand, in the industrial domain, the most important input for the scheduling problem is the ISA-88 master recipe, which provides the set of data that uniquely defines the production requirements of a specific product batch. Recipes are recursive structures containing five components: *Header, Formula, Procedure, Equipment requirements* and *Other Information*. See for example Fig. 1, which depicts the master recipes of P1 and P2, which are the final products of the STN shown in Fig. 2 of Giménez et al. (2009). Fig. 1 shows that the procedure component of the P1 master recipe is defined in terms of the T2, T1 and T3 operations. The INT3 recipe entity is also shown in Fig. 1 and the ones corresponding to the other intermediates can be found in VH (2014). An analysis of Fig. 1, the material in VH (2014), along with Figs. 1 and 2 of Giménez et al. (2009) shows that these recipe representations are quite different and that a direct mapping is not possible. On top of the recipe information, the scheduling problem needs additional input data, such as demands to be fulfilled, plant topology with unit features, etc. This last type of information is not represented neither in the STN/RTN graphs nor in the ISA-88 recipe model. Usually, industry specifies it in the so called *physical model* proposed by ISA-88, while in academia it is handled in an informal way that is not machine procesable and can lead to misinterpretations.

Having all this input information, a mathematical model is built and then solved. The resulting production schedule needs to be communicated to the adjacent levels in the planning pyramid: (i) to the lower process control layer to materialize batch execution and (ii) to the upper production planning and control (PPC) level for plan management activities. In practice, the results included in the solver output file need to be translated into the *control recipe* (the one that according to ISA-88 standard is employed by the control system to perform batch execution) and into the *operations schedule*, an explicit representation of the schedule according to the ISA-95 standard.

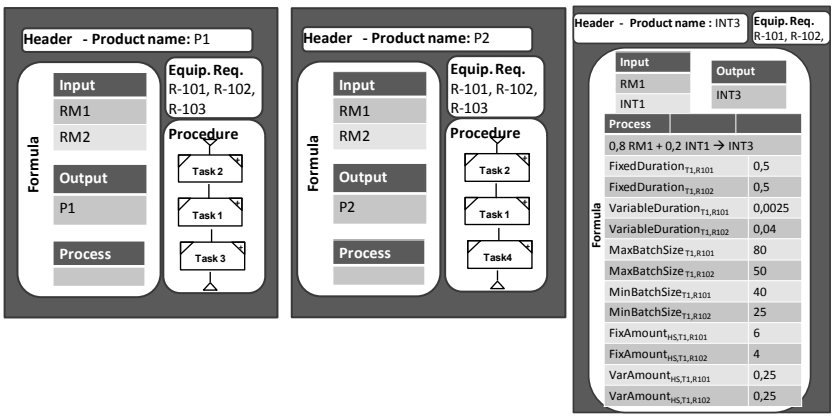

Figure 1. Recipe entities for products P1, P2 and INT3

As a result, it can be seen that in order to perform scheduling activities and to articulate them within the planning pyramid, several knowledge representations and models need to interplay. For instance, to transform a given master recipe into a control one, the procedure that is conceptualized in Fig. 2 would need to be executed (actually, such an approach was never made explicit by researchers devoted to the industrial scheduling field and it is presented in this contribution). Currently, the translation from one representation to another is manually done, in the few cases it is indeed carried out. In fact, none of the academic proposals take into account the automatic translation of the solver output file into representations that are useful from an industrial point of view, i.e. control recipes and explicit schedule representations. In addition to the manual translation workload, these heterogeneous data models employ distinct terms to refer to the same concepts. Besides these semantic issues, since the models are not formal, they cannot be interpreted by a computer and can also be ambiguous. Moreover, an analysis of the ISA-88 and ISA-95 standards (Vegetti and Henning, 2014) reveals some overlappings on the information and activities handled by them (e.g. product definition vs. recipe specification; equipment capability vs. physical model), which discloses some collision points. The problems pointed out in the previous paragraphs are some of the difficulties preventing the integration of scheduling activities within the planning pyramid and, more specifically, precluding the adoption of advanced scheduling approaches in industry.

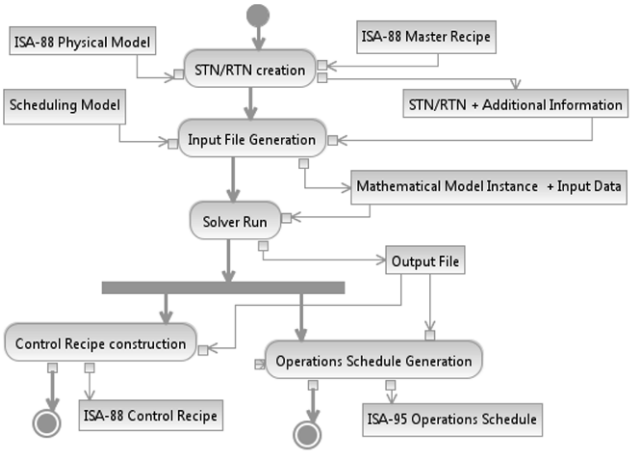

Figure 2. Data manipulation and model translation associated with scheduling

3. Ontological approach that supports scheduling activities

In order to tackle the problems posed in the previous section an ontological approach is addressed in this contribution. An ontology is a "formal, explicit specification of a shared conceptualization" (Gruber, 1993). Ontologies have been recognized as key elements to reach semantic integration, since they provide formal models that establish a consensual and precise meaning to the information communicated among different sources.

Following the interlingua approach (Ciocoui et. al, 2000), this contribution proposes the construction of a network of ontologies (see Fig. 3), having the *Schedule Reference Ontology* (SRO) as a common vocabulary. This network also contains local ontologies that formalize the different sources of information supporting scheduling activities: for instance, it contains ontologies of the ISA-88 and ISA-95 standards, the STN/RTN

representations, of the mathematical programming models (whenever MILP/MINLP-based solution approaches are pursued), of timed automata-based solution procedures, etc. The implementation of this ontology network requires the formalization (triangles in Fig. 3), with a previous conceptualization in certain cases (diamonds in Fig.3), of the various information sources. This is done by means of the OWL (Ontology Web Language; W3C, 2004) and RDF (Resource Description Framework; W3C, 2014) languages. Moreover, the development of ontology alignment agents (circles in Fig. 3), which map concepts in the local ontologies to their definitions in the SRO common vocabulary, is also required. This core ontology plays a central role in the network, acting as a bridge between the different ontologies in the net.

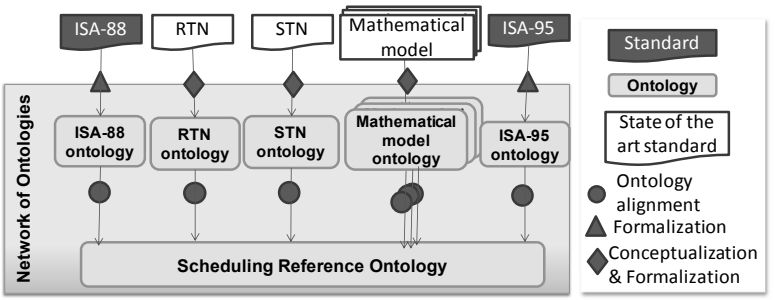

Figure 3. The proposed network of ontologies

The development of the proposed network of ontologies is the starting point for the automatic construction and translation of models that are employed during the scheduling activities. Fig. 4 presents the architecture that is proposed for an application supporting this task, considering the case in which an MILP-based scheduling solution approach is adopted. This architecture has two main components: the RDB2RDF and the automatic constructor and translator (AC&T). The aim of the first component is to create an OWL view of the relational databases that provides information about the master recipe and the physical model. Based on a mapping file and on the ontology network, RDB2RDF creates a populated ontology in RDFS/OWL from these relational databases. The populated ontology is then published by the SPARQL-endpoint, which can reply to the SPARQL queries that are issued from the AC&T component.

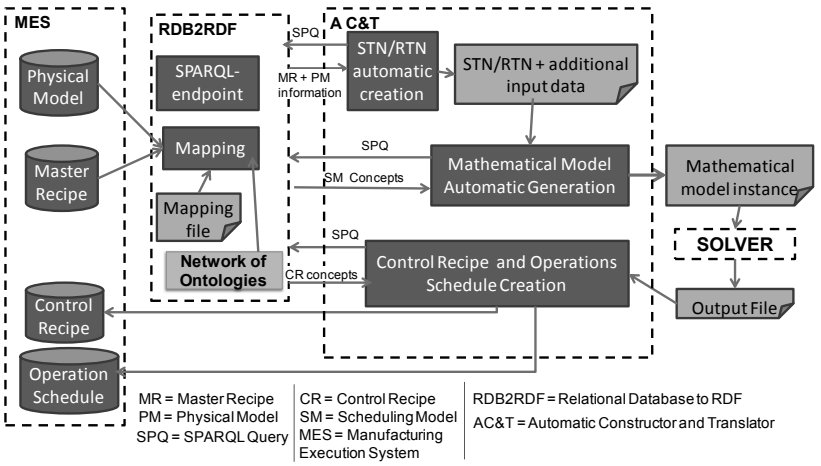

Figure 4. Automatic construction and translation framework

The AC&T component has two objectives. On the one hand, it is responsible for the automatic creation of two representations: the STN/RTN intermediate model and the mathematical model instance, which are the inputs to the solver. On the other hand, it translates the solver output file into the needed control recipes (one per product batch) and the operations schedule models. To execute these tasks, the AC&T component obtains information from the RDB2RDF one through the SPARQL query language. The development of these components is based on JENA, a Java framework for building Semantic Web applications that provides a programmatic environment for RDF, RDFS, OWL, SPARQL and includes a rule-based inference engine. In addition, there are many tools that support the RDB2RDF functions, like the D2RQ platform, Asios' SBRD, RDBtoOnto, among others.

4. Development of the ontology network. ISA-88 example.

The formalization of the ISA-88 standard has been tackled first as it is the data model having the major semantic inconsistencies in its term definitions and because of its central role in scheduling activities. Vegetti and Henning (2014) presented the initial steps towards the formalization of the ISA-88 master recipe, in particular focusing on its recipe procedure component. Therefore, the main concepts in the corresponding ontology are related to recipes and their components. The *RecipeEntity* is the combination of a *ProceduralElement* with associated recipe information, which includes a *Header*, *EquipmentRequirements* and a *Formula* (See VH, 2014). Each *Recipe Entity* is built up of lower-level recipe entities. But these levels should be hierarchically organized according the procedural control model. Therefore, the concepts *Procedure RecipeEntity*, *UnitProcedureRecipeEntity*, *OperationRecipeEntity* and *PhaseRecipe Entity* have been added to the ontology in order to represent recipe entities at *Procedure*, *UnitProcedure*, *Operation* and *Phase* Levels, respectively. All *Recipe Entities,* except the ones at *Phase* level, which do not have components, should include *composedOf* recipe entities belonging to the immediate lower level.

In the remaining of this section, the formalization of the recipe *Formula* component is described for illustration purposes. For space reasons, only a brief sketch of the concepts is shown, along with their definitions. For more details on its OWL implementation refer to VH (2014). According to ISA-88, the *Formula* is a category of recipe information that includes various parameters (see Fig. 1). Therefore, as shown in Fig. 5, a *Formula* is modeled as a parameter set, which may be categorized as inputs, outputs, or process parameters. Parameter values may be simple values, expressions, or references to parameters that are defined at the same level or at higher levels in the associated procedural hierarchy. Values that are expressions may include references to other parameters (*ReferenceTo* association in Fig. 5). An input parameter represents the identification and quantity of a resource required to make the product batch. These resources may be raw materials, energy, manpower or utilities. Moreover, the Resource class may be specialized to take into account others pertaining to specific industrial domains. Similarly, an output parameter specifies a certain material and the quantity that is expected to be obtained from the execution of a recipe. A process parameter details information, such as temperature, pressure, batch size bounds, that is relevant to the product batch. Each parameter is associated with a value type, a unit of measure, a scaling factor and a reference type. The corresponding definitions are given below:

Value type: specifies how the parameter value is interpreted. It includes: basic data types, data sets that define material transactions (transfer, consumption, generation of material); or data series (e.g., a temperature profile that will be tracked).

UnitofMeasure: identifies the engineering units of measure for the Value (e.g., kg, pounds).
ReferenceType: specifies the way parameters are related if the associated parameter has references to others. The types of relations may be: Algebraic or Boolean equations, Product specific entry forms that work on one or more parameters, Deferral of parameters to different recipe entities (at the same or another level), among others.
Scaling Factor: defines the scaling rule, which indicates how the parameter should be scaled with the batch size.

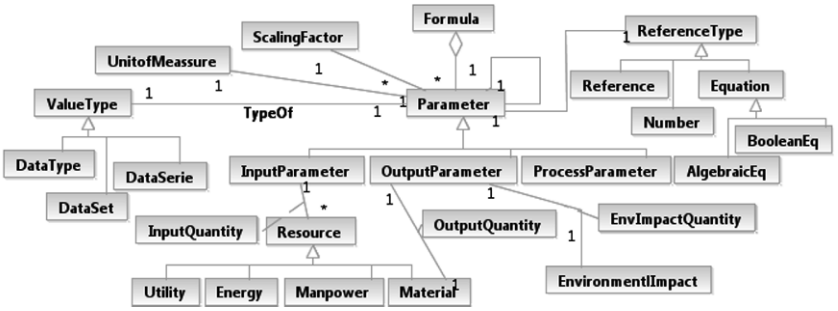

Figure 5. Formula Definition

5. Conclusions

Ontologies support interoperability by providing semantic terminology in a computer understandable format. This article proposes the definition of a network of ontologies to solve the interoperability problems associated with the execution of scheduling activities and their interplay with other functions within the Planning pyramid. This ontology network, whose architecture is presented in this contribution, is the starting point for the automatic construction and translation of models that are employed during the scheduling activities. In addition, one of the main ontologies of this network is described along with its implementation in OWL (VH; 2014).

References

ANSI/ISA–88.00.01: Batch Control Part 1: Models and Terminology, 2010.
ANSI/ISA-95.00.01-2000: Enterprise-Control System Integration. Part 1: Models and terminology, 2000.
Ciooui, M., Gruninger, M., Nau, D. (2000). Ontologies for integrating Engineering Applications, Journal of Computing and Information Science and Engineering, 1, 12-22.
Giménez, D. Henning, G., Marevelias, C. (2009). A novel network-based continuous-time representation for process scheduling: Part I. Main concepts and mathematical formulation. Computers and Chemical Engineering, 33, 1511–1528.
Gruber, T. (1993).A Translation Approach to Portable Ontology Specifications. Knowledge Acquisition, 5, 199-220.
Vegetti, M. and Henning, G. (2014). ISA-88 formalization. A step towards its integration with the ISA-95 standard, FOMI 2014 Proceedings, Brasil.
VH (2014) SRO Data Repository https://sites.google.com/site/sropse2015/Last access: 30th November 2014.
W3C (2004) OWL 2 Web Ontology Language Document Overview. www.w3.org/TR/owl2-overview/ . Last access: 28th November 2014.
W3C (2014) Resource Description Framework (RDF). http://www.w3.org/RDF/. Last access: 28th November 2014.

Krist V. Gernaey, Jakob K. Huusom and Rafiqul Gani (Eds.), 12th International Symposium on Process Systems Engineering and 25th European Symposium on Computer Aided Process Engineering.
31 May - 4 June 2015, Copenhagen, Denmark.

Constructing an ontology for physical-chemical processes

Heinz A Preisig

Department of Chemical Engineering; NTNU; Trondheim, Norway
Heinz.Preisig@chemeng.ntnu.no

Abstract

An ontology is a formal collection of pieces of knowledge that specify the behaviour of entities in a domain. Our domain is physical-chemical-biological systems, processes that we describe with a set of concepts or principles. These ontologies are not used to reason about the system, but to construct process models that adhere to these concepts, in particular the conservation principles and the behaviour of materials, the geometrical concepts in space and time.

Simplicity of the ontology is a design criteria, both in the definition and implementation of its utilisation. A simple generic structure building on defining the containment as a directed graph, which is populated with tokens. The two enable us to apply our concept in a very broad field of contexts. So whilst we discuss the structure based on physical systems with control, it can be applied much wider. The extension to multi-scale models is or particular interest.

Keywords: model-based engineering, computer-aided, design, operations

1. Why ontoloy-based modelling

Over the past decade this term is increasingly used in science and technology and since by definition the term is context dependent, the usage varies greatly, Adding natural variations in interpretation, it cannot be a surprise that people raise their eyebrows when being confronted with the term. So let us argue on why then we still want to use the term here: Ontologies are loosely defined as the basic knowledge, the template on which we construct and derive the knowledge of a field. Since we attempt to capture the representation of physical systems, we think of ontology to be indeed an appropriate term to use. Our application is in stark contrast to other uses of ontologies, which more lean towards knowledge-based systems. Our application constructs the ontology as a lower triagonal structure, thus the resulting knowledge representation is anything than loose, it is highly structured.

2. The architecture

2.1. Frame

Our objective is to construct an ontology for mechanistic models of physical systems Preisig (2012, 2010). Physical systems live in time and space. The space they occupy is a part of the universe and they move in time.

```
Ontology.physical: frame := [time, space]
```

With this statement we introduced not only a ontology statement, but also an attribute to the ontology, making the ontology context dependent.

2.2. Containment

We further state that space being occupied by the physical system can be subdivided into smaller parts without imposing any further limitations on how "small" this he parts may get. For practical reasons we implement the break-down mechanism as a hierarchical procedure, purely for making the handling of large scale systems feasible; so complexity handling is the issue, but latter is separated from generating an ontology because the model is always the collection of the leave nodes of the hierarchical decomposition.

The process is embedded in its environment thus defining an initial split into two basic parts. The next step is to structure the physical space the plant occupies. The granulation of the process is motivated by time-scale and or some kind of grouping considerations. As mentioned the granulation process is done recursively, which though is not relevant for the ontology in the first place. Without introducing limitations, we specify the environment to consist of infinitely large volumes, and call them *reservoir* thereby following the nomenclature of classical thermodynamics. The observant reader may argue that this will limit the models to constant boundaries. This is not the case as we can always construct a time varying input from a combination of constant reservoirs and perfect control, which though also defines the need for adding control as part of the basic ontology. Once the plant's volume has been divided, one defines the interactions between the different parts across the common boundaries. In the case of a physical process, they will exchange extensive quantities by which means the state of the two interacting volume parts are changing. The interactions carry flow direction information, which must be related to the geometry. Thus we introduce the interaction as directional interaction, physically speaking as a reference co-ordinate. The result is a network of interacting volume elements represented as a directed graph with the nodes being capacities and the arcs representing the exchange of extensive quantities.

We have seen the need for representing control systems. We map them also into a directed graph, though here the nodes represent information processing units and the arcs signals. Again the direction is used to give signals a flow direction.

In both cases we have as a basis a directed graph. So for the ontology we define:

```
Ontology.<context>: containment :: directed graph := [nodes, arcs]
```

The nodes are a list of node identifiers, whilst the `arcs` is a list of tuples each tuple consisting of a tail node identifier and a head node identifier. The `arcs` is thus the incidence list of the graph. At least for physical systems, the graph is a simple one, meaning it has no loops (arcs with identical head and tail). The same usually applies to information systems.

2.3. Tokens

The containment definition together with the frame represent the foundation of the model ontology, whilst the main body is a supergraph of equations and variables. Since the latter is context dependent, the part between must define the context in more detail. We do this by adding one more base component, namely token. The token represents what is living in the containment. In the case of a physical system this will essentially be what is associated with the conserved extensive quantities. The token in a node than gives raise to the definition of the state.

```
Ontology.<context>: tokens := [<token>]
```

with `<token>` representing a context dependent token.

2.4. Index structures

In order to associate the equations to the objects, we introduce index structures, which when implemented will contain two elements, namely a running index and a set. In the ontology we

define the base sets as being the lists of the base objects. Thus there is a index structure for the list of nodes, list of arcs, list of tokens. And since the tokens are living in the network we add product index structures of nodes*tokens and arcs*tokens.

```
Ontology.<context> :
index_structs := [graphs, nodes, arcs, tokens, nodes*tokens, arcs*tokens]
```

2.5. Attributes - colours

In order to enable the specification of the context dependences in more detail, we introduce attributes to all base objects, thus for graph, node, arc and token. The attributes add a kind of ”colour” to objects. They provide the means to further classify the objects and use them in structuring the equation/variable network.

2.6. Variable - equations

The mathematical representation of the model is a super graph of variables and equations.

2.6.1. Completeness

A proper model consists of a ”complete” set of equations and variables. The ontology is the ”mother” of all models, thus it is a type of super structure that captures a range of models, it can be thought of a combination of possible models. It is only when utilising the ontology, the model for the application is being identified or ”extracted” from the ontology. Apparently the term ”complete” is essential and needs to be defined. Models are used for many applications and plant-related problems that are eventually mapped into mathematical / numerical problems that then are solved to get insight into the original plant-related problem. Taking the view of the problem space, the utilisation of the ontology is a priori not defined and a suitable method of guaranteeing ”completeness” must be defined. We found it convenient to define ”completeness” to use simulation as the basis for the definition. It must be noted, though, that this does not constrain the further use of the ontology to simulation. It merely serves the purpose of guaranteeing completeness, and is thus not to be mistaken for instantiation of a mathematical / numerical problem. In general a simulation problem is defined as a set of differential equations augmented with a set of algebraic equations, thus a differential-algebraic problem, whereby differential can also be exchanged with any approximation, such as difference equation or population related description of the dynamic behaviour. A complete simulation problem thus consists of this differential-algebraic system augmented with a set of known parameters, initial conditions and boundary conditions. So we utilise this structure to define completeness: The model is properly specified if the set of equations satisfies a zero-degree of freedom condition given the initial conditions, the boundary conditions and the parameters.

We impose the rule that the definition of the equation set must be done in a lower-triangular manner, meaning that once an initial set of variables is defined, all consecutive definitions can only use what has already been defined. Thus the equation / variable incidence matrix of this bipartite graph is required to be strictly lower diagonal. The ”completeness” condition then implies that we require for each dependent variable a corresponding equation. This makes it possible to guarantee for the completeness of the model in terms of a zero degree of freedom.

2.6.2. Behaviours - variable classes

Often a model is seen as a mapping of the behaviour of the modelled system, though leaving a feel of arbitrariness. Mathematical system theory defines behaviour as a subset of all possible events

in the defined signal space (Willems, 2014, 2007). We use this view defining a set of signal spaces that are in some sense minimal, but add sufficient structure to make the definition of the dynamic system convenient and well aligned with the physical view.

The definition needs a starting point. The starting point is the frame, in our case time and space for the physical containment. Next we define a class of signals called ”state” for the tokens in the capacities. The tokens thus provide us with the philosophical link between the network and the state. The state reflects the minimal information required to predict the future of the system a statement that goes back to Kalman. For the physical systems we base the description on the conservation principles thus define the state as the conserved quantities. The conservation principle balances the system's accumulation of an extensive quantity with the flow across the system's boundary. Thus the second class we introduce is the flows of extensive quantities. In order to allow for the conversion between extensive quantities we also introduce the signal class transposition. The description of transport and transposition is indirectly a function of the state, namely a set of intermediate variables that to a large degree describe the driving forces for the transport and transposition of tokens. Since these intermediate variables are a function of the state, we introduce the term ”secondary state”. To complete the description we also introduce ”parameters” and a class ”incidence” to capture the network structure.

Defined variable classes / types for physical systems:

```
Ontology.physical : signal classes :=
  [state, secondary state, transport, transposition, parameter, incidence]
```

For the information processing systems we use the standard classification of control:

```
Ontology.information : signal clases := [state, input, output]
```

2.6.3. Objects

The variable object is used to form together with operators expressions and equations. The object has a number of default attributes:

- symbol : ID unique at least within variable class. Alternatively globally in variables.
- doc : documentation string
- units : physical units
- index_structs : list of index structures
- type : variable type / class
- equations : list of rhs expressions for the variable

The equation is defined for the variable and not only one equation is allowed, but several. This enables for alternatives, a basic feature of the ontology. The equation is represented as a string of the right-hand-sides, a permissible mathematical expression. The rules for the expression are captured in the definition of a small language for which the definition is to attached to the ontology to facilitate compilation into different target languages.

The rhs-string is to be read by a parser implementing the language definition, build an abstract syntax tree for each of the rhs-expressions, which then can be used to generate different target code using the templates for the target language.

2.7. Parser

Finding a minimal representation is the major challenge in defining the structure of the ontology. This also applies to the language that is used to represent the mathematical expression. At this point in time we believe that we can capture macroscopic systems with the simple language defined below in Extended Backus Naur form using standard regular expressions for the token defintions:

```
token UFunc     : '\b(sqrt|exp|log|ln|sin|cos|tan|asin|acos|atan)\b';
token Root      : '\b(root)\b';
token VarID     : '\w[\w]*'; #matches first word char followed by word
token Index     : '\[.*\]'

expr ::= term { ( "+" | "-" ) term }
term ::= fact { ( "." index "." | "*" index "*" | "\" ) fact }
fact ::= atom "^" ( "+" | "-" ) VarID
atom ::= func | "(" expr ")"| VarID
func ::= unitary_func "(" expr ")"
         | root "(" expr ")"
         | integral "(" VarID "," VarID "," VarID "," VarID ")"
         | differential "(" VarID "," VarID ")"
```

For the different items: the `Ufunc` are the standard unitary functions all of which with exception of the sqrt have an argument with no units. The `root` keyword is used to define implicit equations. `Integral` introduces the integral with the arguments (derivative, integration variable, initial condition, upper limit). For the derivative it is the two variables.

The variable definition `VarID` is composed of characters. There are two operations that depend on the index structure, namely the product `.[IndexID].` and the Khatri-Rao product `*[IndexID]*`. The syntax is including the index structure the operator is reducing.

In the implementation each of the above definition lines will trigger an action which generates a new variable being the result of the operation keeping track of the variables and the applies the rules for the units and the index structures. For example for the addition one gets as a result the sum of the two variables being added, adds the variable to the abstract syntax tree together with the two operands and applies the rule of having equal index structs for both operands which is then also the index structs for the result. The units must be equal and are copied to the result.

By doing so, one builds an abstract syntax tree, which can be evaluated for any output language, given a set of templates one for each of the actions, here term, fact, unitary functions, root, integral and differential.

3. Realisation

The implementation uses probably one of the simplest file formats, namely the cfg file format. It is used for specifying configurations of tasks which fits the purpose of ontologies as base structure. The format is a section keyword `[<section>]` wrapped in rectangular brackets, followed by a series of lines with `<keyword> = <string>` essentially representing a dictionary (Python does load it as an ordered dictionary, for example). The type of ontology we pack into the file name itself. Currently we initialise the ontologies in the configuration files defining the frame, the containment and the tokens. Next we use an special-purpose editor to build the ontology. This editor imposes the rules for the construction foremost it imposes the lower-triagonal definition structure for the supergraph of variables and equations.

4. Oportunities

With the structure as suggested one can think of defining different types of networks and then a separate entity that represents the connection between these networks. In our case it would be the connection between the physical network and the information network. In the real world

these are the sensors and the manipulators. Taking this approach lefts these special objects clearly out and the added structure will be beneficial when controlling the construction of models that involve both types of networks. This thought can also be extended to multi-scale models in which the connections upwards are some agglomeration/averaging mechanisms and downwards design of experiments controlled inputs. So also here a very clear benefit arises from having such a structured approach.

5. Conclusions

We are able to capture process ontologies using a very few structural elements. The design is such that we believe we can capture macroscopic systems and it will also apply to microscopic systems, where the particulate nature of the material description matters. Proof of concept is ongoing and will is done through applications.

The goal was not only wide applicability, but also simplicity. The defined objects are few and the parser for interpreting the strings for the right-hand-side definition of equations is context free and very simple indeed. So the implementation of the parser is very simple and compilation of the expressions into different target languages is also simple indeed.

Where to go from here? Main issue is to implement the ontology in the graphical editor supporting the construction of models using a graphical interface, thus to re-establish the capabilities we generated in 2003 (Westerweele, 2003) but now fully build on the above simple ontology design.

Next will be the extension to particulate models, such as population balances. We do not expect any problems as they all fall into the class we can capture with the given ontology language.

References

Preisig, H. A., 2010. Constructing and maintaining proper process models. Comp & Chem Eng 34(9), 1543–1555.

Preisig, H. A., 2012. Thinking ontologies. Proceedings of the 11th International Symposium on Process Systems Engineering, 15-19 July 2012, Singapore, 1682–1686.

Westerweele, M. R., 2003. Five septs for building consistent dynamic process models and their implementation in the computer tool modeller. Ph.D. thesis, The Netherlands: Eindhoven University of Science and Technology.

Willems, J. C., 2007. The behavioral approach to open and interconnected systems. IEEE Control System Magazine.

Willems, J. C., last accessedkal 2014. personal webpage, lists and links to publications and lectures. URL `http://homes.esat.kuleuven.be/ jwillems/`

Krist V. Gernaey, Jakob K. Huusom and Rafiqul Gani (Eds.), 12th International Symposium on Process Systems Engineering and 25th European Symposium on Computer Aided Process Engineering.
31 May – 4 June 2015, Copenhagen, Denmark

Improved Design Strategies for Flexible Hydrogen Networks

Chuei-Tin Chang, Che-Chi Kuo

Depratmentof Chemical Engineering, National Cheng Kung University, Tainan 70101, Taiwan, R.O.C.

Abstract

Although MINLP models have already been developed for generating the optimal hydrogen networks, improvements are still needed to circumvent their common drawbacks concerning (1) unreasonable unit models and (2) incomprehensive design considerations. These issues are addressed in this study by modifying the conventional formulations so as to produce realistic multi-period designs. In addition to the programming approach, a systematic timesharing algorithm is also devised to manually integrate multiple single-period designs to form a less economical but more flexible structure for operation in different periods. One example is provided to illustrate these two design strategies.

Keywords: Hydrogen network, Multi-period design, Timesharing scheme.

1. Introduction

The development of an efficient scheme for hydrogen integration and distribution in a given refinery is a popular research issue nowadays. Although several MINLP models have already been developed to synthesize the optimal networks, there is still room for further improvements. Specifically, the applicability of available formulations is hampered by two common deficiencies, i.e., (1) oversimplified unit models and (2) incomprehensive design considerations. In the former case, the hydrotreaters and hydrocrackers were unreasonably described in the past according to fixed operating conditions and, also, the steam reforming plant was modelled simply as a hydrogen provider without any provisions for possible recycle. Although Jiao et al. (2012) treated the inlet flow rates and concentrations of hydrogen users as variables, their models were still logically inconsistent since the corresponding outlet conditions were fixed. In the latter case, the often-encountered seasonal variations in model parameters and the design options to add extra processing units were often ignored in the conventional approach. Although Ahmad et al. (2010) proposed a model to generate flexible networks which are suitable for operation in multiple periods, this approach is limited to scenarios in which only the throughputs of hydrogen users were time dependent. This study aims to circumvent all such drawbacks by modifying and improving the conventional model formulations.

2. Problem statement and superstructure

It is assumed in this work that the typical structure of conventional networks can be represented with the sketch given in Fig. 1. The hydrogen producer (which is enclosed in a dotted box), the compressors, the hydrogen users and the fuel gas system are arranged sequentially in different steps, while different units in the same step may be placed in parallel. The goal of the present study can be considered as optimally restructuring this given network with the available units and also a few new ones (such as additional compressors, PSA units and fuel cells) when necessary. Note also that the mathematical programming model for identifying this optimal revamp design can be

formulated on the basis of a superstructure, which is essentially a collection of all possible links between hydrogen sources and sinks. The connection rules for building such a structure can be found in Chiang and Chang (2014). To facilitate model formulation, a distinct label is first assigned to each unit in the superstructure and these labels are then classified and collected in two separate sets to identify their sources and sinks respectively. More specifically,

$\mathbf{I} = \{i \mid i \text{ denotes the label of a hydrogen source in superstructure}\}$

$\mathbf{J} = \{j \mid j \text{ denotes the label of a hydrogen sink in superstructure}\}$

It is important to note that, since the label of every unit may be used to identify both its source and its sink, some elements of **I** and **J** are identical.

3. Improved unit models

Only the unit models of the hydrogen users and the hydrogen producers have been modified in the present work. A summary of the modified formulations is given below:

3.1. Hydrogen using units

As mentioned before, the inlet and outlet conditions in the conventional models were fixed. Since this practice clearly precludes other feasible options which may also be favourable, these constants are replaced with variables in the improved model to facilitate more reasonable consideration. Also, methane was assumed to be the sole impurity in every hydrogen-containing stream in the past. For computation simplicity, the same convention is adopted in the present study and, also, the hydrogen consumption rate of each unit is assumed to be kept at a given value based on the argument that the production rates of fuels and petrochemicals in a refinery are usually predetermined. Such an assumption implies that the overall generation rate of all other gases can also be treated as an unchanged parameter. Consequently, the model constraints at the sink end of a hydrogen user can be written as

$$\sum_{i\in\mathbf{I}} F_{i,sk} = fs_{sk}, \quad \sum_{i\in\mathbf{I}} F_{i,sk} y_i = fs_{sk} ys_{sk}, \quad fs_{sk} ys_{sk} \geq \overline{fy}_{sk}^{\min}, \quad ys_{sk} \geq \overline{y}_{sk}^{\min} \tag{1}$$

where, $sk \in \mathbf{SK}$ and **SK** is a label set for identifying the inlets of hydrogen using units; fs_{sk} and ys_{sk} are variables respectively denoting the total flow rate and hydrogen concentration at inlet sk; $F_{i,sk}$ is also a variable which denotes the flow rate of the stream from source i to sink sk; $\overline{fy}_{sk}^{\min}$ and $\overline{y}_{sk}^{\min}$ are design parameters representing the lower bounds of the inlet hydrogen flow rate and concentration, respectively. On the other hand, the model constraints at the source end can be expressed as

$$\sum_{j\in\mathbf{J}} F_{sr,j} = fr_{sr}, \quad fr_{sr} = fs_{sk} - \overline{f}_{sr}^{\mathrm{H_2}} + \overline{f}_{sr}^{\mathrm{CH_4}}, \quad fr_{sr} yr_{sr} = fs_{sk} ys_{sk} - \overline{f}_{sr}^{\mathrm{H_2}}, \quad yr_{sr} \leq \overline{y}_{sr}^{\max} \tag{2}$$

where, $sr \in \mathbf{SR}$ and **SR** is a label set for identifying the outlets of hydrogen users; fr_{sr} and yr_{sr} are variables respectively denoting the total flow rate and hydrogen concentration at outlet sr; $F_{sr,j}$ is a variable which denotes the flow rate of the gas stream from source sr to sink j; $\overline{f}_{sr}^{\mathrm{H_2}}$ and $\overline{f}_{sr}^{\mathrm{CH_4}}$ are given model parameters which are used to represent the hydrogen consumption rate and the net rate of generation of all other gases, respectively; $\overline{y}_{sr}^{\max}$ denotes the upper bound of hydrogen concentration at source sr.

3.2. Hydrogen production plants

As mentioned before, the steam reforming plant is traditionally treated as a source of the hydrogen network. Since the hydrogen consumption level can be reduced significantly

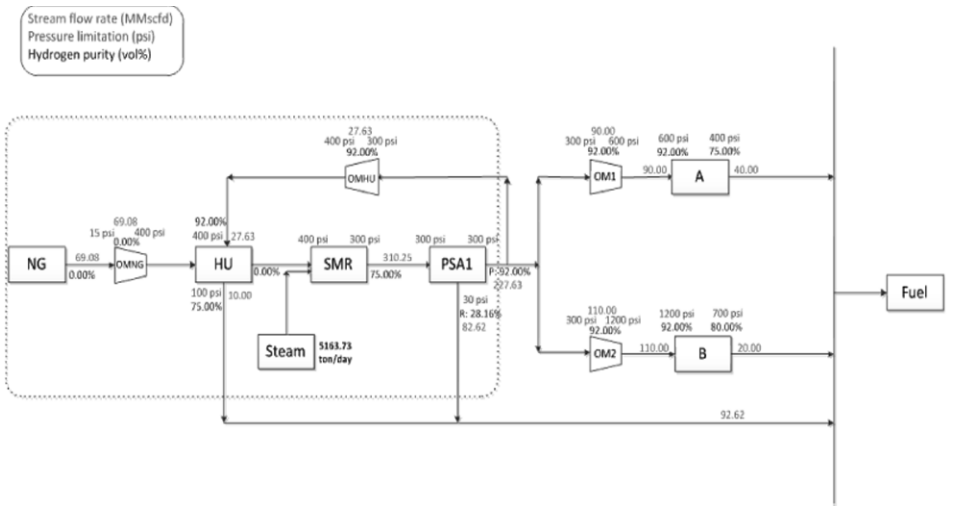

Figure 1. The typical structure of traditional hydrogen networks.

by restructuring the given network, it is desirable to develop schemes that make good use of the consequent overcapacities in the existing units. For this reason, the hydrogen production process is modelled as the following three consecutive steps:

Step I (hydrogenation reactions): The hydrogenation unit is essentially a hydrogen user, which can be modelled in a similar fashion:

$$F_{\mathrm{NG,H2P_I}} \le \overline{f}^{\mathrm{NG}}_{\mathrm{H2P_I}}, \quad \sum_{i\in\mathbf{I}} F_{i,\mathrm{H2P_I}} y_i = \overline{r}^{\mathrm{in}}_{\mathrm{H/N}} F_{\mathrm{NG,H2P_I}}, \quad \sum_{i\in\mathbf{I}} F_{i,\mathrm{H2P_I}} y_i = \overline{y}^{\mathrm{in}}_{\mathrm{H2P_I}} \sum_{i\in\mathbf{I}} F_{i,\mathrm{H2P_I}} \tag{3}$$

where, $F_{\mathrm{NG,H2P_I}}$ is the feed rate of natural gas and $\overline{f}^{\mathrm{NG}}_{\mathrm{H2P_I}}$ is its upper bound; $\overline{r}^{\mathrm{in}}_{\mathrm{H/N}}$ is the proportionality constant used to characterize the linear relation between the feed rates of hydrogen and natural gas; $\overline{y}^{\mathrm{in}}_{\mathrm{H2P_I}}$ is the hydrogen concentration at the inlet, which is fixed at a given value to simplify calculation. The flow rate and concentration of the spent hydrogen stream at the outlet are also fixed at given values. If it is desirable to utilize this stream as a source of the hydrogen network, positive values may be assigned to both parameters. If otherwise, the flow rate of spent hydrogen stream can be set to zero.

Step II (steam reforming reactions): The second group of units represents a complex intermediate step that converts natural gas to hydrogen. In order to simplify computation, all model formulations are approximated with linear functions, i.e.

$$F_{\mathrm{H2P_{II},H2P_{III}}} = \overline{r}_{\mathrm{III/II}} F_{\mathrm{H2P_I,H2P_{II}}}, \quad Z = F_{\mathrm{NG,H2P_I}} / k = Stm_{\mathrm{H2P}} / k' = Pwr_{\mathrm{H2P}} / k'' = Q_{\mathrm{H2P}} / k''' \tag{4}$$

where, $F_{\mathrm{H2P_I,H2P_{II}}}$ and $F_{\mathrm{H2P_{II},H2P_{III}}}$ respectively denote the input and output flow rates of step II, and $\overline{r}_{\mathrm{III/II}}$ is the corresponding proportionality constant; Z is the flow rate of final product of the hydrogen plant which is produced with feed coming solely from step II; k is the proportionality constant that relates Z to the consumption rate of natural gas; Stm_{H2P}, Pwr_{H2P} and Q_{H2P} denote the consumption rates of steam, electricity and heating utility respectively, and k', k'' and k''' are the corresponding proportionality coefficients.

Step III (pressure swing adsorption): Although the PSA unit in the steam reforming plant can be described adequately with a conventional model (Chiang and Chang, 2014), there is an extra need for computing the production rate Z:

$$\overline{y}^{\mathrm{prod}}_{\mathrm{H2P_{III}}} Z = R_{\mathrm{H2P_{III}}} \overline{y}^{\mathrm{out}}_{\mathrm{H2P_{II}}} F_{\mathrm{H2P_{II}},\,\mathrm{H2P_{III}}} \tag{5}$$

where, $\bar{y}_{\mathrm{H2P_{II}}}^{\mathrm{out}}$ and $\bar{y}_{\mathrm{H2P_{III}}}^{\mathrm{prod}}$ denote the known hydrogen concentrations at the outlets of step II and III, respectively, and $R_{\mathrm{H2P_{III}}}$ is the constant hydrogen recovery ratio of the PSA unit in steam reforming plant. This is due to the fact that all sources in the hydrogen network are admissible here.

4. Two effective multi-period design strategies

4.1. Programming approach

The single-period MINLP model can be reformulated for synthesizing multi-period designs. Since the aforementioned unit models are applicable in any period during a year, it is only necessary to introduce an extra subscript p to every process variable and every model parameter so that they can assume different values in different periods. By summing the contributions in all periods, the total annual operating cost can then be determined in a straightforward fashion. On the other hand, to calculate the total capital investment, additional logic constraints should be imposed to determine if new units and new pipelines are needed in the modified design:

$$e_{neq,p}\mathrm{B}_{neq}^{\mathrm{L}} \le \sum_{i\in\mathbf{I}} F_{i,neq,p} \le e_{neq,p}\mathrm{B}_{neq}^{\mathrm{U}}, \quad e_{neq,p} \le e_{neq}, \quad e_{i,j,p}^{\mathrm{pipe}}\mathrm{B}_{i,j}^{\mathrm{L}} \le F_{i,j,p} \le e_{i,j,p}^{\mathrm{pipe}}\mathrm{B}_{i,j}^{\mathrm{U}}, \quad e_{i,j,p}^{\mathrm{pipe}} \le e_{i,j}^{\mathrm{pipe}} \tag{6}$$

where, $e_{neq,p}, e_{neq}, e_{i,j,p}^{\mathrm{pipe}}, e_{i,j}^{\mathrm{pipe}} \in \{0,1\}$ and i, j, neq and p are labels of a source, a sink, a new unit and a period, respectively; $F_{i,neq,p}$ denotes the flow rate of a stream in superstructure between source i and the sink end of unit neq in period p; $F_{i,j,p}$ denotes the flow rate of a stream in superstructure between source i and sink j in period p; $\mathrm{B}_{neq}^{\mathrm{L}}$ and $\mathrm{B}_{neq}^{\mathrm{U}}$ respectively denote the lower and upper capacity limits of unit neq; $\mathrm{B}_{i,j}^{\mathrm{L}}$ and $\mathrm{B}_{i,j}^{\mathrm{U}}$ respectively denote the lower and upper flow-rate limits between source i and sink j.

4.2. Heuristic approach

The above programming approach calls for construction of a mathematical program that minimizes the total annual cost (TAC) under the assumption that the given durations of all periods are fixed. Other than the obvious computational difficulties in solving the MINLP model, the resulting designs are often suboptimal in actual operations since the given period lengths may have to be adjusted in response to unexpected disturbances. A heuristic approach is thus taken in the present study to address this issue. In particular, a single-period model is first constructed and solved to produce the optimal design for each period individually. These individually optimal designs are in general of different structures. A timesharing design strategy is then applied to integrate all such single-period designs so as to reduce the overall capital investment as much as possible while still keeping the operating costs in each period at the desired levels. This integrated design should be considered to be more flexible since it is optimal despite unforeseen schedule changes. In this work, only the PSA units and compressors are allowed to be shared. A systematic manual procedure has been developed to identify the suitable timesharing mechanisms from multiple single-period designs (Kuo, 2014). The detailed steps are omitted here due to space limitation.

5. An illustrative example

The traditional network in Fig. 1 is again considered here. The steam reforming plant consists of a hydrogenation unit (**HU**), the steam reforming reactors (**SMR**) and a purifier (**PSA1**). The other existing units in this network include two hydrogen users (**A** and **B**) and four compressors (**OM1**, **OM2**, **OMNG** and **OMHU**). It is assumed that units **A** and **B** have to be operated differently in three distinct periods according to Tables 1 and 2. The unit costs of natural gas are expected to be 3535, 4600 and 4302

($/MMscf) in these periods respectively. The corresponding costs of electricity and steam also fluctuate. The former are predicted to be 0.18, 0.07 and 0.09 ($/kWh) respectively, while the latter 8.86, 12.51 and 9.06 ($/ton). Two approaches were applied:

(1) To facilitate implementation of the heuristic procedure in subsection 4.2, it is necessary to first produce an "optimal" single-period design for each period. It was found that, if these designs are to be operated respectively in their intended periods, a total of three new compressors (labelled as **NM7**, **NM19** and **NM20**) are required and each is idle in at least one period. One can then manually produce a timesharing scheme in which only the first two are required to be put in use.

(2) By following the programming approach described in subsection 4.1, a multi-period design can also be generated for the present example. For the sake of brevity, only the network structure in period 1 is given in Fig. 2. Note that the idle units are not shown here.

The operating costs, capital costs and total annual costs of all aforementioned designs are compared in Table 3. It can be observed that, by incorporating the proposed model modifications, the TAC of any single-period design is significantly lower than that of the original network. Since any such design is optimal only in one period but may not be suitable for the other time intervals, the proposed timesharing approach should then be utilized to effectively integrate all single-period structures. On the other hand, since a proper trade-off between operating and capital costs can only be achieved with a comprehensive multi-period formulation, the corresponding TAC was found to be the lowest among all options. However, the required optimization run often lasts a very long time which is, in average, 10 times as much as that needed to obtain a single-period design.

6. Conclusions

The conventional programming approach to synthesize hydrogen networks has been modified in this work to circumvent drawbacks concerning unreasonable unit models and incomprehensive design considerations. As an alternative to the brute-force numerical optimization method for producing multi-period designs, a systematic timesharing algorithm has also been devised to manually integrate the single-period designs to form a less economical but more flexible structure for operations in all periods. An example is presented to show the effectiveness of the proposed approaches.

Table 1. Nominal inlet conditions of existing hydrogen users.

Sink	Flow rate in period 1 (MMscfd)	Flow rate in period 2 (MMscfd)	Flow rate in period 3 (MMscfd)	Purity (vol %)	Pressure (psi)
A	90.00	94.00	98.00	92.00	600
B	110.00	112.00	117.00	92.00	1200

Table 2. Nominal outlet conditions of existing hydrogen users.

Source	Flow rate in period 1 (MMscfd)	Flow rate in period 2 (MMscfd)	Flow rate in period 3 (MMscfd)	Purity (vol %)	Pressure (psi)
A	40.00	43.00	45.00	75.00	400
B	20.00	21.00	23.00	80.00	700

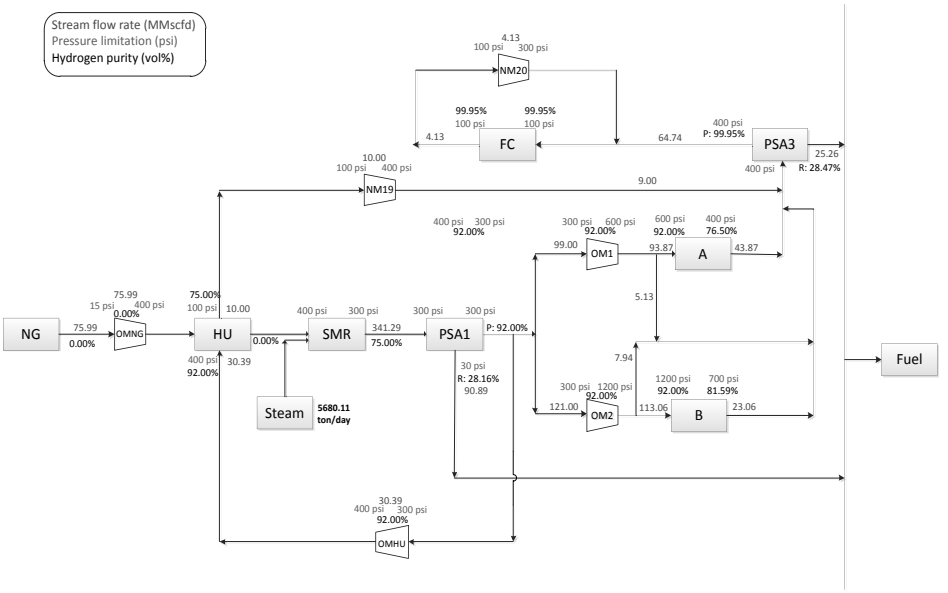

Figure 2. The optimal multi-period design for period 1.

Table 3. Cost summary (million $/year)

	Original network	Heurisitc approach	Programming approach
Operating cost (period 1)	35.59	5.09	9.77
Operating cost (period 2)	38.24	31.35	31.12
Operating cost (period 3)	38.6	31.78	30.59
Total operating cost (total)	112.42	68.22	71.49
Compressor	0.00	3.08	1.98
PSA	0.00	52.86	42.02
Fuel cell	0.00	215.13	175.04
Piping	0.00	6.66	4.73
Annualized total capital cost	0.00	23.75	19.13
TAC	112.42	91.97	90.62

References

M. I. Ahmad, N. Zhang, and M. Jobson, 2010, Modelling and Optimisation for Design of Hydrogen Networks for Multi-Period Operation, J. Clean. Prod., 18, 889–899.

Y. C. Chiang, and C. T. Chang, 2014, Single-Objective and Multiobjective Designs for Hydrogen Networks with Fuel Cells, Ind. Eng. Chem. Res., 53, 6006−6020.

Y. Jiao, H. Su, and W. Hou, 2012, Improved Optimization Methods for Refinery Hydrogen Network and Their Applications, Control Eng. Practice, 20, 1075−1093.

C. C. Kuo, 2014, An Improved Mathematical Model for Flexible Hydrogen Network Designs, MS Thesis, National Cheng Kung University, Tainan, Taiwan.

Krist V. Gernaey, Jakob K. Huusom and Rafiqul Gani (Eds.), 12th International Symposium on Process Systems Engineering and 25th European Symposium on Computer Aided Process Engineering.
31 May – 4 June 2015, Copenhagen, Denmark

An Integrated Reactive Distillation Process for Biodiesel Production

Eduardo S. Perez-Cisneros,[a] Ricardo Morales-Rodriguez,[a] Mauricio Sales-Cruz,[b] Tomás Viveros-García,[a] Ricardo Lobo-Oehmichen[a]

[a]*Departamento de Ingeniería de Procesos e Hidráulica. Universidad Autónoma Metropolitana Unidad Iztapalapa. 09430 D.F., México D.F.*
[b]*Departamento de Procesos y Tecnología. Universidad Autónoma Metropolitana-Cuajimalpa Artificios No. 40, C.P. 01120, México, D.F., México*
espc@xanum.uam.mx

Abstract

An integrated reactive distillation process for the production of biodiesel is proposed. The reactive separation process consists of two coupled reactive distillation columns considering the kinetically controlled reactions of esterification of the fatty acids (FFAs) and the trans-esterification of the tri-di and mono glycerides with methanol, respectively. The conceptual design of each reactive distillation column was performed through the construction of reactive residue curve maps in terms of elements. The design of the esterification reactive distillation column consisted of one reactive zone loaded with a solid catalyst (titanium oxide supported on silica TiO_2/SiO_2) and for the trans-esterification reactive column two reactive zones loaded with solid catalyst (hydrotalcites (CHT) and MgO). Intensive simulation of the integrated reactive process including the complex kinetic expressions for the different reactions and the Cubic-Plus Association (CPA) thermodynamic model was performed using the computational environment of ASPEN Plus. Results showed that the amount of fatty acids (FFAs) and water in the oil fed play a key role on the performance of the trans-esterification reactive distillation column while for the esterification column is not significant.

Keywords: reactive distillation, biodiesel production, conceptual design.

1. Introduction

Biodiesel represents a valuable alternative to petroleum derived fuels due to both its renewable nature and its substantially reduced net carbon dioxide emission. This biofuel is conventionally produced through batch or continuous trans-esterification of highly refined vegetable oils with methanol by using homogeneous alkaline catalysts such as sodium or potassium hydroxides or methoxides (Fukuda et al. 2001). The mentioned technology is not compatible with oils which free fatty acids (FFAs) content exceeding a threshold value of about 0.5% by weight. A possible solution to this drawback could be the development of new technologies enabling to employ waste raw materials such as fried oils or mixture of oils from various sources that cannot be treated in the conventional process for their high content in free fatty acids. This perspective discloses the way toward the development of innovative biodiesel production processes such as those based on supercritical methanol (Kusdiana and Saka, 2001), or the two-stage process (Suwannakarn, K. and E. Lotero, 2009). In the two-stage process, the FFAs in the feed are first esterified by acid catalysis to produce alkyl esters. This step prevents soap formation during the second step, which is the trans-esterification of the unreacted

triglyceride with alkali catalyst to obtain alkyl esters. This two-step process may be able to reduce the overall processing time and permit processing of feed stocks with high FFA content. However, the separation of product and catalyst is required in both the acid and alkali catalyzed steps, which again costs time and money. To avoid the separation required in a homogeneous catalytic system, researchers have explored the use of heterogeneous catalysts. Tesser et al. (2010) studied trans-esterification of soybean oil with both basic and acidic heterogeneous catalysts. For basic catalysts, hydrotalcites (CHT) and MgO were used. For acidic catalysts, titanium oxide supported on silica TiO_2/SiO_2 (TS) and vanadyl phosphate $VOPO_4 \cdot 2H_2O$ (VOP) were used. Therefore, it is generally accepted that a process employing a solid acid catalyst, if technically feasible, would be preferred on economic grounds. All of this evidence supports that there exist a need for improvement in the technological and economic feasibility of biodiesel production. Reactive distillation may be considered as an alternative process for biodiesel production. Especially for equilibrium limited and consecutive reactions, reactive distillation is a promising process alternative. Therefore, in the present work, an integrated reactive distillation process for the production of biodiesel is proposed.

2. The Reactive System

The generic esterification reaction of a carboxylic acid (oleic acid in this case) with methanol, producing methylester and water, is schematically shown below:

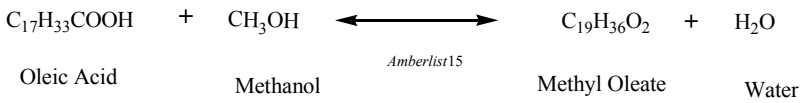

Figure 1. Overall reaction scheme for esterification of oleic acid.

The esterification processes for FFAs abatement are generally promoted by homogeneous acid catalyzed reaction or by ionic exchange acid resins as heterogeneous catalysts. The trans-esterification of triolein with methanol to methyl oleate has been selected as a model process for the trans-esterification of rapeseed oil to produce biodiesel. Figure 2 shows the overall trans-esterification reaction of triolein and Figure 3 shows the stepwise reaction scheme.

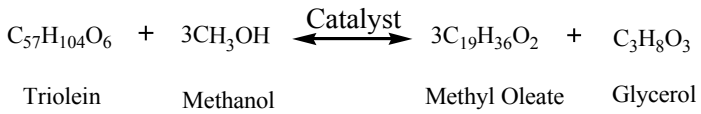

Figure. 2. Overall reaction scheme for trans-esterification of Triolein

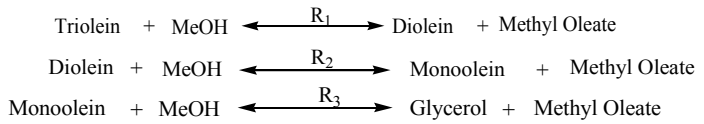

Figure. 3. Stepwise reaction scheme for trans-esterification of Triolein

The reactions described in Figures 1 and 2 can be represented in terms of elements as proposed by Pérez-Cisneros et al. (1997). Table 1 shows the elements definitions and the balanced reactions in terms of such elements.

Table 1. Representation of the reactive system in terms of elements

Reaction	Elements	Reactions in terms of elements
Esterification	A= $C_{18}H_{32}O$	
	B= H_2O	AB + C⇔AC + B
	C= CH_3OH	
Trans-Esterification	A= $C_{18}H_{32}O$	A_3B + C⇔ A_2B + AC
	B= $C_3H_8O_3$	A_2B + C⇔ AB + AC
	C= CH_3OH	AB + C⇔ B + AC

3. Residue Curve Maps and the Integrated Reactive Distillation Process

In this work, the residue curve maps were calculated for each reaction scheme separately following the procedure described by Granados-Aguilar et al. (2008). The heterogeneous kinetic models employed for the esterification reaction and for the transesterification reaction are reported by Tesser et al. (2010) and by Dossin et al. (2006), respectively. For the phase equilibrium computation, the Cubic-Plus-Association Equation of State (CPA) was used with the required parameters reported by Oliveira et al. (2010).

3.1. Esterification Reaction

For the esterification residue curve map a reactive mixture with methanol excess was used as initial composition point (x_{OA}=0.006, x_{MeOH}=0.99, x_{MO}=0.002, x_W=0.002). Figure 4a shows the residue curve map for different values of the reaction-separation parameter (α), which represents the amount of catalyst loaded into the boiling pot. Also, in Figure 4a, (OA) represents the oleic acid, (MeOH) methanol, (MO) methyl oleate and (W) indicates water compounds. It can be observed in Figure 4a that as the amount of catalyst loaded increases (α=0.0001 - 40) the residue curves tend to the AC node, which represents the methyl oleate (MO) pure compound. Figure 4b shows the corresponding liquid composition and temperature profile for the residue curve with α= 40. It can be noted in Figure 5a that the main conversion to methyl oleate occurs between the temperatures 340 K and 450 K, and as the methanol vaporizes and is consumed the remaining liquid phase in the boiling pot is pure methyl oleate.

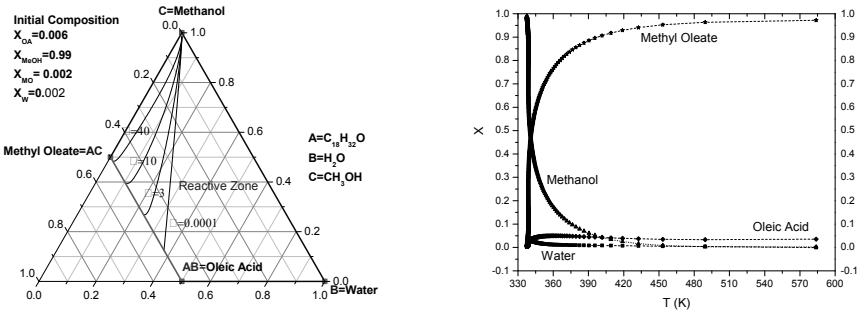

Figure 4. a) Residue curve map for esterification reaction; b) Liquid Composition and temperature profile for the residue curve at α = 40

3.2. Trans-Esterification Reaction

For the trans-esterification residue curve map a reactive mixture with methanol excess was used as initial composition point (xTG=0.04, xMeOH=0.95, xMO=0.004, xDG=0.002, xMG=0.002, xG=0.002). Figure 5a shows the residue curve map for different values of the reaction-separation parameter (α). Also, in Figure 4b, (TG) represents the tri-olein species, (MeOH) methanol, (MO) methyl oleate, (DG) di-olein, (MG) mono-olein and (G) indicates glycerol compounds. It can be observed in Figure 5a that as the amount of catalyst loaded increases (α =0.0001 - 0.01) the residue curves tend to the AC node, which represents the methyl oleate (MO) pure compound. Figure 5b shows the corresponding liquid composition and temperature profile for the residue curve with α= 0.01

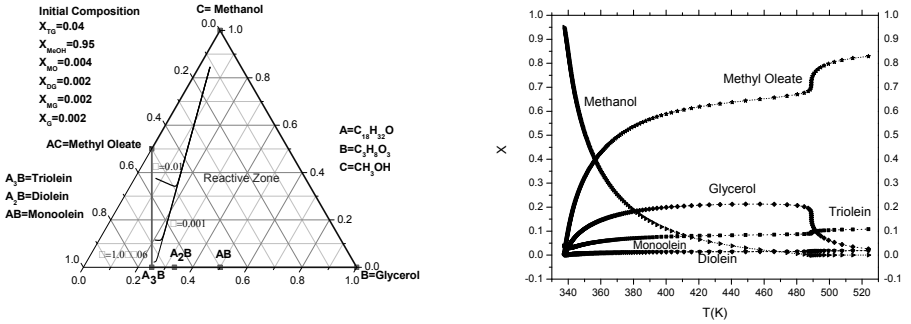

Figure 5. a) Residue curve map for trans-esterification reaction; b) Liquid Composition and temperature profile for the residue curve at α = 0.01

It can be noted in Figure 5b, in opposition to the esterification reaction, that the conversion to methyl oleate increases continuously from 340 K to 490 K, and as the methanol is consumed completely, vaporization of some glycerol occurs leading to an increment in liquid composition of methyl oleate. It should be pointed out that the final mixture in the boiling pot for the trans-esterification reaction is not pure methyl oleate, rather a mixture containing some tri-olein, di-olein and mono-olein should be considered.

4. Intensive Simulation

With the analysis of the reactive residue curve maps and through intensive simulations performed into the ASPEN plus environment a final integrated reactive distillation process to produce biodiesel was obtained. Figure 6 shows the process considering two reactive distillation columns: RDC-1, for esterification reaction loaded with a solid catalyst (titanium oxide supported on silica TiO_2/SiO_2) with one reactive section and RDC-2, for trans-esterification reaction loaded with solid catalyst (hydrotalcites (CHT) and MgO). The firs reactive distillation column (RDC-1) is fed with a mixture of oleic acid and triolein and methanol.

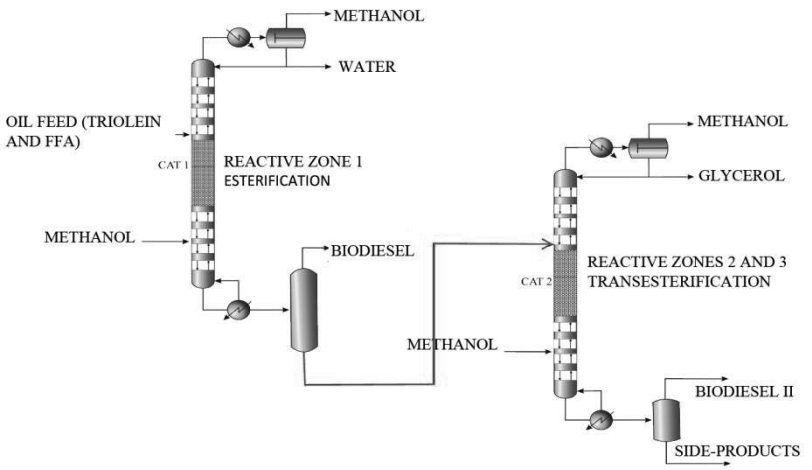

Figure 6. Integrated reactive distillation process for biodiesel production

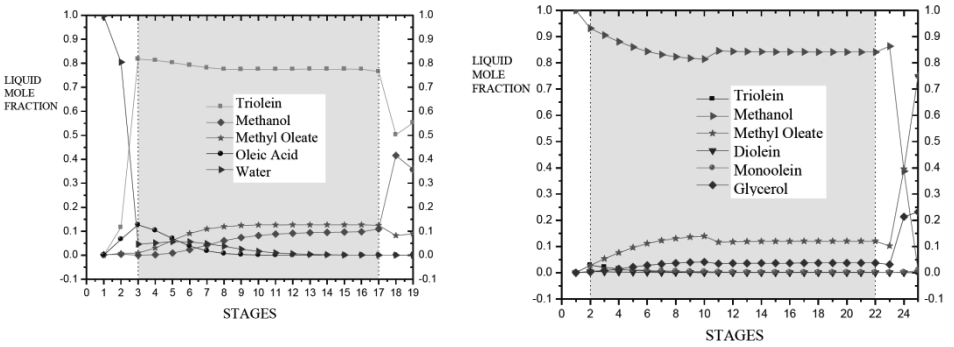

Figure 7. Liquid composition profile a) RDC-1 (Esterification); b) RDC-2 (Trans-esterification)

Table 2 shows the design specifications of the two reactive distillation columns. It should be pointed out that the reflux ratio for the trans-esterification reaction column required is higher than the esterification column and the methanol used is around six times greater. Therefore, it could be concluded that the RDC-2 is more sensitive to changes in the operating conditions. Figure 7a shows the liquid composition profile along the RDC-1 (esterification). It can be noted that the exit stream leaving the bottom of the column is a mixture rich in triolein, methanol and methyl oleate. The Oleic acid is completely consumed and water is vaporized. This bottom stream is further separated in a flash drum and the first biodiesel is produced at the top of the equipment. Figure 7b shows the liquid composition profile along the RDC-2 (trans-esterification). It can be noted that the exit stream leaving the bottom of the column is a mixture rich in methyl oleate and glycerol. The glycerol in the mixture is decanted and separated to produce biodiesel from the trans-esterification column. It is clear that the amount of methanol in

the stages of the RDC-2 must be high in order to achieve complete conversion of the triglycerides.

Table 2. Design specifications for the reactive distillation columns.

Variables	RDC-1	RDC-2
Column Pressure	1 atm	1 atm
Total stages	19	25
Reactive Stages	15 (from 3 to 17)	21 (from 2 to 12 and from 14 to 22)
Reflux Ratio	0.1 (Kmol)	2.5 (Kmol)
Feed Stage (oil)	3	2
Feed Stage (methanol)	18	13 and 23
Oil Feed Flow	14/86 (OA/TG)kmol/h	
Methanol Feed Flow	70 kmol/h	400 kmol/h ; 500 kmol/h
Catalyst loaded in stage	800 (kg)	1000 (kg)

5. Conclusions

An integrated reactive distillation process considering the esterification and trans-esterification reactions has been developed. The reactive residue curves posed in term of elements reveal the optimal operating conditions to render a high purity biodiesel in a coupled reactive distillation process. The complex kinetics and the CPA equation of state have been incorporated into the ASPEN plus environment to perform intensive simulations. Simulation results shown that the trans-esterification reactive distillation column is more sensitive to changes in the operating conditions.

Acknowledgments

The authors kindly acknowledge the Mexican National Council for Science and Technology (CONACyT, project number 230107) for the financial support on the development of this project.

References

T.F. Dossin, M.-F. Reyniers, R.J. Berger, G.B. Marin, 2006, Simulation of heterogeneously MgO-catalyzed transesterification for fine-chemical and biodiesel industrial production, Applied Catalysis B: Environmental, 67, 136–148.

H. Fukuda, A. Kondo, H. Noda, 2001, Biodiesel fuel production by transesterification of oils, Journal of Bioscience and Bioengineering, 92, 405–416.

A.S. Granados-Aguilar, T. Viveros García, E.S. Pérez-Cisneros, 2008, Thermodynamic analysis of a reactive distillation process for deep hydrodesulfurization of diesel: effect of the solvent and operating conditions, Chemical Engineering Journal,143, 210–219.

D. Kusdiana, S. Saka, 2001, Kinetics of transesterification in rapeseed oil to biodiesel fuel as treated in supercritical methanol, Fuel, 80, 693–698.

M.B. Oliveira, A.J. Queimada, J.A.P. Coutinho, 2010, Modeling of Biodiesel Multicomponent Systems with the Cubic-Plus-Association (CPA) Equation of State, Industrial and Engineering Chemistry Research, 49, 1419–1427.

E.S. Pérez-Cisneros, R. Gani, M.L. Michelsen, 1997, Reactive separation systems I. Computation of physical and chemical equilibrium, Chemical Engineering Science, 54, 527-543.

K. Suwannakarn, E. Lotero, 2009, Simultaneous Free Fatty Acid Esterification and Triglyceride Transesterification Using a Solid Acid Catalyst with in Situ Removal of Water and Unreacted Methanol, Industrial and Engineering Chemistry Research, 48, 2810-2818.

R. Tesser, L. Casale, D. Verde, M. Di Serio, E. Santacesaria, 2010, Kinetics and modeling of fatty acids esterification on acid Exchange resins, Chemical Engineering Journal, 157, 539-550.

Krist V. Gernaey, Jakob K. Huusom and Rafiqul Gani (Eds.), 12th International Symposium on Process Systems Engineering and 25th European Symposium on Computer Aided Process Engineering.
31 May – 4 June 2015, Copenhagen, Denmark

A Sequential Algorithm for the Rigorous Design of Thermally Coupled Distillation Sequences

José A.Caballero,[a*] Juan A. Reyes-Labarta,[a] Ignacio E. Grossmann.[b]

[a]*Department of Chemical Engineering, University of Alicante, Ap. Correos 99. 03080,Alicante, Spain*
[b] *Department of Chemical Engineering,Carnegie Mellon University, 5000 Forbes Av. Pittsburgh, PA. 15213,USA.*
caballer@ua.es

Abstract

A sequential design method is presented for the design of thermally coupled distillation sequences. The algorithm starts by selecting a set of sequences in the space of basic configurations in which the internal structure of condensers and reboilers is explicitly taken into account and extended with the possibility of including divided wall columns (DWC). This first stage is based on separation tasks (except by the DWCs) and therefore it does not provide an actual sequence of columns. In the second stage the best arrangement in N-1 actual columns is performed taking into account operability and mechanical constraints. Finally, for a set of candidate sequences the algorithm try to reduce the number of total columns by considering Kaibel columns, elimination of transfer blocks or columns with vertical partitions. An example illustrate the different steps of the sequential algorithm

Keywords: Distillation, Thermally Coupled Distillation, MINLP, Process Integration, Process intensification.

1. Introduction

Thermally Coupled Distillation (TCD) has acquired a renewed interest because, when compared to conventional systems, it is possible to reach over 30% in energy reduction. Besides, if the search space includes Divided Wall Columns (DWC) important investment savings can also be achieved.

One of the major difficulties in the synthesis involving TCD is that the number of alternatives grows up much faster than when only conventional columns are considered. i.e. for a 5 component mixture there are 203 basic configurations (Giridhar & Agrawal, 2010) if we consider also the internal structure of heat exchangers there are around 10^4 alternatives, and if we consider the thermodynamically equivalent configurations the number of alternatives is around $2 \cdot 10^5$. (Caballero & Grossmann, 2003).

In this work we propose a sequential algorithm, that combines shortcut models (based on Fenske – Underwood –Gilliland (FUG) methods) and rigorous process simulators to the rigorous design of complex TCD sequences. A description of the different stages is as follows:

1. Search in the space of basic configurations (Giridhar & Agrawal, 2010) augmented with the internal structure of heat exchangers (Caballero & Grossmann, 2006). Even

though, consider only the basic configurations, and then optimize the internal structure of heat exchangers usually produce good results, Caballero and Grossmann (2013) showed that the optimal sequence of separation tasks can be lost in a sequential approach. Besides, those authors also showed that DWCs could have an important impact on the total cost of a given sequence and therefore it is convenient explicitly include DWCs in this stage. However, it is important that thermodynamically equivalent alternatives are not taken into account at this stage. Thermodynamically equivalent alternatives share the same sequence of separation tasks and, in most cases; the differences in cost are negligible. Therefore, except for the DWCs, we use an approach based on separation tasks instead of final columns. The final model is a MINLP model. A detailed description of this approach can be found in Caballero and Grossman (2013). Note that the sequence of task must be rearranged in actual columns (see points 3 and 4), that could have a considerable impact on the final cost especially if a configuration with less than N-1 columns is generated.
Besides, in TCD it is common to find several solutions near the optimal one, which must be also taken into account. As a consequence we calculate all the sequences of separation tasks inside a given tolerance, say inside the 10% of the best one.

2. FUG equations assume constant volatilities and constant molar overflow. In actual systems these assumptions not always hold either in a single separation tasks or in different separations. The accumulation of errors could produce inaccurate results. A rigorous simulation (i.e. Aspen-Hysys) allows checking the model and, if necessary, we modify relative volatilities for each separation tasks until we get a good agreement between both models.

3. Selection of the best sequence of columns with exactly N-1 columns (N is the number of key components to be separated). At this point we must take into account two considerations. 1. A thermal couple –two streams, a liquid and a vapour connecting two sections- could induce sections with important differences in diameter. Although it is possible to build columns with different diameters, a column with three or four different diameters did not seem, at least practical. 2. Agrawal and Fidkowski (1998) showed that the sections must be arranged in actual columns in such a way that the vapour flows from higher to lower pressures. The vapour flow between columns can be controlled by a valve. Caballero & Grossmann (2003) showed that for a given feasible sequence of separations tasks it is always possible to get that configuration using N-1 columns. Therefore, in this stage we search for the minimum cost feasible sequence formed by N-1 columns with a single diameter in which the vapour flows from higher to lower pressures. This usually means increasing the diameter of some sections, with its corresponding cost penalty. The feasibility must be checked to ensure that modifications in diameters do not create operability problems (i.e. weeping, flooding, etc.).

4. Selection of the best sequence with less than N-1 columns (Intensification). Some basic sequences of separation tasks allow reducing the number of columns to less than N-1 with a small or moderate penalty in energy consumption. There is a trade-off between the reduction in the investment cost and the increase in the energy consumption. It would be possible to generate all the possible sequences with «reduced number» of columns (Shenvi et al, 2012), and try to select the best one. However a more practical approach consists of studying only the set of best

sequences generated in step 1. If the maximum reduction in investment cost identifies a possible optimal sequence then the intensified sequence is rigorously calculated. Three possible intensification alternatives are taken into account: 1) Kaibel columns (Kaibel, 1984) –separate four key components using a DWC-. 2) Elimination of transfer blocks (Rong and Massimiliano, 2012). These blocks appear in sequences which have columns formed by a single section connecting other two columns. 3) Columns that can be merged in a single shell to form «columns with vertical partitions» (Agrawal, 2001). Or any combination of those.
It is also possible to reduce the number of columns by extracting some products as side streams, but in this case high purity requirements are difficult to get. But it must be taken into account if no high recoveries are necessary.

There are other modifications that could facilitate the operability of the sequence and can be taken into account. DWCs or Kaibel columns can be thermally coupled with the rest of the sequence, which could produce difficulties in the operation. In those cases it is convenient 'decouple' those columns by forcing the existence of a reboiler and a condenser. Shah and Agrawal (2010) suggested that some bi-directional flows (a liquid and a vapour stream exiting from some point in the middle of a column and entering in the middle of another column) can be substituted by a single liquid stream with a small energy penalty, but improving the operability of the column.
Finally, the existence of thermal couples makes that some separation tasks are working far away of their optimal conditions (conditions in which separation task would be operated if there were no interaction with other tasks). That excess of vapour (liquid) in some sections could be use as heating (cooling) media in other parts of the plant (Navarro et al, 2013). But of course, this analysis can be performed only taking into account the whole plant. Alternatively, if the excess of flow is too large (with also large diameters in the actual column) we should consider the possibility of include side heat exchangers. A comprehensive discussion can be found in the work by Navarro et al (2013)
We illustrate all these points with the following example.

2. Example

Consider a mixture of four lineal hydrocarbons; from n-hexane to n-nonane (All relevant data are shown in Table 1).

Table 1. Data for the example.(Rest of physical data from Aspen–Hysys ™ database)

Components	Feed flow (kmol/h)		
A = n-hexane	120	Pressure	1.2 atm
B = n-heptane	90	Feed liquid fraction	1
C = n-octane	60	Vapour Steam cost	14.05 $/GJ
D = n-nonane	30	Cooling water cost	0.354 $/GJ
		Cost data source	Turton et al (2013)

The following constraints have been added to the model in order to generate non-difficult to operate sequences: 1) Divided wall columns must have a condenser and a reboiler. In other words, they cannot be thermally coupled with the rest of the system. 2) The flow transfer between two columns using side streams is forced to be saturated

liquid. 3) We search for actual columns with a single diameter, and configurations for which it is possible to establish a gradient of pressures in such a way that the vapour flows from higher to lower pressures. 4) We consider only columns with a single internal wall.

As commented before we obtained not only the best solution but a set of solutions inside a given tolerance. For this example there are 6 different solutions with a TAC that differ in less than 10%. The best solution obtained corresponds to a fully thermally couple configuration (extended Petlyuk arrangement) with a total annualized cost (TAC) equals to 2261.9 k$/y. If we rearrange the sequence of tasks in actual columns there is an increment of cost, because the increase in the diameter of some sections, to 2336.7 k$/y. (around 3.3%). Figure 1 shows the best solution of stage 1 after the rearrangement in actual columns.

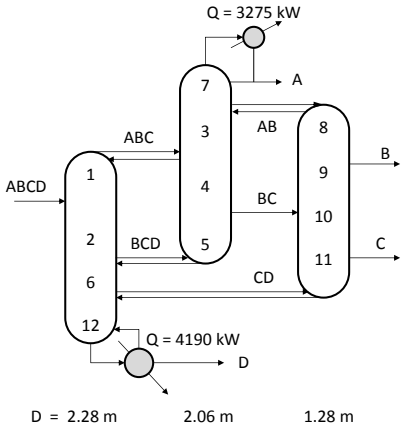

Figure 1. Best solution after steps 1 and 2

A Kaibel sequence can be generated from a fully TCD sequence by removing intermediate mixtures that do not include extreme volatility components (BC in this case). If the energy penalty is not too large the reduction in the number of shells could become the Kaibel column the optimal one. In this example, a simple calculation at minimum reflux conditions shows that there is an energy penalty around 18.5%. Taking into account energy consumption is around the 70% of the TAC we can discard the Kaibel column.

The first, second, third and fourth solutions share the same sequence of separation tasks, and differs each other only in some heat exchangers, therefore we skip here these alternatives (second solution includes a reboiler in the separation BC/CD; the third one includes reboilers in separation tasks ABC/BCD and BC/CD; and the fourth solution a reboiler in ABC/BCD).

Especial mention deserves the fifth solution. For this solution the TAC increases to 2455 k$/y (around 8% higher). In this case it is possible to identify a 'transfer block', which allows reducing by one the number of columns, with almost no penalty in energy consumption, (see Figure 2). We can go a step forward and merge these two columns in a single divided wall column. Remark also that in the final configuration the areas of each section do not need to be modified!

The TAC for the sequence in Figure 2.d is reduced to 2276 k$/y. Therefore, the intensified configuration in Figure 2d has the same TAC than the best sequence formed by N-1 columns (difference around 1%). The final decision on what sequence to build must be based in other kind of considerations.

It is worth remarking that the first sequence with a DWC has a TAC equal to 2821.3 k$/y (around 25% higher). This is due to the fact that we have forced the DWC not to be coupled with the rest of the system. In other words, the DWC must have a condenser and a reboiler (see Figure 3a). Intermediate heat exchangers could have an important impact on the total cost. For example, if for the best solution we force a condenser in the separation task AB/BC (this heat exchanger does not appear in any of the best solutions) the cost increases almost in a 30% (2910 k$/y.)

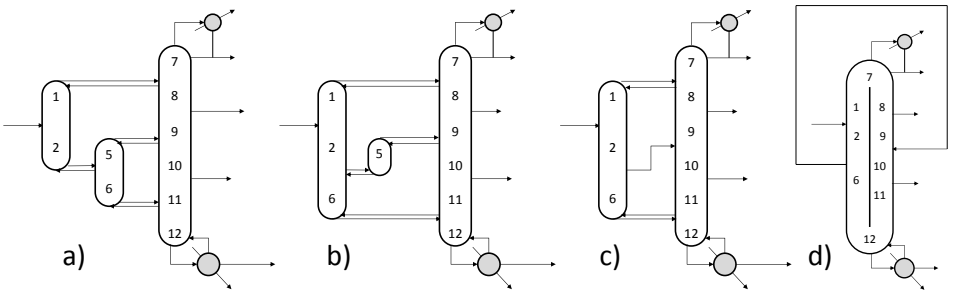

Figure 2. Process intensification for the 5th sequence. a) A feasible arrangement in actual columns. b) A thermodynamically equivalent configuration with a «transfer block». c) Configuration removing section 5. d) Divided wall column thermodynamically equivalent to configuration c.

If we allow the DWCs to be coupled with the rest of the system then the optimal solution is a fully TCD with an internal wall (See Figure 3b).

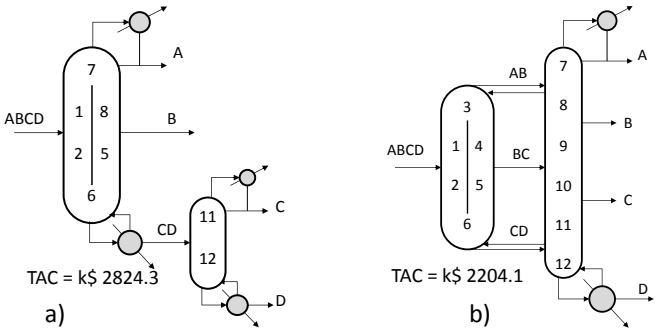

Figure 3. a) Best solution with a divided wall in which the DWC is forced to have reboiler and condenser. b) Best solution if DWCs can be thermally coupled.

3. Conclusions

A systematic procedure for the synthesis and intensification of column configurations for multicomponent distillation is presented. The algorithm starts by searching in the space of basic configurations extended with the internal structure of heat exchangers (reboilers and condensers do not associated to final products). It has been shown that some internal heat exchangers can have a large impact on the performance of the complete system. If this internal structure of heat exchangers is not taken into account there is a large probability of losing the optimal solution. On the other side it is not convenient to explicitly consider, at this stage, the final arrangement in actual columns. This is because there are a potential very large number of thermodynamically equivalent

configurations with similar cost. So a good approach is to use a task based instead of a column based approach.

The optimal sequence of tasks must be rearranged in actual columns. To that end the algorithm takes into account operability constraints and some necessary modification in the diameter of some column sections to avoid building columns with three or more different diameters. Other considerations like limiting the total length can be addressed either by increasing the number of columns or modifying the internals in the column (i.e. tray separation). However, all these modifications must be carefully checked to avoid column malfunctions.

Finally, it is possible try to intensify the total system by reducing the number of column shells. Different alternatives where considered: Kaibel columns, elimination of transfer blocks and merge columns using vertical partitions. However, except in some DWCs, the reduction in the number columns involves a penalty in energy and as a consequence the trade-offs must be carefully studied. But the example shows that these alternatives must be considered

4. Acknowledgements.

The authors wish to acknowledge the financial support by the Ministry of Economy and Competitiveness from Spain, under the project CTQ 2012-37039-C02-02.

References

R. Agrawal, 2001. Multicomponent distillation columns with partitions and multiple reboilers and condensers. Industrial & Engineering Chemistry Research 40(20) 4258-4266.

R. Agrawal, Z. T. Fidkowski, 1998. More operable arrangements of fully thermally coupled distillation columns. AIChE Journal 44(11) 2565-2568.

J. A Caballero, I. E. Grossmann, 2003. Thermodynamically Equivalent Configurations for Thermally Coupled Distillation. AIChE Journal, 49(11) 2864-2884.

J. A. Caballero, I. E. Grossmann, 2006. Structural considerations and modeling in the synthesis of heat-integrated-thermally coupled distillation sequences. Industrial and Engineering Chemistry Research 45(25) 8454-8474.

J. A. Caballero, I. E. Grossmann, 2013. Synthesis of complex thermally coupled distillation systems including divided wall columns. AIChE Journal 59(4) 1139-1159.

A. Giridhar, R. Agrawal, 2010. Synthesis of distillation configurations: I. Characteristics of a good search space. Computers & Chemical Engineering, 34(1) 73-83.

G. Kaibel, 1987. Distillation Columns with Vertical Partitions. Chemical Engineering Techology 10(1) 92-98.

M A. Navarro-Amoros, R. Ruiz-Femenia, J. A. Caballero, 2013. A new technique for recovering energy in thermally coupled distillation using vapor recompression cycles." AIChE Journal 59(10) 3767-3781.

B. G. Rong, M. Errico, 2012. Synthesis of intensified simple column configurations for multicomponent distillations. Chemical Engineering and Processing: Process Intensification 62, 1-17.

V. H. Shah, R. Agrawal, 2010. Are All Thermal Coupling Links between Multicomponent Distillation Columns Useful from an Energy Perspective? Industrial & Engineering Chemistry Research 50(3) 1770-1777.

A. A. Shenvi, ,V.H. Shah, J. A. Zeller, R. Agrawal, 2012. A synthesis method for multicomponent distillation sequences with fewer columns. AIChE Journal 58(8): 2479-2494.

R. Turton, R. Bailei, R. C., Whiting, B. Wallace, J. A. Shaeiwitz, D. Bhattacharyya. 2013. Analysis, Synthesis and Design of Chemical Processes. 4th Edition. Upper Saddle River, NJ. USA., Pearson Education, Inc.

Krist V. Gernaey, Jakob K. Huusom and Rafiqul Gani (Eds.), 12th International Symposium on Process Systems Engineering and 25th European Symposium on Computer Aided Process Engineering.
31 May – 4 June 2015, Copenhagen, Denmark

Discovery of New Zeolites for H_2S Removal through Multi-scale Systems Engineering

Tingting Liu, Eric L. First, M. M. Faruque Hasan[‡], Christodoulos A. Floudas[*]

Department of Chemical and Biological Engineering, Princeton University, Princeton, NJ 08544, USA

[‡] *Present Address: Artie McFerrin Department of Chemical Engineering, Texas A&M University, College Station, TX 77843, USA*

[*]*To whom all correspondence should be addressed, Email: floudas@titan.princeton.edu*

Abstract

Removal of H_2S from industrialgas mixturesis important to avoid operational hazards, and to meet stringent environmental regulationto curb H_2S emission. Zeolites are microporous materialswhich have shown excellent potential as adsorbents for molecular gas separation, and can be applied for separating H_2S from other gases. We apply a multi-scale systems engineering framework to discover or identify highly selective, feasible and cost-effective zeolites for pressure swing adsorption (PSA)-based H_2S separation. Using the *in silico* framework, several new and cost-effective zeolites are identified for adsorption-based H_2S separation. We demonstrate the applicability of the multi-scale approach for H_2S separation fromrepresentative binary gas mixtures such as acid gas (H_2S/CO_2), tail gas (H_2S/N_2), and natural gas (H_2S/CH_4). A key component of the proposed approach is an efficient and hierarchical computational screening that combines selection of materials with advanced process optimization. We anticipate that this approach is suitable for the discovery of novel materials for other molecular gas separation of industrial importance.

Keywords: hydrogen sulfide removal, zeolite, pressure swing adsorption, process optimization, multi-scale systems engineering

1. Introduction

H_2S is a toxic gas found in many chemical and industrial plants, including natural gas processing and utilization, power plants, coal gasification, refineries, petrochemical processing, wastewater treatment, and semiconductor manufacturing. The presence of H_2S in natural gas leads to pipeline corrosion during natural gas transportation. Furthermore, H_2S is one of the major air pollutants found in tail gases and flues gases from chemical and power plants. Removal of H_2S from industrial gas streams with high CO_2 and H_2S concentrations is important due to stringent environmental regulations. Several technologies are available for H_2S removal, which include absorption, adsorption, Claus conversion, catalytic oxidation, catalytic membrane contactor, and microbial treatment.

Pressure swing adsorption (PSA), which involves passing a gas mixture through a column packed with a microporous adsorbent that selectively adheres one gas over others, has been the technology of choice for many industrially important gas separation problems including air separation, carbon capture, and natural gas purification. Microporous adsorbents such as zeolites and metal–organic frameworks (MOFs) have

been shown to be excellent candidates for molecular gas separation for CO_2 capture (Hasan *et al*., 2012a, 2012b, 2013, 2014) and natural gas purification (First *et al*., 2014). There are numerous choices for zeolites as adsorbents, and an efficient computational framework is therefore required to screen for the most promising candidates.

In this work, we apply a multi-scale framework to screen highly selective, feasible and cost-effective zeolites for PSA-based H_2S separation from representative and binary gas mixtures such as acid gas (H_2S/CO_2), tail gas (H_2S/N_2), and natural gas (H_2S/CH_4). We present an *in silico* framework (Figure **1**) that combines zeolite screening with process optimization to identify the most cost-effective materials for these separations involving H_2S. Several materials-centric metrics are used to filter a database of zeolites to a short list of candidates. The PSA process using each of these zeolites is modeled using a detailed system of nonlinear algebraic and partial differential equations. The process topology and conditions are optimized for each zeolite to minimize the total cost of separation, which serves as the final ranking criterion.

2. Screening based on Shape, Size, and Pore Selectivities

Our hierarchical screening procedure (shown in Figure **1**) starts with a three-dimensional pore characterization method to filter the ZEOMICS database of 199 zeolite structures (First *et al*., 2011) to obtain a short list of candidate zeolites as potential adsorbents for H_2S separation. We use three geometric-level metrics: shape selectivity, size selectivity, and pore selectivity. For the case of binary gas mixture, shape selectivity describes the difference in energetic cost of transport of two gases through a zeolite's pores and their networks due to strain and distortion caused by shape and size (Gounaris *et al.*, 2006a, 2006b, 2009; First *et al*., 2013). Shape selectivity is calculated as the absolute difference in Boltzmann factors of the minimum pathway energies of the two gases. The metric of size selectivity was first introduced by Hasan *et al.* (2013) to consider the entire distribution of pore sizes. While shape selectivity is focused on the most dominant pathway through a zeolite, size selectivity is calculated as the relative difference in accessible pore volume between two gases by approximating the gas molecules as hard spheres to determine accessibility.

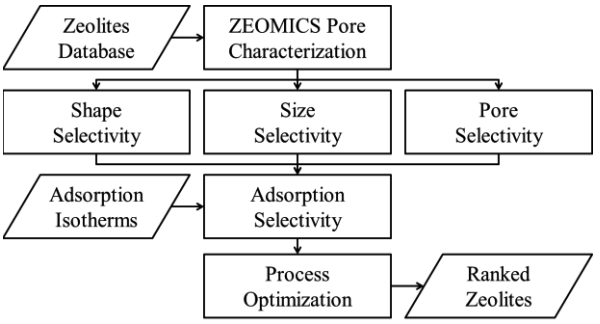

Figure 1. Flowchart of the multi-scale framework for adsorbent screening using combined material characterization and process optimization methodologies.

Pore selectivity is another metric originally proposed for natural gas purification (First *et al.*, 2014). It is calculated as the relative difference in energetically-accessible pore volume. The concept of pore selectivity is based on combining the energetic calculations of shape selectivity with the accessible pore volume calculations of size selectivity.

Each of these metrics is calculated as a number between 0 and 1, with 0 indicating low selectivity and 1 indicating high selectivity. Minimum cut-off values of 0, 0.1, and 0.1 are introduced for shape, size, and pore selectivity, respectively, to filter the full database of zeolites. Out of 199 zeolites, 29 zeolites show shape selectivity, 26 zeolites show size selectivity, and 33 zeolites show pore selectivity higher than 0.1 for H_2S for CH_4/H_2S system. All 33 zeolites which are pore-selective also show shape and size selectivities for this separation. We have also identified 57 out of 199 zeolites which show either shape selectivity, size selectivity or pore selectivity for H_2S removal from CO_2/H_2S.Similarly, 64 candidate zeolites are screenedas preliminary candidates for H_2S removal from H_2S/N_2 mixture, which exhibit either shape, size and pore selectivity.

3. Screening based on Adsorption Selectivity

Adsorption selectivity is determined by performing grand canonical Monte Carlo (GCMC) simulations to calculate the Henry constants for the two gases in each zeolite. The details of the GCMC simulations are reported elsewhere (Hasan *et al*., 2013, First *et al*., 2014). For each system, we consider top zeolites with adsorption selectivitygreater than 10 for further consideration duringdetailed process optimization. The selected zeolites for H_2S/CO_2, H_2S/N_2, and H_2S/CH_4 separation are listed in Table **1**. Note that the reported adsorption selectivities correspond to the more adsorptive component of the two gases present. In zeolites, the adsorption affinities for gases are usually as follows: CO_2> H_2S >CH_4>N_2. Therefore, Table **1** reports the selectivities of CO_2, H_2S, and CH_4 for CO_2/H_2S, H_2S/N_2, and CH_4/H_2S mixtures, respectively.

Table 1. Candidate zeolites for H_2S removal based on materials-centric metrics.

Zeolite	Shape selectivity	Size selectivity	Pore selectivity	Adsorption selectivity
H_2S removal from CO_2/H_2S mixture				*CO_2/H_2S*
AHT	0.396	0	0.4258	38849.16
LOS	0.5864	0	0.9765	2276.41
ABW	0	0	0.2836	627.46
NSI	0.2461	1	0.3365	200.77
BIK	0	1	0.1283	51.97
MON	0	1	0.0762	50.88
AEN	0	1	0.0083	29.93
APC	0	1	0.1936	26.40
H_2S removal from H_2S/N_2 mixture				*H_2S/N_2*
AWO	0	0.22	0.22	227.80
APD	0	1.00	0.12	170.40
DFT	0	0.27	0.00	122.00
ATV	0	0	0.22	118.00
SBN	0.27	1.00	0.28	108.70
TOL	0.84	0	0.96	89.79
ZON	0	0.17	0.06	88.89
SOD	0.94	1.00	0.94	81.77
BRE	0.26	1.00	0.27	77.07
MER	0	0.20	0	73.83

H_2S removal from H_2S/CH_4 mixture				H_2S/CH_4
AWO	0	0	0.1095	32.9
SBN	0.2701	0	0.2736	19.71
MER	0	0.3879	0	14.17
LOV	0.3201	0	0.3188	13.59
RWR	0	1	0	13.01
DAC	0	0.4487	0	12.71
JRY	0	1	0.0046	11.75
GOO	0	0	0.1838	11.53
GIS	0	1	0	11.3
ATN	0	0	0.1272	11.04
SIV	0	0.5369	0.0016	10.33
SOF	0	0.3975	0.0001	10.14
ITW	0.1296	0	0.1472	10.1

4. Process Optimization for Pressure Swing Adsorption (PSA)-based H_2S Separation

The PSA process that we consider for H_2S removal is illustrated in Figure **2a**. The feed may pass through a compressor to bring it to the desired adsorption pressure. Then one or more columns packed with a zeolite adsorbent (selected from Table 1) are used for adsorption. For CO_2/H_2S and H_2S/CH_4 mixtures, the clean gas(CO_2 or CH_4) is collected using a desorption vacuum pump. When we separate H_2S from H_2S/N_2 mixture, H_2S is collected using the desorption vacuum pump.

The process is operated using a 3-step PSA cycle (Figure **2b**) consisting of (i) column pressurization, and (ii) adsorption and (iii) counter-current desorption of the more adsorptive gas. During pressurization, the column fills from the feed-end with the feed mixture until the adsorption pressure, P_{ads}, is reached. Then, during the adsorption step, the other end of the column opens and less adsorptivegas exits the column while the more adsorptive gas is adsorbed by the zeolite. Finally, during desorption, the other end of the column is again closed, and the more adsorptive gas is evacuated from the feed-end of the column at the desorption pressure, P_{des}. A typical pressure profile during a cycle is provided in Figure **2b**. Multiple adsorption columns can be used to maximizethe utilization of the feed compressor and the desorption vacuum pump.

The PSA process is modeled using a detailed system of nonlinear algebraic and partial differential equations (NAPDE), which can be found elsewhere (Hasan *et al*., 2012, 2013; First *et al*., 2014). These equations describe mass and energy balances, flow through porous media, temperature and pressure effects, and heat transfer resistance across the column wall (Hasan *et al*., 2012, 2013). A candidate zeolite is represented in the model by parameters describing the adsorption isotherms and heats of adsorption of the gases present in the feed, which are readily available through GCMC simulation.

The model is optimized to identify the column length (L), adsorption (P_{ads}) and desorption (P_{des}) pressures, and adsorption (t_{ads}) and desorption (t_{des}) step durations. The pressurization time is fixed to 20 s (Hasan *et al*., 2012), and the column diameter and number of columns are determined using analytical expressions described in Hasan *et al*. (2013). To efficiently optimize the large, complex process model, an efficient Kriging-based grey-box constrained optimization approach is used (Hasan *et al*., 2013).

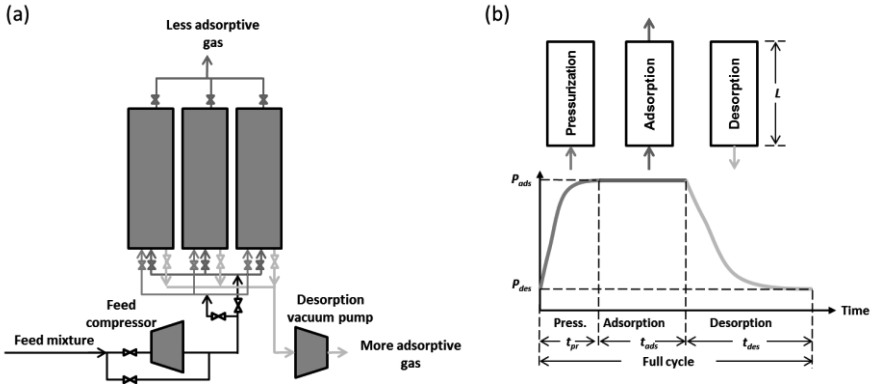

Figure 2. PSA process for H_2S separation: (a) process flow diagram with multiple columns, feed compressor and desorption vacuum pump, and (b) pressure profile of the 3-step PSA cycle, which includes (i) pressurization, (ii) adsorption, and (iii) desorption.

5. Cost-effective Zeolites for H_2S Separation

5.1. H_2S Removal from CO_2/H_2S Mixture

The feed mixture consideredin this problem contains 80% CO_2 and 20% H_2S.The feed flow rate is 0.1 kmol/s. We optimize the total annualized cost (TAC) of the PSA process, where TAC includes the investment, operating and material costs. The optimized results are shown in Table 2. We have identified ABW, LOS, NSI, BIK, MON, AEN and APC, which can remove H_2S and increase the CO_2 purity to 93 – 99% with CO_2recovery of 85 – 92% at reasonable cost.

Table 2. PSA results for the top zeolites for H_2S separation from CO_2/H_2S mixture.

Zeolite	P_{ads}(bar)	P_{evac}(bar)	t_{ads}(s)	t_{evac}(s)	L (m)	CO_2Purit (%)	CO_2Recovery (%)	Cost (MM$)
ABW	1	0.01	9.91	150	1	93	90	3.28
LOS	1.03	0.01	6.58	100	1	98	85	3.27
NSI	1.03	0.01	15	200	1	97	92	3.15
BIK	2	0.01	18.74	300	1	98	92	3.35
MON	2.08	0.01	16.78	150	1	95	91	3.47
AEN	2.31	.005	15.32	231	1	99	88	3.57
APC	2.36	0.01	16.04	150	1	94	89	3.74

5.2. H_2S Removal from H_2S/N_2 Mixture

We have optimized the PSA process for the top zeolites listed in Table **1**. We consider a feed composition of 10% H_2S and 90% N_2. The best zeolite is found to be AWO which can meet the clean gas (N_2) requirement in terms of purity (98%) and recovery (97%). The cost of N2 purification from a feed containing 20% H_2S and with a flow rate of 0.1 kmol/s is $1.51 MM. Therefore, AWO is a promising zeolite for H_2S removal.

5.3. H_2S Removal from H_2S/CH_4Mixture

We consider the feed mixture to be 80% CH_4 and 20% H_2S. This is a challenging problem with high initial concentration of H_2S. We have investigated the top zeolites

suggested by the materials-centric metrics, and found that the zeolite AWO is a promising zeolite which has not been suggested in any previous studies for H_2S separation for removing H_2S from natural gas (CH_4).

6. Conclusions

Using the combined material screening and process optimization methodology, we have discovered several new zeolites for removing H_2S from a variety of industrial gas mixtures with applications in carbon capture, acid gas removal, natural gas purification and tail gas purification. The most economical sorbents, zeolites ABW and AWO, are attractive for use in a PSA process to separate H_2S from sources containing H_2S with high concentrations (as high as 20%). The PSA process can achieve CO_2 purity to 93 – 99% with CO_2 recovery of 85 – 92% for CO_2/H_2S system, 98% purity and 97% recovery of N_2 for H_2S/N_2 system, and more than 90% purity and recovery for H_2S/CH_4 system. The costs of separation are also reasonable.We anticipate that our approach is suitable for the discovery of novel materials for other molecular gas separation.

Acknowledgements

This work was partially supported by the National Science Foundation under awards EFRI-0937706 and CBET-1263165. E.L.F. is thankful for his National Defense Science and Engineering Graduate (NDSEG) fellowship. A portion of the computation was performed at the TIGRESS high performance computer center at Princeton University. Tingting Liu acknowledges support from the China Scholarship Council, (CSC), (No. 201306880009).

References

First, E. L., Gounaris, C. E., Floudas, C. A. (2013). Predictive framework for shape-selective separations in three-dimensional zeolites and metal–organic frameworks. *Langmuir*, 29(18):5599–5608.

First, E. L., Gounaris, C. E., Wei, J., Floudas, C. A. (2011). Computational characterization of zeolite porous networks: an automated approach. *Physical Chemistry Chemical Physics*, 13(38):17339–17358.

First, E. L., Hasan, M. M. F., Floudas, C. A. (2014). Discovery of novel zeolites for natural gas purification through combined material screening and process optimization. *AIChE Journal*, accepted for publication.

Gounaris, C. E., Floudas, C. A., Wei, J. (2006a). Rational design of shape selective separation and catalysis–I: Concepts and analysis. *Chemical Engineering Science*, 61(24):7933–7948.

Gounaris, C. E., Wei, J., Floudas, C. A. (2006b). Rational design of shape selective separation and catalysis–II: Mathematical model and computational studies. *Chemical Engineering Science*, 61(24):7949–7962.

Gounaris, C. E., Wei, J., Floudas, C. A., Ranjan, R., Tsapatsis, M. (2009). Rational design of shape selective separations and catalysis: Lattice relaxation and effective aperture size. *AIChE Journal*, 56(3):611–632.

Hasan, M. M. F., Baliban, R. C., Elia, J. A., Floudas, C. A. (2012). Modeling, simulation and optimization of CO_2 capture for variable feed CO_2 concentration and feed flow. 2. Pressure swing adsorption and vacuum swing adsorption processes. *Industrial & Engineering Chemistry Research*, 51(48):15665–15682.

Hasan, M. M. F., First, E. L., Floudas, C. A. (2013). Cost-effective CO_2 capture based on *in silico* screening of zeolites and process optimization. *Physical Chemistry Chemical Physics*, 15(40):17601–17618.

Krist V. Gernaey, Jakob K. Huusom and Rafiqul Gani (Eds.), 12th International Symposium on Process Systems Engineering and 25th European Symposium on Computer Aided Process Engineering.
31 May – 4 June 2015, Copenhagen, Denmark

Optimization of a Fusel Oil Separation System Using a Dividing Wall Column

José de Jesús Mendoza – Pedroza[a], Juan Gabriel Segovia – Hernández[a], Álvaro Orjuela – Londoño[b]. Salvador Hernández[a]

[a] *Campus Guanajuato, Departamento de Ingeniería Química, Universidad de Guanajuato,Noria Alta s/n, 36050, Guanajuato, Gto., México.*
[b] *Departamento de Ingeniería Química y Ambiental, Universidad Nacional de Colombia. Bogotá Colombia. Carrera 45 N° 26-85 - Edificio Uriel Gutiérrez Bogotá D.C. - Colombia*

Abstract

Fusel oil is a valuable byproduct of the fuel ethanol industry that can be used to isolate C6 alcohols and other fragrances and flavor ingredients. In this work we propose two distillation schemes for obtaining isoamyl alcohol from fusel oil: a conventional distillation sequence and a dividing wall column. After validation of thermodynamic models to accurately describe phase equilibria of fusel components (VLE and LLE), a dividing wall column (DWC) separation scheme was developed. Both traditional sequential distillation and DWC system were optimized using differential evolution and tabu list coupled to ASPEN PLUS. Results indicate that significant energy and economic savings can be obtained in the purification of fusel oil (a non ideal mixture) using a DWC scheme compared to conventional configuration.

Keywords: Optimization; fusel; dividing wall column

1. Introduction

Through the years, the production of ethanol by fermentation has increased due to the biofuels demand, and consequently generation of by-products of this industry such as fusel oil has increased as well. Fusel has been characterized as a liquid waste and used as fuel in the boilers within distilleries. It is a mixture obtained as a side cut during ethanol distillation, mainly composed of i-amyl alcohol, water, *iso*butanol, ethanol and other short chain alcohols (C3-C5). These alcohols can be considered valuable raw material for various products of industrial interest such as: biosolventes, extractants, flavors, fragrances, pharmaceuticals and plasticizers, among others. According to different characterizations, major components of fusel oil are isoamyl alcohol, water and ethanol, accounting for ~98% of the total mixture. In this context, two distillation schemes to purify isoamyl alcohol and ethanol were developed. Such schemes were constructed taking into account continuous distillation sequences currently used in ethanol distilleries. A traditional scheme (Figure 1) is comprised of three distillation columns where most ethanol and water are separated in the top of the first column. This stream is sent to a subsequent column where azeotropic ethanol can be extracted on the top and water at the bottoms product. Bottoms product from first column is sent to a third distillation column connected to a decanter, where isoamyl alcohol is obtained as a bottoms pure product.

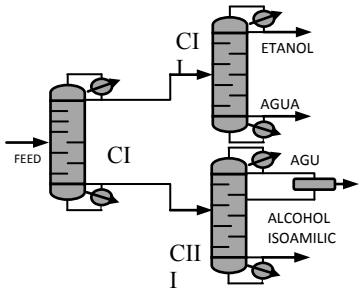

Figure 1. Conventional distillation system for fusel purification.

Dividing wall column has been used in the purification of ternary systems with significantly savings in energy consumption and capital costs over conventional simple column configurations (Hernández et al., 1996). Specifically, the dividing wall column (DWC) has been successfully implemented in many industrial separations (Olujic et al., 2003). In the dividing wall distillation (DWC) scheme proposed in this work (Figure 2), azeotropic ethanol is obtained as the top product of the main column, while isoamyl alcohol is removed from the bottoms product. Water is removed using a side stream connected to a decanter taking advantage of the liquid phase immiscibility

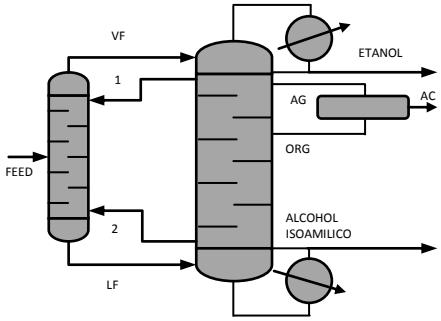

Figure 2. DWC system for fusel purification.

2. Case study

Composition of fusel oil was established according to the analysis performed to six different samples from different sugar mills in Colombia. Samples were characterized by gas chromatography coupled to mass spectrometry. The following components were detected: ethanol, water, n-butanol, isobutanol, isoamyl alcohol and 2-ethylhexanol. The composition of the mixture of study is presented in Table1.

Table 1 Composition of the mixture of study.

T= 25ºC P = 1 atm	
Component	composition % mol
Etanol	0.1258
Water	0.143
isoamyl alcohol	0.7047
n-butanol	0.0139
isobutanol	0.012599
2-ethyl-hexanol	1x10^{-}6

Thermodynamic of phase equilibria was validated by regression of binary and ternary equilibrium literature reports using a NRTL-HOC activity-based model. To obtain the corresponding thermodynamic parameters, NIST equilibrium data incorporated within ASPEN PLUS were used. Using the regression tool included in the same software, VL and LL data were simultaneously fit to accurately model the phase behavior within the distillation system

3. Optimization problem

During optimization of distillation schemes, total annual cost (TAC) minimization was used as objective function. This function takes into account energy consumption, utilities, and column size. The minimization of this objective is subjected to the required recoveries and purities of each product stream, i.e.:

$$\text{Min (TAC)} = f\left(N_{tn}, N_{fn}, R_{rn}, F_{rn}, D_{cn}\right) \quad (1)$$

$$\text{Constrain: } \vec{y}_m \geq \vec{x}_m$$

where Ntn and Nfn are the total number of stages and the feed stages of column respectively, Rrn is the reflux ratio, Frn is the distillate flow, Dcn is the column diameter, ym and xm are the obtained and required purities vectors of the m components, respectively. This minimization implies the manipulation of 14 continuous and discrete variables for each route process, where 5 variables are used for the design of each column. Note that since the product streams flows are manipulated, the recoveries of the key components in each product stream must be included as a restriction for the optimization problem. During each optimization, a Pareto front was generated, plotting the objective function (total annual cost) against the flow of impurities. Impurities flow in each product stream is the sum of the components which are not present in high purity in out flowrate. A list of manipulated variables for both schemes are listed in Table 2.

Table 2 Manipulated variables during process optimization

Manipulated variable	Conventional scheme			DWC	
	CI	CII	CIII	PREF	PETLYUK
number of stages C_n, N_{Cn}	x	X	x	x	x
feed stage in column C_n, $N_{F,Cn}$	x	X	x	x	x
distillate streamflow of column C_n, R_{Cn}	x	X			x
reflux ratio in column C_n	x	X	x		
bottoms streamflow of column C_n			x		x
feed stage of liquid interconnection flow FL in column C_i, N_{FL},C_i					x
feed stage of liquid interconnection flow FV in column C_i, N_{FL},C_i					x
feed stage of liquid interconnection flow FL in column C_i, N_{FL},C_i					x
vapor interconnection flow, FV					x
liquid interconnection flow, FL					x

4. Results

In this section, we present the set of optimal designs in Pareto front, for both schemes: conventional (Figure 3) and divided wall column (Figure 4).

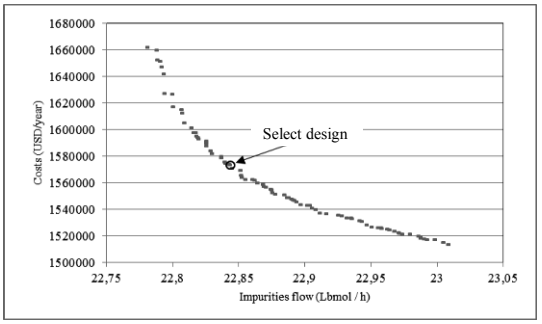

Figure 3. Pareto front of the conventional scheme.

In the conventional configuration, in column CI the number of stages and reflux ratio determine the value of the objective function (TAC) as it is where is performed the separation of water from alcohols including ethanol which forms a minimum temperature azeotrope. Overall, this column represents over 80% of energy consumption scheme. In column CII there is a close relationship between energy consumption, the purity of ethanol and the reflux ratio, due to the higher reflux, there is greater demand for energy and it results in greater purity of ethanol. This was seen as a high purity of ethanol increases energy consumption by 12%.In column CIII was observed the higher flowrate in the bottom stream, the reboiler duty is increased.

Figure 3 shows the Pareto front obtained after optimization, it is clear that both objective functions evaluated are in conflict each other. The Pareto front is formed for several points that accomplish all purity and recovery restriction (84 %, 70 % and 99 % mol). In a general way, the Pareto front consists in three sections, one section where are located designs which have preferably a high number of stages and a high reflux ratio. On the other hand at the end of Pareto front are located some sequences which showed a minor economic impact due to these designs include relative few stages. At the middle of the Pareto front is located a feasible zone, where are designs with suitable values of TAC and impurities flows comparing extremes of plot.

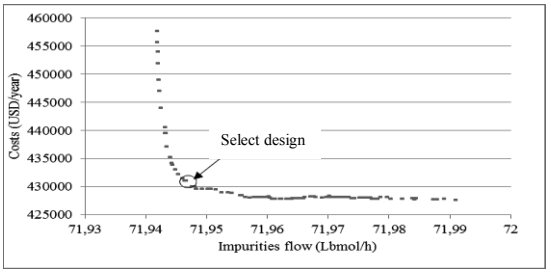

Figure 4. Pareto front Petlyuk scheme.

For the divided wall column, a clear relationship is showed between the reboiler duty and TAC, and high reflux ratio presents a high reboiler duty. Besides, when divided wall column (Figure 4) was evaluated with the same objective functions, and the same restrictions purity of the components of interest, from the Pareto front we appreciate a section with high cost associated to high reflux ratio to achieve a low impurities flow.

Table 3. Design specifications of proposed schemes.

Design specifications						
Equipment		Pref	Petlyuk	CI	CII	CIII
Stages		10	26	16	21	7
Feed stage		8	22	11	15	5
Distillate flow (Lbmol/hr)			13	20	8	---
Reflux ratio			6	6	6	---
Bottom flow (Lbmol/hr)			---	---	---	5
Feed stream	FV		17			
	FL		24			
	ORG		22			
	ETHANOL		1			
	ISOAMYL ALCOHOL		26			
Feed products	AC		22			
	1		16			
	2		25			
Flow interconnection (Lbmol/hr)	AC		60			
	1		12			
	2		95			
Composition	Ethanol		0.84		0.84	
	Water		0.71		0.72	
	Isoamyl		0.99			0.99
Energy consuption (Btu/h)		8´130,642.04		10´214,657.14		
Costs (USD/year)		430,231.31		1´573,677.43		

Characteristics of the design highlighted in Figure 4 are presented in Table 3. Notice that this design includes few stages considering 50 stages as limit. Nevertheless all purity restrictions were accomplished. As well, Table 3 shows general characteristic of design highlighted in Figure 4 such as stages, reflux ratios and interconnection flows values. This design satisfied in the same manner all restrictions. When comparing both schemes, savings of 73% in the total annual costs (TAC) and a 20% saving in energy consumption are obtained. In order to know purity values through stages in divided wall column, Figure 5 shows a concentration profile, which confirms the high isoamyl alcohol and ethanol purities obtained in this column. This behavior of divided wall column projecting itself as a good alternative in fusel purification due to energy and costs savings.

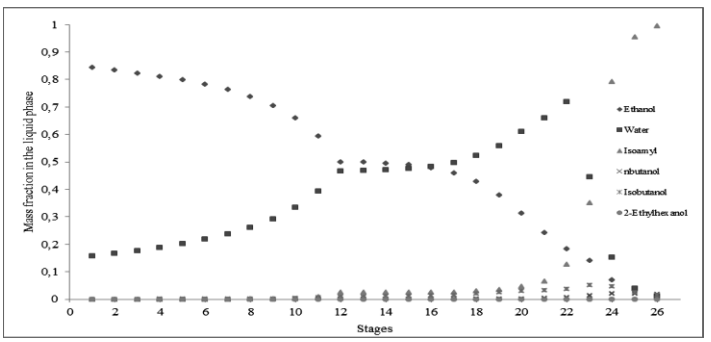

Figure 5. Composition profile for the DWC scheme.

5. Conclusions

In this work, an optimization procedure, based in differential evolution and tabu list coupled to ASPEN PLUS, was proposed for the optimization of complex distillation columns. The results show that divided wall column represents a good option for fusel oil distillation due to the benefits that would be obtained in terms of reduction in total

annual cost (TAC) over the traditional distillation sequence used in industry. The separation of isoamyl alcohol at a high purity and low cost using a dividing wall column represents an excellent option for purification of fusel oil in industry. These results represent a new vision in regard to highly nonideal mixture, where heterogeneous azeotropes are present in multicomponent systems and they are purified in a DWC.

References

C. Floudas, and C. Gounaris, 2009, A review of recent advances in global optimization, Journal of Global Optimization, 45, 1, 3-38

S. Hernández, and A. Jiménez, 1996, Design of optimal thermally coupled distillation, systems using a dynamic model, Chemical Engineering Research and Design,74 -357

K. Muralikrishna, and Madhavan, 2002, Development of dividing wall distillation column design space for a specified separation, Chem. Eng. Res, Des, 155–166

Z. Olujic, and B. Kaibel, 2003, Distillation column internals/configurations for process intensification, Chemical and Biochemical Engineering Quarterly, 17-301

G. Segovia, and V. Rico, 2006, Thermodynamically equivalent distillation schemes to the Petlyuk column for ternary mixtures, Energy, 31, 2176-2183

M. Srinivas, and G. Rangaiah, 2007, Differential Evolution with Taboo List for Solving Nonlinear and Mixed -Integer Nonlinear Programming Problems , Ind. Eng. Chem. Res, 46, 7126-7135

R. Storn, and K. Price, 1997, Differential evolution A simple and efficient heuristic for global optimization over continuous spaces, Journal of Global Optimization, 11, 341–359

M. Srinivas, and G. Rangaiah, 2007, Differential Evolution with Taboo List for Solving Nonlinear and Mixed-Integer Nonlinear Programming Problems, Ind. Eng. Chem. Res, 46, 7126-7135

C. Triantafyllou, and R. Smith, 1992, The Design and Optimization of Fully Thermally Coupled Distillation Columns, Trans. Inst. Chem. Eng, 70, 118-132

J.M. Zamora, and I. E. Grossmann, 1998, Continuous global optimization of structured process systems models, Computers & Chemical Engineering, 22, 12, 1749-1770

Krist V. Gernaey, Jakob K. Huusom and Rafiqul Gani (Eds.), 12th International Symposium on Process Systems Engineering and 25th European Symposium on Computer Aided Process Engineering.
31 May – 4 June 2015, Copenhagen, Denmark

Silane Production through Reactive Distillation with Intermediate Condensers

J. Rafael Alcántara – Avila[a], Hugo Alberto Sillas – Delgado[b], Juan Gabriel Segovia – Hernández[b], Fernando I. Gómez – Castro[b], Jorge A. Cervantes - Jauregui[c]

[a]*Department of Chemical Science and Technology, The University of Tokushima, 2-1 Minami Josanjima-cho, Tokushima 770-8506, Japan.*
[b]*Departamento de Ingeniería Química, División de Ciencias Naturales y Exactas Universidad de Guanajuato, Campus Guanajuato, Noria Alta s/n, Guanajuato 36050, Mexico.*
[c]*Departamento de Química, División de Ciencias Naturales y Exactas Universidad de Guanajuato, Campus Guanajuato, Noria Alta s/n, Guanajuato 36050, Mexico.*

Abstract

This work shows that it is feasible to obtain a high purity of silane over 99% and almost complete conversion of trichlorosilane to silane and silicon tetrachloride by a typical reactive distillation column. Nevertheless, the normal reactive distillation column possesses the shortage of high refrigeration requirement. By removing heat at temperature higher than that at the condenser it is possible to reduce cooling requirements at the condenser. In this work, a superstructure representation, rigorous simulations, and optimization problems were combined to derive optimal reactive distillation columns which can realize heat integration between stages and utilities. The results showed that the installation of two inter-condensers results in the best option with economic savings.

Keywords: Reactive distillation, energy savings, silanes.

1. Introduction

Photovoltaics (PV) use semiconductor materials to generate electricity from solar energy. Semiconductors have electrical conductivities greater than insulators but lower than metals which are good conductors. At low temperatures and high level of purity, they are insulators but at high temperatures and/or when they are doped and excited by sunlight, they conduct electrons. The most commonly used semiconductor element is silicon. Therefore silicon today is the most important material in PV industry. The most well-known chemical route to produce solar-grade silicon is the Siemens process. However, the extremely high consumption of electrical energy as well as the corrosion caused by the byproduct (hydrochloric acid) in some way has limitations in the production of low-cost polysilicon. Other very well known route to produce silane is the disproportionation reactions of $SiHCl_3$ involving the formation of dichlorosilane (SiH_2Cl_2) and monochlorosilane (SiH_3Cl) as intermediates and tetrachlorosilane ($SiCl_4$) as by product (Bakay, 1976) The conventional process for highly pure silane production from trichlorosilane disproportionation is through two reactors and several separation units. However, due to unfavorable chemical equilibrium, this reaction and separation process requires an extremely large recycle ratio and thus the cost of energy as well as

investment is very high. In this context, Reactive Distillation (RD) can be suitable for the disproportionation reactions because it eliminates conversion and phase equilibrium limitations by continuous removal of products from the reaction zone unit (Sundmacher and Kienle, 2003). It can be considered that one of the major disadvantages in using reactive distillation for the disproportionation of trichlorosilane is the low boiling point (-112°C) of the target product at the top of the column (silane) and enforces the use of refrigeration services to condensate it. To alleviate this issue, the use of intermediate condensers can be proposed to reduce the energy consumption. In this work, we investigate the feasibility of applying reactive distillation to the production of silane through the disproportionation of trichlorosilane. The design and rigorous optimization, considering all feasible alternatives, of reactive distillation column with inter-condensers has been studied as a feasible alternative to alleviate this drawback.

2. Case Study

The production of silane (SiH_4) through disproportionation of thrichlorosilane ($SiHCl_3$) in a reactive distillation column has been studied. The reaction occurs in three steps, having as intermediates dichlorosilane (SiH_2Cl_2) and monochlorosilane (SiH_3Cl) and as by-product chlorosilane ($SiCl_4$), as follows:

$$2SiHCl_3 \leftrightarrow SiH_2Cl_2 + SiCl_4 \quad (1)$$

$$2SiH_2Cl_2 \leftrightarrow SiH_3Cl + SiHCl_3 \quad (2)$$

$$2SiH_3Cl \leftrightarrow SiH_4 + SiH_2Cl_2 \quad (3)$$

The L-V equilibrium has been modelled using the Peng-Robinson equation of state (Huang et al., 2013). The reaction occurs in liquid phase, using as catalyst Amberlyst A-21. For the disproportionation of trichlorosilane using such catalyst, a pseudo-homogeneous kinetic model has been proposed (Li, 1988). To model the reactive distillation column, the RadFrac module of Aspen Plus V8.0 has been used. The feed stream has a flow rate of 10 kmol/h of pure trichlorosilane, and enters to the column at 5.5 atm and 50°C. Silane is obtained at the top of the column with a purity of 99 mol%, while silicon tetrachloride is the bottoms product, with a purity of 99 mol%. The condenser operates at 506 kPa, with a pressure drop of 0.5 kPa per stage. A representation of a reactive distillation column is shown in Figure 1a. Since the condenser operates at temperatures lower than 0°C, the use of a refrigerant is necessary, increasing the cost of the separation.

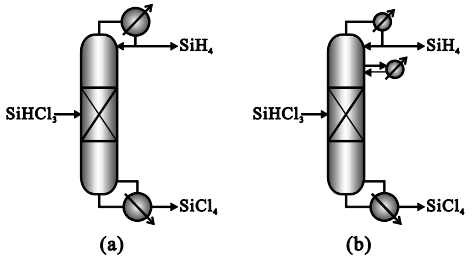

Figure 1. (a) Reactive distillation column, (b) Reactive distillation column with an intermediate heat exchanger.

To reduce the cooling duty at the condenser, the use of intermediate heat exchangers is investigated in the next section. A representation of a reactive distillation column with a single intermediate exchanger is shown in Figure 1b.

3. Installation of Inter-condensers and Inter-reboilers in Reactive Distillation: Optimization Procedure

The vapor stream leaving at the top of a distillation column must be condensed at the lowest temperature condition while the liquid stream leaving at the bottom must be heated at the highest temperature condition. For our reactive column, silane is obtained at the top and it must be condensed at about -78 °C, thus an expensive refrigeration system is required to provide cooling at temperatures below -85 °C. Typically, to avoid condensing at such low temperature levels, the column operating pressure could be increased, however, this option would be impractical because of catalyst deactivation at high pressure. A second alternative, which is exploited in this work, implies cooling at higher temperatures than that at the condenser, allowing the use of less expensive cooling utilities. The cooling and heating utilities used are shown in Table 1 where R1, R2, and R3 denote refrigeration systems at three different temperatures, CHW and CW denote chilled and cooling water, respectively; and MS denotes steam at 6.1 atm.

Table 1. Utilities for cooling and heating.

ID	Inlet temperature (ºC)	Outlet temperature (ºC)	Cost (USD/MWh)
R1	-88	-88	151.94
R2	-30	-30	34.67
R3	-20	-20	28.40
CHW	5	15	15.95
CW	30	40	1.274
MS	160	160	50.58

The selection of the best locations and utilities for heat integration must consider two important features in heat-integrated stages:

1. The heat removed or added at a stage in a rectifying or stripping section is not equal to the net condenser or reboiler duty reduction.
2. The heat removed or added at stages modifies the stage vapor-liquid equilibrium composition, thus the temperature profile changes in the column.

The installation of inter-condensers and inter-reboilers affect both the reaction rate and vapor-liquid equilibrium which results in changes of the equipment size and in operating conditions. A previous work by Huang et al., (2013) studied the disproportionation of trichlorosilane through extensive simulations to find feasible locations and heat loads in inter-condensers. In this work, all the possibilities for cooling at locations other than the condenser and for heating at locations other than the reboiler for a reactive distillation column are comprised in the superstructure shown in Figure 2, which is formulated as an optimization problem.

The adopted objective function, which minimizes the operating cost in a reactive distillation column by finding optimal locations and heat loads in inter-condensers and/or inter-reboilers, is as follows:

$$\min OC = OH\left[\sum_{\substack{i\in REC\\ j\in CU}} C_j^{\text{cool}} Q_{i,j}^{\text{ex}} + \sum_{\substack{i\in HU\\ j\in STR}} C_i^{\text{heat}} Q_{i,j}^{\text{ex}}\right] \tag{4}$$

where *REC* is the set of stages in the rectifying section subject to the installation of a condenser and inter-condensers, *STR* is the set of stages in the stripping section subject to the installation of a reboiler and inter-reboilers, *CU* is the set of cooling utilities, and *HU* is the set of heating utilities. C^{cool} is the cost of cooling utilities while C^{heat} is the cost of heating utilities. $Q_{i,j}^{\text{ex}}$ is the amount of heat exchanged between heat sources *HSO* (i.e., $HSO = REC \cup HU$) and heat sinks *HSI* (i.e., $HSI = STR \cup CU$). Finally, *OH* are the annual operation hours.

Changes in the condenser and reboiler duties due to heat integration at stages in a column are predicted through the use of compensation terms (Alcántara-Avila et al., 2013). Other constraints for the problem are the energy balances, equations for the calculation of the log mean temperature difference (ΔT_{LM}), which is used to determine the temperature driving force for heat transfer in exchangers; and additional constraints to enforce a determined number of heat exchangers in the rectifying and stripping sections and to allocate heat exchangers in feasible heat exchange networks. The log mean temperature difference is used as feasibility criterion for heat integration. The feasibility criterion based on the "Big-M" formulation is as follows:

$$Q_{i,j}^{\text{ex}} - M\Delta T_{\text{LM}i,j} \le 0 \quad i \in HSO, j \in HSI \tag{5}$$

where *M* is a large number.

Since distillation is inherently characterized by a set of nonlinear and nonconvex equations, a simulation software was used to handle them to find optimal values of continuous variables. However, to find optimal values of integer variables (i.e., locations of inter- condensers and/or inter-reboilers) an optimization software was used. Figure 3 shows a flowchart for the proposed iterative procedure, which combines the simulation and optimization software, to find the best reactive distillation column with inter-condensers and/or inter-reboilers. The procedure in Figure 3 was adopted to avoid the solution of complex mixed integer nonlinear and nonconvex mathematical problems.

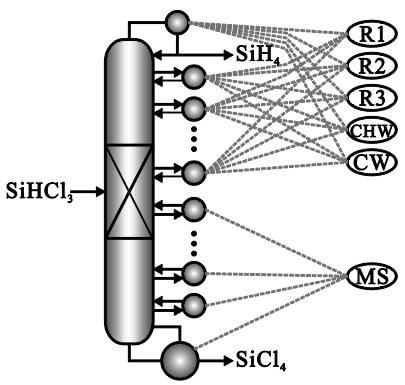

Figure 2. Superstructure representation of the reactive distillation column

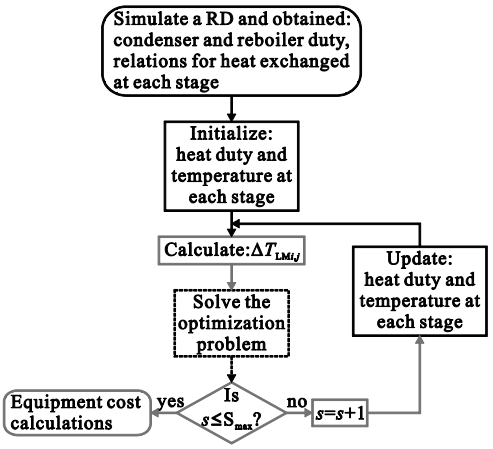

Figure 3. Flowchart of the iterative optimization procedure: Simulation software (solid black lines), optimization software (dasshed lines), interface (solid grey lines).

4. Results

A typical reactive distillation column was investigated first which composed of three sections: the rectifying, catalytic reaction and stripping sections, located at the upper, middle, and lower part, respectively, with the solid catalyst packed in the middle of the column. Trichlorosilane is fed into the column at the middle of the reaction section. Then disproportionation takes place in the reaction section and vaporous product mixture containing light components ascend to the rectifying section while the heavy components descend to the stripping section. Unreacted intermediate products, which rise in the rectifying section towards the condenser, return to the reaction section with the help of the top reflux flow, and unreacted intermediate products, which fall in the stripping section towards the reboiler, return to the reaction section with the help of the boilup stream.

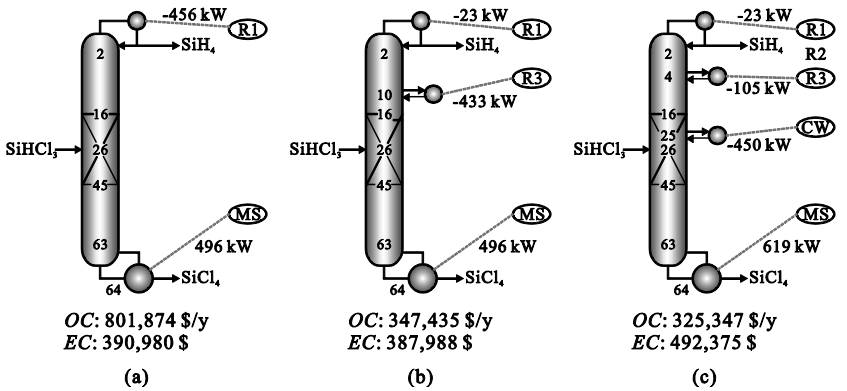

Figure 4. (a) Conventional RD, (b) RD with one inter-condenser, (c) RD with two inter-condensers

To generate the optimal design, the number of stages in the column, the number of reactive stages, the position of the reactive stage, the position of the feed stage, the reflux ratio and the operating pressure were manipulated. The optimum RD column without any intermediate heat exchangers is shown in Figure 4a. The RD with one inter-condenser is shown in Figure 4b, and the RD with two inter-condensers is shown in Figure 4c. The *OC* remarkably drops due to the installation of inter-condensers while the *EC* (Equipment Cost) slightly increases for Figure 4c. In all cases, the liquid residence time of 2.5 s on each stage which is defined as hold-up/liquid-flow-rate. The column is operated at a top pressure of 506.6 kPa with a pressure drop through each stage of 0.5 kPa. The purity of silane in distillate in mole fraction is 0.99. 10 kmol/h of trichlorosilane were fed at 50 °C and 557.3 kPa.

The installation of inter-condensers above the feed stage in the catalytic reaction section (Figure 4c) lowers the temperature profile resulting in higher concentrations of SiH_2Cl_2 and SiH_3Cl in the liquid phase, thus SIH_4 generation is boosted. In addition, although all cases in Figure 4 had the same trichlorosilane conversion (99.25%), the total liquid amount of intermediate species ($SiHCl_3$, SiH_2Cl_2, SiH_3Cl) entering at the top of the catalytic reaction section is 82 kmol/h for Figures 4a and 4b, and 22.7 kmol/h for Figure 4c, respectively. The previous results show how the installation of inter-condensers can effectively reduce the flow rate of intermediate species.

5. Conclusions

It has been proved that it is feasible to obtain a high purity of silane over 99% and a conversion above 99% of trichlorosilane to silane and silicon tetrachloride by the presented reactive distillation columns. The heat removal and addition at stages result in changes of the temperature profile, vapor-liquid equilibrium and reaction rate inside the reactive column. In this work, an optimization procedure was proposed to deal with these changes by iteratively updating the temperature profile and locations of side heat exchangers. In the optimization, the combinatorial problem between stages and utilities was solved while in the simulation, the synthesis problem for the obtained optimal heat integration network was solved. The location of side heat exchangers depend on the estimation of changes in the condenser and reboiler energy requirements due to heat integration, for these purposes, the concept of compensation terms was effectively adopted.

References

J.R. Alcántara–Avila, M. Kano, S. Hasebe, 2013, New synthesis procedure to find the optimal distillation sequence with internal and external heat integrations, Ind. Eng. Chem. Res., 52, 13, 4851-4862.

C.J. Bakay, 1976, Process for Making Silane. U.S. Patent 3,968,199.

X. Huang, W.J. Ding, J.M. Yan, W.D. Xiao, 2013, Reactive distillation column for disproportionation of trichlorosilane to silane: Reducing refrigeration load with intermediate condensers, Ind. Eng. Chem. Res., 52, 18, 6211-6220.

K.Y. Li, 1988, Redistribution reaction of trichlorosilane in a fixed-bed reactor, Ind. Eng. Chem. Res., 27, 9, 1600-1606.

K. Sundmacher, A.Kienle, 2003, Reactive distillation: Status and future direction, Wiley, 1st ed. Germany.

Krist V. Gernaey, Jakob K. Huusom and Rafiqul Gani (Eds.), 12th International Symposium on Process Systems Engineering and 25th European Symposium on Computer Aided Process Engineering.
31 May – 4 June 2015, Copenhagen, Denmark

Optimal production of Furfural and DMF from algae and switchgrass

Mariano Martín[a], Ignacio E. Grossmann[b]

[a]*Departamento de Ingeniería Química. Univ Salamanca.Plz. Caídos 1-5, 37008, Salamanca, Spain*
[b]*Department of chemical Engineering. Carnegie Mellon University. Pittsburgh, PA, 15213, USA.*

Abstract

In this paper we present conceptual designs of optimal integrated processes for the production of DMF and furfural from biomass, switchgrass and algae. The processes consist of four stages, (1) biomass pretreatment into intermediates such as oil and glucose from algae and glucose and xylose from switchgrass, (2) dehydration of the sugars, (3) HMF and furfural purification and (4) synthesis of DMF out of HMF and FAEE synthesis from oil in the case of using algae. Simultaneous optimization and heat integration is performed for the processes using each raw material. For switchgrass, the use of AFEX pretreatment is recommended for a production of 9 MMgal of furfural and 14 MMgal/yr of DMF. The production cost is $3/kg of biofuel ($570MM of investment cost). When using algae, its composition should be 60% oil, 30% starch and 10% protein to obtain 98 MMgal/yr of biofuels, 16% of DMF, at the cost of $1.98/gal, $0.61/kg of biofuel, requiring $693 MM of investment.

Keywords: Algae, Switchgrass, DMF, Furfural, Mathematical optimization

1. Introduction

Biomass is a rich and diverse raw material for a number of products that have sugars or oil as building blocks. In particular, sugars are the starting block for most biochemical process including bioethanol production. However, we can use sugars to produce added value products and/or intermediates. Furans are a family of chemicals that serve as fuels but can also be used as a building block. Algae biomass comprises lipids, proteins and starch, while lignocellulosic raw materials contain celluloses and hemicelluloses which are a source for pentoses and hexoses. Thus, it is expected we can produce dimethyl furfural (DMF) out of the algae starch, and from switchgrass we should be able to obtain not only DMF but also furfural. Lately, a number of papers have evaluated the production of furan and HMF and DMF from sugars, xylose, fructure or glucose, but all of them start with the sugars without evaluating the production of those sugars from non edible biomass, which is a highly energy and capital intensive stage (Kazi et al 2011, de Ávila & Guiradello 2012). In this work we present conceptual optimal designs for processes from the biomass to furans.

2. Process description

The process is divided into four stages: (1) biomass pretreatment into intermediates such as oil and glucose from algae and glucose and xylose from switchgrass, (2)

dehydration of the sugars, (3) HMF and furfural purification and (4) synthesis of DMF out of HMF and FAEE synthesis from oil in the case of using algae.

2.1. Sugar production from algae

The algae are grown in ponds, harvested using a capillarity based belt. The dry algae biomass is assumed to be composed of oil, up to a maximum of 60 %w/w, starch and protein with a minimum of 10%w/w. On the one hand, the oil, extracted using a hybrid method combining mechanical action and the use of solvents, will be transesterified with ethanol using enzymes. The yield of the reaction is predicted using a surface response model as a function of the excess of ethanol, the load of catalysis and the operating temperature. The excess of ethanol is recovered in a distillation column and the polar and organic phases are separated recovering the glycerol and biodiesel which is finally purified by distillation. On the other hand, the biomass containing the starch and protein is liquefied, 85ºC, and saccharified, 65 ºC, to breakdown the structure into maltose and glucose. (Martín & Grossmann, 2013). Figure 1 shows the flowsheet for the use of algae for the production of DMF and biodiesel.

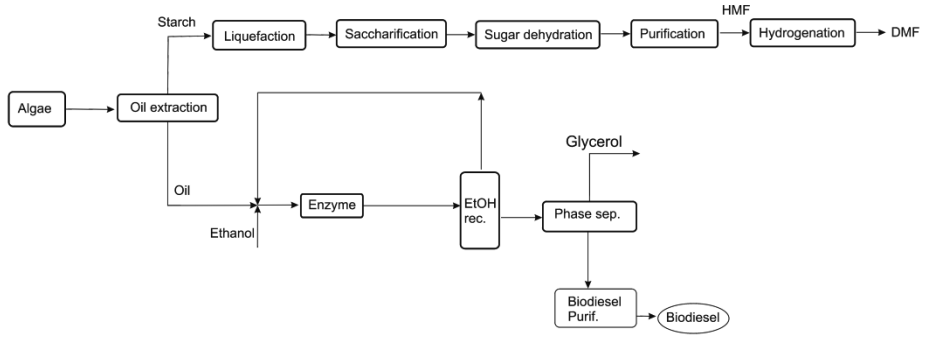

Figure 1.- Flowsheet for the production of DMF and biodiesel from algae

2.2. Sugars production from switchgrass

Two pretreatments are considered for breaking up of the biomass into cellulose, hemicelluloses and lignin, dilute acid and ammonia fiber explosion (AFEX). Once the physical structure of the switchgrass has been broken down, the cellulose and lignocellulose are next hydrolyzed at 50ºC obtaining pentoses and hexoses (Martín & Grossmann, 2012). Figure 2 shows the superstructure for the production of furfural and DMF from switchgrass.

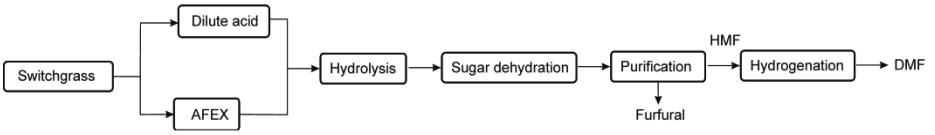

Figure 2.-Superstructure for the production of furfural and DMF from switchgrass

2.3. Sugar transformation into furfural and HMF

The stream containing sugar stream is mixed with butanol, HCl, $CrCl_3$ and NaCl together with recycled streams coming from different separation stages such as the

filter, where the solid catalyst ($CrCl_3$) is recovered, the first distillation column, where mainly water and butanol are recycled, and the distillate of the second distillation column consisting mainly of the same species. The $CrCl_3$ – HCl is the catalyst system and we use a two phase liquid reactor (organic, butanol, - aqueous) to extract the product from the mixture. The NaCl increases the recovery ratio of the products.

In the reactor, the sugars, glucose and xylose, are dehydrated, eqs. (1)-(2). In case of using algae only reaction (1) takes place. The operating temperature and pressure at the reactor are fixed to be 180ºC and 11 bar since it is a common temperature for both sugars to be dehydrated. With this operating conditions the conversion from glucose to HMF becomes 0.67 (Roman –Leshkov et al., 2007) and from xylose to furfural to 0.56 (Marcotulio et al., 2010).

Glucose dehydration: $C_6H_{12}O_6 \rightarrow C_6H_6O_3 + 3H_2O$ (1)

Xylose dehydration: $C_5H_{10}O_5 \rightarrow C_5H_4O_2 + 3H_2O$ (2)

Figure 3 shows the detailed flowsheet for the sugar dehydration process and the subsequent purification process. In case when there is only glucose in the feed, one column is not needed.

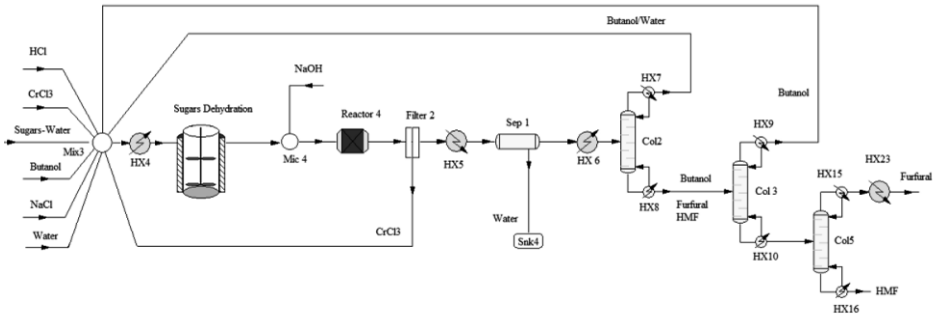

Figure 3.-Sugar dehydration and purification stages

2.4. Products purification.

The purification stage consists of neutralization, filtration, phase separation and a sequence of distillation columns.

The HCl is neutralized using NaOH so that the resulting salt is already in the system. Next, the solid catalyst, $CrCl_3$, is recovered in a filter. After the filter, a phase separation is performed. Based on experimental results from the literature, an operating temperature of 37 ºC is selected (de Álvila et al., 2012) The partition coefficient of the HMF and furfural is taken to be 3 in volume ratio towards the organic phase (Roman-Leshvok, 2009; Roman-Leskov et al., 2007). The polar phase contains butanol, water and NaCl and part of the sugars.

The organic phase coming from the phase separator is distilled. The column operates at low pressure, 0.5 atm, to avoid species decomposition. From the distillate we recover 99,9% of butanol and the water in the feed together with the rest of the sugars. From the bottoms we obtain HMF, furfural and the rest of butanol. A second column recovers

butanol as distillate, and HMF and furfural at the bottoms. Finally, the third column separates furfural to be sold from the HMF that is further used for the production of DMF. In case only hexoses are available, only two columns are needed.

2.5. DMF production from HMF

The production of DMF from HMF is carried out in a catalytic reactor at 120 ºC and 16 bar using CuRu as catalyst. HMF and butanol are fed so that the concentration of the first one is 5% of the liquid mixture. The reactor operates with an excess of hydrogen 12 times the one given by the stoichiometry. The conversion is reported to be 100% (Kazi et al. 2011). The excess of hydrogen is recovered using a flash, and the DMF, butanol and water are sent to a distillation column. The reaction taking place is given in eq. (3). Figure 4 shows the detailed flowsheet for this stage.

$$C_6H_6O_3 + 4H_2 \rightarrow C_6H_8O + 2H_2O \tag{3}$$

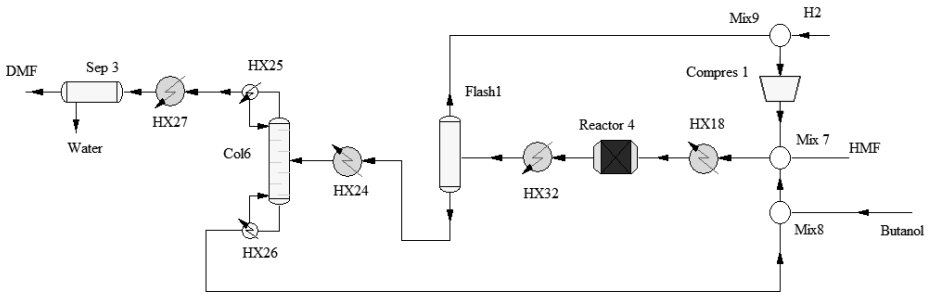

Figure 4.- Production of DMF from HMF

3. Solution procedure.

We formulate the problem for the use of *switchgrass* as raw material as an MINLP where the objective function is a simplified production cost involving the income due to the furfural and the DMF assumed to have a cost of $2/kg and the energy consumed in the process. Due to the fact that there is only one integer variable we decompose the problem into two NLP with 3000 equations and 3600 variables each to solve simultaneously optimize the operating conditions of the pretreatment and heat integrate the entire flowsheet using Duran & Grossmann's (1986) model. In the case of the use of *algae*, the problem is formulated as an NLP with 4100 equations and 5400 variables where the main decision variables are the algae composition, the operating pressures of the distillation columns and the operating conditions of the transesterification reactor. Again simultaneous optimization and heat integration is performed. We use multiple initialization points to solve the problems with CONOPT 3.0 as the preferred solver.

Next, we develop the optimal heat exchanger network using SYNHEAT (Yee & Grossmann 1990). Finally, the cost analysis is performed following Sinnot´s method (Sinnot 1999).

4. Results

4.1. Lignocellulosic based DMF and furfural

If we use lignocellulosic switchgrass as raw material we have as main products DMF and furfural and as byproduct lignin. We consider a price for the switchgrass of \$75/t. AFEX turns out to provide the better performance for a production cost of \$11.3/gal (\$3/kg) versus \$12.15/gal (\$3.20/kg) for the acid based pretreatment with an investment cost of \$570 MM (vs. 764MM). We obtain 23MMgal of products, 9 MMgal of furfural and 14 MMgal/yr of DMF, representing 15% by weight of the initial biomass for the best of the two processes. Due to the need of energy for the process, the lignin produced is fully used to provide part of it

4.2. Algae based DMF

In this case we have as variable the algae composition to produce as main products FAEE and DMF while as byproducts we can obtain glycerol and protein. The algae composition that yields the optimal production facility corresponds to 60% oil, 30% starch and 10% protein, as in previous studies. The reason is that the production of biodiesel is cheaper in terms of energy consumption and investment cost while the use of starch as raw material is much more expensive. The operating conditions at the transesterification reactor are given in Table 1. They match the ones of other integrated processes for the production of biodiesel and starch based products such as ethanol (Martín & Grossmann, 2013).

Table 1.- Operating conditions at the transesterification reactor

	Algae based FAEE + DMF
Temperature(ºC)	30
Pressure(bar)	4 (fixed)
Molar ratio (EtOH/oil)	4.2
Time (h)	8.0
Cat/lipase(%)	13.0
Water added	0.0

The total production capacity of biofuels is 98 MMGal /yr where 81MMGal/yr correspond biodiesel (FAEE) and 17 MMGal/yr of DMF. The investment cost for this facility is high, \$693 MM. In terms of production cost for the main products, namely FAEE and DMF, is \$1.98/gal, \$0.61/kg of biofuel.

5. Conclusions

When switchgrass is used, the preferred pretreatment is AFEX followed by hydrolysis so that the xylose and glucose are available for dehydration. If algae are used, we can not only produce DMF due to the starch within the algae, but also biodiesel that we assume is FAEE for which we need ethanol.

The resulting optimal processes reveal interesting production prices, around \$3/kg if switchgrass is used and \$1.7/gal in the case of producing biodiesel and DMF from algae. However, the energy consumption as well as the water consumption are higher

due to the purification and separation stages for the intermediates. It is technologically feasible to produce furfural and DMF out of algae and switchgrass but at a cost.

The energy consumption of the process is highly dependent on the composition of the mixture in the dehydration reactor. The experimental optimization of the dehydration process is suggested to reduced the amount of butanol so that the separation of the products from the separating agent is less expensive and /or the use of a different agent that has a lower vaporization heat. This can somehow be obtained if the concentration of sugars in the aqueous phase is increased. The concentration of the sugars in the fed can also be adjusted with evaporation previous to the dehydration as long as there is no such need for aqueous phase during the synthesis.

References

F. de Ávila Rodrigues, R. Guirardello, 2012, Techno-Economic Evaluation of Large Scale 2.5-Dimethylfuran Production from Fructose. Chap. 17 In_Advances in Chemical Engineering Intech

M.A. Duran, I.E. Grossmann, 1986, Simultaneous optimization and heat integration of chemical processes. AIChE, Journal, 32, 123-138

F.K. Kazi, A.D. Patel, J.C. Serrano-Ruiz, J.A. Dumesic, R.P. Anexa, 2011, Techno-economic analysis of dimethylfuran (DMF) and hydroxymethylfurfural (HMF) production from pure fructose in catalytic processes Chemical Engineering Journal 169, 329–338

G. Marcotullio, W. De Jong, 2010, Chloride ions enhance furfural formation from D-xylose in dilute aqueous acidic solutions Green Chem., 12, 1739–1746

M. Martín, I.E. Grossmann, 2012, Energy optimization of lignocellulosic bioethanol production via Hydrolysis of Switchgrass. AIChE Journal, 58, 5, 1538-1549

M. Martín, I.E. Grossmann, 2013. Optimal engineered algae composition for the integrated simultaneous production of bioethanol and biodiesel AIChE Journal, 59, 8, 2872–2883

Y. Roman-Leshkov, C.J. Barrett, Z.Y. Liu, J.A. Dumesic, 2007, Production of dimethylfuran for liquid fuels from biomass-derived carbohydrates. Nature, 447, 982-986

R.K. Sinnot, 1999, Coulson and Richardson, Chemical Engineering 3ªEd. Singapore: Butterworth Heinemann, 1999

T.F. Yee, I.E. Grossmann, 1990, Simultaneous optimization models for heat integration. II. Heat exchanger networks synthesis. Computers and Chemical Engineering, 28, 1165-1184

Krist V. Gernaey, Jakob K. Huusom and Rafiqul Gani (Eds.), 12th International Symposium on Process Systems Engineering and 25th European Symposium on Computer Aided Process Engineering.
31 May – 4 June 2015, Copenhagen, Denmark

CO_2 as feedstock: a new pathway to syngas

Flavio Manenti[a]

[a]*Politecnico di Milano, CMIC Dept. "Giulio Natta", Piazza Leonardo da Vinci 32, 20133 Milano, Italy. Email: flavio.manenti@polimi.it*

Abstract

A novel pioneering route to synthesize syngas (CO/H_2) from hydrogen sulphide (H_2S) and carbon dioxide (CO_2) is broached. H_2S in acid gases and flue gases rich in CO_2 represent an environmental issue and an industrial cost as neither H_2S nor CO_2 is presently used as a major industrial feedstock or commodity. Acid gases mainly come from desulphurization from fossil fuels, and they cannot be simply released in the atmosphere, due to their toxicity. H_2S is then usually neutralized by conversion to elemental sulphur, with a minor industrial use. Flue gases are massively produced in power, petrochemical and manufacturing plants and CO_2, final combustion product, is generally vented to atmosphere. CO_2 capture and sequestration is still object of a relevant debate and environmental concern. By the new chemical route, potential value of H_2S and CO_2 will be brought out by means of a radically new conversion process: H_2S will be thermally activated in a high temperature reactor and will reduce the CO_2 to produce H_2 via a complex chemical mechanism. Preliminary reactor and process design, along with identification of relevant equipment and operating conditions, carried out using CAPE tools led to initial very promising results. A detailed kinetic scheme, extensively validated in a broad range of oxidation and combustion of sulphur components, further supports this oxy-reduction process, marginally observed also in the Claus process. Complete recycle of H_2S, relevant reduction of CO_2, and syngas production from these pollutants represent the valuable environmental, energy and commercial benefits of the new route, which could also involve a wider field of industrial applications.

Keywords: waste to energy; waste to hydrogen; hydrogen; syngas; CO_2 as feedstock.

1. Introduction

Hydrogen sulphide (H_2S) and carbon dioxide (CO_2) are two of the most critical chemical by-products generated by power, petrochemical and manufacturing plants. First of all, despite their massive production, they do not represent a major feedstock or commodity for subsequent industrial purposes. Then, they are considered pollutants and their venting to atmosphere, when admissible, leads to environmental issues; otherwise, expensive neutralization processes must be adopted. Hydrocarbons, coal and some natural gases contain significant amounts of H_2S and other sulphurous species. H_2S is a poison for industrial and automotive catalysts and a source of corrosion for process equipment. Moreover, if present in fossil-fuels, its combustion products (SO_x) are strong pollutants. Consequently, desulphurization of hydrocarbons and coal, but also biomasses, and sweetening of natural gas are mandatory operations. Due to chemical acid behaviour, gaseous effluents from desulphurization units are commonly called "acid gases"; H_2S content can reach up to 90% by volume. Since H_2S is malodorous and toxic, it can not be vented to atmosphere, but must be properly neutralized. Then, acid gases represent a dangerous and costly waste.

At H_2S concentrations above 40%, the most important and spread neutralization method is based on oxidation of H2S by air (Claus process): the acid gas is fed to a furnace along with a sub-stoichiometric amount of air and then oxidized to sulphur dioxide (SO_2) at high temperature: $H_2S + 1.5O_2 \rightarrow SO_2 + H_2O$. The SO_2 is next reduced by residual H_2S by means of catalytic reactors for obtaining elemental sulphur: $2H_2S + SO_2 \rightarrow 3S(\downarrow) + 2H_2O$. The elemental sulphur is partially used in process industry for producing sulphuric acid; nevertheless, since most portion of sulphur is stocked and commercial demand for sulphuric acid can be weak, the neutralization process represents a significant plant cost. CO_2 is the major responsible for impacts on ecological and environmental system, involving the greenhouse effect. It is produced in conventional combustion processes in all the fossil-fuel-based power plants and in all combustors installed for providing heat to petrochemical, chemical and manufacturing processes. The so-called "flue gas", at ambient pressure and with a CO_2 content normally up to 15% by vol., is generally vented to the atmosphere. On the other hand, capture of CO_2 from flue gas by chemical or physical washing processes leads to questionable issue of disposal. CO_2 is also produced in some petrochemical processes as by-product in the main stream, as in reforming units: catalytic conversion (steam reforming) of a mixture of hydrocarbons/steam to a mixture of hydrogen/carbon monoxide and subsequent water-gas-shift reaction lead to large co-production of CO_2. On the whole, it is estimated that, including non-industrial emissions, a lot of tons per year of CO_2 are released to atmosphere. Due to its thermodynamic stability and low chemical value, CO_2 has presently minor industrial uses; one of its most important consumptions in chemical plants is in urea synthesis. Viable applications of CO_2 are represented by catalytic "dry" CO_2 reforming and catalytic CO_2 hydrogenation. Nevertheless, these have not been successfully applied to industrial scale yet, because of considerable energy consumption and need for large amounts of hydrogen (CO_2 reforming leads to the ratio $H_2/CO = 1$). Direct production of methanol from CO_2 is also a potential route but catalysts and reactors are still in a research phase.

2. A new point of view

H_2S and CO_2 are strongly undesired industrial by-products, to be accounted as a huge cost in the budget of industrial plants. Nonetheless, despite his bad reputation, H_2S is quite an interesting chemical since it contains a highly noble species, the hydrogen. The trouble is how to pull-out H_2 from H_2S. H_2S is the hydrogen richest molecule after methane (CH_4 and hydrocarbons in general), methanol (CH_3OH), ammonia (NH_3), and water (H_2O). Consequently, H_2S should deserve more attention than to be considered just a waste product and then oxidized in Claus plants to obtain elemental sulphur and water. By this conventional approach, hydrogen in H_2S is finally fixed in water and then lost. Besides, as shown in above reforming synthesis reactions, CO_2 is a potential interesting molecule as well since it may work as oxidizing agent. All these considerations have pushed the research to invest for a captive use of H_2S and CO_2, to improve the accounting of these by-products. For recovering H_2, decomposition of H_2S can be an achievable method; proposals date back decades. A complete review of available techniques is presented by Cox et al. (1998). In the same work, thermal decomposition of pure H_2S flowing in a multi-tubular reactor, externally heated by hot flue gas, is specifically discussed; results appear interesting from technological standpoint, but the overall process is not commercially competitive with regard to traditional steam reforming. More recent studies (Villasmil and Steinfeld, 2010) investigated the possibility to obtain H_2 by

thermal pyrolysis of H_2S, driven by concentrated solar energy. Nevertheless, it is general understanding that H_2S decomposition processes are not economically attractive at the present and therefore they are considered an unsuccessful technological approach for bringing out value from waste acid gas. In this paper, proven and mature technology used in the Claus process has been realized to be potential source of innovation by means of CAPE tools. Taking advantage of extensive scientific works and operating experience on acid gas oxidation by air at high temperatures, H_2S and CO_2 have been observed under a different light, like a couple of oxidizing and reducing species; so, reduction of CO_2 by means of H_2S looks to be a promising and valuable new route. Although some aspects are still unresolved, thermodynamics, kinetics and process control of Claus process have been plentifully studied so far; as a consequence, H_2S and CO_2 conversion process starts from a conceptual and technological sound basis. The threefold advantage of recycling acid gas, reducing CO_2 and producing H_2 makes this new synthesis route not only of interest for process/environmental engineering, but also strategic for industrial plants economy.

3. CAPE tools

Contrarily to the conventional way to operate, the proposed process was not identified at the laboratory scale with the observation of main reactions and conversions, but its studies started from modelling and well-established CAPE tools. Conversion of H_2S and CO_2 to syngas is based on a complex reaction mechanism, involving more than 100 molecular and radical species and thousands of chemical reactions. The conversion mechanism consists of the following macro-steps: (1) decomposition of H_2S into radical species; (2) reduction of CO_2 into CO by free radicals; (3) increase of oxygen-based free radicals; (4) formation of sulphurous oxides and inhibition of reverse reaction from CO to CO_2 according to inhibition effect observed by Mueller et al. (2003); and (5) formation of stable SO_2 from SO. An existing package of modular kinetic models, developed and tested by the research group at Chemical Engineering Department of Politecnico di Milano, has been used to predict thermal process behaviour (Manenti et al., 2013). Such a package includes more than 800 chemical species and 30000 reactions, including sulphur and carbon compounds. Chemical reactions are grouped according to the species involved in the process and in hierarchical modules that progressively include families of reactions which makes such kinetic package as viable tool to be extended to new mechanisms and to estimate kinetic parameters of the reactive system by numerical solution of large-scale nonlinear regression. The kinetic package has been validated over several operating acid gas combustors (Manenti et al., 2013). The chemical kinetics has been then implemented in non-ideal reactor models and, next, in process simulations with commercial packages (AspenHysys™). Another CAPE tool adopted in this work for the industrial feasibility study of Section 5 is the GasDS Suite for the dynamic simulation of coal and/or biomass gasification units. Multi-phase, multi-component, and multi-scale phenomena are included in the GasDS model to properly characterize different kinds of gasifiers. More details and industrial examples are given in Ranzi et al. (2014).

4. New process description

The conversion process of H_2S and CO_2, that is oxidation of acid gases by carbon dioxide at high temperature, is a radically new, interesting route for recycling acid gases and CO_2, and therefore for bringing out the potential value of these by-products. Since the conversion takes place at high temperatures, above 1000 °C, the reactive system is of homogeneous and gas-phase type, with chemical thermodynamics and, specially, kinetics

typical of high temperature systems; for this reason, the conversion chamber can be named as "thermal reactor". An alternative approach is the use of a catalytic reactor instead of the thermal one, where the oxidation is not promoted by temperature but by catalytic active sites. At a glance, this may appear attractive and competitive, but a more accurate analysis driven by experience on Claus process, however, leads to consider the catalytic route much more challenging due to the intrinsic nature of reagents. In fact, acid gases are available at different operating conditions and concentrations, and typically they contain also several minor species that act as catalyst poisons and corrosion precursors. Moreover, presence of elemental sulphur in the combusted gas makes difficult the use of conventional catalysts. The thermal process is more robust and tolerant against acid gas inlet conditions and presence of minor species; furthermore, investigation by means of mathematical models of homogeneous gas-phase reactive systems is nowadays reliable. The kernel of the process is a Regenerative Thermal Reactor (RTR, Figure 1a). It consists of a regenerative section, where the inlet feed is preheated by the hot effluent, and a thermal section, where the conversion takes place at high temperature and the oxygen is provided to sustain the process (Fig. 1). The reliable simulation of the RTR can not be carried out using commercial packages since the most widespread process simulators do not include any complex kinetic scheme for high-temperature reaction systems. Some special tools (Manenti et al., 2013), also validated by the field on more than 20 industrial plants, have been used for this purpose. CO_2, H_2S and a small portion of oxygen are supplied to the RTR according to the Figure 1b. The residence time is in the order of 0.4 s at 1.2 bar at a temperature of 1300 °C. Syngas and elemental sulphur are the main products. It is worth saying that the H_2/CO ratio strongly varies with the residence time and the conversion of reactants is related to the RTR operating temperature. The overall reaction for the new process is: $CO_2 + 2H_2S \rightarrow CO + H_2 + S_2 + H_2O$. For instance, considering a high reaction temperature of 1500 °C, 1.5 bar, and 10 kmol/s of CO_2 and 30 kmol/s of H_2S with proper oxygen supply, the outflow molar flows are [kmol/s]: CO_2, 4.47; H_2S, 4.32, S_2, 11.25; H_2, 6.32; CO, 5.40; SO_2, 2.25; H_2O, 19.16; COS, 0.13.
The benefits coming from this new conversion process are different:

- Recycle of acid gases produced by desulphurization units, converting H_2S into a valuable chemical. This has the twofold advantage to neutralize H_2S and bring out a value of acid gases, besides to reduce plant costs and improve processes sustainability.

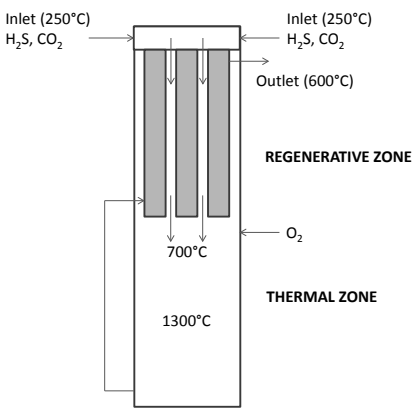

Figure 1a. RTR scheme.

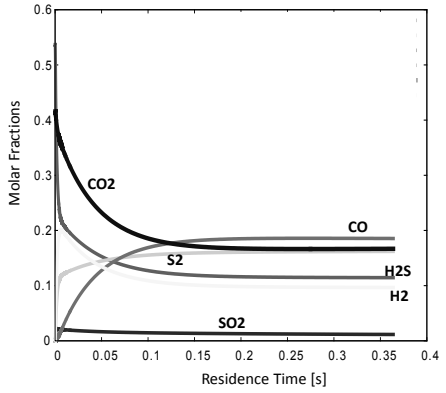

Figure 1b. CO_2/H_2S conversion in the RTR for non-optimal temperature and non-optimal feedstock conditions.

- Recycle of CO_2 as a reactant, and therefore reduction of emissions to atmosphere. CO_2 can be captured from flue gas or taken from separation units installed on main process stream of petrochemical plants.
- Synthesis of syngas or H_2.
- Improvement of Claus process. By means of the new synthesis, the hydrogen contained in H_2S is no longer fixed in water, but is delivered. On the other hand, the sulphur reacts with oxygen to form mainly SO_2. For that reason, the regenerative thermal reactor can be followed by the catalytic conversion from SO_2 to elemental sulphur typical of Claus process. In other words, the overall process can also be seen as a Claus process with a new thermal reactor installed upstream.
- Exploitation of new energy sources without environmental impact. Coal with relevant sulphur content (e.g., Sulcis-Italian coal with 9.5% of sulphur, Inner Mongolia-Chinese coal up to 18% of sulphur) becomes a novel energy/chemical source for low/zero-emission gasification processes.
- Beyond urea and methanol plants, this is a new opportunity to use CO_2 as feedstock.
- Full compliancy with EC Horizon2020 and Energy RoadMap 2030.

From an industrial standpoint, the attractive and promising character of the new process resides in the resemblance with the proven Claus process. This provides not only for a sound basis for process modelling and equipment sizing, but also and specially makes any technological and industrial consideration more concrete. The energy sustainability of the conversion process and mechanical feasibility of equipment are guaranteed by their similarity to H_2S oxidation by air and combustion chamber of Claus units, respectively.

5. Industrial feasibility study: intensification of coal gasification process

The new process is effective in reducing CO_2 emissions and to achieve zero-emissions in different areas, such as gas-to-liquid, methanol synthesis, coal gasification, hydrodesulphurization, to quote a few. Specifically, the selected industrial feasibility study is the coal gasification process using a Texaco's basic layout and a sulphur content of 9.5%. The process line-up simulated using the CAPE tools mentioned above fully integrated with AspenHysys environment is reported in Figure 2. Validation of the GasDS Suite is also given in Figure 3. Coal with sulphur content, steam for gasification and oxygen to sustain the gasification via partial combustion of the coal are fed to the downdraft gasifier of Figure 3a. Water obtained as by-product in the coal gasification is removed in dewatering process. Downstream a sweetening process (MDEA 1) is adopted with a special mixture of MEA/DEA and water to obtain the complete separation of H_2S and the optimal ration of CO_2 to be supplied to the RTR. The remaining portion of CO_2 is sent to the second sweetening process (MDEA 2) for sequestration. The optimal feedstock H_2S/CO_2 from the first sweetening process is then converted in the RTR in syngas. The outflow is sent to the catalytic conversion and the final stream obtained consists of elemental sulphur, water, syngas, and unreacted H_2S/CO_2. After the removal of water and sulphur, syngas and unreacted species could either enter a third sweetening process (MDEA 3) to have direct recycle to the RTR or go back to the MDEA 1 to recovery the additional syngas. It is worth remarking that the only by-product obtained by the process is the elemental sulphur, which is in any case a chemical product with market (30 to 130 $/t according to market price fluctuations of the last years). Considering the lower price of currently unexploited coal with high sulphur content, the additional syngas production, the reduction of CO_2 emissions and the relatively small investment to revamp existing plants, the additional net income for a medium-size gasification process is estimated in the order of 18M€/y.

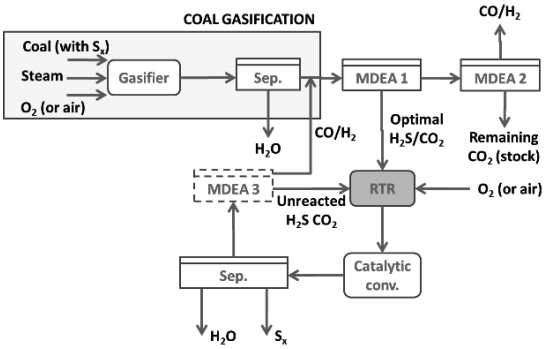

Figure 2. Process line-up for revamped coal gasification process.

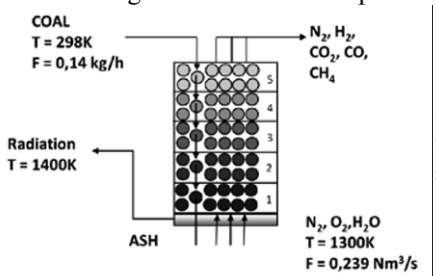

Figure 3a. Downdraft coal gasifier.

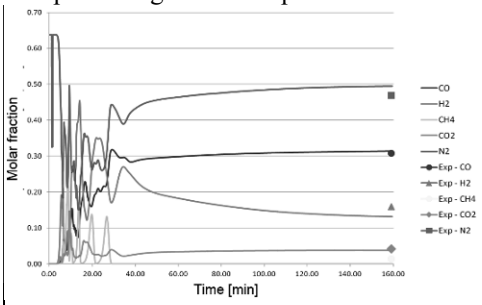

Figure 3b. Model validation (start-up).

6. Conclusions

A novel process to reduce CO_2 and use it as feedstock for chemical/fuel conversion is presented. The process has been studied and engineered using different CAPE tools and then validated by the field, demonstrating its effectiveness and environmental appeal. High conversion of CO_2 and total conversion of H_2S in the oxy-reduction reaction to syngas ensure positive economical impact. The industrial feasibility study on the coal gasification process showed a payback of 2 months for a medium-size plant.

Acknowledgments

The author gratefully acknowledges the support of Prof. Sauro Pierucci and Prof. Eliseo Ranzi, Politecnico di Milano; Ing. Lucio Molinari, Tecnimont-KT; and Ing. Gennaro Perego, Siirtec-Nigi.

References

B. G. Cox, P. F. Clarke, B. B. Pruden, Economics of Thermal Dissociation of H2S to Produce Hydrogen. Int. J. Hydrogen Energy 1998, 23, (7), 531-544.

F. Manenti, D. Papasidero, A. Frassoldati, G. Bozzano, S. Pierucci, E. Ranzi, Multi-scale modeling of Claus thermal furnace and boiler using detailed kinetics and reactor network. Computers & Chemical Engineering 2013, 59, 219-225.

M. A. Mueller, R. A. Yetter, F. L. Dryer, Kinetic Modeling of the CO/H2O/O2/NO/SO2 System: Implication for High-Pressure Fall-off in the SO2+O(+M)=SO3(+M) Reaction. International Journal of Chemical Kinetics 2003, 35, 564-575

E. Ranzi, M. Corbetta, F. Manenti, S. Pierucci, Kinetic Modeling of the Thermal Degradation and Combustion of Biomass, Chemical Engineering Science, 110, 2-12, 2014

W. Villasmil, A. Steinfeld, Hydrogen production by hydrogen sulfide splitting using concentrated solar energy - Thermodynamics and economic evaluation. Energy Conversion and Management 2010, 51, 2353–2361.

Krist V. Gernaey, Jakob K. Huusom and Rafiqul Gani (Eds.), 12th International Symposium on Process Systems Engineering and 25th European Symposium on Computer Aided Process Engineering.
31 May – 4 June 2015, Copenhagen, Denmark

Design and Optimization of Intensified Non-sharp Distillation Configurations

C.E. Torres-Ortega[a], K. Stricker[a], M. Errico[b], B.-G. Rong[a*]

[a]*Department of Chemical Engineering, Biotechnology and Environmental Technology, University of Southern Denmark, Niels Bohrs Allé 1, DK-5230 Odense M, Denmark*
[b]*Universitá degli Studi di Cagliari, Dipartimento di Ingegneria Meccanica, Chimica e dei Materiali, Via Marengo 2, 09123 Cagliari, Italy*
bgr@kbm.sdu.dk

Abstract

For an N-component mixture, a separation sequence with only sharp splits needs the minimum number of N-1 simple columns with 2(N-1) heat exchangers to achieve N pure products. As the number of columns and heat exchangers are the dominant criteria to evaluate a distillation configuration, traditional distillation configurations with only sharp splits have been the preferred alternatives. However, sharp split separations present intrinsic thermodynamic inefficiencies, and one way to reduce these inefficiencies is by means of non-sharp splits. This refers to the possibility of obtaining one product in more than one stream. Moreover, the increasing in both the number of columns and heat exchangers due to the non-sharp splits can be reduced by combining the individual columns and by introducing thermal couplings. In this work, the non-sharp distillation sequence for the separation of a four component mixture of hydrocarbons is considered. Using the aforementioned method, different alternative sequences were designed by the rigorous method with Aspen PlusV8.0, going from 4 to 3 and to 2 columns; then optimized by minimizing the total annual cost by means of a platform consisting in Aspen PlusV8.0 (rigorous simulation) and Visual Basic (stochastic optimizer Differential Evolution), to finally compare the sequences. Moreover, the synthesis methodology used allows deriving two types of intensified systems, the systems with less column sections or the systems with dividing wall columns.

Keywords: non-sharp multicomponent distillation, recombination of column sections, stochastic optimization, dividing wall columns.

1. Introduction

Distillation is one of the most used separation methods in the process engineering and at the same time is responsible of high energy consumptions. According to the U.S. Department of Energy, there are more than 40,000 distillation columns in North America only, and they consume about 40 % of the total energy used to operate refining and bulk chemical industries. Therefore, the research on process synthesis aimed to find new distillation systems with the potential to significantly reduce both energy consumption and capital investment. Defining a simple distillation column as a column with one reboiler and one condenser, this can perform a sharp or a non-sharp split of a mixture. Non-sharp splits refer to a partial or sloppy separation of one or more middle components that are allowed to distribute in the distillate and in the bottom stream. Only sharp-splits configuration allows the minimum number of columns and heat exchangers; thus they have been the preferred alternatives for a quite long time for both academic

research and industrial applications. One way to reduce the high energy consumption of sharp-split systems is to introduce non-sharp splits. However, if non-sharp splits are considered, the corresponding distillation configuration has more columns and heat exchangers than configurations with only sharp splits, leading to an increase in the capital and control costs.

With the introduction of the process intensification concept, several strategies have been proposed for improving the efficiency and environmental-friendly features of different processes. Inside the process separation field, one type of intensified distillation system for multicomponent separations is the dividing wall column (DWC), where the number of shells and the heat exchangers are reduced. The DWCs for ternary separations have been widely studied, and many applications have demonstrated that the energy consumption can be reduced by 30–50 % compared to the conventional columns.

In order to obtain the design for DWCs, the analysis and recombination of column sections, where a column section is defined as a portion of the column not interrupted by mass or energy streams, as well as the inclusion of thermal coupling has the main advantage of relating the design parameters between the original simple column sequences and DWCs. These principles were previously used for the synthesis, design, performance analysis and optimization for mainly ternary mixtures, including side stripper and rectifier configurations, as well as for fully thermally sequences (Fidkowski and Królikowski 1986, Hernández and Jiménez 1996), just to mention a few works. Rong et al. (2003) presented a method which can synthesize all possible distillation configurations with equal to N-1 or more than N-1 columns for an N-component mixture considering both sharp and non-sharp sequences. Moreover, a systematic method has demonstrated to be able to derive the possible distillation configurations with less than N-1 columns for the sharp sequences (Errico et al., 2009). Such distillation configurations with less than N-1 columns for an N-component separation are considered as intensified distillation systems which have the potential to reduce both energy and capital costs. The purpose and novelty of this work is focusing on the intensification of the non-sharp distillation configuration with more than N-1 columns. The objective here is twofold: first, the synthesis of the possible intensified schemes with N-1 or less than N-1 columns is presented, which include the side-stream columns and DWC columns. Second, the design and optimization for all the versions of the considered schemes are implemented for the evaluation of their potential savings in energy and capital costs.

2. Systems synthesis, design and optimization

2.1. Synthesis

In the present work the introduction of thermal couplings together with the possibility of column section recombination were used as a tool to generate the alternative configurations. The reference configuration is reported in Figure 1.a), which first obtained as the feasible distillation configurations with more than N-1 columns in the complete space for an N-component mixture by Rong et al. (2003). Considering only the possibility to introduce thermal couplings in the non-product streams in the first column, three corresponding thermally coupled sequences (TCS) can be generated.

The introduction of the thermal couplings makes some sections movable and recombinable. Then, the thermodynamically equivalent sequences (TES) are obtained. The presence of a single column section in the TES gives the opportunity to reduce the number of columns. If the single column section does not perform a separation task, i.e. is a transportation section, then it is possible to substitute it by a side stream generating

the simple intensified sequence (SIS). Otherwise is still possible to integrate the single section inside the column to which is connected; then dividing wall column (DWC) can be generated. Figure 1 depicts a representative example of the whole synthesis procedure. The evaluation of the separation task of the single column sections were performed through the analysis of the composition profiles.

2.2. Case Study

A 100 kmol h^{-1} of a four component hydrocarbon mixture was considered as a case study to show how the current methodology is implemented for different structures; the authors believe this approach can be extended to other zeotropic mixtures. The composition and the properties of the mixture are presented in Table 1.

All the configurations contained the following features:

- all the components are obtained at the molar purity of 99 %
- only the first column of the sequence performs a non-sharp split
- only the n-hexane is obtained pure in two different product streams
- the split ratios of the intermediate components were fixed at 55 % for n-hexane, and 7.5 % for n-octane; values based on energy consumption via sensitivity analysis.

Table 1. Composition and physical properties of the mixture

Component	x_F
A: C_4H_{10}	0.1
B: C_6H_{14}	0.4
C: C_8H_{18}	0.4
D: $C_{10}H_{22}$	0.1
P (bar)	2
q (feed condition)	1

2.3. Simulation

All the sequences derived from the reference case have been simulated by means of Aspen Plus V8.0. The thermodynamic method selected was the generalized correlation method BK10 that applies for nearly ideal mixtures. The value of the operating pressure for all the columns was defined independently in order to allow the use of cooling water in the condensers. The shortcut design method, based on the Underwood-Gilliland-Winn equations, was used to get the initial parameters, and then these parameters were used in the rigorous RadFrac model. Total condensers, partial reboilers and sieve trays were considered.

A two-step procedure was defined for evaluating the sequences. In the former, all the alternatives were simulated taking the reference case as a basis for the parameters design, and then the reference sequence and the most promising alternative were optimized. However, before the optimization procedure a sensitivity analyses was carried out using Aspen Plus in order to identify the promising alternative via an energy consumption comparison.

2.4. Optimization

The formulation of these problems belongs to a mixed integer non-linear programming problem (MINLP). Among the solver's alternatives, differential evolution (DE) has shown good performances in different theoretical and practical problems. Like others population-based evolutionary algorithms, DE samples the search space, generates new points, evaluate the fitness values and select the best individuals for next generations. The distinctive characteristic of DE is the way the new individuals are generated by means of the scaled difference of random vectors for obtaining a trial vector that will compete against the other individuals of the population.

The DE parameters and stop criterion, as well as the link between Aspen Plus (rigorous process simulations) and Excel (DE coded in Visual Basic) are described in detail in several previous works (Torres-Ortega et al. 2013). The objective function for the final design was to minimize the total annual cost (TAC). The TAC was evaluated following the Guthrie's method (Turton et al. 2004) considering 10 years of investment according to the Eq. (1).

$$TAC = \sum \left[\left(\frac{Capital\ Cost}{Time\ of\ Investment} \right)_i + (Cost\ of\ Utilities)_i \right] \quad (1)$$

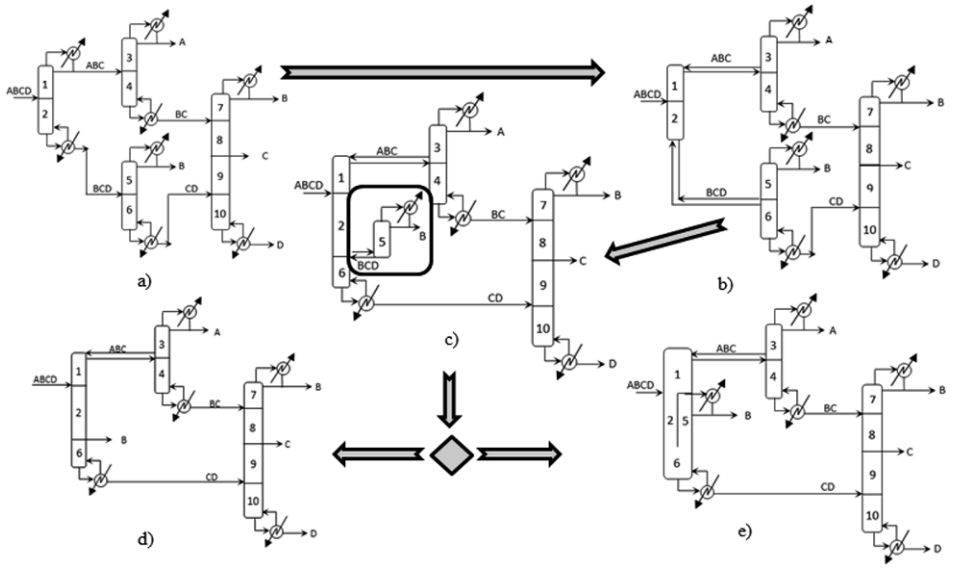

Figure 1.Representative case for the whole synthesis procedure. a) Reference case, and representative derived schemes for: b) TCS, c) TES, d) SIS and e) DWC. In the case depicted, the difference between d) and e) relies in section 5 inside the rectangle of c).

3. Results and discussion

3.1. Simulation analysis

Regarding the energy consumption, the most attractive sequence was the one corresponding to the substitution of both condenser and reboiler of the first column with thermal couplings. Then TES were evaluated and again those obtained from the best TCS presented the lowest energy consumption.

3.2. Simple Intensified Sequences (SIS)

For all the analyzed cases, the single column sections showed a clearly separation function that precludes the possibility to remove these sections and reach the design specifications required. This separation task was more noticeable for single column sections directly related to a product stream than an intermediate section.

3.3. Dividing wall column (DWC)

The derived dividing wall columns from Figure 1a are presented in Figure 2. The energy consumption of these sequences was consistent but slightly lower with their respective TES. However only 4 of the 5 DWC systems, Figure 2.b) to e) presented

lower energy consumption than the reference case and unlike the TES, the DWC arrangements also reduced the number of columns. Again, those derived from the TCS with two thermal couplings reported the major savings.

For intensification purposes, only the systems with energy savings and reduction in the number of equipment were considered for consecutive analyses. Table 2 depicts a more detailed economic analysis comparing the reference case with promising DWCs from Figure 2 b) to e). For the DWC's TAC calculation, the height of the shell was approximated taking into account the total number of stages for the main column and the higher sectional diameter as the overall diameter for the column. The sections just next to the partition wall were considered as complex internal elements, and then an extra factor in the capital cost for these trays was included.

All the promising DWC presented a lower TAC than the reference case. However, the barely improvement in DWC_e can be explained considering the more expensive utility costs associated to a higher pressure in the DWC reboiler. The configuration DWC_d showed the lower energy consumption and TAC; thus it was selected to be optimized together with the reference case.

3.4. Optimization of the reference case and most promising DWC

The modified process variables were related to the number of stages, location of feeds and internal flow division due to the partition wall (in the case of DWC). The own parameters of the DE selected were Cr = 0.8, F = 0.9 for both cases, and Np = 80 and 8,000 simulations for the reference case, and Np = 100 and 9,000 simulations for the DWC. The term Cr stands for the crossover factor, F = mutation factor and Np the population number. Last three rows in Table 2 summarize the main results for the optimal sequences, as well as the percentage of reduction with respect the reference case. According to the data from Table 2, the difference in the energy consumption, the size of the equipment and the TAC were not significantly improved by the optimization from the starting values. However, the alternative DWC configuration moderately outperformed the reference case.

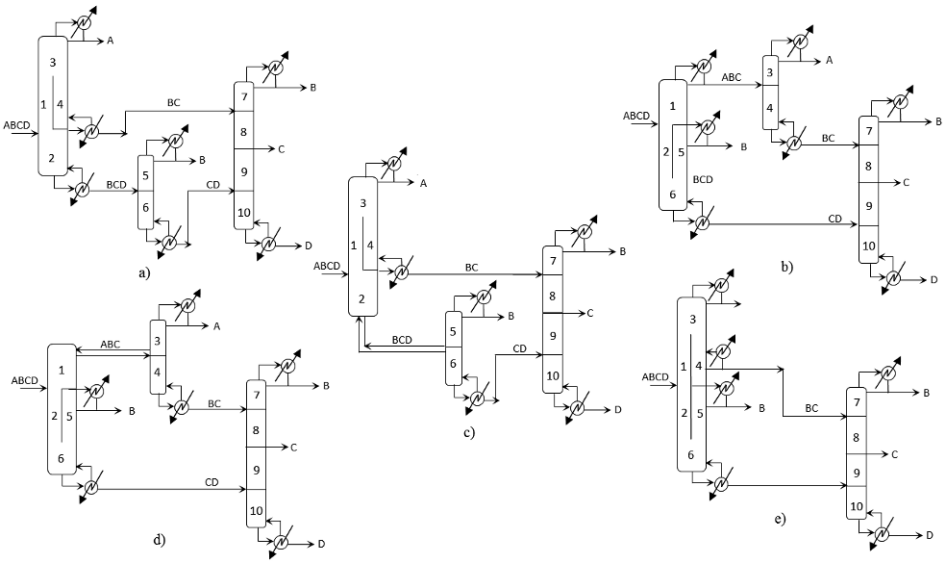

Figure 2. The DWC configurations obtained for the reference case Figure 1a).

Table 2. Economic analysis via sensitivity analysis of the most promising DWC and the reference case, as well as the optimal configuration results. The number in parentheses before the name stands for the number of column shells in every separation train.

Sequence	Total energy consumption [kW]	Capital costs [USD Year^{-1}]	Utility costs [USD Year^{-1}]	TAC [USD Year^{-1}]
(4) RefSC	3023	123742	788638	912381
(3) DWC_b	2804	118012	757772	875783
(3) DWC_c	2679	109302	716633	825935
(3) DWC_d	2567	106138	693910	800048
(2) DWC_e	2737	122582	788890	911472
Optimal (4) RefSC	2950	125382	769985	895367
Optimal (3) DWC_d	2459	115017	673115	788132
% of Reduction	16.6	8.3	12.6	12.0

4. Conclusions

This work has successfully showed that the traditional non-sharp distillation configuration with more than N-1 columns can be intensified into distillation configurations with less than N-1 columns for an N-component mixture. Among the different sub-spaces of the alternatives, DWC showed the highest reductions in both energy consumption and capital costs. Regarding the TAC, the most promising DWC sequence achieved 12 % reduction compared to the reference case. The systematic methodology based on recombination of column sections, sensitivity analysis and stochastic optimization provides a robust and reliable methodology towards looking for the optimal intensified distillation systems.

5. References

M. Errico, B.-G. Rong, G. Tola, I. Turunen, 2009, A method for systematic synthesis of multicomponent distillation systems with less than N-1 columns, Chem Eng Proc, 48, 907-920.

Z.T. Fidkowski, L. Królikowski, 1986, Thermally Coupled System of Distillation Columns: Optimization Procedure, AIChE J, 32, 537-546.

S. Hernández, A. Jiménez, 1996, Design of optimal thermally coupled distillation systems using a dynamic model, Chem Eng Res Des, 74, 357-362.

B.-G. Rong, A. Kraslawski, I. Turunen, 2003, Synthesis of functionally distinct Thermally Coupled Distillation configurations for quaternary distillations, Ind Eng Chem Res, 42, 1204-1214.

B.-G. Rong, M. Errico, J.G. Segovia-Hernández, 2014, New Intensified Distillation Systems for Quaternary Petlyuk Configuration, Comp Aid Chem Eng, 33, 97-102.

C.E. Torres-Ortega, J.G. Segovia-Hernández, F.I. Gómez Castro., S. Hernández, A. Bonilla-Petriciolet, B.-G. Rong, M. Errico, 2013, Design, optimization and controllability of an alternative process based on extractive distillation for an ethane-carbon dioxide mixture, Chem Eng Proc, 74, 55-68.

R. Turton, R.C. Bailie, W.B. Whiting, J.A. Shaeiwitz, 2004, Analysis, Synthesis and Design of Chemical Process, 2nd ed., New Jersey: Prentice Hall.

Krist V. Gernaey, Jakob K. Huusom and Rafiqul Gani (Eds.), 12th International Symposium on Process Systems Engineering and 25th European Symposium on Computer Aided Process Engineering.
31 May - 4 June 2015, Copenhagen, Denmark.

Deterministic Global Optimization of Multistage Melt Crystallization Processes in Hydroformylation

Christian Kunde[a] and Achim Kienle[a,b]

[a]*Otto von Guericke University Magdeburg, Magdeburg, Germany*
[b]*Max Planck Institute for Dynamics of Complex Technical Systems, Magdeburg, Germany*
christian.kunde@ovgu.de

Abstract

This paper deals with the deterministic global optimization of multistage melt crystallization processes with application to mixtures of n-/iso-aldehydes resulting from hydroformylation. For this purpose we adopt a process model including experimentally determined parameters from the literature. We extend that model from commonly used countercurrent cascades to arbitrary process configurations and reformulate it for better computational performance. The resulting model is a MINLP due to operational and structural degrees of freedom. Global optima for the process costs with respect to an economical cost function are determined using BARON/GAMS. The results show that there are new process configurations outperforming the conventional countercurrent cascade, depending on parameter values.

Keywords: deterministic global optimization, MINLP, melt crystallization, multistage

1. Introduction

Separation of closely boiling mixtures is a challenging problem in process synthesis and process design. A typical example given by Micovic et al. (2013) is the separation of mixtures of isomers like n/iso-aldehyde mixtures arising from hydroformylation based on renewable resources. Standard distillation is often not favorable due to high process costs. A more efficient separation process for such closely boiling mixtures may be obtained by using melt crystallization either in combination with distillation or as a stand-alone process, as studied by Micovic et al. (2013). To achieve the desired crystal purity, often a multistage melt crystallization process is required. Standard approaches focus on countercurrent crystallizer cascades. However, due to restricted process topology this process configuration tends to be suboptimal. Hence, in the present contribution restrictions on process topology are relaxed also allowing new process configurations which have not been studied so far by other researchers to the best of our knowledge. Optimal operating conditions and optimal process structures are determined simultaneously using mixed integer nonlinear (MINLP) optimization. Due to nonconvexity, standard MINLP solution procedures based on local or stochastic optimization algorithms can not guarantee to find the global optimum, which however is essential for identifying also new and probably counterintuitive solutions. Therefore deterministic global optimization using BARON/GAMS is applied, see Tawarmalani and Sahinidis (2005). A suitable model of a multistage melt crystallization process for the separation of an isomeric mixture of n-dodecanal and 2-methylundecanal by Micovic et al. (2013) is used. The model is adapted to allow arbitrary process topologies and the resulting model complexity is reduced by reformulating the model equations and excluding redundant crystallizer network configurations. The influence of important model parameters on the performance of new process structures is discussed and the results are compared to the standard countercurrent cascade process.

2. Model description

The crystallization model describes the behavior of a binary, eutectic system corresponding to the intended application of separating binary mixtures of the isomers 2-methylundecanal and n-dodecanal. We assume that crystal product impurities can be described by a constant differential distribution coefficient as in Wellinghoff and Wintermantel (1991) and Micovic et al. (2013). The experimental data for mixtures of 2-methylundecanal and n-dodecanal is published in Beierling and Ruether (2012), Micovic et al. (2013) and Beierling et al. (2014). The position of the eutectic point is close to pure 2-methylundecanal, practically only allowing crystallization of n-dodecanal with impurities of 2-methylundecanal.

We consider a crystallizer network with stages $n = 1,\dots,n^{\mathrm{Cr}}$ numbered downwards. Each stage n separates the molar feed flow F_n into the crystal product S_n and the liquid remainder L_n with the molar flows of the impurity denoted as $F_{\mathrm{iso},n}$, $S_{\mathrm{iso},n}$ and $L_{\mathrm{iso},n}$, respectively. The feed of each stage F_n is the sum of all crystal product flows S and liquid remainder flows L connected to that stage and, if applicable for that stage, the crystallizer feed flow $F^{\mathrm{In_{Cr}}}$. The distribution of the crystallizer feed flow and the connections between stages are implemented using binary variables $\beta_n^{\mathrm{In_{Cr}}} \in \{0,1\}$, $\beta_{l,n}^{\mathrm{S}} \in \{0,1\}$ and $\beta_{l,n}^{\mathrm{S}} \in \{0,1\}$, $n = 1,\dots,n^{\mathrm{Cr}}$, $l = 1,\dots,n^{\mathrm{Cr}}$. The variables $\beta_n^{\mathrm{In_{Cr}}}$, $\beta_{l,n}^{\mathrm{S}}$ and $\beta_{l,n}^{\mathrm{L}}$ attain a value of one if and only if the feed enters at stage n, the crystal product output of stage l is fed to stage n and the liquid remainder output of stage l is fed to stage n, respectively.

$n = 1,\dots,n^{\mathrm{Cr}}$:

$$F_n = F^{\mathrm{In_{Cr}}}\beta_n^{\mathrm{In_{Cr}}} + \sum_{l=1}^{n^{\mathrm{Cr}}} S_l\beta_{l,n}^{\mathrm{S}} + \sum_{l=1}^{n^{\mathrm{Cr}}} L_l\beta_{l,n}^{\mathrm{L}}, \tag{1}$$

$$F_{\mathrm{iso},n} = F_{\mathrm{iso}}^{\mathrm{In_{Cr}}}\beta_n^{\mathrm{In_{Cr}}} + \sum_{l=1}^{n^{\mathrm{Cr}}} S_{\mathrm{iso},l}\beta_{l,n}^{\mathrm{S}} + \sum_{l=1}^{n^{\mathrm{Cr}}} L_{\mathrm{iso},l}\beta_{l,n}^{\mathrm{L}}, \tag{2}$$

We ensure that the feed enters exactly one stage by

$$\sum_{n=1}^{n^{\mathrm{Cr}}} \beta_n^{\mathrm{In_{Cr}}} = 1. \tag{3}$$

We make sure that the output flow of each stage is connected to exactly one stage input or one crystallizer product output by

$$\sum_{n=1}^{n^{\mathrm{Cr}}} \beta_{l,n}^{\mathrm{S}} + \beta_l^{\mathrm{S,Out1_{Cr}}} = 1, \quad l = 1,\dots,n^{\mathrm{Cr}} \tag{4}$$

$$\sum_{n=1}^{n^{\mathrm{Cr}}} \beta_{l,n}^{\mathrm{L}} + \beta_l^{\mathrm{L,Out2_{Cr}}} = 1, \quad l = 1,\dots,n^{\mathrm{Cr}}, \tag{5}$$

with $\beta_l^{\mathrm{S,Out1_{Cr}}} \in \{0,1\}$ attaining value 1 if and only if the crystal product output of stage l is connected to output $\mathrm{Out1_{Cr}}$ and with $\beta_l^{\mathrm{L,Out2_{Cr}}} \in \{0,1\}$ attaining value 1 if and only if the liquid remainder output of stage l is connected to output $\mathrm{Out2_{Cr}}$.

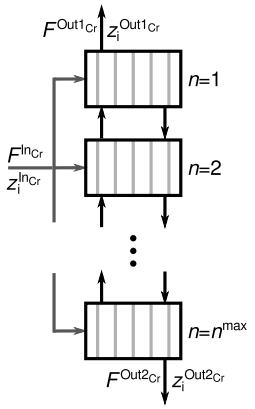

Figure 1: Countercurrent crystallizer cascade with n^{Cr} stages and arbitrary feed stage ($\beta_{l,l-1}^{\mathrm{S}} = 1$, $l = 2,\dots,n^{\mathrm{Cr}}$, $\beta_{l,l+1}^{\mathrm{L}} = 1$, $l = 1,\dots,n^{\mathrm{Cr}}-1$, $\beta_1^{\mathrm{S,Out1_{Cr}}} = 1$, $\beta_{n^{\mathrm{Cr}}}^{\mathrm{L,Out2_{Cr}}} = 1$).

We also require that each stage has at least one input.

$$\sum_{l=1}^{n^{\mathrm{Cr}}} \left(\beta_{l,n}^{\mathrm{S}} + \beta_{l,n}^{\mathrm{L}}\right) + \beta_n^{\mathrm{In_{Cr}}} \geq 1, \quad n = 1,\dots,n^{\mathrm{Cr}} \tag{6}$$

The countercurrent cascade depicted in Figure 1 will serve as the benchmark for any other configuration within this superstructure.

The model equations describing the separation on each stage according to Wellinghoff and Wintermantel (1991) read

$$\begin{aligned} &n = 1,\ldots,n^{\mathrm{Cr}}: \\ &\begin{aligned} S_n &= Y_n F_n, & w_{\mathrm{iso},n} &= k_{\mathrm{int},n} z_{\mathrm{iso},n}, \\ L_n &= F_n - S_n, & x_{\mathrm{iso},n} L_n &= z_{\mathrm{iso},n} F_n - w_{\mathrm{iso},n} S_n, \\ k_{\mathrm{int},n} &= \tfrac{1-(1-Y_n)^{k_{\mathrm{diff}}}}{Y_n}, \end{aligned} \end{aligned} \tag{7}$$

with the yield $Y_n \in [0,1]$, the integral distribution coefficient $k_{\mathrm{int},n} \in [0,1]$ and the molar fractions of the impurity in the feed $z_{\mathrm{iso},n}$, in the crystal product $w_{\mathrm{iso},n}$ and in the liquid remainder $x_{\mathrm{iso},n}$. Note that the distribution coefficient was defined using weight fractions in Wellinghoff and Wintermantel (1991). Weight fractions are equivalent to molar fractions if all chemical species have the same molar mass, as is the case for mixtures of isomers.
With regard to global optimization, it is often desireable to reduce the number of variables and nonlinearities in the model or at least to simplify the nonlinearities. This is done for the crystallization model by reformulating the model using the molar flows of the impurity instead of molar fractions.

$$S_{\mathrm{iso},n} = w_{\mathrm{iso},n} S_n, \qquad L_{\mathrm{iso},n} = x_{\mathrm{iso},n} L_n \qquad F_{\mathrm{iso},n} = z_{\mathrm{iso},n} F_n \tag{8}$$

The resulting equation for $S_{\mathrm{iso},n}$ then reads

$$S_{\mathrm{iso},n} = k_{\mathrm{int},n} Y_n F_{\mathrm{iso},n}. \tag{9}$$

We further introduce new variables $\tilde{k}_{\mathrm{Y},n} \in [0,1]$ and $\tilde{Y}_n \in [0,1]$ as

$$\tilde{k}_{\mathrm{Y},n} = 1 - k_{\mathrm{int},n} Y_n \tag{10}$$

$$\tilde{Y}_n = 1 - Y_n \tag{11}$$

to write the set of equations for the crystallizer that was used for the computational studies in this work.

$$\begin{aligned} &n = 1,\ldots,n^{\mathrm{Cr}}: \\ &\begin{aligned} L_{\mathrm{iso},n} &= \tilde{k}_{\mathrm{Y},n} F_{\mathrm{iso},n}, & S_{\mathrm{iso},n} &= F_{\mathrm{iso},n} - L_{\mathrm{iso},n} \\ L_n &= \tilde{Y} F_n, & S_n &= F_n - L_n \\ \tilde{k}_{\mathrm{Y},n} &= \tilde{Y}_n^{k_{\mathrm{diff}}}. \end{aligned} \end{aligned} \tag{12}$$

Molar fractions are used for the inlet composition $z_{\mathrm{iso}}^{\mathrm{In_{Cr}}}$ and the product specifications $z_{\mathrm{iso}}^{\mathrm{Out1_{Cr}}}, z_{\mathrm{iso}}^{\mathrm{Out2_{Cr}}}$. An interface is implemented by the following equations.

$$F_{\mathrm{iso}}^{\mathrm{In_{Cr}}} = z_{\mathrm{iso}}^{\mathrm{In_{Cr}}} F^{\mathrm{In_{Cr}}} \tag{13}$$

$$F_{\mathrm{iso}}^{\mathrm{Out1_{Cr}}} = z_{\mathrm{iso}}^{\mathrm{Out1_{Cr}}} F^{\mathrm{Out1_{Cr}}} \tag{14}$$

$$F_{\mathrm{iso}}^{\mathrm{Out2_{Cr}}} = z_{\mathrm{iso}}^{\mathrm{Out2_{Cr}}} F^{\mathrm{Out2_{Cr}}} \tag{15}$$

$$F^{\mathrm{Out1_{Cr}}} = \sum_{n=1}^{n^{\mathrm{Cr}}} \beta_n^{\mathrm{S,Out1_{Cr}}} S_n, \quad F_{\mathrm{iso}}^{\mathrm{Out1_{Cr}}} = \sum_{n=1}^{n^{\mathrm{Cr}}} \beta_n^{\mathrm{S,Out1_{Cr}}} S_{\mathrm{iso},n} \tag{16}$$

$$F^{\mathrm{Out2_{Cr}}} = \sum_{n=1}^{n^{\mathrm{Cr}}} \beta_n^{\mathrm{L,Out2_{Cr}}} L_n, \quad F_{\mathrm{iso}}^{\mathrm{Out2_{Cr}}} = \sum_{n=1}^{n^{\mathrm{Cr}}} \beta_n^{\mathrm{L,Out2_{Cr}}} L_{\mathrm{iso},n} \tag{17}$$

Inequalities are added to the model to implement the physical constraint of the eutectic composition x^{eut} and the technical constraint of a minimum cooling temperature. The solid-liquid phase

equilibrium for mixtures of 2-methylundecanal and n-dodecanal given in Micovic et al. (2013) was used to calculate a minimum molar fraction of n-dodecanal $x_{\mathrm{N}}^{\mathrm{min_T}}$ from the minimum cooling temperature. Only one of the following inequalities is active in the model, depending on the parameters.

$$(1-x_{\mathrm{N}}^{\mathrm{eut}})L_n \geq L_{\mathrm{iso},n}, \quad n=1,\ldots,n^{\mathrm{Cr}} \tag{18}$$

$$(1-x_{\mathrm{N}}^{\mathrm{min_T}})L_n \geq L_{\mathrm{iso},n}, \quad n=1,\ldots,n^{\mathrm{Cr}} \tag{19}$$

Without loss of generality we assume that the stages are ordered in terms of purity of the stage feed.

$$F_{\mathrm{iso},n}F_{n+1} \leq F_{\mathrm{iso},n+1}F_n, \quad n=1,\ldots,n^{\mathrm{Cr}}-1 \tag{20}$$

Based on the ordered purity the search space is further reduced by demanding that the crystal output of each stage is not fed to a stage below that stage and that the liquid remainder of each stage is not fed to a stage above that stage. Connecting an output of a stage to the feed of that same stage leads to redundant configurations and is therefore also excluded.

$$\beta_{l,n}^{\mathrm{S}} = 0 \quad \text{for all} \quad 1 \leq l \leq n, \quad n=1,\ldots,n^{\mathrm{Cr}} \tag{21}$$

$$\beta_{l,n}^{\mathrm{L}} = 0 \quad \text{for all} \quad n \leq l \leq n^{\mathrm{Cr}}, \quad n=1,\ldots,n^{\mathrm{Cr}} \tag{22}$$

All potential connections within the crystallizer network used in this work for a fixed number of stages $n^{\mathrm{Cr}}=3$ are illustrated in Figure 2.

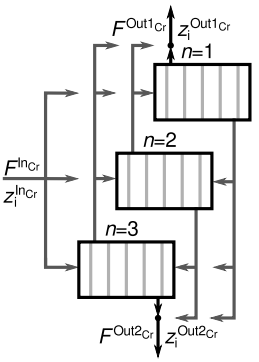

Figure 2: Crystallizer network consisting of $n^{\mathrm{Cr}}=3$ stages with arbitrary configuration.

The process costs are determined according to correlations from Towler and Sinnot (2008). The cost function accounts for annualized installed investment costs of the crystallizer vessel as a heat exchanger, a storage tank for each crystallization stage with the same capacity as the crystallizer and for the energy costs of the process. The dimensioning of the crystallizer is done as in Franke et al. (2008) and the required cooling is calculated according to Wellinghoff and Wintermantel (1991); Franke et al. (2008). Physical parameter values were taken from Beierling and Ruether (2012); Beierling et al. (2014). The resulting cost function can be written in a condensed form as

$$\begin{aligned} cost = (\quad & 86849 \sum_{n=1}^{n^{\mathrm{Cr}}} S_n \text{ s mol}^{-1} + 5215 \\ & + n^{\mathrm{Cr}}(1605.7(\sum_{n=1}^{n^{\mathrm{Cr}}} S_n \text{ s mol}^{-1})^{0.7} + 2123.2) \quad) \text{ \$ a}^{-1}. \end{aligned} \tag{23}$$

3. Results

The results were obtained by applying BARON 11.5.2 (GAMS 23.9.5) to the model described above, minimizing the process costs. CONOPT and CPLEX were facilitated as subsolvers for BARON. The solver options were left at default values except for the termination condition "optcr", the relative difference between upper and lower bound, which was set to 0.000001. In the case of multiple global optima with identical values of the cost function, it should be noted that only one global optimum is found using these options.
The parameters given in Table 1 are chosen to fit the case of constant k_{diff} studied in Beierling et al.

(2014). The value of $x^{\min_T}$ is set according to a minimum cooling temperature above the eutectic temperature. The product specification for $\mathrm{Out2_{Cr}}$ is chosen corresponding to a cooling temperature above the minimum cooling temperature. All molar flow rates are bounded from above by the feed flow rate $F^{\mathrm{In_{Cr}}}$ multiplied by 20.

Table 1: Parameter and domain specifications.

parameter / variable	k_{diff}	$z_{\mathrm{iso}}^{\mathrm{In_{Cr}}}$	$F^{\mathrm{In_{Cr}}}$	$x_{\mathrm{N}}^{\min_T}$	$z_{\mathrm{iso}}^{\mathrm{Out1_{Cr}}}$	$z_{\mathrm{iso}}^{\mathrm{Out2_{Cr}}}$
value / domain	0.08	0.1	1.8838 mol $\mathrm{s^{-1}}$	0.1	$[0, 0.01]$	$[0.89, 1]$

The results for different numbers of stages n^{Cr} are given in Table 2. The countercurrent cascade (see Figure 1) serves as a reference for the evaluation of the optimization results with arbitrary process configurations. The optimal costs for the countercurrent cascade are achieved for $n^{\mathrm{Cr}} = 2$. For configurations with $n^{\mathrm{Cr}} \geq 3$ only the first two stages have a non-zero crystal yield for optimal costs. The optimal costs for arbitrary configurations are achieved at $n^{\mathrm{Cr}} = 3$. Although an additional stage is used the overall costs are reduced by over 2 % compared to the optimal countercurrent cascade. The optimal crystallizer network configurations are depicted in Figure 3.

Table 2: Globally optimal cost values for the countercurrent crystallizer cascade and abitrary crystallizer networks.

number of stages	1	2	3	4	5
countercurrent	infeasible	225468 \$ $\mathrm{a^{-1}}$	230559 \$ $\mathrm{a^{-1}}$	235674 \$ $\mathrm{a^{-1}}$	240776 \$ $\mathrm{a^{-1}}$
arbitrary	infeasible	225468 \$ $\mathrm{a^{-1}}$	220665 \$ $\mathrm{a^{-1}}$	225567 \$ $\mathrm{a^{-1}}$	230101 \$ $\mathrm{a^{-1}}$

The optimal configuration for an arbitrary crystallizer network enables lower overall costs due to a lower crystallization effort $\sum_{n=1}^{n^{\mathrm{Cr}}} S_n$, see Equation (23). This may be explained as follows. The crystallization mechanism used in this work leads to an asymmetric separation, i. e. the purity of the crystal product increases much more compared to the feed than that of the liquid remainder. Using a countercurrent cascade therefore is inefficient due to the mixing of crystal product and liquid remainder with highly different compositions. In arbitrary crystallizer networks there are more degrees of freedom for placing connections to avoid mixing flows with highly different compositions. Consequently, the potential cost reduction depends on the parameters of the model. As an example, lower values of k_{diff} emphasize the asymmetric separation and thereby increase the potential cost savings. Also, the cost reduction seems to be more pronounced if the optimal length of the countercurrent cascade is close to being infeasible. In such a case the yield on each stage is adjusted to fulfill the product specifications and can be used less freely to reduce mixing inefficiencies. Table 3 shows optimization results for $z_{\mathrm{iso}}^{\mathrm{Out1_{Cr}}} \in [0, 0.007]$ with a cost reduction of over 10% compared to the

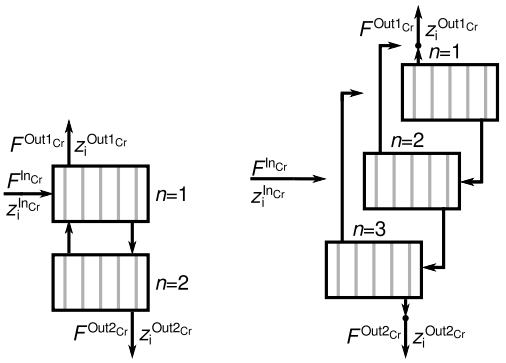

Figure 3: Left: Optimal configuration for a countercurrent cascade ($\beta_{2,1}^{\mathrm{S}} = \beta_{1,2}^{\mathrm{L}} = \beta_1^{\mathrm{In_{Cr}}} = 1$). Right: Optimal configuration for an arbitrary crystallizer network ($\beta_{3,1}^{\mathrm{S}} = \beta_2^{\mathrm{S,Out1_{Cr}}} = \beta_{1,2}^{\mathrm{L}} = \beta_{2,3}^{\mathrm{L}} = \beta_2^{\mathrm{In_{Cr}}} = 1$).

countercurrent crystallizer cascade.

Table 3: Globally optimal cost values for the countercurrent crystallizer cascade and abitrary crystallizer networks with $z_{\mathrm{iso}}^{\mathrm{Out1_{Cr}}} \in [0, 0.007]$.

number of stages	1	2	3	4	5
countercurrent	infeasible	295042 \$ a^{-1}	300804 \$ a^{-1}	306521 \$ a^{-1}	312288 \$ a^{-1}
arbitrary	infeasible	295040 \$ a^{-1}	260752 \$ a^{-1}	265619 \$ a^{-1}	269694 \$ a^{-1}

For the sake of completeness we also report the observed computational time needed to solve the problem cases studied in this work. On a standard desktop computer (Intel® Core™ i7-3770 @ 3.40 GHz) the computational time for the countercurrent cascade is in the range of seconds for $n^{\mathrm{Cr}} \leq 5$. Solutions for arbitrary crystallizer networks require a computational time in the order of seconds for $n^{\mathrm{Cr}} \leq 3$, minutes for $n^{\mathrm{Cr}} = 4$ and hours for $n^{\mathrm{Cr}} = 5$. This increase is caused largely by the combinatorial complexity of the problem.

4. Conclusion

We have presented a suitable model formulation for the deterministic global optimization of melt crystallization processes and applied it to the separation of a mixture of n-/iso-aldehydes, arising from hydroformylation. The results show that the costs of such a process may be reduced considerably by using crystallizer network configurations different from the well-established countercurrent cascade. It is postulated that the mixing of flows with highly different compositions causes inefficiencies in the countercurrent cascade, which can be reduced by using more suitable configurations.

5. Acknowledgements

This work is part of the Collaborative Research Center “Integrated Chemical Processes in Liquid Multiphase Systems”. Financial support by the Deutsche Forschungsgemeinschaft (DFG) is gratefully acknowledged through TRR 63.

References

Beierling, T., Micovic, J., Lutze, P., Sadowski, G., 2014. Using complex layer melt crystallization models for the optimization of hybrid distillation/melt crystallization processes. Chemical Engineering and Processing: Process Intensification 85, 10–23.

Beierling, T., Ruether, F., 2012. Separation of the isomeric long-chain aldehydes dodecanal/2-methylundecanal via layer melt crystallization. Chemical Engineering Science 77, 71–77.

Franke, M., Nowotny, N., Ndocko, E., Górak, A., Strube, J., 2008. Design and optimization of a hybrid distillation/melt crystallization process. AIChE Journal 54 (11), 2925–2942.

Micovic, J., Beierling, T., Lutze, P., Sadowski, G., Górak, A., 2013. Design of hybrid distillation/melt crystallisation processes for separation of close boiling mixtures. Chemical Engineering and Processing: Process Intensification 67, 16–24.

Tawarmalani, M., Sahinidis, N., 2005. A polyhedral branch-and-cut approach to global optimization. Mathematical Programming 103 (2), 225–249.

Towler, G., Sinnot, R., 2008. Chemical Engineering Design - Principles, Practice and Economics of Plant and Process Design. Elsevier.

Wellinghoff, G., Wintermantel, K., 1991. Melt crystallization - theoretical presumptions and technical limitations [Schmelzkristallisation - theoretische Voraussetzungen und technische Grenzen]. Chemie-Ingenieur-Technik 63 (9), 881–888, 89.

Krist V. Gernaey, Jakob K. Huusom and Rafiqul Gani (Eds.), 12th International Symposium on Process Systems Engineering and 25th European Symposium on Computer Aided Process Engineering.
31 May – 4 June 2015, Copenhagen, Denmark

Design and Economic Evaluation of Alternatives to Effluents Treatment on Biodiesel Production from Soybean Oil and Palm Oil

André F. Young,[a]* Fernando L. P. Pessoa,[a] Eduardo M. Queiroz [a]

[a]*Chemistry School, Federal University of Rio de Janeiro, 149 Athos da Silveira Ramos ave, 21941-909, Rio de Janeiro, Brazil*
andreyoung@ufrj.br

Abstract

Biodiesel production by homogeneous alkali catalysis was simulated in PRO/II ® from crude soybean oil and crude palm oil at industrial level, with ethanol. Actual compositions were assumed and thermodynamic properties were estimated by a group contribution method. The main effluents from biodiesel production are streams rich in unreacted oil, water, ethanol and glycerine. Some alternatives to the treatment of these effluents were proposed, including hydrous or anhydrous ethanol production, production and recycle of pure glycerol and unreacted oil recycle. An economic evaluation was done to find out the potential of each treatment possibility. It was demonstrated that, in the case of Brazil in mid-2014, it was not profitable to produce biodiesel from these oilseeds and ethanol without tax reductions or subsidy, but it is possible to reduce production costs and biodiesel prices with effluents treatment, generating more economical and sustainable plants.

Keywords: biodiesel, effluents treatment, soybean, palm.

1. Introduction

In the last few years, the improvement of environmental concerns, allied with the progressive decrease of the worldwide petroleum production, have motivated the study and development of sustainable energy sources and technologies. In this context, the biofuels arise, among them the biodiesel. Biodiesel is a renewable fuel, normally produced from vegetable oils or animal fats, through transesterification of these components with an alcohol, usually methanol or ethanol. It is biodegradable, nontoxic and its burning emits fewer pollutants than traditional petroleum diesel burning (Zhang et al., 2003a).

Regarding the raw material, vegetable oils and animal fats consist mainly in triglycerides (glycerol and fatty acids esters). They can be obtained from a wide variety of sources. In Brazil, special attention is given to soybean, which corresponded to 78 % of the total raw material used in May 2014 (ANP, 2014). Planting of palm, which is the second most used feedstock to biodiesel production in the world, has tripled in Brazil in the last four years (Neher, 2014). Compared to soybean oil, palm oil has a higher content of free fat acids (FFA), which must be removed before transesterification for biodiesel production (Zhang et al. 2003a).

2. Process Design and Simulation

The simulations were performed in PRO/II ®, developed by Invensys Systems, Inc. Due to the presence of highly polar components, like ethanol and glycerol, the NRTL (Non-Random Two Liquid) model was used to predict the activity coefficients. The

binary interaction parameters that were not present in the simulator's database were estimated from the UNIFAC structures of the compounds (Zhang et al., 2003a; West et al., 2008).

The fatty components (triglycerides, FFA and biodiesel), from both the raw materials, were simulated as pseudo-components. The critical properties, boiling point and acentric factor were estimated by the Constantinou-Gani group contribution method (Constantinou and Gani, 1994). It was assumed an average composition for the oils, based on literature data (Knothe et al., 2005). The other properties were estimated based on the linoleic compounds for soybean derivatives and based on the palmitic compounds for palm derivatives.

The plant capacity was specified as the average production per plant in Brazil in mid-2014. In June, there were 61 licensed production plants, producing a total of 21,167.79 m³/day. It corresponds to about 12,625 kg/h per plant (ANP, 2014).

2.1. Pre-treatment: esterification

Alkali catalysis is the most common way to produce biodiesel. However, before entering the transesterification reactor, the FFA content and humidity must be removed, to avoid the production of soap. Lepper and Frisenhagen (1986) have developed a process to esterify the FFA present in vegetable oils, which was first reproduced in a process simulator by Zhang et al. (2003a) and, later, by other authors (West et al. 2008; Morais et al., 2010). This was the process adopted in this work, which is exposed in Figure 1.

A pure ethanol stream is firstly mixed with the catalyst, H_2SO_4, and then conducted to the esterification reactor, which works continuously at 70 °C and 400 kPa. The esterification kinetics was assumed to be of reversible second order, based on the study of Pisarello et al. (2010). The quantity of ethanol added in the reactor was equal to 15 % in volume of the quantity of crude soybean oil (0.5 % FFA) and 45 % in volume of the quantity of crude palm oil (5 % FFA). This greater amount for palm is needed to displace the equilibrium in the products direction.

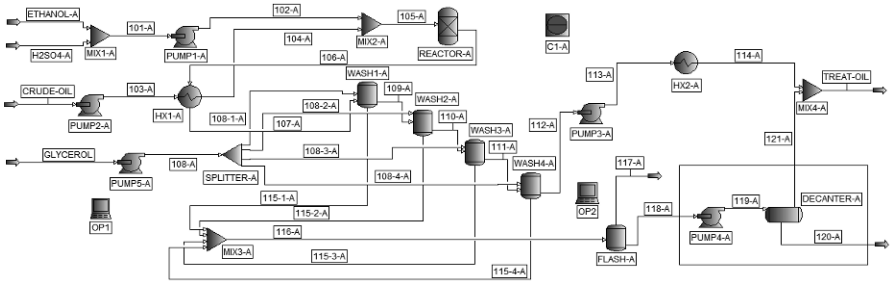

Figure 1 – Pre-treatment module, with (palm) and without (soy) the decanter, indicated by the rectangle

It was necessary a residence time of 0.3 h for the conversion of 50 % of the FFA in soybean oil and 7.1 h for the conversion of 95 % of the FFA in palm oil. After esterification, the oil goes to a sequence of four mixers and settlers (simulated as flash vessels) where a glycerine washing is performed. The objective is to remove all the FFA

and humidity. A flash vessel operating under vacuum (30 kPa) is used to separate glycerine and ethanol. For soy, the ethanol obtained is still under specifications to be sold as anhydrous fuel (ANP, 2011). But the effluent obtained in the palm oil process, which has an ethanol mass fraction of 98.9 %, need to be treated before it can be sold as anhydrous. It is important to note that even if the ethanol could be classified as anhydrous fuel, it cannot be recycled to the esterification reactor, because of the little content of water that could be carried to the transesterification reactor.

There is another difference between the soybean oil process and the palm oil process. Because of the higher quantity of ethanol and solvent needed for washing in the palm oil process, some volume of biodiesel is lost in the extract. To recover this volume, the glycerine goes to a decanter. The biodiesel and the oil recovered in the decanter meet the raffinate stream and go to transesterification.

2.2. Transesterification

The process adopted to perform the homogeneous alkali transesterification is similar to the process used by Zhang et al. (2003a), West et al. (2008) and Morais et al. (2010), showed in Figure 2. Although in the process with methanol it is recommended an alcohol to oil ratio of 6:1 (Freedman et al., 1984), when the vegetable oil is processed with ethanol, a higher ratio is generally used. So, it was adopted a molar ratio of 9:1 in this work. The transesterification reactor works continuously at 50 °C and 400 kPa. An irreversible second order kinetics was assumed, based on the work of Shahla et al. (2012).

Pure ethanol is mixed with the catalyst, NaOH, and is added in the reactor. The same occurs with the pre-treated oil. Based on the contribution of Garnica (2009), who studied these reactions for soybean oil and palm oil in the same conditions, the residence time for 95 % conversion was estimated as 6.6 h for soy, while for palm it was 8.9 h. The reaction product goes to a distillation column, to recover the ethanol excess. The column operates with six theoretical stages, including condenser and reboiler, and reflux ratio of two. It is necessary to operate under vacuum (10 kPa at the top and 30 kPa at the bottom) to avoid degradation of the biodiesel or the glycerol

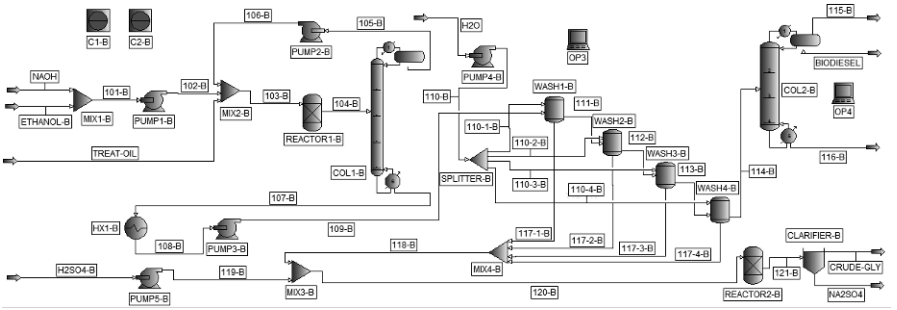

Figure 2 – Alkali-catalysed transesterification module

(Zhang et al., 2003a). Almost 99 % of the ethanol present in the product stream could be recovered and recycled to the reactor. Then, the product goes to a water washing, in a sequence of four mixers and settlers (simulated as flash vessels). The objective is to separate the catalyst and the glycerine. The biodiesel goes to a purification column, which operates with five theoretical stages and under vacuum. The biodiesel produced

in the condenser is under Brazilian and American specifications. The effluent at the top consists of ethanol and water, and must be treated. The effluent at the bottom consists mainly of unreacted oil. The crude glycerine goes to a neutralizer reactor, which also receives the glycerine used in the esterification and a H_2SO_4 load. The reactor works at 60 °C and 110 kPa. After a residence time of five minutes, it is assumed that all the sodium hydroxide reacts with the sulphuric acid, forming sodium sulphate (Na_2SO_4). The solid is separated in a clarifier and the glycerine can be sold as crude glycerine.

2.3. Effluent treatment proposals

The first effluent treatment proposal is the recycle of the unreacted oil obtained at the bottom of the biodiesel purification column directly to the transesterification reactor. The exigency here is just a pump, to put the oil at 400 kPa, and a heat exchanger, to correct the temperature.

The second proposal is the treatment and recycle of the crude glycerine. The glycerine feed a flash vessel, operating under vacuum (30 kPa), which separates the glycerol from water and ethanol. The glycerol obtained has a purity of about 98 % to 99 %. Part of this product can be recycled to the glycerine washing vessels and the rest can be sold as technical grade glycerol.

For both soy and palm, the possibility of mixing the three effluents and producing hydrous ethanol fuel (HEF) was evaluated. This option is showed in Figure 3.

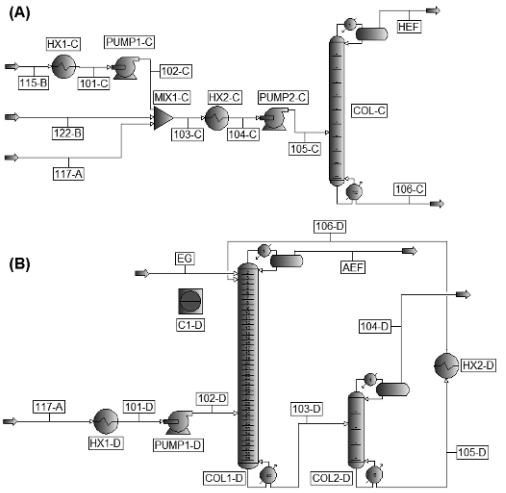

Figure 3 – Treatment of the effluents rich in ethanol
(a) Hydrous ethanol fuel production (b) Anhydrous ethanol fuel production

According to the Brazilian National Agency of Petroleum, Natural Gas and Biofuels (ANP, in Portuguese) specifications, HEF must have an ethanol concentration between 92.5 % and 93.8 %. To obtain this purity, the three effluents feed a column with 12 theoretical stages and reflux ratio of five. Heat exchangers are used to condensate the gaseous effluents, so that they could be pumped up to the column. The column operates

at ambient pressure. At the top, HEF is obtained. The bottom product, rich in water, must be correctly disposed.

The other option is to produce anhydrous ethanol fuel (AEF) from the effluent 117-A of the palm biodiesel plant. According to ANP, AEF must have an ethanol concentration of at least 99.3 %. The process proposed is based on the work of Ravagnani et al. (2010). The effluent feeds a column of 40 theoretical stages and reflux ratio of three, operating at atmospheric pressure. The effluent enters in the column at the thirtieth stage, while the solvent, ethylene glycol, enters at the third stage. The solvent is recovered pure in a six stages column with a reflux ratio of five. The scheme of this treatment module is presented in Figure 3.

3. Equipment Sizing and Economic Evaluation

All the equipment was sized according to empirical guidelines described in Seider et al. (2003). The flash vessels were projected according to Towler and Sinnott (2008). The reactors volumes were obtained multiplying the entering flow rate by the residence time. A headspace of 20 % of the liquid volume was considered. The atmospheric pressure columns were packed with 1 inch carbon steel Pall rings and the vacuum columns with 2 inches carbon steel Pall rings. Equipment that work with sulphuric acid were projected with stainless steel and all the other equipment with carbon steel. The economic evaluation was similar to the works of Zhang et al. (2003b) and West et al. (2008), except by the inclusion of a Lang factor of 4.8, following the guidelines proposed by Seider et al. (2003). Table 1 shows the scenario of prices considered in this work. These were the medium prices practiced in Brazilian foreign and internal trades in the first semester of 2014. Table 2 shows the main economic parameters evaluated.

4. Conclusions

As can be seen in Table 2, it is possible to produce HEF without considerable cost improvements, although AEF production was not economically attractive in this scenario. Unreacted oil recycle contributes with about 5 % of cost reduction and glycerine treatment and recycle contribute with about 10 %. The best results obtained are more economical and sustainable, but without subsidies or tax reductions they were still not profitable in the considered scenario. The authors expect that this work could be a basis for comparison of different biodiesel production technologies and raw materials, aiming more sustainable and even profitable processes.

Table 1. Price scenario in Brazil mid-2014. Medium prices of foreign and internal trades (US$/kg).

RM and Products	Prices	Catalysts and Solvents	Prices	Utilities	Prices
Soybean Crude Oil	0.8790	Tec. Grade Glycerol	0.7900	Superheated Vapour	0.0100
Palm Crude Oil	0.8690	Crude Glycerine	0.3300	Vapour 400 psi	0.0015
Anhydrous Ethanol	0.7461	NaOH	0.5100	Natural Water	0.00005
Hydrous Ethanol	0.6993	H_2SO_4	0.2000	Ammonia 34 °F	0.0005
Biodiesel	0.9600	Na_2SO_4	0.1200	Electricity (US$/KWh)	0.1375
Effluent Disposal	0.1500	Ethylene Glycol	0.9100		

Table 2. Economic results. Values are in 10^6 US$/year, unless specified. A: base case; B: unreacted oil recycle; C: glycerol recycle; D: HEF production; E: AEF production.

Economic Indicators	**Soybean Biodiesel**				**Palm Biodiesel**				
	A	**AB**	**ABC**	**ABCD**	**A**	**AB**	**ABC**	**ABCD**	**ABCE**
Total Investment (US$)	21.6	21.5	21.8	22.8	35.1	34.7	35.0	36.2	36.9
Direct Costs	141.0	134.2	120.6	120.5	156.6	149.3	134.6	134.6	136.9
Raw Material									
Crude Oil	88.1	83.5	83.5	83.5	86.5	82.3	82.2	82.2	82.2
Ethanol	20.0	19.5	19.6	19.6	34.8	33.6	33.6	33.6	33.6
Other	32.9	31.2	17.5	17.4	35.3	33.4	18.8	18.8	21.1
Indirect Costs	1.3	1.3	1.3	1.4	2.0	1.9	2.0	2.0	2.1
General Expenses	25.4	24.2	21.8	21.8	28.4	27.1	24.5	24.5	25.0
Total Annual Manufacturing Costs	167.7	159.7	143.8	143.7	187.0	178.4	161.1	161.2	163.9
Total Annual Revenues	114.7	113.7	111.6	112.4	127.7	126.0	122.7	125.6	123.8
Annual Net Profit	-53.1	-46.1	-32.2	-31.3	-59.3	-52.3	-38.4	-35.6	-40.2
Biodiesel Break-even Price (US$/Kg)	1.53	1.46	1.32	1.32	1.62	1.55	1.41	1.38	1.43

References

Brazilian National Agency of Petroleum, Natural Gas and Biofuels (ANP), 2011, ANP Resolution Number 7, Nov. 2 (in Portuguese).

Brazilian National Agency of Petroleum, Natural Gas and Biofuels (ANP), 2014, Biodiesel Monthly Bulletin of June (in Portuguese).

L. Constantinou, R. Gani, 1994, New group contribution method for estimating properties of pure compounds, AlChE Journal, 40 (10), 1697-1710.

B. Freedman, E.H. Pryde, T.L. Mounts, 1984, Variables Affecting the Yields of Fatty Esters from Transesterified Vegetable Oils, JAOCS, 61 (10), 1638-1643.

J.A.G. Garnica, 2009, Experimental determination of kinetic data from vegetable oils transesterification reaction, State University of Campinas, Campinas, Brazil.

G. Knothe, J.V. Gerpen, J. Krahl, 2005, The Biodiesel Handbook, AOCS Press, Champaign, US.

H. Lepper, L. Friesenhagen, 1986, Process for the production of fatty acid esters of short-chain aliphatic alcohols from fats and/or oils containing free fatty acids, US Patent 4608202.

S. Morais, S. Couto, A.A. Martins, T.M. Mata, 2010, Designing Eco-Efficient Biodiesel Production Processes from Waste Vegetable Oils, ESCAPE20, Ischia, Naples, Italy.

C. Neher, 2014, Controversial, palm planting in Brazil triples in four years <http://www.dw.de/controverso-plantio-de-dend%C3%AA-no-brasil-triplica-em-4-anos/a-17429621> accessed 28.10.2014 (in Portuguese).

M.L. Pisarello, B. Dalla Costa, G. Mendow, C.A. Querini, 2010, Esterification with ethanol to produce biodiesel from high acidity raw materials knetic studies and analysis of secundary reactions, Fuel Processing Technology, 91 (9), 1005-1014.

M.A.S.S. Ravagnani, M.H.M. Reis, R. Maciel Filho, M.R. Wolf-Maciel, 2010, Anhydrous ethanol production by extractive distillation: A solvent case study, Process Safety and Environmental Protection, 88 (1), 67-73.

W.D. Seider, J.D. Seader, D.R. Lewin, 2003, Product and Process Design Principles - Synthesis, Analysis, and Evaluation, John Wiley and Sons, Chichester, UK.

S. Shahla, G.C. Ngoh, R. Yusoff, 2012, The evaluation of various kinetic models for base-catalyzed ethanolysis of palm oil, Bioresource technology, 104, 1-5.

G. Towler, R. Sinnott, 2008. Chemical Engineering Design - Principles, Practice and Economics of Plant and Process Design, Butterworth-Heinemann, Elsevier, Amsterdam, the Netherlands.

A.H. West, D. Posarac, N. Ellis, 2008, Assessment of four biodiesel production processes using HYSYS.Plant, Bioresource Technology, 99 (14), 6587-6601.

Y. Zhang, M.A. Dubé, D.D. McLean, M. Kates, 2003a, Biodiesel production from waste cooking oil: 1 Process Design and Technological Assessment, Bioresource Technology, 89 (1), 1-16.

Y. Zhang, M.A. Dubé, D.D. McLean, M. Kates, 2003b, Biodiesel production from waste cooking oil: 2. Economic assessment and sensitivity analysis, Bioresource Technology, 90 (3), 229-240

Krist V. Gernaey, Jakob K. Huusom and Rafiqul Gani (Eds.), 12th International Symposium on Process Systems Engineering and 25th European Symposium on Computer Aided Process Engineering.
31 May – 4 June 2015, Copenhagen, Denmark

Synthesis of transcritical ORC-integrated heat exchanger networks for waste heat recovery

Cheng-Liang Chen [a], Po-Yi Li , Hui-Chu Chen , and Jui-Yuan Lee [b]

[a] *Department of Chemical Engineering, National Taiwan University, Taipei 106, Taiwan, ROC*
[b] *Department of Chemical Engineering and Biotechnology, National Taipei University of Technology, Taipei 106, Taiwan, ROC*
CCL@ntu.edu.tw

Abstract

This article aims to present a mathematical model for synthesis of a heat-exchanger network (HEN) which can be integrated with a transcritical organic Rankine cycle (T-ORC) for recovering low-grade waste heat from the heat surplus zone of the background process. This work is a direct extension of previous one where the working fluid was operated under subcritical pressure. A T-ORC integrated stagewise superstructure considering all possible match of process hot/cold streams and the re-circulated working fluid is proposed. Based on this superstructure, a mathematical model for synthesizing T-ORC integrated HENs is formulated as a mixed-integer nonlinear program (MINLP), therein the objective is to maximize the net work produced from waste heat in the heat surplus zone below the process pinch. A literature example is solved to demonstrate the application of the proposed model for industrial waste heat recovery. For a given heat source, some organic fluids can be used in both subcritical and transcritical status. After a minor modification, the model can be applied for not only subcritical but also transcritical ORC. Based on the results from the modified model, it is found that the T-ORC-involved HEN can produce higher net power over the heat recovery system where the ORC is operated under subcritical state.

Keywords: Waste heat, Transcritical organic Rankine cycle (T-ORC), Heat exchanger network (HEN), Superstructure, Mixed-integer non-linear programming (MINLP)

1. Introduction

The oil price has increased for several times over the past 20 years. Energy conservation is one of the most visible methods for reducing the energy bill. In industrial processes, there are streams that need heating and streams that need cooling, usually achieved by using hot and cold utilities with some kind of heat recovery. Heat exchanger network (HEN) is the main method to obtain heating and cooling by process streams energetic integration, by using hot streams to heat up cold streams and cold streams to cool down hot streams. In this way, it can reduce the use of external hot and cold utilities. However, a large amount of energy is lost as low-temperature waste heat in industrial and daily processes. Due to the rising cost of energy, effective utilization low-grade waste heat has attracted more and more attention. Organic Rankine cycle (ORC) is widely used to generate electricity from these heat sources. Unlike in a conventional steam Rankie cycle, a low boiling point organic fluid is used as working fluid. Because the organic fluids have lower critical temperatures and pressures, they can be compressed directly to their supercritical pressures and heated to supercritical state before expansion.

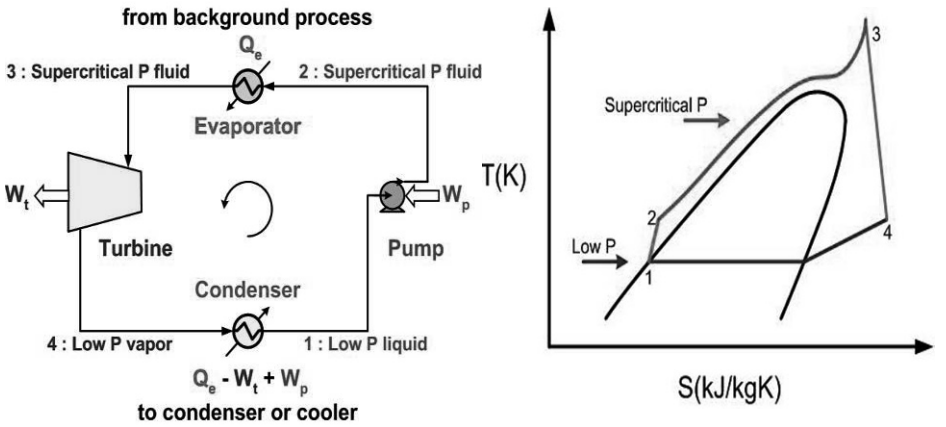

Figure 1a (left) Schematic diagram of transcritical ORC cycle.
1-2: irreversible compression, supply work to the cycle;
2-3: isobaric supply of heat (evaporator);
3-4: irreversible expansion, useful work done by the cycle;
4-1: isobaric removal of heat (condenser);
Figure 1b (right) T-s diagram for a typical transcritical ORC

The heating process of this kind of ORC, which called transcritical ORC, does not pass through a two-phase region like a subcritical ORC, resulting in a better thermal match in the evaporator with less irreversibility, which is confirmed by Saleh et al (2007).This article present mixed-integer nonlinear program (MINLP) model for HENs involving a transcritical ORC for recovery of low-grade waste heat from the background process.

Figure 1 shows the typical transcritical ORC cycle, as well as the temperature-entropy (T-S) diagram. The working fluid is pumped from a lower pressure level (state 1) to a higher pressure level above the critical pressure of working fluid (state 2). Between states 2 and 3 the fluid in supercritical area absorbed the waste heat from background process. The supercritical fluid is expanded in a turbine (state 4). The remaining heat is removed by transferring heat to a cooling medium in the condenser and the complete the cycle.

2. Problem Statement

The problem of integrating a transcritical ORC with the background process can be stated as follows. Givens are a set of hot process streams to be cooled and a set of cold process streams to be heated. The heat capacity flow rates of the process streams, available external hot and cold utilities for heating and cooling, and available dry organic working fluids to be used are also given. It is desired to synthesize an optimal transcritical ORC-integrated HEN to maximize heat recovery among the process streams, while maximizing the recovery of waste heat from the background process for electricity generation.

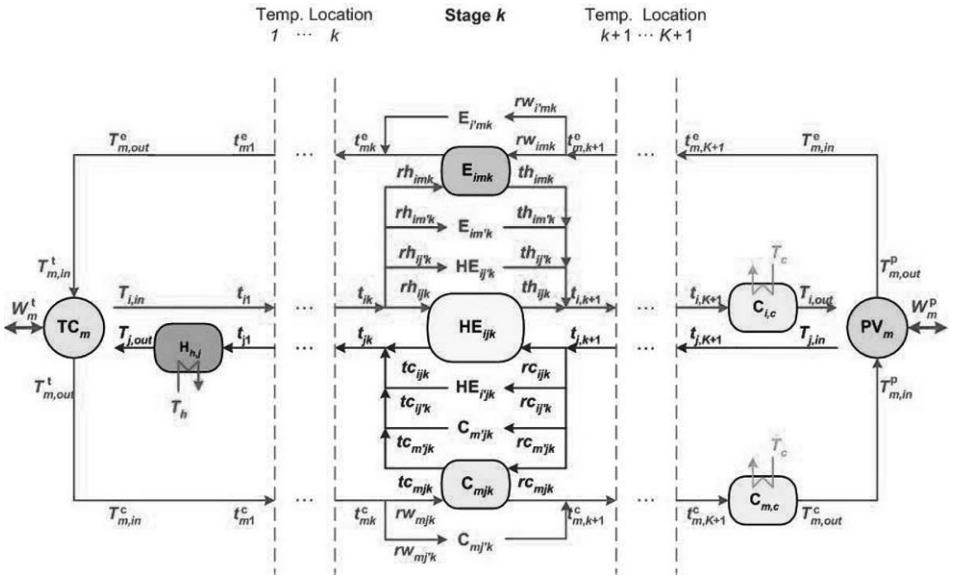

Figure 2. Stagewise superstructure for synthesis of transcritical ORC-integrated HEN

3. Superstructure

Figure 2 illustrates the superstructure for the synthesis of transcritical ORC-integrated HENs for recovery of low-grade waste heat from the background process. This superstructure, an expansion of the stage-wise HEN superstructure of Yee and Grossmann (1990) and Chen et al. (2014), incorporates an ORC and assumes non-isothermal stream mixing.

In the superstructure, HE_{ijk} is the process-to-process heat exchanger; H_{hj} and C_{ic} are the heater and cooler for providing extra hot or cold utilities at the end of process streams; rh_{ijk} and rc_{ijk} are the split ratios for the hot and cold process streams at stage k; t_{ik} and t_{jk} denote the intermediate temperatures; PV_m and TC_m denote the pump and the turbine for working fluid m in the ORC; evaporators E_{imk} and condensers C_{mjk} are used for exchanging the waste heat between the process streams and the working fluid m; t^e_{mk} and t^c_{mk} are intermediate temperatures around the evaporators or the condensers.

4. MINLP Formulation

Mathematical optimization models have commonly relied on the following assumptions for synthesizing HENs:

(1) Heat loss to the surrounding is negligible.
(2) Pressure drops in the pipes and heat exchangers are negligible.
(3) Constant heat capacity flowrates and heat transfer coefficients
(4) Single-pass countercurrent heat exchangers

The objective is to maximize the output net work (W^{net}) from the recovered waste heat, such as shown in Equation (1).

$$\max_{x\in\Omega} J = \sum_{m\in M} W_m^t - \sum_{m\in M} W_m^p \tag{1}$$

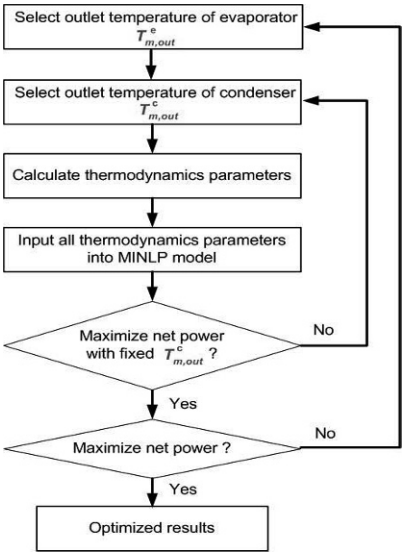

Figure 3. Optimization flowsheet

where W^{t}_{m} represents turbine work of medium m and W^{p}_{m} represents pump work of medium m.

The feasible solution is searched with the limitation of constraints based on the optimization procedure shown in Figure 3. These constraints include energy/mass balances, existence of heat exchangers, temperature difference of heat exchangers, temperature assignments, etc. Under the assumption of the fixed evaporate pressure (P_{max}), there are two remaining design variables for transcritical ORC configuration, which are the evaporator and the condenser outlet temperatures ($T^{e}_{m,out}$ and $T^{c}_{m,out}$). Optimized result can be found by method as shown in Figure 3.

5. Numerical example

The example from the work of Desai and Bandyopadhyay (2009) and Chen et al. (2014) involves three hot and four cold streams with steam and cooling water as the heating and cooling utilities. Given data for the problem, including the inlet and outlet temperatures, heat capacity flow rates, the available utilities of hot and cold process streams are showed in Table 1. The T-ORC is used to recover the waste heat from the heat surplus region of the background process under the pinch temperature 244°C.

Table 2 shows the results by varying two main design variables, the outlet temperatures of evaporator ($T^{e}_{m,out}$) and condenser ($T^{c}_{m,out}$). The net power shown in this table is defined in Equation (2):

$$W^{net} = f \times w^{net} = W^{t} - W^{p} \tag{2}$$

where W^{net}, W^{t}, W^{p}, w^{net} and f are net power output, power done by the turbine, power consumed by the pump, specific net power output and working fluid flow rate. With the selected evaporator outlet temperature $T^{e}_{m,out}$ = 210°C, higher condenser outlet temperature brings more working fluid flow rate and less specific net power output. In similar, with the selected condenser outlet temperature ($T^{c}_{m,out}$ = 102°C), higher evaporator outlet temperature leads to less working fluid flow rate and higher specific

Table 1. Process stream data

Stream	FCp (kW/K)	T_{in} (^{o}C)	T_{out} (^{o}C)
H1	9.802	353	313
H2	2.931	347	246
H3	6.161	255	80
C1	7.179	224	340
C2	0.641	116	303
C3	7.627	53	113
C4	1.690	40	293
T^{hot}_{pinch}=244^{o}C, T^{cold}_{pinch}=224^{o}C		$\Delta T_{min} = 20^oC$	
Isentropic efficiency: turbine = 0.8; pump = 0.65			
Working medium: n-pentane; Pc = 33.6 bar; Tc = 196.6 ^{o}C			

Table 2. Results under different outlet temperatures in evaporator and condenser (P_{max} = 1.1P_c = 36.96 bar)

$T^e_{m,out}$	$T^e_{m,in}$	$T^e_{m,out}$	$T^c_{m,in}$	f	w^{net}	W^p	W^t	W^{net}	eff	Q^e	Q^{CU}
(^{o}C)				(kg/s)	(kJ/kg)	(kW)			(%)	(kW)	
80	83.07	210	133.72	0.599	61.10	5.31	41.89	36.58	12.37	295.66	136.02
90	93.20	210	138.73	0.739	52.79	6.51	45.51	39.00	11.30	345.21	133.60
100	103.34	210	143.68	0.884	45.05	7.70	47.53	39.83	10.24	388.92	132.77
102	105.37	210	144.67	0.915	43.56	7.95	47.79	39.84	10.03	397.23	132.75
105	108.42	210	146.16	0.961	41.38	8.31	48.10	39.79	9.71	409.46	132.81
102	105.37	215	153.60	0.907	46.19	7.88	49.79	41.91	10.10	414.98	130.87
102	105.37	220	161.22	0.901	48.33	7.83	51.40	43.57	10.13	430.16	129.03
102	105.37	224	166.83	0.897	49.85	7.79	52.52	44.73	10.13	441.37	127.87
103	106.39	224	167.31	0.913	49.06	7.91	52.69	44.77	10.03	446.30	127.83
104	107.40	224	167.79	0.918	48.28	7.95	52.29	44.34	9.92	446.58	128.26

net power output. There is a trade-off between working fluid flow rate and specific net power output. The optimized result, which is showed in Figure 4, demonstrates that 44.77 kW net power can be found under $T^e_{m,out}$ = 224^{o}C and $T^e_{m,out}$ = 103^{o}C. Note that 224 ^{o}C is the highest possible evaporator outlet temperature because of the limitation of hot pinch temperature. Compared to the results under subcritical ORC, T-ORC-involved HEN can be operated in higher temperature and pressure, thus can absorb more waste heat and can produce more net work with higher working fluid flow rate.

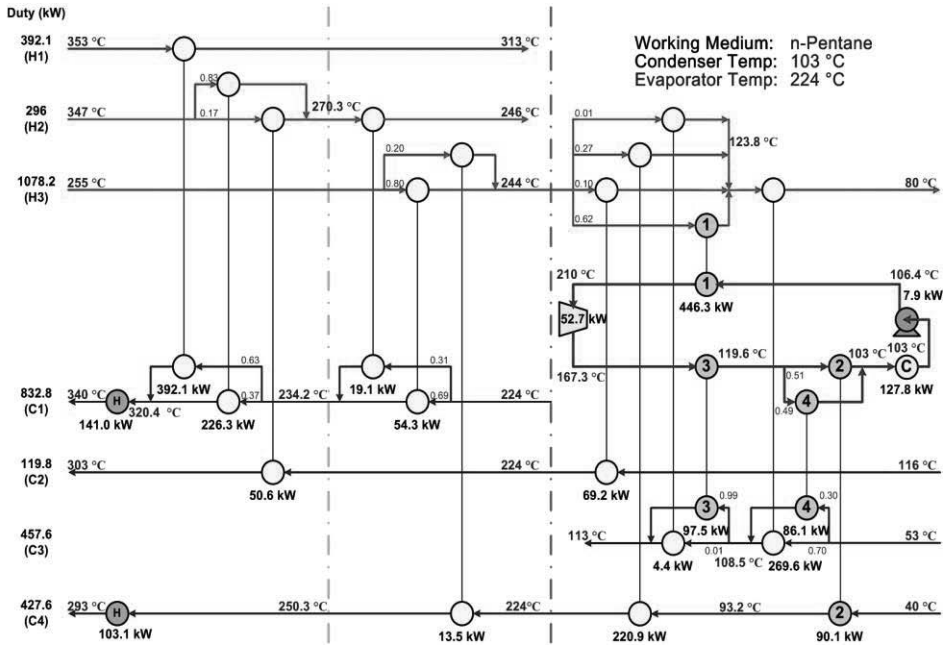

Figure 4. Optimized case with $T^{c}_{m,out}$ = 224 °C and $T^{c}_{m,out}$ = 103 °C

6. Conclusions

A mathematical model for the synthesis of transcritical ORC-integrated HENs has been developed in this paper. Based on a generic stagewise superstructure representation incorporating an ORC and considering non-isothermal stream mixing, the synthesis problem is formulated as an MINLP. A literature example was solved to demonstrates the proposed approach for waste heat recovery from background processes. Based on the results from the modified model, it is found that the T-ORC-involved HEN can generate higher net power over the heat recovery system where the ORC is operated under subcritical state.

References

C.L. Chen, F.Y. Chang, T.H. Chao, H.C. Chen, J.Y. Lee, 2014, Heat-exchanger network synthesis involving organic Rankine cycle for waste heat recovery, *Ind. Eng. Chem. Res.,* 53 (44), 16924–16936

N.B. Desai, S. Bandyopadhyay, 2009, Process integration of organic Rankine cycle. *Energy*, 34, 1674-1686.

B. Saleh, G. Koglbauer, M. Wendland, J. Fischer, 2007,Working fluids for low temperature organic Rankine cycles, *Energy*, 32, 1210-1217.

T.F. Yee, I.E. Grossmann, 1990, Simultaneous optimization models for heat integration-II Heat exchanger network synthesis, *Comp. Chem. Eng.*, 14, 1165-1184.

Krist V. Gernaey, Jakob K. Huusom and Rafiqul Gani (Eds.), 12th International Symposium on Process Systems Engineering and 25th European Symposium on Computer Aided Process Engineering.
31 May – 4 June 2015, Copenhagen, Denmark

Efficiency Comparison of Different Design Schemes of Reactive Distillation Process for Ethyl Lactate Production from Fermentation-Derived Magnesium Lactate

Boonpradab Dangpradab, Panarat Rattanaphanee*

School of Chemical Engineering, Suranaree University of Technology, 111 University Avenue, Suranaree, Muang, Nakhon Ratchasima, 30000, Thailand.
panarat@sut.ac.th

Abstract

Process flow diagram of a reactive distillation process for ethyl lactate production is designed and optimized in this study. In an attempt to intensify a process for ethyl lactate production, magnesium lactate obtained directly from fermentation was used, instead of highly purified lactic acid as in a conventional process, as a starting material. Ethyl lactate produced by esterification in the reactive distillation column is purified in a series of fractional distillation columns until its impurity-free aqueous solution is received as a final product. Process optimization is performed using Aspen Plus simulator equipped with RADFRAC module. Sulfuric acid is used as a homogeneous catalyst, and all the kinetic parameters of the esterification reaction are taken from our previous work. Production efficiency of two process schemes was explored. In the first process scheme, ethyl lactate was collected at the top of the reactive distillation column along with other light compounds in the process, i.e. water and ethanol. In the second process, ethyl lactate was discharged from the bottom of the reactive distillation column. Configurations of each operating unit as well as the optimal process conditions were obtained. The first process is more efficient in terms of lactic acid conversion, ethyl lactate recovery, yield, and production rate. The second process, on the other hand, is more beneficial in terms of heat requirement and concentration of ethyl lactate achieved in the final product solution.

Keywords: Lactic acid, Ethyl lactate, Reactive Distillation, Process Design,

1. Introduction

Ethyl lactate ($C_5H_{10}O_3$) is an ester of lactic acid that can be considered as a green chemical due to its nontoxic, biodegradable and excellent solvent properties. It was used in many industries with general application as solvent for production of nitrocellulose, food additive, perfumery, flavor chemicals as well as drug industries (Lewix, 2007).

Conventional production of ethyl lactate is from esterification of lactic acid with ethanol as shown in Eq.(1). The reaction proceeds well in an acid environment so either homogeneous or heterogeneous acid catalysts are normally used to accelerate the reaction. This approach is, however, expensive due to the costly lactic acid separation and purification processes, which has been estimated to be about a half of the total cost for production of highly purified lactic acid (Pereira at al., 2011). Synthesis of ethyl

lactate directly from lactate salts obtained from lactic acid fermentation might help reducing the production cost of this compound (Kasinathan et al., 2010).

$$Lactic\ acid + Ethanol \underset{k_{-1}}{\overset{k_1}{\rightleftharpoons}} Ethyl\ lactate + Water \quad (1)$$

In this study, preliminary design of reactive distillation process for production of ethyl lactate from fermentation-derived magnesium lactate is proposed. The process simulation and optimization are performed using ASPEN Plus simulator equipped with RADFRAC module. Process efficiency, evaluated from lactic acid conversion, ethyl lactate recovery, yield and production rate, as well as heat requirement of the process is investigated and compared between two different process schemes.

2. Process description

The process for production of ethyl lactate proposed in this work consists of one reactive distillation (RD) column, where esterification is proceeded, and a series of fractional distillation columns (DIS) to purify ethyl lactate until its aqueous solution that is free from ethanol and other impurities is received as a final product.All the columns are tray-type. Tray diameter and tray spacing of 0.1 m and weir height of 1 in are assumed in this study. Equilibrium stages are numbered down from the top to the bottom of each column. A condenser is, therefore,always the first stage. All the columns are operated under atmospheric pressure.

An acidified magnesium lactate solution is used as a source of lactic acid. Procedure for preparing this solution is described in detail in our previous publication (Daengpradab and Rattanaphanee, 2012). In short, powdery magnesium lactate is mixed with sulfuric acid until it is completely dissolved. Any remained residue is removed by filtration. Water is partially vaporized out of the solution in order to lessen its interference in esterification. Concentrated sulfuric acid, the reaction catalyst, is added into the solution before it is charged into the reactive distillation column in feed stream F1, and ethanol isin feed stream F2, as shown in Figure 1 and 2. Compositionsanalysis of both feed streams is performed. The result is shown in Table 1. It should be noted that the reaction zone in the reactive distillation column extended between these two feed stages.

Production efficiency of the proposed process is determined in terms of lactic acid conversion, as well as ethyl lactate yieldand recovery. These parameters are expressed in Eq.(3), Eq.(4) and Eq.(5), respectively. Ethyl lactate production rate, expressed in grams of ethyl lactate produced per hour of the operation,as well as the ester concentration in the final product are also considered. Process heat requirement, which is evaluated from heat duty of all the concerned process units, is another efficiency-evaluating parameter in this work.

Table 1. Feed composition and molar flow rate.

Feed stream	Component	Normal boiling point (ºC)	Molar flow rate (mol/h)	Mole fraction
F1	Lactic acid	216.63	2.12	0.077
	Water	100.02	23.53	0.859
	Magnesium sulfate	9726.85	1.37	0.050
	Sulfuric acid	274.80	0.38	0.014
F2	Ethanol	78.31	6.35	1

$$\%X_{LA} = \frac{Mole\,of\ ethyl\,lactate\,produced\,in\ RD\,column}{Mole\,of\ lactic\,acid\,fed\,in\ stream\,F1} \times 100 \tag{2}$$

$$\%Y_{EtLA} = \frac{Mole\,of\ ethyl\,lactate\,in\ final\,product}{Mole\,of\ lactic\,acid\,fed\,in\ stream\,F1} \times 100 \tag{3}$$

$$\%R_{EtLA} = \frac{Mole\,of\ ethyl\,lactate\,in\ stream\,TP}{Mole\,of\ ethyl\,lactate\,produced\,in\ RD\,column} \times 100 \tag{4}$$

Production efficiencies of two process schemes are compared. The first scheme is called Process A. Here, ethyl lactate is collected at the top of reactive distillation column, along with ethanol and water, while the heavy components, i.e. magnesium sulfate, sulfuric acid, and unreacted lactic acid are removed at the bottom. In the second scheme, Process B, ethyl lactate is discharged as bottom product of the reactive distillation column together with all the heavy components. Ethyl lactate-containing streams in both processes are subjected to a series of fractional distillation columns, where ethanol is recovered and recycled back to the reactive distillation column and all the heavy components are eliminated. The final product is thus received as an aqueous solution of ethyl lactate.

3. Reaction kinetics

Kinetic parameters of esterification of ethanol with lactic acid in magnesium lactate solution using sulfuric acid as the catalyst were obtained experimentally in our previous work. The detailed procedure was described elsewhere (Daengpradab and Rattanaphanee, 2012).Due to non-ideal nature of the reactive quaternary mixture containing lactic acid (*LA*), ethanol (*EtOH*), ethyl lactate (*EtLA*) and water (*W*), the reaction rate, $-r_{LA}$, is expressed in term of activity (*a*) instead of concentration as shown in Eq.(5). Dependence of reaction rate constant for forward (k_1) and backward (k_{-1}) reaction on reaction temperature followsEq.(6) and (7), respectively.

$$-r_{LA} = k_1\ a_{EtOH} a_{LA} - k_{-1}\ a_{EtLA} a_W \tag{5}$$

$$k_1 = 13300 \exp\left(-\frac{30400 J/mol}{RT}\right) \tag{6}$$

$$k_{-1} = 0.799 \exp\left(-\frac{7022.67 J/mol}{RT}\right) \tag{7}$$

4. Phase equilibria

General equation for vapor-liquid equilibrium (VLE) of a particular mixture at constant low pressure, *P*, and temperature, *T*, is given by Eq.(8), where γ_i is the activity coefficient of component *i*, ϕ_i is the fugacity coefficient, and x_i and y_i are mole fraction of *i* in liquid and vapor phase, respectively. P_i^{sat} is the component's vapor pressure at

temperature, T, and ϕ_i^{sat} is the fugacity coefficient of pure saturated vapor i at temperature, T, and the corresponding pressure, P_i^{sat}.

$$\phi_i y_i P = \gamma_i x_i P_i^{sat} \phi_i^{sat} \tag{8}$$

To account for non-ideal vapor-liquid equilibrium (VLE) behavior of the quaternary solution, the activity coefficient of every component in the liquid phase was calculated using the UNIQUAC model with the binary interaction parameters obtained from Delgado et al., 2007. The vapor phase was assumed to be ideal; therefore, the fugacity coefficients of all the components in this phase are unity.

5. Process simulation

Process simulation and optimization was carried out using Aspen Plus® equipped with RADFRAC module. Design variables are total number of stages, feed location and reflux ratio.

6. Results and discussion

Process flow sheet for Process A, where ethyl lactate is collected at the top of the reactive distillation column, is illustrated in Fig. 1. Composition of each stream in this process is given in Table 2. As seen, magnesium sulfate is totally removed at the bottom of the distillation column. Sulfuric acid and unreacted lactic acid are found along ethyl lactate-containing streams and are completely removed in the second distillation column. The ethanol-free aqueous solution of ethyl lactate is received at the bottom of the third distillation column with its final concentration of 8.27 % by mole of ethyl lactate.

Process B, where ethyl lactate is collected as the bottom product of the reactive distillation column, is depicted in Fig. 2. Stream composition, Table 3, shows that Process B gives the final product as 33.52 % by mole of ethyl lactate, which is much higher than the one obtained in Process A.

Optimal designs for both process schemes are displayed in Table 4 and Table 5. The last fractional distillation column in Process B appears to be the tallest column with the total number of equilibrium stages of 18. Nonetheless, the last fractional distillation column in Process A is the most energy-intensive one.

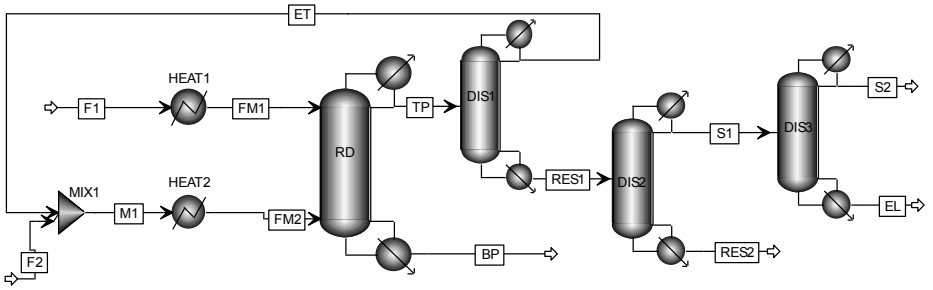

Figure 1. Process flow sheet of Process A, where ethyl lactate is collected in stream TP.

Table 2. Stream composition of Process A.

Description	Stream									
	FM1	FM2	BP	TP	ET	RES1	S1	RES2	S2	EL
Temperature (°C)	110.00	75.00	254.58	84.42	78.40	88.14	87.95	239.77	79.70	99.42
Molar flow rate (mol/h)	27.39	13.45	1.71	39.13	7.10	32.03	31.87	0.15	8.00	23.87
Mole fraction										
Ethanol	0	0.874	0.010	0.247	0.761	0.134	0.134	0	0.535	0
Lactic acid	0.077	0	0.002	0.002	0	0.002	0	0.397	0	0
Ethyl lactate	0	0	0.020	0.052	0	0.063	0.063	0.003	0.005	0.083
Water	0.859	0.126	0.002	0.697	0.239	0.799	0.802	0	0.460	0.917
Sulfuric acid	0.014	0	0.166	0.002	0	0.003	0	0.600	0	0
Magnesium sulfate	0.050	0	0.800	0	0	0	0	0	0	0

Production efficiency of both process schemes is comparatively shown in Table 6. Higher lactic acid conversion as well as ethyl lactate recovery and yield are achieved in Process A. This process also renders the higher ethyl lactate production rate of 233.28 g_{EtLA}/h, while Process B produces 183.35 g_{EtLA}/h.

The superiority of Process B comes in terms of the process heat requirement. This parameter is determined by dividing the total heat duty of concerned process units by the ethyl lactate production rate. In this study, only heat duties of heaters and distillation columns, both reactive and non-reactive, are taken into account. The heat requirement of Process A is 111.768 kJ/g_{EtLA}, which is almost twice higher than that of 70.772 kJ/g_{EtLA} required in Process B.

Another advantage of Process B that is worth to be noted lies in the fact that it gives a much more concentrated final ethyl lactate solution than Process A. This will benefit a downstream processing if further increase in the ester concentration is required.

7. Conclusion

Reactive distillation process for production of ethyl lactate by esterification of ethanol and fermentation-derived magnesium lactate is designed and optimized. Efficiency of two process schemes is studied and compared. Higher lactic acid conversion, as well as ethyl lactate recovery, yield and production rate is achieved in the process scheme where ethyl lactate is collected at the top of the distillation column. On the contrary, when ethyl lactate is collected as the bottom product of the reactive distillation column, higher concentration of ethyl lactate is obtained in the final solution. Heat requirement in the latter process is also found to be lower than the former one.

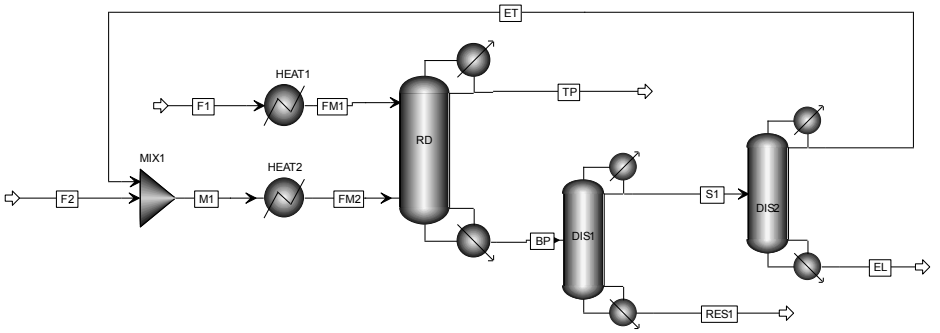

Figure 2.Process flow sheet of Process B, where ethyl lactate is collected in stream BP

Table 3. Stream composition of Process B.

Description	Stream							
	FM1	FM2	BP	TP	S1	RES1	ET	EL
Temperature (°C)	110.00	60.00	86.29	84.27	82.10	239.48	78.19	100.48
Molar flow rate (mol/h)	27.39	14.30	14.70	26.99	12.59	2.12	7.95	4.63
Mole fraction								
Ethanol	0	0.918	0.461	0.166	0.538	0.001	0.852	0
Lactic acid	0.077	0	0.014	0.002	0	0.099	0	0
Ethyl lactate	0	0	0.116	0.006	0.123	0.075	0	0.335
Water	0.859	0.082	0.290	0.826	0.338	0.001	0.148	0.665
Sulfuric acid	0.014	0	0.026	0	0	0.177	0	0
Magnesium sulfate	0.050	0	0.093	0	0	0.647	0	0

Table 4. Optimal design result for Process A.

	HEAT1	HEAT2	RD	DIS1	DIS2	DIS3
Column diameter (m)			0.1	0.1	0.1	0.1
Tray space (m)			0.1	0.1	0.1	0.1
Total number of stages			14	10	10	10
Feed stage			2(F1),13(F2)	5	8	6
Distillate rate (mol/h)			39.13	7.10	31.87	8.00
Bottom rate (mol/h)			1.71	32.03	0.15	23.87
Reflux ratio			0.001	3.306	0.333	24.565
Condenser heat duty (W)			466.13	333.70	491.83	2276.04
Reboiler heat duty (W)			280.25	335.63	492.62	2282.14
Heater heat duty (W)	272.98	11.27				

Table 5. Optimal design result for Process B.

	HEAT1	HEAT2	RD	DIS1	DIS2
Column diameter (m)			0.1	0.1	0.1
Tray space (m)			0.1	0.1	0.1
Total number of stages			9	13	18
Feed stage			2(F1),6(F2)	12	6
Distillate rate (mol/h)			26.99	12.59	7.95
Bottom rate (mol/h)			14.70	2.12	4.63
Reflux ratio			0.011	0.500	13.039
Condenser heat duty (W)			317.62	221.12	1213.76
Reboiler heat duty (W)			116.43	244.70	1216.14
Heater heat duty (W)	272.98	2.69			

Table 6. Comparison of process efficiency.

	$\%X_{LA}$	$\%R_{EtLA}$	$\%Y_{EtLA}$	Production rate (g_{EtLA}/h)	Final product (% by mole EtLA)	Heat requirement (kJ/g_{EtLA})
Process A	96.13	95.76	93.94	233.28	8.27	111.768
Process B	87.68	83.07	73.54	183.35	33.5	70.772

References

B. Daengpradab and P. Rattanaphanee, 2012, Kinetic study of ethyl lactate synthesis from magnesium lactate, Engineering Transaction, 15, 2, 84-90.

P. Delgado, M.T. Sanz, and S. Beltran, 2007, Isobaric vapor-liquid equilibria for the quaternary reactive system: Ethanol+water+ethyl lactate+lactic acid at 101.33 kPa, Fluid Phase Equilibria, 255, 17-23.

P. Kasinathan, H. Kwak, U. Lee, D.W. Hwang, Y.K. Hwang, J. Chang, 2010, Synthesis of ethyl lactate from ammonium lactate solution by coupling solvent extraction with esterification, Separation and Purification Technology, 76, 1-7.

R.J. Lewix, 2007, Hawley's Condensed Chemical Dictionary, John Wiley and Sons, Inc., New York.

C.S.M.Pereira, V.M.T.M. Silva, A.E. Rodrigues, 2011, Ethyl lactate as a solvent: Properties, applications and production processes – a review, Green Chemistry, 13, 2658-2671.

Krist V. Gernaey, Jakob K. Huusom and Rafiqul Gani (Eds.), 12th International Symposium on Process Systems Engineering and 25th European Symposium on Computer Aided Process Engineering.
31 May – 4 June 2015, Copenhagen, Denmark

Tailor-Made Green Diesel Blends Design using a Decomposition-Based Computer-Aided Approach

Li Yee Phoon[a], Haslenda Hashim[a], Ramli Mat[b], Azizul Azri Mustaffa[a,*]

[a]*Process Systems Engineering Centre (PROSPECT), Faculty of Chemical Engineering, Universiti Teknologi Malaysia, 81310 UTM Johor Bahru, Johor, Malaysia*
[b] *Department of Chemical Engineering, Faculty of Chemical Engineering, Universiti Teknologi Malaysia, 81310 UTM Johor Bahru, Johor, Malaysia*
azizul@cheme.utm.my

Abstract

In this study, the tailor-made green diesel blend design problem is mathematically formulated and solved by a decomposition-based computer-aided approach. The green diesel design problem is solved in three main stages to identify the feasible green diesel blend candidates that meet the product property constraints (density, kinematic viscosity, cetane number, higher heating value and flash point) with the desired performance criteria. An optional additives identification step is introduced to enhance the blends. The shortlisted green diesel blends are evaluated on the basis of cost, cetane number and higher heating value. To ensure that the shortlisted candidates have acceptable functional reliability, their compatibility with the engine compartment, engine performance, and emission requirements should be addressed in future works.

Keywords: Lignocellulosic biofuel; Green diesel blends; Computer-aided tools; Mixture design algorithm; Product design

1. Introduction

Tailor-made green diesel blends (the blend of either diesel with biofuel, or of different biofuels) represent one of the most promising solutions to reduce the impact of fuel consumption on the environment while retaining or even improving the performance of diesel fuel. Several studies have clearly demonstrated that biofuels are able to enhance the combustibility of diesel in the engine combustion chamber, and hence, reduce the particulate matter and soot in the exhaust stream (Christensen et al., 2011, Wei et al., 2014). At present, mixtures involving lignocellulosic biofuel (e.g. alcohol, levulinic ester) have been receiving a significant amount of attention. In connection with this issue, one of the main challenges related to green diesel blends involves how to identify the blends that match the blend target properties with the various types of lignocellulosic biofuels.

A systematic computer-aided approach can efficiently address these issues and provide a more efficient solution method than the iterative trial and error approach. The computer-aided technique is able to rapidly narrow down the search space of feasible green diesel blends so that costly and time-consuming experimental work can be reserved for only the most promising candidates (Yunus et al., 2012).

The highlight of this paper is the solution of the tailor-made green diesel blends design problem by using a decomposition-based computer-aided approach, in which the Mixed Integer Non-Linear Programming (MINLP) problem is solved in three main stages: (1)

generation of feasible green diesel blend candidates; (2) generation of the feasible green diesel blends that match the specified target properties, (the design constraints) with or without additives; and (3) ranking of the feasible green diesel blends according to an index of desired performance. Finally, the paper is concluded with suggestions for future work.

2. Tailor-Made Green Diesel Blends Design

The tailor-made green diesel blends are designed by blending commercial diesel with lignocellulosic chemical(s) to reduce the dependency on diesel fuel while mitigating the pollution issue. To ensure that the designed green diesel is able to run the commercial diesel engine without significant reduction in engine efficiency, a set of target properties, as listed in Table 1, should be satisfied. The tailor-made green diesel blends design problem is mathematically formulated (see Table 1), and the problem is solved by using a decomposition-based computer-aided approach. Density, kinematic viscosity and cetane number is calculated using the linear mixing model proposed by (Ariffin Kashinath et al., 2012). The model for higher heating value (Eq.(4)) is taken from (Chen et al., 2009). The flash point of the fuel blends is predicted using the Liaw model (Liaw et al., 2002), and the mixture stability is checked based on the trend of the second derivative of the Gibbs energy of mixing (Eq.(6)) (Yunus et al., 2011). In Table 1, subscripts *i* and *mix* represent the i^{th} compound and mixture; x represents the volume fraction; *C* is the cost; and *n* is the number of components. P_i^{sat} and $P_{i,FP}^{sat}$ are the vapor pressure at mixture flash point and pure compound flash point, respectively. γ_{VLE} and γ_{LLE} are the activity coefficient calculated using the UNIFAC group contribution method for vapor liquid equilibrium (Fredenslund et al., 1975, Fredenslund et al., 1977) and liquid-liquid equilibrium (Magnussen et al., 1981), respectively.

3. Decomposition-Based Optimisation Strategy

3.1. Stage 1: Generation of Feasible Green Diesel Blends Candidates

In this step, the feasible green diesel compounds are generated using computer-aided molecular design technique software (ICAS-ProCAMD). The pure component constraints of the green compounds are first defined according to the benchmark of the existing diesel fuel (Table 2). The potential candidates that satisfy the specific constraints are generated by using ICAS-ProCAMD. Subsequently, the stability of each possible pseudo binary blend is analysed by using Eq.(6).

3.2. Stage 2: Generation of Feasible Green Diesel Blends

The miscible green diesel blends from stage 1 are further tested according to product property constraints. The linear property constraints (density, kinematic viscosity, cetane number and higher heating value) are solved first using Eq.(1) to Eq.(4)), followed by the non-linear property constraint of flash point (Eq.(5)). An optional additive identification step is applied to enhance the blend; for example, the fuel combustion quality can be enhanced by increasing the cetane number. The compatibility of the additive with green diesel blends is verified by using Eq.(6).

Table 1. Mathematical constraint models with target values

Objective function: $F_{obj} = \min \sum x_i C_i$				
Constraint	**Equation**	**Eq.**	**Lower Bound**	**Upper Bound**
Product property constraints				
a) Linear Property Constraints				
Density at 15°C, ρ (kg/m^3)	$\rho_{mix} = \sum_{i=1}^{n} x_i \cdot \rho_i$	(1)	810	870
Kinematic Viscosity at 40°C , η (mm^2/s)	$ln\,\eta_{mix} = \sum_{i=1}^{n} x_i \cdot ln\,\eta_i$	(2)	1.5	5.8
Cetane Number, CN	$CN_{mix} = \sum_{i=1}^{n} x_i \cdot CN_i$	(3)	4.9	-
Higher Heating Value, HHV (MJ/kg)	$HHV_{mix} = \sum_{i=1}^{n} x_i \cdot HHV_i$	(4)	35	-
b) Non-Linear Property Constraint				
Flash Point, T_{FP} (°C)	$\sum_i \frac{x_i \gamma_{VLE,i}(T_{FP}) P_i^{sat}(T_{FP})}{P_{i,FP}^{sat}} = 1$	(5)	60	-
Mixture constraint				
Stability	$\frac{dln\gamma_{LLE,i}}{dx_i} + \frac{1}{x_i} > 0$	(6)	-	-
Process model constraint				
Mass balance	$\sum_i x_i - 1 = 0$	(7)	-	-

Table 2. The requirements of green diesel bio-compounds, translated target properties, and the target value

Requirement	**Target Property**	**Target Value (Pure Component Constraints)**
• Compatible with diesel	Boiling point, T_b	50 °C < T_b< 300 °C
• Enhance engine efficiency • Environmental concern	Choose of chemical types	aliphatic compounds of hydrocarbon, alcohol, ester, ether, aldehyde, ketones, acides
• Liquid at ambient temperature	Melting point, T_m	T_m<20 °C
• Safety	Flash point,FP	FP > 30 °C

3.3. Stage 3: Ranking of Feasible Green Diesel Blends According to Desired Performance Index

The final stage is to select the best solution from all of the feasible blends based on cost and the index of desired performance, which are cetane number and higher heating value. Before considering the cetane number and higher heating value, the following objective function, F_{obj}, is used to identify the binary and ternary fuel blends with minimal cost. The designed green diesel blends must contain a minimum of 10 % of bio-component(s). The composition of bio-component(s) $x_{bio,i}$ is limited to no more than 30 % to ensure that the designed green diesel blend can be used in commercial diesel engines.

$$F_{obj} = \min \sum x_i C_i$$

subjected to

$$\sum x_i - 1 = 0$$

$$0.1 \leq \sum x_{bio,i} \leq 0.3$$

4. Results and Discussion

4.1. The Feasible Green Diesel Blends Candidates

A total number of 6,822 compounds that met the requirements of the pure component constraints were generated in ICAS-ProCAMD. The number of the possible compounds was further narrowed down by comparing the pure component properties with the target property values. Five bio-compounds were selected to illustrate the mixture design algorithm proposed in this paper: ethyl levulinate (EL), butyl levulinate (BL), butanol (BU), pentanol (PEN), and hexanol (HE). The results of the stability test of diesel components with the selected bio-compounds at room temperature (298.15 K) are shown in Table 3. Only the bio-components that are miscible (M) or partially miscible (P) with diesel components were considered as feasible green diesel blend candidates. Based on the previous studies, phase separation only occurred when high concentrations of EL were present in diesel (≥ 15 % of EL) (Wang et al., 2012), while BL can mix with diesel up to 20 % without a miscibility gap at room temperature (Christensen et al., 2011).

4.2. The Feasible Green Diesel Blends

Initially, there were approximately 49,000 possible binary and ternary blend candidates for diesel blending with EL, BL, BU, PEN and HE (with the variation of 1 % blending volume changed). The search space for the feasible blends was sufficiently narrowed down after solving for the linear and non-linear property constraints. For instance, only 49 feasible binary blends were found to meet the linear and non-linear property constraints from the total of 332 possible binary blends. To enhance the fuel combustion quality, a higher cetane number is preferred. Dibutyl ether (DBE) was selected as the cetane enhancer as it is completely miscible with diesel while having a higher cetane number (CN = 91) (Arteconi et al., 2011).

4.3. The Optimum Green Diesel Blends

The best green diesel blends were selected based on cost, cetane number, and higher heating value, as both of these fuel properties are closely related to the fuel combustion quality. The shortlisted green diesel blends with or without additive are ranked according to cost in Table 4. The correlation between cost and the total percentage of CN and HHV loss compared with the conventional diesel is illustrated in Figure 1. All of the shortlisted green diesel blends have competitive cost with the conventional diesel (USD 0.90 per L), except GD 2 (USD 2.33 per L) and GD 4 (USD 1.54 per L). Among the cheaper options (except GD 2 and GD 4), GD 3 and GD 7 have preferable CN and HHV over the other shortlisted blends, especially for the case of GD 3 (see Figure 1). Further testing is essential to evaluate the engine performance and emission of these blends in order to identify the best option for diesel replacement. Meanwhile, the present study has shown that the addition of DBE significantly improved the CN and the HHV of the fuel blends (e.g. GD 3, GD 4 and GD 7).

Table 3. The results of the stability test of each diesel component with the selected bio-compounds

Diesel component	Bio-compounds				
	EL	BL	BU	PEN	HE
n-Decane	P	M	M	M	M
n-Undecane	P	M	M	M	M
n-Dodecane	P	P	M	M	M
n-Tetradecane	P	P	M	M	M
n-Pentadecane	P	P	M	M	M
n-Hexadecane	P	P	M	M	M
n-Octadecane	P	P	M	M	M
n-Icosane	P	P	M	M	M

Table 4. The optimum solutions of the binary and ternary blends with or without additive (DBE)

Blend	Formulation*	Properties					Cost, (USD/L)
		ρ kg/m^3	CN	η mm^2/s	HHV MJ/kg	FP °C	
	Binary Blends						
GD 1	D + 14HE	837.76	55.93	3.90	45.72	60.3	0.89
GD 2	D + 10EL	857.00	52.88	3.60	44.73	72.6	2.33
	Binary Blends + additive						
GD 3	D + 8HE + 2DBE	837.38	57.56	3.78	46.1	60.3	0.92
GD 4	D + 4EL + 6DBE	842.78	58.04	3.42	45.73	61.8	1.54
	Ternary Blends						
GD 5	D + 1PEN+ 10HE	838.15	56.2	3.90	45.94	60.1	0.91
GD 6	D + 1EL + 15HE	839.30	55.24	3.85	45.44	60.2	1.03
	Ternary blends + additive						
GD 7	D + 1EL + 8HE + 2DBE	839.08	57.03	3.83	45.90	60.4	1.05

*diesel + volume % of bio-component/additive

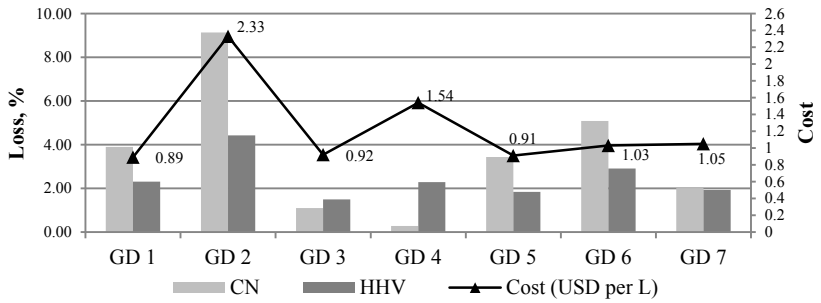

Figure 1. Correlation between cost and the percentage of CN and HHV loss of the shortlisted blends (see Table 4) compared with diesel

5. Conclusions

This paper presents a systematic computer-aided mixture algorithm for solving the MINLP problem of green diesel blend design using a decomposition-based approach. The search space of the possible green diesel blends was sufficiently narrowed down through an iterative computational technique. Only seven different feasible blends that satisfied all of the target properties with minimal cost are shortlisted at the end of this

study. By comparing the cost, cetane number and heating value, GD 3 and GD 7 have competitive price (USD 0.92 and 1.05 per L, respectively) with diesel (USD 0.90 per L), and preferable cetane number and acceptably high heating value. In order to identify the best solution, its behaviour in the diesel engine, including emission, should be evaluated; this will be addressed in future work.

Acknowledgements

The valuable guidance and advice provided by Professor Dr. Rafiqul Gani at the Computer Aided Process Engineering Centre (CAPEC) of the Technical University of Denmark (DTU) are gratefully acknowledged. The authors would like to acknowledge CAPEC for providing the ICAS license (version 17.0) to accomplish this work. Finally, we are grateful for the financial support provided by the Ministry of Education (MoE) Malaysia and the Universiti Teknologi Malaysia (UTM) under the Vote No. Q.J130000.2444.00G53 to perform this research work.

References

S. A. Ariffin Kashinath, Z. Abdul Manan, H. Hashim,S. R. Wan Alwi, 2012, Design of Green Desel from Bofuels using Cmputer Aded Technique, Computers & Chemical Engineering, 41, 0, 88-92

A. Arteconi, A. Mazzarini,G. Di Nicola, 2011, Emissions from Ethers and Organic Carbonate Fuel Additives: A Review, Water, Air, & Soil Pollution, 221, 1-4, 405-423

Z. Chen, X. Ma, S. Yu, Y. Guo,J. Liu, 2009, Physical-Chemical Properties of Ethanol-Diesel Blend Fuel and Its Effect on the Performance and Emissions of a Turbocharged Diesel Engine, International Journal of Automotive Technology, 10, 3, 297-303

E. Christensen, A. Williams, S. Paul, S. Burton,R. L. Mccormick, 2011, Properties and Performance of Levulinate Esters as Diesel Blend Components, Energy & Fuels, 25, 11, 5422-5428

A. Fredenslund, J. Gmehling, M. L. Michelsen, P. Rasmussen,J. M. Prausnitz, 1977, Computerized Design of Multicomponent Distillation Columns Using the UNIFAC Group Contribution Method for Calculation of Activity Coefficients, Industrial & Engineering Chemistry Process Design and Development, 16, 4, 450-462

A. Fredenslund, R. L. Jones,J. M. Prausnitz, 1975, Group-Contribution Estimation of Activity Coefficients in Nonideal Liquid Mixtures, AIChE Journal, 21, 6, 1086-1099

H.-J. Liaw, Y.-H. Lee, C.-L. Tang, H.-H. Hsu,J.-H. Liu, 2002, A Mathematical Model for Predicting the Flash Point of Binary Solutions, Journal of Loss Prevention in the Process Industries, 15, 6, 429-438

T. Magnussen, P. Rasmussen,A. Fredenslund, 1981, UNIFAC parameter table for prediction of liquid-liquid equilibriums, Industrial & Engineering Chemistry Process Design and Development, 20, 2, 331-339

Z.-W. Wang, T.-Z. Lei, L. Liu, J.-L. Zhu, X.-F. He,Z.-F. Li, 2012, Performance Investigations of a Diesel Engine Using Ethyl Levulinate-Diesel Blends, BioResources, 7, 4, 5972-5982

L. Wei, C. S. Cheung,Z. Huang, 2014, Effect of n-Pentanol Addition on the Combustion, Performance and Emission Characteristics of a Direct-Injection Diesel Engine, Energy, 70, 172-180

N. A. Yunus, K. V. Gernaey, Z. A. Manan, J. M. Woodley,R. Gani. Design of Tailor-Made Chemical Blend using a Decomposition-Based Computer-Aided Approach. Modeling, Simulation and Applied Optimization (ICMSAO), 2011 4th International Conference on, 2011. IEEE, 1-6.

N. A. Yunus, K. V. Gernaey, J. M. Woodley,R. Gani, 2012, An Integrated Methodology for Design of Tailor-Made Blended Products, In: IAN DAVID LOCKHART, B. & MICHAEL, F. (eds.), Computer Aided Chemical Engineering. Elsevier

Krist V. Gernaey, Jakob K. Huusom and Rafiqul Gani (Eds.), 12th International Symposium on Process Systems Engineering and 25th European Symposium on Computer Aided Process Engineering.
31 May – 4 June 2015, Copenhagen, Denmark

A Mathematical Programming Targeting Method to Select Treatment Technologies Ahead of Design

Athanassios Nikolakopoulos [a *], Antonis Kokossis[a]

[a]*National Technical University of Athens, School of Chemical Engineering, Heroon Polytechneiou 9, Zografou Campus, Athens, 15780, Greece*
nikolako@mail.ntua.gr

Abstract

The paper proposes a two stage mathematical programming approach for screening wastewater treatment technologies ahead of design, when the limiting concentrations and mass loads of contaminants for a set of water using operations are the only available data. The first stage of the methodology calculates the target for minimum fresh water flowrate further identifying the concentrations and the flowrates of the flows of the wastewater mains. The second stage selects the most effective treatment technologies and calculates targets for minimum wastewater treatment flows. The method is illustrated by a set of examples featuring the different aspects of the problem and characteristics of the solution.
Keywords: Wastewater treatment, Targeting, Water Integration.

1. Introduction

The growing scarcity of water resources and the increasingly stringent legislative framework on discharge limits force the chemical industry to adopt water management practices with ever increasing costs. The minimization of fresh water consumption and waste treatment costs must be synchronized since the effluent flowrates are directly related to the fresh water consumption. Treatment costs depend on the effluent flowrates and the selected treatment processes. Prior to detailed designs it is useful to quantify the target for minimum water consumption and the maximum potential of a wastewater treatment configuration in terms of the selected processes to integrate and minimum wastewater treatment flowrates (Kuo and Smith 1997). Graphical targeting methods (Wang and Smith 1994) are unable to screen treatment technologies and target flowrates for multiple treatment units, while shortcut models for the selection of treatment processes are absent from literature (Bagajewicz 2000, Foo 2009 and Nikolakopoulos et al. 2012). The method proposed in this paper links two transshipment models. The first model (Argaez et al. 1999 and Nikolakopoulos et al. 2013), which targets the flowrate of fresh water, is extended in identifying the flowrates and concentrations of the effluent water mains. The second model (Nikolakopoulos et al. 2014), which originally targets treatment flowrates is extended in screening treatment technologies. The method offers the additional advantage of detecting the critical parameters of the system, where retrofitting changes improve on total cost. The two models are connected by identifying the flowrates and concentrations of the wastewater mains, which are allocated at the *pinch points* of the concentration interval diagram of the residual cascade (Argaez et al. 1999) which in turn correspond to the *pinch points* of the *limiting composite curve* (Wang & Smith 1994). The method is illustrated by a set of examples featuring the different aspects of the problem and characteristics of the solution.

The next section describes the model used for targeting fresh water flowrates and identifying wastewater mains. Section 3 presents the transshipment model for screening

treatment technologies and minimizing treatment flowrates. Section 4 illustrates the method using two examples from literature. The paper concludes in Section 5.

2. Targeting fresh water flowrates and allocating wastewater mains

Let us denote by $I = \{i \mid i = 1,2,...,No\}$ the index set of the water using operations. Associated with each operation are maximum inlet and outlet concentrations $C_i^{in,\max}$ and $C_i^{out,\max}$ respectively. The mass load of the contaminant transferred to each water-using operation is M_i^c. The limiting water flowrate, for the water-using operation i is $F_i^l = M_i^c / \left(C_i^{out,\max} - C_i^{in,\max}\right)$. The index set of concentration intervals is $CI = \{k \mid k = 1,2,...,K\}$, and C_k is the inlet concentration of interval k. The mass transferred from water-using operation i through the k^{th} concentration interval is $W_{i,k}^P = F_i^l \left(C_k - C_{k+1}\right)$, and the residual mass from water using operation i leaving interval k, is $r_{i,k}$. Equations (1-7) are the targeting model for water flowrate F^{fw}:

$$\min F^{fw} \tag{1}$$

$$r_{i,k} - r_{i,k-1} + W_{i,k} = W_{i,k}^P, \ \forall i,k \tag{2}$$

$$\sum_i W_{k,i} = W_k^W, \qquad \forall k \tag{3}$$

$$W_k^W = F^{fw}\left(C_k - C_{k+1}\right), \ \forall k \tag{4}$$

$$0 \le F^{fw} \le F^{fw,U} \tag{5}$$

$$\sum_i r_{i,k} \le y_k M, \ \forall k \tag{6}$$

$$r_{i,0} = r_{i,k} = 0, \ \ r_{i,k} \ge 0, \forall i \ \ and \ \ y_k \in \{0,1\}, \forall k \tag{7}$$

Equation (2) is the mass balances around interval k for every operation i. If $\sum_i r_{i,k} \ge 0$, then k is one of the pinch points. M is a sufficiently large number. If $y_k = 1$, then from (Eq. 6) k is a pinch point; and $KP = \{k^p \mid k^p = 1,...,K\}$ is the index set of all pinch points, including the pseudo pinch K. The total mass of contaminant is $MC^{tot} = \sum_i M_i^c$.

The element that bridges the two targeting models is the allocation of the pinch points at the upper limit of the concentration intervals where the sum of the residuals of the contaminant obtains positive values, while at any other interval the residuals are vanishing. The flowrate in the identified water mains is not influenced by the particulars of the water reuse network. Thus, let $W_{k^p} = \sum_i \sum_{k=k^p-1}^{k=k^p} W_{i,k}, \ \forall k^p$, be the mass of contaminant removed between pinch points $k^p - 1$ and k^p. Then the flowrate of the wastewater main of pinch point k^p is $F_{k^p} = W_{k^p} / \left(C_{kp} - C_{k^p+1}\right), \ \forall k^p$, where C_{kp} is the concentration of the effluent stream k^p. The effluent streams participate at the wastewater treatment optimization configuration to be assessed at the next stage.

3. Screening of treatment processes and targeting treatment flowrates

The design of a waste water network can be described with reference to a set of S_K wastewater mains: $KP = \{k^p \mid k^p = 1,...,K\}$, and a set of S_J treatment processes $J = \{j \mid j = 1,2,...,S_J\}$. Associated with each wastewater main are the original inlet concentrations $C^{in}_{o,k^p} = C_{kp}$. The outlet concentrations of all treated waste streams are equal to the original discharge concentration limits C^{out}_{o,k^p}. The mass load W_{k^p} of the contaminant transferred from main *k*, is already calculated. The minimum water flow rate, MWF_{k^p} for the waste water stream *k* in treatment process *j* is given by: $MWF_{k^p} = W_{k^p}\left(C^{in}_{o,k^p} - C^{out}_{o,k^p}\right), \forall k^p$. Let $IN = \{n \mid n = 1,2,...,N\}$ be the index set of the concentration intervals. C_n is defined as the outlet concentration of interval *n*. The mass transferred from main k^p through the n^{th} interval is given by: $M^P_{n,k^p} = MWF_{k^p}\left(C_{n+1} - C_n\right)$. Similarly, the mass transferred to stream *j* through the n^{th} interval is $M^W_{j,n} = Ft_j\left(C_{n+1} - C_n\right)$. The solution will select a cost effective set of treatment processes and determine the minimum treatment flowrates Ft_j. If fc_j is the fixed cost and $coef_j$ is the coefficient of the variable cost of the j^{th} treatment unit, the problem of selecting treatment processes and minimizing the treatment flowrates is represented by equations (8-14), where u_{n,k^p} is the residual mass of main k^p leaving interval *n*:

$$\min Cost = \sum\left(fc_j x_j + coef_j Ft_j\right) \tag{8}$$

$$u_{n-1,k^p} - u_{n,k^p} + \sum M_{n,j,k^p} = M^P_{i,k^p}, \ \forall n, k^p \tag{9}$$

$$\sum M_{k,j,n} = M^W_{j,n}, \qquad \forall j, n \tag{10}$$

$$M^W_{j,n} = Ft_j\left(C_{n+1} - C_n\right), \ \forall n \tag{11}$$

$$0 \le Ft_j \le Ft^U_j, \ \forall j \tag{12}$$

$$x_j M \ge Ft_j, \ \forall j \tag{13}$$

$$u_{N+1,k^p} = u_{1,k^p} = 0, \ u_{n,k^p} \ge 0, \ \forall n, k^p \ \ and \ \ x_j \in \{0,1\}, \ \forall j \tag{14}$$

The constraint set (9) is the mass balance of the contaminant around each interval. $M_{k,j,n}$ is the mass of contaminant transferred from waste stream *k* to through interval *n* to treatment process *j*. For treatment processes with fixed outlet concentration, before the construction of the concentration intervals the concentrations of all waste streams must be shifted by the minimum of the outlet concentration of the treatment units $C^{out}_{\min} = \min_j\left\{C^{out}_j\right\}$, thus the concentration leaving the treatment processes will have virtually zero value and can be assigned to the first concentrations interval: $C^{in}_{k^p} = C^{in}_{o,k^p} - C^{out}_{\min}$ and $C^{out}_{k^p} = C^{out}_{o,k^p} - C^{out}_{\min}, \forall k^p$. The same shift applies for the inlet and

outlet concentrations of all treatment processes: $C_{s_j}^{in} = C_j^{in} - C_{\min}^{out}$ and $C_{s_j}^{out} = C_j^{out} - C_{\min}^{out}$, $\forall j$. The intervals are defined by the shifted limiting concentrations.

4. Illustrative examples

4.1. Example 1

Table 1 contains the data for four water-using operations (Kuo & Smith 1994) and three waste water treatment processes.

Table 1 Data for example with four water using processes and three waste treatment processes

Water using operations					
Operation No	Contaminant Mass load (kg/h)	C_{in} (ppm)	C_{out} (ppm)	Limiting water flowrate (t/h)	
1	2	0	100	20	
2	5	50	100	100	
3	30	50	800	40	
4	4	400	800	10	
Wastewater treatment processes					
Process No		C_{in} (ppm)	C_{out} (ppm)	Fixed cost K€	Variable cost coefficient K€/t/h
I		50	10	200	15
IIa		900	30	50	10
IIb		900	30	150	8
	Environmental discharge limit		C_e = 20 ppm		

Figure 1a shows the pinch points on the composite curve and Figure 1b shows the resulting water mains that. Treatment processes I and IIb are selected, at cost of 2.5M€.

Table 2 Results for Example 1

Water using operations			Wastewater treatment processes	
Minimum fresh water flowrate		90 t/h	Selected treatment processes	TP I and TP IIb
Water mains	Concentration (ppm)	Flowrate (t/h)	Total cost	2,535 K€
ST I	100	44.3	Wastewater treatment flows (t/h)	
ST II	800	45.7	TP I	90
			TP IIb	64.28

The selection of a TP is sensitive to waste flowrates; if the flowrate of the ST II was 38.46 t/h then TP IIa would have selected instead of TP IIb, with a flowrate of 59.1 t/h.

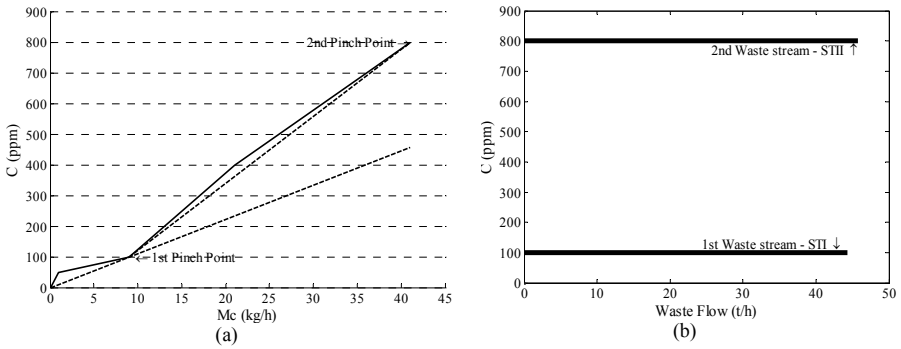

Figure 1 Pinch points and waste streams for example 1

Figure 2 presents an optimal water reuse network for Example 1, where the flows of the two wastewater mains have the same concentration and flowrates as the ones in Figure 1b calculated by solving problem (1-7).

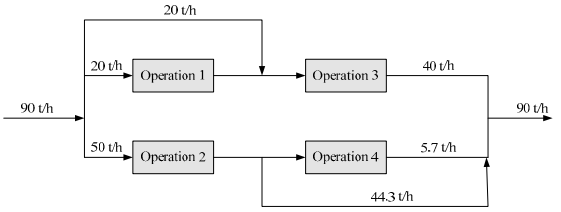

Figure 2 Optimal network for water reuse in example 1 (Smith, 2005)

The pinch points reveal the critical parameters of the water using operations and the treatment units. For example, if the maximum outlet concentration of operation 2, which is involved in the 1st pinch, is increased by 100 ppm, then the minimum fresh water flowrate is reduced by 28% to 65 t/h. This effect propagates to the second stage with an analogous reduction in the treatment flowrates. However a similar increase of the outlet concentration of the 4th operation will have no positive impact.

4.2. Example 2

The data for five water-using operations and three waste water treatment processes are shown in Table 3 (Smith 2005).

Table 3 Example with five water using processes and three waste treatment processes

Water using operations					
Operation No	Cont. Mass load (kg/h)	C_{in} (ppm)	C_{out} (ppm)	Limiting flowrate (t/h)	
1	8	0	200	40	
2	5	100	200	50	
3	6	100	400	20	
4	6	300	400	60	
5	8	400	600	40	
Wastewater treatment processes					
Process No		C_{in} (ppm)	C_{out} (ppm)	Fixed cost K€	Variable cost coefficient K€/t/h
I		200	5	200	15
IIa		1000	50	50	10
IIb		1000	50	150	8
Environmental discharge limit		C_e = 30 ppm			

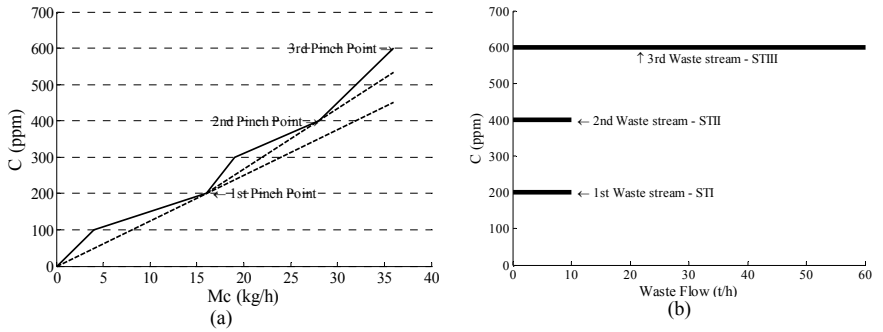

Figure 3 Pinch points and waste streams for example 2

Figure 3a shows the pinch points on the composite curve and Figure 3b shows the wastewater mains that result from this configuration. Treatment processes I and IIb are selected, at a cost of ~2 M€.

Table 4 Results for Example 2

Water using operations			Wastewater treatment processes	
Minimum fresh water flowrate		80 t/h	Selected treatment processes	TP I and TP IIb
Water mains	Concentration (ppm)	Flowrate (t/h)	Total cost	1,986 K€
ST I	200	10	Wastewater treatment flowrates (t/h)	
ST II	400	10	TP I	80
ST III	600	60	TP IIb	54.54

If the flowrate of the ST III was 53 t/h then TP IIa would have been selected instead of TP IIb, with a treatment flowrate of 49.45 t/h.

5. Conclusions

A mathematical programming tool consisting of two interlinked models is proposed for synchronized targeting of fresh water flowrate, screening of wastewater treatment technologies and targeting of treatment flowrates. There is scope to expand the models for multiple water sources, multiple contaminants and treatment processes with removal ratio. Finally, future integration of the two models will offer the possibility to assess the option of regeneration and recycle.

6. Acknowledgements

Financial support from the Marie Curie European Research Program RENESENG (FP7- 607415) is gratefully acknowledged.

References

A. Alva-Argáez, A. Vallianatos, A. Kokossis, 1999, A multi-contaminant transhipment model for mass exchange networks and wastewater minimisation problems, Computers and Chemical Engineering, 23, 1439–1453

M. Bagajewicz, 2000, A review of recent design procedures for water networks in refineries and process plants, Computers and Chemical Engineering, 24, 9-10, 2093-2113

D.C.Y. Foo, 2009, State of the art review of pinch analysis techniques for Water network synthesis, Industrial and Engineering Chemistry Research, 48, 11, 5125-5159

W.C.J. Kuo and R. Smith, 1997, Effluent treatment system design Chemical Engineering Science, 52, 23, 4273-4290

A. Nikolakopoulos, P. Karagiannakis, A. Galanis, A. Kokossis, 2012, A water saving methodology for the efficient development of biorefineries, Computer Aided Chemical Engineering, 30, 7-10

A. Nikolakopoulos, A. Galanis, P. Karagiannakis, A. Kokossis, 2013, An Integrated Targeting and Design Method for Saving Water in 2nd Generation Biorefineries, AIChE 2013 - 2013 AIChE Annual Meeting, Conference Proceedings

A. Nikolakopoulos, L. Thomaidis, A. Kokossis, 2014, Mathematical Programming Shortcut Screening Models for the Design of Integrated Waste Treatment Systems, Computer Aided Chemical Engineering, 34, 381-386

R. Smith, 2005, Chemical Process Design and Integration, John Wiley & Sons, Chichester, UK

Y.P. Wang and R. Smith, 1994, Design of distributed effluent treatment systems, Chemical Engineering Science, 49, 18, 3127-3145

Krist V. Gernaey, Jakob K. Huusom and Rafiqul Gani (Eds.), 12th International Symposium on Process Systems Engineering and 25th European Symposium on Computer Aided Process Engineering.
31 May – 4 June 2015, Copenhagen, Denmark

Optimal Structure Synthesis of Ternary Distillation System

Hiroshi Takase and Shinji Hasebe*

Department of Chemical Engineering, Kyoto University, Kyoto 615-8510, Japan
hasebe@cheme.kyoto-u.ac.jp

Abstract

A new process synthesis method for ternary distillation processes is proposed. First the composition space of the ternary mixture is discretized, and each of the discretized compositions is assigned to a module corresponding to a tray of distillation columns. Then, the superstructure connecting all modules by vapor and liquid flow paths is constructed. In the proposed formulation, the liquid composition of each module is determined in advance. Thus, all of the constraints can be expressed by linear equations and linear inequalities even if the vapor-liquid equilibrium is expressed by a complicated function. Finally, by solving the problem formulated as a linear programming problem, the optimal process structure and design condition can be derived. When the composition space is discretized, the optimization result includes unessential flows among modules to satisfy the material and energy balance at the modules. Such unessential flows are effectively removed by prohibiting the ineffective mixing at each module. The developed synthesis procedure was applied to the separation problem of a ternary mixture consisting of benzene, toluene, and o-xylene. The results showed that a process structure close to the Petlyuk column is created without assigning any process structure in advance.

Keywords: Ternary distillation, Process synthesis, Petlyuk column, Optimal design

1. Introduction

As distillation needs a large amount of energy, various energy-saving techniques have been proposed and implemented for energy conservation. For more than two-component separation, the separation sequence is one of the important design variables that affect the possibility of external heat integration, i.e., heat exchange between the top vapor of a column and the bottom liquid of another column. By considering these facts, many researchers have proposed synthesis procedures that optimize the separation sequence, column design and external heat integration (Andrecovich and Westerberg, 1985, Novak et al., 1996). A superstructure is effectively used to formulate synthesis problems as an MILP or MINLP problem. In these researches, a conventional column, rectifying and stripping sections of a conventional column have been used as the building blocks of the synthesis problem.

The other energy conservation method of distillation system is to use thermally coupled columns such as a Petlyuk column or a side rectifier. Synthesis problems, including thermally coupled columns, have also been discussed by many researchers (Sargent and Gaminibandara, 1976, Alcántara-Avila et al., 2013, Caballero and Grossmann, 2014). In these researches, thermally coupled columns and/or their component structures are embedded as building blocks in the superstructure of the

synthesis problem. In other words, a structure having thermally coupled columns cannot be derived if such structures are not included in the model.

To consider flexible process structures, Ghougassian and Manousiouthakis (2012) adopted a tray of a column as a building block of the synthesis problem. By deciding the composition of each tray in advance, they presented the linear formulation for multi-pressure distillation processes of a binary homogeneous azeotropic mixture. Thanks to LP formulation, this procedure has no assumptions about process structure. However, a heat balance was not considered in their model. Takase and Hasebe (2014) extended their formulation so that a heat balance could be embedded in the formulation. In their method, the heat transfer from trays in the rectifying section to trays in the stripping section is considered as well as that between the condenser and reboiler. The developed method was applied to the design problem of internally heat integrated distillation processes of binary mixture. In this research, the method developed by Takase and Hasebe (2014) is extended to a synthesis problem of a ternary distillation system.

2. Method

2.1. Problem formulation

In this research, problems of separating ternary components are studied. The following assumptions are introduced in the problem. The flow rate of feed and its composition are given in advance. All products are saturated liquid, and the specification of each product is given as the lower bound of the concentration of key component. The pressure of the feed is the same as those of products, and the pressure drop in the system is negligible. Several heating and cooling utilities with different temperatures are available, and the utility costs depend on its temperature. The column cost is negligible compared with the utility cost.

For the above conditions, the problem deciding the process structure that minimizes the operation costs is discussed.

2.2. Modules and superstructure of the system

In the proposed design procedure, each tray is treated as a separation module, and the flow paths among these modules are assumed to be not decided in advance. First, the entire range of liquid composition is divided into N_S different compositions. Then, each of the divided compositions is assigned to a module. For a ternary separation problem, the mole fractions of two components must be decided to identify the composition.

In the proposed method, a vapor-liquid equilibrium is assumed between the output vapor and liquid flows at each separation module. As the pressure at each module has been given in advance, the temperature and the vapor composition are uniquely decided from vapor-liquid equilibrium condition. Molar enthalpies of the vapor and liquid are also decided for the output vapor and liquid flows of each module. These values can be calculated before the optimization. Thus, precise thermodynamic models can be used for the calculation of these values.

Figure 1 shows the input and output relationship of a separation module. There are two input nodes. One is the material flow that consists of the mixture of vapor and liquid flows from other modules. The other is the energy flow that shows the heat added to the module. There are three output nodes: liquid and vapor flows and the energy flow. When some amount of heat is removed from a module, it is regarded as energy flow from the module. In the proposed model, heat can be added to or removed from any modules. Therefore, reboilers and condensers are also treated as separation modules.

Feed and products are treated as special modules; the feed module does not have any input flows, and the product modules do not have any output flows. Each module is numbered as follows: The feed module is regarded as module 0, the separation modules are assigned to module 1 to module N_S, three product flows are assigned to module N_S+1 to module N_S+3. In product modules, it is assumed that the boiling temperature of module N_S+1 is the lowest, and that of module N_S+3 is the highest.

The heating and cooling utilities are treated as other types of special modules. Module N_S+4 to module N_S+N_H+3 correspond to heating utilities with different temperatures, and module N_S+N_H+4 to module N_S+N_H+N_C+3 correspond to cooling utilities with different temperatures. A module showing heating utility has only an energy output node, and a module showing cooling utility has only an energy input node.

The feature of the proposed design procedure is that the vapor and liquid flow paths among modules are treated as decision variables. So, this procedure can derive not only conventional distillation systems but also unexplored process structures. Figure 2 shows the superstructure which is adopted in this research. Each box in the figure corresponds to a module. To easily identify the flow connection, each separation module is shown as two divided parts: output part and input part. Thus, two boxes with the same number correspond to the same module. The solid lines, dashed lines, and alternate long and short dashed lines among the nodes are the liquid flow paths, vapor flow paths, and energy flow paths, respectively.

2.3. Mathematical formulation

The total material balances at the feed module, product modules, and separation modules are expressed by Eqs. (1) to (3), respectively.

$$\sum_{j=1}^{N_S+3} L_{0j} = L^F, \quad \sum_{j=1}^{N_S} V_{0j} = V^F \tag{1}$$

$$\sum_{i=0}^{N_S} L_{ij} \geq L^P_{j-N_S} \qquad (j = N_S+1, N_S+2, N_S+3) \tag{2}$$

$$\sum_{i=0}^{N_S} (L_{ij} + V_{ij}) = \sum_{i=1}^{N_S+3} L_{ji} + \sum_{i=1}^{N_S} V_{ji} \qquad (j = 1, 2, \ldots, N_S) \tag{3}$$

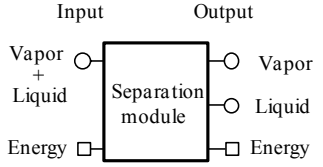

Figure 1 Input-output relationship at a separation module

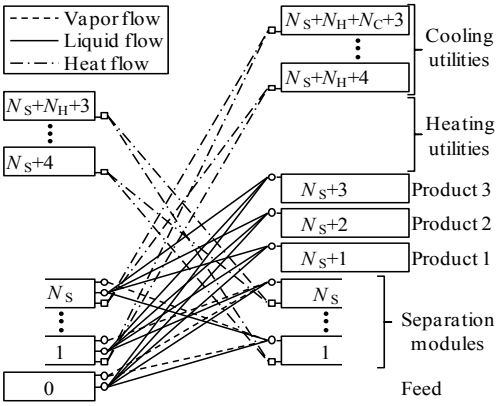

Figure 2 Superstructure of ternary distillation system

where L_{ij} and V_{ij} are liquid and vapor flow rates from module i to module j, respectively. L^{F} and V^{F} are liquid and vapor flow rates of feed, respectively. L_k^{P} is the minimum amount of kth product, and is given in advance. It is assumed that there is no vapor inlet flow to the product modules. The left hand side in Eq. (3) is the sum of inlet flows to module j, and the right hand side of Eq. (3) is the sum of outlet flows from module j.

The enthalpy balance at module j is expressed by Eq. (4).

$$\sum_{i=0}^{N_{\mathrm{S}}} L_{ij} h_i^{\mathrm{L}} + \sum_{i=0}^{N_{\mathrm{S}}} V_{ij} h_i^{\mathrm{V}} + \sum_{k \in U_j^{\mathrm{H}}} Q_{kj} = \sum_{i=1}^{N_{\mathrm{S}}+3} L_{ji} h_j^{\mathrm{L}} + \sum_{i=1}^{N_{\mathrm{S}}} V_{ji} h_j^{\mathrm{V}} + \sum_{k \in U_j^{\mathrm{C}}} Q_{jk} \quad (j = 1, 2, \ldots, N_{\mathrm{S}}) \tag{4}$$

where h_i^{L} and h_i^{V} are molar enthalpy of liquid and vapor flows from module i, respectively. Q_{ij} is the heat flow rate from module i to module j. U_j^{H} and U_j^{C} are sets of heating and cooling utilities which can be used at module j, respectively. By deciding the minimum approach temperature for heat exchange, the content of these sets can be decided in advance.

The specification of the kth product is given as the lower bound of the mole fraction of key component, x_k^{P}, and the corresponding constraint is expressed by the following inequalities:

$$\sum_{i=0}^{N_{\mathrm{S}}} L_{ij} x_{ij} \geq x_{j-N_{\mathrm{S}}}^{\mathrm{P}} \sum_{i=0}^{N_{\mathrm{S}}} L_{ij} \qquad (j = N_{\mathrm{S}}+1, N_{\mathrm{S}}+2, N_{\mathrm{S}}+3) \tag{5}$$

Since the composition is discretized in the proposed method, it is difficult to strictly satisfy the component balance at each separation module. Thus, the component balance at each separation module is given by inequality constraints:

$$-\varepsilon \leq \frac{\sum_{i=0}^{N_{\mathrm{S}}} (L_{ij} x_{ik} + V_{ij} y_{ik}) - x_{jk} \sum_{i=1}^{N_{\mathrm{S}}+3} L_{ji} - y_{jk} \sum_{i=1}^{N_{\mathrm{S}}} V_{ji}}{\sum_{i=0}^{N_{\mathrm{S}}} (L_{ij} + V_{ij})} \leq \varepsilon \quad (j = 1, 2, \ldots, N_{\mathrm{S}},\ k = 1, 2) \tag{6}$$

where ε is a parameter which shows the maximum acceptable error on the composition. (y_{i1}, y_{i2}, y_{i3}) is the vapor composition which is equilibrium to (x_{i1}, x_{i2}, x_{i3}).

In this research, we assumed that the column cost is negligible compared with the utility cost, and that the objective function, PI, is expressed by

$$PI = \sum_{k=1}^{N_{\mathrm{H}}} \left(c_k^{\mathrm{H}} \sum_{i=1}^{N_{\mathrm{S}}} Q_{N_{\mathrm{S}}+3+k,i} \right) + \sum_{k=1}^{N_{\mathrm{C}}} \left(c_k^{\mathrm{C}} \sum_{i=1}^{N_{\mathrm{S}}} Q_{i,N_{\mathrm{S}}+N_{\mathrm{H}}+3+k} \right) \tag{7}$$

where c_k^{H} (c_k^{C}) is the unit cost of kth heating (cooling) utility.

All of the equations and inequalities in Eqs. (1) to (7) are linear. Thus, the problem is formulated as a linear programming problem.

2.4. Prohibition of ineffective mixing

When the problem formulated in the previous section is solved, the obtained result has many flow paths among the modules. Some of them are caused by the effect of the discretization of the composition space. To avoid ineffective mixing at a module, flow paths that satisfy the following conditions are prohibited.

$$L_{ij} = 0 \ \text{ for } {}^{\forall}(i,j) \in \left\{ (i,j) \,|\, (\boldsymbol{x}_j - \boldsymbol{x}_i)^{\mathrm{T}} (\boldsymbol{y}_i - \boldsymbol{x}_i) > 0,\ i, j = 1, 2, \ldots, N_{\mathrm{S}} \right\} \tag{8}$$

$$V_{ij} = 0 \ \text{ for } {}^{\forall}(i,j) \in \left\{ (i,j) \,|\, (\boldsymbol{x}_j - \boldsymbol{x}_i)^{\mathrm{T}} (\boldsymbol{y}_i - \boldsymbol{x}_i) < 0,\ i, j = 1, 2, \ldots, N_{\mathrm{S}} \right\} \tag{9}$$

where $\boldsymbol{x}_i$ and $\boldsymbol{y}_j$ are vectors that show the liquid and vapor compositions of the output of module j. The qualitative meaning of these constraints is that the vapor of a module must flow into the module whose composition is richer in lighter components, and the liquid must flow into the module whose composition is richer in heavier components.

3. Case Study

The proposed method was applied to the separation problems of a benzene, toluene and o-xylene mixture. The feed is the saturated liquid of equimolar mixture of three components and its flow rate is 300 kmol/h. The pressure is assumed to be 101.3 kPa in entire system. The specification for each product is 0.80 for key components, and the flow rate of each product is 100 kmol/h. Only a kind of heating utility is available and its cost coefficient c^{H} is 11.0 \$/GJ, and only a kind of cooling utility is available and its cost coefficient c^{C} is 0.25 \$/GJ. The pitch of composition discretization is 0.025.

First, the vapor composition, temperature, and vapor and liquid enthalpies are calculated for each module. These values are calculated by the NRTL fluid package of Aspen HYSYS®. Then, Eq. (7) is minimized under the linear constraints of Eqs. (1) to (6) and Eqs. (8) and (9). CPLEX 12.5® was used for optimization.

The result is expressed in Fig. 3. The left figure shows the liquid flow paths, and the right figure shows the vapor flow paths. The obtained result still has many flows whose flow rates are very small so as to adjust the material balance. Thus, in Fig. 3, the flow paths whose flow rate is less than 10 % of product flow are not depicted.

In Fig. 3, separation modules are classified into six groups circled by dashed lines. When each group of modules is treated as a column, the process structure in Fig. 4 is obtained. In Fig. 4, solid and dotted lines express liquid and vapor flows, respectively. There are many vapor and liquid flows among the columns. However, by merging five columns, columns 2, 3, 4, 5 and 6, in Fig. 4, the structure shown in Fig. 5 is obtained. This structure is almost the same as the Petlyuk columns except that the obtained structure has several bypass flows among the columns.

4. Conclusion

A systematic synthesis method of a ternary distillation system was proposed. In the method, a tray is treated as a module, and the vapor and liquid flow paths are treated as design variables. By discretizing the composition space of the ternary system and assigning each composition to a module, all the constraints were expressed by linear equations. As the synthesis problem was formulated as a linear programming problem, the optimal structure could be obtained even when the problem size became large. The developed method was applied to the synthesis problem of a benzene, toluene and o-xylene mixture, and a process structure similar to the Petlyuk column was obtained. In the proposed method, there are no constraints on the flow paths among trays. Thus, the proposed method has a high possibility of generating innovative structures which are not derived by human experience.

In the current model, the column cost is not included in the objective function because a large number of 0-1 variables are needed to express the tray number of a process structure. Furthermore, there is no guideline on how to discretize the composition space. This guideline is essential, when purer products are requested or when azeotropes exist. These problems are regarded as future works.

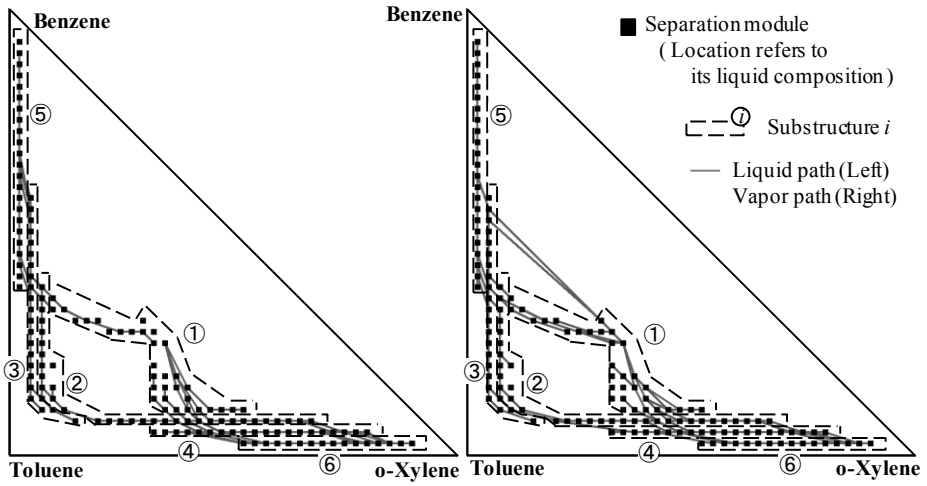

Figure 3 Optimal flow paths for ternary separation (Left: liquid, Right: vapor)

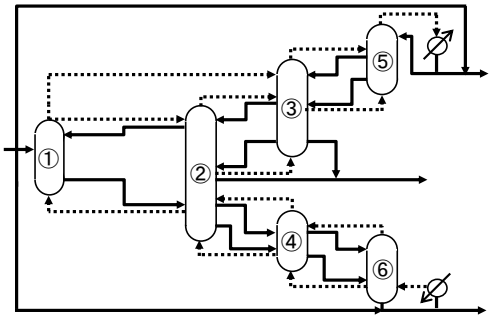

Figure 4 Optimal process structure

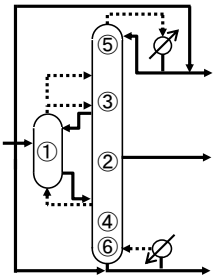

Figure 5 Merged process structure similar to Petlyuk column

References

J. R. Alcántara-Avila, S. Hasebe, & M. Kano, 2013, New Synthesis Procedure to Find the Optimal Distillation Sequence with Internal and External Heat Integrations, Ind. Eng. Chem. Res., 52, 4851–4862

M. J. Andrecovich, & A. W. Westerberg, 1985, An MILP formulation for heat-integrated distillation sequence synthesis, AIChE J., 31, 1461–1474

J. A. Caballero, & I. E. Grossmann, 2014, Optimal synthesis of thermally coupled distillation sequences using a novel MILP approach, Comput. Chem. Eng., 61, 118–135

P. G. Ghougassian, & V. Manousiouthakis, 2012, Globally Optimal Networks for Multipressure Distillation of Homogeneous Azeotropic Mixtures, Ind. Eng. Chem. Res., 51, 11183–11200

Z. Novak, Z. Kravanja, & I. E. Grossmann, 1996, Simultaneous synthesis of distillation sequences in overall process schemes using an improved minlp approach, Comput. Chem. Eng., 20, 1425–1440

R. W. H. Sargent, & K. Gaminibandara, 1976, Optimum Design of Plate Distillation Columns, Optimization in Action, 267–314.

H. Takase, & S. Hasebe, 2014, Optimal Synthesis of Internally Heat Integrated Distillation Column, J. Chem. Eng. JAPAN, accepted

Krist V. Gernaey, Jakob K. Huusom and Rafiqul Gani (Eds.), 12th International Symposium on Process Systems Engineering and 25th European Symposium on Computer Aided Process Engineering.
31 May – 4 June 2015, Copenhagen, Denmark

Optimization and Analysis of Chemical Synthesis Routes for the Production of Biofuels

Douglas Allan, W. Alex Marvin, Srinivas Rangarajan, and Prodromos Daoutidis*

University of Minnesota, 421 Washington Avenue Southeast, Minneapolis 55455, USA
daout001@umn.edu

Abstract

In this work we extend a recently proposed method to concurrently select biofuel blends which satisfy ASTM standards and their optimal synthesis routes by using thermochemistry based post-processing analysis to compare these routes. Gas phase thermochemistry, estimated from group additivity, was used to calculate the equilibrium extent of reaction for each synthesis step. Situations of reaction, phase, and site coupling were subsequently identified to overcome equilibrium limited steps and reduce the number of reaction systems required. This method can aid process designers in screening and ranking large numbers of potential biofuel candidates and synthesis routes simultaneously from an energetic, thermochemical, economic, or kinetic standpoint.

Keywords: Optimization, Reaction network, Biofuels, Thermochemistry, Coupling

1. Introduction

Ethanol is currently the world's most common biofuel, with over 88 billion gallons being produced worldwide in 2013 (Renewable Fuels Association, 2014). However, its miscibility with water, lower heating value, and the high vapor pressures of ethanol-gasoline mixtures are significant drawbacks to its use as a gasoline replacement. Therefore, other oxygenates that can be derived from biomass have been proposed as alternate fuel components, such as 1-butanol and dimethylfuran (Christensen et al., 2011). Furthermore, olefins and alkanes that can be blended with gasoline can also be synthesized from biomass (Bond et al., 2010). To design blend components and their synthesis routes from biomass, Marvin et al. (2013) proposed a method to find the optimal synthesis route of a fuel additive that would be blended with an existing blendstock to create gasoline which satisfies ASTM specifications.

This method combines two chief components: a rule-based reaction network generator, RING (Rangarajan et al., 2012), and a mixed integer linear programming (MILP) problem. The former takes a set of biomass-derived oxygenates identified as possible platform chemicals (Bozel and Petersen, 2010) and uses reaction rules to exhaustively generate a network of reactions and intermediates that upgrade biomass to a plethora of compounds including the desired biofuel blend components. These reaction rules include aldol condensation, to create carbon-carbon bonds, dehydration, to break carbon-oxygen bonds, and (de)hydrogenation to remove oxygen, increase molecule size and saturate or unsaturate bonds as desired. This reaction network, represented by a stoichiometric matrix, is then used in the optimization problem. The optimizer solves the MILP problem subject to blending constraints. The objective function minimized is the total energy loss-the difference in low heating values between reactants and products-which is empirically

linked to the overall process economics. Thermodynamic data was generated for all the intermediate compounds using group contribution methods. A combination of group contribution methods and experimental data was used to ensure the resultant blend satisfied ASTM standards.

In this work we extend the above method by providing metrics and process analysis features to compare and contrast the multiple routes. At the algorithmic level we add post-processing to automatically identify equilibrium-limited reactions. Subsequently, we scan the solutions for possible site, phase, and reaction coupling. These features are applied to the gasoline blend networks generated in Marvin et al. (2013).

2. New Post-processing Features

We start by calculating the equilibrium extent of reaction, X, for each synthesis step in the gas phase, aiming to identify reactions and process conditions with strong equilibrium limitations (i.e. low X). The following expressions are used to this end:

$$exp\left(-\frac{\Delta G_j}{RT}\right) = \prod_i (y_i P)^{\nu_{ij}} \; ; \qquad -\frac{\Delta G_j}{RT} - \sum_i \nu_{ij} \, ln(P) = \sum_i \nu_{ij} \, ln(y_i) \tag{1}$$

$$y_i = \frac{n_i}{\sum_i n_i}; n_i = |\nu_{ij}|X \;\; if \; \nu_{ij} > 0; \; n_i = |\nu_{ij}|(1 - X) \; if \;\; \nu_{ij} < 0 \tag{2}$$

where y_i is the gas phase mole fraction of species i, n_i is the number of moles of species i, ν_{ij} is the stoichiometric coefficient of species i in reaction j, ΔG_j is the Gibbs free energy of reaction j, R is the ideal gas constant, P is the system pressure, and T is the system temperature. Since y_i increases monotonically with X for reactants and decreases monotonically for products, the right hand side in the second equation in (1) increases monotonically with X, and the left hand side must be maximized to maximize X. The only maxima with respect to pressure arise at the lowest or highest pressures in the optimization region, in accordance with Le Chatelier's principle. For temperature, there is the possibility of non-boundary optima. Taking the first two partial derivatives with respect to temperature we get:

$$\frac{\partial}{\partial T}\left(-\frac{\Delta G_j}{RT} - \sum_i \nu_{ij} \, ln(P)\right) = \frac{\Delta H_j}{RT^2} \; ; \quad \frac{\partial}{\partial T}\left(\frac{\Delta H_j}{RT^2}\right) = \frac{1}{RT^2}\frac{\partial \Delta H_j}{\partial T} - \frac{2\Delta H_j}{RT^3} = \frac{\Delta C_{p,j}}{RT^2} \tag{3}$$

where ΔH_j is the enthalpy of reaction j and where $\Delta C_{p,j}$ is the constant pressure heat capacity of reaction. The extrema with respect to temperature, therefore, occur when $\Delta H_j = 0$, and in order for an extremum to be a maximum, $\Delta C_{p,j}$ must be negative. Group contribution methods are used to calculate the heat capacity of each species. In the particular gasoline blend application, the search for maxima was limited to the range of 450-550 K, in order to balance concerns of phase change on the low end and thermal decomposition on the high end. With these restrictions in place, only 0.3% of the reactions in the network and only a single reaction in the top ten synthesis routes, have maxima which do not lie on the boundary of the temperature range. Equilibrium extents of reaction were calculated at 1 bar at 450 K, the optimal temperature, and 550 K using Newton's Method under the assumption of stoichiometric feed. Once the optimal Xs were obtained for each candidate synthesis route, the worst X and the number of reactions with optimal $X < 0.2$ were identified.

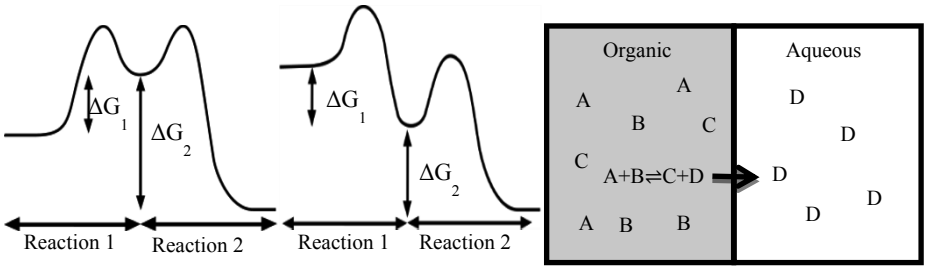

Figure 1. Free energy diagrams demonstrating reaction coupling (left) and site coupling (middle), and a diagram of phase coupling (right).

Many of the reactions can potentially have their *X* enhanced through coupling (Simonetti and Dumesic, 2009) to mitigate equilibrium limitations and to reduce the number of reactors/reaction systems required. Three possibilities arise: (a) reaction coupling wherein a spontaneous reaction consuming the products of an equilibrium-limited reaction can drive the equilibrium forward, (b) phase coupling - differences in hydrophobicity of reactants and products allow for in situ product separation, thereby driving an equilibrium-limited reaction forward or reducing cost of separation, and (c) site coupling whereby two equilibrium-favored reactions are combined in a single process. All of these are illustrated in Figure 1. For site coupling, the intermediate species needs to be consumed mostly or entirely in order to avoid creating a separation challenge. For reaction coupling, the second reaction must be spontaneous enough to increase the overall *X* of the two reactions. As a result, a free energy criterion can be chosen for the second reaction of both types of coupling. For the application here we chose: ΔG_2<-20 kJ/mol. It should be noted that the criterion for reaction coupling identifies potential candidates and the success of the coupling ultimately depends on the kinetics. For phase coupling, octanol-water partition coefficients (log P values), calculated using group contribution methods for all species, were used as a measure of hydrophobicity. Three criteria were used to establish phase coupling: that no two reactants have a difference in log Ps greater than 0.5, that at least two products have a difference of log Ps greater than 1, and that, excluding water, a difference of log Ps greater than 0.5 exists between reactants and products. The first ensures that the reactants do not have tendency to phase separate, the second ensures that the products do, and the third ensures that the coupling assists in separation.All situations which fulfill these criteria are automatically identified and reported in the optimization output, alongside the underlying thermochemistry.

3. Analysis of Gasoline Additives Synthesis Routes

The utility of these post processing steps will be demonstrated by applying them to the same system as in (Marvin et al., 2013). From the optimization results, four synthesis routes are presented here. Figure 2 contains the synthesis routes to create the blends listed in Table 1. These synthesis routes particularly show examples of potential coupling. All of these routes require some external hydrogen source. The two sources of hydrogen identified by the optimization are the decomposition of glycerol or methanol into hydrogen and carbon monoxide. The carbon monoxide is converted into more hydrogen using the water-gas shift reaction. Note that in the second sequence, the ethanol in the final blend comes from the hydrogenation of acetaldehyde. Many of these reactions have been proposed in the literature (see Marvin et al., 2013).

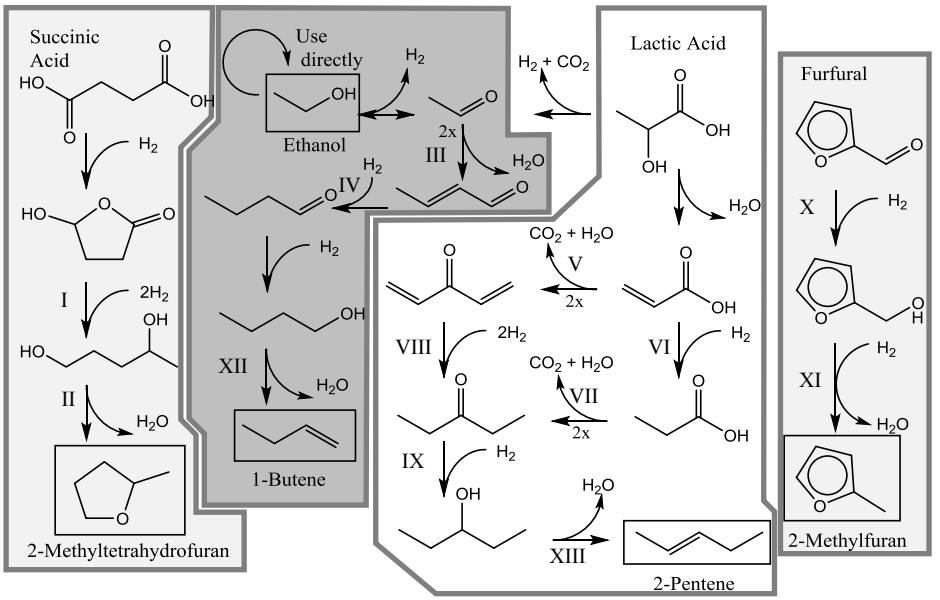

Figure 2. Diagram of the chosen synthesis routes.Note that "2x" denotes a dimerization reaction. Certain reactions are numbered for easy reference in the text.

Reaction I has $X < 10^{-4}$ at both 450 and 550K. It does have a favorable enthalpy of reaction, but this is overbalanced by the loss of entropy from the consumption of two gas phase molecules. This suggests a condensed phase reaction at much lower temperatures and high pressures, but that might not be sufficient to achieve an adequate *X*. Reaction II is equilibrium favored, and could potentially help drive Reaction I if they were conducted together, although reducing temperature and increasing pressure would probably still be required. Reaction II also has optimum *X* at 456 K, and as such is the

Table 1. Reactant and blend fluxes for the four presented blends. The same blendstock used by Marvin et al (2013) is used here.

Synthesis Route:		1	2	3	4
Reactant flux in 10^{-3}mol/min	Ethanol	3.79		1.00	4.01
	Lactic Acid		4.73		
	Succinic Acid				1.23
	Furfural			0.61	
Blend flux in 10^{-3}mol/min	Ethanol	1.05	1.06	1.00	1.08
	1-Butene	1.37	0.65		1.46
	2-Pentene		1.18		
	2-Methylfuran			0.61	
	2-Methyl THF				1.23
	BOB	7.95	7.56	8.22	6.93

only reaction presented here with a non-boundary optimum. The synthesis route from acetaldehyde to 1-butene is important to all but one of the pathways presented here. The aldol condensation of acetaldehyde (Reaction III), however, is equilibrium limited, with $X = 28\%$ at 550K. Its equilibrium cannot be manipulated by changing pressure. However, it has potential for both reaction and phase coupling. 2-Butenal is lipophilic, with a log P equal to 0.76. As a result it will phase separate from the released water, and the equilibrium can be driven forward. Second, the hydrogenation of 2-butenal's carbon-carbon double bond (Reaction IV) is very thermodynamically favorable, and by carrying out these reactions together, the first step's equilibrium can potentially be driven forward. The self-ketonization and hydrogenation of acrylic acid (Reactions V through IX) to make 3-pentanol is a sequence which could benefit from site coupling. As is shown in Figure 2, options exist for the order of the ketonization and hydrogenation. Thermodynamics allow for the site coupling of the self-ketonization of acrylic acid with the subsequent hydrogenation of the carbon-carbon double bonds. However, it is simpler to site-couple the hydrogenation steps together. Finally, the consecutive hydrogenation of furfural into 2-methylfuran is an instance of site coupling identified by both our method and Yan et al (2014). Reactions XII and XIII are spontaneous at both 450K and 550K, but the large difference in log P between reactants and products suggest that they could be carried out at much lower temperatures and without a subsequent extraction step using phase coupling.

From an equilibrium perspective, Route 4 seems to be infeasible. Significant work is needed to achieve an adequate X in Reaction 1, and the other three routes are much more promising. In Routes 1 and 3, the dehydrogenation of ethanol has $X = 18\%$ at 450K, but can be run at 550K for a much better $X = 71\%$. In Route 2, the hydrogenation of 3-pentone has $X = 2\%$ at 550K, but can achieve 22% at 450K and would improve at lower temperatures. Kinetic considerations favor high temperature reactions, but safety considerations favor milder conditions. Routes 2 and 4 contain 13 and 10 reactions, respectively, while Route 1 only contains 5. However, Route 2 synthesizes its own ethanol from lactic acid while Route 1 uses ethanol as a reactant. Route 4 contains

Reaction	ΔG_{rxn} (kJ/mol)	ΔH_{rxn} (kJ/mol)	ΔS_{rxn} (J/(molK))
I	47.8	-47.4	-190.
II	-43.2	-0.67	85.2
III	14.2	7.8	-12.8
IV	-66.2	-125	-119.
V	-60.7	4.4	130.
VI	-74.1	-136.	-125.
VII	-55.0	8.8	127.
VIII	-142.	-268.	-252.
IX	8.2	-56.5	-129.
X	8.2	-54.1	-125.
XI	-102.	-101.	1.7

Table 2 (left) contains ideal gas reaction thermochemistry calculated at 500K for selected reactions. Table 3 (bottom) contains the calculated log P values for selected species.

Species	Log P
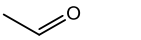	0.21
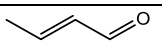	0.76
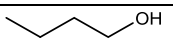	0.78
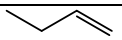	1.58
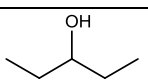	1.17
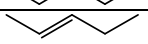	1.97

Route 1 within it, supplementing Route 1's blend with 2-methyltetrahydrofuran. It should be noted that the high number of reactions in Routes 2 and 4 come from parallel, not serial reactions. Not counting hydrogen generation reactions, at most 5 reactions occur in series in Routes 1, 2 and 4, and only two occur in series in Route 3. This analysis has focused on equilibrium properties, but information about reaction kinetics would be necessary to determine what operating temperatures and pressures are feasible.

4. Conclusion and Future Work

Reaction thermochemistry was used to evaluate different synthesis routes for biofuel blends on the basis of equilibrium extent of reaction (*X)* and potential for coupling. The conditions which give optimal *X* for an ideal gas reaction system were derived and the optimal *X* for the reactions present in these synthesis routes were found. Reactions with low *X* were identified, and potential instances of reaction, phase, and site coupling were identified to help compare synthesis routes. Routes 1-3 are all viable based on equilibrium concerns, and they all benefit from moderate amounts of coupling. The final decision between those routes would require a more detailed analysis of kinetics as well as analysis of feedstock costs. The current objective function only takes into account the synthesis route's absolute heat duty, and a more complicated objective function could factor in feedstock cost and equilibrium concerns. Each reaction's thermochemistry and *X* are automatically calculated prior to the optimization, so a complex objective function could easily factor in a term penalizing equilibrium-limited reactions.

5. Acknowledgements

Financial support from the National Science Foundation, CBET award number 1307089, is gratefully acknowledged.

6. References

J. Q. Bond, D. M. Alonso, D. Wang, R. M. West, and J. A. Dumesic, 2010, Integrated Catalytic Conversion of γ-Valerolactone to Liquid Alkenes for Transportation Fuels, Science, 327, 1110−1114.

J. J. Bozel and G. R. Petersen, 2010, Technology Development for the Production of Biobased Products from Biorefinery Carbohydrates—the US Department of Energy's "Top 10" Revisited, Green Chemistry, 12, 539-554.

E. Christensen, J. Yanowitz, M. Ratcliff, and R. L. McCormick, 2011, Renewable Oxygenate Blending Effects on Gasoline Properties, Energy & Fuels, 25, 10, 4723–4733.

K. Yan, G. Wu, T. Lafleur, and C. Jarvis, 2014, Production, Properties and Catalytic Hydrogenation of Furfural to Fuel Additives and Value-added Chemicals, Renewable and Sustainable Energy Reviews, 38, 663–676.

W. A. Marvin, S. Rangarajan, and P. Daoutidis, 2013, Automated Generation and Optimal Selection of Biofuel-Gasoline Blends and Their Synthesis Routes, Energy Fuels, 27, 6, 3585–3594.

S. Rangarajan, A. Bhan, and P. Daoutidis, 2012, Language-oriented Rule-based Reaction Network Generation and Analysis: Description of RING, Computers and Chemical Engineering, 45, 114-123.

Renewable Fuels Association, 2014, Falling Walls and Rising Tides: 2014 Ethanol Industry Outlook, <http://www.ethanolrfa.org/page/-/rfa-association-site/Resource%20Center/2014%20Ethanol%20Industry%20Outlook.pdf> accessed 8/1/2014.

D. A. Simonetti and J. A. Dumesic, 2009, Catalytic Production of Liquid Fuels from Biomass-Derived Oxygenated Hydrocarbons: Catalytic Coupling at Multiple Length Scales, Catalysis Reviews, 51, 3, 441–484.

Krist V. Gernaey, Jakob K. Huusom and Rafiqul Gani (Eds.), 12th International Symposium on Process Systems Engineering and 25th European Symposium on Computer Aided Process Engineering.
31 May – 4 June 2015, Copenhagen, Denmark

Design and Economic Evaluation of Coal to Synthetic Natural Gas (SNG) Process

Bor-Yih Yu and I-Lung Chien

[a] *Department of Chemical Engineering National Taiwan University Taipei 10617, Taiwan*

Abstract

In this work, the steady state design and the economic evaluation for coal to Synthetic Natural Gas (SNG) process are rigorously studied. For those countries which lack energy resources, importing natural gas is very costly due to the requirement of liquefaction and compression. SNG holds very similar composition and heat value to typical natural gas, and can be used as a replacement directly in industrial and home usages. Thus, producing SNG from gasification route will be an attractive alternate for those countries which lack energy sources. From the simulation results, the plant-wide energy conversion efficiency is about 60.38%, and the SNG production cost is 11.433 (USD/MMBTU).

Keywords: Coal; Synthetic Natural Gas (SNG); Process Simulation; Economical Evaluation

1. Introduction

Natural gas has long been considered as a cleaner energy source all over the world, due to its lower C/H ratio. In Taiwan, there are several natural gas power plants that provide electricity to local industries, with over 1300 MWe generated each year. The largest natural gas power plant is in Datan, Taoyuan, which has six NGCC cycles and produces about 438 MWe, to support the electricity needed in northern Taiwan. Thus, natural gas utilization is important in our country.

However, over 99% of annually energy source depends on importation in Taiwan. For Natural gas, it is imported in form of Liquefied Natural Gas (LNG), and the requirement of liquefying and pressurizing makes the importation price expensive (ranged from 15~18 USD/MMTU). Compared with LNG, coal has good advantages of lower price, great abundance, and easier transportation. These advantages lead to the fact that coal is the major energy source used annually in Taiwan. Thus, the route that converts coal into SNG is expected to have both practical and economical advantages. SNG is a product with similar composition as natural gas, which can be used as a replacement of natural gas directly.

In this work, the design and the economical evaluation of a plant-wide coal to SNG process are illustrated. The conversion process starts from gasification to form syngas, and the syngas is then passes through the treating section, including Water-Gas-Shift Reaction (WGSR), Acid Gas Removal (AGR), and finally methanation section to form SNG. The possible heat integration strategy and waste heat recovery in/between different parts are also proposed to produce electricity for using inside the coal to SNG plant. After designing, the plant-wide economical evaluation is studied based on the proposed economic model. The SNG production cost is calculated and compared with the importation price of LNG in Taiwan.

Although the concept of gasification-based process has been proposed earlier, the overall detailed analysis of the plant-wide process with rigorous modeling for each part inside the process is rarely found. The primary aim of this work by the authors is to provide a baseline analysis for coal to SNG process for Taiwan, and any other country holds similar situation as Taiwan. Due to the recent decrease of oil price, there might be other alternative ways to generate syngas for producing SNG. The authors are welcome possible improvement and suggestions for further design of the plant.

2. Design of Coal to SNG Process

The overall block flow diagram for Coal to SNG process is illustrated in Figure 1. The plant-wide process is describing in detail separately in the following subsections. In this work, Aspen Plus V7.3 is used for simulation. The reactions included in the system are listed in Table 1, while the coal properties are listed in Table 2. The detailed information for the process is illustrated in the work by Yu and Chien (2015).

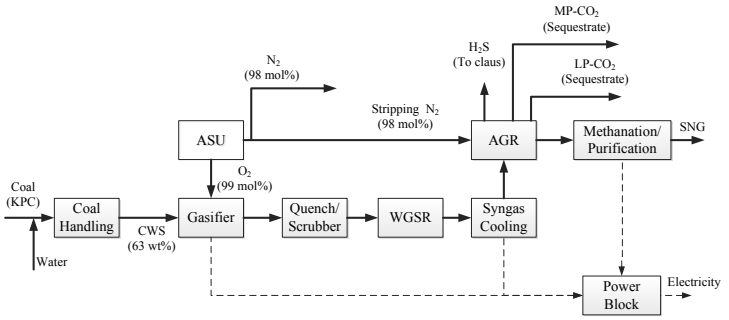

Figure 1. Overall block flow diagram of coal to SNG process.

2.1 Coal Handling

In coal handling section, the coal is uploaded from the silo, dried, crushed, screened, and then transported to plant. In this SNG plant, the gasification system is operated by a slurry-feed, entrained flow gasifier. Thus, a step for slurry preparation is necessary. The processed coal sample in this work is Kaltim-Prima coal (KPC) from Indonesia, which actually imported in Taiwan annually.

2.2. Air Separation Unit and Gasification

Cryogenic separation is used to produce large quantities of pure oxygen and nitrogen. The whole process can be divided into four blocks, including Main Air Compressor (MAC), further compression, Main Heat Exchanger (MHE), and rectifying section. The purity of the oxygen product is assumed to be 99 mol%, so that the amount of inert compounds sent into gasifier could be decreased to let the heat value of final SNG product meet regulation. For nitrogen product, it can be used in recovering the physical solvent in AGR, as well as in ammonia plant downstream. The purity of nitrogen product is set as 98 mol%, with the remainder to be 0.93% Ar and 1.07% O_2.

For gasification system, an industrial scale, slurry-feed, entrained flow, oxygen blown gasifier is used to convert coal into syngas. It is simulated by a simplified 1-dimensional kinetic gasifier model proposed by Yu and Chien (2015). The processed coal flow rate is 240 (ton/hr), with two gasifier trains operate in parallel. The residence time inside

gasifier is assume to be 3 seconds, the operating pressure is 56.7 (bar). The coal particle is assumed to be homogeneously spherical, with 80 (μm) diameter.

Table 1. Reactions included in the plant-wide coal to SNG process.

	Reactions	References
	Homogeneous Reactions	
Gasification Section	$CO + H_2O \leftrightarrow H_2 + CO_2$ (In gasifier)	Kumar and Ghoniem (2012)
	$CO + H_2O \leftrightarrow H_2 + CO_2$ (In RSC)	Karan et al. (1999)
	$COS + H_2O \leftrightarrow H_2S + H_2O$	Svoronous and Bruno (2002)
	$C_{18}O_{20} + 9\ O_2 \rightarrow 18CO + 10\ H_2$	Westbrook and Dryer (1981)
	$CO + 0.5\ O_2 \rightarrow CO_2$	Kumar and Ghoniem (2012)
	$H_2 + 0.5\ O_2 \rightarrow H_2O$	Kumar and Ghoniem (2012)
	$CO + 3H_2 \leftrightarrow CH_4 + H_2O$	Watanabe and Otaka (2006)
	Heterogeneous Reactions	
	$C + 0.5O_2 \rightarrow CO$	Wu et al. (2010)
	$C + H_2O \rightarrow CO + H_2$	Wu et al. (2010)
	$C + CO_2 \rightarrow 2CO$	Wu et al. (2010)
	$C + 2H_2 \rightarrow CH_4$	Wu et al. (2010)
SWGSR Section	$COS + H_2O \rightarrow H_2S + CO_2$	Svoronous and Bruno (2002)
	$CO + H_2O \leftrightarrow CO_2 + H_2O$	Lund (1996)
Methanation Section	$CO + 3H_2 \leftrightarrow CH_4 + H_2O$	HTR: Xu and Froment (1989)
	$CO_2 + 3H_2 \leftrightarrow CH_4 + 2H_2O$	LTR: Kopyscinski et. al (2010)
	$CO + H_2O \leftrightarrow CO_2 + H_2S$	

Table 2. Proximate and Ultimate analysis of Kaltim Prima Coal (KPC),

Proximate Analysis (wet basis, wt%)				**Ultimate Analysis (daf basis, wt%)**					**HHV (dry basis)**
Moist	FC	VM	Ash	C	H	N	S	O	MJ/Kg
10.50	51.58	43.16	5.26	80.00	5.50	1.60	0.70	12.20	31.231

At gasifier outlet, a Radiant Syngas Cooler (RSC) is used to cool the syngas. High temperature syngas is slowly cooled by heat exchange with cooling medium, thus an amount of heat could be recovered as medium (or high) pressure steam. Due to the low cooling rate for radiant quench, some reversible reactions, mainly WGSR, is expected to continue even if the raw syngas has already left gasifier. The raw syngas is cooled to 866 K in RSC as suggested by Tampa Electric Company (2002).

After RSC, a water quench unit is used to cool the syngas to its dew point. The outlet temperature of syngas after water quench is 472 K. The low temperature quench water is having direct contact to syngas, which makes it cool quickly without any remaining reactions. After the water quench, a scrubber is used to wash out the solvable components in raw syngas.

2.3 Syngas Treating Section: WGSR, Syngas Cooling, AGR, and methanation

In this work, the H_2/CO ratio is adjusted to 3.5 by WGSR to enhance the reaction rate of methanation stage. Besides, the sulfur content in coal is appeared in the form of carbonyl sulfide (COS) in syngas, it will also be hydrolyzed to hydrogen sulfide (H_2S)

in WGSR stage. The reaction catalyst for COS hydrolysis is aluminum-based, while the catalyst for WGSR is Mo/Al_2O_3, which will not deactivate under the presence of sulfur.

Because WGSR is exothermic and the reactor is operated in adiabatic mode, the reacted syngas should be further cooled to the operating temperature in AGR. The cooling step is separated into three stages, and part of the waste heat could be recovered by generating different levels of steam. Process condensate contains water and other soluble contaminants that removed from the syngas, which need to be further treated before disposed or recycled.

In Acid Gas Removal (AGR) process, H_2S and CO_2 are captured in two stages. The captured H_2S could be sent into Claus process for sulfur recovery, which is not considered in this work, while CO_2 is assumed to be compressed and sequestrated. In this work, SELEXOL process is used for AGR, in which a mixture of diethylene glycol is used as the solvent. For simulation, PC-SAFT is chosen as the thermodynamic model, with the binary interaction parameter cited from literature, and the aspen built-in DEPG component is used to represent the solvent (Field and Braisington, 2011). The capturing targets are assumed to be 99.7% for H_2S and 92% for CO_2.

The operation of AGR process is complex, with many operating variables to be determined. Thus, in order to simplify the problem, several assumptions are made. First, the temperature of DEPG solvent is assumed to be 283 K. Second, the pressure for the H_2S absorber is set at 5.17 MPa, while 3.03 MPa for CO_2 absorber. Third, the pressure level of the regenerative flash units is assumed to be 1.9/0.9/0.15 (MPa). Finally, because the boiling point of DEPG solvent is very high, the thermal regeneration is expected to operate at a vacuumed pressure (0.02 MPa).

In optimization works, three design variables are selected to study, including the total stage of H_2S absorber (NT_{H2S}), total stage of CO_2 absorber (NT_{CO2}), and the pressure of the concentrator (P_{CONC}). The objective function for AGR is minimized total annual cost. Based on the above assumptions, the optimized opeating condition will be at NT_{H2S} equals to 60, NT_{CO2} equals to 14, and P_{CONC} at 2.21MPa.

In methanation reaction section, a configuration with four adiabatic reactors in series and inter-stage cooling is arranged to react the treated syngas from AGR to form SNG. The possible reactions and the references for kinetic data are also listed in Table 1. The overall process could be roughly divided into two stages, High Temperature Reaction (HTR) stage and Low Temperature Reaction (LTR) stage. This is because methanation reactions are exothermic, thus the reaction equilibrium is favored to the product side at lower temperature.

After the two-staged methanation reaction, the produced gas still contains some CO_2 and H_2O, thus another separation step is required. In this work, molecular sieve is used to separate 99% of remaining CO_2 and all water inside the SNG product as suggested by DOE/NETL (2011). The treated SNG is then compressed to the pipeline pressure, and cooled to required temperature. The molar composition of final SNG product is 95.5% CH_4, 4.2% for combination of N_2 and Ar, while CO is only 7 ppm. The high heat value of SNG product is 36.06 (MJ/m^3), which matches the regulation.

2.4 Power Block

The waste heat inside the system is recovered by generating different level of steam through a Heat Recovery Steam Generator (HRSG). Most of the generated is used to

drive steam turbine for producing electricity, while the remainder of them could be used in the SNG plant. Apart from the SNG product, the net electricity produced (29.15 MW) is viewed as the bonus from the plant-wide process.

2.5 Summary

The overall energy conversion efficiency for this SNG plant is at 60.39%; for energy that transferred from coal to SNG, it is at 58.66%.

3. Economic Evaluation

In According to open literature (Chen, 2005; DOE/NETL, 2011), the items to be studied include capital investment (CAPIN), fixed operating and maintenance cost (Fixed O&M cost), and variable operating and maintenance cost (Variable O&M cost). Each part is explained in detail separately.

In this study, for CAPIN calculation, the cost parameters and terminology used are based on the methodology developed from Electric Power Research Institute (EPRI). The input parameters, the calculation stage, and the items for calculating capital expense for coal to SNG plant include direct and indirect construction costs, general facility cost, engineering & home office fees, project and process contingency costs, royalty fees and start-up costs.

For calculating Fixed O&M, The items studied in this part are operating labor cost, maintenance cost, taxes and insurances, and administrative and support cost. For Variable O&M, the items studied are fuel price, maintenance material cost, consumable cost, and also the profit of by-products. Here in this work, the coal price sold by Tai-power company in Taiwan is used. The primary by-products are sulfur and electricity for this SNG plant. However, KPC is coal sample with very low-sulfur content, thus the credits for selling sulfur is omitted in this work. The consumables included the cost for WGSR catalyst, methanation reaction catalyst, and DEPG solvent that used in AGR.

In this work, a simpler financial structure is assumed that only inflation rate and capital depreciation are accounted. It is assumed that the operation target is that the payback period for capital investment is 20 years, with 3.5% inflation rate during the operation period. All the capital investment will be linearly depreciated in 20 years. According to Gibsin Engineers, Ltd (GIBSIN), a Taiwan-U.S. joint venture consulting company, these assumptions will be corresponded to the investment regulation for public enterprises in Taiwan.

The results for CAPIN, fixed O&M and variable O&M are listed in Table 3. The detailed information for the economics is also illustrated in the work by Yu and Chien (2015).The production cost is calculated in US dollar per unit heat value of SNG, thus the overall energy conversion efficiency will also influence the results of economical evaluation. Here in this work, the calculated SNG production cost is at 11.433 (USD/MMBTU), which is much less than the LNG import price in Taiwan (15~18 USD/MMBTU). If this SNG plant could be co-operated with other country that has large amount of coal reserves, the SNG production cost will become even lower. It seems to be economically attractive for Taiwan in the foreseeable future.

Table 3. Energy and Economic calculation results

Economic Calculation Result		**Energy Calculation Result** (unit: MW)	
CAPIN	3.871	Energy input (Coal)	1690.45
Fixed O&M	1.276	Energy Output(SNG)	991.63
Variable O&M	6.286	Energy Output (Electricity)	29.15
Total Cost	11.433	Overall Energy Conversion	60.38(%)
(Unit:USD/MMBTU)		Coal to SNG Energy Conversion	**58.66(%)**

4. Conclusions

In this work, the plant-wide Coal to SNG process is rigorously studied. Coal is first converted to syngas through gasification, adjusted composition by WGSR, cleaned though AGR process, and reacted to form SNG through methanation reaction. A waste heat recovery system is also studied to produce different levels of steam, and then it is used in the SNG plant or to generate electricity for auxiliary use. From economical evaluation, the cost to produce SNG is at 11.433 (USD/MMBTU), which is much lower than the price to import LNG in Taiwan. Thus, to establish a SNG plant will have practically and economically advantages in the near future.

References

C. A. Chen, 2000, Techmocal and Economic Assessment of CO2 capture Technology for IGCC Power Plants, Ph.D. Thesis, Carnegie Mellon University.

DOE/NETL, 2011. Cost and Performance Baseline for Fossil Energy Plants, Volume 2: Coal to Synthetic Natural Gas and Ammonia.

R. P. Field, R. Brasington, 2011, Baseline Flowsheet Model for IGCC with Carbon Capture. *Ind. Eng. Chem. Res.* 50, 11306-11312.

D. Jones, D. Bhattacharyya, R. Turton, S. Zitney, 2011, Optimal Design and Integration of an Air Separation Unit (ASU) for an Integrated Gasification Combined Cycle (IGCC) Power Plant with CO2 Capture, *Fuel Processing Technology*, 92, 1685-1695.

J. Kopyscinski, T. J. Schildhauer, S. M. A Biollaz, 2011, A. Fluidized-Bed Metahnation: Interaction between Kinetics and Mass Thansfer, *Ind. Eng. Chem. Res*, 50, 2781-2790.

M. Kumar, A. F. Ghoniem, 2012, Multiphysics Simulations of Entrained Flow Gasification. Part two: Constructing and validating the overall model, *Energy Fuels*, 26, 464-479.

K. Karan, A. K. Mehrota, L. A. Behie, 1999, A high-temperature experimental and modeling study pf homogeneous gas-phase COS reactions applied to Claus Plants, *Chem. Eng. Sci*., 54, 2999-3006.

C. R. F. Lund, 1996, Microkinetics of Water-Gas Shift over Sulfided Mo/Al_2O_3 Catalysts , Ind. Eng. Chem. Res, 35, 2531-2538.

P. D. N. Svoronos, T. J. Bruno, 2002, Carbonyl Sulfide: A Review of Its Chemistry and Properties *, Ind. Eng. Chem. Res*., 41, 5321-5337.

Tampa Electric Polk Power Station Integrated Gasification Combined Cycle Project, Final Technical Report, 2002, Tampa Electric Company, Tampa, FL

H. Watanabe, M. Okata, 2006, Numerical simulation of coal gasification in entrained flow coal gasifier, *Fuel*, 85, 1935-1943.

C. K. Westbrook, F. L. Dryer, 1981, Simplified Reaction Mechanism for the Oxidation of Hydrocarbon Fuels in Flames, *Combustion Science and Technology*, 27, 31-43.

Y. Wu, J. Zhang, P. J. Smith, H. Zhang, C. Reid, J. Lv, G. Yue, 2010, Three-dimantional Simulation for an Entrained Flow Coal Slurry Gasifier, *Energy & Fuels*, 24, 1156-1163.

J. Xu, G. F. Froment, 1989, Methane Steam Reformimg, Methanation and Water-Gas Shift: I. Intrinsic Kinstics, *AICHE J.*, 35, 88-96.

B. Y. Yu, I. L. Chien, 2015, Design and Economic Evaluation of Coal to Synthetic Natural Gas (SNG) Process, *Ind. Eng. Chem. Res.* (Submitted)

Krist V. Gernaey, Jakob K. Huusom and Rafiqul Gani (Eds.), 12th International Symposium on Process Systems Engineering and 25th European Symposium on Computer Aided Process Engineering.
31 May – 4 June 2015, Copenhagen, Denmark

Water networks synthesis for industrial parks involving inter-plant allocation

Lin-lin Liu[a,b], Jian Wang[a], Jian-ping Li[a], Jian Du[a]*, Feng-lin Yang[b]

[a] *Institute of Chemical Process Systems Engineering, School of Chemical Engineering, Dalian University of Technology, Dalian, 116024, China*
[b] *Key Laboratory of Industrial Ecology and Environmental Engineering (MOE), School of Environmental Science and Technology, Dalian University of Technology, Dalian, 116024, China*

Abstract

An industrial park is a cluster of multiple company individuals, so there is requirement to develop specific reuse strategies to improve the utilization of resources across plants. Differing from the direct reuse strategy of 'unit-based' mode which is originally proposed for intra-plant water integration, this article presents a 'plant-based' mode for water allocation within industrial parks. Wherein, mixers and splitters are involved to present the mixing, transmission and splitting operations for reusing streams across plants. Such that, the mixing possibilities can also be investigated and many redundant solutions can be avoided by considering the number limit of inter-plant stream connections at the building stage of network superstructures. On base of this mode, both direct and direct-indirect-mixed integration problems are studied in this study. Superstructures are established and mathematically formulated aiming to the minimum fresh water consumption. At last, an example from literature is illustrated. With the obtained results, the effectiveness of the approach has been successfully demonstrated.
Keywords: inter-plant, allocation, water network, industrial park, superstructure

1. Main Text

Nowadays, the shortage and pollution of water have become serious barriers to the development of human society. As a promising way of planning individual plants, industrial parks can provide more opportunities for resources saving and sharing, as well as the centralized treatment of waste. So exploring the reusing possibility in industrial parks, especially investigating the allocation, using and regeneration by breaking process or plant boundary limits would be very meaningful for the global saving and pollution reduction of water in process industries.

Olesen and Polley (1996) carried out the earliest water integration study for inter-plant problem in 1996. However, an extensive discussion about this issue was mainly concentrated in last seven years. Wherein, Lovely et al. (2007) proposed an optimization approach so as to reduce the water consumption and discharge in pulp and paper plants. Later, source-interception-sink representation was used by Castro et al (2012) to retrofit existing networks for eco-industrial parks. Chew and his co-workers have conducted a series of works about inter-plant water integration, including the proposing of direct and indirect integration schemes (Chew et al. 2008), an automated targeting technique based on pinch technology (Chew and Foo, 2009), and the application of game theory (Chew et al. 2009). In order to improve the practicability of system, Chen et al. (2010) presented a mathematical model for integration by placing central and decentralized water mains within and between individual plants. Boxi et al.

(2012) studied a multi-objective optimization problem, in which the fresh water, regenerated water as well as the connection number were minimized. Then in the recent reports, the flexibility and multi-period water planning problem of industrial parks have been discussed by Montastruc et al. (2013), Bishnu et al. (2014) and Avios (2014).

In mentioned works, the 'unit-based' mode would generate many redundant solutions when having connections limits for streams. To avoid this defect and also to consider the allocation of water from plant but unit, a so called 'plant-based' mode is proposed in this study. Based on this mode, the direct integration and the mixed integration, which is studied as the combination of direct and indirect integrations in this work, are both developed for synthesis.

2. Problem Statement

Aim of the work is to make an optimal management of water, respecting to the overall consideration of process requirement of each plant in an industrial park. In this study, the water network synthesis task is illustrated via an industrial park example from Olesen and Polley (1996) and Chew et al. (2008). Table 1 has shown the flow rate and concentration limits of 15 water sources and 15 sinks in example. These sources and sinks, being distributed into three individual companies (A, B and C) as indicated, will be schemed to constitute the intra-plant networks as well as the inter-plant portion. Synthesis purpose is to achieve an optimal network for the park, where all water sources are well managed to satisfy the requirement of sinks. Within the numerous alternatives, the selected network should feature the minimum fresh water consumption and the lowest inter-plant delivery amount of water.

Table 1. Limit data of example

water network	sink SK_j	flowrate F_{SK} ($t \cdot h^{-1}$)	concentration C_{SK} (ppm)	source SR_i	flowrate F_{SR} ($t \cdot h^{-1}$)	concentration C_{SR} (ppm)
A	1	20.00	0	1	20.00	100
	2	66.67	50	2	66.67	80
	3	100.00	50	3	100.00	100
	4	41.67	80	4	41.67	800
	5	10.00	400	5	10.00	800
B	6	20.00	0	6	20.00	100
	7	66.67	50	7	66.67	80
	8	15.63	80	8	15.63	400
	9	42.86	100	9	42.86	800
	10	6.67	400	10	6.67	1000
C	11	20.00	0	11	20.00	100
	12	80.00	25	12	80.00	50
	13	50.00	25	13	50.00	125
	14	40.00	50	14	40.00	800
	15	300.00	100	15	300.00	150

3. Method

3.1. Proposing of plant-based mode

Resource sharing is one of the most important characters of industrial parks. To promote sharing, the distribution of materials between companies should be studied. In previous works, the 'unit-based' mode was always directly applied to manage the inter-

plant water, through building direct connection from a source unit to a sink unit as Figure 1-(a) shows. However, this will on one hand limit the participation of sources because there usually has number constraint toward the stream connections between plants. And on another hand, will generate many infeasible solutions because of the excess inter-plant connections during synthesis. To avoid above defects, a so called 'plant-based' mode is proposed in this study.

A basic structure of 'plant-based' mode is presented in the schematic diagram of Figure 1-(b), in which the sources of a same plant are intensively delivered to another plant and distributed to sinks as shown. Such that the allocation/reuse of water between plants is no longer directly dependent on the outlet streams of sources but that of plants. In another words, the monitoring on each source is moved to the outlet of each plant. This change of allocation/reuse will produce more possibilities for crossing-plant streams especially when their number is strictly limited. Jump out of Figure 1-(b), it's worth noting that the mixing and splitting points of each plant can be multiple if allowed. In this study, the proposed 'plant-based' mode is applied to construct networks for the optimal synthesis.

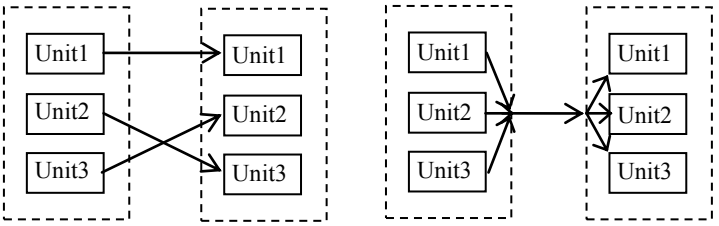

(a) Unit-based mode (b) Plant-based mode

Figure 1. Sketch of inter-plant allocation modes

3.2. Direct and mixed integration superstructures

Define direct integration of reuse are only carried out via cross-plant pipelines, while the indirect kind must go through a centralized regeneration unit. In this article, direct integration and the mixed integration which combines direct and indirect allocation together are both studied to design the water networks within industrial parks.

On basis of 'plant-based' mode, the superstructures presenting cross-plant allocation for direct and mixed water integration are displayed in Figure 2-(a) and (b), respectively, wherein the allocation superstructures for plants are not detailed because they follow a general allocation pathway of 'unit-based mode'. In 'plant-based' mode, cross-plant steams are intensively collected and distributed through mixers and splitters. This way, the in and out steams of plants are able to be used to define superstructure schemes when considering connection complexity. Two typical scenarios are both provided in Figure 2-(a) and (b). For direct integration, 'one in-one out' scenario means one collected stream at most will run out of a plant, then after the inter-plant allocation, one collected stream at most will enter a plant. To investigate more in and out alternatives, the bottom half of Figure 2-(a) has given a scenario having multiple inlets and outlets for a plant. Regeneration operation (indicated with R) is considered in mixed water integration in this study. Add R into Figure 2-(a), then the two scenarios of mixed integration superstructures are presented as Figure 2-(b) shows. Through analysis, two major features of the proposed superstructures can be condensed into:

(1) the number constraint of inter-plant stream has been considered at the building of network superstructure, so there will not generate many redundant solutions.
(2) by adjusting the numbers of mixing and splitting operations, the superstructures in this paper are able to cover the all 'unit based' connection possibilities.

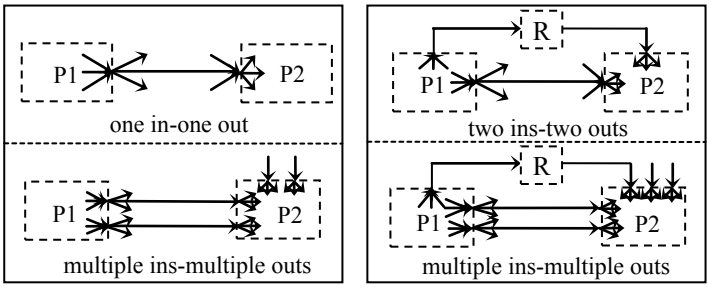

(a) Direct integration (b) Mixed integration

Figure 2. Sketch of direct and mixed integration

3.3. Synthesis and optimization

Alternatives consisted in network topologies of Figure 2 should be investigated and contrastively analyzed in order to do an appropriate decision-making for planning. To carry out this work, mixed integer non-liner programming mathematical models are formulated respecting to the superstructures of different design scenarios. The optimization process is carried out in two steps, where the fresh water consumption is obtained at first and the inter-plant water flow rate is minimized on its basis then. The inter-plant connections between plant and plant, as well as between regeneration unit and plant, should comply with the number constrain. The final results should tell the network details, including concentrations, flow rates, inter-plant stream number, network structure, fresh water consumption, as well as the collection and redistribution of water among individual plants.

4. Problem Solutions

The optimization problem mentioned in Section 2 was solved by means of CPLEX GAMS. In which, the 'one in-one-out' superstructure of direct integration and 'two in-two out' superstructure of mixed integration are both implemented and coded for synthesis. To get rational results from the consideration of actual practice of transportation, set lower boundaries to cross-plant flow rate and intra-plant flow rate as 5 and 0.5 $t \cdot h^{-1}$, respectively.

Apply the two-steps optimization procedure to minimize fresh water consumption and inter-plant water flow rate orderly, then the direct integration results are obtained and summarized in Table 2. At a same inter-plant connection number it can be noted that, the minimum fresh water requirements received in this study are all no larger than that in literature, and the total inter-plant water flow rates follow about the identical relation if the fresh water consumptions are close (as the cases of connection number=2 and 4 indicate). These results can demonstrate the ability of centralized operations (mixing and splitting) on providing more stream options for their reusing into other plants. Figure 3 showing is the network structure of connection number=3 in this study.

Table 2. Results comparisons

content	literature (Chew et al. 2008).			this paper		
minimum fresh water /t·h^{-1}	316.3	316.4	314.4	316.3	314.4	314.4
minimum inter-plant water /t·h^{-1}	61.2	78.5	97.0	61.7	87.8	74.1
inter-plant connections	2	3	4	2	3	4

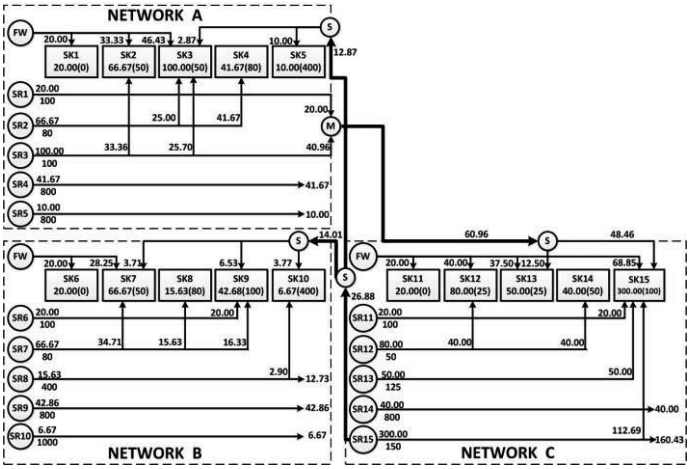

Figure 3. The optimal water network for direct integration

Figure 4. presenting is the optimal network of mixed integration at regeneration rate of 0.5, unit cost of 1.160 $ for per kg removed impurities (Chew et al. 2008). This network features of 138.5 t·h^{-1} fresh water consumption and 557.5 t·h^{-1} inter-plant water. This mixed integration has considered the possibilities of direct reuse, however none exists between any two plants in Figure 4. Observe Figure 3 and Figure 4, then one common feature can be found that: the two networks both have mixers (presented by M) and splitters (presented by S) involved rather than having only direct unit-to-unit inter-plant connections. Thus results can show the necessity of considering mixers and splitters, and also demonstrate the reasonability of the 'plant-based' method.

5. Conclusions

A 'plant-based' mode has been developed for inter-plant water allocation of industrial parks in this work. By involving mixers and splitters, this mode is able to include more inter-plant reuse possibilities and also reduce redundant solutions at the building stage of network superstructures. On its basis, both direct and mixed integration were studied for synthesis, wherein the network superstructures of several scenarios have been presented. Finally for verification, an example adopted from literature was solved for illustration, and the results indicated that the involving of mixing and splitting operations would generate a better solution.

Acknowledgements

The authors gratefully acknowledge the financial support from the Fundamental Research Funds for the Central Universities of China (DUT14RC(3)046). Funding from China Postdoctoral Science Foundation (2014M551091) and Natural Science

Foundation of China (No. 21406026) are deeply appreciated.

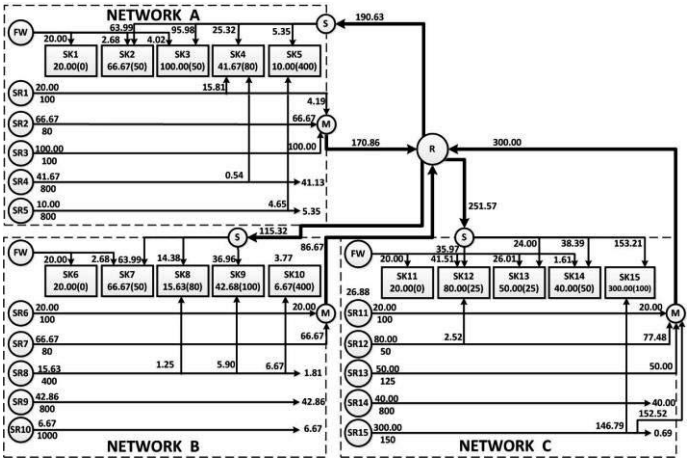

Figure 4. The optimal water network for mixed integration

References

C. L. Chen, S. W. Hung, J. Y Lee, 2010, Design of inter-plant water network with central and decentralized water mains. Computers & Chemical Engineering, 2010, 34, 1522−1531.

E. C. Castro, J. M. P. Ortega, M. S. Gonzalez, M. M. El-Halwagi, 2012, Optimal reconfiguration of multi-plant water networks into an eco-industrial park. Computers & Chemical Engineering, 44, 58−83.

E. M. Lovelady, M. M. El-Halwagi, G. A Krishnagopalan, 2007, An integrated approach to the optimization of water usage and discharge in pulp and paper plants, International Journal of Environment and Pollution, 2007, 29, 274−307.

I. M. L. Chew, D. C. Y. Foo, 2009, Automated targeting for inter-plant water integration, Chemical Engineering Journal, 153, 23-36.

I. M. L. Chew, R. R. Tan, D. K. S. Ng, D. C. Y. Foo, A. S. F. Chiu, 2009, Game theory approach to the analysis of inter-plant water integration in an eco-industrial park, Journal of Cleaner Production,17,1611–1619.

I. M. L. Chew, R. R. Tan, D. K. S. Ng, D. C. Y. Foo, T. Majozi, J. Gouws, 2008, Synthesis of direct and indirect interplant water network, Industrial & Engineering Chemistry Research, 47, 23, 9485–9496.

K. B. Aviso, 2014, Design of robust water exchange networks for eco-industrial symbiosis, Process Safety and Environmental Protection, 92, 2, 160-170.

L. Montastruc, M. Boix, L. Pibouleau, C. A. Pantel, S. Domenech, 2013, On the flexibility of an eco-industrial park (EIP) for managing industrial water, Journal of Cleaner Production, 43,1−11.

M. Boix, L. Montastruc, L. Pibouleau, C. A. Pantel, S. Domenech, 2012, Industrial water management by multiobjective optimization: From individual to collective solution through eco-industrial parks, Journal of Cleaner Production, 22,85−97.

S. G. Olesen, G. T. Polley,1996, Dealing with plant geography and piping constraints in water network design. Transactionsof the Institute of Chemical Engineering, Part B, 74, 4, 273–276.

S. K. Bishnu, P. Linke, S. Y. Alnouri, M. El-Halwagi, 2014, Multiperiod Planning of Optimal Industrial City Direct Water Reuse Networks, Industrial & Engineering Chemistry Research, 53, 21, 8844-8865.

Krist V. Gernaey, Jakob K. Huusom and Rafiqul Gani (Eds.), 12th International Symposium on Process Systems Engineering and 25th European Symposium on Computer Aided Process Engineering.
31 May – 4 June 2015, Copenhagen, Denmark

Energy-saving design and control of a hybrid extraction/distillation system for the separation of pyridine and water

Yi-Chun Chen, [a] I-Lung Chien[a*]

[a]*Department of Chemical Engineering, National Taiwan University, Taipei 10617, Taiwan*
ilungchien@ntu.edu.tw

Abstract

In this study, design and control of a hybrid extraction/distillation system for the separation of pyridine and water are studied. The same separation has been studied in the previous paper (Wu et al, 2009) by using the design of a heterogeneous azeotropic distillation system where a two-column heterogeneous azeotropic column system was devised making use of the new minimum-boiling azeotrope between toluene and water. A further intensified dividing-wall column was recently proposed by Wu et al. (2014) to thermally-couple the two columns for further reduction of the overall reboiler duty.

In the hybrid extraction/distillation design, pyridine is extracted from aqueous solution by using N-propyl formate as a solvent in an extraction column. Combining two strippers with the extraction column, a simple hybrid extraction/distillation process can be devised achieving the same product purity specifications as the original design. By comparing the optimized design of this newly proposed system with the previously mentioned heterogeneous azeotropic design, significant reductions of 58.8 % in the total annual cost and 65.6 % in the steam cost can be obtained. Furthermore, in comparison with the complex design of dividing-wall column system, this proposed hybrid extraction/distillation system can still significantly save total annual cost and steam cost by 41.2 % and 50.8 %, respectively.

The plant-wide control of the proposed system is also studied. Overall control strategy with tray temperature control loops are proposed for the plant-wide control structure. The dynamics results show a trade-off between economical design and controllability due to selecting of an optimal solvent flow rate at low constraint in the design stage. However, the case with 20% more solvent (which results in 6.15 % more total annual cost than the optimized case) is capable of holding product qualities under various feed disturbances by a proposed plant-wide control structure.

Keywords: hybrid extraction/distillation system, plant-wide control, separation

1. Introduction

The use of hybrid extraction/distillation system is a very promising process design, allowing significant energy reduction for the separation of azeotropic mixtures without a reboiler. In this study, a pyridine and water separation system that was studied by Wu and Chien (2009) will be used as a demonstrating example to investigate the energy-saving potential of the hybrid extraction/distillation system.

In Wu and Chien (2009), a two-column heterogeneous azeotropic column system was devised making use of the new minimum-boiling azeotrope between toluene and water. However, from residue curve maps and material balance lines of this system, potential economical pitfall of this heterogeneous azeotropic distillation processes can be predicted due to large recirculation rate inside the system. In Wu et al. (2014), a dividing-wall column design for the same separation system was proposed to thermally-couple the two columns for further reduction of the overall reboiler duty. Nevertheless, the design flowsheet and the control structure are more complex and more interactive than the conventional column system. In this study, a conventional design of hybrid extraction/distillation system is proposed. Moreover, economical analysis and energy consumption of the proposed design are compared with that of the previous mentioned heterogeneous distillation design and the dividing-wall column design.

Besides the issue on energy-saving, dynamics controllability of the hybrid extraction/distillation system will also be closely examined. Certain amount of solvent is necessary for the extraction process. Less solvent leads to less total annual cost (TAC), but reduce the controllability of the system. Thus, a trade-off between economical design and controllability is observed for this studied system.

2. Conceptual Design and Simulation Details

The hybrid extraction/distillation system includes a liquid-liquid extraction column following by two strippers, as shown in Figure 1. Liquid-liquid extraction, which is also known as solvent extraction, is a method to separate compounds based on their relative solubilities in two different immiscible liquids, usually water and an organic solvent. For the extraction process in the proposed design, pyridine is extracted from aqueous solution by using N-propyl formate as a solvent in a countercurrent extraction column. The extract contains most pyridine and solvent and is further purified in a stripper (named STRIP1) to obtain high purity pyridine as bottom product; the raffinate contains very little pyridine and mostly water will also be purified in a stripper (named STRIP2) to obtain high purity water as bottom product. Top vapor products of both strippers will be cooled down by coolers separately, and fed into a decanter where two liquid phases will form. The organic phase contains mostly the solvent, and is treated as recycled solvent used repeatedly in the extraction column; the aqueous phase contains almost the same composition as the raffinate, and thus is combined with raffinate stream as the feed to STRIP2. Two specifications are met for all simulations. The bottoms of STRIP1 is kept to be 99.9mol% pyridine, and the bottoms of STRIP2 is kept to be 99.9mol% water.

There are four design variables for the proposed design flowsheet which are total number of trays for each stripper, total number of extraction column stages, and the ratio of extraction solvent and fresh feed flow rate. The ratio of extraction solvent and fresh feed flow rate is the most important design variable, and should be assigned as the outer-most variable in the optimization procedure. All product specifications are met in the optimization steps. Figure 2 shows the simulation result. Note that from Figure 2, the optimized case reaches a low constraint for the system. When using less entrainer, no more converge run can be obtained because certain amount of entrainer is necessary for extraction process. Thus, this optimized case would not be able to handle feed composition disturbance in dynamics simulation. A trade-off between design and control should be used in this case and will be discussed in the next section.

Table 1 compares the total annual cost (TAC) of the optimized results for hybrid extraction/distillation system, heterogeneous azeotropic distillation system, and dividing-wall column system. All the calculations are based on the TAC calculation basis in Luyben (2013). TAC calculation includes annual total operating cost, total capital cost divided by a payback period assumed to be three years. Operating cost includes the cost of steam, cooling water, and solvent; capital cost includes the costs of columns, vessels, and heat exchangers. Compared the optimized design of the hybrid extraction/distillation system with the previously mentioned heterogeneous azeotropic design, significant reductions of 58.8 % in the total annual cost and 65.6 % in the steam cost can be obtained. Furthermore, in comparison with the complex design of dividing-wall system, the proposed hybrid extraction/distillation system can still significantly save total annual cost and steam cost by 41.2 % and 50.8 %, respectively.

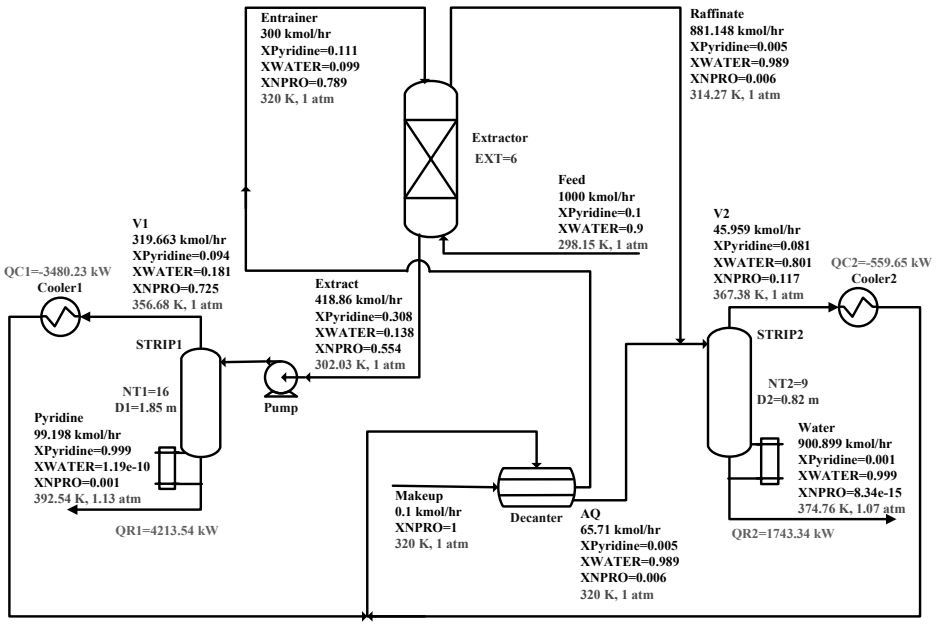

Figure 1. Optimized Flowsheet of Hybrid Extraction/Distillation System

Table.1 Results Comparison of the Three Designs for the pyridine Dehydration System

		Hybrid Extraction/Distillation System			Heterogeneous Azeotropic Distillation System		Dividing-wall Design	
		C1	C2	Extraction Column	C1	C2	C1	C2+C3
annualized column capital cost	1000$/yr	233.04	58.94	308.99	291.97	163.27	81.34	205.53
annualized reboiler capital cost	1000$/yr	215.88	96.00	-	314.82	318.30	170.69	292.31
annualized condensor capital cost	1000$/yr	331.23	91.38	-	181.66	172.87	275.19	-
steam cost	1000$/yr	944.10	390.62	-	1825.76	2053.28	655.30	2059.53
cooling water cost	1000$/yr	35.48	5.71	-	76.76	70.33	102.92	-
reboiler duty	MW	4.21	1.74	-	8.15	9.16	2.92	9.19
makeup cost	1000$/yr	18.09			3.71		3.71	
total reboiler duty	MW	5.96			17.31		12.12	
total steam cost	1000$/yr	1334.72			3879.04		2714.83	
total energy cost	1000$/yr	1375.91			4026.12		2817.75	
total capital cost	1000$/yr	1335.46			1442.90		1025.06	
TAC	1000$/yr	1839.16			4510.80		3159.43	

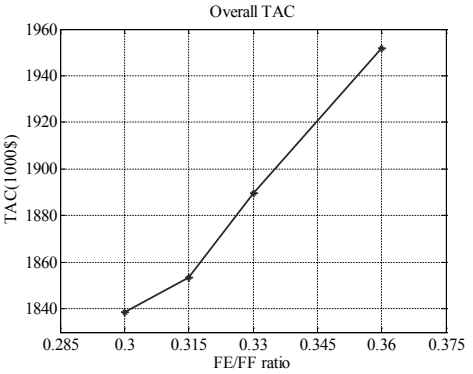

Figure 2. Summary of TAC plots at various FE/FF ratio

3. Control Strategy Design

In this section, dynamics and control of the hybrid extraction/distillation design is examined. As we mentioned above, the optimized case reaches a low constraint for the design flowsheet as shown in Figure 2. Once there is an increase of pyridine in feed, the system will not be able to converge, and thus the optimized case would not be able to handle disturbances. When increasing entrainer flowrate to 360 kmol/h, the case is able to hold product specifications despite disturbances from throughput and feed composition changes by the proposed plant-wide control structure. Figure 3 shows the TAC minimized case when the ratio of extraction solvent and feed flowrate fixed as 0.36. Although this case in Figure 3 has greater TAC (6.51% increase) than the optimized case result in Figure 1, this design case should be able to handle feed composition disturbances. We will examine the dynamic responses under throughput and feed composition changes in the followings.

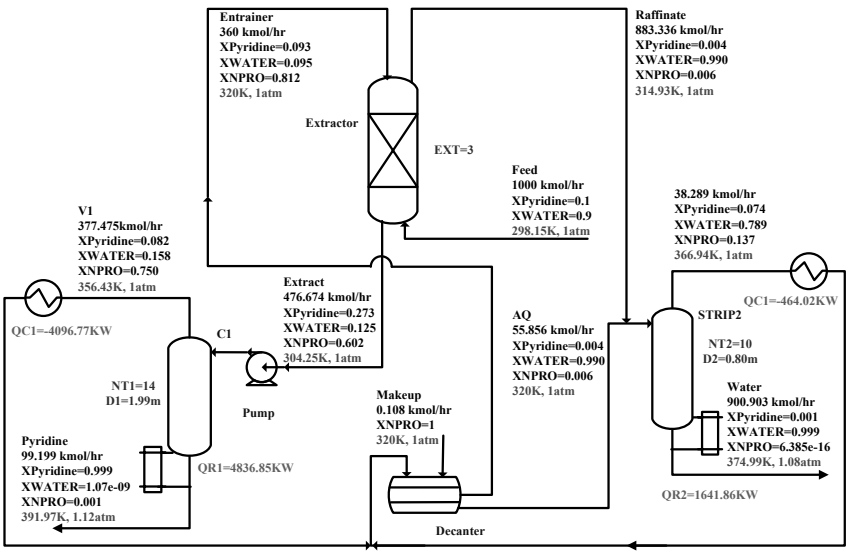

Figure 3. Optimized Flowsheet under FE/FF=0.36

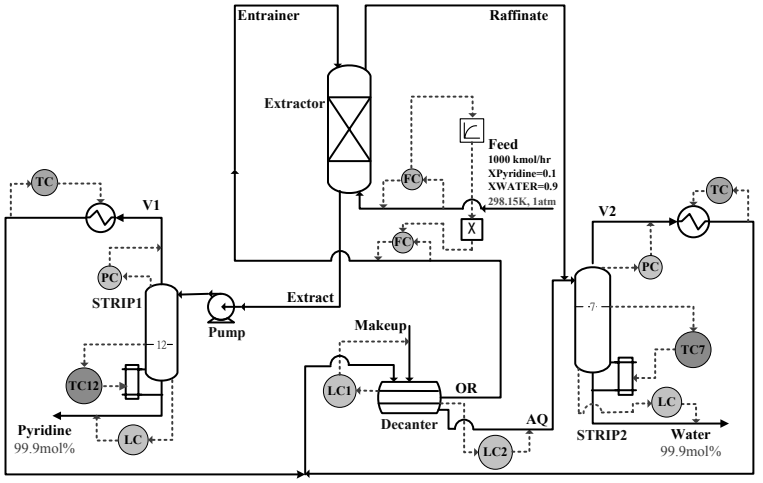

Figure 4. Proposed Overall Control Strategy

The overall control strategy as shown in Figure 4 is developed to hold both specifications in spite of feed flowrate and composition deviation. In control strategy development, no online composition measurement is necessary. It will be inferred by tray temperature control strategy. There are ten inventory control loops included level controls, temperature controls, pressure controls and flow controls. A ratio scheme between feed flow and entrainer flow is established and ten minutes lag is added to smooth out the dynamic response. With the information of closed-loop and open-loop sensitivity tests, the 12th stage temperature of STRIP1 and the 7th stage temperature of STRIP2 are selected to be controlled by reboiler duties. The temperature control loops contain 1-min deadtimes and are tuned by Tyreus-Luyben tuning rules.

The set point of temperature controller is further investigated. To hold both specifications, we pre-investigate the value of set-point of temperature controllers during throughput change as shown in Figure 5. Figure 6(a) displays the responses of ±20% in throughput change. For throughput change, temperature set point values are manually adjusted according to the result of pre-investigation in Figure 5. The two products purities returned quickly back to their specifications. Figures 6(b) gives responses for ±20% composition change of pyridine in feed. The two controlled temperatures returns quickly to their set point values and the two products are still maintained at high purity.

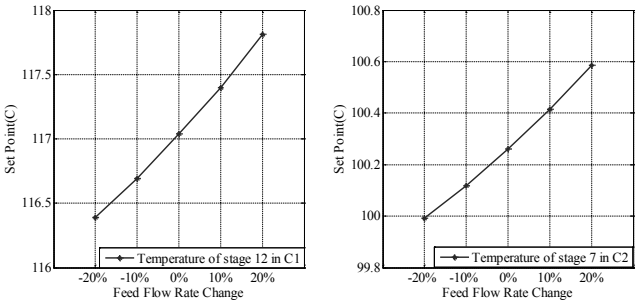

Figure 5. Set-point Values of Tray Temperature Control under Throughput Change

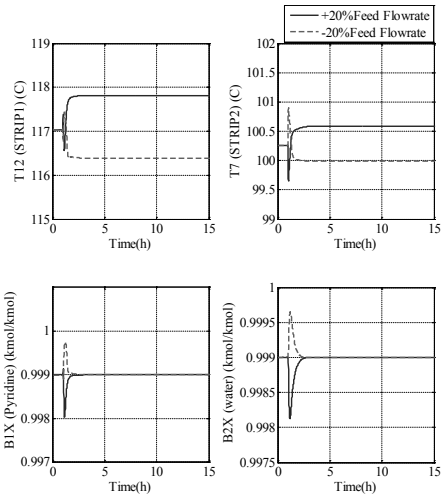

Figure 6(a). Responses of ±20% in throughput change

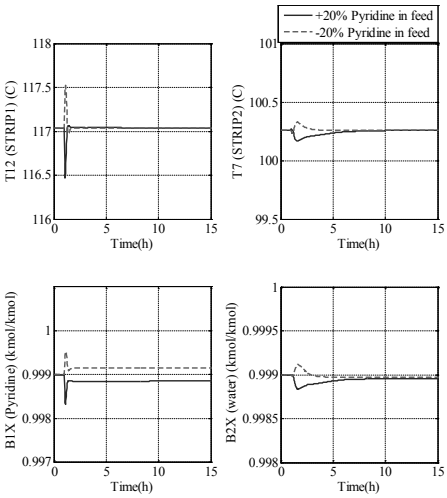

Figure 6(b). Responses of ±20% pyridine in feed

4. Conclusions

Design and control of a hybrid extraction/distillation system for the separation of pyridine and water are studied. In the extraction column, N-propyl formate has been selected as the solvent. Compared with the previously mentioned heterogeneous azeotropic design and dividing-wall column system, significant reductions in the total annual cost and in the steam cost can be obtained.

The dynamics results show a trade-off between economical design and controllability. With the adjustment of solvent flow rate, proposed plant-wide control structure is capable of holding product specifications despite disturbances from throughput and feed composition changes.

References

Y.C. Wu, I.L. Chien, 2009, Design and control of heterogeneous azeotropic column system for the separation of pyridine and water, Ind. Eng. Chem. Res., 48, 10564-10576

Y.C. Wu, H.Y. Lee, H.P Huang, I.L Chien, 2014, Energy-saving dividing-wall column design and control for heterogeneous azeotropic distillation systems, Ind. Eng. Chem. Res., 53, 1537-1552

W.L Luyben, 2013, Comparison of extractive distillation and pressure-swing distillation for acetone/chloroform separation, Comp. Chem. Eng., 50, 1-7

Krist V. Gernaey, Jakob K. Huusom and Rafiqul Gani (Eds.), 12th International Symposium on Process Systems Engineering and 25th European Symposium on Computer Aided Process Engineering.
31 May – 4 June 2015, Copenhagen, Denmark

Alternative Hybrid Liquid-Liquid and Distillation Sequences for the Biobutanol Separation

M. Errico[a*], E. Sanchez-Ramirez[b], J.J. Quiroz-Ramìrez[b], J.G. Segovia-Hernández[b], B.G. Rong[c]

[a] *Universitá degli Studi di Cagliari, Dipartimento di Ingegneria Meccanica, Chimica e dei Materiali, Via Marengo 2, 09123 Cagliari, Italy*
[b] *Universidad de Guanajuato, Campus Guanajuato, División de Ciencias Naturales y Exactas, Departamento de Ingeniería Química, Noria Alta S/N, Guanajuato, Gto., 36050, México*
[c] *Department of Chemical Engineering, Biotechnology and Environmental Technology, University of Southern Denmark, Niels Bohrs Allé 1, DK-5230 Odense M, Denmark*
massimiliano.errico@dimcm.unica.it

Abstract

Recent technologies for biobutanol production by fermentation have resulted in higher final biobutanol concentrations, less fermentation by-products and higher volumetric productivities during fermentation, together with less energy intensive separation and purification techniques. These new technology developments have the potential to provide a production process for biobutanol that is economically viable in comparison to the petrochemical pathway for butanol production. This study compares four different possible process designs for purification of biobutanol by means of a multiobjective optimization process having two objective functions: the total annual cost (TAC) as an economical function and the associated eco-indicator 99 as an environmental function.

Keywords: biofuels, biobutanol, thermal coupling, process synthesis.

1. Introduction

With the depletion in petroleum resources, an increasing attention has been paid to the research of new energy sources. The use of biofuels for transport is becoming very relevant for a number of reasons, such as environmental concerns relating to climate change, depleting fossil fuel reserves, and reducing reliance on imports (Wingren et al., 2003). This is leading to international, national and regional focus on alternative energy sources. In the EU, the transport is responsible for an estimated 21 % of all greenhouse gas emissions (Searchinger et al., 2008). More than 90 % of the total transport emissions are due to the road transport. Biofuels, processed from biomasses, which are considered as a renewable resource, are suggested as a direct substitute for fossil fuels in transport. Thus, the current research and development drivers are the identification of potential renewable energy sources or biomass feedstock and their processing in order to produce alternatives to fossil fuels in transport, such as biobutanol.
The aim of this work is to perform the process design, multiobjective optimization and comparison of different possible process routes for industrial scale biobutanol production. Process modelling in Aspen Plus was performed and the optimization was conducted using the stochastic optimization method Differential Evolution with Tabu list, having two objective functions, the total annual cost as an economic objective,

whereas the environmental objective function is measured through the eco-indicator 99 based on the LCA methodology.

2. Hybrid extraction-distillation process

The combination of extraction and distillation is considered as one of the most promising separation alternatives for the ABE purification (Van der Merwe et al., 2013). The extraction column is located after the fermentor, the mass separation agent or extractant, is fed from the bottom and the fermentation broth from the top. The raffinate phase contains water and traces of acetone, butanol and water. The extract phase contains the extractant, acetone, butanol and ethanol. The selection of the extractant is of meaningful importance for the economy of the process because directly affects the composition of the extract phase. It is possible to generalize that a good extractant, besides its economicity and low toxicity, should have a high distribution coefficient for the butanol and a high selectivity between butanol and water.
The extract phase obtained from the extractor is feed to the distillation section where acetone, butanol and ethanol can be recovered following different arrangements, with simple and/or complex columns. The liquid-liquid extraction may eliminate the request of azeotropic distillation making the process more competitive compare pure distillation flowsheets. The nine configurations reported in Figure 1 are considered and compared in the present study.

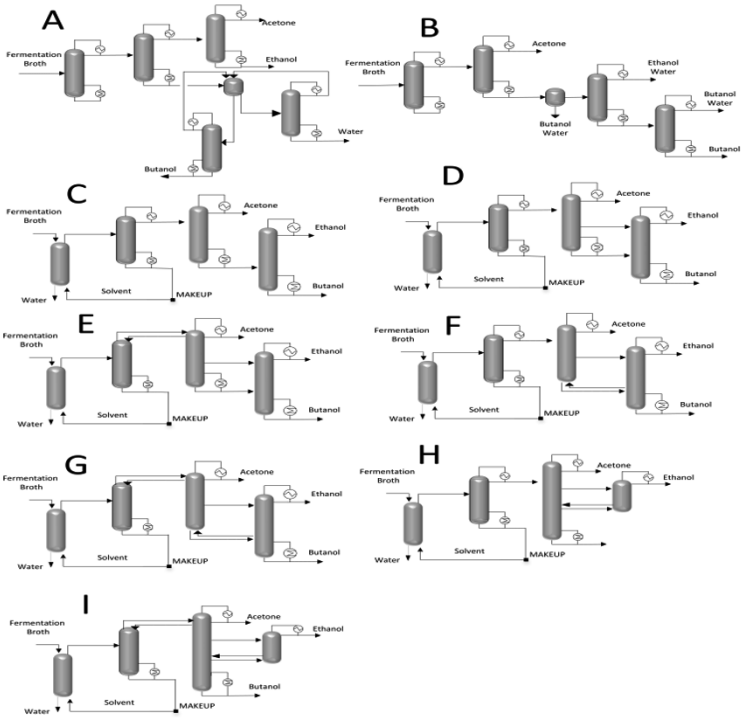

Figure 1. Sequences considered for the biobutanol production.

3. Case study

All sequences in Figure 1 were subject to a rigorous optimization, all these design cases were initially simulated using Aspen Plus process models. Note that these process models were robust and thermodynamically rigorous. According to Van der Merwe et al. (2013) and Chapeaux et al., NRTL-HOC was the most accurate thermodynamic model for the calculation of the physical property available for the components used at the specified conditions. It was assumed that all process designs have the same stream feeds except LLE design where it was added hexyl acetate as extractant. The feed composition reported by Wu et al. (2007) was used. The required purities are 99.5 wt % for biobutanol, 98 wt % for acetone, 94 wt % for ethanol and 95 wt % for the solvent recovered.

4. Optimization problem

The optimization of the biobutanol purification section is essential to run a biobutanol industry that can effectively compete with the current butanol derived from the petrochemical route. Moreover the environmental impact must be also taken in count in order to satisfy all governmental restriction.

4.1 Economic objective function

The objective function is the minimization of the total annual cost (TAC), which is directly proportional to the heat duty, services and the columns size. The minimization of this objective is subject to the required recoveries and purities in each product stream, i.e.:

$$\text{Min (TAC)} = f(N_{tn}, N_{fn}, R_{rn}, F_{rn}, F_{vn}, D_{cn}) \quad (1)$$
$$\text{Subject to } y_m \geq x_m$$

where N_{tn} are total column stages, N_{fn} is the feed stages of all streams in column, R_{rn} is the reflux ratio, F_{rn} is the distillate fluxes, F_{vn} is the vapor flow in interconnections at coupled sequences and D_{cn} is the column diameter, y_m and x_m are vectors of obtained and required purities for the m components, respectively. This minimization implies the manipulation of 22-26 continuous and discrete variables for each configuration, where 5-7 variables are used for the design of each column. Note that since the product streams flows are manipulated, the recoveries of the key components in each product stream must be included as a restriction for the optimization problem. In the configuration reported in Figure 1(a) the acetone, biobutanol and ethanol must be recovered; while in the configuration of Figure 1(b), the acetone and biobutanol must be recovered.

4.2 Environmental objective function

The environmental indicator is measured through the eco-indicator 99 based on the methodology of the life cycle analysis (Geodkoop and Spriensma, 2001) and is stated as follows:

$$\textit{Min (Eco indicator)} = \Sigma_b \Sigma_d \Sigma_k \delta_d \omega_d \beta_b \alpha(b,k)$$

Where β_b represents the total amount of chemical b released per unit of reference flow due to direct emissions $\alpha(b,k)$ is the damage caused in category k per unit of chemical b released to the environment, ω_d is a weighting factor for damage in category d, and δ_d is the normalization factor for damage of category d.
In the eco-indicator 99 methodology, 11 impact categories are considered:

1. Carcinogenic effects on humans
2. Respiratory effects on humans that are caused by organic substances
3. Respiratory effects on humans caused by inorganic substances
4. Damage to human health that is caused by climate change
5. Human health effects that are caused by ionizing radiations
6. Human health effects that are caused by ozone layer depletion
7. Damage to ecosystem quality that is caused by ecosystem toxic emissions
8. Damage to ecosystem quality that is caused by the combined effect of acidification and eutrophication
9. Damage to ecosystem quality that is caused by land occupation and land conversion
10. Damage to resources caused by the extraction of minerals
11. Damage to resources caused by extraction of fossil fuels.

These 11 categories are aggregated into three major damages categories: (1) human health, (2) ecosystem quality, and (3) resources depletion. These 11 categories are aggregated into three major damages categories: (1) human health, (2) ecosystem quality, and (3) resources depletion.

5. Global stochastic optimization strategy

In order to optimize the processes routes for biobutanol production, a stochastic optimization method, Differential Evolution with Tabu List (DETL) was used. Differential Evolution (DE) has its basis in Darwin's natural selection theory, and is similar to genetic algorithms (GAs) except for one important factor: several GAs, particularly earlier versions, encode decision variables as bit strings whereas DE encodes them as floating-point numbers. Srinivas and Rangaiah (2007) showed that the use of some concepts of the metaheuristic tabu can improve the performance of DE algorithm. In particular, the tabu list (TL) can be used to avoid the revisit of search space by keeping record of recently visited points, which can avoid unnecessary function evaluations. A comprehensive description of the DETL algorithm is provided by Srinivas and Rangaiah (2007).
The implementation of this optimization approach was made using a hybrid platform using Microsoft Excel and Aspen Plus. The vector of decision variables (i.e., the design variables) is sent to Microsoft Excel to Aspen Plus using DDE (Dynamic Data Exchange) through COM technology. In Microsoft Excel, these values are attributed to the process variables that Aspen Plus need. After simulation it is done, Aspen Plus return to Microsoft Excel the resulting vector. Finally, Microsoft Excel analyzes the values of the objective function and proposes new values of decision variables according to the stochastic optimization method used. For the optimization of process routes analyzed in this study, we have used the following parameters for DETL method: 200 individuals, 300 generations, a tabu list of 50 % of total individuals, a tabu radius of

0.0000025, 0.80 and 0.6 for crossover and mutation fractions, respectively. These parameters were obtained through a tuning process via preliminary calculations. The tuning process consists of performing several runs with different number of individuals and generations, in order to detect the best parameters to allow better convergence performance of DETL.

6. Results

In Figure 2 the results for the sequences of Figure 1(a) and 1(b) are reported. Only conventional columns are involved in separation and purifications of solvents. Pareto front from sequence 1(b) has a lower TAC and Eco 99 compare to the sequence 1(a), however it must be considered than in sequence 1(b), some part of biobutanol is wasted in the decanter, which means that recovery of biobutanol can not reach the target of 95 wt %.

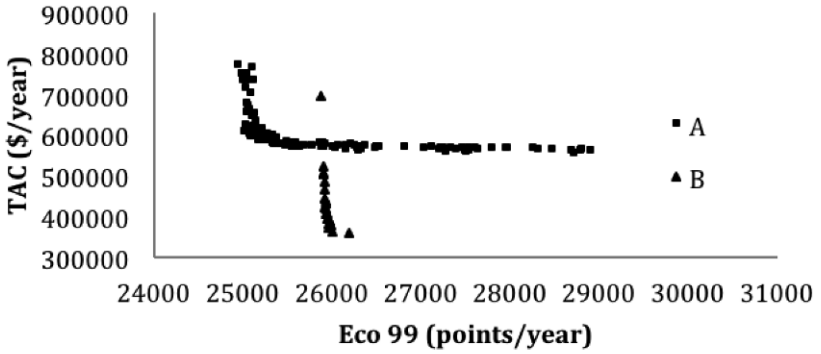

Figure 2. Pareto fronts from sequence of Figure 1(a) and 1(b).

In Table 1 the results of the TAC and the Eco-indicator 99 for all the alternatives considered, were reported. In general it is possible to notice that all the configurations with one or two thermal couplings are able to outperform the TAC and the Eco-indicator 99 of the classical configurations. Among all, configuration 1(h) reports the lowest value of TAC together with the second best environmental indicator.

Table 1: TAC and Eco 99 index for all the configurations of Figure 1.

Process Design	TAC ($/y)	Eco 99 (points/y)
A	580658	25351
B	363832	26009
C	128176	12975
D	133791	14974
E	104868	11056
F	123413	11499
G	107022	11729
H	101026	11434
I	108580	11168

7. Conclusions

A set of nine possible separation sequences for the biobutanol separation has been presented. Pure distillation alternatives together with liquid-liquid extraction plus distillation were considered and compared. The inclusion of thermal coupling in some liquid-liquid extraction based sequences reduced significantly the economic and environmental impact measured by TAC and Eco-indicator 99, comparing with some other sequences that do not include thermally coupling or a liquid-liquid extraction.
Compare to a pure distillation alternative, a liquid-liquid sequence with one thermal coupling was able to reach a 83 % reduction of the TAC together with 55 % reduction of the environmental indicator. This decreasing in economic and environmental issues, combined with other research efforts, could lead to be more profitable the use of biobutanol as an alternative energy source.

References

A. Chapeaux, L.D. Simoni, T.S. Ronan, M.A. Stadtherr, J.F. Brennecke, Green Chemistry 10.1039/b807675h.

M. Geodkoop, R. Spriensma, 2001, The eco-indicator 99. A damage oriented for life cycle impact assessment. Methodology report and manual for designers, Technical report, PRe´ Consultants, Amersfoort, The Netherlands.

T. Searchinger, R. Heimlich, R.A. Houghton, F. Dong, A. Elobeid, J. Fabiosa, S. Tokgoz, D. Hayes, T-H. Yu, 2008, Use of U.S. Croplands for Biofuels Increases Greenhouse Gases through Emissions from Land Use Change, Science, 319,1238-1240.

M. Srinivas M., G.P. Rangaiah, 2007, Differential Evolution with Taboo List for Solving Nonlinear and Mixed-Integer Nonlinear Programming Problems, Ind. Eng. Chem. Res, 46, 7126-7135.

A.B. Van der Merwe, H. Cheng, J.F. Gorgens, J.H. Knoetze, 2013, Comparison of energy efficiency and economics of process designs for biobutanol production from sugarcane molasses, Fuel, 105, 451-458.

A. Wingren, M. Galbe, G. Zacchi, 2003, Techno-Economic Evaluation of Producing Ethanol from Softwood: Comparison of SSF and SHF and Identification of Bottlenecks, Biotechnol Prog, 19, 1109-1117.

M. Wu, M. Wang, J. Liu, H. Huo, 2007, Life-Cycle Assessment of Corn-Based Biobutanol as a Potential Transportation, Fuel, ANL/ESD/07-10.

Krist V. Gernaey, Jakob K. Huusom and Rafiqul Gani (Eds.), 12th International Symposium on Process Systems Engineering and 25th European Symposium on Computer Aided Process Engineering.
31 May – 4 June 2015, Copenhagen, Denmark

Integrated Product and Process Design for the Optimization of Mayonnaise Creaminess

Arend Dubbelboer,[a]* Jo Janssen,[b] Ardjan Krijgsman,[b] Edwin Zondervan,[a] Jan Meuldijk[a]

[a]*Technical University of Eindhoven, Department of Chemical Engineering and Chemistry, PO Box 513, 5600 MB Eindhoven, The Netherlands*
[b]*Unilever Research and Development, Olivier van Noortlaan 120, 1330AC, Vlaardingen, The Netherlands*

a.dubbelboer@tue.nl

Abstract

To optimize the sensory product attributes by changing the processing conditions or product recipe was the main objective of this research. A mathematical framework was built containing process and sensory models. First, a typical mayonnaise production line was modeled. The line consisted of two mixing steps; in mixer 1 the objective was to prepare an oil-in-water emulsion; while in mixer 2 the required product specifications had to be reached. The droplet size and emulsion viscosity were coupled in the processing model for mixer 2. The physicochemical emulsion properties were subsequently correlated to the sensory attributes with a Neural Network. This allowed us to estimate panel scores on sensory attributes. Second, an optimization case study was formulated with the objective to increase mayonnaise creaminess while fixing the oil concentration to a minimal value of 0.65 w/w. The overall result was that the creaminess could be increased by 22 %, but at the expense of other sensory attributes.

Keywords: optimization, mayonnaise, sensory attributes

1. Introduction

It has been a long term goal of many fast-moving consumer goods companies to optimize the sensory profile of their products. Fast-moving consumer goods (FMCG) are products which are frequently purchased, consumed on a daily basis, have a low cost-price and are sold in large quantities; for example, foods, drinks, detergents and cosmetics. The sensory perception of these types of products determines why a consumer favors one product over another. During panel tasting sessions products are rated on sensory attributes such as mouth feel, taste, odor and appearance, which together form the sensory profile of a product. The physics and physical chemistry of the product influence its sensory perception. Many studies in the past have been focusing on relating the sensory attributes to physicochemical product properties (see e.g. Maruyama et al., 2007; Terpstra et al., 2009; Van Aken et al., 2011). What has been lacking until now was a relationship between the sensory attributes and the formulation and processing of the product. Eventually the manufacturer would like to manipulate the sensory profile by changing the recipe and/or processing conditions.

In this context a mathematical framework was built which was able to estimate panel scores on sensory attributes for mayonnaise from formulation and processing decisions.

Mayonnaise is an oil-in-water emulsion stabilized by egg yolk. Other important ingredients are vinegar, salt, sugar, mustard and water. Because the original mayonnaise contains dispersed 70 – 85 % vegetable oil, mayonnaise behaves as a semi-solid with viscoplastic and time dependent properties (Perissini et al., 1998). Mayonnaise is often modelled as a Herschel-Bulkley liquid, see e.g. Singla et al., (2013). In literature there are relations available which explain emulsion viscosity, yield stress and elasticity based on oil fraction and droplet size distribution. When the oil phase is decreased, for low fat products, the continuous phase must be structured with food additives to mimic the behavior of the full fat mayonnaise.

A typical mayonnaise production process consists of two mixers, see Figure 1. The first mixer is a fed batch system, where the oil phase is slowly added to the water phase to ensure an oil-in-water emulsion. The second mixer is usually a high shear mixer, which breaks up the oil droplets to reach the required specifications. While breaking the oil droplets the viscosity of the emulsion increases which influences the emulsion flow and in turn the rate of droplet breakup. Modeling this interaction is stipulated by Janssen and Hoogland (2013) as the top of the modeling hierarchy in terms of complexity and solving the problem in full detail remains far out of reach for practical industrial cases. There are mixers available which operate in the laminar regime and therefore need only one parameter to describe the flow. When a mean field viscosity model is opted for, the interaction between emulsion flow and droplet breakup should be feasible, even in an optimization context.

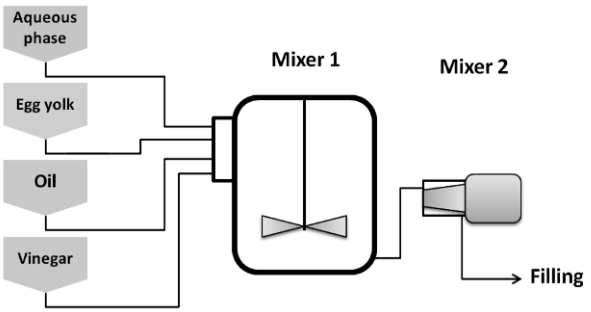

Figure 1: Simplified flow diagram of a typical dressings production line

2. The Framework

The optimization framework connects the processing variables and the product recipe on the left to the sensory attributes on the right, via several interconnected models, see Figure 2. All the models used in the framework will be briefly discussed here:

2.1. The population balance model (f_1)

A population balance tool was used to estimate the emulsion droplet sizes coming out of the second mixer. The inlet droplet size, coming out of Mixer 1, constitutes the initial condition for the population balance. It was experimentally shown that the initial droplet size distribution did not have a significant impact on the outlet droplet size, therefore it was deemed unnecessary to model mixing step 1. The breakage and coalescence rates were similar to those published in Maindarkar et al. (2014). The population balance was integrated over the axis of the mixer head so that at every length step the emulsion viscosity was recalculated using the mayonnaise viscosity model (f_2).

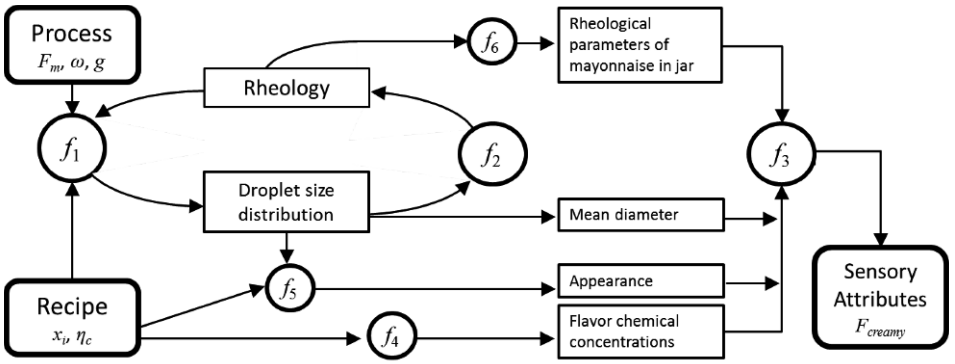

Figure 2: Detailed optimization framework; the arrows indicate the flow of information; the circles are the mathematical functions and the boxes are the variables

2.2. Mayonnaise rheology models (f_2)

To model the mayonnaise viscosity the empirical model of Jansen et al. (2001) was applied. This model is based on a modified Cross model, which contains a viscosity plateau at very low shear rates, a shear thinning region and a high shear plateau. The free parameters in the model are fitted to actual mayonnaise viscosity data. The yield stress and the elastic modulus were calculated using the models of Scheffold et al. (2013). The yield stress is an input parameter for the viscosity model and the sensory model (f_3). The elastic modulus is only an input for the sensory model. The other rheological variables needed for the sensory model are: the critical modulus; the tangent of the phase angle; the shear thinning index; the viscosity at 50 s^{-1}, which is a characteristic for in-mouth shear; and the Stevens value, which is the force necessary to push a grid through the mayonnaise.

2.3. The sensory model (f_3)

An artificial neural network model was selected as the best model from a range of statistical models, see Dubbelboer et al. (2014). The neural network correlates the physicochemical properties to the sensory attributes. The model inputs are rheological variables, mean oil droplet size, yellow index (appearance) and concentrations of flavor chemicals. The model has 25 different outputs estimating the panel scores on various sensory attributes.

2.4. Models predicting flavor chemical concentrations (f_4)

The concentrations of flavor chemicals were detected by Mass Spectrometry and were found to be linear with the amount of added ingredients, except for the pH.

2.5. Model to predict color based on droplet size distribution and recipe (f_5)

Emulsion color is very much affected by droplet size and the ingredients. There are mechanistic models available which are able to estimate emulsion color based on oil droplet size and concentrations up to 20 % (Chantrapornchai et al., 1998). The present case only considers mayonnaises with more than 65 % oil. Besides that many mayonnaises contain food colorants and no information was available which could correlate the concentration of colorants to the yellow index. For the time being the average yellow index was used from the dataset.

2.6. Model describing the increase in product structure due to the setting of mayonnaise in a jar (f_6)

The proteins from the egg yolk are known to gel the emulsion (Kiosseoglou, 2003), which takes roughly 1 to 2 days. The mayonnaise gains in structure while it stays in the

jar. Before it reaches a consumer the rheological properties have changed. Currently there are no models available taking this effect into account. Therefore the rheological properties attained directly after mixing were correlated to the sensory attributes.

3. The case study

The framework models are able to estimate scores on 25 sensory attributes. The case study presented here focuses on the optimization of one particular attribute which is mayonnaise creaminess. Therefore the cost function predicts the sensory score as would be given by a tasting panel. A correlation was found between the oil content of mayonnaise and the panel scores on creaminess see Figure 3. The framework was used to answer the following question: can product creaminess be increased while the oil concentration is kept to a minimum? Here 0.65 w/w is the minimum according to the standard of identity in some countries like US. Besides that the rheology for high internal phase emulsions acquires its characteristics around and above the maximum packing limit of hard spheres.

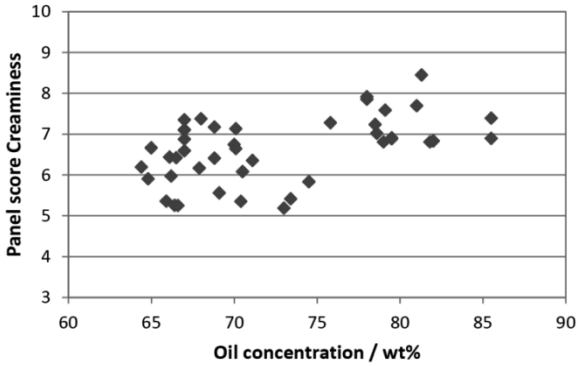

Figure 3: Creaminess scores by a panel on various types of mayonnaise versus the oil concentration

4. Optimization

The optimization problem has the following structure:

$$\max \quad Y_{creamy} = f(x_i, \eta_c, F_m, \omega, g)$$

subject to:

$$\sum x_i = 1$$

$$x_i > 0$$

$$10^{-3} \leq \eta_c \leq 10^{-1} \text{ Pa·s}$$

$$25 \leq F_m \leq 100 \text{ kg/h}$$

$$3{,}000 \leq \omega \leq 10{,}000 \text{ rpm}$$

$$0.2 \leq g \leq 0.64 \text{ mm}$$

It is the objective to maximize the model output creaminess, Y_{creamy}, which is basically an NLP. The model inputs are the formulation variables, x_i, as mass fractions; the continuous phase viscosity, η_c, because there is not a good correlation available to estimate this quantity based on the recipe; and the processing variables: flow rate F_m,

rotor speed ω, and gap size, g. For the optimization case x_{oil} was fixed to 0.65 w/w. The first step in the optimization of the framework a Genetic Algorithm (GA) was used from the MATLAB global optimization toolbox. Then, in the second step, the outcome of GA forms the initial guess for the simplex search method using the fminsearch algorithm with constraints also from MATLAB. From 100 optimization runs the 10 highest creaminess scores were evaluated.

5. Results and discussion

The maximum creaminess score found in the optimization was realized by the input values listed in Table 1. The 10 highest optimization runs had all the same combination of input variables except for 2 runs which were only slightly off. The maximum creaminess score of 7.3 for a 65 wt% oil mayonnaise was an increase of 22% compared to tested mayonnaises with similar oil content. The average creaminess score of mayonnaises in the range 80 – 85 wt% oil was 7.3. This showed that it is possible to increase product creaminess for 65 wt% oil mayonnaises. It appeared that mustard was not beneficial for the sensory attribute creaminess. It does, however, not mean that mustard should be removed from the recipe because other sensory attributes like taste might be influenced by the mustard flavor content.

The vegetable oils used in mayonnaise and dressings contribute the most to the cost price of these types of products. Lowering the oil content while maintaining same product quality is one of the major challenges in the development of mayonnaise and dressings. Also from a sustainability point of view it is desirable to limit the use of vegetable oils. The oil phase gives structure to the products, i.e. an increase in viscosity, elasticity and yield stress. When the oil phase is reduced the loss of structure must be compensated by the viscosity of the continuous phase or the droplet size distribution.

Table 1: optimization results

Product formulation variables	Optimized values	Dimensions
x_{oil}	0.65	w/w
$x_{egg\ yolk}$	0.04	w/w
$x_{vinegar}$	0.01	w/w
$x_{mustard}$	≈ 0	w/w
x_{water}	0.3	w/w
η_c	0.023	Pa*s
Processing variables		
F_m	25	kg/h
ω	10,000	rpm
g	0.64	mm
Model output		
Y_{creamy}	7.3	
$D32$	2.2	µm

The optimization results showed that the viscosity of the aqueous phase had to increase to 23 times that of pure water. With all the components already present in the aqueous phase, the viscosity rises to about 10 times that of pure water. Therefore the aqueous phase must be structured with food additives such as starches or gums to increase the creaminess score of 65% oil mayonnaise. The addition of thickeners could very well influence the perception of creaminess and other attributes. Unfortunately the effect of additional thickeners is not yet included in the sensory model. Likewise the effect of salt and sugar addition on the sensory attributes has not been quantified. Salt and sugar are part of most mayonnaise recipes and are likely to influence the sensory perception of the product.

6. Conclusions

A mathematical framework was presented in this work which could optimize sensory attributes of mayonnaise by changing the product recipe and/or processing variables. Although the framework did not yet contain all desirable correlations it was put to the test by a case study. The case study involved the optimization of mayonnaise creaminess scores while fixing the oil level to a minimal value of 0.65 w/w. An optimum was found by comparing 100 optimization runs. According to the optimization the creaminess scores of mayonnaise containing 0.65 w/w oil could be increased by 22%. However, this meant virtually removing all mustard flavor components and thickening the aqueous phase. Removing the mustard components might have detrimental effects on other sensory attributes and thickening the aqueous phase with food additives could result into other sensory effects. The next step would be to test the result of the framework, from mayonnaise formulation and production to panel tasting sessions.

References

G.A. van Aken, M.H. Vingerhoeds, R.A. de Wijk, 2011, Textural perception of liquid emulsions: Role of oil content, oil viscosity and emulsion viscosity, Food Hydrocolloids, 25, 789-796

W. Chantrapornchai, F. Clydesdale, D.J. McClements, 1998, Influence of Droplet Size and Concentration on the Color of Oil-in-Water Emulsions, J. Agric. Food Chem. 46, 2914-2920

A. Dubbelboer, H. Hoogland, E. Zondervan, J. Meuldijk, 2014, Model Selection for the Optimization of the Sensory Attributes of Mayonnaise, proceedings of OPT-i: An International Conference on Engineering and Applied Sciences Optimization M. Papadrakakis, M.G. Karlaftis, N.D. Lagaros (eds.)

K.M.B. Jansen, W.G.M. Agterof, J. Mellema, 2001, Viscosity of surfactant stabilized emulsions, J. Rheol. 45, 1359-1371

J.J.M. Janssen, H. Hoogland, 2013, Modelling Strategies for Emulsification in Industrial Practice, Can. J. Chem. Eng., 92, 198-202

V. Kiosseoglou, 2003, Egg Yolk Protein Gels and Emulsions, Curr. Opin. Colloid Interface Sci., 8, 365-370

S.N. Maindarkar, A. Dubbelboer, J. Meuldijk, H. Hoogland, M. Henson, 2014, Prediction of Emulsion Drop Size Distributions in Colloid Mills, Chem. Eng. Sc., 118, 114–125

K. Maruyama, T. Sakashita, Y. Hagura, K. Suzuki, 2007, Relationship between Rheology, Particle Size and Texture of Mayonnaise, Food Sci. Technol. Res., 13, 1-6

D. Peressini, A. Sensidoni, B. de Cindio, 1998, Rheological Characterization of Traditional and Light Mayonnaises, J. Food Eng., 35, 409-417

F. Scheffold, F. Cardinaux, T.G. Mason, 2013, J. Phys.: Condens. Matter, 25, 502101

N. Singla, P. Verma, G. Ghoshal, S. Basu, 2013, Int. Food Res. J., 20, 2009-2016

M.E.J. Terpstra, R.H. Jellema, A.M. Janssen, R.A. De Wijk, J.F. Prinz, E. Van Der Linden, 2009, J. Text. St., 40, 82–108.

Krist V. Gernaey, Jakob K. Huusom and Rafiqul Gani (Eds.), 12th International Symposium on Process Systems Engineering and 25th European Symposium on Computer Aided Process Engineering.
31 May – 4 June 2015, Copenhagen, Denmark

Synthesis of indirect work exchanger network based on transshipment model

Jian Du，[a] Yu Zhuang，Lin-lin Liu[a, b]，[a] Ji-long Li，[a] Jie Fan，[c] Qing-wei Meng

[a] *Institute of Chemical Process Systems Engineering，School of Chemical Engineering，Dalian University of Technology，Dalian* 116024，*China*
[b] *Key Laboratory of Industrial Ecology and Environmental Engineering, Ministry of Education, School of Environmental Science and Technology, Dalian University of Technology, Dalian 116024, China*
[c] *State Key Laboratory of Fine Chemicals, Dalian University of Technology, Dalian 116024, China*

Abstract:

The synthesis of indirect work exchanger network (WEN) based on transshipment model is first studied considering the compression ratio and expansion ratio as the variables in this paper. Compared with superstructure method, the transshipment model is simpler to obtain the minimum utility consumption taken as the objective function, which is also easier to get the optimal WEN configuration in which the number of units is minimized. The proposed approach for WEN synthesis is a linear program model applied to isothermal process. All the streams are divided into several pressure intervals, also called sub-networks. Then the energy balance is calculated in each sub-network according to the analysis of work cascade in isothermal process. In addition, the adjacent intervals are merged according to the proposed merging rules in order to decrease utility consumption and optimize the network structure. Finally, this method is proved to be feasible and effective by an example.

Keywords: indirect work exchanger network; transshipment model; process synthesis; compression/expansion ratio

1. Main Text

Energy is a major concern in the 21st century, the worldwide demand of which is predicted to rise by 57% during 2004-2030 (Del et al., 2010). The two common forms of energy in chemical plants are heat and work. As work is much more expensive than heat, which also has higher energy quality, work exchanger network is an important part of energy recovery system, the design level of which will have significant influence on energy consumption in process system.

Work can be exchanged between work sources and work sinks through indirect work exchangers. In the indirect work exchanger, the energy is exchanged in two steps: the pressure energy of work sources is converted to mechanical energy through turbines at first and further converted to the pressure energy of the work sinks through compressors (Liu et al., 2011, 2014). Shin et al. (2007) proposed a mixed integer linear programming method to optimize boil-off gas (BOG) compressor operations targeting the minimization of the total average energy consumption in an LNG receiving and re-gasification terminal. M.S.Razib et al. (2012) proposed a superstructure for the WEN

configuration and developed a MINLP to minimize the total annualized cost for a constant speed of the single shaft on 2-stream single-shaft-turbine-compressor (SSTC) units. Furthermore, Viviani C. Onishi et al. (2014) introduced a multi-stage superstructure to optimize WEN configuration with heat integration simultaneously at a constant speed of the single shaft for SSTC.

Based on the literature researches, no study on the integration of WEN with multiple streams in the indirect work exchanger using transshipment model has been reported. Hence, we employ the transshipment model with work cascades taken into account and formulate the synthesis of work exchanger network as a linear program in isothermal process. Also an example is used to demonstrate the benefits of this method.

2. Problem Statement

A set of gaseous streams at high pressure (HP) and low pressure (LP) are present in a chemical process, with known volume flows, inlet pressure and outlet pressure. In addition, the work efficiency and the maximum compression/expansion ratio are also provided. The main objective is to synthesize an optimized WEN with the minimum utility consumption and the number of units minimized through work recovery between HP and LP streams, utilizing turbines and compressors running on a common shaft. Compression ratio, expansion ratio, inter-stage pressure, energy requirement and number of units are variables in the synthesis of this work exchanger network. Also for purpose of simplifying synthesis process, we assume the following:

(1) All streams are in ideal gas phase.
(2) Only isothermal reversible compression/expansion is considered.
(3) The work efficiency is constant in different pressure intervals.
(4) The condition of temperature constrain is not taken into account.

3. Model Formulation

3.1. Sets definitions

The following sets are defined to meet the requirements for the development of the model:

$HP = \{HP_i / i = 1,2,...,N_H\}$, N_H is the number of high-pressure streams.

$LP = \{LP_j / j = 1,2,...,N_L\}$, N_L is the number of low-pressure streams.

$SN = \{SN_k / k = 1,2,...,K\}$, K is the number of pressure intervals.

1.2 Division of pressure intervals

The first step to establish the transshipment model is to divide all the pressure of streams into several intervals, marked as SN_k. Since no pressure difference constrain is demanded for work exchange, a new strategy is proposed in accordance with the maximum compression ratio $CR_{\max}$ and the maximum expansion ratio $ER_{\max}$ rather than that in the HEN. This strategy for division of pressure intervals guarantee that one high-pressure stream matches with one low-pressure stream through one SSTC unit. The pressure intervals consist of two pressure endpoints of all the streams and the constructed intermediate pressure, arranged in a sequence pressure values from high to low. The intermediate pressure of all streams is constructed as follows.

$$P_{HP_i}^{\text{int}} = P_{HP_i}^{OUT} \times ER_{\max} \tag{1}$$

$$P_{LP_j}^{\text{int}} = P_{LP_j}^{IN} \times CR_{\max} \tag{2}$$

$$P_{HP_i}^{OUT} \le P_{HP_i}^{\text{int}} \le P_{HP_i}^{IN} \tag{3}$$

$$P_{LP_j}^{IN} \le P_{LP_j}^{\text{int}} \le P_{LP_j}^{OUT} \tag{4}$$

3.2. Compression and expansion analysis in sub-networks

As mentioned above, the essence of work exchange between high-pressure streams and low-pressure streams for SSTC is analogous to threshold problem of HEN, which means that only one kind of utility (pressurization utility or depressurized utility) is used for the synthesis of WEN. In each pressure interval, the inlet and outlet pressure of all streams are limited between the minimum and maximum value of the inlet and outlet pressure in the WEN. Additionally, the pressure relationship in these sub-networks is presented as follows.

$$P_{HP_i,IN} = P_{HP_i,k} \quad (HP_i \in HP, k \in K) \tag{5}$$

$$P_{HP_i,OUT} = P_{HP_i,'k} \quad (HP_i \in HP, k' \in K, k' \ge k) \tag{6}$$

$$P_{LP_j,IN} = P_{LP_j,k} \quad (LP_j \in LP, k \in K) \tag{7}$$

$$P_{LP_j,OUT} = P_{LP_j,'k} \ (LP_j \in LP, k' \in K, k' \le k) \tag{8}$$

Let $W_{HP_i,k}$ be the energy extracted by turbines while $W_{LP_j,k}$ is energy required by compressors. In addition, consider $W_{PU,k}$ and $W_{EU,k}$ as pressurized and depressurized utilities. Hence, the transshipment model is represented as Figure 1.

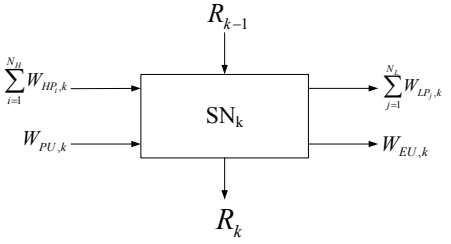

Figure 1: Work exchange in pressure interval k

In conclusion, the objective function and constrains can be obtained as follows according to the above analysis.

$$\min Z = \sum_{k=1}^{K} (W_{PU,k} + W_{EU,k}) \tag{9}$$

$$\sum_{i=1}^{N_H} W_{HP_i,k} + W_{PU,k} + R_{k-1} = \sum_{j=1}^{N_L} W_{LP_j,k} + W_{EU,k} + R_k \tag{10}$$

$$\mathrm{W}_{\mathrm{HP_i},k} = -P_{i,k} V_{i,k} \ln\left(\frac{P_{HP_i,k,t}}{P_{HP_i,k,s}}\right) \cdot \eta \tag{11}$$

$$\mathrm{W}_{\mathrm{LP_j},k} = -P_{j,k} V_{j,k} \ln\left(\frac{P_{LP_j,k,t}}{P_{LP_j,k,s}}\right) \tag{12}$$

$$R_0 = R_K = 0 \tag{13}$$

Where the R_k, $W_{PU,k}$, $W_{EU,k}$ are all non-negative.

3.3. Merging of adjacent pressure intervals

Although the minimum utilities can be worked out based on the proposed transshipment model, an excess of units have to be utilized in order to recover more work, which results in a complex work exchanger network. Therefore, it is essential to reduce the number of units with utility consumption unchanged. And then a new strategy is proposed to solve this problem, which is the merging of adjacent pressure intervals. A stream existing in any of the original pressure intervals being merged is contained in the new interval. All properties of these streams keep the same while the pressure drop ratio in the new interval is enlarged. However, this new pressure drop ratio must be equal or lesser than the required maximum compression/expansion ratio. Furthermore, the work recovery between work sources and work sinks does not change, which indicates no redundant utility is needed.

4. Case Study

Table 1: Stream data for the case

Stream	P_{IN} (MPa)	P_{OUT} (MPa)	F ($dm^3 \cdot s^{-1}$)
HP_1	5.734	2.217	990.49(outlet)
HP_2	3.114	0.196	763.37(outlet)
LP_1	0.244	5.734	725.52(inlet)
LP_2	0.113	2.217	504.71(inlet)
LP_3	1.735	3.114	832.77(inlet)

In this example, WEN is designed to allow work integration between two high-pressure streams (HP_1, HP_2) and three low-pressure streams (LP_1, LP_2 and LP_3), the problem data of which are presented in Table 1. In this case, we set some variables equal to const where the efficiency is 0.85 and both the maximum compression ratio and expansion ratio are 3. For ideal gas, the product of pressure and volume for all streams in different pressure intervals is identical. Subsequently, all the pressure value of streams are divided into 12 pressure intervals and then the above model is employed to solve each sub-network taking the minimum utility as the objective function. The minimum utility consumption is 551.71kW, less than 557.90kW of Zhou et al. (2011). However, more

than 30 units are needed to complete the work exchange in the WEN. Hence, the optimized work cascade diagram is illustrated as Figure 2 according to the proposed strategy with the purpose of reducing the number of units. The corresponding work exchanger network configuration is shown as Figure 3.

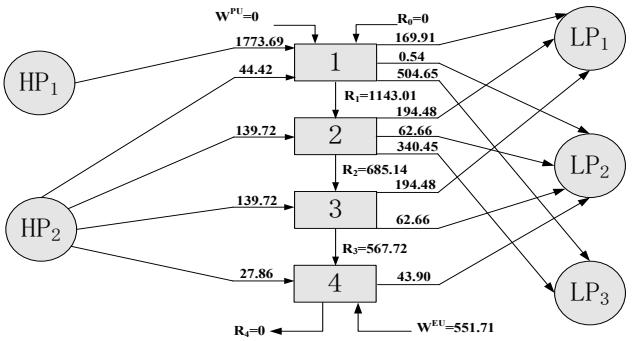

Figure 2: The optimized work cascade diagram for the case

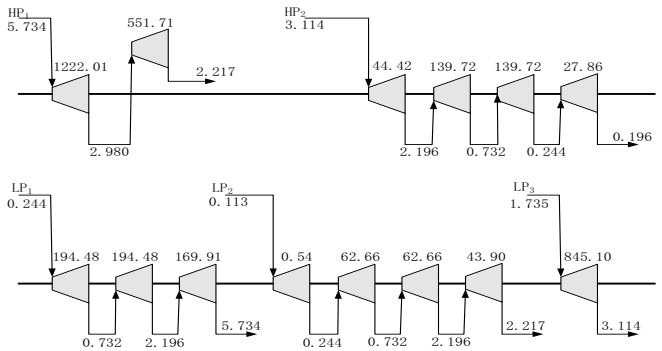

Figure 3: The work exchanger network for the case

5. Conclusions

In this paper, a new optimization methodology for synthesis of WEN based on transshipment model was first proposed, by introducing division of pressure intervals and putting forward pressure-interval merging principles to reduce the number of units and optimize WEN configuration. Finally, a numerical example from literature has been studied and the satisfactory solution justifies the feasibility of the proposed method.

Acknowledgements

The authors gratefully acknowledge the financial support from “Natural Science Foundation of China” (No. 21406026). Funding from Natural Science Foundation of Chinese Liaoning (214020007) are deeply appreciated.

References

Del Nogal F L, Kim J K, Perry S, et al, 2010, Synthesis of mechanical driver and power generation configurations, Part 2: LNG applications, AIChE journal, 56, 9, 2377-2389.

Liu G, Zhou H, Shen R,et al, 2014, A graphical method for integrating work exchange network, Applied Energy, 114, 588-599.

Zhou hua, Liu Guilian, Feng xiao, 2011, Problem table method for work exchange network with efficiency considered, CIESC Journal, 62, 06. 119.

Shin M W, Shin D, Choi S H, et al, 2007, Optimization of the operation of boil-off gas compressors at a liquified natural gas gasification plant, Industrial & Engineering Chemistry Research, 46, 20, 6540-6545.

M.S.Razib, Hasan MMF, Karimi IA, 2012, Preliminary synthesis of work exchange networks, Computers and Chemical Engineering, 37, 262–277.

Viviani C. Onishi, Mauro A.S.S. Ravagnani, JoseA. Caballero, 2014, Simultaneous synthesis of work exchange networks with heat integration, Chemical Engineering Science, 112, 87-107.

Krist V. Gernaey, Jakob K. Huusom and Rafiqul Gani (Eds.), 12th International Symposium on Process Systems Engineering and 25th European Symposium on Computer Aided Process Engineering.
31 May – 4 June 2015, Copenhagen, Denmark

Development of sustainable CO_2 conversion processes for the methanol production

Kosan Roh,[a] Tuan B.H. Nguyen,[b] Uthaiporn Suriyapraphadilok,[b] Jay H. Lee,[a*] Rafiqul Gani[c*]

[a]*Department of Chemical and Biomolecular Engineering, Korea Advanced Institute of Science and Technology (KAIST), 291 Daehak-ro, Yuseong-gu, Daejeon, 305-701, Republic of Korea*
[b]*The Petroleum and Petrochemical College, Chulalongkorn University, 254 Phyathai Road, Patumwan,Bangkok, 10330, Thailand*
[c] *CAPEC, Department of Chemical and Biochemical Engineering, Technical University of Denmark, Søltofts Plads, Kongens Lyngby, 2800, Denmark*
rag@kt.dtu.dk

Abstract

Utilization of CO_2 feedstock through CO_2 conversion for producing valuable chemicals as an alternative to sequestration of the captured CO_2 is attracting increasing attention in recent studies. Indeed, the methanol production process via thermochemical CO_2 conversion reactions is considered a prime candidate for commercialization. The aim of this study is to examine two different options for a sustainable methanol plant employing the combined reforming and CO_2 hydrogenation reactions, respectively. In addition, process improvement strategies for the implementation of the developed processes are also considered. The two methanol plants are developed using Aspen Plus®, the commercial process simulator. The net CO_2 flows and methanol production costs are evaluated using ECON® and compared with those of the conventional methanol plant, which uses two-stage reforming. It is verified that the combined reforming process has to be integrated with the existing conventional methanol plant to obtain a reduced CO_2 emission as well as lowered production costs. On the other hand, the CO_2 hydrogenation based methanol plant could achieve a reduction of net CO_2 emission at a reasonable production cost only with utilization of renewable energy resources (hydroelectric power and biomass) for the H_2 feedstock.

Keywords: CO_2 conversion, Methanol production, Sustainable process design, Process integration, Renewable energy utilization

1. Introduction

As CCUS (Carbon capture, utilization and storage) is becoming a popular R&D theme due to the mounting concerns about climate change, CO_2 conversion has attracted much attention lately. Basically, the aim of CO_2 conversion is to utilize the concentrated CO_2 (from CO_2 capture) as a feedstock to produce valuable chemicals via various conversion processes including thermochemical reaction, electrochemical reduction, photo-catalytic reduction, and bio-enzymatic reduction (Adebajo and Frost, 2012; Taheri Najafabadi, 2013). However, for CO_2 conversion to become widely practical, significant hurdles will need to be overcome. Slow kinetics and high energy demand associated with most CO_2 conversion reactions can lead to high economic penalties and additional CO_2 emission.

In spite of much research done on CO_2 conversion reactions in recent years, works on their process development, optimization, and analysis of their economic feasibility and impact on reduction have been scarce. In this paper, two thermochemical CO_2 conversion reactions, namely the combined reforming and CO_2 hydrogenation, are investigated. Designs of sustainable methanol plants employing these reactions and the conventional methanol plant are developed, respectively. Moreover, the net CO_2 flow and economic feasibility, crucial factors for sustainable process development, of the two methanol plants are compared. Finally, for those infeasible cases, either in terms of net CO_2 flow or economics, strategies are suggested to make them feasible.

2. Process description

In this study, three methanol production processes are developed and compared with one another. Two of the three utilize CO_2 as feedstock and the third represents a conventional process for methanol production. In the conventional process, syngas (the mixture of H_2 and CO) is produced through two-stage reforming (steam reforming and partial oxidation) and methanol is synthesized from the produced syngas (Dahl et al., 2014). The combined reforming (also referred to as mixed reforming or bi-reforming) can also produce syngas for methanol synthesis as in the conventional case, but it uses CO_2 as well as methane as feed and there is only one reforming stage combining the steam reforming and dry reforming steps (Holm-Larsen, 2001; Olah et al., 2009). Finally, methanol can be synthesized from CO_2 hydrogenation using CO_2 and H_2 (Van-Dal and Bouallou, 2013). The reactions taking place in each of the three processes are listed in Table 1.

The two CO_2 conversion reactions (see Table 1) are based on mature technologies already tested in large scale and therefore have the potential for further development. Most other CO_2 conversion options are currently in small-scale experimental stage. For example, a commercial-scale methanol plant (3,030 MTPD) adopting combined reforming has started up in Iran in 2004 (Aasberg-Petersen et al., 2008) and another commercial methanol plant (5 million liters per year) adopting CO_2 hydrogenation has been successfully launched in Iceland in 2011 (CRI, 2011).

Flowsheet simulations of the three methanol plant have been developed in Aspen plus® with the design specifications taken from Holm-Larsen (2001), Van-Dal and Bouallou (2013), and Dahl et al. (2014), respectively. The feed and reactor (including the primary reformers and the CO_2 hydrogenation reactor) operating conditions are optimized further through the simulator (see Table 2).

Table 1. Three different reactions for the methanol production

	Reaction equation	Operating conditions
Combined reforming	$CH_4 + H_2O \rightarrow 3H_2 + CO, \Delta H^\circ = 206.3$ kJ/mol	850~950 °C
	$CH_4 + CO_2 \rightarrow 2H_2 + 2CO, \Delta H^\circ = 247.3$ kJ/mol	20~30 bar
CO_2 hydrogenation	$CO_2 + 3H_2 \rightarrow CH_3OH + H_2O$	200~300 °C
	$\Delta H^\circ = -49.32$ kJ/mol	50~100 bar
Two-stage reforming	$CH_4 + H_2O \rightarrow 3H_2 + CO, \Delta H^\circ = 206.3$ kJ/mol	850~950 °C
	$CH_4 + 0.5O_2 \rightarrow H_2 + CO, \Delta H^\circ = -35.6$ kJ/mol	20~30 bar

Table 2. Feed and operating conditions of three methanol plants

	S/C_nH_m	CO_2/ C_nH_m	O_2/ C_nH_m	H_2/CO_2	T (°C)	P (bar)
Combined reforming	1.79	0.29	-	-	950	22.5
CO_2 hydrogenation	-	-	-	3.00	200	70
Two-stage reforming	1.80	-	0.46	-	890	25

3. Process evaluation and results

In principle, net CO_2 flow and economic feasibility are essential criteria for discussing the feasibility of CO_2 conversion processes.

$$Net\ CO_2\ flow = \sum_i F_{CO_2,i}^{Generated} - F_{CO_2}^{Input} \quad (1)$$

The feasible CO_2 conversion process must achieve a reduction of net CO_2 flow defined as in Eq.(1). Here, the input flow ($F_{CO_2}^{Input}$) is being converted while the generated CO_2 ($F_{CO_2,i}^{Generated}$) is the amount emitted through purge (direct emission) and/or produced for energy used by the process (indirect emission) (Frauzem et al., 2015). Also, positive profit should be guaranteed, based on the mass and energy balance information of the process simulation. The cost of each methanol plant is evaluated by using ECON®. For the costs and energy supply, the equivalent of CO_2 generated is calculated. For the CO_2 feedstock, it is assumed to be captured at a H_2 plant (Metz et al., 2005). H_2 is produced via steam methane reforming (SMR) (Bartels et al., 2010), and the power demand is supplied from the conventional gas-fired power plant (U.S. EIA, 2013). Also, the natural gas is assumed to be 3.915 USD/MMBTU.

Table 3 lists the net CO_2 flow and the corresponding methanol production costs. However, its net CO_2 flow is positive because of the high heat demand in the reformer that resulted in significant CO_2 emission from the reformer furnace (accounting for 92.8 % of total emission, see Table 4). The CO_2 hydrogenation based methanol plant generates the most CO_2 because of the large demand for H_2 which is very expensive and gives significant indirect emission of CO_2 (97.8 %, see Table 4). Therefore, both of the CO_2 conversion based methanol plants are not feasible as is, and follow-up strategies are required.

Table 3. Net CO_2 flow and the methanol production cost of the three methanol plants

	Net CO_2 flow (kg_{CO2}/t_{MeOH})	Production cost ($/$t_{MeOH}$)
Combined reforming	253.56	227.68
CO_2 hydrogenation	1,202.07	596.72
Two-stage reforming	311.36	260.31

Table 4. CO_2 flows of three methanol plants

	CO_2 input rate (kg_{CO2}/t_{MeOH})	Direct CO_2 emission		Indirect CO_2 emission	
		Rate (kg_{CO2}/t_{MeOH})	Portion (%)	Rate (kg_{CO2}/t_{MeOH})	Portion (%)
Combined reforming	375	583	92.8	45	7.2
CO_2 hydrogenation	1,456	60	2.2	2,599	97.8
Two-stage reforming	0	264	84.9	47	15.1

4. Strategies toward the sustainable CO_2 conversion process

A new standalone installation of neither of the developed methanol plants utilizing CO_2 seems promising owing to their positive net CO_2 flow and/or too high production costs. To make them more attractive, process integration and utilization of renewable energy sources are considered.

4.1. Process integration of the combined reforming-based methanol plant with an existing methanol plant

Although an economic advantage is seen from the combined reforming based methanol plant, the problem is that more CO_2 is released from the process than the input amount. Instead of an independent implementation, if integration of two methanol plants in operation, a conventional methanol plant and the CO_2 conversion process, is considered, actual reduction of CO_2 emission can be achieved. In fact, both the conventional methanol plant and the combined reforming based methanol plant produce the syngas necessary for synthesizing methanol. Therefore, for given methanol production capacity, the syngas production rate from the two-stage reforming processing section can be reduced and the reduced amount can be supplemented by the combined reforming section. This "process integration" strategy is illustrated in Figure 1.

For various integration ratios (0.1~0.7, ratio 0.7 means 70 % of original syngas production rate at the two-stage reforming process is generated by combined reforming process and returned to the methanol synthesis section), several performance indices including the CO_2 abatement rate, CO_2 credit benefit, and the methanol production cost saving have been calculated and given in Table 5. Here, 4.63 EUR/t_{CO2} of carbon credit is applied in the calculation of the carbon emission credit benefit.

Consequently, increasing the process integration ratio (producing more syngas by the combined reforming process) leads to a decrease in CO_2 emission and an increase in the production cost saving. The reason is that syngas production via combined reforming is less costly and also emits less CO_2 than the two-stage reforming.

Eventually, depending on the desired CO_2 reduction rate, the proper integration ratio can be decided. This way one can obtain a more sustainable solution without any economic sacrifice. In addition, extra income may be earned from the carbon emission credit trading but it is rather minor (0.166 USD/t_{MeOH} for 50 % integration) at the current rate of carbon emission credit.

Table 5. CO_2 and economic-related performances with respect to the integration ratio

Integration ratio	0.1	0.3	0.5	0.7
CO_2 abatement rate (%)	1.82	5.45	9.09	12.7
Carbon credit benefit \$/tMeOH	0.0332	0.0997	0.166	0.233
Production cost saving \$/tMeOH	0.765	2.30	3.83	5.36

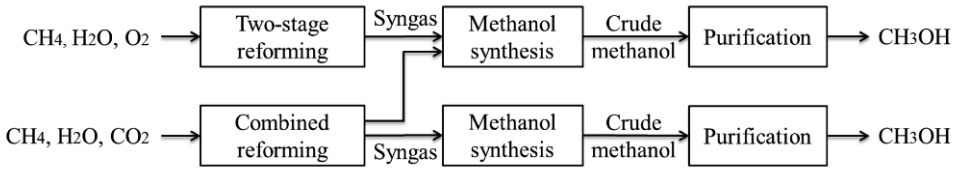

Figure 1. Schematic diagram of the integration of two methanol plants

4.2. Utilization of renewable energy sources for the CO_2 hydrogenation based methanol plant

Large demand of H_2, which is both expensive and laden with sizable CO_2 footprint, is the biggest hurdle to achieve a more sustainable solution for the methanol production via CO_2 hydrogenation. Instead of the conventional H_2 production via SMR, utilization of various renewable energy sources is an alternative worthy of consideration. Here, six different renewable energy sources for H_2 production are considered (Bartels et al., 2010; Yumurtaci and Bilgen, 2004): biomass, hydroelectric power, nuclear power, photovoltaic, solar thermal power, and wind power. For each case, the calculated net CO_2 flow and methanol production cost are plotted along with those of the SMR based H_2 production case and the conventional methanol plant case in Figure 2.

Most cases utilizing H_2 from renewable energy sources result in a reduction of net CO_2 flows except for the photovoltaic case. On the other hand, reasonable methanol production costs (less than 400 USD/t_{MeOH}) are obtained only in the case of hydroelectric power and biomass based H_2 production. The other cases are not found to be economically competitive because of their currently high power generation costs. Therefore, methanol production via CO_2 hydrogenation with H_2 production using hydroelectric power or biomass based is a more sustainable choice in terms of both the CO_2 flow and economic feasibility, at least at the current stage of development. Most likely, the wind and solar thermal power based H_2 production options can also become economically feasible if their power generation costs decrease further in the future.

5. Conclusion

CO_2 conversion technologies are currently attracting much interest due to the mounting concerns on climate change. To argue for the feasibility of CO_2 conversion processes, two promising reactions for methanol production, combined reforming and CO_2 hydrogenation, have been investigated. Plants employing the two reactions were designed and their net CO_2 flows and methanol production costs were evaluated and compared with those of the conventional methanol plant. The combined reforming based methanol plant showed an economic feasibility but it is found to release more CO_2 than it utilizes as input. In particular, direct CO_2 emission from the reformer furnace accounts for more than 90 % of the total CO_2 emission. For the case of CO_2 hydrogenation based methanol plant, the main problem was found to be the large demand for H_2 and its high cost and large CO_2 footprint. Since building a new installation of a standalone CO_2 conversion process based on these reactions is found to be not sustainable, two strategies to make them more sustainable have been investigated. First, integrating the combined reforming process with a methanol plant using the conventional two-stage reforming technology resulted in reduction of CO_2 emission as well as the methanol production cost saving. For the CO_2 hydrogenation based case, utilization of various renewable energy resources has shown to decrease the indirect CO_2 emission at the H_2 production step. In particular, use of the hydroelectric power or biomass in producing the required H_2 has led to a more sustainable solution. The interested reader can obtain the calculation details and simulation results by contacting the corresponding author.

Acknowledgement

Financial support from the Saudi Aramco-KAIST CO_2 Management Center is gratefully acknowledged.

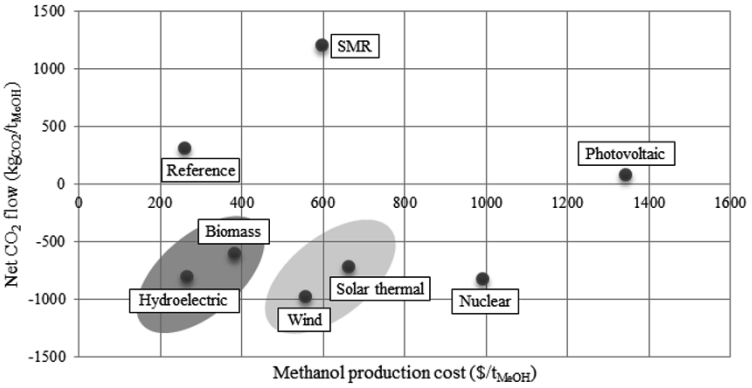

Figure 2. Net CO_2 flow and the methanol production cost of CO_2 hydrogenation based methanol plant with various H_2 production methods

References

K. Aasberg-Petersen, C. S. Nielsen, I. Dybkjær, J. Perregaard, 2008, Large Scale Methanol Production from Natural Gas, Company research article of Haldor Topsøe, Denmark

M. O. Adebajo, R. L. Frost, 2012, Recent Advances in Catalytic/Biocatalytic Conversion of Greenhouse Methane and Carbon Dioxide to Methanol and Other Oxygenates, Greenhouse Gases: Capturing, Utilization and Reduction, 31-56, InTech Europe, Rijeka, Croatia

J. R. Bartels, M. B. Pate, N. K. Olson, 2010, An economic survey of hydrogen production from conventional and alternative energy sources, International Journal of Hydrogen Energy, 35, 8371-8384.

CRI (Carbon Recycling International), 2011, http://www. carbonrecycling.is (accessed November 2014)

P. J. Dahl, T. S. Christensen, S. Winter-Madsen, S. M. King, 2014, Proven autothermal reforming technology for modern large-scale methanol plants, Nitrogen+Syngas 2014 International Conference & Exhibition, Paris, 24-27 February

H. Holm-Larsen, 2001, CO2 reforming for large scale methanol plants—an actual case, Studies in Surface Science and Catalysis, 136, 441-446

Intergovernmental Panel on Climate Change (IPCC), 2007. Climate Change 2007: Mitigation of Climate Change, Cambridge University Press, Cambridge, United Kingdom

B. Metz, O. Davidson, H. De Coninck, M. Loos, L. Meyer, 2005, Carbon dioxide capture and storage: Special Report of the Intergovermental Panel on Climate Change, Cambridge University Press, Cambridge, United Kingdom

G. A. Olah, A. Goeppert, G. S. Prakash, 2009, Beyond oil and gas: the methanol economy, Wiley-VCH Verlag GmbH & Co. KGaA, Weinheim, Germany

R. Frauzem, P. Kongpanna, K. Roh, J. H. Lee, V. Pavarajarn, S. Assabumrungrat, R. Gani, 2015, Sustainable process design: Sustainable Process Networks for Carbon Dioxide Conversion, Sustainability of Products, Computer Aided Chemical Engineering, 36.

A. Taheri Najafabadi, 2013, CO2 chemical conversion to useful products: An engineering insight to the latest advances toward sustainability, International Journal of Energy Research, 37, 485-499

U.S. Energy Information Administration (EIA), 2013, Levelized Cost of New Generation Resources in the Annual Energy Outlook 2013, U.S. Department of Energy (DOE), Report number : DOE/EIA-0383ER(2013), Release date : January 28, 2013

É. S. Van-Dal, C. Bouallou, 2013, Design and simulation of a methanol production plant from CO2 hydrogenation, Journal of Cleaner Production, 57, 38-45

Z. Yumurtaci, E. Bilgen, 2004, Hydrogen production from excess power in small hydroelectric installations, International Journal of Hydrogen Energy, 29, 687-693

Krist V. Gernaey, Jakob K. Huusom and Rafiqul Gani (Eds.), 12th International Symposium on Process Systems Engineering and 25th European Symposium on Computer Aided Process Engineering.
31 May – 4 June 2015, Copenhagen, Denmark

Optimal Design of Algae Biorefinery Processing Networks for the production of Protein, Ethanol and Biodiesel

Peam Cheali, Anthony Vivion, Krist V. Gernaey and Gürkan Sin*

Department of Chemical and Biochemical Engineering, Søltofts Plads, Building 229, Technical University of Denmark, DK-2800 Lyngby, Denmark
**gsi@kt.dtu.dk*

Abstract

In this study, optimal design of algal biorefinery using microalgae with respect to techno-economic criteria is studied. A systematic methodology using superstructure-based optimization is used to this end. A superstructure representing a wide range of technologies developed for processing microalgae to produce end products is formulated. The corresponding technical and economic data is collected and structured using a generic input-output mass balance models. An optimization problem is formulated and solved to identify the optimal designs. The effect of uncertainties inherent in economic analysis such as microalgae production cost, composition of microalgae (e.g. oil content) and biodiesel/bioethanol market prices is considered. New optimal processing paths are found with potential of producing higher amount of biodiesel. Last, the methodology is intended as decision support tool for early-stage concept screening to enhance the future development of algal biorefinery.

Keywords: Algae biorefinery, superstructure-based optimization, process synthesis.

1. Introduction

Sustainability in particular resource availability is a serious challenge to economic growth of chemical/biochemical industries. This motivates the development of technologies for utilizing more sustainable and renewable feedstock. This study is focusing on microalgae as an alternative renewable platform for manufacturing biofuels and co-products.

In development of algal biorefinery, there are a number of alternatives potentially available to choose from depending on types of microalgae and the processing technologies used to produce biodiesel, glycerol, ethanol and protein-based compounds. One of the challenges in identifying optimal algal biorefinery concept is the underlying uncertainties in data used for comparison and evaluation. These include the volatility of market prices, process conversion factors and yields inherent in new technologies. Therefore, it is important to use a systematic methodological approach at early stage design phase to identify the optimal designs under uncertainties.

In this study, a systematic framework that uses superstructure-based optimization is used to identify the optimal algal biorefinery concept. The study considers the effect of uncertainties in raw material composition and product prices on the decision making as well. First, a superstructure representing design space of algal biorefinery is developed containing various types of microalgae and subsequent pretreatment, reaction and

separation technologies to produce biodiesel, ethanol and protein-based compounds.. Subsequently, the database (generic model and parameters and data) is collected The superstructure which is formed by the combination of the alternatives (types of feedstock, technologies, and products) together with the collected data, is then mathematically formulated as optimization problem and solved to identify the optimal designs with respect to techno-economic constraints . Further product market prices and algae oil content uncertainties are analysed for robust decision making purposes.

2. Framework

2.1. Step 1: Problem formulation: (i) problem definition; (ii) superstructure definition and data collection; (iii) model selection and validation.

The first step consists of defining the problem scope by selecting objective function and optimization scenarios with respect to economic/business metrics, engineering performance, or sustainability criteria. The superstructure (processing network) is also defined and the necessary data are collected. The model selection and validation task is then performed, i.e. a consistency check. Each processing technology is simulated in GAMS to reproduce the collected results to verify the input parameters and models used prior to the optimization problem.

2.2. Step 2: Uncertainty characterization.

In this step, the domain of uncertainty is defined and characterized. Monte Carlo simulation and Latin Hypercube Sampling with correlation control are then used to sample uncertain data. The sampling of uncertain data yields the potential scenarios that are to be analyzed in the next step.

2.3. Step 3: Identification of optimal designs under deterministic basis.

The optimization problem which is formulated in step 1 is performed and solved in this step using the nominal values for the parameters – in case a parameter is characterized by a certain statistical distribution (hence uncertain input) then its mean value is used here. The result in this step is the deterministic optimal processing path, i.e. yielding one optimization scenario on the basis of mean value of the input data.

2.4. Step 4a: Identification of optimal designs under uncertainties (deterministic problem)

In this step, the deterministic optimization problem is performed separately for each sample generated from the uncertainty domain (in Step 2). The results are the probability distribution of the objective function value and the frequency of occurrence of the optimal processing path candidates that are selected for given uncertain inputs.

2.5. Step 4b: Identification of optimal designs under uncertainties (stochastic problem, sample average approximation)

In this step, the optimization problem is modified as a stochastic programming problem by including uncertainty domain (inputs, parameters, etc). To this end, the objective function is reformulated as to minimize or maximize the expected value of the objective function over the uncertain domain.

2.6. Step 4c: Identification of optimal designs under uncertainties (stochastic problem, optimal flexible network)

In this step, the optimal trade-off between the investment cost and the ability of the network to adapt its structure in order to mitigate the negative consequences of the uncertainty is identified. The problem is reformulated as a two-stage stochastic programming problem. This step is beyond the scope of this study.

3. Identification of algae biorefinery optimal designs

In this section, synthesis and design of algal biorefinery networks under uncertainty was performed using the systematic framework presented in earlier section.

3.1. Step 1: Problem formulation: (i) problem definition; (ii) superstructure definition and data collection; (iii) model selection and validation

The problem statement was formulated as the identification of optimal biorefinery concepts with respect to techno-economic specifications under a specific objective function aiming at maximizing company earnings. The superstructure (Figure 1) of the algae biorefinery processing network was generated producing biodiesel and co-products by processing microalgae cultivated by raceway pond with 1300 tpd (the same basis as Pacific Northwest National Laboratory, Jones, et al., 2014). The superstructure has 4 four main processing steps consisting of 12 harvesting technologies; 4 pretreatment technologies; 4 extraction technologies; 6 transesterification alternatives; and 4 conversion technologies of co-products, resulting in total of 1920 alternative processing paths. The data collection including model verification was performed against the experimental data published prior to the identification of optimal processing paths in the next steps. This step was performed in the previous study (Cheali et al., 2014a) to form the basis in this study.

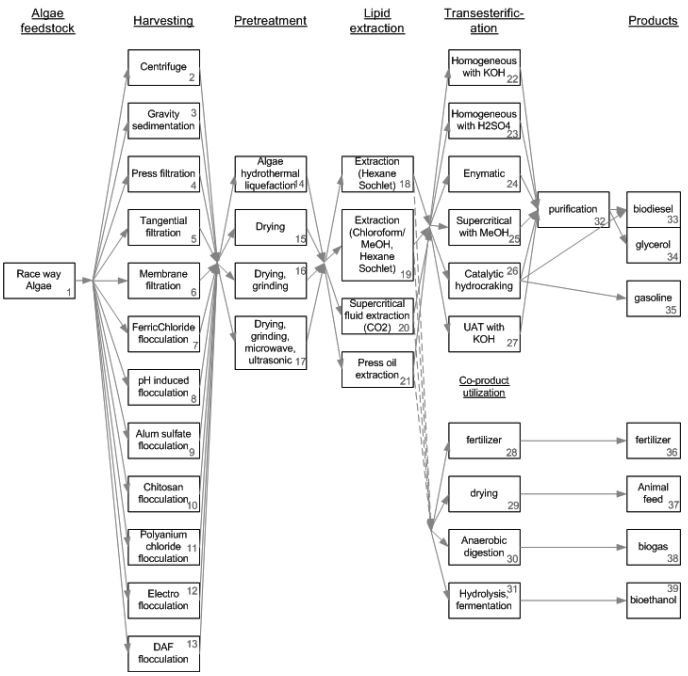

Figure 1. The superstructure of algae biorefinery processing networks

3.2. Step 2: Uncertainty characterization.

In this study, the uncertainties of market prices (biodiesel and bioethanol prices) and oil content in microalgae were identified as the important sources of uncertainty affecting the decision making. Other potential sources of uncertainties (i.e. yields, reaction conversions, efficiencies) were not considered due to low values of uncertainties

reported. A summary of the input uncertainties and the correlation coefficient if available used in this study is presented in Table 1. These data forms the input uncertainty domain, which were then sampled to generate 200 samples of the uncertain inputs. Latin Hypercube Sampling (LHS) technique was used to this end.

Table 1. Input uncertainty and correlation control coefficient

	mean	**Std**	**Reference**	
Biodiesel price ($/kg)	1,43	0,07	EIA	
Bioethanol price ($/kg)	0,72	0,08	USDA	
	min	**Max**		
Oil content (Raceway pond)	7,5	22,5	Alabi et al. (2009)	
Raw algae cost ($/ton)	300	560	Jones et al. (2014)	
Correlation matrix				
	DO	EtOH	RC	Algae
Biodiesel price (DO)	1	0,194	0	0
Bioethanol price (EtOH)	0,194	1	0	0
Oil content (RC)	0	0	1	0
Algae cost	0	0	0	1

3.3. Step 3: Identification of optimal designs under deterministic basis.

In this study, the objective function was defined as maximizing the operating profit (MM$/y) for the biodiesel scenario. The formulated MIP/MINLP was solved in this step under the deterministic basis (mean input values), in particular, maximizing Earnings Before Interest, Taxes, Depreciation and Amortization (EBITDA). The optimization solutions are presented in Table 3. The results show that a new optimal processing paths was found compared to the case study from PNNL report (Jones et al., 2014).

Objective function:

$$\max. EBITDA = Revenue - Expenses\ (excluding\ interest,\ taxes, depreciation\ and\ amortization$$

3.4. Step 4a: Identification of optimal designs under uncertainties (deterministic problem)

In this step the 200 samples generated from the LHS sampling were used as the input data for the MIP/MINLP problem, resulting in 200 optimal solutions. The full results were then analysed to identify the optimal solution under uncertainty. As presented in Table 2, two processing paths were selected under uncertainty.

From the 200 considered scenarios under uncertainty, network 1 and network 2 are identified as the best candidates. Moreover, network 1 resulted in higher EBITDA, however, standard deviation is slightly higher compared to network 2 meaning that further analysis should be performed to mitigate the impact of uncertainties such as flexible network solution.

Table 2: The frequency of selection of the optimal processing paths for 200 input scenarios under uncertainties

Network no.	Processing path	Frequency of selection	EBITDA (MM$/a)	Std.
1	Algae, hydrothermal liquefaction, transesterification with H_2SO_4	130/200	351	26
2	Algae, hydrothermal liquefaction, transesterification with KOH	70/200	316	25

3.5. Step 4b-4c: Identification of optimal designs under uncertainties (stochastic problem, sample average approximation and optimal flexible network)

The mathematical formulation used in Step 3 and Step 4a were reformulated as stochastic programming and solved in this step. Table 3 presents the optimal solutions (processing paths and operating profits) under uncertainty. As regards the optimal network solutions under uncertainty, the process topologies selected were slightly different from the deterministic case, which was the trade-off between conversion and utility cost (higher conversion but more expensive using H_2SO_4), therefore confirming the robustness of the deterministic solution and a strong impact of uncertainties.

Table 3: Optimal solutions under uncertainty

Solution	Network	EBITDA (MM$/a)	Capital cost (MM$)	Operating cost (MM$/a)		
				Microalgae cost	Natural gas	Catalyst/Chemicals
Optimal network (Step 3)	Algae, hydrothermal liquefaction, transesterification with H_2SO_4	316	252	190	6.6	4.5
Network under uncertainty (Step 4b)	Algae, hydrothermal liquefaction, transesterification with KOH	314	252	190	6.6	3.8

To sum up, based on the techno-economic analysis of optimal biorefinery network presented in the previous steps of the methodology, the network presented in Figure 2 is found as the optimal solution both under deterministic case and under uncertainty in particular market uncertainties. Hence the result from optimal flexible network (Algae, hydrothermal liquefaction, transesterification with H_2SO_4 and KOH) is the recommended as the best candidate among the design space for further research and development efforts.

Moreover, it is important to note that 90% of biodiesel production cost is related to the microalgae production cost (1300 tpd of microalgae, 190 MM$/y) which is much higher compared to lignocellulosic biomass (67 %, Cheali et al., 2014b). Furthermore, at the same capital investment, algal biorefinery has a lower production capacity compared to lignocellulosic biorefinery meaning that it is significantly more capital intensive and expensive to realize with the current cost of microalgae production (Jones et sl., 2014). However, biodiesel yield is higher, 51% for algal biorefinery and 28% for lignocellulosic biorefinery (Cheali et al., 2014b).

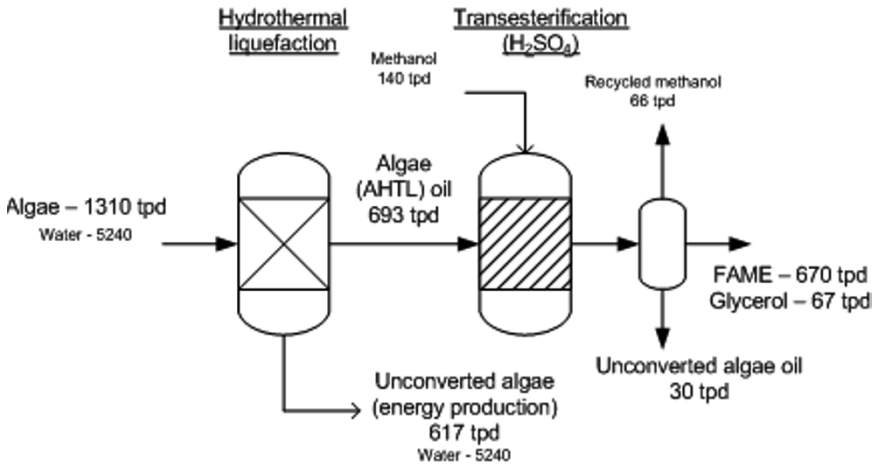

Figure 2. The optimal processing network (simplified flowsheet)

4. Conclusion

In this study, the systematic framework for synthesis and design of processing networks under uncertainty was applied for designing optimal algal biorefinery processing networks. A new optimal processing path was identified which includes the following processing scheme: hydrothermal liquefaction and transesterification with acid (H_2SO_4) or KOH. Moreover, the solutions under deterministic basis and under uncertainties in product market prices, algae cost and oil content are slightly different. These confirm the strong impact of oil content in algae and biodiesel market prices for algae biorefinery processing networks. It is also important to note that the microalgae cost is around 90% of the biodiesel production which indicates that research and development efforts need to focus to bring down the production costs of microalgae by and large.

Using the framework, many processing network alternatives are generated and evaluated at their optimality resulting in the identification of the optimal processing paths. The generated database and superstructure provides a versatile process synthesis toolbox to support designing future and sustainable algal biorefinery.

References

AO. Alabi, M. Tampier, E. Bibeau, 2009, Microalgae technologies & processes for biofuels/bioenergy production in british Columbia, The british Columbia council.

P. Cheali, C. Gargalo, KV. Gernaey, G. Sin, 2014, A framework for sustainable design of Biorefineries: life cycle analysis and economic aspects, Algal Biorefinery, Vol.2. Submitted.

P. Cheali, A. Quaglia, KV. Gernaey, G. Sin, 2014, Effect of Market Price Uncertainties on the Design of Optimal Biorefinery Systems—A Systematic Approach, Ind. Eng. Chem. Res., 53(14), 6021-6032.

S. Jones, Y. Zhu, D. Anderson, R. Hallen, D. Elliott, A. Schmidt, K. Albrecht, T. Hart, M. Butcher, C. Drennan, L. Snowden-Swan, Process design and economics for the conversion of algal biomass to hydrocarbons: whole algae hydrothermal liquefaction and upgrading, Pacifica Northwest National Laboratory, U.S. department of energy, PNNL-23227.

United States Department of Agriculture (USDA) website, http://www.ams.usda.gov/AMSv1.0/LPSMarketNewsPage.

United States Energy Information Administration (EIA) website, http://www.eia.gov/petroleum/gasdiesel/

Krist V. Gernaey, Jakob K. Huusom and Rafiqul Gani (Eds.), 12th International Symposium on Process Systems Engineering and 25th European Symposium on Computer Aided Process Engineering.
31 May – 4 June 2015, Copenhagen, Denmark

Synthetic Methane from CO_2: Dynamic Optimization of the Sabatier Process for Power-to-Gas Applications

Ali El Sibai[a], Liisa Rihko-Struckmann[b] , Kai Sundmacher [a,b,*]

[a] *Otto-von-Guericke University Magdeburg, Process Systems Engineering, Universitätsplatz 2, D-39106 Magdeburg, Germany*

[b] *Max Planck Institute for Dynamics of Complex Technical Systems, Process Systems Engineering, Sandtorstrasse 1, D-39106 Magdeburg, Germany*

* *Corresponding author: sundmacher@mpi-magdeburg.mpg.de*

Abstract

This paper deals with the design and optimization of the Sabatier process for the production of methane from renewable sources with emphasis on the reactor section. It is designed to produce Synthetic Natural Gas (SNG) ready to be injected into existing natural gas grids after downstream drying of the gas via water absorption in glycol. The investigated process configuration is a cascade of polytropic fixed bed reactors with intermediate condensation steps for water removal. The temperature profile and feed conditions of the reactors are optimized simultaneously together with the design parameters of the process, thereby minimizing the production cost of (SNG). It is shown that a cascade of three tube bundle reactors with two intermediate condensation steps is the best process configuration in terms of production cost and practical implementation.

Keywords: Dynamic optimization, CO_2 utilization, H_2 storage, Methanation, Reactor design, Process economics.

1. Introduction

Meeting future energy demands and ensuring sustainable energy supply are two main challenges modern societies are facing. Depletion of fossil fuel reserves, geopolitical struggles, continuous increase of fuel prices, and environmental concerns are factors that push the development of efficient technologies which can exploit renewable energy sources, in particular wind and solar energy. However, electricity generated from these sources is characterised by significant fluctuations posing challenges to the electrical grid. To overcome this, electricity in excess is stored such that it can be fed into the grid at a future point. Unlike batteries and pumped hydro storage which can provide only limited capacities (Stolten et al., 2013), mass storage of surplus electrical power can be realized by converting it into gas. Due to its high selectivity (100%), efficiency (80%), positive impact on environment, and the existing infrastructure for natural gas storage and distribution, the Sabatier process is considered an attractive power-to-gas process route. It converts CO_2, obtainable from biogas plants or coal-fired power plants, by use of H_2, producible by water electrolysis, to synthetic methane which can be used as a fuel or a chemical feedstock whenever needed. The main reaction is:

$$\mathrm{CO_2 + 4\,H_2 \Leftrightarrow CH_4 + 2\,H_2O} \;\; ; \;\; \Delta_R H^0 = -165 kJ/mol$$

In this work we aim at designing and optimizing the Sabatier process with focus on the reactor. The optimal reaction concept is identified from a process-wide perspective to account for its coupling with the other units in the process. This is done by applying our

Elementary Process Function (EPF) methodology (Peschel et al., 2010). Using this flux-oriented approach, the reactor and process design parameters are identified from the solution of a dynamic optimization problem. The objective is to minimize the production cost of SNG which has to meet the following gas grid quality specifications: $0 < x_{out,\,H_2} < 0.02,\ 0 < x_{out,\,CO_2} < 0.05,\ 0.95 < x_{out,\,CH_4} < 1, 0 < c_{out,H_2O} < 200\ \mathrm{mg/m^3}$ (see: DVGW G260/A, 2013; DIN 51624).

2. Optimal Reaction Concept and Process-wide Optimization

2.1. Sabatier Process

Since reducing the number of purification steps can have significant impact on reducing the overall cost of the process, the downstream processing of SNG in the considered design is limited to a final drying step using glycol. The selectivity of the methanation catalyst is normally very high (almost 100%) such that CO separation is not an issue here. But the H_2 conversion must be more than 99 % to meet the product specifications. The whole process thus consists of two main parts: reaction section and drying section.

2.2. Optimal Reaction Route

The design of an optimal reactor based on our EPF methodology follows three decision levels. Predefined devices are avoided on Level 1; instead a general fluid element in the thermodynamic state space is considered. The fluid element is manipulated over time by unlimited mass and heat fluxes such that one obtains optimal profiles of the state variables (e.g. T, x_i), i.e. the optimal reaction route. By investigating the potential of the different options for flux manipulation, the best possible reaction concept can be identified. On Level 2, the effects of mass and heat transfer limitations are taken into account and practically realizable control variables for flux manipulation are determined. On Level 3, the best control variable profiles are technically approximated and additional non-idealities are considered based on a detailed reactor model.

Due to the proposed layout of the Sabatier process and the given constraints (X > 99 %, quality specifications), dosing of the reactants CO_2 and H_2 during the reaction turns out to be not favorable, whereas extraction of products is inevitable in order to overcome thermodynamic limitation of the methanation reaction. According to our knowledge, no simple technology for extracting CH_4 from CO_2/H_2 mixture exists so far. Thus, CH_4 extraction is not an option here. But several methods are available for extracting water either continuously or in discrete manner, namely via hydrophilic membranes or simply by condensation. In addition to water removal, since the Sabatier reaction is highly exothermic, intensive cooling is necessary. This leads to one technically possible integrated concept, namely a reactor section with simultaneous water extraction by use of active cooling. For the sake of brevity, the integration concept developed on Level 1 will not be outlined in more detail here. Instead, the next focus is on Level 2, namely on a process system which applies intermediate condensation steps for water extraction and heat removal during the methanation reaction.

2.3. Model Formulation on Level 2

2.3.1. Reactors

We consider a cascade of polytropic tube bundle reactors with interstage condensation. The reactors are assumed to be randomly packed with spherical pellets. Optimization variables for each reactor of the cascade are: inlet temperature (573 K $\leq T_{in} \leq$ 673 K), inlet pressure (5 atm $\leq p_{in} \leq$ 10 atm), tube diameter (1 cm $\leq d_t \leq$ 5 cm), length of reactor (0.3 m $\leq L \leq$ 10 m), and inlet composition of the first reactor ($0.79 \leq x_{H2,in} \leq 0.81$, $0.19 \leq$

$x_{CO2,\ in} \leq 0.21$). The particle diameter of the catalyst in the tubes is an optimization variable which was varied such that $d_t / d_p \geq 10$.
The tubular reactors are described using a 1D pseudo homogeneous plug flow model. The component mass balances, Eq. (1), and the energy balance, Eq.(2), are given by:

$$\frac{d(\rho_i v_i)}{dz} = \left(\rho_c \frac{1-\varepsilon}{\varepsilon} M_i \right) \sum_j \nu_{ij} r_j \tag{1}$$

$$\rho_g C_p \frac{dT}{dz} = -\left(\frac{4}{d_t \varepsilon} q + \sum_j \Delta H_j r_j \rho_c \frac{(1-\varepsilon)}{\varepsilon} \right) \frac{1}{v_i} \tag{2}$$

The reaction rate expressions r_j for the main reaction (methanation) and the main side reaction (reverse water gas shift) are taken from the work of Xu and Froment (1989).
The heat transfer between the reactor and the coolant was described by

$$q = \alpha_w (T - T_c) \tag{3}$$

where T_c, bounded between 550 and 700 K, is used to control the heat flux q. The heat transfer coefficient across the wall of the reactor is calculated using the correlation given by Yagi et al. (1959). Ergun's equation was used to estimate the pressure drop:

$$\frac{dp}{dz} = -\left(150 \mu_g \frac{(1-\varepsilon)^2}{d_p^2 \varepsilon^3} + 1.75 \frac{v_s \rho_g (1-\varepsilon)}{d_p \varepsilon^3} \right) v_s \tag{4}$$

2.3.2. Condensers
Each condenser is represented by two heat exchangers in series: the first uses steam as coolant while the second uses liquid water. The phase separation in the condenser is calculated using a standard equilibrium flash model (see e.g. Biegler et al., 1997). At equilibrium, the dew point equation must be satisfied. The temperature and split factor defined as $\xi_i = n_{i,vapour} / n_{i,feed}$ $(0 \leq \xi_i \leq 1, 298 \leq T_{cond} \leq 400K)$ are optimization variables while the condensation pressure p_{cond} is set equal to the reactor pressure upstream. The phase distribution constants, $K_{i,cond} = y_{i,cond} / x_{i,cond}$, are calculated using temperature- dependent correlations (Fernandez-Prini et al., 2003) which also account for the solubility of the gaseous components in the liquid phase.

2.3.3. Downstream Dehydration Process
Since natural gas distribution grids require extremely low water content, downstream drying of the generated SNG is indispensable. Several technologies are available for drying natural gas. The most widely used technology is the dehydration of the gas by water absorption using triethylene glycol (TEG). This technology is easy to operate, cheap to install, and the TEG regeneration requires a relatively low amount of energy. In order to estimate the size of the water absorption column and further operating conditions of the glycol unit, we used correlations proposed by Bahadori and Vuthaluru (2009) who calculated the water removal efficiency as a function of the following optimization variables: number of theoretical stages, circulation rate and glycol purity

which is a function of boiler pressure and boiling temperature (Bahadori et al., 2014). The boiler uses steam for heating the glycol-rich solution. The pressure of the absorber column was fixed at 41 bar, the inlet temperature of the wet gas at 311 K and that of the lean glycol at 317 K.

2.3.4. Compressors and Heat Exchangers

The heat exchangers considered are counter-current tube-shell exchangers. The heat exchange area is calculated in terms of the heat duty, mean logarithmic temperature difference, and the heat transfer coefficient. While the heat duties are calculated based on energy and mass balances, overall heat transfer coefficients can be estimated in dependence on the heat transfer media and typical flow conditions.

The outlet temperature and theoretical electric power consumption of the gas compressors are calculated by assuming ideal isentropic compression. The resulting brake power is estimated with the help of compressor and motor efficiencies. Sizing the heat exchangers and compressors is done using the method reported in Biegler et al. (1997).

2.4. Process Optimization

The objective is to minimize the production cost of the proposed process for a given volumetric SNG production rate of 891 m_N^3/h. The production costs include the raw materials, operating costs, and investment costs of the main utilities (heat exchangers, compressors, reactors, glycol water absorption unit). Typical values for the costs of raw materials, electricity, steam, and cooling water are used. The plant is assumed to operate for 10 years, 330 days a year. The investment cost of the sized equipment is estimated using power law correlations developed first by Guthrie in 1969 (see e.g. Biegler et al., 1997), corrected by use of cost updating factors (Chemical Engineering Plant Index, 2012). As mentioned earlier, three different reactor cascades with different number of intermediate condensation steps (1 -3 steps) are investigated and compared on the basis of the production costs of the overall process. Each reactor of the cascade is assumed to consist of 500 parallel tubes filled with catalyst as sketched in Figure 1.

The resulting optimization problem was solved using CONOPT 3.14 G in AMPL. It can be stated as follows:

$$\min_{DoF} \; Cost$$

s.t:

- Component balance equations
- Energy balance equation
- Pressure drop equation
- Chemical reaction kinetics
- Heat transport kinetics
- Ideal gas law
- Inequality constraints (e.g. $d_t/d_p \geq 10$)
- Shortcut models for other process units(e.g.condensers, compressors,absorber)

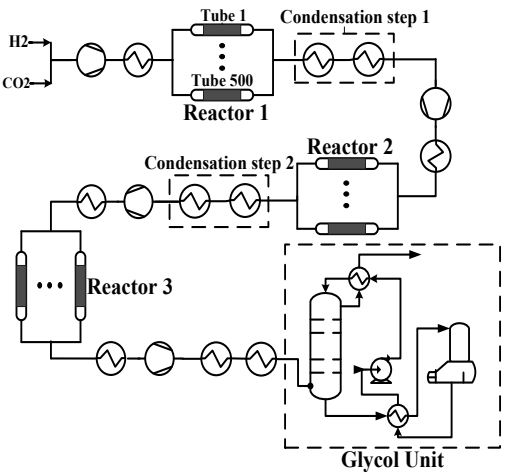

Figure 1: Process flow sheet: Cascade of 3 reactors, each with 500 parallel tubes, and 2 intermediate condensation steps.

3. Results

Although increasing the number of condensation steps enhances the performance of the reactor cascade, as reflected by the space time yield (STY=4.1; 8.8; 10.1 mol/(m^3 s), for 1,2 and 3 condensation steps, respectively), it is not always beneficial on the economical level. The results in Figure 2 shows that having two intermediate condensation steps instead of only one step reduces the production cost by around 440,000 USD. However, adding one condensation step (i.e. 3 intermediate condensation steps with 4 reaction segments) leads to an increase of the cost by more than 2 million USD. This is due to the fact that the incremental enhancement in the performance of the reactors decreases with increasing the number of condensation steps. Beyond two steps, this enhancement does not compensate the increased investment and operating cost for the additional equipment needed (e.g. heat exchangers).

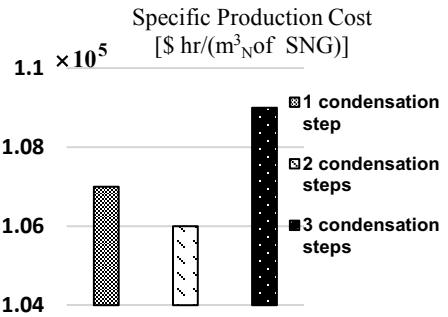

Figure 2: Specific production cost of the process for different number of condensation steps in the reactor cascade.

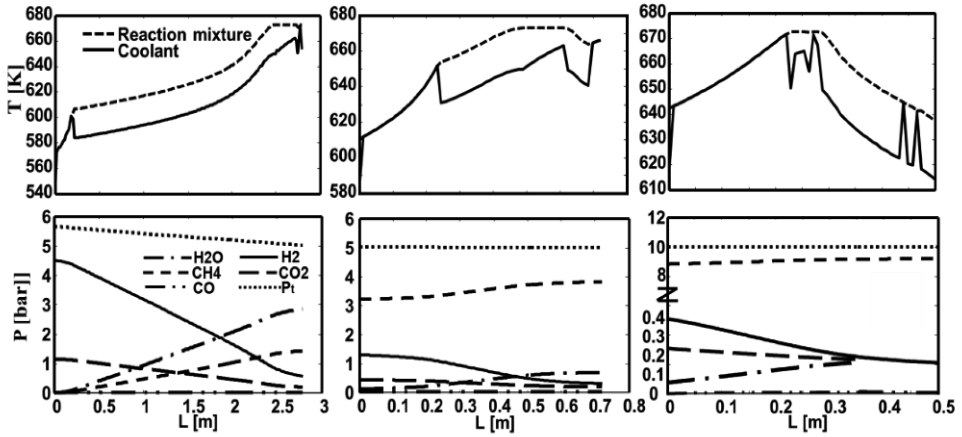

Figure 3: Optimal temperature profiles (upper row), total pressure and partial pressures (lower row) in the tubes of the three reactors (from left to right: reactors 1, 2, 3).

Thus, the best process configuration is a cascade of three tube bundle reactors with two intermediate condensation steps. The optimal temperature profiles of the coolant and reaction mixture in the tubes of the three reactors are presented in Fig. 3. These profiles can be approximated using a combination of adiabatic operation and active cooling using cocurrent (reactor 1 and 2) and counter current (reactor 3) heat exchange. The oscillations of the coolant temperature in reactor 3 are difficult to realize technically. They can be either approximated using countercurrent heat exchange or by partly adiabatic operation. Figure 3 also shows the partial pressure of the different components as well as the total inlet pressure. The optimal inlet pressure of the first and second reactor is 5.6 and 5 bars respectively. Although a higher pressure is favorable from the kinetic as well as from the thermodynamic perspective, a low pressure should be preferred since it reduces the cost of compression. However, the optimal inlet pressure of the third reactor is equal to the upper bound (10 bars) which shifts the methanation

equilibrium towards the product, thereby achieving the desired high level of H_2 conversion (X > 99%), and also increases the reaction rate. Furthermore, a high pressure in the last reactor reduces the power for gas compression to 41 bars, which is a typical pressure level in the absorber column of the glycol unit. The results also show that the concentration of the reactants increase due to intermediate condensation, leading to a sudden increase of reaction rates in the next reactor. The mole fraction of methane at the end of the reactor cascade is 94.7%. This increases further after drying the produced gas in the glycol unit such that the SNG quality requirements are met. Due to the condensation steps, the gas entering the absorber contains a low amount of water. For this reason only two theoretical stages are needed to purify the produced SNG.

4. Conclusions and Outlook

In this work, we design and optimize a process producing SNG from H_2 and CO_2. It consists of reaction section and a drying section. The cost optimal reaction section is a cascade of three fixed bed tube bundle reactors with two intermediate condensation steps for water removal. The results clearly show the importance of considering the coupling between the reaction section and the other process units when determining the optimal process operating conditions. Several advantages of water extraction in the reaction section are visible: (1) overcoming the thermodynamic limitation of the methanation reaction, (2) enhancing the chemical kinetics, and (3) reducing the energy duty of the glycol unit used for final gas drying. Within the reactor tubes, optimal temperature profiles should be realized in order to follow the optimal reaction route. In the future, we will compare the here proposed process configuration with a reactor equipped with an integrated hydrophilic membrane for in situ water removal. Based on this comparison one can step into detailed reactor design (Level 3 of our EPF methodology).

5. References

A. Bahadori and H. B. Vuthaluru, 2009, Simple methodology for sizing of absorbers for TEG gas dehydration systems. Energy, 34,1910-1916.

A. Bahadori, G. Zahedi, S. Zendehboudi and A. Jamili, 2014, A new method estimates TEG purity versus reconcentrator temperature at different levels of pressure in gas dehydration systems. Int. Journal Oil, Gas and Coal Technology, 7(1), 85-94.

L.T. Biegler, A.W. Westerberg, I.E. Grossmann, 1997, Systematic methods of chemical process design. Prentice Hall PTR.

R. Fernandez-Prini, J. L. Alvarez and A. H. Harvey, 2003, Henry's constants and vapor-liquid distribution constants for gaseous solutes in H_2O and D_2O at high temperatures. Journal of Physical and Chemical Reference Data, 32, 903-916.

A. Peschel, H. Freund and K. Sundmacher, 2010, Methodology for the design of optimal chemical reactors based on the concept of Elementary Process Functions, Ind. Eng. Chem. Res., 49, 10535–10548.

D. Stolten, B. Emonts, T. Grube and M. Weber, 2013, Hydrogen as an enabler for renewable energies, in: Stolten, D.; Scherer, V. (Eds.) Transition to renewable energy systems, Wiley-VCH, Weinheim,195-216.

J. Xu and G. Froment, 1989, Methane steam reforming, methanation and water-gas shift: 1. Intrinsic Kinetics. AIChE Journal, 35, 88-96.

S. Yagi and N. Wakao, 1959, Heat and mass transfer from wall to fluid in packed beds, AIChE Journal, 5, 79–85

Krist V. Gernaey, Jakob K. Huusom and Rafiqul Gani (Eds.), 12th International Symposium on Process Systems Engineering and 25th European Symposium on Computer Aided Process Engineering.
31 May – 4 June 2015, Copenhagen, Denmark

Inter-process Heat Integration by Coordination among Agent Systems for Heat Exchanger Network Design

Naoki KIMURA*, Tetsuo KAYA, Shintaro MIYAMOTO, Yoshifumi TSUGE

Department of Chemical Engineering, Faculty of Engineering, Kyushu Univerisity, 744 Motooka, Nishi-ku, Fukuoka 819-0395 Japan
nkimura@chem-eng.kyushu-u.ac.jp

Abstract

Pinch technology is one of the commonly used energy-saving technologies in chemical industries. We have proposed a simulation framework using multiagent into the design of heat exchanger network (HEN) to save the energy usage and to reduce the emissions of greenhouse gases. We set up several HEN Design Agents and each agent had different strategy to search candidate segments of HEN to modify. In our previous study, HENs for only a single process was optimized by the multiagent system at a time. However in general, there are some abutting chemical processes in a site. The inter-process heat integration, that is heat giving and heat receiving between a process and the others, is effective for energy saving in addition to the internal heat integration in a single process.

In this study, we introduced Coordinator agent within the multiagent framework to achieve both inner-process and inter-process heat integration simultaneously.

Keywords: Multiagent system; Coordinator agent; Pinch technology; Heat Recovery; Heat exchanger network;

1. Introduction

Design of heat exchanger networks (HENs) is one of the important levers to save the energy consumption and to reduce emissions of greenhouse gases, in chemical industries. Although the concept of pinch technology is involved in some process simulation software, the skilled engineers' considerations are still necessary to obtain preferable HENs. We have proposed a multiagent oriented framework for HENs design using pinch technology (Kimura 2010, 2012). We have set up several kinds of agent, for example "Project Manager", "Energy Cost Manager" and "HEN Design Agent". And also we have set up some different strategies to HEN Design Agents. In our previous study, our multiagent system could design only a single process at a time. However, there are some abutting chemical processes in a site. Inter-process heat integration or total site heat integration is starts to garner attention. Cheng et al. (2014) proposed a game-theory based optimization strategy and demonstrated their method with a vinyl chloride monomer process. Onishi et al. (2014) proposed a multi-stage superstructure using MINLP to synthesize work exchange and heat integration simultaneously. Liew et al. (2014) developed Total Site Heat Storage Cascade, which can transfer the heat

between several batch processes. In their work, the detailed information of sub processes is necessary to provide to make integration scheme. However in the point of information management, information sharing is not always enthusiastic.

In this study, coordinator agent is introduced to our multiagent framework in order to achieve heat integration both respective sub processes and inter-process simultaneously. And also coordination mechanism is investigated.

2. Multiagent Framework

2.1. Agent framework

We have developed a multiagent framework with "Pinch technology" to design energy-saving chemical processes. In our previous study, HENs for only a single process was optimized at a time. However, there are several adjoining chemical processes in a site, several sub processes in a plant. In order to achieve inter-process heat integration, we introduced new agent named coordinator agent who accommodates heat from a certain sub process to another sub processes. Figure 1 shows the outline of our multiagent framework with coordinator agent. There are three multiagent systems, namely there are three sub processes A, B and C—which are represented by dashed shapes. In each sub process, there are one project manager, one targeting agent, one equipment cost

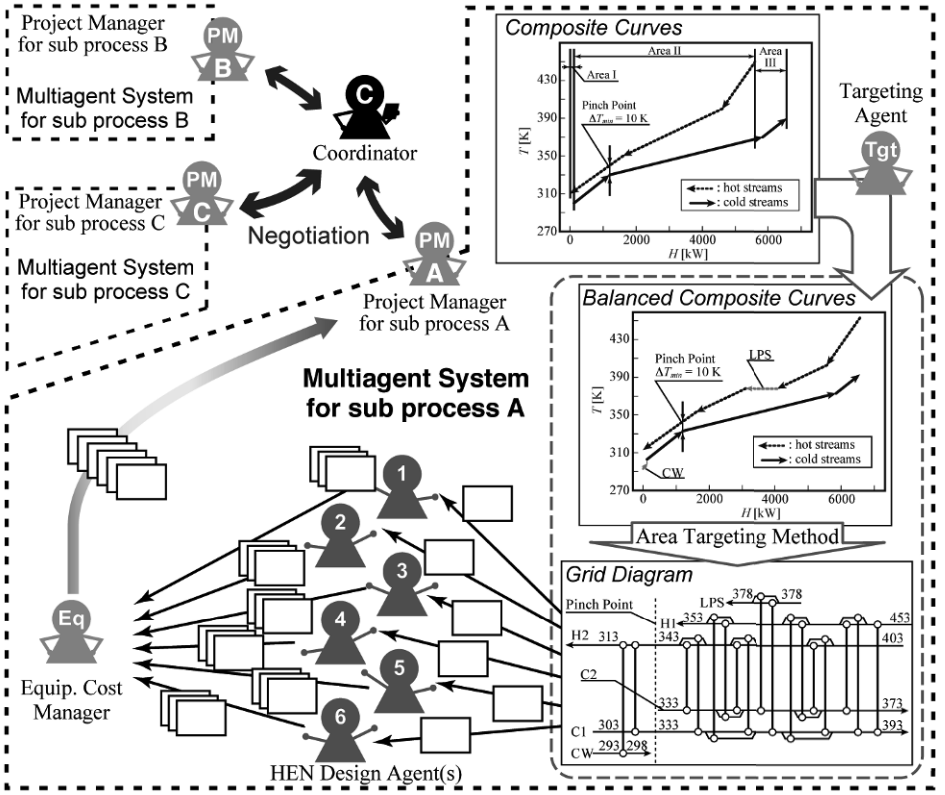

Figure 1: Schematic diagram of multiagent system with coordinator agent.

manager and some HEN design agents. Each multiagent system is able to optimize heat exchanger network for a single process. And process managers negotiate with coordinator agent based on their own result of the internal heat integration.

2.2. Negotiation protocol

Figure 2 shows an outline of communication sequence for the coordination mechanism. In the figure, there are three Project Managers named "PM-A", "PM-B" and "PM-C" for sub processes A, B and C respectively. For each sub process, there are also some agents (e.g. Targeting Agent, Cost Manager, Heat Exchanger Network Design Agent) to design and optimize its own heat exchanger network, but they are omitted in this figure. Each Project manager, named PM-A, PM-B or PM-C, sends a "Heat Demand" message—which contains the specification and quantity of utility— to the coordinator after the planning of the its internal heat integration. In the figure, PM-A needs to consume the high-pressure steam (HP) by 1.3 MW, PM-B can supply the HP by 18.9 MW and PM-C needs to consume the HP by 25.0 MW. When coordinator receives the Heat Demand messages from all the project managers, coordinator starts negotiation sessions with each project manager. Firstly, based on the heat demand from PM-A, coordinator sends a "Negotiation" message to PM-B to ask whether the HP (from PM-A) by 1.3 MW is receivable. Then, PM-B recalculate its internal heat integration and resend "Heat Demand" message with altered quantity of utility (-18.9 MW + 1.3 MW = -17.6 MW). After that coordinator sends other "Negotiation" message to PM-C to ask whether the HP by 17.6 MW can be supplied. If PM-C replies negative, coordinator starts another negotiation session based on the heat demand from PM-B.

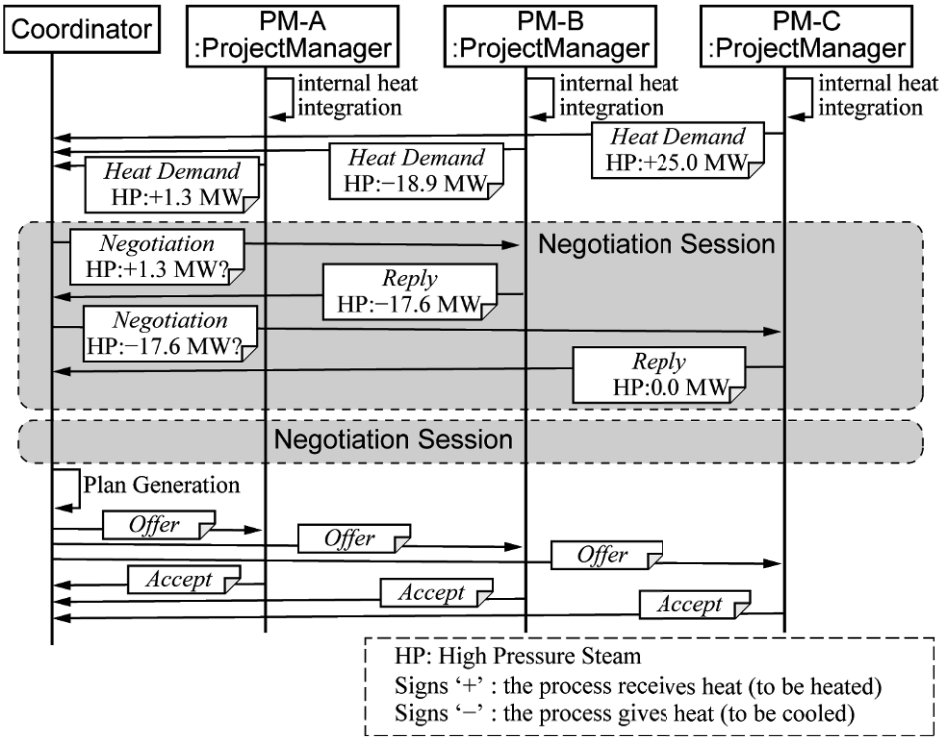

Figure 2: Communication sequence of coordination mechanism.

After the negotiation sessions, coordinator makes several inter-process heat integration plans by the matching between heat demands on the plan generation step. Then, coordinator sends “Offer” message to all the project managers with one of the heat integration plans. If coordinator receives "Accept” messages from all the project managers, the coordination is completed. If not, coordinator offers another plan, one after another. When the consensus obtained among coordinator and project managers, project managers respectively call their own Heat Exchanger Network Design Agents for HEN design based on the accepted inter-process heat integration plan.

3. Simulations and Results

3.1. The target process

3P-1 problem was applied to the above-mentioned multiagent system to achieve inter-process heat integration. This problem was originally introduced by Ahmad et al. (1991) and altered marginally by Hui et al. (1994). There are three sub processes—in other words “region”— A, B and C in the 3P-1. And there are certain distances between these three sub processes. The stream data of each sub processes are shown in Table 1(a)–(c), and the available utilities are shown in Table 1(d). Flue gas is a heating utility and chilled water is a cooling utility. Both HP-ex and HP-cycle mean ‘High Pressure steam’. HP-ex is a heating utility introduced from external energy plant. HP-cycle can be used not only as a heat giving (heating) utility but also as a heat receiving (cooling) utility to achieve the in-direct heat transfer between sub processes.

Table 1: Stream data of three sub processes and available utilities for 3P-1 problem.

(a): Sub process A

Stream Name	Temperature		*CP* [MW/°C]	Heat load *ΔH* [MW]
	Inlet T_{in} [°C]	Outlet T_{out} [°C]		
HotA1	250.0	120.0	0.30	39.00
ColdA1	185.0	220.0	0.50	17.50

(b): Sub process B.

Stream Name	Temperature		*CP* [MW/°C]	Heat load *ΔH* [MW]
	Inlet T_{in} [°C]	Outlet T_{out} [°C]		
HotB1	500.0	120.0	0.25	95.00
ColdB1	139.0	500.0	0.15	54.15
ColdB2	20.0	250.0	0.10	23.00

(c): Sub process C

Stream Name	Temperature		*CP* [MW/°C]	Heat load *ΔH* [MW]
	Inlet T_{in} [°C]	Outlet T_{out} [°C]		
HotC1	120.0	119.0	15.0	15.00
HotC2	200.0	30.0	0.20	34.00
ColdC1	110.0	160.0	0.25	12.50
ColdC2	200.0	201.0	25.0	25.00

(d): Available utilities.

Utility Name	Temperature		Annual cost [£/kW-y]
	Supply T_s [°C]	Return T_r [°C]	
Flue gas	1000.0	550.0	100.0
HP-ex	300.0	300.0	80.0
HP-cycle	300.0	300.0	120.0
Chilled water	5.0	6.0	10.0

3.2. Simulation result

Table 2 shows the utility distribution results, that is heat demands, after the internal heat integration of each sub process (i.e. before “negotiation session”). In the table, the above numeric numbers in a cell represent heating/cooling demands where the sign ‘+’ means consumption of the utility in its sub process, in contrast, the sign ‘–’ means providing. The below numeric numbers with parenthesis in a cell represent annual utility cost (or annual sales). Due to the internal heat integrations, the utility usage and

costs are minimized individually. However the net amount of annual utility cost for entire plant is over three million pounds.

Table 2: Utility distribution results for 3P-1 problem before inter-process heat integration.

Utility Name	Sub process			Net
	A	B	C	
Flue gas [MW]		+1.65		+1.65
(Cost [k£/yr])		(165)		(165)
HP-ex [MW]	+1.30		+25.00	+26.30
(Cost [k£/yr])	(140)		(2,000)	(2,140)
HP-cycle [MW]				0
(Cost [k£/yr])				(0)
Chilled water [MW]	+22.80	+19.50	+36.50	+78.80
(Cost [k£/yr])	(228)	(195)	(365)	(788)
Amount cost [k£/yr]	(332)	(360)	(2,365)	(3,057)

After the negotiation sessions among coordinator agent and three project managers, coordinator agent obtained nine feasible alternatives of inter-process heat integration plans out of 115 suggestions. Table 3 shows two alternatives of the inter-process heat integration. As compared with table 2, HP-cycle is used both in the plan 1 and 2 of table 3. Sub process B provides HP-cycle by 18.90 MW for sub process C instead of the chilled water demand. And the demand of HP-ex of sub process C is decreased in the both plans of table 3. Also the demand of HP of sub process A is changed from HP-ex to HP-cycle in the plan 2. As a consequence of the negotiation among coordinator agent and three project managers, the net amount of annual utility cost for entire plant is reduced more than half. Although the amount utility cost of entire plant and the cost sub process B are drastically reduced, the costs of sub processes A and B are the same or increased from table 2. In these cases, coordinator agent and project manager of sub process B are willing to agree to these plans. In contrast, project managers of sub processes A and C resist these plans because of the increasing utility costs.

Table 3: Utility distribution results for 3P-1 problem after inter-process heat integration.

	Plan 1				Plan 2			
	Sub process			Net	Sub process			Net
	A	B	C		A	B	C	
Flue gas [MW]		+1.65		+1.65		+1.65		+1.65
(Cost [k£/y])		(165)		(165)		(165)		(165)
HP-ex [MW]	+1.30		+6.10	+7.40			+7.40	+7.40
(Cost [k£/y])	(140)		(488)	(592)			(592)	(592)
HP-cycle [MW]		-18.90	+18.90	0	+1.30	-18.90	+17.60	0
(Cost [k£/y])		(-2,268)	(2,268)	(0)	(140)	(-2,268)	(2,112)	(0)
Chilled water [MW]	+22.80	+0.60	+36.50	+59.90	+22.80	+0.60	+36.50	+59.90
(Cost [k£/y])	(228)	(6)	(365)	(599)	(228)	(6)	(365)	(599)
Amount cost [k£/y]	(332)	(-2,097)	(3,121)	(1,356)	(384)	(-2,097)	(3,069)	(1,356)

4. Conclusions

In this study, “coordinator agent” had been introduced to the multiagent framework in order to achieve inter-process heat integration. And also the communication protocol

had been investigated. The results shows that it was possible to obtain several feasible inter-process heat integration alternatives using our multiagent system.

Acknowledgement

This work was supported by JSPS KAKENHI Grant Number 25730137.

References

S. Ahmad, D. C. W. Hui, 1991, “Heat Recovery between Areas of Integrity,” Computers & Chemical Engineering, 15, 809–832.

S.L. Cheng, C.T. Chang, D. Jiang, 2014, “A game-theory based optimization strategy to configure inter-plant heat integration schemes,” Chemical Engineering Science, 118, 60–73.

C. W. Hui, S. Ahmad, 1994, “Minimum Cost Heat Recovery between Separate Plant Regions,” Computers & Chemical Engineering, 18, 711–728.

N. Kimura, K. Yasue, T. Kou, Y. Tsuge, 2010, "A Multiagent Approach for Sustainable Design of Heat Exchanger Networks," Lecture Notes in Computer Science, 6277, 409–416.

N. Kimura, K. Yasue, K. Kobayashi, Y. Tsuge, 2012, "Improvement in Strategy for Design of Heat Exchanger Networks using Multiagent Framework," in Proc. of the 11th International Symposium on Process Systems Engineering (PSE2012), 1557–1561, Singapore.

P.Y. Liew, S.R. Sharofah, R.W. Alwi, J.J. Klemeš, P.S. Varbanov, Z.A. Manan, 2014, “Algorithmic targeting for Total Site Heat Integration with variable energy supply/demand,” Applied Therman Engineering, 70, 1073–1083.

V.C. Onishi, M.A.S.S. Ravagnani, J.A. Caballero, 2014, “Simultaneous synthesis of work exchange networks with heat integration,” Chemical Engineering Science, 112, 87–107.

Krist V. Gernaey, Jakob K. Huusom and Rafiqul Gani (Eds.), 12th International Symposium on Process Systems Engineering and 25th European Symposium on Computer Aided Process Engineering.
31 May – 4 June 2015, Copenhagen, Denmark

Design and synthesis of batch processing plants: A consideration of utility aspect and using a robust scheduling platform

Esmael R. Seid and Thokozani Majozi*

School of Chemical and Metallurgical Engineering, University of the Witwatersrand, 1 Jan Smuts Avenue, Johannesburg, 2000, South Africa
*Corresponding author email address: thokozani.majozi@wits.ac.za

Abstract

The aim of this contribution is to address design, synthesis and scheduling simultaneously with the consideration of economic savings in utility requirements. The recent design and synthesis model by Seid and Majozi (2013) is extended to incorporate the design of the associated utility facility, since it is proven to result in better design objective and computational efficiencies. Additional feature of the proposed model is the determination of optimal pipe connection between processing equipment. The model is implemented in a case study in order to demonstrate its application. From the case study, the profit is increased by 20% and the total utility requirement is reduced by 41.1% for the design and synthesis of energy integrated batch plant compared to the basic design.

Keywords: Design; synthesis; multipurpose batch plant; energy integration; optimization; scheduling.

1. Introduction

There is a great deal of interest in the manufacture of fine chemicals, pharmaceutical products, polymers, food and beverages using batch operations because of their suitability for producing low-volume, high value products, their flexibility to adopt complex operations due to fast market change and their capability to manufacture different products using the same facility. In these batch facilities the different products compete for the available resources, (equipment, utility, manpower and storage) which renders the design and operation of these plants a challenging task. Great effort has been made in the last two decades to develop efficient models for design and synthesis problems.

Papageorgaki and Reklaitis (1990) proposed a mixed integer linear programming (MILP) formulation which accommodated equipment used in and out of phase, units available with different sizes in a processing stage and tasks which can be processed in different equipment. Most of the previous published work were restricted by the following key assumptions: (a) there was a prespecified assignment of equipment items to product tasks, (b) parallel production was only allowed for products that had no common equipment requirements, (c) all units of a given type were identical and could be used in the out of phase mode, (d) all units of a given type were devoted to the production of only one product at a time. Xia and Macchietto (1997) presented a general formulation considering linear/nonlinear models for capital cost of processing units/storage vessels and processing task models with fixed, linear and nonlinear processing time in a general form. The formulation resulted in a mixed integer nonlinear

programming (MINLP) solved by a stochastic MINLP optimizer. A short term scheduling model was implemented based on discrete time representation that allowed multiple batches of a product to be processed in any sequence. This deviated from previous published literature that considered campaign mode of operation. Lin and Floudas (2001) presented a formulation based on the scheduling formulation of Ierapetritou and Floudas (1998) using a unit specific event point and continuous time representation. The formulation addressed a single campaign production approach where multiple batches of a product can be produced in the given time horizon. A comparison with earlier formulation was given. The increasing importance of utilities rationalization within the design of multipurpose batch plants was first addressed by Barbosa-Povoa et al. (2001) who presented a mathematical formulation for the detailed design of multipurpose batch process facilities. This work was later extended by Pinto et al. (2003) where economic savings in utility requirements were obtained while also considering the cost of the auxiliary structures, i.e. heat-exchanger transfer area, and the design of the utility circuits and associated piping costs. Pinto et al. (2008) presented a review on the design of batch plants where both the grassroots and the retrofit design problems are analysed. Two types of plants are considered, the multi-product and the multipurpose plants. They also discussed the limitations and gaps in the published methods in literature.

2. Mathematical model

The mathematical model comprises the following sets, variables, parameters and constraints:

Sets

$J = \{ j \mid j$ is an equipment including heat exchanger$\}$, $P = \{ p \mid p$ is a time point$\}$, $S = \{ s \mid s$ is any state$\}$, $I_c = \{ i_c \mid i_c$ is a task that requires heating$\}$, $I_h = \{ i_h \mid i_h$ is a task that requires cooling$\}$, $I_{rm} = \{ i_{rm} \mid i_{rm}$ is a task that requires raw material$\}$

Continuous variables

$cw(i_h, p)$ = external cooling required by task i_h at time point p, $st(i_c, p)$= external heating required by task i_c at time point p, $w(i_h, i_c, p)$= amount of heat exchanged between the cold and hot task, $tp(i, p)$ = time at which a task finish, $tu(i, p)$ = time at which a task start, A = optimal heat exchanger area required, $mu(i_h, p)$ = amount of material processed by the hot task, $mu(i_c, p)$ = amount of material processed by the cold task, $q(s^p, p)$= amount of product delivered

Binary variables

$x(i_h, i_c, p)$ = 1 if hot task i_h is integrated with the cold task i_c at time point p; 0 otherwise, $y(i, p)$= 1 if task i is active at time point p; 0 otherwise, $e(j)$= 1 if unit j is selected; 0 otherwise

Parameters

C_p = specific heat capacity of fluid, $E(i)$= constant coefficient of amount of heat required or removed corresponding to task i, $\xi(i)$= variable coefficient of amount of heat required or removed corresponding to task i, M= any large number $T(i)$= operating temperature for a task i, $\Delta T^{\min}$ = minimum allowable thermal driving force, C_c = cost unit for cooling, C_h = cost unit for steam, U = overall heat transfer coefficient, $price(s^p)$=selling price for a product, AWH = annual working hour, H = time horizon of interest, FOC = fixed operating cost for a task, VOQ = variable operating cost for a task, FEC = fixed capital cost of equipment, VEQ = variable capital cost of equipment, RCS = raw material cost

Constraints

The recent robust design and synthesis formulation for multipurpose batch plants by Seid and Majozi (2013) is used as a platform. In addition to the design and synthesis model of Seid and Majozi (2013) the following energy integration constraints are used.

Constraints (1) and (2) are active simultaneously and ensure that one hot unit will be integrated with one cold unit when direct heat integration takes place.

$$\sum_{i_c} x(i_h, i_c, p) \le y(i_h, p), \forall\ p \in P,\quad i_h \in I_h \tag{1}$$

$$\sum_{i_h} x(i_h, i_c, p) \le y(i_c, p), \forall\ p \in P,\ i_c \in I_c \tag{2}$$

Constraint (3) ensures that minimum thermal driving forces are obeyed.

$$T(i_h) - T(i_c) \ge \Delta T^{\min} - M(1 - x(i_h, i_c, p)), \forall\ p \in P,\ i_c, i_h \in I \tag{3}$$

Constraint (4) states that the cooling of a heat source will be satisfied by direct heat integration as well as external utility if required.

$$(E(i_h) y(i_h, p) + \xi(i_h)\, mu(i_h, p))(tp(i_h, p) - tu(i_h, p)) = cw(i_h, p) + \sum_{i_c} w(i_h, i_c, p), \forall\ p \in P,\quad i_h \in I_h \tag{4}$$

Constraint (5) ensures that the heating of a heat sink will be satisfied by direct heat integration as well as external utility if required.

$$(E(i_c) y(i_c, p) + \xi(i_c))(tp(i_c, p) - tu(i_c, p)) = st(i_c, p) + \sum_{i_h} w(i_h, i_c, p), \forall\ p \in P,\quad i_c \in I_c \tag{5}$$

Constraint (6) states that the amount of heat exchanged between the hot and cold unit is limited by the total duration of the cold unit.

$$w(i_h, i_c, p) \le (E(i_h) y(i_h, p) + \xi(i_h)\, mu(i_h, p))(tp(i_c, p) - tu(i_c, p)), \forall\quad p \in P,\ i_c \in I_c,\ i_h \in I_h \tag{6}$$

Constraint (7) ensures that the amount of heat transferred from the hot unit to the cold unit is limited by the duration of the hot unit.

$$w(i_h, i_c, p) \le (E(i_c) y(i_c, p) + \xi(i_c)\, mu(i_c, p))(tp(i_h, p) - tu(i_h, p)), \forall\ p \in P,\quad i_c \in I_c,\ i_h \in I_h \tag{7}$$

Constraint (8) states that the amount of heat exchanged between the hot and cold unit cannot exceed a predetermined maximum value *M*.

$$w(i_h, i_c, p) \le M x(i_h, i_c, p), \forall\ p \in P,\quad i_c \in, I_c,\ i_h \in I_h \tag{8}$$

Constraints (9) and (10) are used to determine the heat exchanger area required.

$$UA(T(i_h) - T(i_c))(tp(i_h, p) - tu(i_h, p)) \ge w(i_h, i_c, p), \forall i_h \in I_h, i_c \in I_c, p \in P \tag{9}$$

$$UA(T(i_h) - T(i_c))(tp(i_c, p) - tu(i_c, p)) \ge w(i_h, i_c, p), \forall\ i_h \in I_h, i_c \in I_c, p \in P \tag{10}$$

Constraints (11) and (12) are used to synchronize units when heat integration takes place.

$$tp(i_h, p) \ge tp(i_c, p) - M(1 - x(i_h, i_c, p)), \forall\ p \in P,\quad i_c \in I_c,\ i_h \in I_h \tag{11}$$

$$tp(i_h, p) \le tp(i_c, p) + M(1 - x(i_h, i_c, p)), \forall\ p \in P,\quad i_c \in I_c,\ i_h \in I_h \tag{12}$$

Constraint (13) and (14) are used to cater for external utilities.

$$u_c = \sum_p \sum_{i_c} cw(i_c, p), \forall p \in P\ , i_c \in I_c \tag{13}$$

$$u_h = \sum_p \sum_{i_h} st(i_h, p), \forall p \in P\ ,\ i_h \in I_h \tag{14}$$

Constraint (15) is the objective function expressed as maximization of profit.

$$\text{maximize} \left(\begin{array}{l} \sum_{s^p} price(s^p)\, q(s^p, p) - \sum_p \sum_{i \in I_{rm}} RCS * mu(i, p) - \\ \sum_p \sum_{i \in I} FOC * y(i, p) + VOC * mu(i, p) \\ - C_c u_c - C_h u_h \end{array} \right) * (\text{AWH/H}) - \sum_{j \in J} FEC * e(j) + VEQ * ss(j) \tag{15}$$

3. Case study

This example, which was first examined by Sundaramoorthy and Karimi (2005), is studied extensively in literature. It is a relatively complex problem and is often used in literature to check the efficiency of models in terms of optimal objective value and CPU time required. The plant has many attributes of a multipurpose batch plant, with the following features: units performing multiple tasks, multiple units suitable for a task, states shared by multiple tasks and different products produced following different production paths. The state task network representation (STN) for this case study is depicted in Figure 1. The scheduling and design data are presented in Table 1. The raw material costs for state A, B and C are 1, 0.5 and 0.2 cost units (c.u/kg) respectively. The selling price for product 1 and 2 are 4 and 7 c.u/kg. respectively. Reaction 1 operates at 200 ^{o}C and it is exothermic which requires 0.167 kw/kg of cooling load. Reaction 2 operates at 70 ^{o}C and it is endothermic which requires 0.222 kw/kg of heating load. Reaction 3 operates at 160 ^{o}C and it is exothermic which requires 0.194 kw/kg of cooling load. Steam cost and cooling water cost are 0.7 and 0.15 c.u/MJ respectively. The plant operates 300 days/year.

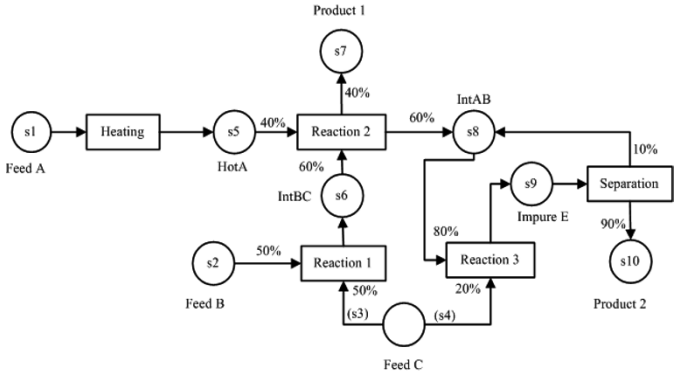

Figure 1. STN representaion for the case study.

Table 1. Equipment and scheduling data for the case study.

Unit	Capacity (ton/m^2)	Suitability	Processing time	Cost model (k c.u.)
Heater	5.0-30.0	Heating	1	200.0+10*s*
Reactor 1	5.0-50.0	Reaction 1	2	5000.0+15*s*
		Reaction 2	2	
		Reaction 3	1	
Reactor 2	5.0-50	Reaction 1	2	5000.0+10s
		Reaction 2	2	
		Reaction 3	1	
Still	5.0-20.0	Separation	2,5	150.0+5*s*
Vessel 4	5.0-50.0	(Hot A)		50.0+3*s*
Vessel 5	5.0-50.0	(Int BC)		70.0+3*s*
Vessel 6	5.0-50.0	(Int AB)		60.0+4*s*
Vessel 7	5.0-50.0	(Impure E)		90.0+5*s*
Heat exchanger 1	0.0-200.0	RX1-RX2		60+5s
Heat exchanger 2	0.0-200.0	RX2-Rx3		60+5s

Results and discussion

The computational results found are depicted in Table 2 and Table 3. An overall profit of 2.6x10^8 c.u. was obtained using the model that catered for energy integration which is much better than the objective value of 2.08x10^8 c.u. obtained by the model without considering energy integration. Consequently, a 20% increase in profit was achieved by

allowing heat integration between the hot and cold tasks. From Table 3 a significant saving in hot utility can be attained by integrating the hot and cold tasks leading to supplanting most of the external utility requirement (160 GJ hot utility required by energy integrated batch plant vs. 271.9 GJ hot utility required by the basic design without energy integration). Consequently a saving of 41.1% in hot utility requirement is achieved. This indicates that solving a design and synthesis problem for batch plants by considering scheduling and heat integration results not only in efficient use of equipment resources for maximum production of products but also rational use of energy for sustainable operation. It is worth mentioning that this comprehensive model also determines the optimal heat exchanger area required in order to allow the heat transfer. An optimal area of 25.6 m^2 for heat exchanger 1 and 43.2 m^2 for heat exchanger 2 was obtained. Figure 2 details the possible amount of energy integration between the cold and hot units and the time intervals during which energy integration occurred. The energy requirements of reactor 1 and reactor 2 during the interval 4 h to 6 h is highlighted to elaborate on the application of the proposed model. The cooling load of reactor 2 between 5 h and 6 h was 25 GJ. This cooling requirement is fully satisfied through energy integration with reactor 1 in the same time interval, resulting in supplanting an external cooling requirement if it operated in standalone mode. At the beginning of the operation of reactor 1 from 4 h to 5 h, the heating requirement was 25.8 GJ. This value was obtained using the time average model by multiplying the duration (5 – 4 h) and the energy demand per hour (51.6 GJ/2 h (total duration of the task) = 25.8 GJ) where the heating requirement is fully satisfied by external heating. For the rest of its operation between 5 h to 6 h, the heating requirement was 25.8 GJ, satisfied partly with energy integration (25 GJ) and the difference by external heating with energy requirement of 0.8 GJ. The amount of material each unit is processing, the type of task each unit is conducting at a specific time point and the starting and finishing times for each task is also presented in Figure 2.

Table 2. Equipment design capacity for the case study.

Unit	Equipment capacity range	Design capacity with consideration of energy integration	Design capacity without consideration of energy integration
Heater	5-30	19	13.3
Reactor 1	5-50	47.7	20
Reactor 2	5-50	50	20
Still	5-20	20	33.3
Vessel 4	5-50	19	13.3
Vessel 5	5-50	30.6	28.7
Vessel 6	5-50	32.1	14
Vessel 7	5-50	33.3	0
Heat exchanger 1	0-200	25.6	-
Heat exchanger 2	0-200	43.2	-

Table 3. Computational results for the case study.

Method	Time point	Objective value	Binary variables	Continous variables	Constraints	CPU time (s)	Cold utility	Hot utility
Design without energy integration	11	$2.08*10^8$	176	793	2079	19	220.4 GJ	271.9 GJ
Design with energy integration	11	$2.6*10^8$	222	887	2367	198	34.4 GJ	160 GJ

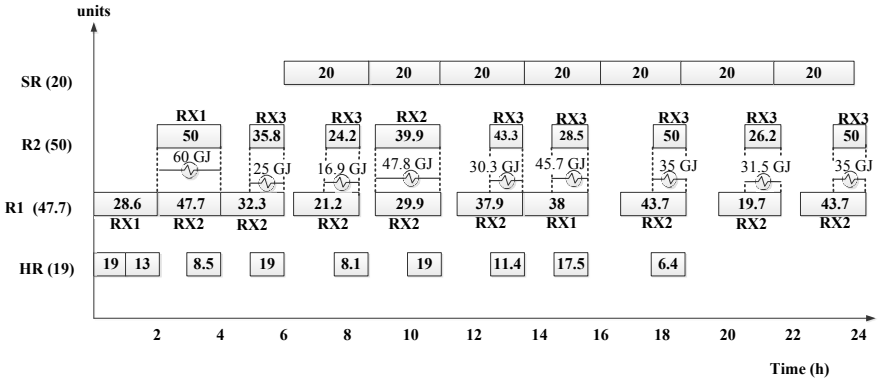

Figure 2. Gantt chart for the case study.

4. Conclusions

An efficient method for the design and synthesis of batch plants that incorporates energy integration was presented. The developed model simultaneously solved scheduling and energy integration within the same design framework leading to optimal design of equipment and rational use of energy. From the case study, the profit maximization was increased by 20% in the energy integrated batch plant compared to the basic design where utilities were the only option to satisfy the heating and cooling load requirements demanded by the tasks. The total hot utility requirement was reduced by 41.1% for the energy integrated batch plant compared to the basic design. From this it can be concluded that for efficient design of batch plants, energy integration must be incorporated in the design problem.

References

Barbosa-Póvoa, A.P., Pinto, T., Novais, A.Q., 2001. Optimal design of heat-integrated multipurpose batch facilities: A mixed integer mathematical formulation, Comput. Chem. Eng. 25, 547–559.

Ierapetritou, M.G., Floudas, C.A., 1998. Effective continuous-time formulation for short-term scheduling: 1. Multipurpose batch processes. Ind. Eng. Chem. Res. 37, 4341-4359.

Lin, X, Floudas, C.A., 2001. Design, synthesis and scheduling of multipurpose batch plants via an effective continuous-time formulation. Comput. Chem. Eng. 25(4–6), 665–674.

Papageorgaki, S., Reklaitis, G.V., 1990. Optimal design of multipurpose batch plants. 1. Problem formulation. Ind. Eng. Chem. Res.. 29(10), 2054–2062.

Pinto, T., Barbosa-Povoa, A.P., Novais, A.Q., 2003. Optimal design of heat-integrated multipurpose batch facilities: A mixed integer mathematical formulation. Comput. Chem. Eng. 25, 547–559.

Pinto, T., Barbosa-Povoa, A.P., Novais, A.Q., 2008. Design of multipurpose batch plants: A comparative analysis between the STN, m-STN, and RTN representations and formulations. Ind. Eng. Chem. Res. 47, 6025-6044.

Seid, E.R., Majozi, T., 2013. Design and synthesis of multipurpose batch plants using a robust scheduling platform. Ind. Eng. Chem. Res. 52, 16301-16313.

Xia, Q.S., & Macchietto, S., 1997. Design and synthesis of batch plants MINLP solution based on a stochastic method. Comput. Chem. Eng. 21, S697–S702.

Krist V. Gernaey, Jakob K. Huusom and Rafiqul Gani (Eds.), 12th International Symposium on Process Systems Engineering and 25th European Symposium on Computer Aided Process Engineering.
31 May - 4 June 2015, Copenhagen, Denmark.

A Novel Approach for the Identification of Economic Opportunities within the Framework of a Biorefinery

A. I. Torres[a], I. Cybulska[b], C. J. Fang[b], M. H. Thomsen[b], J. E. Schmidt[b] and G. Stephanopoulos[a]

[a]*Department of Chemical Engineering, Massachusetts Institute of Technology, Cambridge, MA 02139, USA*
[b]*Department of Chemical and Environmental Engineering, Masdar Institute of Science and Technology, Masdar City, United Arab Emirates*
geosteph@mit.edu

Abstract

In this paper we propose a novel mathematical framework for the study of biorefinery networks. The framework is based on a natural decomposition of the biorefinery network in two sub-problems: a supply of intermediates and a demand of intermediates. The two sub-problems can be optimized independently of each other and their solutions are later coordinated to yield the optimal feasible biorefinery complex. Based on this separability, a computer aided computational environment that emulates the proposed framework is presented.

Keywords: Biorefinery, multi-objective optimization, computer aided collaborative environment

1. Introduction

Advances in technologies for processing biomass feedstocks have resulted in the development of a large number of potential processing schemes for the production of biomass-based fuels, chemicals and materials. To address questions such as which is the most attractive set of products that can be produced from a particular feedstock, which are the best processing pathways, and which are the costs and environmental benefits associated with these conversions, detailed techno-economic analysis of particular combinations of feedstock-technology-products have been performed (Torres et al., 2010; Sen et al., 2012), and more recently, frameworks to systematize the analysis and evaluation of multiple-feedstock multiple-product integrated biorefineries have been proposed (Kim et al., 2013; Murillo-Alvarado et al., 2013).

These frameworks are based on constructing the superstructure of all potential technologies that link biomass feedstocks to the desired products and then the most promising pathways and combination of processes are found through mathematical programming, where the degrees of freedom for optimization involve the type of technologies to be used, and the optimal values of the process design parameters. A common feature of these approaches is that the whole conversion process, *i.e.* from biomass feedstocks to products, is assumed to take place in the same facility, a single actor biorefinery. Moreover, an a-priori fixed, and limited in size, set of target products is considered in all case studies.

In this paper, we propose an alternative framework for the design and optimization of biorefineries in which we aim to introduce the flexibility required for the simultaneous and independent assessment of processes for the production of new bio-based compounds that are being developed

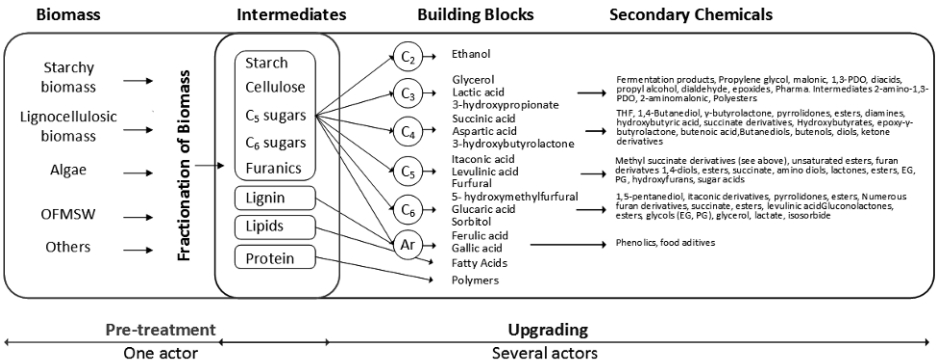

Figure 1: Schematic of a biorefinery complex. Adapted from Werpy and Petersen (2004).

by multiple actors. Within this framework, at the final stage of the design problem, the optimal profitability of the biorefinery complex as a whole will also be guaranteed.

We propose to do so by establishing a natural decomposition of the biorefinery network in a supply and a demand sub-problems which are linked through a set of intermediates. Through the formulation of a multi-actor multi-objective optimization problem, and using a two level Lagrangian approach, in Section 2 we will show that the proposed biorefinery network is separable and that each actor can separately optimize its own process. Furthermore, in Section 3 we will outline the structure of a computer-aided collaborative design environment which was designed to emulate the proposed mathematical framework.

2. Framework for the design of biorefineries

2.1. Problem Statement

Figure 1 shows a schematic of a general biorefinery complex. It comprises several biomass feedstocks that upon fractionation produce a number of "intermediate compounds". These intermediates can in turn serve as feedstocks for different thermochemical or biochemical processes, and be converted into a large variety of chemicals, such as those reported in Werpy and Petersen (2004).

All types of biomass can be seen as composed of a complex mixture of the same major compounds namely carbohydrates (poly and monosaccharides), lignin, lipids and proteins, where differences in their relative amounts and inter and intramolecular chemical bonds give rise to differences in physical structure and reactivity. Processes such as solvent extraction, hydrothermal or organosolv pre-treatment and enzymatic hydrolysis, among others, aim to separate and break down these compounds. Therefore, upon fractionation any type of biomass subject to an appropriate sequence of pre-treatment processes will result in different streams containing the above mentioned major compounds, mixtures of them (in polymeric and monomeric form) and in some cases products of their decomposition. As a first approximation, we will define these streams as our intermediates. Then, downstream processes can use them as feedstocks provided that their quality (highly dependent on the choice of pre-treatment method) and cost are acceptable for their own technologies.

A set of intermediates defined in this way naturally divides the biorefinery complex in two: a supply of intermediates problem and a demand of intermediates problem. The supply of intermediates problem entails finding the set and sequence of pre-treatment technologies to optimally produce the different intermediates; the demand of intermediates problem entails finding an appropriate intermediate and set of technologies to optimally produce a desired product. Then, once the cus-

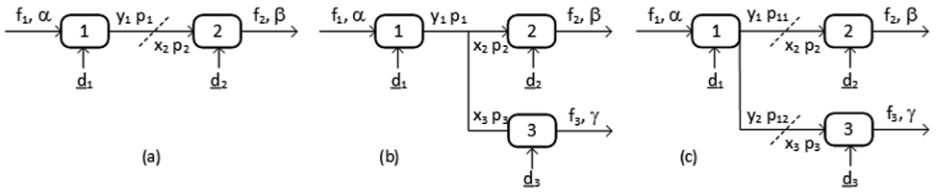

Figure 2: Prototypical network for the biorefinery complex. (a) two actor biorefinery: one supplier one consumer one intermediate; (b) three actor biorefinery: one supplier two consumers competing for the same intermediate (c) three actor biorefinery: one supplier, two consumers of different intermediates.

tomers on the demand side have selected the set of intermediates that are technologically feasible, as the starting points of their processes, the optimal biorefinery complex is completed by defining the optimal flowrates and transfer prices for these intermediates.

2.2. Separability of the biorefinery complex

Based on the division of the biorefinery complex discussed before, we have identified three prototypical networks that describe it: (a) one supplier and one consumer linked to one intermediate, (b) one supplier and two consumers competing for the same intermediate and (c) one supplier producing two intermediates for two different consumers (see Figure 2). Then other configurations of the biorefinery can be expressed by combining these three.

In what follows, we will assume that the inlet flowrate of the biomass feedstock (f_1), the outlet flowrate of products (f_2, f_3) and their corresponding prices (α, β, γ) are known, and our goal is to find the optimal set of design variables for each actor ($\underline{d_I}$) and the optimal transfer flowrates (x_j, y_i) and prices (p_i) . We will consider the profit, defined as the difference between the revenues obtained from selling the product and the feedstock and operational costs, as the function to be maximized by each independent actor.

2.2.1. Two actor biorefinery

For the simplest case (Fig. 2a), the profits of each actor can be expressed as: $P_1 = p_1 y_1(f_1, \underline{d_1}) - c_1(f_1, \underline{d_1}) - \alpha f_1$ and $P_2 = \beta f_2(x_2, \underline{d_2}) - c_2(x_2, \underline{d_2}) - p_2 x_2$. Clearly $y_1 = x_2 = x_I$ and $p_1 = p_2 = p_I$. Therefore maximizing both profits at the same time is not possible as an increase in the term $p_I x_I$ results in an increase of P_1 and a decrease in P_2. Then, the multiobjective optimization problem (MOP) in Eq.1 is formulated to find the solution that maximizes the composite profit.

$$\begin{aligned} Max \quad & P_1 + sP_2 \qquad (1) \\ s.t. \quad & y_1 = x_2 \\ & p_1 = p_2 \\ & P_1 \geq 0 \\ & P_2 \geq 0 \\ & \underline{d_i} \in \mathscr{D}_i \quad \text{i=1,2} \end{aligned} \qquad s = 1 \implies \qquad \begin{aligned} min \quad & c_2(f_1, \underline{d_1}) + c_2(x_2, \underline{d_2}) \qquad (2) \\ s.t. \quad & y_1 = x_2 \\ & -p_1 y_1(f_1, \underline{d_1}) + c_1(f_1, \underline{d_1}) + \alpha f_1 \leq 0 \\ & -\beta f_2(x_2, \underline{d_2}) + c_2(x_2, \underline{d_2}) + p_2 x_2 \leq 0 \\ & \underline{d_i} \in \mathscr{D}_i \quad \text{i=1,2} \end{aligned}$$

By using the Karush-Khun-Tucker conditions it can be proven that the only solution that results in positive profit for both parties is when the value of s, the trade-off between P_1 and P_2, equals 1, and any other value for s leads to a solution where one of the actors has no profit.

Then, by substituting $s = 1$ in Eq.1 it can be shown that the MOP simplifies significantly resulting in the minimization of the summation of the *operational costs* of both units subject to the mass

balance constraint at the connection point, as shown in Eq.2.

The Lagrangian of this optimization problem (Eq.2) can be rearranged in a sum of two terms one depends only on variables from unit 1 and the second depends only on variables from unit 2, where the only common variable among these two parts is the Lagrange multiplier (λ) corresponding to the satisfaction of the mass balance at the connection point.

The solution of the optimization problem in Eq.2 can be found through a two-level Lagrangian approach in which, first, for different values of the Lagrange multiplier, each actor separately minimizes its own *operational burden* defined as $\ell_1(\lambda, f_1, \underline{d}_1) = c_1(f_1, \underline{d}_1) - \lambda\, y_1(f_1, \underline{d}_1)$ for actor 1, and $\ell_2(\lambda, x_2, \underline{d}_2) = c_2(x_2, \underline{d}_2) + \lambda\, x_2$ for actor 2; and second the dual function $\mathscr{D}(\lambda) = \min\ell_1(\lambda) + \min\ell_2(\lambda)$, is maximized with respect to λ to find the optimal values for the design variables $\underline{d}_1^*$, $\underline{d}_2^*$ and transfer flowrate $y_1^* = x_2^* = x_I^*$.

It can be seen that the optimal price for the intermediate p_I^* is not defined by the solution of the previous problem and that, given $\underline{d}_1^*$, $\underline{d}_2^*$ and x_I^*, any price that satisfies the non-negative profit constraint for both units is equally optimal for the overall network, although not for the individual actors. The prices at which these inequality constraints become equality constraints (*i.e.* one of the profits is zero) provide the bounds for the price of this intermediate, which should be compared against the market price of similar intermediates.

However, by examining the units of the terms for the operational burdens (see above) it can be seen that the Lagrange multiplier, λ, has units of \$/(unit of mass of the intermediate), and thus can be interpreted as the price to be paid for the intermediate, and λ^*, the value at the optimal and feasible solution as the price of the intermediate that offers the optimal balance between the *operational burdens* of both units, *i.e.* $\lambda^* = p_I^*$. A detailed discussion on the mathematical approach can be found in Torres and Stephanopoulos (2014).

2.2.2. Extension to multiple-actors biorefinery network

The procedure outlined above for a two-actor biorefinery, can be easily extended to the other two prototypical networks of Fig. 2: two consumers that compete for the same intermediate (Fig. 2b) and one supplier that produces two intermediates for two different consumers (Fig. 2c).

In both cases, a MOP analogous to the one in Eq.1 was proposed to maximize a composite function of the three profits subject to the mass and cash balance constraints for each intermediate. With similar arguments as before, it can be shown that:

1. only when the trade-offs $s_i = 1$ all actors have positive profits
2. the problem is separable and the two-level Lagrangian approach can be used to solve it, where for the general case of one supplier providing multiple intermediates for j different consumers the operational burdens to be minimized by each actor are as follows:
   - operational burden for the supplier s
     $\ell_s(\underline{\lambda}, f_s, \underline{d}_s) = c_s(f_s, \underline{d}_s) - \sum_{i=1}^{\#\text{ of intermediates}} \lambda_i\, y_i(f_s, \underline{d}_s)$
   - operational burden for the consumer j
     $\ell_j(\lambda_j, f_j, \underline{d}_j) = c_j(f_j, \underline{d}_j) + \lambda_j x_j$
3. the Lagrange multipliers that maximize the dual function can be interpreted as the transfer price for the intermediates produced by the supplier.

3. Computer Aided Collaborative Environment

Based on the separability of the biorefinery, we have designed a computer aided collaborative environment to emulate the proposed framework. This environment is implemented in the commercial software Aspen Plus, and a screenshot of it is presented in Fig. 3, where the division in a supply side, a line of intermediates and a demand side with several consumers is clearly identified.

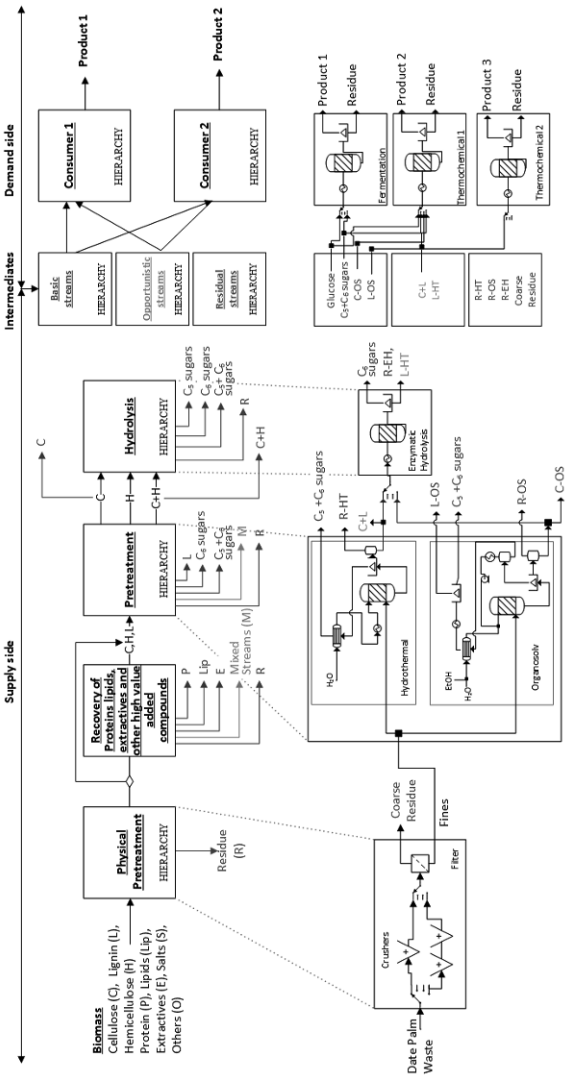

Figure 3: Computer Aided Collaborative Environment: main flowsheet and example of accesible processing options

The supply side of the problem coincides with the pretreatment of biomass and we have identified four main blocks that need to be applied in sequence in order to systematically fractionate the biomass. These blocks are (1) a "physical pretreatment" block which includes oopertions that reduce the size of biomass and remove debris, water and salt; (2) a "recovery of high value added compounds" block which includes operations for the separation of sensitive intermediates (e.g. proteins) which will be destroyed by subsequent processing are recovered, (3) a "traditional" pretreatment block that targets the separation of cellulose, lignin and hemicellulose using for example hydrothermal, steam explosion or organosolv processes, and (4) a "hydrolysis" block that breaks down polymeric compounds, present in the streams that exit the previous blocks, into monomeric ones.

As shown in Fig. 3 for the processing of date palm waste (a lignocellulosic type of biomass) each of these blocks contains flowsheets for several alternative processes. By combining or by-passing them, different fractionation sequences that result in streams that differ in their quality (composition of major and minor compounds) and production cost are obtained. The choice of processes, their operating conditions, as well as whether a stream exiting each of the supply side blocks is considered to be an intermediate or connected to the next block in the sequence for further processing, represent the decision variables for this part of the problem.

We have included three blocks for intermediates streams and hierarchically classified them as follows: Basic streams: those streams that are expected to serve as a starting point for a large number of consumers, such as cellulose, lignin and glucose rich streams, basically those that align with the intermediates proposed in Fig:1; Opportunistic streams: streams containing by-products, or partially fractionated biomass, that have not yet been considered in the literature as feedstocks for bio-based chemicals, but whose characteristics indicate that might be used as a much cheaper source, and streams that target a very specific set of specialty products; Residual streams: streams that can clearly not be used for the production of specialty biomass based compounds as for example solid residues, but would need to be treated for disposal.

Within this computer-aided collaborative environment, we aim to provide actors working on the demand and supply sides, the design capabilities for independent and parallel assessment of processing options. In such setting, realistic estimates of flows and compositions of the intermediate streams, along with economic and environmental assessment is provided. Thus, customers, researchers working on the upgrade of the intermediates, can, independently of each other, test and optimize their processes for different intermediates, be aware of the presence of minor compounds that might be detrimental for their own technologies, have the option of considering less processed but less expensive streams, and propose new technologies to process intermediate streams that they might not currently be aware of.

Finally, it should be mentioned that the assignment of streams as intermediates as well as the definition of the supply-demand side boundary is expected to evolve as more knowledge on the consumer side is acquired. As an example, processes that convert some of the current intermediates (for example, glucose rich streams) into a particular building block (for example a C_3 building block) could be also included in the supply side (and offered as an intermediate) if it proves to dominate the pathway to feasible consumer side processes.

4. Conclusions

A multiactor biorefinery network composed by one supplier and several consumers has been proposed as the natural framework for designing biorefineries. A multi-objective optimization problem that aims to find the solution that maximizes the overall profit of the network has been proposed for its analysis. It was found that the proposed MOP is separable and that by using a two-level Lagrangian approach the optimal design variables for each actor as well as the optimal flowrates and prices for the transfer of intermediates could be computed. A computer aided environment which emulates the proposed framework and allows actors on the supply and demand side to work independently on their processes is presented.

5. Acknowledgements

This project- Biorefinery: Integrated Sustainable Processes for Biomass Conversion to Biomaterial, Biofuels and Fertilizer - was funded by the Cooperative Agreement between the Masdar Institute of Science and Technology (Masdar Institute), Abu Dhabi, UAE and the Massachusetts Institute of Technology (MIT), Cambridge, MA, USA - Reference 02/MI/MI/CP/11/07633/GEN/G/00 for work under the Second Five Year Agreement.

References

Kim, J., Sen, S. M., Maravelias, C. T., 2013. An optimization-based assessment framework for biomass-to-fuel conversion strategies. Energy Environ. Sci. 6, 1093–1104.

Murillo-Alvarado, P. E., Ponce-Ortega, J. M., Serna-González, M., Castro-Montoya, A. J., El-Halwagi, M. M., 2013. Optimization of pathways for biorefineries involving the selection of feedstocks, products, and processing steps. Industrial & Engineering Chemistry Research 52 (14), 5177–5190.

Sen, S. M., Henao, C. A., Braden, D. J., Dumesic, J. A., Maravelias, C. T., 2012. Catalytic conversion of lignocellulosic biomass to fuels: Process development and technoeconomic evaluation. Chemical Engineering Science 67 (1), 57 – 67.

Torres, A., Daoutidis, P., Tsapatsis, M., 2010. Continuous production of 5-hydroxymethylfurfural from fructose: a design case study. Energy & Environmental Science 3 (10), 1560–1572.

Torres, A. I., Stephanopoulos, G., 2014. A multi-actor multi-objective framework for optimization of biorefinery processes. Internal Report.

Werpy, T., Petersen, G., 2004. Top value added chemicals from biomass, volume I - Results of screening for potential candidates from sugars and synthesis gas. Tech. rep., U.S. Department of Energy.

Krist V. Gernaey, Jakob K. Huusom and Rafiqul Gani (Eds.), 12th International Symposium on Process Systems Engineering and 25th European Symposium on Computer Aided Process Engineering.
31 May – 4 June 2015, Copenhagen, Denmark

Integrated Design and Control of Semicontinuous Processes Using Mixed Integer Nonlinear Dynamic Optimization

Vida Meidanshahi, Thomas A. Adams II*

Department of Chemical Engineering, McMaster University, 1280 Main St. West, Hamilton, Ontario, Canada, L8S 4L8
tadams@mcmaster.ca

Abstract

Semicontinuous separation is a distillation based process intensification technique devised for the purification of ternary mixtures to desired purities. It is particularly promising for small scale production processes where the semicontinuous system has a lower total annualized cost relative to the conventional continuous process, thus it can be a suitable option for the purification of biofuels. Semicontinuous systems are dynamic, control driven processes that work in a stable limit cycle with several modes of operations. Therefore, designing the system and its controllers is a challenging task which has not been thoroughly considered in the literature. In this work, for the first time, a methodology is presented to simultaneously obtain the optimum design parameters of the semicontinuous system such as the number of column stages, feed and side stream locations, as well as the optimum tuning parameters for the PI control structure. To design the semicontinuous process, it is formulated as a mixed integer nonlinear dynamic optimization problem using the equation oriented gPROMS software which has built-in deterministic optimization packages. The benzene, toluene and *o*-xylene mixture is chosen as a case study to demonstrate the methodology. The optimization took 1.03 CPU hours and the optimum design parameters are obtained. The results show that the total annualized cost of the designed semicontinuous system is lower than the respective conventional continuous process.

Keywords: Semicontinuous Separation; Integrated Design and Control; Mixed Integer Nonlinear Dynamic Optimization; gPROMS

1. Introduction

The goal of process intensification is to reduce equipment sizes, improve the efficiency of processes and increase profitability. Semicontinuous separation is a process intensification technology which is capable of reducing the capital cost, and potentially the total annualized cost (TAC) of distillation processes. Semicontinuous separation utilizes a storage tank integrated with a distillation column to achieve ternary purification, whereas two distillation columns are typically required in a conventional system (Phimister and Seider, 2000). In a semicontinuous setup, the side stream of the distillation column is constantly recycled back to the storage tank (which is called middle vessel), and after first charging it with the feed to be separated, the contents of the tank are continuously fed to the column. The light and the heavy boiling point components are continuously removed in the distillate and bottom streams of the distillation column, respectively, resulting in the concentration of the intermediate

boiling point component in the middle vessel. Upon the achievement of the desired purity for the intermediate component, the content of the middle vessel is discharged and it is subsequently charged with fresh feed. However, the column works continuously with no start-ups and shut-downs. Due to the cyclic behaviour of the system the composition and the flow rate of the feed to the distillation column changes over the cycle time of the process. Furthermore, the system is control driven, working in three distinct modes of operation: charging, processing and discharging.

Semicontinuous separation is particularly interesting for biofuel production processes, as small scale distributed plants with low capital costs are typically desired. Pascall and Adams (2013) used a semicontinuous system for purification of bio-DME and achieveda remarkable reduction in the cost of producing bio-DME for small-scale distributed networks. Also, Niesbach et al. (2013) studied separation of butyl acrylate from a mixture of several impurities by utilizing the semicontinuous separation technique. Changes in the bio-resource feedstock in the production of butyl acrylate introduce different impurities in the product. However, the semicontinuous system is flexible in terms of impurities and without changing operating conditions of the system, the desired product purities are obtained.

To design the semicontinuous system for any arbitrary ternary mixture, appropriate design parameters such as number of stages, feed and side draw locations, column diameter, middle vessel volume and controller settings must be determined. These design parameters are crucial to guarantee best performance of the system as well as the lowest TAC of the system. This results in a mixed integer nonlinear dynamic optimization (MINLDO) which is one of the most challenging classes of optimization problems, but is the proper framework to simultaneously design the system and its control structure. However, in the case of highly complex semicontinuous systems (hybrid nature, high number of integer variables and expensive computational times) previous attempts at dynamic optimization were limited to stochastic methods such as particle swarm optimization (PSO) and a subset of decision variables.

Adams and Seider (2008) proposed a bi-level optimization algorithm for high dimensional hybrid systems. In this method the decision variables are divided into global and local variables. However, the authors considered only the continuous design variables and control parameters without any integer variables as decision variables. In 2013, Pascal and Adams optimized a semicontinuous system for bio-DME production. They linked Aspen Dynamics software with Excel Visual Basic for Applications (VBA) and used a PSO technique to optimize only the controller tuning parameters of the system. In each of these cases, the required computation time was over a CPU-month and was effective only for smaller subsets of the decision variables of interest.

In this work, a methodology for the synthesis of semicontinuous systems is presented using a deterministic mixed integer nonlinear dynamic optimization algorithm. The separation of benzene, toluene and o-xylene (BTX) is selected as a case study and the system is modelled in gPROMS v4. The resulting MINLDO is solved with a gradient based method. An economic evaluation is performed to compare the conventional distillation system and the optimally designed semicontinuous system.

2. Process Modelling

The optimum conventional continuous configuration for separation of an equimolar mixture of benzene, toluene, and *o*-xylene (BTX) to products with 99 mole% purity consists of two distillation columns with 30 and 28 stages, respectively, as shown in Figure 1(a) (Ling and Luyben, 2009). The semicontinuous counterpart of this system is shown in Figure 1(b). Meidanshahi and Adams (2014) presented a detailed procedure for designing the semicontinuous system for the BTX mixture. Their simulations were performed in Aspen Plus Dynamics V8 which provides a rigorous distillation column model (RadFrac). For the semicontinuous system the optimum number of stages is between a minimum of 28 to a maximum of 58 (summation of stages in the conventional continuous configuration). As the number of stages decreases, the total direct cost of the system decreases but the operation cost increases. On the other hand, the tuning parameters for the PI controllers (which are the main drivers of the process) affect the cycle time, the production rate and the operating costs of the process. Therefore, to have the lowest TAC, the optimum number of stages, optimum locations for feed and side draw and optimum tuning parameters are needed.In this work,a MINLDO is proposed to design an optimum semicontinuous configuration. Although, Aspen Dynamics provides a good rigorous model for simulation purposes,the built-in dynamic optimization solver are not suitable for MINLDO purposes. Therefore, the process is simulated in gPROMS V4 using its process model library (PML).

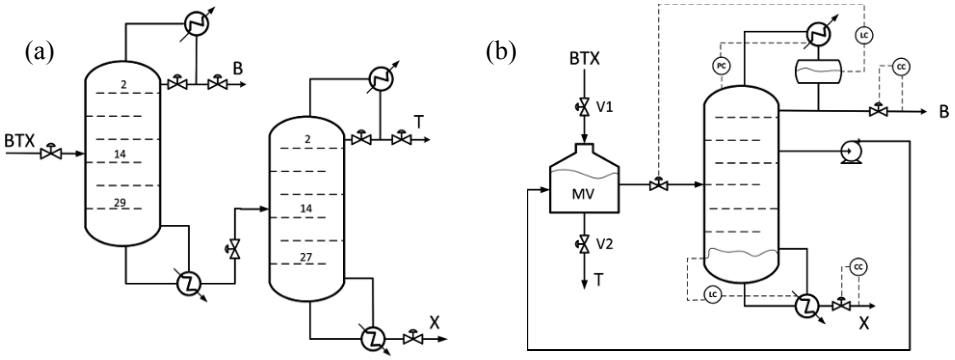

Figure 1- Schematic of the (a) conventional continuous and (b) semicontinuous configuration for BTX separation system.

3. Optimization

The semicontinuous separation is a hybrid process with three modes of operation: charging, processing and discharging. However, the processing mode constitutes the main fraction of the cycle time thus this work focuses only on the optimization of the processing mode. The problem of dynamically optimizing all modes of operation is the focus of future work. To synthesize the optimum process, some design parameters such as column diameter (1.2 m) and the control structure are fixed while other design parameters such as number of column stages, location of feed and side streams and middle vessel height (integer variables) as well as gains and reset times of all five PI controllers (continuous variables) are optimized. The superstructure considered for the distillation column is shown in Figure 2. It has 50 stages with the feed introduced at stage 30 and the side stream withdrawn at stage 20. For detailed information on the value of design parameters and initial conditions, refer to Meidanshahi and Adams (2014).

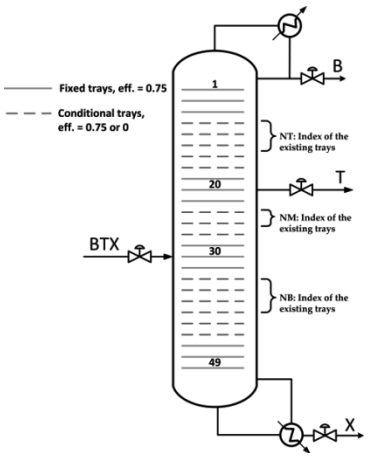

Figure 2- Superstructure for optimization of the column in the semicontinuous system.

To optimize the design parameters of the distillation column, the method proposed by Javaloyes-Antón et al. (2013) is employed.The superstructure of the distillation column consists of four sets of permanent and three sets of conditional trays. Also included in the structure are the feed location, location of side draw, condenser and reboiler. The permanent trays have a defined Murphree efficiency (0.75 in this work) while the Murphree efficiency of the conditional trays are either 0.75 or zero depending on their existence (active) or non-existence (inactive).

The total number of stages as well as the location of feed and side streams is determined by the total number of active and fixed trays. In order to avoid problems associated with non-unique solutions (which would happen if a set of conditional trays were permitted to alternate between active and inactive trays, for example), an integer variable is defined for each set of conditional trays which represents the number of active trays in that set. Consequently, all model equations associated with the conditional trays are structured such that all conditional trays within a set at or below this integer value are active, and all conditional trays above this integer value are inactive. Thus only one possible permutation of inactive/active trays exists for each value of the integer variable. The objective of the dynamic optimization is to minimize the TAC of the system per annual processed feed, as shown in Eq. (1). The optimization problem is subjected to some constraints as shown in Eqs. (2)-(6).

$$\text{Min:} \quad \left(\frac{\textit{Total Direct Cost}}{\textit{Payback Period}} + \textit{Annual Operating Cost}\right)/\textit{Processed Feed} \tag{1}$$

$$0.1 \leq \text{Condenser liquid level fraction} \leq 0.9 \tag{2}$$

$$0.3 \leq \text{Reboiler liquid level fraction} \leq 0.9 \tag{3}$$

$$\text{Average distillate purity} \geq 99 \text{ mole\%} \tag{4}$$

Average bottom purity ≥ 99 mole% (5)

Purity of toluene in the middle vessel by the end of cycle ≥ 99 mole% (6)

The operating costs were calculated considering only the utility costs of steam and cooling water according to the method discussed in Towler and Sinnott (2012).The cost of the distillation column is calculated using the equations reported in Bansal et al. (2002). The MINLDO is solved using the gPROMS optimization toolbox. To solve the MINLDO, gPROMS uses control vector parameterization with the single shooting sequential method and solves the resulting mixed integer nonlinear problem (MINLP) by employing the outer approximation with equality relaxation and augmented penalty method (OAERAP) (Viswanathan and Grossmann, 1990).

4. Results

Due to the nonconvexities of the problem, the OAERAP method only guarantees the local optimality of the solution but not its global optimality. However, the computational time of this deterministic method linked with equation oriented solver is promising compared to heuristic optimization methods. Where 40 CPU days were required to optimize only the tuning parameters of the semicontinuous system using Aspen and PSO (Pascal and Adams, 2013), the MINLDO proposed in this work, took 1.03 CPU hours to solve the problem and obtain a locally optimum solution for both integer and continuous decision variables. Table 1 shows the optimum values of the design parameters for semicontinuous system while Table 2 shows the optimum values of the tuning parameters.

Table 1- Semicontinuous design parameters.

	No. of stages	Feed stage	Side stage	Middle vessel height (m)
Base-case design	50	30	20	6
Optimum design	37	22	13	4

Table 2- Gains (k) and reset times (τ) of distillate composition controller (1), bottoms composition controller (2), reflux drum liquid level controller (3), sump level controller (4) and column pressure controller (5).

	k_1	τ_1	k_2	τ_2	k_3	τ_3	k_4	τ_4	k_5	τ_5
Base-case design	1	100	1	100	0.5	100	0.5	100	0.5	100
Optimum design	0.1	88	5	328	2.2	81.3	0.72	94.2	0.55	102

Table 3- Economic evaluation.

	Operating cost ($/y)	Direct cost ($)	Total annualized cost ($/y)	Cycle time (h)	Feed processed (Mkg/y)	Objective function ($/Mkg)
Semicontinuous base-case design	67,533	216,186	139,595	3.48	33.7	4,137
Semicontinuous optimum design	71,271	158,193	124,002	0.74	46.7	2,655
Conventional continuous	45,276	275,004	136,944	—	46.5	—

The optimum semicontinuous design has fewer stages and consequently has lower direct costs relative to the original base-case semicontinuous design created using standard heuristic methods, and the conventional continuous system (Table 3). However, having fewer stages, the operating costs of the optimum semicontinuous system is higher than the other considered systems. A payback period of 3 years is considered for calculation of TACs. Most notably, the optimum semicontinuous system has the lowest TAC. The cycle time of the semicontinuous system was a decision variable in the optimization problem. The optimum values of the tuning parameters have resulted in lower cycle time for the optimum configuration.

5. Conclusions

A successful method for the determination of an optimal integrated design and control problem with integer variables for semicontinuous systems has been demonstrated for the first time in this work. Most prior studies on semicontinuous systems over the last decade were focused on the feasibility and the applicability of the process. Most prior studies acknowledged the importance of optimization of this cyclic process. However, huge computation times, complex system dynamics, and an inability to handle complex design decisions requiring integer variables were hindering factors to achieve this goal. In this work, the problem was addressed by a mixed integer nonlinear dynamic optimization framework to optimize both integer and continuous design parameters of the system. gPROMS, was used to simulate the system and its deterministic optimization toolbox is employed to solve the optimization problem. The computational time was 1.03 CPU hours and the results show significant promise that the methodology can be rapidly applied to all semicontinuous systems studied to date. For future work, more operational details of the cycle will be considered, such as charge and discharge modes. Then, future studies will consider a superstructure that can choose the best control structure, or potentially more complex controllers such as model predictive controllers instead of PI controllers.

References

T.A. Adams II, W.D. Seider, 2008, Semicontinuous distillation for Ethyl Lactate production, AIChE J., 54, 10, 2539-2552.

V. Bansal, J.D. Perkins, E.N. Pistikopoulos, 2002,A Case Study in Simultaneous Design and Control Using Rigorous, Mixed-Integer Dynamic Optimization Models,Ind. Eng. Chem. Res. 41, 760-778.

J. Javaloyes-Antón, R. Ruiz-Femenia, J.A. Caballero, 2013, Rigorous Design of Complex Distillation Columns Using Process Simulators and the Particle Swarm Optimization Algorithm, Ind. Eng. Chem. Res., 52, 15621−15634.

H. Ling, W.L. Luyben, 2009, New Control Structure for Divided-Wall Columns, Ind. Eng. Chem. Res., 48, 6034–6049.

V. Meidanshahi, T.A. Adams II, 2015, A new process for ternary separations: Semicontinuous distillation without a middle vessel, Chemical Engineering Research and Design, 93, 100-112.

A. Niesbach, T.A. Adams II, P. Lutze, 2013, Semicontinuous distillation of impurities for the production of butylacrylate from bio-butanol and bio-acrylic acid, Chemical Engineering and Processing, 74, 165-177.

A. Pascall, T.A. Adams II, 2013, Semicontinuous separation of Dimethyl Ether (DME) produced from biomass, The Canadian Journal of Chemical Engineering, 91, 6, 1001-1021.

J.R. Phimister, W.D. Seider, 2000, Semicontinuous, middle-vessel distillation of ternary mixtures, AIChE J., 46, 8, 1508-1520.

G. Towler, R. Sinnott, 2012, Chemical Engineering Design: Principles, Practice and Economics of Plant and Process Design, 2nd Ed., Butterworth-Heinemann, Massachusetts.

J. Viswanathan, I.E. Grossmann, 1990, A combined penalty function and outer-approximation method for MINLP optimization, Comput. Chem. Eng., 14, 769-785.

Krist V. Gernaey, Jakob K. Huusom and Rafiqul Gani (Eds.), 12th International Symposium on Process Systems Engineering and 25th European Symposium on Computer Aided Process Engineering.
31 May – 4 June 2015, Copenhagen, Denmark

A Computational Platform for Simulation, Design and Analysis of a Poly(Lactic) Acid Production Process From Different *Lignocellulosic* Raw Materials

Eduardo S. Pérez-Cisneros[ab], Lourdes Avilés-Cabrera[b], Verónica Medina-Bañuelos[d], Mauricio Sales-Cruz[c], Alberto Ochoa-Tapia[a] , Tomás Viveros-García[a] Ricardo Lobo-Ohemichen[ab]

[a]*Departamento de Ingeniería de Procesos e Hidráulica, Universidad Autónoma Metropolitana-Iztapalapa, Av. San Rafael Atlixco 186, C.P. 09340, México, D.F., México.*
[b]*Posgrado en Energía y Medio Ambiente, Universidad Autónoma Metropolitana-Iztapalapa, Av. San Rafael Atlixco 186, C.P. 09340, México, D.F., México.*
[c]*Departamento de Procesos y Tecnología, Universidad Autónoma Metropolitana-Cuajimalpa, Artificios 40, CP. 01120, México D.F., México.*
[d]*Departamento de Ingeniería Eléctrica, Universidad Autónoma Metropolitana-Iztapalapa, Av. San Rafael Atlixco 186, C.P. 09340, México, D.F., México.*
espc@xanum.uam.mx

Abstract

A computational platform for the simulation, design and analysis of the Polylactic (PLA) acid production process using different lignocellulosic raw materials has been developed. The computational platform considers three main reactive-separation processes: 1) the bio-conversion process, where an hydrolysis-saccharification-culture process to produce the inoculated hydrolysate is coupled with a fermentation-separation process producing the broth with crude lactic acid; 2) the purification process, where a sequence of conventional and reactive distillation columns to perform the esterification and hydrolysis reactions, respectively, are used to produce a polymer grade lactic acid; and 3) the polymerization process, where a ring-opening polymerization reaction scheme to produce high molecular weight PLA is carried out. The platform was constructed on the Aspen Plus Environment. The implementation of the platform in a systematic manner allowed the evaluation of various mono and disaccharide materials to produce PLA. The results show that with a higher concentration of glucose the molecular weight of the PLA produced increased. However, the operation of the purification section, that is, the reactive distillation columns should be carried out carefully in order to obtain a purified lactic acid near to 88% mass fraction.

Keywords: Polylactic acid, computational platform, reactive-separation process

1. Introduction

Polylactic acid (PLA), a biodegradable poly hydroxy alkanoate (PHA), it is a promising replacement for synthetic polymers. The advantages of Polylactic acid are its high tensile strength, high modulus, thermoplastic property, biodegradability and bioenvironmental compatibility/absorbability. It is used in making of biodegradable sutures, clamps, bone plates and biologically active controlled release devices (Jamshidian *et al*., 2010).

The production of PLA can be divided into two main steps: production of lactic acid and its polymerization to PLA. The production of lactic acid follows a fermentation process to produce a broth containing crude lactic acid and a downstream processing of the fermentation broth to obtain polymer grade lactic acid. Most frequently used procedures for lactic acid production are batch, repeated batch and continuous fermentation. For the separation and purification different procedure are used for example: electrodialysis, liquid extraction and reactive distillation. Various mono and disaccharide materials are generally used for its production i.e., glucose (dextrose) and glucose syrup as end product of starch conversion; maltose as a product from barley malt or other source; sucrose as end product of beet and cane sugar production. The amount of these cheap raw materials in México is significant all along the country. Therefore, the requirement of a computational tool to evaluate the economical and environmental feasibility of a PLA production plant is highly required. The present work proposes a computational platform based on three different reaction-separation sections: 1) Bio-conversion process: a hydrolysis-saccharification-culture process to produce the inoculated hydrolysate is coupled with a fermentation-separation process producing the broth with crude lactic acid; 2) Purification process: a sequence of conventional and reactive distillation columns to perform the esterification and hydrolysis reactions, respectively, are used to produce a polymer grade lactic acid, and 3) Polymerization process: a ring-opening process to produce high molecular weight PLA. The platform was constructed on the Aspen Plus Environment. Figure 1 shows a simplified flowsheet of the computational platform to produce PLA.

2. The Bio-conversion Process

For the bioconversion different carbohydrate transformation processes on the basis of experimental and literature data were used (Ali *et al.*, 2013).A pretreated lignocellulosic material was used as feedstock for this purpose (45 % cellulose, 20 % hemicelluloses, 30 % lignin, 5 % acetate groups, in weight). Lignin, cellulose and hemicelluloses were defined by their chemical structure and physical properties, which were obtained from the National Renewable Energy Laboratory (NREL) database (Wooley and Putsche, 1996), whereas other conventional components were selected from the ASPEN PLUS data bank. The proposed lactic acid production process started with a fermentator, where glucose and xylose are transformed into lactic acid. The formed lactic acid is precipitated from the fermentation liquid as calcium lactate, $Ca(OH)_2$ is added in aqueous form (in a ratio lime-water of 15:85 wt/wt). The produced lactic acid is then separated by filtration and subsequently washed in a two-steps operation. A design specification is defined to control the amount of water necessary to achieve a solid content less than 1% wt/wt in the liquid part. In the dissolution reactor, the acidification of this slurry is carried out in order to obtain lactic acid in solution and to remove the calcium salt. For this purpose, an aqueous H_2SO_4 stream (15:85 wt/wt sulphuric acid-water) is added. The calcium sulphate formed is separated by filtration and the liquid mixture containing lactic acid is submitted to the evaporation equipment. Table 1 shows the simulation results of the bioconversion section for selected streams of the reference study case.

3. The Purification Process

Many methods for purification of lactic acid have been proposed, including ultrafiltration, reverse osmosis, adsorption, and reactive extraction. However, these methods all have disadvantages. For example, ultrafiltration and osmosis are impractical

for large raw material capacity. Adsorption and reactive extraction have particle selectivity, capacity, and regeneration problems. Most importantly, all of these methods suffer from low lactic acid recovery.

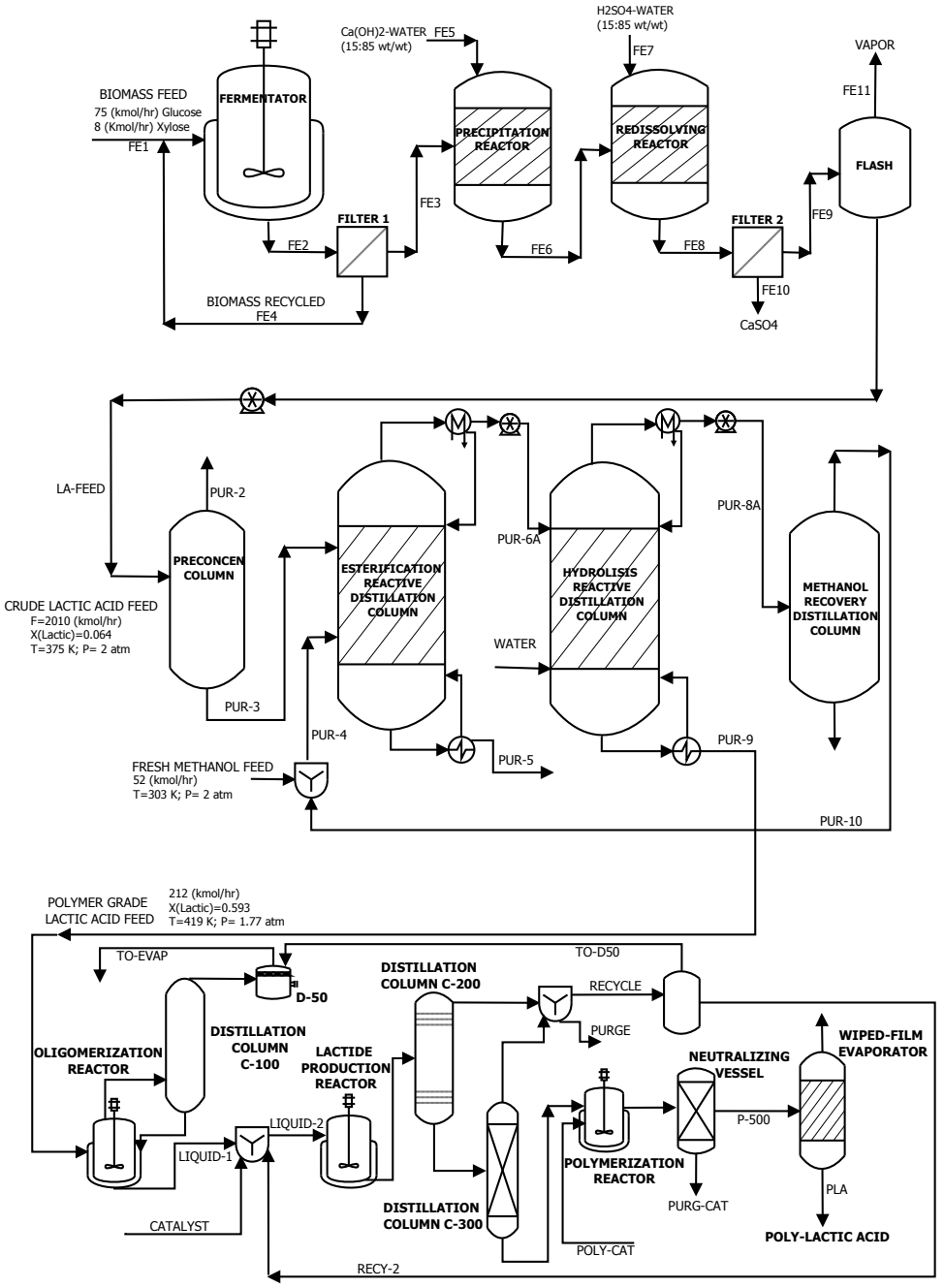

Figure 1. Simplified flowsheet of the computational platform for polylactic acid production

Table 1. Simulation Results for the **Fermentation** Section(Reference Case)

STREAM	FE1	FE2	FE5	FE6	FE7	FE9
Total Flow (kmol/hr)	83.00	146.20	1555.57	1683.57	2038.45	3722.02
Total Flow (kg/hr)	14712.88	14712.88	31613.01	43143.10	41847.47	76277.46
Temperature K	303.15	303.15	368.15	368.15	293.15	293.15
Pressure atm	1.00	1.00	1.00	1.00	1.00	1.00
Mass Frac						
GLUCOSE	0.918	0.184	0.000	0.000	0.000	0.000
XYLOSE	0.082	0.033	0.000	0.000	0.000	0.000
LACTIC	0.000	0.784	0.000	0.000	0.000	0.151
CA(OH)2	0.000	0.000	0.150	0.000	0.000	0.000
WATER	0.000	0.000	0.850	0.676	0.850	0.849
CA-LACTA	0.000	0.000	0.000	0.324	0.000	0.000
H2SO4	0.000	0.000	0.000	0.000	0.150	0.000
CASO4	0.000	0.000	0.000	0.000	0.000	0.000

In view of these limitations, the most attractive method for purification of lactic acid from fermentation broth is a two-step reactive-distillation process in which the acid is first reacted with an alcohol to form a more volatile ester which can be purified by distillation. Then, pure lactic acid is recovered by hydrolysis of the ester. This purification method not only can handle large raw material capacity but also can achieve high lactic acid recovery. In the present work, the vapor−liquid and vapor−liquid−liquid equilibria were estimated for each process using NRTL activity model for the liquid phase and Hayden-O´Conell second virial coefficient model for the nonideality of the vapor phase. The alcohol considered for the esterification reaction is methanol and the corresponding ester is methyl lactate (METHY-01). Also, solid-catalyzed reaction kinetics are used for each reaction and the reactive zones can be located in different sections of the reactive distillation columns. Kinetic data on solid-catalyzed lactic acid esterification and hydrolysis reactions have been reported by Su *et al.* (2013). Table 2 shows the simulation results of the purification section for selected streams of the reference study case.

Table 2. Simulation Results for the **Purification** Section (reference study case)

Stream	LA-FEED	PUR-3	PUR-4	PUR-5	PUR-6A	PUR-7	PUR-8A	PUR-9
Total Flow (kmol/hr)	2009.89	259.89	530.00	1.63	788.26	500.00	1075.89	212.37
Total Flow (kg/hr)	45394.96	13867.12	16982.34	169.31	30680.15	9007.64	26793.82	12893.97
Temperature K	374.68	348.84	303.15	383.32	312.80	303.15	350.25	419.39
Pressure atm	2.00	0.20	2.00	0.35	1.30	2.00	1.20	1.76
Mass Frac								
LACTIC	0.253	0.828	0.000	0.000	0.000	0.000	0.000	0.879
WATER	0.746	0.172	0.000	0.000	0.153	1.000	0.368	0.121
METHANOL	0.000	0.000	1.000	0.002	0.420	0.000	0.632	0.000
METHY-01	0.000	0.000	0.000	0.000	0.427	0.000	0.000	0.000
SUCCI-01	0.001	0.000	0.000	0.998	0.000	0.000	0.000	0.000

4. The Polymerization Process

Once the upstream from the fermentation and purification sections where lactic acid is generated and concentrated upto 88 wt% in aqueous solution (LA-FEED), the solution is fed to the oligomerization reactor, which further concentrates the lactic acid solution by removing water. The resulting product contains a mixture of lactic acid and predominately linear oligomers in an aqueous solution. A column is used to separate vaporized lactic acid, which is returned to the process. A catalyst (SnO) is added to the oligomer from the first reactor through a static mixer. The liquid is fed to a continuous wiped film evaporator/reactor, where the oligomers decompose to form lactide rings. The first column (C200) removes residual water from the mixture. The second column (C300) removes residual lactic acid from the lactide stream. Lactide from the first section of the plant is mixed with an appropriate polymerization catalyst and a phosphite stabilizer in a polymerization reactor. The lactide polymerizes back to polylactide, approaching very close to the ring/chain equilibrium point. The resulting mixture is passed on to a neutralizing vessel where the catalyst is neutralized. This residual lactide is removed in another wiped-film evaporator (WFE) and recycled as vapor and the final PLA polymer is produced. The process described above is a modified version of the proposed by Savey and Liu (2008). Table 3 shows the simulation results of the polymerization section for selected streams of the reference study case.

Table 3. Simulation Results for the **Polymerization** Section(Reference Case)

Stream	LA-FEED	LIQUID-1	CAT.	RECY-2	LIQUID-3	LACTIDE	PLA
Mass Frac							
WATER	0.121	0.007	0.000	0.000	0.005	0.000	0.000
LA	0.879	0.125	0.000	0.000	0.002	0.001	0.000
LACTIDE	0.000	0.000	0.000	0.014	0.119	0.999	0.011
PLA	0.000	0.867	0.000	0.986	0.874	0.000	0.989
CATALYST	0.000	0.000	1.000	0.000	0.000	0.000	0.000
Total Flow (kmol/hr)	212.29	133.49	0.04	1338.00	1416.90	67.25	122.50
Total Flow (kg/hr)	12892.79	9647.80	5.00	97093.41	106746.21	9685.04	8876.36
Temp. C	25.00	170.00	24.85	209.96	220.00	145.00	187.00
Pressure torr	760.00	400.00	760.00	10.00	10.03	10.00	2.00
DPN		7.55		59.71	62.24		865.13
MWN		561.94		4321.00	4503.57		62362.29

5. Study Case and Results

To implement the computational platform a reference study case was used. This is, a hypothetical mixture with 75 % of glucose and 8 % of xylose producing a broth of lactic acid from the fermentation process of 0.59 mole fraction of lactic acid and 0.41 of water. This broth if fed to the purification section and a mixture of polymer grade lactic acid and water of 88% and 12 % mass fraction respectively is produced. The above mixture is driven to the lactide generation and to the opening ring polymerization reactors and a PLA with a molecular weight of 62362 units is produced. Further, four scenarios of composition in glucose and xylose were stated to test the computational platform: a) sugar cane residuals were used as raw material with glucose-xylose content of 39 and 23% respectively, that is, a residual lower in glucose concentration than the reference case;

b) beets with 18 and 53%; c) pineapple with 19.4 and 22.4 % and d) banana with 9.6 and 9.4%. Table 4 shows the different composition scenarios of the lignocellulosic raw materials, the lactic acid broth composition produced and the lactic acid polymer grade purified. Also, it can be noted the final PLA flow produced and its molecular weight respectively. It can be observed from the results that the reduction in the lactic acid composition in the broth from the fermentation step affects significatively the purified polymer grade lactic acid flow. However, it has small influence on the flow of the PLA produced. Nevertheless, the molecular weight of the PLA, which is the key property indicating the biodegradability of the biopolymer, is strongly affected. It should be pointed out that these differences in the PLA weights are a consequence that the lactic acid exit purity required of the purification section is not achieved (88% mass fraction).

Table 4. Composition scenarios of *lignocellulosic* raw materials

RAW MATERIAL	COMPOSITION % (dry)		LACTIC ACID BROTH (mole fraction)	POLYMER GRADE LACTIC ACID FLOW (Kg/hr)	POLYLACTIC ACID PRODUCED (Kg/h)	PLA MOLECULAR WEIGHT
Reference	Glucose 75 Xylose 08		0.59	11335.2	8778.1	62,362
Sugar Cane	Glucose 39 Xylose 23		0.40	7525.7	8778.1	44,387
Beets	Glucose 18 Xylose 53		0.38	7203.7	9199.6	35,432
Pineapple	Glucose 19.4 Xylose 22.4		0.25	4467.1	9460.1	31,710
banana	Glucose 9.6 Xylose 9.4		0.11	2101.7	9698.5	23,800

6. Conclusions

A computational platform for the simulation, design and analysis of the Polylactic (PLA) acid production process using different lignocellulosic raw materials has been developed. The implementation of the platform in a systematic manner allowed the evaluation of various mono and disaccharide materials to produce PLA. The results show that with a higher concentration of glucose the molecular weight of the PLA produced increased. However, the operation of the purification section, that is, the reactive distillation columns should be carried out carefully in order to obtain a purified lactic acid near to 88% mass fraction.

References

Abdel-Rahman Mohamed Ali, Yukihiro Tashiro , Kenji Sonomoto, Recent advances in lactic acid production by microbial fermentation processes, Biotechnology Advances 31 (2013) 877–902

Chien-Yuan Su, Cheng-Ching Yu, I-Lung Chien and Jeffrey D. Ward, Plant-Wide Economic Comparison of Lactic Acid Recovery Processes by Reactive Distillation with Different Alcohols, Ind. Eng. Chem. Res. 52 (2013) 11070-11083

Kevin C. Seavey and Y. A. Liu, Step Grow Polymerization Process Modeling and Product Design, John Wiley & Sons, Inc., Hoboken, New Yersey (2008).

Majid Jamshidian, Elmira Arab Tehrany, Muhammad Imran, Muriel Jacquot and Stéphane Desobry, Poly-Lactic Acid: Production, Applications, Nanocomposites, and Release Studies. Comprehensive REVIEWS in Food Science and Food Safety, Vol. 9 (2010) 552-571

Wooley R.J., Putsche V., 1996, Development of an ASPEN PLUS Physical Property Database for Biofuels Components. NREL/MP-425-20685, National Renewable Energy Laboratory, Golden, Colorado, USA.

Krist V. Gernaey, Jakob K. Huusom and Rafiqul Gani (Eds.), 12th International Symposium on Process Systems Engineering and 25th European Symposium on Computer Aided Process Engineering.
31 May – 4 June 2015, Copenhagen, Denmark

Simultaneous Design of Desalination Plants and Distribution Water Network

Sebastián Herrera[a], Luis A. Cisternas[a,b,*], Edelmira D. Gálvez[c,b]
[a]*Depto. de Ing. Química y Procesos de Minerales, Universidad de Antofagasta, Antofagasta, Chile.*
[b]*Centro de Investigación Científico Tecnológico para la Minería, Antofagasta, Chile*
[c]*Depto. de Ing. Metalurgia y Minas, Universidad Católica del Norte, Antofagasta, Chile.*
luis.cisternas@uantof.cl

Abstract

Northern Chile is characterized by significant mineral resources, particularly copper, nitrate, lithium, molybdenum, rhenium, among others. Moreover, these resources are located in the Atacama Desert, the driest in the world. Water resources are exhausted, but Chile has an extensive coast from where to get water. Then, any new operation or expansion of a current operation must use seawater. The distance from the coast to mining operations ranging from a few kilometers to about 300 kilometers, but even more significant, these operations can be found from 600 to 4,000 meters above sea level. Then, the cost of transporting desalinated water can be greater than the cost of desalination.

This paper presents a methodology to design the system of desalination plant and desalinated water transport. The objective is to determine the location and size of desalination plants and the water distribution system that minimizes capital and operational costs. The methodology uses a superstructure that represents the set of alternatives on which the optimal solution is found. A mathematical model is generated to represent the desalination plant and water distribution system. The end model corresponds to a MINLP problem which is solved in two steps using commercial software. A case study is used to demonstrate the applicability of the methodology developed.

Keywords: process design, desalination, distribution network, mining, seawater.

1. Introduction

The Atacama Desert is commonly known as the driest place in the world, especially in Antofagasta Region (Chile). The average rainfall in the Chilean region of Antofagasta is just 1 millimeter (0.04 in) per year. On the other hand, Antofagasta has represented one of main point of investment for Chile due to the extraordinary mineral wealth of its soils. The region has contributed with 7% of Chilean GDP over the last decade and 60% of the regional GDP is contributed by the mining industry. Chile produces around 35% of world copper production and more than half of that is extracted from Antofagasta Region. Antofagasta also produces gold, silver, molybdenum, potassium nitrate, iodine (50% of the world supply) and lithium carbonate (world's largest producer). Furthermore, mining investment in Chile for the next nine years exceeded 105 billion dollars, being the Antofagasta region the zone of greater investment. The especial

weather conditions and the economic development have increased water and energy demands.

Water scarcity is one of the main problems for the mining industry whether for mine expansion, exploitation of existing mines or development of new mines. The mines are typically located at elevations between 600 and 4,000 m above the sea level, where the main local water supply is from groundwater sources. The increase in the demand of water has been the main cause that regional basins are now depleted and practically all the existing areas with sub-aquifers have been declared under official protection in order to safeguard the fertile plains and wetlands they nourish.

Given this lack of water, the use of seawater has become the most appropriate one. Then, several desalination plants by reverse osmosis (RO) have been installed to provide drinking water. Also, most of the new mining projects have considered, and continue including, the use of seawater or desalinated water to supply their operations. However, the implementation of large systems of seawater desalination and water transport face other issues such as local geography, community relations, environmental impacts, corrosion, adaptation of mineral processes, and energy requirements.

Considerable efforts have been made for the research of the optimum design of RO system and water supply systems. For example, El-Halwagi (1992) investigated the synthesis of RO networks which involve multiple feed streams using a mixed integer nonlinear programming (MINLP) model. Malek et al. (1996) provided an economic model that relates the various operational and capital cost elements to the RO design variable values. Then, Maskan and Wiley (2000) used a directed graph and connectivity matrix to represent the RO networks superstructure. Lu et al. (2012) considered a RO-based desalination process for the production of fresh water from three raw feeds (seawater, brackish and regenerated water). A systematic methodology was presented for the optimal design of RO desalination system that processes multiple feed streams simultaneously, and at the same time, supplies various water streams of different quality. Alnouri and Linke (2013) presented a methodology for optimal design of seawater RO desalination system that addresses the issue of boron removal. The development of water supply systems without the use of optimization provides non-optimal structures. For this reason, several methodologies have been presented for the optimal design of water supply systems. These methodologies usually result in MINLP models. A good review on these issues is given by Coelho and Andrade-Campos (2014).

Despite the advances described above, few studies have considered the simultaneous design of desalination plants and water supply network. Atilhan et al. (2012) introduced an optimization-based approach for the integrated design and operation of macroscopic water networks. A structural representation approach was developed to embed all potential configurations of interest. This representation accounts for water resources, desalination plants, water users, wastewater treatment facilities, and storage. However, the water supply system and the cost of water transportation were not included in the methodology. Also, Atilhan et al. (2011) introduced an approach to the design and decision making of desalination and distribution networks for water supply in regions; however a linear model was considered for the cost of water piping and pumping, without considering aspects such as geometric height differences between source and destination and the pipe design.

In this work, a methodology to design the system of desalination plant and desalinated water transport is presented. The objective is to determine the location and size of desalination plants and the water distribution system that minimizes capital and operational costs.

2. Methodology

2.1 Description of the problem

The problem can be defined as: given the requirements of desalinated water from mining companies, the potential locations of pumping stations, and potential locations of desalination plants; identify the location of the desalination plants and pumping stations; the size of desalination plants, pumping stations and pipe diameter; and operational conditions of pumping stations and water distribution network, which pose a minimal cost.

To find this optimal a superstructure containing a set of feasible water desalination plants and transport system is used, as shown in Figure 1. This superstructure is defined in So_n potential RO plants with known location and maximum production capacity, in N_n potential pumping stations with known location and elevation, and in Si_n mining industries with known demand for desalinated water, location, and elevation.

2.2 Mathematical model

In the mathematical representation of this superstructure four main sets are used: the set of RO plants, SO = {so | so is a RO plant}, the set of pumping stations N = {n | n is a pumping station}, the set of mining plant SI = {si| si is a mining plant}, and the set of pipe diameters D = {d | d is a pipe diameter}. In addition, possible connections between sites within the network were established, being defined distance and geometric height difference between each of them.

Part of the mathematical model describing the superstructure is presented below, and in it appropriate relationships and constraints between variables representing the entire system are defined. These relationships are the equations of continuity in each of the sites, Eqs. (1) - (3),

$$Q_{so}^{*} = \sum_{n \in N} Q_{so,n} \qquad \forall so \in SO \tag{1}$$

$$\sum_{i \in input} Q_{i,n} = \sum_{j \in output} Q_{n,j} \qquad \forall n \in N \tag{2}$$

$$Q_{si}^{*} = \sum_{n \in N} Q_{n,si} \qquad \forall si \in SI \tag{3}$$

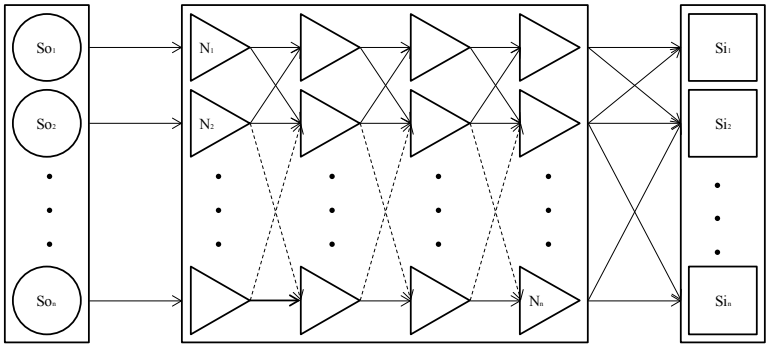

Figure 1. Superstructure of feasible water desalination and transport system

where $Q_{i,j}$ is the volumetric flow rate pumped from site *i* to *j*. The constraints associated with the maximum production capacity, C_{so}, of RO plants, ($Q_{so}^{*} \leq C_{so}$), and desalinated water demands, R_{si}, set by the mining industries ($Q_{si}^{*} \geq R_{si}$) are also included.

For the selection of the pipe diameter between *i* and *j*, a disjunction is used (Eq. 4), which is expressed using the convex hull method.

$$\bigvee_{d \in D} \begin{bmatrix} y_{i,j,d} \\ D_{i,j} = D_d \\ f_{i,j} = f_d \end{bmatrix} \qquad \forall\ (i,j) \in FIJ \tag{4}$$

where FIJ is the set of streams allowed between all the sites *i*, *j*; and *i* & *j* are elements of the set $SI \cup SO \cup N$. In Eq. (4) the friction factor ($f_{i,j}$) is assumed a function of the pipe diameter (and roughness), this is the Reynold number is big enough to not consider its contribution to the friction factor (see Swamee and Jain, 1976).

2.3 Objective function

The objective function minimizes the total annualized cost of all desalination plants, pipelines, and pumping stations required to meet water demands defined by mining industries plants, namely:

$$TC = \sum_{so \in SO} TC_{so} + \sum_{i,j \in FIJ} TC_{i,j} + \sum_{n \in N} TC_n \tag{5}$$

The cost of producing desalinated water is highly variable and dependents on several factors such as energy, chemicals, and labor, among others (Karagiannis and Soldatos, 2008). In this work, the cost function associated with RO plants was extracted from the database of costs raised by Wittholz (2008), and introduced here as a disjunction,

$$\bigvee_{c \in C} \begin{bmatrix} y_{so,c} \\ TC_{so} = PA \cdot UPC_{so,c} \cdot Q_{so}^{*} \\ Q_c^{LO} \leq Q_{so}^{*} \leq Q_c^{UP} \end{bmatrix} \qquad \forall\ so \in SO \tag{6}$$

where $UPC_{so,c}$ is unit cost of producing desalinated water ($/m^3) if $Q_c^{LO} \leq Q_{so}^* \leq Q_c^{UP}$, including capital and operational costs.

As proposed by Swamee (2001), the cost function of water transport network is composed by the annualized capital cost of the pipeline Eq. (7) and operational cost of pumping stations Eq. (8),

$$TC_{i,j} = \frac{k_P \left(1 + \frac{H_{i,j}}{H_b}\right) L_{i,j} {D_{i,j}}^m}{PL} \qquad \forall\, (i,j) \in FIJ \tag{7}$$

$$TC_n = \left(\frac{k_N (1 + s_b)\rho g}{\eta PL} + \frac{8.76 F_D F_A E_c \rho g}{\eta}\right) \cdot \sum_{j \in output} Q_{n,j} \cdot H_{n,j} \qquad \forall\, n \in N \tag{8}$$

In calculating the necessary pumping head, $H_{n,j}$, the Darcy-Weisbach equation was used to calculate the friction losses in the system, so $H_{n,j}$ is established in the follows:

$$H_{n,j} = \Delta Z_{n,j} + H_0 + \frac{8 f_{n,j} L_{n,j} {Q_{n,j}}^2}{\pi^2 g {D_{n,j}}^5} \tag{9}$$

where $\Delta Z_{n,j}$ is the elevation difference from site *n* to *j*, $L_{n,j}$ is the length of pipe from site *n* to *j*, and H_0 is the terminal head.

3. Case study

The case study considers the supply of water for three mining plants located at 1,500, 2,500 and 3,000 m above sea level, and with desalinized water demand of 5,400, 1,800 and 7,200 m^3/h respectively. If the current strategy of mining companies is used, then three RO plants must be built, each one to satisfy a mining plant. Thus three RO plants, each with a capacity sufficient to meet all mining plants water demand was considered. The pumping system is constituted by eleven pumping stations.

The problem was resolved using BARON under GAMS environment and not solution was found after 7,200 s. Then, the problem was resolved in two steps: first for each diameter the optimal solution was found; then the water network was fixed and the pipe diameters were calculated to find the optimal solution. Table 1 shows the results, where the alternative 3 is the best solution. The other two alternatives, local optimum, are included for discussion. Alternative 1 is the strategy currently used by mining companies.

Table 1. Local solutions for the case study. Cost in million $ per year

Alternative	Number of RO plant	RO cost	Number of pumping stations	Pumping cost	Total length of pipes	Piping cost	Total cost
1	3	78	9	126	690 km	55	259
2	1	61	6	125	527 km	46	232
3	1	61	4	125	357 km	36	222

Based on the results of Table 1, desalination costs are between 27 and 30 % of total costs, pumping costs between 48 and 56% of the total, and the costs of pipelines between 16 and 21 % of total cost. The best solution has the lowest cost of pumping, pipelines and desalination. Based on others results observed, there is a tradeoff between the three aforementioned costs to obtain the best solution. Therefore, the simultaneous design of desalination plants, pipelines and pumping system is desirable.

4. Conclusions

The problem of supplying desalinated water to mining plants that are between 600 and 4000 m above sea level was addressed. The proposed methodology considers the design of the desalination plant together the distribution system of desalinated water. A case study was included to illustrate and validate the methodology. The results indicate that the methodology is an appropriate tool to analyze these problems and their application to similar problems is easily adaptable. Also, there is a tradeoff between costs of desalination plant, pumping system, and pipeline system.

Acknowledgements
The authors thank CONICYT and the Regional Government of Antofagasta by their funding through PAI program, Project Anillo ACT 1201.

References

S.Y. Alnouri, P. Linke, 2013, Optimal Design of SWRO Desalination Processes with Boron Level Considerations, Computer Aided Chemical Engineering, 32, 799-804.
S. Atilhan, A. B. Mahfouz, B. Batchelor, et al., 2012, A systems-integration approach to the ptimization of macroscopic water desalination and distribution networks: a general framework applied to Qatar's water resources, Clean Techn Environ Policy, 14, 161–171.
S. Atilhan, P. Linke, A. Abdel-Wahab, et al., 2011, A systems integration approach to the design of regional water desalination and supply networks, Int. J. Process Systems Engineering, 1 (2), 125-135
B. Coelho, A.Andrade-Campos, 2014, Efficiency achievement in water supply systems—A review, Renewable and Sustainable Energy Reviews, 30, 59–84.
I.C. Karagiannis, P.G. Soldatos, 2008, Water desalination cost literature: review and assessment. Desalination, 223(1), 448-456.
M.M. El-Halwagi, 1992, Synthesis of reverse osmosis networks for waste reduction, AIChE J., 38, 1185–1198.
Y. Lu, A. Liao, Y. Hu, 2012, The design of reverse osmosis systems with multiple-feed and multiple-product, Desalination, 307, 42-50.
F. Maskan, D.E. Wiley, 2000, Optimal design of reverse osmosis module networks, AIChE J., 46, 946–954.
A. Malek, M.N.A. Hawlader,1996, Design and economics of RO seawater desalination, Desalination, 105, 245–261.
P.K. Swamee, 2001, Design of high-rise pumping mains. Urban water, 3(4), 317-321.
P.K. Swamee, A.K. Jain, 1976, Explicit equations for pipe-flow problems. Journal of the hydraulics division, 102(5), 657-664.
M.K. Wittholz, 2008, Estimating the cost of desalination plants using a cost database. Desalination, 229(1), 10-20.

Krist V. Gernaey, Jakob K. Huusom and Rafiqul Gani (Eds.), 12th International Symposium on Process Systems Engineering and 25th European Symposium on Computer Aided Process Engineering.
31 May – 4 June 2015, Copenhagen, Denmark

Optimal Design of Microfluidic Platforms for Diffusion-Based PCR for "One-Pot" Analysis of Cells

Jordan Crow[a], Luke E. K. Achenie[a*], Chang Lu[a], Sai Ma[b], Despina Nelie Loufakis[a], Zhenning Cao[b], and Yiwen Chang[a]
[a]*Department of Chemical Engineering, Virginia Tech, Blacksburg, Virginia, 24061, USA*
[b]*School of Biomedical Engineering and Sciences, Virginia Tech, Blacksburg, Virginia, 24061, USA*
achenie@vt.edu

Abstract
Polymerase chain reaction (PCR) is routinely used for analysis of genes from targeted cells leading to an understanding of the fundamental molecular biology involved in cellular events and for detecting abnormal pathways involved in disease development. In a previous paper we argued that the three commonly known strategies to alleviate the impact of cell pretreatment on PCR had serious shortcomings. Furthermore microfluidic strategies that permit simple operation, simple device design and are compatible with Taq polymerase are highly in demand. In this paper, we discuss optimization of microfluidic platform designs, which may be more efficient than the current one we have developed. The microfluidic reactor modelled in this paper relies on the diffusion of molecules from the loading chambers into a small reaction chamber. This results show that diffusion into the reaction chamber can be modified using different loading chamber geometries. Based on the results we have began to develop a mixed integer optimization model to automatically design the geometry to meet the desired transport rates of species in PCR.

Keywords: PCR, microfluidics, optimization, diffusion

1. Introduction
Polymerase chain reaction (PCR) is routinely used for analysis of genes from targeted cells leading to an understanding of the fundamental molecular biology involved in cellular events and for detecting abnormal pathways involved in disease development. Microfluidic devices allow genetic analysis using only tiny amounts of cell samples with high sensitivity and high degree of integration (Ottensen et al., 2006; Marcus et al., 2006; Easley, et al., 2006; Muddu et al., 2011; Agrawal et al., 2007; Bailey et al., 2007; Qavi et al., 2010). The first step in genetic analysis of cells is the lysis of cells leading to a release of genes. Subsequently the genes are isolated, purified, amplified and analysed using PCR (Kim et al., 2009; Chen et al., 2007). The integration of these steps on a microfluidic platform is complicated and needs careful design. The entire process involves various chemical and biological reagents; unfortunately this leads to some reagents interfering with the functions of others. For example chemical reagents used for cell lysis (such as sodium dodecyl sulphate and Triton X-100) may inhibit PCR by reducing polymerase activity (Wilson, 1997; Radstrom et al., 2004; Erlich, 1989). In addition intracellular molecules such as proteins (Hall et al., 2013), polysaccharides (Monteiro et al., 1997), and ions (Al-Soud and Radstrom, 2001) (including Ca^{2+}, Fe^{3+}

and EDTA) in the cell lysate may interact with a polymerase leading to reduced PCR amplification. There are three main strategies for mitigating the impact of cell pretreatment on PCR as follows: (i) Institute an isolation step to remove the lysis reagent and undesired intracellular molecules while preserving nucleic acids. This is typically done by adsorption of nucleic acids on solid surfaces (for example beads or matrices) while replacing the solution (Marcus et al., 2006; Easley et al., 2006; Legendre et al., 2006; Hong et al., 2004). These adsorption and desorption processes increase the complexity of the procedure. Additional chambers and structures may also be needed on the chip to accommodate the procedure. (ii) Use lysis methods that interfere with PCR to a less degree than surfactants, typically in combination with dilution. Freeze-thaw (Toriello et al., 2008) or heating (White et al., 2011; Lien et al., 2007) has been applied to cell lysis in the context of genetic analysis. These methods are less efficient than surfactant-based lysis (Gilbert et al., 2006). In Toriello (Toriello et al., 2008), lysis and PCR were conducted in connected chambers of different sizes so that the lysis reagent was diluted 100-fold when PCR was carried out. Such dilution compromises the limit of detection and requires complex device structure and operational procedure. (iii) Use Direct PCR kit based on Phusion polymerase that is tolerant to surfactant-based lysis reagents (Manage et al., 2011). However, Phusion polymerase can be inhibited by SYBR green and other dyes (Mao et al., 2007) and lacks 5' to 3' exonuclease activity (Wang et al., 2004). Thus commonly used fluorescence-based quantification is impossible with the Phusion polymerase system. Overall microfluidic strategies that permit simple operation, simple device design and are compatible with Taq polymerase are in very high demand. Such strategies will be particularly beneficial for precise and demanding operations such as genetic analysis based on single cells (Novak et al., 2011; Liu et al., 2011; Leung et al., 2012). Our research seeks to address this need.

2. Methodology

In our paper (Ma et al., 2014) and as discussed in the introduction, we argued that the three commonly known strategies to alleviate the impact of cell pretreatment on PCR had serious shortcomings. Furthermore microfluidic strategies that permit simple operation and device design and are compatible with Taq polymerase are highly in demand. To this end we have developed a microfluidic device that permits "one-pot" strategy for multi-step PCR analysis starting from cells (i.e. using one reactor for successive reactions without separation and purification, Ma et al., 2014). The strategy exploits diffusivity differences, effectively replacing the smaller reagent/intracellular molecules in the reaction chamber by diffusion while retaining the larger DNA molecules inside. This simple scheme effectively removes reagents from the previous step to avoid interference and thus *permits multi-step processing in the same reaction chamber*. Our approach shows high efficiency for PCR and potential for a wide range of genetic analysis including assays based on single cells.

Our microfluidic device includes a reaction chamber connected with two loading chambers on both sides. Closing two-layer valves could cut off the connections between the reaction chamber and the two loading chambers. The lysis buffer and the PCR mix are introduced into the chamber by concentration-gradient-driven diffusion. During such diffusion, the new solution replaces the solution and molecules from the previous step without removing the slow-diffusing genomic DNA. The single chamber ("one-pot") design drastically minimizes the complexity of the microfluidic device. We envision

that this may be a general approach for on-chip multi-step assays on genomic DNAs. In this paper we discuss some optimization of microfluidic platform designs, which may be more efficient than the current one we have developed. We are beginning to build these devices to efficiently carry out PCR; the data collected would also be employed to validate our modeling effort. Using the PDE toolbox (pdetool) in MATLAB as a basis, we developed additional code to model diffusion through the reactor. We considered the following components: Primers, Taq Polymerase (Tag), dNTP, small ions, intracellular proteins and Triton X-100. Figures 1 through 5 show different reactor geometries with mesh points. We calculated the average relative concentration in the reaction chamber at each time point.

3. Results

The main focus of this modeling effort is on the diffusion from the loading chamber into the PCR reactor. In Figure 6, *for a given species* we have plotted the results for the different geometries. In contrast in Figure 7, *for a given geometry*, we have plotted the results for the different species. The first three geometries in Figure 6 (Geo 1, 2 3) show essentially no differences in diffusion rates; note that time is in minutes and "concentration" is percent of starting concentration. This is likely due to similar geometry closer to the reaction chamber. Since the reaction chamber is significantly smaller than the loading chamber, the diffusion rates will not change so long as there is a large volume of solution in direct contact with the reaction chamber. Only when this volume is restricted, do changes in diffusion rates appear.

Geo 4 and 5 in Figure 6 show significant changes in the results. The diffusion rate for Geo 4 is slower. The most notable difference is in the small ions. Geo 4 has a 16% lower concentration of small ions than that of Geo 1 at the end of one hour. Geo 5, on the other hand, has some more interesting results. For small ions and dNTP the results for Geo 5 look nearly identical to Geo 4. However for Taq Polymerase and primers the diffusion rates for these two components are highest in Geo 5.

4. Conclusions

Polymerase chain reaction is routinely used for analysis of genes from targeted cells leading to an understanding of the fundamental molecular biology involved in cellular events and for detecting abnormal pathways involved in disease development. In this paper, we have discussed optimization of microfluidic platform designs, which may be more efficient (experimentally) than the current one we have developed. The results show that diffusion into the reaction chamber can be modified using different loading chamber geometries. The geometries in Figure 4 and Figure 5 display this idea with their slowed diffusion in most components. The study also showed that smaller changes in the geometry do not affect diffusion rates in any significant way. If the bulk geometry in direct contact with the diffusion chamber is unchanged, the diffusion rates will remain unchanged. We also realize that in the near future we need to add advection to the PDE model in order to improve the transport through advection-diffusion. Based on the current results we have begun to develop a mixed integer optimization model to automatically design the geometry to meet the desired transport rates of species in PCR. The automatic generation of the geometry would employ Bezier curves often used in computer graphics; Sharifi and Achenie (2007) employed a similar concept. After experimental validation, the results will be reported in a paper.

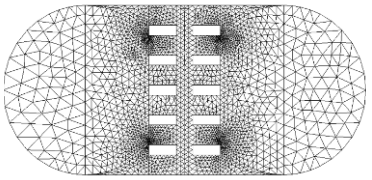

Figure 1: Geometry design # 1 – top view

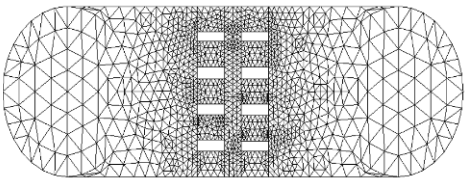

Figure 2: Geometry design # 2 – top view

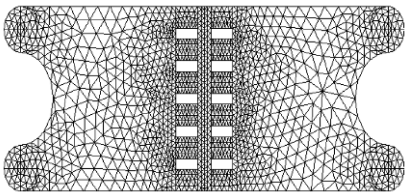

Figure 3: Geometry design # 3 – top view

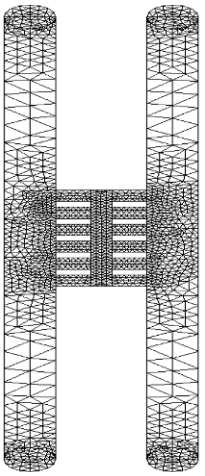

Figure 4: Geometry design # 4 – top view

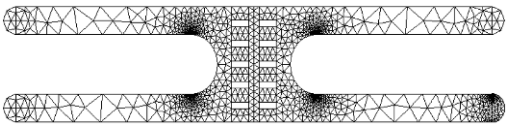

Figure 5: Geometry design # 5 – top view

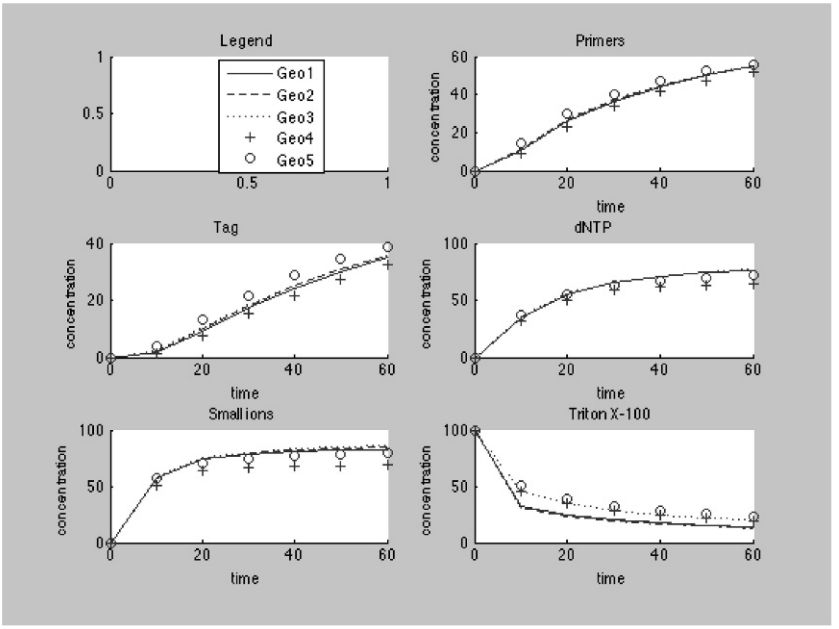

Figure 6: Results for different geometries for a given species

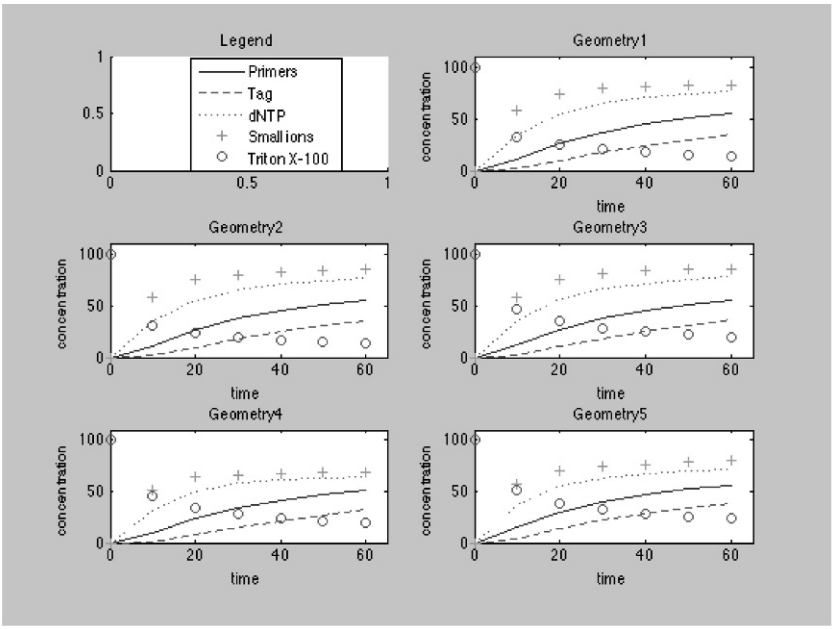

Figure 7: Results for different species for a given geometry

References

N. Agrawal, Y.A. Hassan, and V.M. Ugaz, 2007, A pocket-sized convective PCR thermocycler. Angew. Chem. Int. Edit., 46(23): p. 4316-4319.

W.A. Al-Soud and P. Rådström, 2001, Purification and characterization of PCR-inhibitory components in blood cells. J. Clin. Microbiol., 39(2): p. 485-493.

R.C. Bailey, G.A. Kwong, C.G. Radu, O.N. Witte, J.R. Heath, 2007, DNA-encoded antibody libraries: A unified platform for multiplexed cell sorting and detection of genes and proteins. J. Am. Chem. Soc., 129(7): p. 1959-1967.

L. Chen, L., A. Manz, and P.J.R. Day, 2007, Total nucleic acid analysis integrated on microfluidic devices. Lab Chip, 7(11): p. 1413-1423.

C. J. Easley, J. M. Karlinsey, J. M. Bienvenue, L. A. Legendre, M. G. Roper, S. H. Feldman, M. A. Hughes, E. L. Hewlett, T. J. Merkel, J. P. Ferrance, J. P. Landers, 2006, A fully integrated microfluidic genetic analysis system with sample-in–answer-out capability. P. Natl. Acad. Sci., 103(51): p. 19272-19277.

H. A. Erlich, 1989, PCR technology. Principles and applications for DNA amplification, Stockton press.

T.W. Gilbert, T.L. Sellaro, and S.F. Badylak, 2006, Decellularization of tissues and organs. Biomaterials, 27(19): p. 3675-3683.

A. T. Hall, A. M. Zovanyi, D. R. Christensen, J. W. Koehler, T. D. Minogue, 2013, Evaluation of Inhibitor-Resistant Real-Time PCR Methods for Diagnostics in Clinical and Environmental Samples. PloS one, 8(9).

J. W. Hong, V. Studer, G. Hang, F. W. Anderson, S. R. Quake, 2004, A nanoliter-scale nucleic acid processor with parallel architecture. Nat. Biotechnol., 22(4): p. 435-439.

J. Kim, M. Johnson, P. Hill, B. K. Gale, 2009, Microfluidic sample preparation: cell lysis and nucleic acid purification. Integr. Biol., 1(10): p. 574-586.

L. A. Legendre, J. M. Bienvenue, M. G. Roper, J. P. Ferrance, J. P. Landers, 2006, A simple, valveless microfluidic sample preparation device for extraction and amplification of DNA from nanoliter-volume samples. Anal. Chem., 78(5): p. 1444-1451.

K. Leung, H. Zahn, T. Leaver, K. M. Konwar, N. W. Hanson, A. P. Pagé, C. C. Lo, P. S. Chain, S. J. Hallam, C. L. Hansen, 2012, A programmable droplet-based microfluidic device applied to multiparameter analysis of single microbes and microbial communities. P. Natl. Acad. Sci., 109(20): p. 7665-7670.

K. Y. Lien, W. C. Leeb, H. Y. Leic, G. B. Leea, 2007, Integrated reverse transcription polymerase chain reaction systems for virus detection. Biosens. Bioelectron., 22(8): p. 1739-1748.

P. Liu, X. Li, S. A. Greenspoon, J. R. Scherer, R. A. Mathies, 2011, Integrated DNA purification, PCR, sample cleanup, and capillary electrophoresis microchip for forensic human identification. Lab Chip, 11(6): p. 1041-1048.

S. Ma, D. N. Loufakis, Z. Cao, Y. Chang, L. E. K. Achenie, C. Lu, 2014, Diffusion-based microfluidic PCR for one-pot analysis of cells. Lab Chip, 14: p. 2905-2909.

D. P. Manage, Y. C. Morrissey, A. J. Stickel, J. Lauzon, A. Atrazhev, J. P. Acker, L. M. Pilarski, 2011, On-chip PCR amplification of genomic and viral templates in unprocessed whole blood. Microfluidic. Nanofluidic., 10(3): p. 697-702.

F. Mao, W.-Y. Leung, and X. Xin, 2007, Characterization of EvaGreen and the implication of its physicochemical properties for qPCR applications. BMC Biotechnol., 7(1): p. 76.

J. S. Marcus, W.F. Anderson, and S.R. Quake, 2006, Microfluidic Single-Cell mRNA Isolation and Analysis. Anal. Chem., 78(9): p. 3084-3089.

L. Monteiro, D. Bonnemaison, A. Vekris, K. G. Petry, J. Bonnet, R. Vidal, J. Cabrita, F. Mégraud, 1997, Complex polysaccharides as PCR inhibitors in feces: Helicobacter pylori model. J. Clin. Microbiol., 35(4): p. 995-998.

R. Muddu, Y.A. Hassan, and V.M. Ugaz, 2011, Chaotically Accelerated Polymerase Chain Reaction by Microscale Rayleigh-Benard Convection. Angew. Chem. Int. Edit., 50(13): p. 3048-3052.

R. Novak, Y. Zeng, J. Shuga, G. Venugopalan, D. A. Fletcher, M. T. Smith, R. A. Mathies, 2011, Single-Cell Multiplex Gene Detection and Sequencing with Microfluidically Generated Agarose Emulsions. Angew. Chem. Inte. Edit., 50(2): p. 390-395.

E. A. Ottesen, J. W. Hong, S. R. Quake, J. R. Leadbetter, 2006, Microfluidic Digital PCR Enables Multigene Analysis of Individual Environmental Bacteria. Science, 314(5804): p. 1464-1467.

A. J. Qavi and R.C. Bailey, 2010, Multiplexed Detection and Label-Free Quantitation of MicroRNAs Using Arrays of Silicon Photonic Microring Resonators. Angew. Chem. Int. Edit., 49(27): p. 4608-4611.

P. Rådström, R. Knutsson, P. Wolffs, M. Lövenklev, C. Charlotta Löfström, Pre-PCR processing. Mol. Biotechnol., 2004. 26(2): p. 133-146.

Y. Sharifi, L. E. K. Achenie, 2007, Effect of substrate geometry on deposition rate in CVD, Journal of Crystal Growth, 304: p. 520–525.

N. M. Toriello, E. S. Douglas, N. Thaitrong, S. C. Hsiaob, M. B. Francisb, C. R. Bertozzi, R. A. Mathiesa, 2008, Integrated microfluidic bioprocessor for single-cell gene expression analysis. P. Natl. Acad. Sci. USA, 105(51): p. 20173-20178.

Y. Wang, D. E. Prosen, L. Mei, J. C. Sullivan, M. Finney, P. B. Vander Horn, 2004, A novel strategy to engineer DNA polymerases for enhanced processivity and improved performance in vitro. Nucleic Acids Res., 32(3): p. 1197-1207.

A. K. White, M. VanInsberghe, O. I. Petriv, M. Hamidi, D. Sikorski, M. A. Marra, J. Piret, S. Aparicio, C. L. Hansen, 2011, High-throughput microfluidic single-cell RT-qPCR. P. Natl. Acad. Sci.

I. G. Wilson, 1997, Inhibition and facilitation of nucleic acid amplification. Appl. Environ. Microb., 63(10): p. 3741.

Krist V. Gernaey, Jakob K. Huusom and Rafiqul Gani (Eds.), 12th International Symposium on Process Systems Engineering and 25th European Symposium on Computer Aided Process Engineering.
31 May – 4 June 2015, Copenhagen, Denmark

A Systematic Methodology for Optimal Mixture Design in an Integrated Biorefinery

Lik Yin Ng, Viknesh Andiappan, Nishanth G. Chemmangattuvalappil*, Denny K. S. Ng

Department of Chemical and Environmental Engineering/Centre of Sustainable Palm Oil Research (CESPOR), The University of Nottingham Malaysia Campus, Broga Road, Semenyih 43500, Malaysia.
Nishanth.C@nottingham.edu.my

Abstract

An integrated biorefinery is a processing facility that integrates multiple biomass conversion pathways to produce value-added products. To date, various biomass conversion pathways are available to convert biomass into a wide range of products. Hence, there is a need for a methodology capable of evaluating the integrated processes in order to identify the optimal products possible to be produced from biomass and the optimal conversion pathway in producing them. In many cases where the desired properties cannot be met by a single molecule, an optimal mixture of chemicals would be required. In this respect, product and process design decisions would be a challenging task for an integrated biorefinery. In this work, a two-stage optimisation approach is developed to identify the optimal conversion pathways in an integrated biorefinery which convert biomass into an optimal mixture with desired properties. In the first stage, the optimal mixture is designed via computer aided molecular/mixture design (CAMD) tools. Once the optimal mixture is established, the second stage determines the optimal conversion pathway via superstructural mathematical optimisation approach. With such approach, the optimal conversion pathway can be determined based on different optimisation objectives. To illustrate the proposed methodology, a case study on the design of fuel additives as a mixture of different molecules from palm-based biomass is presented.

Keywords: product design, mixture design, integrated biorefinery, integrated product and process design, inverse design techniques.

1. Introduction

Fossil fuels have been widely utilised as the main source of energy for heat and power production. Besides, fossil fuel has also been an important feedstock for various commodity and specialty chemical productions. However, vast consumption of fossil fuels also contributed to significant environmental issue such as the increased level of greenhouse gases in the atmosphere (Panwar et al., 2011). With the increasing awareness toward clean and sustainable development, biomass has been identified as one of the most promising sources of renewable energy. To convert biomass into energy and value-added products, an integrated processing facility known as an integrated biorefinery is needed. An integrated biorefinery is a processing facility that integrates multiple chemical reaction pathways to convert biomass into value-added products along with heat and power (Fernando et al., 2006). To date, there are a large number of established biomass conversion pathways available for implementation in an integrated

biorefinery to convert biomass into a wide spectrum of products. As such, there is a need to screen all potential pathways systematically and determine the optimum pathway that produces the desired products. Various approaches have been developed for process synthesis and screening of potential conversion pathways for integrated biorefineries.

It can be seen that most of the current works in this area are focused on identifying and designing the optimal processing routes that leads to the product without considering the requirement of product needs. To address this issue, the product design aspects have to be taken into consideration to design integrated biorefinery. This can be achieved by integrating the chemical product design steps during the synthesis and design of integrated biorefinery. According to Cussler and Moggridge (2001), chemical product design is a process of choosing the optimal product to be made for a specific application. Most of the time, functionality of a product are defined in terms of physical properties rather than chemical structure of the product. Hence, chemical product design can be considered as an inverse property prediction problem where the preferred attributes of the product are represented in terms of physical properties (Gani and O'Connell, 2001). As product specifications are often extracted from customer needs, it is required to translate qualitative attributes into quantitative parameters in order to design a product (Achenie et al., 2003). The process of representing product attributes by using measurable parameters is often done by CAMD techniques. CAMD techniques are important for product design because they are able to predict and design molecules with a given set of properties. CAMD techniques have been extensively applied in designing different chemical products over the recent decades. Hechinger et al. (2010) presented a work for the design of biofuels from biomass by integrating product and process design. The work identifies the molecular structures of the biofuels by using CAMD techniques while searching the alternative production pathways by utilising reaction network flux analysis. Chemmangattuvalappil et al. (2010) developed a general framework for the integration of process and molecular design problem for the design of industrial solvent. Roughton et al. (2011) proposed a methodology for the simultaneous design of ionic liquids and azeotropic separation processes. Recently, Mattei et al. (2014) presented a virtual product-process design laboratory for the design and analysis of blended liquid products and emulsion-based products. Despite the usefulness of the aforementioned works, it is found that the development on simultaneous process and product design of integrated biorefinery is still in its early stages. In cases where a single component/molecule is insufficient to meet desired properties, it is an opportunity to explore the potential of designing an optimal mixture from an integrated biorefinery. Therefore, this remains as the scope of this work.

2. Methodology: Two stage optimisation approach

This work presents a systematic methodology for simultaneous process and product design for an integrated biorefinery. A two-stage optimisation approach is utilised to identify the optimal product in terms of mixture of several individual components as well as the optimal conversion pathway for the mixture.

2.1. Mixture design

In this stage, the optimal mixture is designed by utilising signature based molecular design techniques (Chemmangattuvalappil et al. 2010). The main component of the mixture is first identified from the available products or designed based on the target

properties. The additive components required for the mixture are then designed such that when mixed together with the main component, the properties of the mixture will fall within the target property ranges as shown in Eq.1.

$$v_{mp}^{\mathrm{L}} \le \sum_i x_{ip} V_{ip} \le v_{mp}^{\mathrm{U}} \qquad p = 1, 2, \ldots P \tag{1}$$

where x_{ip} is the fraction of chemical component i for target property p, V_{ip} is the value of target property p for chemical component i, v^{L}_{mp} and v^{U}_{mp} are the lower and upper limits of mixture m for target property p respectively. According to Churi and Achenie (1997), the main purpose in designing mixtures is that mixtures have the potential for giving a good mix of target properties which are unattainable by individual chemical components. For example, for refrigerant design, although difluoromethane (CH_2F_2) is a better refrigerant in terms of low compressor displacement and zero ozone depletion, its vapor pressure it too high for an efficient refrigerant. This can be overcome by mixing chloromethane (CH_3Cl) and CH_2F_2 (Duvedi and Achenie, 1997). Hence, mixtures offer greater flexibility in matching multiple target properties. To design an optimal mixture in terms product properties by mixing different chemical components, multiple mixture target properties are needed to be considered and optimised simultaneously. This can be solved as multi-objective optimisation problem where multiple target properties are optimised during the design of the mixture. Fuzzy optimisation approach is applied in this work to trade off different target properties simultaneously. The application of fuzzy set theory in optimal decision-making is introduced by Bellman and Zadeh (1970). Zimmermann (1978) later extended the approach to address mathematical programming problems which involve multiple objectives by integrating multiple objectives into a single objective. An optimised trade-off solution can be obtained by solving the overall objective based on the predefined fuzzy limits. To maximise the mixture property, trade-off between properties to be optimised is done by introducing a degree of satisfaction, λ which is bounded within the interval of 0 and 1.

$$\lambda_p = \frac{v_{mp}^{\mathrm{U}} - V_{mp}}{v_{mp}^{\mathrm{U}} - v_{mp}^{\mathrm{L}}}, \quad \lambda_p = \frac{V_{mp} - v_{mp}^{\mathrm{L}}}{v_{mp}^{\mathrm{U}} - v_{mp}^{\mathrm{L}}} \tag{2}$$

where λ_p is the degree of satisfaction for property p. The first equation in Eq.(2) is used for properties to be maximised while the second equation in Eq.(2) is utilised for properties to be minimised. To obtain the optimal solution, max-min aggregation is applied (Zimmermann, 1978), where the least satisfied degree of satisfaction of these properties is maximised.

2.2. Integrated biorefinery design

In the second stage, an integrated biorefinery is synthesised based on the components designed for the optimal mixture in the first stage. This is done by utilising superstructural mathematical optimisation approach. A superstructure which includes all the possible conversion pathways and technologies that process the biomass into the intermediate, and convert the intermediates into the final products is constructed as the representation of an integrated biorefinery. As such, the optimal conversion pathway based on different optimisation objectives that leads to the desired optimal mixture can be determined in this stage. For cases where the conversion pathway leads to the formation of products as a mixture of several components, separation processes are included.

3. Case study: Production of biofuel additives from palm-based biomass

In this case study, a mixture design problem of bio-based fuel additives with a specified set of properties is produced from palm-based biomass. The optimal mixture is designed such that it possesses target properties which fall within the specified target property ranges. These target properties include higher heating value (*HHV*) which is estimated by group contribution (GC) model developed by Yunus (2014), lethal concentration ($\log LC_{50}$) estimated by connectivity index from Koch (1982), viscosity (η) estimated by GC model from Conte et al. (2008), heat of vaporisation (H_v) estimated by GC model from Marrero and Gani (2001) and oxygen content (*OC*). The target property range for *HHV* is within 3500 and 5500 kJ/mol, *OC* within 2.00 and 6.70 wt %, $\log LC_{50}$ within 2.40 and 3.60, H_v within 30 and 50 kJ/mol and η within 0.30 and 0.90 cP. The main component (MC) of the fuel is predetermined by using a pseudo-component consists of different types of hydrocarbons. The objective of the mixture design is to improve *HHV* and *OC* of the main component by designing additive component made from alkane and alcohol for the fuel. In this work, linear mixing rule is applied to estimate *HHV*, $\log LC_{50}$, *OC* and H_v of the mixture. For η, a mixing rule developed based on property integration as proposed by Qin et al. (2004) is utilised. In order to target the multiple objectives, fuzzy optimisation approach has been applied along with CAMD techniques. Following the proposed approach, the best five solutions for the design of additives made from both alkane (Alk) and alcohol (Alc) are obtained and summarised in Table 1.

Table 1. Possible designs of additives made from alkane and alcohol

Sol.	Properties				
	HHV (kJ/mol)	*OC* (wt %)	log LC_{50}	H_v (kJ/mol)	η (cP)
Alk. A	6767	0.00	1.08	44.32	0.89
Alk. B	6765	0.00	0.86	46.24	0.69
Alk. C	6751	0.00	0.90	44.60	0.60
Alk. D	6126	0.00	1.16	42.97	0.64
Alk. E	6112	0.00	1.25	41.33	0.56
Alc. A	2683	21.62	3.05	50.90	2.50
Alc. B	2669	21.62	3.11	49.25	2.18
Alc. C	3335	18.18	2.60	55.80	3.09
Alc. D	3321	18.18	2.63	54.16	2.70
Alc. E	3307	18.18	2.78	52.52	2.36

By mixing the MC with the identified additive components, the best five mixtures identified together with the mixing ratio of main and additive components are shown in Table 2. Mixture A possesses *HHV* of 4626 kJ/mol, *OC* of 4.34 wt %, $\log LC_{50}$ of 2.97, H_v of 40.22 kJ/mol and η of 0.83 cP.

Table 2. Possible designs of mixture

Mixture	MC (wt %)	Alk (wt %)	Alc (wt %)
A.	52.30	Alk. A (23.85)	Alc. C (23.85)
B.	53.30	Alk. D (23.44)	Alc. D (23.26)
C.	53.74	Alk. A (26.90)	Alc. A (19.36)
D.	53.71	Alk. C (26.99)	Alc. B (19.30)
E.	52.30	Alk. B (23.85)	Alc. C (23.85)

Once the optimal mixture is identified in stage one, the optimal conversion pathways that convert palm-based biomass into the identified additive components is determined in stage two. The superstructure model of this case study is shown in Figure 1.

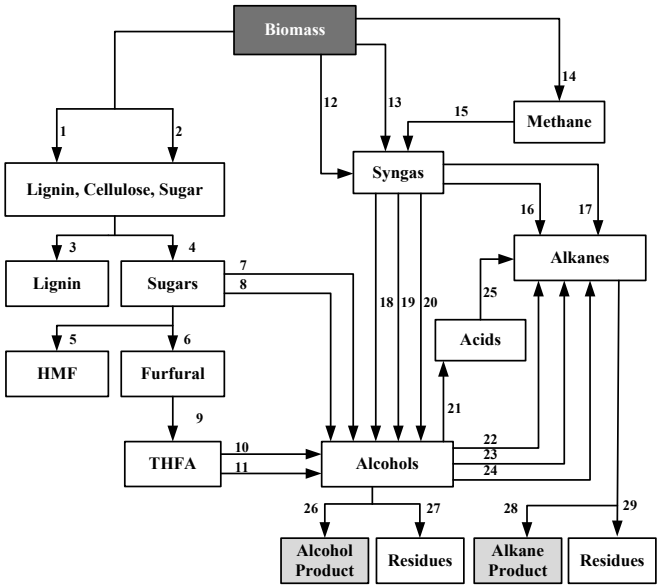

Figure 1. Superstructure of conversion pathways to produce additive components

The numbers in Figure 1 represent different conversion pathways and technologies that process the biomass into the intermediates, and convert the intermediates into the final product. In this case study, the optimisation objective of the integrated biorefinery is to identify the conversion pathways with maximum product yield (Scenario 1) and maximum economic potential (Scenario 2). From the optimal mixture generated in the first stage of the methodology, it is identified the mixing ratio of additives alkane (Alk. A) and alcohol (Alc. C) for mixture A is 1:1. Thus, the production ratio of alkane and alcohol in the integrated biorefinery is fixed as 1:1. With a feed of 50,000 tonnes per year of palm-based biomass, superstructural optimisation model is formulated and solved. The results are shown in Table 3.

Table 3. Comparison of results for Scenario 1 and 2.

Scenario	1	2
Conversion pathways	1,3,4,6,9,11,12,16, 23,26,27,28,29	1,3,4,6,9,10,12,17, 23,26,27,28,29
GP^{Total} (U.S $/y)	5.43×10^6	19.71×10^6
Alkane production rate (t/y)	1169.38	406.33
Alcohol production rate (t/y)	1169.38	406.33
Alkane by-product production rate (t/y)	10303.30	10831.65
Alcohol by-product production rate (t/y)	2710.84	9650.45

In scenario 1, Alc.C is produced from biomass in the sequence of ammonia explosion, Organosolv separation, dehydration of sugars, hydrogenation of furfural, hydrogenation of THFA 2 and fractional of distillation of alcohols. Meanwhile, Alk. A is produced from fractional distillation of alkanes, which are produced from pyrolysis of biomass followed by Fischer-Tropsch process 1 together with dehydration of alcohols 2. In scenario 2, most of the conversion pathways of scenario 2 are similar to those of scenario 1. However, hydrogenation of THFA 1 is chosen instead of hydrogenation of THFA 2 and Fischer-Tropsch process 2 is selected over Fischer-Tropsch process 1 in order to produce the additives while generating maximum profit.

4. Conclusions

This paper introduces a systematic two-stage optimisation approach for optimal mixture design in an integrated biorefinery by integrating product and process design. In the first stage, mixture design is done by CAMD technique. Main component of the mixture is first identified from the target properties. This is followed by the identification of additive components to form the mixture with the main component. Hence, the optimal mixture that possesses optimal product properties can be designed by mixing the identified main component and additive components together. In the second stage, the optimal conversion pathway is determined via superstructural mathematical optimisation approach. Future efforts will be focused on improving the completeness of the methodology. Product stability analysis and verification can be investigated to improve the accuracy of the mixture design methodology.

References

L.E.K. Achenie, R. Gani & V. Venkatasubramanian, 2003, Computer aided molecular design: Theory and practice, Elsevier Science Inc.

R. Bellman & L. Zadeh, 1970, Decision-Making in a Fuzzy Environment, Management Science 17, 4, 141–164.

N.G. Chemmangattuvalappil, C.C. Solvason, S. Bommareddy & M.R. Eden, 2010, Molecular signature descriptors for integrated flowsheet and molecular design, Computers Aided Chemical Engineering, 28, C, 1267–1272.

N. Churi & L.E.K. Achenie, 1997, The optimal design of refrigerant mixtures for a two-evaporator refrigeration system, Computers & Chemical Engineering, 21, S349–S354.

E. Conte, A. Martinho, H.A. Matos & R. Gani, 2008, Combined group-contribution and atom connectivity index-based methods for estimation of surface tension and viscosity, Industrial & Engineering Chemistry Research, 47, 20, 7940–7954.

E. L. Cussler & G. D. Moggridge, 2001, Chemical Product Design, Cambridge University Press.

S. Fernando, S. Adhikari, C. Chandrapal & N. Murali, 2006, Biorefineries: Current Status, Challenges, and Future Direction, Energy & Fuels, 20, 4, 1727–1737.

A. Duvedi & L.E.K. Achenie, On the design of environmentally benign refrigerant mixtures: a mathematical programming approach, Computers & Chemical Engineering, 21, 8, 915–923.

R. Gani & J.P. O'Connell, 2001, Properties and CAPE: from present uses to future challenges, Computers & Chemical Engineering, 25, 1, 3–14.

M. Hechinger, A. Voll & W. Marquardt, 2010, Towards an integrated design of biofuels and their production pathways, Computer & Chemical Engineering, 34, 12, 1909–1918.

R. Koch, 1982, Molecular connectivity and acute toxicity of environmental pollutants, Chemosphere, 11, 9, 925–931.

J. Marrero & R. Gani, 2001, Group-contribution based estimation of pure component properties, Fluid Phase Equilibria, 183-184, 183–208.

M. Mattei, N.A. Yunus, S. Kalakul, G.M. Kontogeorgis, J.M. Woodley, K.V. Gernaey & R. Gani, 2014, The virtual product-process design laboratory for structured chemical product design and analysis, Computer Aided Chemical Engineering, 33, 61–66.

N.L. Panwar, S.C. Kaushik & S. Kothari, 2011, Role of renewable energy sources in evironmental protection: A review, Renewable and Sustainable Energy Reviews, 15, 1513–1524.

X. Qin, F. Gabriel, D. Harell & M.M. El-Halwagi, Algebraic Techniques for Property Integration via COmponentless Design, Industrial & Engineering Chemistry Research, 43, 14, 3792–3798.

B.C. Roughton, J. White, K.V. Camarda & R. Gani, 2011, Simultaneous design of ionic liquids and azeotropic separation processes, Computer Aided Chemical Engineering, 29, 1578–1582.

N.A. Yunus, 2014, Systematic Methodology for Design of Tailor-Made Blended Products: Fuels and Other Blended Products, Technical University of Denmark.

H. J. Zimmermann, 1978, Fuzzy Programming and Linear Programming with Several Objective Functions, Fuzzy Sets and Systems, 1, 44–45.

Krist V. Gernaey, Jakob K. Huusom and Rafiqul Gani (Eds.), 12th International Symposium on Process Systems Engineering and 25th European Symposium on Computer Aided Process Engineering.
31 May – 4 June 2015, Copenhagen, Denmark

A Systematic Visual Approach to Ionic Liquid Design for Carbon Dioxide Capture

Fah Keen Chong,[a] Nishanth G. Chemmangattuvalappil,[a]* Dominic C.Y. Foo,[a] Mert Atilhan,[b] Fadwa T. Eljack[b]

[a]*Department of Chemical and Environmental Engineering/Centre of Excellence for Green Technologies, University of Nottingham Malaysia Campus, Broga Road, 43500, Selangor DE, Malaysia*
[b]*Department of Chemical Engineering, College of Engineering, Qatar University, PO Box 2713, Doha, Qatar*
Nishanth.C@nottingham.edu.my

Abstract

Ionic liquids (ILs) have been introduced as potential replacement of conventional CO_2 capturing solvents, for their negligible vapour pressure and high thermal stability. Besides, through matching cations and anions, ILs provide a flexibility to tune their properties. However, due to vast number of potential ILs, time and expense required determine suitable ILs for CO_2 capture is unaffordable. In this work, a systematic visual approach to design IL as CO_2 solvent, via property clustering technique and group contribution method has been developed. This approach allows visualisation of high-dimensional problem into two or three dimensions. A case study has been presented to elaborate application of the developed approach.

Keywords: Ionic liquid design, property clustering, group contribution.

1. Introduction

Carbon dioxide (CO_2) emission is now a major issue faced by society, which is closely related to the global energy demand and supply. Fossil fuel remains dominant and supply up to 80 % of global energy consumption, and thus accounts for two-thirds of global CO_2 emissions (IEA, 2013). Carbon capture and storage (CCS) is a possible solution to this, by separating CO_2 from emission sources and storing it in secure geological storage. Ionic liquids (ILs) have recently emerged as green solvents and suggested as possible CO_2 capturing solvents. ILs have very unique combination of properties, including large liquid phase range, negligible vapour pressure, and high thermal stability (Plechkova and Seddon, 2008). They are also called "designer" solvents, for their thermophysical properties can be tuned by switching cations and anions, and thus can be designed for specific application. However, it was reported that there are 10^6 unique combinations of cations and anions (Plechkova and Seddon, 2008). It is a challenging task to find potential ILs for specific task and fulfil certain properties, by trial-and-error approach.

To address this problem, works have recently been done to synthesise novel ILs structure through systematic approach. Roughton et al. (2011) presented simultaneous process and ILs design for azeotropic separation process, by using a newly developed UNIFAC model. Hada et al. (2013) proposed a methodology combining group

contribution (GC) method, chemometric and property clustering technique to design IL. Chong et al. (2014) presented a mixed-integer nonlinear programming formulation to design optimal ILs to capture CO_2. The aforementioned works are based on mathematical optimisation techniques, which is preferable when solving relatively complex problem. However, these techniques do not provide insights of the problem, which might be useful for people without mathematical optimisation background. In addition, nonlinear property prediction models used in previous works increase the complexity of the approach that can lead to sub-optimal solutions. This work introduces a property based visual representation of IL design problem, by using property clustering technique and GC method.

2. Property Clustering

Property clustering is a tool developed by Shelley and El-Halwagi (2000) to represent and track properties in a process streams following a conserved manner. This technique allows for representation of process from a properties perspective and visualisation of process design problems (Eljack and Eden, 2008). Eljack et al. (2006) extended this technique and introduced molecular property operators that can solve molecular design problems. This technique allows for simple linear additive rules of the groups, as described in Eq. (1).

$$\psi_j\left(P_{ji}\right) = \sum_{g=1}^{N_g} n_g\left(P_{jg}\right) \tag{1}$$

In Eq. (1), $\psi_j(P_{ji})$ is the molecular property operator of the j^{th} property of component i, n_g is the number of group g, and N_g is the total number of molecular groups. This equation shows that the property operator will follow simple linear mixing rules, regardless of the linearity of the raw property. Through the following steps shown in Eq. (2), property clusters can be obtained from property operators (Eden et al., 2004). In Eq. (2), Ω_{jg} is normalised property operator for property j, $\psi_j(P_{jg})$ is reference operator of j^{th} property, AUP_g is augmented property index of group g, and C_{jg} is property cluster for property j of group g.

$$\Omega_{jg} = \frac{\psi_j\left(P_{jg}\right)}{\psi_j^{ref}\left(P_j\right)}, \qquad AUP_g = \sum_{j=1}^{NP} \Omega_{jg}, \qquad C_{jg} = \frac{\Omega_{jg}}{AUP_g} \tag{2}$$

3. Visualisation of the Problem

Using property clustering technique, the IL design problem can now be visualised in a ternary diagram. In the ternary diagram, each vertex represents a pure property cluster. It should be noted that the number of clusters is limited to three for visualisation purpose, but this does not indicate that the number of properties considered in IL design is also limited to three. Besides, properties with no available GC prediction models can also be included as addition considerations, as long as there are appropriate prediction models for these properties. All considered properties of designed IL should be within the property constraints. For properties included in ternary diagram, El-Halwagi et al. (2004) showed that the constraints can be represented as a feasibility region defined by six unique points. To ensure the designed ILs are valid solutions, following design and optimisation rules have also been developed, based on rules previously developed by Eden et al. (2004) and Eljack and Eden (2008).

Rule 1: When two groups, G_1 and G_2, are added linearly on the diagram, the AUP values and distance between them provide information of G_1-G_2 structure.
Rule 2: More groups can be added if the free bond number, *FBN* of the structure is not zero
Rule 3: The final IL molecular structure must not have any free bond, to ensure the structure is complete and feasible (i.e. $FBN = 0$).
Rule 4: Location of the final formulation is independent of the order of group addition.
Rule 5: In pure IL design, only one cation core and one anion group can be chosen.
Rule 6: The cluster value of the designed IL must be located within the feasibility region on the ternary diagram.
Rule 7: The AUP value of the designed IL must be within the range of target AUP. If the AUP value is outside the range of target AUP, the IL is not a feasible solution.

In the case where properties with no GC prediction models are considered, these properties must be calculated for the designed IL using appropriate prediction models. The calculated property values must be within the range of target properties for the designed IL to be a valid solution. It is common that there is negative GC data, and this will lead to negative property operator and cluster value. In this situation, the group will reside outside the ternary diagram, and using this group will violate Rule 1. Solvason et al. (2009) has discussed about this limitation and another rule is developed to overcome this. Without Rule 8, a negative AUP is mathematically possible, but it gives an infeasible solution. This can be avoided by adjusting reference values of the properties.

Rule 8: All AUP values of the groups must be positive.

4. Case Study

An illustrative case study is included to demonstrate the proposed approach. As shown in Table 1, three cation cores, two anions and three organic functional groups are considered in this design problem. The main objective is to determine a list of potential ILs for carbon capture purpose. In this IL design formulation, the three properties considered for visualisation purpose are density (ρ), heat of vaporisation (ΔH_{vap}), and specific heat capacity (c_p), which are denoted as C_1, C_2, and C_3 respectively. In addition to these, viscosity (μ) and solubility of CO_2 (x_{CO2}) are included for screening purpose. The GC prediction models for density (Qiao et al., 2010), heat of vaporisation (Verevkin, 2008), and specific heat capacity (Gardas and Coutinho, 2008) are shown in Eq. (3).

$$\rho = \rho_0 + \sum_g n_g \rho_g, \qquad \Delta H_{\text{vap}} = \sum_g n_g \Delta H_{vap,g}, \qquad c_p = R\left(\sum_g n_g c_{p,g}\right) \tag{3}$$

Table 1: Organic function groups, cation cores, and anions considered

Type	k	Groups	Type	k	Groups
Organic groups	1	CH_3	Cation cores	6	$[MIm]^+$
	2	CH_2		7	$[Py]^+$
	3	OH		8	$[MPyr]^+$
Anions	4	$[BF_4]^-$			
	5	$[Tf_2N]^-$			

where ρ_0 is the adjustable parameter for density and R is gas constant. From Eq. (3), the property operators can be identified and property clusters are then determined using Eq. (2). Group contribution model for density is possible in pure component design because it is not estimation of mixture density. The viscosity of IL is determined using Eqs. (4) and (5).

$$\ln \frac{1{,}000\mu}{\rho M} = A + \frac{B}{T} \tag{4}$$

$$A = \sum_g n_g A_{g,\mu}, \qquad B = \sum_g n_g B_{g,\mu} \tag{5}$$

where M is IL molecular weight, T is the system temperature in K, $A_{g,\mu}$ and $B_{g,\mu}$ are contributions of group g to parameters A and B respectively. The solubility of CO_2 is determined through equilibrium relationships as shown in Eq. (6). The nonideality of liquid phase, due to presence of ionic and organic compounds, is modelled through activity coefficient γ_i. Activity coefficient is estimated using UNIFAC model for systems containing ILs (Lei et al., 2013).

$$y_i P \varphi_i(T, P, y_i) = x_i \gamma_i P_i^s \tag{6}$$

where x_i and y_i are the mole fractions of component i in liquid and gas phases respectively, P is the system pressure in MPa, P_i^S is the saturated vapour pressure of component i, and $\varphi_i(T,P,y_i)$ is the gas-phase fugacity coefficient. The target property ranges are shown in Table 2. Designed ILs should possess similar properties as current CO_2 solvents, i.e. ethanolamines (The Dow Chemical Company, 2003). Low viscosity of IL is desired to minimise pumping power required to circulate IL solvent within the system. Therefore, the target viscosity is set between 0 to 0.1 Pa.s. Solubility of CO_2 is measured in terms of CO_2 mole fraction in liquid phase at equilibrium. Using the proposed approach, the problem is visualised and shown in Figure 1. The dotted line represents the feasibility region based on the target property ranges in Table 2. The maximum and minimum AUP is determined to be 2.703 and 11.502 from this boundary. Note that, G_1 and G_2 locate out of ternary diagram because they have negative property cluster values.

Eight candidates ILs are formulated, as shown in Figure 2, as potential CO_2 solvents reside within feasibility region. The AUP values of these candidates are determined, as shown in Table 3, and they are all within the range of AUP of feasibility region determined from the six point bounding. Lastly, the properties of all ILs, including the screening properties, are back calculated, and included in Table 3. These designed ILs fulfill all the property constraints set in Table 2.

Table 2: Target property ranges to design IL for carbon capture purpose

Property	Lower Bound	Upper Bound
ρ (g/cm^3)	1	2
ΔH_{vap} (kJ/kmol)	40,000	200,000
c_p (kJ/kmol.K)	100	600
μ (Pa.s)	0	0.1
x_{CO2}	0	1

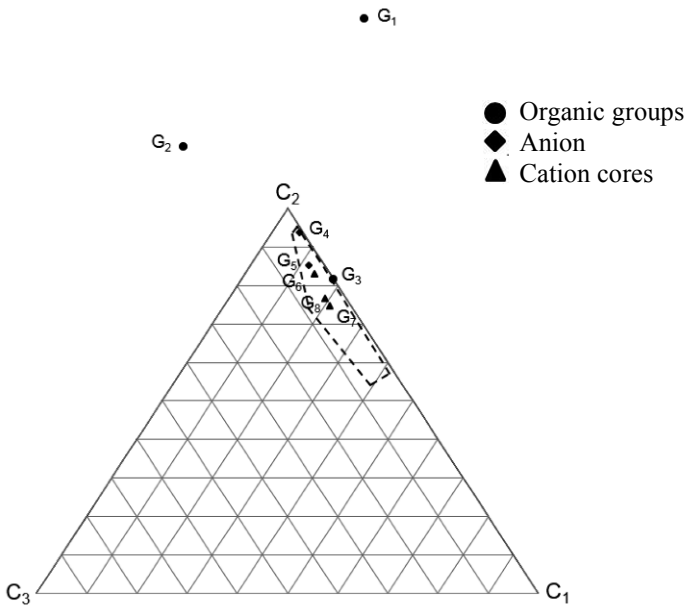

Figure 1: Ternary diagram representing visualisation of IL design problem

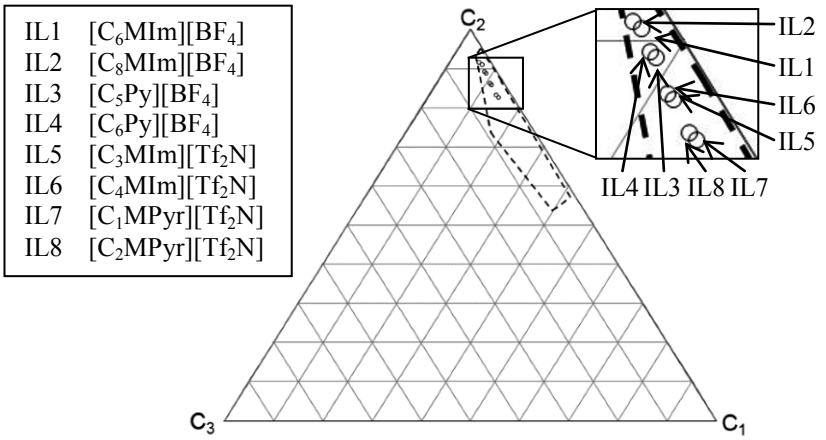

Figure 2: Ternary diagram representing IL design results

Table 3: Ionic liquids design results

Ionic Liquids	ρ (g/cm^3)	ΔH_{vap} (kJ/kmol)	c_p (kJ/kmol.K)	μ (Pa.s)	x_{CO2}	AUP
$[C_6MIm][BF_4]$	1.132	155.4	450.3	44.505	0.0871	8.545
$[C_8MIm][BF_4]$	1.070	160.4	518.4	60.959	0.102	8.761
$[C_5Py][BF_4]$	1.184	129.1	417.8	44.014	0.0655	7.269
$[C_6Py][BF_4]$	1.153	131.6	451.8	51.860	0.0731	7.376
$[C_3MIm][Tf_2N]$	1.446	135.4	560.1	15.152	0.231	7.903
$[C_4MIm][Tf_2N]$	1.415	137.9	594.2	17.524	0.237	8.010
$[C_1MPyr][Tf_2N]$	1.467	106.6	480.2	15.243	0.0776	6.452
$[C_2MPyr][Tf_2N]$	1.436	109.1	514.3	17.673	0.0873	6.559

5. Conclusions

A systematic visual approach to design IL as CO_2 capturing solvent is presented in this work. This approach utilises property clustering technique, and group contribution methods to estimate properties of ILs. The proposed approach provides insight to the user when designing ILs as CO_2 capturing solvents.

Acknowledgement

This paper was made possible by NPRP grant No 5-351-2-136 from the Qatar National Research Fund (a member of Qatar Foundation). The statements made herein are solely the responsibility of the authors.

References

F.K. Chong, F.T. Eljack, M. Atilhan, D.C.Y. Foo, N.G. Chemmangattuvalappil, 2014, Ionic Liquid Design for Enhanced Carbon Dioxide Capture – A Computer Aided Molecular Design Approach, Chemical Engineering Transactions, 39, 253–258.

M.R. Eden, S.B. Jørgensen, R. Gani, M.M. El-Halwagi, 2004, A novel framework for simultaneous separation process and product design, Chemical Engineering and Processing, 43, 595–608.

M.M. El-Halwagi, I.M. Glasgow, X. Qin, M.R. Eden, 2004, Property integration: Componentless design techniques and visualization tools, AIChE Journal, 50, 1854–1869.

F.T. Eljack, M.R. Eden, 2008, A systematic visual approach to molecular design via property clusters and group contribution methods, Computer & Chemical Engineering, 32, 3002–3010.

F.T. Eljack, M.R. Eden, V. Kazantzi, M.M. El-Halwagi, 2006, Property Clustering and Group Contribution for Process and Molecular Design, In: W. Marquardt, C. Pantelides (Eds.), 16th European Symposium on Computer Aided Process Engineering and 9th International Symposium on Process Systems Engineering, Elsevier B.V., Garmisch-Partenkirchen, Germany, 907–912.

R.L. Gardas, J.A.P. Coutinho, 2008, A Group Contribution Method for Heat Capacity Estimation of Ionic Liquids, Industrial & Engineering Chemistry Research, 47, 5751 – 5757.

S. Hada, R.H. Herring, M.R. Eden, 2013, Design of Ionic Liquids Using Property Clustering and Decomposition Techniques, In: A. Kraslawski, I. Turunen (Eds.), 23rd European Symposium on Computer Aided Process Engineering, Elsevier B.V., Amsterdam, 955–960.

IEA, 2013, World Energy Outlook Special Report 2013: Rewarding the Energy Climate Map, Paris.

Z. Lei, C. Dai, W. Wang, B. Chen, 2013, UNIFAC model for ionic liquid-CO_2 systems, AIChE Journal, 60, 716–729.

N.V. Plechkova, K.R. Seddon, 2008, Applications of ionic liquids in the chemical industry, Chemical Society Review, 37, 123–150.

Y. Qiao, Y. Ma, Y. Huo, P. Ma, S. Xia, 2010, A group contribution method to estimate the densities of ionic liquids, The Journal of Chemical Thermodynamics, 42, 852–855.

B.C. Roughton, J. White, K.V. Camarda, R. Gani, 2011, Simultaneous Design of Ionic Liquids and Azeotropic Separation Processes, In: E.N. Pistikopoulos, M.C. Georgiadis, A.C. Kokossis (Eds.), 21st European Symposium on Computer Aided Process Engineering, Elsevier, Amsterdam, 1578–1582.

M.D. Shelley, M.M. El-Halwagi, 2000, Component-less design of recovery and allocation systems: a functionality-based clustering approach, Computer & Chemical Engineering, 24, 2081–2091.

C.C. Solvason, N.G. Chemmangattuvalappil, F.T. Eljack, M.R. Eden, 2009, Efficient Visual Mixture Design of Experiments using Property Clustering Techniques, Industrial & Engineering Chemistry Research, 48, 2245–2256.

The Dow Chemical Company, 2003, Ethanolamines.

S.P. Verevkin, 2008, Predicting enthalpy of vaporization of ionic liquids: a simple rule for a complex property, Angewandte Chemie, 47, 5071–5074.

Krist V. Gernaey, Jakob K. Huusom and Rafiqul Gani (Eds.), 12th International Symposium on Process Systems Engineering and 25th European Symposium on Computer Aided Process Engineering.
31 May – 4 June 2015, Copenhagen, Denmark

Intensification of C5 separation process by heat integration and thermal coupling

Hsiao-Ching Hsu[a], San-Jang Wang[b*], John Di-Yi Ou[a], David Shan Hill Wong[a*]

[a] *Department of Chemical Engineering, National Tsing Hua University*
101 Section 2,Kuang Fu Road, Hsinchu, Taiwan
[b] *Center for Energy and Environmental Research, National Tsing Hua University,*
101 Section 2,Kuang Fu Road, Hsinchu, Taiwan
**corresponding authors: wangsj@mx.nthu.edu.tw , dshwong@che.nthu.edu.tw*

Abstract

C5 fraction, which accounts for 15-25% in naphtha, consists of molecules such as isoprene (IP), pentadiene (PD), cyclopentene(CP), and cyclopentadiene (CPD) can be used to manufacture petroleum resin and other high value-added products. Yet it is often burned as fuel and not fully utilized because separation of these products with close boiling points is difficult. One common process is to react CPD itself to form di-cyclopentadiene (DCPD) so that it can be separated from the other C5 molecules. Extractive distillation was also used to recover alkynes from light ends. Such a process involves use of multiple separation columns and reactors. Furthermore, it was found that the reactor is highly coupled with one of the separation columns by a recycle stream, leading to snowball effect and difficulty in control. Hence a wide range of opportunities for process intensification and integration was available. It was found that the entire separation process can be substantially simplified by reducing number of reaction zones from 2 to 1 and number of columns from 8 to 6. Such a simplification increases product concentration of DCPD from a range between 85wt% and 92wt% to 99wt%, while maintains the high purity (>99.75wt%) for the IP stream and specified purity (>89.90wt%) for the PD plus CP stream. This process can be further simplified by using thermal coupling and external heat integration. Such simplifications and intensified techniques lead to substantial reduction in capital costs, energy costs as well as process operability.

Keywords: Intensification, steady-state simulation, plant-wide process, heat integration, thermal coupling.

1. Introduction

Diolefins, including CPD, IP, CP, and PD in C5 fraction, are the byproduct of ethylene industry. They were obtained from naphtha cracking process by conventional distillation and extractive distillation. The rise of the shale gas industry, where light oil can be used for the ethylene synthesis enabled ethylene to be obtained easily, lowering its production cost. Therefore, the current processes in the naphtha industry need to be improved in order to increase their competitive strength.

Various strategies were provided for treating hydrocarbon streams comprising CPD and other dienes. The multiple dimerization and depolymerization method was embodied by Owen et al. (2001), Liu et al. (2012), and etc. They have showed that it is capable of achieving high concentration of DCPD by the use of multiple reactors combined with

recovery processes of other materials.
IP is the main component and is mixed with close boiling-point components in C5 crude. Some azeotropes can be found between them. Extractive distillation is commonly used in the industry to separate these azeotropes. Three solvents can be used in the extraction distillation for the purification of IP. They are acetonitrile (ACN), dimethylformamide (DMF), and n-methyl-2-pyrrolidone (NMP). (Shu et al., 2009; Liu et al., 2014)

The separation processes are normally complicated involving multiple reactors and distillation units. The aforementioned literature suggested varies of improving the process. However, to our best knowledge, an unified benchmark of various processes and a systematic approach to improving the process have not been found in open literature. The objective of this study is therefore to develop an ASPEN Plus steady state model and use it to investigate how such a process can be simplified using process intensification and integration techniques.

2. Conventional process

The main purpose for the separation process of crude C5 elements is to recover high value-added components, such as CPD, IP, and PD/CP. In this study, a conventional plant-wide process of the crude C5 was simulated and shown in Figure 1 on the basis of the US patent 20032100809A1 (Tian et al., 2003) and the CN patent 102951989 A (Sun et al., 2003). In this conventional process, the target specifications commonly used in the industry are given in Table1. Using the simulation model we developed, the product purities and recovery was also listed. In addition, for a 75,000 Ton per annum plant, the total reboiler duty required was found to be 34.5 MJ. With an 8-year payback period, the amortized capital expenditure (ACAPEX) was found to be 2,316,000 USD/yr. The annual operating cost (AOC) was found to be 2,856,000 USD/yr and the total annual cost (TAC) equals 5,172,000 USD/yr. The above costs were estimated using the method described in Douglas (1988).

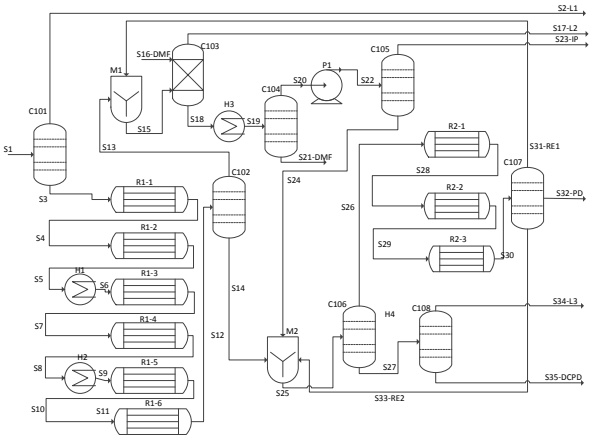

Figure 1 Conventional process flowsheet (CP).

In general, the conventional process CP can provide an effective way to recover the valuable materials in crude C5. However, the main issue of the complexity in the design and control remains unsolved. First, the bottom recycle stream from column 107 is the

key factor to affect the reaction conversion and may cause the snow-ball effects in the second reaction zone and product PD/CP: the rest CPD in the second zone is mostly reacted into DCPD, resulting in the PD/CP stream concentrated without CPD. However, the different CPD concentration and conversion would be found in different recycled rates. Then the snow-ball effect would happen with inadequate CPD conversion and cause the faulty concentration of PD/CP. Second, the whole process containing at least 8 columns and reactors with the length of 98 meters needs high capital costs. In the following, the problems mentioned above are solved by simplifying the conventional process.

Table 1 Targets specifications and simulated performance.

	Target	Conventional process
IP product concentration (wt%)	99.75	99.82
IP product recovery (%)	>90	90.52
PD+CP product concentration (wt%)	89.81	90.79
PD+CP product recovery (%)	-	92.84
DCPD product concentration (wt%)	83.27	86.73
DCPD total recovery (%)	-	89.30
Process duty (MW)	-	34.50
Operating Cost ($1000/y)	-	2,856
Capital Cost ($1000/y)	-	2,316
TAC ($1000/y)	-	5,172

3. Simplified process

In the study, a simplified process (SP) shown in the Figure 2 is presented by deleting the first reaction zone, columns 106 and 108, and two recycle streams from column 107. The first reaction zone is deleted because the presence of IP can increase the concentration of by-products that will decrease the purity of DCPD. With IP removed, the second reaction zone is sufficient to maintain the high conversion of CPD without the use of the first reaction zone. In IP extraction zone, IP can be separated and recovered properly by adjusting temperature and pressure conditions. The stream S31, riches in IP and CPD, can then be deleted by ignoring the tiny impurity of the product PD/CP. This simplification might cause little loss of IP. However, higher recovery can be achieved by reducing the side reactions involved IP. The omission of the columns 106 and 108 in the conventional process can avoid the use of the recycle stream S33, because column 6 in the simplified process is sufficient to directly separate the heavy components (L3) and DCPD.

Table 1 also contained the target specifications of product recovery and product concentrations to be achieved in the simplified process. From the proposed simplified process, high purity products were obtained along with highly improved recovery ratios. The resulting DCPD product stream with 98.84wt% DCPD makes this production process more competitive. In addition, the recovery of the IP product can be increased by 7.1%, the recovery of the PD/CP product can be improved by 1.2%, and the recovery of the main product, DCPD is raised by 4.9%. Overall, the total reboiler duty required for the simplified process can be reduced by 8.1% due to non-recycle of the two streams from column 107 in the conventional process.

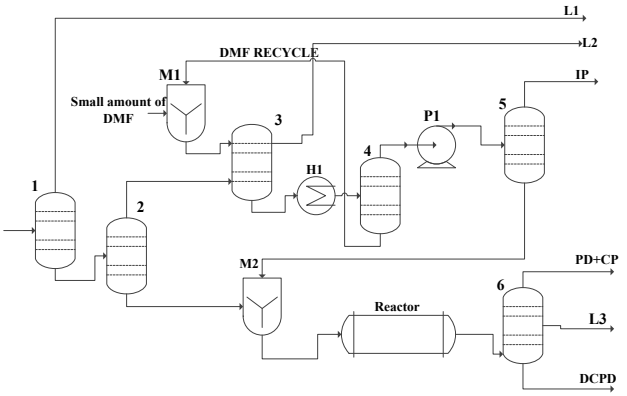

Figure 2 A simplified process flowsheet (SP).

4. Intensified process

The simplified process given in Figure 2 still consists of 6 distillation columns in IP removal and C5 recovery units. They can be intensified by using thermal coupling and heat integration. However, column 3 is operated at high pressures than the other columns. Hence a logical choice would be to combine columns 4 and 5 and columns 1 and 2 as the divided-wall column (DWC) first.

In Figure 3, the intensified process was shown. Columns 4 and 5 were integrated into a DWC 4&5 by sharing a condenser. The bottom product containing enriched DMF of 99.98wt% is recycled to mixer 1 while other containing mixed C5s is sent to mixer 2. The distillate product of the DWC is high purity of IP above 99.75wt%, the same product specification as in the simplified process, showed in Figure 2. The DWC configuration can reduce 30% of the total reboiler duty in columns 4 and 5.

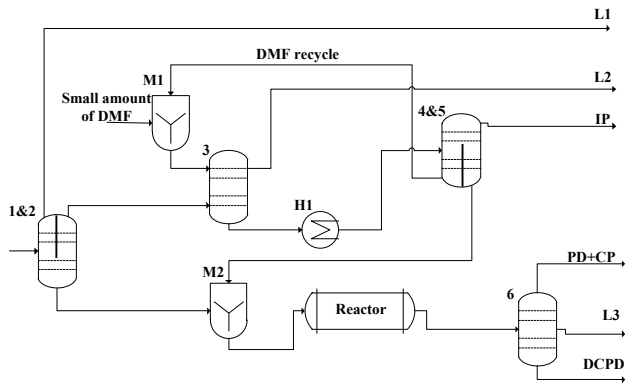

Figure 3 2DWC: Intensification process with DWCs 1&2 and 4&5.

Figure 3 also illustrated the process in which columns 1 and 2 are further integrated into a DWC 1&2 by sharing a reboiler. The DWC configuration can reduce 13% of the total reboiler duty in columns 1 and 2.

In addition to implementing thermal coupling between two columns to reduce reboiler

duty, more heat duty can be recovered from the bottom stream of column 3. To effectively extract IP, column 3 is operated at high pressure, resulting in high temperature of 220 ºC at the column bottom. The bottom stream of column 3 must be cooled to 50 ºC before it was sent into column 4 for further separation as the energy source of external heat integration (EHI). Figure 4 shows the process of 2DWC+EHI. The bottom stream in column 3 can be used to heat the bottom streams in column 6, DWC 4&5, and DWC 1&2, and it can also pre-heat H2. The reboiler duty needed in column 6 can be completely deleted by the heat integration in heat exchanger E1 given in Figure 4. The reboiler duties of the DWC 4&5 and DWC 1&2 are partially supplied by heat integration in heat exchangers E2 and E4 and E5. In addition, the inlet stream of the adiabatic reactor is pre-heated by heat integration in heat exchanger E3. The reaction temperature is then raised from 70 to 135 ºC, and results in faster reaction rate. At the same time, the reactor length can be reduced from 30 meters to 15 meters under the same reaction situation.

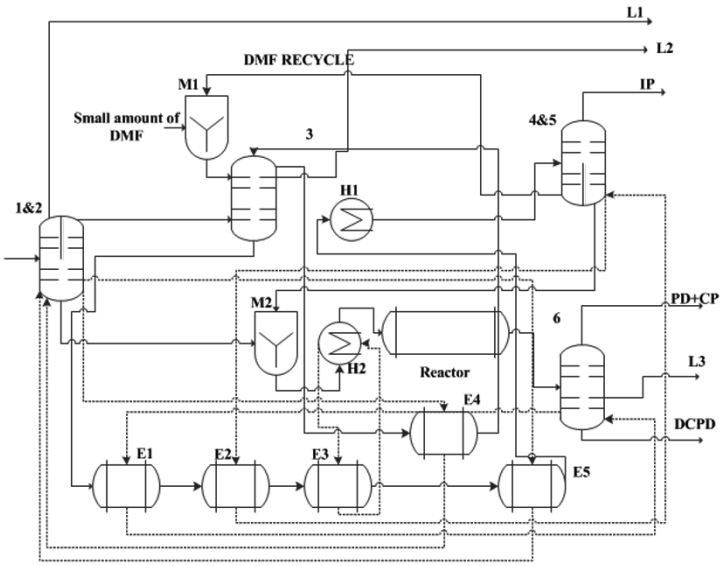

Figure 4: 2DWC+EHI: intensified process with two DWCs and external heat integration.

The reboiler duty can be decreased by 43% with contributions in the order of external heat integration (20%), integration of DMF recovery (10%) and elimination of the first reactor section (8%), and integration of light recovery and IP separation columns (5%). Figure 5 illustrates the reduction of ACPAEX, AOC, and TAC, for different process configurations. The simplified process deleted many columns and reactors, resulting in sharp decrease of the ACAPEX about 35%. With further integration using DWC and EHI, the total reduction in process ACAPEX was found to be about 41%. The total reduction in annual operating cost can be reduced by 29%, and hence the TAC can be reduced by 34%.

5. Conclusions

In the study, the conventional process of the crude C5 for the separation of IP, PD/CP, and DCPD can be substantially simplified by (1) separating IP first before CPD

dimerization, (2) using a side-draw column in the final separation, (3) using divided wall columns and (4) external integration. The needs 60% of the original capital cost under the same product purity requirements. The intensification process designed by the use of thermal coupling and heat integration technologies can further reduce heat duty 38% and operating cost 29% of the simplified process. The recovery and purity of the main product, DCPD, can be increased by reducing the numbers of reaction zones and changing the position of the reaction zones. Simulation results demonstrate that the economic benefit of the crude C5 conventional process can be enhanced by the intensification technologies of thermal coupling and heat integration.

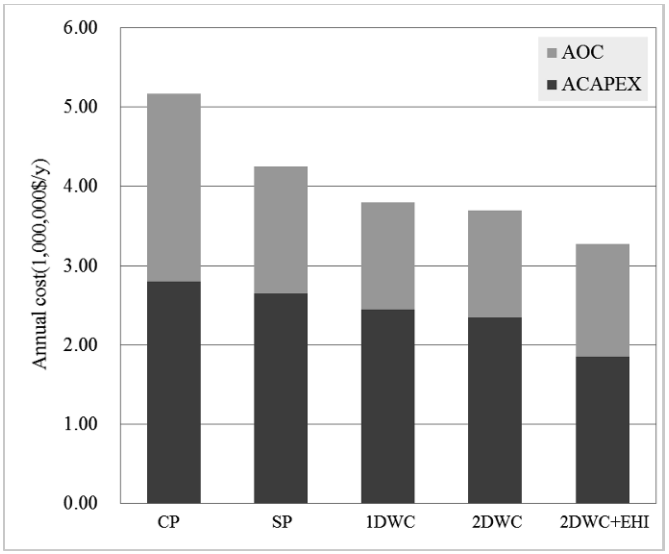

Figure 5: Reduction in costs with various intensification and integration techniques.

Acknowledgment

This work is financially supported by Ministry of Science and Technology: MOST 102－2622－E－007－029－CC1.

References

J. M. Douglas, 1988, Conceptual Design of Chemical Processes, McGraw Hill.
Z.X. Liu, D.F. Li, J.M. Cheng, L.H. Liao, S.F. Li, S.J. Luo, 2014, A C5 Segregation Based Mixed Ionic Liquid Solvent, CN102452882 B.
Z.X. Liu, L.H.Liao, D.F. Li, D.C. Peng, W. Jing, J.M. Cheng, L. Guo, 2012, Method for Separating C5 Fraction by One-Stage Extraction and Rectification, CN 101450885 B.
S. A. Owen, M.M. Johnson, T.T.P. Cheung, M.E. Lashier, 2001, Hydrocarbon Upgrading Process, US006258989B1.
Q.J. Shu, F.H. Wang, X.W. Zhao, H.G. Lui, L.J. Lui, S.C. Wu, 2009, Domestic Technological Advances Separate, China Elastomerics, 19 (5); 71 ~ 75.
C. Sun, F.S. Fu, B.T. Yao, Z.S. Yang, Y.J. Yao, J.Y. Wang, Z.P. Wu, D.M. Zhang, 2013, Separation Method of C5 Fraction, CN 102951989 A.
B. Tian, P. Li, C. Du, H. Xu, H. Feng, J. Hu, J. Gao, M. Ma, 2003, Process for Separating C5 Cuts Obtained from a Petroleum Cracking Process, US 0100809 A1.

Krist V. Gernaey, Jakob K. Huusom and Rafiqul Gani (Eds.), 12th International Symposium on Process Systems Engineering and 25th European Symposium on Computer Aided Process Engineering.
31 May – 4 June 2015, Copenhagen, Denmark

Conceptual Design of Post-Combustion CO_2 Capture Processes - Packed Columns and Membrane Technologies

Mathias Leimbrink*, Anna-Katharina Kunze, David Hellmann, Andrzej Górak, Mirko Skiborowski

TU Dortmund University, Laboratory of Fluid Separations, Emil-Figge-Straße 70, 44227 dortmund, Germany
Mathias.Leimbrink@bci.tu-dortmund.de

Abstract

CO_2 removal from flue gas emitted by coal fired power plants is an important objective for process sustainability. However, solvent regeneration in state-of-the-art absorption processes results in power plant efficiency losses of 7 to 15 % (Neveux et al., 2013). Process intensification, combining different and innovative technologies for gas separation, can result in highly efficient processes capable of reducing the energy penalty caused by CO_2 capture. Current approaches for conceptual process design (CPD) however rarely consider emerging technologies like membrane contactors or hybrid process configurations. We present a multi-stage approach to overcome this drawback, which bases on process decomposition in different levels, combined with an efficient screening of promising materials and process design variants by means of shortcut methods. The approach follows the idea of an iterative refinement, in which the modeling accuracy increases while the number of process variants decreases.

Keywords: Process intensification, design approach, carbon dioxide capture, hybrid processes, membrane technologies.

1. Introduction

Since CO_2 is considered as a major greenhouse gas, its emissions have to be reduced significantly. Current state-of-the-art for CO_2 removal is the reactive absorption using aqueous amine solutions (e.g. MEA). Due to the loss in process efficiency, caused by the high energy demand for the solvent regeneration, CO_2 removal is practically not used at large scale industrial application. In the last decades a lot of research effort was directed towards the investigation of alternative solvents to reduce the energy requirements of ab/desorption processes (see recent review of Le Moullec et al. (2014)). Gas membranes (GM) (Merkel et al., 2010) and membrane contactors (MC) (Favre and Svendsen, 2012) are potential alternatives to absorption columns to increase energy efficiency of CO_2 capture. MC provide a constant volume-specific interfacial area which can be orders of magnitude higher than for conventional equipment (Li et al., 2013). Moreover, GM and MC can be combined with ab/desorption processes to hybrid process configurations. Such hybrid processes can create synergies which potentially compensate for the drawbacks of the involved technologies, compared to stand-alone processes. Only few articles have recently considered the design of such hybrid process configurations (e.g. Bock et al., 2014). Even less research covers systematic CPD methodologies for hybrid processes related to gas separation (e.g. Hasan et al., 2014).

Hence, a systematic approach allowing for Process Intensification from the beginning of a CPD is essential. An approach towards such a holistic CPD is introduced in the subsequent sections and illustrated for CO_2 capture from a coal fired power plant.

2. Approach for CPD of post-combustion CO_2 capture process

2.1. Problem statement

The separation process design is decomposed in four subordinated levels which are arranged in a hierarchical order as illustrated in Figure 1. The decomposition provides a universal perspective on general separation processes.

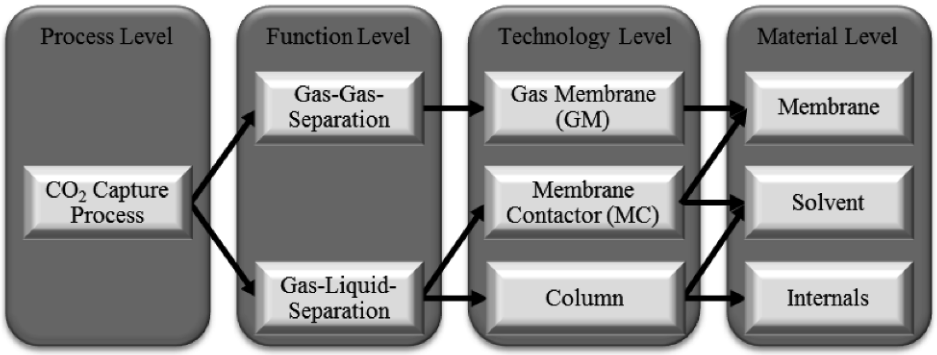

Figure 1: Illustration of process decomposition in subordinated levels

The applied decomposition is illustrated for CO_2 capture process. In order to solve the separation problem, different functions from the "function level" can be utilized and potentially combined. For CO_2 capture two feasible functions are considered, which are gas-gas and gas-liquid-separation. Since gas-liquid-separation necessitates a solvent, a second gas-liquid-separation for solvent recovery is also required, resulting in an ab/desorption process. The considered functions can be achieved by different technologies, applying several materials.

2.1.1. Technology level

Each technology can be operated within its specific operating window. The operation of columns is mainly limited by critical L/G ratios which can result in flooding, foaming or loading (Kenig and Górak, 2005). While such limitations do neither exist for MC nor for GM, there are certain limitations for the applicable operating temperature and pressure. Exceeding these boundaries can lead to membrane deformation due to the polymeric nature of the membrane (Merkel et al., 2010). The pressure difference for MC can not exceed a certain limit to avoid breakthrough of either the liquid or the gas phase. The performance and limitations of the different technologies also depend on the specific materials. Therefore, the available technologies can only be fully characterized in combination with the specific materials, which are defined in the "material level".

2.1.2. Material level

While GM performance depends strongly on operating conditions and the membrane material, MC performance is by definition not determined by the membrane material. However, selection of thermally and chemically stable material is important, but can only be determined experimentally. Hence, a membrane material selection for MC is not further considered, since the separation performance of MC is determined by the selected solvent. This also applies to columns such as the limitation by the gas-liquid

equilibrium, specified by the selected solvent as well. An additional material that needs to be selected for columns represents the type of internals.

2.1.3. Process variants

Regarding all presented technologies and corresponding materials as potential variants for the given separation process, this results in a tremendously complex CPD task. The complexity increases even more if the combination of technologies to hybrid process configurations is taken into account, as illustrated in Figure 2.

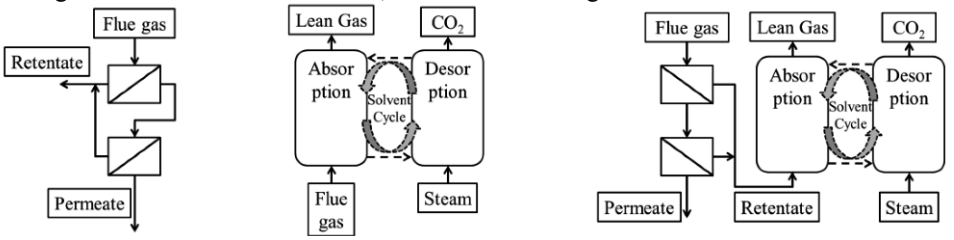

Figure 2: Schematic illustration of GM (left), ab/desorption (middle) and hybrid processes (right)

For the current study 14 different GM materials taken from Merkel et al. (2010) can be installed in two different configurations. While a single-stage configuration purifies the gas stream once, a two-stage configuration further processes the permeate of the first stage in a subsequent stage. Each stage can be operated in either counter-current or cross-flow mode. This results in 56 GM variants as standalone solution. For gas-liquid separation 7 solvents from Schäffer (2013) are considered, which already present a pre-selection based on economic and environmental considerations. Taking into account three different column internals (trays, random and structured packing) results in 21 combinations of solvents and internals for the absorption column. In combination with the MC, there are 28 potential variants only for the absorption. As the solvent is fixed by the absorption, only 4 different variants for desorption are feasible, resulting in 112 possible ab/desorption processes. Taking into account hybrid process configurations, in which gas-gas-separation is performed as pre-treatment step upstream of a gas-liquid-separation, adds additional $112 \cdot 56 = 6272$ potential hybrid processes to a total 6440 potential process variants. Additional structural combinations further increase this number, which already emphasizes the need for a systematic approach to handle this complex CPD problem.

2.2. Methods

In order to solve the complex CPD problem a multistage approach, based on an iterative refinement and successive reduction of the number of process variants, is applied in this work. Similar to the idea of the process synthesis framework of Franke et al. (2004) or Marquardt et al. (2008), the tremendous number of process variants is first screened by means of simple shortcut methods. The simplifying assumptions of the shortcut methods are discarded in the subsequent steps, in which more detailed models are used to determine more accurate performance estimates for a steadily decreasing number of considered process variants. The focus of this work is on the first shortcut-screening step. As it is applied in an early phase of CPD, they need to operate with little information and allow for a qualitatively accurate evaluation in order to reduce the large number of potential process variants. A first material screening is therefore performed based on key performance indicators of the different technologies. For the evaluation of GM materials a shortcut-model, similar to that proposed by Scholz et al. (2015), is utilized. The required membrane area is calculated based on literature data for permeabilities and selectivities. Beside the membrane properties, the operating mode

(cross-flow and counter-current) and the operating conditions ($p_{Feed}/p_{Permeate}$) are taken into account. The final performance is evaluated based on cost calculations for capital investment and operation. Since 70-80% of the separation costs for gas-liquid-separations are caused by solvent regeneration (Notz et al., 2011), the minimal energy requirement (MER) for solvent regeneration is used for a first evaluation of the potential solvents, which can be investigated without fixing the technology, as MER is the same for MC and columns. The MER depends on the gas-liquid equilibrium, accounting for the chemical reaction in the liquid phase, as well as the loading of the solvent after ab- and desorption. To account for these factors the modified Kremser-method, as presented by Notz et al. (2011), is utilized and the liquid to gas ratio (L/G) ratio is optimized. Besides the screening of different solvents for MER, the method further allows for the determination of an optimal L/G and number of theoretical stages, in terms of cost estimates, such that the different technologies can be compared on a common basis. Based on the shortcut screening a selection of promising process variants will be taken to the next evaluation level, for which simplifying assumptions, like isothermal and isobaric operation and constant inert gas and liquid streams, as assumed for the Kremser method, will be subsequently removed. MESH models can be applied in order to consider heat effects for the columns, while a final design will be determined by detailed rate-based models, accounting for heat and mass transfer as well as the hydrodynamics of the process. This iterative refinement is crucial to reconsider the selection, depending on the change in performance estimate due to the increased accuracy. In the current paper, only the best process determined in the shortcut screening is evaluated by means of a detailed rate-based design, to illustrate the projected approach.

3. Case Study

CO_2 capture from a coal fired power plant is chosen as a case study. The corresponding separation task is characterized by a typical CO_2-content in the flue gas of 13.73 Vol.-%, a total flue gas stream of 673.5 kg/s and a capture rate of 90% is targeted.

3.1. Material screening

Assuming comparable membrane material cost, a first material screening is performed based on the minimum area required in a two-stage configuration and constant high driving force (cf. Figure 3 (left)). Due to the large differences, from the set of 14 membranes only the two membranes with the lowest required membrane area are further investigated. The results of a first solvent screening for ab/desorption processes by means of the MER are also illustrated in Figure 3 (right). As MER for most of the investigated solvents are in a similar range, only AP is discarded. This material screening already reduces the number of potential process variants from 6440 to 872.

3.2. Process evaluation

For GM two-stage configurations operated in cross-flow (CF) or counter-current (CC) mode are considered. The operating conditions ($p_{Feed}/p_{Permeate}$) are optimized for total annualized cost (TAC), based on cost correlations taken from Woods (2010). Assuming a constant price of 50 € m^{-2} for all investigated membranes, the economic performance strongly correlates with the membrane area. Here, CC was determined as best operation mode such that only results for CC of both promising membranes (No. 1 and 14 in Figure 3) are illustrated in Figure 4. For each of the remaining six solvents gas-liquid-separation is evaluated in columns and MC. Internals for columns are selected based on the optimized L/G ratio, resulting in random packed columns. A HETP value of 0.9 m was considered for column sizing and cost calculations (Woods, 2010), for which an

adapted L/G ratio was determined by means of the extended Kremser method assuming 10 theoretical stages for absorption and 15 for desorption, similar to Notz et al. (2011).

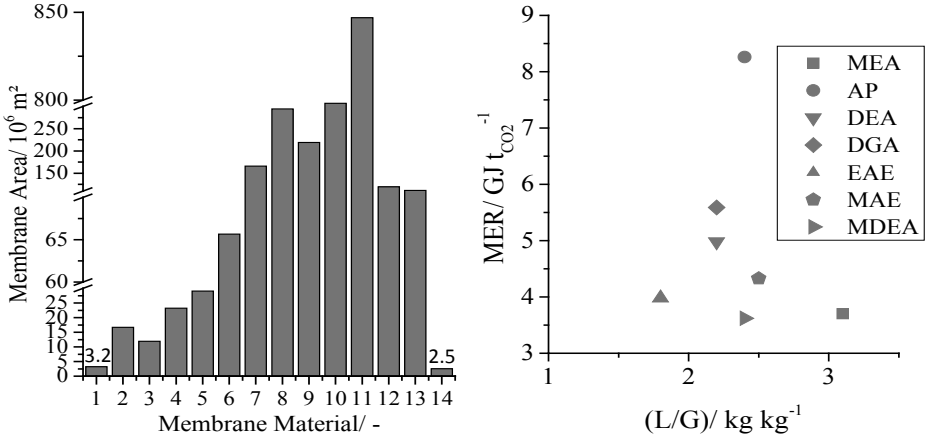

Figure 3: Material screening for (left) GM membranes and (right) solvents

The determination of the required membrane area for the MC process is performed in accordance to Li et al. (2013). Here, similar to the constant HETP value of the column, an average value of 0.4 kg_{CO2} m^{-2} h^{-1} for the trans-membrane flux of CO_2 in the MC is assumed. The price per m² is assumed with 50 €. Due to the fact that gas-liquid equilibrium data for desorption is restricted to temperatures of 120 °C, MC cannot be considered for desorption. Hence, columns are used as desorption technology for MC processes, presenting already a combination of different technologies. Finally, hybrid GM and ab/desorption processes are taken into account.

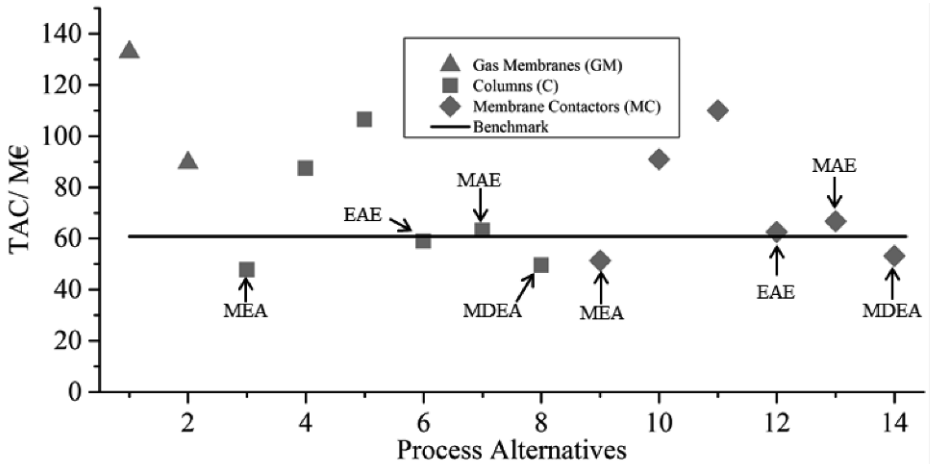

Figure 4: Results of process evaluation

Here, the best performing GM process (No. 2 in Figure 4) is combined with the best performing column and MC process (No. 3 and 9 in Figure 4) respectively. However, the hybrid processes do not make use of the GM, resulting in the simple MEA-based column process as best solution. The results of the short-cut-based economic evaluation of the remaining 16 variants are illustrated in Figure 4. MEA-based ab /desorption in columns, which is currently the state-of-the-art process, is also identified as most

promising process by means of the shortcut-screening. Since the results of a detailed rate-based design calculation, illustrated by the black line in Figure 4, provide a difference between short-cut and detailed calculation of about 21 %, which is in a proper range for shortcut estimations, it indicates the potential of all processes in below that line to be competitive. Thus, based on the utilized available data, stand-alone GM and the considered hybrid processes seem to be less promising. Nevertheless, research on more efficient membrane materials continue, to develop GM into a valuable technology for future processes (Sandru et al., 2013). Based on the current calculations either the GM performance has to be increased or the membrane price has to be reduced by 70% in order to be competitive.

4. Conclusions and Outlook

A systematic multi-stage approach for Process-Intensification-focused CPD of gas separation processes is developed and successfully applied to CO_2 capture from flue gas as a case study. The most promising process alternatives are identified and evaluated by shortcut methods and compared against the rate-based modelled MEA-process as benchmark. Hereby, the MEA and MDEA process are found as most promising and have to be investigated in more detail.
Intermediate evaluation steps are required in order to reduce the experimental effort before starting a final detailed rate-based optimization. In addition the “technology & material level” will be extended to include additional intensified gas separation technologies, like rotating-packed-beds, or enzyme-activated solvents.

5. Acknowledgements

The research leading to these results has received funding from the European Union Seventh Framework Programme FP7/2007-2013 under grant agreement n° 608535.

References

C. Bock, E. Esche, D. Müller, G. Wozny, 2014, Computer Aided Chemical Engineering, 34, 267-272
M. M. Hasan, E.L. First, F. Boukouvala, C.A. Floudas, 2014, Computer Aided Chemical Engineering, 34, 98-107
E. Favre, H.F. Svendsen, 2012, J. Membr. Sci., 407-408, Pages 1-7
M. Franke, A. Górak, J. Strube, 2004, Chem. Ing. Tech., 76(3), 199-210
E.Y. Kenig, A. Górak, 2005, Reactive absorption, In: Integrated Chemical Processes: Synthesis, Operation, Analysis and Control, Wiley-VCH, Weinheim, 265–311
Y. Le Moullec, T. Neveux, A. Al Azki, A. Chikukwa, K.A. Hoff, 2014, Int. J. Greenh. Gas Control, 31, 96-112
S. Li, D. Rocha, S. James Zhou, H. Meyer, B. Bikson, Y. Ding, 2013, J. Membr. Sci., 430, 79-86
W. Marquardt, S. Kossack, K. Kraemer, 2008, Chin. J. Chem. Eng., 16, 3, 333-342
T. C. Merkel, H. Lin, X. Wei, R. Baker, 2010, J. Membr. Sci., 359, 126–139
T. Neveux, Y. Le Moullec, J.P. Corriou, E. Favre, 2013, Chemical Engineering Transactions, 35, 337-342
R. Notz, I.Tönnies, H.P. Mangalapally, S. Hoch, H. Hasse, 2011, Int. J. Greenh. Gas Control, 5, 3, 413-421
M. Sandru, T.-J. Kim, W. Capala, M. Huijbers, M.-B. Hägg, 2013, Energy Procedia, 37, 6473-6480
A. Schäffer, 2013, Amine und Aminmischungen zur CO_2-Absorption aus Kraftwerksrauchgasen und ihr Energiebedarf zur Regeneration, PhD-thesis, Shaker, ISBN: 978-3-8440-2392-3
M. Scholz, M. Alders, T. Lohaus, M. Wessling, 2015, J. Membr. Sci., 474, 1-10
D. R. Woods, 2007, Rules of Thumb in Engineering Practice, Wiley-VCH, Weinheim

Krist V. Gernaey, Jakob K. Huusom and Rafiqul Gani (Eds.), 12th International Symposium on Process Systems Engineering and 25th European Symposium on Computer Aided Process Engineering.
31 May – 4 June 2015, Copenhagen, Denmark

Natural Gas to Liquid Transportation Fuels and Olefins (GTL+C2_C4)

Onur Onel,[a] Alexander M. Niziolek,[a] Christodoulos A. Floudas[a*]

[a]*Department of Chemical and Biological Engineering, Princeton University, Princeton, NJ 08544, USA*
floudas@titan.princeton.edu

Abstract

Co-production of liquid transportation fuels and olefins from a natural gas feedstock is investigated. A superstructure of alternatives is presented with multiple natural gas conversion routes, hydrocarbon production and upgrading methods, and olefins purification options. The superstructure, which is modeled as a mixed integer nonlinear optimization problem (MINLP), is solved to global optimality using a rigorous branch-and-bound framework. The co-production of fuels and olefins from natural gas is found to be profitable,and the net present value increases at higher olefins production levels.

Keywords: Liquid fuels, olefins, natural gas, global optimization.

1. Introduction

The United States produced about 7.45 million barrels of petroleum per day in 2013, while consuming 18.95 million barrels per day (EIA, 2014). High crude oil prices, volatility of the global oil market, and political instabilities in petroleum supplying countries pose serious challenges for crude oil imports.Advances in the shale gas production that provide inexpensive and abundant natural gas to the market, combined with commercially existing natural gas reforming technologies, make natural gas an attractive alternative for liquid fuels production.

Previous studies have shown the viability of liquid transportation fuels production from single and hybrid feedstock systems (Baliban et al., 2010, 2012b, 2013). C_2 to C_4 olefins (ethylene, propylene, butenes, and butadiene) are high value petrochemicals that are mid-products of petroleum refining and are used in subsequent industries (Onel et al., 2014). Therefore, an alternative process towards the production of liquid fuels should also consider the production of these high value petrochemicals. In this study, co-production of liquid fuels and olefins is investigated from a natural gas feedstock. The existing superstructure (Baliban et al., 2010, 2012b, 2013) is enhanced to allow for the production and purification of the olefins. A global optimization-based process synthesis framework with simultaneous heat, power, and water integration is applied to investigate the refinery across different case studies.

2. GTL+C2_C4 Superstructure and Mathematical Modeling

A process superstructure that converts natural gas to liquid transportation fuels was previously developed (Baliban et al., 2013). Additionally, process alternatives for the production of C_2 to C_4 olefins and liquid fuels were investigated for a refinery that uses biomass and natural gas as feedstocks (Onel et al., 2014). The following subsections will describe the key sections of the GTL+C2_C4 refinery.

2.1. Natural Gas Conversion

The natural gas can be directed to six different processes in the refinery: auto thermal reforming, steam reforming, oxidative coupling, partial oxidation, heat generation via fuel combustion, and electricity generation via a gas turbine. The reformers can be utilized to produce the syngas intermediate, whereas oxidative coupling produces olefins and partial oxidation produces methanol for further upgrading. The auto thermal reformer requires high purity oxygen to allow for the partial combustion of natural gas that will provide heat for the endothermic steam reforming reactions. The steam reformer requires an external heat supply to provide required heat for the same endothermic reactions. The reformers can operate at three discrete temperatures (ATR: 900 °C, 950 °C, or 1000 °C, SMR: 800 °C, 850 °C, or 900 °C). The syngas produced is sent to the syngas treatment section, and the raw hydrocarbons produced in the oxidative coupling and partial oxidation processes are sent to the hydrocarbon upgrading section.

2.2. Syngas Treatment

The raw syngas can be sent to a dedicated reverse-water-gas-shift (rWGS) reactor to adjust the H_2/CO ratio.If the H_2/CO ratio of the raw syngas is above the favorable ratio required by the hydrocarbon production processes, CO_2 in the process can be recycled to the rWGS to enhance the overall carbon conversion. The syngas can also bypass the rWGS and be sent directly to the scrubbing system after being cooled down to 185 °C.

The syngas can then be directed to the Rectisol process to remove CO_2 if CO_2-lean syngas is required by the hydrocarbon production alternatives. The recovered CO_2 is either vented, sequestered, or recycled back to the refinery, while the syngas is sent to the hydrocarbon production section.

2.3. Hydrocarbon Production and Upgrading

The clean syngas can be converted to raw hydrocarbons using a methanol synthesis reactor or one of six Fischer-Tropsch (FT) reactors (two cobalt-based and four iron-based). The cobalt based reactors can achieve 60% per-pass CO conversion, whereas the iron-based reactors can facilitate the WGS reaction to convert recycled CO_2. The FT effluent contains a liquid waxy phase and an effluent containing raw hydrocarbons. The waxy liquid phase is sent to a wax hydrocracker to produce distillate range products (Bechtel, 1998). The raw hydrocarbons can be either separated via standard upgrading by a system of hydrocarbon recovery column, reformers, a C_5/C_6 isomerizer, a $C_3/C_4/C_5$ alkylation reactor, and a saturated gas plant (Bechtel, 1998) or passed through a ZSM-5 based catalytic process to be upgraded into gasoline and distillate (Mobil, 1983).

The clean syngas can be directed to a methanol synthesis reactor. The methanol synthesis reaction (Eqn. 1) and WGS reaction (Eqn. 2) reach equilibrium in the effluent:

$$CO + 2H_2 \leftrightarrow CH_3OH \quad (1)$$

$$CO + H_2O \leftrightarrow CO_2 + H_2 \quad (2)$$

The raw methanol is flashed and degassed to remove the unreacted gases. The unreacted gases are recycled back to enhance the overall conversion, whereas the methanol is sent to either methanol-to-gasoline (MTG) or methanol to olefins (MTO) processes. The MTG reactor is a ZSM-5 based reactor that converts methanol into gasoline range hydrocarbons, which are subsequently upgraded in a series of processes (NREL, 2011). The MTO is a SAPO-34 based reactor that is used to convert methanol to olefins at high selectivity (95 wt%). The effluent is fractionated to separate light gases and gasoline range hydrocarbons. The olefins are sent to either a ZSM-5 based MOGD unit to be converted into fuels (Tabak and Yurchak, 1990) or to the olefins purification section.

2.4. Olefins Purification Section

In this section, the olefins produced throughout the refinery are purified. Light gases and C_3-C_5 gases from FT upgrading, and olefins from the MTO process are fed into this section. The CO_2 is removed from light gases which is followed by a demethanizer that separates light gases from olefins. The demethanizer effluent is combined with mixed olefins from the MTO process and directed to a deethanizer column. The distillate is directed to a series of selective hydrogenation and distillation columns to separate ethylene from ethane. Ethylene is sold as a product, whereas ethane is recycled back.

The C_3-C_5 hydrocarbons are sent to a distillation column to separate out C_5 content, and then mixed with the deethanizer bottom which also contains C_3-C_4 hydrocarbons. These hydrocarbons are seperated via a depropanizer. The distillate that essentially contains propane and propylene is distilled one more time to produce propylene. The propane is either recycled back or mixed with the LPG outlet (Onel et al., 2014).

The C_4 hydrocarbons (butanes and butenes) are separated from each other by means of extractive distillation that uses a polar solvent,dimethyl formamide (DMF), because the boiling points of butanes and butenes prevent them from being separated via simple distillation. The butane mixture can be recycled back or mixed with the LPG outlet, whereas the crude butenes can be (1) sold as a mixture, (2) separated to 1-butene and 2-butene to be sold, or (3) converted to butadiene via an Oxo-dehydrogenation process (Onel et al., 2014). The Oxo-D process converts 100% of 1-butenes and 92.7% of 2-butenes with a selectivity of 95% towards butadiene.

2.5. Light Gas Handling

The main sources of light gases in the refinery are (1) unreacted syngas from the hydrocarbon production units, (2) light gases produced in the hydrocarbon upgrading section, and (3) light gases separated in the olefins purification section. An internal gas loop configuration is designed to recycle light gases back to the reformers, FT or methanol synthesis reactors to increase the overall carbon conversion. An external gas loop configuration is also designed to avoid accumulation of inert species in the refinery. The external loop utilizes a fuel combustor to provide high-temperature heat and a gas turbine to provide electricity for the process.

2.6. Hydrogen and Oxygen Production

Hydrogen and oxygen are produced within the refinery by pressure-swing adsorption (only H_2), air separation unit (only O_2), and electrolysis (both H_2 and O_2) processes.

2.7. Waste Water Network

The waste water treatment network incorporates a biological digestor and a sour stripper to remove sulfur species, NH_3, and oxygenates. The effluent water can be discharged, utilized for steam production, or sent to the electrolyzers.

2.8. Heat and Power Integration

An optimization based heat-integration approach is adapted for simultaneous heat integration (Papoulias and Grossmann, 1983; Duran and Grossmann, 1986; Floudas et al., 1986). A series of heat engines are included to convert excess heat into electricity (Elia et al., 2010) for simultaneous power integration.

2.9. Unit costs

Different literature sources and the Aspen PEA is used to assign a base cost function to each unit in the refinery (Baliban et al., 2012b, Onel et al., 2014). The balance of plant (*BOP = 0.32*) and indirect costs (*IC = 0.20*) are also included to calculate the Total Plant Cost (TPC) of a unit, shown in Eqn. 3:

$$TPC = (1 + IC).(1 + BOP).Co.\left(\frac{Sr}{So}\right)^{sf} \quad (3)$$

The $C_o.(S_r/S_o)^{sf}$ stands for the base cost function that is obtained from the literature or Aspen PEA. The total overnight capital of the refinery is converted to an annualized capital charge(15.41%/yr) using the methodology in Kreutz et al. (2008).

2.10. Objective Function

The profit is maximized (or –profit is minimized) in this large scale nonconvex MINLP with the objective function shown in Eqn. 4:

$$MIN \sum_{F \square Feed} Cost^{F} + Cost^{El} + Cost^{Seq} + \sum_{u \square U_{inv}} Cost_{u}^{U} - \sum_{P \square Products} Cost^{P} \quad (4)$$

All of the terms in the objective function are levelized with the energy output of the refinery to obtain the total cost in \$/GJ. $Cost^{F}$ includes the contributions from the feedstocks, $Cost^{El}$ is the electricity cost, $Cost^{Seq}$ is the CO_2 sequestration cost, $Cost_u^{U}$ is the investment cost of unit u, and $Cost^{p}$ is the sales revenues from the products.

The overall model has 13849 continuous variables, 34 binary variables, 16304 constraints, and 735 nonconvex terms. A branch and bound algorithm is used to solve this MINLP to global optimality. At every node, piecewise linear underestimators are used to relax the problem into a mixed integer linear (MILP) problem. The MILP is solved with CPLEX to provide a lower bound to the real problem. At each node the optimal set of binary variables from CPLEX are fixed to convert MINLP to an NLP. NLP is solved to local optimality using CONOPT to provide an upper bound solution (Baliban et al., 2012a, 2012b)The optimality gap is tightened by finding better upper and lower bounds within the branch and bound algorithm. A more detailed explanation of the algorithm can be found in the textbooks of Floudas (1995, 2000).

2.11. Net Present Value Analysis

Net present value analysis is performed to evaluate process economics in a more comprehensive manner. The operating days are assumed to be 330 days. The discount rate is taken to be 10 % and the total tax rate (including federal and state) is taken to be 40 %. 10 year MACRS depreciation scheme is used and the investment period is taken to be 3 years with 30 years plant lifetime (Onel et al., 2014). Net present value is calculated using Eqn. 5:

$$\sum_{i=-2}^{30} (Inv_i + W_i + NAE_i + D_i)(1 + Discount\ Rate)^{0-i} \quad (5)$$

where Inv_i is the investment in year i, W_i is the working capital in year i, NAE_i is the net annual earnings in year i, and D_i is the depreciation credit gained in year i.

3. Computational Studies

The process synthesis model is solved to global optimality within a branch-and-bound framework to determine the optimal process topology that produces liquid fuels and olefins at the maximum profit. Six (6) distinct case studies are examined that investigate the effect of refinery scale and olefins production levels on the overall profit of the GTL+C2_C4 plant. Two refinery scales are investigated: 10 thousand and 50 thousand barrels per day of liquid fuels. No restriction is placed on the type of liquid fuels products nor the composition of olefins output from the refinery. The olefins produced are dependent on the refinery scale and are investigated parametrically. For the 10 kBD refineries, the amount of olefins produced daily will be 100, 500, or 1000 metric tons. Likewise, for the 50 kBD refineries, the amount of olefins produced daily will be 500,

2500, or 5000 metric tons. The case studies are denoted as $N - C - O$, where N represents the fuel compositions (U for unrestricted), C represents the refinery capacity, and O represents the amount of olefins produced daily. Additionally, the process synthesis model includes an environmental constraint that precludes the GTL+C2_C4 refineries from having higher life-cycle GHG emissions than current petroleum-based processes. The cost parameters used in the model are illustrated in Table 1:

Table 1.Cost Parameters Used in the GTL+C2_C4 process

Item	Cost	Item	Cost	Item	Cost
Natural Gas	$5.00/TSCF	Butanes	$1.84/gallon	Electricity	$0.07kWh
Freshwater	$0.50/MT	LPG	$1.40/gallon	CO_2TS&M	$5/MT
Gasoline	$2.86/gallon	Diesel	$3.04/gallon	Kerosene	$2.96/gallon
Ethylene	$1.38/kg	Propylene	$1.34/kg	Mixed	$0.35/kg
Budadiene	$1.87/kg	1-Butene	$2.05/kg	Butenes	

The overall profit breakdown, as well as the net present value, is shown Table 2:

Table 2. Overall Profit Breakdown of the GTL+C2_C4 refineries.

$/GJ of products	U-10-100	U-10-500	U-10-1000	U-50-500	U-50-2500	U-50-5000
Natural Gas	7.99	7.84	7.65	8.12	7.87	7.72
CO_2 Seq.	0.00	0.00	0.00	0.00	0.00	0.00
Investment	4.64	4.15	3.73	3.50	3.19	2.93
O&M	1.22	1.09	0.98	0.92	0.84	0.77
Electricity	0.25	0.31	0.45	0.12	0.29	0.37
Gasoline	-19.56	-14.84	-11.40	-19.56	-14.84	-11.40
LPG	-1.85	-1.45	-1.15	-1.85	-1.45	-1.15
Ethylene	-0.81	-3.08	-4.74	-0.81	-3.08	-4.74
Propylene	-1.15	-4.36	-6.70	-1.15	-4.36	-6.70
1-Butene	-0.48	-1.82	-2.80	-0.48	-1.82	-2.80
2-Butene	-0.07	-0.27	-0.42	-0.07	-0.27	-0.42
Butadiene	0.00	0.00	0.00	0.00	0.00	0.00
Mixed Butenes	0.00	0.00	0.00	0.00	0.00	0.00
Total ($/GJ)	-9.82	-12.43	-14.41	-11.27	-13.65	-15.41
NPV (MM$)	509	1055	1754	3756	6597	10180

Each of the case studies utilized an auto thermal reformer operating at 1000 °C as the natural gas conversion technology. Synthesis gas is converted to methanol, and then the methanol is split between the MTG and MTO reactors to produce the liquid fuels and olefins, respectively. In the optimal topology, gasoline and LPG are the liquid fuels that are produced, whereas the mixed butenes are separated to 1-butene and 2-butene for olefins production. The total figure, "Total ($/GJ)", shown in Table 2 is the difference between the costs associated with the production of olefins and liquid fuels and the total revenue obtained from selling these products. A more negative value corresponds to a more profitable GTL+C2_C4 refinery. The overall profit of the refineries increases as the amount of olefins produced increases and economies of scale are evident as the refinery capacity increases. The most profitable GTL+C2_C4 plant, U-50-5000, has an overall profit of $15.41/GJ and a net present value of 10180 MM$.

4. Conclusions

A superstructure is introduced that allows for the co-production of liquid fuels and olefins from natural gas. The optimal solution and topology is obtained using a global

optimization framework across different case studies. Two different plant scales are investigated to show the effects of economies of scale. The olefins production is varied parametrically to observe the effect it has on the plant profitability. The profit and the net present value are observed to increase as the olefins production increases. All the case studies provided highly profitable refineries that suggest that co-production of liquid fuels and olefins from natural gas is an economically viable alternative.

5. Acknowledgements

The authors acknowledge partial financial support from National Science Foundation (NSF EFRI-0937706 and NSF CBET-1158849).

References

Baliban, R. C.; Elia, J. A.; Floudas, C. A., 2010, Toward novel hybrid biomass, coal, and natural gas processes for satisfying current transportation fuel demands, 1: Process alternatives, gasification modeling, process simulation, and economic analysis, Industrial & Engineering Chemistry Research, 49, 7371-7388

Baliban, R. C.; Elia, J. A.; Floudas, C. A., 2013, Novel Natural Gas to Liquids Processes: Process Synthesis and Global Optimization Strategies, AIChE Journal, 59 (2), 505-531

Baliban, R. C.; Elia, J. A.; Misener, R.; Floudas, C. A.,2012a,Global optimization of a MINLP process synthesis model for thermochemical based conversion of hybrid coal, biomass, and natural gas to liquid fuels, Computers & Chemical Engineering,42, 64-86

Baliban, R. C.; Elia, J. A.; Weekman, V.; Floudas, C. A.,2012b,Process synthesis of hybrid coal, biomass, and natural gas to liquids via Fischer–Tropsch synthesis, ZSM-5 catalytic conversion, methanol synthesis, methanol-to-gasoline, and methanol-to-olefins/distillate technologies, Computers & Chemical Engineering,47 (12), 29-56

Bechtel, 1998, Aspen Process Flowsheet Simulation Model of a Battelle Biomass-Based Gasification, Fischer-Tropsch Liquefaction and Combined-Cycle Power Plant, Contract Number: DE-AC22-93PC91029

Biegler, L. T.; Grossmann, I. E.; Westerberg, A. W.; Kravanja, Z., 1997, Systematic methods of chemical process design, Prentice Hall

Duran, M. A.; Grossmann, I. E, 1986, Simultaneous optimization and heat integration of chemical processes, AIChE Journal, 32(1), 123-138

Energy Information Administration, 2014, Short-Term Energy Outlook, March 2014

Floudas, C. A., 1995, Nonlinear and Mixed-Integer Optimization, Oxford University Press

Floudas, C. A., 2000, Deterministic Global Optimization: Theory, Methods and Applications, Kluwer Academic Publishers

Floudas, C. A.; Ciric, A. R.; Grossmann, I. E., 1986, Automatic Synthesis of Optimum Heat Exchanger Network Configurations, AIChE Journal, 32, 276

Kreutz, T. G.; Larson, E. D.; Liu, G.; Williams, R. H., 2008, Fischer-Tropsch Fuels from Coal and Biomass, Proceedings of the 25th International Pittsburgh Coal Conference

Mobil Research and Development Corporation, 1983, Slurry Fischer-Tropsch/Mobil Two Stage Process of Converting Syngas to High Octane Gasoline, Contract Number: DE-AC22-80PC30022

National Renewable Energy Laboratory, 2011, Gasoline from Wood via Integrated Gasification, Synthesis, and Methanol-to-Gasoline Technologies, Contract Number: DE-AC36-08GO28308

Onel, O.; Niziolek, A. M.; Elia, J. A.; Baliban, R. C.; Floudas, C. A.,2014,Biomass and Natural Gas to Liquid Transportation Fuels and Olefins (BGTL+C2_C4), submitted

Papoulias, S. A., Grossmann, I. E., 1983, A Structural Optimization Approach in Process Synthesis Part II: Heat Recovery Networks, Computers and Chemical Engineering, 7, 707

Tabak, S. A.; Yurchak, S., 1990, Conversion of methanol over ZSM-5 to fuels and chemicals, Catalysis Today

Krist V. Gernaey, Jakob K. Huusom and Rafiqul Gani (Eds.), 12th International Symposium on Process Systems Engineering and 25th European Symposium on Computer Aided Process Engineering.
31 May – 4 June 2015, Copenhagen, Denmark

Life-Cycle Assessment Principles for the Integrated Product and Process Design of Polymers from CO_2

Niklas von der Assen,[a] Matthias Lampe[a], Leonard Müller,[a] André Bardow[a*]

[a]*Chair of Technical Thermodynamics, RWTH Aachen University, Schinkelstr. 8, 52062 Aachen, Germany*
andre.bardow@ltt.rwth-aachen.de

Abstract

To minimize environmental impacts, coupling integrated product and process design with life-cycle assessment (LCA) is a powerful yet challenging approach. A challenge in LCA is the proper accounting for all co-products occurring along the entire supply chain, known as allocation problem. In this paper, we provide a systematic analysis for LCA-based product and process design including alternative allocation methods. We apply the approach to polyol production from CO_2. Here, alternative allocation methods lead to very different polyol products and processes. Finally, we derive general principles regarding co-product allocation in LCA-based product and process design.

Keywords: Life-cycle assessment, product-process design, CO_2 utilization, polymers.

1. Introduction

Today, most polymers are synthesized from fossil-based feedstocks. As alternative and renewable carbon feedstock, carbon dioxide (CO_2) has recently been successfully utilized as building block for polyols, a direct precursor of polyurethanes (Langanke et al., 2014). In addition to the direct utilization of CO_2 as feedstock for polyols, CO_2 can also be used indirectly to produce further chemicals in the polyol supply chain.

Both direct and indirect utilization of CO_2 provide novel degrees of freedom to design the polyol supply chain. These degrees of freedom can be exploited to minimize environmental impacts in the design of a polyol polymer with desired properties and the associated processes in the supply chain. For this purpose, we conduct an integrated design of both product and processes coupled with life-cycle assessment (LCA).

Integrated product and process design is a challenging problem by itself (Gani, 2004; Adjiman et al., 2014). Coupling the integrated design problem with LCA introduces further challenges; in particular the evaluation of co-products has to be addressed since many products are co-produced in the chemical industry, e.g., in (bio-) refineries, steam crackers and also for CO_2 capture from CO_2 point sources (von der Assen et al., 2013). In this case, the environmental impacts have to be allocated to the individual co-products. A set of allocation methods exists in LCA. The choice of the allocation method is known to often lead to strongly varying product footprints (Curran, 2007).

The goal of this work is to analyse the effect of alternative allocation methods in LCA-based product and process design of polyols. The design approach consists of the integrated optimization of the polyol supply chain and the polyol product with respect to minimal environmental impacts (Section 2). As representative environmental impact, the carbon footprint is chosen as single LCA metric to avoid further complexity by multiple environmental objectives. The polyol product has to meet target properties such as the molar mass, OH number, and glass transition temperature. The polyol supply chain includes all processes for production of feedstocks and energy from cradle to gate. We illustrate how

alternative allocation methods change both the optimal monomer composition and the supply chain of the polyol (Section 3). We finally derive general principles regarding allocation approaches in LCA-based product and process design (Section 4).

2. Formulation of Optimization Problem

The aim of LCA-based product and process design is to identify a product and its supply chain with minimal environmental impact. The design problem can be generally formulated as the following non-linear program (NLP):

$$\begin{aligned} \min_{s,\nu} \quad & h = C^T \cdot s && \text{minimal environmental impacts} \\ \text{s.t.} \quad & g(\nu, s) \leq 0 && \text{Constraints from supply chain processes} \\ & l \leq D \cdot \nu \leq u && \text{product design constraints} \\ & s \in \mathbb{R}^k && \text{n process variables} \\ & \nu \in \mathbb{R}^l && \text{m product variables} \end{aligned} \tag{1}$$

The following sections specify the details of problem (1) for CO_2-based polyols.

3. Synthesis and Properties of Polyols

3.1. Polyol Supply Chain Superstructure

Polyether polyols are the most common type of polyols. They can be synthesized from the reaction of a multi-functional alcohol starter (glycerol in this work) with epoxides such as propylene oxide (PO). PO can partly be substituted by CO_2 making the overall reaction more energy efficient since the production of PO is energy intensive (von der Assen and Bardow, 2014). Each molecule of CO_2 reacts with one molecule of PO forming a poly-carbonate (PC) unit in the polymer chains. In addition to PC units and the conventional poly-ether (PE) units from PO, poly-oxy-methylene (POM) units from complete polymerization of formaldehyde can also be incorporated into the polyol. The overall reaction for a hypothetical statistical polyol from the considered feedstocks is:

$$\nu_1\,\mathrm{PO} + \nu_2\,(\mathrm{PO}{+}\mathrm{CO_2}) + \nu_3\,\mathrm{FA} + \mathrm{Starter} \rightarrow \mathrm{HO}\text{-}\{(\mathrm{PE})_{\nu 1}\,(\mathrm{PC})_{\nu 2}\,(\mathrm{POM})_{\nu 3}\}\text{-}\mathrm{OH} \tag{2}$$

Figure 1 shows the considered cradle-to-gate supply chain superstructure for production of polyols. The supply chain illustrates that CO_2 can be incorporated into the polyol both directly and indirectly through methanol and/or formaldehyde.

3.2. Estimation of Polyol Properties

Reaction (2) is thermodynamically feasible for all combinations of ν_i, i.e., $\Delta g^R \leq 0$. However, the product composition ν_i alters the polyol properties. The considered polyol properties in this work are the molar mass M, the OH number, and the glass transition temperature T_g. The properties are estimated from the polyol structure via group contribution methods (van Krevelen and te Nijenhuis, 2009):

$$M = \sum\nolimits_i \nu_i M_i + M_S \;; \qquad OH = \frac{1000\; M_{KOH} F}{M} \;; \qquad T_g = \frac{\sum_i \nu_i Y_{g,i} + Y_{g,S}}{M} \tag{3}$$

The molar mass M of the polyol can be computed from the molar masses M_i of the monomer units PE, PC and POM, and the molar mass M_S=92 g/mol of glycerol as starter. The OH number is a common metric for polyols and can be determined via M and the number F of hydroxyl groups in the starter. Since we fix F=3 for glycerol and M_{KOH}=56 g/mol, bounds for OH are equivalent to further bounds on M. The glass

transition temperature T_g is obtained from the corresponding group contributions $Y_{g,i}$ and $Y_{g,S}$ of the monomers and starter, respectively. Although T_g is non-linear in ν_i, the product design constraints in Eq. (1) can be formulated in a linear way:

$$\sum_i \left(T_{g,min}\, M_i - Y_{g,i}\right) \nu_i \leq Y_S - T_{g,min} M_S \tag{4}$$

$$\sum_i \left(Y_{g,i} - T_{g,max}\, M_i\right) \nu_i \leq T_{g,max} M_S - Y_S \tag{5}$$

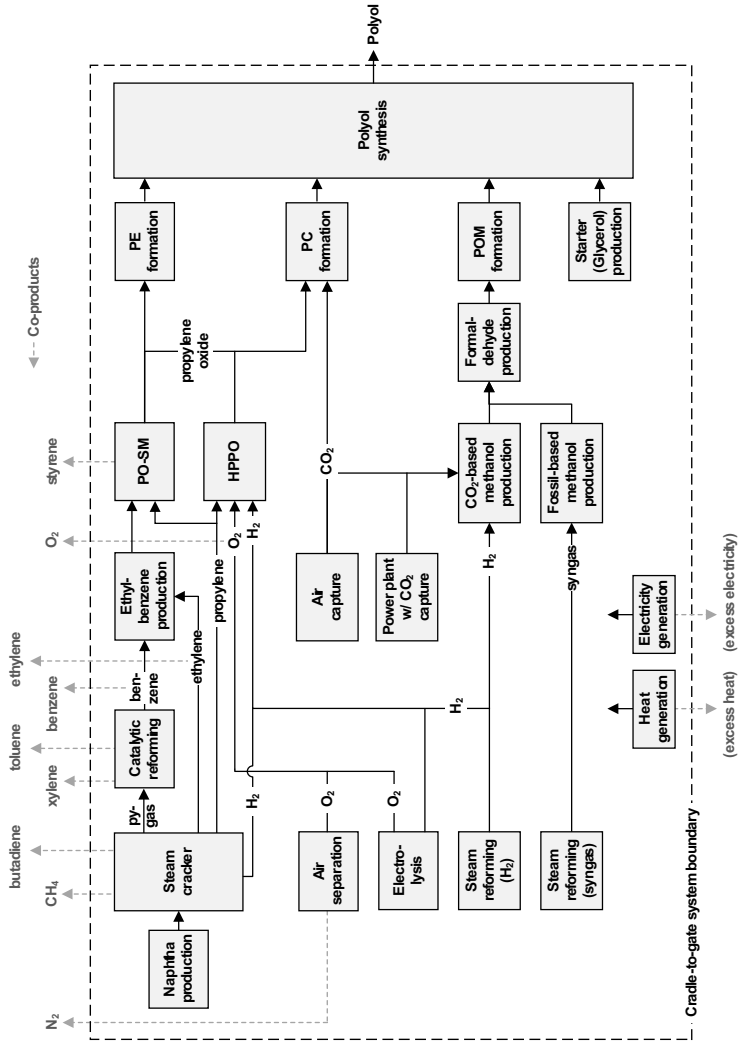

Figure 1. The supply chain superstructure for polyol production illustrating the major feedstocks propylene oxide, CO_2, and formaldehyde as well as glycerol as starter. Co-products in the upstream processes (grey, dashed arrows) leave the cradle-to-gate system boundaries. Energy flows as heat and electricity are also considered (omitted in figure for better visualization).

4. Evaluation of Co-Products in Life-Cycle Assessment

In LCA, process systems are typically modelled as set of linear equations. The product under study is specified in the functional unit as vector $f \in \mathbb{R}^m$. LCA process data is given as technology matrix A and intervention matrix B. Each entry $a_{i,j}$ of A quantifies the flow of product i to process j. To supply only the product flow in f, matrix A is scaled with a scaling vector s (Heijungs and Suh, 2002):

$$A(v) \cdot s = f. \tag{6}$$

For the process of polyol synthesis modelled by Eq. (2), the corresponding entries in A contain the product variables ν. Thus, the mass balances for PE, PC and POM in equations in (6) are non-linear with respect to the design variables s and ν. The environmental impacts h associated with production of the product flow in f are

$$h = (Q \cdot B) \cdot s, \tag{7}$$

where matrix B contains the emissions and resources (rows in B) exchanged between processes (columns in B) and the environment. Matrix Q contains characterization factors to aggregate emissions and resources into environmental impact indicators.
The process superstructure in Figure 1 shows that many upstream processes of polyol production generate co-products. Due to these co-products, the set of equations (6) is over-determined and, in general, no scaling vector s exists to supply only the polyol without any co-products. To still obtain specific environmental impacts for polyol production, three approaches exist in LCA: system expansion, avoided burden and allocation.

4.1. System expansion

System expansion includes all co-products in an expanded functional unit $f_{exp} = f + \tilde{f}$, where f contains only the original product, here the polyol, and $\tilde{f}$ contains the unknown quantities of the co-products. Thereby, the environmental impacts are determined for a basket of products. For system expansion, the first two equations of NLP (1) can be re-formulated as follows:

$$\min_{s,\tilde{f},\nu} \quad h = (Q \cdot B) \cdot s \tag{8}$$

$$\text{s.t.} \quad (A(\nu) \quad -I) \cdot \begin{pmatrix} s \\ \tilde{f} \end{pmatrix} = f \tag{9}$$

4.2. Avoided burden

The co-products of the polyol supply chain can be considered to avoid the production of these products by alternative processes. The alternative processes cause environmental burdens. These burdens can thus be avoided by co-production. The co-products are therefore credited with an ‘avoided burden’. Process data of the alternative, ‘avoided burden’ processes are contained in matrices A_{avo} and B_{avo}. For the avoided burden approach, the first two equations of NLP (1) can be re-formulated as follows:

$$\min_{s,s_{avo},\nu} \; h = Q \cdot (B \quad -B_{avo}) \cdot \begin{pmatrix} s \\ s_{avo} \end{pmatrix} \tag{10}$$

$$\text{s.t.} \quad (A(\nu) \quad -A_{avo}) \cdot \begin{pmatrix} s \\ s_{avo} \end{pmatrix} = f \tag{11}$$

4.3. Allocation

Allocation splits a process with *n* co-products into *n* processes with only one product each. The inputs in A and emissions in B are allocated to the single-product processes according to the co-products' share in mass, energy content or economic value. The allocation criteria can be cast into a matrix C (Jung et al., 2014). With matrices T_1, T_0 and U that handle the process splitting, the first two equations of NLP (1) can be re-formulated for allocation as follows (Jung et al., 2014):

$$\min_{\tilde{s},\nu} \quad h = Q \cdot (B \cdot T_0) \cdot C \cdot \tilde{s} \tag{12}$$

$$\text{s.t.} \quad [U \circ (A(\nu) \cdot T_1)] \cdot C \cdot \tilde{s} = f \tag{13}$$

Since the process splitting increases the number of processes, the dimension of $\tilde{s}$ in Eqs. (11+12) is also increased compared to s in Eqs. (6+7).

5. Results and Discussion

5.1. System expansion

If there are no constraints on the expanded functional unit, all products can be added to $\tilde{f}$ in Eq. (9). In this case, the optimal expanded functional unit includes the polyol and an infinite amount of CO_2 from air capture. The air-capture process provides a net GHG sink for the cradle-to-gate scope. The optimal polyol contains only glycerol and CO_2-based POM units, which are produced without any co-products. However, this solution is degenerate in the context of polyol design since the mono functional process air capture is employed beyond the amounts actually needed for polyol production. To avoid these solutions, the expanded functional unit $\tilde{f}$ should contain only those co-products that leave the system boundaries in Figure 1; for other co-products i we set $\tilde{f}_i = 0$. In this case, the optimal expanded functional unit contains 1,000 kg polyol, 145 kg styrene, 101 kg N_2, 63 kg CH_4, 51 kg butadiene, 26 kg toluene, 19 kg ethylene, and 3 kg xylene. Not all potential co-products, i.e., benzene, O_2, heat and electricity, are included in $\tilde{f}$. Still, the interpretation of such largely expanded functional unit might be difficult. The optimal polyol composition in this case is shown in Figure 2.

5.2. Avoided burden

The superstructure is expanded by avoided burden processes for co-products leaving the system boundaries. For production of 1,000 kg polyol, this approach leads to assigning credits for co-production of 661 kg styrene, 460 kg N_2, 285 kg CH_4, 232 kg butadiene, 118 kg toluene, 85 kg ethylene and 13 kg xylene; in total 1,854 kg co-products. Hence, the avoided burden approach favours co-production compared to system expansion where no credits are assigned to co-products. The polyol consists of mostly PC units which are always produced together with various co-products (Figure 2).

5.3. Allocation

We applied allocation based on mass, energy and price to processes for co-products leaving the system boundaries. The optimal polyols consist of glycerol, POM and PC units. PC content is highest for mass allocation due to low footprints of PO from PO-SM where most emissions are allocated to styrene. For price allocation, the allocation factor for PO from PO-SM is highest and thus, PC content is lowest.

For all considered allocation methods (5.1-5.3), the molar mass M equals the upper bound M_{max}. Methanol required for POM is produced exclusively by the CO_2/H_2 process. In almost all cases, CO_2 is captured from the power plant. H_2 is always produced in the fossil-fuelled processes steam cracker and steam reforming.

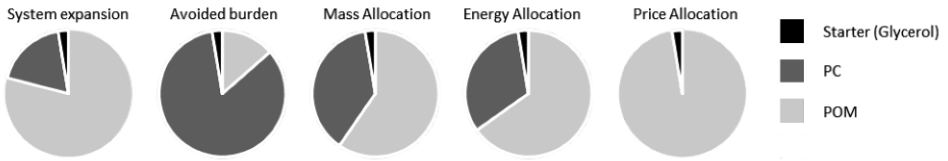

Figure 2. Environmentally optimal polyol compositions (wt %) for alternative allocation methods.

6. Conclusions

In this work, we have presented an approach for coupling an integrated product and process design problem of polyols with LCA. In particular, we systematically integrated allocation methods from LCA to account for co-products in the supply chain. The influence of allocations methods on LCA results has received much attention in the LCA literature. This experience from LCA can be used for in product and process design for co-product evaluation. In the presented example of CO_2-based polyols, we found that alternative allocation methods lead to very different products and processes. Furthermore, general principles for allocation methods in an LCA-based product and process design can be derived: System expansion is always applicable since no additional data are required. Since system expansion does not assign credits to co-products, a supply chain with no or few co-products is favoured. Including all co-products in the functional unit, however, might create too big a basket of goods where interpretation might be difficult. For avoided burden, LCA process data for alternative production technologies without co-products are required. In practice, such data are not always available. As expected, application of the avoided burden approach in the design problem favours co-production across the supply chain. For allocation, results depend strongly on the allocation criterion.

References

C.A. Adjiman, A. Galindo, G. Jackson, 2014, Molecules Matter: The Expanding Envelope of Process Design, Computer Aided Chemical Engineering, Vol. 34, 55-64.

N. von der Assen, J. Jung, A. Bardow, 2013, Life-cycle assessment of carbon dioxide capture and utilization: avoiding the pitfalls, Energy & Environmental Science, Vol. 6, 2721-2734.

N. von der Assen, A. Bardow, 2014, Life cycle assessment of polyols for polyurethane production using CO_2 as feedstock: insights from an industrial case study, Green Chemistry, 16, 3272-3280.

M.A. Curran, 2007, Co-Product and Input Allocation Approaches for Creating Life Cycle Inventory Data: A Literature Review, The International Journal of Life Cycle Assessment, Special Issue Vol. 12, 1, 65-78.

R. Gani, 2004, Chemical product design: challenges and opportunities, Computer & Chemical Engineering, Vol. 28, 2441-2457.

R. Heijungs, S. Suh, 2002, The computational structure of Life Cycle Assessment, Kluwer Academic Publishing, Dordrecht, Netherlands.

J. Jung, N. von der Assen, A. Bardow, 2014, Sensitivity coefficient-based uncertainty analysis for multi-functionality in LCA, The International Journal of Life Cycle Assessment, Vol. 19, 3, 661-676.

D.W. van Krevelen, K. te Nijenhuis, 2009, Properties of Polymers: Their Correlation with Chemical Structure; their Numerical Estimation and Prediction from Additive Group Contributions, 4th edition, Elsevier, Oxford, UK.

J. Langanke, A. Wolf, J. Hofmann, K.Böhm, M.A. Subhani, T.E. Müller, W. Leitner, C. Gürtler, 2014, Carbon dioxide (CO_2) as sustainable feedstock for polyurethane production, Green Chemistry, 16, 1865-1870.

Krist V. Gernaey, Jakob K. Huusom and Rafiqul Gani (Eds.), 12th International Symposium on Process Systems Engineering and 25th European Symposium on Computer Aided Process Engineering.
31 May – 4 June 2015, Copenhagen, Denmark

Optimization-based methodology for wastewater treatment plant synthesis – a full scale retrofitting case study

Hande Bozkurt, Krist V. Gernaey and Gürkan Sin*

CAPEC-PROCESS, Department of Chemical and Biochemical Engineering, Technical University of Denmark, DK-2800 Lyngby, Denmark
gsi@kt.dtu.dk

Abstract

Existing wastewater treatment plants (WWTP) need retrofitting in order to better handle changes in the wastewater flow and composition, reduce operational costs as well as meet newer and stricter regulatory standards on the effluent discharge limits. In this study, we use an optimization based framework to manage the multi-criteria WWTP design/retrofit problem for domestic wastewater treatment. The design space (i.e. alternative treatment technologies) is represented in a superstructure, which is coupled with a database containing data for both performance and economics of the novel alternative technologies. The superstructure optimization problem is formulated as a Mixed Integer (non)Linear Programming problem and solved for different scenarios - represented by different objective functions and constraint definitions. A full-scale domestic wastewater treatment plant (265,000 PE) is used as a case study in order to highlight the use of the framework for generating optimal retrofitting solutions.

Keywords: cold anammox, retrofit, optimization, wastewater treatment, Sharon

1. Introduction

Wastewater treatment process synthesis can be defined as the step in the design of a WWTP where the design engineer selects unit processes from a number of alternatives and interconnects them to create the process flow diagram (i.e. WWTP network). Process synthesis is also performed during retrofitting studies in the sense that a new task can be added to the existing treatment line or one or several processes can be changed as a result of emerging needs. For instance, increased nitrogen limitation in the regulations for the WWTP effluents (Water Framework Directive, 2000/60/EC) gave rise to development of innovative nitrogen removal technologies mostly used for water streams resulting from sludge treatment (Lackner et al., 2014). Similarly, recovery possibilities for clean water, energy and materials shifted the perception about wastewater towards being a valuable resource rather than being a waste. While the regulations change to impose stricter effluent limit values for the contaminants, the increasing population and the size of the cities makes the expansion of the existing WWTPs harder. In this study, we use our previously developed framework using superstructure based optimization in order to perform a retrofitting study focusing on improving the performance of a full-scale WWTP – in particular the Avedøre WWTP treating municipal wastewater and located in Copenhagen, Denmark. The objective is to find novel solutions in terms of enhancing the nitrogen removal capacity and reducing utility consumption needs.

2. The Framework

The superstructure optimization based framework, illustrated in Figure 1, is previously developed for chemical process synthesis (Quaglia et al., 2012) and then modified and adapted for the WWTP design/retrofitting cases. The steps of the framework are recalled briefly in this section, while the details including the mathematical formulation and database generation for alternative treatment technologies can be found elsewhere (Bozkurt et al., 2014). After defining the wastewater characterization, sink limitations and objective function in the first step, the superstructure is generated consisting of the base case of the existing WWTP (i.e. the existing treatment units, only in the retrofitting studies) and other alternative treatment technologies under the existing or new treatment tasks. The formulation of the superstructure is then finalized by defining the feasible connection streams between the treatment tasks. Each treatment unit in the superstructure is defined using a generic model based on mass input-output. The parameters of the generic model are maintained in a database, e.g. process performances (yields, stoichiometry etc.), utility consumptions, volumes and sludge production. The optimal wastewater network problem is then formulated as a mixed integer (non)linear programming (MI(N)LP) problem and solved for deterministic conditions and under uncertainty by defining several scenarios.

3. Case study

3.1. Problem definition

Avedøre WWTP is located west of Copenhagen (Denmark) and receives wastewater from 10 suburban municipalities with a population of approximately 265,000 people. Annually, around 25-30 million m^3 of wastewater is treated in the plant by physical, biological and chemical means. The wastewater treatment line consists of solids separation by means of sedimentation in the primary treatment and removal of organics and nutrients together with solids in the secondary treatment prior to the discharge of the treated water into Køge bay. Organics, nitrogen and partly also phosphorus are removed by the activities of a mixed culture of organisms in activated sludge (AS) reactors operated under alternating oxic/anoxic conditions (Tchobanoglous, 2003). The remaining phosphorus (from biological removal) is precipitated chemically by iron chloride addition. The resulting sludge, on the other hand, is stabilized in an anaerobic digester prior to be incinerated to produce heat and electricity. Table 1 illustrates the influent wastewater characterization and effluent water quality, given as a yearly average of 2012 data.

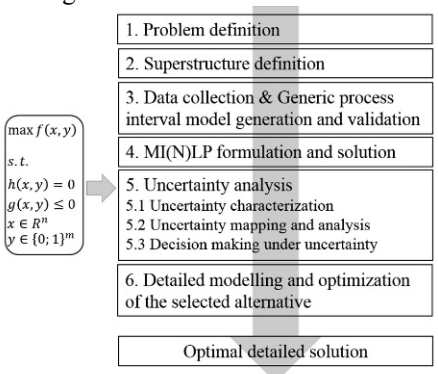

Figure 1. The superstructure based optimization methodology

Table 1. Influent and effluent composition for Avedøre WWTP (yearly average, 2012)

Parameter	Unit	Influent	Effluent
COD	g / m^3	476	23
BOD	g / m^3	180	2
NH_4-N	g / m^3	33	1.2
NO_X-N	g / m^3	-	3.0
Total-N	g / m^3	43	4.8
Total-P	g / m^3	6.5	0.6
SS	g / m^3	209	4.6
Flow rate	m^3 / d	72,000	

The retrofitting problem is defined so that the feasibility of extending the existing treatment line will be analysed in two ways: (1) addition of a new task and alternative technologies in the sludge reject water line; and (2) evaluating an innovative nitrogen removal technology in the main wastewater treatment line. The objective function is defined such that it covers the annual operational and capital cost (only for the new treatment units), which is to be minimized.

3.2. Superstructure definition

The superstructure developed for the case study is illustrated in Figure 2. The process intervals shown in gray are the existing units (i.e. PC – primary clarifier, AS – activated sludge type biological treatment unit, Thick – sludge thickener, AD – anaerobic digester and Dewat – dewatering unit) and the wastewater source and sinks are illustrated in the first and last columns of the superstructure. On the other hand, nitrogen removal alternatives are added in the reject water line, which comprises 5 – 20 % of the total nitrogen load into the system. Furthermore, as an alternative to the AS unit, a combination of a high rate oxic system and an anammox reactor is considered.

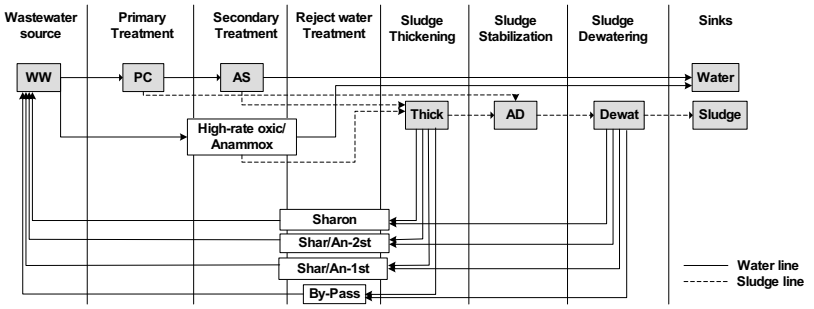

Figure 2. Avedøre WWTP retrofitting case study superstructure

3.3. Data collection & generic process interval model generation

In order to design the individual treatment technologies, the systematic data collection and design procedure, which is developed in the context of the superstructure based optimization methodology, has been used (Bozkurt et al., 2014). Accordingly, the base case of Avedøre WWTP is designed based on the design data obtained from the treatment plant by following the design methodology.

3.3.1. Main stream treatment alternatives

- The high-rate oxic system is characterized by its short solids retention time (SRT) and hydraulic retention time (HRT), as well as its effectiveness in terms of COD removal at low energy cost. It is preferred also because it diverts high organic loads to sludge treatment, which further contributes to biogas production. In this study, it is designed such that it is working with 0.5 days of SRT and 2 hours of HRT resulting in approximately 60% reduction in the biodegradable organic matter. Since the SRT is short, hardly any nitrifiers grow in the medium; therefore, there is no nitrogen removal in this reactor (Versprille et al., 1984). However, it is coupled with a novel technology (i.e. anammox), which is proven to effectively treat nitrogen rich streams at high temperatures (e.g. sludge reject water stream); recent studies showed, however, the effectiveness of the annamox technology in cold and dilute municipal wastewater streams (Winkler et al., 2011; Wett et al., 2013). In this particular case study, the anammox reactor is designed so that there is heterotrophic activity (i.e. denitrification) and ammonium oxidizing bacteria (AOB) and anammox activity (i.e. two step reaction summarized in Eq. 3 and 4) in the medium. Accordingly: (1) The heterotrophic SRT is

selected as 10 days resulting in 80% biodegradable COD removal, (2) As a result of AOB and anammox activity, 88% NH_4-N and 76% total-N is removed and (3) The sizing of the reactor is done based on volumetric nitrogen loading rate, which is selected as 0.2 kg N /m^3 d (Wett et al., 2013).

3.3.2. Side stream treatment alternatives

Three different nitrogen removal alternatives with different mechanisms and reactor configurations are placed in the superstructure under the reject water treatment task. The Sharon reactor operates with the nitritation/denitritation mechanism (as shown in Eq.1 and Eq.2, respectively) in a single CSTR type of reactor. The system can be operated without any sludge retention, and therefore its SRT is equal to its HRT and the sizing of the reactor is done accordingly. The second reaction completes the nitrogen cycle by converting the nitrogen compounds into nitrogen gas and also produces alkalinity which helps maintain the system pH, which otherwise decreases as a result of proton production in the first reaction. This mechanism needs oxygen for nitritation and carbon addition for denitritation. Since the COD in the reject water stream is usually low, carbon is added as methanol. This route reduces the aeration and carbon addition requirements by almost 25 and 40%, respectively, as compared to the conventional nitrification/denitrification route. The other two technologies (i.e. Sharon/Anamox-2stage and Sharon/Anamox-1stage) are operated with the partial nitritation/anammox mechanism as illustrated in Eq.3 and Eq.4, respectively. The difference is, in the Sharon/Anammox-2stage technology, partial nitritation and anammox occur in physically separated reactors, whereas Sharon/Anammox-1stage is a single reactor in which two different microorganism types (i.e. Ammonium oxidizing bacteria for partial nitritation and anaerobic ammonium oxidizers for anammox) are present in granular form or on a support medium. Different performance evaluations have been reported for different reactor configurations, and therefore both are included in the superstructure.

$$NH_4^+ + 1.5O_2 \rightarrow NO_2^- + H_2O + 2H^+ \quad (1)$$

$$NO_2^- + 0.5CH_3OH + 0.5CO_2 \rightarrow 0.5N_2 + HCO_3^- + 0.5H_2O \quad (2)$$

$$NH_4^+ + HCO_3^- + 0.75O_2 \rightarrow 0.5NH_4^+ 0.5NO_2^- CO_2 + 1.5H_2O \quad (3)$$

$$NH_4^+ + 1.124NO_2^- + 0.014HCO_3^- + 0.121H_2CO_3 \rightarrow 0.987N_2 + 0.138NO_3^- + 0.27C_5H_8N_{0.5}O_2 + 2.185H_2O \quad (4)$$

Table 2. Data for side stream treatment alternatives

	Sharon	**Shar/An-2st**	**Shar/An-1st**
Reactor type	CSTR	CSTR-granular sludge	Granular sludge
Mechanism	Nitritation / denitritation	Partial nitritation/Anammox	Partial nitritation/Anammox
Utility requirement	Oxygen, external carbon	Oxygen	Oxygen
Vol. N removal rate (kg N / m^3.d)	-	10	-
Vol. N loading rate (kg N / m^3.d)	-	-	1.5
Efficiency	86% for 1st reaction 60% for 2nd reaction	50% in 1st reactor 80% in 2nd reactor	90% for NH_4-N 80% for Total-N
Volume	Based on HRT = 1 d	Based on vol. N removal rate	Based on vol. N loading rate
References	Hellinga et al., (1998)	Van Dongen et al., (2001) and van der Star et al., (2007)	Abma et al., (2010)

4. Results and Discussion

The deterministic superstructure optimization problem is formulated as a Mixed Integer Linear Programming (MILP) problem and solved under two scenarios.

4.1. Scenario 1

In the first scenario, the base line for wastewater and sludge treatment is maintained and the effect of side stream treatment alternatives on the system performance (i.e. operational cost and nitrogen removal performance) is investigated. When the optimization problem is solved, the Shar/An-1st technology is selected among the side stream treatment alternatives, in addition to the base case; Table 3 summarizes the results comparing the base case with the selected alternative. In the current formulation of the base case, the reject water stream contributes to the total nitrogen load (which is mostly in the form of NH_4-N) by 7%. When a simple mass balance calculation is done around nitrogen and the associated oxygen consumption in the entire treatment plant, it can be seen that around 5.5% of the NH_4-N load (134 kg N/d) is removed in the side stream unit. This means that less NH_4-N needs to be nitrified in the AS unit. It is known from stoichiometry that conventional nitrification/denitrification in the main AS unit consumes around 60% more oxygen as compared to the partial nitritation/anammox route (for the first route it is 4.57 kg O_2/kg NH_4-N whereas this value is 1.71 kg O_2/kg NH_4-N for the latter case). The nitrogen mass removed in the side stream accounts for a daily reduction of the oxygen consumption with 395 kg. Reduction in oxygen demand means a reduction in the operational cost needed to supply the air, hence explaining the improvement obtained in the utility consumption (2,920 unit cost annually) in Table 3. Another point to note with respect to the performance of the system is that the base case (with respect to yearly average values) already performs well in terms of nitrogen removal. Despite that, a slight improvement is observed with the addition of Shar/An-1st reactor into the plant layout. The fact that the improvement is not too significant is mostly related to the nitrogen load of the reject water stream, which is very low (i.e. 7% of the total-N load into the treatment plant and is known to increase up to 20-30% in practice) in this yearly averaged case. Future work will consider evaluation of daily and weekly peak load to the plant as alternative scenario to compare the performance of the side stream technologies with the base case plant operation.

Table 3. Scenario 1 cost breakdown: the analysis is carried out at average influent load

	Utility cost (unit cost)	**Landfill cost (unit cost)**	**Capital cost (unit cost)**	**OBJ (unit cost)**	**Eff. Total N (g N/m^3)**
Base case	201,115	565,385	-	67,478	7.8
Shar/An-1st	198,195	565,020	3,342	67,217	7.5

4.2. Scenario 2

In the second scenario, together with the alternatives of the reject water stream, an alternative treatment technology in the main wastewater treatment line is also considered as shown in Figure 2. The deterministic solution of the network selection problem, which is formulated as a MILP problem with an objective function definition of minimizing the capital and operational cost of the WWTP, resulted in the selection of the base case together with the Shar/An-1st technology. In Table 4, a comparative analysis of the system performance is shown for the selected network and a simulation made by fixing the High-rate oxic/Anammox process interval. Consequently, when the operational costs are compared, it is seen that the high-rate oxic/anammox system is favored as compared to the current AS system (i.e. low aeration requirement, low sludge production and high biogas production associated with higher organic content entering the anaerobic digester). However, when capital cost requirement is considered as well,

the high-rate oxic/anammox technology is not found optimal. It should be noted here that this system has almost 50 % less footprint than the AS system which has traditionally very large reactor volumes (e.g. 5,000–10,000 m^3). Therefore, the potential savings made in land requirement (as well as reduced size for reactor construction) are likely to favor the cold anammox technology for greenfield projects.

Table 4. Comparative system performance analysis for scenario 2

	Network	Utility cost	Landfill cost	Biogas price	Capital cost	OBJ	Eff.TotN (g N/m^3)
Selected	**PC-AS**-Thick-AD-Dewat-Shar/An-1st	198,195	565,020	699,340	3,342	67,217	7.5
Simulated	**High-rate oxic/Anammox**-Thick-AD-Dewat-Shar/An-1st	176,295	555,530	1,151,940	595,392	175,277	6.6

5. Conclusions

An optimization based framework is successfully used to evaluate novel retrofitting solutions for a full scale municipal WWTP. The decision on which technology to employ is rendered on quantitative metrics which complements the experience based approach predominantly used today. Among retrofitting alternatives, the so-called anammox technology is found promising candidate for greenfield project applications where savings in land requirement is factored in to the decision making. Overall the tool is expected to support and facilitate generation and evaluation of ideas for identifying optimal solutions to design and retrofit WWTPs.

References

W.R. Abma, W. Driessen, R. Haarhuis, M.C.M. van Loosdrecht, 2010, Upgrading of sewage treatment plant by sustainable and cost-effective separate treatment of industrial wastewater, WaterSciTechnol, 61,7, 1715-1722.

H. Bozkurt, A. Quaglia, K.V. Gernaey, G. Sin, 2014, A mathematical programming framework for early stage design of wastewater treatment plants, Environ Modell Softw, (accepted).

C. Hellinga, A.A.J.C. Schellen, J.W. Mulder, M.C.M. van Loosdrecht, J.J. Heijnen, 1998, The Sharon process: An innovative method for nitrogen removal from ammonium-rich waste water,Water Sci. Technol.,37, 9, 135-142.

S. Lackner, E.M. Gilbert, S.E. Vlaeminck, A.Joss, H.Horn, M.C.M. van Loosdrecht, 2014, Full-scale partial nitritation/anammox experiences–An application survey, Water Res, 55, 292-303.

A. Quaglia, B. Sarup, G. Sin, R. Gani, 2012, Integrated business and engineering framework for synthesis and design of enterprise-wide processing networks. Comput Chem Eng, 38, 213-223.

G. Tchobanoglous, F.L. Burton, H.D. Stensel, 2003, Wastewater engineering: Treatment and Reuse, McGraw-Hill Publishing, New York.

U. van Dongen, M.S.M. Jetten, M.C.M. van Loosdrecht, 2001, The Sharon-Anammox process for treatment of ammonium rich wastewater, Water Sci Technol, 44,1, 153-160.

A.I. Versprille, B. Zuurveen, Th. Stein, 1984, The A-B process: A novel two stage wastewater treatment system, Water Sci Technol, 17, 235-246.

B. Wett, A. Omari, S.M. Podmirseg, M. Han, O. Akintayo, M. Gómez Bradón, S. Murthy, C. Bott, M. Hell, I. Takács, G. Nyhuis, M. O'Shaughnessy, 2013, Going for mainstream deammonification from bench to full scale for maximized resource efficiency, WaterSciTechnol, 68,2, 283-289.

M.K.H. Winkler, R. Kleerebezem, J.G. Kuenen, J.Yang, M.C.M. van Loosdrecht, 2011, Segregation of biomass in cyclic anaerobic/aerobic granular sludge allows the enrichment of anaerobic ammonium oxidizing bacteria at low temperatures, Environ Sci Technol, 45, 7330-7337.

Krist V. Gernaey, Jakob K. Huusom and Rafiqul Gani (Eds.), 12th International Symposium on Process Systems Engineering and 25th European Symposium on Computer Aided Process Engineering.
31 May – 4 June 2015, Copenhagen, Denmark

An Integrated Framework for Controllability Assessment and Solvent Selection in Post-Combustion CO_2 Capture Processes

Theodoros Damartzis[a,b], Athanasios I. Papadopoulos[a], Panos Seferlis[a,b*]

[a]*Chemical Process and Energy Resources Institute (CPERI) – Centre for Research and Technology – Hellas (CERTH), Thermi-Thessaloniki 57001 Greece*
[b]*Department of Mechanical Engineering, Aristotle University of Thessaloniki, Thessaloniki 54124, Greece*
seferlis@auth.gr

Abstract

The current work addresses the assessment of alternative solvent/process flowsheet combinations in amine based CO_2 capture plants based on economic and static controllability criteria. Various amine solvent blends are employed within an integrated framework that supports optimal design while also considering process performance under multiple variations in process parameters and disturbances. Process operability is explored through the implementation of a multi-variable control scheme that prioritizes control objectives and resource utilization. The steady-state process behavior is investigated through nonlinear sensitivity analysis and quantified in terms of an overall operability index that encompasses the steady-state effort required by the control system to compensate for the effects of exogenous disturbances on the control objectives. Aqueous mono-ethanol-amine (MEA) and 3-amino-1-propanol (MPA) solutions employed in different flowsheet structure configurations enabling material and energy distribution options are evaluated in terms of economic and operability performance.

Keywords: CO_2 capture, optimal design, static controllability, amine solvents.

1. Introduction

CO_2 capture plants are generally required to operate under variable process conditions due to either variations in production levels dictated by both the preceding CO_2 generation plant and the capture plant operating strategy or the influence of unexpected exogenous disturbances. In order to ensure optimal performance and the satisfaction of the operating and economic specifications for such plants, reliable and efficient control systems are designed so that the effects of disturbances on the control objectives can be successfully alleviated. An integrated approach in the process and the control system design requires the investigation, assessment, and rank-ordering of a set of candidate flowsheet and control structure configurations under the presence of multiple and large in magnitude disturbances representing real-time operating scenarios.

The analysis is performed by a disturbance nonlinear sensitivity technique and reveals an inherent property of the process/control system (Seferlis and Grievink, 2001). Disturbance sensitivity analysis have been combined with process optimization by selecting suitable pairings among controlled and manipulated variables with the help of steady state gain matrices (McAvoy, 1999) and frequency domain calculations (Lewin, 1996). Ricardez-Sandoval et al. (2011) studied worst case scenarios during the integration of design and control for large-scale processes. Papadopoulos and Seferlis

(2009) have proposed a generic framework for integrated solvent selection, process design and controllability assessment using a sensitivity analysis approach.
Control strategies for CO_2 capture plants have been investigated by Panahi and Skogestad (2011, 2012) by implementing a self-optimizing control scheme that enables the tracking of the economically optimal process trajectory. Nittaya et al. (2014) have proposed plant-wide control structures based on relative gain array considerations, Léonard et al. (2013) explored the dynamics and control, and McDowell and Shah (2014) studied the dynamic behavior of complex capture configurations. The current work investigates the interactions among solvents for different flowsheet configurations and control structures under multiple disturbance variation through a systematic nonlinear sensitivity analysis.

2. Methodology

The employed approach involves a rigorous, effective, and systematic two-stage screening and evaluation method of CO_2 capture flowsheets and solvents, based on economic and controllability performance. Flowsheet configurations are initially selected based on an economic criterion through a design optimization stage (stage 1). The design optimization stage calculates the optimal flowsheet configuration utilizing a superstructure representation of the plant with flexible process models and operating conditions. A specific flowsheet is derived for each employed solvent in the capture plant. Obviously, all flowsheets are optimized subject to the same process targets and constraints.
However, CO_2 capture processes operate under essentially dynamic environments susceptible to variations in operating parameters and exogenous disturbances. Based on the overall operating policy the capture plant may function at variable capacity whereas disturbances may affect flue gas volumetric flow rate, composition and CO_2 concentration. The steady-state response of the capture process under the effect of simultaneous multiple disturbances of finite magnitude is assessed in a disturbance sensitivity stage (stage 2). For each combination of solvent/flowsheet the control objectives are defined. Such objectives may include the amount of captured CO_2, the purity of the CO_2 stream, the energetic penalty for the separation, and the replenishment of the solvent. These objectives are directly or indirectly linked with variables associated with the process itself. Following Seferlis and Grievink (2004) the disturbance sensitivity problem is formulated as:

$$\begin{aligned} &\underset{\mathbf{y},\mathbf{u}}{\text{Min}} \quad f = \left(\mathbf{y}-\mathbf{y}_{sp}\right)^{\mathbf{T}}\mathbf{W}_y\left(\mathbf{y}-\mathbf{y}_{sp}\right)+\left(\mathbf{u}-\mathbf{u}_{ss}\right)^{\mathbf{T}}\mathbf{W}_u\left(\mathbf{u}-\mathbf{u}_{ss}\right) \\ &\text{s.t.} \quad \mathbf{h}\left(\mathbf{x},\mathbf{y},\mathbf{u},\mathbf{p}\right)=\mathbf{0} \quad \mathbf{g}\left(\mathbf{x},\mathbf{y},\mathbf{u},\mathbf{p}\right)\le\mathbf{0} \\ &\qquad \mathbf{y}^{lb}\le\mathbf{y}\le\mathbf{y}^{ub}, \quad \mathbf{u}^{lb}\le\mathbf{u}\le\mathbf{u}^{ub} \end{aligned} \tag{1}$$

where $\mathbf{W}_y$ represents weights that are used to penalize the deviation of each controlled variable, $\mathbf{y}$, from their desired level value ($\mathbf{y}_{sp}$), whereas $\mathbf{W}_u$ represents the weights that penalize the deviations of manipulated variables, $\mathbf{u}$, from an optimal operating point ($\mathbf{u}_{ss}$). In addition, $\mathbf{x}$ denotes the state variable vector and $\mathbf{p}$ the vector of model parameters and exogenous disturbances. Problem (1) is solved for different values of the parameters vector by pathfollowing the parameterized Karush-Kuhn-Tucker optimality conditions of (1). The aggregate disturbance variation is represented by a single scalar variable, ζ, that acts as the coordinate in the disturbance space. A static controllability performance index constitutes the tool for the assessment and ranking of the alternative solvent/flowsheet/control structure combinations. The static controllability index Ω_{SC}

expresses the deviations of the controlled variables from target values in a least squares sense along the disturbance magnitude coordinate, ζ, and is defined as follows:

$$\Omega_{SC}(\zeta) = \sum_i w_{u,i}(\zeta) \left\| \frac{u_i^*(\zeta) - u_i^*(0)}{u_i^*(0)} \right\|^2 + \sum_i w_{y,i}(\zeta) \left\| \frac{y_i^*(\zeta) - y_i^*(0)}{y_i^*(0)} \right\|^2 \quad (2)$$

The weighting terms, w, in Equation 2 determine the significance of each calculated segment along the perturbation direction and set the hierarchy in achieving the set targets. Generally, from Equation 2, a large value for Ω_{SC} would imply large errors in the controlled variables during the dynamic transition from one steady state operating point to another. A predictor-corrector type of continuation method as implemented in PITCON (Rheinboldt, 1986) is used with ζ acting as the independent continuation parameter for the calculation of the optimal solution trajectory.

3. Controllability case study

Two different flowsheet structures and two amine solvents are evaluated using disturbance sensitivity analysis (Figure 1). The conventional flowsheet (CF) consists of the basic absorption-stripping loop. An alternative flowsheet with a double section stripper and an intercooled absorber (DSS-ICA) flowsheet combines the beneficial effect of material redistribution in the stripper with temperature control in the absorber (Damartzis et al., 2014).

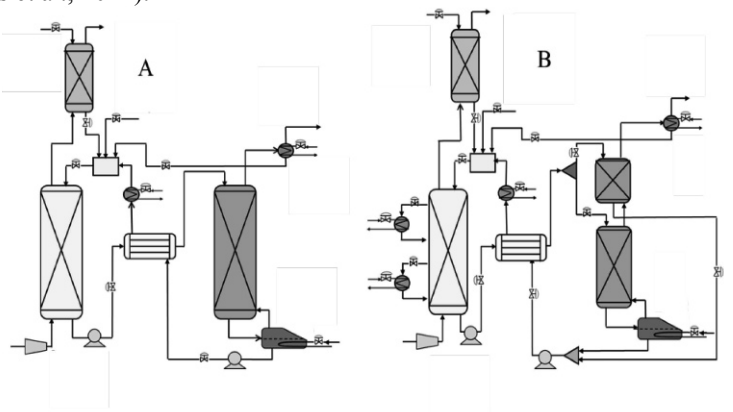

Figure 1. CF (A) and DSS-ICA (B) flowsheet configurations

A flue gas stream typical in quicklime production units is treated by aqueous solutions of monoethanolamine (MEA) 30 % wt and 3-amino-1-propanol (MPA) 30 % wt in the presented CO_2 capture flowsheets. In both cases the controlled variables constituting the process targets include: (a) the CO_2 capture efficiency (% CO_2 captured), (b) the lean stream temperature, and (c) the lean stream loading. Manipulated variables that are used in order to achieve the process targets include: (a) the reboiler duty, (b) the cooler duty, (c) the water and amine make-up flows and in the case of the DSS-ICA flowsheet (d) the intercooler duties and (e) the split ratio of the stream splitter. Manipulated variable upper bounds of 20% the nominal values calculated in the optimization stage are imposed except the reboiler duty where only a 5% upper bound is imposed. The tight bound in the reboiler duty simulates a constrained situation, which aims to examine the behavior of the process/control system under a severe lack of resources The examined

disturbance scenario involves a total increase in the flue gas stream flow rate by 20%, with a simultaneous increase of 10% in the flue gas inlet temperature (Figure 2). Emphasis is given in the achievement of a 90% CO_2 capture level enforced by applying a large weight in the respective entries of $\mathbf{W}y$ in Equation 1.

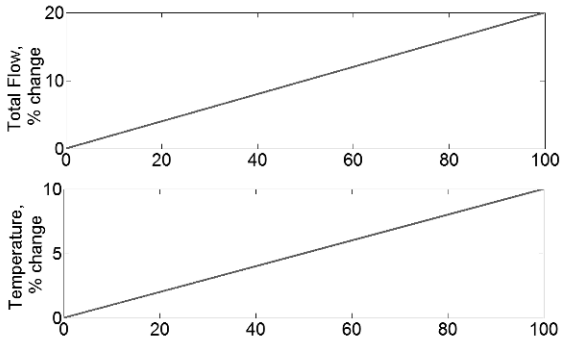

Figure 2. Change in flue gas stream properties in the disturbance scenario. The abscissa represents the independent continuation ζ variable.

4. Results and discussion

The reboiler duty response is shown in Figure 3 with the strict bound imposed being clearly visible. The MPA/DSS-ICA combination seems to handle the disturbance slightly better than the other tested combinations as it exhibits a smaller initial slope during the increment of the reboiler duty. This is attributed to the additional resources available in the DSS-ICA flowsheet (e.g., use of intercoolers) to compensate for the increased flue gas temperature. MPA also seems to be able to handle the disturbance in a more efficient way than MEA, in terms of reboiler duty use, for both flowsheet configurations as indicated by the static behavior in Figures 3-8.

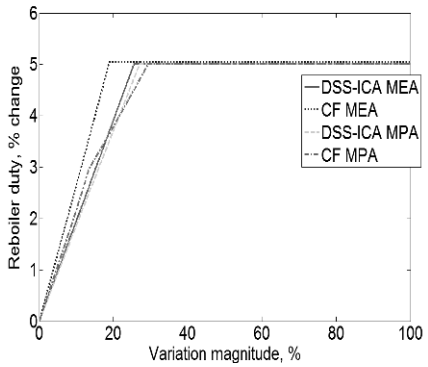

Figure 3. Reboiler duty variation.

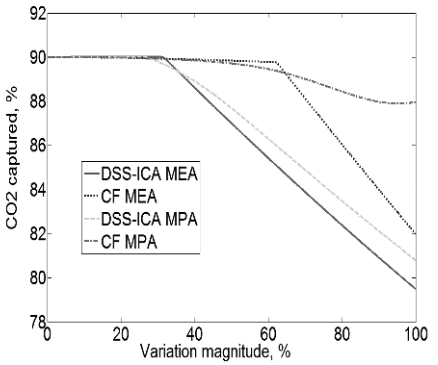

Figure 4. CO_2 capture variation.

The CO_2 capture efficiency as presented in Figure 4 strongly favors the MPA/CF combination. Sharp slope changes in Figure 4 can be explained by considering the responses in the rest of the process resources. Indeed, these changes in the slope occur when some other degree of freedom (manipulated variable) are lost due to saturation. Specifically, for the MEA/CF case, this corresponds to the upper bound of the cooler duty (Figure 5), whilst for both DSS-ICA cases, the CO_2 capture efficiency starts to

drop as soon as both intercoolers reach their upper bound (Figure 6). A diversification is also observed between the two solvents in terms of intercooler usage. It is observed that the MEA plant preferentially utilized both intercoolers in an effort to maintain the captured CO_2 close to the set point; however the result was worse than in the case of the MPA plant by almost 2%.

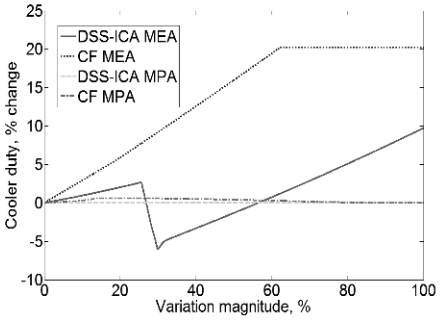

Figure 5. Cooler duty variation

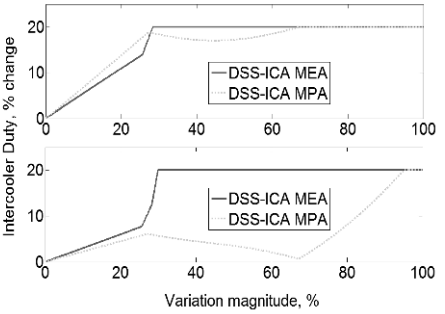

Figure 6. Intercooler duty variation

A key parameter in the operation of the capture plant is the amount of make-up solvent needed to compensate for the lost amine in the vapor phase (Figure 7). Amine make-up is a decisive factor that strongly affects the total operating process cost together with the reboiler duty. It is therefore imperative to maintain low flow rates in the make-up streams in the process to keep the cost at acceptable levels. It is observed that the combination of MPA/DSS-ICA flowsheet achieves low amine make-up flowrates and hence records a superior economic performance over the other combinations.

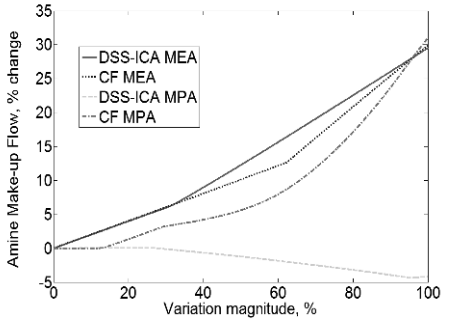

Figure 7. Amine make-up flow variation

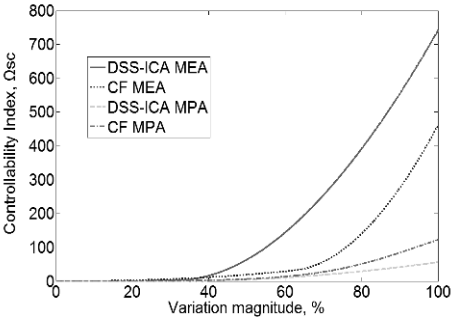

Figure 8. Controllability index variation

Overall, the superiority of the MPA/DSS-ICA pair in terms of disturbance handling is clearly visible in Figure 8, which shows the response of the operability index Ω_{SC} over the extent of the disturbance magnitude variation. Not only the MPA/DSS-ICA combination results to small Ω_{SC} throughout the disturbance span leading to a better disturbance handling, but also both MPA cases show decreased values compared to the cases where the MEA solvent is used. The reason of the superior performance the MPA plant has over the MEA plant can be attributed to the low sensitivity the CO_2 loading behavior shows as conditions such as temperature and CO_2 partial pressure change.

5. Conclusions

A systematic, rigorous, and efficient procedure for the evaluation, rank ordering, and screening of alternative combinations of solvents, process flowsheet, and control structure configurations of CO_2 capture plants has been presented. The ability of the solvent-flowsheet-control structure configurations to compensate for the effects of frequently occurring disturbances due to variable operating conditions is investigated thoroughly with an example testing the integrity of the control system to simultaneous exogenous disturbances. The MPA/DSS-ICA flowsheet exhibited the best performance among the explored plants. The controllability study acts complementary to the solvent selection and the design optimization steps and adds another dimension in which the plant performance must be evaluated and analyzed.

Acknowledgements

The authors would like to thank Prof. Claire Adjiman, Dr. Alexandros Chremos, Prof. Amparo Galindo, and Prof. George Jackson of Imperial College London for providing the SAFT-VR thermodynamic models for the tested solvents. The financial support of the European Commission through project FP7-ENERGY-2011-282789 is gratefully ackowledged.

References

T. Damartzis, A.I. Papadopoulos, P. Seferlis, 2014, Optimum synthesis of solvent-based post-combustion CO_2 capture flowsheets through a generalized modeling framework, Clean Technologies and Environmental Policy, 16,1363–1380.

G. Léonard, B.C. Mogador, S. Belletante, G. Heyen, 2013,. Dynamic modelling and control of a pilot plant for post-combustion CO_2 capture, Computer Aided Chemical Engineering, 32, 451–456.

D. R. Lewin, 1996, A simple tool for disturbance resiliency diagnosis and feedforward control design, Computers and Chemical Engineering, 20, 13–25.

T.J. McAvoy, 1999, Synthesis of plant-wide control systems using optimization, Industrial & Engineering Chemistry Research, 38, 2984.

N. McDowell, N. Shah, 2014, Dynamic modelling and analysis of a coal-fired power plant integrated with a novel split-flow configuration post-combustion CO_2 capture process, International Journal of Greenhouse Gas Control 27, 103–119.

T. Nittaya, P.L. Douglas, E. Croiset, L.A. Ricardez-Sandoval, 2014, Dynamic modeling and control of MEA absorption processes for CO_2 capture from power plants, Fuel, 116, 672-691.

M. Panahi, S. Skogestad, 2011, Economically efficient operation of CO_2 capturing process part I: Self-optimizing procedure for selecting the best controlled variables, Chemical Engineering and Processing 50, 247-253.

M. Panahi, S. Skogestad, 2012, Economically efficient operation of CO_2 capturing process. Part II. Design of control layer, Chemical Engineering and Processing 52, 112– 124.

A.I. Papadopoulos, P. Seferlis, 2009, A framework for solvent selection based on optimal separation process design and controllability properties, Computer Aided Chemical Engineering 26 , 177-18.

W.C. Rheinboldt, 1986, Numerical Analysis of Parameterized Nonlinear Equations, J. Wiley & Sons, New York.

L.A. Ricardez-Sandoval, P.L. Douglas, H.M. Budman, 2011, A methodology for the simultaneous design and control of large-scale systems under process parameter uncertainty, Computers and Chemical Engineering, 37, 307-318.

P. Seferlis, J. Grievink, 2001, Process design and control structure screening based on economic and static controllability criteria, Computers and Chemical Engineering, 25, 177-188.

P. Seferlis, J. Grievink, 2004, Process design and control structure evaluation and screening using nonlinear sensitivity analysis, Computer Aided Chemical Engineering, 17, 326-351.

Krist V. Gernaey, Jakob K. Huusom and Rafiqul Gani (Eds.), 12th International Symposium on Process Systems Engineering and 25th European Symposium on Computer Aided Process Engineering.
31 May – 4 June 2015, Copenhagen, Denmark

Using Product Driven Process Synthesis in the Biorefinery

Alexandra Kiskini[a,b], Edwin Zondervan[b], Peter Wierenga[a], Edwin Poiesz[c], Harry Gruppen[a]

[a]*Laboratory of Food Chemistry, Wageningen University, Postbus 17, Wageningen, 6700AA, The Netherlands*
[b]*Department of Chemical Engineering and Chemistry, Eindhoven University of Technology, P.O. Box 513, Eindhoven, 5600MB, The Netherlands*
[c]*Cosun Food Technology Centre, Oostelijke Havendijk 15, Roosendaal, 4704RA, The Netherlands*

Abstract

In this work, we propose the use of the product-driven process synthesis (PDPS) methodology for the product and process design stage in biorefinery. The aim of the biorefinery is to optimize the total use of the whole feedstock – with focus being on various products simultaneously – rather than to maximize the extraction yield of one single product. The challenge is therefore two-fold; first to identify the main compounds of interest, i.e. the products of the biorefinery, and second to design a process scheme that will allow for an optimal quantity and quality of the identified compounds. To illustrate how PDPS can be used in biorefinery a case study based on sugar beet leaves is described. The identification of the main compounds of interest is based on the functionalities that they can deliver in the final applications, rather than on their quantities in the feedstock. To design the process scheme for the extraction of the selected compounds, task networks, currently used for the extraction of the individual compounds of interest, are used after adaptations. These adaptations are done on the basis of the qualitative and/or quantitative changes that certain tasks – used for the extraction of one compound – may cause on another compound of interest. By using the sugar beet leaves biorefinery case, we show that the PDPS methodology can be a useful tool for structured decision making during the product and process design stage in biorefinery.

Keywords: biorefinery, sugarbeet-leaves, functionalities, product-driven-process-synthesis.

1. Introduction

In the last fifteen years the biorefining industry has gained great momentum. The biorefinery concept describes the process for an integrated extraction of various compounds from one feedstock. The aim of the process is to optimize the total use of the whole feedstock (focus on various products) rather than to maximize the extraction yield of one single product. As such, the volume of the waste is decreased and the economic potential of the process increases, given that the value of the separated compounds is significantly higher than the value of the feedstock.

The challenge is then to design a process scheme that will allow optimization of the different process parameters to yield an optimal quantity as well as quality of the different compounds. The first step in this process is to define which products should be obtained. For instance, sugarbeet leaves contain different types of proteins, carbohydrates, lipids, minerals, phenolics and other minor compounds that can be used in various applications (e.g. pastry products, mayonaise) and in different fields (e.g. food, feed, non-food). The second step is to identify which process steps can lead to obtaining these products. Thus, the main difference in biorefinery compared to traditional approaches is that the sequence of activities in the value chain needs to be inverted. This change in approach has been already acknowledged by other researchers, but has not been studied in details (Marquardt *et al*., 2010).

The product driven process synthesis (PDPS) methodology was introduced to describe the production of a set of (structured) products starting from several raw materials (Bongers and Almeida-Rivera, 2012). This methodology combines the conceptual process synthesis methodology with the product design. It consists of a number of hierarchical levels, where decisions related to the framing level of the design until the design of the task networks and the equipment needed are made (Bongers and Almeida-Rivera, 2012). The aim of this work is to demonstrate how PDPS could be used in the field of biorefinery. Given the fact that PDPS has been originally designed for the production of a set of products from a set of raw materials, it is conceivable that there are some limitations in its application in biorefinery. Therefore, we also propose some adaptations that allow for a successful application of the PDPS in biorefinery. In the following part, we present a case of a sugar beet leaves biorefinery as an example to demonstrate the main steps and adaptations in this approach. As an illustration, only the first four levels of PDPS are discussed (Bongers and Almeida-Rivera, 2012). Depending on interest and the starting material, different choices can be made. Notice that, for this case study, in each step choices have been made that in other cases can be made in a different way leading to different results.

2. PDPS application in sugar beet leaves biorefinery

2.1. Framing level

Sugar beet leaves are currently not used in the industry. After the sugar beets are harvested, the sugar beet leaves are embed in the soil. In this way, a plethora of compounds, such as proteins, carbohydrates, phenolic compounds, lipids, minerals that are present in the sugar beet leaves are left unexploited. These compounds, once extracted from the leaves could be used in various applications, and thus increase the value of the feedstock. Taking into account, for instance, that in the Netherlands the sugar beets cultivation covers an area of 73,200 Ha, it becomes clear that the economic output that could be potentially derived from the exploitation of the sugar beet leaves is significant (FAOSTAT, 2014).

The challenge is then to identify the main compounds of interest; i.e. the output/products of the biorefinery. To facilitate this process of identifying the compounds of interest, we propose the addition of a set of hierarchical steps, as part of this PDPS level, that can lead to a pre-selection of the main compounds of interest in a structured way. The first step in this process is the decomposition of the sugar beet leaves in major and minor compound classes (e.g. proteins, minerals), as shown in Table 1. Based on the compounds identified in sugar beet leaves, a list with commercially available products containing the same or similar compounds is composed. The functionality of each of these compounds in the final product is

identified and added to this list. The functionalities as described and presented in this list refer both to the health-related functionalities (e.g. lowering the glycemic index) and to the techno-functional properties (e.g. emulsifying capacity) of the compounds. It is important to note that the same functionality can be derived from more than one compounds. In principle, the different functionalities can be further assigned to different sales prices. The selection of the compounds of interest is then based on both the quantity of the compounds present in sugar beet leaves and on their potential price. In this respect, both compounds present in sugar beet leaves in high quantities that could potentially yield a low price and compounds present in low quantities that could potentially yield high prices are selected. We here identify three main compounds of interest, namely proteins, carbohydrates and phenolic compounds.

Table 1. Chemical composition of sugar beet leaves (% w/w in dry matter basis)

Protein	Neutral carbohydrates	Uronic acids	Lipids	Chlorophyll	Lignin	Ash	Phenolics	***Total***
33.1 (±0.4)	19.5 (±0.6)	7.7 (±1.4)	8.0 (±1.0)	0.5 (±0.2)	10.1 (±0.6)	15.2 (±0.5)	4.8 (±0.1)	98.9

Table 2. Example of compounds used in various commercial preparations and the link to the specific functionalities that they deliver in these preparations.

	Compounds	Functionality	Applications
Proteins		**Food**	
	Caseinates	Foaming agent	Desserts
	Caseinates	Emulsifying agent	Desserts
	Egg yolk	Emulsifying agent	Confectionary/Dressings
	Soy proteins	Binding agent	Gels
	...	...	...
		Feed	
	Soy proteins	Nutrition	Animal feed
	...	...	...
		Non-food	
	Soy proteins	Nutrition	Culture media
	...	...	...
Carbohydrates		**Food**	
	Cellulose	Gelling agent	Jam
	Cellulose	Water binding	Jam
	Glactooligosaccharides	Nutrition	Prebiotics
	Starch	Viscosifying	Soups/Sauces
	Sucrose	Taste	Sweetener
	...	...	...
		Non-food	
	Cellulose	Water binding	Diapers
	Galactomannan	Emulsions stabilizer	Cosmetics
	...	...	...

2.2. Consumer preferences and product ideas

The output of the sugar beet leaves biorefinery are products that are used in industry as ingredients for other products, and they can thus be used as alternatives for existing ingredients (food, feed, non-food). Hence, a list of product ideas can be extracted from

analysis of the currently available industrial preparations (e.g. starches, protein isolates etc.) that are presented in Table 2. Using this list, we define the final products of the sugar beet leaves biorefinery as following:

a) Proteins for food applications
b) Carbohydrates for non-food applications
c) Phenolic compounds for non-food applications

The consumer preferences can also be derived from the analysis of the currently available industrial preparations ("applications" as shown in Table 2). For instance, a coffee creamer (based on whey protein) is a white powder, that dissolves easily in water and does not aggregate upon heating. Based on these characteristics we could extrapolate what the consumer preferences were, and thus define the consumer preferences for the proteins derived from the sugar beet leaves. The next step is to link the consumer preferences to product specifications that can be controlled and objectively measured. To form this link typically a house-of quality is used (Benner *et al.*, 2003). In Table 3, the characteristics (product specifications) of the three products of the sugar beet leaves biorefinery are summarized.

Table 3. Example of typical product characteristics given a specific field of application.

Proteins (food applications)	**Carbohydrates (non-food applications)**	**Phenolics (non-food applications)**
Free of color	Type/modifications	Purity
No off-taste	Solubility	
Solubility	Color	
Nutritional quality (amino acid balance)	Water binding capacity	
Digestibility	Purity	

2.3. Input-Output level

The input of the process refers to the sugar beet leaves. The specifications of the input are thus described by the chemical composition of the sugar beet leaves, as shown in Table 1. The output of the process refers to the three products (proteins, carbohydrates, phenolics) and their characteristics, as they have been defined in the previous levels.

Task networks

Since the most commonly used plant protein source is soy, we based the task networks for the extraction of proteins from sugar beet leaves on the typical task networks used for the extraction of proteins from soy (Figure 2a) (Kuipers *et al.*, 2005). The extraction of carbohydrates and phenolics presented here are based on protocols currently used for the extraction of these compounds from stover and tea leaves, respectively (Figure 2b, 2c) (van Dongen *et al.*, 2011, Lin *et al.*, 1996).

Table 4. Example of fundamental steps during the extraction of proteins, carbohydrates and phenolics from sugar beet leaves and their expected effects.

Compounds	**Fundamental steps**	**Effect**
Proteins	Heating	Denaturation (loss of solubility)
Carbohydrates	Heating pH>10	Depolymerization (low water binding capacity)
Phenolics	Heating pH>10	Oxidation Polymerization

The next step is to integrate the three task networks used for the extraction of individual compounds to one integrated task network that describes the simultaneous or sequential extraction of the three compounds from the sugar beet leaves. This integration is rather complex due to the different characteristics of the final products For instance, a task network designed to yield the maximum quantity and/or quality of one output might hinder the quantity and/or quality of another output. In the same line, the loss of quality or quantity of one product may be compensated by the increase in quality or quantity of another product. To tackle this challenge, we propose an extra step before the final design of an integrated task network, which is the identification of the critical tasks during the extraction of the individual outputs. In Table 4 the fundamental tasks that could affect the characteristics of the individual compounds are identified (Table 4).
Using these fundamental tasks as a guideline as well as some heuristics and domain knowledge, one integrated task network is designed (Figure 3). It is conceivable that in practice more than one integrated task networks can be designed based on different fundamental tasks. The next levels of the PDPS can be further used for the selection and optimization of one final integrated task network, based also on experimental data. In addition, the equipment needed for the process can be also selected and designed.

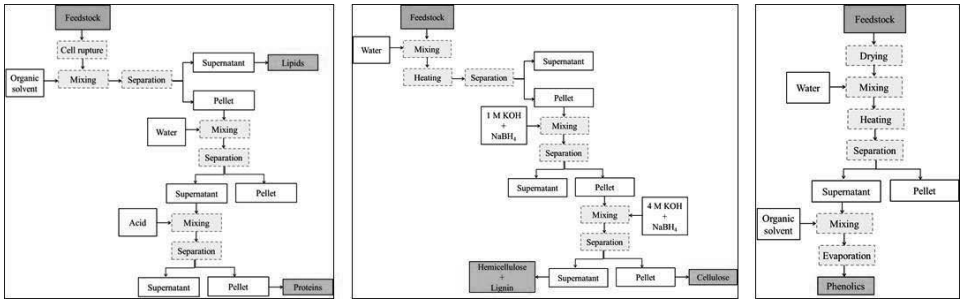

a b c

Figure 2. Example of Individual task networks for extraction of proteins (a), carbohydrates (b) and phenolics (c) from sugar beet leaves.

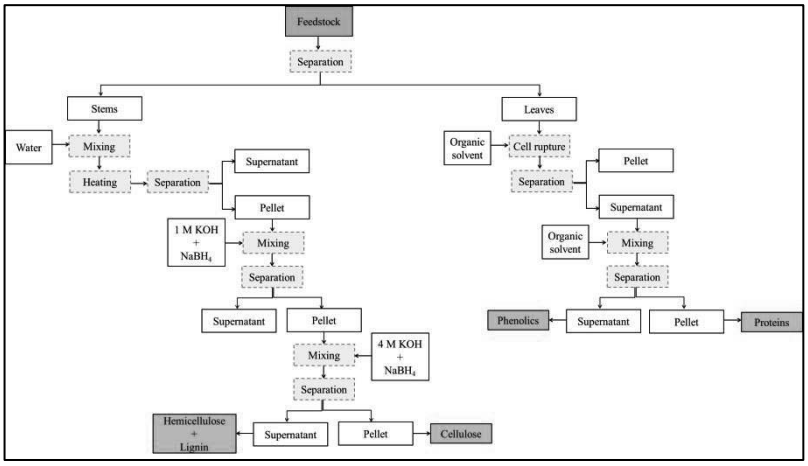

Figure 3. Example of an integrated task network for extraction of proteins, carbohydrates and phenolics from sugar beet leaves.

3. Conclusions

The challenge in designing a biorefinery is related to the various outputs, differing in their physical characteristics, deriving from one initial input (feedstock). To tackle this challenge, the first step is to invert the sequence of activities in the value chain by using the adapted version of PDPS that is described in this manuscript. The adaptations refer both to the identification of the main compounds of interest, i.e. the outputs of the biorefinery and the design of an integrated task network for the different products. To facilitate this process of identifying the main compounds of interest, we propose to link the compounds present in the feedstock to functionalities that are typically ascribed to them in different industrial applications. The benefit of this process is that the selection of the major compounds of interest is not merely based on their quantity but also on their potential sales price, which is different for different functionalities. The task networks developed and optimized for the extraction of independent compounds, do not yield the same results when used as parts of an integrated task network. The identification of the fundamental tasks before the task network integration is thus an extra fundamental step added in the traditional PDPS that can facilitate the selection of one integrated task network. In conclusion, the PDPS methodology can be a useful tool for structured decision making during the product and process design stage in biorefinery.

Acknowledgements

This work has been carried out within the framework of ISPT (institute for sustainable process technology). Dr. Cristhian Almeida-Rivera is gratefully acknowledged for his critical feedback on the manuscript.

References

B. J. H., Kuipers, G. A., van Koningsveld, A. C.,Alting, F., Driehuis, H.Gruppen and A. G. J., Voragen, 2005. Enzymatic hydrolysis as a means of expanding the cold gelation conditions of soy proteins. J Agric Food Chem 53, 1031-1038.

F. E. M., van Dongen, D., van Eylen, and M. A., Kabel, 2011. Characterization of substituents in xylans from corn cobs and stover. Carbohydr Polym86, 722-731.

FAOSTAT 2014. Sugar beets area harvested (Ha) in 2013 in Netherlands.

M., Benner, A. R., Linnemann, W. M. F., Jongen, P., Folstar, 2003. Quality Function Deployment (QFD) - can it be used to develop food products?. Food Qual Prefer 14, 327-339.

P. M. M., Bongers and C., Almeida-Rivera, 2012. Product Driven Process Design Method. Proceedings of the 11th International Symposium on Process Systems Engineering.

W., Marquardt, A., Harwardt, M., Hechinger, K., Kraemer, J., Viell, and A., Voll, 2010. The biorenewables opportunity - toward next generation process and product systems. AlChe 56, 2228-2235.

Y. L., Lin, I. M., Juan, Y. L, Chen, Y. C., Liang, and J. K., Lin, 1996. Composition of polyphenols in fresh tea leaves and associations of their oxygen-radical-absorbing capacity with antiproliferative actions in fibroblast cells. J Agric Food Chem 44, 1387-1394.

Krist V. Gernaey, Jakob K. Huusom and Rafiqul Gani (Eds.), 12th International Symposium on Process Systems Engineering and 25th European Symposium on Computer Aided Process Engineering.
31 May – 4 June 2015, Copenhagen, Denmark

Integrating expanders into sub-ambient heat exchanger networks

Chao Fu, Truls Gundersen

Department of Energy and Process Engineering, Norwegian University of Science and Technology,Kolbjoern Hejes vei 1.A, NO-7491 Trondheim, Norway

Abstract

The Appropriate Placement of expanders in heat exchanger networks is complex, since both heat and work are involved. In addition, the role of streams (as hot or cold) may temporarily change. This paper proposes four theorems for the integration of expanders into sub-ambient heat exchanger networks with a target of minimizing exergy consumption. A systematic methodology for heat exchanger network design including expanders is developed on the basis of traditional Grand Composite Curves (GCCs). It is concluded that in order to achieve a design with minimum exergy consumption, expansion should preferably be done at pinch temperatures, and/or ambient temperature.

Keywords: Appropriate Placement; Pinch Analysis; Pinch Expansion; Exergy.

1. Introduction

The concept of Appropriate Placement is fundamental in Pinch Analysis and addresses how different pieces of equipment should be integrated with heat recovery processes, also referred to as Correct Integration (Linnhoff and Vredeveld, 1984; Linnhoff and Parker, 1984). The placement of expanders refers to the inlet temperature of expansion processes. The appropriate placement of expanders has been discussed by Aspelund *et al.* (2007) and Gundersen *et al.* (2009), and formulated as the following heuristic rule: expansion provides cooling to the system and should thus preferably start at pinch temperature. However, such observations are not based on strict mathematical or thermodynamic analysis. When designing a heat exchanger network (HEN) including expanders, the application of the rule is not straightforward.

A systematic methodology for in the integration of expanders into sub-ambient HENs is developed in this paper. Since both heat and power are involved, the objective of this work has been to minimize exergy consumption for the integrated processes. A set of theorems has been proposed for sub-ambient processes, indicating that Pinch Expansion (expander inlet is at pinch temperature T_{PI}) is the preferred scheme with respect to exergy consumption. A graphical design procedure is developed, based on the Grand Composite Curve (GCC).

2. Theorems

The following four theorems are proposed for the integration of expanders into sub-ambient HENs (the proof is not included due to space limitation):

(1) A HEN design with Pinch Expansion consumes the smallest amount of exergy if the following conditions are satisfied: (i) the outlet temperature of Ambient Expansion (expansion starts at ambient temperature T_0), $T_{exp,0}$, is higher than cold utility temperature (T_{CU}), and (ii) Pinch Expansion does not introduce a new pinch point.

(2) After the cooling demand has been satisfied by Pinch Expansion, the remaining expansion should be done at T_0 if $T_{exp,0} \geq T_{PI}$.

(3) The cooling by Ambient Expansion should be utilized before using Pinch Expansion, if new pinch points are introduced by Pinch Expansion and $T_{exp,0} < T_{PI}$.

(4) Ambient Expansion should be used if $T_{exp,0} < T_{CU}$.

3. Design procedure

Theorem 1 indicates that new pinches may be introduced when Pinch Expansion is used. The maximum fraction of the stream that can be expanded at the pinch, $(mc_p)_{exp,PI,\max}$, is thus limited. Figure 1 shows the GCC for Pinch Expansion without pressure manipulation. Modified temperatures (T') are used, which means that for cold streams $T' = T + 0.5\Delta T_{\min}$, and for hot streams $T' = T - 0.5\Delta T_{\min}$, where $\Delta T_{\min}$ is given as the minimum temperature difference for heat transfer. The outlet temperature of Pinch Expansion is $T'_{exp,PI}$. A temperature is defined as a Potential Pinch Point if it may create a new pinch after a portion of the cooling effect caused by Pinch Expansion is included. The following temperatures are Potential Pinch Points: (i) the convex kink points on the GCC in the region between $T = T'_{PI}$ and $T = T'_{exp,PI}$ (such as points *b* and *c*); (ii) the point $T = T'_{exp,PI}$ on the GCC (point *e*) or the point with the lowest temperature on the GCC (point *f*) if $T'_{exp,PI}$ is lower than this temperature; (iii) the intersection point between the constant temperature line $T = T'_{exp,PI}$ and a pocket (point *g*) in the GCC.

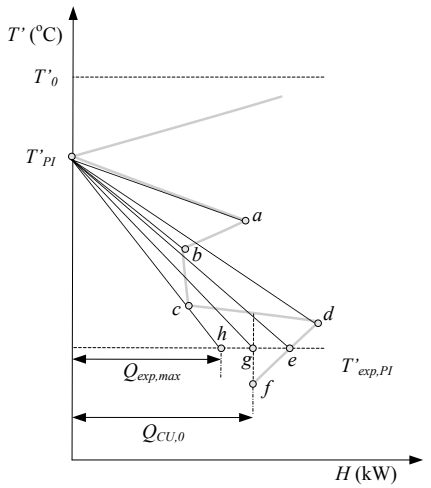

Figure 1. GCC without pressure manipulation

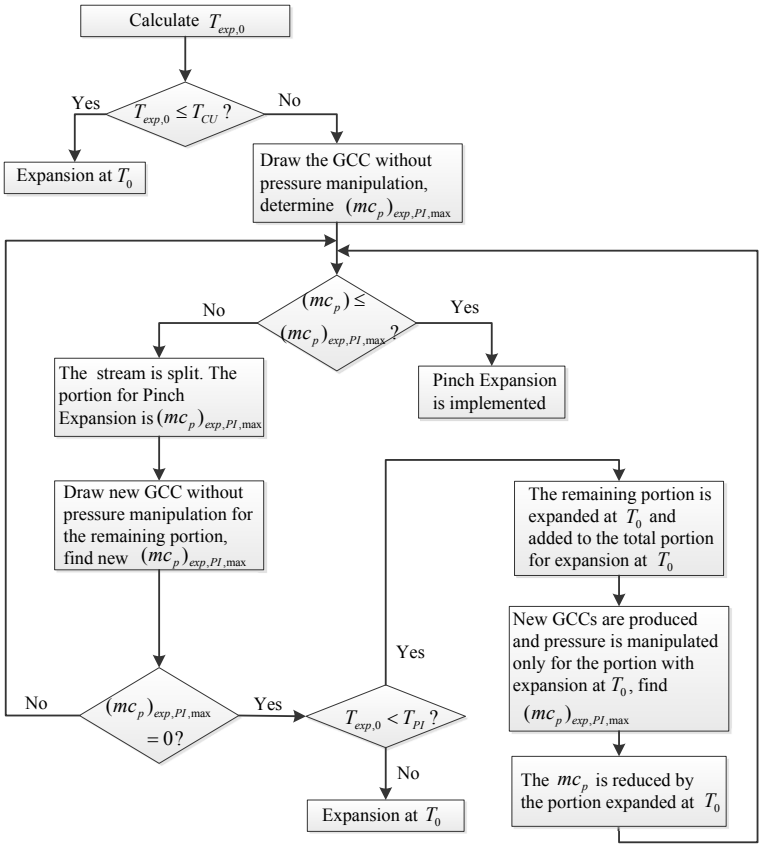

Figure 2. Design procedure for integrating expanders into sub-ambient HENs

The maximum fraction of the stream that can be expanded at the pinch, $(mc_p)_{exp,PI,\max}$, is determined by the following steps: (1) starting at the pinch point (T'_{PI}), draw lines between the pinch point and Potential Pinch Points and extend the line with the largest negative slope until it intersects with the constant temperature line ($T = T'_{exp,PI}$). The corresponding cooling demand $Q_{exp,\max}$ at the intersection (point *h* in Figure 1) is then determined; (2) this cooling demand is equal to the maximum work resulting from Pinch Expansion, and $(mc_p)_{exp,PI,\max}$ can thus be determined as $Q_{exp,\max}/(T'_{PI} - T'_{exp,PI})$. If the mc_p of the stream to be expanded is larger than $(mc_p)_{exp,PI,\max}$, a new pinch point will be created. Stream splitting is required and the fraction of the stream using Pinch Expansion is $(mc_p)_{exp,PI,\max}$.

On the basis of the four theorems, a design procedure has been developed and is illustrated in Figure 2. The first step is to calculate $T_{exp,0}$ and compare it with T_{CU}. According to Theorems 1 and 4, expansion should start at T_0 if $T_{exp,0} < T_{CU}$ and at T_{PI} if $T_{exp,0} \ge T_{CU}$. When Pinch Expansion is used, the maximum portion that can be

expanded, $(mc_p)_{exp,PI,\max}$, is limited by the cooling demand below pinch. Using the concept of Potential Pinch Points, $(mc_p)_{exp,PI,\max}$ can be determined. According to Theorem 1, the entire stream is expanded at T_{PI} if its heat capacity is smaller than $(mc_p)_{exp,PI,\max}$. Otherwise, the stream is split and Pinch Expansion is used for the portion $(mc_p)_{exp,PI,\max}$. A new GCC is then produced, where the pressure manipulation of the portion with Pinch Expansion, i.e. the heating or cooling of the portion from T_s to T_{PI} before expansion and from $T_{exp,PI}$ to T_t after expansion are included. The pressure manipulation of the remaining portion should not be included. The portion available for expansion at new pinch temperatures can then be determined. The procedure is repeated until either the entire stream has been expanded or the cooling demand has been completely satisfied (i.e. the pinch problem has become a threshold problem, $(mc_p)_{exp,PI,\max}=0$). In the latter case, according to Theorem 2, the remaining portion of the stream is expanded at T_0 if $T_{exp,0} \geq T_{PI}$. Otherwise, and according to Theorem 3, the portion for expansion at the original T_{PI} should be reduced and an iteration procedure is required: A new GCC is produced by including pressure manipulation only for the portion of the stream with expansion at T_0 (the other portion of the stream is included in the GCC without pressure manipulation), and the procedure for implementing Pinch Expansion is repeated. The procedure stops if the entire stream has been expanded, otherwise the portion for expansion at T_0 increases until $T_{exp,0}$ is higher than the new pinch temperatures (which means that the pinches above $T_{exp,0}$ have been removed). When the cooling demand has been completely satisfied by expansion at the new pinch point(s) below $T_{exp,0}$, the remaining portion of the stream should be expanded at T_0.

According to the design procedure, it can be observed that in order to achieve a design with minimum exergy consumption, expansion of streams should preferably be implemented at pinch temperatures and/or ambient temperature.

4. Example

The stream data is shown in Table 1, indicating that a hot stream (H1) is expanded. The following assumptions are made: (1) expander polytropic efficiency=1, (2) $\Delta T_{\min}=4$ K, (3) T_0=288 K, and (4) the fluid to be expanded is ideal gas with constant specific heat ratio κ=1.4. $T_{exp,0}$ is calculated to be 210.4 K> T_{CU}=120 K, thus Pinch Expansion should be used. A first case (O) without pressure manipulation is studied to find T_{PI}= 242 K (for hot streams) and $(mc_p)_{exp,PI,\max}$. The GCCs for Case O and the following cases are not presented due to space limitation.

The following cases are compared: Case A - Ambient Expansion is used and $T_A = T_s = T_0$ (288 K); Case B - Pinch Expansion is used for the entire stream; Case C - stream splitting is used: the portion for Pinch Expansion is $(mc_p)_{exp,PI,\max}$ and the remaining portion is expanded at T_0 (expansion at the new pinch is thus not applied); Case D - stream splitting is used: expansion at the original and new pinches are applied

Table 1. Stream data

Stream	T_s, K	T_t, K	mc_p, kW/K	ΔH, kW	p_s, bar	p_t, bar
H1	288	124	4	656	3	1
H2	242	148	9	846	-	-
C1	120	208	7	616	-	-
C2	168	284	8	928	-	-
Heat source	288	288	-	-	-	-
Cooling source	120	120	-	-	-	-

until the cooling demand has been satisfied, and the remaining portion is expanded at T_0 (thus Ambient Expansion as mentioned in Theorem 3 is not utilized); Case E - the proposed procedure is used, i.e. the cooling resulting from Ambient Expansion is utilized before Pinch Expansion is used. Stream H1 becomes different new streams in each case, as shown in Table 2. For example, H1 is split into three portions in Case D: the portion α=1.07 kW/K is expanded after being cooled from T_s to T_{PI}, and then cooled from $T_{exp,PI}$=176.8 K to T_t; the second portion β=1.56 kW/K is expanded after being cooled from T_s to the new pinch $T_{PI,new}$=172 K, and then cooled from the outlet temperature of this expansion $T_{exp,PI,new}$=125.7 K to T_t; the remaining portion γ=1.37 kW/K is expanded at T_0 (= T_s) and then cooled from $T_{exp,0}$=210.4 K to T_t.

Table 2. Stream data for H1

Cases	T_s, K	T_t, K	mc_p, kW/K	ΔH, kW	p_s, bar	p_t, bar
Case A						
H1	210.4	124	4	345.6	1	1
Case B						
H1_1	288	242	4	184	3	3
H1_2	176.8	124	4	211.2	1	1
Case C						
H1_α1	288	242	1.07	49.2	3	3
H1_α2	176.8	124	1.07	56.5	1	1
H1_β	210.4	124	2.93	253.2	1	1
Case D						
H1_α1	288	242	1.07	49.2	3	3
H1_α2	176.8	124	1.07	56.5	1	1
H1_β1	288	172	1.56	181.0	3	3
H1_β2	125.7	124	1.56	2.7	1	1
H1_γ	210.4	124	1.37	118.4	1	1
Case E						
H1_β1	288	172	1.56	181.0	3	3
H1_β2	125.7	124	1.56	2.7	1	1
H1_γ	210.4	124	2.44	210.8	1	1

Table 3. Performance comparison

Cases	O	A	B	C	D	E
Hot utility demand, kW	184	424.4	374.8	411.1	290.3	303.6
Cold utility demand, kW	142	72	72	72	0	0
Pinch temperature, K	240	170	170	170	122	122
Expansion work, kW	-	310.4	260.8	297.2	248.1	261.3
Exergy consumption, kW	-	-209.6	-160.0	-196.4	-248.1	-261.3

The performance comparison is shown in Table 3. The exergy consumption in all cases is negative, indicating that exergy is produced. Case A (Ambient Expansion) is used as the basis for comparison. Direct Pinch Expansion for the entire stream (Case B) reduces the exergy production by 23.7%. When the cooling demand has been completely satisfied by Pinch Expansion (Case D), the exergy production increases by 18.4%. Maximum exergy production (a 24.7% increase) is achieved in Case E. Although less work is produced by expansion, the cooling demand has been completely satisfied by Pinch Expansion in both Cases D and E. As a result, the exergy consumption is smaller (or the exergy production is larger) compared to Case A.

5. Conclusions

A systematic methodology for the integration of expanders into sub-ambient heat exchanger networks has been developed. The objective has been to minimize exergy consumption (or maximize exergy production). Four theorems are proposed and used as the basis for the design. A straightforward graphical design procedure based on the Grand Composite Curve is presented. It is concluded that in order to achieve a HEN design with minimum exergy consumption, expansion should preferably be done at pinch temperatures and/or ambient temperature.

Acknowledgement

This publication has been produced with support from the BIGCCS Centre, performed under the Norwegian research program Centres for Environment-friendly Energy Research (FME). The authors acknowledge the following partners for their contributions: ConocoPhillips, Gassco, Shell, Statoil, TOTAL, GDF SUEZ and the Research Council of Norway (193816/S60).

References

A. Aspelund, D.O. Berstad and T. Gundersen, 2007, An Extended Pinch Analysis and Design procedure utilizing pressure based exergy for subambient cooling,Applied Thermal Engineering, 27, 16, 2633-2649.

T. Gundersen, D.O. Berstad and A. Aspelund, 2009, Extending Pinch Analysis and Process Integration into pressure and fluid phase considerations, Chemical Engineering Transactions, 18, 33-38.

B. Linnhoff and D.R. Vredeveld, 1984,Pinch technology has come of age, Chemical Engineering Progress, 80, 7, 33-40.

B. Linnhoff and S. Parker, 1984, Heat exchanger networks with process modification, IChemE Annual Research Meeting, Bath, UK.

Krist V. Gernaey, Jakob K. Huusom and Rafiqul Gani (Eds.), 12th International Symposium on Process Systems Engineering and 25th European Symposium on Computer Aided Process Engineering.
31 May – 4 June 2015, Copenhagen, Denmark

Water free XTL processes: Is it possible and at what cost?

Xinying Liu[a], Bilal Patel[b], Diane Hildebrandt[a,b]

[a]*Material and Process Synthesis Engineering, University of South Africa,PO Box X6, Florida, 0710, South Africa*
[b]*Department of Chemical Engineering, University of South Africa, PO Box X6, Florida 0710, South Africa*
liux@unisa.ac.za

Abstract

Coal to Liquid (CTL) processes have received renewed attention in recent years. However, these processes face significance challenges in terms of the very high water consumption, and high CO_2 emissions if Carbon Capture and Sequestration is not applied. Although the water consumption of a CTL process can be reduced when a closed cooling water system is applied and air cooling is used instead of cooling water, the overall mass balance for a CTL process still requires water as a feedstock(, to provide the hydrogen needed in the process. Our previous analysis shows that 1.3 tons of water is needed as feedstock to produce one ton of CH_2 assuming coal as pure carbon. On the other hand, when biomass is used in the XTL (X= Coal, Biomass, Natural Gas, Waste etc.) process, there is a potential that water is actually produced from the process. As the composition of biomass is close to a very low quality coal, it raises questions that for some low quality coal, it is possible that extra water is not really needed for the overall mass balance.

In this contribution, basic process synthesis tools including mass and energy balances are applied to investigate the possibility of a water free XTL process. It is found that as long as there is hydrogen in the feedstock, a water free XTL process is possible at the cost of a lower carbon efficiency as the result of imbalance of the hydrogen / carbon ratio in the feed. The region where a water free XTL process can be achieved with reasonable carbon efficiency is investigated. Addition of water in the feed can improve the carbon efficiency of the process, therefore a balance between the water requirements and carbon dioxide produced needs to be considered.

Keywords: XTL processes, - water consumption, process synthesis, carbon efficiency.

1. Introduction

Coal to liquid (CTL) process has received renewed attention in recent years. However, these processes face significant challenges in terms of the very high water consumption, and high carbon dioxide emissions, if Carbon Capture and Sequestration is not applied. Water shortages can be an issue when planning a new CTL plant especially since many undeveloped coal resources lie in areas with limited water supply.

It is interesting to note that although there have been some recent publications by King et.al. (2008), Mielke et. al. (2010), US DoE (2006) providing the water consumption figures of a CTL plant, all of them refer to a report prepared for the US Department of Energy (DoE) by Marano et al (2001), which refers to the water consumption data from an earlier study by

DoE (1998), where the overall plant design was considered but raw water consumption wasn't really been optimized. There was also an earlier study by Choi (1997)which provides the water consumption for a natural gas to liquid (GTL) plant even though water consumption was not the focus of the study. Thus the water consumption figures in the literature, especially in terms of coal-to-liquid (CTL) and biomass-to-liquid (BTL) are limited. The actual water consumption of a plant depends strongly on the process chosen and the feedstock composition. For example, Shell (2014) claims on its website that its mega size Pearl GTL plant, which is the world biggest commercial GTL plant, "run the plant without drawing on Qatar's scarce natural fresh water resources or on seawater". In other words, this GTL process is actually 'water free'. Gabriel (2014) et al. has also shown that water can be produced in a well-designed GTL process. There is no reason to doubt that the water consumption of a CTL process can also be reduced if needed.

The fresh water consumption of a XTL (X=Coal, natural Gas, Biomass, Waste, etc.) composes of two parts; firstly as feed in the process, and secondly in the utility section, especially as cooling water. Cooling water is used to remove heat from the process. The return water can be either discharged into the environment or be cooled and recycled. Modern chemical plants prefers to use evaporation tower to cool down the cooling water before it is recycled, the water loss in the evaporation tower normally mainly contributes to the water loss of the process. If an evaporation tower is not used, the cooling water is a closed-loop and other techniques such as air cooling or refrigeration are used to cool down the cooling water, in order to reduce the water consumption. Shell's Pearl GTL plant has demonstrated that this is feasible. In the case of CTL processes, the overall mass balance for a CTL process doesn't really favours a 'water free' process as there isn't enough hydrogen in the coal and extra hydrogen is needed in the process, and this is normally provided by water. The hydrogen to carbon monoxide ratio in the synthesis gas fed to the Fischer Tropsch section also has to be corrected by the water gas shift (WGS) reaction, where further water is also required.

Patel et. al. (2007a) has calculated that a minimum of 1.3 tons of water is needed as feedstock to produce one ton of $-CH_2-$, assuming coal as pure carbon. Metzger et. al. (2013) showed that when biomass is used in an XTL process, there is potential that water is actually produced from the process. As the composition of biomass is close to a very low quality coal, it raises the question that, for some low quality coal, as to whether the extra water is really needed for the overall mass balance.

2. Methodology

Patel et al. (2007b) stated that chemical processes are limited by certain fundamental constraints, such as: (1) Mass balance constraints, where all atoms of material entering as feed must leave in a product stream; (2) Energy balance constraints, where all energy entering the system that is not used in chemical transformation must be rejected. This means that the change in enthalpy between the products and the feed material must be less than zero ($\Delta H_{process} \leq 0$). When $\Delta H_{process} > 0$, energy must be provided by burning some fuel, and the products of this burning then need to be accounted for as part of the products.

In this study, process mass balance and energy balance are applied to the XTL process to determine how much water is really needed in the process and what the cost of the water-free process is.

The feedstock utilized in XTL processes can be very complex, ranging from natural gas, liquid fuels, coal, coke, biomass and waste etc. The formula of the feedstock used in a XTL process can be simplified as CH_xO_y, where x is the atomic ratio of hydrogen and carbon in the feedstock, and y is the atomic ratio of oxygen and carbon. In most cases other than methane, x is not greater than 2.2 and y is not greater than 1. There are normally other elements in the feedstock, such as sulphur and nitrogen. These are ignored in this calculation. The higher heating value of the feedstock is estimated by using the formula developed by Channiwala et al. (2002), based on over 50 fuels covering gas, liquid, coal, biomass and waste. The equation is as follows:

$$HHV = 0.3491\ C + 1.1783\ H + 0.1005\ S - 0.1034\ O - 0.0151\ N - 0.0211\ A \quad (1)$$

$0\% \le C \le 92.25\%$, $0.43\% \le H \le 25.15\%$, $0\% \le O \le 50\%$, $0\% \le N \le 5.6\%$, $0\% \le S \le 94.08\%$, $0\% \le A \le 71.4\%$, $4.745\ MJ/kg \le HHV \le 55.345\ MJ/kg$, where C, H, O, N, S and A represents carbon, hydrogen, oxygen, nitrogen, sulphur and ash contents of material, respectively, expressed in mass percentage on a dry basis. This formula gives an average absolute error of 1.45% to the measured values of HHV, as claimed by Channiwala et al. (2002). This formula was chosen in this study as it covers a wide range of all different kinds of fuel, and has an acceptable error.As nitrogen, sulphur and ash are not consider in this calculation, Eq. (1) is simplified as

$$HHV = 0.3491\ C + 1.1783\ H - 0.1034 \quad (2)$$

Eq. (2) is employed in this study.

3. Calculations and Discussion

3.1. Overall reactions without adding water

If no water is used in the feed, the overall reactions of a XTL process can be written as

$$CH_xO_y \rightarrow aCH_2 + bCO_2 \quad (3)$$

CH_2 is used here to represent the hydrocarbons formed in the XTL process. All produced hydrocarbon is considered as a product, to simplify the calculation. A basis of 1 mol of CH_xO_y is considered. Furthermore, a and b represent the quantity (in moles) of CH_2 and CO_2 produced respectively.

Eq. 3 only holds in cases where $x + y = 2$. As an indication, the value of x + y for bituminous coal is around 0.8, approximately 0.3 for anthracite and 2.5 for cellulose. In cases where $x + y \neq 2$, either oxygen is needed as feed to provide necessary oxygen, or water is to be produced as a product, as shown in Eq. (4) and (5) respectively:

$$CH_xO_y + dO_2 \rightarrow aCH_2 + bCO_2 \quad (4)$$

or

$$CH_xO_y \rightarrow aCH_2 + b\,CO_2 + eH_2O \quad (5)$$

where for reaction (4), the sum of x and y need to be not greater than 2, and for reaction (5), the sum of x and y need to be not less than 2.

Carbon efficiency is used to measure how efficient the process is. Carbon efficiency is defined as the molar ratio between the carbon in the product, in this case, the CH_2, and the carbon in the feedstock, i.e. CH_xO_y. It is easy to calculate the carbon efficiency when only the mass balance is considered. For Eq. (4), where all the hydrogen in the feed only ends up in the product, the carbon efficiency is x/2, while for Eq. (5), the carbon efficiency is less than x/2, depending on the amount of water produced. The calculated carbon efficiency, as a function of the values of x and y is shown in Figure 1(a). Figure 1(b) shows the enthalpy change of the process $\Delta H_{process}$. For easy interpretation, fuel compositions used in Channiwala (2002)'s calculation are also listed, categorized in groups of biomass, coal/coke, liquid fuel and waste.

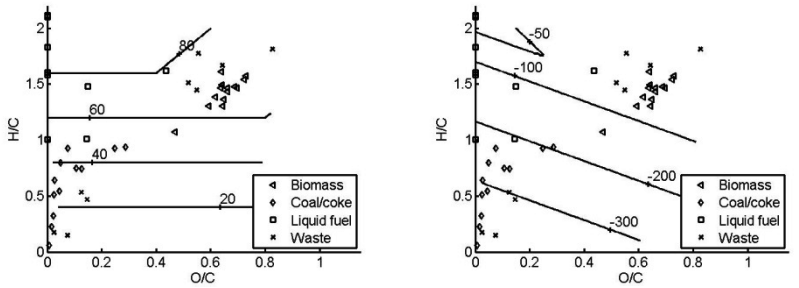

(a) (b)

Figure 1 (a) carbon efficiency of XTL overall process (%); (b) Heat of XTL overall process (kJ/mol)

It can be seen that for the range of feedstock studied, the ΔH of processes are all negative, indicating these processes are all feasible when energy balances are also considered i.e. there is no need for any further external energy supply. This means that as long as there is hydrogen in the feedstock, the water free XTL processes are possible, when both mass and energy balances are considered.

It should also be noted that this water free XTL process comes at the cost of carbon efficiency. For feedstock with excess hydrogen, such as biomass, the carbon efficiencies are at an acceptable range of about 50-80%, where for certain biomass water is actually rejected from the system, in agreement with our previous calculation. For feedstock with insufficient hydrogen, especially in the case of high quality coal, the carbon efficiencies of water free XTL processes are very low.

This is obvious because if no water is added in the process, all the hydrogen which ends up in the products must come from feedstock, and the balance of the carbon has to be ejected as carbon dioxide. The more hydrogen in the feedstock, the more hydrocarbons can be formed as products, thus the higher the carbon efficiency. This also indicates that adding water into the system can improve the carbon efficiency. Thus there is an intricate balance between the carbon efficiency and the water requirements of an XTL process

3.2. Overall mass balance with water in the feedstock

If water is allowed in the feed, the XTL process can be written as

$$CH_xO_y + dO_2 + eH_2O \rightarrow aCH_2 + bCO_2 \quad (6)$$

When $x + y > 2$, it is actually the same mass balance as Eq. (5) where water is produced and oxygen is not needed in the feed. When $x + y \leq 2$, water is needed in the feed and oxygen might be needed to balance the oxygen.

Eq. (6) can be balanced with multiple solutions, but the maximum amount of water needed can be found, as shown in Figure 2a, where the negative amount of water means water is produced as a product. The carbon efficiency and $\Delta H_{process}$ are also shown in Figure 2b.

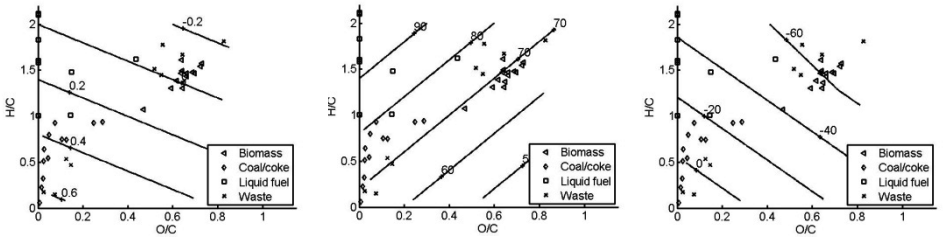

(a) (b) (c)

Figure 2, (a) maximum amount of water needed for XTL process, shown as molar ratio of water and carbon in the feed. (b) Carbon efficiency of XTL processes where maximum amount of water is used in the feed. (c) $\Delta H_{process}$ of XTL processes with maximum amount of water is fed, in kJ/ mol(Carbon in feed)

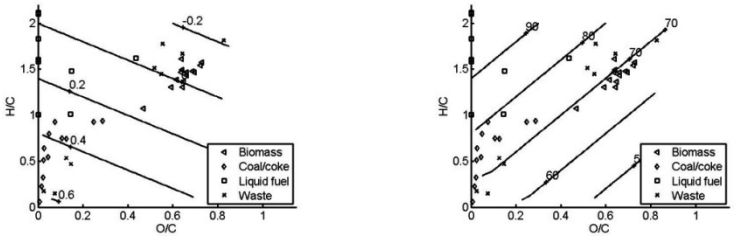

(a) (b)

Figure 3, (a) maximum amount of water allowed to keep a negative $\Delta H_{process}$ (b) carbon efficiency of XTL processes with the water added as shown in figure 3(a).

The calculation shows that for most of the region covering biomass and low quality coal, the $\Delta H_{process}$ is still negative when maximum amount of water is fed as feed in the XTL processes. Carbon efficiencies of the XTL processes improve dramatically when water is added, especially for a feedstock with limited hydrogen. For example in the case of high quality coal carbon efficiency improves from about 20% to about 70% when water is added at a water carbon molar ratio of about 0.6. But the $\Delta H_{process}$ turns positive in the case of high quality coal, indicating further energy is needed in this process. We can provide the energy needed by burning the feedstock, which lowers the carbon efficiency but also consume less water. The maximum amount of water needed and their carbon efficiencies to maintain a negative $\Delta H_{process}$ is shown in Figure 3.

It is worth noting that there is normally water in the feedstock, especially the case of low quality coal and biomass. 20% moisture in a feedstock with about 50% mass percentage of carbon gives a water carbon molar ration of about 0.26. When we check the region where maximum amount of water needed over carbon is less than 0.26, we find that it covers the whole biomass region and is very close to the region of low quality coal. This indicates that extra water is not necessarily required when using biomass or low quality coal as the feedstock in a XTL process.

4. Conclusion

We can conclude that for overall XTL processes where hydrocarbon is produced from a carbon resources,

1. Water free XTL processes are possible, at the cost of lower carbon efficiency;
2. Carbon efficiency can be improved by adding water in the feed, where only a limited amount of water is actually needed;
3. For biomass and low quality coal, when the water content in the feed is normally high, no fresh water is actually needed in the XTL processes, thus a water free XTL process is possible.

References

S. A.Channiwala, P.P.Parikh, 2001, A unified correlation of estimation HHV of solid, liquid and gaseous fuel, Fuel, 81, 1051-1063.

G.H. Choi, S. J. Kramer, S. S. Tan, 1997, Design and economics of a Fischer Tropsch plant for converting natural gas to liquid transportation fuels, report to DoE.

K. J. Gabriel, P. Linke, A. Jimenez-Gutirrez, D. Y. Martinez, M. Noureldin, M M. El-Halwagi, 2014, Targeting of the water energy nexus in gas to liquid processes : a comparison of syngas technologies, Ind.Eng. Chem. Res., 53, 7087-7102

C. W. King, M. E. Webber, 2008, Water Intensity of Transportation, Environmental Science and Technology, 42(21), 7866-7872.

J. J. Marano, J. P. Ciferno, 2001, Life-cycle Greenhouse-Gas Emissions Inventory for Fischer Tropsch fuels. US DoE report.

M. J. Metzger, B. J. Glasser, B. Patel, J. Fox, B. C. Sempuga, D. Hildebrandt, D. Glasser, 2013, Liquid fuels from alternative carbon sources minimizing carbon dioxide emissions, AIChE Journal, 59, 6, 2062-2078.

E. Mielke, L. D. Anadon, V. Narayanamurti, 2010, Water Consumption of Energy Resource Extraction, Processing and Converstion, , Energy Technology Innovation Policy Discussion paper Series, Harvard Kennedy School.

B. Patel, D. Hildebrandt, D. Glasser, B. Hausberger, 2007a, Synthesis and Integration of Chemical Processes from a Mass, Energy, and Entropy Perspective, Ind.Eng.Chem.Res.,46, 8756-8766

B. Patel, D. Hildebrandt, D. Glasser, B. Hausberger, 2007b, Coal to Liquid, an environmental friend or foe? Proceedings of the 24th International Pittsburg Coal Conference, Johannesburg

Shell, 2014, Producing water in the desert, http://www.shell.com/global/aboutshell/major-projects-2/pearl/water-treatment.html, Retrieved 28 Nov 2014

US DoE, 1998, Aspen process flowsheet simulation model of a battelle based gasification, Fischer Tropsch Liquefaction and Combined cycle power plant, Refining and End Use of Coal Liquids, Topical Report.

US DoE, 2006, Energy Demands on Water Resources, report to congress on the interdependency of energy and water.

Krist V. Gernaey, Jakob K. Huusom and Rafiqul Gani (Eds.), 12th International Symposium on Process Systems Engineering and 25th European Symposium on Computer Aided Process Engineering.
31 May – 4 June 2015, Copenhagen, Denmark

Energy and Yield Evaluation of an Alcohols and Hydrocarbons Production Plant using Rh-based Catalysts with Different Promoters

Júlio C. C. Miranda[a], Gustavo H. S. F. Ponce[a], Harvey Arellano-Garcia[b], Rubens Maciel F.[a], Maria R.Wolf M.[a]

[a]*Laboratory of Optimization, Design and Advanced Control, School of Chemical Engineering, Campinas-SP 13083-852, Brazil*
[b]*University of Bradford, Bradford, West Yorkshire, BD7 1DP, United Kingdon*

Abstract

Synthesis gas (syngas), mainly constituted by carbon monoxide (CO) and hydrogen gas (H_2), is produced mostly through biomass gasification and methane reforming. In the last decade, the thermochemical route to produce ethanol and higher alcohols from syngas has been gaining space as a possible route to produce synthetic fuels and additives. This kind of process presents a series of advantages as: short-time reaction, abundant and lower-price feedstocks, the use of lignin and the almost complete conversion of syngas, having the potential to exceed ethanol production by fermentative route. Aiming to produce ethanol through thermochemical route, a singular process (a small-scale plant with capacity to process 100 kmol/h of syngas) was proposed for a first evaluation using the commercial simulator ASPEN Plus v7.3. Four different Rh-based catalysts were tested in the process (RhFe, RhLa, RhLaV, and RhLaFeV), trying to take advantage of the characteristics of Rh-based catalysts as high ethanol selectivity and hydrocarbons production. The process design took into account the reactor selectivity and conversion. Through sensitivity analysis, the downstream process were configured searching for the best possible design of separation steps, making possible to obtain ethanol (>99 % wt.), methanol (>90 % wt.), Liquified Petroleum Gas (LPG, mixture of C_2H_6, C_3H_8 and C_4H_{10}, > 99 % wt.) and pentane (>95% wt.).

Keywords: syngas, ethanol, hydrocarbons, simulation.

1. Introduction

Analysing the world's energy scenario it is possible to observe the continuous rise of petroleum prices, the constant growth of world's population and the consequent increase of energy demand, making attractive the development of renewable, alternative and sustainable energy sources derived from biomass or industrial co-products. Due to the present demands, the interest on the thermochemical route, that converts synthesis gas (syngas) to alcohols, has been renewed and now this route is seen as a possible alternative to supply the fuels market in the near future.

Biomass and coal gasification generates the syngas, a mixture of mostly CO and H_2 known by its use in the production processes of ammonia (Harber-Bosch) and hydrocarbons (Fischer-Tropsch). However, the catalytic conversion of syngas to alcohols, studied during the last 90 years has been gaining space in the last few years as a possible route to produce synthetic fuels and additives (Subramani and Gangwal, 2008; Christensen, 2011). In this route, the initial feedstock is gasified to syngas and

then reformed, cleaned, compressed and catalycally converted into a mixture of high-weight alcohols. This process has also advantages as: short-time reaction, abundant and cheap feedstocks, use of lignin and almost complete conversion of syngas.
Among several catalysts, Rhodium (Rh) is known for its position in the periodic table, between those metal that dissociate CO, forming long-chain hydrocarbons (Fe, Co), and those that do not dissociate CO and produce methanol (Pd, Pt, Ir). Thus, the Rh-based catalysts can form long-chain oxygenate compounds from CO hydrogenation (Spivey and Egbebi, 2007). However, one of the drawbacks of Rh-based catalysts is the high selectivity to hydrocarbons production, generally varying in their chain size from C_1-C_5.
In this work, using the commercial simulator ASPEN Plus v7.3, it was possible to propose a first process design that uses Rh-based catalysts with different promoters (RhFe, RhLa, RhLaV, RhFeLaV), find its best operational settings based on the demands required by each catalyst taking advantage of their characteristics, analyse it regarding energy consumption and production, and finally, point out possible solutions and future developments.

2. Process Design

2.1. Reaction kinetics

The reaction kinetics was obtained from Gao et al. (2011). In their studies, the authors considered the formation of hydrocarbons (CH_4, C_2H_n, C_3H_n) and ethanol, obtaining the kinetic parameters for the Arrhenius model. To obtain a more extended model, considering the formation of alcohols (oxygenates portion) and hydrocarbons (C_{2+} portion) until C_5, we used the Anderson-Schulz-Flory (ASF) distribution (Gunturu et al.,1998). The use of ASF distribution is only reflected in the pre-exponential factors of the reaction kinetics, which were recalculated and properly introduced in the simulator.

2.2. Process Layout

The process layout, shown in Figure 1, was heuristically defined for the four different catalysts. Starting from the products obtained in the reactor, a mixture of alcohols, hydrocarbons, water and non-reacted syngas, the downstream operations were chosen in a way to obtain the desired products for the following steps. After choose a unit operation, according to the stream demands, it was improved using sensitivity analysis.

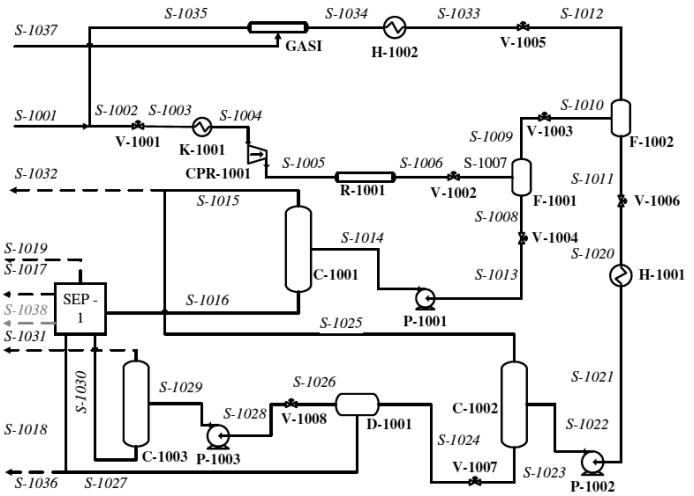

Figure 1. Process flowchart

The syngas enters in the process through S-1001 stream, which is mixed with the recycle stream S-1035, and the resulting stream (S-1002) is then heated, compressed and introduced in the reactor. From the reactor (R-1001) a mixture of alcohols, hydrocarbons, water and non-reacted syngas (S-1006) is obtained, which goes to the first flash drum (F-1001) for a gross separation of water and alcohols (S-1008). The flash's top stream (S-1009), which contains most of hydrocarbons and non-reacted syngas, is directed to the second flash (F-1002) which operates at moderate pressure and very low temperature. The top stream of F-1002, containing the major part of non-reacted syngas and methane, goes to the GASI reactor, which emulates the total conversion of this stream to pure syngas, when this stream reacts with oxygen (S-1031). As seen from the flowchart in Figure 1, the recycle generated by the GASI reactor can be "turned on" and "off" by just disconnecting S-1035, then S-1001 is automatically adjusted to supply the syngas demanded by the process. The goal of the recycle section is to calculate the amount of syngas that can be recovered from the process, admitting total use of the effluent stream (S-1012).

The bottom stream of F-1001 (S-1008) is directed to the distillation column C-1001, in which the rest of hydrocarbons (S-1015) are separated from the water/alcohols mixture (S-1016). The stream S-1011, originated from F-1002, goes to the distillation column C-1002, which operates at moderate pressure. Two streams are generated in this column, the top stream (S-1025), which is rich in C_2-C_4 hydrocarbons (LPG), while the bottom stream (S-1023) is composed by pentane and a small fraction of water and alcohols. S-1023 is sent to the decanter (D-1001), in which the aqueous phase (S-1027) and the pentane-rich phase (S-1026) are split. This stream is directed to the distillation column C-1003, where pentane is obtained in the top stream (S-1031) and a mixture of alcohols and water in the bottom stream (S-1030).

The design used in SEP-1 (Figure 2) is already known from the first generation ethanol production (Dias et al., 1009). It consists of a set of four distillation columns. The first distillation column (C-101) receives a mixture of two streams (S-1009 and S-1031) containing water, alcohols, and traces of hydrocarbons.

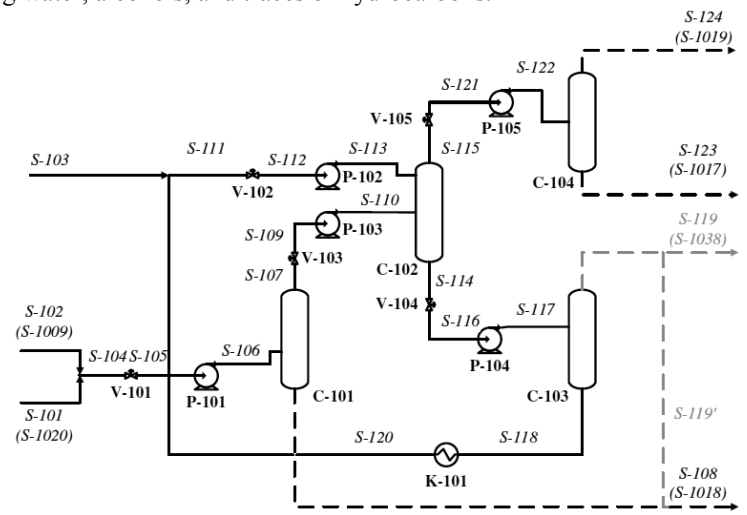

Figure 2. SEP-1 flowchart

In its top stream, C-101 has a concentrated alcohols/water mixture, while in its bottom a water stream (>99 % wt.). In the second column (C-102) is promoted an extractive

distillation (with ethylene glycol), where the mixture entering the column is dehydrated. In its top stream (S-115), C-102 has the mixture methanol/ethanol, which is directed to C-104, where the two alcohols are obtained separately. In the distillation column C-103, the solvent is recovered (S-118) being reintroduced to the system through S-111. The water-rich stream (S-119), highlighted in gray, depending on its composition, can be mixed with S-108 resulting in a stream with >99 % wt. water or, when it has a fraction of higher alcohols, stored to be separated by other unit.

3. Results and Discussion

Four simulations were carried out using the commercial simulator ASPEN Plus v7.3. Based on the properties of the components generated in the reactor and the operating conditions, two thermodynamic packages were chosen. Thus, for the operations containing polar compounds at pressures below 10 bar, the UNIQUAC thermodynamic package was used, and, for operations involving hydrocarbons at pressures above 10 bar, the PENG-ROBINSON thermodynamic package was used.

3.1. Products

The reactor is continuously fed with 100 kmol/h of syngas at a mole ratio of 1:2 ($CO:H_2$). This value was found by sensitivity analysis to result in the best relation between carbon monoxide conversion and ethanol selectivity for the four simulations.
Temperature and pressure were maintained respectively at 270 °C and 1.8 bar, while the catalyst load, obtained through sensitivity analysis, varied between catalysts (17500 kg of $RhFe/SiO_2$, 15000 kg of $RhLa/SiO_2$, 8500 kg $RhLaFeV/SiO_2$ and 8500 kg $RhLaV/SiO_2$). The reactor's conversion was limited by the H_2 supply. In the sensitivity analysis, when the conversion suffered no significant increase (1% from the last point), the catalyst load stop increasing, obtaining the results for conversion (CO mass basis) of: 73.21 % ($RhFe/SiO_2$), 78.73 % ($RhLa/SiO_2$), 86.23 % ($RhLaFeV/SiO_2$) and 85.47 % ($RhLaV/SiO_2$).

In the process, four products are generated, ethanol (the desired oxygenated product), methanol, pentane and LPG (liquefied petroleum gas, a mixture of C_2-C_4 hydrocarbons). As seen from Figure 3, the catalysts generate different amounts of each product. The most prominent product is the LPG, generally followed by ethanol, except in the RhLaFe catalyst, where pentane is the secondary product.

All the product streams were obtained at or above 99 % wt. purity except stream S-1031 (pentane) for the catalyst $RhFe/SiO_2$. Due the low pentane mass flow, this stream attained only 95 % wt. of pentane, which is contaminated with methanol.
The process generates, besides the product streams, three other streams. S-1018 containing most of the water generated in the reactor, while S-1035 recycles the syngas and S-1038 carries water and a small amount of alcohols (C_{3+}). Using the catalyst $RhFe/SiO_2$, the recycle stream attains 624.9 kg/h of syngas with a mole ratio of 1:1.29 ($CO:H_2$), the water stream 385.9 kg/h (99.4 % wt.) carries all the water, being other stream not necessary. In turn, using the catalysts RhLa, RhLaFeV and RhLaV, the process produces respectively water: 435.9 kg/h (99.7 % wt.), 441.4 kg/h (99.8% wt.) and 390.3 kg/h (99.7 % wt.) and syngas: 404.4 kg/h (1:1.3), 230.6 kg/h (1:0.78) and 230.57 kg/h (1:0.86). The mass flows of the stream containing higher alcohols residues in the three cases were respectively: 23.6 kg/h (96.4 % wt. water, 0.8 % wt. propanol, 1.0 % wt. butanol and 1.1 % wt. pentanol), 54.3 kg/h (66.8 % wt. water, 0.6 % wt. ethanol, 9.2 % wt. propanol, 11.0 % wt. butanol and 12.2 % wt. pentanol) and 103.4

kg/h (64.0% wt. water, 0.1 % ethanol, 10.6 % wt. propanol, 12.1 % wt. butanol and 13.0 % wt. pentanol).

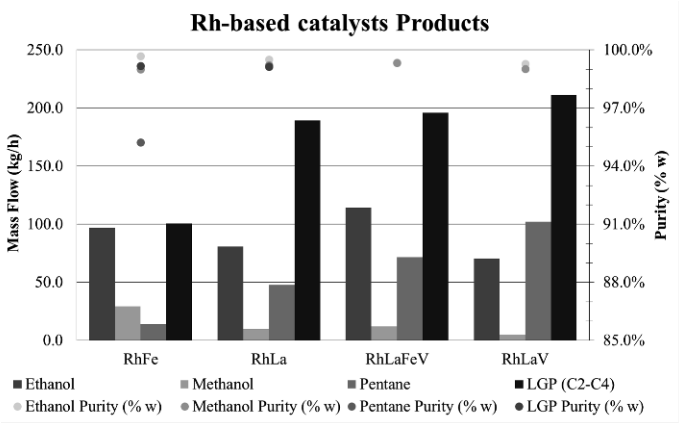

Figure 3. Mass Flow and Purity of Products

3.2. Energy Consumption

The unit operations were set based on sensitivity analysis. For the two flash drums, temperature and pressure were varied in order to obtain in F-1001 the best ratio between alcohols and water (S-1008) and syngas and hydrocarbons (S-1009) recoveries and in F-1002 the recovery of 99.9 % wt. of syngas and methane of the feed stream. The three distillation columns were configured regarding the energy spent in the reboiler. C-1001 had the alcohols and water recovery 99.9 % wt. from the inlet flow established as the goal for its operation, varying the number of stages (N_{STAGE}), feed stage (F_{STAGE}) and the mass reflux ratio (M_{RR}). In C-1002, using the same variables of the prior case, the analysis had as restrictions: the recovery of 99.9 % wt. of the LPG from inlet stream above 99 % wt. purity. Fixing pentane recovery (95 % and 99 % wt.) in C-1003, and varying N_{STAGE}, F_{STAGE} and M_{RR} its final design was obtained.

In SEP-1 the same analysis procedure was followed, the columns were set varying $N_{STAGE,}$ F_{STAGE} (in the case of C-102 both feed stages were varied) and M_{RR}. In the first distillation column of this set (C-101) the main obstacles for its best operation were the azeotropes ethanol/water, propanol/water and butanol/water. Thus, knowing that a reasonable quantity of water would be carried to the second column (C-102), it was possible to best configure the column related to two variables: the recovery of ethanol in the top stream and water purity in its bottom stream. In C-102 the top stream purity was prioritized, in order to have a mixture of at least 99 % wt. of ethanol and methanol with a recovery of both from the feed stream of 99.9 % wt., ethylene glycol at a mass ratio of 1:1 (solvent: feed stream) was introduced in the column. About 99.9% of this solvent is recovered by the distillation column C-103, which produces also a water-rich mixture in its top. The alcohols streams are obtained in column C-104, in which ethanol and methanol are obtained at minimum 99 %wt. purity.

The analysis were carried out in order to achieve the minimum energy required to obtain the desired products with the restrictions described above. In this way, Figure 4 shows the contribution in energy consumption of each unit of the process. Due the exothermic nature of the reactions, the net energy consumption is positive. The reactor appears as the main contributor for cooled units followed by F-1001, which receives all the mass flow coming from the reactor and needs to cool it down to send streams pure enough to

C-1001 and F-1002. SEP-1 is represented as one whole block and has a contribution in both, heated and cooled units. As can be seen, among the cooled units, SEP-1 is the third biggest energy consumer, while among the heated units, the first. Its energy consumption is directly related to the data observed in Figure 3. When the catalyst produces more alcohols, the energy is proportional in SEP-1, in both ways, heating and cooling. The same behavior can be seen in the distillation columns C-1002 and C-1003 but this time related to LPG and pentane production.

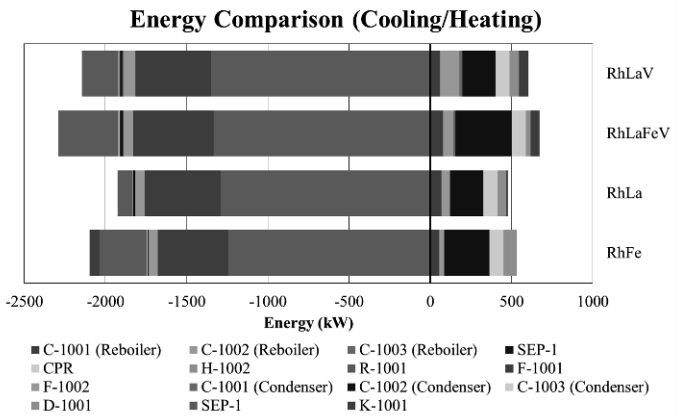

Figure 4. Energy Consumption Comparison

4. Conclusion

Regarding energy aspects, the process showed itself viable due the exceeding energy generated by the reactor that, through energy integration, can be used in the process or in cogeneration. Considering the ratio(catalyst load)/(products mass) the process using RhLaV and RhLaFeV are more favourable, however with different focus, hydrocarbons and ethanol production, respectively. Three further steps can be taken from the results obtained here; the energy integration with other biofuels production processes, the scale-up considering the recovery of the higher alcohols and the catalyst improvement.

References

V. Subramani and S.K. Gangwal, 2008, A review on recent literature to search an efficient catalytic process for conversion of syngas to ethanol, Energy and Fuels, 22, 2, 814-839.

J.M. Christensen, P.A. Jensen, A.D. Jensen, 2011, Effects of feed composition and feed impurities in the catalytic conversion of syngas to higher alcohols ver alkali-promoted cobalt-molybdenum sufide, Industrial & Engineering Chemistry Research, 50, 7949-7943.

J.J. Spivey, A. Egbebi, 2007. Heterogenous catalytic synthesis of ethanol from biomass-derived syngas, Chemical Society Reviews, 36, 1514-1528.

J. Gao, X. Mo. J.G. Goodwin Jr, 2009. La, V, and Fe promotion of Rh/SiO2 for CO hydrogenation: Detailed analysis of kinetics and mechanism, Journal of Catalysis, 268, 142-149.

A.K. Gunturu, E.L. Kugler, J.B. Cropley, D.B. Dadyburjor. A Kinetic Model for the Synthesis of High-Molecular-Weight Alcohols over a Sulfided Co-K-Mo/C Catalyst. Ind. & Eng. Chemistry Research, 37, 2107-2115.

M.O.S. Dias, A.V. Ensinas, S.A. Nebra. R. Maciel F°, C.E.V Rossel, M.R. Wolf. M., 2009 Production of bioethanol and other bio-based materials from sugarcane bagasse: Integration to conventional bioethanol production process, Chemical Engineering Research and Design, 87, 9, 1206-1216.

Krist V. Gernaey, Jakob K. Huusom and Rafiqul Gani (Eds.), 12th International Symposium on Process Systems Engineering and 25th European Symposium on Computer Aided Process Engineering.
31 May – 4 June 2015, Copenhagen, Denmark

Computer-aided process analysis of an integrated biodiesel process incorporating reactive distillation and organic solvent nanofiltration

Kathrin Werth,* Kolja Neumann, Mirko Skiborowski

TU Dortmund University, Laboratory of Fluid Separations, Emil-Figge-Straße 70, 44227 Dortmund, Germany
Kathrin.Werth@bci.tu-dortmund.de

Abstract

To enable the use of alternative cheap feedstock in the production of biodiesel, such as waste cooking oils, the contained free fatty acids have to be separated from the triglycerides. For that purpose an integrated process incorporating reactive distillation and organic solvent nanofiltration is proposed. To determine the potential of the integrated process a detailed model was developed for computer-aided process analysis. Necessary parameters such as permeabilities and kinetics were estimated based on experimental investigations. Process analysis revealed that reactive distillation is a suitable process for the pre-treatment of waste cooking oil and that the application of organic solvent nanofiltration could enhance profitability of the process.

Keywords: Process intensification, rate-based model, esterification, free fatty acids.

1. Introduction

Biodiesel based on renewable resources shows a great potential as alternative future fuel. Until now no economic production of biodiesel is possible because of the high raw material costs of virgin vegetable oil that account for three-fourth of the total production costs (Lim and Teong, 2010). A promising and cheap alternative feedstock are waste cooking oils, which reduce the raw material cost by a factor of three (Yaakob et al., 2013) and upgrade the produced biodiesel to a second generation biofuel. The main drawback of these low-quality oils is the high amount of free fatty acids (FFA) which tend to hydrolyse under the alkaline conditions in the transesterification reaction of biodiesel. Therefore, the amount of FFA in the waste cooking oil has to be minimised in a pre-treatment step to avoid this undesired side reaction in the transesterification.

One possibility to reduce the amount of FFA is the esterification of the acids with an alcohol in a pre-treatment step. Since this reaction is equilibrium limited the application of reactive distillation (RD) is favourable. However, as indicated by Marchetti and Errazu (2008), the low concentration of FFA in the column due to the high amount of non-reacting triglycerides (TG) in the waste cooking oil might result in a reduced reaction rate and conversion. To overcome these challenges, which might restrict the operation window of RD, an integrated process combining RD with organic solvent nanofiltration (OSN) is proposed. Thereby, OSN facilitates an energy efficient separation of FFA and TG due to its mild operation conditions.

In order to prove the feasibility of this concept a systematic experimental and theoretical investigation is performed. As model system the esterification of oleic acid and ethanol

in presence of vegetable oil is chosen. A rigorous model for the integrated process incorporating RD and OSN is developed for the purpose of process analysis and design. To determine missing parameters for reaction kinetics and permeabilities, the esterification of FFA as well as OSN and RD are investigated experimentally. The model is validated based on the experimental results and used for a process analysis of RD and OSN in order to determine suitable operation windows for a further integration and later process design.

2. Modelling of integrated process

In order to provide a rigorous model for the integrated process, comprehensive models for the RD column and an OSN cascade are developed in Aspen Custom Modeler® (ACM). Thermodynamic and physical properties are calculated using Aspen Properties®.

2.1 Reactive distillation

For modelling of RD a rate-based model incorporating heat and mass transfer equations as well as correlations describing the fluid dynamics is used. A detailed description of the RD model is given by Keller and Górak (2013). To adapt the model to the integrated biodiesel process, suitable kinetics for the esterification of FFA with ethanol are necessary. The temperature dependence of the reaction rate is taken into account according to the Arrhenius approach which describes the reaction rate constant as a function of pre-exponential factor k_0 and activation energy E_A. Both parameters have to be estimated based on experimental results.

2.2 Organic solvent nanofiltration

The OSN cascade comprises of various membrane modules which can be connected in parallel or series and can be operated at different temperature and pressure. The optimal configuration for the OSN cascade can be determined based on a superstructure model approach (cf. Micovic et al., 2014). Mass transfer through the membrane is described by the solution-diffusion model (Wijmans and Baker, 1995), in which the flux J of component i represents the product of permeability P_i and driving force ΔDF_i (see Eq. (1)).

$$J_i = P_i \cdot \Delta DF_i \tag{1}$$

The driving force is determined by the difference in chemical potential across the membrane, calculated based on the operating conditions and concentration in feed and permeate. The permeability accounts for the complex interactions between membrane, solvent and solute and is influenced by concentration, temperature and pressure. Till now no accurate prediction of separation performance in OSN is possible because it depends on various factors (e.g. molecular size of components, solubility parameters, solvent interactions, membrane material etc.). Therefore, permeabilities have to be determined experimentally.

3. Experimental investigation and parameter estimation

Since few data is available experimental investigations were performed for the esterification of oleic acid with ethanol and the membrane separation of waste cooking oils to determine the missing parameters.

3.1. Kinetics of esterification of free fatty acids

Experiments of the esterification of oleic acid and ethanol to produce ethyl oleate and water were performed in a batch reactor at different temperatures. To achieve high conversion of oleic acid an excess of ethanol of 6:1 was applied. This ratio was chosen according to preliminary tests and to ensure feasible and stable conditions in the RD experiments. First, a screening of homogeneous and heterogeneous catalysts was performed. For the tested heterogeneous catalysts, Amberlyst^{TM}-15 very low conversion of FFA was observed and thus no application in RD is possible because of the short residence time in the column. The homogeneous catalyst sulphuric acid was identified as a suitable catalyst which leads to high conversion of FFA ($X_{FFA} \sim 80\,\%$) in reasonable reaction times.

Subsequently, the impact of TG from which a high amount is present in waste cooking oils on the conversion of FFA was investigated. As expected the experimental results show that the initial reaction rate is reduced (see Figure 1) since the concentrations of reactants and products are decreased by the present TG. The parameters for the reaction kinetics were determined from the experimental reaction data. The simulated conversions of FFA are in satisfying accuracy with the experimental results for a first process analysis (see Figure 1).

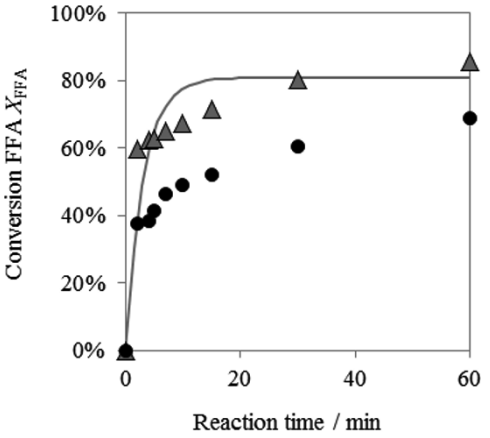

Figure 1: Conversion of oleic acid without triglyceride in the reaction mixture (grey) and in presence of triglyceride (black) at a temperature of 71 °C. Symbols represent experimental data and the solid line represents the simulated data in the absence of triglyceride.

3.2. Membrane permeabilities

A screening of the commercial available membranes GMT-ONF^{TM} 1, GMT-NC^{TM} 1 (both PDMS) and PuraMem^{TM} 280 (polyimide), which differ in polymer material and molar weight cut-off, was performed to determine the potential of this separation step. Furthermore, the influence of different solvents (n-hexane and ethanol) on the selectivity of the separation of oleic acid from TG was investigated, because it is known that solvents can significantly influence the separation behaviour (Schmidt et al., 2013).

Permeabilities of each component are estimated based on the partial permeate fluxes. As exemplarily shown for the investigated membrane GMT-ONF^{TM} 1 (see Figure 2) the

permeate fluxes calculated by the solution-diffusion model are in good agreement with the measured fluxes. For this membrane the flux of n-hexane is considerably higher than for ethanol which also results in higher selectivities for n-hexane. However, for the dense membrane PuraMem^{TM} 280 an appropriate permeability of FFA is found while TG is fully rejected if ethanol is used as solvent instead of n-hexane. For the overall process the application of ethanol as solvent is favourable because it is used as reactant in the following esterification step. Since the membrane PuraMem^{TM} 280 shows high ethanol flux and full rejection of FFA, only this membrane type is considered in the subsequent process analysis.

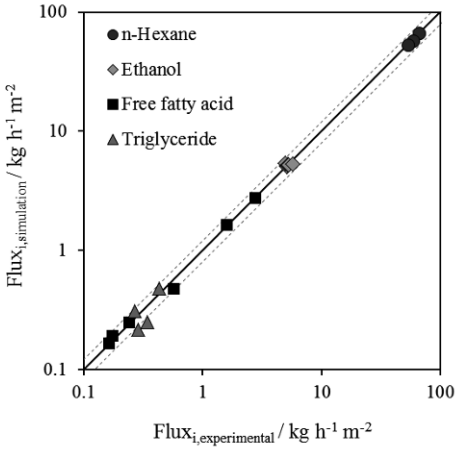

Figure 2: Measured and calculated partial permeate fluxes for the membrane GMT-ONF^{TM} 1.

4. Process analysis

Within process analysis, the influence of various parameters on the process performance of RD and OSN was investigated to determine suitable operation windows for both unit operations. A feed of 1400 kg/h waste cooking oil with a FFA content of 30 wt% was assumed.

In the process analysis of RD the influence of reflux ratio, distillate-to-feed (DF) ratio as well as packing height on the conversion of FFA was investigated (see Figure 3). For the esterification of pure FFA a required packing height of 2.4 m were determined to achieve full conversion of FFA whereby no rectifying section is necessary. If waste cooking oil is applied as feedstock, the energy demand is drastically increased compared. But it is found that the reduced reaction rate due to the presence of TG only slightly affects the conversion of FFA in RD and thus the performance of RD.

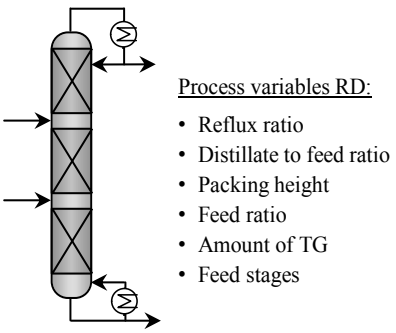

Figure 3: Model setup for RD column (process variables considered in analysis indicated).

A sensitivity analysis was performed in order to identify the influence of different process and design variables and to determine the feasible operation regions of RD for further process optimization. Figure 4 illustrates the results of the sensitivity analysis for a fixed column set-up and indicates that a low reflux ratio and thus a low amount of the by-product water in the column are favourable to achieve full conversion of FFA. Additionally higher DF ratios result in increased conversion but are directly linked with increasing reboiler duty. This trade-off between high conversions and operational costs (in this case reboiler duty) has to be addressed by further process optimization, which will be part of future work.

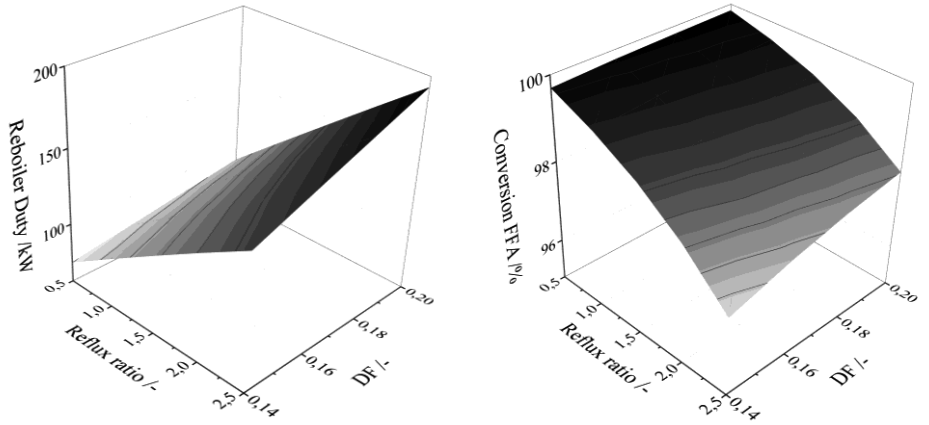

Figure 4: Dependency of reboiler duty (left) and conversion of FFA (right) on reflux ratio (RR) and distillate to feed ratio (DF) for the esterification of pure FFA. Packing height, feed ratio and position of the feed stages are kept constant.

The process analysis of the OSN cascade was performed by means of an evolutionary multi-objective algorithm (Micovic et al., 2014) which allows to analyse the influence of contradicting objectives. Here, membrane area minimization and the maximization of the retentate mass fraction of TG was accomplished by manipulating the different design degrees of freedom and operating conditions of the OSN cascade (see Figure 5).

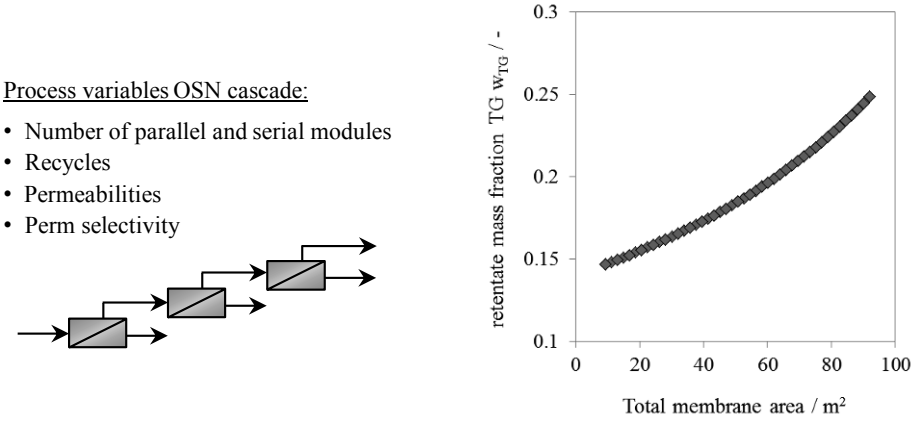

Figure 5: Model setup for OSN cascade with considered process variable in analysis indicated (left). Mass fraction of triglyceride in the retentate in dependence of total membrane area for a three stage OSN cascade equipped with the PuraMem^{TM} 280 membrane (right).

Since only the PuraMem^{TM} 280 membrane was considered (cf. Section 3.2), the permeability and the perm selectivity were kept constant, while the number of parallel and serial modules, the recycle flow rates and the operating pressure of the three-stage OSN network, for which the retentate of the previous stage is processed in the subsequent stage, were optimized. The results of the optimization are illustrated on the right side of Figure 5. These results indicate that for the maximum considered membrane area of 92 m^2 the maximal separation of FFA is achieved. In the retentate an amount of 24.8 wt% TG and 6.4 wt% FFA is obtained, while the permeate contains only FFA and ethanol. This allows processing the FFA to more valuable products (e.g. nitriles, amines), which would lead to enhance the profitability of the overall process. Additionally, it has been shown recently that a separation of saturated and unsaturated FFA via OSN might be possible (Bowden, 2014) and thus new building blocks for chemical production can be generated.

5. Conclusion and future work

Comprehensive models for RD and OSN were developed in order to investigate an integrated biodiesel process. The necessary parameters such as kinetics and permeabilities were estimated based on experimental results. The models were subsequently used for a detailed process analysis in order to determine suitable process configurations and favourable operating conditions. It was found that performance of RD is only slightly affected when TG is present in the reaction mixture. However, by incorporating OSN the profitability of the process might be increased. Based on the current results a detailed process design will be performed considering energy efficiency as well as production costs to determine the most promising process configuration. Furthermore, the developed models facilitate the investigation of the influence of fluctuating feedstock composition, which will also be done in future work.

References

N. Bowden, 2014, Development of the first efficient membrane separations of cis fatty acids, Inform, 25, 9, 558-561

T. Keller, A. Górak, 2013, Modelling of homogeneously catalysed reactive distillation processes in packed columns: Experimental model validation, Computers and Chemical Engineering, 48, 74-88

S. Lim, L.K. Teong, 2010, Recent trends, opportunities and challenges of biodiesel in Malaysia: An overview, Renewable and Sustainable Energy Reviews, 14, 3, 938-954

J.M. Marchetti, A.F. Errazu, 2008, Esterification of free fatty acids using sulfuric acid as catalyst in the presence of triglycerides, Biomass and Bioenergy, 32, 892-895

J. Micovic, K. Werth, P. Lutze, 2014, Hybrid separations combining distillation and organic solvent nanofiltration for separation of wide boiling mixtures, Chemical Engineering Research and Design, 92 (11), 2131-2147

P. Schmidt, T. Köse, P. Lutze, 2013, Characterisation of organic solvent nanofiltration membranes in multi-component mixtures: Membrane rejection map sand membrane selectivity maps for conceptual process design, Journal of Membrane Science , 429, 103-120

J.G Wijmans, R.W. Baker, 1995, The solution-diffusion model: a review, Journal of Membrane Science, 107, 1-21

Z. Yaakob, M. Mohammad, M. Alherbawi, Z. Alam, K. Sopian, 2013, Overview of the production of biodiesel from Waste cooking oil, Renewable and Sustainable Energy Reviews, 18, 184-193

Krist V. Gernaey, Jakob K. Huusom and Rafiqul Gani (Eds.), 12th International Symposium on Process Systems Engineering and 25th European Symposium on Computer Aided Process Engineering.
31 May – 4 June 2015, Copenhagen, Denmark

A Thermodynamic Targeting Approach for the Synthesis of Sustainable Biorefineries

Bilal Patel[a*]

[a]*Department of Chemical Engineering,University of South Africa, Corner of Christiaan de Wet Road and Pioneer Avenue, Florida 1709, South Africa*
patelb@unisa.ac.za

Abstract

One of the major challenges of achieving a sustainable integrated biorefinery lies in the systematic synthesis and design of such systems. There is a need to develop quick and efficient methods to screen the various product options in order to determine which products best utilise the feedstock.

This contribution develops upfront conceptual-level design targets for the production of fuels and chemicals from biomass. These targets aim to provide insight into the design of sustainable biorefineries, prior to the detailed design, with an aim of maximising feedstock utilisation thereby increasing the process efficiency and reducing the emissions from such processes. The targets for these different products are compared using sustainability metrics such as Atom Economy and E-factor. Products which maximise the Atom Economy are determined. This work further identifies integration opportunities and assesses whether combining the production of fuels and chemicals can achieve higher process efficiencies.

Keywords: Biorefineries, design targets, Van Krevelen diagram, process synthesis.

1. Introduction

One of the major challenges of achieving a sustainable bio-refinery lies in the systematic synthesis and design of an integrated biorefinery (Kokossis and Yang, 2010). The key aim is to improve the efficiency, economics and reduce the environmental impact of such processes. In addition, there are many possible products that can be produced, ranging from low-value bulk products (such as fuels) to high-value specialty chemicals (Fernando et al., 2006). Quantitative accounts of the highest efficiency, minimum amount of energy or lowest amount of carbon dioxide that is emitted i.e. design performance targets, can provide essential insight into efficient material and energy utilization. Yuan et al (2013) provides a comprehensive review of various process synthesis methodologies and tools for the optimal synthesis of biorefineries. These methods include classical process synthesis methodologies including hierarchical decomposition, mathematical programming and graphical insight.

This study aims to develop systematic process synthesis tools for the conceptual design of a biorefinery based on the work of Patel et al. (2007, 2010). The study will develop targets for a biorefinery by determining the optimal overall process mass balance by investigating the choice of end-product on the efficient utilisation of the feed-material.

2. Approach

There are three fundamental properties that are utilised on a macroscopic level to determine overall targets for biomass conversion processes, i.e. mass, energy and entropy (or exergy).

In terms of mass, an atomic species balance as a process synthesis tool provides significant insight into the efficient utilization of raw materials. It is important to note here that the overall process mass balance can be determined before any detailed simulation of the process. Here it is proposed that the designer should dictate the overall process mass balance, instead of allowing the process to dictate the mass balance. A graphical approach will be employed to determine the overall mass balances as will be explained in section 3. The energy balance can also be applied to a process without taking the details of the flowsheet or units into consideration. The energy balance gives an indication of the quantity of energy flowing into or out of the process, thus providing a target for the minimum amount of energy required or produced by the overall process. Furthermore, the second law of thermodynamics (entropy/exergy analysis) can also be employed to provide a target for processes as the second law provides a limit to the amount of work required or produced by a process. The maximum theoretical work produced (or minimum work required) from a process is related to the change in the Gibbs energy of the process.

Process design targets will be assessed and compared using three sustainability metrics: carbon efficiency, Atom Economy and E-factor (Sheldon, 2011; Constable et al., 2002). The exergetic efficiency is also used to compare various targets. All three metrics are easily calculated once the overall process mass balance is known. The definitions of the metrics are as follows:

$$Atom\ Economy = \frac{Mass\ of\ desired\ product}{Total\ mass\ of\ feed} \quad (1)$$

$$Carbon\ Efficiency = \frac{Moles\ of\ C\ in\ desired\ product}{Moles\ of\ C\ in\ feed} \quad (2)$$

$$E - factor = \frac{Mass\ of\ waste\ produced}{Mass\ of\ desired\ product} \quad (3)$$

$$Exergetic\ Efficiency = \frac{Chemical\ exergy\ of\ desired\ product}{Chemical\ exergy\ of\ feed} \quad (4)$$

Eqs.(1) to (3) provide a useful indication of raw material utilization and waste generation. Eq.(4) provides an indication of the thermodynamic efficiency of the process. The exergetic efficiency provides a target in terms of the work losses associated with a process.

3. Targets for Biorefineries

3.1. Case Study: BTL

Consider converting biomass with a chemical formula of $CH_{1.5}\ O_{0.7}$ (representing biomass with an ultimate analysis of 48 % C, 45 % O and 6 % H, which is typical for wood) into hydrocarbons (i.e. single feedstock, single product process) i.e. Biomass-to-

liquids (BTL). Hydrocarbons will be denoted as $-CH_2-$.The higher heating value (HHV) of the specified biomass is taken to be 20 MJ/kg.

The overall process mass balance can be determined for this process and as is as follows (Metzger et al., 2013):

$$1.463CH_{1.5}O_{0.7} \xrightarrow[Mass\ Balance]{} -CH_2- + 0.098H_2O + 0.463CO_2 \quad (5)$$

It is clear from Eq. (5) that for every mol of $-CH_2-$ produced, almost half a mol of carbon dioxide is produced. The carbon efficiency of the overall process can be calculated to be 68%. Since the desired product consists only of C and H atoms, the oxygen atoms in the biomass end up as carbon dioxide. Note that according to Eq. (5), BTL processes have the potential of producing water. The Atom Economy and E-factor for the overall BTL process was determined to be 39% and 1.6 respectively, suggesting that the raw material is not being used efficiently.

Therefore by deoxygenating biomass to produce liquid fuel (hydrocarbons), we end up losing 32% of the carbon resource. Furthermore, addition of further oxygen into the system will reduce the carbon efficiency. For example, adding 0.3 mol of oxygen reduces the carbon efficiency to 49%.

The process energy and work requirements can also be determined. For the mass balance given by Eq. (5), the change in enthalpy and Gibbs energy were found to be negative (ΔH = -74 kJ/mol, ΔG = -104 kJ/mol), suggesting that no external heat or work is required. In principal, energy could be produced from the process.

3.2. Van Krevelen Diagram

A graphical representation known as the Van Krevelen diagram (Prins et al., 2007) can be utilised to synthesise the overall mass balances for various biomass conversion processes. The diagram plots the atomic ratios H/C and O/C. The diagram is a useful synthesis tool as the composition of various biomass as well as other compounds containing C, H and O can be represented on the diagram. However, the limitation of the diagram is that compounds such as H_2O, O_2 and H_2 cannot be explicitly represented.

As an example, consider using a biomass with a known composition ($CH_{1.5}O_{0.7}$) to produce liquid fuels ($-CH_2-$) as discussed in section 3.1. The other components involved are H_2O and CO_2. These components are identified on the Van Krevelen diagram, except for water. Water addition or removal can be represented by a straight line with a slope of 45°. In order to move from biomass to $-CH_2-$, one would need to add hydrogen and remove oxygen. In this case, this occurs by converting the biomass into CO_2 and point A (a combination of $-CH_2-$ and H_2O). The quantities of each component can be determined from the lever rule. This mass balance corresponds exactly to the mass balance as given by Eq. 5.

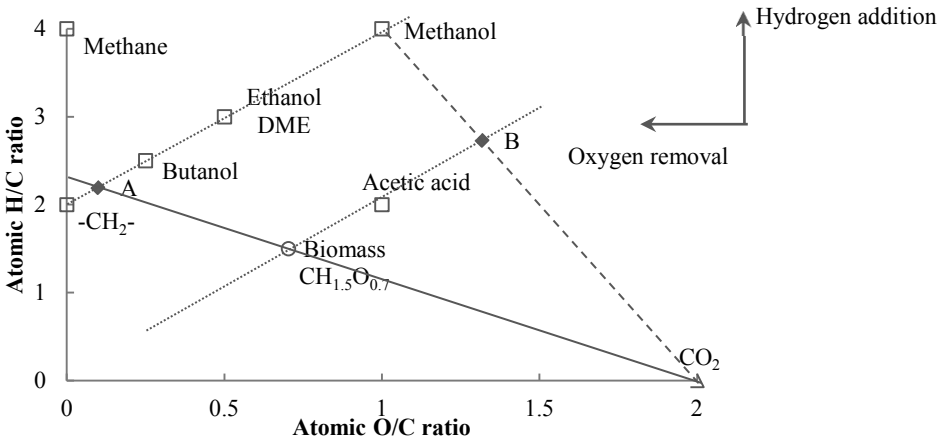

Figure 1. Van Krevelen diagram for the synthesis of biomass conversion processes

Consider a second example, producing methanol from biomass (again considering CO_2 and water as components as well). In this case, both hydrogen and oxygen addition is necessary (which suggests water addition). Point B, the point of intersection between the 45° line passing through the biomass point (the line that represents water addition) and the line between methanol and CO_2 represents the intersection point of feed materials and products. Once again, the quantities of each component can be determined from the lever rule.

3.3. Comparison of performance targets (overall mass balances) for fuel production from biomass

The overall mass balances for various fuels (methanol and hydrocarbons) produced from biomass can be evaluated either from the Van Krevelen diagram. The change in enthalpy and Gibbs energy of each mass balance can also be calculated. The metrics for each mass balance can be determined. All these parameters are summarized in Table 1.

For the case of methanol, the overall mass balance requires water as a feedstock. As previously mentioned, the BTL process could potentially produce water. It is also interesting to note that both processes have exactly the same carbon efficiency of 68%. In terms of Atom Economy and E-factor, the methanol-based process has the highest Atom Economy and the lowest E-factor (even when compared to ethanol or butanol).

This suggests that producing methanol from biomass utilises the feed material more efficiently and generates the least amount of waste (on a mass basis). From an energy and work perspective, it is clear that both processes have a negative change in enthalpy and Gibbs energy (except for the methanol process, which has a slightly positive ΔH). This implies that all processes should potentially be feasible from a heat and work perspective and the processes do not require external heat or work supply. The exergetic efficiency for all the processes are quite high, with the methanol process having the highest efficiency.

Table 1. Comparison of overall mass balances for various fuels produced from biomass.

Product	Overall Mass Balance	ΔH (kJ/mol)	ΔG (kJ/mol)	Carbon Efficiency (%)	Atom Economy (%)	E-Factor	Exergetic Efficiency (%)
Hydro-carbons (-CH_2-)	1.463 $CH_{1.5}O_{0.7}$ ⇒ 0.098 H_2O + -CH_2- + 0.463 CO_2	-73.7	-100.4	68	39	1.6	85
Methanol	1.463 $CH_{1.5}O_{0.7}$ + 0.902 H_2O ⇒ CH_3OH + 0.463 CO_2	3.6	-34.6	68	61	0.64	94

3.4. Performance targets (overall mas balances) for production of chemicals from biomass

Performance targets for the production of chemicals such as acetic acid from biomass are shown in Table 2.

Table 2. Comparison of overall mass balances for chemical produced from biomass.

Product	Overall Mass Balance	ΔH (kJ/mol)	ΔG (kJ/mol)	Carbon Efficiency (%)	Atom Economy (%)	E - Factor	Exergetic Efficiency (%)
Acetic Acid	1.951 $CH_{1.5}O_{0.7}$ + 0.537 H_2O + 0.049 CO_2 ⇒ $C_2H_4O_2$	-89.7	-109.6	100	100	0	89

In order to produce acetic acid from the specified biomass, both hydrogen and oxygen addition is necessary. However, the hydrogen addition is far less than that required for methanol, whereas the oxygen addition for both processes is equal. The consequence of this provides an overall mass balance for acetic acid production which has a carbon efficiency and Atom Economy of 100% i.e. such a process could potentially produce no waste. In fact, as can be seen from the mass balance, a small amount of carbon dioxide is required as feed material.

3.5. Targets for the co-production of fuel and chemicals

Considering the high carbon and atom economy of the acetic acid process, there may be significant advantages in co-producing acetic acid and a fuel. Consider, as an example, co-producing acetic acid and hydrocarbons (-CH_2-). The overall mass balance for such a process could be determined using the Van Krevelen diagram and by determining the limiting variable (either ΔH or ΔG). The overall mass balance is shown in Table 3.

The finding summarized in Table 3 shows that it is possible to co-produce hydrocarbon and acetic acid in a ratio of 1:0.9 with a carbon efficiency and Atom Economy of 87% and 79% respectively.

Table 3. Overall mass balance for the co-production of fuel and chemicals from biomass

Product	Overall Mass Balance	ΔH (kJ/mol)	ΔG (kJ/mol)	Carbon Efficiency (%)	Atom Economy (%)	E - Factor	Exergetic Efficiency (%)
Hydrocarbons ($-CH_2-$) and Acetic acid	$3.246\ CH_{1.5}O_{0.7} + 0.393\ H_2O \Rightarrow -CH_2- + 0.913C_2H_4O_2 + 0.419\ CO_2$	-155.9	0	87	79	0.27	87

This is a substantial increase from simply producing fuel ($-CH_2-$), where the Atom Economy was 39%. It can also be noticed that the water requirement has also decreased from the case where only acetic acid was produced. Note that the process was found to be limited by ΔG and that the process has a high exergetic efficiency.

4. Conclusions

This study introduces a graphical approach for the conceptual design of biorefineries using the Van Krevelen diagram. The approach provides a quick method of screening, evaluating and comparing various biomass conversion processes. The study establishes the overall process mass balance target for the production of various fuels as well as chemicals from biomass. The study also incorporates sustainability metrics such as carbon efficiency, Atom Economy and E-factors to assess these overall mass balance targets. The exergetic efficiency of the various overall mass balances are also determined and compared. These targets, combined with the metrics, provide meaningful insight into maximising feedstock utilisation and process efficiency. Opportunities for co-producing fuels and chemicals can also be assessed.

References

D.J.C. Constable, A. D. Curzons, and V.L. Cunningham, 2002, Metrics to 'green' chemistry—which are the best?, Green Chemistry, 4, 521-527

S. Fernando, S. Adhikari, C. Chandrapal, and N. Murali, 2006, Biorefineries: Current status, Challenges, and Future Direction, Energy & Fuels, 20, 1727-1737

A.C. Kokossis and A. Yang, 2010, On the use of systems technologies and a systmatic approach for the synthesis and design of future biorefineries, Comp. Chem. Eng., 34, 1397-1405

M.J. Metzger, B.J. Glasser, B. Patel, J. Fox, B.C. Sempuga, D. Hildebrandt and D. Glasser, 2013, Liquid Fuels from Alternative Carbon Sources Minimizing Carbon Dioxide Emissions, AIChE Journal, 59, 2062-2078

B. Patel, D. Hildebrandt, and D. Glasser, 2010, An Overall thermodynamic view of Processes: Comparing fuel producing processes, Chem. Eng. Res. Des., 88, 844-860

B. Patel, D. Hildebrandt, D. Glasser, and B. Hausberger, 2007, Synthesis and Integration of Chemical Processes from a Mass, Energy, and Entropy perspective, Ind. Eng. Chem. Res., 46, 8756-8766

M.J. Prins, K.J. Ptasinski, and F.J.J.G. Janssen, 2007, From coal to biomass gasification: Comparison of thermodynamic efficiency, Energy, 32, 1248-1259

R.A. Sheldon, 2011, Utilisation of biomass for sustainnable fuels and chemicals: Molecules, methods and metrics, Catalysis Today, 167, 3-13

Z. Yuan, B. Chen, and R. Gani, 2013, Application of process synthesis: Moving from conventional chemical processes towards biorefinery processes, Comp. Chem. Eng., 49, 217-229

Krist V. Gernaey, Jakob K. Huusom and Rafiqul Gani (Eds.), 12th International Symposium on Process Systems Engineering and 25th European Symposium on Computer Aided Process Engineering.
31 May – 4 June 2015, Copenhagen, Denmark

A Sustainability Driven Methodology for Process Synthesis in Agro-Food Industry

Jochem Jonkman,[a]* Jacqueline M. Bloemhof,[a] Jack G.A.J van der Vorst,[a] Albert van der Padt[bc]

[a]*Operations Research and Logistics Group, Wageningen University, PO. Box 8130, 6700 EW, Wageningen, The Netherlands*
[b]*Food Process Engineering Group, Wageningen University, PO. Box 8129, 6700 EV, Wageningen, The Netherlands*
[c]*FrieslandCampina, Stationsplein 4, 3818 LE, Amersfoort, The Netherlands*
jochem.jonkman@wur.nl

Abstract

Within the agro-food industry, agro-materials are converted into a range of valuable semi-finished and finished products. To reach a sustainable, resource efficient food system, the optimal process pathways converting the agro-material into these products have to be identified. To identify these pathways, a systematic Process Synthesis (PS) method is needed for the agro-food industry. This sustainability driven PS method should enable the synthesis of the optimal process pathways, converting an agro-material into a range of valuable products, producing minimal waste or low-value by-products. In this paper, the elements required for such a method are proposed. The relevance of these elements is illustrated with a simple illustrative case for the processing of tropical fruit. The proposed approach uses Multi-Objective Optimisation methods, to provide decision support for PS to decision makers in the agro-food industry. This leads to new insights in optimal pathways for processing agro-materials for the agro-food industry.

Keywords: Process Synthesis, Agro-Food Industry, Multi-Objective Optimisation, Decision Support.

1. Introduction

In a sustainable, resource efficient food system, agro-materials have to be converted into a range of valuable products. To find the process pathways that enable this optimal conversion, a systematic approach to process (re-)design is necessary.

The design of most food manufacturing processes is historically grown. In a stepwise manner, new technologies were included and processes were reshaped to meet new requirements (legislations, consumer demands, competition). At the start of the 20th century, the agro-food industry generally extracted one product from an agro-material, for example starch from potatoes and sugar from sugar beet. Environmental concerns and decreasing margins forced the industry to valorise and reduce waste streams, extracting for instance whey proteins from whey and using sugar beet pulp for yeast production (van der Padt 2014). In this approach to process design, or Process Synthesis (PS), process pathways are designed sequentially. This evolutionary approach is illustrated in the left side of Figure 1.

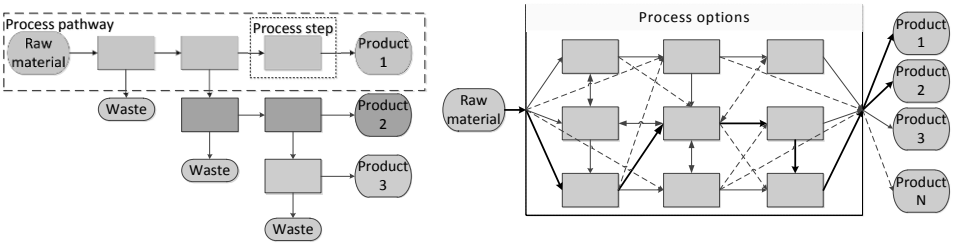

Figure 1: Evolutionary process design (left) and integral process design (right)

A more integral approach to the (re-)design of food manufacturing processes is needed to valorise the full potential of agro-materials (right side of Figure 1).

Recently, Bongers and Almeida-Rivera (2009) showed that PS methods developed for the chemical industry do not suffice in the food assembly industry. Unlike basic chemical products, the functionality and quality of food products is often dependent on their internal structure. They introduce a Product Driven Process Synthesis (PDPS) methodology, taking into account the specific nature of food products and production processes. This methodology maps and optimises a process pathway while considering consumer needs and raw material sourcing (Bongers et al. 2012).

Similar to the chemical industry, the raw materials used by the food assembly industry (such as sucrose and cream) are standardised commodities that can be purchased at the global market. The agro-food industry however, relies on agro-materials for raw materials. Renewable materials, such as agro-materials, vary more in quality than raw materials used by the chemical industry, are subject to seasonality and are only produced in certain areas (Halasz et al. 2005). Additionally, agro-materials contain many components, which in turn have functionalities like foaming capacity or emulsifying capacity. For example, a sugar beet contains sucrose, but also other sugars, proteins, cellulose, lignin and salts (Kuhnel et al. 2011). The choice to primarily extract sucrose from the sugar beet greatly influences the potential use of the other components, as, for example, the proteins and their functionality are lost during the current extraction process of sucrose. The focus on a single end product in a product oriented method like PDPS, although applicable for food products, is not effective to ensure full valorisation of an agro-material. Instead, similar to for instance (Simasatitkul et al. 2012), multiple products should be considered. This is necessary to arrive at a sustainable food production system. To find the process pathways that optimally convert an agro-material into valuable finished and semi-finished products, a range of products and alternative process pathways have to be considered. In this paper the elements relevant for such a sustainability driven PS method for the agro-food industry are proposed (section 2) and illustrated with a small illustrative case (section 3). Conclusions and ideas for future research are presented in section 4.

2. Sustainability driven PS for agro-food industry

A product portfolio has to be defined to find those process pathways that convert the agro-material into a range of valuable products. The availability and structure of the agro-material and its functionalities and a database of food and non-food products and usage are used to develop a perceived product portfolio.

Next the process pathways necessary to convert the agro-material into these products are synthesised. To manage and evaluate the number of alternatives, and choose among the better ones, decision support is needed. Meeuse (2007) states that optimisation

based mathematical programming has limited applicability for structured food products, due to the absence of rigorous models describing the relevant physical and chemical phenomena. However, to determine the boundary conditions within which a certain process pathway is preferable, only a limited level of detail is needed. Abstract representations of separation, structuring, transformation and stabilisation processes are used to build a type of superstructure. Because any process design problem has multiple objectives (Westerberg 2004), Multi-Objective Optimisation (MOO) methods are needed to find the better designs among the many alternatives and support decision making. The sustainability driven PS method we propose, consists of the following steps:

1. Develop a product portfolio based on agro-material composition and functionalities.
2. Synthesise process pathways, using abstract representations of processes, to create a superstructure.
3. Use MOO methods to find the better designs among the alternatives and support decision making.

The method should explicitly consider structure, functionalities, seasonality and regional aspects like transportation. In the following section we illustrate this method with an illustrative case for a tropical fruit process.

3. Illustrative case

Tropical fruits are harvested and can generally be directly send for export as whole fruits, or further processed into many food (e.g. snacks, drinks, ingredients) and non-food (e.g. peels as cattle-feed, seeds for landfill) products.

3.1. Product portfolio development

In this illustrative case, a limited product portfolio is considered, as it is sufficient to illustrate the proposed elements of the PS method without adding too much detail. The first step is therefore bypassed by choosing a basic product portfolio, consisting of whole fruits, fresh cut fruit and dried fruits for the local market and whole and dried fruits for the global market. Additional products like peels and seeds are considered to be waste (see Figure 2).

3.2. Synthesise process pathways

When the processor á priori decides to export whole fruits (pathway 1), he may want to stabilise ripening processes in the fruits to extend their shelf life, increase the time available for sorting and making a larger part of the fruits suitable for long distance transport. A mild heat treatment can be used for this purpose (Tharanathan et al. 2006). However, quality development in these fruits is related to the ripening processes (Tharanathan et al. 2006). Therefore, stabilising the ripening process will negatively affect the potential of the fruits that cannot be sent for export. When considering the full product portfolio instead, the ‘ripening functionality’ of the whole fruits can be maintained by omitting the stabilising step. This reduces the amount of fruit suitable for export, but increases the quality and value of the remaining product portfolio. In the illustrative case, the other options are producing fresh cut fruits (pathway 2) and dried fruits (pathway 3). An overview of the process pathways is given in Figure 2.

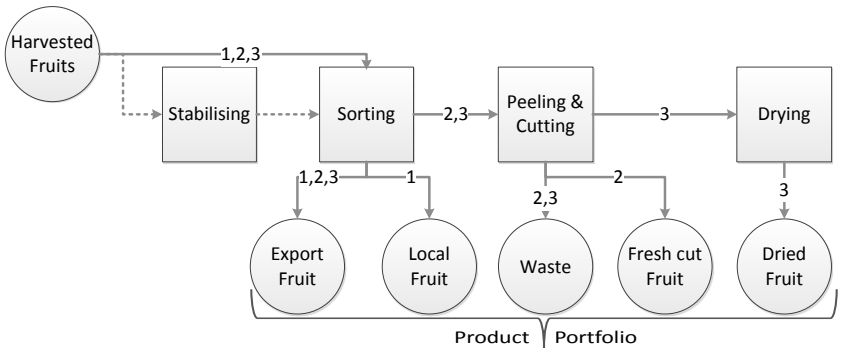

Figure 2: Product portfolio and three process pathways (indicated 1, 2, 3) of the illustrative case

3.3. Decision support

Fresh cut fruits can only be sold locally due to shelf life limitations. They will fetch a lower price than exporting whole fruits or sales of dried fruit, because they can only be sold during the fruit its season, in which the fruits are abundant and prices generally drop. Although sales of dried fruits drop when the fresh fruits are available, dried fruits can be sold outside of the season, due to their extended shelf life, and will therefore fetch a higher price. These issues are examples of seasonal and regional aspects relevant for the agro-food industry. The revenue for each product, energy input for each process step and conversion rates assumed, are shown in Table 1.

The processor has to decide which process pathway and product portfolio has his preference, based on his objectives. To enable easy graphical representation, two objectives are considered in this example. We assume the processor wants to maximise revenue and minimise energy consumption.

In Figure 3 the Pareto optimal (or efficient) solutions for the showcase are presented, and example product portfolios are shown. These solutions are the solutions that cannot be improved respective to one objective, without compromising at least one of the other objectives (Mavrotas 2009).

Table 1: Assumed revenue and energy input values and conversion rates

Revenue (€ / kg)				Energy input (kJ / kg)		
Export Fruit	Local Fruit	Fresh Cut	Dried Fruit	Sorting	Peeling	Drying
0.80	0.25	0.70	9.00	2.16	4.32	2500

Suitable for export	Obtained fresh cut after peeling	Drying ratio
30%	65%	1:10

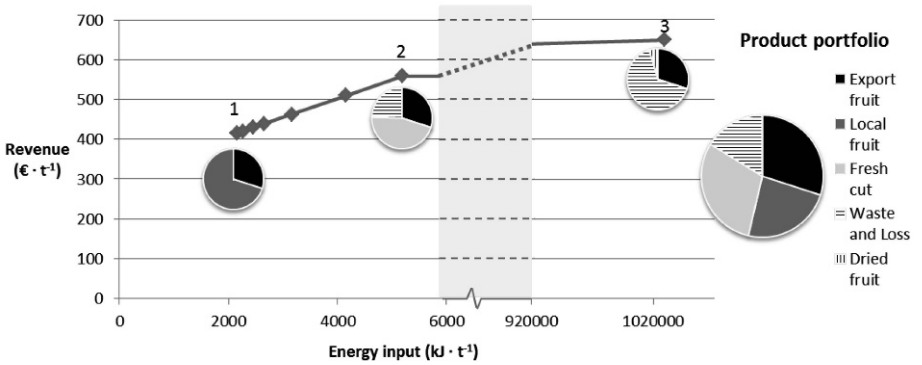

Figure 3: Pareto optimal solutions of the illustrative case, process pathways 1, 2 and 3 are indicated accordingly

Several MOO methods exist that can identify the Pareto optimal solutions. For a priori methods, the decision maker specifies his preferences before finding solutions to the problem (e.g. by assigning weights or target values to the objectives). A posteriori methods first generate the set of Pareto optimal solutions, after which the decision maker chooses from among the options. In a linear problem like this illustrative case, the weighting method will only provide extreme solutions (Mavrotas 2009). To generate a set of Pareto optimal solutions that includes non-extreme Pareto optimal solutions, the augmented ε-constraint method as described by Mavrotas (2009)Mavrotas (2009) is used. The product portfolios resulting from pathway 1, 2 and 3 are indicated in Figure 3. These are the extreme Pareto optimal solutions. The other points shown are examples of non-extreme Pareto optimal solutions.

The Pareto curve and related product portfolios provide insight in the relation between the performance of a process pathway and the resulting product portfolio. It is clear that a lot of energy is needed to produce dried fruits. On the other hand, the shelf life of dried fruits is much longer than the shelf life of fresh cut fruits, and they can be stored at ambient conditions, while fresh cut fruits require chilled storage and transportation. In this example, product portfolios with dried fruits require much more energy than product portfolios with only whole fruits or fresh cut fruits. However, if the scope is extended to include transportation, the energy requirement of portfolios containing fresh cut fruits will increase compared to the portfolios containing dried fruits. This shows the importance of considering regional aspects like transportation in PS for the agro-food industry, to prevent obtaining a sub-optimal Food Supply Chain (FSC) by optimising only the agro-food industry part of the chain.

The processor can use the Pareto-curve obtained through MOO, to determine the desired combination of process pathway and product portfolio. Decision making is influenced by the relative importance of the objectives, and preferences for a certain product portfolio. The preferred solution is influenced by external factors, such as changes in energy price and demand. An (expected) increase in energy price can cause the preferred product portfolio to shift to a portfolio with less energy consumption. These uncertainties are not yet taken into account, but should be considered, to obtain robust results with the proposed PS method, and determine the boundary conditions

within which a process pathway is preferred. This will provide new insights into optimal process pathways for the agro-food industry, and helps to identify potential for process development.

4. Conclusions and future research

A PS method for systematic design of process pathways for Agro-Food industry is proposed. Starting point for the method is the potential of the agro-material, related to its structure and functionalities. MOO methods are used to find Pareto optimal solutions to the problem and enable evaluation of the alternative process pathways to support decision making. This sustainability driven PS method should explicitly consider structure, functionalities, seasonality and regional aspects like transportation, as is illustrated by the case. Sensitivity analysis is needed to determine the boundaries within which a certain process pathway is attractive. The decision support provided by this abstract representation leads to identifying opportunities for process development. This link between decision support and process engineering provides a novel way of PS.
The potential of the proposed method needs to be explored by application to real life industrial cases, using different agro-materials. The elements relevant for the agro-food industry should be taken into account. Additionally, the agro-food industry is only one part of a FSC. Extending the method, considering the entire FSC, will prevent finding optimal solutions for the agro-food industry leading to sub-optimal FSCs.

Acknowledgements

The project is carried out within the framework of the Institute for Sustainable Process Technology (the Netherlands)

References

P. M. M. Bongers and C. Almeida-Rivera (2009). "Product driven process synthesis methodology." Computer Aided Chemical Engineering 26: 231-236.

P. M. M. Bongers, C. Almeida-Rivera, A. K. Iftekhar and S. Rajagopalan (2012). Product Driven Process Design Method. Computer Aided Chemical Engineering, Elsevier. Volume 31: 195-199.

L. Halasz, G. Povoden and M. Narodoslawsky (2005). "Sustainable processes synthesis for renewable resources." Resources, Conservation and Recycling 44(3): 293-307.

S. Kuhnel, H. A. Schols and H. Gruppen (2011). "Aiming for the complete utilization of sugar-beet pulp: Examination of the effects of mild acid and hydrothermal pretreatment followed by enzymatic digestion." Biotechnology for Biofuels 4: 14.

G. Mavrotas (2009). "Effective implementation of the ε-constraint method in Multi-Objective Mathematical Programming problems." Applied Mathematics and Computation 213(2): 455-465.

F. M. Meeuse (2007). "Process synthesis for structured food products." Computer Aided Chemical Engineering 23: 167-179.

L. Simasatitkul, A. Arpornwichanop and R. Gani (2012). Design methodology for bio-based processing: Biodiesel and fatty alcohol production. Computer Aided Chemical Engineering, Elsevier. Volume 31: 855-859.

R. N. Tharanathan, H. M. Yashoda and T. N. Prabha (2006). "Mango(Mangifera indica L.), “The King of Fruits”—An Overview." Food Reviews International 22(2): 95-123.

A. van der Padt (2014). Sustainable Production of Food. Wageningen, Wageningen University, Wageningen UR.

A. W. Westerberg (2004). "A retrospective on design and process synthesis." Computers & Chemical Engineering 28(4): 447-458.

Krist V. Gernaey, Jakob K. Huusom and Rafiqul Gani (Eds.), 12th International Symposium on Process Systems Engineering and 25th European Symposium on Computer Aided Process Engineering.
31 May – 4 June 2015, Copenhagen, Denmark

Evaluation of Dimethyl Carbonate and Ethylene Glycol Production from Biomass

Chayanit Choomwattana[a], Aksornchan Chaianong[a], Worapon Kiatkittipong[b], Pichayapan Kongpanna[a], Suttichai Assabumrungrat[a,c,*]

[a]*Center of Excellence in Catalysis and Catalytic Reaction Engineering, Department of Chemical Engineering, Faculty of Engineering, Chulalongkorn University, Phayathai Road, Wang Mai, Phatumwan, Bangkok 10330, Thailand*
[b]*Department of Chemical Engineering, Faculty of Engineering and Industrial Technology, Silpakorn University, Nakhon Pathom 73000, Thailand*
[c]*PTT Group Frontier Research Center, PTT Public Company Limited, Bangkok 10900, Thailand*

suttichai.a@chula.ac.th

Abstract

In this study, an integrated process of dimethyl carbonate (DMC) and ethylene glycol (EG) production from biomass was proposed. The process was started from biomass gasification, CO_2 separation and CO_2 conversion to ethylene carbonate. DMC and EG were produced via transesterification using reactive distillation and extractive reaction. A variety of key parameters of each part was examined to optimize operating condition, which is focused on heat consumption. DMC and EG can achieve 99.5 % mole of purity. The overall production can sustain itself without any external heat sources by using biomass combustion, and all performance indicators were considered under the energy self-sufficient conditions. The ratio of biomass fed to the gasifier and the combustor was found to be 0.34:0.66 (under energy self-sufficient conditions) where the C, H and O atom efficiencies of the process achieved were 32.87, 48.96 and 37.72%, respectively. Since all energy was supplied by biomass itself, the process was considered as carbon neutral with a fraction of carbon dioxide fixation from biomass into chemicals of 0.24.

Keywords: Aspen Plus; Biomass gasification; Process design; Process simulation

1. Introduction

Over several decades, greenhouse gases such as carbon dioxide (CO_2) and methane (CH_4) have been concerned as a crucial problem because it causes global warming and climate change (Song, 2006, Xu et al., 2010). Many attempts have been paid to search for new processes to utilize CO_2 (Aresta et al., 2007). Recent researches have shown that utilization of CO_2 as a chemical feedstock can produce a variety of chemical products via chemical and electrochemical processes (Olah et al., 2009). The products are for example dimethyl ether, formic acid, methane or DMC (Sakura et al., 2007).

DMC is one of significant chemical products as it can be used as methylating reagent, solvent, intermediate,or fuel additive etc. (Delledonne et al., 2001, Tundo et al., 2002). DMC can also be produced by various types of reaction pathways which have potential for utilizing the CO_2. One of those is the reaction between CO_2 and methanol. However, in this manner, it has to be operated at critical temperature and pressure (Guo et al.,

2008), leading to high energy consumption. Hence, other reaction pathways such as urea route, propylene carbonate route and ethylene carbonate route are currently explored.

The primary objective of this research is to develop a new DMC and ethylene glycol production from biomass via transesterification of ethylene carbonate and methanol. ASPEN Plus simulator was employed in order to optimize operating conditions in each main section, i.e. biomass gasification, methanol synthesis, CO_2 separation, ethylene carbonate synthesis, and DMC and EG synthesis, by focusing on heat consumption optimization. The atom efficiency and amount of CO_2 fixation into chemical is evaluated under energy self-sufficient condition where the process could sustain itself without any external heat source by partially utilizes biomass to generate heat.

2. Process Description

Figure 1 shows a simplified process flow diagram of DMC and EG production from biomass. Biomass was fed to the gasifier where autothermal reforming takes place. The product stream was further fed to CO_2 separation unit to produce a mixture of H_2 and CO before entering to the methanol production process. The separated CO_2 was utilized by reacting with ethylene oxide to produce ethylene carbonate. DMC and EG was produced via transesterification of methanol and ethylene carbonate in reactive distillation. In the purification process of DMC, an extractive distillation of DMC/methanol can be used to separate azeotropic mixture of DMC/methanol. For this work, aniline is used as entrainer in the extractive distillation as proposed by Hsu et al. (2010). In order to operate under energy self-sufficient condition, biomass was splitted and sent to a combustor for providing heat and electricity.

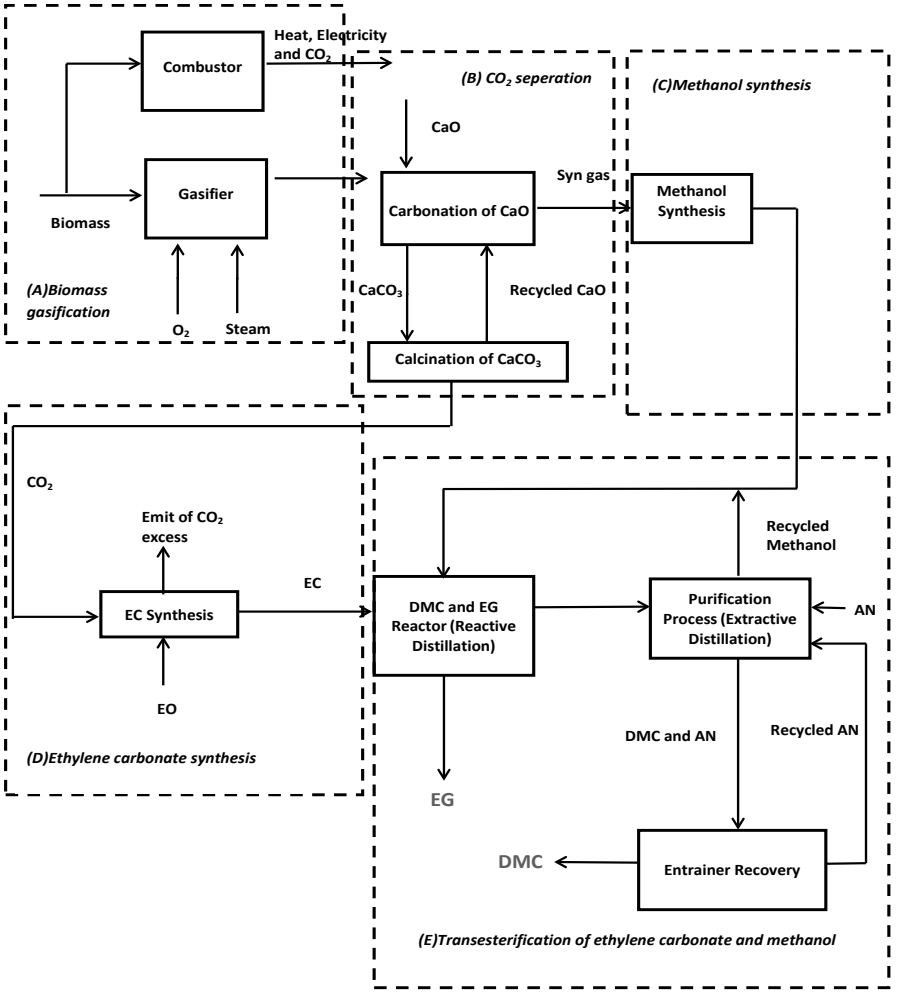

Figure 1 Diagram of integrated process of DMC and ethylene glycol production from biomass

3. Results and Discussion

3.1 Process design

Biomass gasification

The gasifier temperature of 900 °C was selected in this study following the previous report (Franco et al., 2013) which showed that this temperature favors energy and carbon conversions, as well as gas yield. The target of the gasifier in this study is to produce a mixture of H_2 and CO with H_2/CO of 2 for further methanol synthesis. The amounts of H_2O and external oxygen (represented by steam to biomass ratio (SBR) and equivalence ratio (ER), respectively) were adjusted to obtain H_2/CO ratio of 2 accompanying to balance endothermic and exothermic heat for the operation of energy self-sufficient gasification. The investigation to find suitable SBR and ER at the temperature of 900 °C found that SBR of 1.77 and ER of 0.718 could satisfy H_2/CO ratio of 2 and heat duty of 0.

Carbon dioxide separation
CaO was used as CO_2 sorbent. The $CaCO_3$ was regenerated in a calcination reactor. RGibbs model with the Peng-Robinson EOS property method was used to model both carbonation and calcination reactors w. The carbonation and calcination reactors were operated at a pressure of 1 bar with suitable operating temperatures of 600 and 860 °C, respectively.

Ethylene carbonate synthesis
The optimum operating condition for the ethylene carbonate reactor was found to be 30 °C and 25 bar in order to achieve high yield of ethylene carbonate.

Transesterification of methanol and ethylene carbonate for DMC and ethylene glycol production
The design flow sheet of this section integrated the reaction section and the separation section including reactive distillation reboiler, extractive distillation reboiler and entrainer recovery distillation reboiler by minimizing energy consumption.

- Design of reactive distillation column

For the given product specifications, the configuration of reactive distillation column reported by Hsu et al. (2010) was firstly adopted in our simulation. With respect to reactive distillation reboiler, recycled methanol flow rate seems to be the most important factor that affects the reboiler heat duty. The optimal design flowsheet of this column indicated that the output stream of EG could achieve mole fraction purity of 0.995 as the bottom product with an overall EG yield of 0.995. As the process was set up using optimal design specifications, the lower energy consumption in our proposed reactive distillation comparing to the previous study (Hsu et al., 2010) could be achieved.

- Design of extractive distillation and entrainer recovery column

Considering the top stream of reactive distillation column (63 °C, 1 bar, methanol mole fraction of 0.833), azeotropic composition of DMC and methanol could be found. Thus, the process was set up by using optimal design specifications of both columns, so the lower energy consumption in our proposed extractive and entrainer recovery comparing to the previous study (Hsu et al., 2010) could be obtained. Energy consumption was optimized by adjusting distillate rate of two distillation columns as process specifications were set up. According to extractive distillation, the following steps of calculation are applied to obtain a near optimal design: 1) Place the heavy-boiling entrainer ($N_{Aniline}$) and mixture of methanol and DMC feed location ($N_{methanol+DMC}$) on the top and the lowest of the extractive section, and 2) vary the number of stages in the rectifying, extractive and stripping section.

3.2 Overall integrated process of the optimal base case study
According to the suitable operating condition of each section including biomass gasification, CO_2 separation, methanol synthesis, ethylene carbonate synthesis, and DMC synthesis, the energy requirements of different units were calculated. Atom efficiency (or atom economy) was chosen as a criterion for considering reaction efficiency. For the base case study, it is found that the values of atom efficiency are C: 73.20, H: 92.95, O: 58.69. However, note that with this criterion definition, atom efficiency is not referring to energy efficiency for the overall chemical process.

3.3 Overall integrated process with an operation under energy self-sufficient condition

The operating condition and system performance of DMC production from biomass under energy self-sufficient condition is summarized in Table 1. The appropriate fraction of biomass fed to combustor and gasifier should be 0.66 and 0.34, respectively, in order to sustain the energy of overall process. However, the amount of CO_2 from CO_2 separation unit is more than that required for chemical production, an excess of CO_2 was purged from the chemical production process, therefore, a fraction of total CO_2 emission (combustion and purge) from biomass input is 0.76, while carbon dioxide fixation into chemicals is 0.24. Considering atom efficiency, it is found that the atom efficiencies under energy self-sufficient conditions are C: 32.87, H: 48.96, O: 37.72.

Table 1 Operating conditions and system performance of DMC production from biomass under energy self-sufficient condition

Operating conditions and performance indicators	
Overall biomass mass flow rate	1,100 (kg/h)
Biomass mass flow rate to the gasifier	376.68 (kg/h)
Biomass mass flow rate to the combustor	723.32 (kg/h)
Biomass fraction to the gasifier	0.34 (-)
Overall product yield	43.76 (wt.%)
Carbon atom efficiency	32.87 (%)
Hydrogen atom efficiency	48.96 (%)
Oxygen atom efficiency	37.72(%)
CO_2 fixation to chemicals	0.24 (-)

4. Conclusion

In this study, the simulation of overall process for DMC and ethylene glycol production from biomass was developed using the ASPEN Plus simulator. The process consists of five main sections i.e. biomass gasification, CO_2 separation, methanol synthesis, ethylene carbonate synthesis and DMC synthesis. The key performance indicators of biomass to chemical i.e. 1) atom efficiency under energy self-sufficient condition and 2) carbon dioxide fixation from biomass into chemicals under energy self-sufficient condition were defined. It is found that the atom efficiencies are C: 32.87, H: 48.96, O: 37.72 with carbon dioxide fixation from biomass into chemicals value of 0.24 could be achieved under energy self-sufficient conditions.

5. Acknowledgement

Financial support from The Thailand Research Fund and PTT Group Research Scholar from PTT Group Frontier Research Center is gratefully acknowledged. P. Kongpanna

would like to acknowledge the Ph.D. scholarship from Dussadeepipat Scholarship, Chulalongkorn University.

References

M. Aresta, 2010, Carbon Dioxide as a Chemical Feedstock. Wiley-VCH

D. Delledonne, F. Rivetti, U. Romano, 2001, Development in the production and application of dimethylcarbonate, Applied catalysis A: General, 221, 241-251

C. Franco, F. Pinto, I. Gulyurtlu, I. Cabrita, 2003, The study of reactions influencing the biomass steam gasification process, Fuel, 82, 835-842

X.C. Guo, 2008, Critical temperatures and pressures of reacting mixture in synthesis of dimethyl carbonate with methanol and carbon dioxide, Chinese Chemical Letters, 19, 249-252

K.Y. Hsu, Y.C. Hsiao, I.L. Chien, 2010, Design and control of dimethyl carbonate-methanol separation via extractive distillation in the dimethyl carbonate reactive-distillation process, Ind. Eng. Chem. Res., 49, 735–749

P. Kongpanna, V. Pavarajarn, R. Gani, S. Assabumrungrat, 2014, Techno-economic evaluation of different CO_2 based processes for dimethyl carbonate production. Chemical Engineering Research and Design , http://dx.doi.org/10.1016/j.cherd.2014.07.013

G.A. Olah, A. Goeppert, G.K.S. Prakash, 2009, Beyond oil and gas: The methanol economy. Wiley-VCH

T. Sakura, J.C. Choi, H. Yasuda, 2007, Transformation of carbon dioxide. Chem.Rev., 107, 2365-2387

C. Song, 2006, Global challenges and strategies for control, conversion and utilization of CO_2 for sustainable development involving energy, catalysis, adsorption and chemical processing, Catalysis Today, 115, 2-32

T. Song, J. Wu, L. Shen, J. Xiao, 2012, Experimental investigation on hydrogen production from biomass gasification in interconnected fluidized beds. Biomass and Bioenergy, 36, 258-267

P. Tundo, M. Selva, 2002, The chemistry of dimethyl carbonate, ACC.Chem., 35, 706-716

Y. Xu, L. Isom, M.A. Hanna, 2010, Adding value to carbon dioxide from ethanol fermentations, Bioresource technology, 101, 3311-3319

Krist V. Gernaey, Jakob K. Huusom and Rafiqul Gani (Eds.), 12th International Symposium on Process Systems Engineering and 25th European Symposium on Computer Aided Process Engineering.
31 May – 4 June 2015, Copenhagen, Denmark

Simulation of Carbon-Dioxide-Capture Process using Aqueous Ammonia

Akrawin Jongpitisub[a], Kitipat Siemanond*[a], Amr Henni[*,c]

[a]*Petroleum and Petrochemical College,Chulalongkorn University, 254 Pathumwan, Bangkok 10330, Thailand*
[b]*Center of Excellence on Petrochemical and Materials Technology, Thailand*
[c]*Faculty of Engineering and Applied Science, University of Regina, Canada*

Abstract

Recently, carbon dioxide (CO_2) emissions to the atmosphere have become an issue for many industries, especially coal-fired power plants, due to their contribution to global warming. Many research projects were directed towards the development of effective solvents to combat these severe environmental problems. Aqueous ammonia is a solvent that has been proposed as a replacement to conventional aqueous monoethanolamine (MEA) in post-combustion CO_2 capture. In this study, an aqueous ammonia based CO_2 capture process was simulated by Aspen Plus simulator for capturing about 90 % by weight of CO_2 with a purity of 98 % by weight from a post-combustion flue gas based on a 180 MW_e coal-fired power plant. The simulation of this process was performed to meet the ammonia emission standard which allowed less than 2 kg/hr of ammonia emission. An ammonia-based simulation process consists of two parts: the CO_2 absorption process and the ammonia abatement process. To minimize the energy consumption of the process, heat integration was applied by adding a Heat Exchanger Network (HEN). HEN was designed by stage-wise model (Yee and Grossmann, 1990) and validated using the Aspen Plus simulator. Furthermore, capital investment and annual costs were investigated using Aspen Plus and some economic parameters to assess the feasibility of this process based on standard environmental regulations. The results showed that the performance of actual aqueous ammonia plants using process integration reduced the energy requirement from a "non-integrated process" by 58 % on the heaters, coolers and electrical units, resulting in a theoretical decrease of 47 % in the annual cost of utilities, compared to the cost without process heat integration.

Keywords: Post Combustion CO_2 Capture, MEA Scrubbing Process, Ammonia Scrubbing Process, Simulation Modelling, Heat Exchanger Network.

1. Introduction

Post-combustion capture (PCC) with chemical absorption has been considered as a feasible way for capturing huge amount of CO_2 emissions from coal-fired power plants. Commercially available chemical absorption technologies are mainly based on amines, especially monoethanolamine (MEA) due to the advantages of stable operation, high reactivity and high absorption capacity. However, the MEA process suffers from several critical disadvantages, such as high energy requirement for solvent regeneration and amine degradation as a result of high temperature in the regeneration section which is around 120 ºC. These facts cause the process to be unattractive for large scale operation. Compared to MEA, aqueous ammonia has advantages of high CO_2 loading capacity, no absorbent degradation and a low temperature in regeneration section (85-95 ºC) where

low-grade thermal energy can be used. Moreover, aqueous ammonia has the potential to capture CO_2, SO_2 and NO_x in the flue gas simultaneously. However, ammonia abatement is a necessary system for the aqueous ammonia process as ammonia can be volatile at operating conditions. In this study, an aqueous ammonia flow sheet for post-combustion CO_2 capture was simulated and optimized using a commercial simulation program (Aspen Plus). Then, a process heat integration by HEN using stage-wise model with General Algebraic Modelling System (GAMS) software was applied to optimize the energy requirement of heaters and coolers of the process. Finally, Aspen Plus was also used to calculate the investment cost to assess the feasibility of the aqueous ammonia based process for CO_2 capture.

2. Ammonia-based scrubbing system.

In this study, the Redlich–Kwong equation of state and the Electrolyte-NRTL model were used to compute the properties of the vapour phase and liquid phase, respectively. Flue gas from a 180 MW_e coal burning power plant with a flow rate 32 of ton/hr, and a gas composition of 84 % N_2, 12 % CO_2, and 4 % water vapour in standard volume (Khonkaen, 2014) was simulated in this study. The flow sheet development was divided into two parts including the CO_2 capture system and the ammonia abatement system.CO_2 capture system was designed to capture CO_2 about 90 % by weight from the flue gas. The flowsheet was optimized by varying the concentration of ammonia solution in a range between (2 and 8) wt. % and CO_2 lean loading of ammonia solution from 0.20 to 0.35 mole CO_2/mole NH_3. Then, 98 % by weight of CO_2 purity entering storage section was specified by varying the reflux ratio (mass), distillation rate and liquid holdup in the stripping section. The ammonia abatement system was used to recycle the volatized ammonia and also minimize ammonia vent to the atmosphere due to restriction of environmental standards. Vented ammonia flow rate was kept below 2 kg per hour based on ammonia emission standards. This limitation was set as the target of the absorber in the ammonia abatement system and achieved by varying aqueous ammonia concentration at the high loading. Obviously, a sequential optimization was observed (Zhang and Guo, 2013).

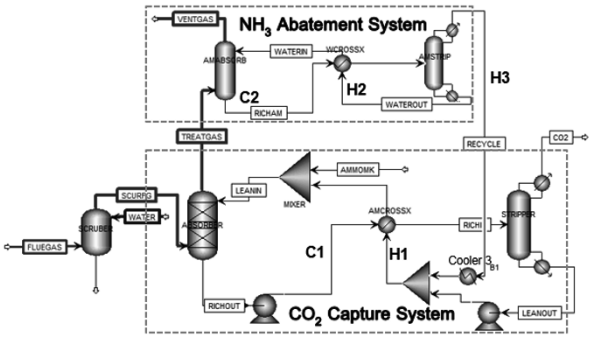

Figure 1. Simplified process flow diagram of aqueous ammonia-based scrubbing system.

2.1. Carbon-dioxide capture system

A simplified process flow diagram of CO_2 capture system was shown in Figure 1. At first, flue gas at high temperature from coal-fired power plant was cooled down to 46.1 ºC with a pressure near atmospheric pressure (115.1 kPa) in the scrubbing section by cooling water before entering to the absorber. Then, the flue gas with CO_2 contacted the

aqueous ammonia solution as counter-current flow to separate CO_2 from the flue gas stream. In the absorber column section, the equivalent equilibrium stages of the absorber were set at 20 stages. The packing type was chosen as DZ-II-750Y for economic evaluation, one of the CY structured packings, which has high mass transfer efficiency (Haroun et al., 2012; Zhao et al., 2011).

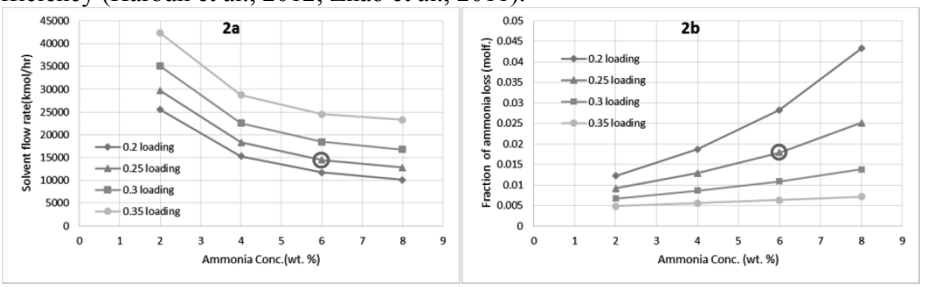

Figure 2a/2b.Optimization of ammonia solvent in the CO_2 capture system.

It is known that the annual cost is mainly due to the energy requirement from the regeneration of the solvent and utilities. Therefore, optimization of the solvent usage was adopted to find minimum-energy-usage condition for CO_2 capture process. Solvent circulation rate and fraction of ammonia loss (TREATGAS) were effectively related to the overall energy requirement of the system as shown in Figures 2a and 2b. Solvent flow rate and the fraction of ammonia loss were optimized by varying the ammonia concentration and CO_2 loading based on 90% CO_2 recovery. The result showed more ammonia concentration in the solvent flow caused more fraction of ammonia loss in TREATGAS stream resulting in more energy requirement in the ammonia abatement system. Increasing the ammonia concentration led to a decrease in the required solvent flow rate. The crucial parameter which affected the energy performance of ammonia-based system was the loading. Loading refers to the moles of CO_2 carrying species over the moles of NH_3 carrying species as specified in Equation 1.

$$\textbf{Loading} = \frac{[CO_2] + [HCO_3^-] + [CO_3^{2-}] + [NH_2COO^-]}{[NH_3] + [NH_4^+] + [NH_2COO^-]} \quad (1)$$

In case of increasing loading in the LEANIN stream, the fraction loss of ammonia decreased while the solvent flow rate deceased because of reduction in term of ammonia species and the availability to capture CO_2 from the flue gas. The optimal concentration of ammonia solution and CO_2 lean loading at 111 kPa and 25 ºC were 6 wt. % and 0.25 mole CO_2/mole NH_3, respectively. The optimal condition resulted in a solvent flow rate and ammonia loss equal to 14666 kmol/hr and 16.75 kmol/hr, respectively. Rich CO_2 ammonia solution had a loading of approximately 0.36 mole CO_2/mole NH_3 left from the bottom of the absorber to the stripping section for regeneration. The rich CO_2 ammonia solution was pumped and heated up at around 120 kPa and 60 ºC, respectively, before entering to the stripper. Heat from the reboiler was used to dissociate the chemical bonds of the formed carbamates and other compounds between ammonia and CO_2. Then, over 98 wt. % of CO_2 purity was stripped out at the top and the regenerated ammonia that exited from the bottom of the stripper. The condenser and reboiler temperatures were simulated in the ranges of (25 to 30) ºC and (85 to 95) ºC, respectively. Ammonia solution was mostly recycled back to the absorber section in order to minimize the ammonia usage. Ammonia solution and make-up water were used to maintain the concentration and CO_2 lean loading of the aqueous ammonia solution.

2.2. Ammonia abatement system

Process flow diagram of ammonia abatement system is shown in Figure 1. This system consists of an absorber to remove ammonia from the treated flue gas (TREATGAS stream) by using water, and a stripper to recover ammonia from the used absorbent (RICHAM stream). The TREATGAS stream is the flue gas with some ammonia contamination, leaves the absorber in CO_2 capture system and is then treated by counter-current flowing water stream with low-ammonia concentration and high CO_2 loading. The number of equivalent equilibrium stages of the absorber of this abatement system was set at 15 stages. The WATERIN stream at ambient condition with the flow rate, ammonia concentration and CO_2 loading of 832 kmol/hr, 9 ppm (by mass) and 1.2 mole CO_2/mole NH_3, respectively, were used to capture volatized ammonia in TREAT GAS stream from the CO_2 capture system. The flow rate of the treated flue gas (VENTGAS stream) in this abatement system was around 1.7 kg/hr which was acceptable for environmental emission standards. The used absorbent stream with rich ammonia (RICHAM stream) from the bottom of the absorber was regenerated in the stripping section. After regeneration, the stream with rich ammonia (RECYCLE stream) from the top of stripper of the abatement system was recycled to the absorber of CO_2 capture system to save ammonia usage in the overall process. The regenerated absorbent stream with lean ammonia (WATEROUT stream) from the stripper of the abatement system was regenerated and sent to the ammonia absorber to minimize water usage in ammonia abatement system. The most important operating conditions of the main streams are shown in Table 1.

Table 1. Optimal operating parameters of main streams in overall CO_2 capture process.

Streams	Optimal Operating Conditions
FLUEGAS	32 ton/hr, at 46.1ºC and 115.1 kPa
LEANIN	270 ton/hr, 6 wt. % NH_3 and 0.25 CO_2 loading at 25 ºC and 111kPa
TREATGAS	26 ton/hr, at 29 ºC and 101.325 kPa
VENTGAS	25.5 ton/hour at 32 ºC and 101.325 kPa
CO_2	6 ton/hr, 98 wt. % CO_2 at 25 ºC and 101.325 kPa

3. Process heat integration

Process heat integration is an important tool to reduce energy usage in the designed process by applying HEN. In the scratch process has three hot process streams from the scratch; H1, H2 and H3, and two cold process streams; C1 and C2, from the simplified CO_2 capture process, as shown in Figure 1, consumed heating and cooling duties of 24567 and 25284 kW, respectively. Heat integration was applied by GAMS program using the stage-wise model (Yee and Grossmann, 1990), as shown in Figure 4. The result from the GAMS model was the conceptual HEN design as shown in Figure 5a with two exchangers for H1-C1 and H2-C2 matches and heating and cooling duty savings of 9987 and 10705 kW, respectively. This conceptual process design with process heat integration, shown in Figure 5a, was validated by Aspen Plus (Figure 5b) simulator to ensure the feasibility of the process. The results showed that the relative error between the conceptual process and the validated process was very small.

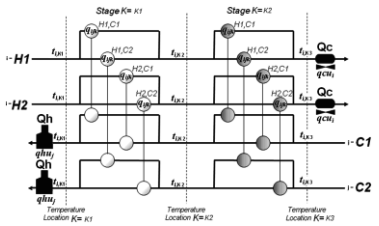

Figure 4.Stage-wise model for HEN (Yee and Grossmann, 1990)

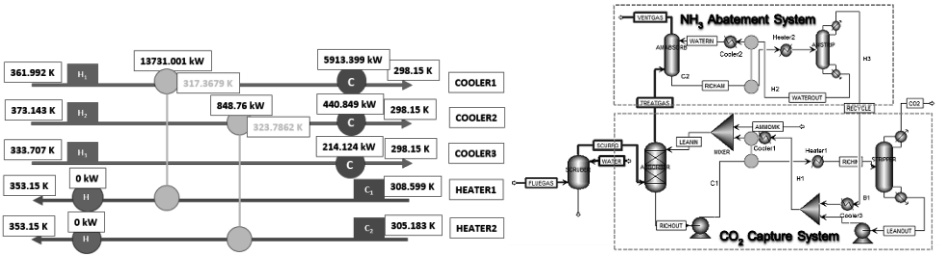

5a 5b

Figure 5a/b.Conceptual process integration from GAMS and validated process flow diagram of improved aqueous ammonia-based scrubbing system (Aspen Plus) with process heat integration.

The validated result showed that the energy requirement of the overall system was reduced by 58.1% compared to the ammonia-based process without process integration. The saving in hot and cold utilities were 59.3% and 57.7%, respectively as shown in Table 2. Furthermore, the overall energy used in regeneration of both CO_2 capture system and NH_3 abatement system was 8601 kJ/kg CO_2 which was a bit higher than the value reported as 8472 kJ/kg CO_2 by Zhangand Guo (2013) for a 550 MW plant size.

4. Economic evaluation

The economic evaluation of the process indicated the feasibility of the process design. In this study, the economics of the ammonia process was divided into two parts including the capital investment and the annual costs of the plant. The capital investment and annualized operating costs of the base-case process and the integrated process by process heat integration were shown in Tables 2 and 3. The purchased equipment cost was mainly performed on a commercial package in Aspen Plus v.8.6. The capital investment and operating costs were estimated using basic utility costs reported by Hassan et al. (2007). The result showed that the annual cost of the integrated process was reduced by 26.5% and resulted from savings in utility usage in the system of close to 58 %. The capital cost of integrated process increased by 39% compared to the process without heat integration. The overall results illustrated that the optimization of the based-case process and process integration application were beneficial in terms of savings in energy requirement and operating expenses of the process compared with basic process.

Table 2. Energy requirement in section for aqueous ammonia process

Parameters	Base Case	Integrated Case
Electricity (kW)	231	306
Hot Utility (kW)	24567	9987
Cold Utility (kW)	25283	10705
Overall Duty (kW)	50081	20998

Table 3. Economic evaluation of aqueous ammonia based processes

Parameters	Base Case	Integrated Case
Purchased Equipment Cost (MMUSD)	2.96	4.12
Capital Investment Cost (MMUSD)	21.51	29.95
Annual Cost (MMUSD/year)	6.72	4.94
Total Utilities Cost (MMUSD/year)	3.49	1.84

Table 4 Assumptions used for the economic estimation(Hassan et al., 2007)

Operating cost assumptions	Rate	Rate units
Electricity	0.06	USD/kWh
Industrial cooling water	0.015	USD/m^3
Steam at 100 Psi	9.18	USD/Ton

Conclusion

In CO_2 capture ammonia system, the optimal concentration and CO_2 lean loading of aqueous ammonia solution were found to be 6% by weight and 0.25 mole CO_2/mole NH_3. In the ammonia abatement system, the optimal concentration and CO_2 loading were 6 ppm by weight and 1.2 mole CO_2/ mole NH_3. These conditions led to the minimum energy consumption. The overall optimal energy used in the regeneration of both CO_2 capture system and NH_3 abatement system was 8601 kJ/kg CO_2. The study focused also on the comparison of energy requirement and capital investment cost of ammonia based process from post-combustion carbon dioxide capture process with and without heat integration based on the flue gas from a coal burning 180 MW_e power plant. The conceptual HEN design using the GAMS model and the validated one using the Aspen Plus simulator were in good agreement in terms of heat reduction. Energy requirement and utility costs savings of the integrated process compared to the basic process were about 58.1 % and 47.3 %, respectively. The total capital investment cost of the integrated process was 29.95 MM$ and the annualized operating costs were less than the ones from the base-case process by about 1.78 MM$/yr. Finally, the regeneration temperature was around 85 to 95 ºC where low-grade thermal energy could be utilized.

Acknowledgements

Petroleum and Petrochemical College, Chulalongkorn University, PETROMAT and Thai Government Budget for funding support.

References

Haroun Y., Raynal L., Legender D., 2012, Mass Transfer and Liquid Hold-up Determination in Structured Packing by CFD, Chemical Engineering Science, 75, 342-348.

Hassan N., Douglas P., Croiest E., 2007, Techno-Economic Study of CO_2 Capture from an Existing Cement Plant Using MEA Scrubbing, International Journal of Green Energy, 4, 197-220.

Khonkaen K., Siemanond K., Henni A., 2014, Simulation of Carbon Dioxide Capture Using Ionic Liquid 1-Ethyl-3-methylimidazolium Acetate, Computer Aided Chemical Engineering, 33, 1045-1050

Niu Z., Guo Y., 2013, A Novel Process for Capturing Carbon Dioxide using Aqueous Ammonia, Fuel Processing Technology, 108, 154-162.

Zhang M., Guo Y., 2013, Process Simulations of large-scale CO_2 Capture in Coal-fired Power Plants using Aqueous Ammonia Solution, International Journal of Greenhouse Gas Control, 16, 61-71.

Zhang M., Guo Y., 2013, Process Simulations of NH_3 Abatement System for Large-scale CO_2 Capture using Aqueous Ammonia Solution, International Journal of Greenhouse Gas Control, 18, 114-127.

Zhao X., Smith H. K., 2011, Comparison of Several Packing for CO_2 Chemical Absorption in a Packed Column, International Journal of Greenhouse Gas Control, 5, 1163-1169

Krist V. Gernaey, Jakob K. Huusom and Rafiqul Gani (Eds.), 12th International Symposium on Process Systems Engineering and 25th European Symposium on Computer Aided Process Engineering.
31 May – 4 June 2015, Copenhagen, Denmark

Energy Efficient Bioethanol Purification by Heat Pump Assisted Extractive Distillation

Anton A. Kiss[a,b*], Hao Luo[c,d],Costin Sorin Bildea[e]

[a] *AkzoNobel Research, Development & Innovation, Process Technology SRG, Zutphenseweg 10, 7418 AJ Deventer, The Netherlands. Tony.Kiss@akzonobel.com*
[b] *Sustainable Process Technology Group, Faculty of Science and Technology, University of Twente, PO Box 217, 7500 AE, Enschede, The Netherlands*
[c] *State Key Laboratory of Multi-Phase Complex Systems, Institute of Process Engineering, Chinese Academy of Sciences, Beijing 100190, China*
[d] *Sino-Danish Center for Education and Research, Beijing 100190, China*
[e] *University "Politehnica" of Bucharest, Polizu 1-7, 011061 Bucharest, Romania*

Abstract

The purification of bioethanol fuel requires an energy demanding separation process to concentrate the diluted streams obtained in the fermentation stage and to overcome the azeotropic behaviour of ethanol-water mixture. The classic separation sequence consists of three distillation columns that carry out several energy demanding tasks: pre-concentration of ethanol, extractive distillation and solvent recovery.

To solve this problem, we propose a novel heat pump assisted extractive distillation process taking place in a dividing-wall column (DWC). In this configuration, the ethanol top vapour stream of the extractive DWC is recompressed from atmospheric pressure to over 3.1 bar (thus to a higher temperature) and used to drive the side reboiler of the DWC, which is responsible for the water vaporization. The results show that the specific energy requirements drop from 2.07 kWh/kg (classic sequence) to only 1.24 kWh/kg ethanol (VRC assisted extractive DWC), thus energy savings of over 40 % and 24 % reduced total annual costs are possible, as compared to the conventional process.

Keywords: extractive distillation; dividing-wall column; heat pump; energy savings

1. Introduction

The industrial production of bioethanol relies on various routes: corn-to-ethanol, sugarcane-to-ethanol, basic and integrated lignocellulosic biomass-to-ethanol. In all cases, the raw materials undergo several pre-treatment steps before entering the fermentation stage where bioethanol is produced. A common feature is the production of diluted bioethanol (typically 5-12 %wt ethanol) that is further concentrated to reach the requirements of the international bioethanol standards (Vane, 2008). To reach the purity targets (max. 0.2 %vol water), an energy demanding separation is needed in practice, in order to overcome the presence of the binary azeotrope ethanol-water (95.63 %wt ethanol). The separation is typically carried out by distillation, the first step being a pre-concentration distillation column (PDC) that increases the ethanol content from 5-12 %wt up to 91-94 %wt (Frolkova and Raeva, 2010). The second step consists of the ethanol dehydration, up to concentrations exceeding the azeotropic composition. Quite a number of separation alternatives are available as described in the open literature: pervaporation, adsorption, pressure-swing distillation (PSD), extractive distillation

(ED), azeotropic distillation (AD), and hybrid methods combining these options (Vane, 2008; Frolkova and Raeva, 2010). Among them, extractive distillation (ED) is still the option of choice in case of large scale production of bioethanol fuel (Kiss and Ignat, 2012). Typically, ED is performed in a sequence of two columns, one being the extractive distillation column (EDC) which separates ethanol, while the other one is the solvent recovery column (SRC) that recovers the mass separating agent (MSA) which is recycled back in the process. Further improvements to the distillation process were proposed, with the aim to increase the energy efficiency of bioethanol purification: e.g. ED process optimization (Kiss and Ignat, 2013); thermally coupled distillation columns; azeotropic and extractive dividing-wall columns (Kiss, 2013).
This work proposes a novel heat pump assisted ED process that efficiently combines vapour recompression (VRC) heat pump with dividing-wall column technology, and allows a major reduction of the energy requirements. A 100 ktpy plant is considered, processing a feed with 10 %wt ethanol, by extractive distillation using ethylene glycol as solvent. Simulations were carried out in Aspen Plus, using NRTL model, and for a fair process comparison the same approach was used as in previous studies (Kiss, 2013).

2. Problem statement

For its use as biofuel or additive, bioethanol must have a purity of min. 99-99.8 %wt but this can be reached only by paying a large energy penalty. Although most of the water present in the diluted ethanol/water mixture (5-12 %wt) from the fermentation step can removed by ordinary distillation, the ethanol purity is limited to max. 95.6 %wt due to the presence of its binary azeotrope with water. Using process optimization and advanced distillation technologies, the energy requirements were reduced by 20 % from about 2.5 down to almost 2 kWh/kg bioethanol (Kiss, 2013). However, to put this into perspective, the energy needed for purification is still considerably high, especially when taking into account the energy content of the ethanol fuel (7.45 kWh/kg fuel).
To solve this issue we integrate VRC technology with an extractive dividing-wall column (E-DWC) capable of purifying bioethanol in a single distillation unit. As shown later, this integration unit allows significant energy savings, less CO_2 emissions and a reduced footprint, as compared to the conventional separation process.

3. Results and discussion

3.1. Classic extractive distillation process

Figure 1 presents the process flowsheet, including the mass and energy balance along with the key process parameters of the classic ethanol purification sequence based on extractive distillation (Kiss and Ignat, 2013).
The process consists of three distillation columns: pre-concentration distillation (PDC), extractive distillation (EDC) and solvent recovery (SRC). The PDC unit separates water as bottom stream and a near-azeotropic composition mixture as distillate (91%wt ethanol being the optimal value as reported by Kiss and Ignat, 2013). The second column (EDC) uses ethylene glycol as solvent that is added at a solvent-to-ethanol ratio of 1.25 mol/mol, on a stage above the feed stage of the near azeotropic ethanol-water mixture. The presence of the solvent changes the relative volatility of ethanol-water such that their separation becomes possible. High purity ethanol is collected as top distillate product of the EDC, while the bottom stream contains solvent and water. The third column (SRC) in the sequence separates the remaining water as distillate and completely recovers the solvent as bottom product, which is cooled in a feed-effluent heat exchanger (FEHE) and then recycled back to the extractive distillation column.

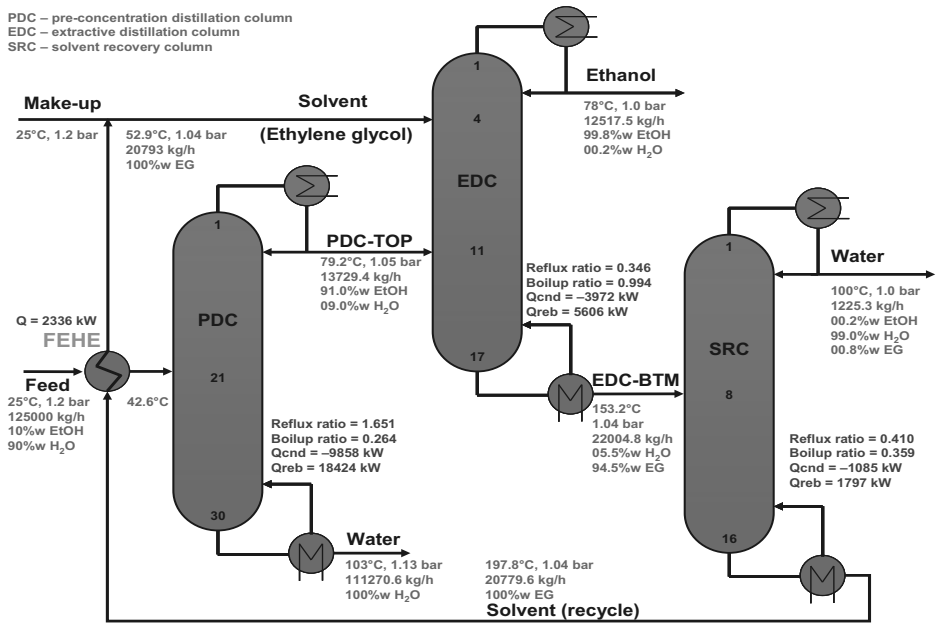

Figure 1. Flowsheet including key process parameters of the classic bioethanol separation by extractive distillation (the numbers on columns indicate the top, bottom and feed stage)

3.2. Vapour recompression assisted extractive DWC

Heat pump assisted distillation can be applied to classic columns (Kiss et al., 2012) but only to a lesser extent to dividing-wall columns (Chew et al., 2014) as the temperature span across the DWC is larger. Kiss et al. (2012) provided a useful scheme for the quick selection of appropriate heat pumps, while Plesu et al. (2014) introduced a criterion depending on the Carnot efficiency to decide whether a heat pump is worth considering:

$$Q / W = 1/\eta = T_c / (T_r - T_c) > 10 \quad (1)$$

where Q is the reboiler duty, W the work provided, while η is the Carnot efficiency, T_r the reboiler temperature and T_c the condenser temperature. When the Q/W ratio exceeds 10, then a heat pump should be considered, while when the ratio is lower than 5 then using a heat pump will not bring any benefits (Plesu et al., 2014). In case of the ethanol separation, the ratio Q/W is 16 (T_r=100 °C, T_c=78 °C) which is clearly favourable.

Notably, the use of a DWC was already explored as an attractive process alternative for bioethanol purification (Kiss and Ignat, 2012). Hereby we go further, by combining the E-DWC technology with vapour recompression (VRC) in order to increase more the energy efficiency. Figure 2 presents the flowsheet of the novel process based on VRC assisted extractive distillation in a DWC. For the reader's convenience, the mass and energy balance, as well as the key process parameters are also provided.

The feed side (prefractionator) acts as the PDC unit of the classic sequence. Water is removed as liquid side stream, but an additional side reboiler is needed in order to return the required amount of water vapours to the column. The liquid feed stream is fed on top of the prefractionator side, thus serving as a reflux to the PDC section. The vapour leaving the feed side of the E-DWC is enriched in ethanol. Solvent is added at the top of the E-DWC, this section acting in fact as the EDC unit of the conventional sequence.

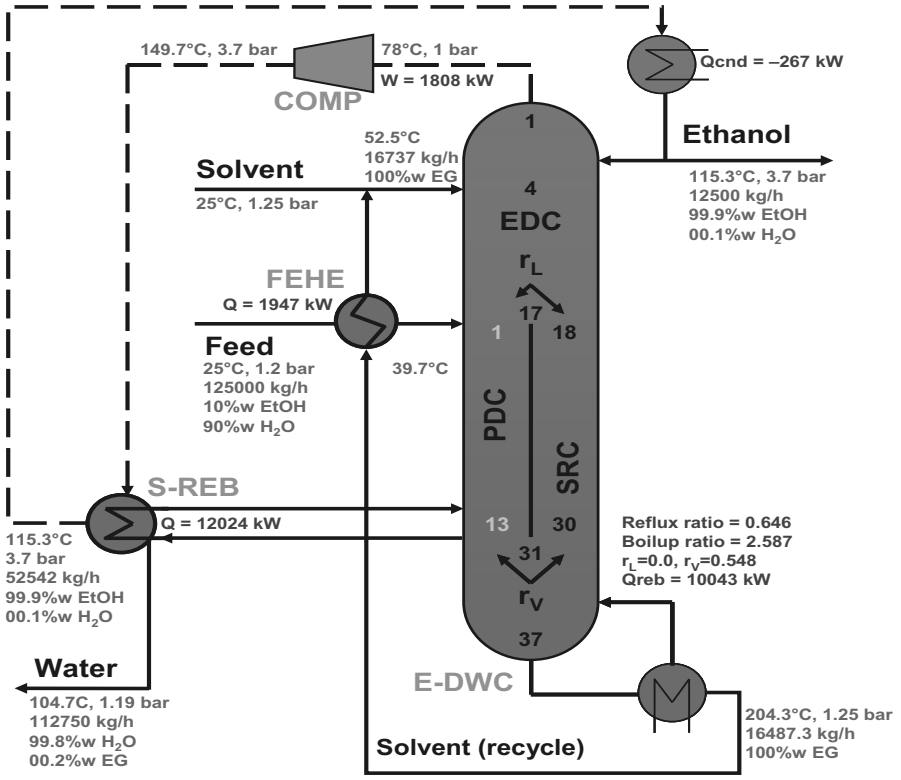

Figure 2. Flowsheet including the mass balance and key parameters of the novel process for bioethanol purification based on VRC assisted extractive distillation in a DWC.

Ethanol is separated here as high purity vapour distillate that is compressed to a higher pressure and temperature level, and then used to drive the side reboiler of the column and being eventually condensed and removed as main product. The liquid flowing down the top section (EDC) is collected and distributed only to the (SRC) side opposite to the feed side and further down the bottom of the E-DWC. This complete redistribution of the liquid flow is required in order to avoid the presence and loss of solvent on the feed side (PDC section). In the SRC section, the solvent is separated as bottom product then cooled in a heed-effluent heat exchanger (FEHE) and recycled to the E-DWC unit. The vapour from the bottom of the E-DWC to the lower part of the dividing-wall is not sufficient for the PDC section, thus the need for an additional side reboiler – which can be driven by a heat pump (VRC in this case). In spite of the high degree of integration of E-DWC, the controllability of such systems is satisfactory (Tututi-Avila et al., 2014).

3.3. Sensitivity analysis

Integrating a vapour recompression heat pump with an extractive DWC requires the setting of the appropriate discharge pressure from the compressor. Figure 3 shows the dependence of the compressor duty and the inverse of the log-mean temperature difference (LMTD) on the discharge pressure of the compressor involved by the VRC system. In terms of reducing the VRC costs, the compressor duty should be as low as possible (smaller and cheaper compressor), while the LMTD should be as high as possible (larger driving force and smaller heat exchanger).

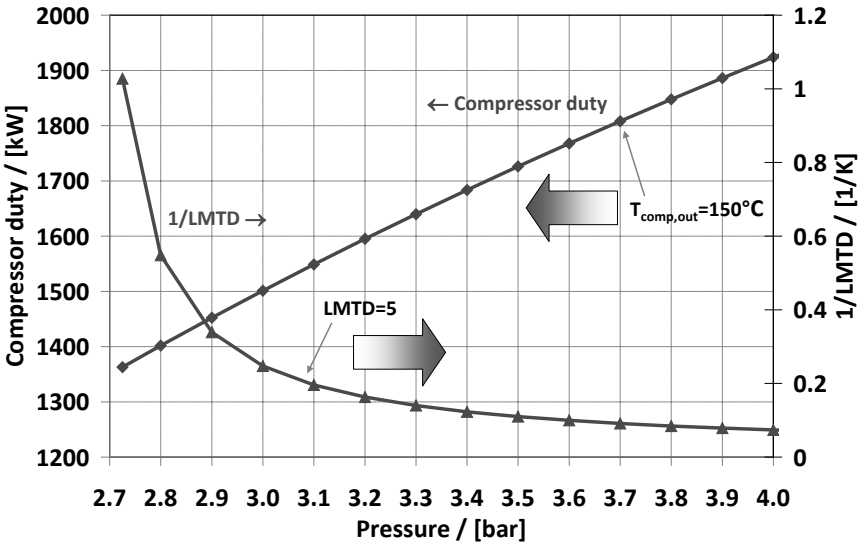

Figure 3. Dependence of compressor duty and the log-mean temperature difference (LMTD) in the side-reboiler, on the discharge pressure of the compressor (VRC system)

However, practical limitations are imposed and these reduce the available range for the discharge pressure to 3.1-3.7 bar. For the heat exchanger (side reboiler of E-DWC) which is part of the VRC loop, the LMTD must exceed 5 K to obtain a reasonable sized and inexpensive side-reboiler – as the heat exchange area (A) depends proportionally with the inverse of LMTD (e.g. $A = Q/U \times 1/LMTD$), when considering a constant heat duty (Q) and heat transfer coefficient (U). Similarly, the compressor is also limited not only by the compression ratio (typically up to 2.5-4.0), but mainly by the discharge temperature (DCT) which should not exceed 150°C for safety reasons – at higher temperatures the system may fail from worn rings, acid formations and oil breakdown.

4. Economic evaluation

The total investment costs (TIC), total operating costs (TOC) and total annual costs (TAC) were calculated according to the procedure described in our previous work (Kiss and Ignat, 2013). The equipment costs are estimated using correlations, based on the Marshall & Swift equipment cost index (M&S=1468.6 in 2012). A price of 600 US $\$/m^2$ was used for the sieve trays cost calculations. For the TAC calculations, a plant lifetime of 10 years was used. Furthermore, the following costs were considered for different types of utilities: 0.03 \$/t cooling water and 15, 17 and 20 \$/t steam of low, medium and high pressure, respectively.

Table 1 provides more details about the rest of key performance indicators. Due to the use of a compressor and a larger side-reboiler required by the VRC system, the total investment cost of the proposed VRC E-DWC process is about 29 % higher than for the classical process, but this is largely compensated by the significant energy savings, which exceed 60 % at a direct comparison. When taking into account the inefficiencies in power generation – e.g. by considering that the ratio of heat to electrical kW is about 3, then the equivalent energy requirements are $0.805 + 3 \times 0.145 = 1.24$ kWh/kg ethanol – the real savings in primary energy become 40 % which is still a remarkable figure.

Table 1. Process performance comparison (*E-DWC as reported in Kiss and Ignat, 2012)

Key performance indicator	Conventional	E-DWC*	VRC E-DWC
Total investment costs, TIC (k$)	3462	3626	4477
Total operating costs, TOC (k$/yr)	5784	5355	4221
Total annual costs, TAC (k$/yr)	6130	5718	4668
CO_2 emissions (kg CO_2 / ton product)	288.94	288.31	173.04
Thermal energy use (kWh / kg product)	2.07	2.07	0.80
Electrical energy use (kWh / kg product)	n/a	n/a	0.14
Equivalent energy requirements (kWh / kg)	2.07	2.07	1.24

Considering both the investment and operating costs, the total annual cost (TAC) is reduced by about 24 %, while the CO2 emissions – which are closely linked to the primary energy requirements – are reduced by 40 % (or even 60 % when the electricity for the compressor comes from renewable sources).

5. Conclusions

The novel heat pump assisted extractive distillation process proposed here is based on an efficient combination of vapour recompression (VRC) and DWC technology. In this configuration, the ethanol top vapour stream of the extractive DWC is recompressed from atmospheric pressure to 3.1-3.7 bar thus to a higher temperature, and used to drive the side reboiler responsible for water vaporization. The results show that the specific energy requirements drop from 2.07 kWh/kg (classic sequence) to only 1.24 kWh/kg ethanol (VRC assisted extractive DWC) hence energy savings of 40 % being possible. Considering the requirements for a compressor and use of electricity in case of the heat pump assisted alternative, about 24 % decrease of the total annual costs is possible for the novel process (in spite of the 29 % increase of total investment costs), as compared to the classic extractive distillation.

References

J. M. Chew, C.C.S. Reddy, G.P. Rangaiah, 2014, Improving energy efficiency of dividing-wall columns using heat pumps, Organic Rankine Cycle and Kalina Cycle. Chemical Engineering and Processing, 76, 45-59.

A. K. Frolkova, V. M. Raeva, 2010, Bioethanol dehydration: State of the art. Theoretical Foundations of Chemical Engineering, 44, 545-556.

A. A. Kiss, 2013, Novel applications of dividing-wall column technology to biofuel production processes. Journal of Chemical Technology and Biotechnology, 88, 1387-1404.

A. A. Kiss, S. J. Flores Landaeta, C. A. Infante Ferreira, 2012, Towards energy efficient distillation technologies - Making the right choice. Energy, 47, 531-542.

A. A. Kiss, R. M. Ignat, 2012, Innovative single step bioethanol dehydration in an extractive dividing-wall column. Separation & Purification Technology, 98, 290-297.

A. A. Kiss, R. M. Ignat, 2013, Optimal economic design of a bioethanol dehydration process by extractive distillation. Energy Technology, 1, 166-170.

V. Plesu, A. E. Bonet Ruiz, J. Bonet, J. Llorens, 2014, Simple equation for suitability of heat pump use in distillation, Computer Aided Chemical Engineering, 33, 1327-1332.

S. Tututi-Avila, A. Jimenez-Gutierrez, J. Hahn, 2014, Control analysis of an extractive dividing-wall column used for ethanol dehydration. Chemical Engineering and Processing, 82, 88-100.

L. M. Vane, 2008, Separation technologies for the recovery and dehydration of alcohols from fermentation broths, Biofuels, Bioproducts and Biorefining, 2, 553-588.

Krist V. Gernaey, Jakob K. Huusom and Rafiqul Gani (Eds.), 12th International Symposium on Process Systems Engineering and 25th European Symposium on Computer Aided Process Engineering.
31 May – 4 June 2015, Copenhagen, Denmark

Process Design of a Multi-Product Lignocellulosic Biorefinery

Aristide Giuliano[a], Massimo Poletto[a], Diego Barletta[a,*]

[a] *Department of Industrial Engineering, University of Salerno, Via Giovanni Paolo II, 132, 84084 Fisciano (SA), Italy*
dbarletta@unisa.it

Abstract

Several alternative process pathways including biochemical and thermochemical conversions are available for the second generation biorefineries. In this view conceptual design of a superstructure and optimization methods for process synthesis are widely used in order to find the optimal process flowsheet (Stefanakis et al., 2014). In the present work the flowsheet resulting from the economic optimization of a multi-product lignocellulosic biorefinery superstructure was simulated by a process simulator (Aspen Plus). As a result, rigorous methods were used to calculate the stream thermodynamic properties and to model the process units. Economic analysis was applied to assess the economic feasibility of the process. Sensitivity analysis on the size of the plant, the product prices and the biomass price was carried out as well.

Keywords: biorefinery, process design, ethanol, succinic acid, levulinic acid.

1. Introduction

Second generation biorefineries are considered promising non-petroleum based processes for the production of fuels and chemicals with low greenhouse gas emissions. Process synthesis methods have been widely used in the conceptual design, optimization and simulation of sustainable and cost-effective biorefinery processes for the bioethanol production (Fumero et al., 2011). Lignocellulosic biomass can be converted not only to biofuels for transportation, but also to added-value chemicals (Werpy and Peterson, 2004). Several works aimed to determine which process is the best way to produce one or more products using lignocellulosic biomass. Stefanakis et al. (2014) considered eight possible products using sugars and lignin as chemical intermediates. Okoli and Adams (2014) evaluated the techno-economic feasibility of a lignocellulosic biorefinery producing biobutanol using thermochemical processes. A useful tool to evaluate rigorously the biorefinery performance is the process simulation software, as Aspen Plus. It has been widely used also to simulate biomass conversion plants exploiting combustion/gasification processes to produce electricity (Sofia et al., 2014) and also biorefining and fermentation processes (Humbird et al., 2011). Moreover, only few studies addressed the simulation and assessment of integrated biorefineries co-producing alcohols (ethanol or butanol), high-value chemicals (i.e. succinic acid) and electrical power.

In this paper a more rigorous simulation approach is presented and applied to assess the economic feasibility of an integrated multi-product biorefinery co-producing ethanol and two of the top value added chemicals (Werpy & Peterson, 2004), levulinic acid and succinic acid. The innovative features of this study are based on the algorithm proposed to reach the scope. In fact, first the optimal multi-product flowsheet was derived by applying mixed integer linear programming (MILP) methods to the initial

superstructure; then the obtained optimal flowsheet was simulated by the more rigorous process modelling software Aspen Plus. This procedure is the first step of an iterative algorithm using the results of the rigorous process simulation to recalculate the optimal flowsheet by the MILP method. This paper presents only the results of the first calculation sequence MILP – Aspen Plus. The economic results obtained by the two methods were compared to assess the influence of simplified process design equations and of the linear approximation on the overall process optimization. Sensitivity analysis on the size of the plant, the product prices, the biomass price was carried out as well.

2. Process optimization methodology of the lignocellulosic biorefinery

A previous work (Giuliano et al., 2014) addressed the construction of a superstructure for a multi-product lignocellulosic biorefinery producing levulinic acid, succinic acid and ethanol. The superstructure consisted in six alternative pretreatment processes. Furthermore, two types of acid for acid hydrolysis reactor, several enzymatic reactors and fermenters for hydrolysis and fermentation section were considered. At least two different process pathways for each purification section of each product were included. Finally, two alternative combustion processes were considered in the lignin valorisation section. All heat duties and all secondary streams (catalysts, reactants, solvents) were evaluated. Constraints about manufacturing and capital costs were also added. A mixed integer non-linear problem was obtained and, in order to solve it, the linear approximation and the discretization of the non-linear variables were used. Thus, mixed integer linear programming (MILP) was used to find the optimal solution in terms of process flowsheet and biomass allocation. The economic objective function was based on the net present value (NPV) of the biorefinery production. The objective function optimal value was affected by the approximations arising from the use of approximated methods for the sizing of the equipments and from the linearization of all nonlinear equations.

In the present work, the process simulation software Aspen Plus was used to simulate more rigorously the biorefinery and to optimize the operating conditions of each process unit of the flowsheet derived from the MILP solution. As a result, process simulations were expected to provide more precise values of the process yields and of the equipment size with respect to those obtained with the MILP analysis. Finally, economic analysis was applied to assess the economic feasibility of the process.

3. Process design of the lignocellulosic biorefinery

The flowsheet resulting from the process optimization of the lignocellulosic biorefinery consists in four sections. The first one is the biomass pretreatment. The second section consists in hydrolysis and fermentations. The third one is product purification. In the fourth one steam and electricity are generated (Figure 1). Three products are considered: levulinic acid, succinic acid and ethanol. The lignin stream is used in order to produce steam and electricity.

Biomass allocation coming from the optimization of the superstructure was used to split the pretreated biomass streams to the different process pathways of the flowsheet: 49.0 % of biomass fed to levulinic acid, 40.8 % to succinic acid, 10.2 % to ethanol. Lignocellulosic biomass is fed to pretreatments, where electricity request to mill biomass is required (Humbird et al., 2011).

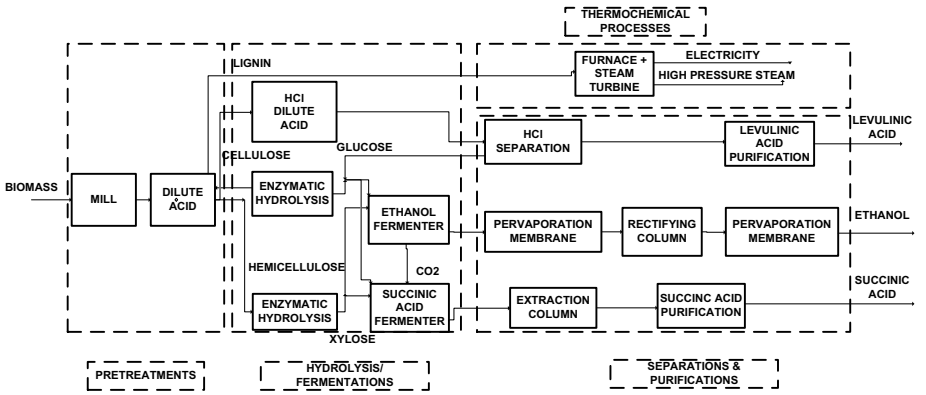

Figure 1. Flowsheet of the multi-product biorefinery.

Main design parameters are shown in Table 1. RSTOIC blocks (stoichiometric reactors) were used in pretreatment and hydrolysis and fermentation sections to set the conversions. Dilute acid pretreatment, using H_2SO_4, was necessary to separate cellulose and hemicellulose. A neutralization reactor was used to neutralize H_2SO_4 using NH_3. The solid fraction of cellulose and lignin essentially was sent to hydrolysis and fermentation section, while liquid fraction of hemicellulose, xylose and other soluble compounds were sent to enzymatic hydrolysis of hemicellulose. In the hydrolysis and fermentation section, part of the solid fraction (60 %) was sent to levulinic acid reactor, in which the glucose converts to levulinic acid and formic acid at 200 °C and 30 bar with HCl as catalyst. RSTOIC block was used in this stage and the conversions derived from Shen and Wyman (2012). Enzymatic hydrolysis was used to convert cellulose to glucose and to convert hemicellulose to xylose (Kadam et al., 2004). The glucose and xylose from hydrolysis reactors were mixed with the glucose rich stream from levulinic purification section. This mixed stream was separated in a stream sent to ethanol fermentation (20 %) and in a stream sent to succinic acid fermentation (80 %).

Ethanol fermenter performance was derived from Leksawasdi et al. (2001) and the beer stream was sent to a flash, at 32 °C and 1 bar, to separate the CO_2 gas. This CO_2 rich stream was sent to succinic acid fermentation section. Here glucose and xylose react with CO_2 to form succinic acid and oxygen. These reactions were simulated using a RSTOIC block assuming conversions derived from Song et al. (2008).

Table 1. Main design assumptions.

Unit	Parameters
Dilute acid pretreatment	T = 160 °C
Enzymatic hydrolysis	Cellulose conversion = 52 %
HCl hydrolysis and levulinic acid formation	T = 200 °C Cellulose conversion = 48 %
Ethanol fermentation	Glucose conversion = 92 % Xylose conversion = 93 %
Succinic acid fermentation	Glucose conversion to succinic acid = 53 %
Levulinic acid purification	Levulinic acid purity = 98.0 %wt
Ethanol purification	Ethanol purity = 99.5 %wt Membrane recovery = 90 %
Succinic acid purification	Succinic acid purity = 99.0 %wt
Heat integration	ΔT_{MIN} = 20 °C

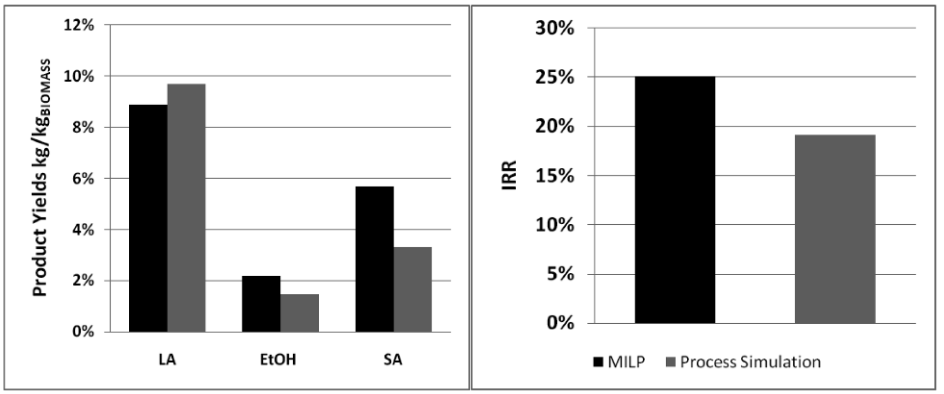

Figure 2. Product yields for the MILP model (dark bar) and for process simulation (light bar).

The purification section of the three products consists in several distillation and extraction columns. In this section the thermodynamic model used for the simulation was the NRTL. In the previous work (Giuliano et al., 2014) all separation yields of separation columns were assumed from data available in the literature. Instead, using the process simulator Aspen Plus it was possible to obtain more accurate separation yields for these equipment accounting for the system thermodynamics. Furthermore, it was also possible to optimize the operating conditions to minimize operating and capital costs using a rigorous multistage vapour-liquid equilibrium approach (RADFRAC block). Levulinic acid purification consisted in a flash in order to separate volatile HCl catalysts and in a distillation column to obtain levulinic acid 98.0 %wt from the bottom (Rackemann and Doherty, 2011). A sequence of three units were used to purify the ethanol. The first was a pervaporation membrane (O'Brien et al., 2000), the second a distillation column to reach to azeotropic composition and the third a pervaporation membrane in order to obtain ethanol 99.5 %wt (Alvarez et al., 2008). Succinic acid at 99.0 % was obtained by separating solids and then using a extraction column with octanol as solvent (Huh et al., 2006). This unit was necessary in order to remove other fermentation acids (formic acid, acetic acid, lactic acid). A vacuum distillation column was used to separate octanol from succinic acid. The last step was the crystallization of succinic acid. Process heat integration was performed by means of Aspen Energy Analyzer in order to obtain the required utilities and the size of the heat exchangers. Economic analysis of flowsheet was carried out as well. The capital expenditure was evaluated by scaling factors and cost index. The latter economic parameters relevant to biorefinery sections were taken from Hamelinck et al. (2005). Manufacturing costs, including reactants, catalysts and utilities, were assessed from data available in Humbird et al. (2011). The total investment cost (TIC) and the total annual costs (TAC) were derived. Finally, a profitability analysis based on the discounted cash flow method assuming a plant lifetime of 20 years was performed to derive the return on investment (ROI) and the internal rate of return (IRR).

4. Results of process design and sensitivities

The base case optimization problem was solved for a 50.0 t_{dry}/h biomass flowrate with a composition of 50.0 $\%_{wt}$ of cellulose, 16.0 $\%_{wt}$ of hemicellulose and 34.0 $\%_{wt}$ of lignin and ash. The base case values of the price of the three products are: 5.0 $/kg for levulinic acid, 7.5 $/kg for succinic acid and 0.75 $/kg for ethanol. The biomass price was assumed 40.0 $/t.

Table 2. Sensitivity analysis on plant size, biomass and product price.

Fed Biomass (t/h)	5	50	500
TIC (M$)	56.6	352.4	1,860.6
TAC (M$/y)	18.1	144.9	854.9
ROI (%)	4.6	20.9	60.0
IRR (%)	2.0	19.1	42.5
Levulinic Acid Price ($/kg)	2.50	5.00	7.50
Rev (M$/y)	180.2	267.6	354.9
ROI (%)	6.0	20.9	35.7
IRR (%)	4.2	19.1	29.2
Succinic Acid Price ($/kg)	3.75	7.50	11.25
Rev (M$/y)	237.9	267.6	312.1
ROI (%)	15.8	20.9	28.5
IRR (%)	14.9	19.1	24.5
Biomass Price ($/t)	20	40	60
TAC (M$/y)	137.7	144.9	152.1
ROI (%)	22.1	20.9	19.7
IRR (%)	20.0	19.1	18.1

The comparison between results of optimization using the mathematical programming (black bar) and results of process simulation (light bar) is reported in Figure 2. Products yields in terms of mass flow of products per unit mass flow of biomass do not vary significantly for levulinic acid and ethanol in both cases. The yield of succinic acid, instead, obtained from process simulation is 58.0 % of that calculated from the mathematical programming. This result is significantly affected by the simulation results of the extraction column of succinic acid using octanol as solvent. For this process unit A more accurate model accounting for complex thermodynamic interactions would be necessary for this process unit. The Internal Rate of Return (IRR) is equal to 25.1 % for the MILP and 19.1 % for the process simulation. This difference is mainly due to the lower revenues of the succinic acid for the second case. A sensitivity analysis was performed on the effect of the price of the products by varying the base case values by ± 50 %. Corresponding values are reported in the Table 2. Varying the biomass flow inlet the plant and, thus, the size of the biorefinery, the TIC and the TAC increase less than linearly with the size. The Internal Rate of Return increases much more from 2.0 % using 5 t/h to 42.5 % with 500 t/h because of economies of scales.

The levulinic acid price affects more significantly the revenues and the economic indexes. This is due to the higher production of levulinic acid (4.85 t/h) than the production of succinic acid (1.65 t/h). The effect of the biomass price on economic analysis is almost negligible: IRR varies from 18.1 % to 20.0 % and ROI from 19.7 % to 22.1 %. This can be explained considering that the feedstock cost covers only 10 % of total annual costs for the base case, 5 % for the lower price value and 14 % for the higher price value.

5. Conclusions

A more rigorous simulation approach affects the prediction of the product yields, in particular a lower value was obtained for the succinic acid. Furthermore, the IRR is lower for the process simulation of about 6 % with respect to evaluations derived from MILP. As expected, the plant profitability increases with the plant size due to the economies of scale. IRR and ROI are significantly influenced by the levulinic acid price while the biomass price has a negligible effect. Future work will consist in updating the

process conditions and yields and the unit size obtained by process simulations into the superstructure. An iterative procedure coupling MILP method and process simulation will be proposed.

References

M.E.T. Alvarez, E.B. Moraes, W.A. Araujo, R. Maciel Filho, M.R. Wolf-Maciel, 2008, Development of a Mathematical Model for Studying Bioethanol-Water Separation Using Hydrophilic Polyetherimide Membrane, Journal of Applied Polymer Science, 107, 2256 – 2265

Y. Fumero, G. Corsano, J.M . Montagna, 2011, Simultaneous design and scheduling of a plant for production and derivates, Computer Aided Chemical Engineering, 29, 1416 – 1420

A. Giuliano, R. Cerulli, M. Poletto, G. Raiconi, D. Barletta, 2014, Optimization of a Multiproduct Lignocellulosic Biorefinery using a MILP Approximation. Computer Aided Chemical Engineering, 33, 1423 – 1428

K.L. Kadam, E.C. Rydholm, J.D. McMillan, 2004, Development and Validation of a Kinetic Model for Enzymaic Saccharification of Lignocellulosic Biomass, Biotechnology Progress, 20, 698 – 705

C.N. Hamelinck, G. van Hooijdonk, A.P.C. Faaij, 2005, Ethanol from lignocellulosic biomass: techno-economic performance in short-, middle- and long-term, Biomass and Bioenergy, 28, 384 – 410

Y.S. Huh, Y.S. Jun, Y.K. Hong, H. Song, S.Y. Lee, W.H. Hong, 2006, Effective purification of succinic acid from fermentation broth produced by Mannheimia succiniciproducens. Process Biochemistry, 41, 1461–1465

D. Humbird, R. Davis, L. Tao, C. Kinchin, D. Hsu, A. Aden, P. Schoen, J. Lukas, B. Olthof, M. Worley, D. Sexton, D. Dudgeon, 2011, Process Design and Economics for Biochemical Conversion of Lignocellulosic Biomass to Ethanol: Dilute-Acid Pretreatment and Enzymatic Hydrolysis of Corn Stover. NREL/TP-5100-47764

N. Leksawasdi, E.L. Joachimsthal, P.L. Rogers, 2001, Mathematical modelling of ethanol production from glucose/xylose mixtures by recombinant Zymomonas mobilis; Biotechnology Letters, 23, 1087 – 1093

D.J. O'Brien, L.H. Roth, A.J. McAloon, 2000, Ethanol production by continuous fermentation-pervaporation: a preliminary economic analysis, Journal of Membrane Science, 166, 105 – 111

C.O. Okoli, T.A. Adams, 2014, Techno-economic Analysis of a Thermochemical Lignocellulosic Biomass-to-Butanol Process. Computer Aided Chemical Engineering, 33, 1681 – 1686

D.W. Rackemann, W.O.S . Doherty, 2011, The conversion of lignocellulosics to levulinic acid, Biofuels Bioproducts & Biorefinering, 5, 198 – 214

J. Shen, C.E. Wyman, 2012, Hydrochloric Acid-Catalyzed Levulinic Acid Formation from Cellulose: Data and Kinetic Model to Maximize Yields, American Institute of Chemical Engineers Journal, 58, 1, 236 - 246

D. Sofia, P. Coca Llano, A. Giuliano, M.I. Hernandez, F. Garcia Pena, D. Barletta, 2014, Co-gasification of coal–petcoke and biomass in the Puertollano IGCC power plant, Chemical Engineering Research and Design, 92, 1428 – 1440

H. Song, S.H. Jang, J.M. Park, S.Y. Lee, 2008, Modelling of batch fermentation kinetics for succinic acid production by Mannheimia succiniciproducens, Biochemical Engineering Journal, 40, 107 – 115

M.E. Stefanakis, K.A. Pyrgakis, A.D. Mountraki, A.C. Kokossis, 2014, The Total Site Approach as a Synthesis Tool for the Selection of Valorization Paths in Lignocellulosic Biorefineries, Computer Aided Chemical Engineering, 33, 1567 – 1572

T. Werpy, G. Peterson, 2004, Top Value Added Chemicals From Biomass, Volume I: Results of Screenin for Potential Candidates from Sugars and Synthesis Gas. U.S. Department of Energy

Krist V. Gernaey, Jakob K. Huusom and Rafiqul Gani (Eds.), 12th International Symposium on Process Systems Engineering and 25th European Symposium on Computer Aided Process Engineering.
31 May – 4 June 2015, Copenhagen, Denmark

MINLP Optimization Model for Water/wastewater Networks with Multiple Contaminants

Kittichai Pungthong, Kitipat Siemanond*

The Petroleum and Petrochemical College, Chulalongkorn University, 254 Pathumwan, Bangkok 10330, Thailand
Kitipat.S@chula.ac.th

Abstract

Water is the main resource for process industry both direct and indirect usages. The saving on water usage helps decrease the operating cost for process industry. This paper presents a method to design water/wastewater network with multiple contaminants to minimize amount of water used in the existing process. It includes two steps of calculations. The first step is initialization step with non-linear programming (NLP) to generate the topology of water network and the second step is optimizing step with mixed-integer non-linear programming (MINLP) to minimize amount of fresh water in the network. The main objective of this model is minimizing water usage and wastewater discharge in overall network. The result from this model is compared with one from the case study in the literatures of Koppol et al. (2003). All mathematical models of this work are solved by DICOPT solver in General Algebraic Modelling System (GAMS). The result shows that our model gives better total annual cost (TAC) than one from literatures.

Keywords: Water network, wastewater network, multiple contaminants, water treatment, mixed-integer non-linear programming (MINLP)

1. Introduction

Fresh water is one of the most important resources used in many industrial processes. One of many ways to reduce fresh water usage is to create the efficient flow network of water streams, called Water Network. Wastewater is generated from water-using processes and disposed to environment. Wastewater containing high concentration of contaminants is treated by treatment process before discharge. Treated wastewater can be re-used as fresh water for water-using process by the network. The problem of wastewater minimization in the industrial processes has been solved by mass exchange calculation unit by unit in a water network (Wang et al., 1994) under mass-balance constraint. The mathematical programming is another way to design the efficient water network. The linear optimization is used as initialization of non-linear optimization for calculating water network with fixed outlet concentration of contaminants (Doyle et al., 1997). The water utilization systems in process plants are divided into two parts; water-using processes and wastewater treating processes. The fresh water is reduced by the water network of the first part. The treatment cost is reduced by the wastewater network of the second part. Simultaneous design of these two networks reduces more fresh water usage by generating the water/wastewater network (Bagajewicz 2000). The mathematical programming is an approach to analyze the feasibility of zero liquid discharge by using different treatment technologies and economical feasibility (Koppol et al., 2003). Water allocation problems have more nonlinearity. The non-linear programming (NLP) is used by providing the lower bound of contaminant

concentration, resulting in reducing the gap between lower and upper bounds. And MINLP minimizes water usage by the water allocation (Faria et al., 2008). The grid diagram of water network model helps create the MINLP model to design the network with the good bounding point (Sarut et al., 2014). Our work proposes the easy way to find the initial point to solve the MINLP model for the optimal solution by comparison with the work from Koppol et al. (2003).

2. Problem Statement

Water/wastewater network model is stated as shown in Figure 1 with a set of water-using units with fixed load of contaminant, maximum allowable inlet and outlet concentration of each contaminant and a set of water treatment unit with outlet concentration of each contaminant. The fresh water without contaminants is water utility for the process. The main purpose of this paper is to use MINLP to generate the water network and water/wastewater network with minimum cost of fresh water usage and wastewater treatment. There are two design steps: the initialization step using NLP model and the final design step using MINLP model.

3. The NLP Model

The proposed NLP model initiates the topology of the Water Network by calculating the lower-bounds of water flowrate for each process ($Flowin_j$) which will be used in MINLP model of the second step as shown in Figure 2 for the final design of network. NLP model is written in terms of fixed contaminants load ($LoadA_{i,j}$) equations:

Step 1 NLP: minimize OFW = $\sum_j FW_j$

$$LoadA_{i,j} = Flowin_j \bullet (SA_i\text{-}DA_j) \qquad \forall i = j \qquad (1)$$

$$Flowin_j = \sum_i (FS_i \bullet x_{i,j}) + FW_j \qquad \forall j \qquad (2)$$

$$xF_{i,j} = FS_i \bullet x_{i,j} \qquad \forall i,j \qquad (3)$$

NLP model requires the maximum allowable fresh water flowrate (FW_j^{MAX}) as a starting point for Eq. (4). At first, it is assumed the process industrials use all freshwater without water network. It uses water flowrate as a FW_j^{MAX} calculated by Eq. (5). SA_i and DA_j must be lower than or equal maximum allowable concentration.

$$FS_i \geq FW_j^{MAX} \qquad \forall i = j \qquad (4)$$

$$LoadA_{i,j} = FW_j^{MAX} \bullet DA_j \qquad \forall i = j \qquad (5)$$

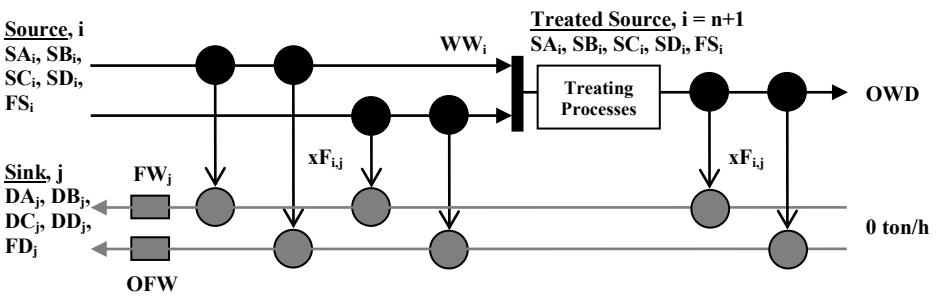

Figure 1. Grid Diagram of Water/wastewater network with four contaminants (A, B, C and D) and the end of pipe regeneration

4. The MINLP Model

After the water flowrates of processes ($Flowin_j$) are found, they are used as lower-bounds of flowrate of sources i (FS_i) in MINLP model under the objective of minimizing total annual cost (TAC) of Freshwater annual cost (FAC) and Treatment annual cost (TTC) in both Water Network and Water/wastewater Network. Additional equations are:

Step 2 MINLP: minimize TAC = Cost of freshwater+Cost of wastewater treatment

$$WW_i = (1-\sum_j x_{i,j}) \bullet FS_i \qquad i = 1 \text{ to } n \qquad (6)$$

$$FT = \sum_i WW_i \qquad i = 1 \text{ to } n \qquad (7)$$

$$OWD = FT - \sum_{i,j} xF_{i,j} \qquad i = n+1, \forall j \qquad (8)$$

$$TAC = (OFW \bullet CostFW \bullet HY) + (FT \bullet CostT \bullet HY) \qquad (9)$$

Where, n is number of water-using processes, CostFW is cost of fresh water ($/ton), CostT is cost of treatment water ($/ton) and HY is working time (h/yr)

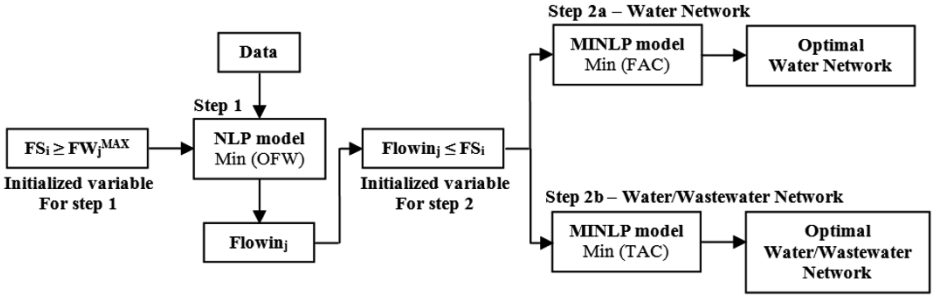

Figure 2. Design flow chart for generating Water Network and Water/Wastewater Network with multiple contaminants

5. Example

This example is a case study from published work of Koppal et al. (2003) consisting of six process sources, six process sinks with the four contaminants (Salts, H_2S, Organics and Ammonia) and three treatment processes. The limiting data of water using units and water treatment units are shown in the original paper. Cost of fresh water in process without treatment process is 2.00 $/ton and cost of fresh water with treatment process at end of pipe regeneration is 0.32 $/ton. The working time is 8400 hr/y. First NLP model calculates $Flowin_j$ as shown in Table 1 and the total annual cost (TAC) of 2.43 Million$^{\$}$/yr. Second MINLP model is run by defining FS_i to be higher than or equal to $Flowin_j$. MINLP model is applied to generate two water networks; one for water-using processes and the other one for water-using processes and wastewater treating processes. Water network alone has six source streams but water/wastewater network has seven source streams (six from water using process and one from end of pipe treatment process). The results from all calculation steps are shown in Table 1. The TAC of water network is 2.031 Million$^{\$}$/yr and one of water/wastewater network is 1.858 Million$^{\$}$/yr. The grid diagrams of water network and water/wastewater network are shown in Figure 3 and 4, respectively the comparison between our results and one from the publication is shown in Table 2.

Table 1. Result by two-step calculation procedure

Result	Step 1 Initialization	Step 2a Water Network	Step 2b Water/Wastewater Network
FW_j (ton/h)	$FW_1 = 2.4$	$FW_1 = 2.67$	$FW_2 = 25.00$
	$FW_2 = 25$	$FW_2 = 25.00$	$FW_3 = 8.574$
	$FW_3 = 8.574$	$FW_3 = 8.574$	
	$FW_4 = 10$	$FW_4 = 10.345$	
	$FW_5 = 25$	$FW_5 = 25.415$	
	$FW_6 = 73.846$	$FW_6 = 48.912$	
$Flowin_j$ (ton/h)	$Flowin_1 = 2.67$	$Flowin_1 = 2.67$	$Flowin_1 = 2.67$
	$Flowin_2 = 25.00$	$Flowin_2 = 25.00$	$Flowin_2 = 25.00$
	$Flowin_3 = 8.574$	$Flowin_3 = 8.574$	$Flowin_3 = 8.574$
	$Flowin_4 = 10.345$	$Flowin_4 = 10.345$	$Flowin_4 = 10.345$
	$Flowin_5 = 28.125$	$Flowin_5 = 28.125$	$Flowin_5 = 28.125$
	$Flowin_6 = 87.27$	$Flowin_6 = 87.270$	$Flowin_6 = 87.270$
			$Flowin_7 = 125.285$
$xF_{i,j}$ (ton/h)	$xF_{1,1} = 0.27$	$xF_{1,5} = 1.490$	$xF_{3,6} = 8.574$
	$xF_{3,4} = 0.112$	$xF_{2,5} = 1.220$	$xF_{5,6} = 28.125$
	$xF_{5,4} = 0.233$	$xF_{2,6} = 1.659$	$xF_{7,1} = 2.67$
	$xF_{5,5} = 3.125$	$xF_{3,6} = 8.574$	$xF_{7,4} = 10.345$
	$xF_{6,6} = 13.424$	$xF_{5,6} = 28.125$	$xF_{7,5} = 28.125$
			$xF_{7,6} = 50.571$
WW_i (ton/h)	$WW_1 = 2.4$	$WW_1 = 1.180$	$WW_1 = 2.67$
	$WW_2 = 25$	$WW_2 = 22.121$	$WW_2 = 25.00$
	$WW_3 = 8.462$	$WW_4 = 10.345$	$WW_4 = 10.345$
	$WW_4 = 10.345$	$WW_6 = 87.27$	$WW_6 = 87.27$
	$WW_5 = 24.767$		
	$WW_6 = 73.846$		
OFW (ton/h)	144.80	120.916	33.574
FT (ton/h)	-	-	125.285
OWD (ton/h)	144.80	120.916	33.574
nX (unit)	5	5	6
nF (unit)	6	6	2
FAC (M$/yr)	2.430	2.031	0.090
TTC (M$/yr)	-	-	1.768
TAC (M$/yr)	2.430	2.031	1.858

Table 2. Result comparison

Result	Water Network		Water/Wastewater Network	
	Koppol et al. (2003)	Our work	Koppol et al. (2003)	Our work
Freshwater flowrate (ton/h)	119.33	120.916	33.571	33.574
Waste disposal (ton/h)	119.33	120.916	33.571	33.574
Number of connecting unit	6	5	6	6
Freshwater cost (M$/yr)	2.005	2.031	0.090	0.090
Treatment cost (M$/yr)	-	-	1.799	1.768
Total annual cost (M$/yr)	2.005	2.031	1.889	1.858

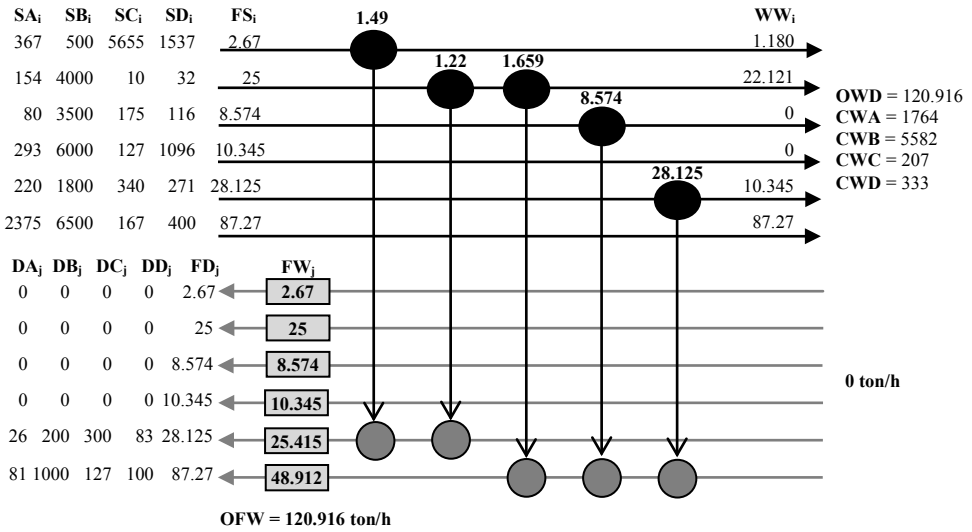

Figure 3. Grid diagram of water network

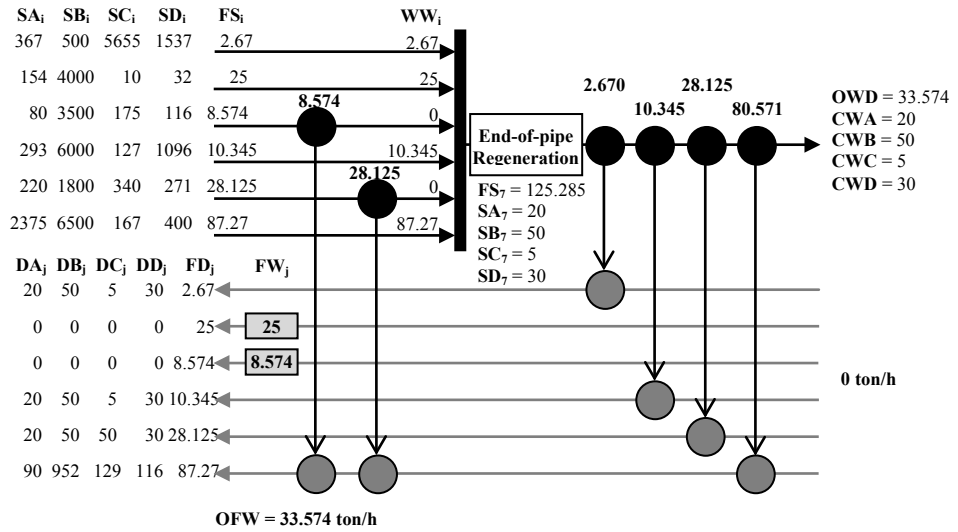

Figure 4. Grid diagram of water/wastewater network with the end of pipe regeneration

6. Conclusion

The MINLP model is another method to generate water network with minimum amount of fresh water. Our calculation is easy to do water network synthesis with optimum freshwater flowrate under a set of freshwater data (FW_j^{MAX}). The first calculation by NLP model is to calculate the initial point of flowrate ($Flowin_j$) of the network which is used for the second calculation by MINLP model to get the optimal results as shown in Table 2. The optimal water network and water/wastewater network results are close to the results from literature (Koopal et al., 2003). The computational time for water

network is 0.3 seconds and one for water/wastewater network is 0.8 seconds. Our future work is to do the retrofit design for water/wastewater network.

Nomenclature

FS_i Flowrate of sources i (ton/h)
FW_j Freshwater usage of sink j (ton/h)
SA_i A concentration of sources (ppm)
SB_i B concentration of sources (ppm)
SC_i C concentration of sources (ppm)
SD_i D concentration of sources (ppm)
FD_i Flowrate of sinks j (ton/h)
WW_i Wastewater from source i (ton/h)
DA_j A concentration of sinks (ppm)
DB_j B concentration of sinks (ppm)
DC_j C concentration of sinks (ppm)
DD_j D concentration of sinks (ppm)
$xF_{i,j}$ Flowrate from i to j (ton/h)
FT Flowrate of treatment water (ton/h)
OFW Overall freshwater (ton/h)
OWD Overall wastewater disposal (ton/h)
CWA A concentration of waste (ppm)
CWB B concentration of waste (ppm)
CWC C concentration of waste (ppm)
CWD D concentration of waste (ppm)
FAC Freshwater annual cost ($/yr)
TTC Treatment annual cost ($/yr)
TAC Total annual cost ($/yr)

Acknowledgements

Authors would like to express our gratitude to the Petroleum and Petrochemical College, Chulalongkorn University, The Center of Excellence on Petrochemical and Materials Technology, PETROMAT and Government Budget Fund for funding support

References

A.P.R. Koppol, M.J. Bagajewicz, B.J. Dericks, M.J. Savelski, 2003, On zero water dischange solutions in the process industry, Advances in Environmental Research, 8, 151-171.

D.C. Faria, M.J. Bagajewicz, 2008, A new approach for the design of multicompoment water/wastewater network, European Symposium on Computer Aided Process Engineering, 18, 43-48.

M.J. Bagajewicz, 2000, A review of recent design procedures for water networks in refineries and process plants, Computer and Chemical Engineering, 24, 2093–2113.

S.J. Doyle, R. Smith, 1997, Targeting water reuse with multiple contaminants, Trans IChemE, 75, 181-189.

T. Sarut, K. Siemanond, 2014, Water Network Design with Treating Units by Four-Step Calculation Procedure, European Symposium on Computer Aided Process Engineering, 24, 1309-1314.

Y.P. Wang, R. Smith, 1994, Wastewater minimization, Chemical Engineering Science, 49, 7 , 981-1006.

Krist V. Gernaey, Jakob K. Huusom and Rafiqul Gani (Eds.), 12th International Symposium on Process Systems Engineering and 25th European Symposium on Computer Aided Process Engineering.
31 May – 4 June 2015, Copenhagen, Denmark

Design of Separation Processes with Ionic Liquids

Worawit Peng-noo,[a] Kusuma Kulajanpeng,[a] Rafiqul Gani,[b] Uthaiporn Suriyapraphadilok*[a]

[a]*The Petroleum and Petrochemical College, Chulalongkorn University, Phayathai Road, Pathumwan, Bangkok 10330, Thailand.*
[b]*CAPEC-PROCESS, Department of Chemical and Biochemical Engineering,Technical University of Denmark, Søltofts Plads, DK-2800 Kgs., Lyngby, Copenhagen, Denmark.*

Abstract

A systematic methodology for screening and designing of Ionic Liquid (IL)-based separation processes is proposed and demonstrated using several case studies of both aqueous and non-aqueous systems, for instance, ethanol + water, ethanol + hexane, benzene + hexane, and toluene + methylcyclohexane. The best four ILs of each mixture are [mmim][dmp], [emim][bti], [emim][etso4] and [hmim][tcb], respectively. All of them were used as entrainers in the extractive distillation. A process simulation of each system was carried out and showed a lower both energy requirement and solvent usage as compared to conventional organic solvent process.

Keywords: systematic methodology, separation processes, ionic liquid, and extractive distillation

1. Introduction

One of several challenging problems in the petrochemical and chemical fields is a separation of binary azeotropic or close-boiling mixtures. The mixtures cannot be easily separated by a simple distillation because the vapor phase has the same composition as the liquid phase. Most of them are homogeneous which are classified as two main systems; (1) aqueous systems (i.e. one component in the mixture is water) and (2) non-aqueous systems such as alcohol + aliphatic hydrocarbons (e.g. ethanol + hexane), aromatic + aliphatic hydrocarbons (e.g. benzene + hexane) and aromatic + cyclic hydrocarbons (e.g. toluene + methylcyclohexane). Several alternative technologies for separation processes have been developed to solve this problem, for example, adsorption, extraction, membranes, extractive distillation and pressure swing distillation (Pereiro et al., 2012). Extractive distillation (ED) is the most efficient separation process considering on the energy requirement and solvent usage (Hernández, 2013).

ED involves the addition of heavy chemical (entrainer) to extract one of the components in the mixtures (target solute) causing the change in the relative volatilities of the mixture (Pereiro et al., 2012). However, some conventional organic solvents, which are usually employed for these separations, may cause some environmental impacts as volatile organic compounds emitted to the atmosphere. A number of environmental issues are influenced how to select the suitable entrainers (Kerton et al., 2013). Ionic liquids (ILs) are proposed as eco-friendly innovative compounds for the next generation, which are initially synthesized from simple anions, cations, and alkyl chains (on cation). Their molecular structures and properties are calculated through group contribution (GC) methods such as liquid densities and critical properties (Valderrama

et al., 2012). Recently, ILs have become the potential entrainers used in the ED for difficult separations. However, The design and selection of the suitable ILs as entrainers is a significant topic especially when a systematic methodology is established one can reduce extensive experimental work and time consuming (Roughton et al., 2012). The objectives of this research are to further develop the systematic methodology for IL selection and design simulation of the best IL-based separation processes. The proposed methodology was tested and demonstrated on several applications: ethanol + water, ethanol + hexane, benzene + hexane, and toluene + methylcyclohexane.

2. Methodology

In order to get the best IL-based separation process, the systematic methodology in Figure 1 has been mainly designed into three stages; selection, verification, and comparison.

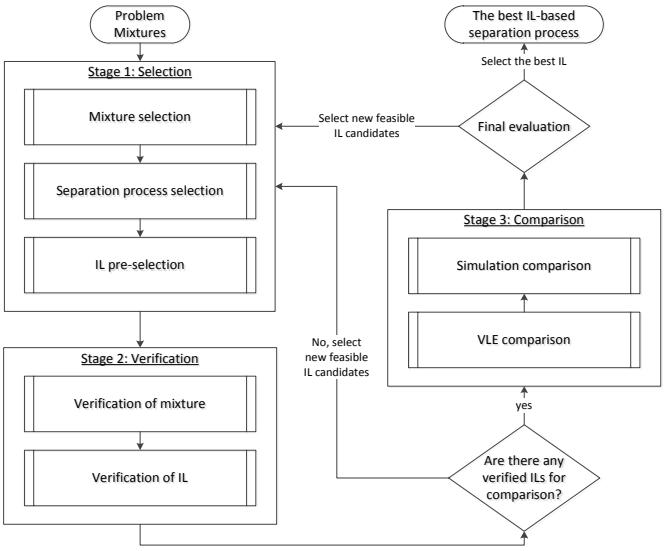

Fig. 1 the systematic methodology of IL-based separation processes

2.1. Stage 1: Selection

2.1.1. Mixture selection

Firstly, homogeneous binary problem mixtures are collected from literature databases and then classified the mixtures as two systems (e.g. aqueous or non-aqueous systems). The final lists are selected based on their wide usage in industry.

2.1.2. Separation process selection

Several alternative technologies of separation process can be performed but this work has been focused on ED because it is the most common and efficient separation process (Hernández, 2013).

2.1.3. IL pre-selection

The following parameters are used as criteria for screening of feasible ILs as entrainers in selected azeotropic systems: (1) Hildebrand solubility parameter (δ), (2) capacity (C_2^{∞}) in Equation 1, and (3) selectivity (S_{12}^{∞}) in Equation 2. The Hildebrand solubility

parameters of ILs (δ_{ILs}) are successfully calculated using the group contribution concepts (Roughton et al., 2012 and Kulajanpeng et al., 2014). The capacity (C_2^∞) and selectivity (S_{12}^∞) are calculated from the activity coefficient at infinite dilution at 298 K of every component in the mixture (e.g. γ_1^∞ and γ_2^∞). Two vertical lines shown in Figure 2 represent the Hildebrand solubility parameters of the each solute in the mixture (e.g. $\delta_{solute1}$ and $\delta_{solute2}$). Hence, One line is selected to be the target solute (e.g. $\delta_{solute1}$) and further calculated the capacity (C_2^∞) and selectivity (S_{12}^∞) of feasible ILs in the target solute. The calculated Hildebrand solubility parameters of feasible ILs are plotted in the *x-axis* against the capacity (C_2^∞) and selectivity (S_{12}^∞) in the primary and secondary *y-axis*, respectively. An example of these plots is illustrated in Figure 2.

$$C_2^\infty = 1/\gamma_2^\infty \quad \text{(Eq.1)}$$

$$S_{12}^\infty = \gamma_1^\infty / \gamma_2^\infty \quad \text{(Eq.2)}$$

The feasible IL candidates were selected based on the closest to the Hildebrand solubility parameter (δ) of the target solute (i.e. shaded area in the vicinity of $\delta_{solute1}$ shown in Figure 2). Beyond that, these feasible IL candidates should have both high capacity (i.e. ~0.5-1.5) and high selectivity (i.e. ~5-15). However, the minimum and maximum ranges of the capacity and selectivity are reasonably flexible to change depending on the availability of ILs in the database.

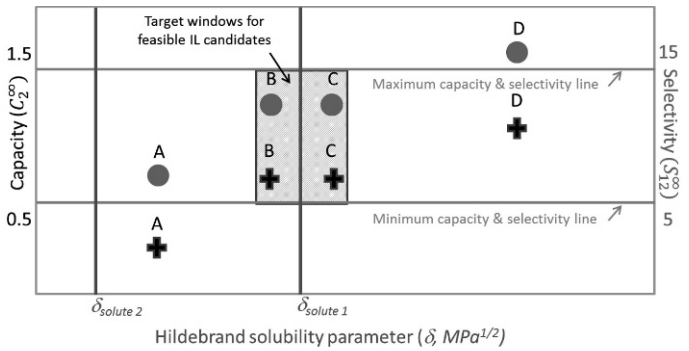

Fig. 2 IL pre-selection graph: ✚ and ● represent the capacity (primary *y-axis*) and selectivity (secondary *y-axis*) of feasible ILs in target solute.

2.2. Stage 2: Verification

2.2.1. Verification of mixture

A vapor-liquid equilibrium (VLE) graph is plotted using the ICAS program to find out the composition of azeotrope. The solute with less concentration at azeotrope is tentatively selected i.e. ethanol is the target solute in the ethanol + hexane azeotrope since the amount of ethanol is ~21 % mol at azeotrope. Two graphs of vapor pressure and heat of vaporization from ProPred program are plotted to verify whether the target solute plus ILs are the bottom product in the ED column.

2.2.2. Verification of IL

Since IL properties are not available in any commercial chemical database, the predictive equations proposed by Valderrama (2012) are employed to calculate the

critical properties. Next, VLE graph of the target azeotrope with the addition of IL as entrainer is generated using non-random two liquid model (NRTL) binary parameters from experimental data of each feasible IL candidate in IL pre-selection step to ensure the capability for breaking the azeotrope or increasing the relative volatility of the mixtures.

2.3. Stage 3: Comparison

2.3.1. VLE comparison

The VLE graphs from verification of IL step are compared each other at the same concentration of ILs to observe the most capable IL for breaking the azeotrope or increasing the relative volatility of the mixture as the best IL. However, the final evaluation of the best IL is considered in advance along with simulation comparison.

2.3.2. Simulation comparison

In order to get the best IL-based separation process in the final evaluation, ProII software is employed to simulate the separation process and design other parameters especially the energy requirement and solvent usage based on the minimum values as compared to the conventional organic solvent process.

3. Results and Discussion

The proposed methodology was demonstrated through several case studies: ethanol + water, ethanol + hexane, benzene + hexane, and toluene + methylcyclohexane mixtures to ensure the viability. The summarized results are expressed in Table 1.

Table 1 the summarized results from each stage of the systematic methodology

Stage 1: Selection				
Mixture selection	Aqeueous system Ethanol + Water (organic solvent: EG)	Non-aqueous system Ethanol + Hexane (organic solvent: sulfolane)	Non-aqueous system Benzene + Hexane (organic solvent: NMP)	Non-aqueous system Toluene + MCH (organic solvent: NMP)
Separation process selection	ED	ED	ED	ED
IL pre-selection	Target window: capacity (2-12), selectivity (1-6) and solubility (23-46 $MPa^{1/2}$)	Target window: capacity (0.5-1.5), selectivity (5-15) and solubility (23-31 $MPa^{1/2}$)	Target window: capacity (0.3-2.1), selectivity (6-42) and solubility (18-28 $MPa^{1/2}$)	Target window: capacity (0.5-1.5), selectivity (5-15) and solubility (18-28 $MPa^{1/2}$)
	Feasible IL candidates: 9 ILs	Feasible IL candidates: 8 ILs	Feasible IL candidates: 34 ILs	Feasible IL candidates: 11 ILs
Stage 2: Verification				
Verification of mixture	Azeotrpic mixture□ (target solute: water)	Azeotrpic mixture□ (target solute: ethanol)	Azeotrpic mixture□ (target solute: benzene)	Close-boiling mixture□ (target solute: toluene)
Verification of IL	Verified ILs for comparison: 3 ILs ([mmim][dmp], [emim][N(CN)2], and [emim][etso4])	Verified ILs for comparison: 2 ILs ([emim][bti] and [bmim][bti])	Verified ILs for comparison: 2 ILs ([emim][bti] and [emim][etso4])	Verified ILs for comparison: 2 ILs ([hmim][bti] and [hmim][tcb])
Stage 3: Comparison				
VLE comparison	Capability for increasing relative volatility: [mmim][dmp] > [emim][N(CN)2] ≈ [emim][etso4]	Capability for increasing relative volatility: [emim][bti] > [bmim][bti]	Capability for increasing relative volatility: [emim][etso4] > [emim][bti]	Capability for increasing relative volatility: [hmim][tcb] > [hmim][bti]
Simulation comparison	Target purity (%mol): ethanol (99.8) and water (99.6)	Target purity (%mol): hexane (99.8) and ethanol (99.9)	Target purity (%mol): hexane (99.7) and benzene (99.9)	Target purity (%mol): MCH (99.5) and toluene (99.9)
	Energy requirement (MW): [mmim][dmp] (5.39) < [emim][etso4] (5.66) < [emim][N(CN)2] (6.02) EG (6.33)	Energy requirement (MW): [emim][bti] (45.60) < [bmim][bti] (49.50) < sulfolane (60.50)	Energy requirement (MW): [emim][etso4] (23.30) < NMP (25.60) < [emim][bti] (30.00)	Energy requirement (MW): [hmim][tcb] (35.52) < NMP (37.30) < [hmim][bti] (66.79)
	Solvent usage (kmol/hr): [mmim][dmp] (40) < [emim][etso4] (60) < [emim][N(CN)2] (90) < EG (210)	Solvent usage (kmol/hr): [emim][bti] ≈ [bmim][bti] (400) < sulfolane (1500)	Solvent usage (kmol/hr): [emim][etso4] (400) < NMP (1200) < [emim][bti] (1300)	Solvent usage (kmol/hr): [hmim][tcb] (250) < NMP (1370) < [hmim][bti] (2600)
Final evalution (the best IL)	[mmim][dmp]	[emim][bti]	[emim][etso4]	[hmim][tcb]

3.1. Stage 1: Selection

3.1.1. Mixture selection

From several homogeneous binary problem mixtures, they could be divided into two main systems; aqueous and non-aqueous systems. Based on industrial applications, the

following problem mixtures were selected in this study. For aqueous system, ethanol + water were represented. Non-aqueous system composed of alcohol + aliphatic hydrocarbons (e.g. ethanol + hexane), aromatic + aliphatic hydrocarbons (e.g. benzene + hexane), and aromatic + cyclic hydrocarbons (e.g. toluene + methylcyclohexane).

3.1.2. Separation process selection

All selected mixtures were employed in IL-based ED.

3.1.3. IL pre-selection

A system of ethanol + hexane azeotrope was employed as an example in this step. Figure 3 illustrates the Hildebrand solubility parameter versus the capacity and selectivity of ILs in ethanol as the target solute. The target windows of feasible IL candidates are highlighted. Only 8 feasible IL candidates were selected for the ethanol + hexane mixture.

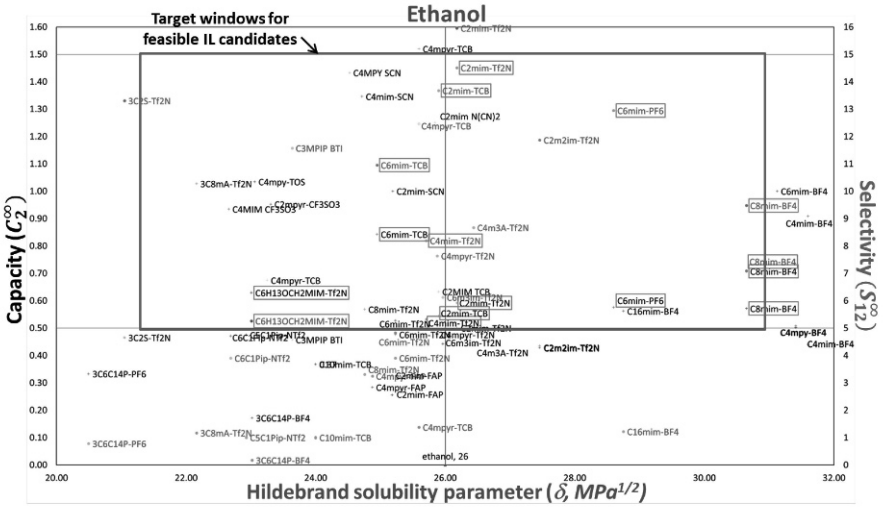

Fig. 3 Hildebrand solubility parameter of ILs vs Capacity and selectivity of ILs in ethanol for ethanol + hexane mixture.

3.2. Stage 2: Verification

3.2.1. Verification of mixture

In ethanol + hexane mixture, the mixture behavior showed ~21 % mol of ethanol at azeotrope and ethanol was guaranteed to select as the target solute due to (1) its lower vapor pressure and higher heat of vaporization than hexane, confirming that ethanol is present as the bottom product in the ED; (2) its lower concentration at azeotrope, i.e. easier to extract ethanol since smaller quantity is present at azeotrope. For other mixtures, the target solutes are water, benzene and toluene of ethanol + water, benzene + hexane, and toluene + methylcyclohexane, respectively.

3.2.2. Verification of IL

After confirming the breaking of azeotropic mixture through VLE plots, the following ILs for each system were selected. For aqueous system, 3 suitable IL candidates were [mmim][dmp], [emim][N(CN)2], and [emim][etso4]. Due to limitation in availability of the NRTL binary parameters from experimental data in several literatures of feasible IL candidates in non-aqueous systems, only 2 suitable IL candidates of each system were found: [emim][bti] and [bmim][bti] for ethanol + hexane mixture, [bmim][tcb] and

[hmim][tcb] for toluene + methylcyclohexane mixture, and [emim][etso4] and [emim][bti] for benzene + hexane mixture.

3.3. Stage 3: Comparison

3.3.1. VLE comparison

At the same concentration, for instance, 30 % mol of ILs, [mmim][dmp] was the best IL for ethanol + water mixture. For ethanol + hexane mixture, [emim][bti] was better than other ILs, whereas [emim][etso4] could perfectly break the azeotrope of benzene + hexane mixture. In addition, [hmim][tcb] was the most efficient IL to increase the relative volatility in toluene + methylcyclohexane mixture.

3.3.2. Simulation comparison

According to Table 1, the best IL candidate of each system as screened required the lowest both energy requirement and solvent usage. Moreover, they performed better than the conventional organic solvent processes.

4. Conclusions

The proposed systematic screening methodology has been successfully demonstrated for one aqueous system (e.g. ethanol + water) and three non-aqueous systems (e.g. ethanol + hexane, benzene + hexane, and toluene + methylcyclohexane). All results showed that the best IL of each azeotropic mixture gave a lower energy requirement while using less solvent usage as compared to the conventional organic solvent processes.

Abbreviations of ILs and conventional organic solvents

[mmim][dmp]	1-methyl-3-methylimidazolium dimethylphosphate
[emim][$N(CN)_2$]	1-ethyl-3-methylimidazolium dicyanamide
[emim][etso4]	1-ethyl-3-methylimidazolium ethylsulfate
[emim][bti]	1-ethyl-3-methylimidazolium bis(trifluoromethylsulfonyl)imide
[bmim][bti]	1-butyl-3-methylimidazolium bis(trifluoromethylsulfonyl)imide
[hmim][bti]	1-hexyl-3- methylimidazolium bis(trifluoromethylsulfonyl)imide
[hmim][tcb]	1-hexyl-3-methylimidazolium tetracyanoborate
EG	Ethylene glycol
MCH	Methylcyclohexane
NMP	N-methyl-2-pyrrolidone

References

K. Kulajanpeng, U. Suriyapraphadilok, and R. Gani, 2014, Ionic-Liquid Based Separation of Azeotropic Mixtures, Chemical Engineering transactions, 39, 517-522.

J.P.G. Hernández, 2013, Extractive distillation with ionic liquids as solvents: selection and conceptual process design / Juan Pablo Gutierrez Hernandez, Eindhoven: Technische Universiteit Eindhoven, 8, 147 p.

J.O. Valderrama, L. A. Forero, and R. E. Rojas, 2012, Critical properties and normal boiling temperature of ionic liquids. Update and a new consistency test, Industrial & Engineering Chemistry Research, 51(22), 7838-7844.

F.M. Kerton, and R. Marriott, 2013, Alternative solvents for green chemistry, Royal Society of chemistry.

B.C. Roughton, B. Christian, J. White, K.V. Camarda, and R. Gani, 2012. Simultaneous design of ionic liquid entrainers and energy efficient azeotropic separation processes, Computers & Chemical Engineering, 42, 248-262.

A. Pereiro, J. Araújo, J. Esperança, I. Marrucho, and L. Rebelo, 2012, Ionic liquids in separations of azeotropic systems–a review, The Journal of Chemical Thermodynamics, 46, 2-28.

Krist V. Gernaey, Jakob K. Huusom and Rafiqul Gani (Eds.), 12th International Symposium on Process Systems Engineering and 25th European Symposium on Computer Aided Process Engineering.
31 May – 4 June 2015, Copenhagen, Denmark

Systematic Screening of Fermentation Products as Future Platform Chemicals for Biofuels

Kirsten Ulonska[a], Birgitta E. Ebert[b], Lars M. Blank[b], Alexander Mitsos[a], Jörn Viell[a]

[a]*Aachener Verfahrenstechnik – Process Systems Engineering, RWTH Aachen University, Turmstr.46, 52064 Aachen, Germany, joern.viell@avt.rwth-aachen.de*
[b]*Institute of Applied Microbiology, RWTH Aachen University, Worringerweg 1, 52074 Aachen, Germany*

Abstract

The production of biofuels must be economically and ecologically viable, in particular due to the competition with existing mature fossil-based fuels. There are many alternative products and pathways to generate biofuels. Hence, focusing on the most promising products and process alternatives requires identification of corresponding pathways from biomass to biofuel candidates using scarce data of high uncertainty. This contribution presents a methodology for i) process evaluation of fermentation and downstream processing (DP) in terms of costs and primary energy demand (PED) as main sustainability criteria and ii) identification of the most promising platform chemicals gained by fermentation for a biofuel production. The methodology considers the energy requirement already at an early design stage bridging the gap between performance screenings solely based on reaction stoichiometry and time-consuming process design, enabling an early process analysis, detection of bottlenecks and ranking of various processes. The focus herein is on lignocellulosic biomass.

Keywords: screening methodology, process performance, platform chemical, biofuels

1. Motivation

With the increasing relevance of sustainability and the desired raw material change from fossil towards renewable sources, a high number of potential processes for the production of biofuels have been proposed. The most prominent ranking of products was already published in 2004 by the US Department of Energy (Werpy and Petersen, 2004) considering chemically as well as biochemically gained molecules synthesized from biomass. The evaluation criteria comprised the number of related publications, possible applications and technical barriers. Recently, Bomgardner et al. (2014) ranked the products according to their probability of soon entering the market and identified succinic, fumaric and malic acid as the most promising platform chemicals from biomass. In contrast to these market studies, Klein-Marcuschamer et al. (2013) proposed a first framework for the selection of fermentation products according to their yield and productivity and the resulting raw material and investment cost identifying ethanol and butanol as superior fermentation products.

A selection of the most promising processes and products to guide future research is clearly mandatory. The potential of the process ideas is usually evaluated using a conceptual process design. However, a full conceptual process design for a varying feedstock composition and for all different processing possibilities faces a lack of data

and is usually too expensive for screening purposes. Consequently, process designs only exist for a few processing pathways starting from very specific raw materials. These designs are mostly evaluated according to their primary energy demand (PED) or global warming potential (Caspeta et al., 2013). Both parameters are based on the process energy requirement and indicate the sustainability of a process.
Bridging the gap between first rankings and time-consuming conceptual process design, this contribution presents for the first time a comprehensive evaluation of the process performance for fermentative products as future platform chemicals for biofuels. For these early-stage design decisions Reaction Network Flux Analysis (RNFA) has been developed as a rapid screening methodology to identify optimal processing pathways based on the reaction stoichiometry (Voll and Marquardt, 2012). Up to now, the process energy requirement was not explicitly addressed, hence neglecting one of the most important metrics for process and sustainability analysis. In this contribution, the RNFA methodology is extended to include the process energy requirement. This is illustrated for the example of fermentation products and the required downstream processing (DP).

2. Methodology

In a first step, the potential of the fermentative products as future platform chemicals for a biofuel production is analyzed by comparing the raw material costs resulting from the highest yield reported in literature with the raw material costs based on the theoretical maximum. In a second step, the PED, and the minimum production costs (MPC) are calculated and benchmarked to existing fuels. The comparison is done per unit enthalpy of combustion of the product (as opposed to per unit mass or volume) due to the envisaged production of biofuels where the energy content of the fuel is the most important criterion. The results of the case study are presented in Section 3 identifying the most promising fermentative products for a subsequent biofuel production. All calculations are executed using Matlab.

2.1. Analysis of process potential based on a comparison between literature and theoretical yield

Directed evolution or genetic engineering can improve selectivity and conversion rate of microorganisms. As raw materials are typically the main cost-driver in the production of bulk chemicals and fuels, the yield is a key parameter for viable processing. Any improvement is however limited by the theoretical yield due to the overall stoichiometry of the fermentation. In order to establish a robust ranking, both the theoretical yield and the maximum yield reported in literature are used. This reveals both the actual research status and any future improvement potential. The maximum yield reported in literature is then benchmarked to the theoretical yield by calculating the resulting raw material costs to provide unit energy. The raw material costs c_R are calculated by

$$c_R \left[\frac{\$}{MJ}\right] = \frac{c_{sugar}}{Y \cdot h_{comb}} \tag{1}$$

with a sugar price c_{sugar} of 0.33 \$/kg (Viell et al., 2013), the yield Y (theoretical or reported maximum) of the fermentations and the enthalpy of combustion h_{comb}. By comparing the raw material costs to E10 as a state-of-the-art fuel with an average price in Germany of 0.625 \$/l without taxes (Sommer, 2014), the potential of the fermentation products as future platform chemical for the production of biofuels is determined.

2.2. Process energy requirement

The PED is based on the energy requirement for fermentation as well as for DP. For a low specific energy requirement, a high yield, productivity and titer are required. By changing the operating conditions during fermentation, e.g., by altering the stirrer speed or aeration rate, an improvement of the yield or the productivity (space time yield) is possible. However, typically there is a tradeoff between these two important metrics. Moreover, the conditions for minimal energy requirement per unit product are difficult to identify. Hence, herein different fermentation strategies are analyzed for each product, first the strategy with the highest reported yield in literature (dataset I) and second the highest productivity (dataset II). An additional key parameter is the titer of the product in the fermentation broth. A lower titer at shorter fermentation time gives a lower energy demand of the fermentation. Conversely, the lower titer increases the separation effort.

The electricity requirement for agitation and aeration during fermentation is based on a value of 0.5 $\mathrm{kW/m^3}$ for anaerobic and 3 $\mathrm{kW/m^3}$ for aerobic fermentations (Hermann and Patel, 2007). For DP, a binary mixture of the fermentation product and water is considered representative of the minimum energy requirement of the separation. In this first assessment, evaporation and distillation are applied for DP since they are established technologies. Evaporation is considered if the products exhibit a higher melting point than the boiling point of water. In the other cases, the energy demand for distillation is estimated by computing the minimum energy requirement using the rectification-body-method by Bausa et al. (1998) for a simple distillation or pressure-swing distillation in case of azeotropes. The PED is then calculated as

$$PED = \frac{f_P \cdot E_{Elec} + f_Q \cdot E_{Heat}}{\dot{m}_{product} \cdot h_{comb,product}}. \quad (2)$$

It considers the product mass flow $\dot{m}_{product}$, the electricity requirement E_{Elec} for fermentation with a fermenter volume set to 5000 m³, as well as the heating requirement E_{Heat} for DP and primary energy factors $f_P = 2.5$ for electricity generation and $f_Q = 1.1$ for steam production.

2.3. Cost evaluation of fermentation processes

For a final selection of platform molecules for an envisaged biofuel production, the MPC is determined and again benchmarked to the price for E10. For reasons of simplicity, only the fermentation routes with the lowest overall PED are herein considered. The MPC consists of the investment cost for the fermenter, the raw material costs as well as the utility costs for fermentation and DP. The investment costs are estimated using the values given by Kumar et al. (2012). The raw material costs are based on the yield (cf. Section 2.1), while the utility costs for heat and electricity are assessed using the demand calculated above (cf. Eq.(2)). Hence the MPC considers the overall process performance based on these early design criteria, often available already at lab-scale. The price of electricity and steam is 0.07 \$/kWh and 0.036 \$/kWh, respectively (Viell et al., 2013).

3. Case Study

A set of 10 fermentation products is analyzed including alcohols as well as various carboxylic acids. The molecules are benchmarked to ethanol and E10 as state-of-the-art fuel and finally ranked as future platform chemical for the production of biofuels.

3.1. Potential analysis of fermentative products

In Figure 1, the raw material costs resulting from the maximum reported and theoretical yield are depicted. The actual market price of E10 is indicated as dashed line. While the worst performance is shown by 3-hydroxypropionic acid (3-HPA), the lowest costs can be observed with ethanol, 2,3-butanediol, 1,3-propanediol, succinic and lactic acid, all achieving a yield equal or very close to the theoretical maximum. Interestingly, 1,3-propanediol seems to offer the largest potential for further improvement of the fermentation yield. While ethanol is already a promising fuel candidate, the other four are only platform molecules requiring a subsequent conversion into biofuels, which might be competitive if high yields are achieved. The production of biofuels could become even more interesting when being produced from cheaper raw materials. Therefore, sugar prices lower than 0.33 $/kg are mandatory for a viable production of future biofuels.

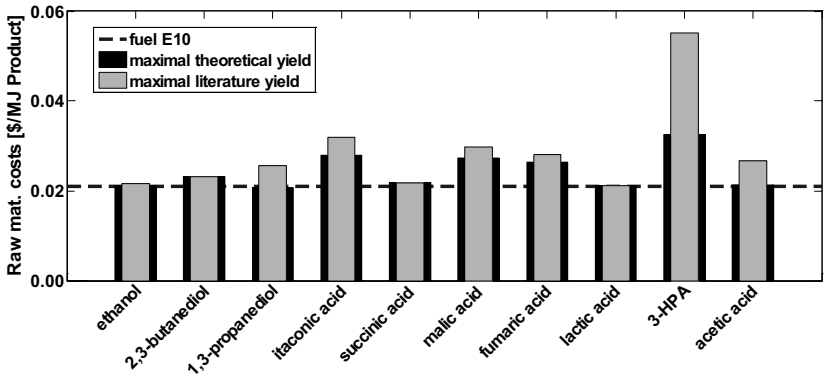

Figure 1: Analysis of process potential of fermentation products according to the reported yield in literature and the theoretical yield.

3.2. Primary energy demand of fermentative products

The PED for fermentation and DP is presented in Figure 2, comparing the performance of the fermentation strategies with the highest yield (wide bars) as well as the highest productivity (narrow bars). The figures are based on evaporation of water after fermentation, if the products are marked with a star. Distillation is applied for the unmarked ones except ethanol and acetic acid that form an azeotrope with water and were separated by pressure swing distillation.

While the worst performance is observed in the case of acetic acid, the lowest total PED is calculated for the fermentation of ethanol, 2,3-butanediol, 1,3-propanediol and lactic acid. Remarkably, all of these four fermentations have a productivity of at least 1.8 g/l/h and titers higher than 110 g/L.

In most cases, the operating conditions corresponding to highest productivity show a lower PED compared to the conditions corresponding to maximum yield. This is caused by the dominating energy factor for electricity. The only exception is succinic acid. The PED of 2,3-butanediol and 3-HPA at maximum yield differs by an order-of-magnitude in comparison to the value for maximum productivity rendering an application as a fuel precursor prohibitive.

While the resulting ranking is similar to Section 3.1, an analysis of the medium performing fermentations reveals an improvement of the productivity in case of itaconic

and malic acid and an increase of the titer for succinic, fumaric, acetic and 3-HPA as the key factors for increasing the competitiveness to ethanol. The improvement of the titer comes along with a reduction of the energy demand in DP. While evaporation and distillation are the most common unit operations in industry, further methodological work is necessary for a fast assessment of additional DP options such as heat integration measures, crystallization or extraction.

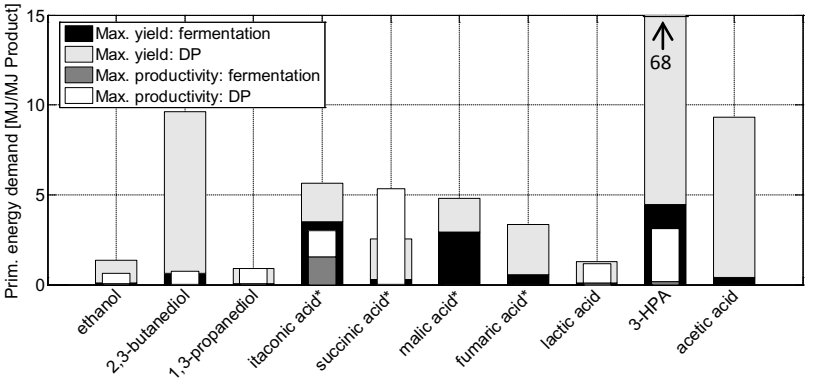

Figure 2: Primary energy demand of fermentation and downstream processing. In case of malic, fumaric and acetic acid the dataset for maximum productivity equals the one for maximum yield.

3.3. Cost performance of fermentation products

A comprehensive cost analysis is shown in Figure 3 revealing the influence of the investment, raw material and utility costs to the overall costs for each product. In addition, the benchmark of E10 is shown as dashed line. Only the best performing fermentation strategies identified in Section 3.2 are considered in this step.

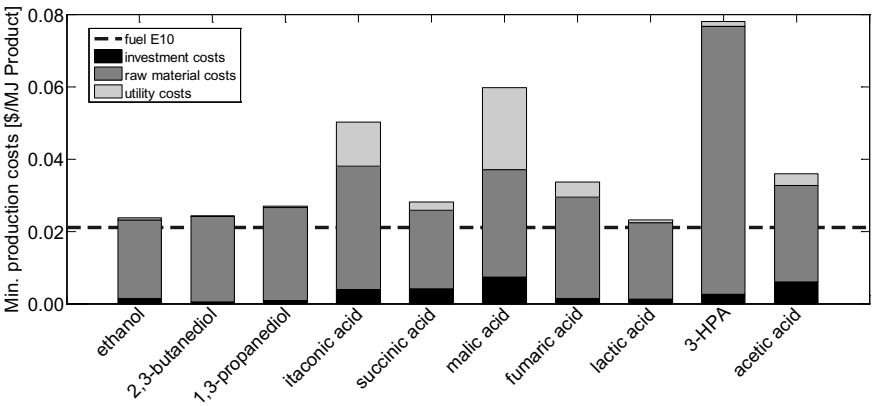

Figure 3: MPC of fermentation products considering only datasets with a lower PED.

The processes for ethanol, 2,3-butanediol, 1,3-propanediol, succinic and lactic acid show again the lowest MPC, which is in line with the ranking in Section 3.1. These similar results are due to the high contribution of the raw material costs to the total costs. The investment costs only play a minor role and the contribution is only relevant for fermentations with a low productivity or aerobic fermentations. In comparison with

E10 the overall difficulty of producing competitive biofuels is obvious, which can only be overcome by using cheap raw materials gained from high yield biomass pretreatment processes with a low PED and capital costs.

4. Summary and conclusion

In this contribution, a methodology is presented for a fast evaluation of fermentation processes at an early conceptual design phase. The methodology consists of an analysis by benchmarking the literature yield to the theoretical maximum and comparing the fermentation product to E10 as a state-of-the-art fuel. The comparison identified the need for raw material prices lower than 0.33 $ per kg of sugar in order to make biofuels competitive with existing fuels. In a second step, the PED of the production is estimated by considering the energy demand of the fermentation and product recovery by evaporation or distillation. In general, an acceptable energy demand requires a titer larger than 110 g/L and a productivity of at least 1.8 g/L/h. Finally, a comprehensive cost evaluation of the processes emphasizes the need for cheap raw materials and low PED. The most promising fermentation products in all analysis steps are ethanol, 2,3-butanediol, 1,3-propanediol, succinic and lactic acid. The methodology proves to be a fast and thorough evaluation of processes based on minimal information, but already considering the process energy requirement at this early design stage and hence identifying bottlenecks and key parameters for future improvement.

5. Acknowledgements

This work was performed as part of the Cluster of Excellence “Tailor-Made Fuels from Biomass”, which is funded by the Excellence Initiative by the German federal and state governments to promote science and research at German Universities. In addition the authors like to gratefully acknowledge Mirko Skiborowski for support with the rectification-body-method.

References

T. Werpy and G. Petersen, 2004, Top value added chemicals from biomass Volume I: Results of Screening for Potential Candidates from Sugars and Synthesis Gas, National Renewable Energy Laboratory, Department of Energy (DoE), USA

M. Bomgardner, 2014, Biobased polymers, Chemical & Engineering News, 92, 43, 10-15

D. Klein-Marcuschamer and H. Blanch, 2013, Survival of the fittest: An economic perspective on the production of novel biofuels, AIChE Journal, 59, 12, 4454-4460

L. Caspeta and J. Nielsen, 2013, Economic and environmental impacts of microbial biodiesel, Nature Biotechnology, 31, 9, 789-793

A. Voll and W. Marquardt, 2012, Reaction network flux analysis: optimization-based evaluation of reaction pathways for biorenewables processing, AIChE Journal, 58, 6,1788-1801

J. Viell, A. Harwardt, J. Seiler, W. Marquardt, 2013, Is biomass fractionation by Organosolv-like processes economically viable?A conceptual design study, Bioresource Technology, 150, 89-97

B. Sommer, 2014, Aral, http://www.aral.de/kraftstoffe-und-preise/kraftstoffpreise/preisbildung-und--struktur.html, accessed 25.11.2014

B. G. Hermann and M. Patel, 2007, Today’s and tomorrow’s bio-based bulk chemicals from white biotechnology, Applied Biochemistry and Biotechnology, 136, 361-388

J. Bausa, R. v.Watzdorf and W. Marquardt, 1998, Shortcut methods for nonideal multicomponent distillation: 1. Simple columns, AIChE Journal, 44, 10, 2181-2198

M. Kumar, Y. Goyal, A. Sarkar, K. Gayen, 2012, Comparative economic assesment of ABE fermentation based on cellulosic and non-cellulosic feedstocks, Applied Energy, 93, 193-204

Krist V. Gernaey, Jakob K. Huusom and Rafiqul Gani (Eds.), 12th International Symposium on Process Systems Engineering and 25th European Symposium on Computer Aided Process Engineering.
31 May – 4 June 2015, Copenhagen, Denmark

From Fed-batch to Continuous Enzymatic Biodiesel Production

Jason Price, Mathias Nordblad, John M. Woodley and Jakob K. Huusom*

Department of Chemical and Biochemical Engineering, Technical University of Denmark, Building 229, DK-2800 Kgs. Lyngby, Denmark.
jkh@kt.dtu.dk

Abstract

In this this paper, we use mechanistic modelling to guide the development of a continuous enzymatic process that is performed as a fed-batch operation. In this work we use the enzymatic biodiesel process as a case study. A mechanistic model developed in our previous work was used to determine the reactor operating conditions for a desired conversion. However, in using a detailed mechanistic model, given the large number of parameters and few experimental data points, the parameters were found not identifiable. The model is then only applicable within the limited operating range for which the model was validated. We hypothesize that fitting this model to fed-batch and continuous stirred tank reactor (CSTR) data together will enable us to use the model for determination of residence times to reach a specified conversion in a CSTR. With this approach, the model fits the experimental data for the five measured components (triglycerides, diglycerides, monoglycerides, free fatty acid and fatty acid methyl esters (biodiesel)) much better than using fed-batch data alone given the smaller residuals. We also observe a reduction in the correlation between the parameters.
The model was then used to predict that 5 reactors are required (with a combined residence time of 30 hours) to reach a final biodiesel concentration within 2 % of the 95.6 mass % achieved in a fed-batch operation, for 24 hours.

Keywords: Process modelling, Parameter estimation, Enzymatic Biodiesel

1. Background

When using a liquid lipase as a biocatalyst for biodiesel production by transesterification, the reaction is conventionally performed in fed-batch operation with respect to methanol to minimize inhibition and deactivation of the biocatalyst (Nordblad et al. 2014). The main disadvantage of fed-batch operation is the downtime between batches. Continuous operation will afford many advantages, such as, steady state operation, smaller reactors which mean that higher mixing rates are possible and easier handling of cheaper, high melting point substrates. However, it is unclear how the continuous enzymatic biodiesel process needs to be designed and operated to ensure optimal economics. The use of conventional Levenspiel plots is an easy and effective way for sizing continuous reactors based on batch reaction data (Levenspiel 1999). Under certain conditions fed-batch data can also be used to guide reactor sizing for other reactor configurations, provided that the rate of change in the reactor volume is substantially smaller than the initial reactor volume. However, Levenspiel plots are only valid for one reaction trajectory and are not an optimization tool. This makes the mechanistic modelling approach quite attractive. The downside to a detailed mechanistic model for a biocatalytic process is that, given the large number of

parameters and the often limited experimental data points, the parameters found are not identifiable. The model is then only applicable within the operating range for which it was validated (Vasić-Rački et al. 2011). In such cases, the non-identifiable parameters may be fixed, while the others are estimated, resulting in reasonable parameter values rather than "true parameter values" (Brun et al. 2002).

To aid in the model calibration, we follow a modelling work flow based on the work by Heitzig et al. (2011). The methodology is based on the concept of decomposing the modelling work into a sequence of modelling tasks and the associated methods, tools and data needed to perform such tasks. What we add to the work flow is the use of differences in the mass balance of the system (different modes of operation between fed-batch and CSTR operation) to aid in the model fitting process. The developed mechanistic kinetic model from our previous work describing the transesterification reaction is used to evaluate the feasibility of a continuous process using a soluble lipase formulation (Price et al. 2014).

2. Modelling workflow

What we add to the modelling workflow of Heitzig et al. (2011) is illustrated in Figure 1. When acquiring the experimental data in step one of the modelling workflow, the reaction is carried out using different modes of operation (e.g. running as fed-batch then switching to CSTR operation) to aid in the model development step where the parameter estimation is performed.

We use the model developed in our previous work describing the transesterification reaction using a liquid lipase, Callera™ Trans L to evaluate the feasibility of a continuous process using a soluble lipase formulation (Price et al. 2014). As part of the statistical analysis, in this work, we will only focus on the parameter confidence intervals and cross correlation.

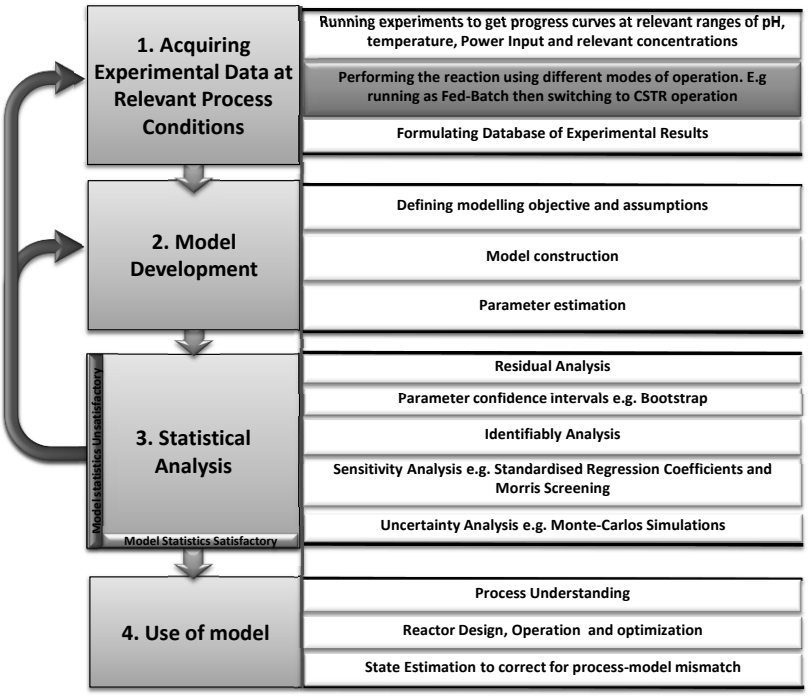

Figure 1 Work flow in the model development for the reaction system

3. Experimental Methods

Information on the chemicals, biocatalyst and analytical method used in this work can be found in Price et al. (2014). In the following sections we present the experimental setup and procedure.

3.1. Experimental Setup

The reaction was carried out in a 2.5 L glass reactor with a tank diameter of 12 cm (T) and 5 baffles, each 0.1×T wide. Two Rushton turbines (impeller diameter 0.42 T), spinning at 515 rpm provided the mixing (power input approximately 0.6 W/L). Temperature control in the reactor was maintained at 35 °C (DT Hetotherm, Apeldoorn, Netherlands). The substrates were fed to the reactor using a KNF STEPDOS .03 pump (KNF Neuberger AB, Stockholm, Sweden), calibrated prior to each experiment. Where the oil, water-enzyme solution and methanol each had their own pump.

3.2. Fed-batch into CSTR Experiment (Fitting and model evaluation dataset)

The reactor was charged with 1980 g of rapeseed oil and 0.525 equivalents (eq.) methanol based on the oil in the reactor. One equivalent corresponds to the stoichiometric amount of alcohol needed to convert all fatty acid residues in the oil to biodiesel (i.e. 1 mol oil : 3 mol alcohol). When the reaction mixture reached the reaction temperature, the reaction was then started as a fed-batch operation. The amount of water (5 wt%) and enzyme (0.5 wt %), was then added to the reactor and methanol feeding started (0.152 eq./hr). After 2 hours and 20 minutes the outlet of the reactor was opened (switched to CSTR operation) and the flow rate of oil (7.52 mL/min), water-enzyme solution (0.41 mL/min) and methanol (0.47 mL/min or 1.5 eq./hr) to be used in the experiment, was then continuously added to the reactors with a resulting residence time of 5 hours. After steady state was reached, a step change in the methanol feed rate from 1.5 eq./hr to 3 eq./hr (based on the feed rate of oil to the reactor) was made. The reaction progress was then monitored until a new steady state was achieved.

4. Numerical Methods

4.1. Model calibration

The 20 unknown kinetic constants (k_1-k_{10},k_{-1}-k_{-10}), were estimated by fitting the model equations with the experimental data for the fed-batch part of the reaction (first 2 hrs and 20 min of the reaction) and the initial CSTR part of the reaction where the methanol feed rate was 1.5 eq./hr.

4.2. Model evaluation

To judge the quality of the fitting, the second part of the CSTR reaction where the methanol feed rate was changed to 3 eq./hr was used.

4.3. Parameter estimation and confidence intervals

The differential equations were solved using a stiff variable order solver based on numerical differentiation formulas (*ode15s*). For the parameter fitting, the squared-sum of the relative errors between the simulated and experimental values for triglycerides (TAGs), diglycerides (DAGs) , monoglycerides (MAGs), free fatty acids (FFAs), and fatty acid methyl esters (FAME) were minimized using *fminsearch* (based on a simplex search algorithm). Using the bootstrap method, 5,000 samples were used to estimate the confidence interval of the parameter, where the mean of the distribution is used as the mean parameter estimate. The 95^{th} and 5^{th} percentiles of the re-estimated parameters were then used as the upper and lower bounds of the parameter estimates, respectively (Joshi et al. 2006).

5. Results and discussion

5.1. Parameter estimates and confidence intervals of the parameters

The model captures the dynamics for the five components over the entire course of the reaction for the three different stages of the reaction as seen in Figure 2. The simulation using the previously obtained kinetic constants (fitted only to fed-batch data) from our previous work is also shown (Price et al. 2014). The combined fed-batch and CSTR experiment fitting has much smaller residuals compared to the previous kinetic constants for all the measured components. The model qualitatively follows the model evaluation part of the dataset (after 19.5 hours) and gives good predictions for the endpoint value compared to using the previous kinetic constants. This is important to note given that being able to predict the concentration of the acylglycerides and FFA at the end of the reaction is just as crucial as the FAME concentration given that a product specification has to be met. It should also be noted (results not shown) that the newly determined kinetic constants also fits the fed-batch validation dataset (biodiesel conversion over 90%) from our previous work (Price et al. 2014). Also, an interesting observation is that a reasonably good fitting is obtained (residuals on the same order of magnitude of the experimental error) by the fitting of the fed-batch into CSTR experiment which required much less data (one experiment, 240 data points) compared to the previous fitting (eight fed-batch experiments, 580 data points (Price et al. 2014)).

As part of the methodology, statistical analysis of the parameter estimates is essential. The parameter estimates and confidence intervals are shown in Table 1. Most of the parameters have quite reasonable confidence intervals except for the inhibition constants (k_{10} and k_{-10}) whose range compared to the mean parameter estimate is over 100%. What is observed is that the strong correlation between most of the parameters have been reduced (between ±0.65) compared to the correlation for the parameter estimates in our previous work (a correlation coefficient of ±0.75 was used to signify strongly correlated parameters) (Price et al. 2014). Usually to arrive at better parameter estimates and reduce correlation between parameters various experiments are performed at different experimental conditions (e.g. variance in enzyme and methanol concentrations). To our knowledge this is the first time that it is shown that by using differences in the reactor mass balance (fed-batch into CSTR operation) that the

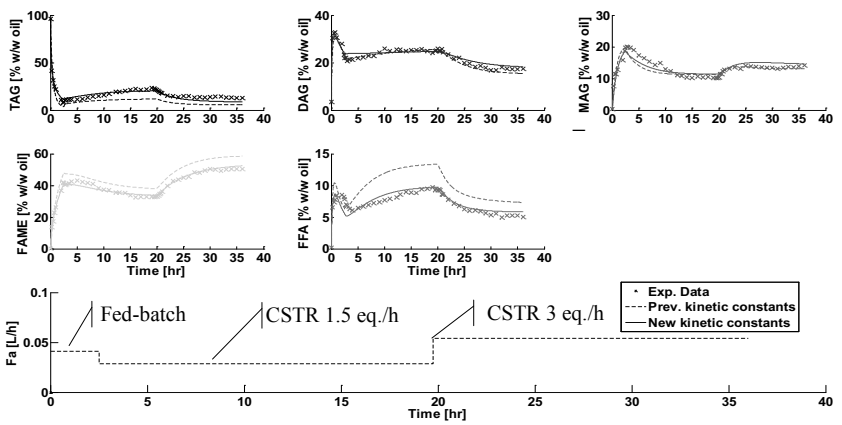

Figure 2 Comparison of the previously reported kinetic constants to the new kinetic constants for the fitting of the combined fed-batch and CSTR experimental data. Switching from fed-batch to CSTR operation can be seen on the methanol flowrate (F_a) plot

Table 1 Mean Parameter estimates and confidence intervals from the 5000 bootstrap samples

Parameter	Mean Estimate	Confidence Intervals	
		Lower	Upper
k_1 [L/mol.min]	1.32×10^5	1.14×10^5	1.43×10^5
k_{-1} [1/min]	4.35×10^0	4.17×10^0	4.49×10^0
k_2 [L/mol. min]	1.66×10^6	1.23×10^6	1.85×10^6
k_{-2} [1/min]	7.15×10^4	6.21×10^4	7.54×10^4
k_3 [1/min]	1.46×10^6	1.36×10^6	1.66×10^6
k_{-3} [L/mol. min]	5.58×10^7	5.06×10^7	6.36×10^7
k_4 [L/mol. min]	6.84×10^6	5.71×10^6	7.32×10^6
k_{-4} [1/ min]	7.10×10^5	6.74×10^5	7.86×10^5
k_5 [1/ min]	4.21×10^4	3.95×10^4	4.75×10^4
k_{-5} [L/mol. min]	1.42×10^6	1.24×10^6	1.59×10^6
k_6 [L/mol. min]	4.39×10^4	3.93×10^4	4.64×10^4
k_{-6} [1/min]	1.02×10^7	9.09×10^6	1.11×10^7
k_7 [L/mol. min]	4.14×10^6	3.95×10^6	4.37×10^6
k_{-7} [L/mol.min]	2.91×10^0	2.74×10^0	2.96×10^0
k_8 [L/mol.min]	1.39×10^5	1.26×10^5	1.58×10^5
k_{-8} [L/mol.min]	3.62×10^5	3.28×10^5	3.83×10^5
k_9 [L/mol.min]	3.29×10^5	3.08×10^5	3.75×10^5
k_{-9} [L/mol.min]	4.61×10^4	4.33×10^4	5.14×10^4
k_{10} [L/mol.min]	2.73×10^3	1.51×10^3	7.94×10^3
k_{-10} [1/min]	3.07×10^5	2.47×10^4	4.06×10^5

correlation between the parameters can be reduced.

5.2. Reactor simulations

Number of CSTR's and conditions to achieve comparable fed-batch performance: The model was then used to investigate for continuous operation, the number of tanks and operating conditions to achieve the same biodiesel conversion as the best fed-batch experiment; in which the final biodiesel value after 24 hours (t_{batch}) was 95.6 mass % (plant productivity 28.2 g FAME L^{-1} h^{-1}) using 0.5 wt% enzyme and 5 wt% water (Price et al. 2014).

The most favourable simulation is shown in Figure 3 which was for 5 tanks with a residence time of 6 hours in each reactor. A FAME conversion of 93.9 mass % is achieved which corresponds to a plant productivity of 22.0 g FAME L^{-1} h^{-1}. However, considerably longer time (40 h) is required to reach the same FAME conversion in the CSTR system compared to the fed-batch system. The simulations show for the CSTR case, that compared to fed-batch operation, plant productivity is sacrificed in favour of continuous operation. Given the reaction slows down in the latter half of the reaction this indicates that the best way of running this process is likely a combination of CSTR operation in the first reactor followed by fed-batch operation. Having a CSTR up front means that the converted FAME in the first reactor (a CSTR) can solubilise higher melting point substrates that are cheaper than virgin oils (e.g. animal fats) which can have a significant positive effect on the economy of the process. To achieve continuous operation in this alternative setup (CSTR into fed-batch) requires proper scheduling of the tanks which adds some complexity to the system, which need to be further evaluated.

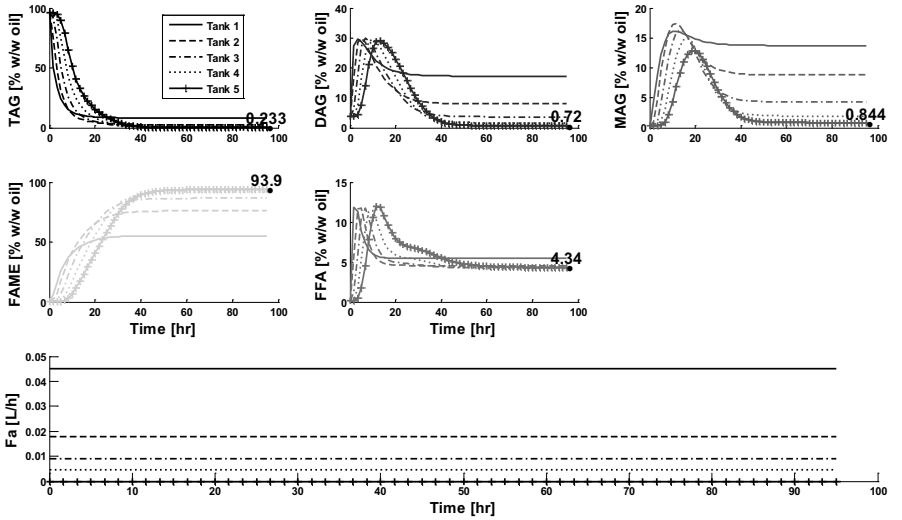

Figure 3 Simulation of the concentration profile of the main components in the oil for 5 CSTR's with a combined residence time of 30 hours. The concentrations in tank 5 are reported.

6. Conclusions

A mechanistic kinetic model is employed to carry out a study dealing with the moving from fed-batch to continuous enzymatic biodiesel production. The method of fitting fed-batch into CSTR data was superior to fitting fed-batch data alone to predict how the continuous process should be operated for the enzymatic biodiesel process. Also, fitting fed-batch into CSTR data reduced the number of data points necessary to calibrate the model compared to fitting fed-batch data alone.The simulations show that in terms of the plant productivity fed-batch operation is better than CSTR operation. However, we propose an alternative setup (CSTR into fed-batch operation) which takes advantage of having a CSTR up front to easily be able to utilise higher melting point substrates followed by a fed-batch reactor which is more efficient in the last half of the reaction.

References

R. Brun, M. Kuhni, H. Siegrist, W. Gujer, P. Reichert, 2002, Practical identifiability of ASM2d parameters - systematic selection and tuning of parameter subsets, Water Res., 36, 4113–4127.

M. Heitzig, G. Sin, M. Sales-Cruz, P. Glarborg, R. Gani, 2011, Computer-Aided Modeling Framework for Efficient Model Development, Analysis, and Identification: Combustion and Reactor Modeling. Ind Eng Chem Res., 50, 5253–5265.

M. Joshi, A. Seidel-Morgenstern, A. Kremling, 2006, Exploiting the bootstrap method for quantifying parameter confidence intervals in dynamical systems. Metabolic Eng., 8, 447–455.

O. Levenspiel, 1999. Chemical reaction engineering, Wiley.

M. Nordblad, V.T.L. Silva, P.M. Nielsen, J.M. Woodley, 2014, Identification of critical parameters in liquid enzyme-catalyzed biodiesel production, Biotech. Bioeng., 111, 2446–2453.

J. Price, B. Hofmann, V.T.L. Silva, M. Nordblad, J.M. Woodley, J.K. Huusom, 2014, Mechanistic Modelling of Biodiesel Production using a Liquid Lipase Formulation. Biotech Prog., 30, 1277-1290.

D. Vasić-Rački, Z. Findrik, A. Vrsalović Presečki, 2011, Modelling as a tool of enzyme reaction engineering for enzyme reactor development, Appl Microbiol Biotechnol., 91, 845–56.

Krist V. Gernaey, Jakob K. Huusom and Rafiqul Gani (Eds.), 12th International Symposium on Process Systems Engineering and 25th European Symposium on Computer Aided Process Engineering.
31 May – 4 June 2015, Copenhagen, Denmark

Feed Flexibility of CH_4 Combined Reforming for Methanol Production

Benjamín Cañete,[a,b] Nélida B. Brignole,[a,b] Carlos E. Gigola[a*]

[a]*Planta Piloto de Ing. Quím (UNS-CONICET), Cno. La Carrindanga km 7, B. Blanca, 8000, Argentina*

[b]*LIDeCC-Laboratorio de Investigación y Desarrollo en Computación Científica, Depto. De Ciencias en Ing. de la Computación, Univ. Nacional del Sur, Av. Alem 1253, B. Blanca, 8000, Argentina*

cgigola@plapiqui.edu.ar

Abstract

Natural gas with high CO_2 content is a readily available resource, whose application for synthesis gas (syngas) production through dry reforming is strictly limited to processes that require low H_2/CO ratios. In a recent work we have demonstrated that methanol production through a process scheme based on combined reforming of methane (with $CO_2 + H_2O$) becomes a viable alternative from both technical and economic viewpoints. The use of a H_2 separation membrane, as well as a partial H_2 reinjection into the loop reactor, has been considered for the syngas composition adjustment to stoichiometric conditions ($M \approx 2$). The reformer and the methanol synthesis reactor were assumed to be working at thermodynamic equilibrium conditions, i.e. at 950 °C and 20 bar for the former, and at 250 °C and 71 bar for the latter. By using a natural gas feed containing 30 % CO_2 and $H_2O/CH_4 = 2$, it is feasible to operate the synthesis reactor with a lower recycle ratio, as well as a CO_2 concentration close to the one employed in industrial practice. Under the operating conditions mentioned above, the use of combined reforming for methanol synthesis turns out to be economically advantageous over the classical steam reforming process.

In this work a study of the feed flexibility for combined reforming is carried out taking into account the existence of gas fields with CO_2 contents higher than 30 %. Feed mixtures containing 35 % and 40 % CO_2 were analyzed, while maintaining the operating conditions for the reformer (P, T, H_2O/CH_4) and the synthesis reactor (P, T, M). For comparative purposes, a methanol plant producing 400,000 mtpy was considered. A higher CO_2 content in the feed does not significantly alter the CH_4 conversion, but increases the CO_2 conversion and lowers the H_2/CO ratio. Consequently, it is necessary to increase the separation and reinjection of H_2 to keep stoichiometric conditions in the synthesis reactor. However, a moderate increase in CO_2 concentration in the synthesis reactor cannot be avoided. It is also shown that the recycle ratio should be markedly reduced in order to achieve stable operation. This situation reduces the operating cost of the recycle compressor. On the other hand, the flow of $CH_4 + CO_2$ to the reformer should be increased for a constant methanol production, which in turn affects the reformer's energy balance. The main operating costs of the methanol plant, with respect to the reference case ($CO_2/CH_4 = 0.43$), grow for $CO_2/CH_4 = 0.55$ and $CO_2/CH_4 = 0.67$ by 9.5 % and 25 %, respectively. This preliminary technical and economic analysis shows that combined reforming of natural gas with CO_2 content up to 40 % is a feasible process to produce methanol without CO_2 removal.

Keywords: CO_2/CH_4, methanol, CO_2 removal, energy, natural gas.

1. Introduction

More than 40 % of the world's conventional gas reserves are estimated to lie in reservoirs that contain significant amounts of Hydrogen Sulfide (H_2S) and CO_2 (Duissenov, 2013). Natural gas (NG) with a high CO_2 content can be found in many different places all around the world at various regions of economic interest, such as Indonesia (Suhartanto et al., 2000), the Colorado Plateau on the South of the United States (Allis et al., 2001), Norway (Nørstebo et al., 2012) and also Argentina (Crotti et al., 2007). As some of these fields are located far away from main natural gas processing areas, they are usually kept in reserve.

For the recovery of NG Liquids cryogenic processes are nowadays preferred (Kidnay and Parrish, 2006). Under low temperature conditions CO_2 might solidify, hence obstructing pipes and other equipment items. Then, prior to NG fractionation, the addition of a CO_2 removal stage becomes necessary. Moreover, in Argentina the highest allowable CO_2 content for transportation and domestic use is limited to 2 %, since CO_2 contributes not only to lower NG's heat capacity, but also to cause corrosion. Therefore, processing NG with a high CO_2 content in order to obtain conventional NG is difficult and above all uneconomical. Without requiring a previous CO_2 removal, it might be interesting to employ the NG stream with its high CO_2 content as a feedstock for the production of higher value derivatives.

Over the last few years the production of liquid fuels or methanol through the Combined Reforming (CR) process (with $CO_2 + H_2O$) of NG has gained special interest (Roh et al., 2008), due to the employment of two of the most important greenhouse gases: CO_2 and CH_4. CR allows obtaining synthesis gas (syngas) with a higher H_2/CO ratio than the one obtained in Dry Reforming (DR), while avoiding the troublesome carbon formation. In Cañete et al. (2014) we have shown that for a NG feed with 30 % CO_2, it is economically feasible to produce methanol through CR without the need of a partial CO_2 removal. In the present work, the effect of higher CO_2 concentrations in the feed gas on the main operating conditions and the economy of the process are analyzed.

2. Methodology

The simulation of the scheme shown in Figure 1 was made by means of GAMS software (Brooke et al., 2014), where both the reformer and the synthesis reactor were considered to operate at thermodynamic equilibrium conditions. For these calculations the Gibbs-free-energy minimization method was employed, also taking into account carbon formation for the reformer. Table 1 shows the main operating conditions for both the reformer and the methanol synthesis reactor.

Table 1. Simulation parameters

Unit	Inlet Temp. (°C)	Outlet Temp. (°C)	Inlet Pressure (bar)	Pressure Drop (bar)	Thermal Efficiency (%)
Reformer	600.0	950.0	20.0	0.0	50.0
Synthesis reactor	250.0	255.0	71.0	3.0	----

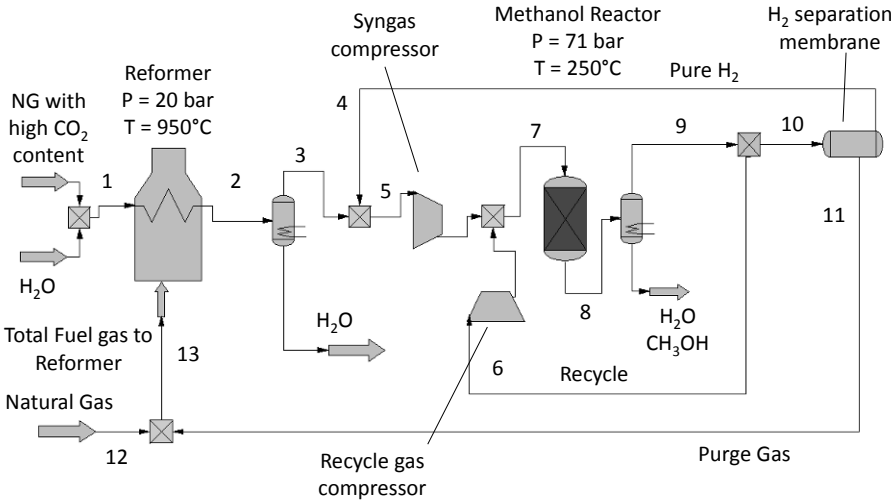

Figure 1. Simplified process scheme

For this analysis a methanol production of 400,000 metric tonnes per year (mtpy) has been set. The simulations aim at analysing the effect of the CO_2/CH_4 feed ratio on the process operating conditions and their impact on the overall energy balance. The M module (H_2-CO_2/CO+CO_2), which is commonly employed to characterize the obtained syngas, was fixed in 2.05 after H_2 reinjection (Stream 5 in Fig. 1). This number is close to the stoichiometric value (M = 2) and was determined to be a suitable composition for methanol synthesis (Cañete et al., 2014).

An important design parameter that has been set free was the CO_2 concentration at the methanol reactor inlet. Although a high value has a negative effect over methanol synthesis kinetics (Lim et al., 2009), it is inconvenient to set an upper limit for this composition, since in this analysis the requirement of a CO_2 separation stage is intended to be avoided. However, the resulting CO_2 concentrations were closer to those employed at industrial practice. For example, Lim et al. (2009) have concluded that the maximum methanol concentration obtained with a $Cu/ZnO/Al_2O_3/ZrO_2$ catalyst corresponds to a CO_2 concentration around 10 %. A common value for reformer efficiency (50 %) was established by Dybkjaer (1995). It relates the total heat transferred to reaction (the one required for heating the feed up to the outlet temperature level plus the heat of reaction) to the total heat generated by fuel combustion.

It is important to remark that both purge gas flow (Stream 11 in Fig. 1) and recycle gas flow (Stream 6 in Fig. 1) have strong influence on the overall energy balance. Therefore, they affect the economy of the process.

3. Results and discussion

For CO_2/CH_4 feed ratios of 0.55 and 0.67 and H_2O/CH_4 = 2.1, Tables 2 and 3 show the effect of CO_2 content on the CH_4 and CO_2 conversions, as well as on the compositions of the main streams for the methanol plant. Stream numbers correspond to the flowsheet given in Figure 1. It can be envisaged that a higher CO_2/CH_4 ratio implies a growth in the consumption of feed gas (Stream 1 in Fig. 1) and fuel gas (Stream 12 in Fig. 1). NG with higher CO_2/CH_4 ratio shows a major tendency for DR, resulting in higher CO_2 conversion (XCO_2 in Tables 2 and 3) at the reformer unit and a syngas with lower

H_2/CO ratio. Meanwhile, CH_4 conversion (XCH_4 in Tables 2 and 3) is only slightly altered by changes in CO_2/CH_4 feed ratio.

Table 2. Computational results (CO_2/CH_4 = 0.55: 35 % CO_2 in NG)

Stream	Flow (Kmol/h)	Composition (vol. %)						XCH_4 (%)	XCO_2 (%)
		CH_4	CO_2	CO	H_2	H_2O	CH_3OH		
1	4770.0	0.274	0.151	0.0	0.0	0.575	0.0	93.9	31.7
2	7229.8	0.011	0.068	0.202	0.478	0.241	0.0		
4	1034.0	0.0	0.0	0.0	1.0	0.0	0.0		
5	6521.4	0.012	0.075	0.224	0.688	0.0	0.0		
6	7600.0	0.117	0.127	0.051	0.705	0.0	0.0		
7	14121.4	0.076	0.097	0.130	0.697	0.0	0.0		
8	10964.9	0.098	0.106	0.043	0.590	0.019	0.144		
11	595.9	0.320	0.346	0.140	0.193	0.0	0.0		
12	935.0	0.994	0.006	0.0	0.0	0.0	0.0		
13	1530.9	0.732	0.138	0.055	0.075	0.0	0.0		

Table 3. Computational results (CO_2/CH_4 = 0.67: 40 % CO_2 in NG)

Stream	Flow (Kmol/h)	Composition (vol. %)						XCH_4 (%)	XCO_2 (%)
		CH_4	CO_2	CO	H_2	H_2O	CH_3OH		
1	5020.0	0.265	0.177	0.0	0.0	0.558	0.0	94.9	36.4
2	7537.8	0.009	0.075	0.210	0.459	0.247	0.0		
4	1482.0	0.0	0.0	0.0	1.0	0.0	0.0		
5	7158.0	0.009	0.079	0.221	0.690	0.0	0.0		
6	4620.0	0.046	0.165	0.069	0.720	0.0	0.0		
7	11778.0	0.024	0.113	0.161	0.702	0.0	0.0		
8	8626.6	0.033	0.135	0.056	0.575	0.018	0.183		
11	806.4	0.117	0.480	0.199	0.204	0.0	0.0		
12	1200.0	0.994	0.006	0.0	0.0	0.0	0.0		
13	2006.4	0.642	0.196	0.080	0.082	0.0	0.0		

Figure 2 shows partial methane conversion for DR and Steam Reforming (SR) reactions. It is evident that a higher CO_2/CH_4 feed ratio produces a higher CH_4 partial conversion by DR and a slightly lower methane partial conversion by SR.

Due to the lower H_2/CO ratio the pure H_2 flow to be separated at the membrane unit (Stream 4 in Fig. 1) is also higher. In addition, the feed with a higher CO_2/CH_4 ratio leads to a lower recycle ratio (Stream 6/Stream 5 in Fig. 1) that is beneficial for the economy of the process, because the compression work at the methanol loop reactor decreases. For CO_2/CH_4 = 0.55 the recycle ratio is 1.2, while for CO_2/CH_4 = 0.67 it is 0.65. Even when syngas compression requirement slightly increase with CO_2/CH_4 ratio (Stream 5 in Fig. 1), a considerably lower value appears for the recycle stream.

The results in Tables 2 and 3 also show that the CO_2 concentration at the methanol reactor inlet increases with CO_2/CH_4 ratio, which might be detrimental for methanol production. As mentioned before, this concentration is commonly limited to a maximum of approximately 10 %, which is close to the figures shown in Tables 2 and 3 (Stream 7

in Fig.1). Nevertheless, our results indicate that the methanol concentration increases, thus revealing a higher syngas conversion. This behaviour is another consequence of the large reduction in recycle ratio.

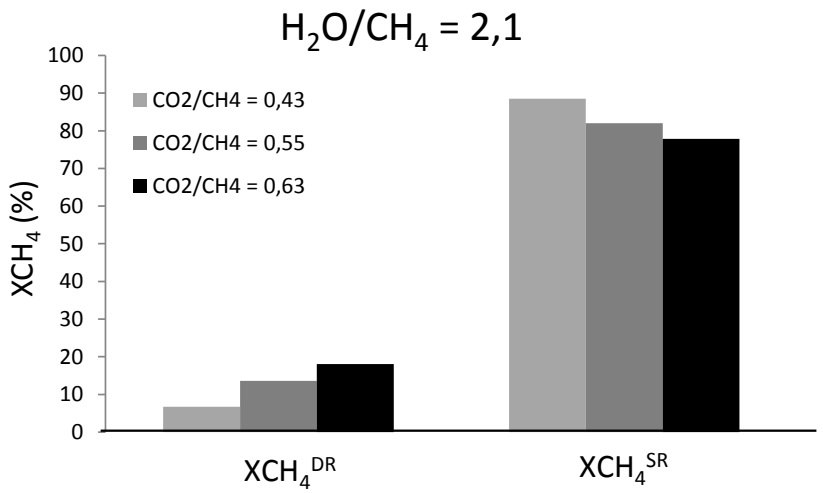

Figure 2. CH_4 partial conversion for DR and SR reactions dependence on CO_2/CH_4 ratio for a feed gas with $H_2O/CH_4 = 2.1$

In this work the considered CO_2 emissions account for the amount present in the flue gas at the reformer unit. For a conventional 400,000 mtpy methanol plant based on SR, CO_2 emission rounds 367 tpd (tonnes per day). In contrast, for CR the CO_2 emissions are approximately 1495 tpd and 1945 tpd for $CO_2/CH_4 = 0.55$ and $CO_2/CH_4 = 0.67$, respectively. There is a net CO_2 production for each alternative of 735 tpd and 1007 tpd, respectively. Total fuel gas (Stream 13 in Fig. 1) for SR is rich in H_2 (≈ 80 %, v/v), while fuel gas for CR is almost exclusively composed of CH_4 (60-75 %). Due to this fact, for CR a significant amount of CO_2 is yielded through CH_4 combustion.
The main operating costs for the process scheme shown in Fig. 1 are those related to the NG requirement (as feedstock and fuel gas), as well as costs arising from recycle and syngas compressor operation. Compared with $CO_2/CH_4 = 0.43$ (Cañete et al., 2014), for CR the operating costs rose steadily in 9.5 % and 25 % for a feed gas with $CO_2/CH_4 = 0.55$ and $CO_2/CH_4 = 0.67$, respectively. Besides, in comparison with SR, operating costs increased to about 2.1 % and 14.3 %, thus indicating that the CR alternative would still remain competitive, even for CO_2 content in NG higher than 30 %. In short, while the capital costs of a CR plant are considerably lower than those for SR, the operating costs are only slightly higher for CR.

4. Conclusions

Natural gas with a high CO_2 content is a promising resource for the production of valuable derivatives, like methanol. For a process plant where H_2 is partially separated and reinjected to the inlet of the methanol loop, augmenting CO_2/CH_4 ratio in the feed gas produces an increase in the CO_2 conversion at the reformer because of a major contribution from DR reaction. Methane conversion is only slightly altered with

changes in CO_2/CH_4 ratio. The increase in CO_2/CH_4 ratio leads to higher NG consumption (as feed gas and fuel), lower H_2/CO ratio, higher H_2 separation rate, higher CO_2 concentration in the syngas and a lower recycle ratio. The latter reduction results in less operating costs as a consequence of lower compression requirements. The operating costs for CO_2/CH_4 = 0.55 and CO_2/CH_4 = 0.67 are approximately 9.5 % and 25 % higher than the alternative design with CO_2/CH_4 = 0.43, while these costs become 2.1 % and 14.3 % higher than that for SR. Then, the Combined Reforming of NG with CO_2 content up to 40 % is a feasible process to produce methanol without CO_2 removal.

References

R. Allis, T. Chidsey, W. Gwynn, C. Morgan, S. White, M. Adams, J. Moore, 2001, Natural CO_2 reservoirs on the Colorado Plateau and Southern Rocky Mountains: Candidates for CO_2 Sequestration First National Conference on Carbon Sequestration, NETL, 1-19.

A. Brooke, D. Kendrick, A. Meeraus, R. Raman, 2014, GAMS Dev. Corp.: Washington.

B. Cañete, C.E. Gigola, N.B. Brignole, 2014, Synthesis Gas Processes for Methanol Production via CH_4 Reforming with CO_2, H_2O and O_2, Ind. Eng. Chem. Res., 53, 17, 7103-7112.DOI: 10.1021/ie404425e

M. A. Crotti, G. Fernández, M. Terrado, 2007, Improving Reserves and Production Using a CO_2 Fluid Model in El Trapial Field, Argentina, Latin American & Caribbean Petroleum Engineering Conference, 15-18 April, Buenos Aires, Argentina, 1-8.

D. Duissenov, 2013, Production and processing of sour crude and natural gas – challenges due to increasing stringent regulations, Norwegian University of Science and Technology (NTNU), 1-101.

I. Dybkjaer, 1995, Tubular reforming and autothermal reforming of natural gas – an overview of available processes, Fuel Proc. Tech., 42, 2-3, 85-107.

A.J. Kidnay, W.R. Parrish, 2006, Fundamentals of Natural Gas Processing, CRC Press

H-W. Lim, M-J. Park, S-H. Kang, H-J. Chae, J.W. Bae, K.W., 2009, Modeling of the Kinetics for Methanol Synthesis using $Cu/ZnO/Al_2O_3/ZrO_2$ Catalyst: Influence of Carbon Dioxide during Hydrogenation, Ind. Eng. Chem. Res., 48, 10448-10455.

S.V. Nørstebo, K.T. Midthun, T.H. Bjørkvoll, L. Kolbeinsen, 2012, Use of Natural Gas with high CO_2 content in an Integrated Industrial Park , ISIJ Int., 52, 8, 1439-1446.

H.S. Roh, K.Y. Koo, U.D. Joshi, W.L. Yoon, 2008, Combined H_2O and CO_2 Reforming of Methane Over Ni-Ce-ZrO_2 Catalysts for Gas to Liquids (GTL), Catal. Lett., 125 (3-4), 283-288.

T. Suhartanto, A.P. York, A. Hanif, H. Al-Megren, M.L. Green, 2000, Potential utilisation of Indonesia's Natuna natural gas field via methane dry reforming to synthesis gas, Cat. Lett., 71 (1-2), 49-54.

Krist V. Gernaey, Jakob K. Huusom and Rafiqul Gani (Eds.), 12th International Symposium on Process Systems Engineering and 25th European Symposium on Computer Aided Process Engineering.
31 May - 4 June 2015, Copenhagen, Denmark.

Process Alternatives for Second Generation Ethanol Production from Sugarcane Bagasse

Felipe F. Furlan[a], Roberto C. Giordano[a], Caliane B. B. Costa[a], Argimiro R. Secchi[b] and John M. Woodley[c]

[a]*Chemical Engineering Graduate Program, Universidade Federal de São Carlos, PPGEQ/UFSCar, Via Washington Luiz, km 235, São Carlos, SP, 13565-905, Brazil*
[b]*Chemical Engineering Program, COPPE, Universidade Federal do Rio de Janeiro, Av. Horácio Macedo, 2030, Rio de Janeiro, RJ, 21941-972, Brazil*
[c]*Department of Chemical and Biochemical Engineering, Technical University of Denmark, Building 229, DK-2800. Lyngby, Denmark*
felipef.furlan@gmail.com

Abstract

In ethanol production from sugarcane juice, sugarcane bagasse is used as fuel for the boiler, to meet the steam and electric energy demand of the process. However, a surplus of bagasse is common, which can be used either to increase electric energy or ethanol production. While the first option uses already established processes, there are still many uncertainties about the techno-economic feasibility of the second option. In this study, some key parameters of the second generation ethanol production process were analyzed and their influence in the process feasibility assessed. The simulated process includes the enzymatic hydrolysis of sugarcane bagasse pretreated with liquid hot water, and the analyzed parameters were the solid consistency in the hydrolysis and pretreatment reactors and the hydrolysis reaction time. The solid consistency in the hydrolysis reactor had the highest influence on the economic feasibility of the process. For the economic scenario considered in this study, using bagasse to increase ethanol production yielded higher ethanol production costs compared to using bagasse for electric energy production, showing that further improvements in the process are still necessary.

Keywords: Bioethanol, sugarcane, techno-economic analysis, process simulation

1. Introduction

The production of ethanol from sugarcane juice is well established in Brazil. In this process, sugarcane juice is extracted and used to produce ethanol, while sugarcane bagasse is sent to boilers, producing steam and electric energy to meet the process demands. However, a surplus of bagasse is frequently possible and this opens opportunities to produce and sell electric energy to the grid or alternatively to increase ethanol yields through second generation (2G) ethanol production. It is expected that these processes would be integrated to the already existing first generation (1G) ethanol process, taking advantage of the economy of scale and decreasing transportation costs. This system will be a highly integrated one with the steam and electric energy demands being met by the burning of by-products of ethanol production. Therefore, it is not a trivial task to infer the effect of some process parameters on the overall process economic performance. In this sense, process systems engineering (PSE) tools can be applied to assess these effects for some key parameters in order to provide insights about the process. Additionally, it will allow

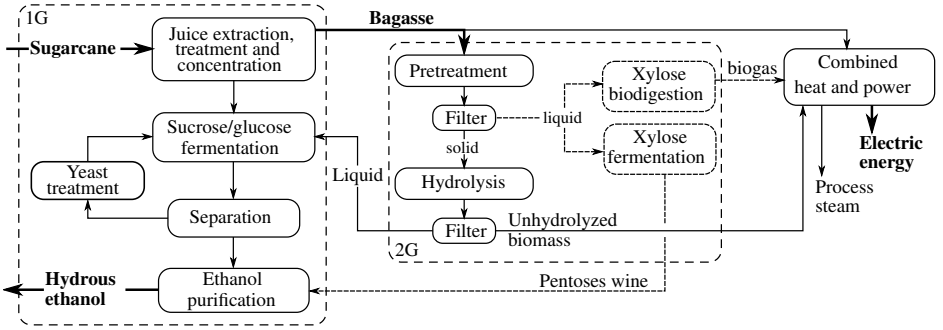

Figure 1: First and second generation ethanol production process. 1G stands for the first generation process, adapted to the integrated process, while 2G stands for the specific second generation process.

new experimental datasets to be quickly evaluated from the whole process perspective and search directions to be derived.

In this study, second generation ethanol production following the biochemical route is considered, including the enzymatic hydrolysis of sugarcane bagasse, pretreated with liquid hot water. The influence of key process parameters on the economic feasibility of the integrated process (first and second generation ethanol) was assessed. The solid consistency in the pretreatment unity and in the hydrolysis reactor were considered, along with the hydrolysis reaction time. Additionally, both fermentation and biodigestion of the pentoses produced in the pretreatment stage are studied.

2. Methodology

The process considered in this study uses liquid hot water for pretreatment of the sugarcane bagasse. The solid fraction from the pretreatment stage is hydrolyzed and the glucose solution is subsequently fermented by *Saccharomyces cerevisiae* along with the treated sugarcane juice. The liquid fraction, consisting mainly of xylose from the hemicellulose hydrolysis, can also be fermented or, alternatively, it can be anaerobically digested to produce biogas. The ethanol solution is sent to the purification stage and hydrous ethanol is produced. Unhydrolyzed cellulose and remaining lignin are separated from the liquid fraction after the hydrolysis reactor and sent to the boiler. The process steam and electric energy demands are still met by the burning of bagasse (in addition to biogas and the solid fraction from the hydrolysis reactor), which limits the amount of bagasse that can be diverted to 2G ethanol production. Therefore, the amount of bagasse diverted to this process varies for each case studied. Figure 1 shows the second generation process and how it is integrated to the (1G) ethanol process: bagasse is diverted to the 2G process, glucose liquor from cellulose hydrolysis is fermented with sugarcane juice and xylose wine is purified with 1G ethanol.

Minimum ethanol selling price (MESP) was determined as the ethanol price that yields a zero net present value. The investment costs for the first generation process were derived from Pinto (2010) and adapted to represent the integrated process. The investment in the combined heat and power stage was based on Dantas (2013) and the investment for the xylose biodigestion system was based on Procknor (2009). Finally, the investment cost of the second generation stage was based on the technical report from the National Renewable Energy Laboratory (Humbird et al., 2011). Other parameters used for the economic analysis are described in Furlan et al. (2013), while the enzyme price was updated to 10.14 USD/kg of enzyme, as reported by Klein-Marcuschamer et al. (2012)

and represents the baseline production cost for the enzyme. Additionally, since sugarcane bagasse does not have an established market price, to assess the feasibility of the process, its opportunity cost regarding electric energy production was considered. This was accomplished by comparing the surplus of electric energy produced with a base case were all bagasse is burnt.

The software EMSO (Environment for Modeling, Simulation and Optimization, Soares and Secchi (2003)) was chosen as the platform for the simulations. This is an equation-oriented simulator with its own modelling language enabling the user to add models to the ones already present in the software. EMSO has several numerical packages for solving algebraic and differential-algebraic systems and also a thermodynamic package, where the user can add compounds and properties as needed.

3. Results and Discussion

Three process parameters were considered in this study: solid consistency (solid mass fraction) in the pretreatment reactor, in the hydrolysis reactor and the hydrolysis reaction time. Table 1 shows the range considered for each parameter. The effect of the parameters were analyzed for three levels of conversion in the hydrolysis reactor: 45, 60 and 75% of the theoretical, i. e., for each set of solid consistencies in the hydrolysis reactor, in the pretreatment reactor and reaction time, three levels of conversion were evaluated.

Table 1: Ranges considered for the parameters studied. Underlined values were used as standard for each parameter when the values of the other parameters were varied.

	Solid fraction in hydrolysis reactor	Solid fraction in pretreatment reactor	Hydrolysis reaction time
Range	10, <u>20</u>,30 and 40%	10, <u>20</u> and 30%	48, <u>72</u> and 96h

As a general case, the biodigestion of xylose allowed a higher amount of bagasse to be diverted to 2G ethanol, resulting in higher ethanol production (23.0 % increase (biodigestion) vs. 21.5 % (fermentation), for the highest increase). However, it also increases investment costs, due to the biodigestors and bigger boilers. Consequently, the MESP of the biodigestion option was on average 46 USD/m^3 higher than the fermentation one. Table 2 shows the cases with the lowest MESP for the xylose fermentation and biodigestion and compares it to 1G base case, with all bagasse being burnt and electric energy surplus being produced. The use of biogas as fuel for steam production allowed 61.9 % of the bagasse to be diverted to 2G production in the biodigestion case. In this case, 50.8 % of the steam demand is met by burning the biogas and the unhydrolyzed fraction of bagasse. At the same time, the higher sugar concentration decreased the specific steam demand (kg of steam/l of ethanol) in 4.4 % compared to the 1G ethanol process. It is worth noticing that this study does not consider the use of sugarcane trash as fuel for the boiler.

As it can be seen in Table 2 the MESP for the best 1G+2G ethanol process with xylose fermentation is 6.3 % higher than the base case, although only 3.1 % higher than the ethanol selling price considered (513.7 USD/m^3, relative to the average price between Jan/2003 and Dez/2012 in Brazil). This shows that second generation ethanol still needs further development in order to compete with electric energy production, at least for the electricity prices used in this study (80.8 USD/MWh), which correspond to the average value of auctions in Brazil in the period 2005-2011.

Among the parameters considered in this study, the solid consistency in the hydrolysis reactor had the most significant effect on the economic feasibility of the process, as it can be seen in Figure 2 for the xylose fermenting case, while the other parameters had only marginal effect on the MESP. Interestingly, 2G MESP is not monotonic with respect to the solid consistency in the hydrolysis reactor, which can be related to a decrease in glucose recovery in the separation step after the

Table 2: Base case (1G burning all bagasse) and best cases (lowest 2G MESP) for the 1G+2G process, for xylose biodigestion and fermentation. Hydrolysis reaction time was 72h for the last two cases.

	1G	1G+2G (xylose biodigestion)	1G+2G (xylose fermentation)
Solid consistency (hydrolysis)	–	20 %	20 %
Solid consistency (pretreatment)	–	10 %	30 %
Hydrolysis reaction yield	–	75 %	75 %
Bagasse fraction burnt	100 %	38.1 %	48.3 %
Increase in ethanol production	–	17.6 %	20.4 %
1G+2G MESP (USD/m^3)	498.4	565.2	529.6
2G MESP (USD/m^3)	–	943.9	682.0
Steam produced (kg/TC)	522.9	404.6	380.4
Contribution to steam production (bagasse /unhydrolyzed biomass/ biogas)	100 % / 0 % / 0 %	49.2 % / 37.4 % / 13.4 %	66.4 % / 33.6 % / 0 %

hydrolysis. This suggests the importance of a washing step to increase sugar recovery when high solid consistencies are used, although in this case there will be a trade-off between sugar recovery and its final concentration in the stream.

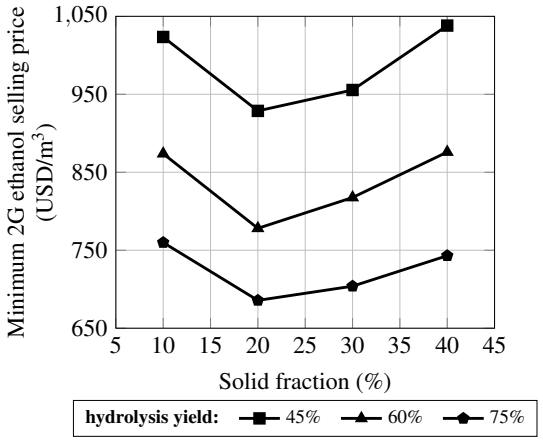

Figure 2: Influence of the solid consistency in the hydrolysis reactor on the minimum 2G ethanol selling price when xylose is fermented.

For the overall cost of ethanol (1G + 2G), sugarcane cost clearly dominated the contribution, followed by capital expenditures (CAPEX) and other operating expenses (OPEX) related to 2G production (enzyme cost, electric energy opportunity cost and other raw material costs), as shown in Figure 3a. The specific 2G cost, on the other hand, is highly dominated by the enzyme costs which is on average 42 % of the total production costs, while the CAPEX cost (second higher) accounts for 23 % of the total cost. The solid consistency in the hydrolysis reactor has a clear effect on the enzyme and CAPEX cost contributions while its effect on the other components of 2G ethanol costs are much weaker, as shown in Figure 3b. Also, it can be inferred that the effect of solid consistency on MESP decreases for higher yields. Since more ethanol is produced for higher yields, the influence of the parameter is softened.

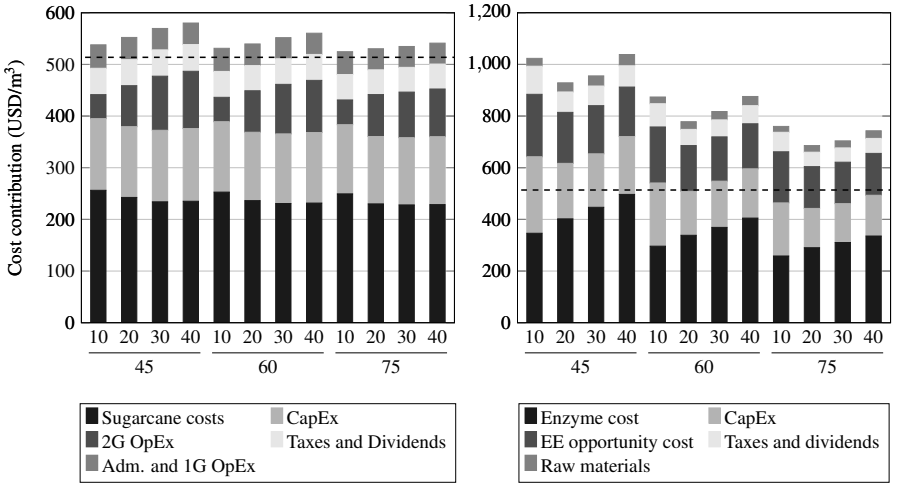

(a) Overall production cost of ethanol.

(b) production cost of 2G ethanol.

Figure 3: Influence of the solid consistency in the hydrolysis reactor (10–40% m/m) and of the hydrolysis yield (45–75% of the theoretical) on the overall production cost of ethanol (a) and on 2G ethanol (b) when xylose is fermented. The dashed line represents the current selling price for ethanol.

To assess the current state of the technology and its feasibility, the yields reported by Souza et al. (2014) for the enzymatic hydrolysis of sugarcane bagasse pretreated with liquid hot water were used. Based on these data, Figure 4 shows the 2G MESP obtained, for the process with xylose fermentation to ethanol. It can be seen that 2G MESP generally decreased for the whole time range considered in the study, showing that the negative effect of the reaction time on 2G MESP is in general lower than the positive effect of the increase in the yield. Only for the higher solid consistency (20%), an increase in 2G MESP is seen in the final hours of reaction. If results similar to the best experimental ones (solid consistency of 15 % and 72 hour of hydrolysis reaction) could be obtained in industrial scale, an increase in ethanol production of 13.9%, with a MESP of 540.3 USD/m^3 (841.9 USD/m^3 for the 2G MESP) could be expected.

4. Conclusions

An integrated first and second generation ethanol industrial plant based on the enzymatic hydrolysis of sugarcane bagasse pretreated with liquid hot water was simulated, and its economic feasibility assessed. In general, for the economic scenario considered, the second generation ethanol cost was higher than the first generation one, even when high solid consistencies in the reactors was considered. This shows that the process still needs further developments in order to compete with electric energy production. Xylose fermentation to ethanol yielded lower MESPs than its biodigestion, although the latter option allowed a higher ethanol production. Among the process parameters considered, the solid consistency in the hydrolysis reactor showed the strongest influence on 2G MESP: the lowest prices were between 20 and 30% of solids, with a slight increase after that. Additionally, simulations based on experimental yields reported in the literature showed that, for the time range considered for the hydrolysis reaction, its negative effect on the 2G MESP was lower than the positive effect of the increase in the yield. For the experimental data considered, a MESP of 540.3 USD/m^3 could be reached if similar results were to be achieved in industrial scale. This is 5.2% higher than the prices in Brazil in the period 2002-2012, but 8.4%

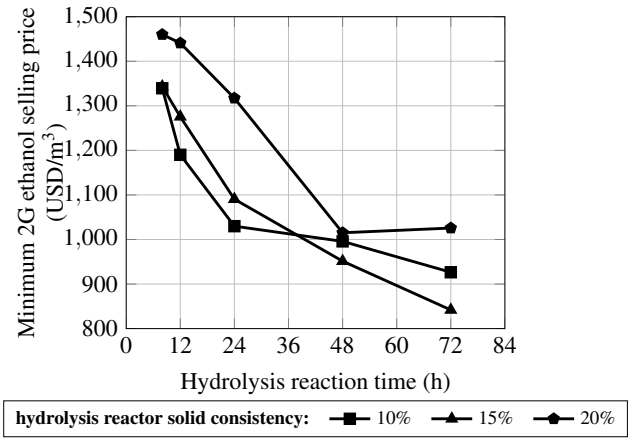

Figure 4: Minimum ethanol selling price considering experimental data reported by Souza et al. (2014) and xylose fermentation.

higher than the MESP for the stand alone 1G process.

5. Acknowledgements

The authors would like to thank CAPES (fellowship process n° 2608/14-6) for the financial support.

References

Dantas, G. A., 2013. Investment alternatives for the sugarenergetic sector for exploitation of sugarcane bagasse and straw. PhD thesis, Universidade Federal do Rio de Janeiro, Rio de Janeiro, in Portuguese.

Furlan, F. F., Filho, R. T., Pinto, F. H. P. B., Costa, C. B. B., Cruz, A. J. G., Giordano, R. L. C., Giordano, R. C., 2013. Bioelectricity versus bioethanol from sugarcane bagasse: is it worth being flexible? Biotechnology for Biofuels 6 (142), 1–12.

Humbird, D., Davis, R., Tao, L., Kinchin, C., Hsu, D., Aden, A., Schoen, P., Lukas, J., Olthof, B., Worley, M., Sexton, D., Dudgeon, D., 2011. Process design and economics for biochemical conversion of lignocellulosic biomass to ethanol. Tech. rep., National Renewable Energy Laboratory.

Klein-Marcuschamer, D., Oleskowicz-Popiel, P., Simmons, B. A., Blanch, H. W., 2012. The challenge of enzyme cost in the production of lignocellulosic biofuels. Biotechnology and bioengineering 109 (4), 1083–1087.

Pinto, F. H. P. B., 2010. Cellulosic ethanol: a study of economic and financial viability. Masters thesis, Universidade de São Paulo, São Paulo, in Portuguese.

Procknor, C., 2009. Electric energy from vinasse. In Portuguese. http://www.unica.com.br/convidados/2564115692033771508 1/energia-eletrica-a-partir-da-vinhaca/.

Soares, R. P., Secchi, A. R., 2003. Emso: A new environment for modelling, simulation and optimisation. Computer Aided Chemical Engineering 14, 947–952.

Souza, R. B. A., Corrêa, L. J., Suarez, C. A. G., Cruz, A. J. G., 2014. Evaluation of the effect of the solid consistency in the enzymatic hydrolysis of sugarcane bagasse and comparisson between different comercial enzymatic mixtures. In: Brazilian Congress in Chemical Engineering. pp. 1–8, in Portuguese.

Krist V. Gernaey, Jakob K. Huusom and Rafiqul Gani (Eds.), 12th International Symposium on Process Systems Engineering and 25th European Symposium on Computer Aided Process Engineering.
31 May – 4 June 2015, Copenhagen, Denmark

Simulation Study of Heat Transfer Enhancement due to Wall Boiling Condition in a Microchannel Reactor Block for Fischer-Tropsch Synthesis

Krishnadash S. Kshetrimayum, Park Seongho, Jong Ikhwan, Na Jonggeol, Han Chonghun*

School of Chemical and Biological Engineering, Seoul National University, Seoul 151-744, Republic of Korea
chhan@snu.ac.kr

Abstract

A microchannel reactor block, with process and coolant channel planes arranged in alternate fashion and cross flow mode was considered for Fischer-Tropsch(FT) synthesis. Computational Fluid Dynamic (CFD) simulation of heat transfer in the microchannel block was carried out to gain insights on the complex thermal behavior. Cooling oil, subcooled water and saturated water were chosen as coolants to simulate the heat transfer phenomena.The study revealed significant enhancement in heat transfer across the channel walls due to wall boiling condition which occures in case of saturated water as coolant. Consequently, near isothermal condition was able to achieve by adjusting saturated water flow rate. Scenario for partial boiling, with saturated water as coolant, was investigated. Simulations were carried out to study effects of different conditions of heat generation and coolant flow rate on reactor performance parameters.

Keywords: Computational fluid dynamics, wall boiling, heat transfer, microchannel, Fischer-Tropsch synthesis.

1. Introduction

Fischer-Tropsch(FT) synthesis is the main step in Gas-to-Liquid(GTL), coal-to-liquid(CTL) and biomass-to-liquid(BTL) processes(Arzamendi et al., 2010). In GTL, natural gas is used as feedstock to produce syn-gas (a mixture of carbon-monoxide-CO and hydrogen-H_2) needed for FT reaction where the reaction then produce liquid hydrocarbon fuels(Fischer and Tropsch, 1930). In CTL and BTL, syn-gas is produced from coal and biomass through coal and biomass gasification. GTL is particularly of interest to oil and gas industry today, partly due to rising fuel price, and partly due to environmental restrictions of flaring offshore stranded and associated gas. FT synthesis involves complex hydrodynamic, chemical and thermal interaction of three material phases: reactant gases in the form of bubbles, liquid as FT product and solid catalyst particles loaded as filled or coating on the microchannel internal walls. The reaction can be represented as the following: $n\mathrm{CO} + (2n+1)\mathrm{H_2} \rightarrow \mathrm{C}_n\mathrm{H}_{2n+2} + n\mathrm{H_2O}$. The reaction is highly exothermic (heat of reaction = 165 kJ/mol CO) with reaction products showing selectivity based on reaction temperature and catalyst deactivation highly sensitive to temperature. Hence, adequate heat removal and temperature control in the reactor is demanded for high reactor yield(Deshmukh et al., 2010).

Microchannel reactors are said to shorten the diffusion distance, and lower heat and mass transfer resistance thereby standing out as a promising candidate for FT synthesis applications. Reduced mass and heat transfer distances provides enhanced process intensification, when compared to conventional reactors. Also, the high exothermic nature of the reaction and shorter residence time of microchannel reactor demands that a coolant having high heat removal capacity, for instance, saturated water be used (Deshmukh et al., 2010). They tested a pilot scale microchannel reactor with 276 process channels and 132 coolant channels arranged in cross-flow mode using saturated water as coolant. Arzamendi et al.(2010) studied the buoyancy effect on the thermal behavior of a microchannel reactor block through CFD simulation considering partial boiling of coolant. However they considered wall coated catalytic reaction zone. Gamze and Ahmet (2011) carried out parametric analysis of FT synthesis, also for wall coated catalytic microchannel reactor, but considering only 2D simulation to represent a unit cell of a parrallely arranged microchannels and using steam a coolant. Shin et al.(2013,2014) presented experimental and simulation study of catalytic bed modular microchannel reactor. But they considered 40 mm wide and 140 mm long channels stacked up to form plate heat exchanger configuration and using silicon oil as coolant.

In this work, we considered a microchannel network in the form of microchannel block, adapted from the microchannel reactor block of Arzamendi et al.(2010), to carry out heat transfer simulation using different coolant types and process channels as catalyst packed bed. The aim of this work is to simulate the complex phenomena associated with two-phase wall boiling heat transfer and quantitatively evaluate the heat transfer enhancement due to wall boiling condition as compared to the non-boiling single phase convective flow of coolant. Effect of practically relevant scenarios: higher or lower heat generation rate and coolant flow rate were studied. Further, we investigated scenario for partial wall boiling condition to avoid critical heat flux and ensure reactor safety.

2. Model Description

2.1 Reactor block model

Microchannel reactor block used by Arzamendi et al.(2010) and adapted in the present work is shown in figure 1. It has dimensions: 21mm x 21mm x 17mm, with four process channel planes and four coolant channel planes stacked up in alternate fashion. Each channel planes has 10 parallel channels of 1mm x 1mm x 17 with gap between adjacent channels as 1mm.

2.2 Process channels

Process channels are assumed to be filled with catalyst and modeled as pack bed reactor with certain void fraction determined by the catalyst and inet material loading. Reaction scheme and kinetics as proposed by Marvast et al.(2005) for Fe-based byfunctional catalyst was considered for the present study, the detail of which is not shown here for brevity. Heat is continuously generated in the process channels as the syn-gas ($CO + H_2$) undergoes catalytic conversion to various hydrocarbon products.

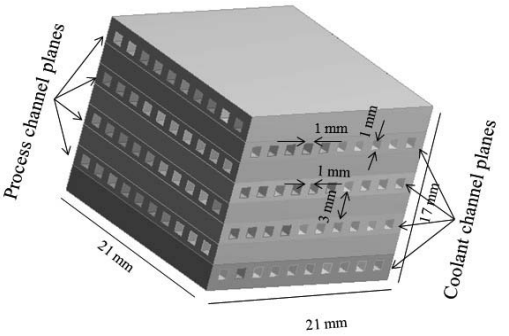

Figure 1: Microchannel reactor block

2.3 Coolant channels

For single-phase coolant flow as is the case with subcooled oil and subcooled water, convective heat transfer is assumed to be the only means of heat removal. In case of saturated water as coolant, the fluid comprises of saturated liquid water and water vapor, with pure liquid at the inlet. The flow of liquid water and vapor is modeled as Eulerain-Eulerian multiphase flow with continuity and momentum equations described by Navier-Stokes equations, separately for both the phases. Mass transfer from the liquid phase to vapor is accounted by the rate of evaporation or wall boiling. Heat transfer between the two phases is assumed to be insignificant as compared to the heat transfer from the channel wall. Details information including the mathematical description is not given here for brevity and can be found in ANSYS FLUENT 14.5 Manual.

2.4 Wall boiling

In the microchannel block, heat is transferred from the process channel, where exothermic reaction occurs, to the adjacent coolant channels through channel walls. If the coolant is saturated water, phase change occurs in the coolant channel due to wall boiling. Mechanistic wall heat flux partioning model for boiling heat transfer as proposed by Podowski (2012) is used for heat transfer from heated channel wall to saturated water. Under the heat flux partitioning model, the total heat flux through the wall is partitioned into convective, quenching and evaporative heat flux as follows:

$$\dot{q}_{Wall} = \dot{q}_F + \dot{q}_Q + \dot{q}_E \tag{1}$$

where $\dot{q}_{Wall}$ represents the total wall heat flux, $\dot{q}_F$, $\dot{q}_Q$, and $\dot{q}_E$ the convective, quenching and evaporative heat flux, respectively. The detail equation of heat flux is not given here for brevity. For the coolant as subcooled oil and subcooled water without phase change, only convective heat transfer is expected to occur.

3. Simulation Conditions

3.1 Single channel

Reaction in a single channel packed bed with void fraction 0.4, dimensions as given in figure 1, at isothermal condition using multiple reactions and kinetic data of Marvest et al.(2005) was considered. Syn-gas composition of H_2/CO ratio of 1 and 1.5, and reactor pressure at 20 bar was used. Temperatures of both syn-gas feed and reactor were assumed to be constant at 503 and 523 K. Catalyst density of 50 - 1060 kg/m^3 was used along with inert. Simulation was carried out using commercial software-ASPEN.

3.2 CFD Model

Simulation was carried out using commercial CFD software- ANSYS FLUENT. Hui et al. (2012) satisfactorily simulated micro-reactor for various configurations using the software tool to demonstrate the applicability. Since heat transfer study is the focus here, fluid flow inside a process channel is neglected and CFD model consist of two types of solid zones--one for process channels and other for reactor body; and one fluid zone for coolant flow. Process channels are zones for constant heat source with heat profile as obtained from single channel reactor simulation and implemented into CFD model using User Defined Function (UDF). Coolant channels are zones for heat sink. Zones are meshed with tetrahedral and hexagonal elements with grid count as 2.2 million to ensure fine mesh quality. Eulerain-Eulerian model of multiphase flow is

applied for multiphase coolant type, as in saturated water, and single phase model for single phase coolant type, as in cooling oil and subcooled water. Simulation model setups are as follows: Laminar for single phase coolant; SST-k Omega for turbulent model in multiphase; SIMPLE algorithm for pressure velocity coupling; second order discretization for momentum and energy equatio; RPI boiling model (Podowski, 2012) for wall boiling. Reactor body is assumed to be made of stainless steel with density 2820 kg/m^3 and heat capacity as 473.3 J/Kg-K with thermal conductivity of 23.2 J/s-m-K. Densities of subcooled oil, subcooled water and water vapor as taken as 936 kg/m^3, 998.2 kg/m^3 and 1.55 kg/m^3 ; heat capacity as 1967 J/Kg-K, 4182 J/Kg-K and piecewise polynomial; thermal conductivity as 0.0974 J/s-m-K, 0.261 J/s-m-K and 0.261 J/s-m-K, respectively. Saturation temperature for wall boiling model was set as 500 K, which is the value at operating pressure of 20 bar. Coolant flow rates in the range of 0.4 g/min to 43.2 g/min were considered.

4. Results and Discussion

4.1. Mole fraction of CO and H_2

Deshmukh et al. (2010) in their experiments on microchannel reactor achieved 71.8 % CO conversion. A conversion value between 71 to 72 % was taken as constraint in our simulation too, by adjusting the catalyst loading (50 - 1060 kg/m3) for syn-gas feed rate considered. Figure 2 shows, mole fraction of syn-gas (CO and H_2) for H_2/CO ratio of 1 and 1.5, and heat generation for different syn-gas flow rates from single channel catalyst packed bed simulation. H_2 consumption rate was observed to be faster than that of CO and mole fraction profile crosses at a point along the channel in case of H_2/CO ratio 1.5. For same final CO conversion, heat generation was higher for higher syn-gas flow rate.

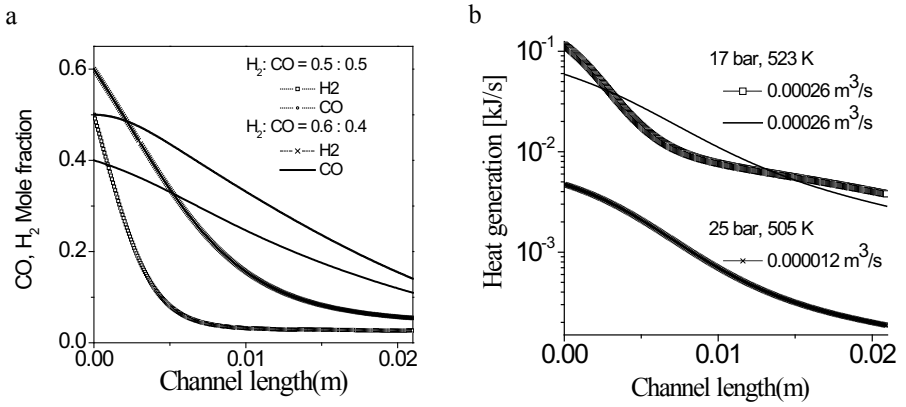

Figure 2. Single channel packed bed simulation, (a) mole fraction of CO, and H_2 for H_2/CO ratio of 1 and 1.5, (b) heat generation for different syn-gas flow rates for same final CO conversion.

4.2 *Wall boiling CFD simulation and heat transfer enhancement*

For better performance of a microchannel reactor, temperature inside the reactor internal is desired to be maintained within temperature difference lesser than about 15 K. This condition is obtained in the CFD simulation with wall boiling heat transfer in coolant channels, as can be seen from temperature profile in Figure 3(a). Figure 3(b) shows

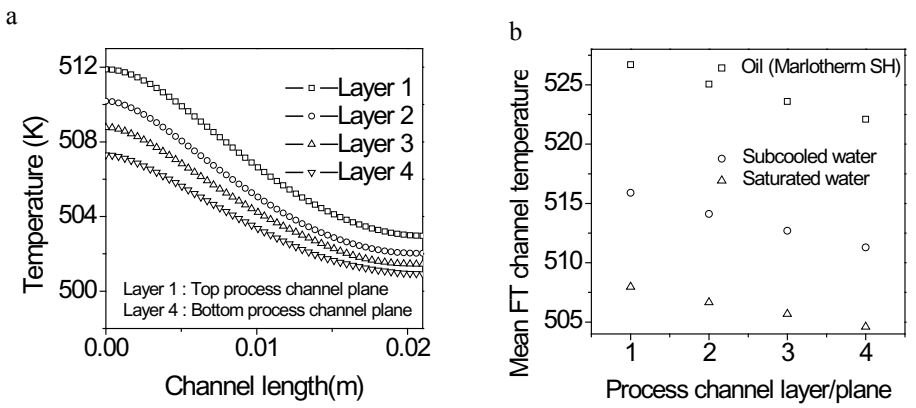

Figure 3. (a)Temperature profile in process channel from wall boiling CFD simulation, (b) Mean FT channel temperature showing heat transfer enhancement due to wall boiling.

mean FT temperature for three cases of coolant type: cooling oil, subcooled water and saturated water. With saturated water as coolant, all FT channel layers have mean temperature below 510 K, whereas in case of subcooled oil and subcooled water, temperatures are above 512 K. Lower mean FT temperature in case of saturated water implies heat transfer enhancement due to wall boiling condition in coolant channels.

4.2 Effect of heat generation and coolant flow rates

In a typical operation, there can be situations of higher or lower heat generation than the normal condition. Accordingly, coolant flow rate has to be adjusted to maintain reactor temperature to the desired value. Effect of heat generation and coolant flow rates are explored. Figure 4(a) shows higher extend of wall boiling for higher heat generation rate, which is evident from lower liquid fraction at coolant channel exit. As expected mean FT channel temperature is larger for higher generation rate, as in figure 4(a) secondary y-axis, and smaller for larger coolant flow rate, as in figure 4(b).

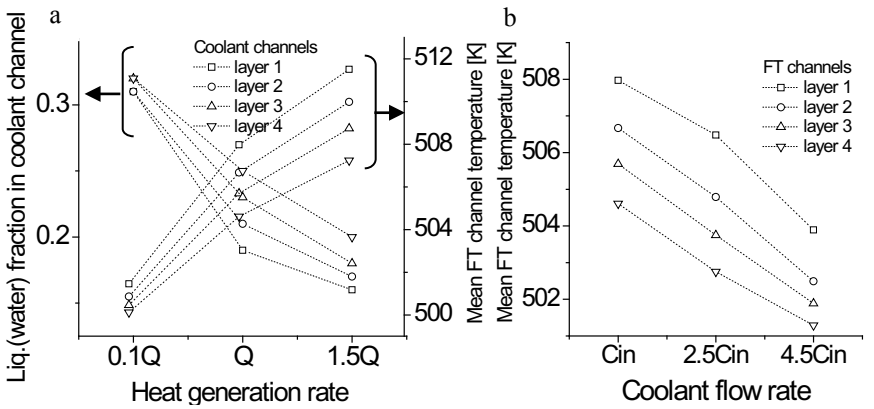

Figure 4. (a) Heat generation rate[Q = heat generation for syn-gas flow rate 0.0026 m^3/s] vs. liquid (saturated water)fraction and FT channel temperature , (b) coolant flow rate[Cin = 1.2 g/min] vs. mean FT channel temperature.

A common concern in microchannel wall boiling heat transfer is critical heat flux. Therefore, flow regime in coolant channels has to be such that situation for critical heat flux is avoided. Adjusting coolant flow rate can ensure flow regime limiting only to partial boiling. For instance, flow regime under partial boiling condition as shown in figure 5, where liquid fraction in coolant channels are high enough, can ensure safe operation of microchannel reactor.

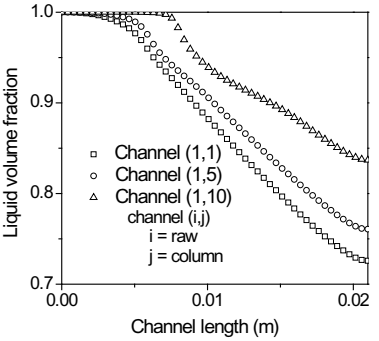

Figure 5: Partial boiling condition in coolant channels (flow rate=3g/min).

5. Conclusions

A systematic simulation study of heat transfer in a microchannel reactor block is presented. Study revealed enhancement in heat transfer due to wall boiling condition which occurs with saturated water as coolant. Concequently, adjusting saturated water flow rate can achieve near isothermal condition in microchannel reactor. Effect of heat generation and coolant flow rate on reactor parameters are investigated. A method to avoid critical heat flux is suggested. Further, Song et al. (2004), from their experimental work, proposed a correlation for chain-growth probability as a function of temperature and H_2/CO ratio. At the maintained FT channel temperature range, 500 K - 510 K, the value of chain-growth probability was calculated to be between 0.79 to 0.85 for H_2/CO molar ratio as 1. This value falls under the desired growth-probability of FT synthesis.

Acknowledgement

This research was respectfully supported by Engineering Development Research Center (EDRC) funded by the Ministry of Trade, Industry & Energy (MOTIE).

References

G. Arzamendi, P.M. Dieguez, M.Montes, J.A. Odriozola, E. F. Sousa-Aguiar, L.M. Gandia, (2010) Computational fluid dynamics study of heat transfer in a microchannel reactor for low-temperature Fischer-Tropsch synthesis, Chem. Eng. J. 160, p915-922.

F. Fischer, H. Tropsch, (1930) Process for the production of paraffin-hydrocarbons with more than one carbon atom. U.S. Patent 1,746,464.

S.R. Deshmukh, A.L.T. Tonkovich, K.T. Jarosch, L.Schrader, S.P. Fitzgerald, D.R. Kilanowski, J.J. Lerou, T.J. Mazanec, (2010) Scale-up of microchannel reactors for Fischer-Tropsch Synthesis. Ind. Eng. Chem. Res. 2010;49: 10883-10888.

M.A. Marvast, M. Sohrabi, S. Zarrinpashne, G. Baghmisheh, (2005) Fischer-Tropsch Synthesis:Modeling and Performance Study for Fe-HZSM5 Bifunctional Catalyst. Chem. Eng & Tech.; 28-1:p78-86

M.S. Shin, N. Park, M.J. Park, K.W. Jun, K.S. Ha, (2013) Computational fluid dynamics model of a modular multichannel reactor for Fisher-Tropsch synthesis: Maximum utilization of catalytic bed by microchannel heat exchangers. Chem. Eng. J. 234, p23-32

M.S. Shin, N. Park, M.J. Park, J.Y. Cheon, J.K. Kang, K.W. Jun, K.S. Ha, (2014) Modeling a channel-type reactor with a plate heat exchanger for cobalt-based Fischer-Tropsch synthesis. Fuel Process. Technol. 118, p235-243

M.Z.Podowski, (2012), Towards mechanistic modeling of boiling heat transfer. Nuclear Eng & Tech., vol 44-8, p889-896

H. An, A. Li, A.P. Sasmitro, J.C. Kurnia, S.V. Jangam, A.S. Mujundar, (2012), Computational fluid dynamics analysis of micro-reactor performance: Effect of various configurations, Chem. Eng. Sc. 75, p85-95

H.S. Song, D.Ramkrishna, S.Trinh, H.Wright, (2004), Operating Strategies for Fischer-Tropsch Reactors: A Model-Directed Study, Korean J. Chem. Eng.21(2), p308-317

www.ansys.com/ANSYS FLUENT 14.5 Manual, 2013

Krist V. Gernaey, Jakob K. Huusom and Rafiqul Gani (Eds.), 12th International Symposium on Process Systems Engineering and 25th European Symposium on Computer Aided Process Engineering.
31 May – 4 June 2015, Copenhagen, Denmark

CO_2 vs Biomass: Identification of Environmentally Beneficial Processes for Platform Chemicals from Renewable Carbon Sources

André Sternberg,[a] Holger Teichgräber,[a] Philip Voll[a] and André Bardow[a*]

[a]*Chair of Technical Thermodynamics, RWTH Aachen University; Schinkelstr. 8; 52477 Aachen; Germany*
andre.bardow@ltt.rwth-aachen.de

Abstract

Conventionally, platform chemicals are produced from fossil feedstock. In recent years, the production of chemicals from renewable feedstock has been considered. One possible renewable carbon source is biomass. Another option is carbon dioxide (CO_2). A rigorous comparison of processes employing renewable carbon sources is missing today. We therefore identify the environmentally most beneficial process routes for platform chemicals. All processes are integrated into a single superstructure, which is analyzed using linear optimization minimizing global warming impacts. The optimal solutions exploit synergies between the different process routes and feedstocks.

Keywords: LCA, optimization, CO_2, Biomass, platform chemicals

1. Introduction

The dependency on fossil fuels and the related global warming impacts can be reduced through the utilization of renewable carbon sources such as biomass and CO_2. The utilization of renewable carbon sources is therefore drawing increasingly attention in the chemical industry (Peters et al. 2011). In biomass-based process routes (Biomass-to-Chemicals), biomass provides the required C-building block and also energy for the chemical reaction. In contrast, in CO_2-based process routes (CO_2-to-Chemicals), CO_2 provides only the C-building block. Thus, most CO_2-based reactions require hydrogen as additional high energy feedstock (Peters et al. 2011). However, conventional hydrogen production based on steam-methane-reforming has very high environmental impacts (Cetinkaya et al. 2012) conflicting with the motivation for renewable carbon sources utilization. To minimize the environmental impacts of hydrogen production, electrolysis using surplus power is a promising option. The multitude of process routes is further complicated as hydrogen can not only be used for CO_2-to-Chemicals process routes but also for Biomass-to-Chemicals process routes to increase the product yield (Gassner and Maréchal 2008; Clausen et al. 2010).

We aim to identify the environmentally most beneficial process routes for platform chemicals from renewable carbon sources. For this purpose, CO_2-to-Chemicals and Biomass-to-Chemicals process routes are integrated into a single superstructure model, which is analyzed using linear optimization minimizing the environmental impacts. The conversion of biomass and CO_2 relies on biomass and surplus power which are limited feedstocks. From a macro perspective, the limited feedstocks should only be used for process routes with highest environmental impact reduction potential. In fact, these feedstocks could also be used outside the chemical industry, e.g., in the energy or transportation sector. Hence, our analysis also considers utilization of the limited

feedstocks outside the chemical industry (Biomass-to-Alternative, Power-to-Alternative).

2. Identification of environmentally beneficial process routes

We use superstructure-based optimization to identify environmentally most beneficial process routes. First, a mathematical superstructure model is formulated incorporating all potential process routes (section 2.1). Secondly, the generated model is analyzed using optimization algorithms to identify process routes minimizing the total environmental impacts (section 2.2).

2.1. Superstructure

The superstructure contains the following process routes (cf. Figure 1): (I) Biomass-to-Chemicals process routes, (II) CO_2-to-Chemicals process routes, (III) hydrogen production processes, (IV) conventional process routes for chemicals, and (V) alternative utilization of biomass and surplus power. The process routes are modeled by constant conversion factors representing the ratio between inputs and outputs. Note that the process routes are coupled in the superstructure model, thus enabling an integrated analysis to exploit possible synergies of the considered process routes: Hydrogen is mandatory for the CO_2-to-Chemicals process routes and optional for the Biomass-to-Chemicals process routes; CO_2 for the CO_2-to-Chemicals process routes could also be supplied from biomass-based process routes.

Process route (V) represents alternative utilization of the limited feedstocks biomass and surplus power outside the chemical industry. An alternative utilization would lead to environmental impact reductions by substituting a conventional process and its related environmental impacts (cf. section 3.4). For the alternative utilization, we do not consider specific technologies but determine threshold values for the environmental impact reduction of these alternative utilization pathways. The threshold value indicates when the alternative utilization achieves higher environmental impact reductions than the utilization for production of chemicals.

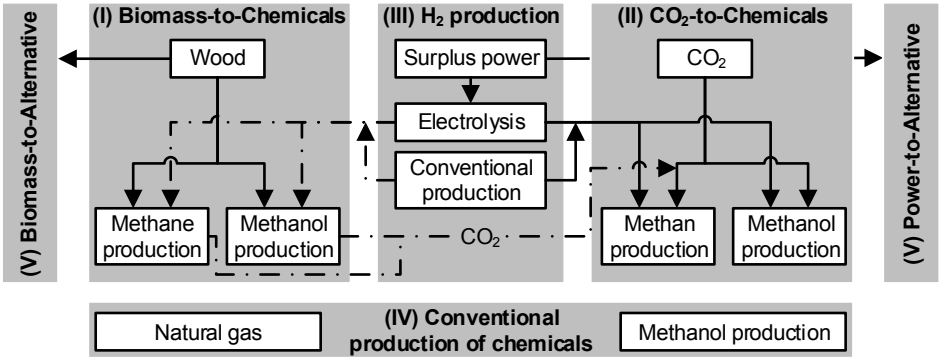

Figure 1: Superstructure embedding all considered process routes for platform chemicals. Dashed/dotted lines indicate optional connections, solid lines indicate mandatory connections.

2.2. Linear optimization model

In this work, optimization is carried out minimizing the total environmental impacts of the considered system (cf. Figure 1):

$$\min z = \underline{EI}^T \underline{x}, \tag{1}$$

$$\text{s.t.} \quad A\underline{x} = 0. \tag{2}$$

The objective function is formulated in terms of the environmental impacts $\underline{EI}$ of the single processes and the scaling factors $\underline{x}$ of the single processes (decision variables). The scaling factors $\underline{x}$ represent the choice and the utilization level (continuous value $\underline{x}$) of the single process routes. Total environmental impacts are to be minimized such that mass and energy balances are fulfilled (Equation 2), where A contains all inputs and outputs of the considered processes.

3. Methanol and methane from renewable carbon sources

In section 3.1, a case study is presented for the production of methanol and methane. The approach is exemplified using global warming impact (GW) as environmental impact category. The results of the case studies for methanol and methane are presented in section 3.2 and 3.3, respectively.

3.1. Problem setting

3.1.1. Considered feedstocks

For the Biomass-to-Chemicals process routes, waste wood with a global warming impact of -0.418 kg CO_2-eq/kWh_{LHV} (Gassner and Maréchal 2008) is considered as feedstock. The CO_2-to-Chemicals process routes use CO_2 captured from a coal-fired power plant. The global warming impact of CO_2 is -0.654 kg CO_2-eq/kg (Gerdes et al. 2013). Furthermore, both process routes can use surplus power with a global warming impact of zero.

However, wood and surplus power are limited feedstocks. Thus, the useable amount is constraint by maximum 1 kWh_{LHV} wood and 1 kWh surplus electricity.

3.1.2. Considered Wood-to-Chemicals and CO_2-to-Chemicals process routes

Most of the considered Wood-to-Chemicals and CO_2-to-Chemicals process routes require additional hydrogen (cf. Table 1). Hydrogen can either be produced from electrolysis using surplus power with an efficiency of 55 kWh/kg H_2 (Schüth 2011) or from steam-methane-reforming with water-gas-shift (GW = 10.8 kg CO_2-eq/kg). All considered chemical processes routes require additional grid electricity for compression and separation of reactants and products. The global warming impact of grid electricity is 0.4 kg CO_2-eq/kWh (German target for 2020).

3.1.3. Conventional production of considered platform chemicals

The following conventional processes are considered (PE International 2013):

- Methanol: production from natural gas-based syngas (GW = 0.88 kg CO_2-eq/kg)
- Methane is assumed as natural gas (GW = 0.034 kg CO_2-eq/kWh_{LHV}).

3.1.4. Alternative utilization of wood and surplus power

While we vary global warming impact reductions ($GW_{reduction}$) for the alternative utilization of wood and surplus power, we also define two reference cases with very high $GW_{reduction}$.

- Wood can be converted to electricity. If the wood-fired power plant replaces a coal-fired power plant, the $GW_{reduction}$ is 0.35 kg CO_2-eq/kWh (Steubing et al. 2012).
- Surplus power can be stored in a pumped hydro storage. If electricity from the pumped hydro storage replaces electricity from a natural gas turbine $GW_{reduction}$ is 0.5 kg CO_2-eq/kWh (Sternberg and Bardow 2015).

Table 1: Inputs, outputs and direct greenhouse gas emissions of considered Wood-to-Chemicals and CO_2-to-Chemicals process routes. All values for Wood-to-Chemicals and CO_2-to-Chemicals process routes are per 1 kWh_{LHV} wood input and 1 kg CO_2 input, respectively. Positive values are inputs and negative values are outputs. For CH_4, inputs are natural gas and outputs are methane.

	H_2	CH_3OH	CH_4	Electricity	Emissions
	kg	kg	kWh	kWh	kg CO_2-eq
CO_2 (+H_2)-to-CH_4[a]	0.172		-4.73	0.112	0.066
CO_2 (+H_2)-to-CH_3OH[b]	0.136	-0.696		0.926	0.032
CO_2 (+H_2, NG)-to-CH_3OH[c]	0.075	-1.537	8.71	0.953	0.583
Wood-to-CH_4[d]			-0.86	0.032	0.246
Wood-to-CH_3OH[e]		-0.103			0.212
Wood (+H_2,min)-to-CH_4[d]	0.001		-0.89	0.033	0.240
Wood (+H_2,max)-to-CH_4[d]	0.035		-1.77	0.066	0.066
Wood (+H_2)-to-CH_3OH[c]	0.014	-0.216		0.140	0.036
Wood (+H_2, NG)-to-CH_3OH[c]	0.011	-0.306	0.76	0.190	0.060

[a]Müller et al. 2013, [b]Rihko-Struckmann et al. 2010, [c]Clausen et al. 2010, [d]Gassner and Maréchal 2008, [e]C. N. Hamelinck and A.P.C. Faaij 2002

3.2. Minimal global warming impacts for methanol production

Figure 2 shows the optimal process routes for methanol production as function of global warming impact reductions ($GW_{reduction}$) for the alternative utilization of wood and surplus power. Five process combinations (zones) are identified. In each zone, the given process route has the lowest overall global warming impacts. Thus, the product (methanol or methane) was not specified. However, the production of methanol from renewable carbon sources always achieves lower global warming impacts than the production of methane.

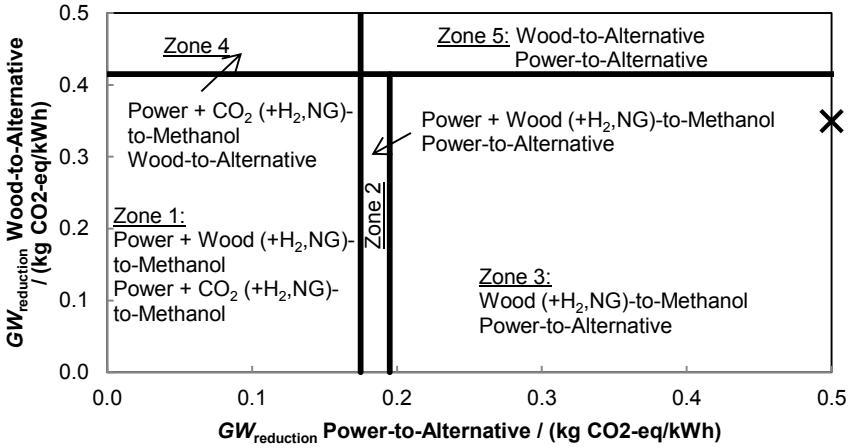

Figure 2: Process routes for methanol production with lowest global warming impacts depending on the global warming impact (*GW*) reduction for Power-to-Alternative and Wood-to-Alternative. "Power +" means that the required hydrogen is produced from surplus power. The cross indicates the considered reference case Power-to-Alternative and Wood-to-Alternative processes.

The combination of Wood-to-Methanol and CO_2-to-Methanol (Zone 1) achieves the lowest global warming impacts as long as the $GW_{reduction}$ for alternative utilization of wood and surplus power is lower than 0.41 and 0.18 kg CO_2-eq/kWh, respectively. Both processes use also natural gas and hydrogen from surplus power. If the $GW_{reduction}$ for Wood-to-Alternative is higher than 0.41 kg CO_2-eq/kWh, Wood-to-Methanol processes are no longer used (Zone 4). If the $GW_{reduction}$ for Power-to-Alternative is higher than 0.18 kg CO_2-eq/kWh, CO_2-to-Methanol processes are not used (Zone 2). In Zone 2 and 3 the production of methanol from wood achieves the lowest global warimg impacts. The difference between Zone 2 and 3 is only the production process for the required hydrogen. The threshold value (0.2 kg CO_2-eq/kWh) between Zone 2 and 3 is exactly the $GW_{reduction}$ for the hydrogen production from surplus power and the subsequent substituion of conventional produced hydrogen. Thus, for higher $GW_{reduction}$ it is environmentally more beneficial to produce the hydrogen conventionally and use the surplus power alternatively. In Zone 5, both wood and surplus power are used alternatively and the methanol is produced conventionally.
If the global warming impact of CO_2 is lower than -0.73 kg CO_2-eq/kg (not shown in Figure 2), the lowest global warming impacts are achieved for CO_2-to-Methanol together with conventional produced hydrogen and natural gas.
For the reference alternative utilization of surplus power and wood presented in section 3.1.4 (Cross in Figure 2), Methanol-to-Wood is the prefered conversion route.

3.3. Minimal global warming impacts for methane production

We repeat the analysis by specifying methane as product. Fig. 3 shows six zones with optimal processes routes for methane production.
In Zone 1, the maximal possible amount of wood and surplus power is used to produce methane. In Zone 4, the maximal possible amount of surplus power is used but only a part of wood is used to produce methane. In Zone 2, the maximal possible amount of wood is used but only part of surplus power. The difference between Zone 2 and 3 is the production of hydrogen (cf. section 3.2.). If the $GW_{reduction}$ for Wood-to-Alternative is higher than 0.25 kg CO_2-eq/kWh, all wood is used for alternative processes. As long as

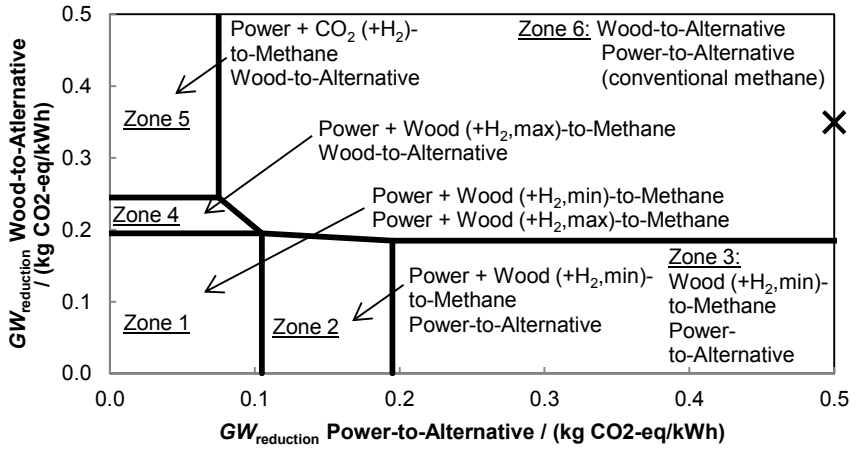

Figure 3: Process routes for methane production with lowest global warming impacts depending on the global warming impact (*GW*) reduction for Power-to-Alternative and Wood-to-Alternative. "Power +" means that the required hydrogen is produced from surplus power. The cross indicates the considered reference case Power-to-Alternative and Wood-to-Alternative processes.

the $GW_{reduction}$ for Power-to-Alternative is lower than 0.07 kg CO_2-eq/kWh, CO_2 and surplus power are used to produce methane (Zone 5). In Zone 6, surplus power and wood are both used alternatively and methane is no longer used to replace natural gas.

4. Conclusions

We present a superstructure-based optimization of chemical process routes based on renewable carbon sources. The approach identifies the environmentally most beneficial process routes for platform chemicals from a macro perspective. Thus, the approach also includes alternative utilization options for the limited feedstocks wood and surplus power. The results are presented as function of global warming impact reductions of the alternative utilization of wood and surplus power.

Our reference case allows alternative utilization of wood for electricity and surplus power in pumped hydro storage. In this case, wood is converted to methanol to achieve the lowest global warming impacts.

Acknowledgements

Funding by the European Institute of Innovation & Technology, Climate Knowledge and Innovation Community (EIT Climate-KIC) is gratefully acknowledged.

References

M. Peters, B. Köhler, W. Kuckshinrichs, W. Leitner, P. Markewitz and T. E. Müller, 2011, Chemical technologies for exploiting and recycling carbon dioxide into the value chain, ChemSusChem, 4, 9, 1216-1240

E. Cetinkaya, I. Dincer and G.F. Naterer, 2012, Life cycle assessment of various hydrogen production methods, Int. J. Hydrogen Energy, 37, 3, 2071-2080

M. Gassner and F. Maréchal, 2008, Thermo-economic optimisation of the integration of electrolysis in synthetic natural gas production from wood, Energy, 33, 2, 189-198

L. R. Clausen, N. Houbak and B. Elmegaard, 2010, Technoeconomic analysis of a methanol plant based on gasification of biomass and electrolysis of water, Energy, 35, 5, 2338-2347

K. Gerdes, J. Haslbeck, N. Kuehn, E. Lewis, L. L. Pinkerton, M. Woods, J. Simpson, M. J. Turner and E. Varghese, 2013, Cost and performance baseline for fossil energy plants - volume 1: Bituminous coal and natural gas to electricity (revision 2a). Report DOE/NETL-2010/1397, National Energy Technology Laboratory, Washington DC, USA

F. Schüth, 2011, Chemical compounds for energy storage, Chem. Ing. Tech., 83, 11, 1984-1993.

PE International, 2013, GaBi 6, Software-System and Database for Life Cycle Engineering

B. Steubing, R. Zah and C. Ludwig, 2012, Heat, electricity, or transportation? The optimal use of residual and waste biomass in europe from an environmental perspective, Environ. Sci. Technol., 46, 1, 164-171

A. Sternberg and A. Bardow, 2015, Power-to-What? – Environmental assessment of energy storage systems, Energy Environ. Sci., DOI: 10.1039/C4EE03051F

B. Müller, K. Müller, D. Teichmann and W. Arlt, 2011, Energiespeicherung mittels Methan und energietragenden Stoffen - ein thermodynamischer Vergleich, Chem. Ing. Tech., 83, 11, 2002-2013 (in German)

L. K. Rihko-Struckmann, A. Peschel, R. Hanke-Rauschenbach and K. Sundmacher, 2010, Assessment of methanol synthesis utilizing exhaust CO2 for chemical storage of electrical energy, Ind. Eng. Chem. Res., 49, 21, 11073-11078

C. N. Hamelinck and A.P.C. Faaij, 2002, Future prospects for production of methanol and hydrogen from biomass, Journal of Power Sources, 111, 1, 1-22

Krist V. Gernaey, Jakob K. Huusom and Rafiqul Gani (Eds.), 12th International Symposium on Process Systems Engineering and 25th European Symposium on Computer Aided Process Engineering.
31 May – 4 June 2015, Copenhagen, Denmark

Design and Optimization of Intensified Quaternary Petlyuk Configuration

Massimiliano Errico[a*], Pietro Pirellas, Ben-Guang Rong[c], Juan Gabriel Segovia-Hernández[b]

[a] *Universitá degli Studi di Cagliari, Dipartimento di Ingegneria Meccanica, Chimica e dei Materiali, Via Marengo 2, 09123 Cagliari, Italy*
[b] *Universidad de Guanajuato, Campus Guanajuato, División de Ciencias Naturales y Exactas, Departamento de Ingeniería Química, Noria Alta S/N, Guanajuato, Gto., 36050, México*
[c] *Department of Chemical Engineering, Biotechnology and Environmental Technology, University of Southern Denmark, Niels Bohrs Allé 1, DK-5230 Odense M, Denmark*
massimiliano.errico@dimcm.unica.it

Abstract

From its first introduction in 1965, the Petlyuk column received a high interest in the research community. Applied for the separation of three-component mixtures, the Petlyuk column is able to perform the separation with a reduced number of equipment and with a consistent reduction of the energy consumption compared to the classical sequences with simple columns. For a three-component separation the Petlyuk arrangement is composed by a prefractionator fully coupled with a main column that performs the separation of the products. Considering the great potential of these sequences it is natural to think about a possible extension to more than three component separations. In the present work a four component case is examined. If the divided wall column configuration is considered, the presence of three walls inside the main column makes the design and the control too complex to attract the industrial interest for a real application. New intensified sequences were proposed for the separation of four-component mixtures. These configurations use a less number of columns compared to the Petlyuk configuration. The case study reported proves the potential of the alternative configurations.

Keywords: Petlyuk configuration, distillation sequencing, design, energy saving.

1. Introduction

Two milestones are recognized by the research community as meaningful improvements in separations performed by distillation. The former is the introduction of structures with a partition wall inside the shell and the latter can be considered the definition of the Petlyuk configuration. Both of them were introduced almost fifty years ago but only recently have been successfully applied into the industrial practice for a limited number of feed components. Considering three-component separations, the Petlyuk configuration is composed by a prefractionator connected by two thermal couplings to the main column where the three products are obtained. If the prefractionator is included in the main column, the corresponding divided wall column (DWC) configuration is obtained. In both cases only one condenser and one reboiler are employed. It was clearly demonstrated that for a three-component mixture the Petlyuk configuration can

save up to 30 % of the energy consumption compare to the classical separation sequences (Emtir et al, 1999). Despite this evidence at least three valid hurdles contributed in the late development of Petlyuk and DWC configurations in the industrial practice. The first is the absence of recognized design methods, the second is the complexity of the structure and the third reason is the difficult in the process control. The research efforts, focused around these three points, contributed to reach more than one hundred operative DWCs around the world.
It is possible to assert that for the case of three component separations the Petlyuk and its equivalent DWC configuration has the potential of a noteworthy energy saving, different design methods are available, structure complexity are overcame by using the thermodynamically equivalent configurations and moreover the control issues are solved. It is clear that the same results are aimed for different number of feed components. Moving from three to four components the complexity of the Petlyuk and DWC structure increases and up to now only few studies are focused on the possible applications of these configurations. The aim of the present work is to propose alternative configurations to the Petlyuk/DWC configuration for a four-component separation. The benefit of the alternatives proposed is a simple design with a less or comparable total annual cost compare to the corresponding Petlyuk/DWC configuration. A case study is presented to support the new sequences.

2. Synthesis Procedure

The synthesis procedure is a systematic methodology that allows the prediction of all the alternatives generable from a sequence chosen as a reference. For a four-component mixture, the non-sharp configuration reported in Figure 1 is considered to start the generation procedure.

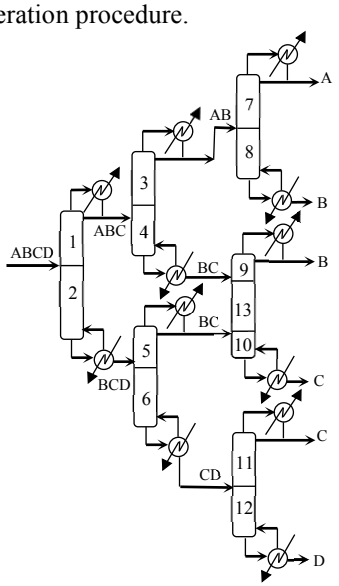

Figure 1. The six-column sequence for the fully sloppy separation of a quaternary mixture.

In this six-column sequence, usually referred as fully sloppy configuration, all the mixtures with three or more components are separated by symmetric sloppy splits. The corresponding Petlyuk configuration can be obtained in two steps: in the first one the

column sections where the same mixture or component is separated are merged. In the case considered sections 4 and 5, 8 and 9, 10 and 11 are combined reducing the number of column to three. Then, considering that in the Petlyuk configuration there is only one condenser and one reboiler independently from the number of component to be separated, all the condensers and reboilers associated to non-product streams can be substituted with a thermal coupling. The corresponding configuration is showed in Figure 2.

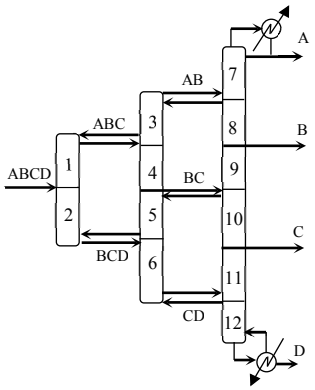

Figure 2: quaternary Petlyuk configuration

The Petlyuk configuration has three columns and five thermal couplings. Intensified sequences alternative to the Petlyuk arrangement can be obtained starting from the fully sloppy configuration of Figure 1 applying four different strategies (Rong at al, 2014):

1. Closed-Heat-Integration strategy to combine individual columns. This strategy is used to combine two columns by heat integration between a condenser and a reboiler co-producing a same product. This will reduce the number of columns.
2. Thermal coupling strategy to eliminate a condenser or a reboiler. This strategy is used to eliminate a condenser or a reboiler associated to a mixture of two or more components. This will reduce the number of heat exchangers.
3. Rearrangement of column sections strategy to generate thermodynamically equivalent structures. This strategy is used to recombine the column sections in a thermally coupled configuration through movement of the movable column sections. This will generate the thermodynamically equivalent structures which have different columns than the original thermally coupled configuration.
4. Elimination of the single-section-side columns strategy to produce the intensified distillation systems. For a thermally coupled configuration, there are thermodynamically equivalent structures in which there are single-section-side columns. This strategy is used to eliminate the single-section-side columns to generate the intensified distillation systems with fewer columns.

Applying the four point strategy presented the five configurations reported in Figure 3 are obtained. In particular the configuration reported in Figure 3(a) is obtained applying the strategy 1 to merge section 8 with section 9 and section 10 with section 11, then following the strategy 2 the condenser associated to the submixture ABC and the reboiler associated to the submixture BCD are substituted by thermal couplings. Strategy 3 is used to rearrange section 3 above section 1 and section 6 below section 2, finally single sections 4 and 5 are eliminated as indicated in the strategy 4. Similarly the configurations reported in Figure 3 (b-e) are obtained. Analyzing all the configurations generated is possible to notice that are all composed by two columns, moreover in

sequences 3(b) and 3(d) the stream C is obtained twice, in sequences 3(c) and 3(e) the component B is recovered in two separate streams. Only the sequence 3(a) is associated to the minimum number of streams.

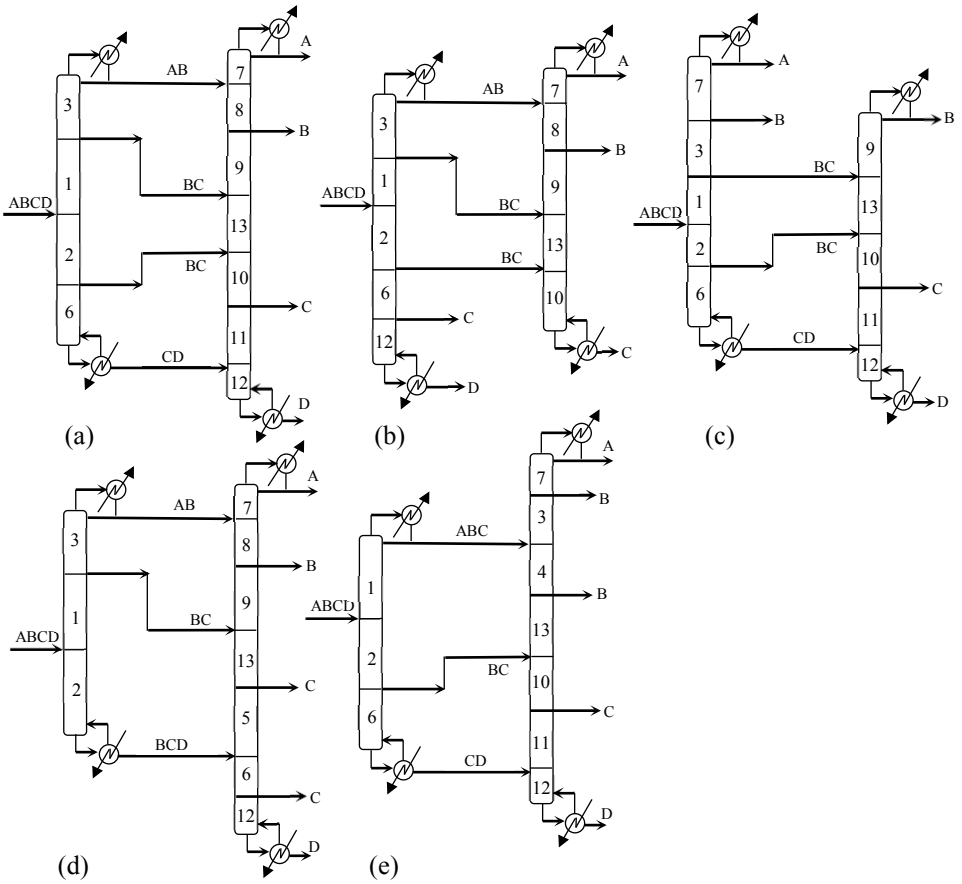

Figure 3: The intensified distillation alternatives for quaternary Petlyuk configuration

3. Case Study and Comparison Indexes

To test the applicability of the new intensified sequences, a case study has been considered. The composition and the product purity targets are shown in Table 1.

Table 1: feed composition and purity target

	Component	Feed composition [mol frac.]	Purity target [mol frac]
A	Butane	0.05	0.990
B	Hexane	0.10	0.970
C	Heptane	0.10	0.974
D	Nonane	0.75	0.997

A saturated liquid feed flowrate of 100 kmol h^{-1} is considered. All the configurations were simulated by means of Aspen Plus V8.0. The NRTL thermodynamic method was used and sieve trays columns were considered. The column pressure was optimized for

each column considering the possibility to use water in the condenser. The minimum temperature for the columns overhead vapor was defined to 323K.
Three different indexes were selected for the configurations comparison: the total annual cost, the thermodynamic efficiency and the carbon dioxide emission. The Total Annual Cost (TAC) is obtained as a sum of the operative and the annualized capital costs as reported in Eq. (1).

$$TAC = \sum \left[\left(\frac{Capital\ Cost}{Time\ of\ Investment} \right) + (Operative\ Costs) \right] \quad (1)$$

The operative costs were evaluated taking into account the cost of the water and the vapor in the condenser and reboiler respectively. The costs of the auxiliary fluids were obtained from Rev et al., 2001. The capital costs were considered as the sum of the costs of the condensers, reboilers, column shell and trays, evaluated according to the Guthrie's method reported in Turton et al., 2004. A mean investment time of 10 years was used to annualize the capital costs. The second index considered is how efficient the energy is being used. This information is expressed by the thermodynamic efficiency (η) evaluated as reported by Seader et al., 2009 and defined in Eq. (2)

$$\eta = -W_{min}/(-LW - W_{min}) \quad (2)$$

where W_{min} is the minimum work of separation and LW the lost work.
The last index used to compare the different configurations is the carbon dioxide emission (m_{co2}) since as a greenhouse gas is directly related to the global warming. The amount of carbon dioxide emitted was evaluated by the Eq. (3) following the method reported by Gadalla et al., 2005:

$$m_{CO_2} = \left(\frac{Q_{FUEL}}{NHV} \right) \left(\frac{\%C}{100} \right) \alpha \quad (3)$$

where Q_{fuel} is the heat generated by the combustion reaction, NHV the net heating value of a fuel with a carbon content of %C and α the ratio of molar masses of CO_2.

4. Simulations and results

In order to get the design parameters of all the alternative sequences, the fully sloppy configuration of Figure 1 was first simulated using the short-cut method of Underwood-Gilliland-Winn already implemented in Aspen Plus. The parameters obtained were used to initialize the stage-to-stage rigorous method RadFrac. The number of stages, feed location, reflux ratio were then optimized for the minimum energy consumption.
The design of the Petlyuk configuration was performed considering the correspondent among the column sections functionality (Errico et al., 2014). In this way once the design of the fully sloppy configuration of Figure 1 was obtained the configuration parameters were transposed to the analogous sections. The thermal coupling the flowrates were defined as the minimum possible value to assure the products purity targets. Following the same design methodology cited for the Petlyuk configuration, the alternative configurations reported in Figure 3 have been simulated using the correspondence of column functionality. Only the results for the configuration of Figure 3(a) are reported in Table 2 since, for the composition cases considered, was most convenient from the energy consumption point of view. Among all the alternatives predicted, the one in Figure 3(a), is the only sequence that performs the separation of the middle components once.

Table 2: Sequences comparison

	Petlyuk	Fig. 3(a)
TAC [$/y]	433	432
η [%]	47	52
CO2 [kg/h]	601	598

5. Conclusions

The work presented a new space of alternatives to the Petlyuk configuration for quaternary separation. The motivation of the work starts from the interest in the Petlyuk configuration due to its potential in energy reduction. Anyway for a four-component separation, the complexity of the design and control limit its application. A synthesis methodology is presented to generate a complete space of alternatives with a simpler design. For the case considered, among all the sequences it was obtained once with similar or better performance compare to the Petlyuk configuration. It is possible to conclude that the alternatives proposed are a valid alternative to the complexity of the Petlyuk configuration but still with the same benefit of less energy consumption.

References

M. Emtir, E. Rev, P. Mizsey, Z. Fonyò, 1999, Comparison of integrated and coupled distillation schemes using different utility prices, Computers & Chemical Engineering, 23, S799-S802

M.Errico, B.-G.Rong, C.E.Torres-Ortega, J.G.Segovia-Hernandez, 2014, The importance of the sequential synthesis methodology in the optimal distillation sequence design, Computers and Chemical Engineering, 62, 1-9

M.A. Gadalla, Ž. Olujić, P.J.Jansens, M. Jobson, R. Smith R., 2005,. Environ. Sci. Reducing CO2 emissions and energy consumption of heat-integrated distillation systems Technol, 39, 6860-6870

E. Rev, M. Emtir, Z. Szitkai, P. Mizsey, Z. Fonyo, 2001, Energy Savings of Integrated and Coupled Distillation Systems, Computers & Chemical Engineering, 25, 119-140

B.-G. Rong, M. Errico, J.G. Segovia-Hernandez, 2014, New intensified distillation systems for quaternary Petlyuk configuration, 24th European Symposium on Computer Aided Process Engineering-ESCAPE 24

W.D. Seider, J.D. Seader, D.R. Lewin, S. Widagdo, 2009, Product and Process Design Principles. Synthesis, Analysis and Evaluation, John Wiley and Sons, Inc: Asia

R. Turton, R.C. Bailie, W.B. Whiting, J.A. Shaeiwitz, Analysis, 2004, Synthesis and Design of Chemical Process, Second ed., Prentice Hall: USA

Krist V. Gernaey, Jakob K. Huusom and Rafiqul Gani (Eds.), 12th International Symposium on Process Systems Engineering and 25th European Symposium on Computer Aided Process Engineering.
31 May – 4 June 2015, Copenhagen, Denmark

Techno-economic analysis of power and hydrogen co-production by an IGCC plant with CO_2 capture based on membrane technology

Daniele Sofia[a], Aristide Giuliano[a], Massimo Poletto[a], Diego Barletta[a]*

[a] *Department of Industrial Engineering, University of Salerno, Via Giovanni Paolo II, 132, 84084 Fisciano (SA), Italy*
dbarletta@unisa.it

Abstract

The techno-economic analysis of an IGCC plant for power and hydrogen production with CO_2 capture by means of Pd-based H_2 membranes was carried out. The case studies were referred to the modifications of the existing 330MWe Integrated Gasification Combined Cycle (IGCC) plant of ELCOGAS based on entrained flow gasification of a dry mixture of coal and pet-coke. The pre-combustion section consisting in a sour water gas shift reactor integrated with Pd-based H_2 selective membranes and CO_2 selective membranes was simulated by process simulation techniques. Heat integration of the new process section was also addressed to minimize the energy loss. Power and energy penalty were evaluated as a function of the CO_2 capture percentage and of the electricity and hydrogen output.
Economic assessment of the additional capital and production costs was also performed to evaluate the mitigation cost of the carbon capture and storage (CCS) based on membrane technology. Sensitivity analysis was carried out to derive the breakeven price and the threshold performance of hydrogen membranes. The results on the cost of electricity, calculated without accounting for the revenues of the hydrogen sales, provided preliminary data for the economic feasibility of H_2 membranes in the IGCC process.

Keywords: IGCC, CO_2 capture, membranes, hydrogen.

1. Introduction

In recent years the interest for IGCC plants has increased, since it is a highly efficient and low emissions technology to produce energy from coal. This technology is also currently used to convert the pet-coke produced from petroleum processing in several refineries (e.g. ISAB Energy plant, ELCOGAS plant) with limited emissions of pollutants. Moreover, the flexibility of IGCC plants allows using also renewable fuels like biomass materials to reduce the greenhouse gas (GHG) emissions (Emun et al., 2008). Alternative solutions to address the GHG reduction are based on the introduction of CO_2 capture units in the process before the gas turbine combustion (Cormos et al., 2011). Some studies have also assessed the possibility to combine co-gasification with biomass and CO_2 capture by different technologies (Maxim et al., 2011) In general, the results of these analyses indicate that the improved process requires significant additional capital costs for the new CO_2 capture units and, therefore, implies high marginal cost of electricity per ton of avoided CO_2 (i.e. mitigation cost). Also the co-

production of electricity and hydrogen has been assessed in several studies with a range of technologies (Cormos et al., 2010).

This work is part of the FECUNDUS EU funded project aiming at demonstrating for IGCC plants the feasibility of co-gasification with biomass and of pre-combustion CO_2 capture process schemes based the combination of water gas shift reactors and two alternative product removal technologies: solid sorbents for CO_2 capture and metallic membrane selective to H_2. The present paper reports the techno-economic assessment of the process flowsheet based on H_2 selective membranes.

2. Process flowsheet synthesis and simulation

The IGCC process flow diagram of the ELCOGAS plant in Puertollano was modeled using the steady-state process simulator Aspen Plus Version 8. The gasifier was simulated assuming chemical equilibrium for all reactions except two for which "temperature approach to equilibrium" was assumed. Optimal ΔT values for these two reactions were found by searching the best fitting between the simulation results and the experimental data of raw syngas. Main gas cleaning units (Venturi scrubber and methyl diethanolamine absorber) were modeled by rigorous multistage vapor-liquid equilibrium approach accounting for electrolytic reactions in the liquid phase. Simplified methods were used for other process units (carbonyl sulfide hydrolysis reactor, Sour Water Steam stripper, sulphur recovery Claus process). The units of the combined cycle (gas turbine, gasifier heat recovery, heat recovery steam generator and steam turbine) for power generation were modeled in detail accounting for heat integration. More details on the model and on its validation with industrial data are reported by Sofia et al. (2014).

A new process section for the pre-combustion capture of CO_2 was developed in the simulation flowsheet after the gas cleaning section (Figure 1). The core of the new section is based on the combination of the water gas shift reactor with hydrogen selective Pd-based membranes (Barreiro et al., 2014) in an integrated water gas shift membrane reactor (WGSMR). The latter is fed with the clean syngas, leaving the purification section of the plant, sand with intermediate pressure steam. The membrane permeate stream consists in a mixture of hydrogen and waste nitrogen, coming from the air separation unit (ASU), used as sweep gas in the membrane. The retentate stream mainly formed by CO_2, H_2O and N_2 is dehydrated by partial condensation of water and then sent to a carbon dioxide polymeric membrane unit to separate CO_2 from N_2. The CO_2 permeate is compressed and cooled down up to storage conditions (30°C, 110bar). The N_2 in the retentate stream is used to further dilute the hydrogen in the H_2-waste N_2 stream before sending it to the gas turbine. The co-production of electricity and hydrogen was considered by splitting part of the the H_2-waste N_2 stream and sending it to further hydrogen separation units.

Simulation of the new process section was addressed as follows. The WGSMR was simulated as an adiabatic multistage catalytic reactor (RPlug blocks) with interstage hydrogen separation (Sep2 blocks). HT-WGS kinetics reported by Adams et al. (2009) was assumed for operating conditions in the range 300 °C-400 °C and 20-22 bar.

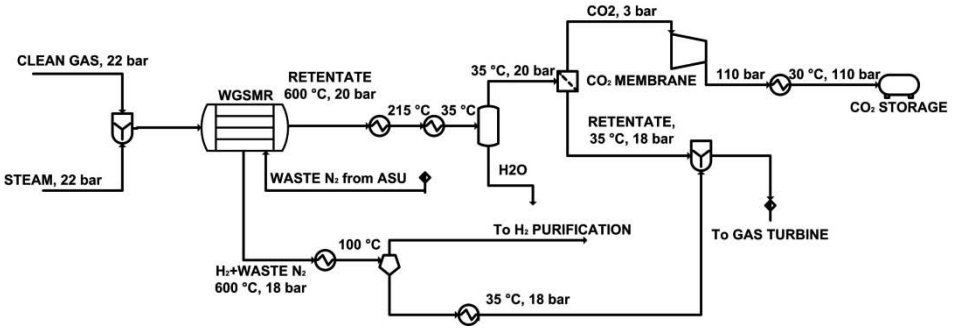

Figure 1 Flowsheet of the CO_2 capture section of the IGCC plant.

The sizing of the area of the membranes was approached by a simplified design equation assuming characteristic values of the molar flow of Pd membranes for H_2 (Barreiro et al., 2014) and polymeric membrane for CO_2 (Grainger and Hägg, 2008). The compressor train for CO_2 was simulated by a multistage compressor model (MCompr block). Process heat integration was performed in the new process section in order to obtain the required utilities and the size of the heat exchangers.

3. Results

Simulations were carried out for the design fuel feed of the IGCC plant consisting in a blend of coal and petroleum coke 50 % in weight with a LHV of 24.89 MJ/kg and 686 MW thermal power input. Further details on the design fuel are reported by Sofia et al. (2013). The technical performances of the WGSMR and of whole IGCC plant was studied as a function of the H_2O/CO feed ratio to the WGSMR. As expected, the water gas shift reaction conversion increases from 85 % to 98 % for increasing values of the H_2O/CO ratio in the range 2-3 due to the beneficial effect of the H_2O/CO ratio on the WGS equilibrium conversion. Moreover, the continuous hydrogen product removal in the membrane reactor allows the conversion exceeding the thermodynamic equilibrium conversion boundary. This reactor performance affects the overall CO_2 capture increasing from 77.8 % to 81.1 % with increasing H_2O/CO feed ratio. On the other hand, the net electrical power produced by the plant decreases from 286 MW obtained without CO_2 capture to 220 MW and 219 MW for 77.8 % and 81.1 % CO_2 capture, respectively. The corresponding net electrical efficiency drops from 41 % of the conventional IGCC to 32.1 % and 32.0 % for 77.8 % and 81.1 % CO_2 capture, respectively. The resulting energy penalty is about 9 %.

The co-production of hydrogen was assessed as well by introducing a split on the H_2-N_2 waste stream coming out of the WGSMR. Results indicate that the hydrogen flow rate is limited by an upper bound value due to the thermal sustainability of the whole IGCC plant. In fact, increasing the H_2 split, the power produced by the gas turbine and by the steam turbine decreases. The steam turbine power has lower bound given by the critical value corresponding to the minimum flow rate of intermediate pressure steam required to feed the gasifier and the WGSMR. As a result, it is possible to increase the maximum H_2 split ratio by decreasing the H_2O/CO ratio of the WGSMR. In fact, the maximum H_2 split ratio that is achievable for H_2O/ equal to 3, 2.5 and 2 is 24 %, 28 % and 30 %, respectively. These results correspond

Table 1 Plant performance and economic analysis results for the CO_2 capture schemes.

	without CO_2 capture	with CO_2 capture		
H_2O/CO to WGSMR [-]	-	2	2.5	3
Gross power [MW]	320.7	281.4	281.1	281.0
Net power [MW]	285.7	220.5	219.8	219.4
Net efficiency	41.6	32.1	32.0	32.0
Capital costs [M€]				
IGCC base installed costs	458	458	458	458
Total new installations	-	215.9	222.2	225.9
Specif. investment [€/kW]	1603	3057	3095	3117
COE [€/MWh_{net}]	55.5	84.7	85.5	86.0
CO_2 captured [%]		77.8	80.0	81.1
CO_2 emitted [kg/MWh_{net}]	828	216	192	181
Mitigation cost [€/tCO_2]	-	47.8	47.2	47.1

On the other hand, the reduction of the H_2O/CO ratio causes a lower conversion of CO to CO_2 in the WGSMR and, thus, a lower pre-combustion CO_2 capture. Obtained results are summarized in Figure 2 in terms of power distribution and CO_2 emissions per MWh as a function of the H_2 spilt ratio.

Economic analysis of the flowsheet was carried out only for the case of power production with CO_2 capture. A total investment cost of 458 M€ was assumed for the Puertollano IGCC plant at the time of the project (Campbell et al., 2000). This cost was not updated intentionally since the aim is to estimate the effect of the different fuel cost and plant performance on the COE over the entire life of a plant built years ago. The capital expenditure for the additional equipment of the new CO_2 capture section was evaluated by scaling factors and cost index methods. For Pd membranes H_2 molar flow of 0.1 kmol m^{-2} h^{-1} (Barreiro et al., 2014) and unit cost of 3500 €/m^2 were assumed for the base case. Manufacturing costs, including reactants, catalysts and utilities, were assessed from data available in the literature. The total investment cost (TIC) and the total annual costs (TAC) were derived.

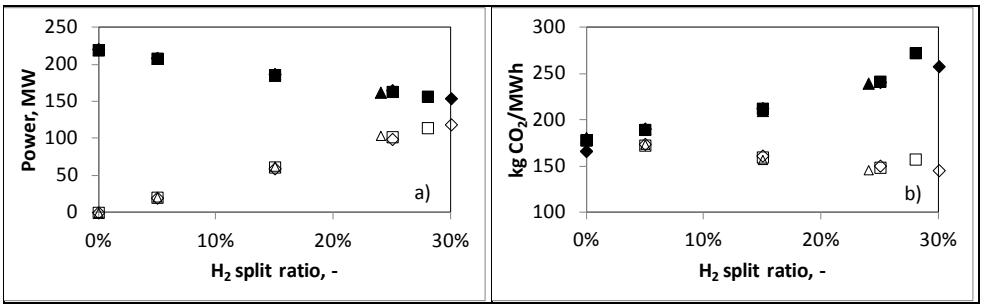

Figure 2 Plant performance for the CO_2 capture schemes with H_2 co-production: a) electric power (solid symbols), H_2 power (hollow symbols); kg CO_2/MWh of electricity (solid symbols) kg CO_2/MWh of electricity and H_2 (hollow symbols). H_2O/CO = 2 (diamonds), 2.5 (squares), 3 (triangles).

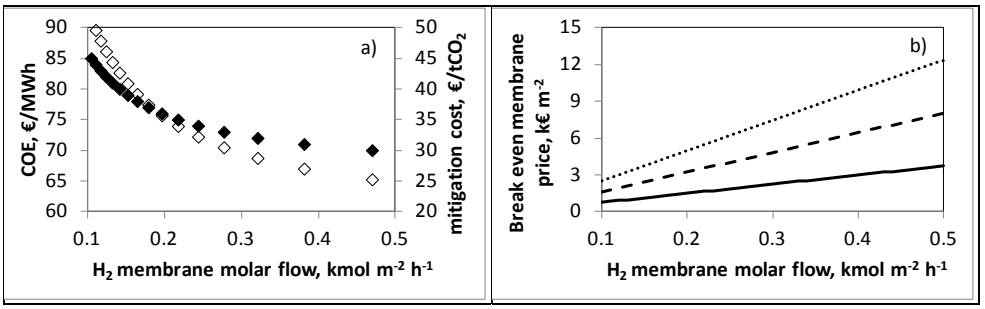

Figure 3 Effect of the H_2 membrane molar flow on a) COE (solid diamonds) and mitigation cost (hollow diamonds); b) break even membrane price for COE = 70 €/MWh (continuous line), 75 €/MWh (dashed line), 80 €/MWh (dotted line). All results are for the 80% CO_2 capture case.

Finally, a profitability analysis based on the discounted cash flow method assuming a plant lifetime of 25 years and an interest rate of 7.5 % was performed to derive the cost of electricity (COE) as the break even cost of electricity (i.e. the value of the cost of electricity which makes the net present value equal to zero). Moreover, the additional cost of electricity due to carbon capture was related to the avoided CO_2 emissions in terms of the so called mitigation cost, defined as follows:

$$\text{mitigation cost} = \frac{\text{COE}_{\text{CCS}} - \text{COE}_{\text{base}}}{\text{CO}_{2\,\text{base}} - \text{CO}_{2\,\text{CCS}}} = \left[\frac{€}{\text{tCO}_2}\right] \quad (1)$$

where COE_{base} and COE_{CCS} are the cost of electricity for the base case IGCC and for the IGCC with CCS, respectively, CO_{2base} and CO_{2CCS} are the corresponding tons of CO_2 emitted per MWh.

Membrane technology for H_2 separation is still under development and continuous improvement since membranes with satisfactory H_2 molar flow values are still really expensive. Thus, it is necessary to find a trade-off between satisfactory separation performance and sustainable cost of the membranes. As a result, a sensitivity analysis on the effect of the membrane molar flow an of the membrane price for unit area on the economic indicators of the whole process as a function of was carried out to preliminary address this point for the 80% CO_2 capture (H_2O/CO to WGSMR = 2.5). In particular, Figure 3a reports the COE and the mitigation cost as a function of the H_2 membrane molar flow. Results indicate a decrease of the COE from 86 to 70 €/MWh and a decrease of the mitigation cost from 47 to 25 €/tCO_2 for increasing membrane molar flow in the range 0.1-0.4 kmol m^{-2} h^{-1}. Furthermore, the break even price (i.e. the price value which makes the net present value equal to zero) of the membrane per unit area was calculated as a function of the H_2 membrane molar flow assuming different values of COE (70, 75 and 80 €/MWh), and, thus, different mitigation cost values (25, 34 and 43 €/tCO_2). Results reported in Figure 3b indicate a linear increase of the break even price with increasing H_2 membrane molar flow. Of course, further calculations are necessary to account for the additional investment costs for H_2 purification and the revenues of the H_2 sales. It is expected that these further evaluations will significantly affect the profitability indicators of the whole plant and the break even price of the membranes.

4. Conclusions

The technical feasibility of an innovative process section including a WGSMR and CO_2 selective membranes to address the CO_2 capture and separation was demonstrated for an IGCC plant fed with a coal-petcoke blend. A CO_2 capture between 77.8 % and 81.1 % was achieved as a function of the H_2O/CO feed ratio to the WGSMR. The maximum carbon capture value achieved corresponds to an energy penalty of about 9%. The conceptual design of a hydrogen co-production revealed that the maximum H_2 flow rate achievable was limited by the steam demand of the WGSMR.
Economic analysis confirmed that the membrane technology for H_2 separation is still very expensive for plants producing only electrical power. This results in high cost of electricity and high mitigation cost. The significant effect of the H_2 molar flow and the price of membrane per unit area on the profitability indicators was also highlighted. Economic improvement deriving from the co-production of electricity and H_2 will be addressed in the future work. Co-firing with biomass could be also considered in combination with the CCS section in order to reduce the fossil carbon in the feedstock and to aim at CO_2 emissions closer to zero.

5. Acknowledgements

The European Commission Research, Research Fund for Coal and Steel is acknowledged for the supporting to the FECUNDUS project (RFCR-CT-2010-00009).

References

T.A. Adams II, P.I. Barton, 2009, A dynamic two-dimensional heterogeneous model for water gas shift reactors, International Journal of Hydrogen Energy, 34, 8877–8891.
M.M. Barreiro, M. Maroño, J.M. Sánchez, 2014, Hydrogen permeation through a Pd-based membrane and RWGS conversion in H2/CO2, H2/N2/CO2 and H2/H2O/CO2 mixtures, International Journal of Hydrogen Energy, 39, 4710-4716.
P.E. Campbell, J.T. McMullan, B.C. Williams, 2000, Concept for a competitive coal fired integrated gasification combined cycle power plant, Fuel 79, 1031–1040.
C.-C. Cormos, A.-M. Cormos, P.S. Agachi, 2011, Techno-economical and environmental evaluations of IGCC power generation process with carbon capture and storage (CCS), Computer Aided Chemical Engineering, 29, 1678-1682.
C.-C. Cormos, F. Starr, E. Tzimas, 2010, Use of lower grade coals in IGCC plants with carbon capture for the co-production of hydrogen and electricity, International Journal of Hydrogen Energy, 35, 556-567.
F. Emun, M. Gadalla, L. Jiménez, 2008, Integrated Gasification Combined Cycle (IGCC) process simulation and optimization, Computer Aided Chemical Engineering, 25, 1059-1064
D. Grainger, M.-B. Hägg, 2008, Techno-economic evaluation of a PVAm CO2-selective membrane in an IGCC power plant with CO2 capture, Fuel, 87, 14-24.
V. Maxim, C.-C. Cormos, P.S. Agachi, 2011, Design of Integrated Gasification Combined Cycle plant with Carbon Capture and Storage based on co-gasification of coal and biomass, Computer Aided Chemical Engineering, 29, 1904-1908.
D. Sofia, P. Coca Llano, A. Giuliano, M. Iborra Hernández, F. García Peña, D. Barletta, 2014, Co-gasification of coal-petcoke and biomass in the Puertollano IGCC power plant, Chemical Engineering Research and Design, 92, 1428-1440.
D. Sofia, A. Giuliano, D. Barletta, 2013, Techno-economic assessment of co-gasification of coal-petcoke and biomass in IGCC power plants, Chemical Engineering Transactions, 32, 1231-1236.

Krist V. Gernaey, Jakob K. Huusom and Rafiqul Gani (Eds.), 12th International Symposium on Process Systems Engineering and 25th European Symposium on Computer Aided Process Engineering.
31 May - 4 June 2015, Copenhagen, Denmark.

Synthesis of Water Treatment Processes using Mixed Integer Programming

Mariya N. Koleva[a], Eleftheria M. Polykarpou[a], Songsong Liu[b], Craig A. Styan[a] and Lazaros G. Papageorgiou[b]

[a]*School of Energy and Resources, UCL Australia, 220 Victoria Square, Adelaide, South Australia, 5000, Australia*
[b]*Centre for Process Systems Engineering, Dept. of Chemical Engineering, UCL, Torrington place, London, WC1E 7JE, United Kingdom*
l.papageorgiou@ucl.ac.uk

Abstract

With exerting pressures on water systems, efforts have recently been focused on optimisation of existing, and design of new treatment facilities. Modelling, specifically, offers the advantage of early stage processes synthesis at minimum design change expenses. Current research and industry gaps lie in overall construction of water treatment flowsheets by crossing various disciplines.

In the current work a systematic approach for the synthesis of water treatment processes is proposed. The design combines technological robustness, improved economic performance and environmental reliability. The problem is formulated as a mixed integer non-linear programming (MINLP) model. A case study of seawater desalination is presented where conventional and non-conventional treatment technologies are considered. The flowsheet structure is selected based on units separation and recovery efficiencies, operating and capital costs, and carbon footprint. The model is solved for desired water purity to meet drinking water standards with the objective to minimise water production costs. The results are analysed to investigate the applicability of the presented approach.

The developed methodology can have a significant impact on reducing the design time and simultaneously, increasing the cost effectiveness of water treatment processes.

Keywords: water treatment synthesis, mixed integer non-linear programming, technological robustness, economic performance, environmental aspects

1. Introduction

Water treatment is assigned a major role in mitigating the current and future demographic, geographic and industrial global water resource challenges. Early stage optimisation with design of treatment facilities conduce to technically, economically and environmentally more advantageous systems. However, so far little work has been done on their systematic synthesis where both, individual units and their interconnections, are optimised.

Desalination of seawater for drinking water purposes, in particular, has recently been a focus of attention worldwide. The most common alternatives used in the process include coagulation-flocculation, sedimentation, dissolved air flotation, media filtration (conventional pretreatment), microfiltration, ultrafiltration (non-conventional pretreatment), nanofiltration and reverse osmosis (non-conventional desalting).

Various optimisation models have been developed to correlate the separation performance of those technologies and their characteristics and operating conditions. Vlaški (1998) investigated the separation efficiency of dissolved air flotation and sedimentation with respect to algae and particles. Tabatabai (2014) worked on the assessment of coagulation and ultrafiltration for reverse osmosis desalination. Ahsan (1995) studied the optimisation of direct horizontal filtration.

Other work has been published on reviewing the principles of design in seawater desalination. Voutchkov (2010) analysed the strategies for choosing pretreatment systems whereas Lior (2013) examined in detail the technical, economic and environmental aspects of the process. Lu et al. (2007) proposed an optimum design of reverse osmosis system for seawater desalination formulated as a mixed integer non-linear program (MINLP) problem. A methodology for overall water treatment synthesis has been suggested by the current authors in previous work (Koleva et al., 2013) where the mathematical model was tested on seawater desalination.

The present work develops the model further and incorporates the environmental aspect of carbon emissions as an inseparable part of overall systems design. The following sections of the paper are organised as follows: Section 2 gives a frame of the study, Section 3 presents the constraints necessary for the fullfilment of the various criteria, Section 4 shows a theoretical case study in seawater desalination and results and Section 5 gives observations and conclusions of the applicability of the model.

2. Problem statement

The current work presents a methodology for design of seawater desalination facilities with technical, economic and environmental aspects. Total suspended solids (TSS), total dissolved solids (TDS) and boron (B) were considered in the model as major contaminants. To the best available technologies pool belong 9 candidates, i.e. coagulation-flocculation (CF), sedimentation (SED), dissolved air flotation (DAF), multi-media filtration (MMF), microfiltration (MF), ultrafiltration (UF), nanofiltration (NF), reverse osmosis (RO) for TDS and reverse osmosis for boron removal. The major criteria for selection are the technical performance to meet final quality product and total annual cost including carbon emissions where production of minimum water net cost is sought. The problem is formulated as an MINLP model and the overall problem definition is stated as follows:

Given:

seawater contaminants groups; best available seawater treatment technologies; seawater feed flowrate and initial contaminants concentrations; technologies operating conditions and characteristics ranges for pressures, temperatures, chemical dosage, mixing input power, flocculation times, media size and load, membrane molecular weight cut-off, hydrophobicity, hydrogen ion concentrations; efficiency parameters such as recovery, pumps and motors efficiencies; cost data such as electricity charge, carbon tax, maintenance and replacement rates

Determine:

conceptual flowsheet design, operating conditions for the selected units, contaminants and flowrates profiles, and annual operating and capital costs

So as to:

minimise the water production cost which is equal to the total annualised cost divided by the annual plant capacity.

3. Mathematical model

The methodology presented below consists of a group of constraints that assist in the selection of the best combination of technologies. For the technical performance, the mass balance constraints are explained next.

3.1. Mass balance constraints

The mass balance constraints relate the potential contaminants concentrations and flowrates from the inlet and outlet of every candidate unit. The method has been described as a MILP model in previous work (Koleva et al., 2013) where the linearity arises from the discrete values of the operating conditions. For the proposed model, the operating conditions are continuous variables taking lower and upper boundaries and an additional, integer variable, U_t, is introduced that accounts for the number of passes for every potential unit.

$$c^P_{s,t} = W_t \cdot c^F_{s,t} \cdot (1 - R_{s,t})^{U_t} + (1 - W_t) \cdot c^F_{s,t}, \qquad \forall t, s \qquad (1)$$

where $c^P_{s,t}$ and $c^F_{s,t}$ $[mg/L]$ are the permeate and feed concentrations of contaminant s for technology t, $R_{s,t}$ is a removal coefficient of contaminant s for technology t, W_t is a binary variable equal to 1 when a unit is selected and equal to 0 otherwise. The removal coefficients are calculated on the basis of regression models and therefore, they are a function of the operating conditions, specific for every technology. The flowrate profiles can be calculated on a similar principle where the main efficiency factor is the recovery, Y_t, that determines the permeate flow profiles, Q^P_t $[m^3/h]$.

$$Q^P_t = W_t \cdot Q^F_t \cdot Y^{U_t}_t + (1 - W_t) \cdot Q^F_t, \qquad \forall t \qquad (2)$$

where Q^F_t $[m^3/h]$ is the feed flowrate to technology t.

3.2. Target constraints

The final water purity should not exceed the conditions imposed by the following constraint:

$$c^P_{s,t} \leq M^{CONC}_s, \qquad \forall s, \forall t = T \qquad (3)$$

where M^{CONC}_s $[mg/L]$ is the maximum allowable concentration of contaminant s after the last candidate technology t. An additional constraint for the minimum effluent at the final stage is enforced by Eq.(4).

$$Q^P_t \geq M^{FLOW}_t, \qquad \forall t = T \qquad (4)$$

where M^{FLOW}_t $[m^3/h]$ is the minimum allowable effluent flow.

3.3. Logical constraints

The number of passes is ensured to be equal or greater than one if a technology is selected, which is expressed by Eq.(5).

$$U_t - M_{max} \cdot W_t \leq 0, \qquad \forall t \qquad (5)$$

where M_{max} is the maximum number of passes corresponding to common industrial practices. To set the passes to non-zero when a technology is selected, the following equation is used:

$$W_t - U_t \leq 0, \qquad \forall t \qquad (6)$$

3.4. Cost constraints

3.4.1. Operating constraints

The operating costs include electricity for pumps, mixers and saturators, and chemicals cost as the major components of ongoing costs.

Chemicals costs: The primary chemical used is for the coagulant which is ferric chloride as often predominating due to the more satisfactory results obtained downstream (Voutchkov, 2010). The annual cost for it is calculated from Eq.(7).

$$OC^{CHEM}_t = a \cdot CD_t \cdot C_{chem} \cdot Q^F_t \cdot U_t, \qquad \forall t = CF \qquad (7)$$

where a is a constant accounting for annualisation, CD_t $[t/L]$ is the coagulant dose selected and C_{chem} $[\$/t]$ is the cost of coagulant.

Saturator costs: The technical and economic performance of DAF depends mainly on its recirculation ratio and saturator. The former is disregarded in this study and the latter is calculated by:

$$OC_t^{SAT} = \frac{a \cdot Q_t^F \cdot U_t \cdot C_e \cdot P_t}{\eta_t}, \qquad \forall t = DAF \quad (8)$$

where P_t $[MPa]$ is the saturator pressure and C_e $[\$/kWh]$ is the electricity cost rate.

The carbon taxation is calculated from Eq.(9) with the assumption that the carbon tax does not increase throughout the lifetime of the project. The largest component for the emissions is the power used, reflected in the equation.

Carbon tax emissions:

$$CO_2C_t = \frac{a \cdot C_{CO2} \cdot CO_2e \cdot Q_t^F \cdot U_t \cdot P_t}{\eta_t}, \qquad \forall t \quad (9)$$

where C_{CO_2} $[\$/t]$ is the carbon tax and CO_2e $[t/kWh]$ is the carbon equivalent emitted.

3.4.2. Capital constraints

The capital costs incorporate economies of scale and are related by correlations for the candidate technologies.

$$CC_t = n_t \cdot U_t \cdot (Q_t^P)^{m_t}, \qquad \forall t = T \quad (10)$$

where n_t and m_t are constants and they differ for every candidate. For the annualisation of the capital costs, the capital recovery factor has been further integrated.

3.5. Objective function

The objective function is to minimise the water production cost, WC $[\$/m^3]$, where PY is the annual production yield and TC is the summation of all the annualised operational and capital costs.

$$minimise \;\; WC = \frac{TC}{a \cdot PY \cdot Q_{t=T}^P}, \quad (11)$$

subject to mass balance, target, logical and cost constraints.

4. Case study

4.1. Data

In this section a theoretical case study is presented to test the applicability of the model. Design parameters and data recommended in various literature sources are used. Influent of $Q_t^{F,IN} = 20{,}000\ m^3/h$ is chosen and for minimum allowable effluent $M_t^{FLOW} = 5000\ m^3/h$ which will ensure a medium size desalination facility. Additional water quality and cost parameters are reported in Table 1.

For conventional and non-conventional pretreatment technology full recoveries are assumed based on recommended values (U.S. Interior Reclamation Department, 2013). For high pressure membranes, NF and RO, 80 % and 40 % recoveries are assumed, respectively, to agree with published values (Lu et al., 2006; Mickley et al., 1993). The pumps and saturator efficiencies vary between 0.75 and 0.85.

It is assumed that cleaning or replacement takes place simultaneously for all trains, there are no pressure losses from pump to membrain train, every pass contains the same number of membrane modules, cleaning is performed every 6 months, replacement is recommended every 5 years, the annual maintenance and shut down time is 65 days a year, and annual production yield 95 %.

Table 1: Water quality and cost parameters

Parameter	initial c^P [TSS/ TDS/ B] $[mg/L]$	final c^P [TSS/ TDS/ B] required $[mg/L]$	C_e $[\$/kWh]$	C_{chem} $[\$/FeCl_3\,t]$	C_{CO_2} $[\$/CO_2\,t]$
Value	30/ 40,000/ 5	1/ 600/ 2.4	0.08	250	23

Source: (Lu et al., 2006; U.S. Energy Information Administration, 2013; World Health Organization, 2011)

4.2. Results

The mathematical model was tested in GAMS 23.9 on a Dell PC OptiPlex 9010 Core i5-3570 at 3.4 GHz and 3.89 GB RAM. The model was solved using BARON with a relative gap 0%. It took the solver 3.4 seconds to return an optimal solution.

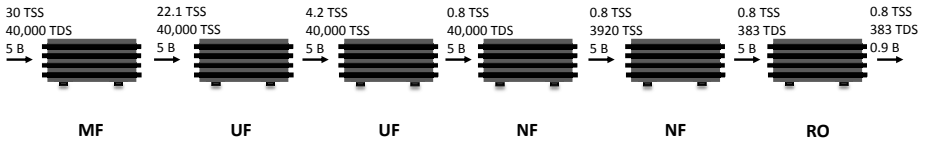

Figure 1: Optimum configuration for the given case study

The flowsheet configuration of the case study is shown in Figure 1 where 1 MF pass and 2 UF passes for the removal of suspended matter were selected, 2 NF passes for the separation of dissolved solids and 1 RO pass for the rejection of boron. The production capacity of the facility was 120,000 m^3/day.

For the selected system, the capital cost was $135 million which agrees with magnitudes for seawater desalination projects reported in reviews (UNESCO Centre for Membrane Science and Technology, 2008). The annual operating cost breakdown showed that electricity cost represented 69 % followed by the carbon emissions cost of 21 %, the labour cost of 8 % and the maintenance cost of 2 %. The water net cost was 1.07 $\$/m^3$. The costs breakdown exhibits 18 % lower maintenance cost, whereas electricity and labour costs approach published values (UNESCO Centre for Membrane Science and Technology, 2008).

The slightly higher percentage for energy consumption stems from the assumption that no energy recovery devices are used, power is taken from the grid, no offsetting for the greenhouse emissions is done by renewable energies and electricity charge is constant throughout the day. The low value of maintenance cost in comparison with the rest is due to the assumptions of cost rates and membrane modules for each unit as well as no cleaning chemicals for the maintenance cost were taken into consideration.

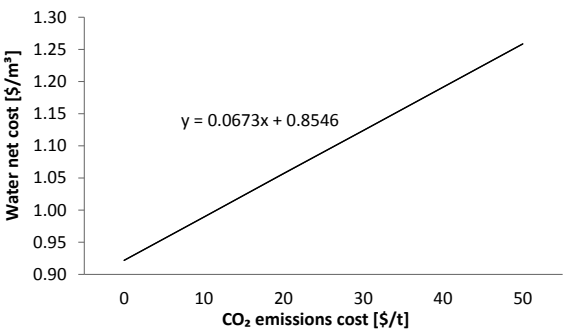

Figure 2: Sensitivity analysis of water cost with carbon price

The carbon emissions of the facility were 786 tCO_2/day assuming 24 hours of operation. For a plant of a capacity 100,000 m^3/day, UNESCO Centre for Membrane Science and Technology (2008) reported carbon footprint of 660 tCO_2/day. Next, we investigated the sensitivity of the production cost with various carbon costs that can be imposed by governments depending on time frame or plant location (Figure 2). When carbon tax at 50 $\$/t$ is included in the estimations, the water net cost increases with 27 %, 10 % more than reported

in literature sources. The elevated sensitivity of the water cost is due to the previously observed low values for the rest of the cost components.

5. Discussion and conclusions

In the current work a systematic approach for the design and optimisation of water treatment facilities was proposed. The problem was formulated as MINLP model with the objective to minimise the water net cost and was applied to a seawater desalination case study.

The optimum result fell within the values reported by AWWA (2011) for medium size seawater desalination facilities, between 0.82 $\$/m^3$ and 1.25 $\$/m^3$. With regard to the annual cost breakdown, the highest percentage allocated to electricity is due to the absence of energy recovery devices.

Nevertheless, the result demonstrates the method and model can be applied in the conceptual design of water treatment facilities. With taking into account technological, economic and environmental constraints at early stage, further design stages would rely on more robust results. Additionally, the tool could help cutting down industrial expenses and time.

Work on refining the model in order to eliminate some of the assumptions along its development would provide more accurate results on units selection and their various cost components. Additional features, such as managing the water net cost when a location specific emissions trading scheme is introduced and allowing for concentrate disposal management, will add significance to advancing in sustainable projects design.

6. Acknowledgements

The authors would like to acknowledge the financial support of BHP Billiton and the advisory help of Prof. John van Leeuwen from University of South Australia.

References

T. Ahsan, 1995, Process Analysis and Optimization of Direct Horizontal - Flow Roughing Filtration, 1 – 212.

AWWA, 2011, Desalination of Seawater, M61, 1 – 99.

M.N. Koleva, E.M. Polykarpou, L.G. Papageorgiou, 2013, An MILP Model for Cost - Effective Water Treatment Synthesis, Modelling and Simulation Society of Australia and New Zealand, 20, 2716 – 2722.

N. Lior, 2013, Advances in Water Desalination, 1, 1 – 688.

Y. Lu, Y. Hu, D. Xu, L. Wu, 2006, Optimum Design of Reverse Osmosis Seawater Desalination System Considering Membrane Cleaning and Replacing, Journal of Membrane Science, 282, 7–13.

Y. Lu, Y. Hu, X. Zhang, L. Wu, Q. Liu, 2007, Optimum Design of Reverse Osmosis System Under Different Feed Concentration and Production Specification, Journal of Membrane Science, 287, 219 – 229.

M.C. Mickley, R. Hamilton, L. Gallegos, J. Truesdall, 1993, Membrane Concentrate Disposal, 52.

S.A.A. Tabatabai, 2014, Coagulation and Ultrafiltration in Seawater Reverse Osmosis Pretreatment, 1 – 227.

UNESCO Centre for Membrane Science and Technology, 2008, Emerging Trends in Desalination: A Review, 1 – 96.

U.S. Energy Information Administration, 2013, Electric Power Monthly.

U.S. Interior Reclamation Department, 2013, Water Treatment Primer for Communities in Need.

A. Vlaški, 1998, Microcystis Aeruginosa Removal by Dissolved Air Flotation (DAF). Options for Enhanced Process Operation and Kinetic Modelling, 1 – 274.

N. Voutchkov, 2010, Considerations for Selection of Seawater Filtration Pretreatment System, Desalination, 261, 354 – 364.

World Health Organization, 2011, Guidelines for Drinking Water Quality, 1 – 564.

Krist V.Gernaey, Jakob K.Huusom and RafiqulGani (Eds.), 12th International Symposium on Process Systems Engineering and 25th European Symposium on Computer Aided Process Engineering.
31 May – 4 June 2015, Copenhagen, Denmark

Viability of Technologies for CO_2 Capture and Reuse in a FPSO: Technical, Economic and Environmental Analysis

Bruna C de S Lima[a], Ofélia Q F de Araújo[a], José Luiz de Medeiros[a], Cláudia R V Morgado[a]

[a]*Federal University of Rio de Janeiro (UFRJ), Av. Athos da Silveira Ramos, 149, Rio de Janeiro, 21941-909, Brazil*
brunacdsl@hotmail.com

Abstract

The recent discoveries of Pre-Salt layers in Brazil require process developments for enhanced sustainability as these reservoirs have oil with associated natural gas exhibiting an expressive amount of CO_2. Monetization of CO_2 by offshore production of methanol in a dedicated FPSO – MFPSO – is a potential alternative to sustainable E&P. Two process alternatives for an MPFSO were previously investigated by the authors, consisting of physical absorption of CO_2 with propylene carbonate and its conversion to yield methanol. Alternative 1 combines dry and steam reforming in one reactor (Bi-Reforming), while Alternative 2 segregates the two reactions - dry reforming occurs in one reactor and water gas-shift reaction in a subsequent reactor. Both alternatives considered Enhanced Oil Recovery (EOR) as a parallel path for CO_2 destination. The economic evaluation employed the software Capital Cost Estimation (CAPCOST) for calculations of CAPEX and OPEX. The software Waste Reduction Algorithm (WAR, EPA) was used to evaluate the potential environmental impacts. The analysis indicated that the performance of Alternative 1 was superior to the performance of Alternative 2: (a) methanol production (17.9 t/h) 4 times higher, (b) lower CAPEX, (c) sales revenue 181% greater, and (d) the potential environmental impact (PEI) 47.7% lower (868 PEI/h). In the present work, Alternative 1was modified by eliminating the EOR step, resulting in enhancement of methanol production as CO_2 was integrally designated to chemical conversion. The modified process (Alternative 3) inherits the environmental feasibility of Alternative 1 and, through elimination of the EOR compression train, has the potential of positive impacts on CAPEX.

Keywords: CO_2 Capture and Utilization, Physical Absorption, Bi-Reforming, Methanol Synthesis, FPSO

1. Introduction

This work approaches the production of remote natural gas exhibiting high CO_2 contents where the separated CO_2 is utilized *in situ* to produce methanol resulting in monetization of CO_2 in an FPSO – MFPSO. The concept of an MFPSO is particularly relevant in the context of Brazilian pre-salt oil reservoirs, 300km distant from the continent and exhibiting high CO_2 - reaching 70% in Jupiter reservoir (Guzzetti, 2010). The sought monetization could contribute to sustainability of natural gas production from such remote fields. The study evaluates three process alternatives where CO_2 is captured from natural gas, by physical absorption with propylene carbonate (PC), producing a natural gas stream poor in CO_2 and a stream consisting of a mixture of CO_2

and hydrocarbons. The evaluated routes for CO_2 conversion to methanol includes Bi-Reforming (Alternative 1 and 3) and Dry-Reforming (Alternative 2). In Alternatives 1 and 2, presented by Lima et al. (2014), part of the captured CO_2 is destined for EOR while Alternative 3 (proposed in the present work) integrally converts CO_2 to methanol. It is worth noting PC was selected as absorption solvent due to its easiness of regeneration, involving a simple expansion valve and a flash vessel.

Also relevant in the scope of the downstream processing of the CO_2 rich stream is that PC has also affinity for hydrocarbons, yet lower than its affinity for CO_2. This benefit is explored by the proposed alternative processes, where absorbed hydrocarbons (CH_4 and, in a lesser extent, heavier molecules) react with CO_2 in dry reforming reactions (e.g., $CH_4 + CO_2 \rightarrow 2CO + 2H_2$), steam reforming reactions (e.g., $CH_4 + H_2O \rightarrow CO + 3H_2$) and bi-reforming reactions (e.g., $3CH_4 + 2H_2O + CO_2 \rightarrow 4CO + 8H_2$). When CO_2 reforming occurs simultaneously with steam reforming, coke deposition is drastically reduced (GANGADHARAN et al., 2012). This combination, named bi-reforming, generates syngas with a H_2/CO ratio of 2, ideal for methanol synthesis (OLAH et al., 2009). Although dry reforming generates syngas with a suboptimal H_2/CO ratio, the water gas-shift reaction (WGS) adjusts the ratio to favour further methanol synthesis (GANGADHARAN et al., 2012). Alternatives 1 and 3 combine dry and steam reforming in one reactor, while Alternative 2 segregates dry reforming in one reactor and WGS reaction in a subsequent reactor. The Alternatives are evaluated with Aspen HYSYS® simulator for calculation of energy and mass balances necessary to assess economic and environment performances. The economic evaluation employed Capital Cost Estimation Software (CAPCOST) for calculations of CAPEX and OPEX, and the Waste Reduction Algorithm Software (WAR) was used to evaluate the potential environmental impacts.

2. Process Simulation

Bi-Reforming (Alternatives 1 and 3) and Dry Reforming (Alternative 2) were evaluated with Aspen HYSYS® simulator. The first process steps relates to CO_2 capture and are common to all evaluated alternatives, which is fed with raw natural gas (NG) stream exhibiting the following molar composition: 60% CH_4, 20% CO_2, 12% C_2H_6, 6% C_3H_8 and 2% N_2. The adopted process premises are: (a) the natural gas, previously dehydrated, enters at 70 bar and 40 ^oC with a volumetric flow rate of 1MMNm^3/d; (b) the treated gas meets selling Brazilian specifications (< 3% in CO_2), and (c) PC flow of 435t/h, necessary to obtain the molar ratio between CH_4 and CO_2 at treated stream suitable for reforming reactions (obtained by successive simulations). Figure 1 shows the Aspen HYSYS® process flow diagram for CO_2 PC absorption. NG enters at the bottom of absorber column (T-100), countercurrent to PC. NG correctly specified is obtained as the top product of absorber, and PC regeneration occurs at the flash vessel (V-100).

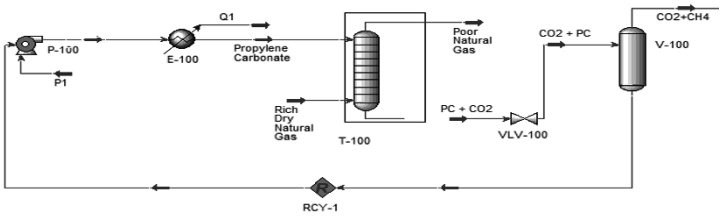

Figure 1. Process flow diagram for CO_2 absorption with PC

2.1. Bi-Reforming Process with CO_2-EOR(Alternative 1)

The stream 'CO_2 + CH_4' is divided into two parts: one goes to a compression train, for CO_2-EOR, and the other is destined to a reactor where both dry and steam reforming reactions occur, shown in Figure 2.

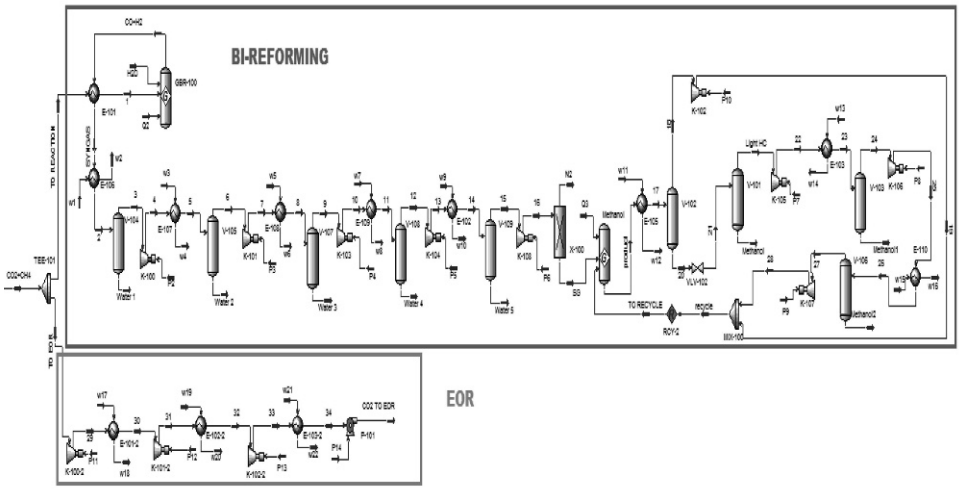

Figure 2. Process flow diagram for EOR and Bi-Reforming process – Alternative 1

With CO_2/CH_4 molar feed ratio of 1:1, GBR-100 operates at 900°C and 1 bar and water vapour is added in reactor at 10.81 t/h. After reaction, the stream 'SYNGAS' passes through a sequence of compressors, heat exchangers and vessels, in order to eliminate water and pressurize gas to 70 bar for methanol synthesis. These heat exchangers utilize seawater for refrigeration. Liquid methanol is recovered at V-101, V-103 and V-106.The remaining hydrocarbons and syngas return to Methanol reactor.

2.2. Dry Reforming Processwith CO_2-EOR (Alternative 2)

Similarly to the Bi-Reforming process, the stream 'CO_2 + CH_4' is divided into two parts. However, the stream 'To Reaction' proceeds to the GBR-100 reactor, where occurs exclusively the dry reforming. GBR-100 operates at 870°C and 1 bar. After reaction, stream 'SYNGAS' passes through a compression and intercooler train. This stream is pressurized to 70.5 bar before entering the Adjust reactor (WGS), where water vapor is added at a rate of 2 t/h. In the sequence, stream "feed" enters in the Methanol reactor. The stream that leaves the Methanol reactor has a high quantity of unreacted methane, which, after methanol recovery, is recycled to GBR-100. Methanol is recovered at V-102, and residual hydrocarbons are recycled (Figure 3).

2.3. Bi-Reforming Process without CO_2-EOR (Alternative 3)

The stream 'CO_2 + CH_4' is integrally directed to methanol conversion, accordingly to Figure 4. Reaction section proceeds as described for Alternative 1.

3. Economic and Environmental Analysis – Alternatives 1 and 2

Alternatives 1 and 2 were evaluated economically, for decision of which reaction path would be more attractive, through CAPEX and OPEX calculations. Equipment sizing

was performed according to procedures described in the literature (e.g., CAMPBELL, 2004; PERRY, 1997; TOURTON et al., 2009). For the economic analysis, the MS Excel spreadsheet CAPCOST, developed by Turton et al (2009), was employed. Table 1 presents the main results from Bi-Reforming (Alternative 1) and Dry-Reforming (Alternative 2) Processes, indicating the resulting CAPEX, OPEX and revenue for each alternative. Alternative 1 has the highest revenue as methanol production (17960 kg/h) was 4 times higher than for the Dry-Reforming Process (Alternative 2).

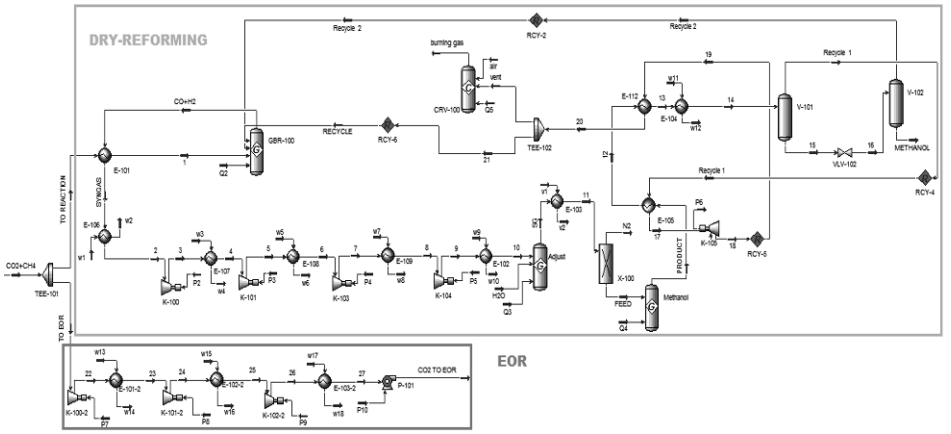

Figure 3. Process flow diagram for EOR and Dry-Reforming process – Alternative 2

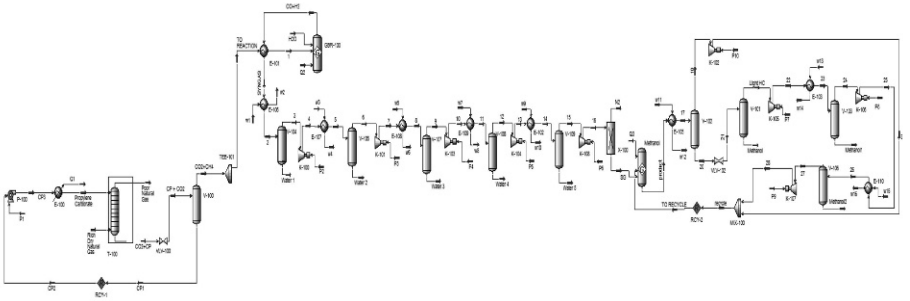

Figure 4. Process flow diagram Bi-Reforming process without EOR – Alternative 3

Table 1. Results of CAPEX, OPEX and Revenue Sales – Alternatives 1 and 2

Cost (U$$)	Bi-Reforming	Dry-Reforming
CAPEX	25,165,709	32,145,906
OPEX	122,575,216	101,189,415
Revenue Sales	144,890,686	51,463,757

The WAR Algorithm (CABEZZAS et al.,1999) was used to comparatively quantify the environmental performance of Alternatives 1 and 2, based on eight categories of environmental impacts, equally weighted. The categories are: Human Toxicity Potential

by Ingestion, Human Toxicity Potential by Exposure, Aquatic Toxicity Potential, Terrestrial Toxicity Potential, Global Warming Potential, Ozone Depletion Potential, Smog Formation Potential, Acidification Potential. WAR measures performance as output rate of PEI (Potential of Environmental Impact). PEI can be described through rates of inlet (Îin), outlet (Îout) and generation (Îgen) of impact in a given system. The mass flow and composition obtained from ASPEN HYSYS simulations were used in the WAR algorithm. Comparing the total impact for these processes two Alternatives (both employing CO_2-EOR), Bi-Reforming (Alternative 1) has a lower impact (868 PEI/hr) than Dry-Reforming (Alternative 2) (1661 PEI/hr).

4. Alternatives 1 and 3 - Bi-Reforming with and without EOR

The comparative economic and environmental analysis indicate that Alternative 1 (Bi-Reforming) is technically, economically and environmentally superior to Alternative 2. Considering the main objective of an MFPSO of enhanced methanol production, Alternative 3 was proposed with removal of the CO_2-EOR section (Figure 4). Based on the conclusion of superior performance of Alternative 1 over Alternative 2, Alternative 1 is the basis of Alternative 3. A preliminary economic analysis (exclusively based on revenue increase) shows enhancement of methanol production of around 2 times over the production achieved in Alternative 1 (35,497.56 kg/h). Consequently, Alternative 3 presents revenue of U$$ 251,502,365, (Alternative 1 showed revenue of US$144,890,686). Furthermore, Alternative 3 and Alternative 1 were compared considering the generation rate of PEI, calculated through WAR Algorithm. It was observed that Alternative 1 (Bi-Reforming) has a negative rate, higher than Alternative 3 (Bi-Reforming without EOR), what means that the first alternative is environmentally superior to Alternative 3, as shown in Figure 5. It is worth noting that methanol contributes to all impact categories evaluated while CO_2 most exclusively impacts in global warming. Consequently, WAR penalises the increase in methanol production achieved in Alternative 3.

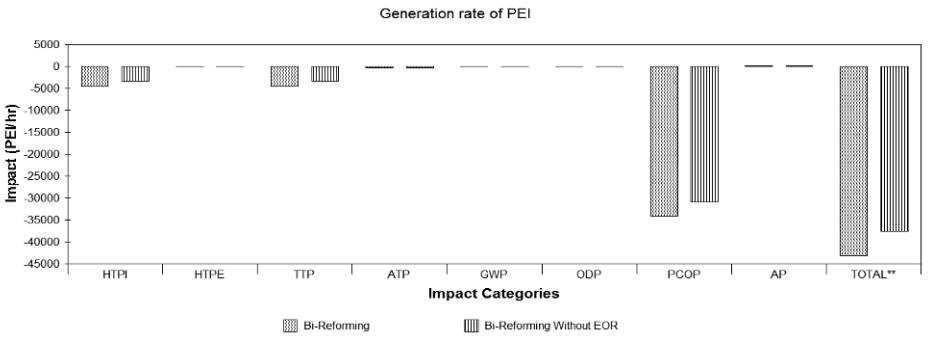

Figure 5. Generation rate of PEI for Bi-Reforming with and without EOR step

5. Discussion and Conclusions

The proposed processes are potentially amenable to methanol floating production system, MFPSO, where the regeneration of PC would present a competitive advantage over alternative CO_2 capturing technologies, since weight and space are the key considerations for floating plants. The treated natural gas stream (248.7 m^3/h) composition is (in molar basis): 90.19% CH_4, 1.67% CO_2, 3.31% C_2H_6, 0.63% C_3H_8 and

4.20% N_2. The main difference of the proposed processes is the fact that at Bi-Reforming (Alternatives 1 and 3) just one reactor is utilized, where occur both dry and steam reforming. On the other hand, for Dry-Reforming (Alternative 2) two reactors are conceived: one for dry reforming and other for WGS reaction. This difference poses a large discrepancy of methanol productivity, as methanol production by Bi-Reforming was 17905 kg/h, 4 times higher compared to Dry-Reforming. Dry reforming occurs not only for methane, but also for ethane and propane, and these last reactions are more favoured than the first one. In consequence, methane is not consumed, but rather produced in the Dry-Reforming alternative, explaining the associated low production of methanol. Since the preliminary conclusions indicate that Bi-Reforming is technically, economically and environmentally superior to Dry-Reforming, a third flowsheet was proposed, considering the elimination of CO_2-EOR section, with dedicated production of methanol. Analysis showed that methanol production in Alternative 3 (35,497.56 kg/h) present revenues around 2 times higher than Alternative 1. Regarding the environmental aspect, Bi-Reforming (Alternative 1) shows superior environmental performance over Bi-Reforming without EOR step (Alternative 3) due to the penalty attributed by WAR algorithm to producing methanol, which contributes to all considered impact categories. However, both alternatives presented negative generation of PEI, which turns Alternative 3 the most sustainable alternative. Although a more detailed economic analysis for Alternative 3 (CAPEX and OPEX) is necessary to reinforce this conclusion, it is foreseen a superior economic performance since the increase in revenues is significant and compression costs associated to CO_2-EOR are eliminated.

Acknowledgments

The authors acknowledge the financial support of PETROBRAS S.A., ANP (PRH-ANP/MCT, PRH-41) and CNPq research grants.

References

H. Cabezas, J. Bare, S. Mallick, 1999, Pollution prevention with chemical process simulators: the generalized waste reduction (WAR) algorithm - full version. Computers and Chemical Engineering, 23, 4–5, 623–634.

J. M. Campbell, 2004, Gas conditioning and processing: the equipment modules. Norman: John M Campbell & Company, 2, 8.

J. Formigli, 2007 Pre-salt reservoirs offshore Brazil: perspectives and challenges, Miami.

C. Guzzetti, Gaffney, Cline & Associates, 2010, Review and evaluation of ten selected discoveries and prospects in the pre-salt play of the deepwater santos basin, Brazil. www.anp.gov.br/?dw=39137.

P. Gangadharan,; K. Kanchi,; H. Lou, 2012, Evaluation of the economic and environmental impact of combining dry reforming with steam reforming of methane. Chem. Eng. Res. Des., 90, 11, 1956–1968.

B. Lima, O. Araújo, J. L. Medeiros, C. Morgado, 2014, Technical, Economic and Environmental Viability of Offshore CO_2, Proceedings of 2014 AICHE Annual Meeting, Atlanta, GA, USA.

G. A. Ola et al., 2013, Bi-reforming of methane from any source with steam and carbon dioxide exclusively to metgas (CO–2H2) for methanol and hydrocarbon synthesis, J. Am. Chem. Soc., 135, 2,648–650.

R. Perry, D. Green, 1997, Perry's Chemical Engineers's Handbook, McGraw-Hill, 1, 7.

R. Turton et al., 2009, Analysis, Synthesis, and Design of Chemical Processes, New Jersey: Prentice Hall, 1, 3.

Krist V. Gernaey, Jakob K. Huusom and Rafiqul Gani (Eds.), 12th International Symposium on Process Systems Engineering and 25th European Symposium on Computer Aided Process Engineering.
31 May – 4 June 2015, Copenhagen, Denmark

A Superstructure-Based Framework for Simultaneous Process Synthesis, Heat Integration, and Utility Plant Design

S. Murat Sen, James A. Dumesic, Christos T. Maravelias*

Department of Chemical & Biological Engineering, University of Wisconsin-Madison, WI 53706, USA
christos@engr.wisc.edu

Abstract

We propose a new framework for simultaneous chemical process synthesis, heat recovery network design, and utility plant design. We generate compact surrogate unit models to describe processes based on new technologies. We also consider (1) process streams with variable heat loads and temperatures, and (2) multiple steam types of variable temperature. We illustrate the applicability of our framework using a novel process for the non-enzymatic production of sugars from lignocellulosic biomass.

Keywords: Superstructure optimization, global optimization, biofuels.

1. Introduction

The goal of this paper is to develop a framework for the systematic generation and evaluation of biomass-to-fuels processes based on novel conversion technologies. One of the challenges in the design of such processes is that no *first-principles* models are available for key conversion steps which are based on novel conversion systems for which no kinetic expressions are available; the same is often true for separations that are found to be effective experimentally but for which limited thermodynamic information is available (e.g., extraction steps with new solvents). Another challenge in the area of biomass-to-fuels strategies stems from the need to design processes that are energetically effective, preferably using lignin and/or biomass residues to provide all necessary process heat and electricity (Stuart and El-Halwagi, 2012; Yuan et al., 2013).

To address these challenges, we propose a superstructure optimization framework that allows us to simultaneously perform (1) structural and parametric optimization for the main chemical plant, (2) heat integration, and (3) utility plant design. Furthermore, we develop surrogate unit models based on (1) experimental results to model unit operations for which rigorous models are not available; and (2) offline simulations to formulate tractable optimization models. Finally, we outline two solution methods for the effective solution of the resulting mixed-integer nonlinear programming (MINLP) model using global optimization solvers. The proposed framework is used to design an integrated strategy for the non-enzymatic production of sugars from biomass.

The integration of the three subsystems is shown in Fig. 1. The chemical plant converts biomass to products and byproducts, as well as biomass residues which can be used to generate process heat and electricity. The hot and cold streams from the main plant and the utilities from the utility plant are inputs to the heat integration subsystem. Finally, using biomass residues and/or fossil fuels, the utility plant produces different types of steam to satisfy heating requirements (after heat integration) and electricity to meet process power requirements, while excess electricity can be sold to the grid.

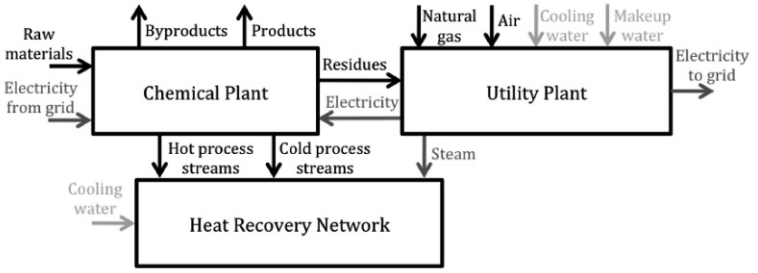

Figure 1. Three basic subsystems and their interactions in the integrated model.

2. Superstructure modelling framework

2.1. Chemical plant

The chemical plant model is based on three sets: (1) compounds, (2) units, and (3) streams. The main variables of the model include component flows, unit operating conditions (T and P), heat loads, conversions (reactors), component recoveries (separation units), and (for some units) compositions. Equality constraints arise from material and energy balances around units, design equations, and correlations of experimental data, while inequality constraints arise from product and design specifications. Unit operations are modelled using surrogate models developed from experimental results or offline process simulations (Henao and Maravelias, 2011), as well as short-cut methods with relatively simple non-linear algebraic expressions. Binary variables are used to *activate* the selected units and the associated variables (Yeomans and Grossmann, 1999). Special care is given to the formulation of the unit models so that the (de)activation of the inlet component molar flows suffices to (de)activate all associated variables, thereby avoiding the introduction of additional nonlinearities.

2.2. Heat recovery network

Steam at different pressure levels (high, medium and low) produced in the utility system is used for heating, while water is used as cooling utility. To minimize total utility requirements, the maximum heat recovery is obtained in a *heat cascade* which can be modelled as a transhipment problem (Papoulias and Grossmann, 1983). Hot streams and heating utilities (sources) supply heat to temperature intervals (intermediate nodes), and these intervals supply heat to cold streams and cooling utilities, while any heat surplus from these intervals are cascaded down to the next interval at lower T).

We propose a generalization of the transhipment model to account for (1) variable heat duties for process streams (determined by the plant subsystem), and (2) variable steam temperature (determined by the utility plant subsystem) (Fig. 2a). The temperatures of process streams are used for the construction of temperature intervals in the heat recovery network. Based on its saturation temperature, each type of steam available for heating is assigned to a temperature interval using binary variables.

2.3. Utility plant

The energy generated from natural gas or process residues is used to produce high-pressure (HP) steam in a boiler (Fig. 2b). HP steam can be used for heating, expanded through back-pressure or vacuum turbines for electricity generation, and/or expanded through a let-down valve to form medium-pressure (MP) or low-pressure (LP) steam to be used for heating and electricity generation. Electricity can be generated by any combination of steam turbines connected with a common shaft on an electric generator,

and/or purchased to meet the electricity demand. In case of electricity surplus (if process residues are used), excess electricity can be sold to the grid to generate extra revenue. Utility demands are simultaneously determined through heat integration of process streams. Selection of how much electricity to produce and/or purchase, selection of the type and amount of steam (HP, MP, LP) to produce and its conditions (temperature and pressure; superheated, saturated or wet steam) are decision variables for the utility plant. Turbines used in the utility system are modelled using isentropic expansion expression, while the total electricity generated in turbines is calculated as a function of the flow rate, enthalpy difference, and turbine efficiency. We use rigorous approaches to determine the steam enthalpy; we take non-ideal behavior of the vapor phase into account through the calculation of vapor compressibility factor as a function of temperature and pressure, which are both continuous variables (Smith et al., 2005). Then, we develop an approximation of the rigorous compressibility factor expression in terms of temperature and pressure of steam. The proposed approximation leads to a maximum error of less than 3%. The consideration of variable pressure/temperature for the three types of steam it potentially allows us to find energetically superior designs where the steam temperature satisfies exactly the minimum ΔT in the heat exchangers.

2.4. Solution methods

Despite the adoption of surrogate unit models, the resulting MINLP models are computationally expensive. They are *nonconvex MINLP* models, which means that global optimization solvers are necessary to obtain globally optimal solutions. To enhance the solution of the resulting models, we developed an algorithm for the calculation of lower and upper bounds on component molar flows. Specifically, starting from component molar flows in the feedstock streams, we *propagate* these bounds moving downstream. For example, using the upper bounds on the flow of reactants in the inlet of a reactor and the maximum yield (experimentally determined), we can calculate upper bounds on the flow of products at the outlet of the reactor. Tearing ideas are used to calculate bounds in the presence of recycle streams. We also calculate bounds for steam condition and properties.

Furthermore, to reduce the solution space, we generate inequalities using unit selection binary variables to enforce logic constraints arising from the connectivity of the units in any feasible solution. Finally, we systematically generate redundant constraints which are found to enhance the solution of the model.

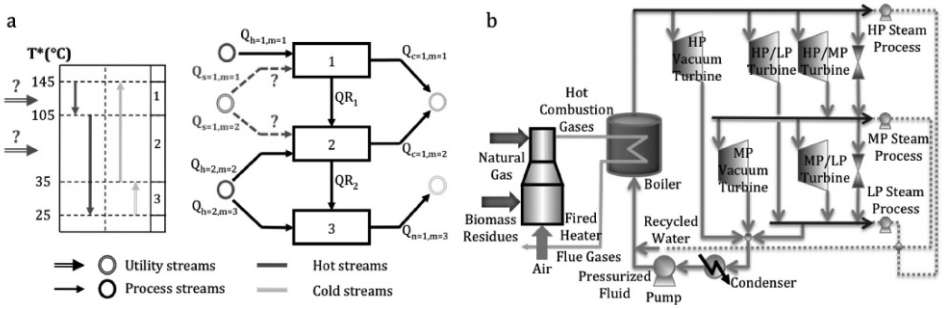

Figure 2. (a) Transhipment model for the heat recovery network. (b) Utility plant design.

3. Case study: Non-enzymatic production of sugars from biomass

To illustrate the applicability of the proposed framework, we study the production of sugars from lignocellulosic biomass via a non-enzymatic conversion technology we proposed recently (Luterbacher et al., 2014). We use the design basis (2,000 dry tons of biomass per day) and assumptions from Kazi et al. (2010).

3.1. Chemical plant superstructure

Luterbacher et al. (2014) proposed a novel non-enzymatic technology for the simultaneous catalytic conversion of hemicellulose and cellulose fractions to soluble C_5- and C_6-sugars, respectively, using biomass-derived γ-valerolactone (GVL) as a solvent. Specifically, sugars are produced in a biomass deconstruction system at 430-490 K using dilute sulfuric acid catalyst in GVL/water (4:1 wt%) solution at a biomass loading of 7 wt%. This reaction system leads to complete conversions of hemicellulose and cellulose with high yields of C_5-sugars from hemicellulose (70-86 mol% depending on the GVL-to-biomass ratio) and C_6-sugars from cellulose (70 mol%). Importantly, the sugar yields were shown to be insensitive to biomass type (Luterbacher et al., 2014). However, a major challenge towards the commercialization of this technology is the recovery of sugars at high purity (to be further converted to ethanol or other chemicals), as well as the separation of GVL (to be recycled to the reactor) from lignin and biomass residues (to be used for heat and power generation). Therefore, for a cost-effective production of fermentable sugars, a series of effective separation technologies should be developed and integrated with the upstream conversion technology.

Accordingly, we generate a superstructure that contains various alternatives for separating biomass-derived sugars from the GVL solvent, lignin and biomass residues. Sugars can be separated from GVL, lignin and residues by multi-stage CO_2 extraction, phase separation upon salt addition, or multi-stage extraction using an alkylphenol solvent as shown in Fig. 3. Following the separation of sugars, GVL solvent can be recovered from lignin and residues using precipitation of solids, or evaporation of GVL. Later, GVL can be recycled back to the sugar production step, while lignin and biomass residues can be sold to generate revenue or utilized in the utility plant for steam and power production. It is not clear that what combination of separation technologies will make the production process more cost-effective, which requires a systematic evaluation of all the alternatives.

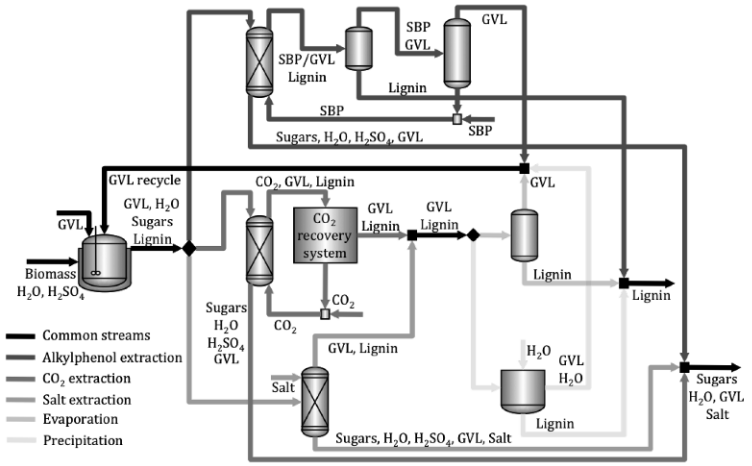

Figure 3. Superstructure for production of sugars.

3.2. The MINLP model

Based on the experimental results of Luterbacher et al. (2014), we developed an optimization model that integrates the sugar production plant with the utility system and heat recovery network. Units for which we developed surrogate models based on experimental results include (1) the reactor for the conversion of biomass to sugars (C_5 and C_6 overall yields as functions of GVL:biomass ratio), (2) the multi-stage sugar extraction using super-critical CO_2 (partition coefficients) (3) the multi-stage GVL extraction using sec-butyl phenol (partition coefficients). We also developed surrogate models based on offline simulations. For instance, Fig. 4 shows the surrogate model for a subsystem of flash tanks and compressors for the recovery and recycle of CO_2. The surrogate model calculates the major variable of this subsystem, the total power requirement, as a function of total feed flow, CO_2 composition, and recovery.

Our objective is to maximize the annual profit: revenue from sugars and by-products (lignin and excess electricity) sales minus the costs of raw materials and utilities minus other operating costs minus the annualized capital cost. The price of sugars is assumed to be 35 cents per kg. The capital costs are annualized using a capital recovery factor of 11.75% based on a 10% discount rate and an equipment lifespan of 20 years. We consider the selection of feedstock among alternatives including corn stover, sugarcane, wheat straw, hybrid poplar, switchgrass, loblolly pine and aspen wood. The model for this case study includes 78 binary variables, 2,314 continuous variables, and 2,156 constraints with 1,248 of them being non-linear.

3.3. Results

Using SCIP global optimization solver in GAMS, we obtained a feasible solution (profit, \$6.5 million/yr) with an optimality gap of 5.8% after 2 hrs of CPU time. The selected configuration includes the non-enzymatic sugar production (br_1) followed by the multi-stage CO_2 extraction (e_1) for separation of sugars, CO_2 recovery system (f_1), and the GVL evaporation (f_2) for its recovery from lignin and biomass residues (see Fig. 5). Sugarcane was selected as feedstock, which has a high total cellulose and hemicellulose content (~66 wt%). The annual feedstock cost was found to be \$28 million. A low GVL-to-biomass ratio (14:1 wt%) is selected despite leading to low C_5-sugar yield. Still, the cost of make-up GVL (\$6.6 million per year at \$120/ton GVL) is a major cost contributor (0.6% of GVL is lost in the 3-stage CO_2 extraction unit). Following the multi-stage extraction, the optimal CO_2 recovery was found to be 99% in the CO_2 recovery subsystem leading to a power demand of 20.5 MW. Then, almost 100% of GVL is separated from lignin and humins in an evaporation unit with a heat duty of 178 MW. The selected process yields 565 tons/day of C_6-sugars and 350 tons/day of C_5-sugars (89% of the sugars are recovered in the aqueous phase in the CO_2 extraction), which can potentially be converted to 47 million gallons of ethanol annually. Utilization of lignin and residues as a fuel in the utility system is a better option than selling them at a price of \$50/ton.

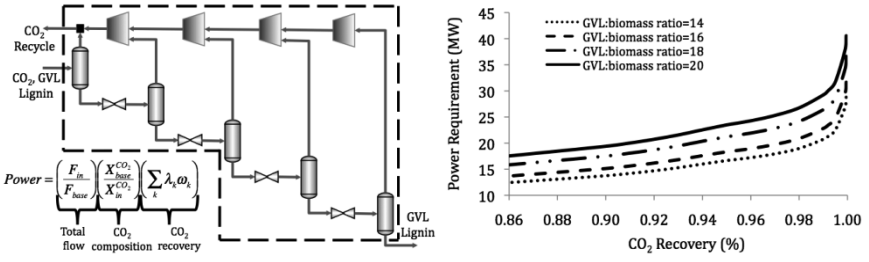

Figure 4. Power requirement for the CO_2 recovery system.

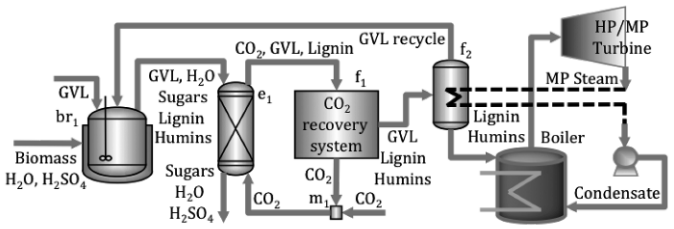

Figure 5. Selected configuration for production of fermentable sugars.

The heating requirement of the selected configuration before heat integration was found to be 178 MW. The heat recovery network, which consists of 13 temperature intervals, allows us to recover 53 MW. The entire cooling requirement is via heat integration, while the remaining heating requirements (125 MW) are satisfied using MP steam at 20.1 bar and 658 K. The boiler produces 71 kg/s of HP steam (at 44.3 bar & 750 K, 176 MW) using the heat released from the combustion of lignin and biomass residues without the need for natural gas purchase. The power requirement of the entire facility is 20.9 MW (chemical plant: 20.5 MW, utility system: 0.4 MW). The majority of the power requirement (18 MW) is satisfied with the HP/MP back-pressure turbine, while the remaining (2.9 MW) is externally supplied.

4. Conclusions

We proposed a framework for the formulation of superstructure optimization models for simultaneous process synthesis, heat integration, and utility plant design. We also proposed methods for the effective solution of the resulting MINLP models, including a bound propagation algorithm. The proposed framework addresses some limitations of previous approaches, namely, it accounts for variable stream heat loads and temperatures for heat integration, and it considers accurate molar enthalpy relationships. We also showed how surrogate models, based on experimental results or offline calculations, can be integrated resulting in computationally tractable models. The proposed framework accounts for the interactions among all three subsystems, which is critical for the generation of strategies for renewable fuels, and allows to quickly generate and evaluate energy-efficient processes that employ newly developed conversion technologies for which rigorous models are not available.

References

C.A. Henao, C.T. Maravelias, 2011, Surrogate-based superstructure optimization framework, AIChE Journal, 57, 1216-1232.

F.K. Kazi et al., 2010, Techno-economic comparison of process technologies for biochemical ethanol production from corn stover, Fuel, 89, S20-S28.

J.S. Luterbacher et al., 2014, Nonenzymatic sugar production from biomass using biomass-derived gamma-valerolactone, Science, 343(6168), 277-280.

S.A. Papoulias, I.E. Grossmann, 1983, A structural optimization approach in process synthesis. II. Heat recovery networks, Computers & Chemical Engineering, 7(6), 707-721.

J.M. Smith, H.C. Van Ness, M.M. Abbott, 2005, Thermodynamic properties of fluids, Introduction to chemical engineering thermodynamics, 7th edition, 199-253.

P.R. Stuart, M.M. El-Halwagi, 2012, Integrated biorefineries: design, analysis, and optimization, CRC Press.

H. Yeomans, I.E. Grossmann, 1999, A systematic modeling framework of superstructure optimization in process synthesis, Computers & Chemical Engineering, 23, 709-731.

Z.H. Yuan et al., 2013, Applications of process synthesis: moving from conventional chemical processes towards biorefinery processes, Computers & Chemical Engineering, 49, 217-229.

Krist V. Gernaey, Jakob K. Huusom and Rafiqul Gani (Eds.), 12th International Symposium on Process Systems Engineering and 25th European Symposium on Computer Aided Process Engineering.
31 May – 4 June 2015, Copenhagen, Denmark

Process Design and Optimization of an Integrated Shale Gas Process for Green Chemicals Production

Chang He,[a,b] Fengqi You[a]

[a] *Northwestern University, 2145 Sheridan Road, Evanston, IL, 60208, USA*
[b] *China University of Petroleum, 18 Fuxue Road, Changping, Beijing 102249, China*

Abstract

This paper is concerned with the process design and optimization of an integrated shale gas process for greener chemicals production. From a sustainability point of view, the bioethanol is incorporated as a renewable feedstock to reduce the environmental footprint of the entire process. The proposed process integrates co-cracking of light NGLs, the oxidative coupling of methane (OCM) reaction, and bioethanol dehydration with raw shale gas processing. Overall, the process consists of four process areas, namely gas treatment, gas to chemicals, methane to ethylene and bioethanol to ethylene. A simulation-optimization method based on the NSGA-II algorithm is developed for the life cycle optimization of the process modelled in HYSYS. An energy integration model is also integrated using the mixed-integer linear programming. The results show that for a "good choice" design, the minimum ethylene selling price is \$877.2/ton and the unit GWP of ethylene (GWP_{E2E}) is 0.360 kg CO_2-eq/kg, when shale gas is considered as a high carbon fuel.

Keywords: shale gas, process design, greener chemicals, simulation-optimization

1. Introduction

The substantial development of shale gas represents a true game changer in the energy and chemical industries in the United States and other countries, including China, Argentina, and Mexico (Varma and Grossmann, 2014). This is because shale gas not only provides low-cost fuels, but also can be used as a basic feedstock in the production of value-added chemicals like plastics, synthetic rubber, adhesives, etc. (Kargbo et al., 2010). It is worthwhile to note that most of the shale formations in the U.S. are reported to be rich in natural gas liquids (NGLs), which are C_{2+} hydrocarbons (Cafaro and Grossmann, 2014). After raw shale gas is purified and fractionated, the NGLs have substantially higher market values than methane. Light NGLs, such as ethane, propane and butanes, can be used as feedstocks in the olefins production, while the remaining heavier fractions can be used as gasoline blending stocks. Currently in the U.S., 99% of NGLs-derived ethane is used as a raw material in cracking facilities because it is cheaper and cleaner than petroleum-derived feedstocks. However, the excessive supply of NGLs has become an issue in regions lacking in abundant NGLs processing and cracking facilities (He and You, 2014). In addition to NGLs, methane is the dominant ingredient in the shale gas. Direct, one-step conversion of methane to value-added chemicals is potentially more attractive. In the pioneering work (Keller and Bhasin, 1982), methane was activated with the assistance of oxygen and further converted into ethylene and ethane; this process came to be known as the OCM reaction. Unfortunately, a standalone OCM process has very little economic potential compared to well-established cracking facilities. The major limitations of the OCM process are its low C_2 yield and selectivity, which lead to a large amount of unreacted gas and byproducts. The

last concern with shale gas is the potential environmental footprint of the increased fugitive CH_4 emissions during drilling. The dispute was initiated because quantitatively assessing the leaking data of methane is complex and varies from well to well, potentially leading to serious environmental issues, in addition to challenges in water management (Gao and You, 2015). It has been concluded that the climate impact of shale gas maybe worse than that of other fossil fuels (Howarth, 2014).

In light of the aforesaid opportunities and challenges, the present work considers shale gas processing with on-site olefins production by co-cracking of NGLs-derived ethane and propane. An OCM process is also integrated to convert methane into short chain alkenes that includes ethylene and ethane. To improve the project economics of the OCM process, a complex co-processing strategy is proposed to purify and separate gas products including the OCM products, co-cracking gas and raw shale gas. The product separation cost is thereby significantly reduced, and the ethylene yield is improved by recovering the OCM-derived ethane and methane. In this process, we address the mitigation of life cycle GHG emissions for shale gas-based chemical processes using carbon capture and storage technology, and sustainable integration of bio-ethylene production. Specifically, bioethanol is incorporated as a renewable feedstock of the process and this hybrid feedstock approach was reported to enhance sustainability of the entire process (He et al., 2014). Overall, the proposed process consists of four process areas, namely gas treatment, gas-to-chemicals, methane-to-ethylene and bioethanol-to-ethylene. Based on rigorous process modeling, a simulation-optimization method based on the NSGA-II algorithm for life cycle optimization (LCO) of the proposed process is developed. In addition, an energy integration model is also fluidly nested in the simulation-optimization using mixed-integer linear programming (MILP). We subsequently conduct a techno-economic analysis, an environmental impact analysis, and energy integration simultaneously.

2. Process description

For the calculations presented in this work, it is assumed that 2,000 kmol/hr of shale gas is supplied at 60.0 bar and 35 ^{o}C, containing 74.25 mol% CH_4, 13.76 mol% C_2H_6, 5.4 mol% C_3H_8, 1.66 mol% i-C_4H_{10}, 1.11 mol% n-C_4H_{10}, 1.11 mol% i-C_5H_{12}, 0.55 mol% i-C_5H_{12}, 0.29 mol% C_6H_{14}, 0.10 mol% C_7H_{16}, 0.09 mol% C_8H_{18}, 1.52 mol% CO_2, 0.16 mol% N_2, 17.1 mg/scf H_2O and 307.2 mg/scf H_2S, based on normalized data reported from Eagle Ford formation (George and Bowles, 2011). Simulations were performed in Aspen HYSYS V7.2, using the Peng-Robinson package throughout the flowsheet, except: Amine package with Kent Eisenberg rule for acid gas (CO_2 and H_2S) removal, and Glycol package for triethylene glycol (TEG) streams.

A chemicals production process from shale gas integrated with bioethanol dehydration is shown in Figure 1. Briefly, the overall process includes four process areas below.

(1) Gas treatment area, where the raw shale gas and OCM product are purified in a gas sweetening unit. H_2S in the removed acid gas is converted into sulfur in a sulfur recovery unit. The acidic CO_2 (SG-CO_2), along with the OCM-derived CO_2 (OCM-CO_2) is collected at point M_1 and is then compressed into the liquid phase in a CO_2 compression unit. CO_2 liquid is transported through pipelines to sequestration sites. Once purified, the sweet gas is mixed with co-cracking gas at point M_2. The mixture is dried in a dehydration unit and then processed in the next process area.

(2) Gas-to-chemicals area. In this area, the heavy NGLs (butanes and natural gasoline) and low-boiling point gases (methane and H_2-rich gas) are successively taken from the dry gas using an NGLs cutting unit. The C_2 and C_3 hydrocarbons included in the

remaining stream are sent to an olefin separation unit where the olefin products are separated from the light NGLs. In the next step, the ethane and propane are mixed at point M_3 and then thermally co-cracked in an olefin production unit. Meanwhile, a pressure swing adsorption (PSA) unit is employed to recover high-quality hydrogen from the H_2-rich gas. The rejected PSA tail gas is mixed with process purges (AGR and TEG purges), a portion of methane (from point S_1), and bio-waste at point M_4. The mixture passes through the point S_2 where the upper branch goes to the bioethanol-to-ethylene area as dehydration fuel, and the lower branch is sent to power plant as gas turbine (GT) fuel. We note that all process waste heat is integrated within this power plant to generate power using the Rankine cycle.

(3) Methane-to-ethylene area, where the incoming methane (from point S_1) is partially oxidized via the OCM reaction in an O_2-rich environment. The OCM product includes ethylene, ethane, hydrogen, carbon dioxide, carbon monoxide, water, and a large quantity of un-converted methane, which is obtained from the first two process areas. As mentioned in the Introduction, bioethanol can be used as a renewable feedstock introduced to the next process area.

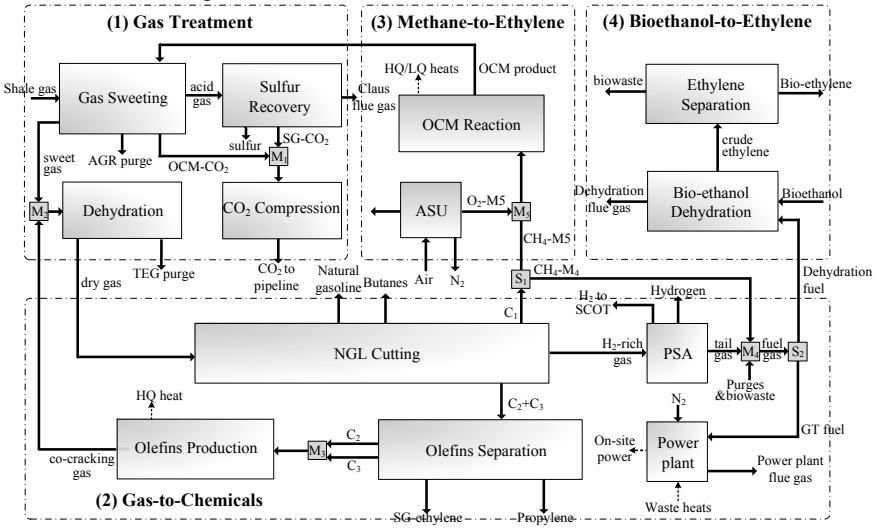

Figure 1. Shale gas/bioethanol to chemicals process

(4) Bioethanol-to-ethylene area. The input amount of bioethanol is fully dependent on that of furnace fuel, that is, by the split ratio at point S_2. The produced crude ethylene is purified via passing through a series of distillations in the ethylene separation unit. In this paper, SG-ethylene, and bio-ethylene refer to the ethylene produced from shale gas, and bioethanol, respectively.

3. Solution procedure

Figure 2 shows the framework of the simulation-optimization method, which performs LCO of the process modeled in Aspen HYSYS. We develop a simulation-optimization method based on the evolutionary NSGA-II algorithm (Deb et al., 2002). An energy integration model is integrated using an MILP approach. First, in the MATLAB control center, the initial decision variables are randomly generated. The MATLAB control center will check the convergence of HYSYS simulation. If feasible, the input/output data taken from simulation results can be mapped and prepared for the next MATLAB

optimization center where two sub-problems are performed. In the first sub-problem, an energy integration model is used to determine the minimum total cost of hot/cold/power utility. Then, the optimal utility cost, combined with the process data (feedstocks, products, emissions, etc.) is passed to a LCO model (Gebreslassie et al., 2013). This model simultaneously maximizes the NPV and minimizes the GWP of the process by using the multi-objective optimization approach (Gong et al., 2014). Sustainable and optimal process designs are then given by Pareto-optimal results (Wang et al., 2013).

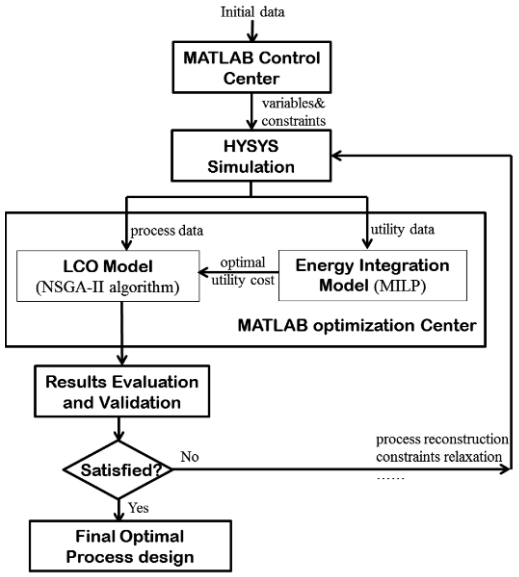

Figure 2. Simplified representation of the simulation-optimization framework

In this work, shale gas is considered as a high carbon fuel and the emission factor (methane leakage/gas produced, v/v%) is assumed to be 3.30% (Howarth, 2014). The corn-derived bioethanol is purchased from market, and the plant-level GHG emissions is equal to 0.042 kg CO_2-eq per GJ bioethanol (You et al, 2012). The decision variables for the proposed process consist of the distribution ratios at points $S_1$and S_2 (X_{S1} and X_{S2}), OCM reaction temperature, pressure and O_2 feed ratio (T_{OCM}, P_{OCM}, and R_{O2}), and co-cracking reaction temperature and pressure (T_{ccr} and P_{ccr}).

4. Result and discuss

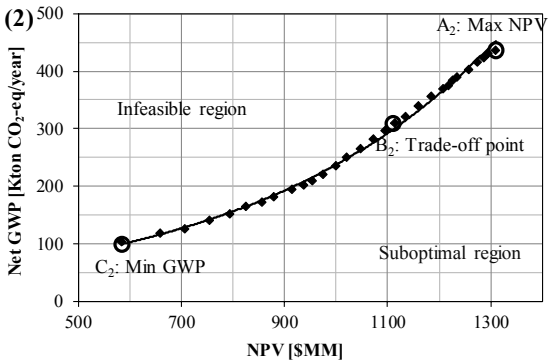

Figure 3. Pareto-optimal solutions of process design

Figure 3 shows the Pareto curve of the proposed process design. Point A on the upper right has the maximum NPV among all feasible solutions. For this design, as the NPV decreases from \$1,322 MM to \$577.7 MM, the annual GHG emissions reduces from 436.2 to 102.9 kton CO_2-eq, as listed in Table 1. In particular, the MESPs of the points A and C are \$712.2/kg and \$1,076/kg, while their corresponding annual GHG emissions are 0.804 and -0.115 kton/CO_2-eq. A comparison between points A and C validates that bioethanol as a renewable fuel can play an important role in reducing the life cycle carbon footprint. To locate a more reasonable point, we note that from point A to point B, the GWP_{E2E} is significantly reduced, while there is only a small rise of the MESP. This implies that the trade-off design of point B is a "good choice" solution.

Table 1. Results of the optimal design

Pareto point	CPU time (hr)	NPV (\$MM)	MESP (\$/ton)	GWP (kton CO_2-eq/year)	GWP_{E2E} ($kgCO_2$-eq/kg)		Bioethanol/SG (mol/mol)
A	104.2	1,322	712.2	436.2	0.804		0.319
B	100.5	1,101	877.2	313.5	0.36		0.576
C	121.2	577.7	1,076	102.9	-0.115		1.092
Pareto point	X_{S1}	X_{S2}	T_{OCM}	P_{OCM}	R_{O2}	T_{ccr}	P_{ccr}
A	0.0002	0.75	817.2	189.2	0.235	789.1	353.5
B	0.045	0.71	845.2	187.0	0.322	770.2	342.4
C	0.202	0.79	852.5	140.2	0.320	755.1	325.0

Table 2. Impacts of GWP reduction options on the CO_2 avoided cost

Reduction option [a]	MESP	GWP_{E2E}	CO_2 avoided cost
BD+CCS	877.2	0.360	197.6
BD	851.0	0.720	218.7
CCS	446.4	2.21	95.60
No reduction	385.2	2.85	baseline

[a] The operating conditions are based on the design of point B. Note that in the CCS option, X_{S2}= 0.

$$\text{Cost of } CO_2 \text{ avoided (\$/kton)} = \frac{(\text{MESP})_{\text{reduction}} - (\text{MESP})_{\text{baseline}}}{(\text{GWP})_{\text{baseline}} - (\text{GWP})_{\text{reduction}}} \quad (1)$$

As previously mentioned, GHGs reduction operations includes CCS and bioethanol dehydration (BD). It is worthwhile understanding the costs behind these two operations. In this work, we investigate the joint and single effect of these operations, as listed in Table 2. The sequence relationship of MESP is "BD+CCS" > "BD" > "CCS" > "no reduction". But as for unit GWP, the sequence reverses. In this work, we adopt the "CO_2 avoided cost" (see Eq. 1) indicator to measure the incremental MESP for a year divided by the difference in unit GWP between the baseline and reduction options. The results clearly show that, the CO_2 avoided cost is increased from \$95.60/kton for the CCS option to \$218.7/kton for the BD option. This indicates that the integration of bioethanol dehydration is an expensive choice. However, with CCS and no reduction options, the GWP_{E2E} are 2.21 and 2.85 kg $CO_{2\text{-eq}}$/kg, respectively, both of which are less competitive than the petroleum-based pathway (1.70 kg $CO_{2\text{-eq}}$/kg). In this case, the integration of bioethanol dehydration becomes a necessary choice if we want to produce greener ethylene. As listed in this table, the GWP_{E2E} can be significantly reduced to 0.720 kg $CO_{2\text{-eq}}$/kg for the BD option, and 0.360 kg $CO_{2\text{-eq}}$/kg for the BD+CCS option.

5. Conclusions

We proposed a novel process design for the conversion of C_1, C_2, and C_3 fractions in shale gas to chemicals. The renewable bioethanol dehydration process is integrated in order to reduce the life cycle GHG emissions of the entire process. Compared to previous process designs, significant production cost and life cycle GHG emissions reductions are achieved. Specifically, the high separation cost and project economics of the OCM process are mitigated by introducing a co-processing strategy of the OCM products, co-cracking gas, and raw shale gas, and recovering OCM-derived ethane and methane efficiently. We formulate a systematic simulation-optimization framework that simultaneously achieves energy integration, and performs a techno-economic analysis and an environmental impact analysis. For a "good choice" optimal design, the MESP is \$877.2/ton and the GWP_{E2E} is 0.360 kg CO_2-eq/kg. The results reveal that, even considered as a high carbon feedstock, shale gas can be converted to greener chemicals in a cost-effective way.

References

D. C. Cafaro, I. E. Grossmann, 2014, Strategic planning, design, and development of the shale gas supply chain network. AIChE Journal, 60(6), 2122-2142.

K. Deb, A. Pratap, S. Agarwal, 2002, A fast and elitist multiobjective genetic algorithm: NSGA-II, Evolutionary Computation, IEEE Transactions on, 6(2), 182-197.

D. L. George and E. B. Bowles, 2011, Shale gas measurement and associated issues, Oil & Gas Journal, 238(7).

J. Gao, F. You, 2015, Optimal Design and Operations of Supply Chain Networks for Water Management in Shale Gas Production: MILFP Model and Algorithms for the Water-Energy Nexus. AIChE Journal, DOI: 10.1002/aic.14705

B. H. Gebreslassie, M. Slivinsky, B. Wang, B., F. You, 2013, Life cycle optimization for sustainable design and operations of hydrocarbon biorefinery via fast pyrolysis, hydrotreating and hydrocracking. Computers & Chemical Engineering, 50, 71-91.

J. Gong, F. You, 2014, Global optimization for sustainable design and synthesis of algae processing network for CO2 mitigation and biofuel production using life cycle optimization, AIChE Journal, 60, 9, 3195-3210.

C. He, F. You, 2014, Shale gas processing integrated with ethylene production: novel process designs, exergy analysis, and techno-economic analysis, Industrial & Engineering Chemistry Research, 53(28), 11442-11459.

C. He, F. You, X. Feng, 2014, A Novel Hybrid Feedstock to Liquids and Electricity Process: Process Modeling and Exergoeconomic Life Cycle Optimization. AIChE Journal, 60, 3739-3753.

R. W. Howarth, 2014, A bridge to nowhere: methane emissions and the greenhouse gas footprint of natural gas, Energy Science & Engineering, 2(2), 47-60.

D. M. Kargbo, R. G. Wilhelm, D. J. Campbell, 2010, Natural gas plays in the Marcellus shale: Challenges and potential opportunities. Environmental Science & Technology, 44, 5679-5684.

G. E. Keller, M. Bhasin, 1982, Synthesis of ethylene via oxidative coupling of methane: I. Determination of active catalysts, Journal of Catalysis, 73(1), 9-19.

A. Varma, I. E. Grossmann, 2014, Evolving trends in chemical engineering education, AIChE Journal, 60(11), 3692-3700.

B. Wang, B. H. Gebreslassie, F. You, 2013, Sustainable design and synthesis of hydrocarbon biorefinery via gasification pathway: Integrated life cycle assessment and technoeconomic analysis with multiobjective superstructure optimization. Computers & Chemical Engineering, 52, 55-76.

F. You, L. Tao, D. J. Graziano, S. W. Snyder, 2012, Optimal design of sustainable cellulosic biofuel supply chains: Multiobjective optimization coupled with life cycle assessment and input–output analysis, AIChE Journal, 58(4), 1157-1180.

Krist V. Gernaey, Jakob K. Huusom and Rafiqul Gani (Eds.), 12th International Symposium on Process Systems Engineering and 25th European Symposium on Computer Aided Process Engineering.
31 May – 4 June 2015, Copenhagen, Denmark

Value-added Chemicals from Microalgae: A Sustainable Process Design Using Life Cycle Optimization

Jian Gong, Fengqi You*

Northwestern University, 2145 Sheridan Road, Evanston, IL 60208 , USA
you@northwestern.edu

Abstract

This paper addresses the sustainable design and synthesis of producing biofuels and bioproducts from microalgae. We propose a comprehensive superstructure with multiple technology alternatives in the seven processing sections. The major products of the superstructure are biodiesel, hydrogen, propylene glycol, glycerol-tert-butyl ether, and poly-3-hydroxybutyrate. Following the life cycle optimization methodology, we propose a bi-criteria mixed-integer nonlinear programming problem to simultaneously optimize the environmental and economic performance. We apply a tailored global optimization algorithm to efficiently tackle the separable concave terms and fractional terms in the objective functions. The most environmentally sustainable processes with respect to various algal bioproducts reduce the life cycle greenhouse gas emissions by 5% to 63%, compared with petrochemical counterparts. Moreover, the minimum biodiesel production cost is $2.79 per gasoline-gallon-equivalent, if all byproducts and value-added bioproducts are considered as credits.

Keywords: Life cycle analysis, glycerol, bioproduct, algal biofuels, global optimization.

1. Introduction

Most fossil-based processes for chemical production are energy- and emissions-intensive (Hermann et al., 2007). In contrast, sustainable bioproducts converted from biomass offer the same chemicals, but tend to cause fewer environmental impacts. Therefore, it could be beneficial to investigate the production of value-added bioproducts in the emerging biofuel processes. Microalgae are very attractive feedstocks owing to high lipid-accumulation rates and minimum competition with food and crops (Silva et al., 2014). Although algal biodiesel production are well studied (Rizwan et al., 2013), little attention is paid to the byproduct converted from glycerol (Pagliaro et al., 2007). Therefore, the goal of this work is to explore the potential environmental and economic benefits of producing both biodiesel and four types of glycerol-derived bioproducts from microalgae: hydrogen, propylene glycol (PG), glycerol-tert-butyl ether (GE), and poly-3-hydroxybutyrate (PHB). We propose a comprehensive superstructure with a number of technology alternatives the conversion of microalgae to biodiesel and bioproducts. Based on the superstructure, we perform a cradle-to-gate life cycle analysis (LCA) focusing on greenhouse gas (GHG) emissions measured by carbon dioxide equivalent. Following a life cycle optimization methodology, we formulate a mixed-integer nonlinear programming (MINLP) problem to simultaneously optimize the environmental and economic performance. A tailored global optimization algorithm is

applied to circumvent the computational difficulties. The results could be used to justify the importance of manufacturing bioproducts in algal biodiesel processes.

2. Process description

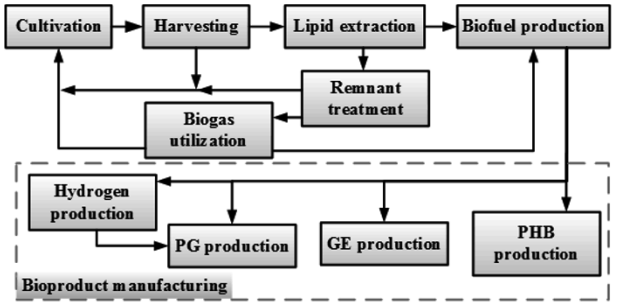

Figure 1. The superstructure for the production of algal biodiesel and bioproducts.

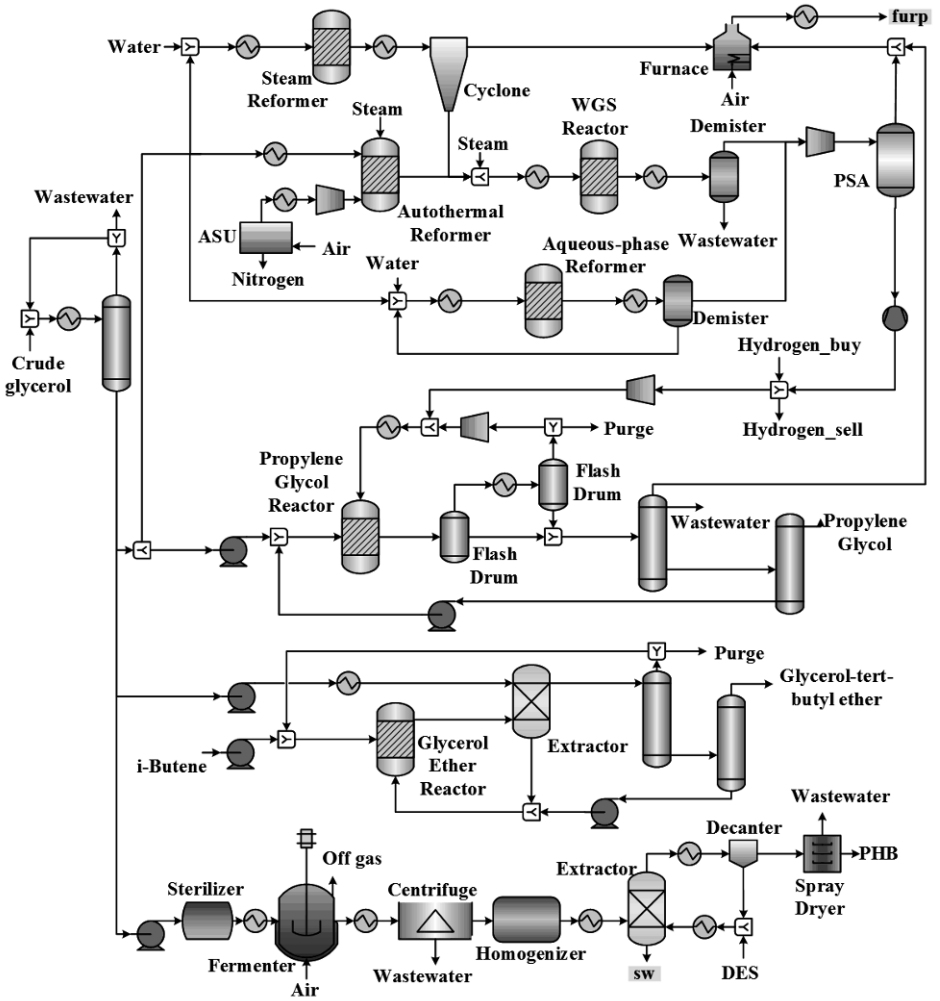

Figure 2. Process diagram of the bioproduct manufacturing section.

We develop by far the most comprehensive superstructure (Figure 1) for the production of biodiesel and bioproducts from the microalgae strain *Chlorella vulgaris*. The superstructure is divided into seven sections: cultivation, harvesting, lipid extraction, remnant treatment, biogas utilization, biofuel production, and bioproduct manufacturing (Gong and You, 2014b). Multiple technology alternatives are incorporated in the superstructure (Gebreslassie et al., 2013b). Pressure filtration and centrifugation are included in the harvesting section; bead beating, microwaving, high pressure homogenization, and sonication in the cell disruption section; hexane, n-butanol, and supercritical carbon dioxide as alternative solvents in the lipid extraction; direct combustion (Gutierrez-Arriaga et al., 2014) and methanol synthesis in biogas utilization; sodium methoxide-catalyzed, heterogeneously catalysed, enzyme-catalyzed, and supercritical methanol-catalyzed transesterifications in biofuel production. Hydrogen, PG, GE, and PHB can be produced in the bioproduct manufacturing section (Figure 2). Three alternative methods, including steam reforming, autothermal reforming, and aqueous-phase reforming, are considered for the hydrogen production . The steam reforming reaction converts glycerol to carbon monoxide, hydrogen, methane, ethylene and char. The autothermal reforming, however, achieves a net zero energy consumption by combining the endothermic reforming reaction and the exothermic oxidation of glycerol. The aqueous-phase reforming takes place under a relatively mild condition, but can only achieve a 9% single loop conversion. The direct product of the catalytic hydrogenolysis of glycerol is a mixture of water, PG, propanol, acetone, and unreacted reactants. Two flash drums and two distillation columns are employed sequentially to separate unreacted hydrogen and impurities from the PG product. In the GE production, the purified glycerol stream extracts most of the intermediate products from the etherification reaction, while the raffinate is introduced into a distillation column to purify the products. In the PHB process, the sterilized glycerol is converted to intracellular PHB. Next, centrifugation, extraction, and drying are employed to separate the products.

3. Model formulation and solving strategies

3.1. Model formulation

(P1)	min	$totalcost / v^{diesel}$
	min	$totalGHG / t$
	s.t.	Mass balance constraints
		Energy balance constraints
		Economic evaluation constraints
		Life cycle environmental impact analysis constraints

A bi-criteria MINLP model is formulated to simultaneously minimize the annualized cost per gasoline gallon equivalent (GGE) of biodiesel and GHG emissions per MJ of biodiesel. In the mass balance constraints, integer variables are introduced to model technology selection decisions (Gebreslassie et al., 2013a). The separation units are described based on the split fractions and mass conservation of every species. The reactions are described with stoichiometric coefficients and conversions, or product distributions. In the energy balance constraints, the consumption and generation of electricity, heating, and cooling utilities are calculated based on the mass flow rates of the input and output materials (Wang et al., 2013). The economic evaluation constraints calculate annualized investment cost based on equipment capital costs following a nonlinear scaling rule (Garcia and You, 2015). These constraints also determine the annual operating cost, taken as the sum of feedstock cost, utility cost, operating &

maintenance cost, and waste treatment cost. Next, the total annualized cost is calculated as the sum of the annualized investment cost and the annual operating cost. In order to quantify the environmental behaviour, a cradle-to-gate life cycle analysis is integrated into the multiobjective optimization problem following the life cycle optimization methodology (You and Wang, 2011). The functional unit is defined as 1 kg of bioproduct manufactured. The system boundaries of this LCA cover three life cycle stages: feedstock acquisition, transportation, and algal biodiesel and bioproduct manufacturing. The environmental impact considered for optimization is the amount of GHG emissions measured by carbon dioxide equivalent. The evaluation methods and co-product allocation methods are consistent with ISO guidelines (Institution, 2006).

3.2. Global optimization algorithm

$$\text{(P2)} \quad \min \; obj = totalcost - Q \cdot v^{diesel} \tag{1}$$

$$\text{s.t.} \quad \text{Original constraints}$$

$$totalGHG \le \varepsilon \cdot t \tag{2}$$

$$\text{Piecewise linear approximation constraints}$$

There are two types of nonlinear terms in nonconvex multiobjective MINLP: the fractional term in the objective function and separable concave functions to evaluate the equipment capital costs. Despite solvable with the ε-constraint method, it could still be computationally demanding for general purpose solvers. To enhance the computation efficiency, we further apply a tailored global optimization algorithm (Gong and You, 2014a) and relax (P1) to a mixed-integer linear problem (P2).This algorithm integrates two algorithms: parametric algorithm based on Newton's method and the branch-and-refine algorithm based on successive piecewise linear approximations to ensure the relaxed formulation achieves enough approximation accuracy. The pseudo-code of this method is shown in Figure 3.

Global Optimization Algorithm

Set $Q = 0$, $Iter^{out} = 1$
While $obj \ge TOL^{out}$
  Set $LB = 0$, $UB = +\infty$, $Iter^{in} = 1$, $G = +\infty$, build (P2) with two insertion points
  While $G \ge TOL^{in}$
    Solve (P2) and obtain optimal results (x^*, obj^*)
    Evaluate the original objective function with x^*, and obtain obj°
    Rebuild (P2) by adding x^* as a new partition point
    Set $LB = obj^*$,UB = min[UB, obj°],$G = 1\text{-}LB/UB$, $Iter^{in} = Iter^{in} + 1$
  end while
  Update $Q = totalcost^*/v^{diesel*}$, $Iter^{out} = Iter^{out} + 1$
end while
Return Q

Figure 3. Pseudo-code of the global optimization algorithm.

4. Results and discussion

4.1. Optimal environmental performance of producing bioproducts

If the bioproduct manufacturing section is devoted to hydrogen production, the lowest unit GHG emissions are 4.28 kg CO_2-eq/kg H_2. In contrast, producing hydrogen by steam reforming of methane results in 11.59 kg CO_2-eq/kg H_2, which is 2.7 times that of algal hydrogen. If we fix PG as the only bioproduct, the minimum unit GHG emissions of the proposed superstructure and three other methods are shown in Table 1. We note that environmental impact of the PG production in the superstructure achieves a 51.5% GHG emissions reduction compared with that of the petroleum-based PG. Regarding

GE, we obtain unit GHG emissions of 2.37 kg CO_2-eq/kg GE. In terms of PHB production, the optimal unit GHG emissions are 4.10 kg CO_2-eq/kg PHB, which is sustainably competitive compared with fossil-based plastic products. Overall, bioproducts in the proposed superstructure proves to be environmentally sustainable, especially compared to fossil-based chemical products. The excellent performance is primarily due to the biogas for electricity generation. The allocation of surplus electricity leads to a significant reduction in GHG emissions. Furthermore, the allocation method also averages the environmental benefit of the entire process and reduces the unit environmental impact of each product.

Table 1. Life cycle CO_2 equivalent emissions of the PG production.

PG production method	Unit GHG emissions (kg CO2-eq/kg PG)
Petroleum-based	3.75
ADM®	3.24
Zemea®	2.18
Algal glycerol-based	1.82

4.2. Optimal biodiesel production

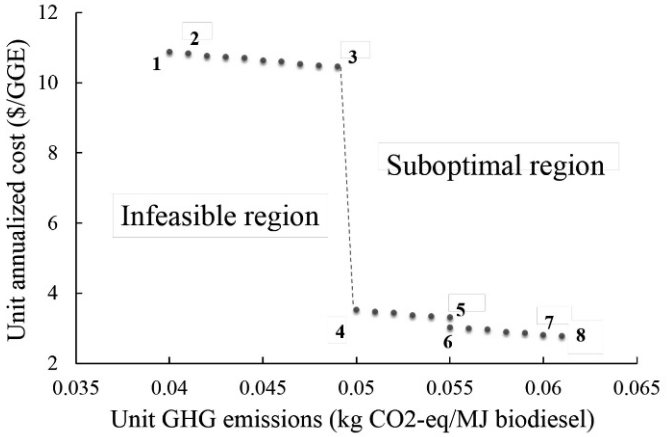

Figure 4. Pareto-optimal curve associated with the unit annualized cost and unit GHG emissions.

As shown in Figure 4, we obtain a Pareto-optimal profile if we optimize the bi-criteria problem with the global optimization strategy and the ε-constraint method. Overall, the curve demonstrates trade-offs between the two competing objective functions: that is, the minimum unit annualized cost decreases when the corresponding minimum unit GHG emissions increase. With no technology selected in the cell disruption and hydrogen production sections, the process selected by point 1 employs pressure filtration in the harvesting section, hexane as the lipid extractant, direct combustion for biogas utilization, enzyme-catalyzed transesterification for biofuel production, and GE synthesis for bioproduct manufacturing. The minimum unit GHG emissions are 0.04 kg CO_2-eq/MJ biodiesel, and the minimum unit cost corresponds to $10.89/GGE. In contrast, the optimal process selected by points 4 to 5 favours supercritical carbon dioxide in the lipid extraction section. Eventually, the optimal process selected by point 8 achieves a unit cost of $2.79/GGE and unit GHG emissions of 0.06 kg CO_2-eq/MJ biodiesel by using centrifugation and heterogeneously catalyzed transesterification. Overall, this result has a 74% decrease in unit cost with a 34% increase in unit GHG emissions, indicating that large economic savings can be achieved.

5. Conclusion

We proposed by far the most comprehensive superstructure for the production of biodiesel and four types of bioproducts from microalgae. Based on the superstructure, we conducted a cradle-to-gate LCA and incorporated it into a bi-criteria MINLP model to simultaneously optimize the environmental and economic performance following a life cycle optimization framework. Manufacturing bioproducts resulted in reduction of unit life cycle GHG emissions by 5% to 63%, compared with the petrochemical counterparts. The co-production of value-added bioproducts reduced the biodiesel production cost to \$2.79/GGE with centrifugation, supercritical CO_2 extraction, direct combustion, heterogeneously catalyzed transesterification, and GE synthesis.

References

D. J. Garcia and F. You, 2015, Multiobjective optimization of product and process networks: General modeling framework, efficient global optimization algorithm, and case studies on bioconversion, AIChE Journal, 61, 2, 530-554.

B. H. Gebreslassie, M. Slivinsky, B. L. Wang and F. Q. You, 2013a, Life cycle optimization for sustainable design and operations of hydrocarbon biorefinery via fast pyrolysis, hydrotreating and hydrocracking, Computers & Chemical Engineering, 50, 71-91.

B. H. Gebreslassie, R. Waymire and F. You, 2013b, Sustainable design and synthesis of algae-based biorefinery for simultaneous hydrocarbon biofuel production and carbon sequestration, AIChE Journal, 59, 5, 1599-1621.

J. Gong and F. Q. You, 2014a, Global Optimization for Sustainable Design and Synthesis of Algae Processing Network for CO2 Mitigation and Biofuel Production Using Life Cycle Optimization, AIChE Journal, 60, 9, 3195-3210.

J. Gong and F. Q. You, 2014b, Optimal Design and Synthesis of Algal Biorefinery Processes for Biological Carbon Sequestration and Utilization with Zero Direct Greenhouse Gas Emissions: MINLP Model and Global Optimization Algorithm, Industrial & Engineering Chemistry Research, 53, 4, 1563-1579.

C. G. Gutierrez-Arriaga, M. Serna-Gonzalez, J. M. Ponce-Ortega and M. M. El-Halwagi, 2014, Sustainable Integration of Algal Biodiesel Production with Steam Electric Power Plants for Greenhouse Gas Mitigation, Acs Sustainable Chemistry & Engineering, 2, 6, 1388-1403.

B. G. Hermann, K. Blok and M. K. Patel, 2007, Producing bio-based bulk chemicals using industrial biotechnology saves energy and combats climate change, Environmental Science & Technology, 41, 22, 7915-7921.

B. S. Institution, 2006, ISO 14040:2006 Environmental Management–Life Cycle Assessment–Principles and Framework. London.

M. Pagliaro, R. Ciriminna, H. Kimura, M. Rossi and C. Della Pina, 2007, From glycerol to value-added products, Angewandte Chemie-International Edition, 46, 24, 4434-4440.

M. Rizwan, J. H. Lee and R. Gani, 2013, Optimal processing pathway for the production of biodiesel from microalgal biomass: A superstructure based approach, Computers & Chemical Engineering, 58, 305-314.

C. Silva, E. Soliman, G. Cameron, L. A. Fabiano, W. D. Seider, E. H. Dunlop and A. K. Coaldrake, 2014, Commercial-Scale Biodiesel Production from Algae, Industrial & Engineering Chemistry Research, 53, 13, 5311-5324.

B. Wang, B. H. Gebreslassie and F. Q. You, 2013, Sustainable design and synthesis of hydrocarbon biorefinery via gasification pathway: Integrated life cycle assessment and technoeconomic analysis with multiobjective superstructure optimization, Computers & Chemical Engineering, 52, 55-76.

F. Q. You and B. Wang, 2011, Life Cycle Optimization of Biomass-to-Liquid Supply Chains with Distributed-Centralized Processing Networks, Industrial & Engineering Chemistry Research, 50, 17, 10102-10127.

Krist V. Gernaey, Jakob K. Huusom and Rafiqul Gani (Eds.), 12th International Symposium on Process Systems Engineering and 25th European Symposium on Computer Aided Process Engineering.
31 May – 4 June 2015, Copenhagen, Denmark

The Effect of Charge Composition on the Optimal Operational Parameters of a Batch Extractive Distillation Process

Laszlo Hegely, Peter Lang*

Budapest University of Technology and Economics, Muegyetem rkp 3-9., H-1111 Budapest, Hungary

Abstract

The recovery of methanol by batch extractive distillation using water as entrainer from an azeotropic waste solvent mixture (acetone(A)-methanol(B)-THF(C)-water(D)-toluene(E)) is optimised by a genetic algorithm (GA) coupled with a professional flowsheet simulator performing the dynamic simulation. Optimization variables are the reflux ratios of the different operation steps, the location, the flow rate and duration of entrainer (water) feeding. The objective function to be maximized is the profit. The effect of changing the charge concentration of methanol and the two main organic impurities (THF and toluene) on the profit and optimal values of the operational variables was studied.

Keywords: batch distillation, extractive distillation, entrainer, optimization, genetic algorithm.

1. Introduction

For the separation of azeotropic mixtures a special (e.g. extractive) distillation method must be applied. In batch extractive distillation (BED, Yatim et al, 1993), an entrainer is fed continuously into the column, changing the relative volatilities favourably. BED is usually applied to extract pollutants of moderate concentration from the main component to be recovered. In this case the main component is extracted from beside the pollutants of low concentration forming minimum azeotropes with it. These pollutants can be removed in fore-cuts, and by using BED, it is possible to reduce the loss of the main component with the fore-cuts. However, the high amount of entrainer fed renders the separation of the main component from it more difficult.

Hegely et al. (2013) studied the recovery of methanol (in purity of 99.5 mass %) from a waste solvent mixture containing THF(C) and toluene (E) as main pollutants. The recovery of methanol (B) is disturbed by the azeotropes B–C (30 % B, 59.5 °C) and B–E (71.5 % B, 63.6 °C). The influence of water (D) as a potential entrainer on the relative volatilities was investigated. We stated that by BED using water as entrainer C and E can be removed in the fore-cuts more efficiently (with lower B loss) than by BD. The laboratory and industrial-size experiments gave also much higher recovery for the BED than for the BD. Hegely and Lang (2014) performed the optimization of both the BD and BED processes by a genetic algorithm (GA). The highest profit was reached by the optimized BED process.

The aim of this paper is to study the effect of changing the concentration of methanol (B) and the two main organic pollutants (C and E) on the profit and on the optimal

values of the operational variables of the BED. Optimization variables are reflux ratios of all operation steps, and the parameters of water feeding (feed plate, flow rate, duration). The optimization was performed by a genetic algorithm with ChemCAD performing the dynamic simulation. The objective function to be maximized is the profit.

2. The separation process

The charge (25 m^3, 22,675 kg.) contains 0.07 mass % A (acetone), 37.14 % B, 4.89 % C, 56.34 % D and 1.56 % E. The boiling points of the components and azeotropes, with the azeotropic compositions were given by Hegely and Lang (2014).
The BED separation of one batch has the following separation steps (Hegely et al., 2013):

- Step 0: heating-up of the column under R=∞. This step can be divided into two parts:
  a: heating-up of the charge without water feeding.
  b: heating-up with water feeding which decreases $x_{D,B}$ and increases $x_{D,C}$. The step is ended when the change in these concentrations becomes slow.
- Step 1: 1st fore-cut containing a high amount of C and E besides B. It is incinerated.
- Step 2: 2nd fore-cut, which contains more B and less pollutant than the first fore-cut. The 2nd fore-cut is recycled to the next batch in order to decrease the loss of B.
- Step 3: Main-cut (production of B in high purity).
- Step 4: After-cut (aqueous B). The aim is to remove B from the still residue, so that the residue can be sent to biological purification. It is recycled to the next batch.

Water feeding can be stopped at the end of Step 0b or it can be still continued in Steps 1 and 2, as well. In the latter case, the loss of B in the fore-cuts can be further reduced, but B must be recovered from a more dilute mixture B-D and the amount of the fore-cuts can also increase raising the cost of incineration and energy.

The column has 25 theoretical plates (excluding the condenser and reboiler). The top pressure of the column is atmospheric, the pressure drop: 0.25 bar. The hold-up of the condenser: 0.45 m^3, that of the column: 0.05 m^3/plate. The duration of Step 0a was 160 min, after which water feeding (of 15 °C) was started. Step 0b was 200 min long. The termination criteria for Steps 1 and 2 are optimization variables (Cr_1 and Cr_2), while the criterion for Step 4 is based on industrial experiences:

- Step 1: $x_{D,C}<Cr_1$ (mass fraction of C in the distillate)
- Step 2: $x_{D,C}<Cr_2$
- Step 3: $x_{MC,A}<99.52$ mass%
- Step 4: $x_{SR,B}<0.25$ mass% (mass fraction of B in the still residue)

The optimization was performed for 4 different charge compositions, which were chosen based on a list of compositions reported by the plant. As the variation of the A content was slight and without significant effect, it was considered to be constant. Charge 1 has the highest B and the highest organic impurity contents. The further charges were the obtained from Charge 1 by reducing the B (to 27.43%, Charge 2) or the C (to 3.27%, Charge 3) content to minimal reported value, or by reducing the E content to the average reported value (0.84%, Charge 4). This decrease of the charge concentration of the organic components was compensated by increasing that of water.

3. Optimisation method

The objective function (OF) to be maximized is the profit of the processing of one batch. It is defined as:

$$OF = p_B m_{MC} - c_{inc} m_{FC1} - c_{st} \frac{\dot{Q}_{st}}{r_{st}} t - c_{cw} \frac{Q_{cond}}{cp_{cw} \Delta T_{cw}} - c_{bio} m_{SR} \quad (1)$$

where m_{MC} is the mass of the main-cut, m_{FC1} is that of the first-fore-cut, m_{SR} is that of the still residue. p_B is the price of methanol (0.46 \$/kg), c_{inc} is the cost of incineration (0.21 \$/kg), c_{st} is cost of heating steam of 3 bar (57.6 \$/t), r_{st} is its heat of condensation (2263.5 MJ/t), $\dot{Q}_{st}$ is the heat duty (1800 MJ/h) and t is the duration of the whole process. Q_{cond} is total heat withdrawn by the cooling water, cp_{cw} is the specific heat of the cooling water and ΔT_{cw} is the increase in its temperature. c_{cw} is the cost of cooling water and c_{bio} is the cost of biological purification, which are neglected. (These are not debited to the solvent recovery plant). Therefore, operation cost is the term related to the heating steam.

The nine optimization variables were the reflux ratios of the steps: R_1 (1st fore-cut), R_2 (2nd fore-cut), R_3 (main-cut), R_4 (after-cut), the termination criteria of Steps 1 and 2 (Cr_1 and Cr_2) and the variables connected to water feeding: feed plate (f, integer variable, counted from the top of the column with plate 1 being the condenser), flow rate (F_{water}) and duration (t_F, even integer). The lower and upper bounds for all reflux ratios were 0.6 and 15. The lower bound of both termination criteria was 0.05 mass%, the upper bounds were 40 % (Step 1) and 10 % (Step 2), respectively. However, the value of Cr_1 also acted as an upper bound for Cr_2. The ranges of the variables connected to water feeding were: $1 \leq f \leq 13$; flow rate: $0 \leq F_{water} \leq 3000$ kg/h; duration: $0 \leq t_F \leq 1000$ min. (Water feeding was always stopped at the end of Step 2, even if t_F had been longer.) Another constraint is added in order to ensure the recyclability of the second fore-cut to the next batch: the B/C and B/E ratios in the second fore-cut cannot exceed those of the traditional batch distillation process applied in the plant (9.36 and 8.31, respectively).

The optimization is performed by a real-coded elitist GA written in VBA under Excel. GA was chosen as OF can only be evaluated by simulation, that is, with a black box approach. The parameters of the GA: mutation probability: 5 %, population size: 30, crossover probability: 70 %. The number of generations was 100 in all cases. OF is evaluated by dynamic simulation using different modules of the flowsheet simulator ChemCAD. The failure to reach the specified purity of B (99.5 mass%), is penalized by changing the value of OF to -10,000 \$.

4. Optimization results

The optimal value of the parameters, different costs and profits calculated for the different charges are shown in Table 1. The detailed data of the cuts are given in Tables 2-5. The optimal operational policies (water flow rate and reflux ratio as a function of time) are shown in Figure 1.

Some results were common for all charges: optimal location of entrainer feeding was always the top tray, and water feeding was stopped during Step 1.

In the basic case, the first fore-cut was taken by high reflux ratio, while the reflux ratio of Steps 2 and 3 were moderate and almost identical. The water flow rate was low, but the water feeding was continued for a long time. The recovery of B was 77.1%.

Table 1. Optimization results for the different charge compositions.

	R_1	R_2	R_3	R_4	Cr_1 %	Cr_2 %	f	F_{water} kg/h	t_F min	Income $	Incin. cost	Oper. cost	Profit
Charge 1	7.74	3.41	3.48	4.72	18.7	3.83	2	283	574	3003	390	1820	793
Charge 2	5.22	4.47	5.07	9.45	19.5	2.80	2	773	444	2054	348	1776	-70
Charge 3	7.56	3.20	3.16	7.56	19.9	3.16	2	433	408	2946	266	1718	962
Charge 4	7.59	3.97	3.49	7.70	19.1	3.79	2	424	384	3001	361	1803	837

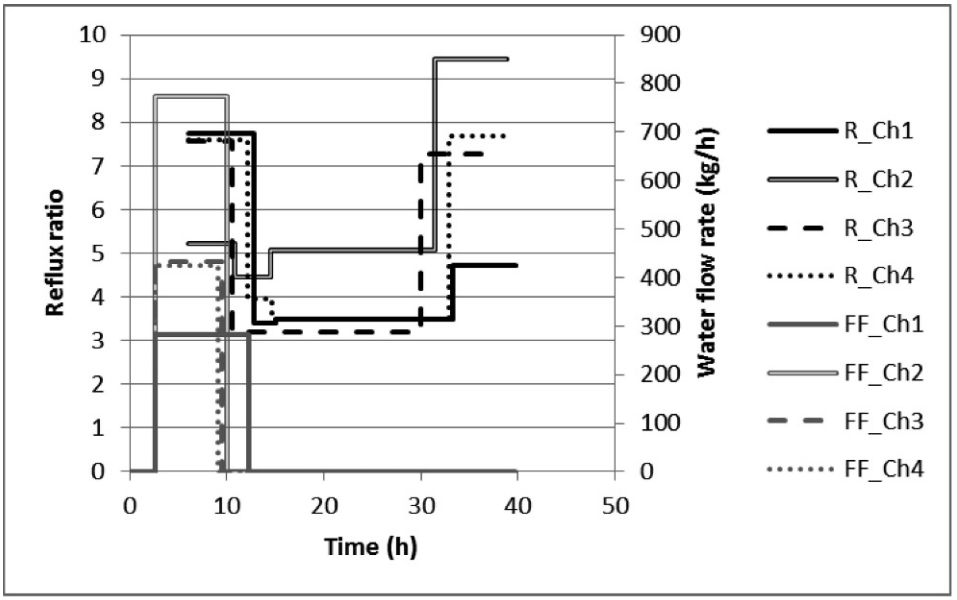

Figure 1. The optimal parameters for the different charge compositions.

The strong decrease of B content (Charge 2) resulted in an uneconomical operation, as the income dropped considerably. The decrease of income was not proportional to that of the B content, as the recovery was also lower (71.4%). The lower B concentration required higher reflux ratio in both Steps 2 and 3. The increase in R_3 was especially sharp. At the same time, the water flow rate was also considerably higher. Step 3 started later, as well. On the other hand, R_1 decreased, and Cr_1 increased, resulting in a shorter Step 1 with lower amount of first fore-cut. Nevertheless, the decrease of incineration cost could not compensate that of the income.

If the C content was reduced (Charge 3), the profit increased considerably. The reason of this was not an increased recovery of B (75.6%), but rather the significantly decreased incineration cost, which was the consequence of higher Cr_1 and lower R_1. All reflux ratios (except R_4) were lower, which resulted in faster operation and contributed to the increased profit. The flow rate of the water was higher, but the feeding duration was lower. The lower R_3 was balanced by lower Cr_2, that is, a later start of Step 3.
In the case of lower E content (Charge 4), the parameters changed less in comparison with those of Charge 1, than for Charge 3, which is explained by the fact that the change of charge composition is also smaller. The profit increased slightly, once again due to

the reduced incineration cost, achieved by a slight increase in Cr_1. R_1 was lower, R_2 was higher, while R_3 was the same as for Charge 1. The parameters of water feeding were similar to those for Charge 3. The recovery of B was the same as for Charge 1.

Table 2. Optimization results for Charge 1 (basic case).

	Fore-cut1	Fore-cut2	Main-cut	After-cut
Duration, min	408	136	1092	388
Mass, kg	1855	896	6529	1157
A, mass%	0.7	0.2	0.0	0.0
B	22.9	85.2	99.5	52.3
C	54.1	9.1	0.4	0.0
D	6.0	0.5	0.0	47.7
E	16.3	5.1	0.1	0.0

Table 3. Optimization results for Charge 2 (lower methanol content).

	Fore-cut1	Fore-cut2	Main-cut	After-cut
Duration, min	292	222	1014	438
Mass, kg	1656	1181	4465	782
A, mass%	0.8	0.2	0.0	0.0
B	14.4	83.9	99.5	62.9
C	61.3	8.8	0.3	0.0
D	6.8	0.3	0.1	37.1
E	16.7	6.9	0.3	0.0

Table 4. Optimization results for Charge 3 (lower C content).

	Fore-cut1	Fore-cut2	Main-cut	After-cut
Duration, min	276	162	1004	448
Mass, kg	1276	1142	6404	1013
A, mass%	1.0	0.2	0.0	0.0
B	24.0	82.9	99.5	63.6
C	48.9	8.8	0.3	0.0
D	5.7	0.2	0.1	36.4
E	20.4	7.9	0.1	0.0

Table 5. Optimization results for Charge 4 (lower E content).

	Fore-cut1	Fore-cut2	Main-cut	After-cut
Duration, min	364	154	1096	388
Mass, kg	1721	896	6523	821
A, mass%	0.79	0.2	0.0	0.0
B	27.3	87.9	99.5	61.5
C	58.2	9.3	0.3	0.0
D	4.2	0.0	0.1	38.5
E	9.5	2.6	0.0	0.0

5. Conclusions

The recovery of methanol from a multicomponent azeotropic waste solvent mixture was studied by dynamic simulation and optimization. The components (acetone-methanol-THF-water-toluene) form several minimum azeotropes limiting the recovery of methanol by traditional batch distillation. By batch extractive distillation (BED) using water as entrainer the process can be made more profitable. The optimization of the BED process was performed by a genetic algorithm coupled with the ChemCAD flow-sheet simulator performing the dynamic simulation. The objective was to maximize the profit for one batch. The optimization variables were the reflux ratios of all operation steps, termination criteria of the two fore-cuts, location, flow rate and duration of water feeding. The effects of changing the feed concentration of methanol and of the two main organic pollutants (THF and toluene) on the optimal values of the variables and on the profit of the process were determined. The decrease of organic pollutant content increased the profit, mainly because the incineration cost was lower due to the lower reflux ratio and duration of first fore-cut. The reflux ratios of the second fore-cut and the main-cut, and the water feeding duration decreased; the flow rate of water increased. If the methanol content of the charge was lower, the reflux ratios of the second fore-cut and the main-cut increased, as well as the flow rate of water. However, the operation was uneconomical. The optimal feeding location was the top tray in every case.

References

L. Hegely, P. Lang, G. Kovacs, 2013, A New Batch Extractive Distillation Operational Policy for Methanol Recovery, Chemical Engineering Transactions, 35, 949-954

L. Hegely, P. Lang, 2014, Optimization of Entrainer Feeding in Batch Extractive Distillation, Computer Aided Chemical Engineering, 33, 1172-1182.

H. Yatim, P. Moszkowicz, M. Otterbein, P. Lang, 1993, Dynamic Simulation of a Batch Extractive Distillation Process, Comput. Chem. Eng., 17, S57-62.

Krist V. Gernaey, Jakob K. Huusom and Rafiqul Gani (Eds.), 12th International Symposium on Process Systems Engineering and 25th European Symposium on Computer Aided Process Engineering.
31 May – 4 June 2015, Copenhagen, Denmark

VPPD Lab -The Chemical Product Simulator

Sawitree Kalakul[a], Rehan Hussain[b], Nimir Elbashir[b] and Rafiqul Gani[a]

[a]*Department of Chemical and Biochemical Engineering, Søltofts Plads, Building 229, Technical University of Denmark, DK-2800 Lyngby, Denmark*
[b]*Department of chemical Engineering, 162 Texas A&M Engineering building, Texas A&M University at Qatar, 23874 Doha, Qatar*

Abstract

In this paper, the development of a systematic model-based framework for product design, implemented in the new product design software called VPPD-Lab is presented. This framework employs its in-house knowledge-based system to design and evaluate chemical products. The built-in libraries of product performance models and product-chemical property models are used to evaluate different classes of product. The product classes are single molecular structure chemicals (lipids, solvents, aroma, etc.), blended products (gasoline, jet-fuels, lubricants, etc.), and emulsified product (hand wash, detergent, etc.). It has interface to identify workflow/data-flow for the inter-related activities between knowledge-based system and model-based calculation procedures to systematically, efficiently and robustly solve various types of product design-analysis problems. The application of the software is highlighted for the case study of tailor made design of jet-fuels. VPPD-Lab works in the same way as a typical process simulator. It enhances the future development of chemical product design.

Keywords: Chemical product design, Blended product, Jet-fuels.

1. Introduction

In chemical product design, it is not only important to find the chemical product that exhibits certain desirable properties but improving the product performance and making products more versatile have become growing concerns in recent times. Chemical products can be classified in terms of molecule and mixtures. Several frameworks have been developed to design basic chemical/functional chemical products (Smith et al., 2009, and Hill, 2004). However, for more complex chemical products such as cosmetic creams, films, and detergents, no generic methodologies exist. While product design is still based on trial and error experimental approaches, it is now generally accepted that application of model-based methodologies can help to design/improve products so as to reach the market faster by reducing costly and time-consuming experiments (Gani, 2004). That is, experiments are only performed during the last stage as a verification tool. Since thousands of products involving mixtures/blends of chemicals need to be designed and/or evaluated, a huge amount of data on physico-chemical properties of chemicals and their mixtures and/or models that can reliably predict them are needed so that model-data based methods for tailor-made design of products can be developed and routinely applied. This is a challenging task requiring data acquisition, data testing, model development and model-based design method development, etc., that needs to be integrated in a computer-aided framework so that chemicals based products can be designed, analyzed and verified in a fast, efficient and systematic manner (Conte et al., 2012, Mattei et al., 2014). These motivate the development of a systematic framework for product design and evaluation.

In this study, the systematic framework employs its in-house knowledge-based system to (1) identify target properties of a desired product; (2) provide suitable property models to calculate the necessary properties classified as primary, secondary, functional, and mixture properties; (3) formulate and solve the design-analysis problems in a fast, robust and systematic manner; and (4) guide the user to the final experimental verification tasks. The framework has built-in libraries of product performance models and product-chemical property models. The built-in knowledge base has a suit of databases containing properties of different classes of chemicals (lipids, solvents, aroma, etc.) and design templates for molecular (solvents, refrigerant, etc) and blended products (gasoline, jet-fuels, lubricants, hair spray, etc.). The property models and the database together provide a very wide range of application for the various chemicals-based products. The large amount of data, models and calculation-algorithms are managed through specially developed ontology, which is implemented as the framework within VPPD-Lab. It has interface to identify workflow/data-flow for the inter-related activities between knowledge-based system and model-based calculation procedures to systematically, efficiently and robustly solve various types of product design-analysis problems. Furthermore, the flexibility of its architecture allows it to be integrated with toolboxes from ICAS (Integrated Computer Aided System) (ICAS Documentation, 2003) such as ProPred (property prediction tool), ModDev and MOT (modeling tools), ProCAMD (hybrid methodology for computer aided molecular design), and process design tools (Kalakul et al, 2014). VPPD-Lab uses template approach for specific type of chemicals-based products. The current version has design templates for microcapsule, active ingredients uptake in plant, homogeneous formulated products, emulsified products, blended products, single chemical-based products (solvents, refrigerants, polymers), and, an option to create templates for new products. The developed computer aided framework is generic and applicable to a wide range of problems. The VPPD-Lab works in the same way as a typical process simulator.

2. Framework

The framework is divided into 2 problems (as shown in Fig. 1); (1) product design, and (2) product evaluation. Each problem follows instruction steps which is integrated with VPPD-Lab knowledge base containing the links for the tools (as shown in Fig. 2).

2.1. Product design

Step A1: Define problem

Tool 1 starts with selection of sub problem (molecular or mixture design), number and type of phases, and available template/ new template corresponding to the user's product design problem. Templates are stored in VPPD-Lab KB. Each template guides the user to identify product needs and translate needs to target properties and property values using Tool 1 Problem definition

Step A2: Go to template

Tool 2: Template guides the user to follow the work-flow for the product design problem such as solvent design, blend design, and emulsion design. Each task in the work-flow is connected with the necessary toolboxes (Figure 2). Tool 3: Chemical database store the experimental property values and needed property values calculated using Property model library. Therefore, it can calculate 55 pure component properties and 10 functional properties for a very wide range of organic chemicals. In addition, it

has data for more than 24,000 compounds and contain more than 50,000 entries of various types of mixture data and several thermodynamic models to calculate mixture properties. Tool 4: Routine/Algorithm contains mixture calculation models (linear and non- linear mixing models), thermodynamic models (UNIFAC, NRTL, UNIQUAC, and PC-SAFT).

Step A3: Go to product evaluation

See 2.2. Product evaluation

Step A4: Further develop selected product-process

After evaluation of the performances of product in step A3, the performances of the process need to be evaluated. The framework has options to link with the process synthesis and evaluation tools such as PROCAFD (computer aided flowsheet design), SustainPro (process sustainability analysis tool), ECON (economic analysis tool), and LCSoft (Life cycle assessment tool).

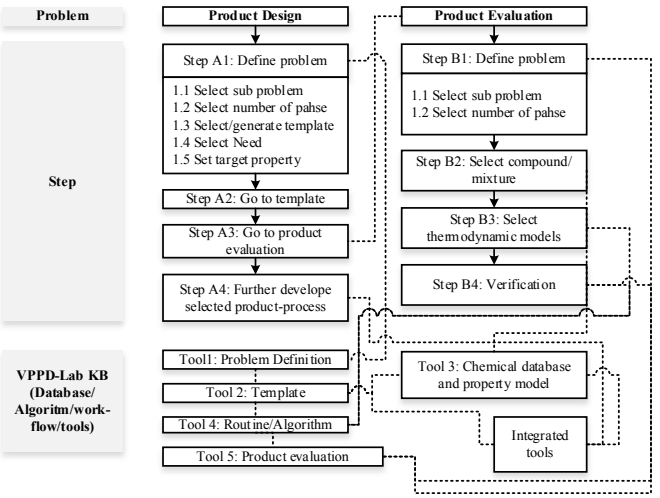

Figure 1.VPPD-Lab Framework

2.2. Product evaluation

Step B1: Problem definition

The selected product's performances need to be evaluated. Experimental verification toolbox helps user to design the experimental tests that may be needed in addition to the molecular and blended products. Product evaluation model toolbox contains product specific performance models (uptake of active ingredient for pesticide, and active ingredient delivery on surface) to evaluate their performances. Depending on the type of the product, these can be model-based, experimental based or a combination of both.

Step B2: Select compound/mixture

This step connects with the chemical database. The user selects the product that can be a single compound or mixture.

Step B3: Select thermodynamic model

This step the thermodynamic model that suitable for the product is selected. Note that, the primary, secondary, and functional properties needed for product performance

calculations are retrieved from chemical database using the suggested property models by VPPD-KB.

Step B4: Verification

This step calculates product performances or behaviors of the product.

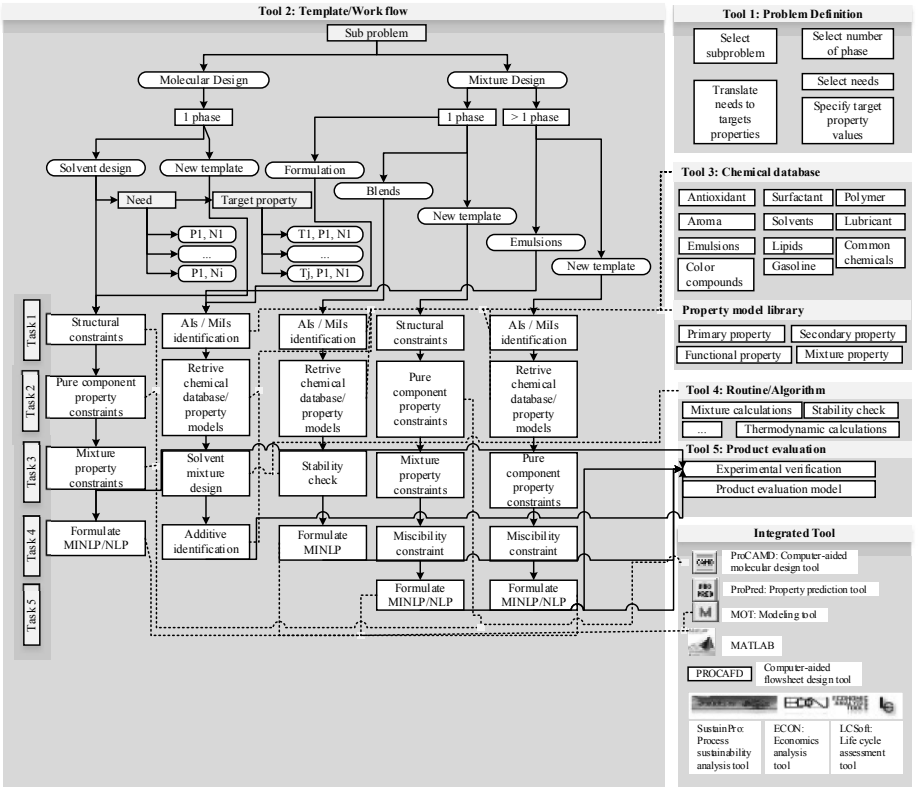

Figure 2.The structure of VPPD-Lab knowledge base (VPPD-Lab KB)

3. Case study

The application of the software is highlighted through the tailor-made fuel blends of jet-fuels.

3.1. Step A1: Define problem

The problem is product design, the sub-problem is blends. The user needs for jet-fuels in terms of target properties, and target property values are identified as shown in Table 1.

3.2. Step A2: Go to template

VPPD-Lab KB guides the user to follow the work-flow of blend design template starting from Task 1 to Task 5.

Table 1.Product needs and translated target properties

Need	**Target Property**	**Target Value**
Ability to be burned	Reid vapor pressure (RVP)	RVP > 1 kPa at 310.95 K
Engine efficiency	Higher heating value (HHV)	HHV > 6125 kJ/mol
Consistency of fuel flow	Dynamic visocosity (η) Melting point (T_m)	η< 6.8 cP at 253.15 K 775 <ρ< 840 kg/m3 at 288.15
Flammability	Flash point (T_f)	T_f>310.95 K
Stability	Gibbs energy of mixing (ΔG^{mix})	ΔG^{mix}< 0
Enviromental impacts	Toxicity (LC_{50}) Carbon footprint (CF)	$-logLC_{50}(mol/L) < 3.6$ CF < 1.8 CO_2 eq.

Task 1: AIs/MiIs identification

The case study of binary mixtures is highlighted where active ingredient (AIs) is the mixture of conventional jetA-1 which is considered as 1 component and The Additives (Minor ingredient or MiIs) are selected from 221 chemicals from different molecular types such as alkanes, cycloalkanes, aromatics, olefins, alcohols with low carbon numbers, ethers, ketones, acid and furan derivatives.

Task 2: Retrieve chemical databases/property models

Primary properties related to target property calculations; molecular weight (Mw), critical temperature (Tc), critical pressure (Pc) ,acentric factor (ω),constant of the Modified Rackett equation (Z_{RA}),LC_{50}, heat of combustion (ΔH_c), RON, and $Wt_{O2}$are retrieved from the chemical databases. The functional properties of pure chemicals; ρ, Dynamic viscosity (μ), and vapor pressure (P_{vap}) are calculated.

Task 3: Stability check

The UNIFAC-LLE group representations of MIs and MiIs are retrieved to calculate the liquid miscibility at 298.15 K (ambient temperature). The stability test is performed using the STABILITY tool (Conte et al., 2011) to check the miscibility of the blends. The blends that are totally immiscible are rejected.50 binary mixtures were found to be partially miscible with jet-fuels.

Task 4: formulate MINLP

The tailor-made blend design problems of jet fuels are formulated as MINLP problem. The objective is to minimize fuel consumption subject to product stability and target properties. The results are the formulation of blended jet-fuels and calculated target properties as shown in Figure 3.

3.3. Step A3: Go to product evaluation

The blended jet-fuels from Task 4 need to satisfy the desired target properties and aviation standards. Experimental verification toolbox in Tool 5: Product evaluation suggests to perform experimental tests to verify η, Tm, Tf, ρ, LHV, RVP. Furthermore, distillation profiles and JFTOT ΔP at 260 ∘C will be tested in order to ensure that the final blends meet the aviation fuel standards based on these properties.

3.4. Step A4: Further develop selected product-process

The process to produce the jet-fuel does not consider in this work since mixing of chemicals in order to obtain blends is a routine mixing operation.

Chemicals	Composition, vol (%)
n-dodecane	20.4
n-tetradecane	13.6
isooctane	6.8
Methylcyclohexane	13.6
tetralin	3.4
p-Xylene	10.2
Decane	0.32

Properties							
HHV	Tm	ρ	η	log(LC50	RVP	Tf	CF
6395.4	210.7	0.775	2.0	2.9	1.87	325.5	1.49
6128.2	224.5	0.802	2.1	4.0	1.48	326.8	1.57
6127.7	224.1	0.801	2.1	4.0	1.44	347.1	1.66

Figure 3.Results for jet-fuels blend problem from VPPD Lab

4. Conclusion

A computer-aided framework for design of chemical products has been developed and implemented into VPPD-Lab. Knowledge base system has been employed to manage data-flow, making it more flexible and capable of solving a wide range of product design problems. The use of the framework has been highlighted through the case study involving a tailor-made design of jet-fuels blend. The results show that adding additive improves jet-fuel properties and reduce the consumption of conventional gasoline. VPPD Lab as the new product simulator that works in the same way as a typical process simulator, it can guide a user to design product, study product behaviors, systematically formulate and robustly solve various type product design problems. Future work is to integrate the software with the process design software in order to systematically solve product-process design problems.

References

B. Smith, M.G. Ierapepritou, 2009, Framework for consumer-integrated optimal product design planning, Expert System with Applications, 35, 1-2, 338-349.
M. Hill, 2004, Product and process design for structrued products, AICHE Journal, 50, 8, 1656-1661.
R. Gani, 2004, Chemical product design: challenges and opportunities, Computers and Chemical Engineering, 28, 2441-2457.
M. Mattei, N. A. Yunus, S. Kalakul, G. M. Kontogeorgis, J. M. Woodley, K. V. Gernaey, and R. Gani, 2014, The Virtual Product-Process Design Laboratory for Structured Chemical Product Design and Analysis, Computer Aided Chemical Engineering, 33, 61-66.
ICAS Documentation, Internal report, 2003, CAPEC, KT-DTU, Lyngby, Denmark.
S. Kalakul, P. Malakul, K. Siemanond, R. Gani, 2014, Integration of life cycle assessment software with tools for economic and sustainablity analyses and process simulation for sustainable process design, Journal of Cleaner Production, 71, 98-109.
E. Conte, and R. Gani, 2011, Chemical-Based Formulation Design: Virtual Experimentations, Computer Aided Chemical Engineering, 29, 1588-1592.
E. Conte, R. Gani, Y. S. Cheng, and K. M. Ng, 2012, Design of Formulated Products:Experimental Component. AIChE Journal, 58, 173-189.

Krist V. Gernaey, Jakob K. Huusom and Rafiqul Gani (Eds.), 12th International Symposium on Process Systems Engineering and 25th European Symposium on Computer Aided Process Engineering.
31 May - 4 June 2015, Copenhagen, Denmark.

Synthesis of Flexible Heat Exchanger Networks Integrated with Reconfigurable Control Design

Lautaro Braccia[a], Patricio Luppi[b], Maximiliano García[b] and Marta S. Basualdo[a,b]

[a]*Computer Aided Process Engineering Group (CAPEG) Technological National University; Faculty of Rosario (UTN-FRRo); Zeballos 1341, S2000BQA, Rosario, Argentina ;*
[b]*French Argentine International Center for Information and Systems Sciences (CIFASIS - CONICET - UNR - AMU); 27 de Febrero 210 bis, S2000EZP, Rosario, Argentina*
basualdo@cifasis-conicet.gov.ar

Abstract

In this work, a new systematic methodology, which extends the synthesis of a flexible heat exchanger network (HEN),proposed by Braccia et al. (2013), with a designing technique of a fully-decentralized reconfigurable control structure(CS) given by Luppi et al. (2014), is presented. The strategy to design the HEN allows the optimal flexible operation inside an expected range of the plant conditions. The CS is done in the context of reconfigurable control structure which are characterized by: (i) the integration of the variables selection task (CVs and MVs) with the corresponding pairings definition (CVs-MVs), (iii) the consideration of scalar indexes to set a rank of the potential solutions. The advantage of the method is that provides alternative control structures able to act at different operating points. In addition, it only utilizes steady-state process information. One example is given in this work to illustrate the potentiality of the proposed methodology and to support the final conclusions.

Keywords: Flexible Heat Exchanger Network Synthesis, Reconfigurable controller design, Systematic methodology;

1. Introduction

The aim of the HEN synthesis consists of finding a network that minimizes the total annualized cost and the operating cost in terms of utilities consumption. Performing a successful synthesis is important because the HEN configuration has a great impact on the process energy efficiency. In addition, since the HEN introduces interactions, the process dynamic behavior is affected turning more difficult its operation and control. The need of considering control issues at early stages of process design is widely accepted and has motivated the integration presented here. Escobar et al. (2013) proposed a computational framework (Synflex) for the synthesis of flexible and controllable HEN. Synflex can be enhanced by performing the HEN design through a global optimization strategy (GOS). Braccia et al. (2013) proposed the incorporation of a new global optimization approach to Synflex for the synthesis of HEN presented by Björk and Westerlund (2002). The main objective is to generate an efficient decentralized control system able to work well over a specified range of expected variations in the inlet temperatures of the process streams. The main concepts given at Luppi et al. (2014) for designing reconfigurable controller for fault-tolerance purposes are adopted here to give an efficiently operable HEN. In the next sections the overall steps of the proposed methodology are given together with a demonstrative application example.

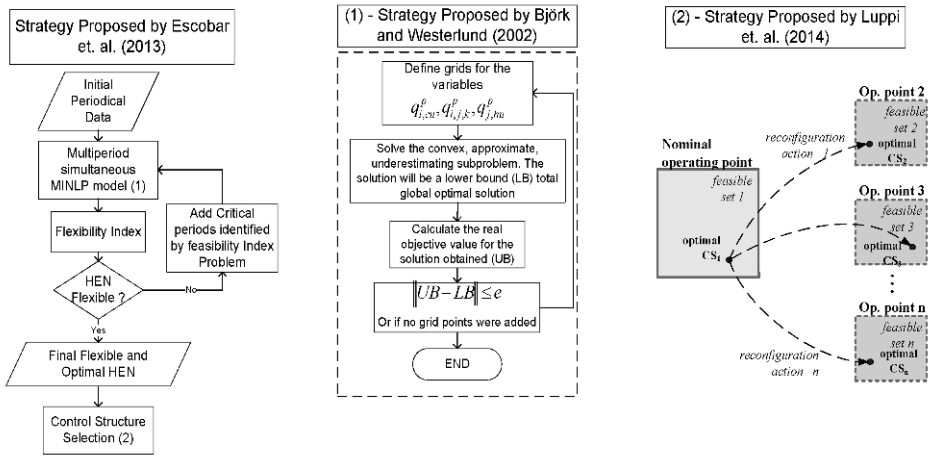

Figure 1: New methodology scheme

2. New Proposed Strategy

2.1. Multiperiod Flexible Heat Exchanger Networks Synthesis with Strategy of Global Optimization.

The synthesis of the network is accomplished based on uncertainty on the inlet temperatures. The first step consists on choosing the number and dimension of the equipments. The second one is an operation stage, for which is checked whether the selected design in the previous step is able to operate over the space of uncertain parameters. If the design is feasible it is assumed to be flexible; otherwise, the critical point obtained from the flexibility evaluation is included in the current set of periods, and a new multiperiod formulation is solved in order to obtain a new design. The GOS used here relies on a convex transformation of the non-convex terms instead of a using a branching procedure.This transformation technique will give rise to a sequence of convex problems that needs to be solved to ensure a global optimal solution. Without a global optimization procedure, one cannot easily know if it is possible to obtain better solutions or not, since there is no information to define whether the solution is a local optimum or the global one. By this procedure is possible to be sure that Synflex model does not exclude optimal configuration.

2.2. Reconfigurable control design methodology.

At Fig. 1 (2) can be seen the complete procedure for obtaining the reconfigurable control structure. By switching between alternative controllers through reconfiguration actions, the system can compensate the effects of the different operation conditions. For each particular scenario, the design of the corresponding optimal decentralized controller involves the selection of q controlled variables (CV) from m available outputs, and q manipulated variables (MV) from n available inputs, including the $q \times q$ pairing. In this work, the considered process has more inputs than outputs, i.e. $n > m$. In addition, all outputs must be controlled due to the control requisites, i.e. $q = m$. Then, in the framework of the well-known Internal Model Control (IMC) theory, at steady-state (SS) the selected MVs can be expressed as (Zumoffen (2013)):

$$\mathbf{u}_s = \mathbf{G}_s^{-1}\mathbf{y}_s^{set} - \mathbf{G}_s^{-1}\mathbf{D}_s\mathbf{d} - \mathbf{G}_s^{-1}\mathbf{G}_s'\mathbf{u}_r \tag{1}$$

where $\mathbf{G}_s$, $\mathbf{D}_s$, $\mathbf{G}_s'$, and $\mathbf{G}_r$ represent transfer function matrices of appropriate dimension, and the vectors $\mathbf{y}_s^{set}$ and $\mathbf{d}$ are setpoint and disturbance vectors, respectively. Therefore, the individual

squared deviations of the selected MVs from its operating point are available in the following vector (Luppi et al. (2014)):

$$\mathbf{e}_{us} = \sum_{i=1}^{n} \mathbf{e}^2_{us_{set}}(i) + \sum_{j=1}^{p} \mathbf{e}^2_{us_d}(j) \tag{2}$$

where:

$$\mathbf{e}_{us_{set}}(i) = (\mathbf{G}_s^{-1})\mathbf{y}^n_{set}(i) \tag{3}$$

$$\mathbf{e}_{us_d}(j) = (\mathbf{G}_s^{-1}\mathbf{D}_s)\mathbf{d}^p(j) \tag{4}$$

The SS deviations stated in eq. 2 result useful to compare alternative MVs-CVs selections. Considering a process with $n > m$ and $q = m$, the design methodology proposes to find solutions to:

$$\min_{\mathbf{C}_i} \|\mathbf{e}_{us}(\mathbf{C}_i)\|_1 \tag{5}$$

subject to:

$$\det(\mathbf{G}_s(\mathbf{C}_i)) \neq 0 \tag{6}$$

$$\mu[E(\mathbf{C}_i)] < 1 \tag{7}$$

where $\mathbf{C}_i$ is the vector of binary variables associated to the selection of the MVs, ($\mathbf{C}_i(j) = 1$ indicates that the input j is selected as MV, and $\mathbf{C}_i(j) = 0$ the opposite case). In addition, $\|.\|_1$ represents the sum of the elements of the vector $\mathbf{e}_{us}$. The constraint of eq. 6 guarantees the feasibility of the selection of the MVs. Finally, the inequality of eq. 7 corresponds to a sufficient condition for decentralized integral controllability (Skogestad and Morari (1988), Braatz (1993)). Here, the matrix E represents a normalization of the interactions introduced by the off-diagonal elements of $\mathbf{G}_s$ (Skogestad and Postlethwaite (2005)), assuming that $\mathbf{G}_s$ is arranged with the CVs-MVs pairings along its diagonal. And $\mu(E)$ corresponds to the structured singular value of E (Grosdidier and Morari (1986)). The inequality of eq. 7 ensures the stability of the control structure despite the interactions of the process and when specific change of operating condition occurs (Luppi and Basualdo (2014)).

3. Results

3.1. Alternative HEN synthesis: calculation of G and D matrices

The data for the illustrative example is given at Table 3. In Braccia et al. (2013) different HEN which consider alternative operation conditions were presented (see Table 2). Total annual cost

Table 1: Input and output variables

Input	Description	Output	Description
$uh_{i,j,k}$	bypass of hot side for exchanger between hot stream i and cold stream j in stage k	$Thout_i$	Outlet Temperature of hot stream i
$uc_{i,j,k}$	bypass of cold side for exchanger between hot stream i and cold stream j in stage k	$Tcout_j$	Outlet Temperature of cold stream j
Disturbance	Description		
$Thin_i$	Inlet Temperature of hot stream i (i=1)		
$Tcin_j$	Inlet Temperature of cold stream j (j=1,2)		
Fh_i	flow capacity of hot stream i		
Fc_j	flow capacity of cold stream j		

Table 2: Operating Conditions

$Thin_1$	$Tcin_2$	$Tcin_2$	
nominal operating point	150	60	0
second operating point	147.3	57.3	17.3

Table 3: Stream and cost data for the example .

Stream	T_{in} (C)	T_{out} (C)	Heat transfer coefficient (kWC^{-1})	Flow Capacity $(kWC^{-1}m^{-2})$
Hot 1	150	45	2	20
Cold 1	60	120	2	13
Cold 2	20	120	2	12
Hu	210	210	1	
Cu	5	15	1	

Cost of heat exchanger $(y^{-1}) = 4000 + 560 \times \mathbf{area}^{0.8}$, *Cost of utility* $(y^{-1}) = 4000 + 700 \times \mathbf{area}^{0.8}$, *Cost of Cooling utility* $(kW^{-1}y^{-1}) = 20$, *Cost of Heating utility* $(kW^{-1}y^{-1}) = 80$.

(TAC) for the first period (nominal condition) was $52,427.28(\$y^{-1})$, the Flexibility Index was 2.7° and the number of heat exchangers and utility in the obtained HEN was 4. In this example the achievable flexibility index was increased up to 20° with a global optimal solution of 5 heat exchangers producing a reasonable higher investment and operating cost corresponding to higher TAC when the second period was calculated. In this period the nominal condition and critical point identified for the first HEN was considered.As stated in section 2.2, the matrix $G(s)$ relates the set of potential manipulated variables (bypass and heats of cold and hot utilities) to the outputs (Outlet temperatures of the hot and cold streams). And matrix $D(s)$ relates the perturbation variables (Inlet temperatures and heat flow of the hot and cold streams) with outputs. For the first heat exchanger network (HEN_1), obtained in the synthesis for nominal operating point, $G(s)$ and $D(s)$ are:

$$G(s) = \begin{bmatrix} 11.355 & 10.591 & 3.173 & 7.513 & 7.482 & 4.411 & -0.133 \\ -8.139 & 0 & 0 & -5.385 & 0 & 0 & 0 \\ 1.720 & -6.620 & -1.983 & 1.138 & -4.676 & -2.757 & 0 \end{bmatrix}$$

$$D(s) = \begin{bmatrix} 0.117 & 0.310 & 0.462 & 1.249 & -0.170 & -0.542 \\ 0.222 & 0.111 & 0 & 0.259 & -0.369 & 0 \\ 0.242 & 0.047 & 0.044 & 0.375 & -0.026 & -0.481 \end{bmatrix}$$

Where the inputs, outputs and disturbances are: (i) u: uh_{111}, uh_{121}, uh_{122}, uc_{111}, uc_{121}, uc_{122}, qc_1, (ii) y: Th_1^{out}, Tc_1^{out}, Tc_2^{out}, (iii) d: Th_1^{in}, Tc_1^{in}, Tc_2^{in}, fh_1^{in}, fc_1^{in}, fc_2^{in}. Second heat exchanger network (HEN_2) obtained in the synthesis for nominal operating point and critical point (second operation point):

-HEN_2 working at nominal operating point

$$G(s) = \begin{bmatrix} 11.457 & 10.630 & 3.025 & 7.534 & 6.509 & 4.190 & -0.133 & 0 \\ -8.146 & 0 & 0 & -5.357 & 0 & 0 & 0 & 0 \\ 1.664 & -6.644 & -1.890 & 1.095 & -4.068 & -2.619 & 0 & 0 \end{bmatrix}$$

$$D(s) = \begin{bmatrix} 0.113 & 0.313 & 0.464 & 1.249 & -0.171 & -0.552 \\ 0.222 & 0.111 & 0 & 0.260 & -0.370 & 0 \\ 0.245 & 0.045 & 0.044 & 0.380 & -0.025 & -0.482 \end{bmatrix}$$

Where the inputs are: uh_{111}, uh_{121}, uh_{122}, uc_{111}, uc_{121}, uc_{122}, qc_1, qh_1.

-HEN_2 working at second operation point

$$G(s) = \begin{bmatrix} 11.611 & 11.155 & 2.814 & 7.022 & 8.182 & 3.898 & -0.054 & 0 \\ -8.144 & 0 & 0 & -4.925 & 0 & 0 & 0 & 0.034 \\ 1.566 & -6.972 & -1.759 & 0.947 & -5.114 & -2.436 & 0 & 0 \end{bmatrix}$$

$$D(s) = \begin{bmatrix} 0.111 & 0.310 & 0.468 & 1.171 & -0.156 & -0.571 \\ 0.217 & 0.116 & 0 & 0.269 & -0.405 & 0 \\ 0.251 & 0.041 & 0.041 & 0.375 & -0.021 & -0.486 \end{bmatrix}$$

Note that $G(s)$ and $D(s)$ are different for each HEN because HEN_2 includes an additional heat exchanger. Firstly can be observed a small change in the gain matrix for HEN_1 and HEN_2 (working at nominal conditions). This is caused by the increase in the area of the heat exchangers in the HEN_2 relative to the HEN_1. Furthermore, it can be seen that for HEN_2 working at nominal condition the heats of hot utilities for the first cold current (q_1)do not affect the outlet temperature (the matrix $G(s)$ has a zero column for this manipulated variable). It is produced because this utility does not work at this condition. While the HEN_2 , working at the condition generated for changes in the inlet temperature requires that this utility begins to operate. This can be seen in the column of zeros considered in the above test. Now it changes taking different values of zero for Tc_1^{out}.

3.2. Alternative decentralized control structures

Table 4: Alternative decentralized control structures

	CS_1	CS_2	CS_3	CS_4
Pairings	$Thout_1 - qc_1$ $Tcout_1 - uh_{111}$ $Tcout_2 - uh_{121}$	$Thout_1 - qc_1$ $Tcout_1 - uh_{111}$ $Tcout_2 - uh_{121}$	$Thout_1 - qc_1$ $Tcout_1 - qh_1$ $Tcout_2 - uc_{122}$	$Thout_1 - qc_1$ $Tcout_1 - qh_1$ $Tcout_2 - uh_{121}$
$\|\mathbf{e}_{us}(\mathbf{C}_i)\|_1$	887.43	887.43	4322.7	4322.5
$\mu[E(\mathbf{C}_i)]$	<1	<1	<1	<1

In this section, the procedure for reconfigurable control design is applied to the HEN process, subject to two operation modes: the nominal operating point (OP) and the second OP (critical point). In Table 1 a list of all the process variables is presented. Here, the normalized SS gain matrices G and D presented above are employed to solve the optimization problem. The objective is to

define one decentralized structure for each considered operating condition. Then, any switching mechanism can be implemented to perform a smooth reconfiguration between controllers. Taking into account that $q = 3$ (all outputs must be controlled, $q = m$), the problem is to select 3 MVs from n available inputs ($n = 7$ for the nominal OP and $n = 8$ for the second OP), together with the 3×3 CVs-MVs pairing. In this context, the length of $\mathbf{C}_i$ results 7 (or 8), according to the number of decision variables for the MVs selection. Due to the dimension of the combinatory problem, an exhaustive search was performed. Furthermore, two algorithms were utilized to pair the CVs with the MVs: (i) the Branch and Bound (BAB) solution proposed in Kariwala and Cao (2010), (ii) the iterative RGA (IRGA, Skogestad and Postlethwaite (2005)).

Finally, four alternative control structures were obtained: (i) CS_1 for HEN_1 at nominal OP,(ii) CS_2 for HEN_2 at nominal OP,(iii) CS_3 for HEN_2 at second OP, using BAB for the pairing task,(iv) CS_4 for HEN_2 at second OP, using IRGA for the pairing task. Table 4 presents these optimal solutions, including the values of $\|\mathbf{e}_{us}(\mathbf{C}_i)\|_1$ and $\mu[E(\mathbf{C}_i)]$ associated with CS_1, CS_2, CS_3 and CS_4.

4. Conclusions

In this work a novel strategy to integrate synthesis and design of control applied to a flexible HEN was presented. It is obtained from the integration of different strategies available in the literature. It was found through the example analyzed here that flexible heat exchanger synthesis generate optimal structure which must work at two operating point. For this reason, it is necessary to design a reconfigurable control capable of controlling the network at these points. The obtained CS_1 and CS_2 for controlling HEN_1 and HEN_2 result equivalent. This is because the corresponding matrices G and D are practically the same, as can be seen in section 3.1. On the other hand, two alternative control structures were designed for HEN_2 at the critical operating point (OP): CS_3 and CS_4. Both structures present similar values of $\|\mathbf{e}_{us}(\mathbf{C}_i)\|_1$ (and $\mu[E(\mathbf{C}_i)] < 1$), but the advantage of CS_4 over CS_3 is that the latter requires minimal reconfiguration. That is, CS_4 only requires the reconfiguration of the loop $Tcout_1 - uh_{111}$ by $Tcout_1 - qh_1$. While CS_3 also demands reconfiguring $Tcout_2 - uh_{121}$ by $Tcout_2 - uc_{122}$.

References

Björk, K., Westerlund, T., 2002. Global optimization of heat exchanger network synthesis problems with and without the isothermal mixing assumption. Computers and Chemical Enginering 26, 1581– 1593.

Braatz, R., 1993. Robust loopshaping for process control. PhD thesis, California Institute of Technology.

Braccia, L., Nieto Degliuomini, L., Luppi, P., Basualdo, M., 2013. Global Optimization for Flexible Heat Exchanger Network Synthesis of Chemical Plant. The Scientific Press.

Escobar, M., Trierweiler, J., Grossman, I., 2013. Simultaneous synthesis of heat exchanger networks whit operability considerations: Flexibiliy and controllability. Computers and Chemical Enginering 55, 158–180.

Grosdidier, P., Morari, M., 1986. Interaction measures for systems under decentralized control. Automatica 22 (3), 309–319.

Kariwala, V., Cao, Y., 2010. Branch and bound method for multiobjective pairing selection. Automatica (46), 932–936.

Luppi, P., Basualdo, M., 2014. Nominal controller design based on decentralized integral controllability in the framework of reconfigurable fault-tolerant structures. Industrial Engineering Chemistry Research. In Press.

Luppi, P., Nieto Degliuomini, L., Garcia M.P., and Basualdo, M., 2014. Fault-tolerant control design for safe production of hydrogen from bio-ethanol. International Journal of Hydrogen Energy 39 (1), 231–248.

Skogestad, S., Morari, M., 1988. Variable selection for decentralized control. AIChE Annual Meeting, Washington DC, Paper 128c.

Skogestad, S., Postlethwaite, I., 2005. Multivariable feedback control. Analysis and design. John Wiley & Sons.

Zumoffen, D., 2013. Oversizing analysis in plant-wide control design for industrial processes. Computers and Chemical Engineering (59), 145–155.

Krist V. Gernaey, Jakob K. Huusom and Rafiqul Gani (Eds.), 12th International Symposium on Process Systems Engineering and 25th European Symposium on Computer Aided Process Engineering.
31 May – 4 June 2015, Copenhagen, Denmark

Computer-Aided Approach for Designing Solvents Blend for Herbal Phytochemical Extraction

Siti Nuurul Huda Mohammad Azmin[a], Nor Alafiza Yunus[a],
Azizul Azri Mustaffa[a], Sharifah Rafidah Wan Alwi[a*], Lee Suan Chua[b]

[a]*Process Systems Engineering Centre (PROSPECT), Faculty of Chemical Engineering, Universiti Teknologi Malaysia, 81310 UTM, Johor Bahru, Malaysia.*
[b]*Institute of Bioproduct Development (IBD), Universiti Teknologi Malaysia, 81310 UTM, Johor Bahru, Malaysia.*
shasha@cheme.utm.my

Abstract
There are many methods to obtain herbs phytochemicals such as the use of solvents as a phytochemical transfer medium in the extraction process. Currently, solvent is preliminarily selected based on the target phytochemicals and solvent polarities. This is followed by performing experiments to determine the potential solvents blends which give the highest desired phytochemicals content. The method uses a trial-and-error approach and is time consuming as well as resource intensive. The combination of property predictive models with computer-assisted search is one way to reduce the needs for huge amount of experiments needed to be conducted. Thus, the main objective of this work is to design solvent blends for the extraction of herbal phytochemicals using computer-aided approach. The methodology is divided into four levels which are pure component constraints (level 1), linear constraints (level 2), non-linear constraints (level 3) and stability checks (level 4). The proposed method has been applied to design a solvent mixture for the extraction of kaempferol from Kacip Fatimah herb as a case study. From the analysis, 12 feasible binary solvents mixture have been identified to be suitable for the extraction as it was within range of the design target. Thus, the optimal search has been performed to find the mixture solvents that can produce the highest kaempferol extraction yield with the lowest cost. Here, five binary solvents showed the highest kaempferol yield with the lowest solvent cost.

Keywords: Herbal extraction, Kacip Fatimah, Phytochemicals, Product design, Solvent blend.

1. Introduction

Natural products are now being extensively marketed in the form of dietary supplements, nutraceuticals, health products, traditional medicines, or as prescriptions written from national pharmacopeias such as Chinese and Indian (Khan and Smillie, 2012). One of the premier Malaysian traditional medicinal plants, *Labisia pumila* (*L. pumila*) is being investigated scientifically for their medicinal properties. *L.pumila*, or locally known in Malaysia as Kacip Fatimah has their own unique characteristic such as anti-oxidant (Shahidi et al., 1992), anti-carcinogenic (Yamamoto and Gaynor, 2001), anti-stress (Choi et al., 2010), high in vitamin C (Tsao and Deng, 2004) and induced cancer cell death (Wei et al., 1990). These characteristics are due to the presence of phytochemicals in *L.pumila* such as flavonoids, phenolic and gallic acid compound.

There are many methods that have been applied to obtain these phytochemicals, where solvent are used. Every solvent will attract different active ingredients as the "like dissolve like" theory is implemented (Barton, 1990). This is the reason why different solvent will give different result (or yield) in the extraction process. In the case of herbal extraction, the main issue need to be considered is the current solvent selection used in extraction is only based on trial-and-error method. Besides, traditional methods have focused on experiments using classes of solvent (polarity) with different classes giving rise to different solute (Karunanithi et al., 2009). This method is limited by the effort, cost and time required (Samudra and Sahinidis, 2013). In addition, in order to extract one type of phytochemical, at least six solvent are needed. If the quantity of these solvents can be reduced, the amount of waste can be minimized, the productivity can be increased or maintained and the time can be saved (Kerton and Marriott, 2013). Thus, the combination of property predictive models with computer-assisted search (Samudra and Sahinidis, 2013) is one way to overcome these drawbacks. From the literature, there is no publication reported on the computer-aided design of solvent blends to optimize the extraction of phytochemicals from herbs. Previously, Karunanithi et al. (2005) designed an optimal extractant/solvent for the separation of acetic acid from water by Liquid-Liquid Extraction (LLE) while (Conte et al., 2011, 2012) designed a solvent blend for the formulation of paint and insect repellent. Besides, Yunus et al. (2014) designed a framework to obtain the optimal blends of gasoline and lubricant base oils. In this study, phytochemicals and, solvent properties and their relationship will be considered to design a blended solvent that can extract the maximum amount of phytochemicals from herbs. The solvent to be designed will consider all the safety, economic and environmental issues. The main objective of this work is to develop a new solvent blend model for the maximum extraction of herbal phytochemicals by using computer-aided approach. The method is demonstrated by designing a solvent blend for Kacip Fatimah herb as a base case study.

2. Methodology of Solvent Design for Herbal Extraction

The systematic methodology employs the reverse design approach (Gani, 2004), where the targets of the design problem are defined and the solvent blends that match the targets are identified. This reverse design approach has been chosen because it is ideally suited to handle with the "define target - match target" problems. In this methodology, the reverse approach is applied when the target properties of solvents mixture are set then solvents mixtures that could be mixed and matched the design target are identified. Normally, a set of solvents are systematically generated and screened. It is possible to generate and screen all potential feasible blend candidates (Yunus et al., 2014). In this solvent design method, it only considers binary mixtures, but it can be easily extended to multicomponent mixtures.

The first and very important task in designing the solvent mixtures is problem definition as shown in Figure 1. In this task, an understanding of the consumers need would be the performance criteria. For herbal extraction, the solvent must have all of these criteria performance which are: can effectively extract the selected phytochemicals from herb, can be removed from the crude extract mixture (so that the pure phytochemical can be obtained), have low toxicity, must be miscible to each other and to herbs phytochemicals and stable, low price and good solvent appearance. According to the knowledge base, the solvent needs are translated to the target properties. Therefore, the target properties affecting the above performance criteria are listed in Table 1.

This method applies four levels to find the optimum solvent mixtures that match the target properties. For the Level 1 until 4, solvent mixtures that do not satisfy the properties constraints would be rejected meanwhile those that satisfy the properties constraints would be considered for the next level. Every target properties listed in Table 1 have their own constraints and solvent mixture selected must have all the properties values within that constraints.

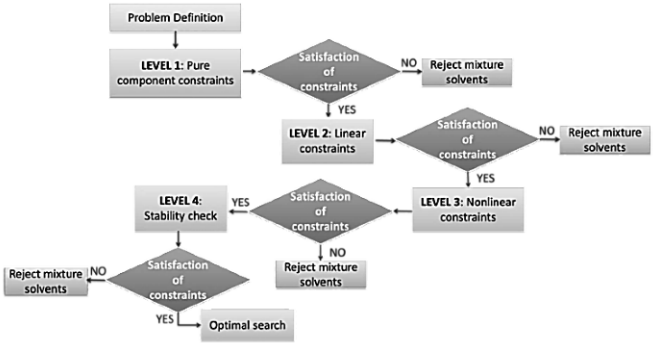

Figure 1. Work-flow diagram for the solvent design in herbal extraction.

Table 1. Translation of the performance criteria into target properties

Solvents Mixture Performance Criteria	Target Properties
Effectively extract the selected phytochemicals	$\log_p$, δ, T_m
Can be removed from crude extract (after extraction process)	μ, T_b,
Low toxicity	LC_{50}
Miscible to each other and stable	δ, $\Delta Gmix$
Low price	ρ, C
Good solvent appearance	μ

For Level 1, pure component properties of solvent in the database and target phytochemicals are compared with respect to the target values. The aim for this level is to get a list of pure solvent that match the phytochemical target properties value. For this step, three properties which are solubility parameter (δ), partition coefficient ($\log_p$), and melting point (T_m) are considered. These properties have the interrelation between solvent and phytochemicals which affect the extraction process efficiency while the other properties are used for the solvent selection only to make sure their safety and compatibility to the extraction process.

At Level 2, binary mixtures of solvents are screened according to the linear constraints. Linear models follow the linear mixing rule to compute the mixture target properties. This level considers toxicity (LC_{50}), density (ρ) and viscosity(μ) properties.

For Level 3, the non-linear mixture properties for the remaining binary mixtures which satisfy the non-linear constraints at the overall composition range are determined. Then, new composition ranges are obtained. This level considers boiling point ($T_{b)}$ properties which using model by Klein et al. (1992).

For Level 4, the stability analysis is performed. The input data consist of the UNIFAC-LLE group representation (Magnussen et al., 1981) of the solvent mixture and the temperature used in herbal extraction process. The stability routine which is Gibbs energy of mixing ($\Delta Gmix$) is solved for each mixture; result from the non-linear design constraints. The result obtained is the information of binary mixtures indicated as either stable or unstable. Then finally, the satisfying solvent mixtures are identified to search the optimal solvents that fulfill the objective of the study.

3. Case Study

The aim of this case study is to design a solvent blend that can maximise the extraction yield of kaempferol, which is one of the main phytochemical in Kacip Fatimah herb. The blend solvent formulation is considered for non-consumable phytochemicals product, to be used for the conventional extraction and the temperature considered is 90 ^{o}C. The results is then compared with the experimental data obtained from Karimi et al. (2011). 30 solvents data were used consisting of alcohol, hydrocarbon, ether and ester solvent categories. From this number of solvents, 870 possible binary solvent combination have been identified (total combinations of binary solvents (n-1) x n, where n is number of solvent in database). Meanwhile, only the main phytochemicals in Kacip Fatimah are taken into consideration, which is kaempferol. In this paper, the case study is solved using the systematic methodology as illustrated in Figure 1.

At Level 1, all 870 possible binary solvent combination were screened by comparing the solubility parameter, partition coefficient, and melting point of kaempferol with the solvents properties. Solvents that have properties value within the pure kaempferol properties will be considered in the next level. After the evaluation of Level 1, only 119 binary solvent combinations satisfy all the specified constraints. These binary solvent combinations will be further screened in Level 2. Only linear model for binary solvent properties is considered in this level. Firstly, the composition of solvent mixtures is set at 0.01 until 0.99 with an interval of 0.01. Then toxicity, density and viscosity for the binary solvents are calculated using the linear mixing rule. The solvent mixtures are then screened according to the property limit as shown in Table 2.

Table 2. Target property constraints for herb solvent blends design.

	Target property value	
Property	**Solvent constraints**	**Phytochemical constraints**
Partition coefficient	Log K_{ow}(depends on phytochemicals)	-0.3 ≤Log K_{ow}≤ 4.44
Boiling point	333.15 K ≤T_b ≤ 348.15 K	-
Toxicity parameter	-2.5 ≤-log LC_{50}≤ 2.5	-
Viscosity	1.20 cP ≤ μ ≤1.24cP	-
Density	1.0g/cm^3≤ρ≤ 1.5g/cm^3	-
Solubility parameter	δ (depends on phytochemicals)	16≤ δ≤48 Mpa$^{1/2}$

From the screening, 36 binary solvents are left and will be considered in Level 3. Level 3 is only for the properties that apply non-linear model for binary properties calculation. The overall binary solvent composition will be obtained in this level. Only one property which is boiling point was applied for this non-linear model case. After Level 3, only 12 binary solvents still remain as shown in Figure 2. These 12 binary solvents would be analyzed in level 4 which is the stability test. This test is very important to make sure that the solvent mixtures are miscible to each other. After stability test, the remaining binary solvents would be further analyzed for optimal search. This optimal search only focuses on two main objectives which are: reducing solvent mixture cost and maximizing phytochemicals yield in extraction process.

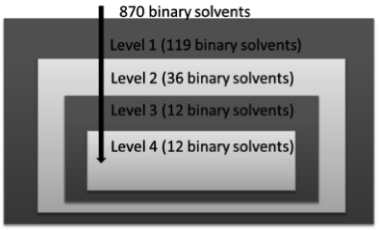

Figure 2. Number of solvent blend reduced after screening using reverse design approach.

From the solvent mixture selected, the price and kaempferol composition were calculated. Price of every pure solvent was obtained from ICIS (2008) meanwhile the kaempferol composition was calculated using Eq.(1). Figure 3 shows the solvent price and yield of kaempferol for each of the selected binary solvent

$$x_i\gamma_i = exp\frac{\Delta H_i}{RT_m}(\frac{T-T_{mi}}{T}) \quad (1)$$

where x_i is solubility of phytochemicals expressed as mole fraction, γ_i is phytochemicals activity coefficients in the solution, T_{mi} is phytochemicals melting temperature, ΔH_i is phytochemicals heat of fusion and T is extraction operating temperature. The activity coefficient, γ_i can be determined using models such as Original UNIFAC, Modified UNIFAC (Dortmund), NRTL and COSMO-SAC. In this work, Original UNIFAC and Modified UNIFAC (Dortmund) models were used to estimate the activity coefficients. The estimated activity coefficients were verified with experimental data from Karimi et al. (2011). Original UNIFAC gave 85.12% error while Modified UNIFAC (Dortmund) gave 21.46% error when compared with the experimental data. Thus, this work considered the Modified UNIFAC (Dortmund) to calculate kaempferol composition in Kacip Fatimah herb based on the lower error obtained.

The top five of solvent mixtures that give the highest kaempferol yield with their cost are plot to observe the trend. From Figure 3, it shows that methanol: isobutylraldehyde (M: IB) solvent mixture has the highest kaempferol composition yield followed by methanol: n-propionedehyde (M: PP), methanol: water (M:W), methanol: ethyl acetate (M: EA) and methanol: acetic acid (M:AA). M: W gives the lowest solvent mixture price in combination with the third place of kaempferol extraction yield as shown in Figure 3. Therefore, M: W is the best solvent mixture that could be used to extract kaempferol from Kacip Fatimah herb.

4. Conclusion

A systematic methodology for the design of blended solvent for extracting phytochemicals from herb has been developed and was tested on the extraction of kaempferol phytochemical from Kacip Fatimah herb. A decomposition method has been applied to solve the blending problem, where the objectives are to quickly screen out a large number of alternatives and to reduce the search space at each hierarchical step. The methodology applied can be used to design blended solvent for extracting phytochemicals from any herb where the scope and size depend on the solvent database available and models availability. For future work, this systematic methodology needs to be verified with different herbs as case studies.

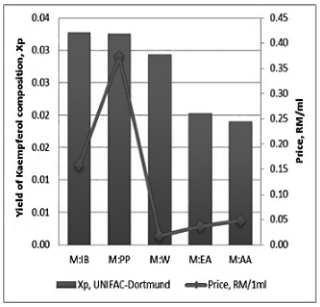

Figure 3. Solvent price on yield of kaempferol composition.

Acknowledgement
This work was supported by the Fundamental Research Grant Scheme, FRGS Research University Grant, RUG (Vote number: R.J130000.7809.4F488Q.J130000.2544.03H44), Universiti Teknologi Malaysia,UTM and the Ministry of Education, Malaysia. This support is gratefully acknowledged.

References

A. F. Barton 1990, polymer-liquid interaction parameters and solubility parameters, Boca Raton Florida, USA, CRC press.
H.-K. Choi, D.-H. Kim, J. W. Kim, S. Ngadiran, M. R. Sarmidi,C. S. Park 2010, Labisia pumila extract protects skin cells from photoaging caused by UVB irradiation. Journal of Bioscience and Bioengineering, 109**,** 291-296.
E. Conte, R. Gani, Y. S. Cheng,K. M. Ng 2012, Design of formulated products: Experimental component. AIChE Journal, 58**,** 173-189.
E. Conte, R. Gani,K. M. Ng 2011, Design of formulated products: a systematic methodology. AIChE Journal, 57**,** 2431-2449.
R. Gani 2004, Computer-aided methods and tools for chemical product design. Chemical Engineering Research and Design, 82**,** 1494-1504.
E. Karimi, H. Z. Jaafar,S. Ahmad 2011, Phytochemical analysis and antimicrobial activities of methanolic extracts of leaf, stem and root from different varieties of Labisa pumila Benth. Molecules, 16**,** 4438-4450.
A. T. Karunanithi, L. E. Achenie,R. Gani 2005, A new decomposition-based computer-aided molecular/mixture design methodology for the design of optimal solvents and solvent mixtures. Industrial & engineering chemistry research, 44**,** 4785-4797.
A. T. Karunanithi, C. Acquah, L. E. Achenie, S. Sithambaram,S. L. Suib 2009, Solvent design for crystallization of carboxylic acids. Computers & chemical engineering, 33**,** 1014-1021.
F. M. Kerton,R. Marriott 2013, Alternative solvents for green chemistry, Cambridge, UK, Royal Society of chemistry.
I. A. Khan,T. Smillie 2012, Implementing a “Quality by Design” Approach to Assure the Safety and Integrity of Botanical Dietary Supplements. Journal of Natural Products, 75**,** 1665-1673.
J. Klein, D. Wu,R. Gani 1992, Computer aided mixture design with specified property constraints. Computers & chemical engineering, 16**,** S229-S236.
T. Magnussen, P. Rasmussen,A. Fredenslund 1981, UNIFAC parameter table for prediction of liquid-liquid equilibriums. Industrial & Engineering Chemistry Process Design and Development, 20**,** 331-339.
A. P. Samudra,N. V. Sahinidis 2013, Optimization-based framework for computer-aided molecular design. AIChE Journal, 59**,** 3686-3701.
F. Shahidi, P. K. Janitha,P. D. Wanasundara 1992, Phenolic antioxidants. Critical Reviews in Food Science and Nutrition, 32**,** 67-103.
R. Tsao,Z. Deng 2004, Separation procedures for naturally occurring antioxidant phytochemicals. Journal of Chromatography B, 812**,** 85-99.
H. Wei, L. Tye, E. Bresnick,D. F. Birt 1990, Inhibitory effect of apigenin, a plant flavonoid, on epidermal ornithine decarboxylase and skin tumor promotion in mice. Cancer research, 50**,** 499-502.
Y. Yamamoto,R. B. Gaynor 2001, Therapeutic potential of inhibition of the NF-κB pathway in the treatment of inflammation and cancer. The Journal of Clinical Investigation, 107**,** 135-142.
N. A. Yunus, K. V. Gernaey, J. M. Woodley,R. Gani 2014, A systematic methodology for design of tailor-made blended products. Computers & chemical engineering, 66**,** 201-213.

Krist V. Gernaey, Jakob K. Huusom and Rafiqul Gani (Eds.), 12th International Symposium on Process Systems Engineering and 25th European Symposium on Computer Aided Process Engineering.
31 May – 4 June 2015, Copenhagen, Denmark

Evolutionary Algorithm for De Novo Molecular Design Considering Multi-Dimensional Constraints

Robert H. Herring III and Mario R. Eden*

Department of Chemical Engineering, Auburn University, Auburn, AL 36849, USA
edenmar@auburn.edu

Abstract

The area of computer-aided molecular design has benefited from significant advances in technology and methodologies through consideration of problems with increasing complexity and size. The development of increasingly accurate and predictive property models, through application of powerful variable selection and improved mapping techniques, requires new approaches for designing structures meeting property requirements as informed by these models. Additionally, the long-standing desire to model and search an increasingly larger region of chemical space maintains. As such, the necessity of developing algorithms for solving these complex property models, most often containing molecular descriptors of varying type (e.g. information theoretic, charge based, constitutional) and dimensionality (e.g. 1D, 2D, 3D), within a large search space is realized. One such approach involves the implementation of guided stochastic algorithms, such as an evolutionary algorithm. This contribution outlines an evolutionary algorithm for solving computer-aided molecular design problems, with multi-dimensional criteria, in terms of spatial signature descriptors. The effect that various user defined variables have on this algorithm, and the resultant solutions, will be considered in further detail.

Keywords: Molecular Design, Evolutionary Algorithm, Descriptors

1. Introduction

Computer-aided molecular design relies on the generation of accurate and predictive structure-property (activity) relationships. When used in a forward manner, these models can predict a given property as a function of various molecular descriptors. Molecular descriptors provide a quantitative reference to structural features in a molecule and can be superficially characterized by the dimensionality of information they capture. This ranges from 0D descriptors, an example of which could be a simple atom count, to the more complex 4D descriptors, which can capture the spatial characteristics of interacting molecules (e.g. ligand/receptor binding). Additionally, there are thousands of molecular descriptors available today, each capturing a unique molecular feature. Recent advances in variable selection techniques (Nicholls et al., 2004) have enabled the identification of an optimal subset of descriptors which best captures the property or activity of interest. It is also becoming increasingly evident (Nettles et al., 2006; Kar & Roy, 2010) that a combination of descriptors with varying dimensionality is best at describing the variance seen with many properties for a wide range of data sets.

While the forward application of these multi-dimensional property models can be straightforward, significant challenges arise when using the same models in an inverse manner, which involves the identification of structures meeting a desired property value

or range of values. Previous approaches (Harper et al., 1999) have considered the lower dimensional criteria first, while consecutively narrowing the chemical search space as more complex criteria are considered. However, this technique would not be suitable for CAMD problems with property models containing both topological (2D) and topographic (3D) descriptors. While the lower dimensional descriptors are invariant with sufficient structural representation, spatial descriptors depend on the conformational space of each molecule. This space has the dimensionality of $3N$-6, with N being the number of atoms in the molecule, and can be quite complex. There are almost always multiple conformers, representing a spatial arrangement of atoms within the molecule, present in bulk chemicals, with larger, more flexible, structures having the largest set of accessible conformations.

The solution of most CAMD problems follows as the combinatorial optimization of molecular fragments, collections of which are meant to represent potential solutions. This approach works well but can fall prey to combinatorial explosion, especially with the extension to include varying spatial information within each fragment. Evolutionary algorithms have been successfully applied within the field of CAMD (Venkatasubramanian et al., 1995) and provide a potential tool for tackling the nonlinearities arising from the mapping of spatial descriptors into chemical space as well as the accompanied combinatorial explosion. As such, this contribution outlines a methodology for solving CAMD problems utilizing property models with multi-dimensional criteria. The approach utilizes spatial molecular fragments as building blocks to generate potential solutions, while estimating the accessible conformational space associated with these structures. The user defined variables associated with the genetic algorithm applied within this methodology, along with their effect on the outcome of an illustrative case study, will be considered in detail as the foundation for this work has been established (Herring and Eden, 2014).

2. Methodology

The steps developed for setting up and solving these molecular design problems with multi-dimensional criteria in a guided stochastic, specifically a genetic algorithm, manner are as follows: (1) Identify necessary property models along with desired property targets; (2) Perform conformational analysis on the common data set among all models; (3) Develop spatial atomic signatures; (4) Apply genetic algorithm, with graph based representation of population members, to identify potential solutions.

2.1. Spatial Signature Descriptors

The signature descriptor, developed by Visco et al. (2002), was created with the intent of being able to represent various types of descriptors on a common platform as well as solve molecular design problems within what is termed ‘signature space.’ This descriptor is rooted in graph theoretical concepts and essentially represents a molecular fragment in which the environment around a central atom, up to a pre-defined height, has been encoded. The representation of this information, known as an atomic signature, is canonical and follows a line notation, which is concise and suitable for programming applications. Each atom within a molecule has its own atomic signature, and the collection of these represents a potential molecular signature.

Since these atomic signatures capture the environment around each atom within a molecule, such a representation is suitable for deriving whole-molecule topological descriptors from the information contained within each fragment before their connectivity has been established. This allows one to displace the computational

expense of arranging these fragments to establish structural isomers, until certain topological constraints are satisfied. The benefits of representing physicochemical properties in terms of molecular fragments are well known from the implementation of group contribution property models in various molecular design applications (Gani et al., 1991). The use of signature descriptors affords the same benefits of reconstructing solution molecules, while extending CAMD efforts to simultaneously consider topological constraints as well.

The extension of atomic signature to include spatial information was facilitated through the fact that these descriptors overlap, by definition. This can be taken advantage of in developing a molecular geometry from fragment geometry information. A full conformational analysis is performed on the set of molecules common to all data sets used to develop the property models applied within the chosen case study. The conformers generated are broken into unique atomic signatures, and the spatial information developed within the conformational study is stored within each of these. Redundant spatial information is eliminated by compressing the data such that the effects of combinatorial explosion are minimized. These fragments are utilized to build potential solution molecules within the evolutionary algorithm discussed below.

2.2. Genetic Algorithm

The genetic algorithm developed begins with the creation of a starting population, which is meant to capture diversity within the chemical search space in terms of molecular features as well as size. To accomplish this task, a desired size range is first established, along with an initial population size. An atomic signature is chosen at random to begin a graph, which is grown until it reaches an acceptable size, which was chosen at random from the desired range. The 'growing' process involves the identification of atomic signatures which overlap with the existing structure, and satisfy the structural overlap and saturation constraints (Herring and Eden, 2014). This is facilitated through information stored within a 'bonding network', which pre-calculates and stores all possible overlaps between atomic signatures such that it only needs to be calculated once.

Once an initial population has been established, the recursive process of selecting certain graphs to undergo various changes, in an attempt to improve the overall fitness of the subsequent population and ultimately identify solutions, begins. These graphs are selected based upon their 'fitness' value, which represents closeness to the chosen property constraints and is meant to mimic the pressure of natural selection. The fitness function chosen for this methodology is shown in Eq. (1).

$$f_i = exp\left(-\alpha\left[\sum_i^n \frac{(P_i - P_{i,bar})^2}{(P_{i,max} - P_{i,min})^2}\right]\right) \quad (1)$$

This format is well suited for application within molecular design problems, which often require candidate solutions to fall within an acceptable property range or a set of property ranges. These ranges are established with $P_{i,max}$ and $P_{i,min}$, which represent the desired upper and lower bounds for a given property, respectively. With $P_{i,bar}$ being the average between this upper and lower limit, this formulation allows the fitness to be expressed as a smooth Gaussian function with values ranging from zero to one. In this case, α represents a tunable parameter known as the Gaussian decay rate, which controls how quickly the fitness value falls off as the property values leave the desired region. Graphs exhibiting a higher fitness value have an increased likelihood of being chosen to

undergo the operations of mutation and crossover. The mutation operator has been designed to drive graphs towards an optimal size identified throughout the algorithm, and as such has three forms: insertion, deletion, and random mutation. While the mutation operators require only one graph, the crossover operator requires two, which are then spliced and recombined at acceptable points, as determined through information in the bonding network, and is meant to break free from any local minima 'traps' which might be found within the chemical search space.

3. Case Study

3.1. Property Model

The property model utilized within this case study was generated through principal component regression (PCR) with principal components identified by the Dragon 6 molecular descriptor program (Talete, 2014), which utilizes the single value decomposition (SVD) algorithm. 245 structures, representing a diverse group of potential solvents with experimentally measured boiling points between 90 and 140 °C, were obtained through the ChemSpider database. These structures were downloaded as mol files and sent through Avogadro (Hanwell et al., 2012) to develop an initial geometry, which was subsequently explored in more detail through a Monte Carlo conformational search within the BOSS (Biochemical and Organic Simulations System) (Jorgensen and Tirado-Rives, 2005) program. Traditional topological descriptors, as well as geometric descriptors, were utilized in the development of principal components and six factors were able to capture around 90% of the variance seen within the chosen data set. Upon regression into property space, this model had an explained variance (R^2) of 81.3% and a standard error (s) of 15.6 °C.

3.2. Population Size

One of the first variables chosen for running a genetic algorithm is the initial population size. Within this study, varying the initial population size would have the assumed effect of considering a larger region of the designated chemical search space, which could potentially provide improved starting points, or seeds, for the continued search for feasible solutions. The effect of varying the starting population size for a case study utilizing the above property model, in an attempt to identify solutions exhibiting a predicted boiling point of between 110 and 120 °C is considered. The number of solutions identified as a function of run time is plotted in Figure 1 for varying starting population sizes.

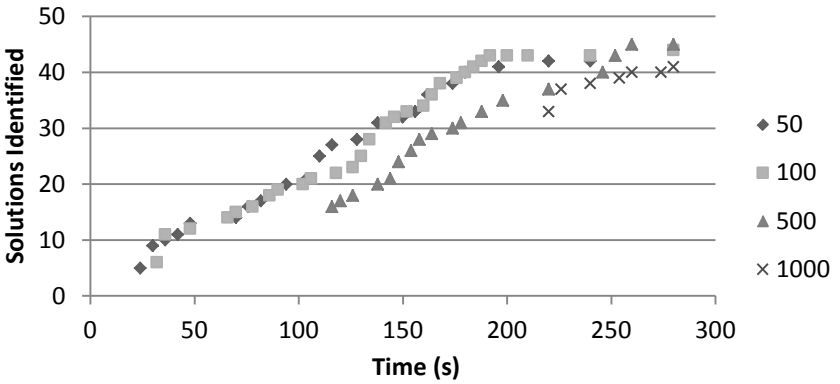

Figure 1 – Effect of initial population size on solutions generated.

Within this study, the initial population is maintained at 100, running population is 50, Gaussian decay rate variable is 10 and the crossover probability was set to 0.05. Predictably, the simulations with a larger starting population were able to begin with more solutions. However, this time sacrifice did not have a large effect on the continuation of the simulation in terms of identifying solutions. The implementation of the designed genetic operators was sufficient to explore varying regions of the search space to make up for the limitation of a smaller set of starting points. However, this phenomenon is likely to vary with respect to the complexity of a chosen chemical search space. In this case, the mutation operators were designed to control the size of solutions generated, which has a strong correlation to the respective boiling point for many groups of solvents.

Another decision to be made within this algorithm is the running population size, which is the number of new candidates generated with each iteration, or generation. It would seem that there should be an optimal running size, which could be determined by the total number of solutions generated after a given amount of time. This effect was considered in the search for solutions falling within the same property range as before, while the initial population size has been fixed at 100 and the running population size is varied. Varying the running population size from 50 to 200, in increments of 50, reveal an optimal size of 50. While all simulations were able to ultimately identify an equivalent number of total solutions, an increase in running population only had the effect of taking longer to attain these solutions.

3.3. Crossover and Mutation

The effect of varying crossover and mutation rates is considered within this section. The target property range is set between 110 and 120 °C, Gaussian decay rate variable is 10, initial population is 100, and the running population is 50. The results are exemplified below in Figure 2, where the crossover rate is varied from 0 to 0.2.

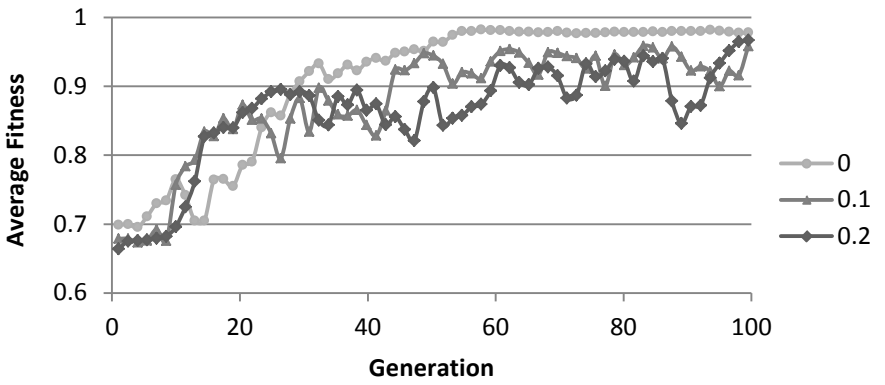

Figure 2 – Average fitness values for simulations with varying crossover rate.

The intended effect of crossover mutation is to help perpetuate diversity, in size and structural features, within the population that is unattainable through pure mutation alone. The effects of an increasing crossover rate can be seen as stochastic in relation to the average fitness of each consecutive generation. While the simulation with only mutations was able to steadily increase the population fitness towards an optimal value,

increasing the chance of encountering a crossover operation resulted in a less stable fitness improvement. However, the simulation with a crossover rate of 0.1 was able to ultimately identify the most solutions satisfying the given constraints. These results could be explained by the fact that similar solutions are likely to be revisited through implementation of the mutation operator, whereas the crossover operation increases the likelihood of arriving at unique solutions but could also create structures with a highly deviant structure and poor fitness value.

4. Conclusions

The effects of varying the starting population size, along with the rates of various genetic operators, have been considered for a genetic algorithm developed to solve CAMD problems with multi-dimensional characterization. The starting population was found not to have a huge effect on the ultimate number of solutions identified as the genetic operators, with a smaller starting population, were able to effectively search the initially uncovered regions of chemical space. Increasing the size the generations had a more pronounced effect of inflating the runtime taken to identify an equivalent number of solutions. The solution density of the chemical search space likely plays a large role in tuning this value and perhaps searching the chemical space established by a more congeneric set of structures would have an opposite effect. The crossover rate was found to induce a stochastic progression of fitness values; however, an optimal setting could potentially be established for exploring chemical search spaces of varying complexity. Future studies will consider the effects that these parameters have on data sets of varying complexity such that a more general consensus can be developed.

References

R. Gani, B. Bielsen, A. Fredenslund, 1991, A group contribution approach to computer-aided molecular design, AIChE Journal, 37.9, 1318-1332.

M. Hanwell, D. Curtis, D. Lonie, T. Vandermeersch, E. Zurek, G. Hutchison, 2011, Avogadro: An advanced semantic chemical editor, visualization, and analysis platform, J. Cheminform., 4, 1, 4-17.

P. Harper, R. Gani, P. Kolar, T. Ishikawa, 1999, Computer-aided molecular design with combined molecular modeling and group contribution, Fluid Phase Equilibria, 158, 337-347.

R. Herring and M. Eden, 2014, De Novo Molecular Design using a Graph-Based Genetic Algorithm, Computer Aided Chemical Engineering, 33, 7-12.

W. Jorgensen and Tirado-Rives, 2005, Molecular modeling of organic and biomolecular systems using BOSS and MCPRO, J. Comput. Chem., 26, 16, 1689-1700.

S. Kar and K. Roy, 2012, First report on development of quantitative interspecies structure-carcinogenicity relationship models and exploring discriminatory features for rodent carcinogenicity of diverse organic chemicals using OECD guidelines, Chemosphere, 87.4, 339-355.

J. Nettles, J. Jenkins, A. Bender, Z. Deng, J. Davies, M. Glick, 2006, Bridging Chemical and Biological Space: "Target Fishing" Using 2D and 3D Molecular Descriptors, J. Med. Chem., 49, 6802-6810.

A. Nicholls, N. MacCuish and J. MacCuish, 2004, Variable selection and model validation of 2D and 3D molecular descriptors, Journal of computer-aided molecular design, 18.7-9, 451-474.

Talete srl, 2014, Dragon (Software for Molecular Descriptor Calculation) Version 6.0 – http://www.talete.mi.it/

V. Venkatasubramanian, K. Chan, J. Caruthers , 1995, Evolutionary Design of Molecules with Desired Properties Using the Genetic Algorithm, J. Chem. Inf. Comp. Sci., 35, 188-195.

D. Visco, R. Pophale, M. Rintoul, J.-L. Faulon, 2002, Developing a methodology for an inverse quantitative structure-activity relationship using the signature molecular descriptor, Journal of Molecular Graphics and Modelling, 20.6, 429-438.

Krist V. Gernaey, Jakob K. Huusom and Rafiqul Gani (Eds.), 12th International Symposium on Process Systems Engineering and 25th European Symposium on Computer Aided Process Engineering.
31 May – 4 June 2015, Copenhagen, Denmark

Data Mining and Regression Algorithms for the Development of a QSPR Model Relating Solvent Structure and Ibuprofen Crystal Morphology

Shounak Datta, Robert H. Herring III, Mario R. Eden*

Department of Chemical Engineering, Auburn University, Auburn, AL36849, USA
edenmar@auburn.edu

Abstract

Computer Aided Molecular Design (CAMD) has been used to supplement and guide experimental efforts in various fields. Currently, highly predictive models can be developed as a result of improved computing hardware along with novel methodologies for model development. Decreasing dependency on experimental efforts can also reduce the environmental footprint of companies involved in product design and development. Though being a well-practiced process, crystallization is comparatively a much less studied separation unit operation. Not much is known about the variables that affect quality and usefulness of the end product gained from crystallization. Studies suggest that the interactions between solute and solvent are quite difficult to quantify and large variance can be noticed with every solute-solvent combination. Pharmaceutical companies are widely known for using crystallization operations to develop their end product. Additionally, crystal morphology has a significant impact on how the drug is metabolized in the human body. This contribution describes the development of a quantitative structure-property relationship (QSPR) model which relates the crystal aspect ratio of ibuprofen to the structure of the solvent utilized. The work focuses on applying various data mining and regression algorithms such as PCA/PCR (Principal Component Analysis/Regression), GA-MLR (Genetic Algorithm - Multiple Linear Regression), ANN (Artificial Neural Network) to generate a QSPR model. The validation results of the models generated from these algorithms are thoroughly analyzed and explained. Three-dimensional (3D) descriptors are often found to cause degeneracy issues when applied within QSPR studies. For these reasons, singular value decomposition (SVD) was used as an alternative to PCA for its increased stability in primary component prediction. Both internal and external validation methods were used to test the predictive capabilities of the developed models.

Keywords: QSPR, modeling, crystallization

1. Introduction

CAMD has become quite an attractive field of research for its ability to identify compounds with desired properties and activities through computational efforts. The drawback, however, is the computational complexity of the calculations required for evaluation of the compounds considered (Harper et al., 1999). A requirement of any CAMD study is a property model that can predict certain properties of the compounds with reasonable confidence.

The major aim of QSPR studies is to find a mathematical model relating a specific activity or property with one or more numbers of descriptors that are related to the molecular structure. The result of such studies is a model, which, if acceptable, can be used to provide an idea of how the property and molecular structure are related. These kinds of models are widely used by synthetic chemists for making choices between alternative molecular structures (Katritzky et al., 1995). Because of their known applicability, QSPR models are widely studied within academia, industry and government settings. In this stage of expansion of QSPR modeling, it is obvious that collaboration between computational and experimental experts is needed to ensure the highest level of success for such modeling practice (Cherkasov et al., 2013).

Study of crystal morphology is required to understand the difference in crystalline products due to changes in the solvent structure. In many pharmaceutical products, slight change of crystal shape is reported to bring a significant level of variance in the metabolic characteristics of the drugs (Datta and Grant, 2004). Solvent properties that contribute to the attributes of the crystal products are not yet fully understood. The pharmaceutical industry, being a field which heavily utilizes crystallization operations, has to apply extensive experimental efforts to identify the optimal crystallization conditions for newly discovered drugs. Understanding solvent influence on crystal shape can provide a basis upon which to design experiments efficiently, potentially decreasing both the environmental impact of experiments and time consumption of crystal engineering.

Ibuprofen [2-(4-isobutyl-phenyl) propionic acid], shown in Figure 1, is a well-known anti-inflammatory drug. While insoluble in water, it is however soluble in various organic liquids. Currently, the drug is crystallized from ethanol and aqueous ethanol in industrial practice (Rashid et al., 2013). To capture the variance in Ibuprofen crystal morphology with respect to the chosen crystallization solvent, the crystal shape is considered along with the structural features of the respective solvent. Additionally, varying force fields, such as GAFF (Generalized AMBER Force Filed), Ghemical and MMFF94s (Merk Molecular Force Field for Static molecules) provided in the Avogadro software, were used to determine their effects on the resulting models. GAFF was developed by Wang et al. (2004) to better represent drug like molecules and molecules they interact with. Ghemical is highly applicable in the case of simple organic molecules. MMFF94s was developed by Halgren (1999). This force field was selected as the compound classes used in its core parameterization are expansive and each of the solvents used in this work fall within that expansive space. QSPR model development algorithms were coded using MATLAB, which was chosen for its built-in tools and functions.

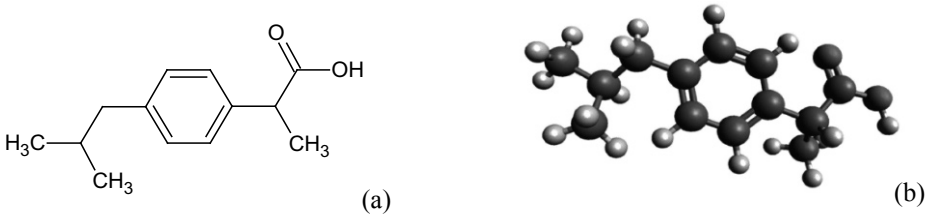

Figure 1: (a) 2D Ibuprofen structure; (b) Optimized 3D Ibuprofen structure

2. QSPR Model Development

Figure 2 highlights the steps taken for the model development methodology, which begins with geometry optimization.

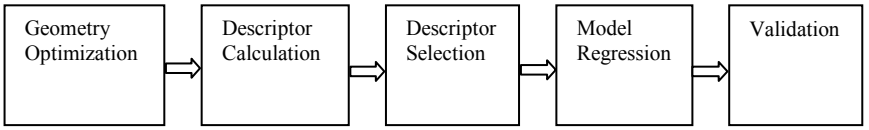

Figure 2: Steps taken in QSPR model development methodology.

Geometry optimization of molecular structures within the chosen data set is necessary to generate spatial molecular data, which is utilized in calculating 3D descriptor values. The chosen geometry optimization algorithm, along with the applied force field, is important because it determines the quality of structures produced. As mentioned before, the geometry optimization for the chosen solvents was performed using three different force-fields available within the Avagadro software package. For each optimization process, the steepest descent algorithm was used. The convergence value was kept to 10^{-7} and 500 iterations were performed. The results generated were saved as MDL mol files for further use.

The MDL mol files generated from the geometry optimization using Avogadro were used to generate molecular descriptors. This project focuses on 3D descriptors calculated using Dragon 6.0 software. To further elaborate, descriptors of the following classes were generated:

- Randic molecular profiles
- Geometrical descriptors
- RDF descriptors
- 3D-MoRSE descriptors
- WHIM descriptors
- GATEWAY descriptors

The calculated descriptors were stored in text files for ease of loading in MATLAB. The next step was to remove descriptors from each matrix that had values of zero for multiple solvents within the data set. If a descriptor had values of zero for more than ten solvents, that descriptor was removed from the data matrix. Finally, experimental results concerning crystal aspect ratio of Ibuprofen for different solvents were considered for regression purposes.

Principal component analysis (PCA) was used to develop a QSPR model relating solvent structure to crystal aspect ratio. PCA is very different from other methods because it does not eliminate descriptors from the analysis, but instead transforms the large, highly correlated data matrix into a smaller matrix of uncorrelated factors that are linear combinations of the original data set. Each factor covers a certain percentage of the variance within the original data matrix, which denotes importance of the factors to be considered. PCA gives a proper understanding of model feasibility and a basic idea on factors governing the model. In addition, principal component regression (PCR) is

used to map these components into property space, generating a model which can be further validated.

A genetic algorithm (GA), in combination with multiple linear regression (MLR) was also used to develop a QSPR model to further understand how solvent properties are related to the respectively produced crystal shape. GA, being an algorithm of optimization through random selection and objective function calculation, can in some cases be tricky if not controlled properly. Its prime operating variables, probabilities of crossover and mutation gives it a unique ability to control the approach to an optimal result after several simulated generations. Gharagheizi (2007) reported in his studies, of QSPR relating solubility parameters, that GA-MLR can be used to develop a QSPR model of high predictability.

Artificial Neural Network (ANN) is used in a wide range of applications. The algorithm designs artificial neurons, connected with coefficients (also known as weights), creating organized layers to develop neural structures (Zupan and Gasteiger, 1999). Here, Feed Forward Neural Network was used for data fitting over the results of a GA to produce a GA-FFNN system with potentially improved accuracy. This regression was performed using the nntool, available within MATLAB. GA-FFNN was performed using default settings with an increased number of neurons. Using the same tool, a radial basis approach was used to perform Radial Basis Function-NN (RBFNN) for a tighter fit.

Ultimately, the developed models are required to be validated. For this purpose, both internal and external validations were performed. This ensures model feasibility for representing a training set of the available data as well as the predictability of the model for external data (e.g. test set separate from the training set). The importance of external validation in light of internal validation is that it ensures reasonable property predictions of a material not included in model development, which is desirable of QSPR models. R^2 values of the models for both the training set and test set were used as a measure of the model correctness and predictability, respectively. R^2 values indicate how well the data fit the models that are to be used for prediction. A 5:1 ratio was maintained for training and test data partitioning.

3. Results and Discussion

The results from PCA/PCR were very useful in determining the best geometry optimization algorithm for these studies. As shown for the internal validation in Figure 3(a), descriptor sets of each geometry optimization process reaches an R^2 value of 1 for models with 9 principal components. The path of external validation shown in Figure 3(b) was not as smooth as the internal validation. With various points of ups and downs, it can be seen that when 9 principal components are added in the model, the best external prediction is achieved by MMFF94s optimized descriptors. This sets a basis for further calculations using the described algorithms provided with information about the optimal types of descriptors and number of principal components.

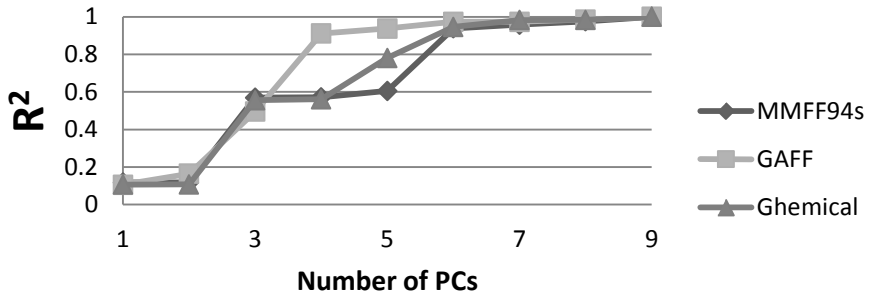

(a)

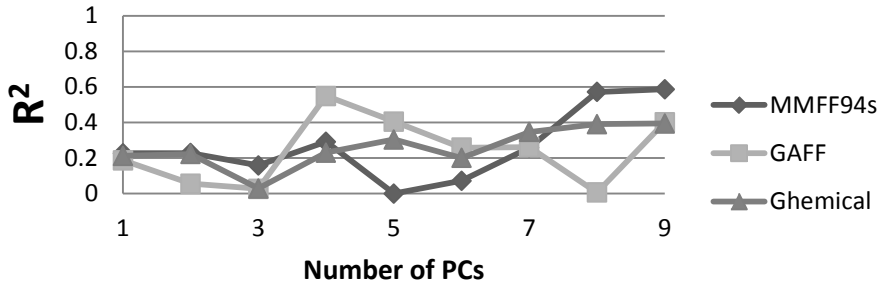

(b)

Figure 3: (a) Internal validation and (b) External validation of PCA-PCR model for descriptor sets of three geometry optimization algorithms.

For further QSPR study, descriptors generated with the MMFF94s force field were used. Influenced by the results of the PCA-PCR model, 9 descriptors were allowed to be chosen in random manner by GA for further optimization. The best results achieved from the trials are presented in Figure 4. It should be noted that, in the case of GA-MLR, the model worked better for the test set than the training set. The results indicate that a combination of GA and RBFNN has produced an acceptable model with external validation R^2 value of 0.8624 and internal validation R^2 value of 0.9834.

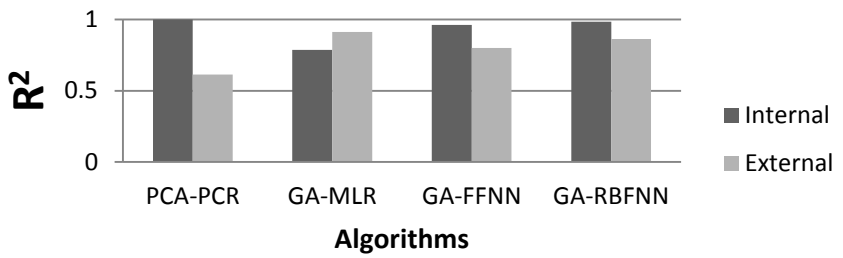

Figure 4: Performance of models developed using MMFF94s descriptors.

4. Conclusions

The necessity of developing predictive models for use within the field of computer-aided molecular design has been established. Specifically, the inclusion of spatial (3D) descriptors within these models requires certain considerations regarding the origin of the spatial data used to estimate these descriptor values. The impact of choosing a proper force field for geometry optimization is discussed in this work and investigations show that, for this case, MMFF94s serves as the optimal choice. With an exception for GA-MLR, all the models show comparatively better response for the training set data than test set data. This is likely the result of a small, and significantly diverse, data set. This study was effective in exemplifying the applicability of modern model development techniques, as applied in the area of crystallization. However, its influence on crystallization process is a matter of further studies.

5. Acknowledgements

The authors greatly appreciate the support of Dr. Charles Acquah, University of Connecticut, and Dr. Arunprakash Karunanithi at the University of Colorado for providing the experimental data which form the basis of this work. Also, thanks to Samir Hasan of Auburn University for providing advice on efficient coding strategies.

References

Zupan, J. and J. Gasteiger, 1999, Neural networks in chemistry and drug design, Wiley-VCH Germany, 2nd edition

Wang, J., R. Wolf, J. Caldwell, P. Kollman and D. Case, 2004, Development and testing of a general amber force field. Journal of Computational Chemistry, Vol. 25,Issue 9, 1157–1174.

Rashid, A., E.T. White, T. Howes, J.D. Litster and I. Marziano, 2013, Crystallizer design methods for direct crystallization of ibuprofen as a pharmaceutical formulation, Chemeca 2013: Challenging Tomorrow, 13-21, ISBN: 9781922107077

Katritzky, A. R. and V. S. Lobanov, 1995, QSPR: The correlation and Quantitative Prediction of chemical andphysical properties from structure,Chem. Soc. Rev., Vol. 24, 279-287

Harper, P. M., R. Gani, P. Kolar and T. Ishikawa, 1999, Computer-aided molecular design with combined molecular modeling and group contribution, Fluid Phase Equilibria, 337-347, DOI:10.1016/S0378-3812(99)00089-8

Halgren, T. A., 1999, MMFF VI. MMFF94s option for energy minimization studies, Journal of Computational Chemistry, Vol. 20, Issue 7, 720–729

Gharagheizi, F., 2007, QSPR studies for solubility parameter by means of Genetic Algorithm-Based Multivariate Linear Regression and Generalized Regression Neural Network, QSAR and Combinatorial Science, DOI: 10.1002/qsar.200630159

Datta, S. and David J. W. Grant, 2004, Crystal structures of drugs: advances in determination, prediction and engineering, Nature Reviews Drug Discovery, Vol. 3, 42-57

Cherkasov, A., E. N. Muratov, D. Fourches, A. Varnek, I. I. Baskin, M. Cronin, J. Dearden, P. Gramatica, Y. C. Martin, R. Todeschini,V. Consonni,V. E. Kuz'min, R. Cramer, R. Benigni, C. Yang, J. Rathman, L. Terfloth, J. Gasteiger, A. Richard and A. Tropsha, 2014, QSAR Modeling: Where have you been? where are you going to?, J. Med. Chem., Vol. 57, 4977−5010

Krist V. Gernaey, Jakob K. Huusom and Rafiqul Gani (Eds.), 12th International Symposium on Process Systems Engineering and 25th European Symposium on Computer Aided Process Engineering.
31 May – 4 June 2015, Copenhagen, Denmark

Designing Reactants and Products with Properties Dependent on Both Structures

Vikrant A. Dev[a], Nishanth G. Chemmangattuvalappil[b], Mario R. Eden[a,*]

[a]*Department of Chemical Engineering, Auburn University, Auburn, AL 36849, USA*
[b]*Department of Chemical and Environmental Eng., University of Nottingham, Malaysia*
edenmar@auburn.edu

Abstract

Computer aided molecular design (CAMD) in the past has successfully been performed to design chemicals for a variety of processes including those involving reactions. However, the problem of design of reactants and products with optimal properties has not received much attention. Recently attempts have been made to address this problem. The majority of these contributions, however, are restricted to design of reactants and products when only a single reactant and product can be structurally varied. An attempt to include variation of structures of multiple reactants and products was also restricted in scope. Only the dominant properties of the product molecules could be optimized such that each product molecule was subjected to its respective set of property constraints. In this work, an algorithm has been developed that designs reactants and products such that properties that are functions of structures of reactants and products are optimized. Also, the reactants and products are subjected to their respective set of property constraints. Certain thermodynamic properties of reactions like standard Gibbs free energy change of a reaction can be optimized using the developed algorithm. Linear and nonlinear property-structure relationships based on group contributions and/or topological indices (TIs) have been utilized. They have been treated on a single platform using signature descriptors. Signatures have also been utilized to relate structures of reactants and products.

Keywords: Reactive Systems, Molecular Design, Signature Descriptors, CAMD

1. Background

1.1. Molecular Design in Reactive Systems

CAMD is progressively being carried out in reactive systems to design solvents that enhance reaction kinetics, catalysts, reactants and products. For the design of reactants and products, the reaction(s) occurring in the system is known prior to the design. The reactants and products however are structurally variable. Chemmangattuvalappil *et al.* (2012) developed an algorithm to generate structures of a single unknown reactant and product, albeit restricted to linear property models. De Vleeschouwer *et al.* (2012) employed density functional theory and optimized the photoacidity of a single variable candidate, but, without provision for property constraints. Also, quantum mechanical methods suffer from escalating computational expense with increasing number of electrons (Adjiman *et al.*, 2014). However, problems tackled by De Vleeschouwer *et al.* (2012) cannot be completely addressed using standard thermodynamic models. Dev *et al.* (2014) developed an algorithm to generate structures of reactants and products irrespective of their numbers such that the respective dominant properties of the products were optimized. The products were also subject to their respective set of

property constraints. The algorithm could also deal with nonlinear models. In this work an algorithm has been developed that designs reactants and products such that properties dependent on structures of reactants and products are optimized. Reactants and products are also subjected to property constraints.

1.2. Atomic Signature Descriptors in Molecular Design

If G is a molecular graph and x is an atom of G, the atomic signature of height h of x is a canonical representation of the subgraph of G containing all atoms that are at a distance h from x (Faulon *et al.*, 2003). Thus, a signature consists of a root atom, x, and atoms in each n^{th} out-neighborhood of x, where n varies from 1 to h. The size of each atom's first out-neighborhood is the out-degree. It can be used as a coloring function to distinguish various atom types in a molecule. Atomic signatures can be used as building blocks to form molecules. Use of signature descriptors in molecular design offers the advantage of enabling utilization of quantitative structure property/activity relationships (QSARs/QSPRs) and group contribution models (GCMs) on a single platform. Thus a wide variety of property targets can be tracked. Faulon *et al.* (2003) identified the relationship between topological indices (TIs), which constitute QSARs/QSPRs, and signatures. If k is a constant, ${}^{h}\alpha_G$ is the vector of occurrences of atomic signature of height h and *TI(root (*${}^{h}\Sigma$*))* is the vector of TI values calculated for each root of atomic signature:

$$TI(G) = k\left[{}^{h}\alpha_G \cdot TI\left(root\left({}^{h}\Sigma\right)\right)\right] \tag{1}$$

2. Molecular Design of Reactants and Products

Molecular design of reactants and products involves their structural variation until the dominant properties of interest are optimized without violation of property and structural constraints. All allowable variation in the structures is captured in the set of possible signatures. This set is generated for each atom in each reactant and product taking into account the general structural formula. In this set, different signatures for the same root atom may exist. This is due to the appearance of different possible atoms from variable groups, in the root atom's neighbourhood. Each instance of variation in molecular structure results in a subset being chosen from the set of possible signatures. The elements of this subset when combined suitably in correct numbers generate a feasible structure. The heights of utilized signatures, h, are those that are able to capture the structural information encoded in the TIs and/or groups used in the property models.

2.1. Root Atom Balance of Signatures

Chemical reactions, barring those that are nuclear reactions, involve only the rearrangement of atoms of reactants to yield products. Thus, the number of atoms is conserved in a reaction and the reactants and products are structurally related. The new position of a reactant atom in the molecular graph of the corresponding product is revealed by the reaction mechanism. Consequently, given a signature from a reactant's set of possible signatures, not only the root atom but atoms in each level of the signature tree can be tracked to the products they get repositioned to. Thus, the change, if any, in the signatures can be inferred.

As mandated by the reaction mechanism, some or all of the atoms in the n^{th} out-neighborhood ($1 \le n \le h$) of a reactant atom may appear in the n^{th} out-neighborhood of the repositioned reactant atom. The common atoms may appear in a different n^{th} out-neighborhood after the reaction. The uncommon atoms can also be tracked from

different positions in the reactants. Thus, identification of a product signature obtained from transformation of a reactant signature, with the same root atom, can be carried out. But, due to variability of molecular structures, some atoms in reactants will exist whose *n* out-neighborhoods can be filled by different sets of possible atoms. If these different possible sets do not appear in the *n* out-neighborhoods of the repositioned reactant atom then different possible reactant signatures will exist for a corresponding product signature. Conversely, it may happen that different sets of possible atoms can be filled in the *n* out-neighbourhoods of the repositioned reactant atom. If they do not originate from the *n* out-neighbourhoods of the original reactant atom then different possible product signatures will exist. Thus, to identify the corresponding product signatures obtained after transformation of certain reactant signatures, the atoms common to the *n* out-neighborhoods of the root atom should appear in both reactant and product signatures as mandated by the reaction mechanism. The uncommon atoms if variable will generate different possible reactant and/or product signatures for the same set of common atoms. Since in a reaction, the number of atoms is conserved, the total number of tracked root atoms of signatures need to be conserved. Since, each root atom has an associated signature, a generalized root atom balance can be written as:

$$\sum_{a=1}^{p}\left(n_a \sum_{b=1}^{q} \alpha_{a,b,root\ v} \right) = \sum_{c=1}^{r}\left(n_c \sum_{d=1}^{s} \beta_{c,d,root\ v} \right) \tag{2}$$

Where p is the number of reactants, n_a is the stoichiometric coefficient of each reactant, and q is the number of possible signatures belonging to a reactant that due to the reaction transforms into specific signatures in the products. Also, r is the number of products, n_c is the stoichiometric coefficient of each product and s is the number of possible signatures in a product that are obtained by transformation of signatures in the reactants under consideration. $\alpha_{a,b,root\ v}$ is the occurrence number of possible atomic signatures of *root v* belonging to one of the reactants. These signatures can transform into possible atomic signatures of *root v* belonging to one of the products having an occurrence number $\beta_{c,d,root\ v}$. *root v* is an atom of the same element and can have different colors associated with the vertex degree in the reactants and products. Also, the occurrence numbers appearing in the sum may not be the total occurrence number.

Consider the transesterification reaction, shown below, as an example to demonstrate the application of Eq. (2). The numbers adjoining the atomic symbols are the vertex degrees, used as colors. The dashed bond between C4 and O2 is a bond that will break. R, R′ and R″ are assumed to be acyclic saturated groups.

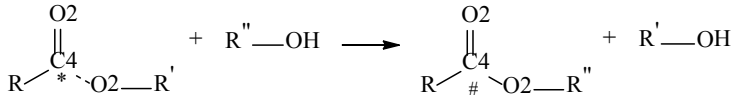

(3)

From the mechanism it is known that the C4 atom (marked *) double bonded to the O2 atom in the reactant ester appears only in the product ester also as C4 (marked #) double bonded to same O2. Let all the possible signatures of height 3 of the reactants and products be generated. Then the root atom balance that can be written for the C4 atom when R is possibly CH_3 i.e. C1 is the following:

α[C4(=O2C1O2(C1))] + α[C4(=O2C1O2(C2(C)))] + α[C4(=O2C1O2(C3(CC)))] + α[C4(=O2C1O2(C4(CCC)))] = β[C4(=O2C1O2(C1))] + β[C4(=O2C1O2(C2(C)))] + β[C4(=O2C1O2(C3(CC)))] + β[C4(=O2C1O2(C4(CCC)))]

Where, α and β are occurrence numbers of the signatures, in square brackets, of reactant and product C4, respectively. The above holds because according to the mechanism, along with C4, the R group is also transferred to the product ester. Thus, the atoms of R group are common and will appear as is in the n neighborhoods of C4 in both reactant and product signatures. In this sub-example we have taken R to possibly be C1. So, C1 makes an appearance in each of the signatures. Also, the OR′ group is transferred to the product alcohol and the OR″ group from the reactant alcohol becomes a part of the product ester. These are the variable groups that do not share any common atom. Thus, the branch of the C4 signature tree containing atoms of OR′ can be varied. The same is done for C4 bonded to OR″. Hence, the summation on both sides includes this variation where single bonded O2 is bonded to differently colored atoms. For this example, different variations in R will have different relationships involving signatures rooted at C4. Since in the above reaction only one C4 double bonded to O2 will appear in each ester, an additional condition where the sum of occurrences of all signatures with C4 root atom equals 1 will be imposed on each ester.

2.2. Optimizing Properties dependent on Structures of Reactants and Products

In this work, properties that are functions of structures of each reactant and product are to be optimized to design reactants and products. Examples of such properties include standard entropy of reaction, standard free energy of reaction, standard enthalpy of reaction, etc. Such properties, which are to be optimized, will be impacted by property constraints and structural constraints on each of the reactants and products. Additionally, for a reaction, structures of reactants and products are related. Thus, constraints capturing this relationship will also impact the property being optimized. The previous section details a general procedure to derive such relationships.

2.3. Problem Formulation

A mixed integer nonlinear programming (MINLP) problem is formulated to optimize the property of interest. The problem is subjected to property constraints of each reactant and product. Each of the properties involved are ultimately expressed in terms of the occurrence number of atomic signatures. Structural constraints for each reactant and product need to be added to ensure that feasible structures are obtained. For this, the structural constraints developed by Chemmangattuvalappil and Eden (2013) are utilized. Additionally, to capture the structural relationships between the reactants and products, root atom balances for each of the root atoms of signatures are added to the set of constraints. The solution obtained by solving the MINLP problem consists of values of occurrence numbers of signatures of reactants and products. Using these values, the signatures are then combined to provide structures of reactants and products using the structure enumeration algorithm of Chemmangattuvalappil and Eden (2013).

3. Case Study

The aim of this case study is to design reactant and product esters RCOOR′ and RCOOR″, and reactant and product alcohols R″OH and R′OH such that the standard Gibbs free energy change of the transesterification reaction, ΔG^o_{rxn}, is minimized. RCOOR′ and R″OH are constrained by log(P) and log(LC_{50}) respectively. P is the octanol-water partition coefficient and LC_{50} is the acute toxicity. RCOOR″ and R′OH are subjected to their respective set of boiling and flash point constraints. The property ranges are listed in Table 1. ΔG^o_{rxn} has been evaluated using the following definition:

$$\Delta G^o_{rxn} = \sum a_{product} G_{f,\,product} - \sum b_{reactant} G_{f,\,reactant} \tag{4}$$

Where, $G_{f,\ product}$ and $G_{f,\ reactant}$ are standard Gibbs energy of formation values and $a_{product}$ and $b_{reactant}$ are stoichiometric coefficients of each product and reactant, respectively. The free energy of formation (G_f) of each reactant and product was expressed in terms of their structures using a GCM developed by Hukkerikar *et al.* (2012). In the GCM, C_i, D_j and E_k are contributions of first, second and third order groups of type i, j and k respectively. N_i, M_j and O_k are their respective occurrence numbers. The other property models utilized have been listed in Table 2. In the log(P) model (Soskic and Plavsic, 2005), ${}^1\chi^{opt}$ is the optimized first-order molecular connectivity index. I_{MET}, I_{PHYD}, I_{ALRIN} and I_{CONJUG} are indicator variables (IVs) for compounds containing methyl group attached to heteroatoms, H atom bonded to strongly electronegative group, an aliphatic ring and conjugation, respectively. I_{HG2} and I_{HG3} are IVs representing 2 and 3 geminal halogens on a C atom, I_{HVIC} represents halogens bonded to vicinal carbons and I_{PG2} and I_{PVIC} represent polar groups separated by 1 and 2 carbons respectively. In the log(LC_{50}) QSAR (Juric *et al.*,1992), ${}^0\chi^v$ is the zero-valence connectivity index. The boiling and flash point GCMs (Hukkerikar *et al.*, 2012) have the same form as GCM of G_f.

Table 1. Property Constraints on Reactants and Products

Reactant/Product	Property	Upper Bound	Lower Bound
All	ΔG^o_{rxn} (kJ/mol)	Minimum	
RCOOR′	log(P)	5	-
R″OH	log(LC_{50})	-	-1
RCOOR″	Boiling Point (K)	485	395
	Flash Point (K)	375	295
R′OH	Boiling Point (K)	470	385
	Flash Point (K)	380	300

Table 2. Property Models

Property	Property Model
Std. Gibbs energy of form., G_f (kJ/mol)	$G_f - G_{f0} = \sum_i N_i C_i + \sum_j M_j D_j + \sum_k E_k O_k$
log(P)	$\log(P) = 0.829 + 1.055 \times {}^1\chi^{opt} + 0.580 \times I_{MET} + 0.367 \times I_{PHYD} - 0.627 \times I_{ALRIN} + 0.454 \times I_{CONJUG} + 0.658 \times I_{HG2} + 1.726 \times I_{HG3} + 0.381 \times I_{HVIC} + 1.271 \times I_{PG2} + 0.605 \times I_{PVIC}$
log(LC_{50})	$\log(LC_{50}) = 2.975 + 1.169 \times \log {}^0\chi^v - 7.309 \times (\log {}^0\chi^v)^2$
Flash Point, F_p (K)	$F_p - F_{p0} = \sum_i N_i C_i + \sum_j M_j D_j + \sum_k E_k O_k$
Boiling Point, T_b (K)	$exp(T_b / T_{b0}) = \sum_i N_i C_i + \sum_j M_j D_j + \sum_k E_k O_k$

An optimization problem consisting of the objective function, minimize the standard Gibbs energy change of transesterification reaction, was set up in GAMS. Additionally,

the structural and property constraints of the reactant and product esters and alcohols along with the root atom balances of signatures were included. The optimization problem was solved using the DICOPT solver. Since, some of the second order groups in the group contribution models can only be represented by signatures of height 3, the maximum height of signatures utilized was 3. Also, R, R′ and R″ are assumed to be acyclic saturated groups. The optimum value of ΔG^{o}_{rxn} is obtained as -13.6 kJ/mol. A set of structures of reactants and products obtained for the minimum value is:

- Reactant ester: 2-methylpentan-3-yl pentanoate $[CH_3(CH_2)_3C(=O)OCH(CH_2CH_3)CH(CH_3)CH_3]$
- Reactant alcohol: ethanol $[CH_3CH_2OH]$
- Product ester: ethyl pentanoate $[CH_3(CH_2)_3C(=O)OCH_2CH_3]$
- Product alcohol: 2-methylpentan-3-ol $[CH_3CH_2CH(OH)CH(CH_3)CH_3]$

4. Conclusions

An algorithm has been developed to design reactants and products such that properties dependent on their structures are optimized. Additionally the reactants and products are subjected to their respective set of property constraints. Thus, certain thermodynamic properties of reactions like the standard Gibbs free energy change of a reaction can be optimized with the developed algorithm. The algorithm takes into account the information provided by reaction mechanisms to relate the structures of reactants to those of products using signatures. Future efforts include developing an algorithm where each reactant and product's respective properties are to be optimized. In such an algorithm the reactants and products are to be subjected to their respective set of property constraints. Additionally properties that are functions of structures of reactants and products are to be optimized and/or are to be added as constraints.

References

C.S. Adjiman, A. Galindo, G. Jackson, 2014, Molecules Matter: The Expanding Envelope of Process Design, Computer Aided Chemical Engineering, 34, 55-64.

N.G. Chemmangattuvalappil, M.R. Eden, 2013, A Novel Methodology for Property-Based Molecular Design Using Multiple Topological Indices, Industrial & Engineering Chemistry Research, 52, 7090-7103.

N.G. Chemmangattuvalappil, C.B. Roberts, M.R. Eden, 2012, Signature Descriptors for Process and Molecular Design in Reactive Systems, Computer Aided Chemical Engineering, 31, 1356-1360.

F. De Vleeschouwer, W. Yang, D.N. Beratan, P. Geerlings, F.D. Proft, 2012, Inverse Design of molecules with optimal reactivity properties: acidity of 2-naphthol derivatives, Physical Chemistry Chemical Physics, 14, 16002-16013.

V.A. Dev, N.G. Chemmangattuvalappil, M.R. Eden, 2014, Reactant Structure Generation by Signature Descriptors and Real Coded Genetic Algorithm, Computer Aided Chemical Engineering, 34, 291-296.

J.L. Faulon, D.P. Visco Jr., R.S. Pophale, 2003, The Signature Molecular Descriptor 1. Using Extended Valence Sequences in QSAR and QSPR Studies, Journal of Chemical Information and Computer Sciences, 43, 707-720.

A.S. Hukkerikar, B. Sarup, A.T. Kate, J. Abildskov, G. Sin, R. Gani, 2012, Group-Contribution^{+} (GC^{+}) Based Estimation of Properties of Pure Components: Improved Property Estimation and Uncertainty Analysis, Fluid Phase Equilibria, 321, 25–43.

A. Juric, M. Gagro, S. Nikolic, N. Trinajstic, 1992, Molecular topological index: An application in the QSAR study of toxicity of alcohols, Journal of Mathematical Chemistry, 11, 1, 179-186.

M. Soskic, D. Plavsic, 2005, Modeling the Octanol-Water Partition Coefficient by an Optimized Molecular Connectivity Index, Journal of Chemical Information and Modeling, 45, 930-938.

Krist V. Gernaey, Jakob K. Huusom and Rafiqul Gani (Eds.), 12th International Symposium on Process Systems Engineering and 25th European Symposium on Computer Aided Process Engineering.
31 May – 4 June 2015, Copenhagen, Denmark

Conceptual Design of an Internally Heat-Integrated Reactive Distillation Column Based On Thermodynamic and Hydraulic Analysis

Zixin Lin[a,*], Weizhong An[a,*],Yawei Xu[a], Jianmin Zhu[b]

[a]*Department of Chemistry and Chemical Engineering, Ocean University of China, Qingdao, 266100, China*
[b]*Liaoning Oxiranchem Group, Liaoyang 111003, China*
linzixin@ouc.edu.cn, awzhong@ouc.edu.cn

Abstract

This work introduces an efficient approach to the conceptual design of an internally heat-integrated reactive distillation column (HIRDiC) synthesizing ethylene glycol (EG) through the hydration of ethylene oxide (EO). A systematic method is proposed to obtain a feasible physical configuration with maximum possible extent of heat integration, in which the column diameter, the number of panels and the panel size on each plate are iteratively examined and determined according to thermodynamic and hydraulic analysis. Evaluated by the total annualized capital cost (TAC), the comparison results showed that neither of the two commonly used heat distribution schemes, i.e. uniform heat transfer area and uniform heat duty distribution, was as good as the design acquired from the proposed methodology.

Keywords: HIRDiC; Heat integration; Reactive distillation; Ethylene glycol

1. Introduction

Reactive distillation (RD) is a process in which chemical reaction and distillation occur simultaneously in one single apparatus. RD has attracted much attention in the last two decades because of its potential for lower capital investment, improved selectivity, and increased yield (Thery et al., 2005). However, because of the nature of distillation, the RD process is energy intensive in the process industries. Significant effort has been devoted to the development of novel schemes with high energy efficiency, such as the dividing-wall reactive distillation column (Sun et al., 2011), and heat pump-assisted RD processes (Jana and Mane, 2011). The latest scheme gaining researchers' attractions is the internally heat-integrated reactive distillation column (HIRDiC) (Vanaki and Eslamloueyan, 2012), with the concepts originated from internally heat-integrated distillation column (HIDiC). Unlike the conventional distillation column which has only one shell with two sections, the HIDiC configuration consists of two separate columns linked by a compressor and a throttling valve. Operated at different pressures and temperatures, the internal heat transfer from the high pressure column to the low pressure column becomes possible which has shown great potentials in energy saving (Olujic et al., 2006). Since the first illustration of the concept of HIDiC, research has focused on the modelling (Nakawaii et al., 2001), control (Ho et al., 2009), and experiments (Nakito et al., 2000). Gadalla et al. (2007) and Suphanit (2011)studied the geometric feasibility from the aspect of hydraulic analysis. In this work, we apply the concept of HIDiC into RD processes, and develop a design framework based on iterative calculations to exploit maximum possible and feasible internal heat integraion.

2. A Design Case of HIRDiC

2.1. Description of a Conceptual Design

The concept of internal heat integration is applied to the ethylene glycol (EG) RD column, which is used as an illustration example. As shown in Eq.(1-3), EG is formed from the hydration of ethylene oxide (EO) and can continue to react with EO to form (diethylene glycol) DEG and (triethylene glycol) TEG. EG is the desired product; hence, the RD process has been designed to satisfy the target selectivity to EG (≥90%). The reaction kinetics was taken from literature (Altiokka and Akyalcin, 2009).

$$C_2H_4O\ (EO) + H_2O \rightarrow C_2H_6O_2\ (EG) \quad (1)$$

$$C_2H_4O\ (EO) + C_2H_6O_2\ (EG) \rightarrow C_4H_{10}O_3\ (DEG) \quad (2)$$

$$C_2H_4O\ (EO) + C_4H_{10}O_3\ (DEG) \rightarrow C_6H_{14}O_4\ (TEG) \quad (3)$$

The boiling points at atmospheric pressure of the components are as follows: EO, 283.6 K; H_2O, 373.2 K; EG, 470.5 K; DEG, 518.0 K; TEG, 561.5 K. To maintain the temperature of the reaction, the reactive zone of the RD column favours a higher pressure, while the operating pressure for separation can be lower because of the obvious differences in the boiling points among pure components. Thus, the RD column for the production of EG is well suitable to be divided into two separate columns with the two sections operated at different pressures and temperatures. Besides, as all reactions are highly exothermic (approximately −100 kJ/mol of EO reacted), the internal heat transfer from reactive section to stripping section is allowable and applicable in theory. Figure 1 shows a schematic diagram of the HIRDiC. The reactive section contains a total condenser with total reflux. The vapour flow from the stripping section enters the compressor and delivered to the reactive section, while the liquid from the bottom of the reactive section pass through the throttling valve entering the low pressure stripping section.

2.2. Simulation Tool

The Aspen Plus software package was employed as the simulation tool for the calculation of the thermodynamic properties and phase behaviour of the studied systems. The UNIQUAC activity coefficient model for the liquid phase and the Redlich−Kwong equation of state for the vapour phase were used for phase equilibrium calculations which were verified with our previous experimental data. The heat transfer area requirement and the equipment cost of the HIRDiC were estimated by an interactive sequential calculation using Aspen and Excel.

2.3. Thermodynamic Analysis

To identify the thermodynamic feasibility of internal heat integration, the two columns were first simulated without any internal heat transfer. From Figure 2 which shows the temperature profiles of the two columns, one can see that the temperature changes little in both reactive and stripping section, leading to a nearly constant temperature difference around 32 K. This temperature difference is sound enough for a thermodynamically feasible HIRDiC design. But if it is less than allowable minimum temperature difference, the pressure of reaction column should be considered to be revised (if allowed). In later section, the two commonly used heat distribution schemes will be investigated and compared, i.e. uniform heat transfer area and uniform heat duty distribution. However, we want to point out here that the results of both schemes should

not have much difference given the nearly constant temperature differences and the same heat transfer coefficient (1000 W/m^{2}K).

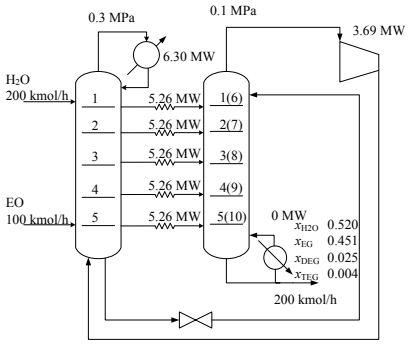

Figure 1 A schematic diagram of HIRDiC.

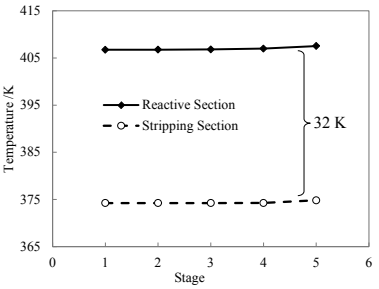

Figure 2 The temperature profile.

The uniform heat duty distribution scheme was employed for a sensitivity analysis to investigate the maximum possible internal heat integration. The results are shown in Figure 3 and 4. When the internal heat duty on each stage increases from 1 to 5 MW, the heat duty of the reboiler and condenser will decrease. The electricity consumption will increase though quite slightly, which can be attributed to the increased reversibility and undermined separation effect. However, the total energy consumption (reboiler heat duty + 3 × compressor break power) decreases. On the other hand, the vapour and liquid flow vary dramatically as the internal heat duty changes.

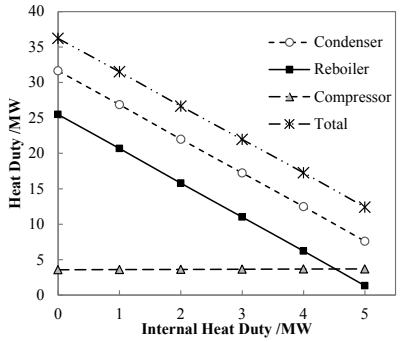

Figure 3 Effects of internal heat duty on the duty of condenser, reboiler and compressor.

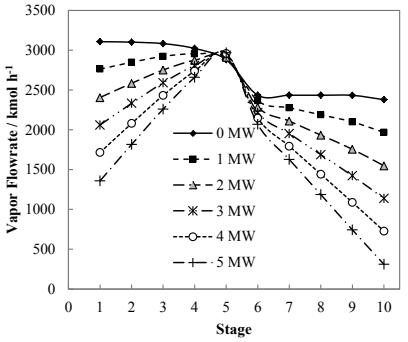

Figure 4 Effects of internal heat duty on the vapour flowrate profile.

According to the sensitivity analysis, it is thermodynamically feasible to reduce the heat duty of the reboiler to 0. Thus, an ideal HIRDiC with no external heat utilities can be obtained as shown in Figure 1. However, a trim reboiler should be considered for system start up and operation flexibility.

2.4. Hydraulic Analysis

Once a reasonable HIRDiC design based on thermodynamic analysis is obtained, its feasibility should be examined again according to hydraulic analysis. In this research we consider a typical concentric configuration with panels placed in the stripping column, as shown in Figure 5. The hot vapour enters the panel, while the cold liquid flows across the outer surface. Under the effect of temperature difference, the vapour condenses inside the panel and the liquid vaporises on the surface. The heat panel has a

fixed thickness and height. The panel length determines the panel area and it is determined by the space available between the two column sections, with the consideration some space allowances (d/L = 0.25 in this work) to ensure the fluid liquidity. However, a tray with the active area fully occupied by a multiplicity of parallel heat transfer panels implies a significant reduction in the free area available for the vapour flow and consequently a faster approach to the entrainment flooding limit. This can be counteracted by a corresponding increase in the tray cross sectional area, i.e. the diameter of the stripping section will be justified by adding up the occupied area of the heat panels.

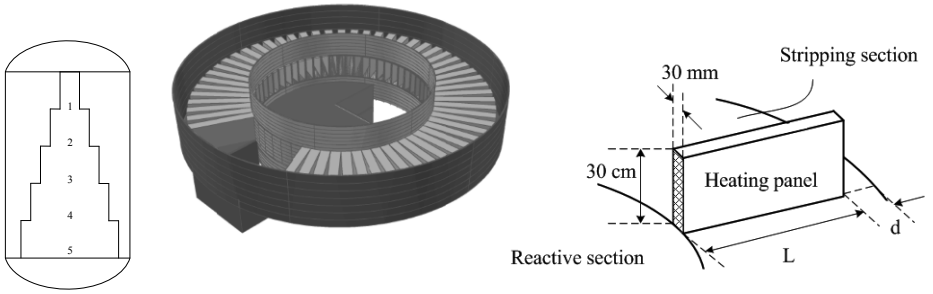

Figure 5 Geometrical analysis of concentric HIRDiC configuration.

Take the ideal HIRDiC design in Figure 1 for example. After determining the internal heat duty on each stage, it is easy to calculate the required heat transfer area on each stage upon updated temperature profile. With the information of liquid and vapour flowrates along the column, the diameter is able to be identified based on the panel layout as well as the flooding limit (0.8 in this work), in terms of which the available heat transfer area can then be calculated. Figure 6 displays the required heat transfer area vs. the available heat transfer area along the column, which shows clearly that not a single stage can provide sufficient transfer area, reflected by the feasibility indicator (required area divided by available area) greater than 1. One can claim that the diameter of stripping section could be increased to provide more heat transfer area. However, this will affect the tray performance. Thus, an appropriate choice is to decrease the internal heat duty of each stage to satisfy the available area, generating a partial HIRDiC design. Moreover, we should point out that, if the internal heat duty is decreased, the vapour and liquid flowrates will increase (according to Figure 4), which requires a larger column diameter. Then, more heat transfer areas are available which in turn allows a higher internal heat duty. Thus, to determine the hydraulically feasible design is not a one-step work. The iteration of calculations cannot be avoided.

3. Design Framework for a Feasible HIRDiC

A two-stage design framework is proposed to obtain a feasible physical configuration with maximum possible extent of heat integration, as shown in Fig 7. The first stage is based on thermodynamic analysis to ensure that the temperature difference between the columns is feasible. In the second stage, the column diameter, the number of panels and the panel size on each tray are iteratively examined and determined according to hydraulic feasibility analysis. To fully utilize the available heat transfer area, a threshold of the feasibility indicator is specified as 0.99 – 1. We emphasize that after the iteration,

the obtained internal heat distribution normally is neither uniform heat duty nor uniform heat transfer area, but a scheme with maximum possible heat integration on each stage restricted by the available heat transfer area.

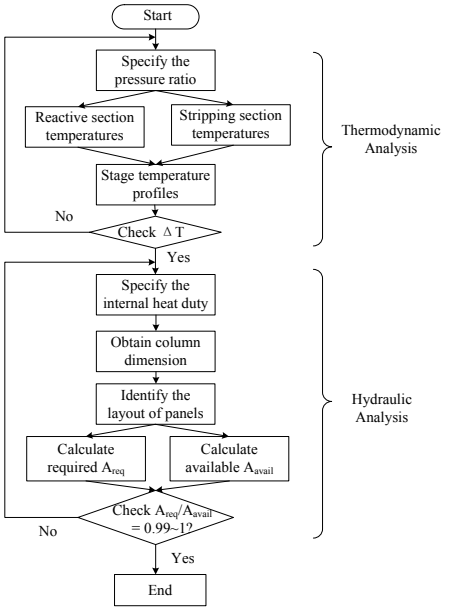

Figure 7 Design framework of feasible HIRDiC based on thermodynamic and hydraulic analysis.

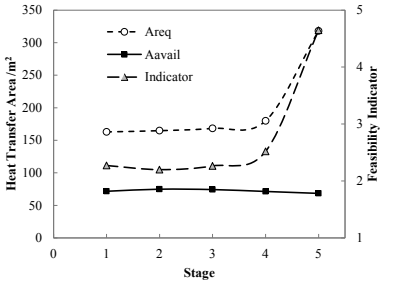

Figure 6 Required and available heat transfer area on each stage.

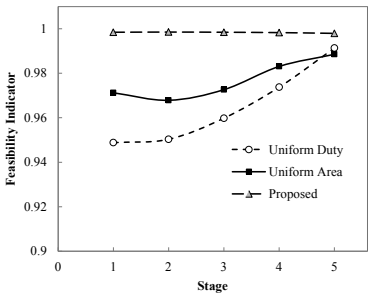

Figure 8 Hydraulic feasibility indicator of different design schemes.

Table 1 Cost information of different HIRDiC design schemes.

Cost Information	Uniform Duty	Uniform Area	Proposed
Column /M$	0.13	0.13	0.13
Panels /M$	0.72	0.72	0.74
Heat Exchangers /M$	1.47	1.45	1.42
Compressor /M$	11.1	11.1	11.1
Annualized Capital Cost /M$·y^{-1}	4.48	4.48	4.47
Electricity /M$•y^{-1}	7.31	7.31	7.31
Cooling Water /M$·y^{-1}	1.86	1.85	1.81
Steam /M$·y^{-1}	9.94	9.75	9.39
Operating Cost /M$·y^{-1}	19.1	18.9	18.5
Total Annual Cost /M$·y^{-1}	23.6	23.4	23.0
Reduction /%	base	0.92	2.58

4. Results and Discussion

Three heat distribution schemes, i.e. uniform heat duty, uniform heat transfer area, and the one obtained from the proposed design framework, were examined and compared. Figure 8 shows the hydraulic feasibility indicator of different schemes, from which one can discover that no matter uniform heat duty or uniform heat transfer area scheme, the

available heat transfer areas were not fully utilized. The scheme obtained from the proposed design framework had the maximum usage of the available heat transfer area and consequently maximum total internal heat duty as well. Table 1 lists the economic analysis results of the three schemes, showing that the uniform heat transfer area scheme is slightly better than the uniform heat duty scheme, although the difference is less than 1%. However, the best design comes from our proposed framework, reducing the total annual cost by some 2.6% compared with the uniform heat duty scheme.

5. Conclusions

A new approach has been proposed for the conceptual design of internally heat-integrated reactive distillation columns. This approach is based on the stage temperature profiles and the physical area availability by the column hydraulic capacity. Through iterative examinations and calculations, a feasible design is obtained with maximum utilization of available heat transfer area and maximum possible internal heat integration. The HIRDiC column synthesizing EG is used as an illustration. The ideal IHRDiC design without external heat utilities is proved to be infeasible according to hydraulic analysis. The feasible design scheme acquired by the proposed framework has the lowest TAC compared with uniform heat duty scheme and uniform heat transfer area scheme.

Acknowledgement

This research was financially supported by the National Natural Science Foundation of China (21306179).

References

M. R. Altiokka, S. Akyalcin, 2009, Kinetics of the Hydration of Ethylene Oxide in the Presence of Heterogeneous Catalyst, 48, 10840 – 10844

M. Gadalla, L. Jimenez, Z. Olujic, P.J. Jansens, 2007, A thermo-hydraulic approach to conceptual design of an internally heat-integrated distillation column (i-HIDiC), Computers and Chemical Engineering, 31, 1346 – 1354

T. J. Ho, C. T. Huang, J. M. Lin, L. S. Lee, 2009, Dynamic simulation for internally heatintegrated distillation columns (HIDiC) for propylene propane system, Comp Chem Eng, 33, 1187 – 1201

A. K. Jana, A. Mane, 2011, Heat pump assisted reactive distillation: Wide boiling mixture, AIChE Journal, 54, 11, 3233 – 3237

K. Naito, M. Nakaiwa, K. Huang, A. Endo, K. Aso, T. Nakanishi, 2000, Operation of a bench-scale ideal heat integrated distillation column (HIDiC): an experimental study, Comp Chem Eng , 24, 495 – 499

M. Nakaiwa, K. Huang, K. Naito, A. Endo, T. Akiya, T. Nakane, 2001, Parameter analysis and optimization of ideal heat-integrated distillation columns, Comp Chem Eng, 25, 737 – 744

Z. Olujic, L. Sun, A. de Rijke, P.J. Jansens, 2006, Conceptual design of an internally heat integrated propylene-propane splitter, Energy, 31, 3083 – 3096

B. Sulphanit, 2011, Optimal heat distribution in the internally heat-integrated distillation column (HIDiC), Energy, 36, 4171 – 4181

L. Sun, R. Wang, J. Li, X. Liu, 2011, Simulation of reactive dividing wall column, Chemical Engineering (China), 39, 7, 1 – 6

R. Thery, X. Meyer, X. Joulia, M. Meyer, 2005, Preliminary design of reactive distillation columns, Chem. Eng. Res. Des., 83, 379

A. Vanaki, R. Eslamloueyan, 2012, Steady-state simulation of a reactive internally heat integrated distillation column (R-HIDiC) for synthesis of tertiary-amyl methyl ether (TAME), Chemical Engineering and Processing, 52, 21 – 27

Krist V. Gernaey, Jakob K. Huusom and Rafiqul Gani (Eds.), 12th International Symposium on Process Systems Engineering and 25th European Symposium on Computer Aided Process Engineering.
31 May – 4 June 2015, Copenhagen, Denmark

Carbon Capture and Utilisation: Application of Life Cycle Thinking to Process Design

Rosa Cuéllar-Franca[a], Ioanna Dimitriou[b], Pelayo García-Gutierrez[b], Rachael H. Elder[b], Ray W.K. Allen[b] and Adisa Azapagic[a*]

[a]*School of Chemical Engineering and Analytical Science, The Mill, Sackville Street, The University of Manchester, Manchester M13 9PL,UK*
[b]*Department of Chemical and Biological Engineering, Mappin Street, University of Sheffield, Sheffield S1 3JD, UK*

**Correspondence to: adisa.azapagic@manchester.ac.uk*

Abstract

Applying life cycle thinking at an early design stage can help engineers to deliver sustainable systems by design. To demonstrate how this can be carried out at a practical level, this paper proposes a simplified methodology for integrating life cycle considerations into process design. Combining flowsheeting and life cycle assessment, it shows how environmental 'hotspots' can be identified and translated into key design targets to improve the sustainability of a system from 'cradle to grave'.The method is applied to a carbon capture and utilisation system using waste CO_2 to produce synthetic diesel in a Fischer-Tropsch process. Although the system is energy intensive, applying life cycle thinking helps to make synthetic diesel competitive not only with fossil but also with biodiesel in terms of the climate change impact.

Keywords: carbon capture and utilisation, life cycle assessment, process design, fuels.

1. Introduction

Global emissions of CO_2 from fossil fuels are increasing steadily and are currently 60% above the 1990 levels, despite the need to reduce them by at least 50% to limit the rise of the global average temperature to 2°C by 2050 (IPCC, 2013). A range of options that could help towards this target are being considered, including carbon capture and utilisation (CCU) which converts waste CO_2 to valuable products such as fuels (Styring et al., 2011). However, conversion of CO_2 to fuels is very energy intensive because of its thermodynamic stability, as well as requiring the use of different chemicals, so that it is not clear if this option is environmentally more sustainable than conventional fossil or biofuels. As CCU technologies are currently being developed, this presents an ideal opportunity to evaluate and optimise their potential for mitigating climate change, the main driver for their development. This is best carried out at an early design stage, taking a life cycle approach to avoid shifting of environmental burdens from one life cycle stage to another (Azapagic et al., 2006). Therefore, this paper sets out to demonstrate how this can be achieved by considering a CCU system for the production of synthetic diesel from waste CO_2.

2. Methodology

The methodology for applying life cycle thinking to process design applied in this work follows the method for process design for sustainability (PDfS) previously proposed by

Azapagic et al. (2006). It takes into account the whole life cycle of a process plant and its product(s) (Figure 1a). However, in this work we consider only environmental impacts with a focus on climate change, excluding economic and social aspects integral to PDfS. Therefore, the PDfS method has been adapted for the purposes of this work and, as outlined in Figure 1b, it involves the following five steps: 1. preliminary process design; 2. life cycle assessment (LCA) of the design; 3. identification of environmental 'hotspots'; 4. identification of design targets for improvements; and 5. identification of correlations between key design variables to help optimise the design at a glance in the next design iteration. These steps are described in more detail in the next section.

3. Applying life cycle thinking to process design: Producing fuels from CO_2

3.1. Preliminary design

The carbon capture and utilisation system considered here produces synthetic diesel in a Fischer-Tropsch process using waste CO_2 from anaerobic digestion of sludge produced during wastewater treatment.The system has been modelled in Aspen Plus (Aspentech, 2014). As shown in Figure 2, it consists of an anaerobic digester that produces biogas and digestate from sewage sludge at mesophilic conditions (308 K and 0.1 MPa). The CO_2 is separated from the biogas using a 15-35 % (wt) monoethanolamine (MEA) solution. It is then recovered from the MEA in a regeneration column, with more than 99 % of the MEA recycled (Zhu et al., 2013). CO_2 and upgraded biogas are converted into syngas through a reverse water-gas shift and steam-methane reforming processes, respectively. This is followed by Fischer-Tropsch synthesis to produce diesel and a mixture of gaseous fuels (methane, ethane, propane and butane).

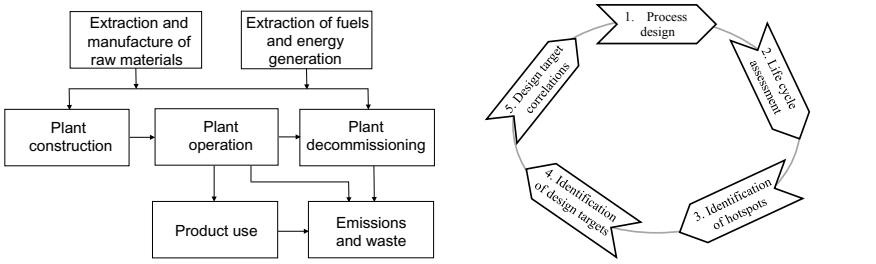

a) The life cycle of a process plant and its product(s) b) Improving environmental sustainability by design

Figure 1 Applying life cycle thinking to process design (adapted from Azapagic et al., 2006).

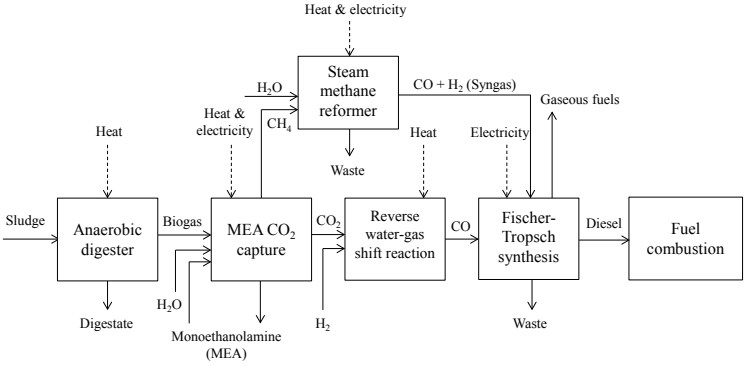

Figure 2. Outline of the process for the production of synthetic fuels from waste CO_2.

3.2. LCA of preliminary design

Following the completion of the preliminary design, LCA is carried out to estimate environmental impacts and identify hotspots which can then be targeted for improvements in the next design iteration. The scope of the study is from 'cradle to grave' and the unit of analysis (functional unit) is defined as 'the production and consumption of 1 MJ of synthetic diesel'. It is assumed that the system is based in the UK. The life cycle inventory data are obtained from Aspen design flowsheets as summarised in Table 1. Hydrogen is assumed to be produced via steam reforming of natural gas as this is the primary production route in Europe (IEA, 2007). Heat is generated from natural gas and electricity is sourced from the UK grid. All liquid waste is treated as industrial wastewater. The transport distances are assumed at 100 km for the sludge and 50 km for hydrogen and MEA. It is also assumed that the nutrients in the digestate displace an equivalent amount of artificial fertilisers (Table 2), for which the system has been credited (Mills et al., 2014). Since the system co-produces gaseous fuels together with diesel, the impacts between the co-products have been allocated in proportion to their mass flows (64 % to diesel and 36 % to gaseous fuels). The biogenic CO_2, originating from the sludge and emitted during the combustion of the fuel, is not considered.

The LCA methodology follows the ISO 14044 guidelines (ISO, 2010). The LCA modelling has been carried out in CCaLC V3.3 (CCaLC, 2014) and the CML 2001 method (Guinée et al., 2002) has been used to estimate the environmental impacts. The background LCA data have been sourced from the Ecoinvent (2010) V2.2 database.

Table 1. Life cycle inventory for the production of 1 MJ of synthetic diesel from waste CO_2.

Life cycle stage	Raw material	Amount (g/MJ fuel)	Heat (MJ/MJ fuel)	Electricity (MJ/MJ fuel)	Waste (g/MJ fuel)
CO_2 capture & separation	Sludge	4500	1.40	9.25×10^{-4}	290
	MEA[a]	9.43×10^{-3}	–	–	–
	Water	2.89×10^{-4}	–	–	–
Syngas production	Water	53	0.71	0.11	1
	Hydrogen	5	–	–	–
Fuel production	–	–	–	0.25	140
Total		4558	2.11	0.36	431

[a] Monoethanolamine

Table 2. Co-products and assumptions for system credits.[a]

Co-products	Displacing	Amount (g/MJ fuel)
Digestate		
Nitrogen	Artificial nitrogen fertiliser (as N)	7
Phosphate	Artificial phosphate fertiliser (as P_2O_5)	13
Sulphur	Artificial sulphur fertiliser (as SO_4)	7
Gaseous fuels[b]	Natural gas	13
Liquid fuels[c]	–	23

[a] The system is credited for displacing artificial fertilisers and gaseous fossil fuels (natural gas). There are no credits for synthetic diesel as that is the main product from the system.
[b] A mixture of methane (67 % wt), ethane (9 % wt), propane (11 % wt) and butane (13 % wt).
[c] A mixture of liquid fuels (C5-C30), in this study assumed to be diesel with a lower heating value of 43.25 MJ/kg.

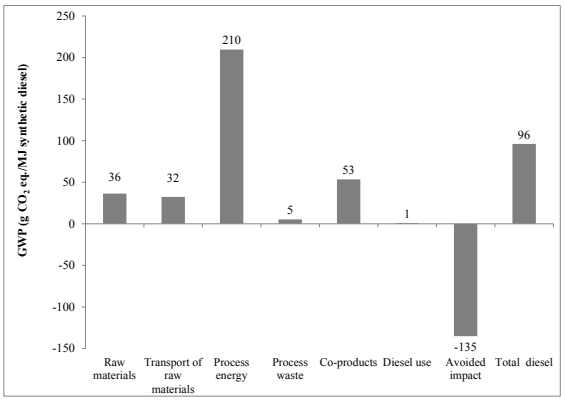

Figure 3.Global warming potential (GWP) of production and consumption of 1 MJ of synthetic diesel (The GWP of co-products refers to gaseous fuels, allocated on a mass basis (36%). The avoided impact refers to the GWP avoided by displacing artificial fertilisers – see Table 2).

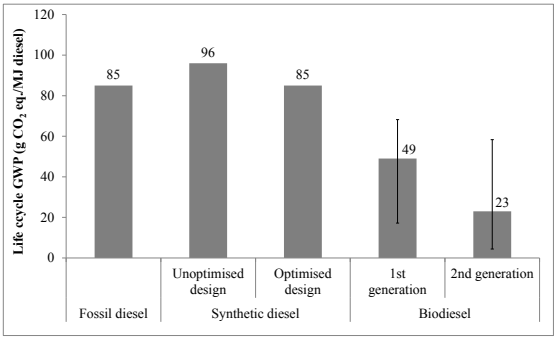

Figure 4. Global warming potential (GWP) of different types of diesel (Data for fossil and biodiesel are from Jeswani and Azapagic (2012). All results are from 'cradle to grave', including fuel use in vehicles. Biogenic carbon for synthetic and biodiesel is excluded).

3.3. Identifying hotspots

With the LCA completed, the next step involves identification of hotspots which will be targeted for optimising the system. As an example, we consider climate change impact as a key driver for CCU, in LCA expressed as the global warming potential (GWP). The GWP can also be used as a proxy for some other impacts, including depletion of fossil fuels, acidification and photochemical smog.

Using the preliminary (unoptimised) design data, the GWP of synthetic diesel from 'cradle to grave' is estimated at 96 g CO_2 eq./MJ (Figure 3). This is 12% higher than the GWP of fossil diesel (see Figure 4). It can also be noted that the GWP of synthetic diesel is 2 times higher than for 1st generation biofuels and 4 times greater than for 2nd generation. Therefore, the design is unsustainable and needs to be improved by targeting the hotspots. Figure 3 shows that the main hotspot in the system is energy consumption, accounting for 74 % of the total GWP. This is due to the high energy requirements in the anaerobic digester, the MEA capturing unit, the steam-methane reforming reactor and compressors. The raw materials and their transport contribute 13 % and 11 % of the total GWP, respectively. Among the raw materials, hydrogen is the highest contributor to the impact, followed by the rate of MEA recycling. The use of diesel in vehicles contributes little to the GWP as most of the CO_2 is biogenic, originating from sewage.

Therefore, energy, hydrogen and MEA recycling rates should be targeted for design optimisation. This is discussed in the next section.

3.4. From hotspots to key design targets

Now that the hotspots have been identified, key design targets can be defined. In this study, the GWP of fossil diesel (85 g CO_2 eq./MJ) is taken as a reference point, aiming to optimise the system so that the GWP of synthetic diesel is equal to or below that of the fossil fuel. As indicated in Figure 5a, for the current industrial practice of MEA recycling of 99.997 %, the process energy consumption must be reduced by 8 %. If the recycling rate is lower, for example 98 %, then the energy reduction of 19 % is necessary. Alternatively, switching from carbon-intensive sources of H_2 such as natural gas (7.5 kg CO_2 eq./kg H_2) to water electrolysis (0.95 kg CO_2 eq./kg H_2) or naphtha cracking (1.7 kg CO_2 eq./kg H_2) would reduce the GWP without the need to decrease energy consumption (Figure 5b). For instance, the GWP of synthetic diesel using H_2 from water electrolysis or naphtha cracking is equal to 76 and 78 g CO_2 eq./MJ, respectively; this is 8-10 % below the GWP of fossil diesel. It is also possible to match the GWP of synthetic diesel with that of 1st generation biodiesel (49 g CO_2 eq./MJ fuel, see Figure 4) with these two sources of H_2 but the energy consumption must be reduced by around 20 % (Figure 5b). Doubling the energy reduction to around 43 % would also make synthetic diesel competitive with 2nd generation biodiesel (23 g CO_2 eq./MJ fuel).

3.5. Correlations between key design targets

To help process designers see at a glance how the key design targets influence the environmental performance of the system, it is useful to plot their correlations for a range of feasible values. For example, if the target is for the synthetic diesel to be competitive with the fossil fuel in terms of the GWP, the correlation in Figure 6 indicates how this can be achieved taking into account three variables: energy consumption, H_2 sources and MEA recycling rates. The correlations suggest that using H_2 from natural gas requires energy reductions ranging from 8 % for the 99.997 % MEA recycling rate to 19 % for 98 % of MEA recycled. For the other two sources of H_2 (naphtha cracking and water electrolysis), no or little energy reduction is needed until the recycling rate of MEA falls below 99 %. At 98% of MEA recycled, the energy consumption must be reduced by 4–5 %. These correlations can be used in the next design iteration to help guide engineers in delivering a more sustainable system.

4. Conclusions

A simplified methodology for applying life cycle thinking to process design has been proposed in this work to help identify hotspots and translate them into key design targets, with the aim of improving the environmental sustainability of processes. One of the advantages of the methodology is that it is relatively simple and enables designers to identify improvement opportunities at a glance. The methodology has been applied to a process producing diesel from waste CO_2. The results show that the main hotspots are energy consumption, sources of H_2 and MEA recycling rates. Optimising these parameters can make diesel from CO_2 competitive with both fossil and biofuels in terms of the climate change impact. Therefore, the study demonstrates that applying life cycle thinking at an early stage can help engineers to deliver sustainable systems by design.

Acknowledgements

This work was carried out as part of the “4CU” Programme Grant funded by the UK Engineering and Physical Sciences Research Council, EPSRC (Grant No. EP/K001329/1).

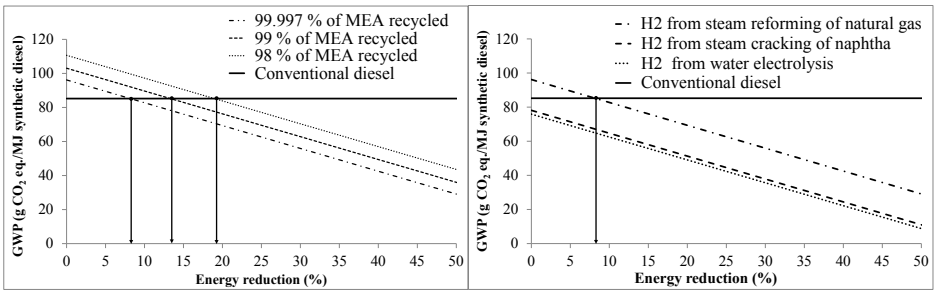

a) Energy reduction targets for different MEA recycling rates (H_2 from natural gas reforming)

b) Energy reduction targets for different sources of hydrogen (MEA recycling rate: 99.997 %)

Figure 5. Identification of design targets for energy reduction for different system variables.

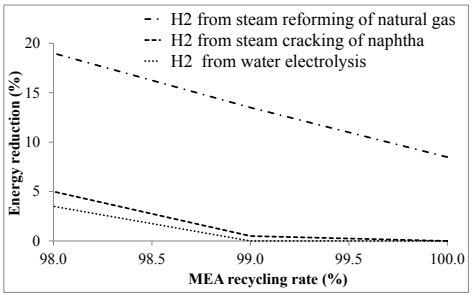

Figure 6 Correlations between key design targets.

References

Aspen Technology, 2014, Aspen Plus, www.aspentech.com.

A. Azapagic, A. Millington, A. Collett, 2006, A methodology for integrating sustainability considerations into process design, Chemical Engineering Research & Design, 84, 6, 439-452.

CCaLC, 2014,CCaLC software and database, www.ccalc.org.uk.

Ecoinvent, 2010, Swiss Centre for Life Cycle Inventories, www.ecoinvent.org/database.

J.B. Guinée, M. Gorrée, R. Heijungs, G. Huppes, R. Kleijn, L. van Oers, A. Wegener Sleeswijk, S. Suh, H.A. Udo de Haes, H. de Bruijn, R. van Duin, M.A.J. Huijbregts, 2002, Handbook on life cycle assessment: Operational guide to the ISO standards, Springer, The Netherlands.

IPCC, 2013, Climate change 2013: The physical science basis,Intergovernmental Panel on Climate Change, www.ipcc.ch/report/ar5/wg1.

IEA, 2007, Hydrogen production & distribution, International Energy Agency,Paris, France, www.iea.org/publications/freepublications/publication/iea-energy-technology-essentials-hydrogen-production--distribution.html.

ISO, 2010, ISO 14044:2006 Environmental management – life cycle assessment – requirements and guidelines, International Organization for Standardization, Geneva, Switzerland.

H. Jeswani, A. Azapagic, 2012, Life cycle sustainability assessment of second generation biodiesel, in R. Luque, J. Melero (eds.), Advances in biodiesel production: processes and technologies, Woodhead Publishing, Oxford, UK.

N. Mills, P. Pearce, J. Farrow, R. B. Thorpe, N. F. Kirkby, 2014, Environmental & economic life cycle assessment of current & future sewage sludge to energy technologies, Waste Management, 34, 1, 185-195.

P. Styring, D. Jansen, H. de Coninck, H. Reith, K. Armstrong, 2011, Carbon capture and utilisation in the green economy, Centre for Low Carbon Futures, York, UK.

L. Zhu, G. W. Schade, C. J. Nielsen, 2013, Real-time monitoring of emissions from monoethanolamine-based industrial scale carbon capture facilities, Environmental Science & Technology, 47, 24, 14306-14314.

Krist V. Gernaey, Jakob K. Huusom and Rafiqul Gani (Eds.), 12th International Symposium on Process Systems Engineering and 25th European Symposium on Computer Aided Process Engineering.
31 May – 4 June 2015, Copenhagen, Denmark

Topology optimization for biocatalytic microreactor configurations

Inês P. Rosinha[a], Krist V. Gernaey[a], John M. Woodley[a] and Ulrich Krühne[a]

[a]*CAPEC-PROCESS Center, Department of Chemical and Biochemical Engineering, Technical University of Denmark (DTU), Building 229, DK-2800 Kgs. Lyngby, Denmark*
inros@kt.dtu.dk

Abstract

The aim of this study is to present an innovative strategy for selecting a reactor for a specific process. Instead of adapting the process to a well-known reactor shape, a topology optimization method is used to obtain the best reactor configuration, and is applied to a biocatalyic reaction system as a case study. The Evolutionary Structure Optimization (ESO) method is applied using an interface between Matlab® and the computational fluid dynamic simulation software ANSYS CFX®. In the case study, the ESO method is applied to optimize the spatial distribution of immobilized enzyme inside a microreactor. The results allow evaluating which regions in the microreactor have more importance for the product formation. In fact, it was possible to simulate the improvement of the outlet product concentration per same amount of enzyme by modifying the spatial distribution of the immobilized enzyme.

Keywords: topology optimization, biocatalysis, immobilized enzymes, CFD

1. Introduction

Topology optimization has been used by mechanical and civil engineers for many years, for example in order to minimize the amount of used material and the strain energy of structures while maintaining their mechanical strength (Bendsoe et al., 2003).Topology optimization is a mathematical method which spatially optimizes the distribution of material within a defined domain, by fulfilling given constraints previously established and minimizing a predefined cost function. For such an optimization procedure, the three main elements are design variables, the cost function and the constraints.

The traditional solutions for structural optimization problems in buildings were determined by the use of direct search methods on an Isotropic Solid and Empty (ISE) topology. In an ISE topology, the elements are either filled by a given isotropic material or do not contain any material. However, due to the large number of elements, the application of direct search methods on an ISE topology was found to be computationally extremely expensive. Therefore, since the 1980s, the main focus in this area has been to develop more efficient methods to obtain faster solutions. In the scientific literature, there are numerous techniques to perform a topology optimization; the two most popular methods are the Solid Isotropic Material with Penalization (SIMP) technique and the Evolutionary Structural Optimization (ESO) technique.

The SIMP technique is based on determining the optimum structure by varying the material density within the predefined domain. The predefined domain is discretized in elements and a finite element (FE) analysis is applied to determine the structure performance. Conceptually, the SIMP method comprises a FE analysis of the domain followed by an optimization of the density of each element of the domain. Afterwards,

the configuration with the new element densities is analyzed and the optimization is performed again. The optimization procedure continues until convergence (Bendsoe et al., 2003).
The ESO method was developed by Xie and Steven (1993) and it has been applied in various optimization research areas. The ESO method is based on the simple concept of progressively removing inefficient material from a structure. The unneeded material is removed by using a rejection criterion (RC) which identifies the ineffective material. This method has the advantage that it is easy to understand and to learn. Moreover, this method is also simple to program and to link with existing computer-aided engineering software e.g. ANSYS CFX®, ANSYS Fluent® or Nastran®.
This contribution presents a novel adaptation of the ESO method to optimize the catalyst spatial distribution inside microreactors considering a reaction carried out by a biological catalyst, an enzyme. The goal is to improve the product formation per same amount of enzyme by optimizing the immobilized enzyme spatial distribution. This contribution applies commercially available tools such as the computational fluid dynamics(CFD) software, ANSYS CFX®, and Matlab®, and will link them with a self-programmed topology optimization method.
Previously, selected studies dealing with topology optimization of catalyst inside microreactors have been reported by Okkels et al. (2007) and by Schäpper et al. (2010) where they used the porosity of the catalyst carrier as the design variable.This study changes the surface concentration of the enzyme instead of changing the porosity of the catalyst carrier, which consequently would modify the fluid dynamic properties inside the microreactor. The optimization procedures considering porosity as design variable have resulted in configurations with large void spaces within the carrier material. These configurations are mechanically unstable and, since in the real reactor such carrier material cannot be packed at fixed locations, the material might change the locations due to the fluid flow. Therefore it is not possible to validate these results experimentally.
The consideration of the enzyme concentration as a design variable, will allow new configurations by depositing the enzyme on favourable areas of the microreactor, either on a surface or on an immobilization carrier. Therefore, the presented topology optimization procedure will allow for the first time that future experimental validations of the simulated design can be performed.

2. Materials and Methods

The shape of the investigated microreactor is an extension of the two dimensional shape presented by Okkels et al. (2007) into a three dimensional design. The view from the top of the microreactor shows that the microreactor consists of a parallelepiped measuring 30 mm of width and depth, combined with two channels for the inlet and outlet located on opposite sides of the square. The width of the inlet and outlet channels is 10 mm. The height of the microreactor corresponds to 0.5 mm. The shape of the reactor is presented in Figure 1.In this investigation, the enzyme is immobilized at the top and bottom surfaces of the reactor. Since the flow profile is symmetric on the central vertical and central horizontal planes, symmetry boundaries were created at half of the height and through the middle of the inlet and outlet as presented in Figure 1b.In this way only a quarter of the whole reactor geometry is simulated which provides an acceleration of the computational solution. The flow velocity at the inlet is set to 0.01 m/s for all simulations. The choice of the residence time was made in order to ensure that the velocity close to the bottom wall is different from zero and varies between

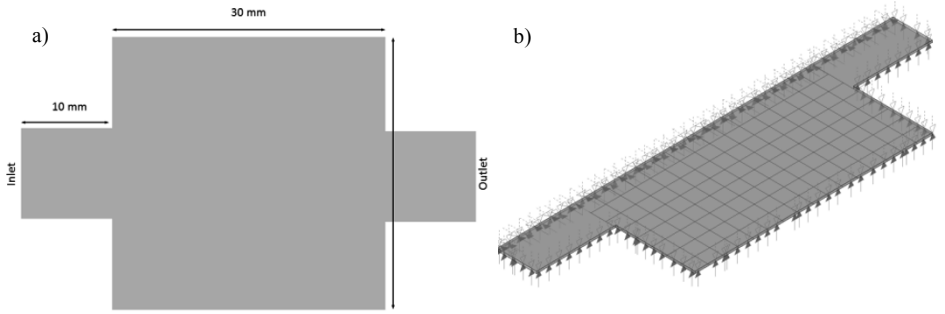

Figure 1- Microreactor configuration: a) full microreactor configuration; b) configuration with symmetry planes, horizontal and vertical planes

different locations on the bottom and top surfaces due to effects of the lateral walls and narrow inlet and outlet.The studied reaction rate (r) in this case study follows the mechanism of an enzyme, which is characterized by a Michaelis-Menten mechanism. The Michaelis-Menten reaction equation is described by Eq 1:

$$r = kcat \cdot [E] \frac{[S]}{[S] + K_M} \tag{1}$$

where *kcat* is the turnover number, [E] the enzyme concentration, [S] the substrate concentration and K_M is the Michaelis-Menten constant. In this case, the values considered for the reaction are equivalent to the values determined experimentally for a catalase reaction, *kcat* = 10^7 mol·m^{-3}·s^{-1} and K_M= 25 mol·m^{-3}(Díaz et al., 2001). The reaction catalysed by catalase corresponds to the conversion of two molecules of hydrogen peroxide forming one molecule of oxygen and two molecules of water:

$$2H_2O_2 \xrightarrow{\text{catalase}} 2H_2O + O_2 \tag{2}$$

In this study, the maximum enzyme concentration was determined considering that the molecular weight of catalase is 315 kDa and assuming that the amount of enzyme that is possible to immobilize on the surface is 4 mg·m^{-2}. From here it is possible to calculate that the maximum enzyme concentration on the surface is $1.2 \cdot 10^{-11}$ mol·m^{-2}.At the inlet, the substrate concentration, hydrogen peroxide, is 1 mM.

The method applied to this study is an adaptation of the ESO method for the topology optimization of enzyme inside the microreactor. The procedure for the topology optimization is presented in Figure 2.In this case, the design variable is the enzyme concentration immobilized on the surface and the cost function to be maximized is the concentration of one of the products at the outlet. There is only one constraint to this problem which is to maintain the same amount of enzyme (number of moles) inside of the microreactor between iterations. This constraint makes the procedure different from the original ESO method. In the ESO method, the ineffective elements are simply eliminated, but in this case study it is not meaningful to simply remove an element. If an element is removed, the amount of enzyme inside of the microreactor will be less and consequently the product concentration at the outlet will decrease. Therefore the ESO method has been modified. When an element is removed the amount of enzyme corresponding to that element is distributed evenly between all the elements which still contain immobilized enzyme.

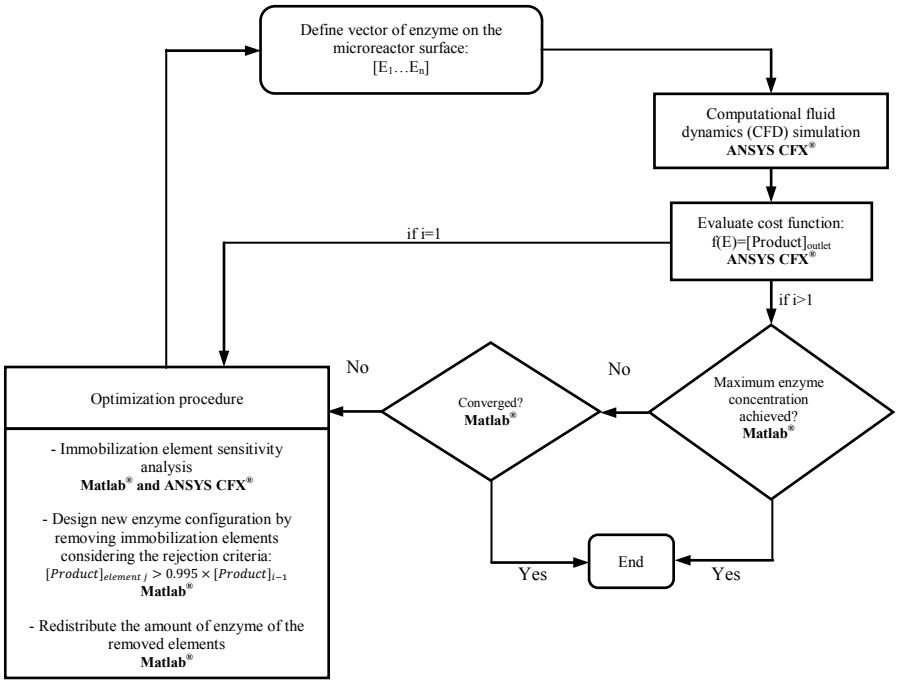

Figure 2 – Flowchart for topology optimization of enzyme in a microreactor using the ESO method through a routine coupling Matlab® and ANSYS CFX®.

The design of the microreactor is implemented into ANSYS CFX® and for this purpose the bottom surface of the microreactor was divided in small areas, in this case 128 immobilization elements as shown in Figure 1b. Then, the whole microreactor volume is discretized using a fine mesh of cells. The dynamics and the reaction parameters of the system are configured according to the conditions and the reaction system for the case study mentioned above.

The optimization procedure consists of a routine which couples the commercial computational fluid dynamics (CFD) software ANSYS CFX® to Matlab®. The optimization loop starts by setting a vector in Matlab® in which the enzyme concentration of the different locations on the surface ($[E_1 \ldots E_n]$) is defined. The enzyme was initially uniformly distributed at half of the maximum concentration on the surface of the microreactor $5.6 \cdot 10^{-12}$ mol·m^{-2}. Afterwards, the ANSYS CFX® script is changed according to the defined vector, a computational fluid dynamics simulation is carried out by ANSYS CFX® and the cost function is evaluated.

The optimization procedure starts with a sensitivity analysis of each immobilized element in order to evaluate its influence on the product concentration at the outlet. One by one the enzyme concentration of each of the immobilization elements is set to zero. This is controlled by a self-programed routine in Matlab® which makes the necessary modifications in the ANSYS CFX® script while ANSYS CFX® carries out the

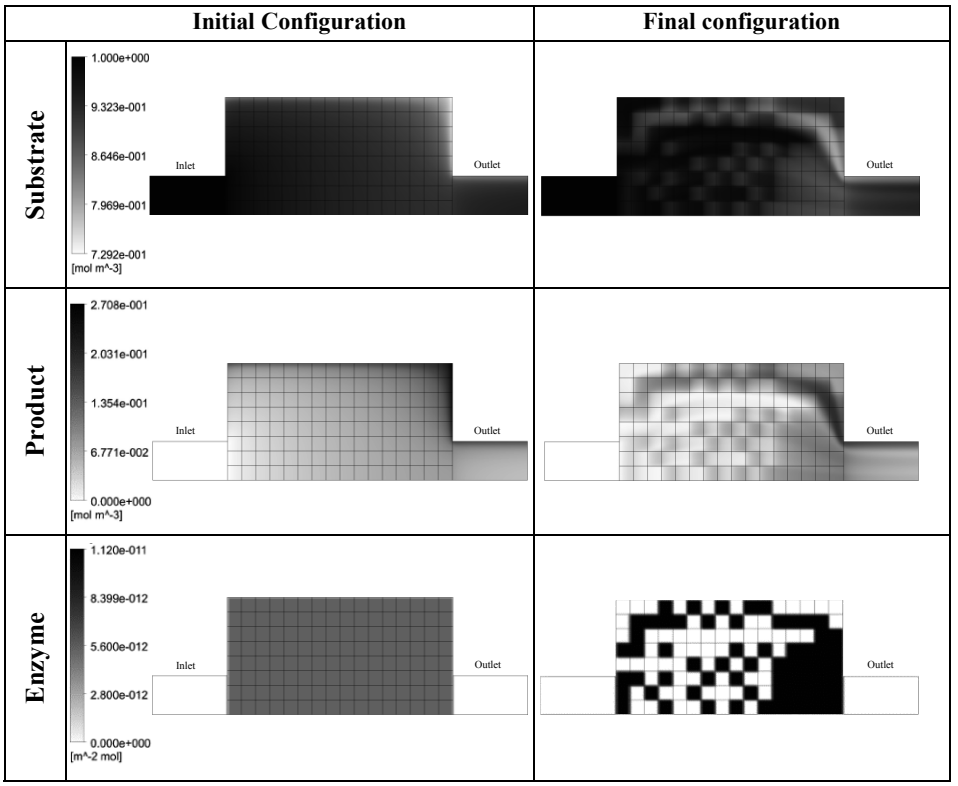

Figure 3 – Results from the topology optimization: Concentration of substrate (hydrogen peroxide) and product (water)inside the microreactor for initial and final configurations and immobilized enzyme (catalase) on the bottom surface of the microreactor.

computational fluid dynamics analysis using the new script. The Matlab® code removes the immobilized elements with the lowest sensitivity according to a predefined rejection criterion (RC). In this study the RC is defined for the immobilized element j which is removed if the product concentration at the outlet is:

$$[Product]_{element\ j} > 0.995 \times [Product]_{i-1} \quad (3)$$

being *i* the iteration number and *j* is number of the element. That means if an element is not contributing substantially to the formation of the product it is removed. The amount of enzyme present in the removed elements is distributed within all other elements that have not been removed in order to keep the same amount of enzyme (mol) inside the microreactor. Subsequently the alterations of the enzyme configuration on the surface of the microreactor and its new concentration are inserted in the ANSYS CFX® script through Matlab® and a CFD simulation is repeated to evaluate the performance of the new enzyme configuration. The procedure is repeated until the maximum product concentration is achieved, the concentration of the enzyme has reached the maximum possible value or the optimization converges.

3. Results and Discussion

The optimization loop ends when the maximum enzyme concentration ($1.2 \cdot 10^{-12}$ $mol \cdot m^2$) was achieved. On the one hand, $6.75 \cdot 10^{-2}$mM of substrate were converted with the initial configuration, on the other hand, $6.89 \cdot 10^{-2}$ mM of substrate were converted with the final shape. In the end, the topology optimization resulted in an improvement of 2%of conversion of the substrate per same amount of enzyme compared with the initial enzyme configuration. It is expected that the application of a topology optimization to a more complex reaction mechanism (with product or/and substrate inhibition) will result in larger improvements. The results of the topology optimization as well as the optimal enzyme configuration can be found in Figure 3.The final configuration of the enzyme is characterized by a higher concentration of enzyme close to the walls and in immobilization elements close to the outlet. This demonstrates that immobilized molecules at locations with higher residence time, due to low fluid velocity, contribute more to the product formation. In addition, within the immobilization elements with maximum velocity, the elements which are close to the outlet are the ones which seem to have more influence on the product formation.

4. Conclusion

The presented work demonstrates that it is possible to use existing methods and tools in an efficient way in order to use topology optimization for finding better reactor configurations for a particular reaction system. The application of the ESO method by combining a CFD software, ANSYS CFX®, with Matlab® revealed to be a feasible implementation to optimize the spatial distribution of immobilized enzyme in a microreactor. In this study, the product formation per same amount of enzyme was improved by optimizing the immobilized enzyme spatial distribution. This study contributes to the development of future innovative solutions for establishing a reactor with immobilized catalyst within a process. Currently, the studies are made in microreactors, because it will be easier to validate the results experimentally. Nevertheless, the topology optimization of catalysts can contribute to an improvement of production also at industrial scale, since the product formation is not uniform in full-scale reactors. The application of topology optimization will potentially change the development of reactors and contribute to the improvement of reaction yields.

Acknowledgments

The research leading to these results has received funding from the European Union FP7 (FP7/2007-2013) Project BIOINTENSE – Mastering Bioprocess integration and intensification across scales (Grant Agreement number 312148).

References

M. P. Bendsoe, O. Sigmund, 2002, Topology Optimization: Theory, Methods and Applications, 2nd ed., Heidelberg: Springer, Berlin, Germany

A. Díaz, P. Rangel, Y, M Oca, F. Lledías, W. Hansberg, 2001, Molecular and kinetic study of catalase-1. A durable large catalase of *Neurospora crassa,* Free Radical Biology & Medicine, 31 (11), 1323-1333.

F. Okkels, H. Bruus, 2007, Design of micro-fluidic bio-reactors using topology optimization, Journal of Computational and Theoretical Nanoscience, 4 (4), 814-816.

D. Schäpper, R. L. Fernandes, A. E. Lantz, F. Okkels, H. Bruus, K. V. Gernaey, 2010, topology Optimized Microbioreactors, Biotechnology and Bioengineering, 108 (4), 786-796.

Y. M. Xie and G.P. Steven, 1993, A simple evolutionary procedure for structural optimization, Computers and Structures, 49 (5), 885-886.

Krist V. Gernaey, Jakob K. Huusom and Rafiqul Gani (Eds.), 12th International Symposium on Process Systems Engineering and 25th European Symposium on Computer Aided Process Engineering.
31 May – 4 June 2015, Copenhagen, Denmark

Design of Hybrid Heat-integrated Configuration for Indirect Reactive Distillation Processes

Kuo-Chun Weng, Hao-Yeh Lee*

Department of Chemical Engineering, National Taiwan University of Science and Technology, Taipei 10607 Taiwan
haoyehlee@mail.ntust.edu.tw

Abstract

In this work, hybrid configuration which combines the concepts of thermally coupled and multi-effect heat-integrated methods has been studied. Moreover, the potential energy saving of other individual heat-integrated methods has been compared with the hybrid configuration. Ideal IIp reactive distillation process and diphenyl carbonate process are chosen as examples to demonstrate the performance of the hybrid configuration. The result shows hybrid configuration displays the highest ability in energy saving for both processes.

Keywords: Reactive distillation; Heat integration; Thermally coupled; Multi-effect; Hybrid configuration

1. Introduction

The ascension of crude oil price and global warming problem has attracted more and more attention in recent years. The development of energy savings becomes an important purpose for the research of chemical processes. Reactive distillation (RD) that integrating multifunctional unit(reaction and separation) to substitute a single function unit has been published and demonstrates its advantages in selectivity, productivity improvement and energy requirement reduction (Malone and Doherty, 2000).

In order to improve more economic benefit, the combination of two famous process intensification techniques for reducing energy usage named multi-effect and thermally coupled with RD configurations are studied in some literatures (Lee et al., 2010; Wang et al., 2010; Cheng et al., 2013). Thermally coupled configuration can eliminate the remixing effect to reduce the total energy requirement. The energy efficiency can be increased in multi-effect configuration by energy reusing. However, in indirect thermally coupled configuration such as IIp case in Wang et al (2010), it is found that more vapor is condensed in the top of second column due to energy transferred from top vapor of the first column to the middle location of the second column. It means more energy is wasted in the top of second column. To overcome the drawback of energy waste in RD process, the hybrid heat integrated configuration which combines the concepts of multi-effect and thermally coupled arrangement is investigated to improve energy efficiency and reduce overall energy requirement simultaneously in this paper. Notice the commercial simulator Asepn Plus is used for all cases.

2. Case 1: IIp ideal RD process

The ideal RD process with quaternary components can be classified into six types according to relative volatilities of reactants and products (Tung and Yu, 2007). IIp type indirect ideal RD process is used in this study to demonstrate superiorities of hybrid

heat-integrated configuration. Four components (C, D, A, B) with relative volatility 8/4/2/1 are assumed in this process. The flowsheet and information of columns refer to Lin's work (Lin, 2007). The thermodynamic and kinetic models are taken from Tung and Yu (2007). Ideal thermodynamic model and Arrhenius form kinetic equations with pseudo homogeneous expression are applied in this study.

2.1. Conventional RD configuration

An ideal reaction is assumed for IIp process. Reactants are A and B and products are C and D. IIp ideal RD process is constituted by a RD column (C1) and a separation column (C2). The reactants A and B are fed into the bottom of RD column. The C1 column only contains reactive section and rectifying section. Due to the higher boiling point of reactants, there is no bottom product at C1 column to avoid the loss of reactants. The rectifying section and the reactive section including column sump in C1 column are set between 6 and 10 stages, respectively. Both reactants are fed into the bottom of the C1 column because of their smaller relative volatility. The flow rates of both reactants are the same and set as 45.36 kmol/h. The holdup of column sump is assumed 10 times than each stage. Top product of C1 column with component C and D is fed into 19th stage of C2 column. 35 stages are in the C2 column. Component C is produced at the top of C2 column and its specification is designed in 99 mol %. Product D with 95 mol % purity can be obtained at the bottom of C2 column. The operating pressures of C1 and C2 columns are 6 and 2 bars, respectively. The overall flowsheet of conventional RD configuration is displayed in Fig. 1(a).

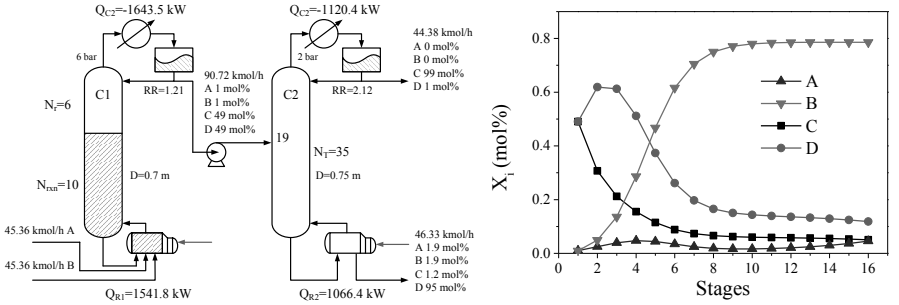

Figure 1: (a) Flowsheet of IIp RD process; (b) Composition profile of C1 column

The liquid composition profile of C1 column is shown in Figure 1(b). In Figure 1(b), the D composition represents in sphere symbol. In the upper section of RD column, the D composition shows to reach the maximum value and then decrease. This phenomenon is well-known as "remixing effect" and it means that there is potential to design a thermally coupled configuration for energy reduction.

2.2. Thermally coupled configuration

Thermally coupled configuration has widely been studied in open literatures to eliminate remixing effect and save energy. To eliminate the remixing effect of C1 column, the thermally coupled configuration of IIp process had been designed by Wang et al. (2010). In this configuration, a liquid sidedraw flow from 19th stage of C2 column is sent back to C1 column as the liquid reflux. The simulation result of thermally coupled configuration is shown in Figure 2(a). The remixing effect can be eliminated and 27.6 % energy requirement can be saved by this arrangement. However, the observation of condenser duty of C2 column presents a higher value than conventional

configuration. This larger condenser duty means a larger column diameter is required and higher energy waste is found at the top of column.

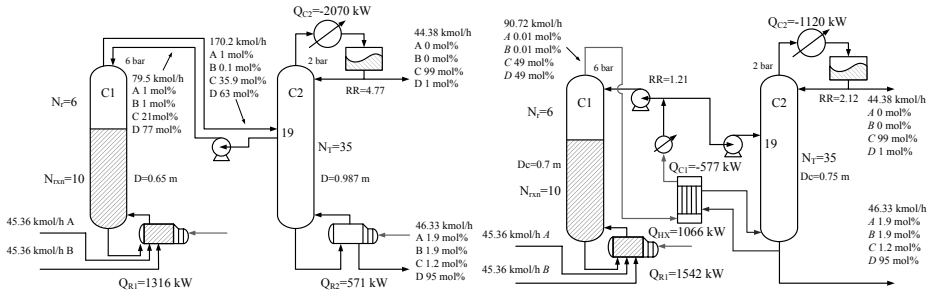

Figure 2: (a) Thermally coupled and (b) Double-effect configurations of IIp RD process

2.3. Double-effect configuration

According to different operating pressure of two columns, the higher operating pressure of C1 column shows an opportunity of double-effect heat integration. The temperature difference between top vapor of C1 column and bottom of C2 column is 22.7 ^{o}C. The top vapor temperature of C1 column will decrease after energy exchange to C2 column. An important assumption of log mean temperature difference between C1 top and C2 bottom must be higher than 10 ^{o}C for energy transfer. The heat exchanger area can be calculated by following equation:

$$A = Q/(U \cdot \Delta T_{ln}) \tag{1}$$

In Eq. (1), Q is the energy of heat transfer and relates to the overall heat transfer coefficient (U), heat exchanger area (A) and log mean temperature (ΔT_{ln}). The overall heat transfer coefficient refers to Douglas (1988) and is set as 0.17 kW/m$^2 \cdot$ h.

The double-effect configuration is shown in Figure 2(b). The energy requirement of C2 column is supplied from heat of C1 column top vapor. An auxiliary condenser is needed to remove the remaining energy. The overall energy exchange in HX unit is 1,066 kW and the calculated heat exchanger area is 300.3 m^2. The double-effect configuration has 40 % energy saving however the remixing effect cannot be eliminated.

2.4. Hybrid configuration

By observing the simulation result of thermally coupled configuration, the energy can be saved in this arrangement because of the elimination of remixing effect. However, larger condenser duty of C2 causes a larger column diameter. Energy efficiency is much higher in double-effect configuration but it cannot overcome the drawback of remixing effect. To overcome the drawback of energy waste in RD process, the hybrid heat integrated configuration which combines the concepts of multi-effect and thermally coupled arrangement is investigated to improve energy efficiency and reduce overall energy requirement simultaneously

The hybrid configuration is based on thermally coupled configuration. However, the top vapor product of C1 column is not fed to C2 directly. Energy is transferred from top vapor of C1 column to C2 bottom first and then fed to 19th stage of C2. A sidedraw flow is also needed to be as liquid reflux of C1 column. The flowsheet of hybrid configuration and liquid composition profile of C1 column is shown in Figure 3(a) and (b). The simulation result in Figure 3(a) shows the energy usage of C2 is 728 kW and all can be supplied from top vapor of C1 column. Total energy requirement can be saved around 50 % by hybrid configuration and the heat exchanger area of heat

exchanger HX is only 63 % of double-effect configuration. Condenser duty of C2 also shows a smaller value than the result of thermally coupled configuration.

The liquid composition profile of C1 column in Figure 3(b) demonstrates the composition of component D monotonic increases to the column top. It means that the remixing effect in hybrid configuration also can be eliminated as the configuration with thermally coupled arrangement.

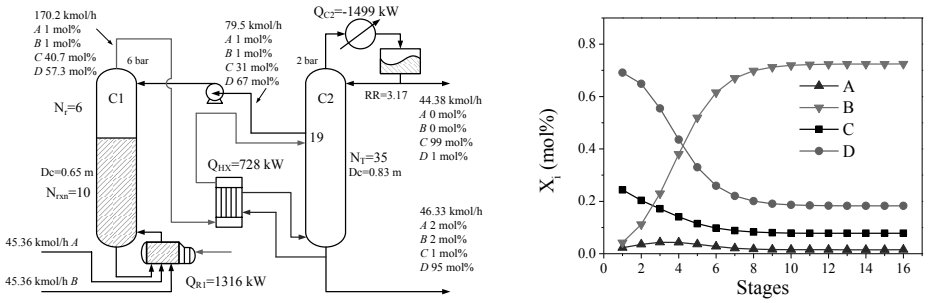

Figure 3: (a) Flowsheet (b) Composition profile of RD column of hybrid configuration

3. Case2: DPC reactive distillation process

With the issue of environmental production, phosgene-free process has gradually replaced the conventional process. Phosgene-free diphenyl carbonate (DPC) RD process has been proposed in Cheng et al. (2013). The ideal thermodynamics and power law kinetic model are taken from their work.

3.1. DPC RD configuration

The overall reaction of diphenyl carbonate production is shown in below:

$$DMC + PA \Leftrightarrow MPC + MA \quad (2)$$

$$MPC + PA \Leftrightarrow DPC + MA \quad (3)$$

The reaction is an endothermic reaction. Two reactants are dimethyl carbonate (DMC) and phenyl acetate (PA). The intermediate component is methyl-phenyl carbonate (MPC) The product and by-product are DPC and methyl acetate (MA). Due to lower reaction rate, the excess reactant, DMC, is fed into reactive section of C1 column. The overall flowsheet of DPC RD process is displayed in Figure 4(a).

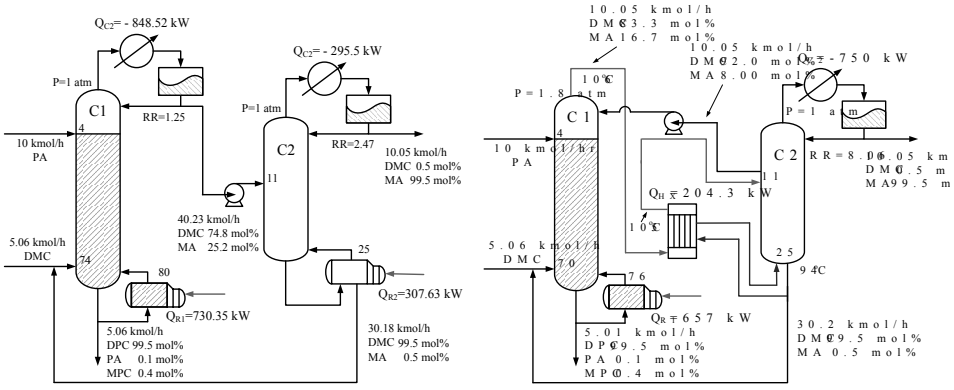

Figure 4: (a) Conventional DPC RD configuration; (b) DPC hybrid configuration

The RD process of DPC production contains a RD column (C1) and a reactant recovery column (C2). The C1 column only contains reactive section and rectifying section. The

upper 3 stages are rectifying section and another 77 stages are reactive section in C1 column. The production rate of DPC is designed to the value of 5 kmol/h. It can be estimated that the fresh feed flow rates of DMC and PA are 5 and 10 kmol/h, respectively. The DMC is chosen as excess reactant and the excess ratio is 6 in the result of Cheng et al. (2013). Therefore, 30 kmol/h of DMC should be recovered and recycle back to C1 column. Fresh feed of DMC mixes with recycle DMC first and then fed to 74th stage of C1 column. The higher boiling point reactant, PA, is fed at 4th stage of C1 column. 99.5 mol% DPC is produced from the bottom of C1column. Byproduct MA and excess DMC are removed from top of C1 column and fed to C2 column for separation. C2 column contains 25 stages and the feed location is 19th stage. The top product of C2 is 99.5 mol % MA and bottom stream contains 99.5 mol % DMC for recycling back to C1 column.

3.2. DPC hybrid configuration

Hybrid configuration in ideal RD process shows a higher energy saving potential. To compare the result of ideal RD process, the hybrid configuration of DPC RD process is discussed in this section. Operating pressure of RD column also should be examined due to minimum temperature difference requirement. 1.8 atm is required for RD column to achieve a minimum temperature difference for energy transfer. The flowsheet of hybrid configuration of DPC RD process is displayed in Figure 4(b). It is found that there is only 204.3 kW is transferred to the bottom of C2 column. Only 70 % energy of double-effect configuration is required for the hybrid configuration. Besides, the smaller energy transfer rate means a smaller heat transfer area. The overall energy requirement of DPC hybrid configuration is 657 kW, only 67 % less than the configuration without heat integration. And also, the remixing effect can be eliminated by this configuration.

4. Discussion

4.1. Remixing effect elimination for heat transfer

The RD column in both cases all shows the top compositions are quite different when the remixing effect is eliminated by the hybrid configuration. Different top compositions also mean the different vapor temperature at the top of RD column. In Case 1, the hybrid configuration shows a higher log mean temperature of heat transfer than the double-effect configuration. Figure 5 represent the temperature of RD top vapor composition location in T-xy diagram for Case 1.

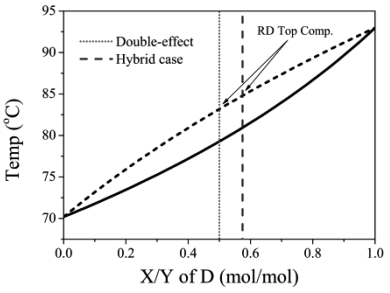

Figure 5: Top composition of RD column for IIp RD process

In Figure 5, dash-dot line shows the top liquid composition location of double-effect configuration. Top composition of D in double-effect configuration locates in 0.5 because of the remixing effect. The dash line represents the top composition location of hybrid configuration. The higher top composition in hybrid configuration can be observed because of the elimination of remixing effect. This phenomenon indicates

hybrid configuration can have higher top vapor temperature. In other words, hybrid configuration can have higher log mean temperature for heat transfer. It also implies that the heat transfer area of would be smaller under the same energy requirement.

4.2. The comparison of energy reduction

Following the simulation result in above sections, energy usage of each configuration for both cases is presented in Figure 6(a) and (b).

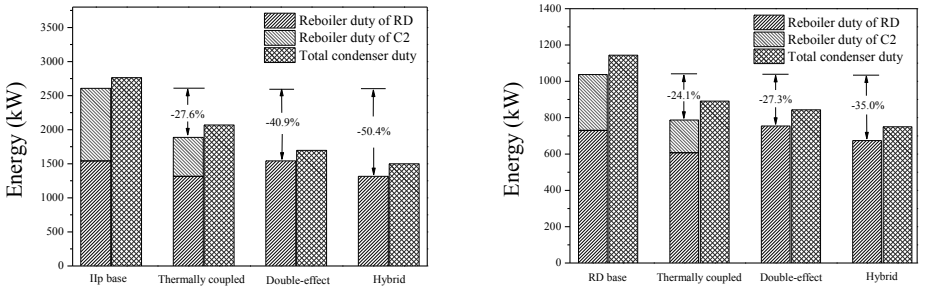

Figure 6: Energy usage for (a) IIp ideal RD process; (b) DPC RD process

The hybrid configuration that combines the concepts of thermally-coupled and double-effect configuration demonstrates the largest energy saving ability. In both cases, around 50 % and 36 % energies can be saved by the hybrid configuration.

5. Conclusions

In this study, the potential energy-saving of various heat-integrated configurations are investigated for ideal IIp and DPC RD process. A new heat-integrated method named hybrid configuration that combines the concepts of thermally coupled and double-effect configuration has been proposed. Smaller heat exchanger can be applied in hybrid configuration in contrast to the case of double-effect configuration. Energy waste in condenser of C2 in hybrid configuration is smaller than thermally coupled configuration. Simulation result shows that remixing effect phenomenon can be eliminated and 50 % and 36 % energy reductions can be achieved by the hybrid configuration.

Acknowledgement

This work was supported by Ministry of Science and Technology: NSC102-2221-E-011-144

References

K. Cheng, S. J. Wang, D. S. H. Wong, 2013, Steady-State Design of Thermally Coupled Reactive Distillation Process for the Synthesis of Diphenyl Carbonate, Comput. Chem. Eng., 52, 262-271

J. M. Douglas, 1988, Conceptual Design of Chemical Processes, McGraw-Hill, NewYork.

H. Y. Lee, Y. C. Lee, I. L. Cheng, H. P. Hung, 2010, Design and Control of a Heat-Integrated Reactive Distillation System for the Hydrolysis of Methyl Acetate, Ind. Eng. Chem. Res., 49, 7398-7411

L. C. Lin, 2007, Effects of Relative Volatility Ranking to the Design of Reactive Distillation: Excess-Reactant Design, Master Thesis, National Taiwan University, Taipei, Taiwan

M. F. Malone, 2000, M. F. Doherty, Reactive Distillation, Ind. Eng. Chem. Res., 39, 3953-3957

S. T. Tung, C. C. Yu, 2007, Effects of Relative Volatility to the Design of Reactive Distillation Systems, AIChE J., 53, 1278-1297

S. J. Wang, H. Y. Lee, J. H. Ho, C. C. Yu, H. P. Huang, M. J. Lee, 2010, Plantwide Design of Ideal Reactive Distillation Processes with Thermal Coupling, Ind. Eng. Chem. Res., 49, 3262-3274

Krist V. Gernaey, Jakob K. Huusom and Rafiqul Gani (Eds.), 12th International Symposium on Process Systems Engineering and 25th European Symposium on Computer Aided Process Engineering.
31 May – 4 June 2015, Copenhagen, Denmark

Optimization of ionic liquid recycling in Ionic Liquid-based Three Phase Partitioning processes

Enrique Alvarez-Guerra,* Angel Irabien

*Departamento de Ingenierías Química y Biomolecular, Universidad de Cantabria, Avda. de los Castros s/n, 39005 Santander, Spain, *e-mail: alvarezge@unican.es*

Abstract

The economic viability of Ionic Liquid-based Three Phase Partitioning (ILTPP) processes, which have been proposed to recover proteins from waste streams, highly depends on the recyclability of the salt and, especially, the ionic liquid used in this technique. For this reason, the economic optimization of the recovery of ILTPP reagents is carried out, considering the main operational costs (reagents and energy). Results show that the process configuration with which costs are minimized is based on the use of vacuum evaporation to remove water from the salt-rich phase of the process. Therefore, the increase of salt concentration is not an economically efficient alternative to recycle the ionic liquid, even though this alternative is usually proposed in the literature. The optimum costs vary between 51.5 – 307 € kg protein^{-1} for almost all protein concentrations in the feed stream, which are significantly lower than the lowest price reported for the target protein (lactoferrin), so ILTPP processes seem to be economically viable. In addition, the price of reagents and energy has very little influence on the optimum solutions, because very large changes of prices are required to modify the obtained results.

Keywords: protein recovery, ionic liquid consumption, recycle, operating cost.

1. Introduction

The major bottleneck of the economic and technical viability of protein production processes is downstream processing, since the conventional methods to purify these biomolecules are time and cost consuming (Pei et al., 2009). In this way, Ionic Liquid-based Three Phase Partitioning (ILTPP) has been proposed as a novel technique to recover proteins at the liquid-liquid interface formed by ternary systems ionic liquid/salt/water, which combines the use of Ionic Liquid-based Aqueous Two Phase Systems (ILATPS) with results that are characteristic of Three Phase Partitioning (TPP) (Alvarez-Guerra and Irabien, 2014). However, the development of ILTPP processes highly depends on the consumption of the reagents involved, and especially of ionic liquid, because of its relative high price.

For this reason, the net consumption of ionic liquid in this process has been assessed in previous works, concluding that between 0.8 and 5% of the ionic liquid cannot be reused, depending on experimental conditions. Therefore, two additional steps to enhance the ionic liquid recyclability have been considered: the increase of the salt concentration to reduce the ionic liquid fraction in the waste stream, and the water removal by means of evaporation to increase the fraction of liquid phases that can be recirculated in the process (Alvarez-Guerra et al., 2014a). Nevertheless, the previous studies have assessed these additional recovery steps individually.

The aim of this work is the economic optimization of the ionic liquid recovery in ILTPP processes so that the costs associated with this recycling, which constitute the objective function, are minimized. This approach makes it possible to analyze simultaneously all the different alternatives to recycle the ionic liquid in the most efficient way: the individual additional recovery steps previously mentioned, a combination of them or the performance of the process without any of these steps. The target protein considered in this work for its recovery by means of ILTPP is lactoferrin, a high-added value whey protein which stands out due its nutraceutical properties (Wakabayashi et al., 2006).

2. Mathematical formulation

Figure 1 shows the general block diagram of the ILTPP process, which considers the alternatives proposed in previous works simultaneously (Alvarez-Guerra et al., 2014a). Therefore, once the protein recovery has been carried out in the first separation tank, the overall salt mass fraction may be increased to reduce the fraction of ionic liquid present in the salt-rich phase. Furthermore, a fraction of the water present in the salt-rich phase can be removed to increase the fraction of ionic liquid and salt contained in this phase that is recirculated, keeping the overall mass of the system constant. Nevertheless, the consideration of these additional recovery steps in the general diagram of the process does not imply that these alternatives to enhance the ionic liquid recyclability are actually included in the process, since they will be discarded if the amount of extra salt added or the fraction of water evaporated is equal to zero.

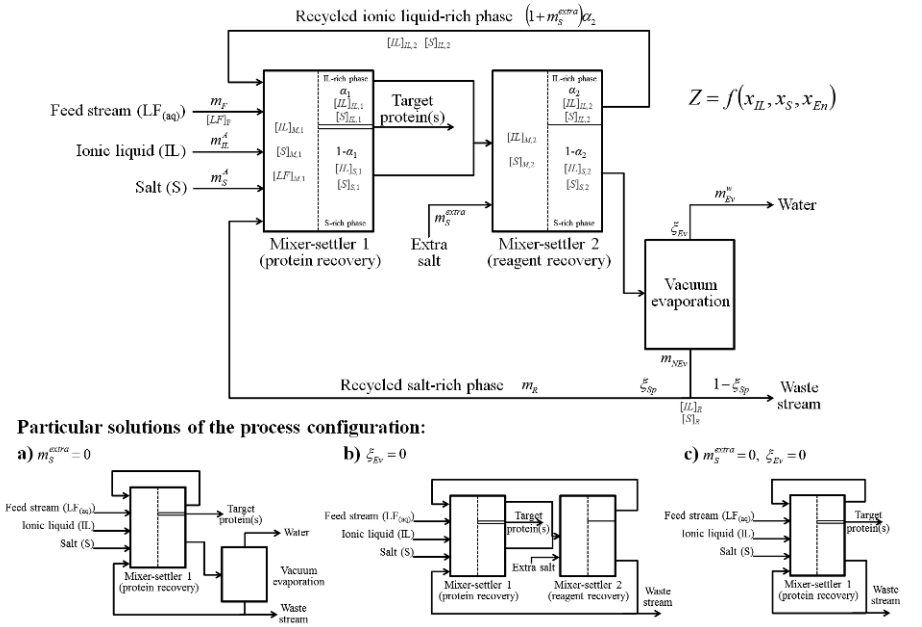

Figure 1-General block diagram and particular solutions of the ILTPP process.

The optimization of the ionic liquid recovery is based on the minimization of operating cost of the process associated with this objective. For this purpose, the three main operating costs related to the ionic liquid recyclability are: the net consumption of both ionic liquid and salt and the energy required to carry out the vacuum evaporation. However, due to the relative simplicity of the equipment involved in the process,

investment costs are considered to be neglected. In fact, for a production of 1 t LF y^{-1} and an amortization period of 10 y, the maximum fixed costs related to the equipment that is added to the process in the different particular solutions of the process configuration are estimated to be around 6 € kg LF^{-1}, according to the Guthrie's modular method (Biegler et al., 1997). These maximum fixed costs only represent around 10 % of the minimum operating costs obtained at high protein concentrations in the feed stream, as shown in the next section. Consequently, results demonstrate the applicability of the previous assumption. Therefore, the mathematical model for the optimization of the ionic liquid recovery is formulated as Figure 2 shows.

$$Min \quad Z = f_{LF}\left(\sum_i c_i x_i + c_{En} x_{En}\right) \tag{1}$$

s.t.

$$x_i = 0.01\left(1-\xi_{Sp}\right)[i]_R m_{NEv} \tag{2}$$

$$x_{En} = \frac{m_{Ev}^w RT \ln\left(P_{out}/P_{in}\right)}{M^w \eta_m \eta_c} + \lambda_{Ev}^w m_{Ev}^w \tag{3}$$

$$m_{IL}^A + m_S^A + m_F + \left(1+m_S^{extra}\right)\alpha_2 + m_R = 1 \tag{4}$$

$$[i]_{M,1} = 100 m_i^A + [i]_{IL,2}\left(1+m_S^{extra}\right)\alpha_2 + [i]_R + m_R \tag{5}$$

$$[IL]_{M,2} = \frac{[IL]_{M,1}}{1+m_S^{extra}} \tag{6}$$

$$[S]_{M,2} = \frac{[S]_{M,1} + 100 m_S^{extra}}{1+m_S^{extra}} \tag{7}$$

$$m_{NEv} = \left(1-\xi_{Ev}\right)\left(1+m_S^{extra}\right)\left(1-\alpha_2\right) \tag{8}$$

$$m_{Ev}^w = \xi_{Ev}\left(1+m_S^{extra}\right)\left(1-\alpha_2\right) \tag{9}$$

$$m_R = \xi_{Sp} m_{NEv} \tag{10}$$

$$[i]_R = [i]_{S,2}/\left(1-\xi_{Ev}\right) \tag{11}$$

$$[IL]_{S,j} = a_S \exp\left(b_S [S]_{S,j}\right) \tag{12}$$

$$[IL]_{IL,j} = a_{IL}[S]_{S,j} + b_{IL} \tag{13}$$

$$[S]_{IL,j} = d_{IL} \tag{14}$$

$$\frac{[IL]_{M,j} - [IL]_{IL,j}}{[S]_{M,j} - [S]_{IL,j}} = \frac{[IL]_{S,j} - [IL]_{M,j}}{[S]_{S,j} - [S]_{M,j}} \tag{15}$$

$$\alpha_j = \frac{[S]_{S,j} - [S]_{IL,j}}{[S]_{S,j} - [S]_{M,j}} \tag{16}$$

$$\xi_{Ev} \le 0.01\left(100 - [IL]_{S,2} - [S]_{S,2}\right) \tag{17}$$

$$x_i, \xi, m, \alpha \le 1 \tag{18}$$

$$[i] \le 100 \tag{19}$$

$$x, \xi, m, \alpha, [i] \ge 0 \tag{20}$$

$$x, \xi, m, \alpha, [i] \in \Re^n$$

Figure 2-Mathematical model for the optimization of the ionic liquid recovery. Notation: x_i is the net consumption of i; x_{En} is the energy consumption required for water removal by means of vacuum evaporation; $[i]$ is the mass fraction of i expressed as percentage; m is the mass fraction of the stream with respect to the total input streams in the first piece of equipment; α is the mass fraction of the ionic liquid-rich phase; ξ is the fraction of the stream evaporated (ξ_{Ev}) or split (ξ_{Sp}); f_{LF} is a conversion factor to express the cost per kg of target protein (lactoferrin, LF) recovered; η_m and η_c are the motor and compressor efficiencies; i denotes the component (IL: ionic liquid; S: salt) and j denotes the number of the mixer-settler (1 and 2: pieces of equipment where the protein recovery and the reagent recovery take place, respectively). Further details about the notation of the variables can be found in Figure 1.

The energy consumption is equal to the latent heat added to the system to keep temperature constant during evaporation and the energy required to create vacuum so that evaporation can be carried out at room temperature. For the last purpose, a vacuum pump is used that is modeled as a compressor that works isothermally due to the relatively low mass flow (McCabe et al., 2005). The compressor is modeled according to Biegler et al. (1997) for the case in which P_{out} = 1 atm and $P_{in} = P^o_{w,\ 25\ ^oC}$. Regarding the constraints of the optimization problem, Eq. 4 and 5 show the overall mass balance and the mass balance to IL and S, respectively, which assures the constancy of the total mass and composition of the system. Eq. 6-11 are also mass balances to connect the streams and compositions among the different pieces of equipment. The thermodynamic equilibrium characterization of the ILTPP systems which allows the determination of

the composition and phase ratio in the mixer-settlers is introduced by means of Eq. 12-16 (Alvarez-Guerra et al., 2014b). It should be noted that in this work $[S]_{IL,j}$ is considered to be constant, since at very high mass fraction of ionic liquid this variable shows a relatively low variability with system composition. Eq. 17 introduces the idea that the maximum fraction that can be evaporated from the salt-rich phase is equal to its water content, since the other components are not volatile (salt and ionic liquid). Eventually, a complete recovery of lactoferrin at the liquid-liquid interface in the first mixer settler, where the concentration of this protein is equal to 0.016 wt% (Alvarez-Guerra et al., 2014b), is assumed in the model.

The optimization problem, which is non-linear (NLP), is solved by means of the CONOPT solver of GAMS (v. 23.3.3). MINOS solver is also used to check the sensitivity of the solution to the resolution algorithm, obtaining almost identical results.

3. Results and discussion

The minimum operation costs of ILTPP process are assessed for different protein concentrations in the feed stream ($[LF]_F$ = 0.32 – 2.00 g kg^{-1}; Alvarez-Guerra et al., 2014a) using BmimTfO and NaH_2PO_4 as ionic liquid/salt system. Table 1 shows the values of the main variables and parameters fixed in the optimization model. The values of other parameters that characterized the thermodynamic equilibrium of the BmimTfO/NaH_2PO_4 system have been previously reported by Alvarez Guerra et al. (2014b).

Table 1-Values of the main variables and parameters fixed in the optimization model.

f_{LF}	6250 kg kg^{-1} [a]	d_{IL}	0.5 % [a]
c_{IL}	895 € kg^{-1} [b]	$[IL]_{M,1}$	26.3 % [a]
c_S	47.5 € kg^{-1} [b]	$[S]_{M,1}$	23.3 % [a]
c_{En}	0.12 € kWh^{-1} [c]	P_{in}	0.0313 atm [e]
η_m	0.9 [d]	λ_{Ev}^{w}	2430 kJ kg^{-1} [e]
η_c	0.8 [d]	T	298.15 K

[a] Alvarez-Guerra et al. (2014b); [b] Commercial suppliers; [c] Foro Nuclear (2014); [d] Biegler et al. (1997); [e] Yaws (2014)

Figure 3 shows the values of the objective function (the main operating cost of the ILTPP process) for different values of $[LF]_F$. In the range 335.3-2000 mg kg^{-1}, moderate costs are obtained (within the range 51.5 – 307 € kg LF^{-1}), which correspond to the vacuum evaporation of water from the salt-rich phase. Therefore, the lower the protein concentration, the higher the cost, because a higher fraction of water must be evaporated to achieve the complete recovery of both the ionic liquid and the salt. In this case, $m_S^{extra} = 0$, which corresponds to the process configuration of Figure 1.a. However, for $[LF]_F \leq$ 335.2 mg LF kg^{-1}, ionic liquid and salt losses are obtained and $m_S^{extra} > 0$, so operating costs increase dramatically. This region is strongly related to that previously reported by Alvarez Guerra et al. (2014a) for which water evaporation could not recycle all the reagents, even though in the present work this behaviour is exhibited for a slightly broad range of concentrations due to the combination of vacuum evaporation and increase of salt concentration ($m_S^{extra} > 0$).

Even though the price of LF is very variable depending on the commercial supplier and the quantity purchased, 600 € kg^{-1} is approximately the cheapest price that can be found for this protein. For this reason, ILTPP seems to be an economically viable process, because the price of lactoferrin is clearly higher than its main operating costs for the reagent recovery when only vacuum evaporation is performed. In fact, for $[LF]_F$ > 850 mg LF kg^{-1}, the analyzed operating costs represent a lower percentage than 20 % of the lowest price reported for LF. Nevertheless, for the production of commercial LF, additional up- or downstream processes not included in the ILTPP may be required, which might imply additional costs.

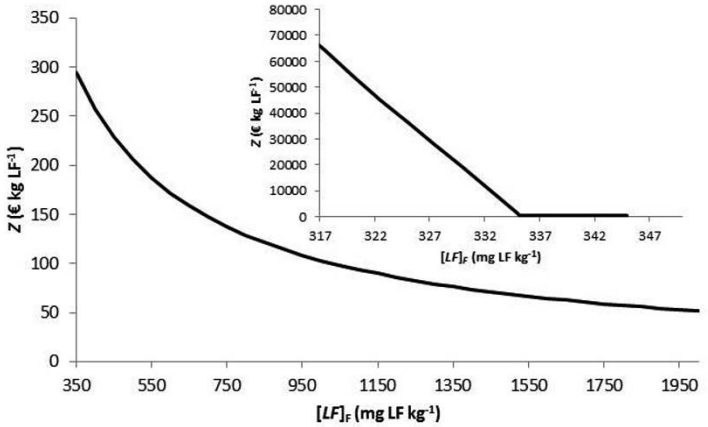

Figure 3-Minimum operating costs of the ILTPP process at different protein concentrations in the feed stream.

Due to the uncertainties associated with the cost of the reagents (ionic liquid and salt) and energy, which are the coefficients of the objective function, a sensitivity analysis is carried out. According to previous trends, it is expected a decrease of the price of reagents (especially the ionic liquid) and an increase of the cost of energy, so their coefficients are multiplied or divided by different factors as follows:

$$Z = f_{LF}\left[\frac{1}{f_{\mathrm{Re}}}\left(c_{IL}x_{IL} + c_S x_S\right) + f_{En}c_{En}x_{En}\right] \tag{21}$$

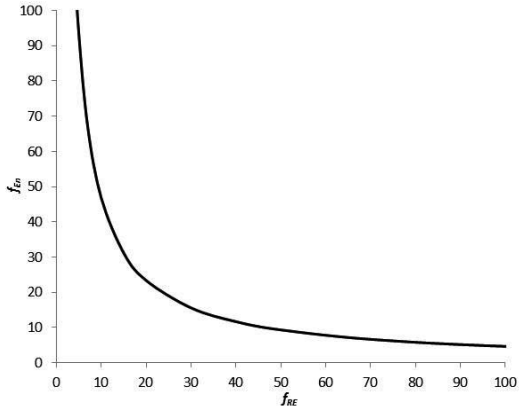

Figure 4-Combinations of the maximum values of f_{Re} and f_{En} for which m^S_{extra}=0.

It is observed that the maximum value of the product $f_{Re}{\cdot}f_{En}$ for which $m_S^{extra} = 0$ (i.e., evaporation remains as the unique reagent recovery step) is kept constant at 468 for all the protein concentrations in the feed stream. Therefore, at least an increase of f_{Re} or f_{En} higher than 468 will be required to change the optimum solution exclusively based on the use of vacuum evaporation to enhance the recovery of reagents. In this sense, Figure 4 graphs the combinations of the maximum values of f_{Re} and f_{En} for which $m_S^{extra} = 0$.

As a consequence, water removal by means of evaporation is a clear more advantageous alternative to recycle the ionic liquid and salt, even when significant changes in the price of reagents and energy occur. In this way, not only is the increase of salt concentration less effective in terms of ionic liquid recovery, but it also leads to higher operating costs, even though this approach is usually suggested in the literature to recycle the ionic liquid (Deng et al., 2009; Li et al., 2010) according exclusively to thermodynamic data.

4. Conclusions

The minimization of operating costs related to the recyclability of ILTPP reagents involves exclusively the water removal from the salt-rich phase by means of vacuum evaporation for almost all protein concentrations in the feed stream. Moreover, this optimum solution is very little sensitive to the price of reagents or energy, leading to operating costs that are significantly lower that the price of the protein to be recovered (lactoferrin), which may assure the economic viability of ILTPP processes.

References

E. Alvarez-Guerra, A. Irabien, 2014, Ionic Liquid-Based Three Phase Partitioning (ILTPP) for Lactoferrin Recovery, Separation Science and Technology, 49, 7, 957-965.

E. Alvarez-Guerra, S.P.M. Ventura, J.A.P. Coutinho, A. Irabien, 2014a, Ionic Liquid Recovery Alternatives in Ionic Liquid-Based Three-Phase Partitioning (ILTPP), AIChE Journal, 60, 10, 3577-3586.

E. Alvarez-Guerra, S.P.M. Ventura, J.A.P. Coutinho, A. Irabien, 2014b, Ionic liquid-based three phase partitioning (ILTPP) systems: Ionic liquid recovery and recycling, Fluid Phase Equilibria, 371, 67-74.

L.T. Biegler, I.E. Grossmann, A.W. Westerberg, 1997, Systematic Methods of Chemical Engineering Process Design, Prentice-Hall, Upper Saddle River, USA.

Y. Deng, T. Long, D. Zhang, J. Chen, S. Gan, 2009, Phase diagram of [Amim]Cl + salt aqueous biphasic systems and its application for [Amim]Cl recovery, Journal of Chemical & Engineering Data, 54, 9, 2470-2473.

Foro Nuclear, 2014, Energy 2014 (‘Energía 2014’), Algor, Madrid, Spain.

C. Li, J. Han, Y. Wang, Y. Yan, J. Pan, X. Xu, Z. Zhang, 2010, Phase behavior for the aqueous two-phase systems containing the ionic liquid 1-butyl-3-methylimidazolium tetrafluoroborate and kosmotropic salts, Journal of Chemical & Engineering Data, 55, 3, 1087-1092.

W.L. McCabe, J.C. Smith, P. Harriott, 2005, Unit Operations of Chemical Engineering (7th edition), McGraw-Hill, New York, USA.

Y. Pei, J. Wang, K. Wu, X. Xuan, X. Lu, 2009, Ionic liquid-based aqueous two-phase extraction of selected proiteins, Separation and Purification Technology, 64, 3, 288-295.

H. Wakabayashi, K. Yamauchi, M. Takase, 2006, Lactoferrin research, technology and applications, International Dairy Journal, 16, 11, 1241-1251.

C.L. Yaws, 2014, Yaws’ Critical Property Data for Chemical Engineers and Chemists, Knovel, http://app.knovel.com/hotlink/toc/id:kpYCPDCECD/yaws-critical-property/yaws-critical-property (last access: October 2014).

Krist V. Gernaey, Jakob K. Huusom and Rafiqul Gani (Eds.), 12th International Symposium on Process Systems Engineering and 25th European Symposium on Computer Aided Process Engineering.
31 May – 4 June 2015, Copenhagen, Denmark

Optimization of the Integrated Gasification Combined Cycle using Advanced Mathematical Models

Bongani Mvelase and Thokozani Majozi*

Department of Chemical Engineering, University of Witwatersrand, 1 Jan Smuts Avenue, Braamfontein, Johannesburg, 2000, South Africa
**Corresponding author: thokozani.majozi@wits.ac.za; Tel: +27 11 717 7384; Fax: +27 86 565 7517*

Abstract

Entrained flow gasifiers are known to operate under very severe conditions in order to achieve very high conversions of up to 99%. The extreme conditions impact negatively on the capital and operating investments of the gasifier and the downstream units. There is, however, no evidence on the published models that the extreme conditions are the optimal conditions in achieving the maximum fuel gas heating value. The first part of this work presents a 1-D simulation model for a dry-fed entrained flow gasifier with oxygen and steam used as oxidizing agent. The model is then validated against published models for the similar reactor configuration and then extended to an existing entrained flow gasifier for an IGCC power plant in Puertollano, Spain. The second part then presents the optimization model in which the objective function is to maximize the heating value of the fuel gas. The results obtained during optimization of the gasifier indicate a 12% increase in heating value with a decrease of about 500K in operating temperature. A 3MPa increase in operating pressure only results in less than 2% increase in fuel gas heating value. Milder operating conditions signify the possibility of a decreasing operating and capital investments, thereby improving the operating cycle of the power plant.

Keywords: IGCC, power generation, heating value, fuel gas, simulation and optimization

1. Introduction

Integrated Gasification Combined Cycle (IGCC) is a technology to increase efficiency and reduce environmental emission associated with fossil fuels. The performance of an IGCC plant and its economic feasibility mainly depend on the cost of the gasifier island (Campbell *et al.,* 2000 and USDoE, 2001). The majority of problems experienced during gasifier operation are associated with an increase in temperature (Ruiz *et al.,* 2013). The refractory life has been identified as a limiting factor in worldwide use of this technology (Schnake, 2012). Several simulation models to study the performance of an IGCC power plant, particularly focusing on the gasification unit, have been proposed and published in open literature. These range from a less intricate 1-Dimensional model (Mitta *et al.,* 2006, Rodrigues *et al.,* 2009 and Rasid *et al.,* 2011) to complex 2-D and 3-D Computational Fluid Dynamics (CFD) models (Chui *et al.,* 2009, Ma and Zitney, 2012 and Jeong *et al.,* 2014). The gasifier which is commonly used in IGCC, the entrained flow gasifier, is known to operate under severe operating conditions of up to 2000^{o}C (Zheng and Furisky, 2005, Sun *et al.,* 2012) and pressures in

excess of 8MPa (Minchener, 2005). The entrained flow gasifier achieves very high conversions of up to 99% due to its severe operating conditions. However, the extreme conditions impact negatively on the capital and operational investments of the gasifier and the downstream units. Developed simulation models on the entrained flow gasifiers have mainly focused on maximizing the carbon conversion, and therefore resulting in the gasifier being operated at the extreme conditions. These models include but not limited to the work of Wen and Chaung (1979), who developed a mathematical model to simulate a Texaco downdraft coal gasifier. Vamvuka *et al*. (1995) proposed a steady state model to study the performance of the entrained flow coal gasifier based on the mass and energy balances of the solid-gas and homogeneous gas-phase equilibria. A simple process model for dry-feeding entrained bed coal gasifier was also proposed by Lee *et al*. (2011) to study the effect of operating conditions on key performance indicators such as conversion and cold gas efficiency. Kasule *et al.* (2012) developed a very comprehensive 1-D steady state model of a slurry-fed entrained flow gasifier to simulate an IGCC process. These are, however, simulation models aimed at predicting the performance of the gasifier under prespecified operating conditions.

Limited work has been conducted on the optimization of the IGCC, mostly focusing on the gas circuit. Madzivhandila *et al.* (2009) were amongst the first researchers to focus on the optimization of an IGCC steam-path, by applying pinch analysis. Emun *et al.* (2010) proposed a simulation tool aimed at improving the efficiency and minimizing adverse effect of the IGCC power plant on the environment. Lang *et al.* (2011) proposed the optimization of the IGCC processes using reduced order CFD models. In their comprehensive work, Lang and co-workers considered the integration of the CFD (reduced order) within steady-state process simulators and the subsequent optimization of the integrated system. Similar to the published simulation models, the optimization of the IGCC, particularly the entrained flow gasifier, has been studied under almost fixed temperatures or the operating conditions such as oxygen-to-fuel ratio and steam-to-fuel ratio have been varied discretely. There is currently no evidence indicating that the extreme conditions are the optimal conditions in achieving the maximum fuel gas heating value.

This work focuses on the gas-side of the IGCC particularly the gasifier and gas turbine. The first part of this work presents a 1-D simulation model for a dry-fed entrained flow gasifier with oxygen and steam used as oxidizing agents. The model is then validated against published models for the similar reactor configuration and then extended to an existing entrained flow gasifier for an IGCC power plant in Puertollano, Spain. The second part then presents the optimization model in which the objective function is to maximize the heating value of the fuel gas. These models were formulated using differential and algebraic equations of mass and energy balance. gPROMS platform was used as a simulation and optimization tool. Multiflash for Windows was chosen as a thermodynamic property model to obtain the physical property data for the gaseous mixture.

2. Model formulation

The mathematical model presented in this work is based on mass and energy balances of the gasifier and the gas turbine. The differential and algebraic equations defining the performance of the system were solved in *g*PROMS while the required thermodynamic data such as enthalpies, heat capacities, thermal conductivities, etc., were obtained from Multiflash for Windows. The model is divided into simulation and optimization

modules. The simulation module considers both the gasifer and the gas turbine while the optimization module only focuses on the gasifier where there objective is to maximize the fuel gas heating value. The summary of the mass and energy balance equations is provided in Table 1.

Entrained Flow Gasifier Simulation Model

There are two models generally used for modelling heterogeneous solid-gas reactions and these are Langmuir-Hinshelwood (Klose and Wolki, 2005, Roberts and Harris, 2006, Boreto *et al.,* 2013) and the *n*-order models (Tremel and Spliethoff, 2013, Lee *et al.,* 2014). *n*-order modelling has been selected for this work because of its simplicity and the available reaction kinetics data. Although this is a simplified model, the accuracy is not lost and *n*-order models have been widely used in solid-gas reaction modelling (Vamvuka *et al.,* 1995, Watanabe and Otaka, 2006, Xu and Qiao, 2012). The mass balances of the homogeneous gas-phase and heterogeneous solid-gas phase reactions are shown in Eq. (1) and (2) respectively.

$$\frac{d\dot{m}_{gi}}{dL} = A_c(Mw_i)\sum_{j=1}^{n} \nu_{ji} r_j(T_g, L) + aA_c(Mw_i)\sum_{k=1}^{m} \nu_{ki} \frac{r_{k(T_p,L)}}{Mw_c} \tag{1}$$

$$\frac{d\dot{m}_c}{dL} = aA_c \sum_{k=1}^{m} r_k(T_p, L) \tag{2}$$

The chemical reaction rates for the homogeneous gas phase and heterogeneous solid-gas reactions are calculated using Eq. (3) and (4) respectively. The pre-exponential factor k_j and k_k are determined from Arrhenius equations.

$$r_j = k_j C_a^x C_b^y \tag{3}$$

$$r_k = k_k P_a^n (1 - X_C)\sqrt{1 - \Psi_k \ln(1 - X_C)} \tag{4}$$

The model only considers two modes of heat transfer in the energy balance. Radiation heat transfer between particle-gas, gas-wall and particle-wall and convection heat transfer between particle-gas and gas-wall have been considered. The respective energy balances for gas phase and particles are shown in Eq. (5) and (6), respectively.

$$\frac{dH_p}{A_c dL} = ah_{gp}(T_g - T_p) + a\varepsilon_p\sigma(T_g^4 - T_p^4) - \frac{4}{D_R}\varepsilon_p\sigma(T_p^4 - T_w^4) \tag{5}$$

$$\frac{dH_g}{A_c dL} = -ah_{gp}(T_g - T_p) - a\varepsilon_p\sigma(T_g^4 - T_p^4) - \frac{4}{D_R}h_{gw}(T_g - T_w) - \frac{4}{D_R}\varepsilon_w\sigma(T_g^4 - T_w^4) \tag{6}$$

Where subscripts *j* refers to homogeneous gas phase reactions, *k* refers to solid-gas reactions and *i* is gaseous component in the gas mixture. a is the contact area between particle and gas per unit volume of the reactor. Subscripts *g* and *p* refer to the gas and particle, respectively. X_c is the carbon conversion, A_c is the cross sectional area of the gasifier, *T* is the temperature and P_a is the oxidizing agent partial pressure, while h_{gp} and h_{gw} are the convection heat transfer coefficients of gas-particle and gas-wall respectively.

The formulation of the optimization model to maximize the heating value of the fuel gas is described in Eq. (7) with the constraints shown in Eq. (8) to (13).

$$Maximize\ HV_{FG} = \sum_i x_i HV_i \tag{7}$$

Subject to:

$$T_R \leq T_{MAWT} \tag{8}$$

$$P_R \leq P_{MAWP} \tag{9}$$

$$T_{g,min} \geq T_{AFT} \tag{10}$$

$$\sum_i^n x_i = 1 \tag{11}$$

$$X_c < 0.9999 \tag{12}$$

$$R_{min} \leq R_{CO/H_2} \leq R_{max} \tag{13}$$

T_{MAWT} and P_{MAWP} are the maximum allowable working temperature and pressure, respectively, and they are the design constraints of the gasifier. HV_i is the heating value of the contributing gas in the fuel gas while x_i is the corresponding mass fraction of the contributing gas. The solution procedure of the model is shown in Figure 1

.

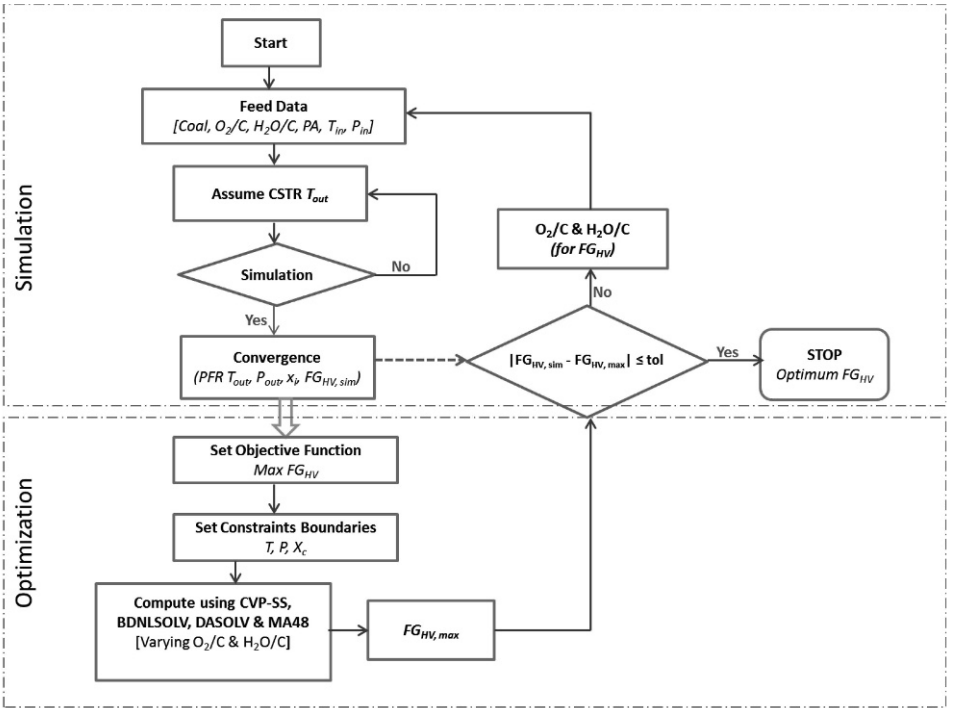

Figure 1: Mathematical model solution procedure

3. Results and discussion

A simulation model developed in this work is compared to published 1-D entrained flow gasifier models at the same input conditions. The mathematical models of Vamvuka *et al.* (1995), Lee *et al.* (2011) and an Aspen Plus model of Sofia *et al.* (2013) are used to validate the simulation model. The validation is also extended to the IGCC power plant of Elcogas in Puertollano, Spain. The performance indicators that were considered crucial were fuel gas composition, gasifier peak temperature, exit fuel gas temperature, conversion and fuel gas heating value. The simulation was based on a 45-55% coal/petcoke feed mixture. The simulation results of the key performance indicators such gasifier peak temperature ($T_{g,P}$), carbon conversion (X_C) cold gas efficiency (η_{CG}) and the fuel gas heating value (FG_{HV}) are presented in Table 1.

Table 1: Comparison of the current model prediction with Elcogas power plant

Variable	Units	Elcogas Gasifier	Current Model
X_c	%	> 98	97.8
$T_{g,P}$	K	> 2273	2882.42
$T_{g,out}$		1623	1539.57
y_{CO+H2}	vol.%	> 85	95.8
y_{CH4}		< 0.1	3.53
η_{CG}	%	-	66.1
η_{CO+H2}		81.02	95.8
FG_{HV}	MJ/kg	-	13.89

A simulated Elcogas gasifier was then optimized to determine the maximum possible heating value of the fuel gas. The resulting NLP model assumes a constant feed into the gasifier with four degrees of freedom; feed pressure, particle size, oxygen-to-coal and steam-to-coal ratios. The feed temperature is assumed to be constant. The optimized performance of the gasifier presented in Table 2 indicates an increase in fuel gas heating value, from 13.9MJ/kg to 16.2MJ/kg.

Table 2: Optimized gasifier performance

Variable	Units	Simulation	Optimized
X_c	%	97.8	64
$T_{g,P}$	K	2882.42	2543.7
$T_{g,out}$		1539.57	1020
y_{CO+H2}	vol.%	95.8	91.93
y_{CH4}		3.53	6.30
η_{CG}	%	66.1	77
η_{CO+H2}		95.8	91.93
FG_{HV}	MJ/kg	13.89	16.21

There is also about 500K decrease in exit gas temperature. The cold gas efficiency also improved as a result of the increase in H_2 and CH_4 content in the fuel gas. There is, however, as significant decrease in carbon conversion. The improved heating value of the fuel gas is preferred in the gas turbine. The increase in H_2 in the fuel gas to the gas turbine increases the expander inlet temperature and the exhaust temperature. This results in an about 2% increase in gas turbine efficiency.

4. Conclusions

The objective of this work was to establish if the severe conditions of high temperature and pressure at which the gasifier is generally operated are indeed the optimum conditions for producing the highest fuel gas heating value. The primary focus was therefore centred on the entrained flow gasifier which is the centrepiece of an IGCC power plant. The gas turbine only receives and combusts the fuel gas to produce power. The developed model was validated against three published models and produces even better results which are comparable to the Elcogas power plant gasifier published data.

The optimized model proves that there exist moderate conditions at which the entrained flow gasifier can be operated to yield the maximum possible fuel gas heating value. An increase of about 14.3% in fuel gas heating value is realized when operating the gasifier at temperatures 500K lower than the extreme temperature reported in literature. The pressure does not have a significant impact on the fuel gas heating value, with only less than 2% increase in heating value being achieved by changing the pressure from 2MPa to 5MPa. Owing to a decrease in operating temperature, the conversion was, however, reduced from 97% to about 64% and this led to a decrease of almost 60% in O_2 and 50% in steam used in the gasifier. The results also indicate an almost 2% increase in the efficiency of the gas turbine when burning the gas of the higher heating value. This is mainly due to the increase in the expander inlet temperature. The gas turbine exhaust temperature and exhaust gas heat capacity also increases, which increases the amount of heat for the HRSG. The overall gas path efficiency also increased by almost 7%. A reduction in operating temperature and pressure of the gasifier will, therefore, guarantee a longer operating cycle of the gasification unit and relatively lower operating and capital costs.

Reference

Emun, F., Gadalla, M., Majozi, T., Boer, D., *Integrated gasification combined cycle (IGCC) process simulation and optimization*, Computers and Chemical Engineering, 2010, 34, 331-338

Kasule, J. S., Turton, R., Bhattacharyya, D., Zitney, S. E., 2012, *Mathematical Modelling of a Single-Stage, Downward-Firing, Entrained-Flow Gasifier*, Industrial & Engineering Chemistry Research, 6429-6440

Lang, Y., Zitney, S. E., Biegler, L. T., 2011, *Optimization of IGCC processes with reduced order CFD models*, Computers and Chemical Engineering, 35, 1705-1717

Madzivhandila, V., Majozi, T., Zhelev, T., 2009, *Process integration as an optimization tool in clean coal technology: A focus on IGCC*, Chemical Engineering Transactions, 941-946

Rasid, R. A., Heggs, P. J., Hughes, K. J., Pourkashnian, M., 2011, *Process Modelling of Entrained Flow Gasification*, 21st European Symposium of Computers Aided Process Engineering – ESCAPE 21, E.N. Pistikopoulus, M. C., Georgiadis and A. Kokossis Editors), Published by Elsevier

Sadhwani, N., Liu, Z., Eden, M. R., Adhikari, S., 2013, *Simulation Analysis, and Assessment of CO_2 Enhanced Biomass Gasification*, Proceeding of the 23rd European Symposium on Computers Aided Process Engineering-ESCAPE 23. June 9-12, 2013, Lappeenranta, Finland, Published by Elsevier

Vamvuka, D., Woodburn, E. T., Senior, P. R., 1995, *Modelling of an entrained flow coal gasifier – 1. Development of the model and general predictions*, Fuel, 1452-1460

Wen, C.Y., Chaung, T.Z., 1979, *Entrainment Coal Gasification Modeling,* Ind. Eng. Chem. Process Des. Dev.

Krist V. Gernaey, Jakob K. Huusom and Rafiqul Gani (Eds.), 12th International Symposium on Process Systems Engineering and 25th European Symposium on Computer Aided Process Engineering.
31 May – 4 June 2015, Copenhagen, Denmark

Nonparametric soft sensor evaluation for industrial distillation plant

Andrei Torgashov,[a,b] Konstantin Zmeu[b]

[a]*Institute of Automation and Control Processes FEB RAS, 5, Radio Str., Vladivostok 690041, Russia*
[b]*Far-Eastern Federal University, Bld. 12(E), Campus FEFU, Russky Island, Vladivostok 690922, Russia*
Torgashov@iacp.dvo.ru

Abstract

The paper improves the existing methods of developing nonlinear soft sensors via a nonparametric approach based on the example of industrial distillation unit. The proposed procedure for soft-sensor design is aimed to overcome obstacles in practice, such as process nonlinearity, unknown model structure and narrow variability ranges of key inputs for soft sensors.

Keywords: soft sensor, distillation column, structural uncertainty, nonparametric methods.

1. Introduction

Soft sensors (virtual on-line analyzers) play a crucial role in any advanced process control (APC) system to optimize the cost of industrial plant operation through their high accuracy in estimating and predicting product quality (Fortuna et. al., 2007).

Nowadays, three methods are used to improve the quality control of the product in technological petrochemical and refining processes: laboratory analysis, the stream analyzer data and the soft sensor data. However, the analysis results, which come from industrial laboratories, are not always full and operative enough; also, they can seldom be used for real-time quality control. The stream analyzers need calibration, are extremely expensive and are sometimes not available. In contrast, the soft sensors, which only have slightly less accuracy, are much cheaper and more reliable. The principle upon which soft sensors work is based on the real-time estimation of quality through a mathematical model that utilizes all available measured process variables, such as flowrates, temperatures and pressures. A review of the existing approaches regarding soft sensor evaluation is given by Kadlec et al., 2009.

However, for industrial plants, such as energy-consuming mass-transfer apparatuses (distillation columns) used in petrochemical and refining production, it is still important to improve methods for soft sensor designs, in order to reach better accuracy, prediction and estimation of products' quality. In uncertain conditions, it is connected with the overcoming of difficulties such as accounting for the variable time of output measurement and a lack of information about the model's structure. Moreover, some of the key (informative) inputs have very low variability ranges because they seldom vary by operator (for instance, the set-point of the distillation column's top pressure). This leads to the statistical insignificance (by t-test) of the corresponding coefficients in the

regression model and contradicts the thermodynamic essence. Therefore, the current paper seeks to handle and overcome such difficulties that arise.

The accuracy of soft sensor predictions is normally investigated by calculating the coefficient of determination (R^2) and root-mean-squared error (RMSE) for both training and test samples. These performance indicators are used in this paper during the further analysis of industrial data.

2. Statement of problem

Let Y be an independent variable (soft sensor output) and $X_1,\ldots, X_n$ be independent variables (inputs). The plant model is described by the following functional relationship:

$$Y = F(\mathbf{X}, \mathbf{B}) + \varepsilon, \tag{1}$$

where $\mathbf{X} = (X_1, \ldots, X_n)^T$ and is the vector of the inputs; $\mathbf{B} = (\beta_1, \ldots, \beta_m)^T$ and is the vector of the model coefficients; and ε is the output error. Suppose that the structure of F in (1) is unknown. From the rigorous (physical-chemical) distillation model, it follows that the structure F should be nonlinear.

This paper deals with the problem of improving the available techniques for soft sensor design in plants like (1), under the following conditions that are widely encountered in practice:

- The process's inherent nonlinearity;
- The unknown model structure;
- The narrow variability ranges of some of the input variables.

The solution to the problem is demonstrated using an industrial case study of a distillation column (Fig. 1) from an FCC unit. The following variables are key inputs of a soft sensor model: x_1 is the flow of distillate (top product) kg/hr; x_2 is the flowrate of reflux, in kg/hr; x_3 is the top pressure of the column, in kgf/cm^2; x_4 is the top temperature of the column, in °C; and x_5 is the bottom temperature of the column, in °C.

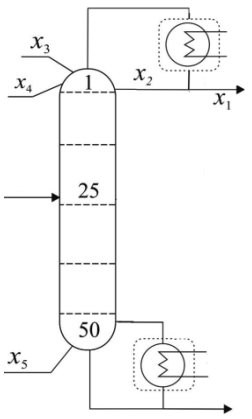

Figure 1: Distillation column: Key inputs of the soft sensor

The soft sensor is intended to predict isopentane (*i*C5) content in the overhead product. The nonparametric approach is proposed in order to solve the stated problem.

3. The use of nonparametric transformations

As pointed out above, industrial plants have a widespread lack of knowledge regarding suitable model structures. The use of a nonparametric approach allows the evaluation of a soft sensor model under structural uncertainty. Thus, the soft sensor model may be found in the following form:

$$\Phi_0(Y) = \sum_{i=1}^{n} \Phi_i(X_i), \tag{2}$$

where Φ_i is the nonparametric transformation. The estimation of transformations for multiple regression using the ACE algorithm was originally proposed by Breiman L. and Friedman J. (1985).

The optimal transformations can be obtained by minimizing the variance between the transformed output and the sum of the transformed inputs. The objective of the ACE algorithm is to minimize the error, e^2, of the transformed output on the sum of transformed input variables, under the constraint $E[\Phi_0^2(Y)] = 1$ ($E[\cdot]$ is mathematical expectation). The error is defined as:

$$e^2(\Phi_0, \Phi_1, \ldots, \Phi_n) = E\left[\left(\Phi_0(Y) - \sum_{i=1}^{n} \Phi_i(X_i)\right)^2\right]. \tag{3}$$

The minimization of the error (3) with respect to $\Phi_1(X_1),\ldots, \Phi_n(X_n)$ and $\Phi_0(X_0)$ proceeds via the following minimization of single functions:

$$\Phi_i(X_i) = E[\Phi_0(Y)|X_i], \tag{4}$$

$$\Phi_0(Y) = E\left[\sum_{i=1}^{n} \Phi_i(X_i)\middle| Y\right] \Big/ \left\| E\left[\sum_{i=1}^{n} \Phi_i(X_i)\middle| Y\right]\right\|. \tag{5}$$

In practice, the conditional expectations in (4) and (5) can be evaluated using smoothing techniques.

The ACE algorithm does not provide a direct calculation of the soft sensor output using (2). However, the nonparametric optimal transformations can be fitted, for example, by a polynomial model as:

$$\Phi_i(X_i) = b_{0,i} + b_{1,i}X_i + b_{2,i}X_i^2 + \cdots + b_{M_i,i}X_i^{M_i}, \tag{6}$$

where M_i is the order of the i-th polynomial for $\Phi_i(X_i)$-transformation ($i = 1,\ldots, n$). The same approximation procedure can be applied for backward calculation of the output (Φ_0 is assumed to be monotonic and invertible):

$$Y = \Phi_0^{-1} = a_0 + a_1\Phi_0 + a_2\Phi_0^2 + \cdots + a_{M_0}\Phi_0^{M_0}, \tag{7}$$

where Φ_0^{-1} is the inverse output transformation and M_0 is the order of polynomial (7).

The 2-step algorithm for calculating the soft sensor output is depicted in Fig. 2. The example for the parameterization of the transformation derived using the ACE algorithm is shown in Fig. 3 with the following equations: $\Phi_0(Y) = 0{,}67 \cdot Y - 12.61$; $\Phi_1(X_1) = -1.25 \cdot X_1 + 28.3$; $\Phi_2(X_2) = -0.3 \cdot 10^{-3} \cdot X_2^2 + 0.17X_2 - 8.4$;$\Phi_3(X_3) = -30.5 \cdot X_3^3 + 156.6 \cdot X_3^2 - 265.7 \cdot X_3 + 149.2$; and $\Phi_4(X_4) = 0.26 \cdot X_4 - 21.7$; $\Phi_5(X_5) = -2 \cdot 10^{-3} \cdot X_5^3 + 0.76 \cdot X_5^2 - 94.3X_5 + 3899$.

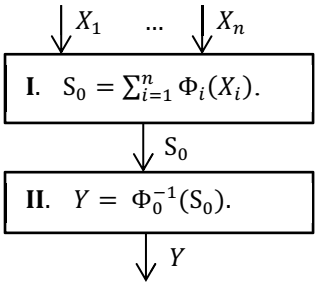

Figure 2: ACE-based 2-step algorithm of output calculation

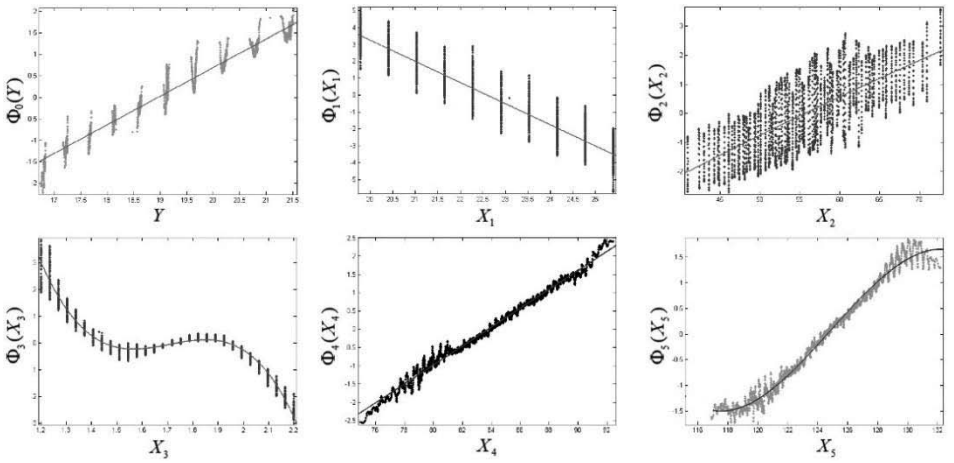

Figure 3: Transformed variables of the soft sensor model

4. Handling the narrow variability ranges of the input variables

4.1. Fitting rigorous model to industrial data

The motivation for using a rigorous distillation model implies that it is necessary to extend the training sample with input variables that have low variability ranges. The fitting procedure involves the selection of the tray efficiency that minimizes the mismatch between industrial data and the rigorous model. The average steady-state operating point is involved when estimating the Murphree efficiency of industrial data.

The following residual function is utilized: $f_{iC5}(\mathrm{E1},\mathrm{E2}) = (x_{iC5}^{rm}(\mathrm{E1},\mathrm{E2}) - x_{iC5})^2$, where $x_{iC5}^{rm}(\mathrm{E1},\mathrm{E2})$ is the isopentane content calculated using a rigorous model; x_{iC5} is the industrial isopentane data; E1 is the absorption section efficiency; and E2 is the stripping section efficiency. Moreover, the data reconciliation problem of the reflux ratio (RR) is solved in conjunction with the residual function's minimization.

The calculation results of the fitting procedure and the Murphree efficiencies' feasible domain are shown in Fig. 4. The point *, with coordinates of E1 = 0.608 and E2 = 0.5, indicates the best-fitted values of the sectional efficiencies, with the optimal reconciled RR value. It should be noted that the fitting of efficiency values for each individual separation stage did not provide significant improvements in the calibration results.

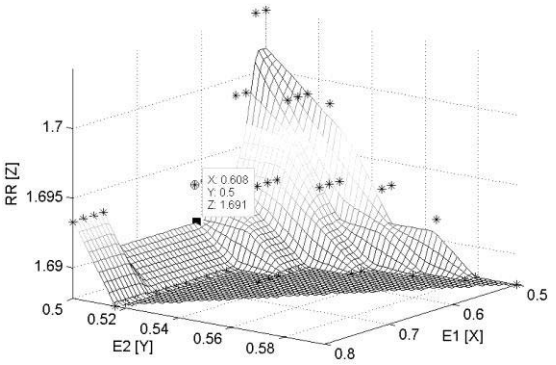

Figure 4: The results of fitting the sectional efficiencies onto industrial data

4.2. Obtaining the model structure

In practice, we have to deal with a situation where a priori information will allow for an understanding that the plant's output is significantly affected by one or more inputs, but that such inputs in the model are not statistically significant. This is due to the fact that, during the plant's operation, the variation ranges are limited by technological reasons, such as safety constraints. Below is a technique that ensures the handling of a priori data about specific input variables within the available data that were obtained from a nonlinear plant with a small range of variation in key (from a physical-chemical sense) input X_m. The model is decomposed in two parts: $\hat{Y} = \hat{Y}_d + Y_m$, where $Y_m = c_m^0 + \sum_{j=1}^{q} c_m^{(j)} X_m^{(j)}$ is obtained based on the data set from the fitted rigorous model; $\hat{Y}_d = c_0 + \sum_{i=1}^{m-1} \sum_{j=1}^{p} c_i^{(j)} X_i^{(j)}$, which is the part for inputs with sufficient variability ranges; and (j) is the j-th order of the polynomial. The resulting model evaluation scheme is as follows: $\hat{Y} = \underbrace{c_0 + \sum_{i=1}^{m-1} \sum_{j=1}^{p} c_i^{(j)} X_i^{(j)}}_{\text{fitting}} + \underbrace{\sum_{j=1}^{q} c_m^{(j)} X_m^{(j)}}_{\text{fix}}$. Note that bias c_0 consumes c_m^0.

As an input variable, pressure was found to be insignificant because of the small range of variability in the available industrial data set. When building the final model to predict the quality of the output product—a concentration of isopentane—without a priori information about the effect of pressure at the top of the column, we get a linear equation of $\hat{Y}_{d,iC5} = 181.3 + 0.39X_1 + 0.05X_2 - 1.25X_4 + 0.2X_5$ using robust regression M-estimator (Maronna et al., 2006). The coefficient of the determination R^2_{iC5} is equal to that for the testing data set and the training sample: 0.1402 and 0.8113 (Fig. 5), respectively.

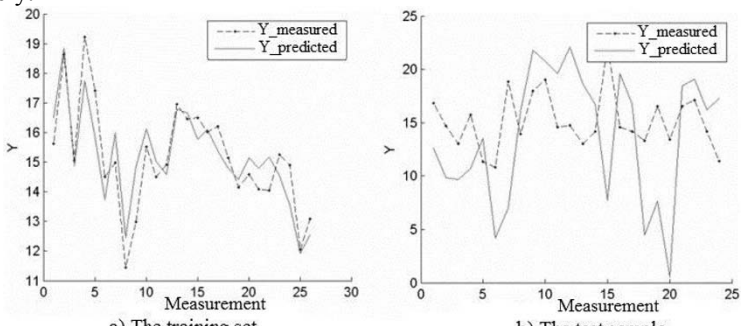

Figure 5: Soft sensor performance without the pressure correction term

Using a priori information about the effect of pressure on the concentration of isopentane in the distillate and rigorous static model, a soft sensor is made as close to the modes of operation for the industrial distillation column as possible. The dependence on the concentration of isopentane in the distillate, along with the pressure change from 1 kg/cm^2 to 2 kg/cm^2, on the fitted rigorous distillation model in form is found using $Y_m = 2.863X_3^2 - 4.432X_3 + 7.708$. Taking into account the influence of pressure, the model of the output product quality using the mass fraction of isopentane was found: $\hat{Y}_{iC5} = 66.46 + 0.48X_1 + 0.12X_2 - 1.04X_4 + 0.08X_5 + 2.863X_3^2 - 4.432X_3$. The coefficient of determination for the test sample R^2_{iC5} is 0.8727; for the training data set, it is 0.7878 (Fig. 6).

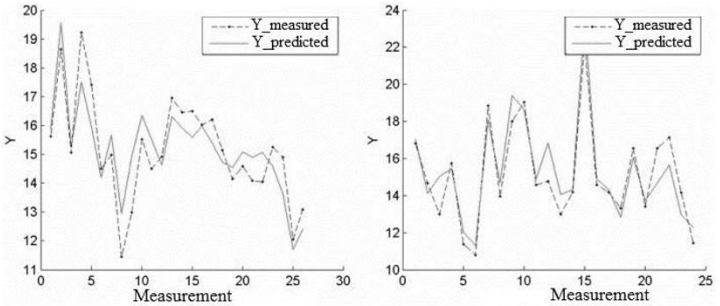

Figure 6: The performance of soft sensor with the pressure correction term

The practical result of using the proposed algorithm (taking into account the a priori information regarding the statistically insignificant inputs) includes improvements in prediction quality by 63.25% in R^2 for the test sample.

5. Conclusions

This article reviews an improved method of evaluating soft sensors for nonlinear industrial plant. The method allows a model structure to be found that counters output uncertainty and avoids the lengthy search and substantiation process for soft sensor's structures. A way to take important (with the physics-chemical meaning) inputs into account, in case of a low variability range, has been proposed. It offers the possibility of increasing the R^2 of the test sample (for example, in comparison with the robust regression *M*-estimator), if it contains new data that are not included in the training set.

6. Acknowledgements

This work was supported by the Ministry of Education and Science of the Russian Federation, through Government Contract No. 02.G25.31.0025.

References

Breiman, L., Friedman, J. 1985. Estimating optimal transformations for multiple regression and correlation // Journal of the American Statistical Association. Vol. 80. pp. 580–598.

Fortuna, L., Graziani, S., Rizzo and A., Xibilia, M.G. 2007. Soft sensors for monitoring and control of industrial processes. London: Springer-Verlag.

Kadlec P., Gabrys B. and Strandt S. 2009. Data-driven soft sensors in the process industry // Computers and Chemical Engineering. Vol. 33. pp. 795–814.

Maronna, R. A., R. D. Martin and V. J. Yohai. 2006. Robust Statistics: Theory and Methods. New York: John Wiley & Sons.

Krist V. Gernaey, Jakob K. Huusom and Rafiqul Gani (Eds.), 12th International Symposium on Process Systems Engineering and 25th European Symposium on Computer Aided Process Engineering.
31 May – 4 June 2015, Copenhagen, Denmark

Comparing Temperature Difference Control Schemes for Dividing-Wall Distillation Columns

Yang Yuan[a], Haisheng Chen[a], Jieping Yu[a], and Kejin Huang[a,] *

[a]*College of Information Science and Technology, Beijing University of Chemical Technology, 15 beisanhuan east road, chaoyang district, Beijing 100029, P.R. China*
**huangkj@mail.buct.edu.cn*

Abstract

The operation of a DWDC, fractionating an ideal ternary mixture of hypothetical components A, B, and C, is studied to compare various temperature difference control schemes proposed so far, including temperature difference control (TDC) scheme, simplified temperature difference control (STDC) scheme, double temperature difference control (DTDC) scheme and simplified double temperature difference control (SDTDC) scheme. The nearly similar system performance of the STDC and SDTDC schemes to the TDC and DTDC schemes, respectively, indicates the great importance to control strictly the two sections along the dividing wall. With the two intermediate sections tightly controlled, the operation of the rectifying and stripping sections should then be tightened to improve further system performance. This gives rise to a novel SDTDC scheme involving two DTDC and two TDC loops, which enriches the potential alternatives to control the DWDC.

Keywords: DWDC, temperature control, temperature difference control, double temperature difference control, simplified double temperature difference control.

1. Introduction

Although dividing-wall distillation columns (DWDCs) can economize 30 % equipment investment and operation cost as compared with the conventional two-column separation sequences in the separations of ternary mixtures, their industrial applications are rather limited due to the complicated process dynamics and control difficulties involved. Many studies have conducted so far, but they focused merely on specific control problems (Kiss and Bildea, 2011; Wang and Wong, 2007). Ling and Luyben (2009) proposed a control structure with four manipulated variables (i.e., reflux flow rate, side-stream flow rate, reboiler heat duty, and liquid split ratio) to control the purities of the top, intermediate, and bottom products. Its major advantages lay in the capability of minimalizing reboiler heat duty. Later, they employed a temperature control (TC) and temperature difference control (TDC) schemes to achieve the same purpose. It was found that while the latter could tolerate 20 % feed composition disturbances the former could not (Ling and Luyben, 2010). Luan et al. (2013) indicated the importance of tight control of the two sections along the dividing wall and developed accordingly a simplified temperature difference control (STDC) scheme. Due to the addition of two temperature measurements, the STDC scheme was demonstrated to be superior to the TC scheme. Wu et al. (2013) devised a double temperature difference control (DTDC) scheme with 12 temperature measurements. It was characterized by great capability of suppressing steady-state deviations and rejecting feed composition disturbances. To reduce its temperature measurements, we recently proposed a simplified double temperature difference control (SDTDC) scheme with 8

temperature measurements. Similar to the DTDC scheme, it still featured relatively great capability of suppressing steady-state deviations and rejecting feed composition disturbances (Yuan and Huang, 2014).

In what follows, the operation of a DWDC separating an ideal ternary mixture of hypothetical components A, B, and C is studied. The purpose is to make a systematic comparison between the TDC, STDC, DTDC, and SDTDC schemes proposed so far and draw potentially useful guidelines for the synthesis and design of control systems for the DWDC.

2. A DWDC Fractionating a Ternary Mixture of Hypothetical Components A, B, and C

The vapor-liquid equilibrium relationship is expressed by

$$P_j = x_{A,j}P_A^s + x_{B,j}P_B^s + x_{C,j}P_C^s \qquad 1 \le j \le N \tag{1}$$

$$y_{i,j} = x_{i,j}P_{i,j}^s / P_j \qquad i = A, B, C, \text{ and } 1 \le j \le N \tag{2}$$

The vapor saturation pressure can be estimated with the following equation

$$lnP_{i,j}^s = A_{vp,i} - B_{vp,i} / T_j \qquad i = A, B, C, \text{ and } 1 \le j \le N \tag{3}$$

Table 1 summarizes the operating conditions and design specifications for the DWDC to be developed. The commercial software Aspen Plus is used to perform steady-state simulation. A stripping distillation column with only a reboiler, two paralleled absorber distillation columns with neither reboiler nor condenser, and a rectifying distillation column with only a condenser are employed to construct the DWDC. The design of the DWDC is conducted via a simple search procedure proposed in our earlier work and the minimization of total annual cost is chosen as the objective function for process screening (Wang et al., 2011). The resultant DWDC is sketched in Figure 1a.

Table 1. Operating Conditions and Design Specifications for the DWDC

Parameter		Value	Parameter		Value
Condenser pressure (bar)		3	Vapor	$A(A_{vp}/B_{vp})$	13.04/3862
Stage pressure drop (bar)		6.8901×10^{-3}	pressure	$B(A_{vp}/B_{vp})$	12.34/3862
Feed	A	33.33	constants	$C(A_{vp}/B_{vp})$	11.65/3862
compositions	B	33.33	Product	A	99
(mol %)	C	33.34	specifications	B	99
Feed flow rate (kmol/s)		1	(mol %)	C	99
Feed thermal condition (liquid fraction)		1	Relative volatility A:B:C		4:2:1

3. Various Temperature Difference Control Schemes Proposed for the DWDC

Figures 1b to 1e sketches, respectively, the TDC, STDC, DTDC, and SDTDC schemes to be studied in the current work. The TDC scheme contains four TDC loops. For the STDC scheme, while two TDC loops are used in the two sections along the dividing wall, two TC loops in the rectifying and striping sections, respectively. The DTDC scheme involves four DTDC loops. In the SDTDC scheme, while two DTDC loops are used in the two sections along the dividing wall, two TC loops in the rectifying and

striping sections, respectively. In all these control schemes, the controlled variables are paired with the nearest manipulated variables in locations (i.e., $T_R/\Delta T_R/\Delta^2 T_R$–D, $T_S/\Delta T_S/\Delta^2 T_S$–$Q_R$, $\Delta T_I/\Delta^2 T_I$–I, and $\Delta T_P/\Delta^2 T_P$–R_L). They are justified, however, by static and dynamic analysis and/or closed-loop operability studies and detailed outcomes can be found, elsewhere (Luan et al., 2013; Wu et al., 2013; Yuan and Huang, 2014).

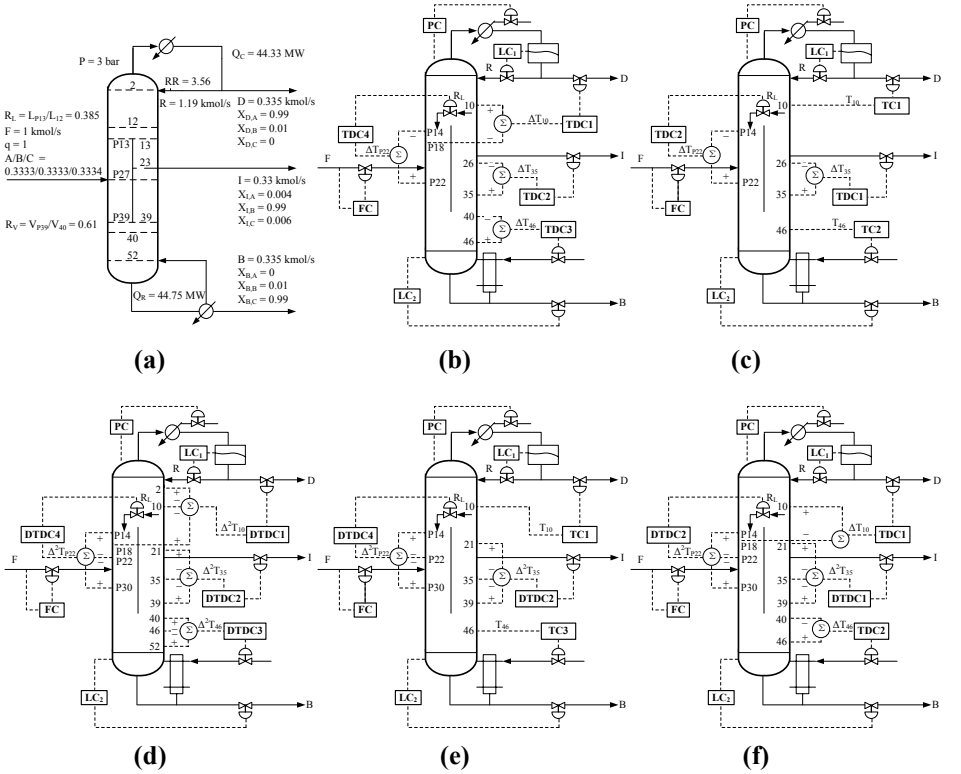

Figure 1. (a) Optimum design of the DWDC, (b) TDC scheme, (c) STDC scheme, (d) DTDC scheme, (e) SDTDC scheme (f) novel SDTDC scheme

Table 2. Controller Parameters for the TDC, STDC, DTDC, SDTDC, and NSDTDC Schemes

Scheme	Controller	K_C	T_I (min)	Scheme	Controller	K_C	T_I (min)
TDC	TDC1	0.279	14.520	STDC	TC1	3.632	13.200
	TDC2	0.745	17.160		TC2	4.020	7.920
	TDC3	0.365	10.560		TDC1	0.731	18.480
	TDC4	0.524	19.800		TDC2	0.508	21.120
DTDC	DTDC1	0.123	14.520	SDTDC	TC1	0.123	14.520
	DTDC2	0.202	17.160		TC2	0.040	10.160
	DTDC3	0.040	10.560		DTDC1	0.202	17.160
	DTDC4	0.700	19.800		DTDC2	0.700	19.800
NSDTDC	TDC1	0.208	13.200	NSDTDC	DTDC1	0.195	17.160
	TDC2	0.359	9.240		DTDC2	0.752	19.800

4. Comparison of Various Temperature Difference Control Schemes Proposed

Closed-loop operations of the DWDC, controlled, respectively, with the TDC, STDC, DTDC, and SDTDC schemes are simulated with the commercial software Aspen Dynamics. All temperature sensors contain a 1-min dead-time element and all the temperature/temperature difference/double temperature difference loops are tuned with the built-in Tyreus-Luyben rule. The detailed parameters are summarized in Table 2.

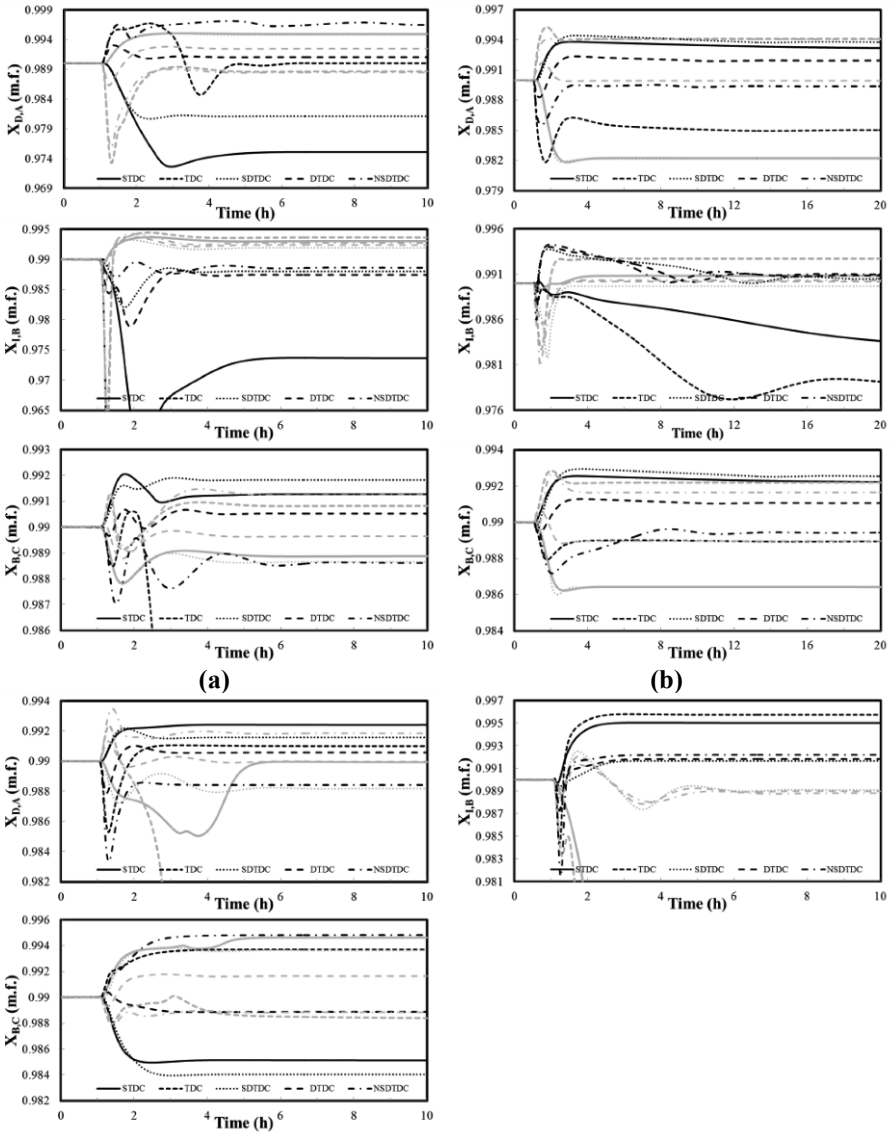

Figure 2. Comparison of various temperature difference control schemes in face of a ±30 % step change in feed compositions of components A, B, and C: (a) component A, (b) component B, (c) component C

In Figure 2, the comparisons of the closed-loop responses of the DWDCs, controlled, respectively, with the TDC, STDC, DTDC, and SDTDC schemes are depicted after the processes have been subjected to a ±30 % step change in feed compositions of components A, B, and C. While the dark lines indicate the responses to the positive changes, the gray lines to the negative ones. The TDC scheme is failed to suppress the disturbances in the cases of positive change in feed compositions of components A and B and negative change in feed compositions of component C. The STDC scheme is unable to reject the disturbances in the case of positive change in feed compositions of component B and negative change in feed compositions of component C. With the inclusion of 4 and 2 temperature measurements, the DTDC and SDTDC schemes can do a better job because they can now suppress a ±30% step change in feed compositions of components A, B, and C. In particular, the DTDC scheme displays smaller steady-state deviations in the three products for step change in feed compositions of components A and C but slightly bigger ones for step change in feed compositions of component B than the SDTDC scheme. Table 3 shows the relative static errors in more detail.

Table 3. Relative Static Errors for a ±30 % Step Change in Feed Compositions of Components A, B, and C

Scenario	Product	Relative static error (%)				
		STDC	TDC	SDTDC	DTDC	NSDTDC
	A	–1.506	0.001	–0.895	0.106	0.652
+30% Z_A	B	–1.649	–33.776	–0.198	–0.259	–0.445
	C	0.127	–3.843	0.184	0.052	–0.143
	A	0.498	–0.137	0.486	0.251	–0.154
–30% Z_A	B	0.305	0.365	0.192	0.241	0.277
	C	–0.114	0.082	–0.136	–0.036	0.127
	A	0.323	–0.501	0.382	0.198	–0.061
+30% Z_B	B	–0.645	–1.098	0.049	0.084	0.099
	C	0.226	–0.106	0.257	0.108	–0.057
	A	–0.782	0.416	–0.791	–0.006	0.413
–30% Z_B	B	0.082	0.272	–0.033	0.018	0.031
	C	–0.361	0.222	–0.363	–0.104	0.167
	A	0.243	0.101	0.159	0.057	–0.159
+30% Z_C	B	0.506	0.580	0.168	0.185	0.221
	C	–0.492	0.374	–0.603	–0.113	0.487
	A	–0.007	–5.734	–0.184	–0.001	0.187
–30% Z_C	B	–29.316	–19.716	–0.092	–0.103	–0.122
	C	0.467	–0.146	0.366	0.166	–0.116

5. Discussions

Generally speaking, the SDTDC scheme can be described to lead to comparable regulatory control performance with the DTDC scheme for a ±30 % disturbance in feed compositions of components A, B, and C. Luan et al. (2013) once demonstrated that the STDC scheme could achieve similar regulatory control performances with the TDC scheme for a ±20 % step change in feed compositions of components A, B, and C. These combined results indicate that for the effective operation of the DWDC it is

extremely important to give strict control of the two sections along the dividing wall and it should be ranked as the top priority in control system synthesis and design. Note the fact that the SDTDC scheme is superior to the STDC scheme coincides also with this interpretation. In case of employing four or more temperature measurements to the two sections along the dividing wall, little enhancement can, however, be secured. Therefore, the DTDC loop should be the best option here.

In Table 3, it can be further observed that the relative static errors in the three products of the DTDC/TDC schemes are smaller than those of the SDTDC/STDC schemes. The result reminds us of the fact that controlling strictly the rectifying and stripping sections helps to improve system performance and it should be taken into account if further improvement is expected from the control system performance of the SDTDC scheme. A novel SDTDC scheme (NSDTDC) with two TDC loops in the rectifying and stripping sections is thus derived as shown in Figure 1f. It yields slight improvement in control system performance in comparison with the SDTDC scheme and the detailed relative static errors are listed also in Table 3.

6. Conclusions

In the current study, the operation of a DWDC separating an ideal ternary mixture of hypothetical components A, B, and C has been examined with the TDC, STDC, DTDC, and SDTDC schemes, respectively. Two conclusions have been drawn on the synthesis and design of the control schemes for the DWDC. Firstly, top priority should be given to the control of the two sections along the dividing wall and usually the DTDC loops should be employed to yield tight control outcomes. Secondly, tightening the operations of the rectifying and stripping sections should then be considered if further improvement in control performance has been required. With the replacement the two TC loops in the SDTDC scheme by two TDC loops, a novel SDTDC scheme has been derived. It enriches the potential alternatives to control the DWDC.

References

S. J. Wang, Wong, D. S. H., 2007, Controllability and Energy Efficiency of High Purity Divided Wall Column, Chemical Engineering Science, 62, 1010.

A. A. Kiss, Bildea, C. S., 2011, A Control Perspective on Process Intensification in Dividing-Wall Columns, Chemical Engineering and Processing: Process Intensification, 50, 281.

H. Ling, Luyben, W. L., 2009, New Control Structure for Divided-Wall Columns, Industrial and Engineering Chemistry Research, 48, 6034.

H. Ling, Luyben, W. L., 2010, Temperature Control of the BTX Divided-Wall Column, Industrial and Engineering Chemistry Research, 49, 189.

S. Luan, Huang, K., Wu, N., 2013, Operation of Dividing-Wall Distillation Columns. 1. A Simplified Temperature Difference Control Scheme, Industrial and Engineering Chemistry Research, 52, 2642.

N. Wu, Huang, K., Luan, S., 2013, Operation of Dividing-Wall Distillation Columns. 2. A Double Temperature Difference Control Scheme, Industrial and Engineering Chemistry Research, 52, 5365.

Y. Yuan, Huang, K., 2014, Operation of Dividing-Wall Distillation Columns. 3. A Simplified Double Temperature Difference Control Scheme, Industrial and Engineering Chemistry Research, 53, 15969.

P. Wang, Chen, H., Wang, Y., Zhang, L., Huang, K., Wang, S. J., 2011, A Simple Algorithm for the Design of Fully Thermally Coupled Distillation Columns (FTCDC), Chemical Engineering Communication, 199, 608.

Krist V. Gernaey, Jakob K. Huusom and Rafiqul Gani (Eds.), 12th International Symposium on Process Systems Engineering and 25th European Symposium on Computer Aided Process Engineering.
31 May - 4 June 2015, Copenhagen, Denmark.

A Decentralised Multi-parametric Model Predictive Control Study for a Domestic Heat and Power Co-generation System

Nikolaos A. Diangelakis[a] and Efstratios N. Pistikopoulos[a,b]

[a]*Department of Chemical Engineering, Imperial College London, London, United Kingdom.*
[b]*Artie McFerrin Department of Chemical Engineering, Texas A&M University, College Station TX, United States.*
e.pistikopoulos@imperial.ac.uk; stratos@tamu.edu

Abstract

The rising interest in heat and power cogeneration, especially in the residential sector, the cost-effectiveness of its operation and environmentally friendly characteristics require attention from both an operational and a design optimisation point of view. In this work, a decentralised control optimisation approach is presented and applied on a natural gas powered, internal combustion engine equipped, domestic cogeneration plant. The approach allows us to not only capture the behaviour of the overall system but also take into account its different operational objectives in terms of either heat or power generation driven production.

Keywords: Decentralised control, multi-parametric Model Predictive Control, Residential scale cogeneration

1. Introduction

Combined Heat and Power (CHP) systems have been receiving a lot of interest as a substitute of traditional power and heat generation resources in residential applications according to Allen et al. (2008) and Ren et al. (2008). Their decentralized production characteristics, cost effective nature and small environmental footprint have added towards that direction. The use of CHP systems aims to reduce the system emissions and increase its operational efficiency via the simultaneous production of usable heat and power in a single process, consuming the same amount of fuel Diangelakis et al. (2014b). Depending on the utilisation of the CHP system, the usable heat is most commonly in the form of high temperature water in liquid or gas form of high pressure and heat bodies of the like. The afore-mentioned heat bodies can be used for a variety of purposes such as (i) heating purposes in other processes, (ii) steam for other process, (iii) space heating, (iv) hot utility water and the like. The basic idea of a cogeneration system is based on the ability of an engine[1] to transform the chemical energy of a fuel into heat and power, most commonly electricity, through a chemical process (i.e. internal/external combustion, etc.). The heat is a byproduct of the power generation process, therefore a heat recovery system, coupled with the prime mover is responsible for transforming the byproduct heat into usable heat. Substantial work has been performed over the last years in the field of cogeneration, employing systems of various scales and power production technologies, focusing on both operational and design aspects, Li et al.

[1]The engine is commonly referred to as the prime mover in such context. An analysis of the most commonly used prime movers can be found in Diangelakis et al. (2014b)

(2010); Wu and Wang (2006); Konstantinidis et al. (2010); Diangelakis et al. (2014a,b); Mehleri et al. (2012). Further attention on this systems is required both on the operational and design level.

The objective of this paper is to introduce a decentralised, multi-parametric Model Predictive Control approach for the operation of a natural gas powered, internal combustion engine equipped, domestic CHP system that exploits its dual operational objectives, namely the electrical power and hot water production. The procedure followed for that purpose is described below, followed by its application in section 2. The full PAROC framework (Figure 1) and the principles presented in Pistikopoulos et al. (2014) are followed in a step-by-step basis. The major difference in this decentralised case is the consideration of a multiple subsystems within the system at hand in order to handle the additional complexity. The 4 steps of the framework are presented below.

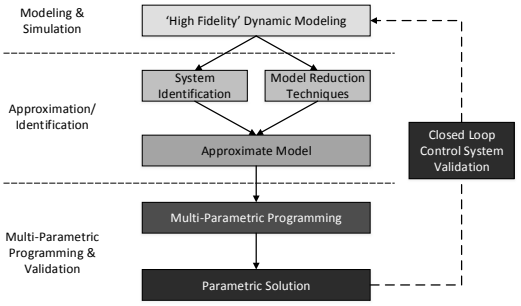

Figure 1: The PAROC Framework.

Step 1: "High Fidelity" Dynamic Modeling – The development of the "high fidelity model", its quality and robustness determine the validity of the framework. The modeling of the system takes place in gPROMS® Process Systems Enterprise (1997-2014).

Step 2: Model Approximation – The resulting highly complex dynamic models of the subsystems of the first step (most commonly DAE or PDAE programs), although sufficiently accurate compared to the real process, are far from ideal in terms of multi-parametric programming utilisation. Therefore, reduction techniques (Lambert et al. (2013) and Lambert (2013)) and identification methods (System Identification Toolbox of MATLAB®) are employed for to (i) reduce the model complexity while (ii) preserving the model accuracy.

Step 3: Design of the Multi-Parametric Model Predictive Controllers – The design of the controllers is based on the validated procedure described in Pistikopoulos et al. (2012) and Bemporad et al. (2002). The resulting multi-parametric program is solved via the POP® toolbox in MATLAB®, thus acquiring the map of optimal control actions.

Step 4: Closed-Loop Validation – The procedure is validated through a closed loop procedure, where the controllers are tested against the original model of Step 1. This can happen either via the interoperability between software tools such as gPROMS® and MATLAB® via gO:MATLAB or via the straight implementation of the controllers in the gPROMS® simulation via the use of C++ programming and the creation of Dynamic Link Libraries.

2. Decentralised mp-MPC for a domestic scale CHP plant

The afore-described framework is put into use on a domestic cogeneration plant utilised to produce electrical power and usable heat in the form of hot water of a certain temperature, in order to cover the electricity and space heating needs of a 10-house district.

2.1. High Fidelity Modeling

The dynamic model of the CHP system is represented in Figure 2 and a full description can be found in Diangelakis et al. (2014b). The mathematical model comprises of a total of 379

equations, 15 of which are differential, with 6 degrees of freedom, 4 of which are dynamic. The model is treated as the interactions between distinct subsystems, namely the power generation subsystem and the heat recovery subsystem. The power generation subsystem comprises the throttle valve, the inlet and exhaust manifolds, the reciprocating internal combustion engine coupled with the crankshaft and the power generator. On the other hand, the heat recovery subsystem comprises of two heat exchangers that facilitate the heat transfer between the high temperature cooling fluid of the internal combustion engine and the exhaust gases towards an external cold water stream.

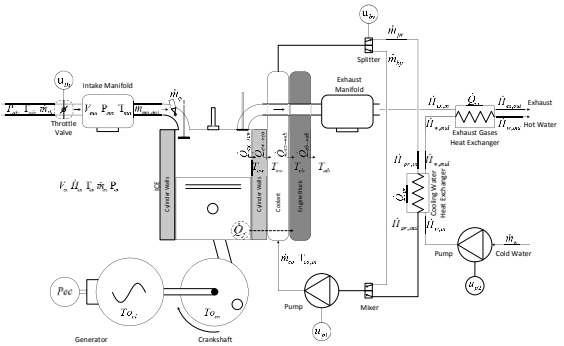

Figure 2: Graphical representation of the CHP System (Acquired from Diangelakis et al. (2014b)).

2.2. Model Approximation

Three subsystems are identified with the use of the System Identification Toolbox of MATLAB®. The first subsystem comprises of the power generation part of the CHP system, including the internal combustion engine, the electrical power generator and their supportive equipment. The approximate model of subsystem 1 is built using the throttle valve position and the electrical power generation output as input-output (I/O) data. The second subsystem comprises of the heat recovery subsystem, including the two heat exchangers and the interaction of the external water stream and the generated heat from the prime mover. The I/O data used for the identification purposes are the electrical power output, the water flowrate in the heat recovery system and the temperature of the water at the outlet of the system. A third subsystem is identified that correlates the inlet water flowrate to the outlet water flowrate of the heat recovery system which for brevity reason won't be thoroughly addressed. Overal 2 single input - single output subsystems and 1 multiple input - single output subsystem are identified. The three sets of equations (Equations 1 to 9) describe the approximate models for the power generation subsystem, the heat recovery subsystem and the flowrate correlation subsystem, respectively.

$$x_{k+1} = 0.9913\,x_k + 0.0044\,u_k \tag{1}$$
$$y_k = 3.5927\,x_k \tag{2}$$
$$T_s = 0.1s \tag{3}$$

$$x_{k+1} = \begin{bmatrix} 0.9712 & -0.0207 & -0.0529 \\ 0.0012 & 0.8169 & -0.0524 \\ -0.0099 & -0.0302 & 0.9551 \end{bmatrix} x_k + \begin{bmatrix} -0.0245 & -0.0079 \\ -0.1009 & 0.0593 \\ -0.02457 & 0.0125 \end{bmatrix} u_k \tag{4}$$
$$y_k = \begin{bmatrix} -158.5 & -9.306 & -155 \end{bmatrix} x_k \tag{5}$$
$$T_s = 0.1s \tag{6}$$

$$x_{k+1} = 0.99\,x_k + 0.01\,u_k \tag{7}$$
$$y_k = 1\,x_k \tag{8}$$
$$T_s = 0.1s \tag{9}$$

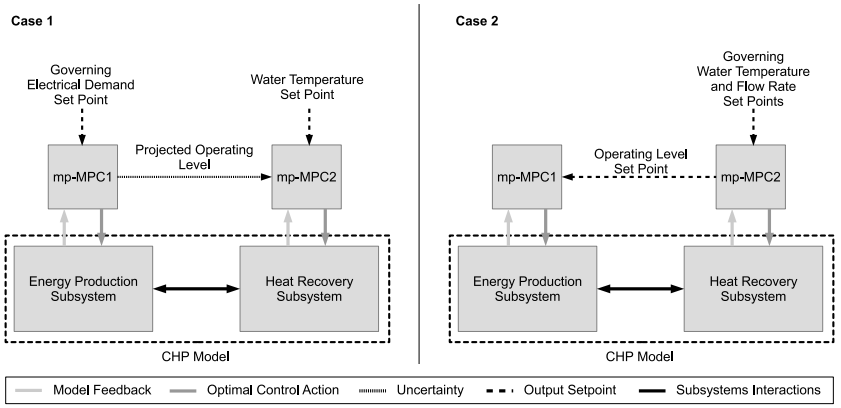

Figure 3: The two distinct control policies.

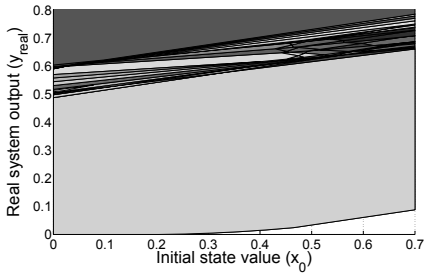

Figure 4: figure
Power generation subsystem mp-MPC

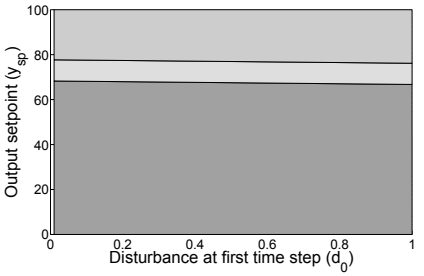

Figure 5: figure
Heat recovery subsystem mp-MPC

2.3. Multi-parametric Programming and Control

The approximate models identified in the model approximation step are the basis for the design of three multi-parametric controllers. The operation of the CHP system though, is governed by either the demand of electrical power (Case 1) or the demand of hot water (Case 2). To serve both cases, a two stage approach has been adopted for the design of the heat recovery system control. In Case 1, the system attempts to (i) cover the electrical power demand and (ii) produce water of a predefined temperature, regardless of the flow rate. In order for this to happen, the controller of the heat recovery subsystem controls the temperature of the water at the outlet of the heat recovery system via the manipulation of the water flow rate while treating the operational level of the energy generation subsystem as a measured uncertainty. Therefore, for Case 1, only two out of the three sub-suystems ad respective controllers are utilised, rendering the third subsystem In Case 2, the system attempts to produce water at predefined temperature and flowrate values. This is translated into treating both the water temperature and flow rate as control variables while the flow rate set point and the operational level of the electrical power generation subsystem are treated as manipulated variables of subsystem 2 and subsystem 3 respectively. The latter is treated as a power output set point for the energy generation subsystem. A schematic representation of the two control cases is presented in figure 3.

The parameters of the quadratic optimisation problems consist of the initial values of the states, the measured disturbances, the previous control action, the output setpoints and the output setpoint mismatch against the original high fidelity system. A 2-D projection of the critical regions for the

power generation and heat recovery subsystems is presented in figures 4 and 5.

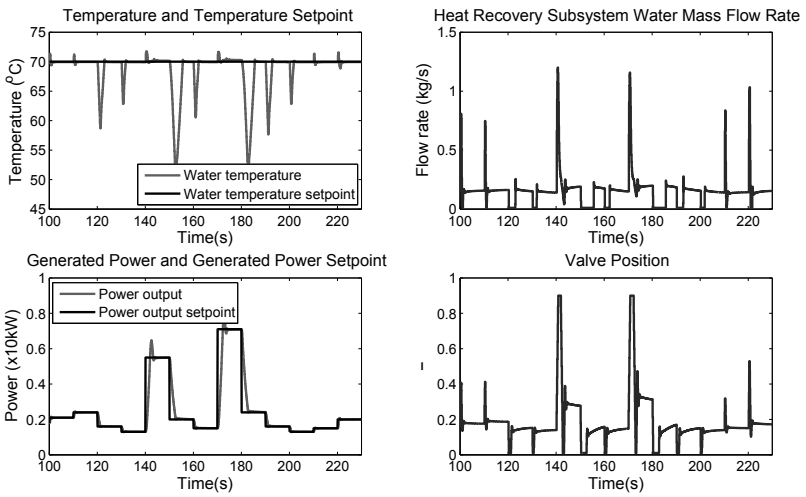

Figure 6: mp-MPC Results for Case 1.

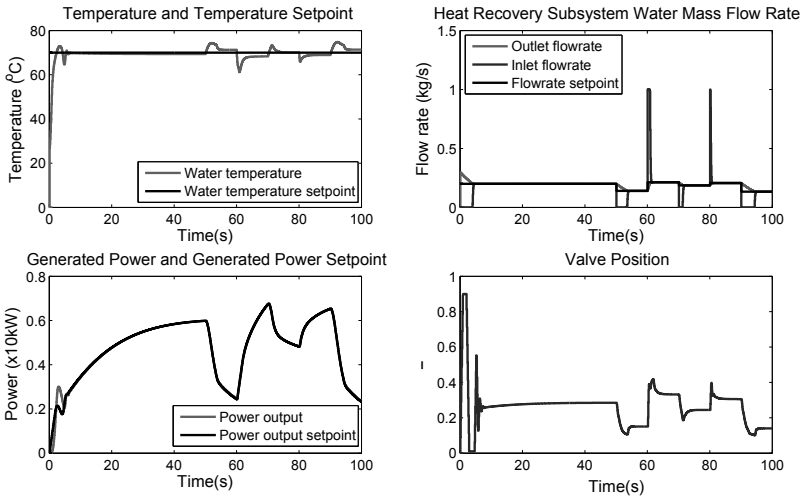

Figure 7: mp-MPC Results for Case 2.

2.4. Closed-Loop Validation and Results

The closed-loop validation takes place for the two cases individually. For the first case, the electrical power generation level is set. The controller of the power generation subsystem follows the pre-set set point while the controller of the heat recovery subsystem treats the electrical power output as a disturbance. The objective of the latter is to maintain the temperature of the water at the outlet of the heat recovery subsystem at 70^oC by manipulating the water flowrate (Figure 6). In the second case, both the flowrate of the water of the heat recovery system and its temperature need to be maintained to a pre-defined level. Therefore, the power generation output is treated as the

manipulated variable of the heat recovery subsystem controller and the setpoint for the electrical power generation controller (Figure 7).

3. Conclusions

Following the procedure described in the Framework we designed two distinct cases for the decentralised control of a domestic CHP system. This scheme decomposes the original system into two major parts thus enabling a more effective approach while ensuring that the operation of the CHP can cover both the heat generation and electrical generation setpoints. In both cases, the controller schemes manage to accurately capture the dynamics of the system and drive it to the desired operational setpoints. This then forms the basis for further exploring the interactions between process design, operational scheduling and model predictive control in a multi-parametric fashion Kopanos and Pistikopoulos (2014); Diangelakis et al. (2014a).

4. Acknowledgments

The financial support from CPSE Industrial Consortium and EPSRC grant (EP/I014640/1) are gratefully acknowledged.

References

Allen, S., Hammond, G., McManus, M., 2008. Prospects for and barriers to domestic micro-generation: A united kingdom perspective. Applied Energy 85 (6), 528–544.

Bemporad, A., Morari, M., Dua, V., Pistikopoulos, E. N., 2002. The explicit linear quadratic regulator for constrained systems. Automatica 38 (1), 3–20.

Diangelakis, N. A., Manthanwar, A. M., Pistikopoulos, E. N., 2014a. A framework for design and control optimisation: Application on a chp system. In: Proceedings of the 8th International Conference on Foundations of Computer-Aided Process Design. Vol. 34 of Computer Aided Chemical Engineering. Elsevier, pp. 765–770.

Diangelakis, N. A., Panos, C., Pistikopoulos, E. N., 2014b. Design optimization of an internal combustion engine powered chp system for residential scale application. Computational Management Science 11 (3), 237–266.

Konstantinidis, D., Varbanov, P., Klemeˇ s, J., 2010. Multi-parametric control and optimisation of a small scale chp. Chemical Engineering Transactions 21, 151–156.

Kopanos, G. M., Pistikopoulos, E. N., 2014. Reactive scheduling by a multiparametric programming rolling horizon framework: A case of a network of combined heat and power units. Industrial & Engineering Chemistry Research 53 (11), 4366–4386.

Lambert, R. S., 2013. Approximation methodologies for explicit model predictive control of complex systems. Ph.D. thesis, Imperial College, London.

Lambert, R. S., Rivotti, P., Pistikopoulos, E. N., 2013. A monte-carlo based model approximation technique for linear model predictive control of nonlinear systems. Computers & Chemical Engineering 54 (0), 60–67.

Li, H., Marechal, F., Favrat, D., 2010. Power and cogeneration technology environomic performance typification in the context of co2 abatement part ii: Combined heat and power cogeneration. Energy 35 (9), 3517–3523.

Mehleri, E. D., Papageorgiou, L. G., Markatos, N. C., Sarimveis, H., 2012. A model predictive control framework for residential microgrids. Computer Aided Chemical Engineering 30, 327–331.

Pistikopoulos, E. N., Diangelakis, N. A., Oberdieck, R., Papathanasiou, M. M., Nascu, I., Sun, M., 2014. PAROC - an integrated framework and software platform for the design, operational optimization and advanced model-based control of process systems, chemical engineering science. Computational Management Science, *Submitted*.

Pistikopoulos, E. N., Dominguez, L., Panos, C., Kouramas, K., Chinchuluun, A., 2012. Theoretical and algorithmic advances in multi-parametric programming and control. Computational Management Science 9 (2), 183–203.

Process Systems Enterprise, 1997-2014. gPROMS.
URL `http://www.psenterprise.com/gproms/`

Ren, H., Gao, W., Ruan, Y., 2008. Optimal sizing for residential chp system. Applied Thermal Engineering 28 (5-6), 514–523.

Wu, D. W., Wang, R. Z., 2006. Combined cooling, heating and power: A review. Progress in Energy and Combustion Science 32 (5-6), 459–495.

Krist V. Gernaey, Jakob K. Huusom and Rafiqul Gani (Eds.), 12th International Symposium on Process Systems Engineering and 25th European Symposium on Computer Aided Process Engineering.
31 May – 4 June 2015, Copenhagen, Denmark

A control strategy for periodic systems - application to the twin-column MCSGP

Maria M. Papathanasiou[a], Fabian Steinebach[b], Guido Stroehlein[c], Thomas Müller-Späth[c], Ioana Nascu[a], Richard Oberdieck[a], Massimo Morbidelli[b], Athanasios Mantalaris[a], Efstratios N. Pistikopoulos[a,d*]

[a]*Dept. of Chemical Engineering, Centre for Process Systems Engineering (CPSE), Imperial College London SW7 2AZ, Lodnon, U.K*
[b] *Institute for Chemical and Bioengineering, ETH Zurich, Wolfgang-Pauli-Str. 10/HCI F 129, CH-8093 Zurich, Switzerland*
[c] *ChromaCon AG, Technoparkstr. 1, CH-8005 Zurich, Switzerland*
[d]*Artie McFerrin Department of Chemical Engineering, Texas A&M, College Station TX*
*e.pistikopoulos@imperial.ac.uk/stratos@tamu.edu

Abstract

In this work we present advanced multi-parametric control strategies for the "Multicolumn Countercurrent Solvent Gradient Purification" (MCSGP) process, which is a continuous chromatographic separation process, governed by a periodic operation profile, linked to the intensification of monoclonal antibody production. We demonstrate a seamless, step-by-step procedure for the development of multi-parametric controllers as part of our recently introduced PAROC framework and software platform. The designed controller assures optimal operating conditions, avoiding pertubations, under continuous operation, while capturing the periodic nature of the process.

Keywords: periodic systems, mp-MPC, chromatography

1. Introduction

Periodic systems form a challenging class of control problems that has been addressed in the open literature (Engell and Toumi, 2005, Kawajiri and Biegler, 2006, Grossmann et al., 2010). Contributions in the field have suggested 'cycle-to-cycle' control approaches (Grossmann et al., 2010), solving a Model Predictive Control (MPC) problem at every cycle. However, ensuring periodic input profiles that can lead to cyclic steady state (CSS) still remains an open challenge. In addition, the development of advanced control strategies for such systems includes handling of complex Partial Differential and Algebraic Equations (PDAEs) models that usually involve nonlinear terms.

In this work, we investigate the design and application of advanced control strategies for the twin-column MCSGP process that is a semi-continuous chromatographic process, described by a nonlinear PDAE model. We demonstrate the seamless development of multiparametric-MPC (mp-MPC)controllers for such systems through the application of the PAROC framework & software platform (Pistikopoulos et al., 2014, PAROC, 2013-2014) that comprises four major steps: (i) the development of a 'high-fidelity' mathematical model, (ii) a model approximation step, (iii) the design and solution of the multi-parametric programming problem and (iv) a 'closed-loop' in silico system

validation step. The steps are described through the application of the framework to a chromatographic system.

2. The System

The development of a multi-parametric control strategy for the twin-column MCSGP is examined. MCSGP (Figure 1a) is a periodic process comprising 2 chromatographic columns that operate in countercurrent mode (Krättli et al., 2011). Both columns are alternated between a batch and interconnected state. The two columns are characterized by the same technical details (e.g. length, diameter, resin material) and are operated in the same way with half a cycle delay. Here we reduce the system to a 5x3 single-column configuration (Figure 1b), considering the modifier concentration, the flow rate and the component concentrations in the feed stream as inputs, while the output set includes: the concentrations of the three mixture components (Weak impurities (W), Product (P) and Strong impurities (S)). MCSGP process aims to separate the product from the early eluting impurity W and the later eluting impurity S, while recycling overlapping regions of the chromatogram. Therefore the control objective is to maintain a high purity of the product stream, while optimizing the recovery yield.

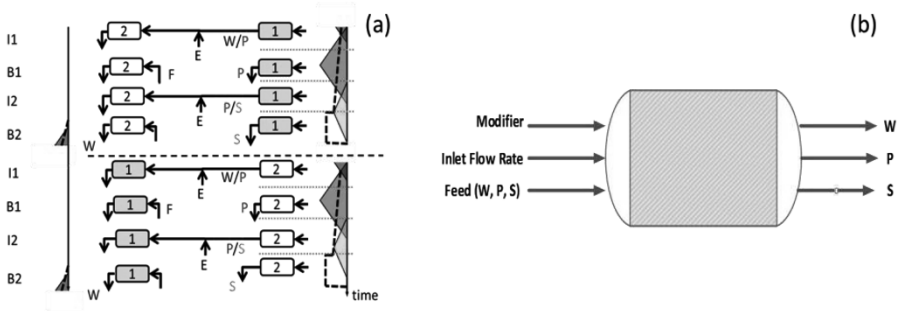

Figure 1 (a) Twin-column MCSGP setup, (b) Input/ Output single-column system based on the principles of the MCSGP process (5x3 system).

2.1 The High-Fidelity Process Model

The system is described by a Partial Differential Algebraic Equation (PDAE) model (Müller-Späth et al., 2008) that was modeled in gPROMS ModelBuilder ® v 4.0.0 (PSE, 1997-2014). The objective is to maintain the process under optimal operating conditions that will ensure high product purity and yield, which are functions of the average concentrations of the three mixture components in the outlet streams (Grossmann et al., 2010).

In this work we track the integral of the outlet concentration of the three mixture components aiming to overcome difficulties with online measurements, as well as to be able to monitor continuous outputs. In that way the controller can operate throughout the process cycle and possibly result in better process monitoring, compared to 'cycle-to-cycle' control. Tracking of the integral of the outlet concentration allows seamless post-calculation of purity and yield. The significance of the inputs was evaluated by the application of a pulse input strategy. As shown in Figure 2, four of the inputs were maintained constant, while the fifth one was varied within the range of interest.

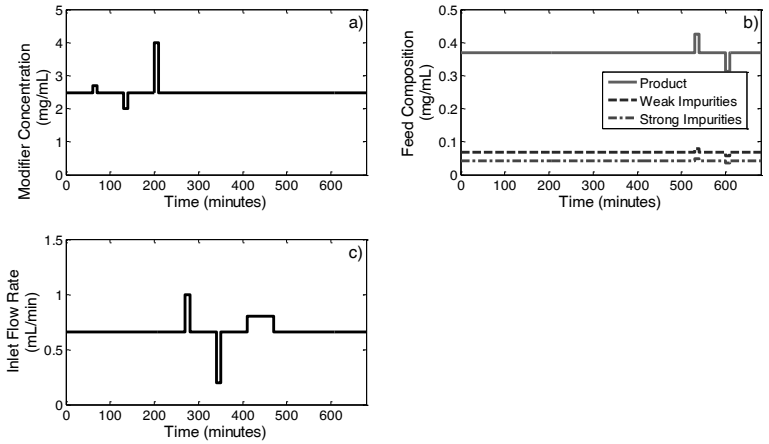

Figure 2 Pulse input strategy as applied for the sensitivity tests for (a) the modifier concentration (mg/mL), (b) feed composition (mg/mL) and (c) the inlet flow rate (mL/min).

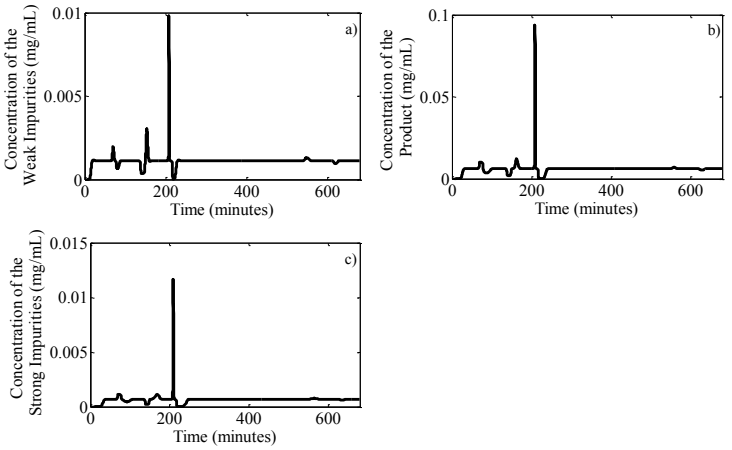

Figure 3 Output profiles as resulted from the sensitivity tests for the outlet concentration of (a) the weak impurities, (b) the product and (c) the strong impurities.

It can be observed that the modifier concentration has the most significant effect on the monitored outputs (Figures 2 & 3), followed by changes in the feed composition. On the contrary, changes in the flow rate values seem have no considerable effect (synergetic and/or antagonistic effects are not considered here). Based on these profiles, we reduce the system to a Single-Input Multiple-Output configuration (Figure 4), considering the modifier concentration as the sole input. This is also in accordance with the process physicochemical properties as the modifier concentration affects greatly the separation performance (Müller-Späth et al., 2008). It is known, however, that the value of the flow rate controls the speed that the components travel through the column and therefore the extraction times. Also, it should be underlined that in reality, the feed composition of the upstream mixture cannot be controlled and should be therefore treated as a disturbance. However, for the purposes of this work disturbances will not be considered.

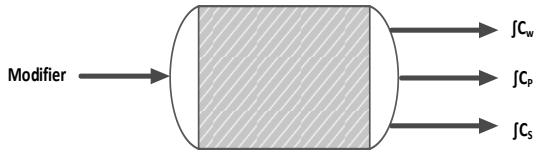

Figure 4 The three Single Input - Multiple Output (SIMO) system, considering the modifier concentration as input and the integral of the three outlet concentrations as outputs

2.2 Model Reduction/System Identification

The process model describing the 1x3 system (Figure 4) is characterized by a large set of PDAEs, involving highly nonlinear terms. Therefore it needs to be simplified in order to be used for control studies (Rivotti et al., 2012, Lambert et al., 2013). The process model was simulated under a random pulse input strategy, ensuring that the system is adequately excited within the range of interest. The input-output (modifier concentration – integral of the outlet concentrations) data set is used for the design of linear, state space model using the identification toolbox in MATLAB®. The reduced models were tested against various sets of inputs and their response and fitting was evaluated. For the selection of the model, the number of states was also considered. The selected reduced model comprises 6 states, 1 input (modifier concentration) and 3 outputs (integrals of the outlet concentrations) and was characterized by the best fit and a relatively small number of states that reduces the computational force needed.

2.3 Design of multi-parametric controllers & 'Closed-loop', in-silico validation

The state space model described above was used for the design of a multi-parametric controller for the nominal single-column design case (Figure 4). The problem was solved for an output horizon of 4 and a control horizon of 2 (using the PAROC software platform (PAROC, 2013-2014)) and the map of solutions comprises a set of 6 critical regions in total. The designed controller was tested in-silico against the original process model and the output behavior was monitored, using the gO:MATLAB interface in gPROMS ModelBuilder® (PSE, 1997-2014). Figure 6 illustrates the comparison between the output and the output setpoint as generated for the input strategy indicated by the controller (Figure 5).

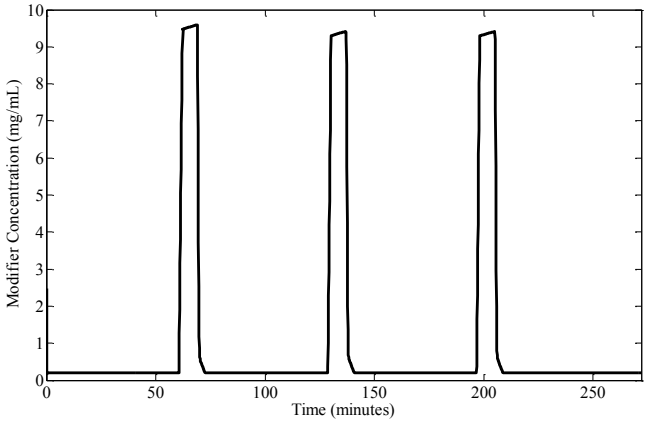

Figure 5. Input profile for the modifier concentration as indicated by the controller during the 'closed-loop' validation.

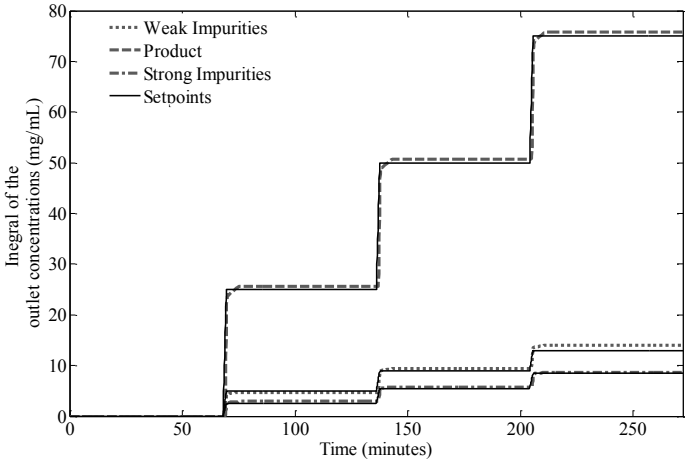

Figure 6 Comparison of the setpoint and the output model output as resulted from the controller closed-loop validation for weak impurities, product and strong impurities over time.

A fairly good agreement between the monitored outputs and the assigned setpoints can be observed (Figure 6), without significant offset (< 3%). However, even this deviation can be tackled by incorporating an integral state that will lead to more efficient setpoint tracking (Sakizlis et al., 2004). Moreover, it can be seen that the controller indicates a cyclic input profile (Figure 5). The latter implies that the design of both the state space and the controller capture the periodic nature of the system and will effectively ensure cyclic steady state (CSS). The results presented are also in agreement with the physicochemical laws that govern the system. In chromatography, elution can only take place with the addition of modifier. This behavior is efficiently captured by the controller, as we observe increase in the modifier concentration (Figure 5) whenever an increase in the setpoint is encountered (Figure 6). A periodic profile is also observed in the selection of critical regions (Figure 7a, 7b). This can be translated into period control laws that could force the system to reach CSS.

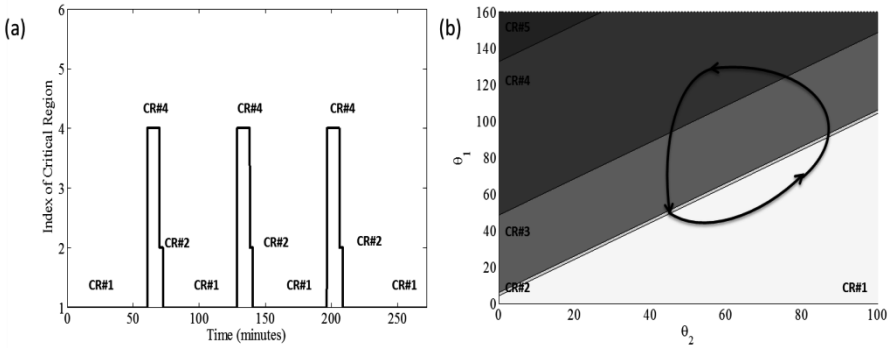

Figure 7 Evolution of the critical regions during the 'closed-loop' controller validation over time: (a) index of critical region, (b) Two-dimensional projection of the critical region polyhedral corresponding to the six state space model.

3. Conclusions

This works presents a detailed approach for the development of model-based multi-parametric controllers for a periodic, chromatographic process. Following the PAROC framework (Pistikopoulos et al., 2014) we demonstrate both the development of the mp-MPC controller and the 'closed-loop' validation against the original process model. We also suggest tracking of the integral of the output concentrations that could result into continuous outputs and effectively continuous process monitoring. The in-silico validation results demonstrate that the controller can efficiently capture the periodic nature of the process by indicating a cyclic input profile that results in cyclic steady state (CSS).

The proposed Single Input – Multiple Output (SIMO) controller could be further robustified against various values of flow rates and disturbances, to account for variations in the composition of the feed stream. Additionally, the addition of an integral state could lead to tighter output monitoring thus eliminating the offsets (Sakizlis et al., 2004).

4. Acknowledgements

This work is performed in the framework of the OPTICO project (G.A. No 280813) for "Model-based Optimization and Control for Process-Intensification in Chemical and Biopharmaceutical Processes".

References

S. Engell & A. Toumi, 2005. Optimisation and control of chromatography. *Computers & Chemical Engineering,* 29**,** 1243-1252.

C. Grossmann, G. Ströhlein, M. Morari & M. Morbidelli, 2010. Optimizing model predictive control of the chromatographic multi-column solvent gradient purification (MCSGP) process. *Journal of Process Control,* 20**,** 618-629.

Y. Kawajiri & L. T. Biegler, 2006. Optimization strategies for simulated moving bed and PowerFeed processes. *AIChE Journal,* 52**,** 1343-1350.

M. Krättli, G. Ströhlein, L. Aumann, T Müller-Späth & M. Morbidelli, 2011. Closed loop control of the multi-column solvent gradient purification process. *Journal of Chromatography A,* 1218**,** 9028-9036.

R. S. C. Lambert, P. Rivotti & E. N. Pistikopoulos, 2013. A Monte-Carlo based model approximation technique for linear model predictive control of nonlinear systems. *Computers & Chemical Engineering,* 54**,** 60-67.

T. Müller-Späth, L. Aumann, L. Melter, G. Ströhlein & M. Morbidelli, 2008. Chromatographic separation of three monoclonal antibody variants using multicolumn countercurrent solvent gradient purification (MCSGP). *Biotechnology and Bioengineering,* 100**,** 1166-1177.

PAROC. 2013-2014. [Online]. Available: http://www.paroc-platform.co.uk/ [Accessed 26.10 2014].

E. N. Pistikopoulos, N. A. Diangelakis, R. Oberdieck, M. M. Papathanasiou, I. Nascu & M. Sun, 2014. PAROC - an Integrated Framework and Software Platform for the Design, Operational Optimization and Advanced Model-Based Control of Process Systems. *Chemical Engineering Science, submitted*.

PSE 1997-2014. gPROMS ModelBuilder (R). Process Systems Enterpise.

P. Rivotti, R. S. C. Lambert & E. N. Pistikopoulos, 2012. Combined model approximation techniques and multiparametric programming for explicit nonlinear model predictive control. *Computers & Chemical Engineering,* 42**,** 277-287.

V. Sakizlis, N. M.P. Kakalis, V. Dua, J. D. Perkins & E. N. Pistikopoulos, 2004. Design of robust model-based controllers via parametric programming. *Automatica,* 40**,** 189-201.

Krist V. Gernaey, Jakob K. Huusom and Rafiqul Gani (Eds.), 12th International Symposium on Process Systems Engineering and 25th European Symposium on Computer Aided Process Engineering.
31 May – 4 June 2015, Copenhagen, Denmark

Design of multiparametric NCO tracking controllers for linear dynamic systems

Muxin Sun[a], Benoît Chachuat[a], Efstratios N. Pistikopoulos[a,b]

[a]*Centre for Process Systems Engineering, Department of Chemical Engineering, Imperial College London, London, SW7 2AZ, UK*
[b]*McFerrin Department of Chemical Engineering, Texas A&M University, College Station, TX, USA* stratos@tamu.edu

Abstract

A methodology for combining multiparametric programming and NCO tracking is presented in the case of linear dynamic systems. The resulting parametric controller contains information regarding the solution structure provided by multiparametric programming and the corresponding feedback control laws for tracking optimality conditions, thus avoiding the need for repetitively solving optimization problems in online real time control. An example of a constrained linear quadratic optimal control problem with initial conditions as parameters is presented to illustrate the approach.

Keywords: multiparametric programming, NCO tracking, feedback control

1. Introduction

On-line optimization and real-time control have been receiving a lot of attention especially driven by the need to reduce economic costs and improve system performance. Many industrial applications are fast dynamic systems operated under constraints, typically reflecting physical operation bounds and/or safety requirements. The optimal control action is obtained by solving the optimization problem based on dynamic model of the system without violating the constraints. One major challenge in such systems is how to effectively deal with uncertainty stemming from model mismatch and process disturbances, where optimal operation needs to be decided online based on real-time feedback. Such optimal control actions can be obtained by solving dynamic optimization problems repeatedly. This is the strategy employed in Model Predictive Control (Rawlings and Mayne, 2009), where uncertainties can be handled by repeatedly solving the optimization problem online to obtain optimal inputs, a quite computationally demanding task. For systems with fast dynamics, this may often cause serious delays, leading to suboptimal performance or even infeasibility. Several approaches have been proposed in the literature to avoid the need for repeatedly solving optimization problems online. One is based on multiparametric programming and control (Pistikopoulos, 2012). Here, optimization problems are solved offline, resulting in priori computations of explicit mapping of solutions, effectively control strategies, as a function of measurable quantities. Another approach is tracking the Necessary Conditions of Optimality (NCO-tracking) (Kadam et al, 2007). Here, feedback control laws are derived in order to track the NCOs along each arc of the nominal optimal solution, as obtained off-line, thereby converting an optimal control problem into a self-optimizing feedback control problem.

The objectives of the work are to combine multiparametric programming and NCO-tracking in unified framework, thereby paving the path towards a theoretical justification for NCO-tracking based on multiparametric programming. A constrained linear quadratic

optimal control problem with parametric initial conditions is presented to illustrate the approach.

2. Multiparametric dynamic optimization

2.1. Problem formulation

Consider the following dynamic optimization problem with linear dynamic system

$$\begin{aligned}&\phi = \min_{u(t)} \tfrac{1}{2}{x_f}^T Q_f x_f + \int_{t_o}^{t_f} \tfrac{1}{2} x(t)^T Q x(t) + \tfrac{1}{2} u(t)^T R u(t) dt \\ &s.t. \quad \dot{x}(t) = Ax(t) + Bu(t), \;\; x(t_0) = x_o, \;\; t_0 \le t \le t_f \\ &\qquad g(x,u) = C_1 x(t) + C_2 u(t) + b_1 \le 0, \;\; e(x_f) = E_1 x_f + b_2 \le 0\end{aligned} \tag{1}$$

where ϕ is the scalar objective function; x and u are the differential state variables and control variables, x_f is the final state variable; t_0, t_f are the initial and final times; g and e are the path and terminal constraints; and $Q_f \succ 0, R \succ 0, Q \succcurlyeq 0$ are the weighting matrix, hence the problem is non-singular.

2.2. Parametric optimal solution structure

For each initial value x_o, treated as parameters, the optimal solution contains a unique sequence of interior and boundary arcs. We define this sequence as the *optimal solution structure*, denoted by $S(x_o)$. Also the entry and exit times for the k-th constraint are denoted by $t_{ken}(x_o)$ and $t_{kex}(x_o)$.

The optimal control and state trajectories should satisfy the following necessary conditions (Kreindler, 1982)

$$\partial\Psi/\partial u = 0, \quad \partial\Psi/\partial x = 0, \quad \partial\Psi/\partial x_f = p_f, \quad \mu^T g = 0, \quad \nu^T e = 0, \quad \mu, \nu \ge 0 \tag{2}$$

Here, $\Psi = \frac{1}{2}{x_f}^T Q_f x_f + \nu^T e(x_f) + \int_{t_0}^{t_f} H(t)dt$ is the Augmented Lagrange function, $H(t), p(t), \mu(t)$ and ν are the corresponding Hamiltonian function, costate variables, path constraints and terminal constraints, respectively.

By applying the above conditions, an optimal pair $(x(t), p(t))$ for (1) can be obtained by solving the following boundary value problem:

$$\begin{bmatrix} x(t) \\ p(t) \end{bmatrix} = e^{G(t-t_k)} \left(\begin{bmatrix} x(t_k) \\ p(t_k) \end{bmatrix} + b \right) - G^{-1} b$$

$$G = \begin{bmatrix} A - BR^{-1}\hat{C}_2^T \left(\hat{C}_2 R^{-1} \hat{C}_2^T\right)^{-1} \hat{C}_1 & -BR^{-1}B^T + BR^{-1}\hat{C}_2^T \left(\hat{C}_2 R^{-1} \hat{C}_2^T\right)^{-1} \hat{C}_2 R^{-1} B^T \\ -Q - \hat{C}_1^T \left(\hat{C}_2 R^{-1} \hat{C}_2^T\right)^{-1} \hat{C}_1 & -A^T + \hat{C}_1^T (\hat{C}_2^T)^{-1} B^T \end{bmatrix}$$

$$b = \begin{bmatrix} -BR^{-1}\hat{C}_2^T \left(\hat{C}_2 R^{-1} \hat{C}_2^T\right)^{-1} \hat{b}_1 \\ -\hat{C}_1^T \left(\hat{C}_2 R^{-1} \hat{C}_2^T\right)^{-1} \hat{b}_1 \end{bmatrix}, \quad \hat{\mu}(t) = \left(\hat{C}_2 R^{-1} \hat{C}_2^T\right)^{-1} \left(\hat{C}_1 x(t) - \hat{C}_2 R^{-1} B^T p(t) + \hat{b}_1\right)$$

Here, $\hat{C}_1, \hat{C}_2, \hat{b}_1$ are defined for the active constraints $\hat{g} = \hat{C}_1 x + \hat{C}_2 u + \hat{b}_1$ that explicitly contain u and $\hat{\mu}(t)$ are the Lagrange multipliers for $\hat{g}$. For the case with active state constraints, solution with similar form can be obtained by taking derivatives of the constraints, one can refer to (Vinter and Zheng, 1998) for details.

Initial costate function $p(t_0, x_0)$ is linear in x_0, for details one can refer to (Sakizlis et al, 2005). The switching times $t_k(x_0)$ can be computed from the continuity conditions $H(t_{ken}^+) = H(t_{ken}^-)$ and $H(t_{kex}^+) = H(t_{kex}^-)$.

Optimal input $u(t) = -R^{-1}B^T p(t) - R^{-1}\hat{C}_2{}^T \hat{\mu}(t)$.
In particular, solution structure can be completely determined by parameter x_0.

Critical regions are defined such that each region corresponds to certain optimal solution structure, which is characterized by a unique sequence of arcs in time domain. For details about how to define the critical regions and the boundaries, one can refer to (Sakizlis et al, 2005). Each critical region contains a set of parameters x_0 with same solution structure. Thus, the solution structure can be a function of parameters, denoted as multiparametric solution structure, providing a mapping for $x_0 \rightarrow S(x_0)$.

3. NCO tracking

3.1. Concept of NCO tracking

The measurement-based method of NCO tracking enforces optimality by directly tracking the necessary conditions of optimality in the presence of uncertainty, thus transforming a dynamic optimization problem into a feedback control problem (Kadam et al, 2007). The optimal control profile of dynamic optimization problem consists of a sequence of arcs, and along each arc, decision variables are linked to different types of NCO, namely, path constraints, terminal constraints and sensitivities conditions, as shown in Equation (2). The adaption laws for constraints and sensitivities is to force NCO variations to be zero (François et al, 2004). Therefore, measurements are used to directly update the inputs by tracking the NCOs at zero.

A restriction for this approach in practise lies in the fact that the solution structure is assumed to remain unchanged in the presence of disturbances. This can be avoided by the use of multiparametric solution structure, as described in section 2.2.

3.2. Solution model

For each solution structure, a feedback controller can be designed based on the corresponding solution model, which includes information about the sequence and types of arcs, input parameterization and adaption for each kind of arcs (Bonvin and Srinivasan, 2013). Such a solution model enforces optimality by defining feedback laws along each arc and switching logic between different arcs. The active constraints can be directly enforced to reach optimality. For sensitivity-seeking arcs input profiles can be parameterized by simple functions and more efforts should be made by pairing the decision variables with control variables (NCOs). It should be noticed that the sequence of arcs in each solution model matches exactly the switching structure for critical regions in the context of multiparametric programming.

4. Multiparametric NCO tracking controller

4.1. Multiparametric solution model

By resorting to the critical regions for optimal solution structure, the general theory of NCO tracking can be extended, where solution structure does not remain unchanged but is determined according to critical regions.

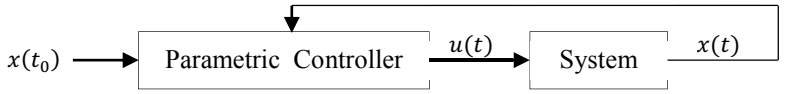

Figure 1 Schematic representation of the algorithm

The parametric controller follows a two-layer online measurement-based control scheme, multiparametric solution structure and input adaption based on NCO conditions, which can be referred to as multiparametric solution model. Here, define the above two-level method as multiparametric NCO tracking.

4.2. Steps for generating controller

The main steps to define feedback control laws in parametric controller are the following:

(1) Define initial feasible region and solve the multiparametric dynamic optimization problem, to find critical regions and their unique solution structures.

(2) Exploit input adaption for NCO conditions of all kinds of arcs in solution structure.

(3) Apply feedback tracking laws according to this multiparametric solution model.

4.3. Application in receding moving horizon control

If the time horizon for the multiparametric dynamic problem is taken as the receding horizon in MPC (Rawlings and Mayne, 2009), multiparametric solution for certain time interval from initial time can be applied as the control action, which is usually the input for first time interval.

During the selected first time interval, tracking method can be used to compute input, thus multiparametric NCO tracking control law is applied in a receding horizon manner. Estimates of states and model parameters can be obtained by online identification approach, enabling solution structure to be updated.

5. Examples

Multiparametric solution model is to be computed for the following problem

$$\min_{x(t),u(t)} \frac{1}{2}{x_f}^T P x_f + \int_0^1 \frac{1}{2}x(t)^T Q x(t) + \frac{1}{2}u(t)^T R\, u(t)$$

$$s.t. \quad \dot{x}(t) = Ax(t) + Bu(t)$$

$$x(0) = x_0$$

$$-2 \le u \le 2$$

$$A = \begin{bmatrix} -3 & -2 \\ 1 & 0 \end{bmatrix}, B = \begin{bmatrix} 1 \\ 0 \end{bmatrix}, R = 0.2$$

$$Q = \begin{bmatrix} 20 & 0 \\ 0 & 20 \end{bmatrix}, P = \begin{bmatrix} 1.6396 & 1.6396 \\ 1.6396 & 21.64 \end{bmatrix}$$

5.1. Solution structure obtained from mpDO

Solving this mpDO by using the method described in Section 2, critical regions are shown in Figure 2. Here, $x_{0,1} \in [-2,2], x_{0,2} \in [-2,2]$ is chosen as the initial region, which can be expanded with critical regions split by same interior boundary definition. It can be found that there are three critical regions, which denote different kinds of structure of optimal inputs. For initial states in CR01, there is no active constraint, which means that the optimal solution needs to only satisfy the sensitivity conditions. Therefore, the optimal control can be obtained the same as in classical LQR problem. For initial states in CR02, the optimal solution is constituted of two arcs, where the first arc corresponds to input reaching its lower bound followed by a sensitivity arc, sharing the same feedback control law as in CR01. For initial states in CR03, reaching its upper bound in first arc following by a sensitivity arc. For any given x_0, there exists an exact optimal solution structure and control profile $u(x_0, t)$.

Select $x_{0\_a} = (1, -0.8) \in$ CR01 and $x_{0\_b} = (1, 1) \in$ CR02, the open-loop optimal trajectories are shown in Figure 3. It can be seen that for x_{0_a}, there is one single arc. While for x_{0_b}, there are two arcs, the first constraint arc $u = -2$ from beginning to switching time around $t_1 = 0.44$, followed by a sensitivity arc.

5.2. Comparison with multiparametric programming

By discretising the continuous time system, the optimization problem can be formulated as conventional multiparametric programming problem (Pistikopoulos, 2012). Critical regions can be obtained by solving mpQP, where input is assumed constant for each time interval, are shown in Figure 4. Critical regions for mpQP are approximations of the regions for mpDO, the smaller the sample time, the more closely the critical regions approach to the exact solutions in Figure 2. A special region in both cases is the middle one, namely CR08 (a) or CR15 (b), which represents the case that no constraint is active. The others are all with the first couple of time intervals containing active constrains, with same solution structure as CR02 or CR03 in Figure 2. This unifies the definition of critical regions for different branches of multiparametric programing and also provides a way to explore the solution structures of mpDO by solving approximate mpQP.

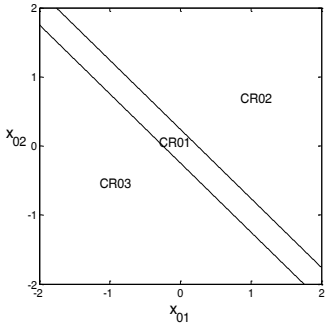

Figure 2 Critical Regions

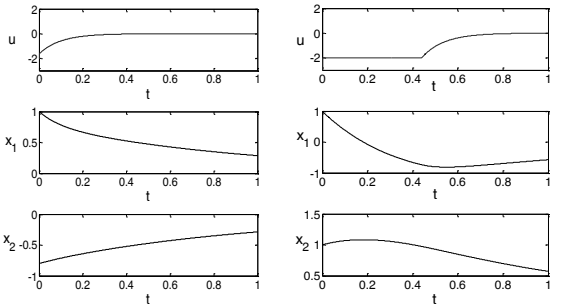

Figure 3 Optimal trajectory from solving mpDO

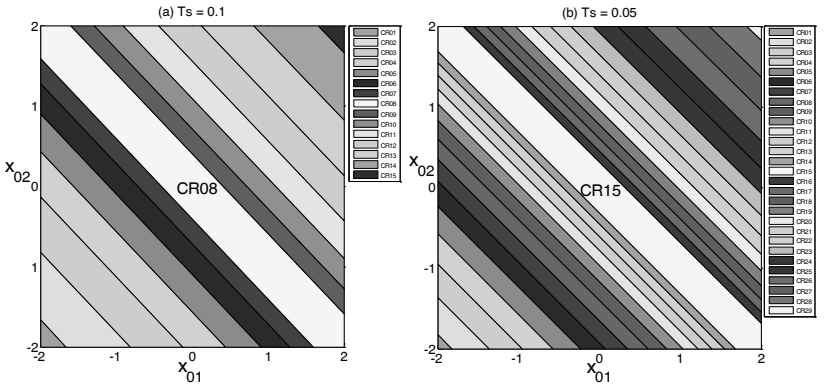

Figure 4 Critical Regions with sampling time (a) Ts = 0.1 and (b) Ts = 0.05.

5.3. Closed-loop simulations with NCO tracking

System response of initial condition x_{0_b} by mp-NCO-tracking as well as the optimal exact solution are shown in Figure 5, two curves coincide. For the first arc, input is kept at its lower bound. And for the second arc, sensitivity condition based on system model is used to force optimality, with feedback control law $u(t) = [-8.198 \ -8.198]\, x(t)$.

Results by applying mp-NCO-tracking in receding horizon scheme, as in section 4.3, coincide with the results shown in Figure 5, with receding time horizon T=1 and first time interval dt = 0.01. It can be seen that multiparametric controller has steered system to its optimal trajectory.

6. Conclusions

The integral framework of multiparametric NCO tracking is justified in the paper by exploiting the multiparametric solution model. An algorithm is proposed to make extension of NCO tracking for linear dynamic systems, which involves computing the multiparametric solution structure mapping via multiparametric dynamic optimization and using it as tracking policy for online feedback control. Critical regions that define the solution structures are determined as a function of uncertain parameters, whereby, the assumption that solution structure remains unchanged in the presence of uncertainty is no longer needed. A constrained linear quadratic optimal control problem is illustrated to show whole application of the algorithm. Critical regions for solution structures are compared with those obtained from solving mpQP, which are in fact approximations of the exact continuous time solution. Multiparametric NCO tracking is implemented for closed-loop control as well as in MPC control scheme, illustrating the use of the parametric controller.

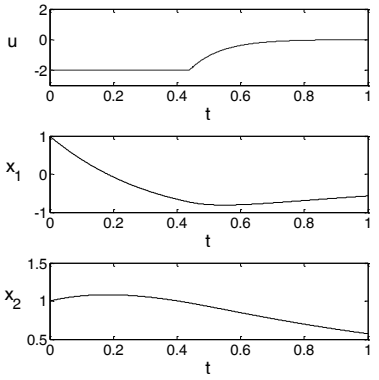

Figure 5 Closed-loop system response

Acknowledgement

This work is funded by the doctoral training award and department studentship from the Department of Chemical Engineering, Imperial College London.

References

E. N. Pistikopoulos, 2009, Perspectives in multiparametric programming and explicit model predictive control. *AIChE Journal*, 55:1918-1925.

E. N. Pistikopoulos, 2012, From multi-parametric programming theory to MPC-on-a-chip multi-scale systems applications. *Computer and Chemical Engineering*, 47:57-66.

E. Kreindler, 1982, Additional necessary conditions for optimal control with state-variable constraints, Journal of Optimization Theory and Applications, 38(2).

D. Bonvin and B. Srinivasan, 2013, On the role of the necessary conditions of optimality in structuring dynamic real-time optimization schemes. *Computers and Chemical Engineering*, 51:172-180.

G. François, B. Srinivasan and D. Bonvin, 2005, Use of measurements for enforcing the necessary conditions of optimality in the presence of constraints and uncertainty. *Journal of Process Control*, 15:701-712.

J. Rawlings and D. Mayne (Eds.), 2009, Model Predictive Control: Theory and Design. Nob Hill Publishing.

J. V. Kadam, M. Schlegel, B. Srinivasan, D. Bonvin and W. Marquardt, 2007, Dynamic optimization in the presence of uncertainty: From off-line nominal solution to measurement-based implementation. *Journal of Process Control*, 17:389-398.

R. B. Vinter and H. Zheng, 1998, Necessary conditions for optimal control problems with state constraints, Transactions of the American Mathematical, 350(3):1181-1204.

V. Sakizlis, J. D. Perkins and E. N. Pistikopoulos, 2005, Explicit solutions to optimal control problems for constrained continuous-time linear systems. *IEE Proceedings: Control Theory and Applications*, 152(4):443-452.

Krist V. Gernaey, Jakob K. Huusom and Rafiqul Gani (Eds.), 12th International Symposium on Process Systems Engineering and 25th European Symposium on Computer Aided Process Engineering.
31 May – 4 June 2015, Copenhagen, Denmark

A Performance-Oriented Robust Framework for the Online Model-Based Optimization and Control of (Fed-)Batch Systems

Francesco Rossi,[a,b] Flavio Manenti,[a,]* Gintaras Reklaitis,[b] Guido Buzzi-Ferraris[a]

[a]*Politecnico di Milano, Dipartimento Chimica, Materiali e Ingegneria Chimica "Giulio Natta", Piazza Leonardo da Vinci 32, Milano 20123, Italy*
[b]*Purdue University, School of Chemical Engineering, Forney Hall of Chemical Engineering, 480 Stadium Mall Drive, West Lafayette, IN 47907-2100, United States*
flavio.manenti@polimi.it

Abstract

A new performance-oriented approach to robust real-time optimization and/or optimal control is developed. It relies on a scenario-based framework and ensures attainment of the robustness of the worst-case approach while allowing significant reduction in the loss in process performance measures, such as profitability. The effectiveness of the proposed robust strategy is demonstrated on the Williams-Otto fed-batch reactor and its profitability is shown to be superior to that of the worst-case approach.

Keywords: robust optimal control, robust dynamic optimization, multi-scenario programming.

1. Introduction

Discontinuous systems are typically employed in the production of high value-added but sensitive products, such as active pharmaceutical ingredients, bio-based chemicals, special polymers and ultra-pure materials for microelectronics. Due to the importance of these products, research is continuing on the development of efficient and reliable optimization and control methodologies for these types of dynamic operations. Among the various proposed options, real-time model-based frameworks, such as DRTO and NMPC, seem to be receiving the most attention in the literature. For example, (Greaves et al., 2003) addresses the DRTO of a batch distillation column and (Joly and Pinto, 2004) investigates the optimal quality control of a Nylon-6,6 production process. In addition, an unconventional optimal control system, aimed at safely reducing the batch cycle time in polymerization processes, has also been proposed in (Finkler et al., 2013). Finally, a screening of the most suitable control laws to be coupled with DRTO for discontinuous systems can be found in (Pahija et al., 2014).
DRTO/NMPC-like approaches are very promising but need a reliable model of the system to be managed, often referred to as a controlled system model (CSM). However, it can be difficult to meet this requirement due to the presence of uncertain parameters in the CSM, such as heat transfer coefficients, kinetic constants and fouling factors. Therefore, there is also a need for robust optimization and control strategies, which are effective even with uncertain parameters in the CSM. This is the goal of the current work. At present, the most common strategy for insuring robustness of DRTO/NMPC-like algorithms in the presence of uncertainties is the so-called worst-case approach (WCA). Worst-case scenario based DRTO/NMPC-like algorithms have been reported in several papers: a bioreactor study (Logist et al., 2011), a reactor for E. Coli bacteria

growth (Santos et al., 2012) and a study of a Siemens process (Vallerio et al., 2014). Moreover, efficient numerical implementations of these methods have also been studied (Diehl et al., 2008). Other strategies for the robust DRTO/NMPC exist but are rarely applicable. Among them, those using online measurements to compensate the CSM uncertainties (Gros et al., 2006, Kadam et al., 2007) are the most common.
The main drawback of the WCA and the typical strategies for insuring robustness lies in the associated optimization/control performance loss. Thus, this work is aimed at proposing a novel scenario-based approach to achieving robustness (SBA), whose main novelty resides in its own structure/configuration, that reduces this performance loss.
In the rest of the paper the SBA structure is outlined and its integration within an NMPC/DRTO-like approach, the BSMBO&C (Rossi et al., 2014a) is demonstrated. The BSMBO&C method is briefly described in section [2]. Subsequently, the combined SBA-BSMBO&C strategy is applied to the Williams-Otto fed-batch reactor and its performance is compared to that resulting from the WCA-BSMBO&C approach, i.e. the BSMBO&C method coupled with the WCA.

2. BSMBO&C schematic structure

BSMBO&C (Batch Simultaneous Model-Based Optimization and Control) is a strategy for the simultaneous dynamic optimization and optimal control of discontinuous systems. The merits of this combined approach are that it is able to: (I) optimally manage a (fed-)batch system by simultaneously adjusting both its manipulated variables and its batch cycle time; and (II) employ a general user-defined objective function. It was first proposed in (Rossi et al., 2014b) and fully elaborated in (Rossi et al., 2014a).
BSMBO&C proceeds by first performing an initialization and then iteratively executing a sequence of operations (*basic step*) until a stopping condition is fulfilled (Figure 1). The initialization is used to provide the algorithm with the user-defined inputs: the CSM, the objective function, the upper/lower bounds and the tuning parameters. The *basic step* consists of three phases: (I) an optimization to compute the next optimal control action; (II) the implementation of this control action on the controlled system; and (III) the measurement of the system response and check of the stopping condition.
BSMBO&C employs BzzMath integrators and optimizers (Buzzi-Ferraris and Manenti, 2012), which are capable of handling strongly non-linear systems. Therefore, it can be applied to almost any kind of system. Moreover, by belonging to the DRTO/NMPC-like methods, BSMBO&C lends itself to be easily integrated with both the SBA and WCA, thus being suitable for the aims of this work.

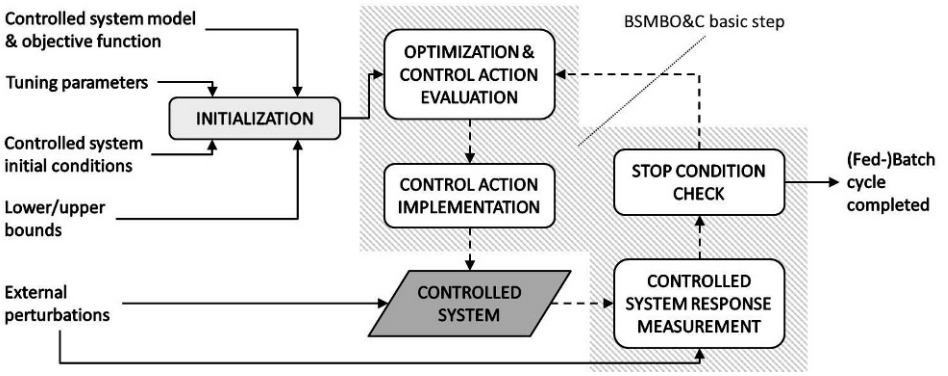

Figure 1. BSMBO&C method simplified scheme

3. The scenario-based robustness strategy

While the SBA is a general strategy for achieving robustness that can be applied within any NMPC/DRTO-like method, in this work we will discuss its application within the BSMBO&C framework. It is based on multiple scenarios and uses four steps in series: (I) definition of a finite space of scenarios; (II) identification of two scenarios, referred to as the nominal and worst case; (III) definition of the number and nature of the additional scenarios to be included; (IV) construction of the multi-scenario CSM and the multi-scenario based performance indicators to be provided to the BSMBO&C.

The identification of the finite space from which to draw scenarios can be readily done, assuming that the probability density function (PDF) of the CSM uncertain parameters is known. It is only necessary to identify the region of the uncertain parameters space corresponding to a cumulative probability that equals a certain confidence threshold.

The identification of the nominal case is straightforward as it corresponds to the maximum of the PDF of the CSM uncertain parameters. Instead, the worst case can be found via sensitivity analysis, performed on the controlled system uncertain parameters and manipulated variables. Indeed, the scenarios space can be mapped, using either Monte-Carlo methods or a uniform grid search, for the scenario that minimizes the distances between the related controlled system states and their upper/lower bounds.

The number of scenarios to be included should be selected in order to ensure the online applicability of the SBA-BSMBO&C. The specific scenarios can be chosen based on a mapping of the level surfaces of the PDF of the CSM uncertain parameters. Once again, either Monte-Carlo or a uniform grid can be employed for this mapping.

Notice that each of the scenarios selected in phases (II) and (III) will be associated with a weighting factor (p_s) that defines its discrete probability density (the p_s sum is one).

For the SBA final step, the multi-scenario CSM is constructed by combining the single-scenario CSMs (Eq. (1)), including the nominal and worst cases, found in step (II), and the other additional scenarios, selected in step (III).

$$\begin{cases} \mathbf{I}_M^s \dfrac{d\mathbf{w}^s}{dt} = \mathbf{h}^s\left(\mathbf{w}^s, \mathbf{m}, \mathbf{d}^*; \boldsymbol{\mu}^s\right) \\ \mathbf{w}^s(t^*) = \mathbf{w}^{s,*} \end{cases} \xrightarrow[\mathbf{h}^R = \{\mathbf{h}^1 \ldots \mathbf{h}^s \ldots \mathbf{h}^{N_s}\}]{\substack{\mathbf{I}_M^R = \{\mathbf{I}_M^1 \ldots \mathbf{I}_M^s \ldots \mathbf{I}_M^{N_s}\} \\ \mathbf{w}^R = \{\mathbf{w}^1 \ldots \mathbf{w}^s \ldots \mathbf{w}^{N_s}\}}} \begin{cases} \mathbf{I}_M^R \dfrac{d\mathbf{w}^R}{dt} = \mathbf{h}^R\left(\mathbf{w}^R, \mathbf{m}, \mathbf{d}^*\right) \\ \mathbf{w}^R(t^*) = \mathbf{w}^{R,*} \end{cases} \quad (1)$$

Moreover, the multi-scenario performance indicators of the controlled system are given as a weighted sum of the single-scenarios performance indicators, where the weighting factors are the p_s values (Eq. (2)). Notice that two performance indicators are needed (f and g) since the BSMBO&C method requires both. Indicators f and g must be chosen so that the product fg measures the controlled system profitability.

$$\begin{cases} f^s \\ g^s \end{cases} \rightarrow \begin{cases} f^R = \sum_{s=1}^{N_s} p_s f^s \\ g^R = \sum_{s=1}^{N_s} p_s g^s \end{cases} \quad (2)$$

In Eq. (1) and Eq. (2), $\mathbf{I_M^R}$ is a diagonal singular/non-singular identity-like matrix, $\mathbf{w}$, $\mathbf{m}$ and $\mathbf{d}$ represent the states, manipulated variables and external perturbations relating to the controlled system, $\boldsymbol{\mu}$ identifies the CSM uncertain parameters and N_s is the total number of included scenarios. In addition, superscript/subscript s refers to the generic scenario while superscript R refers to the entire set of scenarios.

Once steps (I) to (IV) are completed, the SBA can be merged into the BSMBO&C to build the SBA-BSMBO&C by simply setting the multi-scenario CSM and the multi-scenario performance indicators (f^R and g^R) as BSMBO&C input data.

4. The case study: Williams-Otto fed-batch reactor

In this section, the performance obtained via the SBA is tested against that resulting from the WCA and, for the sake of completeness, against that achieved with no attempt to ensure robustness (NCA, i.e. the nominal case approach). Specifically, the results of the online simultaneous optimization and control of a Williams-Otto fed-batch reactor, using the SBA-BSMBO&C, WCA-BSMBO&C and standard BSMBO&C, are reported. Note that the WCA-BSMBO&C is configured by incorporating into the BSMBO&C the CSM and controlled system performance indicators for the worst case while the standard BSMBO&C is configured in the same way but for the nominal case. The SBA-BSMBO&C is set up as described in section [3].

For these illustrative cases, the only CSM uncertain parameter is the overall heat transfer coefficient, which is assumed to be normally distributed. Moreover, the fed-batch reactor model is taken from (Rossi et al., 2014a) and the single-scenario controlled system performance indicators (f^s and g^s) are formulated similarly to those reported in the same reference and test case II. Therefore, the pseudo-scheduling problem is addressed. Finally, the confidence threshold for the SBA step (I) is set to 99.9 % and the SBA steps (II) and (III) are performed based on a uniform search grid. Additional input data for the case study are summarized in Table 1.

Table 1. Case study essential input data

Kinetic scheme, rate equations and kinetic parameters	A + B → C	(1)	$R_1 = k_1^0 \exp\left(-\frac{E_1}{T_R}\right) C_A C_B$	k_1^0 = 2.76650E+5 E_1 = 6.65E+3
	B + C → P + + E	(2)	$R_2 = k_2^0 \exp\left(-\frac{E_2}{T_R}\right) C_B C_C$	k_2^0 = 1.20195E+8 E_2 = 9.05E+3
	C + P → G	(3)	$R_3 = k_3^0 \exp\left(-\frac{E_3}{T_R}\right) C_C C_P$	k_3^0 = 4.45750E+11 E_3 = 1.15E+4
Heats of reaction	$\Delta H_{R,1}$ = -1.095E+5; $\Delta H_{R,2}$ = -1.5425E+5; $\Delta H_{R,3}$ = -3.085E+5			
Thermodynamic properties (reacting mixture and coolant)	Cp_A = 321.204; Cp_B = 127.14; Cp_C = 352.288; Cp_E = 166.212; Cp_G = 844.132; Cp_P = 426.617; Cp_j = 4.186; ρ_j = 1E+3			
Molecular weights (reacting mixture) and reactor structure	PM_A = 142; PM_B = 60; PM_C = 202; PM_E = 81; PM_G = 383; PM_P = 181; D_R = 1; H_R = 3.5; V_j = 0.8236			
Global heat transfer coefficient	U_{ave} = 0.8; $U_{std\ dev}$ = 0.1 (U is normally distributed)			
Relevant lower/upper bounds	$F^{IN,MAX}$ = 1E-3; F_j^{MAX} = 1E-2; T_R^{MAX} = 335; V_R^{MAX} = 2.15;			
Initial conditions	C_A^0 = 1; C_B^0 = 0.5; $C_{i\neq A,B}^0$ = 0; V_R^0 = 1.5; T_R^0 = 308; $T_j^{OUT,0}$ = 308;			
Feed conditions and coolant inlet temperature	C_B^{IN} = 1; $C_{i\neq B}^{IN}$ = 0; T^{IN} = 298; T_j^{IN} = 308;			
Reactants/products price	EV_A = 25; EV_B = 75; EV_C = 200; EV_E = 0; EV_G = 0; EV_P = 40			
Campaign time, dead time and number of selected scenarios	$t_{campaign}$ = 8.64E+4; t_{dead} = 420; N_s = 7;			
Units of measure	amount of substance [kmol]; mass [kg]; length/area/volume [m]/[m^2]/[m^3]; time [s]; temperature [K]; energy [kJ]; prices [€]			

The key results achieved in the case study are reported in Figure 2 and Figure 3. In detail, Figure 2 shows the typical optimal profiles of the reactor temperature (T_R) and manipulated variables (the feed (F^{IN}) and coolant (F_j) flows) observed when the only external perturbation (the coolant inlet temperature (T_j^{IN})) is a step-wise function. Notice that T_R approaches T_R^{MAX}, thus there may be feasibility problems since the reactor model is uncertain. Therefore, this case study is meaningful to test the robustness strategies.

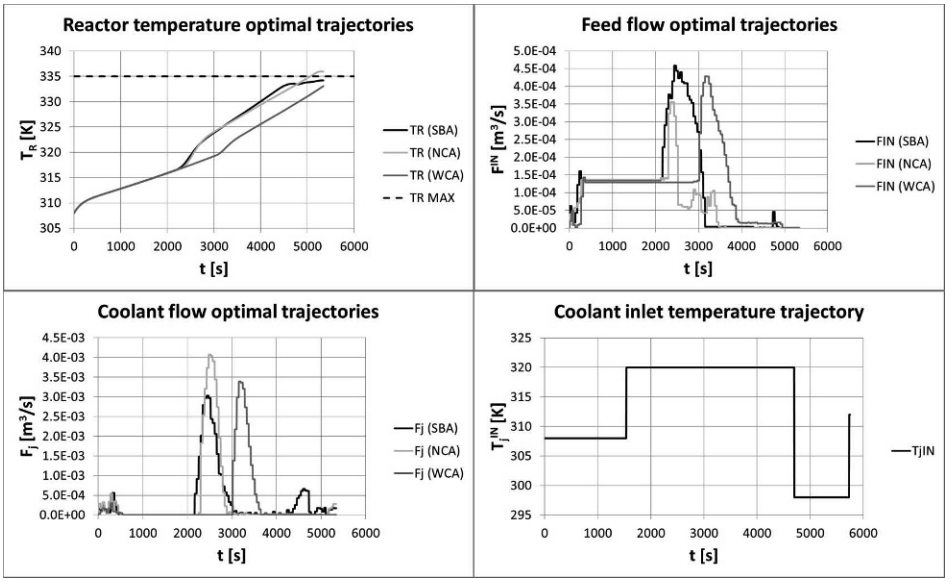

Figure 2. Reactor optimal operation achieved with the SBA-BSMBO&C (SBA), standard BSMBO&C (NCA) and WCA-BSMBO&C (WCA) (U_{real} = 0.625 kW/m^2/K)

Figure 3, shows the performance comparison between the SBA and WCA. It is evident that the SBA is typically much more profitable than the WCA while ensuring the same degree of robustness (both the SBA and WCA allow no bounds violation). In addition, the SBA is more profitable both locally (chart on the left) and globally (chart on the right) and tends to reach almost the same economic performance as the NCA. There is only a very limited zone where the SBA and WCA achieve similar performances. This is probably due to the concurrence of the T_j^{IN} and U_{real} variation along with the linear dependence of the derivatives of the reactor states on the heat transfer coefficient.

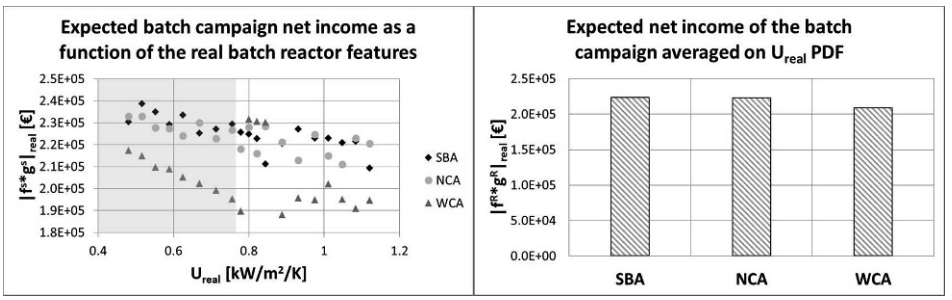

Figure 3. Performance comparison among the SBA-BSMBO&C (SBA), standard BSMBO&C (NCA) and WCA-BSMBO&C (WCA) (Note that the standard BSMBO&C takes the reactor to infeasible operation when U_{real} falls within the shaded region)

We offer two final observations about the SBA. First, it is able to achieve the same robustness as the WCA since the worst case is included in its scenarios set. Moreover, it provides better optimization/control performance because it relies on a more sophisticated objective functions set (Eq. (2)). Secondly, the SBA is suitable for full parallelization because each scenario is independent of the others. This is an additional useful feature and advantage of the SBA over the WCA.

5. Conclusions

A new performance-oriented scenario-based strategy for a robust NMPC/DRTO-like approach, the SBA, is proposed. Its effectiveness is tested against that of the worst-case approach (WCA), the most common conventional alternative. The comparison demonstrates that SBA achieves same robustness as WCA but also an average increase of 6.8 % in the optimization/control performance. Finally, the SBA is also suitable to full parallelization, thus allowing exploitation of multi-core platforms.

References

G. Buzzi-Ferraris, F. Manenti, 2012, BzzMath: Library Overview and Recent Advances in Numerical Methods, Computer Aided Chemical Engineering, 30, 2, 1312-1316.

M. Diehl, J. Gerhard, W. Marquardt , M. Mönnigmann, 2008, Numerical solution approaches for robust nonlinear optimal control problems, Computers and Chemical Engineering, 32, 6, 1287-1300.

T. F. Finkler, S. Lucia, M. B. Dogru, S. Engell, 2013, Simple control scheme for batch time minimization of exothermic semibatch polymerizations, Industrial and Engineering Chemistry Research, 52, 17, 5906-5920.

M. A. Greaves, I. M. Mujtaba, M. Barolo, A. Trotta, M. A. Hussain, 2003, Neural-network approach to dynamic optimization of batch distillation - Application to a middle-vessel column, Chemical Engineering Research and Design, 81, A3, 393-401.

S. Gros, B. Srinivasan, D. Bonvin, 2006, Robust predictive control based on neighboring extremals, Journal of Process Control, 16, 3, 243–253.

M. Joly, J. M. Pinto, 2004, Optimal Control of Product Quality for Batch Nylon-6,6 Autoclaves, Chemical Engineering Journal, 97, 2-3, 87-101.

J. V. Kadam, M. Schlegel, B. Srinivasan, D. Bonvin, W. Marquardt, 2007, Dynamic optimization in the presence of uncertainty: From off-line nominal solution to measurement-based implementation, Journal of Process Control, 17, 5, 389-398.

F. Logist, B. Houska, M. Diehl, J. F. Van Impe, 2011, Robust optimal control of a biochemical reactor with multiple objectives, Computer Aided Chemical Engineering, 29, 1460-1464.

E. Pahija, F. Manenti, I. M. Mujtaba, F. Rossi, 2014, Assessment of control techniques for the dynamic optimization of (semi-)batch reactors, Computers and Chemical Engineering, 66, 269-275.

F. Rossi, F. Manenti, G. Buzzi-Ferraris, 2014a, A Novel All-in-One Real-Time Optimization and Optimal Control Method for Batch Systems: Algorithm Description, Implementation Issues, and Comparison with the Existing Methodologies, Industrial and Engineering Chemistry Research, 53, 40, 15639–15655.

F. Rossi, F. Manenti, I. M. Mujtaba, G. Bozzano, 2014b, A novel real-time methodology for the simultaneous dynamic optimization and optimal control of batch processes, Computer Aided Chemical Engineering, 33, 745-750.

L. O. Santos, L. Dewasme, D. Coutinho, A. V. Wouwer, 2012, Nonlinear model predictive control of fed-batch cultures of micro-organisms exhibiting overflow metabolism: Assessment and robustness, Computers and Chemical Engineering, 39, 143-151.

M. Vallerio, D. Claessens, F. Logist, J. V. Impe, 2014, Multi-objective and robust optimal control of a CVD reactor for polysilicon production, Computer Aided Chemical Engineering, 33, 571-576.

Krist V. Gernaey, Jakob K. Huusom and Rafiqul Gani (Eds.), 12th International Symposium on Process Systems Engineering and 25th European Symposium on Computer Aided Process Engineering.
31 May - 4 June 2015, Copenhagen, Denmark.

Raman-based Advanced Control of an Absorption Desorption System

Erik Esche[a], David Müller[a], Michael Maiwald[b] and Günter Wozny[a]

[a]*Technische Universität Berlin, Department of Process Dynamics and Operation, Str. des 17. Juni 135, D-10623 Berlin*
[b]*BAM Federal Institute for Materials Research and Testing, Richard-Willstätter-Str. 11, D-12489 Berlin, Germany*
erik.esche@tu-berlin.de

Abstract

For absorption processes with fluctuating feed gas compositions it is vital to continuously adjust the operation point to achieve energy efficiency. In this contribution a Raman-based advanced process control (APC) is introduced for the absorption of carbon dioxide (CO_2) using an aqueous solution of monoethanolamine (MEA). The APC is based on a Raman spectroscopic analysis of the composition and CO_2 load of the scrubbing liquid and a non-linear model predictive control (NMPC) to adjust the scrubbing liquid cycle. In addition, an outer real-time optimization loop is set in place to update the set points for the absorption process depending on the current feed gas composition minimizing the energy consumption of the process. Implementation and testing of the APC have been carried out in a mini-plant at TU Berlin. During a plant operation of more than 160 hours robustness and stability of the APC were shown.

Keywords: Raman Spectroscopy, Advanced Process Control, CO_2 Absorption

1. Motivation and Introduction

Process control of steady state systems with fluctuating feeds still is a challenge to date. Both model predictive control and real-time optimization have been applied in industry to improve the performance of such processes with internal or external disturbances (Camacho and Bordons, 2013). The largest challenges still lie in solving the underlying models with greater non-linear parts. This is especially the case for reactive systems such as reactive distillation columns investigated by Kawathekar and Riggs (2007).

1.1. CO_2 Separation

In this contribution, the carbon dioxide removal section of a mini-plant for the oxidative coupling of methane is discussed (Stünkel et al., 2011, 2012). The mini-plant consists of a 4 cm wide absorption column featuring Rombopak 12 M of 6 m of packing height by Sulzer. The desorption column is 10 cm wide and holds Rombopak 9 M of 5 m of packing height. The absorption is carried out at pressures from 5 to 32 bar with a gas flow rate of 10 Nm^3/h. Afterwards the loaded scrubbing liquid is flashed to atmospheric pressure and desorbed in the desorption column by electrically heating the liquid to temperatures around 130 °C at 2.5 bar.

Due to catalyst degradation and general cyclic behavior of the reactors, fluctuations can be observed in the feed to the product purification sections. For the design of this part of the overall

process, two aspects have to be taken into consideration. The first is the minimization of the product loss, namely ethene, the second is the minimization of the energy used to separate the required amount of carbon dioxide. The former is usually mostly achieved by reducing the absorption pressure, but also by using as little scrubbing liquid as possible for removing the carbon dioxide. The latter on the other hand cannot be ensured as straight forward. A model is required to find the optimal combination of desorption heating duty, scrubbing liquid flow rate, etc.

1.2. Optimal Operation

As motivated above, a fixed operation point for the absorption desorption section would not lead to an overall optimal performance. A repetitive reoptimization of the entire system depending on the current reaction conditions is required. For this purpose a model has already been developed to model the performance of the absorption desorption section of the mini-plant and to optimize its performance (Esche et al., 2014b).

In this contribution an overall real-time optimization (RTO) scheme is proposed for the absorption desorption section. The RTO uses the previously mentioned model for the update of the set points. Those are then controlled by nonlinear model predictive control (NMPC). To facilitate the RTO-NPMC structure Raman spectroscopy is applied as fast and reliable process control equipment.

The purpose of this contribution is to highlight the specifics of this new RTO-NMPC-based control scheme with an emphasis on the actual mini-plant implementation.

2. Control Structure Modification

Recently, in (Esche et al., 2014a) an advanced control structure for an amine-based absorption desorption process has been proposed to control the removal of CO_2 from a product gas stream by scrubbing with MEA.

Key aspects of the control structure, shown in Fig. 1, are a Raman spectroscopy-based analysis of the desorbed liquid and an IR analysis of the outlet gas. Raman spectroscopy can be applied to measure both the amine to water ratio as well as the carbon dioxide liquid load (Esche et al., 2014a). The Raman measurement is hence used to control the water to amine ratio by adding fresh amine solution ("QIC 02") and the CO_2 load of the scrubbing liquid at the outlet of the desorption column ("QIC 03") by manipulating the electrical heating of the desorption column. The IR analysis of the outlet gas of the absorption column returns the concentrations of all main gas components, i.e. CO_2, C_2H_4, CH_4, C_2H_6, and N_2. The controller "QIC 01" is able to manipulate the scrubbing liquid flow rate to keep the CO_2 outlet gas concentration at the required minimum level.

Whilst a static set point of 30 wt.-% MEA in water is applied for "QIC 02", deriving an optimal set-point for "QIC 03" and defining the range in which the scrubbing liquid flow may be changed by "QIC 01" can only be done based on the model of the entire process mentioned above.

As part of this contribution, the control structure shown above is applied on the existing mini-plant at TU Berlin.

Raman Spectroscopy: The measurements of the desorbed liquid for "QIC 02" and "03" are carried out using Raman spectroscopy. The calibration of the Raman spectrometer has already been discussed in previous publications (Esche et al., 2014a; Vogt et al., 2011). At this point only a couple of remarks will be made about the applied equipment, measurement positions, and the calibration models. Raman spectroscopy can measure several of the molecular and ionic components appearing in the aqueous technical systems. In this application the components of interest are MEA, CO_2, H_2O, $MEACOO^-$, H_3O^+, OH^-, HCO_3^-, CO_3^{2-}, and $MEAH^+$. Most of them have direct or indirect influences on the Raman spectrum due to changes in functional groups. Here, a

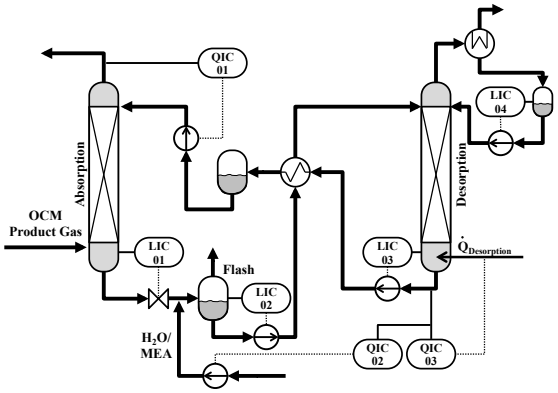

Figure 1: Sketch of the absorption desorption process and all major control loops.

Raman spectrometer RXN1 of Kaiser Optical Systems inc. with an Invictus^{TM} Laser (785 nm) is used covering the spectral range between 400 and 3 400 cm^{-1}. An inflow probe with a half inch diameter is inserted into the piping using a standard T-piece. Calibration models for measuring the CO_2 liquid load as well as the MEA in water concentration were developed. Laboratory calibration experiments based on quantitative NMR spectroscopy as reference method were carried out covering the range between 10 to 50 wt.-% MEA and 0.0 to 0.7 mol CO_2 / mol MEA. These models show a root mean square error of cross validation of below 3 %. First applications in a mini-plant process environment showed, that the transfer of the laboratory based models was successful with respect to robustness and dynamics. Further details may be found in (Esche et al., 2014a).

3. Modeling

To calculate the optimal set-points a model is used to minimize the energy consumption of the process. At a lower level, moving horizon estimation and non-linear model predictive control are employed to ensure a quick return to a steady state to guarantee the validity of the steady state model used for the higher level optimization.

3.1. Mini-plant Process Model

The RTO-NMPC scheme is based on two fundamentally different models for the real-time and the model-predictive control sections. For the RTO part an experimentally validated, steady state model is employed, which contains all necessary information on the most important operation conditions and the required energy inputs. For the NMPC part on the other hand, a dynamic process model is developed, which disregards all chemical compounds and formulates mass balances for all tanks, columns, and actuators of the liquid absorption cycle.

Steady State Model for Real-time Optimization: The steady state model is derived in detail in (Esche et al., 2014b). It has been specifically formulated for the absorption mini-plant at Technische Universität Berlin, but could easily been adapted to different plants. The general idea of the model is a reduction of the amine liquid system to three pseudo components: CO_2, MEA, and water. All ionic components are neglected. Correlations are introduced which relate temperature, CO_2 partial pressure, the amine liquid load α [mol CO_2 / mol MEA], and the heat of absorption based on equilibrium data published by Shen and Li (1992) and Kim and Svendsen (2007). The equilibrium stage model is fitted to experimental data of the mini-plant contained in (Stünkel,

2013) by introducing equilibrium efficiencies and heat loss.

The model allows for a specification of feed volume flow and CO_2 mole fraction, desired degree of CO_2 removal, absorption pressure and is implemented in AMPL using IPOPT (Wächter and Biegler, 2006) as a solver to return the optimal combination of scrubbing liquid flow and scrubbing liquid regeneration to minimize the required energy input.

Dynamic Model for Control: The model for the NMPC part consists of dynamic mass balances for absorption column, flash, desorption column, absorption feed tank, and partial condenser. The liquid content of the packings inside absorption and desorption columns is described by semi-empiric equations by Engel (1999). The correlations are fitted to experimental data obtained from the mini-plant at TU Berlin. In addition, characteristic curves of all control valves and pumps are included. In contrast to most NMPC implementations, the PID controlers are part of the NMPC's dynamic process model. The main reason for this step, is the heightened stability in case of non-convergence of the NMPC (Ławryńczuk, 2014). Consequently, the NMPC's dynamic model consists of a differential algebraic integral equation system (DAIE system).

3.2. Discretization of Differential Algebraic Integral Equation Systems

Instead of refering to the standard solution of employing a DAE solver with a step-integrator for solving the DAIE system, a new approach is tested here. A major disadvantage of the step-integration approach is that it prevents the use of simultaneous optimization schemes, which are often faster than sequential approaches. Here, the whole NMPC process model is fully discretized using fourth order Lagrangian collocation on finite elements. Therefore, the approximation of the offset integration of the PID controllers is performed by the integration of Lagrangian polynomials, which shows a reliable integration estimation within the scope of this contribution. This way, a computationally expensive integration of the differential integral algebraic equation system can be avoided and is replaced by an algebraic equation system with only one finite element per 300 seconds, within similar levels of accuracy as the step-integration method. The approximation of the integral of a function f using Lagrangian orthogonal collocation on finite elements is sketched in Eq. (1):

$$\int_0^{t_{fe,cp}} f(\theta)d\theta \approx fdt_{fe,cp} = fdt_{fe-1,cp=4} + \sum_{pol=0}^{4} a_{fe,cp=pol} \cdot Ldt_{pol,cp} \cdot \Delta t_{fe}, \tag{1}$$

wherein fe denotes the current finite element, cp the collocation position, fdt represents the value of the integral, a is the vector of collocation coefficients, Δt_{fe} the length of the current finite element, and $Ldt_{pol,cp}$ is the value of the integral of Lagrange polynome pol at position cp.

4. Implementation

The actual implementation of the RTO-NMPC scheme features a moving horizon estimation (MHE), which consists of a combined data reconciliation and parameter estimation section as well as the estimation of the states. Fig. 2 shows a schematic of the entire implementation. At the topmost level the Real-Time Optimizer minimizes the specific energy required per kilogram of CO_2 removed from the feed stream. The steady state model discussed above make up the bulk of the constraints for the RTO. A few additional constraints are added to keep the optimizer within the valid range of the model and to require the desired CO_2 separation. From the OPC Server, the RTO level acquires the current gas volume flow and feed concentrations to the absorption column. The optimal set points calculated by the RTO, i.e. CO_2 liquid load at the desorption column outlet α_{Des} and scrubbing liquid flow $\dot{m}$ are written to a "File 1", whenever a new optimal solution is found. This file is accessed by both the NMPC level as well as the process control system. For the

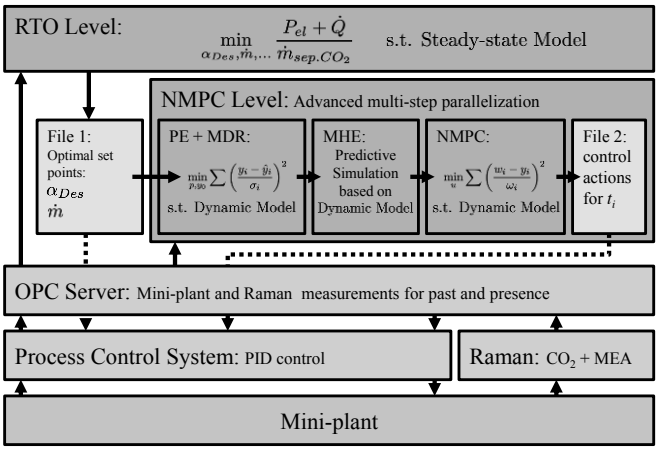

Figure 2: Implementation of the Raman-based RTO-NMPC scheme in the OCM mini-plant.

former $\dot{m}$ sets the window to adjust the liquid feed to the absorption column, for the latter α_{Des} is employed directly as the set-point for the process control system's control circuit "QIC 03".

The NMPC level consists of three separate parts. The first is a combined parameter estimation (PE) and measurement data reconciliation (MDR) section, the second a moving horizon estimation (MHE), and the third the actual nonlinear model predictive control (NMPC). The PE and MDR section has two goals: generate a consistent set of initial conditions for the MHE and further reduce the plant model mismatch by allowing adjustments of model parameters. Among these are the parameters of the correlations describing liquid hold-up of the packings. Based on these results the state of the plant at a time point in the future is estimated using the MHE to reserve time for the solution of the NMPC problem, which in turn minimizes the control offset by plotting a trajectory for the liquid cycle, which is saved in "File 2". The PE and MDR section operates on a time window of 1500 s, the MHE gives an estimation for a time point 300 s later, and the NMPC calculates a trajectory for the next 1200 s. To ensure stability of the entire control scheme, the PID controlers are kept inside the process control system. In addition, redundancy is created at the NMPC level. Every 300 s a new instance of the NMPC level is created as described by Yang and Biegler (2012) and the new control actions are accepted in case the NMPC converges successfully and further reduces the offset.

The content of "File 2" is also read by the process control system and directly translated into control actions for the actuators inside the mini-plant. The Raman spectra are evaluated on an external computer and the results of both carbon dioxide liquid load and MEA concentration model are transferred to RTO and Process Control System via the OPC server. Both "QIC 01" and "QIC 02" run independently from both RTO and NMPC as standard PID control loops on the process control system.

5. Case Study

Parts of the RTO-NMPC implementation discussed above are tested in a mini-plant operation of more than 160 hours. During that time the feed concentrations to the absorption is varied between 5 and 25 mol.-% CO_2, the absorption pressure is set to 5, 10, and 20 bar, and the scrubbing liquid cycle is varied from 30 to 60 kg/h.

The entire process shows a stable performance. Both Raman and IR spectroscopy necessary for

the APC scheme show a robust performance and the feedback time between adjustment of the desorption heating and change in the measured CO_2 liquid load is brief. The NMPC converges within the given time frame and the results of the RTO model show a validity within a range of $\pm$ 5 %. The communication between RTO, NMPC, Process Control System, Raman, and mini-plant is stable, except for a brief crash of the OPC Server, which could quickly be reinitialized. The only other issues, which appeared were a drift of the gas IR used for "QIC 01" and the stability of the parameter estimation inside the NMPC. The drift steadily increased over the operation time to an offset of 10 % of the nitrogen concentration at the gas outlet. The stability of the parameter estimation had to be ensured by quite tight bounds on the parameter values.

6. Conclusions and Outlook

In conclusion, the Raman-based APC has been successfully implemented and shows a robust behavior with respect to the desired minimization of the energy intake. The remaining challenges shall be tackled by improvements to the OPC server scripts and an identifiability analysis of the parameters using a subset selection algorithm. In future work, the Raman measurements shall be extended to more complex amine systems, such as piperazine-activated methyldiethanolamine (aMDEA).

7. Acknowledgements

The authors acknowledge the support from the Cluster of Excellence "Unifying Concepts in Catalysis" coordinated by the Technische Universität Berlin and funded by the German Research Foundation (Deutsche Forschungsgemeinschaft "DFG", Grant no.: DFG EXC 314). Special thanks go to Kaiser Optical Systems inc. for supplying the equipment for the online Raman spectroscopy.

References

Camacho, E., Bordons, C. (Eds.), 2013. Model Predictive Control, second edition Edition. Springer-Verlag.

Engel, V., 1999. Fluiddynamik in Packungskolonnen fr Gas/Flüssig-Systeme. No. 605 in 3. VDI Fortschrittsberichte.

Esche, E., Kraemer, B., Müller, D., Meyer, K., Zientek, N., Maiwald, M., Wozny, G., 2014a. Improved desorption control via raman spectroscopy. In: Proceedings of the 20th International Conference on Process Engineering and Chemical Plant Design. pp. 223–233.

Esche, E., Müller, D., Kraus, R., Wozny, G., 2014b. Systematic approaches for model derivation for optimization purposes. Chemical Engineering Science 115, 215–224.

Kawathekar, R., Riggs, J., 2007. Nonlinear model predictive control of a reactive distillation column. Control Engineering Practice 15 (2), 231–239.

Kim, I., Svendsen, H., 2007. Heat of absorption of carbon dioxide co$_2$ in monoethanoamine (MEA) and 2-(aminoethyl) ethanolamine (AEEA) solutions. Ind. Eng. Chem. Res. 46, 5803–5809.

Ławryńczuk, M., 2014. Computationally Efficient Model Predicitive Control Algorithms. Vol. 3. Springer.

Shen, K., Li, M., 1992. Solubility of carbon dioxide in aqueous mixtures of monoethanolamine with methyldiethanolamine. J. Chem. Eng. Data 37, 96–100.

Stünkel, S., 2013. Kohlendioxid-Abtrennung in der Gasaufbereitung des Prozesses der oxidativen Kupplung von Methan. Ph.D. thesis, Technische Universität Berlin, Berlin, Germany.

Stünkel, S., Drescher, A., Wind, J., Brinkmann, T., Repke, J.-U., Wozny, G., 2011. Carbon dioxide capture for the oxidative coupling of methane process – a case study in mini-plant scale. Chemical Engineering Research and Design 89 (8), 1261–1270.

Stünkel, S., Illmer, D., Drescher, A., Schomäcker, R., Wozny, G., 2012. On the design, development and operation of an energy efficient co$_2$ removal for the oxidative coupling of methane in a miniplant scale. Applied Thermal Engineering 43, 141–147.

Vogt, M., Pasel, C., Bathen, D., 2011. Characterisation of co2 absorption in various solvents for pcc applications by raman spectroscopy. Energy Procedia 4, 1520–1525.

Wächter, A., Biegler, L. T., 2006. On the implementation of an interior-point filter line-search algorithm for large-scale nonlinear programming. Mathematical Programming 106 (1), 25 – 57.
URL http://dx.doi.org/10.1007/s10107-004-0559-y

Yang, X., Biegler, L., 2012. Advanced-multi-step nonlinear model predictive ctonrol. In: Proceedings of the Int. Symp. Adv. Control of Chemical Processes (ADCHEM). pp. 426–431.

Krist V. Gernaey, Jakob K. Huusom and Rafiqul Gani (Eds.), 12th International Symposium on Process Systems Engineering and 25th European Symposium on Computer Aided Process Engineering.
31 May – 4 June 2015, Copenhagen, Denmark

A Comparative study between Neural Networks (NN)-based and Adaptive-PID Controllers for the Optimal Bio-Hydrogen Gas Production in Microbial Electrolysis Cell Reactor

M.Y. Azwar[a,b], M.A. Hussain[b] , A.K. Abdul Wahab[c] and M.F. Zanil [d]

[a]*Chemical Engineering Department, Faculty of Engineering, University of Syiah Kuala, 23111 Banda Aceh, Indonesia*
[b]*Chemical Engineering Department, Faculty of Engineering, University of Malaya, 50603 Kuala Lumpur, Malaysia.*
[c]*Biomedical Engineering Department, Faculty of Engineering, University of Malaya, 50603 Kuala Lumpur, Malaysia.*
[d]*Chemical and Petroleum Engineering, Faculty of Engineering & Built Environment, UCSI University, 56000 Kuala Lumpur, Malaysia.*

Abstract

The main challenge of the hydrogen production study for the MEC reactor is to obtain a good automatic control system due to the nonlinearity and complexity of the microbial interactions. To address this issue an integrated approach involving process modeling, optimization and advanced control has to be implemented. This work focus on the controller's performance in the control system; neural network (NN)-based and Adaptive-PID controllers. The study has been carried out under optimal condition for the production of bio-hydrogen gas wherein the controller output are based on the correlation of the optimal current and voltage to the MEC. A Ziegler–Nichols tuning method and an adaptive gain technique have been used to design the PID controller, while the neural network controller has been designed from the inverse response of the MEC neural network model.

Keywords: **B**io-hydrogen gas, microbial electrolysis cell, neural network-based controller, adaptive-PID controller.

1. Introduction

Microbial electrolysis cells (MEC) is part of the microbial electrochemical cell technology which is one of the renewable energy alternatives today. MEC operation is based on the fundamental of a bio-electrochemical process and is a promising renewable energy technology that produce hydrogen gas. Anodophilic microorganisms in the anaerobic MEC bioreactor is capable of oxidizing substrates containing organic materials in the cell compartment into electrical energy. Anodophilic microorganisms is able to break the organic material and wastewater that has been diluted at low concentrations of organic compounds. In the MEC system, due to the addition of voltage into the cathode of the anaerobic-bioreactor, the reaction between protons and electrons occur leading to the formation of hydrogen gas (Rozendal et al., 2006 and Logan, 2010).

Bio-hydrogen production process in the MEC is a nonlinear and highly complex system due to microbial interaction. Its complexity makes MEC system difficult to operate and control under optimal conditions. However, these problems can be alleviated using an integrated process system engineering approach, which involves process modelling, optimization and control simultaneously. Artificial neural network (ANN) is an effective technique and a powerful tools to be used in modeling of complex processes and unknown systems. ANNs are able to cope with non-linear process between input and output variables without the requirement of explicit mathematical representation. In process control system, ANNs have been widely used when conventional control techniques did not give good performance (Wang and Wan, 2009; Sridevi et al., 2014).

A novel application of using advanced controller including neural network with adaptive PID has been carried out in the MEC bioreactor. This type of controller has not been reported yet in any MEC reactor application especially on control system performance investigation. This study focuses on the performance of the advanced controller in a feedback control system for controlling the MEC reactor. The comparative study including PID, Adaptive-PID, and neural network model-based controller has been discussed. The controller's performance assessment for regulator and servo cases has been investigated. The analysis was conducted in the presence of noise to imitate the real environment in the process system.

2. MEC Model

This section presents a model for the MEC in a fed-batch reactor, which is a modified model from Pinto et al. (2010). The mathematical models presented here aim to simulate the competition of microbial in the MEC. The model represents competition between anodophilic, acetoclastic methanogenic and hydrogenotrophic methanogenic microorganisms for the substrate (Pinto et al., 2011). The dynamic mass balance equations in the reactor system are given below as follows:

$$\frac{dS}{dt} = -q_{max,a}\frac{S}{K_{S,a}+S}\frac{M_{ox}}{K_M+M_{ox}}x_a - q_{max,m}\frac{S}{K_{S,m}+S} \quad (1)$$

$$\frac{dx_a}{dt} = \mu_{max,a}\frac{S}{K_{A,a}+S}\frac{M_{ox}}{K_M+M_{ox}}x_a - K_{d,a}x_a - \alpha_1 x_a \quad (2)$$

$$\frac{dx_m}{dt} = \mu_{max,m}\frac{S}{K_{A,m}+S} - K_{d,m}x_m - \alpha_1 x_m \quad (3)$$

$$\frac{dx_h}{dt} = \mu_{max,h}\frac{H_2}{K_h+H_2} - K_{d,h}x_h - \alpha_2 x_h \quad (4)$$

$$Q_{H_2} = Y_{H_2}\left(\frac{I_{MEC}}{mF}\frac{RT}{P}\right) - Y_h\mu_h x_h V_r \quad (5)$$

$$-E_{applied} = E_{CEF} - \eta_{ohm} - \eta_{conc} - \eta_{act} \quad (6)$$

$$I_{MEC} = \frac{E_{CEF}+E_{applied}-\frac{RT}{mF}ln\left(\frac{M_{Total}}{M_{red}}\right)-\eta_{act,C}(I_{MEC})}{R_{int}} \quad (7)$$

where S is the substrate concentration; x_a, x_m, and x_h are the concentration of the anodophilic, acetoclastic, and hydrogenotrophic microorganisms, respectively; Q_{H_2} is the hydrogen production rate (mL/day); $E_{applied}$ is the electrode potentials (V) and I_{MEC} is the MEC current (A).

3. Controller Design

3.1 Adaptive-PID controllers

Adaptive-PID controller is able to control the system dynamics in the event of a non-nominal process condition. Consider the MEC process model given by:

$$y(k) = A_1 x(k-1) + A_2 x(k-2) + [B_1 u(k-1) + B_2 u(k-2)]u(k) \quad (8)$$

For the case at nominal condition, A_i and B_i for i = 1, 2, and 3 are known through least-square regression technique. The control action is derived as:

$$u(k) = \frac{K_P\left[e(k)+\frac{1}{\tau_I}\int_0^t e(k)dt+\tau_D\frac{d}{dt}e(k)\right]- A_1 x(k-1)+ A_2 x(k-2)}{B_1 u(k-1)+ B_2 u(k-2)} \quad (9)$$

The block diagrams show the method of adaptive PID as in Figure 1.

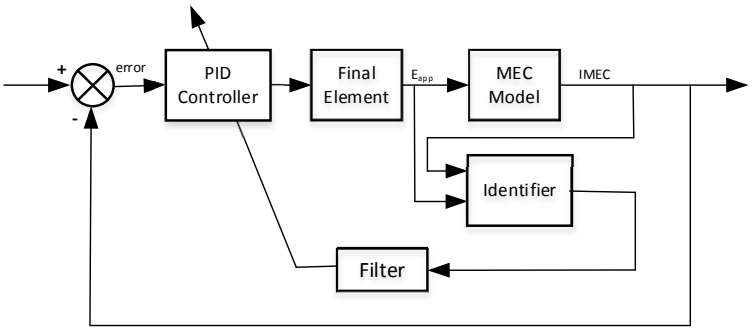

Figure 1. Block diagram of PID-Adaptive gain closed loop design

3.2 Neural network controllers

The NNs controller concept refers to the inverse response of the open loop MEC process. The diagram of the controller and control strategy are shown in Figure 2. In this case, the neural network model is trained to predict the required manipulated variable, Electrode potential $(\mathrm{E_{applied}})$ with the given desire of set-point, MEC current $(\mathrm{I_{MEC}})$.

3.3 Training and Forward Modelling

The forward NNs modeling refers to the open loop response of the MEC process. The networks have been trained to obtain the weights of every node and map the dynamic response of the input-output open loop dataset. The dataset is collected through a moving window approach. The model is made of 14 input nodes; the input nodes consist of data for substrate (S), anodophilic microorganisms (x_a), acetoclastic microorganism (x_m), ammonium nitrogen (x_h), oxidized mediator fraction (M_{ox}), MEC current (I_{MEC}) and the single output node is electrode potentials ($\mathrm{E_{applied}}$).

3.4 Inverse modelling and NNs Controller

However, inverse NNs modelling are the opposite of open loop response which can be used as an ideal controller inside the control system. Inverse model is designed similar to the forward modeling approach. The 14 inputs node and single manipulated output

variable has been selected; $S_{(t)}$, $S_{(t-1)}$; x_a *i.e.* $x_{a(t)}$, $x_{a(t-1)}$; x_m *i.e.* $x_{m(t)}$, $x_{m(t-1)}$; x_h *i.e.* $x_{h(t)}$, $x_{h(t-1)}$; M_{ox} *i.e.* $M_{ox(t)}$, $M_{ox(t-1)}$; I_{MEC} *i.e.* $I_{MEC(t)}$, $I_{MEC(t+1)}$, $I_{MEC(t-1)}$ and output node is the electrode potentials ($E_{applied}$) respectively. The detail network architecture for NNs controller development can refer to Hussain and Mujtaba, 2001.

4. Neural Network Controller Scheme

4.1 Multiple set-point tracking study

In this work, we perform multiple set-point tracking study when the I_{MEC} current has been maintained at the optimal operation value of 0.16 A. Figure 2 shows the comparison of conventional PID, adaptive-PID, and neural networks model-based controllers. Figure 2 shows good tracking performance for neural network controllers. The controlled variable follows the given set points and the result show reasonable control performance. Neural networks controller gives no overshoot compare to the others controller. However, PID controller shows the largest overshoot and longest settling time which indicates the conventional controller is not suitable to be applied in the MEC process. Meanwhile, adaptive-PID controller shows an adaptation progress which the overshoot and settling time performance are improving over time.

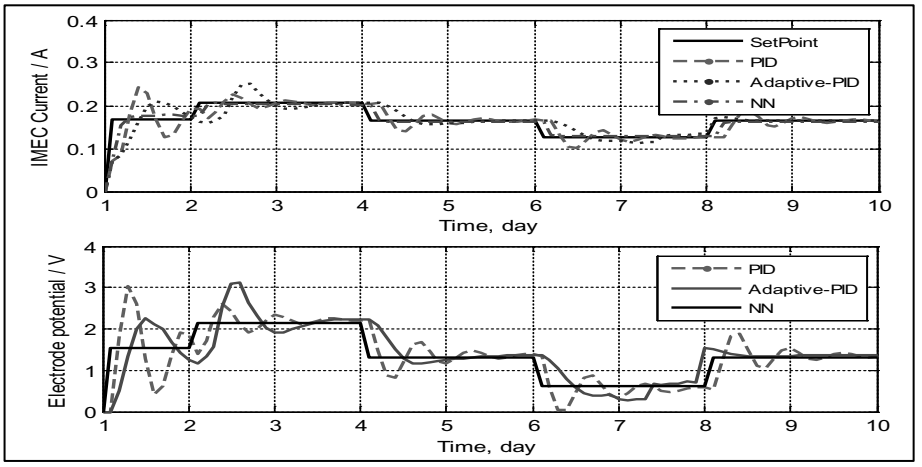

Figure 2**.** Comparison of controlling for set point tracking

The neural network model-based controller can provide better control for the MEC system compared with the conventional PID and adaptive-PID controller.

4.2 Disturbance rejection

Figure 3 shows the control performance comparison of the conventional PID, adaptive-PID and neural network model-based controllers for servo and regulator cases. The disturbance has been generated by changing the counter-electromotive force from the nominal value (from 0.15 V to 0.35 V). Based on Figure 3, all controllers show good performance but the neural network model-based controller is better compare to the rest. However, small offset has been observed from NNs controller and this offset can be compensated by introducing integral effect inside the NNs structure.

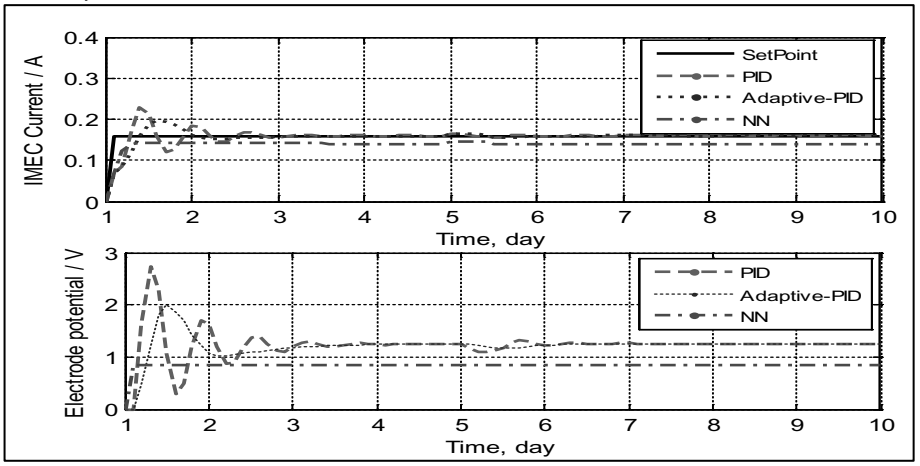

Figure 3. Control performance under disturnabce rejection

4.3 Measurement noise

Figure 4 shows the controller performance with the presence of noise under nominal operating conditions. The noises source are assumed from measurement element inside MEC system. NNs controller responses are more stable with less oscillations compared to the conventional PID and adaptive-PID gain controllers.

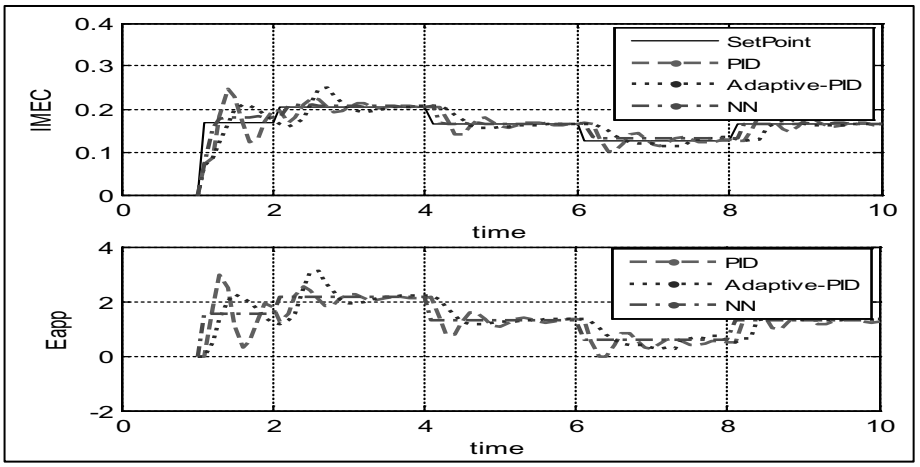

Figure 4. Control performance with measurement noise

In summary, the MEC reactor can be controlled to give an optimum current set-point (simultaneously an optimal hydrogen production rate) using the conventional PID, adaptive-PID and neural network model-based controller. However, the NNs model-based controller is able to give more robust performance compared to this PID and adaptive-PID gain controllers.

5. Conclusions

In this paper, a novel approach for implementing an advanced (NNs) controller for MEC system has been carried out. A comparative study for MEC with various simulation cases involving multiple set-point, disturbance rejection and noise measurement has been achieved. The NNs controller gives fast settling time response, less overshoots, and minimal offset. Thus, NNs controller performances surpass the other types of controller and performs better in all the simulation cases.

Acknowledgment

This research was supported by the "UMRG-RP006H-13ICT" Program, University of Malaya.

References

O. Bernard, Z. Hadj-Sadok, D. Dochain, A. Genovesi, J.-P. Steyer, 2001, Dynamical model development and parameter identification for an anaerobic wastewater treatment process. Biotechnology and Bioengineering, 75 (4), 424–438.

M.A . Hussain and I.M. Mujtaba, 2001, Application of neural networks and other learning technologies in Process Engineering. Imperial College Press, 199-216.

B.E Logan, 2010, Scaling up microbial fuel cells and other bioelectrochemical systems, Applied Microbiology and Biotechnology, 85, 1665–1671.

R. P. Pinto, B. Srinivasan, A Escapa, M. F. Manuel, B. Tartakovsky, 2011, Multi-population model of a microbial electrolysis cell. Environmental Science and Technology, 45, 5039-5046.

R. P. Pinto, B. Srinivasan, M. F. Manuel, B. Tartakovsky, 2010, A twopopulation bio-electrochemical model of a microbial fuel cell. Bioresource Technology, 101 (14), 5256–5265.

R. A. Rozendal, H.V.M. Hamelers, G.J.W. Euverink, S. J. Metz and C.J.N. Buisman, 2006, Principle and perspectives of hydrogen production through biocatalyzed electrolysis, International Journal of Hydrogen Energy, 31(12), 1632-1640.

K. Sridevi, E. Sivaraman, P. Mullai, 2014, Back propagation neural network modelling of biodegradation and fermentative biohydrogen production using distillery wastewater in a hybrid upflow anaerobic sludge blanket reactor. Bioresource Technology, 165, 233-240.

J. Wang & W. Wan, 2009, Application of desirability function based on neural network for optimizing biohydrogen production process. International Journal of Hydrogen Energy, 4, 1253-1259.

Krist V. Gernaey, Jakob K. Huusom and Rafiqul Gani (Eds.), 12th International Symposium on Process Systems Engineering and 25th European Symposium on Computer Aided Process Engineering.
31 May – 4 June 2015, Copenhagen, Denmark

Reaction Monitoring of Cementing Materials through Multivariate Techniques Applied to *In Situ* Synchrotron X-Ray Diffraction Data

Alessandra Taris[a*], Massimiliano Grosso[a], Mariarosa Brundu[b], Vincenzo Guida[b], Alberto Viani[c]

[a]*Dipartimento di Ingegneria Meccanica, Chimica e dei Materiali, Università degli Studi di Cagliari, Via Marengo 2, Cagliari 09123, Italy*
[b]*Procter & Gamble, Pomezia R&D Research Center, Via Ardeatina 100, Pomezia 00040, Italy*
[c]*Institute of Theoretical and Applied Mechanics ASCR, Centre of Excellence Telč, Batelovská 485, Telč CZ- 58856, Czech Republic*
a.taris@dimcm.unica.it

Abstract

In this work, methods for on-line monitoring of the setting reaction of magnesium potassium phosphate ceramic (MKPC) were developed. To this aim, multivariate statistical techniques combined with *in-situ* synchrotron X-ray powder diffraction (XRPD) enabled a fast, real time and reliable analysis of the phenomena occurring even in complex systems as investigated here. Thus, Multivariate Curve Resolution - Alternating Least Squares (MCR-ALS) was employed together with Evolving Factor Analysis (EFA). Comparison with conventional methods for describing reaction kinetic, namely, integrated area of selected diffraction peak for the crystalline phases, show that compounds involved in the process can be correctly distinguished and the main reaction steps, such as reactants consumption, occurrence of intermediate amorphous phase and finally MKPC formation can be clearly identified.

Keywords: reaction monitoring, Multivariate Curve Resolution, ceramic materials.

1. Introduction

Recently, on-line monitoring has become essential for process understanding, particularly in the case of evolving systems where reaction mechanisms and physical phenomena are not completely understood. With this regard, spectroscopic measurements represent a powerful tool for the on-line process monitoring that can provide more information about specific chemical features of the process, such as concentration changes of reacting species. The main drawback in most of the cases is the need of mathematical recipes capable of correlating the raw data gathered in the experiment to informative data. Here, multivariate procedures were implemented to investigate reaction and setting mechanism of MKPC. MKPC is a chemically-bonded ceramic (Wagh, 2004) attractive for applications like waste encapsulation, bone repair, natural fibre composites. When MgO reacts with potassium di-hydrogen phosphate (KDP) in solution, formation of K-struvite (MKP) occurs: $MgO + KH_2PO_4 + 5H_2O = MgKPO_4 \cdot 6H_2O$. Several mechanisms for this reaction have been proposed, but kinetic studies are scarce and none of them provided quantitative data (Ding et al., 2012). Moreover, there are experimental evidences that, besides crystalline MKP, an amorphous phase also forms which can be considered as a precursor of the crystalline

MKP. At the current state of knowledge, the nature of this amorphous phase remains unexplained. Recent kinetic synchrotron diffraction experiments (Viani et al., 2014b) allowed for the description of the reaction as being initially controlled by the dissolution of MgO in aqueous solution to form an intermediate product accumulating at the grain surface. This thickening layer hindered further diffusion of water shifting the mechanism towards a diffusion control one. MKP crystallization reaction was modeled using an Avrami model followed by a first order chemical reaction, as water is available at the interface of the intermediate layer, and K+ and PO_4^{3-} ions readily migrate through the open structure of elongated MKP crystals. Such interpretation should be supported by further evidences since, conventional analysis of X-rays diffraction data allows to evaluate only the crystalline components.
In this work, we propose a procedure based on multivariate techniques, namely the MCR-ALS combined with the EFA algorithm, in order to enable the interpretation and the investigation of the reaction mechanisms and detect the different species involved.

2. Experimental

2.1. Sample preparation

MgO powder obtained by calcination of $MgCO_3$ at 1400°C was mixed with KDP by hand in agate mortar at unity molar ratio and then placed in a capillary 0.7 mm in diameter opened on both ends. The powder was laterally confined between 2 small layers of quartz wool, allowing for the water to flow through the capillary. The capillary was mounted on a goniometric head for data collection with one end connected to a vacuum pump. Water was introduced on the other end, but initially not in contact with the powders. After starting data collection, operating the vacuum pump, the water was gently allowed to flow through the capillary wetting the powder and defining the start of the experiment. The whole process was followed through a high resolution camera. The advantage of such experimental setup, described in more detail elsewhere (Conterosito et al., 2013), is that the reaction can be monitored from the very beginning. The downside was that no exact control on the water/solid ratio was possible.

2.2. XRPD measurements

Data were collected at 20 °C at the beamline BM01a, European Synchrotron Radiation Facility (ESRF), Grenoble (France), employing a wavelength of 0.6895 Å with the pilatus 2M detector (Dectris). The reaction was followed for 111.23 min collecting four scans/min allowing the capillary to swing on its axis of 60 °. Each spectrum was recorded covering a 2θ range 0.97 ° - 43.82 ° with a resolution of 0.0146 °2θ. Eventually, each spectrum $\mathbf{d}^{i}_{(1\times J)}$ recorded at the i-th time (i = 1,… I) can be arranged into a matrix $\mathbf{D}_{(I\times J)}$ representing the I experimental patterns collected at the different J diffraction angles 2θ.

3. Methods

The classical approach to the analysis of decomposition of the reactants and crystallization of MKP implies the integration of the area under Bragg reflection peaks for each one of the phases, their normalization to phase fraction (α) and plot as α vs. time curves. This procedure is time consuming, and is thus usually limited to only one peak for each phase. Furthermore, it requires the preliminary knowledge of each powder pattern in order to exclude the overlap of peaks from different phases that otherwise adversely affects the kinetic interpretation.

Here, the MCR-ALS approach is investigated as a viable alternative to the conventional one. Such technique decomposes the experimental $\mathbf{D}_{(I\times J)}$ matrix in two matrices $\mathbf{C}_{(I\times M)}$ and $\mathbf{S}^{T}_{(M\times J)}$ (de Juan et al., 2009) according to equation (1).

$$\underset{(I\times J)}{\boldsymbol{D}} = \underset{(I\times M)}{\boldsymbol{C}} \cdot \underset{(M\times J)}{\boldsymbol{S^T}} + \underset{(I\times J)}{\boldsymbol{E}} \quad (1)$$

Equation (1) can be considered as the extension of the Lambert–Beer's law in matrix form: **C** is the estimated concentration profile for *M* components; **S** is the matrix representing the estimated spectra for the *M* components. The goal of MCR-ALS is to find iteratively the proper matrices **C** and **S** through the Alternating Least Squares optimization procedure starting from a suitable initial guess $\mathbf{C}^0$ for **C** (or alternatively **S**). During the ALS optimization, several (physical) constraints (e.g. non-negativity, unimodality, mass balance closure) should be applied in order to convey the algorithm towards the most proper estimation of the **C** and **S** profiles. A drawback of MCR-ALS is the lack of ability to separate compounds that behave together (kinetically) in the same manner (e.g. more reactants that decrease together over the time and/or unreacted compounds). Therefore, the method could not lead to the detection of the actual chemicals but may represent a mixture of chemicals appearing in each estimated spectrum $\mathbf{s}^{m}_{(1\times J)}$ (m=1,…,*M*).

In order to improve the performance of the procedure for a more effective separation of the different real compounds in the system, a novel procedure was here adopted and briefly described in the following:

1. EFA algorithm was implemented in order to find the initial estimate $\mathbf{C}^0$ of matrix **C** (De Juan et al., 2004);
2. MCR-ALS was performed and matrices $\mathbf{C}^1$ and $\mathbf{S}^1$ were evaluated.
3. The *pure compounds* diffractograms $\mathbf{S}^2$, were then estimated again with the MCR-ALS procedure by considering an initial guess spectra matrix $\mathbf{S}^{20}$ obtained in the following way: (i) the matrix $\mathbf{S}^1$ is decomposed taking into account the theoretical patterns available from database and (ii) a baseline correction was applied on the resulting diffractograms;

The procedure was implemented with a in-house written Matlab® code and MCR-ALS and EFA algorithms developed by Jaumot et al. (2005).

4. Results and discussion

4.1. Experimental spectra

By comparing XRPD patterns over the time with theoretical ones, three significant changes were identified (dissolution of reactants, amorphous phase formation and growth of MKP crystals) as depicted in figure 1: (i) at t= 0 the spectrum is characterized by a linear combination of the MgO and KDP patterns (Figure 1.a); (ii) at $t\approx$2.6 min broad peaks appear at 1.4 and 13 ° 2θ (Figure 1.b), probably due to the presence of an amorphous phase, in the meantime KDP and MgO begin to dissociate in solution; (iii) at $t\approx$5 min, contribution of the KDP spectra disappears and only magnesia and amorphous phase are present (Figure 1.c); (iv) at $t\approx$15 min MKP crystals start to grow (Figure 1.d); (v) from $t\approx$30 to 111 min (end of the experiment) spectra do not exhibit important changes (Figure 1.e). It should be noticed that MgO is not completely consumed since the reaction is controlled by diffusion as already mentioned in the introduction.

For the forthcoming analysis, data collected in the angular region 1-6 ° 2θ are removed because of the strong contribution coming from incoherent scattering from water. Furthermore spectra collected after 35 min will be not considered because they do not show significant changes. Thus the final data set will be arranged in a matrix $\mathbf{D}_{(80\times 1295)}$.

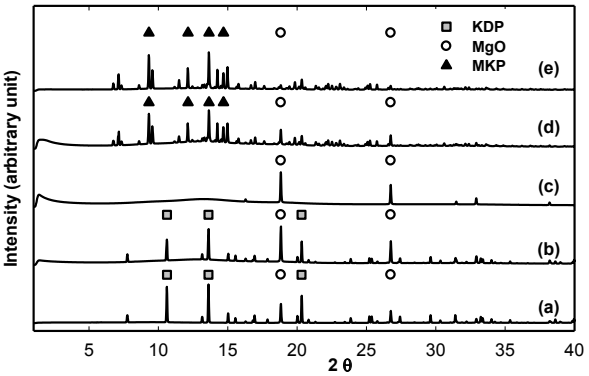

Figure 1. Representative raw spectra at different times: (a) 0 min, (b) 2.6 min, (c) 5 min, (d) 15 min and (e) 30 min. White circles, gray squares and black triangles represent the main characteristic patterns of MgO, KDP, MKP, respectively.

4.2. Data processing

Data processing was performed according to the recipe introduced in section 3.

Step 1: initial estimate $\mathbf{C}^0$ was calculated with the EFA algorithm and reported in Figure 2. It was found that three components adequately capture most of the variance of the matrix **D** and they might be reasonably associated to the following three steps: (i) reactants consumption, (ii) development of intermediate species, (iii) product formation;

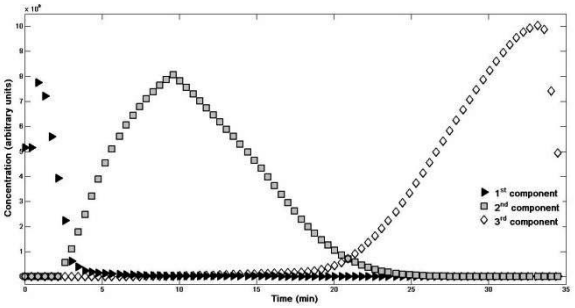

Figure 2. Concentration profiles estimated through EFA algorithm. First component: (►); second component: (■); third component: (◊).

Step (2) matrices $\mathbf{S}^1_{(1295\times3)}$ and $\mathbf{C}^1_{(80\times3)}$ are then evaluated through the MCR-ALS algorithm;

Step (3): spectra $\mathbf{S}^1$ evaluated by MCR, were compared with the theoretical patterns of the pure compounds. It was found that the three spectra correspond to: (i) MgO plus KDP; (ii) MgO and an undefined intermediate species (likely corresponding to the amorphous phase); (iii) MKP and MgO. Therefore, MgO contribution was present in all the $\mathbf{S}^1$ spectra, since it does not react completely. Eventually, four compounds spectra were determined and arranged in the matrix $\mathbf{S}^{20}$.

However, the protocol requires further refinements because of the presence of unreacted species (for the case at hand MgO) that may degrade the effectiveness of the MCR-ALS procedure. For this purpose, the contribution of unreacted MgO diffractogram $\mathbf{d}_{\mathbf{MgO}}$ observed at the end of the experiment was subtracted from the raw matrix **D**. The goal is to obtain a new data set $\mathbf{D}^R$ where $\mathbf{d}^{\mathbf{R}}_{\mathbf{i}}=\mathbf{d}_{\mathbf{i}}-\mathbf{d}_{\mathbf{MgO}}$ (i=1,..,80) where unreacted species are filtered out from the analysis. The matrix $\mathbf{D}^R$ and $\mathbf{S}^{20}$ are then used as input in the MCR-ALS that provides eventually the estimation of the spectra $\mathbf{S}^2$ and $\mathbf{C}^2$. Figure 3 shows

the $\mathbf{S}^2$ spectra together with the main theoretical patterns of the MgO, KDP and MKP. It can be concluded that the first three estimated spectra agree very well with the theoretical patterns of MgO (Figure 3.a), KDP (Figure 3.b), MKP (Figure 3.c), respectively. In addition a spectrum for the intermediate phase is also provided (Figure 3.d). Nevertheless, a perfect separation among the compounds had not been achieved, and this may affect the prediction of the related concentration.

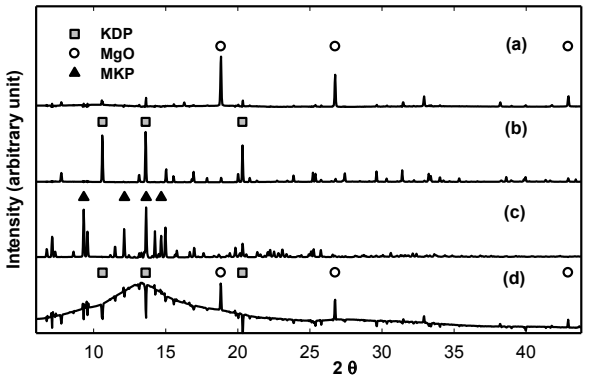

Figure 3. Evaluation of $\mathbf{S}^2$ spectra. White circles, gray squares and black triangles indicate MgO, KDP, MKP main patterns respectively.

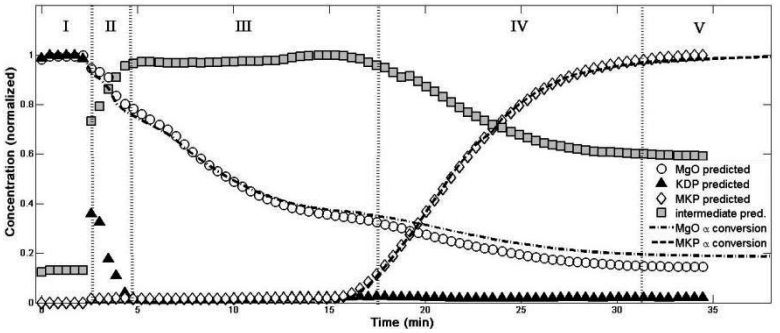

Figure 4. Normalized concentration profiles: MgO (○), KDP (▲), MKP (◊) and amorphous phase (■) are reported. Dashed and dashed-dotted lines represent the estimated α conversion of MKP and MgO, respectively.

Figure 4 shows the concentrations $\mathbf{c}_m^2$ (m=1,…,4) calculated with the proposed procedure and normalized with respect to its maximum value. Moreover the α conversion values obtained from the conventional kinetic analysis (Banford et al., 1980) are also reported for sake of comparison. It is observed a really good agreement between the concentration profiles estimated with the MCR-ALS procedure and the conventional one. It's worth noting that MCR-ALS provides an additional third component, whose contribution comes from the non-crystalline fraction. Its behavior is coherent with previous observations showing a quick formation of an amorphous fraction at the initial stage of the reaction with the subsequent conversion into crystalline MKP (Viani et al., 2014a). Thus, a reliable description of reaction dynamics is achieved. In fact, according to spectra analysis in section 4.1, five regions can be identified in figure 4:

1. *t*= 0÷2.6 min: MgO and KDP are at the maximum values, while the amorphous phase starts from value greater than zero, likely due to the water scattering;
2. *t*=2.6÷5 min: KDP rapidly disappears as dissolves in solution, meanwhile the amorphous phase quickly increases reaching its maximum;
3. *t*=5÷15 min: amorphous phase concentration stays constant, in the meantime MgO keeps dissolving in solution;
4. *t*=15÷30 min: at t=15 min the onset of MKP crystallization and decrease of the amorphous phase are evident;
5. *t*>30 min: a flattening out of the amorphous decay and crystal growth rate is observed and no significant changes in the system are appreciated. This is probably due to a change in mechanism or a diffusion barrier emerging as reaction progresses.

5. Conclusions

In this paper *in situ* x-ray diffraction measurements are used to monitor the K-struvite formation. A procedure based on the MCR-ALS method combined with the EFA algorithm is here proposed to analyse the XRPD data. The main benefits of the algorithm with respect to the traditional analysis are summarized below: (i) it exploits the whole information gathered from data rather than focusing on a limited number of peaks; (ii) it appears less time consuming; (iii) it allows for the detection of the non-crystalline component, otherwise not considered. Thus, the reaction processes are well described and identified. The results here reported demonstrate that the MCR-ALS-EFA method could be a promising framework for generalized treatment of X ray diffraction data and encourage its implementation for the on-line process monitoring. The goals might be: (i) to ensure the achievement of the optimal end-product specifications and (ii) to detect in real time deviations from the nominal process conditions.

References

C.H. Banford, C.F.H. Tipper, 1980,Theory of solid state reaction, in: C.H. Banford, C.F.H. Tipper (Eds.), Comprehensive Chemical Kinetics, 22, 41–113

E. Conterosito , W. Van Beek , L. Palin, G. Croce, L. Perioli et al., 2013, Development of a fast and clean intercalation method for organic molecules into Layered Double Hydroxides, Crystal Growth & Design, 13, 3, 1162-1169

A. de Juan, S. Naveaa, J. Diewokb, R. Tauler, 2004, Local rank exploratory analysis of evolving rank-deficient systems, Chemometrics and Intelligent Laboratory Systems, 70, 11 – 21

A. de Juan, S.C. Rutan, R. Tauler, 2009, Two-Way Data Analysis: Multivariate Curve Resolution – Iterative Resolution Methods, Reference Module in Chemistry, Molecular Sciences and Chemical Engineering from Comprehensive Chemometrics, 325-344

Z. Ding, B. Dong, F. Xinga, N. Hana, Z. Li, 2012, Cementing mechanism of potassium phosphate based magnesium phosphate cement, Ceramics International, 38, 6281–6288

J. Jaumot, R. Gargallo, A. de Juan, R. Tauler, 2005, A graphical user-friendly interface for MCR-ALS: a new tool for multivariate curve resolution in MATLAB, Chemometrics and Intelligent Laboratory Systems, 76, 1, 101-110

A. Viani, A. F. Gualtieri, 2014a, Preparation of magnesium phosphate cement by recycling the product of thermal transformation of asbestos containing wastes, Cement and Concrete Research, 58, 56–66

A. Viani, M. Pérez-Estébanez, S. Pollastri and A. Gualtieri, 2014b, In situ synchrotron powder diffraction study of the setting reaction kinetics of magnesium-potassium phosphate ceramics: influence of MgO reactivity, Journal of the American Ceramic Society, submitted.

AS.Wagh, Magnesium phosphate ceramics, 2004, in: E. Hurst, editor. Chemically bonded phosphate ceramics: 21st century materials with diverse applications, Elsevier, Amsterdam.

Krist V. Gernaey, Jakob K. Huusom and Rafiqul Gani (Eds.), 12th International Symposium on Process Systems Engineering and 25th European Symposium on Computer Aided Process Engineering.
31 May – 4 June 2015, Copenhagen, Denmark

Multivariate fault isolation using lasso-based penalized discriminant analysis

Te-Hui Kuang,[a] Zhengbing Yan,[b] Yuan Yao[a,*]

[a] *Department of Chemical Engineering, National Tsing Hua University, Hsinchu 30013, Taiwan, R.O.C.*
[b] *R and D Center for Membrane Technology, Department of Chemical Engineering, Chung-Yuan Christian University, Chung-Li 32023, Taiwan, R.O.C.*
[*] *Email: yyao@mx.nthu.edu.tw*

Abstract

In multivariate statistical process monitoring (MSPC), isolation of faulty variables is a critical step to discover the source of the detected fault. Although fault detection methods have been intensively investigated, studies on fault isolation are relatively limited, due to the difficulty in analyzing the influences of multiple variables on monitoring statistics. To solve the problems of the existing methods, this paper proposes to conduct fault isolation via a lasso-based penalized discriminant analysis technique. Instead of just offering a suggested set of faulty variables, the proposed method provides more information on the relevance of process variables to the detected fault, which facilitates the subsequent root cause diagnosis step after isolation. The benchmark Tennessee Eastman (TE) process is used as a case study to illustrate the effectiveness of the proposed method.

Keywords: fault isolation, multivariate statistical process monitoring, lasso, discriminant analysis, variable selection.

1. Introduction

For ensuring the safe and efficient operation of manufacturing and chemical industries, multivariate statistical process monitoring (MSPM), which extracts process information from historical operating data, is becoming increasingly important. According to (Chiang *et al.*, 2004), the procedure of MSPM can be summarized into four steps: fault detection, fault isolation, fault diagnosis, and process recovery. The purpose of fault detection is to recognize process abnormality, while fault isolation is for the identification of the variables contributing most to the process faults. Although fault detection methods have been intensively investigated, studies on fault isolation are relatively limited, due to the difficulty in analyzing the influences of multiple variables on monitoring statistics.

For the isolation of faulty variables, contribution plots (Westerhuis *et al.*, 2000) are the most popular tools. Although easy to use, contribution plots often suffer from the "smearing" effect, i.e. the influence of faulty variables on the contributions of non-faulty variables, yielding misleading results (Qin, 2003). The reconstruction-based approaches are also widely used, which re-calculate the values of process variables and monitoring statistics along certain candidate "fault directions" (Dunia and Qin, 1998). A critical assumption for fault reconstruction is that the candidate fault directions are assumed to be known or estimated from sufficient historical fault data, which may not be realistic in real industries. In addition, the unknown faults cannot be handled well by

the reconstruction-based approaches. The reconstruction-based contribution (RBC) was proposed to deal with both known and unknown faults (Alcala and Qin, 2009). However, the smearing effect can still be observed in the RBC plots. To overcome the drawbacks of the reconstruction-based approaches, the branch and bound (BAB) algorithm was combined with the missing variable approach to address the fault isolation problem by solving a combinatorial optimization problem (He *et al.*, 2012). Although BAB is relatively efficient in solving the combinatorial optimization problem, the computational burden of this approach is still heavy, especially for a process with a massive number of variables. As a result, it is difficult to be applied in online process monitoring. In addition to the methods mentioned above, discriminant analysis methods, such as Fisher discriminant analysis (FDA) and support vector machine (SVM), have also been utilized for fault classification, e.g. (Chiang *et al.*, 2004). After a fault is detected, the fault type can be determined by calculating the similarity between the new data and each group of known event data, if sufficient fault data are available in historical database. However, it is unusually to have a complete dataset containing all types of faults. In such situation, the unknown fault may not be isolated.

To solve the mentioned problems of the existing methods, this paper proposes to conduct fault isolation via a lasso-based penalized discriminant analysis technique. Unlike the conventional fault classification, the historical information about the process faults is not needed in the proposed method. Instead, the variables contributing most to the detected fault are automatically selected by solving a penalized discriminant analysis problem formulated in a form of the least absolute shrinkage and selection operator (lasso) (Tibshirani, 1996). Since the lasso can be solved efficiently using state-of-the-art algorithms, heavy computational burden is avoided. In addition, as discussed in (Liu *et al.*, 2014), although the contribution values of process variables follow a certain distribution in the normal operating condition (NOC), the contributions of fault-free variables usually not following the same distribution when a fault occurs. Therefore, it is improper to offer a suggested set of faulty variables based on the control limits derived from normal operating data. In this paper, the proposed method provides more information on the relevance of process variables to the detected fault, which facilitates the subsequent root cause diagnosis step after isolation.

2. Lasso-based penalized discriminant analysis for fault isolation

2.1. Motivations

The basic idea of this paper can be expressed roughly as follows. As mentioned in previous, the goal of fault isolation is to identify variables responsible for the detected process abnormality. In other words, the variables to be isolated are those discriminating the normal process measurements and the fault samples. In a sense, isolating faulty variables is equivalent to identifying discriminating variables in a two-class problem, with the normal operation data regarded as belonging to one class and the data associated with the detected fault as belonging to the other class. Therefore, the task of fault isolation can be transformed into a variable selection problem in discriminant analysis.

In the following of this paper, such problem illustrated using the famous Fisher Discriminant analysis (FDA) technique and solved in a framework of penalized optimization. In previous research, it has been well established that an FDA model can be transformed identically to a least squares regression model with predictors and

response variable chosen properly (Duda *et al.*, 2012). Consequently, the task of identifying discriminating variables is accomplished by doing variable selection for a regression model. In the field of variable selection, the lasso is a promising technique, which minimizes the residual sum of squares under a constraint on the L1-norm of the coefficient vector. By doing so, the lasso tends to produce a number of zero coefficients enforcing sparsity in the solution, and thereby conducts parameter estimation and variable selection simultaneously. The lasso problem can be solved efficiently using a least-angle regression (LARS) algorithm (Efron *et al.*, 2004).

2.2. Relationship between Fisher's linear discriminant and regression analysis

Suppose $\Xi_1 = \{\mathbf{x}_1^1, \cdots, \mathbf{x}_{n_1}^1\}$ and $\Xi_2 = \{\mathbf{x}_1^2, \cdots, \mathbf{x}_{n_2}^2\}$ contain samples from two different classes and $\Xi = \Xi_1 \cup \Xi_2 = \{\mathbf{x}_1, \cdots, \mathbf{x}_n\}$. Fisher's linear discriminant is defined by the vector $\boldsymbol{\omega}$ which maximizes

$$J(\boldsymbol{\omega}) = \frac{\boldsymbol{\omega}^T \mathbf{S}_B \boldsymbol{\omega}}{\boldsymbol{\omega}^T \mathbf{S}_W \boldsymbol{\omega}}, \tag{1}$$

where

$$\mathbf{S}_B = (\mathbf{m}_1 - \mathbf{m}_2)(\mathbf{m}_1 - \mathbf{m}_2)^T, \tag{2}$$

$$\mathbf{S}_W = \sum_{i=1,2} \sum_{\mathbf{x} \in \Xi_i} (\mathbf{x} - \mathbf{m}_i)(\mathbf{x} - \mathbf{m}_i)^T \tag{3}$$

are the between and within class scatter matrices respectively and $\mathbf{m}_i = \frac{1}{n_i} \sum_{j=1}^{n_i} \mathbf{x}_j^i$ are the sample means. By solving the objective function, FDA finds a projection direction maximizing the separation of class means while minimizing the within-class variance, where

$$\boldsymbol{\omega} \propto \mathbf{S}_W^{-1}(\mathbf{m}_1 - \mathbf{m}_2). \tag{4}$$

In order to link the least squares regression solution to FDA, define a predictor matrix

$$\mathbf{X} = \begin{bmatrix} \mathbf{1}_1 & \mathbf{X}_1 \\ -\mathbf{1}_2 & -\mathbf{X}_2 \end{bmatrix}, \tag{5}$$

where $\mathbf{1}_i$ is a column vector containing n_i ones, and $\mathbf{X}_i$ is a matrix whose rows are the samples belonging to Ξ_i. Define a response vector $\mathbf{y}$ as

$$\mathbf{y} = \begin{bmatrix} \frac{n}{n_1}\mathbf{1}_1 \\ \frac{n}{n_2}\mathbf{1}_2 \end{bmatrix}. \tag{6}$$

For a least squares regression problem $\mathbf{X}\boldsymbol{\beta} = \mathbf{y}$, the regression coefficient vector $\boldsymbol{\beta}$ can be obtained by minimizing the residual sum of squares (RSS). Denote $\boldsymbol{\beta} = \begin{bmatrix} W_0 \\ \boldsymbol{\omega} \end{bmatrix}$, where W_0

is the coefficient corresponding to the first column in **X** and the vector **ω** contains the remaining coefficients. Then, it can be proved that **ω** has the same form as in Eq.(4), i.e. the solution of the least squares regression problem is identical to that of FDA.

2.3. Lasso for fault isolation

Since an FDA model can be transformed identically to a least squares regression model, the lasso, which is a penalized regression method, can be adopted to solve the variable selection problem in discriminant analysis. Different from the ordinary least squares (OLS), the lasso minimizes a penalized RSS by introducing an L1 penalty term into the objective function:

$$\min_{\boldsymbol{\beta}}((\mathbf{y}-\mathbf{X}\boldsymbol{\beta})^T(\mathbf{y}-\mathbf{X}\boldsymbol{\beta})+\lambda\|\boldsymbol{\beta}\|_1), \tag{7}$$

where $\|\boldsymbol{\beta}\|_1$ represents the L1-norm of $\boldsymbol{\beta}$ and λ is a tuning parameter. A larger λ usually results in fewer non-zero predictors. There exists a finite sequence: $\lambda_0 > \lambda_1 > \cdots > \lambda_K = 0$. For $\lambda > \lambda_0$, all regression coefficients β_j^λ are shrunk to zero, where β_j^λ is the j-th entry of $\boldsymbol{\beta}$ calculated by solving the optimization problem in Eq.(7). In each interval $(\lambda_{k+1}, \lambda_k)$, the active set $\Gamma(\lambda)=\{j:\mathrm{sgn}[\beta_j^\lambda]\neq 0\}$ and the sign vector $S(\lambda)=\{\mathrm{sgn}[\beta_1^\lambda],...,\mathrm{sgn}[\beta_m^\lambda]\}$ do not change with the value of λ, where $0 \le k \le K-1$ and m is total number of predictors. These λ_k are called transition points. The LARS algorithm (Efron *et al.*, 2004) can be adopted to produce the transition points step by step and obtain the lasso solutions with a similar computational cost to that of OLS.

On the basis of the lasso, the proposed fault isolation procedure is summarized as follows.

1. After a fault is detected, the process data associated with the fault are stored in Ξ_2, while Ξ_1 consists of the historical normal operating data. Without loss of generality, it is assumed that the data have been normalized properly.
2. Construct the predictor matrix **X** and the response vector **y** according to Eq.(5) and Eq.(6).
3. Start with $k = 0$.
4. Set $\lambda = \lambda_k$ and solve the penalized optimization problem described in Eq.(7). The active set $\Gamma(\lambda)$ is achieved.
5. Update $k = k + 1$ and return to step 4, until $\lambda = \lambda_K = 0$.

The order of the process variables appearing in the active set indicates the relevance of the variables to the detected fault. The earlier a variable enters the active set, the more relevant it is. Such information is useful for the subsequent root cause diagnosis step.

3. Case study

In this section, the effectiveness of the proposed fault isolation method is illustrated using the Tennessee Eastman (TE) benchmark process. In the TE process, process data are collected from 41 measured variables and 11 manipulated variables. 20 different types of faults can be simulated. In each fault dataset, the abnormal event is triggered after the 160th sampling interval. More details about the TE process can be found in (Downs and Vogel, 1993).

For illustration, the isolation results of Fault 4 and Fault 5 are introduced. Fault 4 was caused by a step change in the reactor cooling water inlet temperature, which would directly influence the reactor temperature x_9. When the fault occurred, a sudden temperature increase happened in the reactor. Then the feedback controller actioned by adjusting the reactor cooling water flow rate x_{51}. Since such control action is efficient, x_9 returned towards its normal state as shown in Fig. 1, while x_{51} reached a new steady-state value. Other process variables were not affected. Since the steady-state fault signature is informative for root-cause diagnosis, the fault isolation was conducted based on the last 25 observations. Fig. 2 shows the regression coefficients changing with the tuning factor λ, which indicates the isolation results. It is clear that x_{51} is the variable entering the active set first, i.e. the variable most responsible to the fault. The second important variable is x_9.

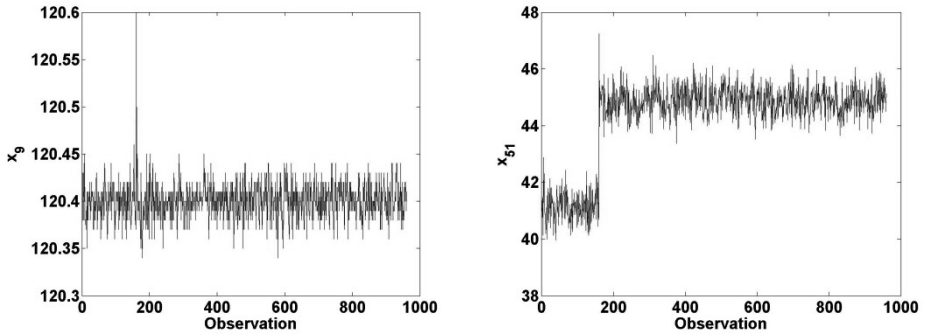

Figure 1. Process variable trajectories for Fault 4

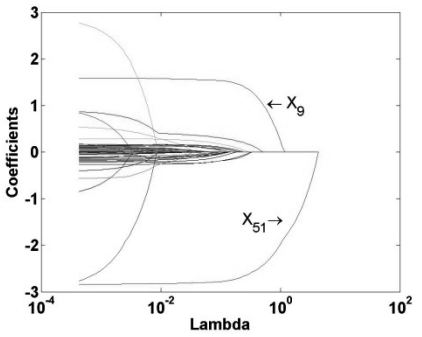

Figure 2. The isolation result for fault 4

Fault 5 was due to a step change in the condenser cooling water inlet temperature. To compensate the effect of such change, the condenser cooling water flow rate x_{52} would be adjusted by the feedback controller. Therefore, when the process reached a new steady-state, x_{52} would not return to its original state. Fig. 3 displays the trajectory of such variable, while Fig. 4 shows the regression coefficients changing with the tuning factor λ. Again, such results are obtained based on the steady-state fault data. According to Fig. 4, x_{52} is considered as the most indicative faulty variable, which is consistent with the process knowledge. The missing data analysis approach based on BAB (He *et al.*, 2012) was also conducted for comparison, which cannot reveal the abnormal variable x_{52}. The second potential faulty variable is x_{18}, which is found to be normal

after further investigation. Therefore, x_{52} is the only abnormal variable in this case, which should be analyzed carefully to reveal the root cause of the fault.

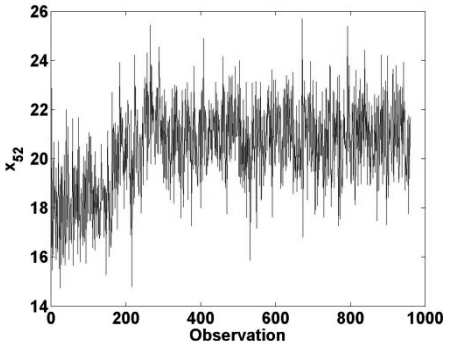

Figure 3. Variable trajectory for Fault 5

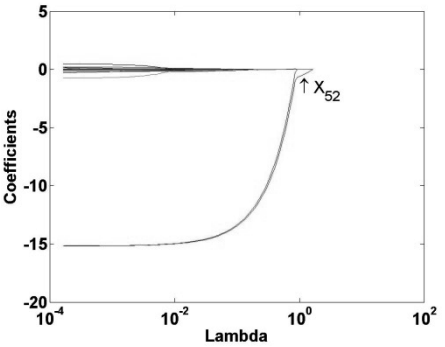

Figure 4. The isolation result for fault 5

4. Conclusions

Isolating faulty variables is a critical step to discover the source of the detected fault. In this paper, the task of fault isolation is transformed to a variable selection problem in discriminant analysis. The lasso approach is adopted to solve such problem. The proposed method does not need any historical fault data or known fault directions, and provides richer information than the conventional methods.

Acknowledgements

This work was supported in part by the Ministry of Science and Technology of R.O.C. under Grant No. Most 103-2221-E-007-123.

References

C. F. Alcala and S. J. Qin, 2009, Reconstruction-based contribution for process monitoring, *Automatica,* 45, 1593-1600.

L. H. Chiang, M. E. Kotanchek and A. K. Kordon, 2004, Fault diagnosis based on Fisher discriminant analysis and support vector machines, *Computers and Chemical Engineering,* 28, 1389-1401.

J. Downs and E. Vogel, 1993, A plant-wide industrial process control problem, *Computers and Chemical Engineering,* 17, 245-255.

R. O. Duda, P. E. Hart and D. G. Stork, 2012, *Pattern classification*, John Wiley and Sons.

R. Dunia and S. Qin, 1998, Subspace approach to multidimensional fault identification and reconstruction, *AIChE Journal,* 44, 1813-1831.

B. Efron, T. Hastie, I. Johnstone and R. Tibshirani, 2004, Least angle regression, *The Annals of Statistics,* 32, 407-451.

B. He, X. Yang, T. Chen and J. Zhang, 2012, Reconstruction-based multivariate contribution analysis for fault isolation: A branch and bound approach, *Journal of Process Control,* 22, 1228-1236.

J. Liu, D. S. H. Wong and D. -S. Chen, 2014, Bayesian filtering of the smearing effect: Fault isolation in chemical process monitoring, *Journal of Process Control,* 24, 1-21.

S. J. Qin, 2003, Statistical process monitoring: basics and beyond, *Journal of chemometrics,* 17, 480-502.

R. Tibshirani, 1996, Regression shrinkage and selection via the lasso, *Journal of the Royal Statistical Society. Series B (Methodological)*, 267-288.

J. Westerhuis, S. Gurden and A. Smilde, 2000, Generalized contribution plots in multivariate statistical process monitoring, *Chemometrics and Intelligent Laboratory Systems,* 51, 95-114.

Krist V. Gernaey, Jakob K. Huusom and Rafiqul Gani (Eds.), 12th International Symposium on Process Systems Engineering and 25th European Symposium on Computer Aided Process Engineering.
31 May – 4 June 2015, Copenhagen, Denmark

Flexible operation of CO_2 capture processes integrated with power plant using advanced control techniques

Ana-Maria Cormos, Mihaela Vasile, Mircea-Vasile Cristea

Babes-Bolyai University, Faculty of Chemistry and Chemical Engineering, Arany Janos 11, RO-400028 Cluj-Napoca, Romania
cani@chem.ubbcluj.ro, vasile.mihaela@ymail.com, mcristea@chem.ubbcluj.ro

Abstract

In this work, a dynamic rate-base model is used to describe CO_2 capture process in aqueous solution of MEA. The model has been implemented in the Matlab/Simulink software in order to do a part-load analysis and elaboration of control strategies of carbon capture process to be used within a power plant. The experimental results published in literature for Esbjerg CESAR pilot plant are used to validate the developed model. A good correlation between absorber's temperature profiles obtained by simulation and experiment was observed, R-squared value is of 0.936 in case of liquid's temperature and of 0.965 for gas's temperature. From environmental protection perspective, the primary control objective for the absorption column is the control of the carbon dioxide concentration in the sweet gas stream. Typical disturbances have been investigated, such as the step/ramp/sinusoidal increment in the flue gas flow rate with respect to its nominal operating point. Two different scenarios have been investigated using both the classical and the advanced control strategy approaches. The simulation results revealed that both PI and MPC controllers were capable to maintain the controlled gaseous mixture close to its imposed set point, rejecting the flue gas flow rate disturbance. Moreover, the MPC is capable to perform efficient control while conforming to constraints imposed on the maximum allowed value of the outlet CO_2 gas concentration and improving the CO_2 capture efficiency.

Keywords: CO_2 capture process, Dynamic rate-base model, Part-load analysis, MPC and PI control strategy.

1. Introduction

In order to reduce CO_2 emissions from flue gases produced by the power generation or other energy-intensive sectors, chemical gas-liquid absorption is an attractive option to be implemented in practice after a well-established scale-up procedure.
CO_2 removal with alkanolamine solvent is the most advanced technology to be deployed on large scale, as worldwide, the CO_2 capture pilot plants had already demonstrated the feasibility of this technology. The use of monoethanolamine (MEA) has considerable interest and led to significant progress in post-combustion CO_2 capture. The advantages of CO_2 capture with alkanolamine are the ability to treat flue gas flows from power stations (CO_2 concentration is of 10–15 vol % for coal and of 3–5 vol % for natural gas) and its suitability for retrofitting existing power plants. The obtained CO_2 product can be made available for chemical and food manufacturing industries (Bui et al., 2014).

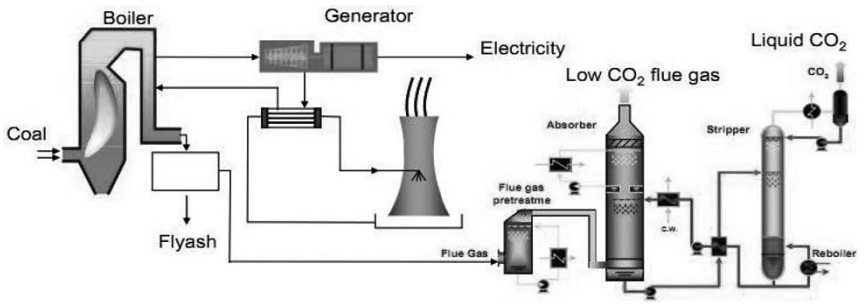

Figure 1. Schematic diagram of CO_2 capture from power station flue gases (http://www.energy-without-carbon.org)

CO_2 capture from power station flue gases using the amine-based process consists in two main packed columns, an absorber and striper (Figure 1). In the absorber, the CO_2 is absorbed from the flue gas by lean amine solvent, being counter-currently contacted. The rich solvent is regenerated in the striper using heat from the steam extracted during the power generation process. A major disadvantage of this technology is the large energy requirement for solvent regeneration. In order to reduce the energy penalty during peak periods of electricity demand, a flexible operation of post-combustion CO_2 capture has been proposed (Bui et al., 2014). Dynamic flexible operation of carbon capture plant is fundamental to successfully implement the process at industrial scale, since full-time continuous CO_2 capture might not be economically feasible. Very few examples of dynamic cases relevant to flexible carbon capture process operation exist in literature at the present time. Dynamic CO_2 capture model simulations have only analysed very small disturbances (Bui et al., 2014).
In this paper, a scale-up dynamic model (for 17 m high absortion column) is used to describe the CO_2 capture process in aqueous solution of MEA. Implemented in Matlab/Simulink software, the model offers the instrument to perform part-load analysis and control strategy design for the carbon capture process to be used within a power plant.

2. Model development and validation

In present work, a dynamic model (previously developed within de group) is scale-up to describe CO_2 capture process in a 17 m high absorption column. The model equations are presented, in detail, in previous works (Gaspar and Cormos, 2011, 2012). The model contain partial differential equations (PDE) to describe the total mass, component and energy balance equations of liquid and gas phases, and algebraic equations for the physical and chemical properties calculation (diffusion coefficients, CO_2 solubility in amine solution, densities, viscosities, specific heat capacities, etc). Two-film theory was used to determine mass and heat transfer processes. Mass transfer coefficient, effective interfacial area and liquid hold up are calculated from Rocha, Bravo and Fair (1996) empirical correlations. The effect of the chemical reaction on the transfer rate is built-in in the transfer equations by the enhancement factor. The reaction mechanism implemented in the model is based on data revised by Versteeg et al. (1996).

The experimental results published in literature for Esbjerg CESAR pilot plant (pilot plant parameters: absorbent 30wt% MEA; packing type: Sulzer Mellapak 2X; absorber diameter 1.1 m, packed height 17 m) are used to validate the developed model. The model parameters are presented in table 1 (Razi et al., 2013).

Table1. Parameter of CESAR pilot plant

Parameters	Value
Packing type	Sulzer Mellapak 2X
Absorber diameter (m)	1.1
Absorber packed height (m)	17
Removal efficiency (%)	87
Flow gas flow (Nm3/h)	50
Lean MEA flow (m3/h)	24
Flue gas temperature (°C)	50
MEA temperature (°C)	40
Lean amine loading	0.2-0.3

The simulation results were used to assess the overall process parameters such as chemical species concentration profiles, liquid and gas flow profiles, temperature profile in the liquid and gas phase along the absorption column. The gas phase CO_2 concentration decreases from the bottom to the top of absorber as it reacts with the solvent (monoethanolamine). The CO_2 removal efficiency to its nominal operating point obtained by simulation is of 83.5 % (experimental is of 87 %). A good correlation between absorber's temperature profiles obtained by simulation and experiment was observed, the R-squared is of 0.936 for the temperature of the liquid and of 0.965 for the temperature of the gas. The temperature profile along the packed column height obtained by simulation and experiment is presented in Figure 2 (Razi et al., 2013).

3. Part-load analysis

Usually, the power plant is operated at full capacity during the day and part-load or even shut down during the night, due to the timely variation of the grid demand. Generally during periods of high electricity demand and, hence spot price, energy penalty of carbon capture process can have a negative impact on the technical and economic performance of the power plant. Flexible operation can significantly reduce the financial impact of integrating carbon capture unit into power plants. The post-combustion CO_2 capture unit is affected by the need of load-following operation imposed by the power block. A complete understanding of the dynamic operability of the power plant with CO_2 capture using amine-based solvents is fundamental to successfully implement this process in commercial scale power plants. The developed dynamic model is used to simulate the transient behavior of the CO_2 capture plant due to changes in the flue gas flow rate, in order to study the effect of the power plants operating conditions on the CO_2 capture process. The CO_2 removal capacity has been studied using step, ramp and sinusoidal input tests to highlight the transient response.

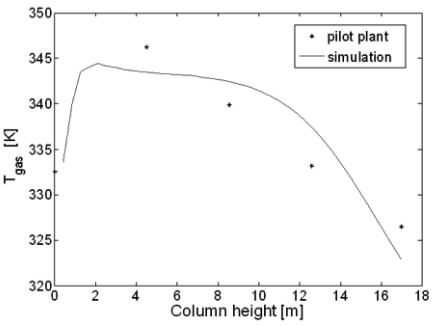

Figure 2. Gas temperature profile

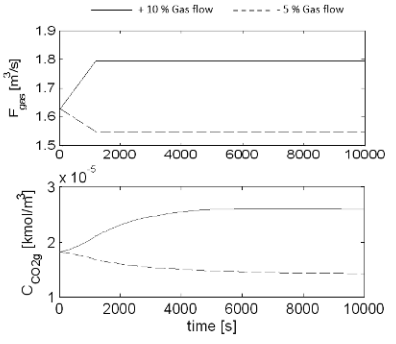

Figure 3. Flue gas flow rate and CO_2 capture rate during the ramp test

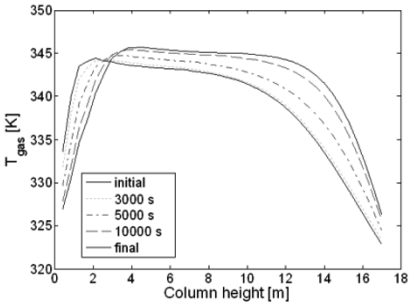

Figure 4. Gas temperature profile during the step test (-20 % in the flue gas flow)

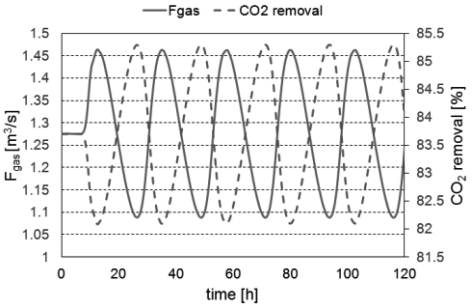

Figure 5. Output gas flow and CO_2 removal percentage during sinusoidal change

The dynamic behavior study of the CO_2 capture process demonstrates that plant performance is reduced significantly with excessive increase of the absorber load and a decrease of FG/FL allowed an increase of CO_2 capture rate. The CO_2 removal capacity of the carbonator was studied during a ramp test which included the increasing/decreasing of inlet gas flow within a 10 % / 5 % range (with respect to its nominal operating point), followed by a constant type disturbance (Figure 3). Figure 4 shows the change of the gas temperature to a typical disturbance, a step increment of -20 % in the inlet gas flow. The response of CO_2 removal efficiency is fast; therefore it is hardly noticeable in an hour scale, as presented in Figure 3 and 4.

The sinusoidal test was introduced in the process model to study the oscillatory behavior of this process, which is ~~a~~ typical for power plant outputs. Consequently, this case study was carried out considering that the amplitude of the sinusoidal function has a change of 15% with respect to the flue gas input base case value. The sinusoidal input was set to complete one cycle within a day. The simulation was performed for five days, as Figure 5 shows. The percentage of CO_2 removal reached a minimal value of 82.2 % when the flue gas flow rate was at its maximum and a maximal value of 85.3 % at the minimum of flue gas flow rate. The changes on CO_2 capture rate are due that the disturbance propagates with delay from beginning to the column end and the absorber are not stabilizes at the new steady-state value. Future studies should provide a dynamic model validated with dynamic pilot plant data.

4. Elaboration of control strategies

Control of the carbon dioxide quantity in the sweet gas stream is the most important objective for flexible operation configuration of post combustion capture plant. In this work, simulations of different control scenarios have been performed using both classical control strategy (proportional-integral controller, PI) and advance control strategy (model predictive control, MPC) (Cristea, et al. 2003; Leonard, et al. 2013).

The two considered control approaches have been investigated in the presence of typical disturbances, such as the step change of the inlet flue gas flow rate, having an increase of 10% with respect to its nominal operating point. The manipulated variable was the liquid flow, adjusted by the controllers to maintain the output CO_2 gas concentration at the setpoint value of 1.81 10^{-5} Kmol/m^3, the latter providing removal of at least 85% CO_2 from the gaseous mixture. As shown in Figure 6, both PI and MPC controllers succeed to reject the effect of the inlet flue gas flow rate change, bringing the output CO_2 gas concentration at the desired value. The advantage of the unconstrained MPC over PI consists in the duration of the time period the controlled CO_2 gas concentration

is exceeding the imposed setpoint. For the MPC case this period is smaller compared to the PI control approach, as shown in Figure 6. This fact has a direct impact on the CO_2 capture increase of efficiency and results in decreased CO_2 emissions. Additionally, the slightly smaller overshoot of the controlled CO_2 gas concentration for the MPC case, compared to the PI case, is emphasizing the same favourable impact. The PI tuning has been based on a trial and error procedure. The control loop with a P controller was brought to oscillation by increasing the proportional gain. The oscillation gain was later halved and the integral gain was increased until the offset was rejected in sufficiently small period of time.

One of the most appreciated features of MPC consists in its optimal characteristic and ability to handle constraints. This may offer flexibility for operation. As an example, this capability is presented in Figure 7 where an upper constraint on the controlled CO_2 gas concentration, at the value of 2.3 10^{-5} Kmol/m^3, was imposed and the results revealed the potential of the constrained MPC to reject the same disturbance while bringing the controlled variable to the desired setpoint. The constraint MPC approach is substantiating the incentives of the unconstrained MPC by further reducing both the period of exceeding the imposed setpoint and the overshoot. The computation of the MPC control law relies on the constrained minimisation of a cost function consisting in the summation of two weighted terms. The first one is the square difference between the desired setpoint and the predicted output, considered over the future prediction horizon, while the second one is the square change of the manipulated variable, considered over the future input horizon. The weighting factors in the cost function have been used for MPC tuning. They have been initially chosen based on the maximum allowed change of the output and respectively, the manipulated variable, values that have been further adjusted until the offset was rejected and the time of return under the setpoint value was minimal.

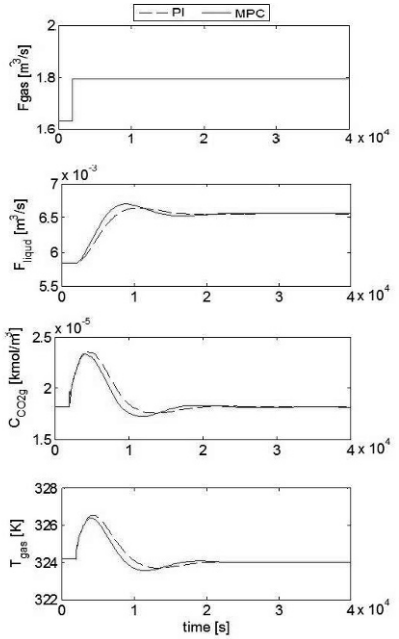

Figure 6. PI vs MPC performance

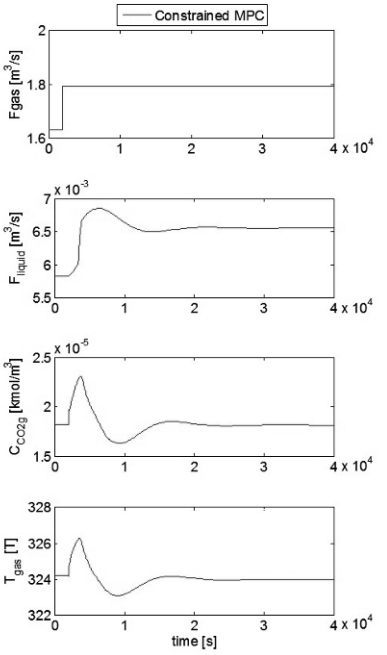

Figure 7. Constrained MPC performance

5. Conclusions

A consistent dynamic rate-base model has been implemented in the Matlab/Simulink in order to do a part-load analysis and design of control strategies of carbon capture process to be used within a power plant. A good correlation between absorber's temperature profiles obtained by simulation and experimental (published in literature for Esbjerg CESAR pilot plant) was observed.

The CO_2 removal capacity has been studied using step, ramp and sinusoidal input tests in order to highlight the transient response of CO_2 capture for a typical load following the behavior of power generation plants. The amount of liquid flow was adjusted to provide absorption of at least 85 % CO_2 of the gaseous mixture.

Two different control strategies have been tested based on the classical PI and the advanced MPC control, in order to enhance the flexibility of the plant operation. The results revealed that the PI and MPC controllers were capable to maintain the concentration of the CO_2 gaseous mixture close to the desired set point, despite the upset produced by the inlet gas flow rate disturbance. Furthermore, the MPC demonstrated to have the very valued potential to perform efficient control by efficiently bringing back the CO_2 concentration under the setpoint imposed limit and reduce overshoot, while complying with operation constraints. This ability results in the improvement of the CO_2 capture efficiency.

Acknowledgements

This work was supported by two grants of the Romanian National Authority for Scientific Research (UEFISCDI): PN-II-PT-PCCA-20113.2-0162: "Technical-economic and environmental optimization of CCS technologies integration in power plants based on solid fossil fuel and renewable energy sources (biomass)".

References

M. Bui, I. Gunawan, V. Verheyen, P. Feron, E. Meuleman, S. Adeloju, 2014, Dynamic modelling and optimisation of flexible operation in post-combustion CO_2 capture plants - A review, Comput. Chem. Eng., 61, 245– 265.

M.V. Cristea, S. P. Agachi, M.V. Marinoiu, 2003, Simulation and Model Predictive Control of a UOP Fluid Catalytic Cracking Unit, Chemical Engineering and Processing, 42, 67-91.

J. Gaspar J., A. M. Cormos, 2012, Dynamic modeling and absorption capacity assessment of CO_2 capture process, Int. J. Green. Gas Control, 8, 45–55.

J. Gaspar, A. M. Cormos, 2011, Dynamic modeling and validation of absorber and desorber columns for post-combustion CO_2 capture, Comput. Chem. Eng., 35, 2044-2052.

G. Leonard, B. C. Mogador, S. Belletante, G. Heyena, Dynamic modelling and control of a pilot plant for post-combustion CO_2 capture, 2013, Computer Aided Chemical Engineering, 32, 451-456

R. Maceiras, E. Alvarez, M.A. Cancela, 2008, Effect of temperature on carbon dioxide absorption in monoethanolamine solutions, Chem. Eng. J., 137, 422-427.

N. Razi, H. F. Svendsen, O. Bolland, 2013, Validation of mass transfer correlations for CO_2 absorption with MEA using pilot data, Int. J. Green. Gas Control, 19, 478–491.

J.A. Rocha, J.L. Bravo, J.R. Fair, 1996, Distilation columns containing structured packings: A comprehensive model for their performance. 1. Mass-transfer models, Ind. Eng. Res. 35, 1660-1667.

G.F. Verstege, L.A.J. Van Dijck, W. Van Swaaij, 1996, On the kinetics between CO_2 and alkanolamines both in aqueous and non-aqueous solutions, Chem. Eng. J., 144, 113-158.

Krist V. Gernaey, Jakob K. Huusom and Rafiqul Gani (Eds.), 12th International Symposium on Process Systems Engineering and 25th European Symposium on Computer Aided Process Engineering.
31 May - 4 June 2015, Copenhagen, Denmark.

Modified Minimum Variance Approach for State and Unknown Input Estimation

Yukteshwar Baranwal, Pushkar Ballal and Mani Bhushan*

Department of Chemical Engineering, Indian Institute of Technology Bombay, India-400076
**mbhushan@iitb.ac.in*

Abstract

For several systems of interest, inputs to the system may be unknown. Thus, one may be interested in estimating the unknown inputs alongwith the states. In this work, we modify the approach proposed by Madapusi and Bernstein (2007) for estimating the states and the unknown inputs. The approach, applicable to systems with feedthrough, obtains a minimum variance unbiased estimate of the states. The inputs are estimated after the filtered states are obtained and do not require any restrictive assumptions about the dynamic variation of the inputs. Compared to Madapusi and Bernstein (2007), our approach differs in the prediction step. In particular, we use the estimated input in the prediction step while it has not been considered in the work of Madapusi and Bernstein (2007). Our proposed modification reduces the number of constraints that need to be satisfied by the filter gain thereby increasing the applicability of the approach. The efficacy of the approach is demonstrated by applying it to estimate unknown inputs and states in a self powered neutron detector, that is widely used in nuclear reactors to monitor the neutron flux.

Keywords: State estimation, unknown input estimation, minimum variance estimation, self powered neutron detector.

1. Introduction

The problem of state estimation is to estimate the states of the system using an uncertain process model and noisy measurements. Most of the state estimation approaches available in literature assume that the inputs to the process are exactly known. However, in several systems of interest the inputs are not directly measured and hence their exact values are unknown. Relatively less attention has been given to problem of state estimation under this scenario. One approach for addressing such problems would be to consider the unknown input to be an unknown parameter and assume a dynamic model (typically random walk) for its variation. The problem is to then estimate the augmented states with this parameter as an additional state. However, arbitrary assumptions about the dynamic variation of the unknown input may be poorly justified specially for inputs varying over a wide range in a deterministic manner.

There are relatively fewer approaches that don't assume any model for the variation of the unknown input. In particular, Kitanidis (1987) developed an unbiased minimum variance estimator for the states in the presence of unknown inputs. Their approach requires the filter gain to satisfy a constraint that ensures that the effect of the unknown input is not felt on the estimated state. However, the focus of their work is on state estimation only and they did not discuss estimation of the unknown inputs. Sanyal and Shen (1974) have considered the problem of state and input estimation but assume the input to be a series of impulses of unknown magnitudes occurring after significant time lapses. Glover (1969) consider mainly estimation of unknown inputs and not the

states themselves. But they assume the initial state to be zero. Madapusi and Bernstein (2007) have presented observability conditions for estimating both states and unknown inputs. They also extend the work of Kitanidis (1987) to deal with feedthrough systems. In both the approaches of Kitanidis (1987) and Madapusi and Bernstein (2007), the prediction step in the filter implicitly assumes the unknown input to be zero.

In this work, we focus on the problem of simultaneous state and unknown input estimation. Our work is applicable to linear systems with feedthrough, namely where the unknown inputs directly affect the measurements. In particular, we modify the approach of Madapusi and Bernstein (2007) in that we use the estimated value of the unknown input in the state prediction step at the next time instant. We show that this modification enables application of the approach to a larger class of systems by reducing the constraints to be satisfied by filter gain to ensure unbiased state estimates. It also results in better (lower variance) state estimates. The approach is thus a modification of traditional Kalman filter and ensures unbiased, minimum variance state estimates while using the estimated values of unmeasured inputs in the state prediction step. The utility of the approach is demonstrated by applying it to the problem of estimating neutron flux in a nuclear reactor. The rest of the paper is structured as follows: in section 2 we present the problem statement and summarize the existing relevant work. The proposed extension is presented in section 3. The approach is applied to a neutron flux estimation problem in section 4. The paper is concluded in section 5.

2. Problem Statement and Existing Approaches

Consider a discrete-time linear system with a linear measurement function,

$$x_{k+1} = A_k x_k + H_k e_k + w_k \tag{1}$$
$$y_k = C_k x_k + G_k e_k + v_k \tag{2}$$

where, $x_k \in \mathbb{R}^n, y_k \in \mathbb{R}^m, e_k \in \mathbb{R}^p, w_k \in \mathbb{R}^n, v_k \in \mathbb{R}^m$ are respectively the states, measurements, unknown inputs, process noise and measurement noise, respectively. w_k and v_k are usually considered to be white, Gaussian discrete time stochastic processes with mean 0 and covariances Q_k and R_k respectively. The subscript k for the various quantities indicates the time instant t_k. The problem in joint state and unknown input estimation is to obtain the best estimates of x_k and e_k given the measurements upto time t_k. Note that while writing the measurement equation above, we have assumed direct feedthrough namely that the unmeasured inputs e_k directly affect the measurements y_k. Further, for simplicity of notation we have not considered known inputs in either the state evolution or measurement equation. Incase some known inputs are present, the proposed methodology can easily be modified to accommodate them. We now summarize the existing relevant technique (Madapusi and Bernstein, 2007) for simultaneous state and unknown input estimation.

2.1. Simultaneous State and Input Estimation

We assume the conditional state density at time t_k to be Gaussian with mean $\hat{x}_{k|k}$ and covariance $P_{k|k}$. In the approach proposed by Kitanidis (1987) and Madapusi and Bernstein (2007), the filter takes the following form:

$$\hat{x}_{k+1|k} = A_k \hat{x}_{k|k} \tag{3}$$
$$\hat{x}_{k+1|k+1} = \hat{x}_{k+1|k} + L_{k+1}(y_{k+1} - C_{k+1}\hat{x}_{k+1|k}) \tag{4}$$

where $\hat{x}_{k+1|k+1}$ is the required filtered (estimated or updated) state while L_{k+1} is the filter gain and $\hat{x}_{k+1|k}$ is the model predicted state based on measurements till time instant k. An important thing to note in the prediction equation (Eq. 3) is that the effect of the unknown input has been ignored while predicting the state.

Define the state estimation error as: $\varepsilon_{k+1|k+1} \triangleq x_{k+1} - \hat{x}_{k+1|k+1}$. Requiring the state estimation error to be 0 mean, leads to the following constraints on the filter gain (Madapusi and Bernstein, 2007):

$$(I - L_{k+1}C_{k+1})H_k = 0 \tag{5}$$

$$L_{k+1}G_{k+1} = 0 \tag{6}$$

The updated error covariance matrix $P_{k+1|k+1}$ is given by,

$$P_{k+1|k+1} \triangleq \mathbb{E}[\varepsilon_{k+1|k+1}\varepsilon_{k+1|k+1}^T] = L_{k+1}\tilde{R}_{k+1}L_{k+1}^T - F_{k+1}L_{k+1}^T - L_{k+1}F_{k+1}^T + P_{k+1|k} \tag{7}$$

$$\text{where, } P_{k+1|k} = A_kP_{k|k}A_k^T + Q_k,\ \tilde{R}_{k+1} = C_{k+1}P_{k+1|k}C_{k+1}^T + R_{k+1},\ F_{k+1} = P_{k+1|k}C_{k+1}^T \tag{8}$$

The unbiased minimum-variance gain L_{k+1} is calculated by minimizing the trace of the error covariance matrix $P_{k+1|k+1}$ subject to the constraints in Eq. 5 and 6 and is given by,

$$L_{k+1} = (F_{k+1} + \Omega_{k+1}(\Phi_{k+1}^T\tilde{R}_{k+1}^{-1}\Phi_{K+1})^{-1}\Phi_{K+1}^T)\tilde{R}_{k+1}^{-1} \tag{9}$$

where,

$$\Phi_{k+1} = [-G_{k+1} \quad V_{k+1}],\ V_{k+1} = C_{k+1}H_k,\ \Omega_{k+1} = [0_{n\times p} \quad H_k] - F_{k+1}\tilde{R}_{k+1}^{-1}\Phi_{k+1} \tag{10}$$

This completes the state estimation step. The estimate $\hat{e}_k$ of the unknown input is subsequently obtained as (Madapusi and Bernstein, 2007),

$$\hat{e}_{k+1|k+1} = G_{k+1}^{\dagger}(y_{k+1} - C_{k+1}\hat{x}_{k+1|k+1}) \tag{11}$$

where, $G^{\dagger}$ is Moore-Penrose generalized inverse, given as $G^{\dagger} = (G^TG)^{-1}G^T$. Note that the presence of the unknown input $e(k)$ in the measurement equation (Eq. 2) enables its estimation using the above expression. Further, it can be shown (Madapusi and Bernstein, 2007) that Eq. 11 provides an unbiased estimate of the unknown input i.e. $\mathbb{E}[\bar{e}_{k+1|k+1}] = 0$ where $\bar{e}_{k+1|k+1} \triangleq e_{k+1} - \hat{e}_{k+1|k+1}$ is the error in estimating the unknown input. The approach in this section is labeled as input reconstruction (InpR) approach.

3. Proposed Approach

In this work, we propose the following filter form,

$$\hat{x}_{k+1|k} = A_k\hat{x}_{k|k} + H_k\hat{e}_{k|k} \tag{12}$$

$$\hat{x}_{k+1|k+1} = \hat{x}_{k+1|k} + L_{k+1}(y_{k+1} - C_{k+1}\hat{x}_{k+1|k}) \tag{13}$$

Comparing with Eqs. 3 and 4, it can be seen that our approach does not ignore the unknown input while predicting the states. Instead, we use the estimated value of the unknown input $\hat{e}_{k|k}$ in the prediction equation. The expected value of the state estimation error $\varepsilon_{k+1|k+1}$ can then be derived to be,

$$\begin{aligned}\mathbb{E}[\varepsilon_{k+1|k+1}] = \mathbb{E}[&(I - L_{k+1}C_{k+1})A_k\varepsilon_{k|k} + (I - L_{k+1}C_{k+1})H_k(e_k - \hat{e}_{k|k}) + (I - L_{k+1}C_{k+1})w_k \\ &- L_{k+1}G_{k+1}e_{k+1} - L_{k+1}v_{k+1}]\end{aligned} \tag{14}$$

Now the filter gain can be derived using a similar procedure as in Kitanidis (1987); Madapusi and Bernstein (2007). If the estimated inputs and the estimated states at previous time step are unbiased, we have $\mathbb{E}[e_k - \hat{e}_{k|k}] = 0$ and $\mathbb{E}[\varepsilon_{k|k}] = 0$. Further, since the unknown input e_k is arbitrary, the following condition needs to hold for obtaining unbiased state estimates at time t_{k+1}:

$$L_{k+1}G_{k+1} = 0 \tag{15}$$

Comparing this condition to Eqs. 5 and 6, it can be seen that the proposed approach results in less restrictive conditions on the filter gain. Further, it can be noted that for the filter gain to exist, the matrix G_{k+1} should have a non-empty left null space i.e. the number of measurements should be more than the number of unknown inputs. Using constraint 15, the state estimation error is,

$$\varepsilon_{k+1|k+1} = (I - L_{k+1}C_{k+1})(A_k\varepsilon_k + H_k\bar{e}_{k|k} + w_k) - L_{k+1}v_{k+1}$$

Thus, the covariance matrix $P_{k+1|k+1}$ of state estimation errors can be derived to be,

$$P_{k+1|k+1} = \mathbb{E}\left[\varepsilon_{k+1|k+1}\varepsilon_{k+1|k+1}^T\right] = P_{k+1|k} - L_{k+1}F_{k+1}^T - F_{k+1}L_{k+1}^T + L_{k+1}\tilde{R}_{k+1}L_{k+1}^T \tag{16}$$

where,

$$P_{k+1|k} = A_kP_{k|k}A_k^T + H_k\xi_{k+1}H_k^T + A_k\sigma_{k+1}H_k^T + H_k\sigma_{k+1}^TA_k^T + Q_k \tag{17}$$

$$\xi_{k+1} = \mathbb{E}[\bar{e}_{k|k}\bar{e}_{k|k}^T] = G_k^\dagger(C_kP_{k|k}C_k^T + R_k - C_kL_kR_k - R_kL_k^TC_k^T)(G_k^\dagger)^T \tag{18}$$

$$\sigma_{k+1} = \mathbb{E}[\varepsilon_{k|k}\bar{e}_k^T] = (-P_{k|k}C_k^T + L_kR_k)(G_k^\dagger)^T \tag{19}$$

$$\tilde{R}_{k+1} = C_{k+1}P_{k+1|k}C_{k+1}^T + R_{k+1}, \quad F_{k+1} = P_{k+1|k}C_{k+1}^T \tag{20}$$

As in the previous section, the optimal filter gain is now computed by minimizing the trace of the estimation error covariance matrix, i.e. trace$(P_{k+1|k+1})$, subject to constraint in Eq. 15 and is derived to be (details are in Baranwal (2012)):

$$L_{k+1} = F_{k+1}(I - \tilde{R}_{k+1}^{-1}G_{k+1}(G_{k+1}^T\tilde{R}_{k+1}^{-1}G_{k+1})^{-1}G_{k+1}^T)\tilde{R}_{k+1}^{-1} \tag{21}$$

Once the state is estimated, the estimate of the unknown input can be computed as,

$$\hat{e}_{k+1|k+1} = G_{k+1}^\dagger(y_{k+1} - C_{k+1}\hat{x}_{k+1|k+1}) \tag{22}$$

It can be shown that this is an unbiased estimate of the unknown input. We label our approach as modified input reconstruction (MInpR) approach to distinguish it from the input reconstruction approach presented in the last section.

4. Case Study

We now implement the proposed approach on a self powered neutron detector (SPND) which is a sensor widely used in nuclear reactors for incore neutron flux estimation. An SPND operates on the principle of activation by neutron interaction, namely that it generates current upon absorption of neutrons. A dynamic model of Vanadium SPND is (Srinivasarengan et al., 2012):

$$\frac{d}{dt}N_{52}(t) = -\lambda_{52}N_{52}(t) + \sigma_{51}N_{51}\phi(t) \tag{23}$$

$$I(t) = k_{pv}\sigma_{51}N_{51}(t)\phi(t) + k_{gv}\lambda_{52}N_{52}(t) \tag{24}$$

where state N_{52} denotes the concentration (atoms.cm^{-3}) of the isotope ^{52}V, while ϕ denotes the neutron flux (neutrons.cm^{-2}.sec^{-1}) which is the unknown input of interest. The measurement $I(t)$ is of the current generated by the SPND. Note that while writing this model, the concentration N_{51} of the stable isotope ^{51}V has been assumed to be a constant. The various parameters occurring in the above equations are listed in Table 1. The constants k_{gv}, k_{pv} reported in this Table are subsequently multiplied by a factor of 1×10^9 to scale the measurement. The sampling interval for the measurements is 1 second. It can be seen that the above is a direct feedthrough linear state space model since the input $\phi(t)$ directly appears in the measurement equation as well. However, the size of the G matrix (Eq. 2) is 1×1. From Eq. 15, this directly leads to filter gain being

zero and the proposed approach (Sec. 3) or the existing approach in literature (Sec. 2) cannot be applied. We thus consider two Vanadium SPNDs with the same, but unknown input. In a nuclear reactor, such a scenario is possible since a typical nuclear reactor has several SPNDs some of which are highly correlated (Razak et al., 2014). The parameters of both the SPNDs are assumed to be the same as given in Table 1. While the proposed modified input reconstruction approach can be applied to estimate states and the unknown input, an analysis of Eqs. 5 and 6 reveals that these constraints cannot be simultaneously satisfied and hence the existing input reconstruction approach cannot be applied. We thus apply the proposed MInpR approach and compare its results with a covariance-reset based Kalman Filter (KF) approach presented in Srinivasarengan et al. (2012). The latter assumes a random walk model for the unknown flux and applies a traditional Kalman filter to the augmented system. However to track sudden changes in the flux, it heuristically resets the variance of the estimated flux to a large value when the mean of norm of the innovations in a moving window exceeds a predefined threshold. Thus, tuning parameters related to the length of the window, the threshold and the value to which the variance is reset, need to be suitably chosen for the approach to work properly.

Three types of input (flux) profiles are generated. The corresponding inputs estimated by the covariance-reset approach and the proposed MInpR approach are shown in Fig. 1 alongwith the true input profiles. The mean squared errors (MSE) corresponding to the estimated fluxes and the estimated states are reported in Table 2. From this table it can be seen the state estimation accuracy is higher (i.e. MSE is lower) with the proposed approach for all the three flux profiles. The accuracy of estimated flux profiles is higher for the covariance-reset approach for first two flux profiles while it is higher for the proposed approach for the third flux profile.

Table 1: Model Parameters

Parameter	Values	Unit
N_{51}	6.86×10^{22}	cm^{-3}
σ_{51}	4.9×10^{-24}	cm^{2}
λ_{52}	3.6×10^{-3}	sec^{-1}
k_{gv}	3.846×10^{-20}	$Amperes.sec$
k_{pv}	3.487×10^{-12}	$Amperes.sec$

Table 2: MSE for Estimated States and Inputs

Flux Profile	Variable	KF (Cov Reset)	MInpR
Flux 1	State: SPND 1	1.1068×10^{14}	1.0590×10^{14}
	State: SPND 2	1.1822×10^{14}	1.1284×10^{14}
	Flux	5.4099×10^{12}	6.7876×10^{12}
Flux 2	State: SPND 1	0.7972×10^{14}	0.7204×10^{14}
	State: SPND 2	0.7997×10^{14}	0.7298×10^{14}
	Flux	6.2910×10^{12}	6.5288×10^{12}
Flux 3	State: SPND 1	0.9375×10^{14}	0.8040×10^{14}
	State: SPND 2	1.0180×10^{14}	0.8890×10^{14}
	Flux	8.6614×10^{12}	7.1141×10^{12}

5. Conclusions

In this work, we present a technique for estimating states and unknown inputs for linear systems with feedthrough. The technique, labeled modified input reconstruction approach, modifies an existing (Madapusi and Bernstein, 2007) technique from literature. The modification is in the prediction step and reduces the number of constraints to be satisfied by the filter gain while obtaining unbiased, minimum variance estimates of the states. The approach is applied to estimate states and the unknown input for a self powered neutron detector, which are widely used in nuclear reactors.

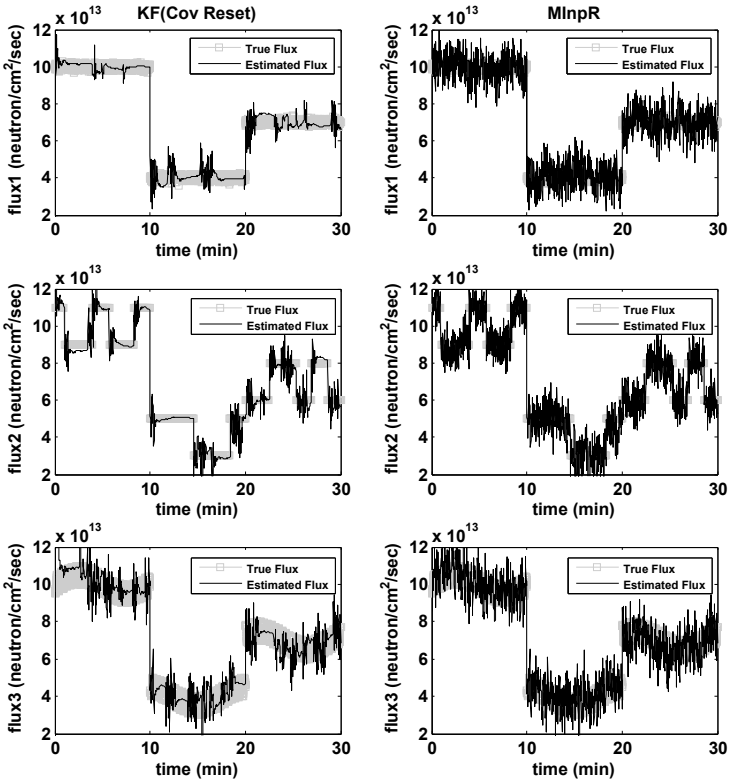

Figure 1: Flux Estimation for Vanadium SPND

The results demonstrate superior quality of state estimation when compared to traditional estimation approach that assumes a dynamic model for the variation of the unknown input, while the quality of estimated inputs is comparable. However, unlike the traditional approach, the proposed approach does not involve any tuning parameters.

References

Baranwal, Y., 2012. Self powered neutron detectors: Model based flux estimation and monitoring based on real time phase detection. Master's thesis, Department of Chemical Engineering, Indian Institute of Technology Bombay, Mumbai, India.

Glover, J. D., 1969. The linear estimation of completely uknown signals. IEEE Transactions on Automatic Control 14, 766–767.

Kitanidis, P. K., 1987. Unbiased minimum-variance linear state estimation. Automatica 23 (6), 775 – 778.

Madapusi, H., Bernstein, D., 2007. Unbiased minimum-variance filtering for input reconstruction. In: Proceedings of the American Control Conference, ACC '07. pp. 5712–5717.

Razak, R. A., Bhushan, M., Belur, M. N., Tiwari, A. P., Kelkar, M. G., Pramanik, M., 2014. Clustering of self powered neutron detectors: Combining prompt and slow dynamics. IEEE Transactions on Nuclear Science 61 (6), 3635–3643.

Sanyal, P., Shen, C. N., 1974. Bayes' decision rule for rapid detection and adaptive estimation scheme with space applications. IEEE Transactions on Automatic Control AC-19, 228–231.

Srinivasarengan, K., Mutyam, L., Belur, M. N., Bhushan, M., Tiwari, A. P., Kelkar, M. G., Pramanik, M., 2012. Flux estimation from vanadium and cobalt self powered neutron detectors (spnds): Nonlinear exact inversion and kalman filter approaches. In: Proceedings of American Control Conference, ACC '12. pp. 318–323.

Krist V. Gernaey, Jakob K. Huusom and Rafiqul Gani (Eds.), 12th International Symposium on Process Systems Engineering and 25th European Symposium on Computer Aided Process Engineering.
31 May – 4 June 2015, Copenhagen, Denmark

A New Software Development Methodology for Controllability Analysis of Forced Circulation Evaporator System

Afshin Sadrieh, Parisa A. Bahri[a]

[a]*Murdoch University, 90 south street, Perth 6150, Australia*

Abstract

Modern chemical process plants are becoming more and more complex due to tighter economic and environmental limitations. As a result, achieving well-controllable process system designs becomes a tedious task. Using software products to evaluate designs in early stages is beneficial in order to reduce the human error and increase the efficiency. However, developing software tools for controllability problems using traditional software development methods is inefficient due to complexity and scale of these problems as well as considerable differences between them. In this work, a graphical domain-specific language (DSL) is introduced for measuring RGA index, to assess the controllability of a process plant with an application to a forced-circulation evaporator system.

Keywords: Domain-specific languages, Forced circulation evaporator, Controllability analysis

1. Introduction

Maintaining controllability measure of modern chemical plants in a safe margin is not only beneficial from economical point of view, but also crucial for safety concerns. A research suggested that Chernobyl disaster could have been prevented if controllability issues of that plant were addressed.

Controllability concept has been defined in various forms, depending on the scope it is being used in. Originally, Ziegler and Nichols defined it back in 1943 and since then it has been emphasized that controllability index of a process system design is dependent on the process design itself, not the controller. As a result, controllability analysis should be conducted during the design stage (Yuan et al, 2011).

However, although the need for controllability evaluation of process systems at design stage was bolded out before, surprisingly, there are only very few software tools dedicated for this purpose and they never became commercialised (Fararooy and Perkins, 1992). This may be due to the fact that controllability problems are complex and sophisticated and also vary significantly from case to case. Therefore, implementing software tools specific to each case becomes inefficient and expensive.

In this work, a new methodology based on graphical domain-specific language (DSL) is introduced to develop software tools to measure controllability index of process system design. The structure of this paper is as follows: first, the proposed methodology and its advantages and disadvantages are discussed followed by introducing the structure of the proposed software product. The product is then tested against a forced-circulation evaporator system case study. The results from evaluating the case study as well as the effort needed to develop the software tool are presented. Finally, the effort needed to

develop this DSL framework is compared with the effort required to develop a DSL framework for a simpler case study.

2. Background

Software development procedures evolved dramatically over the past few years. Novel methodologies are proposed and improvements in traditional procedures are made. domain-specific language (DSL) is a new software development methodology defined as "a computer programming language of limited expressiveness focused on a particular domain" (Fowler and Parsons 2010). In other words, DSL product is a programming language designed and developed for a clearly defined and narrowed down domain. Providing loosely coupled structure and elements, DSL offers a pathway to address complex problems. Moreover, because each DSL product is specially designed for a particular domain, familiar symbols and notations in that domain will be used by the DSL to ease the communication between the programmer and the domain expert. Apart from that, DSL products are relatively small programming languages, which means the symbols and syntax that can be used by them are limited, consequently DSL are often easy to learn and use.

As mentioned above, using DSL methodology in software development process has several advantages; however, it has some drawbacks as well. Similar to any other software tool, it is time consuming to develop, maintain and learn them. This issue is magnified especially when its borders and scope of the domain, on which the DSL is defined, are not clear.

However, one of the reasons that gained attention to DSL is the extensive tool support it requires. In fact, using these tools can reduce the effort of designing, developing, maintaining and using the programming languages by far (Sadrieh and Bahri, 2014). Language workbench is the general term for this category of software and according to Fowler and Parsons (2010), language workbenches can be the "corner stone" of the new software development era.

3. Methodology

In this section the major elements of the proposed framework as well as the procedure of evolution are described.

3.1. DSL Elements

This framework consists of five major elements: Solver, Graphical User Interface (GUI), Semantic model, Code generator and Code generator controller. In the following section, the process of developing framework elements will be explained. It should be noted that MetaEdit+ is used as the language workbench toolbox to generate the DSL framework.

Solver: This part of the framework is responsible for performing the linear and non-linear calculations, which are necessary to evaluate the controllability index of the process system design. The first step for developing the DSL framework is to develop the desired code in the solver environment to generate the final result. In this case, the expected result from the framework is the controllability index of the process system design and the solver is MATLAB software. The input to this element is the state-space model of the process system. During the solver development, the feasibility of solving the problem will be examined via development of a prototype solution, a MATLAB script in this case. This will help to isolate and decouple development of the other elements of the framework.

Graphical User Interface (GUI): DSL notations and rules are designed and used within GUI element. It is essential to use familiar notations in the domain to ensure the software product fits within the definition of a DSL. Moreover, the GUI should be able to gather all the information required to fully describe the process system design. The necessary data from the design is the non-linear model of the process system and the nominal values of the variables. The output of the GUI element is an XML file which contains all the information collected from the user. The structure of the output file depends on how DSL objects and the relationship among the objects are defined.

Semantic model: Based on the properties, relationships and connections among the objects in the DSL, a data structure is implemented. The semantic model is responsible for keeping track of the process system model specification and it should be designed and implemented so that the specifications of process system model can be accessed by other elements of the framework. In this study, a set of classes is chosen as the backbone of the semantic model. Because of the object-oriented nature of the semantic model, an object-oriented programming language is used to parse and analyse the output data from the DSL elements.

As the next sub-element, a parser should be developed to fetch the output data from the DSL element and set it in the semantic model. In this study, to make the evaluation process simpler and more traceable, an XML file is used as an intermediate media and then parsed into the semantic model. However, in real-time cases, where the performance is a concern, it is possible to link the DSL element to the semantic model directly, so that the data from process system model flows straight into the semantic model.

Code generator: The code generator acts as a system which takes the semantic model as the input and generates a set of instructions, which are valid in the solver environment as the output. If run by the solver, this set of instructions calculates the final result.

The crucial role of the prototype, which was generated along with the solver, will be visible in developing the code generator. If the structure of the output of the code generator is similar to solver script prototype, it is guaranteed that the results from running the generated code within the solver environment will also lead to the desirable results.

Code generator controller: So far the framework is capable of assessing single process system design, without any modification in the flow-sheet. However, it is desirable to be able to apply relatively small changes in the process model and the framework to be still capable of analysing it. In this study, the semantic model can be changed based on the disturbances entering the process system. The code generator is then run based on the new semantic model, leading to different generated scripts and different controllability values.

3.2. Assessment procedure

The procedure of assessing the process system design using DSL framework in this study consists of three phases: 1) fetching system information from the user input and calculating the steady state values of state variables, 2) generating the linear model using steady-state values and nonlinear equations and 3) using the linear model to calculate RGA index of the process system design (Figure 1).

In this study, the first phase is carried out autonomously to illustrate this methodology is applicable to any controllability problem, regardless of the complexity and size of process system model. The symbolic math toolbox in MATLAB is used for this task.

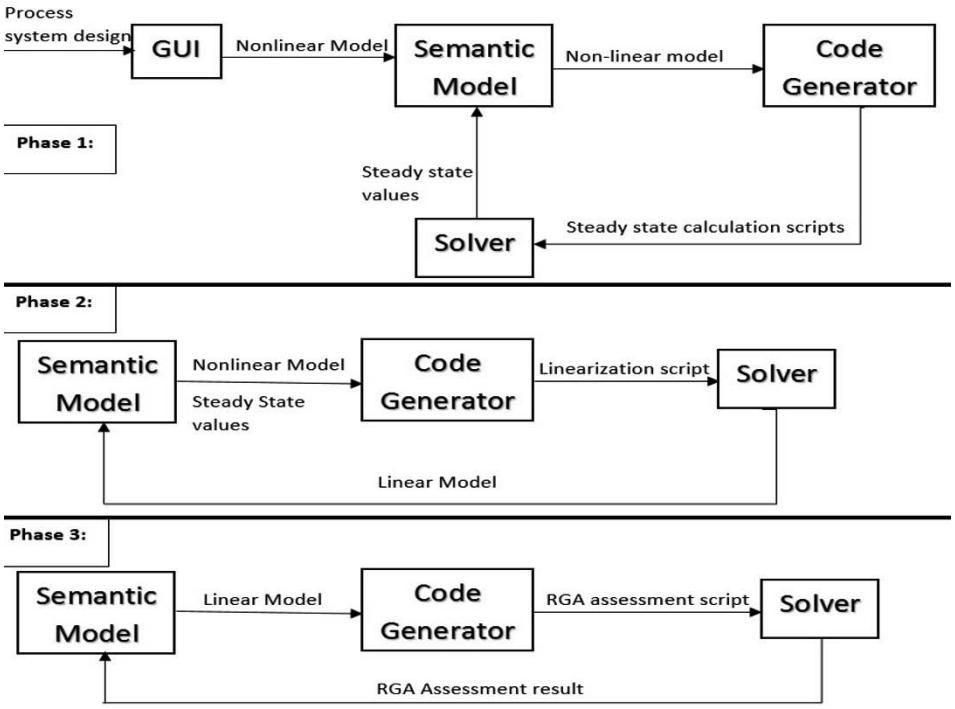

Figure 1 Analyzing process. Phase 1: Fetching process system model data and calculating steady state values. Phase 2: Calculating Linear Model. Phase 3: Calculating RGA Index

4. Case study

In order to verify the scalability of the proposed methodology, an evaporation system is used as a case study. The forced circulation evaporative (FCE) system used in this case study consists of a heat exchanger, a separator, a condenser and a pump (Figure 2). The liquid is circulated at a high rate through the heat exchanger, boiling being prevented within the unit by virtue of a hydrostatic head maintained above the top tube plate. As the liquid enters the separator where the absolute pressure is slightly less than in the tube bundle, the liquid flashes to form a vapour. This process is modelled by Newell and Lee (1989). Table 1 shows the model variables, their types and nominal values.

Table 1. FCE model variable types and nominal steady state values.

Variables	Type	Nominal steady state values
F3, F1, T1, X1, T200,	Disturbance	F1=10 (kg/min), T1=40 (°C), X1=5 (%), F3=50 (kg/min)
L2, X2, P2	Controlled	L2=1 (m), X2=25 (%), P2=50 (kPa)
F2, P100, F200	Manipulated	F2= 2 (kg/min), P100=194 (kPa)

As the FCE behaves relatively linear around its steady state, a controllability measure based on Relative Gain Array (RGA) (Garcia and Morari. 1982), which is a linear

measure, is defined and used in this study. The controllability measure (R) is calculated using Eq.1:

$$R = \sum (\lambda_i - 1)^2 \text{ for each positive } \lambda_i \quad (1)$$

5. Results

The FCE process system is modelled using the proposed DSL framework (Figure 2) and the resulted λ (relative gain) and R values are presented in Table 2. Each row of the table represents the controllability index of the specified conditions of the FCE problem. In each set, a defined value of disturbance (i.e.±7, ±10) is applied to two disturbance variables (T1 and F1) and the RGA index of that configuration is evaluated automatically.

Table 3 illustrates the time needed to implement each element of the two DSL frameworks; one is FCE case study, which is presented in this work, and also another DSL framework which was designed to calculate the same controllability index, but for a different case study consisting of two CSTRs ordered in parallel mode (Sadrieh and Bahri, 2014).

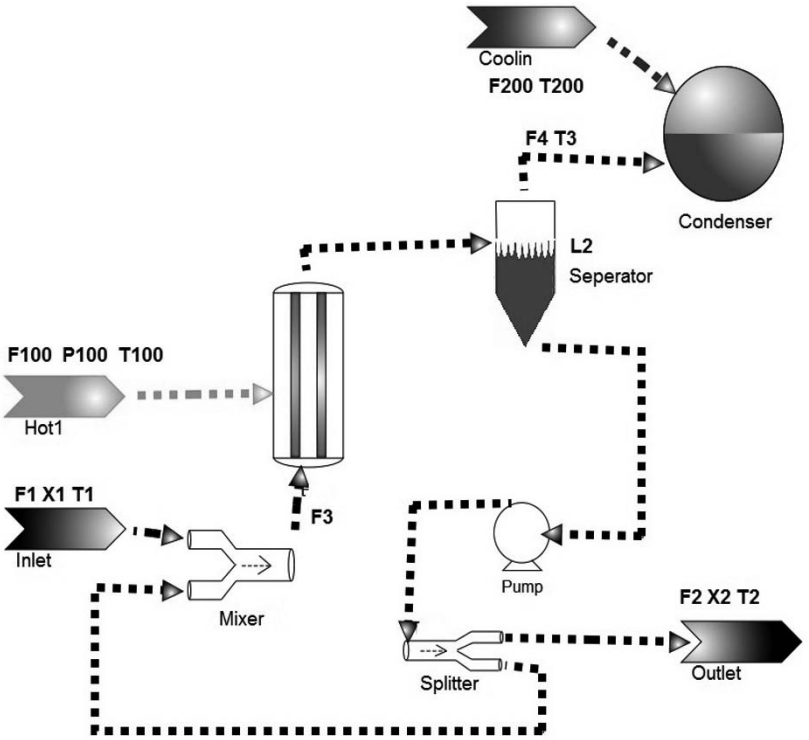

Figure 2. The DSL representation of the FCE case study

6. Conclusion

This study describes a new methodology to produce software tools for controllability analysis of process systems. The product is tested using a Forced Circulation Evaporator (FCE) case study and the results are presented. Moreover, it is concluded that different process model sizes (FCE with 26 equations and CSTR with 4 equations) slightly affect

the effort needed to develop the DSL products. This proves that this methodology is efficient, regardless of the complexity of the process system model.
This is mainly because of the structure of the framework, which isolates the mathematical process from the rest of the framework, and therefore, the size of the model has very little effect on the total effort.

Table 2. Controllability index evaluation results including disturbances

Disturbance Percentage (%)		**Disturbance Values**	**Manipulated Variables Steady state values**					**λ**	**R**
T1	**F1**	**T200**	**T1**	**F1**	**X1**	**P100**	**F200**		
-10	-7	25	36	9.3	5	182.9	149.06	0.5086	0.2414
0	-7	25	40	9.3	5	181.12	149.06	0.5086	0.2414
10	-7	25	44	9.3	5	179.33	149.06	0.5086	0.2414
-10	0	25	36	10	5	196.58	208.05	0.5017	0.2483
0	0	25	40	10	5	194.68	208.05	0.5017	0.2483
10	0	25	44	10	5	192.78	208.05	0.5017	0.2483
-10	7	25	36	10.7	5	209.93	317.16	0.4953	0.2547
0	7	25	40	10.7	5	207.93	317.16	0.4953	0.2547
10	7	25	44	10.7	5	205.92	317.16	0.4953	0.2547

Table 3. Time needed to develop elements of DSL product.

	Solver Script (H)	**Semantic Model (H)**	**GUI (H)**	**Code Generator (H)**	**Total (H)**
FCE Case study	16	7	5	4.5	32.5
CSTR Case study	14.5	5.5	6	4	30

References

S. Fararooy, J. D. Perkins, T. I. Malik.1992, A software package for process controllability analysis, Computers & Chemical Engineering, Volume 16, Supplement 1,S517–S522

M. Fowler, R. Parsons, 2010, Using Domain-Specific Languages, Domain-Specific Languages, Addison Wesley, Massachusetts, USA, 27-42.

M. Garcia , M. Morari, 1982, Internal model control a unifying review and some new results. ,Ind Eng Chem Process Des, Dev., 21, 308– 323.

R.B. Newell, P.L. Lee, 1989, The evaporator model, Applied process control: a case study, Prentice hall, Qld, Australia, 7-13.

A. Sadrieh, P.A. Bahri, 2013, A Novel Graphical Method for Controllability Analysis of Chemical Process Designs, Computer Aided Chemical Engineering, 32, 655-660.

A. Sadrieh, P.A. Bahri, 2014, Novel Domain-Specific Language Framework for Controllability Analysis, Computer Aided Chemical Engineering, 33, 559-564.

M.Salge, P.Milling, 2006, Who is to blame, the operator or the designer? Two stages of human failure in the Chernobyl accident, System Dynamics Review, 22, 89–112.

J. Tolvanen, S. Kelly, 2009, MetaEdit+: defining and using integrated domain-specific modeling languages, OOPSLA '09 Proceedings of the 24th ACM SIGPLAN conference companion on Object oriented programming systems languages and applications, 819-820

Yuan, Chen Zhihong, Bingzhen, 2011, An Overview on Controllability Analysis of Chemical Processes, AIChE Journal, 57, 5,1185-1201

Krist V. Gernaey, Jakob K. Huusom and Rafiqul Gani (Eds.), 12th International Symposium on Process Systems Engineering and 25th European Symposium on Computer Aided Process Engineering.
31 May - 4 June 2015, Copenhagen, Denmark.

A nonlinear quasi-unknown input observer for the chemostat Droop model

Alexander Schaum[a] and Thomas Meurer[a]

[a]*Chair of Automatic Control, Christian-Albrechts-University Kiel, Germany*
alsc@tf.uni-kiel.de

Abstract

An unknown input observer is designed for the Droop model for microalgae growth in the chemostat considering the feed concentration as unknown input. Based on a biomass measurement, the nutrient quota and substrate are estimated together with the unknown (piecewise constant) feed concentration using a nonlinear observation scheme with PI-like correction mechanism. The estimation performance is illustrated with numerical simulations.

Keywords: Microalgae growth, Droop model, unknown-input observability, state and input estimation

1. Introduction

Microalgae processes have received increasing attention in recent years due to the fact that these microorganisms produce high-value compounds like fatty-acids, vitamins or pigments and have a great potential use in the production of energy sources like hydrogen and biofuels (Havlik et al., 2013). Furthermore, microalgae show a comparatively rapid growth, making them even more interesting from a production point of view.

Nevertheless, like all biological processes, microalgae growth processes have to face the complex interaction of (possibly unmeasured) dynamically evolving states, like the extracellular and intracellular nutrient, the biomass and potentially others. This leads to the need of monitoring devices, commonly known as software sensors or observers (Bastin and Dochain, 1990; Havlik et al., 2013). The design of a software sensor is based on a mathematical model for the underlying biological process, which, in combination with a measurement injection mechanism, is used to reconstruct the actual process state from the knowledge of the measurements and the actual (known) inputs. The most commonly used model for microalgae growth is the Droop model (Droop, 1968), which gives a quantitative relation between the dynamics of the biomass growth and nitrogen uptake from an extracellular resource. Several approaches to software sensor design for microalgae production processes have been presented so far, like high-gain observers (Bernard et al., 2001), interval observers (Goffaux et al., 2009a,b), and Lipschitz observers (Toroghi et al., 2013). In the case of unknown inputs, like the dilution rate or the feed concentration, these observation schemes can not achieve exact state reconstruction. When some structural properties of the input are known, e.g. for piecewise constant inputs, so-called quasi-unknown input observers can be designed (Moreno, 2001a,b; Rocha-Cozatl and Vande Wouwer, 2011). The structural property associated to the possibility of observing the state of a system with unknown input is called strong observability and in case of estimating both state and input, state and unknown input observability (Hautus, 1983; Moreno et al., 2014). Classically, the existence of a state observer for the (complete) unknown input case relies on the condition that the unknown input has relative degree one

with respect to the measured output – a property leading to the strong*-detectability concept – (Hautus, 1983; Moreno et al., 2014; Rocha and Moreno, 2010; Rocha-Cozatl and Vande Wouwer, 2011). For this case, recently, a local quasi-unkown input observer based on the linearized Droop model has been proposed for estimating both state and unknown feed flow rate in (Rocha-Cozatl and Vande Wouwer, 2011). The results of this study are quite convincing and highlight the possibility of reconstructing unknown feed perturbations in the Droop model.

In the present study a different scenario is addressed: the biomass is measured and the (piecewise constant) feed concentration is considered as (quasi) unknown input. This leads to the underlying structural burden of having an unknown input with relative degree three, making it impossible to design a complete unknown input observer for the system. Nevertheless, it is shown that for the case of piecewise constant (or slowly varying) feed concentrations that a nonlinear quasi-unknown input estimator can be designed to reconstruct both the state and the unknown feed input. For this purpose, a nonlinear model plus PI-like observation scheme is employed and the observer convergence is rigorously established in the sense of semi-global asymptotic stability using Lyapunov's direct method. Numerical simulations illustrate the estimator performance.

2. Droop's microalgae growth model

Consider Droop's model for microalgae growth (Droop, 1968) in the chemostat

$$\begin{array}{ll} \dot{b} = -db + \mu(q)b, & b(0) = b_0 \\ \dot{q} = \rho(s) - \mu(q)q, & q(0) = q_0 \\ \dot{s} = d(s_{in} - s) - \rho(s)b, & s(0) = s_0 \\ y = b & \end{array} \tag{1}$$

where b is the biomass concentration, q is the internal nutrient quota (i.e. the intracellular nutrient concentration per biomass unit), s is the extracellular nutrient concentration, s_{in} is the *piecewise constant, unknown* feed concentration, μ is the growth rate, ρ is the uptake rate, d is the dilution rate (i.e. the flow-colume quotient q/V), and y is the biomass measurement.

The growth and uptake rates are given by the monotonic functions

$$\mu(q) = \bar{\mu}\left(1 - \frac{k_q}{q}\right), \quad \rho(s) = \frac{k_0 s}{K_s + s}, \tag{2}$$

where $\bar{\mu}$ is the hypothetic maximum growth at infinite quota, k_q is the minimum quota necessary for biomass growth, k_0 is the maximum uptake rate $\rho(s)$, and K_s is the half-saturation constant.

By the change of variables

$$\theta = q - k_q$$

the growth rate μ can be written in the standard Monod form

$$\nu(\theta) := \mu(\theta + k_q) = \frac{\bar{\mu}\theta}{k_q + \theta}. \tag{3}$$

and the dynamics (1) become

$$\begin{array}{ll} \dot{b} = -db + \nu(\theta)b, & b(0) = b_0 \\ \dot{\theta} = \rho(s) - \bar{\mu}\theta, & \theta(0) = q_0 - k_q \\ \dot{s} = d(s_{in} - s) - \rho(s)b, & s(0) = s_0 \\ y = b & \end{array} \tag{4}$$

In vector notation the preceding dynamics are written as

$$\dot{\mathbf{x}} = \mathbf{f}(\mathbf{x}, u, s_{in}), \quad y = \mathbf{c}^T \mathbf{x}. \tag{5}$$

with

$$\mathbf{x} = [b, \theta, s]^T, \quad h(\mathbf{x}) = x_1.$$

It can be directly verified that the $\mathbb{R}^3_+$ is a positively invariant set for the dynamics (4), given that $x_i = 0$ implies $\dot{x}_i \geq 0$, $i = 1,2,3$. For the purpose at hand the following analysis and design are based on the model (4).

3. Observability analysis and observer design

In this section, it is shown that the model (4) is state and unknown input observable with respect to the unknown piecewise constant feed concentration s_{in} and a nonlinear observer with PI-like innovation scheme is designed for the simultanous estimation of the state $\mathbf{x}$ and exogeneous input s_{in}. For this purpose, the extended state vector

$$\mathbf{x}_e = \left[b, \theta, s, s_{in}\right]^T \tag{6}$$

is introduced.

3.1. Unknown input observability

Here, the approach for the analysis of state and unknown-input (or strong) observability discussed in (Schaum and Moreno, 2007; Moreno et al., 2014) is followed. Before going into detail on the observability analysis, it should be recalled from (Lemesle and Mailleret, 2008) that for $d < \max \nu$ the washout $\mathbf{x}_w = [0, \theta_w, s_{in}]'$ with $\theta_w = \rho(s_{in})/\bar{\mu}$ is a repulsor. Based on this property it can be shown that $\mathbf{x}$ moves within a subset $\mathscr{X} \subset \mathbb{R}^3_+$ and in particular that $b > 0$ for $b_0 > 0$.

Proposition 1 *The Droop model* (4) *with $y = b$ and unknown input s_{in} is state and unknown-input (or strongly) observable.*

Proof: Let the claim be false. Then there exist two indistinguishable extended trajectories $\mathbf{x}_{e1} \neq \mathbf{x}_{e2}$ (driven by the same input $d(t)$) satisfying $b_1(t) \equiv b_2(t)$ over some time interval. Let $\varepsilon_b = b_2 - b_1$, $\varepsilon_q = \theta_2 - \theta_1$, $\varepsilon_s = s_2 - s_1$ and $\varepsilon_i = s_{in2} - s_{in1}$ denote the differences between the two trajectories and introduce $\varepsilon = [\varepsilon_b, \varepsilon_q, \varepsilon_s, \varepsilon_i]^T$. From $b_1 \equiv b_2$ it follows directly that $\varepsilon_b = 0$. Furthermore,

$$\dot{\varepsilon}_b \equiv 0 = -d\varepsilon_b + [\nu(\theta_1 + \varepsilon_q)(b_1 + \varepsilon_b) - \nu(\theta_1)b_1] = \nu(\theta_1 + \varepsilon_q)b_1 - \nu(\theta_1)b_1$$

Given that $b_1 > 0$ this holds only if $\nu(\theta_1 + \varepsilon_q) \equiv \nu(\theta_1)$ and, given the monotonicity feature of the growth rate ν, this implies $\varepsilon_q \equiv 0$. Next, it holds that

$$\dot{\varepsilon}_q \equiv 0 = \rho(s_1 + \varepsilon_s) - \rho(s_1) - \bar{\mu}\varepsilon_q = \rho(s_1 + \varepsilon_s) - \rho(s_1)$$

which means that $\varepsilon_s \equiv 0$ due to the monotonicity of the uptake rate ρ. Finally,

$$\dot{\varepsilon}_s \equiv 0 = d(\varepsilon_i - \varepsilon_s) - [\rho(s_1 + \varepsilon_s)(b_1 + \varepsilon_b) - \rho(s_1)b_1] = d\varepsilon_i$$

implying that $\varepsilon_i \equiv 0$. This shows that $\mathbf{x}_{e2} = \mathbf{x}_{e1} + \varepsilon = \mathbf{x}_{e1}$ which contradicts the initial assumption. Thus, model (4) is unknown-input (or strongly) observable. Q.E.D.

3.2. Unknown-input observer

Based on the state and unknown-input observability property derived in the preceding section a nonlinear unknown-input observer is designed for the Droop model (4). For this purpose, the following (full order) nonlinear observer with PI-like correction scheme is considered

$$\begin{aligned}
&\dot{\hat{b}} = -d\hat{b} + \nu(\hat{\theta})\hat{b} - l_b(\hat{b}-y), && \hat{b}(0) = \hat{b}_0\\
&\dot{\hat{\theta}} = \rho(\hat{s}) - \bar{\mu}\hat{\theta} - l_q(\hat{b}-y), && \hat{\theta}(0) = \hat{\theta}_0\\
&\dot{\hat{s}} = d(\hat{s}_{in}-\hat{s}) - \rho(\hat{s})\hat{b} - l_s(\hat{b}-y), && \hat{s}(0) = \hat{s}_0\\
&\hat{s}_{in} = \hat{s}_{in,0} - l_i\int_0^t (\hat{b}(\tau)-y(\tau))d\tau\\
&\hat{q} = \hat{\theta} + k_q.
\end{aligned} \tag{7}$$

with observer gains l_b, l_q, l_s and l_i.

The following proposition states the semi-global asymptotic convergence of the observer over a domain of interest $\hat{\mathscr{X}_e}$.

Proposition 2 *For a piecewise constant input s_{in}, and a given domain of interest $\hat{\mathscr{X}_e} \subset \mathbb{R}^4_+$, the observer gains l_b, l_q, l_s and l_i can be chosen so that*

$$\forall \hat{\mathbf{x}}_e \in \hat{\mathscr{X}_e}: \quad \lim_{t\to\infty} ||\hat{\mathbf{x}}_e - \mathbf{x}_e|| = 0.$$

Proof: Introducing the estimation error

$$e_b = \hat{b} - b, \quad e_q = \hat{\theta} - \theta, \quad e_s = \hat{s} - s, \quad e_i = \hat{s}_{in} - s_{in}, \quad \mathbf{e} = \left[e_b, e_q, e_s, e_i\right]^T$$

the associated observation error dynamics are given by

$$\begin{aligned}
\dot{e}_b &= -(d + l_b - \nu(\hat{\theta}))e_b + [\nu(\theta+e_q)b - \nu(\theta)b]\\
\dot{e}_q &= -l_q e_b - \bar{\mu}e_q + [\rho(s+e_s) - \rho(s)]\\
\dot{e}_s &= -(l_s + \rho(\hat{s}))e_b - de_s + de_i - [\rho(s+e_s)b - \rho(s)b]\\
\dot{e}_i &= -l_i e_b
\end{aligned} \tag{8}$$

or equivalently (summing and subtracting $-e_i$ in the last line) in vector notation

$$\dot{\mathbf{e}} = (\hat{A} - \mathbf{l}\mathbf{c}_e^T)\mathbf{e} + G(y)\left(\varphi(\mathbf{x}_e+\mathbf{e}) - \varphi(\mathbf{x}_e)\right), \quad \mathbf{e} = \left[e_b, e_q, e_s, e_i\right]^T, \quad \mathbf{c}_e = \left[\mathbf{c}^T, 0\right] \tag{9}$$

with

$$\hat{A} - \mathbf{l}\mathbf{c}_e^T = \begin{bmatrix} -(d + l_b + \nu(\hat{\theta})) & 0 & 0 & 0\\ -l_q & -\bar{\mu} & 0 & 0\\ -(l_s + \rho(\hat{s})) & 0 & -d & d\\ -l_i & 0 & 0 & -1 \end{bmatrix}, \quad G(y) = \begin{bmatrix} y & 0 & 0\\ 0 & 1 & 0\\ 0 & -y & 0\\ 0 & 0 & 1 \end{bmatrix}, \quad \varphi(\mathbf{x}_e) = \begin{bmatrix} \nu(\theta)\\ \rho(s)\\ s_{in} \end{bmatrix}$$

Introduce the Lyapunov fuction

$$V(\mathbf{e}) = \mathbf{e}^T P\mathbf{e}, \quad P = P^T > 0 \tag{10}$$

set $\hat{A}_\mathbf{l} = \hat{A} - \mathbf{l}\mathbf{c}_e^T$ and take the time derivative of V

$$\dot{V}(\mathbf{e}) = \mathbf{e}^T\left(\hat{A}_\mathbf{l}^T P + P\hat{A}_\mathbf{l}\right)\mathbf{e} + \mathbf{e}^T PG(y)\left(\varphi(\mathbf{x}_e+\mathbf{e}) - \varphi(\mathbf{x}_e)\right) + \left(\varphi(\mathbf{x}_e+\mathbf{e}) - \varphi(\mathbf{x}_e)\right)^T G^T(y)P\mathbf{e}$$

Due to the Lipschitz continuity of ν and ρ over $\mathbb{R}_+$ there exists a matrix-valued function $M(y)$ such that

$$\mathbf{e}^T PG(y)\left(\varphi(\mathbf{x}_e+\mathbf{e}) - \varphi(\mathbf{x}_e)\right) = \mathbf{e}^T PG(y)\left(\int_0^1 \frac{\partial\varphi}{\partial\mathbf{x}_e}(\mathbf{x}_e + \eta\mathbf{e})d\eta\right)\mathbf{e} \le \mathbf{e}^T PM(y)\mathbf{e}. \tag{11}$$

By the particular observability structure of the pair $(\hat{A}, \mathbf{c}_e^T)$ (for any $\hat{x}_e \in \hat{\mathscr{X}_e}$ the eigenvalues of $\hat{A}_\mathbf{l}$ can be arbitrarily assigned) it holds that $\mathbf{l}$ can be chosen such that the Lyapunov inequality

$$(\hat{A}_\mathbf{l}^T + M^T(y))P + P(\hat{A}_\mathbf{l} + M(y)) < 0 \tag{12}$$

is satisfied for all pairs $(\mathbf{x}_e, \hat{\mathbf{x}}_e) \in \mathscr{X}_e \times \hat{\mathscr{X}_e}$. This means that $\dot{V} < 0$ over $\mathscr{X}_e \times \hat{\mathscr{X}_e}$, implying the observer convergence. Q.E.D.

Note that this result also implies that in presence of (zero-mean) measurement noise the observed trajectories will move within bounded tubes (with size depending on the observer gain) around the actual reactor trajectories.

4. Simulations

In order to verify the theoretic assessment, numerical simulations have been carried out for the parameter set (taken from (Toroghi et al., 2013)) $K_s = 0.105$, $\bar{\mu} = 2$, $k_q = 1.8$, $k_0 = 9.3$ using MATLAB with *ode15s*, and the unknown feed concentration input was set to $s_{in}(t) = 100 + 10\sigma(10) - 20\sigma(20)$ where $\sigma(T)$ is the unit step at T.

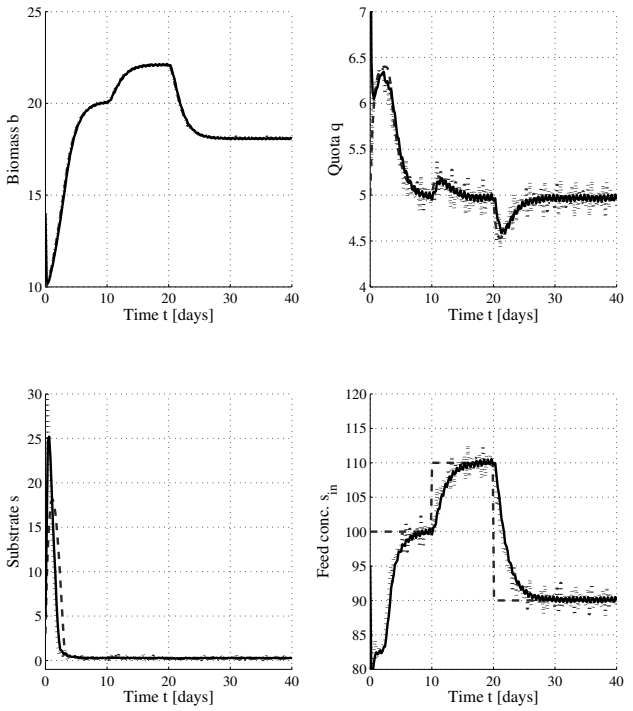

Figure 1: Time response of the Droop model (4) and the state and unknown-input estimator (7): actual plant (dashed lines), estimated state (dotted lines) and filtered state estimates (continuous line).

The measurement was perturbed by a high frequency noise with 1% amplitude. The dilution rate input is set to $d = 1.275$ and the initial condition of the system is given by

$$\mathbf{x}_0 = [10, 5, 3]^T$$

and for the extended state-input observer

$$\hat{\mathbf{x}}_{e0} = [14, 7, 5, 95]^T.$$

The observer gains are chosen as $l_b = 20$, $l_q = 45$, $l_s = 400$, and $l_i = 700$. Given that due to the measurement noise the observed state is noisy, a filtered version of the state estimate is obtained using a simple first-order low-pass filter. Note that the convergence of the filtered estimates is ensured by the convergence (in mean) of the observer state to the actual reactor trajectory.

In Figure 1 the reactor response is shown by the dashed line, the observed (noisy) state by the dotted line, and a filtered version of the observed state by the continuous line. It can be seen that the observed state (dotted line) and its filtered version (continuous line) recover the actual value of the extended state vector $\mathbf{x}_e = [b, q, s, s_{in}]^T$ (dashed line) despite of the unknown feed input.

5. Conclusions

The Droop model for microalgae growth is analyzed with respect to its observability with unknown feed input and it is shown that the model is state and unknown input observable. A nonlinear state-unknown input observer is designed with PI-like innovation scheme and ensured asymptotic stability over a sufficiently large domain of interest. Numerical simulations illustrate the observer performance for constant and time-varying feed flows.

References

G. Bastin, D. Dochain, 1990. On-line estimation and adaptive control of bioreactors. Elsevier, Amsterdam.

O. Bernard, A. Sciandra, O. Sallet, 2001. A non-linear software sensor to monitor the internal nitrogen quota of phytoplanktonic cells. Oceanol. Acta 24, 435–442.

M. Droop, 1968. Vitamin b12 and marine exology iv: the kinetics of uptake growth and inhibition in monochrisis lutheri. Journal of the Marine Biological Association 48 (3), 689–733.

G. Goffaux, A. Vande Wouver, O. Bernard, 2009a. Continuous-discrete interval observers for monitoring microalgae cultures. Biotechnol. Prog. 3 (3), 667–675.

G. Goffaux, A. Vande Wouver, O. Bernard, 2009b. Improving continuous-discrete interval observers with application to microalgae-based bioprocesses. Journal of Process Control 19, 1182–1190.

M. Hautus, 1983. Strong detectability and observers. Linear Algebra and its Applications 50, 353–368.

I. Havlik, P. Lindner, T. Scheper, K. Reardon, 2013. On-line monitoring of large cultivations of microalgae and cyanobacteria. Trends in Biotechnology 31 (7), 406–414.

V. Lemesle, L. Mailleret, 2008. A mechanistic investigation of the algae growth "droop" model. Acta Biotheor DOI 10.1007/s10441-008-9031-3.

J. A. Moreno, 2001a. Existence of unknown input observers and feedback passivity for linear systems. Proc. 40th IEEE Conference on Decision and Control (CDC), 3366–3371.

J. A. Moreno, 2001b. Quasi-unknown input observers for linear systems. Proc. IEEE Conference on Control Applications, Mexico-City, 732–737.

J. A. Moreno, E. Rocha-Czatl, A. Vande Wouwer, 2014. A dynamical interpretation of strong observability and detectability concepts for nonlinear systems with unknown inputs: application to biochemical processes. Bioproc. and Biosys. Eng. 37 (1), 37–49.

E. Rocha-Cozatl, J. A. Moreno, 2010. Dissipative design of unknown input observers for systems with sector nonlinearities. Int. J. Robust and Nonlinear Control 21 (14), DOI: 10.1002/rnc.1656., p. 1623–1644.

E. Rocha-Cozatl, A. Vande Wouwer, 2011. State and input estimation in phytoplanktonic cultures using quasi-unknown input observers. Chemical Engineering Journal 175, 39–48.

A. Schaum, J. A. Moreno, 2007. Dynamical analysis of global observability properties for a class of biological reactors. Proc. 10th IFAC Int. Symposium on Computer Applications in Biotechnology (CAB), Cancun, Mexico, 209 – 2014.

M. Toroghi, G. Goffaux, G., M. Perrier, 2013. Observer-based backstepping controller for microalgae cultivation. Ind. Eng. Chem. Res. 52, 7482–7491.

Krist V. Gernaey, Jakob K. Huusom and Rafiqul Gani (Eds.), 12th International Symposium on Process Systems Engineering and 25th European Symposium on Computer Aided Process Engineering.
31 May – 4 June 2015, Copenhagen, Denmark

PAT for Reactive Crystallization Process Optimization for Phosphorus Recovery from Sewage Sludge

Yi Liu, Haiyan Qu*

Department of Chemical Engineering, Biotechnology and Environmental Technology, University of Southern Denmark, Campusvej 55, DK-5230, Odense, Denmark.
haq@kbm.sdu.dk

Abstract

Recovery of high-purity phosphorus product from sewage sludge ash requires the production of crystals with optimized particulate properties, which will significantly facilitate the down-stream filtration operation and therefore ensure a high purity of the final products. Our previous study has demonstrated that there is a great potential to recover high-purity $CaClH_2PO_4 \cdot H_2O$ crystals from sewage sludge ash that contains high concentration of iron and aluminum. However, $CaClH_2PO_4 \cdot H_2O$ crystals produced from the reactive crystallization process possess poor particulate properties (e.g. small particle size and wide size distribution). In the present work, the effects of different operation parameters on the reactive crystallization of $CaClH_2PO_4 \cdot H_2O$ have been studied in a pure artificial system ($CaCl_2$ + H_3PO_4). The quality of $CaClH_2PO_4 \cdot H_2O$ crystals varied with changing temperature and pH of the solution. It has been found that increasing the processing temperature (>50 ^oC) and the pH of solution will improve the particle size distribution of the crystalline products.

Keywords: Reactive crystallization, Phosphorus recovery, monocalcium chlorophosphate.

1. Introduction

Phosphorus is an essential element for ecosystem, because the function of phosphorus as a nutrient for plants can not be replaced by any other substance (Steen, 1998). Currently, the phosphorus fertilizers are produced from the processing of phosphate rock, which is a natural source with limited deposits. However, as the demand of population and agricultural increases, it is predicted that the current exploitable reserves of phosphate rock will run out within 60-130 years (Steen, 1998). The production of phosphorus is rather concentrated; China, Morocco and the United States occupy almost two-thirds of global phosphate (Steen, 1998). European has only very limited resources (in Finland) and is largely dependent on imports. Therefore, recovery of phosphorus from sewage sludge ash provides an opportunity of supplying phosphorus with sustainable development.

The sewage sludge ash may contain high concentrations of iron and aluminum since iron and aluminum salts are frequently used to precipitate phosphate at wastewater treatment plants (WWTPs). The crude products containing phosphorus can be obtained from the ash in an acidic environment (Tan and Lagerkvist, 2011) (Schaum et al., 2007), and then they can be further processed with reactive crystallization to obtain a purer product in the form of monocalcium chlorophosphate ($CaClH_2PO_4 \cdot H_2O$). 75 years ago,

Fox (1939) observed that $CaClH_2PO_4 \cdot H_2O$ can be precipitated by treating the phosphate rock (CaO/P_2O_5) with hydrochloric and phosphoric acid. The further growth of $CaClH_2PO_4 \cdot H_2O$ crystals took place when the suspension was kept at or near its boiling point. However, the growth of $CaClH_2PO_4 \cdot H_2O$ was very slow and the resulted fine particles led to a very difficult solid-liquid separation via filtration. The poor filterability of the crystals also caused a significant reduction of the final products purity due to the high residual of mother liquor in the filter cake. This poor particle size hinders the application of this process to the large-scale production of phosphorus in industry. In order to improve the filterability of the $CaClH_2PO_4 \cdot H_2O$ crystals, the mechanism of the reactive crystallization process needs to be understood and the key operation parameters that significantly influence the growth kinetics of the $CaClH_2PO_4 \cdot H_2O$ crystals have to be identified.

The objective of this work is to gain insight into the mechanism of reactive crystallization of $CaClH_2PO_4 \cdot H_2O$ in an artificial system of calcium chloride and phosphoric acid. The properties of the produced crystals were characterized with various process analytical technologies, such as Laser Diffraction Particle Size Analyzer, Raman Spectroscopy, X-ray Powder Diffraction (XRPD). The effects of different operation parameters (reactants concentration, temperature, pH) on the reactive crystallization process and the properties of the crystal products have been investigated. Key operation parameters for the optimization of the process have been identified.

2. Experimental Methods

2.1. Reactive crystallization

The solid calcium chloride was purchased from Sigma-Aldrich and the 85 % wt ortho-phosphoric acid was purchased from Merck. $CaClH_2PO_4 \cdot H_2O$ crystals can be produced through the reactive crystallization described in Eq. (1) (Fox, 1939) as follows:

$$CaCl_2+H_3PO_4+H_2O=CaClH_2PO_4 \cdot H_2O+HCl\uparrow \quad (1)$$

The calcium chloride was firstly dissolved in distilled water and then mixed with diluted phosphoric acid in 1:1 ratio of molal quantities. The feed speeds of calcium chloride solution and phosphoric acid were controlled by two peristaltic pumps (Ole Dich Instrumentmakers, Denmark), respectively, assuring to mix calcium chloride and phosphoric acid in equimolecular amounts. An IKA C-MAG HS7 magnetic stirrer (IKA, Denmark) was applied to stir and to heat the mixture up during crystallization. The temperature of the mixture solution was monitored with a thermometer. After the crystallization process, the crystals were separated by vacuum filtration from the mother liquor through a glass fiber filter paper (ADVANTEC GC-50). The whole procedure was carried out in a fume hood.

2.2. X-ray Powder Diffraction (XRPD) Analysis

The products obtained in the present work were analyzed with an X´Pert Pro diffractometer by using Cu $K\alpha_1$ (λ=1.5406 Å) radiation, operating at 40 mA, 45 kV, at room temperature. The pattern were recorded in the range of $2\theta = 5^o - 60^o$ with a step size $2\theta=0.02^o$ and the scan step time was 100 s. Phase of $CaClH_2PO_4 \cdot H_2O$ was identified by using the standard PDF card No. 00-044-0746.

2.3. Raman Analysis

The Raman analysis of crystals was carried out with a SENTERRA/ Dispersive Raman Spectrometer (Bruker, Germany) with a 785 nm laser at 100 mW.

2.4. Particles Size Distribution

The particle size distribution of the solids obtained from the reactive crystallization was measured with a LS13320 Laser Diffraction Particle Size Analyzer (Beckman Coulter). Because $CaClH_2PO_4 \cdot H_2O$ is highly soluble in water, a saturated solution of the testing solids in 70 % (v/v) ethanol (VWR) was chosen as the background solution for analyzing.

3. Results and Discussion

3.1. The effects of temperature

When calcium chloride and phosphoric acid were mixed in an equal molar concentration of higher than 2.9 mol/L, $CaClH_2PO_4 \cdot H_2O$ tends to crystallize as white crystals from the liquid phase at room temperature (22-25 ^oC). It was found that the filterability of the crystals produced at a higher temperature (>50 ^oC) was much better than that of the crystals processed at room temperature (22-25 ^oC). Figure 1 shows the particle size distribution of the crystals prepared at 25 ^oC and at 54 ^oC, respectively. It is evident that the crystals formed at 54 ^oC possess larger sizes, most of which are 200~400 μm, while the particle sizes of the crystals formed at 25 ^oC mainly are 50~200 μm. The micrographs of such $CaClH_2PO_4 \cdot H_2O$ crystals formed at 25 ^oC (upper) and 54 ^oC (down) inset in Figure 1 also demonstrates that the crystals formed at 54 ^oC possess bigger sizes.

The purity of $CaClH_2PO_4 \cdot H_2O$ crystals increases with increasing processing temperature, which is proved by the XRPD analysis,as shown in Figure 2. The solid line in Figure 2 represents the pattern of crystals formed at 25 ^oC and the dash line indicates the pattern of crystals formed at 54 ^oC. Besides the characteristic peaks attributed to the $CaClH_2PO_4 \cdot H_2O$ crystals, it still exists other sharp peaks which are assigned to calcium phosphate hydrate ($Ca_2P_2O_7 \cdot 2H_2O$, $2\theta=7.720^o$, highlighted with ♣) and calcium hydrogen phosphate hydrate ($Ca(H_2PO_4)_2 \cdot H_2O$, $2\theta=22.902^o$ and $2\theta=24.098^o$, highlighted with ♥) in the pattern regarding crystals formed at 25 ^oC. It is obvious that such typical peaks related to impurities are much weaker in the pattern of crystals formed at 54 ^oC. Thus, it demonstrates that a higher processing temperature ($\geq$ 54 ^oC) will be of great benefit to increase the purity of $CaClH_2PO_4 \cdot H_2O$ crystals.

The two crystals prepared at 25 ^oC and 54 ^oC were also checked by Raman spectroscopy, respectively. The results are shown in Figure 3. The crystals prepared at 54 ^oC yields two single significant peaks at the position of 900 cm^{-1} and 1105 cm^{-1}, respectively (dash line, in Figure 3). By comparison, the crystals formed at 25 ^oC shows a single sharp peak at 1110 cm^{-1}, a broad peak at 1014 cm^{-1} and a double peak at 902 cm^{-1} and 913 cm^{-1} (solid line, in Figure 3).The pure $Ca(H_2PO_4)_2$ solid contains such three peaks at similar positions (dash-dot line, in Figure 3), which are the signals assigned to the $H_2PO_4^-$ species. This result reveals that the crystals formed at 25 ^oC contain major impurity of $Ca(H_2PO_4)_2$.

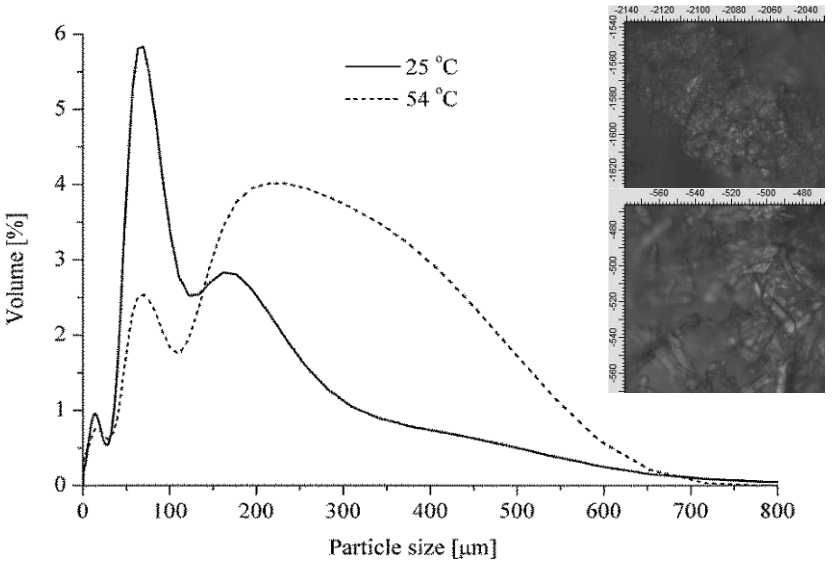

Figure 1: Particle size distribution of $CaClH_2PO_4 \cdot H_2O$ crystals produced at different temperatures. The original concentrations of $CaCl_2$ and H_3PO_4 were both 3.1 mol/L. The attached two photos are the micrographs (×20) of $CaClH_2PO_4 \cdot H_2O$ crystals formed at 25 °C (upper) and at 54 °C (down).

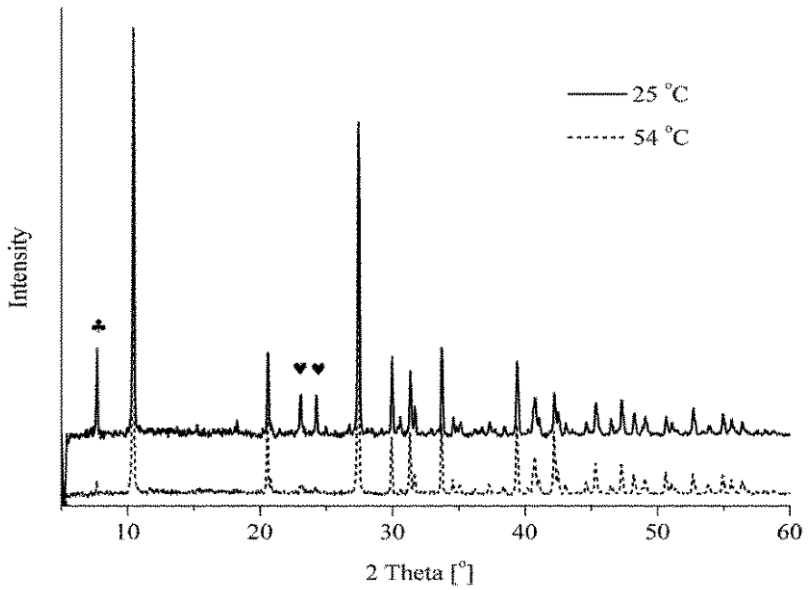

Figure 2: XRPD pattern of $CaClH_2PO_4 \cdot H_2O$ crystals produced at 25 °C (solid line) and at 54 °C (dash line). The original concentrations of $CaCl_2$ and H_3PO_4 were both 3.1 mol/L. ♣ - peak for $Ca_2P_2O_7 \cdot 2H_2O$at $2\theta=7.720^o$; ♥- peaks for $Ca(H_2PO_4)_2 \cdot H_2O$ at $2\theta=22.902^o$ and $2\theta=24.098^o$.

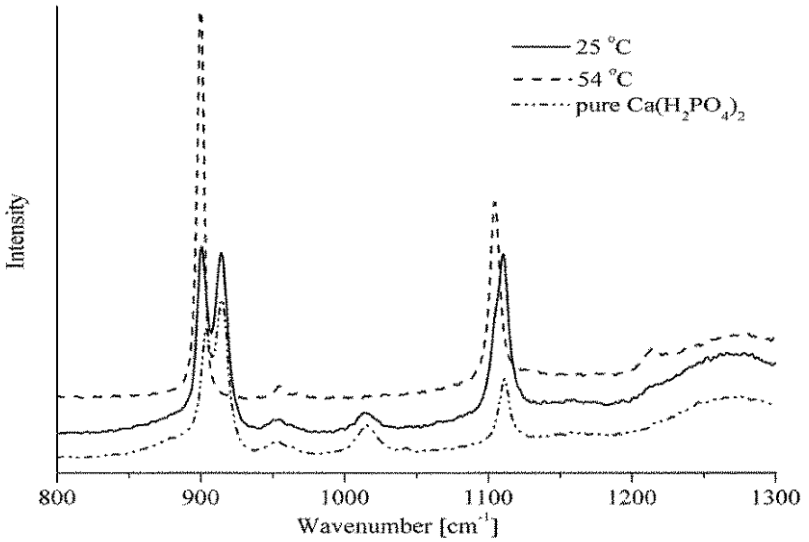

Figure 3: Raman spectra of $CaClH_2PO_4 \cdot H_2O$ crystals produced at 25 °C (solid line), at 54 °C (dash line) and the pure solid of $Ca(H_2PO_4)_2$ (dash-dot line). The original concentrations of $CaCl_2$ and H_3PO_4 were both 3.1 mol/L.

3.2. The effects of pH values

The pH of the mixture solution ($CaCl_2$ + H_3PO_4) in this work is always minus. The relative fraction of the dissociated species of phosphoric acid in water as a function of pH is illustrated in Figure 4 (Wolfe-Simon et al., 2009). The relative concentration of $H_2PO_4^-$ reaches a maximum around pH 4-5. Although the high concentration of $H_2PO_4^-$ will facilitate the formation of $CaClH_2PO_4 \cdot H_2O$ crystals, the other heavy metals (such as Fe and Al) in the sewage sludge ash will precipitated out at pH ≥3 (Schaum et al., 2007). In order to obtain the $CaClH_2PO_4 \cdot H_2O$ crystals without Fe and Al, the pH of the solution must be kept below 3.

In the present work, the pH of the mixture solution was adjusted by adding saturated $Ca(OH)_2$ solution. Since the phosphoric acid can exist as different species, changing the pH of the solution, might lead to the formation of other intermedia phases during the crystallization process, such as dicalcium phosphate dihydrate (DCPD), octacalcium phosphate (OCP), tricalcium phosphate (TCP) and hydroxyapatite (HAP) (Johnsson and Nancollas, 1992). Therefore, it is necessary to check if changing pH will influence the composition of the product.

The XRPD pattern of $CaClH_2PO_4 \cdot H_2O$ crystals prepared at different original pH have been compared and it has been observed that increasing the pH up to 0.42 didn't cause the formation of the phosphate products other than $CaClH_2PO_4 \cdot H_2O$. Meanwhile, the filterability of the crystals has been improved probably due to the higher concentration of $H_2PO_4^-$, which favored the growth of $CaClH_2PO_4 \cdot H_2O$ crystals.

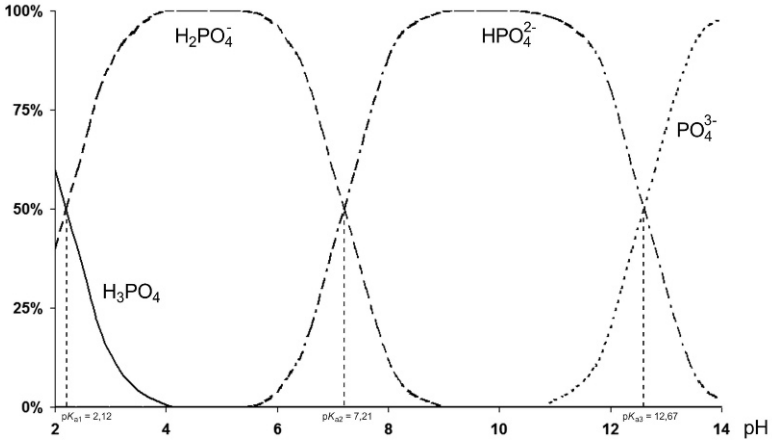

Figure 4: The relative fraction of phosphoric acid in water as a function of pH (Wolfe-Simon et al. 2009).

4. Conclusions

$CaClH_2PO_4 \cdot H_2O$ crystals were produced with a reactive crystallization by mixing calcium chloride solution and diluted phosphoric acid solution in equimolal proportions. The properties of the obtained products have been characterized with different process analytical technologies, such as XRPD, Raman spectroscopy and particle size analyzer. It can be concluded that increasing the processing temperature (>50 ^oC) and pH of the crystallization solution promote $CaClH_2PO_4 \cdot H_2O$ product properties in terms of high purity and larger particle size. The increased particle size will improve the filterability of the crystals and thus lead to a better solid-liquid separation in the down-stream filtration operations. Results obtained in the present work provide guidance for the development and optimization of reactive crystallization process for recovery of phosphorus product from sewage sludge ash that is heavily contaminated by ferrum and aluminum.

References

E. Fox, 1939, Process for the production of monocalcium chlorophosphate. US Patent No. 2143438.

M. Johnsson and G. Nancollas, 1992, The role of brushite and octacalcium phosphate in apatite formation. Critical Reviews in Oral Biology and Medicine, 3 (1/2): 61-82.

C. Schaum, P. Cornel and N. Jardin, 2007, Phosphorus recovery from sewage sludge ash-a wet chemical approach. Proceedings of IWA Specialist Conference on Moving Forward - Wastewater Biosolids Sustainability: Technical, Managerial and Public Synergy, 24-27 June 2007, Moncton, Canada, 583-590.

I. Steen, 1998, Phosphorus availability in the 21st Century: Management of a non-renewable resource. Phosphorus &Potassium, 217: 25-31.

Z. Tan and A. Lagerkvist, 2011, Phosphorus recovery from the biomass ash: A review. Renewable and Sustainable Energy Reviews, 15(8): 3588-3602.

F. Wolfe-Simon, P. Davies and A. Anbar, 2009, Did nature also choose arsenic?. International Journal of Astrobiology, 8 (2): 69-74.

Krist V. Gernaey, Jakob K. Huusom and Rafiqul Gani (Eds.), 12th International Symposium on Process Systems Engineering and 25th European Symposium on Computer Aided Process Engineering.
31 May – 4 June 2015, Copenhagen, Denmark

Time-optimal Operation of Diafiltration Processes in the Presence of Fouling

M. Jelemenský[a], A. Sharma[a], R. Paulen[a,b] and M. Fikar[a]

[a]*Faculty of Chemical and Food Technology, Slovak University of Technology in Bratislava, Slovakia.*
[b]*Process Dynamics and Operations Group, Technische Universität Dortmund, Germany*

Abstract

This paper deals with time-optimal operation of a batch diafiltration process in the presence of membrane fouling. Fouling causes a decrease in membrane area and hence, a decrease in permeate flux. Pontryagin's minimum principle is applied to characterize the structure of the optimal operation. Due to the specific structure of the problem, it is possible to derive and verify an explicit analytic solution. Obtained results are used in a case study where we provide a comparison between traditional operation and the herein developed time-optimal operation.

Keywords: optimal control, membrane fouling, Pontryagin's minimum principle, diafiltration.

1. Introduction

Diafiltration (DF) is a unique membrane process for separation of two or more solutes in a solution, used in the pharmaceutical, food and biotechnological industry. The process is designed to increase the concentration of high molecular weight components (macro-solute) and to decrease the concentration of low molecular weight components (micro-solute).

One of the major problems encountered in membrane separation processes is the fouling of the membrane. Fouling causes a decrease in effective membrane area resulting in reduction of permeate flow, and hence the increase of the processing time. Hermia (1982) provided a unified fouling model, from which four different standard fouling models can be derived considering different ways the solutes deposit on the membrane surface. These models are expressed in the terms of decrease in effective membrane area or the permeate flux (Bolton et al., 2006; Vela et al., 2008).

In the recent years, several papers (Foley, 1999; Paulen et al., 2012) have discussed the optimization of the diafiltration processes. They exploited several ways to efficiently run the diafiltration process in minimum time, but have not considered any fouling behavior. In the paper by Jelemenský et al. (2014b) a time-optimal operation in the presence of fouling has been proposed. It considers that the fouling causes a gradual decrease in the effective membrane area. Pontryagin' minimum principle is applied and optimal operation combines analytic structure with numerical optimization. In this paper we assume explicit dependency of permeate flux on processing time as proposed by Vela et al. (2008). The optimal operation derived in this paper is improved and completely given by simple rules and avoids any on-line optimization. A comparison between the proposed time-optimal operation and the traditionally used control strategy is presented further by means of a case study.

2. Problem Formulation

2.1. Process Description

A diafiltration process consists of a feed tank and a membrane unit. The solution from the feed tank consisting of a solvent and solutes is brought to the membrane unit by means of mechanical energy. The membrane is designed to retain the macro-solute and to allow the passage of micro-solute. Part of the filtered solution rejected by the membrane (retentate) returns back to the feed tank. Permeate stream leaves the system at a flowrate $q = A \cdot J$, where A represents the effective membrane area and J is the concentration- and time-depedent permeate flux subjected to unit membrane area.

The process control is achieved by adjusting the flowrate of solute-free diluant into the feed tank. The control variable α is defined as a ratio between the inflow of diluant into the feed tank, and the outflow of the permeate q. There are several control strategies according to the rate of the diluant utilization: (a) concentration (C) mode with α = 0; (b) constant-volume diafiltration (CVD) mode with α = 1; (c) dilution (D) mode with $\alpha \in (1, \infty)$, where $\alpha \to \infty$ represents an instantaneous dilution that maintains the ratio of solutes concentrations. One of the widely used control strategy in industry is a two-step operation, wherein the first step uses concentration mode (C) to increase the concentration of the product, and the second step is CVD to decrease the concentration of impurities (i.e. C-CVD). The mathematical model of the process is given by material balances of solutes and the overall material balance (Fikar et al., 2010):

$$\frac{dc_i}{dt} = \frac{c_i}{V} \cdot A \cdot J \cdot (R_i - 1), \qquad c_i(0) = c_{i,0}, \qquad i = 1,2,\dots,n \tag{1a}$$

$$\frac{dV}{dt} = A \cdot J \cdot (\alpha - 1), \qquad V(0) = V_0, \tag{2b}$$

where c_i represents the concentration of the *i*th solute, V is the volume of the processedsolution. R_i represents the rejection coefficient for the *i*th solute defined as $R_i = 1 - c_i/c_{p,i}$ where $c_{p,i}$ is concentration of component *i* in permeate.

2.2. Membrane Fouling

Membrane fouling causes decrease of the permeate flux in time as a consequence of the effective membrane area being reduced due to the deposit of the solutes on or in the membrane pores. In Hermia (1982); Vela et al. (2008) a unified model is provided from which four standard fouling models can be derived.The permeate fluxes in these models can be characterized as:

$$\text{(a)complete fouling model: } \ln J = \ln J_0 - K_c \cdot t, \tag{2a}$$

$$\text{(b)intermediate fouling model: } \frac{1}{J} = \frac{1}{J_0} + K_i \cdot t, \tag{2b}$$

$$\text{(c)standard (internal)fouling model: } \frac{1}{\sqrt{J}} = \frac{1}{\sqrt{J_0}} + K_s \cdot t, \tag{2c}$$

$$\text{(d)cake fouling model: } \frac{1}{J^2} = \frac{1}{{J_0}^2} + K_g \cdot t, \tag{2d}$$

where J_0 is the initial flux and K is a fouling constant. These results were obtained for dead-end filtration. We will use the intermediate model (2b) in the subsequent sections for cross-flow regime and J_0 will represent the permeate flow of unfouled membrane.

2.3. Optimization Problem

The optimization goal is to find such time-dependent function $\alpha(t)$ which guarantees transition from given initial to final concentrations in minimum time. We assume that the membrane is absolutely impermeable to macro-solute (c_1), the permeability of micro-solute (c_2) changes as a function of concentrations, and is expressed using rejection coefficient $R_2 = R_2(c_1, c_2)$. Consequently, the optimization problem reads as:

$$\min_{\alpha\in[0,\infty)} \int_0^{t_f} 1 \cdot dt \tag{3a}$$

$$\text{s.t.} \quad \frac{dc_1}{dt} = {c_1}^2 \cdot \frac{A \cdot J}{c_{1,0} \cdot V_0} \cdot (1-\alpha), \qquad c_1(0) = c_{1,0}, \qquad c_1(t_f) = c_{1,f}, \tag{3b}$$

$$\frac{dc_2}{dt} = c_1 \cdot c_2 \cdot \frac{A \cdot J}{c_{1,0} \cdot V_0} \cdot (R_2 - \alpha), \qquad c_2(0) = c_{2,0}, \qquad c_2(t_f) = c_{2,f}, \tag{3c}$$

where we use the fact that $V = c_{10} \cdot V_0 / c_1$, since $R_1 = 1$.

3. Optimal Operation

We use Pontryagin's minimum principle (PMP) (Pontryagin et al., 1962; Bryson, Jr. and Ho, 1975) to identify the candidates for optimal control. A care has to be taken as the process model depends explicitly on time, thus the problem is non-autonomous. There are two possible approaches to handle optimal control of non-autonomous systems. The first approach considers time explicitly in the process model. Then, the optimal Hamiltonian function is zero only at final time. Therefore, there are two variables (concentrations) and PMP has to supply two equations for optimality. The second approach adds a third state variable $\dot{x}_3 = 1$ with initial condition $x_3(0) = 0$ and replaces t with x_3. Therefore, the new problem is autonomous with increased number of variables. In this case, Hamiltonian function is zero along the optimal trajectory and this fact can be used to provide additional equations for finding an optimal solution. When we consider the first approach, the process model can be written as

$$\dot{x} = f(t,x) + g(t,x) \cdot \alpha, \tag{4}$$

where $x = (c_1, c_2)^T$. The Hamiltonian function can then be constructed as

$$H(t,x,\lambda,\alpha) = 1 + f^T(t,x) \cdot \lambda + g^T(t,x) \cdot \lambda \cdot \alpha = H_0(t,x,\lambda) + H_\alpha(t,x,\lambda) \cdot \alpha, \tag{5}$$

where $\lambda = (\lambda_1, \lambda_2)^T$ is the vector of adjoint variables defined from

$$\dot{\lambda} = -\,\partial H/\partial x = -(f_x + g_x \cdot \alpha) \cdot \lambda\,, \quad f_x(t,x) = \frac{\partial f^T(t,x)}{\partial x}, \quad g_x(t,x) = \frac{\partial g^T(t,x)}{\partial x}. \tag{6}$$

Since the Hamiltonian is affine in α, its minimum is attained with α on its boundaries as

$$\alpha = \begin{cases} 0 & \text{if } H_\alpha > 0, \\ \infty & \text{if } H_\alpha < 0. \end{cases} \tag{7}$$

If Hamiltonian is singular in α, the singular case is characterized by equations $H_\alpha = 0$, $\dot{H}_\alpha = 0$. This gives a set of equations which are linear in λ

$$H_\alpha(t,x,\lambda) = g^T \cdot \lambda = 0, \tag{8}$$

$$\dot{H}_\alpha(t,x,\lambda) = h^T \cdot \lambda = (g_x \cdot f - f_x \cdot g + \partial H_\alpha/\partial t)^T \cdot \lambda = 0 \tag{9}$$

Elimination of λ from (8) and (9) results in characterization of the singular surface:

$$S(t, c_1, c_2) = (R_2 - 1) \cdot \left(J + \sum_{i=1}^{2} c_i \cdot \partial J / \partial c_i \right) + J \cdot \left(\sum_{i=1}^{2} c_i \cdot \partial R_2 / \partial c_i \right) = 0 \quad (10)$$

Note that the expression (10) is actually identical to the one without fouling, as derived in Paulen et al. (2012). The only difference lies in the fact that J (and thus S) is not only a function of concentrations but also of time. To obtain the control which keeps the states on the singular surface, we differentiate the singular surface (10) w.r.t. to time. The obtained singular control is:

$$\alpha(t, c_1, c_2) = \frac{c_1 \cdot \partial S / \partial c_1 + c_2 \cdot R_2 \, \partial S / \partial c_2}{\sum_{i=1}^{2} c_i \cdot \partial S / \partial c_i} + \frac{\partial S / \partial t}{c_1 \cdot J / c_{10} \cdot V_0 \cdot (\sum_{i=1}^{2} c_i \cdot \partial S / \partial c_i)}. \quad (11)$$

The optimal operation hence deduced, consists of following three steps:

1. In the first step, depending on the initial concentrations, we use either concentration mode or pure dilution mode until the condition $S(t, c_1, c_2) = 0$ is met.
2. During the second step we stay on singular surface where the singular control (11) is used.
3. The last step is characterized by saturated control until the final conditions for concentrations are met.

It is necessary to point out that any step can be missing from the optimal operation. This depends solely on the initial and final conditions. For instance, if there does not exist any three-step strategy fulfilling the final conditions, the middle step is skipped, and the optimal control is saturated on constraints. It is also worth mentioning that the developed optimal operation can be applied to a general batch diafiltration process with arbitrary type of membrane module and nature of filtered species.

4. Case Study

A case study on the separation of lactose (with concentration c_2) from proteins (with concentration c_1) originally formulated in Rajagopalan and Cheryan (1991) is solved here. The authors experimentally obtained a model for the permeate flux as,

$$J_0(c_1, c_2) = b_0 + b_1 \cdot \ln c_1 + b_2 \cdot \ln c_2 = 63.42 - 12.439 \cdot \ln c_1 - 7.836 \cdot \ln c_2. \quad (12)$$

The fouling model for the permeate flux (2b) is used here. Goal is to drive the concentrations from initial point $[c_{1,0}, c_{2,0}] = [3.3\ \text{g/dL}, 5.5\ \text{g/dL}]$ to final point $[c_{1,f}, c_{2,f}] = [9.04\ \text{g/dL}, 0.64\ \text{g/dL}]$ for 100dL of solution. Further on, we consider that the membrane is absolutely permeable to lactose ($R_2 = 0$), and the membrane area is 1 m^2. The analytic results for singular surface (10) and singular control (11) are

$$S(t, c_1, c_2) = b_1 + b_2 + J_0 + K_i \cdot t \cdot [b_0(b_0 + 2 \cdot F) + F^2] = 0, \quad (13)$$

where $F = b_1 \cdot \ln c_1 + b_2 \cdot \ln c_2$, and (14)

$$\alpha(t, c_1, c_2) = \frac{b_1}{b_1 + b_2} + \frac{c_{10} \cdot V_0 \cdot K_i \cdot J_0 \cdot (K_i \cdot J_0 \cdot t + 1)}{A \cdot K \cdot c_1 \cdot (b_1 + b_2) \cdot (2 \cdot K_i \cdot J_0 \cdot t + 1)}, \quad (15)$$

respectively, with V_0 as the initial volume. We can observe that besides concentrations, singular surface and control also depend on fouling rate and time. From the results

above, time-optimal operation in the presence of fouling comprises a sequence of following three steps:

1. The first step is concentration mode ($\alpha = 0$) till the singular surface (13) is reached.
2. Then, in the second step, the states reside on the singular surface with the singular control (15). This step is performed until the condition $c_1(t)/c_2(t) = c_{1,f}/c_{2,f}$ is satisfied.
3. In the last step we perform pure dilution mode with $\alpha = \infty$ until the final concentrations are reached.

Figure 1 depicts the optimal control strategy (states and control) for the minimum-time operation for different fouling rates. The control structure in all the cases is a three-step strategy, as mentioned above. In the state diagram the circle represents the initial concentrations and the cross depicts the final ones. We can observe that the switching concentration to singular surface (13) is changing with different fouling rates K_i. Furthermore we can observe that the increase of these values translates to longer processing time, as expected.

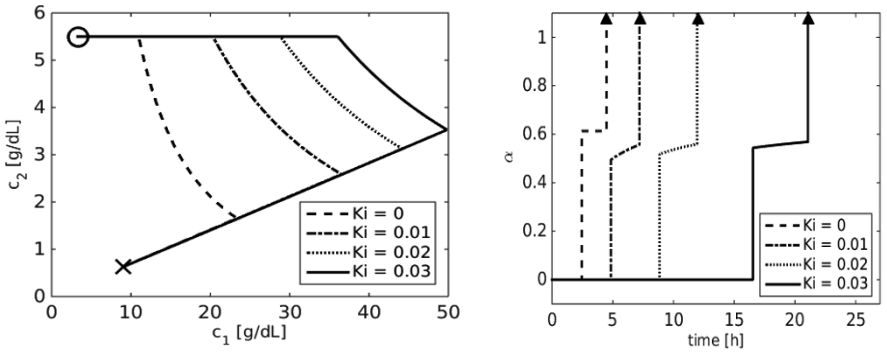

Figure 1: Comparison of different control strategies (left – state space, right – control profiles).

Table 1 presents a comparison of the final processing time in case of minimum-time operation, derived in this paper, and the traditionally used operation (C-CVD). The differences in the duration of the respective operations get more significant as the fouling rate increases. For the highest rate of fouling considered here, the savings in terms of processing time are more than threefold. Therefore we can conclude that it would be substantially beneficial to employ the time-optimal operation for reducing the costs in the separation of macro-solute in this case study.

A care must be taken when applying this optimal operation on a real process. The traditional C-CVD operation and model (11) operate with concentration $c_1 < 10$ g/dL.The proposed optimal operation uses much higher concentrations, up to 50 g/dL. Therefore, a new model has to be estimated that also covers this area.

Table 1: Time-optimal operation compared to traditional operation for different fouling rates.

K_i [10^{-3} m^{-1}]	minimum time t_f [h]	C-CVD t_f [h]	Δ[%]
0	4.49	4.74	5.57
10	7.24	10.52	45.30
20	12.02	26.70	122.13
30	21.27	75.57	255.29

Such high concentrations can cause strong polarization effects and necessity to move the operation in lower-concentration region. In that case, the singular surface would not be attained and constraint-based operation would be applied, as in Jelemenský et al. (2014a).

5. Conclusions

In this paper we studied the time-optimal control of a batch diafiltration process in the presence of fouling. The fouling behavior was described by the reduction of the permeate flux caused by the deposit of the solutes on the membrane. Using Pontryagin's minimum principle we derived the candidates for optimal control. The derived optimal operation is completely analytic, and consists of three steps with singular control being the second one. The developed theory was applied on an example for separating proteins and lactose. The obtained results indicate that by using advanced control strategy we can reduce the production costs compared to traditionally used operations.

Acknowledgement

The authors gratefully acknowledge the contribution of the Scientific Grant Agency of the Slovak Republic under the grant 1/0053/13 and the Slovak Research and Development Agency under the project APVV-0551-11. This publication is also the partial result of the Research & Development Operational Programme for the project University Scientific Park STU in Bratislava, ITMS 26240220084, supported by the Research & Development Operational Programme funded by the ERDF.

References

G. Bolton, D. LaCasse, R. Kuriye, 2006. Combined models of membrane fouling:Development and application to microfiltration and ultrafiltration of biological fluids, J. Membr. Sci. 277 (1–2), 75 – 84.

A. E. Bryson, Jr., Y. C. Ho, 1975, Applied Optimal Control : Optimization, Estimation and Control, Taylor & Francis Group, New York, USA.

M. Fikar, Z. Kovács, P. Czermak, 2010. Dynamic optimization of batch diafiltration processes. Journal of Membrane Science 355 (1-2), 168–174.

G. Foley, 1999, Minimisation of process time in ultrafiltration and continuous diafiltration: the effect of incomplete macrosolute rejection, Journal of Membrane Science, 163, 1–2, 349–355.

J. Hermia, 1982. Constant pressure blocking filtration laws – application to power-law non-newtonian fluids. Trans.Inst. Chem. Eng., 183–187.

M. Jelemenský, R. Paulen, M. Fikar, Z. Kovacs, 2014a. Time-optimal control of batch multi-component diafiltration processes. In: Klemeš, J. J., Varbanov, P. S., Liew, P. Y. (Eds.), 24th European Symposium on Computer Aided Process Engineering. Budapest, Hungary, pp. 553–558.

M. Jelemenský, R. Paulen, M. Fikar, Z. Kovacs, 2014b. Time-optimal diafiltration in the presence of membrane fouling. In: Preprints of the 19th IFAC World Congress Cape Town (South Africa) August 24 - August 29, 2014. pp. 4897–4902.

R. Paulen, M. Fikar, G. Foley, Z. Kovács, P. Czermak, 2012, Optimal feeding strategy of diafiltration buffer in batch membrane processes, J. Membr. Sci., 411-412, 160–172.

L. S. Pontryagin, V.G. Boltyanskii, R. V. Gamkrelidze, E. F. Mishchenko, 1962. The Mathematical Theory of Optimal Processes. John Wiley & Sons, Inc., New York.

N. Rajagopalan, M. Cheryan, 1991. Process optimization in ultrafiltration: Flux-time considerations in the purification of macromolecules. Chem. Eng. Com 106 (1), 57–69.

M. C. V. Vela, S. A. Blanco, J. L. García, E. B. Rodríguez, 2008. Analysis of membrane pore blocking models applied to the ultrafiltration of PEG. Separation and Purification Technology 62 (3), 489 – 498.

Krist V. Gernaey, Jakob K. Huusom and Rafiqul Gani (Eds.), 12th International Symposium on Process Systems Engineering and 25th European Symposium on Computer Aided Process Engineering.
31 May – 4 June 2015, Copenhagen, Denmark

Supercritical gas recycle analysis for surge control of centrifugal compressors

Sara Budinis*, Nina F. Thornhill

Centre for Process Systems Engineering (CPSE), Department of Chemical Engineering, Imperial College London, London, SW7 2AZ, UK
s.budinis11@imperial.ac.uk

Abstract

This paper presents computer-based analysis and design of control systems for centrifugal compressors when the operating fluid is supercritical CO_2. It demonstrates that the design of the control system of the compressor must take into account the state of the fluid. It also evaluates if the plant configuration allows compressor operation within a given surge margin. The results show the impact of the operating conditions of the compression station on surge prevention, their effect on the energy consumption, and suggest ways of dealing with supercritical fluid while controlling a compressor.
Keywords: supercritical, compressor, control, CO_2, recycle.

1. Introduction

The compression of carbon dioxide for transportation and storage has increased in recent years. This is due to its importance within carbon capture and storage technology with large-scale transportation via pipelines (Zhang et al., 2006).
In order to increase the gas density while reducing the pressure drop along the pipeline, the gas is compressed to supercritical phase via multistage centrifugal compressors. However, practical problems can arise in the operation of such a compressor, especially when dealing with gas recycle for antisurge protection. Prior work on transcritical CO_2 compression operation is found from other research areas such as refrigeration plants and power generation based on a supercritical CO_2 Brayton cycle. However in the refrigeration industry the research goal is the thermal optimization of the cycle and positive displacement machines are employed (Conboy et al., 2013, Salazar and Mendez, 2014). On the other hand, technology involving rotating dynamic compressors, such as power generation based on a supercritical CO_2 gas turbine, is still in the early stage of development (Lettieri et al., 2014). Therefore in the future it will need a suitable control system able to deal with the recycle of supercritical CO_2.
This paper reports on the analysis of supercritical gas recycle with the purpose of surge prevention. It compares different recycle configurations during boundary disturbances in order to evaluate the effect of the recycle temperature on surge occurrence and power consumption.

2. Model of the compression system

The model of the compression system consists of a fully validated non-linear dynamic model based on a model present in the literature (Greitzer, 1976) that has been modified by other authors in order to include the shaft dynamics (Fink et al., 1992) and the equations for the torque of the compressor and of the electric driver (Gravdahl et al., 2002). The main equations of the model include the mass and momentum balance for

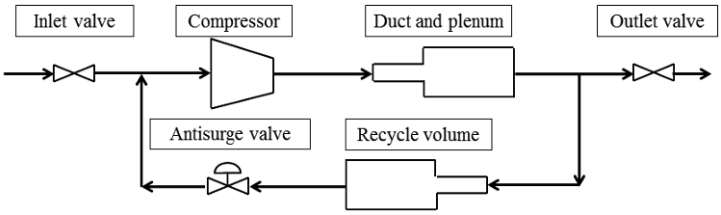

Figure 1. Sketch of the compression system

the compressor and the moment of momentum balance for the rotating shaft. The model of the compression system also includes the equations of the mass flow rate through inlet, outlet and recycle antisurge valve. The mass flow rate has been defined as a function of the upstream density according to Morini et al. (2007). The density of the gas as a function of its temperature and pressure is estimated using the Span and Wagner equation of state (Anwar and Carroll, 2010).

3. Simulation scenarios and control system

Two different configuration scenarios have been modelled. The first scenario includes a cold gas recycle where the recycled gas is cooled from the outlet temperature of the compressor T_{02} to the same temperature as the freshly fed gas T_{in}. The second scenario includes a hot gas recycle where the gas is not cooled before being recycled and therefore affects the inlet temperature of the compressor T_{01}. These two configuration scenarios have been compared during disturbances consisting of step changes of the opening position of the boundary valves. The response of the two systems has been recorded and compared via graphic representation and also by means of dimensionless indicators representing respectively the amount of gas recycled, the energy requested by the system and the performance of the pressure controller, according to the equations (1) - (3). m_r is the recycle mass flow rate, m is the compressor mass flow rate, t_{final} is the time period under analysis, P is the power consumption due to gas compression, Q is the power consumption due to heat removal in the cold gas recycle configuration, p is the compressor outlet pressure and p_{sp} its set point. Equation (4) expresses the corrected mass flow rate as a function of the inlet conditions of the gas (Boyce, 2003). m_{corr} is the corrected mass flow rate while m_{act} is the actual mass flow rate. p_{01} and T_{01} are respectively the compressor inlet pressure and temperature while p_{ref} and T_{ref} are respectively the reference pressure and temperature.

$$M = \frac{\int_{t=0}^{t_{final}} m_r dt}{\int_{t=0}^{t=1h} m dt} \tag{1}$$

$$E = \frac{\int_{t=0}^{t_{final}} (P+Q) dt}{\int_{t=0}^{t=1h} P dt} \tag{2}$$

$$ISE_p = \int_{t=0}^{t_{final}} (p(t) - p_{SP}(t))^2 dt \tag{3}$$

$$m_{corr} = \frac{m_{act}\sqrt{T_{01}/T_{ref}}}{p_{01}/p_{ref}} \tag{4}$$

Finally supercritical gas recycle has been compared with subcritical gas recycle.
A standard control system has been proposed and implemented. It consists of a cascade pressure controller and an antisurge controller. The interaction between these two controllers is a known issue in industrial application. However this is still the most employed control system for compressors and therefore it has been selected for the analysis. In the cascade control structure, the slave loop is a speed controller while the master loop is a pressure controller. The driver torque τ_d is the manipulated variable. The antisurge controller opens the recycle valve ASV when the inlet flow rate of the compressor m falls below the control flow rate m_{ctrl}. A margin of 20 % between the surge flow rate m_{surge} and m_{ctrl} has been imposed.
All the variables reported in the paper have been scaled according to their design value at the inlet of the compressor. This is due to non-disclosure agreement with the partner of the project that has provided the industrial case study. It consists of a multistage centrifugal compressor driven by an electric motor and mounted in a single shaft configuration. The fourth and last stage of compression has been the reference for the supercritical compression case while the third stage has been the reference for the subcritical compression case, and the two machines have the same model.

4. Dynamic simulations and results

4.1. Cold gas recycle

The opening position of the inlet and of the outlet boundary valves has been modified according to negative step changes from the fully open position OP=100 % to the opening positions specified in Table 1. Step disturbances took place at time t=100s and simulations were performed for 30 minutes. Performance indexes for some representative cases have been reported in the table below. For inlet boundary disturbances, four cases have been reported. The first case is the steady state simulation and then the other three cases represent three different step changes. For the second and third case where OP is equal respectively to 80 % and 50 % the compressor does not

Table 1. Performance indexes for inlet and outlet disturbances (cold gas recycle)

	Inlet valve V_{in}				Outlet valve V_{out}				
OP (%)	100	80	50	20	100	80	78	75	72
M	0.00	0.00	0.00	1.35	0.00	0.00	0.00	0.35	5.23
ISE_p	0.00	0.02	0.51	3869.70	0.00	7.75	9.43	12.35	16.01
E	0.50	0.50	0.52	0.63	0.50	0.40	0.39	0.41	0.88

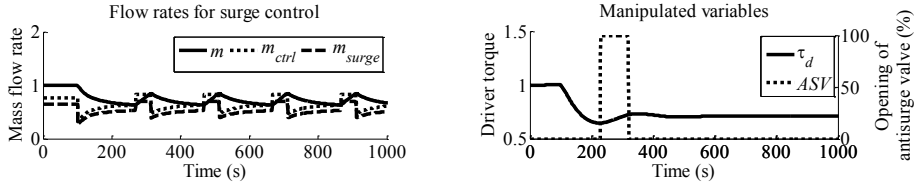

Figure 2. Cold gas recycle. a.Inlet valve step change from fully open position to 20 % (left) – b.Outlet valve step change from fully open position to 75 % (right)

recycle gas as its inlet flow rate m is still above the control flow rate m_{ctrl}. Therefore for these two cases M is equal to zero and E depends only on the compression process. As expected ISE_p increases with the disturbance magnitude. When m and m_{ctrl} cross each other at OP=20 % the antisurge controller opens ASV in order to increase m. However this action influences the value of m_{surge}, according to equation (4). The actual value of m_{surge} increases if p_{01} increases and for this reason m and m_{surge} cross right after the opening of ASV. The operating point of the compressor goes below the surge value and the response of the system starts oscillating as represented in Figure 2.a. The overall control system is not able to stabilise the system. The control over pressure is poor (ISE_p=3869.7). This is due to the saturation of the pressure controller, when the rotating shaft speed achieves its upper boundary.

Negative step disturbances have been performed for V_{out} as well. As it happened for inlet disturbances, until ASV is closed M is equal to zero and ISE_p increases. In this case E decreases because of the decrease of m. When m crosses m_{ctrl} at V_{out}=75 % part of the gas is recycled back to the inlet of the compressor and this case has been represented Figure 2.b. The ASV opens for a short period until m goes above m_{ctrl}. M and therefore E increase with the magnitude of the disturbance.

4.2. Hot gas recycle

The same disturbances as above have been tested in the hot gas recycle configuration. Results have been summarised in Table 2. Until ASV is closed the system behaves as did the cold gas recycle configuration, as the recycle line is not engaged in the process operation. However when ASV opens the system responds in a different way. For the case V_{in}=20 %, the compressor does not go into surge however the response of the system oscillates. This is due to the recycle of hot gas that causes T_{01} to increase and therefore m_{surge} to decreases, according to equation (4), as represented in Figure 3.a. Moreover in this case the power consumption decreases and this is due to both the reduction of m and the missing cost due to gas cooling.

Similarly for the output boundary valve, in the case when OP is equal to 75 % ASV oscillates because of the effect of the hot gas recycle on T_{01} and therefore m_{ctrl}. The time series for the manipulated variables has been represented in Figure 3.b. For this

Table 2. Performance indexes for inlet and outlet disturbances (hot gas recycle)

	Inlet valve V_{in}				Outlet valve V_{out}				
OP (%)	100	80	50	20	100	80	78	75	72
M	0.00	0.00	0.00	0.21	0.00	0.00	0.00	0.04	0.19
ISE_p	0.00	0.02	0.51	6578.80	0.00	7.72	9.39	12.85	17.69
E	0.50	0.50	0.52	0.40	0.50	0.40	0.39	0.38	0.36

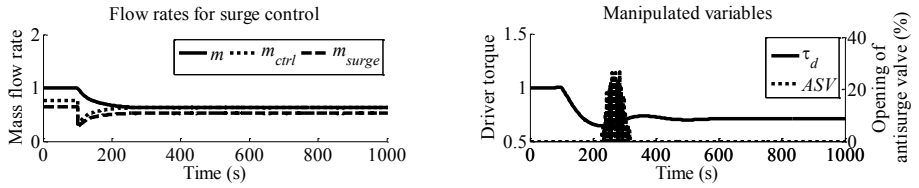

Figure 3. Hot gas recycle. a.Inlet valve step change from fully open position to 20 % (left) – b.Outlet valve step change from fully open position to 75 % (right)

specific case M was higher while ISE_p and E lower. Therefore the hot gas recycle configuration has prevented the surge of the compression system during inlet disturbances and has a lower energy consumption. However it has caused a very strong oscillation of the antisurge valve. This oscillation is caused by the effect of the recycled hot gas on the location of the surge region.

In order to further clarify this point, Figure 4 shows the surge flow rate and the opening of the antisurge valve for the cold gas recycle configuration and for the hot gas recycle configuration. For both inlet and outlet disturbances, the results demonstrate that in the cold gas recycle configuration the opening of the antisurge valve causes the increase of the surge flow rate. This is due to the increase of p_{01} caused by the opening of the recycle valve itself. In the hot gas recycle configuration, the opening of the antisurge valve decreases the surge flow rate. In this case both T_{01} and p_{01} increase because of the gas recycle. However the rate of change of T_{01} is higher than the rate of change of p_{01} and therefore m_{surge} decreases, according to equation (4). In conclusion this behaviour causes the oscillation of ASV, as m and m_{ctrl} keep crossing each other every time the antisurge valve moves towards the opening or closing position.

4.3. Comparison between supercritical and subcritical compression

Additional analyses have been performed in order to compare supercritical gas recycle with subcritical gas recycle for surge prevention. In the selection between cold and hot gas recycle the process parameters that are usually considered include time delay in the process response and machine integrity (Botros, 2011). However when dealing with supercritical compression operation it is also important to take into account the amount of gas recycled. In the present case study, results show that the subcritical compressor operating in full recycle mode is able to recycle 22.64 % more gas by means of a cold gas recycle rather than a hot gas recycle. However in the supercritical compressor this amount rises to 81.50 %. This is due to the dramatic change of density of a supercritical gas especially when it is cooled down toward its critical point. This result is decisive

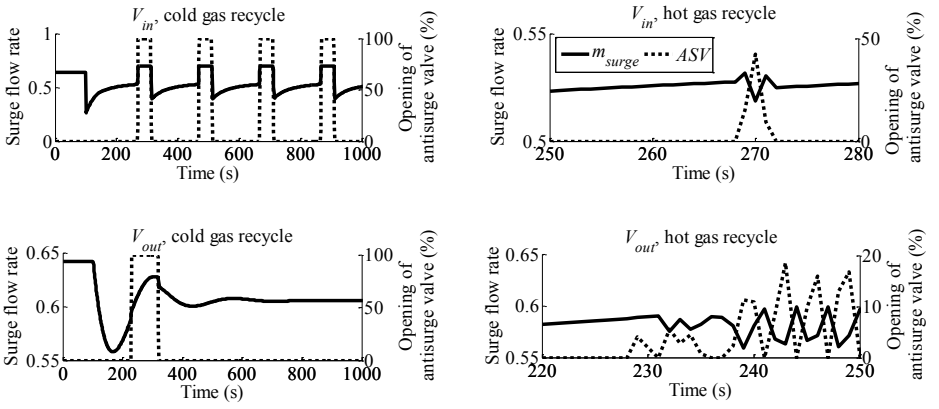

Figure 4. Surge flow rate and opening of the antisurge valve for input (top) and output (bottom) valve disturbances, in cold (left) and hot (right, zoomed views) gas recycle configurations

when full recycle is needed and a hot gas recycle configuration may not provide a sufficient amount of gas for surge protection.

5. Conclusion

This paper reports on the effect of the gas recycle configuration for surge protection on the compression system when dealing with supercritical fluid. Results demonstrate that a hot gas recycle configuration protects the system from boundary disturbances and has a lower energy request. However the response of the antisurge control system and therefore the antisurge valve oscillates. This is due to the effect of the recycle temperature on the location of the surge region. Moreover the amount of gas recycled must be taken into account especially when full recycle is needed. In fact, a supercritical compression station is able to recycle more than three times more gas in a cold gas recycle configuration than a subcritical compression station.

Acknowledgements

Financial support from the Marie Curie FP7-ITN project "Energy savings from smart operation of electrical, process and mechanical equipment– ENERGY-SMARTOPS", Contract No: PITN-GA-2010-264940 and from EPSRC EP/J020788/1 Gas-FACTS: Gas - Future Advanced Capture Technology Options is gratefully acknowledged.

References

Anwar, S. & Carroll, J. J., 2010, Density (kg/m^3) of Carbon Dioxide as a Function of Temperature and Pressure, Carbon Dioxide Thermodynamic Properties Handbook, John Wiley & Sons, Inc.

Botros, K. K., 2011, Single versus dual recycle system dynamics of high pressure ratio, low inertia centrifugal compressor stations, Journal of Engineering for Gas Turbines and Power-Transactions of the ASME, 133**,** 122402: 1-12.

Boyce, M. P., 2003, Centrifugal Compressors - A Basic Guide, PennWell.

Conboy, T., Pasch, J. & Fleming, D., 2013, Control of a Supercritical CO_2 Recompression Brayton Cycle Demonstration Loop, Journal of Engineering for Gas Turbines and Power-Transactions of the ASME, 135**,** 12.

Fink, D. A., Cumpsty, N. A. & Greitzer, E. M., 1992, Surge dynamics in a free-spool centrifugal-compressor system, Journal of Turbomachinery-Transactions of the ASME, 114**,** 321-332.

Gravdahl, J. T., Egeland, O. & Vatland, S. O., 2002, Drive torque actuation in active surge control of centrifugal compressors, Automatica, 38**,** 1881-1893.

Greitzer, E. M., 1976, Surge and rotating stall in axial-flow compressors. 1. Theoretical compression system model, Journal of Engineering for Power-Transactions of the ASME, 98**,** 190-198.

Lettieri, C., Baltadjiev, N., Casey, M. & Spakovszky, Z., 2014, Low-Flow-Coefficient Centrifugal Compressor Design for Supercritical CO_2, Journal of Turbomachinery-Transactions of the ASME, 136**,** 9.

Morini, M., Pinelli, M. & Venturini, M., 2007, Development of a one-dimensional modular dynamic model for the simulation of surge in compression systems, Journal of Turbomachinery-Transactions of the ASME, 129**,** 437-447.

Salazar, M. & Mendez, F., 2014, PID control for a single-stage transcritical CO_2 refrigeration cycle, Applied Thermal Engineering, 67**,** 429-438.

Zhang, Z. X., Wang, G. X., Massarotto, P. & Rudolph, V., 2006, Optimization of pipeline transport for CO_2 sequestration, Energy Conversion and Management, 47**,** 702-715.

Krist V. Gernaey, Jakob K. Huusom and Rafiqul Gani (Eds.), 12th International Symposium on Process Systems Engineering and 25th European Symposium on Computer Aided Process Engineering.
31 May - 4 June 2015, Copenhagen, Denmark.

Software sensors design and selection for the production of biodiesel from grease trap wastes

Efrén Aguilar-Garnica[a] and Juan Paulo García-Sandoval[b]

[a]*Departamento de Química; Universidad Autónoma de Guadalajara (UAG); Zapopan, México*
[b]*Departamento de Ingeniería Química; Universidad de Guadalajara (UdG); Guadalajara, México*
efren.aguilar@edu.uag.mx

Abstract

In this paper, a couple of software sensors were designed for CSTR processes and they were tested in the esterification of grease trap wastes which is a low-cost feedstock for biodiesel production. Both software sensors were designed for the estimation of the concentration of Free Fatty Acids (FFAs) from discrete CSTR's temperature measurements. One of these software sensors, called asymptotic observer, is recognized for its capacity to provide estimates without the knowledge of the process kinetics. It has been also designed an estimation algorithm known as reset fuzzy observer. This approach has been recently proposed and is able to update the estimated states at each instant when discrete measurements are available. Both observers were built regarding the structure of a validated dynamical model for the esterification of grease trap wastes and they were tested considering experimental data. The results show that the asymptotic observer offers a very poor performance when some process's disturbances (e.g. input concentration of FFAs, jacket temperature) are carried out, whereas the reset fuzzy observer is able to reconstruct satisfactorily the concentration of FFAs in the presence of such disturbances. Therefore, this fuzzy observer can be selected as reliable monitoring approach that could be further used as a key part of robust control schemes conceived for this specific biodiesel production process.

Keywords: software sensors, biodiesel, grease trap wastes

1. Introduction

An observer (i.e. software sensor) is an algorithm derived from a mathematical model which is able to reconstruct state variables (whose measurement is technically difficult or relatively expensive) from variables that can be captured constantly from common instruments such as thermocouples, phmeters, etc. An Asymptotic Observer (AO) is able to handle uncertainties in reaction kinetics. Probably, this characteristic has allowed the successful implementation of the asymptotic observer in chemical and biotechnological processes. There exists another class of observer which is known as Fuzzy Reset Observer (FRO) because its structure is derived from the Takagi-Sugeno fuzzy representation of a dynamical model and besides, is able to update the estimation scheme at every instant where measurements are available. This observer has been been successfully applied in biotechnological processes.

On the other hand, biodiesel is a renewable blend of organic esters that has received attention recently due to its ability of reducing CO_2 emissions in comparison to the petroleum diesel fuel. The main barrier for the commercialization of biodiesel is the relatively high cost of this biofuel when it is produced from refined oils (Wen et al., 2010). This economical issue can be improved if biodiesel is produced from cheaper, lower quality feedstock (e.g. waste cooking oils or grease

trap wastes) that is characterized by their high content of Free Fatty Acids (FFAs) (Canakci and Van Gerpen, 2001). In this case, biodiesel is usually produced by the esterification of FFAs with methanol in the presence of sulfuric acid as an homogeneous catalyst.

To the best of our knowledge, little attention has been paid to the design of software sensors in biodiesel production processes, with the remarkable exception of the work conducted by Price et al. (2014). In the present contribution, an AO and a FRO are proposed as monitoring tools for the esterification of a very complex blend of FFAs known as grease trap wastes that are abundantly and routinely collected from grease interceptors before entering the sanitary sewer lines (Park et al., 2010; Canakci, 2007). Specifically, these observers are designed in order to estimate the concentration of FFAs from reactor's temperature measurements.

2. Material and methods

2.1. Materials

Grease tap wastes were provided by Solución Ambiental de México (Guadalajara, Jalisco, México) containing 83.61% FFAs. Industrial reagent grade methanol (0.3% moisture content) and H_2SO_4 were supplied by Pochteca and Químicos Marquez (Mexico), respectively.

2.2. Esterification of grease trap wastes and its dynamical model

The esterification of grease trap wastes was conducted in a three necked glass Continuous Stirred Tank Reactor (1L, 200rpm) that was immersed in a water bath at temperature T_J. The CSTR's temperature, T, was recorded *every minute*. In addition, the methanol and the FFAs' molar ratio was around 20:1. Grease trap wastes and a reagent mixture of methanol/H_2SO_4were pumped to the reactor with volumetric flows F_{FFA} and F_{mix}, respectively, while the output flow F was adjusted to avoid any total mass accumulation within the reactor. The dynamical model for this esterification process is given in (Aguilar-Garnica et al., 2014):

$$\frac{dC_A}{dt} = \frac{F_{FFA}C_{Ai}}{V} - \frac{FC_A}{V} - k_1 C_M(0)\left(C_A - \frac{C_E C_W}{K_{eq} C_M(0)}\right) \tag{1}$$

$$\frac{dT}{dt} = \frac{F_{FFA}\rho_{FFA}\gamma_{FFA}}{\rho V \gamma_P}(T_{AG} - T) + \frac{F_{Mix}\rho_{Mix}\gamma_{Mix}}{\rho V \gamma_P}(T_{Mix} - T) + \frac{U}{\rho V \gamma_P}(T_J - T) - \frac{\Delta H}{\rho \gamma_P} k_1 C_M(0)\left(C_A - \frac{C_E C_W}{K_{eq} C_M(0)}\right) \tag{2}$$

$$\frac{dC_E}{dt} = -\frac{FC_E}{V} + k_1 C_M(0)\left(C_A - \frac{C_E C_W}{K_{eq} C_M(0)}\right) \tag{3}$$

$$\frac{dC_W}{dt} = -\frac{FC_W}{V} + k_1 C_M(0)\left(C_A - \frac{C_E C_W}{K_{eq} C_M(0)}\right) \tag{4}$$

In this model, t is time, while T_{AG} and T_{mix} denote the input temperature for the grease trap wastes and the mixture methanol/H_2SO_4, respectively. Besides, V is the (known) effective volume of the reaction medium, ρ_{FFA}, ρ_{Mix}, ρ, γ_{FFA}, γ_{Mix} and γ_P represent the densities and heat capacities of the grease trap wastes, the reagent mixture methanol/H_2SO_4 and the reaction products, respectively. In addition, U is the overall heat transfer coefficient, ΔH is the entalphy of the reaction and C_{Ai} is the inflow concentration of FFAs. The state variables C_A, C_E and C_W represent the concentration of FFAs, organic esters (i.e. biodiesel) and water, respectively, whereas $C_M(0)$ is the initial concentration of the methanol, that is considered as a constant because it is the reagent in excess. Besides, k_1 and K_{eq} are described by Arrhenius and Van't Hoff expressions, respectively. The dynamical model represented by equations (1)-(4) has been experimentally validated

with the numerical values for densities, heat capacities, kinetic parameters, operating conditions and disturbances that are described in (Aguilar-Garnica et al., 2014).

2.3. Model Fuzzification

Let us define the following premise variables: $z_1(t) = k_1 C_M(0)$, $z_2(t) = k_1 \frac{C_E}{K_{eq}}$ and $z_3(t) = k_1 \frac{C_W}{K_{eq}}$ that remain bounded as follows: $a_1 \leq z_1(t) < a_2$, $b_1 \leq z_2(t) < b_2$ and $c_1 \leq z_3(t) < c_2$. Then, the dynamical model given by equations (1)-(4) can be alternatively expressed as

$$\frac{dx}{dt} = A\left(z_1(t), z_2(t), z_3(t)\right)x + Bu \tag{5}$$

In equation (5) $x = \left[\begin{array}{cccc} C_A & T & C_E & C_W \end{array}\right]^T$, $u = \left[\begin{array}{cccc} C_{Ai} & T_{AG} & T_{Mix} & T_J \end{array}\right]^T$ and

$$A\left(z_1(t), z_2(t), z_3(t)\right) = \begin{pmatrix} -\frac{F_{FFA}}{V} - z_1(t) & 0 & z_3(t) & 0 \\ -\frac{\Delta H}{\rho \gamma_P} z_1(t) & -A_{22} & 0 & \frac{\Delta H}{\rho \gamma_P} z_2(t) \\ z_1(t) & 0 & -\frac{F}{V} - z_3(t) & 0 \\ z_1(t) & 0 & 0 & -\frac{F}{V} - z_2(t) \end{pmatrix} \tag{6}$$

$$B = \begin{pmatrix} \frac{F_{FFA}}{V} & 0 & 0 & 0 \\ 0 & \frac{F_{FFA}\rho_{FFA}\gamma_{FFA}}{\rho V \gamma_P} & \frac{F_{Mix}\rho_{Mix}\gamma_{Mix}}{\rho V \gamma_P} & U \\ 0 & 0 & 0 & 0 \\ 0 & 0 & 0 & 0 \end{pmatrix} \tag{7}$$

Here $A_{22} = \left(\frac{F_{FFA}\rho_{FFA}\gamma_{FFA}}{\rho V \gamma_P} + \frac{F_{Mix}\rho_{Mix}\gamma_{Mix}}{\rho V \gamma_P} + \frac{U}{\rho V \gamma_P}\right)$ is an element of matrix A given by equation (6) Now, let us define the following membership functions $E_1 = \frac{z_1(t)-a_2}{a_1-a_2}$, $E_2 = \frac{a_1-z_1(t)}{a_1-a_2}$, $N_1 = \frac{z_2(t)-b_2}{b_1-b_2}$, $N_2 = \frac{b_1-z_2(t)}{b_1-b_2}$, $M_1 = \frac{z_3(t)-c_2}{c_1-c_2}$ and $M_2 = \frac{c_1-z_3(t)}{c_1-c_2}$ that make possible to propose the following Tagaki-Sugeno fuzzy model for the esterification process (see further details in Guillén-Flores et al., 2013):

$$\frac{dx}{dt} = \sum_{i=1}^{8} h_i \left(A_i x + Bu\right) \tag{8}$$

where $h_i = E_{\phi(i,1)} N_{\phi(i,2)} M_{\phi(i,3)}$, $A_i = A\left(a_{\phi(i,1)}, b_{\phi(i,2)}, c_{\phi(i,3)}\right)$, B is given by equation (7) and

$$\begin{aligned} 2^4 \phi(i,j) = {} & 3 \cdot 2^{j-1}\left(3 + (-1)^j\right) - 2^j \sin\left(\frac{j\pi}{2}\right)(-1)^{i+1} \\ & + \sqrt{2}\left(-1 + 5(-1)^j + 2j\right)\cos\left(\frac{(2i+1)\pi}{4}\right) + \left(5 - (-1)^j - 2j\right) i \end{aligned} \tag{9}$$

This fuzzy model represents exactly the nonlinear dynamical model described by equations (1)-(4) in the local region defined by the bounds of $z_1(t)$, $z_2(t)$ and $z_3(t)$ according to an approach known as sector nonlinearity (Tanaka and Wang, 2001).

2.4. Observers design

2.4.1. Asymptotic observer

A state variable partition is necessary to design the AO . The variables to be estimated are gathered in ξ_1 $\left(i.e.,\ \xi_1 = \left[\begin{array}{ccc} C_A & C_E & C_W \end{array}\right]^T\right)$ and the measured variables in ξ_2 (i.e. $\xi_2 = T$). Thus, the dynamical model for the esterification process can be partitioned into: $\frac{d\xi_1}{dt} = K_1 f + D_{11}\xi_1 + D_{12}\xi_2 + H_1$ and $\frac{d\xi_2}{dt} = K_2 f + D_{21}\xi_1 + D_{22}\xi_2 + H_2$ where $f = k_1 C_M(0)\left(C_A - \frac{C_E C_W}{K_{eq} C_M(0)}\right)$ is the nonlinear term, $K_1 = \left[\begin{array}{ccc} -1 & 1 & 1 \end{array}\right]^T$, $K_2 = -\frac{\Delta H}{\rho \gamma_P}$, $D_{11} = -\frac{F}{V} I_{3X3}$, $D_{12} = 0_{3X1}$, $D_{21} = 0_{1x3}$, $D_{22} = -A_{22}$, $H_1 = \left[\begin{array}{ccc} \frac{F_{FFA} C_{Ai}}{V} & 0 & 0 \end{array}\right]^T$ and

$$H_2 = \left(\frac{F_{FFA}\rho_{FFA}\gamma_{FFA}T_{AG}}{\rho V \gamma_P} + \frac{F_{Mix}\rho_{Mix}\gamma_{Mix}T_{mix}}{\rho V \gamma_P} + \frac{UT_J}{\rho V \gamma_P}\right) \tag{10}$$

In addition, it is possible to obtain a couple of matrices $\Lambda_1 = I_{3\times 3}$ and $\Lambda_2 = \left[\begin{array}{ccc} -\frac{\rho\gamma_P}{\Delta H} & \frac{\rho\gamma_P}{\Delta H} & \frac{\rho\gamma_P}{\Delta H} \end{array}\right]^T$ such that $\Lambda_1 K_1 + \Lambda_2 K_2 = 0$. The AO's structure remains as follows (Bastin and Dochain (1990)):

$$\frac{d\hat{w}}{dt} = W\hat{w} + ZT + \Lambda_1 H_1 + \Lambda_2 H_2 \tag{11}$$

$$\hat{w}(0) = \hat{\xi}_1(0) + \Lambda_2 T(0) \tag{12}$$

$$\hat{\xi}_1 = \hat{w} - \Lambda_2 T \tag{13}$$

Notice that this observer effectively does not require the knowledge of the nonlinear term f that is related with the process kinetics. Besides, $\hat{\xi}_1$ is the estimate provided by the AO for ξ_1 whereas $H_2$is given by equation (10) while W and Z have the following structure

$$W = Z\Lambda_1 D_{11} + \Lambda_2 D_{21} = -\frac{F}{V} I_{3X3} \qquad Z = \Lambda_1 D_{12} + \Lambda_2 D_{22} - W\Lambda_2 \left(\begin{array}{ccc} Z_{11} & 0 & 0 \\ 0 & Z_{22} & 0 \\ 0 & 0 & Z_{33} \end{array}\right)$$

with $Z_{11} = \frac{F_{FFA}\rho_{FFA}\gamma_{FFA} + F_{Mix}\rho_{Mix}\gamma_{Mix} + U + F\rho\gamma_P}{V\Delta H}$ and $Z_{22} = Z_{33} = -Z_{11}$.

2.4.2. Fuzzy reset observer with discrete measurements of T

A FRO can be derived for any process whose dynamical model might be expressed in terms of the fuzzy representation (8)-(9) (Guillén-Flores et al. (2013)). Since the dynamical model of the esterification process matches this fuzzy representation then it is possible to derive a FRO whose structure is given by

$$\frac{d\hat{x}}{dt} = \sum_{i=1}^{8} h_i\left(A_i\hat{x} + Bu\right) \quad t \neq k\delta \tag{14}$$

$$\hat{x}(k\delta^+) = \hat{x}(k\delta) - G_d\left(T(k\delta) - \hat{T}(k\delta)\right) \quad t = k\delta \tag{15}$$

where $\hat{x}$ is the estimate of x, δ is the sampling period, $k = 1, 2, 3, ..., x(k\delta^+)$ is the updated initial condition defined as $\hat{x}(k\delta^+) = \lim_{\varepsilon\to 0}\hat{x}(k\delta^+ + \varepsilon)$ and $G_d = Q^{-1}R$ is the observer's gain with matrices $Q > 0$, R and a constant ϑ derived from Linear Matrix Inequalities specified in (Guillén-Flores et al., 2013).

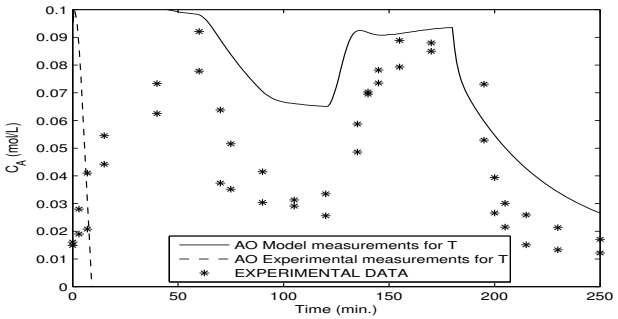

Figure 1: Experimental results for the concentration of FFAs and asymptotic observer performance

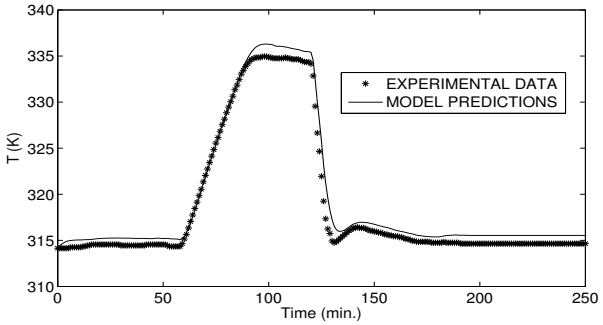

Figure 2: Experimental data and model predictions for the Reactor Temperature T

3. Results, discussion and conclusion

The esterification process was carried out in duplicate over a period of 250 minutes with disturbances on C_{Ai} and on T_J. Samples were analyzed in order to be determined the concentration of FFAs (i.e. C_A) considering the AOCS official method Ca 5a-40. The proposed observers are able to estimate C_A, C_E and C_W but for validation purposes it was decided to measure only C_A because it can be obtained by a very simple titration method compared with the tests to determine C_E and C_W. The experimental results of C_A and T are shown as star points in Figure 1 and Figure 2, respectively. In Figure 2, the solid line corresponds to the temperature that is obtained from the mathematical model eqs. (1)-(4). Note that the experimental results for T remain very close to the temperature described by the model.

The AO, which is described by equations (11)-(13), has been initialized with $\hat{C}_A(0) = 0.1 molL^{-1}$ and its performance is shown in Figure 1. The solid line corresponds to the AO with temperatures provided by the model and in this case, the AO's performance can be considered as satisfactory. Nevertheless, when the model measurements are replaced by the experimental measurements for T, the AO simply does not work well (see Figure 2, dashed line) in spite that both measurements and the model values for T remains very close. *The poor performance of the AO when actual temperature measurements are being used can be associated to a deficient model. This performance can also be due to the relatively high magnitude of the element Λ_2 that enhances slight variations on the measured variable when the estimated state is being computed (see eq. 13).* Thus, the AO can be considered as highly sensitive in temperature variations for this specific es-

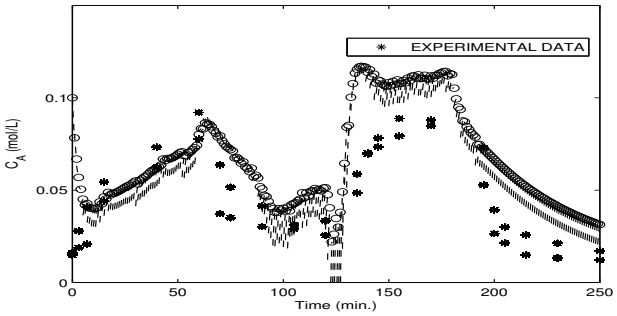

Figure 3: Fuzzy reset observer performance with sampling period $\delta = 1$ min

terification process and then, it is necessary to consider alternative estimation schemes such as the FRO. The performance of this fuzzy observer is shown in Figure 3. Is this case, the estimation scheme was updated according with equations (14)-(15) including experimental temperature measurements captured every minute (i.e. $\delta = 1min$). For $\delta = 1min$, the observer gain was determined to be $G_d = \begin{bmatrix} -0.046 & -1.8 & 0.062 & 0.056 \end{bmatrix}^T$. The FRO was initialized with the same initial condition than the AO and the discrete actualization is clearly visible every minute where a jump on the states estimation can be seen. The circles depict the reset observer result at $\delta = 1$, whereas the dashed lines describe the reset observer performance among sampling periods. It can be concluded that the FRO provides the best performance among the proposed monitoring tools for the esterification of grease trap wastes.

Acknowledgments:

The author gratefully acknowledge financial support from the Consejo Nacional de Ciencia y Tecnología (CONACyT) through the project CB2009-133554 to perform this study.

References

Aguilar-Garnica, E., Rodríguez-Palomera, F., García-Sandoval, J. P., Escalante, F. M., Sep 2014. Dynamical modeling for biodiesel production from grease trap wastes. Chemical Engineering Science 117, 396–406.

Bastin, G., Dochain, D., 1990. On line estimation and adaptive control of bioreactors. Elsevier.

Canakci, M., 2007. The potential of restaurant waste lipids as biodiesel feedstocks. Bioresource Technology 98 (1), 183–190.

Canakci, M., Van Gerpen, J., 2001. Biodiesel production from oils and fats with high free fatty acids. Transactions of the ASAE 44 (6), 1429–1436.

Guillén-Flores, C., Castillo-Toledo, B., Garcia-Sandoval, J., Di Gennaro, S., Gonzalez Alvarez, V., 2013. A reset observer with discrete/continuous measurements for a class of fuzzy nonlinear systems. Journal of the Franklin Institute 350 (8), 1974–1991.

Park, J.-Y., Lee, J.-S., Wang, Z.-M., Kim, D.-K., 2010. Production and characterization of biodiesel from trap grease. Korean J. Chem. Eng. 27 (6), 1791–1795.

Price, J., Nordblad, M., Woodley, J. M., Huusom, J. K., Dec 2014. Real-time model based process monitoring of enzymatic biodiesel production. Biotechnology Progress.

Tanaka, K., Wang, H. O., 2001. Fuzzy Control Systems Design and Analysis: A Linear Matrix Inequality Approach. John Wiley & Sons, Inc.

Wen, Z., Yu, X., Tu, S.-T., Yan, J., Dahlquist, E., 2010. Biodiesel production from waste cooking oil catalyzed by tio2-mgo mixed oxides. Bioresource Technology 101 (24), 9570–9576.

Krist V. Gernaey, Jakob K. Huusom and Rafiqul Gani (Eds.), 12th International Symposium on Process Systems Engineering and 25th European Symposium on Computer Aided Process Engineering.
31 May - 4 June 2015, Copenhagen, Denmark.

Improving Data Reliability for Process Monitoring with Fuzzy Outlier Detection

Harakhun Tanatavikorn[a] and Yoshiyuki Yamashita[a]

[a]*Department of Chemical Engineering; Tokyo University of Agriculture and Technology; Tokyo, Japan*
harakhun@hotmail.com

Abstract

To implement on-line process monitoring techniques that utilize principal component analysis (PCA) or partial least squares (PLS) models, it is important to use reliable data that represents normal process operation when constructing the models. In this paper, a novel flexible fuzzy treatment method is developed for the detection of outliers in process data. This method utilizes a combination of fuzzy C-means clustering algorithm to separate the data into clusters and a fuzzy inference engine to assign a degree of outlier to data points. The current iteration of the fuzzy inference engine performs an evaluation based on distance as a measure of standard deviation and fuzzy membership values to determine the degree of outlier. This method can be considered a hybrid method that incorporates statistical parameters into a fuzzy strategy. Decisions on how to handle the data can then be made based on the degree of outlier. This degree of outlier can be conveniently translated into a relative weight assigned to an outlier entering downstream data processes.

The fuzzy treatment method was applied to benchmark penicillin production process data containing artificial outliers data points. The proposed method was able to detect the outliers in the process data. Though data points in the transient region were prone to high degree of outlier. Additionally it is possible to modify the fuzzy inference engine to utilize different criteria, such as data density or spread to evaluate outlierness. The result is presented along with a discussion on the advantages of this method as a flexible treatment of process data. The methodology will be applied to future investigation on PCA based process monitoring.

Keywords: Process Monitoring, Process Data, Outlier Detection, Fuzzy logic, Batch, Fuzzy C-means

1. Introduction

The advances in the field of sensors, computers, and informatics have exponentially increased the amount of available process data. Large plants record process variables, product quality, production, and maintenance information on a frequent basis. Reliable process data is a vital component in the implementation of on-line process monitoring techniques that control these large facilities. Data reliability, in this context, refers to the accuracy and completeness of data, given the intended purpose for use. Reliability does not mean that the data is error-free; it means that any errors present and found in the data are within a tolerable range. This tolerance is dependent upon evaluation that the associated risks have been assessed and determined that the errors are not significant enough to doubt the findings or conclusions based on the data.

Given a set of process data, an outlier is an element that deviates significantly from normal or

sometimes meaningful range. They represent either errors or interesting observations; such as mechanical faults, changes in system behavior, instrument error, or simply through human error. The presence of outliers may lead to inaccurate process models and wrong analytical conclusions. Therefore outlier detection is used to detect and, when appropriate, remove anomalous entries from process data to improve their reliability for process monitoring. Conventional outlier detection methods rely on statistical tests to perform a screening of a dataset. Classical test are the Grubbs (1950) and the Dixon (1950) ones; other similar tests have also been formulated by Quesenberry and David (1961), and Ferguson (1961). In essence, all these tests provide a statistic to be compared with a critical value in order to evaluate whether a data point is an outlier. Their difference is mainly construction of the statistic and the selection of critical value. Since ultimately outlier detection and analysis is a subjective exercise, classical methods are often rigid and sometime face limitations posed by their statistical nature.

In this paper, a novel flexible fuzzy treatment method is developed for the detection of outliers in process data. This method utilizes a combination of fuzzy C-means clustering algorithm to separate the data into clusters and a fuzzy inference engine to assign a degree of outlier to data points. The main advantage of the method is the flexibility of the inference engine where different evaluation criteria can be implemented. This provides a adjustable subjective framework for evaluating large size data sets. The organization of the paper is as follows: Section 2 describes the components and methodology of the fuzzy treatment method. Section 3 presents selected results of applying the fuzzy treatment method on simulated process data. Finally, Section 4 concludes the paper.

2. Methodology

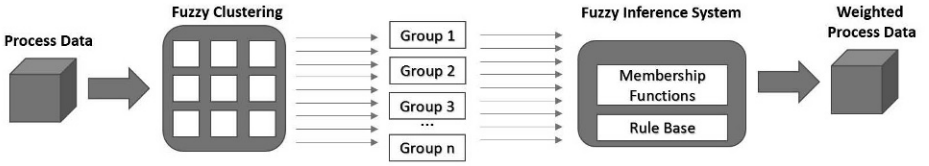

Figure 1: Fuzzy treatment method

2.1. Fuzzy c-means Clustering

The main purpose of fuzzy c-means clustering is the partitioning of data into a collection clusters, where each data point is assigned a membership value for each cluster. Fuzzy c-means clustering involves two processes: the calculation of cluster centers and the assignment of points to these centers using a form of Euclidian distance. These processes are repeated until the cluster centers stabilize. The algorithm is similar to crisp clustering, such as k-means clustering, in several aspects but incorporates fuzzy set concepts of partial memberships by allowing data points to belong to more than one cluster. This can be observed in the form of overlapping clusters. Additionally many crisp clustering techniques tend to have difficulties in handling extreme outliers but fuzzy clustering algorithms tend to give them small membership degree in surrounding clusters (Looney, 1999). The algorithm also needs a fuzzification parameter m which determines the degree of fuzziness in the clusters. When the value of m is 1 the algorithm works like crisp clustering, while larger values of m increases the fuzzification of the clustering algorithm thus allowing a higher degree cluster overlap.

Based on the clustering results, k different data groups are prepare from the initial data. The assignment of x_i to a data group depends it's membership value corresponding to each cluster, u_{ik}. x_i gets assigned to a cluster based on the following conditions:

- The highest value of u_{ik} denotes which group k the x_i is placed in;
- If the difference between highest u_{ik} and the next highest $u_{i(k-1)}$ is less than the threshold value, then x_i gets placed in both groups;
- Additionally if the highest valuest of u_{ik} is below 0.2 then the top 3 u_i are placed 3 groups.

It is important to note that, the selection of the threshold value δ depends on the selecting of the number of clusters n for the fuzzy clustering. In this work, a plot of the *within groups sum of squares* by number of clusters extracted is used to determine the appropriate number of clusters based on the bend in the plot (Everitt and Hothorn, 2006). This is often referred to as the "elbow" method.

2.2. Fuzzy Inference System

Fuzzy inference is the process of formulating the mapping from a given input to an output using fuzzy logic. The mapping then provides a basis from which decisions can be made, or patterns discerned. The FIS selected for implementation in this paper was proposed by D'Errico and Murru (2012) with modifications to the FIS rule base and input variables. The modified FIS includes two inputs (distance and grouping) and one output (degree of outlier). The inference engine is the basic Mamdani Model was constructed using the R Statistical Software 'frbs' package.

The fuzzy distance is obtained after a fuzzification of the crisp distance input $d = d(x_i, \mu)$, according to:

- if $d(x_i, \mu) \geq 4\sigma_{max}$, then distance is very long;
- if $3\sigma_{max} \leq d(x_i, \mu) \leq 5\sigma_{max}$, then distance is long;
- if $2\sigma_{max} \leq d(x_i, \mu) \leq 4\sigma_{max}$, then distance is medium;
- if $d(x_i, \mu) \leq 3\sigma_{max}$, then distance is short.

where
σ_{max} : is the highest observed standard deviation among the chosen variables of the in the corresponding group.
The fuzzy grouping is obtained after a fuzzification of the highest membership values $g = g(x_i, uik)$ from the results of the fuzzy clustering, according to:

- if $g(x_i, u_{ik}) \geq 0.4\sigma$, then grouping is grouped;
- if $0.25 \leq g(x_i, u_{ik}) \leq 0.45$, then grouping is moderate;
- if $0.2 \leq g(x_i, u_{ik})$, then grouping is spread;

where
u_{ik} : is the membership value of the data point i to the data group k.
As to outlierness:

- if $\rho \geq 0.5\sigma$, then outlierness is high;
- if $0.25 \leq \rho \leq 0.75$, then outlierness is intermediate;
- if $0.5 \leq \rho$, then outlierness is low;

The inference system is based on the following 11 rules:

1. if (distance is short) and (grouping is grouped), then outlierness is (low)
2. if (distance is short) and (grouping is moderate), then outlierness is (intermediate)
3. if (distance is short) and (grouping is spread), then outlierness is (intermediate)
4. if (distance is medium) and (grouping is grouped), then outlierness is (low)
5. if (distance is medium) and (grouping is moderate), then outlierness is (intermediate)
6. if (distance is medium) and (grouping is spread), then outlierness is (high)
7. if (distance is long) and (grouping is grouped), then outlierness is (intermediate)
8. if (distance is long) and (grouping is moderate), then outlierness is (intermediate)

9. if (distance is long) and (grouping is spread), then outlierness is (high)
10. if (distance is very long), then outlierness is (high)
11. if (grouping is spread), then outlierness is (high)

This degree of outlier can be conveniently translated into a relative weight that allows a fuzzy outlier to still contribute to a certain extent to any subsequent processes.

2.3. Simulation Example: Fed-batch Penicillin Cultivation Process

Birol et al. (2002) developed a simulation software based on a detailed unstructured model for penicillin production in a fed-batch fermentor. The model extends the mechanistic model of Bajpai and Reuß (1980) by adding input variables such as pH, temperature, aeration rate, agitation power, and feed flow rate of substrate along with introducing the CO2 evolution term. The model is used to generate process data for testing the fuzzy treatment method.

A batch was simulated based on an integration step size of 0.02 h and a sampling interval of 0.5 h. In the simulation, an initial batch culture is followed by a fed-batch operation depending on the depletion of the carbon source. The process switches to fed-batch mode of operation when the level of glucose concentration reaches 0.3 g/l. Fermenter Temperature and pH have a strong influence on product quality. They are controlled by PID controllers whose settings in the simulation software were left at default values for normal operation. The main variables extracted for fuzzy treatment were pH and fermenter temperature.

5 artificial outlier points based on standard deviations were inserted into the simulated data:

1. Outlier$[0.615\sigma_T, -2\sigma_{pH}]$ in Transient region of pH @ 20
2. Outlier $[3\sigma_T, 3\sigma_{pH}]$ (in Temperature and pH @ 200
3. Outlier $[3\sigma_T, -0.3925\sigma_{pH}]$in Temperature @ 400
4. Outlier $[-0.217\sigma_T, -3\sigma_{pH}]$ in pH @ 600
5. Outlier $[6\sigma_T, 6\sigma_{pH}]$ in Temperature and pH @ 800

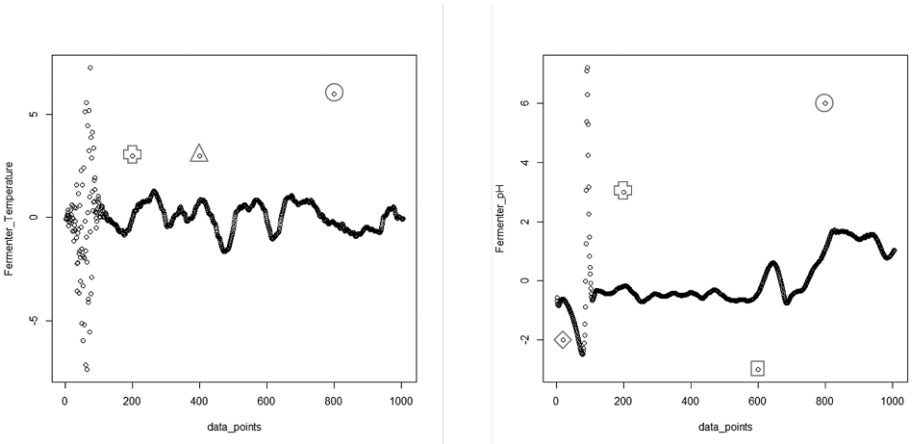

Figure 2: Fuzzy treatment method

3. Result and discussion

As previously mentioned, the elbow method was used to determine the number of cluster for the fuzzy c-means clustering. The number of clusters selected is 10. Additionally a corresponding

threshold value of $\delta = 0.2$ was chosen for the clustering. The group assignment and outlierness value for each artificial outlier point is presented in Table1.

The Fuzzy Treatment Method is able to evaluate and assign an appropriately high outlierness to the artificial outlier points. It is also observed, as seen in Table 2, that the method assigns high outlierness to extreme values, such as those found in the transition region (approx. $0 \leq$ index≤ 150). This is expected due to the fact that the 2 basic input criteria, distance and fuzzy c-means membership values, used to evaluate the outlierness of a data point are sensitive to extreme and/or isolated values. In particular it is interesting to note that a low fuzzy c-means membership value or an evenly spread out membership value distribution between the groups signifies that a data point is relatively isolated from data clusters.

The transient region, where large and rapid fluctuations occur, remain a challenge for the fuzzy treatment method. It is speculated that changing or increasing the numbers of input parameters will improve performance in the transient region. Integration of pattern based outlier detection methods, such as PLS or neural networks, may improve the performance in the transient region. Though this is subjected to further study.

Table 1: Group assignment and outlierness of artificial outliers

Data Point Index	**Group Assignment and Outlierness**			**Variable with Artifical Outlier**
20	3	5	7	pH
	0.583	0.583	0.583	
200	8	9	10	Temp. and pH
	0.75	0.75	0.75	
400	5	7		Temp.
	0.75	0.75		
600	1	2	3	pH
	0.75	0.75	0.75	
800	8	9	10	Temp. and pH
	0.75	0.75	0.75	

Table 2: Group assignment and outlierness of selected data points

Data Point Index	**Group Assignment and Outlierness**			**Remarks**
70	3	5	7	Transient Region
	0.75	0.75	0.75	
100	7	8		Transient Region
	0.583	0.75		
130	1	2		
	0.516	0.456		
300	1			
	0.25			
700	7			
	0.25			

A summary and comparison of the fuzzy treatment method can be seen in Table 3. It is compared to a multivariate outlier detection proposed by Filzmoser et al. (2005) and the Local Outlier Factor (LOF) proposed by Breunig et al. (2000). All three methods yield similar results and have difficulties in the transient region of the data; resulting in false positives or being unable to distinguish the artificial outlier from extreme data points. Though it is important to note that it is possible to integrate the outlier detections proposed by Filzmoser et al. (2005) and Breunig et al. (2000) into the fuzzy treatment methodology.

Table 3: Summary and comparison of fuzzy outlier treatment method

Data Point Index	**Fuzzy Treatment Method (Outlierness)**	**Robust mahalanobis distance based on the adjusted mcd estimator**	**Local Outlier Factor**
20	0.5833	Detected	1.02261 (rank 595/1005)
200	0.75	Detected	1.890222 (rank 43/1005)
400	0.75	Detected	1.822154 (rank 49/1005)
600	0.75	Detected	1.425353 (rank 107/1005)
800	0.75	Detected	2.619494 (rank 21/1005)

4. Conclusion

The presence of suspected outlier values in process data has been a long-standing problem. The difficulty of the problem is mainly due to the subjective nature of outlier detection. A single criteria to distinguish different types of outliers is generally insufficient and does not address the subjective nature of outlier detection. To overcome this issue a novel fuzzy logic approach has been proposed and a system has been implemented. The system performance has been manually tuned: optimization of input parameters along with investigation into automatic-tuning (self-learning) is envisaged for further developments.

The fuzzy treatment method utilizes fuzzy c-means clustering to separate multi-variate data into clusters. Data points can belong to more than a single cluster due to the nature of fuzzy clustering. The concept of fuzzy outlier is then adapted from D'Errico and Murru (2012) with modifications to FIS input parameters and rule-base. Utilizing individual cluster standard deviation and fuzzy c-means clustering membership values as inputs, the outlierness of a data point is computed as a result of a 2-input/1-output fuzzy inference system. The overall fuzzy treatment methodology is a generalize approach and can be modified to suit the application. It provides a flexible and highly subjective framework for outlier detection.

From the results of the research conducted so far, the following conclusions can be pointed out:

1. The fuzzy treatment method provides a subjective framework for integrating various outlier detection parameters.
2. The fuzzy c-means clustering membership values have correlation to extreme and isolated values. These values may potentially be outliers.

References

Bajpai, R. K., Reuß, M., 1980. A mechanistic model for penicillin production. Journal of Chemical Technology and Biotechnology 30 (1), 332–344.

Birol, G., Ündey, C., Çinar, A., 2002. A modular simulation package for fed-batch fermentation: penicillin production. Computers & Chemical Engineering 26 (11), 1553 – 1565.

Breunig, M. M., Kriegel, H., Ng, R. T., Sander, J., 2000. LOF: identifying density-based local outliers. In: Proceedings of the 2000 ACM SIGMOD International Conference on Management of Data, May 16-18, 2000, Dallas, Texas, USA. pp. 93–104.

D'Errico, G. E., Murru, N., 2012. Fuzzy treatment of candidate outliers in measurements. Adv. Fuzzy Systems 2012.

Dixon, W. J., 12 1950. Analysis of extreme values. Ann. Math. Statist. 21 (4), 488–506.

Everitt, B., Hothorn, T., 2006. A Handbook of Statistical Analyses Using R. Chapman and Hall.

Ferguson, T. S., 1961. On the rejection of outliers. In: Proceedings of the Fourth Berkeley Symposium on Mathematical Statistics and Probability, Volume 1: Contributions to the Theory of Statistics. University of California Press, Berkeley, Calif., pp. 253–287.

Filzmoser, P., Garrett, R. G., Reimann, C., Jun. 2005. Multivariate outlier detection in exploration geochemistry. Comput. Geosci. 31 (5), 579–587.

Grubbs, F. E., 1950. Sample criteria for testing outlying observations. Ann. Math. Statistics 21, 27–58.

Looney, C., 1999. A fuzzy clustering and fuzzy merging algorithm. Tech. rep., Technical Report CS-UNR-101-1999.

Quesenberry, C. P., David, H. A., Dec. 1961. Some tests for outliers. j-BIOMETRIKA 48 (3/4), 379–390.

Krist V. Gernaey, Jakob K. Huusom and Rafiqul Gani (Eds.), 12th International Symposium on Process Systems Engineering and 25th European Symposium on Computer Aided Process Engineering.
31 May - 4 June 2015, Copenhagen, Denmark.

Inversion-based feedforward control design for the Droop model

Alexander Schaum[a] and Thomas Meurer[a]

[a]*Chair of Automatic Control, Christian-Albrechts-University Kiel, Germany*
alsc@tf.uni-kiel.de

Abstract

An inversion-based feedforward control for the Droop model for microalgae growth in the chemostat is presented. The dilution rate is manipulated in such a way that a desired biomass trajectory for set point changes is tracked. For this purpose a stable inversion technique is employed exploiting the asymptotic stability of the internal dynamics due to mass-conservation. The impact of unknown feed substrate step changes on the controller performance is analytically delimited using the mass-conservation-based bounded input-bounded output stability property. Numerical results show that the transition time can be significantly reduced by the proposed approach in comparison to a simple step change in the feed flow showing the bounded downgrade due to unknown variations in the feed concentration.

Keywords: Feedforward control, microalgae growth, Droop model, set point transition

1. Introduction

The production of high-value compound production like fatty-acids, vitamins, or pigments have great impact in the biotechnology market. Particularly usefull resources for these products with relatively rapid growth are microalgae. Additionally, microalgae are also of interest as sources for hydrogen and biofuel production (Havlik et al., 2013).

Typically process control is used to improve the process response times and robustness with respect to unknown (and unpredictable) perturbations in the feed variables, etc. In several process control application examples (Graichen et al., 2009; Hagenmeyer and Nohr, 2008; Kleinert et al., 2010) it has been numerically and experimentally shown that substantial improvement can be achieved using model-based feedforward control. This motivates the design of a feedforward control strategy for microalgae growth processes to reduce the time requirements for set-point changes. Furthermore, as such processes are typically subject to fluctuations, specially in the feed concentration, the effects of such variations has to be carefully delimited. This taks are addressed in the present paper, by exploiting the stable inversion technique (Chen and Paden, 1996; Devasia, 1999). For this purpose, using mass-conservation arguments and the reactor bifurcation behavior it is rigurously shown that bounded feed perturbation will lead to bounded deviations from the reference output. Numerical simulation results illustrate the obtained performance.

2. Droop's microalgae growth model

The Droop model for microalgae growth in the chemostat is given by (Droop, 1968; Lemesle and Mailleret, 2008)

$$\begin{aligned} \dot{b} &= -db + \mu(q)b, & b(0) &= b_0 \\ \dot{q} &= \rho(s) - \mu(q)q, & q(0) &= q_0 \\ \dot{s} &= d(s_{in} - s) - \rho(s)b, & s(0) &= s_0 \\ y &= b, \end{aligned} \tag{1}$$

where b is the biomass concentration, q is the internal nutrient quota (i.e. the intracellular nutrient concentration per biomass unit), s is the extracellular nutrient concentration, s_{in} is the *piecewise constant, unknown* feed concentration with nominal value $\bar{s}_{in}$, μ is the growth rate, ρ is the uptake rate, d is the dilution rate (i.e. the flow-colume quotient q/V), and y is the biomass measurement.

The growth and uptake rates are given by the monotonic relations

$$\mu(q) = \bar{\mu}\left(1 - \frac{k_q}{q}\right), \quad \rho(s) = \frac{k_0 s}{K_s + s}, \tag{2}$$

where $\bar{\mu}$ is the (hypothetic) maximum growth at infinite quota, k_q is the minimum quota necessary for biomass growth, k_0 is the maximum uptake rate $\rho(s)$, and K_s the half-saturation constant.

By the change of variables

$$\theta = q - k_q \tag{3}$$

the growth rate μ can be written in the standard Monod form

$$\nu(\theta) := \mu(\theta + k_q) = \frac{\bar{\mu}\theta}{k_q + \theta} \tag{4}$$

and the dynamics (1) become

$$\dot{b} = -db + \nu(\theta)b, \qquad b(0) = b_0 \tag{5a}$$

$$\dot{\theta} = \rho(s) - \bar{\mu}\theta, \qquad \theta(0) = q_0 - k_q \tag{5b}$$

$$\dot{s} = d(s_{in} - s) - \rho(s)b, \quad s(0) = s_0 \tag{5c}$$

$$y = b. \tag{5d}$$

In vector notation the preceding dynamics are written as

$$\dot{\mathbf{x}} = \mathbf{f}(\mathbf{x}, u, s_{in}), \quad y = h(\mathbf{x}). \tag{6}$$

with

$$\mathbf{x} = [b, \theta, s]', \quad h(\mathbf{x}) = x_1.$$

For the purpose at hand, the subsequent analysis and design are based on the model (5).

3. Reactor dynamics

In this section the reactor dynamics are characterized in terms of the input-output behavior including steady-state multiplicity, bifurcation and bounded-input-bounded-output stability properties, which are essential for the subsequent design of a feedforward control strategy. The discussion presented here verifies and complements the one reported in (Lemesle and Mailleret, 2008) and forms the basis of the subsequent characterization of the bounded-input bounded-output stability of the reactor with the feedforward controller designed in Section 4.

3.1. Bifurcation behavior

Consider the equilibrium conditions

$$0 = -db + \nu(\theta)b, \quad 0 = \rho(s) - \bar{\mu}\theta, \quad 0 = d(s_{in} - s) - \rho(s)b \tag{7}$$

Clearly, the washout solution $\mathbf{x}_w = \begin{bmatrix} 0 & s_{in} & \rho(s_{in})/\bar{\mu} \end{bmatrix}^T$ is a solution. For $b > 0$ the following conclusion sequence is valid

$$d = \nu(\theta) \quad \Leftrightarrow \quad \theta = \nu^{-1}(d) = \frac{dk_q}{\bar{\mu} - d} = \sigma_\theta(d) \tag{8a}$$

$$s = \rho^{-1}(\bar{\mu}\theta) = \rho^{-1}(\bar{\mu}\nu^{-1}(d)) = \sigma_s(d) \tag{8b}$$

$$b = \frac{d(s_{in} - \sigma_s(d))}{\rho(\sigma_s(d))} = \sigma_b(d, s_{in}). \tag{8c}$$

In particular, these relations imply that for $d < \max \nu = d_*$ there are two biomass steady states, with the washout being an unstable saddle respulsor and the reactor operation point as asymptotically stable attractor node. At $d = d_*$ a transcritical bifurcation takes place, leading to the disappearance (in a physically feasible regime) of the operation point, and leaving the washout as unique global (in $\mathbb{R}^3_+$) attractor. The associated solution diagram is presented in Figure 1.

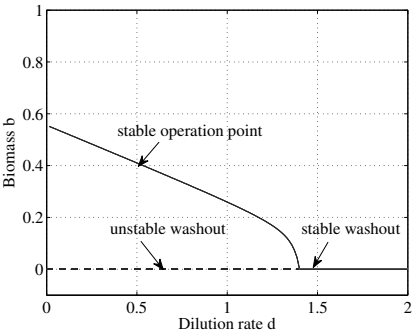

Figure 1: Solution diagram for the Droop model (5) showing the equilibrium dilution rate input-to-biomass output relation.

Note that the sensitivity of the bifurcation point d_* with respect to the feed concentration s_{in} satisfies for $s_{in} \gg k_s$

$$\frac{\partial d_*}{\partial s_{in}} = \frac{\partial d_*}{\partial \rho}\frac{\partial \rho}{\partial s}|_{s=s_{in}} \ll 1$$

given that the slope of $\rho(s)$ attains its minimum over $[0, s_{in}]$ at s_{in} which is much less than one.

3.2. Practical stability

The notion of practical stability (Salle and Lefschetz, 1961) ensures on the one hand asymptotic stability in the absence of perturbations and on the other hand bounded input bounded output stability with respect to perturbations. Mathematically, this can be formulated for the reactor (5) by the existence of a class-KL (increasing-decreasing) function α and a class-K (increasing) function β, so that

$$||\mathbf{x}(t) - \mathbf{x}_r(t)|| \leq \alpha(||\mathbf{x}_0 - \mathbf{x}_r(t)||, t) + \beta(|s_{in}(\cdot) - \bar{s}_{in}|), \tag{9}$$

where $\mathbf{x}_r$ is the reference trajectory for the state $\mathbf{x}$. Typical examples are $\alpha(||\mathbf{z}||, t) = ||\mathbf{z}||e^{-t}$ for some vector $\mathbf{z}$ and $\beta(|s_f(\cdot) - \bar{s}_f|) = \sup_{t \geq 0}|s_f(t) - \bar{s}_f|$. This property will be analyzed in the sequel.

Notice that from (5b) it follows that $\theta \in [0, \theta^+]$ where $\theta^+ = \rho(s_{in}^+)/\bar{\mu}$ and s_{in}^+ are the maximum nutrient quota and feed concentration, respectively. Similarly, from (5c) it follows that $s \in [0, s_{in}^+]$. Furthermore, $\theta = 0$ corresponds to a repulsor set as well as $s = 0$. Now, introduce the total substrate content in the reactor at time t

$$\mathfrak{S} = s + (\theta + k_q)b, \quad \dot{\mathfrak{S}} = d(s_{in} - \mathfrak{S}), \quad \mathfrak{S}(0) = s_0 + (\theta_0 + k_q)b_0. \tag{10}$$

It follows that $\mathfrak{S} \in [0, s_{in}^+]$ and thus $b \in [0, b^+]$ with $b^+ = s_{in}^+/k_q$ in consequence of (10). This shows that the compact pyramidal set (see Figure 2)

$$\mathscr{X} = \left\{ \mathbf{x} \in \mathbb{R}^3 | 0 \le x_2 \le \theta^+, 0 \le x_3 \le s_{in}^+, 0 \le x_3 + (x_2 + k_q)x_1 \le s_{in}^+ \right\} \subset \mathbb{R}_+^3 \tag{11}$$

is a positively invariant set for (5). The face corresponding to $b = 0$ (washout) is an invariant subset of $\mathscr{X}$.

The compact set $\mathscr{X}$ contains the planar compact set

$$\Sigma = \left\{ \mathbf{x} \in \mathbb{R}^3 | \mathfrak{S} = \bar{s}_{in} \right\} \tag{12}$$

which separates $\mathscr{X}$. For $s_{in}(t) = \bar{s}_{in}$ the set Σ is an attractor set for $\mathscr{X}$ and in Σ the operation point $\bar{\mathbf{x}}$ is the unique attractor. Actually, the dynamics in Σ are given by

$$\begin{aligned} \dot{b} &= \left[(\bar{\mu} - d) - \frac{k_q b}{s_{in} - s} \right] b, \\ \dot{s} &= d(s_{in} - s) - \rho(s) b \end{aligned}$$

and have $\bar{\mathbf{x}}$ as unique attractor node for $d < d_*$ accompanied by the repulsor washout $\mathbf{x}_w$, as follows from Poincaré-Bendixson's theorem over the positively invariant compact state set Σ. Note that for a general feed input $s_{in}(t)$ the response is given by

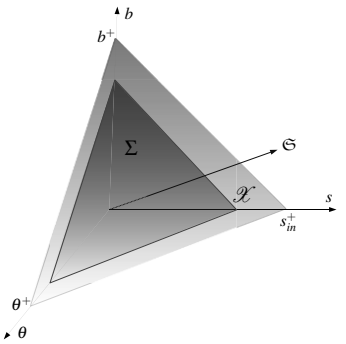

Figure 2: Compact state space sets $\mathscr{X}$ and Σ.

$$\mathfrak{S}(t) = e^{-\int_0^t d(\tau)d\tau} \mathfrak{S}(0) + \int_0^t e^{-\int_0^t d(\vartheta)d\vartheta + \int_0^\tau d(\vartheta)d\vartheta} d(\tau) s_{in}(\tau) d\tau$$

which for $s_{in}(t) = \bar{s}_{in}$ reduces to the nominal one $\bar{\mathfrak{S}}(t) = \bar{s}_{in} + e^{-\int_0^t d(\tau)d\tau}(\mathfrak{S}_0 - \bar{s}_{in})$. Thus for $|s_{in}(t) - \bar{s}_{in}| \le \delta_{in}/2$ it holds that $|\mathfrak{S}(t) - \bar{\mathfrak{S}}(t)| \le \delta_{in}/2$, meaning that the trajectories converge towards a set $\tilde{\Sigma} \supset \Sigma$ of thickness δ_{in}. Hence, for $\tilde{s}_{in}(t) \neq 0$ the reactor trajectories move within a δ_{in}-tube around the nominal one and converge towards an δ_{in} neighborhood of $\bar{x}$ (for $d < d_*$). This implies the practical stability of the reactor with respect to feed perturbations.

4. Feedforward control

In this section a feedforward control is designed to achieve trajectory tracking for operation-point changes in the Droop model. For this puropse, the stable inversion technique (Chen and Paden, 1996; Devasia, 1999) is employed. Having the biomass as output variable, denote the reference trajectory by $y^*(t) = b^*(t)$ with dynamics

$$\dot{y}^*(t) = -d^*(t)y^*(t) + \nu(\theta^*(t))y^*(t), \quad y^*(0) = y_0^*. \tag{13}$$

The requirement of transition between the two steady-states corresponding to $y(0) = b_0$ to $y(T) = b_T$ yields four boundary conditions for the reference trajectory y^*, i.e.

$$\begin{aligned} y^*(0) &= b_0, \quad y^*(T) = b_T \\ \dot{y}^*(0) &= 0, \quad \dot{y}^*(T) = 0 \end{aligned} \tag{14}$$

which are satisfied by the reference trajectory

$$y^*(t) = b_0 + (b_T - b_0)\left(3\left(\frac{t}{T}\right)^2 - 2\left(\frac{t}{T}\right)^3 \right). \tag{15}$$

The corresponding input $d^*(t)$ is thus given at each time instant by (having in mind $y = b > 0$)

$$d^*(t) = \frac{\nu(\theta^*(t))y^*(t) - \dot{y}^*(t)}{y^*(t)} \qquad (16)$$

with $\theta^*(t)$ being the solution of the reference internal dynamics

$$\dot{\theta}^*(t) = \rho(s^*(t)) - \bar{\mu}\theta^*(t)$$
$$\dot{s}^*(t) = d^*(t)(\bar{s}_{in} - s^*(t)) - \rho(s^*(t))y^*(t),$$

with $d^*(t)$ being defined in (16). This equation can be solved numerically for the pair $(\theta^*(\cdot), s^*(\cdot))$, so that $d^*(\cdot)$ can be completely determined *off-line*.

It should be noted that for arbitrary s_{in}, using the coordinate change (10), the internal dynamics can be written as

$$\dot{\mathfrak{S}} = d(s_{in} - \mathfrak{S}), \quad \dot{s} = d(s_{in} - s) - \rho(s)b$$

which, according to the analysis in Section 3, are bounded-input bounded-output stable with respect to the feed concentration.

From the preceding analysis of the reactor dynamics, it follows immediately, that due to mass conservation the reference trajectory will be exactly tracked for the nominal feed concentration $\bar{s}_{in}$ using the feedforward control (16), while for bounded perturbations in s_{in} of size δ_{in}, the reactor trajectories will move within an δ_{in}-tube around the reference trajectory, in the sense of practical stability (cp. eq. (9)).

5. Numerical simulations

In order to verify the theoretic assessment, numerical simulations using MATLAB with *ode15s* have been carried out for the parameter set (taken from (Toroghi et al., 2013)) $K_s = 0.105$, $\bar{\mu} = 2$, $k_q = 1.8$, $k_0 = 9.3$.

In Figure 3 the reactor response for the biomass set-point change from $b_0 = 52.78$ to $b_T = 27.76$ in $T = 1$ day is illustrated. The nominal trajectory is represented by the thin grey continuous line and the reactor feedforward response by the dashed green line.

For comparison purposes the open-loop response for a simple step change in the dilution rate is shown by the dash-dotted line.

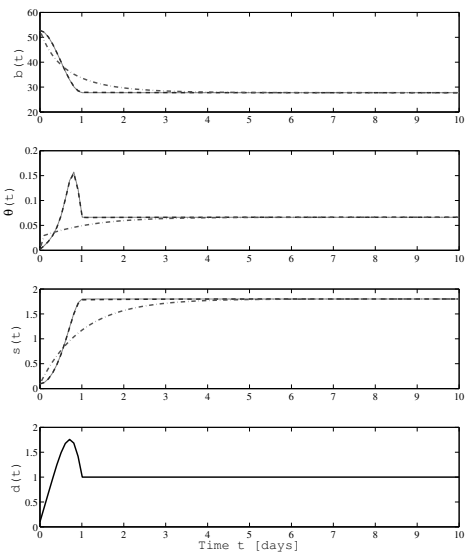

Figure 3: Nominal time response of the Droop model for a biomass set point change from $b_0 = 52.78$ to $b_T = 27.76$ in $T = 1$ day: reference trajectory (thin continuous line), FF response (dashed line), Step response (dash-dotted line).

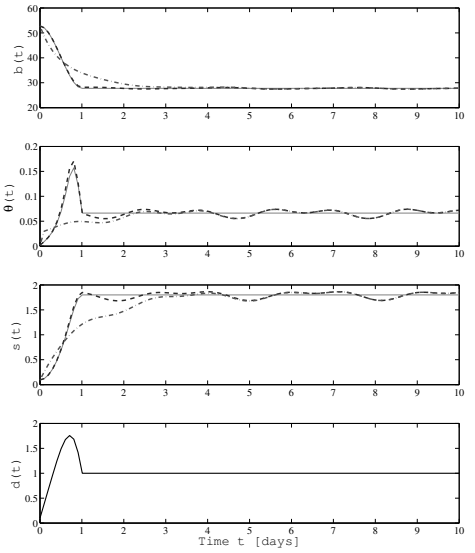

Figure 4: Time response for a biomass set point change from $b_0 = 52.78$ to $b_T = 27.76$ in $T = 1$ day with feed perturbation: reference trajectory (thin continuous line), FF response (dashed line), Step response (dash-dotted line).

It can be seen that the biomass reference trajectory is exactly followed leading to a significant improvement in convergence speed of about a factor of four in comparison to a simple step change.

In Figure 4 the corresponding behavior with a periodic feed perturbation with 10% amplitude according to $s_{in}(t) = \bar{s}_{in} + 10\sin(t)\sin(3t)$ is shown. It can be seen that the improvement in convergence speed is maintained and the deviations from the nominal trajectories lie entirely within a bounded neighborhood of this, verifying the practical stability property.

6. Conclusions

An inversion-based feedforward control for the Droop model for microalgae growth in the chemostat is presented. The dilution rate is manipulated in such a way that biomass set point changes are followed in finite time with practical stability with respect to feed perturbations. The asymptotic stability of the internal dynamics due to mass-conservation is exploited to show this property. Numerical results show that the steady-state to steady-state transition time can be significantly reduced by a factor of four using the proposed approach in comparison to a simple step change in the feed flow, and show the robustness with respect to unknown feed perturbations.

References

Chen, D., Paden, B., 1996. Stable inversion of nonlinear non-minimum phase systems. International Journal of Control 64, 81–97.

Devasia, S., 1999. Approximated stable inversion for nonlinear systems with nonhyperbolic internal dynamics. IEEE Trans. Autom. Cont. 44, 1419–1425.

Droop, M., 1968. Vitamin b12 and marine exology iv: the kinetics of uptake growth and inhibition in monochrisis lutheri. Journal of the Marine Biological Association 48 (3), 689–733.

Graichen, K., Hagenmeyer, V., Zeitz, M., 2009. Design of adaptive feedforward control under input constraints for a benchmark CSTR based on a BVP solver. Comp. & Chem. Eng. 33, 473–483.

Hagenmeyer, V., Nohr, M., 2008. Flatness-based two-degree-of-freedom control of industrial semi-batch reactors using a new observation model for an extended Kalman filter approach. Int. J. Control 81 (3), 428–438.

Havlik, I., Lindner, P., Scheper, T., Reardon, K. F., 2013. On-line monitoring of large cultivations of microalgae and cyanobacteria. Trends in Biotechnology 31 (7), 406–414.

Kleinert, T., Weickgenannt, M., Judat, B., Hagenmeyer, V., 2010. Cascaded two-degree-of-freedom control of seeded batch crystallisations based on explicit system inversion. J. Proc. Cont. 20, 29–44.

Lemesle, V., Mailleret, L., 2008. A mechanistic investigation of the algae growth "droop" model. Acta Biotheor DOI 10.1007/s10441-008-9031-3.

Salle, J. L., Lefschetz, S., 1961. Stability By Liapunov's Direct Method, With Applications. Academic Press.

Toroghi, M. K., Goffaux, G., Perrier, M., 2013. Observer-based backstepping controller for microalgae cultivation. Ind. Eng. Chem. Res. 52, 7482–7491.

Krist V. Gernaey, Jakob K. Huusom and Rafiqul Gani (Eds.), 12th International Symposium on Process Systems Engineering and 25th European Symposium on Computer Aided Process Engineering.
31 May – 4 June 2015, Copenhagen, Denmark

Effect of Solvent Content on Controllability of Extractive Distillation Columns

W. B. Ramos, M. F. Figueirêdo, K. D. Brito, R. P. Brito.
Federal University of Campina Grande – Chemical Engineering Department.
Av. Aprígio Veloso, 882, Bodocongó, Campina Grande – Brazil.

Abstract

This paper arose from a new approach to evaluating separation and energy consumption of extractive distillation columns using as primary analysis parameter the solvent content throughout the column. This new approach allows to find a range of possible solutions that contemplates the global optimal point of operation. In view of this, the objective of this paper is to investigate the influence of the solvent content throughout the column and the size (number of stages) of the column on controllability. The results showed that the columns with smaller number of stages operating with lower solvent content have a better controllability when applied disturbances in the composition of the azeotropic mixture that feeds the column. The production of anhydrous ethanol by extractive distillation using ethylene glycol as solvent was used as a case study for this work.

Keywords: Extractive distillation, Solvent content, Dehydration of anhydrous ethanol, Controllability.

1. Introduction and Problem Definition

Considering that the design of an extractive distillation column is fixed, the variables that result in major impact on energy consumption are the reflux ratio and solvent flowrate (Bruggemann and Marquardt et al., 2004). Recently, a paper published by Figueiredo et al. (2014) included a new parameter in the analysis of extractive distillation, the solvent content in the extractive section. When evaluating the solvent content, the reflux ratio and solvent flowrate are considered simultaneously. According to the authors, the use of this parameter allows to find the range of possible solutions that will necessarily include the global optimum operating point. The specification of the solvent content in the feed stage of the extractive column together with product specifications represent a new phase for the understanding and search for optimal operating conditions of this process as it eliminates one of the main problems of extractive distillation: the existence of various local optimums.

On the results from the analysis procedure suggested by Figueiredo et al. (2014), it was observed that the operating point with higher solvent content in the extractive section provides lower energy consumption by the reboiler of the extractive column. The results also indicate that increasing the solvent content causes the energy consumption to become independent of the number of stages of the column.

However, the idea of using the solvent content in the search for the global optimum operation point is recent and still requires additional studies to support its use in extractive distillation problems. The analysis of the dynamic behavior and controllability of the extractive distillation process is very important for the usefulness

of this separation process in an industrial plant. In view of the non-approach in the literature about the influence of the solvent content in the dynamic and controllability of the extractive distillation process and the intention to complement the study of Figueiredo et al. (2014) based on the analysis of the solvent content, this paper proposes to investigate this aspect, more specifically, answer the following question: Is a column with higher number of stages operating at lower EG content easier to control than a column with smaller number of stages operating at higher levels of EG?

2. Dynamic and Control

Obtaining anhydrous ethanol by extractive distillation using ethylene glycol (EG) as solvent is the case study of this work. The modeling and simulations at steady state, using Aspen Plus®, were based on Figueiredo et al. (2014). By following the procedure suggested by the authors, the Aspen® *design spec* tool was used to obtain ethanol in the distillate with the desired specification of 99.5 mol% and recovery fraction of 99.99%. As specification of the solvent content in the solvent feed stage ($x_{EG}^{\#solv}$), two values were used: 20 % and 75 %, these spoken by the authors as the minimum and maximum solvent content, respectively, that guarantee the specifications of the required product.

In addition, the simulations were performed considering two sizes of the column, 24 and 50 stages, in order to be able to respond to the questions that arose from the sequencing of study of the authors. It totaled in four simulated cases, these described in Table 1. The variables that were manipulated to achieve these specifications were: solvent flowrate (S) and reflux ratio (R) in the extractive column. Table 1 also shows the values of the main variables that resulted in lower specific energy consumption (SEC) for the four simulated cases where it can be seen that the lowest specific energy consumption occurs in a column with a higher content of solvent.

The simulations (Case I, II, III, IV) were exported to Aspen Dynamics® using the pressure-driven mode. Pump head and valve pressure drops (usually 3 atm) were specified to provide reasonable rangeability so that a 20 % increase in transfer rate is handled without valve saturation. The reflux drum and the sump height of the columns, for all cases, were sized to provide 5 min of holdup when 50 % full, at steady state.

Table 1 - Optimal results for minimum specific energy consumption for extractive distillation columns.

Case study	Case I	Case II	Case III	Case IV
Parameter	Values			
Number of stages	24	24	50	50
Ethylene glycol content (mole fraction): $x_{EG}^{\#solv}$	0.2	0.75	0.2	0.75
Solvent flowrate, kmol/h	48.86	78.08	33.81	74.36
Reflux ratio	2.6040	1.4504	1.7892	0.2906
Number of stages of the extractive section	15	15	30	30
Specific energy consumption, kW/kmol	42.67	19.41	33.24	19.21
Internal diameter, m	2.0	2.0	0.8	0.8

Figure 1 shows the basic control structure used for the water-ethanol-ethylene glycol system. All four cases use essentially the same structure with some modifications that account for different temperature profiles and sensitivities to disturbances.

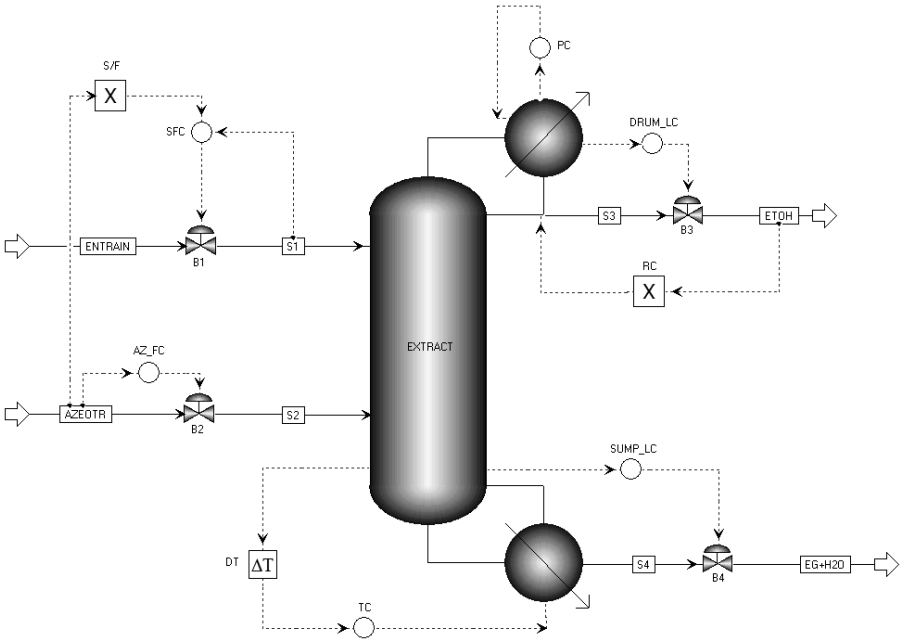

Figure 1. Control structure

The control strategy used in the 4 studied cases was established in accordance with the strategies proposed by Luyben (2008), Gil et al. (2012), Fan et al. (2013) and Tututi-Avila et al. (2014). The control structure consists of the following loops: (1) The sump level is controlled by manipulating the bottom flowrate; (2) The top pressure is controlled by manipulating the condenser duty; (3) The reflux drum level is controlled by manipulating the distillate flowrate; (4) The reflux ratio was kept constant while the disturbances were applied (Arifin and Chien, 2008; Luyben, 2008; Gil et al., 2012); (5) The ratio between the solvent feed flowrate and azeotropic mixture feed flowrate (S/F) is kept constant by using a multiplier together with a controller in cascade; (6) The temperature control is performed by manipulating the vapor flowrate of the reboiler; (7) A flow controller was added to the azeotropic feed stream in order to apply feed flowrate disturbances.

Two criteria were used to determine the best stage to have its temperature controlled: the stage that has the highest slope in the temperature profile, as well as the stage with the highest sensitivity to changes in heat duty, by manipulating the vapor flowrate in the reboiler in ± 0.1 %. It was observed that for the column with 24 stages, the stage 23 is the most suitable to have its temperature controlled for the two solvent contents analyzed. For the column with 50 stages, the results indicated the stage 49 for the column operating with 75 % EG content and stage 39 for the column operating at 20 % EG content.

The level controllers are Proportional olny, with Kc = 2 for the reflux drum level (Luyben, 2002) and Kc = 10 for the sump level (Gil et al., 2012). The pressure controller is Proportional-Integral with Kc = 20 and τ_I = 12 min (Aspen Dynamics default values). The flow controllers are Proportional-Integral with Kc = 0.5 and τ_I = 0.3 min and the filter time constant F = 0.1 min (Luyben, 2002). The parameters of the temperature controllers were tuned using the Tyreus-Luyben method (Tyreus and Luyben, 1992). The results are shown in Table 2. A dead time block was inserted before the temperature controllers with dead time of 1 minute.

2.1. Dynamic Performance

To analyze the effect of the solvent content in the controllability of the the extractive column, disturbances of ±10 % were applied, in the time equal to 2 hours, in the feed flowrate of azeotropic mixture by changing the setpoint of the AZ_FC controller. Disturbances in feed composition of the azeotropic mixture were also applied by changing the mole fraction of ethanol from 0.85 to 0.88 and 0.80.

Figure 2 shows the comparison between the dynamic responses to the disturbances in the azeotropic feed flowrate in the the column with 24 stages, for 20 % and 75 % solvent content in the extractive section, where it can be seen that the control system can maintain the purity of ethanol in the distillate close to the specification value for both EG content, with a slightly better performance when the column operates with 75% EG content. However, the column operating with 20 % EG content has reached the steady state faster, in about 2.5 hours, for disturbances in the feed flowrate and approximately 2 hours for disturbances in the composition.

Figure 3 shows the dynamic responses related to the temperature control of stage 23, where can be seen that the temperature has returned to its setpoint value in about 1 hour. Figure 4 shows the comparison between the dynamic responses to disturbances in the composition of the azeotropic mixture, where can be seen that the control is more efficient when the column operates with a lower solvent content.

The same disturbances were applied to the columns with 50 stages. Similar results were obtained for disturbances in the feed flowrate, as shown in Figures 6 and 7. For disturbances in the azeotropic feed composition, it was also observed that the column operating with lower solvent content has a better controllability (Figure 8). However comparing the results presented in Figures 4 and 8, it is noted that the column with 24 stages is able to better control the composition. The temperature control of the stages 39 and 49 proved to be efficient, as can be seen in Figures 7 and 9.

Table 2. Temperature controllers parameters.

	Case I	Case II	Case III	Case IV
Controlled variable	$T_{I,23}$ = 381.2 K	$T_{II,23}$ = 368.7 K	$T_{III,49}$ = 385.3 K	$T_{IV,39}$ = 371.4 K
Manipulated variable	Reboiler vapor flow	Reboiler vapor flow	Reboiler vapor flow	Reboiler vapor flow
Kc	1.9944	1.5767	0.7283	0.5141
τ_I	7.92 min	9.24 min	9.24 min	9.24 min

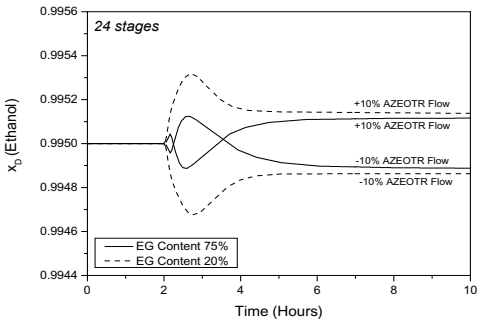

Figure 2. Comparison between the dynamic responses to disturbances in the azeotropic feed flowrate for 20% and 75% solvent content in the the extractive section.

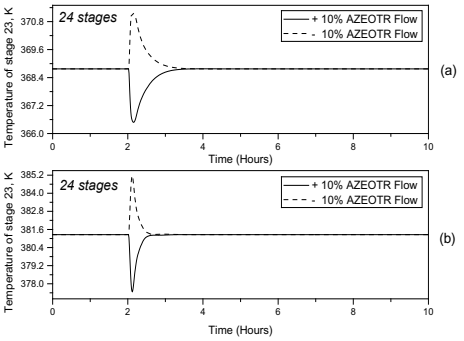

Figure 3. Dynamic responses to disturbances in the azeotropic feed flowrate for (a) 20 % EG content and (b) 75% EG content.

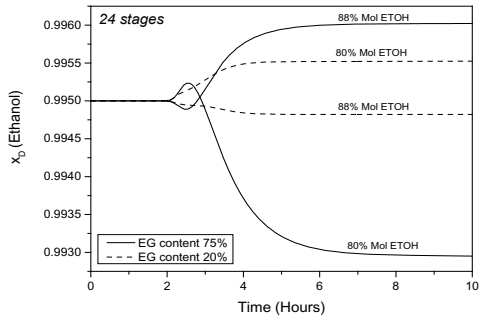

Figure 4. Comparison between the dynamic responses to disturbances in the composition of the azeotropic mixture for 20% and 75% solvent content in the extractive section.

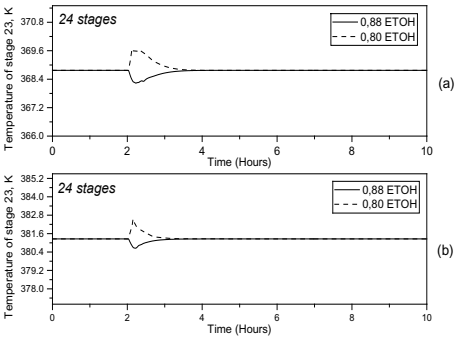

Figure 5. Dynamic responses to disturbances in the azeotropic feed composition for (a) 20% EG content and (b) 75% EG content.

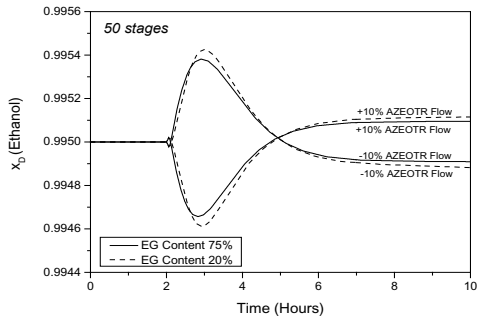

Figure 6. Comparison between the dynamic responses to disturbances in the azeotropic feed flowrate for 20% and 75% solvent content in the the extractive section

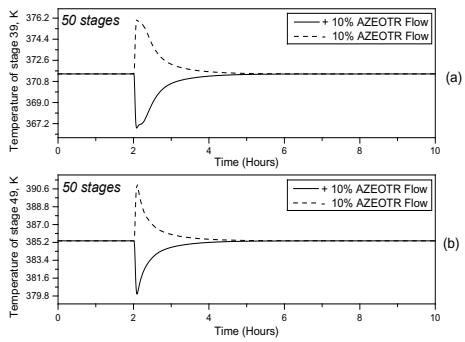

Figure 7. Dynamic responses to disturbances in the azeotropic feed flowrate for (a) 20 % EG content and (b) 75% EG content.

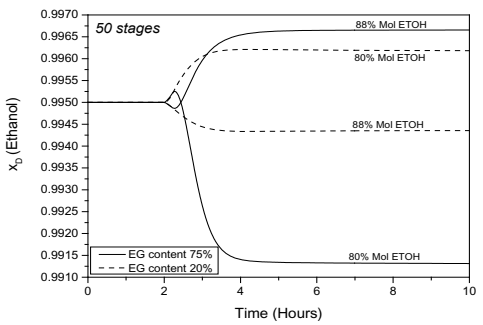

Figure 8. Comparison between the dynamic responses to disturbances in the composition of the azeotropic mixture for 20% and 75% solvent content in the extractive section.

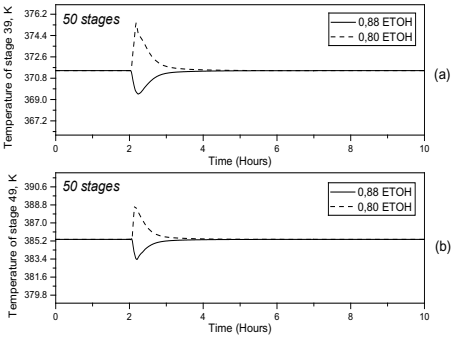

Figure 9. Dynamic responses to disturbances in the azeotropic feed composition for (a) 20% EG content and (b) 75% EG content.

3. Conclusions

Disturbances in the azeotropic feed composition caused poor performance in controlling the top product purity of the the extractive column operating with high solvent content; this poor performance is even sharper in columns with higher number of stages.

Disturbances in the azeotropic feed flowrate had small impact on the control of the top product composition in the four studied cases, however the column with higher number of stages took longer to reach steady state.

These results showed that controlling smaller extractive distillation columns is easier than controlling columns with higher numbers of stages, especially columns operating with low solvent content.

References

S. Brüggemann and W. Marquardt, 2004, Rapid screening of design alternatives for nonideal multiproduct distillation processes, Comput. Chem. Eng., 29, 165-179.

M. F. Figueirêdo, K. D. Brito, W. B. Ramos, L. G. S. Vasconcelos and R. P. Brito, 2014, Effect of Solvent Content on the Separation and the Energy Consumption of Extractive Distillation Columns, Chemical Engineering Communications, 10.1080/00986445.2014.900053.

W. L. Luyben, 2008, Comparison of extractive distillation and pressure-swing distillation for acetone–methanol separation, Industrial and Engineering Chemistry Research, 47(8), 2696–2707.

W. L. Luyben, 2002, Plantwide dynamic simulators in chemical processing and control, New York, Marcel Dekker.

S. Arifin and I. L. Chien, 2008, Design and control of an isopropyl alcohol dehydration process via extractive distillation using dimethyl sulfoxide as an entrainer, Industrial and Engineering Chemistry Research, 47 (3), 790–803.

B. D. Tyreus and W. L. Luyben, 1992, Tuning of PI controllers for integrator dead time processes. Industrial and Engineering Chemistry Research, 31, 2625–2628.

I.D. Gil, J.M. Gómez and G. Rodríguez, 2012, Control of an extractive distillation process to dehydrate ethanol using glycerol as entrainer, Comput. Chem. Eng., 39, 129–142.

Z. Fan, X. Zhang, W. Cai and F. Wang, 2013, Design and control of extraction distillation for dehydration of tetrahydrofuran, Chem. Eng. Technol., 36, 829–839.

S. Tututi-Avila, A. Jiménez-Gutiérrez and J. Hahn, 2014, Control analysis of an extractive dividing-wall column used for ethanol dehydration, Chem. Eng. and Processing, 82, 88-100.

Krist V. Gernaey, Jakob K. Huusom and Rafiqul Gani (Eds.), 12th International Symposium on Process Systems Engineering and 25th European Symposium on Computer Aided Process Engineering.
31 May - 4 June 2015, Copenhagen, Denmark.

High purity, high recovery, multi-component methanol distillation control

Isuru A. Udugama[a], Tajammal Munir[b], Robert Kirkpatrick[a], Brent R. Young[a] and Wei Yu[a]

[a]*Department of Chemical Engineering; The Univeristy of Auckland; New Zealand*
[b]*Industrial Information and Control Centre; The University of Auckland; New Zealand*

Abstract

High purity distillation is a well-established area of research. In an industrial setting most columns are operated at high recovery rate due to economic factors. However, most research work in this area overlooks high recovery as well as the fact many operations have multi-component feeds. In high-purity ($<$ 10ppm) multi-component methanol distillation the columns are typically operated at a recovery of 97.5%. Despite this relatively high value, even a 1% increase in recovery carries a significant financial incentive. In this work a validated model of a methanol distillation column was built in a commercial process simulator and used to study the dynamic behaviour of a real column operating high recovery levels. Based on the analysis the a novel control scheme has been developed and tested for 99.5% recovery: The control scheme extracts flow and composition information from feed, product and side draw streams to dynamically calculate the mass and energy requirements. The information is then used to set reboiler duty, and to manipulate the set points of the decentralized product ethanol composition controller and side draw flow controller. These actions manage the energy requirement, methanol and ethanol mass balances respectively.

Keywords: High purity, High Recovery Distillation, Industrial distillation

1. Introduction and Background

The determination of control system structure is an important step in process control design. The selection of control system structure is based on the type of control used for the process/plant. A centralized multi-input multi-output (MIMO) controller or a set of single-input single-output (SISO) controllers can be used to control a distributed or decentralized process. A decentralized type of control system is more common than the centralized control system in the process industry, as it has more captivating advantages: it is easy to understand, uses uncomplicated hardware, and employs simple working algorithms Morari and Evanghelos (1989); Marlin (2000); Svrcek et al. (2014). On the other hand, centralized type of control (e.g. Model Predictive controllers (MPC)) has many limitations such as: 1) higher maintenance cost, 2) difficulties in operation, 3) complicated structure, and 4) lack of flexibility that can result in fragile controller that is not profitable (Camacho and Alba , 2013). However, centralized controllers have the potential to operate systems at optimal levels, that can potentially have noticeable economic benefits. Distillation columns are an example of a process with sever nonlinear behaviour when their operations lie in the high-purity region. As a result they are challenging to control. Furthermore, gain directionality also becomes more severe near the high purity region (i.e. $x_D > 95\%$ and $x_B < 5\%$). Directionality issues of high-purity distillation columns makes the process response dominated by the higher gain direction (i.e. one product composition can be made further purified), which significantly

limits the performance of linear SISO controllers for dual composition control. A MIMO controller, such as MPC, is often used to address this directionality issue however MPC has its own challenges as discussed. Non-linear behaviour of high-purity distillation columns also results in different dynamics as a result of a small deviation from the operation point. This emphasises that a linear process model and linear SISO controller are insufficient to describe the system dynamics and control respectively over changing operating conditions (Fuentes and Luyben , 1983; Carcia et al. , 1989). The control of industrial multi-component methanol distillation columns is complex due to high product purity specifications ($<$ 10 ppm ethanol in products), and the need to achieve 97.5% product recovery rates or higher. In addition a strict bottoms composition ($x_B < 5$ ppm) needs to be maintained. In current operations producers employ basic control loops together with continuous human intervention to keep the columns operating at these specifications. This operating strategy results in notable financial loses. Thus, there is an industrial requirement for a robust, practical control scheme that can regulate industrial methanol distillation columns both at high recovery and high purity. A MPC can serve most of these purposes, but will require a complex model and mathematical execution algorithms to capture the highly non-linear behaviours at high purity and high recovery. In an industrial setting the MPC will also incur high installation cost and the requirement of a dedicated MPC expert on site, making MPC unviable. This manuscript will attempt to employ constraint based control on a real industrial distillation column (Figure 1 & Table 1) to create a robust control scheme that can optimize recovery and maintain purity, without the complexity of MPC.

2. Control Scheme Developments

2.1. Control Objectives

The main objective of this control scheme is to optimize the economic performance of methanol distillation columns. To achieve this objective the following parameters were found to be important from both previous work (Udugama et al. , 2014) as well as initial analysis:

- Real time management of the ethanol inventory
- Maintaining an average product ethanol specification of $<$ 10 ppm
- Real time tracking of methanol inventory
- Managing reboiler duty to meet the heat requirement for incoming feed disturbances

2.2. Control scheme

Based on the control objectives and initial analysis, the control scheme in Figure 1 has been designed. Table 1 gives the average industrial mass and energy balance data for this type of column in normal operation. In this particular type of methanol refining column, marginal savings in reboiler duty does not carry any financial benefits. The control scheme displayed in Figue 1 consists of a basic PID reboiler level controller and a condenser pressure controller. The set points to the fusel flow rate the distillate flow rate controllers are set by the Recovery constraint controller (RCC), while the steam to the reboiler (reboiler duty) is controlled by a feed-forward controller (FF).

2.3. FF controller

The feed forward controller is a simple static feed forward controller that increases or decreases reboiler duty based on the feed flow rate. Equation (1) has been empirically derived based on both plant performance and model output to achieve 99.5% recovery.

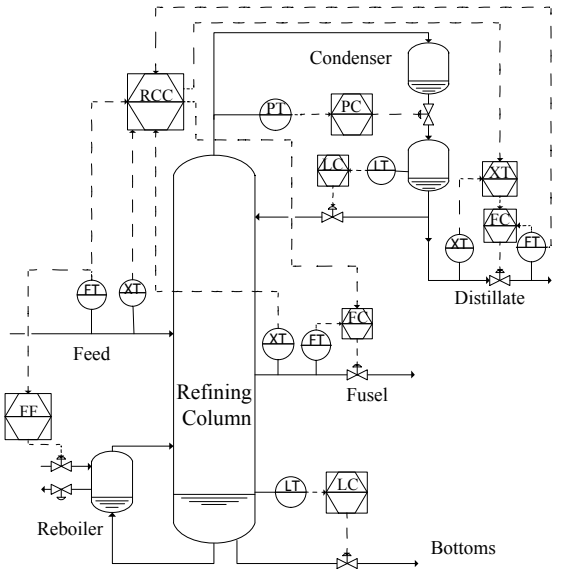

Figure 1: Proposed control scheme

Table 1: Distillation column flow and composition information

		Plant data	Units
Feed	Flow	142500	kg/h
	Methanol	0.82	Mass Frac (%)
	Ethanol	150	ppm
	Water	0.18	Mass Frac (%)
Distillate	Flow	115000	kg/h
	Methanol	99.99	Mass Frac (%)
	Ethanol	8	ppm
	Water	0.1	ppm
Bottom	Flow	25485	kg/h
	Methanol	5	ppm
	Ethanol	0	ppm
	Water	100	Mass Frac(%)
Fusel	Flow	3015	kg/hr
	Methanol	84	Mass Frac (%)
	Ethanol	0.61	Mass Frac (%)
	Water	16	Mass Frac (%)
Reflux ratio		1.687	-
Reboiler duty		88.25	MW
Methanol recovery		97.5	%

$$\text{Power (kW)} = 0.6707 \times \text{feed mass flow rate (in kg/h)} - 801 \tag{1}$$

The simple nature of the control algorithm means it can be easily auto calibrated on a daily / weekly basis to prevent the control scheme from drifting by changing the gradient and constant

values. This is a common practice in many advanced process control (APC) applications (Taube , 2014).

2.4. RCC controller

This recovery constraint controller acts as a central controller that influences the mass flow rate of the distillate and fusel draw to keep both ethanol and methanol inventories at acceptable levels.

The required fusel flow rate is calculated based on the hourly average accumulation / depletion of ethanol and the current fusel ethanol composition. The set point for the fusel flow rate is then adjusted to ensure no accumulation or depletion occurs. A Maximum flow rate set point of 3700 kg/h has been enforced due to practical limitations of the disposal system. While a minimum flow rate set point of 2600 kg/h has been set to maintain column stability.

Comparatively, the calculation of the set point to the product ethanol controller is more complex. In this instance the product ethanol set point is manipulated (within limits) to increase the product recovery when it is $< 99.5\%$. The controller also manipulates the ethanol set point to decrease the product recovery when it is $> 100\%$, as initial analysis illustrate that exceeding 100% methanol recovery for long durations leads to poor column control, leading to poor finical performance.

In situations where the recovery is above 99.5% , the product ethanol set point should be reduced below the 8 ppm limit. Based on Eq. (2),

$$\text{High recovery SP} = 8ppm + 2 \times (99.5 - \text{Product Recovery}) \tag{2}$$

This will force the composition controller to reduce the distillate flow rate which in turn would reduce the recovery rate while taking advantage of the favourable conditions to make product with ≤ 8 ppm ethanol. In situations where the recovery is 99.5% or below the controller should attempt to bring the recovery back to 99.5% as soon as possible by increasing the product specification by the following Eq. (3) up to 10 ppm where a maximum limitation is set.

$$\text{Low recovery SP (LRSP)} = 8ppm + 6 \times (99.5 - \text{Product Recovery}) \tag{3}$$

Both these equations are linear equations. In these equations the constant value is set as the average product ethanol value the operators and plant management would set for steady state operations. The gradient value is set based on how aggressively the set point should be changed per 1% change in recovery. In this instance at lower product recovery the controller acts more aggressively in comparison to a high product recovery situation. The rate at which the controller can change the set point is limited to 0.5 ppm/minute to ensure stability and unwanted reaction to high frequency disturbances. Due to the simple nature equations, these constants and gradient value can be changed by a plant engineer if required. The output of this controller with the current parameters is displayed in Figure 2.

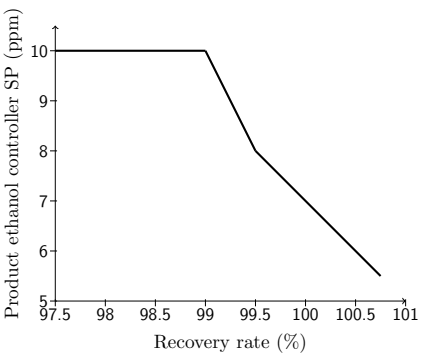

Figure 2: Ethanol controller SP Vs recovery rate

The conceptual frame work of this type of control structure has existed for some time (e.g Luyben (1992) preferred this type of constraint control over a MPC approach). In this paper this conceptual framework has been applied to a real world control situation, where all practical limitations and potential issues of introducing new control structure have been considered. The conceptual frame

work has been simplified to the point where all the supervisory/constraints equations used in the two centralized (RCC and FF) controllers can be manipulated by operators/plant engineers without the need for an expert control person.

In case of sensor faliure, the RCC control scheme can be simply switched off and the underlying control structure can provoide sufficent control to continue operations. In case of misleading/incorrect sensor signals the contraints in the RCC controller will garuntee reasonable operation. In the specific case of feed stream composition sensor failure, there is the possibility of not meeting both the product and bottoms specification. To counter this the FF Controller will be set to maximum. This will increase the refulx ratio as well as the energy cost.

3. Testing and comparison

In order to analyse the control schemes ability to produce AA grade (10ppm ethanol) methanol while keeping a high product recovery it is necessary to introduce process disturbances into the column. To test the column against feed disturbances performance against random flow disturbance sine waves with amplitude of 5 t/h was assessed. The period of the sine wave was changed between 50 minutes and 2000 minutes to simulate short process disturbances to long term process upsets. This also ensured that the designed control scheme does not create "resonance" at expected frequencies of disturbances.

To test the column for long term process upsets a sinusoidal feed disturbance that has a period of 2000 minutes (Left) and 50 minutes (Right) was introduced. The results from this test are displayed in Figure 3 (a)- (d) .

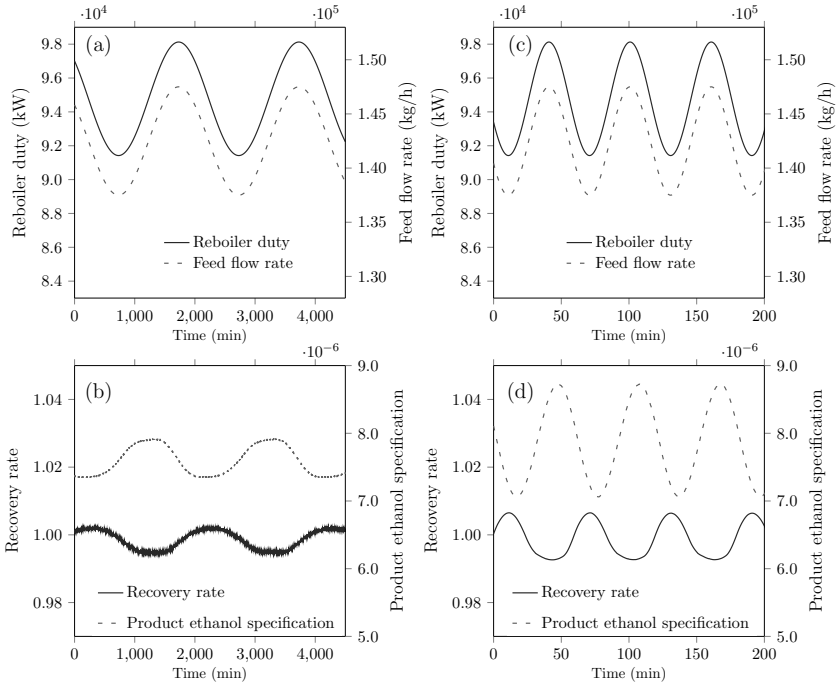

Figure 3: Controller performance for 2000 (min) and 50 (min) disturbances

Figure 3 (a) and (c) show that the reaction of reboiler duty to a fluctuating feed flow rate. In these cases the static feed forward controller has almost immediately adjusted the reboiler duty to maintain the energy balance. Figure 3 (b) and (d) show the behaviour of product recovery and product ethanol specification during the disturbances.

In the 2000 minutes case (Figure 3 (b)), as expected the product ethanol specification is fluctuating around 7 and 8 ppm which is acceptable. Despite significant changes the product recovery is stably tracking between 100.5 and 99.95% which in the long term will help column stability and profitability. Similar results can be observed in the 50 minute figures where the recovery fluctuated between 100.6 and 99.4% (Figure 3 (d)).

Overall the controller seems to be performing it objective of making AA grade methanol at improved level of recovery. To quantify the value of the new control scheme, a control scheme with a classic DV control arrangement was built and tested against similar disturbances. In this instance the average product recovery reached by the classic control for 50 minute fluctuation is scheme is 97.8% while the proposed control scheme reaches a recovery of 99.8%. For 2000 minute fluctuations the classic control scheme reached a recovery of 98.1% while the proposed control scheme reaches a recovery of 99.9%. On average this is an improvement of 1.5%. This will add up to 15000 (t) of extra methanol recovered per year per column which gives a significant financial incentive to implement such a system in the field. Similar results have been observed for other alternatives.

4. Conclusions

In this work an examination has been carried out to quantify the difficult of constantly operating an industrial methanol distillation column at a recovery of 99.5% or above. Based on this analysis a novel control scheme has been propose and tested that can achieve high recovery while being practical to implement. When compared to a classic DV control arrangement the proposed controlled outperformed the classic control scheme where on average it achieved a recovery $> 1.5\%$ than that of a classical DV controller. Considering the financial impact of this extra recovery, simplicity and robustness of the proposed control scheme will be well received in an industrial setting. Furthermore, even if a MPC perfectly control the process further gains in recovery would be limited to 0.15% as the proposed scheme is already operating at 99.85% (average). The only upside of a MPC would be savings made in reboiler duty consumed, which is this particular type of case study is irrelevant.

References

Camacho, E. F., Alba, C. B.(2013). *Model predictive control*, New York: Springer.

Fuentes, C., Luyben, W. L.(1983). Control of high-purity distillation columns. *Industrial & Engineering Chemistry Process Design and Development* **22**(3): 361-366.

Garca, C. E., Prett, D. M., Morari, M. (1989). Model predictive control: Theory and practiceA survey. *Automatica* **25**(3): 335-348.

Luyben, W.L. (1992). Diagonal controller tuning. In: Luyben, ed. *Practical distillation control*. New York: Van Nostrand Reinhold.

Marlin, T. E. (2000). *Process control: design process and control system for dynamic performance*. New York: McGraw Hill.

Morari, M., Evanghelos, Z. (1989). *Robust Process Control*. Englewood Cliffs, NJ: Prentice Hall.

Svrcek, W.Y., Mahoney, D.P., Young, B.R. (2014). *A real-time approach to process control*. 3rd edition, New York: John Wiley & Sons Inc.

Taube, M. (2104), Personal Communication with Michael Taube from S&d Consulting LLC, at The University of Auckland, New Zealand.

Udugama, I.A., Munir, T.M., Kirkpatrick, R., Young, B.R., Yu, W. (2104). Advanced dual composition control for high-purity multi-component distillation column. Proceedings of the Adconip Conference, Hiroshima, Japan.

Krist V. Gernaey, Jakob K. Huusom and Rafiqul Gani (Eds.), 12th International Symposium on Process Systems Engineering and 25th European Symposium on Computer Aided Process Engineering.
31 May – 4 June 2015, Copenhagen, Denmark

Implementation of Model Predictive Control in Industrial Gasoline Desulfurization Process

Kornkrit Chiewchanchairat[a], Pornchai Bumroongsri[b], Veerayut Lersbamrungsuk[c], Amornchai Apornwichanop[a], Soorathep Kheawhom[a*]

[a]*Computational Process Engineering, Department of Chemical Engineering, Faculty of Engineering, Chulalongkorn University, Bangkok, 10330, Thailand*
[b]*Department of Chemical Engineering, Faculty of Engineering, Mahidol University, Nakhonpathom, 73210, Thailand*
[c]*Department of Chemical Engineering, Faculty of Engineering, Silpakorn University, Nakhonpathom, 73200, Thailand*
soorathep.k@chula.ac.th

Abstract

Sulfur is an important pollutant that can severely prevent an implementation of all major pollution control strategies. Thus, to reduce air pollution and to comply with strict environmental regulations, sulfur content in all types of fuel produced is required to be lowered to a certain level. A selective desulfurization process is used to reduce sulfur content of fluidized catalytic cracked (FCC) naphtha, which is a blending component for gasoline product. Though, the desulfurization process can considerably lower sulfur content of the naphtha. Some undesirable olefin saturation reactions are also occurred, resulting in octane loss of the gasoline product. The octane loss depressingly influences economic performances of the plant. Thus, optimizing the operation in order to minimize the octane loss while still complying with sulfur specification and other process constraints is necessary. The operation optimization can be accomplished by implementing model predictive control (MPC). In this work, we focus on the implementation of MPC in the selective desulfurization process in order to strictly control sulfur content in the gasoline product while minimizing octane loss. A soft-sensor for on-line estimating sulfur content in gasoline product was designed and implemented. A series of step tests were performed to build empirical dynamic models. The models obtained were validated and used in MPC design. Analysis of benefit was performed with data collected before and after MPC implementation. The results showed that after MPC implementation, the control performances were improved by shifting mean of sulfur content in product close to the high limit operation. Thus, energy consumption was significantly decreased.

Keywords: model predictive control, desulfurization process, fluidized catalytic cracked naphtha.

1. Introduction

Sulfur is an important pollutant in transportation sector. It can severely prevent an implementation of all major pollution control strategies. Thus, to reduce air pollution and to comply with strict environmental regulations, sulfur content in all types of fuel produced is required to be lowered to a certain level.

Gasoline products are blended from various streams with different properties and sulphur contents. Fluidized catalytic cracked (FCC) naphtha is one of the blending components generally used. Unfortunately, without a pretreatment, FCC naphtha usually contains high sulfur content.

A selective desulfurization process can be used to significantly reduce sulfur content of fluidized catalytic cracked (FCC) naphtha. This process consists of three major units including selective hydrogenation unit, FCC-naphtha splitter unit, and hydrodesulfurization unit. Though, the desulfurization process can considerably lower sulfur content of the naphtha. Some undesirable olefin saturation reactions are occurred, resulting in octane loss of the gasoline product. The octane loss depressingly influences economic performances of the plant. Thus, optimizing the operation in order to minimize the octane loss while still complying with sulfur specification and other process constraints is necessary. The operation optimization can be accomplished by implementing model predictive control (MPC). MPC have been implemented in various industrial processes (Haktanir et al., 2013; Kemaloglu et al., 2009).

In this work, we focus on the implementation of MPC in the selective desulfurization unit of one oil refinery in Thailand. The control objective of the MPC implemented is to strictly control sulfur content in the gasoline product while minimizing octane loss. A soft-sensor for on-line estimating sulfur content in gasoline product was designed and implemented. A series of step tests were performed to build empirical dynamic models. The models obtained were validated and used in MPC design, Shell Multivariable Optimization Controller (SMOCPro). Analysis of benefit was performed with data collected before and after MPC implementation.

2. Selective desulfurization process

A selective desulfurization process composes of three major sections including selective hydrogenation unit (SHU), FCC-naphtha splitter unit, and hydrodesulfurization (HDS) unit. A simple flow diagram of this process is shown in Fig.1.

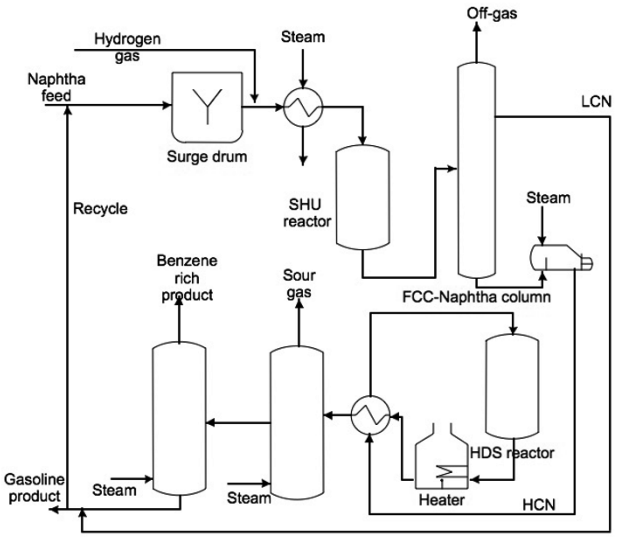

Figure 1. Process flow diagram of the selective desulfurization process.

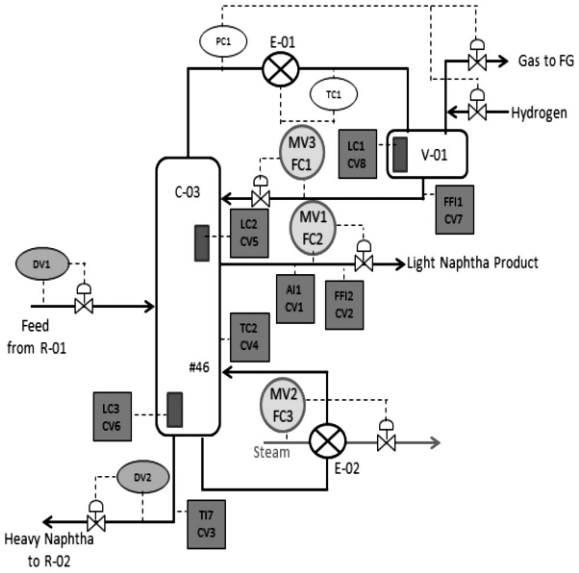

Figure 2. Control structure of the FCC-naphtha splitter unit.

FCC naphtha is fed to the selective desulfurization process through the SHU. In this unit, di-olefins are converted into olefins and light mercaptans are converted into heavier sulfur-containing compounds in the SHU reactor.

The effluent of the SHU reactor is then fed to FCC-naphtha splitter unit at tray #28 of the column, in which light-cut naphtha (LCN) and heavy-cut naphtha (HCN). LCN, which has low sulfur content and high octane number, is drawn from tray #7 in the column. In comparison, HCN, which contains high amount of sulfur and lower octane number, is drawn from the bottom of the column. The top stream of the column is condensed and collected in an overhead drum. The condensed liquid is fed back to the column as reflux. The non-condensable gas leaves the column as off-gas.

The HCN stream leaving from FCC-naphtha splitter unit is processed in the HDS unit. In the HDS reactor, heavy sulfur-containing compounds are converted into hydrogen sulfide. At the same time, undesirable olefin saturation reactions are occurred in the HDS reactor, resulting in octane loss of the gasoline product. The effluent of the HDS reactor is then fed to a stabilizer column to remove all gas by-products. Benzene is removed from the effluent in the benzene splitter column. The final HCN product is then combined with the LCN product drew from FCC-naphtha splitter unit, and sent to gasoline pool.

3. Control objectives and MPC design

The main control objectives of the desulfurization process include maximizing sulfur content in the final product within permissible limits. Thus, the upper limit of sulfur content is satisfied with Euro IV specifications, and octane loss minimization is also achieved. Other objectives are to minimize steam consumption in each column. To achieve these objectives, the main controller was decomposed into two sub controllers. The first controller regards the operation of the SHU, and the FCC-naphtha splitter unit. The other one regards the HDS unit, the stabilizer column, and the benzene splitter column. In this work, we considered the design of the first controller. However, the

Table 1. The effects of manipulated variables and disturbances on controlled variables.

	CV_1	CV_2	CV_3	CV_4	CV_5	CV_6	CV_7	CV_8
MV_1	+	+	+	+	-	-		
MV_2			+	+				
MV_3			-	-			+	-
DV_1		-					-	
DV_2						-		

+ represents positively proportional relation, - represents negatively proportional relation

di-olefin concentration in the SHU reactor cannot be measured online or predicted. Thus, the SHU reactor is excluded from our MPC design. Consequently, design of MPC for FCC-naphtha splitter unit was focused. Figure 2 shows the control structure of the FCC-naphtha splitter unit. Pressure of the column is maintained by adjusting off-gas or hydrogen gas streams. Column pressure must be kept constant. Thus, this loop was not included in the MPC design.

Sulfur content in LCN strongly depends on temperature of the column, and thus LCN draw. Before MPC implementation, a tray temperature is controlled by LCN draw. However, control of sulfur content in LCN was not implemented, as an online analyzer is not available. By utilizing an inferential property, sulfur content in LCN can be predicted from temperature of tray #45, temperature of LCN draw tray, and reflux-to-feed ratio. Real industrial data were collected and multiple linear regression was used to construct the prediction model. The prediction model is shown in Eq.(1).

$$CV_1 = 0.358T_{45} + 0.772T_{LCN} - 1.83r_{R/F} - 136 \quad (1)$$

CV_1 represents sulfur content in LCN. T_{45} and T_{LCN} are temperatures of tray #45 and LCN draw tray, respectively. $r_{R/F}$ is reflux-to-feed ratio. Model validation was done by using another set of industrial data. Good agreement between prediction and industrial data has been obtained.

The MPC designed targets sulfur content in LCN at 20 ppm. The higher sulfur contents lead to a violation of final product specification, while lower sulfur content increases octane loss and energy consumption.

The controlled variables of MPC designed included sulfur content in LCN (CV_1), LCN draw-to-feed ratio (CV_2), bottom column temperature (CV_3), temperature of tray #14 (CV_4), naphtha level at tray #7 (CV_5), naphtha level at bottom (CV_6), reflux-to-feed ratio (CV_7), and condenser level (CV_8). The manipulated variables of MPC designed included LCN draw (MV_1), reboiler steam (MV_2), and reflux flow (MV_3). The measurable disturbances were also included in MPC design. These disturbances were feed flow rate (DV_1), which is adjusted by upstream process, and HCN draw at the bottom (DV_2), which is manipulated by the HDS unit. Some of the CVs may not be maintained at the setpoint as the number of CVs is much greater than the number of

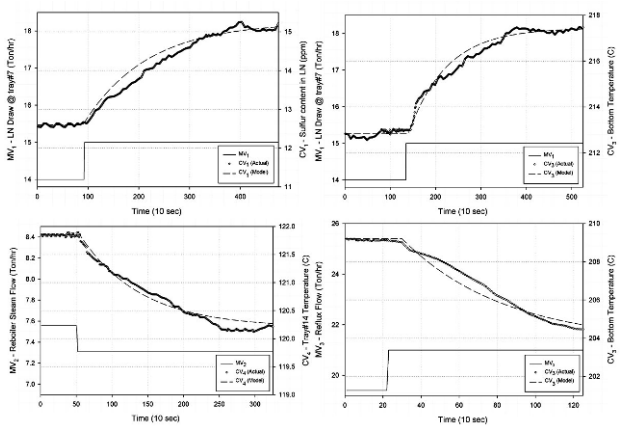

Figure 3. Some of the results from step response tests.

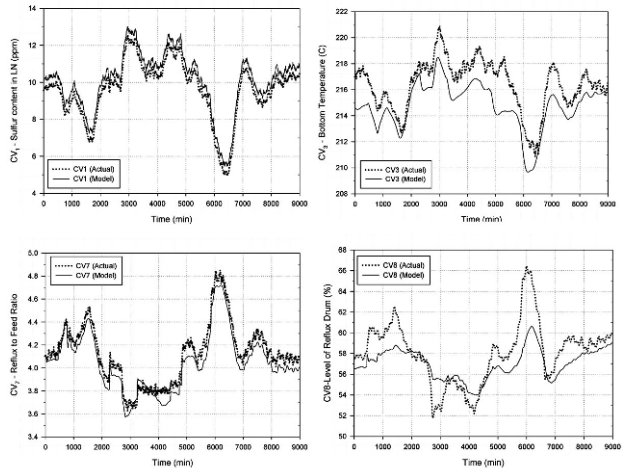

Figure 4. Some of the results from model validation.

MVs. Table 1 shows the effects of manipulated variables and disturbances on controlled variables.

A series of step test was performed, and each dynamic model was then identified as first order plus time delay system. Figure 3 shows some of the results from step response tests. The models obtained are omitted here for brevity.

These empirical models were then validated with another set of real operating data. The prediction data and real operating data were in good agreement as shown in Fig 4. Then, MPC was designed based on these models in SMOCPro.

The MPC uses optimization to minimize a cost function specified while satisfying constraints given. The objective function used was formulated as $\sum_{i=1}^{p} w_1 \| \hat{y}(n+i) - r(n+i) \|^2 + \sum_{j=1}^{c} w_2 \| \Delta u(n+j-1) \|^2$. Where $\hat{y}$, r, and u are a control

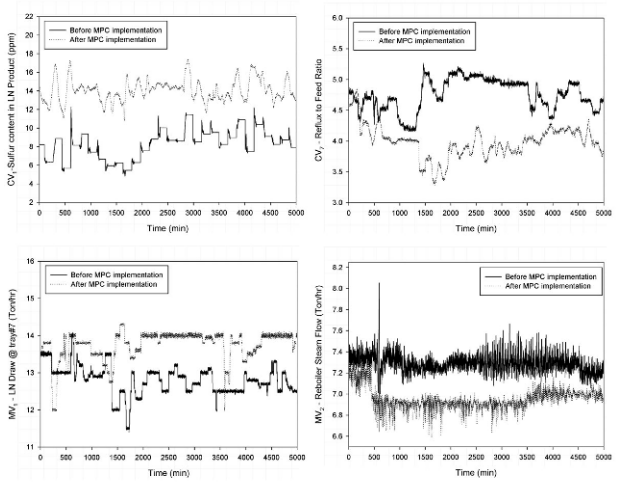

Figure 5. Performances of the process before and after MPC implementation.

vector predicted, a desired reference vector, and a manipulated vector, respectively. $\boldsymbol{p}$ and $\boldsymbol{c}$ are prediction and control horizons, respectively. $\boldsymbol{w_1}$ and $\boldsymbol{w_2}$ are adjustable weighting factors.

4. Results and discussion

Figure 5 shows the results of MPC implementation in normal operation, where disturbances were similar. By implementing MPC, the control performances were improved by shifting mean of sulfur content in product close to the high limit operation. The reflux flow was much lower than that of before MPC implementation. Thus, energy consumption was significantly decreased.

5. Conclusions

In this work, a model predictive control (MPC) was designed and implemented on a FCC-naphtha splitter unit of a selective desulfurization process. The results showed that after MPC implementation, the control performances were significantly improved. Further, reboiler steam consumption was drastically reduced.

Acknowledgment

This research has been supported by National Research University Project, Office of Higher Education Commission (WCU-041-EN-57).

References

S. Kemaloglu, E. Kuzu, D. Gokce, O. Cetin, 2009, Model Predictive Control of a Crude Distillation Unit, An Industrial Application, 7th IFAC International Symposium on Advanced Control of Chemical Processes, July 12-15, 2009, Istanbul, Turkey.

B. Haktanir, M. Aygun, D. G. Kuzu, 2013, Model Predictive Control of an Industrial Gasoline Hydrodesulphurization Unit, International Conference on Process Control. June 18-21, 2013, Slovakia.

Krist V. Gernaey, Jakob K. Huusom and Rafiqul Gani (Eds.), 12th International Symposium on Process Systems Engineering and 25th European Symposium on Computer Aided Process Engineering.
31 May – 4 June 2015, Copenhagen, Denmark

Maximizing Profit of Semi Batch Autocatalytic Esterification Process in the Presence of Disturbance: Application of Cascaded-Conditional Based Online Dynamic Optimization

F.S. Rohman, S. Abdul Sata and N. Aziz*

School of Chemical Engineering, Universiti Sains Malaysia, Engineering Campus
14300 Nibong Tebal, Seberang Perai Selatan, Penang, Malaysia
**Corresponding Author's Phone: +604-5996457; Fax: +604-6941013; E-mail: chnaziz@usm.my*

Abstract

This work addresses the implementation of an online dynamic optimization cascaded with a dual mode PID control strategy for improving the product quality and profit of an autocatalytic esterification of Propionic Anhydride with 2-Butanol. An orthogonal collocation method is implemented to re-optimize the feed rate and temperature trajectories to compensate the deviation of end product due to disturbance (variation of feed concentration). The problem of dynamic optimization is formulated to maximize the profit. The spec of final product (±5% of conversion) constraint is denoted as an active constraint which is applied as the trigger for activating re-optimization. The simulation results show that the proposed strategy offers a large improvement in semi batch reactor performance if compared to the method which the optimal trajectories set point is pre-determined (offline). Moreover, the online dynamic optimization of temperature and feed flowrate trajectories obtained able to sustain the limiting reactant concentration within active constraint. Meanwhile, the offline optimization failed to handle the effect of disturbance thus the end concentration produced is off-spec and can lead to loss in profit.

Keywords: Online dynamic optimization; Semi batch; Autocatalytic esterification,

1 Introduction

To improve the batch processes performance, the dynamic optimization is preferable to be implemented due to its ability to capture the dynamic behavior of the process. Dynamic batch system is very sensitive to uncertainties and disturbances in the process operation. In semi batch esterification process, a disturbance such as variation concentration in the feed stream may cause the final product differs from the desired value. This discrepancy may risk the violation of safety constraints, production off-spec products, and more vitally the loss of invaluable profit. Under these circumstances it is desirable to implement online dynamic optimization strategy to desired trajectories to reach the optimal performances (Kadam and Marquadt, 2007). The aim of the online dynamic optimization for semi batch reactor is to generate the optimal trajectories of process variables such as flow rates of feeds and temperature, which are typically re-adjusted to optimize the objective function in the presence of significance disturbance (Würth et al., 2009). The cascaded-conditional based optimization is applied in this

study because it is found to be an effective technique for updating system with uncertainty. It is solving the optimization and control problem separately by decomposing the overall problem into two levels (Alonso et al., 2013). As the significance uncertainty and disturbance occurred, the re-optimizer will generate a new/modified optimal trajectory in order to ensure optimum performance is obtained. However, the existing techniques implements cascaded – conditional based optimization using a combination of sensitivity-based updates and adaptive control vector parameterization strategy which highly complex. Moreover, it also causes a slower rate of convergence if exact Hessian matrix is miscalculated (Kadam and Marquadt, 2007, Würth et al., 2009). Therefore, the development of effective way for activating the re-optimizer is a must which can lead to the more efficient optimal solution computation.

In this work, orthogonal collocation method (OC) is implemented for cascaded-conditional based optimization to optimize the feed flowrate and temperature reactor trajectories in the presence of disturbance. The process considered is Catalyzed Esterification of Propionic Anhydride with 2-Butanol in a semi batch reactor. The optimal trajectories obtained are based on maximum profit problem.

2. Modeling of autocatalytic esterification process

Esterification of propionic anhydride with 2-butanol is producing sec-butyl propionate and propionic acid. It exhibits a kind of autocatalytic behaviour when sulphuric acid is introduced. The reaction kinetics of this esterification has been investigated and the data of parameters is depicted from Zaldivar et al. (1993). The semi batch reactor model which consist of the mass and energy balances are represented by following equations:

$$\frac{dC_B}{dt} = -((k_1 + k_2 C_{cat1}) C_A C_B + k_3 C_{cat2} C_B) + \frac{F_o}{V}(C_{B0} - C_B) \tag{1}$$

$$\frac{dC_C}{dt} = \frac{dC_D}{dt} = ((k_1 + k_2 C_{cat1}) C_A C_B + k_3 C_{cat2} C_B) - \frac{F_0 C_C}{V} \tag{2}$$

$$\frac{dC_{cat1}}{dt} = -\frac{dC_{cat2}}{dt} = -(k_4 10^{-H} C_{cat1} C_A) - \frac{F_0 C_{cat1}}{V} \tag{3}$$

$$\frac{dT}{dt} = \frac{-\Delta Hr_{total}}{\rho C_p} + \frac{UA}{\rho C_p V}(T_j - T) + \frac{F_O}{V}(T_{feed} - T) \tag{4}$$

$$\frac{dT_j}{dt} = \frac{F_j}{V_j}(T_{jin} - T_j) + \frac{UA}{\rho_j V_j C_j}(T - T_j) \tag{5}$$

where C_A, C_B,C_C, C_{Cat1}, and C_{cat2} are the concentration of 2-butanol, propionic anhydride; propionic acid, sulphuric acid and mono-butyl sulphuric acid, respectively. F_o , V are the feed rate and the volume of solution within reactor. F_j is the jacket flowrate, T_j is the jacket temperature; T_{jin} is the inlet jacket temperature; T_{feed} is the feed temperature; A is the heat exchange area; V_j is the volume of jacket; U is the heat exchange coefficient; C_p, C_j is heat capacity of solution in the reactor and the jacket, respectively; H is the acidity function; ΔHr is the heat of reaction; ρ is density of solution in reactor; ρ_j is density of jacket solution. Those pertaining constant value is depicted from Ubrich et al. (1999). The initial value of C_A, C_B, C_C, C_D, C_{cat1}, C_{cat2} V, T and T_j is 3.4M, 0M, 0M, 0M, 1.02 x 10^{-2}M, 0M, 1L, 303K and 303K, respectively.

3. Design of online cascaded-conditional based optimization

The cascaded-conditional based optimization is constructed by the integration of process model, initial optimal control trajectory, estimator, controller and dynamic re-optimization mechanism which consists of trigger and dynamic re-optimizer. The framework of this strategy is adopted from the works of Alonso et al. (2013), Würth et al. (2009), and Kadam and Marquadt (2007) as shown in Figure 1.

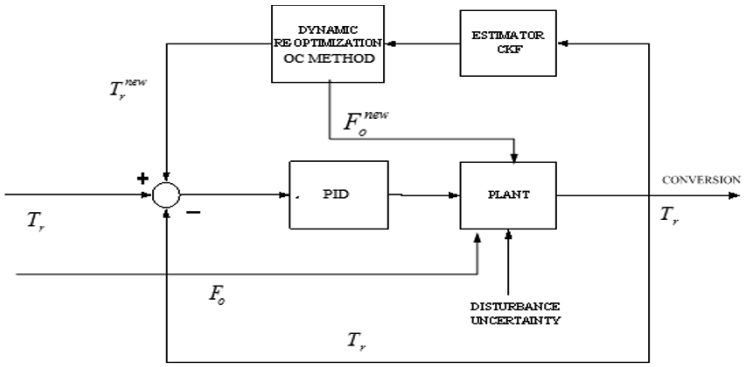

Figure 1: Scheme diagram of online dynamic optimization framework

The distinct of this research from the previous work on cascaded-conditional based optimization is the application of conventional controller and simple dynamic re-optimizer mechanism. Since the value of feed flowrate is assumed to be measurable, the temperature trajectory can be tracked by the dual mode of adaptive PID controller. The details of controller and its tuning can be found in Landau (1990). Meanwhile, the dynamic re-optimization mechanism uses the spec of final product (±5% of conversion) as the activator re-optimizer (trigger) for handling the significance disturbance. All the state variables presented in mass balance are required to calculate the updated values by using Cubature Kalman Filter technique which the algorithm code package is developed by Solin (2010). The measurements available which consider as the CKF input are C_A, jacket and reactor temperature. The noises incriminated in the states are maintained at low level.

The optimal feed flowrate and temperature trajectories were pre-determined from an offline dynamic optimization study. Meanwhile, online dynamic re-optimizer generates new optimal trajectories in order to re-optimize plant for rejecting impact on disturbance. Both offline optimal and online re-optimized trajectories are evaluated by OC method for maximizing profit. In this work, the OC was implemented within the MATLAB® environment by using the dynopt code package developed by Cizniar and co-workers (2005). The operation profit is derived from the price of the product. The operation profit (RM/min) expression is presented by Equation 6 (Aziz, 2001):

$$P = \frac{V\left(C_C P_C + C_D P_D\right) - \left(C_{A0} - C_A\right) P_A V - P_B \left(C_{BF} + C_B\right) V}{t} \tag{6}$$

where P_A, P_B, P_c and P_D, are the prices of A, B, C and D, E and F with numerical values [26.75, 34.39, 10.17, 339.1], respectively (Xingtai, 2014, Sigma-Aldrich, 2014). All values are in RM/mol.

In this study, volume of solution, the reactant, catalyst and product concentration were considered as states variables. The control variables considered were feed flowrate and temperature reactor. The objective function was to maximize profit. The inequality constraint associated was end concentration of limiting reactant and total volume reactor. The dynamic optimization formulations for both problems are shown as:

Problem:

$$\max_{T,F_0} \Im = P$$

Subject to semi batch dynamic model Eq.1-5;
Inequality constraints: $V \leq 2.2L$; Bounds: $0 \leq F_0 \leq 5x\ 10^{-4} L\ s^{-1}$ and $303K \leq T \leq 343K$.

4. Results and discussion

The simulation of cascaded-conditional based optimization was carried out in the SIMULINK® environment. The significance disturbance and parameter that can violate the active constraints and generate the off-spec product (±5% of conversion) was introduced in the plant. The alleviation of feed concentration C_{B0}, i.e. 1M, at 25-35 min of process time was considered as disturbance.

The conversion obtained in online dynamic optimization study is shown in Figure 2. The optimal temperature trajectories together with control response for tracking temperature trajectory obtained for maximizing profit problem under effect of disturbance is shown in Figure 3. Meanwhile, the optimal feed flowrate trajectories obtained are shown in Figures 4. From Figure 2, it is found that the decrease of the feed concentration decrease the amount of product. Therefore, the conversion obtained was also decrease when the disturbance occurs. When the conversion exceeded the active constraint, the dynamic re-optimization was activated to generate the new optimal feed flowrate and temperature trajectories as shown in Figure 3 and 4, respectively. The update mechanism in cascaded dynamic optimization was able to capture the effect of the disturbance by re-optimizing the optimal trajectories which bring the conversion back to the specified constraints region, i.e. conversion = 99.86%. Meanwhile, the offline mode (without the re-optimizing mechanism) produces an off-spec end conversion with value of 94.62%. The online strategy maintained the process to obtain profit at RM 12.89 RM/min. whereas the offline strategy only manages to give profit at 10.89 RM/min. From Figure.3, it is also found that the action of adaptive PID controller to track temperature trajectory is acceptable since the controller can drive the system from current set point value to a new one and maintain it at the set point. This observation signifies the feasibility of the conventional control implemented for the process considered.

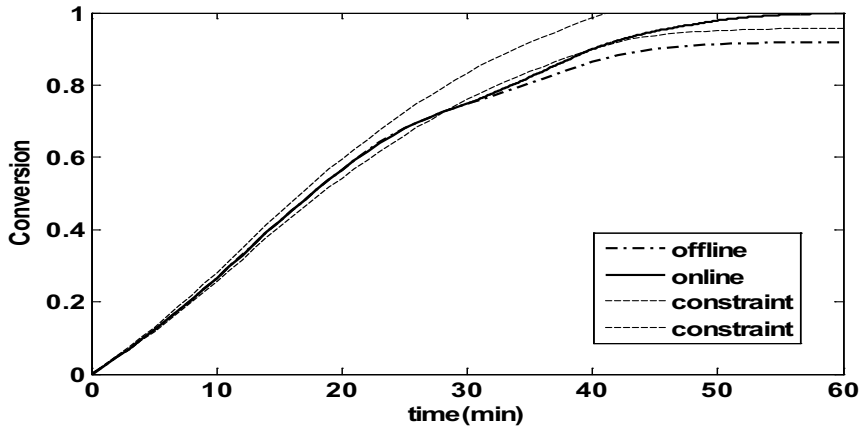

Figure 2: Conversion profile for dynamic optimization study

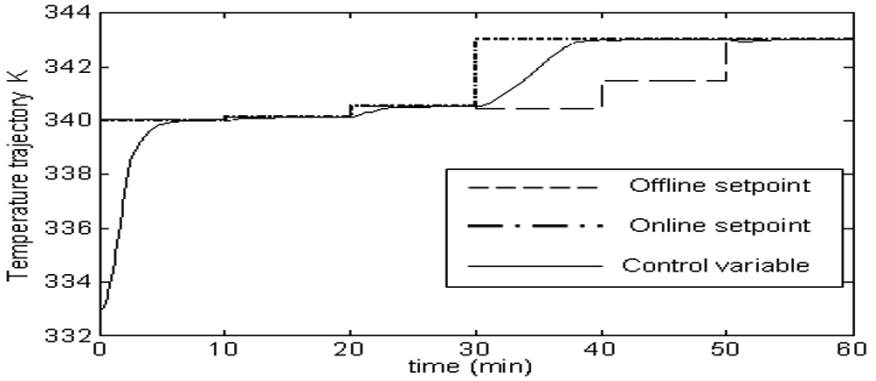

Figure 3: Optimal temperature trajectory for dynamic optimization study

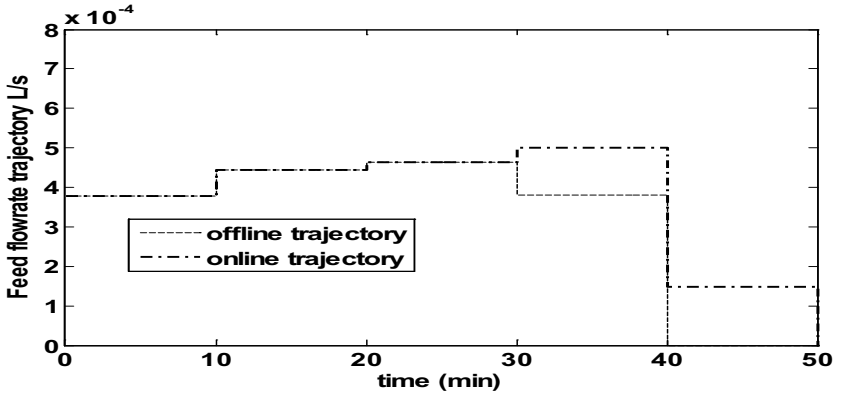

Figure 4: Optimal feed flowrate trajectory for dynamic optimization study

5. Conclusion

The online dynamic optimization of Catalyzed Esterification of Propionic Anhydride with 2-Butanol in semi batch has been carried out. The cascade optimization strategy was implemented to update the optimal trajectories when a significant disturbance occurs in the process. The re-optimized temperature and feed flowrate trajectories drove the conversion within the active constraint which maintains the profit of process. Meanwhile, the offline optimization mode cannot capture the effect disturbance which led to off-spec end product.

Acknowledgement

The financial support from Ministry of Science, Technology and Innovation (MOSTI), Malaysia through Sciencefund grant and Universiti Sains Malaysia through RU grant is greatly acknowledged.

References

Alonso, A.A., Arias-Méndez, A., Balsa-Canto, E.,García, M.R., Molina, J.I., Vilas, C, Villaf´ın, M. (2013) Real Time Optimization for Quality Control of Batch Thermal Sterilization of Prepackaged Foods, *Food Control*, 32: 392–403

Aziz, N (2001) Dynamic Optimization and Control of Batch Reactor, PhD Thesis, University of Bradford

Cizniar, M (2005) Dynamic Optimisation of Processes, Diploma Work, Slovak Technical University in Bratislava

Kadam, J.V and Marquardt, W (2007) Integration of Economical Optimization and Control for Intentionally Transient Process Operation *Lecture Notes in Control and Information Science* 358: 419-434

Landau, I. D (1990) System Identification and Control Design, Prentice Hall International

Sigma-Aldrich (2014) Chemical Invoice, www.sigma-aldrich.com

Solin, A (2010) Cubature Integration Methods in Non Linear Kalman Filtering and Smoothing, Thesis, Aalto University School of Science and Technology

XingtaiYuetai (2014) Chemical Invoice, www.xt-chem.com

Ubrich, O, Srinivasan, B, Bonvin, D, Stoessel, F (1999) Optimal Feed Profile for a Second Order Reaction in a Semi-Batch Reactor under Safety Constraints. Experimental Study, Journal *of Loss Prevention in the Process Industries* 12 (6): 485-493

Würth, L, Hannemann, R, Marquardt,W (2009) Neighboring-extremal updates for nonlinear model-predictive control and dynamic real-time optimization,*Journal of Process Control*, 19: 1277–1288

Zaldivar, J. M., Hernandez, H., Molga, E., Galvan, I. M., & Panetsos, F. (1993) The use of neural networks for the identification of kinetic functions of complex reactions. In Proceedings of the third European symposium on computer aided process engineering, ESCAPE 3

Krist V. Gernaey, Jakob K. Huusom and Rafiqul Gani (Eds.), 12th International Symposium on Process Systems Engineering and 25th European Symposium on Computer Aided Process Engineering.
31 May – 4 June 2015, Copenhagen, Denmark

MIMO Neural Wiener Based Model Predictive Control (NWMPC) For MTBE Reactive Distillation Using Simulated Annealing- Particle Swarm optimization (SA-PSO)

Sudibyo, Murat, M. N. and Aziz, N*

School of Chemical Engineering, Universiti Sains Malaysia, Engineering Campus 14300 Nibong Tebal, Seberang Perai Selatan, Penang, Malaysia
**Corresponding Author's Phone: +604-5996457; Fax: +604-6941013; E-mail: chnaziz@usm.my*

Abstract

MTBE is commonly produced using reactive distillation column which combine reactor and distillation column in single unit process. To achieve high MTBE purity and reactant conversion is a challenging task due to strong interaction between control variables and due its highly nonlinear behaviour of the process. In this work, nonlinear model predictive control (NMPC) is developed and applied to control tray temperature of MTBE reactive distillation. To increase the performance of NMPC, the Neural Wiener model and Simulated Annealing–Particle swarm optimization (SA-PSO) are chosen to be implemented in NMPC. In this work, the MTBE reactive distillation was modelled using Aspen dynamic, meanwhile the control study has been carried out using Simulink (Matlab) which is connected with Aspen dynamic model. The results obtained show that the multi input multi output (MIMO) Neural Wiener based model predictive control (NWMPC) using SA-PSO can successfully control the tray temperatures in MTBE reactive distillation. The NWMPC is able to track the set point change and to reject the disturbances very well with small value of error.

Keywords: Neural Wiener, NMPC, Simulated annealing, PSO, Nonlinear Optimisation

1. Introduction

Maximum production of the MTBE can be achieved using reactive distillation (RD) which the reaction and separation process are combined and run at the optimum operating conditions and column configuration. Meanwhile, to maintain the product purity at a specified range, a feasible controller is required. Control of RD is major problem in MTBE production due to its high degree of nonlinearity, steady state multiplicity, time delay, strong interactions, process uncertainties and the large number of possible control configurations (Satyanarayana and Saha, 2005). One of the advanced control system which can be applied in reactive distillation is a nonlinear model predictive control (NMPC). The NMPC consists of three main components namely the process, the nonlinear model and nonlinear optimizer (Konakom et al., 2011).

Neural Wiener Based MPC (NWMPC) is a relatively new scheme of NMPC which can be applied in a MTBE RD. Neural Wiener model is simple block oriented model that can be solved at lower computational time. It is also flexible in representing the nonlinear processes and can avoid the interactions among control variable thus make NWMPC more attractive for real application (Lawry´nczuk, 2011). The advanced

nonlinear optimization is proposed to increase the performance of NWMPC which must have ability to find both the global and local optimum result. Particle swarm optimization (PSO) is one of nonlinear optimizer which has good performance to find global optimum result but difficult to find a local minimum. Meanwhile, Simulated Annealing (SA) has a strong ability to find the local optimum result but less superior in finding the global optimum. Hence, the combination of SA and PSO will enhances the convergence and accuracy of the controller optimization. Wang et al. (2005) have used SA- PSO to solve the optimization problem in a single input and output (SISO) NMPC to control a thermal power unit load system. Meanwhile, in this work, a NWMPC combined with SA-PSO optimizer is designed and developed to control a reactive distillation for MTBE production.

2. Development MTBE reactive distillation model

The most promising technique of producing MTBE is from methanol and isobutene, where the liquid-phase reaction is catalyzed by ion exchange resin (heterogeneous reaction). The reaction scheme is:

$$\text{i-C4H8} + \text{CH3-OH} \rightleftharpoons \text{C5H12O} \qquad (1)$$

The specification MTBE RD considered here can be found in Fig. 1(Higler et al., 1999). In this work, MTBE reactive distillation model has been developed in Aspen dynamic .

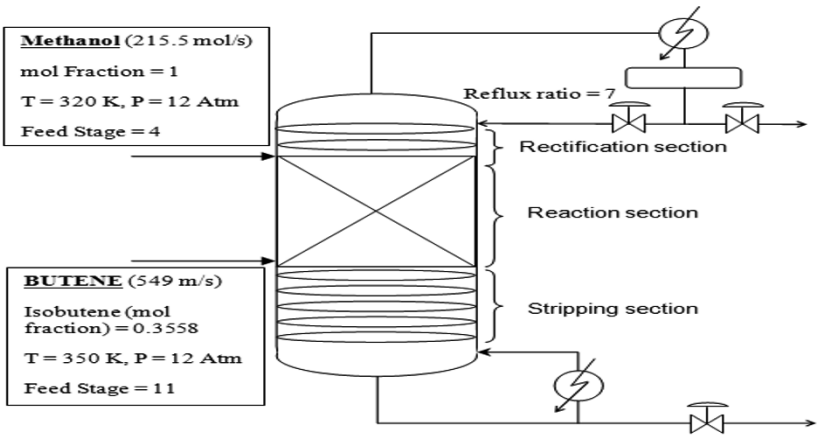

Fig. 1. MTBE Reactive Distillation Column

3. Neural Wiener model identification

Neural Wiener (N-W) model consist of linear block and nonlinear block as shown in Fig. 2. The N-W identification algorithm is begun by data generation in order to collect dynamic input-output data. Then, a linear model is identified to produce the intermediate variable of v(k) from the input data. The v(k) output is a linear dynamic part of state space model which consist of v1 and v2. Finally, neural network model is identified using intermediate variable as input variable. The N-W model block arrangement is shown in Fig. 3.

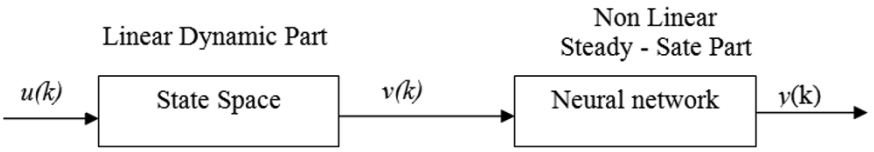

Fig. 2. Neural Wiener model configuration

In this work, state space model is used as the linear block and MIMO neural network model is used as the nonlinear block. The MIMO Neural network used is a feed forward neural network with 15 hidden nodes and 1 hidden layer. The output y(k) of the N-W model is described below:

$$y(k) = w_0 + \sum_{i=1}^{K} w_i^2 \varphi\{w_{i,0}^1 + w_{i,1}^1[C\,x(k) + D\,u(k) + e(k)]\} \quad (2)$$

where w_0 is the bias, $w_{i,j}$ is the weight of first layer, and w_i is the weight of second layer, φ is a nonlinear transfer function such as hyperbolic tangent sigmoid transfer function and tansig, K is the number of hidden nodes.

4. Development of simulated annealing–particle swarm optimization (SA-PSO)

The description of original PSO can be found in Shi and Eberhart (1999). In this research, the first modification done was the addition of weighting function (w) in the inertia of velocity equations shown below:

$$v_i^{t+1} = w.v_i^t + \varphi_1 U_1^t (Pb_i^t - x_i^t) + \varphi_2 U_2^t (gb_i^t - x_i^t) \quad (3)$$

where, v_i^{t+1} is velocity of agent i at iteration k, φ_1 and φ_2 is weighting factor, U_1^t and U_2^t is uniformly distributed random number between 0 and 1, x_i^t is the current position of agent i at iteration k, Pb_i^t is the best known position of particle i. Meanwhile, gb_i^t is the best known position of the entire swarm. The value of the inertia weight (w) is decreased automatically during a run as a proposed by Shi and Eberhart [11]. The combination of simulated annealing (SA) and PSO has been proposed by Wang et al. (2005). The combination of SA and PSO algorithm's have similar searching process which is also started from initializing a group of random particles. In the process of simulated annealing, the new individuals are given randomly around the original individuals. The changing range of original particles as a parameter r1, to each particle is given by following equation:

$$\text{Present} = \text{present} + r1 - r2.2.\ \text{rand}(1) \quad (4)$$

where rand (1) is a random number between 0 and 1, the parameter r1 here also reduces step by step as the generation increasing. The SA method which is activated using 50% of total particle. In SA calculation, the new individuals are given randomly around the original individuals and the changing range of original particles as a parameter r1, to each particle reduces step by step as the generation increasing, hence the SA formulation become:

$$r_1 = \left(\frac{(lb-ub)(0-(0-w_{max})}{(it_{min}-it_{max})(it_{max}-it)}\right) \quad (5)$$

$$x_{(i\to n)} = x_{(i\to n)} + r_1 - r_1 * 2 * \text{rand}\,(1) \quad (6)$$

Where lb = is lower bound, ub is upper bond, lb is lower bound and x is the final result and rand (1) is a random number between 0 and 1 (Wang and Xiao, 2005).

5. Development of Neural Wiener Based MPC (NWMPC)

The N-W model developed and the SA-PSO optimizer proposed are embedded in the Neural Wiener NMPC as shown in Fig. 3.

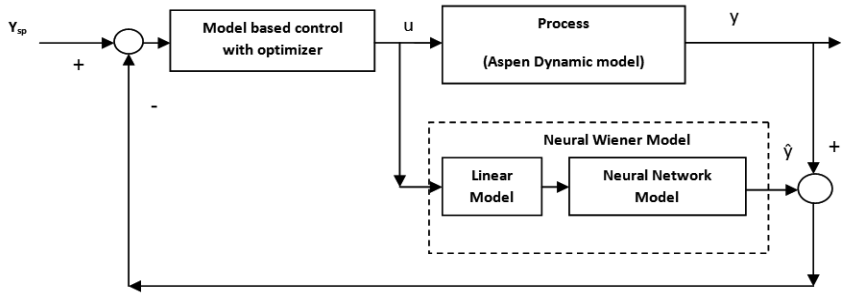

Fig. 3. General structure of Neural-Wiener Based model predictive control

The NWMPC objective function for the MIMO case consists of the quadratic error between each controlled variable and its set-point and the quadratic change of each manipulated variable. The control variables chosen are tray temperature no.3 (CV1) and no.8 (CV2). Meanwhile the manipulated variables are reboiler duty (MV1) and reflux flowrate (MV2). The control and manipulated variables are chosen based on SVD test (Sudibyo*et al*., 2012).The MPC objective function for the 2 × 2 system is defined as follows:

$$j_k = \sum_{i=1}^{P} \left((y_{f1|k+i} - y_{sp1|k+i})^2 Q_1 + (y_{f2|k+i} - y_{sp2|k+i})^2 . Q_2\right) + (\Delta u_{f1|k+i})^2 . R_1 + (\Delta u_{f2|k+i})^2 . R_2 \quad (6)$$

where y_f is predicted future output, y_{sp} is set point, Q is error penalty, R is input change penalty, Δu_f is future input change and k is current sampling time.

6. CONTROL STUDY

NWMPC using SA-PSO as a nonlinear optimizer was tuned to obtain the best control configuration. The NWMPC tuned parameters obtained are tabulated in Table 1.

Table 1.NWMPC and PSO Parameter after tuning

MPC Parameter	Value		PSO Parameter	Value
Prediction horizon	5		Number of particle	110
Control horizon	2		weight function minimum	0.4
Error penalty	1	1	weight function maximum	0.9
Input change penalty	98000	4500	Number of iteration	60
input constraint upper bounds	0.05;	0.05	Rho1 (weighing factor 1)	1.25
input constraint lower bounds	-0.05;	-0.05	Rho2 ((weighing factor 2)	1.25

6.1 Set point change

In this test, the set point CV1 is set at value of 0, 5.4966, 4 and 5.4966, meanwhile set point CV2 is set at value of 0, 0.424, 0.2708 and 0.424 where the switching time of all changes is 2 hours. The changing of set point of tray temperatures in this test was aim to achieve the MTBE purity at 95%, 97.5% and 99%.The profiles of control variables (CV1 and CV2) obtained in this set point test are shown in Fig. 4a and 4b, respectively. Fig. 4a shows that the proposed NWMPC is able to track the set point change with a small amount of overshoot and error (the value ITAE is 1.59). Meanwhile, CV2 profile shows that the controller is also able to track the set point with the settling time less than 0.5 hour and small value of error (ITAE value is 0.237) as shown in Fig. 4b. The result achieved has managed to obtain more that 99% isobutene conversion.The respective MV1 and MV2 profiles achieved are shown in Fig. 5 which are within the specified range with acceptable pattern of changing.

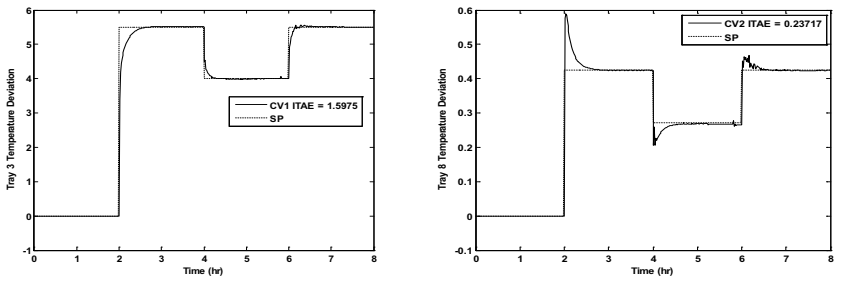

(a) (b)

Fig. 4. Set point change (a) CV1 profile and (b) CV2 profile

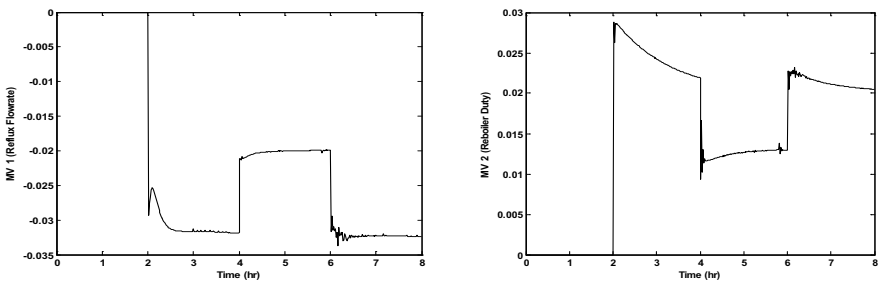

(a) (b)

Fig. 5. Set point change (a) MV1 profile and (b) MV2 profile

6.2 Disturbances rejection test

In this test, +30% change in methanol feed flow rate was introduced as disturbance that occur from 3 until 3.2 hour. Using SA-PSO optimizer, the proposed controller is able to reject the effect of disturbance change after 0.5 and 0.7 hour for CV1 and CV2, respectively as shown in Fig. 6. The ITAE value for CV1 and CV2 are 0.71042 and 0.215, respectively. Meanwhile, the respective MV profiles are shown in Fig. 7.

7. Conclusion

NWMPC using SA-PSO has been successfully developed and applied to control tray temperatures in the MTBE reactive distillation model. The performance test of set point change and disturbance rejection showed that the proposed controller have good performance with small amount of overshoot, low settling time and small amount of error.

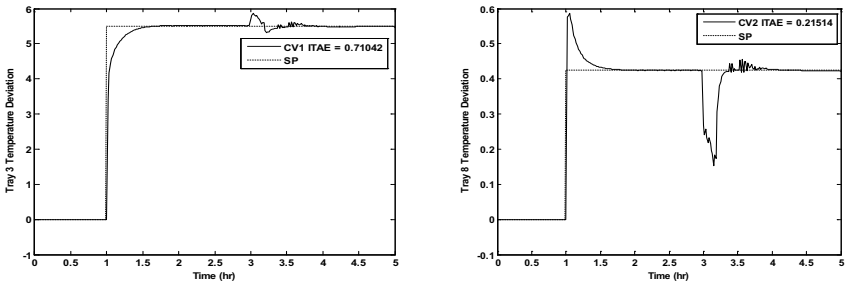

(a) (b)

Fig. 6. Disturbance rejection test (a) CV1 profile(b) CV2 profile

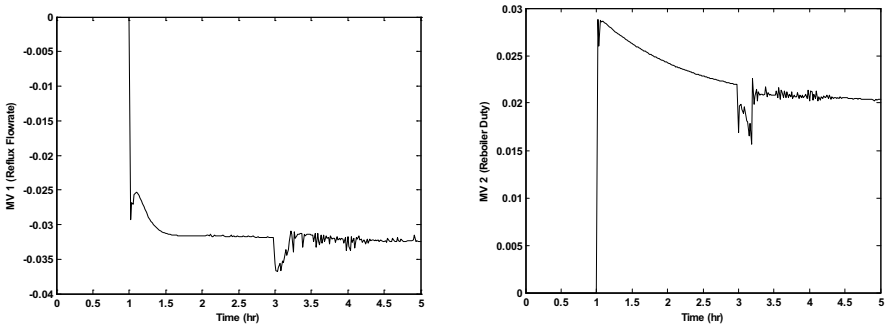

(a) (b)

Fig. 7. Disturbance rejection test (a) MV1 profile (b) MV2 profile

Acknowledgement

The financial support from Universiti Sains Malaysia through Research University (RU) Grant and Graduate Assistant (GA) to the first author are greatly acknowledged.

References :

A.P. Higler, R. Taylor and R. Krishna,1999, The influence of mass transfer and mixing on the performance of a tray column for reactive distillation, Chem. Eng. Science, vol. 54, 2873-2881

L. Wang, K. Chen, and Y. S. Ong, 2005, PSO-Based Model Predictive Control for Nonlinear Processes, Springer-Verlag Berlin Heidelberg, ICNC 2005, 196 – 203.

K. Konakom, P. Kittisupakorn and I. M. Mujtaba,2011, Neural network-based controller design of a batch reactive distillation column under uncertainty, Asia-Pac. J. Chem. Eng. (M. Lawry´nczuk, Precise and Computationally Efficient Nonlinear Predictive Control Based on Neural Wiener Models, Springer-Verlag Berlin Heidelberg, 663–672.

T. Satyanarayana and P. Saha, P. ,2005, Modeling and Control Structure Selection for Reactive Distillation Process using Aspen Custom Modeler, CHEMCON, Newdelhi, 05.

Y. Shi and R. Eberhart,1999, Empirical study of particle swarm optimization, In Proceedings of the 1999 IEEE Congress on Evolutionary Computation, 1945–1950.

Sudibyo, Murat, M. N. and Aziz, N., 2012, Dynamic Modeling and Sensitivity Analysis of Methyl Tert-butyl Ether Reactive Distillation, Computer Aided Chemical Engineering, Vol. 31, 130–134.

Krist V. Gernaey, Jakob K. Huusom and Rafiqul Gani (Eds.), 12th International Symposium on Process Systems Engineering and 25th European Symposium on Computer Aided Process Engineering.
31 May – 4 June 2015, Copenhagen, Denmark

A real time particle size control framework in non-isothermal antisolvent crystallization processes

N. Ghadipasha[a], S. Tronci[b], R. Baratti[b], J. A. Romagnoli[a]

[a]*Department of Chemical Engineering, Louisiana State University, Baton Rouge, LA*
[b]*Dipartimento di Ingegneria Meccanica, Chimica e dei Materiali, Università degli studi di Cagliari, Via Marengo 2, I-09123 Cagliari, Italy*

Abstract

This paper focuses on the design and implementation of on-line optimal control strategies of crystal properties for non-isothermal antisolvent crystallization processes. The one-dimensional Fokker-Planck equation (FPE) is used to represent the dynamic characteristics of the crystal growth and to generate iso-mean and iso-standard deviation curves. Using controllability tools it is shown that the system is ill conditioned in the operational range, posing limitations on the achievable control performance. A novel digital image texturing analysis approach is implemented to track crystal's size distribution along the experiment, thus providing the on-line information for further feedback control action. Subsequently, alternative control strategies are implemented and tested to achieve a desired crystal size distribution (CSD).

Keywords: Crystallization, Optimal control, image analysis

1. Introduction

Crystallization is a main physical separation process in many chemical industries. It is an old unit operation which can separate solids of high purity from liquids, and is widely applied in the production of food, pharmaceuticals and fine chemicals. There are significant properties of the final product in crystallization process such as purity and stability of crystalline particles, growth morphology and size distribution that affect downstream unit operations including filtration, granulation and drying. Hence, to fulfill the product specification it is important to properly control the process which necessitates understanding the dynamic of the system and underlying phenomena. For the control of CSD, one typical approach used is based on model-developed optimal profiles which are then implemented on-line with or without any feedback action. Recently, cooling has been combined with antisolvent crystallization and the joint process has been modeled (e.g., Lindenberg et al. 2009). In contrast to model-developed optimal profiles, there has been alternative ways to control anti-solvent processes. These have been supersaturation control (e.g., Sheikhzadeh et al., 2008). In supersaturation control, the aim is to control the supersaturation at a constant level to maximize crystal growth, while in indirect nucleation control the aim is to control the number of particle counts using an on line particle counter, such as the Lasentecs FBRMs (focused beam reflectance measurement). This prevents excessive nucleation, thus increasing the product crystal sizes. Various methods of robust optimal control have also been studied (e.g., Yang and Nagy, 2014).

Despite the described contributions, there are not publications that directly control the CSD in a feedback fashion. This is basically due to the lack of proper on-line

characterization of the crystal characteristics. This contribution proposes an online strategy to directly control crystal size distribution in joint cooling antisolvent crystallization processes. Crystallization of sodium chloride in water using ethanol as antisolvent is performed in an experimental bench-scale semi-batch crystallizer. Results demonstrate in some cases poor performance of the PIs control strategy, due to ill-conditioning of the process. On the other hand excellent behavior on the CSD control is achieved when the FF and the proposed FF/FB controllers are applied.

2. Theoretical background

The recent development of a stochastic approach to model the non-isothermal antisolvent crystallization processes (Grosso et al., 2010), allowed an accurate analysis on the controllability property of such system. In this novel approach the dynamics of a single crystal size L is described as

$$\frac{dL}{dt} = Lg(L,\theta) + L\,\eta(t) \tag{1}$$

Where g(L;θ) represents the growth rate with θ indicating the vector of model parameters, t is the time, and η(t) is the Langevin force including the growth fluctuation. The dynamic behavior of the probability density distribution of the crystal size (ψ) had been obtained by recurring to the Fokker-Planck equation after performing a nonlinear variable transformation y=ln (L) in Eq. (1):

$$\partial_t \psi = D\partial_{yy}\psi - \partial_y[g(y,t,\theta)\psi] \tag{2}$$

The growth rate function in the variable y, allowing the most simple and accurate representation of the crystallization system is the logistic equation:

$$g(y,\theta) = ry\left(1 - {}^{y}\!/_{K}\right) \tag{3}$$

Simple relationships had been developed to correlate the parameters r and K along with the noise intensity (D) to the antisolvent flow rate and temperature leading to a stochastic model that can be applied to the whole operating range of the experimental system.

The stochastic modeling approach provides a convenient way to analyze the input-output relationships in order to evaluate the process characteristics such as stability and transient response. In recent works it was shown that, representing the asymptotic mean and variance on an antisolvent (q) vs. temperature (T) plane, input multiplicities were obtained (Cogoni et al, 2014) for a certain window of operating conditions. This means that it is possible to obtain an asymptotic CSD, characterized by its mean and variance, by using two different sets of input values. This particular behavior has been corroborated experimentally (Cogoni et al., 2014), and it is due to the presence of competing effects of the process inputs. From a control perspective, input multiplicities implies that the steady-state gains of the system may change sign as the system moves from one operating point to another, therefore if a conventional feedback control is applied, it can lead to undesired output values, unstable or oscillatory responses (Kumar et al., 2005). For the problem at hand, it is possible to analytically solve Equation (2) at the stationary solution (Tronci et al., 2011) obtaining the expression of the asymptotic distribution. Choosing a mean size value, the analytical expressions can be iteratively solved in the domain of the operating conditions to calculate all the possible standard deviations for that specific mean size. This allows constructing the asymptotic iso-mean

(blue line) and iso-standard deviation (red line) curves reported in an antisolvent flowrate - temperature plane (Figure 1).

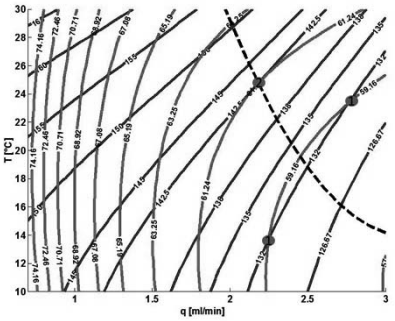

Figure 1: Asymptotic standard deviation (solid red lines) and the mean size (solid blue lines). The catastrophe locus is also reported (dashed black line)

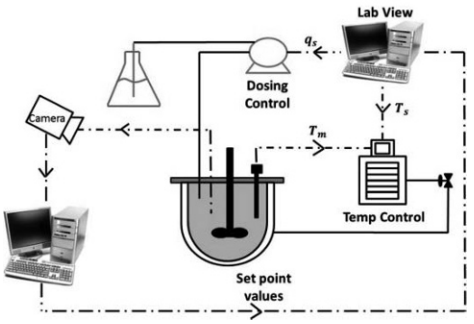

Figure 2: Schematic representation of the experimental system

The region in the (q,T) plane where the matrix of the process gain at asymptotic condition is singular is called catastrophe locus, and it is represented with a black dashed line in Figure 1. As illustrative examples to consider different behaviors of the dynamical system, two asymptotic conditions are chosen as targets, which are: (μ, σ)=(132 μm, 59.16 μm) and (μ, σ)=(142.5 μm, 61.24 μm). According to the operational map these points are feasible and the second one is on the catastrophe locus of the system as shown by gray circles in Figure 1. These two set-points will be considered during the implementation and testing alternative control strategies.

3. Experimental set-up and CSD characterization

Crystallization of sodium chloride in water using ethanol as antisolvent is considered as a case study. Reagent grade sodium chloride (99.5%), 190 proof ethanol and only purified water are used. The initial solution consists of 34 g of NaCl in 100 g of deionized water. All the experiments are carried out in 1 l bench scale crystallizer which is submerged into a temperature control bath. Temperature is measured using an RTD probe that is wired up to a slave temperature control system capable of heating and cooling. Ethanol is added to the solution using a calibrated peristaltic pump. Mixing is provided by a magnetic stirrer at the speed of 400 RPM. Along the experiment, particles are circulated throw a pump into a cell where they are lighted up by an illumination system. Images are taken continuously using a USB microscope camera which fits into the side tube on the side of the microscope with one of the supplied adapters and connects to a computer. Using image-based texture analysis crystal size distribution is determined and the results are compared with the desired set points that have already been defined in the computers by master controller. A schematic representation of the experimental apparatus is shown in Figure 2.

The controller strategies proposed in this work use the mean crystal size and variance of the CSD estimated by a sensor recently developed by Zhang et al., (2014). The novel approach is based on image processing of the crystals, and it is able to extract the required information on textural properties irrespective of whether it is applied to single particles or overlapped as clusters. In this method, which is based on combining

thresholding and wavelet-fractal-energy algorithm, images are considered as a 2D array of pixels with various intensities. Otsu's global thresholding method and an optimum threshold value for the intensity can be exerted to identify the intensity of crystal edges and remove the background. In this way, location of crystal clusters that have different intensities from the background can be detected and the information regarding intensities of those points will be restored into a vector. Discrete wavelet transformation (DWT) is then applied to the signal obtained by processing the image. DWT should extract textural characteristics of crystals by decomposing the signal into several details, which are crystals' edges in our case and an approximation, called the intensity variance caused by illumination. The new information in terms of variance of wavelet coefficients are further processed in order to obtain the fractal dimension (FD). This last property has been selected as texture feature since it has been demonstrated that dynamics of crystal growth follows fractal process. An artificial neural network is then designed using the texture information (FD, energy signatures for details level from 2 to 5) in conjunction with the available online process conditions (flow rate, temperature and time) as inputs for the estimation of the crystal properties (mean size and standard deviation) as output in the whole operating range.

4. On-line control of the Crystal size distribution

Different control strategies have been applied to the crystallization system in order to achieve a desired asymptotic CSD using antisolvent flow rate and temperature to reach the target CSD. For the present system, the target CSD could be assumed lognormal(Grosso et al, 2010), and it is characterized by selecting a proper mean and standard deviation, thus the objective of the controller is to reach the selected mean and standard deviations by manipulating the antisolvent flow rate and temperature. Target selections have been conducted exploiting the model of the process presented in Section 2 and its operative map (Figure 1).

The first strategy applied is a conventional feedback, where two loops are considered to control mean and standard deviation of the CSD by respectively manipulating antisolvent flow rate and temperature. As an alternative to the PIs structure, an open loop (feed-forward) control was also implemented. This approach is introduced because eliminating feedback action should avoid the problems related to ill-conditioning of the gain array matrix (Kumar et al., 2005) and time-varying characteristics of the system (Bovin, 1998). The latter aspects imply that using a linear feedback control ignores the fact that controller parameters should be adapted, as process moves along the given path. The input trajectory for the feed-forward action has been obtained minimizing the area between targets values and outputs calculated by the stochastic model (Cogoni et al., 2014). The feed-forward (FF) approach has the potential to provide minimum residual area and minimize the consumption of antisolvent but will not be able to compensate if any disturbance hits the process or in case of model-plant mismatch, since no feedback action is deployed. Consequently, a two-stage controller (FF/FB) has been also implemented, where a FF strategy is combined with a feedback controller (FB). In particular, the FF action is used to bring the system close to the asymptotic condition at around 5% of the desired set-point, and then the PI controller is activated to remove the offset for the crystals' mean size. As it will be observed, by relinquishing strict control on standard deviation it is possible to have a more efficient control on particles' mean size avoiding problems related to ill-conditioning if they should arise.

5. Results and discussion

The performance of the three different control strategies were be analyzed considering two different cases, which differ from the position of the mean and standard deviation set-points in the (q ,T) plane. Case 1 considers the targets far from the catastrophe locus (point 1 in Figure 2), whereas Case 2 set the target values belonging to the catastrophic locus (point 2 in Figure 2). Due to space restrictions only results for FB and FF/FB configurations for Case 2 are presented. This choice aims to assess the control configurations in a more demanding situation with respect to the previous one, because of the singularity of the input-output relationships.

The results obtained when using the PI controllers are shown in Figure 3 where the inputs and outputs behavior are shown along with the distribution at the end of the batch and the salt concentration. In this case the PI controllers are able to track the system to the desired set-points, thanks to the presence of a higher concentration within the first three hours of the run. In order to adjust the mean crystal size, the antisolvent flow rate is increased after 2 hours and a half to its maximum value by the controller, because it is favored the creation of new nuclei lowering the mean of CSD. However, it is interesting to analyze the shape of the final distribution (bottom of Figure 3) as given by the images taken at the end of the batch. As we can see the final distribution is bimodal showing the effects of secondary nucleation (small crystal are created at the end of the run). This can also be observed by analyzing the images at the end of the run, where small particles are observed jointly with the large particles already created. Consequently, even if the PI controller appears to achieve the control targets in terms of mean and standard deviation, it is not able to bring the system to the target CSD (unimodal lognormal distribution with a specified mean and variance). The poor performance of the conventional PI when operating close to the ill-conditioned region confirms what evidenced in the previous studies (Cogoni et al., 2014). The next experiment reported here has been conducted in order to test the system when either disturbances and/or modeling errors are present and a FF action cannot assure offset-free performance. To accomplish this task, an error in the model estimation of antisolvent flow rate was introduced, and it is set equal to 1.8 ml/min instead of 2.1 ml/min. We should notice that this situation may also represent a calibration error in the feed pump. As presented previously the FF control action is coupled with a PI controller (FB) which is switched on towards the end of the batch to perform final adjustments for the mean size (5% of the final mean size). The performance of the two-step controller are rather good and very close to the results obtained with the FF strategy, both in terms of the two moments and considering the shape of the distribution at the end of the batch, as shown in Figure 3. This clearly shows the importance of a FF/FB combination for realistic situations due to presence of unexpected disturbances.

6. Conclusions

In this contribution an online strategy to directly control crystal size distribution in joint cooling antisolvent crystallization processes was proposed. Alternative control strategies were implemented and tested to achieve a desired CSD. They include multi-loop PIs approach, a feedforward strategy (FF) based on off-line calculated profiles and a two stages control strategy using a combination of feedforward and feedback algorithm (FF/FB). Results demonstrate in some cases poor performance of the PIs control strategy, due to ill-conditioning of the process. On the other hand excellent behavior on the CSD control is achieved when the FF controller was applied. The two

stage (FF/FB) strategy exhibits a perfect control over the mean size and it was able to achieve the asymptotic conditions faster as well as eliminating the natural effect of both model and process disturbances.

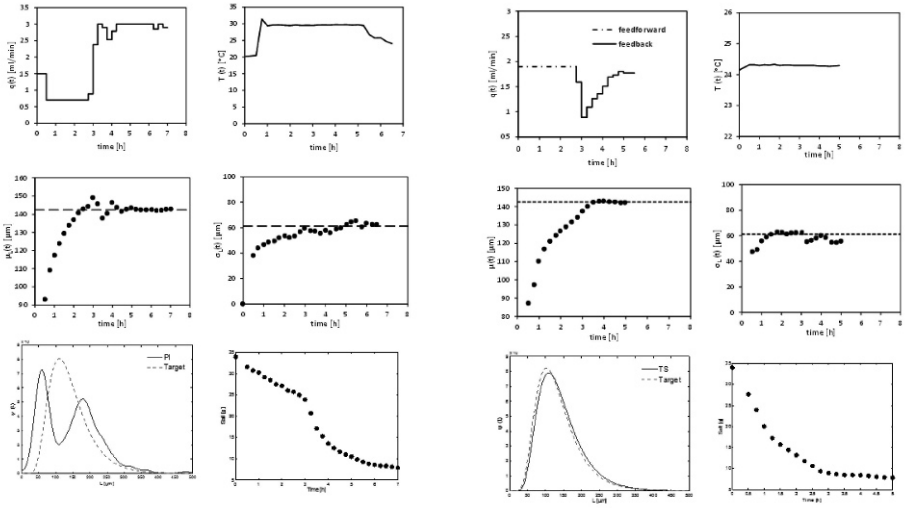

Figure 3: Closed loop responses a) for PI FB and b) combined FF/FB controllers. Upper panel- Antisolvent flow rate (left) and temperature (right) profile. Bottom panel- evolution of mean (left) and standard deviation (right) for the PI controller

References

D. Bonvin, 1998, Optimal operation of batch reactors: A personal view, J. Process Control, 8, 355-368.

G. Cogoni, S. Tronci, R. Baratti, J.A. Romagnoli, 2014, Controllability of semibatch nonisothermal antisolvent crystallyzation process, Ind. Eng. Chem. Res., 53, 7056-7065.

M. Grosso, O. Galàn, R. Baratti, J.A. Romagnoli, 2010, Stochastic formulation for the description of the crystal size distribution in antisolvent crystallization processes. AIChE J., 56, 2077.

S.V. Kumar, V.R. Kumar, G.P. Reddy, 2005, Nonlinear control of bioreactors with input multiplicities: An experimental work, Bioprocess Biosyst. Eng**.,** 28, 45-53.

C. Lindenberg, M. Krattli, J. Cornel, M. Mazzotti, J.Brozio, 2009, Design and optimization of a combined Cooling/Antisolvent process, Cryst. Growth Des., 9, 1124−1136.

M. Sheikhzadeh, M. Trifkovic, S. Rohani, 2008, Real-time optimal control of an anti-solvent semi-batch crystallization process*,* Chem.Eng. Sci.**,** 63, 829-839.

S. Tronci, M. Grosso, R. Baratti, J.A. Romagnoli, 2011, A stochastic approach for the prediction of PSD in crystallization processes: Analytical solution for the asymptotic behavior and parameter estimation, Comput. Chem. Eng., 35, 2318-2325.

Y. Yang, Z.K. Nagy, 2014, Model-Based Systematic Design and Analysis Approach for Unseeded Combined Cooling and Antisolvent Crystallization (CCAC) Systems, Cryst. Growth Des., 14, 687-698.

B. Zhang, R. Willis, J.A. Romagnoli, C. Fois, S. Tronci, R. Baratti, R, 2014, Image-Based Multiresolution-ANN Approach for Online Particle Size Characterization. Ind. Eng. Chem. Res., 53, 7008-7018.

Krist V. Gernaey, Jakob K. Huusom and Rafiqul Gani (Eds.), 12th International Symposium on Process Systems Engineering and 25th European Symposium on Computer Aided Process Engineering.
31 May – 4 June 2015, Copenhagen, Denmark

Multivariable Adaptive Lyapunov Fuzzy Controller for pH Neutralisation Process

M.F. Zanil[a] and M.A. Hussain[b]

[a] *Chemical and Petroleum Engineering, Faculty of Engineering & Built Environment, UCSI University, 56000 Kuala Lumpur, Malaysia.*
[b] *Chemical Engineering Department, Faculty of Engineering, University of Malaya, 50603 Kuala Lumpur, Malaysia.*

Abstract

A multivariable fuzzy logic controller with Lyapunov adaptive control scheme has been developed for a pH neutralisation process. In this study, the nominal neutralisation process condition exhibit nonlinear dynamics and multi-delayed-effects input variables. The proposed controller uses a Takagi-Sugeno fuzzy inference system and it has been optimised by genetic algorithm which minimizing the closed loop error in feedback control system. The optimised structure is used to predict three-difference control action simultaneously. The Lyapunov function is integrated in the fuzzy inference calculation at output membership function. The proposed controller has been tested and compared in several cases such as for set-point tracking, model plant mismatch and unknown disturbance. The adaptive fuzzy controller demonstrate better performance over the conventional PID controller in all the tested cases.

Keywords: Non-linear control; Fuzzy Controller; Adaptive control.

1. Introduction

The pH neutralisation is a typical process in chemical wastewater treatment plant. The effluent from the treatment plant must be neutralised before it can be safety discharged to the environment. Problem that occurs in pH neutralisation control are due to the process characteristics involved in such a process as strong nonlinear respond among acid, neutral, and base regions, wide-ranging time delay of the titration, and the complexity of inlet composition. The characteristic might vary from case to case and thus, the conventional controller can only work at a single desired point and could fail to compensate when the controlled region is changed. There are many solutions in the literature that has been reported, but an ideal solution still depend on the cases involve and it has not been totally solved due to vigour and complexity of the control and process. Thus, the need of an advanced control system is necessary for this situation.

The adaptive technique with a fuzzy logic system has been investigated in this case study is controlling the pH neutralisation for set point tracking and load disturbance. Previously, Salehi (2009) had used fuzzy as an estimator to the adaptive model based control framework , Min (2006) work on adaptive algorithm of universal learning network, and Menzl et al. (1996) had developed self-adapting mechanism inside fuzzy logic controller at neutralisation point. All of these work focus on utilising the fuzzy system for neutralisation control at nominal conditions with satisfactory performance. Related literatures are given in Goodwin (1982), Gustafsson (1984), Henson (1994), Narayanan (1997), Sung (1998), and Boling (2007). However, fuzzy controller incorporated with adaptive mechanism is not easy to build and furthermore an effective control performance

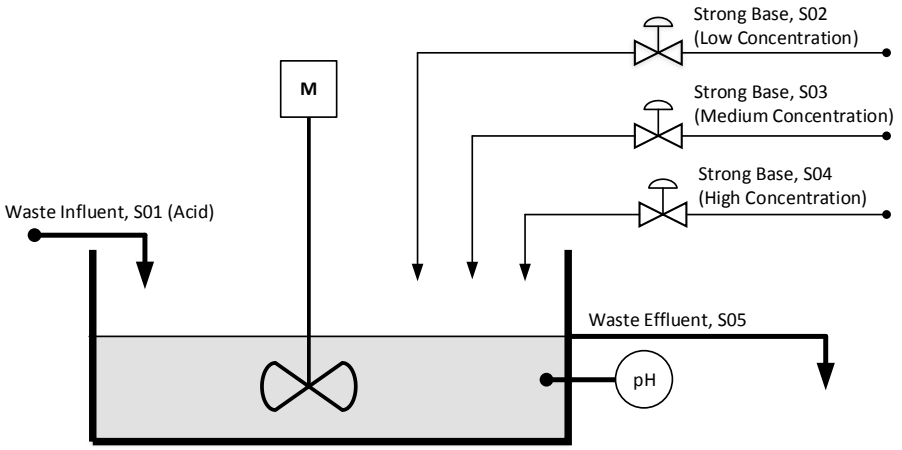

Figure 1: Scheme of pH neutralisation process

for multiple pH regions is very hard to generalize. Therefore, the need of robust controller performance in this field arise significantly.

The objective of this study is to investigate the multivariable controller for the control of nonlinear pH neutralisation process in continuous stirred tank reactor by using the Lyapunov based adaptive Fuzzy Logic approach. The process using the strong acid equivalent model (Zanil et al., 2014). The control system has been set to regulate the pH reactor at neutral point (pH = 7.0) by manipulating several acid flow rates.

2. pH Neutralisation

The potential of hydrogen, pH is mathematically defined the negative logarithm of concentration of ion hydrogen. In pH neutralisation modelling, the nonlinearity characteristic are from the logarithm term in the equation. The model (Eq.1) which follows the law of conservation of mass and chemical equilibrium (Gustafsson et al., 1995). The process is assumed isothermal with constant fluid density and no solid formation occurring during experiment. The schematic diagram (Figure 1) illustrate the multi titration streams with single influent and effluent stream.

The model used in the study is as follows:

$$V\frac{dx}{dt} = F_a C_{a0} - (F_a + \sum_{i=1}^{3} u_{b,i})x - \sum_{i=1}^{3} u_i(t-\theta_i)C_{b0,i} \quad (1)$$

Where x is the remaining acid concentration in the reactor, C_e , C_{p0} and $C_{b0,i}$ is the concentration of the component in the effluent stream, influent stream, and titrating stream, respectively. The input time-delay is used to approximate the dynamics of the pH sensor and non-ideal mixing condition (Sung et al., 1998). In an aqueous solution, the electro neutrality and water-equilibrium theories are used to express the electrolyte disassociations (Eq.2) at an isothermal temperature of 27 ^{o}C, and water equilibrium constant of K_w at 1×10^{-14}.

$$x = [H^+] - \frac{K_w}{[H^+]} \tag{2}$$

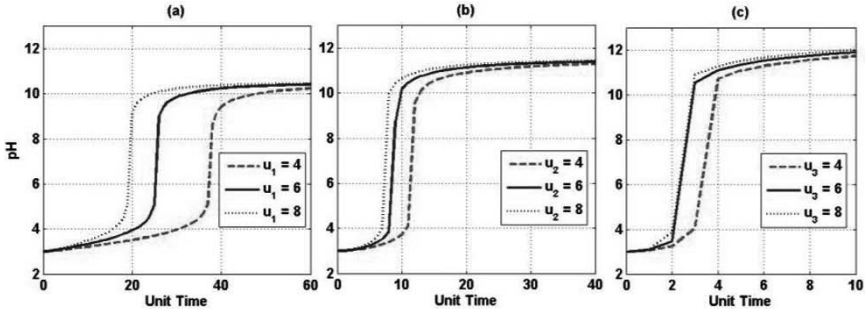

Figure 2: Open loop studies for variation of titration flow rate: (a) Low, (b) Medium, (c) High.

Thus, the hydrogen ion, $[H^+]$ as in Eq.3 can be used to simulate the dynamic profile of hydrogen concentration and pH value of the stirred tank reactor.

$$V\frac{d}{dt}\left([H^+] - \frac{K_w}{[H^+]}\right) = F_a C_{a0} - (F_a + \sum_{i=1}^{3} u_{b,i})\left([H^+] - \frac{K_w}{[H^+]}\right) - \sum_{i=1}^{3} u_i(t-\theta_i)C_{b0,i} \tag{3}$$

The pH value is calculated by taking the logarithm of hydrogen concentration. The simulated result for several titration flow rates has been demonstrate in Figure 2 and it is observed that the variation time response over the titration flow rates has significant effect. The pH value inside the reactor shows several dynamic responses over time. The nominal condition that shows in Table 1 has been used for the simulation study.

3. Control Mechanism

Fuzzy logic consist a set of fuzzy inference that works on approximate reasoning that give a consequence action as the outcome. The structure has been set to receive three inputs and three outputs. The fuzzy logic inference mechanism were computed from the product of input membership function (e, ce and AV) and the fulfilment of fuzzy rules (R_i). i.e.;

$R_i : IF\ e\ is\ A_i\ AND\ ce\ is\ A_i\ AND\ AV\ is\ A_i THEN\ u_1$is $U_{1,i}\ AND\ u_2 is\ U_{2,i}\ AND\ u_3\ is\ U_{3,i}$

Every output membership function can be written as

$$U_{j,i}(k) = A_{1,i}\ e + A_{2,i}\ ce + A_{3,i}\ AV + A_{4,i}\ ; j = 1,2,3\ and\ i = 1,2..N \tag{4}$$

The output parameter, $A_{j,i}$ has been optimised by genetic algorithm depending on the close loop error analysis; Integral Square Error (ISE). The controller output can be formulated as the summation of average weighted inference value for the active rule, R_i.

$$u_i = \frac{\sum_i^n w_i(e,ce,AV)U_{j,i}}{\sum_i^n w_i(e,ce,AV)} \tag{5}$$

$$w_i(e,ce,AV) = min[\mu_i(e), \mu_i(ce), \mu_i(AV)] \tag{6}$$

Table 1: Parameters and value for nominal

Parameter	**Value**	**Unit**
Reactor Volume, V_r	100	Litre
Influent flow rate, F_b	2.5	Litre/Min

Inlet Influent Concentration, C_{b0}	3E-3	Mole/Litre
Inlet Base Concentration (Low) , $C_{a0,1}$	3E-4	Mole/Litre
Inlet Base Concentration (Medium) , $C_{a0,2}$	3E-3	Mole/Litre
Inlet Base Concentration (High) $C_{a0,3}$	3E-2	Mole/Litre

Where w_i is degree of input membership function as Eq. 6 and $\mu_i(e), \mu_i(ce)$, and $\mu_i(AV)$ are the input membership function (triangular types) of error, change of error, and acidic region respectively.

3.1. Adaptive Mechanism

The used of adaptive mechanism is to improve the fuzzy controller performance during the model-mismatch operation in the plant. Let the model identifier approximate the nominal plant response and thus the model error, $\varepsilon = y_m - y$ which detect the existing of model-mismatch condition. So, the adjustable parameter, γ is introduced to minimise Eq. 7 in the negative gradient;

$$\frac{d\theta_i}{dt} = -\gamma_i \left(\frac{1}{2}\varepsilon^2\right) \tag{7}$$

The adaptation law is formulated as in Eq. 8

$$U_i = \frac{d\theta_i}{dt} u_i = -\gamma_i \left(\frac{1}{2}\varepsilon^2\right) u_i \tag{8}$$

3.2. Control System

The study use a conventional closed loop control strategy as in Figure 3 and the neutralisation models as stated in Section 2 has been used for the plant block. Measured disturbance is the signal from influent flow rate (base) and the manipulated variable signal at different concentrations. The fuzzy controller send three-output signals to every individual control valve before the change of titration effect takes place.

In the study, unmeasured disturbance and limited-band white noise has been introduced. A servo and regulator case study has been performed throughout the simulation. Several analysis for servo cases has been carried out; acid/base region at the neutral point and within neutral region. Beside, regulator case analysis has been conducted for ± 5% variation in the measured disturbance flow rate. Plant mismatch of ± 10% from nominal volume reactor has been carried out to test the control performance robustness.

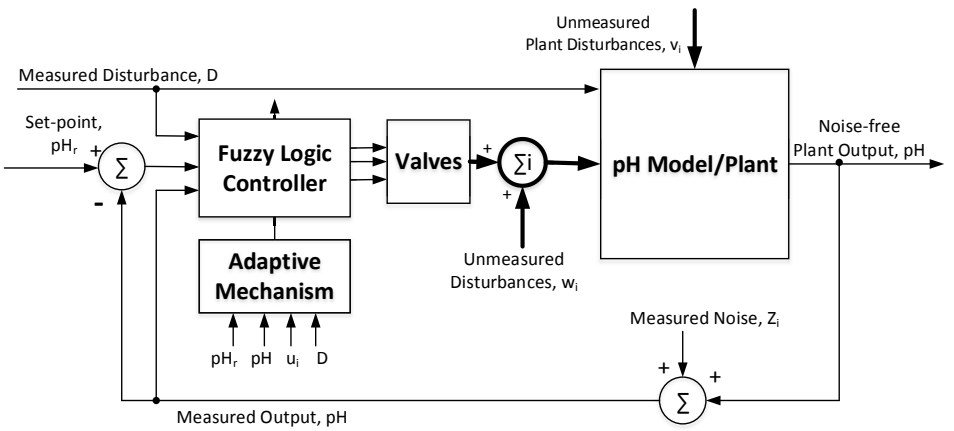

Figure 3: Adaptive Multiple Output Fuzzy Control Scheme for pH Neutralisation

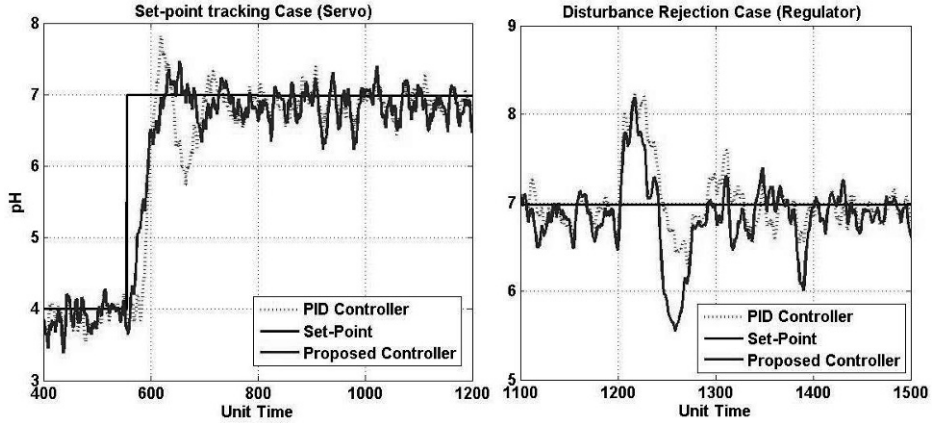

Figure 4: Comparison of control performance for set-point and disturbance rejection cases.

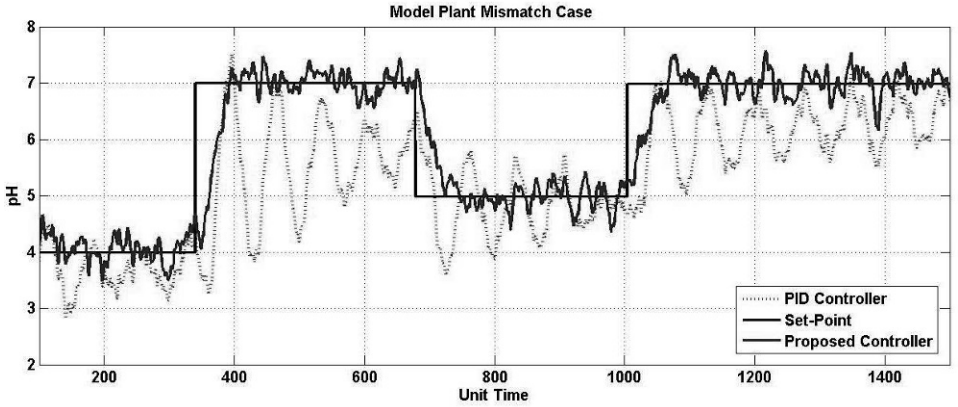

Figure 5: Comparison of control performance for plant mismatch case.

4. Result and Discussion

Simulation result for set point tracking, load rejection of proposed adaptive controller responses are shown in Figures 4 and 5 respectively. Considering the adaptive fuzzy logic controller, its set point and load changes show smoother response over the entire nonlinear region. Furthermore, there is no oscillation or overshoot in proposed control responses. PID controller has showed slightly overshoot and the settling time is more compared to propose controller. This is due to the sluggish control action at the neutralisation region.

The controller performance based on Integral Square Error (ISE), Integral Absolute Error (IAE), and Integral Total Absolute Error (ITAE) as shown in Table 2.

Table 2. Error analysis of control performance according to the case.

Case	Controller Type	ISE	IAE	ITAE
Disturbance Rejection	PID	224,92	367.21	2.57E5
	Proposed Controller	203.95	322.60	2.19E5
Set-point tracking	PID	681.93	582.83	3.64E5
	Proposed Controller	576.07	533.23	3.15E5
Plant mismatch	PID	1.94E3	1.29E3	9.16E5
	Proposed Controller	597.16	624.46	3.90E5

The result shows that the proposed controller gives best performance, which indicate less error analysis compared to conventional controller for all cases. The conventional controller unable to adapt with the plant mismatch case and therefore the error analysis give large value compare to the proposed controller.

5. Conclusions

A multivariable adaptive fuzzy logic controller has been proposed for the nonlinear pH neutralisation control system. It is the integration of empirical optimisation fuzzy logic controller with Lyapunov adaptive law. The results has shown superior performance for the proposed controller compared to conventional controller in all studied cases. The proposed controller has a promising potential for other nonlinear control applications.

Acknowledgement

Special thanks to the Department of Chemical & Petroleum Engineering, UCSI University and to University of Malaya Research Grant (Grant number: RP006G-13ICT) for the research funding.

References

S. Salehi, M. Shahrokhi, and A. Nejati, 2009, Adaptive nonlinear control of PH neutralisation processes using fuzzy approximators. Control Engineering Practice, 17(11), 1329-1337.

H. Min, H. Bing, and G. Wei, 2006, Process control of pH neutralisation based on adaptive algorithm of universal learning network. Journal of Process Control, 16(1), 1-7.

S. Menzl, M. Stühler, and R. Benz, 1996, A self adaptive computer-based pH measurement and fuzzy-control system. Water Research, 30(4), 981-991.

S.F. Graebe, M.M. Seron, and G.C. Goodwin, 1996,Nonlinear tracking and input disturbance rejection with application to pH control. Journal of Process Control, 6(2-3), 195-202.

T.K. Gustafsson and K.V. Waller, 1983, Dynamic Modeling and Reaction Invariant Control of Ph. Chemical Engineering Science, 38(3), 389-398.

M.A. Henson and D.E. Seborg, 1994, Adaptive nonlinear control of a pH neutralisation process. Control Systems Technology, IEEE Transactions on, 2(3), 169-182.

N.R.L. Narayanan, P.R. Krishnaswamy, and G.P. Rangaiah, 1997, An adaptive internal model control strategy for pH neutralisation. Chemical Engineering Science, 52(18), 3067-3074.

S.W. Sung, I.B. Lee, J.Y. Choi, and J. Lee, 1998, Adaptive control for pH systems. Chemical Engineering Science, 53(10), 1941-1953.

J.M. Boling, D.E. Seborg, and J.P. Hespanha, 2007, Multi-model adaptive control of a simulated pH neutralisation process. Control Engineering Practice, 15(6), 663-672.

R.A.W. Wright, M. Soroush and C. Kravaris, 1991, Strong acid equivalent control of pH process. Ind. Engng Chem. Res, 30, 2437-2443.

T.K. Gustafsson, B. O. Skrifvars, K. V. Sandstrom, and K.V. Waller, 1995, Modeling of Ph for Control. Industrial & Engineering Chemistry Research, 34(3), 820-827.

McAvoy, 1972, Dynamics of pH in controlled stirred tank reactor. Ind. Engng Chem. Process. Des. Develop, 11, 68-70.

M.F. Zanil, A. M. Norhuda, M. A. Hussain, and R. Omar, 2014, Hybrid model of pH neutralisation for a pilot plant. Journal of Intelligent and Fuzzy Systems, 26(2), 551-561.

Krist V. Gernaey, Jakob K. Huusom and Rafiqul Gani (Eds.), 12th International Symposium on Process Systems Engineering and 25th European Symposium on Computer Aided Process Engineering.
31 May – 4 June 2015, Copenhagen, Denmark

Detection of changes in fouling behavior by simultaneous monitoring of thermal and hydraulic performance of refinery heat exchangers

Emilio Díaz-Bejarano,[a] Francesco Coletti,[b] and Sandro Macchietto[a,b]*

[a] *Department of Chemical Engineering, Imperial College London, South Kensington campus, London, SW7 2AZ, UK.*
[b]*Hexxcell Limited, Imperial College Incubator, Bessemer Building Level 2, Imperial College London, London, SW7 2AZ, UK*
s.macchietto@imperial.ac.uk

Abstract

Monitoring of pre-heat trains in oil refineries is a crucial activity to assess the gradual decay in performance of heat transfer equipment due to fouling. It is also important to assist in operational decisions with respect to fouling mitigation options and cleaning strategies. In this paper, a novel graphical representation of time varying operational data is proposed to monitor crude oil fouling. This dynamic thermo-hydraulic plot, named the TH-λ plot, simultaneously captures both thermal and hydraulic performance and presents it in a way easily interpreted by field engineers. Its features and applications are demonstrated here for typical situations using data generated using an advanced dynamic simulation model for shell-and-tube heat exchanger undergoing fouling. The results show that consideration of thermal and hydraulic effects, together with process dynamics, is essential to adequately monitor performance, detect changes in fouling behaviour and properly interpret available data. They also show this is achievable using only measurements of inlet and outlet streams to heat exchangers.

Keywords: crude oil, fouling, monitoring, energy efficiency, operational performance.

1. Introduction

The performance of pre-heat trains, extensive energy recovery networks at the front end of oil refineries, is gradually degraded by fouling of heat exchangers, leading to severe energy losses, increased costs and operational problems. Typical refinery monitoring techniques assess the thermal performance of heat exchangers by calculating and following over time fouling resistances or heat duties using temperature and flow measurements. However, the thermal performance only tells part of the story and hydraulic performance (i.e. pressure drop increase due to gradual build-up of fouling inside the tubes) is also important and sometimes dominating over the thermal one.

Few publications in the literature address the interaction between hydraulic and thermal effects of fouling. Yeap *et al.* (2004) presented the performance of individual heat exchangers by plotting the thermal effects of fouling, represented by either the fouling Biot Number or the exchanger effectiveness, against the ratio between fouled and clean pressure drop. Lumped models involving simplifying assumptions were used to simulate the effects of fouling for a number of heat exchangers under ideal conditions. This representation was used by Ishiyama *et al.* (2008) to infer the impact of the thermal-conductivity of the deposit, which ultimately determines which effect, hydraulic or thermal, is dominant. Yeap *et al.* (2004) also proposed a "Modified

Temperature Field Plot" to include thermal and hydraulic effects into network analysis by plotting inlet and outlet temperatures and pressure drops at the beginning and end of an operation period. These methods provide some insights, however present several practical disadvantages: the use of thermal performance indicators which are rather difficult to interpret, limited capabilities to include process dynamics, and unclear application with actual plant data.

To overcome the disadvantages listed above and to broaden the scope of application, a new graphical representation for monitoring the performance of a single exchanger is presented in this paper. Here, the approach is illustrated and its results are compared with those obtained from traditional monitoring methodologies (based on fouling resistance calculations, e.g. R_f-based method). For simplicity the time-varying performance is simulated using a state-of-the-art thermo-hydraulic model, the shell-and-tube exchanger model in the Hexxcell Studio^{TM} software from Hexxcell Ltd., based on the work by Coletti and Macchietto (2011). The model is dynamic, distributed, and evaluates fluids and deposit physical properties, fouling rates and deposit growth as a function of local conditions, as well as fluid velocities and pressure drops. The resulting model can capture the combined thermal-hydraulic behaviour experienced in industrial systems undergoing distinct types and rates of fouling, as shown in the reference paper.

A recent modification (Diaz-Bejarano *et al.*, 2014a) implemented in Hexxcell Studio^{TM} allows simulating multi-component deposits, partial and total cleaning actions, and the effect of composition in fouling behaviour. In the general formulation, the rate of change in deposit thickness ($\dot{\delta}_n$) is given by the sum of net deposition rates (during operation) or by the cleaning rate (during cleaning). In refinery preheat trains, organic matter deposition is the main fouling mechanism. In that case, during operation, the local (time and axially varying) $\dot{\delta}_n$ for each pass is assumed to follow a modified version of the threshold model by Panchal *et al.* (1997):

$$\dot{\delta}_n = \frac{d\delta_n}{dt} = \lambda_0 \alpha Re_n^{-0.66} Pr_n^{-0.33} \exp\left(\frac{-E_f}{R_g T_{f,n}}\right) - \lambda_0 \gamma \tau_n \quad (1)$$

where δ_n is the deposit thickness, n is the pass number, τ_n is the shear stress at the layer surface, $T_{f,n}$ is the film temperature, R_g is the ideal gas constant, λ_0 is the conductivity of the fresh deposit or gel, and α, γ, and E_f are fouling parameters. Following previous works, the fresh foulant is assumed to be formed by organic gel, with a thermal-conductivity of 0.2 W/m K. The organic deposit gradually undergoes ageing at high temperatures (depending on temperature history), eventually transforming it into coke, with a conductivity of 1 W/m K. All examples in this paper are for a single shell exchanger with the geometry (number of tubes (N_t), tube outer diameter (d_o), number of passes (N_p), tube length (L_t), shell diameter (D_s)), fluid properties (*API,* Mean average boiling point (*MeABP*) and viscosity at 38°C ($v_{38°C}$)) reported in (Coletti and Macchietto, 2011) (Table 1). Crude oil is in the tube-side. In this paper, constant inlet conditions are used to illustrate the novel graphical representation.

Table 1. Exchanger geometry, fluids properties, inlet conditions and fouling/ageing parameters

Geometry		*Inlet conditions*			*Fouling/ageing*		
Parameter	Value	Parameter	Shell	Tube	Parameter	Set A	Set B
N_t	900	T_{in}[°C]	330	204	α [m^2 K/J]	0.00165	0.00114
d_o [mm]	25.4	Flow [m^3/h]	161	443	E_f [kJ/mol]	28.5	28.0
N_p	4	API	17.4	37	γ [m^4 K/J N]	$9.3 \cdot 10^{-13}$	$7.3 \cdot 10^{-12}$
L_t	6.1	MeABP[°C]	736	350	A_a [s^{-1}]	0.01	0
D_s [m]	1.4	$\nu_{38°C}$ [cSt]	29	4	E_a [kJ/mol]	50	-

2. TH-λ: A Dynamic Thermo-Hydraulic Monitoring Plot

To monitor effectively a refinery heat exchanger, it is desirable to have as much information as possible on a simple plot: its thermal and hydraulic performance, time evolution of performance to easily visualize its trends, approach to operating limits, and ideally some indication of the underlying causes of fouling. This plot should help refinery operators to assess at a glance the performance of units, identify critical ones and take remedial actions if necessary. Here we propose a novel graphical representation, the dynamic thermo-hydraulic TH-λ plot, meeting these requirements. The performance of a heat exchanger is represented using the following indicators:

1) Thermal: Ratio of fouled to clean heat duty ($Q(t)/Q_c$).
2) Hydraulic: Ratio of fouled to clean tube-side pressure drop ($\Delta P(t)/\Delta P_c$).
3) Temporal: Daily data (monthly points emphasized and labelled with month number). More frequent data, actual dates as label, etc. could be used.

An example of this plot is shown in Figure 1(a), where a performance line, named "TH Line" (continuous line) is shown for 12 months of operation, starting from a clean state. Here, the variation in performance of the unit as a result of fouling (Case A) is simulated using the fouling (α, γ, and E_f) and ageing parameters (A_a and E_a) corresponding to Set A in Table 1 (Coletti and Macchietto, 2011). In practice, the TH Line would be based on plant measurements of inlet and outlet temperatures, flow rates, and tube-side pressure drop. Each point along the line simultaneously reflects the thermal and hydraulic performance w.r.t clean conditions. The time trend reflects how fast the relative change is happening. A displacement in the X axis (hydraulic) implies addition or removal of fouling material (increase or decrease in deposit thickness). A displacement in the Y axis (thermal) indicates a change in the heat exchanged, which may be due to: i) addition or removal of deposit; ii) change in the conductivity of the foulant (e.g. due to ageing); iii) change in the type of foulant, also with consequent change in conductivity (hence the λ in the TH-λ name).

The TH-λ plot becomes even more useful when monitored data and trends are complemented with additional reference lines of practical interest:

a) Thermal and hydraulic limit lines, TH and TL (dashed lines in Figure 1(a)).

Useful limits refer to minimum performance and may be operational constraints (e.g. maximum allowable pressure drop) or design targets (e.g. minimum heat duty). In Figure 1(a), the hydraulic limit (HL), indicated by the vertical line, was set at 4 times the value of the clean pressure drops whilst the thermal limit (TL), indicated by the horizontal line, was set so that the minimum heat duty is 30% of the clean one.

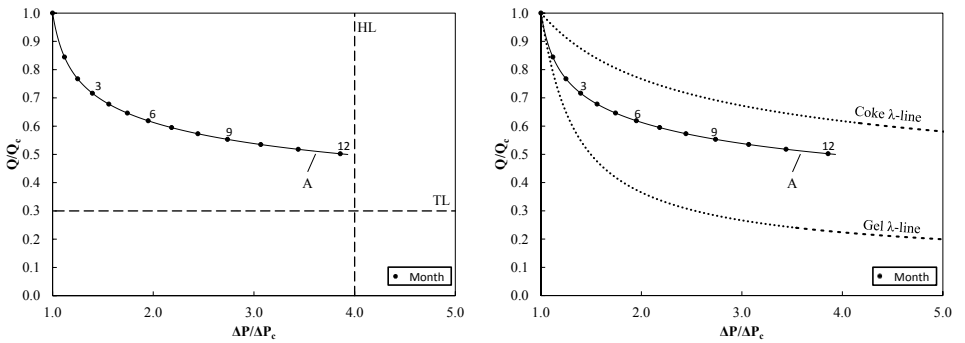

Figure 1. TH-λ Plot (Case A) with added operating limit lines (a) and organic limit λ-Lines (b).

a) Reference conductivity lines, named "λ-Lines" (dotted lines in Figure 1(b)).
Hydraulic and thermal performances are not independent but linked by the thickness and thermal-conductivity of the deposit as it grows (or is removed). As a result, if a suitable thermo-hydraulic model of the exchanger is available, it may be possible to calculate and plot its limiting behaviour. For example, assuming constant inlet conditions, it is possible to calculate two reference lines for fixed deposit conductivities. For organic fouling, for instance, the lines for gel (fresh deposit) and completely coked deposits can be calculated and represented as shown in Figure 1(b). These lines delimit the area of expected performance of the exchanger with organic crude oil fouling. Useful insights on the evolution of the deposit due to ageing can be gained by comparing the TH Line with the reference λ-Lines. For instance, in Figure 1(b), the TH Line gradually moves away from the gel reference line to approach the coke line, indicating significant deposit ageing at month 12. It should be noted that the use of λ-lines as here described is limited to cases where the contribution of shell-side fouling to the overall thermal performance is negligible. This is the most common case in refinery heat exchangers (Coletti and Macchietto, 2011).

3. Applications of the TH-λ Plot – Case studies

3.1. Organic fouling: identification of underlying phenomena

The behaviour of a heat exchanger undergoing fouling depends on the relative values of deposition and ageing rates. Traditional monitoring techniques (e.g. R_f-based method) are inherently unable to discriminate between these phenomena. For instance, consider the two curves A and B in Figure 2(a) (simulated using fouling/ageing parameters Set A - Coletti and Macchietto (2011) and Set B - Yeap *et al.* (2004) in Table 1). Case B seems to clearly indicate substantially greater fouling rate and deposition. On the other hand, using the TH-λ plot for the same 12 months data (Figure 2(b)) some different and more informative conclusions can be extracted straight away: i) the net deposition rate is actually greater in Case A than Case B, as evidenced by a faster increase in ΔP; ii) In Case B, the TH Line follows the lower limit for organic fouling, and therefore the deposit does not age; iii) In Case A, a strong deposit ageing effect is evidenced, which significantly attenuates the thermal losses of fouling; iv) In Case A the hydraulic limit HL will be reached before TL, while the opposite is true in Case B.
The R_f-based monitoring in this case is misleading as it does not evidence ageing effects, whilst the proposed TH-λ representation helps to correctly identify the underlying phenomena and the selection of appropriate operational decisions.

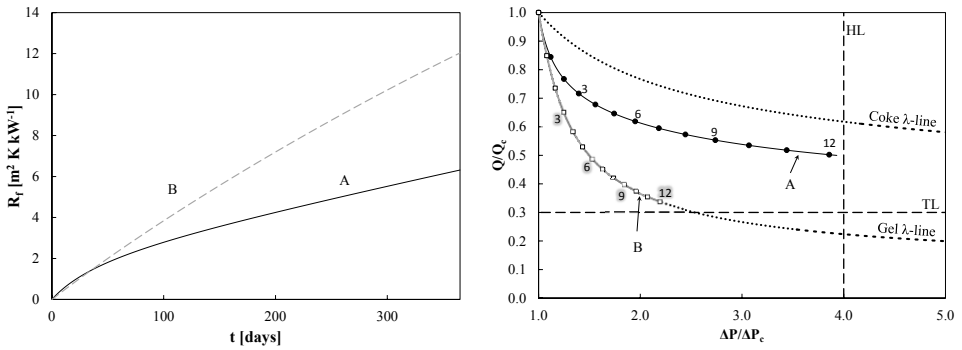

(a) (b)

Figure 2. (a) Fouling resistances over time for Cases A and B; (b) TH-λ Plot for Cases A and B.

3.2. Detection of deviations in fouling behaviour

Most current practices not only ignore the hydraulic performance, but also have limited ability to detect changes in fouling behaviour. Here, the heat exchanger is initially assumed to foul as in Case A in the previous examples. After three months of operation an event leading to a change in fouling behaviour is assumed to occur. Two cases are considered:

a) Deviation due to acute organic fouling

The first case is a change in oil blend or type of oil being processed (e.g. to high fouling propensity oils such as slag or heavy oil) leading to acute organic fouling. The composition of the fresh deposit remains unchanged (only gel), but the fouling rate becomes twice as fast. The R_f-based method (Figure 3(a)) shows a sudden increase in the fouling resistance after the event. A change in behaviour is detected, but no information is provided about the hydraulic impact, which may be relevant due to the fast build-up of material. The TH-λ plot (Figure 3(b)) evidences the change as a large increase in pressure drop. This, together with a deviation towards lower values of thermal efficiency, indicates that the additional foulant has low conductivity and is most likely organic in nature. The increase in the relative contribution of fouling rate with respect to ageing explains the offset in thermal efficiency compared to the expected trend. Therefore, although the R_f-based method shows a deviation, the TH-λ plot provides much more complete and useful information as to its causes and effects.

b) Deviation due to inorganic fouling

In this second case, an inorganic material is assumed to start depositing after 3 months in addition to the usual organic fouling. This might be due to failure of upstream equipment (e.g. desalter), upstream corrosion, or change in the composition of the oil to sour or high metal content oils. Inorganic salts generally have greater conductivity than organic deposits, leading to enhanced thermal properties of the fouling deposit. This effect has been recently shown in a case study based on refinery data for a unit undergoing inorganic and organic fouling due to desalter malfunctioning (Diaz-Bejarano et al. (2014b). Here, iron oxide (Fe_2O_3), which has 3 times the conductivity of coke, is considered to deposit. The deposition rate of Fe_2O_3 is assumed to follow the same fouling law as organic fouling (Eq. (1)), leading after the onset of this event to a doubling of total deposition rate and a fresh deposit containing 50% of organic gel and 50% of Fe_2O_3. In this case, the R_f-based method completely fails to show the change in underlying behaviour (Figure 3(a)). In fact, it indicates that fouling becomes less severe than expected, which is incorrect and could potentially lead to erroneous interpretation and mitigation or cleaning decisions.

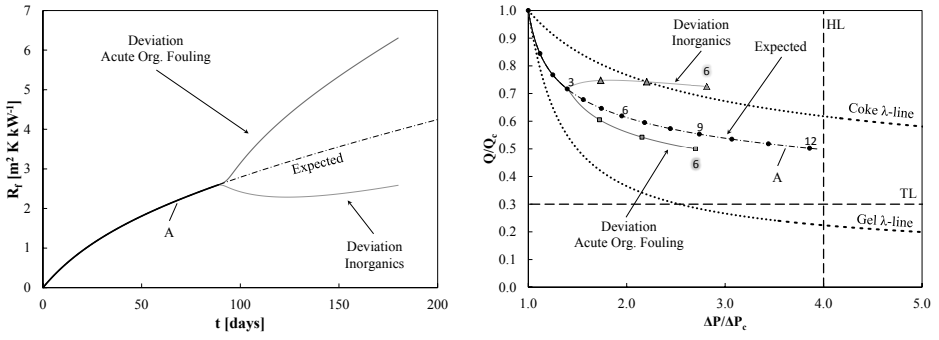

(a) (b)

Figure 3. Performance of the exchanger undergoing fouling (Case A) for a change in behavior after 3 months: (a) Fouling resistances over time; (b) TH-λ Plot.

In the TH-λ plot (Figure 3(b)), a change in behaviour is evidenced, as in case a), by a higher and much faster increase in pressure drop compared to the expected trend. In this case b), however, a deviation of the TH Line towards greater thermal efficiency also indicates that the new foulant is highly conductive and, probably, of inorganic nature. The fact that the TH Line crosses the reference coke λ-line confirms the latter inference.

4. Conclusions

A new dynamic thermo-hydraulic plot (TH-λ) for monitoring of heat exchangers has been presented. Its features and practical uses have been demonstrated using data produced by a sophisticated novel thermo-hydraulic simulation of shell-and-tube heat exchangers undergoing fouling and cleaning, considering constant inlet conditions of temperature and mass flow rates. It has been shown that this monitoring approach is useful to: a) simultaneously evaluate and trend the interacting thermal and hydraulic performance over time; b) highlight underlying mechanism contributing to overall performance, such as fouling rate and ageing; c) detect deviations from expected performance due to change in fouling behaviour; d) help in the identification of potential fouling causes. The results show that simultaneous consideration of thermal and hydraulic effects, together with process dynamics, is essential to adequately detect changes in fouling behaviour. They also show that this can be achieved merely using measurements of inlet and outlet streams to heat exchangers. The use of the monitoring approach described with actual (time-varying) plant data and its application to heat exchanger networks will be reported in future works.

Acknowledgments

This research was partially performed under the UNIHEAT project for which EDB and SM wish to acknowledge the Skolkovo Foundation and BP for financial support. The support of Hexxcell Ltd, through provision of the Hexxcell Studio™ software and modelling framework, is also acknowledged.

References

F. Coletti, F., and Macchietto, S. (2011). A Dynamic, Distributed Model of Shell-and-Tube Heat Exchangers Undergoing Crude Oil Fouling. *Industrial & Engineering Chemistry Research*, *50*(8), 4515–4533.

Diaz-Bejarano, E., Coletti, F., and Macchietto, S. (2014a). A new dynamic model of crude oil fouling deposits and its application to the simulation of fouling-cleaning cycles. In Preparation.

Diaz-Bejarano, E., Coletti, F., and Macchietto, S. (2014b). Detailed Thermo-Hydraulic Modelling of Crude Oil Heat Exchangers: Abnormal Fouling Behaviour Due to Inorganic Deposits. AIChE Annual Meeting, Atlanta, GE (USA), 15-21 Nov.

Ishiyama, E. M., Paterson, W. R., and Wilson, D. I. (2008). Thermo-hydraulic channelling in parallel heat exchangers subject to fouling. *Chemical Engineering Science*, *63*(13), 3400–3410.

Panchal, C. B., Kuru, W. C., Liao, C. F., Ebert, W. A., and Palen, J. W. (1997). Threshold conditions for crude oil fouling. In T. R. Bott (Ed.), *Understanding Heat Exchanger Fouling and its Mitigation* (pp. 273–281). Lucca, Italy: Begell House.

Yeap, B. L., Wilson, D. I., Polley, G. T., and Pugh, S. J. (2004). Mitigation of crude oil refinery heat exchanger fouling through retrofits based on thermo-hydraulic fouling models. *Chemical Engineering Research and Design*, *82*(1), 53–71.

Krist V. Gernaey, Jakob K. Huusom and Rafiqul Gani (Eds.), 12th International Symposium on Process Systems Engineering and 25th European Symposium on Computer Aided Process Engineering.
31 May - 4 June 2015, Copenhagen, Denmark.

Dosage of Filter Aids in the Case of Pure Surface Filtration – An Optimal Control Approach

Michael Kuhn and Heiko Briesen

Chair for Process Systems Engineering, TU München, Freising, Germany
briesen@wzw.tum.de

Abstract

Filter-aid filtration is widely used to remove impurities which tend to clog the filter medium. In many processes, filter aid is continuously dosed to the suspension to be purified. In these cases, a suitable filter-aid concentration is important to assure good separation with a minimal energy consumption. We here present the first optimal control approach to filter-aid filtration. The optimal dosage trajectories in case of constant and variable impurity concentrations in the suspension are derived for the case of pure surface filtration. These findings are compared to other dosage strategies and the benefits are shown. Consequences of the presented results for process control and further modeling and optimization approaches are highlighted.

Keywords: filtration, filter aid, optimal control, surface filtration

1. Introduction

Filter-aid filtration is widely used to remove impurities which tend to clog the filter medium, e.g. gelatinous particles. Hereby, the septum is covered with a small layer of filter aid, known as the precoat, before the separation takes place. Subsequently, filter aid, known as the body feed, is constantly added to the suspension during the actual separation (Sutherland and Hidi, 1966). This strategy assures increased filtration times and low energy expenditure due to high filter-cake permeabilities. Because of its flexibility concerning the separation task, filter-aid filtration is applied in a whole range of fields, such as in biotechnology and the chemical industry, in water treatment and the production of foodstuff and beverages.

Various researchers emphasized the role of the right amount of body feed for successful filtration (Carman, 1938, 1939; Sutherland and Hidi, 1966; Babbitt and Baumann, 1954; Haba and Koch, 1978; Heertjes and Zuideveld, 1978). Some of these works also present a model that relates cake resistance to the ratio of impurity and filter-aid concentration. They assume that separation only takes place by pure cake filtration, i.e. directly at the surface of the cake (Sutherland and Hidi, 1966; Haba and Koch, 1978; Heertjes and Zuideveld, 1978). Other results also showed that in some cases deep-bed filtration contributes to the overall separation (Heertjes and Zuideveld, 1978; Husemann et al., 2003).

Despite the available research and despite the fact that in various applications the amount of impurities to be separated varies over the course of one process cycle, a constant body-feed concentration is common industrial practice. It is suggested here, that this strategy can be improved by a rigorous application of optimal control theory. Dynamic optimization has scarcely been used in the field of filtration. Some works showed its potential to optimize the operation and cleaning strategies in membrane filtration (Blankert et al., 2006, 2007; Zondervan and Roffel, 2008). However, to the best of our knowledge, optimal control theory has never been applied to filter-aid

filtration. We here show its use to derive the dynamically optimal body-feed concentrations for different process scenarios under the assumption of pure surface filtration employing and modifying classical models from the filtration literature.

2. Derivation

2.1. Mathematical Problem Formulation

If the filter-aid concentration in the suspension c is much smaller than its concentration in the filter cake $\rho_{fa,c}$, the velocity of cake growth can be written as

$$u_s = \frac{c}{\rho_{fa,c}} \cdot q\,, \tag{1}$$

compare e.g. Hackl et al. (1993, p. 11). q is the suspension's superficial velocity which is assumed to be constant in the following, i.e. we here consider filtration at a constant flow rate. It is commonly assumed that the impurities captured at the surface do not contribute significantly to cake growth or, if they do, this usually means that too little filter aid is added to the suspension (Sutherland and Hidi, 1966; Hebmüller, 2003). Therefore, the velocity of cake growth u_s is modeled as only being depended on filter-aid concentration c. Cake resistance is given as

$$R = \int_0^{t_e} (u_s(t) \cdot \rho_{fa,c} \cdot r(t))\,dt = \int_0^{t_e} (c \cdot q \cdot r(t))\,dt\,, \tag{2}$$

where t_e is the total time of filtration which is determined by the volume per area to be filtered and the suspension's superficial velocity. r is the specific cake resistance and can be modeled as

$$r = r_0 \cdot e^{k \cdot \frac{w}{c}}\,, \tag{3}$$

with w being the impurity concentration in the suspension, r_0 the specific resistance of the pure filter-aid cake, and k a model constant characterizing the specific combination of filter aid and impurities at hand. This relation was first found by Sutherland and Hidi (1966) and validated by Haba and Koch (1978); it was later on derived again by Heertjes and Zuideveld (1978) and further used e.g. in Hackl et al. (1993). It should be mentioned that r is formulated here as a purely local property of the filter cake. Therefore, R is its integral value over time because r is explicitly allowed to change over the cake height and therefore over time as well. This is a generalization compared to the studies mentioned above which can be reduced to those solutions for the particular case of a constant w and c. In this study, the resistances of the filter medium and the precoat layer are not taken into account because their effect on the overall resistance is relatively small and they contribute nothing to the optimal control problem that is addressed here. The filter cake height is computed in the following way:

$$h(t) = \int_0^{t_e} u_s\,dt = \int_0^{t_e} \frac{c}{\rho_{fa,c}} \cdot q\,dt\,. \tag{4}$$

2.2. Dynamic Optimization

The following question is addressed in this paper: What is the optimal filter-aid dosage trajectory in the case of pure surface filtration in order to minimize cake resistance, i.e. energy expenditure? This optimal control problem is framed in the following way: The filter-aid concentration c is the control variable, the system state is represented by the filter cake height $h(t)$, and the total filter-cake resistance R is used as the performance index. Due to the form of R, this problem can be classified as being of the Lagrangian type with a fixed final time t_e and a free final state $h(t_e)$. The corresponding Hamiltonian reads as follows:

$$H = c \cdot q \cdot r_0 \cdot e^{k \cdot \frac{w}{c}} + \lambda \cdot \frac{c}{\rho_{fa,c}} \cdot q\,. \tag{5}$$

λ is the costate vector which – in this case – contains only one element. The three necessary condition for an extremal solution are the state equation

$$\frac{dh}{dt} = \frac{\partial H}{\partial \lambda}, \tag{6}$$

the control condition

$$\frac{\partial H}{\partial c} = 0, \tag{7}$$

and the adjungate ordinary differential equation

$$\frac{d\lambda}{dt} = -\frac{\partial H}{\partial h}. \tag{8}$$

The optimal control theory used so far can be found e.g. in Bryson Jr. and Ho (1975) and Lewis et al. (2012). It can be easily checked that the first of the conditions above is naturally fulfilled here. The second condition leads to the costate

$$\lambda = \left[\frac{k \cdot w}{c} - 1\right] \cdot \rho_{fa,c} \cdot r_0 \cdot e^{k \cdot \frac{w}{c}}. \tag{9}$$

An evaluation of the third condition shows that

$$\frac{\partial H}{\partial h} = 0 \tag{10}$$

because H does not explicitly depend on h. Combining the equations above gives

$$\frac{d\lambda}{dt} = \frac{\dot{w} \cdot c - w \cdot \dot{c}}{c^2} \cdot \frac{k \cdot w}{c} \cdot \rho_{fa,c} \cdot r_0 \cdot e^{k \cdot \frac{w}{c}} = 0. \tag{11}$$

That the extrema found by these conditions are indeed the best and not the worst scenarios is shown below by a comparison to other constructed trajectories. In the meantime, the found solutions are already referred to as optima.

3. Results

3.1. Constant Impurity Concentration

In case of a constant impurity concentration w, i.e. $\dot{w} = 0$, Equation (11) only holds if $\dot{c} = 0$, i.e. if the body-feed concentration is kept constant, excluding the irrelevant case of a completely clean suspension ($w = 0$). The question remains which filter-aid concentration to choose. Therefore, a thin filter cake slice grown within the time increment Δt at the beginning of filtration is considered. Its total resistance is

$$R = c \cdot q \cdot r_0 \cdot e^{k \cdot \frac{w}{c}} \cdot \Delta t. \tag{12}$$

The optimal filter-aid concentration c is found by

$$\frac{\partial R}{\partial c} \stackrel{!}{=} 0 \tag{13}$$

which gives

$$c = k \cdot w. \tag{14}$$

At first glance, it may be surprising that there is an optimal body-feed concentration at all because Equation (3) appears to suggest that with respect to cake resistance it is desirable to add as much filter aid as possible. But there are two mechanisms at work at the same time: On the one hand, a higher body-feed concentration leads to a lower cake resistance (Equation 3), on the other hand, an increased body-feed concentration leads to a more pronounced cake growth (Equation 4). The found optimum is the trade-off between these two effects.

3.2. Variable Impurity Concentration

In case of a time-variable impurity concentration w, it must hold that

$$\frac{\dot{c}}{c} = \frac{\dot{w}}{w}, \tag{15}$$

as can be seen from Equation (11). Integration leads to

$$c = e^{ln(w)+a} = a^* \cdot w, \tag{16}$$

where a and a^* are constants resulting from integration and rearrangement, respectively. The optimal start concentration can be determined by the same consideration as presented in Equations (12) to (14) because during the time increment Δt w and c can considered to be constant even in the case of variable concentrations. It follows by comparison of coefficients that a^* must be equal to k in the optimal case. This proves that the global optimum derived by Heertjes and Zuideveld (1978) also leads to the optimal trajectory in case of a variable impurity concentration if their condition is fulfilled at each point in time.

Two examples shall illustrate the benefits of a time-variable dosage of filter aid compared to a constant one. In the first case the impurity concentration varies linearly between $w = 0.025$ kg/m^3 and $w = 0.075$ kg/m^3 within the filtration time of 8 h; in the second case it covers the same range quadratically with time. The resulting impurity and optimal filter-aid concentrations are shown in Figure 1.

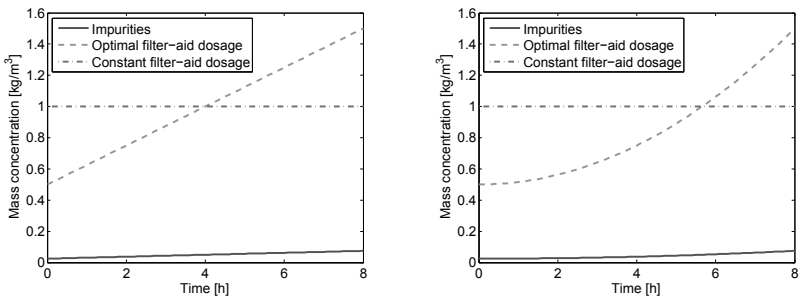

Figure 1: Profile of linearly (left) and quadratically (right) increasing impurity concentration and corresponding optimal filter-aid concentrations.

The required energy per filter area e follows from

$$e = \int_0^{t_e} q \cdot \Delta p \, dt. \tag{17}$$

If Δp is substituted by Darcy's law, one gets

$$e = q^2 \cdot \eta \cdot \int_0^{t_e} R \, dt, \tag{18}$$

with η being the fluid's viscosity. The energy expenditure is computed for both scenarios over the same process time of 8 h with a fluid viscosity $\eta = 1.5$ mPas and a superficial velocity q of $1.4 \cdot 10^{-4}$ m/s. r_0 was set to $2 \cdot 10^{10}$ m/kg and K to 20. These values were taken from Heertjes and Zuideveld (1978). If those results are compared to a constant filter-aid dosage with c at the

arithmetical mean value between its optimal values at $t = 0$ and $t = t_e$ (marked in Figure 1 with the orange dash-dotted line), 4.4 % less energy is consumed in case of the linear impurity profile and 8.9 % in case of the quadratic one. The corresponding energy profiles are shown in Figure 2. However, it is unlikely that the dosage is indeed conducted with the mean value between start and end, because w is only known in the beginning and therefore the dosage is adjusted to fit that value and kept constant there. Therefore, even higher energy savings seem possible in industrial practice.

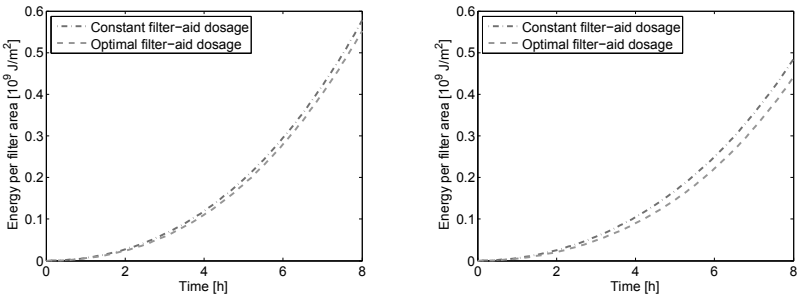

Figure 2: Development of energy expenditure over time in case of linearly (left) and quadratically (right) increasing impurity concentration.

From the presented results also follows that the conditions for extremality evaluated above yield indeed an optimal behavior here because the constant dosage scenarios lead to worse results than the variable ones. Had we incidentally found the worst case, all other scenarios would naturally perform better.

It should be also mentioned that the identified condition only guarantees optimality with respect to filter cake resistance which is not necessarily the economic optimum in every case. To take e.g. the used amount of filter aid into account, an overall cost model would be needed, which is not the aim of this paper. However, it does follow that the concentration of filter aid at each time should not exceed the here determined optimal value because then both filter-aid consumption and pressure drop would be unnecessarily large (compare Section 3.1). Further, the optimality condition also allows to react to discontinuous changes in impurity concentration, as long as they can be detected sufficiently early. A hint on how to implement this practically will be given in the following conclusion.

4. Conclusion

Using dynamic optimization, it was shown that under the assumption of pure surface filtration a constant dosage of filter aid is optimal as long as the impurity concentration is constant. So far this confirms established industrial practice. However, in many processes the impurity concentration varies with time. Therefore, in a second step the corresponding optimal control problem was solved. It was derived that an overall condition from the literature for optimal body-feed concentration in case of constant impurity and filter-aid concentrations also leads to the optimal dosage trajectory if fulfilled at each point in time. This is a far-reaching generalization with benefits e.g. for process control. On-line measurements of impurity mass concentration in the suspension, e.g. by a calibrated turbidity sensor, can be used to determine the optimal body-feed concentration at each time. The insights gained in this study suggest that an optimal control approach may be also beneficial in applications of filter-aid filtration where deep-bed filtration contributes significantly

to the overall separation. The very effect of deep-bed filtration is that earlier filter-cake layers are exposed to ever more impurities over the course of the process. This leads to the hypothesis that in this case, even if the impurity concentration stays constant, more filter-aid should be dosed in the beginning and this dosage should be constantly decreased over time in order to assure a higher capacity for impurities in the earlier filer-aid layers. This more challenging optimal control problem cannot be solved analytically, as done in this paper, but will require sophisticated numerical techniques; it will be addressed in future work.

References

H. E. Babbitt, E. R. Baumann, 1954. Effect of body feed on the filtration of water through diatomite. University of Illinois Bulletin 51 (81), 1–40.

B. Blankert, B. H. L. Betlem, B. Roffel, 2006. Dynamic optimization of a dead-end filtration trajectory: blocking filtration laws. J. Membr. Sci. 285 (1-2), 90–95.

B. Blankert, C. Kattenbelt, B. H. L. Betlem, B. Roffel, 2007. Dynamic optimization of a dead-end filtration trajectory: non-ideal cake filtration. J. Membr. Sci. 290 (1-2), 114–124.

A. E. Bryson Jr., Y.-C. Ho, 1975. Applied optimal control. Taylor & Francis.

P. C. Carman, 1938. The action of filter aids. Ind. Eng. Chem. Res. 30 (10), 1163–1167.

P. C. Carman, 1939. The action of filter aids. Ind. Eng. Chem. Res. 31 (8), 1047–1050.

J. Haba, R. Koch, 1978. Analyse des Filtrationsprozesses unter Einsatz von Filterhilfsmitteln. Chem. Techn. 30 (2), 91–94.

A. Hackl, E. Heidenreich, W. Höflinger, R. Tittel, 1993. Filterhilfsmittelfiltration. VDI-Verlag.

F. Hebmüller, 2003. Einflussfaktoren auf die Kieselgurfiltration von Bier. Ph.D. thesis, Technischen Universität Bergakademie Freiberg, Fakultät für Maschinenbau, Verfahrens- und Energietechnik.

P. M. Heertjes, P. L. Zuideveld, 1978. Clarification of liquids using filter aids. Powder Technol. 19 (1), 17–64.

K. Husemann, F. Hebmüller, M. Esslinger, 2003. Importance of deep bed filtration during kieselguhr filtration (part 2). Monatsschrift für Brauwissenschaft 56 (9-10), 152–160.

F. L. Lewis, D. L. Vrabie, V. L. Syrmos, 2012. Optimal control. John Wiley & Sons.

D. H. Sutherland, P. Hidi, 1966. An investigation of filter-aid behaviour. Trans. Instn. Chem. Engrs. 44 (4), T122–T127.

E. Zondervan, B. Roffel, 2008. Dynamic optimization of chemical cleaning in dead-end ultra filtration. J. Membr. Sci. 307 (2), 309–313.

Krist V. Gernaey, Jakob K. Huusom and Rafiqul Gani (Eds.), 12th International Symposium on Process Systems Engineering and 25th European Symposium on Computer Aided Process Engineering.
31 May – 4 June 2015, Copenhagen, Denmark

Best of Breed Control of Platinum Precipitation Reactors

Rotimi Agbebi[a] , Carl Sandrock[b]

[a]*University of Pretoria, 1 Lynnwood Road, Pretoria 002, South Africa*
[b]*University of Pretoria, 1 Lynnwood Road, Pretoria 002, South Africa*
carl.sandrock@up.ac.za

Abstract

An existing batch precipitation reactor in the mining industry was modelled from first principles using MATLAB S-function language and wrapped into Simulink custom blocks. The model was validated with open loop simulations to evaluate the response to step changes in the model inputs. Two PID controllers with different parameters were implemented on the model at different operating points and their temperature control performance was evaluated based on their ability track a temperature of the industrial reactor as a set-point. The performance of the controllers was measured and compared using an integral time-domain performance measure. A commercial advanced process controller (APC) was implemented on the model, a communication interface between the model in Simulink and the commercial controller was developed with Industrial Data Xchange (IDX); an OPC client and server.

Keywords: Batch Reactors, PID, APC, Aspen DMC plus, OPC

1. Introduction

Batch reactors are integral to the refining process of platinum group metals and their effective control is essential to ensure safe and efficient process in minerals industry (Singh et al. 2010). In these reactors various process phases are encountered in a single process batch; they are heating, cooling and reaction phase. These reactions occur as either an exothermic or endothermic reaction and the control of the batch reactors is essentially treated as a temperature control problem (Friedrich and Perne, 1996). A change from one batch to another batch could necessitate a change in control actions and this makes the control more difficult as different models are applicable for different batch process recipes operating at different operating conditions (Singh et al. 2010).

In many industrial applications, the temperature control of the reactor is carried out with PID controllers in a cascade structure, however rapid and precise temperature control is hard to achieve with these controllers (Stampar et al. 2013).

In terms of a PID controller, the two actuators on the steam and cooling inlet valve to the jacket can be considered as one manipulated variable and a split-range algorithm can be implemented as part of the controlled system (Balaton et al. 2012). Using one controller as long as the system state is close to the corresponding operating point and switching to another when the operating point is sufficiently close to the next operating point gives a better controller performance (Rugh and Shamma, 2000). The use of advanced process control (APC) systems has the potential to improve the control of batch reactors employed in the refining of PGMs (platinum group metals) (Singh et al. 2010). Most of the literature covers process control of continuous reactors in petrochemical industries, reactors with individual heating and cooling jackets. A few literatures cover the application of advanced process control on batch reactors in the minerals industry (Singh et al. 2010). Our aim is to build a platform on which the

performance of the various controllers can be compared and an algorithm to switch between the various controllers for particular process conditions.

2. Process Model Description

The first phase in the reactor involves heating, inflow of steam to achieve a desired temperature set-point. The reaction phase starts at the desired temperature where reagents are added, this result to an exothermic reaction which requires cooling, and then the cooling phase starts with inflow of cooling water (Singh et al. 2010). The temperature control performance mainly depends on the heating-cooling system associated with the reactor. The different configurations of heating-cooling systems cited in literature can be classified into two types: multifluid and monofluid systems (Louleh et al.1999). The commercial reactor modeled in this study has a multifluid system where steam is used as heating medium and water used as a cooling medium as shown in the figure 1 below. The transfer of heat energy to and from the jacket and the reactor is achieved with the transfer fluid through the wall of the reactor. Two exothermic chemical reactions were modelled in the reactor;
Dissolution of Ruthenium

$$Ru_s + 3Cl_{2(g)} \rightarrow RuCl_{3(l)} \quad (1)$$

Evaporation of Ruthenium Chloride

$$2H_2O_{(l)} + 2RuCl_{3(l)} + 2NaClO_{3(l)} \rightarrow 4HCl_{(l)} + 2RuO_{4(g)} + Cl_{2(g)} + 2NaCl_{(l)} \quad (2)$$

The model was developed in an explicit formulation using MATLAB s-function which could be used directly in custom blocks in SIMULINK in pursuit of getting the reactor model to interact effectively with external platform i.e. commercial controllers

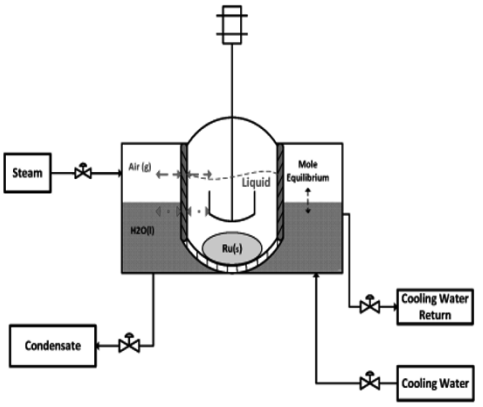

Figure 1: Reactor Model Description

3. PID Control

The process operating conditions are different from phase to phase and also from batch to batch. As such, a requirement on the controller is that it regulates the plant at each operating point or regime. The reactor temperature control is dependent on the control of the steam valve and the cooling water valve of a reactor with a single jacket.
For this design requirement to be correctly modeled using a PID Controller, a split-range algorithm was implemented. The split-range algorithm is preferred in the control of cascaded reactor, to operate two actuators which control the inflow of utilities at the different times during the different phases of a single batch (Balaton et al. 2012).
The two actuators on the steam and cooling water inflow valve to the jacket were considered as one manipulated variable (MV) and the temperature of the reactor as the controlled variable (CV). The PID controllers perform better on operating points they were tuned on. The performance of PIDs degrades with change in process regimes and operating points (Singh et al. 2010). Two PID controllers with different controller

parameters and set points were implemented on the SIMULINK model at different model operating points.

4. Control Objective and Performance Measure

The controller design objective was its set-point tracking ability; its performance can be measured with several integral time-domain performance measures. They are Integral of the Square of the Error (ISE), the Integral of the Absolute value of the Error (IAE), and the Integral of the time-weighted Absolute Error (ITAE).

$$E = \int_0^\infty f(t)\delta t \tag{3}$$

Where f (t) is a function of $\epsilon(t) = y_{sp}(t) - y(t)$

These were all implemented in the performance block of the Simulink model; however the Integral of the Square of the Error (ISE) was used to evaluate the performance of the controllers.

5. Advanced Process Control.

A commercial MPC controller called DMCplus; which is a multivariable controller from AspenTech was developed to control the temperature of the reactor model in Simulink. The DMCplus controller implemented in this work has two manipulated variables (steam and cooling water valves to the same reactor jacket), no feed forward variables and one controlled variable (reactor temperature). As both manipulated variables use the same jacket, they cannot be used at the same time. The controller executes periodically in cycles, the following steps were followed in developing the controller;

- Configuration of MVs and CV tags using Aspen DMC plus Build
- Calculate the open loop prediction for the controlled variable based on step change in manipulated variables which is the model development
- Steady State Simulation using Aspen DMC plus Model
- Determine the path by which the manipulated variables move from their current positions to the end positions i.e. the move plan of the controller.
- Prediction and Tuning of Controller using ASPEN APC web Interface

5.1 Model Interaction with external platforms.

The communication between the Simulink model and the commercial controller shown in figure 2 is very important and this was achieved using MATLAB OPC toolbox and Industrial Data Xchange (IDX); an OPC client and server. The IDX makes the outputs and inputs of the Simulink model available to the ASPEN DMC plus as data tags through the Aspen Cim-IO.The Aspen Cim-IO is an interface solution for AspenTech systems.

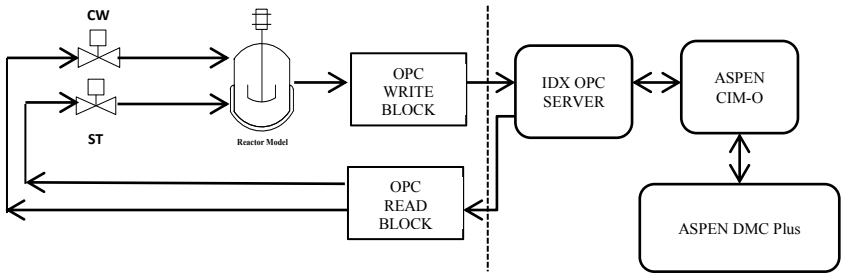

Figure 2 : Simulink model interaction with commercial controller

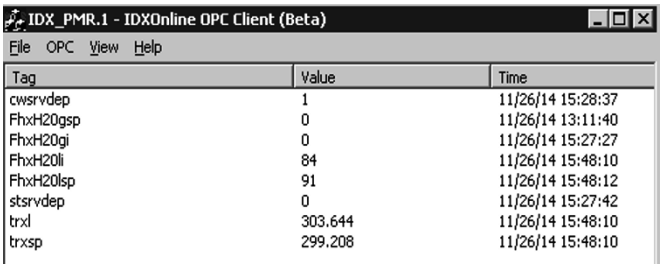

Figure 3 shows the IDX OPC client interface with the MVs and CVs data communication between the Simulink model and commercial controller.

Figure 3: IDX OPC Client

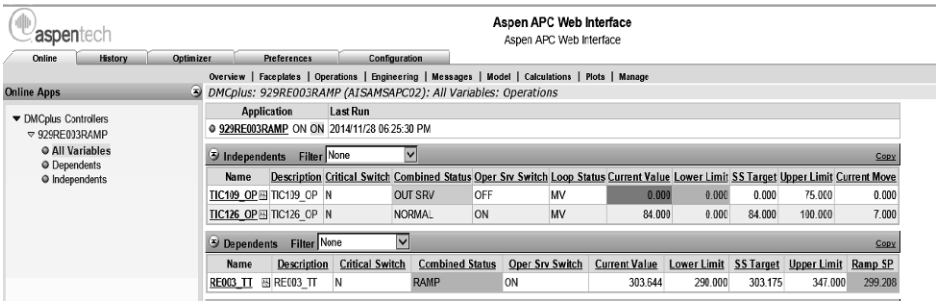

Figure 4: ASPEN APC Web Interface

Figure 4 shows the independent and dependent variables of the controller configuration developed using Aspen DMC plus Build, and monitored on the APC Web Interface. A controller model was built using the Aspen DMC plus Model, the open loop prediction of the model is shown in figure 5. This shows a test controller with cooling phase; increase in cooling water and decrease in steam.

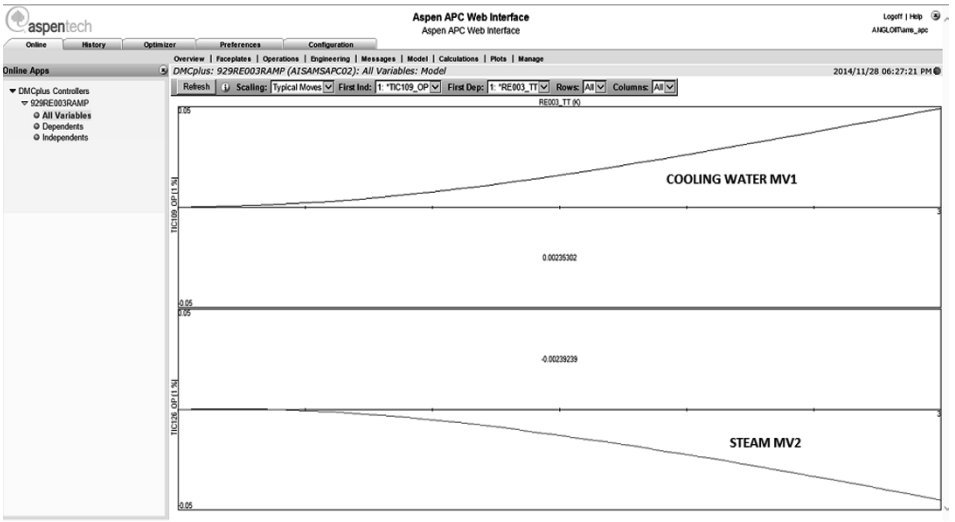

Figure 5: Open Loop Simulation.

Figure 6 shows a closed loop test simulation of the model, the response of the CV to predicted moves of the MVs; this validates the communication between the variables.

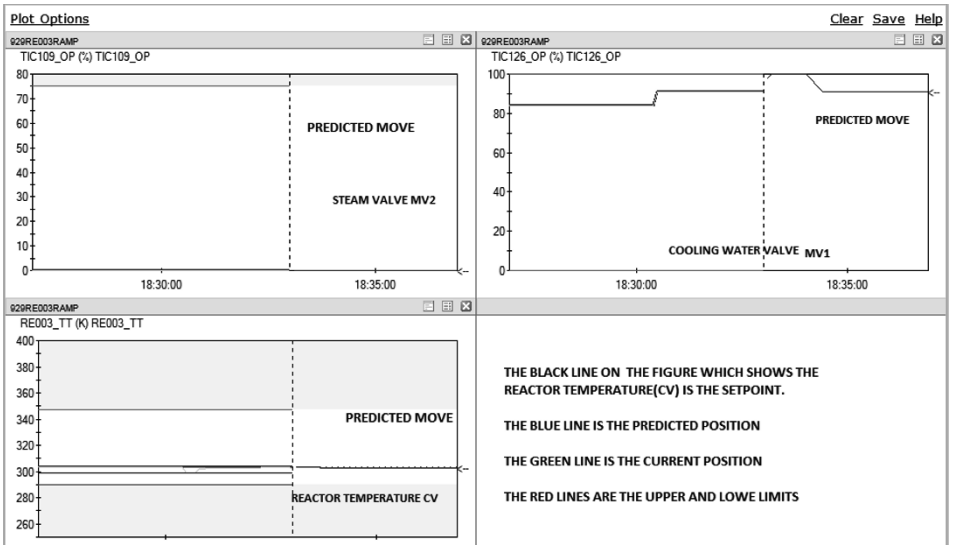

Figure 6: Closed Loop Simulation Response

6. Results and Discussion

The Simulink model was linearized to obtain linear time-invariant state-space models at two different steady state operating points, open loop simulations were ran on two the models and closed loop models were developed using Simulink PID compensator design tool.

The open loop response of the reactor temperature to a step change in the inflow of utilities; steam inflow for heating and cooling water inflow for cooling was done. This validates the response of the model to a unit step change in input at set utility temperatures which are cooling water at 278K and steam at 400.15K.

The closed loop performance results of the PID controllers show the model reactor tracking the set point temperature which is the plant temperature data.

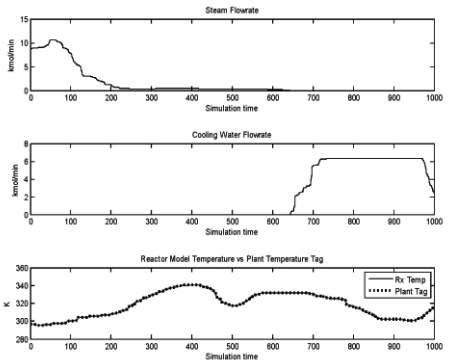

Figure 10: Simulation results of PID 1 on model 1

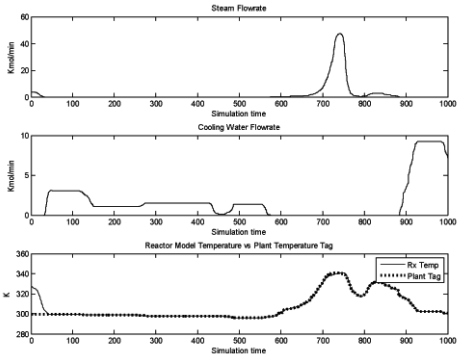

Figure 11: Simulation with PID 2 on model 1

Figure 10 and Figure 11 shows closed loop simulation using using temperature from plant data as PID set point. In Figure 10, PID controller 1 tuned on model 1 shows a very good set-point tracking performance with a lower integral square error of 5.995.

In Figure 11, PID controller 2 tuned on model 1 shows a bad set-point tracking performance with a higher integral square error of 132.62.

Table 1 shows different operating point of the linearized state-space models and Table 2 shows the performance of different controllers implemented on different models using temperature from plant data as reference temperature. The PID 1 performed better on model 1 and PID 2 performed better on model 2

Table 1: Model operating points

Operating Points	Model 1	Model 2
Reactor Temperature (K)	303.1040	292.1161
Jacket Temperature (K)	304.1142	299.0432

Table 2: Controller Performance Values

Controller	Model	Integral Square of Error (ISE)
PID 1	1	**5.995**
PID 1	2	87.61
PID 2	1	132.62
PID 2	2	7.993

7. Further Work

The Advanced Process Controller (APC) implemented on the reactor model will be tuned to its best performance and the performance will be compared to that of the PID controllers and a combination of controllers will be implemented on the model in order to assess if the hybrid controller will out-perform a single controller.

8. Conclusions

PID controllers perform better on model operating points there were tuned on with a lower integral square error (ISE) and their performance degrades with change in process operating points and batches (Noguchi and Kobari, 2005). To overcome these limitations, a commercial APC (Aspen DMC Plus) which has been successfully connected to the Simulink model will be tuned and completely implemented to validate (Singh et al. 2010)'s work on the actual commercial reactors which proves that the APC controller out-performs PID controller. The platform needed to compare ability of the PID and the APC control system with the reactor model is now developed.

9. References

M.G. Balaton, L. Nagy, F. Szeifert, 2012, Model-Based Split-Range Algorithm for the Temperature Control of a Batch Reactor. Scientific Research Eng, 4, 515-525

M. Friedrich and R. Perne, 1995, Design and Control of Batch Reactors - An Industrial Viewpoint, Comp & Chem Eng, 19, S357-S368.

Z. Louleh, M. Cabassud, M.V. Le Lann, 1999, A New Strategy for Temperature Control of Batch Reactors: Experimental Application, Chem Eng Jour 75, 1, 11-20.

Y. Noguchi and M. Kobari, 2005, Model Predictive Control with single heat transfer fluid for Batch Reactor temperature control, SICE Annual Conference, 449 – 452

W. J. Rugh and J. S. Shamma, 2000, Research on gain scheduling, Automatica, 36, 1401 – 1425

A. Singh, P.G.R. De Villiers, P. Rambalee, G. Gous, J. De Klerk, Humphries G. , 2010, A Holistic approach to the application of Model Predictive Control to batch reactor, Automation in Mining, Mineral and Metal Processing, 13, 172-132

S. Stampar and S. Somkolic, 2013, Nonlinear Control of Hybrid Batch Reactor, Journal of Mech Eng , 59, 112 – 123

Krist V. Gernaey, Jakob K. Huusom and Rafiqul Gani (Eds.), 12th International Symposium on Process Systems Engineering and 25th European Symposium on Computer Aided Process Engineering.
31 May – 4 June 2015, Copenhagen, Denmark

Multivariate Analysis of Industrial Scale Fermentation Data

Lisa Mears[a], Rasmus Nørregård[a], Stuart M. Stocks[b], Mads O. Albaek[b] , Gürkan Sin[a], Krist V. Gernaey[a], Kris Villez[c*]

[a]*Department of Chemical and Biochemical Engineering, Technical University of Denmark, Lyngby, 2800, Denmark*
[b]*Novozymes A/S, Pilot plant, Krogshoejvej 36, Bagsværd, 2880, Denmark*
[c] *Eawag: Swiss Federal Institute of Aquatic Science and Technology, Überlandstrasse 133, 8600 Dübendorf, Switzerland*
**kris.villez@eawag.ch*

Abstract

Multivariate analysis allows process understanding to be gained from the vast and complex datasets recorded from fermentation processes, however the application of such techniques to this field can be limited by the data pre-processing requirements and data handling. In this work many iterations of multivariate modelling were carried out using different data pre-processing and scaling methods in order to extract the trends from the industrial data set, obtained from a production process operating in Novozymes A/S. This data set poses challenges for data analysis, combining both online and offline variables, different data sampling intervals, and noise in the measurements, as well as different batch lengths. By applying unfold principal component regression (UPCR) and unfold partial least squares (UPLS) regression algorithms, the product concentration could be predicted for 30 production batches, with an average prediction error of 7.6%. A methodology is proposed for applying multivariate analysis to industrial scale batch process data.

Keywords: Multivariate Data Analysis, Bioprocess, Process Optimisation

1. Introduction

There is a vast amount of batch process data generated in industry, which can be investigated with the aim of identifying desirable process operating conditions, and therefore areas of focus for optimising the process operation. Although multivariate methods are highly established for analysis of large data sets, their application to batch processes is less common due to the additional challenges associated with data dimensionality, as well as high measurement noise. Data mining of such a complex data set requires additional pre-processing stages, however the importance of these steps prior to modelling is often underappreciated (Gurden et al. 2001).

Nomikos and Macgregor (1994, 1995) pioneered the application of multivariate statistical methods to batch processes. With a lack of mechanistic models which can define the non-linear process dynamics and unsteady-state operation, and a lack of sensors which measure key process variables, empirical modelling shows promise for characterizing batch operations (Nomikos and MacGregor 1995).

Fermentation processes are highly sensitive to operational changes, however the underlying mechanisms are often poorly understood. Multivariate methods are therefore suitable tools for gaining process insight (Formenti et al. 2014). Such biological processes are also sensitive to system variations between batches and are often hard to implement in a reproducible manner. In addition, there is evidence to suggest that not only the main fermentation conditions, but also the seed fermentation conditions are vital in order to dictate the resulting yield of the process (Ignova et al. 1999). An additional benefit of multivariate methods is that offline data can be incorporated into the model which helps to account for differences observed between batches (Kourti et al. 1995).

In this work, a 30 batch dataset from a filamentous fungus production process operating at Novozymes A/S is analysed by multivariate analysis with the aim of predicting the final product concentration, which is measured offline at the end of each batch. By investigating the contribution of each variable to the model prediction (Kourti et al. 1995), differences between batches can be diagnosed. This diagnosis procedure can be used to understand the process, and therefore guide future process optimisation efforts.

2. Methodology for applying multivariate analysis to batch data

The multivariate methods require a two dimensional dataset, however batch production processes have dimensions of time, batch number and variable. It is also a requirement for UPCR and UPLS that the data matrix for each batch should have the same dimensionality, however this is not the case due to different data logging and data compression for each variable, as well as different batch durations. These issues must be addressed as part of the data pre-processing. There are then considerations for data scaling, so that all variables have the same weighting in the resulting model. Finally the method of model validation should be discussed in order to validate the conclusions drawn from the regression model. Each of these challenges will now be approached with a discussion of the options available. Figure 1 provides the general methodology for applying the methods discussed.

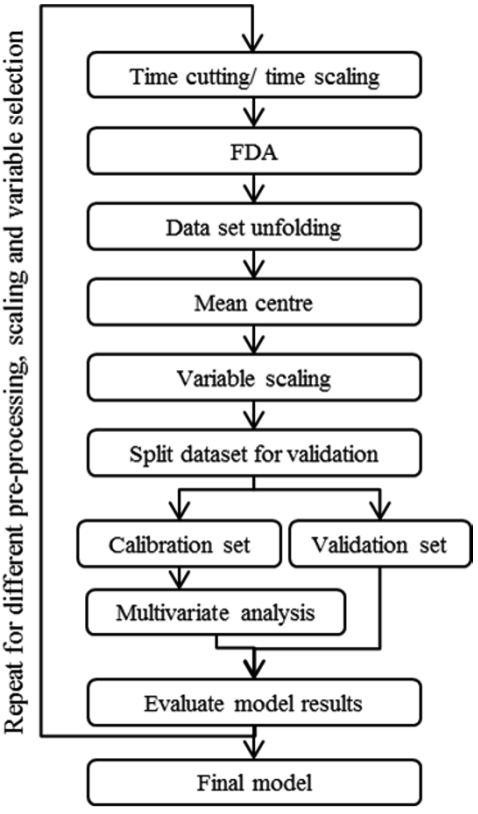

Figure 1: Proposed methodology for multivariate analysis of batch process data.

2.1. Time Scaling Methods

Since batch operations have different durations, the time must be scaled in order to compare multiple batches. The most simple method is to cut the data to the length of the shortest batch, however this is only applicable if the batches show only small variations in duration, otherwise key

data may be lost. There is also the option to cut the data from the beginning, so that the data which is removed is only lag phase data which contains limited relevant dynamics, however the implications of the lag phase can then not be captured, and this may also have an impact on the process.

Alternatively there is the option to linearly scale the time, so that the index of a time unit is scaled such that all batches have the same dimensionality, but with different absolute times. This maintains all data, however it affects the relevance of certain time dependent variables, such as rates or cumulative variables, since the scaling removes this time dependence. Time scaling is highly compatible with functional data analysis (FDA) pre-processing, by fitting the same number of functions across the different batch lengths, which is the method applied in figure 2, and discussed in the next section.

More advanced methods include dynamic time warping which is an example of time series alignment (Keogh and Ratanamahatana 2002). This is a non-linear time scaling, whereby the time series is warped in order to align events in the series, which can be defined by a numerical property of the data, for example a maxima in a variable. This allows batch profiles to be compared relative to key events. As an example, aligning DO limitation profiles in the initial stages, which represents the initial exponential growth phase ending. This method is suitable to aligning events on batch data which can show between batch variations in timing (Kassidas et al. 1998). This method was not applied in this work.

2.2. Data set pre-treatment

It is common that the data logging algorithms result in very different data dimensionality for each variable. In order to avoid large-dimensional datasets, one approach is to log values only after a specified magnitude of change and in addition after a set amount of time. This causes each variable to have a different number of samples, and at different batch times. In order to apply uPCR and uPLS algorithms, data pre-processing stages must create a data matrix for each variable, and each batch with an even time distribution. In addition, variables can be measured with varying degrees of precision, meaning measurements capture different levels of noise. In the literature

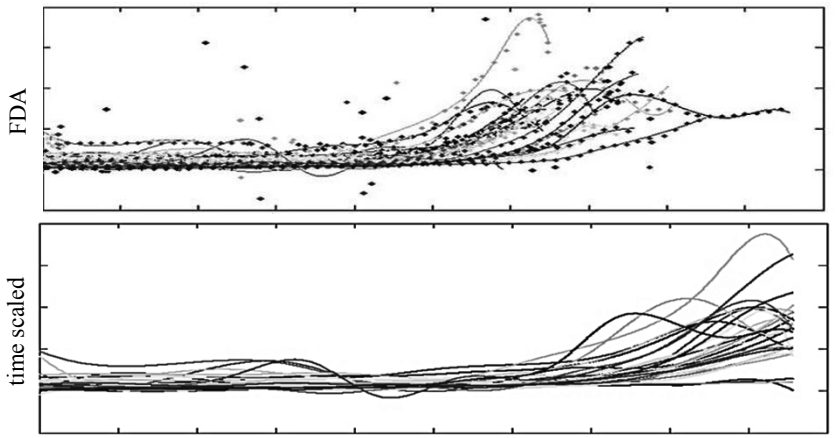

Figure 2: Variable pretreatment, showing the results for FDA (top) plotted with the raw data, and the results of time scaling using functional data analysis (bottom). No axis for confidentiality.

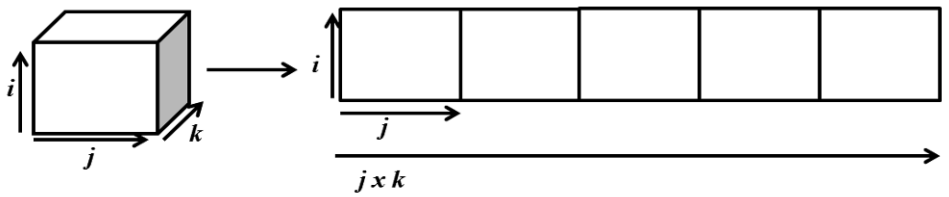

Figure 3: Batchwise unfolding, for i batches, j time, and k variables.

there are different methods used to approach this issue ranging from manual outlier removal (Albert and Kinley 2001), moving average filters, and data interpolation (Le et al. 2012), showing that there is no consensus on the optimal approach.

In this work, the application of functional data analysis (FDA) prior to multivariate methods (Baert et al. 2012) has proven highly valuable in order to greatly reduce the dimensionality of the dataset whilst also filtering noise from the measurements and dealing with outliers in the data in a single processing step. FDA involves fitting of a function across intervals of the data. This method is highly suited, as it allows flexibility in the function output so that the same method can be applied in series to multiple variables. Since this work focusses on non-periodic data, only the spline basis system is considered. Optimal fitting parameters were determined by means of the leave-one-out procedure discussed in James and Silverman (2005).

2.3. Data unfolding

The uPCR and uPLS algorithms apply to a two dimensional data set, therefore dataset unfolding is required (Nomikos and MacGregor 1995). Given a three dimensional matrix with i batches, j time index, and k variables, as shown in Figure 3, unfolding refers to taking slabs from the dataset to create multiple two dimensional matrices of [i x j]. These are aligned to give a two dimensional matrix [i x jk]. This method is most applicable to regression methods for end of batch quality variables, as is discussed in this work.

2.4. Variable Scaling Methods

Column scaling is applied to each time index, so that each time point has equal variance. This is commonly used, however there is the risk that noise is amplified in variables where the overall trend in the data is important but there is high background noise present (Gurden et al. 2001). For example for a cumulative flow profile, implementing column scaling may amplify noise at the start of the batch, where the variance in the values is lower, and lose important information on the final cumulative flow profile as the variance is scaled equally at each time index.

In single-slab scaling all time points for a single variable are scaled for equal cumulative variance. This means that the trajectory shape is maintained more than in column scaling. Figure 4 shows the effect of the variable scaling method on the data profiles.

Model validation methods

In order to assess the resulting model, it is important that suitable model validation is in place, where there is a balance between the fit of the model to the validation dataset, compared to the number of components in the multivariate model. A simple but

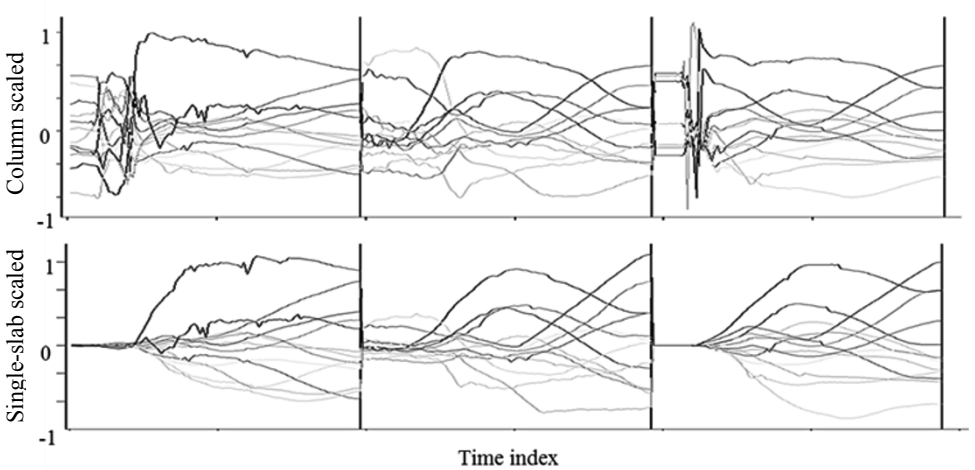

Figure 4: Column scaling (top) and single-slab scaling (bottom) applied to three variables unfolded batchwise. Column scaling affects the cumulative profile, and amplifies noise in the initial time indexes. Variable names and time indexes are excluded for confidentiality reasons.

computationally expensive validation method is leave-one-out, whereby every batch is used as a validation batch. Alternatively the full data set can be split into calibration and validation sets, however the results can then be dependent on the division of the dataset. Leave-one-out validation is suitable for regression applications, since it is then possible to see the effect of individual batches on the model prediction at each calibration stage. This means that if individual batches are outlying, this is seen in the results.

3. Multivariate analysis results from Novozymes A/S industrial dataset

The 30 batch dataset has been analysed by utilising PCR and PLS algorithms implemented in Matlab at Eawag. The discussed data pre-processing stages have been applied, in order to assess the effect on the resulting regression. Many iterations of the modelling were completed, following the methodology in Figure 1, and the effect of the different scaling methods is apparent, as shown by an example in figure 5.

For the final model, time cutting to the shortest batch length was always found to be most effective. Then FDA was applied, with fitting using a roughness penalty (James and Silverman 2005). After dataset unfolding, mean centring was applied followed by

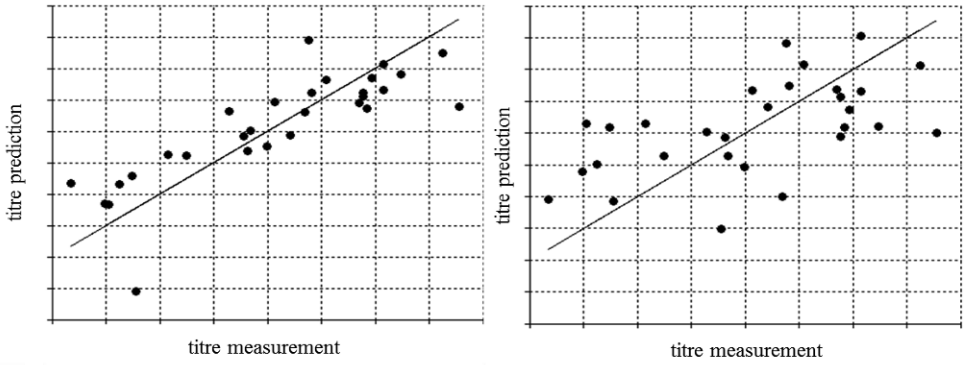

Figure 5: UPCR titre regression models for 30 batch production scale data set at Novozymes A/S. Single slab scaling (left), Column scaling (right). Axis values removed for confidentiality.

single-slab scaling. This resulted in the regression shown to the left in Figure 5.

Based on analysis of the regression coefficients, variables were removed if they had low influence on the resulting model. The accuracy of the model was greatly improved by removal of some variables, which shows that certain variables, although showing high variability, did not show variance relevant to the product concentration prediction, and this therefore affects the model results. The final model included only five online variables, making the model interpretation more straight forward for process optimisation. By analysis of the regression coefficients, it is possible to identify the trend in the data responsible for a higher product concentration prediction. This can lead to identification of potential process optimisation leads.

4. Conclusions

This work discusses how pre-processing is an important and integral stage in multivariate analysis of batch process data, and the choice of methods has an effect on the resulting model, which in this case has been proven by analysis of an industrial fermentation data set from Novozymes A/S. This study was initiated following the observation of practical challenges met during application of conventional statistical process control techniques to an industrial data set. Figure 5 shows that with successful pre-processing it is possible to predict the titre from an industrial fermentation process with an average prediction error of 7.6%. The methodology proposed aims to provide a framework for approaching the multivariate analysis of batch process data.

References

Sarolta A., Kinley R. D. 2001. “Multivariate Statistical Monitoring of Batch Processes: An Industrial Case Study of Fermentation Supervision.” Trends in Biotechnology 19(2):53–62

Baert A., Villez K., and Steppe K. 2012. “Functional Unfold Principal Component Analysis for Automatic Plant-Based Stress Detection in Grapevine.” Funct Plant Biol 39(6):519.

Formenti L R, Nørregaard A, Bolic A, Hernandez D Q, Hagemann T, Heins A, Larsson H, Mears L, Mauricio-Inglesias M, Krühne U, Gernaey K V. 2014. “Challenges in Industrial Fermentation Technology Research.” Biotechnology journal 9(6):727–38.

Gurden S. P., Westerhuis J. A., Bro R., and Smilde A. K. 2001. “A Comparison of Multiway Regression and Scaling Methods.” Chemometr and Intell Lab 59(1-2):121–36.

Hastie T., Tibshirani R., Friedman J. 2009. The Elements of Statistical Learning - Data Mining, Inference, and Prediction, Second Edition.

Ignova M., Montague G. A., Ward A. C., Glassey J. 1999. “Fermentation Seed Quality Analysis with Self-Organising Neural Networks.” Biotechnology and bioengineering 64(1):82–91.

Ramsey J., and Silverman B. 2005. Functional Data Analysis.

Kassidas A, MacGregor J F, and Taylor P A. 1998. “Synchronization of Batch Trajectories Using Dynamic Time Warping.” AIChE Journal 44(4):864–75.

Keogh E., Ratanamahatana C A. 2002. “Exact Indexing of Dynamic Time Warping.”, Knowledge and Information Systems, 7(3), 358–386.

Kourti T, Nomikos P, MacGregor J F. 1995. “Analysis, Monitoring and Fault Diagnosis of Batch Processes Using Multiblock and Multiway PLS.” Journal of Process Control 5(4):277–84.

Le H, Kabbur S, Pollastrini L, Sun Z, Mills K., Johnson K, Karypis G, Hu W. 2012. “Multivariate Analysis of Cell Culture Bioprocess Data--Lactate Consumption as Process Indicator.” Journal of biotechnology 162(2-3):210–23.

Nomikos P, MacGregor J F. 1994. “Monitoring Batch Processes Using Multiway Principal Component Analysis.” AIChE Journal 40(8):1361–75.

Nomikos P, MacGregor J F. 1995. “Multi-Way Partial Least Squares in Monitoring Batch Processes.” Chemometrics and Intelligent Laboratory Systems 30(1):97–108.

Krist V. Gernaey, Jakob K. Huusom and Rafiqul Gani (Eds.), 12th International Symposium on Process Systems Engineering and 25th European Symposium on Computer Aided Process Engineering.
31 May – 4 June 2015, Copenhagen, Denmark

Model-based Observation and Design of Crystal Shapes via Controlled Growth-Dissolution Cycles

Holger Eisenschmidt,[a] Naim Bajcinca,[b] Kai Sundmacher[a,b*]

[a] *Otto-von-Guericke University Magdeburg, Process Systems Engineering, Universitätsplatz 2, D-39106 Magdeburg, Germany*

[b] *Max Planck Institute for Dynamics of Complex Technical Systems, Sandtorstraße 1, D-39106 Magdeburg, Germany*

* Corresponding author: *sundmacher@mpi-magdeburg.mpg.de*

Abstract

Control of multivariate population balance systems is a challenging task in process engineering, which is in particular due to difficulties in observing the state of the dispersed phase. In this article, we present a setup based on video microscopy and Kalman filtering to observe the evolution of a crystal population in batch crystallization processes. We demonstrate the applicability of our methods on the cyclic batch crystallization of potassium dihydrogen phosphate. It is shown that the cyclic process strategy can lead to crystal shapes which would not have been attainable via pure growth processes.

Keywords: crystallization, crystal shape, crystal shape observation, growth-dissolution cycles, Kalman filter

1. Introduction

The final crystal size and shape distribution is a product property that is decisively influencing the final solid state properties of crystalline materials. For example, elongated or platelet like crystal shapes are known to cause difficulties during filtration and drying, and hence these downstream processes may become the bottleneck of the entire crystallization process. However, due to the high surface-to-volume ratio, such crystals might be desirable in specific application areas like catalysis. Hence, crystal shape control offers the possibility to directly adjust the final product properties. However, for this purpose reliable measurement techniques are required to observe the crystal shape distribution over time. For this purpose, video microscopy has received much attention during the last decade, as it offers an immediate impression on the state of the crystalline phase. Recently, Borchert et al. (2014) presented an algorithm to estimate crystal shapes from the recorded videos, which is used in this work to construct an observer for the crystal shape evolution. This observer is then used to monitor the state of the dispersed phase during a cyclic growth-dissolution process of potassium dihydrogen phosphate. Such a process concept was found to be suitable to attain a wider region of crystal shapes, compared to pure growth processes, as demonstrated on the single crystal level by Lovette et al. (2012). In the present contribution this strategy is applied to an entire batch crystallization process, i.e. a system containing a crystal population distributed w.r.t. size and shape.

This article is organized as follows. The experimental setup which has been used is presented in the next section. In Section 3, the experimental results are presented and discussed, and a technique to filter the measured mean crystal shape evolution is presented. Finally, Section 4 concludes this work.

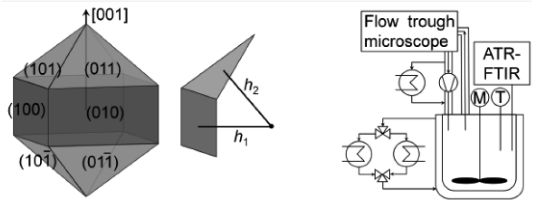

Figure 1: Left: Idealized geometry of a KDP crystal consisting of prismatic {100} faces (dark gray, index 1) and pyramidal {101} faces (light gray, index 2). The crystal shape is represented by the orthogonal face distances h_1 and h_2 of the {100} and {101} faces to the crystal center; right: schematic of the experimental setup.

2. Experimental

Potassium dihydrogen phosphate (KDP) is chosen as a model substance in this work. KDP crystallizes in the tetragonal space group I-42d with a = 7.460 Å and c = 6.982 Å and exhibits prismatic {100} and pyramidal {101} faces on the outer crystal surface, see Figure 1, left. The geometrically possible crystal shapes of KDP range from elongated crystals with a high prominence of {100} faces to compact crystals as depicted in Figure 1 and in an extreme case to octahedral crystals exhibiting only {101} faces on the crystal surface. The solubility of KDP in water is rather high, and can be described with the empirical correlation:

$$w_{\mathrm{eq}} = 4.6479 \cdot 10^{-5} T^2 - 0.022596T + 2.8535 \tag{1}$$

where w_{eq} is the mass of KDP which is in equilibrium dissolved in 1 kg water. The supersaturation is then defined as the ratio of the actual concentration w to the equilibrium concentration w_{eq}:

$$\sigma = \frac{w}{w_{\mathrm{eq}}} - 1 \tag{2}$$

Recently, Eisenschmidt et al. (2015) have presented the face specific growth and dissolution rates of the {100} and {101} faces of KDP, respectively. It was found, that growth at low and intermediate supersaturations is strongly influenced by impurities present in the solution and hence, growth under these conditions is affected by batch to batch variations. Therefore, the authors conclude that KDP crystals should preferably be grown at high supersaturations, which is in accordance to the conclusions of Zaitseva et al. (1999). Due to these constraints on the applicable supersaturation range, the region of possible crystal shapes which are attainable by pure growth is rather confined; see the gray shaded region in Figure 2d. To overcome these limitations, growth-dissolution cycles are performed in this study, by using an experimental setup as depicted in Figure 1. To realize the temperature switches that are required for this cyclic operating policy with minimal time effort, two thermostats are employed, which have been connected to the crystallization vessel via two tree-way valves. KDP is purchased from Carl Roth GmbH Analytica (purity 98%, pH = 4.12 at T_{eq} = 35 °C) and used without further purification. The suspension is stirred with an overhead pitch bladed impeller (d = 4.5 cm) at a speed of 400 rpm to achieve a homogeneous solution. The temperature is measured using a standard PT100 thermo couple and an ATR-FTIR is used to monitor the solute concentration. To monitor the state of the crystalline phase, a flow through microscope (QicPic, Sympatec) has been used, which is fed by an external sampling

loop. Videos of the crystal suspension with a length of 10 seconds are collected at a rate of 20 frames/s with a resolution of 1024 x 1024 pixels. The field of view has a size of 5000 µm by 5000 µm. The videos are processed after the experiment using the algorithms presented by Borchert et al. (2014), to obtain the evolution of the crystals size and shape distribution over time.

According to Bajcinca (2010, 2013), the time optimal operating policy for a cyclic growth-dissolution process is composed of growth and dissolutions phases at constant levels of super- and undersaturations. The corresponding optimization problem is solved for the constraints $0.10 \leq \sigma_G \leq 0.14$, to ensure reproducible growth conditions and to avoid massive nucleation, and $-0.025 \leq \sigma_D \leq 0$ to guarantee dissolution conditions which are well controllable. An initial temperature of $T = 35°C$ is chosen and a mass of 602.0 g KDP is dissolved in 1.8 kg water, corresponding to a supersaturation level of $\sigma = 0.1$. After complete dissolution of the raw material, the temperature is lowered to 35°C and 0.8 g KDP crystals of a sieve fraction between 212 µm – 300 µm has been added to the solution as seed crystals. Afterwards, a temperature control program, calculated in a feedforward manner, is started to achieve growth and dissolution phases at constant super- / undersaturation levels, see Eisenschmidt et al. (2015) for details. The durations of the individual growth and dissolution phases are chosen such that a supersaturation switch is completed when the mean seed crystals reach a maximal or minimal crystal volume. These times are determined in preliminary experiments which are, for the sake of brevity, not shown here. Therefore, the concentration signal is expected to oscillate between a maximal and minimal value as well, which allows for process control based on concentration measurements as well, see Bajcinca et al. (2010).

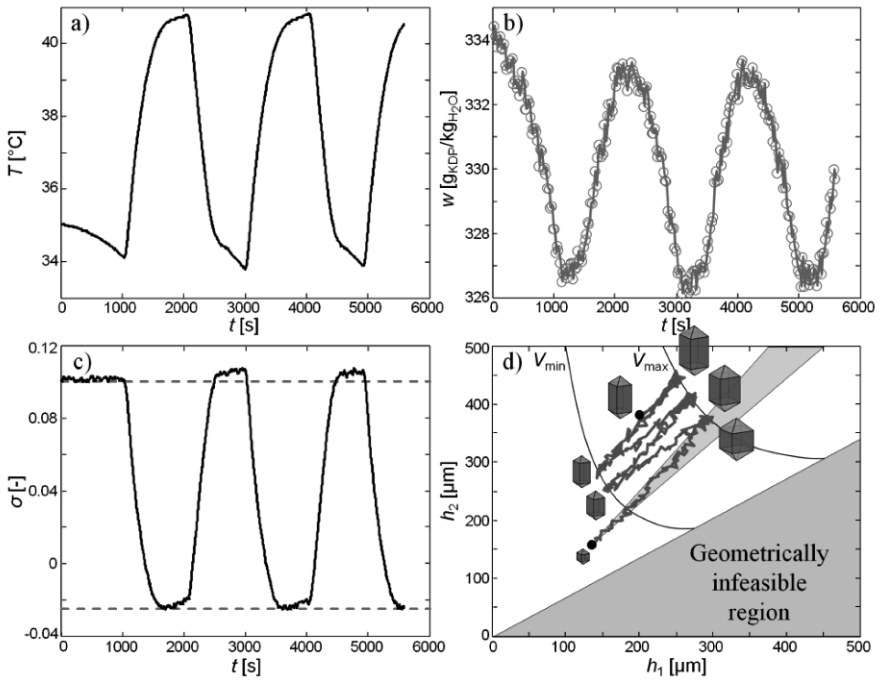

Figure 2: Experimental realization of growth-dissolution cycles. a) applied temperature profile; b) measured concentration profile; c) resulting supersaturation profile (solid lines) together with the set point supersaturation levels (dashed lines); d) observed mean crystal shape trajectory with example crystal shapes.

3. Results and Discussion

Figure 2 depicts the experimental results that were obtained by the procedure described in the previous section. As can be seen, the supersaturation can be controlled reasonably well with the applied temperature profile. Also the concentration profile is oscillating between a minimal and maximal value and hence a control setup based on concentration measurements as proposed by Bajcinca et al. (2010) is indeed feasible. In Figure 2d the measured mean crystal shape evolution of the seed crystal population is depicted. As can be seen, the region which is attainable by growth, indicated as gray cone originating at the starting point, can be left with this approach, which results in the successive mean crystal shape evolution towards elongated crystals.

However, the observed mean crystal shape evolution is significantly affected by the occurring measurement noise, which makes potential feedback control difficult. Therefore, a Kalman filter was applied to the measured mean crystal shapes. To apply this filter, the error covariance matrix $\mathbf{R}_k$ for the measured mean crystal shapes was determined to be:

$$\mathbf{R}_k = \frac{1000}{N_{\mathrm{cryst,k}}} \begin{bmatrix} 1.09 & 0.18 \\ 0.18 & 0.18 \end{bmatrix} \tag{3}$$

where $N_{\mathrm{cryst,k}}$ denotes the number of observer seed crystals. The necessary a priory state estimates can be obtained by integrating the kinetic data presented by Eisenschmidt et al. (2015) and hence an a priory estimate error covariance matrix $\mathbf{Q}_k$ can be defined:

$$\mathbf{Q}_k = 0.01 \begin{bmatrix} \left(\int_{t_{k-1}}^{t_k} G_1(\tau)\, d\tau\right)^2 & 0 \\ 0 & \left(\int_{t_{k-1}}^{t_k} G_2(\tau)\, d\tau\right)^2 \end{bmatrix} \tag{4}$$

where an average error of the kinetic data of 10 percent was assumed. The filtered measurements are shown in Figure 3. As can be seen, the measurement noise can be significantly reduced. However, some systematic deviations in the order of 15 µm between filtered observation and measurements are occurring during the dissolution phases; see the magnification on the right side of Figure 3. These deviations can be attributed to larger errors in the dissolution kinetics. To reduce this bias, we extended the space of the estimated states by two variables δ_1 and δ_2. In this framework, the estimated mean crystal shapes can be calculated by

$$\overline{\mathbf{h}} = \begin{bmatrix} 1 & 0 & 1 & 0 \\ 0 & 1 & 0 & 1 \end{bmatrix} \cdot \begin{bmatrix} \tilde{h}_1 & \tilde{h}_2 & \delta_1 & \delta_2 \end{bmatrix}^T \tag{5}$$

With these two additional states, also the a priory estimate error covariance matrix $\mathbf{Q}_k$ has to be adjusted. In this particular case, the matrix

$$\mathbf{Q}_k = 2.5 \cdot 10^{-5} \begin{bmatrix} \left(\int_{t_{k-1}}^{t_k} G_1(\tau)\, d\tau\right)^2 & 0 & 0 & 0 \\ 0 & \left(\int_{t_{k-1}}^{t_k} G_2(\tau)\, d\tau\right)^2 & 0 & 0 \\ 0 & 0 & 100\,(\Delta t_k)^2 & 0 \\ 0 & 0 & 0 & 100\,(\Delta t_k)^2 \end{bmatrix} \tag{6}$$

was found to result in a reasonably good filter performance, see Figure 4. As can be seen from this equation, the assumed error for the model predictions is significantly decreased while the model error for the additional states δ_i is rather high. Therefore, deviations between model predictions and observations are essentially attributed to the states δ_i, which results in a significant decrease of the deviation between measurement and filtered observations; see Figure 4 left and middle. Besides the improvement of the filter performance, the estimated states δ_i provide additional information about the quality of the kinetics applied for the a priori state estimates. On the right side of Figure 4, the temporal evolutions of the states δ_i are depicted. As can be seen, these evolutions are approximately constant during each growth phase, compare to Figure 2c, whereas they are decreasing during the dissolution phases.

This information can be used in turn to re-estimate the crystallization kinetics. This has been done by adjusting the pre-exponential factors of the growth and dissolution kinetics respectively. The new parameters are determined on the basis of the first growth and dissolution phase using a nonlinear regression approach. The resulting kinetics are afterwards used to re-calculate the observed mean crystal shape evolution. As can be seen in Figure 5, there are significant deviations between observations and model predictions. This is particularly due to the uncertainties in the dissolution kinetics. However, if the adjusted kinetics are applied, model predictions and observations match almost perfectly, and hence the new kinetic data can be used for further process control.

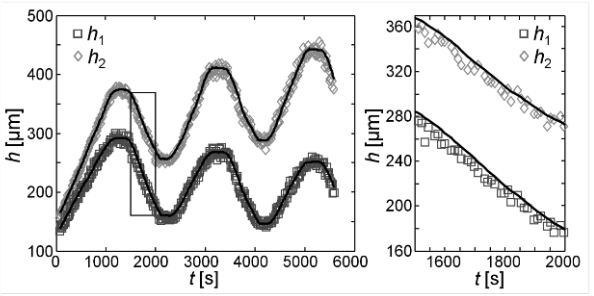

Figure 3: Measured evolution of the face distances of the {100}-faces (squares) and {101}-faces (diamonds) and the filter results of directly filtering the mean crystal shape estimates (solid lines).

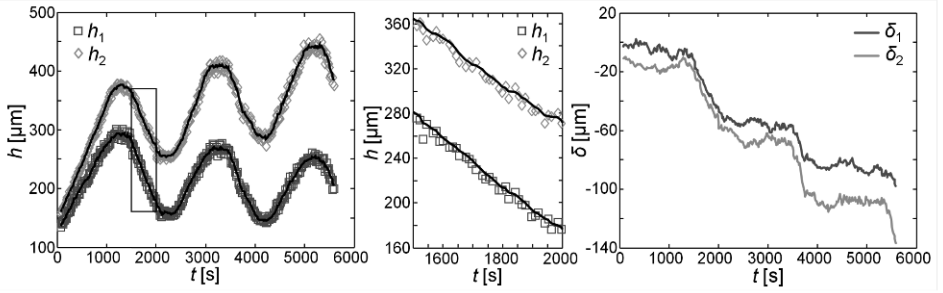

Figure 4: Left, middle: Measured evolution of the face distances of the {100}-faces (squares) and {101}-faces (diamonds) and the results of filtering the states by applying eq. (5) (solid lines); right: evolution of the additional states δ_i over time.

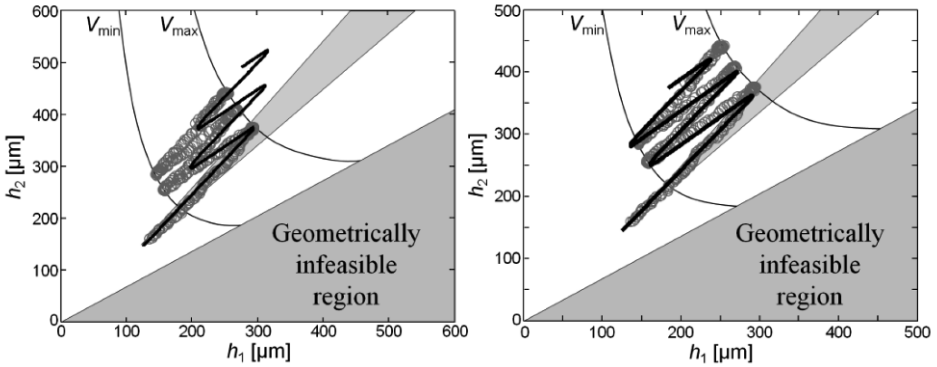

Figure 5: Filtered crystal shape evolution during growth dissolution cycles (circles) together with the model predicted evolution (solid line) with the initial kinetics (left) and adjusted kinetics (right).

4. Conclusions

In this article, the observation of a multivariate population balance system is exemplified on the cyclic crystallization of potassium dihydrogen phosphate. The observations that were obtained by video microscopy are passed to a Kalman filter which serves to reduce the measurement noise significantly. The filtered observations are shown to be robust against process noise and can therefore be used for the re-estimation of the governing process kinetics. The application to growth-dissolution cycles of KDP confirms the usefulness of the observer in generating a feedback which can be used for process control. Furthermore, the investigated cyclic crystallization process provides a promising novel process concept for crystal shape engineering without using any additives.

Acknowledgements

The authors gratefully acknowledge the financial support of this work by the German Research Foundation (DFG) under the grant SU 189/5-1.

References

N. Bajcinca, 2013, Time optimal cyclic crystallization, Computers and Chemical Engineering, 58, 381-389

N. Bajcinca, V. De Oliveira, C. Borchert, J. Raisch, K. Sundmacher, 2010, Optimal control solutions for crystal shape manipulations, Computer Aided Chemical Engineering, 28, C, 751-756

C. Borchert, E. Temmel, H. Eisenschmidt, H. Lorenz, A. Seidel-Morgenstern, K. Sundmacher, 2014, Image-Based in Situ Identification of Face Specific Crystal Growth Rates from Crystal Populations, Crystal Growth & Design,14, 3, 952-971

H. Eisenschmidt, A. Voigt, K. Sundmacher, 2015, Face-specific Growth and Dissolution Kinetics of Potassium Dihydrogen Phosphate Crystals from Batch Crystallization Experiments, Crystal Growth & Design, 15, 1, 219-227

M.A. Lovette, M. Muratore, M.F. Doherty, 2012, Crystal Shape Modification Through Cycles of Dissolution and Growth: Attainable Regions and Experimental Validation, AIChE Journal, 58, 5, 1465-1474

N. Zaitseva, L. Carman, I. Smolsky, R. Torres, M. Yan, 1999, The effect of impurities and supersaturation on the rapid growth of KDP crystals, Journal of Crystal Growth, 204, 4, 512-524

Krist V. Gernaey, Jakob K. Huusom and Rafiqul Gani (Eds.), 12th International Symposium on Process Systems Engineering and 25th European Symposium on Computer Aided Process Engineering.
31 May – 4 June 2015, Copenhagen, Denmark

Adsorption based competitive purity control in crystallization

Akos Borsos,[a] Zoltan K Nagy[a,b*]

[a]*Loughborough University, Chemical Engineering Department,Loughborough, LE11 3TU, United Kingdom*
[b]*Purdue University, School of Chemical Engineering, West Lafayette, IN 47907-2100, USA*
zknagy@purdue.edu

Abstract

Impurities often have influence on crystallization and properties of the crystal product such as nucleation and growth kinetics, polymorphism or particle size and shape distribution. In most cases, these effects are undesired and thus purification of the product is necessary. This paper represents a novel purity control method based on competitive adsorption. Additive which competes with the undesired impurity for the available active sites on the crystal surface leads to changed adsorption equilibria and finally results lowered impurity concentration. This method is tested numerically by using the developed population balance model. The study shows that competitive purity control (CPC) which uses model based optimization can be an effective alternative for lowering undesired impurity concentration in the crystal product without additional purification steps in the production line.

Keywords: Cooling crystallization, competitive adsorption, population balance model, purity control.

1. Introduction

Crystallization is an industrially often applied separation and purification unit operation. The properties of the obtained product such as particle size and shape distribution, stability are important especially in pharmaceutical industry. Effect of impurity on the crystal properties is widely investigated and numerous studies focuses on the impact of impurities on the crystal growth and thus changes in the crystal size and shape distribution. For instance Fu et al., (1999) experimentally investigated the effect of anionic impurities on the growth habit of an inorganic crystal, while Prasad et al., (2001) compared and studied experimentally the Paracetamol crystallization in the presence of impurity and in pure media. Since the crystal size and morphology has impact on the possible application in the production line, considerable number of researches looks into impurity effect on the physical and chemical properties of the pharmaceutical products. Variankaval et al., (2008) focused not only for the impurities, but listed some often occurred challenges in production of active pharmaceutical ingredients (API) e.g., polymorphism, impurity/additive or solvent effect.
Different types of models were also developed in order to describe the impact of impurity on crystal properties. The mathematical model developed by Cabrera and Verilyea (1958) was the earliest which considered impurity adsorption. Rosenberg and Riveros (1974) take into account the relation between impurity and heat of mixing terms. The most widespread impurity adsorption model is based on Langmuir's

adsorption isotherms and ait is originally developed and investigated by Kubota and Mullin (1995). Langmuir type adsorption model was discussed substantially in Ruthven's work (1984). The Kubota-Mullin model was further extended and combined with population balance model in numerous researches such as numerical study by Borsos et al., (2014) who developed a shape control method by using multiple crystal growth modifiers (CGMs).
Additional aspects of product behaviour are required to be considered in pharmaceutical production such as bioavailability, toxicity, and stability which can also be influenced by impurities, thus limited impurity concentration of product is required (Goole et al., 2010). Different methods are used in order to achieve the desired concentration level in the API product. Recrystallization is widely used as an effective purification technique of crystallization (e.g. Nara, 1997; Morito et al., 2013). However this technique does strongly influence the productivity. Further techniques are also available as additional step in the production line: Membrane filtration (e.g., Peeva et al., 2014) and also chromatographic methods (Amanullah and Mazzotti, 2006; Szekely et al., 2011) are also often used as purification unit operation.
The aim of this work is to present a new purity control method which does not require additional unit operation and does not have significant impact on the productivity. Adsorption based competitive purity control (CPC) is proposed and investigated. A morphological population balance model including nucleation, growth, and competitive impurity adsorption kinetics is developed to describe the process when multiple impurities can competitively adsorb on the crystal surface. The numerical study presented in the paper shows that the method may be a useful technique when appropriate control additive is available.

2. Competitive purity control

Competitive purity control is a method which helps lowering the concentration of undesired impurity in crystal products. Figure 1 shows a schematic representation of competitive adsorption mechanism with a harmful impurity which has a suitable active group (orange part of impurities on Fig 1) for connecting to the active sites (orange rectangles on the moving front) on the growing surface layer of crystal, while a harmless additive with same adsorption behaviour also has same/similar group. In this case competitive adsorption occurs between the undesired impurity (Impurity_1) and the control additive (Impurity_2) on the same type of active sites.

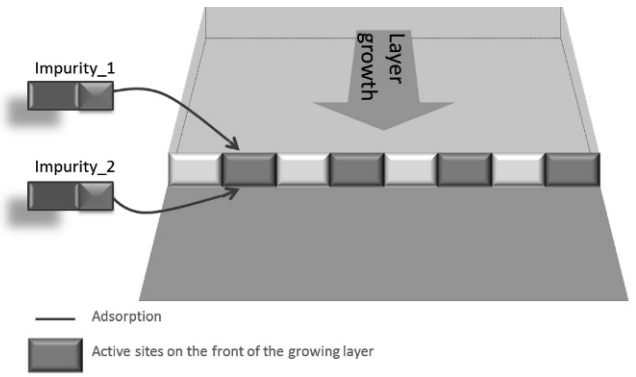

Figure 1 Schematic image of the competitive adsorption mechanism of two crystal growth modifiers.

Hence, competitive adsorption leads to changed equilibria of Langmuir isotherms in accordance of the impurity/additive concentrations in the system. These changes of the equilibria result in lowered level of the harmful impurity concentration in the solid crystal product.

Mathematical models including impurity adsorption have been developed previously in order to investigate the impurity effect on the crystal properties. In the present work, morphological population balance based competitive multi-impurity adsorption model is developed. The effect of growth modifiers on the distribution function leads to an extended population balance model formulation (Fevotte and Fevotte, 2010). The new distribution function includes the time of crystals spending in impure media. The modified distribution function takes the form

$$n(t,\boldsymbol{x}) = \int_0^t \phi(t,\boldsymbol{x},\eta)d\eta \tag{1}$$

where $\phi(t,\boldsymbol{x},\eta)$ defines the new distribution function and $\boldsymbol{x}$ is vector of characteristic crystal sizes.Then the morphological population balance equation is determined as the follow

$$\frac{\partial}{\partial t}\phi(t,\boldsymbol{x},\eta) + \nabla_x\left[\boldsymbol{G}\phi(t,\boldsymbol{x},\eta)\right] + \frac{\partial}{\partial \eta}\phi(t,\boldsymbol{x},\eta) = B_p\delta(\boldsymbol{x}-\boldsymbol{x}_0)\delta(\eta-0) \tag{2}$$

The initial and boundary conditions of the PBE are

$$\phi(0,\boldsymbol{x},0) = \phi(\boldsymbol{x}); \boldsymbol{G}\phi(t,\boldsymbol{x},\eta) = 0, \boldsymbol{x} \in \partial\Omega_x, \ \eta = 0 \tag{3}$$

The $\partial\Omega_x$ is the boundary of the size space.

Primary nucleation is considered and determined in the right side of the PBE. Nucleation rate can be written as the function of the actual and saturation concentrations, c and c_{sat}:

$$B_p = k_p \exp\left[-k_e \ln^{-2}\left(c_{sat}^{-1}c\right)\right] \tag{4}$$

The k_p and k_e are coefficient and kinetic constant of primary nucleation, respectively.

The growth kinetics according to the competitive adsorption mechanism can be written as (Borsos et al., 2014)

$$G_i = k_{gi}\sigma^{g_i}\left\{1 - \sum_j\left(\frac{\beta_i K_{i,j}c_{CGM,j}}{T\sigma\left[1+\sum_j K_{i,j}c_{CGM,j}\right]}\left[1-\exp\left(-\frac{\eta}{\tau_{i,j}}\right)\right]\right)\right\} \tag{5}$$

where G_i is the growth rate of the i^{th} characteristic crystal face, $\sigma = (c - c_{sat})/c_{sat}$, g_i and k_{gi} are the growth exponent and kinetic coefficient. The $\beta_i = \gamma_i a_i/(kL_i)$ which are the edge free energy on the i^{th} crystal face per unit length, the area per growth

unit appearing on the i^{th} surface, Boltzmann constant and average distance between the active sites, respectively. The Langmuir constant, $K_{i,j}$, of the j^{th} CGM on i^{th} characteristic face of the crystal. The adsorption time constant, τ, is the function of adsorption and desorption rates as well as impurity concentration as it is defined by Kubota and Mullin (1995).

The method of moment was used to solve the PBE as it provides effective solution. In the case of morphological population balance the PBE is transformed into a closed set of ordinary differential equation system of cross-moments. The general form of the moment equation system is written as the follows

$$\frac{d\mu_{0,0}}{dt} = B_p \text{ and } \frac{d\mu_{m,r}}{dt} = mG_1\mu_{m-1,r} + rG_2\mu_{m,r-1} \tag{6}$$

It is well known that the first moment is related to the particle number, while the third cross-moment is proportional to the particle volume.

The mass balance is also important in order to describe the crystal purity. The following equation represents the mass balance of solute

$$\frac{dc}{dt} = -\rho_c k_v \frac{d\mu_{1,2}}{dt} \tag{7}$$

The ρ_c is the density of the crystal, k_v is the shape factor. The mass balance of the impurities can be written as the follows

$$\frac{dc_{CGM_j}}{dt} = \frac{\chi_{c,j}}{1-\sum_j \chi_{c,j}} \frac{M_{CGM_j}}{M_c} \frac{dc}{dt} \tag{8}$$

where M_{CGM_j} and M_c are the molecular weights of the impurities/CGMs and solute. The $\chi_{c,j}$ determines the mole fraction of the j^{th} CGM in the crystal phase (Maeda et al., 2006; Borsos et al., 2014). The closed set of differential equations with the mass balance is suitable to describe competitive adsorption of multiple impurities during crystallization.

3. Simulation and results

The presented morphological population balance model was implemented in Matlab environment in order to investigate and control the crystal purity by using multiple impurities or additives in the system.

The sensitivity of crystal purity was studied at the end of the crystallization by applying various mixtures of the impurity/additive. Figure 2a shows how the concentration of adsorbed impurity in the product depends on the initial concentration of the impurity and control additives in the system. The surface shows that increased amount of control additive results in reduced impurity concentration in the solid phase. Figure 2b describes the dependence of the total impurity in the crystal product on impurity and the control additive concentration. It can be seen that a small amount of control additive leads to lowered level of total impurity concentration while further addition of it increases the amount of adsorbed impurity.

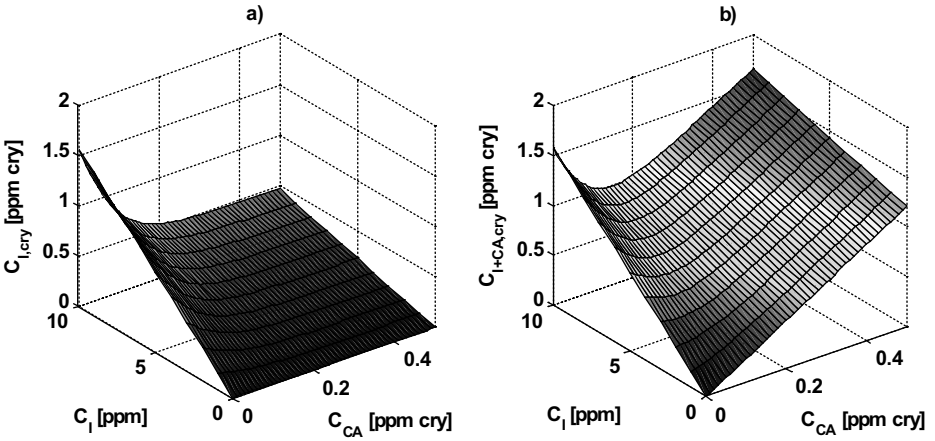

Figure 2 Study on the effect of initial impurity and control additive concentration on the adsorbed amount of a) impurity and b) sum of impurity and control additive in crystal product

A case study of the application of CPC is presented in Fig 3. The objective function of the optimization is defined as the minimization of the weighted multiplication of impurity and total impurity concentration, which are important quality indicators in pharmaceutical crystallization. Fig 3a shows the results of a simulated scenario of 20 batches with batch to batch variation of impurity concentration when the initial concentration of the impurity varies. The squares represent the impurity concentration level in the system without treatment, while the stars indicate the case of applied CPC according to the model based optimization on the basis of the objective function. Figure 3b shows the model based calculation of the optimal amount of control additives used.

4. Conclusions

A new purification method so called competitive purity control is presented in this paper. This method is based on competitive multi-impurity adsorption theorem which was combined with the developed morphological population balance model including primary nucleation, growth of the two characteristic sizes and competitive multi-adsorption kinetics.

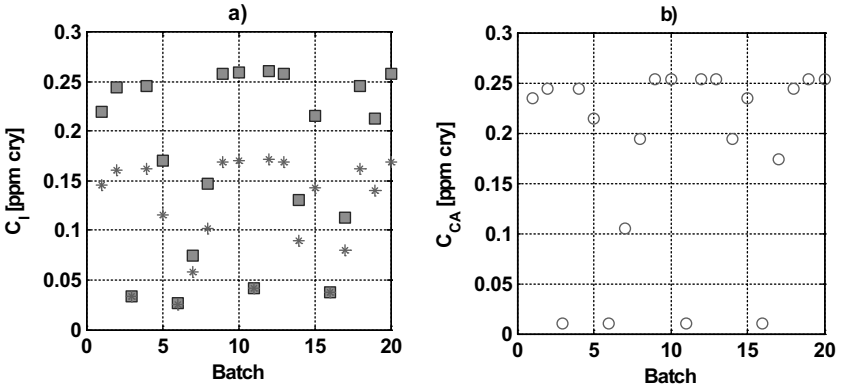

Figure 3 a) Batch to batch variation of impurity concentration in the crystal product; b) optimal amount of control additives in each batches

The CPC method was numerically studied in order to examine the effectiveness on the crystal product purity. The simulation based case study shows that the impurity concentration could be lowered to around 60% of the non-treated system by using CPC method with the chosen kinetic, process parameters and objective function. While alternative purification methods can be more effective, all of those have unfavorable properties such as reduced productivity or cost and time consuming additional unit operations. Furthermore, combinations of the presented and existing purification methods may be considerable solution in order merge the benefits of the techniques.

5. Acknowledgements

Financial support provided by the European Research Council grant no. [280106-CrySys] is gratefully acknowledged.

References

M., Amanullah, M., Mazzotti, 2006. Optimization of a hybrid chromatography-crystallization process for the separation of Troger's base enantiomers. Journal of Chromatography A, 1107, 36-45.

A., Borsos, A., Majumder, Z. K., Nagy, 2014. Model development and experimental validation for crystal shape control by using tailored mixtures of growth modifiers. Computer Aided Chemical Engineering, 33, 781-786.

N., Cabrera, D.A., Vermilyea, 1958. The growth of crystal from solution. In: Dormeus, R.H., Roberts, B.W., Turnbull, D.: Growth and perfection of crystals, Chapman and Hall, London.

F., Fevotte, G., Fevotte, 2010. A method of characteristics for solving population balance equations (PBE) describing the adsorption of impurities during crystallization processes. Chemical Engineering Science, 65, 3191-3198.

Y-J., Fu, Z-S., Gao, J-M., Liu, Y-P., Li, H., Zeng, M-H., Jiang, 1999. The effect of anionic impurities on the growth habit and optical properties of KDP. Journal of Crystal Growth 198-199(1), 682-686.

J., Goole, D.J., Lindley, W., Roth, S.M., Carl, K., Amighi, J-M., Kauffmann, G.T., Knipp, 2010. Effect of excipients on transporter mediated absorption. International Journal of Pharmaceutics, 393, 17-31.

N., Kubota, J.W., Mullin, 1995. A kinetic model for crystal growth from aqueous solution in the presence of impurity. Journal of Crystal Growth 152(3), 203-208.

K., Maeda, R., Tabuchi, Y., Asakuma, K., Fukui, 2006. Distribution of metallic ions in single KDP crystal grown from aqueous solution. Cryst. Res. Technol., 41(10), 955-960.

H., Morito, M., Uchikoshi, H., Yamane, 2013. Boron removal by dissolution and recrystallization of silicon and sodium-silicon solution. Separation and Purification Technology, 118, 723-726.

O., Nara, 1997. Effective purification of ellagic acid by successive automatic recrystallization and absolute determination of purity by absorptivity ratio. Analytica Chimica Acta, 338, 247-253.

K.V.R., Prasad, R.I., Ristic, D.B., Sheen, J.N., Sherwood, 2001. Crystallization of paracetamol from solution in the presence and absence of impurity. International Journal of Pharmaceutics 215(1-2), 29-44.

F., Rosenberg, H.G., Riveros, 1974. Segregation in alkali halide crystallization from aqueous solutions. The Journal of Chemical Physics, 60(2), 668-674.

D.M., Ruthven, 1985. Principles of adsorption and adsorption processes. John Wiley and Sons, Canada.

Gy., Szekely, J., Bndarra, W., Heggie, B., Sellergren, F.C., Ferreira, 2011. Organic solvent nanofiltration: a platform for removal of genotoxins from active pharmaceutical ingredients. Journal of Membrane Science, 381, 21-33.

N., Variankaval, A.S., Cote, M.F., Docherty, 2008. From form to function: Crystallization of active pharmaceutical ingredients. AIChE Journal 54(7), 1682-1688.

Krist V. Gernaey, Jakob K. Huusom and Rafiqul Gani (Eds.), 12th International Symposium on Process Systems Engineering and 25th European Symposium on Computer Aided Process Engineering.
31 May – 4 June 2015, Copenhagen, Denmark

Stabilizing control for reactor/separator processes with gas and liquid recycles

Hiroya Seki

Chemical Resources Laboratory, Tokyo Institute of Technology, 4259-R1-19, Nagatsuta, Midori-ku, Yokohama 226-8503, Japan

Abstract

A reactor/separator process with gas and liquid recycles is one of the most common process configurations in chemical plants. A control system design problem for such processes is discussed using the two representative plant-wide control benchmark problems, VAM (vinyl acetate monomer) production and HDA (hydrodealkylation of toluene) plants. The most commonly used control configuration for such systems is to introduce the gas feed as a pressure controller handle, while the fresh liquid feed is provided as a make-up to the liquid feed inventory. Installation of a liquid hold-up tank, to which the liquid recycle and fresh feed streams are introduced, is most helpful for eliminating the positive feedback effect due to the material recycle and making control system design easy. This paper seeks the possibility of eliminating such buffer tanks from the viewpoint of process safety (the concept of inherently safer processes), and configures a stable control system despite the positive feedback effect. The liquid feed stream to the reactor is put on flow control by manipulating the fresh feed stream. Locally, configuring a simple mixing control may seem sufficient, but it is shown that the stability depends on the reaction kinetics and the gas component inventory control: the elimination of the buffer tank results in an open-loop unstable process for both benchmark problems, but an appropriate control scheme, ex. PI control, can easily realize a stable closed-loop system

Keywords: process control, plant-wide control.

1. Introduction

Material recycles are common in chemical processes. When a reactor is so designed that the per-pass conversion is well below 100%, separators are introduced to recover and recycle the unconsumed reactants. Often, a reactor per-pass conversion is designed at a moderate value due to increased side reactions and increased reactor construction costs for a higher conversion.

The simplest configuration of the reactor-separator-recycle (RSR) process, which comprises a CSTR and distillation column with one material recycle as shown in Fig. 1, has been extensively studied as one of the representative examples of plant-wide control problems (Luyben,1994; Larsson et al., 2003), since the existence of even a single material recycle complicates the overall behaviour of the combined units.

This paper deals with multiple recycle processes, which include liquid and gas recycles. By using the two representative benchmark problems as examples, namely the VAM (vinyl acetate monomer)

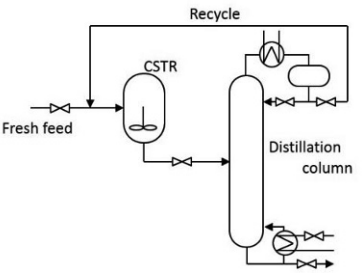

Figure 1 Example of reactor-separator-recycle (RSR) process, consisting of a CSTR and distillation column.

production process (Luyben et al., 1998) and the HDA (hydrodealkylation of toluene) plant (Douglas, 1988; Luyben, 2002), plant-wide control system design is discussed.

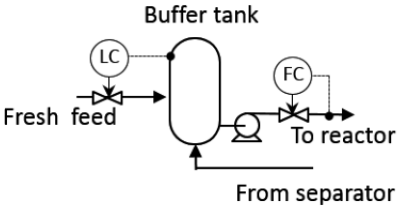

Figure 3 Use of a feed buffer tank to introduce fresh feed (Bildea et al., 2003)

The most commonly used control configuration for gas and liquid recycle systems is to introduce the gas feed as a pressure controller handle, while the fresh liquid feed is provided as a make-up to the liquid feed inventory. Installation of a liquid feed buffer tank may be the most straightforward way of realizing an operable process (Bildea et al., 2003), but an alternative process configuration which does not use the extra buffer tank is considered in this paper. The liquid feed stream to the reactor is put on flow control by manipulating the fresh feed stream: the liquid feed to the reactor is the sum of the fluctuating recycle stream and the fresh feed stream. Locally, configuring simple mixing control may seem sufficient for such systems, but it is shown that the stability depends on the reaction kinetics and the gas component inventory control. Simulation results using dynamic simulators are shown.

2. Control configuration for liquid feed introduction in recycle processes

2.1. Luyben's rule

Luyben (1994) introduced so-called "Luyben's rule" for configuring control system for plants with recycles. Luyben's rule states that at least one stream on the recycle path should be put on flow control: in the RSR system of Fig.1, the reactor effluent and the distillate (recycle stream) should not be used as the level control handles at the same time. Otherwise, "snow ball effect" arises: the recycle flow rate may increase significantly when the fresh feed is provided over the reaction capacity. He pointed out that the reactor effluent should be put on flow control and the fresh feed has to be used to regulate the CSTR level. He also showed that the control configuration violating Luyben's rule introduces very slow dynamics, which can be understood from the block diagram shown in Fig.2 (Luyben, 2012).

Later, Bildea et al. (2003) pointed out the reactor inlet stream is the most appropriate place where the flow control should be applied. To realize this, they suggested a process configuration as shown in Fig. 3 which incorporates a buffer tank: the fresh feed is provided as the level controller handle. If the buffer tank is inserted, positive feedback due to the material recycle is eliminated, and control system design becomes considerably easy. Without a feed buffer tank, it would not be always obvious where to configure level control for introducing the fresh feed.

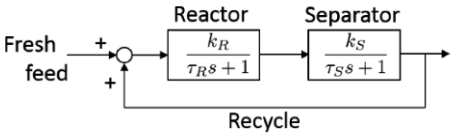

Figure 2 Block diagram of a recycle process configuring positive feedback

However, from the viewpoint of process safety (the concept of inherently safer processes), the extra inventory would not be preferable (Bollinger, 1996). The fresh feed can be introduced into the

reflux drum of a separator to be used as the manipulated variable of the reflux drum level control, but such a configuration limits the control system design for the distillation column.

2.2. Proposed configuration

Figure 4 shows the process and control configuration we employ in this study. Simply, the feed buffer tank is eliminated and the total feed flow to the reactor, which is the sum of the fresh feed flow and the recycle flow, is put on flow control by manipulating the fresh feed flow. The advantage of this configuration is that there is no extra feed buffer tank, and the recycle flow can be used for control system design of the separator. The drawback is that we have to take the positive feedback effect into consideration when we design control system.

Let the fresh feed flow, the total feed flow to the reactor, and the recycle flow be F, F_{tot}, and F_{rec}, respectively. The transfer function from the reactor feed F to the recycle flow F_{rec} is denoted as $G(s)$. Then the transfer function from F to F_{rec}, for which the flow controller is to be designed, can be expressed as

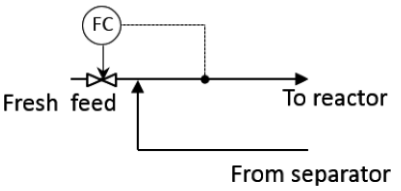

Figure 4 Proposed process and controller configuration. Elimination of the feed buffer tank and introduction of the total liquid feed control by the fresh feed

$$\frac{F_{tot}}{F} = \frac{1}{1-G(s)}. \quad (1)$$

The flow control shown in Fig. 4 has to be designed for the process whose transfer function is described above. We have to be aware of the effect of the positive feedback on the dynamics of the process to be controlled. As shown in the next section, the open-loop dynamics may become unstable.

3. Examples

3.1. VAM plant

3.1.1. Process description

Figure 5 shows a process flow of the vinyl acetate monomer production plant. This process was proposed as a benchmark problem for plant-wide control study (Luyben et al., 1998; Chen et al., 2003). It is a typical reactor/separator process with gas and liquid recycles. Acetic acid is provided as liquid feed, and ethylene and oxygen are provided as gaseous feed.

In the plug flow reactor, the following gas-phase reactions are assumed to occur:

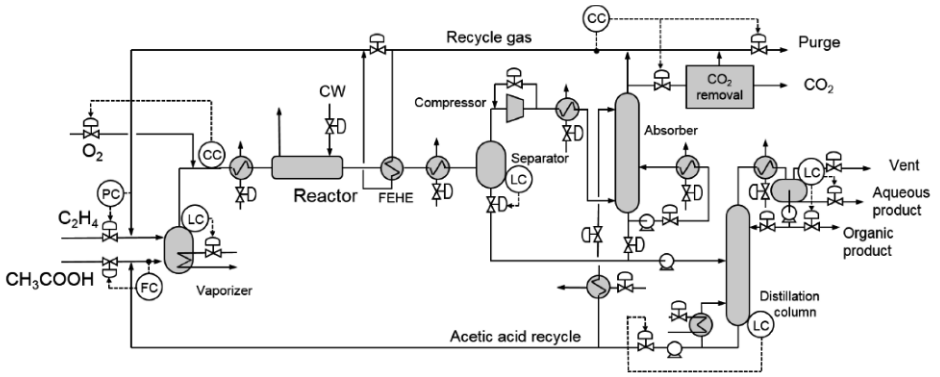

Figure 5 Process flow of the VAM plant with basic inventory control loops

Main reaction

$$C_2H_4 + CH_3COOH + \frac{1}{2}O_2 \xrightarrow{r_1} CH_2 = CHOCOCH_3 + H_2O$$

Side reaction

$$C_2H_4 + 3O_2 \xrightarrow{r_2} 2CO_2 + 2H_2O$$

The rate of the main reaction [mol/min/g-catalyst] is expressed as

$$r_1 = 3.16 \times 10^{-4} \exp\left(\frac{-3670}{T}\right) \cdot p_E \cdot \frac{p_A}{1 + 0.986 p_A} \cdot \frac{p_O(1 + 0.247 p_W)}{1 + 0.0846 p_O(1 + 0.247 p_W)}, \qquad (2)$$

where T [K] is a reactor temperature, p_E, p_A, p_O, and p_W are the partial pressure [kPa] of ethylene, acetic acid, oxygen, and water, respectively. The throughput manipulator is the reactor outlet temperature, which is controlled by the cooling water flow.

3.1.2. Simulation

Figure 6 shows a simulation result. The simulation was performed on the commercial dynamic simulator Visual Modeler (Seki et al., 2010; Yumoto et al., 2010). During t=2 – 15 h, the flow controller for the total liquid feed was turned off and the fresh feed was held constant. The recycle acetic acid continued to decrease: this implies the open-loop is unstable. After the controller was turned on (t=15 h), the recycle flow rate was stabilized.

The instability of the transfer function from the acetic acid fresh feed to the liquid recycle, $1/(1-G(s))$, can be explained as follows. When the total acetic acid feed is increased, the partial pressure of acetic acid p_A should increase. This would lead to increased reaction rate according to (2), but the total pressure is controlled at the reactor inlet, decreasing the partial pressure of ethylene p_E. Consequently,

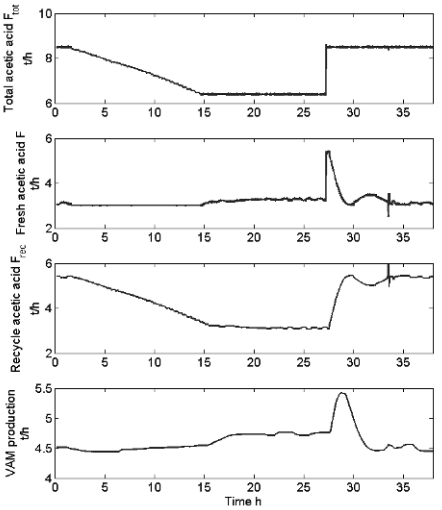

Figure 6 Simulation result for the VAM plant

the reaction rate decreases. This results in $G(0)>1$(increasing the acetic acid feed to the reactor leads to increased amount of acetic acid recycle), which destabilizes the transfer function $1/(1-G(s))$. If the gas-phase pressure is controlled at the separator where it is free from the acetic acid partial pressure, such instability does not occur.

Although the process is open-loop unstable, it is not a difficult task to configure a stable closed-loop. Simply, integral control was sufficient.

3.2. HDA plant

3.2.1. Process description

The HDA process, shown in Fig. 7, is for producing benzene through hydrodealkylation of toluene (Douglas, 1988). It consists of an adiabatic plug flow reactor and separators with gas and liquid recycle streams. Fresh toluene and hydrogen are introduced to the process and they are mixed with the recycled liquid and gas streams. The reactant mixture is pre-heated by the feed-effluent heat exchanger (FEHE) and then heated up to the reaction temperature by the furnace before being fed to the PFR. The following two reactions are considered:

Main reaction:

$$C_6H_5CH_3 + H_2 \longrightarrow C_6H_6 + CH_4$$

Side reaction:

$$2C_6H_6 \longleftrightarrow C_{12}H_{10} + H_2$$

The model of the HDA process used in this study is a modified version of the model by Luyben (2002) and it has been implemented on the commercial dynamic simulator UniSim. The throughput manipulator in this control configuration is the total toluene flow rate; the reactor inlet temperature is controlled by manipulating the fuel to the furnace so that the per pass toluene conversion becomes 85% by looking at the liquid composition of the stabilizer bottom outlet stream.

3.2.2. Simulation

Figure 8 shows a simulation result. During t=2~12 h, the total toluene flow controller was put into manual. As shown in the figure, the open-loop dynamics was found to be unstable with the growing oscillation in the recycle toluene, although the steady state gain $G(0)$ was smaller than 1 in this process. After t=12 h, the controller was turned on

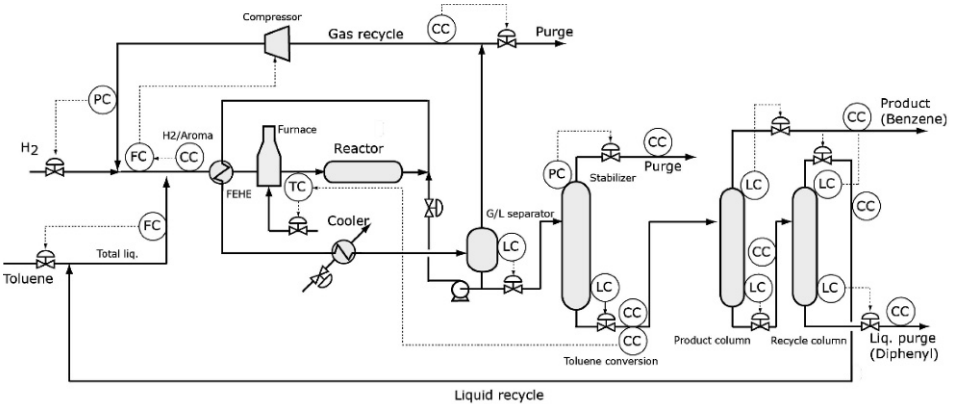

Figure 7 Process flow of the HDA plant with basic inventory control loops

and the closed loop was stabilized. PI control with the control parameter K_p=1 (kmol/h/kmol/h) and T_i=1 min was used.

At t=22 h and 32 h, step changes in the total toluene flow rate were made. As shown in the bottom plot, the production rate was successfully controlled.

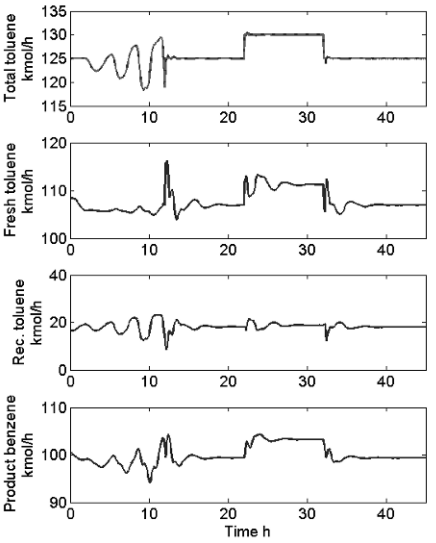

Figure 8 Simulation result for the HDA plant

4. Conclusion

By using the two representative benchmark plants with gas and liquid recycles, a control system design problem concerning liquid feed introduction was discussed. Fresh feed was introduced as the manipulated variable of the controller which regulates the total liquid feed to the reactor. No feed buffer tank was used. In both cases, the open-loop processes were found unstable, but PI or I-control was capable of stabilizing the closed-loop.

Acknowledgement

The Workshop 31 (Process Control Technlogy) of the Japan Society for the Promotion of Science (JSPS) 143rd Committee on Process Systems Engineering was gratefully acknowledged for the use of the VAM simulator on Visual Modeler.

References

C.S. Bildea, A.C. Dimian, 2003, Fixing flow rates in recycle systems: Luyben's rule revisited, Ind. Eng. Chem. Res., 42, 4578-4585

R.E. Bollinger, D.G. Clark, A.M. Dowell III, R.M. Ewbank, D.C. Hendershot, W.K. Lutz, S.I. Meszaros, D.E. Park, E.D. Wixom, 1996, Inherently safer chemical processes, CCPS.AIChE

R. Chen, K. Dave, T. McAvoy, M. Luyben, 2003, A nonlinear dynamic model of a vinyl acetate process, Ind. Eng. Chem. Res., 42, 4478-4487

J.M. Douglas, 1988, Conceptual Design of Chemical Processes, McGraw-Hill Book Company

M.L. Luyben, B.D. Tyreus, 1998, An industrial design/control study for the vinyl acetate monomer production process, Computers Chem. Engng., 22, 867-877

W.L. Luyben, 1994, Snowball effect in reactor/separator processes with recycle, Ind. Eng. Chem. Res., 33, 299-305

W.L. Luyben, 2002, Plantwide dynamic simulators in chemical processing and control, Marcel Dekker Inc., New York

W.L. Luyben, 2012, Heuristics for plantwide control,Plantwide control - Recent developments and applications, Chapter 6, G.P. Rangaiah and V. Kariwala, Eds., John Wiley & Sons

H. Seki, M. Ogawa, T. Itoh, S. Ootakara, H. Murata, Y. Hashimoto, and M. Kano, 2010, Plantwide control system design of the benchmark vinyl acetate monomer production plant, Computers Chem. Engng., 34, 1282-1295

T. Yumoto, S. Ootakara, H.Seki, Y. Hashimoto, H. Murata, M. Kano, and Y. Yamashita, 2010, Rigorous dynamic simulator for control study of the large-scale benchmark chemical plant, IFAC Symp. Dynamics and Control of Process Systems, 49-54, Leuven, Belgium

Krist V. Gernaey, Jakob K. Huusom and Rafiqul Gani (Eds.), 12th International Symposium on Process Systems Engineering and 25th European Symposium on Computer Aided Process Engineering.
31 May – 4 June 2015, Copenhagen, Denmark

Extended VRFT Method for Controller Design of Nonlinear Systems Based on Block-Oriented Model Structures

Jyh-Cheng Jeng,[a]* Yi-Wei Lin,[a] Min-Wei Lee[b]

[a] *National Taipei University of Technology, Taipei 106, Taiwan*
[b]*China Steel Corporation, Kaoshiung 812, Taiwan*
jcjeng@ntut.edu.tw

Abstract

This paper presents a novel data-based controller design for nonlinear systems based on the VRFT design framework and block-oriented modeling. Identification of a complete dynamic model of the nonlinear system is not required, whereas only the static nonlinearity has to be estimated. Moreover, the nonlinearity estimation and the controller design are performed simultaneously without the needs of iterative procedures or nonlinear optimization. Simulation studies of a distillation column and a pH neutralization process confirms the effectiveness of the proposed design method.

Keywords: Nonlinear process control; Hammerstein system; Wiener system; VRFT.

1. Introduction

Most dynamical systems exhibit nonlinear characteristics so that they can be better represented by nonlinear models. One of the most frequently studied classes of nonlinear models is the block-oriented nonlinear model. Two typical block-oriented model structures are the Hammerstein and Wiener models. In the Hammerstein structure, the linear dynamic element is preceded by the static nonlinearity. The order of connection is reversed in the Wiener structure. Traditional model-based control design approaches require identification of an empirical model for the system. The identification process, however, usually relies on some prior assumptions such as model structure and order, which are often unavailable or subject to uncertainties. Hence, the complexity and modeling errors associated with such models increase the difficulty of the control design task, and lead to considerable degradation of control performance.

Data-based control design methods are very useful in many practical control applications, where obtaining a suitable model is a very difficult task. The virtual reference feedback tuning (VRFT) method (Campi et al., 2002) can be used to design the controller by directly utilizing plant I/O data without resorting to plant models. Most existing results on the VRFT design are however restricted to linear systems. Campi and Savaresi (2006) explored the extension of VRFT to nonlinear systems, which requires iterative procedure. Adaptive VRFT design (Yang et al., 2012) was proposed for adaptive PID controller parameter tuning. Unlike the linear VRFT, these extended versions of VRFT are no longer one-shot method so that a significant advantage of VRFT is lost. In this study, we propose a novel controller design method for nonlinear systems based on the one-shot (noniterative) VRFT design framework and the Hammerstein/Wiener modeling for the system. Combining the parameterization of the nonlinearity with VRFT framework enables putting the system in linear regressor form,

so that least-squares techniques can be used to determine parameters of the nonlinearity and the controller simultaneously, without identifying the linear dynamic subsystem.

2. Controller design based on Hammerstein modeling

The control scheme for Hammerstein system is shown in Figure 1 where f, G, f^{-1}, and C denote the static nonlinear element, linear dynamics, inverse of nonlinearity, and controller, respectively. This linearizing control scheme results in an equivalent linear control system shown in Figure 2(a). The static nonlinear function is parameterized as

$$v_k = f(u_k) = \sum_{i=1}^{s} a_i B_i(u_k) \tag{1}$$

where B_i are (known) basis functions, and a_i are unknown coefficients. A linear controller with integral action is given by

$$C(z) = \frac{c_0 + c_1 z^{-1} + \cdots + c_r z^{-r}}{1 - z^{-1}} \tag{2}$$

Because the gain of a Hammerstein system can be arbitrarily distributed in nonlinear and linear blocks, it is assumed, without loss of generality, that $c_0 = 1$. The problem of controller design is to determine the controller parameters c_i (i = 1,2,…,r) and the unknown coefficients a_i (i = 1,2,…,s), from an N-point data set $\{u_k, y_k\}_{k=1\sim N}$ of observed input-output measurements.

We apply the VRFT method to the equivalent linear control system (Figure 2(a)), so that a model-reference problem, as depicted in Figure 2(b), is to be solved. The reference model $T(z)$ describes the desired behavior of the closed-loop system, which is specified as the following second-order dynamics:

$$T(z) = \frac{(\alpha + \beta z^{-1}) z^{-d-1}}{1 - 2Az^{-1} + A^2 z^{-2}}; \quad \alpha = 1 - A + A\ln A; \quad \beta = A^2 - A - A\ln A \tag{3}$$

where d is related to the time delay of the system and A is a user-specified tuning parameter related to the speed of response. The design goal is to determine the controller parameters c_i and the unknown coefficients a_i, such that the control system in Figure 1 behaves as similarly as possible to the reference model $T(z)$. Based on the virtual reference signal $\tilde{r}(z) = T^{-1}(z)\, y(z)$, the virtual controller output is calculated as

$$\begin{aligned} \tilde{v}(z) &= C(z)\left[\tilde{r}(z) - y(z)\right] \\ &= \left(\frac{1 + c_1 z^{-1} + \cdots + c_r z^{-r}}{1 - z^{-1}}\right)\left[\frac{1 - 2Az^{-1} + A^2 z^{-2} - (\alpha + \beta z^{-1}) z^{-d-1}}{(\alpha + \beta z^{-1}) z^{-d-1}}\right] y(z) \end{aligned} \tag{4}$$

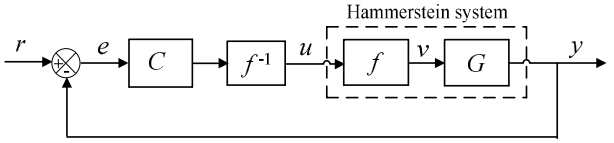

Figure 1. Linearizing control scheme for Hammerstein system.

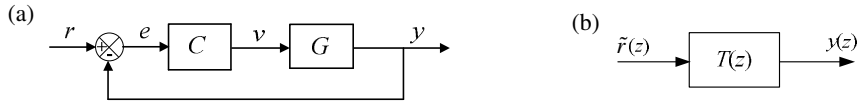

Figure 2. (a) Equivalent linear control system for Hammerstein system and (b) its reference model.

Equation (4) can be rewritten as

$$Q(z)y(z)=\left(\alpha+\beta z^{-1}\right)\tilde{v}(z)-\left(c_1z^{-1}+c_2z^{-2}+\cdots+c_rz^{-r}\right)Q(z)y(z) \tag{5}$$

where

$$Q(z)=z^{d+1}-\left(2A-1\right)z^{d}+\left(1-A\right)^2\sum\nolimits_{\ell=1}^{d-1}z^{\ell}+\beta \tag{6}$$

When the linear block is fed by v_k, it generates y_k. Therefore, a controller that shapes the closed-loop behavior to the reference model generates v_k when the error signal is given by $\tilde{r}_k-y_k$. The task of controller design then becomes minimizing the difference between v_k (Eq.(1)) and $\tilde{v}_k$ (Eq.(4)), or equivalently, minimizing the difference between $\varphi_{k,0}$ and $\boldsymbol{\psi}_k\boldsymbol{\theta}$, where

$$\begin{aligned}
&\varphi_{k,j}=y_{k+d+1-j}-\left(2A-1\right)y_{k+d-j}+\left(1-A\right)^2\sum\nolimits_{\ell=1}^{d-1}y_{k+\ell-j}+\beta y_{k-j};\quad j=0,1,\cdots,r\\
&\boldsymbol{\psi}_k=\begin{bmatrix}-\varphi_{k,1} & -\varphi_{k,2} & \cdots & -\varphi_{k,r} & \eta_{k,1} & \eta_{k,2} & \cdots & \eta_{k,s}\end{bmatrix}\\
&\eta_{k,i}=\alpha B_i\left(u_k\right)+\beta B_i\left(u_{k-1}\right);\quad i=1,2,\cdots,s\\
&\boldsymbol{\theta}=\begin{bmatrix}c_1 & c_2 & \cdots & c_r & a_1 & a_2 & \cdots & a_s\end{bmatrix}^T
\end{aligned} \tag{7}$$

Therefore, the parameter $\boldsymbol{\theta}$ is computed by solving the following minimization problem:

$$\min_{\boldsymbol{\theta}}J\left(\boldsymbol{\theta}\right)=\min_{\boldsymbol{\theta}}\sum_{k=1}^{N-d-1}\left[\varphi_{k,0}-\boldsymbol{\psi}_k\boldsymbol{\theta}\right]^2=\min_{\boldsymbol{\theta}}\left\|\boldsymbol{\varphi}-\boldsymbol{\Psi}\boldsymbol{\theta}\right\|_2^2 \tag{8}$$

where

$$\boldsymbol{\varphi}=\begin{bmatrix}\varphi_{1,0} & \varphi_{2,0} & \cdots & \varphi_{N-d-1,0}\end{bmatrix}^T;\quad \boldsymbol{\Psi}=\begin{bmatrix}\boldsymbol{\psi}_1^{\,T} & \boldsymbol{\psi}_2^{\,T} & \cdots & \boldsymbol{\psi}_{N-d-1}^{\,T}\end{bmatrix}^T \tag{9}$$

The solution can be calculated using the least-squares technique given by

$$\hat{\boldsymbol{\theta}}=\left(\boldsymbol{\Psi}^T\boldsymbol{\Psi}\right)^{-1}\boldsymbol{\Psi}^T\boldsymbol{\varphi} \tag{10}$$

The controller parameters c_i and estimates of the coefficients a_i can be obtained by partitioning the estimate $\hat{\boldsymbol{\theta}}$, according to the definition of $\boldsymbol{\theta}$ in Eq.(7).

3. Controller design based on Wiener modeling

The control scheme for Wiener system is as shown in Figure 3, which results in an equivalent linear control system shown in Figure 4(a). It is assumed that the inverse function of the static nonlinearity is parameterized as

$$v_k=f^{-1}\left(y_k\right)=\sum\nolimits_{i=1}^{s}a_iB_i\left(y_k\right) \tag{11}$$

The problem of controller design is to determine the controller parameters c_i ($i=0,1,\ldots,r$) and the unknown coefficients a_i ($i=1,2,\ldots,s$) from an N-point I/O data set $\{u_k, y_k\}_{k=1\sim N}$. The VRFT method is applied to the equivalent linear control system shown in Figure 4(a), so that a model-reference problem, as depicted in Figure 4(b), is to be solved. The design goal is to determine the controller parameters and the unknown coefficients a_i, such that the control system in Figure 3 behaves as similarly as possible to the prespecified reference model $T(z)$. Based on the virtual reference signal $\tilde{r}_v(z)=T^{-1}(z)v(z)$, the virtual controller output is calculated as

$$\begin{aligned}
\tilde{u}(z)&=C(z)\left[\tilde{r}_v(z)-v(z)\right]\\
&=\left(\frac{c_0+c_1z^{-1}+\cdots+c_rz^{-r}}{1-z^{-1}}\right)\left[\frac{1-2Az^{-1}+A^2z^{-2}-\left(\alpha+\beta z^{-1}\right)z^{-d-1}}{\left(\alpha+\beta z^{-1}\right)z^{-d-1}}\right]v(z)
\end{aligned} \tag{12}$$

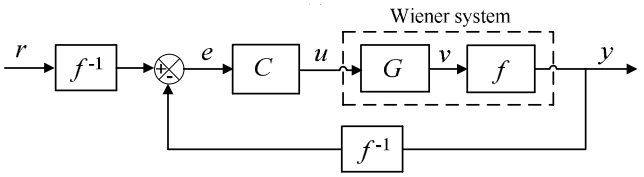

Figure 3. Linearizing control scheme for Wiener system.

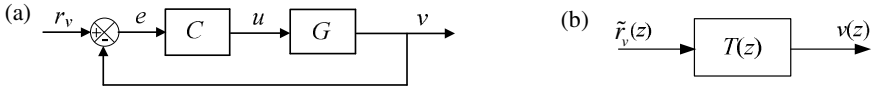

Figure 4. (a) Equivalent linear control system for Wiener system and (b) its reference model.

When the linear block is fed by u_k, it generates v_k. Therefore, a controller that shapes the closed-loop behavior to the reference model generates u_k when the error signal is given by $\tilde{r}_{v,k} - v_k$. The task of controller design becomes minimizing the difference between u_k and $\tilde{u}_k$. Equation (12) can be rewritten as

$$\left(\alpha + \beta z^{-1}\right)\tilde{u}(z) = \left(c_0 + c_1 z^{-1} + c_2 z^{-2} + \cdots + c_r z^{-r}\right)Q(z)v(z) \tag{13}$$

Substituting Eq.(11) into Eq.(12) and rearranging yields $\tilde{\phi}_k = \boldsymbol{\psi}_k \boldsymbol{\theta}$, where

$$\begin{aligned}
&\tilde{\varphi}_k = \alpha\tilde{u}_k + \beta\tilde{u}_{k-1} \\
&\boldsymbol{\psi}_k = \begin{bmatrix} \psi_{k,1} & \psi_{k,2} & \cdots & \psi_{k,s} \end{bmatrix}; \quad \psi_{k,i} = \begin{bmatrix} \psi_{k,i,0} & \psi_{k,i,1} & \cdots & \psi_{k,i,r} \end{bmatrix} \\
&\psi_{k,i,j} = B_i\left(y_{k+d+1-j}\right) - (2A-1)B_i\left(y_{k+d-j}\right) + (1-A)^2 \sum_{\ell=1}^{d-1} B_i\left(y_{k+\ell-j}\right) + \beta B_i\left(y_{k-j}\right) \\
&\boldsymbol{\theta} = \begin{bmatrix} \vartheta_1 & \vartheta_2 & \cdots & \vartheta_s \end{bmatrix}^T; \quad \vartheta_i = \begin{bmatrix} c_0 a_i & c_1 a_i & \cdots & c_r a_i \end{bmatrix}
\end{aligned} \tag{14}$$

By defining $\varphi_k = \alpha u_k + \beta u_{k-1}$, minimizing the difference between u_k and $\tilde{u}_k$ is equivalent to minimizing the difference between φ_k and $\tilde{\varphi}_k$. Thus, the parameter $\boldsymbol{\theta}$ is computed by solving the following minimization problem:

$$\min_{\boldsymbol{\theta}} J(\boldsymbol{\theta}) = \min_{\boldsymbol{\theta}} \sum_{k=1}^{N-d-1} \left[\varphi_k - \boldsymbol{\psi}_k \boldsymbol{\theta}\right]^2 = \min_{\boldsymbol{\theta}} \left\|\boldsymbol{\varphi} - \boldsymbol{\Psi}\boldsymbol{\theta}\right\|_2^2 \tag{15}$$

where

$$\boldsymbol{\varphi} = \begin{bmatrix} \varphi_1 & \varphi_2 & \cdots & \varphi_{N-d-1} \end{bmatrix}^T; \quad \boldsymbol{\Psi} = \begin{bmatrix} \boldsymbol{\psi}_1^T & \boldsymbol{\psi}_2^T & \cdots & \boldsymbol{\psi}_{N-d-1}^T \end{bmatrix}^T \tag{16}$$

The solution can be calculated using the least-squares technique given by Eq.(10). The problem is how to obtain the controller parameters c_i and estimates of the unknown coefficients a_i from the estimate $\hat{\boldsymbol{\theta}}$. Define

$$\boldsymbol{\Theta} = \begin{bmatrix} \vartheta_1^T & \vartheta_2^T & \cdots & \vartheta_s^T \end{bmatrix} = \mathbf{c} \cdot \mathbf{a}^T \tag{17}$$

where $\mathbf{c} = \begin{bmatrix} c_0 & c_1 & \cdots & c_r \end{bmatrix}^T$ and $\mathbf{a} = \begin{bmatrix} a_1 & a_2 & \cdots & a_s \end{bmatrix}^T$. An estimate $\hat{\boldsymbol{\Theta}}$ of the matrix $\boldsymbol{\Theta}$ can be obtained from the estimate $\hat{\boldsymbol{\theta}}$. Let the economy-size SVD of $\hat{\boldsymbol{\Theta}}$ be given by

$$\hat{\boldsymbol{\Theta}} = \mathbf{U}\boldsymbol{\Sigma}\mathbf{V}^T = \begin{bmatrix} U_1 & U_2 & \cdots & U_{r+1} \end{bmatrix} \cdot \mathrm{diag}\begin{bmatrix} \sigma_1 & \sigma_2 & \cdots & \sigma_{r+1} \end{bmatrix} \cdot \begin{bmatrix} V_1 & V_2 & \cdots & V_{r+1} \end{bmatrix}^T \tag{18}$$

Then, the closest, in the 2-norm sense, estimates of the parameter vectors $\mathbf{c}$ and $\mathbf{a}$ can be computed as (Gómez and Baeyens, 2004)

$$\hat{\mathbf{c}} = U_1; \quad \hat{\mathbf{a}} = \sigma_1 V_1 \tag{19}$$

4. Simulation examples

4.1. Example 1: Distillation column

The proposed controller design method for Hammerstein systems was applied to a binary distillation column (Horton et al., 1991). The distillate composition x_D is controlled by manipulating the reflux ratio R. A time delay of 2 min is assumed for the composition measurement. At the steady-state of $R = 3$ and $x_D = 0.935$, a uniform random signal was introduced to the reflux ratio R and the resulting x_D was simulated with a sampling time of 2 min, as shown in Figure 5. To simulate a more realistic condition, measurement noise with NSR = 15% was added to the output data. A set of 600 data points were used for implementing the proposed controller design, with parameters in the reference model chosen as $A = 0.67$ and $d = 3$. The static nonlinearity was represented by the third-order B-splines. Using a third-order controller ($r = 3$), the estimated nonlinearity is plotted in Figure 6. For the purpose of comparison, a linear control system was also designed based on the (linear) VRFT method using the same process data and reference model. Figure 7 shows the response of the proposed nonlinear control system and the linear control system to successive set-point changes. The response of proposed nonlinear control system is close to the reference trajectory and better than that of the linear control system for the set-point changes, indicating that the proposed controller effectively compensates the process nonlinearity. The robustness of the proposed control was evaluated through varying the process parameters. The result (not shown due to page limitation) is still satisfactory.

4.2. Example 2: pH neutralization process

The proposed controller design method for Wiener systems was applied to a pH process (Palancar et al., 1998). The pH of the effluent solution is controlled by manipulating the base flow rate q_b. A set of 3000 data points were generated around the steady-state of q_b = 14.2 mL/s and pH = 9.407, as shown in Figure 8. The estimated inverse of nonlinearity is plotted in Figure 9. Figure 10 shows the closed-loop performance of the proposed nonlinear control system and the linear control system to successive set-point changes.

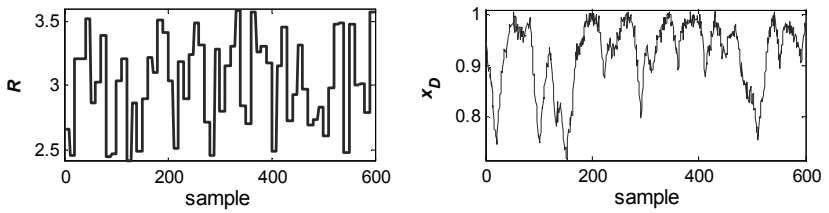

Figure 5. Input-output data used for controller design (Example 1).

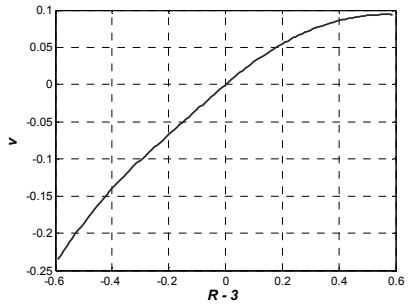

Figure 6. Estimated nonlinearity (Example 1).

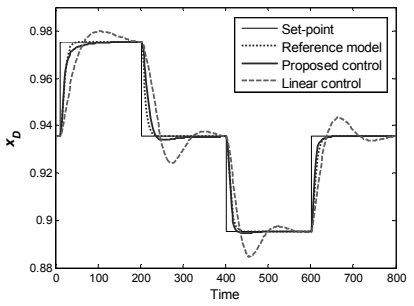

Figure 7. Closed-loop response (Example 1).

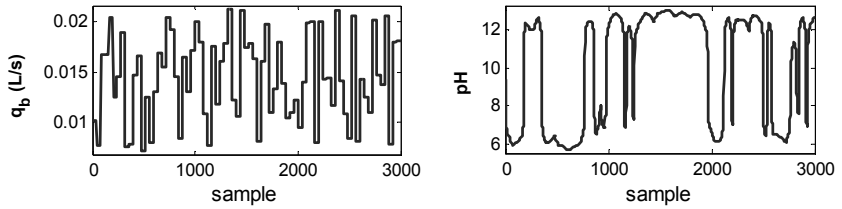

Figure 8. Input-output data used for controller design (Example 2).

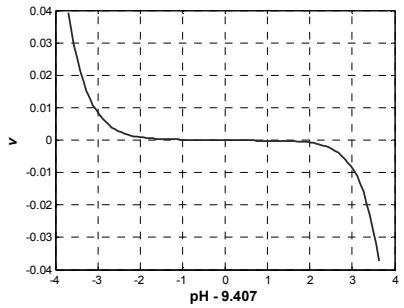

Figure 9. Inverse of nonlinearity (Example 2).

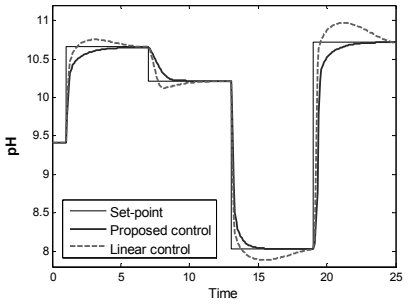

Figure 10. Closed-loop response (Example 2).

The nonlinear control system shows favorable and almost the same control performance for the set-point changes, which verifies the effectiveness of the proposed method.

5. Conclusions

We proposed extended VRFT methods for nonlinear controller design based on the Hammerstein/Wiener modeling for nonlinear systems. The controller parameters and system nonlinearity are simultaneously obtained based directly on a set of plant data. This is in sharp contrast to the model-based design methods that require first identifying an approximate process model, which is often difficult and subject to modeling errors. The proposed algorithms combine the basis function representation of the nonlinearity with the VRFT framework to enable putting the system in linear regressor form, which avoids implementation problems due to computational limitations. The superiority of the proposed nonlinear control design over linear control has been illustrated using two benchmark processes (i.e., a distillation column and a pH neutralization process).

References

M.C. Campi, A. Lecchini, S.M. Savaresi, 2002, Virtual Reference Feedback Tuning: A Direct Approach for the Design of Feedback Controllers, Automatica, 38, 1337–1346.

M.C. Campi, S.M. Savaresi, 2006, Direct Nonlinear Control Design: The Virtual Reference Feedback Tuning (VRFT) Approach, IEEE Trans. Automatic Control, 51, 14–27.

X. Yang, Y. Li, Y. Kansha, M.S. Chiu, 2012, Enhanced VRFT Design of Adaptive PID Controller, Chem. Eng. Sci., 76, 66–72.

J.C. Gómez, E. Baeyens, 2004, Identification of Block-Oriented Nonlinear Systems Using Orthonormal Bases, J. Process Control, 14, 685–697.

R.R. Horton, B.W. Bequette, T.F. Edgar, 1991, Improvements in Dynamic Compartmental Modeling for Distillation, Comput. Chem. Eng., 15, 197–201.

M.C. Palancar, J.M. Aragon, J.S. Torrecilla, 1998, pH-Control Systems Based on Artificial Neural Networks, Ind. Eng. Chem. Res., 37, 2729–2740.

Krist V. Gernaey, Jakob K. Huusom and Rafiqul Gani (Eds.), 12th International Symposium on Process Systems Engineering and 25th European Symposium on Computer Aided Process Engineering.
31 May - 4 June 2015, Copenhagen, Denmark.

Linear or Nonlinear? Comparing Measures of Nonlinearity

Malik M. Tahiyat[a] and M.A.A Shoukat Choudhury[b]

[a]*Department of Chemical Engineering; Bangladesh University of Engineering and Technology, Dhaka, Bangladesh*
[b]*Department of Chemical Engineering;Bangladesh University of Engineering and Technology, Dhaka, Bangladesh*
shoukat@che.buet.ac.bd

Abstract

Nonlinearity plays a significant role in the closed loop performance of a controller/process as it can render controller tuning ineffective. Nonlinearities can initiate oscillations in process variables that may cause plantwide oscillations, which in turn results in loss of plant profitability and rapid wear and tear of plant machinery. Thus, quantification of nonlinearity is important for designing appropriate controllers, troubleshooting process faults and ensuring smooth operation of a process plant. In this paper, two data-based nonlinearity measures namely, bicoherence and surrogate-data based measures are compared using physical models of a few common processes to identify which method works better for which process.

Keywords: nonlinearity, bicoherence, surrogate, modeling

1. Introduction

Study of Nonlinear systems have been of foremost interest to researchers because most physical systems in reality are nonlinear. Nonlinear systems are defined by those, which do not follow the principle of superposition. Nonlinearities in process variables can be caused by stiction in control valves, which, in turn, sets up oscillations that propagate throughout the whole plant. So, quantification of nonlinearity takes precedence over implementing linear or nonlinear control methods. Two broad approaches exist for measuring nonlinearity of a a process: Model based measures and Time-series or Data-based based measures. The preference of the Data-based approaches over the Model-based resides on the fact that Model-based approaches, like Best Linear Approximation and Curvature-Based methods, require a process model which is often unavailable or difficult to obtain (Choudhury et al. (2008)). Therefore, in recent times, data based methods are gaining popularity because they require time series data of the process which are readily available from the DCS or data historian. The data-based approaches include bicoherence based approach, surrogate data-based approach, Lyapunov exponents and Correlation Dimension.

Most notable data based methods include Bicoherence-Based Measures, proposed by Emara-Shabaik et al. (1996) and Choudhury et al. (2004), Surrogate Data-based Measures by Kantz and Schreiber (1997) and Theiler et al. (1992) and Harmonic Analysis by Paulonis and Cox (2003), Ruel and Gerry (1998), and Thornhill and Hägglund (1997). Correlation dimension and maximal Lyapunov exponent have been examined for the diagnosis of nonlinearity in chemical processes by Zang and Howell (2005a,b).

In this paper, an overview of nonlinearity is given in section 1. Two data based methods are briefly reviewed in section 2. Two common processes, which include a 'Continuous Stirred Tank Reactor'(CSTR) and a 'Spherical Tank' are described in section 3. The nonlinearities of the aforementioned systems are quantified using data-based measures of nonlinearity in section 4. The paper ends with a conclusion.

2. Nonlinearity Measures

2.1. Bicoherence-based Method

The bispectrum is the simplest of the various frequency domain HOS (Higher Order Statistics) measures. It is the frequency domain counterpart of the third-order moments. The bispectrum is normalized in the following way to give a measure called bicoherence whose magnitude is bounded between 0 and 1:

$$bic(f_1,f_2)^2 \triangleq \frac{|E\left[X(f_1)X(f_2)X^*(f_1+f_2)\right]|^2}{E\left[|X(f_1)X(f_2)|^2\right]E\left[|X(f_1+f_2)|^2\right]} \tag{1}$$

where $X(f)$ is the Fourier transform of the data series $x(t)$. Significance of bicoherence magnitude at each individual bifrequency is given by

$$P\{bic(f_1,f_2)^2 > \frac{c_\alpha^{\chi^2}}{2K}\} = \alpha \tag{2}$$

where K is the number of data segments used in bicoherence estimation and $c_\alpha^{\chi^2}$ is the critical value calculated from the central χ^2 distribution table for a significance level of α with two degrees of freedom. Those bicoherence values which satisfy the above condition are called $bic^2_{significant}$. Then Choudhury et al. (2008) quantified the total nonlinearity present in the time series as the following index:

$$TNLI \triangleq \sum bic^2_{significant} \tag{3}$$

2.2. Surrogate-data based Method

The purpose of surrogate data methods is to create synthetic data sets called surrogate time series, having the same power spectrum, but with the phase coupling removed by randomization. A key property of the test time series is then compared to that of its surrogates, and nonlinearity is diagnosed if the property is significantly different in the test time series (Theiler et al. (1992); Kantz and Schreiber (1997)). For a time-series, the surrogate data is calculated by:

$$\text{z}=FFT(\text{test time series}) \quad ,$$

where, FFT=Forward Discrete Fourier Transform; then,

$$z_{surr} = \begin{array}{ll} z[i] & i=1 \\ z[i]\,e^{j\phi_{i-1}} & i=2,.....,N/2 \\ z[i] & i=N/2+1 \\ z[i]\,e^{-j\phi_{N-i+1}} & i=(N/2+2),.....N \end{array} \tag{4}$$

N = number of samples in the time-series. The quantity $\phi_k, k=1,...,(N/2-1)$, is a random phase in the range 0-2π.
Then, surrogate data = IFFT(z_{surr}) , where IFFT=Inverse Discrete Fourier Transform.

An embedded matrix is created of both test and surrogate data. Squared Prediction errors of both test data, Γ_{test} and of surrogate data, Γ_{surr} are calculated as described in Choudhury et al. (2008). Surrogate Nonlinearity Index, N_{surr} is then calculated from :

$$N_{surr} = \frac{\bar{\Gamma_{surr}} - \Gamma_{test}}{3\sigma_{\Gamma_{surr}}} \tag{5}$$

where $\bar{\Gamma}_{surr}$ and $\sigma_{\Gamma_{surr}}$ are mean and variances of M sets of Γ_{surr} , respectively.

3. Processes for Simulation Study

3.1. Continuous Stirred Tank Reactor (CSTR)

The first model is that of a CSTR. The model equations are given by Pottman and Seborg (1992), in which a single exothermic reaction is taking place $A \rightarrow B$. The dynamic behavior of the system is represented by a set of differential equations, portraying the rate of change of concentration of reactants and temperature of the reactor respectively. The equations of the system are given by:

$$\frac{dc_A}{dt} = \frac{q}{V}(c_{Af} - c_A) - k_0 c_A e^{\frac{-E}{RT}} \tag{6}$$

$$\begin{aligned}\frac{dT}{dt} = {} & \frac{q}{V}(T_f - T) - \frac{(-\Delta H)k_0 c_A}{\rho C_p} e^{\frac{-E}{RT}} \\ & + \frac{\rho_c C_{pc}}{\rho C_p V} q_c \left[1 - e\left(\frac{-hA}{q_c \rho_c C_{pc}}\right)\right](T_c - T)\end{aligned} \tag{7}$$

where C_{Ao}=feed concentration, T_{fi}=inlet temperature of the feed, T_c=inlet temperature of coolant, q= feed flow rate, V=reactor's volume, UA=overall heat transfer co-efficient$*$Area, $\rho\&\rho_c$=density of the reactant and coolant respectively, Cp=Specific Heat of the product, k_o=reaction rate constant, ΔH=Heat of reaction. The values of the respective parameters are taken from Luyben (1995).

3.2. Spherical Tank

The second model is that of a spherical tank. The model equation is as follows:

$$\pi R^2 \left[1 - \frac{(R-h)^2}{R^2}\right] \frac{dh}{dt} = F_i(t-d) - F_0(t) \tag{8}$$

Where $F_o(t)$ is the outlet flow rate at time t, h the height of the water level from the bottom of the tank, R the radius of the spherical tank and d corresponds to the delay in the input flow rate. The outlet flow rate, F_o, can be expressed as $F_o(t) = \sqrt{2g(h-h_o)}$, where g is the gravitational constant and h_o the height of the outlet pipe from the base of the vessel. For the open-loop simulation of the system, we use $R = 0.5$ m, $h_o = 0.01$ m. The details of the parameters of the aforementioned model equation can be found in Agrawal and Lakshminarayanan (2003). The control of water level in the tank is accomplished by manipulating the inlet volumetric flow rate, F_i.

4. Simulation Results

Linear systems are said to exhibit *sinusoidal fidelity*, i.e. a sinusoidal input will produce a sinusoidal output of the same frequency; nonlinear systems, however, produce additional frequencies as well. Thus, to incorporate oscillations, a sinusoidal wave of varying frequencies and amplitudes are added to the systems. The measures of nonlinearity are then applied to output data.

4.1. Nonlinearity Study of a CSTR

The inlet reactant concentration, C_{Ai}, was excited using sinusoidal signals of varying frequencies and amplitudes. The data from output concentration was collected and tested for nonlinearity of the system.

Figure 1 shows that for small changes in amplitude, i.e., small changes in reactant concentration, the values of TNLI are close to zero (the lower left portion of the plot). This is expected, because for small excitations, the nonlinear processes can be assumed to be 'locally linear'. Thus TNLI is close to zero. As the amplitude increases, the nonlinearity goes up and so does the TNLI. The nonlinearity has increased monotonically with changes in frequencies and amplitudes. Thus, Total Nonlinearity Index increases with increasing frequency and amplitude.

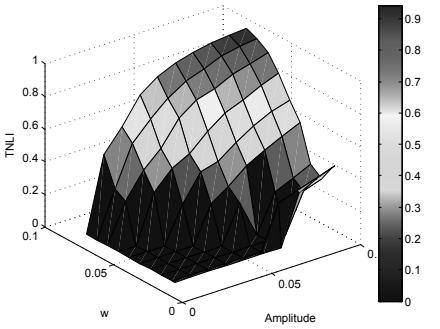

Figure 1: Total Nonlinearity Index (TNLI) Pattern for CSTR

Figure 2 shows the variation in N_{surr}, when Surrogate data-based measure is applied to the same data-set. As seen from the figure, N_{surr} is not monotonically increasing with amplitudes and frequencies, rather, it generates an irregular pattern. The plot shows that the nonlinearity is mostly increasing with increasing frequency. At the same time, the nonlinearity index, N_{surr} does not show good sensitivity with increasing amplitudes. This may be due to the almost sinusoidal nature of the output data because it is known that Surrogate data-based measure, does not work good for purely sinusoidal or strong cyclic signals.

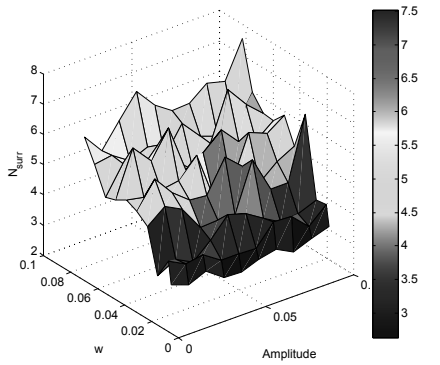

Figure 2: Surrogate Nonlinearity Index Pattern for CSTR

While the the plot of Total Nonlinearity Index appeared to vary between 0 and 1, the plot of N_{surr} showed higher sensitivity to nonlinearity for small excitation signals.

4.2. Nonlinearity Study of a Spherical Tank

In this simulation, the input sinusoidal signal is applied to the inlet flow, F_i, of a spherical tank to introduce sinusoidal disturbance in the water-level of the tank. The data of water-level was collected and nonlinearity measures were calculated from this data. The experiment is operated at a steady-state height of 0.35 m of water in the tank so that the water in the tank neither dries out nor overflows.

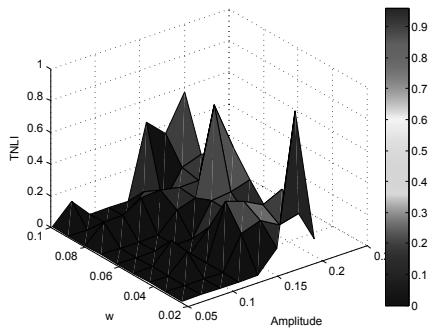

Figure 3: Total Nonlinearity Index (TNLI) Pattern for Spherical Tank

Figure 3 shows that for small magnitudes of input signals, the spherical tank system can also be assumed locally linear as portrayed by the flat regions on the left portion of the plot. As the amplitude of excitation signal increases beyond a certain value, nonlinearity suddenly jumps as visualized from the several peaks at the right portion of the plot. The reason for this can be attributed to the fact that nonlinearity increases at a point where the total surge volume of the tank drops below a certain level. With the decrease in liquid volume, the tank loses its ability to attenuate disturbances, and thus it contributes to an increase in TNLI. Another fact is that the curvature of the spherical tank increases as we move away from the center along the top or bottom direction of the tank. Thus the height of the same volume of water will behave in a more nonlinear fashion when operating closer to the top or bottom portion of the tank than it would while operating near the centre. Another finding is that the nonlinearity of this particular system is not very sensitive to changes in frequency. Therefore, it can be concluded that nonlinearity of the process depends on the size of the excitation signal.

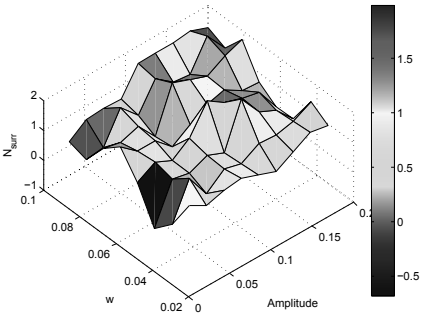

Figure 4: Surrogate Nonlinearity Index Pattern for Spherical Tank

The Surrogate data-based measure is applied to the same data-set. Figure 4 shows that nonlinearity is increasing with both frequency and amplitude. However, the rise in N_{surr} is neither uniform nor monotonic. The dependency of N_{surr} on amplitude can be attributed to the fact as discussed previously.

5. Applicability and Practical Issues

5.1. Applicability

i The comparison of nonlinearity measures will eventually allow the users to find the suitability of each measure for quantifying and finding the degree of nonlinearity for different kinds of processes.

ii The degree of nonlinearity will help to decide whether a linear controller is adequate or a nonlinear controller is required.

iii Multiple nonlinearity measures can be used to increase the reliability of data-based methods for diagnosis of root cause in plant wide oscillations.

5.2. Practical Issues

i For simulation study, sinusoidal excitation was used. In industry, sinusoidal excitations might not be allowed. Since it is widely perceived that often oscillations are existent in industrial processes, the pertaining oscillatory data could itself be used for analyzing purposes. It is to be noted that data-based nonlinearity measures, discussed in this study, are not dependent on sinusoidal excitations only; they can be applied to any time series.

ii It was noted that in case of CSTR, Bicoherence-based measure required approximately 1 minute of computational time while Surrogate data-based measure required around 6.5 hours for execution.

6. Conclusion

The study compares Bicoherence-based measure and Surrogate data-based measure for quantifying nonlinearity. A CSTR and a spherical tank were used for simulation study.

- Bicoherence-based measure appeared to be more sensitive towards changes in amplitude of excitation signals.
- Execution of Bicoherence-based algorithm was much faster than that of surrogate-based algorithm. This makes the bicoherence-based algorithm suitable for application on large data-sets.
- Surrogate data-based measure required a shorter data length in comparison to Bicoherence-based measure for a consistent and reliable estimate of nonlinearity.

7. Acknowledgment

Financial support in the form of scholarship for the first author from BUET Chemical Engineering Forum (BCEF) is gratefully acknowledged.

References

Agrawal, P., Lakshminarayanan, S., 2003. Tuning proportional-integral-derivative controllers using achievable performance indices. Industrial & engineering chemistry research 42 (22), 5576–5582.

Choudhury, M. A. A. S., Shah, S. L., Thornhill, N. F., 2004. Diagnosis of poor control-loop performance using higher-order statistics. Automatica 40 (10), 1719–1728.

Choudhury, M. A. A. S., Shah, S. L., Thornhill, N. F., 2008. Diagnosis of process nonlinearities and valve stiction: data driven approaches. Springer-Verlag, Berlin Heidelberg, Germany.

Emara-Shabaik, H. E., Bomberger, J., Seborg, D. E., 1996. Cumulant/bispectrum model structure identification applied to a ph neutralization process. In: UKACC International Conference on Control. Control '96. IET, pp. 1046–1051.

Kantz, H., Schreiber, T., 1997. Nonlinear Time Series Analysis, vol. 7 of Cambridge Nonlinear Science Series. Cambridge University Press, Cambridge, England.

Luyben, W. L., 1995. Process modeling, simulation and control for chemical engineers. McGraw-Hill Higher Education, New York, USA.

Paulonis, M. A., Cox, J. W., 2003. A practical approach for large-scale controller performance assessment, diagnosis, and improvement. Journal of Process Control 13 (2), 155–168.

Pottman, M., Seborg, D. E., 1992. Identification of non-linear processes using reciprocal multiquadric functions. Journal of Process Control 2 (4), 189–203.

Ruel, M., Gerry, J., 1998. Quebec quandary solved by fourier transform. PULP AND PAPER August (1998), 53–55.

Theiler, J., Eubank, S., Longtin, A., Galdrikian, B., Farmer, J. D., 1992. Testing for nonlinearity in time series: the method of surrogate data. Physica D: Nonlinear Phenomena 58 (1), 77–94.

Thornhill, N., Hägglund, T., 1997. Detection and diagnosis of oscillation in control loops. Control Engineering Practice 5 (10), 1343–1354.

Zang, X., Howell, J., 2005a. Correlation dimension and lyapunov exponent based isolation of plant-wide oscillations. In: Dynamics and Control of Process Systems 2004 (IPV - IFAC Proceedings Volume). Elsevier, pp. 347–352.

Zang, X., Howell, J., 2005b. Isolating the root cause of propagated oscillations in process plants. International Journal of Adaptive Control and Signal Processing 19 (4), 247–265.

Krist V. Gernaey, Jakob K. Huusom and Rafiqul Gani (Eds.), 12th International Symposium on Process Systems Engineering and 25th European Symposium on Computer Aided Process Engineering.
31 May – 4 June 2015, Copenhagen, Denmark

Model Predictive Control for the Self-optimized Operation in Wastewater Treatment Plants

Mario Francisco[a*], Sigurd Skogestad[b], Pastora Vega[c]

[a] *Dept of Computing and Automation. University of Salamanca. 37700 Béjar, Spain*
[b]*Dept. of Chemical Engineering, Norwegian University of Science and Technology. N-7491 Trondheim, Norway.*
[c]*Dept. of Computing and Automation.Univ. of Salamanca. 37008, Salamanca,Spain*
mfs@usal.es

Abstract

This paper describes a procedure to find the best economically controlled variables for the activated sludge process in a wastewater treatment plant despite the load disturbances. A further controllability analysis of those variables including a nonlinear model predictive controller (NMPC) has been performed. The self-optimizing methodology has been applied, considering the most important measurements of the process. A first pre-screening of those measurements has been done based on the nonlinear model of the process and typical disturbances, in order to avoid non feasible operation. The NMPC performance has been compared with a distributed NMPC-PI structure.

Keywords: self-optimizing control; model predictive control; wastewater treatment plant

1. Introduction

The efficiency of most wastewater treatment plants (WWTP) is an important issue that must be improved. In order to fulfil the effluent legal requirements for all weather conditions, which generate large variations of the influent, the operating costs are usually higher than the actually needed. Therefore, the optimization of the WWTP operation can provide a significant cost reduction. In the existing literature, most works only consider the problem from a heuristic viewpoint or stating a particular optimization problem. Only Araujo et al. (2013) provides a comprehensive approach, performing a sensitivity analysis of optimal operation. In Francisco et al. (2011) the process is optimized offline but including also plant design.

In order to minimize the economic loss when disturbances occur, one approach is the re-optimization of the plant by applying Real Time Optimization techniques which can be very demanding computationally, or perform some set point optimization off-line. In this work, a different approach is considered, called self-optimizing control (SOC) (Skogestad, 2000), which consists of determining some primary controlled variables (CVs), also called self-optimized variables, and their corresponding set points, that when kept constant, the economic loss is small with respect to costs if the operation is re-optimized. Although there are many successful works of SOC (see e.g. Umar et al., 2012) the dynamic validation of the results is usually performed by means of decentralized PI controllers (Araujo and Skogestad, 2008).

The first objective of this work is to find the self-optimized variables in a WWTP as a combination of measurements, and the second objective is to evaluate the dynamic behavior of those variables by implementing two control structures: a centralized nonlinear multivariable model predictive controller (NMPC) and a distributed control structure with an NMPC and local PI controllers. The methodology explained has been applied to the activated sludge process using the Benchmark Simulation Model No. 1 (BSM1) (Alex et al., 2008).

2. Local methods for self-optimizing control

The controlled variables selection, particularly for SOC, is a fundamental issue within the plant-wide design. The first step of the methodology is the determination of the optimal operation, assuming here that the economics of the plant are primarily determined by steady state behavior. The following problem is solved, considering nominal disturbances:

$$\min_{\mathbf{u}_0} J_0\left(\mathbf{x},\mathbf{u}_0,\mathbf{d}\right) \tag{1}$$

subject to:

$$\mathbf{g}_1\left(\mathbf{x},\mathbf{u}_0,\mathbf{d}\right)=0\,;\ \mathbf{g}_2\left(\mathbf{x},\mathbf{u}_0,\mathbf{d}\right)\le 0$$

where $\mathbf{x}$ is the state vector, $\mathbf{u}_0$ is the manipulated variables vector (degrees of freedom), $\mathbf{d}$ is the disturbances vector, $\mathbf{g}_1$ is a vector function representing the process model equations and $\mathbf{g}_2$ the process constraints. The active constraints found when solving problem (1) must be controlled tightly for optimal operation (active constraints control), and in this work it is assumed that the set of active constraints does not change for all typical disturbances.

Then, the identification of as many economic controlled variables as the number of remaining degrees of freedom is performed, by using the SOC methodology explained below. The selection is based on the Taylor expansion of the loss function around the equilibrium nominal point $\mathbf{u}_{opt}(\mathbf{d})$:

$$L\left(\mathbf{u},\mathbf{d}\right)=J_c\left(\mathbf{u},\mathbf{d}\right)-J_{opt}\left(\mathbf{u}_{opt}(\mathbf{d}),\mathbf{d}\right)=\frac{1}{2}\left[\mathbf{u}-\mathbf{u}_{opt}(\mathbf{d})\right]^T\mathbf{J}_{uu}\left[\mathbf{u}-\mathbf{u}_{opt}(\mathbf{d})\right] \tag{2}$$

where J_c is the cost value when the set point is kept constant, and J_{opt} is the optimum cost re-optimizing for the corresponding $\mathbf{d}$, $\mathbf{u}_{opt}$ is the optimum value for $\mathbf{u}$ and $\mathbf{J}_{uu}$ is the Hessian of the cost function.

In order to achieve near-optimal operation without the need to re-optimize the process when disturbances occur, the loss must be minimized. Although CV can be selected as a subset of the available measurements, lower loss is achieved by selecting CV as linear combinations of measurements. For that reason, a combination matrix $\mathbf{H}$ with real coefficients is defined as $\mathbf{c}=\mathbf{H}\cdot\mathbf{y}$, where $\mathbf{c}$ is the vector of controlled variables and $\mathbf{y}$ is the vector of available independent measurements, that can include manipulated variables (e.g. flow rate measurements) or measured disturbances. The matrix $\mathbf{H}$ can be found through minimization of the following expression (Halvorsen et al., 2003; Alstad et al., 2009):

$$\min_{\mathbf{H}} \left\| \mathbf{J}_{uu}^{1/2} \left(\mathbf{H}\mathbf{G}^{y} \right)^{-1} \mathbf{H}\mathbf{Y} \right\|_{F} \tag{3}$$

where $\mathbf{Y} = \begin{bmatrix} \mathbf{F}\mathbf{W}_d & \mathbf{W}_e \end{bmatrix}$; $\mathbf{F} = \mathbf{G}_d^{y} - \mathbf{G}^{y}\mathbf{J}_{uu}^{-1}\mathbf{J}_{ud}$; $\mathbf{y} = \mathbf{G}^{y}\mathbf{u} + \mathbf{G}_d^{y}\mathbf{d}$, $\mathbf{W}_d$ and $\mathbf{W}_e$ are scaling matrices for disturbances and implementation errors, $\mathbf{G}^{y}$ and $\mathbf{G}_d^{y}$ are the process transfer matrices (linearized model) , and $\mathbf{J}_{uu}$, $\mathbf{J}_{ud}$ are the hessians.

For problem (3), explicit solutions have been developed, where **Q** is any nonsingular matrix of n_c x n_c (n_c = No. of controlled variables) (Yelchuru and Skogestad, 2011)

$$\mathbf{H}^{T} = \left(\mathbf{Y}\mathbf{Y}^{T} \right)^{-1} \mathbf{G}^{y}\mathbf{Q} \tag{4}$$

3. Methodology applied to the BSM1

3.1. Description of the process

The benchmark simulation model nº 1 (BSM1) (Alex et al., 2008) has been used as a standard activated sludge process model in a WWTP for performance assessment of control strategies and optimization. It consists of five biological reactors connected in series and one secondary settler. The reactors are modeled according to mass balances described in the Activated Sludge Model nº 1 (ASM1), developed by the IWAQ (International Association on Water Quality). An internal recycle (Q_a) from the last tank to the first one is used to supply the denitrification step with nitrate. In order to maintain the microbiological population, sludge from the settler is recirculated into the reactors by means of an external recycle (Q_r), and sludge excess is purged from the bottom of the settler (Q_w). Note that in this benchmark no pH control is considered. More details are given in Alex et al. (2008).

3.2. Operational objectives and constraints

The operational objectives of the WWTP include operational costs and other process and regulations constraints. The cost defined in Alex et al. (2008) has been considered:

$$J = k_E \left(AE + PE + ME \right) + k_D SP \tag{5}$$

where *PE* is the pumping energy, *AE* is the aeration energy, *ME* is the mixing energy, *SP* is the sludge production, and k_E, k_D are the weights representing prices. The constraints needed for process operability are listed in table 1, where COD_e is the chemical oxygen demand, $BOD_{5,e}$ is the 5 day biological oxygen demand, TSS_e is the total suspended solids concentration, and TN_e is the total nitrogen concentration, all measured in the effluent.

For the BSM1 there are eight manipulated variables that correspond to eight degrees of freedom (**u**): Q_a, Q_r, Q_w, $K_La^{(1\text{-}5)}$. The disturbances selected are some of the most important inputs to the plant: $Q^{(in)}$, $COD^{(in)}$, $TSS^{(in)}$. $TN^{(in)}$ is not considered in the methodology in order to simplify the results, but it is inclusion is straightforward. The weather profile events specified in the BSM1 derive the following disturbance vectors: $\mathbf{d}_0$ corresponds to the nominal load conditions, $\mathbf{d}_1$ are the average load values during the rainy weather, $\mathbf{d}_2$ are the average values only for a rain event (extracted from the rain BSM1 disturbances), $\mathbf{d}_3$ are the average during the whole period for storms, $\mathbf{d}_{42}$ are the average values during a storm, $\mathbf{d}_5$ are the average values for one year with average temperature.

Table 1: Process constraints

Effluent constraints and constraints on manipulated variables		
$COD_e \leq 100$ (gCOD/m^3)	$TSS_e \leq 30$ (gSS/m^3)	$Q_w \leq 1844.6$ (m^3/d)
$BOD_{5,e} \leq 10$ (gBOD/m^3)	$S_{NH\,e} \leq 4$ (gN/m^3)	$Q_a \leq 92230$ (m^3/d)
$TN_e \leq 18$ (gN/m^3)	$0 \leq KLa_{1-5} \leq 360$ (1/d)	$Q_r \leq 36892$ (m^3/d)

The nominal optimal operating point has been obtained solving problem (1) for the WWTP, considering cost function (5) and constraints of table 1. This optimization has also been performed for different disturbances, always showing the same three active constraints Q_a (m^3/d)=0, S_{NH_e} (g/m^3)=4, TSS_e (g/m^3)=30. Two of them are output active constraints, so they will be linked to two degrees of freedom, remaining 5 available degrees of freedom.

For the selection of the five self-optimized variables, the Eq. (4) with matrix **Q** selected as the identity has been considered to obtain the corresponding matrix **H**. The initial set of measurements selected has been taken out of Alex et al. (2008), adding also the inputs and disturbances as measurements. In this work, a previous selection of measurements has been performed, very useful to avoid infeasibilities for the CV variables selected later (Larsson et al., 2001). The economic losses have been calculated with Eq. (2) for different weather conditions using the nonlinear model of the process, considering individual measurements. The primary CV candidate variables that make the process infeasible for some load disturbances have been removed, which are in this case S_{NH} for all reactors. Then, based on this study, several sets of measurements have been considered, giving different combination matrices **H**. In order to select the most suitable, as SOC procedure is local, nonlinear losses have been obtained for each set (Table 2) and only $\mathbf{H_3}$ gives feasible solutions for all disturbances.

Set 1 ($\mathbf{H}_1$): $S_O^{(1)}, S_{NO}^{(1)}, S_O^{(5)}, S_{NO}^{(5)}, Q^{(in)}, COD^{(in)}, TSS^{(in)}, K_L a^{(5)}, Q_r$

Set 2 ($\mathbf{H}_2$): $S_O^{(1)}, ..., S_O^{(5)}, S_{NO}^{(1)}, ..., S_{NO}^{(5)}, Q^{(in)}, COD^{(in)}, TSS^{(in)}, MLSS, K_L a^{(5)}, Q_r$

Set 3 ($\mathbf{H}_3$): $S_O^{(1)}, ..., S_O^{(5)}, S_{NO}^{(1)}, ..., S_{NO}^{(5)}, Q^{(in)}, COD^{(in)}, TSS^{(in)}, K_L a^{(5)}, Q_r$

Table 2: Nonlinear losses for different combination matrices and disturbances

	$\mathbf{d}_1$	$\mathbf{d}_2$	$\mathbf{d}_3$	$\mathbf{d}_{42}$	$\mathbf{d}_{43}$	$\mathbf{d}_5$
$\mathbf{H}_1$	Infeas	Infeas	Infeas	Infeas	Infeas	Infeas
$\mathbf{H}_2$	0.223	Infeas	0.127	Infeas	Infeas	1.229
$\mathbf{H}_3$	0.038	0.627	0.069	1.182	0.821	0.300

4. Process controllability analysis

In this section, the dynamic behavior of the selected CV as combination of measurements defined by $\mathbf{H}_3$ is evaluated. This study is important in order to validate the possible implementation of a controller which keeps the selected CV at optimal set points in spite of influent disturbances. The first control structure considered is a

centralized multivariable nonlinear constrained MPC for controlling the active constraints and the self-optimized variables, with the full BSM1 as internal prediction model, and the following objective function:

$$V(k)=\sum_{i=H_w}^{H_p}\left\|\mathbf{y}(k+i\mid k)-\mathbf{r}(k+i\mid k)\right\|_{\mathbf{Q}}^2+\sum_{i=0}^{H_c-1}\left\|\Delta\mathbf{u}(k+i\mid k)\right\|_{\mathbf{R}}^2+\left\|\mathbf{y}(k+H_p\mid k)-\mathbf{r}(k+H_p\mid k)\right\|_{\mathbf{P}}^2$$

where **y** are the controlled outputs, **u** the manipulated variables and **r** the reference, k denotes the current sampling point, $\mathbf{y}(k+i\mid k)$ is the predicted output at time $k+i$, depending of measurements up to time k, $\Delta\mathbf{u}$ are the changes in the manipulated variables, H_c is the control horizon, H_w and H_p are the initial and final prediction horizons respectively, **R** and **Q** are positive definite constant matrices, and **P** is the terminal weight. A second control structure with two PI controllers for the active constraints and the NMPC to control the self-optimized variables has been considered. This control structure has the advantage that if the MPC fails, the PI controllers still keep set points for the active constraints. For selecting a good pairing for the PIs, the RGA matrix has been studied; TSS_e is controlled with Q_w and $S_{NH,e}$ is controlled with $K_La^{(5)}$.

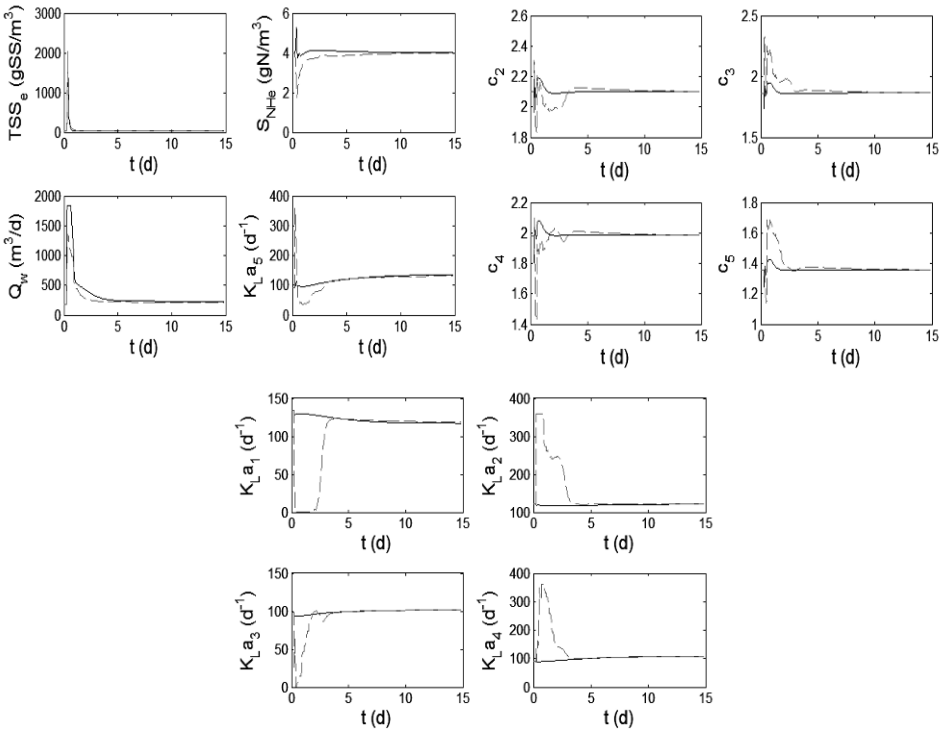

Figure 1: Control performance comparison of NMPC-PI control structure (solid line) and centralized NMPC (dashed line) for rain event disturbance ($\mathbf{d}_2$) at t=0. Active constraints control (top left), self-optimized variables (top right) and manipulated variables (bottom).

In Fig. 1 the dynamic responses are presented, comparing the performance of the control structures when a $\mathbf{d}_2$ step disturbance is applied. They show a good set point tracking both for active constraints and selfoptimized variables, with reasonable control actions. The selfoptimized variable c_1 is not presented because its significance in costs

is negligible. The tuning of the NMPC has been performed by trial and error procedure, choosing $\mathbf{Q}$ = diag(0.1 1 0.001 2 2 2 2) and $\mathbf{R}$ = diag(0.1 0.014 0.014 0.014 0.014 0.014 0.005) for the centralized NMPC; and $\mathbf{Q}$ = diag(0.001 2 2 2 2), $\mathbf{R}$ = diag(0.05 0.01 0.01 0.01 0.01) for the distributed NMPC-PI control. The horizons for both control structures are $H_w = 1$, $H_p = 20$ and $H_c = 1$ .The tuning parameters for the PI control No.1 are K_p= -54.8,T_i= -27.4 and K_p= -12,T_i= -0.2 for No. 2, the first one selected by SIMC guidelines (Skogestad, 2003). For simplicity in the comparative dynamic analysis, the manipulated variables have not been considered in the linear combinations determined by $\mathbf{H}_3$.

5. Conclusions

In this work, the SOC methodology has been applied to find the optimum controlled variables as a combination of measurements in a WWTP. A previous prescreening of measurements to avoid unfeasibilites for large load disturbances has been performed. The dynamic controllability of these variables has also been studied, by implementing two control structures. The results show that both control structures give good set point tracking, despite of a long transient due to the slow process dynamics, particularly for the most severe disturbances. The distributed MPC-PI control shows better transient, particularly for large disturbances, because of the separate treatment of the different time scales of the process and the easier tuning compared to the centralized NMPC.

References

J. Alex, L. Benedetti, J. Copp, K. Gernaey, U. Jeppsson, I. Nopens, M. Pons, L. Rieger, C. Rosen, J. Steyer, P. Vanrolleghem, S. Winkler, 2008, Benchmark Simulation Model no. 1 (BSM1), IWA Taskgroup on benchmarking of control strategies for WWTPs. Dpt. of Industrial Electrical Engineering and Automation, Lund University. Cod.: LUTEDX-TEIE 7229. 1-62.

V. Alstad, S. Skogestad, E.S. Hori., 2009, Optimal measurement combinations as controlled variables, Journal of Process Control, 19, 138-148.

A. Araujo, S. Skogestad, 2008, Control structure design for the ammonia synthesis process, Computers and Chemical Engineering, 32, 2920-2932.

A. Araujo, S. Gallani, M. Mulas, S. Skogestad, 2013, Sensitivity Analysis of Optimal Operation of an Activated Sludge Process Model for Economic Controlled Variable Selection, Ind. Eng. Chem. Res., 52 (29), 9908-9921.

M. Francisco, P. Vega, H. Álvarez, 2011, Robust Integrated Design of Processes with terminal penalty model predictive controllers, Chemical Engineering Research and Design, 89, 1011-1024.

I. J. Halvorsen, S. Skogestad, J. C. Morud, V. Alstad, 2003, Optimal Selection of Controlled Variables. Ind. Eng. Chem. Res., 42, 3273-3284.

T. Larsson, K. Hestetun, E. Hovland, S.Skogestad, 2001, Self-Optimizing Control of a Large-Scale Plant: The Tennessee Eastman Process, Ind. Eng. Chem. Res., 40, 4889-4901.

S. Skogestad, 2000, Plantwide control: The search for the self-optimizing control structure, J. of Process Control, 10, 487-507.

S. Skogestad, 2003, Simple analytic rules for model reduction and PID controller tuning, Journal of Process Control, 13, 291–309.

L. M. Umar, W. Hu, Y. Cao, V. Kariwala, 2012, Selection of Controlled Variables using self-optimizing Control Method: Recent Developments and Applications (eds G. P. Rangaiah and V. Kariwala), John Wiley & Sons, Ltd, Chichester, UK.

R. Yelchuru, S. Skogestad, 2011, Optimal Controlled Variable Selection with structural constraints using MIQP formulations, 18th IFAC World Congress (Milano, Italy).

Krist V. Gernaey, Jakob K. Huusom and Rafiqul Gani (Eds.), 12th International Symposium on Process Systems Engineering and 25th European Symposium on Computer Aided Process Engineering.
31 May – 4 June 2015, Copenhagen, Denmark

Off-Line Tube-Based Robust Model Predictive Control for Uncertain and Highly Exothermic Polymerization Processes

Pornchai Bumroongsri,[a]* Veerayut Lersbamrungsuk,[b] Soorathep Kheawhom[c]

[a]*Department of Chemical Engineering, Faculty of Engineering, Mahidol University, Salaya, Nakhon Pathom 73170, Thailand*
pornchai.bum@mahidol.ac.th
[b]*Department of Chemical Engineering, Faculty of Engineering and Industrial Technology, Silpakorn University, Nakhon Pathom 73100, Thailand*
[c]*Computational Process Engineering, Department of Chemical Engineering, Faculty of Engineering, Chulalongkorn University, Pathumwan, Bangkok 10330, Thailand*

Abstract

Polymerization processes usually contain some uncertain parameters such as those in kinetic rate constants and heat transfer coefficients. An inefficient handling of these uncertain parameters may lead to unexpected thermal runaway of the reaction. In this paper, off-line tube-based robust model predictive control (MPC) is developed. The trajectories of uncertain systems are restricted to lie in a sequence of tubes so robust stability and constraint satisfaction are guaranteed in the presence of both uncertain parameters and disturbances. All of the optimization problems are solved off-line so the proposed algorithm is applicable to fast dynamic polymerization processes. The proposed algorithm is applied to an illustrative example of continuous stirred tank reactor where highly exothermic polymerization reactions occur. The results show that robust stability and constraint satisfaction are guaranteed.

Keywords: Tube-based robust model predictive control; polymerization processes; uncertain parameters; disturbances

1. Introduction

Chemical processes are usually involved with complex chemical reactions. These reactions usually contain some uncertain parameters and disturbances. In order to efficiently control uncertain chemical processes, a multivariable control algorithm that can handle both uncertain parameters and disturbances needs to be developed (Lee, 2011).

Polymerization process is one of the chemical processes that usually contain some uncertain parameters such as those in reaction rate constants and heat transfer coefficients (Gao et al., 2013). Moreover, the polymerization process usually contains some disturbances such as measurement noises. Since most of the polymerization processes are highly exothermic, inefficient handling of these uncertain parameters and disturbances may lead to unexpected thermal runaway of the system (Shamiri et al., 2013). For this reason, it is necessary to develop an efficient multivariable control algorithm for uncertain polymerization process that is able to ensure both robust stability and constraint satisfaction in the presence of uncertain parameters and

disturbances. Additionally, it should be able to handle fast dynamics of exothermic polymerization reactions.

In this paper, an off-line tube-based robust MPC algorithm is developed. Both robust stability and constraint satisfaction are guaranteed in the presence of uncertain parameters and disturbances. Moreover, all of the optimization problems are solved off-line so the developed MPC algorithm is applicable to fast dynamic processes. This paper is organized as follows. The problem description is presented in Section 2. The off-line tube-based robust MPC algorithm is developed in Section 3. An illustrative example is presented in Section 4. The conclusions are drawn in Section 5.

Nomenclature: Given two subsets X and Y of $\mathbb{R}^n$, Minkowski set addition is defined as $X \oplus Y := \{x+y \mid x \in X, y \in Y\}$ and Minkowski set difference is defined as $X \ominus Y := \{x \mid x \oplus Y \subseteq X\}$.

2. Problem Description

Consider the following discrete-time system subject to uncertain parameters and disturbances

$$x^+ = A^\lambda x + B^\lambda u + w \tag{1}$$

where $x \in \mathbb{R}^n$ is the vector of states, $u \in \mathbb{R}^m$ is the vector of control inputs, $w \in \mathbb{R}^n$ is the vector of bounded disturbances and $x^+ \in \mathbb{R}^n$ is the vector of successor states. The system is subject to the constraints $x \in \mathbb{X}$, $u \in \mathbb{U}$ and $w \in \mathbb{W}$ where $\mathbb{X} \subset \mathbb{R}^n$, $\mathbb{U} \subset \mathbb{R}^m$ and $\mathbb{W} \subset \mathbb{R}^n$ are compact, convex and each set contains the origin as an interior point. The matrices A^λ and B^λ satisfy

$$[A^\lambda \; B^\lambda] \in \text{Conv}\{[A_1 \; B_1], \ldots [A_L \; B_L]\} \tag{2}$$

where Conv denotes the convex hull, $[A_j \; B_j]$ are vertices of the convex hull and L is the number of vertices of the convex hull. Any $[A^\lambda \; B^\lambda]$ can be written as

$$[A^\lambda \; B^\lambda] = \sum_{j=1}^{L} \lambda_j [A_j \; B_j] \tag{3}$$

where $\lambda = [\lambda_1, \lambda_2, \ldots \lambda_L]$ is the vector of uncertain parameters satisfying $\sum_{j=1}^{L} \lambda_j = 1$. The objective is to robustly stabilize the system (1) while satisfying all of the state and input constraints. The presence of additive bounded disturbances means it is only possible to drive the states to the neighborhood of the origin.

3. Off-Line Tube-Based Robust MPC Algorithm

In this section, an off-line tube-based robust MPC algorithm is developed. The trajectories of uncertain systems subject to disturbances are restricted to lie in a sequence of tubes so robust stability and constraint satisfaction are guaranteed. Additionally, all of the optimization problems are solved off-line so the developed

algorithm is applicable to fast dynamic processes. Let the nominal system (the system with no uncertain parameters and disturbances) be defined by

$$\bar{x}^{+} = A\bar{x} + B\bar{u} \tag{4}$$

where $A = \frac{1}{L}\sum_{j=1}^{L} A_j$, $B = \frac{1}{L}\sum_{j=1}^{L} B_j$, $\bar{x} \in \mathbb{R}^n$ is the vector of nominal states and $\bar{u} \in \mathbb{R}^m$ is the vector of nominal control inputs. The predicted nominal states and nominal control inputs when the initial state is $\bar{x}_0$ are denoted by $\bar{\mathbf{x}} := \{\bar{x}_0, \bar{x}_1, \ldots, \bar{x}_N\}$ and $\bar{\mathbf{u}} := \{\bar{u}_0, \bar{u}_1, \ldots, \bar{u}_{N-1}\}$, respectively where N is the prediction horizon. Consider the following difference equation between (1) and (4)

$$x^{+} - \bar{x}^{+} = A(x - \bar{x}) + B(u - \bar{u}) + d \tag{5}$$

where the artificial disturbance d is defined as $d := (A^{\lambda} - A)x + (B^{\lambda} - B)u + w$. Since $x \in \mathbb{X}$, $u \in \mathbb{U}$ and $w \in \mathbb{W}$, it is seen that $d \in \mathbb{D}$ where $\mathbb{D} := (A^{\lambda} - A)\mathbb{X} \oplus (B^{\lambda} - B)\mathbb{U} \oplus \mathbb{W}$. In order to counteract the effect of disturbance, the control law $u = K(x - \bar{x}) + \bar{u}$ is employed where K is the disturbance rejection gain. The system (5) can be rewritten as

$$x^{+} - \bar{x}^{+} = (A + BK)(x - \bar{x}) + d. \tag{6}$$

If the disturbance rejection gain K is chosen such that $(A^{\lambda} + B^{\lambda}K)^T P (A^{\lambda} + B^{\lambda}K) - P < 0$, $\forall [A^{\lambda} \; B^{\lambda}] \in \mathrm{Conv}\{[A_1 \; B_1], \ldots, [A_L \; B_L]\}$ where P is a Lyapunov matrix, then we can bound $x^{+} - \bar{x}^{+}$ by a robust positively invariant set Z satisfying $(A + BK)Z \oplus \mathbb{D} \subseteq Z$, $\forall (x - \bar{x}) \in Z$ and $\forall d \in \mathbb{D}$. It is desirable that Z be as small as possible. The minimal Z can be calculated as

$$Z = \bigoplus_{i=0}^{\infty} (A + BK)^i \mathbb{D} = \mathbb{D} \oplus (A + BK)\mathbb{D} \oplus (A + BK)^2 \mathbb{D} \oplus (A + BK)^3 \mathbb{D} \oplus \ldots\ldots \tag{7}$$

The method to approximate the minimal Z in (7) can be found in Raković et al. (2005). In order to ensure the satisfaction of the original state and input constraints $x \in \mathbb{X}$ and $u \in \mathbb{U}$, the tighter constraint sets for the nominal system (4) are employed $\bar{x}_i \in \mathbb{X} \ominus Z$, $\bar{u}_i \in \mathbb{U} \ominus KZ$ for $i \in \{0, \ldots, N-1\}$. In order to ensure robust stability, an additional terminal constraint is employed $\bar{x}_N \in \bar{X}_f \subset \mathbb{X} \ominus Z$ where $\bar{X}_f$ is the terminal constraint set satisfying the usual assumptions (Mayne et al., 2005). Since we can bound $x^{+} - \bar{x}^{+}$ by a robust positively invariant set Z, we can control the nominal system $\bar{x}^{+} = A\bar{x} + B\bar{u}$ in such a way that the uncertain system with disturbance $x^{+} = A^{\lambda}x + B^{\lambda}u + w$ is robustly stabilized while all of the original state and control

constraints are satisfied. At each sampling time, the state x is measured and the following optimization problem is solved on-line

$$\min_{\bar{x}_0,\bar{\mathbf{u}}} \sum_{i=0}^{N-1} \frac{1}{2}(\bar{x}_i^T Q \bar{x}_i + \bar{u}_i^T R \bar{u}_i) + \frac{1}{2}\bar{x}_N^T P_f \bar{x}_N \tag{8}$$

$$\text{s.t. } x \in \bar{x}_0 \oplus Z \tag{9}$$

$$\bar{x}_{i+1} = A\bar{x}_i + B\bar{u}_i,\ i \in \{0,\ldots,N-1\} \tag{10}$$

$$\bar{x}_i \in \mathbb{X} \ominus Z,\ \bar{u}_i \in \mathbb{U} \ominus KZ,\ i \in \{0,\ldots,N-1\} \tag{11}$$

$$\bar{x}_N \in \bar{X}_f \tag{12}$$

where Q, R and P_f are positive definite weighting matrices. Then, the control law $u = K(x - \bar{x}) + \bar{u}$, $\bar{x} = \bar{x}_0$, $\bar{u} = \bar{u}_0$ is implemented to the process.

On-line tube-based robust MPC is computationally demanding because the on-line optimization problem (8) must be solved at each sampling time. The recent advances in multi-parametric optimization (Kvasnica et al., 2004) make it possible to reduce such high on-line computational time. In order to reduce on-line computational burdens, off-line tube-based robust MPC can be formulated as follows

Algorithm 3.1

Off-line: Solve the optimization problem (8) off-line using the Multi-Parametric Toolbox (Kvasnica et al., 2004) to find the explicit nominal control inputs $\bar{u}$ corresponding to the regions of $\bar{x}$.

On-line: At first sampling time ($t = 0$), measure the state x and find $\bar{u}$ corresponding to the region of x (at the first sampling time $x = \bar{x}$). Apply the control law $u = \bar{u}$ to the process and calculate $\bar{x}^+$ from $\bar{x}^+ = A\bar{x} + B\bar{u}$.

At each sampling time ($t > 0$), find $\bar{u}$ corresponding to the region of $\bar{x}$ which is calculated from the previous step. Measure the state x and apply the control law $u = K(x - \bar{x}) + \bar{u}$ to the process. Then, calculate $\bar{x}^+$ from $\bar{x}^+ = A\bar{x} + B\bar{u}$.

4. An Illustrative Example

This section illustrates the implementation of the developed off-line tube-based robust MPC algorithm. The polymerization reaction is assumed to take place in a continuous stirred tank reactor where a cooling coil is used to remove heat from the exothermic reaction. The reaction rate constant (k_o) and the heat of reaction (ΔH_{rxn}) are

considered to be two uncertain parameters. The behaviour of the reactant concentration ($\overline{C}_A$) and the reactor temperature ($\overline{T}$) can be described as

$$\begin{bmatrix} \overline{C}_A(k+1) \\ \overline{T}(k+1) \end{bmatrix} = \begin{bmatrix} 0.85-0.0986\alpha(k) & -0.0014\alpha(k) \\ 0.9864\alpha(k)\beta(k) & 0.0487+0.01403\alpha(k)\beta(k) \end{bmatrix} \begin{bmatrix} \overline{C}_A(k) \\ \overline{T}(k) \end{bmatrix} + \begin{bmatrix} 0.15 & 0 \\ 0 & -0.912 \end{bmatrix} \begin{bmatrix} \overline{C}_{A,F}(k) \\ \overline{F_C}(k) \end{bmatrix} + \begin{bmatrix} 1 \\ 1 \end{bmatrix} 0.01\sin k \tag{13}$$

Where $\overline{C}_{A,F}(k)$ is the feed concentration of reactant and $\overline{F_C}(k)$ is the coolant flow rate. The uncertain parameters $1 \le \alpha(k) = k_o / 10^9 \le 10$ and $1 \le \beta(k) = -\Delta H_{rxn} / 10^7 \le 10$ are randomly time-varying within the predefined range. The state constraint is $\overline{T}(k) \le 7$ K. The input constraints are $\left|\overline{C}_{A,F}(k)\right| \le 0.1$ kmol/m^3 and $\left|\overline{F_C}(k)\right| \le 1$ m^3/min. Figure 1 shows the regions of state computed off-line by Algorithm 3.1.

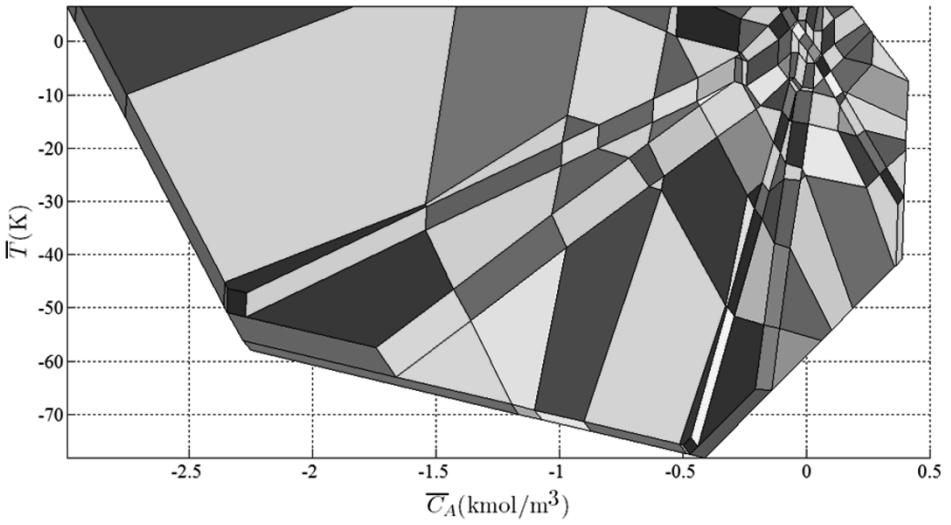

Figure 1 The regions of state computed off-line

Figure 2 shows the state trajectories. The infeasible region of the state constraint is shown in yellow. A sequence of tubes (Z) are shown in green. The trajectory of the uncertain system with disturbances (13) is shown in red line. The trajectory of the nominal system (the system with no uncertain parameters and disturbances) is shown in black line. Starting from the initial point of $(0.2,\ 5)$, the trajectory of uncertain system with disturbances is restricted to lie in a sequence of tubes so robust stability and constraint satisfaction are guaranteed.

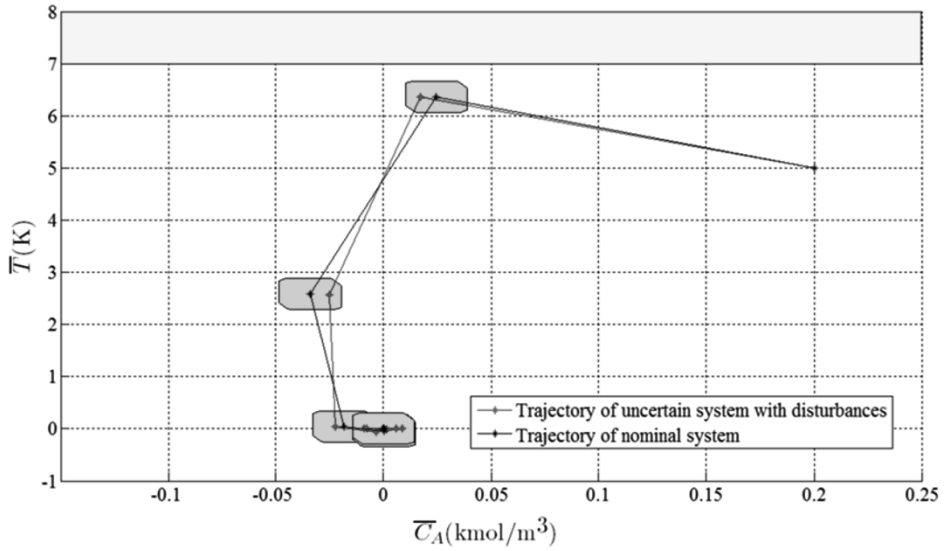

Figure 2 The state trajectories

5. Conclusions

In this paper, off-line tube-based robust MPC is developed. Robust stability and constraint satisfaction are guaranteed in the presence of both uncertain parameters and disturbances. The developed algorithm is applied to an illustrative example of uncertain continuous stirred tank reactor where highly exothermic polymerization reactions occur. The results show that the state trajectory is restricted to lie in a sequence of tubes.

Acknowledgement

This research has been supported by National Research University Project, Office of Higher Education Comission (WCU-041-EN-57). This research project is financially supported by Mahidol University.

References

S.H. Gao, J.S. Wang, X.W. Gao, 2013, Modeling and advanced control method of PVC polymerization process, J. Process contr., 23, 5, 664-681.

M. Kvasnica, P. Grieder, M. Baotić, M. Morari, 2004, Multi-Parametric Toolbox (MPT), Hybrid Systems: Computation and Control, 2993, 448-462.

J.H. Lee, 2011, Model Predictive Control: Review of the three decades of development, Int. J. Control Autom., 9, 3, 415-424.

D.Q. Mayne, M.M. Seron, S.V. Raković, 2005, Robust model predictive control of constrained linear systems with bounded disturbances, Automatica, 41, 2, 219-224.

S.V. Raković, E.C. Kerrigan, K.I. Kouramas, D.Q. Mayne, 2005, Invariant approximations of the minimal robust positively invariant set, IEEE T. Automat. Contr., 50, 3, 406-410.

A. Shamiri, M.A. Hussain, F.S. Mjalli, N. Mostoufi, S. Hajimolana, 2013, Dynamics and predictive control of gas phase propylene polymerization in fluidized bed reactors, Chinese J. Chem. Eng., 21, 9, 1015-1029.

Krist V. Gernaey, Jakob K. Huusom and Rafiqul Gani (Eds.), 12th International Symposium on Process Systems Engineering and 25th European Symposium on Computer Aided Process Engineering.
31 May - 4 June 2015, Copenhagen, Denmark.

Optimization Based Constrained Unscented Gaussian Sum Filter

Krishna Kumar Kottakki, Sharad Bhartiya, Mani Bhushan

Department of Chemical Engineering; Indian Institute of Technology Bombay; Mumbai, India
krishnadfs@gmail.com, bhartiya@che.iitb.ac.in, mbhushan@iitb.ac.in

Abstract

Bayesian state estimation for constrained nonlinear systems involves two main issues: (i) appropriate representation of the underlying non-Gaussian densities, and (ii) use of appropriate techniques to bound the estimates so that they satisfy the give constraints. In this work we present a new constrained state estimation approach, named as Optimization based Constrained Unscented Gaussian Sum Filter. The proposed approach uses Unscented Gaussian Sum Filter to represent the non-Gaussian densities and an optimization approach to incorporate the state constraints. Benefits of the proposed approach are illustrated by applying it to a benchmark case study.

Keywords: Unscented transformation, Unscented Gaussian sum filter, Sum of Gaussians

1. Introduction

Recursive Bayesian estimation for nonlinear dynamical systems uses process and measurement models along with available process measurements to obtain conditional density of states. These process models are often derived from first principles, that is material and energy balances, and are typically nonlinear. Further, the process states inherently satisfy thermodynamic properties/constraints, for e.g. mole fraction of individual species/components in a multi component mixture are positive and their sum is unity. Hence, a practical nonlinear constrained state estimation approach should have the following two features: (i) an ability to approximate non-Gaussian densities arising out of nonlinear transformation or non-Gaussian noise, and (ii) an ability to incorporate constraints on the state estimates.

Several nonlinear state estimation approaches such as Extended Kalman Filter (EKF) (Anderson and Moore, 1979), Unscented Kalman Filter (UKF) (Julier and Uhlmann, 2004), Ensemble Kalman Filter (EnKF) (Gillijns et al., 2006), Gaussian Sum Filters (Sorenson and Alspach, 1971) and Particle Filters (Arulampalam et al., 2002) have been reported in literature that account for the nonlinear transformations and/or the non-Gaussian nature of the densities. While EKF involves linearization of the nonlinear process and measurement models, other approaches utilize deterministically or randomly chosen samples thereby avoiding the explicit linearization. Among these sampling based approaches, UKF is based on unscented transformation (UT) that requires only $(2n+1)$ deterministically chosen sigma points, with n being the number of states. This use of limited number of samples opens up possibilities of applying UKF for solving practical (industrial) state estimation problems (Kolas et al., 2009; Vachhani et al., 2006). However, similar to Kalman Filter (Kalman, 1960), UKF also assumes that the underlying probability densities are Gaussian, an assumption commonly violated for nonlinear systems and/or non-Gaussian noise.

In literature, a few modifications of UKF have been proposed that avoid the Gaussianity assumption. In particular, Gaussian-sum UKF (GS-UKF) (Šimandl and Duník, 2006) is based on the

result that a sum of Gaussians can approximate any density to an arbitrary degree of accuracy (Sorenson and Alspach, 1971). GS-UKF uses $N(2n+1)$ sigma points to obtain a sum of Gaussians based representation of non-Gaussian prior, where N refers to the number of Gaussians used and is a user defined parameter. Recently Unscented Gaussian Sum Filter (UGSF) (Kottakki et al., 2014) has been proposed that enables a sum of Gaussians representation of the non-Gaussian prior using only $2n+1$ sigma points. In particular, the computational effort in UGSF is similar to that in UKF and it can thus be potentially applied to practical systems (Kottakki et al., 2014). The sum of Gaussians prior in UGSF is subsequently updated using Bayes' rule. The updated Gaussian sum posterior in UGSF is reapproximated as a single Gaussian at the next time instant using the first two moments of the updated Gaussian sum density. This reapproximation avoids degeneracy of the individual Gaussians in the sum of Gaussians representation. Implementation on several case studies demonstrated superior performance of UGSF when compared to UKF. While UGSF addresses the issue of non-Gaussianity of the prior density, it does not incorporate constraints on the state estimates making them potentially infeasible and thus unusable.

In this work, we propose an extension of the UGSF approach so that it can effectively incorporate state constraints in the estimation procedure. This is achieved by modifying the sigma point generation step to incorporate constraints as well as using explicit constrained optimization formulation to obtain the posterior density. The resulting approach is labeled as Optimization Based Constrained Unscented Gaussian Sum Filter (OCUGSF). In particular, the proposed OCUGSF solves $2n+1$ optimization problems to obtain a constrained posterior estimate.

Organization of this paper is as follows: Problem statement with a brief summary of elements used in the proposed method is presented in Section 2 and Section 3, respectively. Benefits of the proposed OCUGSF are demonstrated by comparing its performance with other state estimation techniques on a benchmark three state isothermal batch reactor case study in Section 4. The paper is concluded in Section 5.

2. Problem Statement

Consider a sampled data system consisting of nonlinear process dynamics, a linear measurement function and interval constraints on the states as,

$$x(t_k) = x(t_{k-1}) + \int_{t_{k-1}}^{t_k} f(x(t),u(t))dt + w_k, \quad w_k \sim \mathcal{N}(0,Q) \tag{1}$$

$$y_k = Hx(t_k) + v_k, \; v_k \sim \mathcal{N}(0,R) \tag{2}$$

$$d_k \leq x_k \leq e_k \tag{3}$$

where, $x(t) \in \mathbb{R}^n$, $u(t) \in \mathbb{R}^p$, represent the state and input vectors at time t while $y_k \in \mathbb{R}^m$, $w_k \in \mathbb{R}^n$, $v_k \in \mathbb{R}^m$ represent observation, state noise and measurement noise, respectively at time t_k. Function $f : \mathbb{R}^n \times \mathbb{R}^p \to \mathbb{R}^n$ represents the nonlinear state dynamics and $H \in \mathbb{R}^{mxn}$ represents the linear observation model. Measurements y_k are assumed to be available at regularly spaced sampling instants t_k, at $k = 0,1,2,3,\ldots$ with $T_s = t_k - t_{k-1}$ being the sampling interval. For ease of notation, we define $x_k \triangleq x(t_k)$. Eq.(3) specifies the interval constraints on each component of state vector x. The problem is to find a point estimate for x_k, whose dynamics are described in Eq.(1), using available measurements $Y_k = y_1,\ldots,y_k$, in Eq.(2) subject to the interval constraints given in Eq.(3). We limit our attention to the linear measurement model Eq.(2) for ease of presentation. For nonlinear measurement models, the UGSF approach can be extended (Kottakki et al., 2014) using ideas presented in the current work. Now we briefly review the proposed OCUGSF for the given system (Eqs.(1), (2)) and the state constraints (Eq.(3)).

3. Optimization Based Constrained Unscented Gaussian Sum Filter (OCUGSF)

The proposed OCUGSF approach uses a three step framework to obtain constrained state estimate for the problem (Eqs.(1) to (3)). These steps are: (i) use of Interval Constrained Unscented Transformation (ICUT) approach (Vachhani et al., 2006) to generate the constrained sigma points from the given posterior density, (ii) propagation of sigma points through the process model, and (iii) a constrained optimization based update step. These are discussed next.

3.1. Interval Constrained Unscented Transformation (ICUT) Based Sigma Point Generation:

Given that the random variable x_{k-1} has a Gaussian distribution with mean $\hat{x}_{k-1|k-1}$ and covariance $P_{k-1|k-1}$ at time t_{k-1}, the Interval Constrained Unscented Transformation approach deterministically selects $2n+1$ constrained sigma points and corresponding weights as (Vachhani et al., 2006),

$$\chi^{(i),c}_{k-1|k-1} = \begin{cases} \hat{x}_{k-1|k-1}, & w^{(i),c} = b_{k-1}, \quad i = 0 \\ \hat{x}_{k-1|k-1} + \theta_{i,k-1}[\sqrt{P_{k-1|k-1}}]i, & w^{(i),c} = a_{k-1} + \theta_{i,k-1}b_{k-1}, \quad i = 1,\ldots,n \\ \hat{x}_{k-1|k-1} - \theta_{i,k-1}[\sqrt{P_{k-1|k-1}}]i{-}n, & w^{(i),c} = a_{k-1} + \theta_{i,k-1}b_{k-1}, \ i = n+1,\ldots,2n \end{cases} \tag{4}$$

$$a_{k-1} = \frac{(2\kappa - 1)}{2(n+\kappa)\big[\sum_{i=1}^{2n}\theta_{i,k-1} - (2n+1)\sqrt{n+\kappa}\big]}, \ \ b_{k-1} = \frac{1}{2(n+\kappa)} - a_{k-1}\sqrt{n+\kappa} \tag{5}$$

$$\theta_{i,k-1} = \min_{1\le j\le n}(\Theta_{j,i}), \ \ i = 1,2,\ldots,2n \tag{6}$$

where, for $j = 1,2,\ldots,n;\ i = 1,2,\ldots,2n$

$$\Theta_{j,i} \triangleq \begin{cases} \sqrt{n+\kappa} & \text{if } \ S_{j,i} = 0 \\ \min\left(\sqrt{n+\kappa}, \frac{e_{j,k-1} - \hat{x}_{j,k-1|k-1}}{S_{(j,i)}}\right) & \text{if } \ S_{j,i} > 0 \\ \min\left(\sqrt{n+\kappa}, \frac{d_{j,k-1} - \hat{x}_{j,k-1|k-1}}{S_{(j,i)}}\right) & \text{if } \ S_{j,i} < 0 \end{cases} \tag{7}$$

$$\text{with } \ S \triangleq \begin{bmatrix} \sqrt{P_{k-1|k-1}} & -\sqrt{P_{k-1|k-1}} \end{bmatrix} \tag{8}$$

In Eq.(4), $\chi^{(i),c}_{k-1|k-1}, w^{(i),c}$ represent the i^{th} constrained sigma point and its corresponding weight, respectively. It can be noted that these sigma points have been projected away from the mean using a factor $\theta_{i,k-1}$. Since this factor has been chosen according to the state constraints (Eqs.(6) to (8)), the sigma points will be feasible with respect to the interval constraints Eq.(3). Further, if the constraints are not active ($d_k = -\infty$ and $e_k = +\infty$), the expressions (Eqs.(4) to (8)) result in unconstrained sigma points obtained using UT as have been reported in the literature (Julier and Uhlmann, 2004; Vachhani et al., 2006).

3.2. Prediction Step:

The constrained sigma points obtained in Eq.(4) are then transformed through the process model (Eq.(1)) to obtain the predicted sigma points as follows:

$$\chi^{(i),c}_{k|k-1} = \chi^{(i),c}_{k-1|k-1} + \int_{t_{k-1}}^{t_k} f(x(t),u(t))dt, \ \ i = 0,\ldots,2n \tag{9}$$

Without loss of generality, it is assumed that since the sigma points generated by Eq.(4) satisfy the interval constraints, the predicted sigma points $\chi^{(i),c}_{k|k-1}$ (Eq.(9)) will also satisfy these constraints. The proposed OCUGSF uses the UGSF design choices (Kottakki et al., 2014) to obtain non-Gaussian prior as a sum of Gaussians. These design choices are: (i) Number of Gaussians in prior

is the same as the number of sigma points i.e $2n+1$, (ii) $\chi^{(i),c}_{k|k-1}$ is the mean of i^{th} Gaussian in the sum of Gaussians prior, (iii) the covariance of each i^{th} Gaussian, $i=0,\ldots,2n$ is identical and equal to the process noise covariance Q and (iv) weight $w^{(i),c}$ of the i^{th} sigma point is the weight of i^{th} Gaussian, $i=0,\ldots,2n$ in the sum of Gaussians. These design choices result in a constrained non-Gaussian prior:

$$p_{x_k|Y_{k-1}}(\xi_k|Y_{k-1}) = \sum_{i=0}^{2n} w^{(i),c} \frac{1}{(2\pi)^{n/2}|Q|^{1/2}} \exp\left\{\frac{-1}{2}[\xi_k - \chi^{(i),c}_{k|k-1}]^T Q^{-1}[\xi_k - \chi^{(i),c}_{k|k-1}]\right\} \tag{10}$$

Now we illustrate a procedure to obtain a constrained posterior corresponding to the prior (Eq.(10)), measurement model (Eq.(2)) and the state constraints (Eq.(3)).

3.3. Main Contribution: Constrained Update Using Optimization

For the linear measurement model with Gaussian uncertainties (Eq.(2)), the likelihood density is given as,

$$p_{y_k|x_k,Y_{k-1}}(\zeta_k|\xi_k,Y_{k-1}) = \frac{1}{(2\pi)^{m/2}|R|^{1/2}} \exp\left\{\frac{-1}{2}[\zeta_k - H\xi_k]^T R^{-1}[\zeta_k - H\xi_k]\right\} \tag{11}$$

where $\zeta_k \in R^m$ is the random variable corresponding to the measurement y_k. Since the above likelihood density is an unconstrained Gaussian, direct application of Bayes' rule with the non-Gaussian prior (Eq.(10)) and likelihood densities (Eq.(11)), can yield an unconstrained sum of Gaussians posterior density (Vachhani et al., 2006). To avoid this situation, we propose to update the means of the individual Gaussians in the sum of Gaussians prior by using a constrained optimization formulation. This formulation replaces the conventional Bayes' rule based update step as presented by Kottakki et al. (2014). Thus the constrained updated mean $(\chi^{(i),c}_{k|k})$ and updated covariances (Ξ) of i^{th} individual Gaussians are given by,

$$\chi^{(i),c}_{k|k} = \underset{\chi_k : d_k \le \chi_k \le e_k}{arg\ min} \left[(y_k - H\chi_k)^T R^{-1}(y_k - H\chi_k) + (\chi_k - \chi^{(i),c}_{k|k-1})^T Q^{-1}(\chi_k - \chi^{(i),c}_{k|k-1})\right] \tag{12}$$

$$\Xi = Q - QH^T[HQH^T + R]^{-1}HQ \tag{13}$$

while the updated weights $\delta^{(i)}_k$ are given by,

$$\tilde{w}^{(i),c}_k = w^{(i),c} \exp\left\{-\frac{1}{2}(y_k - H\chi^{(i,c)}_{k|k-1})^T[HQH^T + R]^{-1}(y_k - H\chi^{(i,c)}_{k|k-1})\right\},\ i=0,\ldots,2n \tag{14}$$

$$\delta^{(i),c}_k = \tilde{w}^{(i),c}_k \Big/ \sum_{j=0}^{2n} \tilde{w}^{(j),c}_k,\quad i=0,\ldots,2n \tag{15}$$

Conventional Gaussian sum filters often encounter degeneracy in weights in subsequent iterations (Sorenson and Alspach, 1971). The proposed OCUGSF overcomes this problem by approximating the sum of Gaussians posterior density as a single Gaussian for subsequent step of sigma point generation at the next time instant (Kottakki et al., 2014). The mean and covariance of this single Gaussian are chosen to be the mean and covariance of the sum of Gaussians posterior density which are given as:

$$\hat{x}^c_{k|k} = \sum_{i=0}^{2n}\left[\delta^{(i),c}_k \chi^{(i),c}_{k|k}\right],\ P^c_{k|k} = \sum_{i=0}^{2n} \delta^{(i),c}_k \left[\Xi + [\chi^{(i),c}_{k|k} - \hat{x}^c_{k|k}][\chi^{(i),c}_{k|k} - \hat{x}^c_{k|k}]^T\right] \tag{16}$$

To summarize, Eqs.(4) to (16) illustrate the steps involved in the proposed OCUGSF approach for obtaining the constrained posterior moments at k^{th} time instant for the given posterior moments at $(k-1)^{th}$ time instant.

It can be shown that if the state constraints are not active, then the proposed OCUGSF approach reduces to UGSF approach. Further, if the non Gaussian prior density (Eq.(10)) is approximated by a single Gaussian instead of sum of Gaussians, then for the unconstrained and the constrained scenarios, OCUGSF reduces to the UKF (Julier and Uhlmann, 2004) and the Unscented Recursive Nonlinear Dynamic Data Reconciliation (URNDDR) (Vachhani et al., 2006; Narasimhan and Rengaswamy, 2009) approaches, respectively.

4. Results and Discussions

A three state isothermal batch process is chosen to validate the performance of proposed OCUGSF. The process involves gas-phase reversible reactions under isothermal conditions, $A \rightleftharpoons B+C,\ 2B \rightleftharpoons C$. The dynamical process and measurement models are (Kolas et al., 2009):

$$\begin{bmatrix} \dot{x}_1 \\ \dot{x}_2 \\ \dot{x}_3 \end{bmatrix} = \begin{bmatrix} -k_{c_1}x_1 + k_{c_2}x_2x_3 \\ k_{c_1}x_1 - k_{c_2}x_2x_3 - 2k_{c_3}x_2^2 + 2k_{c_4}x_3 \\ k_{c_1}x_1 - k_{c_2}x_2x_3 + k_{c_3}x_2^2 - k_{c_4}x_3 \end{bmatrix} \tag{17}$$

$$y_k = \begin{bmatrix} 32.84 & 32.84 & 32.84 \end{bmatrix} \begin{bmatrix} x_1 & x_2 & x_3 \end{bmatrix}^T \tag{18}$$

Eqs.(17) and (18) represent the nonlinear process model and linear measurement model, respectively. In Eq.(17), x_1, x_2 and x_3 represent the concentrations of the species A, B and C, respectively, and k_{c_i} $(i = 1,\ldots,4)$ represents the rate constant for i^{th} reaction. True states were generated for 100 different noise realizations consisting of 720 sampling time instants, i.e. for 180 seconds. The parameters used for true state generation and for state estimation are reported in Table 1.

Table 1: Process and simulation parameters for isothermal batch reactor (Kolas et al., 2009)

$x_0 = \begin{bmatrix} 0.5 & 0.05 & 0 \end{bmatrix}$	$k_c = \begin{bmatrix} 0.5 & 0.05 & 0.2 & 0.01 \end{bmatrix}$	$P_0 = 4I_{3\times3}$
$\Delta t = 0.25 seconds$	$Q = diag(0.001^2 \ \ 0.001^2 \ \ 0.001^2)$	$\hat{x}^2_{0\|0} = \begin{bmatrix} 0.6 & 0.1 & 0.05 \end{bmatrix}^T$
$\hat{x}^1_{0\|0} = x_0$	$d_k = \begin{bmatrix} 0.0129 & 0.0743 & 0.0243 \end{bmatrix}^T$	$e_k = \begin{bmatrix} 0.4758 & 0.3575 & 0.6601 \end{bmatrix}^T$

The performance of estimation algorithms, namely, OCUGSF, URNDDR, UGSF, and UKF are investigated for two different scenarios of initial posterior densities, i.e Case I: $\hat{x}_{0|0} = \hat{x}^1_{0|0}$ and $P_{0|0} = P_0$, and Case II: $\hat{x}_{0|0} = \hat{x}^2_{0|0}$ and $P_{0|0} = P_0$. Average of sum of the square roots of the estimation errors (ASSREE) was chosen to compare the performance of estimation algorithms and is defined as: $\text{ASSREE} = \frac{1}{100}\sum_{l=1}^{100}\left[\sqrt{\frac{1}{720}\sum_{k=1}^{720}[\hat{x}^{(l)}_{k|k} - x^{(l)}_k]^T[\hat{x}^{(l)}_{k|k} - x^{(l)}_k]}\right]$. Here $x^{(l)}_k$ and $\hat{x}^{(l)}_{k|k}$ represent the true and the estimated states for the l^{th} simulation run, respectively. The ASSREE values for four estimation algorithms along with their computational times are reported in Table 2 for both Cases I and II. The average number of constraint violations is also reported under the heading #violations in this Table. From the ASSREE values reported in Table 2, it can be observed that the proposed OCUGSF results in superior state estimates compared to the other three algorithms with higher, but acceptable computational cost. It can also be noted that OCUGSF estimates have satisfied the state constraints for all the time instants across the simulation runs. Even though the URNDDR approach has reported no constraint violation, the Gaussian approximation of non-Gaussian prior (Narasimhan and Rengaswamy, 2009) has resulted in inferior performance compared to OCUGSF. For UGSF, while the prior approximation is non-Gaussian, it has violated the state constraints at several time instances as it is an unconstrained estimator. Gaussian approximation of non-Gaussian prior and unconstrained state estimation has resulted in inferior performance of UKF. State x_2 tracking for one particular simulation run has been shown in Fig. 1 and illustrates the superior performance of OCUGSF over UKF, UGSF and URNDDR approaches.

Table 2: Performance comparison for three state isothermal batch reactor

	Case-I ($\hat{x}_{0\|0} = x_0$)			Case-II ($\hat{x}_{0\|0} = \hat{x}^2_{0\|0}$)		
Algorithm	ASSREE	#violations	CPU Seconds	ASSREE	#violations	CPU Seconds
UKF	159.39	705	0.0271	155.29	705	0.0320
UGSF	5.9164	645	0.0273	6.0094	643	0.0322
URNDDR	3.5503	0	0.1131	3.4396	0	0.1781
OCUGSF	2.1247	0	0.1400	2.7890	0	0.2172

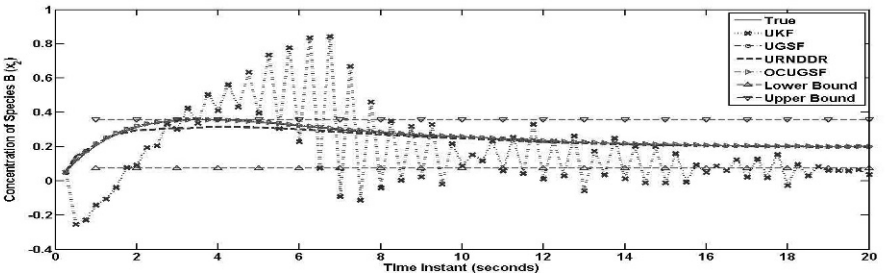

Figure 1: Tracking of state x_2 by UKF, UGSF, URNDDR and OCUGSF for Case-I ($\hat{x}_{0|0} = x_0$)

5. Conclusions

In this work, a new approach, labeled OCUGSF is proposed for constrained state estimation of nonlinear dynamical systems. The approach uses the attractive features of UGSF, in better representation of non-Gaussian densities using a sum of Gaussians, and explicitly incorporates the state constraints. Comparison with UKF, UGSF and URNDDR on a literature case study demonstrated the superior performance of the proposed OCUGSF approach.

References

Anderson, B. D. O., Moore, J. B., 1979. Optimal filtering. Prentice-Hall Englewood Cliffs, N.J.

Arulampalam, M. S., Maskell, S., Gordon, N., Clapp, T., 2002. A tutorial on particle filters for online nonlinear/non-gaussian bayesian tracking. IEEE Transactions on Signal Processing 50 (2), 174–188.

Gillijns, S., Mendoza, O., Chandrasekar, J., De Moor, B. L. R., Bernstein, D., Ridley, A., 2006. What is the ensemble kalman filter and how well does it work? American Control Conference (2006), 4448–4453.

Julier, S., Uhlmann, J., March 2004. Unscented filtering and nonlinear estimation. Proceedings of the IEEE 92 (3), 401 – 422.

Kalman, R., 1960. A new approach to linear filtering and prediction problems. Transactions of the ASME–Journal of Basic Engineering 82, 35–45.

Kolas, S., Foss, B. A., Schei, T., 2009. Constrained nonlinear state estimation based on the ukf approach. Computers and Chemical Engineering 33 (8), 1386 – 1401.

Kottakki, K. K., Bhartiya, S., Bhushan, M., 2014. State estimation of nonlinear dynamical systems using nonlinear update based unscented gaussian sum filter. Journal of Process Control 24 (9), 1425 – 1443.

Narasimhan, S., Rengaswamy, R., 2009. Reply to comments on robust and reliable estimation via unscented recursive nonlinear dynamic data reconciliation (urnddr). Journal of Process Control 19 (4), 719 – 721.

Sorenson, H., Alspach, D., 1971. Recursive bayesian estimation using gaussian sums. Automatica 7 (4), 465 – 479.

Vachhani, P., Narasimhan, S., Rengaswamy, R., 2006. Robust and reliable estimation via unscented recursive nonlinear dynamic data reconciliation. Journal of Process Control 16 (10), 1075 – 1086.

Šimandl, M., Duník, J., 2006. Sigma point gaussian sum filter design using square root unscented filters. Proceedings of the 16th IFAC World Congress 16 (1), 1000–1005.

Krist V. Gernaey, Jakob K. Huusom and Rafiqul Gani (Eds.), 12th International Symposium on Process Systems Engineering and 25th European Symposium on Computer Aided Process Engineering.
31 May – 4 June 2015, Copenhagen, Denmark

Systematic Control Structure Evaluation of Two-Stage-Riser Fluidized Catalytic Pyrolysis Processes

Zhihong Yuan[a], Ping Wang[b], Mario R. Eden[a]

[a]*Department of Chemical Engineering, Auburn University, Auburn, AL 36849, USA*
[b]*Department of Information and Control Engineering, China University of Petroleum (East China), Tsingdao 266580, Shandong, China*

Abstract

Control structure selection plays an important role in achieving an effective control system. Through the application of open-loop and closed-loop steady-state multiplicities, the primary goal of this paper is to obtain the best control structure from candidates selected based on heuristic reasoning for a demonstration Two-Stage-Riser Fluidized Catalytic Pyrolysis (TSRFCP) process which can maximize propylene yield without any significant losses in gasoline/diesel yields. Steady state multiplicity analysis can not only elucidate the relationships between potential manipulated variables and controlled variables over a large operational horizon but can also identify the perfect control action for tackling uncertainties in each control structure. It is illustrated that output temperatures from the two risers and the regenerator controlled by two regenerated catalyst flow rates and the cooling water flow rate, respectively, which have the best controllability characteristics and most superior dynamic behavior, are the most suitable control structure for further control system design of the studied process.

Keywords: Control structures, multiplicity, control actions, TSRFCP process.

1. Introduction

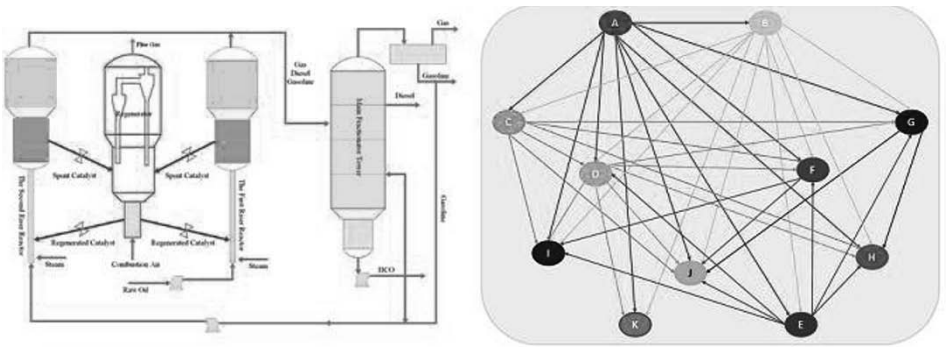

Figure 1. Schematic of the TSRFCP process and the relevant 11-lump kinetic network. (A: Heavy oil; B: Diesel; C: Alkenes; D: Aromatics; E: Paraffins; F: Butane+Propane; G: Butene; H: Propylene; I: Ethylene; J: Ethane+Methane+Hydrogen; K: Coke)

Two-Stage-Riser Fluidized Catalytic Pyrolysis (TSRFCP) for maximizing propylene yield, which applies a subsidiary riser operated under appropriate condition to reprocess crude gasoline from the main riser fed with fresh feedstock, is recognized as an efficient route to handle the expanded propylene supply/demand gap and to moderate the increased propylene price (Li *et al*., 2007). Due to strong interactions between the

exothermic reactions of catalyst regeneration in the regenerator and endothermic pyrolysis reactions in the two risers, the TSRFCP process exhibits complex nonlinear behavior which may lead to difficulties in operation. Furthermore, product quality requirements along with environmental/safety considerations drive the TSRFCP process to operate close to its operational boundaries such as minimization of dry gas yield, or maximization of propylene yield. Clearly, to increase industrial adaption, high-efficient control mechanisms for the TSRFCP process are greatly needed. Selection of the proper primary control structure, to some extent, is far more important than the detailed algorithm used in the design of the actual controllers. Based on the detailed nonlinear model of the TSRFCP process (Liu, 2008; Wang *et al*., 2014) and according to the selected control structures based on heuristic reasoning, this paper focuses on the evaluation of the selected candidates for the TSRFCP process through analyzing the steady-state multiplicity.

2. Control structure candidates

As illustrated by Figure 1, the complex pyrolysis reactions take place in two risers sharing the same regenerator. Fresh feedstock (raw oil) dispersed with steam is fed to the first-stage-riser and subjected to a certain degree of endothermic pyrolysis reactions. The recycling oil (crude gasoline and HCO) from downstream separation units dispersed with steam is introduced into the second-stage-riser under more severe pyrolysis conditions to maximize the selectivity towards light olefins and to increase the octane number of the naphtha. Changes in products from the first-stage-riser can alter the composition and properties of the feedstock for the second-stage-riser and thus affect the final product quality. For the TSRFCP process, spent catalysts with low activity and selectivity, which are separated from the gas products at the end of each riser to suppress further thermal and catalytic pyrolysis, are regenerated in the regenerator. The regenerated catalyst flows through two standpipes from the regenerator to the bottom of each riser. In the studied TSRFCP process, the regenerator is mainly comprised of two distinct regions, i.e. the dense region and the dilute region. In general, the regenerator is designed with a high-efficiency combustor and an external catalyst cooler. The combustor, where the gas and the solid flows are fast-fluidized with excess air, ensures that the coke content of regenerated catalyst is maintained at a very low level. The cooler, on the other hand, is used to remove the excess heat in the regenerator above the requirement for heat balance. Thus, the cooler helps to control regenerator temperature within a desired range especially when the feedstock contains a high percentage of carbon.

With regard to the integrated model of the TSRFCP process, the 11-lump kinetic model and the energy/mass balance equations, which were validated by experimental data sets, are two main components. Because of the short residence time of oil vapour in the two risers (1.1s~1.5s), the two risers are modelled as pseudo-steady state plug flow reactors. The regenerator system is modelled as two continuous stirred-tank reactors (CSTRs) in series. In other words, the high-efficiency combustor and the dense region of the fluidized bed reactor are modelled as CSTRs, and these parts are connected by internal circulated catalyst flows. In total, the integrated model has 34 differential equations. The detailed models can be found in (Liu, 2008; Wang *et al*., 2014).

The selection of control structure traditionally contains manipulated variable (input) selection, measurement (output) selection, and control configuration (input-output partitioning and pairing) selection (Skogestad, 2004). Compared with the control

structure selection, the control structure evaluation, which is the main purpose of this paper, is less complex. In this paper, candidates for the manipulated/controlled variables are decided based on heuristic reasoning. From existing contributions to the control structure selection of conventional fluidized catalytic cracking units and the knowledge of open-loop bifurcation analysis, a total of six control structure candidates are generated. For the riser system, outlet temperatures, $T_{\mathrm{ris},1|z=1}$ and $T_{\mathrm{ris},2|z=1}$, which have the most significant influences on the product distributions along the two riser reactors, are the controlled variables. These two variables can be controlled by the corresponding regenerated catalyst flowrates, $G_{\mathrm{reg},1}$ and $G_{\mathrm{reg},2}$. Moreover, $T_{\mathrm{ris},1|z=1}$ can also be controlled by the inlet temperature of the crude oil, $T_{\mathrm{oil,in}}$. For the regenerator system, oxygen composition of the flue gas, y_{O2} and outlet temperature, T_{rg2} are two potential controlled variables. Combustion air flowrate, F_{g}, combustion air inlet temperature, $T_{\mathrm{air,in}}$, and cooling water flowrate, F_{c} are three candidates for the manipulated variables. In order to facilitate the subsequent investigations, these six control structure candidates are denoted as follows.

- Control structure 1 (CS1): [$T_{\mathrm{ris},1|z=1}$, $T_{\mathrm{ris},2|z=1}$, T_{rg2}; $G_{\mathrm{reg},1}$, $G_{\mathrm{reg},2}$, F_{c}]
- Control structure 2 (CS2): [$T_{\mathrm{ris},1|z=1}$, $T_{\mathrm{ris},2|z=1}$, T_{rg2}; $G_{\mathrm{reg},1}$, $G_{\mathrm{reg},2}$, F_{g}]
- Control structure 3 (CS3): [$T_{\mathrm{ris},1|z=1}$, $T_{\mathrm{ris},2|z=1}$, T_{rg2}; $G_{\mathrm{reg},1}$, $G_{\mathrm{reg},2}$, $T_{\mathrm{air,in}}$]
- Control structure 4 (CS4): [$T_{\mathrm{ris},1|z=1}$, $T_{\mathrm{ris},2|z=1}$, y_{O2}; $G_{\mathrm{reg},1}$, $G_{\mathrm{reg},2}$, F_{g}]
- Control structure 5 (CS5): [$T_{\mathrm{ris},1|z=1}$, $T_{\mathrm{ris},2|z=1}$, y_{O2}; $G_{\mathrm{reg},1}$, $G_{\mathrm{reg},2}$, F_{c}]
- Control structure 6 (CS6): [$T_{\mathrm{ris},1|z=1}$, $T_{\mathrm{ris},2|z=1}$, T_{rg2}; $T_{\mathrm{oil,in}}$, $G_{\mathrm{reg},2}$, F_{c}]

It is apparent that each control structure has three control loops. All these six control structures have two common controlled variables $T_{\mathrm{ris},1|z=1}$ and $T_{\mathrm{ris},2|z=1}$. The remaining issues are to compare the perfect control actions based on closed-loop steady-state multiplicity analysis to rank these candidates.

3. Closed-loop steady-state multiplicity analysis

The TSRFCP process is described as Differential Algebraic Equations (DAEs) which actually can be reformulated as Eqs (1) and (2) through substituting algebraic equations into differential ones.

$$\dot{\boldsymbol{x}} = \boldsymbol{f}(\boldsymbol{x},\boldsymbol{u}) = \boldsymbol{f}(\boldsymbol{x}) + \sum_{j=1}^{m} \boldsymbol{g}_j(\boldsymbol{x})\boldsymbol{u}_j \tag{1}$$

$$\boldsymbol{y} = \boldsymbol{h}(\boldsymbol{x}) \tag{2}$$

Where $\boldsymbol{x} = [x_1, x_2, ..., x_n]^T \in R^n$ are state variables, $\boldsymbol{u} = [u_1, u_2, ..., u_m]^T \in R^m$ are input variables ($n > m$), $\boldsymbol{y} = [y_1, y_2, ..., y_m]^T \in R^m$ are outputs. $\boldsymbol{f}(\boldsymbol{x})$ and $\boldsymbol{g}(\boldsymbol{x})$ are smooth vector functions, $h_i(x), i = 1, 2...m$ is a smooth scalar function. Closed-loop steady-state multiplicity can provide the control actions each control structure should take for dealing with disturbances and set point changes. In order to do so, Eq (1) can be reformulated as Eqs (3) and (4).

$$\dot{\boldsymbol{X}} = \boldsymbol{f}(\boldsymbol{X}, \boldsymbol{X}_1, \boldsymbol{u}_1, \boldsymbol{u}_2) \tag{3}$$

$$\boldsymbol{X}_1 = \boldsymbol{X}_{1,\mathrm{set}} \tag{4}$$

Where $\mathbf{X} \in R^{n-n_1}$ is a $n - n_1$ dimensional vector of the state variables; $\mathbf{X}_1 \in R^{n_1}$ is a n_1 dimensional vector of the state variables which are assumed as constant through

adjusting the relevant input variables. $u_1 \in R^{m_1}$ is a m_1 dimensional vector of primary manipulated variables; $u_2 \in R^{m-m_1}$ is a $m-m_1$ dimensional vector of the remained manipulated variables. The closed-loop steady-state multiplicity can be achieved through solving Eqs (3) and (4). Relationships between the primary manipulated variables and the remained ones can be simultaneously established. In this paper, $T_{\mathrm{ris},1|z=1}$ and $T_{\mathrm{ris},2|z=1}$ will be kept constant by adjusting the corresponding manipulated variables at the operating point to analyse the closed-loop steady-state multiplicity under different scenarios.

4. Evaluation of the control structure candidates

Table 1. Operating conditions at point A.

Variables	$T_{\mathrm{ris},1\|z=1}$	$T_{\mathrm{ris},2\|z=1}$	T_{rg2}	y_{O2}	$G_{\mathrm{reg},1}$	$G_{\mathrm{reg},2}$	F_{c}	F_{g}	$T_{\mathrm{air,in}}$
Units	K	K	K	%	kg/s	kg/s	kg/s	kmol/h	K
Values	786	798	954	0.8	41	24	450	850	428

In this section, all analysis and simulations are based on point A (Table 1) which is a representative operating point of the industrial demonstration TSRFCP plant.

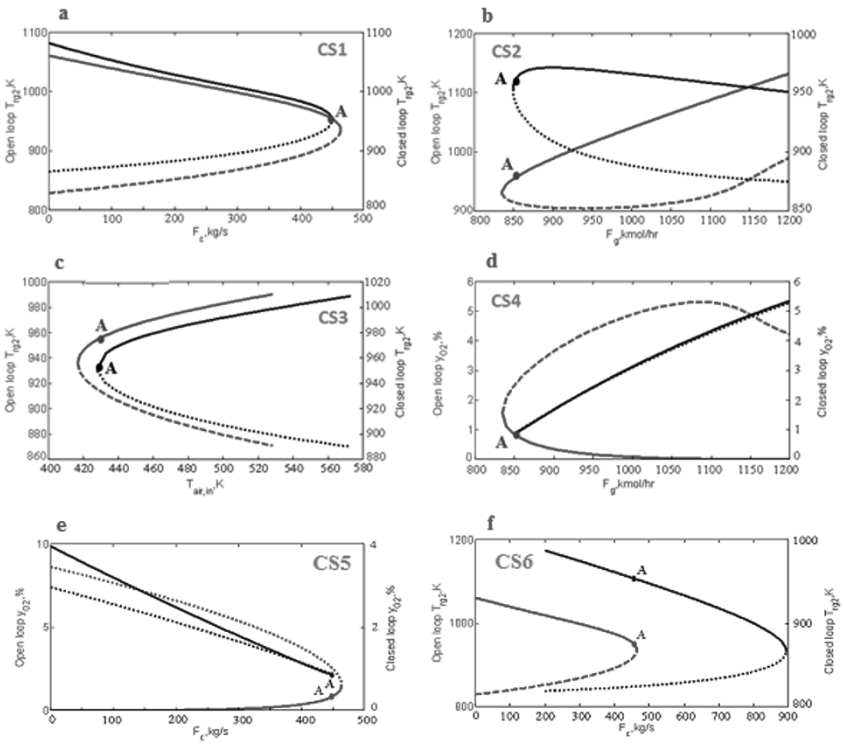

Figure 2. Comparisons of open-loop/closed-loop multiplicity for each control structure.

The implementation of a control system may alter the open-loop topologies representing relationships between the manipulated and controlled variables. Fig. 2 compares the open-loop and closed-loop steady-state multiplicity associated with point A under each

control structure. With regard to CS1, CS3 and CS6, closed-loop steady-state topologies are similar to the open-loop ones and no input multiplicity exists. Illustrated by Fig. 2d, CS4 demonstrates very interesting properties. Point A does not have a reachable counterpoint in the region of interest in the open-loop. However, closed-loop input multiplicity appears, and moreover the distance between the designed operating point and its counterpoint can be ignored. In such situations, even very minor disturbances may suddenly cause the system to become unstable. Hence, employing CS4 for designing a control system at point A is undesirable. As shown in Fig. 2e which is similar with Fig. 2d, CS5 is also undesirable. Illustrated by Fig. 2b, the open-loop/closed-loop steady-state multiplicity, when CS2 is introduced, may promote the TSRFCP process to operate initially at point A and then switch to its counterpoint with higher F_g. Apparently, comparisons on open-loop and closed-loop multiplicity suggest that CS1, CS3, and CS6 are better than CS2, CS4, and CS5. In order to support such conclusion, control actions that each control structure should take for overcoming various disturbances are also investigated.

Table 2. Control actions required for each control structure under various disturbances.

Variables	$k_{0,c}$ (+30%)						$F_{oi,in}$ (+1t/h)					
	CS1	CS2	CS3	CS4	CS5	CS6	CS1	CS2	CS3	CS4	CS5	CS6
$\Delta G_{reg,1}$(%)	0	0	0	-11	-12	0	6.6	6.6	6.6	-5.9	-18.5	0
$\Delta G_{reg,2}$(%)	0	0	0	-13	-14	0	0	0	0	-14.2	-27.9	0
ΔF_c(%)	6.5	0	0	0	-1	7	-8.2	0	0	0	-19	9
ΔF_g(%)	0	42	0	0.2	0	0	0	50.8	0	3.6	0	0
$\Delta T_{air,in}$(%)	0	0	-5.8	0	0	0	0	0	7.2	0	0	0
$\Delta T_{oil,in}$(%)	0	0	0	0	0	0	0	0	0	0	0	8
T_{rg2}	0	0	0	19.4	20	0	0	0	0	21	48	0
y_{O2}	-0.2	4.3	-0.2	0	0	-0.2	-0.3	4.8	-0.3	0	0	-0.2

Table 2 lists the control actions at point A for all six control structures. Increasing $k_{0,c}$ accelerates the combustion in the regenerator and in turn reduces y_{O2}. In order to maintain y_{O2}, action on F_g of CS4 or F_c of CS5 simultaneously increases T_{rg2} which subsequently requires $G_{reg,1}$ and $G_{reg,2}$ to take negative actions to control $T_{ris,1|z=1}$ and $T_{ris,2|z=1}$. Hence, the lowered catalyst-to-oil ratios may negatively affect the product yields from the two risers. In other words, three loops of CS4 or CS5 are heavily coupled with each other. When CS1, CS3, and CS6 are introduced to address the disturbance on $k_{0,c}$, the effects of control actions taken by F_c or $T_{air,in}$ on the other two loops can be ignored. Among these three control structures, CS3 takes the minimum action. Similarly, three control loops of CS4 or CS5 are also heavily coupled to reject the disturbance on $F_{oi,in}$. At the same time, the actions of both CS4 and CS5 cause upsets in T_{rg2}. For dealing with the disturbances on both $k_{0,c}$ and $F_{oi,in}$, effects of CS1, CS3, and CS6 on y_{O2} can be neglected. However, actions of CS2 result in significant influence on y_{O2}. The aforementioned closed-loop multiplicity of CS2 predicted that the saturation of F_g may occur. As can be seen from Table 2, the magnitudes of CS2 for tackling disturbances on $k_{0,c}$ and $F_{oi,in}$ reach 42% and 50.8%, respectively. Obviously, these large actions are undesirable for actual control system implementation. In summary, CS1, CS3, and CS6 are top three candidates.

PID controllers are implemented based on CS1, CS3, and CS6 for tackling an +30% perturbation on $k_{0,c}$, and the behavior of classic PID controllers tuned by critical proportioning method is given in Fig.3. Each of the following simulations takes around 1.5 min. On the other hand, the transient behavior of CS2 is also demonstrated. Shown in Fig.3, CS3 has the longest settling time. CS1 and CS6 have similar settling times and

maximum deviations. Interestingly, CS2 takes the minimum settling time at the cost of almost saturated action. Accounting for the results from closed-loop steady-state multiplicity and the dynamic simulation, CS1 and CS6 are the top two control candidates.

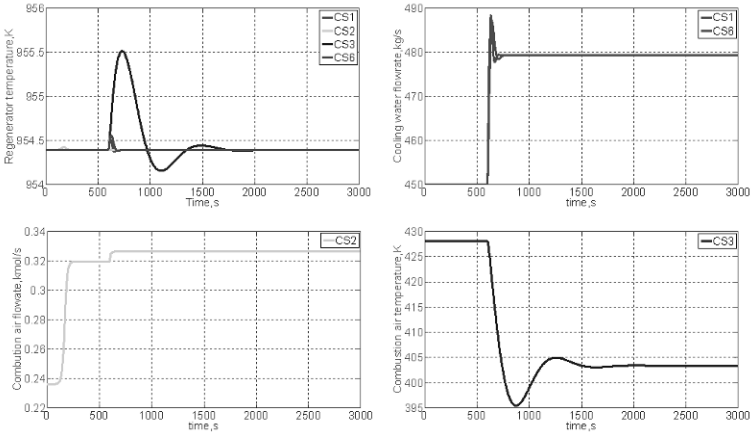

Figure 3. Closed-loop dynamic simulations of disturbance rejections at point A.

5. Conclusions

The performance of a control system for the TSRFCP process in the face of uncertainties and disturbances with minimum performance loss is heavily dependent on the control structure used. Control structure candidates of the demonstration TSRFCP process have been evaluated through applying closed-loop steady-state multiplicity analysis and dynamic simulation validation. Several key conclusions from the control structure selection for the TSRFCP process include: Closed-loop steady-state topologies of the TSRFCP process under CS4 and CS5 are totally different from their open-loop counterparts. For CS1, CS3, and CS6, closed-loop and open-loop steady-state topologies of the TSRFCP process are similar to each other; CS2 is not a suitable control structure due to the uneconomical control actions for F_g. CS3 shows the longest transient time for disturbance rejections when compared to CS1 and CS6. As the studied TSRFCP process is still in its demonstration stage, we believe that the control structure selection and the subsequent control system design will accelerate the scale-up of the demonstration TSRFCP plant to industrial applications.

References

C. Li, C. Yang, H. Shan, 2007, Maximizing propylene yield by two-stage riser catalytic cracking of heavy oil. Industrial Engineering Chemistry Research 46, 4914-4920.

Y. Liu. Study on Catalytic Pyrolysis of FCC Gasoline and Kinetic Model for Two-Stage-Riser Fluid Catalytic Cracking. [Ph.D Thesis]. 2008. China University of Petroleum, Dongying, China.

S. Skogestad, 2004, Control structure design for complete chemical plants. Computers Chemical Engineering 28, 219-23

P. Wang, Z. Yuan, C. Yang. 2014, Model development and validation of two-stage-riser catalytic pyrolysis processes for maximizing propylene yield. Submitted to Industrial Engineering Chemistry Research.

Krist V. Gernaey, Jakob K. Huusom and Rafiqul Gani (Eds.), 12th International Symposium on Process Systems Engineering and 25th European Symposium on Computer Aided Process Engineering.
31 May - 4 June 2015, Copenhagen, Denmark.

Novel Data Segmentation Methods for Data Driven Process Analyses

Rajesh Paul[a] and Dr. M.A.A. Shoukat Choudhury[b]

[a]*Department of Chemical Engineering; BUET, Dhaka, Bangladesh*
[b]*Department of Chemical Engineering; BUET, Dhaka, Bangladesh*
shoukat@che.buet.ac.bd

Abstract

With the advent of computer control and Distributed Control System (DCS), it has become easy for process industries to store a huge amount of data everyday. These data are rich sources of information. Often it requires selecting a window of data from a large data set for calculating or estimating various performance metrics of the control loops or the process itself. For example, if data is collected at a sampling rate of 4s, there will be 21,600 samples for each variable each day. Calculation of a performance measure or metric requires only a few hundred or a couple of thousand data points. The question is which part of the data should be used. This study attempts to find suitable data segmentation methods appropriate for the various purposes of data analysis. This study utilizes various simple statistical measures such as autocovariance function, signal to noise ratio, and skewness for selecting appropriate segment of the data. The performance of the segmentation methods has been evaluated using simulation examples and real industrial data sets. The selection of appropriate window of data largely increases the reliability of the data driven analyses.

Keywords: Autocovariance, Data segmentation, Nonlinearity analysis, Oscillation detection, Signal to noise ratio.

1. Introduction

Choudhury et al. (2008) presented theories to calculate various performance metrics for example process nonlinearity and oscillation for monitoring the performance of a process using routine operating data. In data driven analysis of process, selection of an appropriate data segment is important since computation of performance metric on non-representative data may give erroneous results. For system identification and forecasting, Shardt (2012) proposed entropy based approach for data segmentation. In entropy based approach, the difference in entropy between the input and output signals for routine operating data is used to separate the data into its constituent models. Fu and Mui (1981) reviewed various image segmentation techniques for partitioning of an image into a set of regions that cover it. Various region extraction techniques are applied to find meaningful regions of an image. Similarly, data segmentation techniques are applied to segment a time series for finding appropriate data window to estimate performance metrics of control loops. In this study, suitable data segmentation methods are developed for oscillation detection and nonlinearity analysis using routine operating data. In this paper, section 3 describes a data segmentation method for oscillation detection and section 4 describes a data segmentation method for nonlinearity quantification. Both sections also give application results and the paper ends with a conclusion section.

2. Motivation

The main motivation of this study is to find suitable methods to select a data window (a part of a time series) from a large time series to calculate various performance metrics of the control loops. Figure 1 shows time series data of 16 industrial variables. These data corresponds to 6 hours operation of a fertilizer plant and they are collected at a sampling rate of 4s. As shown in Figure 1, data windows separated by vertical lines, are different from each other, though they correspond to same tag. To calculate performance metrics from such industrial time trends, two common problems are encountered by engineers. First, which data window is to be used and second, what would be the length of each data window. Selection of data window depends on data analysis purposes. For example, less noisy data window is preferred for oscillation detection, but in case of a filter design noisy data window is required. In this study, suitable data segmentation methods are developed for segmenting data into different windows and then choosing the appropriate window of data for analysis. Two common purposes of data analysis are covered in this paper, namely, oscillation detection and nonlinearity quantification.

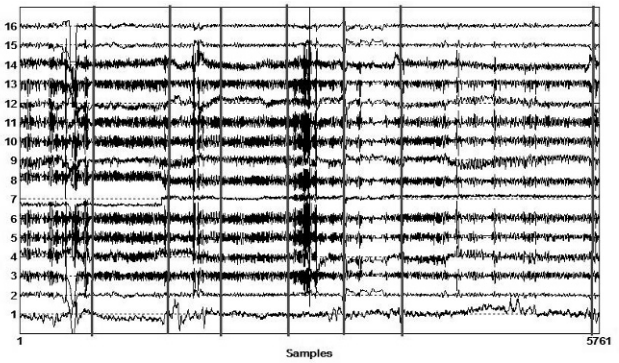

Figure 1: Industrial time trends

3. Data Segmentation for Oscillation Detection

Detection and diagnosis of oscillation is a regular issue in process industries. Oscillatory behavior in a chemical process causes inferior quality products, higher rejection rates, and larger consumption of energy; all of which impact the profitability of the plant. This section presents a method for selection of a window of data from a large data set for detection of oscillation based on regularity of zero crossing of filtered autocovariance function. The first step is to find the data window length.

3.1. Determination of Data Window Length

Data segmentation method allows us to break a time trend into smaller windows of data. Thornhill and Hägglund (1997) proposed zero crossing of autocovariance function (ACF) method for oscillation detection. In their method, intervals between regular zero crossings of autocovarience function are used to determine Oscillation period, T_p and Oscillation regularity, r. But they did not discuss about the minimum required length of a time trend to detect oscillation. Number of data in the selected time trend must be large enough for accurate determination of oscillation period. In this study, minimum required length of a time trend is calculated. Thornhill et al. (2003) proposed the following: *"The 10 intervals between the first eleven zero crossings are used for calculation of $\overline{T_p}$ and σ_{T_p}. The interval from lag zero up to the first zero crossing is excluded from the calculation because it corresponds to only one half of a completed deviation."* Box et al. (1994) stated that for reliable estimation of autocovarience at a lag, r_K, total number of data points must be equal to or greater than four times of the lag value. Ten intervals between the first eleven zero crossings equal

Table 1: Oscillation analysis for different size of data

Data length	Mean oscillation period, T_p	Deviation from actual period	Std of T_p
$\frac{L_m}{2}$ (1 to 1045)	103.78	3.78	4.29
L_m (1 to 2090)	99.56	0.44	0.88
$2L_m$ (1 to 4180)	99.78	0.22	0.67
All data (1 to 20000)	100.22	0.22	1.2

to five times of period and interval from lag zero up to the first zero crossing is equal to the one fourth of the period.

Therefore, the minimum required length of a time trend,

$$L_m = (5+\frac{1}{4})T_{pi} \times 4$$

$$L_m = 21 \times T_{pi} \quad (1)$$

Here, T_{pi} is the initial assumed value of oscillation period. Power spectrum of the time series is used to estimate the value of T_{pi}. The inverse of frequency corresponding to the highest power in the power spectrum gives the value of T_{pi}. In order to minimize the effects of disturbances and sampling errors, a data length more than the minimum length, L_m, should be used. From the experience of analyzing industrial data sets, it is observed a data length twice the minimum length is adequate. Thus, data can be segmented into windows of length $2L_m$.

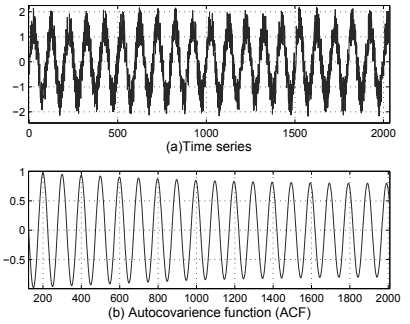

Figure 2: (a) Oscillatory time series (b) ACF of time series

3.1.1. Simulation Study

To observe the effect of length of a time trend on ACF based oscillation detection method, a time series shown in Figure 2, was generated as following:

$$X(t) = \sin(2\pi f_1 t + \phi_1) + d(k) \quad (2)$$

where $f_1 = 0.01\ Hz$, $\phi_1 = 0$, t varying from 1 s to 20000 s and white noise, d(k) with variance 0.2. The value of SNR for this analytical time series was 5. The frequency of the constructed time series was 0.01 Hz. Therefore, the actual oscillation period is 100 s. From Table 1, it is observed that for a selected data length equal to $2L_m$, the deviation of the estimated oscillation period from the actual oscillation period is 0.22 s and the estimated standard deviation of T_p is 0.67. This is the lowest among the four cases presented in Table 1. Therefore, the proposed method of choosing data length provides a better result in estimating oscillation period using ACF method.

3.2. Selection of Data window

After determining minimum required window length, L_m, a time series is divided into data windows each of length $2L_m$. Finally, a data window with high SNR value is selected for oscillation detection. High SNR values indicate less noisy data as variance of the noise is smaller compared to the variance of the signal. Signal to noise ratio (SNR) of a window is estimated indirectly. A

Table 2: Oscillation analysis of an industrial time series using data segmentation methods

Tag no.	Method name	Mean T_p	Std of T_p	r	Power (%)
1	Data segmentation (window length= $\frac{L_m}{2}$)	194.25	19.26	3.36	35
	Data segmentation (window length= L_m)	171.33	29.05	1.97	31
	Data segmentation (window length= $2L_m$)	171.33	18.06	3.16	24
	All data (1 to 16200)	168.00	17.83	3.14	23

simplified Wiener filter is used to separate noise from data windows. After that, all data windows of a particular time trend are filtered and the percentage of power retained in the filtered spectrum by different windows at the specified frequency range are compared. Finally, the window that retains the maximum percentage of power in the filtered spectrum is chosen. The retained power in the filtered spectrum increases with the increase of SNR value. Summary of the proposed data segmentation method for oscillation detection using ACF method is shown in Figure 3.

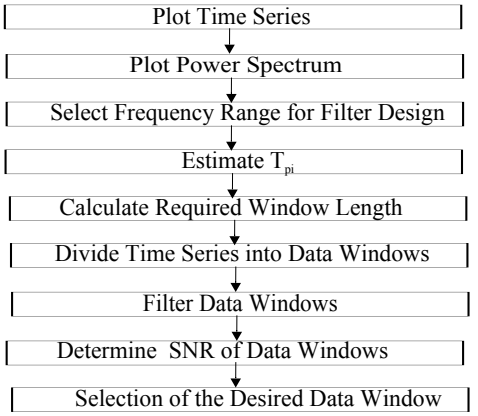

Figure 3: Algorithm for Data Segmentation

3.3. Application to Industrial Data

Figure 4 shows an industrial oscillatory time series data obtained from Karnaphuli Fertilizer Company Limited (KAFCO) located in Chittagong, Bangladesh. This time series data is labeled as Tag 1. Data were collected at a sampling rate of 4s; 16,200 samples were collected corresponding to 18 hours of operation. Table 2 represents the results of oscillation analysis in industrial time series using all data points (conventional method) and data segmentation methods (using a selected data window). By comparing the values of Mean T_p, standard deviation of T_p and oscillation regularity, r calculated from data segmentation methods considering window length $\frac{L_m}{2}$, L_m and $2L_m$, with the results obtained from conventional method (using all data points), it has been concluded that the proposed data segmentation method considering window length equal to $2L_m$, provides representative results for oscillation detection.

4. Data Segmentation for Bicoherence based Measure of Nonlinearity

A linear controller does not perform well for highly nonlinear processes, so the measurement of the degree of nonlinearity of a process is essential to take a decision about the necessity of a nonlinear controller. This section presents a method of data window selection for bicoherence based nonlinearity quantification.

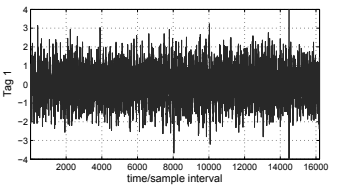

Figure 4: An industrial time trend

4.1. Determination of Data Window Length

Bicoherence method proposed by Choudhury et al. (2008) is a data based approach, which requires only

output time series of a process variable to estimate nonlinearity. For nonlinearity detection and quantification Choudhury et al. (2008) proposed three indices: Non-Gaussianity Index (NGI), Nonlinearity Index (NLI) and Total Nonlinearity Index (TNLI). $NLI > 0$ indicates the presence of nonlinearity; for linear process $NLI \leq 0$. TNLI quantifies the total nonlinearity present in a time series. For bicoherence estimation, a time series of finite length is divided into K segments. Size of data in each segment and length of discrete Fourier transform (DFT length) are two key parameters for bispectral analysis. Hinich (1982) suggested that if no frequency domain filtering is used, number of segments should be equal to or greater than DFT size (M) i.e. $K \geq M$. However, this may not be achievable in real life applications. For determining number of segments, Jamšek et al. (2003) stated the following: *" For a real signal, with a finite number of points, the compromise between bispectral resolution and statistical stability may be expected at K around 30"*. So, the window length should be,

$$L = 30 \times M \tag{3}$$

where, M is DFT length. Since M equal to 128 or 256 is usually used, it demands for a long data window length.

4.2. Selection of Data window

After determining the required length, L, a time series is divided into data windows of length L. After windowing a times series, an appropriate window can be selected based on SNR since higher SNR provides better bispectral estimation (Fackrell, 1996). However, there is no suitable method to determine SNR of an industrial times series having distributed power spectrum over wide frequency range. It is well known that there is a relationship between skewness and nonlinearity. So, skewness is proposed as a criterion for window selection. If the variation of skewness in different windows of a time trend is large, then selecting the window having the highest absolute skewness represents the highest nonlinear portion of the data.

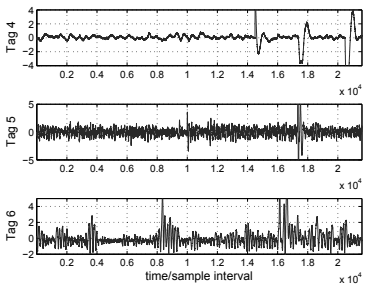

Figure 5: Normalised nonlinear industrial time trends

4.3. Application to Industrial Data Sets

Figure 5 shows three normalised industrial time trends. These data are labeled as tag 4, tag 5 and tag 6. Each time series is divided into three windows, each of length L equal to 7680 corresponding to M = 256. Bispectral analysis for nonlinearity detection is performed on overall time trend as well as data-windows. Results of nonlinearity analysis are presented in Table 3 for both conventional method and proposed data segmentation method. In conventional method (using all data points of a time trend), presence of nonlinearity is detected in all tags. As shown in Table 3, nonlinearity differs from window to window. In tag 4, no nonlinearity is found in window 1 ($NGI = 0$) but found in window 2 ($NGI = 0.47, NLI = 0.84$) and window 3 ($NGI = 0.4, NLI = 0.73$). This may be due to change in the operating points. In tag 5, nonlinearity is present in all data windows, but window 3 ($TNLI = 16.33$) is the most nonlinear. Due to large variation of skewness in windows of tag 4 and 5, maximum nonlinearities are observed in windows having the highest skewness. Variation of skewness is small in different windows of tag 6, so nonlinearity is almost the same in all windows. Therefore, it can be concluded that bicoherence based nonlinearity quantification is sensitive to data skewness and the data window having the highest skewness corresponds to the most nonlinear part of the data.

Table 3: Nonlinearity analysis of industrial time trends

Tag	Window	Skewness	NGI	NLI	TNLI	Max_bicoherence
Tag 4	All Data	-3.08	0.31	0.75	48.05	0.81
	1	0.11	0	0.05	0	0.05
	2	4.3	0.47	0.84	87.2	0.97
	3	-1.71	0.4	0.73	50.12	0.79
Tag 5	All Data	3.68	0.12	0.6	5.86	0.6
	1	-0.08	0.05	0.06	0.55	0.06
	2	-0.014	0.08	0.16	0.85	0.16
	3	3.72	0.26	0.9	16.33	0.91
Tag 6	All Data	2.62	0.04	0.1	0.51	0.1
	1	1.39	0.13	0.36	1.06	0.36
	2	1.9	0.1	0.22	1.25	0.22
	3	2.33	0.08	0.14	1.21	0.14

5. Conclusion

In this paper, data segmentation methods are developed for increasing the reliability of oscillation detection and nonlinearity analysis.

- A method for choosing minimum data window length for oscillation detection has been developed.
- Once data is divided into several windows, the window having the highest SNR value provides the representative results for oscillation detection.
- For nonlinearity analysis based on bicoherence method, a method for finding the data window length has been developed.
- The data window having the highest skewness corresponds to the most nonlinear region of the data.

Work is in progress to improve these data segmentation methods further.

References

Box, G. E., Jenkins, G. M., Reinsel, G. C., 1994. Time series analysis: forecasting and control. Prentice Hall, New Jersey, USA.

Choudhury, A. A. S., Shah, S. L., Thornhill, N. F., 2008. Diagnosis of process nonlinearities and valve stiction: data driven approaches. Springer-Verlag Berlin Heidelberg, Germany.

Fackrell, J. W., 1996. Bispectral analysis of speech signals. Ph.D. thesis, The University of Edinburgh. UK.

Fu, K.-S., Mui, J., 1981. A survey on image segmentation. Pattern recognition 13 (1), 3–16.

Hinich, M. J., 1982. Testing for gaussianity and linearity of a stationary time series. Journal of time series analysis 3 (3), 169–176.

Jamšek, J., Stefanovska, A., McClintock, P. V., Khovanov, I. A., 2003. Time-phase bispectral analysis. Physical Review E 68 (1), 016201.

Shardt, Y., Fall 2012. Data quality assessment for closed-loop system identification and forecasting with application to soft sensors. Ph.D. thesis, University of Alberta, Department of Chemical and Materials Engineering.

Thornhill, N., Hägglund, T., 1997. Detection and diagnosis of oscillation in control loops. Control Engineering Practice 5 (10), 1343–1354.

Thornhill, N., Huang, B., Zhang, H., 2003. Detection of multiple oscillations in control loops. Journal of Process Control 13 (1), 91–100.

Krist V. Gernaey, Jakob K. Huusom and Rafiqul Gani (Eds.), 12th International Symposium on Process Systems Engineering and 25th European Symposium on Computer Aided Process Engineering.
31 May – 4 June 2015, Copenhagen, Denmark

Robust Model Predictive Control Strategy for LTV and LPV Systems of the Internal Reforming Solid Oxide Fuel Cell

Narissara Chatrattanawet, Soorathep Kheawhom, Amornchai Arpornwichanop*

Computational Process Engineering Research Unit, Department of Chemical Engineering, Chulalongkorn University, Bangkok 10330, Thailand
Amornchai.a@chula.ac.th

Abstract

Solid oxide fuel cell (SOFC) is an electrochemical device operating at a high temperature, converting the chemical energy of a fuel directly to electrical energy. Moreover, it can directly convert hydrocarbon fuels to a hydrogen-rich gas via internal reforming inside the fuel cell stack itself. However, the endothermic cooling effect resulting from the reforming reaction at the anode side causes the temperature gradient and thermal stress within the fuel cell stack. This requires an efficient control design for assuring a stability of the system. In this study, a robust linear model predictive control (MPC) based on uncertain polytopic approach is synthesized for controlling the SOFC. Different designs of the robust MPC using linear time-varying (LTV) and linear parameter varying (LPV) models are studied. The state feedback control laws are derived by minimizing an upper bound on the worst-case performance cost and are implemented to the cell voltage and temperature controls of the direct internal reforming SOFC. The simulation results show that under model uncertainties, the proposed robust MPC can control the SOFC when disturbances in the fuel feed and air temperature are introduced and guarantee the stability of the SOFC. The performance of the MPC using different linear models is compared and discussed.

Keywords: robust model predictive control, solid oxide fuel cell, linear time-varying model, linear parameter varying model.

1. Introduction

Model predictive control (MPC) is a multivariable control algorithm that has been widely used in many industries. In general, a MPC problem is solved on-line at each sampling time to compute optimal control inputs based on predicted future outputs. MPC can be designed to guarantee its stability, independence of the controlled plant. However, as a model-based control strategy, it is difficult for the MPC to handle with an uncertain plant model.

In order to improve the MPC robustness property, a number of studies have been focused on the development of a robust MPC algorithm. Kothare at el. (1996) synthesized the robust MPC using linear matrix inequalities (LMIs). The state feedback control law was proposed to minimize a worst-case value of the objective function. The LMIs optimization was implemented to solve input and output constraints and described the uncertain plant. Bumroongsri and Kheawhom (2012) developed a polyhedral off-line robust MPC algorithm for the polytopic uncertain discrete-time system. The nonlinear process model was approximated by a linear time varying (LTV) system with

the polytopic uncertain. They showed that the robust stability of the proposed MPC was guaranteed. Recently, the controller synthesis based on a linear parameter varying (LPV) system has been received considerable attention. Casavola et al. (2012) proposed the MPC for feedback regulation problems. The LPV model was used to explain a nonlinear plant in the MPC algorithm. The performance of the developed MPC based on LPV and LTV models was compared.

A solid oxide fuel cell is regarded as the power generation device with high efficiency. Due to its high operating temperature, SOFC can directly convert hydrocarbon fuels into hydrogen fuel inside a cell stack by a steam reforming process. However, the reforming reaction at the anode side causes the complicated dynamic behavior, and the temperature gradient and thermal stress within the fuel cell stack. As a result, an efficient control is necessary for this process to avoid thermal cracking and ensure system stability. Kouramas et al. (2011) focused on the design of MPC controller to control the cell voltage and cell temperature. The result showed that the controller can manage the SOFC voltage and temperature to its desired value. Because the SOFC model involves many uncertain parameters, the control design should take care this model uncertainty.

The aim of this study is to develop the robust constrained MPC with a state feedback control law for the direct internal reforming SOFC. Uncertain polytopic discrete-time linear time varying (LTV) and linear parameter varying (LPV) models are employed to explain the SOFC behavior and to design the MPC control. Performance of the MPC based on the two different linear models are investigated and compared.

2. Model Description and MPC Formulation

The discrete-time linear time varying (LTV) and linear parameter varying (LPV) systems with multi-model paradigm polytopic uncertainty are considered and expressed in Table 1.

It is noted that $x(k)$ is the state of the plant, $u(k)$ is the control input and $y(k)$ is the plant output. The scheduling parameter $p(k)$ is measurable on-line at each sampling time k. Furthermore, we define the set Ω which is the polytope for polytopic systems. Co represents the convex hull, and A_j and B_j are the vertices in the convex hull. [A(k)B(k)] and [$A(p(k))B(p(k))$] are the linear combination of the vertices and λ is the uncertain parameter vector.

Table 1. Discrete-time model for LTV and LPV systems

Linear time varying system	Linear parameter varying system
$x(k+1) = A(k)x(k) + B(k)u(k)$	$x(k+1) = A(p(k))x(k) + B(p(k))u(k)$
$y(k) = Cx(k)$	$y(k) = Cx(k)$
$[A(k) \quad B(k)] \in \Omega$	$[A(p(k)) \quad B(p(k))] \in \Omega$
$\Omega = \mathrm{Co}\{[A_1 \quad B_1],[A_2 \quad B_2],...,[A_L \quad B_L]\}$	$\Omega = \mathrm{Co}\{[A_1 \quad B_1],[A_2 \quad B_2],...,[A_L \quad B_L]\}$
$[A(k) \quad B(k)] = \sum_{j=1}^{L} \lambda_j [A_j \quad B_j]$	$[A(p(k)) \quad B(p(k))] = \sum_{j=1}^{L} p_j(k)[A_j \quad B_j]$
$\sum_{j=1}^{L} \lambda_j = 1, \quad 0 \le \lambda_j \le 1$	$\sum_{j=1}^{L} p_j(k) = 1, \quad 0 \le p_j(k) \le 1$

At each sampling time k, the robust performance objective is a min-max problem (minimization of worst-case performance cost) in term of the quadratic objective as given in Eq. (1) and (2) for the LTV and LPV systems, respectively.

$$\min_{u(k+i|k),i=0,1,\ldots,m} \max_{[A(k+i)\ B(k+i)]\in\Omega,i\geq 0} J_\infty(k) \tag{1}$$

$$\min_{u(k+i|k),i=0,1,\ldots,m} \max_{[A(p(k+i))\ B(p(k+i))]\in\Omega,i\geq 0} J_\infty(k) \tag{2}$$

$$J_\infty(k)=\sum_{i=0}^{\infty}\left[x(k+i|k)^T Q_1 x(k+i|k)+u(k+i|k)^T Ru(k+i|k)\right] \tag{3}$$

where $Q_1(>0)$ and $R(>0)$ are the symmetric weighting matrices

A state-feedback control law is defined to synthesis the robust MPC algorithm.

$$\begin{aligned} &u(k)=Kx(k), \quad i\geq 0 && \text{For LTV system} \\ &u(k)=K(p(k))x(k), \quad K(p(k))=\sum_{j=1}^{L} p_j(k)K_j && \text{For LPV system} \end{aligned} \tag{4}$$

3. Off-Line Robust MPC Scheme

The optimization problem at each sample time step is formulated as the convex optimization problem involving linear matrix inequalities constraints (Kothare et al., 1996).The Lyapunov function is presented to guarantee the stability for the MPC algorithm. Table 2 shows the proposed MPC algorithm for LTV and LPV systems. For LTV system, the state feedback gains K_i in the control law are defined as $K_i=Y_iQ_i^{-1}$ (Kothare et al., 1996) while the state feedback gains are defined as $K_i=Y_iG_i^{-1}$ for the LPV system(Wada et al., 2006) to stabilize the closed-loop system.The matrix variables Q_i, G_i, and Y_i are achieved from the result of the linear objective minimization problem with the upper bound γ on the worst-case MPC. The symbol * represents the corresponding transpose of the lower block part of symmetric matrices.

Table 2. MPC algorithm for LTV and LPV systems

Linear time varying system	Linear parameter varying system
$\min_{\gamma,Q_i,Y_i}\gamma$	$\min_{\gamma,Q_i,G_i,Y_i}\gamma$
s.t. $\begin{bmatrix}1 & *\\ x_i & Q_i\end{bmatrix}\geq 0$	s.t. $\begin{bmatrix}1 & *\\ x_i & Q_i\end{bmatrix}\geq 0$
$\begin{bmatrix}Q_i & * & * & *\\ A_jQ_i+B_jY_i & Q_i & * & *\\ Q_1^{1/2}Q_i & 0 & \gamma I & *\\ R^{1/2}Y_i & 0 & 0 & \gamma I\end{bmatrix}\geq 0,\quad j=1,2,\ldots,L$	$\begin{bmatrix}G_i+G_i^T-Q_i & * & * & *\\ A_jG_i+BY_i & Q_i & * & *\\ Q_1^{1/2}G_i & 0 & \gamma I & *\\ R^{1/2}Y_i & 0 & 0 & \gamma I\end{bmatrix}\geq 0,\quad j=1,2,\ldots,L$
Input constraint	
$\begin{bmatrix}X & *\\ Y_i^T & Q_i\end{bmatrix}\geq 0,\quad X_{hh}\leq u_{h,\max}^2,\quad h=1,2,\ldots,n_u$	$\begin{bmatrix}X & *\\ Y_i^T & G_i+G_i^T-Q_i\end{bmatrix}\geq 0,\quad X_{hh}\leq u_{h,\max}^2,\quad h=1,2,\ldots,n_u$
Output constraint	
$\begin{bmatrix}S & *\\ (A_jQ_i+B_jY_i)^T C^T & Q_i\end{bmatrix}\geq 0,$	$\begin{bmatrix}S & *\\ (A_jG_i+BY_i)^T C^T & G_i+G_i^T-Q_i\end{bmatrix}\geq 0,$
$S_{rr}\leq y_{r,\max}^2,\quad r=1,2,\ldots,n_y$	$S_{rr}\leq y_{r,\max}^2,\quad r=1,2,\ldots,n_y$

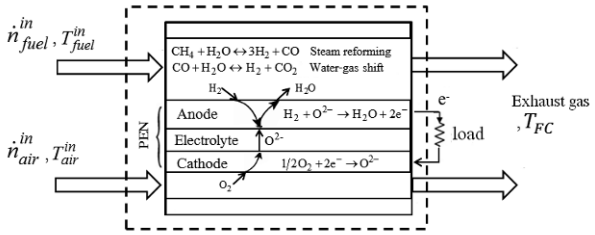

Figure 1. Schematic diagram of the direct internal reforming solid oxide fuel cell.

4. Control of SOFC

4.1. SOFC model

Figure 1 illustrates the direct internal reforming solid oxide fuel cell (DIR-SOFC). Methane as fuel is directly fed at the anode side and air as oxidant is introduced at the cathode side to produce electricity by the electrochemical reactions. The mathematical model including three major elements: electrochemical model and mass and energy balances,is used in the SOFC as shown in Table 3.For the electrochemical model, the operating cell voltage or the actual voltage (V_{FC}) decreases from its open-circuit voltage due to ohmic losses (η_{Ohm}), concentration overpotentials (η_{conc}), and activation overpotentials (η_{act}).The mass and energy balances represented in a lumped-parameter model are implemented to analysis, design, and control the SOFC. In the fuel channel, the chemical species i consist of CH_4, H_2O, CO, H_2, and CO_2, whereas the chemical species i in the air channel are O_2 and N_2.The chemical reactions taking place in the SOFC are shown in Table 4.

Table 3. SOFC model (Chatrattanawet et al., 2014)

Electrochemical models		
Cell voltage	$V_{FC} = E_{OCV} - \left(\eta_{\text{Ohm}} + \eta_{\text{conc}} + \eta_{\text{act}}\right)$	(5)
Open-circuit voltage	$E_{OCV} = E_0 - \frac{RT_{FC}}{2F}\ln\left(\frac{p_{\text{H}_2\text{O}}}{p_{\text{H}_2} p_{\text{O}_2}^{0.5}}\right)$	(6)
Ohmic losses	$\eta_{\text{Ohm}} = jR_{\text{Ohm}}$	(7)
Concentration overpotentials	$\eta_{\text{conc}} = \frac{RT_{FC}}{2F}\ln\left(\frac{p_{\text{H}_2\text{O,TPB}} p_{\text{H}_2}}{p_{\text{H}_2\text{O}} p_{\text{H}_2,\text{TPB}}}\right) + \frac{RT_{FC}}{4F}\ln\left(\frac{p_{\text{O}_2}}{p_{\text{O}_2,\text{TPB}}}\right)$	(8)
Cathode activation overpotentials	$j = j_{0,\text{cathode}}\left[\exp\left(\frac{\alpha nF}{RT_{FC}}\eta_{\text{act,cathode}}\right) - \exp\left(-\frac{(1-\alpha)nF}{RT_{FC}}\eta_{\text{act,cathode}}\right)\right]$	(9)
Anode activation overpotentials	$j = j_{0,\text{anode}}\left[\frac{p_{\text{H}_2,\text{TPB}}}{p_{\text{H}_2}}\exp\left(\frac{\alpha nF}{RT_{FC}}\eta_{\text{act,anode}}\right) - \frac{p_{\text{H}_2\text{O,TPB}}}{p_{\text{H}_2\text{O}}}\exp\left(-\frac{(1-\alpha)nF}{RT_{FC}}\eta_{\text{act,anode}}\right)\right]$	(10)
Mass balances		
Fuel channel	$\frac{dn_{i,f}}{dt} = \dot{n}_{i,f}^{in} - \dot{n}_{i,f} + \sum_{\text{k}\in\{\text{(i)},\text{(ii)},\text{(iii)}\}} \upsilon_{i,\text{k}} R_{\text{k}} A$	(11)
Air channel	$\frac{dn_{i,a}}{dt} = \dot{n}_{i,a}^{in} - \dot{n}_{i,a} + \upsilon_{i,\text{(iii)}} R_{\text{(iii)}} A$	(12)
Energy balances		
	$\frac{dT_{FC}}{dt} = \frac{1}{\rho_{SOFC} Cp_{SOFC} V_{SOFC}}\left(\dot{Q}_{f,in} - \dot{Q}_{f,out} + \dot{Q}_{a,in} - \dot{Q}_{a,out} + \sum_{\text{k}\in\{\text{(i)},\text{(ii)},\text{(iii)}\}}\left(-\Delta H\right)_{\text{k}} R_{\text{k}} A - jAV_{FC}\right)$	(13)

Table 4. Reactions considered in a SOFC

Reaction name	No.	Reaction equation	ΔH (kJ/mol)
steam reforming	(i)	$CH_4 + H_2O \leftrightarrow 3H_2 + CO$	206.10
water-gas shift	(ii)	$CO + H_2O \leftrightarrow H_2 + CO_2$	-41.15
Electrochemical reaction	(iii)	$H_2 + 1/2O_2 \rightarrow H_2O$	-241.83

Table 5. Operating conditions used in this study

Parameters	Value	Parameters	Value
Cell temperature (K)	1058	Power density (W/cm^2)	0.32
Cell voltage (V)	0.72	Inlet temperature (K)	1023
Current density (A/cm^2)	0.45	Steam to carbon ratio	2

The mathematical model is used to perform steady state analysis for the SOFC in order to select the operating point. The operating conditions for designing the SOFC controller are summarized in Table 5.

4.2. Control implementation

The implementation of the off-line robust MPC for LTV and LPV systems is performed by using Matlab. The lumped-parameter model represented by nonlinear ODEs is linearized and then discretized using Euler first-order approximation into discrete-time model with a sampling period of 5 second. The objective is to control the cell temperature to its desired value by manipulating the inlet temperature of air with $Q_1=I$ *and* $R=0.1I$.

Figure 2 shows the closed-loop responses for the robust MPC based on the LTV and LPV systems. The MPC controller for LTV and LPV systems can maintain the cell temperature (T_{FC}) to its setpoint by manipulating the control input ($T_{air,in}$). Moreover, it is observed that the cell voltage (V_{FC}) also moves to its desired value. By comparing the MPC design based on the LTV and LPV systems, it seems that the MPC with the LPV system can achieve a better control performance because the scheduling parameter is taken into the controller synthesis.

5. Conclusions

In this work, the robust constrained MPC algorithm based on uncertain polytopic discrete-time LTV and LPV systems is synthesized for controlling the direct internal reforming SOFC. The state feedback control law minimizing an upper bound on the worst-case objective function is implemented. The lumped-parameter model is used to explain the SOFC dynamic behavior and employed to design the MPC controller. The performance of the MPC controller using the proposed different models is compared. The simulation results show that under model uncertainties, the proposed robust MPC can control the cell voltage and temperature to its setpoint. The proposed control can guarantee the stability of the SOFC. The results also show the control performance of the robust MPC algorithm based on LPV system is better than LTV system.

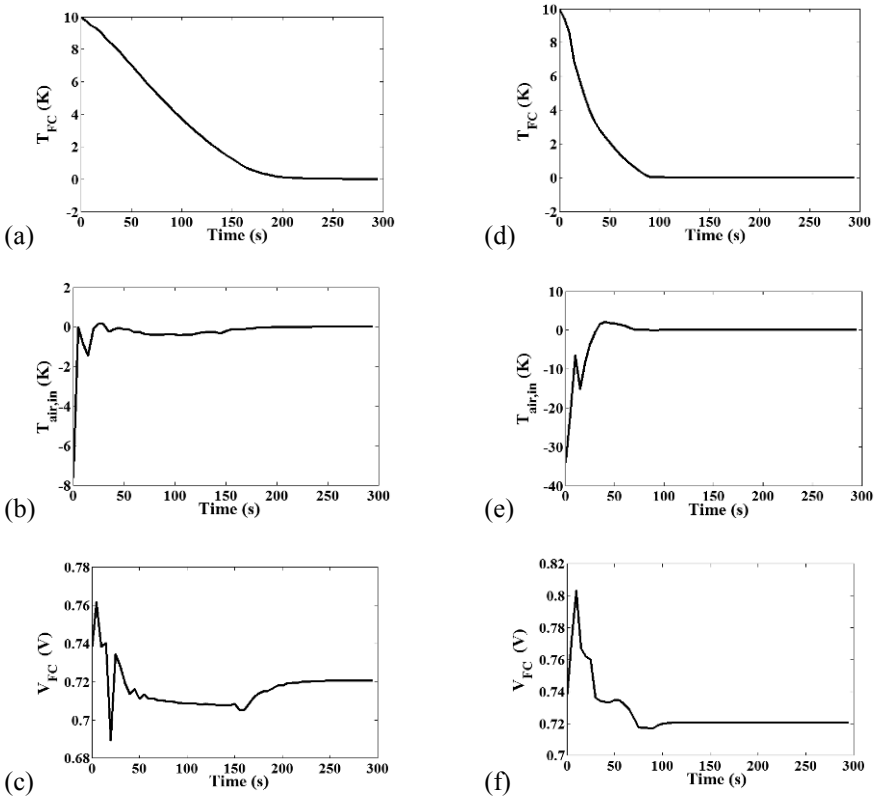

Figure 2. The closed-loop responses of the MPC based on the LTV system ((a)-(c)) and the LPV system ((d)-(f)).

Acknowledgements

Support from The Royal Golden Jubilee Ph.D. Program, The Thailand Research Fund and the National Research University, Office of Higher Education Commission (WCU-040-EN57) is gratefully acknowledged.

References

A. Casavola, D. Famularo, G. Franze, E. Garone, 2012, A fast ellipsoidal MPC scheme for discrete-time polytopic linear parameter varying systems, Automatica, 48, 2620-2626.

K. Kouramas, P.S. Varbanov, M.C. Georgiadis, J.J. Klemes, E.N. Pistikopoulos, 2011, Explicit/Multi-Parametric model predictive control of solid oxide fuel cell, Computer Aided Chemical Engineering, 29, 773-777.

M.V. Kothare, V. Balakrishnan, M. Morari, 1996, Robust constrained model predictive control using linear matrix inequalities, Automatica, 32, 10, 1361-1379.

N.Chatrattanawet, S. Skogestad, A. Arpornwichanop, 2014, Control structure design and controllability analysis for solid oxide model, Chemical Engineering Transactions, 39, 1291-1296.

N. Wada, K. Saito, M. Saeki, 2006, Model predictive control for linear parameter varying systems using parameter dependent Lyapunov function, IEEE Trans. Circuits Syst, 53, 1446-1450.

P. Bumroongsri, S. Kheawhom, 2012, An off-line robust MPC algorithm for uncertain polytopic discrete-time systems using polyhedral invariant sets, Journal of Process Control, 22, 6, 975-983.

Krist V. Gernaey, Jakob K. Huusom and Rafiqul Gani (Eds.), 12th International Symposium on Process Systems Engineering and 25th European Symposium on Computer Aided Process Engineering.
31 May – 4 June 2015, Copenhagen, Denmark

Plantwide Predictive Monitoring of Sulfur Emissions in Tail Gas Treatment Units

Eva M. Speelmanns,[a*] Francesco Rossi,[b,c] Andres R. Leon-Garzon,[b] Flavio Manenti[a,b]

[a] *Technische Universitat Berlin, Chair of Process Dynamics and Operation (dbta), Straße des 17. Juni 135, D-10623, Berlin, Germany*
[b] *Politecnico di Milano, CMIC Dept. "Giulio Natta", Piazza Leonardo da Vinci 32, 20133, Milano, Italy*
[c] *Purdue University, School of Chemical Engineering, Forney Hall of Chemical Engineering, 480 Stadium Mall Drive, West Lafayette, IN 47907-2100, USA*
eva.m.speelmanns@tu-berlin.de

Abstract

Plantwide predictive monitoring is a useful tool for observation of certain compounds of interest (e.g. pollutants) depending on fluctuations in the feed stream and operating conditions of plant sections. A general framework for the dynamic modeling of packed bed reactors (PBRs) in sulfur tail gas treatment is broached and implemented for related processes and a wide range of operating conditions. The model was validated using experimental data from both a miniplant for industrial off gas treatment and an industrial plant for sulfur recovery. After its validation, the model has been coupled with the existing multiscale models for thermal furnace already adopted to simulate Claus processes to get the plantwide prediction of plant emissions. The proposed approach allows to carry out a priori the estimation of environmental impact according to the current feedstock and operating conditions as well as to exploit in advance the hidden potential of the plant in mitigating/removing them before achieving the stack.

Keywords: dynamic modeling; plantwide process monitoring; sulfur emissions.

1. Introduction

In recent years, environmental regulations are becoming more and more stringent and therefore are forcing engineers and technicians to find novel solutions for emission reduction. Beside carbon dioxide, sulfur emissions (mostly in the form of sulfur dioxide) have become a key target for several countries (Guangxiang, 2014). Promising solutions to this are predictive technologies that enable the real-time monitoring of certain components, thus the accurate estimation of final concentrations just by assigning inlet conditions of a plant. Hence, they give in advance the possibility to act on the degrees of freedom of the plant to avoid any threshold overcoming. In addition, it can be realized in real-time what in the operational range is to fulfill the environmental limitations. Dynamic models for entire plants have been developed previously in the fields of CO_2 capture (Bui et al., 2014), gasification (Pérez-Fortes et al., 2009) or cracking units (Berreni and Wang, 2011). Recently, the same methodology has been successfully adopted for the minimization of SO_x emissions of a sulfuric acid plant (Kiss et al., 2010), but many issues are still unresolved to extend it to other chemical and oil & gas areas. In tail gas units, for instance, such as Claus processes, there is the need to characterize complex kinetics to get a reliable prediction of the dynamic behavior of the plants. Nevertheless, a plantwide predictive monitoring is most welcome

especially in these tail gas processes due to their typical strong fluctuations in the feedstock and lack in instrumentation and redundancy. Moreover, sulfur reduction is of great importance in many industrial branches and it is often realized by processes with a thermal section and/or a catalytic section, consisting of heterogeneous catalysis in fixed bed reactors. While thermal models are already discussed elsewhere(Manenti et al., 2013), there is still the need to define computer-aided tools for the catalytic section to bridge the gap between the literature on sulfur removal and the practical expected benefits. On this basis, the paper mainly focuses on the formulation, implementation and validation of a new general dynamic model of packed bed reactors (PBRs). The model is structured to get high generality and modularity and can therefore easily be adapted only by providing geometrical data of the reactor, chemical properties of the species and kinetic data. As a benchmark for tail gas treatment units, the model was employed to simulate a sulfur recovery unit (Selim et al., 2013). Furthermore, the model was validated with experimental data from a miniplant operation for deep desulfurization of industrial off gas.

2. Dynamic modeling of the packed bed reactor (PBR)

The pseudo-homogeneous catalytic (PHoCa) reactor simulation suite (available at http://super.chem.polimi.it) is a first principles model involving spatio-temporal evolution (partial differential-algebraic equation system). Modeling has required the following assumptions, which could progressively be removed in future activities: (1) the fluid phase behaves as perfect gas; (2) thermodynamic properties such as pressure and volume are considered constant with temperature; specific heat and enthalpy of reaction are dependent on temperature and were acquired from the *NIST Chemistry Webbook*; (3) gas transport properties such as axial dispersion, thermal conductivity, viscosity, global heat transfer coefficient are considered constant with temperature and composition; (4) no diffusive limitations inside catalyst (i.e. efficiency factor is one); (5) reactor temperature can be controlled with a phase changing fluid on the lateral area of the reactor, so there is no variation in the coolant temperature profile over the lengths; and (6) gas-catalytic phase gradients are neglected, i.e. a homogenous approach is used. The PBR model includes the mass balances for the *i*-th component and energy balance:

$$\frac{\partial \rho_i^{(G)}}{\partial t} = -\frac{1}{\varepsilon A_{cs}} \frac{\partial}{\partial z}\left(\rho_i^{(G)} Q\right) + D_i^{eff} \frac{\partial^2 \rho_i^{(G)}}{\partial z^2} + \frac{1-\varepsilon}{\varepsilon} PM_i \sum_{j=1}^{N_R} \nu_{ij} R_j^{(r)} \tag{1}$$

$$\frac{\partial T}{\partial t} = \frac{1}{\varepsilon \sum_{i=1}^{N_C} \rho_i^{(G)} Cv_i + (1-\varepsilon)\rho_c Cp_c} \left[\begin{array}{l} -\frac{Q}{A_{cs}} \sum_{i=1}^{N_C} \rho_i^{(G)} Cp_i \frac{\partial T}{\partial z} - (1-\varepsilon) \sum_{j=1}^{N_R} \Delta H_{R_j} R_j^{(r)} + k^{eff} \frac{\partial^2 T}{\partial z^2} + \\ + \frac{U}{A_{cs}} \frac{dA_{exc}}{dz}\left(T_c - T\right) - \frac{P}{A_{cs}} \sum_{i=1}^{N_C} \frac{1}{\rho_i^{(P)}} \frac{\partial}{\partial z}\left(\rho_i^{(G)} Q\right) + \\ + P\left(1-\varepsilon\right) \sum_{i=1}^{N_C} \frac{PM_i}{\rho_i^{(P)}} \sum_{j=1}^{N_R} \nu_{ij} R_j^{(r)} \end{array} \right] \tag{2}$$

Energy balance (2) includes the correction of pressure for internal energy, which provides with a wide application range, from low pressure (e.g., Claus converter) to high pressure PBR (e.g., methanol and ammonia synthesis). For reaction kinetics a general Langmuir-Hinshelwood approach is chosen that can be easily adapted to a more simplified Arrhenius approach:

$$R_j^{(r)} = \frac{k_j^0 e^{Ea_j/RT} \prod_{i=1}^{N_C} P_i^{\gamma_{ji}}}{\left(1 + \sum_{i=1}^{N_C} k_{ji}^{eq,0} e^{Ea_{ji}^{eq}/RT} P_i\right)^{\psi_j}} \tag{3}$$

In addition, the pressure loss over the fixed bed is described by the Ergun equation (Ergun 1952):

$$\frac{\partial P}{\partial z} = -\frac{1-\varepsilon}{\varepsilon^3} \frac{G}{DP_c \sum_{i=1}^{N_C} \rho_i^{(G)}} \left[1.75G + 150(1-\varepsilon)\left(\frac{\mu_{mix}^{(G)}}{DP_c}\right)\right] \tag{4}$$

According to the assumptions above, variations of volumetric flow is as follows:

$$Q = Q_{IN}\left(\frac{T}{T_{IN}}\right)\left(\frac{P_{IN}}{P}\right)\left(\frac{PM_{mix}^{IN}}{PM_{mix}}\right) \tag{5}$$

The model is solved by spatial discretization with finite-difference method based on backward derivative approximation so a set of DAE systems are received. Parallel Gear multi-value methods (Buzzi-Ferraris and Manenti, 2012a, b) are adopted.

3. Model validation

Model validation was carried out on different systems to assess the generality and reliability of the model. Hereinafter, the agreement of model predictions and experimental data is given for the deep desulfurization process of industrial off gas obtained using the mobile miniplant technology available at TU Berlin. This process aims at converting sulfur content of COS and CS_2 into H_2S by heterogeneous catalysis. The desired hydrolysis reactions are:

$$COS + H_2O \leftrightarrow H_2S + CO_2 \quad \text{and} \quad CS_2 + 2H_2O \leftrightarrow 2H_2S + CO_2 \tag{6}$$

The inlet molar fraction was: H_2, 0.61; CH_4, 0.21; CO, 0.06; N_2, 0.07; olefins, 0.02; CO_2, 0.012; and organosulfur compounds, 0.0002.

3.1. Experimental Setup

Experiments were conducted with a mobile and modular test plant that was constructed for testing catalysts under real conditions with industrial gas (Günther et al., 2012). The main part of the plant is a fixed bed reactor with a diameter of 100 mm and a maximum number of 5 catalytic beds, each of which is 100 mm long (Figure 1). The ratio of bed diameter to particle diameter is >8 for most industrial catalysts, which leads to the assumption of negligible radial concentration gradients (Chu and Ng, 1989) as in PHoCa suite. The temperature was measured at the reactor inlet and after each catalyst bed by resistance thermometers PT 100 inside the gas stream, as well as on the outer wall by thermocouples. Values were recorded every second by ABB Freelance control system. Therefore, heat generation and losses over the wall can be determined. For chemical analysis, gas samples were drawn in front of and after the reactor. Relevant components (organosulfur compounds and H_2S) were quantified by gas chromatography at stationary points. The inlet reactor temperature and the Gas Hourly Space Velocity (GHSV) were varied in the experiments and determine the conversion of COS and CS_2.

3.2. PBR simulations and data fitting

The model described above was adapted to the miniplant process by assigning geometric data, inlet conditions and reaction kinetics. The kinetic parameters of the main reactions (6) were estimated by adaption to the experimental data (both temperature and concentration) using a stationary method developed by Schöneberger (2010). The results of the simulations are shown in Figures 2 and 3 for the temperature profiles and concentration of organosulfur compounds, respectively. Due to the heat losses over the wall, a drop of temperature can be seen over the length of the reactor. Upon feeding the process gas to the reactor at t = 0 s, the temperature starts to rise until a stationary profile is reached after approx. 10,000 s. As can be seen in Figure 2, the measured temperatures can be well predicted with the simulations. In addition, the concentrations of the two key components COS and CS_2 were simulated and the result is shown in Figure 3. The simulations show good agreement with the measured outlet concentrations of both components for the relevant operating range.

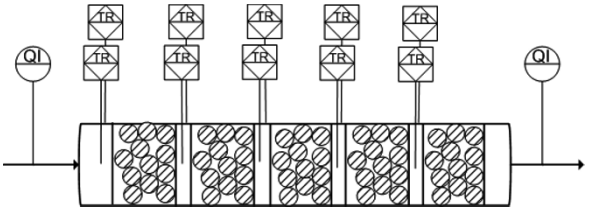

Figure 1. Schematic drawing of miniplant test reactor with temperature and quality measurement.

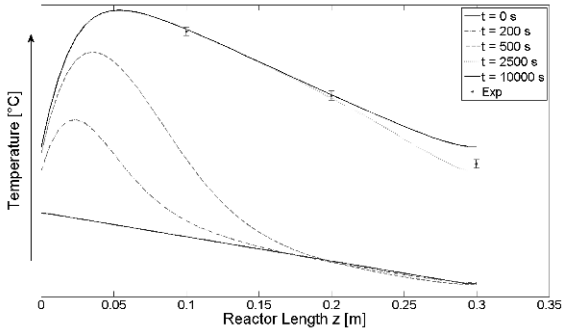

Figure 2. Qualitative gas temperature over the length of the reactor and for different times until a stationary point is reached after 10,000s. Experimental data points are indicated at z = 0.1, 0.2, 0.3.

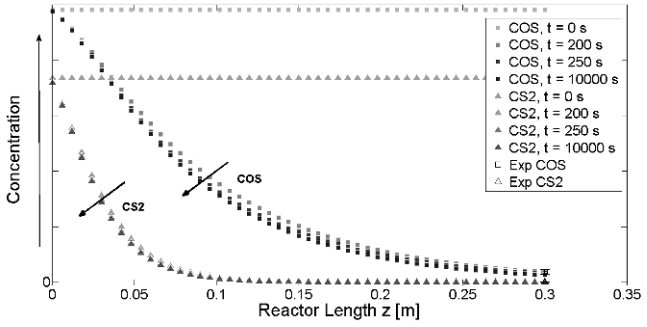

Figure 3. Qualitative concentration of the components COS and CS_2 over reactor length and variation over time. The stationary outlet concentrations of both components were measured and are indicated at z = 0.3.

4. Plantwide predictive monitoring of sulfur emissions of Claus plants

After validation, the dynamic model was applied to model the catalytic units of a Claus process. Claus processes consist of a thermal reactor furnace, where the acid gas (mainly H_2S) is fed together with combustion air, a waste heat boiler to recover heat and generate medium pressure steam, a series of sulfur condenser and a series of catalytic reactors (packed bed reactors for sulfur removal and organosulfur hydrolysis). The most relevant emission for these processes is SO_2; therefore, the reactions of interest is the Claus reaction to produce elemental sulfur:

$$2H_2S + SO_2 \leftrightarrow \frac{1}{2}S_6 + 2H_2O \tag{7}$$

S_6 only is considered in this study as it is the principal allotrope at the reactor operating conditions (sulfur equilibria). The chemical kinetics for reaction (7) were taken from the literature (Tong et al., 1997) and employed to the model. Using the outlet stream of the previously developed model of the thermal furnace and waste heat boiler (Manenti et al., 2013) as an inlet for the newly developed model of PBRs, the entire Claus plant can be simulated. A sensitivity analysis considering the inlet airflow to the thermal furnace was conducted and extreme conditions for the main polluting component SO_2 are displayed in the same graph (Figure 4). The trends show that under optimum conditions, the concentrations of SO_2 is relatively low. However, a change in operating conditions, (here an increase of inlet air mass flow by 25%) shows a major impact on the outlet concentration of SO_2 and therefore a critical condition for emission production is reached.

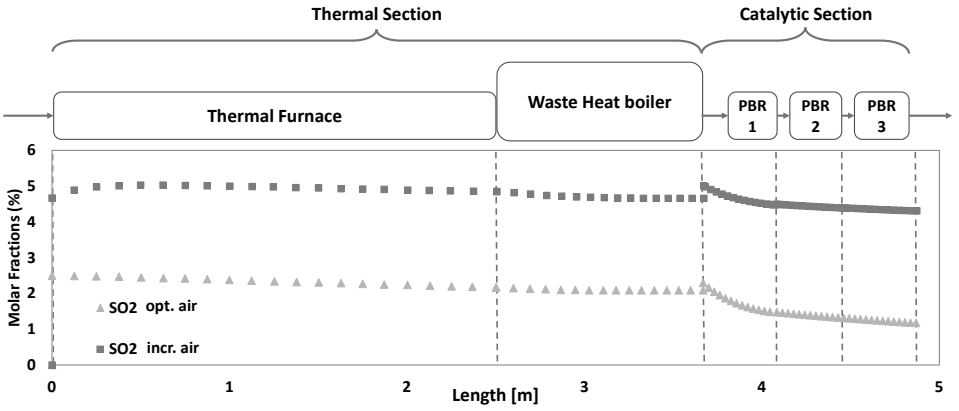

Figure 4. Simulation of relevant sulfur component SO_2 for entire Claus plant including thermal section and catalytic section for two operating conditions concerning airflow.

5. Conclusions

In this work, a first principle fixed bed reactor model based on a partial differential equation system for simulation and monitoring of sulfur recovery units was presented. The predictive monitoring of sulfur emissions was experimentally validated using process data from a miniplant which was coupled to an industrial production line and operated over a wide range. The PBR model was then applied to the catalytic train of a Claus plant which therefore enables plantwide monitoring of relevant species such as

SO_2. Therefore, it is possible to predict in advance which operating conditions lead to a violation of emission limit values.
In contrast to the work of Tong et al. (1997), who developed a stationary and heterogeneous model for the catalytic Claus units in particular with high degree of detail, our model can be used as a first approach for sulfur tail gas treatment units when the level of information on the process is little as this is mostly the case in industrial processes.

Acknowledgments

Alexander von Humboldt Foundation is gratefully acknowledged by the authors for funding professorship and hosting institution. We also thank the student Riccardo Ratti for his contribution on the simulations.

References

M. Berreni, M. Wang, 2011, Modelling and dynamic optimization of thermal cracking of propane for ethylene manufacturing. Computers & Chemical Engineering 35 (12), 2876–2885.
M. Bui, I. Gunawan, V. Verheyen, P. Feron, E. Meuleman,S. Adeloju, 2014, Dynamic modelling and optimisation of flexible operation in post-combustion CO2 capture plants—A review. Computers & Chemical Engineering 61, 245–265. 10.1016/j.compchemeng.2013.11.015.
G. Buzzi-Ferraris, F.Manenti, 2012, BzzMath: Library Overview and Recent Advances in Numerical Methods, Computer-Aided Chemical Engineering, 30, 1312-1316.
G. Buzzi-Ferraris, F. Manenti, 2012b, Improving the Selection of Interior Points for One-dimensional Finite Element Methods, Computers &Chemical Engineering, 40, 41-44.
C.F. Chu,K.M. Ng, 1989, Flow in packed tubes with a small tube to particle diameter ratio. AIChE J. 35 (1), 148–158.
Sabri Ergun, 1952, Fluid flow through packed columns, Chem. Eng. Prog. 48, 89-94.
J. Guangxiang, 2014,The Ways to Bring the SO2 Concentration of the Coke Oven Chimney Emission Down to Standard, Coal Chemical Industry,170, 35-38.
R. Günther, J.C.Schöneberger, H. Thielert, G.Wozny, 2012, Effektive Prozessentwicklung durch modulare Versuchsanlage im realen Prozessverbund, Dortmund.
A.A. Kiss, C.S. Bildea, J. Grievink, 2010, Dynamic modeling and process optimization of an industrial sulfuric acid plant. Chemical Engineering Journal 158 (2), 241–249.
F. Manenti, D. Papasidero, A. Frassoldati, G. Bozzano, S. Pierucci,E. Ranzi, 2013, Multi-scale modeling of Claus thermal furnace and waste heat boiler using detailed kinetics. Computers & Chemical Engineering 59, 219–225.
M. Pérez-Fortes, A.D. Bojarski, E. Velo, J.M. Nougués, L. Puigjaner, 2009, Conceptual model and evaluation of generated power and emissions in an IGCC plant. Energy, 34, 1721–1732.
J.C.Schöneberger, 2010, Entwicklung und Analyse katalytischer Abgasbehandlungsprozesse am Beispiel einer emissionsfreien Schwefelsäureanlage. Dissertation, Berlin.
H. Selim, A.K. Gupta, A. Al Shoaibi, 2013, Effect of reaction parameters on the quality of captured sulfur in Claus process, Applied Energy, 104, 772-776.
S. Tong, Ivo G. Dalla Lana, K.T. Chuang, 1997, Effect of Catalyst Shape on the Hydrolysis of COS and CS 2 in a Simulated Claus Converter. Ind. Eng. Chem. Res. 36 (10), 4087–4093.

Krist V. Gernaey, Jakob K. Huusom and Rafiqul Gani (Eds.), 12th International Symposium on Process Systems Engineering and 25th European Symposium on Computer Aided Process Engineering.
31 May – 4 June 2015, Copenhagen, Denmark

Robust Control of Industrial Propylene-Propane Fractionation Process

Cristian Patrascioiu, Nicolae Paraschiv, Anh Cao Minh, Marian Popescu

[a]*Petroleum-Gas University of Ploiesti, Bd. Bucuresti 39, Ploiesti 100680, Romania*

Abstract

The paper presents some results in the field of the industrial propylene-propane separation process control. The process inputs and outputs, the quality specifications for the separated products and the possible pairs of control agents, based on the relative gain array, are analyzed. The analysis emphasized the fact that the control structure based on L and B control agents is the most suitable. Starting from this result two robust control structures for the quality of the separated products are developed. The first structure refers to the feedback control of the distillate quality, and the second structure is associated with feedforward control of top and bottom products quality. Each structure was tested using dynamic simulation for the same step input of the feed flowrate disturbance. Test results confirmed the superiority of feedforward control.

Keywords: fractionation process, dynamic simulation, robust control, feedback control, feedforward control, quality specification

1. Introduction

A binary distillation process may be described by the following groups of variables: outputs (compositions of distillate and bottom product), disturbances (feed flowrate and composition), control agents (reflux flowrate, bottom product flowrate). In systemic approach this is a 2x2 multivariable process. For this process the distillate composition is a hard target and the bottom product composition is a soft target. A hard target refers to a fixed value of the specification (propylene concentration in distillate x_D), and a soft target indicates a range of variation for the specification (propylene concentration in bottom product x_B) (Patrascioiu et al., 2010). This feature directs the automation of the process to a robust control which may ensure the distillate specification at minimum cost. This objective can be achieved by feedback or feedforward control structures.

2. Analysis of quality control structures

Robust control (viewed as secure, powerful control) of the quality of the separated products in the propylene-propane separation column requires an adequate selection of the control agents used for separated products quality control. A powerful tool for the analysis of theoretical structures for separated products quality control is the Relative Gain Array (RGA). The elements of RGA, denoted by Λ, were calculated using the relations developed by Shinskey (1996) and also based on a steady-state simulation of the process using Unisim® Design simulation environment (Honeywell, 2009). Table 1 presents the calculated values of the relative gains for a series of control structures: *L-V*, *L-B*, *D-V*, *D-B/L*, *D-V/B*, *S-B/L*, *S-V/B*. The significance of the symbols used in table 1 is: *L* – reflux flowrate; *B* – bottom product flowrate; *D* – distillate flowrate; *V* – boilup flowrate; *S* – separation factor.

Table 1. Values of the relative gains for different control structures

Structure name	RGA value	Structure name	RGA value	Structure name	RGA value	Structure name	RGA value
Λ_{DV}	0.841	Λ_{LV_B}	0.828	Λ_{LD}	0.165	$\Lambda_{SL/B}$	0.942
$\Lambda_{DL/B}$	1.019	Λ_{SD}	0.241	Λ_{LB}	1.010	$\Lambda_{SV/B}$	1.015
$\Lambda_{DV/B}$	1.042	Λ_{SV}	2.435	Λ_{LV}	20.831	Λ_{DS}	0.758
$\Lambda_{LL/B}$	0.910						

The criteria used for selecting the best control structure were: value of the relative gains as close to 1 as possible and use of the lowest flowrate (*B* or *D*) as control agent (Mihalache et al., 2008). The analysis of the mentioned structures showed that the *L-B* structure is the most adequate for industrial implementation of a robust control system for separated products quality. Figure 1 shows the control structure of top and bottom compositions using *L* and *B* flowrates as control agents.

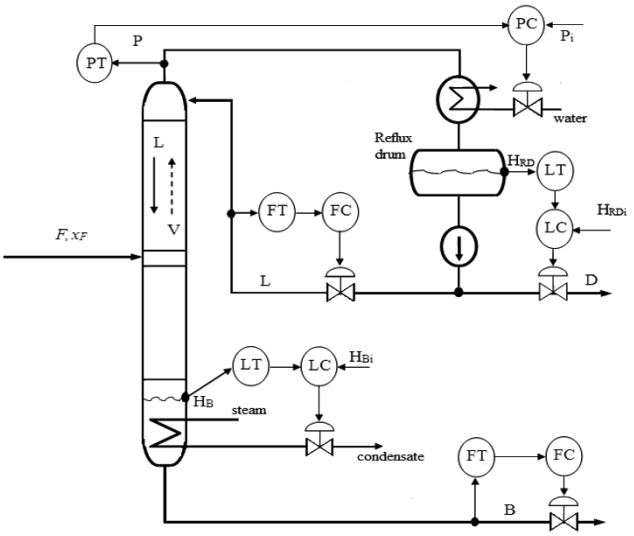

Figure 1 L-B control structure

3. Dynamic simulation of proposed control structures

Performance testing of the proposed control structures for the propylene-propane separation column was done by dynamic simulation using Unisim® Design simulation environment (Honeywell, 2010). In order to achieve this the following steps were completed: steady-state configuration of the separation process, implementation of the *L-B* structure, tuning of the (pressure, level and flowrate) controllers associated with *L-B* structure, implementation of the quality control system and tuning of the related controllers, implementation of the feedforward control structure.

3.1. Steady-state configuration of the separation process using UniSim® Design

The simulator for the propylene-propane separation column was configured using the standard Distillation Column module, taking into account the design and operating parameters presented in table 2.

Table 2 Main design and operating parameters of the column

Parameter	Measurement unit	Value
Number of theoretical trays	-	80
Feed tray	-	30
Feed flowrate	kmole/h	612.4
Feed pressure	bar	20.68
Condenser pressure	bar	19.31
Reboiler pressure	bar	20.68
Reflux flowrate	kmole/h	5500
Bottom product flowrate	kmole/h	150

3.2. Implementation of the L - B control structure

Figure 2 shows a diagram of the simulator obtained by implementing the control structure from figure 1. The control systems in figure 2 have the following meanings: FIC-100 – feed flowrate controller, PIC-100 – top pressure controller, LIC-100 – reflux drum level controller, LIC-101 – reboiler level controller, FIC-101 – bottom product flowrate controller. Some implementation details are presented in (Patrascioiu et al., 2014). As regards the solving of the dynamic models compatibility problems, the Dynamic Assistant function included in Unisim® Design was used.

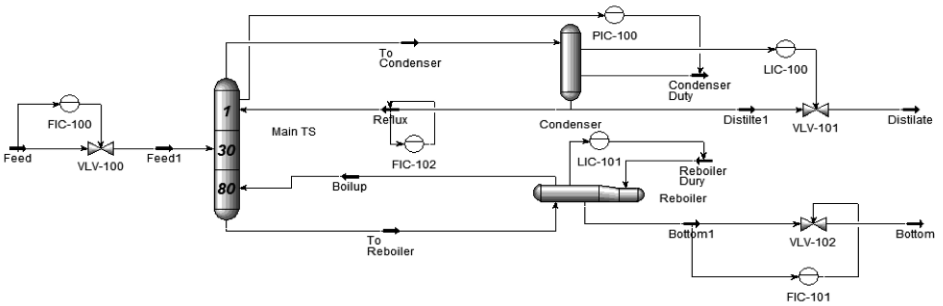

Figure 2 Dynamic simulation diagram of the *L-B* control structure

Table 3. Control system configuration parameters

	Parameter	FIC-100	FIC-101	FIC-102	PIC-100	LIC-100	LIC-101
Controller	Action	Reverse	Reverse	Reverse	Direct	Direct	Direct
	PV min	0 m^3/h	0 m^3/h	0 m^3/h	0 kPa	0 %	0 %
	PV max	80 m^3/h	26 m^3/h	894 m^3/h	3800 kPa	100 %	100 %
	Kc	0.25	0.20	0.25	2	0.05	0.5
	Ti [min]	0.20	0.25	2	0.1	25	0.75
Control valve	Cv	41.10	32.63	-	-	93.80	-
	DeltaP	500 kPa	50 kPa	-	-	50 kPa	-

3.3. Controller tuning of the L-B control structure

The dynamic simulator cannot be used without tuning the controllers associated ~~to~~ with the distillation column and the feed flowrate. Table 3 contains the values of the tuning parameters and other elements related to the control loops configuration (Action, PVmin, PVmax, Cv, DeltaP).

The configured *L-B* structure was tested through simulation to step variation of feed flowrate from 50.62 m^3/h to 55 m^3/h. As shown in figure 3, which displays the simulation results, there are different dynamics on channels F-x_D and F-x_B. This behavior is caused by different speeds of L and V flows through the column and by hydraulic delays introduced by the plates below the feed tray.

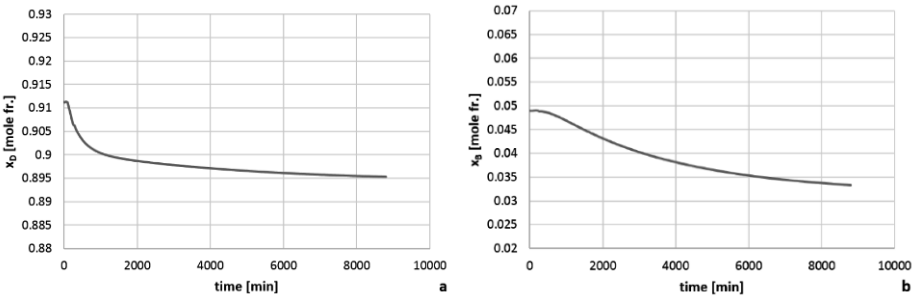

Figure 3 Dynamic response of the propylene concentration in: a) distillate; b) bottom product

Analysis of the time evolutions in figure 3 showed that the dynamic on channel F-x_D can be approximated with a first order element, whereas on channel F-x_B the approximation can be described with a second order element. These results will be starting points for the development of the robust control structure.

3.4. Feedback robust control design

The propylene-propane distillation column is characterized by strong interactions on channels disturbances – propylene concentration and control agents – propylene concentration. These interactions would require the use of a multivariable controller for quality control, solution which is not considered robust because of the fact that the decoupling algorithms are dependent on operating parameters.

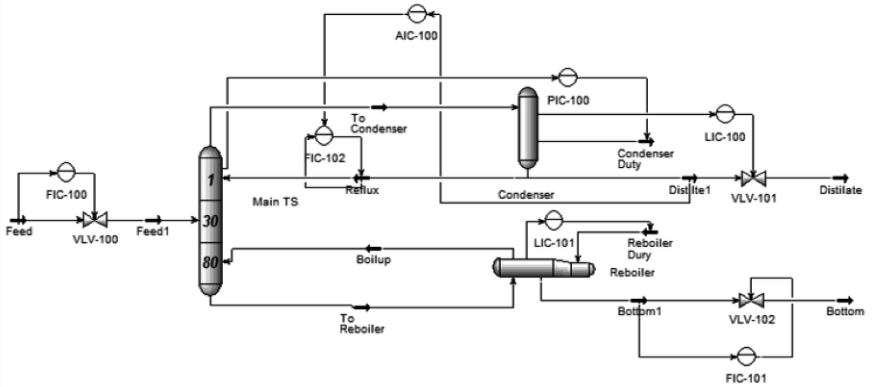

Figure 4 Dynamic simulation diagram of the feedback robust control structure

The design of the feedback robust control structure is based on the fact that only the propylene concentration in distillate requires a fixed value (hard target). The propylene concentration in the bottom product may take values within a range (soft target). In these conditions, the distillate quality control is sufficient. This objective is materialized in a feedback control system for the propylene concentration in distillate with reflux flowrate as manipulated variable. In order to dynamically simulate this system the simulator was reconfigured obtaining the structure in figure 4. For the concentration controller, AIC-100, the following parameters were set: Action = Reverse, PV min = 0, PV max = 1, Kc = 1.2, Ti = 25 min.

The developed control structure was simulated for the same variation of the feed flowrate as in the first case, from 50.62 m^3/h to 55 m^3/h. The time evolutions of the propylene concentration in distillate and bottom product are illustrated in figure 5. It can be observed that this control structure ensures the control of x_D (propylene concentration in distillate), whereas the propylene concentration in the bottom product is allowed to evolve relatively free. The decrease of x_B is explained by the fact that the bottom product flowrate was controlled when the feed flowrate was increased.

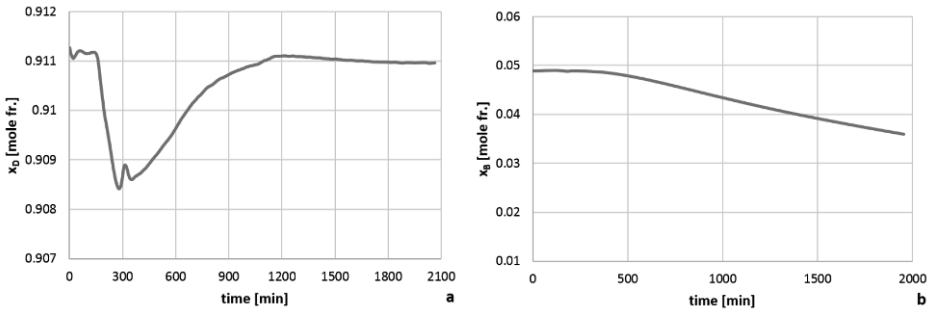

Figure 5 Dynamic response of the propylene concentration in: a) distillate; b) bottom product

3.5. Feedforward control structure

The developed feedforward robust control system is also based on *L-B* structure. The feedforward controller generates set-points for the reflux flowrate and the bottom product flowrate control system. These signals are calculated in real time by processing the two disturbances (feed flowrate - F and concentration of propylene in feed - x_F).

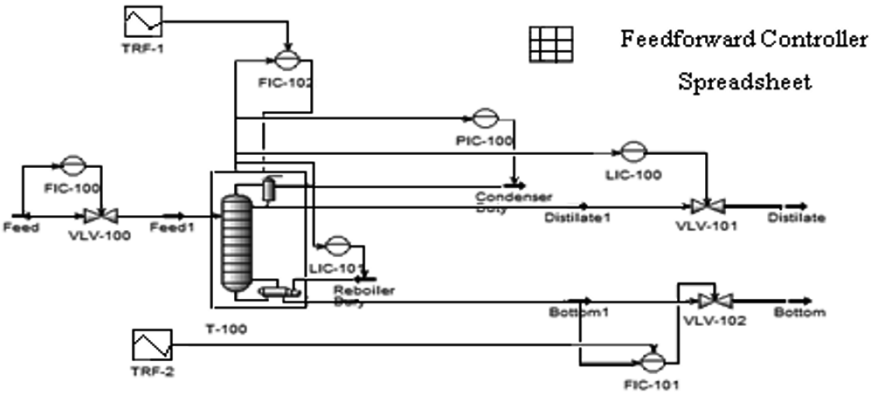

Figure 6 Dynamic simulation diagram of feedforward control structure

The feedforward controller implements the model based on Fenske-Underwood relations and Gilliland correlation (Marinoiu et al., 1986). The steady-state values of the controller outputs were calculated in the simulator using Feedforward Controller Spreadsheet module. Regarding the dynamic components, they have associated first order elements with gain=1 and the time constants T_L = 150 min. and T_B = 175 min., implemented with TRF module.
The feedforward control structure presented in figure 6 was tested for a change of the feed flowrate from 50.62 m^3/h to 55 m^3/h. Analysis of the time evolutions of concentrations x_D and x_B in figure 7 indicated the absence of transient regimes which were present in the case of feedback robust control system.

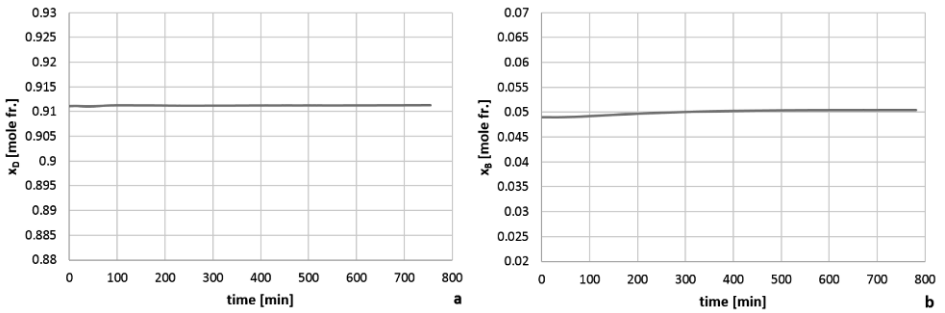

Figure 7 Dynamic response of the propylene concentration in: a) distillate; b) bottom product

4. Conclusions

The paper presents two robust control structures for the quality of products separated in a propylene-propane separation column. Based on relative gain array, the best control structure was selected, respectively *L-B* structure. For this structure, a feedback control system and a feedforward control system for separated products quality control were developed. The dynamic tests performed using Unisim® Design configured for the two robust structures emphasized the superiority of the feedforward control system.

References

Honeywell, 2009, Process Modelling using UniSim® Design Training, Student Guide 4526.
Honeywell, 2010, Dynamic Modelling using UniSim® Design Training, Student Guide 4528.
V. Marinoiu, N. Paraschiv, C. Patrascioiu, 1986, Computer control of propylene separation process (in Romanian), Rev Chim (Bucharest), 37, No. 11, 990-994.
S. Mihalache, C. Patrascioiu, N. Paraschiv, 2008, Pilot Plant for Testing Control Configurations of Binary Distillation Columns, Rev Chim (Bucharest), 59, No. 8, 926-929.
C. Patrascioiu, N. Paraschiv, M. Popescu, 2010, The Quality Control of the Multi-Component Fractionation Process, Petroleum – Gas University of Ploiesti Bulletin, Technical Series, Vol. LXII, No. 4B, 67-74.
C. Patrascioiu, M. Popescu, N. Paraschiv, 2014, Specific Problems of Using Unisim® Design in the Dynamic Simulation of the Propylene-Propane Distillation Column, Rev Chim (Bucharest), 65, No. 9, 1086-1091.
G.F. Shinskey, 1996, Process Control Systems (4th edition), McGraw-Hill, New York.

Krist V. Gernaey, Jakob K. Huusom and Rafiqul Gani (Eds.), 12th International Symposium on Process Systems Engineering and 25th European Symposium on Computer Aided Process Engineering.
31 May - 4 June 2015, Copenhagen, Denmark.

Improved Optimization-based Design of PID Controllers Using Exact Gradients

Chriss Grimholt and Sigurd Skogestad*

Department of Chemical Engineering; NTNU; Trondheim, Norway
**e-mail: skoge@ntnu.no*

Abstract

Finding good controller settings that satisfy complex design criteria is not trivial, even for the simple three parameter *proportional-integral-derivative* (PID) controller. One strategy is to formulate the design problem into an optimization problem. However, when using gradient based optimization with finite differences to estimate the gradients, the algorithm often fails to converge to the optimal solution. This is thought to be a result of inaccuracies in the estimation of the gradients. In this paper we show exact gradients for a typical performance (IAE) versus robustness (M_S, M_T) design problem. We demonstrate increased accuracy in the optimization when using exact gradients compared with forward finite differences.

Keywords: PID control, controller design, optimization, exact gradients, IAE, M_S.

1. Introduction

The simple three parameter *proportional-integral-derivative* (PID) controller is the most adopted controller in the process industry. However, finding good parameter values by trial and error is not only difficult, but also time consuming. In combination with simple models, good parameters are usually found using tuning rules like Ziegler-Nichols or SIMC. When the design complexity increases, in the form of process model complexity or special requirements on controller performance or robustness, it is beneficial to switch to optimization-based design.

Our optimization problem can be formulated as follows,

$$\begin{aligned} \underset{parameters}{\text{minimize:}} \quad & \text{performance cost } (J) \\ \text{subject to:} \quad & \text{required robustness} \end{aligned}$$

where we want the best performance subjected to a required robustness.

The background for this study was to find optimal PID and Smith predictor controller settings for a first-order plus delay process. Here, the performance requirements were to minimize integrated absolute error (IAE) for input and output disturbances, and the robustness criterion was to have a given sensitivity peak (M_S). A similar design formulation has been proposed by Shinskey (1990) where load disturbance was optimized when subjected to sensitivity constraints. By using the link between integral error and integral gain (IE $= 1/k_i$), Åström et al. (1998) formulated the optimization problem for PI control as a set of algebraic equations which could be efficiently solved. In Panagopoulos et al. (2002) the formulation was extended to PID control. However, using IE as the performance criterion can lead to oscillatory response, especially for PID controllers.

Initially, we solved this optimization problem using gradient-free optimization, similar to the work done by Garpinger and Hägglund (2008). Natively, gradient-free approaches, like the simplex

method, does not explicitly handle constraints. To bypass this, the constraints are handled internally by an internal solver. For our application, generating optimal trade-off curves for PID controllers, requiring hundreds of accurate sequential optimizations, the gradient-free method was too slow due to the internal solver and the number of iterations required to converge.

By switching to gradient based methods, using finite-differences to estimate the gradients, we achieved faster convergence. However, the optimization algorithm frequently failed to converge to the solution. Surprisingly, this also occurred even though the initial guess was very close to the local optimum. In our case, it seems that the main problem is not necessarily the non-convexity of the problem and the possibility for local minima, but rather inaccuracies in the estimation of the gradients when using finite-differences. We found that the robustness of the optimization was significantly improved by supplying the exact gradients.

In this paper we show and use exact gradients for IAE of the time response and the peak of the sensitivity functions M_S, and M_T. The main advantage of using accurate gradients is that we improve the convergence properties and make the problem less sensitive to the initial point. The approach has been successfully used to find optimal PID on a first-order with delay processes. But the method can also easily be extended to other processes and controllers.

2. The closed-loop system

In this paper we consider the linear feedback system as shown in Figure 1. Disturbances can enter the system at two different locations, at the plant input (d_u) and the plant output (d_y). The disturbance at the plant output is equivalent to a setpoint change. However, unlike setpoint changes, the output disturbance is not known in advance. Measurement noise (n) enters the system at the measured output (y). This system is represented by four transfer functions nicknamed *the gang of four*,

$$S(s) = \frac{1}{1+G(s)K(s)} \qquad T(s) = 1 - S(s)$$

$$GS(s) = G(s)S(s) \qquad KS(s) = K(s)S(s)$$

where their effect on the control error and plant input is,

$$-e = S(s)\,d_y + GS(s)\,d_u + T(s)\,n \tag{1}$$

$$-u = KS(s)\,d_y + T(s)\,d_u + KS(s)\,n \tag{2}$$

Though we could use any fixed-order controller, we chose in this paper to use the parallel PID controller as an example;

$$K_{\text{PID}}(s;p) = k_p + \frac{k_i}{s} + k_d s = K_c\left(1 + \frac{1}{\tau_I s} + \tau_D s\right); \quad p = \begin{pmatrix} k_p & k_i & k_d \end{pmatrix}^T \tag{3}$$

where $k_p = K_c$, $k_i = K_c/\tau_I$, and $k_d = K_c\,\tau_D$ is the proportional, integral, and derivative gain, respectively. The parallel PID controller can have complex zeros, which we have observed can result in several peaks or plateaux for the magnitude of sensitivity function in the frequency domain $|S(j\omega)|$. This becomes important when adding specifications on the frequency behaviour, which we will show later.

3. Quantifying the optimal controller

3.1. Performance

In this paper we chose one of the most popular ways of quantifying controller performance, the integrated absolute error (IAE);

$$\mathrm{IAE}(p) = \int_0^{t_f} |e(t;p)| \, \mathrm{d}t \tag{4}$$

when subjecting the system to a disturbance. We take both input and output disturbances into account and choose the weighted cost function,

$$J(p) = 0.5 \left(\varphi_{dy} \, \mathrm{IAE}_{dy}(p) + \varphi_{du} \, \mathrm{IAE}_{du}(p) \right); \quad \varphi_{du} = \frac{1}{\mathrm{IAE}^{\circ}_{du}}; \quad \varphi_{dy} = \frac{1}{\mathrm{IAE}^{\circ}_{dy}} \tag{5}$$

where both terms are weighted equally with 0.5 to get a good balance. The φ_{dy} and φ_{du} are scaling factors from IAE-optimal PID controllers for a step load change on the input and output, respectively. To ensure robust reference controllers, they are required to have $M_S = M_T = 1.59$. Note that two different controllers are used to obtain the reference IAE° values, whereas a single controller $K(s;p)$ is used to find $\mathrm{IAE}_{dy}(p)$ and $\mathrm{IAE}_{du}(p)$.

3.2. Robustness

In this paper we have choosen to quantify robustness in terms of M_S and M_T;

$$M_S = \max_{\omega} |S(j\omega)| = \|S(j\omega)\|_{\infty}$$
$$M_T = \max_{\omega} |T(j\omega)| = \|T(j\omega)\|_{\infty}$$

where $\|\cdot\|_{\infty}$ is the H_{∞}-norm. In the Nyquist plot, M_S is the inverse of the closest distance between the critical point $(-1,0)$ and the loop transfer function $L(s) = G(s)\,K(s)$.

The closed-loop system is insensitive to small process variations for frequencies where the sensitivity function $\left|S(j\omega)\right|$ is small (Åström and Hägglund, 2006). On the other hand, small values of the complementary sensitivity function $|T(j\omega)|$ tells us that the closed-loop system is insensitive to larger process variation. The system is most sensitive at the peak of the sensitivity functions (M_S and M_T).

From experience, using only the peaks can lead to cycling between iterations. This is typical for PID control on first order models, where the optimal controller has several peaks of equal magnitude in $S(j\omega)$. The optimizer then discreetly jumps from using one peak to the other between iterations. It is assumed that this results from the peaks having different gradients. To avoid this problem,

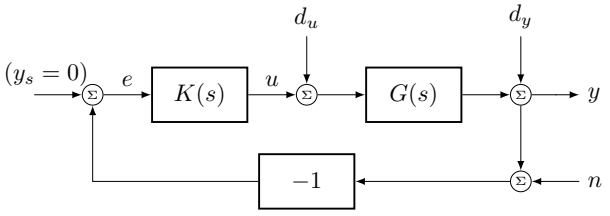

Figure 1: Block diagram of the closed loop system, with controller $K(s)$ and plant $G(s)$.

instead of putting the upper bounds on the peaks, e.g. $M_S \leq M_S^{ub}$, we choose to require

$$\left|S(j\omega)\right| \leq M_S^{ub} \qquad \text{for all } \omega$$

which in addition to handling multiple peaks and plateaux, also improves convergence for infeasible initial controllers. The constrain is approximated by gridding the frequency domain within the interesting region, resulting an inequality constraint for each grid point;

$$\left|S(j\omega)\right| \leq M_S^{ub} \qquad \text{for all } \omega \text{ in } \Omega$$

where Ω is the set of selected frequency points during the gridding of the frequency domain. This results in reduced accuracy and increased computational load. However, the benefit gained towards improved convergence properties makes up for this.

4. Implementation of the optimization problem

The optimization problem can be stated as follows,

$$\begin{aligned}
\underset{p}{\text{minimize}} \quad & J(p) = 0.5\left(\varphi_{dy}\,\text{IAE}_{dy}(p) + \varphi_{du}\,\text{IAE}_{du}(p)\right) \\
\text{subject to} \quad & c_s(p) = |S(j\omega;p)| - M_S^{ub} \leq 0 \quad \text{for all } \omega \text{ in } \Omega \\
& c_t(p) = |T(j\omega;p)| - M_T^{ub} \leq 0 \quad \text{for all } \omega \text{ in } \Omega
\end{aligned}$$

where M_S^{ub} and M_T^{ub} are the upper bounds on $\left|S(j\omega)\right|$ and $\left|T(j\omega)\right|$. If there is a trade-off between performance and robustness, at least one robustness constraint will be active.

5. Gradients

The gradient of a function $\nabla f(p)$ with respects to p is defined as

$$\nabla_p f(p) = \begin{pmatrix} \frac{\partial f}{\partial p_1} & \frac{\partial f}{\partial p_2} & \cdots \frac{\partial f}{\partial p_n} \end{pmatrix}^T \tag{6}$$

where n_p is the number of parameters. In this paper, p_i reference to the parameter i, and the partial derivative $\frac{\partial f}{\partial p_i}$ is called the sensitivity of f. The sensitivities can be approximated by forward finite differences,

$$\frac{\partial f}{\partial p_i} \approx \frac{f(p_i + \Delta p_i) - f(p_i)}{\Delta p_i} \tag{7}$$

requiring $(1+n_p)$ perturbations. For our problem this results in $2(1+n_p)$ step response simulations. The accuracy can be improved by using central differences, which requires $(1+2n_p)$ perturbations.

5.1. Cost function gradient

The gradient of the cost function $\nabla_p J(p)$ is then expressed in terms of the sensitivities,

$$\frac{\partial J(p)}{\partial p_i} = 0.5\left(\varphi_{dy}\,\frac{\partial \text{IAE}_{dy}(p)}{\partial p_i} + \varphi_{du}\,\frac{\partial \text{IAE}_{du}(p)}{\partial p_i}\right) \tag{8}$$

For even relatively simple systems with time delay, these integrals becomes quite complicated, if not impossible, to solve. However, the sensitivities can be found in a fairly straight forward manner by developing them such that the integrals can be numerically evaluated. The sensitivity of IAE can be expressed as,

$$\frac{\partial \text{IAE}(p)}{\partial p_i} = \int_0^{t_f} \text{sign}\left\{e(t;p)\right\}\left(\frac{\partial e(t;p)}{\partial p_i}\right) \mathrm{d}t \tag{9}$$

where $e(t;p) = \mathscr{L}^{-1}\left\{e(s;p)\right\}$ and $\frac{\partial e(t;p)}{\partial p_i} = \mathscr{L}^{-1}\left\{\frac{\partial e(s;p)}{\partial p_i}\right\}$

For the case given in Figure 1 with unit steps load disturbances, the error $e(s;p)$ is $S(s;p)/s$ for the output disturbance dy and $GS(s;p)/s$ for the input disturbance du. The transient $\partial e(t;p)/\partial p$ can then easily found by step response simulations of

$$\frac{\partial S(s)}{\partial p_i} = -GS(s)\, S(s)\, \frac{\partial K(s)}{\partial p_i} \tag{10}$$

$$\frac{\partial GS(s)}{\partial p_i} = -GS(s)\, GS(s)\, \frac{\partial K(s)}{\partial p_i} \tag{11}$$

The gradient of IAE is then calculated by evaluating (9) using numerical integration, and the method is closely related to using direct sensitivities in optimal control problems. This results in $2(1+n_p)$ step response simulations, which is the same as the forward finite differences approximation in (7).

5.2. Constraint gradients

The gradient of the robustness constraints $\nabla c_s(p)$ and $\nabla c_t(p)$ expressed in terms of the parameter sensitivities are,

$$\frac{\partial c_s(j\omega)}{\partial p_i} = \frac{\partial |S(j\omega)|}{\partial p_i} = \frac{1}{\left|S(j\omega)\right|} \mathrm{Re}\left\{S(-j\omega)\, \frac{\partial S(j\omega)}{\partial p}\right\} \qquad \text{for all } \omega \text{ in } \Omega \tag{12}$$

$$\frac{\partial c_t(j\omega)}{\partial p_i} = \frac{\partial |T(j\omega)|}{\partial p_i} = \frac{1}{\left|T(j\omega)\right|} \mathrm{Re}\left\{T(-j\omega)\, \frac{\partial T(j\omega)}{\partial p}\right\} \qquad \text{for all } \omega \text{ in } \Omega \tag{13}$$

If the constrains were instead expressed in terms of the peaks of the transfer functions (e.g. $M_S \leq M_S^{ub}$) the gradients become as follows,

$$\frac{\mathrm{d}}{\mathrm{d}p_i} \|G(j\omega;p)\|_\infty = \frac{\partial}{\partial p_i} |G(j\omega_{peak};p)| \tag{14}$$

where ω_{peak} is the frequency of the peak.

6. Case study

The exact gradients were implemented for the problem;

$$G(s) = \frac{e^{-s}}{s+1};\ \mathrm{IAE}^{\circ}_{dy} = 1.56;\ \mathrm{IAE}^{\circ}_{du} = 1.42;\ M_S^{ub} = M_T^{ub} = 1.3;\ p_0 = \begin{pmatrix} 0.2 \\ 0.02 \\ 0.3 \end{pmatrix} \tag{15}$$

To make the loop function proper, a first order filter with filter time constant $\tau_F = 0.001$ was added to the controller. The error response and parameter sensitivity was found by fixed step integration ($t_f = 25$, $n_{\text{steps}} = 10^4$), with the initial point p_0. The problem was solved using Matlab's fmincon with the active set algorithm. For comparison, forward finite differences was used to approximate the gradients. This problem has two equal M_S peaks at the optimum (Figure 2), and is a typical example of a problem exhibiting cyclic behaviour when using the $M_S \leq M_S^{ub}$ constraint. The optimal error response is shown in Figure 3.

The exact gradients performed better than the finite differences (Table 1). The exact cost function gradients give the best improvement. This signals that the optimum is relatively flat, and that the approximated cost function gradients are not precise enough to find the true local optimum. The same test was performed for different numbers of time steps during the integration. Even with $n_{\text{steps}} = 10^5$, the forward finite differences failed to converge to the local optimum (controller parameter error in the second digit). On the other hand, the exact gradient could still converge to the local optimum with as low as $n_{\text{steps}} = 500$ (control parameters error in the fifth digit). The exact gradient converged for most stable initial guesses, but the forward finite differences failed to

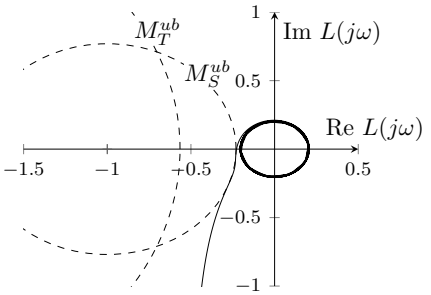

Figure 2: Nyquist plot of $L(j\omega)$ with the optimal controller for the problem given in (15).

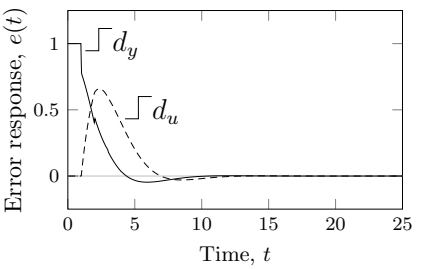

Figure 3: Optimal error response for the problem given in (15).

find the optimum even when started very close to the optimum $p_0 = \begin{pmatrix} 1.001p_1^\star & p_2^\star & p_3^\star \end{pmatrix}^T$. When using central finite differences, the accuracy was increased. However, this requires $2(1+2n_p)$ step simulations.

Table 1: Comparison between optimal solutions with different combinations of gradients.

Gradient type		Cost function	Optimal parameters			number of
Cost-function	Constraints	$J(p^\star)$	k_p	k_i	k_d	iterations
exact	exact	2.0598	0.5227	0.5327	0.2172	13
fin.dif.	exact	2.1400	0.5204	0.4852	0.1812	16
exact	fin.dif.	2.0598	0.5227	0.5327	0.2172	13
fin.dif.	fin.dif.	2.9274	0.3018	0.3644	0.2312	11

7. Conclusion

In this paper we have successfully applied the exact gradients for a typical performance (IAE) versus robustness (M_S, M_T) optimization problem. The exact gradients improved the convergence to the true optimal point when compared to gradients approximated by forward finite difference.

References

Åström, K., Panagopoulos, H., Hägglund, T., May 1998. Design of PI Controllers based on Non-Convex Optimization. Automatica 34 (5), 585–601.

Åström, K. J., Hägglund, T., 2006. Advanced PID control. ISA-The Instrumentation, Systems, and Automation Society; Research Triangle Park, NC 27709.

Garpinger, O., Hägglund, T., 2008. A software tool for robust pid design. In: Proc. 17th IFAC World Congress, Seoul, Korea.

Panagopoulos, H., Å ström, K., Hägglund, T., 2002. Design of PID controllers based on constrained optimisation. IEE Proceedings - Control Theory and Applications 149 (1), 32.

Shinskey, F. G., 1990. How Good are our controllers in absolute performance and robustness. Measurement and Control 23, 114–120.

Krist V. Gernaey, Jakob K. Huusom and Rafiqul Gani (Eds.), 12th International Symposium on Process Systems Engineering and 25th European Symposium on Computer Aided Process Engineering.
31 May – 4 June 2015, Copenhagen, Denmark

Enhancing Xylitol Bio-Production by an Optimal Feeding Policy during Fed-Batch Operation

Oscar Andrés Prado-Rubio,[1*] Héctor Hernández-Escoto,[2] Divanery Rodriguez-Gomez,[3] Sarote Sirisansaneeyakul,[4] Ricardo Morales-Rodriguez[2,5]

[1]*Departamento de Ingeniería Química, Universidad Nacional de Colombia, Caldas, Colombia.*
[2]*Departamento de Ingeniería Química, Universidad de Guanajuato, Guanajuato, Gto., 36050, México.*
[3]*Departamento de Biotecnología, Universidad Autónoma Metropolitana-Iztapalapa, México, D.F., 09340, México.*
[4]*Department of Biotechnology, Faculty of Agro-Industry, Kasetsart University, Bangkok 10900, Thailand*
[5]*Departamento de Ingeniería de Procesos e Hidráulica, Universidad Autónoma Metropolitana-Iztapalapa, México, D.F., 09340, México.*
**oaprador@unal.edu.co*

Abstract

The xylitol production has become an important process to investigate given the diverse product applications, especially in the food industry. The biotechnological xylitol production has been assessed mainly through an experimental approach via batch and fed-batch operation. This study presents an analysis for optimal operation of the fed batch process following a systematic methodology. The model based approach includes the collection, validation and calibration of the mathematical model, followed by the proposal of some operation scenarios. The implementation of such methodology allowed to increase 20% the yield of xylitol compared with the obtained previously in some experiments. Moreover, an analysis for the diauxic phenomenon was also performed, allowing to determine an optimal feeding ratio between substrates.

Keywords: xylitol bioproduction, fed-batch operation, optimal feeding policy

1. Introduction

Due to the gradual increase in worldwide energy consumption, research efforts have been directed to biofuels production mainly employing lignocellulosic material. Nevertheless, economic analyses have shown that production of biofuels and high value-added products should be performed simultaneously to enhance profitability; such high value-added products are xylitol, polylactic acid acid, sorbitol, levulinic acid, furfurals, among others (van Ree and Annevelink, 2007).

Xylitol is a natural five-carbon sugar alcohol usually employed as sugar substitute since it prevents dental caries. Recently, its biotechnological production using yeast from genera *Saccharomyces*, *Candida* and *Pichia* has gained interest (Granström et al., 2007). For instance, *Candida mogii* can produce xylitol from xylose by action of the enzyme xylose reductase. A drawback of this bioprocess is that the produced xylitol can be consumed by the microorganism to generate cell mass and maintenance energy. It has been shown that the addition of glucose in the fermentation broth can improve the

xylitol yield, because glucose can partially substitute xylitol as substrate in the growth metabolic pathway. However, it must be considered that high glucose concentration might inhibit xylose transport into the cell and repress induction of relevant enzymes for the xylose assimilation. From the model-based simulation perspective, a mathematical model describing xylitol batch production has been presented by Tochampa et al. (2005), and it has also been extended by Hernandez-Escoto et al. (2014) for a continuous reactor including some control scenarios. In order to improve the xylitol production, Sirisansaneeyakul et al. (2012) performed some experiments introducing a fed-batch operation for xylitol production, where a feeding policy was proposed to increase the yield xylitol/xylose in the reactor. The experiments showed an improvement in the xylitol production during intermittent fed-batch fermentations; however, there was no certainty whether the findings can be considered as optimal results. In order to address this issue, the objective of this work is to propose fed-batch operation scenarios for xylitol production using a model-based framework. The process system provided by Sirisansaneeyakul et al. (2012) was taken as benchmark.

2. Methodology

The methodology employed to reach the proposed objective is illustrated in Figure 1, which considers 4 main steps.

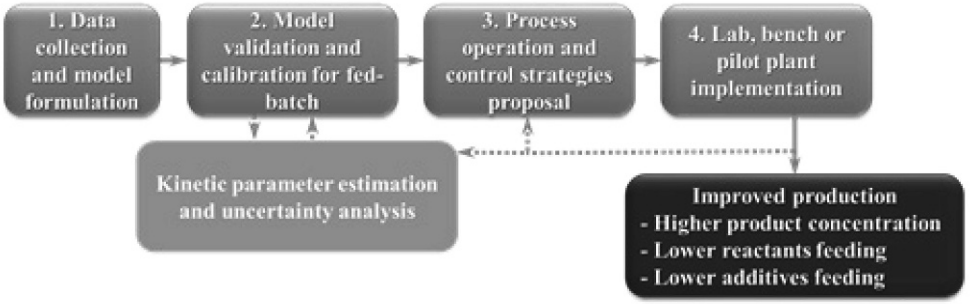

Figure 1. Model-based framework for enhanced and controlled operation of a fed-batch reactor.

The first step is the data collection and model structure formulation, where a kinetic mathematical model is proposed or obtained/extended from the literature. The second step is the model validation employing experimental data; if necessary, a model parameters calibration is performed, and complemented by an uncertainty analysis. Using the model and process insights from step 2, the third step is to propose diverse optimal operation scenarios according to a processing objective, i.e. higher product concentration, enhanced bioreactor productivity and higher biomass growth. The main outcome of the scheme is the final step where experiments are proposed at lab, bench or pilot plant scale, based on the outcomes of step 3. The results of step 4 can be then employed to recalibrate the model or to propose other operational and control scenarios. In general, this methodology could be used for other fed-batch fermentations systems in order to enhance product generation related to certain constraints, such as, product inhibition, substrate inhibition, operational constraints, etc.

3. Results

The implementation of the model-based framework (Figure 1) for optimized operation of a fed-batch reactor was performed for xylitol production employing a biotechnological route.

3.1. Data collection and model formulation

This work considered the mathematical model of xylitol production proposed by Tochampa et al. (2005). Since the mathematical model was originally proposed for a batch operation, the model structure was extended to describe a fed-batch operation.

3.2. Model validation and calibration for fed-batch

The modified mathematical model was then validated using some data previously published by Sirisansaneeyakul et al. (2012), where the authors proposed a fed-batch operation. Figure 2a illustrates the validation performed by comparison of fed-batch model with original kinetics parameters with respect to experimental data. The model trajectories showed mismatch with respect to experimental data, which could be associated with the experimental conditions during fed-batch operation.

Therefore, a calibration of the kinetic parameters was related with low accuracy of the model in the fed-batch operation. The least-squares nonlinear function "lsqrnonlin" of Matlab® was employed to re-estimate the kinetic parameters of the mathematical model using three experimental datasets published by Sirisansaneeyakul et al. (2012). Table 1 shows the parameters modified from the original model.

Table 1. Parameter values obtained after parameter estimation.

Parameter	Value	Parameter	Value
$\mu_{xit}^{\max}$, h^{-1} (maximum specific growth rate on xylitol)	0.189	$q_{xyl}^{\max}$, $g-xylose \cdot g-DWC^{-1} \cdot h^{-1}$ (maximum specific uptake rate of xylose)	0.342
$K_{s,xyl}$, $g-xylose \cdot l^{-1}$ (saturation constant based on xylose)	11.761	$K_{s,xit}$, $g-xylitol \cdot l^{-1}$ (saturation constant based on xylitol)	16.06

The simulation results after parameter calibration are illustrated in Figure 2 (solid line), which showed an improvement and better prediction than original parameters of the model. There is still room for improvements.

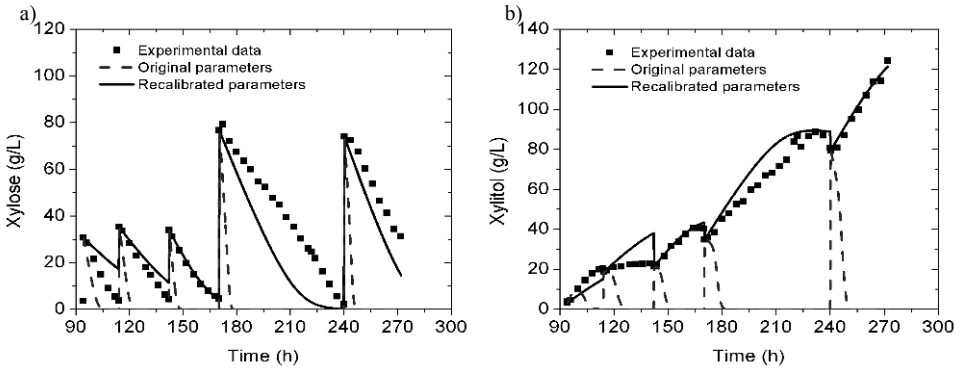

Figure 2. Validation of the recalibrated mathematical model parameters for intermittent operation: a) xylose concentration; b) xylitol concentration.

3.3. Process operation and control strategies proposal

The aim of this part was to investigate operational challenges and potential improvements of the fed-batch fermentation for xylitol production. For this purpose, two case studies were analysed within this contribution: optimal xylose feeding policy and optimal diauxic cultivation. An important characteristic of the implementation is to account for the volume change due to sampling. This is relevant since the final aim is to propose an optimal operation scenario to test at laboratory scale. The constrained optimization problem included the mass balances for the species involved in the reacting system (Eq. 1), the objective function (Eq. 2) and constrains of the problem (Eq. 3).

$$\frac{dX}{dt} = h\left(X, \theta, u\right) \tag{1}$$

$$Max_u\left(F_{obj}\right) = \left(VC_{xylitol} - VC_{xylose}\right)_{final,ts} \tag{2}$$

s.t.

$$g_{operational,l} < g_{operational}\left(X, \theta, u\right) < g_{operational,u} \tag{3}$$

where, X is the set of state variables, u is the model inputs, and θ is the set of model parameters.

The proposed objective function maximizes the amount of xylitol obtained while penalizes the remaining xylose in the fermenter as illustrated in Eq. (2). In this work the influence of weight factors for each contribution in the objective function was not investigated. The optimization problem was subject to operational constraints, which depended on the investigated scenario. The optimization was solved through Matlab® function “fmincon”, based on the interior-point algorithm. During the resolution, the best solution was selected from a series of found local minima.

3.3.1. Optimal xylitol feeding policy

Using selected experimental data from Sirisansaneeyakul et al. (2012) as reference model inputs, the attempt of this study case was to compare the performance of the experimental cultivation and the simulated optimal fed-batch fermentation. The operational constraint imposed in this scenario was that the final reactor volume must not surpass the 70% of the initial value. Each experimental sampling instant was considered as a feeding change instant, where an inlet flow rate was calculated in order to obtain a maximum value of the objective function. The simulation results of the optimal policy for five feeding steps are shown in Figure 3. The biomass concentration remained almost constant since the low growth rate of the microorganism on xylose was compensated with dilution and the simulated bleeding due to sampling. Regarding to xylose concentration, the penalty imposed in the objective function made the feeding policy to dose xylose in order to avoid its accumulation. The final xylitol concentration after almost 180 h reached 48.4 g/L. During the solution of other optimization scenarios for this bioreaction system (not shown here), it was possible to observe that there was a trend in the feeding policy on using a larger amount of substrate at the beginning of the fermentation. The reason was that the system did not exhibit substrate inhibition in the evaluated experimental conditions. Comparing the simulated results with the experimental values used for validation (see Figure 2), lower xylitol production was predicted. The different results are attributed to the model mismatch (especially biomass growth), the different biomass states used during the experiments (pH variations and increasing substrate loads in the intermittent fermentations) and intermittent cultivation

broth dilution with fresh substrate at different concentration. However, the simulation under xylose feeding has shown potential improvement since the xylitol yield from substrate was increased almost 20%. Further work is required in order to find better optimization scenarios.

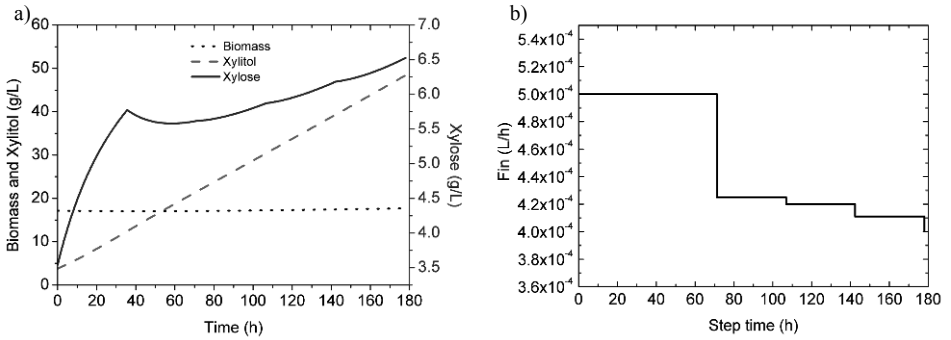

Figure 3. Optimal Fed-batch operation simulation results. The initial conditions are after a batch fermentation to achieve high biomass density. a) Bioreactor concentrations; b) xylose feeding policy at 595 g/L.

3.3.2. Optimal diauxic fermentation

In order to complement the previous efforts using only xylose as substrate, a diauxic growth on xylose and glucose was also investigated; recalling that the addition of glucose in the fermentation broth can improve the xylitol yield, but high concentration can also produce an inhibition on xylitol production (Sánchez et al., 2008; Tochampa et al., 2005). Hence, the objective function was maximized to find the optimal initial concentrations of xylose and glucose as well as the appropriate fermentation time. The problem was subject to maximum concentrations of 100 g/L and fermentation time of 100 h. The optimal solution of diauxic growth and fermentation on xylose are shown in Figure 4. The optimization results indicated that there was an optimal glucose initial concentration and fermentation time in order to exploit the loaded xylose; in this case, the maximum allowed. The optimal glucose addition delayed the xylitol production while favoured the biomass growth. Higher biomass density enhanced the xylose uptake and subsequently the xylitol production. In this case, there is a 40% improvement on xylitol production.

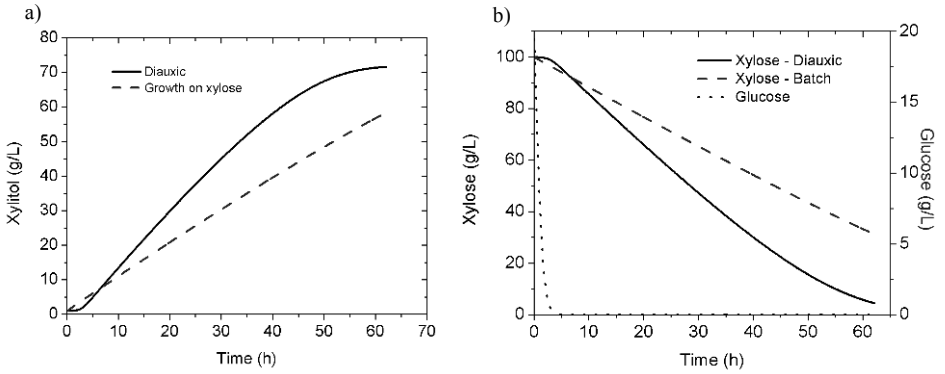

Figure 4. Fed-batch fermentation on xylose compared to fed-batch cultivation on optimal glucose and xylose initial concentrations: a) xylitol; b) xylose and glucose

Despite the main objective of this work that was to generate model-based alternative scenarios to be tested at laboratory, bench or pilot plant scales, an economic analysis was also performed. The economic potential of the processes was evaluated using the current average prices available on-line of product and reactants as bulk chemicals. The results showed that the ratio between the economic potential of the diauxic against batch fermentation was over 2.6. These results are encouraging to validate experimentally the outcomes of the proposed methodology. On the other hand, qualitatively speaking on the basis of results, it is advantageous to use diauxic fermentations since: higher xylitol concentration in the fermentation broth facilitates its downstream separation, and a mixture of substrates makes this process compatible within a biorefinery framework.

4. Conclusion

Due to the challenge of finding optimal operation conditions for bioprocesses from an experimental approach, a model based framework was proposed in this work. The framework was useful to provide system insights that lead to alternative operation scenarios to be tested in the laboratory. Using the xylitol bioproduction as study case, it was shown the potential of using optimal feeding policies in order to enhance productivity and substrate utilization. Comparing the experimental presented by Sirisansaneeyakul et al. (2012) and optimization results obtained in this work, it was possible to observe an improvement in the yield xylitol/xylose by 20%. The analysis of diauxic phenomenon allowed to identify an improvement up to 40% on xylitol production and 260% on the crude economic potential comparing the simulated fed-batch and batch operations. This work showed the potential of a model based approach to bring new perspectives for optimal operation of bioprocesses. Further investigations are required in order to propose and optimal operation scenario to be tested experimentally.

Acknowledgments

The authors kindly acknowledge the Mexican National Council for Science and Technology (CONACyT, project number 230107) and PROMEP-Mexico (project number, UAM-PTC-454) for the financial support on the development of this project.

References

T.B. Granström, K. Izumori, M. Leisola, 2007, A Rare Sugar Xylitol. Part I: The Biochemistry and Biosynthesis of Xylitol, Applied microbiology and biotechnology, 74 (2), 277-281.

H. Hernandez-Escoto, D. Rodriguez-Gomez, R. Morales-Rodriguez, 2014, Process Design and Control of a Xylitol Production Reactor, Computer-Aided Chemical Engineering, 33, 757-762.

MatLab/Simulink. The MathWorks, Inc. 2009. Version 7.9.0.529 (R2009b).

R. van Ree, B. Annevelink, 2007, Status Report Biorefinery 2007, Agrotechnology and Food Sciences Group, ISBN-number 978-90-8585-139-4.

Sánchez, S., Bravo, V., García, J.F., Cruz, N., Cuevas, M., 2008, Fermentation of D-Glucose and D-Xylose mixtures by *Candida tropicalis* NBRC 0618 for xylitol production, World Journal of Microbiology and Biotechnology, 24, 709-716.

S. Sirisansaneeyakul, S. Wannawilai, Y- Chisti, 2012, Repeated Fed-Batch Production of Xylitol by *Candida magnolia* TISTR 5663, Journal of Chemical Technology and Biotechnology, 88, 1121-1129.

W. Tochampa, S. Sirisansaneeyakul, W. Vanichsriratana, P. Srinophakun, H.H.C. Bakker, Y. Chisti, 2005, A Model of Xylitol Production by the Yeast *Candida mogii*, Bioprocess and Biosystems Engineering, 28, 175-183.

Krist V. Gernaey, Jakob K. Huusom and Rafiqul Gani (Eds.), 12th International Symposium on Process Systems Engineering and 25th European Symposium on Computer Aided Process Engineering.
31 May - 4 June 2015, Copenhagen, Denmark.

Performance Evaluation of Bayesian State Estimators for Nonlinear DAE Systems Using a Moderately High Dimensional Reactive Distillation Column Model

Jalesh L. Purohit[a], Sachin C. Patwardhan*[b] and Sanjay M. Mahajani[b]

[a]*Department of Chemical Engineering; Dharamsinh Desai University, Nadiad, India*
[b]*Department of Chemical Engineering; Indian Institute of Technology Bombay, India*
**Email: sachinp@iitb.ac.in*

Abstract

If it is desired to control a reactive distillation (RD) system at an unstable operating point, then use of a reliable nonlinear state estimator becomes an essential step in the controller synthesis. This work aims at carrying out a comparative evaluation of the performances of two recently developed nonlinear Bayesian estimators for systems modelled as DAEs, namely extended Kalman filter (EKF) and unscented Kalman filter (UKF) (Mandela et al., 2010). Efficacies of DAE-EKF and DAE-UKF have been evaluated by simulating state estimation problems associated with a benchmark ideal RD column (Olanrewaju and Al-Arfaj, 2006). When compared on the basis of sum squared estimation errors, the DAE-UKF was found to outperform the DAE-EKF. However, contrary to the claims in the state estimation literature regarding the computational efficiency of UKF vis a vis EKF, the average computation time needed for the DAE-EKF computations was found to be significantly less (by factor of 50) than the average computation time needed for the DAE-UKF computations. Moreover, the performance of DAE-EKF was found to improve if the top and the bottom concentration measurements are included in the estimation problem along with temperature measurements on alternate trays. Thus, DAE-EKF was found to be better suited for development of an observer based control scheme.

Keywords: Reactive Distillation, Differential Algebraic Equations (DAEs), EKF, UKF

1. Introduction

Reactive Distillation (RD) systems can exhibit steady state input and output multiplicity behavior due to complex interaction between reaction and phase equilibrium (Purohit et al., 2013a). Occurrence of the output multiplicity behavior leads to an open loop unstable dynamics at some of the multiple steady states. The behavior of the process in the presence of output multiplicities, thus, depends on the process history and the process output can be different for the identical input moves. The difficulties are further compounded by the fact that dynamic models for RD systems often turn out to be a set of coupled stiff differential algebraic equations (DAEs). Thus, if it is desired to control the system at one of the unstable operating points, then use of a reliable nonlinear state estimator becomes an essential step in the controller synthesis (Purohit et al., 2013b).

With regards to the RD columns, relatively little work has been reported on the application of state estimation methods for estimating compositions (Grüner et al., 2003; Olanrewaju and Al-Arfaj, 2006; Venkateshwarlu and Kumar, 2006). These contributions directly apply the state estimation approach developed for the systems modeled as ODEs. However, since the RD systems are typically modelled as DAEs, a different treatment is needed to handle the associated state estimation

problem. The area of nonlinear Bayesian observers for systems modeled as DAEs is relatively unexplored. The extension of the Kalman Filter to nonlinear DAE systems was developed by Becerra et al. (2001) under the assumption that only the differential states are measured. Mandela et al. (2010) have recently extended the work of Becerra et al. (2001) to accommodate measurements obtained from differential as well as algebraic states. In addition, they also developed a version of unscented Kalman filter (UKF) suitable for the DAE systems.

As a step towards observer based controller synthesis for a RD system, this work aims at carrying out a comparative evaluation of the performances of DAE-EKF and DAE-UKF. Efficacies of these estimators have been evaluated by simulating state estimation problems associated with a benchmark ideal RD column (Olanrewaju and Al-Arfaj, 2006), which exhibits input and output multiplicity behavior simultaneously. In contrast to small dimensional examples considered in the available literature on state estimation of DAE systems, the RD model considered in this work is of moderately high dimension i.e. it consists of 90 differential states and 21 algebraic states. The performances of the DAE observers are investigated in the neighborhood of an unstable operating point of the RD system by assuming that only the temperatures on alternate trays are measured.

This paper is organized in five sections. The modeling assumptions are stated in Section 2. Section 3 briefly presents the DAE-UKF algorithm. The simulation results are presented in Section 4 and main conclusions reached through the simulation studies are presented in Section 5.

2. Model for Plant Simulation and State Estimation

The system under consideration can be represented in abstract form by a semi-explicit DAE of the form

$$\frac{d\mathbf{x}}{dt} = \mathbf{f}[\mathbf{x}(t), \mathbf{z}(\mathbf{t}), \mathbf{m}(t), \mathbf{d}(t)] \text{ and } \mathbf{G}[\mathbf{x}(t), \mathbf{z}(t)] = \overline{0} \tag{1}$$

where, $\mathbf{x} \in \mathbb{R}^{n_d}$ represents the differential state variables, $\mathbf{z} \in \mathbb{R}^{n_a}$ represents the algebraic state variables, $\mathbf{m} \in \mathbb{R}^m$ represents the input variables, and $\mathbf{d} \in \mathbb{R}^d$ represent the unmeasured disturbance variables. The state estimation using this model have been carried out under the following simplifying assumptions:

- The measurements, $\mathbf{y}_m(k), \in \mathbb{R}^r$ are obtained at a regular interval, h, and the measurement equation at $k'th$ sampling instant is given by

$$\mathbf{y}_m(k) = \mathbf{C}\begin{bmatrix} \mathbf{x}(k) \\ \mathbf{z}(k) \end{bmatrix} + \mathbf{v}(k) = \mathbf{C}\mathscr{X}(k) + \mathbf{v}(k) \tag{2}$$

  where $\mathscr{X}(k)$ represents augmented state vector. Here, measurement noise, $\mathbf{v}(k)$, is modelled as a zero-mean Gaussian white-noise process with covariance matrix $\mathbf{R}$, i.e. $\mathbf{v}(k) \sim \mathscr{N}(\overline{\mathbf{0}}, \mathbf{R})$

- In discrete time settings, the true value of the inputs (**m**) are related to the known / computed values of the inputs (**u**) as $\mathbf{m}(k) = \mathbf{u}(k) + \mathbf{w}_u(k)$ where $\mathbf{w}_{u,k} \in \mathbb{R}^m$ denotes an unknown disturbance in inputs such that $\mathbf{w}_u(k) \sim \mathscr{N}(\overline{\mathbf{0}}, \mathbf{Q}_u)$.

- The variation of the unmeasured disturbances around a desired steady state $\overline{\mathbf{d}}$ can be adequately approximated using piecewise constant functions of the form $\mathbf{d}(k) = \overline{\mathbf{d}} + \mathbf{w}_d(k)$ over $[t_k, t_k + h]$ where $\mathbf{w}_d(k) \in \mathbb{R}^{d_u}$ such that $\mathbf{w}_d(k) \sim \mathscr{N}(\overline{\mathbf{0}}, \mathbf{Q}_d)$.

Thus, the plant is simulated by solving the set of DAEs (1) using a suitable DAE solver. For the sake of convenience, the following notation is adopted to represent the DAEs in discrete form

$$\mathbf{x}(k+1) = \mathbf{F}[\mathbf{x}(k), \mathbf{z}(k), \mathbf{u}(k), \mathbf{w}(k)] \quad \text{and} \quad \mathbf{G}[\mathbf{x}(k+1), \mathbf{z}(k+1)] = \overline{0} \tag{3}$$

where $\mathbf{w}(k) \in R^{n_w}$ represents augmented state noise vector, $\mathbf{w}(k) = \begin{bmatrix} \mathbf{w}_u^T(k) & \mathbf{w}_d^T(k) \end{bmatrix}^T$, with covariance matrices $\mathbf{Q} = \mathbf{diag}\begin{bmatrix} \mathbf{Q}_u & \mathbf{Q}_d \end{bmatrix}$.

3. State Estimation

The state estimation has been carried out using two recently developed nonlinear Bayesian estimators for systems modelled as DAEs, namely extended Kalman filter (EKF) and unscented Kalman filter (UKF) (Mandela et al., 2010). For the sake of brevity, only the DAE-UKF algorithm is summarized here. The details of DAE-EKF can be found in Mandela et al. (2010).

Given prior estimates $(\widehat{\mathbf{x}}(k-1|k-1), \widehat{\mathbf{z}}(k-1|k-1))$, and covariance matrix $\mathbf{P}(k-1|k-1)$, generate $2(n+n_w)+1$ sigma points for $\xi(k-1) = \begin{bmatrix} \mathbf{x}^T(k-1) & \mathbf{w}^T(k-1) \end{bmatrix}^T$ are constructed as follows:

$$\mathbf{P}_a(k-1|k-1) = \mathbf{diag}\begin{bmatrix} \mathbf{P}(k-1|k-1) & \mathbf{Q} \end{bmatrix} \tag{4}$$

$$\mathbf{S}(k-1|k-1) = \sqrt{\mathbf{P}_a(k-1|k-1)} \tag{5}$$

$$\widehat{\xi}^{(0)}(k-1|k-1) = \widehat{\xi}(k-1|k-1) \text{ with } w_0 = \frac{\kappa}{(n+n_w)+\kappa} \tag{6}$$

$$\widehat{\xi}^{(i)}(k-1|k-1) = \widehat{\xi}(k-1|k-1) + \rho \mathbf{S}^{(i)}(k-1|k-1) \tag{7}$$

$$\widehat{\xi}^{(n+n_w+i)}(k-1|k-1) = \widehat{\xi}(k-1|k-1) - \rho \mathbf{S}^{(i)}(k-1|k-1) \tag{8}$$

$$w_i = w_{(n+n_w)+i} = \frac{1}{2((n+n_w)+\kappa)} \text{ for } i = 1,2,...,(n+n_w) \tag{9}$$

where, $\mathbf{S}^{(i)}$ represents the i^{th} column of matrix square of $\mathbf{S}$, $\rho = \sqrt{((n+n_w)+\kappa)}$, w_i represents the weight associated with i^{th} sigma point and κ denotes a tuning parameter. The associated algebraic state, $\widehat{\mathbf{z}}^{(i)}(k-1|k-1)$, has to be generated by solving for $\mathbf{G}\left(\widehat{\mathbf{x}}^{(i)}(.), \widehat{\mathbf{z}}^{(i)}(.)\right) = \overline{\mathbf{0}}$. The sigma points are then propagated using a DAE solver to obtain predicted differential, $\widehat{\mathbf{x}}^{(i)}(k|k-1)$, and algebraic states, $\widehat{\mathbf{z}}^{(i)}(k|k-1)$. The mean and covariance of the differential states is then estimated as follows:

$$\widehat{\mathbf{x}}(k|k-1) = \sum_{i=0}^{2(n+n_w)} w_i \widehat{\mathbf{x}}^{(i)}(k|k-1) \text{ and } \mathbf{P}(k|k-1) = \sum_{i=0}^{2(n+n_w)} w_i \varepsilon^{(i)}(k|k-1)\left[\varepsilon^{(i)}(k|k-1)\right]^T$$

where $\varepsilon^{(i)}(k|k-1) = \left(\widehat{\mathbf{x}}^{(i)}(k|k-1) - \widehat{\mathbf{x}}(k|k-1)\right)$. The Kalman gain matrix is computed as $\mathbf{L}(k) = \mathbf{P}_{\mathscr{X}y}(k)\mathbf{P}_{yy}(k)^{-1}$ where

$$\mathbf{P}_{yy}(k) = \sum_{0}^{2(n+n_w)} w_i \left[\left(\mathbf{e}^{(i)}(k)\right)\left(\mathbf{e}^{(i)}(k)\right)^T\right] + \mathbf{R}$$

$$\mathbf{P}_{\mathscr{X}y}(k) = \sum_{0}^{2(n+n_w)} w_i \left(\widehat{\mathscr{X}}^{(i)}(k|k-1) - \widehat{\mathscr{X}}(k|k-1)\right)\left(\mathbf{e}^{(i)}(k)\right)^T$$

Here, $\mathbf{e}^{(i)}(k) = \left(\widehat{\mathbf{y}}^{(i)}(k|k-1) - \widehat{\mathbf{y}}(k|k-1)\right)$ and

$$\widehat{\mathscr{X}}(k|k-1) = \sum_{i=0}^{2n} w_i \widehat{\mathscr{X}}^{(i)}(k|k-1) \text{ and } \widehat{\mathbf{y}}(k|k-1) = \sum_{i=0}^{2(n+n_w)} w_i \mathbf{C}\widehat{\mathscr{X}}^{(i)}(k|k-1)$$

The Kalman Gain corresponding to the differential states $\mathbf{L}_x(k)$ is $n \times n$ matrix constructed using the first n rows of $\mathbf{L}(k)$.The mean and covariance of the differential states is then updated as follows

$$\widehat{\mathbf{x}}(k|k) = \widehat{\mathbf{x}}(k|k-1) + \mathbf{L}_x(k)(\mathbf{y}_m(k) - \widehat{\mathbf{y}}(k|k-1)) \tag{10}$$

$$\mathbf{P}(k|k) = \mathbf{P}(k|k-1) - \mathbf{L}_x(k)\mathbf{P}_{yy}(k)\mathbf{L}_x(k)^T \tag{11}$$

The updated algebraic states, $\widehat{\mathbf{z}}(k|k)$, consistent with $\widehat{\mathbf{x}}(k|k)$ are then estimated by solving for $\mathbf{G}(\widehat{\mathbf{x}}(k|k), \widehat{\mathbf{z}}(k|k)) = \overline{\mathbf{0}}$

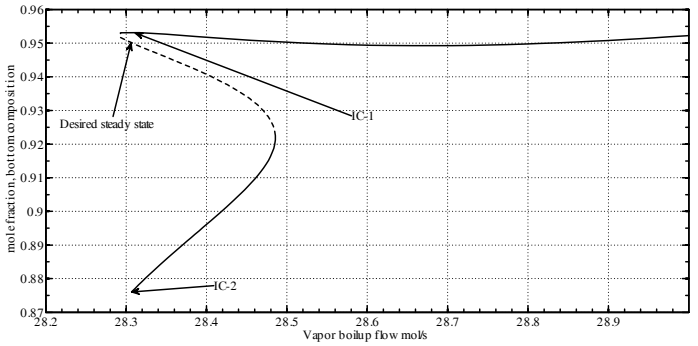

Figure 1: Steady state multiplicity in ideal RD 7/6/7 at constant reflux flow rate

4. Simulation Studies

The simulation exercise is aimed at comparison of the performances of DAE-EKF and DAE-UKF algorithms proposed by Mandela et al. (2010) using an ideal RD system. An example of the RD column with hypothetical quaternary reaction, $a+b \leftrightarrow c+d$, and ideal VLE (Olanrewaju and Al-Arfaj, 2006) is chosen for simulation. The RD model considered here has 90 differential states and 21 algebraic states. The liquid compositions of all the components on all the stages including reboiler and condenser stages and molar holdup of reboiler and condenser are considered as differential states. Temperatures on all the stages are considered as algebraic states. Details regarding the structural parameters, operating parameters, reaction kinetics and mathematical model of this RD column are available in Olanrewaju and Al-Arfaj (2006) and Purohit et al. (2013b). The RD column considered in the present work exhibits nonlinear input and output multiplicities behavior as shown in Figure 1. The desired operating point is indicated in Figure 1 which is an unstable operating point. There are two other stable steady states, indicated as IC-1 and IC-2 in Figure 1, at the same input value of the vapor boil up rate.

To carry out state estimation of the RD system under consideration, it was assumed that, total 11 temperatures on the alternate stages, starting from the reboiler stage, are measured. Also, the temperature measurements are available at regular interval of 30 sec. Details of covariances of the measurement noise and unmeasured disturbances in the manipulated inputs can be found in Purohit et al. (2013b). The value of κ in UKF is chosen as 1. To compare the performances of EKF and UKF for the DAE RD column considered here, the following two performance indices were used: (a) Sum of square of estimation errors (SSEE) defined as $SSEE_i = \sum_{i=1}^{N} \left(\mathbf{x}_i(k) - \widehat{\mathbf{x}}_i(k|k)\right)^2$ where N represents number of data points in a simulation experiment and (b) average computational time (on Intel CORE^{TM} i3 2120 CPU 3.3 GHz with 4 GB RAM).

The process states are maintained at the middle unstable steady state whereas the state estimator is initialized at the either of the two steady states, that is, IC-1 or IC-2 (Figure 1). Initial condition, IC-1 is close to the unstable steady state, whereas IC-2 is far away from the steady state. Thus, these two initial conditions are representative of a *good initial guess* and a *bad initial guess* scenarios. From control point of view, the mole fraction of heaviest component d in bottoms (x_b) and lightest component c in distillate (x_d) are of prime importance and are selected as main indicators of the observer performance. The comparison of state estimates of x_b and x_d generated by UKF and EKF is presented in Figure 2 for both the initialization of state estimates, IC-1 and IC-2.

Since, IC-1 steady state (Figure 1) is a good estimate of desired operating steady state, both the estimators converge close to desired operating steady state in about the same time. SSEE values (Ref. Table 1) for unmeasured differential states (x_b and x_d) and for unmeasured algebraic states

Table 1: SSEE values for UKF and EKF

Estimator⟶	UKF		EKF		
Estimated states↓	IC-1	IC-2	IC-1	IC-2	IC-2*
x_b	0.0026	0.0717	0.0015	2.759	0.1019
x_d	0.0023	0.0563	0.0007	2.913	0.0378

**In presence of concentration measurements*

Table 2: SSEE values for unmeasured algebraic states (Temperatures) generated by UKF and EKF

Initialization⟶	IC-1		IC-2		
Stage Number↓	UKF	EKF	UKF	EKF	*EKF
1	14.50	15.69	920.3	2530	1881
3	50.22	159.6	3549	7260	6296
5	125.15	660.6	2560	39770	3650
7	64.96	337.1	545	78490	364
9	5.38	21.98	67.4	6590	28
11	10.95	6.35	356.7	1390	171.7
13	37.71	27.04	682	14890	72.2
15	153.03	103.9	1375	154700	269.4
17	59.64	21.38	737.3	265550	373.8
19	8.56	2.06	175.2	74080	111

**In presence of concentration measurements*

(Temperatures) are listed in Table 2. It can be seen that, except for stages 11, 13, 15, 17 and 19, UKF outperforms EKF in terms of SSEE values of algebraic states. When the initialization of estimates was chosen as IC-2, which is far from the desired operating steady state, UKF is able to converge (Ref. Fig. 2) to desired operating steady state accurately despite the large initial mismatch. On the other hand, the performance of EKF degrades resulting in large deviations from the desired operating steady state. As a consequence, SSEE values (Ref. Tables 1 and 2) of the unmeasured differential states (x_b and x_d) and for unmeasured algebraic states (Temperatures) for UKF are significantly smaller than those for EKF. Thus, UKF's performance is found to be robust against initial mismatch considered here. However, UKF is computationally significantly more expensive than EKF. The average computation time for DAE-UKF (*41.57 sec for IC1 and 73.03 sec for IC2*) is about 50 times more than for DAE-EKF (*0.8456 sec for IC1 and 2.2433 sec for IC2*). In UKF formulation, it is necessary to integrate the DAEs $2(n+n_w)+1$ (=185) times at each prediction step, which is computationally expensive step. On the other hand, the EKF, only requires computation of Jacobian matrices using finite differences. It was observed that the Jacobian computation is far less computationally intensive than multiple solutions of DAEs needed in UKF.

To examine whether the estimation performance of EKF can be improved by including additional measurements, it was assumed that the measurements of concentrations x_d and x_b are available in addition to the temperature measurements and hold up measurements (Purohit et al. (2013b)). The performance of the EKF with the initial estimate as IC-2 under the assumption of availability of measurements of concentrations is presented in Figure 2. It can be seen that, the EKF now converges to desired operating steady state when bottom and top products concentrations are assumed to be measured. The SSEE values for estimates of differential states (x_d and x_b) and for algebraic states also significantly decreased when compared with the SSEE values in absence of concentration measurements as listed in Tables 1 and 2.

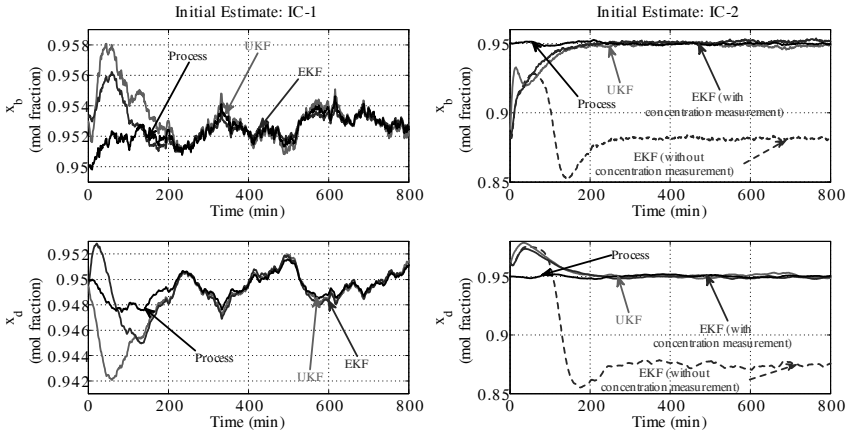

Figure 2: State Estimates of x_b and x_d generated by UKF and EKF

5. Conclusions

In this work, the performance evaluation of two recently developed nonlinear Bayesian estimators for systems modeled as DAEs, namely EKF and UKF have been investigated by simulating state estimation problems associated with a moderately high dimensional RD column. When compared on the basis of sum squared estimation errors (SSEE), the DAE-UKF outperformed the DAE-EKF. Whereas DAE-UKF was able to work even with a large mismatch in the initial state, the DAE-EKF performed satisfactorily only when initial estimation error was relatively small. However, under the identical simulation conditions, the average computation time needed for the DAE-EKF computations is significantly less (by factor of 50) than the average computation time needed for the DAE-UKF computations. Contrary to the claims in the literature regarding the drawbacks of EKF, the calculation of Jacobian for local linearization in the DAE-EKF formulation was found to be significantly faster than the multiple integrations needed in the DAE-UKF formulation for carrying out the prediction step. Moreover, the performance of EKF is found to improve if the top and the bottom concentration measurements are included in the estimation problem. Thus, the DAE-EKF with proper initialization appears to be better suited for development of an observer based control scheme.

References

Becerra, V.M., Roberts, P.D., Grifiths, G.W., 2001. Applying the extended Kalman filter to systems described by nonlinear differential-algebraic equations. Cont. Eng. Pract. (9), 267-281.

Grüner, T. E., Mohl, K. D., Kienle, A., E. D., Fernholz, G., Friedrich, S., 2003. Nonlinear control of a reactive distillation column. Cont. Eng. Pract. (11), 915-925.

Mandela, R. K., Rengaswamy, R., Narasimhan, S., 2010. Recursive state estimation techniques for nonlinear differential algebraic systems. Chem. Eng. Sci. **(**65), 4548-4556.

Olanrewaju, M., Al-Arfaj, M. A., 2006. Estimator-based control of reactive distillation system: Application of an extended Kalman filtering. Chem. Eng. Sci. *(*61), 3386-3399.

Purohit, J. L., Mahajani, S. M., Patwardhan, S. C., 2013a. Analysis of steady state multiplicity in reactive distillation columns. Ind. Eng. Chem. Res. (52), 5191-5206.

Purohit, J. L., Patwardhan, S. C., Mahajani, S., 2013b. DAE EKF based nonlinear predictive control of reactive distillation systems exhibiting input and output multiplicities. Ind. Eng. Chem. Res. (52), 13699-13716.

Venkateshwarlu, C., Kumar, J. B., 2006. Composition estimation of multicomponent reactive batch distillation with optimal sensor configuration. Chem. Eng. Sci. (61), 5560-5574.

Krist V. Gernaey, Jakob K. Huusom and Rafiqul Gani (Eds.), 12th International Symposium on Process Systems Engineering and 25th European Symposium on Computer Aided Process Engineering.
31 May – 4 June 2015, Copenhagen, Denmark

State Estimation in Fermentation of Lignocellulosic Ethanol. Focus on the Use of pH Measurements

Miguel Mauricio-Iglesias,[a,b]* Krist V. Gernaey,[a] Jakob K. Huusom[a]

[a]*CAPEC-PROCESS, Dep. of Chemical and Biochemical Engineering, Technical University of Denmark, Soltøfts Plads, Lyngby, 2800, Denmark*
[b]*Dep. of Chemical Engineering, University of Santiago de Compostela, rúa Lope Gómez de Marzoa, 15706, Santiago de Compostela, Spain. miguel.mauricio@usc.es*

Abstract

The application of the continuous-discrete extended Kalman filter (CD-EKF) as a powerful tool for state estimation in biochemical systems is assessed here. Using a fermentation process for ethanol production as a case study, the CD-EKF can effectively estimate the model states even when highly non-linear measurements such as pH are included. Several configurations of the CD-EKF are tested and it is seen that including pH, which is a readily available measurement in virtually every biochemical process, provides information that significantly improves the performance of the filter.

Keywords: state estimation; non-linear filtering; fermentation; lignocellulosic ethanol

1. Introduction

Monitoring of biochemical processes is essential for fault-diagnosis, control and optimisation. However, a number of factors have hindered the development of advanced monitoring techniques, especially in comparison with standard chemical processes. Lack of appropriate sensors and the high non-linearity inherent to biochemical processes are some of the main obstacles among these factors. In this context, the continuous-discrete extended Kalman filter (CD-EKF) is an appropriate tool for state estimation in biochemical processes. The non-linearity of the model can be efficiently tackled by the CD-EKF since the sensitivity of the dynamic model is updated at each sampling time via ODE integration. Commonly this step consumes a non-negligible computation time. However, the sampling time in biochemical processes is usually relatively slow (>>1 min) and computation time is rarely an issue. Another consequence of the slow sampling is that non-linearity between samples may be significant; other EKF formulations using linear approximations for the forecasting step are then unsuitable.

In this contribution we present the application of the CD-EKF to the monitoring of a fermentation process aimed at producing ethanol from C6 and C5 sugars. The focus is specifically on the use of pH as this is a variable that correlates well with the yeast catabolism (CO_2 is co-produced with ethanol, leading to acidification of the medium) and that can be easily measured online. Several configurations of the CD-EKF are presented and it is concluded that using pH measurements is 1) a suitable means to monitor the process if a good prediction model is available; and, 2) a good complement to other measurements if model mismatch is more severe.

2. Process description and modelling

The process studied here corresponds to the production of second generation bioethanol by fermentation by *Saccharomyces cerevisiae* of C6 and C5 monosaccharides (mainly glucose and xylose respectively), obtained from lignocellulosic biomass. One of the specific challenges of this operation is to minimise the effect of the inhibitory compounds that are produced during biomass hydrolysis such as furfural, 5-hydroxymethylfurfural (HMF) and acetate. Besides, in the case of organic acids, there is evidence that only the unionized form of the acid (e.g. acetic acid and not acetate) is responsible for the inhibition (Casey et al. 2010) and pH must be taken into account.

This simulation case study is based on common configurations for fermentation found in the literature. It is carried out in a 100 m^3 reactor and is run in fed-batch mode as follows: 1) first a batch phase with the inoculum (0.2 m^3) during 1 h; 2) a feeding phase for 7 h with a flowrate of $4 \cdot 10^{-3}$ $m^3 s^{-1}$; 3) finally a batch phase during 92 h. The composition of the inflow, which includes a strong base for pH regulation, is assumed to be known. The model of the process is composed of 11 states: reactor holdup (M), cell biomass (X_{bio}), glucose (Glu), xylose (Xyl), ethanol (Eth), furfural (Fur), total acetate (Ac), 5-hydroxymethylfurfural (HMF), furfuryl alcohol (FA), base conjugated cations (K) and total inorganic carbon (TIC), which includes several species in equilibrium (CO_2, H_2CO_3, HCO_3^- and CO_3^{2-}). Of these, only M is routinely measured at a relatively fast sampling time; Glu, Xyl and Eth are often measured but at slow sampling times. As in virtually every other fermentation, pH is measured at a relatively fast sampling time but it does not correspond directly or linearly to any state.
The total mass balance is expressed as:

$$\frac{dM}{dt} = F_{in}\ \rho_{in} \tag{1}$$

where F_{in} is the feed flowrate (m^3/s) and ρ_{in} is the feed density (kg/m^3). As the reactor is modelled as a stirred tank, the partial mass balances are generically expressed as:

$$\frac{d\,C_i}{dt} = \frac{F_{in}}{V}\left(C_{i,in} - C_i\right) + r_i \tag{2}$$

In Eq.(2), V represents the volumetric holdup of the reactor, C_i represents the concentration of component i in the reactor (kg/m^3) and r_i is a lumped term representing the reaction and gas-liquid transfer of compound i. The reactions describe the fermentation of the C6 and C5 sugars by a generic strain of *Saccharomyces cerevisiae*; it has not been attempted to model any particular strain but to build a multi-purpose model that takes into account the phenomena that impact the fermentation of lignocellulosic ethanol. Hence, several references have been used to describe the consumption of glucose and xylose (Krishnan et al. 1999), the effect of pH on metabolism (Nielsen et al. 2003), and the effect of inhibitors (Hanly and Henson, 2014). The stoichiometric matrix and the process rates description are provided in table 1.

The gas-liquid mass transfer, which in this case is only relevant to CO_2 is described as:

$$J_{CO_2} = k_L a \left(P_{CO_2} - H_{CO_2}\, C_{CO_2}\right) \tag{3}$$

where k_La is the volumetric mass transfer coefficient, P_{CO2} is the partial pressure of CO_2 in the headspace, H_{CO2} is the Henry's constant and C_{CO2} is the liquid concentration of CO_2 which can be obtained from the concentration of TIC and the pH in the liquid.

Table 1. Stoichiometric matrix and process rates for the fermentation process. Note that I represents an inhibitory term for the fermentation process. K_{si} represent affinity constants while J_i and K_{Ii} represent inhibition constants.

Comp.→ Process↓	X_{bio}	Glu	Xyl	Eth	Fur	Ac	HMF	FA	TIC
Glu uptake	$Y_{X/Glu}$	-1	0	$Y_{Eth/Glu}$	0	0	0	0	$Y_{CO2/Glu}$
Xyl uptake	$Y_{X/Xyl}$	0	-1	$Y_{Eth/Xyl}$	0	0	0	0	$Y_{CO2/Xyl}$
Fur uptake	~0	0	0	0	-1	0	0	$Y_{FA/Fur}$	0
Ac uptake	~0	0	0	0	0	-1	0	0	$Y_{CO2/Ac}$
HMF uptake	~0	0	0	0	0	$Y_{Ac/HMF}$	-1	0	0

	Equation expressed as substrate consumption
Glu uptake	$\nu_{Max} X_{bio} \frac{Glu}{K_{SGlu} + Glu + \frac{Glu^2}{K_{IGlu}}} \frac{1}{1+\frac{Fur}{J_{Fur}}} \frac{1}{1+\frac{HMF}{J_{HMF}}} \frac{1}{1+\frac{HAc}{J_{HAc}}} I(Xyl, Eth, pH)$
Xyl uptake	$\nu_{Max} X_{bio} \frac{Xyl}{K_{SXyl} + Xyl + \frac{Xyl^2}{K_{IXyl}}} \frac{1}{1+\frac{Fur}{J_{Fur}}} \frac{1}{1+\frac{HMF}{J_{HMF}}} \frac{1}{1+\frac{HAc}{J_{HAc}}} I(Glu, Eth, pH)$
Fur uptake	$\nu_{Max} X_{bio} \frac{Fur}{K_{SFur} + Fur}$
Ac uptake	$\nu_{Max} X_{bio} \frac{Ac}{K_{SAc} + Ac}$
HMF uptake	$\nu_{Max} X_{bio} \frac{Fur}{K_{SFur} + Fur}$

Finally, pH is calculated as the solution, at every time step, of the algebraic equation accounting for the charge balance.

$$C_{H^+} + K^+ - \frac{K_w}{C_{H^+}} - \frac{K_{Ac} C_{Ac}}{C_{H^+} + K_{Ac}} - \frac{K_{1,C} C_{TIC} C_{H^+}^2 + K^2_{1,C} C_{TIC}\ C_{H^+}}{\left(C_{H^+} + K_{1,C}\right)\left(C_{H^+}^2 + K_{1,C} C_{H^+} + K_{1,C} K_{2,C}\right)} = 0 \qquad (4)$$

where K_w is the ionic product of water, K_{Ac} is the acid constant of acetic acid, $K_{1,C}$ is the pseudo-acid constant between carbon dioxide and the bicarbonate anion and $K_{2,C}$ is the acid constant between the bicarbonate and carbonate anions. Lactic acid bacteria (LAB) in simulation scenario 2 were modelled according to Pinelli et al (1997).

3. State estimation and filter configuration

The system described by Eq. (1-4) can be written in a general non-linear state-space form using the reactor volume as system boundary.

$$\frac{dx}{dt} = f\left(x(t), u(t), d(t)\right) \qquad (5a)$$

where the states (x), inputs (u) and disturbances (d) represent:

$$x = [M \; C_i]^t \qquad u = [F_{in}] \qquad d = [C_{i,in}] \tag{5b}$$

The estimation is indeed computed at discrete time step based on the sample rate in the control or monitoring system. The system (5) takes the following discrete step form:

$$x_{k+1} = F(x_k, u_k, d_k) = x_k + \int_{t_k}^{t_{k+1}} f(x(\tau), u(\tau), d(\tau)) d\tau \tag{6a}$$

$$y_k = G(x_k) + \nu_k, \quad \nu_k \in \mathrm{N}_{iid}(0, R_\nu) \tag{6b}$$

The observer is formulated as a CD-EKF filter as described by Price et al. (In Press). The main particularity of the CD-EKF in the present work is that output matrix C_k is not time invariant. C_k is the partial derivative of the output function $G(x_k, u_k, d_k)$with respect to the states. Commonly, C_k is time invariant as it represents the relation between the measurements and the states. In this case, as pH is one of the outputs:

$$C_k = \left. \frac{\partial G(x_k)}{dx} \right|_{\hat{x}_{k|k-1}} \tag{7}$$

Three possible configurations of the CD-EKF were tested considering different measurements and sampling rates, chosen following realistic implementation (Table 2). It is considered that the total holdup and the pH can be followed on-line and hence to a fast sampling rate. On the contrary, measuring glucose, xylose and ethanol content requires sample preparation and off-line analyses; the sampling rate is necessarily slow.

Table 2. Measured variables for three configurations of the CD-EKF

Configuration	Measurements	Sampling rate (Ts, min)
1	M, pH	20
2	M, Glu, Xyl, Eth	240
3	M, Glu, Xyl, Eth, pH	240

4. Simulation results

A first scenario was defined where the filter is assumed to dispose of perfect knowledge of the plant model (the only difference between the model and the plant is introduced by sensor noise). The performance of the three configurations is very similar when the performance metrics are compared (Table 3). As the space of this contribution is limited, we have decided to focus on the unmeasured states that have the highest influence on the plant evolution: X_{bio}, Fur, Ac and TIC. It can be seen (Table 3) that configurations 2 and 3 outperform configuration 1, as more information is available from the measurements.

A second simulation scenario was set where a certain and realistic model mismatch is assumed: there is contamination in the media by lactic acid bacteria (LAB), simulated by including 0.2% w/w of the yeast biomass in the inflow. The performance of the filter with the three configurations is compared to a simulation that does not take into account the LAB contamination. In this scenario (Figure 2), configuration 1 and 2 present a severe bias, in particular for X_{bio} and Ac. In contrast, X_{bio} is accurately estimated by configuration 3, demonstrating the importance of the information provided by pH. In

general, configuration 3 presents the smallest error of all the filter configurations and the system simulations except for Ac (probably because of the presence of lactic acid produced by the LAB). The performance metrics (Table 3) confirm these results. Additionally, the variance is smallest for configuration 3, showing that a good compromise between the use of measurements and model information was reached.

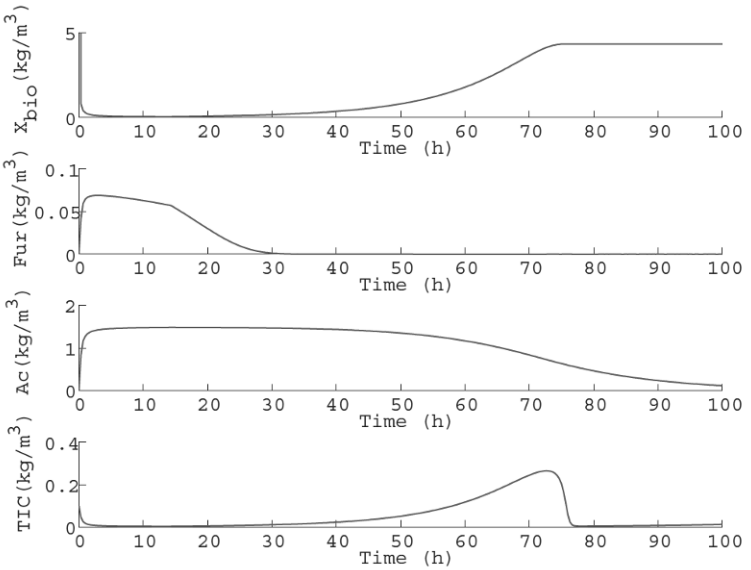

Figure 1. Simulation of the process with LAB contamination. Selection of key states.

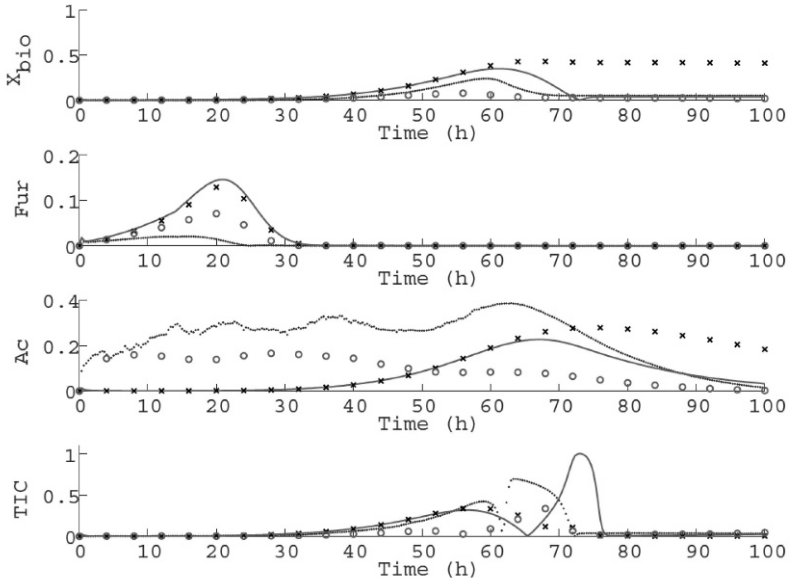

Figure 2. Absolute normalized prediction error of the CD-EKF in scenario 2 (LAB contamination) for pure simulation (line), configuration 1(dots), configuration 2 (crosses) and configuration 3 (empty circles)

Table 3. Estimation statistics: the mean and the standard deviation are given for the absolute estimation error on selected states based on the normalized data. Simulation stands for a simulation with the original plant model (not considering LAB contamination)

Variable→	X_{bio}		Fur		Ac		TIC	
Configuration ↓	$\mu \cdot 10^3$	$\sigma \cdot 10^3$	$\mu \cdot 10^3$	$\sigma \cdot 10^3$	$\mu \cdot 10^3$	$\sigma \cdot 10^3$	$\mu \cdot 10^3$	$\sigma \cdot 10^3$
Scenario 1. Perfect plant model								
1	0.98	1.33	0.73	1.35	1.08	0.87	2.00	6.18
2	0.36	0.50	0.32	0.60	0.39	0.31	0.82	2.22
3	0.36	0.50	0.32	0.60	0.39	0.32	0.82	2.23
Scenario 2. Contamination by lactic acid bacteria (LAB)								
Simulation	96.0	112	21.9	43.2	77.7	73.0	181	286
1	62.0	65.4	2.90	6.70	232	98.7	173	250
2	239	194	19.3	38.7	123	109	117	159
3	27.2	22.0	10.9	21.7	89.0	54.4	66.9	104

5. Conclusions

The CD-EKF was proven as a suitable tool for monitoring of biochemical processes. Its main drawback, i.e. requirement of significant computational resources, is of little relevance in these processes as sampling is relatively slow. Providing pH helps improving the prediction of the filter when comparing several configurations. The use of pH is of great interest for such processes since it is a ubiquitous measurement in biochemical processes, in particular in fermentation. Further application in contamination detection and real time optimisation will follow this study.

6. Acknowledgements

This work is partially financed by BIOPRO funded by the European Regional Development Fund (ERDF), Region Zealand (Denmark) and BIOPRO partners.

References

E. Casey, M. Sedlak, N.W.Y. Ho, N.S. Mosier, 2010, Effect of acetic acid and pH on the cofermentation of glucose and xylose to ethanol by a genetically engineered strain of *Saccharomyces cerevisiae*, FEMS Yeast Research, **10**(4):385–393.

T.J. Hanly, M.A. Henson. 2014 Dynamic model-based analysis of furfural and hmf detoxification by pure and mixed batch cultures of *S. cerevisiae* and *S. stipitis*, Biotechnology and Bioengineering, **111**(2):272–284.

M.S. Krishnan, N.W.Y Ho, G.T. Tsao, 1999, Fermentation kinetics of ethanol production from glucose and xylose by recombinant *Saccharomyces* 1400(plnh33), Applied Biochemistry and Biotechnology, **77–79**:373–388.

J. Nielsen, J. Villadsen, G. Liden, 2011, Bioreaction engineering principles. 3rd Ed, Springer.

D. Pinelli, A. González-Vara, D. Matteuzzi, F. Magelli, 1997, Assessment of kinetic models for the proudction of L- and D-Lactic Acid Isomers by *Lactobacillus casei* DMS 20011 and *Lactobacillus coryniformis* DMS 20004 in continuous fermenation, Journal of Fermentation and Bioengineering, **83** (2), 209-212

J. Price, M. Nordblad, J.M. Woodley, J.K. Huusom, Real-Time Model Based Process Monitoring of Enzymatic Biodiesel Production, (In Press), Biotechnology Progress

Krist V. Gernaey, Jakob K. Huusom and Rafiqul Gani (Eds.), 12th International Symposium on Process Systems Engineering and 25th European Symposium on Computer Aided Process Engineering.
31 May – 4 June 2015, Copenhagen, Denmark

Dynamic Simulation and Analysis of Slug Flow Impact on Offshore Natural Gas Processing: TEG Dehydration, Joule-Thomson Expansion and Membrane Separation

Lara de O. Arinelli[a]*, Ofélia Q. F. Araújo[a], José Luiz de Medeiros[a]

[a]*Federal University of Rio de Janeiro, Av. Athos da Silveira Ramos, 149, Rio de Janeiro 21941-909, Brazil*
**lara.arinelli@gmail.com*

Abstract

Crude natural gas (NG) can contain a significant amount of contaminants that must be removed to guarantee safe transportation and sales specification. Water and hydrocarbon dew point (WDP and HCDP) adjustments are important for conditioning NG. In Brazil, Pre-Salt reservoirs have large amounts of NG with high CO_2 content, which also must be adjusted by a suitable operation like Membrane Permeation (MP). Furthermore, offshore processing requires reduced footprints, which minimize inventories and, consequently, intensify propagation of feed disturbances to downstream units. The dynamic scenario is inherently related to riser oscillations caused by slug flow, that may cause operational problems, losses and environmental and safety issues. Hence, the process control system must be sufficiently robust to ensure stability within such context. This work approaches the dynamical analysis of an offshore NG treating process for a typical Pre-Salt feed with the following operations: phase separation, dehydration with triethylene glycol (TEG) absorption, HCDP adjustment via Joule-Thomson (JT) expansion and CO_2 removal via MP. The objective is to assess the dynamic behaviour of the process and its control framework under slug flow oscillations within HYSYS simulation environment. As MP is not included in the simulator unit library, a dynamic unit operation extension (UOE-D) was developed. This UOE-D extension adequately reproduces MP response to disturbances allowing the entire process to be dynamically assessed. In general, results point to good process controllability and overall robustness despite the severe slug flow feed oscillations.

Keywords: Natural Gas, Slug Flow, Dynamic Simulation, Membrane Permeation.

1. Introduction

Recently, huge oil reserves have been discovered in Pre-Salt fields of Brazil, with high gas-oil ratio (Formigli, 2013) and impressive CO_2 content. The associated natural gas (NG) should be treated for adjusting water dew point (WDP), hydrocarbon dew point (HCDP) and for removal of CO_2, which reduces NG heat value and the transportation capacity of pipelines and, besides, is corrosive in presence of water (Dortmundt and Dosh, 1999). Considering the 300 km distance from coast to Pre-Salt fields, high NG flow rates have to be processed offshore for safe transportation to land facilities and sales specifications. However, high NG capacity requires large equipments, which configure a challenge for offshore rigs where space and weight are serious constraints. Due to its modularity, low weight and footprint, Membrane Permeation (MP) was chosen for CO_2 removal in Pre-Salt projects. Other design choices involve WDP

adjustment via NG dehydration by absorption with TEG (triethylene glycol) and HCDP adjustment via Joule-Thomson (JT) expansion. WDP is necessary to prevent hydrate formation under high pressure and low temperature, and HCDP is necessary to avoid condensation of heavier hydrocarbons in NG pipelines and processing.

Considering the offshore context, platforms are frequently vulnerable to flow and pressure oscillations of feeds caused by multiphase slug flow in production risers. Such instabilities configure a big challenge associated with oil and NG production in deep-water offshore fields. Slug flow is an intermittent flow in which liquid slugs are propelled by large bubbles of gas. The main types of slug flow are: Transient, Hydrodynamic and Severe Slugging (SS). The first one is induced by operational changes, such as start-up or pigging and can have impact on downstream processes. The second one occurs in near horizontal pipelines, being usually weak with limited effects on downstream facilities and is initiated by wave instabilities on gas/liquid interface with a sufficient velocity difference between phases. The third one, Severe Slugging (SS), may occur at low flow rates when a downwards inclined or horizontal pipeline is connected to a vertical riser. SS exhibits a cyclic behavior with characteristics steps: (i) liquid accumulates at the riser base blocking gas flow and increasing pressure upstream; (ii) pressure becomes sufficiently high, causing a sudden ejection of liquid, followed by gas blow-down; (iii) then, some liquid falls back, beginning a new cycle. Sagatun (2004) reported SS field data indicating periods between ≈10 min and ≈15 min. According to Godhavn (2005) SS in pipelines between Tordis field (North Sea) and Gullfaks C platform resulted in severe pressure and level oscillations in inlet separators, leading to instabilities and operational issues in the receiving facilities. Some consequences of SS to downstream facilities are: large disturbances in the separation area affecting oil/water separation; periods of low liquid flow, followed by high liquid production, occasionally causing flooding and shutdowns; impact on gas compression due to pressure variations from gas separation; increased flaring due to separator pressure oscillations, affecting the environment and destroying inventories (Sausen et al., 2012). Therefore, dynamic simulation becomes an important tool for offshore process design and operation, since it allows the analysis of the dynamical behavior of process under feed disturbances. Furthermore, reduced inventories dictated by space constraints in offshore rigs lead to rapid propagation of disturbances along downstream operations and render important the prediction of transient responses caused by SS. This work assesses the impacts of slug flow oscillations on a typical Pre-Salt offshore processing unit.

2. Methodology

The software used for process simulation is Aspentech HYSYS, with Peng Robinson equation of state. For simulation of the MP unit, a Dynamic Unit Operation Extension (UOE-D) was developed in Visual Basic. A base case was defined and simulated in steady state and process design parameters were defined through sensitivity analysis. In order to proceed to the dynamic mode, equipment sizing was performed employing literature correlations (Campbell, 2004) and the HYSYS Sizing tool. Last, the control structure was proposed and tuned in accordance with literature data and procedures (Nunes, Medeiros and Araújo, 2010). A slug flow emulator was developed using a vessel and two valves. The slug cycles were formed by coordinating valves opening and closing (Figure 1a), in a period of 9 minutes. The impact of slug flow on inlet gas and

liquid phases mass flow rates are presented in Figure 1 (b,c). The oil flow rate is reduced to approximately 50% of its base value in each cycle, while gas flow rate is increased to around 160% of base value.

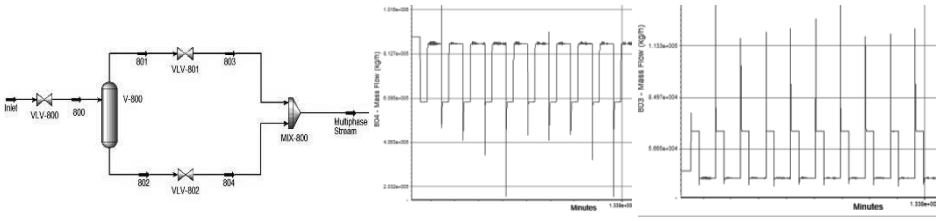

(a) (b) (c)

Figure 1. Slug Flow: (a) Process Emulator, (b) Liquid Flow Pattern, (c) Gas Flow Pattern

3. Base Case

Process premises assumed a multiphase stream of 960 t/h, 75 bar and 40 ºC, with composition adapted from Vaz (2009) to represent a typical Pre-Salt feed (~20% molar base on gas phase - Table 1) similar to Lula field (Formigli, 2013). The treated NG specifications were defined according to ANP (Brazil National Agency of Oil, Gas and Biofuels): WDP ≤ -45 ºC at 1.01 bar; HCDP≤ 0ºC at 45 bar, CO_2 content ≤ 3%mol.

Table 1. Inlet Stream Gas Phase Composition (% mol.)

Component	Composition	Component	Composition	Component	Composition
Methane	59.98%	Water	5.00%	n-Pentane	0.18%
Ethane	6.00%	H2S	0.02%	n-Hexane	0.32%
Propane	4.97%	i-Butane	2.80%	n-Heptane	0.08%
CO2	18.99%	n-Butane	0.40%	n-Octane	0.01%
Nitrogen	0.43%	i-Pentane	0.83%		

3.1. Steady State Simulation

Plant scheme is based on Machado et al. (2012), with phase separation (Vaz, 2009), two MP stages (Pinto et al., 2009) and final NG compression. Fig. 2 shows the overall scheme on HYSYS. Table 2 shows the treated NG composition. Final NG conditions are 49.71 t/h, 94.29 ºC, 204.07 bar, WDP of -54.48 ºC at 1.01 bar, and HCDP of -4.9 ºC at 45 bar.

Table 2. Final Gas Stream Composition

Component	Composition	Component	Composition	Component	Composition
Methane	79.19%	Water	0.00%	n-Pentane	0.02%
Ethane	10.29%	H_2S	0.02%	n-Hexane	0.01%
Propane	5.12%	i-Butane	1.53%	n-Heptane	0.01%
CO_2	2.97%	n-Butane	0.17%	n-Octane	0.01%
Nitrogen	0.52%	i-Pentane	0.15%		

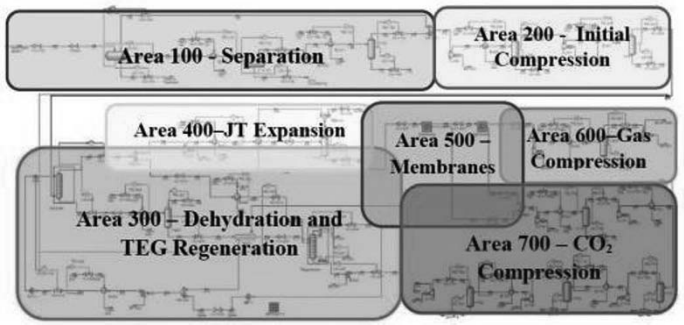

Figure 2. Process Flowsheet Scheme

3.2. Control Structure

Process control on offshore platforms is usually classic, presenting many simple loops with PID controllers in SISO configuration (Nunes et al., 2010). Controllers for the present process are selected in accordance with literature data for each unit operation (Mokhatab et al., 2006). Control loops dedicated to WDP and HCDP are: ratio controller between gas and TEG flow rates at the absorber and temperature controller at JT vessel. It is also important to control reboiler temperature to avoid TEG degradation (206 ºC). Control parameters suggested by HYSYS Dynamic Modelling Manual and by Luyben (2002) were used as base values for initial tuning. Then, process was initialized in dynamic state and a manual fine-tuning step was performed to reduce oscillations.

4. Dynamic Analysis

4.1. Membrane Separation Dynamic Extension

A UOE-D dynamic extension was developed to simulate MP modules for both steady and dynamic states. Extensions also provide customized interface options. The MP transient response is fast, so it was modelled as a first order transfer function with unitary gain. Permeate pressure is fixed, defined by user, according to its downstream application, while a fixed head loss of 1 bar is associated with the retentate product relative to the feed. Permeation rates vary with trans-membrane ΔP (Pinto et al., 2009). To validate the extension, simple MP cases were simulated and their responses were compared with the expected behaviour, resulting in a satisfactory representation.

4.2. Slug Flow Impact

The separation area is responsible for absorbing the first impacts, so vessels pressures and levels are extremely affected (Figure 3a,b). Both separation pressures reach 150% of base case values. The tree-phase separator level fluctuates between 20 and 70%, while the two-phase separator reaches levels near 100% of full scale. The simulation did not identify any errors in this case, however, in a real plant it can lead to flooding and shutdown. Figure 3c shows stage pressure profiles on gas compression. The oscillations amplitude double in each step, reflecting the impact on compression ratio due to inlet pressure variations.

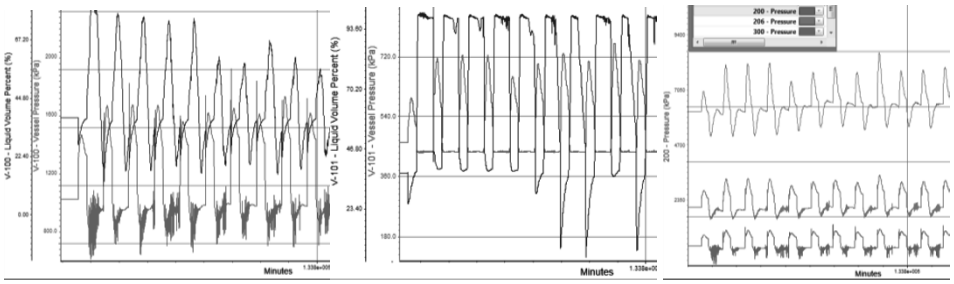

(a) (b) (c)

Figure 3. Slug Flow Impacts: (a) Three-Phase Separator, (b) Two-Phase Separator – level (blue), pressure (red), (c) Compression – inlet (red), 1st stage outlet (pink) and 2nd stage outlet (blue).

At the absorber, inlet gas mass flow rate fluctuations are of ~23 t/h and impact the absorption process. The ratio controller acts in TEG flow rate to maintain an optimum ratio for dehydration. Water content on dry gas still presents oscillations and may have affected gas specification at some points. Figure 4b depicts the strict relation between gas HCDP and JT vessel temperature, which is an expected behavior. The oscillations are of approximately 3 ºC, so it does not loose HCDP the specification. Figure 4c shows flow rate, dew points, methane and CO_2 contents of the final natural gas stream. Export gas properties and conditions presented variations, though dampened when compared to slug flow disturbances. Mass flow rate fluctuates with an amplitude of 10% of base case value. Dew point oscillations are of less than 5 ºC, so export gas can exceed specifications, but in not relevant levels.

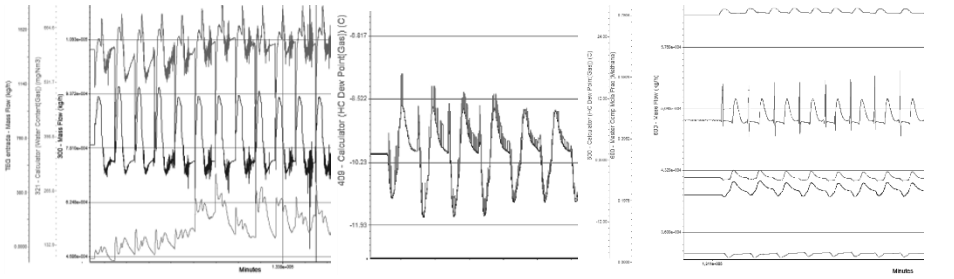

(a) (b) (c)

Figure 4. Slug Flow Impacts: (a) Absorber – inlet gas flow rate (blue), TEG flow rate (red), water content (green), (b) JT – separator temperature (blue), HCDP (pink), (c) Final Gas Stream – gas flow rate (red), HCDP (blue), WDP (green), CO_2 content (light blue), methane content (pink).

5. Conclusions

A satisfactory representation of a NG processing plant on steady state was obtained, with the export NG stream complying with Brazilian ANP specifications for WDP, HCDP and CO_2 content. In general, the proposed control structure was properly tuned, since, despite the severe dynamic scenario, it performs adequately and promotes dampening of the inlet oscillations along downstream processing steps. Although the slug flow emulator is not a completely accurate representation of the real phenomenon, it successfully approaches its inherent intermittent profile. Furthermore, the MP

dynamic extension presents fast responses under system disturbances, according to the behavior expected for this unit operation.

The simulation further elucidates the impact of oscillations on gas dew points, which must be constantly monitored and controlled. It is worth noting that its increase may cause loss of specification and hence potential risk situations. It is relevant in validating the proposed control structure that such situation was not reached in the simulated scenario, in spite of the severe disturbances applied to the inlet stream. Finally, this study denoted the applicability of dynamic simulation in predicting the dynamic behavior in natural gas processing under severe slug conditions, and, hence, its potential application in the analysis and test of control strategies, operator training, HSE (Health, Safety & Environment) assessments, among others.

Acknowledgements

Authors acknowledge financial support from PETROBRAS S.A., ANP and FINEP, through the ANP Human Resources Program for Oil & Gas PRH-13 from Escola de Química, UFRJ. CNPq-Brazil grants are also gratefully acknowledged.

References

ANP – Brazil National Agency of Oil, Gas and Biofuels. "Resolução ANP nº 16." Brasília, 2008.

Aspen Technology Inc. Hysys Dynamic Modelling. Cambridge: Aspentech, 2005.

J. M. Campbell. Gas Conditioning and Processing - Volume 2: The Equipment Modules. Norman, Oklahoma: Campbell Petroleum Series, 2004.

D. Dortmundt, K. Dosh. Recent developments in CO2 removal membrane technology. Des Plaines, IL: UOP LLC, 1999.

J. Formigli. CO2: Challenges & Opportunities. 2nd Brazilian Congress of CO_2 in Oil, Gas and Biofuels Industry, April 8-9, 2013.

J. M. Godhavn, S. Strand, G. Skofteland. Increased oil production by advanced control of receiving facilities. IFAC, 2005.

W. L. Luyben. Plantwide Dynamic Simulators in Chem. Processing & Control. CRC Press, 2002.

P. B. Machado. "Análise comparativa de tecnologia de separação supersônica para o condicionamento de gás natural". MSc Thesis. Rio de Janeiro: UFRJ, 2012.

S. Mokhatab, W. A. Poe, J. G. Speight. Handbook of Natural Gas Transmission and Processing. Burlington: Elsevier, 2006.

G. C. Nunes, J. L. De Medeiros, O. Q. F. Araújo. "Modelagem e Controle na Produção de Petróleo - Aplicações em Matlab". São Paulo: Blucher, 2010.

D. P. Pinto, O. Q. F. Araújo, J. L. De Medeiros. "Curso de Membranas Módulo I: Conceitos Básicos". Rio de Janeiro: UFRJ/H2CIN, November 2009.

S. I. Sagatun. In: Modeling, Identification and Control, Vol. 26, No. 2, 95-109. 2005.

A. Sausen, P. Sausen, M. Campos. The Slug Flow Problem in Oil Industry and Pi Level Control. In: New Technologies in the Oil and Gas Industry, 103-118. Intech, 2012.

J. C. Vaz. "Síntese de Controle e Análise de Cenários em Planta Offshore de Óleo e Gás". MSc Thesis. Rio de Janeiro: UFRJ, 2009.

Krist V. Gernaey, Jakob K. Huusom and Rafiqul Gani (Eds.), 12th International Symposium on Process Systems Engineering and 25th European Symposium on Computer Aided Process Engineering.
31 May – 4 June 2015, Copenhagen, Denmark

Automata Based Test Plans for Fault Diagnosis in Batch Processes

Chuei-Tin Chang, Wei-Chung Hsieh

Depratment of Chemical Engineering, National Cheng Kung University, Tainan 70101, Taiwan, R.O.C.

Abstract

Hardware failures are inevitable but random events in the useful life of any batch chemical plant. If such incidents are not efficiently diagnosed, the consequences may be very serious and sometimes even catastrophic. The present study aims to develop a systematic procedure-synthesis strategy for generating the test plans that minimize the chance of misjudgements. By modelling the components in the given system with timed automata, all possible fault propagation scenarios and their observable event traces (OETs) can be enumerated. The test procedure for every OET can then be conjectured by designing a supervisory controller to achieve the highest level of diagnostic resolution. One example is provided to show the feasibility of the proposed approach.

Keywords: Timed automata, Diagnostic tests, Model checking, Batch processes

1. Introduction

Various high value-added products, such as the specialty chemicals, foods, semiconductors and pharmaceuticals, etc., are manufactured in complex but flexible batch processes. Over the lifespan of any such plant, the hardware failures should be regarded as random but inevitable events. If these fault origins cannot be correctly identified in time, the consequences can be very serious and sometimes even catastrophic. Several studies have already been performed to address various issues concerning fault diagnosis in batch processes. Although satisfactory results have been reported, the available methods are mostly effective for applications in systems with relatively few interconnected units and, also, the diagnostic resolution in cases of coexisting failures may not always be acceptable.

In general, the diagnostic performance can be improved by capturing more online data so as to gain a clearer picture of the current system state and also a deeper understanding of the underlying fault propagation mechanism(s). This improvement is traditionally brought about by installing additional sensors. However, since adding new hardware inevitably requires extra spending and, also, the related issues have already been discussed extensively, there are incentives to consider a nonconventional means without capital investments. To this end, Yeh and Chang (2011) suggested to carry out extra control actions which are not included in the normal operating procedure. Kang and Chang (2014) later developed an effective method to synthesize diagnostic test plans according to untimed automata. However, due to the lack of time-tracking mechanisms in their models, the failure-induced abnormal plant behaviours cannot always be predicted accurately. To circumvent this drawback, it is the goal of present study to devise a procedure synthesis strategy for producing more practical test plans by using the timed automata.

2. Model construction principles

Since the modelling principles proposed by Kang and Chang (2014) are generic enough, their basic approach is also adopted to build time automata in the present study. For the sake of illustration clarity, this model construction method is illustrated here with a simple example. Specifically, let us consider a fictitious liquid transfer system represented by the piping and instrumentation diagram (P&ID) in Figure 1 and also the sequential function chart (SFC) in Figure 2. Notice that the components in this and any other batch process can always be classified into a hierarchy of 4 different levels: (1) the programmable logic controller (PLC); (2) the actuators, i.e., the three-way valves (V-1 and V-3) and the two-way valves (V-2 and V-4); (3) the processing units, i.e., Tank and (4) the online sensor(s). If a three-way valve is closed, the port connecting to the horizontal pipeline in Figure 1, i.e., P-2 in the case of V-1 or P-3 in the case of V-3, is assumed to be blocked. Otherwise, its inlet flow(s) should be directed to every outlet pipeline. It is assumed that all valves except V-4 are placed at the "close" position initially. Thus, it clear from the above SFC that, during the normal operation, the buffer tank is filled with liquid via P-1, P-3 and P-4 by manipulating V-3 and then drained via P-5 by gravity. For the sake of brevity, only four fault origins are considered in this example and they are denoted respectively by f_{1A} (or Tank_LEAK), i.e., a large leak develops in tank, f_{1B} (or Tank_leak), i.e., a minor leak develops in tank, f_2 (or V3SC), i.e., V-3 fails at the "close" position, and f_3 (or V3SO), i.e., V-3 fails at the "open" position.

The plant model can in general be obtained by first building automata to model all components in the given process and then integrating them via the standard parallel decomposition operation. In this work, the controller and the remaining components are modelled differently. Let us first outline the construction principles for the latter components, i.e., the valves, the tank and the sensors. In particular, a timed automaton is used to represent a finite set of identifiable states of the hardware item under consideration and also the specific events facilitating the state transitions. The prerequisite conditions of these events can be imposed with the so-called "guards", while the updated integer and clock variables may also be specified as the attributes of a transition (Behrmann et al., 2006).

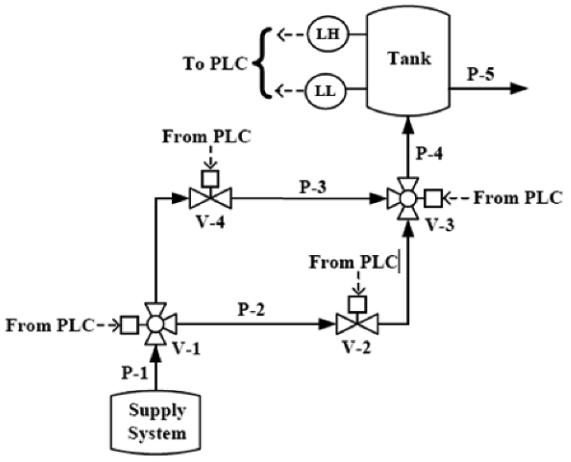

Figure 1. P&ID of a liquid transfer system.

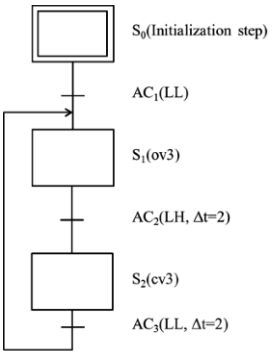

Figure 2. Normal SFC of a liquid transfer operation.

In this example, only the elapsed times of the transitions in tank model are assumed to be nonzero and the corresponding automaton is presented in Figure 3. Note that the places LL and LH are used to represent low and high liquid levels under normal conditions respectively, while LL_leak and LH_leak denote the corresponding liquid levels when a minor leak is present in the tank and LL_TEAK is the low level eventually reached after a large leak. For the sake of brevity, let us consider only the transition from LL to LH. To trigger this transition, three conditions (guards) are imposed with four binary variables (*v1 – v4*) and a clock variable *x*. The former are used to represent the corresponding valve states, i.e., 1 denotes open and 0 otherwise, and the latter is the time needed to complete the state transition. Tank_LH! is the LL-to-LH transition process and "!" denotes that it is an initiator or sender event. The last line is the reset condition, i.e., the liquid level is reset to high (*L=1*) after completing the transition. Finally, due to space limitation, the component models of valves and sensors are not presented here since they are essentially the same as the untimed counterparts given in Kang and Chang (2014).

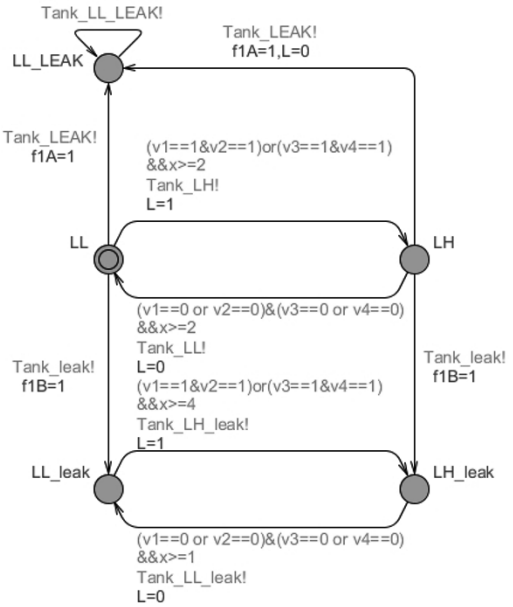

Figure 3. Tank model.

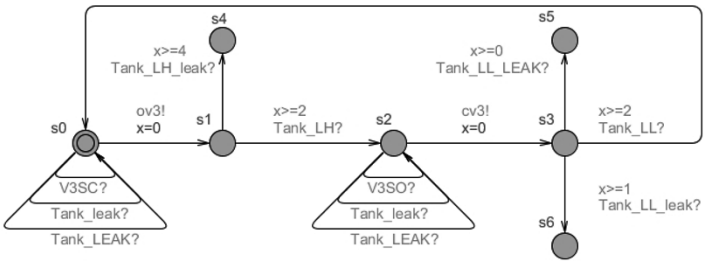

Figure 4. Controller model

The controller model can be constructed according to the normal system behaviours specified in SFC and also the failure-induced events (see Figure 4). The controller controlled actions in this model, i.e., open and close V-3 (*ov3*! and *cv3*!), should naturally be viewed as senders, while the failure induced events, e.g., V3SC?, V3SO?, Tank_leak? and Tank_LEAK?, are receivers.

3. Identification of fault propagation mechanisms

According to Clarke et al. (1986), "model checking" is essentially an algorithmic procedure for verifying whether a given system is compliant with the target specifications. A software verifier can be applied to determine if a set of timed automata conform to the desired system properties. If not, the verifier will provide a counter scenario, from which the user could find error(s) and then modify the models accordingly. In this study, the model checking tool provided in UPPAAL (Behrmann et al, 2006) was utilized for enumerating all fault propagation paths. The required deductive reasoning procedure is summarized in Figure 5.

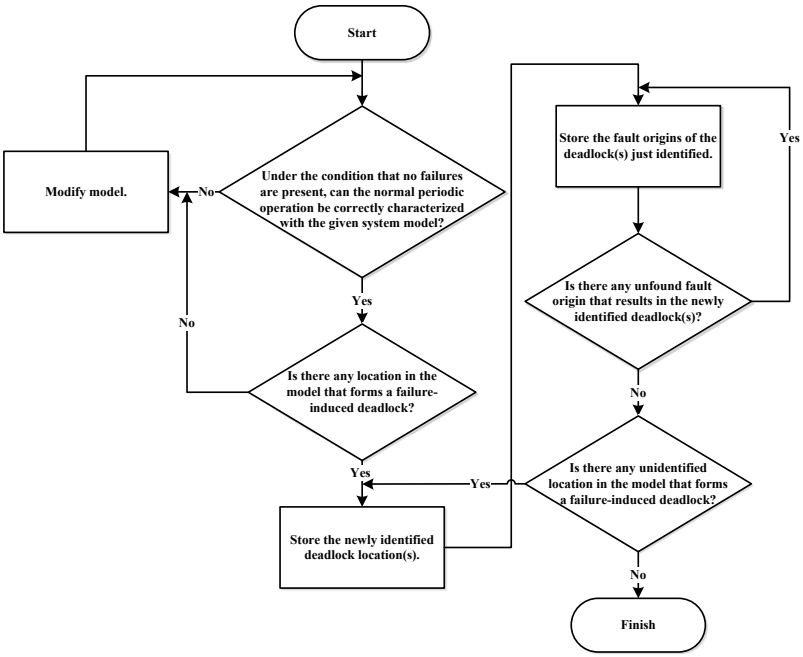

Figure 5. Deductive reasoning procedure for identification of fault propagation paths.

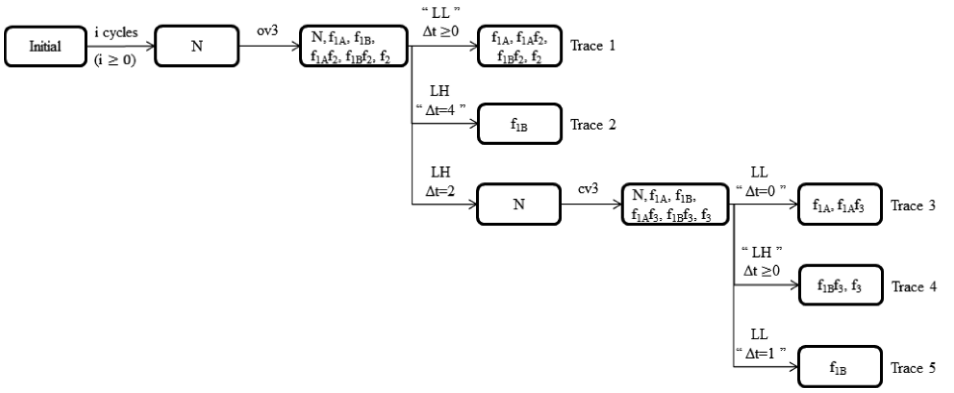

Figure 6. Observable event traces.

As mentioned before, failures may occur at any instance during the batch operation. Since these events are usually not directly observable, the fault origins can only be diagnosed with other available online information. By assuming that the sensor measurements, the actuator actions and the clock readings are observable online, all OETs in the present example can be identified and summarized in Figure 6. The rectangles in this figure are used to specify the implied system states, which may be either normal (N) or under the influence of one or more failure, while the arrows are transitions triggered by the corresponding *observable* events. Note also that every abnormal event is marked with double quote. For the sake of brevity, let us consider only Trace 1 in more detail. The first transition on this trace is used to represent the observable event sequence that may be experienced in *i* completed operation cycles. The subsequent action is the first operation step of SFC, i.e., *ov3*, which should normally result in a high liquid level (LH). However, if the abnormal state "LL" is detected instead, there should be four implied fault origins: (1) f_{1A}; (2) $f_{1A}f_2$; (3) $f_{1B}f_2$; (4) f_2. Note that two coexistent failures are present in the 2nd and 3rd scenarios respectively.

4. Synthesis of diagnostic test plans

If the implied fault origins are not unique after observing a fully developed OET during operation, additional tests should be performed to further enhance diagnostic resolution. The corresponding test plan can also be produced with the model checking tool mentioned above.

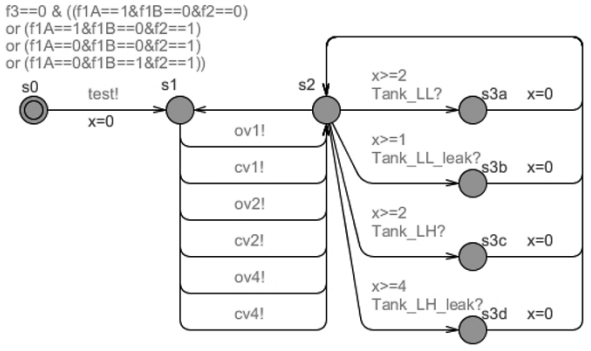

Figure 7. Test model.

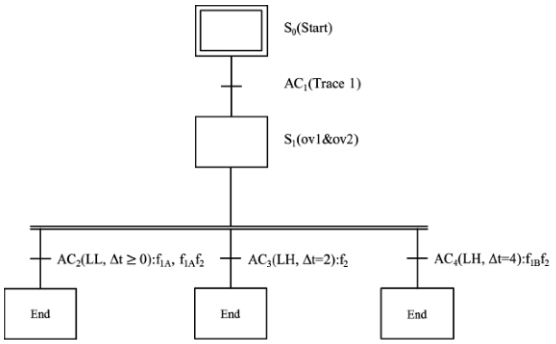

Figure 8. Optimal test procedure.

All component models can be adopted for synthesizing the test plans except that of the controller, which should be modified by introducing an additional transition which points away from a deadlock place reached after failure(s). This transition is activated by a receiver event "test" and terminated at an artificial place without outputs. An additional automaton should also be constructed to facilitate procedure synthesis (see Figure 7). The initial event "test" should be a sender, while its guards limit the scope of fault origins to those implied by the corresponding OET. All possible test actions are placed on the loops between s0 and s1, respectively. On the other hand, every admissible observable event triggers a unique outward transition from place s2 to a downstream place (i.e., s3a, s3b, s3c or s3d), which can then be brought back to the originating state s2 by resetting clock. It should be noted that the aforementioned loops are used mainly for creating multi-step procedures. By appropriately checking these models with UPPAAL, the SFC in Figure 8 can be generated for fault diagnosis after observing Trace 1. Note that the control actions *ov1* and *ov2* in the operation step S_1 are called for as soon as the activation condition AC_1 is satisfied. There may be three resulting scenarios depending on the sensor and clock readings, i.e., (1) AC_2 (LL, $\Delta t \geq 0$), (2) AC_3 (LH, $\Delta t = 2$), and (3) AC_4 (LH, $\Delta t = 4$), and the corresponding fault origins are: (1) f_{1A} or $f_{1A}f_2$; (2) f_2; (3) $f_{1B}f_2$.

5. Conclusions

A standardized methodology has been proposed in this work to construct timed automata for modelling all components in a given batch plant, and to establish the observable event traces accordingly. A generic synthesis procedure has also been developed for conjecturing the test plans of all undiagnosable traces. This diagnosis strategy is featured with the unique capability of differentiating various time delays caused by fault origins of the same type but with different intensities. Further enhancements should include a generalized method for more complex operations.

References

G. Behrmann, A. David, K. G. Larsen, 2006. A Tutorial on UPPAAL 4.0., Department of Computer Science. Aalborg University, Denmark.

A. Kang, C. T. Chang, 2014, Automata Generated Test Plans for Fault Diagnosis in Sequential Material- and Energy-Transfer Operations. Chem. Eng. Sci. 113, 101-115.

M. L. Yeh, C. T. Chang, 2011, An Automaton-Based Approach to Evaluate and Improve Online Diagnostic Schemes for Multi-Failure Scenarios in Batch Processes. Chem. Eng. Res. Des 89, 2652-2666.

Krist V. Gernaey, Jakob K. Huusom and Rafiqul Gani (Eds.), 12th International Symposium on Process Systems Engineering and 25th European Symposium on Computer Aided Process Engineering. 31 May – 4 June 2015, Copenhagen, Denmark

Modelling and Monitoring of Natural Gas Pipelines: New Method for Leak Detection and Localization Estimation

Xinghua Pan, M. Nazmul Karim*

Artie McFerrin Department of Chemical Engineering, Texas A&M University, 3122 TAMU, College Station, Texas 77843, United States
nazkarim@mail.che.tamu.edu

Abstract

Leakage of the chemicals from pipelines is the biggest safety concern about the transportation of the chemicals. Model-based fault detection method is one of the most widely used software solutions for fault identification. In this paper, a new leak detection method for a natural gas pipeline is proposed basing on the non-isothermal modelling of the process. The new software-based method is developed by designing an unknown input observer, which is able to deal with the disturbance from the temperature change and pressure drop from the pump station and estimate the boundary flow rate of the pipeline. A new adaptive model was updated towards the temperature and boundary pressure change for leak location estimation. A simulation of a natural gas pipeline with consumer connection was demonstrated.

Keywords: leak detection, natural gas pipeline, unknown input observer

1. Introduction

Pipeline is one of the most widely applied transportation methods for chemicals. However, the leakage accidents from the pipeline have generated great safety concerns. The software-based method generally use flow rate and pressure measurements at the boundary of the pipeline. Some software methods need temperature measurement such as Real Time Transient Modelling (Geiger, 2005). However, there are some limitations of the software method such as its high sensitivity to the process noise.

A natural gas pipeline is different from water and crude oil pipeline problems because of the change of gas thermal phase. Research have been reported for the leak detection of a natural gas pipeline without considering the thermal effect (Benkherouf and Allidina, 1988; Emara-Shabaik et al., 2002).The effect of the thermal property on the natural gas flow is demonstrated in this paper by non-isothermal modelling. A non-isothermal model of a natural gas pipeline without leak has been demonstrated (Osiadacz and Chaczykowski, 2001). Model-based software methods involve solving the partial differential equations (PDE) of the natural gas flow model both for isothermal and non-isothermal cases. The oscillation in boundary pressure changes the flow rate in the pipeline, further influences the leak detection decision.

In this paper, we designed a linear unknown input observer for the leak detection of a natural gas pipeline. The pipeline is featured with time-variant consumer usage at certain location. An unknown input observer is designed to eliminate the effect of

unknown input (Sename, 1997; Fu et al., 2004). The observer is able to identify the disturbance of pressure oscillation and temperature change without requiring the measurement and real-time modelling.

2. Modelling of the natural gas flow

2.1 Non-isothermal modelling of the natural gas flow in a pipeline

The non-isothermal modelling of a natural gas flow was demonstrated. Briefly, the composition of natural gas is assumed as 95 % methane, 2.5 % ethane, 1.6 % nitrogen, 0.7 % carbon dioxide, and 0.2 % propane. The pressure heat capacity is assumed constant at 2170 (J/kg K). The pipeline is 10 km in length (L = 10 km), and 0.3 m in diameter (D = 0.3 m). Heat transfer coefficient along the pipeline is assumed uniform. The inlet pressure (P_{in}) is 10 bar, and the outlet pressure (P_{out}) is 8 bar. The flow rate, pressure, and temperature across the pipeline cross-section were assumed constant as the flow is highly turbulent. A time-variant consumer usage is applied to the pipeline. The measurement frequency of the consumer usage is every 30 second. The non-isothermal models are developed based on mass, moment, and energy balance which are listed below.

$$\frac{\partial P}{\partial t}=\frac{-\frac{1}{A}\frac{\partial q}{\partial x}-\frac{1}{A\Delta x}q_L+\left[\frac{1}{ZC_P}\frac{\partial Z}{\partial T}+\frac{1}{TC_P}\right]\left[\frac{fq^3Z^2R^2T^2}{2DA^3P^2}-\frac{4U(T-T_g)}{D}-\frac{q}{A}C_P\frac{\partial T}{\partial x}+\left(\frac{T}{Z}\frac{\partial Z}{\partial T}+1\right)\frac{q}{AP}ZRT\frac{\partial P}{\partial x}\right]}{\left[\frac{1}{ZRT}-\frac{P}{Z^2RT}\frac{\partial Z}{\partial P}-\left(\frac{\partial Z}{\partial T}\right)^2\frac{T}{Z^2C_P}-\frac{2}{ZC_P}\frac{\partial Z}{\partial T}-\frac{1}{TC_P}\right]} \tag{1}$$

$$\frac{\partial q}{\partial t}=-A\frac{\partial P}{\partial x}-\frac{AP}{ZRT}g\sin\theta-\frac{fq^2}{2DAP}ZRT-\frac{1}{A}\frac{q_L}{\Delta x}\left(\frac{q}{P}\right)ZRT \tag{2}$$

$$\frac{\partial T}{\partial t}=\frac{\left(\frac{1}{ZRT}-\frac{P}{Z^2RT}\frac{\partial Z}{\partial P}\right)\frac{\partial P}{\partial t}}{\left(\frac{P}{Z^2RT}\frac{\partial Z}{\partial T}+\frac{P}{ZRT^2}\right)}+\frac{\frac{1}{A}\frac{\partial q}{\partial x}}{\left(\frac{P}{Z^2RT}\frac{\partial Z}{\partial T}+\frac{P}{ZRT^2}\right)}+\frac{q_L}{A\Delta x}\frac{1}{\left(\frac{P}{Z^2RT}\frac{\partial Z}{\partial T}+\frac{P}{ZRT^2}\right)} \tag{3}$$

Z is the compressibility factor and q_L is the leak mass flow rate.The isothermal models are developed using constant compressibility as shown in Eq. (4) and (5).

$$\frac{\partial P}{\partial t}+\frac{c^2}{A}\frac{\partial q}{\partial x}+\frac{c^2}{A\Delta x}q_L=0 \tag{4}$$

$$\frac{\partial q}{\partial t}+A\frac{\partial P}{\partial x}+\frac{fc^2q|q|}{2DAP}+\frac{c^2}{A\Delta x}\left(\frac{q}{P}\right)q_L=0 \tag{5}$$

2.2 Model reduction

The nonlinear isothermal model was reduced to a linear model which showed the relationship between consumer usage and boundary flow rate. The model reduction process starts from the isothermal model.

The reduction process is shown as followed. The overall pipeline is divided into three parts: the section before the usage (l_1), the section with the usage (l_2), and the section

after the usage (l_3). The isothermal nonlinear equation holds for each section. q_{usage} is zero for l_1 and l_3. With the assumption of fixed boundary pressure condition, equation becomes the following.

$$l_1 \frac{f(2q_1+\Delta q_1)\Delta q_1}{D} + (l_2+l_3)\frac{f(2q_1+\Delta q_0)\Delta q_0}{D} + \frac{1}{2}(\Delta q_1 - \Delta q_0)(q_1+\Delta q_0) = 0 \tag{6}$$

With the assumption that $(2q_1 + \Delta q_1) \approx 2q_1$ and $(2q_1 + \Delta q_0) \approx 2q_1$, the above equation can be simplified to the following equations with a/b as a constant.

$$q_{in} = q_{st.} + q_{usage} \cdot a \qquad q_{out} = q_{st.} + q_{usage} \cdot b \tag{7}$$

For a time-variant consumer usage, the dynamic of the boundary flow rate can be written as the following equations.

$$q_{in}(t) = q_{st.} + \sum_{i=1}^{n} a_i q_{usage}(t-i) \qquad q_{out}(t) = q_{st.} + \sum_{i=1}^{n} b_i q_{usage}(t-i) \tag{8}$$

3. Design of an unknown input observer with multiple time delays

Without loss of generality, a linear model was showed in Eq. (9). In which, x(t) is the state, y(t) is the measurement, $u(t-\tau_i)$ is the input (consumer usage), and w(t) is the unknown input.

$$x(t) = \sum_{i=0}^{n} A_i x(t-\tau_i) + \sum_{i=0}^{n} B_i u(t-\tau_i) + Ww(t) \tag{9}$$

$$y(t) = Cx(t) \tag{10}$$

The unknown input observer is designed as the following

$$\mathrm{z(t)} = \sum_{i=0}^{n} F_i z(t-\tau_i) + \sum_{i=0}^{n} TB_i u(t-\tau_i) + \sum_{i=0}^{n} G_i y(t-\tau_i) \tag{11}$$

$$\hat{x}(t) = z(t) + Ny(t) \tag{12}$$

Theorem 1: The observer will asymptotically estimate the state if and only if the following conditions hold:

1. $\mathrm{e(t)} = \sum \mathrm{F_i e(t-\tau_i)}$ is asymptotically stable
2. $T+NC=I$
3. $TW=0$
4. $\bar{G}_1 = G_i - F_i N,\ i = 0,1,2,\ldots n$
5. $F_i = TA_i - \bar{G}_1 C,\ i = 0,1,2,\ldots n$

(13)

The unknown input parameter matrix was set as $\begin{bmatrix} 1 & 1 \\ 1 & 1 \end{bmatrix}$, which corresponds to the pressure oscillation, process noise, and temperature change. The observer parameter synthesis is solved using the LMI method. The proof of the theorem is not shown here, which can be found in the reference (Keong et al., 2005).

Theorem 2: The observer estimation error will be asymptotically stable if and only if the following conditions hold: there exist matrices $P = P^T > 0;\ Q_i > 0$ satisfying the LMI.

$$\begin{bmatrix} -P+\sum_{i=1}^{4} Q_i & 0 & 0 & 0 & 0 & F_0^T P \\ * & -Q_1 & 0 & 0 & 0 & F_1^T P \\ * & * & -Q_2 & 0 & 0 & F_2^T P \\ * & * & * & -Q_3 & 0 & F_3^T P \\ * & * & * & * & -Q_4 & F_4^T P \\ * & * & * & * & * & -P \end{bmatrix} < 0 \tag{14}$$

The proof of the theory is to introduce a discrete type Lyapunov-Karsovskii function, which is not shown here. Another restriction for the parameter is that the eigenvalues of the parameter need to be restricted in a certain range. It satisfies the following LMI with λ_1 and λ_2 as constants as shown in the reference (Keong et al., 2005).

$$\begin{aligned} &Q_1 \sum \chi_i + (Q_1 \sum \chi_i)^T - \mathrm{U} \sum \beta_i - \left(\mathrm{U} \sum \beta_i\right)^T + 2\lambda_2 Q_1 < 0 \\ &Q_1 \sum \chi_i + (Q_1 \sum \chi_i)^T - \mathrm{U} \sum \beta_i - \left(\mathrm{U} \sum \beta_i\right)^T + 2\lambda_1 Q_1 > 0 \end{aligned} \tag{15}$$

4. Results and discussion

The effect of the temperature change and pressure drop at boundary of the pipeline was simulated in Matlab. A pattern of consumer usage in a time span is illustrated in Fig. 1, which shows a constant usage at midnight for heating and an increased usage for cooking in the morning.

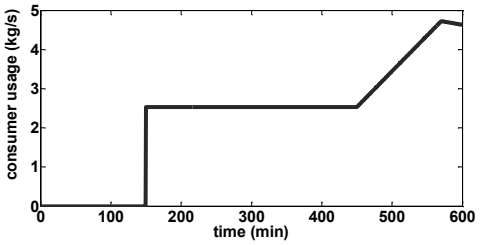

Figure 1. Time-variant consumer usage

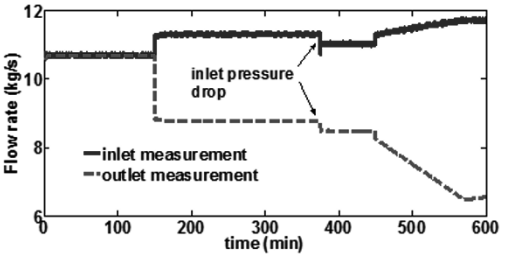

Figure 2. Effect of pressure drop on flow rate

The measurement data is generated by the non-isothermal model. The estimation data is from the unknown input observer which is based on the isothermal model. The measurement and estimation are only limited to flow rate. To study the effect of disturbance such as pump station pressure drop and temperature disturbance on the effect of flow rate, the simulation results are shown in Fig. 2 and 3.

Fig. 2 shows the effect of inlet pressure drop on the boundary flow rate. The inlet pressure drops from 10 bar to 9.9 bar in 30 s. As can be seen in the figure, both inlet and outlet drop, however, the inlet flow rate has a sharp drop and increases back. The effect of temperature change on flow rate is demonstrated in Fig. 3 with a 10 K temperature increase in 30 s. As shown in the figure, both inlet and outlet flow rate decrease after temperature change. The decrease of ground temperature will have the opposite effect which is not shown here.

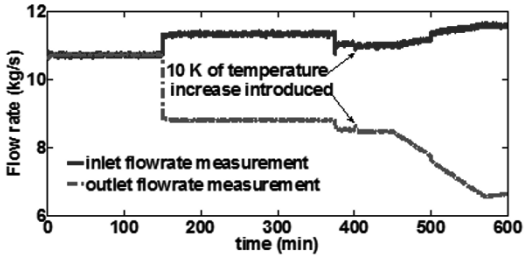

Figure 3. Effect of temperature change on flow rate

Fig. 4 compares the measurement and observer estimation of boundary flow rate. The observer was given an initial estimation error as seen in the figure. The observer is able to estimate the flow rate when disturbance occurs such as pressure drop and temperature change till a leak occurs.

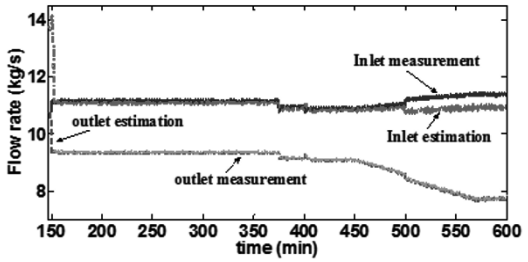

Figure 4. Comparison between flow rate measurement and observer estimation

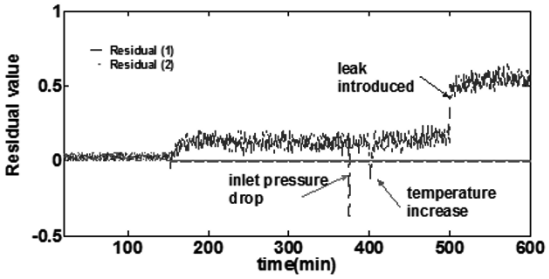

Figure 5. Residual signal of observer

The difference between measurement and observer estimation is defined as a residual. As pointed out in Fig. 5, the pressure drop will generate a sharp negative residual signal. The temperature increase also has a sharp negative residual signal. However, the leak accident creates a constant increase in the residual value, which is a different residual pattern for distinguishing the disturbance of pressure drop and temperature change.

A new location estimation scheme is proposed. The new method involves first identifying the disturbance and leaks basing on the residual signal shown in Fig. 5. If a disturbance was identified, the linear model of the natural gas flow was updated to include the information of disturbance. Once a leak event was distinguished from disturbance, the leak location was calculated based on the measurement and observer estimation. Fig. 6 demonstrated the leak location estimation result. The leak location was estimated using the Eq. (7) and (8).

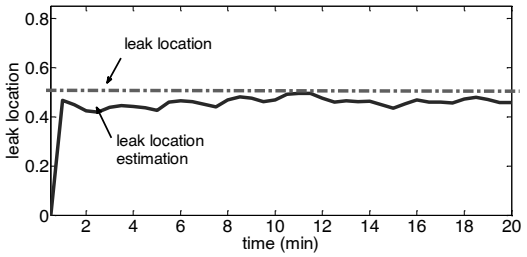

Figure 6. Leak location estimation

5. Conclusions

The non-isothermal modelling of a natural gas flow in a pipeline was developed. The unknown input observer can estimate the boundary flow rate of the pipeline, and also can distinguish the disturbance from the leak accident basing on the different residual signal. A new adaptive model was proposed to incorporate the temperature and pump pressure change for leak location estimation.

References

A. Benkherouf, AY. Allidina, 1998, Leak detection and location in gas pipelines, Control Theory and Applications, IEE Proceedings D, 135, 142-148.

H. Emara-Shabaik, Y Khulief, I. Hussaini, 2002, A non-linear multiple-model state estimation scheme for pipeline leak detection and isolation. Proceedings of the Institution of Mechanical Engineers Part I Journal of Systems and Control Engineering, 216, 497-512.

YM. Fu, GR. Duan, SM. Song, 2004, Design of unknown input observer for linear time-delay systems. International Journal of Control, Automation and Systems, 2, 530-535.

D. Koeing, N. Bedjaoui, X. Litrico, 2005, Unknown input observers design for time-delay systems application to an open-channel. Decision and Control, 2005 and 2005 European Control Conference, 5794-5799.

AJ. Osiadacz, M. Chaczykowski, 2001, Comparison of isothermal and non-isothermal pipeline gas flow models. Chemical Engineering Journal, 81, 41-51.

IG. Geiger, 2005, Principles of leak detection. KROHNE.

O. Sename, 1997, Unknown input observers design for time-delay systems. Proceedings of the 36th IEEE Conference on Decision and Control, 2, 1629-1630.

Krist V. Gernaey, Jakob K. Huusom and Rafiqul Gani (Eds.), 12th International Symposium on Process Systems Engineering and 25th European Symposium on Computer Aided Process Engineering.
31 May – 4 June 2015, Copenhagen, Denmark

Dynamic artificial immune system with variable selection based on causal inference

Yidan Shu[a], Jinsong Zhao[a*]

[a]*Department of Chemical Engineering, Tsinghua University, Beijing 100084, China*
jinsongzhao@tsinghua.edu.cn

Abstract

Large numbers of variables are measured in typical chemical processes. In most of the fault detection and diagnosis methods, all the measured variables are selected. However, the incorporating measured variables that do not provide any additional information about faults degrades monitoring performance.

Dynamic artificial immune system (DAIS) is a new artificial intelligence methodology shows strong ability of self-learning and self-adaptability. Much work has been done on its application in process monitoring and fault diagnosis in chemical processes. However, there is little research in the variable selection in DAIS. In this paper, we propose an approach to select variable used for DAIS. The approach is based on the causal inference among the measured variables. Through causal inference, the cause-effect relations among variables can be found and then variables that do not reflect the main trends of changes of the processes can be picked out. Then the variable selection of the DAIS can be optimized and the performance of the fault diagnosis of DAIS can be improved. Case studies based on the Tennessee Eastman process are performed to illustrate the effectiveness of our approach.

Keywords: Fault diagnosis, artificial immune system, transfer entropy, variable selection

1. Introduction

It is of great importance to detect and diagnose process faults to ensure the stability and safety of chemical processes. The fault detection and diagnosis techniques can be divided into two categories: model-based techniques and data-based techniques (Venkatasubramanian et al., 2003). Model-based techniques require a reliable mathematical model and their application are often limited by the complexity of the chemical processes. On the other hand, data-based techniques mainly depend on the availability of process data, which are usually easy to obtain from modern chemical processes. Therefore, data-based techniques attract lots of focus from the fault detection and diagnosis study.

Among the data-based techniques, the multivariate statistical process monitoring (PSPM) techniques are very popular, such as principal component analysis (PCA), independent component analysis (ICA), partial least square (PLS). Besides PSPM, some methods based on pattern classification also draw much attention, such as artificial neural network (ANN), support vector machine (SVM). Compared with the data-based techniques above, artificial immune system (AIS) shows stronger self-adaptive and self-learning abilities and draws much attention recently (Dai and Zhao, 2011; Ghosh and Srinivasan, 2011; Zhao et al., 2014). In this paper, the fault detection and diagnosis (FDD) are based on dynamic artificial immune system (DAIS), which was proposed by

Dai and Zhao in 2011 to conduct FDD for batch processes as well as steady-state processes.

Although much work has been done in data-based fault diagnosis, few of them considered the selection of variables to be used in the diagnosis. As modern chemical processes are becoming larger and more complex, thousands of variables are measured to monitor the processes. However, for the FDD of a process, the measured variables aren't equally important. The introduction of unimportant variables will obviously increase the computing loads of the FDD techniques and, moreover, degrade the performance like the false alarm rate, the missed detection rate and the detection delay (Ghosh et al., 2014). Therefore, the variable selection is a critical issue of the FDD techniques.

In this paper, we propose a variable selection method based on the causal inference with transfer entropy, and apply it to improve the performance of FDD with AIS. The rest of the paper is organized as follows: Section 2 is a brief introduction of DIAS; Section 3 is the description of our proposed variable selection methods; Section 4 is the case study on Tennessee Eastman process; Section 5 is the conclusion.

2. Dynamic artificial immune system

Artificial immune system (AIS) is a method that tries to mimic the human immune system. As summarized by Timmis in 2008, AIS is a diverse area of research that attempts to bridge the gap between immunology and engineering and it is developed through the application of techniques such as mathematical and computational modeling of immunology, abstraction from those models into algorithm (and system) design and implementation in the context of engineering.

Recently, work on chemical process FDD has been reported (Aguilar in 2004; Wang and Zhao. in 2008; Ghosh and Srinivasan in 2011). To apply AIS in fault diagnosis of batch processes, Dai and Zhao integrated the clonal selection algorithm of AIS with dynamic time warping (DTW) in 2011and afterwards used the so-called dynamic AIS (DAIS) in an online fault diagnosis strategy for full operating cycles of chemical processes in 2014.

In this work, we use DAIS to diagnose faults. In DAIS, antibodies and antigens are represented by matrices of time-sampled data, instead of vectors of data, to reflect data changes in trend. The differences between them are calculated by the DTW algorithm. The details of DAIS can be found in Dai and Zhao's paper in 2011 and Zhao et al.'s paper in 2014. The main steps of DAIS are shown as below.

1) Initialization. Generate original fault and normal antibodies from historical samples. Then clone these antibodies with mutation to construct antibody library of normal state and each type of fault. The threshold of each of the antibody library should also be calculated.
2) Fault detection. Generate detective antigen from the incoming data and calculate the difference between the detective antigen and each antibody in the normal antibody library. If all of the differences are greater than the threshold of the antibody library, then a fault is detected.
3) Fault diagnosis. After a fault is detected, generate diagnostic antigen and calculate the difference between the diagnostic antigen and each antibody in antibody library of each type. If there exist fault antibodies in only one of the fault antibody libraries that have smaller difference degrees than the threshold of the fault antibody library, the fault is recognized of the fault type of the corresponding fault antibody library. If none of the fault antibody libraries contain an antibody that has a smaller

difference degree than the corresponding threshold, the fault is then diagnosed as a new fault.

4) Self-learning. After the fault diagnosis of DAIS, a manual diagnosis should be conducted to double check the diagnosis results by DAIS. According to the manual diagnosis result, a new original fault antibody is then generated and stored into the fault antibody library of the fault type of the manual diagnosis result. Afterwards the fault antibody library is updated through a new round of clone with mutation.

Although DAIS shows strong adaptation capability and independency on the number of training samples, there is still much work worth doing to improve its performance. One of the critical issues is the selection of variables to generate antibodies and antigens. In the next section, the issue of variable selection will be discussed.

3. Variable selection based on causal inference with transfer entropy

In pattern recognition, patterns are recognized based on a vector of features values, the selection of a subset of variables can have a significant effect on the classification performance and therefore feature selection have become an important step of data pre-processing in automated pattern recognition (Jain & Zongker, 1997; Raymer et al., 2000).

Although feature selection (or variable selection) is widely used in pattern recognition and data mining, it is rarely considered in multivariate statistical process monitoring (MSPM) or FDD. Two notable exceptions are: Verron et al. proposed a fault diagnosis method with variable selection based on mutual information in 2008; Ghosh et al. proposed a genetic algorithm (GA) based method for the variable selection in PCA in 2014. However, their method was based on a GA optimization and didn't consider the intrinsic relationships between variables. As a result, the optimized selection PCA may be useless for other FDD method. Verron's method is based on the mutual information between the data and the considered classes. Therefore, a large number of samples of each fault class to be considered are necessary for the variable selection, which may limit its application.

In our proposed selection approach, we utilize transfer entropy to infer the causal relationships between variables. According to the inferred causal relationships, the variables that closely relate to the root cause of a certain fault can be found. Then DAIS can be built with these related variables to diagnose the fault. In detail, our proposed DAIS fault diagnosis method with variable selection can be divided into three steps, which will be described separately as follows:

3.1. Transfer entropy calculation

Based on the concept of information theory and information entropy (Shannon and Weaver, 1949), Schreiber proposed the concept of transfer entropy in 2000 to measure the asymmetric interactions in a system. Transfer entropy is in an asymmetric form, which makes it possible to measure cause-and-effect relationships. To consider time delays, which are common in many practical situations, Bauer et al. in 2007 incorporated the prediction horizon in the transfer entropy. Shu and Zhao in 2013 proposed a modified transfer entropy to make the estimation of time delay more accurate. In this work we use the modified form to calculate transfer entropy that indicates the causal relations of y to x:

$$t(y \to x) = \int \cdots \int \hat{p}(x_{i+h}, x_{i+h-1}^{(k)}, y_i^{(l)}) \log \frac{\hat{p}(x_{i+h} \mid x_{i+h-1}^{(k)}, y_i^{(l)})}{\hat{p}(x_{i+h} \mid x_{i+h-1}^{(k)})} dx_{i+h} dx_{i+h-1}^{(k)} dy_i^{(l)} \quad (1)$$

x and y represent two variables while x_i and y_i represent their values at time i. $y_i^{(l)} = [y_i, y_{i-1}, \cdots, y_{i-l+1}]$ and $x_{i+h-1}^{(k)} = [x_{i+h-1}, x_{i+h-2}, \cdots, x_{i+h-k}]$. The probability density function (PDF) is estimated by a kernel estimator, which can be found in Bauer's work in 2007. As we change h, the value of equation (1) will change and we can find an h to maximize the value. Then the maximized value is the transfer entropy that presents the strength of causal relations from y to x and the corresponding h is the time delay.

3.2. Variable selection

With equation (1), the transfer entropy between variables of the process to be diagnosed can be calculated to measure the causal relations between variables with the normal data in steady state. Then for a certain fault type, pick out the measured variable that directly relates to the root cause of the fault. Afterwards examine the transfer entropy values from that variable to the other variables. Only those variables with transfer entropy values larger than the pre-set threshold, which means they are strongly affected by the fault, should be selected to be used in DAIS.

3.3. DAIS fault diagnosis

After the variables are selected for each fault type, the antibodies of each fault type can also be generated using only the variables selected for that fault type instead of all of the variables. On the other hand, different antigens should also be generated using different selection of variables for different fault types.

4. Case study

The case study is conducted on Tennessee Eastman (TE) process (Downs and Vogel, 1993), which is a benchmark model for studying fault detection and diagnosis. The process was simulated on Matlab Simulink using the control strategy proposed by Ricker in 1996.

In this case study we only use the continuous process measurements (XMEAS (1)-(22)) and the process manipulated variables (XMV (1)-(12)). The sampling interval is 1.8 seconds.

The transfer entropy calculation is based on 1000 sampling points of steady state normal data, with k=l=1 and the search range of h is from 0 to 5 sampling intervals. The threshold of transfer entropy to determine whether to select a variable is 0.1.

Totally 20 types of faults can be introduced into the simulated process to generate fault samples for the validations of FDD methods. In this case study, we choose to introduce fault 4 and 6 because the cause of each of these faults can be directed related to a measured variable. Then the related variables can be found using the results of transfer entropy calculation and selected to build DAIS. The descriptions and selected variables of the introduced fault are listed in Table 1.

Table 1. Fault description and selected variables

Fault No.	Fault description	Selected variable in DAIS
IDV (4)	reactor cooling water inlet temperature step change	Reactor Level; Reactor cooling water outlet temperature; Reactor cooling water flow valve
IDV (6)	A feed loss	A feed; A and C feed; A feed flow valve; A and C feed flow valve

For each fault type, two fault batches are simulated to generate training samples to construct the DAIS antibody libraries. Then two fault batches are simulated to provide test samples. The antibody length is set to be 30 sampling points and the antigen length is set to be 15 sampling points.

The diagnosis delays, which mean how long it takes DAIS to recognize the fault types of the type samples, are shown in Table 2. It can be found that variable selection reduced the diagnosis delays by 1 to 3 sampling intervals, or 1.8 to 5.4 seconds.

Table 2 Diagnosis delay of DAIS

Test sample	Diagnosis delay, all variables are used	Diagnosis delay, only selected variables are used
IDV (4) sample1	12.6 sec	10.8 sec
IDV (4) sample2	14.4 sec	10.8 sec
IDV (6) sample1	23.4 sec	21.6 sec
IDV (6) sample2	27.0 sec	21.6 sec

Then we generate diagnostic antigens from data of 15 sampling points after the fault introduced moment and calculate their difference degrees from the fault antibody libraries. The results are shown in Table 3. The antibody libraries of each fault type can correctly diagnose the two fault samples of its fault type and won't recognize the fault samples of other fault type by mistake, no matter whether the variable selection is implemented. But the variable selection will lead to a more obvious discrimination between antigens of different fault types. For example, when we use antibody library of IDV (6) to diagnose faults, the difference degrees between the antibody library and the samples of IDV (4) will be very close to the difference degrees between the antibody library and the samples of IDV (6) (0.5616 and 0.5083 v.s. 0.4418 and 0.4753). But if we use only the selected variables to diagnose, the differences will have a more significant disparity (0.0964 and 0.0963 v.s. 0.0248 and 0.0320).

Table 3 Difference degrees between antigens of test samples and the antibody libraries

Test sample	Antibody libraries, all variables are used		Antibody libraries, only selected variables are used	
	IDV (4) Threshold: 0.5085	IDV (6) Threshold: 0.4781	IDV (4) Threshold: 0.0661	IDV (6) Threshold: 0.0815
IDV (4) sample1	0.4457	0.5616	0.0457	0.0964
IDV (4) sample2	0.3772	0.5083	0.0401	0.0963
IDV (6) sample1	0.5596	0.4418	0.0691	0.0248
IDV (6) sample2	0.6030	0.4753	0.0766	0.0320

5. Conclusion

Because of the good availability data in modern chemical process, data-based techniques draw much attention from the chemical process fault detection and diagnosis (FDD) research. Although much work has been done on the data-based FDD methods, the selection of variable to be used in the FDD methods is rarely studied. Some research has shown that improper variable selection may degrade the performance of FDD methods. Variable selection is an important issue in FDD.

In this work, we propose a variable selection method based on the causal inference with transfer entropy. With causal inference, the variables that strongly relate to a certain fault type can be picked out. The FDD using only these variables will have a better

performance in diagnosis delays because irrelevant variables will no longer disturb the diagnosis.
The FDD method used in this work is dynamic artificial immune system because it is strong adaptation capability and independency on the number of training samples. However, it should be noted that our variable selection can also be used to improve other FDD methods because it depends on the causal inference rather than optimization of the performance of a certain FDD method.
A case study on TE process is performed to show the improvement of DAIS when our variable selection method is used.

6. Acknowledgement

The authors would like to gratefully acknowledge financial support from the National High Technology Research and Development Program of China (863 Program, Grant No. 2013AA040702) and National Natural Science Foundation of China (Grant No. 61433001).

References

J. Aguilar, 2004, An artificial immune system for fault detection. In Proceedings of the 17th International Conference on Innovations in Applied Artificial Intelligence, Ottawa, Canada, 219-229
M. Bauer, J.W. Cox, M.H. Caveness, J.J. Downs, N.J. Thornhill, 2007, Finding the direction of diturbance propogation in a chemical process using transfer entropy, IEEE Transactions on control systems technology, 15, 1, 12-21
Y. Dai, J. Zhao, 2011, Fault diagnosis of batch chemical processes using a dynamic time warping (DTW) based artificial immune system, Industrial and Engineering Chemistry Research, 50, 8, 4534-4544
J.J. Downs, E.F. Vogel, 1993, A plant-wide industrial process control problem, Computers and Chemical Engineering, 17, 3, 245-255
K. Ghosh, M. Ramteke, R. Srinivasan, 2014, Optimal variable selection for effective statistical process monitoring, Computers and Chemical Engineering, 60, 260-276
K. Ghosh, R. Srinivasan, 2011, Immune-system-inspired approach to process monitoring and fault diagnosis, Industrial and Engineering Chemistry Research, 50, 3, 1637-1651
A.K. Jain, D. Zongker, 2007, Feature selection: evaluation application, and small sample performance, IEEE Transaction on Pattern Analysis and Machine Intelligence, 19, 153-158
M.L. Raymer, W.F. Punch, E.D. Goodman, L.A. Kuhn, A.K. Jain, 2000, Dimensionality reduction using genetic algorithm, IEEE transactions on Evolutionary Computation, 4, 2, 164-171
T. Schreiber, 2000, Measuring information transfer, Physical Review Letters, 85, 2, 461-464
C. Shannon, W. Weaver, 1948. A mathematical theory of communication, The Bell System Technical Journal, 27, 379-423, 623-656
Y. Shu, J. Zhao, 2013, Data-driven causal inference based on a modified transfer entropy, Computers and Chemical Engineering, 57, 173-180
J. Timmis, P. Andrews, N. Owens, E. Clark, 2008, An interdisciplinary perspective on artificial immune systems. Evolutionay Intelligence, 1, 5–26.
V. Venkatasubramanian, R. Rengaswamy, K. Yin, S. Kavuri, 2003, A review of process fault detection and diagnosis. Part I: Quantitative model-based methods, Comupters and Chemical Engineering, 27, 3, 213-311
S. Verron, T. Tiplica, A. Kobi, 2008, Fault detection and identification with a new feature selection based on mutual information, 18, 479-490
C. Wang, Y. Zhao, 2008, A new fault detection method based on artificial immune systems. Asia-Pacific Journal of Chemical Engineering, 3, 706–711
J. Zhao, Y. Shu, J. Zhu, Y. Dai, 2014, An online fault diagnosis strategy for full operating cycles of chemical processes, Industrial and Engineering Chemistry Research, 53, 13, 5015-5027

Krist V. Gernaey, Jakob K. Huusom and Rafiqul Gani (Eds.), 12th International Symposium on Process Systems Engineering and 25th European Symposium on Computer Aided Process Engineering.
31 May - 4 June 2015, Copenhagen, Denmark.

A smart safety system for chemical processes

Rafael M. Soares, Argimiro R. Secchi and José C. Pinto

Universidade Federal do Rio de Janeiro, Chemical Engineering Program / COPPE, Rio de Janeiro 21941-909, Brazil
{*rsoares; arge; pinto*}*@peq.coppe.ufrj.br*

Abstract

Conventional safety systems are designed to mitigate incidents, i.e., they aim to reduce the impact of failures using relief valves, rupture disks and, usually, cause a system emergency shutdown. The design of these systems is based on failure likelihood and the accident severity. However, this basis is normally obtained empirically, leaving the safety system vulnerable to process nonlinearities. To ensure the process safety, the control actions are conservative, so that small deviations from setpoints can lead to shutdown, generating large economic losses. This work proposes the periodic simulation of the reactor behaviour considering several component failures and, from these responses, determine the potential risk to which the system is subjected. Depending on this potential, preventive actions can be taken in order to guarantee the reactor safety and integrity and avoid a potential shutdown. These actions are calculated to provoke the least possible disturbance in order to reduce the impact on product quality, while keeping the process operating. The goal is to increase annual operating time of the plant without compromising the safety of the process and product quality. The results show that the proposal is feasible to real time applications and that, with a reliable model and an efficient fault detection system, unnecessary shutdowns can be avoided.

Keywords: process safety, nonlinear model predictive control

1. Introduction

Although the chemical industry operates on a large scale for tens of decades, only in the last two decades the subject of safety has gained the attention it deserves. Several accidents have marked the history of the chemical industry, such as Chernobyl, Bhopal, Seveso and Sandoz. Important lessons have been learned from these tragedies. Among them, the deep knowledge of the chemical process can be emphasized. In the synthesis of a new process, even after the tests on a pilot scale, the scale-up to industrial scale can bring serious changes in the dynamic behaviour of the system. Besides these changes, the control structure can modify the stability of the system at various operating points. In this case, the use of mathematical models is essential for reliable dynamic analysis. Moreover, with the rapid advancement of computing in recent years, the use of rigorous phenomenological models becomes increasingly feasible (Manenti, 2011). Their penetration in the industrial environment, however, is still limited. In security systems is no different. Despite the obvious gains that non-linear mathematical models can bring regarding the reliability of the analysis, their use still faces difficulties in implementation and hesitancy of industry replacing traditional linear models. In the area of process safety the scenario is even worse because, traditionally, the analyses are based on process empirical knowledge. Often qualitative models are used for that purpose, which are still quite lagged the proposals found in the scientific literature, which has suggested the use of more accurate models and techniques (Venkatasubramanian et al., 2003).

In addition to the difficulties faced during the design of safety systems, new obstacles arise during industrial operation. Detecting the origin of unwanted events can be a complex task, but once found, can be decisive in determining the actions of the security system (Venkatasubramanian et al., 2003). Another important issue is that many decisions involving hazardous situations are taken by operators, whose subjectivity considerably reduces the reliability of the security system. All of that makes these systems to be designed and operated conservatively under close tolerances in deviations from the setpoints and often using the emergency shutdown as a way to ensure safety (Luyben, 2012). These actions, however, lead to considerable loss of production and, consequently, financial losses, since the plant for days will idle until it is ready for the new startup.

This work focuses on industrial operation, putting the emergency shutdown as the last alternative in situations of risk to the integrity of the system. Before it, a step of system dynamics analysis is proposed. A feasible condition for safe operation is calculated in order to avoid an emergency shutdown while disturbing the system as little as possible. The goal is to increase annual operating time of the plant, reducing losses due to idleness without compromising the safety of the process and product quality. The strategy proposed in this work is not opposed to the techniques used in process safety. In other words, it represents a new security layer that can operate in harmony with the traditional layers.

2. Methodology

The smart safety system aims to test the actual responsiveness of the control system against critical failures and take preventive actions in case of risk. The risk in this case refers to a possible violation of the safety limits of the process as a result of a possible undesired behaviour. Thus there are two stages: one to evaluate risks and other to determine the safety action. The first consists of the dynamic simulation of the process in failure scenario. If any controlled variable violates safety limits, the operation is considered unsafe and new setpoints must be calculated. If not found a safe state of operation, the only alternative in case of failure would be the emergency shutdown. The integrated control, security and reconciliation system is outlined in Figure 1. The methodology proposed in this work to calculate these setpoints is to solve the optimization problem described below:

$$\min_{\mathbf{u}} \left(\mathbf{x}_0(k) - \check{\mathbf{x}}(k+P)\right)^T \chi \left(\mathbf{x}_0(k) - \check{\mathbf{x}}(k+P)\right) \tag{1}$$

Subject to:

$$\mathbf{x}(i+1) = f\left(\mathbf{x}(i), \mathbf{u}(i)\right) \qquad i = k, \ldots, k+P-1 \tag{2}$$

$$\mathbf{x}(k) = \mathbf{x}_0(k) \tag{3}$$

$$\check{\mathbf{x}}(j+1) = f\left(\mathbf{x}(j), \mathbf{u}(j), \omega\right) \qquad j = k+P, \ldots, k+P+H-1 \tag{4}$$

$$\check{\mathbf{x}}(k+P) = \mathbf{x}(k+P) \tag{5}$$

$$\check{\mathbf{x}}(k+P+H) - \check{\mathbf{x}}(k+P+H-1) < tol \tag{6}$$

$$\check{\mathbf{x}}(j+1) < \mathbf{x}^{max} \tag{7}$$

$$\left|\mathbf{x}(k+P) - \mathbf{x}(k+P-1)\right| < tol \tag{8}$$

$$\mathbf{u} \in \mathbb{U} \tag{9}$$

From state $\mathbf{x}_0(k)$, which is the current state of the plant (Eq.(3)), varying $\mathbf{u}$, a steady state $\check{\mathbf{x}}(k+P)$ (Eq.(5) and Eq.(8)) should be found such a way that from the initial condition $\check{\mathbf{x}}(k+P)$ a dynamic trajectory simulation with a failure scenario (Eq.(4)) must fulfil the defined safety limits (Eq.(7)). In addition, this dynamic trajectory must not be crescent at the end of prediction horizon H (Eq.(6)). Otherwise, after the prediction horizon H, the safety limits could be violated. The

state $\check{\mathbf{x}}(k+P)$ should be a steady state (Eq.(8)) because after changing the controller from SISO to MIMO the control actions $\mathbf{u}(k+P)$ are repeated. Only T_j remains manipulated. Thus, if $\check{\mathbf{x}}(k+P)$ is a point of a dynamic trajectory, then it is not possible to ensure the fulfilment of the safety limits.

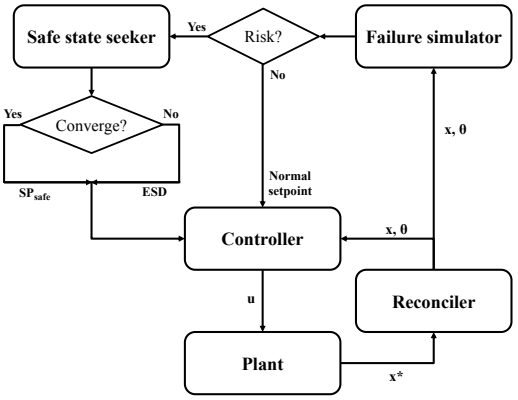

Figure 1: Structure of the proposed system.
ESD: Emergency shutdown. SP_{safe}: Safe setpoint.

In order to illustrate the methodology, the system under consideration consists of a jacketed stirred tank reactor fed by three independent inlet streams (monomer, solvent and catalyst) and an output that in addition to all components of the entry also carries the polymer formed in the chemical reaction. For illustration we consider an A $\rightarrow$ B chemical reaction which simulates a suspension polymerization, wherein the monomer reacts to form polymer in the presence of a solvent. Monomer, solvent, polymer and catalyst are in liquid phase. The mathematical model of this system consists of five differential equations, one related to energy balance (Eq.(14)) and the others relating to the material balance of monomer, polymer, solvent and catalyst (Eq.(10) - Eq.(13), respectively).

$$\frac{dM_{Mon}}{dt} = F_{in}^{Mon} - F_{out}^{Mon} - r \tag{10}$$

$$\frac{dM_{Pol}}{dt} = -F_{out}^{Pol} + r \tag{11}$$

$$\frac{dM_{Sol}}{dt} = F_{in}^{Sol} - F_{out}^{Sol} \tag{12}$$

$$\frac{dM_{Cat}}{dt} = F_{in}^{Cat} - F_{out}^{Cat} \tag{13}$$

$$\frac{dT}{dt} = \frac{F_{in}\,T_{in}}{M_t} - \frac{F_{out}\,T}{M_t} + \frac{\Delta H_r\,r}{M_t\,C_p} + \kappa_c(T_j - T) \tag{14}$$

$$M_t = M_{Mon} + M_{Pol} + M_{Sol} + M_{Cat} \tag{15}$$

$$\kappa_c = \frac{UA}{M_t\,C_p} \tag{16}$$

$$\mathrm{k} = \frac{\mathrm{k}_0\,M_t^2}{V} \tag{17}$$

$$r = x_{Mon}\,x_{Cat}\,\mathrm{k}\,exp\left(\frac{-E_a}{R\,T}\right) \tag{18}$$

$$F_{in} = F_{in}^{Mon} + F_{in}^{Sol} + F_{in}^{Cat} \tag{19}$$

$$F_{out} = F_{in} \tag{20}$$

$$F_{out}^{i} = F_{out}\,x_i,\ i = [Mon, Pol, Sol, Cat] \tag{21}$$

$$x_i = \frac{M_i}{M_t}, \qquad i = [Mon, Pol, Sol, Cat] \tag{22}$$

where F is flow in mol/h, M is amount of substance in mol, r is the chemical reaction rate in mol/h, T is temperature in K and x is molar fraction. The subindex j means jacket, t means total and Mon, Pol, Sol and Cat mean monomer, polymer, solvent and catalyst, respectively. The parameter k_0 is the Arrhenius pre-exponential factor, V is the reaction mixture volume, k is the equivalent kinetic

constant, E_a is the activation energy, R is the universal gas constant, ΔH_r is the reaction heat, C_p is the reaction mixture heat capacity, UA is the overall heat transfer coefficient and κ_c is the jacket equivalent heat transfer coefficient. The model parameters (Table 1) were adjusted empirically to represent a typical dynamics of a tank reactor. This mathematical model was used as a virtual plant and as model of the controller during the simulations.

The control strategy adopted in this work is known as Nonlinear Model Predictive Control (NMPC) an advanced control strategy based on nonlinear model. This controller is based on the concept of Model Predictive Control (MPC), conceived in the 60s, and basically consists of a dynamic optimization problem with multiple objectives and constraints. The NMPC has been gaining attention in the industry in recent years, especially because of three characteristics (Manenti, 2011): (i) is able to handle economical non-linearities and the process dynamics; (ii) can be based on phenomenological mathematical model or nonlinear semi-empirical models; (iii) is able to solve simultaneously the control problem and the problem of dynamic real-time optimization (economic problem), satisfying constraints for state variables and manipulated variables.

The controller was programmed to assume different configurations depending on the risk to which the process is subject. Under normal operating conditions (safe operation), the controller assumes the SISO (Single Input Single Output) configuration, where the manipulated variable is the jacket temperature and the controlled variable is the reactor temperature. When the algorithm detects an adverse safety situation (unsafe operation) new setpoints are calculated. To meet them the controller is reconfigured as MIMO (Multiple Input Multiple Output). In this case, the manipulated variables are: jacket temperature and monomer, catalyst and solvent flowrates. The controlled variables are: reactor temperature and the amounts of monomer, catalyst and solvent in the reactor. Due to the chemical reaction, monomer and polymer cannot be simultaneously controlled. Only one of them can be controlled while the other is given by the chemical reaction. It is noteworthy that the MIMO controller is retained until the safe setpoint is reached. After convergence, the controller returns to SISO, because the algorithm ensures that this configuration is able to keep the system safe.

In most chemical processes, parameter changes occur throughout the operation. To keep the accuracy of the controller model, this work uses a moving horizon data reconciliation algorithm to estimate parameters and states simultaneously in real time. The measured variables were the streams flowrates and temperatures. Only the reactor temperature measurements figure into the objective function of the reconciliation, so it was corrupted with zero mean Gaussian noise with standard deviation of 0.2. The other measurements were not corrupted with noise and were used to feed the prediction model; i.e., they do not contribute to the objective function of the reconciliation problem. The other states were estimated together with the parameter κ_c. The model of the controller is updated in each sampling time with the new estimates of the reconciler. This allows the adaptation of the controller to process changes (Souza et al., 2011).

3. Results and discussions

To test the efficiency of the proposed algorithm a scenario with an unwanted event was simulated. This event refers to a significant loss of reactor cooling capacity. The safety limit considered in the simulation is related to the reactor temperature, which should reach a maximum value of 385 K. The loss of cooling capacity is simulated by varying the parameter κ_c. This type of event is quite common during operation of reactors with jacket. Several failures may cause a decreased capacity for heat exchange between the reactor and jacket. For example, failure in the cooling fluid supply pumps, failure in stirring the reactor, increasing of viscosity of the reaction mixture (gel effect), and fouling.

The performance of the safety system to an abrupt drop in parameter κ_c from 1 to 0.1 is shown in Figure 2. Such an event would be able to raise the reactor temperature at 392 K, which represents

Table 1: Model Parameters

Parameters	Values	Units
k	5.0×10^7	mol/h
E_a	1.0×10^4	J/mol
R	8.32	J/mol.K
T_{in}	350.0	K
ΔH_r	2.5×10^4	J/mol
C_p	125.6	J/mol.K

Table 2: Comparison between initial setpoint and calculated by the security system

States	Initial	Safe
M_{Mon}	36.2	50.21
M_{Pol}	77.2	62.05
M_{Sol}	200.0	201.20
M_{Cat}	0.10	0.09
T	380.0	380.16

security risk to the process. For $t \leqslant 1$ h the system operates normally in SISO mode. At time 1 h, a simulation is performed for the failure in question, whose trajectory is represented by gray x markers in Figure 2. A violation of the safety limit is observed in Figure 2a, and immediately, the safe state seeker is activated. The safe state found is shown in Table 2. The observed good proximity between the variables is a result of the optimization scheme proposed. The dynamic trajectory predicted by the algorithm for the same failure, which has the safe state as the initial condition is represented by gray diamonds markers from the time of 4 h. This trajectory was calculated at time 1 h, but for ease of comparison with the actual trajectory of the plant it was moved graphically to the instant 4 h. Found the safe state, the controller is reconfigured to the MIMO mode in order to pursue the new setpoint. This configuration remains active in the interval $1 \text{ h} < t \leqslant 4$ h. Although not shown, other states follow perfectly to their new setpoints. At time 4 h, the controller returns to the SISO mode and the simulated failure is applied effectively in the plant, in order to test the effectiveness of the algorithm. As it can be seen in Figure 2a, the final reactor temperature remains around the safety limit and the actual trajectory of the plant is similar to the trajectory predicted by the algorithm.

Figure 2b shows the estimated parameter κ_c. The solid line represents the estimated values during operation. The gray "x" markers leaving at time 1 h, are the result of failure simulation. Besides considering the behaviour of the controller, this simulation also considers the behaviour of the reconciliation system, by adding noise to the simulated temperature. The gray diamonds markers in the interval $t > 4$ h are the κ_c values used to predict the trajectory of the system, represented by the same marker in Figure 2a.

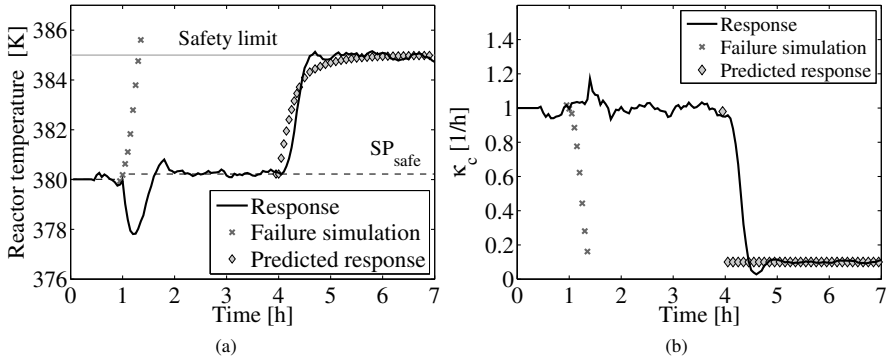

Figure 2: Performance of the safety system (a) to an abrupt drop in parameter κ_c (b).

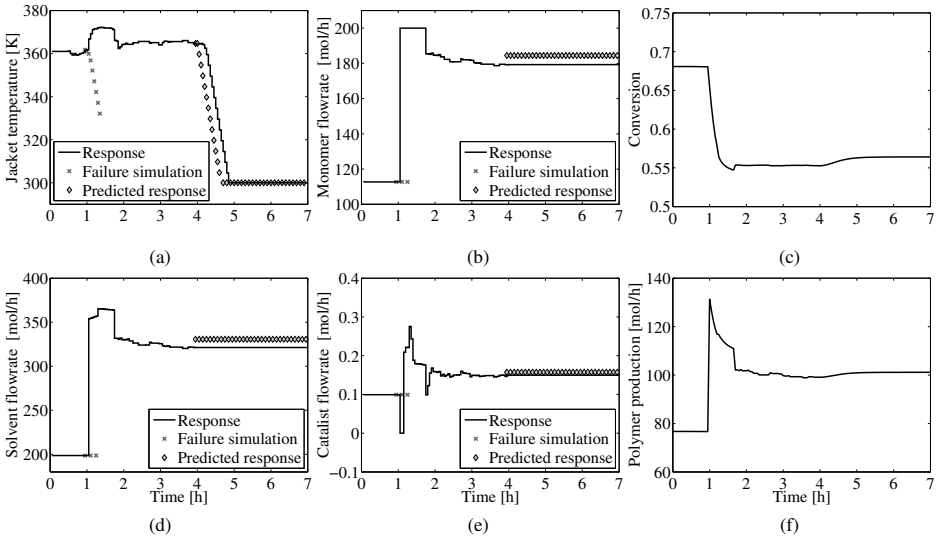

Figure 3: Dynamic trajectories of the manipulated variables, conversion and production.

For this case, therefore, the intelligent safety system was able to reverse a failure which could raise the reactor temperature at about 392 K, well above the safety limit. This failure would activate the emergency shutdown and consequently cause a huge economic loss. The system began operating with a lower conversion but with increased production (Figures 3c and 3f), showing that the losses caused by the preventive security action are questionable. The trajectories of the control actions are also shown in Figure 3.

4. Conclusions

This paper proposes a new security layer, leaving the emergency shutdown as the last alternative in terms of safety actions. The goal is to avoid unnecessary shutdowns, and increase the annual operating time of the plant. The results have shown that the proposed algorithm may be feasible if there is a reliable model of the process. For the discussed case of loss of cooling capacity, the algorithm was effective. It was able to prevent a violation of the safety limit which possibly would cause a system shutdown, thus preventing economic losses as well.

References

Luyben, W. L., 2012. Use of dynamic simulation for reactor safety analysis. Computers and Chemical Engineering 40, 97–109.

Manenti, F., 2011. Considerations on nonlinear model predictive control techniques. Computers and Chemical Engineering 35 (11), 2491–2509.

Souza, P. N., Soares, M., Amaral, M. M., Lima, E. L., Pinto, J. C., 2011. Data Reconciliation and Control in Styrene-Butadiene Emulsion Polymerizations. Macromolecular Symposia 302 (1), 80–89.

Venkatasubramanian, V., Rengaswamy, R., Yin, K., 2003. A review of process fault detection and diagnosis Part I : Quantitative model-based methods. Computers and Chemical Engineering 27, 293–311.

Krist V. Gernaey, Jakob K. Huusom and Rafiqul Gani (Eds.), 12th International Symposium on Process Systems Engineering and 25th European Symposium on Computer Aided Process Engineering.
31 May - 4 June 2015, Copenhagen, Denmark.

Shape Constrained Splines with Discontinuities for Anomaly Detection in a Batch Process

Kris Villez[a] and Jonathan Habermacher[a]

[a]*Department of Process Engineering, Eawag, Swiss Federal Institute of Aquatic Science and Technology; Dübendorf, Switzerland*
kris.villez@eawag.ch

Abstract

A previously developed technique for qualitative trend analysis (QTA) based on shape constrained splines (SCS) has been favourably compared to pre-existing techniques for the purpose of batch process diagnosis. Thanks to the branch-and-bound algorithm, this approach leads to a deterministic and global solution for QTA. One limitation of this method is that local discontinuities in otherwise continuous derivatives of the fitted spline function are not permitted. Recent work however allows to relax the optimization problem further so that provable bounds can be computed for this more complicated case. In this contribution, the resulting shape constrained splines with discontinuities (SCSD) method is applied for anomaly detection in batch process data. Importantly, the QTA approach to anomaly detection proves worthwhile because *(i)* tuning of the SCSD method is limited to setting an upper control limit, *(ii)* the resulting sum of squared errors statistic shows almost no drift for SCSD in contrast to the similar Q-statistic computed by principal component analysis (PCA), and *(iii)* true positive rates by means of SCSD are over 80% while the PCA method delivers at most 70% for false positive rates up to 5% based on a data set consisting of 410 batches.

Keywords: Anomaly detection, Fault diagnosis, Batch process monitoring, Statistical process control, Qualitative trend analysis

1. Introduction

Qualitative trend analysis (QTA) consists of a rather wide set of techniques for segmentation of data series. Such segmentation is popularly used for fault diagnosis applications. For such applications, QTA offers the possibility of an intuitive fault diagnosis mechanism. Its advantages include *(i)* that coarse-grained information about the faults symptomatic effects on measured data is sufficient to characterize and recognize a fault, *(ii)* that the required coarse-grained information corresponds to intuitive notions by human plant operators, and *(iii)* that consequently sparse occurrence of faults can effectively be dealt with. Despite these advantages, available techniques are often based on heuristic rules or greedy optimization schemes tuned for a particular application only. The lack of theoretical optimality makes it challenging to transfer such techniques from their original application context as was observed in Villez et al. (2012). This motivated the conception of a globally optimal approach to QTA based on shape constrained splines (SCS, Villez et al., 2013). This SCS method is limited in a number of ways. One important limitation is that any derivative of a degree smaller than or equal to $o-2$, in which o is the order of the spline function (for cubic splines: $o=4$), must be continuous over the whole function domain. Indeed, knots with multiplicity are not permitted. This is critical for QTA purposes as this means that certain shape constraints are not permitted. For example, one cannot fit a spline function which

is characterized by a segment which is decreasing (negative 1st derivative) and concave (negative 2nd derivative) followed by a segment which is increasing (positive 1st derivative) and concave (negative 2nd derivative). Practically, this is solved by adding a knot of multiplicity $o-1$ when the exact location where the segments meet, a.k.a. transition, is known. This is however not the case in general. Unfortunately, the SCS method does not permit optimizing transitions which imply a discontinuity in one or more derivatives which are otherwise continuous. This paper discusses results obtained with a modified version of the SCS method which accounts for shape-implied discontinuities. The method is therefore further referred to as the shape constrained splines with discontinuities (SCSD) method. Similar to the SCS method, it is based on a combination of second order cone programming (SOCP) and the branch-and-bound algorithm. This algorithm enables the identification of all transitions. The method is successfully demonstrated by means of oxidation-reduction potential (ORP, redox) measurements obtained from a laboratory scale sequencing batch process for wastewater treatment.

2. Methods

2.1. Case study

The data used in this study stems from an experimental side-stream reactor (SSR) setup operated at Eawag for a period of two years by the second author of this contribution. This SSR setup consists of two connected tanks in which the first tank is a sequencing batch reactor (SBR). The second tank is the so called SSR and is operated as a continuously stirred tank reactor for sludge digestion. The SBR is operated with a fixed recipe which lasts 6 hours. Each SBR cycle starts with pumping of sludge from the SSR to the SBR (7 min.) followed by addition of fresh wastewater (10 min.) under anoxic conditions. A reaction phase follows in which air is supplied to provide aerobic conditions in the SBR (285 min.). The SBR cycle ends with excess sludge withdrawal, settling, and decanting (58 min.). Each new cycle starts right after decanting.

The SBR is equipped with an oxidation-reduction potential (ORP) sensor, amongst others. A typical profile of the first 513 data points (85.33 min.) is shown in Fig. 1 (top panel). The first phase corresponds to an almost linear decreasing trend, followed by a convex decreasing trend in the second phase. In the third phase, the trend roughly corresponds to a concave increasing trend. The ORP time series consisting of the first 513 data points of 410 consecutive cycles are studied in this work. The selected batch cycles represent a period of 3.5 months in which no changes were made to the SBR recipe, the installed sensors (e.g., no replacements), or the data acquisition and control system. Each of these time series were inspected visually by two operators which are familiar with the experimental setup and the use of ORP sensors, including the second author of this paper. These operators addressed the question *whether the observed time series can be explained by normal circumstances alone* by means of a simple yes or no. To this end, the time series were visually represented to these operators on separate occasions and in a randomized order. Following this initial classification of the ORP time series as normal or anomalous, batches for which the classification by the two operators was different were visualized again with both operators present so to find a consensus classification result. For 16 cycles out of 410, no consensus could be reached. Only the time series

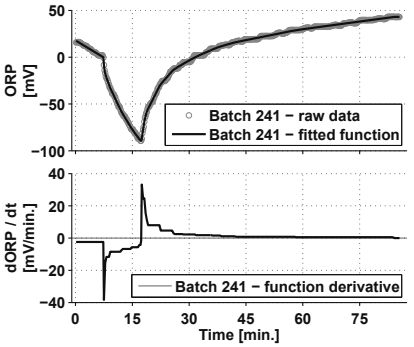

Figure 1: Exemplary time series corresponding to normal operation.

for which consensus was reached (394 batch cycles) are considered in the remainder of this study. The consensus classification is used as the ground truth or true class for each analysed time series.

2.2. Qualitative trend analysis (QTA): Definitions

The identification of so called *qualitative representations* (QRs) is the primary goal of QTA. Such QRs are defined as a sequence of *episodes*. Each of these episodes is completely characterized by means of *(i)* a start time, *(ii)* an end time, and *(iii)* a *primitive*. Such a primitive corresponds a unique combination for the signs of the measured variable and/or one or more of its derivatives with respect to time. A primitive is usually represented by means of a unique character, which can however be chosen arbitrarily. Fig. 2 shows the primitives and characters used in this study. Only the signs of the first and second derivatives are considered relevant. The episodes within a QR are contiguous, meaning that the end time of one episode is the start time of the next episode. The locations (in time) where two episodes meet are known as *transitions*. A sequence of primitives without specification of the transitions is known as a qualitative sequence (QS). Conform these definitions, the QS for a typical profile of ORP measurements as in Fig. 1 reads as EAC. The SCSD method explained in the next paragraphs allows to identify the values for the corresponding transitions.

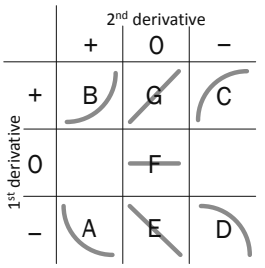

Figure 2: Primitives and associated characters.

2.3. Shape constrained splines (SCS)

In essence, the fitting of a shape constrained spline function can be written as the following mathematical problem:

$$\min_{\beta,\theta} J(\beta,\theta) = J(\beta,\theta,\mathbf{x},\mathbf{y}) \tag{1}$$

subject to:

$$\beta \in \Omega(\theta) \tag{2}$$

$$\theta \in \Theta \tag{3}$$

Table 1: Definitions of variables and parameters for SCSD.

Symbol	Definition
β	Function parameters
θ	Transitions
$\Omega(\theta)$	Feasible set for β
Θ	Feasible set for θ
$\mathbf{x}$	Argument vector
$\mathbf{y}$	Measurement vector
J	Objective function

with definitions given in Table 1. The spline function is defined by a number, m, of parameters represented by the vector β. In Villez et al. (2013), the parameters are the spline coefficients. Given a QR defining the shape constraints, the feasible set for these coefficients, $\Omega(\theta)$, is a convex subset of the real space ($\Omega(\theta) \subseteq \mathbb{R}$). This set depends on the values for the transitions, θ. In the context given by Villez et al. (2013) and this study, optimal values for θ are found by means of the branch-and-bound algorithm. Proofs for the applied bounds were given in Villez et al. (2013). The existing proofs are limited however in the sense that the bounding procedures only apply to spline functions without knot multiplicity and any associated discontinuities of the derivatives in such knots. This limitation is removed in the next paragraphs.

2.4. Shape constrained splines with discontinuities (SCSD)

To enable application of the branch-and-bound algorithm when discontinuities are implied by the imposed QS, the fitted function is now redefined by representing the spline function explicitly as a contiguous set of piece-wise polynomials. Once more, the problem is convex as long as θ

is given. To solve the non-linear search for θ the branch-and-bound algorithm can be applied again. The upper bound procedure is practically the same as in Villez et al. (2013). The lower bound procedure is fairly different however. In Villez et al. (2013) it was sufficient to implement only those constraints on β which are guaranteed to be included for any candidate solution for θ within a given solution set. In this case, one further needs to modify the objective function as well as set of implemented continuity constraints. The details of the lower and upper bounding procedures are given in Villez (2014). Apart from the modified bounding procedures, the branch-and-bound algorithm is applied exactly as in Villez et al. (2013). The branch-and-bound algorithm was solved until a resolution of 1 sampling interval (10 seconds) was reached for the location of the transitions. The fitted function is a natural cubic spline function ($o = 4$) with fixed spline knots placed at each sampling time. The resulting function is an interpolating spline function when no shape constraints are applied. As a result, any deviation of the SSE from zero is only due to a mismatch between the measured time series and the imposed shape (EAC).

2.5. Shape constrained function fitting as a method for process monitoring

To test the shape constrained splines methodology for process monitoring, the following strategy is applied. One optimizes the values for β and θ so to minimize the objective function value J. Importantly, there is no calibration phase for the SCSD method as long as the expected shape is known. In this study, this objective function is the sum of squared errors (SSE). In general, the optimized SSE, further referred to as SSE_{SCS}, will be high when the profile of the analysed data series does not correspond well to the imposed shape on the fitted function. As such, this SSE can be used as a lack-of-fit statistic to detect deviations from the expected shape. To this end, one defines a fixed upper limit, U_{SCS}, a priori and one classifies a data series as anomalous (normal) when the obtained SSE is higher (lower) than this limit. There are no theoretical distributions available for the SSE_{SCS} statistic. As such, an empirical evaluation is obtained by evaluating the false positive rate (FPR, fraction of normal cycles which are erroneously classified as anomalous) as well as the true positive rate (TPR, fraction of abnormal cycles which are correctly classified as anomalous) by varying the value for U_{SCS} between the lowest and highest value for SSE_{SCS} obtained. To this end, the ground truth classification as described above is used as a reference. This leads to the so called receiver operating characteristic (ROC, Fawcett, 2006).

2.6. Principal component analysis (PCA)

Principal component analysis (PCA) is by far the most commonly used method for process monitoring in a multivariate context. PCA is of use primarily when significantly large data sets are available and first principles modelling is impossible or cost-prohibitive. The successful application of classical PCA depends on a number of factors such as *(i)* whether relationships between measured variables are linear and time-invariant, and *(ii)* whether sufficient and representative data is available for PCA modelling of the normal process data variation. Despite these restrictive statistical requirements, PCA has been applied successfully to many processes. In this study, the batch process data is organized in a matrix with rows corresponding individual batches and columns to individual time instants in each of the analysed batches. A PCA model is then fitted to a subset of the data by *(i)* selecting a number of rows corresponding to normal process conditions, *(ii)* subtracting the column-wise mean, and *(iii)* computing a number of principal component loadings and associated scores by means of singular value decomposition. In this study, a simple scree plot is used as the device to select the number of principal components (PCs). Once the PCA model is identified, one projects the data not used for calibration and evaluation the so called reconstruction errors or residuals. Following this step, one computes the corresponding SSE, SSE_{PCA}, which is also known as the Squared Prediction Error (SPE, Kresta et al., 1991) and as the Q statistic (Jackson and Mudholkar, 1979). Theoretical and/or empirical confidence limits can be computed for this statistic (Jackson and Mudholkar, 1979). In this study, the ROC is computed as is done for the SCSD method to enable an effective comparison.

3. Results

3.1. Example

Fig. 1 displays the exemplary oxidation-reduction potential (ORP) time series, the optimized shape constrained spline function with EAC shape, and the 1st derivative of this fitted function. Finding the optimal transitions required 34 branching steps in the branch-and-bound algorithm which is equivalent to solving 69 SOCPs. This took 1.2 minutes on a dedicated desktop machine (Intel® Core™ i7-4770 CPU, 3.40 GHz, 16.0 GB RAM). The optimized SSE_{SCS} is equal to 332.

3.2. Benchmarking

All batch time series were analysed with the SCSD method on a dedicated desktop machine (as above). Computing the optimal transitions took less than 20 minutes in all cases. The PCA model was identified by means of the first 100 normal batch cycles and included two principal components which capture 86.9% and 9.6% of the variability (total: 96.5%). The statistics obtained with SCSD and PCA are shown in Fig. 3 as a function of batch index. The SSE_{SCS} is relatively stable with a number of outlying values sparsely present during the covered time span. In contrast, the SSE_{PCA} shows more variation and is generally higher. This is believed to be a result of non-linear parametric changes of the ORP profiles which are hard to capture by a linear PCA model. The SCSD method is robust to these variations because of a greater parametric flexibility of the spline function compared to PCA. In the top panel, an upper detection limit, U_{SCS}, is set at 610.33 which is the lowest value for which no false alarms (no false positives) result. Similarly, in the bottom panel, the upper detection limit, U_{PCA}, is set at 37659. With SCSD 38 of the 46 abnormal time series have an SSE_{SCS} which is higher than the set limit (TPR: 83%). With PCA only 30 positive detections result (TPR: 65%). Closer inspection reveals that 29 cycles are identified as abnormal by both methods. The SCSD method correctly flags 8 batch cycles as anomalous which are not detected by PCA. One batch cycle not identified with SCSD is identified as anomalous by PCA.

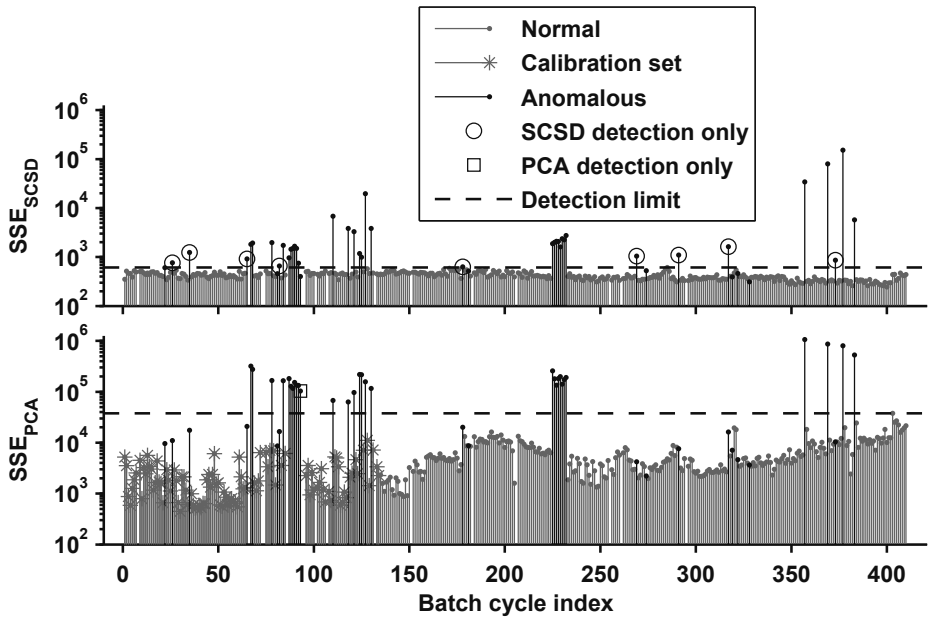

Figure 3: Sum of squared errors (SSE) statistics obtained with SCSD (top) and PCA (bottom).

Decreasing values of the upper limits for the SSR statistics increase both the FPR and the TPR. For example, at an FPR of 5% the TPR for SCSD is 85% while the TPR for PCA is 70%. The complete receiver operating characteristics (ROCs) are shown in Fig. 4. One can observe that the SCSD method performs better for FPRs up to 69%. PCA dominates only for FPRs ranging from 88% to 93%. In other sections of the curve, the methods are performing equally. In the present application as well as for most anomaly detection schemes, normal operating conditions are more frequent than anomalous conditions. It is thus reasonable to give larger weight to a low FPR than a high TPR. Selecting FPRs lower or equal than 5% is common. At such rates, the SCSD method clearly outperforms PCA-based detection.

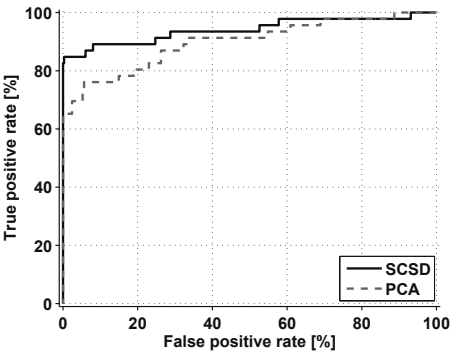

Figure 4: Receiver operating characteristics (ROC) showing the true positive rate (TPR) as a function of the false positive rate (FPR).

4. Conclusion

With this contribution, an extended version of the shape constrained spline (SCS) method for qualitative trend analysis (QTA) has been tested for batch process monitoring. The proposed extension allows to optimize the location of abrupt changes (discontinuities) in one or more derivatives of measured variable trends. Importantly, the identification of shape constrained splines with discontinuities (SCSD) is based on the optimization of the sum of squared errors which is has been successfully used as a lack-of-fit statistic for anomaly detection. A preliminary comparison with principal component analysis underscores the value of a qualitative approach to fault detection.

5. Acknowledgement

The authors want to thank Nicolas Derlon at Eawag for interpreting and classifying the studied data series and for his creative input and constructive feedback during execution and reporting of this study. All computations were executed by joint use of Matlab (The MathWorks Inc., 2012); the Functional Data Analysis software package accompanying Ramsay and Silverman (2002); and MOSEK (MOSEK ApS, 2012). The first author thanks O. Peth for everlasting inspiration.

References

Fawcett, T., 2006. An introduction to ROC analysis. Pattern recognition letters 27, 861–874.

Jackson, J., Mudholkar, G., 1979. Control procedures for residuals associated with principal component analysis. Technometrics 21, 341–349.

Kresta, J., MacGregor, J., Marlin, T., 1991. Multivariate statistical monitoring of process operating performance. Can. J. Chem. Eng. 69, 35–47.

MOSEK ApS, 2012. MOSEK Optimization Software for MATLAB, Version 6.0. Available from http://www.mosek.com/.

Ramsay, J. O., Silverman, B. W., 2002. Applied Functional Data Analysis: Methods and Case Studies. Springer-Verlag.

The MathWorks Inc., 2012. Matlab, version 8.0.0.783 (R2012b). Natick, Massachusetts.

Villez, K., 2014. Bounding Procedures for Shape Constrained Splines with Discontinuities. Eawag, Dübendorf, Switzerland, Technical Report TR-001-01-0.

Villez, K., Rengaswamy, R., Venkatasubramanian, V., 2013. Generalized shape constrained spline fitting for qualitative analysis of trends. Comp. Chem. Eng. 58, 116–134.

Villez, K., Rosén, C., Anctil, F., Duchesne, C., Vanrolleghem, P. A., 2012. Qualitative representation of trends (QRT): Extended method for identification of consecutive inflection points. Comp. Chem. Eng. 48, 187–199.

Krist V. Gernaey, Jakob K. Huusom and Rafiqul Gani (Eds.), 12th International Symposium on Process Systems Engineering and 25th European Symposium on Computer Aided Process Engineering.
31 May – 4 June 2015, Copenhagen, Denmark

Quantifying Model Uncertainty in Scarce Data Regions – A Case Study of Particle Erosion in Pipelines

Wei Dai, Selen Cremaschi*

Department of Chemical Engineering, The University of Tulsa, 800 South Tucker Drive, Tulsa, Oklahoma 74104, USA
selen-cremaschi@utulsa.edu

Abstract

The transport of solids in multiphase flows is common practice in energy industries because of the unavoidable extraction of solids from oil and gas bearing reservoirs. The safe and efficient operation and design of these pipelines requires reliable estimates of erosion rates. The models used to calculate this rate have significant uncertainty due to the complexity of the underlying process. This uncertainty becomes especially important during the design phase for subsea applications, as erosion rate allowance, which is set using the erosion rate predictions and its uncertainty, directly impacts the integrity of the facility. Unfortunately, none of the models provide an estimate of this uncertainty. This paper introduced a systematic approach to quantify the model uncertainty for erosion rate predictions combining Gaussian Process Modeling (GPM) with data transformation and cross-validation techniques. The results reveal that given the available experimental data and the erosion rate prediction model considered, the model uncertainty is on average 3.61 times the model's predictions. Hence, our results suggest at least on average four order of safety factor when designing subsea systems.

Keywords: model uncertainty, erosion prediction, Gaussian Process Modeling

1. Introduction

The solid transport and management systems (STMS) are an integral part of the processes in energy industries, because of the unavoidable extraction of solids from oil and gas bearing reservoirs either onshore or offshore sites. If the amount and velocity of the solids in the fluids (oil and gas) in the transportation lines are too high, they might cause erosion in the pipelines resulting in facility integrity issues. These issues become more important for deep-water applications as these systems are "too costly to fail" due to limited availability of access for repairs and potential for devastating environmental consequences if failed. One of the essential design decisions is the expected erosion allowance for these systems and pipelines throughout their lifetime.

The erosion process, especially in flow systems, is a complex phenomenon and depends on many factors including fluid characteristic, particle characteristics, the construction material properties and the geometry of the flow lines. Given this complexity, most modeling work in this area focuses on developing empirical or semi-empirical models. Although all of these models have been compared to a limited set of experimental data, it has been reported that their predictions for the same input set can vary up to two orders of magnitude (Mazumder, 2004). Our preliminary comparisons of model predictions to experimental data revealed that the predictions may be up to 10 orders of

magnitude higher (resulting in considerable overdesign) for some input sets whereas up to one order of magnitude lower (causing facility integrity issues) for others. There are many sources of uncertainty in these models, e.g., in the model inputs, assumptions, and equations. However, none of the existing models include uncertainty analysis or quantify the confidence intervals in their predictions.

The goal of this paper is to introduce a framework capable of quantifying prediction uncertainty and confidence for erosion models under a wide range of input conditions especially focusing on regions where experimental data is scarce or not available. The framework, utilizing general model uncertainty quantification formulation (Kennedy and O'Hagan, 2001), estimates model bias and its confidence, and incorporates the effect of experimental uncertainty using Gaussian Process Modeling (GPM), and is capable of estimating model-prediction uncertainty due to extrapolation in sparse or no data regions. The framework is developed around 1-Dimensional Sand Production Pipe Saver (1-D SPPS) model (McLaury and Shirazi, 1999), which is used widely by oil and gas industry for predicting erosion rate when designing and operating pipelines and separation systems. A brief overview of 1-D SPPS model is given in the next section. Section 3 introduces the compiled experimental database that is used to train the GPMs for predicting model uncertainty. Section 4 contains the details of the systematic approach, followed by the results in section 5. Finally, conclusions are summarized.

2. The 1-D SPPS model

The 1-D SPPS model predicts maximum erosion rate given system geometry and materials, flow conditions, and particle properties (McLaury and Shirazi, 1999). It calculates the maximum erosion by defining how a hypothetical representative particle will impinge the target material. The abrasion caused by this particle is defined by length loss in the target material, and is calculated using the momentum of impingement, which requires the so-called characteristic impact velocity of this representative particle. Given flow conditions, particle and pipe properties, the model first calculates the characteristic impact velocity. The erosion ratio, which is defined as the ratio of measured target material mass loss to the mass of all particles in the carrier fluid, is calculated using a power law correlation of the characteristic impact velocity. Here, the carrier fluid can be single phase (liquid or gas), or multiphase (liquid/gas mixture). The maximum erosion rate empirical model in 1-D SPPS calculates the target material length loss per unit time, and uses erosion ratio and accounts for pipe geometry, size and material; fluid properties (density and viscosity) and rate; and sand sharpness, density and rate.

The multiphase carrier mixtures result in different flow patterns in the conduit depending on the relative ratios of liquid and gas flow rates, and liquid and gas densities and viscosities. These flow patterns are (1) Annular, (2) Mist, (3) Churn, (4) Slug, and (5) Dispersed Bubble (Zhang, 2006). The 1-D SPPS model can predict erosion rate considering or ignoring the effects of flow pattern in cases of multiphase (liquid/gas) carrier fluids. In the flow-pattern-dependent calculations, the input liquid and gas flow properties are first used to determine the flow regime, and erosion-rate-prediction models specifically developed for each flow pattern are used to calculate the erosion rate. Partly due to its semi-empirical nature and partly due to its efficient algorithm, 1-D SPPS calculates the erosion rate for a single input almost instantaneously.

3. Experimental database

For estimating erosion-rate-prediction uncertainty, we compiled an experimental database of erosion rate measurements from literature. It contains 544 data points in single or multiphase carrier flow. During experiments, the controlled variables were flow rate(s) and viscosity, particle size, and pipe geometry, size and material. The output or the measured variable was the erosion rate. According to the predicted flow regime from 1-D SPPS, eighty percent of the data in the database are collected for gas dominated flows (i.e., gas only, annular, mist and churn flow). For most experiments, the particle density is 2650 kg/m^3. Most experiments used one or more of the following particle types: Silica Flour with an average particle size of 20 µm, Oklahoma #1 with an average particle size of 150 µm, and California 60 Mesh with an average particle size of 300 µm. Superficial gas velocities range from 5 to 200 m/s, but experimental data at higher gas velocity region (>50 m/s) is limited. The superficial liquid velocities range from 0.0001 to 1 m/s. Pressure and temperature is used to change the density and viscosity of the gas phase. The viscosity of water is changed by adding CMC (Carboxy-methyl cellulose), which slightly changes the density of fluid but this effect is too small and is generally neglected (Okita, 2010).

4. Methodology

According to general model uncertainty quantification formulation (Kennedy and O'Hagan, 2001), the experimental response, y^e can be expressed with Eq.(1).

$$y^e = y^m + \delta + \varepsilon \tag{1}$$

In Eq.(1), y^m is the model response, δ is the model bias, and ε is the experimental uncertainty. In our case, the experimental response is the measured erosion rate, which is expressed as the sum of 1-D SPPS's prediction of erosion rate (y^m), a bias function which estimates 1-D SPPS bias (δ), and a random error, which assumed to follow a zero-mean normal distribution accounting for the experimental variability (uncertainty). The model bias includes the uncertainties associated with estimated model parameters in 1-D SPPS, the numerical errors and the model form discrepancies, and can be expressed as a Gaussian random process. As the experimental variability is assumed to follow a zero-mean normal distribution, the model bias and the experimental variability can be combined into one term, which we will refer as model discrepancy for the remainder of the paper. The model discrepancy can then be assumed to be a Gaussian random process (Jiang et al., 2013), and can be represented using Gaussian Process Modeling.

4.1. A Brief Overview of Gaussian Process Modeling (GPM)

The Gaussian process ($\mathcal{GP}(m,k)$) is a natural generalization of the Gaussian distribution, where the GP is fully characterized by its mean and covariance functions (Rasmussen and Williams, 2006). Let x denotes a point in multidimensional space, $m(x)$ is the mean function of the GP, and $k(x,x')$ is the covariance function of the GP, representing the spatial covariance between any two points (x and x') at the process. Once we specify the mean and covariance functions using the available data, the GP can be used to predict values at untested locations, and its prediction variance, i.e., uncertainty, can be calculated by the covariance function. The process of finding the mean and covariance function estimates using available data is referred to as the Gaussian Process Modeling.

In order to define GPM, prior information about the dataset is needed to specify prior mean and covariance functions. This prior information is normally represented by a hierarchical prior, where the mean and covariance functions are parameterized using hyper-parameters. Eq. (2) gives a constant mean and a squared exponential covariance functions for a Gaussian process as examples:

$$\begin{aligned} f &\sim \mathcal{GP}(m, k), \\ m(x) = a, \text{ and } k(x, x') &= \sigma_y^2 \exp\left(-\frac{(x - x')^2}{2l^2}\right), \end{aligned} \tag{2}$$

In Eq.(2), we have introduced hyper-parameters $\theta = \{a, \sigma_y, l\}$, where σ_y and l specify the characteristic length-scale and magnitude of the covariance function. The values of hyper-parameters are determined via maximum likelihood estimation approach, which is generally performed via a gradient based search algorithm (Rasmussen, 2004).

With the prior mean and covariance functions, the value of the function and its uncertainty for the unseen test location, *x*, is inferred by obtaining the posterior distribution using the training data set (*D*):

$$\begin{aligned} f|\mathcal{D} &\sim \mathcal{GP}(m_{\mathcal{D}}, k_{\mathcal{D}}), \\ m_{\mathcal{D}}(x) &= m(x) + \Sigma(X, x)^T \Sigma^{-1}(f - m), \\ k_{\mathcal{D}}(x, x') &= k(x, x') - \Sigma(X, x)^T \Sigma^{-1} \Sigma(X, x'), \end{aligned} \tag{3}$$

where $\Sigma(X, x)^T$ is the covariance vector between the training data (*X*) and x. The computational complexity in estimating Gaussian Process hyper-parameters scales cubically with the size of the dataset. For small problems (e.g. dataset size < 1000), storing and solving the associated linear system is not computationally expensive

4.2. Developing 1-D SPPS Prediction Discrepancy using GPM

In order to express 1-D SPPS discrepancy as a GPM, we need to estimate the hyper-parameters of mean and the covariance function. Based on our experience with the erosion dataset and the 1-D SPPS, a constant mean function and a squared exponential covariance function are deemed appropriate. The maximum-likelihood estimators of the hyper-parameters are determined using the experimental database, specifically, using the difference between experimental erosion rates and the corresponding erosion rate predictions of 1-D SPPS. We will refer to this difference as actual model discrepancy.

For training the GPM, we converted the categorical inputs, such as pipe geometry, to numerical values. The experimental database covers a wide range of input conditions resulting in significantly different erosion rates, and, at times, up to five orders of magnitude differences in actual model discrepancies. Such significant differences in training data may not suitable to train GPMs. Therefore, we applied a data transformation approach, Generalized Box-Cox transformation (Box, 1964) with θ = 1.5 (Eq. (4)), to reduce the range of actual model discrepancies.

$$\mathrm{f}(\mathrm{y}; \theta) = \frac{sign(y)|y|^{\theta} - 1}{\theta} \tag{4}$$

The transformed actual model discrepancy and the corresponding inputs are divided into two subsets: (1) a training set, and (2) a test set. The data in the training set is used to calculate the maximum-likelihood estimators of the GPM, and the test set is used to assess the performance of the GPM for unseen data points. A Matlab® based toolbox,

GPML (Gaussian Process for Machine Learning) (Rasmussen and Williams, 2006), is used to solve the resulting optimization problem for training the GMP. The same toolbox is used to calculate the expected mean and variance at the data points of the test set. Given the expected mean and the variance, the model discrepancy prediction is equal to the expected mean, and the 95% confidence interval of these predictions is equal to the two times of the standard deviation (i.e., square root of variance).

The suggested separation of training and test data sets is three to one (Mitchell, 1997), where around 75 % of the whole dataset is used to train the GPM. However, the maximum-likelihood estimates of the hyper-parameters, and hence, the performance of the GPM at data points in the test set differ based on the data points in the training set. To mitigate the influence of the training data subset on the GPM predictions and to obtain a robust GPM prediction, we applied a four-fold cross validation approach, and repeated this process 30 times. For one repetition of the four-fold cross validation, the dataset is separated to four distinct parts. Then, three of the four parts are randomly picked as the training data set, while the remaining part is used as the test data set. The procedure is repeated four times until all the parts have been used as the test data set. At one repetition of the four-fold cross-validation, we obtain the predicted mean and variance of each data point when it is used as a test point, i.e., as an unseen data point. The 30 repetitions, therefore, provide 30 predicted means and variances for each data point in our database when they are used as an unseen data point. Then, we calculate the average predicted mean and variance of model discrepancy at each data point. The average predicted mean is compared to the actual model discrepancy to assess the quality of the GMP predictions and the average variance is used to estimate the model uncertainty.

5. Results and discussion

Given the 545 data points in our database, 408 randomly selected points are used as training set and the rest as test set for each cross validation fold at each repetition. The performance of the resulting GPM predictions for all data points and for each flow regime data subset are summarized in Table 1. The average difference between the predicted and the actual model discrepancy, Di, is 116 %. If one defines the data points where the actual model discrepancy is outside the 95 % confidence interval predicted by the GPM, there are 53 outliers (O) in our database. If these outliers are ignored, the average difference, $Di_{w/oO}$, becomes 55.5 %. The average of the ratio (R) between the 95 % confidence interval and the model prediction is 9.9. The data points where there is a probability of 1-D SPPS under-predicting erosion, i.e., the points where the 95 % interval intersects the zero line, ($Da_{P<0}$), is of great interest for facility integrity and safe operation. Based on the GPM predictions, 71 % of the data points fall into this category. If we only consider these data points, average of the ratio between the 95 % confidence interval and the model prediction ($R_{Da_{P<0}}$) becomes 13.7. The safety factor at 95% confidence for designing these systems is defined as the ratio of average value of the lower bounds of the confidence intervals prediction by GPM to the average predicted discrepancy calculated using only the data points in $Da_{P<0}$. Our results reveal that this safety factor is equal to 3.61. This safety factor provides a measure of under-prediction ratio for the model and hence aid in avoiding integrity issues at the design stage.

As can be seen from Table 1, except for mist flow, other flow regimes exhibit a smaller average difference, $Di_{w/oO}$, and average ratio, $R_{Da_{P<0}}$, when compared to the whole data

set. We speculate that the large *Di* value and the safety factor yielded for mist flow stems from 1-D SPPS grossly under-predicting experimental erosion rates for a subset of data points. This results in wide range of actual discrepancies, and hence, reduces the reliability of the GPM predictions. Our results suggest caution may be taken when using our GPM approach with 1-D SPPS for erosion-rate-allowance estimates of mist flow.

Table 1. Summary statistical results obtained using the proposed approach

flow regime	Di	O	$Di_{w/oO}$	R	$Da_{P<0}$	$R_{Da_{P<0}}$	safety factor
total	116%	53	56%	9.9	71%	13.7	3.61
gas	71%	21	41%	4.4	62%	6.2	2.68
mist	2703%	27	83%	1.7	31%	19.9	4.97E+3
annular	59%	5	60%	6.2	82%	5.7	1.11
churn	42%	0	42%	4.9	100%	4.9	1.01
slug	358%	0	358%	27.9	100%	27.9	1.00

6. Conclusions

This paper introduced and demonstrated a model uncertainty quantification approach for erosion rate predictions using a well-known erosion model, 1-Dimensional Sand Production Pipe Saver (1-D SPPS), which is used extensively in oil and gas industry for erosion predictions. The results suggest using 3.61 as the safety factor when designing subsea systems, pipelines and auxiliary equipment if they would be exposed to solids. Future work will investigate different data transformation approaches, and consider data clustering approaches prior to GPM training.

Acknowledgements

The financial support for this project is provided by Chevron Energy Technology Company.

References

G. Box and D. Cox, 1964, An analysis of transformations, Journal of the Royal Statistical Society. Series B (Methodological), 26, 2, 211-252.

Z. Jiang, W. Chen, Y. Fu, and R. Yang, 2013, Reliability-Based Design Optimization with Model Bias and Data Uncertainty, SAE International, 10.4271/2013-01-1384.

M.C. Kennedy and A. O'Hagan, 2001, Bayesian calibration of computer models, Journal of the Royal Statistical Society Series B-Statistical Methodology, 63, 425-450

Q. H. Mazumder, 2004, Development and Validation of a Mechanistic Model to Predict Erosion in Single-Phase and Multiphase Flow, PhD. Dissertation, Department of Mechanical Engineering, The University of Tulsa, Tulsa, Oklahoma, USA

B.S. McLaury and S.A. Shirazi, 1999, Generalization of API RP 14E for Erosive Service in Multiphase Production, Society of Petroleum Engineer, 423-432

R. Okita, 2010, Effects of Viscosity and Particle Size on Erosion Measurement and Predictions, M.S. Thesis, Department of Mechanical Engineering, The University of Tulsa, Tulsa, Oklahoma, USA

C.E. Rasmussen and C.K. Williams, 2006, Gaussian Process for Machine Learning, The MIT Press, ISBN 0-262-18253-X.

C.E. Rasmussen, 2004, Gaussian Processes in Machine Learning, Lecture Notes in Computer Science, 3176, 63-71

Y.L. Zhang, 2006, Application and improvement of computational fluid dynamics (cfd) in solid particle erosion modeling, PhD. Dissertation, Department of Mechanical Engineering, University of Tulsa, Tulsa, Oklahoma, USA

Krist V. Gernaey, Jakob K. Huusom and Rafiqul Gani (Eds.), 12th International Symposium on Process Systems Engineering and 25th European Symposium on Computer Aided Process Engineering.
31 May - 4 June 2015, Copenhagen, Denmark.

Leak Identification using Extended Kitanidis-Kalman Filter

C. Ganesh[a], Pushkar Ballal[b], Mani Bhushan[b] and Sachin C. Patwardhan*[b]

[a]*Dept. of Electrical Engineering, Indian Institute of Technology Bombay, Mumbai, India*
[b]*Department of Chemical Engineering, Indian Institute of Technology Bombay, Mumbai, India.*
**Email:sachinp@iitb.ac.in*

Abstract

If it is desired to maintain uniform performance in the face of process faults, then it is important to diagnose them as they start developing. Kalman filter based fault diagnosis approaches are of particular interest in this work. Kitanidis (1987) has proposed a modified version of linear Kalman filter, which modifies the observer gain to make the estimated states insensitive to unknown input / faults of arbitrary character. An extended version of Kitanidis-Kalman filter (EKKF), which can directly employ a nonlinear mechanistic model for fault identification, is proposed in this work. The residuals generated by the EKKF are used to construct the fault magnitude estimates. Efficacy of the proposed EKKF is demonstrated using simulation studies on the benchmark quadruple tank system (Johansson, 2000). The proposed approach successfully identifies the leak type fault (modelled as changes in areas of the tank outlets) introduced either sequentially or simultaneously.

Keywords: Kalman Filtering, Nonlinear Systems, Fault Identification

1. Introduction

Engineered systems are susceptible to faults and failures. If it is desired to maintain uniform performance in the face of the soft faults, such as biases or drifts in system parameters or unmeasured disturbances, or hard faults, such as leaks in storage tanks, then it is important to diagnose them as they start developing and plan remedial measures. In particular, extended Kalman filter based fault detection and diagnosis approaches are of particular interest in this work. Wilsky and Jones (1976) originally proposed a method for identifying time, location and magnitude of a fault using the generalized likelihood ratio (GLR) method. Deshpande et al. (2009) have recently developed a nonlinear version of the GLR method. This approach is based on analysis of innovation or the model residual sequence generated by the extended Kalman filter after occurrence of a fault. One difficulty with the GLR method is that it is necessary to assume a model, such as step or ramp function, for all anticipated faults while carrying out the diagnosis. A commonly used approach for tracking arbitrary variations in fault / parameters is to assume the random walk model for the evolution of faults / parameters and carry out state and fault / parameter estimation simultaneously. This approach, however, requires *tuning* of the covariance matrix of artificially introduced noise in the random walk model. The covariance tuning is non-trivial exercise (Bavdekar et al., 2011).

Kitanidis (1987) has proposed an alternate version of linear Kalman filter (referred to as Kitanidis-Kalman filter or KKF in rest of the text), which modifies the observer gain calculation step to make the estimated states insensitive to unknown input / faults of arbitrary character. Madapusi and Goyal (2011) have recently used this approach to estimate magnitudes of the unknown inputs from the innovation sequence. The KKF, together with the input magnitude identification step, appears to be well suited for carrying out online fault identification. These developments, however,

have been carried out for discrete time linear systems. Majority of the engineered systems, on the other hand, exhibit nonlinear dynamics in the desired range of operation. Thus, an extended version of KKF (referred to as EKKF), which can directly employ a nonlinear mechanistic model for fault / parameter identification, has been proposed in this work. The residuals generated by EKKF are used to construct magnitude estimates of faults / parameters, which can exhibit relatively slow but arbitrary variations. A significant advantage of the proposed estimation scheme is that, despite model plant mismatch, it generates unbiased estimates of the states without requiring any *covariance tuning*. Efficacy of the proposed EKKF algorithm has been demonstrated using simulation studies on the benchmark quadruple tanks system (Johansson, 2000). Leaks occurring in the tanks are modelled as changes in area of the outlets for outflows from the tanks. The simulation study is carried out for sequential as well as simultaneous occurrence of the faults.

This paper is organized in four sections. The development of extended Kitanidis-Kalman filter is presented in Section 2. The simulation results are presented in Section 3 and main conclusions reached through the simulation studies are presented in Section 4.

2. Development of Extended Kitanidis-Kalman Filter

Kalman filter generates minimum variance estimates of states for linear time varying system under the perfect model assumption. However, if the plant dynamics is influenced by unmeasured inputs of unknown character, then the estimates are biased. Kitanidis (1987) proposed a variation of the Kalman filter, which generates unbiased estimate of the plant states even in the presence of unknown inputs. This approach is extended here to deal with fault identification in nonlinear dynamic systems.

The dynamics of systems under consideration in the work can be represented by the following nonlinear difference equation

$$\mathbf{X}(k+1) = F(\mathbf{X}(k), \mathbf{u}(k), \theta(k)) + \mathbf{w}(k) \tag{1}$$

$$\mathbf{Y}(k) = \mathbf{h}(\mathbf{X}(k)) + \mathbf{v}(k) \tag{2}$$

where, $\mathbf{X} \in \mathbb{R}^n$ denotes the system states, $\mathbf{u} \in \mathbb{R}^m$ denotes the manipulated inputs, $\theta \in \mathbb{R}^p$ denotes vector of faults / model parameters and $\mathbf{w}(k) \in \mathbb{R}^n$ represents a zero mean Gaussian white noise process with covariance matrix $\mathbf{Q}$. The measurements of the system outputs $\mathbf{Y} \in \mathbb{R}^r$ are assumed to be corrupted with zero mean Gaussian white noise process $\mathbf{v}(k) \in \mathbb{R}^r$ with covariance matrix $\mathbf{R}$. Moreover, $\mathbf{w}(k)$ and $\mathbf{v}(k)$ are assumed to be mutually uncorrelated. It is further assumed that $\theta(k) \in R^p$ can be represented as, $\theta(k) = \overline{\theta} + \Delta\theta(k)$, where, $\overline{\theta}$ represents the mean or the steady state value of the parameter at some desired operating point and $\Delta\theta(k)$ represent time varying perturbations of unknown characteristics. Moreover, the number of model parameters is less than or equal to the number of measurements, i.e. $p \leq r$.

Given the measurements up to time $(k+1)$, it is desired to construct an unbiased minimum variance estimate of $\mathbf{X}(k+1)$. Let us assume that an unbiased filtered estimate, $\hat{\mathbf{X}}(k|k)$, of $\mathbf{X}(k)$ is available at instant $(k+1)$. Defining estimation error, $\varepsilon(k+1) = \hat{\mathbf{X}}(k+1|k+1) - \mathbf{X}(k+1)$, it is desired to construct the estimate $\hat{\mathbf{X}}(k+1|k+1)$ such that it is unbiased, i.e. $\mathbf{E}[\varepsilon(k+1)] = 0$. Using Taylor series expansion in the neighborhood of $\hat{\mathbf{X}}(k|k)$ and neglecting terms higher than the first order terms, the R.H.S. of equation (1) can be approximated as follows (Soderstrom, 2002)

$$\mathbf{X}(k+1) = \Phi(k)\mathbf{X}(k) + \mathbf{G}(k)\Delta\theta(k) + \mathbf{M}(k) + \mathbf{w}(k) \tag{3}$$

where $\mathbf{M}(k) = \mathbf{F}(\hat{\mathbf{X}}(k|k), \mathbf{u}(k), \overline{\theta}) - \Phi(k)\hat{\mathbf{X}}(k|k)$ and

$$\Phi(k) = \left[\frac{\partial \mathbf{F}}{\partial \mathbf{X}}\right]_{(\hat{\mathbf{X}}(k|k), \overline{\theta})} \quad ; \quad \mathbf{G}(k) = \left[\frac{\partial \mathbf{F}}{\partial \theta}\right]_{(\hat{\mathbf{X}}(k|k), \overline{\theta})} \tag{4}$$

Following Kitanidis (1987), the predicted estimate of $\mathbf{X}(k+1)$ is constructed as follows

$$\widetilde{\mathbf{X}}(k+1|k) = \Phi(k)\hat{\mathbf{X}}(k|k) + \mathbf{M}(k)\left(= \mathbf{F}(\hat{\mathbf{X}}(k|k), \mathbf{u}(k), \overline{\theta})\right) \tag{5}$$

The state to output map can now be locally approximated in the neighborhood of $\widetilde{\mathbf{X}}(k+1|k)$ as follows

$$\mathbf{Y}(k+1) = \mathbf{C}(k+1)\mathbf{X}(k+1) + \mathbf{N}(k+1) + \mathbf{v}(k+1) \tag{6}$$

where

$$\mathbf{C}(k+1) = \left[\frac{\partial \mathbf{h}}{\partial \mathbf{X}}\right]_{\widetilde{\mathbf{X}}(k+1|k)} \quad \text{and} \quad \mathbf{N}(k+1) = \mathbf{h}(\widetilde{\mathbf{X}}(k+1|k)) - \mathbf{C}(k+1)\widetilde{\mathbf{X}}(k+1|k) \tag{7}$$

Following Kitanidis (1987), the predicted output at instant $(k+1)$ is defined as follows

$$\widetilde{\mathbf{Y}}(k+1|k) = \mathbf{C}(k+1)\widetilde{\mathbf{X}}(k+1|k) + \mathbf{N}(k+1)\left(= h(\widetilde{\mathbf{X}}(k+1|k))\right) \tag{8}$$

Using the predicted estimate and the predicted output, the updated state estimate at instant $(k+1)$ can now be constructed as follows

$$\hat{\mathbf{X}}(k+1|k+1) = \widetilde{\mathbf{X}}(k+1|k) + \mathbf{L}(k+1)\mathbf{e}(k+1) \tag{9}$$

$$\mathbf{e}(k+1) = \mathbf{Y}(k+1) - \widetilde{\mathbf{Y}}(k+1|k) = -\mathbf{C}(k+1)\xi(k+1) + \mathbf{v}(k+1) \tag{10}$$

where $\xi(k+1) = \widetilde{\mathbf{X}}(k+1|k) - \mathbf{X}(k+1)$. Using equation (9), the estimation error dynamics can be approximated as follows

$$\varepsilon(k+1) = [\mathbf{I} - \mathbf{L}(k+1)\mathbf{C}(k+1)]\xi(k+1) + \mathbf{L}(k+1)\mathbf{v}(k+1) \tag{11}$$

From equations (3) and (5), it follows that

$$\xi(k+1) = \Phi(k)\varepsilon(k) - \mathbf{G}(k)\Delta\theta(k) - \mathbf{w}(k) \tag{12}$$

and

$$\varepsilon(k+1) = [\mathbf{I} - \mathbf{L}(k+1)\mathbf{C}(k+1)]\,[\Phi(k)\varepsilon(k) - \mathbf{G}(k)\Delta\theta(k) - \mathbf{w}(k)] + \mathbf{L}(k+1)\mathbf{v}(k+1) \tag{13}$$

Taking expectation on both the sides under the assumption that $\mathbf{E}[\varepsilon(k)] = 0$, the unbiasedness condition is satisfied at $(k+1)$ if and only if an additional constraint is imposed

$$[\mathbf{I} - \mathbf{L}(k+1)\mathbf{C}(k+1)]\mathbf{G}(k) = [\mathbf{0}] \tag{14}$$

It may be noted that, matrix $\mathbf{C}(k+1)\mathbf{G}(k)$ is assumed to have full column rank at all k in this work.

To arrive at the minimum variance estimate of $\mathbf{X}(k+1)$, a scalar objective function $\varphi(k)$ is defined as

$$\varphi(k) = tr\left[\mathbf{P}(k+1|k+1) + 2[\mathbf{I} - \mathbf{L}(k+1)\mathbf{C}(k+1)]\mathbf{G}(k)\Lambda(k+1)^T\right] \tag{15}$$

where $\mathbf{P}(k+1|k+1) = \mathbf{E}[\varepsilon(k+1)\varepsilon^T(k+1)]$ and $\Lambda(k+1)$ denotes the matrix of Lagrange multipliers. Defining matrices $\mathbf{P}(k+1|k) = \Phi\mathbf{P}(k|k)\Phi^T + \mathbf{Q}$ and $\mathbf{V}(k+1)$ as

$$\mathbf{V}(k+1) = \mathbf{C}(k+1)\mathbf{P}(k+1|k)\mathbf{C}(k+1)^T + \mathbf{R} \tag{16}$$

the use of the necessary conditions for optimality reduces to the following matrix equation (Kitanidis, 1986)

$$\begin{bmatrix} \mathbf{V}(k+1) & -\mathbf{C}(k+1)\mathbf{G}(k) \\ \mathbf{G}(k)^T\mathbf{C}(k+1)^T & [\mathbf{0}] \end{bmatrix} \begin{bmatrix} \mathbf{L}(k+1)^T \\ \Lambda(k+1)^T \end{bmatrix} = \begin{bmatrix} \mathbf{C}(k+1)\mathbf{P}(k+1|k) \\ \mathbf{G}(k)^T \end{bmatrix} \tag{17}$$

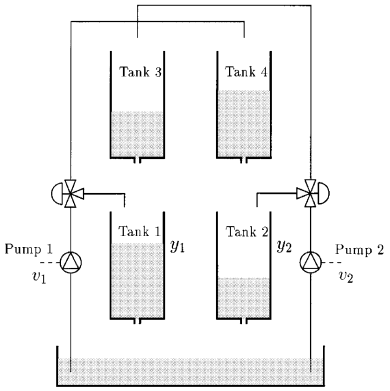

Figure 1: Quudruple Tank System: Schematic Representation (Johanson, 2000)

which can be used to compute $\mathbf{L}(k+1)$. Expressions for update of covariance matrix $\mathbf{P}(k+1|k+1)$ and discussion regarding the second order necessary conditions that ensure the minimality of the covariance can be found in Kitanidis (1987). It may be noted that the proposed EKKF reduces to the conventional EKF when $\mathbf{G}(k)$ equals the null matrix, i.e. in absence of any fault / parameter variations.

The extended Kitanidis-Kalman filter constructed such that the state estimate are insensitive to unknown drift in the parameter. In practice, however, the drifting value of the parameter / faults can be of interest from the viewpoint of monitoring. Estimates of the drifting parameters / faults can be constructed using the innovation sequence generated by EKKF. Consider innovation, $\mathbf{e}(k+1)$,which can be expressed as follows

$$\mathbf{e}(k+1) = \mathbf{C}(k+1)\mathbf{G}(k)\Delta\theta(k) + \upsilon(k+1) \tag{18}$$

where $\upsilon(k+1) = \mathbf{C}(k+1)\left[-\Phi(k)\varepsilon(k) + \mathbf{w}(k)\right] + \mathbf{v}(k+1)$ is a zero mean signal with covariance equal to $\mathbf{V}(k+1)$ given by equation (16). It is further assumed that variations in $\Delta\theta(k)$ are relatively slow and their value remains constant over a window in time $[k+1, k-N+1]$, i.e. $\Delta\theta(k-i) = \Delta\theta(k)$ for $i = 0, 1, ...N$. Under this simplifying assumption, by stacking equations for innovations over the window $[k+1, k-N+1]$, we arrive at $\mathscr{E}(k) = \mathscr{A}(k)\Delta\theta(k) + \mathscr{V}(k)$ where

$$\mathscr{E}(k) = \begin{bmatrix} \mathbf{e}(k+1) \\ ... \\ \mathbf{e}(k-N+1) \end{bmatrix}; \mathscr{A}(k) = \begin{bmatrix} \mathbf{C}(k+1)\mathbf{G}(k) \\ ... \\ \mathbf{C}(k-N+1)\mathbf{G}(k-N) \end{bmatrix}; \mathscr{V}(k) = \begin{bmatrix} \upsilon(k) \\ ... \\ \upsilon(k-N) \end{bmatrix}$$

Here, $E\left[\mathscr{V}(k)\right] = \overline{0}$ and covariance $Cov\left[\mathscr{V}(k)\right] = block\ diag\left[\begin{array}{cccc} \mathbf{V}(k+1) & ... & \mathbf{V}(k-N+1) \end{array}\right]$. Defining weighting matrix $\mathscr{W}(k) = \left[Cov\left[\mathscr{V}(k)\right]\right]^{-1}$, the maximum likelihood estimate of $\Delta\theta(k)$ can be constructed as

$$\Delta\theta(k) = \left[\mathscr{A}(k)^T\mathscr{W}(k)\mathscr{A}(k)\right]^{-1}\mathscr{A}(k)^T\mathscr{W}(k)\mathscr{E}(k) \tag{19}$$

3. Simulation Studies

The efficacy of the proposed EKKF is evaluated by conducting simulation studies on the benchmark quadruple tank system (Johansson, 2000). The system consists of four interconnected tanks as shown in Figure 1. Voltage inputs v_1 and v_2 to Pump 1 and Pump 2, respectively, represent the manipulated inputs and the liquid levels in Tank 1 and Tank 2 are the measured outputs. A

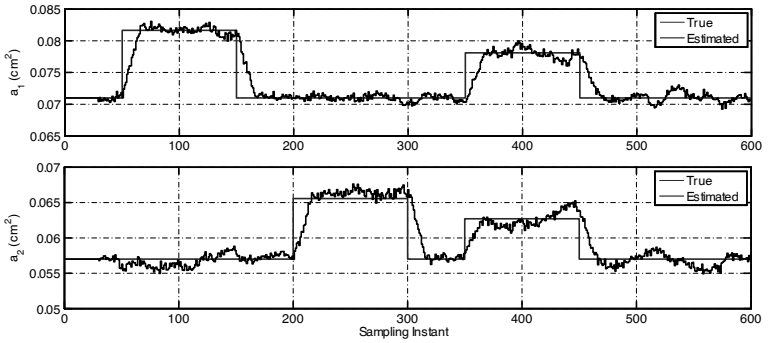

Figure 2: Comparison of variations of parameters a_1 and a_2 generated using EKKF with the true parameter variations

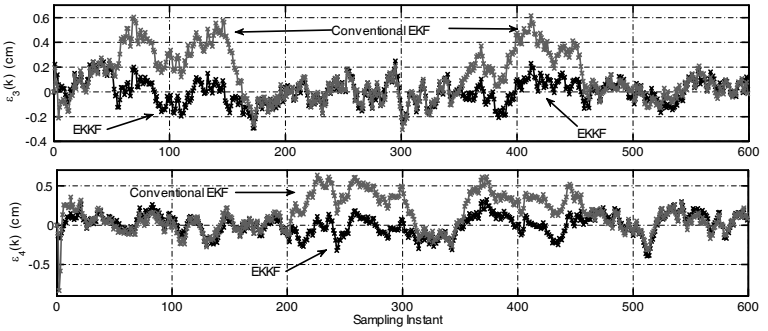

Figure 3: Comparison of state estimation errors generated by EKKF and EKF for the umeasured states h_3 and h_4.

mechanistic model governing the system dynamics, together with the model parameters, is given in Johansson (2000). The system is operated under the non-minimum phase conditions. The sampling interval is selected as 5 seconds. The system is operated in open loop and the manipulated input variations are introduced as random binary inputs (RBS) around the steady state values with amplitude of 0.5 V and in frequency range $[0, 0.05\pi/T]$. The state and the measurement noise covariances are chosen as $\mathbf{Q} = 0.05\mathbf{I}_{4\times4}$ and $\mathbf{R} = 0.05\mathbf{I}_{2\times2}$.

The faults considered here are leaks occurring at the bottoms of Tank 1 and Tank 2. Thus, they are modelled as changes in model parameters a_1 and a_2, i.e. changes in areas of bottom outlets of Tank1 and Tank 2, respectively. At instant $k = 51$, +15 % increase in area a_1 is introduced and a_1 is set equal to the nominal value at instant 150. Subsequently, at instant $k = 201$, +15 % increase in area a_2 is introduced and a_2 is set equal to the nominal value at instant $k = 300$. After introducing faults sequentially, areas a_1 and a_2 are simultaneous changed by 10 % between $k = 351$ to $k = 450$ and set equal to their nominal values subsequently. For fault magnitude estimation, the window size N is chosen as 30. The fault magnitude estimates generated using EKKF are shown in Figure (2). As evident from this figure, the proposed method for parameter / fault magnitude estimation generates fairly accurate estimates of variation in a_1 and a_2 for sequential as well as simultaneous faults. A comparison of the state estimation errors generated by the conventional EKF and EKKF is presented in Figures (3) and (4). The advantages of the proposed EKKF are highlighted by

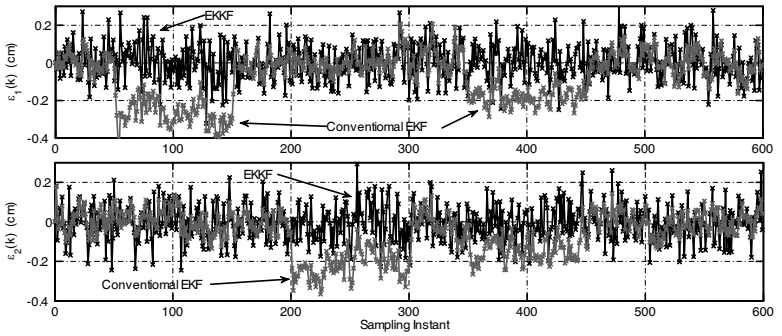

Figure 4: Comparison of state estimation errors generated by EKKF and EKF for the measured states h_1 and h_2.

Figure (3), which compares the estimation errors for the unmeasured states h_3 and h_4. When the faults are introduced, the estimates generated by the conventional EKF become biased. On the other hand, as can be expected from the design conditions, the estimates generated by EKKF remain unbiased throughout the simulation. The behavior of the estimation errors in h_1 and h_2 is qualitatively similar. Both the figures also underscore the fact that EKKF performance becomes similar to that of the conventional in the absence of any fault / parameter drift. However, under the no fault scenario, there is a relative loss of performance with respect to EKF as EKKF seeks a constrained optimum irrespective of occurrence of the faults.

4. Conclusions

In this work, an extended version of Kitanidis-Kalman filter (Kitanidis, 1987) has been developed, which employs a nonlinear mechanistic model for fault identification through successive linearization. The residuals generated by the EKKF are used to construct the fault magnitude estimates. Efficacy of the proposed EKKF is demonstrated using simulation studies on the benchmark quadruple tank system (Johansson, 2001). The proposed approach is able to generate reasonably accurate estimates of the leak type fault (modelled as changes in areas of the tank outlets) introduced either sequentially or simultaneously. Moreover, unlike the conventional EKF, the proposed EKKF formulation generates unbiased estimates of the states even in the presence of moderately large model plant mismatch.

References

Bavdekar, V. A., Deshpande, A. P., Patwardhan, S. C., 2011. Identification of process and measurement noise covariance for state and parameter estimation using extended Kalman filter. *Journal of Process Control*, 21, 585–601.

Deshpande, A. P. , Patwardhan, S. C. , Narasihman, S., 2009. Intelligent state estimation for fault tolerant nonlinear model predictive control, *Journal of Process Control*, 19, 187–204.

Kitanidis, P. K., 1987. Unbiased Minimum-variance Linear State Estimation, *Automatica*, 23(6):775–778.

Johansson, K. H., 2000. The Quadruple-Tank Process: A multivariable laboratory process with an adjustable zero, *IEEE Trans. on Control Systems Technology*, 8(3), 456-465.

Madapusi, H. J. P., Goyal, S., 2011. Robust estimation of nonlinear constitutive law from static equilibrium data for modeling the mechanics of DNA, *Automatica*,47, 1175–1182.

Soderstrom, T., 2002, Discrete Time Stochastic Systems, Springer.

Wilsky, A. S., Jones, H. L., 1976. A generalized likelihood ratio approach to the detection and estimation of jumps in linear systems*IEEE Trans. on Automatic Control*, 21(1),108–112.

Krist V. Gernaey, Jakob K. Huusom and Rafiqul Gani (Eds.), 12th International Symposium on Process Systems Engineering and 25th European Symposium on Computer Aided Process Engineering.
31 May – 4 June 2015, Copenhagen, Denmark

Process Monitoring and Fault Detection in Non-Linear Chemical Process Based On Multi-Scale Kernel Fisher Discriminant Analysis

Norazwan Md Nor,[a] Mohd Azlan Hussain,[a] Che Rosmani Che Hassan[a]

[a]*Department of Chemical Engineering, University of Malaya, 50630 Kuala Lumpur, Malaysia*

Abstract

This paper presents a multi-scale kernel Fisher discriminant analysis (MSKFDA) algorithm combining Fisher discriminant analysis (FDA) and its nonlinear kernel variation with the wavelet analysis. This approach is proposed for investigating the potential integration of wavelets and multi-scale methods with discriminant analysis in nonlinear chemical process monitoring and fault detection system. In this paper, a discrete wavelet transform (DWT) is applied to extract the dynamics of the process at different scales. The wavelet coefficients obtained during the analysis are used as input for the algorithm. By decomposing the process data into multiple scales, MSKFDA analyse the dynamical data at different scales and then restructure scales that contained important information by inverse discrete wavelet transform (IDWT). A monitoring statistic based on Hoteling's T^2 statistics is used in process monitoring and fault detection. The Tennessee Eastman benchmark process is used to demonstrate the performance of the proposed approach in comparison with conventional statistical monitoring and fault detection methods. A comparison in terms of false alarm rate, missed alarm rate and detection delay, indicate that the proposed approach outperform the others and enhanced the capabilities of this approach for the diagnosis of industrial applications.

Keywords: multi-scale, Fisher discriminant analysis, wavelet analysis, process monitoring, fault detection

1. Introduction

Various modelling methodologies have been developed for achieving efficient monitoring and control system for chemical processes. These methodologies are broadly divided into three types: quantitative model-based methods; qualitative model-based methods; and process history based methods (Venkatasubramanian *et al*., 2003). The process history based or data-driven method concerns with the transformation of large amounts of data into a particular form of knowledge representation that will enable proper detection and diagnosis of faults. Availability of vast amounts of plant data has encouraged researchers to develop and improve the data-driven-based and multivariable statistical process monitoring based methods, which use statistic projection technique to extract key process information from theses massive process data. These methods including such as Principal Component Analysis (PCA), Partial Least Square (PLS), Independent Component Analysis (ICA) and Fisher Discriminant Analysis (FDA) have been widely applied to on-line continuous and batch process monitoring, fault detection and diagnosis.

In some context, fault diagnosis problems can be considered as classification problems when lots of historical data are obtained from various faulty conditions, and then feature extraction and pattern recognition or classification methods can be used for fault diagnosis. Linear supervised classification methods such as PCA, discriminant PLS (DPLS) and FDA can be used. PCA represents high-dimensional process data in a reduced dimension, which brings convenience for process monitoring. However, PCA aims at reconstruction but not classification, which degrades the performance in classification problems while FDA provides an optimal lower dimensional representation in terms of discriminating among classes, which is very useful for fault diagnosis. Though it has been proven that FDA outperforms PCA in the classification problems, it is still linear in nature, which degrades the performance of FDA in monitoring the nonlinear system.

Furthermore, a chemical process is often characterized by large scale and non-linear behaviour. When linear FDA is used for fault diagnosis in non-linear system, a lot of incorrect diagnosis results will occur. As solution to deal with the nonlinear system, and to improve the classification ability, kernel-based FDA, called kernel FDA (KFDA), is introduced. The basic idea of the KFDA is to map the input sample data into a kernel feature space by a nonlinear kernel function and then perform linear FDA in the nonlinearly mapped feature space to find the discriminant feature vectors for classification. KFDA has turned out to be effective in many real-world applications due to its power of extracting the most discriminatory nonlinear. However, application of KFDA in fault diagnosis of chemical and biological processes is still limited.

There were also limited application on multi-scale FDA and KFDA that integrates FDA and wavelet packet analysis (Vana *et al.*, 2011). Discrete wavelet analysis decomposes the high-frequency part further, which wavelet analysis not does, and adaptively selects relative frequency bond based on character of signal to be analysed. To further improve de-noising character of multi-scale KFDA, the paper describes a discrete wavelet transform KFDA, which combines the ability of KFDA to de-correlate the variables by discriminating a nonlinear relationship with that of discrete wavelet transform to extract auto-correlated measurements. Then, a novel multi-scale kernel FDA is proposed by combining FDA and its nonlinear kernel variation with the wavelet analysis. Finally, an individuals control charts (XmR charts) and Hoteling's T^2 statistics are used to monitor the fault data in process monitoring and fault detection. The proposed method is evaluated and compared with the T^2 statistical methods based on the PCA in terms of the average run length (ARL). The paper is organized as follows. In Section 2 the background of FDA, KFDA and the discrete wavelet transform (DWT) is introduced. Section 3 introduces the proposed fault diagnosis approach with kernel FDA and integrates it with the wavelet transform. The case study illustrates an application to Tennessee Eastman process is provided in Section 4, and Section 5 concludes the paper.

2. Background

2.1. Fisher Discriminant Analysis

Fisher discriminant analysis is a linear dimensionality reduction technique to find a direction for which data classes are optimally separated. The optimal discriminant direction is determined by maximizing the scatter within the classes (Wang and Romagnoli, 2005). Let the training data for all faulty classes be stacked into a n by m matrix $X \in R^{n \times m}$, where n is the observation number and m is the variable number. The

within-class-scatter matrices S_W and the between-class-scatter matrix S_B contain all the basic information about the relationship within the groups and between them as in Eq.(1) and Eq.(2) respectively.

$$S_W = \sum_{k=1}^{K} \sum_{n \in C_k} (x_n - m_k)(x_n - m_k)^T \tag{1}$$

$$S_B = \sum_{k=1}^{K} N_k (x_n - m_k)(m_k - m)^T \tag{2}$$

where N_k and m_k are the number and mean vector of the points assigned to class k, respectively; m is the total mean of all the samples, and K is the number of classes and x_n is the data sample. Maximizing Eq.(3) with w is the solution is equivalent to maximizing the between-class scatter S_B,and minimizing the within-class scatter S_W.

$$J(w) = \arg\max \frac{|w^T S_B w|}{|w^T S_W w|}. \tag{3}$$

2.2. Kernel Fisher Discriminant Analysis

The idea of KFDA is to solve the problem of FDA in the feature space F. However, since any solution $w \in F$ must lie in the span of all the samples in F, there exists coefficients $\alpha = \{\alpha, i = 1, 2, \ldots, n\}$ and the mapping of sample class, ϕ_i such that

$$w = \sum_{i=1}^{n} \alpha_i \phi_i. \tag{4}$$

K_B and K_W are the between-class kernel matrix and within-class kernel matrix, as in Eq.(5) and Eq.(6) respectively.

$$w^T S_B w = \alpha^T K_B \alpha \tag{5}$$

$$w^T S_W w = \alpha^T K_W \alpha \tag{6}$$

So the solution can be achieved by maximizing Eq.(7) following Fisher criterion

$$J(\alpha) = \arg\max \frac{|\alpha^T K_B \alpha|}{|\alpha^T K_W \alpha|}. \tag{7}$$

2.3. Discrete Wavelet Transform

Wavelets are basis functions that are localized in both time and frequency. Generally, the dyadically discretized form of wavelets is used and it can be represented as

$$\psi_{mk}(t) = 2^{-m/2} \psi(2^{-m} t - k), \tag{8}$$

where, $\psi(t)$ is the mother wavelet, and m and k are dilation and translation parameters, respectively. The translation parameter determines the location of the wavelet in the time domain, while the dilation parameter determines its scale and location in the frequency domain. By projecting a signal on the wavelet basis function, its contributions in different regions of the time-frequency space can be obtained. The

scaling and wavelet coefficients represented in terms of original measured data vector, x, take the form of

$$a_s = H_s x,\ d_s = G_s x \tag{8}$$

where, H_s represents projection m times on the scaling function, and G_s represents projection $(s-1)$ times on the scaling function and once on the wavelet. The sequences H and G are low-pass and high-pass filters derived from the corresponding basis function, respectively. The scaling coefficients represent the lower frequency approximation of the signal while the wavelet coefficients represent the higher frequency components of the signal (Maulud *et al.*, 2005).

3. Methodology

The detailed in multi-scale kernel FDA application procedure of fault diagnosis were discussed briefly in this section. First, each of the m variables is first decomposed individually by applying discrete wavelet transformation (DWT). Then, the Kernel FDA is performed on the wavelet coefficients for each selected scale. Appropriate numbers of component loading vectors are retained and the wavelet coefficients are reconstructed at each selected scale. In this work four scales (s=4) are used for discrete wavelet transformation (DWT) of the original signal. After that, the wavelet coefficients larger than a selected threshold corresponding to a significant event are retained. The variables consisting of deterministic components are reconstructed from the retained wavelet coefficients through inverse discrete wavelet transformation (IDWT) and the loadings of the extracted deterministic components are computed.

The new observations are projected into lower dimensional subspace. This subspaces measures the systematic or state variations occurring in the process. Meanwhile, the lower dimensional subspace corresponding to the $(m-a)$ smaller singular value describes the random variations of the process such as that associated with measurement noise are term as residual space. KFDA is used to search the optimal one-dimensional discriminant direction between the fault data and the normal data. Thus, individuals control charts, also known as XmR charts, are used to monitor the fault data on the optimal discriminant direction with contribution plot based on the optimal discriminant direction from KFDA is also used to improve its performance (Pei *et al.*, 2006). The proposed method is applied to the Tennessee Eastman process. Finally, the proposed method is evaluated and compared with the Hotelling's T^2 statistical methods.

4. Case study

Tennessee Eastman process (TEP) as described by Downs and Vogel (1993) in Figure 1was used as a case study. The process includes a total of 52 variables with 20 different faults were simulated (Yélamos *et al.*, 2006). The data set for the process and the details can be obtained from the Multi-scale Systems Research Laboratory (MIT, 2013).

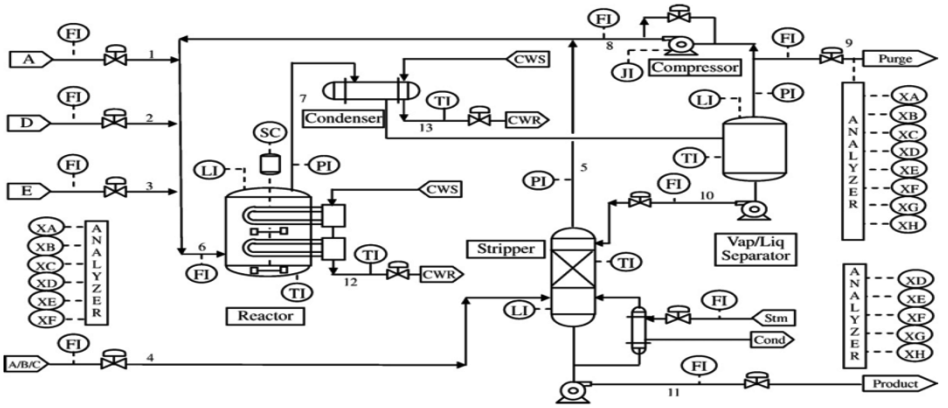

Figure 1 Tennessee Eastman process diagram

Table 1 Selected faults for four combination cases

	ID	*Fault description*	*Type*
Case 1	Fault 3	D feed temperature	Step change
	Fault 4	Reactor cooling water inlet temperature	Step change
	Fault 11	Reactor cooling water inlet temperature	Random variation
Case 2	Fault 8	A, B, C feed composition	Random variation
	Fault 12	Condenser cooling water inlet temperature	Random variation
	Fault 15	Condenser cooling water valve	Sticking
Case 3	Fault 2	B composition, A/C ration constant	Step change
	Fault 9	D feed temperature	Random variation
	Fault 13	Reactor kinetics	Slow drift
Case 4	Fault 9	D feed temperature	Random variation
	Fault 14	Reactor cooling water valve	Sticking
	Fault 17	Unknown	Unknown

These case studies and their respective faults were tabulated in Table 1, covering all fault types in the TEP simulation. Each case study combination includes three different types of faults and each of fault type sampling intervals is set to be 3 min with every sample data contains 52 process variables.

5. Results and Discussion

Table 2 Comparison among diagnosis success rates using different approaches

		Diagnosis success rate (%)		
		FDA	KFDA	MSKFDA
Case 1	Training data set	67.5	100	98.0
	Testing data set	41.7	84.7	92.7
Case 2	Training data set	89.1	100	100
	Testing data set	33.7	72.7	91.3
Case 3	Training data set	100	100	100
	Testing data set	86.7	100	100
Case 4	Training data set	93.7	100	100
	Testing data set	62.7	95.3	98.3

A summary of the classification results for MSKFDA, KFDA and FDA is listed in Table 2. Compared with the classification performance of KFDA, MSKFDA has a significant improvement. After fault data are decomposed by DWT wavelet analysis, KFDA is performed on these multi-scaled fault data, which offers important supplemental classification information to KFDA. Without proper variable weighting, all variables are used in a same level and the data sets are masked with irrelevant information. The integration of DWT with KFDA improved the extraction of features that are relevant to the abnormal operation in both time and frequency domain and lead to better classification. In addition, the high misclassifications rate for FDA shows the advantage of nonlinear technique when the fault data are highly overlapped.

6. Conclusions

In this paper, MSKFDA-based fault diagnosis for the Tennessee Eastman process is presented. The data discrimination and fault detection based on MSKFDA methodology enhanced the diagnosis proficiency by taking into consideration the multi-scale information compared to other methods that considered only single scale nature. Moreover, it can provide a better separation of the deterministic and stochastic features and improve the extraction of features that are relevant to a faulty situation from both time and frequency domain aspects. The application of the proposed MS-KFDA shows better fault diagnosis performance than KFDA and FDA. The high misclassification rate for FDA also shows the advantage of nonlinear technique when the fault data are highly overlapped.

References

Downs, J.J., Vogel, E.F., 1993. A plant-wide industrial process control problem. Computers and Chemical Engineering, 17, 245–255

Massachusetts Institute of Technology, 2013, The Simulation Code of Tennessee Eastman, Department of Chemical Engineering, Massachusetts Institute of Technology, Cambridge, U.S.A.

Maulud, A. H. S., Wang, D., & Romagnoli, J. A., 2005, Wavelet-Based Nonlinear Multivariate Statistical Process Control. In L. Puigjaner & A. Espuña (Eds.), European Symposium on Computer Arded Process Engineering – 15.

Pei, X., Yamashita, Y., Yoshida, M., Matsumoto, S., & Pei, X., 2006, Discriminant analysis and control chart for the fault detection and identification. In W. Marquardt & C. Pantelides (Eds.), 16th European Symposium on Computer Aided Process Engineering and 9th International Symposium on Process Systems Engineering, pp. 1281–1286.

Vana, Z., Privara, S., Cigler, J., & Preisig, H. A., 2011, System identification using wavelet analysis. In E. N. Pistikopoulos, M. C. Georgiadis, & A. C. Kokossis (Eds.), 21st European Symposium on Computer Aided Process Engineering – ESCAPE 21, Vol. 29.

Venkatasubramanian, V., Rengaswamy, R., Kavuri, S. N., & Yin, K., 2003, A review of process fault detection and diagnosis Part III: Process history based methods, Computers and Chemical Engineering, 27, 327–346.

Wang, D., & Romagnoli, J. A., 2005, A Robust Discriminate Analysis Method for Process Fault Diagnosis. In L. Puigjaner & A. Espuña (Eds.), European Symposium on Computer Aided Process Engineering – 15.

Yélamos, I., Escudero, G., & Graells, M., 2006, Fault diagnosis based on support vector machines and systematic comparison to existing approaches. In W. Marquardt & C. Pantelides (Eds.), 16th European Symposium on Computer Aided Process Engineering and 9th International Symposium on Process Systems Engineering, pp. 1209–1214.

Krist V. Gernaey, Jakob K. Huusom and Rafiqul Gani (Eds.), 12th International Symposium on Process Systems Engineering and 25th European Symposium on Computer Aided Process Engineering.
31 May – 4 June 2015, Copenhagen, Denmark

Hierarchical Fault Propagation and Control Strategy from the Resilience Engineering Perspective: A Case Study with Petroleum Refining System

Jinqiu Hu,[a*] Laibin Zhang,[a] Xi Ma,[a] Zhansheng Cai,[a,b]

[a] *College of Mechanical and Transportation Engineering，China University of Petroleum，Beijing 102249，China*
[b] *CNOOC ZHONGJIE PETRO CHEMICALS CO., LTD, Cangzhou City, Hebei Province, 061000, China*
hujinqiu@gmail.com

Abstract

Although fault propagation scenario-based accident analysis can be an effective means to help operators to find the root causes of the current abnormal event, it has not yet been analyzed from the resilience engineering (RE) perspective. Resilience engineering is a new method that can control incidents and limit their consequences. This study introduces a hierarchical fault propagation model (HFPM) as an extension of the Infrastructure Resilience-Oriented Modelling Language (IRML), considering the dynamic behaviour of fault propagation. The method involves two parts: the first part is static analysis for system structure feature and the second part is dynamic analysis for fault evolution mechanism. The performance of the proposed model has been tested on a petroleum refining system with the characteristics of complex, non-linear and multivariate.

Keywords: fault propagation; process safety; resilience engineering; Infrastructure Resilience-Oriented Modeling Language.

1. Introduction

The complexity of the process plants which can be considered as systems of systems, has increased due to extensive heat and mass integration. Thus, the plant operation becomes more demanding with multiple unit operation interactions. It is their scale, nonlinearities, interconnectedness, and interactions with humans and the environment that can make these complex systems fragile, when the cumulative effects of multiple abnormalities can propagate in numerous ways to cause systemic failures. Therefore it is often difficult to develop nonlinear models that accurately describe the system as well as the fault propagation features in all regimes.

Various methods and models for systems of systems have been proposed. The main aim is to reveal fault propagation features, to estimate the process risk or to make resilience analysis. According to previous accidents and disasters, Utne (2011) plotted a cascade diagram to describe the cascading failures process under a specific initiating event. It is a logical method to model the dependencies. Johansson et al (2010) proposed an agent based approaches for vulnerability analysis in critical components. Kjølle et al (2012) proposed an across-sector approach for analysis of critical components and interdependencies between components. Functional Resonance Analysis Method

(FRAM) (Belmonte, 2011) was proposed to establish a fault evolution model in systemic functional perspective. To uncover process variables' interactions, Gabbar et al (2014) employed fault semantic network (FSN) as a novel method for fault diagnosis and fault propagation analysis by using techniques like genetic programming (GP) and neural networks (NN).

Although above fault propagation scenario-based accident analysis can be an effective means to help operators to find the root causes of the current abnormal event, it has not yet been analyzed from the resilience engineering (RE) perspective. Resilience engineering is a new method that can control incidents and limit their consequences. This study introduces a hierarchical fault propagation model (HFPM) as an extension of the Infrastructure Resilience-Oriented Modelling Language (IRML) (Filippini, 2014), considering the dynamic behaviour of fault propagation. It can be used for fault propagation and control strategy analysis from the resilience engineering perspective and also be beneficial to the design and modifications of process plants which will enhance the process safety.

2. Hierarchical fault propagation model (HFPM)

HFPM is an optimization method based on IRML for fault propagation analysis for systems of systems. The core of the method is a network formed by nodes and links, where nodes represent different components and links mimic the functional connections among them. This method is aimed at analyzing the system structure and the fault scenarios to capture the fault propagation behaviors and evaluate the resilience of systems of systems. HFPM has two modules: static analysis module, dynamic analysis module.

2.1. static analysis

Static analysis, i.e. structure analysis, captures the system structure features for fault propagation in a specific system, which includes following steps:

Setp (1): Draw the network. The network can be drawn based on the process flowchart, where nodes are classified into two types, i.e. the subsystem node and secondary node. The subsystem nodes are decided according to the process units, and the devices in subsystems are called the secondary nodes.

Setp (2): Simplify the network. The simplified network is the overall representation of all the relevant functional dependencies with the secondary nodes omitted. Criticality, vulnerability and interdependency node sets are obtained to judge the criticality and vulnerability degree of each subsystem.

Setp (3): Complicate the network. The most critical and vulnerable subsystem nodes determined in step (2) are chosen as the analysis object. The criticality and vulnerability degree of the devices is determined as step (2).

2.2. dynamic analysis

Dynamic analysis module quantifies the fault propagation behavior under different fault modes and working conditions in systems of systems. The procedure used to develop the dynamic analysis is described as: fault propagation scenarios analysis, determination of modeling parameters and state function definition.

Setp (1): Fault propagation scenarios analysis: Combining "what…if…" method, HFPM analyzes the fault propagation scenarios to obtain the event sequences of each subsystem and device in the certain fault mode.

Setp (2): Determination of modeling parameters, which contains disturbance duration (T_D), node buffering time (T_F) and node recovery time (T_R).

Setp (3): State function definition: Resilience is the ability of the network to resist a disturbance and recover back to the initial state. A simple metric of network resilience is the sum of the node's state. HFPM defines the node's state function R, which has two values. If the node operates normally, R=1, otherwise, R=0. If a subsystem node contains n secondary nodes, the subsystem node's state function $R=(r_1+r_2+...+r_n)/n$. The system's state function R is determined based on the fault propagation scenarios and modeling parameters. It can be calculated as the sum of the affected subsystems.
Setp (4): Map the system's state function graph. The fault propagation behavior is reflected in the graph.

Petroleum refining system is an automatic and nonlinear system of systems. Its process parameters are controlled by DCS (Distributed Control System). When parameters fluctuate beyond the threshold due to fault, it will be adjusted to the normal levels. The detected parameter's value has fluctuation in a certain period and eventually returned to the normal value. Therefore, the state function R with two values in HFPM can express the parameter fluctuation in petroleum refining system. Fault acts as the disturbance of the detected parameters. In case study, "Fault" is expressed as "Disturbance".

3. Case study

In petroleum refining system, the atmospheric and vacuum distillation process is a complicated information and mass transfer process. It has many variables, between which there exist a large amount of correlations, intercouplings and interactions among units. It is a typical system of systems. According to the principle technological process, HFPM network is developed and shown in Fig 1.

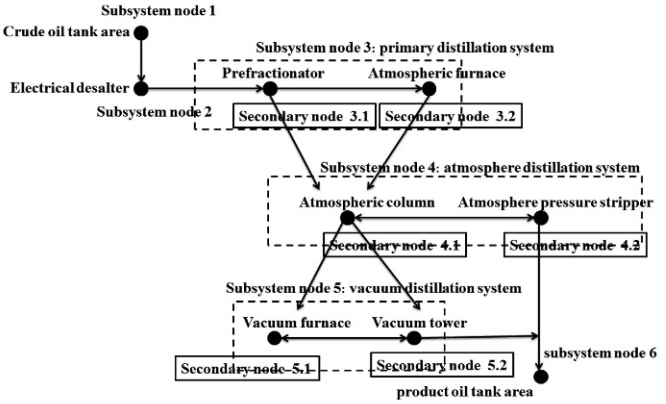

Figure 1 Structure diagram of atmospheric and vacuum system (HFPM network)

3.1. HFPM static analysis

The criticality, vulnerability and interdependency of each subsystem node are achieved by static analysis in table 1 to show that node 1 is the most critical node and node 6 is most vulnerable node. Node 1 represents crude oil tank area and node 6 represents product tank area. The two subsystem nodes determined both contain only one secondary node. Static analysis on the two subsystems is unnecessary.

3.2. HFPM Dynamic analysis

Fault can be detected on devices or product in petroleum refining system. Thus, the disturbance mode is classified into device disturbance mode and product disturbance mode. Taking Device disturbance as an example, the considered fault is prefractionator

disturbance, which triggers fault propagation in an atmospheric and vacuum distillation system.

Table 1: the criticality/vulnerability/interdependency set

	criticality set	vulnerability set	interdependency set
node 1	C(1)={2，3，4，5，6}	V(1)={}	I(1)={}
node 2	C(2)={3，4，5，6}	V(2)={1}	I(2)={}
node 3	C(3)={4，5，6}	V(3)={1，2}	I(3)={}
node 4	C(4)={5，6}	V(4)={1，2，3}	I(4)={}
node 5	C(5)={6}	V(5)={1，2，3，4}	I(5)={}
node 6	C(6)={}	V(6)={1，2，3，4，5}	I(6){}

If the system is under multi-device disturbance, the system's state function is also the sum of the effected subsystems' state functions, which is the sum of the involved secondary nodes' state functions. When *n* devices are disturbed at initial moment, the disturbances from different source reach device *i* in different time points. Device *i* is disturbed at the moment that the first disturbance reaches and recovers at the moment that the last disturbance withdraws. The disturbance affected nodes are *node 3*, *node 4*, *node 5* and *node 6*. Under different working conditions and disturbance modes, the system's state function graphs are drawn according to section 2.2 steps (1) - (4), which represent the fault propagation.

Scenario 1: T_D=2.5; Buffer time parameter and recovery time parameter of each node are set as 1.

The prefractionator (node 3) is disturbed at time=2 for 2.5 time units. Fig 2 (a) shows the system's state function graph. It means that the system will recover to normal state after a period of disturbance. The system resilience can deal with the disturbance of such strength.

Scenario 2: T_D=3.5. Buffering time parameter and recovery time parameter are set the same as scenario 1.

The prefractionator (*node 3*) is disturbed at time=2 for 3.5 time units. Fig 2 (b) shows the system's state function graph. It means that the system will break down after a period of disturbance. The disturbance imposed exceeds the system resilience.

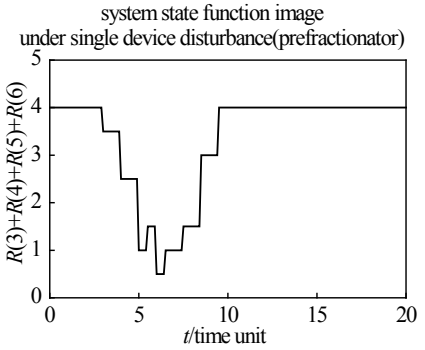

Figure 2(a) single device disturbance in scenario 1

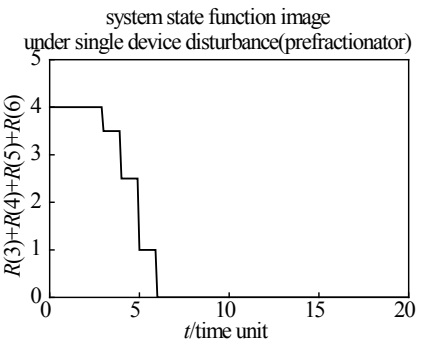

Figure 2(b) single device disturbance in scenario 2

Comparing **scenario 1** and **scenario 2**, it is concluded that the system may recover to the normal state or break down after a period of disturbance and it depends on the

system resilience and the modelling parameters determined by disturbance mode and working condition. The system response varies for different disturbance duration (T_D) in **scenario 1, 2**. In **scenario 3, 4**, buffering time (T_F) or recovery time (T_R) is changed based on scenario 2.

Scenario 3: T_D=3.5; Longer buffering time is set as 1.5 and constant recovery time as 1.

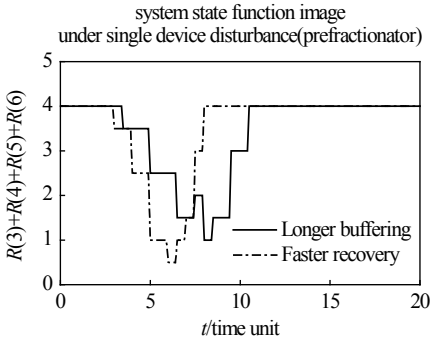

Figure 3: system state function image under single device disturbance in scenario 3/4

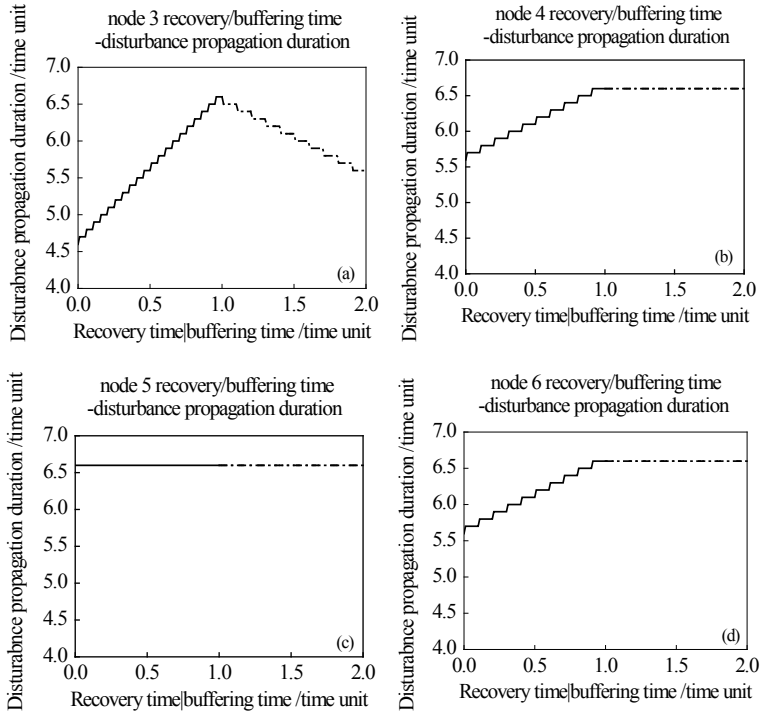

Figure 4: recovery time/buffering time-disturbance propagation duration
(——Recovery time; - - - - -Buffering time)

Scenario 4: T_D=3.5; Constant buffering time is set as 1 and faster recovery time as 0.5.

As Fig 3 shows, in a single device disturbance (prefractionator), longer buffering time or faster recovery may make the break-down resolved. In the case study, faster recovery is more efficient than longer buffering for intervening.

The quantitative relation between recovery time/buffering time and disturbance propagation duration of each effected subsystem node is shown in Fig 4. Each node's sensitivity to disturbance is various. The disturbance propagation duration remains constant when some time parameter of some node is changed, such as buffering time parameters of *node 4, 5, 6* and recovery time parameter of *node 5*. But faster recovery of *node 3, 4, 6* and longer buffering time of *node 3* accelerate the disturbance propagation.

4. Conclusions

Resilience engineering provides a new way to control incidents and limit their consequences. This study introduces a hierarchical fault propagation model (HFPM) as an extension of IRML, involving two parts: static analysis for system structure feature such as the interdependency between nodes; and dynamic analysis for fault evolution mechanism based on the fault scenario simulation. Due to the dynamic and highly nonlinear characteristics of petroleum refining system, the HFPM is applied in the case study, which can not only analyze structure features about the fault propagation, but also can capture quantitative fault propagation features in various fault modes and changeable working conditions.

Acknowledgements

The project is supported by the Natural Science Foundation of China (Grant No. 51104168), the Program for New Century Excellent Talents in University (NCET-12-0972) and Beijing Natural Science Foundation (3132027) and also Supported by Science Foundation of China University of Petroleum (No. YJRC-2013-35).

References

F. Belmonte, W. Schon, L. Heurley, R. Capel, 2011. Interdisciplinary safety analysis of complex socio-technological systems based on the functional resonance accident model: An application to railway traffic supervision. Reliability Engineering and System Safety, 96, 2, 237–249.

R. Filippini, A. Silva, 2014. A Modeling Framework for the Resilience Analysis of Networked Systems-of-Systems Based on Functional Dependencies. Reliability Engineering and System Safety, 125, 82–91.

H. Gabbar, S. Hussain, A. Hossein Hosseini, 2014. Simulation-Based Fault Propagation Analysis – Application on Hydrogen Production Plant. Process Safety and Environment Protection, 92, 6, 723–731.

J. Johansson, H. Hassel, 2010. An approach for modeling interdependent infrastructures in the context of vulnerability analysis. Reliability Engineering and System Safety, 95, 12, 1335–1344.

G. Kjølle, I. Utne, O. Gjerde, 2012. Risk analysis of critical infrastructures emphasizing electricity supply and interdependencies. Reliability Engineering and System Safety, 105, 80–89

I. Utne, P. Hokstad, J. Vatn, 2011. A method for risk modeling of interdependencies in critical infrastructures. Reliability Engineering and System Safety, 96, 6, 671–678.

Krist V. Gernaey, Jakob K. Huusom and Rafiqul Gani (Eds.), 12th International Symposium on Process Systems Engineering and 25th European Symposium on Computer Aided Process Engineering.
31 May – 4 June 2015, Copenhagen, Denmark

Risk Analysis Applied to Bioethanol Dehydration Processes: Azeotropic Distillation versus Extractive Distillation

Adriana Avilés-Martínez,[b] Nancy Medina-Herrera,[a] Arturo Jiménez-Gutiérrez,[a*] Medardo Serna-González[b] and Agustín Jaime Castro-Montoya[b]
[a]*Instituto Tecnológico de Celaya, Departamento de Ingeniería Química, Celaya, Gto., 38010, México*
[b]*Universidad Michoacana de san Nicolás de Hidalgo, Facultad de Ingeniería Química, Morelia, Mich., 58000, México*

Abstract

Production of anhydrous ethanol in large scale has been made by extractive distillation using solvents such as ethylene-glycol or glycerol. In this work, azeotropic distillation is studied to dehydrate bioethanol using n-octane as entrainer. We use a procedure to account for risk and safety, in addition to economic evaluations, in the process design. A probabilistic methodology is applied for the evaluation of a distance likely to cause death as a risk index. The safety assessment combines a frequency and consequence analysis to calculate process total risk. The approach is applied to the design of ethanol dehydration processes, for which azeotropic and extractive distillation systems are compared. The properties of the solvents affect the inherent process safety. The comparison between the two alternatives is done in terms of individual risk, CO_2 emissions and total annual cost. The results show that the azeotropic distillation using n-octane as entrainer presents lower total energy consumption and risk compared to the purification process with extractive distillation using ethylene glycol. The product of the proposed separation scheme is a dehydrated mixture of ethanol and n-octane with 81 % mol (61% vol) ethanol, which can be used to produce gasohol.

Keywords: Safety; Anhydrous ethanol; Azeotropic distillation; Bio-ethanol

1. Introduction

Anhydrous ethanol demand has been increasing in response to environmental policies that promote the use of gasohol. Thus, bio-refineries have gained significant interest. The bioethanol production process has three main steps: pre-treatment, fermentation, and purification. Purification steps have been investigated especially because most of the energy requirements are spent at this point of the process. Ethanol and water form an azeotrope, which makes dehydration process costly, and complex configurations are needed to achieve dehydrated ethanol for fuel use. The selection of an adequate dehydration configuration requires a multi-criteria approach.

Complex distillation systems have been tested for bioethanol dehydration (Luyben, 2013). Azeotropic and extractive distillations employ a separating agent to obtain anhydrous bioethanol. Both distillation schemes require the addition of an external component to the separation process, which implies additional risk and cost. Then, this added agent plays an important role in safety and economics of the dehydration process. In this work, we analyze azeotropic distillation and we compare the results with

extractive distillation in order to select a proper configuration and entrainer considering safety, CO_2 emissions and economics.

2. Methodology and case study

After the fermentation step, ethanol is highly diluted in water, among other components. The first step of the purification process is the concentration of ethanol close to the azeotrope composition using simple distillation. After pre-concentration, a dehydration process is needed, which is the focus of this work. Extractive distillation and azeotropic distillation processes are considered.

Heterogeneous azeotropic distillation is used when there is an immiscibility zone in the ternary diagram that can be used to attain the desired separation. Then, a decanter is used for the liquid-liquid separation. Figure 1 shows the proposed azeotropic distillation flowsheet, where C0 is the preconcentrator column, C1 is the azeotropic distillation column, C2 is the entrainer recovery column and T1 is a decanter.

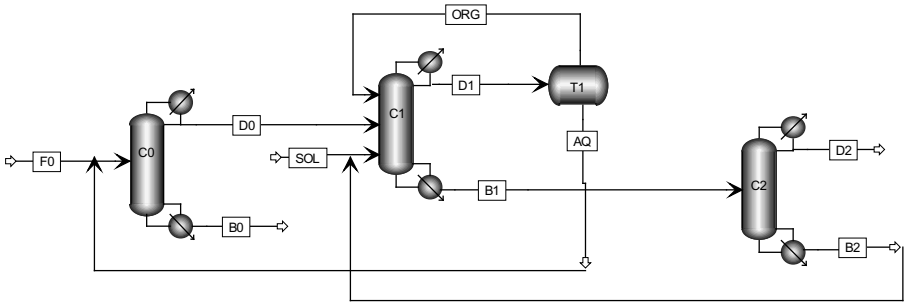

Figure 1. Azeotropic distillation flowsheet.

The dehydration processes are simulated using rigorous models with the ASPEN Plus process simulator. The feed stream for the azeotropic distillation process is 800 kmol/h with a composition of 90% mol water and 10% mol ethanol, which is a typical yield from fermentation of first generation raw materials for biofuels. UNIFAC was used as the thermodynamic model for the vapor-liquid and the liquid-liquid equilibrium. The conventional column C0 was initially designed using the Winn-Underwood-Gilliland method (DSTWU model) and manipulating the reflux ratio until a composition of about 80% mol ethanol was reached. Then, the RadFrac model was used to simulate C0 and C1. The initial design for C1 is assumed to recover the ethanol in F0, and initial guesses are needed for the composition of the organic phase recycle, which is a ternary mixture; the degrees of freedom (number of stages, reflux ratio, solvent to feed ratio, feed stages) are varied one by one aiming to minimize the energy requirements and to separate all of the water in the distillate stream. After the parameters for C1 were determined, C2 was designed applying first the DSTWU model to concentrate the ethanol-n-octane mixture to a composition near the binary azeotrope, and then the three columns with recycles were simulated with RadFrac. Once the simulation is done, risk, CO2 emissions and economic evaluations are carried out.

The methodology proposed by Medina-Herrera et al. (2014) is used to evaluate risk. This probabilistic methodology combines a frequency and consequence analysis to calculate risk. A distance likely to cause death is used as a risk index. The total annual

cost (TAC) is estimated using the Aspen Cost Estimator. A depreciation factor of 0.2 for equipment cost annualization was assumed. The utilities considered are saturated steam at $4.1x10^5$ N/m^2 ($4.7/10^6$ USD / KJ) and water with a cooling cost of 33.44 KJ/Kg (0.0251$/t). The carbon dioxide emission is reported considering the CO_2 emission factor data source US-EPA-Rule-E9 5711. The analysis provides an understanding of safety, environmental and economics behavior. This configuration is then compared with extractive distillation.

Gasohol is a mixture of gasoline and ethanol, which is used as a substitute for pure gasoline. The focus of this work is the dehydration of ethanol for its potential use in the production of gasohol. The main compound of gasoline is octane. Therefore we use n-octane as an entrainer for the azeotropic configuration. The challenge found in this ternary system (see Figure 2) is that n-octane forms azeotropes with water and ethanol. Three binary azeotropes and one ternary heterogeneous azeotrope provide three distillation regions. Therefore, if the mixture to separate is located on the upper left side of the triangle, below the azeotrope ethanol-water (D0), there are two possible regions to explore in order to get dehydrated ethanol. Operating in the top region enables the total purification of ethanol, with the disadvantage that recycle streams with high ethanol composition and relatively high flow rates are required to achieve the purification. On the other hand, operating in the right distillation region presents lower flow rates and thus low energy requirements. Even though the product is not pure ethanol, it is a dehydrated mixture of ethanol and n-octane, which can then be used for gasohol production.

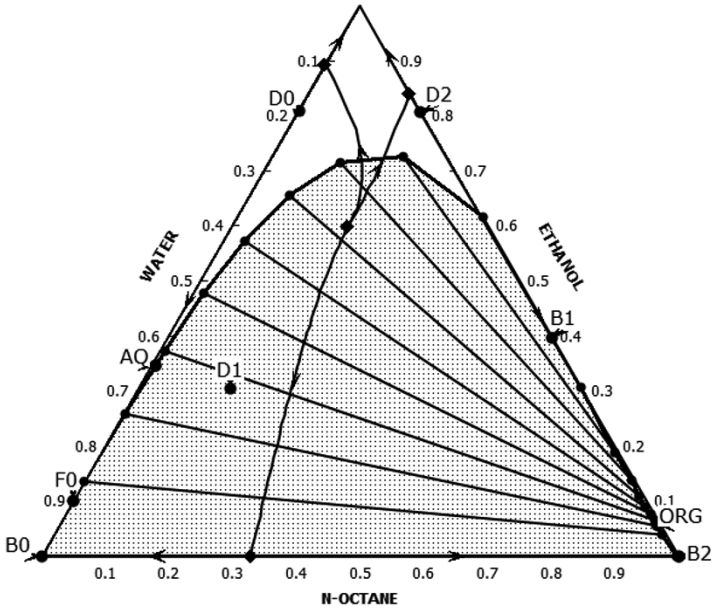

Figure 2. Ternary diagram with stream compositions (mol basis), obtained with the UNIFAC model at 1 atm.

3. Results and Discussion

The stream from the fermentation step enters the column C0 (see Figures 1 and 2) to concentrate the diluted mixture to a composition near the azeotrope composition (D0). The distillate stream is the feed to the azeotropic column C1, where the dehydration step

takes place and the top product (D1), containing mostly water, is located in the immiscibility zone of the ethanol-water-n-octane system. The product is condensed and sent to a liquid-liquid separator to obtain an n-octane rich phase (ORG) that is recirculated to the azeotropic column. The aqueous phase is recycled to the column C0 because it still contains ethanol. The bottom C1 product is an n-octane-ethanol mixture that enters the column C2 to recover the entrainer and obtain the final product, an ethanol-n-octane mixture (B2). The results of the design for the columns and mass flows are presented in Tables 1 and 2.

Table 1. Design parameters of columns for the azeotropic distillation scheme

	C0	C1	C2
Number of stages	40	28	12
Feed stages	F0-20 A-21	D0-10 SOL-2 ORG-3	B1-6
Design Pressure (N/m^2)	101,325	101,325	101,325
Reflux ratio	2	3	0.0002
Heat duty (kw)	4,906.00	1,457.65	1,418.00

Table 2. Mass flowrates for streams

Flows (kg/s)	Ethanol	Water	n-octane	T (*K*)
F0	1.02376	3.60306	-	303.15
D0	1.17127	0.107584	0.00572393	351.15
B0	-	3.60306	-	373.15
SOL	-	-	0.60284	303.15
D1	0.151802	0.107712	0.17818	343.15
B1	1.02376	-	3.85052	350.15
ORG	0.004286	0.000128	0.172461	343.15
AQ	0.147516	0.107584	0.005724	343.15
D2	1.02376	-	0.60284	350.15
B2	-	-	3.24768	399.15

For risk calculations, five catastrophic scenarios are considered. There are two types of mass releases, instantaneous and continuous. In the case of an instantaneous release, the outcomes are boiling liquid expanding vapour explosion (BLEVE), unconfined vapour cloud explosion (UVCE), and flash fire due to instantaneous release (FFI). The other two scenarios correspond to a continuous release, jet fire and flash fire due to continuous release (FFC). The calculations were carried out considering only n-octane within the process. The estimated total distance likely to cause death (DD) was 0.1446371 m/y, which represents the total individual risk of the process considering the extractive and recovery columns. The corresponding risk of the five events can be seen in Figure 3 for columns C1 and C2.

Table 3 shows the distances of impact obtained for all events. Although BLEVE scenarios have the greatest distances, we can see in Figure 3 that flash fire due to a continuous release represents the worst-case scenario for both columns. This is because FFC has a higher probability of occurrence. The probability of occurrence for FFC is 2.48×10^{-4}/y in contrast to the BLEVE probability of occurrence of 5.75×10^{-6}/y, a difference of two orders of magnitude.

As mentioned above, the approach is based on a multi-criteria analysis. Therefore, Table 4 shows the cost of dehydrating the product, with a flow of 800 kmol/h and a composition of 90% mol water. The total purification cost is 0.0752 US$/kg ethanol. Carbon dioxide emissions were estimated assuming crude oil as fuel. The value reported in Table 4 shows CO_2 emissions of 0.007639 Kg/s per kmol of ethanol dehydrated.

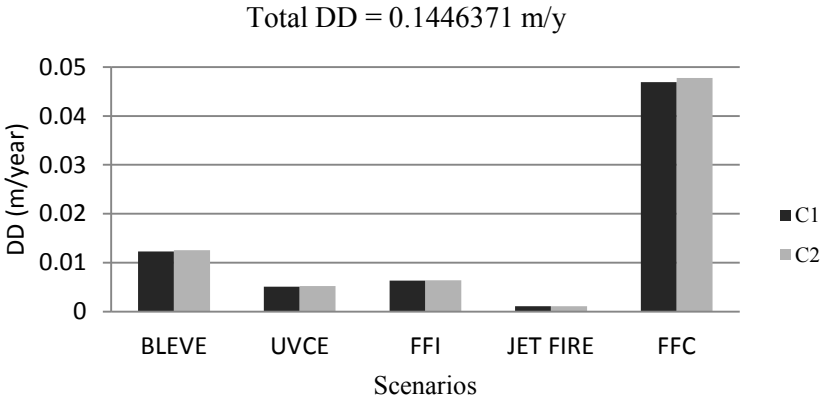

Figure 3. Total distance likely to cause death for the azeotropic distillation scheme.

Table 3. Fatal distances for the different events

	Di (m) C1	Di (m) C2
BLEVE	2136.08	2182.66
UVCE	657.10	667.99
FF INS.	812.00	826.34
JET FIRE	29.06	29.05
FF CONT	189.46	192.72

Table 4. Azeotropic distillation scheme costs for an 80 kmol/h ethanol production

Cost Analysis Result	(USD / year)
Equipment	1,116,920.00
Utilities	1,309,450.00
Total Annual Cost	2,426,370.00
CO_2 Emissions	2200 Kg/hr

In order to compare the results with the extractive distillation process to dehydrate bioethanol, we considered the works reported by Avilés-Martinez et al. (2012) and Medina-Herrera et al. (2014), in which extractive distillation was used to obtain anhydrous bioethanol. Using the same ethanol production rate as in this work, Medina-Herrera et al. (2014) minimized the total individual risk in the extractive column and in the ethylene-glycol recovery column, and reported a distance likely to cause death of 0.2052 m/y, which is higher than the result obtained here of 0.1446 m/y. In the work by Avilés-Martinez et al. (2012), glycerol was considered as entrainer. Based on the design parameters reported in their work, we simulated their extractive distillation process for the diluted water-ethanol mixture considered here. The results include a higher TAC of 3,148,340 US$/y, equivalent to 0.0996 US$/kg ethanol, and a total heat duty of 0.010931 GJ/kg-ethanol. The CO_2 emissions were estimated at 3096.23 kg/h, equivalent to 0.011 Kg/s for every kmol of ethanol purified. Figure 4 summarizes the results obtained for the economic, safety, energy and environmental terms analyzed for the

separation schemes; it can be observed that all of these factors favor the use of azeotropic distillation over extractive distillation for the case study considered here.

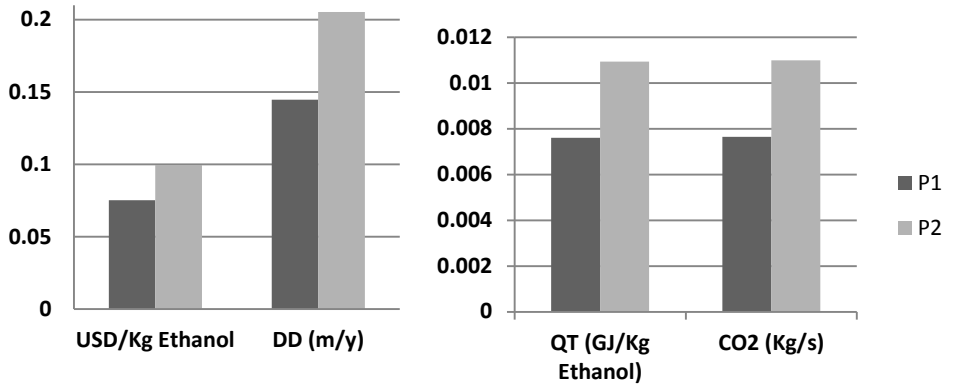

Figure 4. Comparison of total cost, total distances likely to cause death, energy requirements and CO_2 emissions for the azeotropic (P1) and extractive distillation (P2) processes.

4. Conclusions

Two alternatives for the ethanol dehydration process have been considered. The results for the azeotropic distillation option suggest that n-octane is a promising entrainer. Although the product is not highly purified ethanol, the product blend of ethanol and n-octane is dehydrated (with composition near the binary azeotrope of 84% mol of ethanol), which can then be mixed directly with gasoline to produce gasohol. The comparison between extractive and heterogeneous azeotropic distillation has shown that the latter is a promising alternative to the conventional extractive distillation scheme in terms of both safety and economics. Both processes, however, are suitable for dehydration of ethanol because the energy requirements are lower than the ethanol heat of combustion.

References

A. Avilés-Martínez, J. Saucedo-Luna, J.G. Segovia-Hernández, S. Hernández, F.I. Gómez-Castro, A.J. Castro-Montoya, 2012, Dehydration of bioethanol by hybrid process liquid-liquid extraction/extractive distillation, Ind. Eng. Chem. Res., 51, 5847-5855.

W.L. Luyben, 2013, Comparison of extractive distillation and pressure-swing distillation for acetone/chloroform separation. Comput. Chem. Eng., 50, 1-7.

N. Medina-Herrera, I.E. Grossmann, M.S. Mannan, A. Jiménez-Gutiérrez, 2014, An approach for solvent selection in extractive distillation systems including safety considerations, Ind. Eng. Chem. Res., 53, 12023-12031.

12TH INTERNATIONAL SYMPOSIUM ON PROCESS SYSTEMS ENGINEERING AND 25TH EUROPEAN SYMPOSIUM ON COMPUTER AIDED PROCESS ENGINEERING

PART C

Edited by
KRIST V. GERNAEY
JAKOB K. HUUSOM
RAFIQUL GANI

COMPUTER-AIDED CHEMICAL ENGINEERING, 37

12TH INTERNATIONAL SYMPOSIUM ON PROCESS SYSTEMS ENGINEERING

&

25TH EUROPEAN SYMPOSIUM ON COMPUTER AIDED PROCESS ENGINEERING

This page intentionally left blank

COMPUTER-AIDED CHEMICAL ENGINEERING, 37

12TH INTERNATIONAL SYMPOSIUM ON PROCESS SYSTEMS ENGINEERING AND 25TH EUROPEAN SYMPOSIUM ON COMPUTER AIDED PROCESS ENGINEERING

PART C

Edited by

Krist V. Gernaey, Jakob K. Huusom and Rafiqul Gani

Department of Chemical and Biochemical Engineering
Technical University of Denmark
DK-2800 Lyngby, Denmark

Amsterdam – Boston – Heidelberg – London – New York – Oxford
Paris – San Diego – San Francisco – Singapore – Sydney – Tokyo

Elsevier
Radarweg 29, PO Box 211, 1000 AE Amsterdam, The Netherlands
The Boulevard, Langford Lane, Kidlington, Oxford OX5 1B, UK

British Library Cataloguing in Publication Data
A catalogue record for this book is available from the British Library

Library of Congress Cataloging-in-Publication Data
A catalog record for this book is available from the Library of Congress

ISBN (Part C): 978-0-444-63576-1
ISBN (Set): 978-0-444-63429-0
ISSN: 1570-7946

Printed and bound in Great Britain

14 15 16 17 10 9 8 7 6 5 4 3 2 1

Contents

Contributed Papers
T-7: Plant Operations, Integration, Planning /Scheduling and Supply Chain

Krist V. Gernaey, Jakob K. Huusom and Rafiqul Gani (Eds.), 12th International Symposium on Process Systems Engineering and 25th European Symposium on Computer Aided Process Engineering.
31 May – 4 June 2015, Copenhagen, Denmark

Supply chain design and planning accounting for the Triple Bottom Line

Bruna Mota[a*], Maria Isabel Gomes[b], Ana Carvalho[a], Ana Barbosa-Póvoa[a]

[a]*CEG-IST, University of Lisbon, Av. Rovisco Pais, 1049-001 Lisboa, Portugal*
[b]*CMA-FCT, Nova Universtity of Lisbon, Monte de Caparica, 2829-516 Caparica, Portugal*
bruna.mota@tecnico.ulisboa.pt

Abstract

In this work, a multi-objective mixed integer linear programming (moMILP) model is presented for the design and planning of sustainable closed loop supply chains. It includes strategic decisions such as facility location, definition of transportation modes, technology selection and allocation, as well as tactical decisions. The model includes four objectives: 1) The economic pillar, measured through the net present value (NPV); 2) the environmental pillar, which includes Life Cycle Assessment (LCA), through the application of the ReCiPe methodology; 3 and 4) The social pillar measured using two socio-economic indicators applied by the European Union in its Sustainable Development Strategy. The applicability of the model is demonstrated through a representative supply chain case study. Results show that the different objectives influence the supply chain structure and translate in significantly different and conflicting decisions, showing the importance of such type of models to better understand the decisions implications on the different dimensions of sustainability.

Keywords: sustainable supply chain, environmental impact, socio-economic indicators

1. Introduction

The growing pressure from both customers and governments towards sustainable development is redirecting strategies focused on profit to strategies that account for the triple bottom line, where profit, planet and people are considered (Bojarski et al., 2009). However, the complexity inherent to the integration of such decisions has been delaying the growth in both research and implementation of sustainable development practices. A number of different and interdependent factors are involved and have an impact on the economic, environmental and social performances of the supply chains, resulting in highly complex models. Facility location decisions for instance directly influence the costs and environmental impact of transportation, which is often the activity responsible for the major share of both costs and environmental impact within supply chains. However, these decisions also have an impact on the community where facilities are located. Decisions such as transportation policy also have an impact on the three pillars of sustainability. Depending on the transportation mode selected, costs may be higher but compensated by a lower environmental impact or additional job creation. There is also the possibility of selecting either unimodal transportation, in which a single transportation mode is used to distribute the product to its final destination, or intermodal transportation, where the product is carried by a combination of at least two transport modes (e.g. road, rail, sea, air). Another decision variable of significant impact is the technology selection as different technologies might have different operating costs, may use different quantities of raw materials or even different raw materials,

which may result in different environmental impacts, and may require a different workforce. Closing the loop by recovering end-of-life products opens an even more complex path that needs to be carefully designed and planned so as to actually translate a more sustainable supply chain. In addition is the difficulty in quantitatively measuring environmental and social impacts, where a significant research gap is found (Mota et al., 2014). Hence, decision support tools that adequately address such complex problems, both at a strategic and tactical level, are required to help companies adjust to these current and growing sustainability pressures. This work aims to be a step forward in this direction by presenting a model for the design and planning of closed loop supply chains, which introduces the discussed decision variables and incorporates the three pillars of sustainability.

2. Problem definition and mathematical formulation

The proposed model aims at determining the supply chain structure, transportation network, and technology allocation, along with planning decisions (supply and product recovery) that maximize profit, minimize environmental impact and maximize the social benefit of a closed loop supply chain. The modelled supply chain structure is the one depicted in Figure 1, which shows a four-echelon structure where suppliers send the raw materials to the factories, the factories transform them into final products and then send these products to other factories, to distribution centres or directly to the clients. End-of-life products are then recovered at the clients and can be sent back to the distribution centres or directly to the factories. Transhipment is also allowed between distribution centres. In the factories the end-of-life products are remanufactured and sold as final products. Transportation between all facilities can be performed using only one transportation mode (unimodal transportation) or using intermodal transportation. In this latter case a new entity is installed, a hub terminal, where the transfer of cargo from one transportation mode to the other is performed.

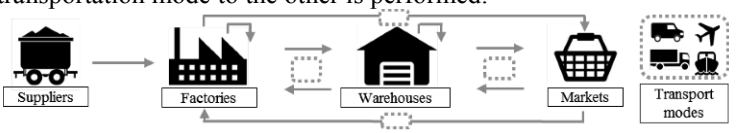

Figure 1. Modelled supply chain structure.

The problem is modelled through a moMILP formulation, evolving from the work presented by Mota et al. (2013, 2014) in three ways. Firstly it moves from a 3-echelon to a 4-echelon structure that includes suppliers. Secondly it incorporates technology selection and allocation decisions as well as transportation network definition, to which an intermodal transportation option is added. Thirdly the social impact indicator is redesigned to consider Gross Domestic Product (GDP) and unemployment rate as socio-economic indicators. The economic objective function is obtained from the maximization of the NPV as described in Cardoso et al. (2013). The net earnings (*NEt*) are given by the difference between the incomes, defined by the amount of products sold, and the costs per time period (Eq. (1)). The costs include:

- raw material costs (first term, where X_{maijt} is the flow of product *m* through transportation mode *a* between entities *i* and *j* in time period *t*);
- production costs (second term, where Ψ_{mgit} is the amount of product *m* produced through technology *g* in entity *i* in time period *t*);
- product recovery (third term) and remanufacturing costs (fourth term, where Φ_{mgit} is the amount of product *m* remanufactured through technology *g* in entity *i* in time period *t*);

- transportation costs for air (fifth term) and for road transportation (sixth term, where Q_{aijt} is the number of trips with transportation mode *a* between entities *i* and *j* in time period *t*), and handling costs at the hub terminal (seventh term);
- inventory costs (eighth term, where S_{mit} is the inventory of product *m* in entity *i* in time period *t*; and
- labour costs at entities (ninth term, where Y_i is a binary variable for entity installation in location *i*), at production and remanufacturing technologies (tenth term, where Z_{gmi} is a binary variable for technology allocation) and at transportation (eleventh term, where K_{aij} is a binary variable for transportation link establishment).

The last term describes the depreciation of the capital invested (*DPt*) with *tr* being the tax rate.

$$
\begin{aligned}
NE_t = (1-tr)\Bigg[& \sum_{m,i,j:(m,i,j)\in F_{INCFP}} psu_m \sum_a X_{maijt} \\
& - \Bigg(\sum_{m,i,j:(m,i,j)\in F_{OUTSUPRM}} rmc_m \sum_{a\in A} X_{maijt} \\
& + \sum_{m,g,i:(m,g)\in G_{PROD}\wedge i\in I_f} opc_g \Psi_{mgit} \\
& + \sum_{m,i,j:(m,i,j)\in F_{OUTCRP}} rpc_m \sum_{a\in A} X_{maijt} \\
& + \sum_{m,g,i:(m,g)\in G_{REM}\wedge i\in I_f} opc_g \Phi_{mgit} \\
& + \sum_{a,m,i,j:(a,m,i,j)\in NetP\wedge a\in A_{plane}} tc_a . pw_m . d_{ij} . X_{maijt} \\
& + \sum_{a,m,i,j:(a,m,i,j)\in NetP\wedge a\in A_{truck}} vtc_a . d_{ij} . Q_{aijt} \\
& + \sum_{a,m,i,j:(a,m,i,j)\in NetP\wedge a\in A_{plane}} hhc . X_{maijt} + \sum_{m,i:(m,i)\in V} sc_m . S_{mit} \\
& + \sum_{i\in I_f \cup I_w \cup I_{air}} w_i . lc_i . mwh . Y_i \\
& + \sum_{m,g,i:(m,g)\in G_{PROD}\cup G_{REM}} w_g . lc_i . mwh . \mathrm{Z}_{gmi} \\
& + \sum_{a,i,j:(a,i,j)\in Net} w_{aij} . lc_i . mwh . K_{aij} \Bigg) \Bigg] + tr . DP_t
\end{aligned}
\tag{1}
$$

The fixed capital investment (FCI) is defined in Eq. (2) and is given by the investment in facilities (first and last term), investment in production and remanufacturing technologies (second term) and investment in transportation links (third term).

$$FCI = \sum_{i \in I_f \cup I_w} ec_i . Y_i + \sum_{m,g,i:(m,g) \in G_{PROD} \cup G_{REM} \wedge I_f} tec_g . \mathrm{Z}_{gmi} + \sum_{a,i,j:a \in A_{truck} \wedge (a,i,j) \in Net} ftc_a . \frac{\mathrm{K}_{aij}}{2} + \sum_{i \in I_{air}} hub_i \, Y_i \quad (2)$$

The environmental objective function is modelled using the ReCiPe methodology as described in Mota et al. (2014). For each midpoint category c the environmental impact of production (first term), transportation (second term) and entity installation (third term) is determined, summed and normalized as shown in Eq. (3).

$$\min EnvImpact = \sum_{c} (\sum_{t \in T} \sum_{m,g,i:(m,g) \in G_{PROD} \cup G_{REM} \wedge I_f} I_{mgc} (\Psi_{mgit} + \Phi_{mgit}) + \sum_{t \in T} \sum_{a,m,i,j:(a,m,i,j) \in NetP} I_{ac} pw_m d_{ij} X_{maijt} + \sum_{i \in I_f \cup I_w} I_{ic} a_i Y_i) \eta_c \quad (3)$$

The social objective function is designed taking into account socio-economic indicators applied by the European Union to its Sustainable Development Strategy, namely GDP and the unemployment rate of each country. These two indicators are applied through μ_i, a regional factor. Hence, two social objective functions are in fact given. One where μ_i results from GDP statistics and the other where the regional factor results from unemployment rate statistics. In this way the models prefers the location of entities (first term), the allocation of technologies (second term) and the establishment of transportation links (third term) in regions of higher unemployment rate or of lower GDP, according to the selected regional factor. Additionally these social objective functions are designed to balance these regional indicators with the maximization of the number of jobs created ($w_i / w_g / w_{aij}$), as shown in Eq. (4).

$$\min SocialAssess = \sum_{i \in I_f \cup I_w \cup I_{air}} \mu_i \frac{Y_i}{w_i} + \sum_{m,g,i:(m,g) \in G_{PROD} \cup G_{REM} \wedge i \in I_f} \mu_i \frac{Z_{gmi}}{w_g} + \sum_{a,i,j:(a,i,j) \in Net} \mu_i \frac{K_{aij}}{w_{aij}} \quad (4)$$

The constraints account for the mass balances, supply capacity, flows of products at entities, inventory levels, production, remanufacturing and transportation capacities.

3. Case-study

The model was applied to a European case-study where decisions regarding facility location, technology selection and allocation, product recovery and transportation modes/network establishment are to be taken, so as to satisfy the demand. Model inputs include:

- Entities: The suppliers location is set in the United Kingdom and Italy, the same two possible locations are available for factories. Seven possible locations exist for warehouses: United Kingdom (UK), Italy (IT), Spain (ES), Germany (DE), Portugal (PT), Hungary (HU) and Bulgaria (BG). All locations are characterized in terms of their socio-economic indicators: GDP and Unemployment rate.

- Markets: The target markets are located in Portugal, Spain, Italy, the United Kingdom and Germany, as shown in Figure 2.
- Products and technologies: Two final products are modelled. Each can be obtained through production or remanufacturing. For product 1 (P1) there are two alternative production technologies and one for remanufacturing. For product 2 (P2) there is one production and one remanufacturing technologies. All technologies are characterized in terms of cost, capacity, environmental impact and workers.
- Product recovery: a minimum product recovery of end-of-life products is imposed per time period.
- Transportation: There are three transportation modes available, two types of trucks and one by airplane. All modes are characterized by different costs, capacities, environmental impact and number of workers. Three airports for intermodal transportation can be used, one in France, one in Spain and one in Belgium. In case a hub terminal is installed, it is also characterized in terms of economic, environmental and social performance.

Figure 2. Superstructure considered for the case-study.

4. Results and discussion

Table 1 summarizes results obtained when considering different sustainability pillars.

Table 1. Summary of results considering the different sustainability pillars.

	Sustainability pillar			
	Economic	**Environmental**	**Social (GDP)**	**Social (Unemployment)**
Entity location	Factories: UK, IT Warehouses: HU, BG	Factories: UK, IT Warehouses: UK, PT	Factories: UK, IT Warehouses: HU, BG	Factories: UK, IT Warehouses: ES, PT
Technology selection and allocation	Only one production technology for product 1	Only one production technology for product 1	Combination of both production technologies for product 1	Combination of both production technologies for product 1
Product recovery and remanufacturing	Minimum imposed	Maximum allowed	In-between limits	In-between limits
Transportation network	Unimodal + Combination of two types of trucks	Intermodal with three airports + Combination of two types of trucks	Unimodal + Combination of two types of trucks	Unimodal + Combination of two types of trucks

When maximizing profit the model installs two factories in the UK and Italy, and two warehouses in Hungary and Bulgaria. This solution minimizes the costs with human resources, which is the largest contributor to this supply chain total cost, by selecting the countries with the lowest hourly labour costs and reducing the number of established transportation links. This implies increasing the number of trips and the labour intensity for truck drivers (even though a maximum is respected). The technology chosen for production of P1 is the one that even though having higher installation costs, has a higher production capacity and lower operating costs. Product recovery is minimized since it is less expensive to produce from raw materials than from recovered products.

Unimodal transportation is selected and a combination of the two types of trucks is used, according to the corresponding capacities.
When minimizing environmental impact the same factories as before are installed but the two warehouses are now installed in the UK and in Portugal. Product recovery and remanufacturing are maximized since the environmental impact of remanufacturing is lower than that of production, even with the necessary increase in transportation. Intermodal transportation is implemented in this case with all the three available airports given the lower environmental impact of air transport. These options translate in a 40% profit reduction.
When optimizing for social performance the structure obtained considering GDP is different from the one obtained considering unemployment rate. In the first case the structure is identical to the one obtained for profit maximization since the countries are the ones with the lowest GDP. In the latter case the warehouses are opened in Spain and Portugal, the countries with the highest unemployment rate, contributing to the decrease in profit by 50%. However, in both cases a combination of both production technologies is used for P1, product recovery is between the imposed limits and unimodal transportation is preferred. A smaller number of workers is obtained in either of these solutions when compared to the number of workers obtained when minimizing environmental impact. This indicates that these social indicators attribute a higher importance to the regional factor than to the number of jobs created. Does more social benefit arise from the creation of jobs in socio-economically challenged regions or from the maximization of job creation throughout the supply chain? This type of questions evidence the importance of such models to better understand the implications of the decisions on different dimensions of sustainability.

5. Conclusions and future work

The presented work proposes a decision support tool to study how sustainability can be introduced in supply chain design and planning. The model allows to understand the impact of decisions such as facility location, technology selection and allocation, and transportation modes choices, on the three pillars of sustainability. Through the model application to a European case-study results show how the different indicators return conflicting solutions. Future work will include the determination of the Pareto front through the augmented ε-constraint method, allowing to address the trade-offs inherent to these conflicting objectives. Further case-studies will also contribute to a better understanding of the implications of the proposed environmental and social indicators.

References

A. Bojarski, J. Laínez, A. Espuña and L. Puigjaner, 2009, Incorporating environmental impacts and regulations in a holistic supply chains modeling: An LCA approach, Computers & Chemical Engineering, 33, 10, 1747-1759

B. Mota, M. I. Gomes, A. Carvalho and A. P. Barbosa-Povoa, 2013, Towards supply chain sustainability: balancing costs with environmental and social impacts. In Computer Aided Process Engineering, 895-900. Elsevier, 2013.

B. Mota, M. I. Gomes, A. Carvalho and A. P. Barbosa-Povoa, 2014, Towards supply chain sustainability: economic, environmental and social design and planning, Journal of Cleaner Production, http://dx.doi.org/10.1016/j.jclepro.2014.07.052

S. Cardoso, A. P. Barbosa-Póvoa and S. Relvas, 2013, Design and planning of supply chains with integration of reverse logistics activities under demand uncertainty, European Journal of Operational Research, 226, 3, 436-451

KristV.Gernaey, JakobK.Huusom and RafiqulGani (Eds.), 12th International Symposium on Process Systems Engineering and 25th European Symposium on Computer Aided Process Engineering.
31 May – 4 June 2015, Copenhagen, Denmark

Planning of a multiproduct pipeline integrating blending and distribution

Diovanina Dimas[a*], Valéria V. Murata[a], Sérgio M. S. Neiro[a], Susana Relvas[b] and Ana Paula Barbosa-Póvoa[b]

[a] *Programa de Pós-Graduação em Engenharia Química (PPGEQ), Universidade Federal de Uberlândia (UFU), Avenida João Naves de Ávila, 2121, 38408-100, Uberlândia, Minas Gerais, Brasil*
[b] *Centro de Estudos de Gestão do Instituto Superior Técnico (CEG-IST), Universidade de Lisboa (UL), Avenida Rovisco Pais 1049-001, Lisboa, Portugal*
diovaninadimas@yahoo.com.br

Abstract

Pipelines play an important role in the oil supply chain linking different supply chain echelons and acting as one of the most sustainable, safe economical transportation mode. In this context, multiproduct pipeline scheduling is a key issue to be addressed in an optimized form, namely when integrating pipeline operation with the operations of the connected entities. In this paper a MILP discrete time formulation is developed for multiproduct distribution scheduling linking both sides of the pipeline, refinery and distribution centre, so as to generate the best product pumping sequence accounting for material availability at the refinery blending process and delivery needs at the distribution centre. The model was applied to a case based on a real world oil supply chain.

Keywords: oil industry, scheduling, multiproduct pipeline, activities integration, MILP.

1. Introduction

Typically, downstream distribution in the oil industry can be accomplished via road, railway and pipelines. Pipelines are widely used since they may connect several refineries, depots and terminals transporting crude oil as well as final products in large quantities for long distances in a more sustainable form. The pipeline operator must decide what products and what quantities should be pumped, operational timing range, and how to distribute all products among several destinations (Rejowski and Pinto, 2008). Additionally, this problem often presents some restrictive requirements associated with the pipeline operational conditions such as reverse operation, pumping rate limits, inventory levels, interfaces and lot sizes. All these aspects taken simultaneously make this operation quite complex and decision support tools to help the solution of such complexity are required. Therefore, according to MirHassani, Abbasi and Moradi (2013), distribution scheduling arises as a modeling tool that should be able to determine the transport details and the best way to fulfill several demands at the right time.

Several works may be found in the literature addressing pipeline scheduling integrated with either up or downstream operations. Rejowski and Pinto (2004) presented a discrete MILP problem composed by a refinery, pipeline and depots considering

intermittent pumping time and logical constraints, adding a set of integer cuts and special interface constraint that resulted in better solutions. The same problem was later improved by the same authors (Rejowski and Pinto, 2008) to develop a MINLP continuous time formulation with pumping cost dependent on booster stations yield rate. Magatão et al. (2012) developed a hierarchical decomposition to solve a planning and assignment\sequencing pipeline network model composed by refineries, harbors, depots and clients applied to a real scenario. More recently, Ghaffari-Hadigheh and Mostafaei (2014) proposed a model which provides input and output pipeline sequences to satisfy different terminals simultaneously with minimum operating costs.

Pipeline scheduling alone has derived over the last years an intense field for publication, consisting in a complex scheduling problem. These complexities are related with the need to model time and volume decisions efficiently and additionally build flexible models aiming to address multiple i) topologies, ii) products iii) operational and cost issues so as to represent any pipeline-based system. Recent works on the area include the work of Cafaro et al. (2015), where pumping costs are detailed, MirHassani and BeheshtiAsl (2013), who use heuristic procedures as solution method for pipeline scheduling and Relvas et al. (2013) where inventory management at destination depots is tackled along with pipeline scheduling.

From the literature review it can be seen that the integration of pipeline scheduling with operations in input and output entities is not widely studied, given the complexity of integrating the pipeline scheduling problem with additional decisions in different echelons. The purpose of this work is to address this problem and to integrate information on product availability at both sides of the multiproduct pipeline (blending and distribution centre) so as to produce an optimal product sequence with minimum operational costs while guaranteeing service levels. The inventory management at the blending and distribution centre is integrated with the pipeline pumping sequence.

2. Problem description

The system considers a single unidirectional multiproduct pipeline that connects a product tank farm at the refinery, blending section, and a distribution centre that has to satisfy the local market, as illustrated in Figure 1. Three different products (gasoline, diesel and jet fuel) are produced and stored at the refinery and transported through a multiproduct pipeline to a distribution centre and to storage tanks with fixed service. When a batch of product arrives at the distribution centre a settling period is required due to regulatory quality assessments.

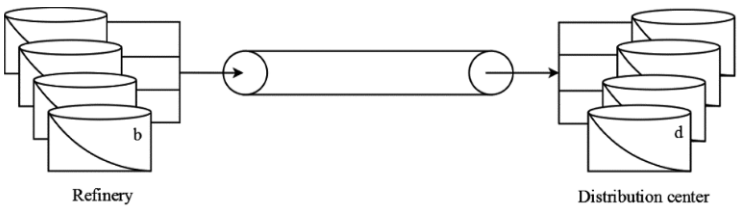

Figure 1 - Schematic system.

Given:

- The scheduling horizon;
- The inventory limits (minimum/maximum storage capacities);
- Initial volume available at each tank and pipeline;
- The feeding flow rate from the refinery blending;
- The pipeline volumetric capacity and batch size limits;
- The minimum settling period;
- The matrix of possible/forbidden products sequence;
- The daily demand;

The goal is to determine the products sequence pumped into the pipeline, which satisfy the demand while controlling the inventory tanks at the refinery blending centre and distribution centre.

3. The mathematical formulation

A discrete time Mixed Integer Linear Programming (MILP) model is formulated which is an extension of the previous work developed by Relvas et al. (2013). This extension links the previous developed model to the blending tank farm where inventory management is also performed. The main assumptions for this problem are:

1. There is a set of dedicated tanks teach product at refinery and distribution centre;
2. A tank at the refinery is not allowed to load and unload simultaneously;
3. The pipeline should be full at any time;
4. At most one tank can be connected to the pipeline at any time;
5. Changeovers time from one tank to another are disregarded;
6. Not all products sequences are allowed in the pipeline;
7. Settling periods are accounted for at the destination depot, making unavailable the settling product for dispatching to local market;
8. The flowrate is assumed to be variable within an acceptable operational range.

This operation is controlled by several constraints that are summarized as follows:

1) Material balance –to determine that the amount of products available in each tank;
2) Timing – to define the initial and final pumping and receiving time of each batch;
3) Inventory control – the minimum and maximum storage tanks limits;
4) Operating rules –referred to allocation constraints;
5) Forbidden sequences – the contact between some products inside the pipeline is prohibited;
6) Demand – to satisfy the local market demand values on time;
7) Batch limits – the volumes pumped should be bounded by the pipeline capacity;
8) Initial conditions –inform on the initial products at each tank and inside the pipeline;

Due to space limitations, we will only present the timing constraints and the objective function. Timing constraints are responsible for connecting the blending to the distribution centre, given the pipeline operation, using a reduced amount of problem information.

3.1 Timing constraints

These constraints are used to synchronize the operations between refinery, pipeline and distribution centre since these operations are continuous. Then, when a tank b start to feed a pipeline with product p simultaneously a tank d begins to receive a product already pumped at previous time. In this way, at the distribution centre the receiving time for batch i (TDS_i) is determined based on the previous receiving time plus the time required to unload the product from the pipeline, as expressed in constraint (1).Similarly, at the refinery the pumping time for batch i (TBS_i) depends on the

transportation time to the distribution centre and the receiving time at the distribution centre, as shown in constraint (2). Both timings are calculated within an interval given by minimum and maximum pipeline flow rate.

$$TDS_{i-1} + \left(\frac{1}{v_{max}}\right) * \sum_{d \in D_p} \sum_{p} \sum_{k} W_{d,i,p,k} \leq TDS_i \leq TDS_{i-1} + \left(\frac{1}{v_{min}}\right) * \sum_{d \in D_p} \sum_{p} \sum_{k} W_{d,i,p,k} \quad \forall\, i \tag{1}$$

$$\frac{pipe}{v_{max}} * \sum_{b \in B_p} \sum_{p} \sum_{k} XR_{b,i,p,k} - TDS_i \leq TBS_i \leq \frac{pipe}{v_{min}} * \sum_{b \in B_p} \sum_{p} \sum_{k} XR_{b,i,p,k} - TDS_i \quad \forall\, i \tag{2}$$

Where v_{min}/v_{max} are the minimum/maximum pipeline flowrate, *pipe* is the pipeline volume, $W_{d,i,p,k}$ is the volume of batch *i* with product *p* received in tank *d* at time *k* and $XR_{b,i,p,k}$ a binary variable that indicates if a batch *i* with product *p* is unloading from tank *b* to pipeline at time *k*.

3.2 Objective Function

The objective function is based in operational indicators and is composed by four terms. The first one corresponds to the difference between the total amount received at the distribution center and the total demand. The second term is used to maximize the pipeline usage so as to avoid stoppages/idle times. The third and last terms represent the lowest inventory level at refinery blending and distribution centre, respectively.

$$\min \; w_1 * \frac{dif}{\sum_p \sum_k Dem_{p,k}} - w_2 * \frac{TDS_{|I|}}{h^{max}} - w_3 * minid - w_4 * minib \tag{5}$$

$$minib \leq \frac{InvR_{b,p,|K|}}{InvR_{b,p}^{max}} \quad \text{and} \quad minid \leq \frac{InvT_{d,p,|K|}}{Inv_{d,p}^{max}} \tag{6}$$

Where $InvR_{b,p,|K|}$ and $InvT_{d,p,|K|}$ are the inventory of each tank at end of the time horizon as well as their maximum limits, *dif* is the difference between the volume arrived at the tank at the distribution centre and the volume sent to clients, $Dem_{p,k}$ is the demand of each product *p* at time *k*, h^{max} is the time horizon and w_1-$w_4$are weights for each of the normalized objective function terms.

4. Results and discussion

Having presented the problem at hand, an example to illustrate the model applicability was built based on data reported by Rejowski and Pinto (2008). The input data are detailed in Table 1 regarding inventory limits and initial conditions for each tank. Note that there are two equal tanks for each product at the refinery, since a tank cannot load and unload simultaneously. The product demands for each day for all products are:

Gasoline=2000m^3, Jet Fuel=2500m^3 and Diesel=6500m^3.The pipeline capacity is 18000 m^3 and pipeline flowrate range is 450-650 m^3/h. A time horizon of 7 days was considered.

Table 1 - Input data.

	Max – Min capacities (m^3)		Initial Inventory (m^3)	
Product	Refinery	Distribution centre	Refinery	Distribution centre
Jet Fuel (A1)	100,000-15,000	14,000-3000	31,500	9000
Diesel (GO)	250,000-40,000	40,000-3000	105,000	10,000
Gasoline (U8)	225,000-40000	19,000-5000	100,000	10,000

The model was implemented using GAMS 23.7.3 system version with CPLEX solver on an Intel(R) Core(TM) i7 platform with 6GB of RAM. The model contains 1614 continuous variables, 1008 binary variables and 1547 constraints. The objective function value obtained was -3.4781after 1.061CPU seconds with a gap of 0.0 %.
The model solution provides the inventory management in both centres as well as the pipeline scheduling that are shown in Figures 2 and 3, respectively.

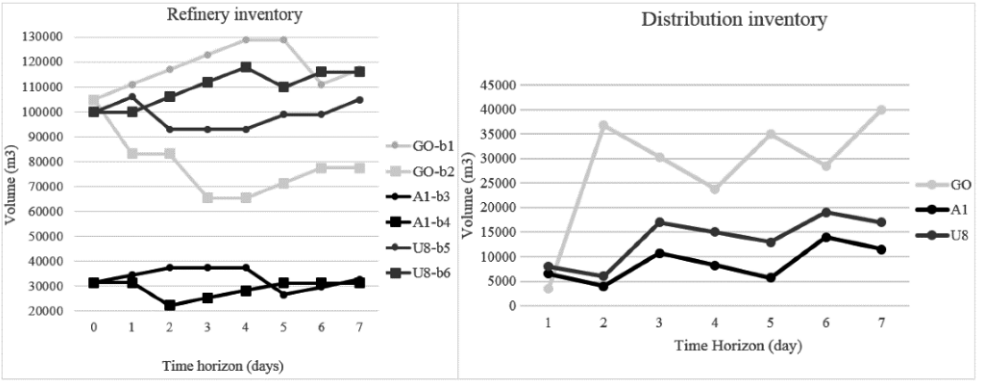

Figure 2 - Inventory at the refinery (left) and distribution centre (right)

Refinery Tank	i=1	i=2	i=3	i=4	i=5	i=6	i=7	
TBSi	0.24	1.08	1.67	2.74	4.01	4.69	5.84	
Day	1	2		3	5		6	7
Distribution tank	pipe	i=1	i=2	i=3	i=4	i=5	i=6	i=7
TDSi		1.39	2.23	2.82	4.41	5.15	5.84	7.0
Day	1	2	3		5	6		7
		GO		A1		U8		

Figure 3 - Pipeline sequence (input/output of the pipeline).

It can be seen in Figure 2 that the first product delivered from the refinery at the beginning (k = 0) is diesel followed by gasoline and jet fuel (when analysing the slopes). When we look to the distribution centre, it is observed that during the day 1diesel volume is increasing, this corresponding to the volume received from the initial pipeline volume and the volume sent by refinery. This is similar for all products and it demonstrates the synchronization operations. All pumping sequences can be seen through Figure 3. In this figure is shown in different colours the product sequence and the transference time due to the pipeline operation. The time variables values, TBS and TDS, represent the exact moment that the last "volume" of batch *i* finished its' pumping or receiving. It is important to note that some products, e.g. in batches 2 and 3, are sent

at the same day but not at the same time. The constraints which do not allow simultaneous products dispatch as well as loading and unloading simultaneous tanks operations are both satisfied, translated into positive or negative slopes. Additionally, between days 3 and 4 the refinery tanks are loading or stopped and, consequently, there is no pipeline operation and the distribution tanks are just delivering the products.

5. Conclusions

This work has presented a model that integrates storage tanks at the refinery blending centre and distribution centre. The scheduling model is capable to coordinate pipeline and the tanks operation at the refinery and distribution centre, while guarantee the demand. Settling periods are considered so as to ensure product quality prior to market delivery. A scenario based on real world data was built to test the model feasibility. This problem allowed testing the model performance even when both pipeline ends are modelled and require having a careful operation with some restrictions. As future work, the model has to be extended in order to include more real world problem features such has blending procedures at the refinery integrated with the market demand, intermediate pipeline inputs/outputs, operational rules at the distribution centre as well as longer time horizons, so as to improve the integration of operations that have different timings along the distribution network.

Acknowledgements

The authors ackowledge finantial support from CAPES (Grant 99999.002568/2014-04).

References

A. Ghaffari-Hadigheh and H. Mostafaei, 2014, On the scheduling of real world multiproduct pipelines with simultaneous delivery, Optimization and Engineering, Springer, DOI 10.1007/s11081-014-9263-9.

R. Rejowski Jr and J.M. Pinto, 2004, Efficient MILP formulations and valid cuts formultiproduct pipeline scheduling, 28, 1511–1528.

R. Rejowski Jr and J.M. Pinto, 2008, A novel continuous time representation for the scheduling of pipelinesystems with pumping yield rate constraints, Computers and Chemical Enginnering, 32, 1042–1066.

S.A. MirHassani, M. Abbasi, S. Moradi, 2012, Operational scheduling of refined product pipeline with dualpurpose depots, Applied Mathematical Modelling, 37, 5723–5742.

S.A. MirHassani, N. BeheshtiAsl, 2013, A heuristic batch sequencing for multiproduct pipelines, Computers and Chemical Engineering, 56, 58–67.

S. N. B. Magatão, L. Magatão, H. L. Polli, F. NevesJr.,L. V. R. Arruda, S. Relvas and A. P. F. D. Barbosa-Póvoa, 2012, Planning and Sequencing Product Distribution in a Real-WorldPipeline Network: An MILP Decomposition Approach, Industrial and Engineering Chemistry Reserach, 51, 4591–4609.

S. Relvas, S. N. B. Magatão, A. P. F.D.Barbosa-Póvoa and F. NevesJr., 2013, Integrated scheduling and inventory management of an oil products distribution system, Omega, 41, 955–968.

V.G Cafaro, D.C. Cafaro, C.A. Mendéz, J. Cerdá, 2015, MINLP model for the detailed scheduling of refined products pipelines with flow rate dependent pumping costs, Computers and Chemical Engineering, 72, 210-221.

Krist V. Gernaey, Jakob K. Huusom and Rafiqul Gani (Eds.), 12th International Symposium on Process Systems Engineering and 25th European Symposium on Computer Aided Process Engineering.
31 May – 4 June 2015, Copenhagen, Denmark

Optimal Multi-Period Investment Analysis for Flexible Pulp Mill Utility Systems

Elin Svensson[a,*]

[a]*Chalmers University of Technology, Dept of Energy and Environment, Heat and Power Technology, SE-412 96 Göteborg, Sweden*
elin.svensson@chalmers.se

Abstract

The techno-economic potential for new technologies in pulp mills is conventionally studied assuming annual averages, based on the assumption that the pulp mill is continuously operated at a constant production rate close to its design capacity. Recent work has shown, however, that a technology, such as lignin extraction, which can improve the operating flexibility of the pulp mill utility system, has a value associated with its flexibility that is not captured in such average-value models. These previous results indicated a risk of significant errors if heat load variations were not properly modelled. This paper presents a multi-period optimization model for the planning of design and operating decisions connected to pulp mill utility systems, which in this work has been extended with back-pressure and condensing turbine models. The model optimizes technology selection, equipment capacities and operating loads under the influence of demand variations, considering part-load efficiencies and operating load limits. Application of the model to an illustrative example showed that lignin extraction can compete with electricity production already at a lignin price of 22 €/MWh in the presence of variations due to poor off-design performance for the turbines. This demonstrates the usefulness of the proposed modelling approach.

Keywords: multi-period, utility system, pulp mill, lignin extraction, steam turbine.

1. Introduction

The pulping process is typically continuous and designed for maximization of quality and throughput of one core product. The operational objective is to maintain the production as close to the design capacity as possible. Consequently, pulp mill energy systems are traditionally modelled using annual averages representing values close to design conditions. However, changes in wood, pulp and energy market conditions motivate a shift towards producing a larger variety of products including traditional pulp mill energy by-products such as electricity and heat, and emerging lignocellulosic biorefinery products such as different kinds of materials and chemicals (Moshkelani et al., 2013). The transition from the traditional pulp mill towards a biorefinery concept will connect the pulp mills to an increased number of external markets. Also for the traditional by-products of heat and electricity, an increased implementation and production rate can be expected when energy prices rise. Pulp mills that are connected to district heating systems, which is common in Scandinavia today, can be strongly affected by large variations in heat demand over the day and over the year. In a typical Nordic district heating grid with an average heat load of about 130 MW, the winter peak load can be over 300 MW while the summer minimum load is about 30 MW (Gadd and Werner, 2013). In combination with the opportunities connected to the diversified product portfolio of a pulp mill biorefinery, there is no lack of incentives for better modelling of variations in investment analyses connected to pulp mill utility systems.

Methodologies for the design optimization of utility systems with varying demands need to simultaneously consider both design and operational decisions. Most published methods rely on a multi-period, mixed-integer linear programming (MILP) formulation. For example, Marechal and Kalitventzeff (2003) optimized the synthesis and operation of the utility system using a multi-period MILP model, after having used a genetic algorithm to identify the minimum number of operating periods needed in the model. During the last decade, the focus has primarily been directed towards the modelling of energy equipment performance. Varbanov et al. (2004) proposed improved models for steam and gas turbines in part-load operation. Shang and Kokossis (2005) considered the performance of turbines and boilers to depend on size, load and operating conditions in their approach, in which they rely on thermodynamic targeting to achieve a reasonably sized MILP formulation. Aguilar et al. (2007) also considered part-load operations and varying energy demands and obtain linearity by starting from the development of linear models for boilers and turbines. Recent advances also include the modelling of variations in steam header properties, either as predetermined parameters (Aguilar et al., 2007) or as variables to be optimized (Chen and Lin, 2011).

The present work suggests a multi-period approach for the specific application to a chemical pulp mill retrofit. The aim is to illustrate the potential advantage and importance of applying this kind of methodology also in an industrial sector such as the pulp and paper industry that traditionally has been served well by simpler approaches. In addition to boilers and turbine, the model proposed in this paper includes the option to invest in lignin separation, an emerging technology for the pulping industry. Previous work has shown that lignin extraction may provide a great opportunity for indirectly increasing the flexibility of the pulp mill utility production in response to demand variations (Svensson, 2014). However, the previous study did not consider competing technologies, such as condensing power generation, which may have similar advantages. The aim of the present work is to extend the previous model with turbine models and investigate to what extent the lignin extraction can compete with the alternative of electricity generation.

2. Studied pulp mill

An overview of the utility system of the pulp mill is shown in Figure 1. The main steam producer is the recovery boiler for which the load is determined by the demand for recovering chemicals from the black liquor, which in turn is set by the pulp production rate. Variations in steam demand are therefore normally controlled by varying the steam production in a supplementary boiler, typically fired with bark. However, for typical market Kraft pulp mills, the steam production from the recovery boiler alone is sufficient for covering the steam demand under most operating conditions. Under such conditions, which can occur during long periods of the year, excess steam will be vented to atmosphere. There are, however, opportunities to reduce the steam production also in the recovery boiler. This can be achieved by extracting lignin from the black liquor in the evaporation plant, thereby reducing the heating value of the black liquor fired in the recovery boiler. During periods of excess steam production, electric power production in a condensing turbine can be an alternative to lignin extraction.

The studied mill is connected to a district heating network. The heat-load variation curve used for the pulp mill has been constructed to represent the typical steam demand of a mill that is the dominant heat supplier in a district heating network (see Figure 2).

The average heat load is approximately the same as in the mill studied by Persson and Berntsson (2009) and the relation between maximum and minimum district heating demand is approximately the same as for a typical medium-sized district heating system as defined by Jönsson et al. (2008). The few days with top-load demand are, however, assumed to be covered by alternative heat supply. The combined heat demand of the mill and district heating system create a demand for the bark boiler. Because of the minimum load limit on the bark boiler and the constant load in the recovery boiler, there will be a steam excess during parts of the year, but the amount is fairly small. However, without any investments to enable reduced steam production or to make use of a potential steam excess, there are few incentives for steam demand savings in this mill, since this would mainly lead to increased steam venting.

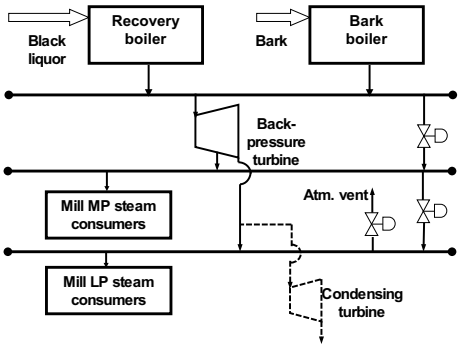

Figure 1. Utility system at a chemical market pulp mill (cond. turbine = investment option).

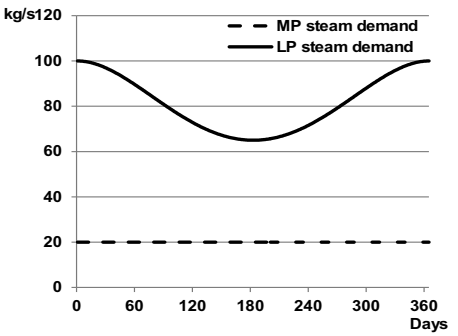

Figure 2. Current steam demand of the pulp mill (incl. district heating).

3. Optimization model

The MILP model is used to identify the optimal steam production and turbine operation at the pulp mill, typically as a response to a steam savings retrofit. The steam header data for high-pressure (HP), medium-pressure (MP) and low-pressure (LP) steam are pre-determined. Potential costs or difficulties associated with daily variations in the operation of the studied processes and steam production units are neglected (see discussion in Svensson, 2014). For the boilers, part-load operation is represented by the use of marginal efficiencies that are estimated to be valid as long as the boiler load is kept above the minimum load limits set in the model. Finally, part-load efficiency effects of the lignin extraction plant are assumed to be negligible.

The objective of the optimization is to minimize the net annual investment cost and the bark costs, and maximize the revenues from lignin exports and electricity production:

$$\text{Minimize} \quad InvCost + BarkCost - LigRev - ElecRev \tag{1}$$

The investment costs $InvCost$ for the lignin extraction plant (Lig) and the condensing turbine (CT) are annualized by the annuity factor r (Eq.2). The cost function $Cost_x(Y_x)$ for investment in technology x is expressed by a piecewise linear function of the capacity, Y_x, of the technology (Eq.3). $C_{inv,x}(i)$ is the investment cost at the breakpoints, $bp_x(i)$, between the segments of the piecewise function and $k_x(i)$ is the linear slope between $bp_x(i)$ and $bp_x(i+1)$. The binary variable z_x is 1 if investment is made in technology x, and 0 otherwise. Eq.(4) represents the valid linearization range.

$$InvCost = \mathrm{r}\big(Cost_{\mathrm{LIG}}(Y_{\mathrm{LIG}}) + Cost_{\mathrm{CT}}(Y_{\mathrm{CT}})\big) \quad (2)$$

$$Cost_x(Y_x) = \begin{cases} 0, & Y_x = 0 \\ \mathrm{C}_{inv,x}(i) + \mathrm{k}_x(i)\big(Y_x - \mathrm{bp}_x(i)\big), & \mathrm{bp}_x(i) \le Y_x < \mathrm{bp}_x(i+1) \end{cases} \quad (3)$$

$$z_x\ \mathrm{bp}_x(1) \le Y_x \le z_x\ \mathrm{bp}_x(\mathrm{n}) \quad (4)$$

$BarkCost$ is the annual bark cost as a function of the bark price, $\mathrm{p}_{\mathrm{bark}}$. The bark use, $Q_{\mathrm{Bark},t}$, is given by the steam production in the bark boiler $M^{\mathrm{prod}}_{\mathrm{BB},t}$, the boiler efficiency η_{BB} and the enthalpies of HP steam and feed water, h_1 and h_{FW}. T_t is the operating time in period t. Similarly, the annual lignin revenues, $LigRev$, associated with lignin exports, $Q_{\mathrm{Lig},t}$, are a function of the lignin price $\mathrm{p}_{\mathrm{lignin}}$ and the recovery boiler's marginal lignin efficiency, $\eta_{\mathrm{RB-LIG}}$. Lignin extraction reduces the steam production in the recovery boiler from its previous level $M^{\mathrm{max}}_{\mathrm{RB}}$. $ElecRev$ represents the annual revenues from electricity produced in the steam turbines, E_t, at an electricity price of p_{el}; E_t is given by the sum of the power output $W_{st,t}$ from all turbine stages *st*.

$$BarkCost = \mathrm{p}_{\mathrm{bark}} \sum_t T_t Q_{\mathrm{Bark},t} = \mathrm{p}_{\mathrm{bark}} \sum_t T_t (\mathrm{h}_1 - \mathrm{h}_{\mathrm{FW}}) M^{\mathrm{prod}}_{\mathrm{BB},t} / \eta_{\mathrm{BB}} \quad (5)$$

$$LigRev = \mathrm{p}_{\mathrm{lig}} \sum_t T_t Q_{\mathrm{Lig},t} = \mathrm{p}_{\mathrm{lig}} \sum_t T_t\,(\mathrm{h}_1 - \mathrm{h}_{\mathrm{FW}})\big(\mathrm{M}^{\mathrm{max}}_{\mathrm{RB}} - M^{\mathrm{prod}}_{\mathrm{RB},t}\big)/\eta_{\mathrm{RB-LIG}} \quad (6)$$

$$ElecRev = \mathrm{p}_{\mathrm{el}} \sum_t T_t E_t = \mathrm{p}_{\mathrm{el}} \sum_t T_t \sum_{st} W_{st,t} \quad (7)$$

The turbine model (Eqs.8-12) is adapted from Aguilar et al (2007). The parameters A_{st}, B_{st} and L_{st} are coefficients calculated from regression and thermodynamic data, $\Delta\mathrm{h}^{\mathrm{is}}_{st}$ is the estimated isentropic enthalpy difference over the turbine stage *st* and $\mathrm{w}^{\mathrm{min}}_{st}$ defines the minimum load of the turbine as a fraction of the design load. $M^{\mathrm{turb}}_{st,t}$ represents the steam flow through a turbine stage. If a turbine stage is in operation, the binary variable $\gamma_{st,t}$, which is introduced in Eq.(8) to avoid a flow through a non-existing turbine, takes the value one and the virtual design output of this turbine stage, W^{VD}_{st}, is set to the design output. If not in operation, both these variables are zero. The existing turbine is assumed to always be in operation (Eq.10) and its virtual design output is a parameter set to the existing design output. For the condensing turbine, the virtual design output, $W^{\mathrm{VD}}_{3\to\mathrm{c},t}$, will instead be a decision variable subject to constraints (Eqs.11-12).

$$W_{st,t} = (\mathrm{L}_{st} + 1)\big(M^{\mathrm{turb}}_{st,t}\Delta\mathrm{h}^{\mathrm{is}}_{st} - \gamma_{st,t}\mathrm{A}_{st}\big)/\mathrm{B}_{st} - \mathrm{L}_{st}W^{\mathrm{VD}}_{st,t} \quad (8)$$

$$\mathrm{w}^{\mathrm{min}}_{st}\ W^{\mathrm{VD}}_{st,t} \le W_{st,t} \le W^{\mathrm{VD}}_{st,t} \quad (9)$$

$$\gamma_{1\to2,t} = \gamma_{2\to3,t} = 1 \quad (10)$$

$$\mathrm{bp}_{\mathrm{CT}}(1)\gamma_{3\to\mathrm{c},t} \le W^{\mathrm{VD}}_{3\to\mathrm{c},t} \le \mathrm{bp}_{\mathrm{CT}}(\mathrm{n})\gamma_{3\to\mathrm{c},t} \quad (11)$$

$$Y_{\mathrm{CT}} - \mathrm{bp}_{\mathrm{CT}}(\mathrm{n})\big(1 - \gamma_{3\to\mathrm{c},t}\big) \le W^{\mathrm{VD}}_{3\to\mathrm{c},t} \le Y_{\mathrm{CT}} \quad (12)$$

Mass balances for steam pressure headers p are formulated in Eqs.(13-15). The process steam demands are given by $\mathrm{M}^{\mathrm{proc}}_{p,t}$, but there will also be an extra LP steam demand S in the evaporation plant if lignin is extracted. $M^{\mathrm{turb}}_{st,t}$, $M^{\mathrm{vlv}}_{st,t}$ and M^{vent}_{t}denote the steam flows through the turbine, expansion valves and atmospheric vent, respectively; $M^{\mathrm{qw}}_{p,t}$ denotes quench water added to steam header p and $M^{by}_{3\to\mathrm{c},t}$ represents a bypass flow around the condensing turbine that preheats the turbine outlet before the feedwater tank.

$$M^{\mathrm{prod}}_{\mathrm{RB},t} + M^{\mathrm{prod}}_{\mathrm{BB},t} = \mathrm{M}^{\mathrm{proc}}_{1,t} + M^{\mathrm{turb}}_{1\to2,t} + M^{\mathrm{vlv}}_{1\to2,t} \quad (13)$$

$$M^{\mathrm{turb}}_{1\to2,t} + M^{\mathrm{vlv}}_{1\to2,t} + M^{\mathrm{qw}}_{2,t} = \mathrm{M}^{\mathrm{proc}}_{2,t} + M^{\mathrm{turb}}_{2\to3,t} + M^{\mathrm{vlv}}_{2\to3,t} \quad (14)$$

$$M^{\mathrm{turb}}_{2\to3,t} + M^{\mathrm{vlv}}_{2\to3,t} + M^{\mathrm{qw}}_{3,t} = \mathrm{M}^{\mathrm{proc}}_{3,t} + \mathrm{S}\ Q_{\mathrm{Lig},t} + M^{\mathrm{turb}}_{3\to\mathrm{c},t} + M^{\mathrm{by}}_{3\to\mathrm{c},t} + M^{\mathrm{vent}}_{t} \quad (15)$$

Energy balances for the MP and LP steam headers are given by Eq.(16). $Q_{p,t}^{\text{ext}}$ represents the estimated heat flow discharged by the turbine to steam header p calculated from estimated inlet enthalpies at each turbine stage, $\text{h}_{j-1}^{\text{in}\prime}$ (Eq.17) (see Aguilar et al., 2007). An energy balance is also set up around the condensing turbine (Eq.18).

$$M_{j-1\to j,t}^{\text{vlv}}\text{h}_{j-1} + Q_{j,t}^{\text{ext}} + M_{j,t}^{\text{qw}}\text{h}_{\text{QW}} = \left(M_{j-1\to j,t}^{\text{vlv}} + M_{j-1\to j,t}^{\text{turb}} - M_{j\to j+1,t}^{\text{turb}} + M_{j,t}^{\text{qw}}\right)\text{h}_j \quad j = 2,3 \tag{16}$$

$$Q_{j,t}^{\text{ext}} = \left(M_{j-1\to j,t}^{\text{turb}} - M_{j\to j+1,t}^{\text{turb}}\right)\left(\text{h}_{j-1}^{\text{in}\prime} - 0.838\Delta\text{h}_{j-1\to j}^{\text{is}}\right) + 0.8097 \quad j = 2,3 \tag{17}$$

$$M_{3\to\text{c},t}^{\text{turb}}(\text{h}_{\text{c}} - \text{h}_{\text{FW}}) + M_{3\to\text{c},t}^{\text{by}}(\text{h}_3 - \text{h}_{\text{FW}}) = 0 \tag{18}$$

A boiler in operation must operate within the limits $\text{M}_b^{\min}$ and $\text{M}_b^{\max}$ (Eq.19). The binary variable $y_{b,t}$ is one if the boiler is in operation, and zero otherwise; it is always one for the recovery boiler (Eq.20). Lignin exports are limited by extraction capacity (Eq.21):

$$y_{b,t}\text{M}_b^{\min} \le M_{b,t}^{\text{prod}} \le y_{b,t}\,\text{M}_b^{\max} \tag{19}$$

$$y_{\text{RB},t} = 1 \tag{20}$$

$$Q_{\text{Lig},t} \le Y_{\text{Lig}} \tag{21}$$

Model data are shown in Tables 1-4. The process steam demand equals the steam demand shown in Figure 2, with the LP steam demand reduced by 15 kg/s after a steam savings retrofit. The year is divided into 365 periods with T_t=24 h. The prices are set to p_{Bark} = 20 €/MWh and p_{elec} = 60 €/MWh, while two levels for lignin price have been analyzed: p_{Lignin} = 20 €/MWh (≈ wood fuel) and p_{Lignin} = 30 €/MWh (≈ oil). Operating costs for lignin extraction are included in the lignin price. The extra steam demand in the evaporation plant when lignin is extracted is S=0.0229 kg/MW.

Table 1. Investment cost data

Investment cost parameter	Lignin extr. plant (LIG)	Cond. turb. (CT)
r [1/y]	0.2	
$\text{bp}_{\text{x}}(i)$[MW], $(i = 1..10)$	$10 + 8(i-1)$	$4 + 2(i-1)$
$\text{C}_{\text{inv,x}}(i)[10^6€]$	$1.02\ \text{bp}_{\text{LIG}}(i)^{0.6}$	$2.38\ \text{bp}_{\text{CT}}(i)^{0.6}$
$\text{k}_x(i)$ [€/MW]	$\frac{(\text{C}_{\text{inv},x}(i+1)-\text{C}_{\text{inv},x}(i))}{(\text{bp}_x(i+1)-\text{bp}_x(i))}$	

Table 2. Performance data for the boilers

Boiler parameters	Rec. boiler (RB)	Bark boiler (BB)
η_{b} $[\frac{\text{MW steam}}{\text{MW "fuel"}}]$	0.92[a]	0.88
$\text{M}_{\text{b}}^{\min}$ [kg/s]	65	8
$\text{M}_{\text{b}}^{\max}$ [kg/s]	90	30

[a] Marginal lignin-to-steam efficiency = Steam output decrease / heat content of extracted lignin

Table 3. Steam and water enthalpies

Steam/water	Enthalpy [MJ/kg]
HP steam, h_1	3.300
MP steam, h_2	2.822
LP steam, , h_3	2.745
Feed water, h_{FW}	0.42
Quench water, h_{QW}	0.084
Cond. turb. out, h_{cond}	0.147

Table 4. Turbine data (see Aguilar, 2007)

Property/ coefficient	Turbine stages 1→2	2→3	3→c
$\Delta\text{h}_{\text{st}}^{\text{is}}$	0.4349	0.1814	0.6581
$\text{h}_{\text{st}}^{\text{in}\prime}$	3.300	2.930	2.776
A_{st}	0.6442	0.2601	0.0343
B_{st}	1.230	1.280	1.418
L_{st}	0.1540	0.1966	0.0276
$\text{W}_{\text{st}}^{\text{D}}$	41.0	13.8	*var*
$\text{w}_{st}^{\min}$	0.25	0.25	0.25

4. Results

The model was formulated in Cplex Optimization Studio and solved in 4–7 seconds on a standard desktop computer. Figure 3 shows the optimal operation of the plant for different levels of the lignin price. At p_{Lignin} = 20 €/MWh, lignin extraction is not competitive, but for p_{Lignin} = 30 €/MWh, the lignin extraction rate is high.

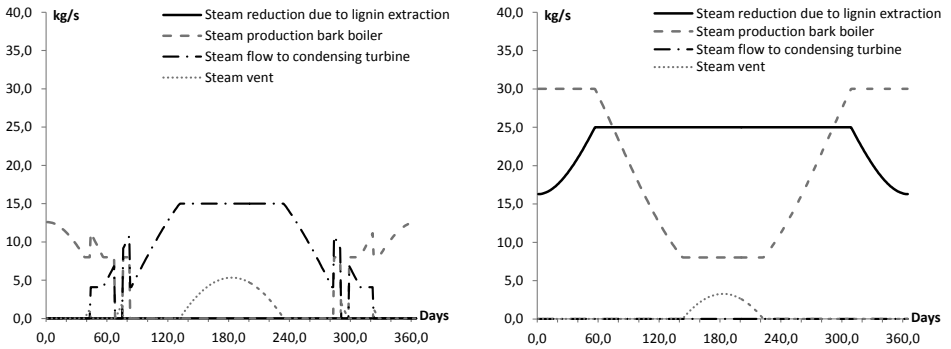

Figure 3. Optimal operation: a) p_{Lignin}=20 €/MWh, b) p_{Lignin}=30 €/MWh

In fact, investment in lignin extraction becomes more profitable than the condensing turbine already at a lignin price of 22 €/MWh. The low value is explained by the poor off-design performance of the condensing turbine.

5. Conclusions

A model has been formulated for optimal investment decisions in lignin extraction and turbine capacity at a pulp mill affected by demand variations. Results indicate an advantage for lignin extraction already at lignin prices above 22 €/MWh due to poor off-design performance of condensing power generation. Further research is needed to investigate the influence of varying operating conditions on the lignin extraction and evaporation plant and the recovery boiler.

Acknowledgements

Financial support from the Swedish Energy Agency is gratefully acknowledged.

References

O. Aguilar, S. Perry, J. Kim, R. Smith, 2007, Design and optimization of flexible utility systems subject to variable conditions: Parts 1 and 2, Chem. Eng. Res. Des. 85, 1136-1168.

C. Chen, C. Lin, 2011, A flexible structural and operational design of steam systems, Appl. Therm. Eng. 31, 2084-2093.

H. Gadd, S. Werner, 2013, Daily heat load variations in Swedish district heating systems, Appl. Energy 106, 47-55.

J. Jönsson, I. Svensson, T. Berntsson, B. Moshfegh, 2008, Excess heat from Kraft pulp mills: Trade-offs between internal and external use in the case of Sweden – Part 2: Results for future energy market scenarios, Energy Policy 36, 4186-4197.

F. Marechal, B. Kalitventzeff, 2003, Targeting the integration of multi-period utility systems for site scale process integration, Appl. Therm. Eng. 23, 1763-1784.

M. Moshkelani, M. Marinova, M. Perrier, J. Paris, 2013, The forest biorefinery and its implementation in the pulp and paper industry, Appl. Therm. Eng. 50, 1427-1436.

J. Persson, T. Berntsson, 2009, Influence of seasonal variations on energy-saving opportunities in a pulp mill, Energy 34, 1705-1714.

Z. Shang, A. Kokossis, 2005, A systematic approach to the synthesis and design of flexible site utility systems, Chem. Eng. Sci. 60, 4431-4451.

E. Svensson, 2014, Flexibility to seasonal demand variations in pulp mill steam production: The effect of steam savings leading to off-design heat loads, Appl. Therm. Eng. 70, 1180-1188.

P. Varbanov, S. Doyle, R. Smith, 2004, Modelling and optimization of utility systems, Chem. Eng. Res. Des. 82, 561-578.

Krist V. Gernaey, Jakob K. Huusom and Rafiqul Gani (Eds.), 12th International Symposium on Process Systems Engineering and 25th European Symposium on Computer Aided Process Engineering.
31 May – 4 June 2015, Copenhagen, Denmark

Scenario-Based Price Negotiations vs. Game Theory in the Optimization of Coordinated Supply Chains

Kefah Hjaila, Luis Puigjaner and Antonio Espuña

Chemical Engineering Department, Universitat Politècnica de Catalunya, ETSEIB, Av. Diagonal 647, 08028 Barcelona, Spain.

Abstract

A scenario-based negotiation (SBN) win-to-win approach is proposed for the optimization of coordinated decentralized multi-site multi-product Supply Chains (SCs) in a competitive environment. Based on non-symmetric roles, the leader aims to settle its offer taking into account the uncertain reaction of the follower, which behavior is represented by a probability of acceptance. Different negotiation scenarios, based on considering Standalone, Cooperative, and Non-Cooperative SCs are analyzed for the negotiation, resulting in different MINLP tactical models, which are illustrated using a case study with different "follower" SCs around an industrial production SC "leader". On the other hand, a Stackelberg non-cooperative bi-level MINLP game model is built and solved for the same case study. The Non-Cooperative Negotiation Scenario (NCNS) proves to be more adequate, leading to higher individual profits expectations.

Keywords: Tactical management, Supply Chain coordination, Game Theory

1. Introduction

The competitiveness among chemical industries is shifting the interest of Process Systems Engineering (PSE) towards SCs coordination based on individual and global benefits. Many works have been carried out to analyze different ways of coordination among SCs, such as the integration of different SCM levels (Varma et al., 2007); or the coordination of suppliers' and producers' SCs at the tactical level (Hjaila et al., 2014). But, these works support decisions through the use of centralized objectives, disregarding the goals of individuals SCs, and thus conflicts of interests may arise.

Solving these conflicts by negotiations has been studied through Game Theory (GT), and specially through the "revenue sharing" based on Stackelberg's-game for one manufacturer and many competing retailers (Cao et al., 2013), or through developing a bi-level MINLP design and planning model under the leading role of the manufacturer (Yue & You, 2014). Price negotiations as a way to prepare a coordination agreement has been also proposed as a form of "timing" between producer and customer (Moon et al., 2011). Nevertheless, most of the negotiation mechanisms focus on the competitiveness among the retailers disregarding the supplier's competitive behavior. Furthermore, the aforementioned approaches are based on dominance leadership, without considering the uncertain behavior of the other partner/s, leading to insufficient coordination.

Accordingly, this work aims to establish the best conditions for the coordination contract through quantitative negotiations built on win-to-win principles considering the uncertain behavior of the follower conditions when optimizing the leader SC. A

scenario-based negotiation approach is developed taking into account the individual and global profits at the tactical level. Furthermore, a Stackelberg-game model is also developed to solve the same negotiation problem.

2. Problem statement

2.1. Scenario-Based Negotiation (SBN)

Based on non-symmetric roles, the SBN is held between two independent SCs: supplier SC (follower), and client SC (leader); actually, both have been considered production SCs with their own independent suppliers/markets. The leader decides to improve its benefits by buying internal product/s (negotiation item) from the follower SC. The negotiation procedure is divided into two main steps: i) analyzing the negotiation scenarios, and ii) the coordination agreement.

2.1.1. Analyzing the negotiation scenarios

Standalone Scenario (SS)"pre-negotiation": based on the individual objectives, this step aims to establish benchmarks for all negotiation methods.

Non-cooperative negotiation scenario (NCNS): based on individual objectives, this scenario considers the contract to be offered to maximize the profit of the leader SC.

Cooperative negotiation scenario (CNS): based on establishing a global objective.

2.1.2. The coordination agreement

In order to push the negotiation towards a win-to-win policy, the benefits of any reduction in the uncertainty of the production scenario associated to the signature of a collaboration agreement are considered. This includes the calculation of a probability of acceptance of this agreement by the follower SC, taking into account the risk associated to the uncertain behavior of the external conditions. Then, the contract proposed by the leader will be the one driving to the most profitable leader's expected profit.

2.2 Game Theory (GT)

The interaction between the leader and the follower is modelled as a single-leader–single-follower no-cooperative non-zero-sum Stackelberg-game, resulting in a bi-level MINLP model. The idea of the bi-level is that the follower (lower-level SC) objective function is represented as constraints in the leader problem (upper-level SC). In this paper, the bi-level model is solved by building the Stackelberg-payoff matrix considering constraints in both leader and follower SCs. The reaction function is identified (price vs. quantity) and, based on complete information "dynamic game", the leader designs its moves by offering prices, and the follower responds by offering the amounts to be supplied according to its best conditions.

3. Mathematical Model

A generic MINLP tactical model is developed as a basis for this paper. A set of supply chains (sc1, sc2… SC) is considered with their new subsets linking each SC to its corresponding negotiation partner (follower F or leader L). The total sales include internal and external markets (M), at different prices ($p_{r',sc',t}$ and $pr_{r,m,t}$ respectively).

$$SALES_{sc} \le \sum_{t\in T}\sum_{r\in R}\sum_{m\in M} pr_{r,m,t}\cdot xdem_{r,sc,m,t} + \sum_{t\in T}\sum_{r'\in R} p_{r',sc',t}\cdot Q_{r',sc',}\forall sc\in SC; sc'\in F \quad (1)$$

The SC Cost along the planning time horizon T is (RM purchase, transport, storage, production, and the negotiation resource total costs, respectively (Eq. 2).

$$COST_{sc} = \sum_{t\in T}(CRM_{sc,t} + CTR_{sc,t} + CST_{sc,t} + CPRD_{sc,t}) + \sum_{t\in T}\sum_{r'\in R} p_{r',sc',t}\cdot Q_{r',sc',t} \quad (2)$$

$\forall sc \in SC; sc' \in L$

$$PROF_{sc} = SALES_{sc} - COST_{sc} \qquad \forall sc \in SC \qquad (3)$$

3.1. Application of negotiation scenarios:

SS: the negotiation resource quantity $Q_{r',sc',t}$ will be substituted by zero.

CNS: the independent SCs seek to optimize the global SC profit (*Tprofit*) (Eq. 4),

$$Tprofit = \sum_{sc \in SC} PROF_{sc} \qquad (4)$$

NCNS: the negotiation resource demand is equal to a constant value $E_{r',sc',t}$ resulted from maximizing the leader SC profit:

$$Q_{r',sc',t} = E_{r',sc',t} \qquad \forall r' \in R; sc' \in L; t \in T \qquad (5)$$

Within the expected leader SC profit expression, $ExPROF_{sc'}$, the uncertainty reduction cost is represented as an "abridged" uncertainty risk, to be represented by a probability of acceptance (Eq. 7)

$$ExPROF_{sc'} = PROF_{sc'} - uncertainty\ risk_{sc'} \qquad \forall sc' \in L \qquad (6)$$

$$prob_{sc'} = \frac{No.\ of\ scenarios\ of\ improved\ profits_{sc'}}{Total\ No.\ of\ scenarios_{sc'}} \qquad \forall sc' \in F \qquad (7)$$

3.2. Application of Game Theory

Mathematically, the Stackelbergy game forms a bi-level model (Chu and You, 2015), which can be represented in Eqs. (8 &9), where Z and z are the upper-level and lower levels objective functions; *X* and *Y* stands for the upper-level and lower-level decision variables; *G* and *H* are the upper-level inequality and equality constraints; while *g* and *h* are the lower-level inequality and quality constraints.

$$\max_{x \in X, y \in Y} Z_{sc' \in L}(x, y) \text{ , subject to } G_{sc' \in L}(x, y) \le 0 \text{ , and } H_{sc' \in L}(x, y) = 0 \qquad (8)$$

$$\text{Where } y \in \max_{y \in Y} z_{sc' \in F}(x, y) \text{ subject to } g_{sc' \in F}(x, y) \le 0 \text{ ,and } h_{sc' \in F}(x, y) = 0 \qquad (9)$$

4. Case Study

The negotiation models have been implemented and solved for a real data case study (Figure 1) modified from Zamarripa et al. (2014). The partners involved are a production/distribution SC (leader), and the Energy generation SC (follower); the energy supplied/demanded represents the negotiation item.

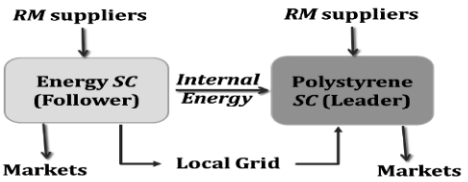

Figure 1- The decentralized global SC network

5. Results and discussion

5.1. Scenario-Based Negotiations (SBN)

The resulting MINLP models have been solved using GloMIQO (Misener & Floudas, 2013). The negotiation starts from the total profit ensuing from the SS (Figure 2 –

purple line). Obviously, if coordination will not allow improvement over this total profit, there is nothing to negotiate. It is worth noticing that the NCNS leads to 10.77 M€ total profit at the contract price 0.21 €/kWh, with a difference of 8.7% and 3.3% comparing with the SS and the CNS, respectively. Furthermore, the NCNS mathematical formulation is less complex and so allows to identify better solutions with less computational effort (32% less than SS and 63% less than CNS).

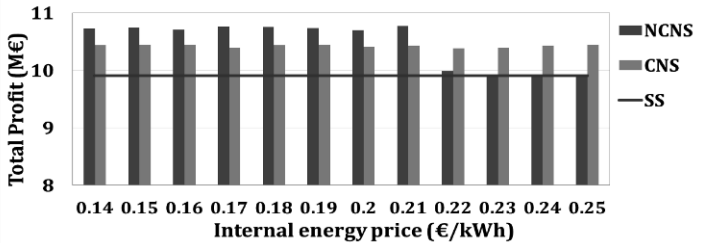

Figure 2- Negotiation scenarios total profits

In turn within the NCNS scenario the leader designs its final offer taking into account the follower uncertain reaction; then, the follower has to assess this offer based on its probability distribution curves (accept or reject):

5.1.1. From the leader side:

The Production SC assesses its expected profit for each contract offer based on the follower probability of acceptance (Figure 3). In general this probability increases as the contract price increases, but at 0.22 €/kWh the leader decides to buy higher energy amounts from the local Grid, resulting in a sudden probability reduction.

The difference between the Production SC contract profit and the expected profit represents the uncertainty cost. The total energy amount needed for the Production SC during the established long term planning horizon is 24.71GWh; 36% of this amount (8.84 GWh) is expected to be supplied from the energy SC, while the rest (15.86 GWh) is to be covered by the local Grid. It is worth mentioning that before considering the uncertainty reduction cost, the contract price 0.14€/kWh was the best option for the leader SC (9.24 M€), but after considering the uncertain reaction of the supplier, the leader offers higher price (0.15 €/kWh), resulting in a 15.5 % profit reduction.

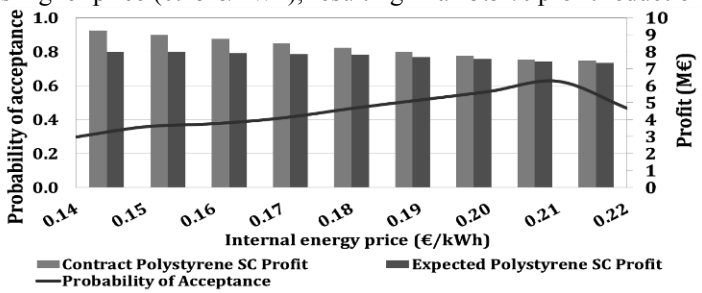

Figure 3- Polystyrene SC contract/expected Profit vs. Probability of acceptance

5.1.2. From the follower side:

The Energy SC seeks to optimize its expected benefit based on the leader offer (8.84 GWh at 0.15€/kWh). This results in 2.29M€ profit. In spite of an initially calculated SS profit of 2.44 M€, based on the Energy SC profit probability curves (Figure 4), the probability from accepting the contract seems to be higher.

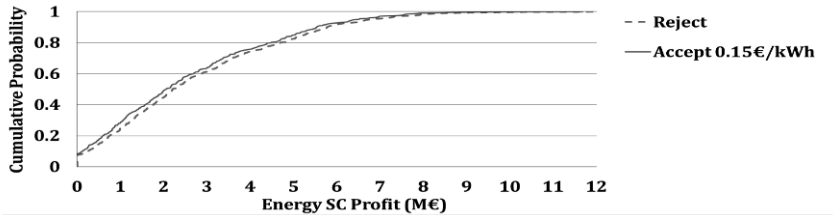

Figure 4- Cumulative probability curves

5.2. Results of Game Theory

The non-cooperative single-leader/single-follower Stackelberg payoff matrix has been built (Table 1), highlighting the follower optimal quantities for each leader offer.

5.2.1. From the leader side:

Stackelberg initial point results in 9.16 M€ profit for the Leader, but this solution is not considered (not win-to-win: The Energy SC Profit is 1.57M€). The final point corresponds the leader SC profit of 7.92 M€ (6% profit improvement vs. the SS). The leader Stackelberg strategy then is to buy 24.71GWh at contract price 0.19 €/kWh.

Table 1- Stackelberg-Payoff Matrix

L (Leader) → action (€/kWh)	0.14		(…)	0.17		0.19		0.20		0.21	
F (Follower) response (GWh)↓	F	L		F	L	F	L	F	L	F	L
0	2.44	7.47		2.44	7.47	2.44	7.47	2.44	7.47	2.44	7.47
(…)											
12.00	2.10	8.29		2.46	7.93	2.70	7.69	2.82	7.58	2.94	7.45
(…)											
23.00	1.69	9.06		2.38	8.37	2.84	7.90	3.07	7.68	3.30	7.45
24.71	1.57	**9.16**		2.31	8.42	2.81	**7.92**	3.06	7.67	3.30	7.43

5.2.2. From the follower side:

The leader contract results in 2.81 M€ Energy SC profit (13 % higher than SS: 2.44M€). The follower then analyses its expected benefits in order to accept or reject. The expected follower SC profit with the coordination contract is 2.99 M€, 8.4% higher than the expected profit resulting from rejecting the contract (2.74 M€). So the follower is expected to accept the coordination contract.

5.3. Scenario-Based-Negotiations (SBN) vs. Game Theory (GT):

Table 2 shows the final SCs coordination contract using the SBN and GT. The SBN results in higher leader SC profit than GT method, with a difference of (74.61 k€).

Table 2- Coordination contract

Negotiation method	Contract price (€/kWh)	Contract amount (GWh)	Leader profit (M€)	Follower profit (M€)
Scenario-Based (SBN)	0.15	8.84	8.00	2.29
Stackelberg Game	0.19	24.71	7.92	2.81

6. Conclusions

A Scenario-Based Negotiation (SBN) approach is proposed to set the best conditions for the coordination of independent multi-site multi-product SCs in a highly competitive

environment. Under the leading role of the client SC, different negotiation scenarios have been analyzed based on Standalone, Non-cooperative, and Cooperative SCs. An uncertainty reduction cost is modelled within the expected leader SC profit as a form of probability of acceptance. From the other hand, a single-leader-single-follower Stackelberg Bi-level MINLP model is developed. Both methods have been illustrated using a case study which coordinates different suppliers' SCs and client "industrial production SC" (leader) through a global scenario. The results show that the Non-Cooperative Negotiation scenario (NCNS) proves to be the most adequate scenario leading to higher global profits (8.7% and 3.3% than the Standalone and Cooperative scenarios). Furthermore, the SBN results in higher profit (1%) than GT, in favor of the leader SC. The proposed approach allows to contemplate the different mechanisms a SC may use to modify its relationships with its clients and suppliers during the optimization procedure, which can be used for further second stage agreements, in a generic and flexible way, so it can be applied in practice to real cases, including centralized/decentralized simple/global SCs, as illustrated in the presented case study.

Acknowledgements

Financial support received from the Spanish Ministry of Economy and Competitiveness and the European Regional Development Fund, both funding the Project SIGERA (DPI2012-37154-C02-01), and from the Generalitat de Catalunya (AGAUR FI program and grant 2014-SGR-1092-CEPEiMA), is fully appreciated.

References

D. Yue, & F. You, 2014, Game-Theoretic Modeling and Optimization of Multi-echelon Supply Chain Design and Operation under Stackelberg Game and Market Equilibrium, Comp & Chem Eng, 71, 347–361.

E. Cao, C. Wan, M. Lai, 2013, Coordination of a supply chain with one manufacturer and multiple competing retailers under simultaneous demand and cost disruptions, Int J. Prod Econ, 141, 425–433.

K. Hjaila, M. Zamarripa, A. Shokry, A. Espuña, 2014, Application of Pricing Policies for Coordinated Management of Supply Chains, Comp Aided Chem Eng, 33, 475–480.

M. Zamarripa, K. Hjaila, J. Silvente, A. Espuña, 2014, Tactical management for coordinated supply chains, Comp & Chem Eng, 66, 110-123.

R. Misener, Ch. Floudas, 2013, GloMIQO: Global mixed-integer quadratic optimizer, J Glob Optim, 57,3–50.

V.A. Varma, G.V. Reklaitis, G. E. Blau, J. F. Pekny, 2007, Enterprise-wide modelling & optimization—An overview of emerging research challenges and opportunities, Comp & Chem Eng, 31,692–711

Y. Chu, F. You, J.M. Wassick, A. Agarwal, 2015, Integrated planning andscheduling under production uncertainties: bi-level model for-mulation and hybrid solution method, Comp. & Chem. Eng., 72, 255–272.

Y. Moon, T. Yao, S. Park, 2011, Price negotiation under uncertainty, Int J. Prod Econ, 134, 413–423.

Krist V. Gernaey, Jakob K. Huusom and Rafiqul Gani (Eds.), 12th International Symposium on Process Systems Engineering and 25th European Symposium on Computer Aided Process Engineering.
31 May – 4 June 2015, Copenhagen, Denmark

On the complexity of production planning and scheduling in the pharmaceutical industry: the Delivery Trade-offs Matrix

Samuel Moniz,[a,b*] Ana Paula Barbosa-Póvoa,[b] Jorge Pinho de Sousa,[a, c]

[a]*INESC TEC, Rua Dr. Roberto Frias, Porto, Portugal*
[b]*Centro de Estudos de Gestão, Instituto Superior Técnico, Universidade de Lisboa, Av. Rovisco Pais, Lisboa, Portugal*
[c]*Faculdade de Engenharia da Universidade do Porto, Rua Dr. Roberto Frias, Porto, Portugal*
samuel.moniz@inesctec.pt

Abstract

The manufacturing of pharmaceutical products is preceded by complex development phases where process design, planning, and scheduling problems must be considered as deeply linked, fact that has not yet been adequately handled by the existing literature. In this perspective, this work discusses the role of the production planning and scheduling decisions in the pharmaceutical industry. It starts by analysing the main aspects that influence planning and scheduling, and defines an extended scope of the related problems, as a way to account for higher levels of integration between process design and operational decisions. We propose a novel conceptual representation, the *Delivery Trade-offs Matrix* (DTM) to help managing the trade-offs occurring in the drug development process and to expose the factors that affect the performance of these manufacturing systems.

Keywords: Planning; scheduling; pharmaceutical industry

1. Introduction

The pharmaceutical industry can be viewed as a complex system of processes, operations, and organizations involved in the discovery, development, and manufacturing of drugs. Companies operating in this industry are responsible for: a) research and development (R&D) activities; b) development and manufacturing of active pharmaceutical ingredients (APIs); and c) drugs manufacturing. Federsel (2009) recognized that, although the pharmaceutical industry has historically tolerated total time investments of more than 10 years from idea to market, the current worldwide paradigm imposes a significant reduction of this time. The pharmaceutical industry is therefore confronted with several challenges that are related to increasing R&D costs, long cycle times, and low probabilities of success (Hynes III, 2009). Additionally, over the years, manufacturers and regulators have created an environment for operations management that strongly conditions the planning and scheduling functions. In this work, we have looked into the literature addressing planning and scheduling problems in the sector, and tried to derive some general principles for defining and extending the scope of these functions, and to identify some current and future research and industrial challenges.

The rest of the paper is structured as follows. Section 2 presents the critical factors that determine how planning and scheduling are done in the pharmaceutical industry.

Section 3 discusses the planning and scheduling functions and proposes an extension of the scope for the related problems, to account for higher levels of integration between process design and operational decisions. In section 4, the *Delivery Trade-offs Matrix (DTM)* is introduced. Finally, in section 5, some concluding remarks are presented.

2. Critical factors for planning and scheduling

Planning and scheduling are functions that primarily aim at reducing costs and improving responsiveness of the manufacturing systems. One recent review on planning and scheduling has been written by Harjunkoski et al., (2013). The critical factors that drive the planning and scheduling functions, in the particular context of the pharmaceutical industry, can be grouped in three categories: market, processes, and plants. Market factors are related to the specific contextual factors of this industry. Process factors have to do with the structure of the chemical processes. Plant factors relate to the operating strategies and resources characteristics of the manufacturing systems. Note that some of the process and plant characteristics discussed in the following subsections are more general and not specific to the pharmaceutical industry.

2.1. Market

The market context has a direct influence on the planning and scheduling functions. First of all the pharmaceutical market is highly fragmented. There is a large variability on the demand, that is also a result of the pressure created by generic drugs, and that leads to larger production mixes in the manufacturing sites. Operations flexibility is therefore required to fit the systems to this heterogeneous demand, and for that reason efficient planning and scheduling methods are required. Manufacturing in a high regulated market has to deal with additional complexities that do not exist in less regulated markets. In fact chemical processes are executed under a close supervision of the regulatory agencies that define rigorous procedures to monitor process changes. Globally, the time-to-market issue and the pressure to reduce costs are imposing operations to run more efficiently and therefore advanced planning and scheduling methods are necessary (Moniz et al., 2014).

2.2. Processes

The production process topology strongly determines the scheduling models that can be applied. The work of Mendez et al. (2006) provides a comprehensive review on the different types of scheduling models. In the manufacturing of APIs, for example, processes require numerous production steps with tasks having short and long processing times, usually spanning across several working shifts. Regulatory and quality procedures define the *lot size* and the *changeover* requirements that must be rigorously followed in the manufacturing sites, thus introducing additional time to the effective production time. Stable intermediaries and final products are produced in lots, and therefore lots traceability must be ensured. The first batches after a *scale-up* are usually more difficult to produce, since this may involve the use of different processing units or even performing changes in the process. For that reason, these processes impose frequent revisions of the production schedule.

2.3. Plants

The plant structure has also implications on how planning and scheduling are performed. Note that, although the modelling approach strongly depends on the process topology (as discussed above), the characteristics of the plants (such as resources, plant structure, operating mode, and batch/continuous manufacturing) lead as well to specific

planning and scheduling problems. Continuous manufacturing of pharmaceuticals is an emergent process mode that relies on flow reactors and is currently being evaluated for the production of drugs. A consequence of using flow reactors, instead of batch reactors, is that the production process moves from a batch mode to continuous operating conditions (Buchholz, 2010). Finally, it is important to mention that for aiming the full operational efficiency the integration with advanced control systems should be performed. However, here there are significant practical and theoretical integration challenges, Engell and Harjunkoski (2012).

3. Extending the scope of planning and scheduling problems

In the context of process development and manufacturing of drugs, R&D, and Operations Management (OM) departments perform critical activities that determine how planning and scheduling are effectively done (see Figure 1).

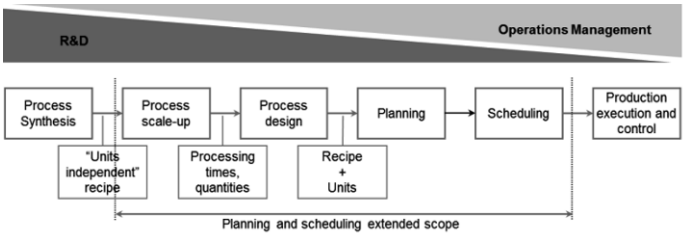

Figure 1 – Scope of the planning and scheduling problems.

We argue that the planning and scheduling functions must be extended in order to integrate decisions made in the *process scale-up* and *design* steps. The planning process, whether long-term or short-term, will clearly benefit from considering decisions taken at the scale-up and process design levels, as these decisions have a direct impact on the determination of the processing units suitable for the process, this leading to different production routes (alternative processes). On the contrary, after schedules have been released to the shop-floor, changes on planning and scheduling decisions can only be very limited, although *rescheduling* is a common practice. The same happens with changes in process design decisions that may not be possible or are not desirable to perform. In summary, we propose that the scope of the planning and scheduling functions is extended to account for design decisions (Barbosa-Povoa (2007)), especially for chemical manufacturing processes that are under development. This will increase the solution space of planning and scheduling decisions, hopefully leading to more globally optimized operations.

4. The Delivery Trade-offs Matrix

The ultimate goal of planning and scheduling is to deliver the right amounts of product at the right time, cost, and quality. Thus, in order to provide guidance on the issues that determine the effectiveness of manufacturing a new drug to the market, we propose a conceptual representation, named the *Delivery Trade-offs Matrix* (DTM) that is depicted in Figure 2. The relative importance of *costs* and *uncertainty* on the manufacturing activities that support the development and delivery of APIs or final products can be assessed in the DTM. It is important to notice that the proposed DTMs were built taking into account a set of estimated values available in the literature. To the best of our knowledge, there are no reliable figures regarding the cost structure and uncertainty associated to the R&D, trials I-III, and commercialization phases. However, the huge development and manufacturing costs in the pharmaceutical industry clearly justify a discussion on the path to follow towards manufacturing efficiency.

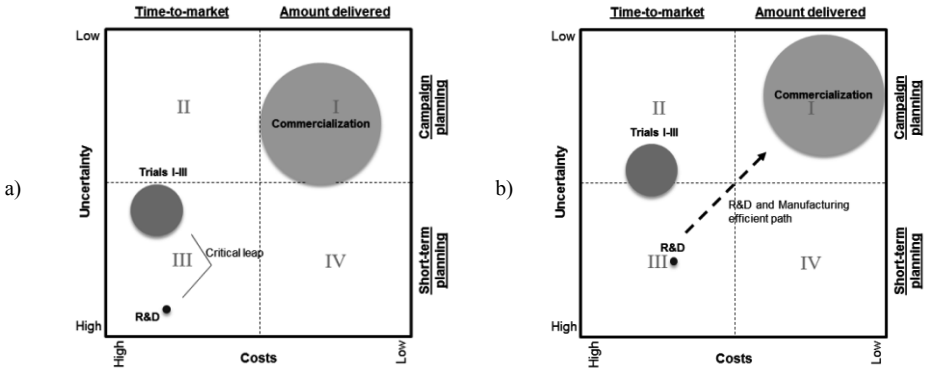

Figure 2 – Delivery Trade-offs Matrix (DTM) of the pharmaceutical industry: a) current state, b) future scenario.

The matrix depicts three phases of the drug development cycle (R&D, trials I-III, and commercialization). The R&D phase accounts for discovery, safety, and toxicology research activities and clinical supplies. Trials I-III relate to clinical studies performed on humans. The commercialization phase includes the manufacturing activities required to deliver the right amounts of product to the market, after approval by the regulatory agencies. Uncertainty and costs are represented in a continuous scale from *high* to *low*. The proportion of the production lot size at each phase is indicated by the size of the associated bubble. The DTM of Figure 2.a) shows the current trade-offs of the industry, while b) depicts a future scenario, as a possible response to the challenges the pharmaceutical industry is facing and needs to overcome. These aspects are next discussed in more detail.

4.1. Uncertainty and costs

At the start of a research program, products and processes have not yet been developed, and therefore there is a high uncertainty associated to the drug structure and to the production process. Uncertainty makes planning decisions more complex, since it is more difficult to estimate the required times and resources. For example, in the development and manufacturing of APIs it is common to allocate production resources 6 to 12 months in advance. Thus, changes in the plans may have a significant impact in manufacturing costs and delivery time. With drug development the uncertainty tends to decrease as product and process characteristics are better understood. In fact at the laboratory scale, only small amounts are produced (around few hundred grams). The delivery of the first scaled up batch (usually between 1 to 5 kg), used to support toxicological and formulation studies, along with phase I trials, is on the critical path of the development process This scale-up is particular difficult to perform since the knowledge obtained at the laboratory scale is seldom sufficient to guarantee a successful process at a plant scale (Federsel, 2009). Moreover, the drug development process requires a series of scale-ups so as to develop an efficient production process.

At the commercialization stage, the need for API or drug products is normally in the order of hundreds of kilograms. The processes are well defined, thus the uncertainty is mainly associated to market parameters such as demand, and to the processing time of the complex production tasks. The current practice demonstrates that there are large costs and high uncertainty at the R&D and trials I-III phases (see Figure 2 a), with the total estimated cost of bringing a new drug to market being larger than 1 billion dollars (Kessel, 2011). In terms of the total cost structure, pharmaceutical R&D costs are

around 30% to 35%, and clinical trials (typically representing the most significant cost) can be between 35% to 40% of the total (Suresh & Basu, 2008).

4.2. Time-to-market and amount delivered

It should be noted that from the planning and scheduling perspective, the delivery of products to Trials I-III phases is of extreme importance. Shah (2004) and Buchholz (2010) pointed out that time-to-market is a critical driver of the pharmaceutical industry. Additionally, Buchholz (2010) highlighted that fast and robust scalability of the production processes is another relevant driver for this industry. In fact it is quite often to have more than one company developing similar drugs, and therefore the importance to respect due dates is even more crucial.

On the other hand, at the commercialization phase there is more flexibility concerning delivery dates, if there is inventory on the supply chain. According to Shah (2004), the whole pharmaceutical chain stock can represent 30% to 90% of the annual demand in quantity. Therefore, at this phase, we can say that delivering the right product amounts is relatively more important than respecting delivery dates. Remember that the production lot sizes at the Trials I-III phases are in the order of few kilograms, while after several scale-up and validation steps, the lot sizes are around hundreds of kilograms. After drug development, the manufacturing costs are lower and tend to decrease with the reduction of the root causes of variability in the production process.
Concerning the operating mode, manufacturing sites run in *short-term mode* to fulfil a small product demand, or run preferably in *campaign mode* to respond to a regular demand. Sometimes the short-term mode is also used for manufacturing products that are in commercialization, this naturally resulting in the production of a smaller number of lots. However, in all cases the process must run with the same lot size as approved by the regulatory agencies.

4.3. The path to efficient R&D and manufacturing activities

All the above issues led the pharmaceutical industry to recognize the need for reducing time-to-market, the costs of new drug development, and the manufacturing costs. The path to efficient R&D and manufacturing activities requires new ways to address uncertainty and reduce costs (see Figure 2 b). This will involve the introduction of new production technologies (Suresh & Basu, 2008), as well as the adoption of innovative process design, planning, and scheduling decision-making tools. For example, according to Roberge et al. (2005), 50% of the reaction tasks in the chemical-pharmaceutical industry could benefit from the adoption of continuous processes based on the micro-reactor technology. In what concerns decision-making, the relevance of applying optimization tools and deploying more integrated decision-making processes is being recognized by the industry, despite the challenges that still exist (Grossmann, 2012). A new path must then be followed as represented in Figure 2 b. Such path must focus on improving the reliability of the drugs delivery by dealing with the uncertainty and the associated costs. The challenge here is to address in a systematic way the huge uncertainty present in the supply chain, so as to decrease the delivery times and meet the delivery quantities, thus improving the delivery reliability and response time. In the manufacturing sites, a more effective utilization of the resources can be achieved by integrating process design, planning and scheduling decisions and reducing the production lot sizes, but without increasing the costs, particularly the ones related to the long production changeovers.

5. Conclusions

This work analyses the main aspects that influence planning and scheduling decisions in the context of the pharmaceutical industry. Extending the traditional scope of planning and scheduling functions is particularly interesting, if drug development and manufacturing activities are simultaneously considered. The critical factors that determine planning and scheduling were identified and grouped in three categories: market, processes, and plants. In our view, comprehensive optimization methods for this sector must take into account these factors. Finally, we propose a conceptual representation, the Delivery Trade-offs Matrix, as a contribution to better managing uncertainty and costs issues, in the drug development and manufacturing activities. The matrix shows that the pharmaceutical industry should focus on the manufacturing and delivery issues knowing that each phase of the development cycle has different challenges. The integration of design decisions in the planning and scheduling is fundamental to do in the early stages of the drug development cycle. While the implementation of high flexible and high efficient manufacturing systems will then require the integration of planning and scheduling and control, especially during the commercialization phase.

References

A. Barbosa-Povoa, 2007, A critical review on the design and retrofit of batch plants, Computers & Chemical Engineering, 31, 833-855

S. Buchholz, 2010, Future manufacturing approaches in the chemical and pharmaceutical industry, Chemical Engineering and Processing: Process Intensification, 49, 993-995

S. Engell, I. Harjunkoski, 2012, Optimal operation: Scheduling, advanced control and their integration, Computers & Chemical Engineering

H. Federsel, 2009, Chemical Process Research and Development in the 21st Century: Challenges, Strategies, and Solutions from a Pharmaceutical Industry Perspective, Accounts of Chemical Research, 42, 671-680

I. Grossmann, 2012, Advances in mathematical programming models for enterprise-wide optimization, Computers & Chemical Engineering

I. Harjunkoski, C. Maravelias, P. Bongers, P. Castro, S. Engell, I. Grossmann, J. Hooker, C. Méndez, G. Sand, J. Wassick, Scope for industrial applications of production scheduling models and solution methods, Computers & Chemical Engineering, Volume 62, 5 March 2014, Pages 161-193

M. Hynes III, 2009, Project and capacity management: An application to drug development, Computers & Chemical Engineering, 33, 1994-1998

M. Kessel, M, 2011, The problems with today's pharmaceutical business an outsider's view, Nature biotechnology, 29, 27-33

C. Mendez, J. Cerda, I. Grossmann, I. Harjunkoski, M. Fahl, 2006, State-of-the-art review of optimization methods for short-term scheduling of batch processes, Computers & Chemical Engineering, 30, 913-946

S. Moniz, A. Barbosa-Póvoa, J. Sousa, P. Duarte, 2014, A solution methodology for scheduling problems in batch plants, Industrial & engineering chemistry research

D. Roberge, L. Ducry, N. Bieler, P. Cretton, B. Zimmermann, 2005, Microreactor technology: a revolution for the fine chemical and pharmaceutical industries, Chemical engineering & technology, 28, 318-323

N. Shah, 2004, Pharmaceutical supply chains: key issues and strategies for optimisation, Computers & Chemical Engineering, 28, 929-941

P. Suresh, P. Basu, 2008, Improving pharmaceutical product development and manufacturing: impact on cost of drug development and cost of goods sold of pharmaceuticals, Journal of Pharmaceutical Innovation, 3, 175-187

Krist V. Gernaey, Jakob K. Huusom and Rafiqul Gani (Eds.), 12th International Symposium on Process Systems Engineering and 25th European Symposium on Computer Aided Process Engineering.
31 May – 4 June 2015, Copenhagen, Denmark

Flare Minimization of Ethylene Plant Start-up via Resource-Task Network Approach

Guang Song, Tong Qiu*, Bingzhen Chen

Department of Chemical Engineering, Tsinghua University, Beijing, China

Abstract

Energy utilization and environment protection has received increasing attention over the last few decades. Therefore, flare minimization has become one of the main concerns for ethylene industry. Currently, the research of flare minimization has two major approaches, which are the experience-based approach and the dynamic simulation approach. The former has some limitations when it has to confront dynamic operations. The latter adopts dynamic simulation to validate the proposed start-up plans, which lacks optimization for the start-up plans. The start-up process of an ethylene plant can be considered as a semi-continuous process. Thus, the short-term scheduling approach based on resource-task network (RTN) is firstly used in this paper to depict the super-structure of the start-up process and optimize the start-up plans. This work developed a flare minimization model for the start-up process of ethylene plant, which could overcome the aforementioned shortcoming. We established the mathematical formulation of the flare minimization model, whose reliability and adaptability was validated by 5 significant case studies. The results showed that the flare minimization model also could effectively reduce start-up durations.

Keywords: flare minimization, ethylene plant, start-up, scheduling, resource-task network

1. Introduction

Energy utilization and environment protection has gotten more and more attention during the last few decades. The complicated start-up operations of ethylene plant would generate huge amounts off-spec product streams that have to be sent to flare systems (Q. Xu, 2009). Flare minimization has become one of the main concerns for the ethylene industry. Currently, the research of flare minimization has two major approaches, which are the experience-based approach and the dynamic simulation approach.

In the experience-based approach, the flare emission sources are firstly identified. Based on this, some improvements have been presented to reduce flare emissions, such as starting charge gas compressors with starting working medium(SWM) before feeding the furnace (A. Shaikh, 1995). However, the experience-based approaches have some limitations when they have to confront dynamic operations. Therefore, a “three step” methodology for flare minimization by using dynamic simulation tools is proposed (Q. Xu, 2008). This methodology is used to study start-up performance of a multistage compression system (X. Yang, 2009) and integrated cryogenic separation system (Y. Zhao, 2014). However, the above methods use dynamic simulation to validate the proposed startup or shutdown plan, which lack optimization for operating parameters. Thus, a flare minimization model of an ethylene splitter system based on the simulation data for different operating situations have been built, which optimizes the operating

* Corresponding author: Tong Qiu. qiutong@tsinghua.edu.cn.

parameters in the shutdown plan (G. Song, 2013). Notwithstanding, the model only involved the ethylene splitter system, and also lacked the optimization for the whole plant. In this work, the start-up process of an ethylene plant is considered as a semi-continuous process. The short-term scheduling approach based on resource-task network (RTN) is firstly utilized to model the flare minimization problem, which includes the whole plant.

2. Resource-Task Network Approach

RTN approach has been implemented to definitely model the main features encountered in ethylene plant start-up process such as the choice of SWM, inventories of products, start-up operations and procedures and units' state, etc. The main characteristic of RTN approach is the entirely uniform description of available resources, such as materials, processing and storage equipment, utilities, and different states of the same equipment. The other concept involved in the RTN approach is that of a task, which can be viewed as an abstract operation that consumes or/and produces a specific set of resources. In this work, not all resources and tasks will be treated in the same manner. The following subsections will describe the semantic elements in detail.

2.1. Equipment Resources.

The equipment resources include all of the equipment units, such as furnace and compressors. An example of an equipment resource is given in Figure 1 as "J1". One equipment resource, at a given time, can be used by a single processing task at most, meaning that any two tasks cannot be executed simultaneously in the same equipment resource.

2.2. Cumulative Resources.

The cumulative resource represents a resource that, at a given time, can be shared by multiple processing tasks. So, they include materials and utilities. The material resources are raw materials, intermediate and finished products that are consumed or produced during the start-up operation. The utility resources represent steam under different pressures. An example of a cumulative resource is given in Figure 1 as "R2", in which the initial stock and the capacity are given.

2.3. State Resources.

The state resource represents a state of an equipment. Some equipment have different operating states. For example, the furnace has three states and needs to follow this sequence: 1) "shutdown"; 2) "steam running"; 3) "feed running". The state resource can be used to manage transitions between modes. An example of a state resource is given in Figure 1 as "R1", in which the initial state and the capacity are given.

2.4. Task.

A task node represents a processing operation that consumes and/or produces a specific set of resources. An example of a task is given in Figure 1 as "T1". The maximum and minimum batch size are given as V_{max} and V_{min}. Moreover, the duration of the task equals to $pf+pv*B$, where B is a variable equal to the batch size of the task.

3. Mathematical Formulation

During the last decade, the research on RTN-based scheduling formulations has made great progress. Castro et al proposed several formulations for batch and continuous processes (P. M. Castro, 2010). Thery et al extended the RTN approach to integrate the production and utility system (R. Thery, 2012). In view of the aforementioned formulation, a continuous time mixed integer linear programming (MILP) model is

presented in this paper based on the global time point representation. The type of event representation and constraints of the formulation are given below.

3.1. Event Representation.

The continuous-time formulation uses a uniform time gird to keep track of events taking place. The time horizon is divided into *n-1* time slots. The boundaries are named event points and global time points, where the events take place. The absolute time of event point is a variable, which needs to be determined via the optimization.

3.2. Allocation constraints.

The three index binary variable $W(i,n,n')$ defines the assignment of task i that starts at event point n and ends at event point *n'* ($n < n'$). A parameter, Δn, is defined as $n < n' \leq n + \Delta n$, to control on the maximum number of event points allowed between the beginning and end of a given task. The allocation constraints have the three following parts.

In every equipment unit *j* ($j \in J$), at most, one task *I* ($i \in I$) can start at each event point *n* ($n \in N$) as given by constraint 1.

$$\sum_{i \in I_j} \sum_{\substack{n' \in N \\ n < n' \leq n + \Delta n}} W(i,n,n') \leq 1 \qquad \forall j \in J, n \in N \tag{1}$$

Similarly constraint 2 states that, in every equipment unit *j* ($j \in J$), at most, one task *i* ($i \in I$) can end at each event *n* ($n \in N$).

$$\sum_{i \in I_j} \sum_{\substack{n \in N \\ n' - \Delta n \leq n < n'}} W(i,n,n') \leq 1 \qquad \forall j \in J, n' \in N \tag{2}$$

Constraint 3 states that, in a given equipment unit a new task can start only if the total number of tasks that started earlier matches the total number of tasks ending.

$$\sum_{\substack{n' \in N \\ n < n' \leq n + \Delta n}} W(i,n,n') \leq 1 - \sum_{\substack{n' \in N \\ n' < n}} \sum_{\substack{n'' \in N \\ n' < n'' \leq n' + \Delta n}} \sum_{i \in I_j} W(i',n',n'') + \sum_{n'' \in N} \sum_{\substack{n' \in N, n' \leq n \\ n'' < n' \leq n'' + \Delta n}} \sum_{i \in I_j} W(i',n'',n') \tag{3}$$

$\forall i \in I_j, j \in J, n \in N, n > 1$

3.3. Capacity constraints.

Constraint 4 states that the amount *R(r, n)* of resource *r* stored at event point *n* should never exceed its maximum storage capacity C_r^{max}.

$$0 \leq R(r,n) \leq C_r^{max} \qquad \forall r \in R, n \in N \tag{4}$$

3.4. Batch size constraints.

For each task, constraint 5 states that the batch size $B(i,n,n')$ is bound by the maximum V_i^{max} and minimum V_i^{min} value.

$$W(i,n,n')V_i^{min} \leq B(i,n,n') \leq W(i,n,n')V_i^{max} \qquad \forall i \in I, n, n' \in N, n < n' \leq n + \Delta n \tag{5}$$

3.5. Cumulative resource mass balance.

In the mass balance eq. 6, the amount $R(r,n)$ of resource *r* stored at event point *n* equals to that at previous event point *n-1* adjusted by the materials coming into and out of the resource at the current *n*. Constraint 6 represents the generalized mass balance that is applicable to all the cumulative resources, in which *I*(*r, i, n*)/*O*(*r, i, n*) defines the amount of cumulative resource *r* ($r \in RC$) entering in/leaving task *i* ($i \in I$) at event point *n* and

governed by a mass balance, and *UI*(*r, i, n*)/*UO*(*r, i, n*) defines those not governed by a mass balance.

$$R(r,n) = R(r,n-1) + \sum_{i\in I} O(r,i,n) - \sum_{i\in I} I(r,i,n) + \sum_{i\in I} UO(r,i,n) - \sum_{i\in I} UI(r,i,n) \qquad \forall r \in R^C, n \in N, n > 1 \tag{6}$$

The initial amount $R0_r$ of resource *r* is given as constraint 7.

$$R(r,1) = R0_r - \sum_{i\in I} I(r,i,1) - \sum_{i\in I} UI(r,i,1) \qquad \forall r \in R^C \tag{7}$$

The demand in resource needs to be constrained as constraint 8.

$$R(r,N) \geq D(r) \quad \forall r \in R^C \tag{8}$$

3.6. Processing of cumulative resource.

Tasks can transform cumulative resources in known or unknown proportions of batch size. In the latter case, the proportions are calculated through the resolution of the optimization problem. Constraint 9~10 state that the batch size *B*(*i, n, n'*) is equal to the sum of the amount *I*(*r, i, n*) of resource r entering in task i as well as the amount *O*(*r, i, n'*) of resource *r* leaving task *i*.

$$\sum_{\substack{n'\in N \\ n<n'\leq n+\Delta n}} B(i,n,n') = \sum_{r\in R_i^{cons}} I(r,i,n) \qquad \forall i \in I, n \in N \tag{9}$$

$$\sum_{\substack{n\in N \\ n'-\Delta n\leq n<n'}} B(i,n,n') = \sum_{r\in R_i^{prod}} O(r,i,n') \qquad \forall i \in I, n' \in N \tag{10}$$

The amount of input flows into a task *i* needs to be constrained as given by constraint 11~12. The amount of output flows out of a task *i* constraint is similar, that is omitted.

$$I(r,i,n) \leq \left(\rho_{i,r}^{cons} + \mu_{i,r}^{cons}\right) \cdot \sum_{\substack{n'\in N \\ n<n'\leq n+\Delta n}} B(i,n,n') \quad \forall i \in I, r \in R_i^{cons}, n \in N \tag{11}$$

$$I(r,i,n) \geq \rho_{i,r}^{cons} \cdot \sum_{\substack{n'\in N \\ n<n'\leq n+\Delta n}} B(i,n,n') \quad \forall i \in I, r \in R_i^{cons}, n \in N \tag{12}$$

3.7. Production/consumption of cumulative resource.

The consumption and production of cumulative resources needs to be constrained as given by constraint 13~14.

$$UI(r,i,n) = u_{i,r}^{cons} \cdot \sum_{\substack{n'\in N \\ n<n'\leq n+\Delta n}} W(i,n,n') \qquad \forall i \in I, r \in R^C, n \in N \tag{13}$$

$$UO(r,i,n') = u_{i,r}^{prod} \cdot \sum_{\substack{n\in N \\ n'-\Delta n\leq n<n'}} W(i,n,n') \quad \forall i \in I, r \in R^C, n' \in N \tag{14}$$

3.8. State resource balance.

Be similar as cumulative resource balance, constraint 15~16 represent the transition among states of a resource.

$$R(r,n) = R(r,n-1) + \sum_{i \in I}\left(\alpha_{i,r}^{prod} \cdot \sum_{\substack{n' \in N \\ n-\Delta n \le n' < n}} W(i,n',n)\right) - \sum_{i \in I}\left(\alpha_{i,r}^{cons} \cdot \sum_{\substack{n' \in N \\ n < n' \le n+\Delta n}} W(i,n,n')\right) \quad (15)$$

$\forall r \in R^S, n \in N, n > 1$

$$R(r,1) = R0_r - \sum_{i \in I}\left(\alpha_{i,r}^{cons} \cdot \sum_{\substack{n' \in N \\ 1 < n' \le 1+\Delta n}} W(i,1,n')\right) \qquad \forall r \in R^S \quad (16)$$

3.9. Duration constraints.

The finish time and start time of a task are constrained by the duration constraints as given by constraint 17~18.

$$T(n') - T(n) \ge pf_i \cdot W(i,n,n') + pv_i \cdot B(i,n,n')$$
$$\forall i \in I, n, n' \in N, n < n' \le n + \Delta n \quad (17)$$

$$T(n') - T(n) \le M\big(1 - W(i,n,n')\big) + pf_i \cdot W(i,n,n') + pv_i \cdot B(i,n,n')$$
$$\forall i \in I, n, n' \in N, n < n' \le n + \Delta n \quad (18)$$

The absolute time of the first time point should be assigned to the start time of time horizon, and similarly that of the last time point should be assigned to the ending time as given in constraint 19.

$$T(1) = 0;\ T(n) = H \quad (19)$$

4. Case Study

In this section, the modeling of an ethylene plant's start-up process is presented to illustrate the use of the proposed flare minimization model. The RTN representation of the start-up process of the ethylene plant is shown in Figure 1, in which the problem data related to resources and tasks are also given. The detailed description of the resource node and task node is given in the list.

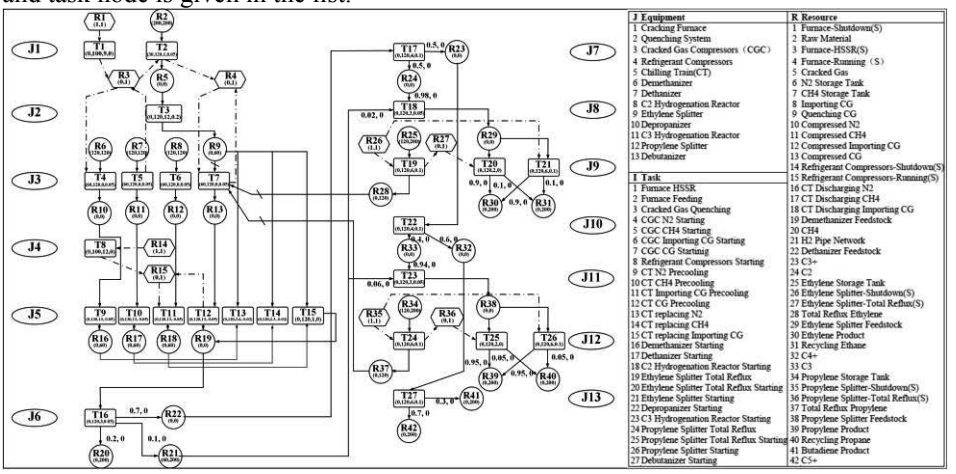

Figure 1. RTN representation of the start-up process of the ethylene plant.

Five case studies with different raw material inventories are presented, and case 5 is the general start-up process. Note that the reduction of starting time means not only the increase of normal manufacturing time and but also the saving of raw materials from flaring. Therefore, the optimal objective is to minimize the start-up duration. Table 1 gives the raw material inventories of each case and computational results. For case 1 and case 2, it can be observed that one more time point could obtain shorter duration but require more computer time. For case 3 and case 4, the reduction of the ethylene and propylene inventories caused the longer durations, because the total reflux operation of product splitter could not be executed. Case 1~4 all require less durations than case 5, thus the flare minimization model could effectively reduce the start-up duration.

Table 1 Case study features and computational results

Case	R6	R7	R8	R21	R25	R34	Duration/h	Time point	Δn	Cplex time[a]
1	120	120	120	60	120	120	60.66	14	4	189.73
2	120	120	120	0	120	120	60.16	15	4	1 000.02
3	120	120	120	0	30	30	82.16	15	4	407.09
4	120	120	120	0	0	0	91.30	15	4	48.08
5	120	120	0	0	0	0	91.78	15	4	57.48

a. Seconds on Intel(R) Core(TM) i7-3770 CPU @3.40GHz 3.90GHz Ram 8GB with CPLEX 12.5

5. Conclusion

This paper firstly used the short-term scheduling approach based on RTN to optimize the start-up plans. The RTN approach was used to depict the super-structure of the start-up process. We developed a flare minimization model for the start-up process of ethylene plant. As shown in computational results for five case studies, the flare minimization model could effectively reduce the start-up duration. Therefore, raw materials are saved from flaring during start-up process.

References

Q. Xu; X. Yang, C. Liu; K. Li; H. H. Lou; J. L Gossage, 2009, Chemical Plant Flare Minimization via Plantwide Dynamic Simulation, Ind. & Eng. Chem. Res., 48 (7), 3505-3512.

A. Shaikh, C. Lee, 1995, Minimize flaring during ethylene plant startup, Hydrocarbon Processing, 74(7), 89-96.

Q. Xu, K. Li, 2008, Dynamic simulation for chemical plant turnaround operation//Integrated Environmental Management Consortium Meeting [C], Houston, TX.

X. Yang, Q. Xu, C. Zhao, K. Li, H. H. Lou, 2009. Pressure-Driven Dynamic Simulation for Improving the Performance of a Multistage Compression System during Plant Startup, Ind. & Eng. Chem. Res., 48(20), 9195-9203.

Y. Zhao, J. Zhang, T. Qiu, J. Zhao, Q. Xu, 2014, Flare minimization during start-ups of an integrated cryogenic separation system via dynamic simulation, Ind. & Eng. Chem. Res., 53(4), 1553-1562

G. Song, T. Qiu, J. Zhao, 2013, Flare minimization model for an ethylene splitter system's shutdown, Ind. & Eng. Chem. Res., 52(26), 9180-9188

P. M. Castro, 2010, Optimal Scheduling of Pipeline Systems with a Resource-Task Network Continuous-Time Formulation, Ind. & Eng. Chem. Res., 49 (22), 11491-11505.

R. Thery, G. Hetreux, M. H. Agha, A. Hait, J. M. Le Lann, 2012, The extended resource task network: a framework for the combined scheduling of batch processes and CHP plants, Int J Prod Res, 50 (3), 623-646.

Krist V. Gernaey, Jakob K. Huusom and Rafiqul Gani (Eds.), 12th International Symposium on Process Systems Engineering and 25th European Symposium on Computer Aided Process Engineering.
31 May – 4 June 2015, Copenhagen, Denmark

Phenomenological Decomposition Heuristic for Process Design Synthesis of Oil-Refinery Units

Brenno C. Menezes,*[a] Jeffrey D. Kelly,[b] Ignacio E. Grossmann[c]

[a]*Refining Optimization, PETROBRAS, Rio de Janeiro, RJ, 20231-030, Brazil*
[b]*Industrial Algorithms, 15 St. Andrews Road, Toronto, ON, MIP-4C3, Canada*
[c]*Department of Chemical Engineering, Carnegie Mellon University, Pittsburgh, PA 15213, United States.*

Abstract

We propose a mixed-integer nonlinear optimization for process design synthesis of oil-refinery units that includes crude-oil mixing, unit processing and product blending. The quantity-logic-quality phenomena involving a non-convex mixed-integer nonlinear problem is decomposed into a two-stage stochastic programming model with complete recourse considering, in a first stage, quantity and logic variables in a mixed-integer linear model and, in a second stage, quantity and quality variables in a nonlinear programming formulation. Iteratively, nonlinear models of each demand scenario are restricted by the multi-scenario process design results. An industrial-sized example that is not solved in a full space model demonstrates our tailor-made decomposition scheme, which yields within 5% gap between the first and the average second stage results.
Keywords: Oil-refinery design synthesis, strategic planning, stochastic programming

1. Introduction

Multi-period and multi-scenario process design synthesis models integrating logic variables and quantity-quality relations gives rise to large scale non-convex mixed-integer nonlinear (MINLP) models that are often difficult to solve. In order to overcome this problem, a method denoted here as the phenomenological decomposition heuristic (PDH) partitions MINLP models into two simpler submodels namely logistics (quantity and logic) and quality (quantity and quality) problems. The logistics model solves a mixed-integer linear (MILP) problem with quantity and logic variables subject to quantity and logic constraints. Quality optimization solves a nonlinear (NLP) model for quantity and quality variables subject to quantity and quality constraints after the logic variables have been fixed at the values obtained from the solution of the logistics optimization.

The PDH algorithm resembles the well-known approach suggested in generalized Benders decomposition where complicating variables (in this case, binary) are fixed such that a simpler problem may be solved, which are later freed again for the new iteration of the master problem (Geoffrion, 1972). A similar method has also been applied for a different purpose, namely that of integrating decentralized decision-making systems through a hierarchical decomposition heuristic (HDH) (Kelly and Zyngier, 2008). In the context of the integration between logistics and quality problems, the coordinator (logistics problem) would send what we call logic pole-offers to the cooperator (quality problem), which would send back logic pole-offsets to the coordinator. This procedure continues until convergence is achieved, hopefully providing a good globally feasible MINLP solution.

A phenomenological decomposition example considering an MINLP crude-oil scheduling problem (Mouret et al., 2009) compares the full space solution and its decomposed MILP-NLP problem by neglecting the pooling or blending nonlinear constraints in the MILP model, and then composing the model in an NLP problem by relating quantity and quality variables for the binary results found in the MILP model. In their work, the full space solution becomes intractable for industrial-sized examples, but they are solved in an MILP-NLP decomposition gap lower than 4%. Only a small example considering low number of time slots is solved using an MINLP formulation, which yields the same result found in the decomposed solution but with higher computational expense.

Another decomposition method, applied in large scale MILP process industry problems (You et al., 2011; Corsano et al., 2014) and relying on relaxations and primal bounding information, is the bi-level decomposition (Iyer and Grossmann, 1998) that requires smaller computational times leading to solutions that are much closer to the global optimum when compared to the full space solution and to Lagrangean decomposition (Guignard and Kim, 1987). A cross-decomposition algorithm (Mitra et al., 2014), combining Benders and scenario based Lagrangean decomposition in two-stage stochastic MILP problems with complete recourse, demonstrates a reduction of iterations and stronger lower bounds compared to pure Benders decomposition.

2. Problem statement

Given future scenarios *sc*, the full design problem (*FDP*) consists of determining the expansion of existing units and installation of new units in petroleum refineries, which are defined by binary variables y_t related to the investment decision and continuous variables x_t that are the size of the new capacities to be expanded and installed.

The objective function (1) maximizes the net present value (NPV) and consists of cash flows (*CF*) from operational gains $\sum_{sc} \pi^{sc} CF_{op}(x_t^{sc})$ and investment costs $CF_{in}(x_t, y_t)$, where π^{sc} is the probability for the scenario *sc* with $\sum_{sc} \pi^{sc} = 1$.

$$(FDP)\ \max NPV = \sum_t \left(\sum_{sc} \pi^{sc} CF_{op}(x_t^{sc}) - CF_{in}(x_t, y_t) \right) \tag{1}$$

$$s.t. \quad A_t x_t + B_t y_t \leq b_t \quad \forall\ t \tag{2}$$

$$D_t y_t \leq d_t \quad \forall\ t \tag{3}$$

$$x_t^{sc} \leq x_t \quad \forall\ sc, t \tag{4}$$

$$h_t^{sc}(x_t^{sc}) = 0 \quad \forall\ sc, t \tag{5}$$

$$x_t, x_t^{sc} \in \mathbb{R}^+, y_t \in \{0,1\} \tag{6}$$

The investment layer in constrains (2) and (3) controls the capacity increase linked to the operational layer by (4), e.g. if capacity is expanded/installed, additional decisions over the scenarios are available in x_t^{sc}. Eq. (5) specifies linear and nonlinear constraints for each scenario *sc*. The PDH algorithm for the *FPD* problem considering scenarios is a two-stage stochastic programming model with the first stage problem (*FS*) comprising the investment and operational layers in an MILP model (logistics optimization), and

the second stage problems (SS^{sc}) in an NLP model (quality optimization), in which the complete recourse in crude-oil diet, processing, and imports permits the problem to match the different demand scenarios despite the first stage investment decisions. To the best of our knowledge, there is no work in the process design synthesis literature handling the following: (i) oil-refinery optimization including the mixing of crude-oils, processing units, and blending of the product streams, (ii) expansion and installation of existing and new units with consideration to their time of execution, and (iii) the decomposition of the oil-refinery process design problem along the phenomenological dimensions of quantity, logic, and quality in order to find good solutions in reasonable time. The need to improve the strategic decision-making to address issues in a quantitative manner rather than the usual qualitative approaches is acknowledged by the industry and still remains an active field of research (Shapiro, 2001).

3. Phenomenological decomposition heuristic algorithm

To formulate the MILP and NLP objective functions, the time horizon comprises investment t and operational t_0 time periods as seen in Figure 1. After project executions over each t with time duration of several years (ΔT_t), a new production framework is considered in the following time periods to determine new operational gains given by throughputs $QF_{u,t}^{sc}$ of crude, imports, and fuel sales ($u \in U_G$). These gains are considered fixed within the investment time period t; otherwise there would be the need to optimize the problem for every t_0, which results in a combinatorial explosive problem with small or no influence in the discrete decisions. Prices pr_{u,t_0} are considered varying annually to improve the accuracy of the NPV calculation. The gains are brought back to the initial time t_i (t_{i1}, t_{i2},…; see Figure 1) for every t_0 at an interest rate ir_t to reflect future gains when they are considered at the present. The investment amounts are withdrawn in t_i for the t with investment under consideration.

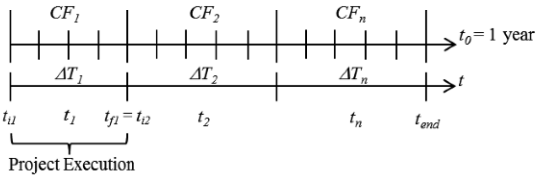

Figure 1. Investment t and operational t_0 time horizon.

The FS problem maximizes the NPV_{MILP} function (7) considering revenues from operational scenarios and costs from investments $y_{u,t}$ (expansions and installations) to among the process units u ($u \in U_I$). Constraints (8) to (12) are the capacity planning equations for adding new capacity $QN_{u,t}$ only once until the next-to-last time period ($t < t_{end}$) considering capital CAP_t, lower and upper bounds of the additions ($QN_{u,t}^{L}$ and $QN_{u,t}^{U}$), and varying and fixed cost coefficients, $\propto_{u,t}$ and $\beta_{u,t}$, respectively. Eq. (12) represents integer constraints to reduce the tree search related to investment in groups of units with the same functionality and considers process unit sequence-dependency investment based on the possible connectivity in the oil-refinery design. Eq. (13) is the linking constraint, where unit throughputs $QF_{u,t}^{sc}$ despite sc is lower than its current capacity $QC_{u,t}$. Eq. (14) represents linear operational constraints, by neglecting the nonlinear relations or linearizing them.

$$(FS)\ \max NPV_{MILP} = \sum_{t}\left(\sum_{t_0=t_i}^{t_0=t_f}\sum_{sc}\sum_{u\in U_G}\frac{\pi^{sc} pr_{u,t_0} QF_{u,t}^{sc}}{(1+ir_t)^{t_0}} - \sum_{u\in U_I}\frac{\propto_{u,t} QN_{u,t} + \beta_{u,t} y_{u,t}}{(1+ir_t)^{\sum_t \Delta t - \Delta t_t}}\right) \quad (7)$$

$$s.t. \quad \sum_{u\in U_I} \propto_{u,t} QN_{u,t} + \beta_{u,t} y_{u,t} \le CAP_t \ \ \forall\ t < t_{end} \quad (8)$$

$$QC_{u,t+1} = QC_{u,t} + QN_{u,t} \ \ \forall\ u \in U_I, t < t_{end} \quad (9)$$

$$QN_{u,t}^{L} y_{u,t} \le QN_{u,t} \le QN_{u,t}^{U} y_{u,t} \ \ \forall\ u \in U_I, t < t_{end} \quad (10)$$

$$\sum_{t<t_{end}} y_{u,t} \le 1 \ \ \forall\ u \in U_I \quad (11)$$

$$D_{u,t} y_{u,t} \le d_{u,t} \ \ \forall\ u \in U_I, t < t_{end} \quad (12)$$

$$QF_{u,t}^{sc} \le QC_{u,t} \ \ \forall\ u, sc, t \quad (13)$$

$$\tilde{h}_{u,t}^{sc}\left(x_{u,t}^{sc}\right) = 0 \ \ \forall\ u, sc, t \quad (14)$$

$$QC_{u,t}, QN_{u,t}, QF_{u,t}^{sc}, x_{u,t}^{sc} \in \mathbb{R}^{+}, y_{u,t} \in \{0,1\} \quad (15)$$

The second stage SS^{sc} problem of each scenario maximizes the NPV_{NLP}^{sc} function (16) for fixed investment decisions $\overline{QN}_{u,t}$ and $\bar{y}_{u,t}$ and unit throughputs lower than the capacities from the *FS* problem, so it means $QF_{u,t}^{sc} \le \overline{QC}_{u,t}$ for existing units ($u \in U_E$) (both previously existing and those installed). Eq (17) represents linear and nonlinear equations for crude-oil mixing, processing, and blending that can be found in Menezes et al. (2013) for the improved swing-cut distillation modeling and in Menezes et al. (2014) for the other equations, in which is also given overall data such as price, crude assay, and product specification. The number of these equations and its variables varies every each MILP-NLP iteration depending on the binaries $y_{u,t}$ found in the *FS* problem. Figure 2 shows the PDH algorithm flow. For the second or later MILP iteration (*FS*), yields and rates are taken from the past NLP or quality optimization (SS^{sc}), which brings processing changes into the MILP problem. The algorithm details is in Menezes (2014).

$$(SS^{sc})\ \max NPV_{NLP}^{sc} = \sum_{t}\left(\sum_{t_0=t_i}^{t_0=t_f}\sum_{u\in U_G}\frac{pr_{u,t_0} QF_{u,t}^{sc}}{(1+ir_t)^{t_0}} - \sum_{u\in U_I}\frac{\propto_{u,t} \overline{QN}_{u,t} + \beta_{u,t}\bar{y}_{u,t}}{(1+ir_t)^{\sum_t \Delta t - \Delta t_1}}\right) \forall\ sc \quad (16)$$

$$s.t. \quad h_{u,t}^{sc}\left(x_{u,t}^{sc}\right) = 0 \ \ \forall\ u \in U_E, sc, t \quad (17)$$

$$QF_{u,t}^{sc}, x_{u,t}^{sc} \in \mathbb{R}^{+} \quad (18)$$

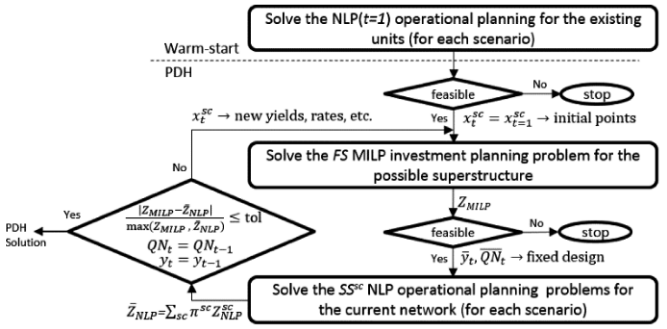

Figure 2. PDH algorithm flowchart.

4. Illustrative example

We apply the proposed decomposition to capacity planning of the São Paulo State supply chain refineries in Brazil, where the investments in new capacities for both expansion and installation of units over a 15-years time horizon (3 periods of 5 years each) are defined in the first stage with the same scenario probability π^{sc} and the operations including the nonlinearities are defined in the second stage.

As shown in Table 1, the decomposition solution converged after 4 iterations, when the investment results between consecutive iterations are nearly identical (4th iteration in Table 2) within a 5% gap between the NPV_{MILP} and the average-NPV_{NLP}^{sc} ($\overline{NPV}_{MILP}$) solutions. The indices r, u, and n in Table 2 correspond to refinery, unit, and number of the unit, respectively. The full space MINLP problem was tested with several solvers, but it was found to be infeasible in the root relaxation. Table 3 shows the model statistics of the problems. Note that the number of equations and variables in the NLP problems change over the time because of different investment decisions. The NLP solver used is CONOPT (v. 3.15P) and the MILP solver is CPLEX (v. 12.6.0.0).

Table 1. São Paulo State refineries example: MILP and NLP solutions (in billions of U.S. dollars).

iteration →		1st	2nd	3rd	4th
NPV_{MILP}		8,063	7,812	7,893	7,934
MILP optimality gap (%)		0.957	0.994	0.998	0.991
NPV_{NLP}^{sc}	sc=1	6,722	8,429	7,856	7,866
	sc=2	6,567	8,287	7,719	7,730
	sc=3	6,099	7,777	7,099	7,139
$\overline{NPV}_{NLP}$		6,462	8,164	7,558	7,578
NPV_{MILP}-$\overline{NPV}_{NLP}$ gap (%)		19.9	4.5	4.2	4.5

Table 2. Capacity expansions (exp) and installations (ins) (in 1,000 m^3/d).

iteration →			1st		4th					1st		4th	
r	u	n	exp	ins	exp	ins	r	u	n	exp	ins	exp	ins
REPLAN	CDU	1	9.7				RPBC	CDU	1	4.0		4.0	
	CDU	2			5.5			VDU	1		2.9	2.9	
	VDU	1			2.0			VDU	3		6.2		
	VDU	2	6.6					DEBUT	2		2.0		2.0
	FCC	1						FCC	2		18.9		12.7
	CLNHT	1	1.1		1.1			LCNHT	2		9.5		6.4
	ST	2		5.1		5.1		CLNHT	2		2.0		2.7
	DC	3		10.0		10.0		ST	2		2.0		2.7
	REF	2		1.3		1.3		REF	2			0.6	
REVAP	CDU	1	12.0		12.0			ALK	1		0.8		
	VDU	1	5.4		6.0		RECAP	SUPER	2		2.0		2.0
	FCC	1	2.5		3.9								
	DC	2		7.5		5.7							
	KHT	3		2.0		2.0							
	LCNHT	2	2.1			2.8							
	CLNHT	2		4.3		3.0							
	ST	2				3.0							
	REF	2		1.4		1.0							

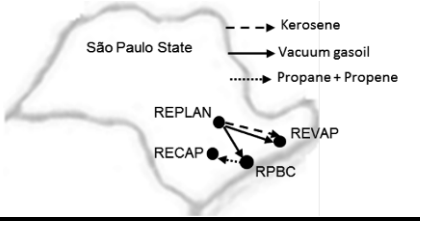

Table 3. MILP and NLP models statistics (with 203 binaries in the MILP problem).

iteration →		1st		2nd		3rd		4th	
		MILP	NLP	MILP	NLP	MILP	NLP	MILP	NLP
equations		10,076	5,406	10,076	5,347	10,076	5,378	10,076	5,349
variables		13,782	5,932	13,782	5,870	13,782	5,899	13,782	5,870
CPU(s)		3.0		4.3		3.4		3.4	
	sc=1		17.5		5.5		3.5		3.7
	sc=2		20.7		0.2		4.2		4.2
	sc=3		20.6		0.2		4.1		4.3

5. Conclusion

We have described how to iteratively solve an MINLP capital investment optimization in a two-stage programming problem using MILP and NLP sub-solvers configured in a coordinated manner that resulted in an MILP-NLP solution gap within 5%. This same technique can be applied to any advanced planning and scheduling MINLP problem in the process industries given our assertion that these problems can be phenomenologically modeled using the QLQP (quantity-logic-quality phenomena) attributes to concatenate the sub-problems. The major advantage of the PDH approach is that each sub-problem can be decomposed and thoroughly investigated to debug inconsistencies and unexpected solutions when they exist. In contrast to existing MINLP and global optimizers that may fail to even obtain feasible solutions, the PDH approach is computationally much more efficient and robust, and yields optimal or near optimal solutions.

References

A. Geoffrion, 1972, Generalized Benders Decomposition, J Optimiz Theory App, 10, 237-260.

S. Mouret, I.E. Grossmann, P. Pestiaux, 2009, A Novel Priority-Slot Based Continuous-Time Formulation for Crude-Oil Scheduling Problems, Ind Eng Chem Res, 48, 8515-8528.

G. Corsano, G. Guillén-Gosálbez, J. Montagna, 2014, Computational Methods for the Simultaneous Strategic Planning of Supply Chain and Batch Chemical Manufacturing Sites, Comput Chem Eng, 60, 154-171.

M. Guignard, S. Kim, 1987, Lagrangean Decomposition: A Model Yielding Stronger Lagrangean Bounds, Math Program, 39, 215–228.

R.R. Iyer, I.E. Grossmann, 1998, A Bilevel Decomposition Algorithm for Long-range Planning of Process Networks, Ind Eng Chem Res, 37(2), 474–48.

J.D. Kelly, D. Zyngier, 2008, Hierarchical Decomposition Heuristic for Scheduling: Coordinated Reasoning for Decentralized and Distributed Decision-Making Problems, Comput Chem Eng, 32, 2684–2705.

B.C. Menezes, J.D. Kelly, I. E. Grossmann, 2013, Improved Swing-Cut Modeling for Planning and Scheduling of Oil-Refinery Distillation Units, Ind Eng Chem Res, 52, 18324-18333.

B.C. Menezes, L.F.L. Moro, W.O. Lin, R.A. Medronho, F.L.P. Pessoa, 2014, Nonlinear Production Planning of Oil-Refinery Units for the Future Fuel Market in Brazil: Process Design Scenario-Based Model, Ind Eng Chem Res, 53, 4352-4365.

B.C. Menezes, 2014, Quantitative Methods for Strategic Investment Planning in the Oil-Refining Industry, Ph.D. thesis, Federal University of Rio de Janeiro, Rio de Janeiro, Brazil.

S. Mitra, P. Garcia-Herreros, I.E. Grossmann, 2014, A Novel Cross-decomposition Multi-cut Scheme for Two-Stage Stochastic Programming, Computer Aided Chemical Engineering, Volume, 32, 241-246.

J.F Shapiro, 2001, Modeling the Supply Chain. Duxbury Press: New York, NY.

F. You, I. E. Grossmann, J. M. Wassick, 2011, Multisite Capacity, Production, and Distribution Planning with Reactor Modifications: MILP Model, Bi-level Decomposition Algorithm versus Lagrangean Decomposition Scheme, Ind Eng Chem Res, 50, 4831–4849.

Krist V. Gernaey, Jakob K. Huusom and Rafiqul Gani (Eds.), 12th International Symposium on Process Systems Engineering and 25th European Symposium on Computer Aided Process Engineering.
31 May – 4 June 2015, Copenhagen, Denmark

A Value Chain Optimisation Model for a Biorefinery with Feedstock and Product Choices

Madeleine J. Bussemaker[a*], Kenneth Day[b], Geoffrey Drage[b], Franjo Cecelja[a]

[a]*Process and Information Systems Engineering Research Centre, University of Surrey, Guildford, GU2 7XH, United Kingdom*
[b]*Bio-Sep Limited, Clapton Revel, Wooburn Moor HP10 0NP, United Kingdom*

Abstract

There is a movement towards implementation of 2nd generation biorefineries producing chemicals from renewable sources or residual feedstock such as woody biomass or woodchips. Value chain optimisation is used as a decision making tool to aide in the development and implementation of biorefining. To this end, an optimisation model for the value chain assessment of a lignocellulosic biorefinery was developed using mixed integer linear programming and verified with a softwood case study. The model allows for the comparison of different feedstock sources with different characteristics such as moisture content and size. Each source may be subjected to alternate pre-processing prior to biorefining to up to three product streams. Optimisation identified the most profitable locations for each process stage, including, collection points and intermediate storages, pre-processing locations, biorefining locations and customers for different production pathways according to the associated transport as well as capital and operational costs. The scene was set in Scotland, UK, with two source streams, logged softwood versus the chipped by-products from the sawmill industry. The biorefinery was based on a technology developed by Bio-Sep Ltd which converts the lignocellulosic feedstock into three product streams, cellulose, hemicellulose and lignin. The results demonstrate the significant effect of moisture content on drying and transportation costs. Overall, it was demonstrated that decision making tools for biomass processing must allow for the consideration of different pre-processing stages with respect to overall costs and/or profit

Keywords: biorefining, lignocellulose, optimisation, value chain,

1. Introduction

Biorefinery value chain analysis from lignocellulosic feedstock has traditionally focussed on ethanol or heat production for fuel (Sharma, Ingalls et al. 2013). However, increasingly, alternative product streams are being considered. Therefore, as biorefining for non-biofuel purposes become more inevitable, tools to evaluate the economic viability of various operations are increasingly needed. It is evident that previous supply and/or value chain works have focussed on the distribution of processing hubs, (Bowling, Ponce-Ortega et al. 2011) comparison of biomass sources, (van Dyken, Bakken et al. 2010) first and second generation bioethanol (Akgul, Shah et al. 2012) and feedstock properties such as moisture content (Dunnett, Adjiman et al. 2007). In addition, transport cost and distance was demonstrated to be an important consideration for biofuel supply chain networks (Yu, Cecelja et al. 2013).

Lignocellulose consists of three main polymeric materials, lignin, hemicellulose and cellulose which undergo further conversion to monomer sugars and aromatic alcohols with potential use across industry. Sources of lignocellulose include woody biomass,

fast growing crops and agricultural residue such as wheat straw, sugar bagasse, rice husks and corn stover.
In this work a mixed-integer linear model is described for the optimisation of the value chain associated with biorefining. The value chain allows for consideration of different moisture contents, biomass sources and indicates the optimal locations and configuration of the value chain. The optimisation is performed relative to maximising the profit received from the sale of three product streams, cellulose, hemicellulose and lignin. The value chain assessment is based on a novel technology which utilises ultrasound to treat the lignocellulose prior to final separation into lignin, cellulose and hemicellulose.

2. Technology description

The technology used in the model is a low capacity technology developed by Bio-Sep Ltd. with three main stages: slurry preparation, sono-assisted fractionation and separation. The slurry preparation involves mixing mechanically reduced biomass with a dilute organic acid solution prior to the addition of appropriate amounts of ethanol and MIBK. The fractionation stage involves treatment at elevated temperature of the slurry with ultrasound prior to centrifuging to separate the liquid and solid streams. Separation involves further treatment of the liquid and solid streams to extract the lignin, hemicellulose and cellulose. The biorefinery is based on a capacity of 1540 ton/y with operational time and labour costs based on 7 days/week, 20 h/day and 44 a week year.
Assuming a solvent recovery percentage of 99%, the key contribution to the cost of the technology is heating. A techno-economic assessment demonstrated significant savings are obtained with a reduction in heat energy price. With a reduction in price from £0.05/ kWh to £0.01/kWh, the contribution of heat energy cost to total operational cost is reduced from around 40% to 10%. Therefore, the base case considered for the technology for the optimisation scenario is to assume the solvents are recycled with >95% efficiency and as a starting point the heating cost was assumed to be £0.05/kWh. This gives a total fixed cost (in both cases) of £753 000 and an operational cost of £358 and £257 y/ton for heating at £0.05 kWh and £0.01 kWh, respectively.

3. Optimisation model formulation

As shown in Figure 1, the value chain model is based on two different feedstock routes, namely the softwood log source and chipped feedstock source from the sawmill. These were pre-processed before refining into three product streams, lignin, hemicellulose and cellulose. A summary of the parameters, objective function and constraints is presented in Table 1 and Table 2. In brief, the total profit was maximised according to the costs, income and constraints. The model optimises the locations of storages, pre-processing sites, biorefining site, selection of customers satisfying the capacity of the biorefinery, as well as the transportation routes and modes. The number of biorefineries available for use is set by the user and the location of each biorefinery is chosen by the model.

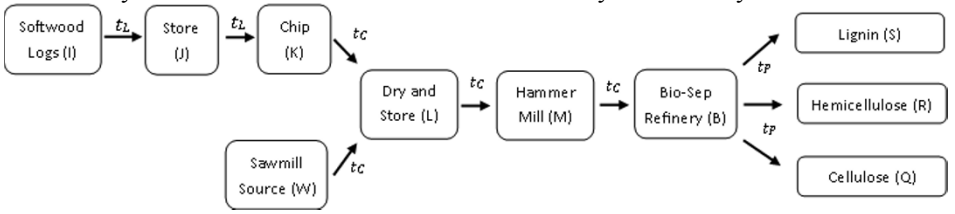

Figure 1. Value chain outline for the Bio-Sep biorefinery

Table 1. Parameters used in the optimisation model

Log source points	$i \in I$	Pre-processing stage	$\{J, K, L, M\} \in O$
Storage locations	$j \in J$	Capacity of pre-processing	$A_p(O)$
Chipping locations	$k \in K$	Fixed cost of pre-processing	$P_{pf}(O)$
Sawmill source points	$w \in W$	Operating cost of pre-processing	$P_{po}(O)$
Dry and store locations	$l \in L$		
Milling locations	$m \in M$	Existence of pre-processing	$E_P(O)$
Biorefining locations	$n \in N$	Conversion rate of pre-processing	$C_p(O)$
Cellulose buyer	$q \in Q$		
Hemicellulose buyer	$r \in R$	Set of biorefineries	$b \in B$
Lignin buyer	$s \in S$	Fixed cost of biorefinery	$P_{bf}(B)$
Feedstock source	$\{I, W\} \in F$	Operational cost of biorefinery	$P_{bo}(B)$
Availability of feedstock	$A_F(F)$	Existence of biorefinery at N	$E_B(N, B)$
Cost of feedstock	$P_p(F)$	Conversion to cellulose	$C_Q(B)$
Material transported	$x \in X$	Conversion to hemicellulose	$C_R(B)$
Transport distance cost	$Pt(T)$	Conversion to lignin	$C_S(B)$
Transport load cost	$Pl(T)$	Capacity of the biorefinery	$A_N(B)$
Capacity of transport	$T_c(T)$	Product buyer	$\{Q, R, S\} \in Z$
Transportation type	$t \in T$	Price of product	$P_z(Z)$
Distances between stages	$d \in D_t$	Capacity of buyer	$A_z(Z)$

Table 2. Functions within the value chain model.

Objective Function:	**Maximise Σ Profit – Σ Cost**	
Cost Functions		
Feedstock purchase	$\sum P_p(F) \cdot X(F)$	(1)
Transportation cost (travelling)	$\sum Pt \cdot X \cdot D_t$	(2)
Transportation cost (loading)	$\sum Pl \cdot X$	(3)
Pre-processing operational cost	$\sum P_{po} \cdot X$	(4)
Pre-processing fixed cost	$\sum P_{pf} \cdot E_P$	(5)
Biorefinery fixed cost	$\sum P_{bo} \cdot X$	(6)
Biorefinery operational cost	$\sum P_{bf} \cdot E_B$	(7)
Income from product sales	$\sum P_z \cdot X(Z)$	(8)
Constraints		
Amount of feedstock used cannot exceed capacity: $\sum X(F) \leq A_F(F),\ \forall i, w \in \{I, W\} \in F$		(9)
Transported material cannot exceed capacity: $\sum X \leq T_c\ \forall t \in T$		(10)
Pre-processing capacity cannot be exceeded: $\sum X(O) \leq A_p(O), \forall j, k, l, m \in \{J, K, L, M\} \in O$		(11)
What is transported away from an operation cannot exceed what is transported to an operation, considering conversion: $\sum X(O_{n+1}) \leq \sum X(O_n) \cdot C_p(O_n), \forall j, k, l, m \in \{J, K, L, M\} \in O$		(12)
There can only be one of each type of pre-process at each location: $\sum E_P(O) \leq 1, \forall j, k, l, m \in \{J, K, L, M\} \in O$		(13)
There can only be one biorefinery at each location: $\sum E_B(N, B) \leq 1, \forall b, n \in B, N$		(14)
What is transported away from the biorefinery is less than what was produced: $\sum X(Z) \leq \sum X(M) \cdot C_Q(B) + \sum X(M) \cdot C_R(B) + \sum X(M) \cdot C_S(B), \forall m, z \in M, Z$		(15)
The buyer capacity cannot be exceeded: $\sum X(N, Z) \leq A_z(Z) \forall q, r, s \in \{Q, R, S\} \in Z$		(16)
The capacity of the biorefinery must be filled $\sum X(M) \geq A_N(B), \forall b \in B$		(17)

Key
Log sources = $\{I_1, I_2, I_3, I_4, I_5\}$
Chip sources = $\{W_1, W_2, W_3\}$
Log storages = $\{J_1, J_2\}$
Biorefinery location options = $\{N_1, N_2, N_3\}$
Customer locations = $\{Z_1, Z_2\}$

Figure 2. Map of candidate points considered

4. Example scenario

The example scenario is set in Scotland with the use of softwood either as logs or as chips from the sawmill by-product. The prices in the model are based on the pound sterling 2012. A summary of the candidate points is presented in Figure 2. The pre-processing operations, chipping, drying and milling could either be located at the log storage sites, the sawmill sources or the biorefinery locations. The data for each route type was made on collation of information collected for the Road Haulage Association (Table 3) (Road-Haulage-Association 2013). Diesel fuel cost was averaged over 2012, as reported by the UK government, (1.4216 £/L).

4.1. Feedstock sources

Trees are bought as sawlogs at an average price of £47.60 per green ton (Forestry Commission 2012) with a moisture content of 60% (wet basis) for Sitka Spruce (Rolls 2009). However if any tree is allowed to air dry, the moisture content can be reduced to 30% in 18 months (Price 2009). Here the price per cubic metre is converted using the mass ratios to a related price of £92/ ton (30% moisture content), with a nominal 10% added to incorporate cost of passive drying.

The sawmill availability is based on three different sawmills in Scotland, considering their annual production of by-products. The sawmills were assumed to provide green chips with 55% (wet basis) moisture content (Price 2009). The wet wood price taken for woodchips was £30 which was an average of public and private sources provided which was corrected for any dryer prices using a mass conversion and adding 10% nominal additional holding cost per ton.

Table 3. Transport costings calculated according to UK data. (Road-Haulage-Association 2013)

Transport Type	**Distance** (£/ton/km)	**Load** (£/ton)	**Capacity** (km.ton/ year)
Forest logs	0.53	6.57	2.42×10^6
Highway logs	0.25	6.57	2.42×10^6
Chips and milled feed stock	0.15	1.88	2.51×10^6
Products - large trucks	0.31	4.37	4.34×10^5
Products – small trucks	0.46	6.59	2.53×10^5

Table 4. Fixed costs and capacities of different pre-processing stages.

Pre-process	Capacity (ton/y)	Fixed cost (£/y)	Operational cost (£/ton)
Storage (J)	20 000	200	1
Chipping (K)			
At log store	23500	48300	0.95
At BioSep Facility	44000	64000	0.95
Milling (M)			
At Dry/Store	5040	20 100	3
At Bio-Sep Site	18000	31800	3

Table 5. Drying Costs. Variations per moisture content to reduce to 10% moisture

Moisture content (MC) (%)	Operating cost (£/ ton(wet))	Capacity (wet ton/y)	Conversion rate
60	125	19000	0.44
55	100	19000	0.50
50	80	19000	0.56
40	50	21100	0.67
30	29	27000	0.78
10	0	30000 (nominal)	1

4.2. Pre-processing stages (J,K,M)

The figures for capacity, fixed cost and operational cost of the various pre-processing costs are summarized in Table 4. Estimates were made for the cost of a storage facility with capacity of 1200 tons. The chipping scenario costs were based on chipping costs with respect to forest logs (Webster 2007). Two different milling capacities were considered (Zhangqiu Yulong Co. Ltd), with an assumed conversion rate of 95%.

4.3. Chip dry and store (L)

Woodchip drying can normally be facilitated to 10% moisture content (MC) based on woodfuel drying, and pelletisation reports (Crown 2001, Price 2009, Price 2011). The calculated cost per dry ton per percent reduction in moisture content was £0.87, and this value was translated into a cost per input (wet ton), as displayed in Table 5. Then the cost of dryers was estimated, with an additional land and labour cost which gave a total of £22600/year (Alibaba, accessed February 2014). The capacity of each drying site was then based on 0.56 h/dry ton/% which correlated to 4704 dry ton/ year.

4.4. Product values

There are three main products for consideration in the value chain, namely; lignin, cellulose and hemicellulose. Mid-range values for cellulose, lignin and hemicellulose were used at £2600, £460 and £1200, respectively. This was based on the organosolv lignin valorisation (Gosselink 2011), cellulose values from the National Non-Food Crops Centre (NNFCC), (Higson 2011), and alibaba.com, and an approximation for hemicellulose using xylose values (alibaba.com).

5. Results

The main cost to the value chain was the biorefining, (>50%) followed by drying (up to 25%) and feedstock transport (5-20%). Overall, sawmill by-products (55% MC) were cheaper overall than green saw logs (60% MC) and the southern sawmill (W3) was the preferred option for a feedstock source due to proximity to the processing sites.

However, passively dried sawn logs were the cheaper option once they reached 40% MC due to transportation and drying cost reduction. Drying was done at either the log storage or collection location to minimise transportation costs. Due to the additional transportation costs and requirements in log processing, the change in moisture content is a more significant factor for the log source compared to the sawmill source. The biorefineries were placed next to potential sources of waste heat and the effect of heating cost on the overall value chain was only 3% when going from £0.05/kWh to £0.01/kWh.

6. Conclusions

The flexibility of the model allowed for analysis of key parameters such as moisture content, feedstock size and hence subsequent downsizing and drying options. Thus the model provides a generic framework for a flexible scenario where one technology may consider more than one simultaneous feedstock type and hence pre-processing route. The significant variation in costs given the alternative scenarios demonstrated the importance of this flexibility in consideration of different feedstock characteristics.
Moreover the availability of various product streams provides a generic framework, useful for the evaluation of a variety of lignocellulosic products. These may be alternatives to heat energy and ethanol or co-production biorefineries where ethanol or heat energy are produced alongside other by-products of lignocellulose processing. With regards to decision making for a biorefinery with multiple options for feedstock sources and products the model can be useful for comparing and identifying the key factors to consider with respect to profitability.

References

O. Akgul, N. Shah and L. Papageorgiou, 2012 An optimisation framework for a hybrid first/second generation bioethanol supply chain. Comput. Chem. Eng. 42,11, p101-114.
I. M. Bowling,, J. M. Ponce-Ortega and A. M. El-Halwagi, 2011, Facility location and supply chain optimization for a biorefinery., Ind. Eng. Chem. Res., 50 p6276-6286.
Crown, 2001, Commercial woodchip drying trials., K. F. P. Ltd, Crown.
A. Dunnett, C. Adjiman and N. Shah, 2007, Biomass to heat supply chains applications of process optimisation., Process. Saf. Environ., 85, B5, p419-429.
Forestry Commission, T., 2012, Sales Results - Scotland 2012., Sales Results Retrieved March, 2014, from http://www.forestry.gov.uk/forestry/infd-8d7gb8.
R. J. A. Gosselink, 2011, Lignin as a renewable aromatic resource for the chemical industry., Doctor of Philosephy, Wageningen University.
A. Higson,, 2011, Cellulose., N. N. F. C. Centre. York.
M. Price,, 2009, Wood Pellet Production., Scotland, Forest Research.
M. Price,, 2011, Woodchip Drying. Scotland, Forest Research.
Road-Haulage-Association, 2013, RHA Cost Tables. D. International, DFF International.
W. Rolls,, 2009, Wood as fuel, technical supplement for fuel suppliers., Wood as fuel. B. E. Centre, Forestry Commission.
B. Sharma, R. G. Ingalls, C. L. Jones and A. Khanchi, 2013, Biomass supply chain design and analysis: Basis, overview, modeling, challenges and future., Renew. Sust. Energ. Rev., 24, p608-627.
S. van Dyken, B. H. Bakken and H. I. Skjelbred, 2010, Linear mixed-integer models for biomass supply chains with transport, storage and processing. Energy 35, p1338-1350.
P. Webster, 2007, Large Chippers., Forest Research., F. Commission, Forestry Commission.
M. Yu, F. Cecelja and S. A. Hosseini, 2013, Design and Optimization of Biofuel Supply Chain Network in UK., Computer Aided Chemical Engineering., K. Andrzej and T. Ilkka, Elsevier., 32, p673-678.

Krist V. Gernaey, Jakob K. Huusom and Rafiqul Gani (Eds.), 12th International Symposium on Process Systems Engineering and 25th European Symposium on Computer Aided Process Engineering.
31 May – 4 June 2015, Copenhagen, Denmark

Downstream Petroleum Supply Chain Planning under Uncertainty

Leão José Fernandes,[ab] Susana Relvas,[b*] Ana Paula Barbosa-Póvoa[b]

[a] *CLC, EN 366, Km 18, 2050125 Aveiras de Cima, Portugal*
[b] *CEG-IST,Instituto Superior Técnico,Universidade de Lisboa,1049001 Lisboa,Portugal*
[*] *susana.relvas@tecnico.ulisboa.pt*

Abstract

Design and planning of petroleum supply chains (PSC) present significant opportunity as financial crunches and variability in crude oil prices continue augmenting volatility among the petroleum product prices, costs, margins and demand. To deal with this challenge, we present a stochastic mixed integer linear program (MILP) that maximizes the expected net present value (ENPV) while simultaneously minimizing a risk measure the conditional value-at-risk (CVaR) under demand uncertainty. The bi-objective MILP model determines the design decisions relating to installation, sizing and operation of infra-structures, the fair price strategic cost and tariffs and tactical decisions concerning periodic depot and route product affectations and inventory levels. Pareto optimal solutions are obtained for the retrofit network design of the Portuguese PSC, wherein computational results are presented and identified opportunities for further research.

Keywords: petroleum supply chain, strategic design, tactical planning, mathematical programming, uncertainty management

1. Introduction

The PSC is a complex network that can be divided into upstream involving exploration and production; and downstream involving refining, transportation, storage and distribution. While world economies struggle amidst financial crunches and volatile crude oil prices, the strain on the reduction of the petroleum products' costs has increased for companies to stay competitive and sustain sales. Market condition adjustments have created volatility among the petroleum prices, margins and product demand. Consequently, inefficiencies resulting from crude oil price fluctuations that are transferred down to the final product prices and customer demand misbalances that scale up the distribution, inventory, production and procurement stages have adversely affected PSC profitability. This presents an opportunity for downstream networks to improve the PSC efficiency and perform well in spite of price and demand uncertainty.

PSCs have always been under focus for supply chain optimization. Lately, considerable research has focused refinery and the distribution network planning, specifically related to process design and operational planning including some references on network design. Nevertheless, the integrated downstream PSC design and planning under uncertainty although less explored, presents an increasing potential. Fernandes et al. (2011) surveyed the supply chain and PSC risk management literature on risk planning in petroleum prospection, exploration, production, refinery process design, scheduling and network design. Interesting directions for the strategic, tactical and operational planning levels under several types of uncertainties were identified.

The crude oil supply chain management has been identified in Sahebi et al. (2014) as a flourishing research area, requiring vertical integration of strategic and tactical decisions and horizontal integration of the complex crude oil supply chain. Uncertainty with global factors such as international taxation, transfer prices, environmental impacts involving multi-stage stochastic and nonlinear modelling still remain unaddressed.

Uncertainties relating to demand and cost were modelled in Lakhanawat and Bagajewicz (2008) using a non-linear program for refinery operations planning, in order to determine the final product prices and the crude purchase and production quantities that maximize profits. The stochastic model incorporates the upper-bound risk curve, opportunity value, and value-at-risk (VaR) to provide higher expected gross margin and lower risks. Later, Conejo et al. (2010) model production, cost, demand and price uncertainty for electrical markets, maximizing net profits and simultaneously minimizing a risk measure. The risk measures included mean variance, variability index, probabilistic financial risk, downside risk, risk premium, VaR and CVaR.

Recently, Oliveira et al. (2014) proposed a two-stage stochastic MILP to make the downstream PSC investment, transportation and inventory decisions that minimize the investment and logistics costs under demand uncertainty. Network design and discrete capacity expansion are modelled using the L-Shaped method (Benders decomposition), for varying demand scenarios, to improve the solution quality and performance. However few works have analysed so far the presence of uncertainty in oil supply chains when dealing with many important aspects that characterize these chains.

In order to contribute to the reduction of this gap we extend our previous work (Fernandes et al. 2014) where several characteristics of the downstream oil supply chain have been considered. Namely, a PSC collaborative design is studied to determine depot locations, transport modes, routes and shared resource capacities under an uncertain context. Tactical decisions are also considered that include the periodic multi-stage importation, exportation, refinery, storage, transportation and inventory volumes for crude oil and petroleum products, for current, grassroots and retrofit redesign considering single-entity and multi-entity networks. Company financial participations determine the resource sharing and incorporation of refinery, transport infrastructure and distribution depot profits. Entity tariffs are determined using piecewise linearization, to ensure economies of scale and efficient sharing of self and competitor installation capacities. The multi-stage and multi-period crude oil and derivative price variations are captured and the procurement, exportation, refining and inventory costs optimized. The stochastic model developed generates Pareto-Optimal network design solutions by varying demand scenarios for the Portuguese PSC. On one side we consider the maximization of the Net Present Value (NPV) while on the other side we minimize the conditional value-at-risk (CVaR).

2. Problem Description and modelling

PSC networks are comprised of petroleum companies that purchase crude oil, import and export or produce petroleum products through refineries, which they commercialize and distribute through distribution depots using different transportation modes and routes to retail customer districts. Considering that multiple entities operate in a market with self-owned or participated installations, the mission of the petroleum companies is to design, construct and manage PSC networks that maximize the profits and reduce risks for the entire PSC. The problem here is to determine the right company participations, depot locations, resources, capacities, transport modes and routes to install and operate per product; the crude importation, production, primary and

secondary distribution volumes, the product inventories at multi-stage nodes and the entity tariffs and prices, in order to construct efficient collaborative networks.
Figure 1 represents the Portuguese downstream PSC where two refineries R1 and R2 produce the petroleum products. The companies purchase the oil products from the local refineries or import them from external sources at a premium of insurance and freight. The product is then transported using the primary distribution to eleven storage depots, D1-D11, where it is stored and distributed using the secondary distribution to the retail stations. The depot capacities as the number of typical capacity tanks are determined for each of the 8 products (C3, C4, U5, U8, GO, FU, A1, B5). The retail stations are aggregated into customer zones corresponding to the eighteen districts of Portugal.

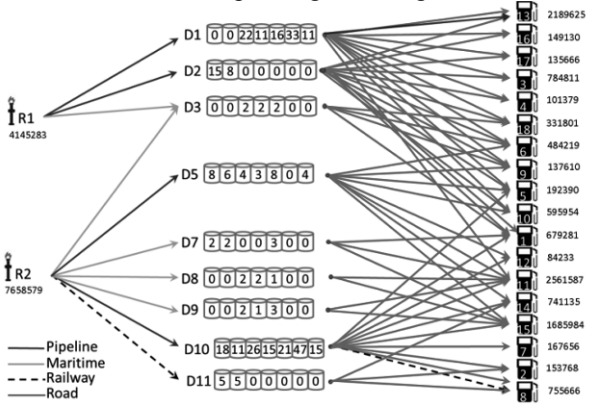

Figure 1. The PSC network in Portugal

The stochastic MILP determines 1) strategic decisions for installation, operation and closure of multi-entity infrastructures and capacities; 2) tactical decisions for crude and product inventories and transfer volumes per PSC stage, entity, time period and scenario. The objective function is an aggregation of value components determined per PSC stage, location, transportation route, product, entity, time period and scenario:

$$= \textit{Refinery Margin} = \textit{(Refinery profits – Exportation costs – Importation costs – Crude Oil, refined product, depot and retail inventory costs)}$$

$$+ \textit{Gross retail margin} = \textit{(Retail profits – Depot tariffs – Transportation tariffs – Shortage costs + Depot profits + Transportation profits)}$$

The PSC collaborative model may consider a current network, a retrofit network or a grassroots network. Hence the network initial conditions for the infrastructure may begin with the existing depots and transport infrastructures with known entity participations which may not change (Current), may begin with the current and are allowed to change (Retrofit), or need to be constructed from scratch (Grassroots).

3. Uncertainty Management

The stochastic scenario dependent MILP simultaneously maximizes ENPV (Expected NPV) and minimizes one risk measure including variance, variability index, downside risk, VaR and CVaR and uses the compact node-variable formulation as explained in Conejo et al. (2010). The authors identify the first four measures as non-coherent risk measures, presenting drawbacks of "fat tail" profit distributions, discouraging diversification and not distinguishing the different levels of losses below the threshold

whereas CVaR is a coherent risk measure ward of such drawbacks. The CVaR is the likelihood that an ENPV will be lower than the NPV given by the VaR with a specific confidence level and can be expressed using a linear formulation.
The ENPV is determined in equation (1) as the aggregate of the product of probability and NPV for all scenarios where the NPV per scenario is given by equation (2) as the summation of the discounted profits per time period, using an arbitrary interest rate. The MILP implements the linear approximation of CVaR for discrete distributions as defined in Rockafellar and Uryasev (2002). Equation (3) derives the CVaR where $a \in (0,1)$ represents a confidence level defined by the decision maker and ΔV_s is a positive difference between the VaR and NPV obtained per scenario in equations (4).

$$Max(ENPV) = \sum_s \psi_s \times NPV_s \tag{1}$$

$$NPV_s = \sum_t \text{Profit}_{ts} / (1+irr)^{t-1} \tag{2}$$

$$CVaR_a = VaR + 1/(1-a) \times \sum_s (\psi_s \times \Delta V_s) \tag{3}$$

$$\Delta V_s \geq VaR - NPV_s \tag{4}$$

$$\Delta V_s \in R_0^+ \tag{5}$$

$$Max(f_1 + 10^{-6}(slack/r)) \qquad | f_2 + slack = f_{2Max} - k(r/n_k) \tag{6}$$

The stochastic model is combined with the improved augmented ε-constraint algorithm from Mavrotas and Florios (2013) to determine the Pareto optimal solutions and the trade-off between the two objective functions f1 = ENPV and f2 = CVaR. Both objective functions are individually optimizing to obtain f1=z1* and f2=z2*. By adding constraint f2=z2*, is optimized F1 to obtain the extreme points of the Pareto curve. The remaining points of the curve are obtained by solving the problem in equation (6) where f_{2Max} is the upper bound of f_2, slack is a non-negative surplus variable, r is the range of objective function f2 and k is the number of efficient solutions between 1 and n_k.

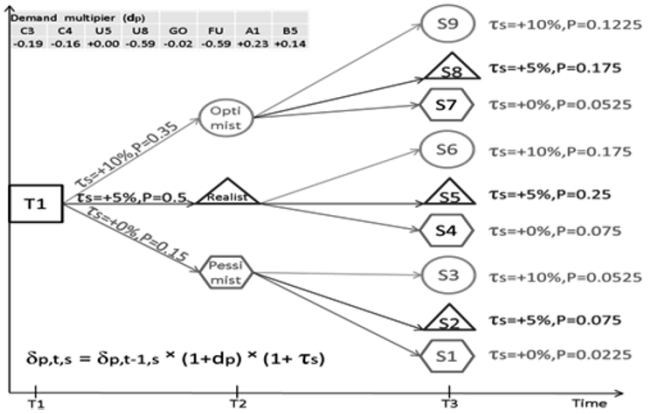

Figure 2. Demand scenario tree construction.

Figure 2 presents the scenario tree for the demand uncertainty which is constructed based on the market demand evolution in recent years, which has increased for some products and decreased for others. After the recent economic crisis, the market evolution is expected to be favourable, so the scenarios are constructed considering an optimistic growth of 10% with 0.35 probability, a realistic growth of 5% with 0.5

probability and a pessimistic growth of 0% with 0.15 probability. The product demand per period and scenario $\delta_{p,t,s}$ is given by expression $\delta_{p,t-1,s}\times(1+dp)\times(1+\tau s)$ where *dp* is the product trend per period and τs is the market tendency per scenario.

4. Computational Results

The MILP model is implemented using GAMS 24.3.3 64-bit and solved with MILP commercial solver CPLEX 12.6 using 4 parallel threads on a dual-core Pentium 2.4 Ghz CPU with 8GB RAM. The stopping criterion is 0.1% optimality gap or 24 hours of CPU time. The MILP models the current, grassroots and retrofit designs for single and multi-entity networks of the Portuguese PSC maximizing ENPV while minimizing CVaR.

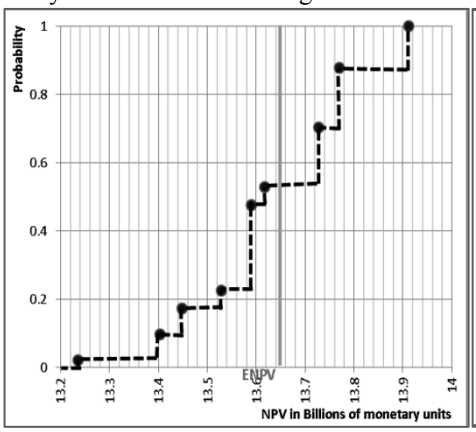

Figure 3. ENPV maximization solutions

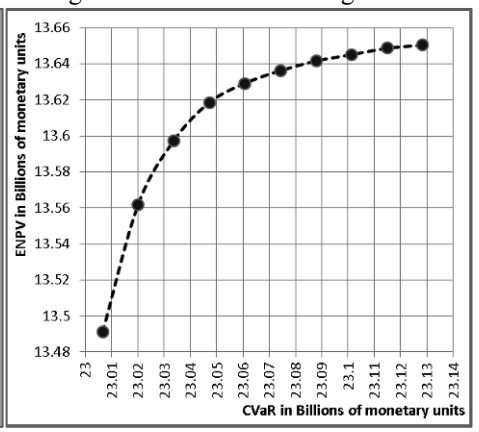

Figure 4. Pareto optimal solutions ENPV/CVaR

Figure 3 presents the cumulative probability distribution for the ENPV maximization problem of the single-entity retrofit. The PSC designs for the 9 scenarios generate NPVs between 13.23 to maximum 13.91 billion monetary units (bmu). The cumulative probability distribution shows that the MILP generated network design has 0.5275 probability of generating NPVs higher than the ENPV which is 13.65 bmu.

Figure 4 presents the Pareto optimal solutions for the Portuguese PSC considering ENPV maximization and CVaR minimization. By fixing the VaR to 13.65 bmu which is the result of the max(ENPV) problem and using a confidence level of 95%, are obtained the minimum CVaR of 23.01 bmu and maximum CVaR of 23.13 bmu. The CVaR range is then calibrated into 10 equidistant grid points and solved the max(ENPV) problem for these CVaR grid points deriving the ENPV values which vary between a minimum of 13.49 up to a maximum of 13.65 bmu. The min(CVaR) problem contrasts with the Max(ENPV) problem where a higher ENPV implies a higher CVaR risk as seen in the Pareto-Optimal curve. The MILP and augmented ε-constraint methodology is seen to adequately model the downstream PSC design and planning under uncertainty.

The methodology may also be used to minimize variance, variability index or downside risk. While variance is the summation of the modulus of the differences between ENPV and NPV per scenario multiplied by its probability, the variability index only considers the positive differences. The downside risk is similar to the variability index, however the reference is not ENPV but a NPV target value defined by the decision maker. The bad news for the variance is that negative differences will nullify positive differences whereas NPVs higher than the target value will be discarded for the variability index and downside risk measures. Hence, the use of CVAR besides the fact that it considers

both the expected profit and the profit variability where the trade-off between the two is modelled using a weighting parameter.

Table 1 – Model Statistics

	Total Variables	Binary Variables	Equations	Gap (%)	CPU(s)
ENPV	433397	4591	101501	0.1	59556
CvaR	433414	4591	101515	0.1 - 3.5	8402 – 86400

Table 1 presents the model statistics for the PSC example. The MILP is executed four times to obtain the payoff table: 1) the maximum ENPV; 2) the minimum CVaR; 3) the minimum ENPV which is max(ENPV) when z2*= min(CVaR); 4) the maximum CVaR which is min(CVaR) when z1*= max(ENPV). These are the extreme points of the Pareto-Optimal curve. The MILP is then executed 10 times to obtain the efficient solutions of max(ENPV) for 10 equidistant CVaR values derived from the payoff table. Each run considered 9 scenarios with execution times varying between 8402 and 86400 seconds. The model statistics demonstrate the problem complexity and the computational load for solving such problems even when considering only 9 scenarios.

5. Conclusions

The current paper presents a stochastic MILP for collaborative strategic and tactical planning of downstream PSC networks where uncertainty management and economies of scale are considered. Besides ENPV, the risk measure CVaR is incorporated using the augmented ε-constraint method, in order to improve planning under demand uncertainty. As result, are obtained improved network designs with stable expected profits, and therefore lower risk for the real-case Portuguese PSC network. These designs improve costs, tariffs, revenues and total profits. As the PSC planning under uncertainty is a large scale problem, our future research will focus decomposition strategies and robust optimization as alternative methods that may better explore time performance difficulties.

References

L.J. Fernandes, A.P. Barbosa-Póvoa, S. Relvas, 2011. Supply Chain Risk Management Review and a New Framework for Petroleum Supply Chains, Quantitive Financial Risk Management, Computational Risk Management Book Series, DD Wu (Ed.), Springer-Verlag, 1, 227-264.

L.J. Fernandes, A.P. Barbosa-Póvoa, S. Relvas, 2014. Collaborative Design and Tactical Planning of Downstream Petroleum Supply Chains, Ind. Eng. Chem. Res., 91, 1557-87.

A. Conejo, M. Carrión, J. Morales, 2010. Decision Making Under Uncertainty in Electricity Markets. International Series in Oper. Res. Manag. Sci., Springer, ISBN 978-1-4419-7420-4.

H. Lakhanawat, M.J. Bagajewicz, 2008. Financial risk management with product pricing in the planning of refinery operations. Ind. Eng. Chem. Res., 47, 6622–6639.

F. Oliveira, I.E. Grossmann, S. Hamacher, 2014. Accelerating benders stochastic decomposition for the optimization under uncertainty of the petroleum product supply chain, Computers & Operations Research, 49, 47-58.

R. Rockafellar, S. Uryasev, 2002. Conditional value-at-risk for general loss distributions. Journal of Banking and Finance, 26, 7, 1443-1471.

G. Mavrotas, K. Florios, 2013. An improved version of the augmented ε-constraint method (AUGMECON2) for finding the exact pareto set in multi-objective integer programming problems. Applied Mathematics and Computation archive. 219, 18, 9652-9669.

H. Sahebi, S. Nickel, J. Ashayeri, 2014. Strategic and tactical mathematical programming models within the crude oil supply chain context - A review, Comp. & Chem. Eng., 68, 56-77.

Krist V. Gernaey, Jakob K. Huusom and Rafiqul Gani (Eds.), 12th International Symposium on Process Systems Engineering and 25th European Symposium on Computer Aided Process Engineering.
31 May – 4 June 2015, Copenhagen, Denmark

Optimal Management of Shuttle Robots in a Laboratory Automation System of a Cement Plant

Christian Schoppmeyer,[a] Christian Sonntag,[b,c] Siddharth Gajjala,[d] Sebastian[b] Engell

[a]*Materna GmbH, Voßkuhle 37, 44141 Dortmund Germany*
[b]*Process Dynamics and Operations Group, Department of Biochemical and Chemical Engineering, Technische Universität Dortmund, Emil-Figge-Str. 70, 44227 Dortmund, Germany*
[c]*euTeXoo GmbH, Behringstraße 65, 44225 Dortmund, Germany*
[d]*ThyssenKrupp Industrial Solutions AG, Resource Technologies, Cement Services, Graf-Galen-Straße 17, 59269 Beckum, Germany*
christian.schoppmeyer@materna.de;{c.sonntag|s.engell}@bci.tu-dortmund.de

Abstract

To meet the quality requirements in the production of cement, samples are taken in the production process, transported to a central lab and analysed partially automatically. The measurements are used to adjust the parameters of the production process. An optimal management of the laboratory system can lead to significant throughput gains and shorter analysis times. In this contribution, we describe the optimal scheduling of the robots-based laboratory automation system a cement plant. The TA-based approach is embedded into a reactive scheduling approach to handle the different uncertainties in the system, e.g. manually inserted jobs. We show that compared to a priority-based dispatching rule, this approach leads to significant throughput gains while meeting all process-related timing restrictions.

Keywords: Process operations, Reactive scheduling, timed automata, laboratory automation.

1. Introduction

The increasing demand for high quality cement in construction calls for an efficient integrated quality analysis process in cement production plants. To analyse the quality of the cement, small samples of material are collected online in several stages of the cement production process, and the composition and the properties of the samples are analysed in a central laboratory. Based on these measurements, various control parameters of the production process are adjusted. In advanced cement plants, the sample collection, transportation and analysis is partially automated. In the automated lab, human operators and robots interact in a cooperative setup. In the automated analysis process, the time between the sample collection and the adjustment of the control parameters is strictly restricted but the actual time depends on the load on the lab and on material composition and quality. Additionally, the human workers can insert new samples that have to be analysed at any point in time and are allowed to switch analysers that are required to process the samples to a manual mode thus disconnecting them from the automatic system. The assignment, sequencing, and timing decisions that are required to execute the automated sample handling and analysis process are taken by a scheduling solution, either in the form of a dispatching rule (He

and Hui (2012)) or by an optimization-based technique, e.g. mathematical programming (Mendez and Cerda (2006)) or TA-based scheduling (Subbiah et al. (2011)). One of the crucial characteristics that make a scheduling problem challenging, especially if strict time limits have to be met, is the presence of uncertainty in the information on the operational level, e.g. varying analysis times, insertion of new samples, decoupling of idle analysers from the automatic system, etc. Such highly dynamic environments demand optimization techniques that can compute new decisions within small amounts of computation time when reacting to unforeseen events.

In this contribution, it is shown that a real-time optimization of the sample handling and analysis system can lead to significant efficiency increases in the shuttle-based laboratory automation system that is connected to a cement production plant. The sample scheduling problem is modelled using timed automata (TA). To handle the different kinds of uncertainties in an efficient and robust fashion, the TA-based approach is extended to a reactive scheduling approach that combines the idea of a moving window approach in which schedules are computed one after the other for temporally overlapping windows with an explicit event handling procedure to quickly cope with unforeseen deviations in the schedule execution and the insertion of new jobs. We show that this approach can successfully handle the different uncertain events and can lead to significant throughput gains compared to priority-based dispatching rules while meeting all process-related timing restrictions.

2. The laboratory Automation System

The industrial case study considered is the shuttle-based laboratory automation system (LAS) of a cement production plant located in Solnhofen, Germany. The layout of the LAS is shown in Fig. 1. The LAS is equipped with seven collectors which are located in different parts of the continuous cement production plant and collect sample material from the production process. The collectors are connected by a single-capsule pneumatic tube system that transfers the material samples - one at a time - to the laboratory. The laboratory itself consists of a cup filling machine, three storage areas, four analysers and two material crushers which are connected by a single-track shuttle lane and one shuttle robot. All parts of the laboratory, except of the cup filling machine, can also be accessed by human workers. In this case they are decoupled from the automatic system. Furthermore the workers can insert additional samples in the storage areas that must be analysed.

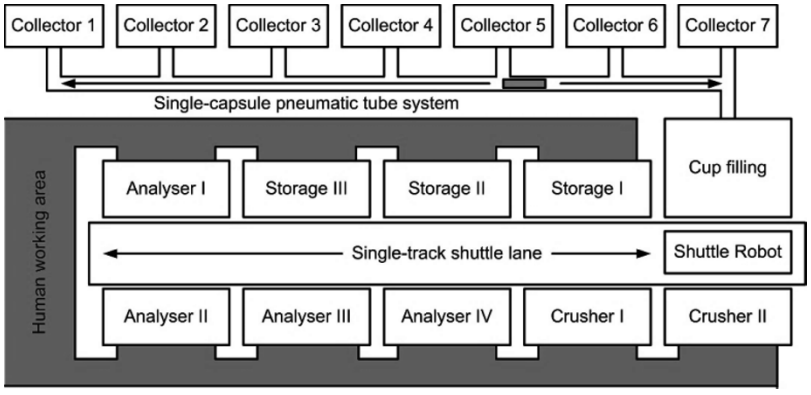

Figure 1: Layout of the laboratory automation system (LAS).

The cyclic sample analysis process starts with the collection of material in one of the collectors. When the collection of the material is finished, the capsule of the pneumatic tube system is sent to the corresponding collector, filled with the material and sent back to the cup filling machine. Once the material has been poured into up to three different cups, each cup can be picked up by the shuttle robots and has to be transported to different units in the laboratory based on a predefined sample route. The time required by the shuttle robot to transport a cup from one of the unit to another is in the range of a few seconds to tens of seconds and depends on the current position of the shuttle robot, hence it is sequence-dependent. Furthermore, the time required to process the sample in one of analysers depends on the material composition and the quality of the current sample, and may vary. In total, 340 different sample routes exist including the transportation from the seven collectors to the laboratory, the splitting into up to three subsamples.

In the current control system, the samples and the shuttle-robot movements are dispatched using a problem-specific algorithm implemented on a programmable logic controller. The complexity of dozens of priority rules makes it challenging to improve the existing algorithm and to implement new features. It can happen that deadlines are missed or that manually inserted samples suffer from starving which means that these samples are not started for a long period of time.

3. Timed Automata-based Scheduling

A relatively new method to model and to solve scheduling problems is by means of reachability analysis of timed automata (TA). Timed automata are finite state automata extended by the notion of clocks. They are used to model and to analyse real time systems with discrete dynamics. The timed automata framework offers a transparent graphical problem representation, and models can be built in a modular fashion, making the approach intuitive and comprehensible also for inexperienced users. Due to the modular nature of the framework, changes in the model formulation can easily be implemented. For a detailed introduction to timed automata, see Behrmann et al. (2005).

The model of the case study was built in a generic fashion taking advantage of the modular framework of the TA formalism. Following the standard modelling approach for batch scheduling problems, see Panek et al. (2008), for each sample route a separate recipe automaton was created. If the material that was collected is split and poured into more than one cup in the cup filling machine, for each of the subsamples a separate recipe automaton was created. Similarly, for each unit in the laboratory, for each collector, for the pneumatic tube system and for the shuttle robots, separate resource automata were created. The movements of the shuttle robot were modelled according to the modelling procedure for sequence-dependent changeovers (Subbiah et al. (2011)), similar to the shuttle management of a high-rise warehouse in a polymer production plant described in Schoppmeyer et al. (2014a).

The large number of 340 different sample and subsample routes made it impossible to create all recipe automata by hand. Therefore the generation of the recipe automata is done online in an automated fashion based on the current state of the system including the current execution state of all samples in the system, the current position of the robot and the current operating mode of the units in the laboratory, i.e. available or decoupled. The automatic procedure developed in Gajjala (2014) works as follows: first, a recipe

automaton for the sample collection and the transportation using the pneumatic tube is created. In a second step, additional subsample recipe automata are created including the shuttle movements to transport the samples in the laboratory.

Once the TA model has been created, the sets of job automata and resource automata are combined on-the-fly by the technique of parallel composition to form a composed global automaton that represents the complete scheduling problem as a directed graph. Every path from the initial node of this graph to a leaf node represents a feasible schedule and the shortest path according to a given cost criterion represents the optimal schedule. To compute the shortest path, the cost-optimal reachability algorithm for TA models is used that was presented in Panek et al. (2008). To enhance the efficiency of the search, different graph search and state space reduction techniques were introduced, see Panek et al. (2008) and Schoppmeyer et al. (2012).

4. Reactive Scheduling Approach

As mentioned in the description of the case study above, the material composition and hence the duration of the operations, the insertion times of manually started samples, and the times at which human workers disconnect idle units from the automatic system are not known to the shuttle management system in advance. To tackle the problem of optimizing the sample scheduling problem with online information on the processing duration and insertions and decoupling times, a reactive scheduling approach has been developed.

The reactive scheduling approach combines the idea of a moving window approach (Schoppmeyer et al., 2014a) in which schedules are computed one after the other for overlapping windows with an explicit event handling procedure to quickly cope with deviations in the execution of the schedule from the nominal schedule. Fig. 2 shows the structure of the reactive scheduling approach. , The monolithic problem is decomposed into overlapping windows where the decisions in later windows are not taken at the beginning of the scheduling horizon but at later points in time. Hence, it is possible to incorporate new information on the execution status and new job arrivals in the later decisions.

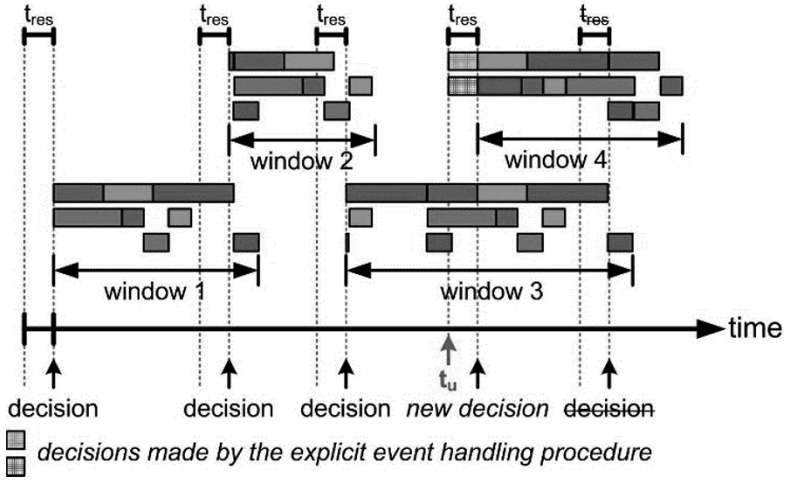

Figure 2: Schematic structure of the reactive scheduling approach.

The response time t_{res} denotes the time that is required to calculate a new decision. In a dynamic production environment where new decisions have to be taken quickly, the response time should be as short as possible. The actual response time of any algorithm does not only include the calculation time to compute new decisions but also the time required for data handling and communication. Hence not all unexpected events can be handled by a re-computation of the schedule in a new window. The moving window approach is therefore combined with a lightweight explicit event handling procedure based on pre-calculated dependencies between operations. Dependencies are defined following the principles introduced in Schoppmeyer et al. (2014b). Dependencies exist between operations of the same recipe, so-called recipe-based dependencies, requiring to stick to the sequence of the recipe, between operations that are scheduled on the same resource (unit), so-called resource-based dependencies, and between operations that share or require a common utility, so-called utility-based dependencies. Based on these dependencies and using the currently valid schedule, the explicit event handling procedure can quickly – in the range of a few milliseconds - determine upon recording of an unexpected event that occurred at time t_u in Fig. 2 which operations can continue, which operations can start as planned and which operation have to be delayed or aborted. Of course, the capabilities of the event handling procedure are limited to re-decide on the operations that were planned in the current window. At the same time at which the event handling procedure is started, a new window in the moving window approach is created and a new schedule is computed. In other words, the explicit event handling procedure only has to bridge the response time t_{res} to avoid that the systems stops while waiting for the computation of a new schedule.

In principle, the reactive scheduling solution can be used with any scheduling algorithm that solves the static problems within the individual windows. The advantages of selecting the TA-based scheduling approach are that good and feasible schedules are found within seconds, even for larger scale problems, and that the developed automatic model builder can adapt the model easily to the current state of the system, exploiting the modular nature of the TA formalism.

5. Numerical Results

To test the performance of the developed approach, a 24 hours scenario that had been recorded in the real plant was simulated. The scenario includes 82 automatically collected samples with strict timing restrictions and 20 additional samples that were inserted at random points in time by human workers – counting the individual subsamples, the total number of orders is 415. Additionally, the scenario includes several delays in the operations that are executed in the analysers caused by the varying material composition and a few disconnections of units by the human workers. In case of any of the uncertain events, the explicit event handling procedure of the reactive scheduling approach is called and a new window is created and scheduled.

Table 1 shows the comparison of the results for the 24 hours scenario between the existing dispatching rule and the proposed reactive scheduling approach. It can be seen that the dispatching rule is not able to meet the timing restrictions for all samples while the proposed approach not only meets these constraints but also reduces the average execution time required to process the samples as shown in the last column. For the manually inserted samples, the proposed approach is able to reduce the average execution time by up to 47%.

Table 1. Comparison of results for the 24 hours scenario.

Recipe type	Time limit	Dispatching rule			Reactive scheduling approach			Perf. difference
		Av. ex. time	Max. ex. time	Constr. vio.	Av. ex. time	Max. ex. time	Constr. vio.	
Raw meal	30	26.55	46.40	5	25.01	28.33	0	+7.1%
Kiln feed	60	28.59	36.46	0	28.56	34.25	0	+0.2%
Hot meal	60	49.37	55.27	0	50.44	51.35	0	-2.3%
Clinker	60	53.58	61.55	1	49.15	53.55	0	+8.8%
Manually inserted	-	124.52	255.01	-	66.11	122.41	-	+47.0%

Times in minutes, av. – average, ex. – execution, t. – time, max. – maximum, constr. – constraint, vio. – violations, perf. - performance

6. Summary

In this paper, a reactive scheduling approach for the sample handling and analysis in the shuttle-based laboratory automation system of a cement production plant was developed. The reactive scheduling approach combines a moving window approach with an explicit event handling procedure to provide an instantaneous reaction to unforeseen events. To solve the scheduling problems in the moving window approach, the TA-based schedule optimization is used, exploiting the advantages of the modular modelling formalism and its performance in calculating good and feasible schedules quickly. The numerical results show that the reactive scheduling approach is able to meet all crucial process-related time restrictions while handling the different uncertain events in a robust fashion. The performance in terms of the throughput of the system is increased by serving all additional samples inserted by the human workers within the required time.

References

Y. He, C.-W. Hui, 2012, Apply heuristics and meta-heuristics to large-scale process batch scheduling, Scheduling Problems and Solutions, 21-83

C. Mendez, J. Cerda, I.E. Grossmann, I. Harjunkoski, M. Fahl, 2006, State-of-the-art review of optimization methods for short-term scheduling of batch processes, Computers and Chemical Engineering, 30, 913-946.

S. Subbiah, C. Schoppmeyer, S. Engell, 2011, An intuitive and efficient approach to process scheduling with sequence-dependent changeovers using timed automata models, Industrial & Engineering Chemistry Research, 50, 5131-5152.

G. Behrmann, K.G. Larsen, J.I. Rasmussen, 2005, Optimal scheduling using priced timed automata, ACM Sigmetrics, 32, 34−40.

S. Panek, S. Engell, S. Subbiah, O. Stursberg, 2008, Scheduling of multiproduct batch plants based upon timed automata models, Computers & Chemical Engineering, 32, 275-291.

C. Schoppmeyer, S. Subbiah, J.M. De La Fuente Valdes, S. Engell, 2014a, Dynamic scheduling of shuttle robots in the warehouse of a polymer plant based on dynamically configured timed automata models, Industrial & Engineering Chemistry Research, 53, 17135-17154.

S. Gajjala, 2014, Development of an Optimizing Shuttle Robots Management for the POLAB Shuttle Laboratory Automation System, Master's thesis, TU Dortmund University.

C. Schoppmeyer, S. Subbiah, S. Bendiganahalli-Deveerappa, S. Engell, 2012, Effective batch scheduling with sequence-dependent changeovers using reachability analysis of timed automata combined with lower bound computations, In: 14th IFAC Symposium on Information Control Problems in Manufacturing 2012, 75−80.

C. Schoppmeyer, S. Fischer, J. Steimel, V.Q. Do, N. Wang, S. Engell, 2014b, Embedding of timed automata-based schedule optimization into recipe driven production, Computer Aided Chemical Engineering, 33, 415-420.

Krist V. Gernaey, Jakob K. Huusom and Rafiqul Gani (Eds.), 12th International Symposium on Process Systems Engineering and 25th European Symposium on Computer Aided Process Engineering.
31 May – 4 June 2015, Copenhagen, Denmark

A Novel Approach to Predict Violations and to Define the Reference Contaminant and Operation in Water Using Networks

Ewerton E. S. Calixto,[a] Flávio S. Francisco,[a] Fernando L. P. Pessoa,[a] Eduardo M. Queiroz[a]

[a]*Departamento de Engenharia Química, Escola de Química da Universidade Federal do Rio de Janeiro. Sala E-201, Bloco E, Centro de Tecnologia, Ilha do Fundão, CEP: 21949-900 Rio de Janeiro, Brazil.*

Abstract

The development of new techniques to the management of industrial water resources has become increasingly necessary in the last years. Many efforts in the field of algorithmic approaches have been made to achieve the minimum fresh water consumption. A common issue to most of those methods is the determination of a reference contaminant when dealing with processes presenting multiple contaminants. An assertive choice of it is crucial, because the calculations of all other contaminants are based on the reference contaminant and all of them require the same flow rate to meet the process constrains. Not only that, but the structure obtained based only on the reference contaminant can lead to violations of concentration limits. One of those techniques is the Water Source Diagram (WSD), which also requires a reference contaminant to deal with multiple contaminants. This work presents a novel and robust algorithm to determine the reference contaminant when applying WSD in Water Using Networks (WUN) problems. The proposed approach can also be used in conjunction with other methods based on the Water Pinch Analysis (WPA). We also present a violation prediction method that informs which contaminant violates (or may violates) the concentration limits and its respective operation. The presented results show the effectiveness and robustness of the algorithm when applied to a process plant example from the literature with four operations and three contaminants.

Keywords: Water Source Diagram, Reference Contaminant, Violation Prediction, Multiple Contaminants, Water Using Networks.

1. Introduction

The world is facing a faster and increasing demand for water resources. The water scarcity has reached regions that are traditionally known for its abundance in the availability of water. This fact has concerned environmental government agencies, private and state-owned companies and motivating them to provide changes in the use and regulation of resource (UNEP, 2008). The increasing demand associated with climate changes and agricultural and industrial sectors are the major responsible for this situation.

In the industrial sector, especially in the chemical process industries, there is a requirement of great amount of water that is distributed to several usages such as vapour generation, cooling water, washing, etc (UNESCO, 2012). Most of this water is loaded with contaminants making it difficult to be reused.

To consider reusing wastewater in a process, the presence and behaviour of multiple contaminants must be investigated. To perform mass transfer calculations, it is necessary

to choose a contaminant to be the reference for the others. This choice involves some assumptions and one of them is to presume that the mass transfer between contaminants presents a linear relation, as shown in Eq. (1) .

$$\Delta \mathrm{m}_{\mathrm{u,c}} = f_u\left(C_{u,c,out}^{max} - C_{u,c,in}^{max}\right) \quad (1)$$

Where $\Delta \mathrm{m}_{\mathrm{u,c}}$ is the mass load of contaminant *c* transferred in the unit *u*, f_u is the flow rate in unit *u* and $C_{u,c,in}^{max}$ and $C_{u,c,out}^{max}$ are the maximum inlet and outlet contaminant concentrations, respectively.

Gomes et al., (2013), in a recent work, proposed a procedure to identify the reference contaminant when dealing with many processes and contaminants in WUN. Some difficulties found by Gomes et al., (2013) are intimately associated with the choice of the reference contaminant.

This paper proposes a novel algorithm to determine the reference contaminant and operation, focusing on improving the procedure developed by Gomes et al. (2013). Moreover, we present a method to identify previously, which contaminant will present violations in its limiting concentrations, and the unit where this occurs. This identification procedure represents an important role to solve not only the WSD but also other methods based on WPA and to remove violation concentration in the network evolution step. This algorithm contributes to most targets achievement procedures in the literature when dealing with multiple contaminants.

2. Reference Contaminant and Operation

The reference operation is the unit, which demands the use of the cleanest external fresh water available and the reference contaminant is the one, which calculations of all other contaminants are based on, and all of them require the same flow rate to meet the process constraints.

Even defining steps to properly use the WSD, they were not enough to avoid the presence of violations. To escape of such problems, Savelski and Bagajewickz (2003) proposed optimality conditions, and one of them is related with a rule of monotonicity used to define the reference contaminant, which can be analysed using the following parameter.

$$G_{u,c}^{w} = \frac{\Delta m_{u,c}}{C_{u,c,out}^{max}} \quad (2)$$

Where *w* indicates the fresh water source as the basis. The reference contaminant is then the one with the highest $G_{u,c}^{w}$ value. In other words, this contaminant reaches first its maximum inlet concentration in a process unit when fresh water is used. This contaminant with the highest $G_{u,c}^{w}$ has a specific nomenclature:$G_{u,c_{ref}}^{w}$.

2.1. The choice of the reference operation

The criteria presented herein to choose the reference operation are based only on the analysis of the maximum inlet contaminants concentration. The reference operation is then the one whose some contaminant requires the cleanest water, i.e., water at a maximum inlet concentration of 0 ppm.

As can be seen in Figure 1, if more than one operation present all of its contaminants with the maximum inlet concentration equal to zero, then to choose the reference operation among them, it is necessary to select the one which presents the lowest outlet concentration. It allows a greater possibility of reuse between operations. The operation having this characteristic is the reference. Furthermore, if no operation present any

contaminants with the maximum inlet concentration equal to zero, the reference operation will be the one with the lowest inlet concentration among all contaminants.

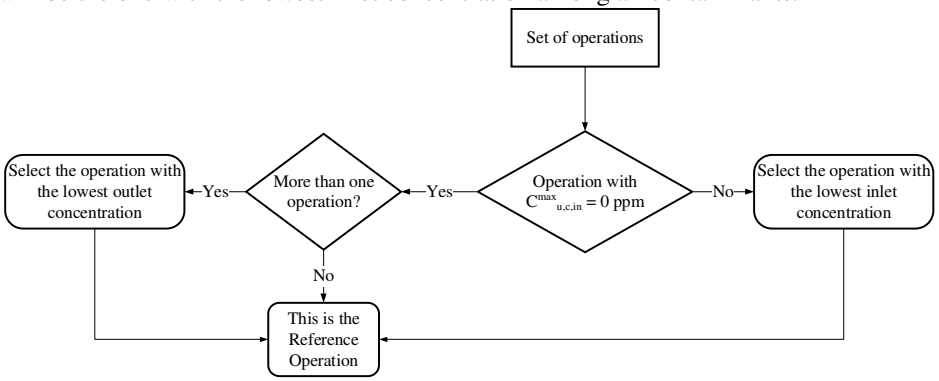

Figure 1. Algorithm for the choice of the reference operation.

2.2. The choice of the reference contaminant

The criteria to choose the reference contaminant are also initially based on the verification of the maximum inlet concentration of all contaminants in the process. However, we now analyse if the contaminants meet the criterion of monotonicity, as it is presented in previous work (Savelski and Bagajewickz, 2003). Figure 2 shows the algorithm to define the reference contaminant. We analyse if there is some contaminant with the maximum inlet concentration equal to zero. If so, then the monotonicity of the contaminant(s) is (are) verified, i.e. the concentration must be rankable and sortable in an ascending order.

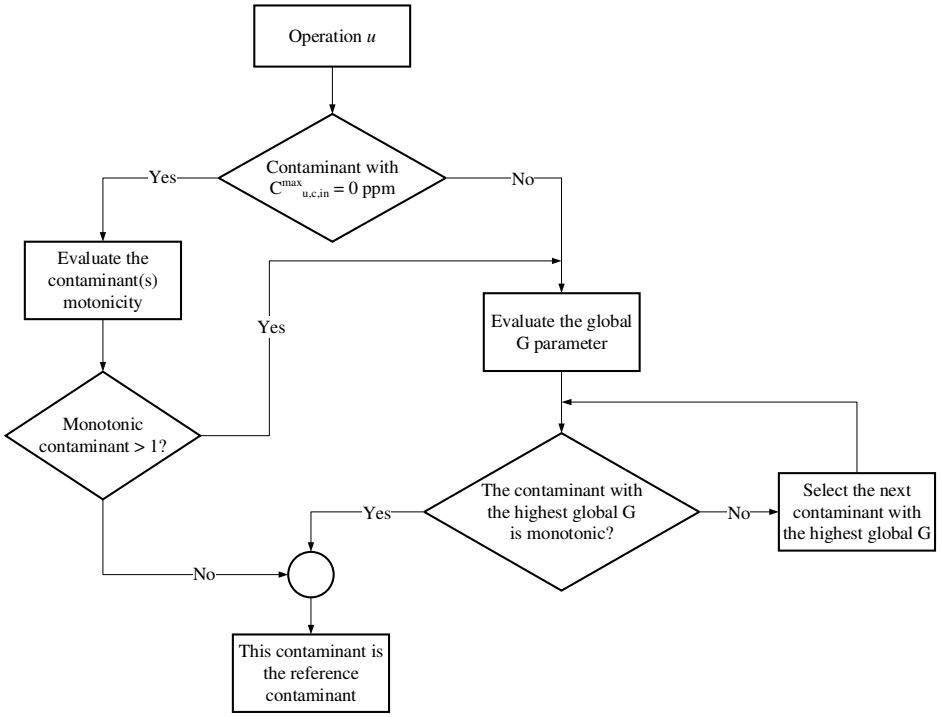

Figure 2. Algorithm for the choice of the reference contaminant.

If only one contaminant is monotonic then it is the reference, otherwise, if more than one is monotonic, the parameter $G_{u,c}^{w}$ presented in Eq. (1) is evaluated. The monotonicity is now verified for the contaminant with the highest $G_{u,c}^{w}$ value among all operations. If this contaminant is monotonic, then it is the reference contaminant, but if is not, the next contaminant with a higher $G_{u,c}^{w}$ is select, and its monotonicity is evaluated. This process continues until find a contaminant that respect the monotonicity criterion.

3. A Method to Predict Concentrations Violations

In order to avoid unnecessary effort in the preparation of the WSD and generation of the WUN and, to identify where will (or may) occur concentration violation, a prediction method is presented. Before introduce the algorithm, it is important to define other parameter as follows.

$$R_{u,c} = \frac{C_{u_{ref},c,out}^{max}}{C_{u,c,in}^{max}} \tag{3}$$

Where $C_{ref,c,out}^{max}$ is the maximum outlet concentration of contaminant c in the reference operation unit u_{ref} and $R_{u,c}$ is a relation that represents the amount of water saved in an operation unit u. Figure 3 shows the steps of the algorithm. Given the set of all operations in the process, the reference operation and contaminant are defined. However, it is possible to have one contaminant in the operation u, which its respective $G_{u,c}^{w}$ is greater than the $G_{u,c_{ref}}^{w}$ of the reference contaminant in that operation. If so, then we evaluate $R_{u,c}$ for it. The contaminant with the highest $R_{u,c}$ will have its concentration violated. Otherwise, if such contaminant does not present the highest $R_{u,c}$, then it is not confirmed the violation, but it is possible to have a one in that contaminant. The $R_{u,c}$ parameter is also evaluated in the case of the operation presents the highest $G_{u,c}^{w}$. If the reference contaminant presents the highest $R_{u,c}$, the violation will not be present in that operation.

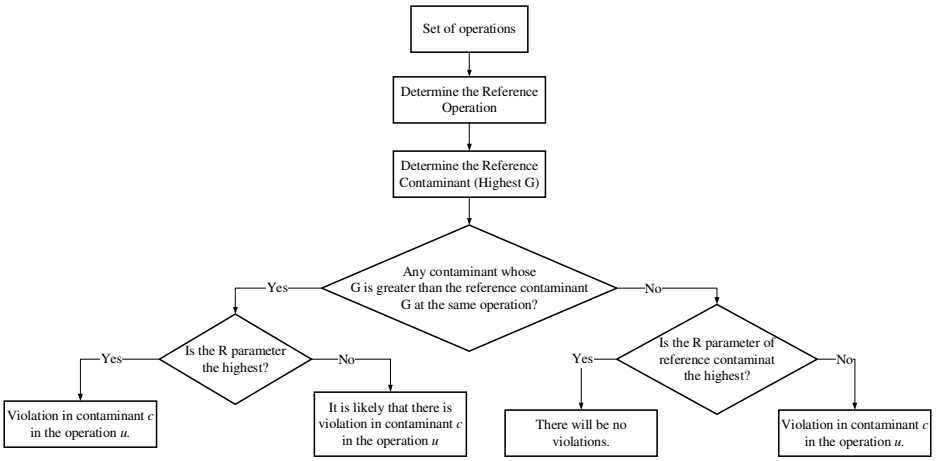

Figure 3. Algorithm to predict violations.

However, if its respective $R_{u,c}$ is not the highest one, then a violation will occur for that contaminant in the operation under evaluation. To make it clear, the three algorithms presented herein will be applied in a case study.

4. Case Study

To a better understanding of the presented algorithms, a problem provided by Doyle and Smith (1997) with four operations and three contaminants will be tested. The limiting data, as well as $G^w_{u,c}$ and $R_{u,c}$ are showed in Table 1. The WSD construction will not be explained here and for more detail, we recommend a reading of the work of Gomes et al. (2013). The first step is to define the reference operation. Using the algorithm given in Figure 1, the operation 1 is the reference, because it is the only one that requires freshwater at 0 ppm. The second step relates to the choice of the reference contaminant. The algorithm in Figure 2, points out that all the three contaminants can be the reference. All of them present the inlet concentration equal to 0 ppm, which increases monotonically. When this happens, the contaminant with highest $G^w_{u,c}$ will be the reference. In this case, the contaminant A is the reference ($G^w_{4,A}$ = 50.00 in operation 4).

Table 1. Data for the Case Study.

Operation (OP_i)	Limiting water flow rate (t/h)	Contaminant (c)	C^{max}_{in} (ppm)	C^{max}_{out} (ppm)	$\Delta m_{u,c}$ (kg/h)	$G^w_{u,c}$	$R_{u,c}$
1	34	A	0	160	5,440	34.00	NA
		B	0	450	15,300	34.00	
		C	0	30	1,020	34.00	
2	75	A	200	300	7,500	25.00	0.80
		B	100	270	12,750	47.22	4.50
		C	500	740	18,000	24.32	0.06
3	20	A	600	1,240	12,800	10.32	0.27
		B	850	1,400	11,000	7.86	0.53
		C	390	1,580	23,800	15.06	0.08
4	80	A	300	800	40,000	50.00	0.53
		B	460	930	37,600	40.43	0.98
		C	400	900	40,000	44.44	0.08

The third step refers to identify which contaminant will present violation. This is made looking at $G^w_{u,c}$, where the contaminant that presents $G^w_{u,c}$ bigger than $G^w_{u,c_{ref}}$ will present violations in its limiting concentrations.

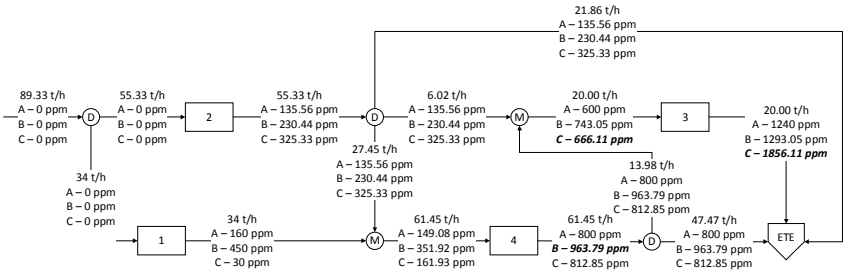

Figure 4. Water Network with concentration violations.

After identifying this contaminant, the concentration of the reference contaminant is adjusted with respect to the reference operation. This modification will be made only in contaminant B in operation 2, because it is the only operation that cannot receive

wastewater from the reference operation to allow reuse. It can be noted that contaminant C in operation 3 has a $G_{3,C}^{w}$ bigger than the reference contaminant and the lowest value of $R_{3,C}$. Therefore, it may occurs violation of contaminant C in this operation. For operation 4, the reference contaminant has the highest value of $G_{u,c}^{w}$ and only the $R_{u,c}$ is important to evaluate whether or not occurs violation in this operation.

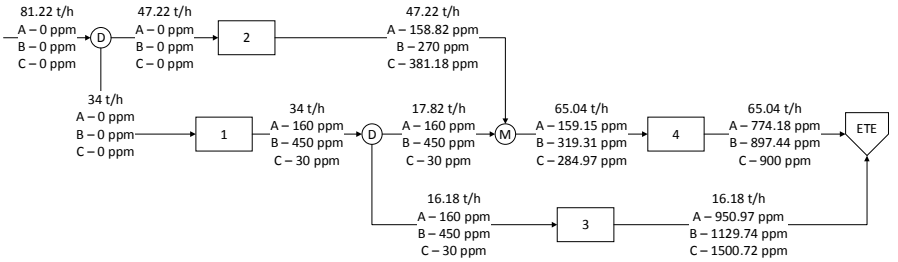

Figure 5. Final Water Network.

The $R_{4,B}$ for contaminant B is the highest, so it will violate its concentration limiting value. Figure 4 shows the WUN with violations and a total water consumption of 89.33 t/h, which is bigger than the one reported by Doyle and Smith (1997). The violations are marked in bold and italic. As expected for the operation 4, the contaminant B presents violation. For operation 3, there was violation in contaminant C that could be occurred or not. Using some rules and heuristics (Gomes et al., 2013), the network evolution is made to remove all the violations and to achieve the minimum water consumption. The new network is showed in Figure 5, with a total water consumption of 81.22 t/h.

5. Conclusions

This work presented a novel way to choose the reference operation and the reference contaminant, as well as to identify where may occur violation(s) in the limiting concentration of the others contaminants. To show this new method, a case study with four operations and three contaminants was analyzed using WSD. The proposed procedure can be employed to other targeting methods based on WPA. It does not guarantee the global optimum, but the monotonicity rule presented herein is the criterion to establish an optimum system. The violations occurred as predicted by the algorithm giving a water network with violation of constraints. Some rules and heuristics are used to remove these violations and to achieve the better water network. The $R_{u,c}$ parameter can be used to avoid computational effort in a future computer package implementation.

References

S. J. Doyle, R. F. Smith. 1997. Targeting Water Reuse With Multiple Contaminants. Insitution of Chemical Engineers 75 (Part B): 181–89.

J. F. S. Gomes, R. C. Mirre, B. E. P. C. Delgado, E. M. Queiroz, F. L. P. Pessoa. 2013. Water Sources Diagram in Multiple Contaminant Processes: Maximum Reuse. Industrial & Engineering Chemistry Research 52 (4): 1667–77. doi:10.1021/ie301537c.

M. Savelski, M. Bagajewickz. 2003. On the Necessary Conditions of Optimality of Water Utilization Systems in Process Plants with Multiple Contaminants. Chemical Engineering Science 58 (23-24): 5349–62. doi:10.1016/j.ces.2003.09.004.

UNEP. 2008. Vital Water Graphics: An Overview of the State of the World's Fresh and Marine Waters. http://www.unep.org/dewa/vitalwater/article32.html.

UNESCO. 2012. Managing Water under Uncertainty and Risk. Vol. 1.

Krist V. Gernaey, Jakob K. Huusom and Rafiqul Gani (Eds.), 12th International Symposium on Process Systems Engineering and 25th European Symposium on Computer Aided Process Engineering.
31 May – 4 June 2015, Copenhagen, Denmark

MDP formulation and solution algorithms for inventory management with multiple suppliers and supply and demand uncertainty

Joohyun Shin,[a] Jay H. Lee[a]*

[a]*Chemical and Biomolecular Engineering Department, Korea Advanced Institute of Science and Technology, Daejeon, Korea*
jayhlee@kaist.ac.kr

Abstract

Supply chain of a manufacturing system contains various functional activities including procurement of raw materials from suppliers considering demands of intermediate products. One of the most important issues for the inventory management is that various sources of supply and demand uncertainty should be considered. In general, these order decisions cannot be made effectively by intuition or heuristic approaches because they oftentimes involve multiple suppliers and competing criteria for their selection. Therefore, in this study, we apply a systematic approach to consider diverse criteria for supplier selection and to incorporate possible realizations of uncertainty into the decision-making process. This multi-period decision problem is formulated as a Markov decision process (MDP) with supply and demand uncertainty. Decision policies are obtained from solving the MDP problem through exact value iteration, as well as approximate approaches intended to overcome the 'curses of dimensionality.' We compare the results from applying them with those from the popular (s, S) policy for a simple benchmark problem.

Keywords: inventory planning, supply and demand uncertainty, Markov decision process

1. Introduction

Supply chain (SC) of a manufacturing system includes the following functional activities: procurement of raw materials from suppliers, transformation of raw materials into valuable products, blending and storage of final products, and distribution of final products to warehouses or customers. Decomposition of the overall SC planning into sub-problems is a common practice in refinery or chemical plants due to the complexity involved in different operations throughout the SC. To optimize the overall production system, it is important to manage the inventories of raw materials effectively.

For a sustainable long-term operation, supply and demand uncertainty should be considered. According to an excellent review of planning under uncertainty by Peidro et al. (2009), many models exist for a random demand, whereas the case of supply uncertainty has been studied far less, despite its significance. Another issue of inventory management for the raw materials is that multiple external vendors are oftentimes used; one should determine which suppliers to choose, and how much order is released to each one. In almost all cases, these decisions involve multiple criteria. Because the criteria for supplier selection often tend to conflict with one another, decision made by intuition or heuristic approaches can be significantly suboptimal.

The above argues for a systematic approach that can consider diverse, conflicting criteria for the supplier selection and incorporate possible realizations of supply/demand uncertainty into the decision-making process. Cheng et al. (2003) state that there are two

modelling approaches to address the problem of "multi-period decision under uncertainty": multistage stochastic programming (SP) with recourse and Markov decision processes (MDP), which is naturally solved by dynamic programming (DP). Since the SP formulation is limited to the problem of only a modest number of scenarios, it is difficult to apply to multi-period decision problems of practical significance (Lee, 2014). On the other hand, since a state-oriented formulation of MDP allows for a sequential decision making capturing both the physical dynamics and the flow of information, it can prove to be more convenient for handling many practical problems.

In this study, the inventory control problem is formulated as a MDP with two exogenous information variables: lead time (delay time from order release to delivery) and demand. By formulating the MDP problem considering both demand and supply uncertainties, a more general inventory system that better reflects the reality can be constructed and serve as a basis for future research. On the demand side, Markovian demands are used to capture the time-correlations that often exist in randomly changing economic and market condition (Cheng and Sethi, 1999). The formulated MDP problem is solved through approximate value iteration with linear separation form of the value function as well as exact value iteration. By employing the approximate solution method, we can alleviate the 'curse of dimensionality' associated with DP, and thus increase the range of applications but performance loss due to the approximation should be evaluated.

The rest of the paper is organized as follows. Section 2 provides a general background of MDP, and solution algorithms. The system and decision problem for the inventory management problem are described and formulated as an MDP in Section 3. In Section 4, usefulness of the MDP formulation is verified by comparing its performance against the popular (s, S) policy for a simple benchmark problem. Section 5 concludes the paper.

2. Markov Decision Process (MDP)

A formal MDP formulation requires following specifications with time index k:

1) State variables, s_k and finite state space S
2) Decision variables, a_k and finite action space A
3) Exogenous information variables, W_k and finite exogenous space Ω
4) Stage-wise cost function, $c(s_k, a_k)$
5) Transition function, $s_{k+1} = S^M(s_k, a_k, W_{k+1})$

A state variable is the minimally dimensioned function of history that is sufficient to compute all the future dynamics of the system (Powell, 2011). Exogenous information, which models uncertainty and becomes realized only at each corresponding time period, forces us to make decisions before all the information is known. It is expressed in the form of random variables governed by probability distributions or an exogenously provided file of scenarios (Powell et al., 2011). Decision is made by decision policy π, which is a map indicating which action to take for any given state should be found by the decision maker. The decision maker receives a cost corresponding to the given state and taken decision. The system state at the next period is determined by the given transition function. The problem of finding the best policy to minimize the overall cost over the entire infinite horizon would be written by Eq. (1). Here, discount factor $\gamma < 1$ is used to ensure the convergence of the infinite horizon cost.

$$\min_{\pi \in \Pi} E\left[\sum_{k=0}^{\infty} \gamma^k c\left(s_k, \pi(s_k)\right) \middle| s_0\right] \quad (1)$$

For convenience, we can represent the optimal infinite horizon cost to as $V(s_0)$, which is also referred to as the value function. Note that it is a function of the starting state.

2.1. Dynamic programming (DP)

We do not have to solve the entire problem (Eq. (1)) at once. Invoking the Markov property of the system, meaning that future state depends on the only current state and decision, the multi-period decision problem can be decomposed into sequential one-period decision problems. The optimality equation includes both the current and future cost of being in the current state (Eq. (2)). In a case of infinite horizon problem, this equation cannot be solved by backward induction. One of the most widely used algorithm for solving this problem is value iteration, of which details can be found in Powell (2011).

$$V(s_k) = \min_{a_k \in A} \{c(s_k, a_k) + \gamma E[V(s_{k+1})|s_k]\} \tag{2}$$

The fact that the value function is a function of the state complicates the calculation significantly. The exact value iteration algorithm essentially has to enumerate over the entire state space for each iteration, thus causing the 'curse-of-dimensionality'.

2.2. Approximate Dynamic Programming (ADP)

A common strategy for alleviating the curse of dimensionality associated with solving the optimality equation is to replace the exact value function with some sort of approximation. In the problem of inventory management, the linear separable function approximation (Eq. (3)) with appropriate basis functions (ϕ_f) is known to be efficient due to only minimal interaction between the states (Kleywegt et al., 2002). Another source of computational complexity is the computation of the expectation in Eq. (2). To facilitate this computation, a sample set of outcomes $\widehat{\Omega}^n$ (in iteration n) is randomly generated for realization of exogenous information. Let $p^n(\widehat{\omega})$ be the probability of outcome $\widehat{\omega} \in \widehat{\Omega}^n$. If we choose M realizations in the set $\widehat{\Omega}^n$, $p^n(\widehat{\omega}) = 1/M$. Then the expectation of values at a future state, $s' = S^M(s^n, a, W)$ could be approximated using a sample average approximation, as in Eq. (4). Estimating the coefficient vector (θ) in a linear form of the value function using batch methods (a whole set of data processed together) such as the conventional least squares would be very expensive and can even be infeasible because of the singularity problem. Therefore we compute the parameters in a recursive manner with an observed value ($\hat{v}^n$) at a visited state (s^n). Refer to Powell (2011) for details of the algorithm of approximate value iteration (AVI).

$$V_k(s) \approx \bar{V}(s) = \sum_{f \in F} \theta_f \phi_f(s) \tag{3}$$

$$\mathrm{E}[\bar{V}^{n-1}(s')] \approx \sum_{\widehat{\omega} \in \widehat{\Omega}^n} p^n(\widehat{\omega}) \bar{V}^{n-1}\left(S^M(s^n, a, \widehat{\omega})\right) \tag{4}$$

3. Problem Formulation

3.1. Problem description

Different types of suppliers are considered together as candidates for providing raw materials to a single manufacturer (Figure 1). A single-echelon system is studied. The inventory level of the raw material is stochastic because of the random lead times and demand. We consider a periodically renewed inventory model under a backorder and assume that the decisions are made sequentially for each period in an infinite horizon. Replenishment costs and inventory holding costs are imposed, and the inventory shortage is controlled by a penalty cost. Exogenous suppliers are assumed to be always available and have infinite capacity. All suppliers are independent of each other, and may have a minimum or maximum order constraint. Replenishment cost for each supplier is known and fixed. Order released for supplier i must arrive within u_i time periods, i.e., lead time (L_i) is a random variable distributed among $\{1, \dots, u_i\}$. At decision epoch k, the sequence

of events occur in the following manner: Stocks being delivered arrive at the beginning of the period, and demand of intermediate products are realized. With these information, the state of the inventory is renewed. Then, by predicting the next state based on the current information, a decision about placing a new replenishment order is made.

3.2. MDP formulation

We model the inventory system, described in the previous section, as a discrete-time infinite horizon Markov decision process (MDP). In our system, s_k consists of three categories: on-hand inventory level (x_k), on-order inventory (o_k), and demand (d_k). Non-negative x will represent items at a storage point and negative x will correspond to a backorder. And o is on-order inventory indicating the items are in the process of being delivered, whose elements are made of orders to supplier i released j periods ago ($o_{k,j,i}$), where $i = 1, \dots, n$, and $j = 1, \dots, (u_i - 1)$. a_k is a vector containing the order amount to each supplier placed at time k. ω_k is new information resulting of items arrival ($r_{k,j,i}$) and demand realization ($\hat{d}_k$). $r_{k,j,i}$ is a binary random variable that is 1 if the corresponding order arrives at time k and 0 otherwise. The probability of order arrival is calculated from $P(L_i = j | L_i \geq j)$ for positive o_k. With the overall number of arrival stocks (N_k) and evolving demand by $d_k = d_{k-1} + \hat{d}_k$, the state of the inventory is reviewed following:

$$x_k = x_{k-1} + N_k - d_k, \qquad o_{k,j,i} = o_{k,j,i}\left(1 - r_{k,j,i}\right) \tag{5}$$

The state transition probability $p(s'|s_k, a_k)$ from the current state $s_k = (x_k, o_k, d_k)$ to the future states $s' = (x', o', d') \in S$ is specified in Eq. (6). The first term is calculated by product of all probability of on-order inventory transition by random arrival $p\left(o'_{j,i} \middle| \tilde{o}_{j,i}\right)$ where $\tilde{o}_{j,i} = a_{k,i}$ if $j = 1$; and $\tilde{o}_{j,i} = o_{k,j-1,i}$ otherwise. In the case of corresponding order arrival, $\left(o_{j,i}{}' = 0 \middle| \tilde{o}_{j,i} > 0\right) = P_r\left(r_{k+1,j,i} = 1\right)$. The second term of Eq. (6) is for the probability of demand evolution by random demand. The last term $p(x'|s_k, o', d')$ is 1 if $x' = x_k + N' - d'$; and 0 otherwise. Here, N' is the number of ordered items arrival at next period.

$$p(s'|s_k, a_k) = p(o'|o_k, a_k)p(d'|d_k)p(x'|s_k, o', d') \tag{6}$$

In this work, one-period cost consists of the replenishment cost and the inventory handling cost as shown in the following:

$$c(s_k, a_k) = \sum_i \left(c_{setup,i}\delta(a_{k,i}) + c_{rep,i}a_{k,i}\right) + h(x_k)^+ + b(-x_k)^+ \tag{7}$$

where c_{setup} is setup cost (a fixed cost incurred for any size order); c_{rep} is the unit replenishment cost; h is unit holding cost; b is unit backorder cost; $\delta(\cdot)$ is the step function which is 0 for zero input and 1 otherwise; and $(\cdot)^+$ is a function defined as $(\cdot)^+ = \max(0, \cdot)$. The first two terms represent the replenishment cost and the last two terms represent the inventory handling cost.

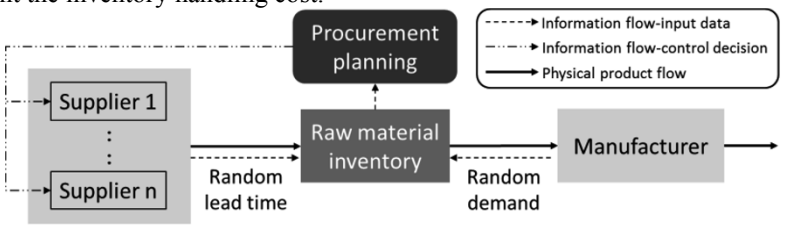

Figure 1. The studied raw material inventory system with multiple suppliers

4. Case Study

We defined a benchmark problem with three different types of suppliers; Supplier 1 and 2 have longer lead time but offer cheaper replenishment costs, while the orders released to Supplier 3 arrive right after the period but the cost is higher. Detailed parameter values are given in Table 1. On-hand inventory and demand space are defined as: $X = \{-7, \dots, 7\}$ and $D = \{2, \dots, 5\}$. We assume that lead times are uniformly distributed with $(1, \dots, u_i)$, and $\hat{d}$ follows a normal distribution, $N(0,\ 1)$. Unit inventory holding cost and backorder cost are specified as 1 and 5, respectively. The problem is formulated as a MDP, and solved by exact VI with γ=0.99. The converged value function from the VI is graphed in Figure 2 (left). In overall, the value function can be approximated as a piecewise linear function with respect to the on-hand inventory (dashed line). The slope on the negative on-hand inventory side is steeper than that on the positive side due to the higher penalty for backorder than the inventory holding cost. By the values of 1 ~ 64 states, which have a same on-hand inventory, we can check that local fluctuations are caused by the differences in the on-order inventory and demand; the values are linearly increased by the demand, and decreased by the sum of the on-order inventories over i and j, $\mathrm{sum}(o) = \sum_i \sum_j o_{j,i}$. Based on these analysis, a basis set for a linear model can be constructed as in Eq. (8). Another significant point is that the effects of on-order inventory and demand become more important as the on-hand inventory value decreases. To reflect this impact, the basis set for the linear approximation can be revised to that in Eq. (9). Coefficient vectors for the different basis sets are calculated by AVI, and the resulting linearly approximated value functions are shown in Figure 2 (right). We can check that ϕ_2 represents a more accurate choice of approximate basis for the value function. In this result, on-order inventory has little marginal effect on the value function when the system has sufficient inventories (x=5~7), whereas it becomes important in the case of severe inventory shortage (x=-5~-7). Thus the significant factors that affect future values change according to the current state.

$$\phi_1 = [1\ \ (-x)^+\ \ (x)^+\ \ \bar{o}\ \ d]^T \text{ where } \bar{o} = \max\{sum(o)\} - sum(o) \tag{8}$$

$$\phi_2 = [1\ \ (-x)^+\ \ (x)^+\ \ \bar{o}\bar{x}^2\ \ d(\bar{x} + \mathrm{c})\ ]^T \text{ where } \bar{x} = x_{max} - x \tag{9}$$

The policies obtained from VI, and AVI with different basis sets are compared with a rule-based (s, S) policy, one of the most widely used inventory policies (Axsater, 2007); if the inventory level is at or below a reordering point (s), a replenishment order will be placed up to S. Table 2 shows the computational time to obtain each policy, and the average cost incurred under the policy. Average cost of the (s, S) policy is much higher than those of the other policies from the MDP formulation because it does not account for the information regarding the on-order inventory and demand of the system. Henceforth it is vulnerable to environmental variability. While the average cost of the policy from exact VI is the lowest, its computational burden is significant even for this simple problem. In addition, it does not scale well with problem size. In this sense, AVI with basis ϕ_2 represents an attractive tradeoff between optimality (average cost) and computational time.

Table 1. Problem parameters for different suppliers

	u_i	O_i	$c_{setup,i}$	$c_{rep,i}$
Supplier 1	2	{0,2,3,4}	0.4	0.5
Supplier 2	2	{0,1,2,3}	0.5	0.6
Supplier 3	1	{0,1,2}	0.8	0.9

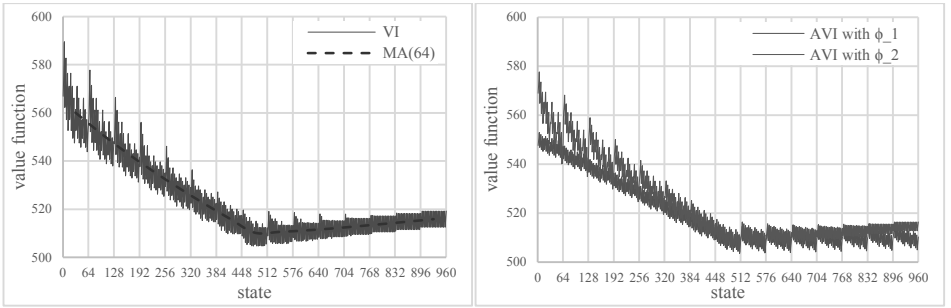

Figure 2. Converged value function (left), and linear approximated value functions (right).

Table 2. Results

	Rule-based (s, S) policy	Policy from VI	Policy from AVI with $\boldsymbol{\phi_1}$	Policy from AVI with $\boldsymbol{\phi_2}$
CPU time (s)	1.56	1007.36	4.72	5.41
Average cost	635.64	515.16	566.88	539.28
Improvement (%)	-	18.95	10.82	15.16

5. Conclusions

In this study, a general inventory control problem for supplying raw materials to manufacturers has been formulated as a MDP to incorporate supply and demand uncertainty. MDP formulation enables the use of both the physical dynamics and the flow of information in sequential decision making. The problem was solved by the dynamic programming method of VI. The performance gain from employing the more rigorous MDP formulation compared to the popular (s, S) policy was verified through a case study. The results showed that the proposed method can reduce the costs by capturing uncertainties, and considering multiple criteria for supplier selection such as lead time, replenishment cost, and limits on the order quantity. Additionally, an approximation framework using stochastic simulations and linear function approximation was tested to reduce the computational burden of exact VI. It can be an excellent alternative to the exact dynamic programming to broaden the applicability of the MDP approach to practically sized problems at minimal performance loss.

References

S. Axsater, 2007, *Inventory control*, 90, Springer

L. Cheng, E. Subrahmanian, and A.W. Westerberg, 2003, Design and planning under uncertainty: issues on problem formulation and solution, *Comput. Chem. Eng.*, 27, 6, 781-801

F. Cheng, and S.P. Sethi, 1999, Optimality of state-dependent (s, S) policies in inventory models with Markov-modulated demand and lost sales, *Prod. Oper. Manag.*, 8, 2, 183-192

A.J. Kleywegt, V.S. Nori, and M.W.P. Savelsbergh, 2002, The stochastic inventory routing problem with direct deliveries, *Transport. Sci.*, 36, 1, 94-118

J.H. Lee, 2014, Energy supply planning and supply chain optimization under uncertainty, *J. Process Contr.*, 24, 2, 323-331

D. Peidro, J. Mula, R. Poler, and F.C. Lario, 2009, Quantitative models for supply chain planning under uncertainty: a review, *Int. J. Adv. Manuf. Tech.*, 43, 3-4, 400-420

W.B. Powell, 2011, *Approximate dynamic programming: solving the curses of dimensionality 2nd edition*, Wiley

W.B. Powell, A. Georage, H. Simao, and W. Scott, 2011, SMART: a stochastic multiscale model for the analysis of energy resources, technology, and policy, *Informs. J. Comput.*, 24, 4, 665-682

Krist V. Gernaey, Jakob K. Huusom and Rafiqul Gani (Eds.), 12th International Symposium on Process Systems Engineering and 25th European Symposium on Computer Aided Process Engineering.
31 May – 4 June 2015, Copenhagen, Denmark

Optimal Design of Closed-Loop Supply Chain Networks with Multifunctional Nodes

Magdalini A. Kalaitzidou,[a] Pantelis Longinidis,[b] Michael C. Georgiadis [a,*]

[a] *Department of Chemical Engineering, Aristotle University of Thessaloniki, University Campus 54124, Thessaloniki, Greece*
[b]*Department of Engineering Informatics & Telecommunications, University of Western Macedonia, Karamanli & Lygeris Street, 50100 Kozani, Greece*
mgeorg@auth.gr

Abstract

This paper introduces a general mathematical programming framework that employs an innovative supply chain network (SCN) composition coupled with forward and reverse logistics activities. The work addresses a multi-product, multi-echelon and multi-period Mixed-Integer Linear Programming (MILP) problem in a closed-loop supply chain network design solved to global optimality using standard branch-and-bound techniques. Applicability, benefits, and robustness of the proposed model are illustrated by using a medium size case study.

Keywords: Supply chain network design; Multifunctional nodes; MILP;

1. Introduction

Over the last years, closed-loop supply chains (CLSC) have gained considerable attention in global organizations, as well as in academic fields. Researchers emphasize that focusing on both forward and reverse logistics, can be achieved maximization of the value creation over the entire life-cycle of a product. Therefore, in order to ensure high profit margins, it is necessary for companies to cope with the design, control and operation of the whole network system while managing different types of products. Some of the recent works found in the literature aiming to optimize both direct forward and reverse supply chain processes are those of Salema et al. (2010) who presented a generic model for coping with the simultaneous design and planning of supply chains with reverse flows using two level of decisions that corresponds into two time scales, macroscale for supply chain network design and microscale for the planning activities, In the same perspective, Cardoso et al. (2013) developed a mixed integer linear programming for the design and planning model for CLSC considering simultaneously all processes and uncertain product demand. Pishvaee et al. (2011) proposed a robust optimization model for handling both opened-loop and closed-loop structures coping with uncertainty in return products, demands and transportation costs while, Ramezani et al. (2014) addressed a multi-period problem in a closed-loop supply chain network design under a fuzzy environment with intergrading activities considering the transportation option, the quality and hybrid processing facilities.

Regarding the existing literature this is the first paper that presents a general mathematical programming framework that employs an innovative SCN composition coupled with forward and reverse logistics activities by introducing a generalized node with fourfold role. The function of the proposed Multifunctional nodes are optimally

defined rather than selected from a set of potential alternatives providing flexibility options to the model on designing and operating SCNs.

2. Mathematical formulation

2.1. Problem description

The problem addresses the design of a multi-product, multi-echelon and multi-period supply chain for closed-loop networks consisting of a set of distributed first class and second class markets whose location is known, and a set of facilities, whose locations are to be determined. The model proposes an innovative configuration to network's structure by entering a level consisted of multifunctional nodes with fourfold role. The generalized Production/Distribution/Recovery/Re-distribution (PDR) nodes will substitute the traditional plants and distribution centers at the forward flow and the traditional collection and re-distribution centers at the reverse flow of the materials. The model permits intra-layer material flow connections that occur in the PDR level.

The objective is to minimize the overall capital and operational cost and determine the optimal structure of the network. The model defines: (i) generalized node's location and role; (ii) suppliers; (iii) recycle centers and disposal sites; (iv) material flow among SCN's levels; and (v) functional elements (capacity, material flow, inventories, purchases etc.).

2.2. Mathematical model

A deterministic MILP model is formulated where each product can be produced at several generalized PDR nodes in different location with known and time-variant product demand. All transportation flows determined are considered to be time-averaged quantities whereas customer zones are single sourced. We denote the set of all nodes and materials in the network as $n \in N$ and $i \in I$ respectively. This includes not only the generalized nodes $n \in PDR$ but also suppliers nodes $n \in S$, first customers nodes $n \in C$, second customers nodes $n \in CC$, recycling centers $n \in Re$ and disposal sites $n \in Di$. Also, the set of raw material will be demonstrated with the set $i \in is$, likewise the set of final and return products with the set $i \in ir$. Overall we have $N = S \cup PDR \cup C \cup CC \cup Re \cup Di$ and $I = is \cup ir$. The objective (Eq.(1)) is to minimize the overall capital and operational cost of the network and is as follows:

$$
\begin{aligned}
&\min \sum_{t\in T} DT(t) \Big\{ \sum_{n\in PDR} \Big(C_n^P Y_n^P + \gamma_n^D D_n + C_n^D Y_n^D + C_n^R Y_n^R + C_n^{DR} Y_n^{DR} + \sum_e \delta_{en}^P \sum_{i\in ir} \lambda_{ine} P_{int} + \\
&+ \sum_{i\in ir} C_{in}^{DH} \Big(\sum_{n'\in S, i'\in is} Q_{i'n'nt} + \sum_{n'\in PDR} Q_{in'nt} + \sum_{n'\in PDR} QR_{inn't-1} + \sum_{n'\in CU PDR} Q_{inn't} \Big) + \\
&\sum_{i\in ir} C_{in}^{DRH} \Big(\sum_{n'\in PDR} QR_{in'nt} + \sum_{n'\in CC} Q_{inn't} \Big) + \sum_{i\in ir} \Big(\sum_{n'\in S, i'\in is} C_{i'n'n}^T Q_{in'nt} + \sum_{n'\in PDR} C_{inn'}^T Q_{inn'} + \\
&\sum_{n'\in C} C_{inn'}^T Q_{inn't} + \sum_{n'\in C} C_{in'n}^T QR_{in'nt} + \sum_{n'\in PDR} C_{inn'}^T QR_{inn't} + \sum_{n'\in CC} C_{inn'}^T QR_{inn't} + \\
&\sum_{n'\in Re} C_{inn'}^T QR_{inn't} + \sum_{n'\in Di} C_{inn'}^T QR_{inn't} \Big) + \sum_{i\in ir, n\in PDR} C_{int}^{IP} \frac{I1_{int} + I1_{in(t-1)}}{2} + \\
&\sum_{i\in ir, n\in PDR} C_{int}^{IDR} \frac{I2_{int} + I2_{in(t-1)}}{2} + \sum_{i\in ir, n'\in C} C_{in}^{RV} QR_{in'nt} + \sum_{i\in ir, n'\in C} C_{in}^{RP} (QR_{in'nt}) RCC + \\
&\sum_{i\in ir, n'\in C} C_{in}^{RM} (QR_{in'nt}) RM \Big) + \sum_{n\in Di} (C_n^{Di} Y_n^{Di} + \sum_{i\in ir, n'\in PDR} C_{in}^{Di} QR_{in'nt}) + \sum_{n\in Re} (C_n^{Re} Y_n^{Re} + \\
&\sum_{n'\in S, i\in ir} C_{i'nn'}^T QR_{i'nn't} + \sum_{i\in ir, n'\in PDR} C_{in}^{Re} QR_{in'nt}) + \sum_{n\in S} (C_n^S Y_n^S + \sum_i C_{in}^S S_{int}) \Big\}
\end{aligned}
\tag{1}
$$

Capital cost is consisted of infrastructure cost whereas handling, production, transportation, purchasing, recovery, remanufacturing, repairing, recycling, disposing and inventory cost contribute to operational cost.

Infrastructure cost is related to the establishment of all capabilities at $n \in PDR$ node, recycling center and disposal site ($C_n^P Y_n^{DP}, C_n^D Y_n^D, C_n^R Y_n^R, C_n^{DR} Y_n^{DR}, C_n^{Re} Y_n^{Re}, C_n^{Di} Y_n^{Di}$) that is the annualized fixed cost required to establish the node (C_n^n) with the binary variable that expresses the establishment of this node (Y_n^n). If a distribution capability is established at a node $n \in PDR$ then its infrastructure cost has also a variable element ($\gamma_n^D D_n$), that is a coefficient expressing the unit cost associated with the distribution capacity (γ_n^D) with the continuous variable expressing the distribution capacity (D_n). Regarding operational cost, handling cost is expressed as a linear function of the total throughput at node $n \in PDR$ both at forward and reverse flow. At the forward direction the total throughput is the sum of the continuous variables expressing the rate of flow of material $is \cup ir$ that arrives at node $n \in PDR$ from node $n \in S$ or/and from other node $n \in PDR$ at time period t ($\sum_{n' \in S \cup PDR} Q_{in'nt}$) whether it is coming from forward or reverse flow and the sum of the continuous variables expressing the rate of flow of material ir that leaves node $n \in PDR$ to node $n \in C$ or/and to other node $n \in PDR$ at time period t ($\sum_{n' \in C \cup PDR} Q_{inn't}$). We apply the same at reverse direction. By multiplying the aforementioned total throughputs with the unit handling cost for material i ($C_{in}^{DH}, C_{in}^{DRH}$) and summarising the resulting products we obtain the handling cost. Production cost is related to the unit cost of consumption of resource e at node $n \in PDR$ multiplied with the total utilization of each resource e at time period t ($\sum_{i \in ir} \lambda_{ine} P_{int}$). Transportation cost is related to the amount of material i transferred between all nodes occurred in the forward and reverse network. This cost summarizes the products of unit transportation cost of material i from a node n to another node n' ($C_{inn'}^T$), and vise versa ($C_{in'n}^T$), and the corresponding continuous variables expressing the rate of flow of material i that arrives at a node n from another node n' ($Q_{inn'}$), and vise versa ($Q_{in'n}$). Purchasing cost is consisted of the cost required to establish a relationship (supplier management costs, technology integration investments, hedging costs for financial risk, etc.) with supplier $n \in S$ ($C_n^S Y_n^S$) plus the sum of the cost for purchasing amounts of raw material i from the selected supplier ($\sum_i C_{in}^S S_{int}$) during time period t, that is the product of the unit purchase price of material i from node $n \in S$ (C_{in}^S) and the continuous variable expressing the purchased amounts of raw material i from the selected node $n \in S$ at time period t (S_{int}). Inventory cost occurred over a given time period t is assumed to be proportional to the average amount of inventory held over this time period. The average amount of inventory held over a time period is expressed as an arithmetic mean of the starting and ending inventories($\frac{I1_{int} + I1_{in(t-1)}}{2}$) for this period and by multiplying with the unit inventory cost for material i in case of established forward (C_{int}^{IP}) or reverse capabilities (C_{int}^{IDR}) we gain inventory cost. Recovery cost is related to the cost of returned or recoverable products at the recovery center $n \in PDR$ and is the product of unit recovery cost ($C_{in'}^{RV}$) with the continuous variables expressing the rate of flow of recoverable materials. Remanufacturing ($C_{in}^{RM}(QR_{in'nt})RM$), repairing ($C_{in}^{RP}(QR_{in'nt})RCC$), recycling ($C_{in}^{Re} QR_{in'nt}$) and disposing ($C_{in}^{Di} QR_{in'nt}$) costs are dealt in the same fashion.

The MILP optimization model has six sets of constraints that formulate the structure of the network, the flow of materials within the network, the core operations in the network (purchasing, operating multifunctional node, recycling and disposing), and customer satisfaction. Constraints (2) to (5) demonstrate the conditions for the establishment of a node $n \in PDR$. In specific, constraint (2) states that if a production capability is established at a node $n \in PDR$ ($Y_n^P = 1$) then the corresponding node

$n \in PDR$ should be established as the binary variable that expresses its establishment is forced to take the value of one ($Y_n = 1$). In the same fashion, constraint (3), (4) and (5) for distribution, recovery and redistribution capability respectively.

$$Y_n \geq Y_n^P, \forall n \in PDR \tag{2}$$

$$Y_n \geq Y_n^D, \forall n \in PDR \tag{3}$$

$$Y_n \geq Y_n^R, \forall n \in PDR \tag{4}$$

$$Y_n \geq Y_n^{DR}, \forall n \in PDR \tag{5}$$

As shown in constraint (6) and (7), considering the forward flow, if a node $n \in PDR$ is established ($Y_n = 1$) should receive material from at least one other node $n' \in S \cup PDR$ and should provide material to at least one other node $n' \in C \cup PDR$. For this reason the binary variable that expresses the establishment of a material transportation link ($X_{n'n}$) or ($X_{nn'}$) is forced to take the value one for at least one pair of $n' \in S \cup PDR$ or $n' \in C \cup PDR$ with $n \in PDR$ and provided that $n \neq n'$.

$$Y_n \leq \sum_{n' \in S \cup PDR \setminus \{n\}} X_{n'n}, \forall n \in PDR \tag{6}$$

$$Y_n \leq \sum_{n' \in C \cup PDR \setminus \{n\}} X_{nn'}, \forall\, n \in PDR \tag{7}$$

Similarly considering reverse flow, if a node $n \in PDR$ is established it should receive material from at least one other node $n' \in C \cup PDR$ and should provide material to at least one other node $n' \in CC \cup PDR \cup Re \cup Di$. Constraint (8) forces the binary variable expressing the contracting of node $n' \in S$ ($Y_{n'}^S$) to be unity when the material transportation link, between a node $n' \in S$ and a node $n \in PDR$, is established ($X_{n'n} = 1$). On the other hand, constraint (9) forces the binary variable expressing the establishment of node $n \in PDR$ to be unity when the material transportation link, between a node $n' \in S$ and a node $n \in PDR$, is established ($X_{n'n} = 1$).

$$X_{n'n} \leq Y_{n'}^S, n' \in S, n \in PDR, n \neq n' \tag{8}$$

$$X_{n'n} \leq Y_n, n' \in S, n \in PDR, n \neq n' \tag{9}$$

In the same manner, we manage all the constraints that force to build links between all permitted nodes occurred in the network. The binary variable ($X_{nn'}, XR_{nn'}$) is fixed to zero, in cases when the model does not allow intra-layer flows between nodes except node $n \in PDR$, flows from suppliers to first/second markets or to recycle centers, from first markets to other nodes, from PDR nodes to suppliers, from disposal sites or recycle centers to PDR nodes. Moreover, the flow of materials at time period t ($Q_{inn't}, QR_{inn't}$) lies between upper and lower bounds provided that the corresponding transportation connection has been established. Constraint (10) states that the available inventory of product $i \in ir$ held in production facility at node $n \in PDR$ at the end of period t is equal to

$$I1_{int} = I1_{in(t-1)} + \left(\sum_{n' \in PDR \setminus \{n\}} Q_{in'nt} + \sum_{n' \in PDR \setminus \{n\}} QR_{in'nt-1} + P_{\text{int}} - \sum_{n' \in C \cup PDR \setminus \{n\}} Q_{inn't} \right) \Delta T_t, \forall t, i, n \in PDR \tag{10}$$

the inflow from other nodes $n \in PDR$ including the remanufacturable products from reverse flow at the end of period *t-1*, plus the rate of production of product $i \in ir$, plus the inventory held at the end of period *t-1* minus the outflow to other nodes $n \in PDR$ at forward flow and to first markets.

The rate of production (P_{int}) of product *i* is limited between a maximum and minimum production capacity while, the usage of manufacture resources *e* must not exceed the total availability of the resource *e*. Additionally, appropriate constraint force to satisfy the demand at first markets. At the reverse direction, provided that a recovery capability is established at node $n \in PDR$, constraint (11) states at period *t* the flow of recoverable material $i \in ir$ exiting from each customer $n \in C$ to all recovery centers is equal to the flow that enters to first markets multiplied with a return ratio (*RC*).

$$\sum_{n' \in PDR} Q_{inn't} = \left(\sum_{n' \in PDR} Q_{in'nt} \right) RC, \forall t, i \in ir, n \in C \tag{11}$$

After collecting and inspecting the return products, repaired products are shipped by recovery center to node $n \in PDR$ provided re-distribution capability it is established, remanufacturable to node $n \in PDR$ with production capability, recycled products to recycled centers and scrapped products to disposal sites. The flow of recyclable products entering recycling centers is re-processed to raw materials. Provided that a re-distribution capability is established at node $n \in PDR$, constraint (12) depicts that the inventory of repaired product $i \in ir$ held at the end of period *t* is equal to the inflow from other $n \in PDR$, plus the inventory held at the end of period *t-1* minus the outflow to second markets.

$$I2_{int} = I2_{in(t-1)} + \left(\sum_{n' \in PDR \setminus \{n\}} QR_{in'nt} - \sum_{n' \in CC \setminus \{n\}} QR_{inn't} \right) \Delta T_t, \forall t, i, n \in PDR \tag{12}$$

Finally, distribution, recovery and re-distribution capacity (D_n, Rc_n, RD_n) lies between higher and lower limits, provided that the capabilities are established while it is approached as linear function of handled material flow that enters/leaves the node.

3. Case study

The applicability of the Generalized SCN design and operation model is illustrated by using a medium-size case study in the European area. This network is comprised by five potential suppliers, ten potential generalized nodes ten first markets, three recycle centers-disposal sites and 5 second markets. The number of materials/products provided by the suppliers is ten. The proposed model (GSCN) is compared with a counterpart model with fixed-echelons (FSCN), both of which were implemented in GAMS 24.1.3 software, using CPLEX 12 solver. Identical data were used for both models while the production process is approached in the same way.

4. Results

Figure 1, presents the optimal network for GSCN and FSCN, respectively. The former establishes 1PDR node with production-distribution-recovery capability (BE) and 1 PDR node with production-distribution-redistribution capability (CH) both of which are provisioned from the same supplier (RO), 1 recycle center (FR) and 1 disposal site (IT), while the latter establishes 3 plants (FI,BE,CH) which are provisioned from two suppliers (RO, TR), 2 distribution centers (BE,CH), 1 recycle center (IT) 1 disposal site (IT). Both models employ the same objective function that was counted 5,323,075 and 6,169,743 relative money units for GSCN and FSCN, respectively. Cost saving of about 15% is due to the fact that FSCN model is forced by the a priori structure to build more facilities (sum of plants, distribution, recovery and re-distribution centers) resulting also in higher inventory (94%) and production (13%) cost. Moreover the GSCN model resulted to lower transportation cost due to the network's flexibility.

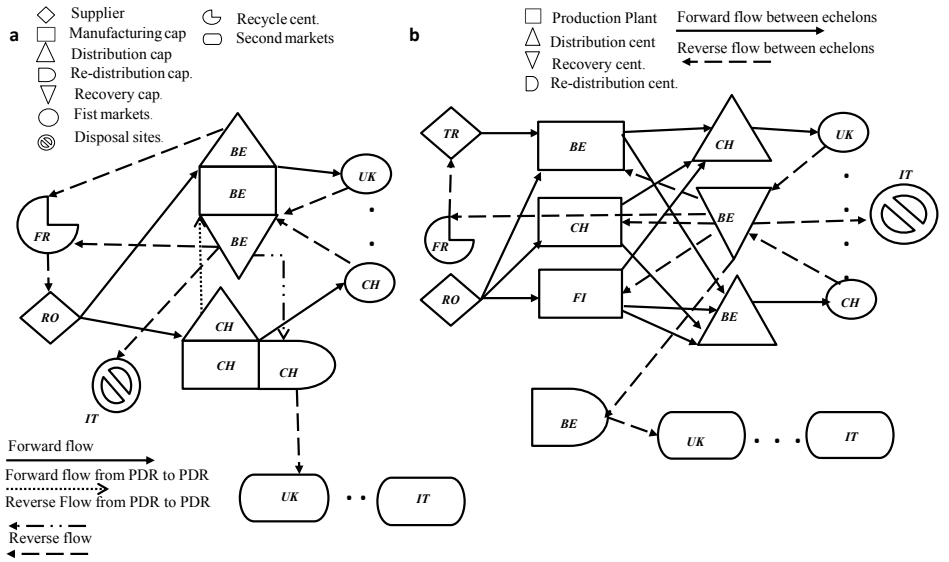

Figure 1. Optimal GSCN configuration (a) against the optimal FSCN configuration (b).

5. Conclusions

This paper introduces a mathematical model that provides flexibility options on designing and operating CLSCNs. The model is capable of deciding the appropriate suppliers and material flow connections including intra-layer flows but mainly the location and role/capability of the generalized nodes. It is concluded that, giving the network the option to have multifunctional nodes (or choose among them) and simultaneously to avoid having separated processes, significant cost savings can be achieved.

6. Acknowledgement

This research has been co-financed by the European Union (European Social Fund – ESF) and Greek national funds through the Operational Program "Education and Lifelong Learning" of the National Strategic Reference Framework (NSRF) - Research Funding Program: Thales.

References

S.R. Cardoso, A.P.F.D. Barbosa-Póvoa, & S. Relvas, 2013, Design and planning of supply chains with integration of reverse logistics activities under demand uncertainty, European Journal of Operational Research, 226, 436-451.

M. S. Pishvaee, M. Rabbani, & S. A. Torabi, 2011, A robust optimization approach to closed-loop supply chain network design under uncertainty, Applied Mathematical Modelling, 35, 637-649.

M. Ramezani, A. M. Kimiagari, B. Karimi, & T. H. Hejazi, 2014, Closed-loop supply chain network design under a fuzzy environment. Knowledge-Based Systems, 59, 108-120.

M. I. G. Salema, A. P. Barbosa-Povoa, & A. Q. Novais, 2010, Simultaneous design and planning of supply chains with reverse flows: A generic modelling framework, European Journal of Operational Research, 203, 336-349.

Krist V. Gernaey, Jakob K. Huusom and Rafiqul Gani (Eds.), 12th International Symposium on Process Systems Engineering and 25th European Symposium on Computer Aided Process Engineering. 31 May – 4 June 2015, Copenhagen, Denmark

Simultaneous Optimisation of Economic and Environmental Objectives with Dynamic Price Signals and Operational Constraints

Tristan Lambert,[a,b] Andrew Hoadley,[a,b*] Barry Hooper[c]

[a]*Cooperative Research Centre for Greenhouse Gas Technologies (CO2CRC), Level 3 Earth Sciences Building, the University of Melbourne, Melbourne 3010, Australia*
[b]*Monash University, Dept. Chemical Engineering Monash University Clayton Campus, Melbourne 3800, Australia*
[c]*UNO Technology, 368 St Kilda Rd Melbourne 3004, Australia*
Andrew.Hoadley@monash.edu

Abstract

Processing plants are often required to be capable of turndown or increased production depending on the demand for their products or changes to the raw materials supply and the design of the process should take into account of these considerations in determining additional capital that may be required to provide this additional flexibility. In this paper the economic and environmental performance of a natural gas combined cycle (NGCC) power plant fitted with post combustion capture (PCC) is optimised under a number of different scenarios using a time-integrated multi-objective optimisation (MOO) framework.

In the base case scenario, the plant is operated in a base-load continuous mode and just accepts the electricity price available. The economic performance of the plant will be modelled and optimised for each day throughout the year accepting the electricity price for that year. The results are provided on a Pareto front multi-objective basis as annual net operating profit plotted against the average fraction of CO_2 captured. This general modelling framework can be applied to a wide range of industries where there are similar economic and/or environmental dynamics.

Keywords: Carbon capture and storage, Multi-objective optimisation, Dynamics, Surrogate Modelling.

1. Introduction

In order to address the problem of global warming, swapping coal fired power plants for natural gas will be insufficient to achieve the emission reduction required for the 2 °C temperature rise scenario (IEA, 2012). Fossil fuel use is also predicted to continue to play a major role in energy production throughout the 21st century (IEA, 2013) and as result carbon capture and storage (CCS) will be required to mitigate the CO_2 equivalent (CO_{2e}) emissions.

CCS is economically detrimental to power plant performance not only due to the capital and operating expenses incurred by the CCS plant, but also from the loss of revenue incurred due to reduction in power plant output. Work by Berstad et al. (2011) showed that although NGCC had a lower efficiency penalty compared to coal fired power

stations the specific work required for capture was higher. This is due to lower CO_2 flue gas concentration in NGCC power plants thus requiring more specific work to capture the CO_2. Exhaust gas recirculation (EGR) has been used to increase the CO_2 concentration in the flue gas by recycling a portion of the flue gas around to the air inlet. Sipöcz et al. (2011) showed a reduction in energy requirement and levelised cost of electricity (LCOE) with the use of EGR. ElKady et al. (2009) showed the maximum EGR rate without turbine modification was 35 %. An additional problem with gas turbine post combustion capture is the high O_2 concentration in the flue gas stream. As shown in work by Supap et al. (2006) the presence of O_2 degrades monoethanolamine (MEA), the most common solvent currently used for solvent based post combustion capture. Similar to Pandit et al (2014) a potassium carbonate (K_2CO_3) solvent process is selected for this work.

Most studies of integration of CCS with the power station have been based on calculating the LCOE using design conditions. Work by Wiley et al. (2011) showed that by adjusting capture rate within the demand cycle, up to 50 % of the CO_2 could be captured for a coal fired power plant without affecting the net power supplied to the grid. Manaf et al (2014) analysed different dynamic post combustion carbon capture control strategies. Whereas Pandit et al (2014) studied the improvements obtained from EGR and heat integration and Harkin et al (2012) studied the economic performance under design conditions, is the current study has applied the first MOO model for dynamic capture based on real market electricity power prices.

2. Methodology

The power plant and capture process were modelled using the Aspen Plus® V8.4 processing modelling software. The steam cycle performance and simple heat integration were calculated from the grand composite curve (Harkin et al., 2012). The gas turbine modelled was a combined cycle Alstom GT26 (Alstom, 2007). Gas turbine performance is shown in Table 1. A simplified flow sheet for the gas turbine with PCC-CCS is shown in Figure 1.

The detailed Aspen model was then used to produce a surrogate model (SUMO) (Gorissen et al., 2010), which takes the inputs to the Aspen simulation and uses an artificial neural network to generate an empirical formula for the simulation outputs. The SUMO is used to reduce CPU time for multiple simulations runs to aid the MOO. A comparison of the SUMO model to the Aspen simulation is provided in Figure 2.

Table 1: Alstom GT26 combine cycle performance (Alstom, 2007)

Gas Turbine	
ISO rating (MW)	288
Exhaust Gas Flow (kg/s)	650
Exhaust Gas Temp (°C)	614
Steam Turbine	
Power Out (MW)	157
HP Pressure/Temp (bar/°C)	135.3/565
MP Pressure/Temp (bar/°C)	28/565
LP Pressure/Temp (bar/°C)	4.74/287

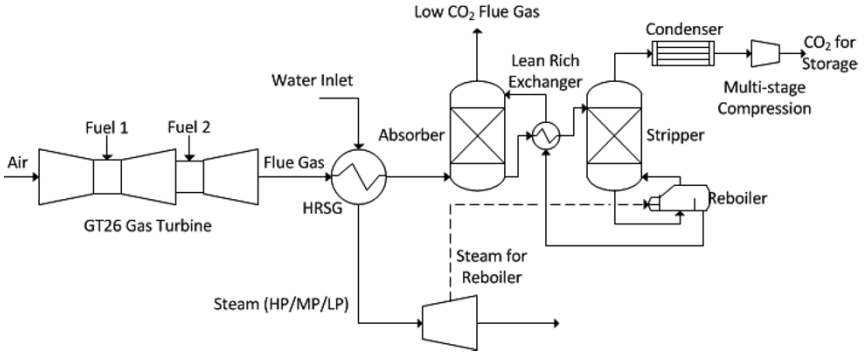

Figure 1. Simplified flow diagram for an Alstom GT26 with PCC.

The MOO is performed using the Genetic Algorithm code NSGA-II developed by Deb et al. (2002) and adapted for use in Microsoft Excel® by Sharma et al. (2012). MOO allows for the simultaneous optimisation of profitability, defined by Net Present Value (NPV) and the capture rate.

The economic framework first defined by Ho et al. (2009) is shown in Table 2. The economic output is given in 2011 Australian dollars ($AU). A new build NGCC power plant without capture would result in a NPV of $AU 255 million under these conditions. The electricity price data is the South Australian market price data (AEMO, 2014) for the 2013-14 financial year. During this period Australia had a carbon price of $AU 24.15 /t CO_{2e} and payment of this tax has been included in the economic analysis.

In the alternative scenarios, a time slice pseudo-steady-state modelling approach is used to integrate the performance of the plant over the full year. However, rather than optimise for each of the 8760 hours individually, a frequency distribution has been used to provide the integration of costs and revenue over the whole year on an hourly basis.
The simulations are optimised with respect to the maximum and minimum capture rates and cut off price. The maximum capture rate is used to set the size of the plant and hence the economic and power plant performance. The cut off price selects whether maximum or minimum capture is used at any given time based on the real electricity price data. When the real price exceeds the cut off price capture is reduced to the minimum capture rate and when the price falls below the cut off rate maximum capture is utilised. Hourly price fluctuations are shown in Figure 3a. Figure 3b shows the fit obtained using both a normal distribution and a log normal distribution, which is preferred. From this distribution it is possible to directly calculate the number of operational hours at both maximum and minimum capture rates. This is done by integrating below the cut off price for minimum capture rate and above the cut off price for maximum capture rate. The price probability is given by a log normal distribution:

$$p = \frac{1}{x\sqrt{2\pi}\sigma} e^{-\frac{\ln x - \mu}{2\sigma^2}} \quad (1)$$

Table 2: Economic parameters used

Discount Rate (%)	7	Load factor (%)	90
Project lifetime (y)	25	Natural gas price ($AU/GJ)	4
Build time (y)	2	Carbon Price (AU/tCO_{2e}$)	24.15
CO_2 storage cost (AU/tCO_2$)	6.03		

Table 3: Simulation case operating parameters. Turndown limit is 30 % (Peplinski, 2011)

Case	*Variable Capture*	*Rich and Lean Solvent Storage*	*Turndown Limitations*
Base	No	No	N/A
Option 1	Yes	No	No
Option 2	Yes	No	Yes (30 %)
Option 3	Yes	Yes - 2 h	No
Option 4	Yes	Yes – 2 h	Yes (30 %)

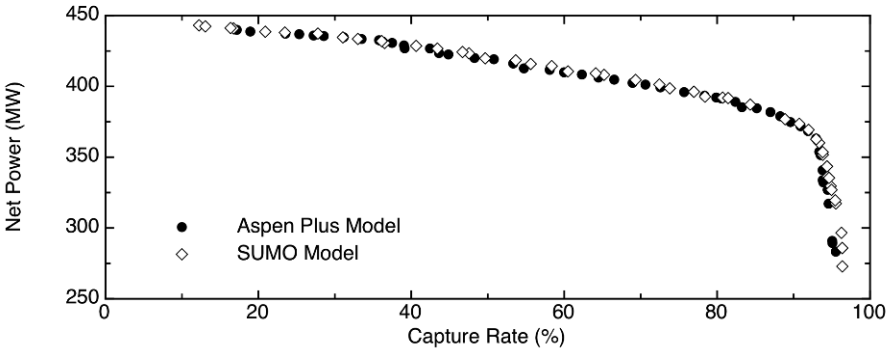

Figure 2. Comparison of the SUMO models to the detailed Aspen Plus® simulations.

The hours (h) of minimum capture can be calculated from the cumulative distribution function:

$$h_{min\,capture} = h_{total} \cdot \int_0^x p\,dx = h_{total} \cdot \left(\frac{1}{2} + \frac{1}{2}\mathrm{erf}\left(\frac{\ln x - \mu}{\sqrt{2}\sigma}\right)\right) \quad (2)$$

where x is the cut of price, μ is the location parameter and σ is the scale parameter and erf is the error function. The hours of maximum capture can also be calculated as the difference. This sets the total CO_2 captured. The SUMO model can then be used to calculate the total amount of power produced by the plant throughout the year. A constraint is imposed within the model to ensure that there is sufficient steam generated to satisfy the reboiler regeneration energy requirements.

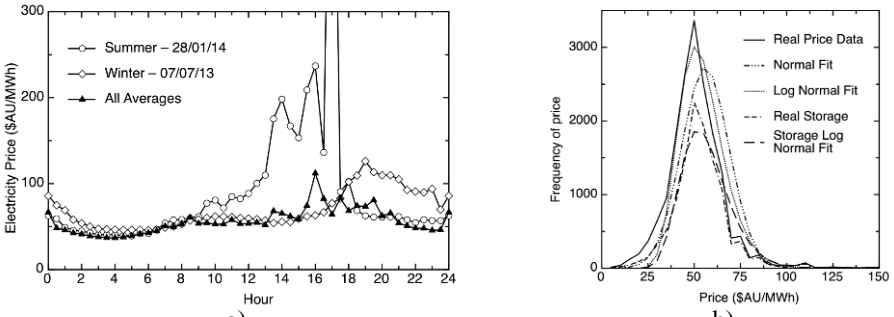

Figure 3. a) Electricity price data showing variability in the price across the most average summer and winter day (dates shown) and the total average. Storage is done during the total average highest 2 h period, from 4pm-6pm. The summer point at17:00 off the scale is 739.89 $/MWh. b) Electricity price histogram with real data and normal and log normal distribution. Log normal is used for this work. Storage peaks reduced due to lower hours total hours the system is free to vary in. Price mean is 56.01 $AU/MWh with a standard deviation of 18.12 $AU/MWh (μ = 3.96, σ = 0.32, R^2 = 0.957). With storage it becomes 58.02 $AU/MWh with a standard deviation of 19.46 $AU/MWh (μ = 4.01, σ = 0.33, R^2 = 0.959).

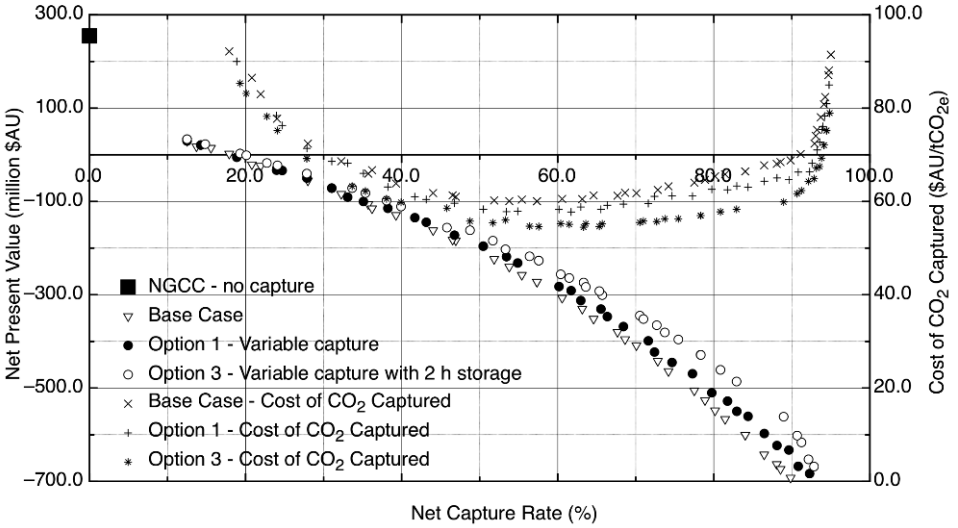

Figure 4. NPV for all cases as a function of capture rate. The cost of CO_2 captured is also shown. Cost of CO_2 capture calculated as $= \frac{\Delta NPV}{\sum discounted\ CO_2\ captured}$.

3. Results and Discussion

The net present value (NPV) for cases without turndown limits are shown in Figure 4. Table 3 shows the turndown NPV at selected capture rates. All cases show an improvement in NPV with dynamic optimisation. With turndown constraints imposed, the improvement compared with the base case is reduced.

The similarity between all cases at lower capture rates is expected as variable operation makes less difference to the plant performance as the difference between maximum and minimum capture rates is reduced. Higher capture rates provide more flexibility for the cases with variable operation and this results in better economic performance. The addition of turndown constraints into the results in reduced performance improvement. Limiting turndown reduces the possible variability and hence reduces the benefits of variable capture. The addition of solvent storage improves the economic performance of the power plant by transferring the energy cost from a time of expensive electricity prices to times with lower electricity prices.

4. Conclusions

A statistical approach was used in conjunction with MOO to allow the optimisation of a NGCC-CCS plant over a whole year. By fitting price data to a log normal distribution and setting a price point as an optimisation variable it was possible to optimise the plant with variable performance. Using this approach the plant could be optimised to achieve economic benefits for the same net plant performance.

5. Acknowledgements

The authors would like to acknowledge the funding provided by the Australian Government through its CRC Program to support this CO2CRC research project.

Table 4: NPV results at selected capture rates to compare the effect of the turndown limitations on the plant performance.

Case	*50 % capture*	*80 % capture*	*90 % capture*
Base Case	-223 m$AU	-548 m$AU	-692 m$AU
Option 1	-196 m$AU	-510 m$AU	-632 m$AU
Option 2	-209 m$AU	-520 m$AU	-677 m$AU
Option 3	-184 m$AU	-460 m$AU	-601 m$AU
Option 4	-193 m$AU	-465 m$AU	-614 m$AU

References

AEMO, 2014, http://www.aemo.com.au/Electricity/Data/Price-and-Demand/Aggregated-Price-and-Demand-Data-Files/Aggregated-Price-and-Demand-2011-to-2015, Last accessed: 15/11/2014.

Alstom, 2007, Transforming Tallawarra: GT26 based plant for booming New South Wales, Australia, Modern Power Systems, TBC 04 03E.

D. Berstad, A. Arasto, K. Jordal, G. Haugen, 2011. Parametric study and bench-marking of NGCC, coal and biomass power cycles integrated with MEA-basedpost-combustion CO_2 capture. Energy Procedia, 4, 1737–1744.

K. Deb, A. Pratap, S. Agarwal, T. Meyarivan, 2002, A fast and elitist multi-objective genetic algorithm: NGSA-II, Evolutionary Computing, IEEE Transactions, 6, 2, 182-197.

A. ElKady, A. Evulet, A. Brand, T. Ursin, A. Lynghjem, 2009, Application of exhaust gas recirculation in a DLN F-Class combustion system for postcombustion carbon capture, Journal of Engineering for Gas Turbines and Power, 131, 034505-1-6.

D. Gorissen, K. Crombecq, I. Couckuyt. T. Dhaene, P. Demeester, 2010, A surrogate modelling and adaptive sampling toolbox for computer based design, Journal of Machine Learning Research, 11, 2051-2055.

T. Harkin, A. Hoadley, B. Hooper, 2012, Optimisation of power stations with carbon capture plants – the trade off between costs and net power, Journal of Cleaner Production, 34, 98-109.

M. Ho, G. Allinson, D. Wiley, 2009, Factors affecting the cost of capture for Australian lignite coal fired power plants, Energy Procedia, 1, 763-770.

IEA, 2012, Energy Technology Perspectives – How to Secure a Clean Energy Future, International Energy Agency (IEA).

IEA, 2013, World Energy Outlook 2013, International Energy Agency (IEA).

N. Manaf, A. Cousins, P. Feron, A. Abbas, 2014, Control analysis of post combustion carbon dioxide capture process (PCC), International journal of Chemical and Environmental Engineering, 5, 4, 250-254.

J. Pandit, T. Harkin, C. Anderson, M. Ho, D. Wiley, B. Hooper, 2014, CO_2 emission reduction from natural gas power stations using a precipitating solvent absorption process, International Journal of Greenhouse Gas Control, 28, 234-247.

S. Peplinski, 2011, Basic design & engineering package, Quest CCS Project, 07-1-AA-7739-0001.

S. Sharma, G. Rangaiah, K. Cheah, 2012, Multi-objective optimization using MS Excel with an application to design of a falling film evaporator system, Food and Bioproducts Processing, 90, 2, 123-134.

N. Sipöcz, A. Tobiesen, M. Assadi, 2011, Integrated modelling and simulation of a 400 MW NGCC power plant with CO_2 capture, Energy Procedia, 4, 1941-1948.

T. Supap, R. Idem, P Tontiwachwuthikul, C. Saiwan, 2006, The roles of O_2 and SO_2 in the degradation of monoethanolamine during CO_2 absorption from industrial flue gas streams, EIC Climate Change Technology, 2006 IEEE, 1-6.

D. Wiley, M. Ho, L. Donde, 2011, Technical and economic opportunities for flexible CO_2 capture at Australian black coal fired power plants, Energy Procedia, 4, 1893-1900.

Krist V. Gernaey, Jakob K. Huusom and Rafiqul Gani (Eds.), 12th International Symposium on Process Systems Engineering and 25th European Symposium on Computer Aided Process Engineering.
31 May – 4 June 2015, Copenhagen, Denmark

Integration of Scheduling and Vessel Routing in Pipeless Plants

Munawar A. Shaik* and Pulkit Mathur

Department of Chemical Engineering, Indian Institute of Technology Delhi, India.
munawar@iitd.ac.in

Abstract

A novel methodology for integrating scheduling and routing of moveable vessels for the optimal operation of pipeless plants is presented in this work. Herring-bone layout is assumed for processing stations. The proposed mathematical model is based on state-task-network process representation and unit-specific event based continuous-time formulation. Vessels are treated as states, the feasible routes for vessel transfer between different stations are considered as units and the movement of vessels on a route is considered as a routing task. The computational performance of the proposed formulation is illustrated through an example drawn from literature.

Keywords: Pipeless Plants, Scheduling, Routing, Vessels

1. Introduction

Pipeless plants offer an alternative flexible and responsive production route to traditional batch plants, where different transferable vessels keep moving between stationary processing stations for performing typical operations such as charging, mixing, heating, cooling, discharging, and cleaning. The vessels are carried on automated guided vehicles (AGVs) between processing stations. Unlike in traditional batch plants, cleaning between product changeovers in the same vessel can be done at another cleaning station without losing production time. Pipeless plants are expected to become a major trend in small to medium scale industries especially for processing of powders and slurries which are difficult to transport using pipelines.

In the operation of pipeless plants, decisions have to be made regarding scheduling of production processes, assignment of orders to stations and vessels, and routing of the AGVs. The efficiency of operation of pipeless plants depends on the optimality of the production schedules (Bok and Park, 1998). The optimal routing of AGVs must be determined for a safe and collision-free operation of transporting vessels from one station to another. Vessels are used for both processing and storage of materials in addition to transporting the batches from one station to another. Owing to this strongly interacting nature of the scheduling and vessel routing aspects for pipeless plants, they need to be addressed simultaneously using an integrating approach (Huang and Chung, 2005).

In this work a novel mathematical formulation is proposed for integrating scheduling and vessel routing in pipeless plants for an assumed fixed layout of processing stations. The proposed model is based on state-task-network (STN) process representation and unit-specific event-based continuous-time formulation adapted from the three-index model for batch plants by Vooradi and Shaik (2012). The development of the STN

depends on the number of vessels available, number of batches to be produced and their relationship. In the proposed novel STN, vessels have been treated as separate states (S^V) and the corresponding tasks have been converted into as many tasks as the number of vessels when the number of vessels available (N^V) is less than the total number of batches of all products (N^B) to be produced ($N^V<N^B$). Otherwise, when there are equal or more vessels available ($N^V \geq N^B$), then splitting of states of material and tasks has not been done. In addition to this, all tasks have been split based on the number of production sequences. The methodology used for handling vessel routing involves addition of vessel routing tasks and the corresponding routes as units. The different possibilities of feasible routes for different production sequences have been considered as separate units. The movement of an empty vessel or a vessel carrying material on a route has been considered to be a routing task. These routing tasks are product specific in order to maintain the identity of the production sequence. The movement of an empty vessel after the end of a particular production sequence to the first processing station has also been accounted for every batch of production. If a routing task repeats for a particular production sequence, it is considered to be different as it involves production and consumption of different states of material. The time of travel of vessels between different processing stations has been considered to be the processing time in the routing units.

This paper is organized as follows. The proposed mathematical formulation has been described in detail in section 2. The application to a benchmark problem from literature (Bok and Park, 1998) and the results for a case study have been discussed in section 3 followed by conclusions given in section 4.

2. Mathematical Model

The integrated scheduling and vessel routing problem addressed in this work can be stated as follows. Given: (i) scheduling horizon or demands for final products, (ii) the production recipe (i.e., the processing times for each task in suitable units, relation between tasks, states and units), (iii) the layout (determines the transfer time between stations) and the amount of available resources (amount of raw materials and number of moveable vessels), (iv) processing units and their capacity limits and (v) the number and type of vessels available and suitable tasks requiring these vessels. Determine: (i) the optimal sequence of tasks taking place in each unit, (ii) the start and end times of different tasks in each unit, (iii) the amount of material processed and stored at each time in each unit and (iv) vessel utilization and routing profiles. The objective considered is minimization of makespan or total production time for a specified horizon to produce specific demands of final products. The layout is fixed (say Herringbone layout) and the transfer times have been assumed on the basis of this type of layout.

The proposed mathematical formulation has been adapted from the three-index unit-specific event-based model for scheduling of batch plants by Vooradi and Shaik (2012) that has been customized for application to pipeless plants through addition of new constraints such as a single sequencing constraint for material flow replacing the two material balance equations in the model from literature, vessel balances to ensure appropriate vessel utilization and intermediate balances for all intermediate states except vessels replacing bounds on excess material to ensure proper material usage. The duration and tightening constraints have been modified to exclude transfer times as they

have been incorporated as processing times in route units. The variables involved have been reduced to a considerable extent by removal of batch sizes and excess material states for all materials since the primary considerations are optimal scheduling and routing which depend only on the number of batches of production of different products and their production sequences. The major constraints in the model are as follow.

2.1. Sequencing Constraints

$$\sum_{\substack{n'\in N\\ n'\le n}} \sum_{\substack{n''\in N\\ n'\le n''\le n'+\Delta n}} \sum_{i\in I_s^c} w(i,n',n'') \le \sum_{n'\in N} \sum_{\substack{n''\in N\\ n'\le n''\le n'+\Delta n\\ n''<n}} \sum_{i\in I_s^p} w(i,n',n'') \tag{1}$$

$$\forall n, s\in S^I, s\notin S^V$$

Eq.(1). ensures proper material flow sequencing as per the specified production recipe for all intermediate states so that production occurs before consumption.

2.2. Vessel Balances

$$ST(s,n) = ST_o(s) + \sum_{i\in I_s^c} \sum_{\substack{n'\in N\\ n\le n'\le n+\Delta n}} \rho_{is}\, w(i,n,n') \tag{2}$$

$$\forall n = 1, s\in S^V, N^V < N^B$$

$$ST(s,n) = ST(s,n-1) + \sum_{i\in I_s^p} \rho_{is} \sum_{\substack{n'\in N\\ n-1-\Delta n\le n'\le n-1}} w(i,n',n-1) + \sum_{i\in I_s^c} \rho_{is} \sum_{\substack{n'\in N\\ n\le n'\le n+\Delta n}} w(i,n,n') \tag{3}$$

$$\forall n > 1, s\in S^V, N^V < N^B$$

Eqs.(2) and (3) ensure appropriate recycle and reuse of vessels for the case when number of vessels are less than the total number of batches of production. For all other states the material balances are given in Eq.(4) and (5).

2.3. Intermediate State Balances

$$\sum_{i\in I_s^p} \rho_{is} \sum_{\substack{n'\in N\\ n-1-\Delta n\le n'\le n-1}} w(i,n',n-1) + \sum_{i\in I_s^c} \rho_{is} \sum_{\substack{n'\in N\\ n\le n'\le n+\Delta n}} w(i,n,n') = 0 \tag{4}$$

$$\forall s\in S^I, s\notin S^V, n\in N, n>1$$

$$\sum_{i\in I_s^c} \rho_{is} \sum_{\substack{n'\in N\\ n\le n'\le n+\Delta n}} w(i,n,n') = 0 \tag{5}$$

$$\forall s\in S^I, s\notin S^V, n\in N, n=1$$

No excess amount of intermediates is allowed to be stored in the vessels in Eq.(4) and (5).

2.4. Duration Constraints

$$T^f(i,n) = T^s(i,n) + \alpha_i\, w(i,n,n) \tag{6}$$

$$\forall i\in I, n\in N, \Delta n = 0$$

$$T^f(i,n') = T^s(i,n) + \alpha_i \; w(i,n,n') \tag{7}$$
$$\forall i \in I, n, n' \in N, n \le n' \le n + \Delta n, \Delta n > 0$$

$$T^f(i,n') = T^s(i,n) + \alpha_i \; w(i,n,n') + M(1 - w(i,n,n')) \tag{8}$$
$$\forall i \in I, n, n' \in N, n \le n' \le n + \Delta n, \Delta n > 0$$

The duration does not include transfer times or waiting times for units as they have been incorporated into the model as processing times through the modifications in the STN involving routing tasks in route units. Hence, the duration constraints in Eq. (6) – (8) are similar to the batch scheduling model of Vooradi and Shaik (2012).

2.5. Tightening Constraints

$$\sum_{i \in I_j} \sum_{n \in N} \sum_{\substack{n' \in N \\ n \le n' \le n + \Delta n}} \alpha_i \; w(i,n,n') \le MS \quad \forall j \in J \tag{9}$$

Since the transfer times have been incorporated in the duration constraints for routing tasks, the tightening constraint in Eq.(9) is written for all units including route units.

The other constraints such as allocation and sequencing and definition of objective function are similar to those in literature (Vooradi and Shaik, 2012).

3. Case Study and Results

The mathematical formulation described above has been implemented on a benchmark problem from literature (Bok and Park, 1998). The layout of processing stations is Herring-bone layout as shown in Figure 1 and the production sequence and processing times in all units for all products have been taken from Example 1 of Bok and Park (1998). The proposed STN is shown in Figure 2 where tasks are split into as many tasks as the number of products and vessels considered. The processing times are given in Table 1. The transfer times on vertical (V_0 to V_7) and horizontal routes (H_0 to H_2) have been assumed to be 0.05 h and 0.1 h respectively.

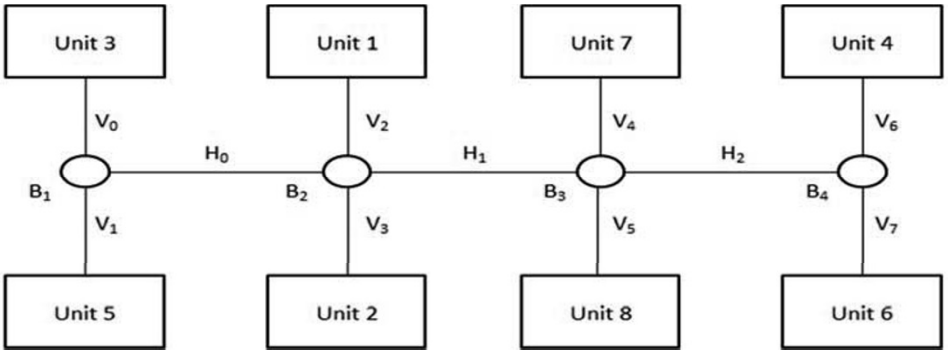

Figure 1. Herring-bone layout of processing stations.

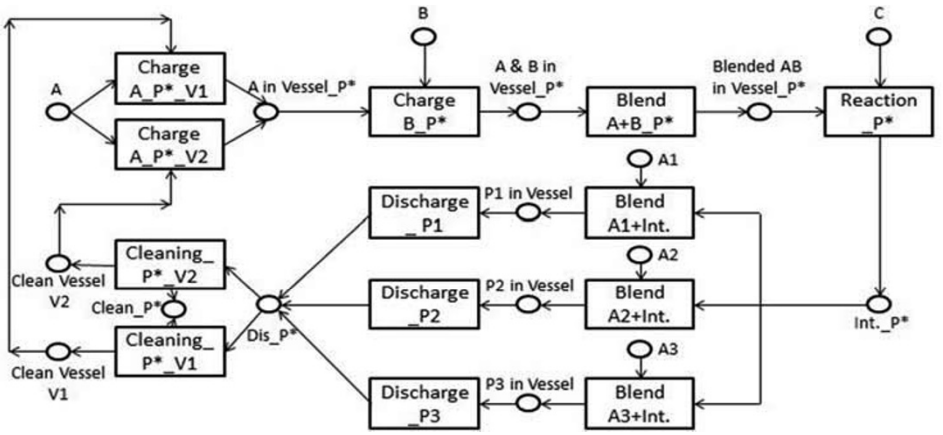

Figure 2. Proposed STN representation showing product and vessel based task splitting.

Table 1. Processing times in all units for all products.

Processing Times (h)	Unit 1 (U1)	Unit 2 (U2)	Unit 3 (U3)	Unit 4 (U4)	Unit 5 (U5)	Unit 6 (U6)	Unit 7 (U7)	Unit 8 (U8)
P1	0.6	0.5	0.5	0.85	0.85	0.6	0.5	0.5
P2	0.5	0.5	0.7	0.75	0.75	0.5	0.5	0.5
P3	0.5	0.6	0.5	0.65	0.65	0.6	0.5	0.5

The proposed mathematical formulation has been implemented on the above sample problem solved in GAMS 23.5 software using CPLEX 12.2 on a 3 GHz Intel Xeon processor with 32 GB RAM running on a Linux operating system. The computational results for this case study are summarized in Table 2.

Table 2. Computational results for the case study.

Number of Vessels	Number of Events	Number of Discrete Variables	Number of Continuous Variables	Number of Constraints	Makespan (h)	CPU time for Non Zero Gap (s)	CPU time for Zero Gap (s)
3	27	4371	9073	66202	6.25	589.8	41252.9
2	47	8286	17015	133601	9.90	240.5	878.8
1	72	12144	24697	195896	14.95	398.8	1869.2

It can be clearly inferred from the above table that the model size is least for the case of equal number of vessels and batches of production because vessels need not be modeled as separate states and there is no need of splitting tasks and states based on the number of vessels available for production. Also, the number of events and makespan increases with decrease in the number of available vessels since vessel reassignment can only take

place after completion of the production sequence. Lastly, there is an interplay of model size and complexity in determining the computational time required for solution. Therefore, computational time is the least for the two vessel case relative to the three vessel case, which is the most complex of the cases considered. A Gantt chart for the two vessel case illustrating both parallel and sequential processing over all units is shown in Figure 3. The gaps in time and event points between different processing tasks are due to the occurrence of routing tasks in route units, which are not explicitly shown.

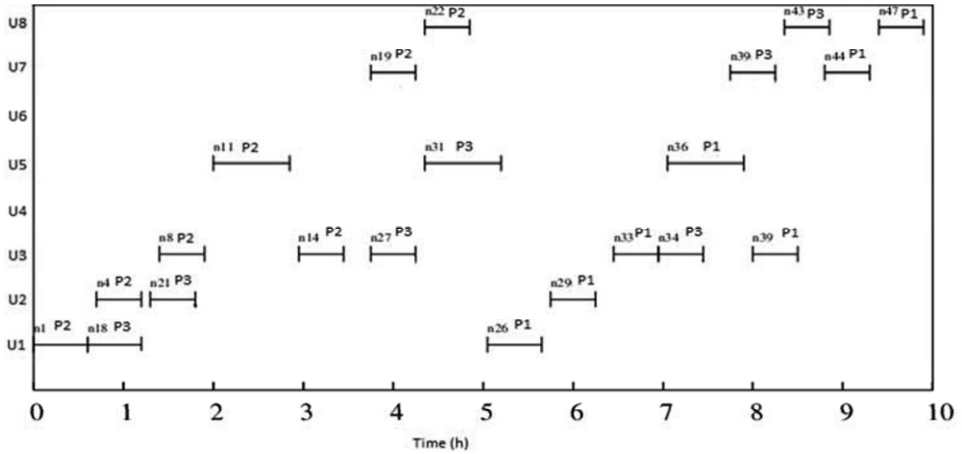

Figure 3. Gantt chart for the two vessel case.

4. Conclusion

A novel mathematical formulation has been proposed for integration of scheduling and vessel routing in pipeless plants for a fixed layout, based on adaptions from scheduling models for batch plants. Accordingly, STN representation has been modified to reflect different cases based on number of batches and number of vessels considered. The proposed formulation is feasible and effective in ensuring optimal scheduling and conflict-free routing of vessels. This approach can be further applied to other layouts of processing stations and more complex case studies to demonstrate its applicability and efficiency.

Acknowledgements

The corresponding author gratefully acknowledges financial support received from Department of Science and Technology (DST), India, under FAST TRACK scheme, grant no. SR/FTP/ETA-0095/2011.

References

J.K. Bok, S. Park, 1998, Continous-Time Modeling for Short-Term Scheduling of Multipurpose Pipeless Plants, Ind. Eng. Chem. Res., 37, 3652-3657.

W. Huang, P.W.H. Chung, 2005, Integrating Routing and Scheduling for Pipeless Plants in Different Layouts, Comp. Chem. Eng., 29, 1069-1081.

R. Vooradi, M.A. Shaik, 2012, Improved Three-index Unit-specific Event-based Model for Short-term Scheduling of Batch Plants, Comp. Chem. Eng., 43, 148-154.

Krist V. Gernaey, Jakob K. Huusom and Rafiqul Gani (Eds.), 12th International Symposium on Process Systems Engineering and 25th European Symposium on Computer Aided Process Engineering.
31 May – 4 June 2015, Copenhagen, Denmark

A Mean Value Cross Decomposition Strategy for Demand-side Management of a Pulping Process

Hubert Hadera[a,b], Per Wide[c], Iiro Harjunkoski[a]*, Juha Mäntysaari[d], Joakim Ekström[c], Guido Sand[a], Sebastian Engell[b]

[a]*ABB Corporate Research, Wallstadter Str. 59, 68526 Ladenburg, Germany*
[b]*Technical University of Dortmund, Emil-Figge-Str. 70, 44221 Dortmund, Germany*
[c] *Linköping University, Campus Norrköping, SE-60174 Norrköping, Sweden*
[d] *ABB Oy Industry Solutions, CPM, Strömbergintie 1 B, 00380 Helsinki, Finland*
**Iiro.Harjunkoski@de.abb.com*

Abstract

Energy is becoming a critical resource for process industries as introduction of new policies drive changes in the energy supply systems. Energy availability and pricing is much more volatile. In this study, we propose a Mean Value Cross Decomposition approach to functionally separate production scheduling from energy-cost optimization. Such a decomposition makes it possible to exploit existing optimization solutions avoiding a need to create a new monolithic model. The proposed framework is applied to a continuous process of thermo-mechanical pulping using a discrete-time Resource-Task Network model. Example case study scenarios show that the approach gives optimal system-wide solutions while keeping the models separated.

Keywords: Scheduling, demand-side management, mean value cross decomposition.

1. Introduction

Today's electricity supply systems face new challenges due to introduction of new policies, volatility of energy availability and prices. One of the important technologies that support the transformation is demand-side response which on the operations level calls for energy-aware scheduling methods. Especially for large scale industrial energy users, energy-aware production scheduling can reduce the operating cost, as shown in case studies available in literature (Hadera et al., 2014). The traditional industrial approach for scheduling of energy intensive operations is to schedule the production first, satisfying all production specific rules, and to predict from that schedule the demand for energy. Next, energy purchase and sale optimization models can be used to find the best contracting strategy. This approach in general is suboptimal on the system level. There could be a schedule for the production that creates a demand with significantly lower total energy cost, out-weighting the sub-optimality of the schedule from the production point of view. The traditional strategy reported in literature is to combine all energy-related information into a single monolithic problem and to solve it. This ensures finding a system-wide optimal solution that satisfies both the scheduling constraints and energy-cost optimization constraints. However, from an industrial point of view, such a monolithic integration usually requires noticeable effort.

2. Problem statement

The goal of this work is to develop a decomposition framework for process scheduling and energy cost optimization while still ensuring a system-wide optimal solution.

The scheduler provides a feasible schedule, and the energy cost optimizer finds the best purchase and sales structure of contracts based on a fixed load curve. This framework helps to utilize already installed industrial solutions of energy contracts optimization. The joint optimization obviously requires an information exchange between the two optimizers. Under specific conditions the structure of the monolithic model can be exploited to develop a Mean Value Cross Decomposition (MVCD) scheme (Van Roy, 1983) – a variant of decomposition without a master problem (Holmberg, 1994). In the next section we show that the two optimizers can be modified such that one forms a part of the subproblem of the Benders' decomposition of the overall problem (energy-cost optimizer) and one forms a part of the subproblem of the Dantzig-Wolfe decomposition (energy-aware scheduler) after decomposing the monolithic model. It is important to note that it is not the goal of this work to develop the best possible scheduling model for the example process, but to develop and demonstrate the decomposition framework.

2.1. Industrial process description

We apply the decomposition approach on an energy-intense industrial process, Thermo-Mechanical Pulping (TMP). We formulate the scheduling model as a Mixed Integer Linear Program (MILP) using a discrete-time Resource-Task Network (RTN) representation (Castro et al., 2009). The model handles all production-specific constraints and includes information concerning the consumption of electricity. The scheduling model is expanded by a formulation for the minimization of deviation penalties which are accounted for when the process load deviates from the pre-agreed load curve (Hadera et al., 2014). Energy-cost optimization uses the Min-Cost Flow Network for the optimization of multiple time-sensitive electricity contracts including base load, time-of-use, day-ahead spot market and onsite power generation, and the opportunity to sell electricity back to the grid with revenues. The example process (Figure 1) consists of identical refiners which produce one type of pulp. The pulp flows to a storage tank and has to satisfy a deterministic demand curve. Additional flexibility is given by the option of buying pulp from an external source at a given cost.

3. Model formulation

In order to develop the decomposition approach we first develop a monolithic model of the problem. The model notation is shown in Table 1.

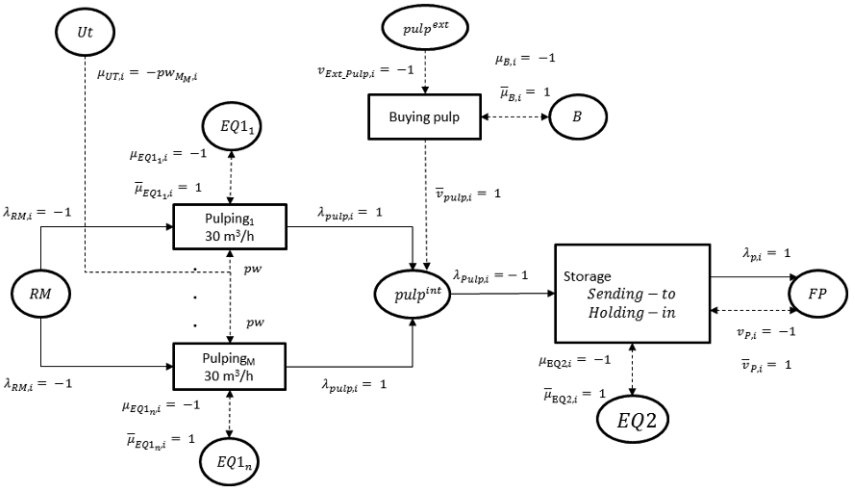

Figure 1. RTN superstructure for the thermo-mechanical pulping process

Table 1. Model notation

Sets: R– resources; I– tasks, T- time intervals, $EQ1/EQ2 \subseteq R$-refiners/storage tank, $EQ3 \subseteq R$-external buy, $RM \subseteq R$-raw material, $pulp^{int}/pulp^{ext} \subseteq R$-pulp from refiners/external source, $UT \subseteq R$-electricity, $CT \subseteq R$-cont. resources, $FP \subseteq R$-final product, I^c- continues tasks, I^B-buying task, I^S-storage task.
Parameters: l^{max}–maximum capacity volume of storage tank, l^{min}-minimum volume in storage, l^{init}-initial volume in storage, u-production rate of refiner in one time slot, u^{max}-maximum production by all refiners in one time slot, b^{max}-maximum pulp amount available to buy, c^{start}/c^{end}-refiner start-up/shut-down cost, $\prod_{r,t}^{in}/\prod_{r,t}^{out}$-resource input (electricity)/ output (final product) to/from the system in time t, c_t^{pulp}-external pulp price in slot t, p^{el}-electricity consumption of one refiner in one time slot.
Variables: $N_{i,t}$-binary, execution of task i in time t, $\xi_{i,t}/\xi_{i,t}^*$- cont. positive, amount handled /continuously send to storage, $R_{r,t}$- cont. positive, amount of r available at time t, $R_{r,t}^{end}$- cont. positive, amount of resource r available immediately before end of time t, $R_{r,t}^0$- cont. positive, amount of initial resource, n_t^{ref}-number of refiners, n_t^{end}/n_t^{start}- cont. positive, number of refiners shut-down/start-up, $pulp_t^{ext}/pulp_t^{int}$- cont. positive, pulp bought externally/produced by refiners, q_t- cont. positive, el. consumption, c^{el}-net electricity cost, c^{ref}-cost of start-up and shut-down of refiners, δ-penalties for load deviation

3.1. Monolithic model formulation

The objective function of the problem is to minimize the cost of energy and the production-specific costs as in Eq. (1). The core of the RTN formulation is the excess resource balance equation, shown in Eq. (2), and the handling of the continuous resources by Eq. (3). Proper balance of the $pulp^{int}$ and final product fp resource is ensured by Eq. (4). Using resource excess variable, we enforce the upper bound of all equipment resources and enforce no intermediate storage by Eq. (5). The storage capacities limits are enforced by Eq. (6). Another constraint restricts the amount handled by the hybrid task (Eq. 7) and continuous tasks (Eq. 8). Buying of pulp from the external source is limited by the desired level b^{max} as in Eq. (9). Some auxiliary variables are introduced in Eq. (10-11). Eq. (12) accounts for the electricity consumption in each time slot. We capture the number of refiners starting up or shutting down with the constraint in Eq. (13). Lastly, we account for the production costs in the objective function. The cost of the pulp bought (Eq. 14) and start-ups and shut-downs of refiners (Eq. 15) are accounted for.

$$min(e + \delta + c^{extpulp} + c^{ref}) \tag{1}$$

$$R_{r,t} = R_{r,t}^0|_{t=1} + R_{r,t-1}^{end}|_{r\in R^{RM}\cup R^{pulp^{int}}\cup R^{FP}} + R_{r,t-1}|_{r\in R^{EQ1}\cup R^{EQ2}\cup R^{EQ3}\cup R^{pulp^{ext}}} + \sum_{i\in I}(\mu_{r,i}N_{i,t} + v_{r,i}\xi_{i,t} + \overline{\mu}_{r,i}N_{i,t-1}) + \sum_{i\in I^S}(\overline{\mu}_{r,i}N_{i,t\,|t=1}) + \Pi_{r,t}^{in}\,|_{r\in R^{UT}} - \Pi_{r,t}^{out}\,|_{r\in R^{FP}} \quad \forall r \in R, t \in T \tag{2}$$

$$R_{r,t}^{end} = R_{r,t} + \sum_{i\in I^c}\lambda_{r,i}\xi_{i,t} + \sum_{i\in I^s}\left(\overline{v}_{r,i}\xi_{i,t} + \lambda_{r,i}\xi_{i,t}^*\right) + \sum_{i\in I^B}\left(\overline{v}_{r,i}\xi_{i,t}\right) \quad \forall r \in r \in R^{RM} \cup R^{pulp} \cup R^{FP}, t \in T \tag{3}$$

$$R_{r,t}^{end} = 0 \;\forall \in R^{pulp^{int}}, t = |T|\;; R_{r,t}^{end} \geq \Pi_{r,t}^{out}\;\forall r \in R^{FP}, t \in T \tag{4}$$

$$R_{r,t}^{max} = 1\;\forall r \in R^{EQ1} \cup R^{EQ2} \cup R^{EQ3}, t \in T\;; R_{r,t}^{max} = 0\;\forall r \in R^{pulp^{int}} \cup R^{FP}, t \in T \tag{5}$$

$$l^{min} \leq R_{r,t}^{end} \leq l^{max}\;\forall r \in R^{FP}, t \in T \tag{6}$$

$$\xi_{i,t} + \xi_{i,t}^* \leq \left(l^{init} + b^{max} + u^{max}\right)\cdot N_{i,t}\;\forall i \in I^S,\;\; \forall t \in T \tag{7}$$

$$\xi_{i,t} = u \cdot N_{i,t} \quad \forall i \in I^c, t \in T \tag{8}$$

$$\xi_{i,t} \leq b^{max} \cdot N_{i,t}\;\forall i \in I^B, t \in T \tag{9}$$

$$n_t^{ref} = \sum_{i\in I^c} N_{i,t}\;\forall t \in T \tag{10}$$

$$pulp_t^{int} = \sum_{i\in I^c}\xi_{i,t}\;\forall t \in T\;; pulp_t^{ext} = \sum_{i\in I^B}\xi_{i,t}\;\forall t \in T \tag{11}$$

$$q_t = p^{el} \cdot \sum_{i \in I^C} N_{i,t} \; \forall t \in T \tag{12}$$

$$n_t^{ref} = n_{t-1}^{ref} + n_t^{start} - n_t^{end} \; \forall t \in T \tag{13}$$

$$c^{extpulp} = \sum_{t=1}^{T} c_t^{pulp} \cdot pulp_t^{ext} \tag{14}$$

$$c^{ref} = \sum_{t=1}^{T} \left(c^{start} \cdot n_t^{start} + c^{end} \cdot n_t^{end} \right) \tag{15}$$

We assume that for the considered production process the energy cost optimization problem has the same structure as the MILP formulation in Hadera et al. (2014). The plant has an option to choose from multiple contracts, onsite generation, and the possibility to sell electricity back to the grid. Therefore the monolithic problem is further extended by the same flow network as in Hadera et al. (2014), Eq. (13-22), and load deviation equations as in Eq. (30-32), which together represent all energy-related cost (net electricity cost e and load deviation penalties δ).

3.2. Functional decomposition approach using MVCD

The monolithic MILP problem can be simplified to the following general form:

$$min \; (C_1^T f + C_2^T y) \tag{16}$$

s.t.

$$A_1 f + D_1 x \leq b_1 \quad \text{[flow network constraints (energy purchase and sale)]} \tag{17}$$

$$A_2 q + D_2 y \leq b_2 \quad \text{[production scheduler constraints (optimize production cost)]} \tag{18}$$

$$q - A_3 f = 0 \quad \text{[complicating constraint]} \tag{19}$$

$$x \in X, \; y \in Y, \; q \geq 0, f \geq 0. \tag{20}$$

In the above equations let x and y represent the variables specific to the flow network and to the energy-aware scheduler, and let X and Y represent all variable bounds and types (continuous and integer requirements). Eq. (19) is a complicating constraint that links the two kinds of variables which are present in Eqs. (17-18). Note that the term $A_3 f$ represents the amount of electricity needed to be bought for the production process, i.e. the flow from the balancing node to the process demand node in any time slot. Any change in the values of any variable in Eq. (19) causes a change in the respective part of the monolithic model (Eq. 17 or 18), thus also in the value of the objective function components in Eq. (16), either the specific cost of the flow network $C_1^T f$ or the production specific cost $C_2^T y$. We consider the load deviation constraints to be integrated into the scheduling problem, i.e. the penalties are part of $C_2^T y$. The monolithic formulation can be decomposed using well known techniques of Benders' and Dantzig-Wolfe (D-W) decomposition. The sub-problems of these two decompositions , shown in Table 2, can be combined in a MVCD scheme (Holmberg, 1994). Note that both sub-problems will separate into two different problems; one related to the scheduling problem, and one related to the energy network. Further, the dual variable of Eq. (19) in the flow network part of Benders' sub-problem is equal to the Marginal Cost (MC) curve used in the D-W's sub-problem. Secondly, the schedule from the scheduler's part of the D-W's sub-problem is equal to the fixed schedule in Benders' sub-problem. Thus by iteratively solving these sub-problems and exchanging the information on production schedule and marginal cost curves (forward related to as the two signals) between them, a Cross Decomposition (CD) scheme can be constructed (Van Roy, 1983). Further, we can identify the flow network part of Benders' sub-problem as the energy cost minimization problem with a fixed production schedule.

Table 2. Decomposed models

Benders' sub-problem		Dantzig-Wolfe sub-problem	
scheduler $f^{EPS}(\bar{q}'_t)$	flow network $f^{MFN}(\bar{q}'_t)$	scheduler $f^{EPS}(\overline{MC}'_t)$	flow network $f^{MFN}(\overline{MC}'_t)$
$min(\delta + c^{extpulp} + c^{ref})$ (21)	$min(c^{el})$ (22)	$min(\delta + c^{extpulp} + c^{ref} + \sum_{t\in T} q_t \cdot \overline{MC}_t)$ (23)	$min(c^{el} - \sum_{t\in T} f_{i5,i7,t} \cdot \overline{MC}_t)$ (24)
subject to:			
Eq. (2-15) – production scheduling constraints	Eq. (13-22) from [3] – flow network constraints	Eq. (2-15) – production scheduling constraints	Eq. (13-22) from [3] – flow network constraints
Eq. (30-32) from [2] – load deviation penalties constraints	$f_{i5,i7,t} = \bar{q}_t \quad \forall t \in T$	Eq. (30-32) from [2] – load deviation penalties constraints	
$q_t = \bar{q}_t \quad \forall t \in T$			

Next, the scheduler part of D-W's sub-problem can be formulated as an energy-aware RTN scheduler with the MC curve as actual costs of energy that are penalized in the objective function. Thus we have identified the two problems which are currently being used in the industrial setting. However, a CD scheme requires the solution of additional complex master problems to guarantee convergence. An alternative is to adopt a MVCD which instead of using a master problem to guarantee convergence makes use of the mean values of the two signals (Holmberg, 1994). To solve the two partial sub-problems in Eq. (22-23) is enough to find a feasible solution of the monolithic problem - a schedule and the corresponding optimal purchasing and selling structure. However, to test the convergence, the value of the objective function of the complete sub-problems is needed (Eq. 21-24). The iterative algorithm (Fig. 2) is initialized by solving the production scheduling model using the day-ahead spot market price. There are a few reported variations of MVCD which differ on how to alter signals (q'_t and MC'_t in Fig. 3) in each iteration. We selected the following option:

- One-sided MVCD (OSWMVCD) – only one of the signals ($MC'_t = y$) is altered by calculating a weighted mean as in Eq. (25), the other (q') is used directly without any changes in order to overcome potential infeasibility problems:

$$y^i = \delta_i \tilde{y}^{i-1} + (1-\delta_i) y^{i-1}, \text{ where: } \delta_i = \frac{\beta+\gamma}{\beta i+\gamma}, \sum_{i=0}^{\infty} \delta_i = \infty, \beta = 1 \text{ and } \gamma = 3 \quad (25)$$

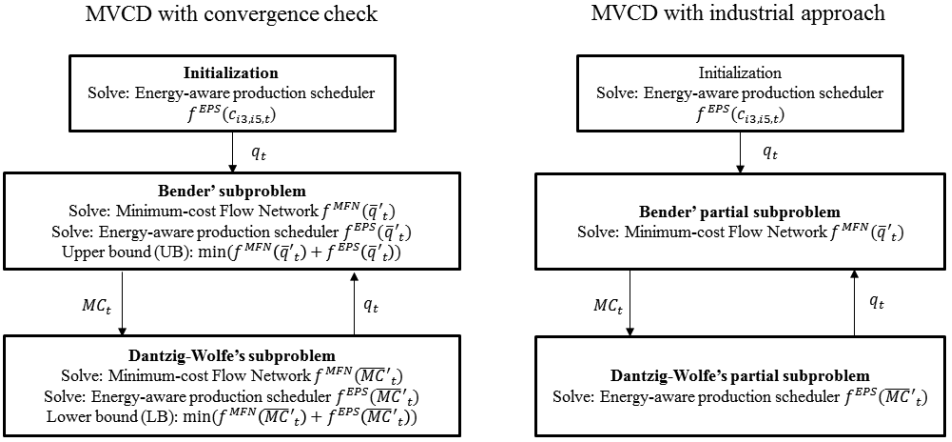

Figure 2. Generic framework for functional separation

4. Numerical case study

Three test instances were solved using GAMS/CPLEX 24.1.2 for the different solution approaches - monolithic model (RTN), convergence test with complete sub-problems (CRTN), and industrial approach (IOWMV), the two latter ones (Fig. 2) using OSWMCD and iterating MC_t only. With such a setup the load curve is always sent directly without mean value smoothing, which could cause infeasibility problems. For all non-monolithic approaches, a CPU limit of 180s is enforced. The results are reported in Table 3. Interestingly the decomposition resulted in higher CPU times than RTN.

Table 3. Numerical results for the case study

Model	Scenario	Best upper bound	Best lower bound	Algorithm iterations (best)	Total CPUs	Gap
RTN		219637,2	-	-	1,14	0%
CRTN*	1	219637,2	219637,2	13	24,60	0%
IOWMV*‡		219637,2	-	2	3,2	0%
RTN		-623600	-	-	1,09	0%
CRTN*	2	-623600	-623600	2	5,96	0%
IOWMV*‡		-623600	-	2	3,55	0%
RTN		122869,2	-	-	340,92	0%
CRTN*	3	123246,3	122681,78	30 (30)	776,84	0,31%
IOWMV*‡		123246,3	-	30 (15)	285,70	0,31%

* solved with max CPUs limit of 180s; ‡ solved with algorithm iterations limit of 30

5. Discussion and conclusion

The tests showed that for both variants of decomposition strategies optimal or close to optimal solutions are obtained for the considered TMP process. In general, the lack of optimality for the developed approach might be due to the duality gap between the objective function values of Benders' and Dantzig-Wolfe sub-problems. In addition, using IOWMV instead of mean values on both signals, there is no guarantee of convergence. Taking mean values on integer variables would produce infeasible solutions, but can be expected to converge to the Lagrangean relaxation (Holmberg, 1994). However, for industrial cases the presented framework allows simultaneously using existing models and solvers for the individual problems resulting in very good system-wide solutions. This re-use of existing solution also eases maintenance problems. Further work could focus on investigating other industrial processes such as steel-making. Another direction is to employ different combination of raw materials and resources as a subject of optimization, instead of energy considered in this work.

Acknowledgements

The Marie Curie FP7-ITN research project "ENERGY-SMARTOPS", Contract No: PITN-GA-2010-264940 is acknowledged for financial support.

References

Castro, P. M., Harjunkoski, I. and Grossmann, I. E., 2009, New continuous-time scheduling formulation for continuous plants under variable electricity cost, I.E.Ch.R.,48, 14, 6701-6714

Hadera, H., Harjunkoski, I., Grossmann, I. E., Sand, G. and Engell, S., 2014, Steel production scheduling under time-sensitive electricity cost, Comp. Aided Chem Eng, 33, 373-378

Holmberg, K., 1997, Mean value cross decomposition applied to integer programming problems, Europ Journal of Oper Res, 97, pp. 124-138

Van Roy, T. J., 1983, Cross Decomposition for Mixed Integer Programming, M. P. 25, 46-63

Krist V. Gernaey, Jakob K. Huusom and Rafiqul Gani (Eds.), 12th International Symposium on Process Systems Engineering and 25th European Symposium on Computer Aided Process Engineering.
31 May – 4 June 2015, Copenhagen, Denmark

Tighter Integration of Maintenance and Production in Short-term Scheduling of Multipurpose Process Plants

Matteo Biondi,[a] Guido Sand,[a] Iiro Harjunkoski[a,]*

[a]*ABB Corporate Research Germany, Wallstadter Str. 59, Ladenburg 68526, Germany*
iiro.harjunkoski@de.abb.com

Abstract

This paper presents an optimization based modelling framework for the integration of maintenance and production in short-term scheduling of multipurpose process plants. An MILP formulation of the integrated approach for a State Task Network (STN) process representation is introduced. Targets and directions for further development of the proposed approach are discussed.

Keywords: maintenance, production, STN, short-term, scheduling

1. Introduction

According to the British Standards Institution (BS 3811:1993), maintenance can be defined as "the combination of all technical and administrative actions, including supervision actions, intended to retain an item in, or restore it to, a state in which it can perform a required function". Therefore, not only the disruptive activities performed in industrial plants every 5-10 years to update or renew the equipment should be accounted as maintenance. Cleaning operations, assets inspection, components lubrication or part-substitutions involving only a partial plant shutdown can also be accounted as maintenance.

In literature in the context of short-term scheduling, the interaction of maintenance and production scheduling has been widely explored. Dedopoulos at al. (1995) considered a set of maintenance tasks to be performed in the scheduling horizon with a penalty to be paid if any of them doesn't take place. Hazaras et al. (2012) account for different types of maintenance: fixed time maintenance intervals as well as a set of maintenance with flexible start time to be determined by the optimization. In summary, in the short-term scheduling context a maintenance task is mainly treated either as a fixed unavailability period of equipment; or as an additional "job" to be scheduled on the plant with some additional constraints which differentiate a maintenance from a production task. Therefore, the overall effect of maintenance activities on the production scheduling (Figure 1) can be summarized in a reduction of overall available time.

In this work, we want to make a step forward and explicitly take into account the effect that production has on maintenance requirements in order to "close the loop" between the two decision processes (Figure 1).

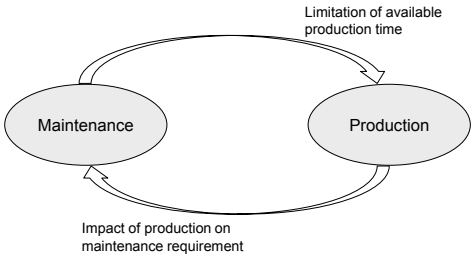

Figure 1 – Impact of maintenance on production schedule and vice versa: closing the loop

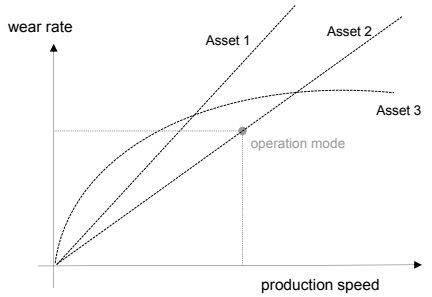

Figure 2 – Asset operation mode and relation between production speed and wear rate

The main objective of the paper is to describe a framework for the integration of maintenance and production in short-term scheduling of complex multipurpose batch process plants. We will highlight strengths and weaknesses of the proposed approach and describe challenges and opportunities for its further development.
The remainder of this paper is organized as follows. Section 2 discusses the concept of *operation mode*, the key element of the proposed integrated approach. In Section 3 we introduce all the other elements of the model which is then introduced and discussed in Section 4. Section 5 gives an insight on how the proposed model can be extended before providing some final conclusion in Section 6.

2. The key of integration: asset operation mode

The key element that we will consider in the following to strengthen the integration of maintenance and production scheduling is the assumption that each equipment of the plant (or at least most of them) has the possibility to work in different operation modes.
The impact of operation mode on the process and production is two-fold. On the one hand, we assume that by modifying the operation mode of an asset it's possible to adapt its production speed, i.e. the throughput for a continuous process or the processing time for a batch production. On the other hand, we assume that the operation mode impacts on the way/speed the equipment wears out. By modulating it, it is therefore possible to extend the *residual useful life* of the equipment, i.e. to prolong the time before the next maintenance (cleaning, lubrication…).
The relation between production speed and asset wear rate might be very process and equipment dependent. We will therefore assume that any equipment of the plant has its own characteristics in the speed/wear plane (Figure 2) which can be linear or nonlinear.

In this particular work we do not consider a specific application for the method we are proposing as our target is to develop a generic approach for the integration of maintenance and production scheduling. On the other hand, it is important to highlight that the concept of operation modes and the relation between production speed and asset wear rate is realistic and can be encountered in several applications, e.g. in the steel making process for stainless steel production (Harjunkoski et al., 2001). In the first production step (the electric arc furnace) steel scrap is molten by means of electric arcs generated by cathodes that are lowered into the metal bath. The length of the arcs (the production mode for this process) can be modified by operators with direct impact on the production time and on the wear of the equipment (in particular on the refractory material of the ladle).

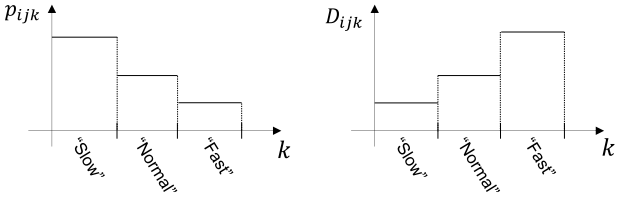

Figure 3 – Production time and wear of product *i* on unit *j* operating in mode *k*

3. Elements of the model

The reference modeling framework for our integrated approach is the State Task Network (STN) formulation as introduced by Shah et al. (1993). A simplified version of it is presented in Eq.(1.a-e) and will be used for our purpose. The key decision variables of the problem are: W_{ijt}(binary) if unit *j* starts processing task *i* at the beginning of time period *t*; B_{ijt} amount of material which starts undergoing task *i* in unit *j* at the beginning of time period *t*; S_{st} amount of material stored in state *s*, at the beginning of time period *t*. Constraint (1.a) ensures that no job can start before the previous one is finished; (1.c) is a material balance constraint for intermediate and final states (where ρ_{is} is the proportion of input of task *i* from state *s* and $\bar{\rho}_{is}$the proportion of output of task i to state *s*); (1.b) and (1.d) are respectively unit and storage capacity constraints. The objective of the optimization problem is assumed to be the maximization of the profit over a given time horizon.

$$\max \quad obj$$

$$\sum_{i\in I_j}\sum_{t'=t-p_i+1}^{t} W_{ijt'} \quad \le 1 \quad \forall j,t \tag{1.a}$$

$$V_{ij}^{min} W_{ijt} \le B_{ijt} \le V_{ij}^{max} W_{ijt} \quad \forall t,j,i\in I_j \tag{1.b}$$

$$S_{st} = S_{s,t-1} + \sum_{i\in \bar{T}_s} \bar{\rho}_{is} \sum_{j\in K_i} B_{ij,t-p_i} - \sum_{i\in T_s} \rho_{is} \sum_{j\in K_i} B_{ijt} \quad \forall s,t \tag{1.c}$$

$$0 \le S_{st} \le C_s \quad \forall s,t \tag{1.d}$$

$$W_{ijt} \in \{0,1\}, B_{ijt}, S_{st} \ge 0 \tag{1.e}$$

We will assume in the following that each unit *j* can work in a finite set of operation modes $k \in K_j$ and that the mode can be changed only if the unit is not active, i.e. only between consecutive jobs. With these assumptions, the relation between production speed and asset wear rate as we introduced it in Figure 2 can be simplified and any complex nonlinearity in the speed/wear dependency eliminated. For each product *i* and unit *j*, the production time p_{ijk} and the wear D_{ijk} will depend on the operation mode *k* as in Figure 3.

For the asset degradation and maintenance requirements, we will consider a model derived from Bock at al. (2012). We assume that each unit has a maximum residual useful life measured in "equivalent" running hours and that the usage of unit *j* for producing product *i* in mode *k* decreases the available residual life by D_{ijk}. When the lifetime of an asset reaches a critical threshold, it can be restored to its maximum level by mean of a maintenance activity which involves fixed costs and down time (τ_j).

4. An integrated model for production and maintenance scheduling

Having described all the elements of the integration model, assume the following variables:

W_{ijkt} equals 1 if unit *j* starts processing task *i* with operation mode *k* at the beginning of time period *t* (binary)

B_{ijkt} amount of material which starts undergoing task *i* in unit *j* with operation mode *k* at the beginning of time period *t*

S_{st} amount of material stored in state *s* at the beginning of time period *t*

R_{jt} remaining useful life of unit *j* at the beginning of time period *t*

M_{jt} equals 1 if maintenance of unit *j* starts at the beginning of time period *t* (binary)

Having defined this set of variables, it is possible to describe the integrated production scheduling problem as an MILP like in Eqs.(2.a-g). The constraints of the model can be interpreted as follows: Eq.(2.a) ensures that no contemporary production and maintenance activities are active on unit *j* at time *t*; Eq.(2.b) is a bound on the amount of product *i* that can be processed on unit *j*; Eq.(2.c) is, like in the original model, a material balance constraint for the intermediate and final states of the production. Eq.(2.d) is the key constraint of the proposed formulation as it takes care of updating the residual life of the units at each time period. In particular, the residual life if decreased by D_{ijk} if a production job starts to be processed in the current time period *t* and it's restored to its maximum value (R_j^{max}) if a maintenance activity is started. Eq.(2.e) is a bound on the amount of material that can be stored in state *s* at any time *t*. Eq.(2.f) is a bound on the residual life of unit *j* and defines the threshold (R_j^{min}) on R_{jt} triggering the start of a maintenance on unit *j* by mean of Eq.(2.d).

$$\max \quad obj$$

$$\sum_{k\in K_j}\sum_{i\in I_j}\sum_{t'=t-p_{ijk}+1}^{t} W_{ijkt'} + \sum_{t'=t-\tau_j+1}^{t} M_{jt'} \le 1 \quad \forall j,t \tag{2.a}$$

$$V_{ij}^{min} W_{ijkt} \le B_{ijkt} \le V_{ij}^{max} W_{ijkt} \quad \forall t, j, i \in I_j, k \in K_j \tag{2.b}$$

$$S_{st} = S_{s,t-1} + \sum_{i\in \overline{T}_s} \overline{\rho}_{is} \sum_{j\in K_i}\sum_{k\in K_j} B_{ijk,t-p_{ijk}} - \sum_{i\in T_s} \rho_{is} \sum_{j\in K_i}\sum_{k\in K_j} B_{ijkt} \quad \forall s,t \tag{2.c}$$

$$R_j^{max} M_{jt} \le R_{jt} \le R_{j,t-1} - \sum_{i\in I_j}\sum_{k\in K_j} D_{ijk} W_{ijkt} + U \cdot M_{jt} \quad \forall j,t \tag{2.d}$$

$$0 \le S_{st} \le C_s \quad \forall s,t \tag{2.e}$$

$$R_j^{min} \le R_{jt} \le R_j^{max} \quad \forall j,t \tag{2.f}$$

$$W_{ijkt}, M_{jt} \in \{0,1\}, B_{ijkt}, S_{st}, R_{jt} \ge 0 \tag{2.g}$$

The objective function of the MILP model can be chosen according to the use case Meaningful objective functions in this context are for example:

- Maximization of the profit on a given time horizon (value of final products minus production costs including maintenance costs)
- Maximization of the profit on a given time horizon with maintenance advance penalties (C. Varnier et al., 2012)
- Maximization of the profit on a given time horizon by assuming variable production costs for each production mode (e.g. due to an increase of electricity consumption)
- Minimization of production costs (e.g. including maintenance costs, variable production costs for each production modes,…) for a predefined demand profile over a given time horizon

We tested the proposed model on the STN process proposed by Kondili et al. (1993) with the objective of maximizing the profit over a time horizon of 50 time slots. For each unit (4), three distinct operation modes were introduced as well as production time and wear for each task (5), unit and mode like in Figure 3. The model was implemented in GAMS and resulted in a MILP with around 3500 equations, 1900 continuous variables and 1400 discrete variables (as reported by GAMS). By solving the model with CPLEX 12.6, the optimal solution was found in 50s but it took 1200s to verify the optimality criterion (0.1% gap).

5. Discussion and model extensions

The above model was shown to be able to describe the integration of the maintenance and production process in a short-term scheduling horizon. In this section, we want to discuss some of the weaknesses of the model in order to set the target for further development.

5.1. Time "dynamics"

One of the unwritten assumptions of the model is that the *dynamic* of the degradation process (and therefore the frequency of maintenance requirements) is fast enough to be captured within the production scheduling horizon. With reference to the model in Eqs.(2.a-g), this means that the average degradation D_{ijk} per time interval is not too small compared to R_j^{max}. Only with this assumption, i.e. only if maintenance requests for every unit appear more than once in any scheduling horizon, it make sense to compare production profits and maintenance costs in the objective function of the optimization problem as we described. Unfortunately, this assumption does frequently not hold in real industrial applications and if the different dynamics between maintenance and production are not explicitly taken into account, the model struggles to find a reasonable solution.

5.2. Asset degradation

In the proposed formulation, it is assumed that the performance of a unit is not changing along the unit life and that a unit is always able to perform any required production task notwithstanding its health. This may not always be the case; the asset degradation might impact the scheduling problem in different ways. For example, the maximum dimension of a batch that a unit can process might be a function of the unit health (e.g. due to quality reasons, physical reasons or health and safety reasons). Another way to account for unit degradation in the proposed modelling framework is to let the set of available operation modes K_j of unit j depend on the unit health, i.e. $K_j=f(R_{jt})$. Any operation mode might be used by the unit right after maintenance is performed (Figure 4), but only few of them might be available when the unit reaches the end of its useful life.

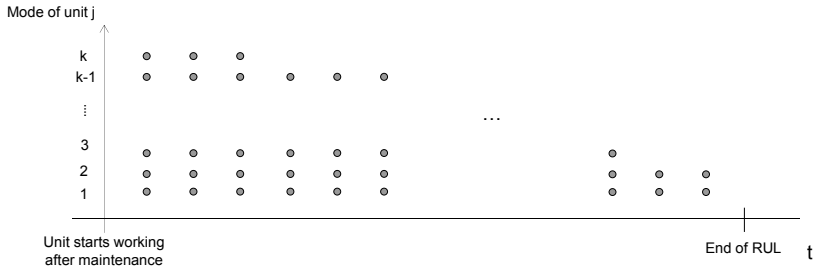

Figure 4 – Available operation mode throughout the useful life of a unit

6. Conclusions

In this paper we addressed the challenge of a tighter integration between production and maintenance scheduling. The key element for the integration of the two decision processes we introduced is the concept of operation mode of a production unit having impact on performance and wear rate. An MILP formulation to model and solve the integrated maintenance and production scheduling problem was proposed and discussed. Finally, further development directions of the model to account for time dynamic challenges and degradation were introduced.

Acknowledgements

The Marie Curie FP7-ITN research project "ENERGY-SMARTOPS", Contract No: PITN-GA-2010-264940 is acknowledged for financial support.

References

S. Bock, D. Briskorn, A. Horbach, 2012, “Scheduling flexible maintenance activities subject to job-dependent machine deterioration”, Journal of Scheduling, Volume 15, Issue 5, 565-578

I.T. Dedopoulos , N.Shah. “Optimal Short-Term Scheduling of Maintenance and Production for Multipurpose Plants”, Industrial Engineering and Chemistry Research, 1995, 34 (1),192–201

I. Harjunkoski, I.E. Grossmann, 2001, “ A decomposition approach for the scheduling of a steel plant production”, Computers & Chemical Engineering, Volume 25, Issues 11–12, 1647–1660

M.J. Hazaras, C.L.E. Swartz, T.E. Marlin, “Flexible maintenance within a continuous-time state-task network framework”, Computers & Chemical Engineering, Vol 46, 167–177

E. Kondili, C.C. Pantelides, R.W.H. Sargent, 1993, “A general algorithm for short-term scheduling of batch operations—I. MILP formulation”, Computers & Chemical Engineering, Volume 17, Issue 2, 211–227

N. Shah, C.C. Pantelides, R.W.H. Sargent, 1993, “A general algorithm for short-term scheduling of batch operations—II. Computational issues”, Computers & Chemical Engineering, Volume 17, Issue 2, 229–244

C. Varnier, N. Zerhouni, 2012, “Scheduling Predictive Maintenance in Flow-shop”, 2012 Prognostics & System Health Management Conference (PHM-2012 Beijing)

Krist V. Gernaey, Jakob K. Huusom and Rafiqul Gani (Eds.), 12th International Symposium on Process Systems Engineering and 25th European Symposium on Computer Aided Process Engineering.
31 May – 4 June 2015, Copenhagen, Denmark

Integrating Control and Scheduling based on Real-Time Detection of Divergence

Preeti Rathi,[a] Shanmukha Manoj Bhumireddy,[a] Naresh N. Nandola,[b] Iiro Harjunkoski,[c] Rajagopalan Srinivasan[a*]

[a] *Indian Institute of Technology Gandhinagar, VGEC Complex, Chandkheda,, 382424 Ahmedabad, India*
[b] *ABB Global Industries and Services Limited, Whitefield, Block1, Bhoruka Tech Park, 560048 Bangalore, India*
[c] *ABB Corporate Research, Wallstadter Str. 59, D-68526 Ladenburg, Germany*
raj@iitgn.ac.in

Abstract
Scheduling and control have been long recognized as the two critical building blocks in many manufacturing execution systems. Operating at the interface between the supply chain and the process, the scheduler generates a detailed schedule that has to be executed by the process so as to meet the demands originating from the supply chain. Given the tight interactions between the two, there has been wide interest in integrating control and scheduling. A variety of methods ranging from monolithic integration into one large integrated problem, to hierarchical cooperative approaches have been proposed in literature. In this paper, we propose a novel approach to the integration problem.

Our key insight is that disturbances which occur post the generation of the original schedule, trigger a divergence between operational targets defined by the schedule and its execution. If left uncorrected, the disturbances will propagate between the process and the supply chain. A timely response could eliminate or minimize such effects. Recognizing this, we propose a novel framework for integrating scheduling and control that detects in real-time when a divergence occurs between the original schedule and its execution in the process, identifies the root-cause(s) of the divergence (i.e. the disturbance), and triggers a suitable response from the scheduler and the process so as to nullify or minimize its effect. In this paper, we will describe the proposed approach and illustrate it using an industrially motivated case study.

Keywords: Advanced control; reactive scheduling, abnormal situations

1. Introduction
A simple supply chain consists of raw material procurement, storage of raw materials, processing, storage of products and its dispatch to customers. In any production plant, customer orders are collected, demand is calculated and based on that a schedule is made which is then sent to the processing unit. The processing unit make products as per the schedule and then dispatch it to customers. After the products are delivered to the customers, the key performance indicators such as number of orders fulfilled, number of partial orders, number of cancelled orders, plant utilization, volume fulfilled, etc. are estimated.

Scheduling and control are very crucial in any production plant. Schedules are a set of tasks having information about the start time, duration, product id, quantity to be produced, equipment on which products ate to be made, grade of the products and set points of the controllers. Schedules are made typically for a time horizon of few days to weeks. Process control deals with real time execution of process. It controls the transformation of raw materials into products as per the set points specified by the schedule while rejecting disturbances. It makes sure that the product quality, production rate and equipment operating limits are within the desired range and evaluates constraints on capacity and quality. It operates typically in a time horizon of seconds or minutes. Even though scheduling and control works using different algorithms and for different users, they have some similarities. Both cope with uncertainties and both makes real time decisions taking into account new information. The uncertainty for scheduler includes rush orders, supplier problems, logistic difficulties, demand fluctuations and for controller includes equipment breakdown, manpower unavailability, low raw material inventory (Bansal et al., 2005). Scheduling interfaces with process control through production schedules, actual production information and production capability information (Harjunkoski et al., 2009).

Today's agile business climate is characterized by changing market trends, increasing competition, and environmental concerns. This has induced manufacturers to vie for faster, cheaper and more flexible production strategies in order to sustain their profitability. Companies have implemented various systems for planning (ERP), scheduling and advanced process control (MES/CPM) but these technologies operate at different spatial and temporal scales in the decision-making hierarchy. Integrated decision making between these levels, especially between production scheduling and advanced control is now considered to be absolutely essential and has received significant attention in the academic literature However, a number of key challenges have impeded the deployment of these techniques in industrial settings. Some challenges include modelling and solution of optimization algorithms, interaction of interface with users, human behavior and organization behavior. In this paper, we seek to develop and systematically evaluate a practicable approach for integrating scheduling and production control.

1.1. Literature Review

A variety of methods are used towards integration of scheduling and control (Harjunkoski and Engell, 2012). One set of method is on a monolithic approach in which scheduling and control are integrated in such a way that it is not possible to distinguish which decision belongs to scheduling and which one belongs to control. The benefit of this approach is that all the information required to make any decision will be available often but the challenge is to solve the mixed integer dynamic optimization problem which is nonlinear and non-convex. Another set of solution use hierarchical approach where three actions; scheduling, optimization and control exchange information with each other. The scheduling layer take decisions about batch sizes, assignment of resources and possible timings of production. Optimization layer computes the optimal batch trajectories and control layer implement these trajectories. Another approach is the classical hierarchical approach in which one scheduling system interacts with multiple control systems for different equipment. Scheduler gives the resource allocation and sequencing details to the optimization and control layers. Optimization layer set the trajectories, and decisions related to time are left for the controller. The problem with this approach is that at the time of uncertainty there will be

a mismatch between model and reality. There should be a repair mechanism that has to be implemented when there is a plant model mismatch to avoid sub optimal schedules. Since the start time decisions are taken by the controller, there will be no possibility that the plant will produce more than planned or before time. This can be removed by frequently giving schedules to the controller. There must be fast and frequent share of information between scheduling and control about the current status of production and availability of resources. Cooperative solution can also be an approach. In this, a schedule is made using a nominal model of system and then it is optimized. After optimization, original schedule is modified. This allows parallel computations.

There have been many advancements in scheduling techniques to handle the complexities introduced by the integration of scheduling with control. These includes use of more efficient mathematical solvers, considering inventory and resource constraints, developing expert systems, implementing neural network, multistage stochastic optimization and robust optimization procedures. Park et al. (2014) proposed an Internal coupling model (ICM) which is an explicit low order model that describes the closed loop input-output behavior of the process under supervisory control. Chu and You (2012) proposed an integration method which is formulated as a mixed integer dynamic optimization problem with discrete variables in scheduling problem and constraints of differential equation from the control problem. They provided an online closed loop solution with fast computational strategy that helps production system to quickly respond to uncertainties and disturbances. In this paper, we develop an alternate approach to the integration problem which focusses on real time performance of the process.

2. Proposed architecture

Our key insight is that the motivation for integration arises primarily when either (1) the process control system is unable to meet the goals set by the scheduler due to various disturbances originating at the process level, or (2) when the scheduler layer requires the process to operate differently at a short-notice due to some unforeseen event in the supply chain. Traditionally, the information exchange between the scheduler and process control layer is limited. The scheduler is ignorant about the process dynamics. It receives only the information about the task lengths, transition times and transition dynamics from the process. Similarly the process is ignorant about the information from supply chain. In general, the scheduling and control layers exchange information periodically (e.g.: weekly / fortnightly) with the scheduling layer transmitting the needs from the supply chain in the form of a periodic schedule and the control layer reporting on the actual performance of the process through a periodic production report. To account for the uncertainties, there is a need for precise and timely exchange of information between the scheduling and control layers which can be achieved by a tighter integration between them. This is accounted for in the proposed attaché framework.

In our framework, the primary purpose of integration is to ensure that any information available to one layer is made available to the other layer in a timely fashion so that it can exploit possible arbitrage opportunities for overall benefit. Consider a case where the process control system is unable to meet the goals set by the scheduler due to various disturbances originating at the process level. Another example is a case when the scheduler layer requires the process to operate differently at a short-notice due to

some unforeseen event in the supply chain. In such cases, disturbances, which occur post the generation of the original schedule, trigger a divergence between operational targets defined by the schedule and its execution. If left uncorrected, the disturbances will propagate between the process and the supply chain. A timely response based on timely information exchange could eliminate or minimize such effects through suitable arbitrage (e.g.: rescheduling). To achieve this in a practicable fashion, the attaché serves as an intermediary between scheduler and controller by serving as a feedback provider for scheduler, as shown in Figure 1. It provides a closer and more frequent interaction between the scheduler and the process by intervening the process at a higher frequency than the scheduler interacts with the process. It continuously observes the operating process as shown in Figure 1 and detects in real-time when a divergence occurs between the original schedule and its execution in the process by detecting the deviation in actual and predicted production. If the deviation is significant, it triggers a suitable response from the scheduler (i.e., rescheduling) so as to nullify or minimize the effect of the disturbance.

3. Case study

A simulation of Thermo Mechanical Pulping (TMP) process is considered as the case study. It consist of two stages (1) primary refiner that produces course pulp and (2) secondary refiner that reduces it to a quality that is suitable for paper making. A detailed description of the process is given by Bemporad et al. (2004). The manipulated variables are feed rate of chips (screw feeder rpm), dilution water flow to each of the refiners, set points to two regulatory controllers that control the gap between the rotating disks in each set of refiners; unmeasured disturbance inputs are fiber filling factor and fiber-water filling factor; measured outputs include primary and secondary refiner consistencies, primary and secondary refiner motor loads and vibration monitor measurements on the two refiners. The process produces three different grades of product each operating at a different throughput and setpoint. The process is controlled using a MPC controller. The parameter, feed RPM, is chosen as the disturbance variable and secondary consistency is the measured output considered. A disturbance generator produces three different cases of operation in the process, (1) plant operating at desired feed RPM, i.e., no disturbance case, (2) operating at a lower throughput, i.e., feed RPM reduces to a lower value, (3) complete shutdown, i.e., the feed RPM is 0.

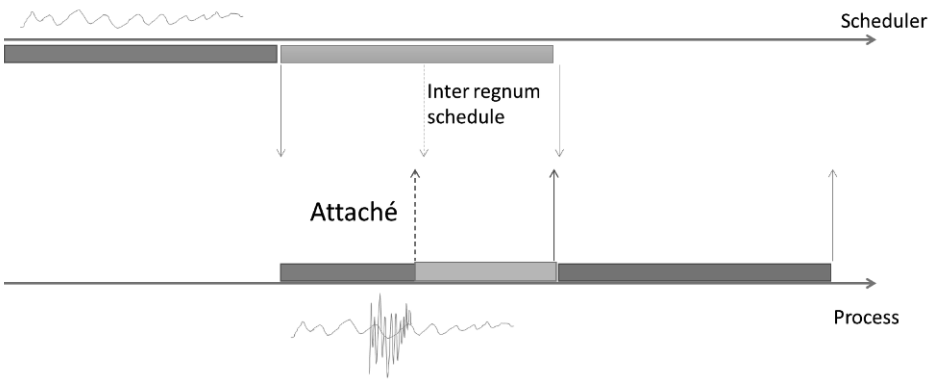

Figure 1: Schematic representation of the attaché framework

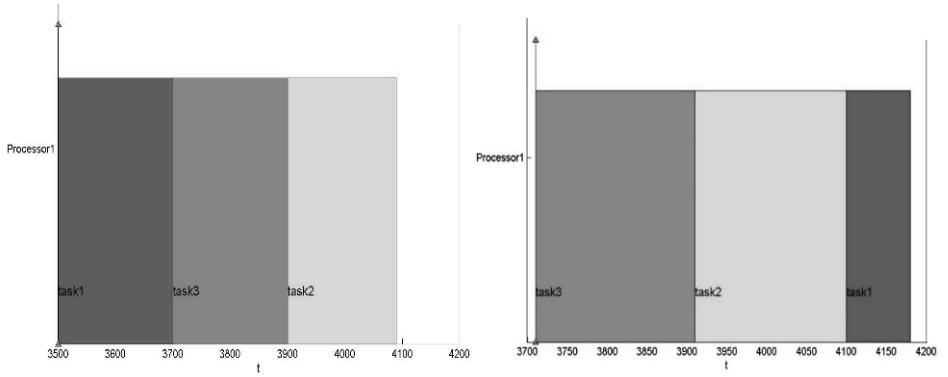

(a) (b)

Figure 2: Production schedule before (a) and after (b) rescheduling

The order type, quantity and due date are generated using random numbers with a maximum and minimum limit. The simulation horizon is of 52 weeks. Schedules are generated on a weekly basis based on the longest processing time strategy and sent to the process. After every intervention interval, attaché gets triggered and tries to detect any deviation in the actual production and the one predicted by the schedule. If the deviation detected is greater than a specified tolerance level, attaché escalates the problem to the scheduler. Rescheduling is done for the remaining time and quantity to be produced. The new schedule generated tries to compensate for the losses incurred during production due to disturbances, in the remaining time of the week. Once the simulation for a week is done, the quality of the products is checked. The qualified products are then used to fulfil the customer orders. No backlog of products are carried forward i.e. the demand of orders not fulfilled is cancelled.

To get an insight on attaché functioning, consider one simulation run. Zooming in to the 6^{th} week (where each week consist of 700 ticks), in Figure 2(a), which starts at 3500^{th} simulation tick, the process operates as per normal operation till 3600^{th} tick, but then due to an equipment problem, the throughput decreased till 3900^{th} tick where it resumes normal operation till the end of the scheduling horizon, i.e., 4200^{th} tick. The intervention frequency for attaché is set to be 100 ticks i.e., at every 100^{th} tick, attaché intervenes and compares the predicted production and actual production in that week for the time span of 100 ticks. Figure 2(a) shows the initial schedule made before the commencement of 6^{th} week. At 3600^{th} tick attaché intervenes and detects no deviation beyond the specified tolerance (10 %) and hence, no rescheduling is done. When attaché intervenes at 3700^{th} tick, it detects a deviation and rescheduling is done. Figure 2(b) shows the new schedule of the 6^{th} week after rescheduling. It can be clearly seen that the production has shifted in the time and the loss incurred in producing product grade 1 (task 1) is made up by shifting it to the end of the week.

A sensitivity study of the effect of the intervention interval and of tolerance level has been conducted. Our results as summarized in Figure 3 show that the performance improvement gained from attaché is relatively insensitive to the settings of these parameters.

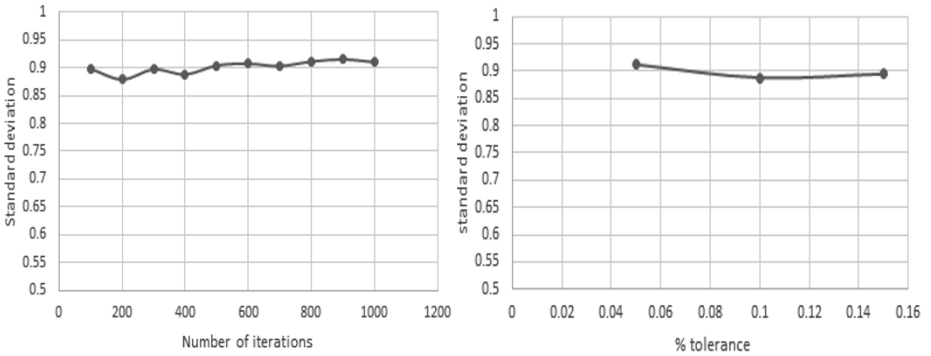

(a) (b)

Figure 3. Standard deviation of percent improvement (a) in volume fulfilled with number of iterations (b) with % tolerance

4. Concluding remarks

In this paper, we proposed a novel framework for the integration of scheduling and control layers. In our method, the attaché observes the process, monitors the important decision variables periodically and detects if there is any significant divergence. When a significant divergence is detected, the problem is escalated to the scheduler, which can then reschedule the production and transfer it over to the process for implementation. To evaluate attaché, we have used the case study of thermo mechanical pulping process. The results show that attaché framework worked well in improving the volume of orders fulfilled during abnormal situations.

References

I. Harjunkoski, R. Nystrom, A. Horch, 2009, Integration of scheduling and control – Theory or practice? Computers and Chemical Engineering, 33, 2009, 1909–1918.

D. Shobrys, D. White, 2000, Planning, scheduling and control system: why cannot they work together. Computers and Chemical Engineering, 24, 2000, 163-173.

S. Engell, I. Harjunkoski, 2012, Optimal operation: Scheduling, advance control and their integration. Computers and Chemical Engineering, 47, 2012, 121– 133.

M. Bansal, A. Adhitya, R. Srinivasan, I.A. Karimi, 2005, An Online Decision Support Framework for Managing Abnormal Supply Chain Events, Computer Aided Chemical Engineering, 20,2005, 985-990.

Y. Chu and F. You, 2012, Integration of scheduling and control with online closed-loop implementation: Fast Computational Strategy and large scale global optimization algorithm, Computers and Chemical Engineering, 47, 2012, 248– 268.

J. Park, J. Dua, I. Harjunkoski, M. Baldea, 2014, Integration of Scheduling and Control Using Internal Coupling Models, Proceedings of the 24th European Symposium on Computer Aided Process Engineering – ESCAPE 24 June 15-18, 2014, Budapest, Hungary.

A. Bemporad, N. Lawrence Ricker, J. Gareth Owen, 2004, Proceedings of the 2004 American Control Conference, Boston, Massachusetts, June 30 – July 2 , 2004

Krist V. Gernaey, Jakob K. Huusom and Rafiqul Gani (Eds.), 12th International Symposium on Process Systems Engineering and 25th European Symposium on Computer Aided Process Engineering.
31 May – 4 June 2015, Copenhagen, Denmark

Resource Efficiency Indicators for Real-Time Monitoring and Optimization of Integrated Chemical Production Plants

Marc Kalliski,[a*] Daniel Krahé,[a] Benedikt Beisheim,[b] Stefan Krämer,[b] Sebastian Engell[a]

[a]*Process Dynamics and Operations Group, Department of Biochemical and Chemical Engineering, Technische Universität Dortmund, Emil-Figge Str. 70, 44227 Dortmund, Germany*
[b]*INEOS Köln GmbH, Alte Straße 201, 50769 Köln, Germany*
Marc.Kalliski@bci.tu-dortmund.de

Abstract

Operational decisions in the day-to-day business of chemical production plants can have a significant impact on the resource efficiency, but this is usually not transparent to managers and operators because of complex interactions in the plants and the lack of real-time resource efficiency indicators (RTREI). As a first step towards real-time decision support to improve resource efficiency, this contribution presents principles for the definition of resource efficiency indicators that capture the performance of a plant on shorter time scales. Guided by these principles, individual RTREI for a specific plant can be chosen. To assess the indicators, an evaluation framework was developed that helps to identify which indicators are capable of reflecting the total resource efficiency best. To demonstrate the approach, indicators for an ethylene oxide production unit that is operated at INEOS in Cologne are presented and compared to the currently used energy efficiency indicator (EnPI), showing that the new indicators are better suited to capture the operational efficiency of the plant.

Keywords: Resource efficiency, energy efficiency, performance monitoring, environmental impact analysis

1. Introduction

Chemical processes are a major consumer of raw materials and energy. Increasing costs of raw material and energy as well as the need to minimize the environmental impact of chemical production processes call for the systematic monitoring and optimization of their resource efficiency. Optimization efforts in the operation of the plant usually focus on the economic optimality within the constraints posed by process limitations and environmental legislation and do not evaluate the resource efficiency during operations. Some companies report environmental KPI of the impact of their production processes on the environment, e.g. the global warming potential and carbon footprint according to the standard ISO/TS 14067 (2013). Such reporting is done in retrospect over long periods of time (usually a business year) and reflects the choice of raw materials, the plant technology used and the operational performance without separating between the different influences. As they are the result of integration over long periods of time and over many factors, they do not support the decision making processes in the daily operations. The European project MORE [www.more-nmp.eu] aims at developing solutions for real-time decision support to improve the resource efficiency of chemical

plants. The first step towards this goal is to define suitable RTREI that can be used for performance assessment over short periods of time (from minutes to days) and provide proper guidance to plant managers and operators. This contribution presents guidelines for the definition of RTREI that reflect the current technical performance of a production plant and can be used to steer the operation in real-time. Further an evaluation framework is described to assess the suitability of existing and proposed indicators. The methodology is applied to the case study of ethylene oxide production proving the relevance for industrial applications.

2. Principles for the definition of real-time resource efficiency indicators

2.1. Gate-to-gate approach

As the goal is to improve the operational performance, the entity of interest is a production site, a plant or a process unit and the boundary of the analysis that defines the inflows and outflows is the limit of the respective entity. The effect of the choice of raw materials or sources of energy and of distribution channels can be added to the effect of the production itself to compute e.g. a carbon footprint value, but in order to correctly assess the operational efficiency of a plant independent of business decisions on procurement and distribution, the scope is limited to the plant or process unit.

2.2. Material and energy flow analysis is the core

Resource efficiency means "more from less". The resource efficiency indicators are based on the physical flows and conversions of raw materials and energy to products and emissions to the environment. All relevant inflows, outflows and environmental impacts must be captured. The material and energy balances must be closed which poses significant challenges to the measurements of flows and concentrations. If the same input material can be either converted into the desired product or serve as a source of energy, an integrated energy and material flow analysis must be performed.

2.3. Resource and output specific

In the first step, the resource efficiency should be measured with a fine granularity, i.e. for all products and inputs of material and energy separately. Product specific RTREI are defined with respect to all resources used and products produced in a process as in Eq. (1).

$$RTREI_{RPS} = \frac{Product\ Output}{Resource\ Input} \tag{1}$$

Product here refers to a product with specific properties (purity, colour, etc.) and different product specifications will lead to a different consumption of energy and raw materials, e.g. because of the need of more intense purification steps. Similarly, the use of different raw materials (in particular if renewable feedstock is used) may lead to different efficiencies which must be reflected in specific indicators. In a second step, the indicators can be aggregated for reporting purposes, or averaged over similar products or different feedstock. This however reduces the potential to correctly assess the limitations and the potential for improvements.

2.4. Normalize to the best possible operation

The value of a resource and product specific RTREI by itself does not show whether the process is operated well. It should therefore be related to a baseline (cf. Eq. (2)), yielding the normalized resource efficiency, which indicates how close the current operation is to a best case. The best case can be obtained from a theoretical analysis (based on a model) or from the best demonstrated practice (based on historical data).

$$RTREI_{norm} = \frac{RTREI_{RPS}}{RTREI_{RPS,best\ case}} \quad (2)$$

2.5. RTREI are needed on different time-scales

In the definition of RTREI the choice of the temporal aggregation interval is crucial. The aggregation interval must be adapted to the decisions which are considered. E.g., for the choice of the operating parameters of an evaporator, its current performance, filtered over short intervals to remove stochastic influences should be used. For the choice of cleaning policies or for the setting of a reactor temperature, that increases the efficiency but reduces the life-time of the catalyst when set to higher values, longer horizons must be considered. Also the filling or depletion of internal storages must be taken into account.

2.6. Include the environmental impact

The impact on the environment must often be taken into account separately to measure the ecological performance. A full energy flow analysis (EFA) and material flow analysis (MFA) will include energy losses and pollutant streams; however the streams of pollutants may be so small that they hardly affect the overall resource efficiency. Therefore emissions to air, water and soil as well as the generation of solid waste should be measured by separate specific indicators. The amount of waste per amount of product manufactured may have to be differentiated according to its use (e.g. incinerated waste that generates or consumes energy, re-used waste or deposited waste). Moreover for reporting and assessment purposes, the RTREI concept can be extended to a Life Cycle Assessment (e.g. CO_2-footprint) by weighting the different streams with the upstream impacts.

2.7. Hierarchy of indicators

For the operation of a unit, the operators need local indicators that measure the performance of the unit, e.g. the amount of steam used by a distillation column. Such RTREI for an individual apparatus may however be misleading because resource utilization can be shifted to other units by different local operational policies. Therefore the primary resource efficiency indicators must be defined on a scale where the net effect of the operational policies on the resource efficiency is measured in a meaningful way (cf. Figure 1). Then secondary indicators can be introduced on the unit level but must be related to carefully chosen specifications of the performance (e.g. a certain purity of the stream leaving a column).

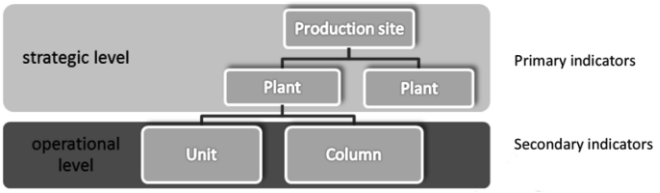

Figure 1: Hierarchy of Resource Efficiency Indicators

2.8. Focus on technical performance independent of external economic factors

The bottom line of a plant is its economic performance to which the resource efficiency contributes significantly. However, the economic figures are strongly influenced by external factors like prices for electricity, gas and oil or revenues from the different products. These economic factors vary independent from the operational performance and therefore the resource efficiency should in the first step be measured independent of e.g. energy prices. As trade-offs e.g. between low emissions or consumption of electric

power and economic performance may exist (sometimes due to pricing schemes or subsidies), resource efficiency and profitability should in the best case be represented as a multicriterial optimization problem.

3. MORE-RACER RTREI evaluation framework

In order to evaluate the real-time resource efficiency indicators, we use ideas from the RACER methodology (European Commission, 2009) and adapted it to the purpose considered here. In RACER, the main categories are Relevant, Accepted, Credible, Easy and Robust. The RTREI are evaluated with respect to the criteria listed under each category in Table 1. A grading system adopted from Lutter (2008) for the main criteria and sub-criteria presented is utilized which enables users to perform a rough screening of the proposed RTREI. The range is between 0 and 2 points, where 0 means "criterion not fulfilled", 1 point represents "partially fulfilled" and 2 point means "completely fulfilled". In the next step, the results for all indicators are visualized in a radar plot as average values per main category (cf. Figure 4).

Table 1: RACER sub-categories for the evaluation of RTREI.

Relevant	Accepted	Credible	Easy	Robust
• Goal related (resource efficiency) • Suitable for the time horizon considered • Influenced by operator actions • Transferability to other units	by • Stakeholders • Plant managers • Operators • Academia • Public	• Sound theoretical background • Consistent in direction and magnitude • Transparent • Clear documentation of assumptions and limitations	• Already in use • Data available in sufficient quality and frequency • Additional instrumentation affordable • Baseline can be provided	• Small influence of measurement errors • Reliable measurement and computation • No uncontrolled influences • No double accounting

4. Case study – ethylene oxide production plant

As an example, we discuss the use of different indicators for an ethylene oxide (EO) production plant. EO is a highly reactive substance used industrially to produce many chemicals and intermediates. The production on a commercial scale is performed by direct oxidation of ethylene on a fixed bed silver catalyst in parallel tubes. CO_2 and water are produced as undesired by-products in a parallel reaction. Both reactions are exothermal, and the full oxidation of ethylene to CO_2 and water has a larger reaction enthalpy than the main reaction. The ethylene oxide process is very interesting from an energy and resource efficiency point of view because the raw material can be converted to product or can be used as source of energy. It is important to obtain a high yield by means of a high selectivity for the main product with small purge streams and minimum external energy consumption. In present-day industrial processes, selectivity towards EO is high (>80%), however, with the ageing of the catalyst, the selectivity decreases, leading to a higher ethylene demand at a constant EO production rate. Consequently, the material efficiency in the sense of generated product mass per converted reactant is decreasing. Besides the selectivity, the process is currently evaluated by the energy performance indicator (EnPI), computed by Eq. (3).

$$EnPI = \frac{m_{EO}}{E_{el} + E_{Steam} + E_{FG}} \tag{3}$$

where m_{EO} denotes the EO product mass, E_{el} the electrical power consumption, E_{Steam} the energy content of the consumed steam and E_{FG} the energy content of the consumed

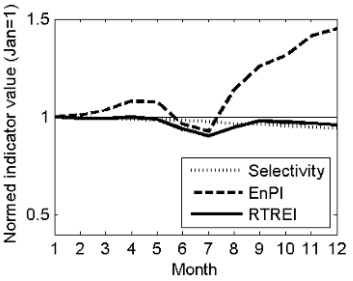

Figure 2: Evolution of selectivity, EnPI and RTREI over one year

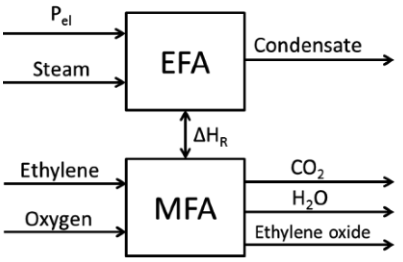

Figure 3: Integrated mass and energy flow analysis for the ethylene oxide plant

fuel gas. The trajectories of the presently used indicators over one year show a decrease in the selectivity (cf. Figure 2), whereas the energy efficiency of the process improves at the same time (increasing EnPI). The decreasing selectivity leads to a decreasing demand of steam but a higher consumption of ethylene per unit of ethylene oxide—more ethylene is used as a fuel. This is not desired because of the significantly higher economic value of ethylene compared to steam or fuel gas. After performing a combined energy and material efficiency analysis (cf. Figure 3), stated before as the second principle, a new indicator for the EO plant, the total energy consumption was introduced. Measurement data for the main in- and outgoing streams of material and energy is available at the plant.

The mass flow analysis is performed only for the ethylene feed under the assumptions:

- Total conversion of ethylene because of a total recycle,
- Only the above mentioned reactions and species are taken into account,
- Enthalpy of the species is only evaluated at standard conditions (standard enthalpy of formation), while temperature, pressure and mixing influences are neglected,
- Purge streams are neglected.

The total absolute energy consumption of this kind of processes is given by:

$$E_{tot} = E_{el} + E_{Steam} - \sum_{i=1}^{n_R} \Delta H_i^R = E_{el} + E_{Steam} - \sum_{j=1}^{n_C} h_{f,j}^0 \left(n_{out,j} - n_{in,j}\right) \quad (4)$$

Where E_{tot} denotes the total energy demand, n_R the number of reactions, ΔH_i^R the reaction enthalpy of reaction i, n_C the number of components, $h_{f,j}^0$ the specific enthalpy of formation of species j at standard conditions and n_j the molar amount of species j. Corresponding to the eighth principle, all sources of energy are weighted equally, irrespective of their financial value. As an alternative to the EnPI, the RTREI is computed as the desired output per used input in agreement with the third principle, shown in Eq. (5).

$$RTREI = \frac{m_{EO}}{E_{tot}}. \quad (5)$$

Figure 2 shows the evolution of the selectivity, the currently used energy performance indicator and the new RTREI for one year on a monthly basis, scaled to 1 at the beginning of the year regarding principle four. The EnPI is improving over time due to a decreasing selectivity of the catalyst whereas the RTREI deteriorates slightly. By evaluating the RTREI and the selectivity, the process performance in the sense of

energy and material efficiency is represented adequately. The results show the superiority of the integrated EFA/MFA based indicators over standard indicators that are currently used. However, for this complex process, the standalone resource efficiency indicators are not sufficient to optimize plant operation. Additional information is necessary which indicates the deviation from the best case scenario. Therefore, a meaningful baseline has to be generated.

5. RACER evaluation of the ethylene oxide plant indicators

The new combined material and energy RTREI was compared to the current energy related EnPI using the MORE-RACER methodology introduced above (cf. Figure 4).

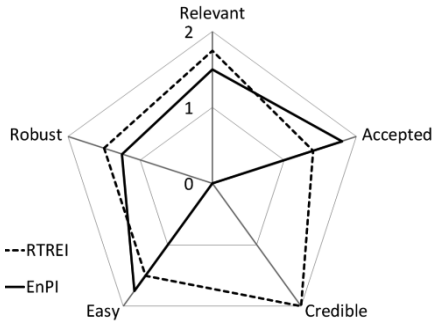

Figure 4: RACER evaluation results.

The EnPI is rated with 0 points for Credible since the indicator is ambiguous for the plant operators. However, compared to the RTREI, the EnPI is rated better in the categories Accepted and Easy. This is related to the higher effort necessary to calculate the RTREI and the less transparent computation since assumptions are necessary to obtain the results. In the categories Robust and Relevant, the results for both indicators differ slightly. The figure reveals the superiority of the RTREI over the EnPI.

6. Conclusions

While standard EnPI might be enough to describe the performance of a production process and its performance over long periods of time, the eight principles introduced enable the user to define RTREI that provide information on the current resource efficiency of the process. Primary and secondary indicators capture the global and local resource efficiency, without being biased by external economic effects. Furthermore, the MORE-RACER methodology was introduced to evaluate the real-time capability of the indicators for the purpose of monitoring resource efficiency in chemical production plants. The relevance for industrial production units was demonstrated for an ethylene oxide example provided by INEOS in Cologne.

Acknowledgement

We would like to acknowledge the European Union for financial support under the grant agreement no. 604068.

References

European Commission, 2009, “Annexes to Impact Assessment Guidelines”, Part III, p.76-77

ISO/TS 14067, 2013, “Greenhouse gases - Carbon footprint of products - Requirements and guidelines for quantification and communication”, International organization for standardization, p.1-52

S. Lutter and S. Giljum, 2008, “Development of RACER Evaluation Framework”, ERA-NET SKEP Project EIPOT “Development of a methodology for the assessment of global environmental impacts of traded goods and services”, p.1-11

Krist V. Gernaey, Jakob K. Huusom and Rafiqul Gani (Eds.), 12th International Symposium on Process Systems Engineering and 25th European Symposium on Computer Aided Process Engineering.
31 May – 4 June 2015, Copenhagen, Denmark

A meta-multiparametric framework: Application to the operation of bio-based energy supply chains

Sergio Medina, Ahmed Shokry, Javier Silvente and Antonio Espuña

Chemical Engineering Department, ETSEIB, Universitat Politècnica de Catalunya, 647 Diagonal Avenue, 08028 Barcelona, Spain.

Abstract

This paper proposes a framework for the analysis of complex optimization problems under uncertainty. The usual multiparametric programing approach is skipped through the use of metamodels to mimic a set of already solved scenarios. Such framework has been applied to the operation of a bio-based energy supply chain, taking into account economic, environmental and social aspects: these objectives might be summarized in a single-objective formulation according to arbitrary economic criteria so, in order to assess the importance of the weighting factors used in the final decisions at different demand levels, a Kriging based metamodeling technique has been used to simplify the optimization procedures, leading to dramatic reductions in both the complexity of the methodology application and the required computational effort.

Keywords: metamodeling, kriging, uncertainty, multiparametric programming.

1. Introduction

The limited availability of fossil fuels and the concern related to the environmental impact associated to the use of these non-renewable resources have motivated the interest in the use of alternative technologies and biofuels for energy generation. One important practice is the use and exploitation of agroindustrial wastes (i.e. biomass) as a fuel for several power generation systems. The management of these situations generally faces to a challenging design and planning optimization problem which involves the capacities, cost and productions of the available energy generation units at each time instant (Silvente et al., 2013). Additionally, the network management is directly affected by several types of uncertainty in which we can highlight the demand uncertainty. Therefore, in order to ensure the reliability of the system, uncertainty must be considered due to the fact that the deterministic solution may become suboptimal or even infeasible (Kopanos and Pistikopoulos, 2013).

Different methods and tools have been proposed to consider uncertainty in the formulation of optimization models at different supply chain levels (demand, weather conditions, biomass supply, price variability across the time, etc). When this uncertainty affects not only the internal and external scenarios, but also the optimization parameters (like the importance of the different terms on the objective function), a way to analyze the effects of this uncertainty is the use of techniques referred as multiparametric programming. The main characteristic of multiparametric programming is its ability to obtain an optimal solution of the problem as a function of the uncertain/varying parameters and the region in the space of the parameters where these functions are valid (Sakizils et al., 2007).

In this work, a methodology based on the metamodeling is proposed in order to create a multimetaparametric framework which provides practical advantages over existing methodologies in terms of simplicity and computational effort, leading to significant decision making information.

2. Problem Statement

The planning of a bio-based energy production supply chain to satisfy highest profit under uncertainty parameters and objective reduction is considered. The basic optimization problem formulation is based on a linear programming framework which considers the production capacity, storage levels, equipment capacity and sales per market as main decision variables. This model takes into account the production of energy through biomass considering the possibility of resizing the equipments of the existing energy plants.

A multiobjective evaluation of production levels to be managed and energy sales to the main power grid have been also included in order to maximize the profit taking care about environmental and social impacts as additional objectives. The mathematical model includes not only the mass and energy balances constraints associated to the energy production, but also the constraints required to describe the technologies involved (Dryer, chipper, Gasifier and transport units).

A kriging metamodeling technique (Shokry and Espuña, 2014) has been applied as a way to manage uncertain parameters based on its properties and potential of accurately approximating complex problems. The next terms describe the problem under study:

2.1 Inputs

- *Process data*

- The set of materials $s \in S$, which includes raw, intermediates and final products.
- The tasks $i \in I$, which include on site treatments, pre-treatments and transportation.
- The set of economic criteria for environmental and social objectives.
- The set of locations (Fixed)$fc \in FC$, composed by suppliers (Biomass providers), intermediates (Pretreatment and treatment sites) and consumers (Markets).
- A time horizon $t \in T$, which represents the months of the year.
- A given expected energy demand profiles: for each short-term period and market, a different (uncertain) target value is considered.

- *Economic, Environmental and Social information*

- Product and consumable prices are considered
- Environmental impacts for raw material production, process and transportation systems are also considered. The importance of this assessment on the decision making procedure is considered uncertain.
- The social impact is considered as a function of the size of the different installed processes, although again, The importance of this assessment on the decision making procedure is considered uncertain.

An optimization model based on the State Task Network formulation allows summarizing the information about the activities from all the SC nodes through a single variable set. The main decisions to be made to maximize the profit are related to:

- Magnitude of the task $P_{i,j,fc,ffc,t}$. This is the most important variable in the model and represents the magnitude of a task *i* performed using technology *j* during period *t*, whose origin is location *fc* and destination is location *ffc*.
- Storage levels at each site and time.
- Size of installed equipment units.

The main equations of the mathematical formulation are now brief described. Storage levels of raw material in each site and at any time are specified in eq.1. Eq. 2 represents the energy balance in which the energy must respect the conservation law. the energy balance must be related to the amount of energy produced and consumed. Eq. 3 ensures that the production level and raw material processed in each facility will be greater or equal than a minimum utilization value defined by the decision maker and lower than the maximum capacity. Eq. 4 ensures that the raw material s purchased form site fc at time t is lower or equal than an upper limit which at the same time is the physical availability of raw material. Eq. 5 is just a constraint that represents the fact that the demand could be satisfied partially for the energy produce using biomass. It is important to notice that even if the solution is treated as an uncertain parameter on the model it must be consider as a deterministic value since each change of demand value implies an isolated optimization procedure.

$$S_{sft} - S_{sft-1} = \sum_{f'} \sum_{i \in \bar{T}_s} \sum_{j \in \left(J_i \cap \widetilde{J_{f'}}\right)} \alpha_{sij} P_{ijff't} - \sum_{f'} \sum_{i \in \bar{T}_s} \sum_{j \in \left(J_i \cap \widetilde{J_{f'}}\right)} \bar{\alpha}_{sij} P_{ijff't} \qquad \forall s, f, t \quad (1)$$

$$\sum_{s \in T_s} HV_s \alpha_{sij} P_{ijff't} = \sum_{s \in \bar{T}_s} HV_s \, \bar{\alpha}_{sij} P_{ijff't} \qquad \forall i \in \bar{I}, j, f, t \quad (2)$$

$$\beta_{jf} F_{jft-1} \leq \sum_{f'} \sum_{i \in I_j} \theta_{ijff'} P_{ijff't} \leq F_{jft-1} \qquad \forall f, j \in \tilde{J}_f, t \quad (3)$$

$$\sum_{f'} \sum_{i \in \bar{T}_s} \sum_{j \in J_i} P_{ijff't} \leq A_{sft} \qquad \forall s \in RM, f \in Sup, t \quad (4)$$

$$\sum_{f' \in M} Sales_{sf'ft} \leq Dem_{sft} \qquad \forall s \in FP, f \in Mkt, t \quad (5)$$

The expected profit of the entire supply chain is calculated considering incomes (Esales) and costs. The costs include fixed cost ($FCost_t$) related at the investment and the variable cost (EPurch) including the transportation, acquisition and production cost in eq. 6, subject to the previous constraints. Environmental impact is related to an LCA analysis. The main form of this analysis is in eq. 7. The social impact is calculated as the number of pretreatment and treatment sites installed as eq. 8 represents. In this equation the binary variable V_{jft} represents if a unit is installed or not. It is important to notice that in the proposed formulation the number of units installed will be the same for each of the parameters set since the superstructure is fixed, but it is considered in the model for comparison purposes.

$$Profit_t = Esales_t - \left(FCost_t + \sum_e EPurch_{et} \right) \qquad \forall t \quad (6)$$

$$Impact^{2002}_{overall} = \sum_f \sum_g \sum_t \sum_{a \in A_g} NormF_g \zeta_{ag} IC_{aft} \qquad \forall g, f, t \quad (7)$$

$$SoC = \sum_{j}\sum_{f}\sum_{t} V_{jft} \qquad \forall j,f,t \qquad (8)$$

For more details of the model and symbology readers are suggested to read (Pérez-Fortes et al., 2012).

The original formulation is a multiobjective one which contemplates the profit, environmental and social impact as objectives. In the presented work the new objective function, which is the one to be maximized, is calculating transforming the objectives environmental and social impacts into an economic one applying an arbitrary criterion (WeightSoc and WeghtEnv). The objective function calculation is described by eq. 9.

$$OF = \sum_{t} Profit_t + (SoC * WeightSoc) - (Impact_{overall}^{2002} * WeightEnv) \qquad \forall t \qquad (9)$$

Notice that if the arbitrary criterion change the optimal solution could be suboptimal since this value affects directly the OF value. For this reason an kriging metamodel will be created in order to facilitate further optimization once the values of the arbitrary criterion changes. The same occurs with the Demand value that in this case is treated as an uncertain parameter.

3. Methodology

The proposed framework could be summarized in a set of steps that must be done in order to ensure its functionality.

1. Identification of the uncertain parameters to be analysed; confirmation of the corresponding upper and lower bounds.
2. Generation of a well distributed (representative) design of experiments.
3. Generation of the set of optimum solutions.
4. Training of the metamodel. In this particular case, the selected technique was "kriging", but any other suitable process may be used (support vector machines, ANNs, etc.). One metamodel for each one of the problem DOFs have to be trained.
5. Validation of the obtained metamodel. According to the results on this step, it may be considered to go back to point 3 and to generate a larger training set of experiments.

4. Case study

The supply chain introduced by Pérez-Fortes et al. (2012) has been used as case-study. It contemplates the bio-based energy production in a small district in Ghana. The 9 most important communities there were taken into account as suppliers, potential production sites and/or market sites for a 3 months planning horizon. The optimal fixed superstructure obtained for this particular case study (Pérez-Fortes et al., 2012) has been considered and, for this superstructure, the objective of this study includes the analysis on how the changes in the uncertain parameters (electricity demand and decision making criterion) affect the planning decissions. In the original work, these parameters were fixed to 50 €/Env_unit, 1000 €/Soc_unit and 50000 kWh/month (WeightEnv, WeightSoc and Demand respectively); now these parameters are considered to vary in a range of 10-100 €/Env_unit, 100-10000€/Soc_unit, 49916-61009 kWh/month.

4.1. Results and discussion

Series of 25, 50, 75, 100, 125 and 150 experiments (combination of variables defining one single scenario) have been generated following Hammersly sampling technique and solved according to the proposed LP formulation using GAMS/CPLEX. Figure 1 shows the optimal objective values as a function of total demand and the environmental weight. The missing parameter under evaluation (Social weight) is not constant but even this it is worth noting that the response surface is clearly irregular, confirming that the parametric function may be nonlinear although the basic problem formulation is linear.

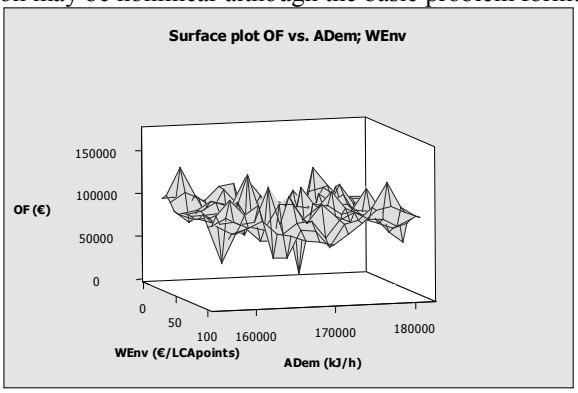

Figure 1. Behavior of the optimal objective function for different values in weightEnv and total demand parameters.

Figure 2 shows the kriging model cross-validation using sets of experiments of different sizes, and exhibits (a) the correlation between the estimated Objective Function obtained by a surrogate model trained using a reduced number of experiments, and the corresponding real optimum values (optimization of the original model), and (b) the quality of the metamodel as a function of the size of the training set. Although an obvious improvement in the quality of the fitting with the size of the training set is observed, the fitting is good enough to justify the use of the surrogate model, even in cases where the size of the training set is quite small. Similar plots are obtaining for the models fitted to reproduce the resulting values of the DOFs at their optimum values.

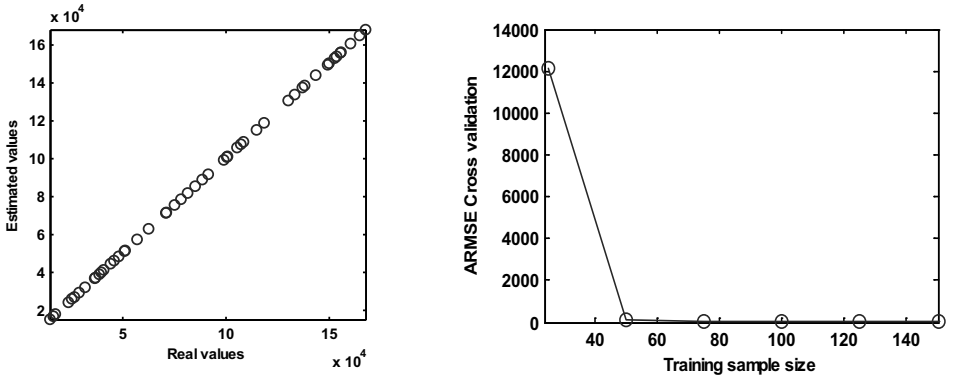

Figure 2. Cross-validation a) for a set of 50 experiments; b) as a function of the size of the training set.

Finally, Table 1 illustrates the reduction in the optimization time with the use of the metamodel. Although the solution of the 150 experiments requires a relatively high computational effort (this problem may become very important when a more complicated model is to be solved), once the surrogate model has been created the optimization time drops dramatically: for this example, the time to obtain the solution is reduced in more than 3 orders of magnitude (1/4,895), and of course higher reductions would be obtained for a more complex optimization problem.

Table 1. Computational effort required.

	Math. Programming (GAMS/CEPPLEX)	**Kriging metamodel**
Training effort (CPU s)	(model building)	(model building + 3300 s (150 experiments) + 70 s (training))
Optimization effort (CPU s)	22	0.00466

(*)HP-dc7900, Intel core 2-duo 3, 16 GHz, RAM 6GB.

5. Conclusions

In order to solve optimization problems under uncertainty, which usually requires programming, can be also successfully solved employing a framework based on Kriging metamodel. The resulting model behaves like a useful metamultiparametric framework. This has been proved in relatively simple case studies. More work is required to develop a robust framework to handle bigger and more complex problems (Highly nonlinear models, MIP problems, etc.).

Acknowledgements

The authors would like to thank the financial support received from the Spanish "Ministerio de Economía y Competitividad" and the European Regional Development Fund (both funding the research Project SIGERA, DPI2012-37154-C02-01) and from the "Ministerio de Economía y Competitividad" (FPI, BES-2010-036099), from the Generalitat de Catalunya (2014-SGR-1092-CEPEiMA) and the Mexican National Council for Science and Technology (CONACyT).

References

G.M. Kopanos, E.N. Pistikopoulos, 2013, Ind. & Eng. Chem. Res., 53, 4366-4386

M. Pérez-Fortes, J.M. Laínez, P. Arranz-Piera, E. Velo, L. Puigjaner, 2012, Energy, 44, 79-95

A. Shokry, A. Espuña, 2014, Applying metamodels and sequential sampling for constrained optimization of process operations, Lecture Notes in Computer Science, 396-407.

V. Sakizils, K.I. Kouramas, E.N. Pistikopoulous, 2007, Linear Model Predictive Control via Multiparametric programming. Multi-Parametric model-Based Control, volume 2, 275 pages.

J. Silvente, A. Aguirre, G. Crexells, M. Zamarripa, C. Méndez, M. Graells, A. Espuña, 2013, Computer-Aided Chemical Engineering, 32, 553-558

Z. Li, M.G. Ierapetritou M.G, 2008, AIChE Journal, 54, 2610-2623.

Pèrez-Fontes M. Conceptual design of alternative energy systems from biomass, PhD. Thesis, UPC, Barcelona, Spain. (2011)

Krist V. Gernaey, Jakob K. Huusom and Rafiqul Gani (Eds.), 12th International Symposium on Process Systems Engineering and 25th European Symposium on Computer Aided Process Engineering.
31 May – 4 June 2015, Copenhagen, Denmark

A Continuous-time MILP Model for Direct Heat Integration in Batch Plants

Pedro M. Castro,[a] Bruno Custódio,[b,c] Henrique A. Matos[c]

[a]*CIO, Faculdade de Ciências, Universidade de Lisboa, 1749-016 Lisboa, Portugal*
[b]*Unilever Jerónimo Martins, 2690-361 Santa Iria de Azóia, Portugal*
[c]*CERENA, DEQ-IST, Universidade de Lisboa, 1049-001 Lisboa, Portugal*

Abstract

We propose a new continuous-time formulation for the short-term scheduling of single stage batch plants with parallel units that allows for direct heat integration between hot and cold streams linked to production tasks of different products. This is in essence a bi-objective optimization problem in which makespan and utility consumption are the conflicting objectives. Using industrial test problems from a vegetable oil refinery, we show that savings in utilities can already be obtained for the minimum makespan but that the optimal synchronization of hot and cold streams requires major production delays. In between, there are multiple Pareto optimal solutions to consider.

Keywords: Energy efficiency; Heat exchanger networks; Mathematical modeling.

1. Introduction

Increasing energy efficiency is an important goal of governments worldwide. The systems approach has been named process integration, involves pinch analysis or mathematical programming and can readily be applied to continuous plants (Fernández et al., 2012). In contrast, in batch plants, hot and cold streams are not always available and direct heat integration is only possible if the streams are synchronized. Indirect heat integration provides additional flexibility since the energy from the hot stream can be collected by a heat transfer medium and stored until the time it is required by the cold stream, but it is not the subject of this paper.

Vaklieva-Bancheva et al. (1996) and Adonyi et al. (2003) highlight that minimum utility consumption through direct integration leads to production delays. Halim and Srinivasan (2009) considered the bi-objective optimization problem through a two-stage decomposition approach but their best schedule featured minimum makespan as well as minimum utility usage. Seid and Majozi (2014) have proposed a general model for direct and indirect heat integration in multipurpose batch plants and found a better solution. However, and despite being suitable for the most complex plant topology, such model may not perform well in single stage batch plants. As an example, Castro et al. (2014b) have shown that a continuous-time formulation tailored for a simpler topology performs orders of magnitude better in a steam-sharing problem from a pulp plant. Computational importance gains relevance when solving multiple-criteria problems.

In this paper, we propose to rigorously tackle the bi-objective optimization problem involved in the simultaneous optimization of product sequencing, timing and heat integration decisions. From the latter point of view, the new formulation can be seen as an extension of the simultaneous targeting and design model of Yee et al. (1990) for

heat exchanger networks of continuous plants. An algorithm relying on the ϵ-constraint method is used for generating the Pareto optimal points.

2. Problem definition

Assume a multiproduct batch plant where the production recipe for product $i \in I$ involves multiple subtasks $k \in K_i$ with processing time $p_{i,k}$ to be executed inside a pre-assigned equipment unit $m \in M_i$. A subset of tasks requires heating or cooling defining respectively cold $c \in C$ and hot streams $h \in H$. Let such union represent a process stream $ps \in PS = C \cup H$ characterized by initial t_{ps}^{in}, final temperature t_{ps}^{out} (K) and heat capacity cp_{ps} (J/K). We assume that only direct heat integration is possible, thus excluding matches between hot and cold streams belonging to the same product. Heat integration between streams of different products is possible if the temperature difference is greater than the minimum approach temperature Δt (K) and the streams overlap in time (at least partially). The goal will be to find the optimal schedule that minimizes two conflicting objectives: (i) makespan; (ii) total utility consumption.

3. Mathematical model

We consider a continuous-time model for a single stage batch plant, similar to the one by Méndez et al. (2001). General precedence sequencing variables $X_{i,i'}$ identify if product i is completed before the start of product i'. Let $S_{i,k}$ and $E_{i,k}$ represent the starting and ending time of subtask k of product i, $|K_i|$ the last subtask of product i and hz an upper bound on the makespan. If product i precedes i' then $X_{i,i'} = 1$, Eq. (1) is enforced and Eq.(2) is relaxed, else it is the other way around. Eq. (3) states that the ending time is equal to the starting plus processing time. The starting time in stage $k+1$ is made equal to the ending time in k to avoid temperature degradation, Eq. (4). The latest ending time defines the makespan MS, Eq. (5).

$$E_{i,|K_i|} \leq S_{i',1} + hz(1 - X_{i,i'}) \; \forall i, i' > i, m \in M_i \cap M_{i'} \quad (1)$$

$$E_{i',|K_{i'}|} \leq S_{i,1} + hz \cdot X_{i,i'} \; \forall i, i' > i, m \in M_i \cap M_{i'} \quad (2)$$

$$E_{i,k} = S_{i,k} + p_{i,k} \; \forall i, k \in K_i \quad (3)$$

$$S_{i,k+1} = E_{i,k} \; \forall i, k \in K_i \backslash |K_i| \quad (4)$$

$$MK \geq E_{i,|K_i|} \; \forall i \quad (5)$$

The direct heat integration part of the model features starting and ending variables linked to process streams, Ts_{ps} and Te_{ps}. These can be linked to the tasks variables through Eqs. (6-7), where set $PS_{i,k}$ holds the single stream linked to task k of product i.

$$Ts_{ps} = \sum_i \sum_{k \in K_i \wedge ps \in PS_{i,k}} S_{i,k} \; \forall ps \quad (6)$$

$$Te_{ps} = \sum_i \sum_{k \in K_i \wedge ps \in PS_{i,k}} E_{i,k} \; \forall ps \quad (7)$$

We assume a superstructure where each hot/cold stream goes through a sequence of two stages from their initial to final temperature. In each stage, matches with different streams are possible but to avoid bilinear terms in the energy balances, isothermal mixing is assumed (Yee at al. 1990), leading to a parallel arrangement (see Figure 1).

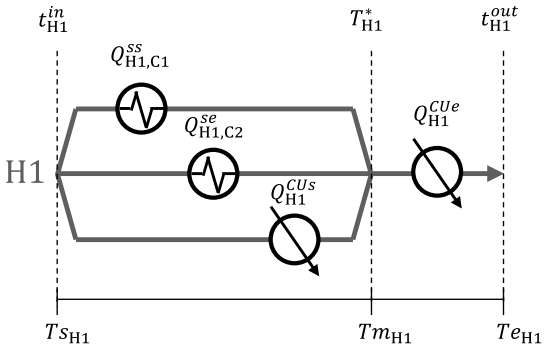

Figure 1. Cooling/heating of stream involves up to two stages, possibly with parallel matches.

Let T^*_{ps} be continuous variables representing the intermediate temperatures and Tm_{ps} the intermediate times. If a hot h and cold c stream exchange energy, four types of interaction are possible, identified through binary variables $Y^j_{h,c}, j \in \{ss, se, es, ee\}$. Taking type se as an example, the hot stream h starts its cooling by exchanging heat with cold stream c, which is in its second stage of heating having previously exchanged heat with another hot stream and/or heating utility. The two points for synchronization thus involve: (i) the starting time of h and the intermediate time of c; (ii) the intermediate time of h and the ending time of c. It should be noted that the complete set of synchronizing constraints given below was generated from a Generalized Disjunctive Programming model (Raman and Grossmann, 1994) using insights from the interaction of tasks with time periods of constant electricity pricing (Castro et al. 2014a).

$$Ts_c - hz(1 - Y^{ss}_{h,c}) \le Ts_h \le Ts_c + hz(1 - Y^{ss}_{h,c})\ \forall h, c \quad (8)$$

$$Tm_c - hz(1 - Y^{ss}_{h,c} - Y^{ee}_{h,c}) \le Tm_h \le Tm_c + hz(1 - Y^{ss}_{h,c} - Y^{ee}_{h,c})\ \forall h, c \quad (9)$$

$$Tm_c - hz(1 - Y^{se}_{h,c}) \le Ts_h \le Tm_c + hz(1 - Y^{se}_{h,c})\ \forall h, c \quad (10)$$

$$Te_c - hz(1 - Y^{se}_{h,c}) \le Tm_h \le Te_c + hz(1 - Y^{se}_{h,c})\ \forall h, c \quad (11)$$

$$Ts_c - hz(1 - Y^{es}_{h,c}) \le Tm_h \le Ts_c + hz(1 - Y^{es}_{h,c})\ \forall h, c \quad (12)$$

$$Tm_c - hz(1 - Y^{es}_{h,c}) \le Te_h \le Tm_c + hz(1 - Y^{es}_{h,c})\ \forall h, c \quad (13)$$

$$Te_c - hz(1 - Y^{ee}_{h,c}) \le Te_h \le Te_c + hz(1 - Y^{ee}_{h,c})\ \forall h, c \quad (14)$$

Eqs. (15)-(18) reflect the temperature driving force (TDF) constraints, where the big-M parameter is calculated through Eq. (19). Notice that no continuous variables appear in Eq. (18) since the minimum driving force Δt occurs between the two final temperatures. Note that TDF decreases throughout integration time, typically reaching Δt at the end.

$$T^*_h \ge T^*_c + \Delta t - bm_{h,c}(1 - Y^{ss}_{h,c})\ \forall h, c \quad (15)$$

$$T^*_h \ge t^{out}_c + \Delta t - bm_{h,c}(1 - Y^{se}_{h,c})\ \forall h, c \quad (16)$$

$$t^{out}_h \ge T^*_c + \Delta t - bm_{h,c}(1 - Y^{es}_{h,c})\ \forall h, c \quad (17)$$

$$Y^{ee}_{h,c}(t^{out}_h - t^{out}_c - \Delta t) \ge 0\ \forall h, c \quad (18)$$

$$bm_{h,c} = -t^{out}_h + t^{out}_c + \Delta t\ \forall h, c \quad (19)$$

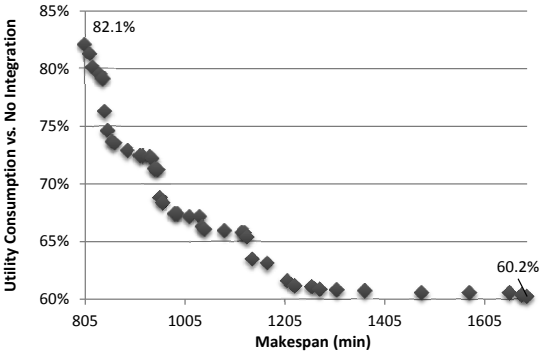

Figure 2. Pareto optimal solutions for a problem involving 33 process streams.

Two process streams are allowed to exchange energy only if the corresponding interaction type is selected, see Eq. (20). The upper bound $q_{h,c}$ is given by Eq. (21). Eq. (22) states that at most one type of interaction can be active.

$$Q_{h,c}^{j} \leq q_{h,c} Y_{h,c}^{j} \; \forall h, c, j \in \{ss, se, es, ee\} \tag{20}$$

$$q_{h,c} = min\left[cp_h\left(t_h^{in} - t_h^{out}\right), cp_c(t_c^{out} - t_c^{in})\right] \forall h, c \tag{21}$$

$$Y_{h,c}^{ss} + Y_{h,c}^{se} + Y_{h,c}^{es} + Y_{h,c}^{ee} \leq 1 \; \forall h, c \tag{22}$$

The remainder constraints deal with the stage energy balances. Let Q_h^{CUs}, Q_h^{CUe}, Q_c^{HUs} and Q_c^{HUe}, represent the energy removed/supplied by the cooling/heating utility (CU/HU) at the start and ending stages. The change in temperature of a stream is due to process streams and/or utilities. The total utility consumption is then given by Eq. (27).

$$cp_h\left(t_h^{in} - T_h^*\right) = \sum_c (Q_{h,c}^{ss} + Q_{h,c}^{se}) + Q_h^{CUs} \; \forall h \tag{23}$$

$$cp_h(T_h^* - t_h^{out}) = \sum_c (Q_{h,c}^{es} + Q_{h,c}^{ee}) + Q_h^{CUe} \; \forall h \tag{24}$$

$$cp_c(T_c^* - t_c^{in}) = \sum_h (Q_{h,c}^{ss} + Q_{h,c}^{es}) + Q_c^{HUs} \; \forall c \tag{25}$$

$$cp_c(t_c^{out} - T_c^*) = \sum_h (Q_{h,c}^{se} + Q_{h,c}^{ee}) + Q_c^{HUe} \; \forall c \tag{26}$$

$$UT = \sum_h (Q_h^{CUs} + Q_h^{CUe}) + \sum_c (Q_c^{HUs} + Q_c^{HUe}) \tag{27}$$

4. Pareto optimal solutions

The decision-making problem involves the minimization of two conflicting objectives, utility consumption and makespan: min (UT, MK). To generate the set of Pareto optimal points we choose the ϵ-constraint method, which involves solving multiple problems of the form (***P***), one for each value of auxiliary parameter ε. The domain of ε is found by solving the two single objective problems.

$$min \; UT$$

$$s.t. \; MK \leq \varepsilon \qquad \textbf{(P)}$$

$$Eqs.(1-27)$$

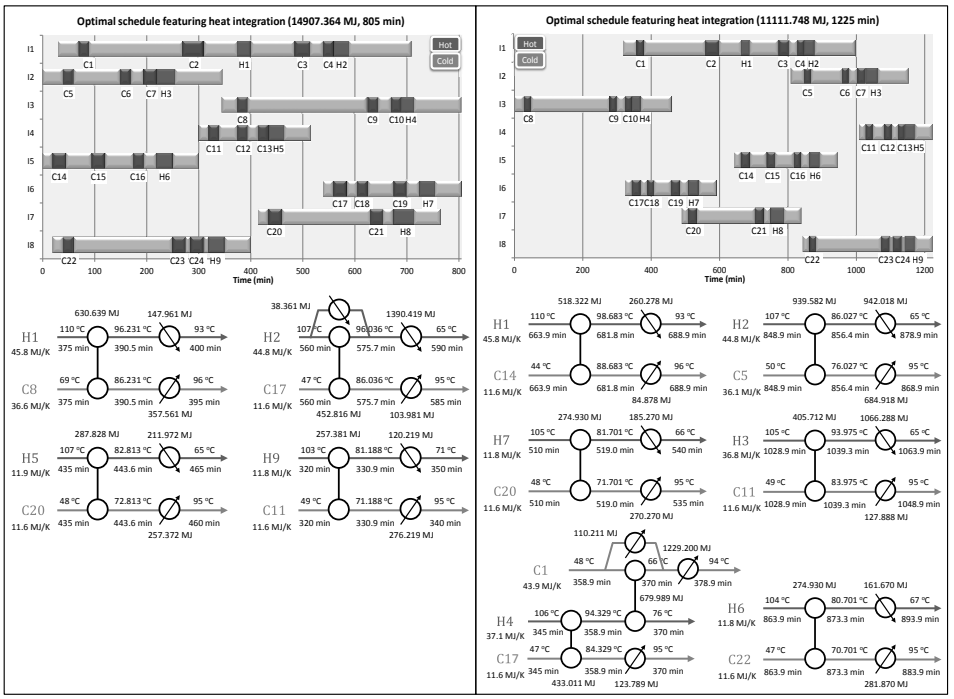

Figure 3. Two Pareto optimal schedules and corresponding matches for 33-stream problem.

Parameter $\varepsilon \in [805,1690]$ (min) for a 33-streams problem from a vegetable oil refinery. A total of 41 optimal solutions arise, ranging from the minimum makespan with 82.1% utility consumption compared to no integration, to the lowest value of 60.2%, for which the production time is more than doubled, see Figure 2. Perhaps the best solution is something in between. In particular, the right-most schedule in Figure 3 features 61.2% utilities and a makespan equal to 1225 min. It can be seen that lowering utility consumption requires additional matches between process streams (7 vs. 4), resulting in a more complex network. The start-start is by far the preferred type of interaction. The other interesting observation is that product sequencing has changed in all three equipment units with more than one product assigned, from (I2-I3, I5-I4-I6, I8-I7) to (I3-I2, I6-I5-I4, I7-I8). This is a clear indication of the importance of solving the scheduling and heat integration problems simultaneously (Seid and Majozi, 2014).

5. Computational studies

We consider four problems ranging from 18 to 46 streams. The general mixed-integer linear programming (MILP) formulation was implemented in GAMS and solved by CPLEX 12.6 running in parallel deterministic mode using up to 8 threads (relative optimality tolerance=10^{-6}). The hardware consisted of a desktop with an Intel i7-4790 CPU (3.6 GHz), 8 GB of RAM and running Windows 7.

Table 1 gives the results for the two extreme points of the Pareto set. The first three problems were generated so as to have the same minimum makespan. As the number of products and streams increases, so does the potential utility savings. The drawback is

that significant production delays may be needed to achieve the proper synchronization of tasks. The added complexity is reflected in the total computational time to generate the full Pareto set, with the 33-streams instance requiring roughly two days. In fact, the reported values in column 7 for 33 and 46 streams involve the solution of makespan-unconstrained problems, needed to find the upper bound on ε, and do not necessarily correspond to minimum utility consumption (large gap at termination). Adding the constraint $MK \leq 1740$ makes it possible to solve the 33-streams problem in less than 1 h. The last important aspect is that the mathematical formulation has a poor relaxation, equal to the difference between the energy requirements of hot and cold streams. Thus, the linear relaxation disregards timing and temperature driving force constraints.

Table 1. Main results from Pareto set generation

$\|I\|$	Streams	MK (min)	UT (MJ)	Savings	MK (min)	UT (MJ)	Savings	TCPUs
4	18	805	11569.5	15.6%	1140	9102.7	33.6%	29.5
6	26	805	13567.5	15.5%	1365	10007.0	37.7%	463
8	33	805	14907.4	17.9%	1740	10951.3[a,b]	39.7%	171971
11	46	1305	19823.2	26.5%	2330	15208.9[a,c]	43.6%	-

[a]Best possible solution up to 3600 CPUs, may be dominated ([b]Gap=19.5%; [c]Gap=52.9%).

6. Conclusions

This paper has addressed the simultaneous scheduling and heat integration problem in a multiproduct batch plant. Through the solution of four industrial cases studies from a vegetable oil refinery, it has been shown that energy efficiency can be improved substantially. There is a clear trade-off between production time and utility consumption, with larger utility savings typically associated to significantly longer production times. This can be interesting in plants operating well below their maximum capacity. Overall, there are a large number of Pareto optimal solutions to choose from.

Acknowledgments

Financial support from Fundação para a Ciência e Tecnologia (FCT) through Investigador FCT 2013, PTDC/EQU-ESI/118253/2010 and SFRH/BDE/51346/2011.

References

R. Adonyi, J. Romero, L. Puigjaner, F. Friedler, 2003, Applied Thermal Engineering, 23, 1743.
P.M. Castro, I.E. Grossmann, P. Veldhuizen, D. Esplin, 2014a, AIChE J. 60, 2083-2097.
P.M. Castro, D. Rodrigues, H.A. Matos, 2014b, Ind. Eng. Chem. Res. 53, 17098-17111.
I. Fernández, C.J. Renedo, S.F. Pérez, A. Ortiz, M. Mañana, 2012, Renewable and Sustainable Energy Reviews, 16, 2260-2277.
I. Halim, R. Srinivasan, 2009, Ind. Eng. Chem. Res., 48, 8551-8565.
C.A. Méndez, G.P. Henning, J. Cerdá, 2001, Comp. Chem. Eng. 25, 701-711.
R. Raman, I.E. Grossmann, 1994, Comp. Chem. Eng., 18, 563-578.
E.R. Seid, T. Majozi, 2014, Energy, 71, 302-320.
N. Vaklieva-Bancheva, B.B. Ivanov, N. Shah, C.C. Pantelides, 1996, Comp. Chem. Eng., 20, 989-1001.
T.F. Yee, I.E. Grossmann, Z. Kravanja, 1990, Comput. Chem. Eng. 14, 10, 1165.

Krist V. Gernaey, Jakob K. Huusom and Rafiqul Gani (Eds.), 12th International Symposium on Process Systems Engineering and 25th European Symposium on Computer Aided Process Engineering.
31 May – 4 June 2015, Copenhagen, Denmark

Improving Pharmaceutical Batch Production Processes with Data-Based Tiered Approach

Lukas G. Eberle[a,b,*], Hirokazu Sugiyama[c], Stavros Papadokonstantakis[a], Andreas Graser[b], Rainer Schmidt[b], Konrad Hungerbühler[a]

[a]*ETH Zurich, Vladimir-Prelog-Weg 1, 8093 Zurich, Switzerland*
[b]*F.Hoffmann-La Roche Ltd., Grenzacherstrasse 124, 4070 Basel, Switzerland*
[c]*The University of Tokyo, 7-3-1, Hongo, Bunkyo-ku, 113-8656 Tokyo, Japan*
lukas.eberle@roche.com

Abstract

Improving the yield of batch-wise production is an increasingly important topic for the pharmaceutical industry; reasons for that include the rising public pressure on drug prices as well as a number of soon-expiring patents. This study defines a data-based, three-level approach for yield enhancements in batch-wise operations that is applied exemplary to the manufacturing of sterile drug products. The application on data of a yearly Parenterals production validated the presented approach by facilitating the identification of the main loss causes (e.g., quality control samples and scratched vials) and by supporting the development of improvements with the result of an increased production yield. As a case study, one loss cause (i.e., rubber stoppers with embedded particles) is discussed, where all three levels were applied and a process enhancement could be realised.

Keywords: Pharmaceutical Production, Industrial Application, Decision-making, Statistical Process Control, Multivariate Data Analysis.

1. Introduction

The growing public pressure on drug prices and the marketing of high-cost drug products renders efficiency of technical operations increasingly important to the success of pharmaceutical companies. Besides more strategically motivated efforts, for example improved scheduling algorithms or large scale supply chain optimisations, also operational improvements, including broadly applicable approaches for yield increases on the shop floor level, should be considered. The importance of research on the operational level is also supported by the fact that the increasing availability of production data provides the required database only since lately and corresponding methodologies are not yet established to the full extent.

Early efforts for yield improvements in pharmaceutical production have, for example, been reported by Nyfeler et al. (2004) with case studies about the production of sterile drug products. More recent industrial research on yield enhancements has considered the variability in raw material qualities and uses the composition of ingredients as decision variable for getting optimal drug product characteristics for all batches within a certain planning horizon (García-Muñoz et al., 2014; García-Muñoz, 2014). These efforts are supported by ongoing academic research on batch applications for model

predictive control (MPC), such as Laurí et al. (2014). The current state of process systems engineering tools tailored to the need of the pharmaceutical industry was reviewed and summarized by Troup and Georgakis (2013).

2. Methodology

This study, an expansion of Eberle et al. (2014), defines a hierarchical three-level approach for yield enhancements in batch-wise manufacturing, which is depicted in Fig. 1. For improving production yield, loss causes are prioritized on the first level (1) by their financial impact or active pharmaceutical ingredient (API) losses as the corresponding main cost driver in the biotechnology production area. The emergence patterns of prioritized loss causes are then characterised (2) by statistical analysis with process control charts and thereby screened for characteristics such as outliers, trends or shifts. Based on heuristics and the consultation of expert knowledge, this information is then considered for deriving improvement ideas. If the information available after the execution of the second level is sufficient for deriving favourable process enhancements, a deeper investigation is not necessary. However, if enhancements cannot be defined, an intra-process investigation (3) is performed. This third level is conducted by performing a fault tree analysis (FTA) first and then assigning measured parameters (e.g., gas pressure, temperatures) for as many branches of the FTA as possible. The branches of the FTA are then either starched or dropped based on statistical findings.

On the first level, processes are ranked by their loss impact L_P, which is calculated according to Eq. 1.

$$L_{\mathrm{p}} = \sum_{i=1}^{d} \sum_{k=1}^{n} Q_{k,i,p} \times F_{i,p} \tag{1}$$

L_{p} is determined for each process p as the sum of n batches and d drug products by multiplying quantity $Q_{k,i,p}$ [litres or units of drug product] and impact factor $F_{i,p}$, i.e., grams of API lost per unit for API losses [e.g., g/L or g/unit drug product] or costs of non-commercialized products [monetary units/L or monetary units/unit drug product]. The impact factor $F_{i,p}$ distinguishes the costs on a certain process stage for different products and accounts for the increasing associated costs during manufacturing. All these L_{p} are then graphed in the order of magnitude, as illustrated in Fig. 2 for the case study on embedded particles.

Then, on the second level, a statistical analysis of the loss emergence pattern is performed based on time-resolved loss data exclusively; production characteristics other than the chronological order and the lost quantities are not yet considered. The concept of this second level of the approach is to identify patterns that are supportive for identifying root causes of lost resources by screening the data for outliers, trends or shifts and assigning rationales.

If enhancements cannot be derived, the investigation is escalated to the third level of the proposed methodology, which starts with the creation of a fault tree analysis (FTA) for each loss cause of concern. An FTA facilitates the identification of influence factors for an observed loss phenomenon, for example moving belt velocities to the share of scratched vials. It is the goal of performing the FTA to first bring in all root causes and

then to list for each root cause as many measured parameters as possible for enabling a later reduction of FTA branches by identifying relevant factors or measured parameters. This is performed by cutting branches that were not supported by statistical findings and starching branches that are supported, indicating significant root causes more clearly and enabling the development of process enhancement opportunities.

3. Industrial Case Study

The presented approach was applied to a drug product facility of Roche in Switzerland, which is producing so-called Parenterals. Parenterals are drug products that reach the body by circumventing the gastrointestinal tract, including liquid drug products such as vials and pre-filled syringes. The process steps considered in this study include the compounding of the drug product solution, the filling into the primary product container and the visual inspection for defects.

The yearly production output of six biopharmaceutical Parenterals was investigated with the goal of increasing the production yield, considering some 111 loss causes that are occurring during the production of either pre-filled syringes, liquid vials or both product types. As can be seen in Fig. 2, which resulted from executing the first level of the presented approach, the five major loss causes trigger more than half of the costs for non-commercialised products, including samples and scratched vials. For these loss causes, improvement initiatives have been initiated or executed and will be discussed in a later publication. The focus of the work presented herein is on the loss cause ranked

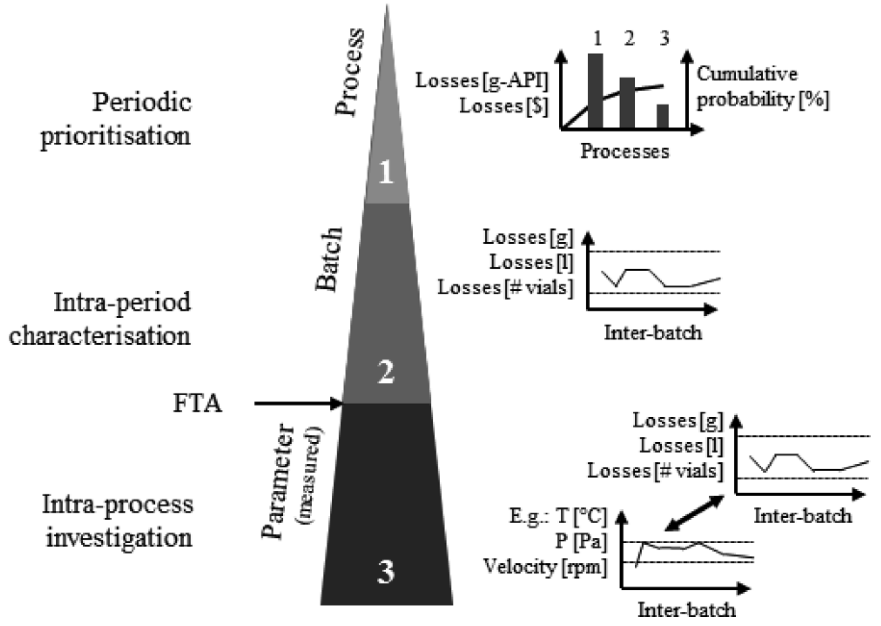

Figure 1: The presented approach is split into three hierarchical tiers that are prioritising (1), characterizing (2) and then investigating (3) loss causes.

sixth, i.e., embedded particles, which is marked in black in Fig. 2. Embedded particles

were selected as case study example in this publication, since the investigation of that loss cause required the application of all three levels of the presented methodology and therefore illustrates all the respective methodological elements to be considered.

The term embedded particles, as defined in this study, includes liquid drug products with impeccable quality that could be applied without a risk of harming a patient. However, the rubber stopper of such vials with embedded particles contains one or few very small areas with discolorations that are hardly visible to the naked eye. This kind of cosmetic defect still leads to the rejection of affected vials. As mentioned above, on the first level, embedded particles are ranked as the sixth most important loss cause in the sampled production period and cause nearly 10 % of costs for non-commercialized products.

On the second level, the emergence of embedded particles was investigated with the help of control charts. A trend or outliers was not detectable and, in more general terms, no solution for decreasing that kind of defect was derivable from available information on the second level. As a consequence of that, the decision was made to proceed to the third level of the presented approach, i.e., establishing an FTA, determining associated measured parameters for each FTA root cause and collecting data accordingly.

From all the vectors that potentially bring a cosmetic defect to the product (product solution, glass container, rubber stopper and isolator air), the rubber stopper was considered as the only relevant vector for embedded particles. A sample of untreated stoppers did not contain embedded particles, which led to the conclusion that the embedded particles must be generated during production processes and was not imported with the supply. Since stoppers are only exposed to conditions other than ambient conditions during their time in the cleaning and sterilisation unit, the focus was on these processes, indicated on the top of Fig. 3. Seven setting characteristics (i.e., batch size of drug product, batch size of stoppers in cleaning vessel, stopper cleaning

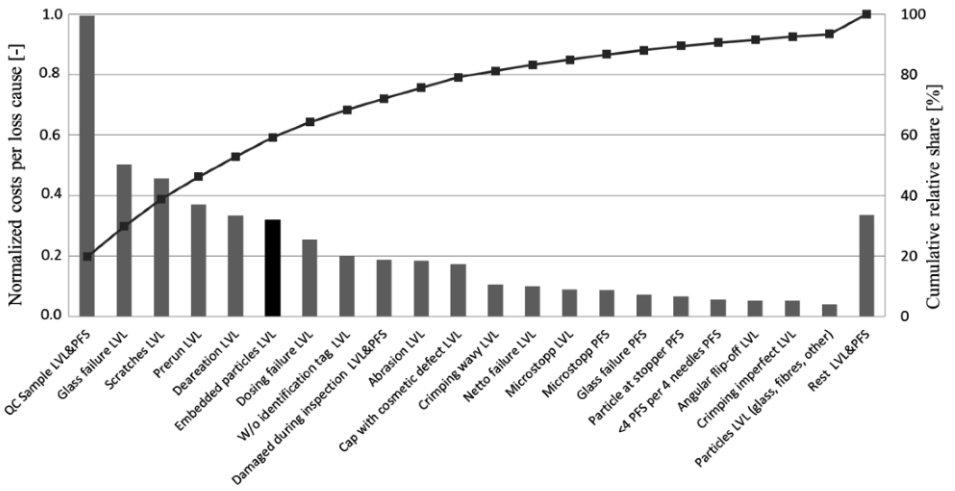

Figure 2: An overview chart for loss causes occurring during the production of Parenterals, indicating the causes on the abscissa in the order of magnitude and the associated absolute but normalized and cumulative relative costs on the left and right ordinate, respectively.

unit, stopper vessel, filled product, format of glass vial and filling period) and three process parameters (i.e., water temperature, water flow and air pressure) for the four process phases (i.e., rinsing, sterilising, drying and cooling) were investigated for all sampled stopper cleaning runs. Since the emergence of embedded particles was not normally distributed, a Kruskal-Wallis test (e.g., Glenberg and Andrzejewski, 2007) was performed and seven parameters that were identified as factors without quality impact could be removed from further analysis. However, the test revealed that the filling period, the batch size of the stoppers in the cleaning vessel as well as the minimal pressure during drying had a significant effect on the emergence of embedded particles, marked black in Fig. 3.

A Bonferroni corrected (Bonferroni, 1936) Mann-Whitney test revealed that embedded particles mostly emerge for the latest filling period, for the biggest stopper batch sizes and stopper cleaning runs with the highest minimal pressure during the drying process. Based on this information and with the support of expert knowledge it was concluded that a vacuum pump in the stopper cleaning unit was underperforming and exposing the stoppers to elevated humidity and temperatures. Hence, the pump was exchanged and the first yield data indicated that this correction measure was successful by reducing the loss by about 20 %.

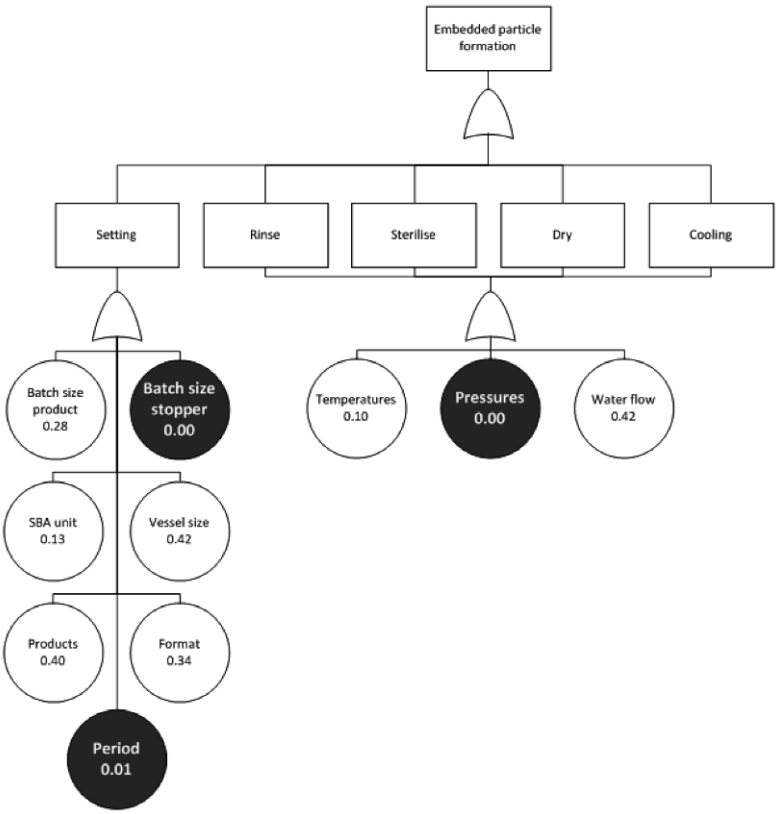

Figure 3: The FTA for embedded particles lists ten investigated parameters; the parameters represented by dark spots have a significant effect on embedded particles. The numbers listed for all parameters indicate the p-value of the Kruskal-Wallis test.

4. Conclusions

The presented approach structures data-based yield improvements in batch-wise productions, for example drug product manufacturing, by applying three hierarchical levels of statistical evaluation. Based on an initial process prioritisation on the first level, loss causes are characterised on the second level and investigated in more detail on the third level. The third level is only executed, if the information gained on the second level is not sufficient for deriving process enhancements. In summary, the developed tiered approach enables a structured use of production data and guides the effort of finding weak points that need improvement. Hence, the approach provides a generic framework for loss causes relevant on the long run but does not substitute process monitoring efforts on a more frequent basis.

Two advantages of the prioritisation as performed on the first level by considering Eq. 1 is that it enables the comparison of losses occurring in different measuring units and account for the increase in value during production processes. Applying the proposed approach to data of a yearly production of Parenterals facilitated the identification, quantification and prioritisation of the main loss causes during production, including QC samples or scratched vials. On the top of that, the information gained from applying the second and third level of the proposed approach allowed the development of enhancements with sustained effects on production yield.

5. Acknowledgement

The support of Sandra Schinzel for the investigation of the embedded particles as well as Markus Mattern and Philip Schneider for providing necessary resources is gratefully acknowledged.

References

C. Bonferroni, 1936, Teoria statistica delle classi e calcolo delle probabilità, Pubblicazioni del R Istituto Superiore di Scienze Economiche e Commerciali di Firenze, 8, 3-62.

L. Eberle, H. Sugiyama, S. Papadokonstantakis, A. Graser, R. Schmidt, K. Hungerbühler, 2014, Data-Based Tiered Approach for Improving Pharmaceutical Batch Production Processes, Proceedings of the 24th European Symposium on Computer Aided Process Engineering, Elsevier, Amsterdam, the Netherlands.

S. García-Muñoz, V. Padovani, J. Mercado, 2014, A computer aided optimal inventory selection system for continuous quality improvement in drug product manufacture, Comput. Chem. Eng., 60, 396-402.

S. García-Muñoz, 2014, Two novel methods to analyze the combined effect of multiple raw-materials and processing conditions on the product's final attributes: JRPLS and TPLS, Chemometr. Intell. Lab., 133, 49-62.

A. Glenberg, M. Andrzejewski, 2007, Comparing Multiple Population Means: One-factor ANOVA, Learning from Data: An Introduction to Statistical Reasoning, 3rd edition,384-387.

D. Laurí, B. Lennox, J. Camacho, 2014, Model predictive control for batch processes: Ensuring validity of predictions, J. Process Contr., 24, 239-249.

P. Nyfeler, 2004, Increased Productivity through Dynamic Process Optimization in Sterile Facility 303 at Novartis Pharma Stein AG, 58, 649-660.

G. Troup, C. Georgakis, 2013, Process systems engineering tools in the pharmaceutical industry, Comput. Chem. Eng., 51, 157-171.

Krist V. Gernaey, Jakob K. Huusom and Rafiqul Gani (Eds.), 12th International Symposium on Process Systems Engineering and 25th European Symposium on Computer Aided Process Engineering.
31 May – 4 June 2015, Copenhagen, Denmark

Integrated Cyclic Scheduling and Operation Optimization for Cracking Furnaces System Considering Feed Changeover

Yangkun JIN[a,b], Jinlong LI[b,*], Wenli DU[a], Feng QIAN[a,*]

[a]*Key Laboratory of Advanced Control and Optimization for Chemical Processes, Ministry of Education, East China University of Science and Technology, Shanghai 200237, China; fqian@ecust.edu.cn*
[b]*School of Information Science and Engineering, East China University of Science and Technology, 200237, China; lijl@ecust.edu.cn*

Abstract

Due to changeable market price and flexible feed resources, the feed changeover for cracking furnace occurs frequently. The integration of scheduling and operation optimization is a promising way to further improve the performance of cracking furnaces system. Motivated by the above situations, a novel integrated cyclic scheduling and operation optimization for cracking furnaces system considering feed changeover is proposed to meet this challenge. This integrated problem is a Mixed-Integer Dynamic Optimization (MIDO) problem. Discretized by the Orthogonal Collocation on Finite Elements (OCFE), the MIDO problem is converted into a large scale Mixed Integer Non Linear Programming (MINLP) problem. A case study is used to demonstrate the efficacy of the developed integrated model.

Keywords: cyclic scheduling, operation optimization, cracking furnaces system, feed changeover, MIDO, MINLP.

1. Introduction

Ethylene cracking furnace is the main unit to produce the fundamental raw materials such as ethylene and propylene in petrochemical industry. For an ethylene plant, once it is set up, the number of ethylene cracking furnaces and their geometry configurations are fixed. Operation of the ethylene cracking furnaces system is the main engineering direction to improve the economic performance, and to meet technical and environmental requirements. With the development of economic and increase of global population, the demand for the petrochemical products such as ethylene and propylene is quite strong in the last several decades. Many ethylene plants nowadays have multiple cracking furnaces to process several different types of feeds. The scheduling and planning activities have been involved on the ethylene cracking furnaces system. Jain & Grossmann (1998) first proposed the cyclic scheduling of cracking furnaces system problem and formulated it as an MINLP problem using the exponential decaying function of ethylene yield. Then based on the exponential decaying functions of product yields, Zhao et al. (2011) proposed an MINLP for scheduling of ethylene cracking furnaces system, which can consider the secondary ethane cracking, no simultaneous cleanup constraints and dynamic scheduling. Wang et al. (2014) proposed a novel synchronized decision-supporting framework for the long term planning and scheduling problem of an ethylene plant. To consider the operation condition, Schulz et al. (2006) incorporated the furnaces models into the scheduling of ethylene cracking furnaces

system with the simplified models of distillation columns and raw material and product storage equations. Lim et al. (2009) incorporated a neural-network based on simulation data of rigorous models to consider the impact of feed processing rate on the product yield.

However, none of these above efforts have been made on the integration of scheduling and operation optimization for the ethylene cracking furnaces system. The integration of scheduling and operation optimization is a promising way to further improve the performance of cracking furnaces system, because it has been proven to make significant improvement for many chemical processes (Chu & You, 2014). Motivated by the above situations, a novel integrated cyclic scheduling and operation optimization for cracking furnaces system considering feed changeover is proposed to meet this challenge. The integrated model considering feed changeover is an MIDO problem. Discretized by the OCFE (Biegler, 2007) method, the MIDO problem is converted into a large scale MINLP problem. To demonstrate the efficacy of the developed integrated model considering feed changeover, the integrated model without allowing no-decoking feed changeover is used as the reference model.

2. Problems Statement

In the integrated cyclic scheduling and operation optimization of an ethylene cracking furnaces system with feed changeover, suppose there are *NJ* cracking furnaces, j=1,2,…,*NJ*. *NI* types of feeds are processed, i=1,2,…,*NI*. The considered products are the products, l=1,2,…,*NL*. The cyclic horizon *H* of each cracking furnace are divided into *NK* time-slots, k=1,2,…,*NK*. Two binary variables $WF_{i,j,k}$ and $WC_{j,k}$ are introduced to determine the feed time-slot matching and the changeover type between two consecutive time slots. The integrated cyclic scheduling and operation optimization of an ethylene cracking furnaces system with feed changeover is to determine scheduling activities: the feed-time slot matching and the changeover type between two consecutive time-slots and the operation activities of time slot utilized for cracking. The illustrated Gant chart of the integrated problem with feed changeover is shown in Figure 1.

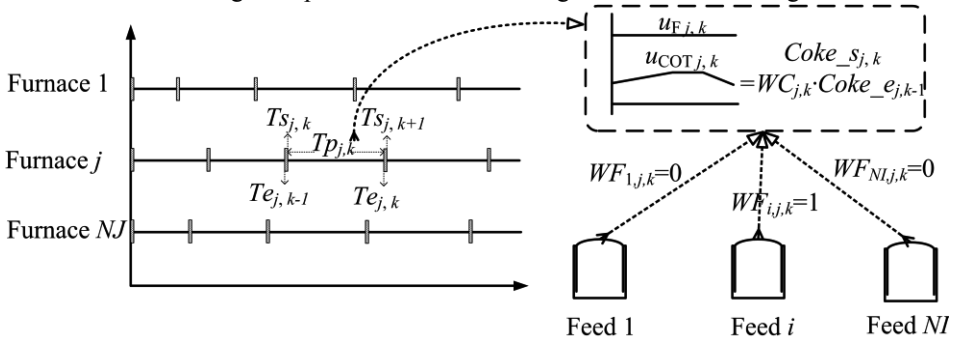

Figure 1 Integrated cyclic scheduling and operation optimization for cracking furnaces system considering feed changeover

3. Integrated Model and Solution Strategy

3.1. Objective Function

In the integrated problem, the maximization of the day mean profit is perused. The day mean profit is sale income of key product minus the clean and changeover cost divided by the cyclic scheduling horizon *H* as:

$$\max\ obj=\frac{\sum_{j=1}^{NJ}\sum_{k=1}^{NK}\left\{\sum_{l=1}^{NL}\left[\int_0^{Tp(j,k)} u_{\mathrm{F}j,k}(t)\cdot y_{j,k,l}(t)\cdot P_l dt\right]-Cc(j,k)\right\}}{H} \tag{1}$$

3.2. Dynamic Models considering Feed Changeover

The dynamic model is expressed as Eq.(2), where f_{FNN} and g_{FNN} mean the Feed-forward Neural Network model, which are obtained by is obtained using combination simulation of rigorous model Coilsim1D (Van Geem et al., 2007) and artificial neural network. Here the subscript l is the outputs of hydrogen (H_2), ethylene (C_2H_4), propylene (C_3H_6), 1,3-butadiene (C_4H_6), benzene (Benz). Here the dynamic models with several disjunctions are reformulated using big M method.

$$\begin{cases} \vee_{i=1,\cdots NI}\begin{bmatrix} WF(i,j,k) \\ \dot{x}_{\mathrm{coke}\,j,k}(t)=f_{\mathrm{FNN},i,j}(x_{\mathrm{coke}\,j,k}(t),u_{\mathrm{F}\,j,k}(t),u_{\mathrm{COT}\,j,k}(t)) \\ y_{j,k,l}(t)=g_{\mathrm{FNN},i,j,k,l}(x_{\mathrm{coke}\,j,k}(t),u_{\mathrm{F}\,j,k}(t),u_{\mathrm{COT}\,j,k}(t)) \\ T_{\mathrm{TMT}\,j,k}(t)=g_{\mathrm{FNN},i,j,TMT}(x_{\mathrm{coke}\,j,k}(t),u_{\mathrm{F}\,j,k}(t),u_{\mathrm{COT}\,j,k}(t)) \\ u_{\mathrm{F}\,j,k}(t)=(Dlo_{i,j}+Dup_{i,j})/2,\ COTlo_{i,j}\le u_{\mathrm{COT}\,j,k}(t)\le COTup_{i,j} \end{bmatrix} \\ T_{\mathrm{TMT}\,j,k}(t)\le 1090,\ Coke\_e_{j,k}=x_{\mathrm{coke}\,j,k}(Tp_{j,k}) \\ x_{\mathrm{coke}\,j,k}(t+1)=x_{\mathrm{coke}\,j,k}(t)+\dot{x}_{\mathrm{coke}j,k}(t)\cdot T_s(t),\ x_{\mathrm{coke}\,j,k}(0)=Coke\_s_{j,k} \\ \forall j,\forall k,\forall t\in[0,Tp_{j,k}] \end{cases} \tag{2}$$

3.3. Scheduling Constraints

3.3.1. Integrality Constraints

In the k time slot of j furnace, it can process no more than one feed at the same time. To express this logical constraint, a binary variable $WF_{i,j,k}$ is introduced. If feed i is processed in the k time slot of j furnace, it is one; otherwise, it is zero. The time slot number NK is a heuristic integer, which is set to a proper number. Thus some time slot may not be used for cracking. To reduce the solution searching space, some additional logical constraints are needed. During the cyclic horizon H, each feed and each ethylene cracking furnace should be utilized. These integrality constraints are expressed as:

$$\sum_{i=1}^{NI} WF_{i,j,k}\le 1,\ \ \sum_{j=1}^{NJ}\sum_{k=1}^{NK} WF_{i,j,k}\ge 1,\ \ \sum_{i=1}^{NI} WF_{i,j,1}=1,\ \ \forall i,\forall j,\forall k \tag{3}$$

$$\sum_{i=1}^{NI} WF_{i,j,k}\ge \sum_{i=1}^{NI} WF_{i,j,k+1},\ \ \forall j,\forall k\le NK-1 \tag{4}$$

3.3.2. Changeover Related Constraints

There are two types of changeovers in the ethylene cracking furnace. One is the decoking process which needs clean time (τ) and clean cost (Cs), and after which the coke is clean and the production efficiency of the ethylene cracking furnace is restored. The other one is the feed changeover without decoking, where a different feed is sent to the ethylene cracking furnace without coke clean process, but with a changeover cost (Co). To express the changeover, another binary variable is $WC_{j,k}$ introduced. $WC_{j,k}$=1

indicates the k time slot of j furnace is operated immediately following a feed changeover. $WC_{j,k}$=0 indicates the k time slot of j furnace is operated immediately following a decoking changeover. Thus the changeover cost ($Cc_{j,k}$) and initial coke thickness($Coke\_s_{j,k}$) can be expressed as Eqs.(5)-(10), where BM is big M parameter.

$$Cc_{j,k} \le \left[(1-WC_{j,k+1})\cdot Cs + WC_{j,k+1}\cdot Co\right] + BM\cdot(1-\sum_{i=1}^{NI} WF(i,j,k)), \forall j, \forall k \le NK-1 \quad (5)$$

$$Cc_{j,k} \ge \left[(1-WC_{j,k+1})\cdot Cs + WC_{j,k+1}\cdot Co\right] - BM\cdot(1-\sum_{i=1}^{NI} WF(i,j,k)), \forall j, \forall k \le NK-1 \quad (6)$$

$$Cc_{j,NK} \le \left[(1-WC_{j,1})\cdot Cs + WC_{j,1}\cdot Co\right] + BM\cdot(1-\sum_{i=1}^{NI} WF(i,j,NK)), \forall j \quad (7)$$

$$Cc_{j,NK} \ge \left[(1-WC_{j,1})\cdot Cs + WC_{j,1}\cdot Co\right] - BM\cdot(1-\sum_{i=1}^{NI} WF(i,j,NK)), \forall j \quad (8)$$

$$Cc_{j,k} \le BM\cdot\sum_{i=1}^{NI} WF(i,j,k),\ Cc_{j,k} \ge -BM\cdot\sum_{i=1}^{NI} WF(i,j,k)), \forall j, \forall k \quad (9)$$

$$Coke\_s_{j,k+1} = WC_{j,k+1}\cdot Coke\_e_{j,k},\ Coke\_s_{j,1} = WC_{j,1}\cdot Coke\_e_{j,NK}, \forall j, \forall k \le NK-1 \quad (10)$$

3.3.3. Timing Constraints

Due to the cyclic scheduling requirement of a round-table problem, the relation of starting time ($Ts_{j,k}$), ending time ($Te_{j,k}$) and feed processing time ($Tp_{j,k}$) can be expressed as Eqs.(11)-(15).

$$Ts_{1,1} = H,\ Ts_{j,1} \le H,\ \forall j \ge 2 \quad (11)$$

$$Ts_{j,1} = Te_{j,NK} + \tau\cdot(1-WC_{j,NK}), \forall j \quad (12)$$

$$Ts_{j,k} = Te_{j,k-1} + \tau\cdot(1-WC_{j,k}), \forall j, \forall k \ge 2 \quad (13)$$

$$Te_{j,1} = Ts_{j,1} + Tp_{j,1} - H, \forall j \quad (14)$$

$$Te_{j,k} = Ts_{j,k} + Tp_{j,k}, \forall j, \forall k \ge 2 \quad (15)$$

3.3.4. Material Balance

The feed arriving amount should be equal to the processed amount by the ethylene cracking furnaces system during the cyclic scheduling horizon H as:

$$F_i \cdot H = \sum_{j=1}^{NJ}\sum_{k=1}^{NK}\left[WF_{i,j,k}\int_0^{Tp_{j,k}} u_{Fj,k}(t)\right]dt,\ \forall i \quad (16)$$

3.4. Variables Bounds

The arriving rate of different feeds F_i, cyclic horizon H, slot starting time $Ts_{j,k}$, ending time $Te_{j,k}$ are bounded as:

$$\begin{aligned} &Flo_i \le F_i \le Fup_i,\ 60 \le H \le 360, 0 \le Ts(j,k) \le 360, \\ &0 \le Te(j,k) \le 360, 0 \le Tp(j,k) \le 360\ \forall i, \forall j, \forall k \end{aligned} \tag{17}$$

3.5. Solution Strategy

The integrated problem is a complex MIDO problem. Discretized by the Orthogonal Collocation on Finite Elements (OCFE) (Biegler, 2007), the MIDO problem is converted into a large scale MINLP problem. All of the models are modelled in the GAMS environment, and the resultant MINLP is solved using SBB as the MINLP solver with CONOPT as the nonlinear sub solver.

4. Case Study

A simple case study of one ethylene cracking furnace with multiple feeds is represented here. In the scope of our study, only an ethylene cracking furnace of GK-VI type is considered and it can process four different types of feeds: light naphtha (LNAP), naphtha (NAP), heavy vacuum gas oil (HVGO) and atmospheric gas oil (AGO). The prices of the high valued products and costs are supposed as in Table 1. The related parameters are supposed as in Table 2. Using the developed framework, the integrated cyclic scheduling and operation optimization of cracking furnaces system considering feed changeover (MIDO problem) is converted into an MINLP model, which is developed with GAMS version 24.1.2 and solved using SBB as the MINLP solver with CONOPT as the nonlinear sub solver. 5 finite elements for each processing time and 3 collocation points per finite element are used in the OFCE process. The resultant MINLP problem involves 77,171 equations, 7990 continuous variables and 25 discrete variables. The solving time with a PC with 64 bit Windows 7 Professional, Intel Core i3 CPU 2.1 GHz and 4 GB RAM is about six hours with a local integer solution. The optimal profiles of the coke thickness are shown in Figure 2(a), which gives a cyclic horizon of 84.9 days and a day mean profit of 2.591 Mil. RMB/day. For comparison purpose, the integrated problem without non decoking feed changeover is also solved as shown in Figure 2(b) of the optimal profiles of the coke thickness. The result gives a cyclic horizon of 253.2 days and a day mean profit of 2.544 Mil. RMB/day. It can be found that the integrated problem with feed changeover can bring more day mean profit, which is result from the more freedom of feed processing with feed changeover.

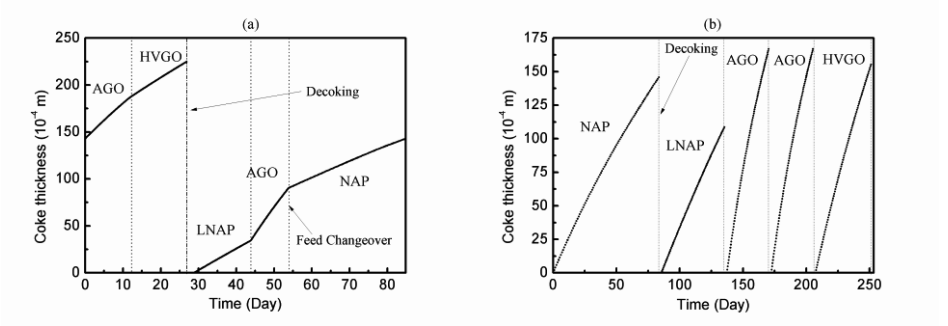

Figure 2 Results of integrated problem (a) with and (b) without non decoking feed changeover

Table 1 Economic indexes

Price of Key Product *l* [RMB/t]					Cost [RMB]		Decoking time [Day]
H_2	C_2H_4	C_3H_6	C_4H_6	Benz	*Cs*	*Co*	τ
14620	8,480	8,210	10,799	10,500	264,052.5	11,000	2

Table 2 Related parameters of the integrated model

Parameters	Feed *i*			
	1 (LNAP)	2 (NAP)	3 (HVGO)	4 (AGO)
Dlo_{ij} (t/d)	504	528	504	528
Dup_{ij}(t/d)	624	672	648	624
$COTlo_{ij}$(°C)	830	820	790	790
$COTup_{ij}$(°C)	845	840	810	810
Flo_{ij}(t/d)	100	150	100	150
Fup_{ij}(t/d)	200	250	200	250

5. Conclusions

The integration of scheduling and operation optimization is a promising way to further improve the performance of cracking furnaces system. In this paper, a novel integrated cyclic scheduling and operation optimization for cracking furnaces system considering feed changeover is proposed to meet this challenge. This integrated problem is a MIDO problem, which is discretized by the OCFE method and it is converted into a large scale MINLP problem. A case study is used to demonstrate the efficacy of the developed integrated model compared with the integrated strategy without allowing no-decoking feed changeover. Future work will be on the multi-furnaces multi-feeds, which needs more efforts to solve it.

Acknowledgements: This is supported by Major State Basic Research Development Program of China (2012CB720500), National Natural Science Foundation of China (U1162202, 21276078), Fundamental Research Funds for the Central Universities, Shanghai Rising-Star Program (13QH1401200) and Natural Science Foundation of Shanghai(13ZR1411300).

References

C.Zhao, C.Liu, Q.Xu, 2011, Dynamic scheduling for ethylene cracking furnace system, Industrial & engineering chemistry research, 50, 21, 12026-12040.

E.P.Schulz, J.A.Bandoni, M.S. Diaz, 2006, Optimal shutdown policy for maintenance of cracking furnaces in ethylene plants, Industrial & engineering chemistry research, 45, 8, 2748-2757.

H.Lim, J.Choi, M.Realff, J.H.Lee, S.Park, 2009, Proactive scheduling strategy applied to decoking operations of an industrial naphtha cracking furnace system, Industrial & engineering chemistry research, 48, 6, 3024-3032.

K.M.Van Geem, R.Žajdlík, M.F.Reyniers, G.B.Marin, 2007, Dimensional analysis for scaling up and down steam cracking coils, Chemical Engineering Journal, 134, 1, 3-10.

L.T.Biegler, 2007, An overview of simultaneous strategies for dynamic optimization, Chemical Engineering and Processing: Process Intensification, 46, 11, 1043-1053.

V.Jain, I.E. Grossmann, 1998, Cyclic scheduling of continuous parallel process units with decaying performance, AIChE Journal, 44, 7, 1623-1636.

Y.Chu, F.You, 2014,Integrated Scheduling and Dynamic Optimization for Network Batch Processes, Computer Aided Chemical Engineering,Volume 33, 523-528.

Z.Wang, Y.Feng, G. Rong, 2014, Synchronized Scheduling Approach of Ethylene Plant Production and Naphtha Oil Inventory Management, Industrial & engineering chemistry research, 53, 15, 6477-6499.

Krist V. Gernaey, Jakob K. Huusom and Rafiqul Gani (Eds.), 12th International Symposium on Process Systems Engineering and 25th European Symposium on Computer Aided Process Engineering.
31 May – 4 June 2015, Copenhagen, Denmark

MINLP Model and two-level Algorithm for the Simultaneous Synthesis of Heat Exchanger Networks and Utility Systems

Emanuele Martelli,[a] Alberto Mian,[b] François Maréchal[b]

[a]*Politecnico di Milano, Via Lambruschini 4, 20156 Milano, Italy*
[b]*Ecole Politechnique Fédérale de Lausanne, Station 9, 1015 Lausanne, Switzerland*

Abstract

This work proposes a novel approach for the simultaneous synthesis of Heat Exchanger Networks (HEN) and Utility Systems. Given a set of hot and cold process streams and a set of available utility systems (e.g., gas turbine, steam cycle, boiler, etc), the method determines the optimal selection of utility systems, their arrangement and design (including steam generator), and the heat exchanger network (between process-process as well as process-utility and utility-utility streams) rigorously considering the trade-off between efficiency and capital costs. The mathematical model is formulated as a Mixed Integer NonLinear Program (MINLP) and it combines the SYNHEAT superstructure for HENs with ad hoc models/superstructures for utility systems. The challenging MINLP is solved with a two-level algorithm using at the upper level the Variable Neighbourhood Search (VNS) algorithm to optimize the integer variables, and at the lower level the SQP algorithm to optimize the real variables. The algorithm is tested on problems with up to 15 streams (corresponding to 465 binary variables).

Keywords: HEN synthesis, utility systems, MINLP, VNS, steam cycle

1. Introduction

The optimal design of energy systems and chemical processes involves also the synthesis of the Heat Exchanger Network (HEN) as well as of the utility systems necessary to provide thermal, refrigeration and electric power to the process units. To the best of our knowledge, all the available synthesis techniques tackle the two problems separately by limiting the set of integration options between the HEN and the set of utility streams. For instance, the well-known sequential approach proposed in the works of (Papoulias & Grossmann, 1983a), (Papoulias & Grossmann, 1983b) and (Floudas, Ciric, & Grossmann, 1986) has the following limitations.

1. HEN and utility systems (e.g., steam cycle) are designed sequentially.
2. As far as steam cycles are concerned, it is assumed that only evaporating/condensing steam can be integrated within the HEN to supply/remove heat from the process. For example, hot process streams cannot heat up boiler feedwater or superheat steam.
3. The matches of each utility stream can only be in parallel (it is considered one utility substream for each match which involves the given utility, as shown in Fig. 1A). This implies that the HEN superstructure excludes the series arrangement shown in Fig. 1B. Note that the parallel arrangement is possible only if the outlet temperature of cold/hot utility stream is lower/hotter than the inlet temperature of the hot/cold streams matched. This constraint does not allow to use cold utility streams with high outlet temperatures (e.g., feedwater of a steam cycle with outlet temperature of 300

°C) or hot utility streams with low outlet temperatures (e.g., flue gases with outlet temperature of 60 °C) excluding potentially advantageous utility systems.

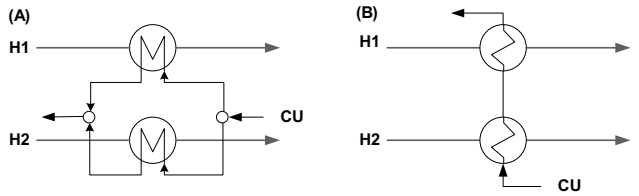

Figure 1. (A): cold utility stream with two matches in parallel (H1-CU and H2-CU). (B): cold utility stream with two matches in series.

Also simultaneous HEN synthesis techniques have limitations which make them not suitable for designing HENs optimally integrated with utility streams. For instance, the MINLP Synheat model of (Yee & Grossmann, 1990) has the following limitations:

1. utility superstructures/models are not included for selection and optimization,
2. the optimization of the utility stream mass flow rates is not tackled because it would lead to nonlinear nonconvex constraints,
3. utility streams are not included in the HEN superstructure but placed at the hot and cold ends of the superstructure (thus, matches of each utility stream can be only in parallel, as shown in Figure 1A).
4. matches between streams of different utilities (e.g., boiler – steam cycle) are not possible.

In utility synthesis techniques the optimization of the process HEN is not dealt with. The utility system is optimized to provide the thermal, electric and refrigeration power required by the process (for fixed process HEN). Synthesis techniques for HENS with multiple utilities, like the one proposed by (Na, Jung, Park, & Han, 2014), do not tackle the design problem of the utility systems (e.g., steam cycle and related boiler) and do not envisage the possibility for utility streams to have matches in series, as in Fig. 1B.

This work proposes a methodology and algorithm for the simultaneous synthesis of HENs and utility systems, which allows to (1) select among several available utility systems, (2) include complex superstructures of utility systems, (3) generate any possible match between process streams and utility streams, (4) optimize the design of the steam generator (arrangement and area of tube banks), (5) include design constraints on the HEN like “forbidden matches”, “restricted matches” and “no stream splitting”.

2. Superstructure, mathematical model, and two-level algorithm

The problem can be stated as below:

“Given a set of hot and cold process streams with given mass flow rates, inlet and outlet temperatures, and a set of available utility systems (e.g., cooling water, boiler, multiple-level steam cycle, refrigeration cycle, heat pump, etc) with given structure or superstructure of possible configurations, the method simultaneously determines the optimal selection of utility systems, their design (arrangement of the steam generator as well as of other heat exchangers of the utility systems, turbine size, mass flow rates of each utility stream, etc), and the heat exchanger network between process-process as well as process-utility and utility-utility streams.”

The proposed synthesis model combines the SYNHEAT temperature-stage HEN superstructure of (Yee & Grossmann, 1990) with models and superstructures of utility systems, as shown in Fig. 2. Utility systems are divided in two categories, U-HEN and

U-END. The streams of utilities in U-HEN can be fully integrated in the HEN, indeed they are dealt with as process streams (e.g., the gas turbine flue gases, the cooling air and the streams of the steam cycle in Fig. 2). Streams of utilities in U-END instead are not included in the HEN superstructure and they are placed at the hot/cold ends of the cold/hot streams (as done in (Yee & Grossmann, 1990)). As a result, utility streams in U-END have limited matching options with other streams. However, they require a much lower number of binary and real variables compared to utility streams in U-HEN. A utility is included in U-END only if its streams have very hot/cold inlet and outlet temperatures compared to those of the cold/hot streams. In such a case, the optimal matching is likely to be at the hot/cold ends of the HEN superstructure. If this condition is not verified, it is advisable to include the utility in U-HEN so as not to exclude better matching options. It is worth noting that the set U-END may be empty if no utility can be reasonably classified as "hot/cold-end" utility, or a stream may not need a "hot/cold-end" utility because its target temperature is variable (e.g., flue gases).
The optimization problems involves the following variables, objective function and constraints.

- Binary optimization variables: activation of utility system (U-END and U-HEN), activation of utility system options (only for utility with superstructure), activation of heat exchangers in the HEN (for process-process and process-utility streams in U-HEN and utility-utility streams both in U-HEN), activation of end utility (in U-END) for each process stream as well as utility stream in U-HEN.

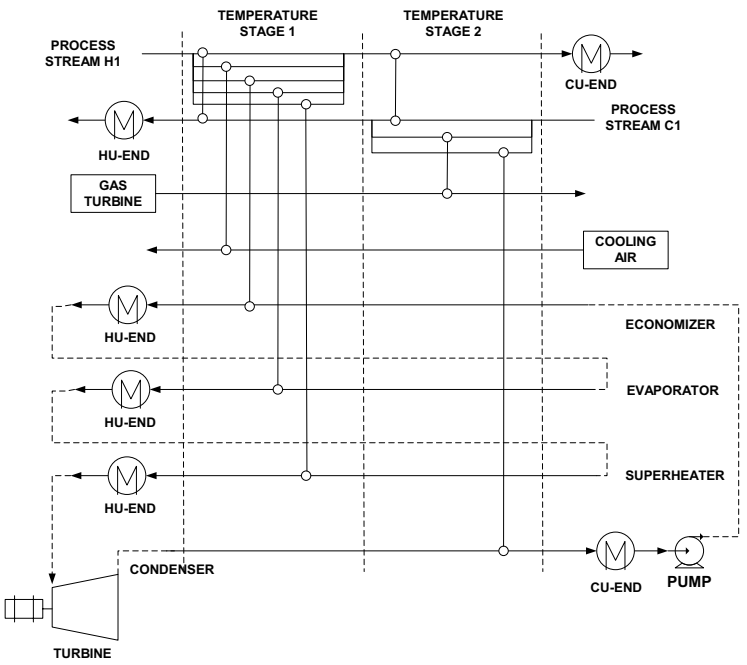

Figure 2. Superstructure of HEN and utility systems. CU-END and HU-END denote respectively "cold/hot-end" utilities.

- Real optimization variables: mass flow rates of utility streams, thermal power exchanged in each heat exchanger, stream temperatures at the inlet/exit of each heat exchanger.

- Objective function: minimum total annual cost, sum of the utility capital cost (fixed activation cost + size depending cost), heat exchanger costs (fixed activation cost + area depending cost) and utility operating cost (energy consumption + other operating costs).
- Constraints: logical constraints to activate/deactivate utility systems and heat exchangers, energy balance equation of each stream, energy balance equation of each stream at each temperature stage, feasibility of stream temperatures in each match, model equations of each complex utility system (e.g., steam cycle), upper and lower bounds on each continuous variable.

It is worth noting that the energy balance equations contain bilinear terms (nonconvex), the products of flow rates and inlet/outlet temperatures of streams in U-HEN.
The challenging MINLP is tackled with a two-level algorithm: at the upper level the Variable Neighborhood Search (VNS) algorithm of (Egea et al., 2014) optimizes the binary variables (dealing with a balck-box integer problem), while at the lower level the SNOPT SQP algorithm optimizes the real variables. In order to minimize the variables and constraints of the lower-level NonLinear Program (NLP), the adaptive reformulation strategy of (Chen et al., 2008) is used. Given the combination of binary variables set by the VNS algorithm, it removes variables and constraints of the NLP.

3. Test case

The algorithm has been tested on several test cases including literature HEN synthesis problems (without utility optimization) and ad hoc problems comprising utility systems. Here we report the computational results for a test problem representative of integrated power plants (e.g., Integrated Gasification Combined Cycles) where the heat recovery steam generator (HRSG) must recover heat from multiple hot streams. Stream data are reported in Table 1. The heat exchangers have an activation cost of 3000 \$/y and area cost of 150 \$/m^{2}y. The boiler has an activation cost (C_A) of 40000 \$/y and energy + size-related cost (C_P) of 200 \$/kWy. For cooling water C_A = 4000 \$/y and C_B = 20 \$/kWy, while for the steam cycle C_A = 1000000 \$/y and C_B = -600000 \$/kWy. A scale factor equal to 0.75 is considered for the area cost of the heat exchangers.

Table 1. Stream data of the test problem.

Stream	F [kW/K]	Tin [°C]	Tout [°C]	h [kW/Km^2]
H1 (process)	200	600	>= 60	0.06
H2 (process)	40	900	250	0.04
H3 (process)	50	350	200	0.04
C1 (process)	20	100	250	0.5
C2 (process)	30	15	150	1.5
BOILER (HU-END)	var	1000	300	0.5
COOLING WATER (CU-END)	var	15	25	1.5
ECONOMIZER (CU-HEN)	var	30	275	1
EVAPORATOR (CU-HEN)	var	275	275	10
SUPERHEATER (CU-HEN)	var	275	565	0.6
CONDENSER (HU-HEN)	var	30	30	2

The optimization has been repeated for ten times with 60000 function evaluations of the VNS algorithm. The best solution is shown in Fig. 3 and its objective function value (total annual cost of the plant) is equal to -19.4587 M\$/y (being a negative value, it is a

revenue). The average objective function of the solutions returned by the algorithm is equal to -19.45259 M$/y, which, being quite close to the best solution value, indicates a good reliability of the VNS algorithm. The CPU computational time of a run is about 800 seconds.

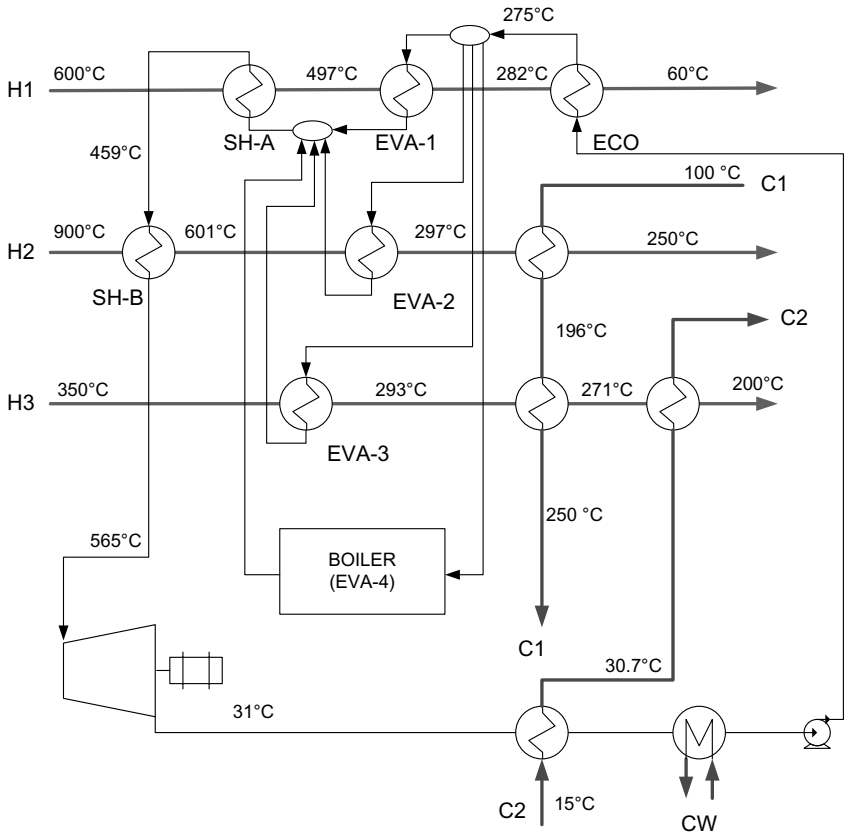

Figure 3. Best solution found by the two-stage algorithm

It is worth noting that the algorithm identifies a solution in which:

- heat exchangers of stream H1 are arranged as a conventional HRSG,
- steam superheating is split into two heat exchangers which are placed in series,
- steam evaporation is split into four heat exchangers (H1, H2, H3, boiler) connected in parallel.
- the steam cycle has been automatically arranged so as to perform cogeneration of power and heat, a particularly efficient thermodynamic solution, as it is heating up the cold stream C2 by means of the heat rejected by the condenser (at turbine outlet).

Such a solution with a so deep integration between the steam cycle and the process HEN cannot be found by other synthesis techniques. Also the layout of the HEN is really interesting as it combines energy efficiency and arrangement simplicity.

The algorithm has been tested also on literature problems with a larger number of streams, up to 15, and up to 465 integer variables. Computational results indicate that the number of function evaluations of the VNS algorithm required to reach close-to-optimal solutions increases considerably. For instance, with 465 integer variables, 300000 function evaluations (corresponding to 10000 s CPU time) are not sufficient to

find the optimal solution. However the returned solution has an objective function value only 3% suboptimal compared to the best-known solutions for the literature problem.

4. Conclusions

Compared to classic HEN synthesis methods, the proposed methodology returns improved HENs and utility system designs in which utility streams are fully integrated within the HEN and advantageous thermodynamic expedients, such as cogeneration, are exploited. The SQP algorithm is extremely efficient and, most important, finds the global optimum also for the problem formulations with variable utility flows (with nonlinear nonconvex constraints). The computational time and convergence rate (in terms of decrease rate of the objective function) of VNS strongly depends on the number of integer variables. However close-to-optimal solutions can be obtained also for problems with a large number of streams within a reasonable computational time (10000 s CPU time), and parallel-computing environment optimized for SQP algorithms, like that proposed by (Kang, Liu, Ren, & Tang, 2014), may significantly decrease the computational time. Future works are aimed at including more complex utility superstructures and testing other optimization algorithms (e.g., branch-bound gradient-based MINLP methods).

Acknowledgements

The authors acknowledge the Swiss National Science Foundation (SNSF) for having supported this work by funding the visiting period of Ass. Prof. Martelli at EPFL (grant number IZK0Z2_157270).

References

X. Chen, Z. Li, J. Yang, , Z. Shao, 2008. Nested Tabu Search and Sequential Quadratic Programming Method, Combined with Adaptive Model Reformulation for Heat Exchanger Network Synthesis, Industrial & Engineering Chemistry Research, 47, 2320–2330.

J.A. Egea, D. Henriques, T. Cokelaer, A. F. Villaverde, A. Macnamara, D. Danciu, J. Saez-rodriguez, 2014, MEIGO : an open-source software suite based on metaheuristics for global optimization in systems biology and bioinformatics, BMC Bioinformatics, 15(136), 1–9.

C.A. Floudas, A. Ciric, I.E. Grossmann, 1986, Automatic synthesis of optimum heat exchanger network configurations, AIChE Journal, 32(2), 276–290.

L. Kang, Y. Liu, Y. Ren, Y. Tang, 2014, Optimal Design of Heat Exchanger Networks by Using SQP Algorithm Based on GPU Acceleration, Computer Aided Chemical Engineering, 33, 295–300.

J. Na, J. Jung, C. Park, C. Han, 2014, Simultaneous Optimization Models for Heat Exchanger Network Synthesis with Multiple Utilities : A New Strategy by Using Utility Sub-stage, Computer Aided Chemical Engineering, 33, 1675–1680.

S. Papoulias, I.E. Grossmann, 1983a, A structural optimization approach in process synthesis—I: utility systems, Computers & Chemical Engineering, 7(6), 695–706.

S. Papoulias, I.E. Grossmann, 1983b, A structural optimization approach in process synthesis—II Heat Recovery Networks, Computers & Chemical Engineering, 7(6), 707–721.

T. Yee, I.E. Grossmann, 1990, Simultaneous optimization models for heat integration—II. Heat exchanger network synthesis, Computers & Chemical Engineering, 14(10), 1165–1184.

Krist V. Gernaey, Jakob K. Huusom and Rafiqul Gani (Eds.), 12th International Symposium on Process Systems Engineering and 25th European Symposium on Computer Aided Process Engineering.
31 May – 4 June 2015, Copenhagen, Denmark

Process Simulations Supporting a Techno-Economic Framework to Optimize Biorefinery Supply Chains

Sumesh Sukumara, Kwabena Darkwah and Jeffrey R. Seay*

Department of Chemical and Materials Engineering, University of Kentucky, 177 F Paul Anderson Tower, Lexington 40508, USA
jeffrey.seay@uky.edu

Abstract

With recent innovations in the field of renewable energy, several promising biorefining techniques have been discovered. While many of these innovations have demonstrated promising outcomes in a small scale, laboratory settings, validation of these for their practical viability must be substantiated. While several contributions exist that captures the economic performance and inherent uncertainties of biorefinery supply chains, further emphasis must be directed towards coupling the models with basic sciences. One of the major voids in this existing body of knowledge is the ability to embody experimental outcomes while identifying the optimum supply chain logistics. This contribution illustrates a novel methodology for capturing the experimental details and coupling it with a techno-economic framework. In order to develop the process simulations, various tools from the Aspen Engineering Suite (Aspen Tech®) are explored extensively and tailored in a unique manner to share critical data for further analyses. This attribute of the proposed approach enables successful linking of the basic sciences with the broader biomass supply chain, guiding the decision making process. The resulting comprehensive framework will provide insight in channelling resources appropriately and acting as a decision support tool for investors, policy makers and related stakeholders.

Keywords: Decision Support Tool, Biofuels, Fermentation, User-Defined Functions, Biomass.

1. Introduction and Motivation

The production transportation fuel, energy and chemicals from renewable resources has increasingly gained attention in the past decade. Researchers around the world are aspiring to discover various bio-based pathways to create fuels and chemicals with biomass as a primary feedstock. While several feedstocks exist, due to the increased availability and choice (Naik *et al.* 2010), second generation (lignocellulosic) biomass is considered to be a promising source in meeting the progressively rising energy demands (U.S. Energy Information 2013). In addition to dedicated energy crops, several second generation processes have the capability to include waste agricultural and forest residues, making this extremely attractive for the production of biofuels. However, recent studies demonstrate that the economic viability of second generation biofuels are subject to higher uncertainties, mainly due to the costs associated with agriculture, upstream and downstream conversion processes (Van Eijck, Batidzirai, and Faaij 2014). Therefore, it is imperative to account for various contributors which are involved in the overall supply chain of converting biomass into biofuels and bio-chemicals. Sukumara *et al.* 2013, have demonstrated a framework that links conversion and transportation

models to evaluate the optimum biorefinery configuration (Sukumara *et al*. 2014). This model is intended towards capturing the broader scope of the supply chain while simultaneously evaluating viability of the operational configurations for second generation biorefineries. However, in the framework presented, details pertaining to the addition of fundamental scientific innovations are limited as the process models are based on generic conversion yields and reaction stoichiometry. In order to make the model accessible to fundamental scientific outcomes, this contribution exhibits a supplementary method that can be applied towards embodying the experimental details to the developed framework. This linking enables researchers involved in the development of novel biomass conversion and biofuel separation processes, a route to evaluate and validate the operational viability of their innovations.

2. Background

The development of sustainable biofuel production systems are challenged by the complex nature of the voluminous decisions that policy makers, stakeholders and producers have to make (Seay and Badurdeen 2014). The production of biofuels and biochemicals from biomass involves complex processes and processing steps. The biochemical conversion of biomass into biofuels, for instance, involves pre-treating, hydrolysis to produce fermentable sugars, fermentation to produce products and concentration and purification of products. The complexity and interdependency of the processing systems, coupled with the numerous assumptions that are made to scale-up such processes to commercial level introduces trade-offs that must be included in assessing the economic viability of such process (Geraili, Sharma, and Romagnoli 2014). Additionally, bio-butanol production using biochemical conversion route and fermentation is crippled by low conversions, yields and final product concentrations due to substrate and product inhibition on the microorganism used in the fermentation step (Abdehagh, Tezel, and Thibault 2014). Given these challenges, the process profitability is sensitive to marginal changes in the processing inputs, process yields and cost estimation of the process inputs and products. These inputs are generally modelled with estimated fixed process parameters, such as, yields, reactions and production rates (Geraili, Sharma, and Romagnoli 2014). Simulation as a major tool in process engineering allows for the scaling up of experimental data and prediction on the performance of processes based on process parameters. Experiments have inherent errors due to measurements sensitivity and subjective biases. Thus, simulation and modeling processes that rely on literature data to be used for profitability assessment of a project could be misleading. Simulation packages, such as Aspen Engineering Suite (Aspen Tech®) have thermodynamics packages and other models that can predict reliable trends of processes with credible inputs. Most simulation processes in the literature rely on simplified models, equations and linear models that give overall estimates of large integrated biorefineries. In order to develop a robust and comprehensive framework that depicts actual trends in conversion technologies and processing (which are inherently non-linear in a biorefinery), policy makers, stake holders and manufacturers rely on the use of a decision support tool that addresses the mentioned shortcomings. Furthermore, such a robust framework can be used to determine the possible sources of experimental errors, eliminating infeasible options and thus saving time to ensure the use of accurate economic measures to assess the profitability of a biorefinery (Geraili, Sharma, and Romagnoli 2014).

Based on the examination of current literature, a major void in the existing state of knowledge is determined as the lack of capacity of the decision support tools to contain novel discoveries (Seay and Badurdeen 2014). Thus, this contribution will illustrate a methodology to incorporate fundamental results into the process simulations which categorically links to the multidisciplinary biorefinery assessment framework.

3. Decision Support Tool

As a characteristic of emerging chemical technologies, the supply chain for the production of biofuels have several pivotal stages and cumulative impacts which determines its practical application in any given locale. In a unique contribution (Sukumara *et al*. 2014), a framework is demonstrated that encompasses major models to capture the impacts pertaining to the conversion and transportation operations. Figure 1, shows a schematic of an extended contribution based on the principal framework (Sukumara et al. 2014), highlighting the current domain of focus for this research. The following sections describe the existing state of knowledge and novel contributions made to enhance the accessibility of the multidisciplinary decision support tool.

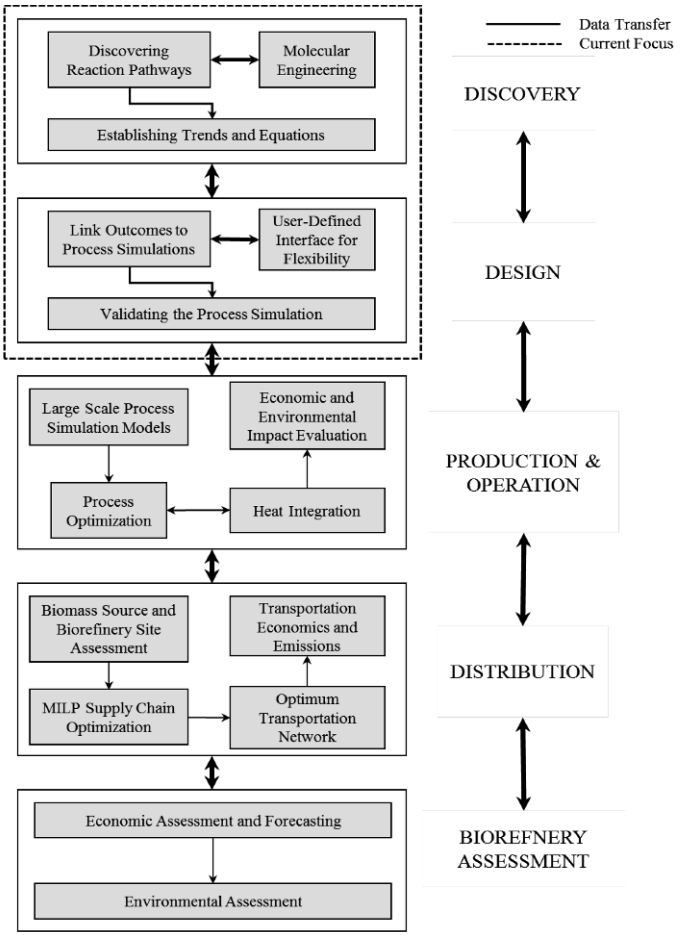

Figure 1. Realms of the decision support framework incorporating experimental outcomes for assessing viability of future biorefinery configurations

3. 1 Overview

Sukumara *et al.*, 2013 illustrated a novel framework that linked gaps in the current state of knowledge by coupling process simulations to the supply chain optimization (Faulkner 2012) and discrete event simulation models (Amundson 2013). The research used Aspen Plus® as a tool to develop process simulations which is further linked to the Mixed Integer Liner Programming (MILP) optimization model.

3.2 Creating and Linking Process Simulations

The deterministic decision support tool is run iteratively, initiated by simulating the conversion models for biorefining processes. In a previous research (Sukumara 2014), simulations are developed for biochemical conversion process, such as, fermentation of corn stover to ethanol. Amongst many, the three major processing challenges for the biological process (mainly from agricultural residue and dedicated energy crops) are determined to be hydrolysis of cellulose, fermentation and finally product purification. Hence, various potential schemes, tolerant micro-organisms and several processing configurations are being investigated to improve the conversion yield of the end products. Therefore, while performing runs, it is necessary to simultaneously import the research outcomes to a broader techno-economic framework to determine the corresponding practical consequences. With the objective of including fundamental details to the framework, the venues to introduce the user-defined data are explored in this contribution.

3.3 Inclusion of Novel Research Outcomes

Aspen Engineering Suite (Aspen Tech®), a versatile process simulation tool which allows for the integration of higher level of details into process models while being able to access the broader economic and operational performances. The simulation has several avenues to incorporate user-defined commands, major ones being: Microsoft Excel®, calculator blocks (Aspen Plus® Built-in model) and dynamically linked FORTRAN subroutine. A common practice is to use the built-in ports available in the simulation; however, biochemical processes have relatively complex conversion mechanisms. Therefore, options towards exploring custom modelling must be considered to incorporate such non-conventional mechanisms. While each of the interfaces could be used in various competencies, the current work demonstrates a procedure to dynamically link user-defined functions to brace the techno-economic framework. In order to illustrate the working of the model, a case study is framed with a decoupled unit operation to explore the capability of the model to adopt data from experimental outcomes.

4. Case Study, Results and Discussions

The objective of this proof-of-concept is to simulate a batch reactor to convert corn stover into glucose using a biological pathway. The data and reaction schemes used for this operation are adopted from a previous contribution (Kadam, Rydholm, and McMillan 2004). Hence, the exploratory goal is to recreate a profile that can portray the original experimental outcome from the literature. A major segment of the process simulation (cellulose hydrolysis) is run to establish the compatibility of this integration. The conversion of cellulose and production of glucose is tracked with respect to the operation time (7 days).

The results from the simulation are plotted to compare with the findings in the literature (Kadam, Rydholm, and McMillan 2004). It is observed that the variations in the

reproduced data are minimal and the accumulation of glucose in the reactor is consistent with the original data. In the perspective of the overall outlook, this is a preliminary success. Nevertheless, this outcome translates into a greater contribution, as it justifies an interconnection and a potential avenue for researchers to validate and assess the viability of their innovations. Figure 2 shows the generated concentration profiles followed by the potential economic results that can be achieved by such implementation.

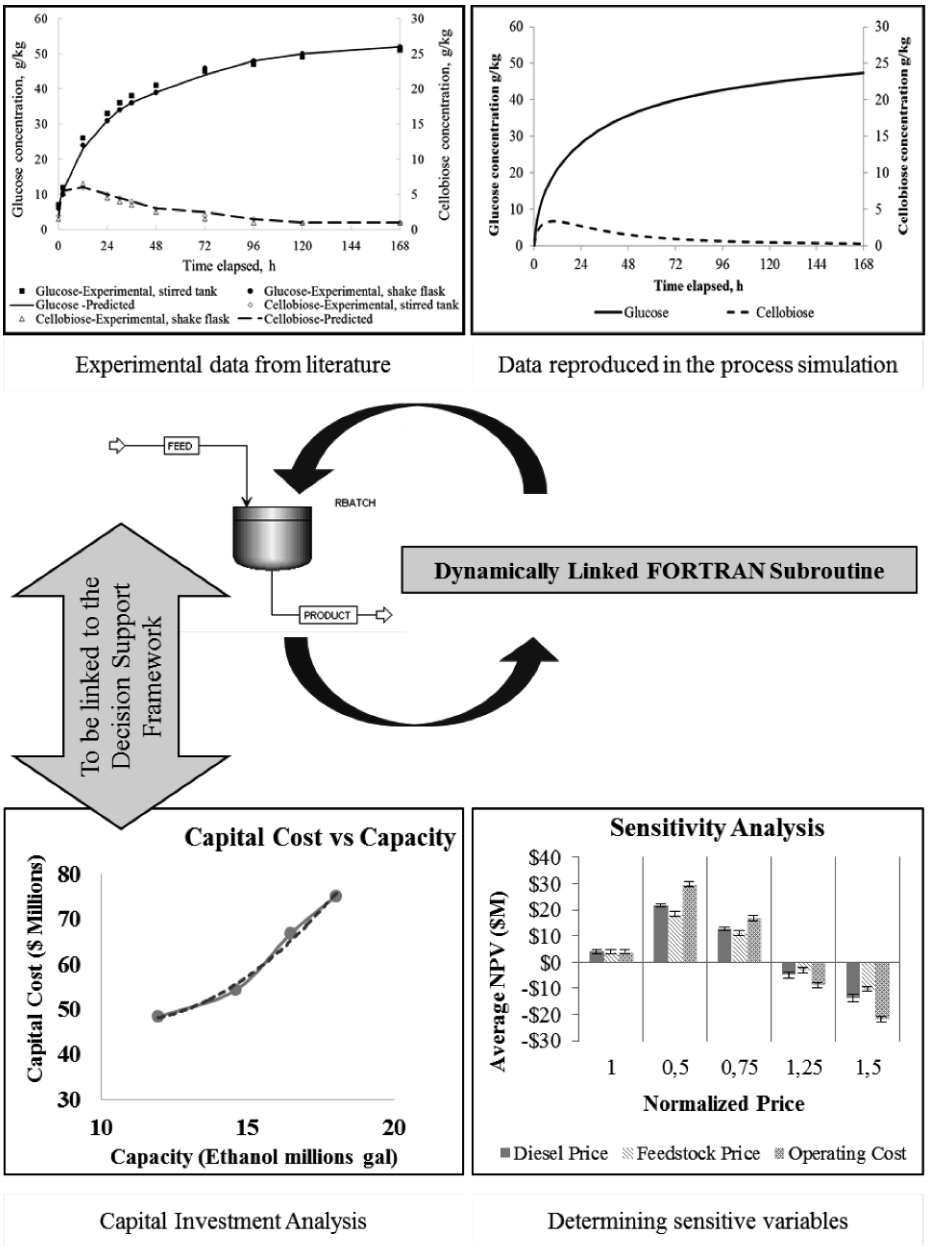

Figure 2. Results on the experimental work from the literature

Note: The top left plot shows the data and predicted trends from the literature (Kadam, Rydholm, and McMillan 2004). The top right plot is the recreated work using the Aspen Plus® user-defined (FORTRAN) function. Bottom plots elaborate on the nature of results that can be determined using this unique integration.

5. Conclusions and Future Work

In conclusion, this contribution demonstrates one of the promising integrations that can be established with the decision support tool to enhance the resolution of the input which in-turn will translate into a practical and bolstered assessment scheme. The contribution paves one pathway to link the fundamental research with an indicator that can answer a range of questions pertaining to the economic viability of a process in a region. This is one of the several potential approaches which captures and couples the discrete domains of basic science and engineering. Similarly, several other user-defined models for processes, such as, fermentation and product purification can be coupled to the framework making it an ideal test venue. In the future, several other novel discovery schemes could be justified to evaluate the feasibility, operability and sustainability of discovered pathways from biomass to biofuels, energy and chemicals.

References

Abdehagh, Niloofar, F. Handan Tezel, and Jules Thibault. 2014. "Separation Techniques in Butanol Production: Challenges and Developments." *Biomass and Bioenergy* 60 (January): 222–46. doi:10.1016/j.biombioe.2013.10.003.

Amundson, Joseph S. 2013. "Modeling of Biorefinery Supply Chain Economic Performance with Discrete Event Simulation." Masters Thesis, University of Kentucky, Lexington, KY, USA

Faulkner, William H. 2012. "Economic Modeling & Optimization of a Region Specific Multi-Feedstock Biorefinery Supply Chain." Masters Thesis, University of Kentucky, Lexington, KY, USA

Geraili, A., P. Sharma, and J.A. Romagnoli. 2014. "Technology Analysis of Integrated Biorefineries through Process Simulation and Hybrid Optimization." *Energy* 73 (August): 145–59. doi:10.1016/j.energy.2014.05.114.

Kadam, Kiran L., Eric C. Rydholm, and James D. McMillan. 2004. "Development and Validation of a Kinetic Model for Enzymatic Saccharification of Lignocellulosic Biomass." *Biotechnology Progress* 20 (3): 698–705.

Naik, S.N., Vaibhav V. Goud, Prasant K. Rout, and Ajay K. Dalai. 2010. "Production of First and Second Generation Biofuels: A Comprehensive Review." *Renewable and Sustainable Energy Reviews* 14 (2): 578–97. doi:10.1016/j.rser.2009.10.003.

Seay, Jeffrey R, and Fazleena F Badurdeen. 2014. "Current Trends and Directions in Achieving Sustainability in the Biofuel and Bioenergy Supply Chain." *Current Opinion in Chemical Engineering* 6 (November): 55–60. doi:10.1016/j.coche.2014.09.006.

Sukumara, Sumesh, William Faulkner, Joseph Amundson, Fazleena Badurdeen, and Jeffrey Seay. 2014. "A Multidisciplinary Decision Support Tool for Evaluating Multiple Biorefinery Conversion Technologies and Supply Chain Performance." *Clean Technologies and Environmental Policy* 16 (6). Springer Verlag: 1027–44.

U.S. Energy Information, A. 2013. "Annual Energy Outlook 2013." *Office of Integrated and International Energy Analysis* 1: 1–244. doi:DOE/EIA-0383(2013).

Van Eijck, Janske, Bothwell Batidzirai, and André Faaij. 2014. "Current and Future Economic Performance of First and Second Generation Biofuels in Developing Countries." *Applied Energy* 135 (0): 115–41. doi:http://dx.doi.org/10.1016/j.apenergy.2014.08.015.

Sukumara, Sumesh. 2014. "A Multidisciplinary Techno-Economic Decision Support Tool for Validating Long-Term Economic Viability of Biorefining Processes" PhD Dissertation, University of Kentucky, Lexington, KY, USA

Krist V. Gernaey, Jakob K. Huusom and Rafiqul Gani (Eds.), 12th International Symposium on Process Systems Engineering and 25th European Symposium on Computer Aided Process Engineering.
31 May – 4 June 2015, Copenhagen, Denmark

A Rescheduling Approach for a Large-scale Reverse Osmosis Desalination Plant under Uncertain Fresh Water Demand

Jian Wang, Aipeng Jiang, Lekai Lian, Guohui Huang,Qiang Ding, Shu Jiangzhou

College of Automation, Hangzhou Dianzi University, Hangzhou 310018, China

Abstract

The scheduling problem of a large-scale seawater reverse osmosis (SWRO) desalination plant is considered as a mixed-integer nonlinear programming problem (MINLP) over the time horizon. It is hard to find out the exact solution directly, especially when the working environment is changing. So, when the variables are changed, it is needed to find out a new scheduling plan quickly to meet the changes. In this paper, a rescheduling model of operational optimization of a large-scale SWRO is built, which is a bi-objective optimization with criterions of efficiency and stability. A rolling horizon approach (RHA) is used to make the solution meet the requirements of accuracy and rapidity. The framework of RHS is structured and a two-stage differential evolution (TSDE) algorithm is used to compute the solution. A simulation based on a real case with fluctuations in freshwater demand in Liuheng Seawater Desalination Plant in Zhejiang province was made, and the results show that the performance of the proposed algorithm is satisfied.

Keywords: reactive scheduling, reserve osmosis, rolling horizon approach, optimization

1. Introduction

There are many uncertainties in the seawater reverse osmosis (SWRO) desalination process (Sassi, 2013). When the uncertainty occurs, the scheduling made based on the steady states will not work well any more. A reschedule problem of SWRO desalination plant under uncertain freshwater demand is studied in this paper. The objective function of this optimization problem contemplates the dual combination of two performances: the optimization performance (OP) and the stability performance (SP). The OP is the total cost of plant, and the SP refers to the degree of deviation between the rescheduling and the original schedule. The rolling horizon approach (RHA) is an excellent method to speed the computation of scheduling problem (Suresh, 1997; Wang, 2005), so it is used to satisfy the requirement of quickly calculation in rescheduling. A case study shows the satisfied performances of the proposed approach.

2. Mathematical formulation

A large-scale SWRO desalination plant is usually structured with a number of independent RO units in parallel, as shown in Figure 1. Each RO unit has different permeate rate $Q_i(k)$. The water product flows into the storage tanks and is supplied to

users after pH adjusting and minerals adding. In this paper, we assume that the capacity of storage tank is large enough for freshwater supply to simplify the scheduling problem.

The operational optimization of SWRO desalination process is carried out by making a schedule to determine how the RO units work in a time horizon, *K*. In the schedule, the on/off state of each RO unit is determined, and if the RO unit is on, the optimal amount of produced fresh water of RO unit is proposed too. A hybrid scheduling approach is proposed to deal with the uncertain freshwater demand, which consists of two parts: a predictive schedule with redundant freshwater to fit the low amplitude uncertainties and a reactive schedule with RHA to deal with high amplitude uncertainties.

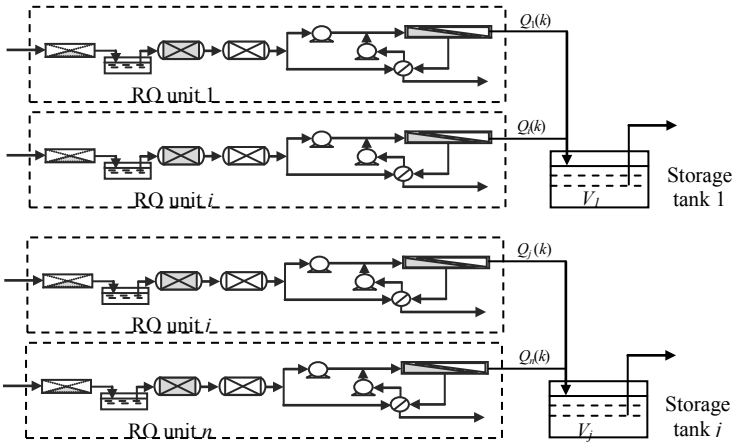

Figure 1: Schematic diagram of a large-scale SWRO desalination plant

2.1. Objective function

The objective function of this rescheduling problem includes two terms: optimization performance and stability performance. The purpose of the operational optimization is to minimize the objective function, which is presented as Eq.(1).

$$\textbf{min} \quad Obj = \alpha \cdot OP + \beta \cdot SP \tag{1}$$

Here, α and β are the weights of OP and SP respectively.

2.1.1. Optimization performance, OP

The OP of this problem is the total cost of plant, which consists of three main parts: the operational cost (OC), the energy cost (EC), and the default fine (DF), shown in Eq.(2).

$$OP = OC + EC + DF \tag{2}$$

The OC includes the maintenance expense when the machine runs and the cleaning & repairing expense when the machine stops. It is presented as Eq.(3).

$$OC = \sum_{k=1}^{K} \sum_{i=1}^{n} \left(\alpha_i(k) \times c_1 \times Q_i(k) + \left(1 - \alpha_i(k)\right) \times C_2 \right) \tag{3}$$

Where, K is the period of scheduling, n is the number of RO units. we consider that the maintenace expense is proportional to freshwater output $Q_i(k)$, and c_1 is the coefficient. The cleaning & repairing expense is a constant C_2. $\alpha_i(k)$ is the on/off status of Unit i at time k, $\alpha_i(k)$=1 when the Unit i is running; $\alpha_i(k)$=0 when it stops.

The EC is the consumption of electrical energy, which is presented as Eq.(4).

$$EC = \sum_{k=1}^{K}\left(P_e(k)\cdot \sum_{i=1}^{n}\left(\alpha_i(k)\times c_3 \times Q_i(k)\right)\right) \tag{4}$$

Where, $P_e(k)$ is electrical price at time k, and c_3 is the coefficient.

The DF is an additional compensation to the shortage of freshwater, which is presented as Eq.(5). Here, $\omega_{DF}(k)$ is the coefficient of default fine.

$$DF = \sum_{k=1}^{K}\omega_{DF}(k)\cdot\left(\left(D(k)+\xi\right) - \sum_{j=1}^{m} S_j(k), \right) \tag{5}$$

Where, ξ is the uncertainty of fresh water demand.

2.1.2. Stability performance, SP

The stability performance refers to the degree of deviation between the rescheduling and the original schedule (here is the predictive schedule), which is shown as Eq.(6).

$$SP = \sum_{\mathrm{k}=1}^{K}\left(\sum_{i=1}^{n} | \alpha_i^r(k)\times Q_i^r(k) - \alpha_i^p(k)\times Q_i^p(k) | + \sum_{j=1}^{m}\left| S_j^r(k) - S_j^p(k)\right| \right) \tag{6}$$

Where, $Q_i^r(k)$, $Q_i^p(k)$ is the amount of freshwater generated by Unit i at time k according the reschedule and predictive schedule respectively, $\alpha_i^r(k)$ and $\alpha_i^p(k)$ is the on/off status of Unit i at time k according the reschedule and predictive schedule respectively.

2.2. Constraints

The constraints include technical limitations and the design requirements, which are as follows.

The permeate rate $Q_i(k)$ of Unit i at time k is subject to Eq.(7).

$$Q_{i,\min} \le Q_i(k) \le Q_{i,\max}, i = 1,2,\cdots,n; k = 1,2,\cdots,K \tag{7}$$

Where, $Q_{i,\max}$, $Q_{i,\min}$ are the upper and lower limits.

The storage tank capacity is subject to Eq.(8).

$$V_{j\min} \le V_j(k-1) + \sum_{i=1}^{n_j}\alpha_i(k)\cdot Q_i(k) - S_j(k) \le V_{j\max}, j = 1,2,...,m; i = 1,2,...,n_j; \forall k \tag{8}$$

Where, $V_j(k)$ is the capacity of storage tank j at time k; $S_j(k) \geqslant 0$ is the supply of freshwater by storage tank j at time k. $V_{j\min}$ and $V_{j\max}$ are the lower and upper capacity limit of storage tank j.

2.3. Rescheduling approach

A reschedule approach is proposed to deal with uncertain fresh water demand in SWRO desalination process, which works as follow.

Step 1. Generating a baseline schedule (S_0) under a certain condition;

Step 2. Generating a predictive schedule (S_p) by adding redundancy amount of freshwater to deal with some low amplitude uncertainties; the added redundancy according Eq.(10).

$$Redu_i(k) = \frac{Q_i(k) \cdot \overline{R}}{\lambda} \tag{10}$$

Here, $\overline{R}$ is the average amount of changed freshwater demand of each RO unit ($\overline{R} = \omega_{re} R / n$, here R is the total changed amount of freshwater demand, ω_{re} is the coefficient), $1/\lambda$ is probability of freshwater demand changing.

Step 3. When uncertainty happens, a criterion is used to judge whether the reactive schedule should be triggered. If necessary, a RHA is used to build a reschedule; otherwise, operating machines according to predictive schedule S_p.

When the real increment of freshwater demand is higher than $\Sigma Redu_i(k)$ at time k, the reschedule will be triggered, and a RHA works in the following steps.

Step 1. Dividing the remained schedule problem into a series local sub schedule S_r with a K' time horizon as its optimal operation period (here, $K' << K$) ;

Step 2. Computing the rescheduling sub problem to get local rescheduling S_r, then implementing a portion of this reschedule S_i to operate the equipments;

Step 3. If the all the sub scheduling are finished, stop; otherwise, repeat Step 1-3.

The rescheduling horizon and implementing horizon are shown in figure 2.

3. Experimentation and discussion

Here, we take a case in Liuheng Island for numerical experimentation (see details in (Wang, 2013)), which has a capacity of 100,000 m^3 freshwater per day provided by a parallel-unit SWRO desalination plant with 8 RO units. The maintenance plan of RO units is made in advance.

The scheduling time period is K=24, the rescheduling horizon K' is 12, and the implementing horizon is l=1. The objective function of rescheduling is shown as Eq.(1),

let α=β=0.5, $\omega_{DF}(k)$=3.65, ω_{re} =0.01. Assuming the occurrence probability of the uncertainty obeys the exponential distribution D_e and the uncertain amount of change of freshwater demand, ξ, obeys the uniform distribution D_u.

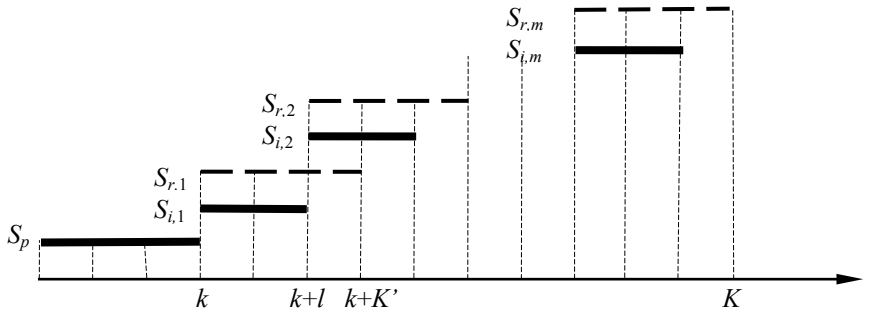

Figure 2: Schematic presentation of rescheduling horizon and implementing horizon

The probability density function of D_e is described by Eq. (11).

$$f_e(x)=\begin{cases}\lambda\cdot x^{e-\lambda x} & x>0\\ 0 & x\le 0\end{cases} \tag{11}$$

The probability density function of D_u is given by Eq. (12).

$$f_u(x)=\frac{1}{b-a}\quad a\le x\le b \tag{12}$$

Here, Eq.(5) is replaced by an expected value model Eq. (13).

$$DF=\sum_{k=1}^{K}\omega_{DF}(k)\cdot\left(\left(D(k)+\mathrm{E}(\xi)\right)-\sum_{j=1}^{m}S_j(k),\right) \tag{13}$$

And, the E(ξ) is described by Eq.(14).

$$E(\xi)=\left(1-\frac{1}{\lambda}\right)\cdot D(k)+\frac{1}{\lambda}\cdot\left(D(k)+\frac{a+b}{2}\right) \tag{14}$$

Here, we use a TSDE algorithm (Wang, 2014) to solve the scheduling problem. The parameters of TSDE are as follows: the maximum number of iterations G_1=300, G_2=700, the population size NP=100, the mutation factor F= 0.1, the crossover rate CR= 0.9, the length of individual D=20, that is, each individual consists of 20 variables: the first 8 variables are real values to represent the amounts of freshwater generated by 8 RO units, the next 8 variables are binary variables representing the on/off states of 8 RO units, and the last 4 variables are real values representing the supplied freshwater by storage tanks.

A comparison of rescheduling with RHA (Case A) and the traditional schedule (Case B, a simulation of workers operating: without adding redundancy, rescheduling when the freshwater demand changes) is shown in table 1 under different conditions. The algorithm is coded in MATLAB R2012 and executed in HP desktop 6300 MT with Intel Core i5-3470 CPU @3.2 GHz and 4 GB RAM. Each of algorithm runs 20 times.

From table 1, it is obvious that the reschedule algorithm has better performance than the traditional schedule, especially for bigger λ values and larger range of (a,b). Additionally, Case A is more time-saving than Case B.

Table 1 the comparisons of different schedules

$[\lambda, (a,b)]$	schedule	Best /￥/×10^4	Worst /￥/×10^4	Meanvalue /￥/×10^4	Std.dev.	Time /s
[0.5,(0,200)]	Case A	93135	94523	93396.8	154.1	423
	Case B	94325	96187	95749.2	138.6	2835
[0.5,(-150,450)]	Case A	88900	89873	89328.8	125.3	438
	Case B	92313	93983	92222.4	189.7	3092
[1.25, (0,200)]	Case A	88166	89365	88381.2	129.7	416
	Case B	93452	94689	93690.4	194	2926
[1.25,(-150,450)]	Case A	89945	91368	90286.2	117.9	433
	Case B	93046	93785	93398.2	137.1	3018

4. Conclusions

This paper discusses the rescheduling problem of a large-scale SWRO desalination plant under uncertain freshwater demand. A rescheduling approach is used to deal with it. A RHA was involved to shorten the computing time by replacing the global scheduling with a series of local schedulings. Experimental results show that the proposed method is satisfactory in solution quality and time consumption. The real-time maintenance plan should be taken into account in future works.

Conflict of interest

The authors declared that they have no conflicts of interest to this work.

References

B. Wang, Y. G. Xi, H. Y. Gu, 2005, An improved rolling horizon procedure for single-machine scheduling with release times. Control and Decision 20, 257–260

C. Suresh, T. Rodney, U. Reha, 1997, Rolling horizon procedures for the single machine deterministic total completion time scheduling problem with release dates. Annals of Operations Research 70, 115–125

J. Wang, X. L. Wang, 2013, Design of Monitoring and Scheduling System for a Large-scale Reverse Osmosis Desalination Plant, Proce. of 32nd China Control Conference, 2480–2485

J. Wang, X. L. Wang, A. P. Jiang, S. Jiangzhou, P. Li, 2014, Operational optimization of large-scale parallel-unit SWRO desalination plant using differential evolution algorithm. Sci. World. J 2014, 1–14

K. M. Sassi, I. M. Mujtaba, 2013, Optimal operation of RO system with daily variation of freshwater demand and seawater temperature, Comp & Chem Eng 59, 101–110

Krist V. Gernaey, Jakob K. Huusom and Rafiqul Gani (Eds.), 12th International Symposium on Process Systems Engineering and 25th European Symposium on Computer Aided Process Engineering. 31 May – 4 June 2015, Copenhagen, Denmark

Water Exchanges in Eco-industrial Parks through Multiobjective Optimization and Game Theory

Manuel Ramos,[a] Marianne Boix,[a] Didier Aussel,[b] Ludovic Montastruc,[a] Patrick Vilamajo,[b] Serge Domenech[a]

[a] *Laboratoire de Génie Chimique, U.M.R. 5503 CNRS/INP/UPS, Université de Toulouse, 4, Allée Emile Monso, 31432 Toulouse Cedex 4, France*
[b] *Laboratoire PROMES, UPR CNRS 8521, Université de Perpignan, Via Domitia, 66100 Perpignan, France*

Abstract

The current environmental context makes urgent the development of robust methodologies able to design innovative industries. Industrial ecology, and most particularly the concept of eco-industrial parks, aims at proposing at several companies to gather in a same geographical site to share several fluxes (water, energy, utilities…) in order to decrease environmental impacts of their industrial activities. A recent literature analysis has shown the emergence of new works devoted to the application of optimization methodologies to design greener and more efficient eco-industrial parks. In this work, the method of goal programming is applied for the first time to design optimal exchanges of water in an academic case of park. Goal programming is employed to deal with several conflicting objectives: the cost for each company included in the park. This method is proven to be reliable in this context because it proposes to obtain one solution instead of a set of optimal solutions that takes directly into account the preferences of the decision maker. Although the solution obtained in this study is quite interesting and is a good compromise, the main perspective of this work is to be extended by being coupled with a game theory approach so that an more equilibrate solution can be obtained.

Keywords: Eco-industrial Park, Water Network, Multiobjective Optimization, Goal Programming, Game theory

1. Introduction

Over the past ten years, most industrialized countries have invested heavily in environmental research thanks to a general awareness about natural resources depletion. Especially in the case of fresh water, there is a real need to reduce its consumption by redefining and designing industrial networks with a low environmental impact. In response to these environmental problems, the concept of industrial ecology is born. Frosch and Gallapoulos (1989) initiated the scientific community to look very closely at the gathering of industries with a common goal of sustainable development. During the last twenty years, many terms and concepts have emerged in the broad field of industrial ecology. Eco-industrial parks (EIP) are a particular manifestation of industrial ecology and a definition commonly admitted was given by Lowe (1997) as: "A community of manufacturing and service businesses seeking enhanced environmental and economic performance through collaboration in managing environmental and resource issues including energy, water, and materials. By working together, the community of businesses seeks a collective benefit that is greater than the sum of the individual

benefits each company would realize if it optimized its individual performance only." Since these preliminary studies, a lot of concrete examples have emerged through the world including the most famous example of the EIP of Kalundborg in Denmark. Other successful examples even more numerous are built all over the world. Most of them were built in industrialized countries of North America, Europe, or Australia but more recently it is in developing countries that many parks are born (such as China, Brazil and Korea for example).

The approach adopted in this work consists in designing optimal EIP networks (carrying water or energy) before its manufacturing. Optimization methods are then implemented in this context so that optimal networks for EIP can be designed. For a most extended bibliographic review to optimization methods applied to the design of eco industrial parks, the reader can refer to Boix et al. (2015). In this study the increasing interest for this research field during the past few years is highlighted. Figure 1 illustrates the number of studies published and cited during the fifteen past years with "optimization" and "eco industrial parks" keywords in the ISI Web of Science database.

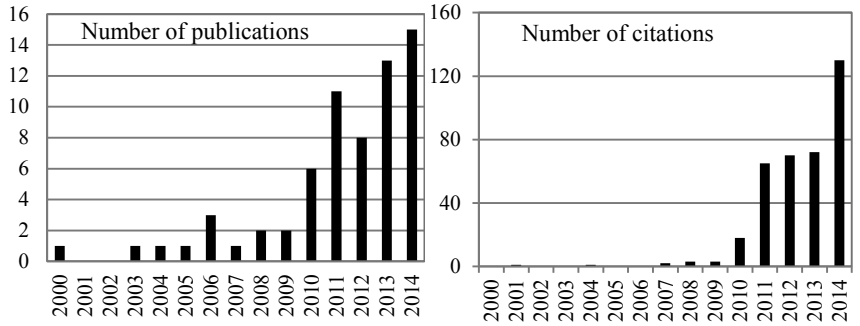

Figure 1. Number of articles referenced in the last 15 years with the keywords: "optimization" and "eco industrial park" (from Boix et al., 2015).

This paper aims at proposing a new methodology to deal with multiobjective optimization of eco-industrial parks. The first part is devoted to the presentation of objective functions, the superstructure and the methodology adopted. Then, a case study illustrates some results applied to the optimal design of a water network in an EIP.

2. Methodology

2.1. Objective functions

The analysis of previous studies has proven the existence of several types of objective functions. The most common is related to the economic cost, one can cite for example: profit of each industry, profit for the local community, transport and logistics or the net present value. However, although the economic cost remains very important for the feasibility of the project, in the context of industrial ecology, many other objectives can also be important. Objective functions in this type of problem are antagonist like for example, the economic cost versus environmental objective. Environmental objectives can be formulated through different ways: minimizing natural resources consumption (water), minimizing greenhouse gases emissions, minimizing water footprint or minimizing health and safety impacts. Another important aspect relative to sustainability development is the social and/or societal criterion. Although most of the time more qualitative than quantitative, social objectives are quite important and include the quality of life of workers, an index of satisfaction for the different participants

(Aviso et al., 2013) or the number of jobs created for example. Finally, topological objectives can also be taken into account as in the work of Boix et al. (2012) so that the network remains feasible.

2.2. Modeling eco-industrial parks

Modeling eco-industrial parks is somewhat a complex problem because of its size (thousands of variables, constraints and hundreds of binary variables) and the number of objectives to take into account. In order to model the network of an EIP, the concept of superstructure is used, it represents all the possible alternatives to connect each process of the network, this systemic approach allows to represent process design. Figure 2 shows the superstructure of an EIP including 3 industries and each industry is composed of process and regeneration units.

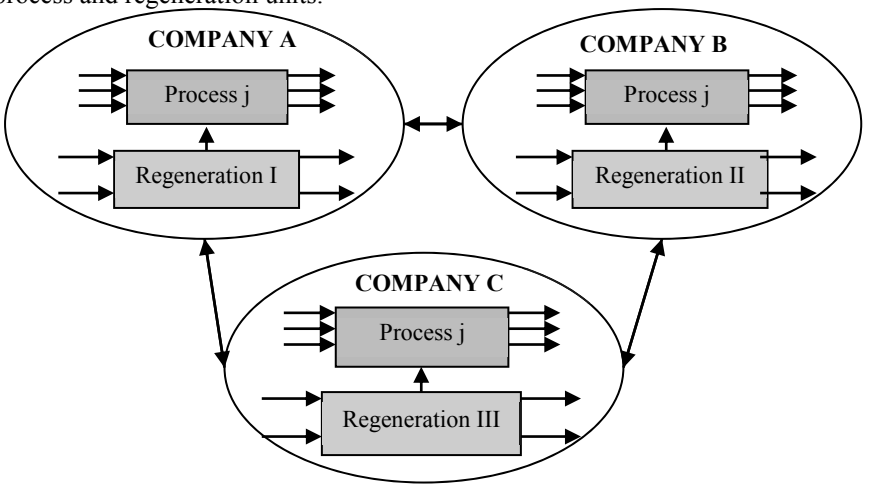

Figure 2.General superstructure of an EIP including 3 industries

After modeling the superstructure, the next step is to model the network with mass balances so that mathematical programming methods can be applied. A "black box" approach is adopted so that each parameter of the different processes are known, for more precision about the modeling stage, the reader can refer to Boix et al. (2012).

2.3. Multi-objective optimization approaches

Resolution methodologies for multiobjective optimization are generally classified depending on the number of generated solutions and on the importance of the decision maker during the resolution. These approaches can be classified into two categories:

- **Generative approaches**: these methods are characterized by the generation of different solutions and the decision maker has to choose one solution among them. These "a posteriori" methods include scalar approaches like weighting method or the epsilon-constraint strategy coupled with mathematical programming and stochastic methods like genetic algorithm. With these methods, a Pareto front is built to propose a set of non-dominated solutions to the decision maker.
- **Preference-based methods**: in this case, decision maker preferences are included along with the resolution and the optimization. These "a priori" approaches like for example, goal programming or interactive methods like NIMBUS directly include the decision maker preferences during the resolution so that one solution is

finally obtained. In this work, we propose to adopt the goal programming approach to solve the case of water allocation in eco industrial parks.

2.4. Characteristics of eco-industrial parks

Boix et al., 2015 highlighted the lack of studies dealing with optimization in order to design optimal configuration of an EIP. However, it is important to develop methodologies able to design an EIP where each industry has a gain compared to the case where it is individual. Furthermore, each company included in a park has its own objective (for example to minimize its costs) and all of these objectives are always antagonists. In this work, a multiobjective optimization approach is adopted in order to take into account each objective function associated to each company of the EIP. This approach has already been applied to the design of industrial water networks but never with the optimal design of the water network in an EIP which is a different problem.

The optimization of eco-industrial parks includes several bottlenecks: one of the main characteristic of this problem is that the structure (represented by the existence or not of connections between processes and numerically modeled by binary variables) is dominating the solution. The resulting model is large and of MILP (mixed integer linear programming) type which constitute a great challenge and it is relatively new to solve this problem with the help of preference-based approaches. Indeed, previous studies have widely explored generation based approaches but some numerical problems were encountered especially when problems involve many binary variables. In most of the cases, the solver does not succeed to return a feasible solution and when it succeeds to build the Pareto front, it remains a very long and tedious task.

In this work, a goal programming (GP) approach is adopted to obtain one solution that already includes the preferences of the decision maker. This approach is based on a recent study (Ramos et al., 2014) where it has been proven that GP can be a very reliable method to design industrial water networks following multiple antagonist objective functions.

Based on an academic example, this paper explores 3 different scenarios of an EIP in order to point out the difficulties encountered with multiobjective optimization of EIP's.

3. Multiobjective optimization through goal programming

3.1. Presentation of the case study

In this study, an EIP including 3 companies is designed, this academic example has been widely explored in the literature (Olesen and Polley, 1996; Boix et al., 2012). For this reason, it remains a good example to test and to validate a new methodology because solutions are well-known. Each company is composed of 5 process units and the parameters are the same as those defined in Boix et al. (2012).

Three different scenarios are explored (Figure 3), where the position of the regeneration unit differs, so that all the configurations are scanned :

- ***Scenario 1***: the three companies exchange water and each company owns its regeneration unit, chosen among three available types (depending on the outlet concentration);
- ***Scenario 2***: the three companies exchange water and share one regeneration unit;
- ***Scenario 3***: a mixed scenario where each company owns its regeneration unit and an additional unit is shared by the three companies.

It is important to notice that for each above mentioned scenario, three objective functions are minimized: the total cost of each company involved in the EIP.

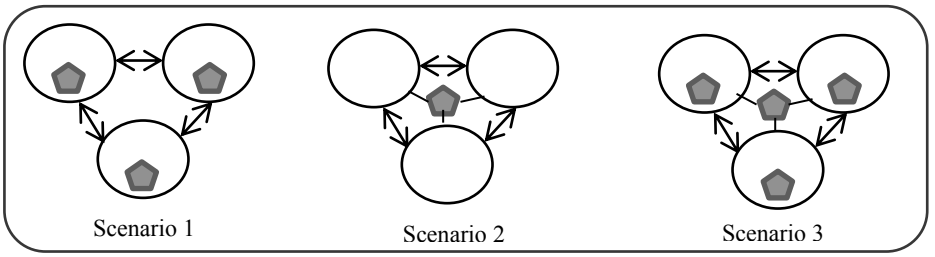

Figure 3. Different configurations of the EIP

In order to show that these objectives are antagonists, table 1 represents the pay-off table that include the values of two objectives while the third is minimized for scenario 2.

Table 1. Pay-off table for scenario 1 (the value in bold is minimized for each line)

Pay-off table	*Cost for ind. A*	*Cost for ind. B*	*Cost for ind.C*
Cost A	**1.143**	4.334	16.985
Cost B	9.349	**1.138**	8.223
Cost C	10.353	9.942	**1.154**

This cost takes into account: fresh water consumption, regenerated water flow rate, cost of external and internal connections between processes and the capital cost of regeneration units.

3.2. Results with the goal programming approach

Results obtained with the goal programming approach are summed up in table 3. Mono-objective optimizations were carried out in a first step in order to obtain minimal (utopia) and maximal (nadir) values of each objective function, that is to say the minimal cost of each company when it is included in the EIP. Then, the goal programming methodology allows to have one solution for each scenario. It is important to note that the optimal solution found by GP leads to an intermediate solutions where all the companies are closed to their personal objective.

Table 2. Results of the multiobjective optimization of the EIP through goal programming, cost are expressed in M$.

	Scenario 1			**Scenario 2**			**Scenario 3**		
	Min	Max	**Solution GP**	Min	Max	**Solution GP**	Min	Max	**Solution GP**
Cost for company A	1.51	6.96	**1.85**	1.14	13.78	**1.98**	1.14	16.09	**2.85**
Cost for company B	1.14	7.05	**1.51**	1.14	6.82	**1.32**	1.14	4.35	**1.34**
Cost for company C	2.81	14.13	**3.52**	1.15	15.36	**2.98**	1.15	12.42	**1.96**

The main interest of this study is to note that for each scenario, one company is favored compared to others. In scenario 1, company A is the closest from its objective whereas in scenarios 2 and 3, it is the company C. Goal programming has been proven to be an efficient approach to design water exchanges in EIP through multiobjective

optimization. Furthermore, it proposes a unique solution that satisfies a goal in very low computational times. Although the optimal solutions are intermediate and satisfying in terms of individual costs, it is of great interest to obtain more balanced solutions so that each company is satisfied at the same time.

3.3. A game theory perspective

Game theory could be a promising approach, particularly adapted to the case of the design of exchanges in an EIP. Several methods can be adopted like a non cooperative approach to preserve confidentiality of companies (Figure 4). Furthermore, the main barrier to integrate an EIP for industry is the lack of confidentiality and this approach could be very promising to overcome this problem. This approach could be useful to overcome the difficulties linked to information exchanges between companies in an IEP. However, it is important to deal with an authority that attends to minimize environmental impacts of the EIP. The existence of an optimal solution satisfying Nash equilibrium could insure that none of each company is prejudiced compared to others.

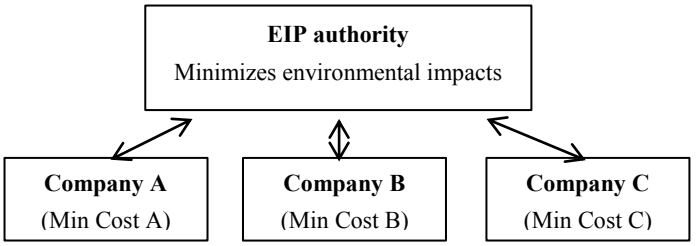

Figure 4. Example of a non cooperative approach to model an EIP through game theory.

4. Conclusions

In this study, water exchanges in an EIP have been optimized by minimizing three objective functions with a goal programming approach. Goal programming is a reliable method of multiobjective optimization and it had been proven to be efficient to find optimal solutions to complex problems. This study dealt with a well-known example to prove the efficiency of the methodology and to make a preliminary study in order to apply further a game theory approach to this work. The development of this method could be coupled with a game theory approach in order to obtain more equilibrate results where no company is favoured to another following the concept of Nash equilibrium.

References

Aviso, K.B., 2013, Design of robust water exchange networks for eco-industrial symbiosis, Proc. Safety Environ. Protect., 92, 160-170.

Boix, M., Montastruc, L., Pibouleau, L., Azzaro-Pantel, C., Domenech, S., 2012, Industrial water management by multiobjective optimization: from individual to collective solution through eco-industrial parks, J. Clean. Prod. 22, 85–97.

Boix, M., Montastruc L, Azzaro-Pantel C, Domenech S, 2015, Optimization methods applied to the design of eco-industrial parks: a literature review, J. Clean. Prod. 87, 303-317.

Frosh, R.A., Gallopoulos, N.E., 1989, Strategies for manufacturing, Sci. Am. 261, 144-152.

Lowe, E.A., 1997, Creating by-product resource exchanges: strategies for eco-industrial parks, J. Clean. Prod., 5, 57–65.

Olesen, S.G., Polley, G.T., 1996, Dealing with plant geography and piping constraints in water network design, Trans. Ind. Chem. Eng., 74, 273-276.

Ramos, M.A., Boix, M., Montastruc, L., Domenech, S., 2014, Multiobjective optimization using goal programming for industrial water network design, Ind. Eng. Chem. Res., 53, 17722-735.

Krist V. Gernaey, Jakob K. Huusom and Rafiqul Gani (Eds.), 12th International Symposium on Process Systems Engineering and 25th European Symposium on Computer Aided Process Engineering.
31 May – 4 June 2015, Copenhagen, Denmark

Conceptual Design of Cost-effective and Environmentally-friendly Configurations for an Integrated Industrial Complex

Chen Chen, Ross Wakelin

Northern Research Institute Narvik AS. Postboks 250, NO-8504 Narvik, Norway.

Abstract

An integrated industrial production complex with natural gas and locally sourced minerals as the main raw materials was studied. Eleven processes including a central synthesis gas plant which uses natural gas were examined in optimization studies considering the exchange of materials and energy. The optimizations included consideration of financial and environmental impacts as well as robustness to unplanned production stops in individual processes.

Material balances for the various chemical processes were built up based on data from literature sources with the production scales assumed according to estimated market demand and economy of scale. Energy quantities and the quality of the streams in and out of the processes were also calculated and are presented in the paper. The potential for material and energy savings by exchange between different processes is quantified by a spreadsheet. The optimization is made using input data from the spreadsheet in Java-based MILP software (reMIND). Apart from improved economic profits, the cases are analyzed also with respect to carbon dioxide emissions and energy requirement in the objective function. A sensitivity analysis examined the response of the financial profit, energy consumption and CO_2 emissions to different operating conditions.

While there are benefits from the integration of the processes, the dependency between different plants also results in exposure to unplanned stoppages by connected processes. The allocation of benefits and liabilities between processes could be calculated in a fair and transparent way by using the model.

Keywords: multi-objective, integration, reMIND

1. Introduction

Norway as the largest source of oil and natural gas reserves in Europe provides gas to all of the major consumer countries in Western Europe. Norwegian gas export covers close to 20 percent of European gas consumption. In contrast, only 1.2% of total Norwegian gas production is consumed in the country (NPD, 2013). The high export of natural gas from Norway and low utilization domestically makes it topical to investigate an added-value integrated industrial complex based on natural gas. With regard to the local situation, the Nordland region is rich in mineral resources and hydroelectric power and is one of the largest export provinces in Norway. In addition the petroleum extraction activities are moving to fields off the coast of Northern Norway. All these conditions support the relevance of a study of the integration of a conceptual industrial production complex with natural gas and locally sourced minerals.

The design of the proposed industrial complex including eleven different chemical processes is aimed at an annual consumption of natural gas around 2-5 billion Sm^3 both as raw materials for chemical reactions and fuel for heating. This amount of natural gas

is considered necessary to justify the costs of building a branch pipeline. More detailed background to the study can be found in an earlier publication publication (Chen and Wakelin, 2013).

2. Method

Material balances for the chemical processes studied were based on data from literature sources with the production scales assumed according to estimated market demand and economy of scale. Energy quantities for the main streams for each process were also calculated and are presented in Figure 3. The potential for financial and energy savings, along with the reduction of CO_2 emissions by exchange between different processes is quantified. A sensitivity analysis of these targets to different operating conditions has also been examined. It is possible to use the model to analyze the industrial complex in order to utilize the internal flexibility for optimization of the operation.

A central process in the study is the production of direct reduced iron (DRI) based on natural gas and iron ore that is currently transported via the ice-free Narvik harbor from mines in Northern Sweden. The DRI produced can either be used in electric arc furnaces for steel production or exported. The other main mineral resources included in the project are carbonates. Based on the large deposits of this mineral in Narvik region (Schaller, A., et al., 2011), it is proposed to produce precipitated calcium carbonate (PCC) with utilization of lower grade carbonates as flux for steel production. Other processes selected to be included in the conceptual complex were mainly for efficient utilization of the syngas and heat as can be seen in Figure 1.

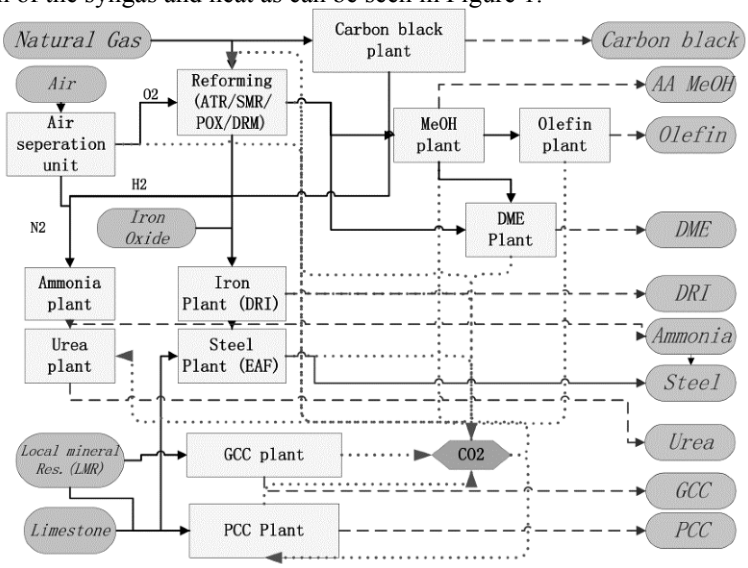

Figure 1 Flow sheet of processes included in the current model

The integration of the processes assists the efficient and profitable utilization of the natural resources by the exchange of by-product materials and energy. The main objective of this study is to quantify the potential savings possible from process integration. Apart from direct cost reductions, savings in energy consumption and carbon dioxide emissions for the integrated production processes are also considered in the objective function. This function has not considered external sale of waste heat. But

the optimization has used the waste heat (of appropriate quality) to offset the consumption of natural gas for heating purposes.
The operational statuses of the individual plants were dependent on variables such as the prices of raw materials and products in the model. Thus, the amount of production is not fixed, instead an upper limit on capacity has been given on each processes except DRI which has a specific capacity set of 1.5 million t/y. Other intermediate products like crude methanol, ammonia in the system have been similarly been assigned 'either-or' choices.
Energy balances for all processes included in Figure 1 have been made with reference to various studies published in the literature on temperature and the pressure of reaction. The changes in enthalpy have been calculated from three parts while treating the reaction processes as black boxes at present. Raw materials are fed to processes after heating them in a preheater to a temperature that is 10°C lower than the reaction temperature. The products then leave the reactor at the temperatures and pressures determined by the various process conditions. It is assumed that the normal state of all the raw materials and products is 298 K and 0.1 MPa.
Enthalpy is a property of state of a substance, having the same value at a given temperature and pressure for a specific material. Then, neglecting work, potential energy and kinetic energy, the thermal energies involved in our study can be calculated based on the rule simplified from the energy balance shown in Figure 2a).

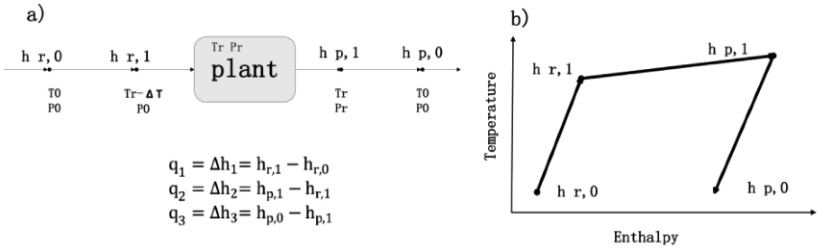

Figure 2a Definition of thermal energies in terms of enthalpy change; 2b Path for enthalpy change

The term q2 is the heat of reaction, while q1 and q3 are thermal energy changes associated with the change of status of inflow and outflow without chemical changes. The amounts of q1 and q3 indicate the potential of energy that could be saved by exchanging heat between high temperature and lower temperature flows, or reusing heat in other ways. Detailed information such as the temperature differences between exchange flows and the efficiency of the transformation of heat energy must be taken into account when considering how to save or use this heat. In the current model, the sum of heat (q1+q2+q3) was considered for each process. Heat from exothermic processes was considered as waste heat which potentially could be used by other processes in the integrated system. All endothermic reactions are assumed to obtain heat from burning natural gas, while pre-heating reactants could utilize waste heat streams.

3. Results

The main heat flows for the base case scenario (natural gas price 2500 NOK/t) is shown in Figure 3. Some exothermic processes with significant reaction heat can be used for steam production. As examples, POX and ammonia production can contribute 8% and 16% respectively of the total heat demand.
Sensitivity analyses for all the prices of raw materials and products have been made using the model. Most of those variables influence the total profit, the amount of CO_2

release and the operational status of different processes. A base case scenario was defined using the current prices of varied materials and other costs. Variation of this base case scenario with respect to natural gas prices greater or lower than 2500 NOK/t is shown in Figure 4a). As expected there is a gradual decrease in total profit with increasing natural gas price. The amounts of consumed and waste heat from the integrated complex are also plotted for each natural gas price level. For natural gas prices between 2500 and 4000 NOK/t the amount of heat consumed (and generated as waste heat) is approximately constant. The waste heat available is around 39% of the heat consumed, indicating potential for energy savings from heat integration. At natural gas prices lower than 1000 NOK/t the optimisation chooses to utilize Steam Methane Reforming (SMR) to generate synthesis gas, with higher heat and CO2 emissions. An increase of the natural gas price to 5000 NOK/t results in the stopping of ammonia production, which releases further heat for reuse.

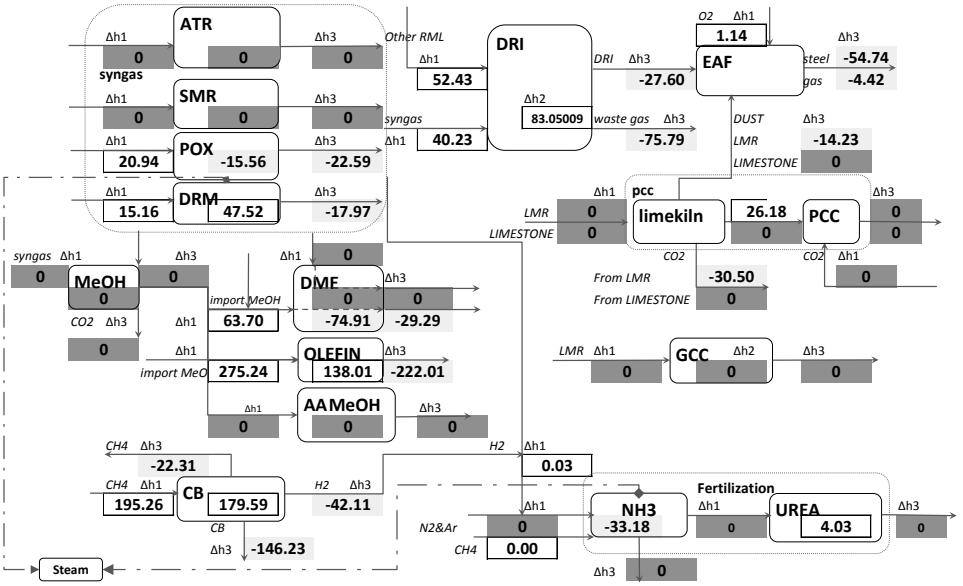

Figure 3 Heat flow in base condition (MJ/s)

Scenarios of CO_2 emission in terms of the total amount and due to burning of natural gas for heating are given in Figure 4b). Since the CO_2 emissions generated from natural gas combustion are the result of providing heat to the system, it shows the same tendency as the heat consumption with changing gas price. CO_2 emissions for a natural gas price under 1000 NOK/t are more than 8 times higher than those for natural gas prices between 2000 and 4000NOK/t, due to the operating characteristic of the Steam Methane Reforming. Once the natural gas price reaches a value of 5000NOK/t, an increase in CO_2 emission is observed due to the stoppage of urea production, which is a CO_2-consuming process. The urea CO_2-sink is also the reason for the net CO_2 emission from system being lower than would be expected from the amount of natural gas consumed.

An important issue within the integrated complex is the inter-dependency between different plants and the allocation of benefits and liabilities between processes. Thus, it is important to find a reasonable way to show the sharing between those processes. The costs for the EAF steel-mill production at the base case scenario is shown in Figure 5. A saving of about 18% on the total cost on steel producing can be seen when comparing

the result from an integrated system with independently operating processes for producing steel at the same capacity. The costs for steel production were divided into five main parts in Figure 5. The Air Separation Unit (ASU) and DRI processes provide the main reactants of oxygen and DRI, respectively to EAF. Meanwhile, the production of DRI is dependent on the up-stream process of syngas production which is selected to be partial oxygen reforming, which in the optimum situation also utilizes oxygen from the ASU.

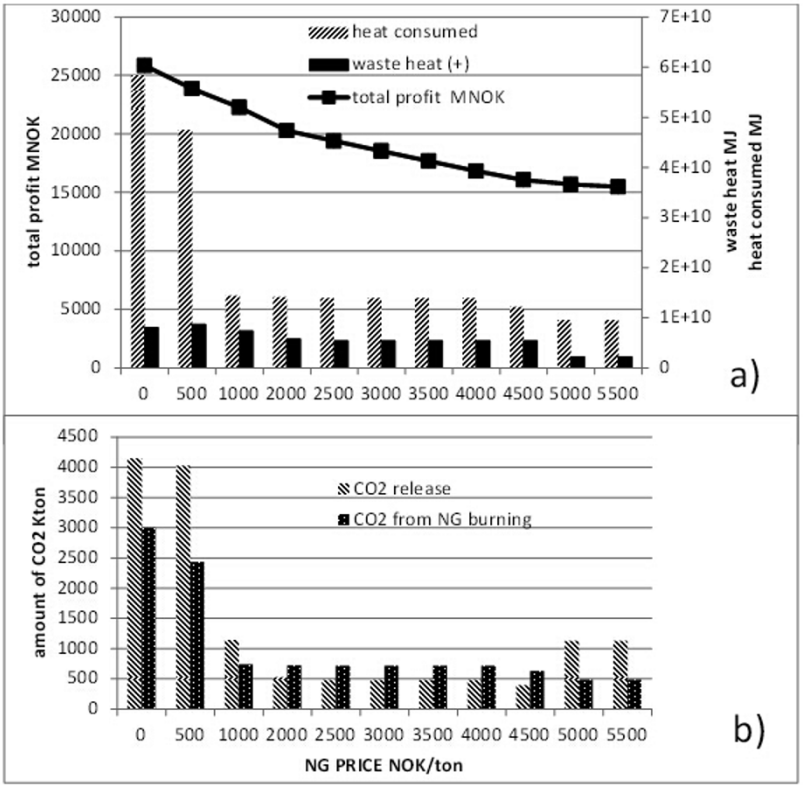

Figure 4 Scenarios of profit, heat, CO_2 and operational status at varied prices of natural gas

The costs or benefits of the up-stream processes were shared by the intermediate product consumer depending on the amount of products utilized, Eq.(1).

$$\text{Allocation of production cost of intermediate product} = \frac{\text{amount of product utilized}}{\text{total amount produced of same product}} \times \text{production cost of that product} \quad (1)$$

In the absence of ammonia production there is a considerable increase in the cost of the ASU, as the ammonia consumes the nitrogen that is 75% by weight of the ASU production. The increase in the specific capital cost of the ASU due to the reduction of production capacity also has been taken into consideration. The costs grouped under 'other' include the cost of raw materials and the cost of heat for the processes. The cost difference on this 'other' part is caused by the lower supply of waste carbonate from PCC processes, requiring the substitution of higher cost flux.

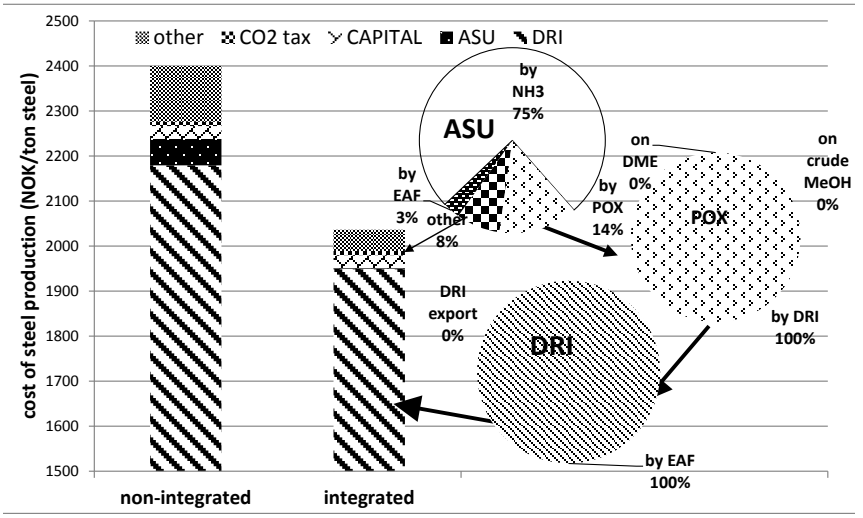

Figure 5 Cost distribution for steel production for the base-case scenario

4. Discussion and conclusion

The results of heat and CO_2 emission changes at various gas prices show a higher consumption of heat and emission of CO_2 from steam methane reforming, while still returning a higher overall economic result. On the other hand, the ammonia and urea processes show advantages from energy saving and CO_2 reduction. The potential for reuse of waste heat can cover as much as 39% of the heat consumed. However, the usability and efficiency on reuse of those heats will depend on their quality. Moreover, it is necessary to consider the influence of the geographical location on the potential for energy saving.

Savings on costs are obtained from several aspects such as effects of scale, sharing of intermediate-products and the utilization of by-products (waste) from other processes. The allocation of production costs for intermediate products used by different downstream processes was presented. In addition, costs arising from unplanned stoppage of specific plants can be included in the optimisation by setting the capacity constraint to zero. This enables the quantification of the contribution of each process to the overall optimal profitability of the system.

The optimisation model responds well to the influence of the variables changing under sensitivity analyses, resulting in different combinations of processes included in the chemical complex. Economic benefits obtained by the exchange of materials have been demonstrated and quantified. Reductions in CO_2 emissions were also observed due to the inclusion of some CO_2 consuming processes (urea production) running at some scenarios.

References

C. Chen, R. Wakelin, 2013, Conceptual Design of a Natural Gas-based Integrated Industry Park, Chemical Engineering Transactions, 35, 1237-1242.

Norwegian Petroleum Directorate (NPD), 2013.03, Facts 2013: the Norwegian petroleum sector, Gas export from the Norwegian shelf, <http://www.npd.no/en/publications/facts/facts-2013/chapter-7/>, accessed 20.01.2014.

A. Schaller, A. M. Raaness and A. Korneliussen, 2011, Description of drill cores from the Rolla and Evenes area, Troms and Nordland countries, NGU report, 2011.039, 177p.

Krist V. Gernaey, Jakob K. Huusom and Rafiqul Gani (Eds.), 12th International Symposium on Process Systems Engineering and 25th European Symposium on Computer Aided Process Engineering.
31 May – 4 June 2015, Copenhagen, Denmark

Modelling of Environmental Impacts and Economic Benefits of Fibre Reinforced Polymers Composite Recycling Pathways

Phuong Anh VO DONG[a], Catherine AZZARO-PANTEL[a], Marianne BOIX[a], Leslie JACQUEMIN[b], Serge DOMENECH[a]

[a] *Laboratoire de Génie Chimique, LGC UMR CNRS 5503 ENSIACET INPT, 4 allée Emile Monso, BP 84234, 31432 Toulouse Cedex 4, France*
[b] *Altran RESEARCH, 4 avenue Didier Daurat, Parc Centreda - Bâtiment Synapse, 31700 Blagnac, France*

Abstract

In the last few years, composites have been used increasingly in different applications (aerospace, automobile, industry, sports…). Both environmental and economic factors have driven the development of recycling pathways for the increasing amount of fibre reinforced polymer (FRP) scrap generated. A recycling system for FRP has to be designed to recover and reuse the fibre and matrix content of the scrap. The objective of this paper is to model and compare the different routes of end-of-life FRP from both environmental and economic viewpoint combining Life Cycle Assessment and Cost-Benefit Analysis. More precisely, mechanical recycling, pyrolysis and fluidized bed are investigated and compared to low value end-of-life solutions (incineration, co-incineration and landfill) both for Glass and Carbon FRPs. Pyrolysis turns out to be an attractive recycling solution for CFRP that satisfies both environmental and economic benefit while co-incineration seems more promising for GFRP.
Keywords: composite recycling, fibre reinforced polymers, waste management, environmental impacts, economic benefits

1. Introduction

Fibre reinforced polymers (FRP) are composite material made of polymer matrix reinforced with fibres. Due to their low density, FRP are increasingly used in structural applications to replace more conventional materials (steel, aluminium, alloys…) in order to design lighter products especially in the aeronautics sector. Despite all advantages associated with FRP, the increasing use generates also an increasing amount of FRP waste. Common sources of waste include out-of-date prepregs, manufacturing cut-offs, testing materials, production tools and end-of-life (EoL) components. The global demand of carbon fibres is expected to exceed production capacity in 2015 if growth remains at this rate and recycling could be a fibre supply solution in order to meet future demand (Black, 2012). However, the complex composition of FRP makes recycling more complex than typical thermoplastic recycling. Unlike thermoplastics, the thermoset FRP scrap cannot be melted down and remoulded, as is often done in plastic recycling. Most of the FRP waste is currently landfilled or incinerated but these solutions are far from being satisfactory from environmental, legislation and economic viewpoints (Yang et al., 2012).

The aim of this study is to use process systems engineering methods to model and compare the recycling pathways of Carbon Fibre Reinforced Polymers (CFRP) and Glass

Fibre Reinforced Polymers (GFRP). Unlike glass fibres that are generally ten times cheaper due to their simple fabrication by fusion, carbon fibres are high-value added products because of their high technical properties and complex production. Despite differences in fibre nature, the recycling techniques of these thermoset composites exhibit similar principles. Due to high durability of polymer matrix, the technologies like torrefaction and fast pyrolysis cannot be applied to FRP. The analysis of the relevant literature highlights that if technical solutions are readily available, they are developed at different scales of process maturity, i.e., industrial scale for mechanical recycling and pyrolysis, pilot and laboratory scales for fluidized bed and chemical recycling (Yang et al., 2012). More precisely, mechanical recycling, pyrolysis and fluidized bed are investigated and compared to low value EoL solutions (incineration, co-incineration and landfill) through a combined use of a Life Cycle Assessment (LCA) and a Cost-Benefit Analysis. The inventory, data collection will be described together with the evaluation of the economic and environmental impacts for the selected scenarios.

2. A methodological framework for recycling pathway evaluation

2.1. FRP recycling pathways

The recycling pathway alternatives considered in this work and the system boundaries are summarized in Figure 1. The recycling units are assumed to be located in France. The composite waste is cut on the dismantling site and then transported either to the landfill site or to any other recovery facility. All the different recycling technologies are assumed to be available to treat the FRP. The typical features of each process will be shortly presented together with the analysis.

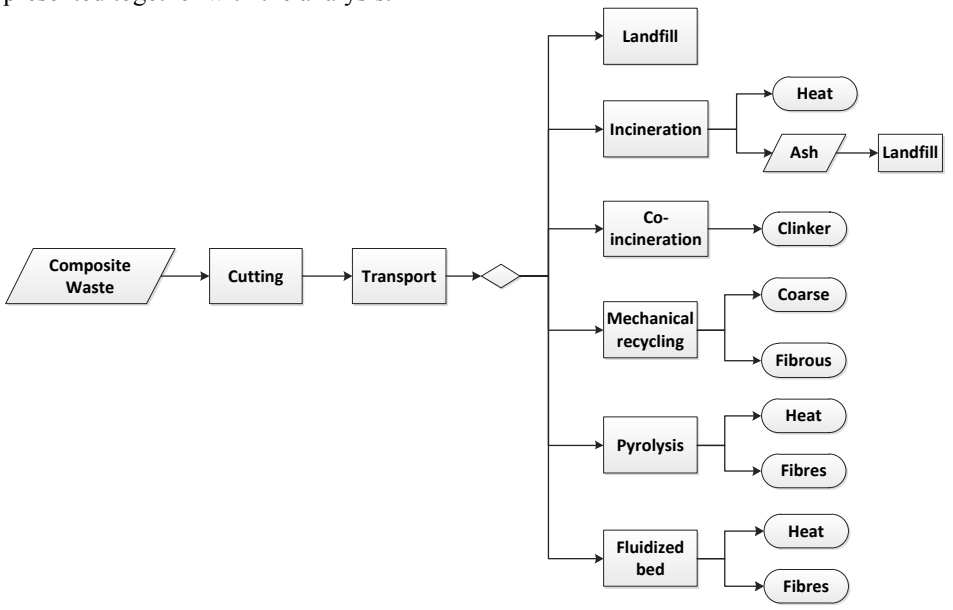

Figure 1: Recycling pathway alternatives and system boundaries

2.2. Life Cycle Assessment

The functional unit (FU) defined for this study is 1 kg of cured FRP waste to be treated by one of the proposed technology. A product life cycle consists in four individual phases: raw material extraction, production, utilization and EoL. Within the limits of this study,

only the environmental impacts of the EoL activities of the composite are assessed. Data on the energy requirements and emissions of the recovered product from the different waste scenarios were collected to analyse the influence of these paths. The calculations are based on elementary environmental impacts coupled with the LCA software SimaPro 7.3. Although LCA is identified as a multicriteria environmental management tool, the analysis is limited in this work to climate change impacts (CCI), evaluated on a kg CO_2 eq. basis performed by the ReCiPe Midpoint (H) v.1.06 assessment method.

2.3. Cost-benefit analysis

Cost-benefit analysis (CBA) is a simple method in which all expenses and incomes of an activity are considered to a cash balance (Farel et al., 2013). Its principle is summarized in Eq. (1).

$$CBA = \sum Benefits - \sum Costs \quad (1)$$

This allows determining whether an activity can promote economic profits or which solutions generate the most profit. This method is applied in this preliminary study to analyse the differences of economic benefits among the pathways of EoL composites. In this context, CBA is simplified and the total expenses are mainly based on the price of the process energy requirement and on the average cost of transport. The benefit of the recovery centres comes from the sale of recycled materials to the manufactures as raw materials and the savings of energy, i.e. "avoided energy", which is released from the production process.

3. Modelling FRP recycling processes and inventory data

3.1. General assumptions

Due to the lack of FRP specific data for recycling, the system is modelled by a "black-box" approach, i.e. changes in waste composition during the treatment are not considered, but only fixed input-output data of the system are studied in this preliminary study. In each process, input-output data are estimated both from typical operating conditions of the considered processed obtained from a literature survey and on the basis of the information available, from SimaPro database. Data were also collected from the European Environment Agency (EEA) and Eurostat. The cost of electricity from French average power mix (with 78 % rate from nuclear energy according to SimaPro 7.3) is fixed at 0.085 €/kWh (Eurostat, 2014). The composite waste is supposed to be a continuous fibre reinforced thermoset resin and composed of 60 vol% in fibre and 40 vol% of resin. No contaminant, metallic insert, flame retardant agent, hazardous substance and filler is considered in the composition of FRP waste. In this study, FRP waste is classified as a non-hazardous waste. In each scenario, the composite is firstly shredded with an amount of energy of 0.0025 MJ/kg (Witik et al., 2013) and then transported over a distance of 100 km from the site of dismantling to the site of treatment by a 40-ton truck with an average cost in Western Europe of 0.14 €/(t.km) (Schade et al., 2006). The avoided impacts and the prices of the recovered products are summarized in the Table 1.

Table 1: Prices and avoided impacts of the recovered products (Witik et al., 2011; Duflou et al., 2012; Job, 2013; SimaPro databases)

	Carbon fibre	Glass fibre	$CaCO_3$
Price (€/kg)	12	1.6	0.25
Climate change Impacts (kg CO_2 eq/kg)	22.4	2.6	0.0132

3.2. Recycling alternatives

3.2.1. Landfill

The environmental impacts of landfill are assessed by the model of "sanitary landfill of mixed plastics" extracted from SimaPro databases because composite material specific data were not available. The total charge of landfill in France is about 80.5 €/t according to EEA (2013).

3.2.2. Incineration

Incineration is a thermal process, which allows recovering energy in heat resulting of waste combustion. The heat can be used directly or converted into electricity. In this scenario, the heat from the process is converted to electricity with an efficiency of 35 % and the process is assumed to be auto-thermal. The emissions of 1 kg FRP from combustion are presented in Table 2. The ash by-product is landfilled as an inert waste.

Table 2: The outputs of 1 kg FRP incineration (Hedlund-Åström, 2005; Job, 2013)

	Ash (wt%)	CO2 emission (kg)	Net heat of combustion (MJ)
CFRP waste	9.65	3.39	31.7
GFRP waste	75	0.61	12

3.2.3. Co-incineration

Although incineration and co-incineration are both based on combustion of waste, co-incineration allows material recovery besides energy recovery. Indeed, in co-incineration, waste is used as a substituted fuel involved in clinker fabrication.

3.2.4. Mechanical recycling

The principle of this technique is to separate fibres from matrix by a grinding process. However, the obtained product is a mixture of polymer and fibres composed of two fractions, i.e., a coarse one, which is rich in matrix and a fibrous part, rich in fibre. Because of the reduction of mechanical properties, the products are generally used for low value-added applications like filler in concrete (Job, 2013). In this scenario, the necessary energy for the process is estimated at 0.27 MJ/kg of composite, the yield is supposed to be 100 %, i.e. all of FRP waste is recovered. In the case of CFRP, according to Palmer et al. (2010), 24 % of composite waste can be used to replace the equivalent quantity of glass fibre in SMC without important degradation of mechanical properties; the remaining is used as calcium carbonate. In the case of GFRP, all products obtained from grinding composite are considered to replace calcium carbonate.

3.2.5. Pyrolysis

Pyrolysis is a thermal recycling process that decomposes the matrix at around 400 to 600 °C according to its thermal properties to recover fibres. The main characteristic of this process is the thermal decomposition in an inert environment or in a controlled atmosphere with a low proportion of oxygen to avoid the oxidation of fibres. A rapid gasification might be needed after the principal step to clean the fibres from char of resin decomposition. Gas fraction produced from the decomposition of matrix can be condensed to be reused as a fuel or burned to recover heat. In this study, the pyrolysis is assumed as the combustion of the matrix. The total energy used in pyrolysis which is estimated at about 30 MJ/kg composite (Witik et al., 2013). This recycling pathway is the most developed until now (Yang et al., 2012). The recovery rate of fibre is considered to be 95 % in this study. The recycled fibres are supposed to be used as reinforcement in composite, such as for SRIM (Structural Reaction Injection Molding).

3.2.6. Fluidized bed

In this process, the sand is fluidized by the hot air flow at a temperature of 450-550 °C with a velocity of 0.4-1.1 m/s. In these conditions, the organic matrix is volatilized and the fibres are thus released. The fibres are sent out of the bed by gas flow. After the fibres are recovered, the gas passes through a secondary combustion chamber where the polymer is completely decomposed. This technique is still at both development stage and pilot scale (Yang et al., 2012). The needs for electricity are estimated at 15.5 kWh/kg of composite and the fibre yield is fixed at 67.5 % in this scenario from the conditions of laboratory test of Pickering et al. (2000). As for the pyrolysis process, the recycled fibres from this technique are used as reinforcement in composite, such as for SRIM.

4. Results and Discussion

4.1. Case 1: CFRP waste treatments

The Climate Change Impacts and the CBA of six EoL scenarios of CFRP are presented in Figure 2 (a). In this case, the material recovery is the most important factor of CFRP waste management because of the high value of carbon fibre in market and reduction of the important avoided impacts by replacement of virgin carbon fibre. All of the recycling techniques studied in this work generate more profits and have less the environmental impacts than the energy recovery techniques (incineration, co-incineration). Composite combustion and landfill of ash are not only penalized from the economic viewpoint since they do not lead material recovery but the resulting emissions also contribute to the total positive Climate Change Impacts of these pathways. At this stage, pyrolysis remains the best solution for recycling CFRP wastes. Indeed, it leads to the best economical profit and generates a low environmental impact. This is probably due to the highest maturity of this technology for carbon fibre recovery compared to other processes.

4.2. Case 2: GFRP waste treatments

In this case (see Figure 2 (b)), the choice of the technology is not as clear as for CFRP if pyrolysis remains a good alternative regarding the economic term. Co-incineration is a better competitor from an environmental point of view. It can also be emphasized that the profit of GFRP pyrolysis is lower than the one of CFRP pyrolysis due to the lowest added value of glass fibre compared to carbon fibre. More generally, the low value of glass fibres influences the environmental benefits of GFRP waste management.

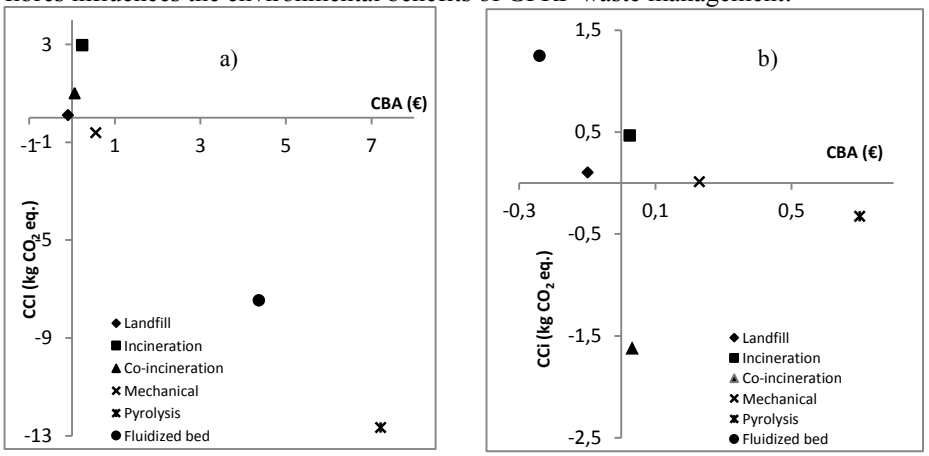

Figure 2: Evaluation of EoL pathways, (a) for CFRP, (b) for GFRP.

A process such as fluidized bed will not present the same advantage for CFRP and GFRP. This technique is outperformed by landfill pathway for GFRP. Since glass fibre is incombustible, the material recovery after combustion in co-incineration seems more promising than the incineration pathway.

5. Conclusions and Perspectives

This study proposed a model of the overall system of FRP waste pathways and an evaluation of environmental and economic impacts of each alternative. The results show the importance of the value of the recovered products and of the maturity of techniques on waste management. For CFRP, pyrolysis is an attractive recycling solution that satisfies both environmental and economic benefit. However, for GFRP wastes, it is not so obvious: mechanical recycling and co-incineration are possible alternatives. A weak point for GFRP waste recycling is the low value of the recovered product that may impact the total benefits.

This model will be then extended to other possibilities for FRP waste management (chemical recycling for example) and to various transport types while considering more complexity in FRP waste composition the multi-purpose nature of the recovered product. Economic impacts will be analysed thoroughly by considering investment, labour cost and other costs (dismantling, collection, stocks…). Environmental assessment will be carried out considering other environmental impacts other than those related to climate change. The recycling chain has indeed to be considered as a whole, and must be managed with respect to all the involved stakeholders. Multiobjective optimization has potential to examine the different compromise solutions to design a recycling system with respect to economic and environmental purposes.

References

S. Black, 2012, Carbon fiber market: Gathering momentum, High-Performance Composites, Composite World, Accessed 16 Avril 2014.

J.R. Duflou, Y. Deng, K. Van Acker, W. Dewulf, 2012, MRS BULLETIN 37, 374-382.

EEA, 2013, http://www.eea.europa.eu/data-and-maps/figures/typical-charge-gate-fee-and#tab-documents, Accessed 27 Ocotober 2014.

Eurostat, European Commision, 2014, Electricity and natural gas price statistics, http://epp.eurostat.ec.europa.eu/statistics_explained/index.php/Electricity_and_natural_gas_price_statistics, Accessed 23 October 2014.

R. Farel, B. Yannou, A. Ghaffari, Y. Leroy, 2013, Res. Conserv. Recycl. 74, 54-65.

A. Hedlund-Åström, 2005, PhD thesis, Royal Institute of Technology, Stockholm.

S. Job, 2013, Reinforced Plastics 57, 19-23.

J. Palmer, L. Savage, O.R. Ghita, K.E. Evans, 2010, Special Issue on 10th Deformation & Fracture of Composites Conference, 41, 1232–1237.

S.J. Pickering, R.M. Kelly, J.R. Kennerley, C.D. Rudd, N.J. Fenwick, 2000, Composites Sci. Technol. 60, 509–523.

W. Schade , C. Doll, M. Maibach, M. Peter, F. Crespo, D. Carvalho, G. Caiado, M. Conti, A. Lilico, N. Afraz, 2006, COMPETE Final Report, DG TREN, Karlsruhe, Germany.

R.A. Witik, J. Payet, V. Michaud, C. Ludwig, J.-A.E. Månson, 2011, Composites: Part A 42, 1694-1709.

R.A. Witik, R. Teuscher, V. Michaud, C. Ludwig, , J.-A.E. Månson, 2013. Composites Part A: Applied Science and Manufacturing 49, 89–99.

Y. Yang, R. Boom, B. Irion, , D.-J. van Heerden, P.Kuiper, H. de Wit, 2012, Chem. Engin. Process. 51, 53–68.

Krist V. Gernaey, Jakob K. Huusom and Rafiqul Gani (Eds.), 12th International Symposium on Process Systems Engineering and 25th European Symposium on Computer Aided Process Engineering.
31 May – 4 June 2015, Copenhagen, Denmark

A MILP Transshipment Model to Integrate and Re-Engineer Distillation Columns into Overall Processes

Konstantinos A. Pyrgakis, Kipouros P. Ioannis, Antonis C. Kokossis

School of Chemical Engineering, National Technical University of Athens, Zografou Campu GR-15780, Greece
akokossis@mail.ntua.gr

Abstract

Heat integration of distillation columns can be succeeded using several schemes. These may include multiple effects and thermally-coupled systems, heat pumping, feed preheating or combinations of all of them. Moreover, setting individual integration of distillations in the scope of overall process integration is possible to secure operation even at zero energy cost. This paper focuses on the scheme of multi-effect distillation due to its high potentials for stand-alone and integration with the overall process. The proposed methodology examines the synthesis specifications (number, pressures and feed split fractions) of multiple effects, scoping for promising structures ahead of analytical design and rigorous optimization analyses. A MILP mathematical formulation is presented to optimally synthesize multi-effect distillation systems taking into consideration the integration of the effects with the overall process at the same time. The model is illustrated through a real-life biorefinery including the integration of three different distillation processes succeeding in energy savings up to 82%.

Keywords: heat integration, multiple effect distillation, transshipment.

1. Introduction

Distillation constitutes a widely used and energy intensive separation process that in most cases features a big share of the overall energy consumption and a high impact on process sustainability. Integration of distillation columns appears indispensable in future designs (ex. biorefineries) as well as in retrofit cases. Several schemes deal with stand-alone integration securing better efficiencies than initial designs. In this paper, the scheme of multiple effects is examined, since the technique succeeds in significant energy benefits from both stand-alone and integration with the overall process.

The application involves adding of separation effects that operate at different pressures, enabling that way energy serving from the condenser of a higher pressure effect to the reboiler of a lower pressure effect, while the initial distillation feed is distributed among them. Linnhoff et al. (1983) originally gave fundamentals concerning the thermodynamic background for the integration of distillation heating and cooling demands along the heat cascade of the overall process. The graphical approach of Grand Composite Curves (GCC) has been extensively applied to detect the feasible heat transfer contexts between the multiple distillation effects and the background needs (hot/cold streams of process that remain if reboilers and condensers of distillations are excluded) previewing options about the number, capacities and operating pressures of

the effects that secure maximum energy savings. The graphical tool has been applied in several recent biorefinery applications for the purification of downstream bioethanol (Dias et al., 2011; Kravanja, 2013) while other robust optimization models (Martín and Grossmann, 2011; 2013) has been also used to determine operating pressures and split fractions of effects (up to three) followed by heat integration with the overall process.

The development of multi-effect distillation schemes has to cope with the selection of number, capacities and pressures of effects as well as with their integration with the overall process so as to take full advantage of available heat sinks and sources of background and minimize the overall energy cost. Since distillation effects and their specifications constitute significant degrees of freedom, the development of multi-effect systems should be approached in a process synthesis approach. This paper presents a MILP mathematical formulation with the capacity to address the additional degrees of freedom and synthesize the portfolio of effects that minimizes utilities cost of the process and investment cost of applied effects. The methodology intends to select the appropriate combination of effects (given a set of candidate pressure effects) and their capacities, securing at the same time their integration with the background. An extended transshipment model (Papoulias and Grossmann, 1983) is proposed to formulate heat flows along the heat cascade incorporating new terms associated with the selection and contribution of effects. Finally, the mathematical model was applied in the courses of a real-life biorefinery, which produces bioethanol and lignin from lignocellulosic biomass, for the integration of three different distillation columns involved in the overall process.

2. The synthesis problem of multi-effect distillation

The three critical challenges of the synthesis problem (number, operating pressures and feed split fractions) are graphically previewed in the illustrative GCC of Figure 1. There, a set of candidate effects are possible to be placed over or below the pinch, while the operating pressures (vertical arrows) and their capacities (horizontal arrows) need to be optimized so as to ensure full integration with the available heat sinks and/or sources of the background. The synthesis problem becomes even complicated as far as more distillation units need to get integrated and the effects, which integrate different distillations, are possible to compete for the appropriate placement within the same background profile. In these cases, investment cost plays a significant role for the selection of the appropriate pressures and capacities of competitive effects.

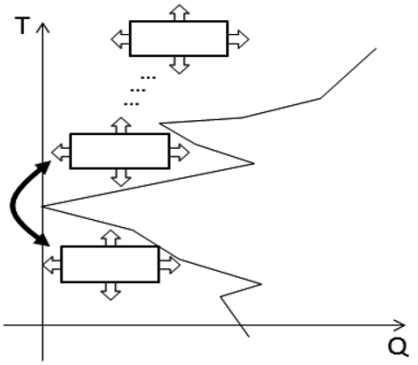

Figure 1: Illustrative Grand Composite Curve and candidate distillation effects

This paper presents a MILP model to describe the heat cascade of the overall process and mathematically formulate the energy interactions between added effects and the background. The proposed methodology intends to select the appropriate portfolio of effects among a given set of effects that operate at a spread range of preselected pressures. The nominal (maximum) heat demands of the candidates can be estimated in advance setting the feed rate and top/bottom product compositions of the initial column. Therefore, the desired compositions of final top/bottom products in the multi-effect system are secured by mixing top/bottom products, respectively, of all effects together. Moreover, the reboiler and condenser heat demands can be safely supposed to be linearly depended on the capacities of distillation effects and consequently approximated as a fraction of their nominal values. This fraction is directly related to the split fraction of the initial distillation feed that is distributed among the effects. As a result, heat demands of all candidate effects can be incorporated into the heat cascade of the overall process as additional streams (condensers are considered as hot streams with Tin−Tout = −1 K and reboilers as cold streams with Tin−Tout = +1 K) and their contribution can be managed through the related split fractions.

In the courses of the proposed mathematical model, the following sets are defined: $K=\{k|k=1,N_K\}$, where N_K is the number of temperature intervals of the heat cascade from higher to lower temperatures; $D=\{d|d=1,N_D\}$, where N_D is the number of distillations of the process that need to get integrated; $H=\{i|i=1,N_H\}$ and $C=\{j|j=1,N_C\}$, where N_H and N_C are the numbers of hot and cold streams respectively including both process streams and condensers/reboilers of candidate effects; $H_k=\{i|i\in H\}$ and $C_k=\{j|j\in C\}$ for hot stream i and cold stream j that are present at interval k; $H_d=\{i|i\in H\}$ and $C_d=\{j|j\in C\}$ for hot stream i and cold stream j that represent the condenser and reboiler respectively of the effect that integrates distillation d; $S=\{m|m=1,N_S\}$ and $W=\{n|n=1,N_W\}$, where N_S and N_W are the numbers of hot and cold utilities respectively; $S_k=\{m|m\in S\}$ and $W_k=\{n|n\in W\}$ for hot utility m and cold utility n respectively that are present at interval k; $HC=\{(i,j)|i\in H,\ j\in C\}$ for i,j pairs that represent the reboiler and condenser respectively of the same effect. Let known parameters Q_{ik}^H and Q_{jk}^C be the heat contents of hot stream i and cold stream j respectively at interval k and c_m and c_n be the unit costs of hot utility m and cold utility n respectively. Let variables Q_m^S and Q_n^W be the heat loads of hot utility m and cold utility n, R_k be the heat residual exiting interval k, y_i^H and y_j^C be the split fractions of hot stream i and cold stream j and the binary variable y_i associated with the selection of hot stream i.

Parameters Q_{ik}^H and Q_{jk}^C for $i\in H_d$ and $j\in C_d$ refer to the nominal heat contents of the related effects, while variables y_i^H and y_j^C are used to manage heat contents of all hot and cold streams as degrees of freedom. On one hand, y_i^H and y_j^C variables for $i\in H\text{-}H_d$ and $j\in C\text{-}C_d$ describe the split fractions of streams that belong to the background and should be fixed to equal to unit, since they must fully contribute the heat cascade in any case. On the other hand, y_i^H and y_j^C variables for $i\in H_d$ and $j\in C_d$ describe the split fractions of the effects and should range between 0 and 1, while in case that $(i,j)\in HC$, y_i^H and y_j^C variables should be equal between them, since they represent split fractions of the same effect and both the condenser and reboiler should be similarly managed.

Adding more separation effects to succeed in better integration with the background has a subsequent impact on the annualized investment cost, which must be retained to

minimum achievable. Therefore, besides energy consumption, investment cost should be also taken into account and needs to be minimized. This cost depends on both pressure and the capacity of the column. The equations of Mullet et al. (1981) were used to estimate the installed cost of towers and trays, while the equations of Douglas (1988) were used to estimate the installed cost of reboilers and condensers. The Annualized Cost (AC) of the effects are then linearly formulated using Taylor series in the form of: $AC = b + a * F$, where F is the capacity and a and b are known parameters that depend on the operating pressure of the effect. In this analysis, capacity F can be decomposed into the form of: $F_{nom} * x$, where F_{nom} is the nominal feed flowrate of the column as defined by the initial distillation and x is the split fraction as selected by the optimization procedure. Consequently, parameter a is redefined by incorporating F_{nom} and further includes the nominal capacity of each distillation. As a result, let a_i and b_i be the costing (known) parameters of each effect and defined through the set of hot streams i (condensers) that belong to set H_d.

3. Mathematical formulation

The mathematical formulation for the selection of the prime portfolio of effects that minimizes (Eq.(1)) utilities and investment cost (Total Annualized Cost–TAC) is presented as follows:

$$min \qquad TAC = \sum_{m \in S} c_m * Q_m^S + \sum_{n \in W} c_n * Q_n^W + \sum_{d \in D} \sum_{i \in H_d} y_i * b_i + y_i^H * a_i \tag{1}$$

s.t.

$$R_{k-1} + \sum_{m \in S_k} Q_m^S + \sum_{i \in H_k} y_i^H * Q_{ik}^H = R_k + \sum_{n \in W_k} Q_n^W + \sum_{j \in C_k} y_j^C * Q_{jk}^C \quad k = 1, \dots K \tag{2}$$

$$y_i^H = y_j^C \qquad \forall (i,j) \in HC \tag{3}$$

$$\sum_{i \in H_d} y_i^H = 1 \qquad \forall d \in D \tag{4}$$

$$y_i^H \geq y_i * MAL \qquad \forall i \in H \tag{5}$$

$$y_i^H \leq y_i \qquad \forall i \in H \tag{6}$$

$$y_i^H = 1 \;\; \forall i \in (H - H_d), \qquad y_j^C = 1 \;\; \forall j \in (C - C_d) \tag{7}$$

$$R_0 = R_K = 0, \qquad 0 \leq y_i^H \leq 1 \;\; \forall i \in H_d, \qquad 0 \leq y_j^C \leq 1 \;\; \forall j \in C_d \tag{8}$$

The above mathematical formulation incorporates the process cascade equation (Eq.(2)) and logical constraints (Eq.(3)-Eq.(8)). A transshipment model is used to formulate the heat flows along the heat cascade (Eq.(2)) by incorporating new terms: $\sum_{i \in H_k} y_i^H * Q_{ik}^H$ and $\sum_{j \in C_k} y_j^C * Q_{jk}^C$, that account for the development of the variable intervals by controlling contribution of streams. Hot and cold streams related to the background are set to fully contribute the cascade by fixing the related y_i^H and y_j^C variables to be equal

to unit through Eq.(7). The heat contents of streams related to the effects are possible to range between zero and their nominal values; thereby, these are managed through y_i^H and y_j^C variables that are set to vary between 0 and 1 through Eq.(8). Eq.(3) secures the simultaneous contribution of the reboiler and condenser streams that belong to the same effect. Full distribution of the initial feed of each distillation d is secured through Eq.(4), where the sum of split fractions related to condensers should be equal to unit. This constraint is also secured for the associated split fractions of the reboilers through Eq.(3). To avoid selection of negligible and industrially impractical capacities of the effects, equations Eq.(5) and Eq.(6) are incorporated into the model to set the lower bound of capacities for the effects that are selected. This is done through a user defined (here is 10%) parameter that determines the Minimum Allowable Limit (MAL) of non-zero split fractions of effects that are selected through binary variables y_i. Equations Eq.(5) and Eq.(6) are also recorded only for split fractions of condensers, since the constraints related to reboilers split fractions are secured again through Eq.(3). The binary variables y_i that refers to the streams of the background will be equal to unit in any case, since the respective split fractions are fixed to unit through Eq.(7). Finally, the transshipment formulation necessitates setting residuals R_0 and R_K to zero (Eq.(8)).

4. Case study

The mathematical formulation has been applied to integrate three distillation columns that are met in the courses of a real-life biorefinery that produces bioethanol and lignin from lignocellulosic biomass. An organosolv process fractionates lignocellulosic biomass into C5 Sugars, C6 Sugars and lignin, while the sugars are then fermented through two separate processes producing C5 based ethanol and C6 based ethanol. Three distillation columns are used along the overall process; the first and most energy intensive is used for the recovery of solvents in organosolv process and the other two for the purification of ethanol from the downstream ethanol/water azeotrope mixtures of the two fermentation processes. The mathematical model selected two effects over the pinch for the first distillation, since more heat sinks are available than the heat sources below pinch, and one effect for each ethanol purification (Figure 2).

The crucial synthesis challenge is identified in the selection of operating pressures for the ethanol purifications, due to tradeoffs between energy and investment costs of the related candidate effects. As long as operating pressure of purification column decreases, the ethanol/water azeotrope mixture becomes richer in ethanol with a subsequent decrease in the energy consumption (easier separation), while investment cost appears minimum prices for operation at atmospheric pressure. This phenomenon appears in both C5-Ethanol and C6-Ethanol purification columns making the synthesis problem more complicated in the courses of simultaneous integration of all three distillations and strongly dependent on the morphology of the energy integrated profile of the background. Eventually, the operating pressures of ethanol purifications were selected so as to operate below pinch, where the background heat sinks are sufficient to integrate both of them, without adding more separation effects and securing full integration of these columns with significant investment cost savings. The energy consumption finally reduced from 129 MW and 120 MW of hot and cold utilities, respectively, to 30 MW and 22 MW, while the selected portfolios of effects contributed 33% of the overall energy savings.

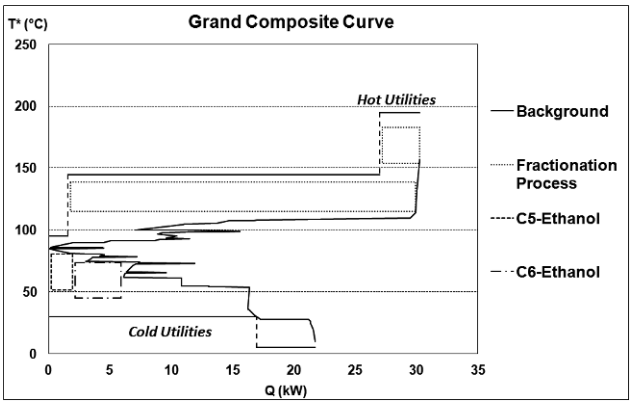

Figure 2: Grand Composite Curve of fully integrated lignocellulosic biorefinery

5. Conclusions

A MILP mathematical formulation is proposed to synthesize multi-effect distillation systems and integrate them with the overall process. Significant answers were given about the number, the pressures and the split fractions of the multiple effects, ahead of analytical design. The model detects promising structures of distillation effects by examining interactions between the synthesis specifications (number, pressure, split fractions) and the morphology of the energy profile of the background, being capable to re-engineer operating conditions without adding more effects (if this is feasible) and secure maximum energy and investment cost savings.

Acknowledgements

Financial support from the European Research Program BIOCORE (FP7-241566) and the Alexander S. Onassis Public Benefit Foundation (Greece) are gratefully acknowledged.

References

M. Dias, M. Modesto, A. Ensinas, S. Nebra, R. Filho, C. Rossell, 2011, Improving bioethanol production from sugarcane: evaluation of distillation, thermal integration and cogeneration systems, Energy, 36, 6, 3691–3703

J. Douglas, Conceptual Design of Chemical Process, International Edition 1988, ISBN 0.07-100195-6, McGraw-Hill Book Co., Singapore

P. Kravanja, A. Modarresi, A. Friedl, 2013, Heat integration of biochemical ethanol production from straw – A case study, Applied Energy, 102, 32–43

B. Linnhoff, H. Dunford and R. Smith, 1983, Heat Integration Of Distillation Columns Into Overall Processes, Chemical Engineering Science, 38, 8, 1175–1188

M. Martín and I. Grossmann, 2011, Energy Optimization of Bioethanol Production via Gasification of Switchgrass, AIChE Journal, 57, 12, 3408–3428

M. Martín and I. Grossmann, 2013, On the Systematic Synthesis of Sustainable Biorefineries, Ind. Eng. Chem. Res., 52, 9, 3044–3064

A. Mulet, A. Corripio, L. Evans, 1981, Estimate costs of distillation and adsorption towers via correlations, Chemical Engineering, 88, pp.77-80, 82

S. Papoulias, I. Grossmann, 1983, A structural optimization approach in process synthesis-II: Heat recovery networks, Computers & Chemical Engineering, 7, 6, 707-721

Krist V. Gernaey, Jakob K. Huusom and Rafiqul Gani (Eds.), 12th International Symposium on Process Systems Engineering and 25th European Symposium on Computer Aided Process Engineering.
31 May - 4 June 2015, Copenhagen, Denmark.

A Duality-based Approach for Bilevel Optimization of Capacity Expansion

Pablo Garcia-Herreros[a], Pratik Misra[b], Erdem Arslan[b], Sanjay Mehta[b] and Ignacio E. Grossmann[*a]

[a]*Department of Chemical Engineering; Carnegie Mellon University; Pittsburgh (PA), USA*
[b]*Air Products and Chemicals, Inc.; Allentown (PA), USA*
[*]*grossmann@cmu.edu*

Abstract

The traditional approach for capacity expansion problem aims to balance investment costs with the returns obtained from production. These formulations ignore the behavior of competitive markets in which buyers select their providers according to their own interest. We propose a bilevel optimization formulation that considers the industrial producer and the markets as independent decision makers. The upper-level problem maximizes the profit of a producer whose revenue is subjected to a lower-level linear program (LP) that minimizes markets expenses. As an alternative to the single-level reformulation based on the KKT optimality conditions, we propose an approach based on strong duality of the lower-level LP. Both reformulations are shown to yield the same solution, but the duality-based reformulation achieves a significant reduction in solution time.

Keywords: capacity expansion, bilevel optimization, strong duality

1. Introduction

Mathematical programming has been used extensively to develop plans involving one-time investments that are recovered over long periods of time. Capacity expansion planning in the process industry is not an exception. In industry, producers plan their capacity such that their market position is not endangered by lack of responsiveness to variations in demand. An intuitive approach for capacity expansion planning is to formulate an optimization problem that maximizes profit over a finite time horizon. This approach has the advantage of exhaustively analyzing a set of expansion strategies, but it implicitly assumes that the producer decides which market share to satisfy. In competitive markets, buyers have the freedom to select their providers from different alternatives. In order to model the conflicting interests of a producer and the markets, we propose a bilevel optimization formulation to find the Stackelberg equilibrium between them. The problem implies finding the investment plan for a company whose revenue is determined by markets that minimize their cost. The bilevel formulation includes mixed-integer variables for the leader's decisions and models the markets' decisions in a lower-level linear program (LP).

The standard solution strategy for bilevel optimization problems with lower-level LPs is to replace the lower-level problem with its KKT optimality conditions. This reformulation maintains linearity of the problem except for the introduction of complementarity constraints. In this article, we use an equivalent reformulation that replaces the lower-level problem by its primal and dual constraints, and guarantees optimality by enforcing strong duality (Motto et al., 2005; Garces et al., 2009).

Most of the literature proposing bilevel optimization for capacity expansion is related to electricity markets. Soyster and Murphy (1989) formulated a capacity expansion problem for a perfectly competitive market. A more realistic model assuming an oligopolistic market was presented by Murphy and Smeers (2005). A bilevel formulation for the expansion of transmission networks was developed by Garces et al. (2009) to maximize the average social welfare over a set of lower-level problems representing different market clearing scenarios. Ruiz et al. (2012) modeled electricity markets as an Equilibrium Problem with Equilibrium Constraints (EPEC) in which competing producers maximize their profit in the upper level and a market operator maximizes social welfare in the lower level. In the context of the process industry, Ryu et al. (2004) developed a bilevel programming formulation for supply chain optimization under uncertainty to model different interests for production and distribution operations. Chu and You (2014) presented a bilevel model for scheduling and dynamic optimization of batch processes. Game theory concepts have also been used to model cooperative and competitive environments in supply chain planning (Zamarripa et al., 2012).

The novelty of our research resides on the application of bilevel optimization for capacity expansion planning in a competitive environment. Bilevel programming for these kind of problems can be seen as a risk reduction strategy given the significant influence of external decision makers in the economic success of investment plans. In particular, we propose a mathematical model that includes a rational behavior for the markets. The investment plans obtained from this approach are found to be less sensitive to changes in the business environment in comparison to the plans obtained from single-level formulations.

2. Problem statement

We consider an industrial producer willing to establish the capacity expansion plan that maximizes its profit during a finite time horizon, subject to revenue that is determined by markets that minimize the cost that they pay. The problem is modeled as a Stackelberg game in which the industrial producer (leader) decides its investment strategy first, and then the markets (follower) respond according their own interest. The Stackelberg game is a strategic game with perfect information: the leader chooses his actions with full knowledge of the follower's decision criterion, and the follower reacts after observing the leader's actions.

The industrial producer controls a set of facilities with limited production capacity. It has the possibility of expanding the existing facilities or investing to open new facilities. The goal of the investment plan is to maximize the Net Present Value (NPV) considering the cost of investments, production, maintenance, transportation, and the revenue obtained from selling a single product to several markets. The capacity expansion problem assumes deterministic demands during the finite time horizon; the prices offered to the markets by all providers are also assumed to be given. The products offered by the competing providers are considered homogeneous and the markets have no other preference for providers than price.

3. Formulation

Bilevel optimization problems are mathematical programs with optimization problems in the constraints (Bracken and McGill, 1973). In our formulation, the upper-level problem determines the optimal capacity expansion plan by selecting the investments that maximize the NPV of the leading producer. The expansions are modeled using binary variables such that the capacity increments are discrete. The lower-level determines the response of markets that select providers with the unique interest of satisfying their demands at lowest cost. The decisions of the markets are modeled with continuous variables that represent the deliveries that they obtain from each provider.

It is assumed that the leading producer offers the same price to each market in a given time period,

regardless of the production facility that is used to satisfy its demand. Therefore, markets have no preference among production facilities of the leader and the leading producer is free to choose the facilities it uses to satisfy demands. This modeling framework, in which degeneracy in the lower-level problem is resolved in favor of the upper-level decision maker, is known as the Optimistic Approach (Loridan and Morgan, 1996). The bilevel optimization formulation for the capacity expansion planning in a competitive environment is presented in Eqn. (1) - (9).

$$\max_{v,w,x} \quad \sum_{t\in T}\sum_{i\in I^1}\sum_{j\in J}\frac{1}{(1+R)^t}P_{t,i,j}y_{t,i,j} - \sum_{t\in T}\sum_{i\in I^1}\frac{1}{(1+R)^t}\left(A_{t,i}v_{t,i}+B_{t,i}w_{t,i}+E_{t,i}x_{t,i}\right)$$
$$-\sum_{t\in T}\sum_{i\in I^1}\sum_{j\in J}\frac{1}{(1+R)^t}\left(F_{t,i}y_{t,i,j}+G_{t,i,j}y_{t,i,j}\right) \tag{1}$$

$$\text{s.t.} \quad w_{t,i} = V_{0,i} + \sum_{t'=1}^{t} v_{t',i} \qquad \forall\, t\in T, i\in I^1 \tag{2}$$

$$x_{t,i} \le w_{t,i} \qquad \forall\, t\in T, i\in I^1 \tag{3}$$

$$c_{t,i} = C_{0,i} + \sum_{t'=1}^{t} H_i x_{t',i} \qquad \forall\, t\in T, i\in I^1 \tag{4}$$

$$\min_{y} \quad \sum_{t\in T}\sum_{i\in I}\sum_{j\in J}\frac{1}{(1+R)^t}P_{t,i,j}y_{t,i,j} \tag{5}$$

$$\text{s.t.} \quad \sum_{j\in J} y_{t,i,j} \le c_{t,i} \qquad \forall\, t\in T, i\in I \tag{6}$$

$$\sum_{i\in I} y_{t,i,j} = D_{t,j} \qquad \forall\, t\in T, j\in J \tag{7}$$

$$y_{t,i,j} \in \mathbb{R}^+ \qquad \forall\, t\in T, i\in I, j\in J \tag{8}$$

$$c_{t,i}\in\mathbb{R}^+,\ v_{t,i},\ w_{t,i},\ x_{t,i}\in\{0,1\} \qquad \forall\, t\in T, i\in I^1, j\in J \tag{9}$$

where T, I^1, I^2, and J are respectively, the index sets for time (t), facilities of the leading producer (i^1), facilities of the independent providers (i^2), and markets (j). The first term in (1) represents the revenue obtained from deliveries. Revenue is proportional to the volume of sales ($y_{t,i,j}$) according to the price paid by the markets ($P_{t,i,j}$). The second term includes the cost of opening new facilities, the maintenance cost of open facilities, and the expansion cost. The binary variable deciding if a new facility is open at location i at time period t is $v_{t,i}$; the parameter $A_{t,i}$ determines the cost to build a new facility with zero capacity. The binary variable $w_{t,i}$ indicates if facility i is open at time period t; if the facility is open at period t, a fixed cost $B_{t,i}$ is paid for maintenance. The expansion in facility j at period t is decided with binary variable $x_{t,i}$; the cost of the expansion is given by the parameter $E_{t,i}$. The third term includes production and transportation costs. Production costs are proportional to the volume of sales ($y_{t,i,j}$) according to the unit production cost ($F_{t,i}$). Transportation cost from production facilities to markets is proportional to the volume of sales ($y_{t,i,j}$) according to the unit transportation cost ($G_{t,i,j}$). All terms are discounted with an interest rate (R).

Constraint set (2) is used for the maintenance cost of facilities during the time periods when they are open; the binary parameter $V_{0,i}$ indicates the facilities that are initially open. Constraint set (3) requires capacity expansions to take place only at open facilities. Constraint set (4) determines the production capacity of facilities according to the expansion decisions; parameters $C_{0,i,k}$ indicate the initial capacities and H_k the magnitude of the potential capacity expansions. Constraints set (6) bounds deliveries according to the production capacities. Finally, constraints set (7) enforces demand satisfaction. The domains are given by Eqn. (8) - (9).

4. Single-level reformulation using strong duality

An optimistic bilevel program with a convex and regular lower-level can be transformed into a single-level optimization problem using its optimality conditions (Colson et al., 2007). The key property of convex programs is that global optimal solutions can be described by the set satisfying their KKT conditions. In the case of linear programs, KKT optimality conditions are equivalent to the satisfaction of primal feasibility, dual feasibility, and strong duality (Gale et al., 1951). Based on this equivalence, we can replace Eqn. (5) - (9) from the bilevel formulation with Eqn. (10) - (13).

$$\sum_{t\in T}\sum_{i\in I}\sum_{j\in J}\frac{1}{(1+R)^t}P_{t,i,j}y_{t,i,j}=\sum_{t\in T}\left[\sum_{j\in J}D_{t,j}\lambda_{t,j}-\sum_{i\in I}c_{t,i}\mu_{t,i}\right] \tag{10}$$

$$\sum_{j\in J}y_{t,i,j}\leq c_{t,i} \qquad \forall\, t\in T, i\in I \tag{11}$$

$$\sum_{i\in I}y_{t,i,j}=D_{t,j} \qquad \forall\, t\in T, j\in J \tag{12}$$

$$\lambda_{t,j}-\mu_{t,i}\leq\frac{1}{(1+R)^t}P_{t,i,j} \qquad \forall\, t\in T, i\in I, j\in J \tag{13}$$

The upper-level problem represented by Eqn. (1) - (4) remains unchanged in the duality-based reformulation. The reformulation introduces dual variables $\mu_{t,i}$ corresponding to Enq. (6) and $\lambda_{t,j}$ corresponding to Enq. (6). Strong duality is enforced by equating the primal and dual objective functions as presented in Eqn. (10). Lower-level primal constraints (11) and (12) are kept in the formulation to guarantee primal feasibility. Dual feasibility of the lower level is ensured with constraint (13).

It is important to note that this reformulation yields a nonconvex Mixed-Integer Nonlinear Program (MINLP). The nonconvexity arises from the dual objective function in the right hand side of Eqn. (10), because of the product of upper-level variable $c_{t,i}$ and lower-level dual variable $\mu_{t,i}$. Fortunately, the problem can be reformulated as a MILP because the continuous variable $c_{t,i}$ only takes values in discrete increments as indicated by Eqn. (4). The linearization procedure is based on eliminating variable $c_{t,i}$ from the formulation by replacing it with Eqn. (4). The resulting bilinear terms are products of continuous variables ($\mu_{t,i,k}$) and binary variables ($x_{t',i}$). Therefore, they can be modeled with a set of mixed-integer constraints by including a continuous variable ($u_{t',t,i}$) for each bilinear term.

The resulting MILP formulation is obtained after replacing Eqn. (10) with Eqn. (14),

$$\sum_{t\in T}\sum_{i\in I}\sum_{j\in J}\frac{1}{(1+R)^t}P_{t,i,j}y_{t,i,j}=\sum_{t\in T}\left[\sum_{j\in J}D_{t,j}\lambda_{t,j}-\sum_{i\in I}c_{0,i}\mu_{t,i}-\sum_{t'=1}^{t}\sum_{i\in I^1}H_i u_{t,t',i}\right] \tag{14}$$

and introducing the mixed-integer constraints presented in Eqn. (15) - (16).

$$u_{t,t',i}\geq\mu_{t,i}-M\left(1-x_{t',i}\right) \qquad \left(t,t'\right)\in\left\{\left(t,t'\right):\, t'\leq t,\, t\in T\right\},\, i\in I^1 \tag{15}$$

$$u_{t,t',i}\in\mathbb{R}^{+} \tag{16}$$

It is interesting to remark that only the two terms presented in Eqn. (15) and (16) are necessary for the linearization of the bilinear terms because they are sufficient to bound the values of $u_{t,t',i}$ in the improving direction of the objective function.

5. Illustrative Example

The duality-based reformulation is implemented to solve a small case study from the air separation industry. This example considers the production and distribution of one product to 15 markets during 20 periods of 90 days (quarters of year). Initially, the leading producer has three production facilities with capacities equal to 7,200 ton/period, 22,500 ton/period, and 45,000 ton/period; it also has one candidate location for a new facility. There are three independent providers with constant capacity equal to 27,000 ton/period, 45,000 ton/period, and 9,000 ton/day. In every time period, the production facilities controlled by the leading producer are allowed to expand by installing additional production lines with a capacity of 9,000 ton/period. Selling prices and costs related to investment, maintenance, production, and transportation increase with time. The total demand of all markets grow from 131,400 ton in the first time period up to 149,929 ton in the last time period. The complete data for the illustrative example is omitted because of the space limitation.

The solution of the problem establishes the investment plan and the distribution strategy during the time horizon. We compare the solution obtained from the bilevel formulation with the solution obtained from a single-level optimization problem in which the markets are assumed to be captive by the leading producer. Additionally, we calculate the performance of the single-level expansion strategy in a competitive environment. Table 1 presents the comparison. The results show that the single-level formulation proposes a more aggressive expansion strategy than the bilevel formulation. This is a consequence of planning for a larger market share when the decision criterion of the markets is ignored. When the single-level expansion strategy is evaluated in competitive markets, the investments remain the same but the revenue reduces from MM $1,265 to MM $931. In contrast, the bilevel formulation proposes a more conservative expansion strategy that obtains a 35 % increase in NPV (from MM $441 to MM $338) in competitive markets when compared to the single-level expansion strategy.

In order to illustrate the benefits of the duality-based reformulation we compare it with its equivalent KKT reformulation. The computational statistics for both of them are presented in Table 2. Both MILP reformulations were implemented in GAMS 24.2.3 and solved using CPLEX 12.6.0.1.

Table 2 shows the increase in model size from the single-level formulation to the bilevel formulations. It is important to highlight that the duality-based reformulation does not require any additional binary variables in comparison to the single level formulation. In contrast, the KKT reformulation requires one additional binary variable for each inequality in the lower level, including bounds on the variables. The significant increase in the number of constraints, continuous variables, and specially binary variables dominates the solution time of the KKT reformulation. However, the solution obtained form the KKT and the duality-based reformulations are identical.

Table 1: Comparison of the results for the single-level and the bilevel formulation

Term in objective function	**Single level without competition**	**Single level with competition**	**Bilevel with competition**
Revenue (MM$):	1,265	931	930
New facilities (MM$):	0	0	0
Maintenance (MM$):	94	94	94
Expansion (MM$):	191	191	85
Production (MM$):	412	296	300
Transportation (MM$):	14	12	10
NPV (MM$):	554	338	441
Total market cost (MM$):	1,494	1,355	1,355

Table 2: Model statistics for the proposed formulations

Model statistic	Single level without competition	KKT reformulation	Duality-based reformulation
Number of constraints:	680	8,540	4,380
Number of continuous variables:	2,240	6,140	4,220
Number of binary variables:	240	3,120	240
Solution time (s) [a]:	0.22	210	3.2

[a] using priority branching on the expansion decisions

6. Conclusions

We have presented a bilevel optimization formulation for the capacity expansion problem in competitive markets. The formulation considers the interactions between two independent decision makers: an industrial producer establishing its expansion plan and a set of markets minimizing the cost that they pay to satisfy their demands. The proposed formulation has the advantage that it models markets as rational decision makers, which avoids overestimating the attainable revenue. The illustrative example demonstrates that the bilevel formulation yields an expansion strategy that is more conservative with respect to capital investments and produces higher NPV when evaluated on competitive markets.

We have also proposed an approach to reformulate the bilevel problem as a single level optimization problem. The reformulation is based on the strong duality property of the lower-level LP, and it is equivalent to the reformulation that uses the KKT optimality conditions. The main benefit of the duality-based reformulation is that it does not require the addition of new binary variables; however, in order to obtain a MILP reformulation the decision of the leader must be discrete. The computational performance of the duality-based reformulation is significantly superior to the performance of the KKT reformulation. The proposed reformulation of the bilevel optimization problem for capacity expansion has the potential to address large-scale problems that support decision making for industrial producers.

References

A.L. Motto, J.M. Arroyo, F.D. Galiana, 2005. A mixed-integer lp procedure for the analysis of electric grid security under disruptive threat. Power Systems, IEEE Transactions on 20, 1357–1365.

A.L. Soyster, F.H. Murphy, 1989. Economic Behaviour of Electric Utilities. Prentice-Hall.

B. Colson, P. Marcotte, G. Savard, 2007. An overview of bilevel optimization. Annals of Operations Research 153, 235–256.

C. Ruiz, A.J. Conejo, Y. Smeers, 2012. Equilibria in an oligopolistic electricity pool with stepwise offer curves. IEEE Transactions on Power Systems 27, 752–761.

D. Gale, H.W. Kuhn, A.W.Tucker, 1951. Activity Analysis of Production and Allocation. New York: Wiley, Ch. Linear programming and the theory of games, p. 317 329.

F.H. Murphy, Y. Smeers, 2005. Generation capacity expansion in imperfectly competitive restructured electricity markets. Operations Research 53, 646–661.

J. Bracken, J.T. McGill, 1973. Mathematical programs with optimization problems in the constraints. Operations Research 21, 37–44.

J-H. Ryu, V. Dua, E.N. Pistikopoulos, 2004. A bilevel programming framework for enterprise-wide process networks under uncertainty. Computers & Chemical Engineering 28, 1121–1129.

L.P. Garces, A.J. Conejo, R. Garcia-Bertrand, R. Romero, 2009. A bilevel approach to transmission expansion planning within a market environment. IEEE Transactions on Power Systems 24, 1513–1522.

M.A. Zamarripa, A.M. Aguirre, C.A. Mendez, A. Espuna, 2012. Improving supply chain planning in a competitive environment. Computers & Chemical Engineering 42, 178–188.

P. Loridan, J. Morgan, 1996. Weak via strong stackelberg problem: New results. Journal of Global Optimization 8, 263–287.

Y. Chu, F. You, 2014. Integrated scheduling and dynamic optimization by stackelberg game: Bilevel model formulation and efficient solution algorithm. Industrial & Engineering Chemistry Research 53, 5564–5581.

Krist V. Gernaey, Jakob K. Huusom and Rafiqul Gani (Eds.), 12th International Symposium on Process Systems Engineering and 25th European Symposium on Computer Aided Process Engineering.
31 May – 4 June 2015, Copenhagen, Denmark

A Hybrid CP/MILP Approach for Big Size Scheduling Problems of Multiproduct, Multistage Batch Plants

Franco M. Novara[a], Gabriela P. Henning[b*]

[a]*FIQ,UNL, Santiago del Estero 2829, Santa Fe, 3000, Argentina*
fra_novara@hotmail.com
[b]*INTEC (UNL-CONICET),Güemes 3450, Santa Fe, 3000, Argentina*
ghenning@intec.unl.edu.ar

Abstract

This contribution presents a novel CP/MILP hybrid approach aimed at solving large size multiproduct, multistage batch plants scheduling problems. This three-phase approach accounts for many real world features. In addition, production orders requiring several batches of each product can be fulfilled by operating in a campaign mode, as it occurs in many industrial facilities. Numerical results show that for large scale examples the approach can perform better than standalone MILP and CP models and can solve problems that could not be solved with either of these methods alone.

Keywords: Batch plant scheduling, Resource-constraints, Hybrid approaches, MILP methods, Constraint-programming

1. Introduction

Since scheduling problems are NP hard, the efficient solution of their corresponding MILP models can become computationally very expensive for large-scale problems. This challenging situation can be tackled by means of hybrid approaches (Harjunkoski et al., 2014) combining the complementary strengths of Mixed-Integer Linear Programming (MILP) and Constraint Programming (CP) techniques. This contribution presents a novel CP/MILP approach aimed at solving multiproduct, multistage batch plants scheduling problems addressing a big number of batches that are manufactured under a campaign mode. The methodology has three phases. In the first one, an MILP model tackles the assignment problem. The second phase, addressed by means of a relaxed CP model, has a twofold goal: first, to check the feasibility of the previously obtained assignment, and second, to solve the sequencing problem taking into account sequence-dependent changeover times. When the assignment turns out to be unfeasible, cuts are generated and the first phase is solved again. The iteration between phases one and two continues until a feasible assignment is reached. In such a case, the third phase, which is a rigorous CP model that optimizes performance measures such as makespan, total or mean tardiness, etc., obtains the final solution. The reduction of CPU time is the reason for having both a relaxed (phase 2) and a tightened (phase 3) CP model, instead of just one, as in other hybrid CP/MILP methodologies. Section 3 presents the models corresponding to this three phase approach. The proposal has been implemented in the IBM ILOG CPLEX Optimization Studio (IBM, 2014), in which both MILP and CP models can be defined. Section 4 shows the results that have been obtained when addressing various case studies and Section 5 presents concluding remarks.

2. Hybrid CP/MILP model

2.1. Nomenclature

2.1.1. Sets/Indexs

B/b: batches
C_p/c: campaigns comprising a set of batches of product *p*
$Csol^n_{u,p,c}$: set of index triplets representing those campaign tasks associated with campaign *c* of product *p* on unit *u* contained within solution *n*
Fp/-: product couples that correspond to forbidden production sequences f=<*p,p'*>. When the campaign mode is adopted, it includes same product sequences
Fu/-: units belonging to stage *s+1* that are not connected to unit *u* belonging to stage *s*
Nsol/n: set of MILP model solutions
P/p, p': products that are demanded during the scheduling horizon
S/s: processing stages
$Sol^n_{b,u}$: set of index pairs representing those processing tasks of batch *b* executed in unit *u* that are contained within solution *n*
U/u: processing units

2.1.2. Parameters

changeOverTimes: <*p,p',u*> triplets containing the changeover time between products *p* and *p'* on unit *u*
$cost_{p,u}$: processing cost of a batch of product *p* on unit *u*
dd_b: due-date of batch *b*
lb_p: minimum number of batches of product *p* that is possible to process in a row
$nbCampaign_n$: number of campaigns included in solution *n*
$pt_{p,u}$: processing time required by a batch of product *p* in unit *u*
rd_u: ready time of unit *u*
rt_b: release time of batch *b*
ub_p: maximum number of same product batches that is possible to process in a row

2.1.3. Variables

$taskAsig_{b,u,c}$: binary variable representing the allocation of unit *u* to processing task of batch *b* that belongs to campaign *c*
$campaignAsig_{u,p,c}$: binary variable representing the allocation of unit *u* to processing campaign *c* of product *p*
mws_s: end time estimator of the last processing task at stage *s*
y_n: binary variable that is equal to 1 when the current solution (*n+1*) has a smaller number of campaigns than solution *n,* and 0 otherwise
$cBin_{u,p,c}$: binary variable employed to reach a feasible solution at the second phase when a campaign mode is considered
$bin_{b,u}$: binary variable employed to reach a feasible solution at the second phase when a campaign mode is not considered
$task_{b,u,c}$: optional interval variable that represents a processing task of batch *b* that belongs to campaign *c* on unit *u*. If campaign mode is not considered, index *c* is ignored
$campaignTask_{u,p,c}$: campaign interval variable that spans over all the processing tasks that belong to the campaign *c* of product *p* carried out unit *u*
$unitBatchSeq_u$: sequence variable defined for each unit *u*. It represents an ordering of task interval variables associated with *u*. Each interval variable (task) in this sequence is characterized by an attribute. When the changeovers between tasks are unit-independent, this attribute specifies the product *p* associated with each task variable. In case the changeovers are unit-dependent, the attribute represents both, the product and the unit where the task is assigned

$unitCampaignSeq_u$: sequence variable defined for each unit u. It represents an ordering of campaign interval variables associated with u. Each interval variable (campaign) in this sequence is characterized by an attribute that specifies the product p associated with the campaign variable
tar_b: tardiness of batch b

2.2. First phase: MILP Model

Each batch must be assigned to just one processing unit at each stage (constraint 1) and to just one campaign that is the same at all stages (constraint 2).

$$\sum_{\forall\, u\in U_s, \forall\, c\in C_p} taskAsig_{b,u,c} = 1 \qquad \forall\, b \in B_p, \forall\, p \in P, \forall\, s \in S \tag{1}$$

$$taskAsig_{b,u1,c1} + taskAsig_{b,u2,c2} \leq 1$$
$$\forall\, b \in B_p, \forall\, c1, c2 \in C_p \,|c1 \neq c2, \forall\, p \in P, \forall\, u1, u2 \in U \tag{2}$$

Constraints (3) and (4) fix the lower and upper bounds on the number of batches that belong to a particular product campaign.

$$\sum_{b\,\in\, B_p} taskAsig_{b,u,c} \geq lb_p \cdot campaignAsig_{u,p,c} \qquad \forall\, c \in C_p, \forall\, p \in P, \forall\, u \in U \tag{3}$$

$$\sum_{b\,\in\, B_p} taskAsig_{b,u,c} \leq ub_p \cdot campaignAsig_{u,p,c} \qquad \forall\, c \in C_p, \forall\, p \in P, \forall\, u \in U \tag{4}$$

When a particular campaign is assigned to a given unit, to allocate another campaign of the same product it is necessary to assign a different product campaign to avoid the consecutive execution of campaigns linked to the same product (constraint 5). Similarly, in order to assign campaigns associated with a forbidden product sequence to a certain unit, is necessary to assign to such unit a campaign belonging to a non-forbidden product (constraint 6).

$$\sum_{\forall\, c1\in C_{p1}} campaignAsig_{u,p1,c1} \leq 1 + \sum_{\forall\, c2\in C_{p2}, \forall\, p2\in P\,|p1\neq p2} campaignAsig_{u,p2,c2}$$
$$\forall\, p1 \in P, \forall\, u \in U \tag{5}$$

$$\sum_{\forall\, c2\in C_{p2}} campaignAsig_{u,p2,c1} \leq 1 + \sum_{\substack{\forall\, c1\in C_{p1}, \forall\, p1\in P, \\ (p,p2)\in Fp\,|p1\neq p}} campaignAsig_{u,p1,c2}$$
$$\forall\, p2 \in P, \forall\, u \in U \tag{6}$$

Constraint (7) enforces topology restrictions by ensuring that batches are not assigned to consecutive units that are not physically connected.

$$taskAsig_{b,u1,c} + taskAsig_{b,u2,c} \leq 1$$
$$\forall\, b \in B_p, \forall\, c \in C_p, \forall\, p \in P, \forall (u2, u1) \in Fu, \forall\, u1, u2 \in U \tag{7}$$

For each product, a given batch cannot be assigned to campaign *c+1* if the previous campaign *c* for the same product is not allocated into a given unit (constraint 8).

$$campaignAsig_{u1,p,c1} \geq campaignAsig_{u2,p,c2}$$
$$\forall\, c1, c2 \in C_p, \forall\, p \in P, \forall\, u1, u2 \in U_s | c1 + 1 = c2 \wedge s = 1 \tag{8}$$

When the assignment turns out to be unfeasible, cuts are generated by means of constraints (9) to (11). For each previous solution, constraint (9) ensures that the new one will comprise at least a different task. Since the new solution may have a different

task but the same campaigns, which will retain the infeasibility, constraints (10) and (11) ensure the presence of a different combination of campaigns.

$$\sum_{(b,u,c)\in Csol_{b,c,u}^{n}} taskAsig_{b,u,c} < nbTasks \quad \forall\, n \in Nsol \tag{9}$$

$$\sum_{\substack{\forall b\in B_p,\forall c\in C_p,\forall p\in P,\\ \forall u\in U|(b,u,c)\in Csol_{b,u,c}^{n}}} campaignAsig_{u,p,c} < nbCampaigns_n \cdot y_n \quad \forall\, n \in Nsol \tag{10}$$

$$\sum_{\substack{\forall b\in B_p,\forall c\in C_p,\forall p\in P,\\ \forall u\in U|(b,u,c)\in Csol_{b,u,c}^{n}}} campaignAsig_{u,p,c} > nbCampaigns_n \cdot (1-y_n)\ \forall\, n \in Nsol \tag{11}$$

Expression (12) is the objective function to be minimized when a cost-based criterion is chosen. When makespan is selected, constraints (13) and (14) have to be included to take into account the maximum workload at each stage.

$$minimize \sum_{\forall b\in B_p}\sum_{\forall c\in C_p}\sum_{\forall p\in P}\sum_{\forall u\in U} taskAsig_{b,c,u}\cdot cost_{p,u} \tag{12}$$

$$minimize \sum_{\forall s\in S} mws_s \tag{13}$$

$$mws_s \geq \min_{\substack{\forall u\in S_u\\ \forall b\in B}} (rd_u, rt_b) + s \cdot \sum_{\substack{\forall b\in B_p,\forall c\in C_p,\\ \forall p\in P\forall u\in U_s}} taskAsig_{b,c,u}\cdot pt_{p,u} \quad \forall s \in S \tag{14}$$

2.3. Second phase: CP model-I

The duration of each task depends on the unit assigned to it. Constraint (14) fixes the duration when UIS or NIS/ZW policies are adopted. To handle a NIS/UW policy, a greater than or equal to symbol has to replace the equality one in constraint (14). To handle a NIS/FW policy, a couple of similar constraints, which are not presented due to lack of space, need to be added.

$$\begin{gathered} sizeOf\big(task_{b,u,c}\big) = pt_{p,u} \\ \forall b \in B_p, \forall c \in C_p, \forall p \in P, \forall u \in U | (b,u,c) \in Csol_{b,u,,c}^{n} \end{gathered} \tag{14}$$

Tasks belonging to a batch recipe must be executed without any overlapping, satisfying the prescribed inter-stage storage and waiting policies, as well as the precedence relationships. Constraint (15) corresponds to a UIS policy. To handle the other policies the *endBeforeStart* constraint has to be replaced by an *endAtStart* one.

$$\begin{gathered} endBeforeStart\big(task_{b,u1,c}, task_{b,u2,c}\big) \qquad \forall b \in B, \forall c \in C, \forall u1, u2 \\ \in U, \forall s1 \in S_{u1}, \forall s2 \in S_{u2} | (b,u,c) \in Csol_{b,u,c}^{n} \wedge \mathrm{s1} + 1 = \mathrm{s2} \end{gathered} \tag{15}$$

By using the *span* CP construct, constraint (16) ensures that each processing task associated with a campaign takes place within the campaign spanning interval.

$$\begin{gathered} span\big(campaignTask_{u,p,c}, all\big(b \in B_p | (b,u,c) \in Csol_{b,u,c}^{n}\big) task_{b,u,c}\big) \\ \forall c \in C_p, \forall p \in P, \forall u \in U \end{gathered} \tag{16}$$

Constraint (17) enforces all the interval variables associated with a given campaign sequence variable, *unitCampaignSeq*$_u$, to not overlap each other, being separated by the corresponding transition times when the problem being faced has sequence (unit) - dependent changeover times. Constraint (18) avoids forbidden production sequences.

When a forbidden sequence is present, the binary variable $cBin_{u,p,c}$ is equal to zero. Both, the *typeOfNext* and *noOverlap* constructs are described in detail in IBM (2014).

$$noOverlap(unitCampaignSeq_u, changeOverTime) \qquad \forall\, u \in U \tag{17}$$

$$TypeOfNext\left(unitCampaignSeq_u, campaignTask_{u,p,c}\right) \neq p' \cdot cbin_{u,p,c} \quad \forall c \in C_p, \forall p \in P, \forall u \in U, \forall\, (p,p') \in Fp | (u,p,c) \in Csol^n_{u,p,c} \tag{18}$$

When the campaign mode is not considered, constraints (17) and (18) are replaced by constraints (19) and (20)

$$noOverlap(unitBatchSeq_u, changeOverTime) \qquad \forall\, u \in U \tag{19}$$

$$typeOfNext\left(unitBatchSeq_u, task_{b,u}\right) \neq p' \cdot bin_{b,u} \quad \forall b \in B_p, \forall p \in P, \forall u \in U, \forall\, (p,p') \in Fp | (b,u) \in Sol^n_{b,u} \tag{20}$$

Constraint (21) is the objective function to be maximized. A value equal to card($Csol^n_{u,p,c}$) means that a feasible solution was reached. When the campaign mode is not considered, the variable $cbin_{u,p,c}$ must be replaced by $bin_{b,u}$.

$$maximice \sum_{\forall c \in C_p, \forall p \in P, \forall u \in U | (u,p,c) \in Csol^n_{u,p,c}} cbin_{u,p,c} \tag{21}$$

2.4. Third phase: CP model-II

The model corresponding to this phase is similar to second-phase model. Constraints (18) or (20) must be replaced by (22) or (23), respectively. To minimize makespan, the objective function (24) is required and to reduce total tardiness, expressions (25) and (26) are to be included. Constraint (26) captures the tardiness of each batch.

$$TypeOfNext\left(unitCampaignSeq_u, campaignTask_{u,p,c}\right) \neq p' \quad \forall c \in C_p, \forall p \in P, \forall u \in U, \forall\, (p,p') \in Fp | (u,p,c) \in Csol^n_{u,p,c} \tag{22}$$

$$typeOfNext\left(unitBatchSeq_u, task_{b,u}\right) \neq p' \quad \forall b \in B_p, \forall p \in P, \forall u \in U, \forall\, (p,p') \in Fp | (b,u) \in Sol^n_{b,u} \tag{23}$$

$$minimize\ max\left(task_{b,u,c}\right) \quad \forall b \in B_p, \forall c \in C_p, \forall p \in P, \forall u \in U_s | (b,u,c) \in Csol^n_{b,u,c} \wedge s = nbStages \tag{24}$$

$$minimize \sum_{\forall b \in B} tar_b \tag{25}$$

$$tar_b = max\left(0, endOf\left(task_{b,c,u}\right) - dd_b\right) \quad \forall b \in B_p, \forall c \in C_p, \forall p \in P, \forall u \in U_s | (b,u,c) \in Csol^n_{b,u,c} \wedge s = nbStages \tag{26}$$

3. Case studies

The MILP-CP formulation has been tested with several examples. Case 1 is based on the pharmaceutical facility addressed by Novara et al. (2013) adding the following characteristics: unit ready times, topological constraints, forbidden product sequences, banned unit-product assignments, as well as sequence- and unit-dependent changeover times. Fifty different product orders with distinct release times are to be scheduled. Each order comprises four batches. The goal is to find good quality schedules for the 200 batches, minimizing makespan under UIS, NIS/FW and NIS/ZW polices (Cases 1.1 to 1.3 in Table 1, respectively). The second case study was introduced by Kopanos et al. (2010). It considers the scheduling of 60 orders, including stage-dependent changeover times, as well as UIS and NIS/ZW policies (Examples 3.1 and 3.2 in Table 1). The goal is to minimize makespan.

Table 1. Comparison with other approaches. Examples 1 and 2

	Kopanos et al. (2010)		Novara et al. (2013)		This approach	
	OF value	CPU Time (s)*	OF value	CPU Time (s)*	OF value	CPU Time (s)*
1.1	--	--	125975	3578	**117828**	3166
1.2	--	--	NS	NS	**156689**	3595
1.3	--	--	**162471**	3543	163989	3247
2.1	48.548	1502	**42.8967**	1969	49.0680	246
2.2	56.061	1718	**48.6045**	3103	49.4946	610

*Time limit: 3600 seconds

Example 3 corresponds to Case 1 environment. Seven different products are to be manufactured. Nine product orders, having between 3 and 10 batches, need to be scheduled. Each order has a different due date and there are four orders that correspond to just two products. The plant operates under a campaign production policy, having different upper and lower bounds on the number of batches per product. Various interstage storage and waiting policies are considered: UIS (3.1, 3.4), NIS/UW (3.2, 3.5) and NIS/ZW (3.3, 3.6). The goal is to minimize cost. At the CP phase, makespan (cases 3.1 to 3.3) or tardiness (cases 3.4 to 3.6) is minimized as a second criterion.

Table 2. Comparison with other approaches. Example 3

	Novara et al. (2013)				This approach			
	Cost	Tardiness	Mk	CPU Time (s)*	Cost	Tardiness	Mk	CPU Time (s)*
3.1	nsf	nsf	nsf	nsf	75800	1403863	99731	1735
3.2	nsf	nsf	nsf	nsf	75800	1564563	122205	277
3.3	nsf	nsf	nsf	nsf	75800	1769265	128087	2835
3.4	nsf	nsf	nsf	nsf	75800	687213	105837	2759
3.5	nsf	nsf	nsf	nsf	75800	1400432	123596	2396
3.6	nsf	nsf	nsf	nsf	75800	1562640	133290	3508

*Time limit: 3600 seconds nsf: no solution found

4. Conclusions

The proposal has been extensively tested by means of several examples (60 to 200 batches). Numerical results show that for large size cases of plants operating under a campaign mode, the approach can perform better than standalone MILP and CP models, and, more importantly, can solve problems that could not be solved with either of these methods alone. In several instances, the first phase of the approach allows obtaining feasible and efficient assignments, thus avoiding the need for iterations and reducing the required CPU time. This decomposition approach has proved to be quite effective.

5. References

IBM, IBM ILOG CPLEX Optimization Studio. http://www-01.ibm.com/software/integration/optimization/cplex-optimization-studio/, 2014.

Harjunkoski, I., Maravelias, C., Bongers, P., Castro, P., Engell, S., Grossmann, I., Hooker, J., Méndez, C., Sand, G., Wassick, J., Scope for Industrial Applications of Production Scheduling Models and Solution Methods, Computers and Chemical Engineering, 62, 161-193, 2014.

Kopanos, G.M., Méndez, C.A., Puigjaner, L., MIP-based decomposition strategies for large-scale scheduling problems in multiproduct multistage batch plants: A benchmark scheduling problem of the pharmaceutical industry. European Journal of Operational Research, 207, 644-655, 2010.

Novara, F.M., Novas, J.M, Henning, G.P.: A comprehensive CP approach for the scheduling of resource-constrained multiproduct multistage batch plants. In: Computer-Aided Chemical Engineering 32, pp. 589-594. Elsevier 2013.

Krist V. Gernaey, Jakob K. Huusom and Rafiqul Gani (Eds.), 12th International Symposium on Process Systems Engineering and 25th European Symposium on Computer Aided Process Engineering.
31 May – 4 June 2015, Copenhagen, Denmark

Optimal Scheduling of Liquid Drug Product Manufacturing

Lukas G. Eberle[a,b,*], Elisabet Capón-Garcia[a], Martin Senninger[b], Hirokazu Sugiyama[c], Andreas Graser[b], Rainer Schmidt[b], Konrad Hungerbühler[a]

[a]*ETH Zurich, Vladimir-Prelog-Weg 1, 8093 Zurich, Switzerland*
[b]*F.Hoffmann-La Roche Ltd., Grenzacherstrasse 124, 4070 Basel, Switzerland*
[c]*The University of Tokyo, 7-3-1, Hongo, Bunkyo-ku, 113-8656 Tokyo, Japan*
lukas.eberle@roche.com

Abstract

Production scheduling in pharmaceutical production must consider a complex set of features, including due dates, shelf-life, reduced possibility for task execution during night shifts or weekends. Especially when dealing with the sterile production of liquid drug products, production is prone to short-term rescheduling; mainly caused by material scarcity, process duration uncertainty and holding time restrictions. The mentioned complexity and rescheduling challenges motivate the development of production models that are accounting for these features and include efficient campaigning by minimizing the duration of sequence dependant activities. A slot-based model was developed to solve these problems with the objective of minimizing the overall makespan.

The model was applied to a filling line of liquid drug products in an industrial case study, which allowed the validation of the presented model and revealed a 2 % optimisation potential on a ten batch planning goal. The successful implementation for one filling line has motivated the expansion of the model to two parallel and three consecutive processing units.

Keywords: Mathematical Optimisation, Mixed-Integer Linear Programming, Scheduling, Batch Production, Industrial Application.

1. Introduction

The increasingly competitive pharmaceutical industry calls for advanced scheduling models, tailored to the specifics of drug product manufacturing. Optimized schedules support reducing the number of required format changes and isolator sterilizations by optimal sequencing and campaigning, i.e. the production of multiple batches in a row without intermediate re-sterilisation or re-decontamination. In real-life, realistic schedules can only be achieved reasonably by fulfilling all major production constraints in one model simultaneously; including demand, shelf-life, due date, workforce availability as well as capacity of utilities and equipment. On top of these constraints, redefining an optimal batch size and rescheduling of batches are frequent issues caused by reprioritization of products, raw material scarcity and sterile holding time limitations. Hence, optimal scheduling on the shop floor level results in a very complex activity, of utmost importance for maintaining efficient production.

A large amount of scheduling models is available in the literature, and they have a broad field of application (Maravelias, 2012). The current state of the literature has recently been summarized by Harjunkoski et al. (2014) in a review article on scheduling models and their relevance in process industries. Fumero et al. (2014) introduce a methodology that includes many of the aspects, including campaigning and the minimisation of sequence dependant activities but lacks to model effects of limited sterile holding times. The consideration of these limitations and the efficient modelling of the resulting constraints is achieved in the presented model.

2. Methodology

In this work, most of the aforementioned challenges have been addressed and a slot-based formulation is presented, which is inspired by a liquid vial production line, as described in the case study. While considering demand, shelf-life, due date, product-dependent processing rates and sterile holding times, the formulation allows finding the optimal batch sequence with respect to makespan minimization. This goal is achieved by the introduction of a model similar to the one presented by Kabra et al. (2013) and by applying the concept of two operation modes, as described by Moniz et al. (2014).

Routine production runs are illustrated schematically in the top row of Fig. 1. The operation mode (OM) referred to as OM-A illustrates a "single" batch, i.e. a batch that is produced by interrupting the sterile state of the filling isolator before and after the production of that batch. This represents the most simple but also inefficient operation mode, which requires one sterilisation run for each batch. However, operation modes OM-B, OM-C and OM-D to the right of the top row in Fig. 1 represent an alternative way of producing batch-wise, namely campaign mode. This concept has also been described lately in the work of Moniz et al. (2014). For sterile drug products, this operation mode requires the validation of a certain time period, during which an isolator is considered sterile after having performed a successful sterilisation run. Furthermore, all batches in a campaign must be filled into the same glass container format, so that the isolator must not be opened for a format change. Likewise, the necessary cleaning activities between two such batches must allow for the isolator to remain sealed. Products fulfilling these criteria of campaign production are referred to as members of the same product family in this study. The advantage of campaign modes, consisting of a first (OM-B), last (OM-D) as well as *n* intermediate (OM-C) batches,

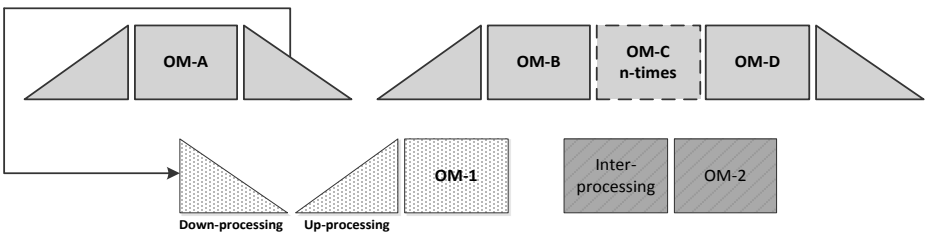

Figure 1: A representation of the operation modes (OM) as performed in pharmaceutical batch production processes. The top row indicates the traditional structure with OM-A as a batch produced individually and the OMs B to D (i.e., OM-B, OM-C and OM-D) in the campaign mode. By performing a task shift, a model reduction to two operation modes OM-1 and OM-2 can be achieved, which requires less computational resources while not reducing the accuracy of the scheduling output.

where *n* can be any natural number including zero, is to maximize production capacity by performing less sterilisation runs per batch.
However, four operation modes (OM-A to OM-D) are computationally expensive and would be difficult to optimise within reasonable time even for small scale problems. A simplification to the problem without limiting the accuracy of resulting scheduling solutions was achieved by executing a task shift, as illustrated by the arrow in Fig. 1, which led to the introduction of OM-1 and OM-2. This model takes advantage of the fact, that up-processing activities must only be performed, if the preceding batch was ending with down-processing and vice versa.
Hence, on the top level the presented solution comprises of batches produced individually (OM-1), and the more time-efficient variant, where multiple batches are produced within a campaign (OM-2), i.e., cleaning and sterilization activities are reduced. A more detailed modelling level is depicted in Fig. 2, which consists of ten tasks and their sequences, which are indicated by arrows.
The execution of all tasks T1 to T7 is necessary for the production of liquid drug product batch in OM-1. However, when filling a batch into the same sort of glass vial as a preceding batch, the format change (T3) must not be executed. Performing tasks T1, T8 and T7 is required for the manufacturing of an OM-2 batch. As can be seen in Fig. 2, the execution of an OM-2 is beneficial when compared to OM-1. The tasks T9 and T10 are included in the model to account for technical services and media fills, respectively. Media fills are batch production runs, during which a culture medium is filled instead of a regular drug product solution in order to assess the sterility of the filling unit.

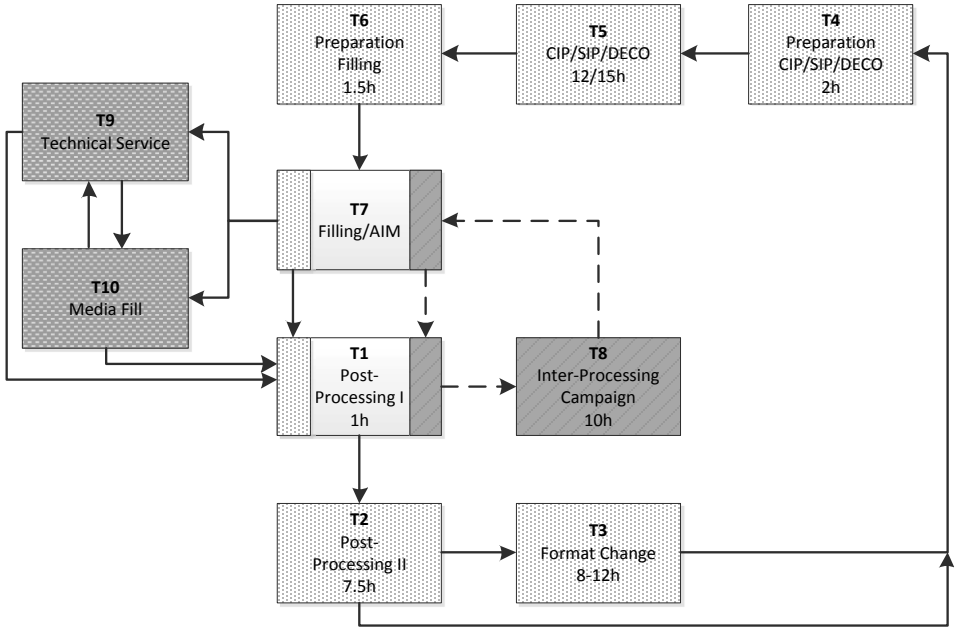

Figure 2: The tasks required for the production of a batch in OM-1 are indicated in the light shaded boxes (T1 to T7). Tasks T1, T8 and T7 are tasks required for executing an OM-2 batch while T9 and T10 are the tasks for technical service and media fill, respectively.

The proposed slot-based scheduling model comprises of Eq. (1) to (13) for a single filling line. The overall objective consists of minimizing the makespan, that is, the sum of the duration of all the batches (Eq. (1)). Eq. (2) defines that the duration of a batch is the sum of the duration of all the tasks that belong to that batch. Therefore, task duration may be either fixed (Eq. (3A)) or batch size dependent (Eq. (3B)). Each batch has to be assigned exactly to one slot (Eq. (4)) and a slot has to be assigned to a single batch (EQ. (5)). In order to determine the operating mode of a certain batch, variable $biS_{s,b}$ is introduced. Eq. (6) imposes that the operating mode of a batch in a certain slot can only be decided if the batch is assigned to that slot. Therefore, the sterility condition imposes that not more than two consecutive batches can be run in OM2 (Eq. (7)). If there is a format change between two consecutive slots, the later has to be run in OM1 (Eq. (8A and 8B)). Finally, it is necessary to define the timing of the different slots. Constraints (9) to (13) assign the starting time of the different tasks of the different slots and impose the conditions on due dates and shelf life.

$$TIME = MIN \sum_{s \in S^{ALL}, b \in B^{ALL}} TB_{s,b} \tag{1}$$

$$TB_{s,b} = \sum_{t \in T^{ALL}} TT_{s,b,t} \quad \forall\, s \in S^{ALL}, b \in B^{ALL} \tag{2}$$

$$TT_{s,b,t} = biT_{s,b} * tasks_t \;\; \forall\, s \in S^{ALL}, b \in B^{ALL}, t \in T^{CONST} \tag{3A}$$

$$TT_{s,b,t} = biT_{s,b} * \frac{q_b}{rf_p} \;\; \forall\, s \in S^{ALL}, b \in B^{API}, t \in T^{VAR}, p \in BP^{ATTACHED} \tag{3B}$$

$$\sum_{s \in S^{ALL}} biT_{s,b} = 1 \quad \forall\, b \in B^{ALL} \tag{4}$$

$$\sum_{b \in B^{ALL}} biT_{s,b} = 1 \quad \forall\, s \in S^{ALL} \tag{5}$$

$$biT_{s,b} \geq biS_{s,b} \;\; \forall\, s, b \tag{6}$$

$$biS_{s,b} + biS_{s+1,b'} + biS_{s+2,b''} \leq 2 \quad \forall\, s \in S^{ALL};\; b, b', b'', p, p', p'' \in BP^{ATTACHED} f, f', f'' \in PF^{ATTACHED};\; f = f' = f'';\; b \neq b' \neq b'' \tag{7}$$

$$biS_{s,b} + biS_{s+1,b'} \leq 1 \quad \forall\, s \in S^{ALL};\; b, b', p, p' \in BP^{ATTACHED};\; f, f' \in PF^{ATTACHED};\; f \neq f';\; b \neq b' \tag{8A}$$

$$biS_{s,b} \geq biS_{s+1,b'} \quad \forall\, s \in S^{ALL};\; b, b', p, p' \in BP^{ATTACHED};\; f, f' \in PF^{ATTACHED};\; f \neq f';\; b \neq b' \tag{8B}$$

$$EP_{s,b,t+1} \geq EP_{s,b,t} + TT_{s,b,t} \;\forall\, b \in B^{ALL};\; s \in S^{ALL};\; t \in T^{ALL} \tag{9}$$

$$EP_{s+1,b,t} \geq EP_{s,b',t'} + TT_{s,b,t} \;\forall\, b, b' \in B^{ALL};\; b \neq b';\; s, s' \in S^{ALL};\; t \in T^{LAST};\; t' \in T^{FIRST} \tag{10}$$

$$EP_{s,b,t} \leq dd_b + M * (1 - biT_{s,b}) \;\forall\, s \in S^{ALL};\; b \in B^{ALL};\; t \in T^{DD} \tag{11}$$

$$EP_{s,b,t} \geq sl_b - M * (1 - biT_{s,b}) \;\forall\, s \in S^{ALL};\; b \in B^{ALL};\; t \in T^{SL} \tag{12}$$

$$EP_{s,b,t} = EP_{s,b',t} \;\; \forall\, s \in S^{ALL};\; b, b' \in B^{ALL};\; b \neq b';\; t \in T^{ALL} \tag{13}$$

Notation: Sets: b,b',b'': batches; s,s',s'': time slots; p,p',p'': products; t: tasks; f,f',f'': product families; B^{ALL}: all batches b; $BP^{ASSIGNED}$: batches b assigned to products p; F^{ALL}: all product families f; $PF^{ASSIGNED}$: products p assigned to product families f; P^{ALL}: all products; S^{ALL}: all time slots; T^{ALL}: all feasible tasks t; T^{CONST}: tasks with a constant

duration; T^{VAR}: tasks with a product dependent duration; T^{DD}: task which is rated as trigger for the due date; T^{SL}: task which is rated as trigger for the shelf life; Parameters: M: big-M; q_b: quantity of all vials in batch b; rf_p: filling rate of product p; dd_b: maximal value of event point $EP_{s,b,t}$ for batch b (i.e. due date); sl_b: minimal value of event point $EP_{s,b,t}$ for batch b (i.e. shelf life); dr_p: product dependent detection rate of AIM; $tasks_t$: duration of all fixed tasks t; Free variables: TIME: makespan of all scheduled batches; Positive variables: $TB_{s,b,t}$: duration of batch b in slot s; $TT_{s,b,t}$: duration of task t of batch b in slot s; $EP_{s,b,t}$ event point of task t of batch b in slot s; Binary variables: $biT_{s,b}$:1 if batch b is performed in slot s; $biS_{s,b}$: 1 if batch b is produced in slot s.

3. Industrial Case Study

The goal of an industrial case study was to validate the proposed model and simultaneously optimize the production schedule, if it was not at optimum yet. As illustrated in Table 1, the case study was performed on a planning horizon of ten production slots and the same amount of batches. Based on expert knowledge and according to the standards of the industry, these ten batches and their respective products were sequenced prior to the study. The production schedule as proposed by company experts is indicated in the second row of the table, termed product.

The case study was performed at a filling line for liquid drug products in a manufacturing facility of Roche in Switzerland. The production at that facility is described in more detail by Eberle et al. (2014), together with a methodology for production time reduction of drug product manufacturing. The sterile production of liquid drug products, so-called Parenterals, is performed batch-wise. Manufacturing processes for Parenterals start with the compounding of a drug product solution, which is then filled into glass vials, sealed and inspected for imperfections before being sent to secondary packaging. The presented case study focuses on the tasks performed at the filling isolator; including the line preparation activities, filling, sealing and post-production tasks. These activities define the line time or makespan necessary for the production of one liquid drug product batch. Since line time is a costly and often scarce commodity, minimizing the required makespan per batch and thereby maximizing the potential productivity is highly desirable.

In Table 1, the third row “family” refers to product families; as described above, these are groups of products that allow for campaign production. The lower three rows of Table 1 indicate the batch sequence for the same ten-slot planning horizon but in the sequence proposed by the presented model. As can be seen, the batches initially scheduled for slots eight and nine were advanced to slots three and four. This change led to the elimination of one format change in the considered planning horizon. However, due to the overall amount of product scheduled for these four batches in product family two, it was not possible to include both batches in one campaign with the batches in slots two and three. The information about the operation modes for the optimized batch sequence is listed in the last row of Table 1. Owing to optimal sequencing, the makespan for the production is reduced by over 2 % compared to the value obtained by company experts; which gives rise to additional production capacities, either for absorbing fluctuations in processing times or for the production of more or larger batches.

Table 1: This table contains the information about the planning horizon considered in the case study. The first line lists the ten production slots in scope, the rest of the table is split in the upper part containing the expert knowledge solution and the corresponding batch sequence as proposed by the presented model. The two batch sequences are in the rows termed product, while the rows termed family indicate whether two batches could be produced in OM-2. The operation mode of the batches as proposed by the model is indicated in the last row, where OM-4 is indicating the media fill scheduled for slot 6.

	Production Slot	1	2	3	4	5	6	7	8	9	10
Expert know-ledge	Product	5	1	4	MF	10	10	10	2	2	5
	Family	I	II	II	III	IV	IV	IV	II	II	I
Model	Family	I	II	II	II	II	III	IV	IV	IV	I
	Product	5	2	1	4	2	MF	10	10	10	5
	Operation Mode	1	1	2	2	1	4	1	2	2	1

4. Conclusions

The proposed methodology allows the simultaneous modelling of multi-product batch production processes, campaign and single-batch operation modes, batch-size dependent processing rates, changeovers, due-date and product shelf-life.

The case study was performed on a planning horizon comprising of ten batches of liquid drug products. The result of the case study validated the usefulness of the proposed model by predicting nearly the same production durations as scheduled by the responsible company experts. On top of that, despite the limited number of batches, a format change could be avoided by more efficient sequencing of batches.

A key feature of this model is the complexity reduction of the filling process, which is performed in several hundred working steps; however, grouping the filling tasks into process elements that need to be performed without major interruptions, e.g., weekends, allowed an efficient modelling with ten tasks only. Due to the promising results on one filling line, the presented model is currently being expanded to account for two additional filling units that run in parallel and the subsequent quality assurance steps.

References

L. Eberle, H. Sugiyama, R. Schmidt, 2014, Improving Production Lead Time of Pharmaceutical Production Processes using Monte Carlo Simulation, Comput. Chem. Eng., 68, 255–263.

Y. Fumero, G. Corsano, J. Montagna, 2014, Simultaneous Batching and Scheduling of Batch Plants That Operate in a Campaign-Mode, Considering Nonidentical Parallel Units and Sequence-Dependent Changeovers, Ind. Eng. Chem. Res., 53, 17059–17074.

I. Harjunkoski, C. Maravelias, P. Bongers, P. Castro, S. Engell, I. Grossmann, J. Hooker, C. Mendez, G. Sand, J. Wassick, 2014, Scope for industrial applications of production scheduling models and solution methods, Comput. Chem. Eng., 62, 161–193.

S. Kabra, M. Shaik, A. Rathore, 2013, Multi-period scheduling of a multi-stage multi-product bio-pharmaceutical process, Comput. Chem. Eng., 57, 95–103.

C. Maravelias, 2012, General framework and modeling approach classification for chemical production scheduling, AICHE J., 58, 1812–1828.

S. Moniz, A. Barbosa-Póvoa, J. de Sousa, 2014, Simultaneous regular and non-regular production scheduling of multipurpose batch plants: A real chemical–pharmaceutical case study, Comput. Chem. Eng., 67, 83–102.

Krist V. Gernaey, Jakob K. Huusom and Rafiqul Gani (Eds.), 12th International Symposium on Process Systems Engineering and 25th European Symposium on Computer Aided Process Engineering.
31 May – 4 June 2015, Copenhagen, Denmark

Optimization of Petrochemical Process Planning using Naphtha Price Forecasting and Process Modeling

Hweeung Kwon[a], Byeonggil Lyu[a], Kyungjae Tak[a], Jinsuk Lee[b], Il Moon[a]

[a] *Department of Chemical and Biomolecular Engineering Yonsei University, Seoul 120-749, Rep. of Korea*

[b] *Samsung Total corporation Dokgot-ri, Daesan-eup Seosan-si, Chungcheongnam-do 356-711, Rep. of Korea*

Abstract

A naphtha price forecasting model based on the time series method is developed to predict the monthly variation of naphtha price using statistics. We used the model to forecast future naphtha prices by looking at historical time series data from January 2008 to September 2011. After forecasting, we perform the normalization of the observed period and implement a simulation using the price forecasting model. In order to check the accuracy of the model, the predicted naphtha price variations are compared with the actual naphtha variation. If the predicted variation of the normalized naphtha price has the same trend as the actual naphtha variation, our prediction value is called "T." Otherwise, the predicted value is called "F." The accuracy of the predicted value is relatively higher than the price forecasting for other products such as crude oil. As a result, our model is useful to industry decision-makers for forecasting the price of naphtha.

Keywords: Forecasting, Naphtha Price, Artificial Neural Network, Exponential Smoothing, Prediction Models

1. Introduction

Naphtha is playing an important role in the world economy, similar to other products such as crude oil. However, the increasing price of naphtha has affected the supply and demand for the product as well as ocean freight costs, both of which have political consequences. Consequently, decision makers hope to reduce the uncertainty of future prices. The naphtha price trend moves mainly in the same direction as that of crude oil, which means that the naphtha and crude oil have a high interoperability. Figure 1 shows the dynamics of WTI (West Texas Intermediate) crude oil and naphtha price in the period between March, 1996 and November, 2011.

Forecasting the price of naphtha is similar to forecasting the price of crude oil and other products. Predictions of crude oil prices have been carried out by many investigators all over the world. Various approach methods of oil price expresses both the linear and nonlinear models. Simple linear regression model predict crude oil prices and stochastic models to calculate patterns of volatility and oil prices. Ye, Zyren and Shore (2006) developed what is known as the multiple linear regression models, which considers

independent variables including GDP, population size, and electricity; a model prediction is then compared with earlier models.

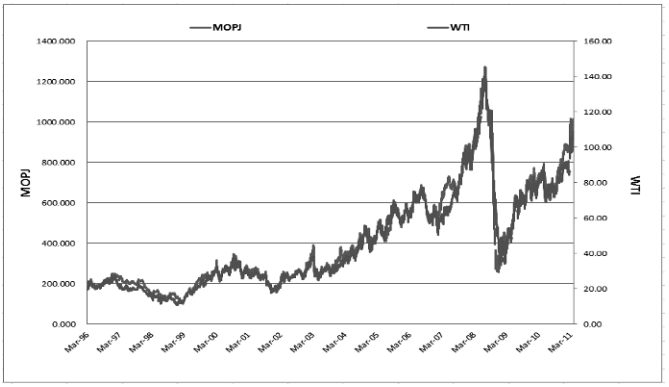

Figure 1. Correlation of MOPJ and WTI.

The purpose of this study is to forecast the correct trend and compare it with the actual naphtha price. In our study, we used two methods based on multiple linear regression and exponential smoothing according to the ratio of training and forecasting intervals. The normalized actual and ANN prediction values are also compared to determine the correct trend for the total period.

2. Forecasting models and simulation results

In this section, the paper considers three different approaches to the forecasting model: (i) statistical; (ii) exponential smoothing; and (iii) the ANN method. The basic concepts of each approach are detailed as follows.

2.1. Statistical model technique

Statistical methods are used to model the linear relationships between dependent and several independent variables. It is based on multiple linear regressions. The statistical model equation, with the error term, is defined as follows:

$$f(x_1, x_{2,} \cdots, x_n) = F_t = \beta_0 + \beta_1 x_{1,n} + \beta_2 x_{2,n} + \cdots + \beta_n x_{n,t} + \varepsilon_n \quad (1)$$

$$F_t = \beta_0 + \sum_{i=0}^{n} i\beta_i x_i \quad (2)$$

β_n is the parameter, and $x_{n,t}$ is each major factor value for a specific time. Each parameter of SMT estimates that the sum of error squares is minimized.

Therefore, the forecasting equation is

$$F_t^{'} = \beta_0^{'} + \beta_1^{'} x_{1,t} + \beta_2^{'} x_{2,t} + \cdots + \beta_n^{'} x_{n,t} \quad (3)$$

Where the symbol ‘ denotes the estimated parameter values. The error term includes multiple regression residuals and, if the model has been predicted, is defined as follows:

$$\varepsilon_n^{'} = F_t - F_t^{'} \quad (4)$$

F_t represents the actual value of a month n; F_t' is the predicted value of a month n. The regression residuals measure the nearness of actual and predicted values in the calibration periods.

The results reported in this section were collected after training data of the statistical models. We proposed a method for time series forecasting using two techniques. In order to carry out the simulation, we divided the data into four datasets (50:50, 60:40, 70:30, and 80:20). The results of each model used for the training and verification parts are compared with real data of the normalized naphtha prices.

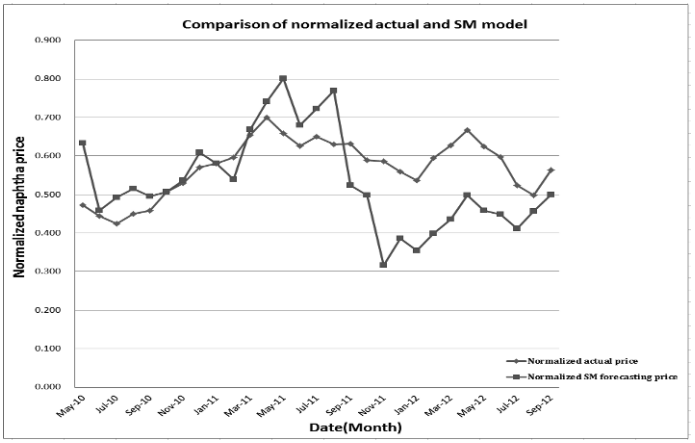

Figure 2. Comparison of normalized actual and predicted SM forecasting values

2.2. Exponential smoothing technique

The exponential smoothing technique was introduced by Robert G Brown. EST can be applies to time series data and is one of the most efficient forecasting methods. When the time series data has no seasonality and no trend, this model is used. The time series data is a sequence of observations. The following simple form of EST is given by

$$F_1 = x_0$$

$$F_t = \frac{Y_1 + Y_2 + \cdots + Y_t}{t} = Y_{t-1} + \frac{Y_t - Y_{t-1}}{t}$$

$$F_t = \alpha x_{t-1} + (1-\alpha) F_{t-1} \tag{5}$$

Where F_t is the forecast value at period t. In this equation, the forecasting value F_t applies the weighting factor of the previous observation data x_{t-1}. α is the weighting factor of EST which ranges from 0 to 1. A small will show a visible EST trend, and a large will provide a quicker response to the recent changes in time series. The exponential smoothing technique was introduced by Robert G Brown. EST can be applied to time series data and is one of the most efficient forecasting methods. When the time series data has neither seasonality nor trend, this model is used.

2.3. Artificial neural network

An Artificial Neural Network (ANN) is a modification of a human brain structure. The neural network (NN) finds a pattern or correlation in a large amount of data with a very complex structure; it is also useful for future predictions. NNs have many features, such as an adaptive system, many simple process elements, and high interconnectivity. ANN is used for computing nonlinear problems and has an enormous number of nonlinear group neurons which fix input and output signals. ANN is a typical method of feed-forward network modeling for time series forecasting. Nonlinear group numbers determine a complex relationship with a high prediction between neurons. The mathematical relationship of ANN between input and output is as follows:

$$F_t = b_0 + \sum_{j=1}^{k} W_j \tan sig(b_{0,k} + \sum_{i=1}^{n} W_{i,j} F_{t-1}) + e_t \tag{6}$$

Where $W_{i,j}$ and W_j are the connecting weight factors of the model parameters, N is the input node number, and K is the output node number. A hyperbolic tangent transfer function is used as a hidden layer, and the equation is as follows:

$$f(x) = \frac{e^x - e^{-x}}{e^x + e^{-x}} \tag{7}$$

This function has a range from -1 to 1. The ANN model using Eq.(7) calculated a nonlinear equation from a past observed date in order to predict a future value.

Figure 3 and figure 4 were comparison of actual and two forecasting models.

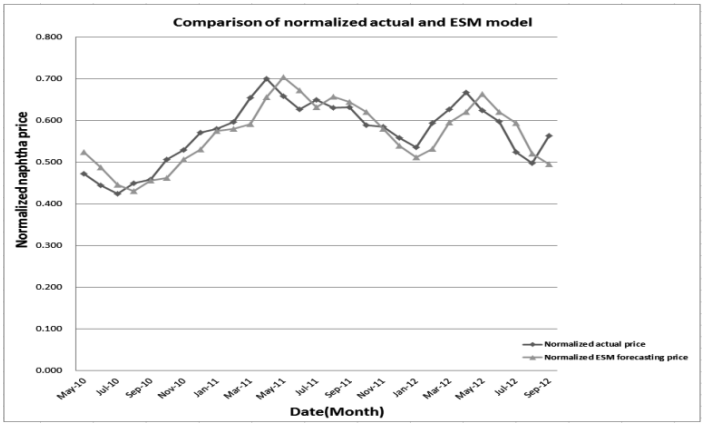

Figure 3. Comparison of normalized actual and predicted ESM forecasting values

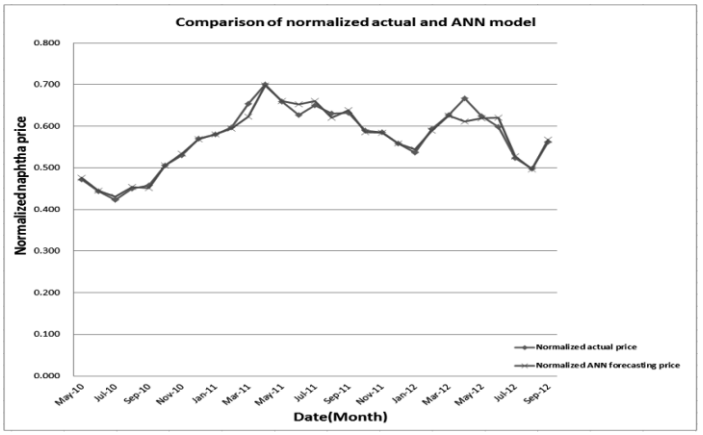

Figure 4. Comparison of normalized actual and ANN model forecasting value

3. Conclusions

In this paper, we developed a method for time series forecasting using two techniques: the EST and statistical methods. This study provides a model to predict naphtha price variation by developing a statistical and EST model. In other words, accurate forecasting for a proportion of a time series is very important for decision making in naphtha purchasing. The best model is analyzed by comparing the forecasting results of the models with the actual values of the naphtha price during several observation periods. The forecasting value of the statistical method is better than the EST method. Furthermore, we predicted the AFP using the ANN method for the time series data. The ANN method was then compared with the actual values and the other two models. The SMT method shows 81.81% and the ANN method shows 93.48% of the total trend AFP. As a result, the AFP of the ANN method is superior to the SMT model.

Acknowledgments

This work was supported by the Ministry of Education (MOE) of Korea by its BK21 **P**rogram.

This research was respectfully supported by Engineering Development Research Center (EDRC) funded by the Ministry of Trade, Industry & Energy (MOTIE).

References

J. Deng, J. Jirutitijaroen, 2010, Short-Term Load Forecasting Using Time Series Analysis: A Case Study for Singapore. 2010 IEEE Conference, 231-236.

Y. Fan, Q. Liang, Y. M. Wei, 2006, A generalized pattern matching approach for multistep prediction of crude oil price. Energy Economy 30, 889-904.

A. Ghaffari, S. Zare, 2009. A novel algorithm for prediction of crude oil price variation based on soft computing. Energy Economy 31, 531-536.

F. Gori, D. Ludovisi, P. F. Cerritelli, 2007, Forecast of oil price and consumption in the short term under three scenarios: Parabolic, linear and chaotic behavior. Energy 32, 1291-1296.

S. H. Kang, S. M. Kang, S. M. Yoon, 2009, Forecasting volatility of crude oil markets. Energy Economy 31, 119-125.

M. Khashei, M. Bijari, G. A. R Ardali, 2009, Improvement of Auto-Regressive Integrated Moving Average models using Fuzzy logic and Artificial Neural Networks(ANN). Neurocomputing 72, 956-967.

A. Lara, M. W. Leger, J. Auers, 2007, Crude Oil Forecasting: A Statistical Approach. Annual Meeting. AM-07-45, National Petrochemical & Refiners Association.

Z, Mohamed, P. Bodger, 2005, Forecasting electricity consumption in New Zealand using economic and demographic variables. Energy 30, 1833-1843.

Z. Raida, 2002, Modeling EM Structures in the Neural Network Toolbox of MATLAB. IEEE Antenna's and Propagation Magazine 44, 46-66.

P. Visetsripong, P. Sooraksa, P. Luenam, W. Chaimongkol, 2008, Naphtha's Price Forecasting using Neuro-fuzzy System. SICE Annual Conference 2008, 659-663.

Y. Wei, Y. Wang, D. Huang, 2010, Forecasting crude oil market volatility: Further evidence using GARCH-class models. Energy Economy 32, 1477-1484.

M. Ye, J. Zyren, J. Shore, 2006, Forecasting short-run crude oil price using high- and low-inventory variables. Energy Policy 34, 2736-2734.

G. Zhang, 2003, Time series forecasting using a hybrid ARIMA and neural network model. Neurocomputing 50, 159-175.

G. Zhang, M. Qi, 2005, Neural network forecasting for seasonal and trend time series. European Journal of Operational Research 160, 501-514.

Krist V. Gernaey, Jakob K. Huusom and Rafiqul Gani (Eds.), 12th International Symposium on Process Systems Engineering and 25th European Symposium on Computer Aided Process Engineering.
31 May – 4 June 2015, Copenhagen, Denmark

Agent-based model of the German Biodiesel Supply Chain

Jorge A Moncada[a,b], Martin Junginger[b], Zofia Lukszo[a], André Faaij[c], Margot Weijnen[a]

[a]*Faculty of Technology, Policy, and Management. Delft University of Technology. Jaffalaan 5, 2628 BX Delft, The Netherlands*
[b]*Copernicus Institute of Sustainable Development. Utrecht University. Heidelberglaan 2, 3584 CS Utrecht, The Netherlands*
[c]*Energy and Sustainability Research Institute. University of Groningen. Nijenborg 4, 9747 AC Groningen, The Netherlands*

Abstract

The production of biodiesel from rapeseed in Germany has been conceptualized using the complex adaptive systems (CAS) theory and formalized using the agent-based modelling approach (ABM). The ABM incorporates farmer's decisions on market choice, and biodiesel producer's decisions on biofuel production and capacity expansion. The ABM was calibrated to replicate the pattern in the evolution of rapeseed, wheat, and biodiesel production in Germany in the period 1992-2012. It was found that complex adaptive systems theory could be used as a conceptual framework to analyse supply chains. In the specific case of biofuels supply chains, where it has been proven that exist due to subsidies and incentives from governments, the agent based modelling approach could be an important tool to analyse the impact of different policies.

Keywords: Agent-based modelling, Biodiesel, Supply chains, Complex Adaptive Systems.

1. Introduction

Complex adaptive systems refers to those systems whose overall behavior is extremely complex, yet whose fundamental components parts are each very simple, and constantly adapt to their environment. Examples of such systems are: Economies, ecologies, immune systems, the brain, and supply chains. Traditionally, supply chains (SC) have been modeled as a pure mathematical formulation (equation-based model). However, the interactions and inter-dependencies among different entities, processes and resources that make the SC a complex network are neglected. This network is highly non-linear, exhibits multi-scale behavior, and evolves and self-organizes making it difficult for an equation-based model to approach it (Surana, Kumara, *et al.,* 2005).

Literature does not provide sufficient sources on analysis of supply chains for biofuels from an agent based modelling perspective. It is worth noting in this area the work done by (van Vliet, de Vries, *et al.*, 2010) where an agent based model to analyze motorists' preferences based on real-world choice mechanisms was developed; (Shastri, Rodríguez, *et al.*, 2011) analysed the dynamics in the adaptation of Miscanthus as an agricultural crop and its impact on biorefinery capacity; the work by (Alexander, Moran, *et al.*, 2013) where the UK perennial crop market, including the interaction of

supply and demand, was modelled using an agent-based approach; and (Singh, Chu, *et al.*, 2014) addressed the problem of biorefinery supply chain network design under competitive feedstock markets. An agent-based model was developed to simulate the feedstock markets.

In the specific case of the German biodiesel supply chain (Kaupa & Selbmanna, 2013) analyzed the drivers that led to the origin of the biofuel industry in Germany. The analysis based on actors and discourse coalitions showed that the German biodiesel industry emerged as a result of national and supranational market interventions. In this work, we developed an agent-based model for the German biodiesel supply chain. The aim of the model is to replicate patterns in the production of feedstock and biodiesel in Germany in the period 1992-2012.

Section 2 introduces the agent-based model development. Agent-based model results for the German biodiesel supply chain are described in section 3. Finally, the main conclusions are drawn in section 4.

2. Model development

The construction of the agent based model starts with the formulation of the problem. The problem is formulated using the generative science approach (Epstein, 2006), which identify and describe the problem based on a macroscopic regularity or pattern in the real world. The methodology proposed by (van Dam, Nikolic, *et al.*, 2013) to build an agent based of a socio technical system was followed.

The aim of the agent-based model is to understand how different policies, either individually or collectively, have triggered: Production of feedstock and biodiesel, and conversion capacity. The impact of these policies on the different actors involved in the supply chain for biodiesel are to be modelled, replicating not only the currently observed pattern, but also exploring what conditions might lead to different outcomes.

Figure 1 presents a biofuel supply chain conceptual scheme. The systems is made up of agents (farmers, oil mill companies, biodiesel producers, distributors, and gas stations), objects (farms, refineries, and facilities), and markets (biomass, oil, diesel, biodiesel). It can be observed how different agents are connected directly (physically) through the flow of rapeseed, oil, biodiesel, and blend biodiesel, respectively. The agents can also interact with the different objects through ownership. The agents interact among themselves through the flow of money (dashed lines) as a result of the trading of products. The decision making of different agents is based on the information (prices) provided by different markets. The environment is composed of the government. The government can influence the price of the different products through incentives in the different markets. To simplify the analysis only three agents are included in the model: Farmers, biodiesel producers, and distributors. The system's environment is composed of the German government which through policies, incentives, and regulations affect some or all of the agents mentioned above.

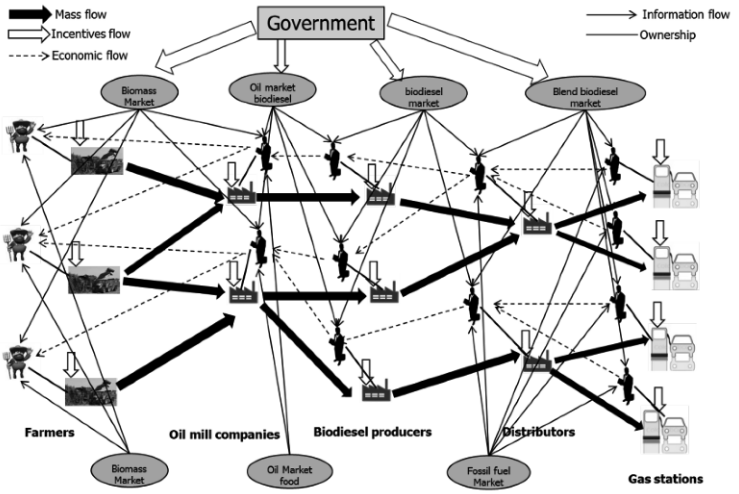

Figure 1. Biofuel supply chain conceptual scheme

Figure 2 shows the simulation sequence used in the agent-based model. The main model's assumptions are summarized below:

- It is assumed that the agents forecast prices for the current year form the very beginning (i.e. 1st January) and schedule their activities for the rest of the year based on the forecasting.
- One tick is equivalent to one year.
- The price of rapeseed does not depend on the type of land (set aside land or arable land).
- Rapeseed transportation costs are charged only to the biodiesel producers.
- Biodiesel transportation costs are charged only to the distributors.
- The penalty is only charged to distributors.
- The length of the link in "NetLogo units" was translated to kilometres based on the longest distance in Germany (North to South, 853 km). Assuming that Germany is a square with 800 km length each patch in the agent based model has a length of 25 km. This value was used as a conversion factor (1 link length = 25 km).

3. Results and discussion

The agent based model for the German biodiesel supply chain was developed in NetLogo. Then, it was calibrated to replicate the pattern in the evolution of rapeseed, wheat, and biodiesel production. From a complex adaptive systems perspective, the German biodiesel supply chain emerged as a result of decisions that are made by the individual agents that cause the collective system behaviour to emerge over time. **Table 1** presents an overview of the base case model parameters. The model was run 50 times to check its robustness. **Figure 3** - **Figure 5** present both historical data and model's results for rapeseed, wheat, and biodiesel production, respectively.

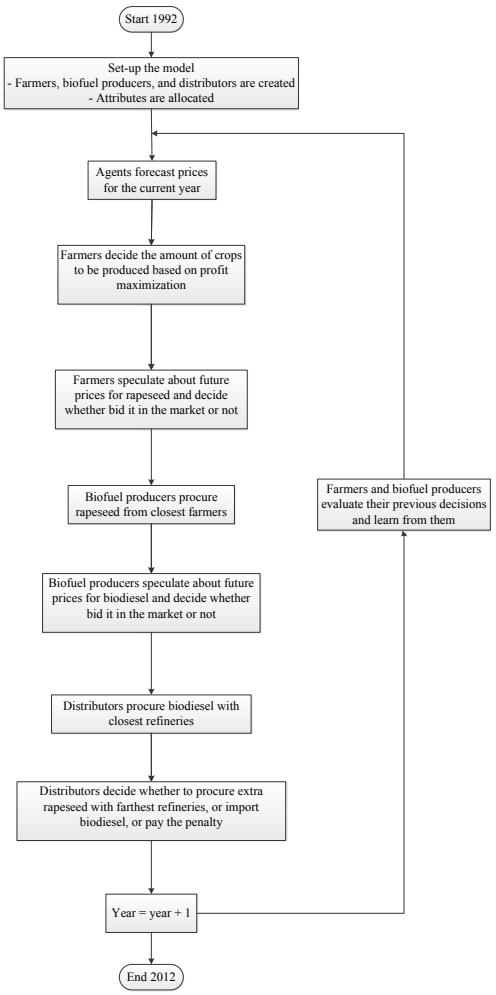

Figure 2. Simulation sequence for the agent-based model

Table 1. Real-world parameter values for the German biodiesel supply chain

Parameter	Value	Unit
Initial land	3,200,000	ha
Set aside land	10	%
Fixed cost biodiesel	0.4 + random[-1.5 - 0.5]	euro/L
Production cost rapeseed	250 + random[-10 - 10]	euro/ton
Production cost wheat	100 + random [-10 - 10]	euro/ton
Yield rapeseed	assigned yearly according to historical data	ton/ha
Yield wheat	assigned yearly according to historical data	ton/ha
Yield biodiesel	1,590	L/ha
Penalty	0.6	euro/L

According to the historical data both production of rapeseed and wheat exhibit an increase in their production as a function of time. Data also shows a higher production of wheat. These characteristics are captured in the model except for the production of rapeseed in 1992 where its production reaches a maximum. This maximum value in the production of rapeseed is due to the high price of rapeseed in 1991 which makes farmers to forecast high prices for rapeseed in 1992 and, as a result it is decided to increase the production of rapeseed. The model's results also exhibits an overproduction of wheat due to it was assumed that farmers are limited to grow only wheat and/or rapeseed. As in the real world farmers have multiple crop choices the wheat overproduction calculated by the model could account for the different crops competing with rapeseed.

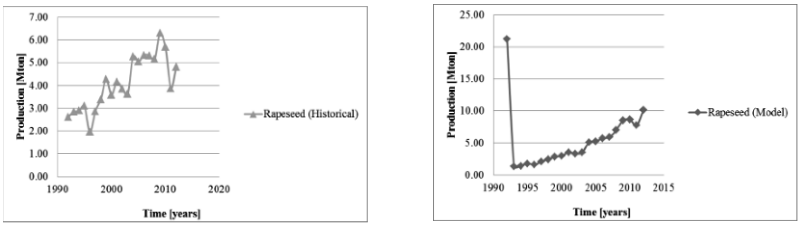

Figure 3. Rapeseed production in Germany according to the historical data (left) and the agent-based model (right)

As shown in **Figure 5** the production of biodiesel reaches a maximum in 2007 since the quota is imposed. Afterwards, the production remains constant. Only a decrease in its production is noted in 2009 possibly because of the economic crisis. The model's results also exhibit these trends. However, the increase in production calculated by the model is not so steep as the reported in the historical data. An explanation for this model's behaviour could be the lack of rapeseed supply close to the facilities. Having an affluence of supply could stimulate the investment on capacity expansion which, eventually, will be translated in bigger productions.

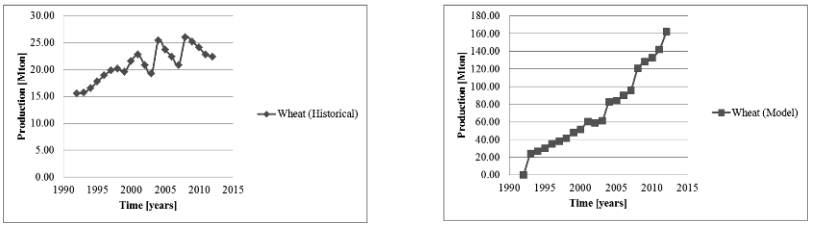

Figure 4. Wheat production in Germany according to the historical data (left) and the agent-based model (right)

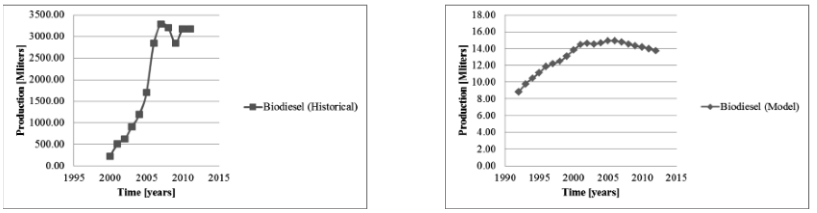

Figure 5. Biodiesel production in Germany according to the historical data (left) and the agent-based model (right)

4. Conclusions

The production of biodiesel from rapeseed in Germany has been conceptualized using the complex adaptive systems (CAS) theory and formalized using the agent-base modelling approach (ABM). Unlike traditional least-cost optimization models, the model includes non-economic attributes and elements of cooperation and competition between different agents. Some lessons were learned:

- Complex adaptive systems theory offers a suitable conceptual frame to analyse complex networks such as supply chains. By using this theoretical framework phenomena such as: emergence, self-organization, and path dependence could be analysed. In this work, the German biodiesel supply chain emerged and self-organized because of the competition and learning effects of the different agents.

- In the specific case of biofuels supply chains (BSC), where it has been proven that exist due to subsidies and incentives from governments, the agent based modelling approach could be an important tool to analyse the impact of different policies on the BSC. Obviously, the validity of the analysis will rely on the model's ability to replicate the actual macroscopic behaviour. Therefore, it is recommended to build the ABM based on historical data if possible.

Finally, it is planned to extend the analysis of the evolution of the German biodiesel supply chain by studying the influence of different policies on the system.

References

A. Rauch, M. Thöne, 2012, Biofuels – At What Cost? Mandating ethanol and biodiesel consumption in Germany, Geneve: Global Subsidies Initiative (GSI) of the International Institute for Sustainable Development (IISD), Switzerland.

A. Singh, Y. Chu, F. You, 2014, Biorefinery Supply Chain Network Design under Competitive Feedstock Markets: An Agent-Based Simulation and Optimization Approach, Ind. Eng. Chem. Res., 53, 15111-15126.

A. Surana, S. Kumara, M. Greaves, U. Nandini Raghavan, 2005, Supply-chain networks: a complex adaptive systems perspective, International Journal of Production Research, 43(20), 4235-4265.

F. Kaupa, K. Selbmanna, 2013, The seesaw of Germany's biofuel policy – Tracing the evolvement to its current state, Energy Policy, 62, 513-521.

J. M. Epstein, 2006, Generative Social Science: Studies in Agent-Based Computational Modeling, New Jersey: Princeton University Press, United States.

K. H. van Dam, I. Nikolic, Z. Lukszo, 2013, Agent-Based Modelling of Socio-Technical Systems. Dordrecht: Springer, The Netherlands.

N. Berghout, 2008, Technological Learning in the German Biodiesel Industry. An Experience Curve Approach to Quantify Reductions in Production Costs, Energy Use and Greenhouse Gas Emissions, Utrecht: Utrecht University, The Netherlands.

O. van Vliet, B. de Vries, A. Faaij, W. Turkenburg, W. Jager, 2010, Multi-agent simulation of adoption of alternative fuels, Transportation Research Part D, 10(326-342), 326-342.

P. Alexander, D. Moran, M. D. Rounsevell, P. Smith, 2013, Modelling the perennial energy crop market: the role of spatial diffusion, J. R. Soc. Interface, 1-10.

Y. Shastri, L. Rodríguez, A. Hansen, K. C. Ting, 2011, Agent-Based Analysis of Biomass Feedstock Production Dynamics, Bioenerg. Res., 4, 258-275.

Krist V. Gernaey, Jakob K. Huusom and Rafiqul Gani (Eds.), 12th International Symposium on Process Systems Engineering and 25th European Symposium on Computer Aided Process Engineering.
31 May – 4 June 2015, Copenhagen, Denmark

A Study of the Sustainable Development of China's Phosphorus Resources Industry Based on System Dynamics

Shujie Ma, Shanying Hu, Dingjiang Chen, Yuzhong Feng

Center for Industrial Ecology, Department of Chemical Engineering, Tsinghua University, Beijing 100084, China

Abstract

As a non-renewable ore, phosphate rock is a very important strategic resource. However, in the process of the exploitation and utilization, there are severe waste and environmental pollution problems which are disadvantageous to the sustainable development of phosphorus resources. In order to promote the sustainable development of China's phosphorus resources industry, this research proposes a system dynamics model with two sub-models for thermal phosphoric acid and wet phosphoric acid separately, considering to the actual situation of regional phosphorus resources industry. This model focuses on industrial, financial, technological and environmental policies for the development of phosphorus resources industry, such as phosphorus resources exploitation, product structure adjustment, waste management and other policies. To find the optimum policy combination of sustainable development, the model which employs resource productivity, economic benefits, ecological efficiency and social satisfaction as objects, explores development situations of phosphorus resources industry and assesses the impacts of the policies by comparative policy scenarios. Results show that under the condition of excess capacity, optimization of phosphate fertilizer product portfolio is more advantageous compared with capacity expansion to increase production value of phosphorus chemical industry. And the combination of total consumption control policy of phosphate rock and acts to promote technical progress improves resource productivity. The implementation of waste recycling policies is conducive to improve continuously the eco-efficiency, and is not conducive to increase economic benefit due to more investment cost. Finally, this study indicates that an effective combination of total consumption control policy, product structure adjustment and appropriate environmental protection will be beneficial to the sustainable development of phosphorus resources industry. In addition, it contributes not only to the conservation of natural resources, but also to a reasonable disposition of the investment which can promote technological progress in industrial weak links. Moreover, the results can provide relevant references for policy makers to make appropriate decisions.

Keywords: system dynamics; phosphorus resources; industrial policy; sustainable development

1. Introduction

As an essential element in national agricultural and industrial development, phosphorus resource is not only to produce a comprehensive and far-reaching impact of economic and social sustainable development but also a very unique strategic resource (Ma et al., 2014). The scarcity of phosphorus recourse will impact the sustainable development of China economy, even the life safety of human being. It is predicted that there is nearly 70 years life- span for the phosphorus reserves, or 10～15 years life- span for the high- grade

phosphorus reserves[w(P2O5) ⩾30%] in China, based on the current phosphate rock (PR) production (Ma et al., 2013). In China, the extraction, production and processing firms of phosphorus rock (PR) gather most in the southwest provinces, such as Guizhou, Yunnan, Sichuan and Hubei province.

Generally speaking, phosphoric acid can be produced from phosphate ore via two major process routes: the thermal phosphoric processes, which produces elemental phosphorus as an intermediate through the burning of the ore in an electric furnace or in a rotary kiln, and the wet phosphoric processes, which uses strong mineral acids to digest the ore. Phosphoric acid produced through the thermal phosphoric process contains fewer impurities such that the resulting acid can be used in "high added value" areas, such as detergents and food additives, whereas phosphoric acid from the wet processes contains more impurities and is primarily used for fertilizers. As it requires more energy consumption, the thermal process will be replaced by the wet process gradually. It is well known that phosphorus resources are non-renewable resources. Due to the exploitation of phosphorus resources, China is facing a shortage of phosphorus resources, environmental pollution, and excess resource waste. To address these problems, we need to optimize the industrial structure of phosphorus resources, to explore new technologies for P recycling and to increase the “three wastes” treatment technology in the manufacturing process of phosphorus resources.

The sustainable development of phosphorus resource is a complex system, contains resources, economy, industry, society, environment and other comprehensive factors. In order to promote the sustainable development of China’s phosphorus resource industry, this study proposes a system dynamics model including four sections for economy, resource, environment and society to research the utilization of phosphorus resources. After verification the model by historical data, and based on four different scenarios, this paper analyses and forecasts the phosphorus resource efficiency in China. The results of analysis can provide implications for industry and governments in China to establish appropriate policies and laws in order to promote sustainable development of domestic phosphorus resource industry.

2. Methodology: System Dynamics Approach

System dynamics (SD), introduced by Jay Forrester in 1960s, is a methodology and mathematical modeling technique for framing, understanding, and discussing complex issues and problems(Yuan et al., 2014). SD models solve the problem of simultaneity (mutual causation) by updating all variables in small time increments with positive and negative feedbacks and time delays structuring the interactions and control. The validation of the model, different policies can be developed by altering certain variables such as retrofitting rate, energy efficiency, construction rate and leave the rest as defined in the base model. The policies are compared to evaluate their impacts on the system behavior and to see their relative effects respect to the baseline.

SD approach has been applied extensively to address critical problems from various fields of studied including social-economic systems (Yuan et al., 2014), ecological systems (Tian et al., 2014), environment issues and sustainability problems (Rehan et al., 2011; Marzouk and Azab, 2014),such as urban energy consumption and CO_2 emissions (Feng, 2013), residential building stock (Onat et al, 2014) , and waste disposal (Yuan et al., 2014).To the best of our knowledge, not much attention has been paid to the research of phosphorus resources industry form the perspective of system dynamics. In this study, a system dynamics model was employed to solve the problem of phosphorus resource sustainable development.

3. A SD model for the Regional Phosphorus Resource Industry

3.1. Model description

The system dynamics model with two sub-models is constructed based on a practical industrial process. Sub-model 1 is a wet-process phosphoric acid (WPA), and the main products are phosphate fertilizer and purified WPA. The representative solid and gas pollution generated in sub-model 1 are phosphor gypsum (PG) and SiF4. Sub-model 2 is a thermal-process phosphoric acid (TPA), and the prime products and pollutants are yellow phosphate, phosphate, phosphorus slag and tail gas.

Fig. 1 illustrates the simplified system dynamics model used in this study, and the actual operations model is more complicated. In the case of phosphorus fertilizer, which is divided into two categories: high-analysis and low-analysis phosphate fertilizer.

The system dynamics model encompasses four sections: economy, resource, environment and society. Many connections of material production and information transmission existed in these sections. In addition to the supply relationship of the upstream and downstream supply, feedback loops also play essential roles in maintaining normal production.

There are two types of feedback loops: reinforcing and balancing. Here take a balancing loop for example: Total Pollution Emission→ (−) Industrial positive impact on society→ (−) Social satisfaction→ (+) Environmental Investment 1-wet/ 2-thermal → (−) Total Pollution Emission.

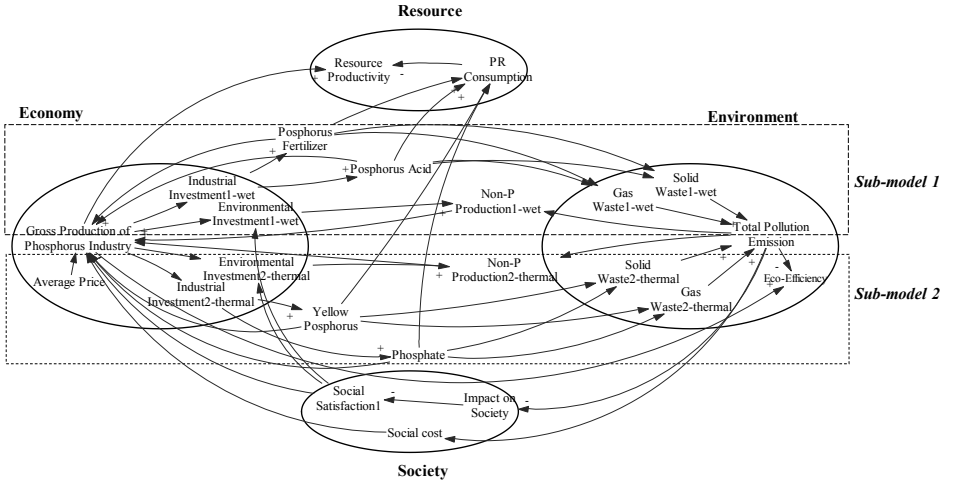

Figure 1. System dynamics model of the phosphorus resources industry illustration

3.2. Variable Definition and Model Assumption

3.2.1 Variable definition

In this paper, Guizhou province is used as a case study. In the current stage, Guizhou also faces the pressures of overcapacity, resource shortages and environmental pollution. The original data available from 2011 to 2013 form the Guizhou phosphate industry are investigated and simplified appropriately. Considering the effect of the five-year plan, the simulation length is 15 years. Given that the comprehension utilization of three types of

waste achieves the required level in Guizhou during this development stage, the societal acceptance of pollution will not be investigated in this study. The indicators of economy, resources and environment are selected as systematic characterizations. These indicators are primarily influenced by the extent of P production. The economic indicators include the gross production of the phosphorus industry and the economic benefit. The environmental indicators include the eco-efficiency and the emission of pollutants. The resource indicators include the resource efficiency and the PR consumption.

3.2.2 Model Assumption and verification

Assumption 1. Considering the constraint of excess capacity and agriculture demand, the production of P fertilizer is assumed to have upper and lower limits. The price of P chemicals are considered to fluctuate according to supply and demand in the market. Assumption 2. In this model, we assume that the environmental impact from the wet and the thermal method follows a 1:1 ratio. Assumption 3. The waste generated from the process is assumed to be discharged according to environmental standards, and environmental investment is used in waste recycling. The comprehensive utilization of wet and thermal wastes is used to produce fine power, methanoic acid and building materials that are based on PG and fluoride-idodine chemicals. Assumption 4. The promulgation and implementation of policies mentioned in this study are almost simultaneous and the time delay is not considered. The model has been verified using operation verification and historical data magnitude verification.

4. Model Simulation and results analysis

4.1. Scenario definition

This study defines four scenarios in which to conduct comparisons and to select different policies, which can be used to draw a rational implementation solution. Specific actions motivating each policy are described below. An expanding industrial policy can be achieved by improving the proportion of industrial investment. The environmental policy can be explained as improving the proportion of the environmental investment and enhancing the comprehensive recycling of solid and gas wastes. Controlling industrial policy can also be achieved by adopting measures contrary to an expanding policy, such as by setting limits on excess P production and by enhancing the deep processing ratio.

Table 1 Strategy and policy description for each scenario

Scenario	Strategy	Policy Description
Baseline	the current situation of P industry	Without compulsive environmental policy
Scenario 1	Expansion of P product production	Individual expanding industrial policy
Scenario 2	Utilization of pollution	Individual environmental policy
Scenario 3	Expansion of P product production, Utilization of pollution	Jointly implement expanding industrial policy and environmental polity
Scenario 4	Improvement of waste recycling efficiency, Control of P products, resource extraction and consumption	Jointly implement controlling industrial and environmental polity

4.2. Analysis of different scenarios

Fig. 2 shows the gross production of the phosphorus industry, the P resource efficiency, the total PR consumption and the P eco-efficiency for different scenarios. The reasons and implications behind the trend curves were analysed. The total PR consumption is coincident with the gross production of the P industry. Similarly, the eco-efficiency follows a similar trend as the resource efficiency. (Refer to Fig. 2. (a), (b), (c), (d)).

Compared with baseline scenario, the gross production has a significant increase in scenario 1, and the increase ranges of the corresponding PR consumption and pollution

emissions can be clearly observed as well. The P resource efficiency and eco-efficiency improve by 50 RMB/ton and 100 RMB/ton, respectively, and the cumulative pollution emissions are reduced in scenario 2. Variations in scenario 2 mean that the comprehensive utilization of the waste can not only reduce the pollution emissions but can also contribute to the economic benefit and efficiencies given the requirements of the technology.

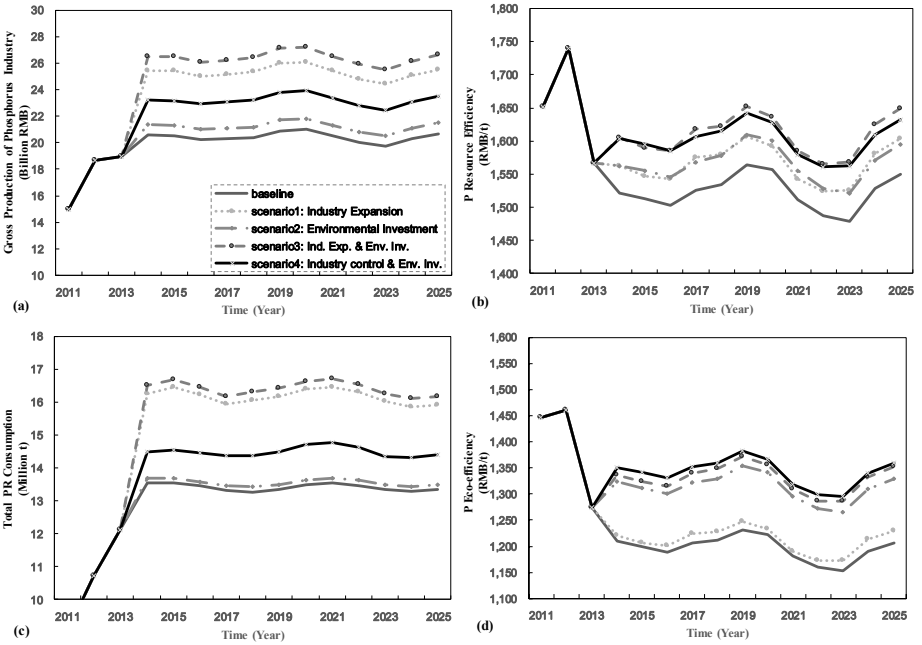

Figure 2. The indicators of economy, resource, environment in each scenario

The P resource efficiencies in scenario 2 are essentially consistent with the change in scenario 1, but the eco-efficiency performs better than in scenario 1. Therefore, compared with a single industrial policy, the implementation of a single environmental policy can both improve efficiencies while compromising fewer economic interests.

Comparing scenario 3 with scenario 1, scenario 2 and the baseline, both the P resource efficiency and the eco-efficiency improve by different amplitudes, which illustrates that the joint implementation of expansive industrial and environmental strategies can achieve a better result than a single implementation. The PR consumption in scenario 3 is greater than in scenario 2 and the baseline and is slightly greater than in scenario 2; however, the gross production increases to 26 billion RMB, which is greater than the other three scenarios, and the pollution emission obviously also declines. Therefore, if the resource consumption remains constant and the two policies are applied together, the amount pollution can be effectively controlled. Meanwhile, a single-minded pursuit of economic growth will not result in a balance between the economy and the environment.

In the case of excess capacity, the P resource efficiency and the eco-efficiency will reach a cyclical peak approximately in the year 2019, correspond to 1643 and 1382 RMB/Ton respectively. Comparing scenario 4 with scenario 1, 2, 3 and the baseline. The gross production and economic benefit in scenario 4 are less than in scenario 3, and the PR consumption is also less, but the resource efficiency is equal. Under these circumstances, the eco-efficiency in scenario 4 is greater than the eco-efficiency in scenario 3. From the perspective of the resource utilization efficiency, the industry should control the production of low-end products and adjust the product structure in a timely manner

instead of consuming more resources, which results in greater pollutant discharge and a smaller increase in income. By comparing scenario 4 with scenario 1, although the former's economic value is higher in the latter scenario, the PR consumption is significantly less than it and the pollutant amount is also less. The results show that even if scenario 4 results in a weaker economy there is the strong advantage with respect to environmental protection, which can be seen in Fig. 2 (b). If the goal is only to expand the product scale without recycling waste, it may not be productive to increase efficiencies. With the main premise of waste management, the curves' performances of scenario 4 and 2 indicate that the consequences of the appropriate expansion of products are beneficial to the productivity efficiency and environment.

5. Conclusions

Based on the theories and methods of system dynamics, we can characterize industrial development situations given different scenarios by adjusting key parameters. By comparing the selected indicators, we can determine the most reasonable and applicable strategies to apply to the current industry standards.

In the case of overcapacity, if increased production is pursued unilaterally by increasing the product scale and if the domestic demand saturation is approached by exporting resource-based, low-end products, the results will not be conducive to the sustainable development of the phosphorus industry. The combination of industrial and environmental policies can contribute to long-term resource productivity and eco-efficiency. Similarly, with respect to technological progress, the comprehensive utilization of waste and the modest expansion of high-end products are favorable conditions to increase the economic benefit, to improve efficiencies and to reduce pollutants. Subsequently, it would be possible to achieve positive outcomes in terms of economic interests, resource conservation and environmental preservation. In the continued studies, the influence of time delay will be added in the system, policies implement and other various factors related with time will also be discussed.

References

D. C. Ma, S. Y. Hu, D. J. Chen, Y. R. Li, 2013, The Temporal Evolution of Anthropogenic Phosphorus Consumption in China and Its Environmental Implications, Journal of Industrial Ecology, 17, 4, 566-577.

H. P. Yuan, J. Y. Wang, 2014, A system dynamics model for determining the waste disposal harging fee in construction, European Journal of Operaional Research, 237,988-996.

M. Marzouk, S. Azab, 2014, Environmental and economic impact assessment of construction and demolition waste disposal using system dynamics, Resource, Conservation and Recycling, 82, 41-49.

N. C. Onat, G. Egilmez, O. Tatari, 2014, Towards greening the U.S. redsidential building stock: A system dynamics approach, Building and Environment, 78, 68-80.

S. J. Ma, S. Y. Hu, D. J. Chen, 2015, A case study of a phosphorus chemical firm's application of resource efficiency and eco-efficiency in industrial metabolism under circular economy, Journal of Cleaner Production, 87, 839-849.

Y. H. Tian, K. Govindan, Q. H. Zhu, 2014, A system dynamics model based on evolutionary game theory for green supply chain management diffusion among Chinese manufacturers, Journal of Cleaner Production, 80, 96-105.

Y. Y. Feng, 2013, System dynamics modeling for urban energy consumption and CO_2 emmissions: A case study of Beijing, China. Ecological Modelling, 252, 44-52.

R. Rehan, M. A. Knight, C. T. Haas, A. J. A. Unger, 2011, Application of system dynamics for developing financially self-sustaining management policies for water and wastewater systems, Water Research, 45, 4737–4750.

Krist V. Gernaey, Jakob K. Huusom and Rafiqul Gani (Eds.), 12th International Symposium on Process Systems Engineering and 25th European Symposium on Computer Aided Process Engineering.
31 May – 4 June 2015, Copenhagen, Denmark

Interplant Carbon Integration Towards Phased Footprint Reduction Target

Dhabia M. Al-Mohannadi, Patrick Linke*, Sumit K. Bishnu, Sabla Y Alnouri

Department of Chemical Engineering, Texas A&M University at Qatar, PO Box 23874, Education City, Doha, Qatar

Abstract

This work presents a first attempt to define and address the multi-period carbon dioxide network synthesis problem for industrial parks. The problem is to determine over time an optimal carbon dioxide reuse networks for reducing the net emissions of the industrial park by utilizing carbon dioxide source flows in carbon dioxide sinks. The formulated optimisation model determines the optimum amount of CO_2 that is to be captured in different time periods with an objective of minimizing total cost of treatment and equipment. It takes into account information on carbon dioxide sources, existing and options for additional sinks, capture and transmission, expansion plans for the industrial park and carbon reduction targets. The approach is illustrated with an example.

Keywords: Carbon Integration, Industrial Park, Multi-Period Optimisation,

1. Introduction

The main purpose of carbon integration is the recovery of carbon dioxide sources into sinks with the goal of reducing the overall carbon footprint of the system at minimum cost. The concept of carbon integration was first introduced by Al-Mohannadi (2014). Other works have been demonstrated in terms of carbon dioxide allocation in geological storage sinks (Middleton and Bielicki, 2009; Tan et al, 2012; He et al, 2013) or in enhanced oil recovery applications (Turk et al, 1987; Alhajaj, 2013; Hasan et al, 2014). Previous work on inter-plant carbon network synthesis (Al-Mohannadi, 2014) does not take into consideration changes to the industrial park over time. In addition, targets for carbon dioxide reductions are typically set over multi-year time periods. This work is a first step towards a systematic approach to explore carbon integration scenarios over time. Such an approach can provide policy makers with important information for the planning of upcoming industrial parks.

2. Carbon Integration in Industrial Parks

Industrial park carbon dioxide emission sources can result either from fuel use or from carbon dioxide byproduct in processes. Therefore, emission reduction can take place at the park input to limit of carbon production and within the park as part of process enhancement through energy integration and the use of clean fuels or at the outlet of the park as end-of-pipe measure by using carbon capture and sequestration. However, carbon dioxide can be converted in many different ways, including chemical or biological conversion into fuel or another value added product (Mikkelsen et al, 2010). Carbon integration presents a systematic approach to integrate carbon dioxide within an industrial park with multiple carbon emitting streams and the potential carbon

utilization options (sinks) that may exist. The approach selects the best sources to be captured with the various utilization options including geological storage and Enhance Oil Recovery (EOR). It determines if the captured carbon dioxide should be purified and takes into account costs of carbon capture, carbon transportation between sources and sinks as well as costs associated with the utilization processes required to determine the most economically attractive footprint reduction solutions. This helps create synergy between plants within the industrial park, help overcome cost limitations in terms of the high carbon capture cost and aids policy makers and designers to plan carbon capture strategies, which cannot be evaluated without considering the aspect of time.

3. Multi-Period Carbon Capture

Multi-period planning helps services and industries negotiate changes over-time.It enables efficient utilization of resources, whether it be for process expansion, or during start up and development phases ensuring smooth transition across various phases of planning. It has been effectively applied for water network synthesis, reactor design, and heat exchange network synthesis. In this work, minimization of cost of carbon network developed across the periods has been set as the objective with aim of reduction of carbon emission. Specific targets have been set for each period and this is one of the constraints in the problem formulation. The concept of specific targets for carbon emission cuts is based on the lines of environmental regulation like GHG protocol, Kyoto protocol and other greenhouse gases emissions reduction agreement.

4. Problem Statement

The model presented aims at synthesizing an optimal cost carbon source-sink allocation network over multiple time periods with target of emission cuts being specified for each period. The problem involves in each time period a number of carbon sources of known flow and composition and a number of carbon sinks with known carbon capture capacity. Carbon flows emanating from can be transferred to sinks either in treated form or without treatment. Both the flows are merged and transported to the concerned sinks using single pipeline.Sinks can collect carbon from various sources and the purity of carbon streams should above specified threshold levels. Emission cuts targets for each period have been specified as a percentage of carbon emission in the first period of planning. Maximum amount of carbon flow from source and sink capacities together with their concentration data are known for each period. Figure 1 presents a general outlay of a carbon network

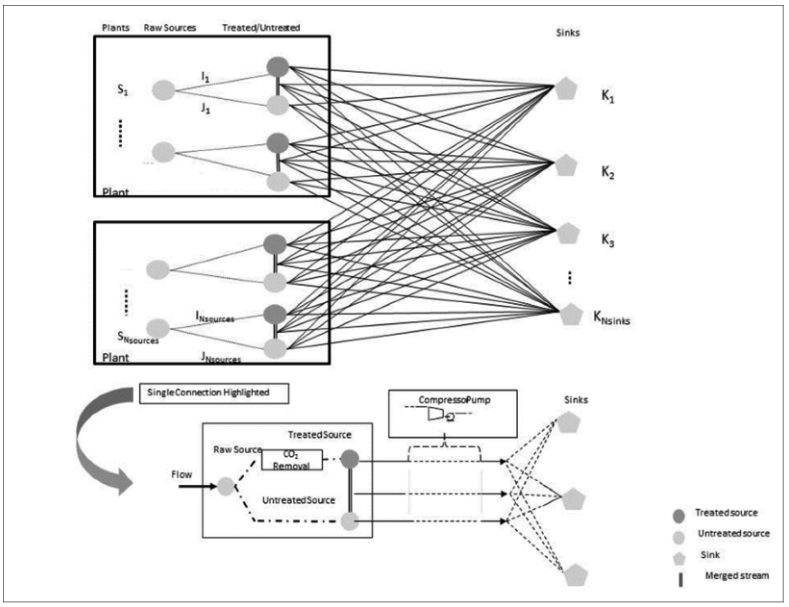

Figure 1. Representation of Carbon Integration Network (Al-Mohannadi, 2014)

5. Model Formulation

The source-sink mapping formulation developed in this work is based on the work by Al-Mohannadi (2014) without consideration of a planning horizon. A Mixed Integer Non-Linear Programming formulation has been developed for the multi-period problem. Each source is split into two kind of streams $F_{i,j,tr,t}$ representing the flow from i^{th} source to j^{th} sink after treatment and a separate stream $F_{i,w,ut,t}$ which represents the flow from each source to sinks without treatment. Constraint on minimum and maximum flow between sources and sinks has been imposed using a binary variable $X_{i,j,t}$ which represents the connection between i^{th} source and j^{th} sink in time period t. The value of X is one if the flow rate associated with the particular stream is non-zero. The objective function used in this work is total network cost over the entire period of planning. The detailed model will be presented in a full-length manuscript.

6. Illustrative example

This example presented here demonstrates the application of multi-period model to a carbon capture network synthesis problem. The case study considers an industrial park layout. The distances are obtained based on a map approximation between different sources and sinks for an industrial park layout in terms of source-to-sink connections is provided in Table 1. Assumptions and calculations of streams data are explained in Al-Mohannadi (2014) based mostly on open literature such as the IPCC Report (Metz et al, 2005).

Detailed information about sources and sinks are provided in Table 2 and Table 3 respectively. Planning has considered for three time periods, each of which spans for three years. Period 1 consists of first three sources while periods 2 and 3 has all the four sources. Carbon capture target for the three periods are 10%, 20% and 30%

respectively. The objective function considered in this work is minimization of total cost which consist of following components-

- Treatment cost of carbon streams.
- Revenues generated from carbon sinks.
- Cost of pipes, pumps and compressors.

Algae, Greenhouses, Storage, Methanol, Urea and Enhanced Oil Recovery (EOR) are the sinks used this work. The capacity of EOR decreases with time. Results may vary according to the estimated capacity for different periods.

Table 1. Distance between Sources and Sinks (km)

Source/sink	Algae	Greenhouse	Storage	Methanol	Urea	EOR
Ammonia	1.72	25.38	1.51	1.51	1.55	1.56
Steel	2.07	25.73	1.86	1.86	1.9	1.91
Power plant	2.77	27.33	2.95	2.95	0.91	0.51
Refinery	2.53	27.09	2.71	2.71	0.66	0.82

Table 2 - Carbon Dioxide Sources

Source	Composition			ρ dry, (kg/m^3)	Estimated C_{si}^T (USD/t CO_2)	CO_2, MTPD
	wt% dry	mol% dry	vol% dry			
Ammonia-CO_2 amine unit	100	100	93	1.85	0	977
Steel-Iron	44	20	21	0.97	29	3451
Power-gas turbine	7	3	3	0.74	43	9385
Refinery-boiler	27	11	11	0.81	35	1092

Table 3- Carbon Dioxide Sinks

Sinks	CO_2 (wt%)	Flow CO_2, MTPD	P(kPa	C^{sink} $/ton CO_2	ε k
Algae	6	283	101	0	0.42
Greenhouses	94	1030	101	-5	0.5
Methanol Solar	99.9	1710	8080	-21	0.098
Urea	99.9	1126	14140	-15	0.29
CO_2-EOR	94	8317	15198	-30	0
Saline Storage	94	8317	15198	8.6	0

The optimization problem for was solved using "What's Best 12.0 " LINDO Global Solver for Microsoft Excel 2013, using a laptop with Intel® Core ™ i7-2620M, 2.7 GHz, 8.00 GB RAM, and a 64-bit Operating System. The results obtained for the multi-period optimization is shown in Tables 4 -7. Cost of pipes, pumps and compressors vary from period to period. This concept is implemented by multiplying fixed

parameters in cost functions of periods 2 and 3. These parameters are ratios of area in the above mentioned periods to area in the first period. Flowrates given are in tons/day.

Table 4 - Time Period 1

Source/sink	Algae	Greenhouse	Storage	Methanol	Urea	EOR
Ammonia	0	0	0	1	0	976
Steel	0	0	0	0	0	7843.18
Power plant	0	0	0	0	0	0

Table 5 - Time Period 2

Source/sink	Algae	Greenhouse	Storage	Methanol	Urea	EOR
Ammonia	0	0	0	0	0	977
Steel	643.18	0	0	0	0	3020.63
Power plant	0	0	0	0	0	0
Refinery	0	0	0	0	0	0

Table 6 - Time Period 3

Source/sink	Algae	Greenhouse	Storage	Methanol	Urea	EOR
Ammonia	0	0	977	0	0	0
Steel	0	0	1096.51	1727.27	0	901.61
Power plant	0	0	0	0	0	501.48
Refinery	1048.15	0	0	0	0	808.87

Table 7 – Piping, Compressors and Pump Cost chart (x 10^6)

Source/sink	Algae	Greenhouse	Storage	Methanol	Urea	EOR
Ammonia	0	0	8.23	0	0	7.02
Steel	3.92	0	9.25	13.06	0	47.05
Power plant	0	0	0	0	0	4.23
Refinery	4.9	0	0	0	0	6.62

The size of a pipe connecting two facilities is chosen in a way that it is able to handle the largest flowrate in any of the time periods in which the connection is present. High pressure natural gas pipes were used to estimate the piping cost while compression cost was approximated using cost correlation based on each connection specific power in a 4-stage compressor. The cost correlations and pumping cost are explained further in Al-Mohannadi (2014). The optimal solution obtained for multi-period optimization has a total cost of - $14958838 over the planning horizon. The negative cost indicates that there is a saving when carbon network integration is done over time.

7. Conclusion

An approach to multi-period planning of carbon network problem has been presented here. A MINLP formulation is solved for a known industrial park expansion plan and emission cut targets for each period of planning. A case study has been developed which illustrates implementation of multi-period optimization. With the assumed parameters for the case study, the solution identifies savings if multi-period optimization approach is adopted for carbon network synthesis especially with the use of EOR. Future works will look into the problem in greater detail and integration of new sinks in the network will be implemented.

Acknowledgements

Support from the Qatar Science Leadership Program (a member of Qatar Foundation) is gratefully acknowledged.

References

A. Alhajaj, N. MacDowell, N. Shah, 2013, Multiscale Design and Analysis of CO_2 Capture, Transport and Storage Networks. Energy Procedia, 37, 2552-61

D. Al-Mohannadi, 2014, A Systematic Approach to Carbon Footprint Reduction Strategies in Industrial Park. MS. Thesis, Texas A&M University at Qatar, Doha.

M. Hasan, F. Boukouvala, E. First, C. Floudas, 2014, Nationwide, Regional, and Statewide CO_2 Capture, Utilization, and Sequestration Supply Chain Network Optimization. Industrial & Engineering Chemistry Research, 53, 7489-506

Y. He, Y. Zhang, Z. Ma, N. Sahinidis, R. Tan, D. Foo, 2013, Optimal Source–Sink Matching in Carbon Capture and Storage Systems under Uncertainty. Industrial & Engineering Chemistry Research, 53, 778-85

B. Metz, O. Davidson, H. De Coninck, M. Loos, L. Meyer, 2005, A. IPCC Special Report on Carbon Dioxide Capture and Storage: Prepared by Working Group III of the Intergovernmental Panel on Climate Change; IPCC, Cambridge University Press: Cambridge, United Kingdom

R. Middleton, J. Bielicki, 2009, A Comprehensive Carbon Capture and Storage Infrastructure Model. Energy Procedia,1, 1611-16

M. Mikkelsen, M. Jorgensen, F. Krebs, 2010, The Teraton Challenge. A Review of Fixation and Transformation of Carbon Dioxide. Energy & Environmental Science, 3, 43-81.

R.Tan, K. Aviso, S. Bandyopadhyay, D. Ng, 2012, Continuous-Time Optimization Model for Source–Sink Matching in Carbon Capture and Storage Systems. Industrial & Engineering Chemistry Research, 51, 10015-20

G. Turk, T. Cobb, D. Jankowski, A . Wolsky, F. Sparrow, 1987, CO_2 Transport: A New Application of the Assignment Problem. Energy, 12, 123-30

Krist V. Gernaey, Jakob K. Huusom and Rafiqul Gani (Eds.), 12th International Symposium on Process Systems Engineering and 25th European Symposium on Computer Aided Process Engineering.
31 May – 4 June 2015, Copenhagen, Denmark

Decision Support by Multicriteria Optimization in Process Development: An Integrated Approach for Robust Planning and Design of Plant Experiments

Michael Bortz,[a,*] Volker Maag,[a] Jan Schwientek,[a] Regina Benfer,[b] Roger Böttcher,[b] Jakob Burger,[c] Erik von Harbou,[c] Norbert Asprion,[b] Karl-Heinz Küfer,[a] Hans Hasse[c]

[a]*Fraunhofer Institute for Industrial Mathematics ITWM, Fraunhofer Platz 1, 67663 Kaiserslautern, Germany*
[b]*BASF SE, Carl-Boschstr. 38, 67063 Ludwigshafen , Germany*
[c] *Laboratory of Engineering Thermodynamics, University of Kaiserslautern, Erwin-Schrödinger-Str. 44, 67663 Kaiserslautern, Germany*
michael.bortz@itwm.fraunhofer.com

Abstract

In simulation-based process design, model parameters, like thermodynamic data, are affected by uncertainties. Optimized process designs should, among different other objectives, also be robust to uncertainties of the model parameters. In industrial practise, it is important to know the trade-off between an increase in robustness and the other objectives – like minimizing costs or maximizing product purities. This contribution describes a practical procedure how to incorporate robustness as an objective into a multicriteria optimization framework. The general procedure is illustrated by a concrete example. Finally, we argue that the same approach is useable for an optimal design of plant experiments.

Keywords: Optimization, robust design, sensitivity analysis, Pareto solutions

1. Introduction

Models for computer-aided process design contain a multitude of physical, chemical and, when it comes to cost functions, also economical and sustainability related parameters. Often these parameters have either been estimated by model adjustment to experimental data, or their values are given by experience. In both cases, these values are not known exactly, but rather within specific uncertainty ranges (we prefer using the term uncertainty range to confidence interval. The term confidence interval has a statistical meaning that is not needed in our discussion). The impact of these ranges on the output functions can be estimated by sensitivity analysis (Saltelli et al. 2008). In sensitivity analysis, different sampling-techniques for scenarios in the space of the uncertain model parameters are available to obtain insight into the importance and the size of the resulting uncertainty ranges in the output functions of the model. The application of Monte-Carlo sampling (e.g. in Xin et al., 2000) demonstrated the importance of analysing the uncertainties in the calculated process designs.
On the other hand, the engineer aims at understanding the influence of the available process parameters on the output functions. This is essential in order to arrive at a process design in the space of process parameters that meets certain criteria in the space

of the output functions. Generally, these optimization problems contain different, often conflicting objectives, like cost and quality measures. In this situation, Multicriteria optimization is a well-established tool to arrive at best compromises (Pareto solutions) between conflicting criteria (adaptive sampling strategies combined with deterministic optimization algorithms have been demonstrated by Bortz et al. (2014)). Navigating the Pareto solutions then visualizes the trade-offs interactively to the planner (Asprion et al. 2011).

In this contribution, we aim at including the sensitivities with respect to uncertain model parameters as further objectives into a multicriteria optimization setting. We call this procedure Robust Planning (RP). The result of RP will be the quantification of trade-offs between increasing robustness to uncertain model parameters and the other objectives. This approach complements the definitions of robust optimization (for a review, see Ben-Tal et al. (2009)) and chance-constraint programming (Ostrovsky et al. 2009). In these approaches, the focus is on an absolute definition of robustness in the sense that solutions can be classified as either robust or non-robust. Our strategy however puts emphasis on the compromise one has to accept in order to arrive at a more robust solution compared to a more sensitive one.

It turns out that in practice, optimal experimental design (OED) is supported in a similar multicriteria setting: On the one hand, the model should be accurate for process designs which are practically relevant (e.g. at low costs, high product qualities). Thus, experiments should preferably be carried out at these designs. On the other hand, in order to reliably estimate model parameters, experiments are favored at which measureable output functions are sensitive to the respective model parameters. A common approach discussed in literature (Franceschini and Macchietto 2008) - focuses on the maximization of different sensitivity measures. Therefore, one defines scalar measures of the sensitivity matrix encoding the sensitivity of certain output functions to relevant model parameters. However, these scalarizations of the sensitivity matrix lead not only to contradictory results (Telen et al., 2012), but also constitute a weighting of matrix entries which has to be known *a priori*. In practice, however, this knowledge does not exist, leading eventually to a loss in optimization potential.

A possible solution suggested in this contribution consists in following a similar route as sketched above for robust process design: For each measurable output function of interest, an adequate sensitivity measure is proposed as one objective to be maximized, among others which also have to be met during the experiment. By doing so, the trade-off between sensitivity, i.e. reliable estimates of model parameters, and good representation of the designs which are practically most relevant is quantified. On this basis, the planner can decide for a process design that realizes the compromise that best suits the current situation. Thus in our approach, RD and OED merely differ in the way how sensitivity measures are treated: As objectives to be minimized for RD, or as objectives to be maximized for OED.

The article is structured as follows. In Section 2 it is described how robustness can be incorporated into a conventional optimization problem. Section 3 contains the illustration of this approach by an example. The article ends with the conclusion in Section 4.

2. Sensitivity as an optimization objective

Sensitivity analysis is used here to quantify the uncertainty range of an output function with respect to given distributions over uncertainty ranges of thermodynamic model

parameters around their reference values. During RP (OED), process parameters are to be adjusted such that, among others, adequate robustness measures derived from the uncertainty ranges of certain output functions are maximized (minimized).
Our starting point is a conventional optimization problem that has been set up and solved, i.e.

- the engineer has chosen one or more meaningful objectives $f_i, i = 1, \dots, N_{obj}$ from the output functions and relevant process parameters $p_j, j = 1, \dots, N_{proc}$;
- one or more (Pareto-) optimal solutions have been obtained by some optimization method. These are given by design points $\boldsymbol{S}_\alpha, \alpha = 1, \dots, N_{Sol}$, with corresponding objective function values $f_{i,ref}(\boldsymbol{S}_\alpha)$. The index *ref* means that the model parameters $x_k, k = 1, \dots, N_{mod}$, are fixed to certain reference values $x_{k,ref}$.

If one now wants to take into account the uncertainty ranges in the x_k one merely has to find out which compromise one has to accept in order to arrive at more (for RP) or less (for OED) robust solutions compared to the $f_{i,ref}(\boldsymbol{S}_\alpha)$. The following steps are recommended:

i. Carry out a conventional sensitivity analysis for a set of design points $\boldsymbol{P}_\beta, \beta = 1, \dots, N_{Points}$, where for each design point a sampling in the N_{mod}-dimensional space of the x_k is done. In order to keep the numerical effort manageable, scenario samplings that scale linearly with N_{mod}, like one-at-a-time or factorial design (Saltelli et al., 2008), should be used. The $\boldsymbol{P}_\beta$ should contain the original Pareto points $\boldsymbol{S}_\alpha$, but do not have to be restricted to them; it is advisable to include some more points, for example, by enumerating points in a suitable neighbourhood around the designs of the Pareto points. The result will be uncertainty ranges in f_i for each $\boldsymbol{P}_\beta$ resulting from the uncertainty of model parameter x_k with lower values $f_{i,k-}(\boldsymbol{P}_\beta)$ and upper values $f_{i,k+}(\boldsymbol{P}_\beta)$. Thus an average relative deviation with respect to the reference value $f_{i,ref}(\boldsymbol{P}_\beta)$ follows:

$$\Delta_{f_i,k}(\boldsymbol{P}_\beta) := \frac{1}{f_{i,ref}(\boldsymbol{P}_\beta)} \sqrt{\frac{1}{2}\left[\left(f_{i,k-}(\boldsymbol{P}_\beta) - f_{i,ref}(\boldsymbol{P}_\beta)\right)^2 + \left(f_{i,k+}(\boldsymbol{P}_\beta) - f_{i,ref}(\boldsymbol{P}_\beta)\right)^2\right]} \quad . \tag{1}$$

This is the measure for robustness used in this contribution. It quantifies the impact of x_k on the objective function f_i at $\boldsymbol{P}_\beta$ and tends to zero if both $f_{i,k-}$ and $f_{i,k+}$ approach $f_{i,ref}$. Without trade-off between the original objectives and minimizing (RP) or maximizing (OED) this measure, then one can stop here.

ii. If there are trade-offs, one includes the corresponding $\Delta_{f_i}(\boldsymbol{P}_\beta)$, into the original optimization problem. In each iteration step during the optimization, a sensitivity sampling has to be done in order to calculate the $\Delta_{f_i}(\boldsymbol{P}_\beta)$, .

It is important that one restricts oneself to the most important *conflicting* objectives in this procedure. The strength of multicriteria optimization is in quantifying trade-offs between best compromises (Pareto-solutions). Objectives that correlate should not be defined as single objectives in the procedure: This would lead to numerical inefficiency and to hiding valuable information.

3. Example

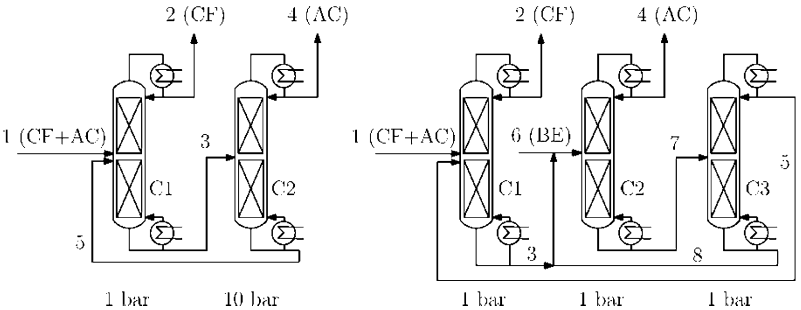

Figure 1: Flow sheets of the pressure-swing (left) and entrainer (right) distillation processes for separating chloroform (CF) and acetone (AC). The entrainer is benzene (BE).

In this section, we want to compare two types of distillation processes for separating a binary mixture of chloroform and acetone into pure components. As these two substances form a maximum boiling azeotrope, a separation in a simple single distillation column is not possible. Two variants for separating the azeotropic mixture are considered: the first is a pressure-swing distillation which takes advantage of the pressure dependency of the azeotrope. In the second one, an entrainer (benzene) is used to influence the phase behavior in a way which makes a separation by distillation feasible. The flow sheets for these two variants are shown in Fig. 1. In Bortz et al. (2014), a comparative multicriteria study of these two variants has been performed with three conflicting objectives: Minimizing the total heat duty and maximizing the product purities in the product streams, i.e. the purity of Acetone in streams 4 and the purity of Chloroform in streams 2; as design parameters, the reboil and split ratios of the columns were taken.

Here we aim at including the robustness of the separation with respect to uncertainties in the VLE data as additional objective that is to be minimized. A NRTL model was taken to model the VLE of the mixtures with reference model parameters given in Bortz et al. (2014). An inspection of original VLE measurements in the Dortmund Data Bank (Onken et al., 1989) revealed that assuming uncertainty ranges in the activity coefficients at infinite dilution, $\gamma^{\infty}_{AC,CF}$ and $\gamma^{\infty}_{CF,AC}$, by ±10 % around their reference values models the accuracy of experimental data well. A Margules approach (Mathias 2014) was then used to incorporate the uncertainties into the corresponding VLE model.

A sensitivity analysis using one-at-a-time-sampling was then performed for a large set of possible design points to analyze the impact of the uncertainty ranges in both $\gamma^{\infty}_{AC,CF}$ and $\gamma^{\infty}_{CF,AC}$. It turned out that the influence of $\gamma^{\infty}_{CF,AC}$ on the objective functions is negligible. Thus in the following, we focus on the impact of the uncertainty range of $\gamma^{\infty}_{AC,CF}$. To keep computational costs moderate, a one-at-a-time-sampling is used here as well to calculate $\Delta_{f_i,\gamma^{\infty}_{AC,CF}}(\boldsymbol{P}_\beta)$, i.e. in Equation (1), one sets $f_{i,k-}(\boldsymbol{P}_\beta) = f_i(\boldsymbol{P}_\beta)\big|_{\gamma^{\infty}_{AC,CF}-10\%}$ and $f_{i,k+}(\boldsymbol{P}_\beta) = f_i(\boldsymbol{P}_\beta)\big|_{\gamma^{\infty}_{AC,CF}+10\%}$. With this set-up, the sensitivity in the product purities of the original Pareto-points was calculated. It turned out that the effect on the Acetone purity dominates the effect on the Chloroform purity by one order of magnitude; furthermore, both effects are highly correlated. Therefore, we restrict ourselves to the uncertainty of the Acetone purity, $\Delta_{Ac,\gamma^{\infty}_{AC,CF}}$, in the following, which we note by Δ_{Ac}. Its values for the original Pareto points are shown in Fig. 3.

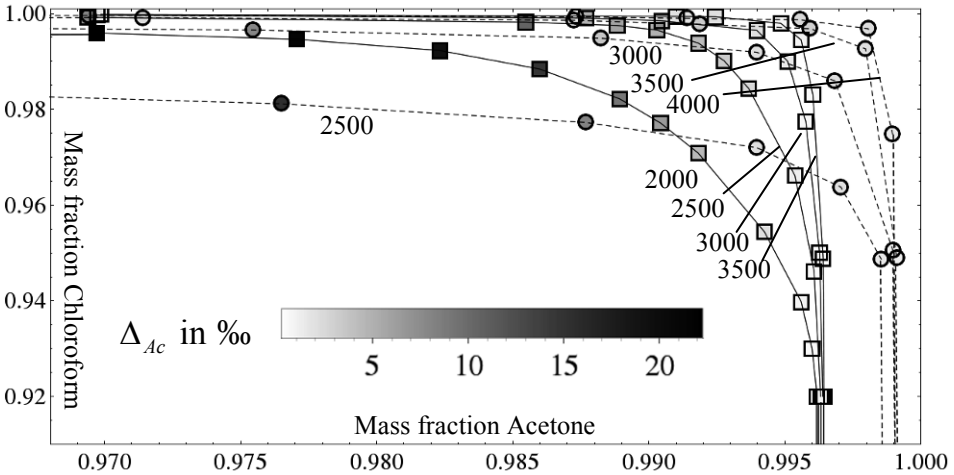

Figure 3: Pareto points for entrainer distillation (squares) and pressure swing distillation (circles) for different heat duties in kW (numbers next to the Pareto sets), calculated by a sandwiching algorithm as in Bortz et al. (2014) maximizing the mass fractions of the two product purities: mass fraction of Acetone (Chloroform) in stream 4 (2)). The grey code denotes the relative uncertainty of the acetone purity.

From the results shown in Fig. 3, two conclusions can be drawn. First, increasing the Acetone purity is not conflicting with its robustness. On the other hand, an increase in the Chloroform purity leads to a decrease in its robustness, which can, however, be counterbalanced by an increase in the heat duty. Thus, in order to achieve certain robustness, one either has to invest sufficient energy, or make a compromise in the Chloroform product purity. This leads to the question how to quantify the trade-off between robustness and product quality.

This question is answered by minimizing Δ_{Ac} as a fourth objective. Since, as argued above, this objective is conflicting with the minimization of the heat duty and the maximization of the Chloroform purity, it can be included into the original Multicriteria framework by introducing appropriate upper bounds and redoing the original problem again. The result is presented in Fig. 4.

Fig. 4 shows the highest possible increase in robustness that can be achieved by accepting a compromise in the Chloroform purity. This gain in robustness at relatively moderate heat duty is similar in value to the robustness obtained by significant increase in the energy invest. Furthermore, Fig 4 demonstrates that the entrainer distillation tends to be more robust to uncertainties of $\gamma_{AC,CF}^{\infty}$ at less energy invest.

4. Conclusions

We presented a practical guideline how to include robustness as one objective among others in a multicriteria optimization framework. If the goal consists in finding robust designs, then robustness as an objective is to be maximized. However, in the framework of optimal experimental design, it is to be minimized. The guideline consists of three steps, starting from the original optimization problem, followed by a sensitivity analysis of the original Pareto points, possibly including an interesting neighbourhood, and leading to the inclusion of robustness as a further objective only where conflicts with the other objectives occur. In order to play to the strength of the multicriteria approach, one should restrict oneself to the representatives of the most important *conflicting*

objectives. The planner then obtains the trade-offs between the objectives. The practicability of our approach was demonstrated by a comparative study between two distillation types, leading to new insights into the competition between maximal product quality, minimal energy invest and maximal robustness.

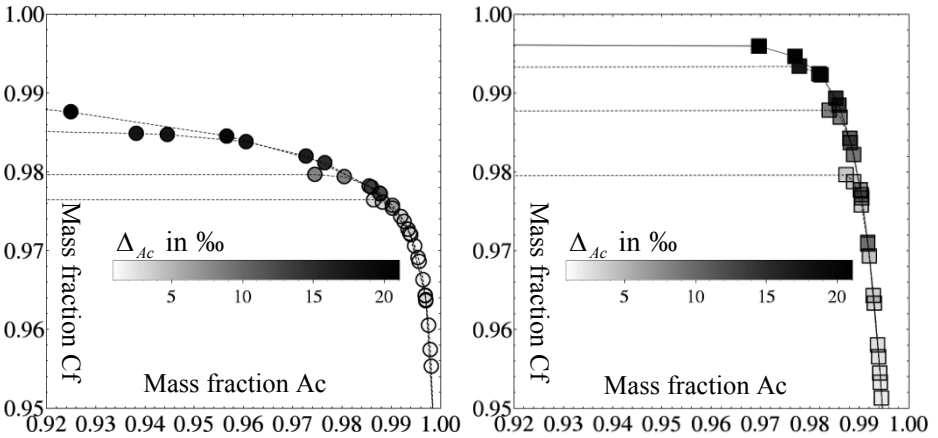

Figure 4: Pareto points for constant heat duty (left panel: 2500 kW, pressure swing distillation; right panel: 2000 kW, entrainer distillation) and bounds on Δ_{Ac}, namely $\Delta_{Ac} \leq 2‰, 5‰, 13‰$ (curves from bottom to top; the grey level is the same in both panels). The uppermost curve represents the case unrestricted in Δ_{Ac}.

References

Asprion N., Blagov S., Ryll O., Welke R., Winterfeld A., Dittel A., Bortz M., Küfer K.-H., Burger J., Scheithauer A., Hasse H., 2011, Pareto-Navigation in Chemical Engineering, European Symposium on Computer Aided Process Engineering, Chalkidiki, Greece, 422-426

Ben-Tal A., El Ghaoui L., Nemirovski A., 2009, Robust Optimization, Princeton University Press

Bortz M., Burger J., Asprion N., Blagov S., Böttcher R., Nowak U., Scheithauer A., Welke R., Küfer K.-H., Hasse H., 2014, Multi-criteria optimization in chemical process design and decision support by navigation on Pareto sets, Comp. Chem. Eng. 60, 354-363

Franceschini G., Macchietto S., 2008, Model-based design of experiments for parameter precision: State of the art, Chem. Eng. Sc. 63 (2008) 4846-4872

Mathias P. M., 2014, Sensitivity of Process Design to Phase Equilibrium – A new Perturbation Method Based Upon the Margules Equation, J. Chem. Eng. Data 59 (2014) 1006-1015

Saltelli A., Ratto M., Andres T., Campolongo F., Cariboni J., Gatelli D., Saisana M., Tarantola S., 2008, Global Sensitivity Analysis, The Primer, John Wiley & Sons.

Telen D., Logist F., Von Derlinden E., Tack I., Van Impe J., 2012, Optimal experiment design for dynamic bioprocesses: A multi-objective approach, Chem. Eng. Sc. 78 (2012) 82-97

Onken U., Rarey-Nies J., Gmehling J., The Dortmund Data Bank: A Computerized System for Retrieval, Correlation, and Prediction of Thermodynamic Properties of Mixtures, Int.J.Thermophys., 10(3), 739-747, 1989, see also http://www.ddbst.com/ddb-search.html

Xin, Y., Whiting, W.B., Case Studies of Computer-Aided Design Sensitivity to Thermodynamic Data and Models, Ind. Eng. Chem. Res. 39 (2000) 2998-3006

Krist V. Gernaey, Jakob K. Huusom and Rafiqul Gani (Eds.), 12th International Symposium on Process Systems Engineering and 25th European Symposium on Computer Aided Process Engineering.
31 May – 4 June 2015, Copenhagen, Denmark

Product and Process Network Modeling and Pathway Optimization with Life Cycle Functional Unit Analysis: The Case of Biofuels

Daniel Garcia, Fengqi You*

Northwestern University, 2145 Sheridan Road, Evanston, Illinois, 60208, USA
you@northwestern.edu

Abstract

Biofuels have been promoted as a possible solution to provide renewable fuels and diminish society's dependence on non-renewable energy sources. However, there are a plethora of possible biofuel product and processes, and an ideal choice is unclear. Furthermore, economic and environmental metrics must be chosen that best analyze the performance of the selected pathway. This work presents a functional unit based approach towards optimization of product and process networks. The mass of ethanol produced in a biofuels network is chosen as the functional unit (FU), and the production cost and global warming potential per FU are computed. Solving the resulting NLFP (nonlinear, fractional program) is reduced to iteratively solving a sequence of MILP by integrating a piecewise linear approximation algorithm using branch and refine methods with the parametric algorithm. A case study processing up to 100,000 tons/hr of a variety of biomass to meet an ethanol demand of 2.88 Mgal/yr is presented.

Keywords: Functional unit, global network optimization, sustainability, biofuels

1. Introduction and Background

Biofuels have generated significant attention in recent years in the business, policy, and research arenas. Much has been made of the potential for biofuels to replace fossil fuels in significant quantities to lessen dependence on petroleum (Yue et al., 2014). Certainly, biofuels can have a prominent position in the clean energy landscape of the future; for some sectors – aviation especially – liquid biofuels are the only viable alternative for petroleum fuels. The United States government also requires that a certain percentage of the nation's fuel consumption be satisfied by biofuels, a policy brought about by the Energy Independence and Security Act (EISA) of 2007. Thus, much research has been directed towards making biofuels economical. In recent years there has been a variety of technoeconomic analyses of biofuel production processes with the goal of demonstrating their economy on a large scale. Examples include algal-based fuel processes (Davis, 2011), hydrothermal liquefaction of woody biomass (Zhu, 2014), cellulosic ethanol processes (Seabra, 2010), ethanol production from corn stover (Kazi, 2010), and ethanol production from switchgrass (Tao, 2011), hydrocarbon fuels frm corn stover (Gebreslassie et al, 2013), among many others. With the advent of these sophisticated technoeconomic analyses, it appears prudent to consider the appropriate way to construct, model, and optimize a biofuels product and process network.

Modeling of biofuel and biomass networks has been identified as critical for the successful implementation and commercialization of biofuel technologies (Yue et al., 2014). To that end, a variety of optimization objectives and methods have been

proposed. Rizwan, Lee, and Gani presented a superstructure-based approach to find the optimal processing pathway for biodiesel production form algae (Rizwan et al., 2013), using objective functions of the yield of biodiesel, gross operating margin, and multi-objective maximization of gross operating margins and minimization of waste. Gong and You also optimized algae fuels networks, but with the objectives of biological carbon sequestration and costs per mass of CO_2 sequestered by the facility (Gong et al., 2014a). Clearly, economics and environmental performance are important considerations when optimizing a biofuels product and process network.

Life cycle optimization has also been applied in the case of biofuels and bioenergy production (You et al., 2011). This optimization style utilizes the ideas behind the life cycle assessment (LCA) methodology, which aims to account for material and energy usage as well as wastes throughout the product's lifetime. A key step in performing an LCA is that of choosing the functional unit (FU), a quantitative unit that aims to relate the process's inputs and outputs (ISO, 1997). Multiple studies have explored using the functional unit methodology for biofuels network optimization in recent years. Gong and You (2014) optimized a algal fuel network using life cycle optimization, with a choice of functional unit of 1 gallon of gasoline equivalent, an energy-based metric. Similarly, Yue et al. (2013) optimized sustainable product system networks and supply chains with a gasoline equivalent metric.

Such energy-based functional units are extremely useful if fuels are the only end product, however, when looking at an overall product and process network where not all products are to be used as fuels, the choice of functional unit becomes murky. A recent Argonne National Lab report on bioproducts – chemicals or other substances made from biomass that are not fuels – presents results on a per mass of bioproducts produced basis (Dunn et al., 2014). If such a functional unit is used, the discussion turns from a sustainable fuels focus to a sustainable product focus. In the case of biofuels, the idea of co-production of bioproducts along with fuels has been proposed, reasoning that this could increase profitability of the selected product and process network, allowing for increased production of sustainable fuels and other products (Bozell, 2010). Thus, a functional unit of kg of products produced is chosen in this work to reflect this slight shift in viewpoint. This shift also has the additional benefit of keeping the presented model general and able to represent a wide variety of product and process networks.

2. Methods

A comprehensive biofuels technology network has been previously constructed to find the optimal processing pathway from a comprehensive product and process network (Garcia et al., 2014); the data and network superstructure was taken from this model. In contrast with the optimization model of that work, however, this work aims to incorporate the functional unit in the optimization methodology. The functional unit chosen for this demonstrative communication will be total mass of products produced per year. It is important to note that any functional unit can be used with the solution strategy employed in this work. A bioconversion technology network with corn, corn stover, hard wood, soft wood, algae, and switchgrass feedstocks available is optimized to produce ethanol (Figure 1). Due to functional unit implementation, a nonlinear fractional programming (NLFP) model is constructed in this work instead of a nonlinear program (NLP). Directly solving NLFP's can consume large computational resources. Thus, a new solving methodology is developed and implemented in this work to obtain reasonable solution times. In the interest of brevity, a full list of the variables,

parameters, and equations will not be presented here; only a summary of our methods is presented along with the pseudo algorithm code of Figure 2.

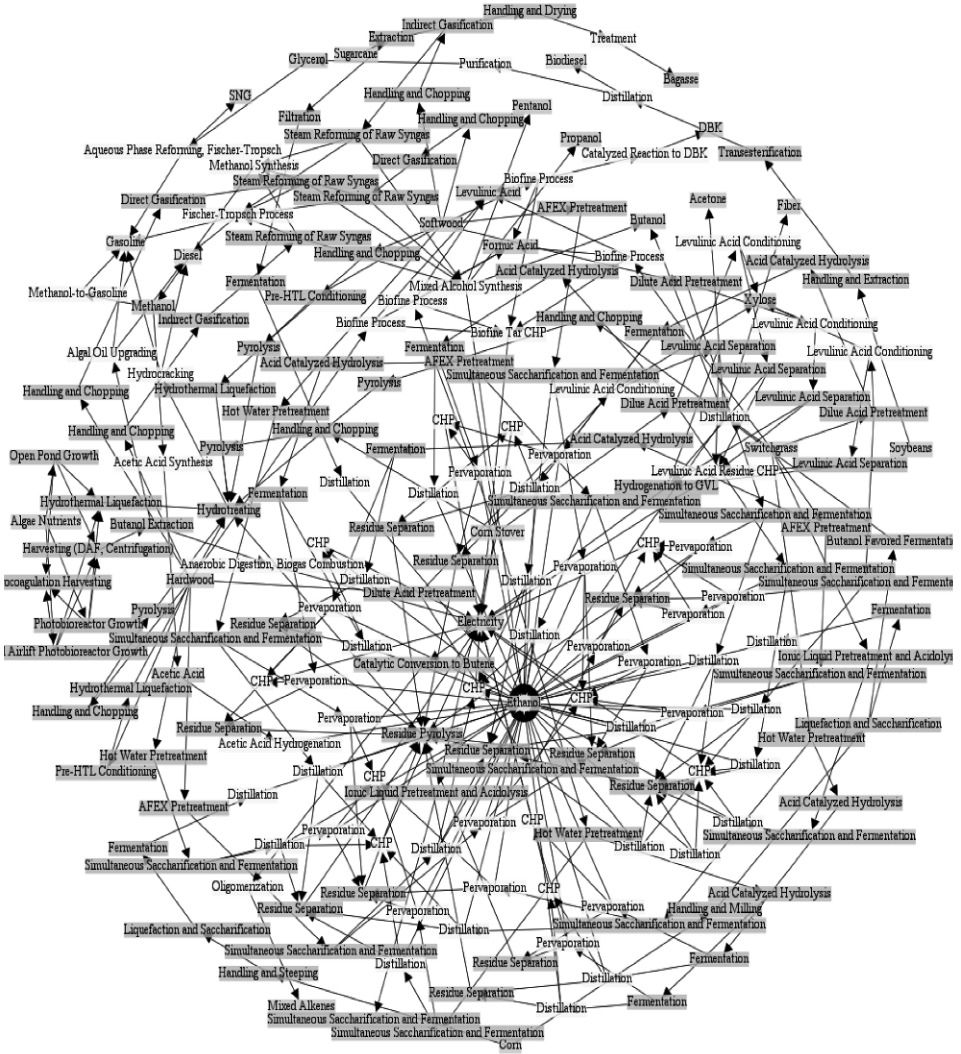

Figure 1. Bioconversion technology network for this problem (Garcia et al., 2014).

The objective function chosen in this work is the production cost per kg of products produced. This choice in objective results in a fractional form of the objective function, potentially complicating the optimization process. A parametric algorithm based on Newton's method is employed to deal with this potential problem, a strategy that has been shown to be very efficient for solving mixed-integer fractional programming problems (Zhong and You, 2014). After implementation of the parametric algorithm, nonlinear, nonconvex terms remain in the calculation of capital costs, as these costs scale nonlinearly with capacity. Once again, in order to reduce the solving times, the capital cost term is approximated by piecewise linear underestimations with an MILP-based branch and refine algorithm (You and Grossman, 2011) using variables of specially ordered sets of type 1 (SOS1), giving a lower bound to the production cost.

This algorithm makes up an inner loop within the parametric algorithm, and iteratively updates its upper and lower bounds until the capital cost convergence is met (see Figure 2). The solution from the branch and refine algorithm is used to update the parametric algorithm parameter. If the parametric algorithm convergence criteria is not met, the parametric algorithm parameter is updated, and the inner loop is revisited. If the convergence criteria of the inner and outer loops are both satisfied, then the solution for the fractional production cost is given by the final value of the parametric algorithm parameter (Gong et al., 2014b). The fractional GWP is then calculated. Prices for feedstocks, fuel products, and bioproducts were taken from a variety of industry, market, and literature sources. Figure 2 describes the procedure for optimizing a model with a fractional production cost objective function.

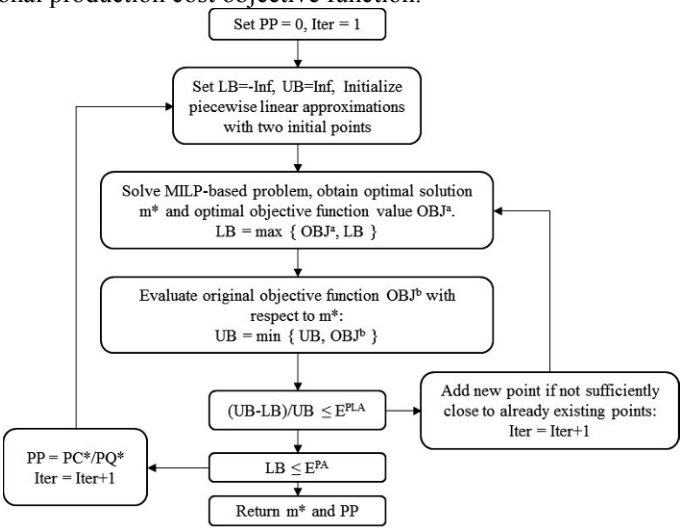

Figure 2. Algorithm flow chart for the proposed parametric algorithm with inner branch and bound piecewise linear approximation loop. PP = parametric parameter; Iter=iteration counter; LB=lower bound; UB=upper bound; Inf=infinite; E^{PLA}=tolerance for piecewise linear approximation; E^{PA}=tolerance for parametric algorithm.

3. Case Study, Results, and Discussion

All experiments were performed on a DELL OPTIPLEX 790 desktop PC with an Intel(R) Core(TM) i5-2400 CPU @ 3.10 GHz and 8 GB RAM. All models and solution procedures were coded in GAMS 24.3.3. The original NLFP problems were solved with BARON 14.0.3. The MILP problem was solved using CPLEX 12.6. The results shown are obtained by solving the MILP problem with the algorithm described above.

An ethanol demand of 2.88 Mgal/yr was to be satisfied by processing any amount of corn, corn stover, switchgrass, hard wood, soft wood, or algae. No feedstock was assigned a minimum purchase amount. The results of this case study are shown in Figure 3. The resulting process makes only ethanol. This is likely due to a lack of demand for other products; making more products will only increase production costs. Another feature of the resulting pathway is the large capacity. The pathway aims to process almost 800,000 tons/yr of soft wood feedstock to make almost 120 million gallons of ethanol per year.

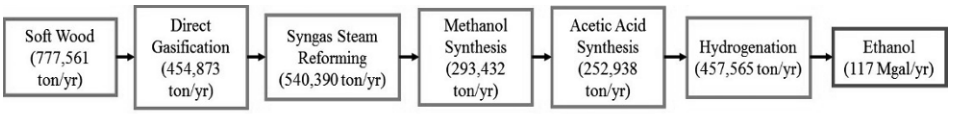

$$\frac{Production\ Cost}{Mass\ of\ Products\ Produced} = \$0.839/kg$$

$$\frac{GWP}{Mass\ of\ Products\ Produced} = 1.413\ kg\ CO_2 - eq/kg$$

Figure 3. Results of the demonstrative case study. Capacities of each technology in the pathway is shown as well as the unit production cost and unit GWP.

The fractional production cost was calculated to be \$0.839/kg of ethanol produced. Since only ethanol was produced in this case study, this production cost can be converted to a cost per gallon: this figure is approximately \$2.50/gal. Thus, the pathway results in a cost per gallon figure that aligns well with current ethanol market prices. The facility produces a large amount of ethanol at an annual operating deficit of less than \$70,000 per year. This large operating scale, however, comes with a high capital cost estimate of approximately \$295 million. Thus, it is clear that reducing the unit production cost arises naturally with economies of scale, as predicted by classical economics.

The fractional GWP of the proposed process is 1.413 kg CO_2-eq/kg of ethanol produced. Similarly to the previous paragraph, we can calculate the kg CO_2-eq/MMBTU as ethanol is the only product; this number is 50.23 kg CO_2-eq/MMBTU. For comparison, burning one kilogram of gasoline results in emissions of approximately 71.3 kg CO_2/MMBTU. No extra GWP is attributed to the combustion of ethanol downstream of the process, as the carbon from the ethanol was assumed to come from the atmosphere during biomass cultivation, resulting in net zero emissions. Thus, this process achieves greenhouse gas savings of ~30% if the produced ethanol is to be used as fuel. A comparison of the performances of BARON 14.0.3 and the proposed algorithm in solving this problem is shown in Table 1. The proposed method displays a clear advantage.

4. Conclusions and Directions for Future Study

In conclusion, it was shown for the first time that functional unit-based optimization of large product and process networks can be seamlessly implemented into existing network optimization methods. In this work, a bioconversion network of

Table 1. Computational performances of the NLP solvers and the proposed algorithm.

	BARON 14.0.3	Proposed MILP-based algorithm
Objective Value (\$/kg)	0.839	0.839
Solution time (s)	2757	20.07

hundreds of technology options and compounds/materials was optimized to find the lowest production cost per mass of products produced. This functional unit was introduced as to offer another analysis method of the impact of potential product and process networks as a whole, instead of focusing on just one aspect of the product portfolio (e.g. fuel/energy content). The algorithm presented was shown to find the optimal solution much faster than off-the-shelf NLP solvers. Thus, this method provides an opportunity for future analysis of integrated product and process network optimization for pathways that produce many types of products – such as the integrated biorefineries of the future.

References

J. Bozell, 2010, Connecting Biomass and Petroleum Processing with a Chemical Bridge, Science, 329, 5991, 522-523.

R. Davis, A. Aden, and P.T. Pienkos, 2011, Techno-economic analysis of autotrophic microalgae for fuel production, Applied Energy, 88, 10, 3524-3531.

J. Dunn, F. Adom, N. Sather, J. Han, S. Snyder, 2014, Life-cycle Analysis of Bioproducts and Their Conventional Counterparts in GREET, Argonne National Laboratory, ANL/ESD-14/9.

D. Garcia, F. You, 2014, Multiobjective optimization of product and process networks: General modeling framework, efficient global optimization algorithm, and case studies on bioconversion, AIChE Journal, 61, 530–554.

B. H. Gebreslassie, M. Slivinsky, B. Wang, F. You, 2013, Life Cycle Optimization for Sustainable Design and Operations of Hydrocarbon Biorefinery via Fast Pyrolysis, Hydrotreating and Hydrocracking. Computers & Chemical Engineering, 50, 71-91.

J. Gong, F. You, 2014a, Optimal Design and Synthesis of Algal Biorefinery Processes for Biological Carbon Sequestration and Utilization with Zero Direct Greenhouse Gas Emissions: MINLP Model and Global Optimization Algorithm, Industrial and Engineering Chemistry Research, 53, 4, 1563-1579.

J. Gong, F. You, 2014b, Global optimization for sustainable design and synthesis of algae processing network for CO2 mitigation and biofuel production using life cycle optimization, AIChE Journal, 60, 9, 3195-3210.

International Organization for Standardization (ISO), 1997, Switzerland, ISO 14040, Environmental management – Life cycle assessment – Principles and framework.

F. Kazi, J. Fortman, R. Anex, D. Hsu, A. Aden, A. Dutta, G. Kothandaraman, 2010, Techno-ecomonic comparison of process technologies for biochemical ethanol production from corn stover, Fuel, 89, Supplement 1, S20-S28.

M. Rizwan, J. Lee, R. Gani, 2013, Optimal processing pathway for the production of biodiesel from microalgal biomass: A superstructure based approach, Computers and Chemical Engineering, 58, 305-314.

J. Seabra, L. Tao, H. Chum, I. Macedo, 2010, A techno-economic evaluation of the effects of centralized cellulosic ethanol and co-products refinery options with sugarcane mill clustering, Biomass and Bioenergy, 34, 8, 1065-1078.

L. Tao, A. Aden, R. Elander, V. Pallapolu, Y. Lee, R. Garlock, V. Balan, B. Dale, Y. Kim, N. Mosier, M. Ladisch, M. Falls, M. Holtzapple, R. Sierra, J. Shi, M. Ebrik, T. Redmond, B. Yang, C. Wyman, B. Hames, S. Thomas, R. Warner, 2011, Process and technoeconomic analysis of leading pretreatment technologies for lignocellulosic ethanol production using switchgrass, Bioresource Technology, 102, 24, 11105-11114.

F. You, I. E. Grossman, 2011, Stochastic inventory management for tactical process planning under uncertainties: MINLP models and algorithms, AIChE Journal, 57, 5, 1250-1277.

F. You and B. Wang, 2011, Life Cycle Optimization of Biomass-to-Liquid Supply Chains with Distributed-Centralized Processing Networks, Industrial & Engineering Chemistry Research, 50, 17, 10102-10127.

D. Yue, M. Kim, F. You, 2013, Design of Sustainable Product Systems and Supply Chains with Life Cycle Optimization Based on Functional Unit: General Modeling Framework, Mixed-Integer Nonlinear Programming Algorithms and Case Study on Hydrocarbon Biofuels, ACS Sustainable Chemistry & Engineering, 1, 8, 1003-1014.

D. Yue, F. You, S. W. Snyder, 2014, Biomass-to-bioenergy and biofuel supply chain optimization: Overview, key issues and challenges, Computers & Chemical Engineering, 66, 36-56.

Z. Zhong, F. You, 2014, Globally convergent exact and inexact parametric algorithms for solving large-scale mixed-integer fractional programs and applications in process systems engineering, Computers & Chemical Engineering, 61, 90-101.

Y. Zhu, M. Biddy, S. Jones, D. Elliott, A. Schmidt, 2014, Techno-economic analysis of liquid fuel production from woody biomass via hydrothermal liquefaction (HTL) and upgrading, Applied Energy, 129, 384-394.

Krist V. Gernaey, Jakob K. Huusom and Rafiqul Gani (Eds.), 12th International Symposium on Process Systems Engineering and 25th European Symposium on Computer Aided Process Engineering.
31 May - 4 June 2015, Copenhagen, Denmark.

Computer-aided design of solvents for the recovery of a homogeneous catalyst used for alkene hydroformylation

Kevin McBride[a] and Kai Sundmacher[a,b,*]

[a]*Max Planck Institute for Dynamics of Complex Technical Systems, Department Process Systems Engineering, D-39106 Magdeburg, Germany*
[b]*Otto-von-Guericke University Magdeburg, Process Systems Engineering, D-39106 Magdeburg, Germany*
sundmacher@mpi-magdeburg.mpg.de

Abstract

Recent works have demonstrated the efficiency of thermomorphic solvent systems (TMS) in the recovery of homogeneous catalysts, especially for the hydroformylation of long-chain alkenes such as 1-dodecene. In this case, the TMS mixture was comprised of dimethylformamide and decane; however, these solvents were not rigorously screened and may represent a suboptimal solution for catalyst recovery. Also, in view of other homogeneously catalyzed reactions, a systematic approach to solvent selection for catalyst recycling is desirable. In this contribution we propose using an established approach by estimating solvent effects on catalyst solubility with the Conductor Like Screening Model for Real Solvents (COSMO-RS). A framework for TMS solvent screening based on the relative solubility of the catalyst ligand, reactant, and product as calculated using COSMO-RS is proposed.

Keywords: computer-aided molecular design (CAMD), COSMO-RS, solvent design, homogeneous catalysis

1. Introduction

Thermomorphic solvent systems (TMS) were proposed by Behr and Fängewisch (2002) as a promising method for recovering homogeneous catalysts from a post-reaction mixture. A TMS consists of polar and non-polar solvents that form a one-phase liquid mixture during the reaction but can be switched into a biphasic mixture upon cooling, thereby enabling separation of the product from the catalyst. These tunable solvent mixtures have been used effectively in recovering homogeneous catalysts, for example, in Behr and Roll (2005) for hydroaminomethylation and in Behr et al. (2005) for hydroformylation, where a general method for the selection of TMS components based on Hansen parameters was presented. Thus, criteria for solvent selection were based on the thermo-regulated phase separation behavior of two or three solvents. This work was expanded upon in Behr et al. (2008) and included many example TMS systems as well as a classification system for different types of TMS depending on the number of solvents and type of miscibility gap formation. In their work, several TMS compositions were investigated for the hydroformylation of 1-dodecene, the example presented in this work. It was shown that a mixture of dimethylformamide (DMF) and decane provided high retention of the catalyst Rhodium-Biphephos while allowing for simple separation of the tridecanal product. They labeled this a Type III TMS, a mixture consisting of only catalyst and product solvents foregoing the use of a third,

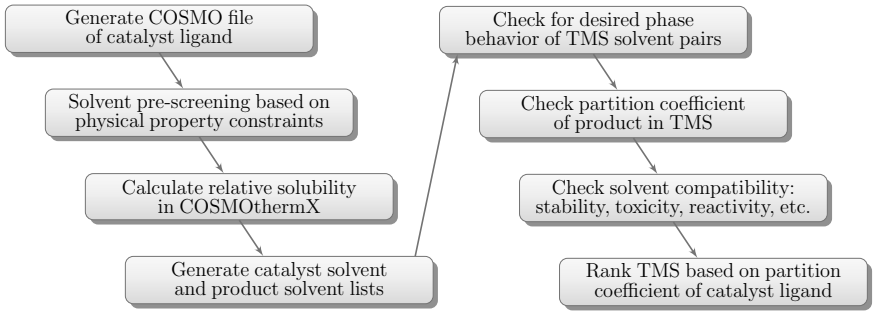

Figure 1: Procedure for TMS design

mediator solvent. This catalyst solvent requires a high affinity for the catalyst while the product solvent should have low catalyst and relatively high product solubilities.

In the present contribution, a method is proposed to identify an optimal type III TMS system with efficiency for catalyst recovery in the hydroformylation of 1-dodecene. This reaction has garnered much attention in recent years, having been the focus of reaction and process optimization by Hentschel et al. (2013). In principle the design of the TMS system should incorporate some aspects of catalyst partitioning into the initial stage of solvent selection. It is proposed that by predicting the thermodynamic properties of the catalyst ligand, a TMS effective at minimizing catalyst loss can be developed from the ground up. Since thermodynamic and experimental data regarding the solvent effects on the catalyst are limited or non-existant, the *ab initio* COSMO-RS model was used as the basis for all thermodynamic predictions.

2. Method and Results

Important criteria for solvent selection have been outlined by Gani et al. (2005), of which several, such as reactivity, solubility, liquid phase at reaction and separation conditions, and phase splitting, are used in this work to judge the physical and mixture properties of TMS solvents. These guidelines as they relate to the task at hand are summarized in Figure 1. The goal is to establish a TMS using a catalyst solvent with high catalyst solubility and to pair it with a product solvent that has low catalyst solubility but also a high affinity for the tridecanal product.

Thermodynamic properties of the catalyst ligand and subsequent solvent screening are calculated using the COSMO-RS method developed by Klamt (1995) as implemented in the commercial software package COSMOtherm by Eckert and Klamt (2014). COSMO-RS is an *a priori* method that combines quantum chemical calculations with statistical thermodynamics allowing for fast calculations of fluid phase interactions. There are many papers in the literature detailing the use of COSMO-RS in its various forms for solvent screening, such as for predicting solubilities of pharmaceuticals by Tung et al. (2008) and Hahnenkamp et al. (2010). A comparison of several thermodynamic models and their ability to predict pharmaceutical solubilities was given by Bouillot et al. (2011). Another important article written relative to this topic is by Wichmann and Klamt (2010), where a detailed description of the COSMO-RS method relating to solvent screening is given. The conclusion in these articles was that COSMO-RS can qualitatively predict the solubility of large and complex molecules in various solvents. Therefore, this method should be suitable for the current task of predicting catalyst ligand solubility.

2.1. Generate COSMO file of catalyst ligand

The first task is to create the COSMO file of the solute used in the process, namely the catalyst ligand Biphephos. Since this molecule is not included in the COSMObase expansion, it must

be computationally modeled and evaluated using a quantum chemical COSMO calculation which evaluates its surface charge in a perfect conductor. The molecular model was developed using TURBOMOLE (2013), at the RI-DFT level of theory from Eichkorn et al. (1997) using the def-TZVP basis set developed by Schäfer et al. (1994). A quantum chemical COSMO calculation for the molecule was performed generating a COSMO file for the Biphephos ligand. This file contains all of the information required for predicting the thermodynamical information required for solvent screening and is used as COSMOtherm input.

2.2. Pre-screening of candidate solvents

To start, a list of candidate solvents from the COSMObase extension is to be generated. Certain molecular properties, such as molecular weight, melting temperature, boiling temperature, screening charge, and component atoms, can be used as constraints to pre-screen solvent candidates. In this example, the search space was left intentionally large with physical property constraints limited to boiling temperature and molecular weight. The boiling temperature was chosen to be between zero and 260 °C, 20 °C less than the boiling point of tridecanal to avoid possible azeotrope formation in a subsequent distillation column. Candidate molecules were also restricted to molecular weights not higher than 200 g/mol leaving 2813 molecules as potential solvents.

2.3. Solvent screening: catalyst solubility

The next step is to estimate the relative solubility of the Biphephos ligand in the candidate solvents. Relative solubility is evaluated using the solvent screening option in COSMOthermX. The relative solubility of Biphephos in all 2813 solvents must be calculated at once in order to compare values. This is predicted using the chemical potential, $\mu_i^{solvent}$, of the solute at infinite dilution in the pure solvent as calculated by COSMO-RS (Eq. 1) based on statistical thermodynamics using sigma profiles of the involved components. All relative solubilities were investigated at 25 °C.

$$\ln(x_i) = \mu_i^{solvent}/RT \tag{1}$$

Two lists are generated: one with solvents predicted to have high relative solubility of the catalyst ligand (HRSC) and the second with those having low relative solubility of the catalyst ligand (LRSC). One solvent from each list will be used as a component in the final TMS. In Table 1 the top five performing HRSC and LRSC solvents are respectfully presented. From the candidate solvents, hydrofluoric acid should have the highest solubility for Biphephos while water should have the lowest solubility, about 18 orders of magnitude less. However, it should be immediately clear that not all molecules in Table 1 are suitable for use as solvents as all of the HRSC solvents are either highly reactive acids, strong oxidizers, or destructive to the ozone. The LRSC solvents are also quite reactive and/or toxic outside of water, which cannot be used due its poor affinity for the product and reactant. Obviously it is undesirable to determine which of the almost 3000 solvents are poor candidates based on reactivity, toxicity, or by some other property at this stage. Therefore, removal of such solvents is done at a later point in the screening process when fewer candidates remain, trading calculation time for research time. To ensure, however, that reliable candidates are found, the HRSC list contains the top 100 solvents for catalyst solubility and the LRSC list contains all molecules from octane down. This is done to compare the effects of shorter alkanes with the performance of decane, for which some data with DMF is available from Brunsch (2013). This leaves 403 solvents in the LRSC list.

2.4. Miscibility gap formation

To generate a functioning TMS, one must ensure that biphasic separation occurs within the post-reaction mixture containing non-converted reactants as well as the product. For this, COSMOtherm was implemented to estimate miscibility gap formation. Liquid-liquid equilibrium calculations were carried out for each HRSC and LRSC solvent pair, 40,300 in total. A temperature of

Table 1: Top 5 high (HRSC) and low (LRSC) relative solubility catalyst solvents

HRSC	$\log_{10}(x_i)$	LRSC	$\log_{10}(x_i)$
Hydrofluoric acid	0.0000	H_2O	-18.4128
Selenic acid	-1.0582	Formamide	-12.7388
Chlorosulfonic acid	-1.2406	Hydroxyacetonitrile	-12.2432
ClO_2	-2.6015	Butanedinitrile	-12.1521
1,1,1-Trifluoro-2-bromoethane	-3.0996	Dicyanomethane	-11.6746

-25 ^{o}C, the lower bound of the method's planned experimental validation, was selected for these calculations. The size of the miscibility gap was not regarded; simple biphasic formation was considered acceptable to avoid potential LLE prediction errors. A total of 5225 TMS mixtures were predicted to form two liquid phases at the desired temperature. Miscibility gap formation at 100 ^{o}C, a reasonable temperature for the reaction, is calculated for the final, valid TMS compositions. Of these, only one did not form a homogeneous mixture.

2.5. Product and ligand distribution

Once candidate solvent pairs have been identified, it is of interest to ensure the TMS extracts the product from the post-reaction mixture as intended. Partition coefficients of tridecanal according to Eq. 2 were used to evaluate this distribution. Solvent mixtures with a partition coefficient of less than 0.25 (lower is better) were considered for further screening, leaving 350 potential solvent pairs.

$$\log_{10}(P_j^{(2,1)}) = \log_{10}(\exp((\mu_j^{(1)} - \mu_j^{(2)})/RT) \cdot V_1/V_2) \tag{2}$$

Here, $\mu_j^{(i)}$ is the chemical potential of species j at infinite dilution in species i, where j stands for the reaction product tridecanal, 1 for the HRSC solvent, 2 for the LRSC solvent, and V for the estimated solvent volume.

2.6. Suitable solvent solutions

At this point, individual solvents were eliminated for the various reasons mentioned in section 2.3. Solvents were also removed when melting temperature data was unavailable, for having a melting temperature above the separation temperature, and for containing double and triple bonds, which may react during hydroformylation. The remaining HRSC solvents included acetaldehyde, DMF, acetone, n,n-dimethylacetamide, n-methyl-2-pyrrolidone, methylacetate, and n,n-diethylformamide, all good hydrogen bond donors with low non-polar profiles. The LRSC solvents are comprised exclusively from linear, branched, and cyclic alkanes. In total, 208 TMS mixtures remain as one TMS was predicted to form a miscibility gap at 100 ^{o}C.

2.7. Analysis

The TMS systems are now ranked according to the partition coefficients in the HRSC and LRSC solvents respectively, calculated using a variation of Eq. 2, with j representing Biphephos and also ignoring the volume quotient of the solvents. Thus, the partition coefficients for Biphephos are simply the logarithm of the relative solubility quotients calculated in the second screening step. The top ten TMS systems based on catalyst partition coefficients are listed in Table 2 (higher is better). Here it can be seen that for good catalyst recovery and functioning product separation, catalyst solvents acetaldehyde and DMF paired with long-chain alkanes as product solvents are recommended. It can also be seen that with increasing alkane chain-length, catalyst recovery

capacity increases due to the increase in non-polarity of the non-polar phase. Tridecanal separation decreases for the same reason.

Since all LRSC solvents are long-chain alkanes, a general comparison of HRSC performance can be made when fixing the LRSC as *n*-decane. This was chosen due to its common use and that some experimental data is available for comparison. Results for the top TMS systems using *n*-decane are given in Table 3. Here we also see acetaldehyde topping the list due to its increased solubility of the catalyst ligand compared to DMF and other HRSC solvent candidates. This might be mainly due to the slight increase in excess entropy when using acetaldehyde over DMF, although both form approximately ideal solutions with Biphephos. It is also noticeable that solvents having similar catalyst solubility have varying tridecanal solubility. For example, DMF and acetone have about the same heat of mixing with tridecanal, but the excess entropy is more negative in acetone leading to a slightly more favorable solution.

A final comparison of solvent pairs with DMF as the HRSC and various length linear alkanes from octane to tridecane as the LRSC are set side-by-side (Table 4). As expected, the solubility of the catalyst and of tridecanal worsens as the length of the alkane chain increases, due to the increased heat of mixing. The change in excess entropy is small, as the molecular order is not drastically influenced by more of the same non-polar interactions. These results are in agreement with the experimental findings by Brunsch (2013).

Table 2: List of top ten TMS mixtures

HRSC	LRSC	$log_{10}(P_{tridecanal})$	$log_{10}(P_{Biphephos})$
Acetaldehyde	Tridecane	0.2060	2.8038
Acetaldehyde	Dodecane	0.1750	2.7655
Acetaldehyde	Bicyclohexyl	0.0663	2.7507
Acetaldehyde	*n*-Undecane	0.1445	2.7231
Acetaldehyde	*n*-Hexylcyclopentane	0.0953	2.7151
Acetaldehyde	2-Methyldecane	0.2042	2.7099
Acetaldehyde	Pentylcyclohexane	0.0896	2.6978
Dimethylformamide	Tridecane	0.2180	2.6959
Acetaldehyde	4-Methyldecane	0.1415	2.6850
Acetaldehyde	Pentylcyclopentane	0.0522	2.6754

Table 3: List of high relative solubility solvents and decane TMS candidates

HRSC	LRSC	$log_{10}(P_{tridecanal})$	$log_{10}(P_{Biphephos})$
Acetaldehyde	*n*-Decane	0.1061	2.6713
Dimethylformamide	*n*-Decane	0.1180	2.5635
Acetone	*n*-Decane	0.2882	2.5627
n,n-Dimethylacetamide	*n*-Decane	0.2184	2.5572
n-Methyl-2-pyrrolidone	*n*-Decane	0.3017	2.5193
Methyl acetate	*n*-Decane	0.1777	2.2222
n,n-Diethylformamide	*n*-Decane	0.1880	2.2166

3. Conclusion

This contribution presents a novel method based on quantum chemical COSMO calculations for selecting TMS solvent pairs for the recycling of homogeneous metal-organic catalysts used for the hydroformylation of 1-dodecene. The benefit of using this method is its simplicity and the

Table 4: Comparison of TMS composed of DMF and linear alkanes

HRSC	LRSC	$log_{10}(P_{tridecanal})$	$log_{10}(P_{Biphephos})$
Dimethylformamide	Octane	0.0267	2.4158
Dimethylformamide	Nonane	0.0759	2.4982
Dimethylformamide	Decane	0.1180	2.5635
Dimethylformamide	Undecane	0.1565	2.6152
Dimethylformamide	Dodecane	0.1870	2.6577
Dimethylformamide	Tridecane	0.2180	2.6959

absence of experimental data for identifying potential solvents with high and low affinity for a specific catalyst ligand. This method is partially corroborated by its ability to identify mixtures of DMF and longer alkanes as satisfactory TMS solvents for recovering the Biphephos ligand, something already empirically confirmed. It also provides a general starting point for further experiments with new TMS compositions that may increase catalyst retention, product separation, and overall process performance.

4. Acknowledgment

This work was conducted in part in cooperation with the Collaborative Research Centre "Integrated Chemical Processes in Liquid Multiphase Systems". The financial support from the German Research Foundation (DFG) under the grant SFB/TRR 63 is gratefully acknowledged.

References

A. Behr, C. Fängewisch, 2002, Temperature-dependent multicomponent solvent systems–an alternative concept for recycling homogeneous catalysts, Chem. Eng. Technol. 25 (2), 143–147.

A. Behr, G. Henze, L. Johnen, C. Awungacha, 2008, Advances in thermomorphic liquid/liquid recycling of homogeneous transition metal catalysts, J. Mol. Catal. A: Chem. 285 (1), 20–28.

A. Behr, G. Henze, D. Obst, B. Turkowski, 2005, Selection process of new solvents in temperature-dependent multicomponent solvent systems and its application in isomerising hydroformylation, Green Chemistry 7 (9), 645–649.

A. Behr, R. Roll, 2005, Hydroaminomethylation in thermomorphic solvent systems, J. Mol. Catal. A: Chem. 239 (1), 180–184.

B. Bouillot, S. Teychen, B. Biscans, Oct 2011, An evaluation of thermodynamic models for the prediction of drug and drug-like molecule solubility in organic solvents, Fluid Phase Equilibria 309 (1), 36–52.

Y. Brunsch, 2013, Temperaturgesteuertes katalysatorrecycling für die homogen katalysierte hydroformylierung langkettiger alkene, Ph.D. thesis, TU Dortmund, Germany.

F. Eckert, A. Klamt, COSMOtherm, version C13, COSMOlogic GmbH & Co. KG, Leverkusen, Germany 2014.

K. Eichkorn, F. Weigend, O. Treutler, R. Ahlrichs, 1997, Auxiliary basis sets for main row atoms and transition metals and their use to approximate coulomb potentials, Theor. Chem. Acc. 97, 119–124.

R. Gani, C. Jiménez-González, D. J. Constable, 2005, Method for selection of solvents for promotion of organic reactions, Comput. Chem. Eng. 29 (7), 1661–1676.

I. Hahnenkamp, G. Graubner, J. Gmehling, Mar 2010, Measurement and prediction of solubilities of active pharmaceutical ingredients, Int. J. Pharm. 388 (1-2), 73–81.

B. Hentschel, A. Peschel, H. Freund, K. Sundmacher, 2013, Simultaneous design of the optimal reaction and process concept for multiphase systems, Chem. Eng. Sci., 69–87.

A. Klamt, Feb 1995, Conductor-like screening model for real solvents: A new approach to the quantitative calculation of solvation phenomena, The Journal of Physical Chemistry 99 (7), 2224–2235.

A. Schäfer, C. Huber, R. Ahlrichs, 1994, Fully optimized contracted gaussian basis sets of triple zeta valence quality for atoms li to kr, J. Chem. Phys. 100, 5829–5835.

H.-H. Tung, J. Tabora, N. Variankaval, D. Bakken, C.-C. Chen, May 2008, Prediction of pharmaceutical solubility via nrtl-sac and cosmo-sac, J. Pharm. Sci. 97 (5), 1813–1820.

TURBOMOLE, V6.5, Program Packager for Ab initio Electronic Structure Calculations, COSMOlogic GmbH & Co. KG, Leverkusen, Germany, 2013.

K. Wichmann, A. Klamt, 2010, Drug solubility and reaction thermodynamics, Chemical Engineering in the Pharmaceutical Industry, 457–476.

Krist V. Gernaey, Jakob K. Huusom and Rafiqul Gani (Eds.), 12th International Symposium on Process Systems Engineering and 25th European Symposium on Computer Aided Process Engineering.
31 May – 4 June 2015, Copenhagen, Denmark 2015 Published by Elsevier B.V.

Computational Molecular Design of Water Compatible Dentin Adhesive System

Farhana Abedin[a, b], Brock Roughton[b], Paulette Spencer[a, c], Qiang Ye[a], Kyle Camarda[d*]

[a] *University of Kansas,Bioengineering Research Center, 1530 W. 15th Street, Lawrence, KS 66045, USA*
[b]*University of Kansas, Bioengineering Graduate Program, 1530 W. 15th Street, Lawrence, KS 66045, USA*
[c]*University of Kansas, Department of Mechanical Engineering, 1530 W. 15th Street, Lawrence, KS 66045, USA*
[d]*University of Kansas, Department of Chemical and Petroleum Engineering, 1530 W. 15th Street, Lawrence, KS 66045, USA*

Abstract

The objective of this work is to develop a framework to a design dentin adhesive system for water compatibility and efficient photo-polymerization applying computer aided molecular design. A dentin adhesive system consists of monomers and photo-initiators which trigger a photo-polymerization reaction when exposed to visible light. In this study a water compatible visible light photosensitizer was designed for dental applications. Quantitative structure property relationships (QSPRs) were developed for relevant properties (octanol/water partition coefficient and molar extinction coefficient) using molecular descriptors. The QSPRs are combined with structural constraints to form a MINLP, which is then solved to near optimality using Tabu search to generate novel candidate photosensitizer molecules with desired properties. Tabu search, a heuristic optimization method, does not yield globally optimal solutions for MINLPs, but it is an efficient and practical method for solving general combinatorial optimization problems. This framework will provide insight regarding possible functional groups for developing water-compatible visible light photosensitizers for dentin adhesive systems.

Keywords: hydrophilic, initiator, optimization, Tabu search, water compatible, QSPR

1. Introduction

1.1 Motivation

Dentin adhesives are sensitive to moisture and undergo phase separation into hydrophobic and hydrophilic-rich phases, when coming into contact with water within wet demineralized dentin (Spencer and Wang, 2002). The major components of a dentin adhesive are monomers (cross-linker and 2-hydroxyethyl methacrylate, HEMA) and a photo-initiator system which enables initiation of a photo-polymerization reaction. Previous investigations have quantitatively exhibited a limited presence of the most popular hydrophobic photo-initiator system (camphoquinone, CQ and ethyl 4-(dimethylamino) benzoate, EDMAB) in the hydrophilic-rich phase (Ye *et al.* 2012). Limited photo-initiator content indicates sub-optimal polymerization of the hydrophilic-rich phase and can cause unreacted monomers and pendant groups to become trapped. The overall impact would be detrimental to the dentin/adhesive bond integrity. The trapped unreacted monomers can also cause leaching of HEMA, which can elicit a cytotoxic effect (Chang *et al.* 2005). The

presence of photo-sensitizer in a higher concentration within the hydrophilic-rich phase is critical for improving the dentin/adhesive bond integrity and reducing cytotoxicity (Ye *et al.* 2009).

1.2 Physical properties

The efficiency of the photo-polymerization is dependent on the absorptivity of the photosensitizer within the activation range (Neumann *et al.* 2005). The absorption of light at a given wavelength by the photosensitizer is governed by its molar extinction coefficient at that wavelength. Therefore, it is important that the emission spectrum of the curing light unit matches with the absorption spectrum of the photosensitizer. A high molar extinction coefficient of a photosensitizer increases the formation of initiating reactive species, which in turn improves the degree of conversion and the photo-polymerization reaction kinetics (Neumann *et al.* 2005). The hydrophilicity of the photosensitizer also plays a vital role in a dentin adhesive system, since this governs the availability or dispersion of the photosensitizer in the hydrophilic-rich phase after infiltration of the adhesive within the wet demineralized dentin. For the current study, the octanol/water partition coefficient (log P) was used to estimate the hydrophilicity of the photosensitizer.

1.3 Background and objective

In this work, a visible light water compatible photosensitizer for dental applications has been designed by applying computer-aided molecular design (CAMD). Two quantitative structure property relationships for properties, the molar extinction coefficient at 480 nm and the octanol/water partition coefficient (log P), have been developed using topological descriptors, specifically connectivity indices (Randić 1975). CAMD consists of a forward and an inverse problem. The development of QSPRs represents the forward problem, where mathematical expressions for predicting properties using known molecular structures are derived. The next step, where novel molecules with desired properties are designed, is the inverse problem. For the inverse problem, QSPRs are used to design molecules which have properties close to the target values. This is an optimization problem where the molecule is formed from various combinations of different molecular sub-structures. Tabu search, a stochastic optimization algorithm, was employed to solve the optimization problem. This method was used previously to design novel molecules with desired properties (McLeese *et al*. 2010). CAMD and connectivity indices have been successfully used previously to design polymers and small molecules (Eslick *et al.* 2009, Roughton *et al.* 2012, Chavali *et al.* 2004). CAMD has been utilized in the past for polymer design (Venkatasubramanian *et al.* 1994) and for the design of ionic liquids and other solvents (Gani *et al.* 1991, Matsuda *et al.* 2007, Folic *et al*. 2008, Gardas *et al*. 2008).

2. Experimental Data and QSPR Development

To build the QSPR for the molar extinction coefficient (ξ), data was collected for candidate molecules which exhibited their peak wavelength in the visible range (unpublished data). The molar extinction coefficient was determined at 480 nm wavelength, which is approximately the peak wavelength generated by the halogen curing light unit used in dental applications. The nine molecules in the model building set for $\ln(\xi)$ were: New Fuchsin, Victoria blue B, Methylene blue chloride, Eosin Y disodium salt, Bromophenol blue sodium salt, Erythrosin B, Fluorescein sodium salt, [3-(3,4-dimethyl-9-oxo-9H-thioxanthen-2-yloxy)-2-hydroxypropyl]trimethylammonium chloride (QTX) and Rose bengal sodium salt. The octanol/water partition coefficients (log P) of similar molecules were obtained from literature (Pellosi *et al.* 2012, Shiekh *et al.* 1976, Wagner *et al.* 1998, Wainright *et al.* 1999). The molecules in the model building set for log P were:

Bromophenol blue, Eosin Y, Erythrosin B, Fluorescein, Methylene blue chloride, Rose bengal, Victoria blue B and Victoria blue R.

2.1 Descriptor selection and QSPRs

Quantitative structure property relationships (QSPRs) mathematically link physical or chemical properties with the structure of a molecule. For example, QSPRs for organic dyes were developed in the past for solar cell applications for properties such as peak wavelength (Xu et al. 2010, Venkatraman *et al.* 2014). In this work, the statistical software R (R-Development-Core-Team, 2010) was used to develop the QSPRs correlating properties with connectivity indices by linear regression. The leaps package (Lumely, 2004) was used to select the descriptors. Descriptors in the model with higher correlation coefficients (R^2) and lowest Mallow's C_p were selected. The Mallow's C_p statistic is a means of determining the optimum number of descriptors, which takes into account the lack of fit as well as complexity in the correlation (Roughton *et al.* 2012). The octanol/water partition coefficient of molecules has been predicted previously by using the group contribution method (Marrero and Gani 2002). Here, a QSPR for log P was built using connectivity indices for a set of relevant molecules which are specific to this type of design problem. The QSPRs models were cross-validated with the leave-one-out method using the package DAAG in R. The predictive squared correlation coefficient, Q^2, was calculated for each model to evaluate the predictive ability of the models. For a model with good predictive capability, $Q^2 \approx R^2$.

2.2 Computer-aided molecular design using Tabu search

For this study, 42 groups were used to build the structures. Two example groups used in the CAMD are given in Figure 1. Tabu search was employed to solve the optimization problem. The advantage of Tabu search is that it avoids becoming stuck around a local optimum by storing previous solutions in the Tabu list, and comparing the new solutions with those in the list. Tabu search was allowed to choose a maximum of 5 groups from the 42 groups for building the new molecules. Therefore, there were approximately 100 million possibilities at maximum within the search space. Being a stochastic approach, Tabu search can generate locally optimal solutions. Since the property prediction expressions are not exact, identification of multiple near optimal solutions is more valuable than a single globally optimal solution. The CAMD framework used by Roughton *et al.* for carbohydrate excipient design was used in this work (Roughton *et al.* 2012). The optimization problem was formulated as an MINLP due to the use of higher order indices. The objective function minimizes the difference between the predicted and the target property values (Eslick *et al.* 2009, Roughton *et al.* 2012). The optimization formulation is given below:

$$\text{Minimize } s = \sum_M \frac{1}{P_m^{scale}} \left| P_m - P_m^{Target} \right|$$
$$P_m = f_m(\chi)$$
$$\chi = g(a_{ij}, w_i)$$
$$h_c(a_{ij}, w_i) \geq 0$$

where P_m is the value of property m given by the QSPR function $f_m(\chi)$ for a given candidate molecule, χ is a connectivity index computed via functions g which are functions of the adjacency matrix a_{ij}, and the identity vector w_i, P_m^{Target} is the target value for the property m, P_m^{scale} is a scaling factor and h_c are the set of molecular structural constraints.

The target values for ln(ξ) were chosen to be 9 and 10, which were close to the maximum values obtained from the known candidates. For log P, the target value was set to -0.55, which is the log P value for HEMA (Fujisawa and Masuhara, 1981). The target for ln(ξ)

was selected close to the maximum values obtained from the model building set because a high molar extinction coefficient will increase the probability that the photosensitizer will absorb light and be promoted to the excited state. The log P value for HEMA was selected as the target value because the major components of the hydrophilic-rich phase were determined to be HEMA and water.

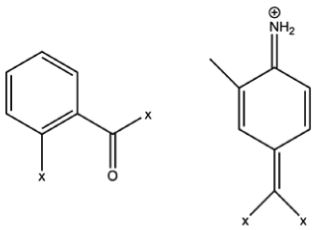

Figure 1. Two example molecule sub-structures (groups) used in CAMD. The connectors are marked as x.

3. Results

A summary of the two QSPRs for ln(ξ) and log P are given in Table 1 along with the C_p values. The QSPR was developed for ln(ξ) using zero and fifth order valence connectivity indices (χ^v) and zero, first, third, fourth order connectivity indices (χ) as given in Eq. (1).

Table 1. Summary of QSPRs for ln(ξ) and log P

Property	Number of descriptors used	R^2	C_p
ln(ξ)	6	0.99999	6.00845
log P	5	0.99996	5.07619

$$ln(\xi) = 32.22723 + (3.95277 \cdot {}^{0}\chi^{v}) - (15.07572 \cdot {}^{5}\chi^{v}) - (4.60663 \cdot {}^{0}\chi) + (0.63374 \cdot {}^{1}\chi) - (0.62536 \cdot {}^{3}\chi) + (4.81887 \cdot {}^{4}\chi) \quad (1)$$

Adjusted $R^2 = 0.99999$, $Q^2 = 0.99272$

The QSPR for log P was obtained using zero and second order valence connectivity indices and first, fourth, fifth order connectivity indices as shown in Eq. (2).

$$log\ P = -9.08869 + (1.61343 \cdot {}^{1}\chi) - (7.86666 \cdot {}^{4}\chi) + (6.86586 \cdot {}^{5}\chi) + (0.98095 \cdot {}^{0}\chi^{v}) - (1.48700 \cdot {}^{2}\chi^{v}) \quad (2)$$

Adjusted $R^2 = 0.99996$, $Q^2 = 0.99813$

It can be seen from above that the Q^2 values are very close to the R^2 values, indicating that the correlations have good predictive capability. The correlations were combined with structural constraints (enforced implicitly by controlling moves) and the resulting MINLP was solved to near optimality via the Tabu search algorithm. Two example potential structures proposed by the CAMD are given in Figure 2 with target ln(ξ) being 9 and 10. In both the cases the target value for log P remained -0.55.

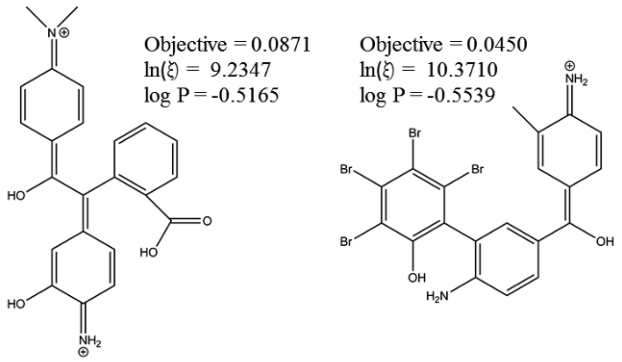

Figure 2. Structures proposed by CAMD for target values, log P = -0.55 (a) $\ln(\xi) = 9$ (b) $\ln(\xi) = 10$

The structures in Figure 2 indicate that combination of amino and/or amine groups with benzene or benzoic acid moieties and hydroxyl groups could play a vital role into imparting desired absorptivity and hydrophilicity to the molecule.

4. Conclusions

Incorporation of a water compatible photosensitizer improves photo-polymerization within the hydrophilic-rich phase of a dentin adhesive system, and also minimizes leaching of monomers. This work demonstrates the design of water compatible photosensitizers by CAMD for dental applications. Tabu search has been employed for solving the resulting MINLPs. The properties for which the photosensitizers have been optimized are $\ln(\xi)$ and log P. The proposed structures provide insight regarding functional groups that possess the potential of imparting desired properties. For design of an efficient water compatible photosensitizer, properties such as the degree of conversion and the rate of polymerization should be taken into account, and this work is currently underway.

5. Acknowledgement

This investigation was supported by Research Grant: R01 DE022054 from the National Institute of Dental and Craniofacial Research, National Institutes of Health, Bethesda, MD 20892.

Dr. Brock Roughton's current affiliation is with the U.S. Food and Drug Administration (FDA), 10903 New Hampshire Avenue, Silver Spring, MD 20993. The opinions and information in this article are of the authors, and do not represent the views or policies of the FDA.

References

H-H. Chang, M-K. Guo, F. H. Kasten, M-C. Chang, G-F. Huang, Y-L. Wang, 2005, Stimulation of glutathione depletion, ROS production and cell cycle arrest of dental pulp cells and gingival epithelial cells by HEMA, Biomaterials, 26, 745-53.

S. Chavali, B. Lin, D. C. Miller, K. V. Camarda, 2004, Environmentally-benign transition metal catalyst design using optimization techniques, Computers and Chemical Engineering, 28, 605-611.

J. C. Eslick, Q. Ye, J. Park, E. M. Topp, P. Spencer, K. Camarda, 2009, A computational molecular design framework for cross-linked polymer networks, Computers and Chemical Engineering, 33, 954-963.

M. Folic, C. S. Adjiman, E. N. Pistikopoulos, 2008, Computer-aided solvent design for reactions: Maximizing product formation, Industrial and Engineering Chemistry, 47(15), 5190-5202.
S. Fujisawa and E. Masuhara, 1981, Determination of partition coefficients of acrylates, methacrylates, and vinyl monomers using high performance liquid chromatography (HPLC), Journal of Biomedical Materials Research, 15, 787-793.
R. Gani, B. Nielsen, A. Fredenslund, 1991, A group contribution approach to computer-aided molecular design, AIChe Journal, 37(9), 1318-1332.
J. Marrero and R. Gani, 2002, Group-contribution-based estimation of octanol/water partition coefficient and aqueous solubility, Industrial and Engineering Chemistry Research, 41(25), 6623-6633.
R. L. Gardas and J. A. P. Coutinho, 2008, A group contribution method for heat capacity estimation of ionic liquids, Industrial and Engineering Chemistry Research, 47(15), 5751-5757.
T. Lumely, 2004, The leaps package, www.cran.r-project.org/doc/packages/leaps.pdf.
S. E. McLeese, J. C. Eslick, N. J. Hoffmann, A. M. Scurto, K. V. Camarda, 2010, Design of ionic liquids via computational molecular design, Computers and Chemical Engineering, 34, 1476-1480.
H. Matsuda, H. Yamaoto, K. Kurihara, K. Tochigi, 2007, Computer-aided reverse design for ionic liquids by QSPR using descriptors of group contribution type for ionic conductivities and viscosities, Fluid Phase Equilibria, 261, 434-443.
M. G. Neumann, W. G. Miranda Jr., C. C. Schmitt, F. A. Rueggeberg, I. C. Correa, 2005, Molar extinctions coefficients and the photon absorptions efficiency of dental photoinitiators and light curing units, Journal of Dentistry, 33, 525-532.
D. S. Pellosi, B. M. Estevao, J. Semensato, D. Severino, M. S. Baptista, M. J. Politi, N. Hioka, W. Caetano, 2012, Photophysical properties and interactions of xanthene dyes in aqueous micelles, Journal of photochemistry and photobiology A: Chemistry, 247, 8-15.
M. Randic, 1975, Characterization of molecular branching, Journal of the American Chemical Society, 97, 6609-6615.
B. C. Roughhton, E. M. Topp, K. Camarda, 2012, Use of glass transitions in carbohydrate excipient design for lyophilized protein formulations, Computers and Chemical Engineering, 36, 208-216.
R-Development-Core_Team, 2010, A language and environment for statistical computing. http://www.R-project.org.
M. I. Sheikh, 1976, Renal handling of phenol red II. the mechanism of substituted phenolsulphophthalein (PSP) dye transport in rabbit kidney tubules *in vitro*, Journal of Physiology, 256, 175-95.
P. Spencer and Y. Wang, 2002, Adhesive phase separation at the dentin interface under wet bonding conditions, Journal of Biomedical Materials Research, 62, 447-456.
V. Venkatasubramanian, K. Chan, J. M. Caruthers, 1994, Computer-aided molecular design using genetic algorithms, Computers nad Chemical Engineering, 18, 9, 833-844.
V. Venkatraman, P.-O. Astrand, B. K. Alsberg, 2014, Quantitative structure-property relationship modeling of gratzel solar cell dyes, Journal of Computation Chemistry, 35(3), 214-226.
S. J. Wagner, A. Skripchenko, D. Robinette, J. W. Foley, L. Cincotta, 1998, Factors affecting virus photoinactivation by a series of phenothiazine dyes, Photochemistry and Photobiology, 67(3), 343-349.
M. Wainwright, S. M. Burrow, S. G. R. Guinot, D. A. Phoenix, J. Waring, 1999, Uptake and cell-killing activities of a series of victoria blue derivatives in a mouse mammary tumour cell line, Cytotechnology, 29, 35-43.
J. Xu, H. Zhang, L. Wang, G. Liang, L. Wang, X. Shen, W. Xu, 2010, QSPR study of absorption maxima of organic dyes for dye sensitized solar cells based on 3D descriptors, Spectrochimica Acta Part A: Molecular and Biomolecular Spectroscopy, 76(2), 239-247.
Q. Ye, J. Park, R. Parthasarathy, F. Pamatmat, A. Misra, J. S. Laurence, O. Marangos, P. Spencer, 2012, Quantitative analysis of aqueous phase composition of model dentin adhesives experiencing phase separation, Journal of Biomedical Materials Research B Applied Biomaterials, 100, 1086-1092.
Q. Ye, J. Park, E. Topp, P. Spencer, 2009, Effect of photo-initiator on the in vitro performance of a dentin adhesive exposed to simulated oral environment, Dental Materials, 25, 452-458.

Krist V. Gernaey, Jakob K. Huusom and Rafiqul Gani (Eds.), 12th International Symposium on Process Systems Engineering and 25th European Symposium on Computer Aided Process Engineering.
31 May – 4 June 2015, Copenhagen, Denmark

An Evaluation of Thermodynamic Models for the Prediction of Solubility of Phytochemicals from *Orthosiphon Staminues* in Ethanol

Mohd Shukri Mat Nor,[a] Zainuddin Abd Manan,[a*] Azizul Azri Mustaffa,[a] Chua Lee Suan[b]

[a]*Process Systems Engineering Centre (PROSPECT), Faculty of Chemical Engineering, Universiti Teknologi Malaysia, 81310 UTM Johor Bahru, Johor, Malaysia*
[b] *Institute of Bioproduct Development (IBD), Universiti Teknologi Malaysia, 81310 UTM Johor Bahru, Johor, Malaysia*

zain@cheme.utm.my

Abstract

Orthosiphon Staminues (OS) is a species of herbs locally known in Malaysia as Misai Kucing. This study aims to analyse the performance of existing group contribution models in predicting the solubilities of phytochemical compounds from OS in ethanol. The compounds are oleanolic acid, ursolic acid and betulinic acid which have properties of pharmaceutical importance. The solubility experimental data of the compounds in ethanol were derived from the literature and were compared with the predictions made by the original UNIFAC, Modified UNIFAC (Dortmund), and Pharma Modified UNIFAC. The very high ranges of ARD values of between 40.86% to 98.6% calculated in this work shows that the models presented in this paper are not able to accurately predict the solubility of the studied phytochemical compounds in ethanol.

Keywords: Orthosiphon staminues, Activity Coefficient, UNIFAC, UNIFAC Modified (Dortmund), Pharma Modified UNIFAC

1. Introduction

Orthosiphon stamineus (OS) is a popular medicinal plant that has been used extensively as a traditional medicine to treat rheumatoid diseases, diabetes, hypertension, tonsillitis, epilepsy, menstrual disorder, gonorrhea, syphilis, renal calculus, gallstone, lithiasis, edema, eruptive fever, influenza, hepatitis, and jaundice (Ameer, et al. 2012). The therapeutic effects of OS have been ascribed mainly to its phytochemicals which are directly related to pharmacological properties such as, antioxidant, anti-inflammatory, anti-bacterial, heptoprotective, diuretic, anti-hypertensive and vasodialative properties (Basheer and Majid 2010, Al-Suede, et al. 2014). Several classes of phytochemicals have been identified from OS, including flavonoids, terpenoids, saponins, hexoses, organic acids, phenylpropanoids (caffeic acids derivatives), chromene and myo-inositol (Ameer, et al. 2012, Ibrahim and Jaafar 2012).

These phytochemicals are typically isolated via solvent extraction, where solubility plays an essential role in influencing the yield of extracts. The tendency of each phytochemical to be solubilized, transferred or diffused into a given solvent is governed by thermodynamic factor called activity coefficient (Queimada, et al. 2009). Due to the

lack of physical property data, studies on these prediction data are very scarce even though solubility in solvents is an important factor for the recovery of phytochemicals.

The objective of the study is to predict the solubility of three phytochemicals from OS in ethanol by testing and analysing existing activity coefficient models (original UNIFAC, Modified UNIFAC (Dortmund), and Pharma Modified UNIFAC). These three thermodynamic models were chosen because they apply the group contribution methods. Practically, these established and simple models have been widely used to predict the solubility of organic compounds in solvents. The advantage of the method is that the number of functional groups is much smaller than the number of possible molecules. These models rely on the use of the database known as group-group interaction parameters between functional groups. This database has been developed through regression of available experimental data.

2. Materials and Methods

2.1. Reference phytochemicals

In this paper, oleanolic acid (OA), ursolic acid (UA) and betulinic acid (BA) were chosen as the phytochemicals of OS. These compounds were selected mainly because of the solubility experimental data for the compounds have been reported in the literature by Cheng, et al. (2011), Liu and Wang (2007), Fan, et al. (2011). In addition, these phytochemicals are categorized into the same phytochemical class as terpernoids. The structures of these compounds are shown in Figure 1.

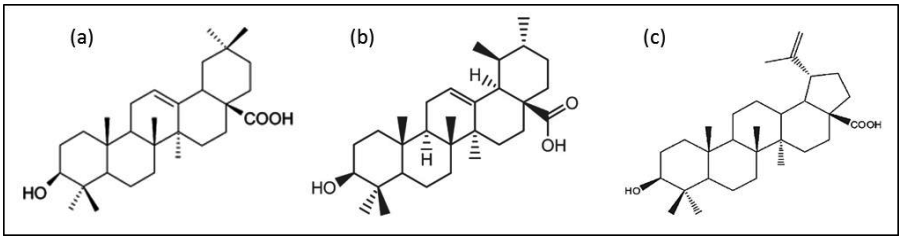

Figure 1. (a) Oleanolic acid, (b) ursolic acid and (c) betulinic acid

2.2. Activity Coefficient Models

The activity coefficient is the thermodynamic property that influences the solubility of solute in solvents. It is a mixture property that provides a measure of the non-ideality of the solution phase. From the solubility data, activity coefficients can be calculated using Eq. (1).

$$\chi_i \gamma_i^l = \exp\left\{ \frac{\Delta H_i^{fus}}{R T_{mi}} \left(\frac{T - T_{mi}}{T} \right) + \frac{\Delta C_{pi}^{fus}}{R} \left[\ln\left(\frac{T}{T_{mi}} \right) - \left(\frac{T - T_{mi}}{T} \right) \right] \right\} \quad (1)$$

ΔH_i^{fus} is the enthalpy of fusion for component i, T_{mi}, the melting temperature for component i, T is the temperature, and ΔC_{pi}^{fus} the difference between the heat capacity of the solid and the liquid phase at equilibrium for component i. However, it is very difficult to measure ΔC_{pi}^{fus} especially for the case of sublimation, decomposition or parallel reactions occuring during melting. Therefore, ΔC_{pi}^{fus} contribution is typically

assumed as negligible (Bouillot, et al. 2011). Equation (1) can therefore be further simplified to give the relationship between solubility and activity coefficients as given by Eq. (2).

$$\chi_i \gamma_i^l = \exp\left[\frac{\Delta H_i^{fus}}{RT_{mi}} \ln\left(\frac{T}{T_{mi}}\right)\right] \tag{2}$$

In this work, the activity coefficients of a phytochemical substance in the ethanol were estimated using the UNIFAC (Fredenslund, et al. 1975), Modified UNIFAC (Dortmund) (Jakob, et al. 2006), and Pharma Modified UNIFAC (Diedrichs and Gmehling 2011) models.

(a) Original UNIFAC

The Original UNIFAC model is a combination of two parts of activity coefficient as stated in Eq. (3):

$$\ln \gamma = \ln \gamma^C + \ln \gamma^R \tag{3}$$

γ^C is the combinatorial term, representing the entropic contribution to the activity coefficient which takes into account the shape and size of the molecules. Expression of $\ln \gamma^C$, as given in Eq. (4) depends on the mole fraction (x_i), area (θ_i), segment fraction (Φ_i), Van der Waals radius (r_i) and volume (q_i). Superscript i designates the type of phytochemical:

$$\ln \gamma_i^C = \ln \frac{\Phi_i}{x_i} + 5q_i \ln \frac{\theta_i}{\Phi_i} + l_i - \frac{\Phi_i}{x_i} \sum_j x_j (5(r_j - q_j) - (r_j - 1)) \tag{4}$$

Meanwhile, γ^R is the residual part which represents the enthalpic contribution (inter and intramolecular interactions). It is a sum of the activity coefficients of the functional groups weighted by their number in solution. The equation for this part is presented in Eq. (5).

$$\ln \gamma_i^R = \sum_k v_k^{(i)} \left[\ln \Gamma_k - \ln \Gamma_k^{(i)}\right] \tag{5}$$

where v_k and v_k^i are the number of groups of type k in the mixture and in component i. Γ_k and Γ_k^i are the residual activity coefficient of group k in the mixture and in a solution of pure component i respectively . They depend on the area and segment fraction of the compounds and adjustable binary interaction parameters a_{mn} that are usually regressed from VLE experimental data. The equations are expressed in Eq. (6) and Eq. (7):

$$\ln \Gamma_k = Q_k \left[1 - \ln\left(\sum_m \Theta_m \psi_{mk}\right) - \frac{\sum_m \Theta_m \psi_{km}}{\sum_n \Theta_n \psi_{nm}}\right] \tag{6}$$

with:

$$\psi_{mn} = \exp\left(-\frac{a_{mn}}{T}\right) \tag{7}$$

(b) Modified UNIFAC (Dortmund) Model

Modified UNIFAC (Dortmund) is a modification of UNIFAC model that takes into account of the temperature in the residual activity contribution. The new combinatorial term and interaction parameter are written as Eq. (8) and Eq. (9), respectively:

$$\ln \gamma_i^C = 1 - \ln \frac{\Phi_i}{x_i} + 5q_i\left(1 - \ln \frac{\Phi_i}{\theta_i} + \ln\left(\frac{\Phi_i}{\theta_i}\right)\right) \tag{8}$$

$$\psi_{mn} = \exp\left(\frac{a_{mn} + b_{mn}T + c_{mn}T^2}{T}\right) \tag{9}$$

(c) Pharma Modified UNIFAC

The Original UNIFAC and Modified UNIFAC (Dortmund) are effective models for many applications. However, these group contribution models have a limited range of applications for active pharmaceutical ingredients (APIs) because of the missing structural groups and group interaction parameters. To overcome this limitation, the Pharma Modified UNIFAC model was developed by Diedrichs and Gmehling (2011) in order to extend the range of applicability of the group contribution methods for APIs. The model is a derivative of the modified UNIFAC (Dortmund) model, created with the intention of overcoming the functional groups diversity limitation of the modified UNIFAC (Dortmund) when applied to API solutions. Therefore, the system of equations of Pharma Modified UNIFAC is the same as the modified UNIFAC (Dortmund) whereby the difference between these models resides solely in the set of available functional groups and its unary (R_k and Q_k) and binary parameters values Ψ_{nm}. Note that, k, n and m represent the functional group indices.

2.3. Models Evaluation

In order to evaluate the performance of these three models, the absolute relative deviation (ARD) was calculated for each method. The ARD was determined using Eq. (10):

$$ARD = \left|\frac{\chi_{\exp} - \chi_{pred}}{\chi_{\exp}}\right| \times 100\% \tag{10}$$

χ_{exp} is the solubility experiment data, and χ_{pred} is the predicted value of solubility point in mole fraction unit.

3. Results and Discussion

The comparison between experimental and predicted values of the solubilities of phytochemicals from OS are shown in Table 1. The experimental value was obtained from the experimental data available from the literature at 288.3 K for oleanolic acid (Liu and Wang 2007), 293.6 K for ursolic acid (Fan, et al. 2011), and 278.2 K for betulinic acid (Cheng, et al. 2011). The predicted values were estimated using the group contribution methods of activity coefficient models at the same operating temperature with the experimental data.

The table illustrates that the Original UNIFAC yields an ARD value of 98.41% (OA), 86.05% (UA), and 98.6% (BA) whereas the Modified UNIFAC (Dortmund) yields an ARD value of 85.71% (OA), 40.86% (UA), and 85.43% (BA). On the other hand, the ARD values obtained from Pharma Modified UNIFAC are 93.87% (OA), 50.61% (UA), and 93.05% (BA). The high ARD values show that all the models are not applicable for the prediction of phytochemicals from OS.

It is known that the original UNIFAC and its modified models are using group contribution method, which do not consider the molecular geometry and isomers of the compounds in the prediction. These may be the possible reasons for the poor prediction results. Moreover, phytochemicals are group of molecules that include hydrogen bonding and strong hydrophobic interactions that can make UNIFAC prediction inaccurate (Sevillano, et al. 2014). Besides, the molecular complexity of the phytochemical compounds makes it difficult to achieve a high accuracy for the models.

Table 1. Comparison between experimental and predicted values of solubility of oleanolic acid, ursolic acid, and betulinic acid.

Phytochemicals	Model	Experimental Value (mol/mol)	Predicted Value (mol/mol)	ARD (%)
Oleanolic acid	Original UNIFAC		0.000083	98.41
	Modified UNIFAC (Dortmund)	0.0052 at 288.3 K	0.000743	85.71
	Pharma Modified UNIFAC		0.000318	93.87
Ursolic acid	Original UNIFAC		0.0004	86.05
	Modified UNIFAC (Dortmund)	0.0030 at 293.6 K	0.0042	40.86
	Pharma Modified UNIFAC		0.0015	50.61
Betulinic acid	Original UNIFAC		0.0001	98.6
	Modified UNIFAC (Dortmund)	0.0038 at 278.2 K	0.0006	85.43
	Pharma Modified UNIFAC		0.0003	93.05

4. Conclusion

In the present work, the capabilities of three thermodynamic models to predict the phytochemical solubility from OS in ethanol were investigated. Very high ARD values of between 40.86% to 98.6% shown in this work indicates that none of the model presented in this paper was able to accurately predict the solubility of the studied phytochemical compounds in ethanol. However, the Modified UNIFAC (Dortmund) showed the lowest ARD value as compared to the ARD values for other models. Work is in progress to increase the prediction accuracy of the models to reduce the ARD value down to 5%.

Acknowledgement

The authors gratefully acknowledge the Ministry of Higher Education (Malaysia) and Universiti Teknologi Malaysia for funding our research through Fundamental Research Grant Scheme (Reference: R.J130000.7844.4F270).

References

O. Z. Ameer, I. M. Salman, M. Z. Asmawi, Z. O. Ibraheem and M. F. Yam, 2012, Orthosiphon stamineus: Traditional Uses, Phytochemistry, Pharmacology, and Toxicology, 15, 678-690.

M. K. A. Basheer and A. M. S. A. Majid, 2010, Medicinal potentials of Orthosiphon stamineus Benth, 1, 12, WMC001361.

F. S. R. Al-Suede, E. Farsi, M. K. B. Ahamed, Z. Ismail, A. S. Abdul Majid and A. M. S. Abdul Majid, 2014, Marked antitumor activity of cat's whiskers tea (Orthosiphon stamineus) extract in orthotopic model of human colon tumor in nude mice, 3, S170-S176.

M. H. Ibrahim and H. Z. Jaafar, 2012, Primary, secondary metabolites, H_2O_2, malondialdehyde and photosynthetic responses of Orthosiphon stimaneus Benth. to different irradiance levels, 17, 1159-1176.

A. J. Queimada, F. L. Mota, S. P. Pinho and E. A. Macedo, 2009, Solubilities of Biologically Active Phenolic Compounds: Measurements and Modeling, American Chemical Society, 113, 3469-3476.

Y. Cheng, Y. Shao and W. Yan, 2011, Solubilities of betulinic acid in thirteen organic solvents at different temperatures, 56, 4587-4591.

L. Liu and X. Wang, 2007, Solubility of oleanolic acid in various solvents from (288.3 to 328.3) K, 52, 2527-2528.

J.-P. Fan, T. Kong, L. Zhang, S. Tong, Z.-Y. Tian, Y.-H. Duan and X.-H. Zhang, 2011, Solubilities of ursolic acid and oleanolic acid in four solvents from (283.2 to 329.7) K, 56, 2723-2725.

B. Bouillot, S. Teychené and B. Biscans, 2011, An evaluation of thermodynamic models for the prediction of drug and drug-like molecule solubility in organic solvents, 309, 36-52.

A. Fredenslund, R. L. Jones and J. M. Prausnitz, 1975, Group-contribution estimation of activity coefficients in nonideal liquid mixtures, 21, 1086-1099.

A. Jakob, H. Grensemann, J. Lohmann and J. Gmehling, 2006, Further Development of Modified UNIFAC (Dortmund): Revision and Extension 5, 7924 − 7933.

A. Diedrichs and J. r. Gmehling, 2011, Solubility Calculation of Active Pharmaceutical Ingredients in Alkanes, Alcohols, Water and their Mixtures Using Various Activity Coefficient Models, 1757–1769.

D. M. Sevillano, L. A. van der Wielen, N. Hooshyar and M. Ottens, 2014, MPP-UNIFAC, a predictive activity coefficient model for polyphenols, 384, 82-88.

Krist V. Gernaey, Jakob K. Huusom and Rafiqul Gani (Eds.), 12th International Symposium on Process Systems Engineering and 25th European Symposium on Computer Aided Process Engineering.
31 May – 4 June 2015, Copenhagen, Denmark

Computer-aided Framework for Design of Pure, Mixed and Blended Products

Stefano Cignitti, Lei Zhang, Rafiqul Gani*

CAPEC-PROCESS, Department of Chemical and Biochemical Engineering, Technical University of Denmark, Søltofts Plads, Building 229, DK-2800 Kgs. Lyngby, Denmark
rag@kt.dtu.dk

Abstract

This paper presents a framework for computer-aided design of pure, mixed and blended chemical based products. The framework is a systematic approach to convert a Computer-aided Molecular, Mixture and Blend Design (CAM^bD) formulation, based on needs and target properties, into a mixed integer non-linear program (MINLP). The MINLP is sequentially solved through a decomposed optimization approach to solve the possibly large MINLP in a smaller set of sub-problems. The framework application is highlighted through a solvent design case study.

Keywords: Product Design, Mixture, Blend, CAMD, MINLP

1. Introduction

Design of novel pure, mixed and blended products with process and application considerations is an emerging topic in the field of chemical and biochemical engineering. Methods, such as Computer Aided Molecular Design (CAMD) (Harper *et al.*, 1999), and Computer-aided Mixture and Blend Design (CAM^bD) (Yunus *et al.*, 2014), provide the possibility of designing such products. However, these product design problems can quickly become large and difficult, if not infeasible, to solve through mathematical optimization. In addition, considerations of process, application, special product attributes, economic feasibility, environmental and sustainability metrics that must be included in today's product designs, consequently makes the problem harder to mathematically define and to solve.

Property prediction methods are the backbone of the any CAMD/CAM^bD methods. The property prediction methods ensure that product generation is not hindered by experimental data resources. Group contribution method is a property prediction method where by knowing the molecular groups present in a molecule the properties can be predicted (Cosntantinou and Gani, 1994). For mixtures and blends, the ensemble properties can as well be predicted (Conte *et al.* 2011). This enables the possibly of generating novel pure compounds, mixtures and blends alike (Gani 2004). Here, the precision and detailed description of molecular groups and structure become important. In group contribution methods, molecular groups are represented as 1^{st} order, 2^{nd} order and 3^{rd} order, where an increase in order gives a more detailed representation of the molecule and increase the precision in property prediction. However, difficulties arise when higher order groups must be found from lower order groups, the structure of the molecules has to be estimated, and when missing groups need to be created (Gani et al., 2005; Apostolakou and Adjiman, 2003).

Given the needs, properties and criteria, the solution strategy for a CAMD/CAM^{b}D problem can be of two types: “generate and test”, and “mathematical optimization”. In generate and test, a molecule or a mixture/blend constituting of a set of molecules are generated. From the group contribution method theory that every molecular group contributes to the property of the ensemble molecule, the molecules and mixtures/blends are designed from a reversed engineering approach. The generated product is then tested to see if the needs and properties are met, if not, a new design target is generated. In the mathematical optimization solution strategy mainly two approaches exist: simultaneous optimization and decomposed optimization. In both approaches the needs are translated into a mixed integer non-linear program (MINLP) with an objective function to be optimized. The MINLP formulated problem can then be solved simultaneously, which means that all constraints are solved in the same program. In the decomposed optimization approach; however, the MINLP formulation is solved sequentially so that in each routine the search space is reduced and the MINLP problem is broken down to a MILP problem, which is divided into a set of smaller NLP problems with fixed integers. This decreases search space and solution time systematically and ensures that a global optimum and all feasible solutions can be found.

In this paper, a computer-aided framework is presented for formulating needs into an MINLP problem, which is solved through a decomposed optimization approach. The framework is capable of finding the optimum product based on the specified needs and properties. The optimum product may be a pure compound, mixture or blend. In addition, given the decomposed optimization approach, it is possible to also obtain all feasible solutions, or a set of feasible solutions close to the objective function. The framework is implemented into a computer-aided tool where the MINLP is formulated. The framework application is demonstrated through a case study.

2. Computer-aided Framework

The computer-aided framework for design of pure, mixed and blended products is presented here. The framework utilizes the needs and target properties to construct the CAMD/CAM^{b}D problem into a MINLP formulation. The MINLP formulation is then solved through a decomposed approach. The framework has four steps represented in Figure 1.

2.1. Step 1:Problem Definition

In step one the product needs, target properties and desired product type are defined. These can be thermodynamic properties, economic, sustainability and environmental needs. The product type refers to the type of desired molecule, such as chain size, chain type (cyclic, acyclic, aromatic etc.), and type of functional groups and occurrence of these groups.

2.2. Step 2: CAMD Formulation

In step two the needs, properties and product types are converted into a CAMD/CAM^{b}D formulation. Here, constraints are given for the product structure and needs with upper and lower bounds for target properties. An objective function is defined, which is a function that is to be optimized. Furthermore, relevant process and/or thermodynamic models are formulated, such as mass balances and phase equilibrium equations.

2.3. Step 3: MINLP Formulation

In step three the formulation from step two is set-up as a MINLP formulation. A general CAMD/CAM^{b}D problem is formulated as the following MINLP problem, which is divided into objective function and four types of constraints.

$$\min/\max f_{obj}(\mathbf{X},\mathbf{N}) \tag{1}$$

s.t. structural constraints: $g_1(\mathbf{N},\mathbf{Y}) \le 0$ (2)

pure component property constraints: $g_2(\mathbf{N}) \le 0$ (3)

mixture property constraints: $g_3(\mathbf{X},\mathbf{N}) \le 0$ (4)

process model constraints: $g_4(\mathbf{X},\mathbf{N}) = 0$ (5)

$$\mathbf{X} \in \mathbb{R}^n, \mathbf{N} \in \mathbb{Z}_+^m, \mathbf{Y} \in \{0,1\}^q$$

N is a vector of integer variables, which are related to the numbers of the building blocks and/or molecules (1st and 2nd order groups). **Y** is adjacency matrix which is related to the description of the molecular structure. **X** is a vector of continuous variables, which are related to the mixture and/or process variables. The first constraint deals with the structural stability of the generated molecules. Here, molecules that do not follow rules such as the octet rule (valency) will be rejected as infeasible molecules. The second constraint includes pure component property constraints. These are, for the case of group contribution methods, often linear equations. In the third property constraint the mixture properties are investigated. Here, both mixture composition dependent properties, such as mixture stability, and mixture independent properties,

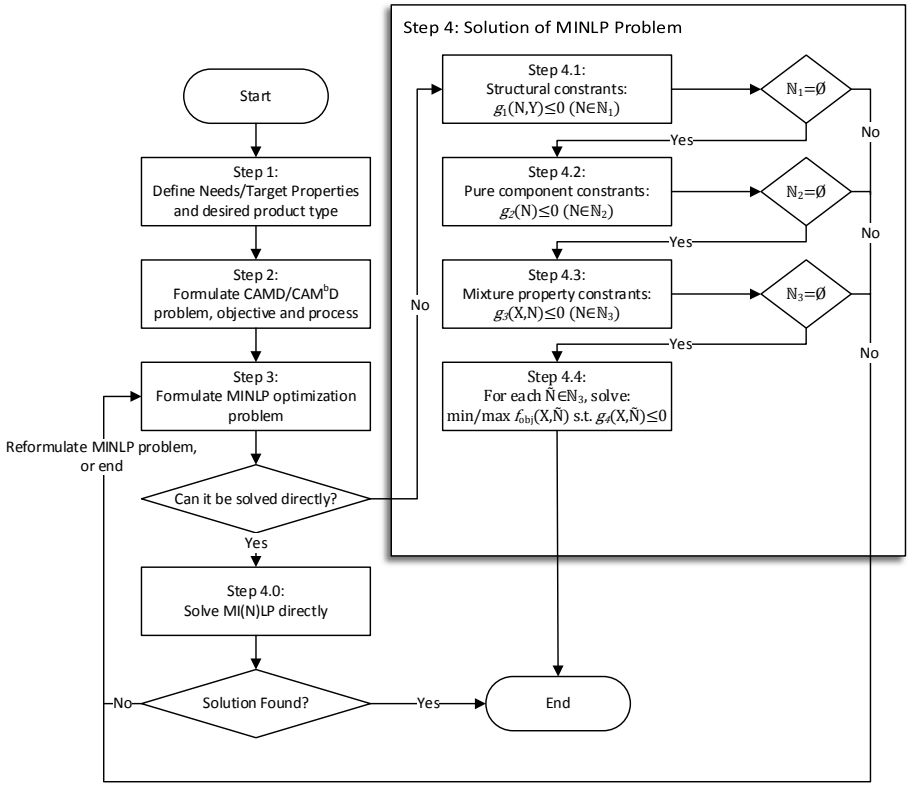

Figure 1: Computer-aided Framework for Product Design

such as solvent selectivity, are considered. There are often nonlinear equations. In the last and fourth constraint type, process models are included, such as mole balance for a unit operation. Other models may also be included here such as phase equilibrium equations.

2.4. Step 4: Solution of MINLP Problem

In step four the MINLP formulation is solved. For this, a database is used for group contribution coefficients for the molecular groups. Group contribution method for pure compound properties used in this work is Cosntantinou and Gani (1994). Mixture/blend group contribution method used in this work is by Fredenslund *et al.* (1975). In most CAM^{b}D problems, the need for using highly nonlinear property models and process models can lead to non-convex and non-smooth problems, which are difficult to solve. Karunanithi et al. (2005) proposed a decomposition-based algorithm to solve this MINLP problem by first solving sub-problems consisting of a set of property constraints only. The search space is reduced by using this decomposition algorithm. The MINLP problem is converted to several Non-Linear Programming (NLP) problems corresponding to fixed values of the integer variables. The decomposition-based algorithm is shown with the rest of the framework in Figure 1 as step 4.1 to 4.4. Step 4.0 is used instead if only linear equations (MIP) are present, or that the problem is small enough to solve simultaneously. Once the decomposed solution strategy is computed, it is checked if the solution or feasible solutions are found. If not, it is necessary to modify the MINLP formulation, thus returning to Step 3, to either loosen the constraints or in another way increase the search space. If the optimum solution is found the framework ends.

3. Case Study

In this case study a solvent is designed for an extraction process. Given a mixture of water (H_2O) and acetic acid (CH_3COOH), find a suitable solvent that is able to extract acetic acid from water. The flow sheet of the extraction process is given in Figure 2. The feed is the acetic acid/water solution, the extract is the acetic acid rich phase, whereas the raffinate (R) is the water rich phase.

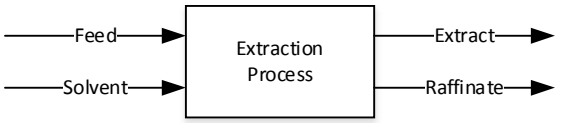

Figure 2: Extraction Process

The combined flow of feed and solvent (F) is 2338.2 mol/h. Mole fractions x_i of acetic acid (A), water (B), and solvent (S) are 0.0077, 0.2951 and 0.6972, respectively. The extraction process is operated at 298 K. Every step of the framework from Figure 1 will be walked through in the following.

3.1. Step 1

From the process description, the process needs can be defined. It is desired to obtain a solvent that likely will split acetic acid from water. Therefore, an efficient solvent for removal of acetic acid from water is needed. As the extraction process is operated at 298 K, it is furthermore needed that the solvent is in a liquid state at this temperature. The boiling point of acetic acid is 391 K. In many cases, the solvent is separated from the solute in the extract phase in a solvent recovery system. Thus, the volatility between solute and solvent must be high.

3.2. Step 2

As the needs have been defined, a CAMD problem can be formulated. Here, the needs will be formulated through lower and upper bounds of the needed properties. It is specified here that, for the sake of this case study, only acyclic solvents containing C, H and/or O atoms are chosen. Thus, the group set u only contains acyclic groups (see Eq. 8) containing C, H and/or atoms ($u \in \{CH_3, CH_2, CH, C, OH, CH_3OH, CHO, CH_3COO, CH_2COO, HCOO, CH_3CO, CH_2O, HCO, COOH, COO\}$). The size of the generated solvents will also be limited. The needs with their respective lower and upper bounds are given in Table 1. N_G is the total number of groups u, N_F is the total number of functional groups. The need regarding efficient solvent is here expressed as distribution coefficient m, solvent loss SL, solvent power SP, and selectivity β.

Table 1: Lower and upper bounds for specified needs

Need	Lower	Upper	Constraint	Need	Lower	Upper	Constraint
$\mathbf{N_G}$	1	6	Eq. 7	**m**	0.49	-	Eq. 12
$\mathbf{N_F}$	0	2	Eq. 9	**SL**	-	0.0038	Eq. 13
$\mathbf{T_m}$	-	270K	Eq. 10	**SP**	0.778	-	Eq. 14
$\mathbf{T_b}$	430K	-	Eq. 11	**β**	11	-	Eq. 15

As the objective function, the molar flow of water in the raffinate and of acetic acid in the extract should be maximized (Eq. 6). The process models will be molar balances for the extraction process and liquid-liquid phase equilibrium (Eq. 16-18).

3.3. Step 3

Based on the CAMD formulation, the MINLP formulation is written:

$$f_{obj} = \max\left(x_A E + x_B R\right) \tag{6}$$

s.t.

$$1 \le \sum_i \sum_j u_{ij} \le 6 \tag{7}$$

$$\sum_i \sum_j u_{ij}\left(2 - v_j\right) = 2 \tag{8}$$

$$0 \le \sum_j u_{ij} \le 2 \tag{9}$$

$$102.425 \times \log \sum_i N_i T_{mi} \le 270 \tag{10}$$

$$430 \le 204.359 \times \log \sum_i N_i T_{bi} \tag{11}$$

$$0.49 \le \gamma^{\infty}_{A,B} MW_B \,/\, \left(\gamma^{\infty}_{A,S} MW_S\right) \tag{12}$$

$$1 / \gamma^{\infty}_{S,B} \le 0.00381 \tag{13}$$

$$0.778 \le 1 / \gamma^{\infty}_{A,\mathrm{S}} \tag{14}$$

$$11 \le \gamma^{\infty}_{B,\mathrm{S}} / \gamma^{\infty}_{A,S} \tag{15}$$

$$\gamma_i^E x_i^E - \gamma_i^R x_i^R = 0, i \in \{A, B, S\} \tag{16}$$

$$x_i^F F - x_i^E E - x_i^R R = 0, i \in \{A, B, S\} \tag{17}$$

$$x_A^p + x_B^p + x_S^p = 1, p \in \{F, E, R\} \tag{18}$$

v, is the free bonds of a molecular group, $\gamma_{i,i}$, is the activity coefficient. Eq. 10-11 are group contribution equations defined in Cosntantinou and Gani (1994).

3.4. Step 4

The MINLP cannot be solved directly due to its size. Thus, the decomposed solution strategy is used (step 4.1 to step 4.4). In step 4.1 constraint 7 to 9 are solved as MIP, which yields 514 solutions. The solutions are screened in step 4.2 through constraint 10 to 11, which yields 196 solutions. These are further screened in step 4.3 in constraints 12 to 15, which yields 19 solutions. These are then solved in a set of 19 NLP with objective function from Eq. 6 with constraints 16 to 18. This yields the optimum solvent, given in Table 2. As it can be seen, a diester (butane-2,3-diyl diformate, groups: 2 CH3, 2 CH, 2 HCOO), was generated that satisfied the constraints and obtained a

maximized objective function value. The recovery is 98.3%. In Seader and Henley (1995) and Karunanithi *et al.*, (2005) methyl ethyl ketone and 2-hexanone were designed, respectively, as solvents for the same problem. It is interesting to note that both of these were in the list of feasible solutions; however, a better solvent was found in this case study, achieving higher recovery. The result should, however, be verified through experimentation. Also, the generate and test approach would have given this results, but not all the constraints can be included.

Table 2: Optimum designed solvent and key properties

Tm [K]	**Tb [K]**	**m**	**SL**	**β**	**Possible Structure**
236.75	455.22	0.7678	0.0021	14.7702	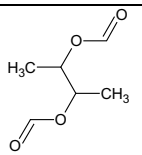
SP	x_A^E	x_B^E	x_S^E	x_A^R	
2.1290	0.00859	0.20005	0.79136	0.00112	
x_B^R	x_S^R	**E [mol/h]**	**R [mol/h]**	f_{obj} **[mol/h]**	
0.99700	0.00188	2059	278.86	295.72	

With the proposed framework other problems have been solved but not reported. These include, but are not limited to, design of polymers based on polymer specific properties (e.g. glass transition temperature) and design of refrigerants for a thermodynamic cycle.

4. Conclusion and Future Works

A computer-aided framework was developed in this work. The framework has been shown to systematically define and solve a large MINLP product design problem. Higher order description of groups both for pure compound and mixture property prediction and the ability to estimate the structure of molecules is subject to future works. In addition, the framework application is to be shown for a larger range of case studies with inclusion of mixture and blend design problems.

References

A. Fredenslund, R. L. Jones, J. M. Prausnitz, 1975, Group-contribution estimation of activity coefficients in nonideal liquid mixtures, AIChE Journal, 21, 6, 1086–1099.

A., Apostolakou, C. S. Adjiman, 2003, Chapter 4: Optimization Methods in CAMD – II, In Computer Aided Molecular Design: Theory and Practice, Elsevier Science, 63–93.

A. T. Karunanithi, L. E. K. Achenie, R. Gani, 2005, A New Decomposition-Based Computer-Aided Molecular/Mixture Design Methodology for the Design of Optimal Solvents and Solvent Mixtures, Industrial & Engineering Chemistry Research, 44, 13, 4785–4797.

E. Conte, R. Gani, K. Ming, 2011, Design of formulated products: A systematic methodology, AIChE Journal, 57, 9, 2431-2449.

J. D. Seader, E. J. Henley, 1998, Separation process principles, Wiley, New York.

L. Constantinou, R. Gani, 1994, New group contribution method for estimating properties of pure compounds, AIChE Journal, 40, 10, 1697–1710.

N. A. Yunus, K. V. Gernaey, J. M. Woodley, R. Gani, 2014, A systematic methodology for design of tailor-made blended products, Computers and Chemical Engineering, 66, 201–213.

P. M. Harper, R. Gani, P. Kolar, T. Ishikawa, 1999, Computer-aided molecular design with combined molecular modeling and group contribution, Fluid Phase Equilibria, 158-160, 337–347.

R. Gani, 2004 Chemical product design: challenges and opportunities, Computers and Chemical Engineering, 28, 2441-2457.

R. Gani, P. Harper, M. Hostrup, 2005, Automatic creation of missing groups through connectivity index for pure-component property prediction. Industrial & Engineering Chemistry Research, 44, 7262–7269.

Krist V. Gernaey, Jakob K. Huusom and Rafiqul Gani (Eds.), 12th International Symposium on Process Systems Engineering and 25th European Symposium on Computer Aided Process Engineering.
31 May – 4 June 2015, Copenhagen, Denmark

Uncertainty in Clinical Data and Stochastic Model for In-vitro Fertilization

Kirti M. Yenkie[a, b] and Urmila M. Diwekar [a, b*]

[a]*Department of Bioengineering, University of Illinois, Chicago, IL-60607, USA*
[b]*Center for Uncertain Systems: Tools for Optimization & Management (CUSTOM), Vishwamitra Research Institute, Clarendon Hills, IL-60514, USA*
urmila@vri-custom.org

Abstract

In-vitro Fertilization (IVF) is the most common technique in Assisted Reproductive Technology (ART). It has been divided into four stages; (i) superovulation, (ii) egg retrieval, (iii) insemination/fertilization and (iv) embryo transfer. The first stage of superovulation is a drug induced method to enable multiple ovulation, *i.e.*, multiple follicle growth to oocytes or matured follicles in a single menstrual cycle. IVF being a medical procedure that aims at manipulating the biological functions in the human body is subjected to inherent sources of uncertainty and variability. Also, the interplay of the hormones with the natural functioning of the ovaries make the procedure dependent on several factors like patient's condition in terms of cause of infertility, actual ovarian function, responsiveness to medication, etc. The treatment requires continuous monitoring and testing and this can give rise to errors in observations. Thus, it becomes essential to look at the process noise and deviations and think of a way to account for them to build better representative models for follicle growth. The purpose of this work is to come up with a robust model which can project the superovulation cycle outcome based on the hormonal doses and patient response in presence of uncertainty. The customized stochastic model results in better projection of the cycle outcome for the patients where the deterministic model has some deviations from the clinical observations and the growth term value is not within the range of '0.3 to 0.6'. It was found that the prediction accuracy was enhanced by more than 70% for some patients by using the stochastic model projections.

Keywords: infertility, assisted reproduction, multiple ovulation, uncertainty

1. Introduction

Infertility is the inability of a couple to achieve conception or to bring a pregnancy to term after a year or more of regular, unprotected intercourse. The World Health Organization has estimated that about 8-10% couples experience some kind of infertility problems. Medical science has come up with ARTs to treat these problems. IVF involves fertilization of oocytes by a sperm outside the body in a laboratory simulating similar conditions as in the human body and then implanting the fertilized eggs back in the uterus of the patient for full term pregnancy (Speroff and Fritz, 2005). The success of superovulation, its first stage, is critical to proceed with the next stages in the IVF cycle. Also it requires maximum medical attention and is cost-intensive when compared to other stages.

The major hormonal drug involved in superovulation is the follicle stimulating hormone (FSH), responsible for follicle growth and development. The deterministic model for

multiple follicle growth, dependent on the amount of FSH dosage was built by drawing similarities with the particulate process of batch crystallization and it fitted very well to the clinical data for most patients. However, the fact remains that IVF is actually a medical procedure involving manipulations in biological functions of human body and specifically to functioning of ovaries, is subjected to inherent sources of uncertainty.

2. The deterministic model

2.1. Model development and validation

The similarities between process of crystallization (Hill et al., 2006) and superovulation used for model development are presented in Table 1. Thus, the concept of moment model in batch crystallization (Hu et al., 2005) was used for modeling superovulation in IVF. The growth term in batch crystallization is temperature dependent and hence it becomes the decision variable for control. On similar lines, in IVF the follicle growth is dependent upon the doses of hormones injected to the patient.

Table 1: Analogy between batch crystallization and superovulation

Batch Crystallization	Superovulation (IVF stage I)
-Production of multiple crystals	-Production of multiple oocytes or eggs
-Crystal quality is determined in terms of maximum size and uniformity	-Oocyte quality is determined in terms of maximum size and uniformity
-The rate of crystallization or crystal growth varies with time and process conditions	-The rate of ovulation or oocyte growth varies with time, drug dosing amounts and interactions
-Process is affected by external variables like agitation, and process operating variables like temperature, pressure, etc.	-Process is affected by externally administered drugs and body conditions of the patient undergoing the process

The follicle size is converted into mathematical moments by assuming the follicles to be spherical in shape. The Eq. (1) is used for converting follicle size to moments. Each moment corresponds to a feature of the follicles; zeroth moment corresponds to the number, first moment to the size, second to area, etc.

$$\mu_i = \sum n_j(r,t) r_j^i \Delta r_j \tag{1}$$

Here, μ_i is the ith moment, $n_j(r, t)$ are number of follicles in j^{th} bin with mean radius as r at time t, r_j is mean radius of j^{th} bin and Δr - range of radii variation in each bin. The follicle growth term (G) is dependent on the amount of FSH injected (C_{fsh}) to the patient at particular time (t) and is represented as Eq. (2). Here, k and α are kinetic constants.

$$G(t) = k\Delta C_{fsh}(t)^{\alpha} \tag{2}$$

In the literature by Baird (1987) it was suggested that number of follicles activated for growth during a particular superovulation cycle is constant for a particular patient, hence zeroth moment has a constant value (Eq. (3)). Also, the 1st to 6th order moments (Eq. (4)) are used in the model, since they help in better prediction of moment values as well as help in efficient recovery of the size distributions.

$$\mu_0 = constant \tag{3}$$

$$\frac{d\mu_i}{dt} = iG(t)\mu_{i-1}(t); \qquad (i = 1,2,\ldots,6) \tag{4}$$

The validation method (Yenkie et al., 2013) requires conversion of predicted moments back to the follicle size and number as a follicle size distribution (FSD) for each day of the cycle. The method (Flood, 2002) is represented in Eq. (5).

$$\bar{\mu} = \mathbf{A}\,\bar{n} \tag{5}$$

Here, $\bar{n}$ is the vector of number of follicles in n bins on ith day; $\bar{\mu}$ is the vector of moments on ith day and **A** is the inversion matrix derived from Eq. (1). The elements in matrix 'A' are evaluated using the formula shown in Eq. (6).

$$a_{i,j} = \bar{r}_j^i \Delta r_j \tag{6}$$

Here, i is the order of the moment (increment in rows), j is the representative bin (increment in columns), $\bar{r}$ is the mean radius of the bin and Δr is the range of the bin.

2.2. Prediction accuracy

The deterministic modelling approach was applied to clinical data on 50 superovulation cycles. The predictions of FSDs were compared with the actual follicle size and numbers reported in clinical data. The mean square error (MSE) for the accuracy of the FSD projections on final FSH dosing day was evaluated using Eq. (7).

$$MSE = \sum \left[\frac{n_{i,obs} - n_{i,sim}}{Max(n_{i,obs}, n_{i,sim})} \right] \tag{7}$$

Here, $n_{i,obs}$ is number of follicles observed and $n_{i,sim}$ is number of follicles predicted by the model in the i^{th} bin on last day of FSH dosing. This error value was evaluated for model projections from the initial two day data. In MSE evaluation, follicles in size bins corresponding to size range of 9-12 mm were used, because it is the desired range for inducing final maturation and egg retrieval. The error analysis as shown in Figure 1 indicates that initial two day data is sufficient for more than 60% cases to project the overall superovulation outcome.

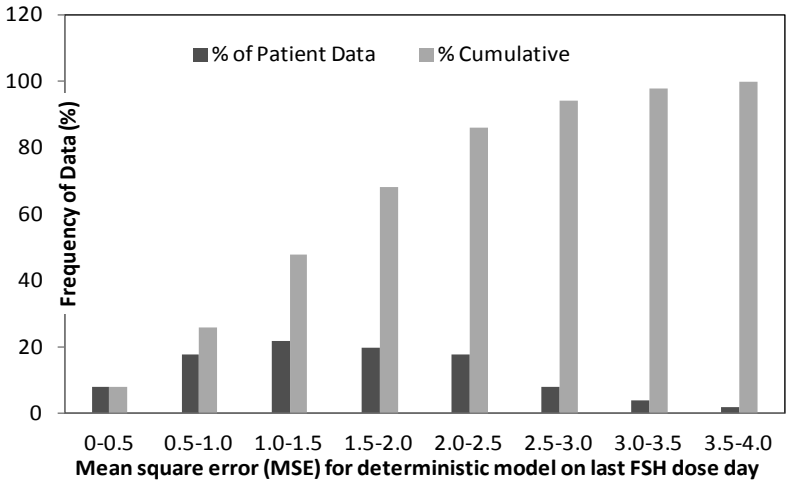

Figure 1. Prediction accuracy analysis for the deterministic model

However, the deterministic model does not match very well for cases with high MSE values and when the growth term (G) value for the patients were not within the range of '0.3-0.6', suggesting the need for additional monitoring and data to predict the superovulation outcome with more accuracy.

3. The stochastic model

In this work, the aim is to develop a stochastic model for the superovulation stage in terms of *Ito* processes. Initially, these *Ito* processes were mostly applied in financial field and stock price modelling to characterize uncertainties. Since they can characterize time-dependent uncertainties and can be integrated and differentiated using rules of *Ito*'s stochastic calculus, they can prove beneficial in modelling biological processes. The simplest example of an *Ito* process is the *Brownian* motion which is also known as *Wiener* process in continuous form. To characterize any stochastic process as a *Wiener* process it must follow following three important properties (Diwekar, 2008).

i. *Markov* property: The probability distribution for all future values of the process depends only on its current value.
ii. It should have independent increments in time. The probability distribution for the changes in the process over any time interval is independent of any other time interval.
iii. Changes in process over finite time interval should be normally distributed, with variance linearly dependent on length of time interval, dt (i.e., N (0, $\sqrt{dt}$) for all t > 0).

The superovulation data is analyzed and checked whether it classifies as a *Wiener* process. As per the current protocols, the hormonal dosage is decided based on daily monitoring of the patient's response from the previous day dose and the follicle size observed. Thus, the next FSD after the injection of hormones is dependent on the FSD at that particular time, hence it is reasonable to categorize the superovulation stage as a *Markov* process. The follicle growth term developed in the deterministic model and which satisfies the data is dependent on the amount of FSH injected (C_{fsh}) to the patient at the particular day (t) in the cycle as shown earlier in Eq. (2). Thus it satisfies the second property, where the FSH dosage can have independent increments.

The follicle growth and number is represented as FSD, where follicle size is divided into equispaced bins and numbers of follicles are represented as discrete markers in each size bin as shown in Figure 2. When these markers are connected with smooth curve, it can be seen that the data tends to follow a normal distribution. As time progresses, it continues to follow the same trend, with a change in mean and variance values. Hence, uncertainties associated with superovulation process can be modelled as *Wiener* processes.

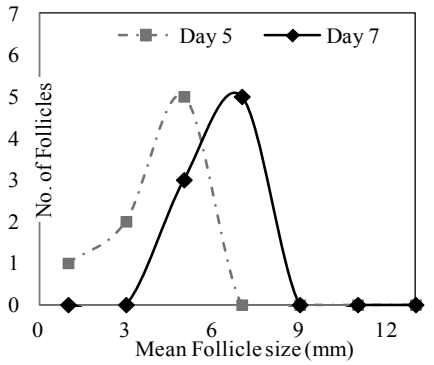

Figure 2. Follicle size showing normal distribution on day 5 and 7.

The *Ito* processes are of various types whose basic building block is a *Wiener* process. Depending upon the behaviour of the system under random influences it can modelled as one of the suitable *Ito* processes. Some examples are simple *Brownian* motion, geometric *Brownian* motion, mean reverting process and geometric mean reverting process. Following a similar approach, we can model the uncertainties associated with the superovulation stage. It was found that the uncertainties could be represented using

the simple *Brownian* motion type of *Ito* process, thus resulting in the following (Eq. (8) to Eq. (13)) set of stochastic differential equations (SDEs).

$$d\mu_1(t) = G(t)\mu_0 dt + \sigma_1 \varepsilon_t \sqrt{dt} \tag{8}$$

$$d\mu_2(t) = 2G(t)\mu_1 dt + \sigma_2 \varepsilon_t \sqrt{dt} \tag{9}$$

$$d\mu_3(t) = 3G(t)\mu_2 dt + \sigma_3 \varepsilon_t \sqrt{dt} \tag{10}$$

$$d\mu_4(t) = 4G(t)\mu_3 dt + \sigma_4 \varepsilon_t \sqrt{dt} \tag{11}$$

$$d\mu_5(t) = 5G(t)\mu_4 dt + \sigma_5 \varepsilon_t \sqrt{dt} \tag{12}$$

$$d\mu_6(t) = 6G(t)\mu_5 dt + \sigma_6 \varepsilon_t \sqrt{dt} \tag{13}$$

Here, μ_i is the i^{th} moment, σ_i are the standard deviation terms for the moment equations corresponding to noise in clinical data, ϵ_t is the set of random numbers derived from unit normal distribution and dt is the time interval.

4. Results and discussions

The parameters for the system are evaluated using the two level approach (Yenkie et al. (2013)), in which parameters in the stochastic part, *i.e.*, the standard deviations (σ_i), are evaluated from variance in the data. The follicle size measurements are converted to moments and the parameters in deterministic part (k, α and integration constants) are evaluated using modified form of objective function involving values of standard deviations. The results for FSDs are shown in Figure 3A and 3B for day 5 and day 9.

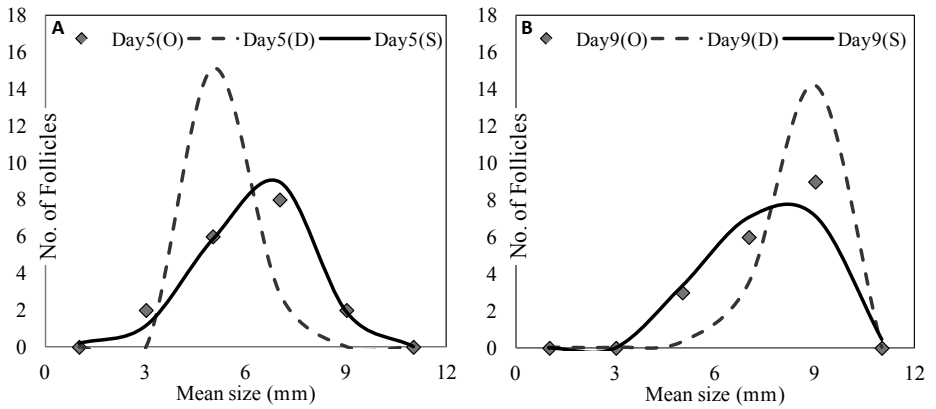

Figure 3. Comparison of FSD from observed clinical data (O), deterministic (D) and stochastic (S) model predictions for Patient-I on day 5 (A) and 7(B).

We can see that the results projected by stochastic model (S) match the data (O) better when compared to the deterministic results (D). Especially when it comes to the final FSH dosing day projections, *i.e.* 9th day in case of Patient-I. This study was done for more patients and the results are reported in Table 2 in terms of the mean square error on final FSH dosing day. For all these patients with a high growth term (G) value, the FSD projections using the stochastic model are greatly improved.

Table 2. Error comparison for deterministic and stochastic model predictions

Patient	Growth term (G)	Mean square error (deterministic)	Mean square error (stochastic)	% Improvement (stochastic over deterministic)
A	0.72	1.1239	0.0748	93.34
B	0.77	0.927	0.1999	78.4
C	1.55	1.4813	1.3740	7.24
D	0.82	1.3009	1.1865	8.79
E	0.70	1.6541	0.9351	43.47

5. Conclusions

The approach to develop a stochastic model for the superovulation stage in IVF in terms of *Ito* form of stochastic differential equations (SDE) is a novel aspect of the study and the results look very promising. The approach used for stochastic model development involving a novel parameter estimation procedure is an added contribution in this work and can eliminate a lot of computation difficulties in development of SDE models.

Predictions obtained from the stochastic model are inclusive of the patient's uncertainty and noise in clinical data and hence match better as compared to deterministic results for the study done on five selected patients with high 'growth term (G)' value. The mean square errors (MSE) in modelling for the deterministic and stochastic cases provide a numerical estimate of the improvements in predictability and robustness of SDE model. The predictions from the stochastic model can be used for predicting robust drug dosing policies using stochastic control methods for achieving desired outcome in superovulation and thus can contribute to the studies on enhancement of success rate of IVF cycles.

References

Baird, D. T. 1987. A model for follicular selection and ovulation: Lessons from Superovulation. *J. steroid Biochem.*, 27**,** 15-23.

Diwekar, U. 2008. *Introduction to Applied Optimization*, 2nd ed.; Springer NY.

Flood, A. E. 2002. Thoughts on recovering particle size distributions from the moment form of the population balance. Developments in Chemical Engineering and Mineral Processing, 10(5/6): 501-519.

Hill, P. J., Korovessi, E. L., Linninger, A. A. 2006. *Batch Processes: Batch Crystallization*. CRC Press, Taylor and Francis, 2006.

Hu, Q., S. Rohani, Jutan, A. 2005. Modelling and optimization of seeded batch crystallizers. *Computers and Chemical Engineering*, 29: 911-918.

Speroff, L., and M. A. Fritz. 2005. *Clinical Gynecology Endocrinology and Infertility*. Philadelphia, USA: Lippincott Wilkins & Williams, 7th edition, 1331-1380.

Yenkie, K. M., Diwekar, U., Bhalerao, V. 2013. Modelling the superovulation stage in in-vitro fertilization. *IEEE Trans. Biomed. Engg.*, 60(11): 3003-3008.

Yenkie, K.M., Diwekar, U., Linninger, A., Kim, S. A new method for parameter estimation in stochastic differential equations. *AIChE Annual Meeting, 2013, 589e*, San Francisco, CA.

Krist V.Gernaey, Jakob K.Huusom and RafiqulGani (Eds.), 12th International Symposium on Process Systems Engineering and 25th European Symposium on Computer Aided Process Engineering.
31 May – 4 June 2015, Copenhagen, Denmark

Mathematical analysis of multistage population balances for cell growth and death

Margaritis Kostoglou[a], María Fuentes-Garí[b], David García-Münzer[b], Michael C. Georgiadis[c], Nicki Panoskaltsis[d], Efstratios N. Pistikopoulos[b],Athanasios Mantalaris[b]

[a]*Department of Chemistry, Aristotle University of Thessaloniki, Thessaloniki, Greece*
[b]*Department of Chemical Engineering Imperial College London, London, UK*
[c]*Department of Chemical Engineering, Aristotle University of Thessaloniki, Thessaloniki, Greece*
[d]*Department of Haematology, Imperial College London, Harrow, Middlesex, UK*

Abstract

The cell cycle is a biologically timed process by which cells duplicate. It consists of 4 phases, during which cells undergo different mandatory transformations. Modelling the cell cycle therefore requires capturing the evolution of those processes inside of each phase. A specific three stage biologically supported population balance model employed to simulate evolution of several cell cultures is studied here in detail. The three governing equations of this model are composed by growth and transition terms. A one equation analogue of the multistage model is formulated and it is solved analytically in the self-similarity domain. The effect of initial conditions at the system evolution is studied numerically. The three model equations are then considered by using asymptotic and numerical techniques. It is shown that in the case of sharp interstage transition the discontinuities of the initial conditions are preserved during cell growth leading to eternal oscillations whereas for distributed transition the cell distribution converges to a self-similar (long time asymptote) shape. It is also illustrated that the closer the initial condition to the self similar distribution the faster the convergence to self-similarity and the smaller the oscillations of the total cell number. Exact results are given for the growth parameters of the population balance and lumped models.

Keywords: multistage, cell cycle, population balance, cell growth and death, analytical solutions.

1. Introduction

Normal cell proliferation occurs following a four-step cycle, known as the cell cycle: G1 phase, when cells grow and stock up on nutrients; S phase, when their DNA is duplicated; G2 phase, when DNA is checked for duplication errors and M phase, when the cell divides giving birth to two new cells. These can in turn enter the cell cycle or stay in a quiescent state (G0) until needed. The cell cycle is inherently regulated by the scheduled expression of cyclinsintracellularly, which activate their partner cyclin-dependent kinases (cdks) in a phase-specific manner leading to progression-related events. More specifically, the concentration of cyclins E and B typically fluctuates and reaches a threshold in G1 and G2 phases respectively as cells come closer to transitioning to the next phase. Cyclin concentration and DNA content are thus excellent candidates for use as progress variables within G1 (cyclin E), S (DNA) and G2 (cyclin B).

Cell cycle modelling is of relevance for two specific applications: leukaemia proliferation according to chemotherapy response and phase-specific production of antibodies in industrial cell lines. Population balance models (PBMs) are particularly suitable as they account both for inter- and intra- phase growth, allowing for distributed phases which give greater accuracy.

Leukaemia is a type of cancer of the blood, involving a loss of cell cycle controls. It requires treatment with chemotherapy drugs, which are toxic to proliferating cells only. Their mechanism is cell cycle phase-specific, i.e. they block cell growth at only one of the phases of the cell cycle. Survival relies not only on the eradication of the malignant cells but also on the maintenance of a minimum level of healthy stem cells (which are also affected due to their proliferative nature). It is therefore very important to minimise the number of cycles and to optimise the dose amount and timing. However, current treatment protocols rely basically on the theoretical maximum tolerance level of the patient (correlated to his height and weight). Total cell quantification and cell cycle distribution of cancer and healthy cells, described by a mathematical model, are clearly needed here to optimise the treatment (Pefani et al., 2013; 2014).

The cell cycle description is of industrial relevance due to the intrinsic heterogeneous nature of these systems at different scales (from the molecular to the bioreactor level). Moreover, the cell cycle plays is intimately related to the growth, death, and productivity of mammalian cell cultures. An accurate description of the cell cycle heterogeneity can therefore provide a systematic platform for model-based applications such as optimising product titres, where a balance between cell proliferation and cell cycle specific productivities needs to be found (Dutton et al., 1998). Therefore, relevant mammalian cell cycle models that capture the complex dynamic relations of the system can advantage the commonly industry-adopted design of experiment (DoE) approach.

2. The mathematical problem

After the appropriate change to the variables notation for clarity, the mathematical model can be written as follows:

$$\frac{\partial G(x,t)}{\partial t} + k_g \frac{\partial G(x,t)}{\partial x} = -r_g(x)G(x,t) \tag{1}$$

$$\frac{\partial S(y,t)}{\partial t} + k_s \frac{\partial S(y,t)}{\partial y} = 0 \tag{2}$$

$$\frac{\partial M(z,t)}{\partial t} + k_m \frac{\partial M(z,t)}{\partial z} = -r_m(z)G(z,t) \tag{3}$$

The three stages communicate to each other through the following boundary conditions (continuity of cell number flux between the stages):

$$k_g G(0) = 2\int_0^\infty r_m(z)M(z,t)dz \tag{4}$$

$$k_s S(0) = \int_0^\infty r_g(x) G(x,t) dx \tag{5}$$

$$k_m M(0) = k_S S(2) \tag{6}$$

The above system of partial differential equations must be solved in the domain $0 \le x,z \le \infty$, $1 \le y \le 2$ with initial conditions $G(x,0)=G_0(x)$, $S(y,0)=S_0(y)$, $M(z,0)=M_0(z)$. A particular cell according to the above model undergoes growth of its content and transition from stage to stage. The transition from M to G stage is accompanied by a splitting of the cell leading to an increase of the total cell number. The form of the transition frequency function is of particular importance. A transition zone can be defined as the zone of cell contents (x or z) between a lower value for which the transition frequency is practically zero and an upper limit for which the transition frequency is very large compared to the growth rate. In case of an uniform or step shape of the transition frequency the transition zone is not well defined but in practical applications r is a relatively steep function of the cell content. A ramp function shape is a good candidate for the transition frequency (with parameters the inception content and the ramp slope). A case of particular interest is the one of zero width transition zone (i.e. infinite slope in the ramp model). This is an important case since it allows further mathematical insight in the structure of the model. The equations in this case are singular at the location of transition and an appropriate modification of the model is needed.

3. The one equation prototype

In order to understand the structure of the solution of the mathematical system and the effect of parameters a one-equation prototype of the problem will be considered first. The prototype has the form:

$$\frac{\partial f(x,t)}{\partial t} + k\frac{\partial f(x,t)}{\partial x} = -r(x) f(x,t) \qquad 0 \le x \le \infty \tag{7}$$

with $kf(0,t) = 2\int_0^\infty r(x) f(x,t) dx$ and $f(x,0)=f_0(x)$. The original problem (1-3) can be cast in the form of the above equation in the particular case of zero width transition zone for G stage and $k_g=k_s=k_m$. In the case of zero transition width for f, the right hand side in equation (7) must be set equal to zero, the definition domain is restricted to $0<x<x_m$ and the boundary condition takes the form $f(0,t)=2f(1,t)$. The present problem can be considered as a non-conventional type of growth-breakage population balance (with no internal coordinate conservation by breakage). The total cell number N(t) is given as $N(t) = \int_0^\infty f(x,t) dx$. It is assumed that there is a solution of the form $f(x,t)=N(t)F(x)$. It can be shown that $\frac{dN}{dt} = \lambda N$ with $\lambda = \int_0^\infty r(x) F(x) dx$. The proper mathematical manipulation leads to:

$$F(x)=\frac{2\lambda}{k}e^{-(\lambda x-\int_0^x r(y)dy)/k} \quad (8)$$

where the constant λ can be found from the solution of a transcendental equation.

The corresponding results for the case of zero width transition zone at $x=x_m$ are $\lambda=k\ln(2)/x_m$, $F(x)=\frac{2\ln(2)}{x_m}2^{-x/x_m}$. It is noticeable that the function F does not depend on growth coefficient k. Furthermore, introducing the normalized variable $\eta=x/x_m$ leads to a universal shape for the function $F(\eta)$ (i.e. $F(\eta)=2\ln(2)2^{-\eta}$).

In the above the self-similar solution of the single equation prototype has been derived in closed form. The question now is the realizability of this solution (i.e. if it is really the long time asymptotics of the dynamic problem) and the way it is approached. A first very important assertion is that if the initial cell distribution has the shape of the self-similar one then the self-similarity solution is the **exact** solution of the dynamic problem at any time. In the case of the monodisperse initial distribution the self-similarity solution is never reached (it is non-realizable). The total cell number increases stepwise by doubling each time interval of x_m/k. On the average it can be considered as an exponential growth like the one suggested by the self-similarity solution. An explanation of the system behavior will be pursued here. In general the system attempts to transform the initial cell distribution to the self-similar one in order to converge to the self-similarity regime. In order to do this it must redistribute cells with respect to x variable. The only dispersion mechanism is through transition process. The largest the width of transition zone the higher the dispersion ability of the system and the fastest the approach to the self-similarity. In the particular case of zero width transition zone there is no mechanism for dispersion so the initial distribution can be never transformed to the self-similar one and the system continuously oscillates. The largest the deviation of the initial distribution from the self-similar one, the largest the amplitude of oscillations.

In order to verify the above statements some results on the evolution of the system will be shown here. The evolution of the total cell number N for the zero width transition zone is shown in Figure 1 for several shapes of the initial cell distribution. The content x is normalized by x_m and time is normalized by x_m/k. The case A corresponds to $f_0(x)=\delta(x)$, the case B to $f_0(x)=2x$, the case C to $f_0(x)=2-2x$, the case D to $f_0(x)=2/3(1-x)+2/3$ and finally the case E to $f_0(x)=1$. The asymptotic solution is practically indistinguishable from case E (less than 1% maximum difference) so it is not presented for clarity. There is a repeated shape of the curve for each doubling period. As it is obvious the closer the initial distribution to the self-similar one the closer the proximity of the total number evolution to the self-similar one. In case of zero width transition zone the system retains the discontinuities of the initial distribution. On the contrary, the finite transition zone smeares out very fast the discontinuities allowing the distribution to converge to the self-similar one.

4. The three stage model

A self-similar solution for the three stage model has also been derived. In the particular case of the same normalized growth rate k in each stage the value of λ for the zero width

transition zone is ln(2)k/3. Regarding the realizability of the self-similar solution the situation is exactly the same with the one shown for the one-equation prototype case.

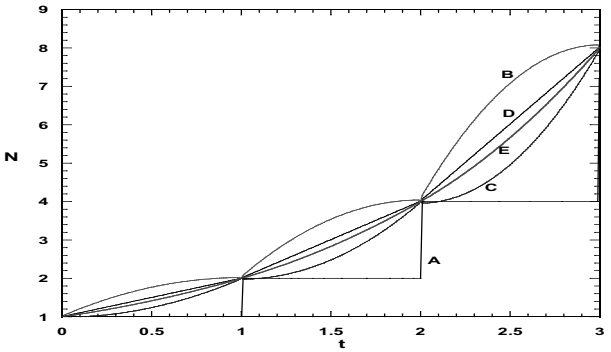

Figure 2: Evolution of total cell number for zero width transition zone and several initial cell distributions (one equation prototype).

The initial distribution of self-similar shape retains its shape during system evolution. The three stage model contains two transition zones (from G to S and from M to G stages). If both transition zones are of zero width then the system oscillates for ever with no convergence to self-similarity. If at least one transition zone is of finite width the system converge to self-similarity for any initial condition.

5. On the reduced (lumped) models

The so called reduced models are mathematical simplifications of the detailed models and they describe the evolution of integral quantities sacrificing higher order information as the detailed cell distribution shapes. Such a model contains parameters with clear physical meaning but different from the parameters of the detailed model. Typically the reduced model parameters can be found using experimental data but it cannot be used to extract the detailed model parameters due to their integral nature. The reduced model for the one equation prototype analysed here is simply dN/dt=KN.

It is clear that the model coincides with self-similar behaviour considering that K=λ. The reduced model is not able to reproduce the approach to the self similarity and the oscillating behaviour but is the best possible single parameter approximation. The parameter K depends on both growth and transition rates as it has been shown for λ.

A reduced model for the three stage model, used extensively in the past has the form (Pefani et al., 2013):

$$\frac{dN_G}{dt} = 2K_M N_M - K_G N_G \tag{9}$$

$$\frac{dN_S}{dt} = K_G N_G - K_S N_S \tag{10}$$

$$\frac{dN_M}{dt} = K_s N_S - K_M N_M \tag{11}$$

where N_i (i=G,S,M) are the numbers of cells in each stage and K_i (i=G,S,M) are the transition between the stages rate constants. The rates K_i are function of the growth rate

and of the transition function in the corresponding stage. The above system admits also a self-similar solution in the sense of $dN/dt=\lambda N$ and of a constant partition between the three stages. By assuming $N=N_o e^{-\lambda t}$, $N_G=\alpha N$, $N_S=\beta N$, $N_M=\gamma N$ substituting in the system (10-12) and performing some algebra leads to

$$\alpha = (1+\frac{\lambda+K_G}{2K_M}+\frac{(\lambda+K_G)(\lambda+K_M)}{2K_MK_S})^{-1} \quad (12)$$

$$\beta = \frac{(\lambda+K_G)(\lambda+K_M)}{2K_MK_S}(1+\frac{\lambda+K_G}{2K_M}+\frac{(\lambda+K_G)(\lambda+K_M)}{2K_MK_S})^{-1} \quad (13)$$

where λ is given from the solution of the algebraic equation $(\lambda+K_G)(\lambda+K_M)(\lambda+K_S)=K_GK_MK_S$ and $\gamma=1-\alpha-\beta$. Let us consider the special case $K_G=K_S=K_M=K$. At this case $\lambda=(2^{1/3}-1)K$ and $\alpha=1/(1+2^{-1/3}+2^{-2/3})$, $\beta=2^{-1/3}/(1+2^{-1/3}+2^{-2/3})$, $\gamma=2^{-1/3}/(1+2^{-1/3}+2^{-2/3})$. Comparing this result with the corresponding zero width transition zone population balance model with equal growth rates reveals that the partition is exactly the same and the ratio of the λ parameters is $3(2^{1/3}-1)/\ln(2)$ (approximately 1.1). The success of the reduced model to describe the self-similarity state of the detailed model should not lead to underestimation of its pathologies. It leads very fast to self-similarity, it is not able to represent complex dynamics of the detailed model and it does not convey any information of cell distribution in the stages. Let us examine here what happens with the addition of a death term with rate constant K_d in S stage. It can be shown that both population balance and lumped models admits self similar solutions. In case of the same growth constant for the three stages the population balance model leads to $\lambda=\ln(2)K/3-K_d/3$ and the lumped model leads to the following equation for λ: $(K+\lambda)^2(K+\lambda+K_d)=2K^3$. The value of λ in the first case decreases linearly with K_d but in the second case exhibits a minimum at $\lambda=-K_d$. In this case the lumped model does not agree with population balance model leading to much smaller apparent cell death rates for the same value of K_d.

6. Conclusions

Multistage population balance models are necessary tools for the study of cell behaviour. A particular model of this type is mathematically examined here. It is shown that the model evolves to a self-similar state or undergoes eternal oscillations depending on the form of functions determining the transition from stage to stage. The amplitude of the oscillations depends on the deviation of the initial cell distribution from the self-similar one. A lumped model can adequately describe the cell growth process but it fails in case of stage-specific cell death.

References

R.L. Dutton, J.M. Scharer, M. Moo-Young, 1998, Descriptive parameter evaluation in mammalian cell culture, Cytotechnology 26, 139-152.

E. Pefani, N. Panoskaltsis, A. Mantalaris, M. C. Georgiadis, E. N. Pistikopoulos, 2013, Design of optimal patient-specific chemotherapy protocols for the treatment of acute myeloid leukemia (AML), Computers & Chemical Engineering, 57, 187-195.

E. Pefani, N. Panoskaltsis, A. Mantalaris, M.C. Georgiadis, E.N. Pistikopoulos, 2014, Chemotherapy Drug Scheduling for the Induction Treatment of patients diagnosed with Acute Myeloid Leukemia, Transactions of Biomedical Engineering Journal, 61, 7, 2049-2056.

Krist V. Gernaey, Jakob K. Huusom and Rafiqul Gani (Eds.), 12th International Symposium on Process Systems Engineering and 25th European Symposium on Computer Aided Process Engineering.
31 May – 4 June 2015, Copenhagen, Denmark

Oxygen transfer rates and requirements in oxidative biocatalysis

Asbjørn Toftgaard Pedersen, Gustav Rehn and John M. Woodley

Department of Chemical and Biochemical Engineering, Søltofts Plads 229, 2800 Kgs. Lyngby, Denmark

Abstract

Biocatalytic oxidation reactions offer several important benefits such as regio- and stereoselectivity, avoiding the use of toxic metal based catalysts and replacing oxidizing reagents by allowing the use of oxygen. In this contribution the oxygen requirements are analysed for different process scenarios, considering different biocatalyst formats and variation of the desired productivity. Also, the applicability of two different oxygen supply methods (bubbling and membrane aeration) is considered. The results indicate that growing cells could be used to reach productivities up to 3.5 g $L^{-1}h^{-1}$ without oxygen supply being limiting. Also, membrane contactors can provide a feasible oxygen supply method when bubble-less aeration is desired. However, in order to support high productivity the oxygen flux using air may be insufficient, thus requiring the use of oxygen.

Keywords: biocatalysis, oxygen requirements, oxygen supply.

1. Introduction

Process Systems Engineering (PSE) methods and tools are of enormous value for evaluation of new manufacturing processes. In particular they can assist in the development of new biological processes. An interesting case concerns the development of biocatalytic oxidation processes, which is a complex task requiring the simultaneous consideration of several issues regarding the process design and operation. For example, the biocatalyst format and method of oxygen supply must be carefully chosen. Thus, mathematical models for assessing the oxygen requirement using different biocatalyst alternatives and the attainable oxygen transfer rate (OTR) using different aeration methods are valuable for predicting process feasibility. Furthermore, such models are essential to efficiently design new and sustainable bioprocesses for the future.

1.1 Oxygen dependent enzymes

Oxidation reactions are highly important in organic chemistry. However, traditional chemical methods are associated with drawbacks such as oxidants based on toxic metal ions, undesired side reactions, ineffective use of oxygen and the difficulty of performing regio and stereoselective oxidations (Faber, 2011). Biocatalytic oxidations (bio-oxidations) provide opportunities to avoid several of these problems and are especially useful due to their stereoselectivity. Also, they allow the use of molecular oxygen, the most inexpensive and harmless oxidant available. Several different enzymes, belonging to several enzyme classes such as dehydrogenases, oxidases, mono- and dioxygenases and peroxidases are used to catalyze many interesting oxidation reactions including oxidation of alcohols and polyols, hydroxylation of phenols, epoxidation of double bonds and heteroatom oxygenation (Hollmann et al., 2011).

1.2 Biocatalyst format

There are several possible ways to use a biocatalyst, whether in the form of an isolated enzyme or in the form of whole-cells. Also, isolated enzymes as well as whole-cells may be used either in solution/suspension or immobilized using numerous techniques available. The choice of biocatalyst format depends on the requirements of the process at hand. However, the choice of biocatalyst format also influences the way the process can be operated. On the one hand, the whole-cell format is attractive because no enzyme purification is needed, thus lowering the biocatalyst cost. Another advantage is that co-factors (e.g. NAD(P)H) can be regenerated within the cell, thus eliminating the need for an additional enzyme and co-factor. On the other hand, the diffusion of substrates and products in and out of the cell may limit the reaction rate compared to that observed using an isolated enzyme. Moreover, side reactions catalyzed by other enzymes present in the cell may lower the reaction yield and result in a more complex product mixture. Also, the stability of some enzymes can be comparatively lower when used in isolated form. In the following section, implications of the biocatalyst format in oxygen demanding bio-oxidation process are discussed.

2. Oxygen requirements

The oxygen consumption of a biocatalyst arises from the oxygen requirement of cellular processes and the consumption of oxygen in the biocatalytic reaction of interest. The cellular processes cover the catabolism of an energy source (typically glucose) to supply energy (in the form of ATP) used in the anabolic reactions synthesizing cell mass. The cellular processes can be described by Eq.(1-4) (Villadsen et al., 2011), here given on a c-mol basis. Glucose is converted to CO_2, NADH and ATP in the glycolysis and tri-carboxylic acid cycle, Eq.(1), and ATP is synthesized via oxidation of NADH in the electron transport chain, Eq.(2). The anabolic reactions require NADPH, which is produced by degradation of glucose in the pentose-phosphate pathway, Eq.(3). Eq.(4) describes the lumped anabolic reactions responsible for cell mass (X) synthesis. These equations are valid for *Escherichia coli* and other organisms that use similar pathways, but will change dependent upon the specific metabolic pathways used by a given microorganism.

The equations describing the cellular processes contain several parameters that depend on the reaction conditions and the type of microorganism. The amount of ATP formed in Eq.(1) (ε) varies depending on the amount of intermediate species that is required for macromolecule synthesis; the maximum value is 2/3. The efficiency of the electron transport chain (P/O) has a theoretical maximum of 3 ATP per NADH, but most often the value is closer to 1.5. The yield coefficients for NADH, NADPH and ATP (Y_{xNADH}, Y_{xNADPH}, Y_{xATP}) in Eq.(4) depend on the type of organism (i.e. the composition of the cell), the substrate, and the conditions of growth (i.e. substrate limitations, etc.). The CO_2 formation, α, is typical between 0.08 and 0.14, and can be calculated via a redox balance if the cellular composition and the yield coefficients for NADPH and NADH are known.

$$CH_2O \longrightarrow CO_2 + 2\,NADH + \varepsilon\,ATP \tag{1}$$

$$NADH + 1/2\;O_2 \longrightarrow P/O\,ATP \tag{2}$$

$$CH_2O \longrightarrow CO_2 + 2\,NADPH \tag{3}$$

$$(1-\alpha)CH_2O + Y_{xNADPH}NADPH + Y_{xATP}ATP \longrightarrow X + \alpha CO_2 + Y_{xNADH}NADH \tag{4}$$

The last reaction required in order to predict the oxygen consumption of a microbial cell that performs a bio-oxidation, is the oxidation reaction itself, as shown in Eq.(5). In the reaction substrate (S) is oxidized to product (P) requiring stoichiometric amounts of oxygen and co-factor, which, dependent on the enzyme, can be either NADH or NADPH. In the following calculation it is assumed that the enzyme of interest is NADH dependent, however, a NADPH dependent enzyme will only slightly increase the oxygen requirements of the biocatalyst.

$$S + NAD(P)H + O_2 \longrightarrow P \tag{5}$$

By combining Eq.(1-5) an expression for the overall oxygen consumption rate for a given whole-cell biocatalyst can be found. To reduce the number of required input variables quasi-steady state is assumed for the concentration of cofactors (NADH and NADPH), as well as the energy carrier (ATP). The oxygen consumption rate is described by Eq.(6), where the constants A, B, and C are defined by Eq.(7-9). The parameter m_{atp}, included in Eq.(8), describes the energy required for cellular maintenance processes, such as protein turnover and membrane potential maintenance. This parameter is highly depended on the type of organism and the conditions the organism is exposed to. Eq.(6-9) describe the oxygen consumption rate for *E. coli* growing on glucose. The expressions will change if another substrate is applied or an organism with different metabolism is employed.

$$r_{O_2} = (A + 1/2\ Y_{xNADH})\,\mu + B + C\ A_{cat} \tag{6}$$

$$A = \frac{Y_{xATP} - Y_{xNADH}\,P/O}{\varepsilon + 2\ P/O} \tag{7}$$

$$B = \frac{m_{ATP}}{\varepsilon + 2\ P/O} \tag{8}$$

$$C = \frac{1}{2} + \frac{P/O}{\varepsilon + 2\ P/O} \tag{9}$$

The oxygen requirements of growing cells, resting cells, and isolated enzymes carrying out an oxidation reaction are plotted in Figure 1 for different volumetric productivities. The volumetric productivity is based on initial rates, meaning that the observed volumetric productivity can be significantly lower. The reported oxygen requirements can therefore be seen as the maximum requirement observed during a reaction.

The volumetric productivity required by biocatalytic processes differs significantly depending on the value of the product produced, i.e. a pharmaceutical might only require 1-10 g/L/day to be economically feasible whereas a bulk chemical requires much higher productivities. The oxygen transfer capabilities in industrial bioreactors set a limit to the maximum volumetric productivity that can be achieved. Depending on the volumetric productivity required, it will be necessary to intensify the oxygen transfer to overcome this limitation. Intensified oxygen transfer can be achieved by e.g. pressurizing the reactor or using alternative oxygen supply methods, such as feeding hydrogen peroxide to reactor, which can be degraded to oxygen using catalase.

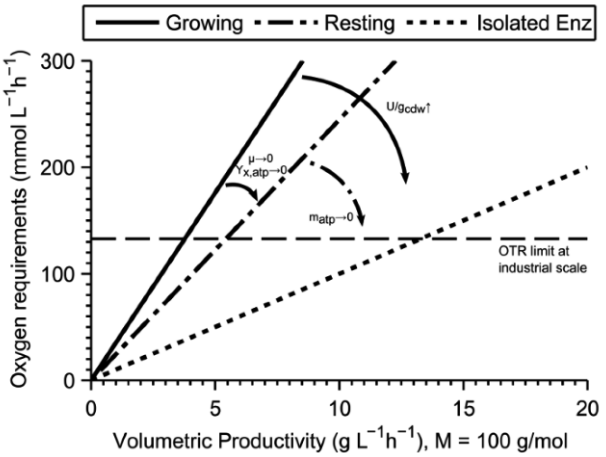

Figure 1 Oxygen requirements of different types of biocatalysts carrying out an oxidation reaction. The calculations are based on *E. coli* and the following parameter values: A_{cat} = 50 U/g_{cdw}, μ = 0.2 h^{-1}, ε = 2/3, P/O = 1.5, Y_{xNADH} = 16.97 mmol/g_{cdw}, Y_{xatp} = 70.2 mmol/g_{cdw}, m_{atp} = 7.9 mmol/g_{cdw}/h(Ingraham et al., 1983; Varma and Palsson, 1994). The maximum oxygen transfer rate (OTR) for bubble aeration at industrial scale is estimated using a $k_l a$ of 500 h^{-1} (Villadsen et al., 2011). The OTR limit is based on the use of air.

3. Supply methods

3.1. Bubble aeration

Supplying oxygen by bubbling air through the reaction medium is the method of choice in most fermentation processes, due to its relatively easy implementation and operation. In general the oxygen transfer rate (OTR) can be assumed to be controlled by the diffusion of oxygen across the liquid boundary layer, and hence described by a simple mass transfer equation, Eq.(10). The OTR depends on the volumetric oxygen transfer coefficient ($k_l a$), the oxygen saturation concentration ($C_{O_2}^{sat}$), and the concentration of oxygen in solution. Several factors influence the OTR; the temperature, pressure, and salt concentration influence $C_{O_2}^{sat}$, while mixing power input, gas flow rate, and liquid viscosity influence $k_l a$.

$$OTR = k_l a \, (C_{O_2}^{sat} - C_{O_2}) \tag{10}$$

The concentration of oxygen in solution is critical in order to ensure that the biocatalyst is not limited by oxygen. The minimum concentration to ensure effective catalysis depends on the affinity of the enzyme of interest towards oxygen and can be as high as 100 μM, corresponding to ≈ 50% air saturation in water at 1 atm. (Duetz et al., 2001). This naturally reduces maximum achievable OTR in such systems, because the driving force for oxygen transfer is lowered. At industrial scale the OTR is also limited by the achievable mixing power input and the maximum aeration rate, typically the maximum OTR for an industrial scale stirred bioreactor is 100-200 mmol/L/h when the oxygen concentration in the reactor is close to zero (Chisti, 1999).

3.2. Membrane aeration

Hollow fibre membrane contactors are widely used for creating large specific areas (area/volume) of liquid/liquid or gas/liquid interfaces and therefore present an interesting alternative for reactor aeration. The contactor can combine a large gas/liquid

interfacial area with bubble-free aeration, thus enabling efficient oxygen mass transfer while also preventing foaming and minimizing undesired evaporation of any volatile components. Due to the modular design of membrane contactors, scaling-up is relatively straight forward (Gabelman and Hwang, 1999), and contactors are implemented for various industrial applications (Klaassen et al., 2005).
The use of isolated enzymes in bio-oxidation processes is potentially challenging because enzymes can be subject to inactivation by the presence of gas/liquid interfaces, with an inactivation rate proportional to the interfacial area (Bommarius and Karau, 2005). Stability data, however, cannot simply be extrapolated to other operating conditions and should therefore be investigated for each case. The successful use of membrane aeration, using a non-porous silicon based membrane, was reported for the oxidation of lactose to lactobionic acid using isolated enzymes (Van Hecke et al., 2011). Based on the above estimations of oxygen requirements, the required specific membrane areas were calculated for different bio-oxidation processes (Figure 2).

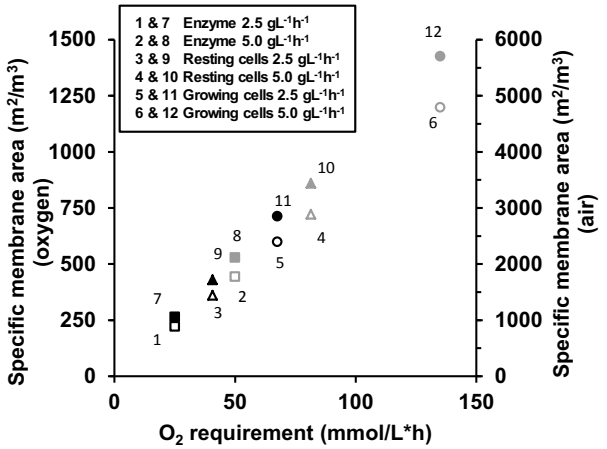

Figure 2 Estimated specific membrane areas required for aeration of bio-oxidation processes, based on a volumetric productivity of 2.5 $gL^{-1}h^{-1}$ (black) or 5 $gL^{-1}h^{-1}$ (grey) respectively. Calculations are based on either the use of oxygen (open symbols) or air (closed symbols). The calculation were conducted as described previously (Côté et al., 1988), assuming an oxygen mass transfer coefficient of 3.8 g $m^{-2}h^{-1}bar^{-1}$) for a polypropylene hollow fibre (Côté et al., 1989) and operation at 1 bar.

Figure 2 indicates that membrane aeration could be feasible for several bio-oxidation processes. Commercially available membrane modules (e.g. from Liqui-Cel®) can provide over 350 m^2 of membrane are in a contactor volume of about 75 L, and several modules can be used in parallel if needed. If air is used instead of oxygen, the lower partial pressure of oxygen results in a lower driving force for the oxygen diffusion. Consequently, the use of air is likely to be limited to processes with relatively low (<50 mmol $L^{-1}h^{-1)}$ oxygen requirement. Similarly, dense membranes with inherently lower oxygen mass transfer coefficients compared to porous fibres may not provide large enough flux of oxygen for many processes, but can be useful for isolated enzyme processes in which the gas/liquid interface causes enzyme inactivation.

4. Conclusions and future outlook

Development a bio-oxidation process is a complex task. While the target productivity is linked to the product value, the maximum achievable productivity is greatly influenced

by the oxygen requirement set by the biocatalyst. The present analysis indicates that a productivity of 3.5 or 5 g $L^{-1}h^{-1}$ could be attainable by conventional bubble aeration, using growing or resting cells, respectively. The use of membrane aeration may necessitate using pure oxygen in order to support whole-cell systems at this level of productivity. Thus, its use may be limited to the production of high value products due to the considerable cost contribution by the pure oxygen. The use of isolated enzymes, however, could benefit from the use of a dense membrane to prevent interfacial inactivation of both the enzyme catalyzing bio-oxidation reaction but also any enzyme used for co-factor regeneration. With the operating conditions assumed here, such a process would require oxygen is used rather than air. Naturally, both the use of oxygen and the membrane contactor would contribute to an increased process cost and the strategy should be evaluated from case to case. In the future, further analysis will be focussed on case-studies of bio-oxidation processes with different characteristics in terms of products, biocatalyst formats and reactor aeration. The use of PSE tools and methods will be important to help provide a clear and excellent quantitative understanding.

Acknowledgements

The research leading to these results has received funding from the European Union's Seventh Framework Programme for research, technological development and demonstration under grant agreement n° [613849].

References

Bommarius, A.S., Karau, A., 2005. Deactivation of formate dehydrogenase (FDH) in solution and at gas-liquid interfaces. Biotechnol. Prog. 21, 1663–72.

Chisti, Y., 1999. Fermentation (industrial): Basic considerations. In: Robinson, R., Batt, C., Patel, P. (Eds.), Encyclopedia of Food Microbiology. Academic Press, London, pp. 663–674.

Côté, P., Bersillon, J., Huyard, A., Faup, G., Pierre, C., 1988. Bubble-Free Aeration Using Membranes : Process Analysis. J. Water Pollut. Control Fed. 60, 1986–1992.

Côté, P., Bersillon, J.-L., Huyard, A., 1989. Bubble-free aeration: Mass transfer analysis 47, 91–106.

Duetz, W.A., Beilen, J.B. Van, Witholt, B., 2001. Using proteins in their natural environment : potential and limitations of microbial whole-cell hydroxylations in applied biocatalysis 419–425.

Faber, K., 2011. Biotransformations in org chemistry, 6th ed. Springer-Verlag Berlin.

Gabelman, A., Hwang, S., 1999. Hollow membrane contactors. J. Memb. Sci. 159, 61–106.

Hollmann, F., Arends, I.W.C.E., Buehler, K., Schallmey, A., Bühler, B., 2011. Enzyme-mediated oxidations for the chemist. Green Chem. 13, 226.

Ingraham, J.L., Maaløe, O., Neidhardt, F.C., 1983. Growth of the bacterial cell. Sinauer Associates Inc., Sunderland, MA, U.S.A.

Klaassen, R., Feron, P.H.M., Jansen, a. E., 2005. Membrane Contactors in Industrial Applications. Chem. Eng. Res. Des. 83, 234–246.

Van Hecke, W., Haltrich, D., Frahm, B., Brod, H., Dewulf, J., Van Langenhove, H., Ludwig, R., 2011. A biocatalytic cascade reaction sensitive to the gas–liquid interface: Modeling and upscaling in a dynamic membrane aeration reactor. J. Mol. Catal. B Enzym. 68, 154–161.

Varma, A., Palsson, B., 1994. Stoichiometric flux balance models quantitatively predict growth and metabolic by-product secretion in wild-type Escherichia coli W3110. Appl. Environ. Microbiol. 60, 3724–3731.

Villadsen, J., Nielsen, J., Lidén, G., 2011. Bioreaction Engineering Principles, 3rd ed. Springer Science+Business Media, New York.

Krist V. Gernaey, Jakob K. Huusom and Rafiqul Gani (Eds.), 12th International Symposium on Process Systems Engineering and 25th European Symposium on Computer Aided Process Engineering.
31 May - 4 June 2015, Copenhagen, Denmark.

Robust process design for the bioproduction of β-carotene in green microalgae

Robert J. Flassig*[a], Melanie Fachet[a], Liisa Rihko-Struckmann[a] and Kai Sundmacher[a,b]

[a]*Max Planck Institute for Dynamics of Complex Technical Systems, Sandtorstraße 1, 39106 Magdeburg/Germany*
[b]*Otto-von-Guericke University Magdeburg, Process Systems Engineering, Universitätsplatz 2, 39106 Magdeburg/Germany*
**flassig@mpi-magdeburg.mpg.de*

Abstract

In this contribution, we present a probabilistic process design approach to derive a robust, optimal process design. Robustness is referred to the consideration of model and process design uncertainties. The probabilistic design approach is based on a hybrid uncertainty propagation strategy using profile likelihood and sigma point samples. At small additional computational effort the presented approach allows to predict the expected process performance and can improve process robustness by identifying design regions of small variability (=variance) in the design objective. As an example, we use the β-carotene production in the microalga *Dunaliella salina* to illustrate the impact of different dynamic nutrient feeding strategies, model and process design uncertainties on the expected biomass yield on absorbed light and its variability.

Keywords: *Dunaliella salina*, uncertainty analysis, profile likelihood, sigma points

1. Introduction

Biotechnological processes using microalgal cell factories are gaining significant importance for sustainable chemicals production based on renewable energy and feedstocks. The biochemical composition of the biomass is strongly affected by environmental conditions such as nutrient availability and light. Mathematical modeling can broaden our understanding of the underlying metabolic mechanisms and enable predictions of dynamics in biomass growth and biochemical composition under different cultivation conditions. Despite the huge progress in analytical cell biology, many model parameters are still unknown and need to be estimated. Natural biological variability in combination with the limited amount of quantitative data results in large parameter uncertainties, and thus model prediction uncertainties. Consequently, model-based process design objectives are rendered uncertain. Additionally, fluctuating operating conditions in combination with general process noise can render a non-probabilistic process design suboptimal (Bestle et al., 2010). Consequently, for a robust biological process design, prediction uncertainties and process design variabilities have to be accounted for. Here we present a hybrid uncertainty propagation strategy joining profile likelihood and sigma point samples (e.g. Royston, 2007; Julier and Uhlmann, 1996). We apply the probabilistic design approach to a growth model of *Dunaliella salina*. *D. salina* belongs to one of the few algal species with commercial relevance, because it accumulates high amounts of β-carotene. High light intensities and the nitrate depletion are the key factors promoting its accumulation. Even though large-scale systems for *D. salina* are already operated in Israel and Australia (e.g. Borowitzka and Borowitzka, 1990), a profound understanding of the optimal process design and operation including the impact of the uncertainties due to

environmental fluctuations and biological variability is largely missing. Indeed, such uncertainties could have a large impact on process yield and robustness especially in view of up-scaling from lab- to large-scale outdoor cultivation scenarios.

2. Methods

2.1. Model formulation

The dynamic evolution of system's states can be described by an ordinary differential equation (ODE) system

$$\begin{aligned} \dot{x}(t) &= f(x(t,\theta_x),u(t),\theta_x) \\ y(t) &= g(x(t,\theta_x),\theta_y)+\varepsilon, \end{aligned} \tag{1}$$

where $x(t,\theta_x)$ represent the states of the system, $u(t)$ indicates external feeds and θ_x a vector of kinetic parameters. Experimental readouts $y(t)$ are modeled by a readout function g, which also accounts for scaling and offset parameters θ_y and an additive white measurement noise model $\varepsilon \propto \mathcal{N}(0,\sigma^2_{\text{exp}})$. Kinetic and readout parameters are combined into the parameter vector θ, including all parameters required to completely characterize the system: $\theta = [\theta_x,\theta_y]^{\text{T}}$.

2.2. Profile likelihood

The profile likelihood is of special use, when analyzing the identifiability of the maximum likelihood estimate (MLE) $\hat{\theta}$ of the model parameters, but also when deriving confidence regions (Venzon and Moolgavkar, 1988; Raue et al., 2009). The profile likelihood of a parameter θ_i is given by (Venzon and Moolgavkar, 1988)

$$\chi^2_{\text{PL}}(\theta_i) = \min_{\theta_{j\neq i}} \chi^2(\theta), \tag{2}$$

which represents a function in θ_i of least increase in the residual sum of squares $\chi^2(\theta)$. For additive, independent, identically and normally distributed measurement noise we have $\chi^2 \propto -2\log L$, with likelihood L. Therefore χ^2 is often referred to as the likelihood. The least increase is achieved by adjusting $\theta_j, j = 1\ldots n_\theta \backslash i$ accordingly. Profile likelihood-based confidence regions CR_θ can be derived via

$$\text{CR}_\theta = \{\theta | \chi^2_{\text{PL}}(\theta) - \chi^2_{\text{PL}}(\hat{\theta}) < \delta_\alpha\}, \tag{3}$$

with δ_α being the α quantile of the χ^2 distribution with $df = 1$ (pointwise) or $df = n_\theta$ (simultaneous) degrees of freedom. A confidence interval of parameter θ_i is given by the borders of CR_θ. Notably, CR_θ represents a set of parameters, which approximates the high dimensional confidence region by n_θ sets of constrained projection samples via Eq. (2).

2.3. Uncertainty propagation by the sigma point method

The sigma point method is a versatile uncertainty propagation method that can be applied to problems of the form

$$Y = h(Z), \tag{4}$$

where h represents a possibly nonlinear function in Z. Z represents a stochastic, possibly multivariate, variable characterized by some known density function ρ_Z or statistical moments thereof.

In the following expectation $E[z]$ and variance-covariance $C[z]$ are used to characterize ρ_Z. Y represents also a stochastic variable that can be characterized by some *unknown* density function ρ_Y, whose shape depends on h and ρ_Z. The capitalized letters Y and Z represent stochastic variables, whereas non-capitalized letters represent the corresponding realizations. As shown by Julier and Uhlmann (1996), the sigma point methods yields efficient and accurate estimates of the first two statistical moments of Y, which can be used to describe ρ_Y. The two statistical moments of Y are derived from the (nonlinearly) transformed stochastic variable Z. The computational effort is of order $\mathscr{O}(2n_z+1)$, with n_z representing the dimension of Z. In brief, the sigma point method works as follows:

1. Select $2n_z+1$ sigma points in the original domain of the stochastic variable according to

$$z^{(0)} = E[z]; \qquad z^{(i)} = z^{(0)} \pm \sqrt{n_z+\lambda}\sqrt{C[z]}^{(i)}, \tag{5}$$

2. Propagate these points through the function h via $y^{(i)} = h(z^{(i)})$.

3. Estimated expectation $E^{\mathscr{S}}[y]$and variance-covariance $C^{\mathscr{S}}[y]$ of Y are given by

$$E^{\mathscr{S}}[y] = \sum_{i=-n_z}^{n_z} w^{(i)} y^{(i)}; \quad C^{\mathscr{S}}[y] = (1-\gamma^2+\beta)\left(y^{(0)}-E[y]\right)\left(y^{(0)}-E[y]\right)^{\mathrm{T}} + \\ + \sum_{i=-n_z}^{n_z} w^{(i)}\left(y^{(i)}-E[y]\right)\left(y^{(i)}-E[y]\right)^{\mathrm{T}} \tag{6}$$

with weights $w^{(0)} = \frac{\lambda}{n_z+\lambda}$, $w^{(\pm i)} = \frac{1}{2(n_z+\lambda)}$ and $\lambda = \gamma^2(n_z+\kappa)-n_z$. The superscript $\mathscr{S}$ indicates that sigma point samples have been used to estimate expectation and variance-covariance. The parameters γ, β, κ can be used to tune the sigma point method (Julier and Uhlmann, 1996).

2.4. Probabilistic process design using profile likelihood and sigma point samples

In this section we show how profile likelihood and sigma point samples can be combined to yield an efficient, probabilistic process design tool that accounts for uncertainty in the model parameters but also variability in the process design. Given significant profile likelihood samples from CR_θ and knowledge on typical process variability, we may derive an expected process design objective and its associated uncertainty in the following way. The scalar design objective O is given by

$$O = h(\Theta, \mathbb{D}), \tag{7}$$

where h represents the simulation of the process model as a function of the stochastic model parameters Θ and stochastic process design variables $\mathbb{D}$. As can be seen, the objective O is also a stochastic variable with realization $o = h(\theta, d)$, which in most of the cases is nonlinearly related to Θ and $\mathbb{D}$. The stochastic process design variable $\mathbb{D}$ can be characterized by mean $\mu_{\mathbb{D}}$ and variance-covariance $\Sigma_{\mathbb{D}}$. Then, using the sigma point approach in combination with a profile likelihood sample $\theta_i \in \mathrm{CR}_\theta$ an expected objective $m_i = E^{\mathscr{S}}[o]_i$ can be derived, including its associated variance $c_i = C^{\mathscr{S}}[o]_i$, to obtain a set of tuples $\{(m_i, c_i)\}$ with $i = 1 \ldots \#\mathrm{CR}_\theta$. From this set, final mean and variance of the process design objective can be derived via

$$\langle O \rangle = E^{\mathscr{S}}[o(\hat{\theta})]_{\mathbb{D}} \tag{8}$$

$$\langle (O - \langle O \rangle)^2 \rangle = \frac{\left(\max(\{m_i + q_\alpha\sqrt{c_i}\}) - \min(\{m_i - q_\alpha\sqrt{c_i}\})\right)^2}{q_\alpha^2} \tag{9}$$

with q_α being the α quantile, which can be derived from the confidence level α of the samples in CR_θ. Assuming normality we have $q_\alpha = 1.96$ for $\alpha = 0.05$. The quantity $\langle O \rangle$ in Eq. (8) represents

the expected process design objective under the fluctuating process design $\mathbb{D}$ at the MLE $\hat{\theta}$. The variability of $\langle O \rangle$ is affected by uncertainties of the model parameters and fluctuations of the process design itself. This range is quantified by the variance $\langle (O - \langle O \rangle)^2 \rangle$ in Eq. (9). A scheme of this hybrid uncertainty propagation strategy is given in Fig. 1a. In this probabilistic formulation, the initial scalar objective is turned into a two criteria objective, consisting of mean and variance of the scalar design objective. In the more general case of a probabilistic multi-objective design approach, we may describe variance-covariances of the objectives in the same way as illustrated here for the scalar case. The computational effort is of order $\mathcal{O}(\#\mathrm{CR}_\theta n_\theta n_d)$.

3. Results

3.1. Model description

The ODE model describing the growth of *D. salina*, proposed by Fachet et al. (2014), is used to demonstrate the here presented probabilistic design approach. The model incorporates light and nutrient effects on growth and pigmentation of *D. salina*. Fachet et al. (2014) further performed a profile likelihood analysis of the parameters, which is used here to supply the profile likelihood samples of the model parameters. The published model equations were slightly modified to solve the proposed equation system explicitly: An estimated biomass yield on absorbed light $Y_{\mathrm{X,E,est}}$ was calculated based on the biomass-specific light availability and nitrogen cell quota ω_{N} as expressed in Eq. (10):

$$Y_{\mathrm{X,E,est}} = \mu_{\max} \cdot \left(1 - \frac{\omega_{\mathrm{N,min}}}{\omega_{\mathrm{N}}}\right) \cdot \left(\frac{\frac{\overline{E}}{\rho_{\mathrm{X,dw}}}}{\frac{\overline{E}}{\rho_{\mathrm{X,dw}}} + K^*_{\mathrm{s,E}} \cdot \frac{\rho_{\mathrm{X,dw}}}{\rho_{\mathrm{Chl}}}} \right) \cdot \rho_{\mathrm{X,dw}} \cdot V_{\mathrm{PBR}} / E_{\mathrm{abs}}, \tag{10}$$

where $\mu_{\max}$ refers to the maximal growth rate and $K^*_{\mathrm{s,E}}$ refers to the light intensity per gram biomass for which the photosynthesis rate is half saturated with respect to light. The parameter values for the additionally introduced parameters $\mu_{\max}$=1 d^{-1} and $K^*_{\mathrm{s,E}}$=5.8 $\times$ 10^{-5} mol m g^{-1} d^{-1} were derived from experiments in batch cultures. Table 1 summarizes the model parameters used for simulations in this work. The carbon-specific photosynthesis rate r_{P}, the growth rate μ and the

Table 1: Summary of the values and parameters used for simulation.

Category	Value	Unit	Description	Comment
Initial conditions				
$\rho_{\mathrm{X,dw}}$	35	g dw m^{-3}	Biomass density	-
$\rho_{\mathrm{N,ext}}$	0.02	g N m^{-3}	Nitrogen density	-
ω_{Chl}	0.04	g Chl g^{-1} dw	Chlorophyll fraction of the biomass	-
ω_{N}	0.02	g N g^{-1} dw	Cell quota for nitrogen	-
Constants				
a^*	10	m^2 g^{-1} Chl	Optical cross section of chlorophyll *a*	-
E_0	168	mol photons m^{-2} d^{-1}	Maximal photon flux density at the reactor surface	-
m_{cell}	7×10^{-11}	g dw cell^{-1}	Cell weight	-
Reactor constants				Fachet et al. (2014)
Model parameters				Fachet et al. (2014)

biomass yield on absorbed light $Y_{\mathrm{X,E}}$ were calculated according to the following equations (Eqs. (11) - (12)):

$$r_{\mathrm{P}} = r_{\mathrm{P,max}} \cdot \left(1 - \frac{\omega_{\mathrm{N,min}}}{\omega_{\mathrm{N}}}\right) \cdot \left(1 - exp\left[\frac{-a^* \cdot Y_{\mathrm{X,E,est}} \cdot \overline{E}}{r_{\mathrm{P,max}}}\right]\right) \tag{11}$$

$$\mu = r_{\mathrm{P}} \cdot \left(\frac{\omega_{\mathrm{Chl}}}{\omega_{\mathrm{C}}}\right) \quad \text{and} \quad Y_{\mathrm{X,E}} = \frac{\mu \cdot \rho_{\mathrm{X,dw}} \cdot V_{\mathrm{PBR}}}{E_{\mathrm{abs}}}. \tag{12}$$

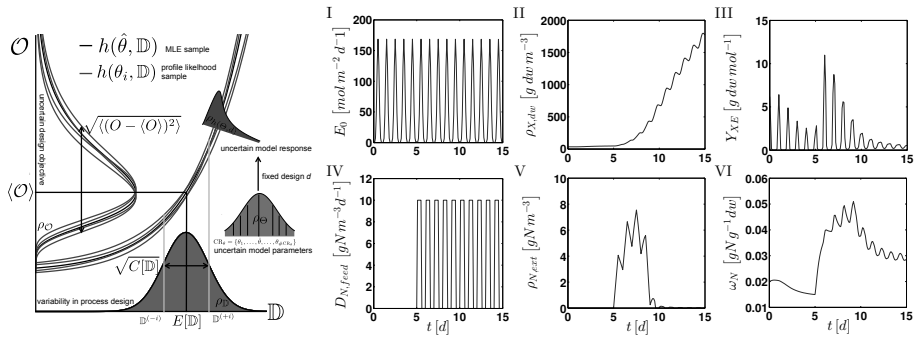

(a) (b)

Figure 1: (a) Scheme of the hybrid uncertainty propagation strategy. (b) Illustration of the influence of a day/night light profile (I) on cell density (II), biomass yield (III), extracellular nitrogen density (V) and intracellular nitrogen fraction (VI) at the MLE $\hat{\theta}$ for a deterministic nutrient feeding profile (IV) with $\tau_{\mathrm{N,feed}} = 5\,\mathrm{d}$ and $D_{\mathrm{N,feed}} = 10\,\mathrm{g\,N\,m^{-3}\,d^{-1}}$.

3.2. Formulation of the probabilistic design problem

The process design problem is to find an optimal nutrient feeding strategy for a day/night light profile with maximal photon flux density of E_0 (see Fig. 1b). Optimality of the feeding profile is measured with the design objective $\bar{Y}_{X,E} = 1/T \int_0^T Y_{X,E}(t)\mathrm{d}t$, which represents the average biomass yield on absorbed light energy over the process time T (in the example $T = 15\mathrm{d}$). A high β-carotene content of the biomass can be assured through a high light intensity day/night profile in combination with a nutrient feeding profile that ensures low nitrogen cell quota. The design of the nutrient feeding profile is parameterized as

$$u_{\mathrm{N,feed}}(t) = \begin{cases} 0 & \text{if } t \leq \tau_{\mathrm{N,feed}} \\ \frac{D_{\mathrm{N,feed}}}{2}\left(1 + \mathrm{sign}[\sin\left(\frac{2\pi(t-\tau_{\mathrm{N,feed}})}{T_{\mathrm{N,feed}}}\right)]\right) & \text{if } t > \tau_{\mathrm{N,feed}}, \end{cases} \tag{13}$$

which is a square wave with the volumetric flow rate of the nutrient feeding $D_{\mathrm{N,feed}}$, period $T_{\mathrm{N,feed}}$ fixed at one day, and feeding delay $\tau_{\mathrm{N,feed}}$. Therefore, the design space $\mathscr{D}$ consist of only two design variable, namely $\tau_{\mathrm{N,feed}}$ and $D_{\mathrm{N,feed}}$. Fig. 1b illustrates the dynamics of *D. salina* under periodic day/night light and nutrient supply. Fluctuations of the nutrient feeding profile are modeled with $\tau_{\mathrm{N,feed}} \propto \mathscr{N}(m_{\tau_{\mathrm{N,feed}}}, \eta m_{\tau_{\mathrm{N,feed}}})$ and $D_{\mathrm{N,feed}} \propto \mathscr{N}(m_{D_{\mathrm{N,feed}}}, \eta m_{D_{\mathrm{N,feed}}})$, where $\mathscr{N}(\mu, \sigma^2)$ represents the normal distribution with mean μ and parameterized variance σ^2. The scaling factor η is used to control the process noise, i.e. level of fluctuations in the nutrient feeding profile. The uncertainties in the model parameters are accounted by the profile likelihood samples at $\alpha = 0.05$. Applying the approach outlined in Sec. 2.4 yields the probabilistic optimal design problem:

$$\begin{aligned} &\underset{[\tau_{\mathrm{N,feed}}, D_{\mathrm{N,feed}}]^{\mathrm{T}}}{\text{minimize}} && [-\langle \bar{Y}_{X,E} \rangle, \langle (\bar{Y}_{X,E} - \langle \bar{Y}_{X,E} \rangle)^2 \rangle]^{\mathrm{T}} \\ &\text{subject to} && [0,0]^{\mathrm{T}} \leq [\tau_{\mathrm{N,feed}}, D_{\mathrm{N,feed}}]^{\mathrm{T}} \leq [20,50]^{\mathrm{T}}, \end{aligned} \tag{14}$$

within the feasible design space $\mathscr{D}$ defined by the bounds of the box constrains (in units of the respective design parameter). A Pareto optimal solution to Eq. (14) is given by the set of best trade-offs between maximal expected average biomass yield on absorbed light energy and minimal variance thereof (e.g. Pardalos et al., 2008). In Fig. 2a, the design objectives are shown over the design parameter space for different process noise levels ($\{\text{low,medium,high}\} \leftrightarrow \eta = \{0.25, 0.5, 0.75\}$). As can be seen, when increasing the process noise, the maximal expected yield decreases, while the maximal observed variance increases. This can also be seen in Fig. 2b, which shows the

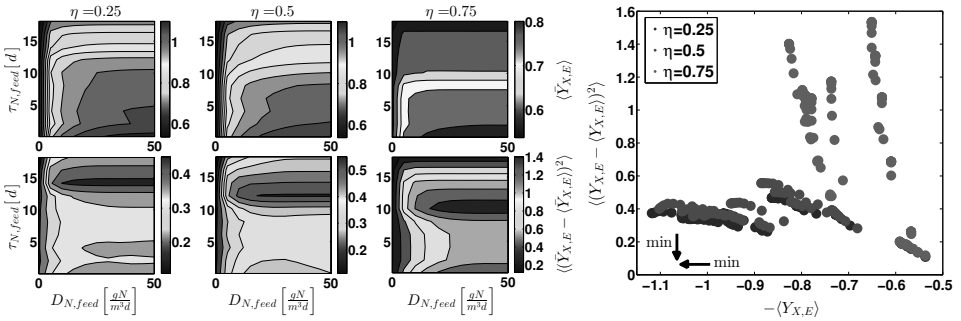

(a) (b)

Figure 2: (a) Design objectives $\langle \bar{Y}_{X,E} \rangle$ and $\langle (\bar{Y}_{X,E} - \langle \bar{Y}_{X,E} \rangle)^2 \rangle$ over the design space $\mathscr{D}$ and associated criterion space (b) for different process noise levels $\leftrightarrow \eta = \{0.25, 0.5, 0.75\}$ and profile likelihood samples from CR_θ at $\alpha = 0.05$.

criterion space for a set of equally sampled design parameters in the feasible design space: In the high level process noise scenario one can only reach the same process robustness, i.e. approximate variance of $\langle (\bar{Y}_{X,E} - \langle \bar{Y}_{X,E} \rangle)^2 \rangle \approx 0.4$ compared to low and medium level noise, by selecting a design point (i.e. nutrient feeding profile) that reduces the expected performance from roughly $\langle \bar{Y}_{X,E} \rangle = 1.1$ to $\langle \bar{Y}_{X,E} \rangle = 0.7$.

4. Conclusions

Here we present a probabilistic nonlinear design approach that allows to account for uncertainties of the model parameters, but also variabilities in the process design, e.g. general process noise or fluctuations of the operation conditions. The approach is based on a hybrid uncertainty propagation strategy using profile likelihood and sigma point samples. The profile likelihood samples are readily available from parameter identification analysis, as for instance performed by Fachet et al. (2014), and can thus be directly used to efficiently sample the confidence region of the typically high-dimensional model parameter space for estimating the uncertainties of the model predictions. Additionally, variability of the process in the form of process noise, e.g. varying feeding profiles or fluctuations of operating conditions, can be efficiently described with sigma point samples. In conclusion, the results of this work pave the way to an efficient probabilistic tool for robust bioprocess design under uncertainties of model parameters and operating conditions.

References

Bestle, D., Flassig, P. M., Dutta, A. K., 2010. Robust design of compressor blades in the presence of manufacturing noise. In: 9th European Conference on turbomachinery, fluid dynamics and thermodynamics. Vol. 1. pp. 1303–1314.

Borowitzka, L. J., Borowitzka, M. A., 1990. Commercial production of β-carotene by *Dunaliella salina* in open ponds. Bulletin of Marine Science 47 (1), 244–252.

Fachet, M., Flassig, R. J., Rihko-Struckmann, L., Sundmacher, K., 2014. A dynamic growth model of *Dunaliella salina*: Parameter identification and profile likelihood analysis. Bioresour Technol 173C, 21–31.

Julier, S. J., Uhlmann, J. K., 1996. A general method for approximating nonlinear transformations of probability distributions. Tech. rep., Technical report, Robotics Research Group, Department of Engineering Science, University of Oxford.

Pardalos, P., Migdalas, A., Pitsoulis, L., 2008. Pareto optimality, game theory and equilibria. Vol. 17. Springer.

Raue, A., Kreutz, C., Maiwald, T., Bachmann, J., Schilling, M., Klingmüller, U., Timmer, J., 2009. Structural and practical identifiability analysis of partially observed dynamical models by exploiting the profile likelihood. Bioinformatics 25 (15), 1923–1929.

Royston, P., 2007. Profile likelihood for estimation and confidence intervals. Stata Journal 7 (3), 376–387.

Venzon, D. J., Moolgavkar, S. H., 1988. A method for computing profile-likelihood-based confidence-intervals. Applied Statistics-Journal of the Royal Statistical Society Series C 37 (1), 87–94.

Krist V. Gernaey, Jakob K. Huusom and Rafiqul Gani (Eds.), 12th International Symposium on Process Systems Engineering and 25th European Symposium on Computer Aided Process Engineering.
31 May – 4 June 2015, Copenhagen, Denmark

Exploring Opportunities for the Production of Chemicals from Municipal Solid Wastes within the Framework of a Biorefinery

Fabian Bonk [a#], Tanmay Chaturvedi [a#], Ana I. Torres [b], Jens Ejbye Schmidt [a], Mette Hedegaard Thomsen [a], George Stephanopoulos [b*]

[a] *Masdar Institute, iEnergy, PO box 54224, Abu Dhabi, United Arab Emirates*
[b] *Massachusetts Institute of Technology, Department of Chemical Engineering, Building 66, 25 Ames Street, Cambridge, MA 02139, USA*
[*] *geosteph@mit.edu;* [#]*both authors have contributed equally.*

Abstract

Technological advances in catalytic and biological engineering have created opportunities for the production of high value chemicals from biomolecules such as glucose. Yet, production of such chemicals from real, complex biomass requires the integration with biomass pre-treatment. This study exemplifies the use of a computer aided collaborative environment that integrates biomass pre- and post-treatment via a limited set of intermediate streams. The cost and composition of intermediate streams from two different pretreatment methods, dark fermentation and enzymatic hydrolysis, were simulated using AspenPlus, using the organic fraction of municipal solid waste (OFMSW) as feedstock. Using these streams in downstream processes was found to have a cost advantage over the use of pure substrates. On the other hand, these streams contain by-products with the potential to inhibit downstream bioprocesses and to complicate downstream product separation.

Keywords: biorefinery, computer aided collaborative environment, organic fraction of municipal solid waste, enzymatic hydrolysis, dark fermentation

1. Introduction

The disposal of organic fraction of municipal solid waste (OFMSW), can lead to health risks and the production of greenhouse gases, if not properly managed. Research on waste treatment technologies has focused on optimizing the conversion of the OFMSW to final products with low market value such as biogas or ethanol. However, advances in biomass-based biological and catalytic engineering have defined opportunities for converting the OFMSW to chemicals with significant added-value, thus creating options which are economically more appealing. This study aims at assessing the economic opportunities of valorising intermediates from such processes within the framework of a biorefinery.

The assessment is performed using a computer-aided collaborative environment developed for the evaluation of biorefinery processes. Within the scope of the computer-aided collaborative environment, the overall problem and the associated biorefinery (biomass to high value added chemicals) is decomposed into two interacting problems: the supply of a (limited) set of intermediates (*supply* side) and the use of these intermediates to produce a wide range of products (*demand* side). In the present paper we focus the attention on the supply side of the problem, and we study two

competitive platforms for the conversion of OFMSW into intermediates. The first platform involves dark fermentation to produce an intermediate stream of volatile fatty acids (VFAs) in addition to hydrogen and the second platform involves enzymatic hydrolysis for the production of an intermediate stream of monomeric sugars. The geographic area for the assessment is Abu Dhabi (United Arab Emirates), one of the largest OFMSW producers per inhabitant in the world. The objective is to assess options and establish a feasible path forward in achieving the goal of the government of Abu Dhabi of establishing a sustainable integrated waste management system.

2. Process Description

The processing pathways for the two studied platforms are shown in Figure 1. It follows the general fractionation sequence, proposed in the computer-aided collaborative environment established in AspenPlus V8.4, which divides the supply side into *physical pretreatment*, *recovery of high value compounds*, *chemical pre-treatment and hydrolysis* operation blocks.

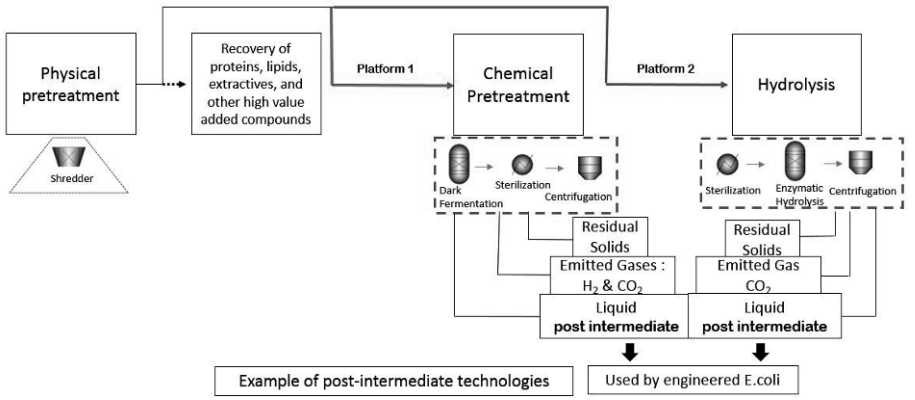

Figure 1: Scheme exhibiting the two platforms for processing the OFMSW stream

The aim of the physical pretreatment is to reduce the size of the OFMSW and give the feed some degree of homogeneity. As the OFMSW encompasses only the organic part of waste from household, commerce, and institutions, such as food, park and garden waste, low speed shearing devices can be used for size reduction (Fitzgerald, 2009). Recovery of protein, lipids and other unknown extractives is not considered in this study. Therefore, this block is by-passed and the homogenized OFMSW stream can either be sent to the "chemical pre-treatment" block, which abstracts the processing flowsheet of the dark fermentation platform, or to the "hydrolysis block", where the processing flowsheet for the enzymatic hydrolysis platform is placed.

Dark Fermentation platform: Dark fermentation is the anaerobic microbial conversion of organic matter to VFAs, H_2 and CO_2. The general biochemical reaction in dark fermentation can be written as:

α Biomass +β $H_20 \rightarrow \gamma$ Acetic acid + δ Propionic acid + ε Butyric acid + ζ valeric acid + θ hexanoic acid + κ H_2 + λ CO_2 + μ Microbial biomass + π others (e.g. ethanol)

The OFMSW is mixed with water and fermented in the dark fermentation reactor. For this study, a mixed microbial culture was chosen, and therefore the stream entering the

reactor does not need to be sterilized prior to the fermentation step. The stream exiting fermentation needs to be sterilized to make it suitable for pure culture downstream processes and to kill pathogens. Sterilization was simulated at 85°C for 1 hour following EU regulations on MSW sterilization (European Comission, 2005). The sterilized stream is then separated into a solid and a liquid intermediate stream. The liquid stream contains the dissolved VFAs, and can be upgraded by the demand side processes, while the solid stream is considered to be a residue.

Hydrolysis platform: The first step of the hydrolysis platform is to sterilize the OFMSW for the same reason as described above. After cooling down the OFMSW to 35 °C, an enzyme mix is added to transform sugar macromolecules into sugar monomers:

Glucan + Xylan + Arabinan + H_2O --> Glucose + Xylose + Arabinose

3. Process Simulation and Techno-Economic Evaluation

Abu Dhabi's OFMSW generation was estimated to be 348,229 t/year, based on 892,895 t/year of MSW generation in 2012 and an organic fraction of 39 % (Statistics Center Abu Dhabi, 2013). Figure 2 shows the assumed OFMSW composition for this study on a dry basis; the moisture content is 64 % (Nwobi et al., 2014).

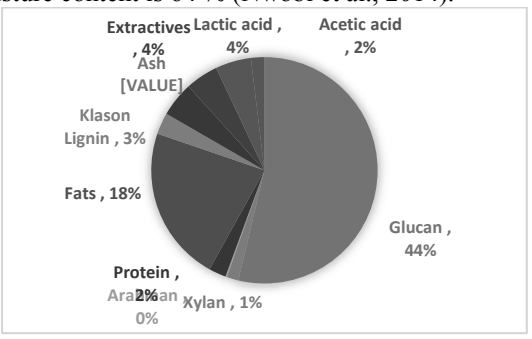

Figure 2: OFMSW composition (dry base) Nwobi et al., (2014)

Yield distribution, based on experimental data from literature, was used to simulate the fermentation reactors in both platforms. The reactor volume was calculated based on the hydraulic retention times (HRT), used in the corresponding experiments. For the sugar hydrolysis platform, an operating temperature of 35°C and a HRT of 12 hours were used (Nwobi et al., 2014). The composition of the enzyme mixture [0.1 % cellulase, 0.1 % amylase, 0.02 % protease, 0.02 % hemicellulase, 0.02 % lipase, and 0.02 % pectate lyase (w/w per TS)] is as reported in the same reference, and the cost of the enzyme was estimated to be USD 2/kg. By-product formation was also based on Nwobi et al. (2014). For dark fermentation a yield of 0.182 gVFA/gOFMSW fed (31 wt.-% acetic, 7 % propionic, 42 % butyric, 20 % hexanoic acid), a temperature of 35 °C, and a HRT of 72 hours were assumed based on literature data (Zahedi et al., 2013). Note that these yields can vary with waste composition and operational parameters.

The simulations were carried out in Aspen Plus V8.4, and equipment and operational costs settings were set at default except for the electricity price in Abu Dhabi, 0.04 USD/kWh (Abu Dhabi Regulation & Supervision Bureau, 2014) and the cost of the fermenters, 380 USD/m^3-working volume (Holtzapple et al., 2002). Centrifugation was modelled with 1% solid load of liquid outlet and 90% liquid to liquid outlet. A plan lifetime of 10 years and a 20 % rate of return were assumed for computation of the total

annualized cost (TAC). The cost of the intermediates streams was calculated by dividing the TAC by the amount of sugar monomers or VFA's produced per year.

4. Results and Discussion

4.1 Composition and cost of the liquid intermediate streams

Under the assumptions made in the previous section, 180 t/h exit as a liquid intermediate product from the dark fermentation process and 24 t/h from the enzymatic hydrolysis process, after solids separation. Figure 3 shows the composition of these liquid streams. It can be seen that the one resulting from the enzymatic hydrolysis process is mainly composed of glucose (75%, on a dry basis), and the presence of minor by-products, such as, acetic and lactic acid (during enzymatic hydrolysis) should be noted, as they could be detrimental to downstream processes. The stream exiting the dark fermentation process is composed of a dilute solution of a mixture of volatile fatty acids. The extractives were excluded from Figure 3 because their fate has not been determined in the referenced experimental data. In addition, many other by-products in small concentrations can potentially occur and hinder downstream processes and product separation.

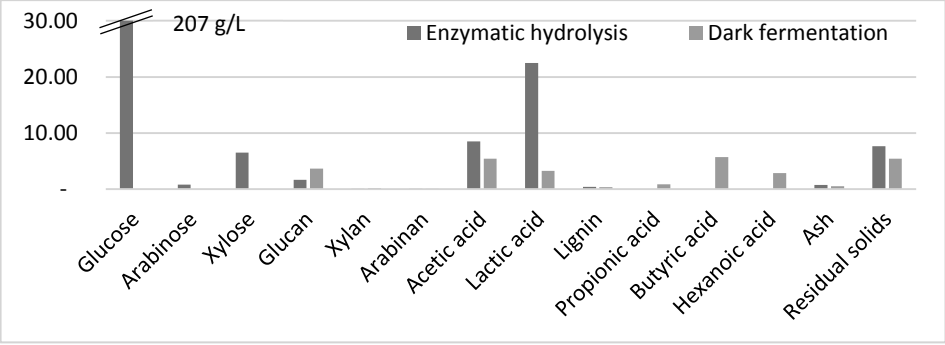

Figure 3: Liquid stream composition for dark fermentation and enzymatic hydrolysis

The cost of the intermediate stream from dark fermentation was estimated to be 335 USD/t-VFA. This cost does not include the separation cost of VFAs from water. The market price of pure VFAs lies between 400 USD/t-VFA (lower range for acetic acid) and 2500 USD/t-VFA (upper range for hexanoic acid) (Zacharof and Lovitt, 2013), and about 1500 USD/t-VFA for the VFA composition obtained in this study, thus leaving an allowance of ~1200 USD/t-VFA for water-VFAs separation and product purification processes.

The cost of the intermediate stream from enzymatic hydrolysis was estimated to be 86 USD/t-sugar monomers. In comparison, the estimated price for a stream containing 127.4 g/l of lignocellulosic sugar monomers is 222 USD/t-sugar monomers (Humbird et al., 2011). This cost is estimated by NREL for intermediate sugar production and is used to distinguish the cost of producing sugars from downstream costs of producing ethanol. The estimated total project capital cost for the dark fermentation platform is USD 13.42 million and operating costs sum up to USD 4 million per year. The estimated total project capital cost of the enzymatic hydrolysis platform is USD 7.07 million and operating costs are USD 1.35 million per year. Figure 4 shows the major cost

contributors for both processes. Operating cost represents the largest component of the intermediate stream cost in both options. In dark fermentation, the share of utilities is higher, due to the higher amount of water to sterilize. The reactor cost is a significant contributor in both cases. The relative contribution is similar in both cases, but the absolute costs for reactor and centrifuge are higher in dark fermentation because of the higher HRT and amount of water.

4.2 Possible uses of the intermediate streams

Following the costs analysis, discussed previously, both intermediate streams seem very promising, when compared to similar streams currently available on the market, and retain ample allowance for covering the cost of separation and purification steps.

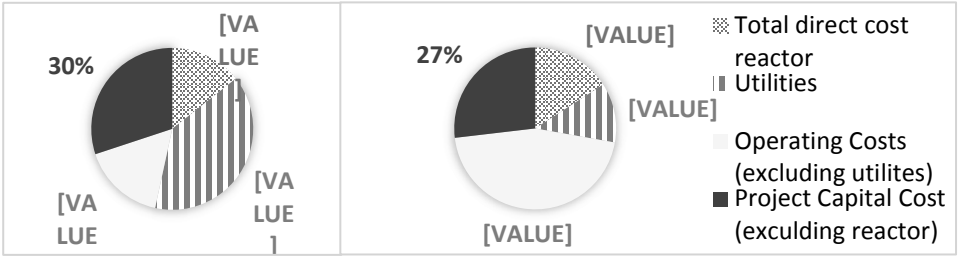

Figure 4: Major contributors to the intermediate stream cost for dark fermentation (left) and enzymatic hydrolysis (right).

However, we would like to explore here their possible use "as is" for the production of value added chemicals. As an example, the glucose-rich stream from the enzymatic hydrolysis process could be used as a feedstock for a pure engineered *E. coli*. Assuming a desired glucose concentration of 15-30 g/l for the downstream process, a dilution by a factor of approximately 10 will be needed. A possible problem is the presence of organic acids like acetic and lactic acid, as they are known to inhibit microbial activity. Vázquez et al. (2011) studied the inhibition of organic acids in *E. coli* CECT 731 at pH 7.4, finding that the concentrations that lead to 50% inhibition of growth were 178 mM (10.7 g/l) for lactic acid and 66 mM (5.9 g/l) for acetic acid. The concentrations of these two acids in the enzymatic hydrolysis stream after considering the dilution will be 2.3 g/l and 0.9 g/l, respectively. Thus, the by-products in the enzymatic hydrolysis stream will probably cause inhibition, but lower than 50%. The inhibition potential of the enzymatic hydrolysis stream depends on various factors, and needs to consider inhibitors produced in the downstream process itself. Inhibition will slow down growth, increasing the reactor volume and thus the capital cost needed. Yet, using the stream "as is" over pure glucose has advantages, such as the presence of micronutrients and other compounds that are necessary for the growth of microbes, which could result in significant savings as they would need to be supplied by, for example, a corn steep liquor of 1 % w/w, which in turn has an estimated price of 200 USD/t (Claypool and Raman, 2013). This idea has been introduced previously by Richter et al. (2013) in the context of coupling dark fermentation with syngas fermentation.

Separation of VFAs is known to be difficult in aqueous solution, due to the presence of azeotropes. Thus, the use of the VFA stream "as is" would be the more cost-effective solution. As an example, VFAs could serve as precursors for biological processes, as demonstrated by Martin et al. (2013), who produced hydroxyacids using VFAs and

glucose as substrate for metabolically engineered *E.coli*. These hydroxyacids can be used for example for the production of biopolymers (Martin et al., 2013).

5. Conclusions

This work studied the generation of streams useful for the manufacturing of value-added chemicals from OFMSW. Two alternative processes for the conversion of OFMSW to intermediate streams were simulated in Aspen Plus and the cost for their production was calculated. The costs obtained, 335 USD/t-VFA for a dark fermentation-based process, and 86 USD/tonne-sugar-monomers for an enzymatic hydrolysis-based process, compare favourably against the market prices of similar compounds. Moreover, these streams are expected to be suitable for use in "as is" form in downstream bioprocesses.

Acknowledgements

This work was funded under the Cooperative Agreement between the Masdar Institute of Science and Technology (Masdar Institute), Abu Dhabi, UAE and the Massachusetts Institute of Technology (MIT), Cambridge, MA, USA (02/MI/MI/CP/11/07633/GEN/G/00, Project 13KAMA1).

References

Abu Dhabi Regulation & Supervision Bureau, 2014, Customer Tariffs. http://rsb.gov.ae /en/sector/new-water-and-electricity-tariffs-structure. Accessed on January 19, 2015.

J.T. Claypool, D.R. Raman, 2013, Development and validation of a technoeconomic analysis tool for early-stage evaluation of bio-based chemical production processes, Bioresource Technology, 150, 486-495.

European Comission, 2005, Comission Regulation (EC) No 93/2005.

G.C. Fitzgerald, 2009, Technical and economic analysis of preshredding municipal solid wastes prior to disposal, M.Sc. Thesis, Department of Earth and Environmental Engineering, Columbia University, USA.

M. Holtzapple, R. Davison, 2002, MixAlco process. http://www.fh-flensburg.de/ct/born /intern/Biomasseverwertung/waste_management.pdf. Accessed on January 19, 2015.

D. Humbird, R. Davis, L. Tao, C. Kinchin, D. Hsu, A. Aden, P. Schoen, J. Lukas, B. Olthof, M. Worley, D. Sexton, D. Dugeon, 2011, Process design and economics for biochemical conversion of lignocellulosic biomass to ethanol, National Renewable Energy Laboratory, Report No. NREL/TP-5100-47764, Golden, USA.

C.H. Martin, H. Dhamankar, H.C. Tseng, M.J. Sheppard, C.R. Reisch, K.L. Prather, 2013, A platform pathway for production of 3-hydroxyacids provides a biosynthetic route to 3-hydroxy-γ-butyrolactone, Nature Communications 4, 1414.

A. Nwobi, I. Cybulska, W. Tesfai, Y. Shatilla, J. Rodríguez, M. Thomsen, 2014, Simultaneous saccharification and fermentation of solid household waste following mild pretreatment using a mix of hydrolytic enzymes in combination with saccharomyces cerevisiae, Applied Microbiology and Biotechnology, DOI 10.1007/s00253-014-5977-z.

H. Richter, S.E. Loftus, L.T. Angenent, 2013, Integrating syngas fermentation with the carboxylate platform and yeast fermentation to reduce medium cost and improve biofuel productivity, Environmental Technology, 34, 13-14, 1983–1994.

Statistics Center Abu Dhabi, Statistical Yearbook of Abu Dhabi 2013 – Environment. http://www.scad.ae/en/statistics/Pages/Statistics.aspx?ThemeID=6&TopicID=47&SubTopicID=189&PublicationID=560. Accessed on January 19, 2015.

M.P. Zacharof, R. Lovitt, 2013, Complex effluent streams as a potential source of volatile fatty acids, Waste and Biomass Valorization, 4, 3, 557-581.

S. Zahedi, D. Sales, L. Romero, R. Solera, 2013, Hydrogen production from the organic fraction of municipal solid waste in anaerobic thermophilic acidogenesis: Influence of organic loading rate and microbial content of the solid waste, Bioresource Technology, 129, 85-91.

Krist V. Gernaey, Jakob K. Huusom and Rafiqul Gani (Eds.), 12th International Symposium on Process Systems Engineering and 25th European Symposium on Computer Aided Process Engineering.
31 May – 4 June 2015, Copenhagen, Denmark

Development of a Macroscopic Model for the Production of Bioethanol with High Yield and Productivity via the Fermentation of *Phalaris aquatica* L. Hydrolysate

Anna Karapatsia[1], Giannis Penloglou[1], Christos Chatzidoukas[1], Costas Kiparissides[1,2*]

[1]*Department of Chemical Engineering, Aristotle University of Thessaloniki (AUTH), Thessaloniki, P.O. Box: 472, 54124, Greece*
[2]*Chemical Process & Energy Resources Institute (CPERI), Centre for Research and Technology Hellas (CERTH), Thermi, Thessaloniki, P.O. Box: 60361, 57001, Greece*
cypress@cperi.certh.gr, ckiparissides@cperi.certh.gr,

Abstract

This study deals with the development of a structured macroscopic model for the dynamic simulation of the bioethanol production through the fermentation of sugars derived from the hydrolysis of lignocellulosic biomass of the perennial herbaceous species *Phalaris aquatica* L. In the proposed model, the growth of Saccharomyces cerevisiae cultures consuming hydrolysate sugars as carbon source in parallel with the intracellular bioethanol production and excretion are quantitatively described accounting for substrate and product inhibition phenomena. A number of different feeding policies were designed and investigated on a model-base and verified experimentally in a real fermentation process. Substantial improvement on the real process performance was attained, resulting in a final ethanol concentration equal to 59.1 g/L corresponding to 2.19 g/(L·h) overall ethanol productivity.

Keywords: Bioethanol, hydrolysate sugars, fermentation, dynamic modelling.

1. Introduction

Bioethanol production from renewable resources has recently attracted worldwide attention as a strategy of enhancing the countries energy security and autonomy. However, the transition from first to second generation biofuels indicated that the potential of bioethanol as direct complementary fuel, without interfering and competing the human nutrition, is conditionally feasible on the restriction that the main resource for such a biofuel will be the abundant lignocellulosic biomass (López-Arenas et al., 2013). *Phalaris aquatica* [*Phalaris aquatica* (L.)] is one of the most promising lignocellulosic biomass feedstock in the South Europe. It is a perennial herbaceous energy grass with high content of structural carbohydrates (e.g., cellulose, hemicellulose) exceeding 70 % wt. of dry mass of the plant, thus providing an excellent source of monomer sugars (e.g., glucose) upon hydrolysis and other biomass pretreatment steps (Engel et al., 2011). It is cultivated in marginal farmlands with low nutrients and water demands, and the biomass production capacity ranges from 6.3 - 11 t/ha dry mass (Pappas et al., 2014).

The microorganism that is widely used for the fermentative ethanol production from hexoses, particularly glucose, is *Saccharomyces cerevisiae* with plenty of industrial applications. Efficient operation of the fermentation process is unambiguously not a trivial task and cannot be based on heuristic decisions, when considering the maximization of sugar to ethanol yield simultaneously with the maximization of product final concentration. An accurate mathematical model that simulates the cultivation process dynamic behaviour will provide the means for effective process operation on a systematic way.

A great deal of effort has been spent towards the development of simple or complex mathematical models for the dynamic simulation of the alcoholic fermentation process. The influence of aeration and mixing profile on the ethanol yield and productivity has been extensively studied in the open literature for cultures with microbial populations (Wan Teng and Samyudia, 2012). A more systematic modelling approach of the product inhibition was proposed by Sriyudthsak and Shiraishi (2010) who introduced the "metabolic bottleneck parameter" caused by the accumulation of an intracellular metabolite in a purely theoretical study though. Despite the various modelling approaches presented in the open literature little attention has been paid on the model-based design of the optimal operating strategy in terms of medium composition and substrate addition policy that will substantially enhance the sugars to ethanol yield and ethanol productivity. Thus, it is the objective of the present study to develop a dynamic model with predicting capabilities that will serve as a tool to optimise the process performance and to build up sufficient understanding over the influence of various process parameters (e.g., substrate and product concentrations, sufficiency or limitation of nutrients, etc.).

2. Materials and Methods

The *Saccharomyces cerevisiae* strain used was the Sigma Type II and was purchased from Sigma Aldrich. The strain was stocked at 4 ^{o}C in agar plates containing solid yeast extract-peptone rich medium. The seed preculture was prepared in Erlenmeyer flasks placed in an orbital shaker incubator (GFL 3033) at 150 rpm, at 30 ^{o}C, for 8 h. Upon sufficient growth of the preculture (i.e., at $O.D_{600}\approx1.5$), it was used to inoculate the main culture. As glucose feedstock for the main culture it was used the biomass hydrolysate, derived from the herbaceous plant *Phalaris aquatica*. The selected protocols regarding the biomass pretreatment, enzymatic hydrolysis and detoxification of the derived sugars solutions, are described in detail in a recent work (Karapatsia et al., 2014).

Fed-batch experiments were conducted in a 3 l stirred-tank glass bioreactor (BioFlo 110 Bioreactor/Fermentor, New Brunswick Scientific Co. Inc.). The bioreactor was initially loaded with 800 ml of the "main culture" medium with the following composition per litre: yeast extract, 3 g; $(NH_4)_2SO_4$, 5 g; KH_2PO_4, 3 g; Na_2HPO_4, 1 g; $MgSO_4.7H_2O$, 1 g; $Ca_2Cl_2.2H_2O$, 0.1 g and 2 ml of trace elements solution. The former solution contains (per liter): $ZnSO_4.7H_2O$, 0.9 g; $FeSO_4.7H_2O$, 0.6 g; H_3BO_3, 2 g; $MnCl_2.4H_2O$, 1.5 g; $Na_2MoO_4.2H_2O$, 0.8 g; $CoCl_2.6H_2O$, 0.8 g; $CuSO_4.5H_2O$, 0.5 g. Initial glucose concentration was adjusted at 20 g/L or 110 g/L with appropriate amount of biomass hydrolysate in the medium. The pH was regulated at 5.5 and the agitation rate of the bioreactor was manipulated in the range of 150-1000 rpm. The aeration of the fermentation broth was set at 1 vvm. The cultivation temperature was controlled at 30 ^{o}C. The nutrients composition in the feeding stream was 7.5 times concentrated compared to the "main culture" medium.

The optical density ($O.D_{600}$) of the culture was measured as light absorbance of the culture at 600 nm wavelength with the use of a UV-Vis spectrophotometer (Hitachi U-1800). Glucose and ethanol concentration in the medium was measured off-line through frequent sampling. The samples were analysed in a high performance liquid chromatograph (HPLC) with a refractive index detector (RI). A Hi-Plex H^+ Analysis column (300 x 7.7 mm) operating at 60 ^oC with 0.5 % sulphuric acid and 95.5 % water as mobile-phase (ml/min) was used. Relative standard deviations of the replicates of the measurements from the respective mean values were in all cases below 5 %.

3. Structured Model

The fermentative production of ethanol by yeast strains is a complex bioprocess involving the ethanol synthesis either simultaneously with the biomass growth (growth associated) or under relatively constant biomass (non-growth associated) with varying production rates. In the present study a structured dynamic model that accounts for the necessary intracellular and extracellular metabolites at minimum complexity and parameterization is proposed to sufficiently describe the kinetics of these metabolic phenomena and the time evolution of biomass, glucose and ethanol concentrations in the culture. It should be noted that at some critical values of glucose and/or ethanol concentrations in the medium, substrate and product inhibition with respect to biomass growth and ethanol production have been observed to occur at a significant extent (Phisalaphong et al., 2006).

The total biomass (X) is considered to be structured into three compartments. Glucose and ethanol are the two intracellular metabolites representing the two biomass compartments. The residual biomass (X_R) constitutes the third compartment. The intracellular glucose, expressed as glucose cellular quota (q_G), is the carbon substrate pool used by the cells for their metabolic activities and is continuously refilled through a glucose assimilation mechanism, as long as there is sufficient glucose (G) in the medium. Similarly, the intracellular ethanol, expressed as ethanol cellular quota (q_E), is the product pool that is accumulated in the medium through a cells excretion mechanism. Thus, a large number of simultaneous metabolic reactions can be lumped for simplicity into three main cellular activities, namely, the residual biomass growth, the maintenance of the residual biomass and the ethanol production. The system of DAEs describing the dynamic evolution of *S. cerevisiae* cultures in a bioreactor is presented below.

Residual biomass concentration, $[X_R]$: $$\frac{d(V[X_R])}{dt} = V\mu_s[X_R] - Q_{out}[X_R] \quad (1)$$

Glucose concentration, [G]: $$\frac{d(V[G])}{dt} = -V r_{Gu}[X_R] + Q_{in}[G]_{in} - Q_{out}[G] \quad (2)$$

Ethanol concentration, *[E]*: $$\frac{d(V[E])}{dt} = Vr_{Es}[X_R] - Q_{out}[E] \quad (3)$$

Glucose cellular quota, q_G: $$\frac{d(Vq_G[X_R])}{dt} = Vr_{Gu}[X_R] - Vr_{Gc}[X_R] - Q_{out}q_G[X_R] \quad (4)$$

Ethanol cellular quota, q_E: $$\frac{d(Vq_E[X_R])}{dt} = Vr_{Ep}[X_R] - Vr_{Es}[X_R] - Vr_{Ec}[X_R] - Q_{out}q_E[X_R] \quad (5)$$

Culture volume, V: $$\frac{d(V)}{dt} = Q_{in} - Q_{out} \quad (6)$$

Total biomass, $[X]$: $$[X] = [X_R] + q_G[X_R] + q_E[X_R] \quad (7)$$

The specific consumption/production rates (e.g., μ_s r_{Gu}, etc.) are defined in Table 1.

Table 1 – Net specific production/consumption species rates.

Specific residual biomass growth rate:

$$\mu_s=\mu_{s,max}\frac{q_G/q_E}{K_G+q_G/q_E}\left(1+\exp\left(-\frac{G_{max}-[G]}{a_1}\right)\right)^{-1}\left(1+\exp\left(-\frac{E_{max}-[E]}{a_1}\right)\right)^{-1}\{1+\mathcal{H}(G/E-GE_c)\}\,\mathcal{H}(q_G-q_{G_{min}}) \quad \text{(i)}$$

Glucose specific uptake rate:

$$r_{Gu}=r_{Gu_{max}}\frac{[G]}{K_{Gu}+[G]}\mathcal{H}(q_{G_{max}}-q_G) \quad \text{(ii)}$$

Intracellular ethanol specific production rate:

$$r_{Ep}=\left(K_{E1}\mu_s^2+K_{E2}\,\mathcal{H}(q_G-q_{G_{min}})\right)\left(1+\exp\left(-\frac{XE_c-[X_R]/[E]}{a_2}\right)\right)^{-1} \quad \text{(iii)}$$

Ethanol specific secretion rate:

$$r_{Es}=r_{Es_{max}}\left(1+\exp\left(\frac{q_{E_c}-q_E}{a_3}\right)\right)^{-1}-r_{Eu_{max}}\frac{[E]}{K_{Eu}+[E]}\left\{1-\mathcal{H}(q_G-q_{G_{min}})\right\} \quad \text{(iv)}$$

where, $r_{Es_{max}}=K_{E1}\mu_{s,max}^2+K_{E2}$

Glucose specific consumption rate:

$$r_{Gc}=\left[\frac{1}{Y_{XG}}\mu_s+K_{Gm}\{1+\mathcal{H}(G/E-GE_c)\}+\frac{1}{Y_{EG}}r_E\right]\mathcal{H}(q_G-q_{G_{min}}) \quad \text{(v)}$$

Ethanol specific consumption rate:

$$r_{Ec}=r_{Eu_{max}}\,\mathcal{H}(q_E-q_{E_{min}})\left\{1-\mathcal{H}(q_G-q_{G_{min}})\right\} \quad \text{(vi)}$$

Heaviside function defined as $\mathcal{H}(Y-Y_c)=\begin{cases}1, \text{ when } Y>Y_c\\ 0, \text{ when } Y\le Y_c\end{cases}$

The proposed specific rates introduce a number of unknown model kinetic and bioprocess parameters. These parameters were determined from a series of batch and fed-batch cultivation experiments through the fitting of the model predictions to experimental measurements using the gPROMS® (PSE Ltd.) parameter estimator, based on the Maximum Likelihood formulation.

4. Results and Discussion

4.1. Screening of operating strategies- Evaluation of model performance

The proposed mathematical model it was primarily tuned using experimental data form a number of batch and fed-batch fermentation processes representing a wide range of cultivation conditions. Then it was used to design and investigate specific fed-batch operating strategies targeting to the improvement of the process performance and to identify the policy that leads to high ethanol production and efficient utilization of substrate.

Two fed-batch operating strategies with different substrate addition profiles were first designed and evaluated on a model-base and then they were tested in the real fermentation process. Both strategies refer to a bioreactor that was initially loaded with the main culture medium with initial glucose concentration equal to 20 g/L. However, in the first operating policy, the culture was supplemented at a constant feeding rate (*constant addition policy*). The onset of the addition was decided from a relatively early stage of culture growth to create sufficiency of every nutritive ingredient and mainly substrate for a long period. In the second strategy, the feeding profile was adjusted so that the glucose provision rate would be close to the consumption rate (*conservative addition policy*).

In the bioreactor operating under the constant feeding strategy, a state of nutrients and substrate sufficiency (not excess) in the medium was induced for a long period of time. Under such conditions biomass production was favored while the ethanol production was of lower priority as shown in Figure 1. After 24 h over 240 g of glucose were consumed, however ethanol concentration did not exceed 23.54 g/L reflecting a yield of only 9.8 % (of the respective theoretical yield) and ethanol productivity 0.98 g/(L h).

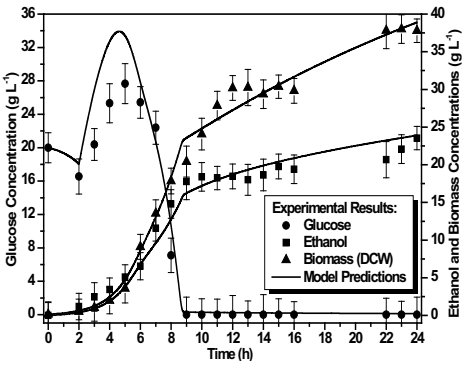

Figure 1. Time profile of glucose, ethanol and biomass concentrations in the bioreactor-scale fed-batch experiment under the *constant addition policy*.

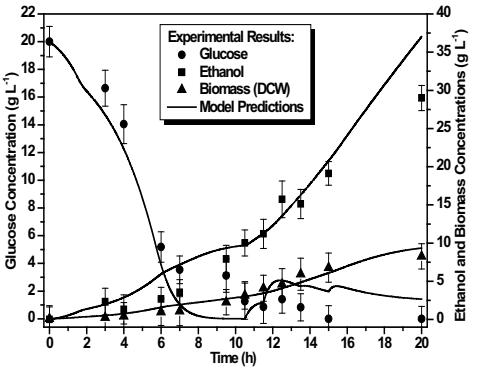

Figure 2. Time profile of glucose, ethanol and biomass concentrations in the bioreactor-scale fed-batch experiment under the *conservative addition policy*.

Upon such a low process performance the *conservative addition policy* was designed aiming at generating such culture conditions under which the culture was exposed at some degree to substrate and nutrients limitation in order to assess the process performance. In that case the feeding started after approximately 10.5 h from the beginning of the culture and the addition rate was progressively adjusted according to the culture response. The final ethanol concentration increased up to 29 g/L raising the ethanol yield to 24.73 % (of the respective theoretical maximum yield) and the ethanol productivity to 1.45 g/(l h). The dynamic simulation of process behavior, with respect to the selected bioprocess variables, is displayed in Figure 2. Note that the model predictions are in satisfactory agreement with the respective experimental data derived under both strategies, which clearly demonstrates adequacy of the estimated model parameters and the predicting capabilities of the proposed model.

4.2. Fed-batch strategy for improved process productivity

In order to investigate the process dependence on the substrate availability at the onset of the cultivation, a bioreactor experiment was conducted with an exponential-like addition policy, initially loaded with 110 g/L glucose. The glucose concentration in the feeding stream was 300 g/L. In Figure 3 the time profile of the three model variables (i.e., glucose, ethanol and biomass concentration) applied in the bioreactor are presented. Due to the high initial glucose concentration and the provoked substrate inhibition effect a retardation of 6 h is observed in both the culture growth and the ethanol production. From that point onwards the cultures progressively proceeded to the exponential growth phase. It should be pointed out that nineteen hours after the beginning of the culture, the ethanol production, the glucose consumption and the biomass growth rates slowed down even though there was sufficient substrate available in the medium. The reason behind this phenomenon was the product inhibition effect which emerged upon a considerable ethanol accumulation in the medium with a consequent osmotic stress on the cells (Maiorella, 1983). The performance criteria for that operating strategy shown a final ethanol concentration equal to 59.1 g/L, however with a large amount of glucose consumed for maintenance of the cells and/or other possible products (such as glycerol), supressing the glucose to ethanol yield to 24.77 % (of the respective theoretical yield), retaining the ethanol productivity to a satisfactory

level, 2.19 g/(L h). That fed-batch strategy was fully verified in the real process. The excellent agreement of the model predictions with the experimentally measured process variables clearly proves the model capability to simulate and predict the metabolic phenomena and the culture growth rate under various environmental conditions.

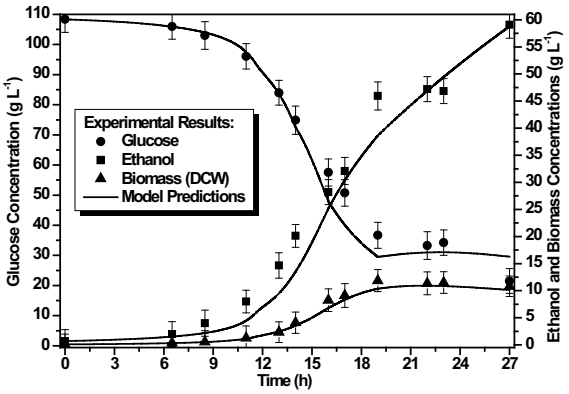

Figure 3. Time profile of glucose, ethanol and biomass concentrations in the bioreactor fed-batch experiment under high initial glucose loading with exponential addition policy.

5. Conclusions

The present work investigated the growth of the *S. cerevisiae* culture and the potential of this culture for ethanol fermentative production on sugars derived from the hydrolysis of lingocellulosic biomass. In this study great emphasis was given on identifying and quantifying the effect of the environmental conditions on the bioprocess dynamic behaviour as well as various inhibition effects (e.g., product and substrate inhibition) and the resulting metabolic bottleneck or metabolic deviations from the desired products they provoke. A comprehensive structured mathematical model for the fermentative ethanol production by *S. cerevisiae* was developed to assist in this objective. The developed model was tuned and validated against experimental data. The predictive capabilities of the proposed model underline its importance as a valuable simulation tool for process optimization and scaling-up studies.

References

P. Engel, B. Bonhage, D. Pernik, R. Rinaldi, P. Schmidt, H. Wulfhorst, A.C. Spiess, 2011, Population balance modelling of homogeneous and heterogeneous cellulose hydrolysis, Computer Aided Chemical Engineering, 29, 1316-1320.

Karapatsia A, Penloglou G, Pappas I, Kiparissides C. Bioethanol production via the fermentation of *Phalaris aquatic*a L. hydrolysate. Chem Eng Transac 2014; 37:289-94.

T. López-Arenas, M. Sales-Cruz, J. Alvarez, A. Schaum, 2013, Modelling, design and operation of a pretreatment reactor for lignocellulosic biomass, Computer Aided Chemical Engineering, 32, 37-42.

B. Maiorella, H.W. Blanch, W. Charles, 1983, By-Product Inhibition effects on ethanolic fermentation by *Saccharomyces cerevisiae*, Biotechnology and Bioengineering, 25, 103-121.

I.A. Pappas, Z. Koukoura, C. Tananaki, C. Goulas, 2014, Effect of dilute acid pretreatment severity on the bioconversion efficiency of *Phalaris aquatica* L. lignocellulosic biomass into fermentable sugars, Bioresource Technology, 166, 395-402.

M. Phisalaphong, N. Srirattana, W. Tanthapanichakoon,2006, Mathematical modelling to investigate temperature effect on kinetic parameters of ethanol fermentation, Biochemical Engineering Journal, 28, 36-43.

K. Sriyudthsak, F. Shiraishi, 2010, Investigation of the performance of fermentation processes using a mathematical model including the effects of metabolic bottleneck and toxic product on cells, Math Bioscience, 228, 1-9.

E.L. Wan Teng, Y. Samyudia, 2012, Nonlinear Control Strategies for a Micro-Aerobic, Fermentation Process, Computer Aided Chemical Engineering, 31, 330-334.

Krist V. Gernaey, Jakob K. Huusom and Rafiqul Gani (Eds.), 12th International Symposium on Process Systems Engineering and 25th European Symposium on Computer Aided Process Engineering.
31 May – 4 June 2015, Copenhagen, Denmark

Enzymatic Reactive Distillation for the Transesterification of Ethyl Butyrate: Model Validation and Process Analysis

Matthias Wierschem[a,]*, Rene Heils[b], Stefan Schlimper[a], Irina Smirnova[b], Andrzej Górak[a], Philip Lutze[a]

[a] *TU Dortmund University, Laboratory of Fluid Separations, Emil-Figge-Straße 70, D-44227 Dortmund, Germany*
[b] *Hamburg University of Technology, Institute of Thermal Separation Processes, Eissendorfer Straße 38, D-21073 Hamburg, Germany*
matthias.wierschem@bci.tu-dortmund.de

Abstract

For the production of new and more sustainable products, new technologies need to be developed. Within process intensification, reactive distillation which is the integration of reaction and distillation in one apparatus is one known technology. A new concept is to integrate enzymes into the distillation column which enables new or more selective reaction routes. However, matching operating windows is difficult due to for example the temperature sensitiveness of the enzyme. Here, modeling is an important tool for design, scale-up, analysis and optimization of chemical and biochemical processing by enzymatic reactive distillation systems. The lipase-catalyzed transesterification of ethyl-butyrate with *n*-butanol is highlighted, which is an equilibrium-limited reaction. Based on kinetic data and investigations of a surface coating to provide the enzyme into the reactive section, a detailed model of a continuous enzymatic reactive distillation is developed in Aspen Custom Modeler®, including hydrodynamic and mass transfer investigations of coated reactive packings. Subsequently, the detailed model is validated against experimental data of a pilot-scale enzymatic reactive distillation column with a diameter of 50 mm to check the agreement between experiments and modeling.

Keywords: Process intensification, process simulation, catalytic distillation, biocatalysis

1. Introduction

Biocatalytic reactions play an important role in development of more sustainable products and processes. Enzymes are enantio- and regioselective catalysts and capable of using a huge range of substrate molecules. But they are still able to produce the desired product with a high selectivity and a high conversion rate. Reactive distillation integrates reaction and separation in one unit operation which allows overcoming an equilibrium-limited conversion as well as thermodynamic boundaries. This leads to savings in operational and capital costs. Thus, the combination of reactive distillation and enzymatic reaction creates synergies enabling efficient production of totally new products. Paiva et al. (2003) and Heils et al. (2012) presented enzymatic reactive distillation (ERD) in batch mode, but no modeling approach of either batch or continuous ERD has been investigated yet.

The challenge of the process is how enzymes are applied in distillation columns to match the operating window of reaction/enzyme and separation. A homogeneous addition of enzyme is not feasible, since it will pass the reboiler and will denature at high temperatures. For the immobilization of enzymes within the column, the method of choice is the coating of wire gauze packing with a sol-gel that contains entrapped enzymes (Figure 1) (Heils et al., 2012). The coating covers not only the wires of the packing, but also seals the gaps between the wires. Hence, the packings mass transfer features are modified which means that hydrodynamics and mass transfer phenomena need to be experimentally investigated. Here, modeling is an important tool for design, scale-up, analysis and optimization of ERD systems. Therefore, an integrated approach of experiments and modeling is performed at different scales from laboratory-scale up to pilot-scale in which the accuracy of the model, the feasibility and performance analysis of the concept is stepwise increased to reduce experimental effort, costs and process uncertainties.

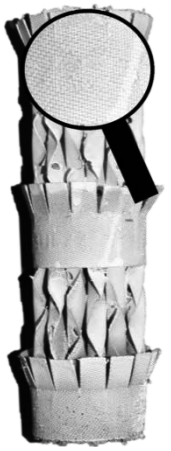

Figure 1: Magnified coated packing Sulzer BX^{TM}.

2. Materials and Methods

The integrated approach is depicted in Figure 2 in which the three subdomains experiments, modeling and process analysis are conducted simultaneously. That is essential to evince process feasibility and to verify the validity and transferability of all three subdomains because of existent uncertainties in model and experiment.

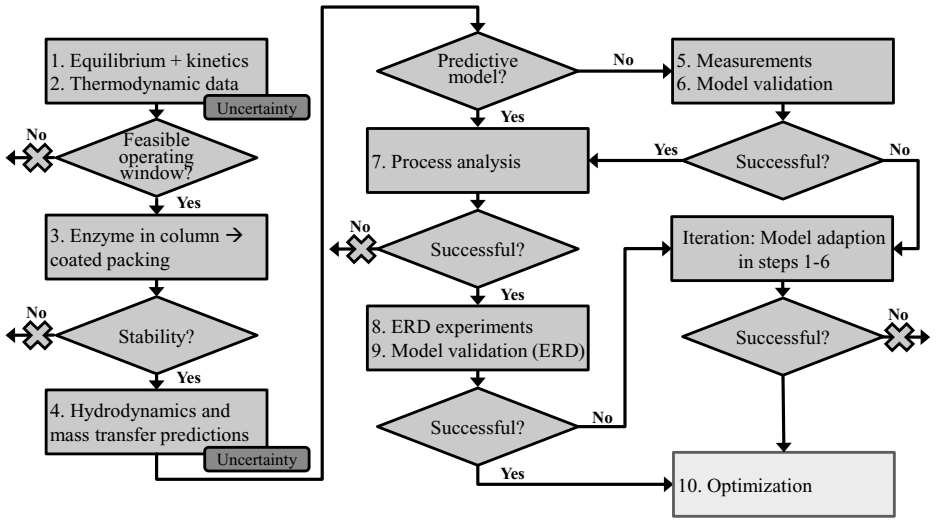

Figure 2: Integrated approach as a way of proceeding for enzymatic reactive distillation (ERD). Rectangles signify steps, that may contain uncertainties and rhombuses signify decisions.

The sizes and features of the experimental set-up as well as the model are shown in the following subsections. As a case-study, the transesterification of ethyl butyrate is used as a model system (Figure 3), catalyzed by *Candida antarctica* lipase B (CalB). For mass transfer investigations of the packing (step 5), the binary system of n-butanol/iso-butanol (nBu/iBu) is used (Table 1).

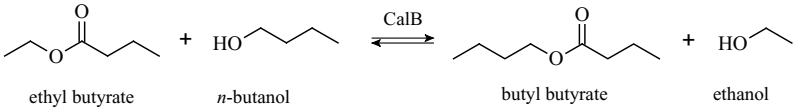

Figure 3: Transesterification of ethyl butyrate (EtBu) and *n*-butanol (BuOH) to butyl butyrate (BuBu) and ethanol (EtOH) catalyzed by *Candida antarctica* lipase B (CalB).

2.1. Experimental set-up

The pilot-scale ERD (step 8, Figure 2) and the distillation set-up to measure HETP values with *n*-butanol/*iso*-butanol (nBu/iBu) system (step 5, Figure 2) are described in Table 1. The column is equipped either with coated or uncoated Sulzer BX^{TM}. The two mid-sections are composed of (enzymatic) reactive packing. The sections are connected by liquid distributors that contain sample withdrawing points and PT100-thermocouples for vapor temperature measurements.

Table 1: Set-up for the distillation column and parameter window for distillation and enzymatic reactive distillation (ERD) experiments.

Distillation Column			
h_{column} [m]		5.12	
d_{column} [m]		0.05	
$N_{sections}$ (reactive/coated) [-]		6 (2)	
Enzymatic reactive distillation		**Distillation**	
Substrate ratio (EtBu/BuOH) [mol/mol]	3.62	Substrate ratio (nBu/iBu) [mol/mol]	9.00
ṁfeed [kg/h]	2	ṁfeed [kg/h]	4
D/F [kg/kg]	0.605	D/F [kg/kg]	-
RR [kg/kg]	2.8	RR	∞
F–factor [$Pa^{0.5}$]	0.96	F–factor [$Pa^{0.5}$]	0.7 – 1.6

2.2. Modeling

Modeling is required in steps 1, 2, 4, 6, 7, 9 and 10 in the integrated approach (Figure 2). An equilibrium stage model by Holtbruegge et al. (2013) and Niesbach et al. (2013) is used for the simulations. It utilizes HETP values to calculate concentration and temperature over the column height, since there is no sufficient knowledge of mass transfer phenomena and hydrodynamic behavior with self-made coated packing (Figure 1) so far.

3. Results

Within this section a short overview on the most important results for each step of the integrated approach is presented.

3.1. Step 1: Equilibrium + Kinetics and Step 2: Thermodynamic data

For kinetic measurements for the enzymatic transesterification of ethyl butyrate granulates of the coating within 1 mm of diameter were used (Heils et al., 2014). The Michaelis-Menten double-substrate kinetic was applied to calculate the reaction rates. Those depend on actual concentrations as well as temperature and are investigated for the concentration and temperature ranges, occurring in the column. Temperature dependency was concerned by using Arrhenius equation. However, the transferability of the lab-scale kinetic measurements based on granulate to the packing concept (step 3) is uncertain. Thermodynamic and physical data, such as vapor-liquid-equilibria and

viscosities, are calculated by Abrams UNIQUAC method (Abrams and Prausnitz, 1975).

3.2. Step 3: Enzyme in Column

Within this work, wire gauze packing with a sol-gel coating that contains entrapped enzymes has been used for incorporating enzymes into the column (Figure 1) and the stability of this coating for several batches has been presented before (Heils et al. 2012). However, within continuous processing the stability is not known. Kinetics and thermodynamic data led to a feasible operating window with a stable enzyme inside the column.

3.3. Step 4-6: Mass transfer and hydrodynamics

The characteristic value to describe mass transfer phenomena in an equilibrium based-on model is the height equivalent to a theoretical plate (HETP). HETP values are received from distillation experiments and differ with liquid and gas load expressed by the F-factor with gas velocity and density (Eq. (1)).

$$F\text{–}factor = w_G\sqrt{\rho_G} \tag{1}$$

In Table 2 the dependency of the HETP-values of coated packing to column pressure and gas loads (F–factor) is presented using measurements of the system nBu/iBu. The HETP-value for F-factors greater than one remains constant at around 0.242 m. For lower F-factors the HETP-value decreases significantly.

Table 2: Measured HETP-values for SulzerBX^{TM} packing depending on the F-factor.

F–factor [Pa$^{0.5}$]	HETP uncoated packing [m]	HETP coated packing [m]
0.75	0.117	0.171
0.94	0.148	0.223
1.18	-	0.241
1.38	0.148 / 0.152	0.242
1.59	-	0.244

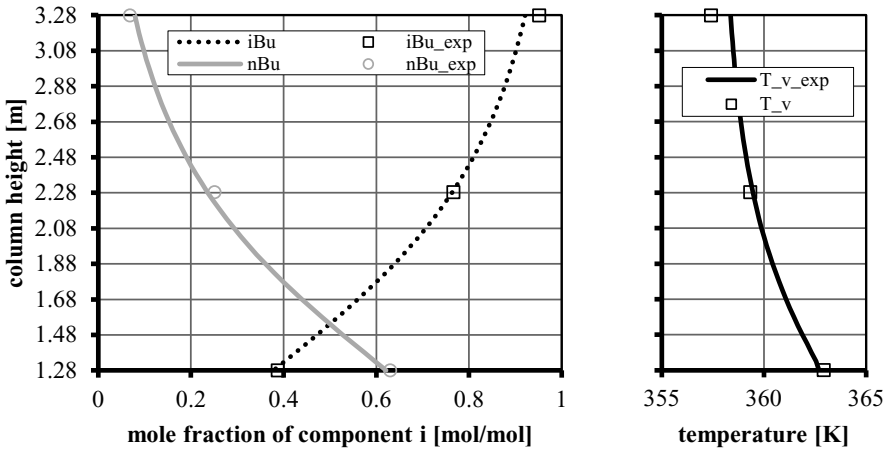

Figure 4: Column profile with mole fractions of the components and vapor temperature, respectively for experimental HETP-value measurements and the simulation thereof for the testing section. Simulated results are represented by lines and the experimental values by marks.

The HETP-values for the coated packing are around 40 % higher than for uncoated packing. The accuracy of the model is shown in Figure 4. The simulated concentration and temperature profile of the coated packing in the column cover the experimental results with only a slight averaged deviation of below 1.5 wt% and 0.27 K. With these results the model is validated regarding mass transfer.

3.4. Step 7-9: Process Analysis, Experiments and model validation of Enzymatic Reactive Distillation

Process analysis is used to assess a suitable operating window (step 7), in which the ERD is stable (step 8). Subsequently, an analysis of experimental data and simulation results is performed for model validation to find out whether prudential adaptions are necessary (step 9). The process analysis (step 7) revealed to a usage of a column pressure of 14.2 kPa and 0.0483 kg/m CalB in the reactive section in order to gain a conversion of 35.79 % for *n*-butanol and 9.90 % for ethyl butyrate with the set-up in Table 1. Nevertheless, experimental conversions (step 8) amount to 85.99 % for *n*-butanol and 23.78 % for ethyl butyrate. Thus, model validation failed (step 9) and the model needs to be improved. Mass transfer issues are not the key for improvement, since conversion is too low. A sensitivity analysis showed that the mass of CalB has a high impact on the conversion, so adjusting the kinetics is a reasonable attempt (iteration step). The kinetics were obtained with granulates of the coating with a diameter of 1 mm (Heils et al., 2014), to the contrary in this study coated packing with a coating width of 34 µm is used. We assume that due to diffusion limitations in the granulate the enzyme in the core of the granulate does not contribute to the conversion. Consequently, the kinetics including the mass of CalB are underestimated. Due to low conversion of the simulation compared to the experiment, CalB mass in the model is increased until simulated and experimental conversions equal each other. This occurs at 0.5 kg/m CalB in the reactive section. A column profile of the simulated (lines) and experimental (marks) components mole fraction and temperature is depicted in Figure 5. The graphs confirm a good agreement of the simulated and experimental profiles.

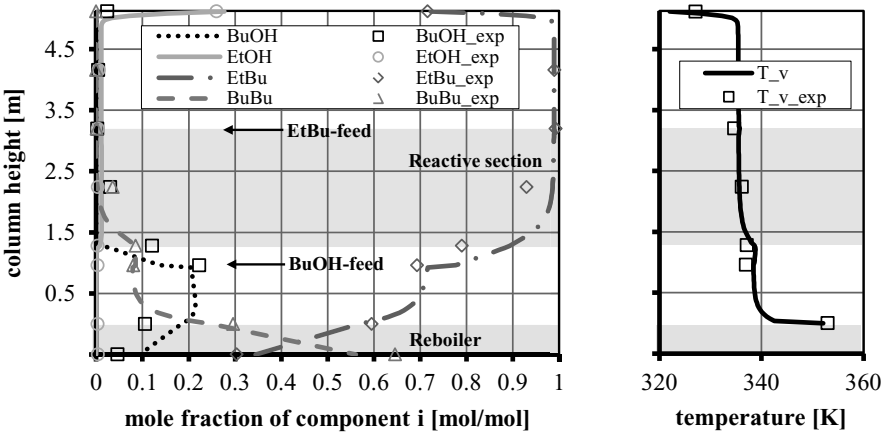

Figure 5: Column profile with mole fractions of the components and vapor temperature T_v, respectively. The reactive section, the reboiling section as well as the position of the feed streams are highlighted in the figure. Simulated results are represented by lines and the experimental values by marks.

Furthermore, it is verified that the temperature in the reactive section below 343 K is sufficient to prevent immobilized CalB from denaturation. Additionally, enzyme leaching from the reactive section into the stripping section of the column might be present due to stability issues of the coating (uncertainty step 3-4). Prospectively, these issues will be investigated. To conclude, an underestimation of the kinetics is only observed because of the simultaneous elaboration of modeling and experimental investigation. Model validation is confirmed by a good agreement of experimental and simulated data. Feasibility of ERD is proven.

4. Conclusions

In this work, feasibility of a continuous ERD was proven. Mass transfer for coated packing to provide enzyme in a distillation column using the HETP was investigated to be 40 % higher compared to uncoated Packing Sulzer BX^{TM}. A simulation model was validated for mass transfer phenomena for coated packing without reaction with only a slight deviation of 1.5 wt%. An approach to investigate ERD being a necessity for a simultaneous elaboration of experiments and modeling is described within this work in order to receive trustful results with small experimental and computational effort. The investigated kinetics are not valid to use in the set-up and an adaption of the kinetics increased the reliability of the model significantly.
In future work, kinetics will be determined for the reactive coated packing in order to validate the ERD model. Additionally, studies for coating stability will be accomplished.

Acknowledgement

The author thanks Sulzer Chemtech Ltd. for the support and provision of Sulzer BX^{TM} wire gauze packing. The author has received funding from the Ministry of Innovation, Science and Research of North Rhine-Westphalia in the framework of CLIB-Graduate Cluster Industrial Biotechnology, contract no: 314 - 108 001 08

References

D. S. Abrams, J. M. Prausnitz, 1975, Statistical Thermodynamics of Liquid Mixtures: A New Expression for the Excess Gibbs Energy of Partly or Completely Miscible Systems, AIChE J., 21, 1, 116–128

R. Heils, A. Sont, P. Bubenheim, A. Liese, I. Smirnova, 2012, Integration of Enzymatic Catalysts in a Reactive Distillation Column with Structured Packings ,Ind. Eng. Chem. Res., 51, 35, 11482–11489

R. Heils, A. Niesbach , M. Wierschem , D. Claus , S. Soboll , P. Lutze, I. Smirnova, 2014, Integration of enzymatic catalysts in a continuous reactive distillation column: reaction kinetics and process simulation, Ind. Eng. Chem. Res., 53, 50, 19612–19619

J. Holtbruegge, S. Heile, P. Lutze, A. Górak, 2013, Synthesis of dimethyl carbonate and propylene glycol in a pilot-scale reactive distillation column: Experimental investigation, modeling and process analysis, Chem. Eng. Process, 234, 448–463

A. Niesbach, P. Lutze, A. Górak, 2013, Reactive distillation for production of n-butyl acrylate from bio-based raw materials, Comput. Aided Chem. Eng., 32, 223–228

A. L. Paiva, D. van Rossum, F. Malcata, 2003, Lipase-Catalyzed Synthesis of Butyl Butyrate by Alcoholysis in an Integrated Liquid-Vapor System, Biotechnol. Prog., 19, 3, 750–754

Krist V. Gernaey, Jakob K. Huusom and Rafiqul Gani (Eds.), 12th International Symposium on Process Systems Engineering and 25th European Symposium on Computer Aided Process Engineering.
31 May – 4 June 2015, Copenhagen, Denmark

Design of a Gene Metabolator under Uncertainty

Asif Hamid Bhatti[a], Geraint Thomas[b], Vivek Dua[a,*]

[a]*Department of Chemical Engineering, University College London, London, WC1E 7JE, United Kingdom.* [*]*E-mail: v.dua@ucl.ac.uk*
[b]*Department of Cell and Developmental Biology, University College London, London, WC1E 7JE, United Kingdom.*

Abstract

This work aims to optimally design a metabolator, which is a metabolic process of Acetyl Co-Enzyme A (Acetyl-CoA) and its co-factors, with a view to incorporate uncertainty. The metabolic process can be described using a dynamic model involving nonlinear differential equations. An artificial neural network (ANN) transformation is utilised in order to transform the dynamic model of the metabolator into a system of simultaneous algebraic equations. The metabolator simulation problem is first solved and then the design problem is formulated as an optimisation problem, where the objective is to control the concentrations of Acetyl-CoA at desired set-points by manipulating the glycolytic flux. A non-linear model predictive control (NLMPC) formulation is then presented for computing the value of the source energy for the system, the glycolytic flux, which is used as the control variable. In this work Zone NLMPC is used to address the effect of uncertainty in the glycolytic flux as the system is allowed to perform within a range rather than at a fixed set point.

Keywords: Artificial Neural Network, Model Predictive Control, Gene Oscillator, Model-Based Design

1. Introduction

Synthetic biology has garnered much interest in the last few years as a means of understanding how biological systems can be adapted or exploited to give more favourable outcomes. Current research within the field of synthetic biology includes research into protein engineering, systems engineering and gene networks. Many of these systems utilise E.Coli as a natural chassis for testing models. E.Coli is used mainly as it can be grown easily in the laboratory and has relatively simple genetics that can be manipulated. Non-infectious strains are able to be constructed for testing purposes; however one of the main disadvantages of using a natural chassis is that one cannot achieve adequate control in biological synthesis.

Early approaches of creating a synthetic oscillatory network have been researched by Elowitz and Leibler (2000) who showed that it is possible to construct gene networks from components that are naturally available in other systems. In this work, we consider the metabolator system presented by Fung et al. (2005). The metabolator consists of two metabolite pools, one for Acetyl-CoA (M1), and another for Acetyl-CoA's upstream and downstream metabolites, Acetate (OAc/HOAc) and Acetyl Phosphate (AcP) respectively. Acetate Kinase (Ack) closes the cycle by catalysing conversion of Acetyl

Phosphate and Acetate and together with this substrate/product pair forms the pool M2. The two pools are connected by a reaction converting Acetyl-CoA to Acetyl Phosphate catalysed by Phosphate Acetyltransferase (Pta) (E1), and a feed-forward reaction from the Acetate formed from Acetyl Phosphate (by Ack in M2 by acetyl synthase (Acs) (E2). The influx of glycerol, fatty acids and sugars (glycolytic flux) into the Acetyl-CoA pool (M1), causes its concentration to oscillate. As a result Pta feeds mass into the metabolite pool M2 to produce acetate. Acetate is then used for various purposes by the cell or protonated and exported or returned to the Acetyl-CoA pool by Acs. However an increase in acetate will also have an additional positive feed–forward effect because the levels of acetate in the M2 pool can upregulate the levels of the Acs enzyme to increase the movement of mass back from the M2 pool to M1. Furthermore the two pools are also connected by a negative feedback reaction to decrease levels of Phosphate Acetyltransferase (Pta, E1) when Acetyl Phosphate concentrations increase and this slows down the rate at which metabolites move from M1 to M2 pools. This synergistic system is presented in Figure 1.

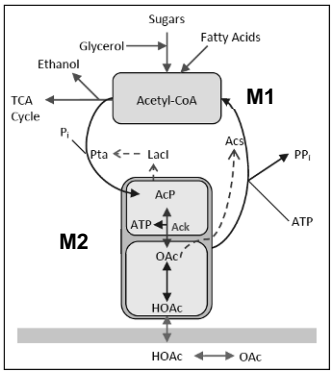

Fig. 1. In vivo realisation of the metabolator. The metabolic pools are represented by M1 and M2, and the enzymes, E1 and E2, are represented by Pta and Acs respectively.

Fung et al. (2005) also formulated a nonlinear ordinary differential equations (ODEs) model that represented the dynamics of the system and simulated the model using MATLAB (Mathworks, 2014). In this paper the main objective is to design the system to deliver a given desired performance by tracking a pre-determined profile of Acetyl-CoA through manipulation of its source energy, glycolytic flux (Vgly). The problem is formulated and solved as a nonlinear model predictive control (NLMPC) problem (Dua, 2006), where concentration of Acetyl-CoA is the controlled variable and the glycolytic flux is the control variable. The resulting NLMPC problem is transformed into a nonlinear programming (NLP) problem by transforming the ODEs into algebraic equations (AEs) using an Artificial Neural Network (ANN) transformation (Dua and Dua, 2012). The resulting NLP problem is solved using GAMS (Brooke et al., 1998).

This work also aims to investigate the use of a control system on a gene metabolator with view to modify the system outcomes through artificial regulation. Further control is achieved using Zone model predictive control (Zone MPC) (Gonzalez et al., 2009) as a means of confining the system in a pre-determined region. It has shown much success in modelling the pancreas and its effect on the glycaemic levels of insulin in the body (Grosman et al., 2010). It is particularly useful in controlling complex dynamic systems as it creates a region within which the system output is constrained, instead of tracking a

fixed set-point. In regards to the metabolator we confine the enzyme and co-factor outputs to a given region. It can also aid with addressing uncertainty in models. In the research by Grosman et al. (2010) the main uncertainty was an external meal announcement factor that affected the glucose levels in the subjects. Three modes were chosen for the meals; announced and unannounced at their normal value and with 40% uncertainty. The results from the Zone-MPC showed that meal announcement decreased the amount of glucose in the body, however once errors in carbohydrate estimation were considered, unannounced Zone-MPC was considered a good alternative in modelling the glycaemic levels in test subjects We believe that in the case of the metabolator Zone-MPC can help with understanding and controlling the effect of uncertainty in the glycolytic flux entering the system, much in the same way as that shown for glucose in patients following meals.

2. Results and Discussion

Figure 2 shows the simulation profiles obtained by using ANNs to transform ODEs to AEs. Here we see a loss of oscillations in the metabolite concentration with an increase in the glycolytic flux rate. The results from the simulation model show good comparison with that of the experimental results achieved in the case study (Fung et al., 2005). Moreover, when the acetate concentration increased there was a distinct change in the system activity and oscillations reach a steady state. This is expected because if acetate is increased there is an increase in the acidity of the environment, which therefore causes breakdown of the metabolator. The simulation results were verified using a Fourth Order Runge Kutta (RK4) method. This was carried out to gain confidence in the ODE to AE transformation using ANNs.

The NLMPC model was then developed with aim to control the system using the glycolytic flux (Vgly). This control variable was able to successfully track the set activity for the enzyme that was programmed into the model. Results for this can be seen in Figures 3 and 4. As can be seen from figure 4a the system is predicted to be able to follow the set points. It can be seen that the system responds well with smaller variation in the set points and is able to track the desired pattern. The next objective was to look at longer time frames and see if the system could adjust to more variations. The system again can be seen to respond well to the variations in the set points. As can be seen in Figure 4b the response from Vgly is expected. When the set concentration of Acetyl-CoA is increased in the system Vgly is also increased to help drive metabolite pool M1. This is typical of the synergistic relationship in the metabolator that was discussed earlier.

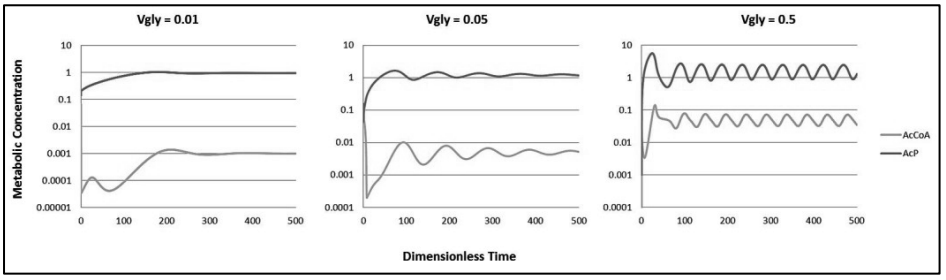

Fig. 2. Oscillation results obtained for the metabolite, Acetyl-CoA, and its co-factor, Acetyl Phosphate against time.

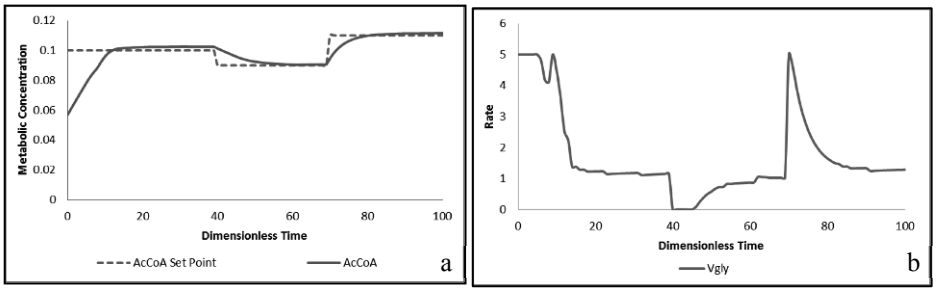

Fig 3. a. graph to show the NLMPC results for Acetyl-CoA at small variations in the set points (dashed) and (solid) shows the tracking of the system, b. graph to show the concentration of Vgly in the system showing the fluctuations required to track the set points.

The Zone NLMPC model was then established with a view to address uncertainty of the glycolytic flux within the model. It creates a range that the system is allowed to oscillate within, and therefore aims to constrain the system output to lie within this range. The results from this can be seen in Figure 5. As can be seen in Figure 5 the system is able to stay within the given range, and the resulting oscillations for glycolytic flux are less varied and extreme when compared to previous NLMPC results. Indeed rapid changes in glycolytic rate are needed only very transiently and are rapidly reset to smaller, stable adjustments in flux that persist until the next desired change in Acetyl-CoA set point. A constraint on the rate of change of Vgly, denoted as Dvgly, is applied to control the rate of glycolytic flux entering the metabolator. This has significant effect on the response of Vgly as the peak values are smaller than when constraints on Dvgly are not imposed. This provides a platform for experimental applications of the metabolator in vivo.

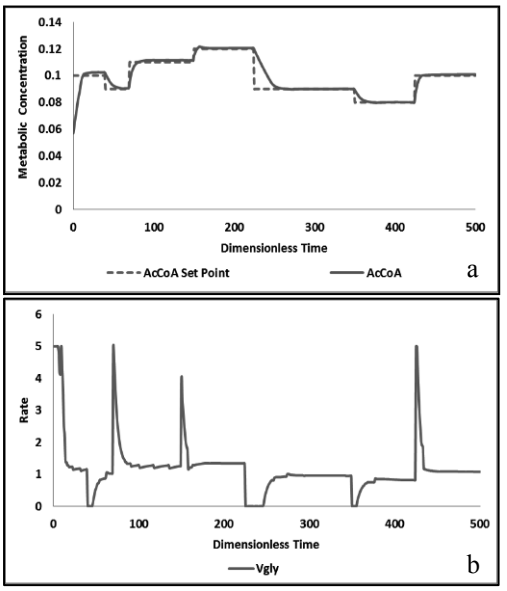

Fig 4. a. graph to show the NLMPC results for Acetyl-CoA at small variations in the set points (dashed) and (solid) shows the tracking of the system, b. graph to show the concentration of Vgly in the system showing the fluctuations required to track the set points.

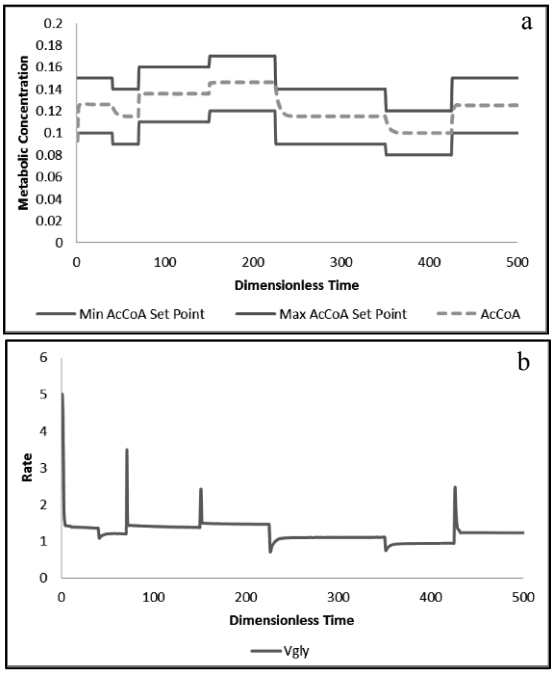

Fig 5. a. graph to show the Zone NLMPC results for Acetyl-CoA at small variations in the set points (solid lines) and tracking of the system (dashed), b. graph to show the rate of Vgly in the system showing the fluctuations required to track the set points, 0.00001 ≤ Dvgly ≤ 10.

3. Methods

A Fourth Order Runge-Kutta transformation (RK4) was utilised in order to validate the metabolator ANN/ODE model. A brief description of the ANN based framework by Lagaris et al. (1998) is presented in Equation (1).

$$G\left(\vec{x}, \Psi(\vec{x}), \nabla\Psi(\vec{x}), \nabla^2\Psi(\vec{x})\right) = 0, \qquad \vec{x} \in D \tag{1}$$

where $\vec{x} = (x_1, \ldots, x_n) \in R^n$, $D \subset R^n$ denotes the definition domain and $\Psi(\vec{x})$ is the solution to be computed. In order to obtain the solution for Equation (1) a collocation method was utilised. This assumes discretisation of the domain D and the boundary S into the set points $\hat{D}$ and $\hat{S}$ respectively. The problem is then transformed into the following Equations (2)-(4).

$$G\left(\vec{x}_i, \Psi(\vec{x}_i), \nabla\Psi(\vec{x}_i), \nabla^2\Psi(\vec{x}_i)\right) = 0, \qquad \forall\vec{x}_i \in \hat{D} \tag{2}$$

If $\Psi_t(\vec{x}, \vec{p})$ symbolises the trial solution with adjustable parameters $\vec{p}$ then the equations is transformed to give:

$$\min_{\vec{p}} \sum_{\vec{x},\in\hat{D}} \left(G\left(\vec{x}_i, \Psi_t(\vec{x}_i, \vec{p}), \nabla\Psi(\vec{x}_i, \vec{p}), \nabla^2\Psi(\vec{x}_i, \vec{p})\right)\right)^2 \tag{3}$$

In their approach the trial solution Ψ_t employs a feed forward neural network and the parameters $\vec{p}$ correspond to the weights and biases of the neural network. A form is

chosen for the trial function $\Psi_t(\vec{x})$ such that it satisfies the boundary conditions by default, Equation (4).

$$\Psi_t(\vec{x}) = A(\vec{x}) + F(\vec{x}, N(\vec{x}, \vec{p})) \quad (4)$$

where $N(\vec{x}, \vec{p})$ is a single output feed forward neural network with parameters $\vec{p}$ and n input units are fed with the input vector $\vec{x}$. The boundary conditions are satisfied by $A(\vec{x})$, which contains no adjustable parameters. The second term, F, is constructed in a way that it does not contribute to the boundary conditions as $\Psi_t(\vec{x})$ must also satisfy them. This term however employs a neural network whose weights and biases are adjustable in order to manage the minimisation problem. It is also noted that the objective function has been reduced from a constrained to an unconstrained optimisation problem.

4. Conclusions

In this paper the metabolator has been successfully simulated using the ANN transformation, with validation achieved through the use of Fourth Order Runge Kutta (RK4). The neural network has been applied to transform the ODEs into algebraic equations and simulation has shown this to mimic results published by Fung et al (2005). The metabolator was then optimally controlled using a control system (MPC) to gauge the effect of glycolytic flux on performance. Uncertainty in flux was then addressed using Zone-MPC, which gave promising results, and will be paramount in future experimental work.

5. References

A. Brooke, D. Kendrick, A. Meeraus & R. Raman, 1998, GAMS – A user's guide, GAMS development corporation, Washington, D.C, United States

V. Dua, 2006, Stability analysis of nonlinear model predictive control: an optimization based approach, 16th European Symposium on Computer Aided Process Engineering and 9th International Symposium on Process Systems Engineering, 1287-1292

V. Dua & P. Dua, 2012, A simultaneous approach for parameter estimation of a system of ordinary differential equations, using artificial neural network approximation, Industrial and Engineering Chemistry Research, 51, 4, 1809-1814

M. Elowitz & S. Leibler, 2000, A synthetic oscillatory network of transcriptional regulators, Nature, 403, 335-338

E. Fung, W. Wong, J. Suen, T. Butler, S. Lee & J. Liao, 2005, A synthetic gene metabolic oscillator, Nature, 435, 118-122

A. Gonzalez, J. Marchetti & D. Odloak, 2009, Robust model predictive control with zone control, IET Control Theory and Applications, 3, 1, 121-135

B. Grosman, E. Dassau, H. Zisser, L. Jovanonic & F. Doyle, 2010, Zone model predictive control: a strategy to minimize hyper- and hypoglycaemic events, Journal of Diabetes Science and Technology, 4, 961-975

I. Lagaris, A. Likas & D. Fotiadis, 1998, Artificial neural networks for solving ordinary and partial differential equations, IEEE Transactions on Neural Networks, 9, 987-1000

The Mathworks, 2014, MATLAB, Inc., Natick, Massachusetts, United States.

Krist V. Gernaey, Jakob K. Huusom and Rafiqul Gani (Eds.), 12th International Symposium on Process Systems Engineering and 25th European Symposium on Computer Aided Process Engineering.
31 May – 4 June 2015, Copenhagen, Denmark

Manufacturability Indices for High-Concentration Monoclonal Antibody Formulations

Yang Yang[a], Ajoy Velayudhan[b], Nina F. Thornhill[a*], Suzanne S. Farid[b*]

[a]*Department of Chemical Engineering, Imperial College London, South Kensington Campus, London SW7 2AZ, UK*

[b]*Department of Biochemical Engineering, University College London, Torrington Place, London WC1E 7JE, UK*

** Joint corresponding authors: n.thornhill@imperial.ac.uk, s.farid@ucl.ac.uk*

Abstract

The need for high-concentration formulations for subcutaneous delivery of therapeutic monoclonal antibodies (mAbs) can present manufacturability challenges for the final ultrafiltration/diafiltration (UF/DF) step. Viscosity levels and the propensity to aggregate are key considerations for high-concentration formulations. This work presents a novel framework for deriving a set of manufacturability indices related to viscosity and thermostability to rank high-concentration mAb formulation conditions in terms of their ease of manufacture. This is illustrated by analysing published high-throughput biophysical screening data that explores the influence of different formulation conditions (pH, ions and excipients) on the solution viscosity and product thermostability. A decision tree classification method, CART (Classification and Regression Tree) is used to identify the critical formulation conditions that influence the viscosity and thermostability. Polynomial regression techniques combined with the impact of protein concentration-time profiles and flux decay behaviour during UF/DF are used to transform the experimental data into a set of stress maps which show viscosity and thermostability as functions of the formulation conditions and time profiles during UF/DF. Manufacturability indices are derived from analysis of the stress maps and the process conditions experienced in the final UF/DF step. The indices are used to identify the optimal formulation conditions that minimize the potential for both viscosity and aggregation issues during UF/DF.

Keywords: data mining, high-concentration protein formulation, manufacturability index, multivariate regression, viscosity, aggregation.

1. Introduction

Therapeutic monoclonal antibodies (mAbs) have been successful in treating a number of chronic conditions such as autoimmune diseases Subcutaneous delivery of mAbs is becoming increasingly preferred over intravenous routes since they allow patient self-administration in the home; this improves patient quality of life and treatment compliance. However, subcutaneous delivery necessitates high-concentration protein formulations of more than 100g/L (Harris et al., 2004; Rao et al., 2012). This can present manufacturability challenges for the final UF/DF step used to achieve the final product concentration and buffer exchange into the formulated conditions. The high concentrations result in high viscosities that can impact the UF/DF performance (He et al., 2010; Shire, 2009). It is critical to be able to choose the optimal formulation for both efficacy and manufacturability in terms of being able to process the material in the final UF/DF step.

This paper presents a proposed methodology for the derivation of viscosity indices that consider the impact of the protein concentration-time profiles on manufacturability, whilst accounting for the expected flux decay behaviour during UF/DF. Multivariate regression and calculus techniques are used to transform experimental data into a set of viscosity stress maps as a function of the formulation conditions and the time profiles during UF/DF and finally to derive the indices. This work demonstrates that viscosity indices can be used as manufacturability predictors to identify the optimal formulation buffer conditions with minimum viscosity issues during the final UF/DF step while meeting the thermostability requirement. Furthermore, the CART decision tree classification method can be applied to identify the major factors that impact viscosity and thermostability and thus inform future experimental designs.

2. Data description

The datasets used in this work have been published by He et al. (2010). The datasets describe the high-throughput measurements of thermostability and viscosity for an IgG2 mAb sample assessed using differential scanning fluorimetry (DSF) method and dynamic light scattering (DLS) methods respectively. .The data was obtained via a full factorial design of experiment (DoE) with four predictor variables, including two continuous variables (pH and formulation concentration) and two categorical variables (presence of ions and excipient). Table 1 describes the summary of DoE predictor variables.

Table 1. Summary of DoE predictor variables

DoE predictors	**Variables**		
pH	5.0	5.5	6.0
Formulation concentration (mg/mL)	89	119	149
Ion	N/A	Ca^{2+}	Mg^{2+}
Excipient	N/A	Sucrose	Proline

In this work, the final product concentration is 100 g/L. There are four sub-steps in the final UF/DF step: initial concentration, diafiltration, overconcentration and flush. A typical overconcentration ratio of 1.5 was used (i.e. the product concentration would reach 150 g/L). The final flush sub-step dilutes the product back to 100g/L.

3. Decision tree analysis and results

3.1. Classification and regression tree (CART)

CART (classification and regression tree) (Grajski et al., 1986) is a decision tree algorithm that divides the data in homogenous subsets using binary recursive partitions. The most discriminative variable is first selected as the root node to partition the data set into branch nodes. The partitioning is repeated until the nodes are homogenous enough to be terminal. So in a tree structure, the terminal nodes (called leaves) represent class labels and branches represent conjunctions of features that lead to those class labels. In this work, CART is realized in Matlab Statistics Toolbox.

3.2. CART tree for key factors identification

The viscosity dataset has 80 data records. Each data record represents one formulation design in terms of a combination of four variables: pH, formulation concentration, presence of ions and excipient. The critical value of solution viscosity for final UF/DF manufacturing was set as 6 cp (He et al., 2010). According to the viscosity values, each

data record in the DoE dataset was classified into one of two groups: high viscosity (≥6 cp) and low viscosity (<6 cp). Figure 1a shows the CART tree for the viscosity dataset which reveals that the major factors impacting solution viscosity are the formulation concentration followed by the presence of ions and then the presence of excipients. For low formulation concentrations (89 mg/ml), low viscosity is expected while for high formulation concentrations (149 mg/ml), high viscosity is expected. When the formulation concentration is 119 mg/ml, the presence of Ca^{2+} or Mg^{2+} ions can reduce the viscosity except when sucrose excipient is added.

Similar to the viscosity dataset, according to the critical value of hydrophobic exposure temperature (Th), the thermostability dataset was split into two groups: stable (≥50 ^{o}C) and unstable (<50 ^{o}C). The CART tree result as shown in Figure 1b reveals that the pH value, presence of ions and presence of excipients are major factors affecting thermostability.For a low pH value of 5.0, the protein is prone to instability while for a higher pH value of 6.0, the protein is more likely to be stable. When the pH is 5.5, Ca^{2+} ions can reduce the protein thermostability under the condition with no excipient.

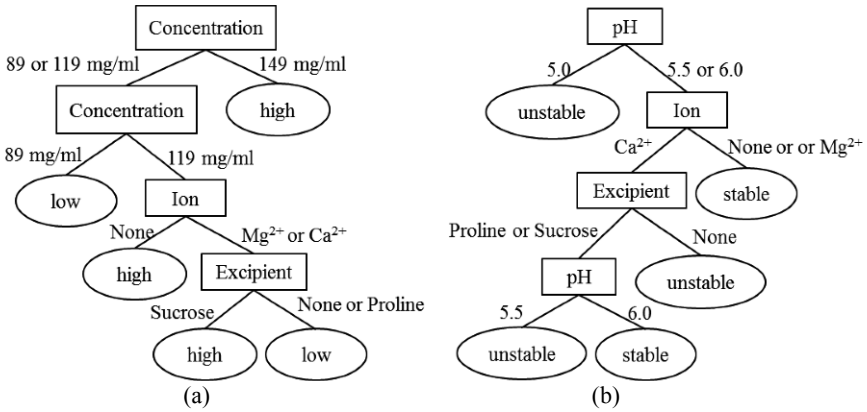

Figure 1. CART tree for (a) viscosity and (b) thermostability analysis. Rectangle nodes are branch nodes (e.g. concentration, pH) which represent the key formulation factors. Values on branches are the threshold levels of the split points for the corresponding split conditions. Circle nodes are leaves representing subsets with different class labels for viscosity (high (≥ 6 cP) versus low (< 6 cP)) and thermostability (unstable (< 50^{o}C) and stable (≥ 50^{o}C)).

4. Manufacturability index analysis and results

4.1. Viscosity stress maps generation using polynomial regression

The viscosity dataset was divided into nine sub-datasets according to the combination of formulation ions and excipients. Nine quadratic polynomial models which describe viscosity as a function of pH and protein concentration have been built by polynomial regression for all formulation conditions. The contour plots of the regression models, named viscosity stress maps, indicate the viscosity values under different pH and protein concentrations. The viscosity stress map for the formulation condition of no ion with no excipient has been shown in Figure 2a.

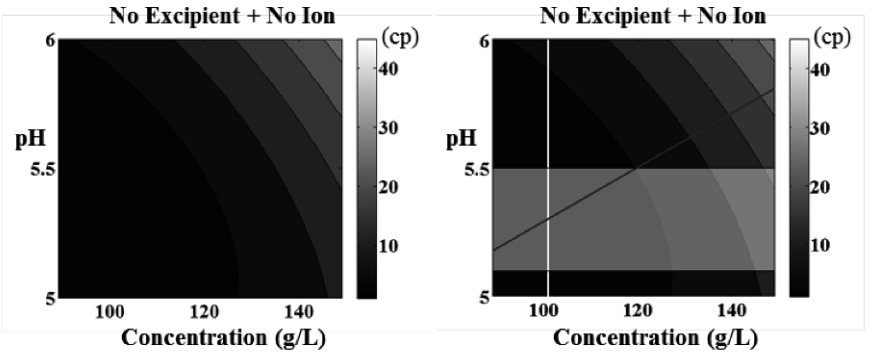

(a) (b)

Figure 2. (a) Viscosity stress map for the formulation condition of no ion with no excipient generated by polynomial regression (R^2 = 0.949). Viscosity value is a function of pH and protein concentration and increases from dark to light; (b) Window of operation (rectangular overlay region) for the formulation condition of no ion with no excipient. The window of operation is determined by the the pH value (±0.2) that meets the thermostability criterion across the ranges of concentration experienced during final UF/DF step.

4.2. Window of operation location using the thermostability criterion

Since the thermostability criterion was set as the hydrophobic exposure temperature (Th) ≥50 ^{o}C, a window of operation has been set up for each formulation design to identify the optimal pH range that meets the thermostability requirement. Figure 2b illustrates the identification of the window of operation for the formulation condition of no excipient with no ion. In Figure 2b, the white line indicates the final product concentration of 100 g/L and the dark line indicates the thermostability criterion. The intersection of the dark and white line indicates the pH value for the final product to meet the thermostability criterion. For the formulation condition of no excipient with no ion, the pH required is 5.3. Considering that a typical pH control range is within ±0.2 units, the window of operation is determined by the ranges of concentration and pH which are 90-150 g/L and 5.1-5.5 respectively as indicated by the rectangular overlay region in Figure 2b.

4.3. Processing time exposed to different viscosity levels in final UF/DF

In the final UF/DF step, the concentration of the product stream, and hence its viscosity, are dynamically changing over time. Furthermore, the flux through the membrane can be significantly lowered by membrane pore blockage and protein fouling that occurs as the concentration factor increases. In order to capture the information about the time exposed to different viscosity levels during UF/DF, a mathematical model for the filtrate flux (Ho and Zydney, 2000) was incorporated. This accounts for initial fouling due to pore blockage and subsequent fouling due to the growth of a protein cake or deposit over these initially blocked regions. Using this model, the variation of protein concentration with processing time during the overconcentration and flush stages of the UF/DF step has been captured, as illustrated in Figure 3a. The viscosity stress map has been transformed as a function of pH and processing time in Figure 3b. The window of operation (overlay area) is determined by the ranges of processing time and pH which are 135-204 mins and 5.1-5.5 respectively.

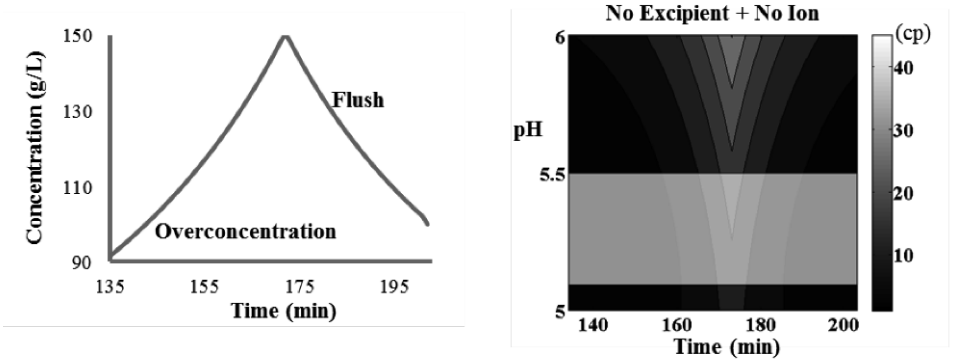

(a) (b)

Figure 3. (a) Time profile of product concentration during overconcentration stage and flush stage of final UF/DF; (b) Transformed viscosity stress map for the formulation of no ion with no excipient as a function of pH and processing time during UF/DF. The rectangular overlay region is the window of operation to meet thermostability criterion.

4.4. Viscosity indices generation and optimal formulation selection

A double integration calculation was applied to the viscosity stress map in order to obtain the average viscosity value within the window of operation, termed the viscosity index. The index indicates the average viscosity value of the product stream during the UF/DF step taking into account the time profiles of pH and concentration. The viscosity index for the formulation condition of no ion with no excipient is 5.5.

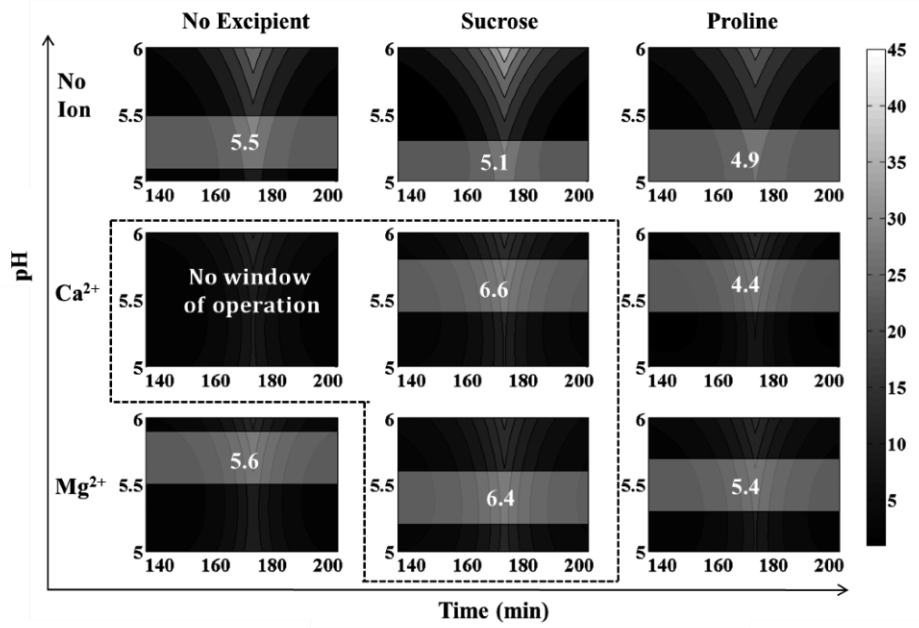

Figure 4. Viscosity indices for all formulation designs. The value of each index indicates the average viscosity value of the product stream during the UF/DF step taking into account the time profiles of pH and concentration while meeting the thermostability criterion (Th ≥50 ^{o}C).

Viscosity indices were generated for all formulation designs as shown in Figure 4. Each set of formulation conditions can be ranked according to their viscosity indices where a low index value indicates a more desirable outcome. From Figure 4, it can be seen that Ca^{2+} with proline excipient is the optimal formulation design with the lowest viscosity index, 4.4. For the formulation of Ca^{2+} ions with no excipient, there is no window of operation since the pH required for the final product to meet thermostability criterion is 6.4 which is outside the experimental range of the dataset (5-6). Furthermore, if the critical acceptable viscosity value for the final UF/DF step is 6 cP, three formulation designs would not be feasible: Ca^{2+} with no excipient, Ca^{2+} with sucrose and Mg^{2+} with sucrose. This approach can be used early in development to rank formulation designs in terms of their potential UF/DF manufacturability.

5. Conclusions

This work presents a novel methodology to derive viscosity indices which can be used as manufacturability predictors to rank different formulation designs. The optimal formulation buffer conditions with minimum viscosity issues during the final UF/DF step that also met the thermostability requirement could be identified. This work also demonstrated that the CART decision tree method could be applied to identify the critical factors for both solution viscosity and thermostability. The decision tree results are meaningful for future high-throughput experimental designs.

Acknowledgments

Funding from the UK Engineering & Physical Sciences Research Council (EPSRC) for the EPSRC Centre for Innovative Manufacturing in Emergent Macromolecular Therapies is gratefully acknowledged. Financial support from the consortium of industrial and governmental users is also acknowledged.

References

Grajski, K.A., Breiman, L., Diprisco, G.V., Freeman, W.J., 1986, Classification of EEG spatial patterns with a tree-structured methodology-CART, IEEE Transactions on Biomedical Engineering, 33 (12): 1076-1086.

Harris, R.J., Shire, S.J., Winter, C., 2004, Commercial manufacturing scale formulation and analytical characterization of therapeutic recombinant antibodies, Drug Development Research, 61 (3): 137-154.

He, F., Becker, G.W., Litowski, J.R., Narhi, L.O., Brems, D.N., Razinkov, V.I., 2010, High-throughput dynamic light scattering method for measuring viscosity of concentrated protein solutions, Analytical Biochemistry, 399 (1): 141-143.

Ho, C.C., Zydney, A.L., 2000, A combined pore blockage and cake filtration model for protein fouling during microfiltration, Journal of Colloid and Interface Science, 232 (2): 389-399.

Rao, S., Gefroh, E., Kaltenbrunner, O., 2012, Recovery modeling of tangential flow systems, Biotechnology and Bioengineering, 109 (12): 3084-3092.

Shire, S.J., 2009, Formulation and manufacturability of biologics, Current Opinion in Biotechnology, 20 (6): 708-714.

Krist V. Gernaey, Jakob K. Huusom and Rafiqul Gani (Eds.), 12th International Symposium on Process Systems Engineering and 25th European Symposium on Computer Aided Process Engineering.
31 May – 4 June 2015, Copenhagen, Denmark

Experimental Validation Of *in silico* Flux Predictions from A Genome-Scale Model (*i*MM518) For Carbon Dioxide Utilization by *M. maripaludis*

Nishu Goyal,[a] Iftekhar A. Karimi,[a]*, Zhi Zhou[b]

[a]*Department of Chemical and Biomolecular Engineering, National University of Singapore, 4 Engineering Drive 4, Singapore 117585*
[b]*Department of Civil and Environmental Engineering, National University of Singapore, 1 Engineering Drive 2, Singapore 117576. Recently moved to School of Civil Engineering and Division of Environmental and Ecological Engineering, Purdue University, USA*
cheiak@nus.edu.sg

Abstract

M. maripaludis, a hydrogenotroph, is capable of reducing CO_2 to methane in the presence of electron donors such as H_2 or formate. To explore the metabolic potential of *M. maripaludis* for CO_2 conversion to methane, it is crucial to quantify its substrate uptake and methane production rates. In this work, we perform a dynamic cell growth study in a batch culture of *M. maripaludis* and estimate three key extracellular fluxes, namely CO_2 uptake, H_2 uptake, and CH_4 evolution for different growth rates. To the best of our knowledge, this is the first study to report CO_2, H_2 consumption and CH_4 production rates under an environment where CO_2 is the sole carbon substrate. We present a process simulation approach for estimating such fluxes from experimentally measured compositional data. Using the same data, we also present an approach to estimate Non-Growth Associated Maintenance (NGAM) energy required for cell survival, and Growth Associated Maintenance (GAM) energy required for growth. We then use *i*MM518, a genome-scale model for *M. maripaludis* [2], to predict the extracellular fluxes (mmol/gDCW-h) and compare the predictions with measured values. Exceptionally high uptake and production rates were observed in *M. maripaludis* with a high growth yield. Based on the results, *M. maripaludis* is capable of reducing 70-95% of CO_2 to methane during exponential phase. This study shows the predictive power of *i*MM518 and helps us investigate the intracellular metabolic profiles underlying the extracellular observations.

Keywords: *i*MM518, hydrogenotroph, extracellular flux, intracellular flux, mass balance

1. Introduction

The ecological role of methanogens to remove CO_2 from environment via methanogenesis has been widely studied. The produced biomethane, major component of natural gas, offers great alternative energy source for heating and electricity. *M. maripaludis* is a rapidly growing, fully sequenced hydrogenotrophic methanogen capable of consuming major components (i.e. CO_2 and N_2) of a flue gas (Jones, 1983; Kessler et al., 2001). It is also a model organism among hydrogenotrophs for studying genetic and regulatory pathways (Kessler & Leigh, 1999; Tumbula et al., 1997; Yu et al., 1994). While several studies have characterized and engineered the metabolic

pathways in *M. maripaludis*, quantitative measurements on carbon utilization and methane production are absent in the literature. To this end, genome-scale models proved extremely useful to quantify specific growth rate, substrate uptake rates, and product production rates.

To understand the metabolic interactions and significant parameters affecting methanogenesis from CO_2, a genome-scale metabolic model of *M. maripaludis* (*i*MM518) has been developed recently (Goyal et al., 2014). Although models are extremely useful to understand hidden insights of metabolism during knockouts or any genetic or environmental perturbations, they need thorough validation. To validate such models, one can accurately measure extracellular fluxes by estimating the change in substrate concentrations in the medium surrounding the cells or measure intracellular fluxes using ^{13}C NMR labeling (Wiechert, 1996). Unlike intracellular measurements, analytes moving in and out of the cells are sensitive indicators of change and measuring them is relatively simpler. Extracellular flux measurements, in combination with genome-scale models can be used for determination of intracellular metabolic fluxes (Zupke & Stephanopoulos, 1995).

In this work, we perform a dynamic batch culture study of *M. maripaludis* and measure cell growth and three extracellular fluxes, namely CO_2 uptake, H_2 uptake, and CH_4 evolution rates. We also present a novel approach to estimate NGAM and GAM with the help of experimentally determined rates. Further, we use *i*MM518 to analyze the distribution of carbon flux between central metabolism and methanogenesis.

2. Flux measurements and flux predictions

2.1. Growth media and culture conditions

Our study used *M. maripaludis* wild type strain S2 from DSMZ-German Collection of Microorganisms and Cell Cultures with accession number DSM14266. The minimal medium used for our growth experiments lacked all possible carbon sources except headspace CO_2. The medium had neither carbon source nor cysteine. Vitamins were also omitted, as they do not affect (Whitman et al., 1987) the growth of *M. mariplaudis*. Reactors were pressurized with 250 kPa 80:20 v/v H_2/CO_2 and incubated at 37 °C under constant stirring at 180 rpm. Cell density and concentrations of CO_2, H_2, and CH_4 in the headspace were measured every hour for about 7 h. The growth experiments were discontinued, when the headspace pressure fell below 100 kPa to avoid the inflow of air into the reactor. All growth experiments were performed in duplicates accompanied by a control.

2.2. Specific growth rates and experimental flux measurements

Specific growth rate (μ) is the rate at which cells divide in the culture. In a chemostat experiment, μ remains constant, as the supply of nutrients is unlimited. However, in a batch culture experiment, the supply of nutrients keeps decreasing continuously with time. The dry cell biomass, X (gram Dry Cell Weight (gDCW)) was computed as O.D. X 0.34 g/L X culture volume. This time profile was then used to compute specific growth rate (μ) at selected points as given in Eq.(1).

$$\mu\left(\frac{1}{h}\right) = \frac{1}{X}\frac{dX}{dt} \tag{1}$$

OD_{600nm} = 1 is chosen to represent 0.34 g DCW/L based on the literature (Lupa et al., 2008).

Estimating extracellular fluxes from a cell culture study is not straightforward, when gases are distributed into both aqueous media and headspace as is the case in our experiment. In order to estimate fluxes precisely, we simulated the dynamics of a 600 ml reactor using Aspen HYSYS V8.2 (Abd Hamid, 2007) for the entire experiment. We accounted for the reduction in medium volume and expansion in headspace at each time point and computed the total moles of H_2 and CH_4 as the sum of moles of gases in headspace and aqueous media. For computing total moles of CO_2, we accounted high solubility of CO_2 into bicarbonates and carbonates. The fluxes (mmol / gDCW-h) for CO_2 and H_2 consumption and CH_4 production were computed by plotting the time profiles of total moles of CO_2, H_2, and CH_4 as shown in Eq.(2).

$$v_i = \frac{1}{X(t)} . \frac{dn(i)}{dt} \tag{2}$$

Where, $n(i)$ are the moles of species i (CO_2, H_2, or CH_4) in the bottle and $X(t)$ is the dry cell mass (gDCW) at time t.

2.3. *In silico flux predictions using i*MM518

*i*MM518 is available in BioModel database as MODEL1304120000 (Goyal et al., 2014). We implemented *i*MM518 in GAMS (build 38380/38394) and used CPLEX and BARON respectively as the solvers for various linear and nonlinear optimization problems. For flux balance analysis, we assumed the cellular objective to be maximum biomass given in Eq.(3). Then, to predict cell growth rate for a given CO_2 uptake rate, we solved the following LP (Linear Programming) using *i*MM518.

$$Maximize\ Biomass = \sum_{j=1}^{j} c_j v_j \ subject\ to\ \ S.v = b \tag{3}$$

Where, maximize biomass is represented as a weighted sum of metabolite fluxes v_j (j = 1,2,..,j) with weights c_j. S is an $I \times J$ matrix of stoichiometric coefficients of the metabolic reactions, I is the number of metabolites, and J is the number of metabolic reactions, and v is a ($j \times 1$) vector of reaction fluxes and b is a ($I \times 1$) vector of net metabolic fluxes.

3. Results and Discussion

M. maripaludis grew extremely well on CO_2 with negligible lag phase and without needing any complex substrates such as acetate, yeast extract, amino acids etc. The dry cell biomass increased by 15.49 mg over a period of 7 h. The doubling time was about 2 h, which is consistent with the literature (Jones, 1983). The lag phase duration varied with the state of inoculum, and found to be the shortest for an inoculum from the late exponential phase. Figure 1 shows the profiles of specific growth rates and extracellular fluxes obtained using cell growth and concentration profiles of gases in the headspace respectively.

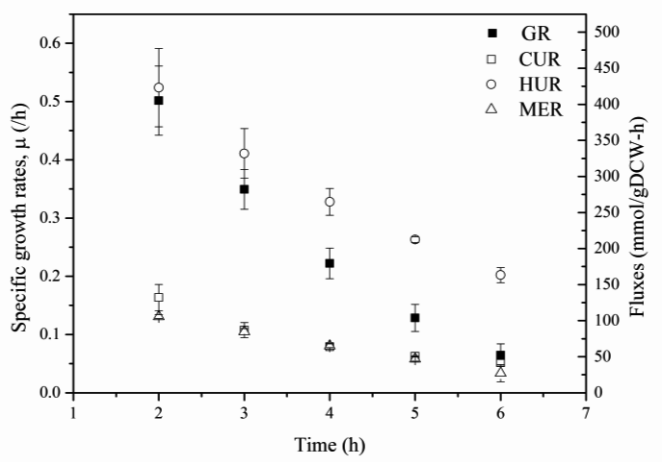

Figure 1: The time profiles of experimentally measured specific growth rates (growth rate denoted as GR) and fluxes (CO_2 uptake rates denoted as CUR, hydrogen uptake rates as HUR, and methane evolution rates as MER).

Based on 95% confidence, the maximum growth rate was estimated to be 0.50 ± 0.05 /h for a CO_2 uptake of 132.13 ± 15.13 mmol / gDCW-h, H_2 uptake of 423.06 ± 44.94 mmol / gDCW-h, and CH_4 production of 105.61 ± 17.75 mmol / gDCW-h. Our study is the first to give a full range of comprehensive growth and flux data for *M. maripaludis*. In fact, in spite of our best efforts, we could not find similar data for any other methanogen except for one study (Adam M Feist, 2006) on *Methanococcus barkeri*. This study reported a maximum hydrogen uptake of 41 mmol / gDCW-h with a corresponding CO_2 uptake of 11.61 mmol / gDCW-h and CH_4 production of 8.82 mmol/gDCW-h. Clearly, our observed fluxes are one order of magnitude higher than those reported for *M. barkeri*. This could be attributed to the much shorter doubling time (~2 h) of *M. mariplaudis* compared to *M. barkeri* (~30 h).

From the plot of dry cell weight (g) versus methane produced over time, we obtained a growth yield of 3.549 ± 0.149 gDCW per molCH_4 for *M. maripaludis* during the exponential phase. This yield matches well with the 2-4 gDCW per mol CH_4 reported for other hydrogenotrophic methanogens growing on H_2/CO_2 in batch cultures (Taylor & Pirt, 1977; Woese et al., 1978). The linear CO_2 flux vs growth rate relationship given in Eq.(4) tells us that cell growth is zero for a CO_2 uptake rate below 23.51mmol / gDCW-h. Using this uptake rate and *i*MM518, we computed NGAM = 7.836 mmol / gDCW-h as the amount of energy spent for maintenance during non-growth.

$$v_{CO2} = 203.25\mu + 23.51 \quad (4)$$

For estimating GAM, we computed total weighted Sum of Squares of Errors (SSE) (Eq.5) between experimentally measured fluxes and model predicted fluxes for different values of GAM. GAM value = 27.14 mmol/gDCW-h resulted in minimum total weighted SSE for *M. maripaludis*. Note that the energy required for growth increases linearly with growth with a slope of GAM. Our measured GAM of 27.14 mmolATP / gDCW-h agrees very well with our theoretically estimated GAM of 30.0 mmolATP / gDCW-h) (Goyal et al., 2014) for *M. maripaludis*. Thus, we fixed

GAM = 27.14 mmolATP / gDCW and NGAM = 7.836 mmolATP / gDCW-h in *i*MM518 and performed further analyses.

We also estimate ATP gains from our NGAM as 0.33 molATP / molCO_2, 0.35 mol ATP / molCH_4, and 0.238 molATP / molH_2. While the ATP gains from CO_2 and CH_4 are close, that from H_2 is much lower. This could be due to the deviations observed in our flux predictions for H_2 in total SSE. The value of 0.35 molATP / molCH_4 is in the acceptable range of 0.2-0.8 molATP / molCH_4 reported for microbes with autotrophic growth on H_2/CO_2 (Kates et al., 1993). Kaster et al., 2011 suggested an ATP gain of less than 1 molATP / molCH_4 for methanogens without cytochromes (e.g. *M. maripaludis*) and more than 1 molATP / molCH_4 for methanogens with cytochromes (e.g. *M. barkeri*). Thus, our estimate of 0.35 molATP / molCH_4 is consistent with the literature.

With GAM = 27.15 mmol / gDCW and NGAM = 7.836 mmol / gDCW-h in *i*MM518, we fixed CO_2 uptake rate at various values and predicted cell growth, MER, and hydrogen uptake rate for maximum biomass growth. Figures 2 compare experimental results with our model predictions. As we can see, our model predictions and experimental results match very well.

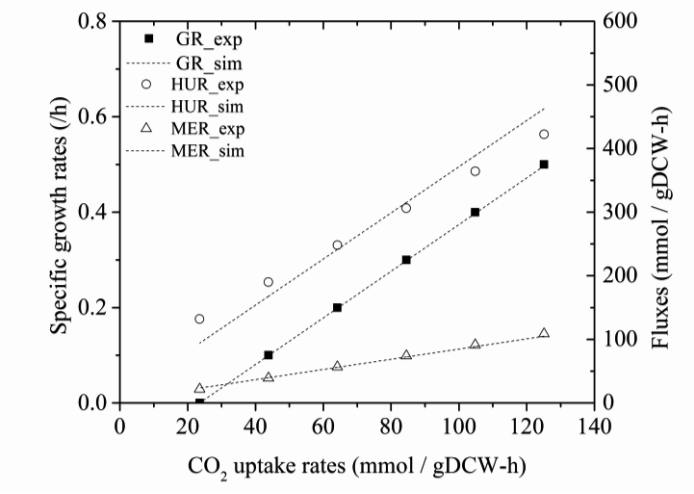

Figure 2: Comparison of experimentally measured fluxes and model predicted fluxes for fixed CO_2 uptake rates at GAM = 27.14 mmol / gDCW and NGAM = 7.836 mmol / gDCW-h

Intracellular flux distribution map for methanogenesis and central metabolic pathways shows the quantitative distribution of CO_2 towards methane production and towards formation of amino acids, cofactors, coenzymes, and other biomass precursors. We observed that CO_2 conversion to CH_4 decreases with increase in CO_2 uptake rate (or equivalently cell growth). This is consistent with the fact that cell growth competes with methanogenesis for carbon (Goyal et al., 2014). The ratio of flux directed towards methanogenesis to the amount of flux directed towards biomass formation can be altered by altering genetic and environmental perturbation, media compositions, growth phase, etc. We identified several environmental factors such as key amino acids, limiting nutrients and genetic perturbations i.e. genes / reactions knockouts to enhance methane production in *M. maripaludis*.

4. Conclusions

In this work, we demonstrated a process simulation approach for flux measurement of gases that partition between headspace and aqueous medium of a batch reactor. Using this experimental flux measurements and genome-scale model of a microbe (in our case *i*MM518), we estimated two key parameters NGAM and GAM along with ATP gain. In this work, *in silico* predictions by *i*MM518 were in excellent agreement with experimental measurements, thus allowed us to elucidate the physiological and metabolic states of the cells during batch culture.

References

A. Hamid, M. Kamaruddin 2007. HYSYS: an introduction to chemical engineering simulation for UTM Degree++ program.

A.M. Feist, J.C.M. Scholten, B. Ø. Palsson, F. J. Brockman, T. Ideker. 2006. Modeling methanogenesis with a genome-scale metabolic reconstruction of *Methanosarcina barkeri*. Molecular Systems Biology, 2.

B. Lupa, E.L. Hendrickson, J.A. Leigh, W.B. Whitman. 2008. Formate-dependent H2 production by the mesophilic methanogen *Methanococcus maripaludis*. Appl Environ Microbiol, 74(21), 6584-90.

C.R. Woese, L.J. Magrum, G.E. Fox. 1978. Archaebacteria. Journal of Molecular Evolution, 11(3), 29-30.

C. Zupke, G. Stephanopoulos. 1995. Intracellular flux analysis in hybridomas using mass balances and in vitro 13C NMR. Biotechnology and bioengineering, 45(4), 292-303.

D.L. Tumbula, Q. Teng, M.G. Bartlett, W.B. Whitman. 1997. Ribose biosynthesis and evidence for an alternative first step in the common aromatic amino acid pathway in *Methanococcus maripaludis*. Journal of bacteriology, 179(19), 6010-6013

G.T. Taylor, S.J. Pirt. 1977. Nutrition and factors limiting the growth of a methanogenic bacterium (*Methanobacterium thermoautotrophicum*). Archives of microbiology, 113(1-2), 17-22.

M. Kates, D. J. Kushner, A.T. Matheson. 1993. The Biochemistry of archaea (archaebacteria). Elsevier.

N. Goyal, H. Widiastuti, I.A. Karimi, Z. Zhou. 2014. Genome-scale metabolic model of *Methanococcus maripaludi*s S2 for CO2 capture and conversion to methane. Molecular BioSystems, 10(5) 1043-1054.

P.S. Kessler, J.A. Leigh. 1999. Genetics of nitrogen regulation in *Methanococcus maripaludis*. Genetics, 152(4), 1343-1351.

P.S. Kessler, C. Daniel, J.A. Leigh. 2001. Ammonia switch-off of nitrogen fixation in the methanogenic archaeon *Methanococcus maripaludis*: mechanistic features and requirement for the novel GlnB homologues, NifI(1) and NifI(2). J Bacteriol, 183(3), 882-9.

W.J. Jones, M. J. B. Paynter, and R. Gupta. 1983. Characterization of *Methanococcus maripaludis* sp. nov., a new methanogen isolated from salt marsh sediment. Archives of Microbiology, 135, 91-97.

W.B. Whitman, S. Sohn, S. Kuk, R. Xing. 1987. Role of amino acids and vitamins in nutrition of mesophilic *Methanococcus spp*. Applied and environmental microbiology, 53(10), 2373-2378.

W. Wiechert, 1996. Metabolic flux determination by stationary 13-C tracer experiments: Analysis of sensitivity, identifiability and redundancy. in: System Modelling and Optimization, (Eds.) J. Doležal, J. Fidler, Springer US, pp. 128-135.

Yu, J.-P., Ladapo, J., Whitman, W.B. 1994. Pathway of glycogen metabolism in *Methanococcus maripaludis*. Journal of bacteriology, 176(2), 325-332.

Krist V. Gernaey, Jakob K. Huusom and Rafiqul Gani (Eds.), 12th International Symposium on Process Systems Engineering and 25th European Symposium on Computer Aided Process Engineering.
31 May - 4 June 2015, Copenhagen, Denmark.

Cell cycle model selection for leukemia and its impact in chemotherapy outcomes

María Fuentes-Garí[a], Ruth Misener[b], Eleni Pefani[a], David García-Münzer[a], Margaritis Kostoglou[c], Michael C. Georgiadis[d], Nicki Panoskaltsis[e], Efstratios N. Pistikopoulos[a,f] and Athanasios Mantalaris[a]

[a]*Department of Chemical Engineering; ICL; London, UK*
[b]*Department of Computing; ICL; London, UK*
[c]*Department of Chemistry; AUTH; Thessaloniki, Greece*
[d]*Department of Chemical Engineering; AUTH; Thessaloniki, Greece*
[e]*Department of Hematology; ICL; London, UK*
[f]*Department of Chemical Engineering; TAMU; Texas, USA*
m.fuentes-gari@imperial.ac.uk

Abstract

The cell cycle is the biological process used by cells to replicate their genetic material and give birth to new cells that are in turn eligible to proliferate. It is highly regulated by the timed expression of proteins which trigger cell cycle events such as the start of DNA replication or the commencement of mitosis (when the cell physically divides into two daughter cells). Mathematical models of the cell cycle have been widely developed both at the intracellular (protein kinetics) and macroscopic (cell duplication) levels. Due to the cell cycle specificity of most chemotherapeutic drugs, these models are increasingly being used for the study and simulation of cellular kinetics in the area of cancer treatment.

In this work, we present a population balance model (PBM) of the cell cycle in leukemia that uses intracellular protein expression as state variable to represent phase progress. Global sensitivity analysis highlighted cell cycle phase durations as the most significant parameters; experiments were performed to extract them and the model was validated. Our model was then tested against other differential cell cycle models (ODEs, delay differential equations (DDEs)) in their ability to fit experimental data and oscillatory behavior. We subsequently coupled each of them with a pharmacokinetic/pharmacodynamic model of chemotherapy delivery that was previously developed by our group. Our results suggest that the particular cell cycle model chosen highly affects the outcome of the simulated treatment, given the same steady-state kinetic parameters and drug dosage/scheduling, with our PBM appearing to be the most sensitive under the same dose.

Keywords: Cell cycle, population balance model, chemotherapy optimization, leukemia, model selection

1. Introduction

AML is a type of leukemia characterized by the sudden increase in immature cells with highly proliferative features. Chemotherapy treatments rely on cell cycle phase-specific (CCS) agents, which act on cells going though one of the four phases of the cell cycle (G1: growth, S: DNA duplication, G2: preparation for division, M: mitosis (cell division)). Efficacy of current treatment protocols is hampered by a lack of patient-specific information related to drug action and cell

cycle kinetics. Blood samples from patients receiving chemotherapy cannot be collected due to their medical condition and to weakening treatment effects. Therefore, modeling patient response *in silico* could provide valuable insights as a helper tool for clinicians. To this end, a complete pharmacokinetic/pharmacodynamic (PK/PD) model of patient response was previously developed by Pefani et al. (2013, 2014). The model considered the infusion, transport and degradation of chemotherapeutic drugs inside the body, as well as the drug effects at the point of action (bone marrow), where leukemia resides. The leukemic cell cycle was represented as a set of 3 ODEs, one per compartment (G1, S and G2/M). Global sensitivity analysis revealed that the cell cycle phase durations (τ_{G1}, τ_S and $\tau_{G2/M}$) were the most significant parameters for treatment outcomes. Since ODEs provide only a simplified representation of cell cycle progression, we hypothesized that the cell cycle model itself, in addition to its parameters, would have an impact on simulated chemotherapy response. More complex types of models such as population balance models (PBM) which are distributed in a second progression-related variable, or delay differential equation models (DDE) which account for the phase-induced time delay, could be more suited for the purpose.

In this paper, we present two new cell cycle models composed of 3 compartments (G1, S, G2/M): a PBM distributed in protein concentration (G1, G2/M) or DNA content (S), and a DDE model featuring phase-specific time delays. All three models (ODE, PBM, DDE) are compared in: (i) their ability to fit chemotherapy-free experimental data Fuentes-Garí et al. (2014); (ii) chemotherapy outcomes when embedded in the pharmacokinetic/pharmacodynamic (PK/PD) model of Pefani et al. (2013).

2. Results

2.1. Developing cell cycle models that can be experimentally validated

The three models are presented with increasing levels of complexity. Phase distributions (percents) will be of importance here as they account for oscillatory behavior, in contrast with phase numbers which increase over time. They can be experimentally measured by aggregating data from single cell measurement techniques such as flow-cytometry. The cell cycle can initially be modeled as a set of ODEs (one per compartment), with the parameters needed being the transition rates and the initial cell populations for each phase. A general example of this scenario with three compartments (G0/G1, S and G2/M) can be found in Pefani et al. (2013) (a chemotherapy death term is added here with value zero for this section and a positive value in the other three models for the results of the next section):

$$\frac{dG}{dt} = 2 \cdot 1/\tau_M \cdot M - 1/\tau_G \cdot G \quad - k_{D,G} \cdot G \tag{1}$$

$$\frac{dS}{dt} = 1/\tau_G \cdot G - 1/\tau_S \cdot S \quad - k_{D,S} \cdot S \tag{2}$$

$$\frac{dM}{dt} = 1/\tau_S \cdot S - 1/\tau_M \cdot M \tag{3}$$

This model quickly stabilizes to its steady-state when subject to a disturbance. In order to account for the fact that stabilization takes 1-2 cell cycles experimentally, a time delay equal to the phase duration can be introduced in each phase by using DDEs:

$$\frac{dG(t)}{dt} = 2 \cdot 1/\tau_M \cdot M(t-\tau_M) - 1/\tau_G \cdot G(t) \quad - k_{D,G}(t) \cdot G(t) \tag{4}$$

$$\frac{dS(t)}{dt} = 1/\tau_G \cdot G(t-\tau_G) - 1/\tau_S \cdot S(t) \quad - k_{D,S}(t) \cdot S(t) \tag{5}$$

$$\frac{dM(t)}{dt} = 1/\tau_S \cdot S(t-\tau_S) - 1/\tau_M \cdot M(t) \tag{6}$$

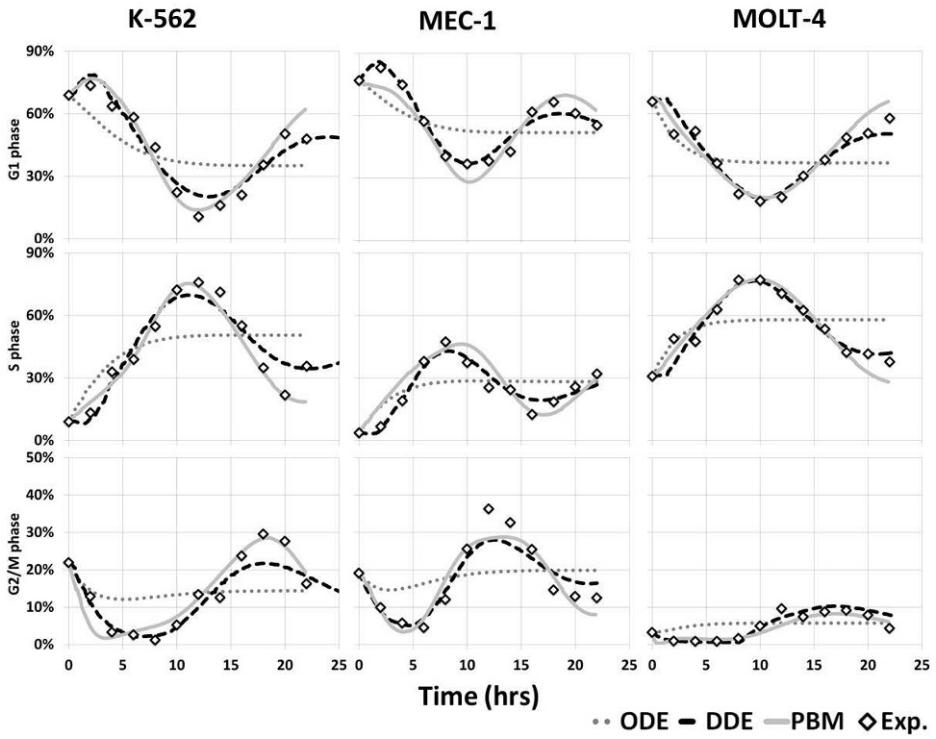

Figure 1: Comparison of experimental phase percents in 3 leukemia cell lines (K-562, MEC-1, MOLT-4) with simulation results for ODEs, DDEs, PBM.

An important advantage of this type of model is that it adds synchrony to the system (i.e., cell populations are not eligible to exit a phase as soon as they enter), so any disturbances in time will be well captured. Furthermore, DDEs do not require any additional parameters and maintain a fast computational execution. Because DDE systems' asynchrony is based on total phase numbers at earlier times, not intra-phase cell numbers, properties related to phase progression cannot be deduced. In order to account for properties varying within each phase, distributed systems such as PBMs must be used. To make this biologically relevant, those properties should be experimentally measurable. In Fuentes-Garí et al. (2014), we presented a PBM of the cell cycle with cyclins (proteins related to phase progression) and DNA as state variables, which was discretized and validated for 3 leukemia cell lines (K-562, MEC-1, MOLT-4) experimentally:

$$\begin{aligned}\frac{dG_e}{dt} =& G_{e-1}\cdot r_G\cdot \nu_E - G_e\cdot r_G\cdot \nu_E - G_e\cdot r_{G\to S,e}\cdot \nu_E + \delta(e-1)\cdot 2\cdot \sum_{b=1}^{n_B} M_b\cdot r_{M\to G,b}\cdot \nu_B \\ & - k_{D,G}\cdot G_e \quad \forall e\in\{1,\ldots,n_E\}\end{aligned} \tag{7}$$

$$\begin{aligned}\frac{dS_d}{dt} =& S_{d-1}\cdot r_S\cdot \nu_D - S_d\cdot r_S\cdot \nu_D + \delta(d-1)\cdot \sum_{e=1}^{n_E} G_e\cdot r_{G\to S,e}\cdot \nu_E \\ & - k_{D,S}\cdot S_d \quad \forall d\in\{1,\ldots,n_D\}\end{aligned} \tag{8}$$

$$\begin{aligned}\frac{dM_b}{dt} =& M_{b-1}\cdot r_M\cdot \nu_B - M_b\cdot r_M\cdot \nu_B - M_b\cdot r_{M\to G,b}\cdot \nu_B + \delta(b-1)\cdot S_{n_D}\cdot r_S\cdot \nu_D \\ & \forall b\in\{1,\ldots,n_B\}\end{aligned} \tag{9}$$

Growth rates (r_G, r_S and r_M) correlate phase progression to its state variable; transition rates ($r_{G\to S,e}$ and $r_{M\to G,b}$) account for the transition probability according to the state variable level.

Table 1: Phase time parameters estimated in each of the three models as compared to the experimental ones

Cell line	Duration	PBM	DDEs	ODEs	Exp. value
K-562	T_G	9h	4.4h	5.8h	6 ± 2h
	T_S	10h	6.6h	12h	10 ± 2h
	T_M	5h	2.7h	3.9h	4 ± 2h
MEC-1	T_G	8.5h	4.6h	8.4h	7 ± 2h
	T_S	7.5h	2.9h	5.6h	8.5 ± 2h
	T_M	3h	2.6h	4.7h	5 ± 2h
MOLT-4	T_G	12h	5.0h	4.2h	10 ± 2h
	T_S	15h	8.5h	10.3h	12 ± 2h
	T_M	2h	1.4h	1.1h	2 ± 2h

In order to compare the ability of all three models to fit experimental data, we used the synchronous experimental data of Fuentes-Garí et al. (2014) together with the PBM simulation results reported. Parameter estimation and simulations are all performed in gPROMS for ODEs and DDEs. Results for all three models can be seen in Figure 1. The PBMs and DDEs presented here can capture synchronous oscillatory behavior while the ODEs fail to account for this intra-phase heterogeneity, resulting in a lack of fit of this particular model. Either a spatial (such as protein expression in PBMs) or temporal (such as the delay history in DDEs) distribution is needed in order to capture the synchronous cell behavior. The model parameters (Table 1) are always lower for DDEs, higher for PBMs and unpredictable in ODEs (likely due to the fact that the parameter estimation optimizer cannot find a good solution for the minimization problem). In addition, the PBM cell cycle times are consistently the closest to the ones measured experimentally and are thus the most biologically meaningful.

2.2. Evaluating cell cycle model sensitivity to chemotherapy

The previous section showed that both PBMs and DDEs are capable of fitting synchronous experimental data, a fact that is critical in modeling chemotherapy due to its phase-specific action (G1 and S phase) and subsequent aggregation of cells into synchronized populations (Sherer et al. (2006)). In this section, each model will be embedded into a PK/PD model of chemotherapy delivery in leukemia (Pefani et al. (2014) and tested for its sensitivity to chemotherapy (as captured by the chemotherapy drug effect parameters $k_{D,S}$ and $k_{D,G}$ for S and G1 phases respectively, see equations 1-9; delayed terms in the DDEs were also subject to the chemotherapy effect over time).

For the comparison to be fair, the total kinetics (so that the cell number is equal) and the cell cycle distribution (so that the percentage of cells likely to be affected when chemotherapy starts) have to be equal at steady-state. All three systems of equations are solved at steady-state resulting in the following three equalities for log-growth (α: ODE; γ: DDE; β: PBM):

$$\alpha = \frac{dT}{dt}\frac{1}{T} = k_3 \cdot M_{SS,\%} \tag{10}$$

$$\gamma = \frac{dT}{dt}\frac{1}{T} = k_3 \cdot M_{SS,\%} \cdot \left(2e^{-\gamma\cdot\tau_M} - 1\right) + k_1 \cdot G_{SS,\%} \cdot \left(e^{-\gamma\cdot\tau_G} - 1\right) + k_2 \cdot S_{SS,\%} \cdot \left(e^{-\gamma\cdot\tau_S} - 1\right) \tag{11}$$

$$\beta = \frac{dT}{dt}\frac{1}{T} = \sum_{b=1}^{n_B} M_{b,SS,T\%} \cdot r_{M\to G,b} \cdot \nu_B \tag{12}$$

In the PBM form, equations are first translated as $\frac{dG_{e,G\%}}{dt} = 0 \quad \text{with} \quad G_{e,G\%} = \frac{G_e}{\sum G_e}$. Next, all populations in each phase are summed: $\frac{dG}{dt} \cdot \sum_{e=1}^{n_E} G_{e,G\%} = 2 \cdot \sum_{b=1}^{n_B} M_b \cdot r_{M\to G,b} \cdot \nu_B - \sum_{e=1}^{n_E} G_e \cdot r_{G\to S,e}\nu_E$. Summing all three phases, the result in Equation 12 is obtained. Similar equations can be derived for cell cycle distributions at steady-state. Equating $\alpha = \gamma = \beta$ and each of the phase fractions

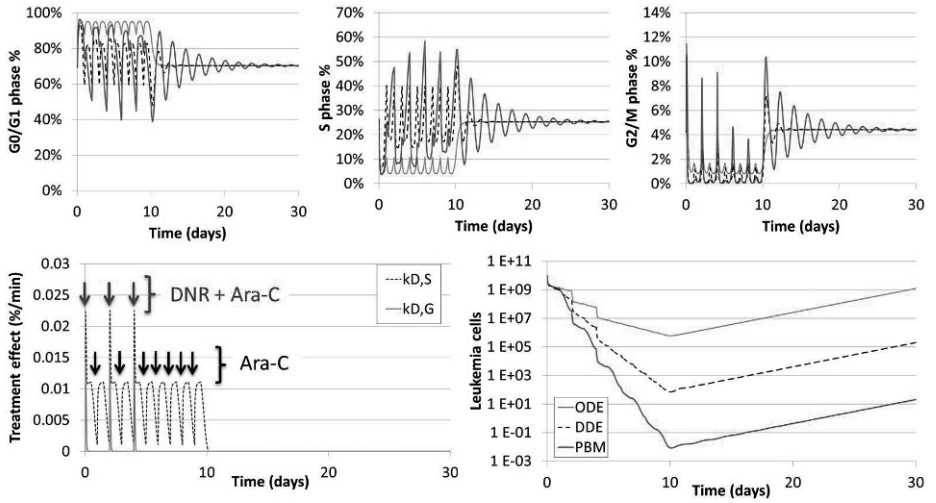

Figure 2: Comparison of cell cycle distribution (top 3 panels) and total cell number(bottom right) under chemotherapy treatment (bottom left panel) in: ODEs, DDEs, PBMs under equivalent growth kinetics (converted from DDE to equivalent parameters in ODE and PBM - see equal cell cycle distribution and total growth kinetics after 10 days of treatment)

($G_{SS,\%,ODE} = G_{SS,\%,DDE} = G_{SS,\%,PBM}$...), cell cycle times can be converted from one system (ODE, DDE, PBM) to another. Given the cell cycle times in the DDE system (which is the most complex to solve practically), all other cell cycle times can be obtained through this process of equaling the total growth rate and the phase distributions at steady-state (Table 2). This lays the foundations for our PK/PD kinetics comparison as we choose a hypothetical female patient that is 156cm tall and 60.7kg in weight, over 60 years old, receiving a chemotherapy treatment of 160 mg/m^2 Ara-C (12h infusion once a day for 10 days) and 80 mg/m^2 DNR (pulse dose on days 1, 3 and 5). The latter are the input parameters for the PK model.

Table 2: CC times converted from DDEs to PBM and ODEs for the steady state conditions chosen ($G_{SS,\%} = 70.36\%$, $S_{SS\%} = 25.23\%$, $M_{SS\%} = 4.41\%$, $\alpha = \beta = \gamma = 0.0161h^{-1}$)

	PBM	DDEs	ODEs
T_G	31.0554h	14h	33.7000h
T_S	13.5147h	7h	15.0075h
T_M	3.0674h	1.4h	2.7380h

Comparing the total cell evolution over the treatment period in the three models (Figure 2), we observe that the ODE sensitivity to chemotherapy is effectively lower due to its inherent tendency to allow the passage of cells from phase to phase (absence of intra-phase distribution). Conversely, the DDE and PBM models allow for cells to be distributed in each phase (temporally and spatially respectively). This can be further confirmed by observing the cell cycle phase distributions: ODEs reach much higher G2/M phase percents, representing the higher fraction of S phase cells coming in and contributing to the overall total cell duplication. Although G1 phase percents are higher throughout the treatment in ODEs, duplication remains the single most important factor affecting overall growth. DDEs response seems to be halfway between PBM and ODEs, in that cell kill is 5 orders of magnitude above PBM and below ODEs, while the oscillatory behavior can be broadly said to be a combination of ODEs (peak timings) and PBMs (peak heights). Oscillations post-treatment are the most sustained for PBM, while DDEs take 1-2 cell cycles to stabilize and ODEs immediately reach steady state.

3. Discussion

Three different models representing cell cycle kinetics were presented here and analyzed for their ability to capture oscillations and their response to chemotherapy under the same steady-state behavior. When fitted to experimental data, only DDEs and PBM performed well, with PBM having the most biologically relevant parameters (additionally to accurately predicting intracellular protein expression as reported in Fuentes-Garí et al. (2014)). In order to compare those cell cycle models under the effect of chemotherapy, cell cycle model parameters were obtained by equaling the steady-state distributions and total exponential growth for all three models and equivalent cell cycle times were obtained. Each of the models was then embedded in a PK/PD model of chemotherapy for AML and a hypothetical case was run. Throughout the treatment, ODEs had the highest percent of cells in the G2/M phase and the lowest amount of cell kill, which was explained by its inability to capture intra-phase distributions, letting cells transition to the next phase as soon as they have entered (thus escaping the chemotherapy effect). Conversely, PBM and ODE put a spatial or temporal restriction to the eligibility of cells to transition to the next phase, and subject those cells for a minimum phase time to the effect of chemotherapy (leading to a lower percent of G2/M cells and a higher cell kill at the end of the treatment).

A strikingly different behavior was observed when using different cell cycle models to simulate patient response to treatment. Current standards in PK/PD rely on cell cycle models that are not always accurate enough and that have not necessarily been validated. The PBM model presented here provides a good trade-off between capturing more complex pathway and protein kinetics, which are normally reported in single-cell models only, and maintaining a computationally efficient solution representing global cell kinetics, of which the ODEs discussed are a clear example. Importantly, treatment personalization requires defining measurable parameters representing patient heterogeneity. Our PBM is seamlessly linked to experimentally measurable parameters that have been reported to be highly heterogeneous among AML patients (Raza et al. (1990); Gong et al. (1994)). Future work will focus on unraveling heterogeneous response of patients to chemotherapy treatments .

4. Acknowledgements

This work is supported by ERC-BioBlood (#340719), ERC-Mobile Project (#226462), by the EU 7th Framework Programme [MULTIMOD Project FP7/2007-2013, #238013, OPTICO Project FP7/2007-2013, #280813], by Northwick Park Hospital R&D and by the Richard Thomas Leukaemia Research Fund. RM is thankful for a Royal Academy of Engineering Research Fellowship.

References

E. Pefani, N. Panoskaltsis, A. Mantalaris, M. C. Georgiadis, and E. N. Pistikopoulos, "Design of optimal patient-specific chemotherapy protocols for the treatment of acute myeloid leukemia (AML)," *Comput. Chem. Eng.*, vol. 57, pp. 187–195, 2013.

E. Pefani, N. Panoskaltsis, A. Mantalaris, M. Georgiadis, and E. Pistikopoulos, "Chemotherapy drug scheduling for the induction treatment of patients with acute myeloid leukemia," *IEEE Trans Biomed Eng*, vol. 24, p. 24, 2014.

M. Fuentes-Garí, R. Misener, D. García-Münzer, E. Velliou, M. C. Georgiadis, M. Kostoglou, E. N. Pistikopoulos, N. Panoskaltsis, and A. Mantalaris, "A mathematical model of sub-population kinetics for the deconvolution of leukaemia heterogeneity," *Submitted*, 2014.

E. Sherer, R. E. Hannemann, A. Rundell, and D. Ramkrishna, "Analysis of resonance chemotherapy in leukemia treatment via multi-staged population balance models," *Journal of Theoretical Biology*, vol. 240, no. 4, pp. 648–661, 2006.

A. Raza, H. D. Preisler, R. Day, Z. Yasin, M. White, J. Lykins, C. Kukla, M. Barcos, J. Bennett, G. Browman, J. Goldberg, H. Grunwald, R. Larson, J. Vardiman, and R. Vogler, "Direct relationship between remission duration in acute myeloid-leukemia and cell-cycle kinetics - a leukemia intergroup study," *Blood*, vol. 76, no. 11, pp. 2191–2197, 1990.

J. P. Gong, B. Ardelt, F. Traganos, and Z. Darzynkiewicz, "Unscheduled expression of cyclin-B1 and cyclin-E in several leukemic and solid tumor-cell lines," *Cancer Research*, vol. 54, no. 16, pp. 4285–4288, 1994.

Krist V. Gernaey, Jakob K. Huusom and Rafiqul Gani (Eds.), 12th International Symposium on Process Systems Engineering and 25th European Symposium on Computer Aided Process Engineering.
31 May - 4 June 2015, Copenhagen, Denmark.

Model-based characterisation of twin-screw granulation system for continuous solid dosage manufacturing

Ashish Kumar[a,b], Krist V. Gernaey[c], Thomas De Beer[b] and Ingmar Nopens[a,*]

[a]*BIOMATH, Dept. of Mathematical Modelling, Statistics and Bioinformatics, Faculty of Bioscience Engineering, Ghent University, Coupure Links 653, B- 9000 Gent, Belgium*
[b]*Laboratory of Pharmaceutical Process Analytical Technology, Dept. of Pharmaceutical Analysis, Faculty of Pharmaceutical Sciences, Ghent University, Harelbekestraat 72, B-9000 Ghent, Belgium*
[c]*CAPEC-PROCESS, Department of Chemical and Biochemical Engineering, Technical University of Denmark, 2800 Kongens Lyngby, Denmark*
[*]*Ingmar.Nopens@UGent.be*

Abstract

Continuous twin-screw granulation has received increased attention as it can be embedded in a continuous manufacturing line allowing 24/7 production capacity eliminating scale-up requirements and intermediate storage. The screws have a modular structure (interchangeable transport and kneading discs) allowing greater flexibility in equipment design. However, process knowledge should be further developed both under steady state and dynamic conditions. Mechanistic models incorporating the underlying mechanisms are therefore applied. In this study, the principle constitutive mechanisms such as aggregation and breakage are included in a population balance modelling framework. Based on an experimental inflow granule size distribution and mean residence time of the granulator, predictions of the outflow granule size distribution were made. Experimental data was used for calibrating the model for individual screw modules in the twin-screw granulator. The results showed that the successive kneading blocks lead to a granulation regime-separation inside the twin-screw granulator. The first kneading block after wetting caused an increase in the aggregation rate, which was reduced after the second kneading block. The breakage rate increased successively along the length of the granulator. Such a physical separation between the granulation regimes will be promising for future design and advanced control of the continuous granulation process.

Keywords: continuous manufacturing, population balance modelling, wet granulation.

1. Introduction

Continuous manufacturing of pharmaceutical solid dosage forms has received great interest in the last decade due to several process and economic benefits associated with it. A continuous process with 24/7 production capacity may eliminate scale-up requirements and intermediate storage. With this in mind, twin-screw granulation has emerged as promising method for particle size enlargement to achieve better flow properties and avoid segregation during successive unit operations. A twin-screw granulator (TSG) can be embedded in a continuous manufacturing line which also includes dryer, screening unit and tabletting machine making continuous powder to tablet production

possible. Moreover, the screws used in the granulator have a modular structure (interchangeable transport and kneading discs) providing flexibility towards adaptation in equipment and process variables depending upon on feed characteristics to achieve the required product characteristics. The available studies have primarily focused on the effect of process variables (such as screw configuration, material throughput, screw speed etc.) (Vercruysse et al., 2012; Dhenge et al., 2011; Thompson and Sun, 2010) and formulation properties (El Hagrasy et al., 2013; Dhenge et al., 2013) on granule properties at the outlet of the TSG due to the opacity of the multiphase system. Thus, little is known about the effect of these variables on the evolution and kinetics of granule formation in the TSG and the resulting granule structure. In a recent study, granule size distribution (GSD) evolution along the TSG screw was experimentally mapped in order to understand the dominant constitutive mechanisms of a granulation system such as growth, aggregation and breakage (Kumar et al., 2014a). However, such measurements provide a semi-quantitative insight regarding the GSD at discrete time steps, making it difficult to apply in process design applications. Population balance equations (PBEs) are a frequently used mathematical tool to describe particulate processes such as granulation (Kumar et al., 2013). An extensive review of the applications of such equations to particulate systems in engineering is given by Ramkrishna (2000). Barrasso et al. (2015) used a multi-component population balance model (PBM) for tracking the liquid content and porosity of each particle size class during the twin-screw granulation. The experimental data from El Hagrasy et al. (2013) used for the study originated from samples collected from the granulator outlet and therefore a lumped-parameter approach was adopted for the development of the model.

In this study, the principle constitutive mechanisms of a granulation system such as growth, aggregation and breakage are included in a population balance modelling framework to track particle size evolution in the different individual screw blocks of a continuous TSG. Based on an experimentally determined inflow GSD (Kumar et al., 2014a) and mean residence time ($\bar{t}$) (Kumar et al., 2014b) of the granulator, predictions of the outflow GSD were made. The experimental data was used for calibrating the model for individual screw modules in the TSG.

2. System analysis and model formulation

2.1. Continuous wet-granulation using TSG

The TSG consists of a barrel enclosing two co-rotating self-wiping screws. At the entrance, raw materials are fed into the transport zone and the granulation liquid is added via two nozzles, one for each screw, before the material reaches the mixing zone which consists of kneading discs (Fig. 1). The powder is hence wetted by the granulation liquid in this region. Further down, since the granulation occurs by a combination of capillary and viscous forces binding particles in the wet state, the wetted material is distributed, compacted and elongated by the kneading discs of the mixing zones, changing the particle morphology from small (microstructure) to large (macrostructure) (Vercruysse et al., 2012). The rotation of the screws conveys the material in axial direction through the different zones of the TSG by the drag and flow-induced displacement forces and thus causing mixing and granulation. The rheological behaviour of the material also changes based on liquid-to-solid ratio (L/S) (Althaus and Windhab, 2012).

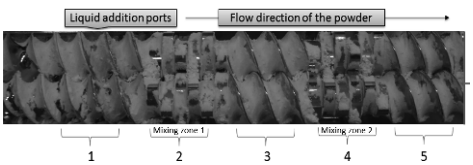

Figure 1: TSG screws with two mixing zones, each containing six kneading discs. Numbers indicate experimental sampling locations used for model calibration and validation.

2.2. Population balance model for twin-screw granulator

A TSG consists of a wetting zone and several mixing zones containing a finite number of kneading elements, which significantly drive the granulation process. The compartmentalisation into two mixing zones for simulation solved the challenge of inhomogeneous distribution in particle properties along the TSG length, due to the geometry of the screw as well as position of the liquid addition port. Introducing an external coordinate can be another possibility to model this inhomogeneity, but that will require implementation of the discrete element method together with population balances which is computationally challenging. In order to model the change in GSD across the individual mixing zone, these mixing zones were assumed as well mixed systems. The granulation rate processes which are considered dominant in the kneading element regions of the granulator, i.e. aggregation and breakage, were included in a population balance modelling framework, which can be represented as:

$$\begin{aligned}\frac{\partial n(t,x)}{\partial t} =& \frac{Q_{in}}{V} n_{in}(x) - \frac{Q_{out}}{V} n_{out}(x) + \frac{1}{2}\int_0^x \beta(t,x-\varepsilon,\varepsilon)\, n(t,x-\varepsilon)\, n(t,\varepsilon)\, d\varepsilon \\ & - n(t,x)\int_0^\infty \beta(t,x,\varepsilon)\, n(t,\varepsilon)\, d\varepsilon + \int_0^\infty b(x,\varepsilon) S(\varepsilon) n(t,\varepsilon)\, d\varepsilon - S(x) n(t,x)\end{aligned} \tag{1}$$

where, $n(t,x)$ is the number density function of particle volume as the internal co-ordinate at time t, Q_{in} and Q_{out} were inflow and outflow of the material based on throughput and V was the volume of the mixing zone. Assuming the material transport across the mixing zone to occur at a steady state, inflow and outflow can be eliminated from Eq. 1. The primary challenge for using PBE is to model the kinetics of the twin-screw granulation process in $\beta(t,x,\varepsilon)$ and $b(x,\varepsilon)$, because of their strong dependence on the time and in a fairly complex way on operating parameters and material properties. The constant aggregation kernel ($\beta(t,x,\varepsilon) = \beta_0$) describing the frequency that particles with diameter ε and $x-\varepsilon$ collide to form a particle of size x was used in this study. For the breakage process, the quadratic selection function, $S(y) = S_0(y)^\mu$, where S_0 and μ are positive constants for reasons of simplicity. The breakage function, $b(x,y)$ proposed by Austin (2002) (eq. 2) describing the formation of particles of size x from the breakup of a particle of size y was used.

$$b(x,y) = \frac{\frac{\phi\gamma x^{\gamma-1}}{y^\gamma} + \frac{(1-\phi)\alpha x^{\alpha-1}}{y^\alpha}}{\frac{\phi\gamma}{\gamma+1} + \frac{(1-\phi)\alpha}{\alpha+1}} \tag{2}$$

where γ, ϕ and α are dimensionless material constants. The term ϕ is called the weight parameter to quantify the mass content of the first breakage distributions. The exponents γ and α represent the width of the fragment distributions ϕ and $1-\phi$, respectively.

2.3. Numerical solution of PBM

To solve this equation numerically we first fix a computational domain]0,R] with R $<$ 1 and the truncated equation is obtained from Eq. 1 replacing 1 by R. A logarithmic grid with 50 bins was used for the discretisation of internal coordinates in order to accommodate particles of a wide size range with a minimal number of bins. Thereafter, a sectional method known as the cell average technique (CAT) was applied to solve the equation (Kumar et al., 2006). As the volumes of the newborn particles due to aggregation and/or breakage may lie between the bins of the logarithmic grid, the CAT allocates these particles into the corresponding nodes.

2.4. Model parameter estimation

The experimental data provided evidence that the aggregation and breakage are the dominant mechanisms in twin-screw granulation (for details see Kumar et al. (2014a)) and a model framework was developed to include these phenomena. However, various parameters in this model are

Table 1: Estimated model parameters with corresponding confidence intervals (95.44 %) at different screw speeds and mixing zones.

Screw speed	Low		High	
Mixing zone	I	II	I	II
β_0	3.02E-03 ± 1.47E-04	1.95E-01 ± 4.56E-02	9.18E-02 ± 4.07E-03	4.99E-02 ± 1.80E-02
S_0	2.53E-02 ± 5.91E-03	7.99E-01 ± 4.35E-02	3.11E-02 ± 2.25E-03	5.72E-01 ± 3.55E-02
α	1.13E-05 ± 8.83E-06	6.11E-01 ± 3.19E-02	1.26E-03 ± 3.29E-04	4.38E-01 ± 9.30E-02
γ	4.05E+00 ± 7.60E-01	3.81E-03 ± 2.18E-04	2.63E-01 ± 9.02E-03	4.49E-02 ± 3.78E-03
ϕ	1.03E+00 ± 2.31E-01	5.43E-02 ± 2.24E-03	1.18E+00 ± 3.89E-01	1.50E-02 ± 2.13E-03

unknown and can vary based on process settings and material properties. Experimental data of volume distributions of granule samples from various locations inside the granulator (Fig. 1) were used to estimate values of five parameters: three dimensionless material constants, γ, ϕ and α and the aggregation constant β_0 and selection function constants S_0. Based on available literature, selection function constants μ was fixed at 0.33. The estimation of these parameters was done by minimising the RMSE as an objective function (eq. 3):

$$\text{RMSE} = \sqrt{\frac{\sum_{i=1}^{n}(\hat{y}_i - y_i)^2}{n}} \tag{3}$$

where $\hat{y}_i$ and y_i are the predicted and experimentally measured values for n bins of the granule size range. In order to find the global minimum of the objective function, the `brute force` method was used, which computed the objective function's value at each point of a multidimensional grid of points, to arrive at the global minimum of the function. This multidimensional grid contained ranges of β_0 (1e-5, 0.4), S_0 (0.001, 3.5), α (3.3e-6, 1), γ (1.6e-4, 5) and ϕ (0.01, 1.5) with linear step length of 0.005, 0.005, 0.000005, 0.05 and 0.05, respectively. The estimated parameter sets were useful to check any correlations between estimated parameters, and also to determine the confidence interval of the fitted parameter using the bootstrap estimation Efron and Tibshirani (1986). Later, to obtain a more precise (local) minimum, the downhill simplex algorithm was used applying the estimation result of brute force minimization as initial guess (Nelder and Mead, 1965). The implementation of PBM solution and parameter estimates were performed using the Python programming language, employing built-in functions in scientific libraries NumPy and SciPy (Oliphant, 2007) and Odespy (Langtangen and Wang, 2014).

3. Results and discussion

3.1. Parameter estimation for predictive modelling

Experimentally measured size distributions from location 1, 3 and 5 in Fig. 1 for runs at low (500 rpm) and high (900 rpm) screw speed were used for model calibration. In order to quantitatively represent these trends in the simulations, the unknown rate parameters of the aggregation and Austin breakage kernels were estimated by comparing the simulation results with experimental data. The estimated parameters used for the numerical computations and their confidence intervals (95.44 %) are listed in table 1. The error estimates (RMSE and R^2) are mentioned in Fig. 2. The low RMSE and high R^2 values for all the screw speeds and mixing zones indicate that numerical results were in excellent agreement with the experimental data for each location inside the granulator subject to different optimal model parameters.

3.2. Simulated dynamic behaviour in the mixing zones of TSG

The simulation results showed that when the screw speed is low (Fig. 2.a), the D_{90} and D_{75} reduced and the D_{25} and D_{50} increased slightly when the material passed the first mixing zone. This indicates that the primary role of the first kneading block at this condition was the breaking of larger wetted lumps. The granules resulting from breakage caused increase in D_{25} and D_{50}. The

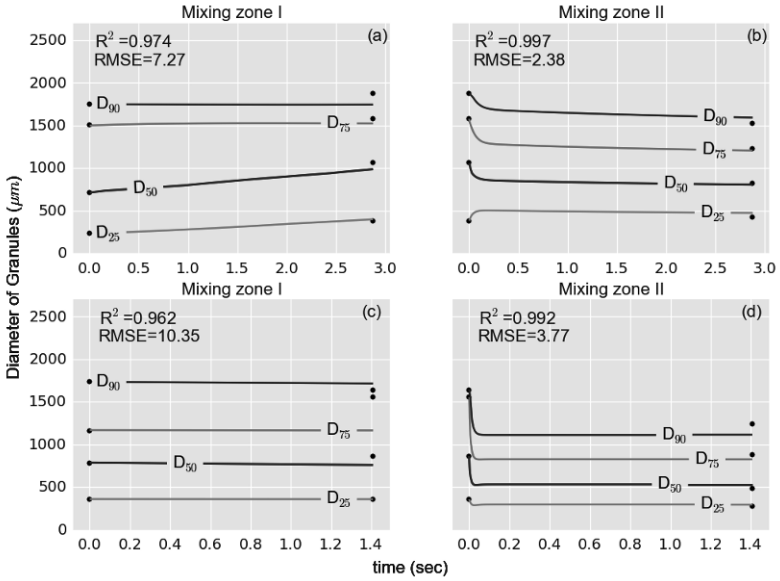

Figure 2: Experimental (•) and simulated (—) trends for dynamic change in quartiles of GSD (D25, D50, D75 and D90) at low (a and b) and high (c and d) screw speeds for first (a and c) and second (b and d) mixing zones.

second mixing zone at this condition caused further breakage of the granules leading to reduction in D_{50} as well together with D_{75} and D_{90} (Fig. 2.b). However, the D_{25} of the GSD remained unaffected by the mixing in the second zone. Overall, the barrel at this condition was highly filled due to the low screw conveying rate at low screw speed leading to less space for material to get distributed. This was also the reason that in experimental study this condition led to an undesirable level of high torque Kumar et al. (2014a).

The simulation of the high screw speed condition showed a significant change in the granulation behaviour in two mixing zones (Fig. 2.c and d). Unlike low screw speed, when the material passed through the first mixing zone at this condition all the quartiles of the GSD increased (Fig. 2.c). This indicates that aggregation was the most dominant mechanism in this condition in this mixing zone, while the level of breakage was very low leading to no reduction in any fraction with time. However, when the material was introduced to the second kneading block, the quartile values D_{90}, D_{75}, D_{50} dropped significantly, which indicates that breakage returned as the dominant mechanism in the second mixing zone (Fig. 2.d). This observation by process simulation is very important as it established that the successive kneading blocks led to a granulation regime-separation inside the twin-screw granulator under this condition. The mixing of the wetted powder in the first kneading block caused an increase in the aggregation rate, which was reduced after the second kneading block. However, the breakage rate increased successively along the length of the granulator. Such a physical separation between the granulation regimes will be promising for future design and advanced control of the continuous granulation process.

In order to further improve the model, future work will focus on introducing the wetting kinetics in the model framework and to obtain particle flux data and collision frequencies using DEM to avoid the parameter estimation by model inversion. Additionally, dedicated mechanistic kernels for the twin-screw granulation can be developed in order to improve the sensitivity of the model towards the change in process condition and other field parameters. Finally, a validated model can be used to define the design space of the process for the future optimization and model-based control of the granulation process.

4. Conclusions

A 1-D PBM including aggregation and breakage subprocesses for a continuous twin-screw granulation process was presented. Unknown model parameters and their 95% confidence range were estimated using experimentally measured particle size distributions from inside the granulator. The calibrated model was then used as a predictive tool within the experimental space. The results showed strong agreement with experimental data. This approach is the better way forward for the development of twin-screw granulation models as multiple factors of twin-screw granulator leading to a experimental output can now constrain the model during calibration. Further analysis revealed that, at high screw speed, the successive kneading blocks can lead to the dominance of different constitutive granulation mechanisms inside the twin-screw granulator. An ability to achieve a physical separation between the granulation regimes inside the granulator can be promising for future design and advanced control of the continuous granulation process using the twin-screw granulator. Furthermore, the study suggested that a model-based approach can be adopted to develop a better understanding of twin-screw granulation processes. A validated model can ultimately be used to define the design space of the process to facilitate process optimization and model-based control.

Acknowledgements

Financial support for this research from the BOF (Bijzonder Onderzoeksfonds Universiteit Gent, Research Fund Ghent University) is gratefully acknowledged.

References

Althaus, T. O., Windhab, E. J., Jan 2012. Characterization of wet powder flowability by shear cell measurements and compaction curves. Powder Technol. 215-216, 59–65.

Austin, L. G., 2002. A treatment of impact breakage of particles. Powder Technol. 126 (1), 85 – 90.

Barrasso, D., Hagrasy, A. E., Litster, J. D., Ramachandran, R., 2015. Multi-dimensional population balance model development and validation for a twin screw granulation process. Powder Technol. 270, Part B (0), 612 – 621.

Dhenge, R. M., Cartwright, J. J., Doughty, D. G., Hounslow, M. J., Salman, A. D., 2011. Twin screw wet granulation: Effect of powder feed rate. Adv. Powder Technol. 22 (2), 162 – 166.

Dhenge, R. M., Washino, K., Cartwright, J. J., Hounslow, M. J., Salman, A. D., 2013. Twin screw granulation using conveying screws: Effects of viscosity of granulation liquids and flow of powders. Powder Technol. 238, 77–90.

Efron, B., Tibshirani, R., 1986. Bootstrap methods for standard errors, confidence intervals, and other measures of statistical accuracy. Stat. Sci. 1 (1), pp. 54–75.

El Hagrasy, A., Hennenkamp, J., Burke, M., Cartwright, J., Litster, J., 2013. Twin screw wet granulation: Influence of formulation parameters on granule properties and growth behavior. Powder Technol. 238, 108–115.

Kumar, A., Gernaey, K. V., De Beer, T., Nopens, I., 2013. Model-based analysis of high shear wet granulation from batch to continuous processes in pharmaceutical production – a critical review. Eur. J. Pharm. Biopharm. 85 (3, Part B), 814 – 832.

Kumar, A., Vercruysse, J., Bellandi, G., Gernaey, K. V., Vervaet, C., Remon, J. P., Beer, T. D., Nopens, I., 2014a. Experimental investigation of granule size and shape dynamics in twin-screw granulation. Int. J. Pharm. 475 (1-2), 485 – 495.

Kumar, A., Vercruysse, J., Toiviainen, M., Panouillot, P.-E., Juuti, M., Vanhoorne, V., Vervaet, C., Remon, J. P., Gernaey, K. V., Beer, T. D., Nopens, I., 2014b. Mixing and transport during pharmaceutical twin-screw wet granulation: Experimental analysis via chemical imaging. Eur. J. Pharm. Biopharm. 87 (2), 279 – 289.

Kumar, J., Peglow, M., Warnecke, G., Heinrich, S., Morl, L., 2006. Improved accuracy and convergence of discretized population balance for aggregation: The cell average technique. Chem. Eng. Sci. 61 (10), 3327–3342.

Langtangen, H. P., Wang, L., 2014. Odespy software package. `https://github.com/hplgit/odespy`.

Nelder, J. A., Mead, R., 1965. A simplex method for function minimization. Comput. J. 7 (4), 308–313.

Oliphant, T. E., 2007. Python for scientific computing. Comp. Sci. Eng. 9 (3), 10–20.

Ramkrishna, D., 2000. Population balances: Theory and applications to particulate systems in engineering. Academic press.

Thompson, M. R., Sun, J., 2010. Wet granulation in a twin-screw extruder: Implications of screw design. J. Pharm. Sci. 99 (4), 2090–2103.

Vercruysse, J., Córdoba Díaz, D., Peeters, E., Fonteyne, M., Delaet, U., Van Assche, I., De Beer, T., Remon, J. P., Vervaet, C., 2012. Continuous twin screw granulation: Influence of process variables on granule and tablet quality. Eur. J. Pharm. Biopharm. 82 (1), 205–211.

Krist V. Gernaey, Jakob K. Huusom and Rafiqul Gani (Eds.), 12th International Symposium on Process Systems Engineering and 25th European Symposium on Computer Aided Process Engineering.
31 May – 4 June 2015, Copenhagen, Denmark

Process-based Method for Reducing Product Losses in Pharmaceutical Manufacturing

Hirokazu Sugiyama,[a*] Masaaki Ito,[a] Hirao Masahiko[a]

[a]*Department of Chemical System Engineering, The University of Tokyo, 7-3-1 Hongo, Bunkyo-ku, 113-8656 Tokyo, Japan*

sugiyama@chemsys.t.u-tokyo.ac.jp

Abstract

We present a method for reducing product losses in sterile drug product manufacturing processes. The method consists of five steps that guides the effort of process improvement, and serves as a fundament for the Plan phase of the Plan-Do-Check-Act (PDCA) cycle. The method considers all product components of the process, e.g., Active Pharmaceutical Ingredients (APIs), excipients and primary packaging materials. In addition, a couple of mechanisms are newly developed for generating effective improvement scenarios as well as comparing effect and effort of different scenarios in a multiobjective manner. In the case study, the method was executed step-by-step using industrial data and the effectiveness of the method was demonstrated.

Keywords: pharmaceutical processes, process improvement, yield

1. Introduction

Due to the increase of healthcare costs and R&D expenses, pharmaceutical manufacturing is requested to become more cost-effective without compromising the product quality. As to the manufacturing cost, one of the major factors is the material cost. With the aim of reducing raw material costs, several authors worked on the yield of APIs, the most value-added component of products. Dassau et al. (2006) applied quality control techniques for improving the API yield as well as product property such pH in the bio-pharmaceutical production processes. With a focus on fractional batch distillation processes, Yang and Tjia (2010) applied process simulators for creating better process understanding, which lead to the enhancement of API throughput and yield. Sugiyama and Schmidt (2013) proposed an indicator for prioritizing loss causes of API, and applied the indicator in a biological drug product manufacturing facility.

However in these previous contributions, there are still rooms for improvement regarding applicability. For instance, the focus so far is more on the effectiveness of reducing losses, and less on the associated efforts or quality risks. Regardless of the effectiveness, no process improvement will be accepted that does not comply with quality regulations known as Good Manufacturing Practice (GMP). In addition, the above mentioned work considers only APIs, and other materials are outside of the scope, e.g., excipients or packaging materials. These raw materials, which also have pharma-grade, can be a relevant factor of the entire material cost.

In this paper, we propose a planning method for reducing product losses in the pharmaceutical manufacturing processes. The primary target of the method is the manufacturing processes of sterile drug products, such as injectables, infusion solutions,

or eye-drops. The method consists of five steps: (1) Analyze process flow, (2) Collect process data, (3) Characterize loss causes, (4) Generate improvement scenarios, and (5) Perform multiobjective evaluation. The outcome is a set of promising improvement scenarios for reducing product losses, which supports the Plan-phase of the PDCA cycle of process improvement. A couple of novel mechanisms are proposed in order to help generating effective improvement scenarios as well as to compare different scenarios in a multiobjective manner. The consideration scope is extended to cover not only API, but also other component materials such as excipients or packaging materials. An industrial case study is performed in order to show the effectiveness of the method.

2. Method

Figure 1 shows a general process for producing sterile drug products. The process is batch-wise. There are different causes of product losses in the process. For instance, a number of samples are taken for quality control (QC) or In Process Control (IPC), for complying with the GMP requirements. The nature of the batch production results in losses associated with the start and the end of the production, e.g., pre-flush of the product solution from the filter unit.

The effective way to reduce these losses would be to investigate the mass flow of the entire process, and to identify the relevant loss causes with high economic damages. However in the pharmaceutical batch processes, this simple work can face difficulties because (i) the concept of taking overall mass balance is weak; (ii) some of the loss data are not measured due to the high-value given to the product; (iii) even when the data are available, they are stored in different places in the organization. Thus, as shown in Figure 2, our method first starts with creating an overview of the process and material flow, before working on concrete improvement.

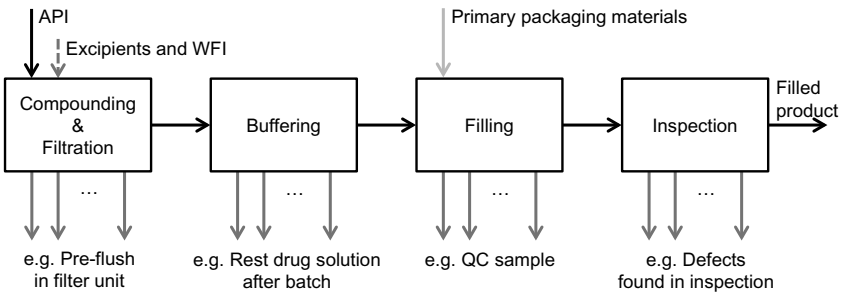

Figure 1 Typical processes of sterile drug product manufacturing

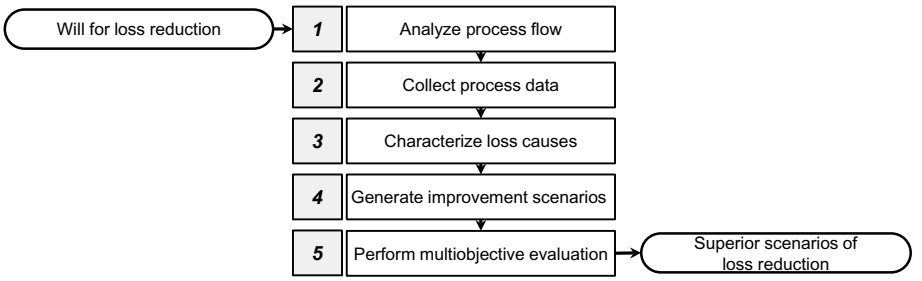

Figure 2 Five-step method for reducing product losses

2.1. Step 1: Analyze process flow

The aim of Step 1 is to create a process flow diagram as shown in Figure 1, where all manufacturing steps as well as entering/exiting flows are identified.

2.2. Step 2: Collect process data

In Step 2 data are collected for the process flows and the quantities of the loss flows m are obtained for product i, loss cause j, batch k, and material l. The term m can have different units such as L, kg, or unit, depending on the material. Manufacturing recipes can provide the quantity of the flows that are fixed over batches, e.g., API inlet, whereas batch record data need to be collected for variable flows, e.g., defectives found in the inspection. In parallel, purchase price P for unit amount of material l is also collected, using information from the financial department.

2.3. Step 3: Characterize loss causes

Based on the collected information, economic damage of each loss cause is calculated. In this method we introduce an indicator termed Annual Cost of Losses (ACL) for loss cause j of product i as:

$$ACL_{i,j} = \frac{N_i}{n_i} \sum_{k,l} \left(P_l \, m_{i,j,k,l} \right) \tag{1}$$

where N_i and n_i are the numbers of batches planed in the year and covered in the data collection, respectively. With this simple indicator, all loss causes that have different units can be now compared on the same basis. The indicator is also flexible in terms of the time span considered, and it can be adjusted from yearly to quarterly or monthly according to the interest of the company. Apparently the value of m needs to be stable over batches, and n_j needs to be sufficient, for the realistic estimation of ACL.

In addition, we propose a qualitative method in Table 1 for distinguishing causes into four categories according the reason of the loss. Category I is the samples collected due to the GMP requirements. If the reduction of the loss is desired, the sampling method needs to be investigated, e.g., frequency or quantity. Category II is the losses planned at the start or the end of the batch production, such as discharge of the product solution in the tank remaining after a batch. Such planned losses are usually defined in the manufacturing procedure, and thus its validity needs to be investigated. Category III covers the losses due to trouble in the production, which happens so frequently that the discard procedure is defined in the procedure. For reducing this type of losses, one approach is to scrutinize the procedure itself, or the other is to identify and prevent the root cause of the trouble. Losses in Category IV are due to unplanned troubles such as defectives found in the visual inspection. The only approach for this type of loss is to identify the root cause and to implement preventive actions.

Table 1 Categorization of product losses as a guide to generate effective improvement scenarios

Category	Reason of the loss	Points to be investigated
I	Sampling due to GMP	Sampling method, frequency and quantity
II	Start and end of batch production	Discard procedure
III	Frequent trouble	Discard procedure, root cause of the trouble
IV	Sudden trouble	Root cause of the trouble

Table 2 Calculation scale for evaluating product quality risk using FMEA. The terms of *SV*, *OC* and *DT* stand for the evaluation scores of severity, occurrence and detectability, respectively.

Severity	*SV*	Occurence	*OC*	Detectability	*DT*
Recall from the market	5	Every batch	5	Patient notices for the first time	5
Total batch rejection	4	Once in a month	4	Not checked in the inspection	4
Partial batch rejection	3	Once in a year	3	Checked in the inspection but judgment is subtle	3
Re-inspection	2	Once in ten years	2	Spot check	2
No effect	1	Once in 100 years	1	100% inspection	1

2.4. Step 4: Generate improvement scenarios

Improvement scenarios are generated in Step 4. A scenario can be an imaginary situation, e.g., abolish the planned discard of remaining solution after a batch, but with a concrete and realistic technical countermeasure. Preliminary measurements would be helpful to justify the appropriateness of the scenario, e.g., quality measurement of the effluent solution. Brain storming by different experts from manufacturing, quality, engineering would be effective for enhancing comprehensive generation of scenarios.

2.5. Step 5: Perform multiobjective evaluation

In this step, all scenarios generated are evaluated in different criteria. Our method gives an evaluation score S to each improvement scenario regarding the following six aspects: reduction potential of ACL (S_1), investment cost (S_2), impact for shift operation (S_3), timing of implementation (S_4), effort of change management (S_5) and product quality risk (S_6). The score S ranges from one to five, with five as the most favorable and one as the least favorable, respectively. Economic evaluation scores (S_1 and S_2) are based on the actual quantities, while the other scores (S_3 to S_6) are assessed in a semi-quantitative manner.

This paper presents the calculation of S_6: product quality risk using Failure Mode and Effect Analysis (FMEA). The first action of this well-established quality method is the generation of failure mode, each of which is secondly evaluated in terms of severity *SV*, occurrence *OC* and detectability *DT*. Table 2 shows the calculation scale. Lastly all the scores are multiplied to obtain so-called Risk Priority Number (*RPN*) for failure mode *f*, and the maximum value represents the *RPN* of a scenario, as defined in Eq. (2).

$$RPN = \max_{f}(SV\ OC\ DT)_f \tag{2}$$

The score S_6 is then obtained by the Eq. (3).

$$S_6 = 6 - \left\lfloor \sqrt[3]{RPN} \right\rfloor \tag{3}$$

Trade-offs between different scenarios can be discussed based on the obtained scores. For supporting management decision, Pareto optimization can be helpful in identifying superior scenarios, which can be selected for detailed planning. If no desirable solution can be found, alternative scenarios need to be generated by repeating Step 4.

3. Case Study

An industrial case study was performed to demonstrate the method. The target of the case study was a plant, which produces two sterile drug products of A and B in different production lines. Although these lines are similar, the products A and B are different in regard to the therapeutic area, pharmaceutical prices, annual production amount and product property. Thus, for the plant management, it was difficult to judge which product loss should be worked on with which priority and approach.

3.1. Step 1: Analyze process flow

As Step 1, process flow diagrams as in Figure 1 were created for the products A and B.

3.2. Step 2: Collect process data

For all the loss causes identified in Step 1, quantities of the mass *m* were collected from different sources in the manufacturing area, e.g., batch record and QC data.

3.3. Step 3: Characterize loss causes

The value of ACL were then calculated for the loss causes of both products A and B, and the major results are shown in Figure 3 (left). Loss categorization in Table 1 was applied.

The first four dominant causes belong to Category II, i.e., losses associated with the start/end of batch production. The first one was found in product A, and was the discharge of the remaining product solution from the buffer tank at the end of the batch. When the process was designed, there were some technical difficulties to fill all the solution in the tank, and a certain amount was set to be discarded in every batch. The second most relevant was in product B, and was due to the pre-flush of the filter unit during the preparation of a batch production. This is commonly practiced in the industry because the product properties, e.g., concentration, are considered to be unstable, when the solution is introduced into the filter. Since the amount to be discarded was determined with a large safety allowance, this cause appeared in a prominent position.

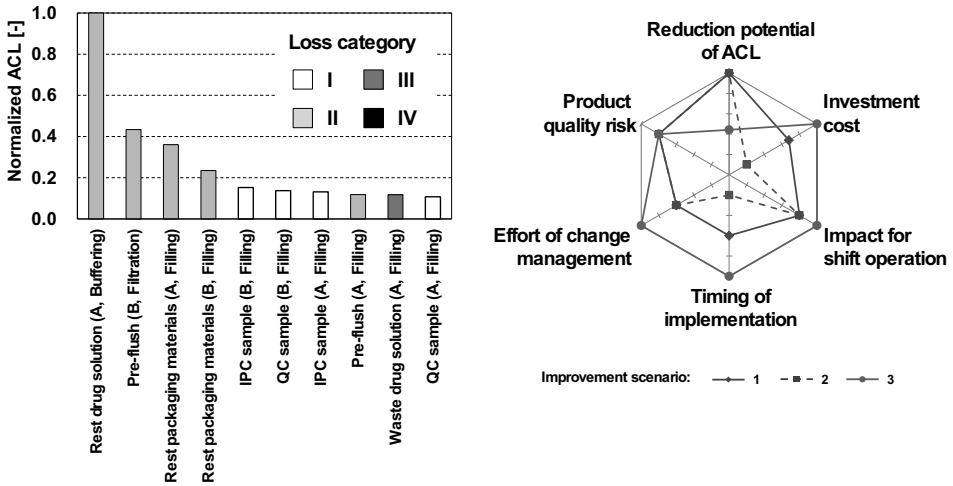

Figure 3 ACL evaluation result (left) and multiobjective evaluation result (right)

3.4. Step 4: Generate improvement scenarios

Regarding the first and second loss cause, an analysis indicated that the discarded solution can have the same quality as the regular product. Based on this preliminary analysis, three scenarios were generated (Scenarios 1 and 2 for the first cause, and Scenario 3 for the second cause). All scenarios are basically to set the discard amount to be zero by implementing either of the following facility changes.

3.5. Step 5: Perform multiobjective evaluation

Figure 3 (right) shows the evaluation of three scenarios in regard to the multiobjective criteria defined the previous chapter. Different characters of all scenario are visualized. Scenarios 1 and 2 show the largest reduction potential of ACL, whereas they are the best in none of the other criteria. Scenario 2 involves construction activities for a long period, which resulted in the worst result of all in investment cost and timing. Scenario 3 has the second largest potential in reducing ACL, and the best score in all other criteria. The score S_6 was four for all scenarios. In Scenario 1, *SV*, *OC* and *DT* of the worst failure mode were 4, 3 and 1, respectively, which resulted in $RPN = 12$ and $S_6 = 4$.

In Figure 3 (right), it can be seen that Scenarios 1 and 3 are the Pareto optima, or the set of non-dominated scenarios. Trade-off can be observed in these two scenarios, i.e., compared to Scenario 1, Scenario 3 is less lucrative regarding ACL reduction, but is easier to be implemented. In this way, Step 5 can help characterization of all scenarios and prioritization of the effort on process improvement.

4. Conclusions and Outlook

In this paper, we presented a process-based method for reducing product losses in sterile drug product manufacturing processes. Five steps defined in the method can guide the effort of process improvement, and support the Plan phase of the PDCA cycle. The method considers all product components used in the process, and both effect and effort of an improvement in the evaluation. Another novelty can be found in the following mechanisms: ACL indicator for comparing different loss causes with different units; loss categorization for generating improvement ideas effectively; multiobjective evaluation indicators for considering economy, operational feasibility and impact on quality management. The method was demonstrated in an industrial case study, where two improvement scenarios are obtained as promising ones. In the future, the method can be combine with process simulation techniques, which can support model-based generation of various scenarios.

Acknowledgements

Financial supports by JSPS Grant-in-Aid for Young Scientists (B) No. 26820343 as well as Research Grant 2014 from Nagai Foundation Tokyo are deeply acknowledged.

References

E. Dassau, I. Zadok, D. R. Lewin, 2006, Combining Six-Sigma with Integrated Design and Control for Yield Enhancement in Bioprocessing, Ind. Eng. Chem. Res., 45, 8299-8309

Y. Yang, R. Tjia, 2010, Process Modeling and Optimization of Batch Fractional Distillation to Increase Throughput and Yield in Manufacture of Active Pharmaceutical Ingredient (API), Comput. Chem. Eng., 34, 1030-1035

H. Sugiyama, R. Schmidt, 2013, Business Model of Continuous Improvement in Pharmaceutical Production Processes, Computer Aided Process Engineering, 32, 697-702

Krist V. Gernaey, Jakob K. Huusom and Rafiqul Gani (Eds.), 12th International Symposium on Process Systems Engineering and 25th European Symposium on Computer Aided Process Engineering.
31 May - 4 June 2015, Copenhagen, Denmark.

Model-based optimization of the primary drying step during freeze-drying

Séverine Thérèse F.C. Mortier[a,b], Pieter-Jan Van Bockstal[b], Ingmar Nopens[a], Krist V. Gernaey[c] and Thomas De Beer[b]

[a]*BIOMATH, Department of Mathematical Modelling, Statistics and Bioinformatics, Faculty of Bioscience Engineering, Ghent University, Coupure Links 653, 9000 Ghent, Belgium*
[b]*Laboratory of Pharmaceutical Process Analytical Technology, Department of Pharmaceutical Analysis, Faculty of Pharmaceutical Sciences, Ghent University, Ottergemsesteenweg 460, 9000 Ghent, Belgium*
[c]*CAPEC-PROCESS, Department of Chemical and Biochemical Engineering, Technical University of Denmark, Building 229, 2800 Kgs. Lyngby, Denmark*
severine.mortier@ugent.be

Abstract

Since large molecules are considered the key driver for growth of the pharmaceutical industry, the focus of the pharmaceutical industry is shifting from small molecules to biopharmaceuticals: around 50% of the approved biopharmaceuticals are freeze-dried products. Therefore, freeze-drying is an important technology to stabilise biopharmaceutical drug products which are unstable in an aqueous solution. However, the freeze-drying process is an energy and time-consuming process. The use of mechanistic modelling to gather process knowledge can assist in optimisation of the process parameters during the operation of the freeze-drying process. By applying a dynamic shelf temperature and chamber pressure, which are the only controllable process variables, the processing time can be decreased by a factor 2 to 3.

Keywords: Dynamic Design Space, Modelling, Optimization, Pharmaceuticals

1. Introduction

Nowadays large molecules receive more attention and the interest in these molecules is growing. The list of the Food and Drug Administration (FDA) and European Medicines Agency (EMA) with the approved biopharmaceutical products (> 300) contains approximately 50% freeze-dried products (Constantino and Pikal, 2004). This is an indication that freeze-drying is the preferred way of stabilizing biopharmaceutical drug products that are unstable in aqueous solution. However, the high cost and energy consumption and long processing time are disadvantegeous (Burns, 2009; Gieseler, 2012). Among the freeze-dried biopharmaceutical products the largest fraction are therapeutic protein formulations and vaccines (Pikal, 2002; Patel et al., 2010).
Conventionally, freeze-drying (or lyophilization) is a batch process, consisting of three consecutive steps: freezing, primary drying and secondary drying. Therefore, vials filled with a solution are placed on temperature-controlled shelves in the drying chamber. The lyophilization process starts with the cooling of these shelves down to approximately -45 °C. During this freezing step most of the water crystallizes to ice. The solutes gradually concentrate between these ice crystals, until they start crystallizing (at the eutectic temperature T_e) or form an amorphous glass (at the glass transition temperature T_g'). After complete solidification, the primary drying step begins by introducing a vacuum, conventionally between 50 and 300 μbar, in the drying chamber.

Additionally the temperature of the shelves is increased to provide the energy necessary for ice sublimation. The sublimation front, the border between the ice crystals and dried product, gradually decreases during the progress of primary drying until ice sublimation is complete. Finally, during the secondary drying step, the remaining unfrozen water is removed by desorption and a dry cake is obtained.
Several Critical Quality Attributes (CQA) are identified for freeze-dried biopharmaceuticals. These product characteristics should be within an appropriate limit to ensure product quality (ICH guidelines on Pharmaceutical Development (Q8)), e.g. the Active Pharmaceutical Ingredient (API) needs to stay stable throughout the lyophilization process to guarantee optimal therapeutic activity (e.g. avoiding loss of protein conformation by adding lyo- and/or cryoprotectants) or the residual moisture level of the dried cake needs to be adequate to ensure product stability (e.g. water-mediated degradation pathways). One of the most important CQA's is cake appearance. For aesthetic purposes and to ensure fast reconstitution of the drug product, loss of structure (cake collapse) should be avoided throughout the lyophilization process. Therefore the product temperature T_p at the sublimation front should always be kept below the collapse temperature T_c and T_e for amorphous and crystalline materials respectively (Kasper and Friess, 2011). T_c is generally a few degrees higher than T_g' because the high viscosity of the glass near T_g' limits molecular motion. On the other hand, primary drying asks for T_p to be as high as possible to shorten the sublimation time. Therefore, the adaptable process variables, shelf temperature T_s and chamber pressure P_c, should not be chosen too conservative. Mechanistic modelling allows to determine the optimum combination of T_s and P_c keeping T_p at the sublimation front below the critical temperature during primary drying. Mechanistic modelling is a powerful tool for both cycle development and optimization. The information obtained from the models allows the development of the Design Space for a specific formulation. The limits of the Design Space are determined by the efficiency of primary drying, the dried cake appearance and the equipment capability. The target T_s and P_c should therefore be within these limits to acquire a good cake within an acceptable process time. The use of the Design Space highly improves the efficiency and control of the lyophilization process.
Since T_p depends on a wide range of varying parameters during sublimation, the optimal combination of T_s and P_c is not constant during drying. For instance, along with the progress of primary drying the thickness of the dried product layer L_{dried} increases which simultaneously leads to an increase in product resistance R_p and T_p at the sublimation interface. Because of the continuous dynamics of dependent variables, the Design Space also changes continuously throughout the lyophilization process and, hence, requires a dynamic Design Space.

2. Objectives

The objective is to use the freeze-drying model (Fissore et al., 2011b,a) to obtain the optimal values for the shelf temperature T_s and the chamber pressure P_c, i.e. a dynamic Design Space is created.

3. Freeze-drying model

The mathematical model consists of two phases, and the equations are based on the principles of mass and energy transfer. In the first instants the chamber pressure is gradually decreasing till the calculated sublimation rate $\dot{m}_{sub}$ (kg/s) is higher than zero. An exponential decrease of the chamber pressure P_c from 100,000 Pa to 10 Pa in 10 minutes is assumed. A faster decrease of the chamber pressure is restricted by the freeze-drying equipment. During this first phase it is assumed that the shelf temperature T_s (K) remains constant at the initial shelf temperature and the temperature at the sublimation front T_i (K) equals the shelf temperature. Moreover, the temperature difference across the ice layer ΔT is fixed at 0 K. As long as the calculated sublimation rate is lower than zero, the sublimation rate is set to zero.

During the second phase, starting when the sublimation rate is higher than zero, the thickness of the dried layer L_{dried} (m) increases.
The full mathematical model describing the freeze-drying process consists of several equations of which some have to be solved simultaneously. The model calculates the evolution of the thickness of the dried layer in function of time. For a fixed set of input values the temperature at the sublimation front T_i (K) and the temperature difference across the ice layer ΔT are calculated using the following equations (Fissore et al., 2011b; Murphy and Koop, 2005):

$$e^{9.550426-5723.265/T_i+3.53068\ln(T_i)-0.00728332T_i} = -\frac{(-A_p\Delta H_{sub}P_c - A_vK_vM\,T_s + A_vK_vR_pM\,T_i + A_vK_vR_pM\Delta T)}{A_p\Delta H_{sub}} \tag{1}$$

$$\Delta T = \frac{24.7\frac{(L_{total}-L_{dried})(P_i-P_c)}{R_p+R_s} - 0.0102\,(L_{total}-L_{dried})\,(T_s-T_i)}{1-0.0102\,(L_{total}-L_{dried})} \tag{2}$$

with A_p and A_v the product and the vial area (m^2), which are respectively equal to the inner and the outer surface of the vial, ΔH_{sub} the latent sublimation heat of ice (J/mol), P_c the pressure in the drying chamber (Pa), K_v the vial heat transfer coefficient (J/(m^2sK)), M the molecular weight of water (kg/mol), T_s the temperature for the temperature-controlled shelf (K), R_p the dry product resistance (m/s), R_s the stopper resistance (m/s), ΔT the temperature difference across the ice layer (K), L_{total} the total thickness of the product layer (m) and L_{dried} the thickness of the dried layer (m). The latent sublimation heat of ice ΔH_{sub} is given by (Murphy and Koop, 2005):

$$\Delta H_{sub} = 46782.5 + 35.8925T_i - 0.07414T_i^2 + 541.5e^{-\left(\frac{T_i}{123.75}\right)^2} \tag{3}$$

The vial heat transfer coefficient K_v is calculated by (Fissore et al., 2011a):

$$K_v = \alpha + \frac{\beta P_c}{1+\gamma P_c} \tag{4}$$

with α (J/(m^2sK), β (J/(m^2sKPa) and γ (1/Pa) constants, which are determined using experimental data.
The dry product resistance R_p is given by (Fissore et al., 2011a):

$$R_p = R_{p,0} + \frac{A_{Rp}L_{dried}}{1+B_{Rp}L_{dried}} \tag{5}$$

with $R_{p,0}$ (m/s), A_{Rp} (1/s) and B_{Rp} (1/m) constants, which are dependent on the product that is freeze-dried and its concentration. The constants are determined by fitting to experimental data.
Once the temperature at the sublimation front is known, the pressure at the interface P_i (Pa) can be calculated using the following relation (Murphy and Koop, 2005):

$$P_i = e^{9.550426-5723.265/T_i+3.53068\ln(T_i)-0.00728332T_i} \tag{6}$$

The sublimation rate $\dot{m}_{sub}$ can be calculated using (Fissore et al., 2011a,b):

$$\dot{m}_{sub} = A_p\frac{(P_i-P_c)}{R_p} \tag{7}$$

The evolution of the thickness of the dried layer is then given by (Tang et al., 2006):

$$L_{dried} = \frac{m_{sub}}{\rho_I\varepsilon A_p} \tag{8}$$

with m_{sub} the mass of ice removed by sublimation (kg), ρ_I the density of ice (kg/m^3) and η the porosity of ice.
The total thickness of the product layer L_{total} is calculated based on the amount of liquid that is filled in the vial:

$$L_{total} = \frac{V 10^{-6}}{\pi r_i^2} \tag{9}$$

with V the volume in one vial (mL).
The nominal values of the parameters are given in table 1. With the inner radius r_i and outer radius r_o of the vial the product area A_p and vial area A_v can respectively be calculated.
The critical temperature at the sublimation front is set at 238.15 K (-35 °C). The limits for the

Table 1: Nominal values of the parameters of the freeze-drying model

Parameter	Numerical value
r_i	0.011 m
r_o	0.0115 m
α	3.2 J/(m^{2}sK)
β	0.7 J/(m^{2}sKPa)
γ	0.02 1/Pa
R_s	0 m/s
$R_{p,0}$	1.1 10^4 m/s
A_{Rp}	2.7 10^8 1/s
B_{Rp}	2.5 10^3 1/m
V	2.5 mL
ρ_I	919.4 kg/m^3
ε	0.97
M	0.018015 kg/mol

freeze-drying equipment for respectively the chamber pressure (Pa) and the shelf temperature (K) are $[10\ 10000]$ and $[-233.15\ 303.15]$.
The sublimation rate is limited by the freeze-drying equipment, known as the Equipment Capability Curve (ECC)-restriction which is function of the chamber pressure:

$$\dot{m}_{sub,max} = -2.7075\,10^{-9} + 8.1232\,10^{-9} P_c \tag{10}$$

To optimise the freeze-drying process the objective is to maximise the sublimation rate without exceeding the critical temperature at the sublimation front and the ECC-criterion. The degrees of freedom are the chamber pressure and the shelf temperature which do not necessarily have to be fixed throughout the process.

4. Results

During freeze-drying the thickness of the dried layer L_{dried} increases over time until L_{dried} equals L_{total}. To determine the optimal values for the chamber pressure and shelf temperature during freeze-drying a grid-search method is used. For each combination of P_c and T_s, feasible using the equipment under study, the sublimation rate is calculated. For each grid point two criteria are verified: (1) the temperature at the sublimation front and (2) the ECC-criterion. As the thickness of the dried layer changes during freeze-drying the optimal values for P_c and T_s are changing as well. To limit the calculation time the limits for the grid-search are restricted to $[5\ 800]$ and $[-16\ 20]$. The underlying reason for the extension of the pressure towards 5 Pa instead of using the equipment limitation of 10 Pa is that the optimal chamber pressure seemed to be on the lower limit. By

using 5 Pa it was possible to verify if a lower value for the chamber pressure would be even more optimal.

In figure 1 the evolution of the thickness of the dried layer is presented. Initially, L_{dried} remains constant at a value of zero, because the sublimation rate is zero. As long as the chamber pressure is higher than the pressure at the interface P_i sublimation does not occur. Once sublimation kicks in, a gradual increase of L_{dried} is observed. The evolution of the chamber pressure and the shelf temperature is presented in figure 2 (logarithmic axes on the right). A steep decrease of the chamber pressure can be noticed. The process starts at ambient pressure and during the first 10 minutes the pressure is decreasing exponentially. Initially, the shelf pressure is kept at -45 °C, subsequently the optimal value for T_s is relatively high, without the risk that the temperature at the sublimation front is exceeded. After this increase, the shelf temperature should be gradually decreased in order to meet the quality standards. Due to the resolution that has been chosen for the grid-search, the evolution of P_c and T_s is step-wise instead of a smooth evolution. The resolution for the grid-search has been limited in order to be able to perform the simulation study in a reasonable time frame. The sublimation rate, presented in figure 3 is initially equal to zero, then evolves to a maximum value, after which it exponentially decreases till it reaches a steady-state value.

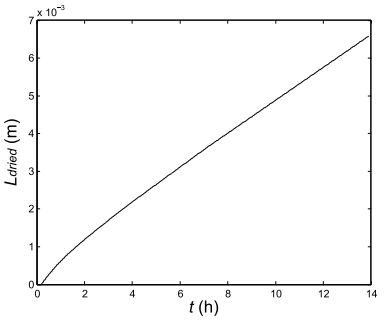

Figure 1: The evolution of L_{dried} in time using optimal values for P_c and T_s

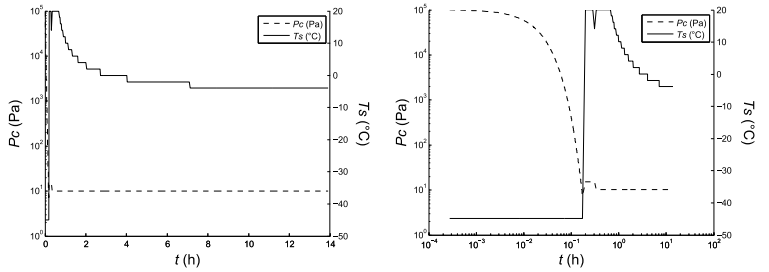

Figure 2: The evolution of P_C and T_s in time. The figure to the right zooms in on the initial time steps by using logarithmic axes

5. Conclusion & further perspectives

The use of a mechanistic model to develop the Design Space is interesting and a cost-effective approach, as it requires no energy and material. However, the model should be a reliable representation of the reality before the model predictions are useful to draw conclusions. Therefore, a

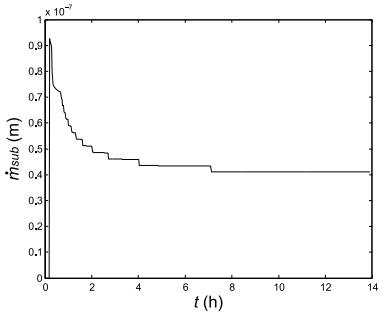

Figure 3: The evolution of $\dot{m}_{sub}$ in time

validation of the model using experimental data is required. Once a validated model is available, it can be used to gather process knowledge and to develop the Design Space.
Additionally, the freeze-drying process will be dependent on the product that is freeze-dried and its concentration and the used equipment. These elements have an influence on the parameters used to calculate the model predictions, and as such, have an effect on the calculated Design Space. An uncertainty analysis is useful to incorporate the impact of parameter uncertainties on the predictions. In order to guarantee the final product quality of the freeze-dried product, the temperature at the sublimation front should be kept under the critical temperature, which is again product-dependent. Therefore, instead of using a shelf temperature and chamber pressure which maximize the sublimation rate, it is recommended to incorporate the uncertainties and work at the 5% percentile. In this case, there is 95% probability that the true sublimation rate will be higher in reality, but only 5% probability that the true sublimation rate is higher. As such, the probability that the critical temperature at the sublimation front is exceeded is relatively low.

References

Burns, L., 2009. The biopharmaceutical sector's impact on the US economy: Analysis at the national, state and local levels. Tech. rep.

Constantino, H., Pikal, M., 2004. Lyophilization of Biopharmaceuticals. AAPS Press, Arlington.

Fissore, D., Pisano, R., Barresi, A., 2011a. Advanced approach to build the design space for the primary drying of a pharmaceutical freeze-drying process. J. Pharm. Sci. 100 (4922-4933).

Fissore, D., Pisano, R., Barresi, A., 2011b. On the methods based on the pressure rise test for monitoring a freeze-drying process. Dry. Technol. 29, 73–90.

Gieseler, H., 2012. Insights in lyophilization. In: Current best practices & research trends. Antwerp.

Kasper, J., Friess, W., 2011. The freezing step in lyophilization: physico-chemical fundamentals, freezing methods and consequences on process performance and quality attributes of biopharmaceuticals. Eur. J. Pharm. Biopharm. 78, 248–263.

Murphy, D., Koop, T., 2005. Review of the vapour pressures of ice and supercooled water for atmospheric applications. Q. J. R. Meterol. Soc. 131, 1539–1565.

Patel, S., Chaudhuri, S., Pikal, M., 2010. Choked flow and importance of Mach I in freeze-drying process design. Chem. Eng. Sci. 65, 5716–5727.

Pikal, M., 2002. Freeze drying. In: Encyclopedia of pharmaceutical technology. pp. 1299–1326.

Tang, X., Nail, S., Pikal, M., 2006. Evaluation of manometric temperature measurement, a process analytical technology tool for freeze-drying: Part II Measurement of dry-layer resistance. AAPS PharmSciTech 7, 1–8.

Krist V. Gernaey, Jakob K. Huusom and Rafiqul Gani (Eds.), 12th International Symposium on Process Systems Engineering and 25th European Symposium on Computer Aided Process Engineering.
31 May – 4 June 2015, Copenhagen, Denmark

Plant-Wide Control of a Continuous Tablet Manufacturing for Quality-By-Design Based Pharmaceutical Manufacturing

Ravendra Singh, Fernando Muzzio, Marianthi Ierapetritou, Rohit Ramachandran

Engineering Research Center for Structured Organic Particulate Systems (C-SOPS), Department of Chemical and Biochemical Engineering, Rutgers University, Piscataway, NJ 08854, USA
ravendra.singh@rutgers.edu

Abstract

The pharmaceutical industry is strictly regulated, where precise control of the end product quality is necessary to ensure the efficiency of the drug products. In this work, a combined feed-forward/feedback (FF/FB) control system has been developed for a direct compaction continuous tablet manufacturing pilot-plant. The feed-forward controller takes into account the effect of process disturbances and raw material variability proactively while the feedback control system ensures the end product quality consistently. The feed-forward control loop is based on real time monitoring of the powder bulk density while the feedback control loops are based on the powder level of instrumented hopper, drug concentration, tablet weight and hardness. Powder blend density has significant effects on the end product quality of the pharmaceutical tablets and therefore has been selected as the feed-forward variable. The coupled FF/FB control system ensures minimum variability in the final product quality irrespective of process and raw material variations.

Keywords: Continuous manufacturing, Control, PAT, QbD, feed-forward.

1. Introduction

Continuous pharmaceutical manufacturing integrated with PAT (Process Analytical Technology) provides a suitable platform for the automatic control of the end product quality as desired by the QbD (quality by design) paradigm, that is mandated by the regulatory authorities (Singh et al., 2014a, 2014b). The precise control of the quality of the pharmaceutical product involving solid dosage forms requires corrective actions on the process/raw material variability before they can influence the product quality. A feedback standalone strategy is therefore insufficient to provide efficient control of the pharmaceutical process. Therefore, this motivates the need for a feed-forward control system to be coupled with the feedback control system. Variations in raw material properties (e.g. particle size), feeder hopper level, amount of lubrication, milling and blending action, applied shear in different processing stages can affect the blend density significantly and thereby tablet weight, hardness, and dissolution. Therefore, the inline real time monitoring of the blend density and its incorporation into the control system so that it cannot affect the end product quality is highly desired.

In the last few years, very few attempts have been made toward the control of a continuous tablet manufacturing process utilizing feedback control algorithm. Singh et al. (2012a) have designed a feedback control system for a roller compaction route of the

continuous tablet manufacturing process. Singh et al. (2013) have developed a model predictive control system (MPC) for direct compaction continuous tablet manufacturing process. Singh et al. (2014a) have implemented a MPC based feedback control system into the direct compaction tablet manufacturing pilot-plant. The performance of the implemented feedback control system utilizing PAT tools have been also demonstrated (Singh et al., 2014b). The control system for wet granulation route of continuous tablet manufacturing process has been also proposed (Singh et al., 2014c). García-Munoz et al. (2010) have proposed a feed-forward controller using latent variable regression methods. However, no attempt has been made to design a plant-wide combined feed-forward/feedback control system for an integrated continuous tablet manufacturing process.

In this work, for the first time a plant-wide combined feed-forward/feedback (FF/FB) control strategy for direct compaction tablet manufacturing process has been developed, tablet weight and hardness control loops have been decoupled and an NIR (Near Infrared) based real time monitoring of the blend density for feed forward control has been proposed.

2. Systematic framework for design and implementation of the combined feed-forward/feedback control system

The design and implementation of the combined feed-forward/feedback control system involves ten hierarchical steps as shown in Figure 1. The starting point is to define the problem in terms of process and product quality specifications. Then the control relevant transfer function process model needs to be developed through step response analysis (steps 1 - 2). The next step is to design the control system (step 3). The design of the control system involves identification of control variables, pairing of control variables with corresponding manipulating variables, identification of the control variables for which a cascade loop is needed and for which single loop is sufficient, and pairing of the control variables with real time inline/online monitoring tools (Singh et al., 2009). Subsequently, the process variables that need to be fed-forward to the control system need to be identified in step 4. Sensitivity analysis can be used to identify the feed-forward process variables. For each identified feed-forward process variables the real time inline/online monitoring tools need to be identified. In step 5, a transfer function model relating a feed-forward variable with corresponding control variable need to be developed. Similarly, in step 6 a transfer function model relating an actuator with the corresponding control variables need to be developed. The feed-forward controller can then be implemented into the process model (step 7). In step 8, feedback control loops need to be implemented. The performance of the combined feed-forward/feedback control system can be analyzed in step 9. If the performance is satisfactory then it can be implemented into the plant in step 10 otherwise steps 5-9 need to be repeated until the satisfactory performance is achieved. Commercially available control platform (e.g. DeltaV (Emersions), PCS7 (Siemens)), PAT data management tools (e.g. synTQ (Optimum), SiPAT (Siemens)), Chemomatric tools and OPC communication protocol can be used to implement the control system. After experimental verification of the performance the combined control system can be used for regular plant operation and control.

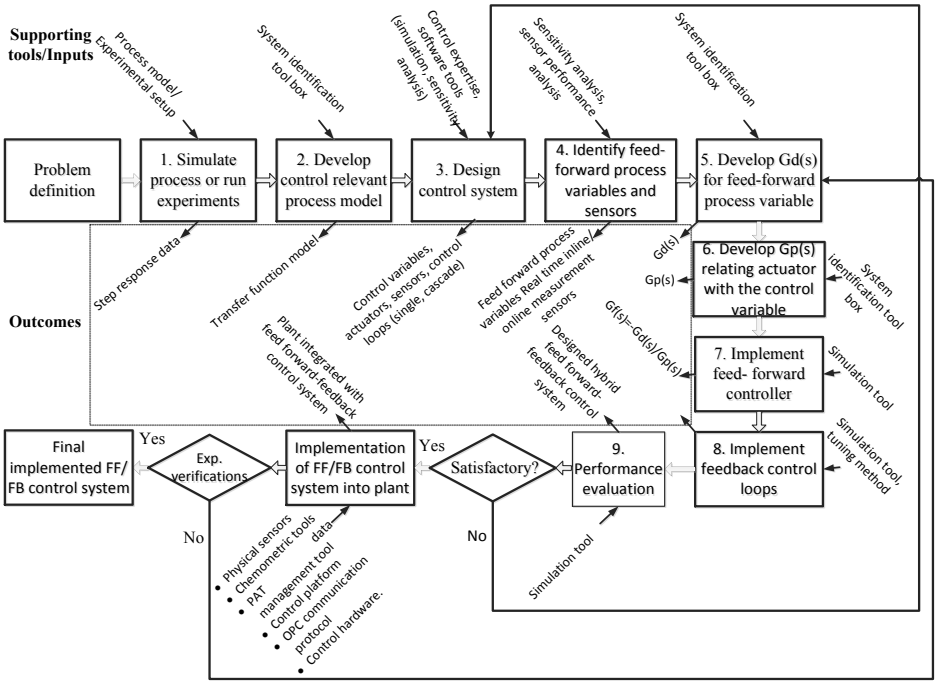

Figure 1: Systematic framework for design of combined feed-forward/feedback control system

3. Continuous tablet manufacturing process and pilot-plant

A continuous direct compaction tablet manufacturing pilot-plant has been installed and situated at C-SOPS, Rutgers University. The snapshot of the pilot-plant is reported in Singh et al. (2014a). The pilot-plant is built at three levels of different heights to take advantage of gravitational material flow. The top level is used for feeder placement and powder storage, the middle level is used for delumping and blending, and the bottom level is used for tablet compaction. There are three gravimetric feeders -with the capability of adding more- that feed the various formulation components (active pharmaceutical ingredient (API), excipient, lubricant). A co-mill is also integrated after the feeder hopper primarily for de-lumping the powders and creating contact between components. The co-mill eliminates any large, soft lumps within the powder. The lubricant feeder is added after the mill to prevent over lubrication of the formulation in the mill. These feed streams are then connected to a continuous blender within which a homogeneous powder mixture of all the ingredients is generated. Subsequently, the outlet from the blender is fed to the tablet press via a rotary feed frame.

4. Plant-wide control architecture of continuous tablet manufacturing process

The local level controllers are inbuilt in each feeder in order to control the powder flow rate. A ratio controller has been added that provides the flow rate set points of API, Excipient and Lubricant feeders for a given total flow rate and API composition. Six supervisory control loops have been then added. First loop is for feed-forward control (FFC) which takes the corrective action on variations in powder bulk density. NIR

sensor together with chemometric tools have been used for real time inline monitoring of the powder blend density. The signal of powder blend density has been then sent to the feed-forward controller that manipulates the fill cam depth of the tablet press proactively. The second loop has been added to control the main compression force of the tablet press. This control loop is in cascade arrangement with a master controller (loop 3) specifically designed to control the tablet weight. The input of this master controller is weight and it generates the set point of main compression force. The loop four has been designed to control the tablet hardness by manipulating the punch displacement. Checkmaster (Fette) has been used for real time monitoring of tablet weight and hardness. This control mechanics allows controlling the tablet weight and hardness independently. The control loop 5 has been added to control the powder level in instrumented hopper. Webcam has been used for online monitoring of powder level. The drug concentration has been controlled through 6th control loop. The NIR sensor has been used for inline real time monitoring of drug concentration. The powder bulk density and drug concentration has been monitored using a single NIR probe. Two PLS models have been used to predict the powder bulk density and drug concentration separately. In order to implement the designed feed-forward/feedback control into the pilot-plant, the signal from the NIR sensor (raw spectrums) has been sent to a chemometric tool that utilizes the NIR calibration models for blend density and drug concentration and real time prediction tool to generate the signals of the control variables in real time. The generated signals are then sent to a commercially available control platform via an OPC communication protocol where the combined FF/FB control loop has been implemented. The blend density is the input for the feed-forward controller while the blend composition together with powder level, tablet weight and hardness are the inputs of the feedback control system. The actuators generated from the control platform are then communicated with the plant through fieldbus devices and serial ports.

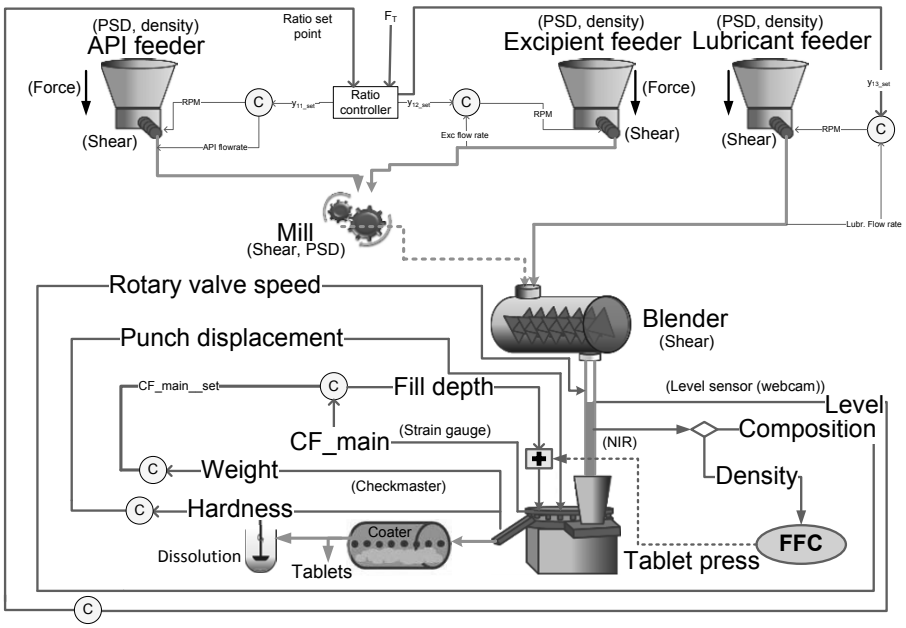

Figure 2: Plant-wide combined feed-forward/feedback control architecture.

5. Results and discussion

The tablet press has been considered to demonstrate the performance of combined feed-forward/feedback control system. The ability of the control system to track the set point and reject the disturbances has been evaluated. A step change in the hardness set point has been introduced while keeping the tablet weight set point at constant value. The powder blend density acts as the disturbance and can affect the tablet weight and hardness significantly. Random disturbances have been added to the blend density throughout the operation. A step change in the blend density has been also introduced at t = 2500 s in order to analyze its effects. Figure 3 shows a closed-loop response of the tablet hardness under two control strategies. As shown in the figure, under the combined control strategy, the feed-forward controller rejects the variation in the blend density before it can affect the tablet hardness. Therefore, in this case, the tablet hardness has been controlled better. A significant variation in the achieved hardness can be seen in case of feedback only control scheme. It should be noted that the hardness variation is more at t = 2500s where the step change in the blend density has been introduced. The results shown in Figure 3 demonstrate the advantages of coupling feed- forward controller with the feedback control system.

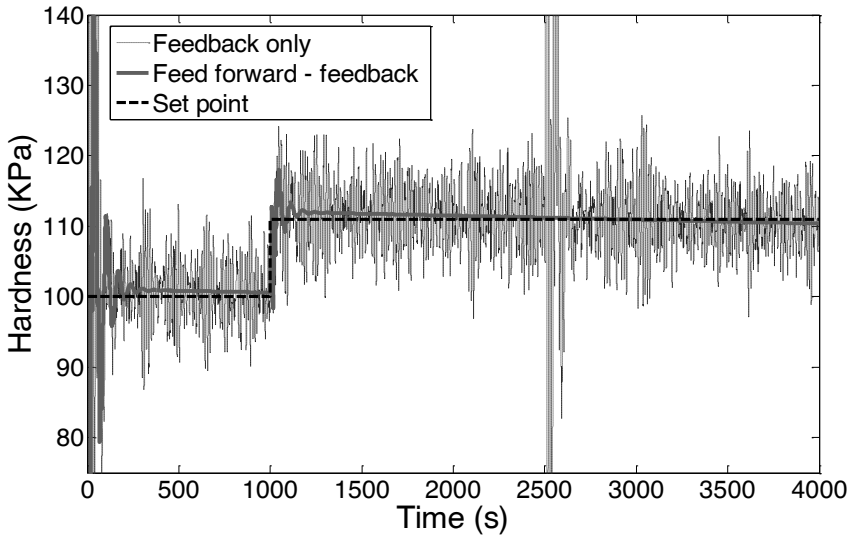

Figure 3: Performance evaluation of combined feed-forward/feedback control strategy.

The closed-loop response of the tablet weight under the combined feed-forward/feedback control strategy and only feedback control strategy is shown in Figure 4. As shown in the figure, the variation in tablet weight is less under combined control scheme in compare to only feedback control scheme. A small oscillation can be seen at t =1000 s where the step change in the hardness set point has been made and this is essentially because the hardness and weight control loops are highly interactive. At t = 2500 s, a step change in the blend density has been introduced but the combined feed-forward/feedback control system has efficiently rejected its effect and thereby a consistent desired tablet weight has been achieved. Similarly, the performance of other combined FF/FB control-loops has been analysed and found to be satisfactory. The tablet content uniformity depends on powder blend uniformity that should be controlled at blending operation (Singh et al., 2014b). For product acceptance, the critical quality

attributes should be within a specified control limits (Singh et al., 2012). The feed-forward controller can only compensate the variation in powder bulk density (or any other variables) within the process capability limits. The main challenges associated with implementation of FF/FB control strategy is the complexity associated with real time monitoring of powder bulk density and control variables.

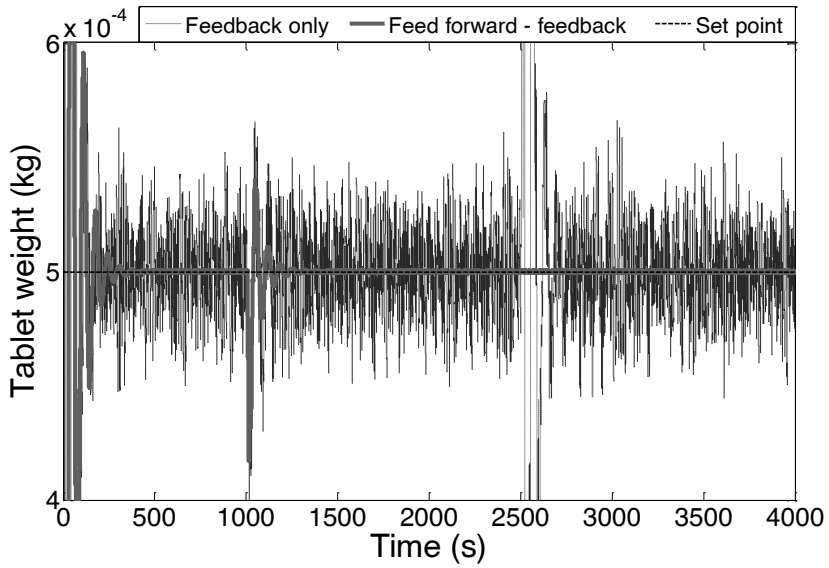

Figure 4. Performance evaluation of combined feed-forward/feedback control strategy.

6. Conclusions

A plant-wide control system has been developed for a direct compaction continuous tablet manufacturing pilot-plant. The control architecture consists of integrated feed-forward and feedback (FF/FB) control loops. The performance of the combined FF/FB control strategy is found to be better in comparison to the feedback only control strategy and therefore demonstrates potential to improve industrial pharmaceutical tablet manufacturing operations. The future work includes the implementation of FF/FB control strategy in our pilot-plant facility.

References

R. Singh, A. Sahay, F. Muzzio, M. Ierapetritou, R. Ramachandran, 2014a, Computers & Chemical Engineering, 66, 186-200.

R. Singh, A. Sahay, K. M. Karry, F. Muzzio, M. Ierapetritou, R. Ramachandran, 2014b, International Journal of Pharmaceutics, 473, 38–54.

R. Singh, D. Barrasso, A. Chaudhury, M. Sen, M. Ierapetritou, R. Ramachandran, 2014c, Journal of Pharmaceutical Innovation, 9, 16-37.

S. García-Munoz , S. Dolph, H. W. Ward II, 2010, Computers and Chemical Engineering, 34, 1098-1107.

R. Singh, K.V. Gernaey, R. Gani, 2009, Computers & Chemical Engineering, 33(1), 22-42.

R. Singh, M. Ierapetritou, R. Ramachandran, 2013, European Journal of Pharmaceutics and Biopharmaceutics, 85(3), Part B, 1164-1182.

R. Singh, M. Ierapetritou, R. Ramachandran, 2012, International Journal of Pharmaceutics, 438 (1-2), 307-326.

Krist V. Gernaey, Jakob K. Huusom and Rafiqul Gani (Eds.), 12th International Symposium on Process Systems Engineering and 25th European Symposium on Computer Aided Process Engineering.
31 May – 4 June 2015, Copenhagen, Denmark

Systematic Retrofitting Methodology for Recrystallization of Thermally Unstable Active Pharmaceutical Ingredients

G. Casola,[a,b*] H. Sugiyama,[b] S. Yoshikawa,[c] H. Nakanishi,[c] M. Hirao[a]

[a]*Department of Chemical System Engineering*, *The University of Tokyo*, *7-3-1 Hongo*, *Bunkyo-ku*, *113-8656 Tokyo*, *Japan*
[b]*Institute for Chemical and Bioengineering*, *ETH Zurich*, *8093 Zurich*, *Switzerland*
[c]*Shionogi & Co., Ltd*, *7 Moriyama*, *Nishine*, *Kanegasaki-cho*, *Isawa-gun*, *029-4503 Iwate*, *Japan*
giocasola@hotmail.com

Abstract

Process optimization has become an increasingly important issue in the pharmaceutical industry in recent years. Due to the high competition, companies are obliged to make quick decisions, with sometimes ending up in sub-optimal solutions. In this paper, we propose a systematic retrofitting methodology for process optimization as method for the optimization of post-design pharmaceutical processes. The use of the combination of measurements, process modeling and computer-aided simulation provides a structured procedure for understanding and quantifying the improvement potential of the plant. The methodology consists of five tasks: gain process understanding (I), create process model (II), recognize constraints and optimization parameters (III) optimize the process model (IV). These tasks are supported by an interpretation/verification/validation step (X). The primary target of this methodology is the recrystallizatoin of thermally unstable Active Pharmaceutical Ingredients (APIs) The secondary target is to elucidate the many features contained in the modeling process. As a case study, the method was demonstrated in an actual plant with dissolution, filtration and crystallization (DFC) units. After performing the five steps, we could identify a better temperature and flow rate of the process with a 0.9% improvement of API yield.

Keywords: Pharmaceutical process, retrofitting, API sterilization, optimization, reactive dissolution

1. Introduction

Process optimization has become an increasingly important issue in the pharmaceutical industry in recent years. Expiration of patents protecting the companies from the competition and increase of the R&D expenses cause economic pressures for many companies. The strong competition forces the realization of the feasible solution in a short time, frequently leading to sub-optimal design in many cases. The high value of the products, especially in pharmaceutical manufacturing, furthermore justifies poor optimization in the first steps of creating a new production line. Currently simulation and process modeling have a secondary importance, however, the pharmaceutical industry could profit from a more engineering-based analysis, including computer simulation. Modeling and problem-approaching skills are crucial for the success of an optimization (Troup and Georgakis, 2013), leading to time and cost reductions. A limitation here is the presence of tough constraints, which need to be satisfied for ensuring the product

quality, e.g., Good Manufacturing Practices (GMP) and the condition set by the Drug and Food Administration (FDA). During the creation and optimization of a process model these constraints have always to be considered. Srinivasan et al. (2002) offered an overview of analytical and numerical technics for the optimization of general batch processes. In a second study, Srinivasan et al. (2003) discussed the role of measurements and their application in the creation, validation and implementation of process models. In this work we aim to develop a systematic methodology capable to assist the retrofitting of pharmaceutical processes. The methodology consists of five tasks: gain process understanding (I), create process model (II), recognize constraints and optimization parameters (III) optimize the process model (IV). These tasks are supported by an interpretation/verification/validation step (X). Altough the entire procedure is structured in a general manner, the second task is the most prominent and specialized for the purification of the crude and thermally unstable API in the crystalline form. The methodology is applied to an industrial case study to prove its effectivness.

2. Methodology

The flowchart (Figure 1, left) shows the sequence of tasks to be followed, while tackling with the model creation and optimization of a running plant. Gain understanding about the plant and its behavior is necessary to ensure the creation of a valuable process model. Measurements coupled with path-flow decomposition (PFD) (Figure 1, right) help in this task (Task I). The PFD facilitates the visualization of the material flow of the process. Task II is responsible for the reproduction of the processes as mathematical models, aiming to imitate the current plant. Subsequently, the model created in Task II is subjected to optimization (Task IV). In order to perform Task IV, the necessary constraints and the optimization parameters have to be identified and defined (Task III). Task X consists of interpretating and verifying the results of each task and validating the process models and the assumption made during the model formulation. Task X is connected to all four tasks and represents a decisional step, which permits to re-evaluate the decisions or eventually re-iterate the tasks.
The primary target of this methodology is the recrystallization plant of crude APIs with dissolution, filtration and crystallization (DFC) operations. The details will be presented in the next section.

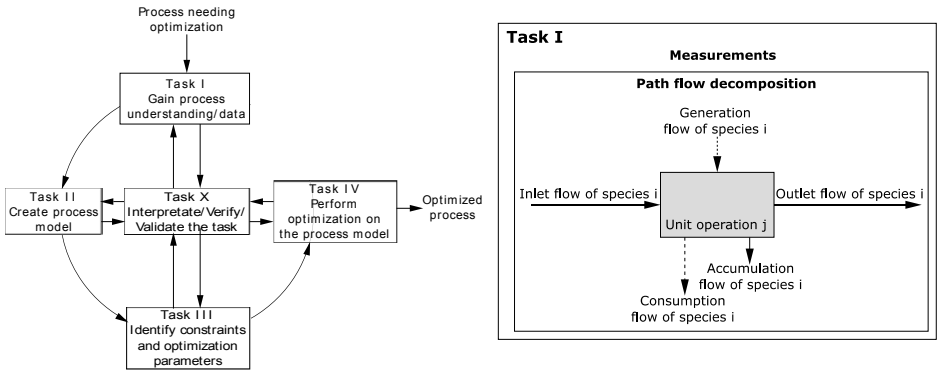

Figure 1: Flow diagram showing the procedural order (left) Insight on Task I showing a generic path flow decomposition (right).

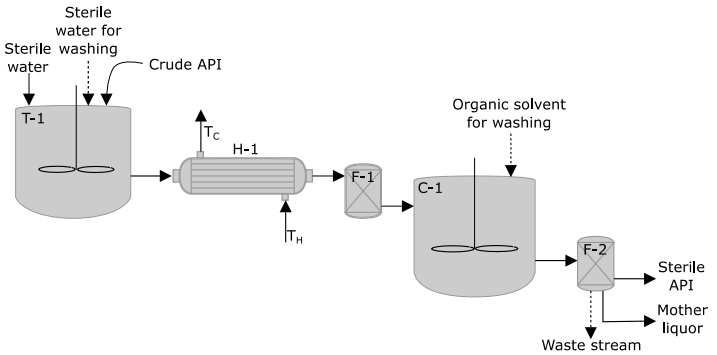

Figure 2: Sketch of the plant performing the dissolution-filtration-crystallization (DFC) process

3. Case Study: Purification of solid drug by DFC process

3.1. Gain process understanding/data

Figure 2 shows a typical process of a DFC plant, consisted of a charge tank (T-1), a heat exchanger (H-1), a filtration unit (F-1), a crystallizer (C-1) and a filter/dryer (F-2). When the API is dissolved in the liquid phase—i.e. over the entire process before the crystallization an endothermic degeneration reaction occurs, reducing the yield of the API. These unwanted reactions are reppresented by the following equations:

$$\text{API} \rightarrow \text{B} \tag{1}$$

$$\text{API} + \text{B} \rightarrow \text{C} \tag{2}$$

Mass balance, temperature profile and particle size distribution (PSD) were measured. The crystals are cylindrical shaped with a narrow PSD (within two order of magnitude). The solubility of the API in water and its reaction rate were characterized. The degradation is a first order reaction with the kinetic constant k_{deg} [s^{-1}]. From the PFD it was possible to recognize five different phenomena affecting the mass balance of the API: reaction coupled dissolution of the API crystals inside H-1, adsorption of the API on the filtration material, reaction during the filling of C-1, crystallization and accumulation of the API along the equipment. Measurements and PFD visualization enabled the partial closure of the mass balance. The mass deficit resulting from the mass balance was attributed to the reaction; the assumption was subsequently confirmed by the result of the modeling, which enabled the closure of the mass balance.

3.2. Create process model

The model aims to imitate the reality as accurate as possible. The dissolution of the crystals in medium-turbulent environment inside T-1 was modeled as follows:

$$\frac{dm}{dt} = -kM_W S(c_s - c) \tag{3}$$

Equation 3 describes the mass transfer between the fluid and the solid phase, where m [kg] represents the mass of the crystal, k [m s^{-1}] the mass transfer coefficient, S [m^2] the surface of the crystal, c [mol m^{-3}] the actual API concentration in the bulk liquid phase, c_s [mol m^{-3}] the saturation concentration of the API and M_W [kg mol^{-1}] the molecular weight of the API. Eq. 3 was reformulated, resulting in the following equation:

$$\frac{dl}{dt} = -\frac{2kM_W}{\rho}\frac{r(l)+l}{r(l)+2l\frac{dr}{dl}}(c_s - c) \tag{4}$$

Equation 4 describes the rate of change of the characteristic length of the crystal, where l [m] represents the height of the crystal, r [m] its radius and ρ [kg m^{-3}] its density.
A mass transfer correlation (Eq. 5), describing the dissolution of cylindrical crystals in a turbulent fluid environment (Bernstein and Churchill, 1977) was employed to solve the ordinary differential equation (ODE) Eq. 4, providing the characteristic length profile along H-1.

$$k = \frac{D}{l}\left[0.3 + 0.62 \cdot Re_D^{0.5} \cdot Sc^{0.33} \cdot \left(1 + \left(\frac{Sc}{0.4}\right)^{-0.66}\right)^{-0.25} \cdot \left(1 + \left(\frac{Re_D}{282000}\right)^{0.63}\right)^{0.8}\right] \tag{5}$$

The parameters Re_D, Sc and D [m^2 s^{-1}] are the particle Reynolds and Schmidt numbers and the molecular diffusion coefficient of the API, respectively.
The crystal length profile was used to characterize the size exclusion phenomena in the filter (F-1). A constant crystal aspect ratio was assumed. The constant B was defined as the diameter to height ratio and was implemented in the population and mass balance, resulting in the following system of ordinary differential equations (SODE)

$$\begin{cases} \frac{dl_i}{dt} = -\frac{2k \cdot M_W}{\rho}\,\frac{(2B+1)}{3}\,(c_s - c); & i = 0,1,2,3,\ldots \\ \frac{dc}{dt} = \frac{\sum_i^M (l_i^2 \cdot N_i \cdot k_i)}{V} \cdot \pi\,\frac{(2B+1)}{2B^2}(c_s - c) - k_{deg} \cdot c \end{cases} \tag{6}$$

The parameter M [–] represents the number of different crystals sizes, the index i indicates the crystal initial size, N_i is the number of crystal of every type of crystals, V [m^3] is the volume of the batch. The measured PSD of the crude product was used as initial values of the sizes l_i [m], to solve the SODE. The slurry exiting T-1 enters in the heat exchanger (H-1), in which the crystals dissolve. The dissolution in this unit was according to Eqs. 3, 4 and 6, considering the mass transfer coefficient proposed by Bedingfield and Drew (1950) (Eq. 7). This mass transfer correlation describes the mass transfer between solid and liquid phase for a cylindrical crystal in turbulent continuous flow:

$$k = 0.281 \cdot v_f Re_D^{-0.4} Sc^{-0.56} \tag{7}$$

The parameter v_f [m s^{-1}] is the fluid velocity in the unit. The temperature profile inside H-1 was modelled with a one-shell, one-tube heat exchanger model (Welty, et al. 2007). The model takes in consideration the heat transfer between the heating and the process fluid along the wall separating the two phases, considering the heat transfer inside the wall as well.

$$\begin{cases} \frac{d^2T_w}{dx^2} = 4 \cdot \frac{(U_s d_o \cdot (T_w - T_s) - U_t d_i \cdot (T_t - T_w)}{k_w \cdot (d_o^2 - d_i^2)} \\ \frac{dT_t}{dx} = \frac{\pi d_i U_t (T_w - T_t)}{c_{p,t} F_t} \\ \frac{dT_s}{dx} = \frac{\pi d_o U_s (T_s - T_w)}{c_{p,s} F_s} \end{cases} \tag{8}$$

The operation properties were defined through the boundary condition. In fact the heat exchanger was operated counter-currently.

$$\begin{cases} T_s(L_{HEX}) = T_H \\ T_t(0) = T_{in} \\ \frac{dT_w}{dx}(0) = 0 \\ \frac{dT_w}{dx}(L_{HEX}) = 0 \end{cases} \tag{9}$$

In Eqs. 8 and 9 T_w [K] is the temperature of the tube-shell wall, T_t [K] the temperature of the liquid inside the tube and T_s [K] the temperature inside the shell of the heat exchanger. The parameters d_o [m] and d_i [m] describe the outer and inner diameter of the tube, while L_{HEX} represents for the length of the heat exchanger. The parameters U_t [W m^{-2} K^{-1}], U_s [W m^{-2} K^{-1}] and k_w [W m^{-1} K^{-1}], are the overall heat transfer coefficient of the tube, shell and the thermal conductivity of the wall, respectively. The coefficients $c_{p,s}$ [J kg^{-1} K^{-1}], $c_{p,t}$ [J kg^{-1} K^{-1}] and the variables F_t [kg s^{-1}] and F_s [kg s^{-1}] are the heat capacity of the fluid in the shell and in the tube, and their flow rates, respectively. Finally T_{in} [K] and T_H [K] are the temperature of the process stream at the inlet of the heat exchanger and the temperature of the heat medium at its inlet. The parameters U_t, U_s, and k_w were obtained through fitting to the measured data. The mass balance measurements performed on the chemical filter revealed the accumulation of API in the unit, enabling the calculation of its efficiency, which was 99.4%. The reaction inside the piping was modeled with an ideal plug flow reactor model. The filling up of the crystallizer (C-1) was represented as homogeneous chemical reaction in a semi-batch reactor. Due to lack of measured data, the crystallization process was modeled with an empirical correlation relating the amount of by-product at the beginning of the crystallization with the total amount of crystals obtained in this process. The amounts of product ending up in the wastewater and in the organic washing streams were modelled in the similar way. The total process had a loss of 10% with respect of the initial amount of crude API. The measurement performed on the plant showed the same loss supporting the reliability of the model. Figure 3, left shows the position of the loss along the plant

3.3. Identify constraints and optimization parameters

The pharmaceutical character of the process led to the consideration of some constraints. The GMP and the quality of product could not be affected by an intervention on the plant. Therefore in this case study, the filtration and the crystallization units were considered to be unchangeable due to their impacts on the product quality. The remaining units and parameters were considered to be modifiable, with exception for the current pipe diameter. The sensitivity analysis performed on the model recognised the process stream flow rate F [–] and the temperature of the heating medium T_H [–] as reasonable parameters for process optimization.

3.4. Perform optimization on the process model

The model created in the previous task was optimized (Eq. 10) with an aim of increasing overall API yield.

$$max\big(f(\boldsymbol{x})\big) \qquad with\ \ \boldsymbol{x} = [x_1, x_2]^T$$
$$h(\boldsymbol{x}) < L_{\text{pore}} \tag{10}$$
$$0 < x_2 < F_{max}$$
$$x_1 < T_{H,max}$$

The variables x_1, x_2 and $h(\boldsymbol{x})$ are the optimization parameters T_H and F, and the function describing the size of the crystals at the inlet of the filtration unit, respectively. The parameters L_{pore}, F_{max} and $T_{H,\,max}$ are the boundary values characterising the maximal crystal size, the flow rate and the heating medium temperature, respectively.

4. Result

In Figure 3, right, all the values are normalized with respect to the current parameters and yield, i.e., base case to indicate only the improvements. The optimality is denoted

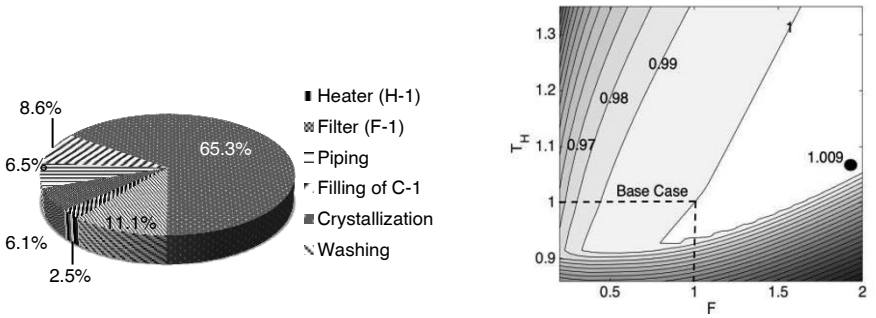

Figure 3: Portion of production relative to the lost position (left). Optimization results (right).

by the dot and shows 0.9% of improvement with respect to the base case showed by the intersection of the dashed lines. Due to the proximity of the current process to the optimum, the process holds a contained margin of improvement within the constraints. From Figure 3, right it is notable that T_H has a bigger influence if compared to F. This effect is justified by the exponential dependency of the temperature of the saturation concentration of the API. Indeed at temperatures lower than the current one, the amount of undissolved crystals increases, decreasing the yield drastically. F plays an important role only at high temperatures; influencing the time, during which the API undergoes the degeneration reaction.

5. Conclusions and Outlook

In this paper we presented a systematic retrofitting methodology applied on a process of recrystallization of a thermally instable API. The results provided a detailed mathematical model of the process. This was subsequently employed for the optimization of the production of sterile API. The mathematical design of the reactive dissolution of an organic API crystals characterized by a PSD is an additional novelty brought by the paper. Moreover the use of an accurate model describing the temperature profile inside the heat exchanger is an additional feature of the model. Furthermore the consideration of specific aspects like GMP and product quality increases the applicability of the methodology in the retrofitting of pharmaceutical production plants. In future studies the optimization could be enlarged to the plant layout, performing therefore a mixed integer non-linear programming (MINLP) optimization. Indeed the introduction of intercooling unit could reduce the loss of API along the piping, therefore increasing the overall yield of the process.

References

C. Bedingfield, T. Drew, 1950, Analogy between heat transfer and mass transfer: A psychrometric study, Ind. Eng. Chem. Res. 42(6), 1164–73.
M. Bernstein, S. Churchill, 1977, A Correlating Equation for Forced Convection From Gases and Liquids to a Circular Cylinder in Crossflow, J. Heat Transfer 99(2), 300–6.
B. Srinivasan, D. Bonvin, E. Visser, S. Palanki, 2003, Dynamic optimization of batch processes II. Role of measurements in handling uncertainty, Comput. Chem. Eng. 27(1), 27–44.
B. Srinivasan, D. Bonvin, S. Palanki, 2003, Dynamic optimization of batch processes I. Characterisation of the nominal solution, Comput. Chem. Eng. 27(1), 1–26.
M. Troup and C. Georgakis. 2013, Process systems engineering tools in the pharmaceutical industry, Comput. Chem. Eng. 51(Special Issue), 157–71.
J. Welty, C. Wicks, R. Wilson, G. Rorrer, 2008, Fundamentals of Momentum Heat, and Mass Transfer, 5th Edition, Wiley, New York, United States of America.

Krist V. Gernaey, Jakob K. Huusom and Rafiqul Gani (Eds.), 12th International Symposium on Process Systems Engineering and 25th European Symposium on Computer Aided Process Engineering.
31 May – 4 June 2015, Copenhagen, Denmark

Modelling of Crystallization of Solid Oral Drug Forms in a Dropwise Additive Manufacturing System

Elçin Içten*, Zoltan K. Nagy, Gintaras V. Reklaitis

School of Chemical Engineering, Purdue University, West Lafeyette, IN, 47906, USA
**eicten@purdue.edu*

Abstract

Melt-based solid oral drug forms are produced using a dropwise additive manufacturing process for pharmaceuticals. A model based on non-isothermal Avrami kinetic equation is developed to model the solidification and crystallization processes of the drug deposits under different cooling profiles using temperature dependent crystallization kinetics. Using the proposed model, the temperature profiles leading to the desired solid-state parameters such as the minimum mean size are determined.

Keywords: crystallization kinetics, solidification, temperature control, drop on demand

1. Introduction

Traditionally, the pharmaceutical industry uses batch processes to manufacture pharmaceutical products, which provide significant challenges for the industry. In recent years, US Food and Drug Administration introduced the Quality by Design approach and Process Analytical Technology guidance to encourage innovation and efficiency in pharmaceutical development, manufacturing and quality assurance. As part of this renewed emphasis on improvement of manufacturing, the pharmaceutical industry has begun to develop more efficient production processes, including the use of on-line measurement and sensing, real time quality control and process control tools. Under the US National Science Foundation supported Engineering Research Center for Structured Organic Particulate Systems (NSF ERC-SOPS), a dropwise additive manufacturing process for solid oral drug production has been developed as an alternative to conventional pharmaceutical manufacturing methods (Hirshfield, et al., 2014). This mini manufacturing process for the production of pharmaceuticals utilizes drop on demand (DoD) printing technology for automated and controlled deposition of melt-based drug formulations onto edible substrates (Içten, et al., 2014a). The advantages of DoD technology, including reproducible production of small droplets, adjustable drop sizing and flexible use of different formulations, enable production of individualized dosing even for low dose and high potency drugs. A supervisory control system, consisting of on-line monitoring, automation and closed-loop control, is implemented on the process, in order to produce individual dosage forms with the desired dosage amount and crystal morphology (Içten, et al., 2014b). Since the product morphology depends on the crystallization temperature, the drop solidification process following the drop deposition on the substrate should be controlled (Nagy and Braatz, 2012). This paper presents a modelling approach for the solidification and crystallization processes of the drug deposits using temperature dependent crystallization kinetics and cooling profiles monitored via an optical microscopy with a hot stage. Using the proposed model, the temperature profiles leading to the desired solid-state parameters such as the mean size can be optimized.

2. Production of Dosage Forms via Dropwise Additive Manufacturing

The dropwise additive manufacturing system consists of a precision positive displacement pump, xy-staging, a hot air based heating system, online imaging and sensing, and temperature, pump and stage controllers. Using this system, melt-based systems, i.e. co-melted polymer-drug systems, or solvent-based systems can be produced reproducibly. For the melt-based formulation, a low melting point polymer such as polyethylene glycol, in which the drug dissolves once the polymer becomes molten, is used. In order to maintain constant rheological properties of the printed formulation, temperature control is established on the whole process using a counter-current hot air based heating system and heating elements with PID controller units. After passing through the precision P/D pump, the drops are ejected through the nozzle and deposited onto an edible substrate. The xy-staging and synchronization logic allows precise drop positioning on the substrate while printing. The main process units and melt-based formulations deposited onto polymeric films are shown in Figure 1.

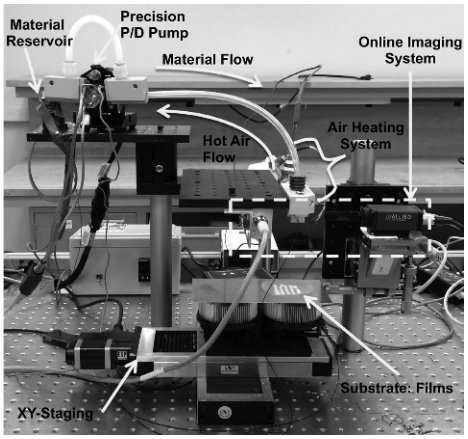

Figure 1. Dropwise Additive Manufacturing System and Melt-based Products

The temperature of the deposited drops is controlled indirectly by controlling the temperature of the substrate using a Peltier device placed beneath the substrate on the xy-stage. This allows control of the rate of solidification of melts and thus control of nucleation and crystallization phenomena. Precise control of the drop solidification process occurring on the substrate is very important since the crystallization temperature profile has a direct effect on product solid-state characteristics, influencing the dissolution properties and hence the bioavailability of the drug (Içten, et al., 2014b). Recently, Içten et al. (2014b) reported that applying a fast cooling rate of 10 °C/min to the deposits containing naproxen results in faster dissolution profiles compared to a slow cooling rate of 1 °C/min. Controlling crystallization temperature profiles can be used to enhance the solubility of dissolution limited drugs such as naproxen.

3. Modelling of Crystallization of Melt-based Dosage Forms

We have modelled the solid-state transformation of the melt-based solid oral dosages produced using the dropwise additive manufacturing process based on the modified Avrami (1939) kinetic equation. The model formulation consists of 15 % drug, naproxen, and 85 % polymer, PEG 3350. The drops are deposited at 60 °C and cooled to 20 °C using two different controlled cooling rates, 1 °C/min and 10 °C/min. In order

to determine the nucleation and growth kinetics experimentally, the solidification process under the same conditions are monitored using optical microscopy with a hot stage. The model formulation undergoes sporadic nucleation and spherical crystal growth. Determination of kinetic parameters is described in Section 4.

The Avrami equation describes isothermal solid-state transformation reactions based on nucleation and growth kinetics, which is widely used for various processes including metal, fat and polymer crystallization. The Avrami model equation for different growth geometries and types of nucleation is given by Eq.(1), where m_s is total mass of solids present in the system at a particular time, m_{max} is maximum total mass of solid at infinity, $(m_{max} - m_s)$ is mass of supercooled material that has not crystallized yet, t is crystallization time (min), s is the geometrical shape factor, I_c is the number of crystals per unit volume in the system (cm^{-3}), A_g is the area of crystal involved in growth (cm^{-2}).

$$\frac{\partial m_s}{\partial t} = (m_{max} - m_s) \cdot s \cdot I_c \cdot A_g \tag{1}$$

For spherical crystal growth, the geometrical shape factor is $s = 4\pi/3$ and crystal growth A_g is described by Eq.(2), where r is linear growth rate of crystal radius in time (cm) and g is growth rate constant for crystals radius per time (cm min^{-1}).

$$A_g = r^2 = g^2 \cdot t^2 \tag{2}$$

For sporadic nucleation, the change in the number of nuclei as a function of time, I_c is described by Eq.(3), where j is nucleation rate constant (cm^{-3} s^{-1}).

$$I_c = j \cdot t \tag{3}$$

In the dropwise additive manufacturing process, we apply different controlled temperature cooling profiles to the deposited drops in order to achieve the targeted dissolution behaviour (Içten, et al., 2014b). Temperature profiles applied to the drug deposits as a function of time and cooling rate are shown in Eq.(4), where the induction time is defined as a function of cooling rate $t_{ind} = t_{ind}(r_{cool})$.

$$T(t) = T_i - r_{cool} \cdot (t + t_{ind}) \tag{4}$$

In order to capture the effect of temperature on crystallization kinetics we use the modified Avrami equation, which is extended for non-isothermal kinetics by using temperature dependent nucleation and growth rates (Ozawa, 1971). Since the cooling profiles are represented as a function of time, the crystallization model we are using can be expressed as in Eq.(5), where both $j(T)$ and $g(T)$ are temperature and therefore time and cooling rate dependent.

$$\frac{\partial m_s}{\partial t} = (m_{max} - m_s) \cdot \frac{4}{3}\pi \cdot j(T) \cdot g(T)^2 \cdot t^3 \tag{5}$$

The growth rate constant is described as $g(T) = \alpha_1 \cdot T + \alpha_2$. The parameters α_1 and α_2 are a function of cooling rate which are determined experimentally as described in Section 4.2. The nucleation rate constant is described as $j(T) = \beta_1 \cdot T + \beta_2$. The parameters β_1 and β_2 are a function of cooling rate which are also determined experimentally as described in Section 4.3.

4. Determination of Kinetic Parameters

The kinetic parameters of the model formulation consisting of 15 % naproxen and 85 % PEG 3350 are determined experimentally, based on the crystallization behavior observed using an optical microscopy with a hot stage when a particular cooling profile is applied. The two cooling rates used in this study are 10 °C/min and 1 °C/min.

4.1. Induction Time

The cooling rates applied to the deposits effect the induction time. Induction times corresponding to 10 °C/min and 1 °C/min are determined experimentally as 2.2 min and 12 min, respectively. In the model development, we assumed that the changes in the induction times are linearly proportional to the change in the cooling rates.

4.2. Nucleation Rate

For a cooling rate, the change in the number of nuclei per volume as a function of time is determined from the images captured using optical microscopy at different times. For the same cooling rate, the parameters β_1 and β_2 are determined by fitting a linear relation to experimental data points. The nucleation rate parameters determined for the two cooling rates used in the experiments are shown in Figure 2a. Next these parameters are used to calculate the nucleation rate parameters β_1 and β_2 when cooling rates $10\ ℃/min \geq r_{cool} \geq 1\ ℃/min$ are applied to the deposits. Here it is again assumed that the changes in the parameters are linearly proportional to the change in the cooling rates.

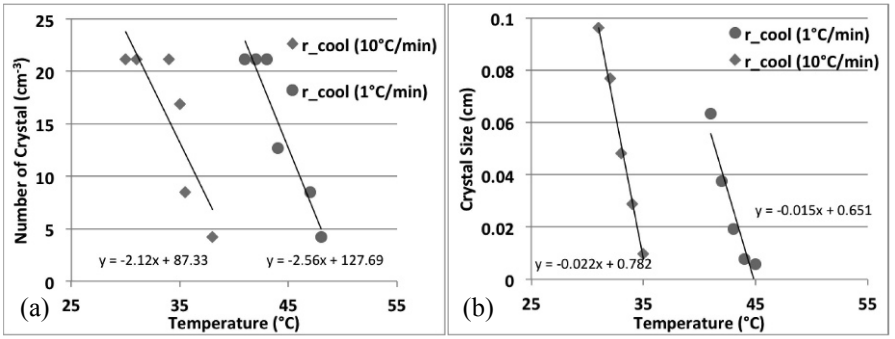

Figure 2. Crystallization Kinetics for Different Cooling Rates (a) Nucleation and (b) Growth

4.3. Growth Rate

For a particular cooling rate, the linear growth rate constants of crystal radius as a function of time is determined from the images captured through optical microscopy. The calculation of linear growth rate of crystal radius is depicted in Figure 3. White arrows represent the dynamic changes in the linear growth rate of crystal radius in consecutive images, when a cooling rate of 1 °C/min is applied to the deposits. By measuring the changes in the growth front throughout different cooling profiles, the dynamic growth rate constants parameters α_1 and α_2 are determined. The growth rates determined for the two cooling rates used in the experiments are shown in Figure 2b. These parameters are used to calculate the growth parameters α_1 and α_2 when cooling rates $10\ ℃/min \geq r_{cool} \geq 1\ ℃/min$ are applied to the deposits. Here it is again assumed that the changes in the crystallization parameters are linearly proportional to the change in the cooling rates.

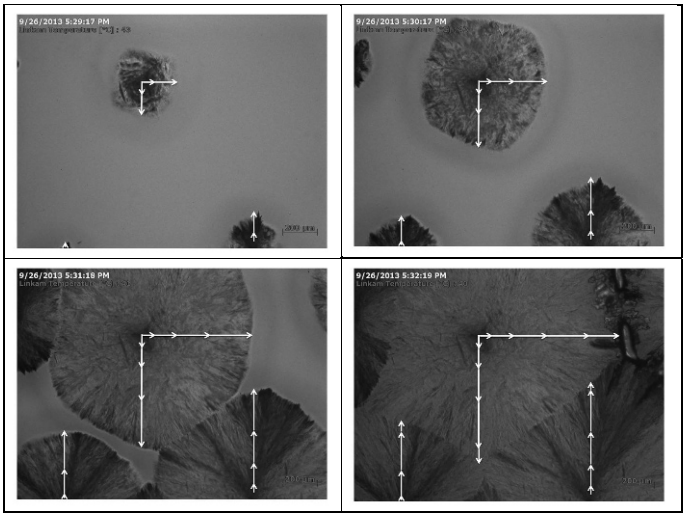

Figure 3. Optical microscopy images used for growth rate estimation with cooling rate 1 °C/min

5. Results and Discussion

Using the modified Avrami model, the solid fraction of the dosage forms produced of the model melt-based formulation by the dropwise additive manufacturing process with different cooling rates is calculated as a function of time. The differential equation, Eq.5, is solved numerically. The time and cooling rate dependence of kinetic parameters are taken into account as explained in Section 3. The nucleation and growth kinetic parameters presented in Section 4 are used in the model. The solidification rates of the dosage forms solidified with cooling rates of 1 °C/min and 10 °C/min is shown in Figure 4. For 10 °C/min, complete solidification occurs after 1.1 min, whereas in experiments this time was observed as 0.8 min. For 1 °C/min, complete solidification occurs after 5 min, whereas in experiments this time was 7 min. The mismatch between the experimentally observed and modeled solidification times could potentially be reduced by using experimental data points corresponding to intermediate cooling rates and checking the validity of the linearity assumptions made during the kinetic parameter estimation.

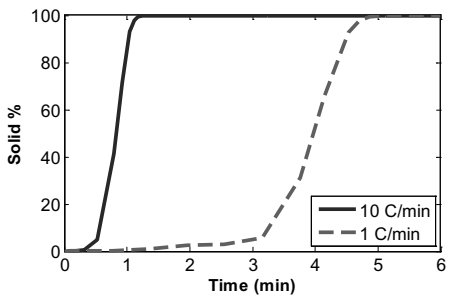

Figure 4. Solid Percentages of the Dosage Forms using the Developed Crystallization Model

The developed model is used to determine the mean size of crystals when different cooling rates are applied. For different cooling rates, the time, t*, to reach 100 % solidification is calculated. The number of nuclei formed per image area at t* is calculated and mean crystal radius is calculated, which are plotted in Figure 5 for cooling rates from 1 to 10 °C/min. By increasing the cooling rate from 1 to 10 °C/min,

the mean size is decreased from 434 to 307 μm, which is in accordance with the increase in the dissolution rate observed by Içten et al. (2014b) when fast cooling rate of 10 °C/min is applied to the same model formulation containing 15 % naproxen and 85 % PEG 3350. According to model results, the minimum radius of 217 μm can be achieved with a cooling rate of 5.5 °C/min. This can be used to further increase the dissolution rate of naproxen for which dissolution is limiting.

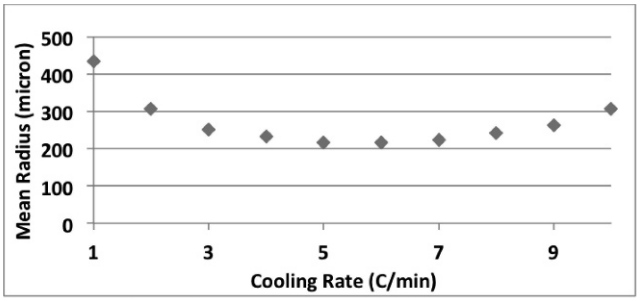

Figure 5. Crystallization model results for mean crystal radius vs cooling rate

6. Conclusions

In this work, we have developed a crystallization model based on non-isothermal Avrami kinetic equation for the cooling temperature dependent solid-state transformation of the melt-based solid oral dosages produced using the dropwise additive manufacturing process. The model is used to calculate the solidification times of the dosage forms and their mean crystal sizes under two different cooling profiles. The experimentally observed and modeled solidification times have the same trend, and the accuracy of the model can be improved by using experimental data points corresponding to intermediate cooling rates and by validating the linearity assumptions made during the kinetic parameter estimation. Using the model, a mean crystal size can be achieved which would lead to the desired product quality, such as dissolution.

Acknowledgments

This work was funded by the National Science Foundation under grant EEC-0540855 through the Engineering Research Center for Structured Organic Particulate Systems. The authors would like to thank IN-MaC for financial support provided to E.I.

References

M. Avrami, 1939, Kinetics of phase change I General Theory, Journal of Chemical Physics, 7, 12, 1103-1112.

L. Hirshfield, A. Giridhar, L. Taylor, M. Harris, G. Reklaitis, 2014, Dropwise Additive Manufacturing of Pharmaceutical Products for Solvent-based Dosage Forms, Journal of Pharmaceutical Sciences, 103, 2, 496-506.

E. Içten, A. Giridhar, L. Taylor, Z. Nagy, G. Reklaitis, 2014a, Dropwise Additive Manufacturing of Pharmaceutical Products for Melt-based Dosage Forms, Journal of Pharmaceutical Sciences, DOI 10.1002/jps.24367.

E. Içten, Z. Nagy, G. Reklaitis, 2014b, Supervisory Control of a Drop on Demand Mini-manufacturing System for Pharmaceuticals, Comp. Aided Process Eng., 33, 535-540.

Z. Nagy, R. Braatz, 2012, Advances and new directions in crystallization control, Annual Review of Chemical and Biomolecular Engineering, 3, 55-75.

T. Ozawa, 1971, Kinetics of non-isothermal crystallization, Polymer, 12, 3, 150-158.

Krist V. Gernaey, Jakob K. Huusom and Rafiqul Gani (Eds.), 12th International Symposium on Process Systems Engineering and 25th European Symposium on Computer Aided Process Engineering.
31 May – 4 June 2015, Copenhagen, Denmark

Macroporous microparticles for pharmaceutical and medical applications

Alexandra Zhukova,[a*] Alexander Troyankin,[a] Alexander Didenko,[b] Natalia Menshutina,[a]

[a]*D. Mendeleev University of Chemical Technology of Russia (MUCTR), International Center for transfer of Pharmaceutical and Biothechnology, 20/1 Geroev Panphilovtcev str., Moscow, 125480, Russia*
[b]*NPO Petrovax Pharm, LLC, 1 Sosnovaya St., Pokrov village, Podolsky district, Moscow region,142143 Russia*
chemcom@muctr.ru

Abstract

Powders and particles from biodegradable polymers and based on biologically active materials of the protein nature were obtained. The way of obtaining such powders is presented and the main characteristics and also possible paths of use of the obtained powders are described.

Keywords: vacuum freeze drying; atmospheric freeze drying; macroporous; microparticles; powders for inhalation.

1. Introduction

Microparticles and fine powders are becoming more and more widely used in different areas. In medicine such particles can be applied as material for implants and surgery, as sorbents for viruses and protein purification, as embolization agents, fillers for cosmetology, plates and matrixes for cell growth and may have many other applications. They can be used in pharmaceutical industry as components of drug delivery systems, as a base for inhalable and nasal products. However, production of particles of a size less than 20 μm today can be done either by using grinding technology, or by the way of atomizing a liquid followed by drying of the formed droplets (Wean Sin Cheow, 2011).
Main disadvantage of the grinding process in comparison with the atomizing technique is that the form of the particles obtained by the first one, is not spherical and uniformed. In the same time, many types and models of atomizing devices with various characteristics were developed and introduced to the market for the last 30 years (A. Troyankin et al., 2009).
Chemical, pharmaceutical industries and medicine are interested in particles of spherical form, low bulk density of about 0.2 g/sm3, with residual moisture content 3% and less, with good stability and flowability. Possibility of production of such particles in an ease and efficient way will significantly increase their areas of applications and usability. It is important to provide new ways of production of micropowders and particles suitable for pharmaceutical and other applications (A.Yu. Troyankin, 2012).
There is also a challenge to create an equipment capable to produce microparticles with predesigned properties, shape and size, that will gently handle product being produced saving its biological properties (N.V. Menshutina, 2008).
Drying process under vacuum, also known as sublimation freeze drying and lyophilisation – is one of the most known, popular and widespread process for the last decades. The process became famous due to high quality of obtained products and nowadays it is very important for pharmaceutical, food industries, biotechnology because it allows drying of heat sensitive, easily oxidized pharmaceutical substances, proteins that require gentle handling (grinding can lead to protein degradation due to

mechanical impact). The process is also widely used in chemistry and other areas (N. Menshutina et al., 2009).

2. Methods for preparing and basic characteristics of the microparticles

At MUCTR new laboratory scale equipment consisting of 3 units combined into 2 technological schemes were created, Figures 1 – 3. The process of production of microparticles with predefined properties and sizes were developed. The formation of the particles in the abovementioned process is done by of atomizing the solution, using two different types of nozzles: pneumatic and ultrasonic, into cryogenic liquid (liquid nitrogen and other) with rapid freezing process followed by freeze drying process.

a) b)

Figure 1. Atomizing of the solution into liquid nitrogen using Sono-Tek ultrasonic nozzle (a) and Glatt pneumatic nozzle (b).

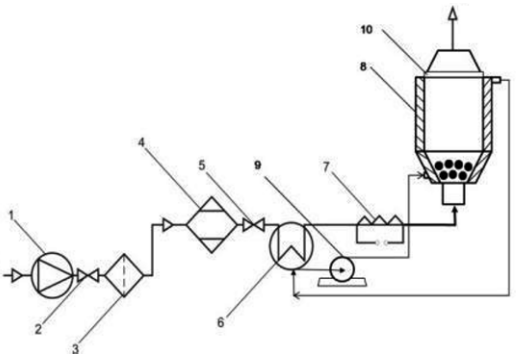

1 - compressor; 2 - valve; 3 - air filter; 4 - air dryer; 5 - valve; 6 - tube-type heat exchanger; 7 - electric air heater; 8 - freeze chamber spouted bed; 9 - casing; 10 - cartridge filters; 11 -frozen material feed line; 12 - ultrasonic nozzle; 13 - tank of freezing material; 14 - liquid nitrogen supply line.

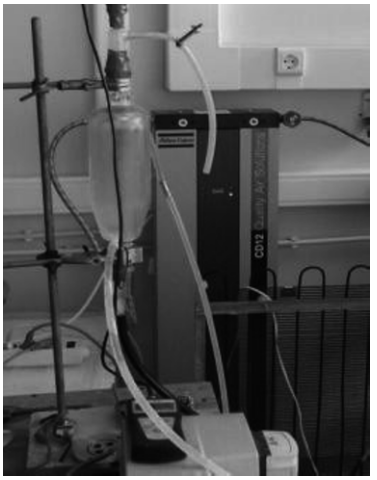

a) b)

Figure 2. Laboratory scale installation for atmospheric freeze drying in a fluidized bed a) – schematic layout; b) – external view.

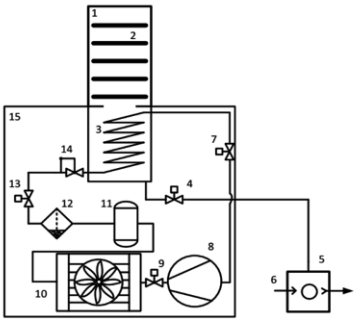

1 - camera freeze set; 2 shelves freeze set; 3 - ice condenser; 4 - main vacuum valve; 5 - vacuum pump; 6 - carrier gas; 7 - solenoid valve; 8 - refrigerant compressor; 9 - refrigerant control valve; 10 - air-cooled condenser; 11 - receiver; 12 - filter drier; 13 - refrigerant flow control valve; 14 - thermostatic expansion valve; 15 - body of the machine

a) b)

Figure 3. Vacuum freeze drier ScanLaf CoolSafe 100-9 PRO:
a) – schematic layout; b) – external view.

Microparticles and powders produced were made of different materials:

- chemically cross-linked modified polyvinyl alcohol, modified PVA were provided by prof. M.I. Shtilman, MUCTR (A.A. Artyukhov et al., 2011);
- physically cross-linked polyvinyl alcohol hydrogels, material provided by Prof. V.I. Lozinskiy, A.N. Nesmeyanov Institute of Organoelement Compounds of Russian Academy of Sciences (V.I. Lozinsky et al., 2014);
- particles of protein based pharmaceutical substance (cytokines), provided by A.I. Burnasyan Federal Medical Biophysical Centre of Federal Medical and Biological Agency.

To produce chemically cross-linked modified polyvinyl alcohol particles of hydrogels, a special atomizing technique was used that combined atomizing of modified PVA in aqueous solution together with catalyst system in Liquid nitrogen followed by radical polymerization and storage and crosslinking at cryogenic conditions (-20ºC) leading to hydrogel matrix formation. Freeze drying, vacuum and own designed atmospheric freeze drying process, was used to produce final dried particles, Figure 4.

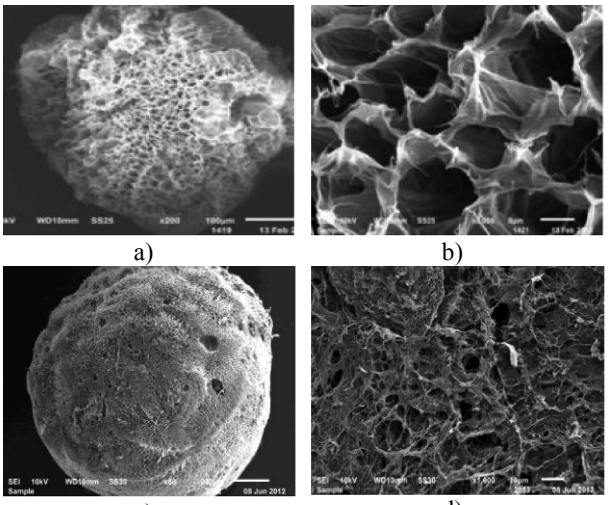

a) b)

c) d)

Figure 4. SEM photos of produced chemically cross-linked PVA hydrogel particles (external view and macroporous structure): a), b) pneumatic nozzle and vacuum freeze drying used; c), d) ultrasonic nozzle and atmospheric freeze drying used.

The process of production of physically cross-linked PVA hydrogel particles consisted of two stages: first stage - atomizing of PVA aqueous solution into cryogenic liquid, storage of the frozen particles under cryogenic conditions (-15ºC) and second stage - slow defreezing at the rate of 0,03 ºC/min to ambient temperature or vacuum freeze drying. Pictures of produced particles are shown in Figure 5.

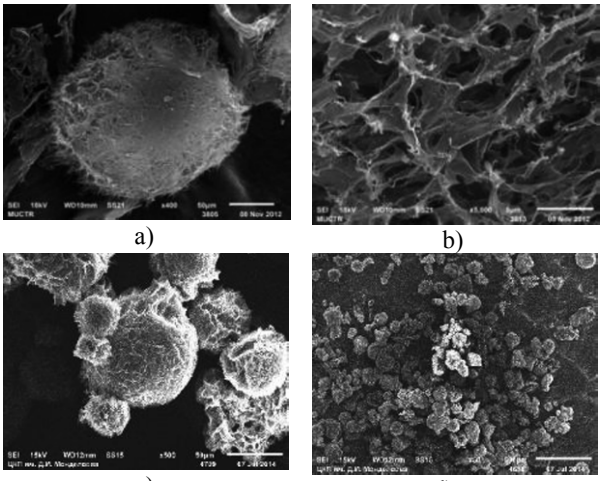

a) b) c) d)

Figure 5. SEM photos of produced physically cross-linked PVA hydrogel particles (external view and macroporous structure)
a), b) pneumatic nozzle and atmospheric freeze drying used;
c), d) pneumatic nozzle and vacuum freeze drying used.

PVA-hydrogels have unique properties and characteristics that make them attractive materials to use in biomedicine and pharmaceutical industry.
Some characteristics of hydrogels produced using two types of nozzles (pneumatic and ultrasonic ones) and two methods of drying – vacuum, Figure 2, and atmospheric freeze drying, Figure 3, respectively, are presented in Table 1.
Such hydrogels are non-toxic, biocompatible materials with high elasticity and good swelling properties. Polyvinyl alcohol macroporous hydrogels are widely used as membranes, components of controlled drug release systems, plates for cell and tissue engineering and have other applications in modern medicine.

Table 1
Characteristics of produced powders

Characteristic	**Pneumatic nozzle**		**Ultrasonic nozzle**	
	Vacuum freeze drying	**Atmospheric freeze drying**	**Vacuum freeze drying**	**Atmospheric freeze drying**
Residual moisture content, mass. %	5,2	6,5	3,89	5,74
Bulk density, g/sm^3	0,18	0,3	0,09	0,25
Mean particle diameter, μm	400		40	
Mean pore diameter, μm	10		5	
Overall porosity (calculated)	~0,95			
Swelling degree, g water/ g PVA hydrogel	~1200 %			

Application of PVA hydrogel as a matrix for drug delivery allows for sustained release drug delivery site in.
Developed process allows to produce spherical macroporous particles with a range of particle diameter of 200 – 1000 μm using pneumatic nozzles and with a range of particle diameter of 10 – 100 μm using ultrasonic nozzles, with overall material porosity up to 95 % and pore diameter of 2 - 10 μm. Pore network is rich and sponge like, that predefines high swelling and adsorption properties.
Development of dry particulate of proteinaceous nature drugs for inhalation applications is being undertaken at MUCTR at the present moment. The process of creating such particles is arranged in a periodic mode of two steps: through atomizing an aqueous solution of the proteinaceous nature drugs into the cryogenic liquid (liquid nitrogen Tb = -196 ºC) or through complete aqueous solution freezing in a flask without spraying and vacuum freeze-drying at the temperature of -50 °C ÷ -5 °C. Powders received in such a way are shown in Figure 6.

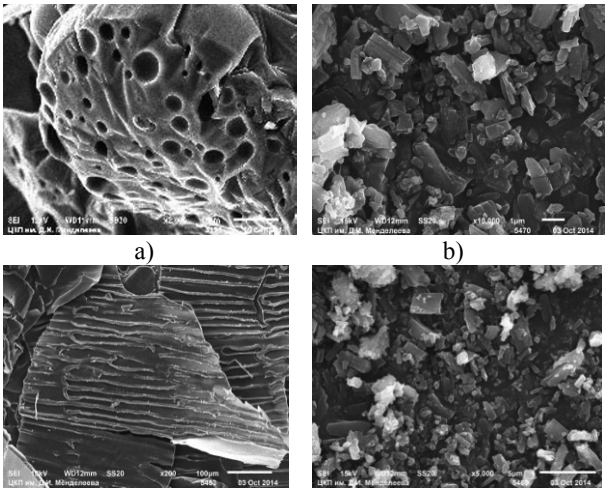

Figure 6. SEM photos of produced proteinaceous nature powders (external view and macroporous structure):
a), b) ultrasonic nozzle and atmospheric freeze drying used;
c), d) pneumatic nozzle and vacuum freeze drying used.

The resultant proteinaceous powders hava a high dispersibility, porosity, rapid and complete solubility in suitable solvents, high flow, it also has a narrow particle size distribution - the particle diameter is of 2 - 20 micrometers, the residual moisture content, is of 1 - 3 mass. % and the bulk density is of 0,09 – 0,18 g/cm3. In addition, the powders are 100 % reducible after freeze drying process without aggregating and do not contaminate due to the excipients.
The finished product – proteinaceous powder - may be used for inhaled, nasal, and transdermal applications. Due to micron particle size, regular shape and their excellent aerodynamic characteristics these powders can be used to create effective drugs based on biologically active substances of protein origin to deliver active ingredients of immunostimulating agents properties by virtue of their specific pharmacological activity, which is higher than that of similar synthetic drugs.

3. Conclusions

Conducted in MUCTR investigation of the powders indicates that the materials created by the higher described method exhibits a high biocompatibility, thermally stable,

substantial water absorption (the total degree of the hydrogel particles swelling in units of g water/g of PVA is 1200 %), mechanical resistance, good adsorptive properties: adsorption rate constant (Brilliant green dye) (k_{ad}) 6,98×10-3 min^{-1}, the effective diffusion coefficient inside the particle(k_p) 1,32×10-5mmol / g×$min^{1/2}$. The developed process allows to produce powders based on resistant to heat substances as well as heat-labile ones.

Biosafety of the obtained powders protein materials and their reducing from a dry powder have been by A.I. Burnasyan Federal Medical Biophysical Centre of Federal Medical and Biological Agency. The results showed excellent biocompatibility and biosafety of the obtained bio-product as well as excellent efficiency of targeting the immune system of experimental animals-rats and no immunotoxic effects of the powders.

There have been conducted an examination of the adhesion of eukaryotic cells to the surface of the particles of PVA by the N.K. Koltzov Institute of Developmental Biology of Russian Academy of Sciences. The results indicate a high cell adhesion and normal proliferation to the surface of the particles, which allows the resulting material to be regarded as a matrix for use in the tissue engineering.

References

Wean Sin Cheow, Mabel Li Ling Ng, Katherine Kho, Kunn Hadinoto, 2011, Spray-freeze-drying production of thermally sensitive polymeric nanoparticle aggregates for inhaled drug delivery: Effect of freeze-drying adjuvants, International Journal of Pharmaceutics, 404, 1–2, 289–300.

A. Troyankin, A. Kozlov, A. Voynovskiy, N. Menshutina, 2009, Quality by design approach in drying process organization, Computer Aided Chemical Engineering, 26, 291–296.

A.Yu. Troyankin, 2012, The process of producing macroporous particles of hydrogels based on polyvinyl alcohol: Author. PhD, Moscow, 16 pp.

N.V. Menshutina, 2008, Nanoparticles and nanostructured materials for the pharmaceutical industry, Kaluga, 192 pp.

N. Menshutina, M. Gordienko, Yu. Makovskaya, A. Kasimova, A. Voinovskiy, 2009, System approach to modeling of pharmaceutical integrated processes: drying, layering and coating, 26, 501–505.

A.A. Artyukhov, M.I. Shtilman, A.N. Kuskov, L.I. Pashkova, A.M. Tsatsakis, A.K. Rizos, 2011, Polyvinyl alcohol cross-linked macroporous polymeric hydrogels: Structure formation and regularity investigation, Journal of Non-Crystalline Solids, 357, 2, 700–706.

V.I. Lozinsky, L.G. Damshkaln, I.N. Kurochkin, I.I. Kurochkin, 2014, Cryostructuring of polymeric systems. 36. Poly(vinyl alcohol) cryogels prepared from solutions of the polymer in water/low-molecular alcohol mixtures, European Polymer Journal, 53, 189–205.

Krist V. Gernaey, Jakob K. Huusom and Rafiqul Gani (Eds.), 12th International Symposium on Process Systems Engineering and 25th European Symposium on Computer Aided Process Engineering.
31 May – 4 June 2015, Copenhagen, Denmark

Optimal Resin Selection for Integrated Chromatographic Separations in High-Throughput Screening

Songsong Liu,[a,b] Spyridon Gerontas,[b] David Gruber,[c] Richard Turner,[c] Nigel J. Titchener-Hooker,[b] Lazaros G. Papageorgiou[a,b]

[a]*Centre for Process Systems Engineering, Department of Chemical Engineering, University College London, Torrington Place, London WC1E 7JE, UK*
[b]*EPSRC Centre for Innovative Manufacture in Emergent Macromolecular Therapies, Department of Biochemical Engineering, University College London, Gordon Street, London WC1H 0AH, UK*
[c]*MedImmune Limited, Milstein Building, Granta Park, Cambridge CB1 6GH,UK*
l.papageorgiou@ucl.ac.uk

Abstract

Chromatography is an essential step of biopharmaceutical production. High-throughput screening (HTS) is widely used in the biopharmaceutical industry to identify optimal conditions for chromatography processes. At the early stage of the purification process development, different resins are tested under various operating conditions, resulting in the generation of large amounts of data. To facilitate the decision-making process, we develop an optimisation-based decision support approach to process data generated from microscale experiments in order to identify the best resins to maximise key performance metrics of the biopharmaceutical manufacturing process. A multiobjective mixed integer nonlinear programming (MINLP) model is developed, for optimal resin selection for chromatographic sequence used for protein purification. The proposed model is solved using the ε-constraint method and applied to an industrially-relevant example with two chromatography steps. The computational results show that the developed approach is an efficient way to identify the best resins.

Keywords: high-throughput screening, chromatography, multiobjective optimisation, mixed integer programming, ε-constraint method

1. Introduction

In the biopharmaceutical industry, high-throughput screening (HTS) is an early critical step in drug development (Bensch et al., 2005), in which the combination of robotic methods, parallel processing and miniaturisation of bioprocess unit operation has allowed a large number of potential process parameters to be examined within a short time. However, facing a huge volume of data generated from microscale experiments, there is a critical need to analyse them rapidly in order to arrive at conditions that result in optimal overall process performance. Different types of resins may be tested using ultra scale down robotic platforms. Various operating conditions, including different pH values, salt concentrations, and flow rates, may then be optimised in order to maximise chromatographic yield and product purity. Thus, determining optimal resins/conditions from the HTS data becomes a critical problem. The optimal resin found through the microscale experiment is usually the best one for the specific conditions that are tested in that experiment. However, in the real practice of commercial manufacturing, a

chromatography sequence, including multiple chromatography separation steps, is implemented. Thus, the selection decision for each resin should not only depend on this resin's performance, but also is related to the selection of other chromatography resins in the chromatographic sequence, and their operating conditions and performance.

Optimisation-based approaches in the biopharmaceutical industry have become more popular recently (Liu et al., 2013, 2014, 2015; Allmendinger et al., 2014). However, the use of systematic approaches for resin selection in HTS is still largely uncommon. Currently, there are only limited optimisation approaches available for the HTS data analysis problem, as well as statistical tools (Malo et al., 2006). Nfor et al. (2011) presented a model-based rational strategy for the selection of chromatographic resins, in which multiple performance metrics, including yield, purity, productivity, resin/solvent cost, and concentration factor, are optimized using a genetic algorithm. This work addresses the rapid selection of resins for HTS data by developing an optimisation-based systematic decision support framework to select optimal resins for integrated chromatographic separations. The approach is based on experiments involving single resins in each, in order to highlight the benefits of the use of optimisation techniques in drug development.

2. Problem Statement

The optimisation problem considered is described as follows:
Given are:

- target protein, and impurity proteins;
- chromatography sequence and candidate resins;
- chromatography operating conditions for each resin;
- multiple time periods dividing the whole chromatography purification process;
- protein mass loaded under each condition in each time period for each resin;
- protein mass collected under each condition in each time period for each resin;
- salt concentration level for elution in each time period for each resin;

to determine:

- resin selection;
- chromatography operating conditions;
- starting and finishing time for protein collection;

so as to maximise key performance metrics of the chromatography sequence, including yield and purity of target protein.

3. Mathematical Formulation

To solve the above optimisation problem, we formulate a multiobjective mixed integer nonlinear programming (MINLP) model.

3.1. Resin selection constraints

At each chromatography step s, only one resin r can be selected:

$$\sum_{r \in R_s} Y_{sr} = 1, \quad \forall s \tag{1}$$

where Y_{sr} is a binary variable that is equal to 1 if resin r is selected at step s; R_s is the set of resins available at step s.

3.2. Operating condition selection constraints

For each resin *r*, only one operating condition *c* should be selected, out of all operating conditions:

$$\sum_{c\in C_s} Z_{sc} = 1, \quad \forall s \tag{2}$$

where binary variable Z_{sc} is equal to 1 if condition *c* is selected at step *s*; C_s is the set of conditions available at step *s*.

3.3. Starting and finishing time constraints

At each step *s*, during the whole chromatography purification process, including load, wash, elution and regeneration stages, there is only operating starting cut-point, as well as finishing cut-point:

$$\sum_t Xs_{st} = 1, \quad \forall s \tag{3}$$

$$\sum_t Xf_{st} = 1, \quad \forall s \tag{4}$$

where binary variables Xs_{st}/Xf_{st} is equal to 1 if the beginning/end of time period *t* is the starting/finishing time cut-point at step *s*. Thus, the time periods selected for protein collection are determined as follows:

$$X_{st} = X_{s,t-1} + Xs_{st} - Xf_{s,t+1}, \quad \forall s,t \tag{5}$$

where binary variable X_{st} is equal to 1 if time period t is selected at step s.

3.4. Logic constraints

The binary variable W_{srct} is defined as $X_{st} \cdot Y_{sr} \cdot Z_{sc}$, i.e., = 1 if time period *t* of resin *r* under condition *c* is selected at step *s* for collection, which can be expressed as follows:

$$\sum_{r\in R_s}\sum_{c\in C_s} W_{srct} \le U \cdot X_{st}, \quad \forall s,t \tag{6}$$

$$\sum_{c\in C_s}\sum_t W_{srct} \le U \cdot Y_{sr}, \quad \forall s, r \in R_s \tag{7}$$

$$\sum_{r\in R_s}\sum_t W_{srct} \le U \cdot Z_{sc}, \quad \forall s, c \in C_s \tag{8}$$

$$W_{srct} \ge X_{st} + Y_{sr} + Z_{sc} - 2, \quad \forall s, r \in R_s, c \in C_s, t \tag{9}$$

where parameter *U* is a large number.

3.5. Step integration constraints

Between the two successive chromatography steps, the salt concentration of elution at the finishing cut-point at a former step ($conc_{st}$) should be less than that of the starting cut-point at a later step ($conc_{s+1,t}$):

$$\sum_t conc_{st} \cdot Xf_{st} < \sum_t conc_{s+1,t} \cdot Xs_{s+1,t}, \quad \forall s \tag{10}$$

3.6. Yield constraints

The yield after each step (Yd_s) is the fraction of the collected mass and the loaded mass of the target protein, *dp*:

$$Yd_s = \sum_{r\in R_s}\sum_{c\in C_s}\sum_t \frac{m_{src,dp,t} W_{srct}}{lm_{src,dp}}, \quad \forall s \tag{11}$$

where $m_{src,dp,t}$ is the mass of target protein *dp* collected under condition *c* in resin *r* in time period *t* at step *s*, while lm_{srcp} is the mass of protein *p* loaded to resin *r* under condition *c* at step *s*.

3.7. Purity constraints

The purity after each step (Pu_s) is the fraction of the collected mass of the target protein and that of all proteins *p*:

$$Pu_s = \frac{\sum_{r\in R_s}\sum_{c\in C_s}\sum_t m_{src,dp,t}W_{srct}}{\sum_{r\in R_s}\sum_{c\in C_s}\sum_p\sum_t m_{srcpt}W_{srct}}, \quad \forall s \tag{12}$$

3.8. Objective functions

We aim to maximise both overall yield and purity of the integrated chromatography steps. We use an performance indicator, z^{Yd}, equalling the product of the yields at all steps, for the overall yield of the whole process (Eq. 13). Also, another performance indicator, z^{Pu}, is used to represent the overall purity, which is approximated by the average purity of all steps involved, in order to reflect all steps' effects on it (Eq. 14).

$$z^{Yd} = \prod_s Yd_s \tag{13}$$

$$z^{Pu} = \sum_s Pu_s / |s| \tag{14}$$

3.9. Summary

Based on the above constraints, the multiobjective optimisation problem can be presented in the following format as problem (15). Note that when $|s| = 1$, this MINLP model can still deal with single-step separation.

$$\begin{aligned} &\max \{z^{Yd}, z^{Pu}\} \\ &s.t. \text{ Eqs. (1)-(14)} \end{aligned} \tag{15}$$

4. Solution Approach

To solve the above multiobjective optimisation problem (15), we apply the ε-constraint method (Haimes et al., 1971), in which all but one objective are converted into constraints by setting an upper or lower bound to each of them, having only one objective to be optimised. Thus, the multiobjective optimisation problem (15) can be transformed into a set of single-objective optimisation problems (16):

$$\begin{aligned} &\max\ z^{Yd} \\ &s.t.\ z^{Pu} \geq \bar{z}^{Pu} \\ &\quad \text{Eqs. (1)-(14)} \end{aligned} \tag{16}$$

where $\bar{z}^{Pu}$ is the minimum bound of the purity indicator. By using multiple values of $\bar{z}^{Pu}$, the Pareto frontier can be achieved. When single-step separation is considered, a mixed integer linear programming (MILP) model is solved in the ε-constraint method.

5. Case Study

Here, we consider a real case study of a biopharmaceutical company, wishing to purify a monomer protein from a protein mixture with aggregates and fragments as the main impurities. We consider a two-step chromatography sequence, including cation-

exchange chromatography (CEX) as step 1 and mixed mode chromatography (MM) as step 2. For CEX, there are 8 candidate resins (CEXR1-CEXR8) with two operating conditions/pH values for each resin (C1-C2), while for MM, there are 4 candidate resins (MMR1-MMR4) with 8 to 12 operating conditions (C1-C12) for each resin. These CEX and MM resins investigated are all commercially available and were selected for evaluation based on their different chemical characteristics and purification capabilities. The whole purification process at each step is divided into 29 time periods (T1-T29). The developed models were implemented in GAMS (Brook et al, 2012) on a Windows based machine with 3.2 GHz processor and 12 GB RAM. BARON was used as the MINLP solver and CPLEX as the MILP solver. The optimality gap was set to 0%.

Firstly, we select the optimal resin for CEX and MM steps, separately, by solving a number of MILP models in the ε-constraint method. Each MILP involved took less than 1 second to find the optimal solution. Figure 1 shows the Pareto frontiers which are obtained by increasing $\bar{z}^{Pu}$ from 85% to 95%. The labels on Figure 1 show the corresponding optimal resin and condition. We can see that CEXR3, CEXR4 and CEXR7 can achieve both high yield and purity, while MMR1 and MMR3 show dominant performance for the MM step. A particular note was that different performances for the same resin and condition result from their different starting and finishing cut-points. Secondly, we consider the integration of the above two steps, including CEX as the first step and MM as the second one. The average CPU time for each integrated MINLP model was around 50 seconds. By increasing $\bar{z}^{Pu}$ from 85% to 95%, we have the Pareto frontier as shown in Figure 2. In the Pareto-optimal solutions, the best chromatography sequence is CEXR7-MMR3. This sequence is able to achieve both high yield and high purity (>90%). Other sequences result in slightly higher purity, but significantly lower yield (<85%). The difference between the best resin for each single chromatography step and the best resins for the two chromatography steps shows the value of the proposed optimisation-based decision support framework of HTS, although the validation in larger scale experiment is still needed.

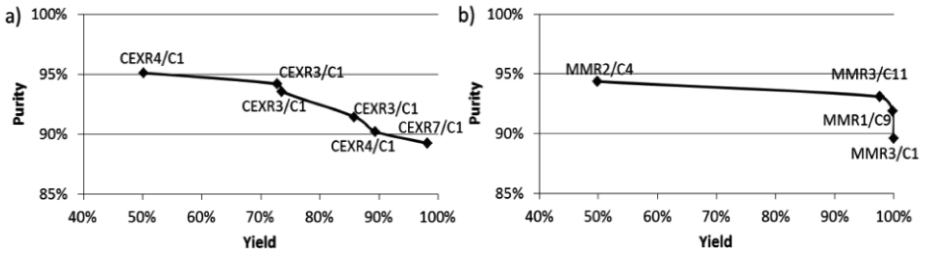

Figure 1: Pareto frontier for a) CEX step and b) MM step.

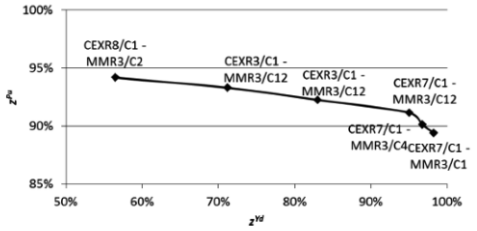

Figure 2: Pareto frontier for the integrated CEX and MM steps.

6. Conclusions

In this work, we address the rapid resin selection problem for the integrated chromatographic separations made available during HTS, by developing an optimisation-based decision support systematic framework for optimal resin selection. A multiobjective MINLP model has been developed to maximise both yield and purity of the integrated chromatographic separations. Then, the classic ε-constraint method has been adapted as the solution approach, in which only yield was optimised in relation to the purity constraints. Then, the developed framework was applied to a real case study to show its applicability. The results show the benefits of the decision-making based on integrated chromatographic separations, by comparing the best resins in terms of yield and purity to be used in each chromatography step independent from the other steps and the optimal best resins when the two chromatography steps have been integrated.

The limitation of this work is the indicator of overall purity is calculated based on the data from experiments for each single resin only. In future work, we will seek to link the two chromatography steps using protein mass balances, and hence calculate the overall purity in a more accurate way.

Acknowledgements

Funding from the UK Engineering & Physical Sciences Research Council (EPSRC) for the EPSRC Centre for Innovative Manufacturing in Emergent Macromolecular Therapies hosted by University College London is gratefully acknowledged. Financial support from the consortium of industrial and governmental users is also acknowledged.

References

R. Allmendinger, A.S. Simaria, R. Turner, S.S. Farid, 2014, Closed-loop optimization of chromatography column sizing strategies in biopharmaceutical manufacture, Journal of Chemical Technology and Biotechnology, 89, 1481-1490.

M. Bensch, P. Schulze Wierling, E. von Lieres, J. Hubbuch, 2005, High throughput screening of chromatographic phases for rapid process development, Chemical Engineering & Technology, 28, 1274-1284.

A. Brooke, D.Kendrick, A. Meeraus, R. Raman, 2012, GAMS - A User's Guide, GAMS Development Corporation, Washington, D.C.

Y.Y. Haimes, L.S. Lasdon, D.A. Wismer, 1971, On a bicriterion formulation of the problems of integrated system identification and system optimization, IEEE Transactions on Systems, Man, and Cybernetics, 1, 296-297.

S. Liu, A.S. Simaria, S.S. Farid, L.G. Papageorgiou, 2013, Designing cost-effective biopharmaceutical facilities using mixed-integer optimization, Biotechnology Progress, 29, 1472-1483.

S. Liu, A.S. Simaria, S.S. Farid, L.G. Papageorgiou, 2014, Optimising chromatography strategies of antibody purification processes by mixed integer fractional programming techniques, Computers and Chemical Engineering, 68, 151-164.

S. Liu, A.S. Simaria, S.S. Farid, L.G. Papageorgiou, 2015, Mathematical programming approaches for downstream processing optimisation of biopharmaceuticals, Chemical Engineering Research and Design, 94, 18-31.

N, Malo, J.A. Hanley, S. Cerquozzi, J. Pelletier, R. Nadon, 2006, Statistical practice in high-throughput screening data analysis. Nature Biotechnology, 24, 167-175.

B.K. Nfor, D.S. Zuluaga, P.J.T. Verheijen, P.D.E.M. Verhaert, L.A.M. van der Wielennd, M. Ottens, 2011, Model-based rational strategy for chromatographic resin selection. Biotechnology Progress, 27, 1629-1643.

Krist V. Gernaey, Jakob K. Huusom and Rafiqul Gani (Eds.), 12th International Symposium on Process Systems Engineering and 25th European Symposium on Computer Aided Process Engineering.
31 May – 4 June 2015, Copenhagen, Denmark

Plantwide Design and Economic Evaluation of Two Continuous Pharmaceutical Manufacturing (CPM) Cases: Ibuprofen and Artemisinin

Hikaru G. Jolliffe, Dimitrios I. Gerogiorgis

School of Engineering, University of Edinburgh, Edinburgh EH9 3JL, UK

Abstract

Continuous Pharmaceutical Manufacturing (CPM) is a rapidly expanding research field with growing industrial importance: challenging the current batch production paradigm, it has a documented potential to deliver key cost, efficiency and environmental benefits. Ibuprofen, the potent painkiller, and artemisinin, a highly effective anti-malarial drug, have been identified as promising CPM candidates, and steady-state flowsheet models have been developed on the basis of published continuous organic synthesis pathways. Reactor design has been conducted using original kinetic parameter estimation results. A comparative economic analysis via published recoveries has computed performance indices which indicate that both CPM designs exhibit high economic potential, even if conservative profit and climate estimates are used to derive capital and operating costs. More detailed technoeconomic analyses can facilitate quicker CPM implementations.

Keywords: Continuous Pharmaceutical Manufacturing (CPM), ibuprofen, artemisinin.

1. Introduction

Continuous Pharmaceutical Manufacturing (CPM) is a vibrant research field addressing challenges due to the ever-increasing R&D costs and globalised corporate competition. Offering a cost-effective alternative to traditional batch processes (Roberge et al., 2008), CPM can reduce cost (Schaber et al., 2011) at high yield, solvent and energy efficiency, allow for easier process scale-up and eliminate intermediate storage needs, while also reducing environmental impact and increasing sustainability (Poechlauer et al., 2013). Process synthesis, modelling and simulation can rapidly assess process potential (Gerogiorgis & Barton, 2009) toward sound CPM business cases (Gernaey et al., 2012). Recently, a series of Active Pharmaceutical Ingredients (APIs) have been identified as promising CPM candidates (Jolliffe & Gerogiorgis, 2015): ibuprofen and artemisinin ranked highest among all, using a set of nine specific technoeconomic criteria (Figure 1)

Ibuprofen is recognised as an essential non-steroidal anti-inflammatory drug (NSAID) by the World Health Organisation; its global annual production exceeds 13,500 tonnes. Artemisinin is the parent substance of the fastest acting and most effective anti-malarial drugs, currently extracted in batch from sweet wormwood, *Artemisia annua* (Tu, 2011). Demand fluctuations and production timescales induce supply and cost unpredictability: between 2005 and 2008, market price varied by an order of magnitude, \$120÷1,200/kg (Artemisinin Enterprise, 2008), with a recent report at \$400/kg in 2013 (Peplow, 2013). This paper focuses on a technoeconomic CPM analysis and comparison of these APIs. Process mass balance simulations for two CPM designs have been performed, and reactor design has relied on novel kinetic and thermodynamic parameter estimations. Annual capacity for both APIs (50 kg) is chosen toward comparative economic analysis.

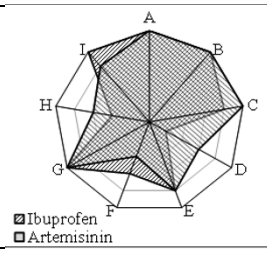

A. Is the process fully continuous?
B. Is the final product a currently marketed API?
C. Low to medium complexity process?
D. Has the process been implemented?
E. Feedstock/reagent availability.
F. Ease of process scale-up.
G. Are intermediate separations eliminated?
H. Price of commercially available product.
I. Global sales volume.

Figure 1. Systematic analysis of CPM potential for the two APIs (Jolliffe & Gerogiorgis, 2015).

2. Continuous flow synthesis of APIs

Continuous organic flow synthesis pathways for ibuprofen (Bogdan et al, 2009) and artemisinin (Kopetzki et al, 2013) illustrate their acknowledged therapeutic importance and serve as precedents for developing both steady-state process models reported here.

2.1. Ibuprofen

Ibuprofen is produced using three reactors: in the first PFR, Friedel-Crafts acylation converts isobutyl benzene (IBB) into intermediate $\mathbf{2_A}$, then transformed in the second PFR (by 1,2-aryl migration) into intermediate $\mathbf{3_A}$. The latter undergoes base hydrolysis in the third PFR, yielding the potassium salt of ibuprofen: we consider this entirely acidified prior to final separation, as the salt is unsuitable for commercial formulations.

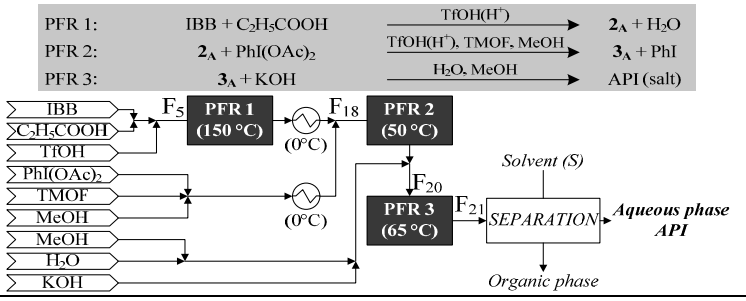

Figure 2. Demonstrated process flowsheet for ibuprofen CPM production (Bogdan et al, 2009).

2.2. Artemisinin

Artemisinin is attainable via a series of two reactors: dihydroartemisinic acid (DHAA, a conventional artemisinin batch extraction waste) is photo-oxidised in a chilled PFR, producing intermediate $\mathbf{3_B}$ and by-products. In the second PFR, $\mathbf{3_B}$ undergoes multiple transformations in presence of trifluoroacetic acid (TFA, acid catalyst), before eventual oxidation to artemisinin; additional by-products are generated (Gilmore et al., 2013).

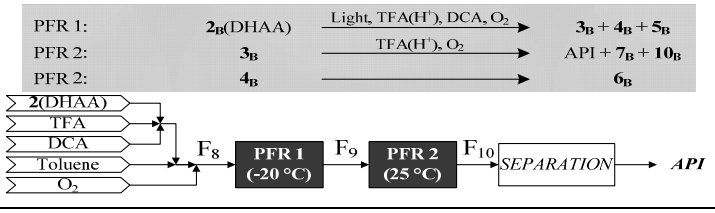

Figure 3. Demonstrated process flowsheet for artemisinin CPM production (Kopetzki et al, 2013).

3. Mass balances and reactor design

Process mass balances for both CPM flowsheets appear in Fig. 4; some flows are scaled for clarity, and by-products (BPD: salts, methyl formate, iodobenzene) are all grouped. For comparative economic evaluation, the annual production is set at 50 kg of pure API without considering any losses in downstream processing or final dosage formation. The summary of essential kinetic parameters for PFR design is presented in Table 1.

3.1. Kinetics

Kinetic rate constants and conversions for the first two ibuprofen reactions are extracted from literature data, using SPARC software for the third (Jolliffe & Gerogiorgis, 2015). Possible side effects (e.g. esterification reactions between organic acids and methanol), the chemical action of by-products and the presence of solids are assumed negligible; reaction orders and constants (hr^{-1} /1st order, $Lmol^{-1}hr^{-1}$ /2nd order) are given in Table 1.

Kinetic parameter estimation for both artemisinin reactions has relied on the first-order assumption, given their nature (large organic molecules react with an excess of e.g. O_2); published conversion and reactor volume data have been used (Kopetzki et al., 2013). The photo-oxidation reaction in the first PFR can achieve a DHAA conversion of 98%. For the second PFR, a conversion of 79% is obtained for the first reaction ($\mathbf{3_B}$→API), using DHAA conversion (98%), artemisinin (59.9%), $\mathbf{7_B}$ (4.5%) and $\mathbf{10_B}$ (2.5%) yields.

The conversion of $\mathbf{4_B}$ (61%) is similarly calculated on the basis of data for overall yield (i.e. including species from the reaction of $\mathbf{3_B}$) of $\mathbf{6_B}$ (6.18%) (Kopetzki et al., 2013); yields have been adjusted to account for small by-product (BPD) quantities (< 1% mol).

3.2. Reactor design

For both CPM plant designs, the present design analysis considers that all PFR reactors perform well at isothermal operation and that sufficient heat transfer can be achieved. Selecting a suitably small diameter ensures radial temperature gradients are negligible. Well-circulating heating media and controlled environments (e.g. ovens, baths) are established state of the art for several CPM reactor prototypes (Bedore et al., 2010).

Plug Flow Reactor (PFR) design has been performed by determining required lengths via integration: a small ID (5 mm) has been selected to ensure adequate heat transfer, in accordance with proven CPM PFR designs at similar length scale (Mascia et al., 2013). No phase change during flow is considered (precipitation can be prevented by design).

Table 1. Continuous reaction parameter estimates and summary of reactor (PFR) design results.

PFR # (reaction)	***T*** (ºC)	k_i (resp. units)	**Flowrate** ($g\ hr^{-1}$)	**Conversion** (%)	***ID*** (mm)	**Volume** (mL)	**Length** (mm)
Ibuprofen							
PFR 1 (IBB→$\mathbf{2_A}$)	150	31.41	41.58	91	5.0	6.392	326
PFR 2 ($\mathbf{2_A}$→$\mathbf{3_A}$)	50	2732.3	115.77	98	5.0	1.997	102
PFR 3 ($\mathbf{3_A}$→API)	65	15.57	306.90	99	5.0	28.912	1472
Artemisinin							
PFR 1 (DHAA→$\mathbf{3_B}$)	-20	39.12	109.86	98	5.0	10.442	532
PFR 2 ($\mathbf{3_B}$→API)	25	2.91	109.86	79	5.0	55.685	2836
($\mathbf{4_B}$→$\mathbf{6_B}$)	25	1.78	109.86	61	5.0	55.685	2836

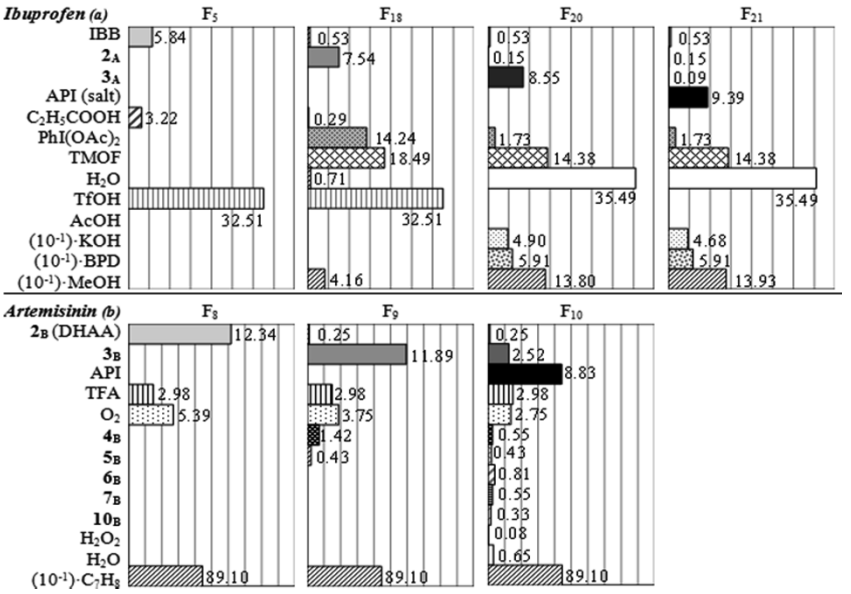

Figure 4. Mass balances for streams of both CPM designs (units: 5 g hr^{-1}/a, 2 g hr^{-1}/b).

4. Separation design

Separation design entails the analysis of candidate solvents and operating conditions: for ibuprofen production, liquid-liquid extraction (LLE) has been considered as a viable choice, to achieve high API recovery before crystallisation and downstream processing. Six solvents (acetonitrile, ethanol, methyl acetate, ethyl acetate, n-hexane, toluene) have been evaluated to assess performance and environmental impact (Alfonsi et al, 2008). Solvent-to-feed mass ratios ($S:F_{21}$) ranging from 0.25 to 5 have been considered for the ones yielding phase split (n-hexane, toluene), at 25 °C (ambient) and 65 °C (PFR3). Stream F_{21} is approximated as a H_2O-MeOH mixture; solubility and phase equilibria modelling enables computation of effluent compositions (Jolliffe & Gerogiorgis, 2015).

The recommended choice is toluene, at a $S:F_{21}$ ratio of 0.75 at 25 °C, resulting in 81.7% final ibuprofen recovery: operation at higher temperature (65 °C) gives higher recovery, but is less preferable due to heating cost and off-gassing (Jolliffe & Gerogiorgis, 2015). While n-hexane performs better in many instances of $S:F_{21}$ ratios and temperatures, it has a grave environmental impact and is not a desirable solvent (Alfonsi et al, 2008). The other solvents considered are unsuitable for this LLE case due to full miscibility. Purification design must consider seamless downstream (e.g. ethanol-based) processing.

Kopetzki et al. (2013) used acetonitrile to dissolve artemisinin, allowing the removal of poorly-soluble DCA by filtration: the latter is followed by two crystallisation stages, both of which use a cyclohexane-ethanol (9:1 v/v) solvent mixture to obtain solid API. The published organic flow synthesis pathway produces artemisinin at a yield of 65%; the subsequent sequential crystallisations achieve respective yields of 57% and 46%, corresponding to an overall API recovery of 70.8%: this can also be improved further to increase CPM efficiency, by means of multicomponent equilibria and solubility models.

5. Environmental impact: the E-factor

The environmental factor (E-factor) is a green engineering metric of process impact: in its simplest form, it is defined as the ratio of waste to product mass (Sheldon, 2012). Highly efficient continuous (e.g. petrochemical) industries have typical E-factors of 0.1, while pharmaceutical industries frequently reach values of 200 or higher (Ritter, 2013). E-factors have been calculated for both CPM designs considered: a very attractively low low E-factor of 25.4 has been calculated for ibuprofen (Jolliffe & Gerogiorgis, 2015), indicating that CPM implementation is a viable option even without solvent integration. The corresponding E-factor of 33.5 for artemisinin is equally appealing (albeit slightly higher): the total mass of material input considers both feedstocks as well as solvent (cyclohexane-ethanol) requirements for both crystallisation stages and API production. The comparable and similar E-factor values underline the importance of systematic environmental impact evaluation, while also illustrating that there is indeed clear scope for improving the efficiency of artemisinin recovery by continuous separation design.

6. Economic evaluation

Economic CPM performance has been analysed using established economic metrics, Net Present Value (NPV), Return on Investment (ROI), and Payback period (PBP); for these, the plant lifetime, τ (20 yr), and the discount rate, r (variable) are key parameters. Prices are taken as £538/kg and £229/kg for ibuprofen and artemisinin, respectively. For CapEx calculations, all equipment costs have been sourced from vendor databases. For ibuprofen, unit prices of all expensive equipment as listed by Bogdan et al. (2009) have been considered and scaled up accordingly; for artemisinin production, a literature figure for equipment cost of similar capacity has been used (Extance, 2012). Assumptions include: equipment delivery cost 5% of price, working capital 3.5% of annual sales, contingency 20% of the battery-limits installed cost (BLIC, i.e. equipment plus delivery) (Schaber et al., 2011); total CapEx is the sum of BLIC and contingency. For OpEx calculations, waste disposal costs £0.33 and £1.98 per litre of water and of solvent have been considered, respectively; utility cost is £0.96 per kg of input material (Schaber et al., 2011). Labour, material handling, tax and quality control have not been considered, but are essential components of a more detailed technoeconomic analysis. Annual operation is set at 7728 and 8000 hr for ibuprofen and artemisinin, respectively. Economic performance indices for CPM design evaluation are summarised in Table .

Table 2. Economic performance comparison for CPM production of both APIs analysed (r =5%).

	Ibuprofen	**Artemisinin**
NPV	£73,500	£108,300
ROI (%)	33.95	82.60
PBP (years)	3.27	1.28
BEP (kg API/year)	7.37	3.03

Artemisinin has a stronger economic potential (higher NPV and ROI), reaching payback (positive NPV) in less than half the time (Fig. 5). Nevertheless, both CPM designs are clearly viable, even if Table values are only useful in preliminary economic evaluation (implementation requires a comprehensive analysis of all equipment and cost factors). The CPM of artemisinin is very attractive as it uses as feedstock waste material from the current artemisinin extraction process: great added value is attainable by implementing this CPM design to address demand. The CPM of ibuprofen is also promising, but a strong competitive advantage is essential to demonstrate in case of no patent protection.

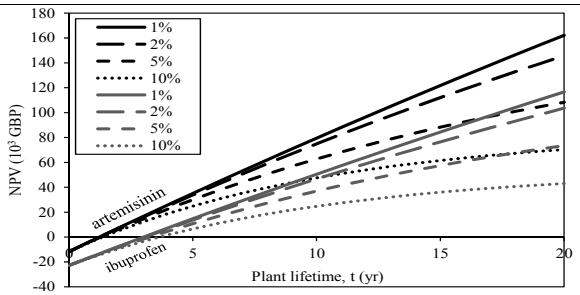

Figure 5. Comparison of projected Net Present Values (NPV) for a wide range of discount rates.

7. Conclusions

Continuous Pharmaceutical Manufacturing (CPM) has great potential to deliver strong cost and efficiency benefits for two APIs (ibuprofen and artemisinin) at a 50 kg/yr scale. Computed PFR volumes range from 2÷55 mL, illustrating CPM applicability benefits, with a positive environmental impact outlook (E-factors of 25.4 and 33.5, respectively), and the enormous sustainability benefit of using batch process waste as CPM feedstock. Both designs thus hold high economic promise (NPV: £73,500 and £108,300, ROI: 34% and 83%, PBP: 3.3 yr and 1.3 yr, respectively) toward CPM pilot plant implementation.

References

Alfonsi, K., Colberg., J. et al., 2008. Green chemistry tools to influence a medicinal chemistry and research chemistry based organisation, *Green Chem.* **10**(1): 31-36.

Artemisinin Enterprise, 2008. *Meeting the malaria treatment challenge*, York, UK.

Bedore, M.W., Zaborenko, N. et al., 2010. Aminolysis of exides in a microreactor system: A continuous flow approach to β-amino alcohols, Org. Proc. Res. Dev. **14**(2):432-440.

Bogdan, A.R., Poe, S.L. et al., 2009. The continuous-flow synthesis of Ibuprofen, *Angew. Chem. Int. Ed*. **48**(45): 8547-8550.

Extance, A., 2012. Tube-wrapped lamp makes malaria drug, *RSC Chemistry World* (online).

Gernaey, K.V., Cervera-Padrell, A.E. et al., 2012. Development of continuous pharmaceutical production processes supported by PSE methods tools, *Future Med. Chem*. **4**(11): 1371-1374.

Gerogiorgis, D.I., Barton, P.I., 2009. Steady-state optimization of a continuous pharmaceutical process, *Comp. Aided. Chem. Eng.* **27**(A): 927-932.

Gilmore, K., Kopetzki, D. et al., 2013. Continuous synthesis of artemisinin-derived medicines, *Chem. Commun.* **50**(84): 12652-12655.

Jolliffe, H.G., Gerogiorgis, D.I., 2015. Process modelling and simulation for continuous pharmaceutical manufacturing of ibuprofen, *Chem. Eng. Res. Des.* (in press).

Kopetzki, D., Lévesque, F., Seeberger, P.H., 2013. A continuous-flow process for the synthesis of artemisinin, *Chem.-Eur. J.* **19**(17): 5450-5456.

Mascia, S., Heider, P.L. et al., 2013. End-to-end continuous manufacturing of pharmaceuticals, *Angew. Chem. Int. Ed.* **52**(47): 12359-12363.

Peplow, M., 2013. Malaria drug made in yeast causes market ferment, *Nature* **494**(7436): 160-161.

Poechlauer, P., Colberg, J. et al., 2013. Pharmaceutical roundtable study demonstrates the value of continuous manufacturing in the design of greener processes, *Org. Proc. Res. Dev*. **17**(12): 1472-1478.

Ritter, S.K., 2013. Greener organic synthesis, *Chem. Eng. News* **91**(15): 22-23.

Schaber, S.D., Gerogiorgis, D.I. et al., 2011. Economic analysis of integrated continuous and batch pharmaceutical manufacturing: a case study, *Ind. Eng. Chem. Res*. **50**(17): 10083-10092.

Sheldon, R.A., 2012. Fundamentals of green chemistry: efficiency in reaction design, *Chem. Soc. Rev.* **41**(4): 1437-1451.

Tu, Y., 2011. The discovery of artemisinin (qinghaosu) and gifts from Chinese medicine, *Nat. Med*. **17**(10): 1217-1220.

Krist V. Gernaey, Jakob K. Huusom and Rafiqul Gani (Eds.), 12th International Symposium on Process Systems Engineering and 25th European Symposium on Computer Aided Process Engineering.
31 May – 4 June 2015, Copenhagen, Denmark

Data-based multivariate modeling of a grain comminution process

Filippo Dal-Pastro[a], Pierantonio Facco[a], Fabrizio Bezzo[a], Helen Thomas[b], Eliana Zamprogna[b], Massimiliano Barolo[a,*]

[a]*CAPE-Lab – Computer-Aided Process Engineering Laboratory, Department of Industrial Engineering, University of Padova, via Marzolo, 9 35131 Padova PD (Italy)*
[b]*Bühler AG, Division Grain Processing, Gupfenstrasse, 5 9240 Uzwil (Switerland)*

max.barolo@unipd.it

Abstract

A grain comminution process is based on a gradual size reduction approach, through repeated milling and sieving units that increase the flour yield. In this study we use latent variable modeling techniques to link process parameters and grain properties to the final product quality. Using experimental data, it is shown how the use of models in their direct form allows one to improve process understanding and to predict the product quality from the process settings and grain properties. Additionally, it is shown that, by inverting the latent variable models, the optimal combination of process parameters and grain properties leading to a desired product quality can be determined.

Keywords: grain comminution, latent variable model, process understanding, product design

1. Introduction

Through direct consumption and indirectly via animal feed, cereals supply more than half of global food consumption. Around 2 billion tons of cereals are produced annually, with wheat contributing around 600 million tons, from which 123 million tons of flour are produced from medium and large mills (Campbell, 2007). The aim of wheat milling is to break open the kernel and to separate its structural components (endosperm, bran and germ) in such a way as to recover endosperm in maximum quantity at minimum contamination (with bran and germ), and at a minimum cost. A wheat milling process typically comprises up to five break stages and a dozen reduction stages, arranged in a complex configuration (Campbell, 2007). Flour milling uses repeated size reduction steps (by roller milling) and repeated separation steps (by sifting) to achieve an effective separation of endosperm from bran and germ, and an appropriate reduction of the endosperm into flour. This gradual reduction approach greatly increases the flour recovery (with minimum bran contamination), but needs profound process understanding to be operated. This is also due to the origin of wheat that, as a natural product, shows a high intrinsic variability. Therefore, the millers' main challenge is to produce flour of consistent uniform quality, in the face of a changing feedstock. Nowadays the process operation is mostly based on the operators' experience. This study focuses on the second break stage of a wheat milling process. The second break is one of the most important passages of the entire process, and only few studies have been reported about this passage. Yuan et al. (2003) considered second break milling in their systematic analysis of the entire break subsystem. Al-Mogahwi

and Baker (2005) included the second break passage in their study of both break and reduction milling.

There is a great interest in finding systematic approaches that can be used to improve process understanding, to support the process operation by predicting the product quality, and to optimize the process operating conditions by suggesting how the process parameters should be set to counteract the changing characteristics of the input materials, as well as to ensure a consistent product quality. Modeling the process by first principles is still a very challenging and unresolved issue. A data-based modeling approach, namely partial least-squares regression (PLS; Wold et al., 2001) is used in this study to analyze the second break process, given the multivariate nature of the process and the correlation showed by the process parameters, wheat properties and product quality.

2. Materials and methods

2.1. Experiments and available data

The dataset used in this study was obtained from an experimental campaign carried out in a pilot-scale roller mill fed with material entering the second break stage of an industrial-scale mill. Experiments were designed following a central composite face-centered design of experiments (DoE) strategy applied to the most important parameters of the process: wheat kernel moisture content (MC), mass flow (MF) to the roller mill and milling gap (MG). The ranges for MC, MF and MG were chosen in such a way as to match typical industrial ranges. In addition, for each experiment, ambient humidity (MC_e) and ambient temperature (T_e) were measured and included in the dataset. Each experiment was repeated at least twice and average values are used in this study. Some other parameters affect the milling operation. These comprise process and equipment parameters (such as roll speed, roll speed differential, roll fluting) and wheat properties (such as hardness of the wheat kernel). Roll speed, speed differential, and fluting were fixed as in the industrial second break roller mill, whereas the kernel hardness was not considered in this study.

The experimental data were organized in a regressor matrix **X** [15×5] and in a response matrix **Y** [15×37]. The **X** matrix included 5 variables referring to process parameters (MF and MG), wheat properties (MC) and ambient conditions (MC_e and T_e) for 15 different averaged observations. The **Y** matrix included 37 variables, where each y_i variable represents the range of diameters of the output particle size distribution (PSD) within bin i; namely, y_1 corresponds to the smallest particle diameter range (0-4 μm), whereas y_{37} represents the biggest diameter range (5958-7399 μm). The value taken by each y_i variable refers to the volume fraction of particles whose diameter is within the diameter range of bin i. The PSDs were measured with the image analysis sensor QICPIC (Sympatec GmbH, Germany). Note that the particle diameter range does not change linearly across the PSD bins (see later on Figure 1b).

2.2. Mathematical methods

PLS (Wold et al., 2001) is a latent variable regression modeling technique that relates input variables (e.g., process parameters and wheat properties) and response matrices (e.g., product PSD) by projecting them onto a space of uncorrelated latent variables (LVs). The LVs explain the major sources of the variability of the inputs that are most correlated to the variability of the response variables. After appropriate data pretreatment (namely, autoscaling; Wold et al., 2001), PLS is applied to the **X** [I×N] and **Y** [I×M] matrices:

$$\mathbf{X} = \mathbf{T}\mathbf{P}^{\mathrm{T}} + \mathbf{E}_{\mathbf{X}} \tag{1}$$

$$\mathbf{Y} = \mathbf{T}\mathbf{Q}^{\mathrm{T}} + \mathbf{E}_{\mathbf{Y}} \tag{2}$$

$$\mathbf{T} = \mathbf{X}\mathbf{W}^{*} \quad , \tag{3}$$

where $\mathbf{T}$ [$I \times A$] is the score matrix, $\mathbf{P}$ [$N \times A$] and $\mathbf{Q}$ [$M \times A$] are the loading matrices and $\mathbf{W}^*$ [$N \times A$] is the weight matrix. $\mathbf{E}_{\mathbf{X}}$ [$I \times N$] and $\mathbf{E}_{\mathbf{Y}}$ [$I \times M$] are the residual matrices accounting for the model mismatch. A represents the number of significant LVs chosen to build the model, i.e. it corresponds to the dimensions of the latent space that should be appropriately selected (Picard and Cook, 1984).

A PLS model correlating $\mathbf{X}$ and $\mathbf{Y}$ explains the systematic variability in the process settings and wheat properties that are related to the variability in the product PSD. This model can be exploited to identify the main driving forces acting on the system. To this purpose, a loading analysis is used. Loading plots are very useful to understand and quantify the correlation between input variables and product characteristics; namely, they allow one to understand the effects of input process parameters on the output PSD.

PLS models can be used in their direct form for predictive purposes (e.g., to predict the PSD from process parameters and wheat properties). On the other hand, PLS model inversion (Jaeckle and MacGregor, 2000) can be exploited to calculate the combination $\mathbf{x}_{\mathrm{NEW}}$ of input conditions (e.g., process parameters and wheat properties) that lead to desired product quality $\mathbf{y}_{\mathrm{DES}}$.

Letting $R_{\mathbf{X}}$=rank($\mathbf{X}$) and $R_{\mathbf{Y}}$=rank($\mathbf{Y}$), if $R_{\mathbf{X}} = R_{\mathbf{Y}}$ (namely, the effective dimension of $\mathbf{X}$ is the same as that of $\mathbf{Y}$) direct model inversion can be done and $\mathbf{x}_{\mathrm{NEW}}$ can be calculated as:

$$\mathbf{x}_{\mathrm{NEW}} = \mathbf{t}_{\mathrm{DES}}\mathbf{P}^{\mathrm{T}} \quad , \tag{4}$$

where:

$$\mathbf{t}_{\mathrm{DES}}^{\mathrm{T}} = (\mathbf{Q}\mathbf{Q}^{\mathrm{T}})^{-1}\mathbf{Q}^{\mathrm{T}}\mathbf{y}_{\mathrm{DES}}^{\mathrm{T}} \quad . \tag{5}$$

Note that the designed input set $\mathbf{x}_{\mathrm{NEW}}$ belongs to the model space and has the same covariance structure of historical data used for PLS model building.

3. Results and discussion

A PLS model using 3 LVs explains a large amount of variability (86.9 % of explained variance) of the $\mathbf{X}$ matrix. Since MF, MC and MG were varied according to a DoE plan, they are uncorrelated, and each LV essentially describes the variability of each input. The 3 LVs describe a large fraction (88.6 %) also of the $\mathbf{Y}$ variability, with the first LV explaining as much as 83.2 % of the variance. This means that the variables describing the PSD are strongly correlated, and one LV is enough to describe almost the entire variability of $\mathbf{Y}$. Hence, the second and the third LVs are mainly used to describe the variability of $\mathbf{X}$. Note that describing a sufficiently large fraction of the $\mathbf{X}$ variability is important for model inversion.

The PLS model is used to: *i*) improve process understanding, by studying the correlation between the input parameters and the output PSD from the second break stage; *ii*) predict the product quality profile (PSD), and *iii*) to identify (by model inversion) the process parameters and wheat properties that are required to obtain a product with desired quality specifications.

3.1. Process understanding

Figure 1 shows the plots of the **P** (Figure 1a) and **Q** (Figure 1b) loadings of the PLS model; each loading is weighted for the explained variance of the relevant LV.

The first latent variable (top plot of Figure 1a) is dominated by the MG. The effects of MG can be understood by comparing the top plot of Figure 1a with the top plot of Figure 1b, which is the loading plot of first LV of matrix **Y**. By looking at the top plot of Figure 1b, it can be seen that the MG has a strong effect on the whole PSD. Namely, when the MG increases, the quantity of particles with a diameter lower than 751 μm decreases (refer to the bars that have a negative value in the top plot of Figure 1b), whereas bigger particles increase. This behavior is meaningful from a physical point of view: when the MG decreases, the possibility of obtaining smaller particles increases. The threshold particle diameter is ~751 μm: a reduction of the particle diameter by MG reduction can be achieved for particles smaller than this threshold, and this is obtained at the expense of the fraction of particles with larger diameters. In fact, the number of particles with diameter larger than the threshold descreases as the MG decreases. Since first LV explains about 83 % of data variability of the output PSD, it can be concluded that nearly the whole data variability in the PSDs is due to the variability of the MG.

The second LV (lower plot of Figure 1a) is dominated by the MC. MC exhibits a negative correlation with MC_e and T_e (which are positively correlated). This correlation is not representative of the process, but simply illustrates the ambient conditions in the days when the experimentation was carried out. MC has a strong effect on particles whose diameter lays in the range 626-751 μm (tallest bar in the lower plot of Figure 1b). MC has a considerable influence also on particles that are bigger than 1081 μm (bars with negative values in the lower plot of Figure 1b). When MC increases, also the amount of these particles increases. This behavior can be explained physically by noticing that particles with diameter bigger than 1081 μm are identified as bran. The bran breakage behavior is highly dependent on the MC: a higher wheat kernel MC has the effect of hardening the bran, with the result that it breaks in larger particles.

The loading plots for third LV are not reported because, even though this LV is explaining a reasonably large amount of data variability for matrix **X** (20.4 %, due to the variability of MF), it explains a very low percentage of explained variance for **Y** (only 1.5 %), meaning that the effects of MF on the output PSDs are negligible.

It is interesting to notice that a threshold diameter range exists around 751-1081 μm, where all PSDs show an "inversion" pattern (namely, the relevant loadings change sign). The physical explanation for this behavior is the difference in the shape of the milled particles. Particles bigger than 1081 μm are identified as bran and are characterized by flat large particles (two-dimensional particles); smaller particles are made of endosperm and have a more spherical shape (three-dimensional particles). In fact, the difference in shape can explain why the PSD bins behave differently when a process parameter is changed.

3.2. Product quality prediction

In this subsection the main idea is to evaluate how the product quality can be predicted once process parameters, wheat properties and ambient conditions are known. A jackknife approach was used (Miller, 1964). Namely, one of the available observations was removed from the database and it was used to validate the model built on the remaining observations. The procedure was then iterated by including that observation in the dataset and removing a different one, until each observation was removed once. Eventually, the results were averaged through all iterations.

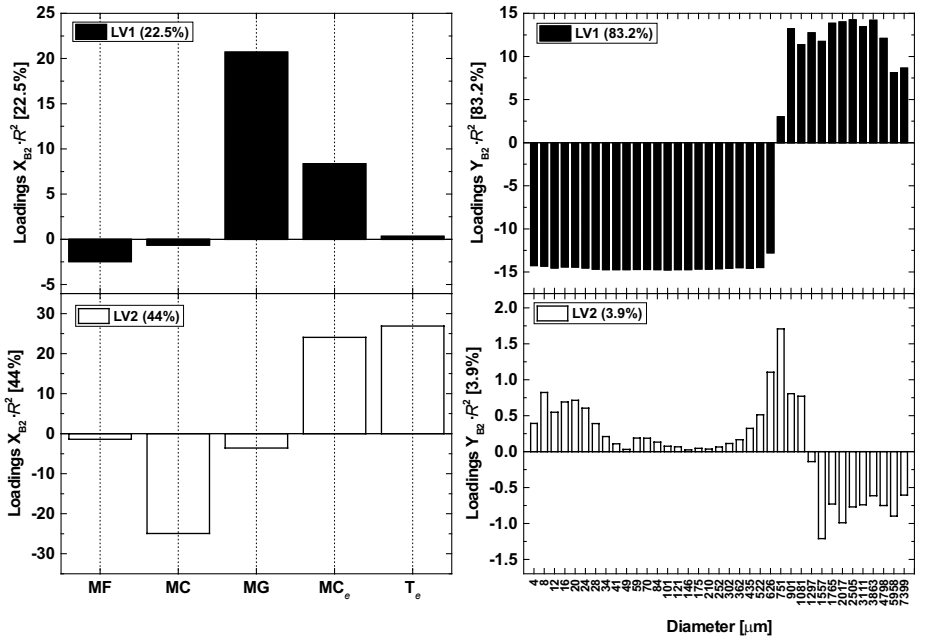

(a) (b)

Figure 1. Loading plots of the PLS model: (a) loadings of matrix **X** and (b) loadings of matrix **Y**.

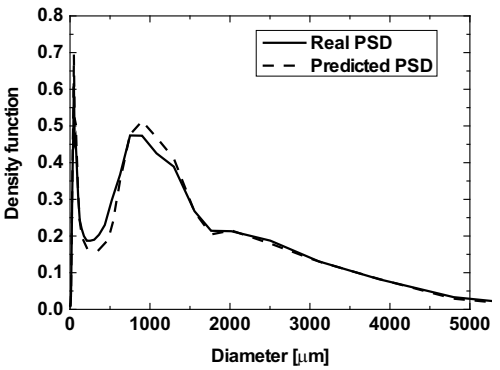

Figure 2. Example of prediction of output PSD from roller mill for the second break step.

Figure 2 shows that the predictions are very good for all observations. The average root mean square error (RMSE) for all predictions is 0.0338 (that corresponds to an average correlation coefficient R^2 of 0.9755); the average RMSE is lower than the average variability of the PSDs (0.1042). The prediction error is usually larger at the distribution peaks (i.e., where the PSD variability increases).

3.3. Milling product design

PLS model inversion can be used to calculate the best combination of process parameters and wheat properties that are needed to obtain a product with assigned PSD. As an illustrating example, the observation related to a product with desired PSD ($\mathbf{y}_{DES}$) was removed from the dataset, and the input combination (MG, MC and MF) required to obtain $\mathbf{y}_{DES}$ was estimated by direct model inversion. The calculated input set is

reported in Table 2 together with the true input set leading to $\mathbf{y}_{DES}$. Unfortunately, a validating experiment was not possible due to a problem in the experimental apparatus. Nevertheless, the calculated and true input sets are in fair agreement, indicating that the model inversion approach has the potential for the design of the optimal operating conditions.

Table 2. Example of product design for the second break step.

	MG [µm]	MC [%]	MF [kg/h]
Input set estimated by model inversion	275	17.22	316.58
True input set	300	14.89	300.00

4. Conclusions

In this study, how PLS modeling can be used in different ways to support the operation of the second break step in a wheat milling process has been discussed.

A loadings analysis improved process understanding, by studying and quantifying the correlation between process parameter, wheat properties and product PSD. The study supported the evidence that the product PSD is mostly affected by the milling gap, but it was found that the correlation between input parameters and output PSD depends on how the different constituents distribute in the milled product, as endosperm and bran have different breakage behavior. The range of particle diameters separating different breakage behavior was found to be around 751-1081 µm.

Latent variables models have been used to predict the product PSD with very promising results. This kind of prediction can greatly support process optimization, allowing one to predict product quality profile reducing costly and time expensive experimental campaigns. Furthermore, it was shown how the same models can be inverted and used to calculate the best combination of input parameters (milling gap, moisture content and wheat mass flow) that leads to a desired PSD. Although this study concentrated on the second break stage, it can be extended to other break and reduction passages.

References

C.M. Jaeckle, J.F. MacGregor, 2000, Industrial applications of product design through the inversion of latent variable models, Chemom. Intell. Lab. Syst. 50, 199–210.

G.M. Campbell, 2007, Roller milling of wheat, in: Handbook of Powder Technology. Elsevier Ltd, Amsterdam (Netherlands).

H.W.H. Al-Mogahwi, C.G.J. Baker, 2005, Performance evaluation of mills and separators in a commercial flour mill, Food Bioprod. Process. 83, 25–35.

J. Yuan, R.A. Flores, D. Eustace, G.A. Milliken, 2003, A systematic analysis of the break subsystems of a wheat flour pilot mill, Food Bioprod. Process. 81, 170–179.

R.G. Miller, 1964, A trustworthy jackknife, Ann. Math. Stat. 1594–1605.

R.R. Picard, R.D. Cook, 1984, Cross-validation of regression models, J. Am. Stat. Assoc. 79, 575–583.

S. Wold, M. Sjöström, L. Eriksson, 2001, PLS-regression: a basic tool of chemometrics, Chemom. Intell. Lab. Syst. 58, 109–130.

Krist V. Gernaey, Jakob K. Huusom and Rafiqul Gani (Eds.), 12th International Symposium on Process Systems Engineering and 25th European Symposium on Computer Aided Process Engineering.
31 May – 4 June 2015, Copenhagen, Denmark

A comprehensive sensitivity and uncertainty analysis of a milk drying process

A. Ferrari[1], S. Gutiérrez[1], G. Sin[2]

[1]*Chemical & Process Systems Engineering Group – Chemical Engineering Institute - Engineering School – Universidad de la República, Julio Herrera y Reissig 565, CP 11300, Montevideo, Uruguay. aferrari@fing.edu.uy*

[2]*CAPEC-PROCESS - Deparment of Chemical and Biochemical Engineeriing - Technical University of Denmark, Søltofts Plads, Building 229, DK-2800 Kgs. Lyngby, Denmark. gsi@kt.dtu.dk*

Abstract

A simple steady state model of a milk drying process was built to help process understanding. It involves a spray chamber and also internal/external fluid beds. The model was subjected to a statistical analysis for quality assurance using sensitivity analysis (SA) of inputs/parameters, identifiability analysis (IA) of parameters, and uncertainty analysis (UA) to estimate confidence intervals on parameters and in model predictions. A local method was used for SA, IA was based in the delta mean square and collinearity index calculation, and Maximum Likelihood Estimation was used as the main UA technique. SA results provide evidence towards over-parameterization in the model, and the chamber inlet dry bulb air temperature was the variable (input) with the highest sensitivity. IA results indicated that at most 4 parameters are identifiable: two from spray chamber and one from each fluid bed dryer. Moreover, the confidence intervals obtained for identifiable parameters were reasonable, although two parameters were found significantly correlated. The obtained confidence intervals for model predictions reflect a low uncertainty for the outputs. The rigorously analyzed model is expected to contribute to model-based decision making for process operation and optimization.

Keywords: Sensitivity analysis, Identifiability analysis, Uncertainty analysis, Milk drying process.

1. Introduction

The most widely used technique for dehydration of dairy products is spray drying. It can preserve food properties as it doesn't involve severe heat treatments since drying occurs within a few seconds (Schuck et al., 2008). The standard process has three sequential stages: spray chamber, internal and external fluid beds as it is shown in Figure 1. There are two fundamental approaches to modeling drying processes: lumped and distributed formulations. The main difference is that the distributed models can include second order terms (diffusion) for air stream and also inside each particle being dried. The lumped models involve the concept of the reaction engineering approach (process kinetics) using a characteristic drying curve (Wang and Langrish, 2009). In this study a simple steady state lumped model for production scale of three stage dryer (not shown due to space restrictions) is built to help process understanding and guide optimization efforts. It is based on a simultaneous convective heat/mass transfer between the mean particle/air trajectories. Figure 1 shows this model and Table 1 exposes the involved variables and parameters. In this work the model is subjected to a comprehensive statistical analysis for quality assurance.The following methods are used: (i) sensitivity

analysis (SA) of inputs/parameters, (ii) identifiability analysis (IA) of parameters for parameter estimation (PE), and (iii) uncertainty analysis (UA) to estimate confidence interval on the identifiable parameter subset and also in model predictions.

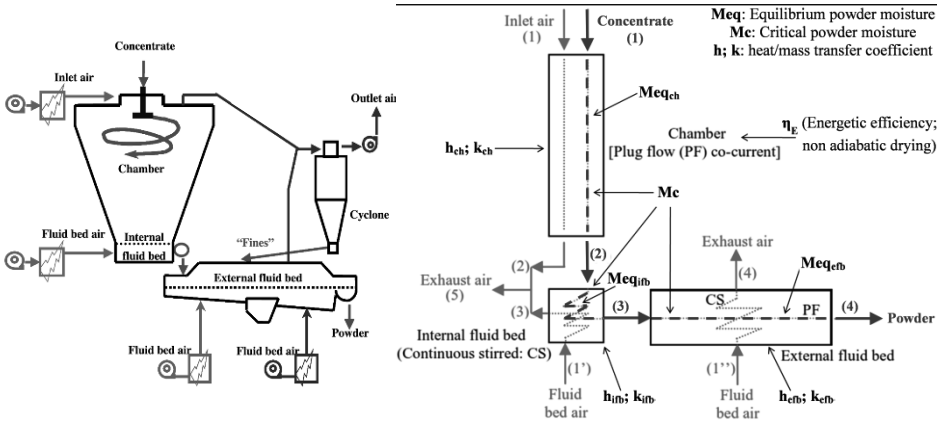

Figure 1. Left: physical system of three stage dryer scheme; right: process model.

Table 1. Description of model variables and parameters

Symbol	Name	Dimension
Inputs		
$W_{P,1}$	Concentrate mass flow rate	$kg_{total}.h^{-1}$
$M_{P,1}$	Concentrate moisture	$kg_{water}.kg_{total}^{-1}$
$T_{P,1}$	Concentrate temperature	K
$Q_{A,1}$	Chamber inlet air volumetric flow rate	$m^3.h^{-1}$
$H_{A,1}$	Chamber inlet air humidity	$kg_{water}.kg_{dry\ air}^{-1}$
$T_{A,1}$	Chamber inlet dry bulb air temperature	K
$Q_{A,1}'$; $Q_{A,1}''$	Internal/external fluid bed inlet air volumetric flow rate	$m^3.h^{-1}$
$H_{A,1}'$; $H_{A,1}''$	Internal/external fluid bed inlet air humidity	$kg_{water}.kg_{dry\ air}^{-1}$
$T_{A,1}'$; $T_{A,1}''$	Internal/external fluid bed inlet dry bulb air temperature	K
Outputs		
$M_{P,2}$; $M_{P,3}$ and $M_{P,4}$	Powder moisture	$kg_{water}.kg_{total}^{-1}$
$T_{P,2}$; $T_{P,3}$ and $T_{P,4}$	Powder temperature	K
$H_{A,2}$; $H_{A,3}$; $H_{A,4}$ and $H_{A,5}$	Exhaust air humidity	$kg_{water}.kg_{dry\ air}^{-1}$
$T_{A,2}$; $T_{A,3}$; $T_{A,4}$ and $T_{A,5}$	Exhaust dry bulb air temperature	K
Parameters		
M_C	Critical dry basis powder moisture	$kg_{water}.kg_{dry\ solids}^{-1}$
Meq_{ch}; Meq_{ifb}; Meq_{efb}	Equilibrium dry basis powder moisture for the chamber, internal fluid bed and external fluid bed	$kg_{water}.kg_{dry\ solids}^{-1}$
h_{ch}; h_{ifb}; h_{efb}	Heat transfer coefficient for the chamber, internal fluid bed and external fluid bed	$kcal.h^{-1}.K^{-1}.m_{axial}^{-1}$
k_{ch}; k_{ifb}; k_{efb}	Mass transfer coefficient for the chamber, internal fluid bed and external fluid bed	$kg_{water}.h^{-1}.(kg_{water}.kg_{dry\ air}^{-1})^{-1}.m_{axial}^{-1}$
η_E	Energetic efficiency for chamber [$0 < \eta_E < 1$]	Dimensionless

2. Materials and methods

2.1. Data

Figure 2 shows the outputs used in this work which are derived from a full scale process (feed concentration: 48% total solids; throughput: 6 ton/h final powder; actual plant) (**Mp**: product moisture; **HA**: air humidity; **Tp/TA**: product/air temperature). The data also agree with profiles showed by Kieviet (1997) and Birchal and Passos (2005).

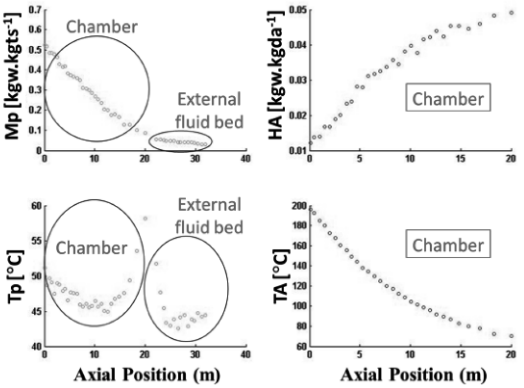

Figure 2. Process data; "axial position": reference independent variable representing the virtual straight way for mean trajectories; kgw = kg_{water}, kgts = $kg_{total\ solids}$, kgda = $kg_{dry\ air}$.

2.2. Sensitivity, identifiability and uncertainty analysis

A differential local SA was implemented. Each input or parameter is perturbed in turn (around a nominal point), and the effect on the outputs is measured by Eq. (1).

$$s_{ij} = \left(\frac{\partial y_i}{\partial \theta_j} \right) \cdot \frac{\theta_j^{\,0}}{y_i^{\,0}} \tag{1}$$

Where **s** is the dimensionless sensitivity; **y** and $\mathbf{y^0}$, the output and its reference value; $\boldsymbol{\theta}$ and $\boldsymbol{\theta^0}$, the input (or parameter) and its nominal value; **i**, an output index; and **j,** an input (or parameter) index.

IA implementation was based in the delta mean square and collinearity index calculation (Sin et al., 2010). It is based in the local SA of the outputs to the parameters, sensitivities that are then used to rank the parameter significance through a measure called $\boldsymbol{\delta^{msqr}}$. Then, parameter subsets are analyzed and the linear correlation between parameters is evaluated through a new measure called collinearity index ($\boldsymbol{\gamma}$). As higher the $\boldsymbol{\gamma}$ value, means more correlation between the parameters. The analysis is used to find the largest size identifiable subset assuming a threshold $\boldsymbol{\gamma}$ value for the identifiability. Table 2 summarizes the steps involved in this IA.

Table 2. Sequential steps for identifiability analysis

Steps	Formulation	
Absolute sensitivity(*)	$S_a = \{s_{a,ij}\}$	$s_{a,ij} = \partial y_i / \partial \theta_j .$
Dimensionless sensitivity	$S_{nd} = \{s_{nd,ij}\}$	$s_{nd,ij} = s_{ij}$ [see Eq. (1)]
Normalized sensitivity	$S_{norm} = \{s_{norm,ij}\}$	$s_{norm,ij} = s_{nd,ij} / \left\| s_{nd,ij} \right\|$
Parameter significance	$\partial_j^{\,msqr} = \sqrt{\frac{1}{N} \cdot \sum_{i=1}^{N} (s_{nd,ij})^2}$	
Collinearity index(*)	$\gamma_K = \frac{1}{\sqrt{\min(\lambda_K)}}$	$\lambda_K = eigen\,(S_{norm,K}{}^T S_{norm,K})$

(*) - **i**, **j** and **K**, refers to an index for outputs, parameters, and parameter subsets respectively.

In order to rank subsets with the same $\boldsymbol{\gamma}$ value, it is used a new measure called subset sensitivity index (**SSI**) which is defined by Eq.(2).

$$SSI = mean(\partial_0^{\,msqr}, \partial_1^{\,msqr}, ...\partial_j^{\,msqr}) \qquad \text{j} = \text{each parameter of the subset} \tag{2}$$

Maximum Likelihood Estimation (MLE) was used as the main UA technique for the estimation of an identifiable parameter subset and output predictions. In this work PE was solved through a least squares method which represents a special case of MLE (Seber and Wild, 1989). Confidence interval of parameters ($\boldsymbol{\theta_{1-\alpha}}$) are estimated in accordance to Eq. (3) and (4).

$$COV(\theta) = \frac{J(\theta)}{N-p}.\left[\left(\frac{\partial y}{\partial \theta}\right)^T Q_m^{-1}\left(\frac{\partial y}{\partial \theta}\right)\right] \quad \text{Covariance matrix of parameter estimators} \tag{3}$$

Where $\mathbf{J(\theta)}$ is the sum of squared errors from least squares method; $\mathbf{(\delta y/\delta \theta)}$, a sensitivity matrix; $\mathbf{Q_m}$, the covariance matrix of errors; and **N** and **p**, the total number of measurements and parameters. All functions are evaluated at the estimated values of the parameter set.

$$\theta_{1-\alpha} = \hat{\theta} \pm \sqrt{diag[COV(\hat{\theta})]}.t\left(N-p, \frac{\alpha}{2}\right) \tag{4}$$

Where $\mathbf{t(N\text{-}p,\alpha/2)}$ is the upper $\boldsymbol{\alpha/2}$ quantile of t-distribution with **N-p** degrees of freedom. The correlation matrix between two estimators [$\mathbf{COR(\theta_l,\theta_u)}$] is given by Eq. (5) and the confidence interval of predictions ($\mathbf{y_{1-\alpha}}$) is estimated using Eq. (6) and (7).

$$COR(\theta_l, \theta_u) = \frac{COV(\theta_l, \theta_u)}{\sqrt{\sigma_{\theta_l}^2 . \sigma_{\theta_u}^2}} \tag{5}$$

$$COV(y) = \left(\frac{\partial y}{\partial \theta}\right) COV(\hat{\theta}) \left(\frac{\partial y}{\partial \theta}\right)^T \quad \text{Covariance matrix of predictions} \tag{6}$$

$$y_{1-\alpha} = y(\hat{\theta}) \pm \sqrt{diag[COV(y)]}.t\left(N-p, \frac{\alpha}{2}\right) \tag{7}$$

Modelling and algorithms for SA, IA and UA were implemented in Matlab 7 (R2010a).

3. Results and discussion

3.1. Sensitivity and identifiability analysis

SA results are shown in Figure 3 where y-axis indicates the local dimensionless sensitivity of an input/parameter to a measured output and x-axis is the location of the measured data points. The results provide evidence about model over-parameterization, which are revealed by the low sensitivity values and close similarity of some sensitivity profiles indicating correlation between the parameters. These could represent difficulties in order to obtain unique estimates for parameters (Sin et al., 2010). Hence, identifiability analysis becomes necessary to identify a parameter subset for PE. The chamber inlet dry bulb air temperature ($\mathbf{T_{A1}}$) was found the variable with major sensitivity as it is showed in Figure 3.

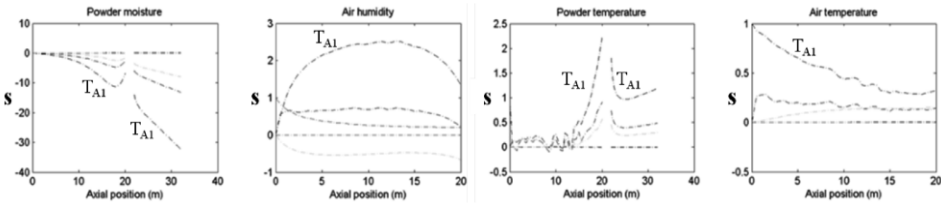

Figure 3. Example of SA results; comparison between sensitivity respect to $\mathbf{T_{A1}}$ and other variables.

With respect to IA results, Figure 4 and Table 3 show the most sensitive parameters ($\boldsymbol{\delta^{msqr}}$) and the ranking of largest size identifiable subsets. Identifiability threshold for collinearity index was assumed 5. The results indicated that identifiable subsets represent a 4.4 % of total subsets and at most 4 parameters are identifiable. These are

two parameters from spray chamber and one parameter from each of fluid bed models. This reflects the major significance of the spray drying process in the model overall. Another observation is that mass and heat transfer coefficients from the same unit are not identifiable simultaneously.

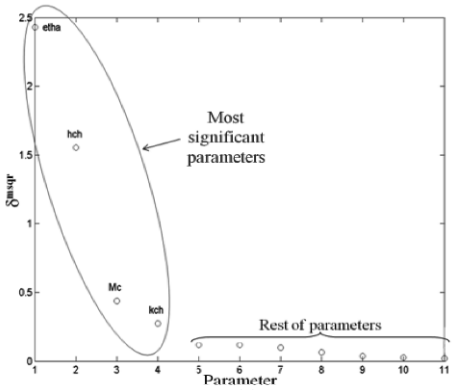

Figure 4. Most sensitive parameters.

Table 3. Ranking of largest size identifiable subsets

Largest size identifiable parameter subsets				Collinearity index	SSI
Meq_{ch}	Meq_{ifb}	h_{ch}	k_{efb}	4.387	0.463
Meq_{ch}	h_{ch}	k_{ifb}	k_{efb}	4.387	0.458
Meq_{ch}	Meq_{ifb}	h_{ch}	h_{efb}	4.602	0.443
Meq_{ch}	Meq_{ifb}	Meq_{efb}	h_{ch}	4.475	0.438
Meq_{ch}	h_{ch}	h_{efb}	k_{ifb}	4.602	0.438
Meq_{ch}	Meq_{efb}	h_{ch}	k_{ifb}	4.475	0.433
Meq_{ch}	Meq_{ifb}	k_{ch}	k_{efb}	4.215	0.143
Meq_{ch}	k_{ch}	k_{ifb}	k_{efb}	4.215	0.138
Meq_{ch}	Meq_{ifb}	h_{efb}	k_{ch}	4.417	0.123
Meq_{ch}	Meq_{ifb}	Meq_{efb}	k_{ch}	4.298	0.119
Meq_{ch}	h_{efb}	k_{ch}	k_{ifb}	4.417	0.118
Meq_{ch}	Meq_{efb}	k_{ch}	k_{ifb}	4.298	0.113
Meq_{ch}	h_{ifb}	h_{efb}	k_{ch}	4.989	0.100

This is reasonable because both phenomena are linked by system fluid-dynamics.

3.2. Uncertainty analysis

The identifiable subset for PE was chosen from a maximum **SSI** point of view, since the minimum collinearity index value of most subsets were close to each other. The selected subset is **{Meq_{ch}, Meq_{ifb}, h_{ch}, k_{efb}}**. The optimization problem was solved using the "lsqnonlin" function with the "trust-region reflective" algorithm. Table 4 summarizes main PE results. Despite confidence intervals for parameters present a reasonable extension, some correlation between h_{ch} and Meq_{ifb} is observed (correlation coefficient: 0.85). Parameters Meq_{ch} and Meq_{ifb} seem to also have a pseudo correlation (coefficient: -0.55). Figures 5 and 6 show the model fit to the data and the posterior simulations. Good fit and low model predictions uncertainties were obtained.

Table 4. PE results ([Meq_{ch}, Meq_{ifb}]: $kg_{water}.kg_{dry\ solids}^{-1}$; [$h_{ch}$]: $kcal.h^{-1}.K^{-1}.m_{axial}^{-1}$; [$k_{efb}$]: $kg_{water}.h^{-1}.(kg_{water}.kg_{dry\ air}^{-1})^{-1}.m_{axial}^{-1}$)

	Meq_{ch}	Meq_{ifb}	h_{ch}	k_{efb}
Mean	0.081	0.031	2126	1889
Conf. interval (95%)	[0.074 - 0.087]	[0.026 - 0.036]	[2103 - 2149]	[1740 - 2038]
		Correlation matrix		
Meq_{ch}	1	-0.55	-0.41	0.17
Meq_{ifb}	-0.55	1	0.85	0.37
h_{ch}	-0.41	0.85	1	0.15
k_{efb}	0.17	0.37	0.15	1

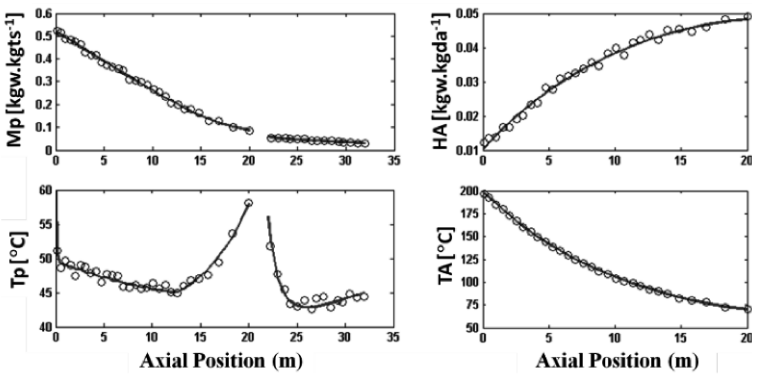

Figure 5. MLE fitting (data: dotted; model: line).

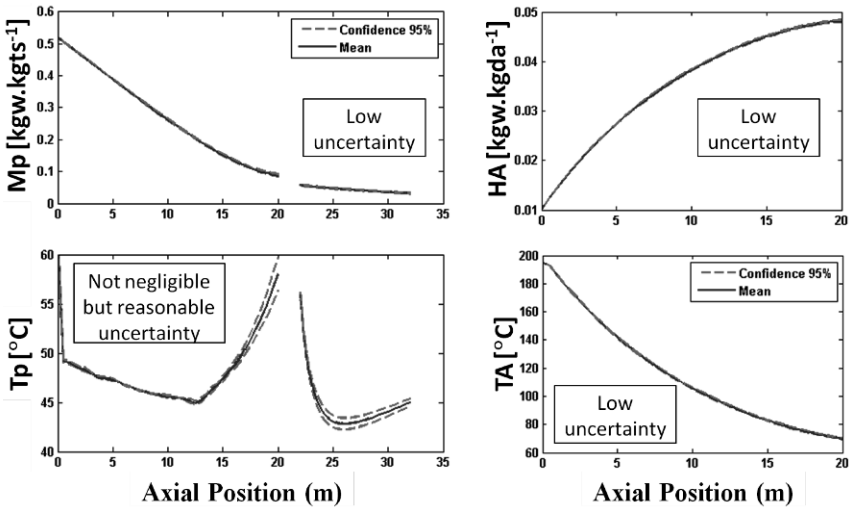

Figure 6. Error propagation in output predictions.

4. Concluding Remarks

A simple steady state model for milk spray and fluid bed drying was developed and implemented in Matlab. The results indicate the presence of some degree of over-parameterization and thus suggesting a potential for model reduction which is a future challenge. As chamber inlet dry bulb air temperature was the variable with major local sensitivity, this point to energy optimization potential since air heating represents the main energy consumption in the system. IA implementation indicated that maximum 4 parameters are identifiable: two from spray and one from each fluid bed. Despite PE was carried out for the best identifiable subset, it was found some degree of correlation between two of the parameters. To reduce this correlation, it is suggested to improve the quality/quantity of available experimental data by means of design of experiments. As posterior simulations present low uncertainty (95% confidence), the developed model is expected to be a robust tool for a model-based decision-making at industrial scale.

References

V. S. Birchal and M.L. Passos, 2005. Modeling and simulation of milk emulsion drying in spray dryers, *Brazilian Journal of Chemical Engineering*, 22(2), 293-302.

F. G. Kieviet, 1997. Modelling quality in spray drying, Laboratory of Separation Processes and Transport Phenomena, Department of Chemical Engineering, Eindhoven University of Technology.

P. Schuck, A. Dolivet, S. Méjean, and R. Jeantet, 2008. Relative humidity of outlet air: the key parameter to optimize moisture content and water activity of dairy powders, *Dairy Science & Technology*, 88, 45–52.

G. Seber and C. Wild, 1989. Nonlinear regression. New York: Wiley.

G. Sin, A.S. Meyer, and K.V. Gernaey, 2010. Assessing reliability of cellulose hydrolysis models to support biofuel process design—Identifiability and uncertainty analysis, *Computers & Chemical Engineering*, 34, 1385-1392.

S. Wang and T.A.G. Langrish, 2009. A distributed parameter model for particles in the spray drying process, *Advanced Powder Technology*, 20, 220–226.

Krist V. Gernaey, Jakob K. Huusom and Rafiqul Gani (Eds.), 12th International Symposium on Process Systems Engineering and 25th European Symposium on Computer Aided Process Engineering.
31 May – 4 June 2015, Copenhagen, Denmark

Optimization of Production Planning and Scheduling in the Ice Cream Industry

Mariana Carvalho[a], Tânia Pinto-Varela[a]*, Ana Paula Barbosa-Póvoa[a], Pedro Amorim[b], Bernardo Almada-Lobo[b]

[a]*CEG-IST, Instituto Superior Técnico, Universidade de Lisboa, Av. Rovisco Pais, 1049-101 Lisboa, Portugal*

INESC TEC, Faculdade de Engenharia, Universidade do Porto, Rua Dr. Roberto Frias, s/n, 4600-001 Porto, Portugal b
**tania.pinto.varela@tecnico.ulisboa.pt*

Abstract

As in other segments of the food industry, the ice-cream industry has its own features that influence the production management of its processes. Amongst these we identify: changeover tasks, products shelf-life, raw-materials (RM) perishability and, multiple deliveries during the planning horizon. These aspects have been often left out when studying the production planning and scheduling within the batch food industries. Thus, the aim of this work is to define an optimal planning and scheduling model based on the Resource Task Network, where the profit maximization is performed taking into account the cost trade-off between the approach based on the perishable RM inventory for the planning horizon versus the just-in-time RM delivery policy. The study is motivated by a Portuguese artisanal ice-cream industry.

Keywords: Production Scheduling, Batch process, RTN, Perishability, Raw-material Inventory Management.

1. Introduction

The food industry has been growing throughout the years. This growth has been driven by the increase of new market competitors, as well as by an increase on the consumers' demand and requirements. These factors combined have changed the trends in the industry and, production optimization is nowadays a need. In this context the production scheduling became an important activity for companies, allowing them to determine when, where and how a set of products should be produced considering the operational aspects. Thus, the scheduling activity has an important role for performance improvement while adjusting the resources consumption/production to demand needs through an accurate allocation. In the ice-cream industry, mainly artisanal ice-creams production, the major challenge is related to the raw-materials (RM) quality aspects as the final products' qualities/freshness is deeply dependent on these characteristics. In this context it is extremely important to address this aspect on the production at the scheduling level.

Nowadays, a wide range of methodologies and techniques to deal with the production planning and scheduling is available in the literature. However, the artisanal ice-cream industry is a food industry niche and the literature regarding this subject is very scarce.

Nevertheless, some research has been made considering the perishable inventory management, such as the work developed by Goyal (1994) and Soman et al.

(2004) based on the application of the Economic Lot Size Problem (ESLP). However, the ESLP has in its base assumptions that are unrealistic for the ice-cream industry. Beyond that, another research stream has been explored considering products shelf-life aspects. Kallrath (2005) presented a MILP formulation for design and planning problems considering products shelf-life limitation at the planning level. Accordingly in these cases limitations on the final products' shelf-life require records control to trace time stamps of products. Entrup et al. (2005) have developed a MILP formulation considering shelf-life restrictions for the final products applied to the yoghurt industry. This aspect was accounted in the objective function, which aims to maximize the margin contribution. Considering the segment of seafood products, Cai et al. (2008) proposed a formulation that takes into account the RM perishability, considering three type of decisions: i) the type of products to be produced, ii) the processing time of resources to be allocated to each type of product, and finally, iii) the sequence of products production . The authors stated that this model can be applied to any system that has limitations in terms of RM and uncertainty in the delivery dates. Amorim et al. (2011) have also presented a MILP formulation exploring two cases; i) a make-to-order and; ii) a hybrid make-to-order /make-to-stock strategy.

Notwithstanding, the research on production planning and scheduling in the ice-cream industry with perishable goods is still at its beginning. Exploring this gap, the present work develops a mathematical formulation for the artisanal ice-cream batch multipurpose and multi-product process. The aim of the model is to explore the characteristics of the artisanal ice-cream industry, accounting for RM perishability, changeover tasks and multiple deliveries simultaneously with the planning and process scheduling.

2. Description of Ice-cream Production Process

The ice-cream industry has different types of ice-creams production, which are often classified into four different categories according to their main ingredient, as it is shown in Figure 1. The ice-cream is classified based on: vanilla, cream, yoghurt and fruits/sorbets. However, when considering the production process of these products they are mainly divided in two categories: sorbets and other types of ice-creams production. Both categories differ in its production process until frozen task is reached.

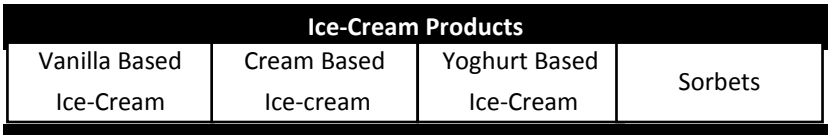

Figure 1 – Classification of the types of ice-creams.

For confidentiality reasons a generic ice-cream production process is characterized in Figure 2, followed by its description.

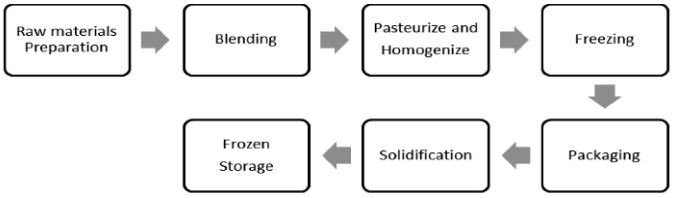

Figure 2 - Generic diagram of the ice-cream production process.

Raw-Materials Preparation: Each product requires a different RM according to its flavor. All RM must have good quality to avoid quality problems in the final products. According to each RM, its chemical characteristics and properties, different types of storage are used: dry, frozen and ambient temperature.

Blending: The blending phase comprises the mix of products according to each recipe of ice-cream. In this phase the ingredients are mixed for the production of a uniform liquid product.

Pasteurization/Homogenization: During pasteurization all the pathogens agents are removed. This task must be performed in a pre-defined temperature and duration. It is also during this phase that the product is homogenized, and particles are diminished in order to create uniform product with the desired consistency.

Freezing: In this phase the product that is in a liquid state is transformed into a mousse.

Packaging: The ice-cream is packaged in tubes to guarantee the safety, integrity and quality of the final product.

Solidification: The tubes go to an area with lower temperature than freezing to perform the solidification task. This task is performed in appropriate solidification equipment.

Frozen Storage: After performed all the phases mentioned before, the ice-creams are stored in a very low temperature environment to maximize the products quality.

3. Problem Statement

This work addresses the scheduling problem in an artisanal ice-cream production line of a multiproduct dairy batch plant. The optimal scheduling of production can be obtained by solving the following problem:

Given:

- Process description, through a Resource Tasks Network representation;
- The maximum amount of each type of resource available (equipment and manpower);
- Resource characteristics and capacities;
- Time horizon of planning;
- Task and resources operating data;
- Raw-material and products shelf-life;
- Spoilage, purchase and storage costs;
- Changeover costs;
- Quantities contracted of raw-material supplies;
- Selling price of ice-creams and sorbets;
- Demand deliveries along the planning horizon.

Determine:

- The amount of each resource used;
- The optimal scheduling satisfying not only the multi-deliveries along the horizon, but also, the demand at the end of the horizon;
- Raw-materials planning for the time horizon.

Based on the problem described, a formulation was developed using the RTN representation proposed by Pantelides (1994) considering a discrete time representation. This formulation was applied under two cases. The first case considers the existence of the current contracts with the RM suppliers, taking advantage of economies of scale, but requiring RM inventory control. Only the RM with shelf-life within the production time horizon are used in the production process. Otherwise, the RM are discarded at the end of the planning horizon and opportunity costs are considered. The second case explores a new policy, where a just-in-time approach is used. The inventory levels diminish but RM acquisition costs increases. A changeover task is required whenever the production between two different products changes.
The two cases were solved with an optimality margin of 0%. A computer with Intel 2.16 GHz processor and RAM memory of 4 GB and GAMS 24.2.2 software package with CPLEX solver were used.

4. Example

The scheduling of an artisanal ice-cream industry is explored considering the profit maximization. The production schedule of six products: 500 l of A- Strawberry, 250 l of B- Mango, 250 l of C- Limon, 200 l of D – Hazelnut, 600 l of E –Chocolate and 300 l of F – Vanilla is to be performed considering an aggregate set of specific RM to produce each flavor. For instance, Amp, Bmp, Cmp, Dmp, Emp and Fmp define the set of RM used to produce A, B, C, D, and F, respectively. For confidentiality reasons, it is not possible to explicitly state each recipe. Along the process, intermediated storage for working-in-process products is considered and a make-to-order strategy is followed. For simplicity, the processing time horizon is two working days with an 8h shift/day. This example is explored for two different cases: a) define the scheduling and perishable RM inventory, taking advantage of economy of scale in its purchase price and b) define the scheduling based on a just-in-time strategy associated to the RM supplies. A cost-benefit analysis of those cases is performed. The present suppliers contracts verify a delivery of 2600 l of RM, at a pre-defined price every second day, the JIT strategy follows the market price, which reflects an average increase of 50% monetary units over the pre-define price for each RM. The two cases differ in purchase costs. The other costs are only considered in case a), such as: storage and opportunity costs that are penalized, in case the RM is spoiled. Two time-windows are considered where the final products can be delivered.

The results obtained are shown in Figures 3 to 5. The RM consumption profile is shown in Figure 3. Case a) is based on the present contracts with the RM suppliers, the RM availability to fulfil the total demand is shown furthermore, the RM spoilage is penalized and discarded in the final of the planning horizon. Analyzing case b) using JIT strategy, the RM purchase is exactly the required to satisfy the order demand, avoid RM spoilage.

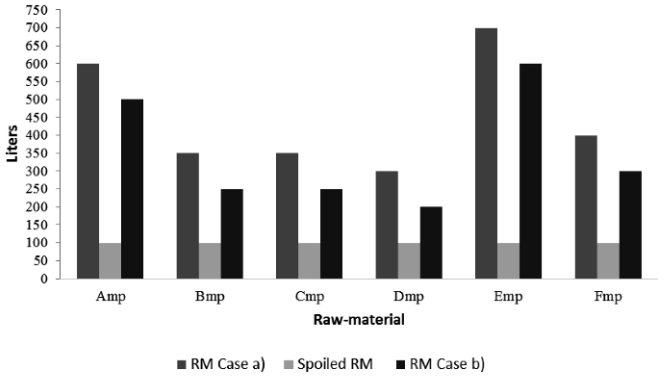

Figure 3 – Raw materials consumption/spoiled.

The production scheduling shown in Figure 4, illustrates only four working hours day –in the morning period. The production is aggregated not only by product, taking into account the change-over tasks, but also its set of equipment, where some are shared. The production starts with product A, followed by E, C, E, A, C, F, A and D till t=4, where 200 l of products A and E are delivered. During the time horizon two time-windows for each product are defined, allowing as many deliveries as necessary to fulfil the demand.

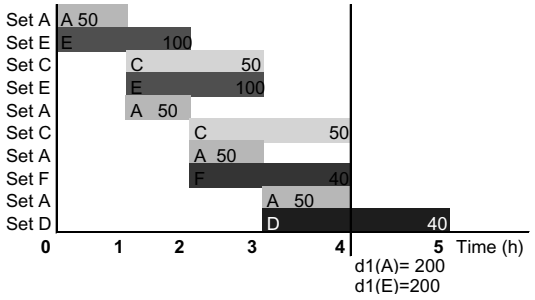

Figure 4 – Schedule Results.

In Figure 5 is shown the final product deliveries profile. Product E has five deliveries, in a total of 600 l and products C and D only one, with 250 l and 200 l, respectively. Product A has four deliveries, two of 200 l (shown in Figure 4) and two of 50 l later on, fulfilling the total demand.

The JIT strategy followed in case b) presented an increase of 25 % of profit over case a). This result is derived mainly from the reduction of RM storage and spoilage costs, despite the increase of RM purchase price of this strategy. Additionally, JIT strategy has a major importance qualitative aspect, which is the RM quality/ freshness that is reflected into the final product quality. As disadvantages is the dependence on the RM deliveries and the suppliers' difficulties to implement it.

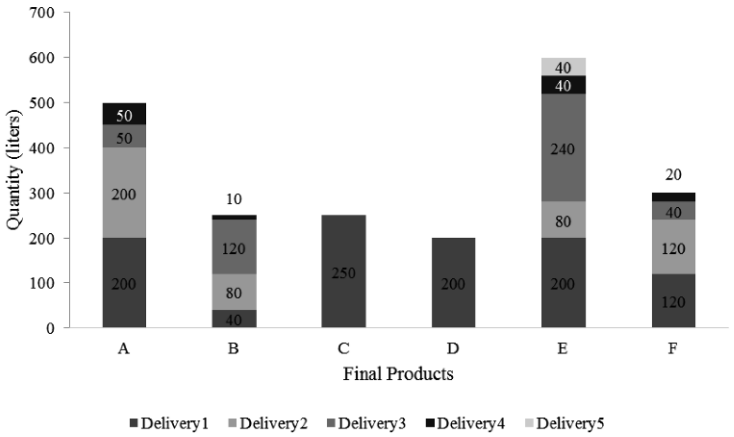

Figure 5 – Final products deliveries profiles.

5. Conclusions

In the present work, the production scheduling problem of a real ice-cream facility and RM inventory management are discussed. A process characterization of the artisanal ice-cream industry is presented. A MILP formulation is developed considering its own industry characteristics and two strategies over the RM inventory management are analysed. Results seem to indicate that the supplier strategy JIT is better to be applied in this type of food industry. Not only it presents better economic results, but also allows better final products quality. The extension of the present work will explore the other main characteristics of this industry, such as changeovers.

Acknowledgements

The authors acknowledge financial support from FCT within project EXPL/EMS-GIN/1930/2013.

References

C.A Soman, D.P. Van Donk, G.J.C Gaalman,2004, A basic period approach to the economic lot scheduling problem with shelf life considerations. International Journal of Production Research, 42(8), 1677–1689.

C. Pantelides, 1994, Unified frameworks for process planning and scheduling Short-term Scheduling of Batch Operations. Centre for Process Systems Engineering, Imperial College of Science, Technology and Medicine of London, 1 – 22.

J. Kallrath, 2005, Solving Planning and Design Problems in the Process Industry Using Mixed Integer and Global Optimization. Annals of Operations Research,140, 339-373.

L. M. Entrup, H.O. Günther, P. Van Beek , M. Grunow, T. Seiler, 2005, Mixed-Integer Linear Programming approaches to shelf-life-integrated planning and scheduling in yoghurt production. International Journal of Production Research, 43(23), 5071–5100.

P. Amorim, C. Antunes, B. Almada-Lobo, 2011, Multi-Objective Lot-Sizing and Scheduling Dealing with Perishability Issues. Industrial & Engineering Chemistry Research, 50(6), 3371–3381

S. K. Goyal, , 1994. A note on effect of production cost shelf life.pdf. , pp.2243 – 2245

X. Cai, J. Chen, Y. Xiao, X. Chu, 2008, Product selection, machine time allocation, and scheduling decisions for manufacturing perishable products subject to a deadline. Computers & Operations Research, 35(5), 1671–1683.

Krist V. Gernaey, Jakob K. Huusom and Rafiqul Gani (Eds.), 12th International Symposium on Process Systems Engineering and 25th European Symposium on Computer Aided Process Engineering.
31 May – 4 June 2015, Copenhagen, Denmark

Evaluation of Energy Integration Aspects for Advanced Chemical Looping Systems Applied for Energy Vectors Poly-generation

Calin-Cristian Cormos,* Ana-Maria Cormos, Paul-Serban Agachi

Babes-Bolyai University, Faculty of Chemistry and Chemical Engineering
Arany Janos 11, Postal code: RO-400028, Cluj-Napoca, Romania

Abstract

Developing advanced conversion ways for fossil fuels and renewable energy sources to electricity or other total or partial decarbonised energy vectors (e.g. hydrogen, heat, synthetic fuels) is of paramount importance in modern energy sector. In addition, the development of carbon capture, utilisation and storage (CCUS) technologies is equally important for transition to low carbon economy. This paper evaluates various integration aspects of energy vectors poly-generation (focussing on power, hydrogen and synthetic fuels) based on chemical looping systems using syngas produced from solid fuel gasification. As illustrative examples, iron-based and calcium-based chemical looping systems were assessed in conjunction with coal gasification plants.

The paper presents in details the evaluated plant configurations, focussing especially on operational and mass & energy integration issues. The plant designs were modelled and simulated using process flow modelling software, the results being used to assess the overall performance indicators. For energy integration analysis, pinch method was used to evaluate in details and to find the best energy integration options of available heat generated in the chemical looping unit into overall steam cycle of the power block. Other mass and energy integration aspects, e.g. air flow mass integration between the air separation unit and the gas turbine, plant flexibility in terms of changing generated energy vectors vs. time, were evaluated as well to assess their influence on overall plant energy efficiency. As the results show, the chemical looping-based conversion systems exhibit both higher energy efficiency and carbon capture rate than current state of the art gasification plants with gas-liquid absorption for carbon capture (benchmark case).

Keywords: Energy vectors poly-generation; Chemical looping; Energy integration; Carbon capture, utilisation and storage (CCUS).

1. Introduction

Chemical looping is an emerging carbon capture method suitable to be applied in advanced energy conversion processes because CO_2 is inherently separated and no significant energy duty is required (Fan, 2010). This technology is attractive for reducing energy and cost penalties associated with carbon capture. Most of the looping systems are applied to gaseous fuels (e.g. natural gas, syngas) due to the fact that no ash contamination of the oxygen carrier occurs. From various energy conversion technologies, gasification has one of the highest potential for CO_2 capture with low penalties in energy and cost due to high partial pressure of carbon species (mainly CO) in the syngas to be treated for carbon capture. In addition, when energy vector poly-generation is targeted, hydrogen production from gasification seems the obvious choice.

The chemical looping with hydrogen production is based on three interconnected fluidized bed reactors, fuel, steam and air reactors, with an oxygen carrier circulating between them (Adanez et al., 2012). For example, the reactions for iron lopping are:
- Fuel reactor:

$$2Fe_2O_3 + 3CO + 3H_2 \rightarrow 4Fe + 3H_2O + 3CO_2 \quad (1)$$

- Steam reactor:

$$3Fe + 4H_2O \rightarrow Fe_3O_4 + 4H_2 \quad (2)$$

- Air reactor:

$$4Fe_3O_4 + O_2 \rightarrow 6Fe_2O_3 \quad (3)$$

A special looping cycle is based on calcium sorbents to push the water gas reaction equilibrium towards hydrogen (Sorbent Enhanced Water Gas Shift - SEWGS). The formed $CaCO_3$ is then regenerated in a separate reactor and the CaO is recycled back:
- SEWGS reactor:

$$CaO + CO + H_2O \rightarrow H_2 + CaCO_3 \quad (4)$$

- Calcination reactor:

$$CaCO_3 \rightarrow CaO + CO_2 \quad (5)$$

As illustrative syngas-based looping systems for energy vectors poly-generation, plant designs with about 400 - 600 MW net power and a flexible hydrogen output (0 to 200 MW_{th} based on lower heating value) were assessed. The product flexibility (the capability to change the generated energy vectors according to timely demand from the grid) is an important aspect for integration in modern energy conversion systems. The carbon capture rate of evaluated energy conversion concepts is almost total (>95%).

2. Description of plant configurations and key model assumptions

Figures 1 and 2 present hydrogen and power co-generation concepts using syngas-based iron and calcium looping cycles. As illustrative gasifier, Shell reactor was used.

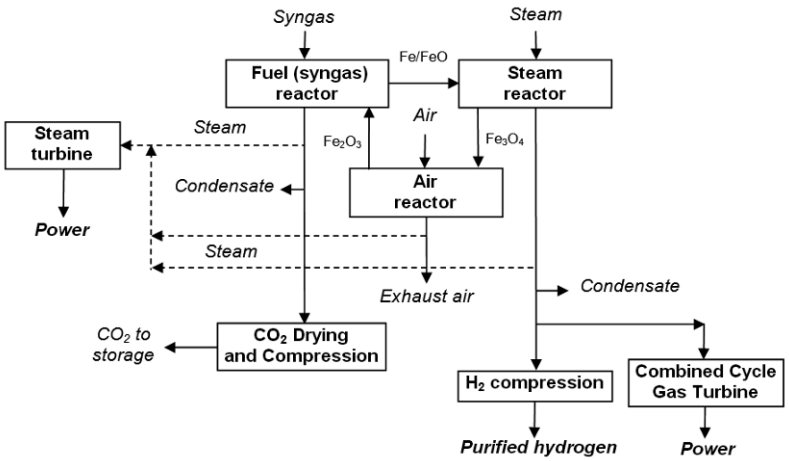

Figure 1. Hydrogen and power co-generation using syngas-based iron looping cycle (Case 1)

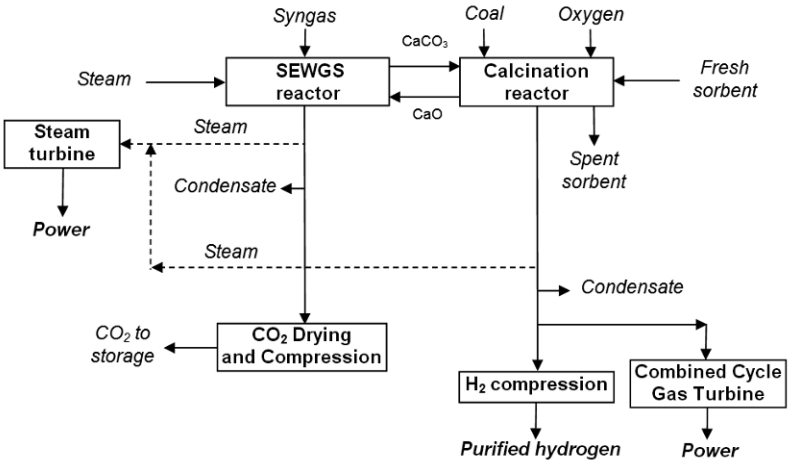

Figure 2. Hydrogen and power co-generation using syngas-based calcium looping cycle (Case 2)

All plant configurations consider a standard Shell-based coal gasification island with Selexol® process for syngas desulphurization (gas-liquid absorption). The main plant sub-systems of investigated plant concepts and theirs design assumptions used in the modelling are presented in Table 1 (Cormos et al., 2013; Tong et al., 2014).

Table 1. Main design assumptions

Unit	Parameters
Air separation unit (ASU)	O_2 purity: 95 % (vol.) Power consumption: 225 kWh/ton O_2
Gasifier (Shell)	Pressure: 40 bar; Temperature: >1400°C Pressure drop: 1.5 bar; Gas quench configuration
Acid gas removal (AGR)	Solvent: Selexol® for H_2S capture
Iron looping cycle (Case 1)	Oxygen carrier: ilmenite ($FeTiO_3$) Fuel reactor parameters: 30 bar / 700 - 750 °C Steam reactor parameters: 28 bar / 700 - 800 °C Air reactor parameters: 26 bar / 850 - 1,000 °C Gibbs free energy minimization model Pressure drop fuel and steam reactors: 1 bar / reactor
Calcium looping cycle (Case 2)	Sorbent: calcium-based ($CaO/CaCO_3$) SEWGS reactor parameters: 30 bar / 650 – 700 °C Calcination reactor parameters: 28 bar / 900 – 950 °C Gibbs free energy minimization model Pressure drop fuel and steam reactors: 1 bar / reactor
CO_2 compression and drying	Delivery pressure: 120 bar Solvent for CO_2 drying: TEG (Tri-ethylene-glycol) Captured CO_2 specification (vol. %): >95 % CO_2; <2,000 ppm CO; <500 ppm H_2O; <100 ppm H_2S
H_2 compression	Delivery pressure: 60 bar Compressor efficiency: 85 %
Gas turbine	Gas turbine type: M701G2 (MHI) Net power output: 334 MW; Net efficiency: 39.5 %
Heat recovery steam generation (HRSG) and steam cycle	Pressure levels: 120 bar / 34 bar / 3 bar & MP reheat Steam turbine isoentropic efficiency: 85 % Steam wetness ex. steam turbine: max. 10 %
Heat exchangers	$\Delta T_{min.}$ = 10 °C; Pressure drop: 3 - 5 % of inlet pressure

3. Results and discussions

Both chemical looping pre-combustion capture coal gasification-based concepts were modelled and simulated using ChemCAD and Thermoflex software. By simulation all required data to evaluate the key performances of investigated concepts are generated. The designs were optimized by performing heat and power integration analysis (using pinch technique) for maximization of power generation (Cormos, 2010). Steam flows generated in the gasification island, syngas conditioning line and chemical looping units were integrated in the steam (Rankine) cycle of the combined cycle. As minimum approach temperature between hot and cold streams, 10 ^{o}C was considered.

Figures 3 presents the hot and cold composite curves (HCC and CCC) for gasification island and iron looping cycle (Case 1). Similarly for the same case, Figure 4 presents the hot and cold composite curves for hydrogen-fuelled combined cycle gas turbine.

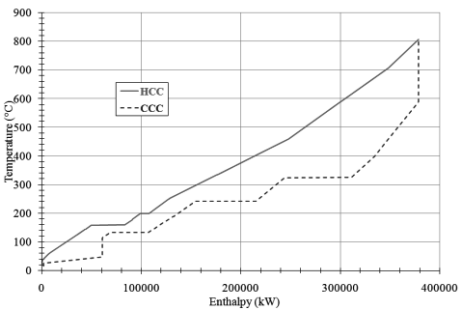

Figure 3. Composite curves for gasification island and iron looping cycle

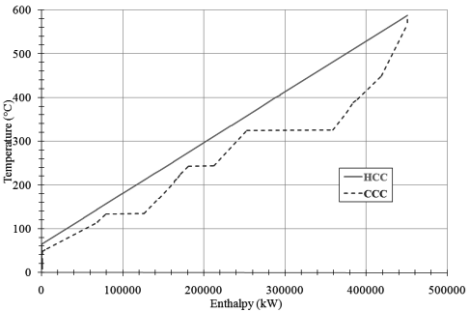

Figure 4. Composite curves for hydrogen-fuelled combined cycle gas turbine

For Case 2, Figure 5 presents the hot and cold composite curves for SEWGS calcium looping cycle. The composite curves for the hydrogen-fuelled combined cycle gas turbine are similar with the one presented in Figure 4 for Case 1.

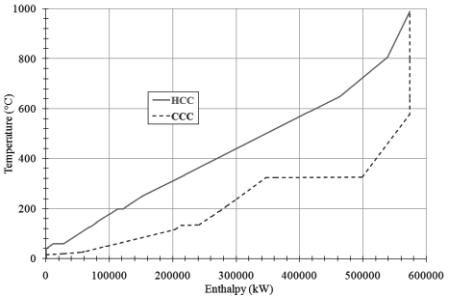

Figure 5. Composite curves for gasification island and calcium looping cycle (SEWGS)

As can be noticed from Figures 3 and 5, the calcium looping case (Case 2) has a higher heat recovery potential than Case 1 (574 MW_{th} vs. 378 MW_{th}) due to the additional coal stream and higher operation temperature (about 1,000 ^{o}C) in the calcination reactor. The good energy integration of plant sub-systems leads to optimum plant energy efficiency.

The first operation scenario was based on power generation only. As can be expected this scenario is susceptible of the greatest importance due to the significance of electricity in overall energy sector. Table 2 presents the main performance indicators for both iron and calcium looping options. As benchmark case (noted as Case 3), an IGCC design based on Shell gasifier fitted with a pre-combustion capture unit using gas-liquid absorption (Selexol®) was considered (Cormos, 2010; Ozcan and Dincer, 2014).

Table 2. Main performance indicators (power generation only)

Main Plant Data	Units	Case 1	Case 2	Case 3
Coal flowrate	t/h	167.21	226.71	165.70
Coal lower heating value (LHV)	MJ/kg		25.353	
Coal thermal energy (A)	MW_{th}	1,177.57	1,596.64	1,166.98
Gas turbine output	MW_e	334.00	334.00	334.00
Steam turbine output	MW_e	205.43	410.49	210.84
Air expander power output	MW_e	3.54	1.40	0.78
Gross electric power output (B)	MW_e	542.97	745.89	545.62
Air separation unit consumption	MW_e	45.13	70.74	44.73
Fuel processing consumption	MW_e	15.52	9.68	9.12
Carbon capture + CO_2 drying & compression	MW_e	15.63	52.35	39.81
Power island consumption	MW_e	21.80	21.97	18.78
Total ancillary power consumption (C)	MW_e	98.08	154.74	112.44
Net power output (D = B - C)	MW_e	444.89	591.15	433.18
Gross electrical efficiency (B/A * 100)	%	46.61	46.71	46.75
Net electrical efficiency (D/A * 100)	%	37.78	37.02	37.11
Carbon capture rate	%	99.71	95.94	90.79
CO_2 specific emissions	kg/MWh	3.88	32.89	86.92

The net power efficiency has the highest value for Case 1 (iron looping); the calcium looping (Case 2) has a lower net efficiency with about 0.8 percentage points. Case 1 has a bit higher net power efficiency than the benchmark case (~0.7 net percentage points) since Case 2 is about the same as the benchmark case. One important aspect to be mentioned is the higher decarbonisation rate of both looping cases (almost total for Case 1). This aspect underlines the good potential of chemical looping options to deliver higher energy efficiency simultaneously with an almost total carbon capture rate.

Any modern power plant has to have the capability to timely adjust the generating load according to the grid demand. The chemical looping cases have the capability of reducing power output by producing high purity hydrogen (mass integration). Figure 6 presents the variation of plant efficiencies vs. hydrogen output for Case 1 (iron looping). As can be noticed the overall plant efficiency is increasing with hydrogen output.

Other potential mass integration option to further increase the energy efficiency by poly-generation would be for instance power and substitute natural gas co-generation (Ozcan and Dincer, 2014). For this option part of the syngas / captured CO_2 is reacted with hydrogen to produce methane. As an illustrative example for Case 1 (iron looping), the energy efficiency is about 70 % and the carbon capture rate is about 60 - 65 %.

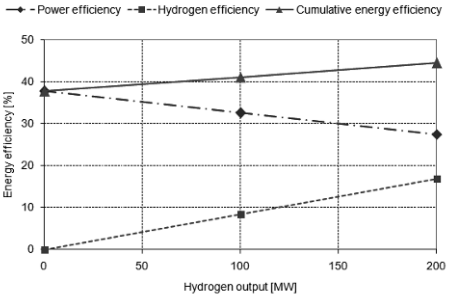

Figure 6. Variation of plant energy efficiency vs. hydrogen output (Case 1)

To increase further the efficiency, an option would be to integrate the air separation unit with the gas turbine compressor (Cormos, 2010). An air bleed from the GT compressor can supply the air required by the ASU. The degree of air mass integration is defined as the percentage of the total ASU air required coming from the GT compressor. Figure 7 presents the variation of plant energy efficiency vs. air integration degree for Case 1.

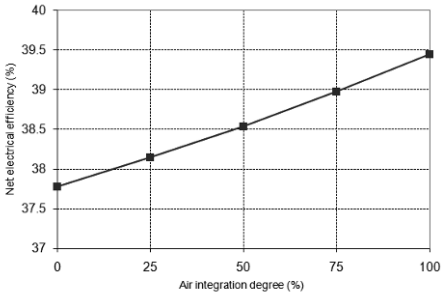

Figure 7. Variation of plant energy efficiency vs. ASU-GT air integration degree (Case 1)

As can be noticed from Figure 7, the ASU-GT air flow (mass) integration lead to an energy efficiency increase and net power output up to 1.7 percentage points and about 20 MW net power for a total air integration compared to non-integration case. Also, the tight energy integration leads to reduction of plant cooling duty (water consumption).

4. Conclusions

The paper evaluates two syngas-based chemical looping configurations for hydrogen and power co-generation. The designs were evaluated in various conditions to assess the energy integration aspects. Both looping cases show superior carbon capture rate compared to the benchmark case. In addition, the iron looping case exhibits superior energy efficiency and the calcium looping case has comparable efficiency.

Acknowledgement

This work was supported by a grant of the Romanian National Authority for Scientific Research, CNCS – UEFISCDI, project ID PN-II-ID-PCE-2011-3-0028: "*Innovative methods for chemical looping carbon dioxide capture applied to energy conversion processes for decarbonised energy vectors poly-generation*".

References

J. Adanez, A. Abad, F. Garcia-Labiano, P. Gayan, L. de Diego, 2012, Progress in chemical-looping combustion and reforming technologies, Progress in Energy and Combustion Science, 38, 215 - 282.

C.C. Cormos, 2010, Evaluation of energy integration aspects for IGCC-based hydrogen and electricity co-production with carbon capture and storage, International Journal of Hydrogen Energy, 35, 7485-7497

C.C. Cormos, A.M. Cormos, S. Agachi, 2013, Evaluation of chemical looping systems as carbon capture option to be applied to gasification processes, Computer Aided Chemical Engineering, 32, 199-204

L.S. Fan, 2010, Chemical looping systems for fossil energy conversions, Wiley-AIChE

H. Ozcan, I. Dincer, 2014, Thermodynamic analysis of a combined chemical looping-based trigeneration system, Energy Conversion and Management, 85, 477-487

A. Tong, S. Bayham, M. Kathe, L. Zeng, S. Luo, L.S. Fan, 2014, Iron-based syngas chemical looping process and coal-direct chemical looping process development at Ohio State University, Applied Energy, 113, 1836-1845

Krist V. Gernaey, Jakob K. Huusom and Rafiqul Gani (Eds.), 12th International Symposium on Process Systems Engineering and 25th European Symposium on Computer Aided Process Engineering.
31 May – 4 June 2015, Copenhagen, Denmark

Synthesis of Biomass-based Trigeneration Systems with Reliability Aspects

Viknesh Andiappan[a], Raymond R. Tan[b], Kathleen B. Aviso[b], Denny K. S. Ng[a,*]

[a] *Department of Chemical and Environmental Engineering/ Centre of Excellence for Green Technologies, The University of Nottingham Malaysia Campus, Broga Road, Semenyih, 43500, Malaysia*

[b] *Chemical Engineering Department, 2401 Taft Avenue, De La Salle University, Manila, Philippines.*

[*] *Denny.Ng@nottingham.edu.my*

Abstract

Trigeneration systems produce heat, power and cooling simultaneously from a single fuel source. With such efficient use of fuel, installing trigeneration systems on-site would be beneficial as it reduces the requirement of external power and fuel, reduces emissions, and improves local power reliability. On the other hand, trigeneration systems need to have a reliable network of component process units, since the high level of integration increases the likelihood of cascading failures. Each unit may not always be available to function because it may require preventive or corrective maintenance during the course of operations. Traditionally, this issue is handled by installing additional process units based on heuristics. This approach, however, may not be able to address complex decisions on whether to purchase a single additional unit with larger capacity or multiple smaller capacity units. Additionally, the decision becomes increasingly complex when seasonal variations in operations are considered. If not addressed appropriately, such decisions may result in excessive capital and/or maintenance costs. To address these issues, this work presents a systematic procedure for the grassroots design of a trigeneration system considering equipment redundancy for variations in raw material and energy demand. To illustrate the proposed approach, a simple case study on designing a grassroots steam turbine configuration for a biomass-based trigeneration system (BTS) is presented.

Keywords: Trigeneration; Reliability; Redundancy Allocation.

1. Introduction

Trigeneration systems are energy (or utility) systems which produce heat, power and cooling simultaneously from a single fuel source. In this respect, installing a trigeneration system on site would be able to reduce the importation of power and fuel (from large distances), reduce environmental impact, and improve local power reliability (Stoijkov et al., 2011). However, such benefits may not be realized if a trigeneration system is not sufficiently equipped to cope with an event of failure (e.g., preventive maintenance, equipment breakdown). Since typical energy systems contain a network of interconnected equipment, an event of failure would disrupt the overall system performance. As such, it is arguable whether an energy system design is suitable for keeping a desired level of reliability in meeting energy demands. In this respect, reliability is defined as the probability that a system will perform a required function at a given point in time, when operated under specific conditions (Ebeling, 1997). It is a quantitative measure (e.g., percentage) of non-failure operation over a given

(operational) time period. Since no equipment in an energy system is fully (100%) reliable, it is necessary to account for the possible failures during its design. A common way of addressing such issue is by implementing redundancy allocation (Kuo and Zhu, 2012). Redundancy allocation is a strategy of employing additional number of equipment connected in parallel to perform the same function, with the intention of achieving higher system reliability. Traditionally, redundancy cases were considered by means of heuristics. The $n + 2$ rule is an exemplary heuristic applied where two extra units are added to an initial design, n (where redundancy was not considered). Besides implementing additional units, safety factors have been used to oversize equipment.

Besides heuristics, optimization studies have been employed to address redundancy allocation in energy systems. For instance, Olsommer et al. (1999a; b) proposed a methodology to optimize the design and operation of a co-generation system subject to different operating scenarios. The methodology also performs a reliability analysis via an automated program and determines all the possible failure modes upon defining the optimal system. Frangopoulos and Dimopoulos (2004) then extended the previous work, by using the same steps but all within one optimization procedure. In their contribution, a search subroutine using genetic algorithm first proposes a design for which reliability analysis is carried out, generating all possible failure scenarios and calculating penalties whenever the demands are not fully met. The corresponding investment and operating costs are then compared with the designs automatically generated from the search, until a near-optimal solution is found. Besides, Aguilar et al. (2008) presented a framework to address reliability issues in the design and operation of a utility system. In their work, a robust optimization framework was presented to handle both grassroots and retrofit problems. In addition, the framework determines the redundancy allocation for the system based on different time horizons and failure scenarios. Recently, Voll et al. (2012) presented a framework on automated superstructure generation and optimization of a trigeneration system based on different demands, available technologies, equipment redundancy and topological constraints.

Based on the aforementioned contributions, it can be seen that there are several opportunities to further explore and improve systematic approaches on redundancy allocation for an energy system. For instance, there is a need for less labor and computationally intensive approaches to address redundancy allocation issues in energy systems. Apart from that, a more comprehensive systematic approach is required to address complex decisions such as whether to install additional large capacity units or multiple smaller capacity units. This is because each option is unique in terms of equipment reliability. Besides, redundancy allocation decisions become increasingly complex when seasonal variations in raw material supply and energy demand are also be factored in. If such decisions are not addressed appropriately, an energy system may perform sub-optimally in certain operational periods and incur unnecessary or excessive capital and maintenance costs. To address such opportunities, this work introduces an alternative approach to tackle redundancy allocation of technological units during the grassroots design of a biomass-based tri-generation system (BTS). This alternative approach adapts the *k*-out-of-*m* system modeling, an approach previously used for reliability optimization of existing systems with pre-defined redundancy (Coit and Liu, 2000). In this work however, *k*-out-of-*m* system modeling is adapted to develop an optimization model to determine the required redundancy allocation for a particular technology in a BTS based on a minimum reliability level. The minimum reliability level is defined using chance-constraint programming. Chance-constraint programming

is an approach that considers the probabilistic level of constraint satisfaction (Charnes and Cooper, 1959). Following this, the developed model is solved via multi-period optimization. In multi-period optimization, the variations in raw material supply and energy demand are discretized into multiple intervals such that each individual interval represents a scenario with an approximated discrete distribution. As such, this approach provides a unique solution that is feasible for the given set of anticipated supply and demand scenarios. To illustrate the proposed approach, a simple grassroots design case study on steam turbines in a BTS is solved.

2. Problem Statement

As various established technologies are available in the market, the grassroots design of a reliable tri-generation system can be a complex problem. The grassroots design problem addressed in this work is stated as follows: Raw material *i* can be converted to product $p \in P$ through technology $j \in J$. The objective of this work is to develop a systematic approach for the grassroots design of a reliable BTS configuration with maximum economic performance while considering multiple supply and demand scenarios, $s \in S$. In each considered scenario, various design capacities $n \in N$ are available for selection within technologies *j*. Based on the aforementioned problem, a mathematical model is formulated for each scenario. The formulated model consists of material and energy balances, and economic correlations for all considered alternatives. Following this, each scenario is represented by a fraction of occurrence, α_s and the required redundancy allocation is determined via *k*-out-of-*m* system modeling and chance-constraint programming as shown in the next section.

3. Mathematical Formulation

The mathematical formulation for this work is shown in Eq.(1 – 6). As shown, F_{jp}^{I} is the flow rate of product *p* in technology *j* while $\mathrm{F}_{jn}^{\mathrm{Design}}$ is the fixed design capacity *n* available for purchase in technology *j*. Meanwhile, z_{jn} and m_{jn} are positive integers which represent the number of operating and installed units with design capacity *n* selected in technology *j* respectively. Besides, P_{jn} is the reliability of design capacity *n* performing its function in technology *j* while R_{jn} $(m_{jn} \geq z_{jn})$ represents the reliability of design capacity *n* in technology *j* whereby at least z_{jn} out of m_{jn} number of units are operational. *C* is the binomial coefficient. R_j is overall reliability of technology *j*. I_{jn} is a binary integer variable which denotes the presence of a selected technology *j* with design capacity *n* in the configuration for each scenario *s*. $\mathrm{R}_{jn}^{\mathrm{Min}}$ is the minimum reliability level of design capacity *n* in technology *j*. *EP,* AOT, C_p and CRF are the economic performance, annual operating time, product selling price and capital recovery factor respectively. Meanwhile, *CAP* and *MAC* are the total capital and maintenance costs respectively. *CAP* and *MAC* are both determined based on m_{jn} units to achieve the specified minimum reliability level.

$$\sum_{n=1}^{N}\left(z_{jn}\right)_s \mathrm{F}_{jn}^{\mathrm{Design}} \geq \left(\sum_{p=1}^{P} F_{jp}^{\mathrm{I}}\right)_s \qquad \forall j \forall s \qquad (1)$$

$$\left(R_{jn}\left(m_{jn} \geq z_{jn}\right)\right)_s = \sum_{k=(z_{jn})_s}^{m_{jn}} {}^{m_{jn}}C_k \left(\mathrm{P}_{jn}\right)^k \left(1-\mathrm{P}_{jn}\right)^{m_{jn}-k} \qquad \forall j \forall n \forall s \qquad (2)$$

$$\left(R_j\right)_s = \left(\sum_{n=1}^{N} R_{jn} I_{jn}\right)_s \qquad \forall j \forall s \quad (3)$$

$$\left(z_{jn}\right)_s \le \left(\mathrm{M} \times I_{jn}\right)_s \qquad \forall j \forall n \forall s \quad (4)$$

$$\left(R_j\right)_s \ge \left(\sum_{n=1}^{N} \mathrm{R}_{jn}^{\mathrm{Min}} I_{jn}\right)_s \qquad \forall j \forall s \quad (5)$$

$$EP = \sum_{s} \alpha_s \left[\mathrm{AOT} \times \left(\sum_{p=1}^{P} F_{jp}^{\mathrm{I}} \mathrm{C}_p \right)_s \right] - \mathrm{CRF} \times CAP - MAC \quad (6)$$

To illustrate this approach, a simple grassroots design case study of a steam turbine configuration for a BTS is presented. In the case study, a mixed integer non-linear programming (MINLP) model consisting of 46 continuous variables, 27 integer variables and 62 constraints is formulated based on Eq. (1 – 5). The developed model is then solved via multi-period optimization in LINGO v14 Global Solver in Dell Vostro 3400 with Intel Core i5 (2.40GHz) and 4GB DDR3 RAM in an average time of 0.1s of CPU time.

4. Case Study

In this case study, it is assumed that the owner of a BTS is interested to design a reliable steam turbine configuration with maximum economic performance. The steam turbine configuration is required to deliver output power based on the seasonal requirements shown in Table 1 (assuming the boiler is able to supply steam at fixed rate). In addition, Table 1 also shows the fraction of occurrence for each respective season. Table 2 shows the design capacity options available for purchase and their respective reliabilities while Table 3 summarizes other economic parameters used for this case study. Besides, the steam turbine configuration is expected to operate on a minimum reliability level of 95%. Subsequently, a simple superstructure is developed to include all considered turbine options (as shown in Figure 1). Note that although only one unit is shown for each option in the superstructure, it is possible to have several pieces in the case where units with small design capacities are selected as described in Eq.(1 – 5). The mass, energy and economic calculations for these options are then mathematically modeled, allowing quantitative analysis and optimization. Following this, the developed model for this case study is solved by maximizing Eq.(6) to determine a reliable steam turbine configuration.

Table 1: Fraction of Occurrence and Power Demand for Seasons 1, 2 and 3

Season	Power Demand (kW)	Fraction of Occurrence, α_s
1	489	$\alpha_1 = 0.417$
2	225	$\alpha_2 = 0.333$
3	289	$\alpha_3 = 0.250$

Table 2: Available Design Capacity Options

Design Capacity Options	Capital Costs (USD)	Maintenance Costs (USD)	Reliability
250 kW	90,549	5,000	0.90
500 kW	122,380	10,000	0.91
1 MW	165,395	20,000	0.92

Table 3: Economic Parameters for Case Study

Operational Hours, AOT	5000/year
Operation Lifespan	15 years
Capital Recovery Factor, CRF	0.13/year
Price of Power Sold, C_p	0.09 USD/ kWh

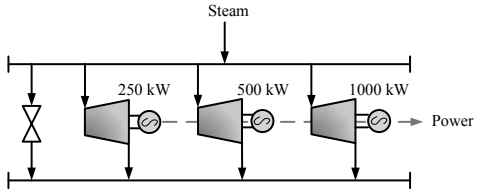

Figure 1: Superstructure of Steam Turbine Options for Case Study

The resulting grassroots steam turbine configuration is shown in Figure 2. As shown, the configuration consists of three 250 kW steam turbine units. Based on the optimized result, the *EP*, *CAP* and *MAC* are determined as 111,187 USD/year, 279,646 USD and 15,000 USD/year respectively. Meanwhile, Table 4 shows the reliability level achieved with this configuration are 0.972, 0.999 and 0.972 for Seasons 1 – 3 respectively. Moreover, Table 4 shows the status (e.g., operational or standby) of the steam turbines in each season. As shown, Season 1 has two operating turbines while the remaining one will be placed on standby. Since one turbine is available on standby in Season 1, the synthesized configuration would still be able to meet demands if one of the operational turbines fails. In Season 2, only one turbine would be operational while the remaining two would be on standby mode. If the turbine in operation experiences failure, two standby turbines are available to meet power requirements. Therefore, a higher reliability value is obtained in Season 2 compared to Season 1. Similar to Season 1, two out of the three turbines would be operating in Season 3. If one of the turbines in operation fails, the remaining turbine on standby is still available and capable to resume operations.

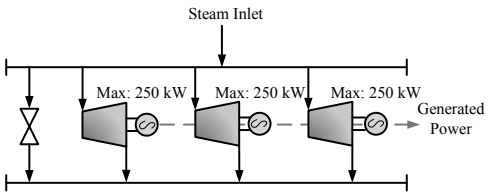

Figure 2: Synthesized Grassroots Design of Steam Turbine configuration

Table 4: Equipment Status for each Season

Season	Status		Reliability
	Operational, $(z_{jn})_s$	Standby	
1	2	1	0.972
2	1	2	0.999
3	2	1	0.972

5. Conclusions

A systematic approach was presented to design a reliable grassroots steam turbine configuration for a BTS with reliability aspects. In this approach, an alternative reliability modeling approach, based on *k*-out-of-*m* system modeling, is adapted to determine the required redundancy allocation for a particular technology in a system. The required redundancy allocation is then determined based on a minimum reliability level specified via chance-constrained programming. The developed model is solved via multi-period optimization. The presented approach is used to determine whether to install a large capacity equipment unit or multiple smaller capacity units based on their unique reliabilities. The proposed approach is illustrated using a simple case study on designing a reliable grassroots steam turbine configuration for a BTS.

Acknowledgement

The financial support from the Ministry of Higher Education, Malaysia through the LRGS Grant (Project Code: NRL 20001) is gratefully acknowledged.

References

O. Aguilar, J. Kim, S. Perry, R. Smith, 2008, Availability and reliability considerations in the design and optimisation of flexible utility systems, Chemical Engineering Science, 63 (14), 3569-3584.

A. Charnes, W. Cooper, 1959, Chance-constrained programming, Management Science, 6 (1), 73-79.

D. Coit, J. Liu, 2000, System reliability optimization with k-out-m subsystems, International Journal of Reliability, Quality and Safety Engineering, 7 (2), 129-142.

C. Ebeling, 1997, An introduction to reliability and maintainability engineering, McGraw-Hill.

C. Frangapoulos, G. Dimopoulos, 2004, Effect of reliability considerations on the optimal synthesis, design and operation of a cogeneration system, Energy, 29 (3), 309-329.

W. Kuo, X. Zhu, 2012, Importance Measures in Reliability, Risk, and Optimization, John Wiley and Sons Inc.

B. Olsommer, D. Favrat, M. Spakovsky, 1999a, An approach for the time-dependent thermoeconomic modeling and optimization of energy system synthesis, design and operation Part I: Methodology and Results, International of Journal Applied Thermodynamics, 2 (3), 97-114.

B. Olsommer, D. Favrat, M. Spakovsky, 1999a, An approach for the time-dependent thermoeconomic modeling and optimization of energy system synthesis, design and operation Part I: Reliability and Availability, International of Journal Applied Thermodynamics, 2 (4), 177-186.

M. Stoijkov, E. Hnatko, M. Kljajin, K. Hornung, 2011, CHP and CCHP Systems Today, Development of Power Engineering in Croatia.

P. Voll, C. Klaffke, M. Hennen, A. Bardow, 2013, Automated superstructure-based synthesis and optimization of distributed energy supply systems, Energy, 50, 374-388.

Krist V. Gernaey, Jakob K. Huusom and Rafiqul Gani (Eds.), 12th International Symposium on Process Systems Engineering and 25th European Symposium on Computer Aided Process Engineering.
31 May – 4 June 2015, Copenhagen, Denmark

Optimization of the cost of compression in the Finnish natural gas pipeline

M. Mikolajková,[a] H. Saxén,[a] F. Pettersson[b]

[a] *Åbo Akademi University, Thermal and Flow Engineering Laboratory, Biskopsgatan 8, Åbo, Finland*
[b] *Åbo Akademi University, Process Design and Systems Engineering Laboratory, Biskopsgatan 8, Åbo, Finland*

Abstract

The ambient temperature strongly influences the demand of heat and electricity in Finland. In order to study a potential expansion of the gas distribution network and the use of new gas sources, a mathematical model for the pipeline network was formulated. The model considers daily variations in the energy demand at the consumers, the gas flow rates and pressures in the pipes, as well as compressor duties. Using the model, the present natural gas system was simulated for a reference year. This gave a basic understanding about the gas flow rates and pressures in the pipes, as well as compressor duties for every day. The possibilities to extend the pipeline to other cities was also studied, and the implications for additional gas supply, using alternative sources, on the system was analysed, revealing an extra need of compression as well as information about the feasibility of the system at these new states. The pipeline network expansion problem was stated and solved as a nonlinear programming cost minimization problem, yielding information about an optimal operation of the network. Finally, an attempt was made to optimize the integration of a new LNG terminal from which regasified natural could be supplied to the pipeline.

Keywords: Natural gas pipeline, nonlinear programming, compression, mass flow.

1. Introduction

In Finland natural gas (NG) is today distributed to the southern parts of the country with a pipeline from Russia (Figure 1). The gas is mainly used for electricity and heat production, and in 2013 about 33.2 TWh of natural gas was delivered to customers in Finland. The extension of the distribution pipeline network to other cities has been considered. Further possibilities to provide natural gas to the users would be to connect regasification facilities from liquid natural gas (LNG) terminals or sites with biogas production to the pipeline. The construction of LNG terminals and storages is seen a means to increase the independence of Finland on the energy deliveries while the use of biogas will lower the emissions considerably.

The problem of an efficient pipeline operation depends to a large extent on the components and size of the distribution network. In order to provide a delivery of gas of sufficient amount and pressure, adequate pressure for the transmission of the gas has to be maintained everywhere in the system. Compression stations built in regular intervals along the pipeline serve this purpose. Work to solve the problem of an efficient pipeline operation, utilising methods such as dynamic programming, was presented already in the 1960's, e.g. Wong and Larson (1968). A dynamic programming approach is also discussed in a more recent article by Borraz-Sanchéz and Haugland (2011).

Other methods, such as an extended simplex algorithm by De Wolf and Smeers (2000) or MINLP formulation by Cobos-Zaletta and Ríos-Mercado (2002) have been presented in the literature. As an alternative solution, meta-heuristic methods such as ant colony optimization have been proposed by, e.g., Chebouba et al. (2009). In the present approach sequential quadratic programming was used to tackle the problem, as the resulting formulation can handle nonlinearities, is flexible and efficient for the studied system.

Figure 1. Present gas distribution network (Kaasuyhdistys 2014)

2. Mathematical Model

The current configuration of the model is designed for simulation of the distribution of natural gas in a NG transmission network in Finland. The simulation is based on the information provided by the Finnish gas company Gasum Oy and their web pages (Gasum Oy 2014a, Gasum Oy 2014b). There are three compression stations placed before Imatra, after Kouvola and after Mäntsälä, which are used to increase the natural gas pressure to a level suitable for the transmission. In the model, the following cities are included as nodes for the base case study (with node numbers reported in parentheses): Imatra (1), Kouvola (2), Orimattila (3), Kotka (4), Lahti (5), Mäntsälä (6) Tampere (7), Helsinki (8), Lohja (9), Porvoo (10), and Hamina (11). As potential extension nodes in the test scenarios, Pori (12) and Turku (13) are considered. In Pori, which has a large port, plans to build an LNG terminal have recently been announced. In the present work, it is assumed that a regasification unit at this terminal would make it possible to supply NG to the network, but gas will also be consumed by the city and local industry. Thus, Pori is at the same time a consumer and a supply point to the gas network, while Turku is assumed to be an additional demand point in the network. All nodes included in the simplified pipeline model are illustrated in Figure 2.

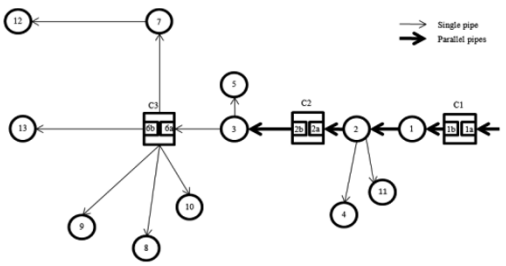

Figure 2. Scheme of nodes and pipes included in the simulation

The pressure and mass flows through the nodes should be determined in an optimal way. The existence of pipelines between the nodes is determined prior to the simulation together with the pipe diameters. There is a double pipe from Russia trough Imatra (node 1) and further to Orimattila (node 3). The pressure of the NG at the Russian-Finnish border is assumed to be known (p_0). Three compression stations are located before Imatra, after Kouvola and after Mäntsälä. Both the inlet pressure and discharge pressure of those compression stations are optimised. The inlet pressure is limited to be at least $p_{c,\mathrm{in}}$ and the discharge pressure to be no larger than $p_{c,\mathrm{out}}$. For the sake of simplicity, the temperature in the pipe is assumed to be proportional to the ambient temperature T_0 and inclination of the pipe is assumed to be negligible.

Mass flows of gas, $m_{i,j}$, between the nodes are balanced based on a balance between the inflows/supply and outflows/demands of the nodes. Assuming static conditions, the mass balances can be expressed as linear equality constraints

$$\sum_j m_{i,j} + D_i = \sum_j m_{j,i} + S_i \quad \forall\, i \quad i \neq j \tag{1}$$

where D_i and S_i are the demand and supply, respectively, at node i. The pressure, p_i, at each node is bounded by minimum and maximum values

$$p_{\min} \leq p_i \leq p_{\max} \quad \forall i. \tag{2}$$

Furthermore, the pressure at (some) demand nodes should fulfil the condition

$$p_i \geq p_{\mathrm{D},i} \tag{3}$$

For the calculation of NG density, it was assumed that the temperature of the gas in the pipe assumes the temperature of the surrounding and that the ideal gas law holds, i.e.,

$$\rho_i = \frac{p_i M}{R T_0} \quad \forall i. \tag{4}$$

where M is the molar mass of the NG. Pressures at the nodes are calculated with the equation for pressure drop in a pipe with a flow of a compressible gas

$$\frac{p_i^2 - p_j^2}{2p_i} = \frac{1}{2} f \frac{l_{i,j}}{d_{i,j}} \rho_i m_{i,j} \left| m_{i,j} \right| \left(\frac{n}{4} \rho_i \pi d_{i,j} \right)^{-2} \quad \forall j \; \forall i \; i \neq j \tag{5}$$

where n is the number for parallel pipes. This general equation also applies if the direction of the mass flow changes. The length of each pipe between nodes i and j, l_{ij}, is determined as in Euclidean distance calculation. The Darcy friction factor, f, is given by the Colebrook-White equation. The average velocity in the pipe is given by

$$w_i = \frac{4 m_{i,j}}{\rho_i \pi {d_{i,j}}^2} \quad \forall i \in I. \tag{6}$$

The cost of the compression depends on the difference between the temperature of the gas and the temperature of the surrounding, assuming that the NG is cooled down after each compression to the ambient temperature. The temperature after an ideal compression stage, $T_{i,\mathrm{id}}$, was determined considering the possible reverse flow by nonlinear inequality constraints, Eqs. (7a,b). The real temperature after the compression, T_i, was the obtained from Eq. (7c) by considering the efficiency factor (η_{ad}) of the compressor

$$T_{i,\mathrm{id}} \geq T_0 \left(\frac{p_{ib}}{p_{ia}} \right)^{\frac{R}{MC_p}} \qquad T_{i,\mathrm{id}} \geq T_0 \left(\frac{p_{ia}}{p_{ib}} \right)^{\frac{R}{M}} \qquad T_i = T_0 + \frac{T_{i,\mathrm{id}} - T_0}{\eta_{\mathrm{ad}}} \qquad \forall i \in I_{\mathrm{cmp}} \tag{7a,b,c}$$

where the set of compressors for the base case is I_{cmp}={1,2,6}. The objective to be minimized is the total energy demand for compression, i.e.,

$$E_1 = \left(m_{1,2}(T_1 - T_0) + m_{2,3}(T_2 - T_0) + m_{3,6}(T_6 - T_0)\right) c_p t \quad (8)$$

where t is the time period. The task is a constrained non-linear programming problem which has been solved using `fmincon` in Matlab [1], employing the sequential quadratic programming algorithm.

3. Results and Discussion

The model developed was applied to optimize the Finnish NG system. The energy demand during the year was estimated based on the information about the average daily consumption during 2009-2011. The total demand was proportionally distributed between the end nodes 4, 5, 7, 8, 9, 10 and 11 for the base case according to the assumed number of consumers in the nodes (roughly yielding the shares 5 %, 5 %, 20 %, 45 %, 5 %, 15 % and 5 %). The demand at every node with a consumer was approximated to follow the outdoor temperature by a linear function adapted to some known consumption in the network. The NG pressure in the network was taken to be bounded (cf. Eq. (2)) by p_{min} = 30 bar and p_{max} = 52 bar. As for the demand pressures, inequalities (cf. Eq. (3)) were imposed for four nodes (Kotka, Tampere, Lohja and Porvoo) with $p_{D,4}$ = 30.5 bar, $p_{D,7}$ = $p_{D,9}$ = 30.0 bar and $p_{D,710}$ = 31.5 bar, while p_0 = 35 bar for the NG entering Finland. For the flow to and from the compressors (cf. Eq. (7)) the pressure limits applied are $p_{c,in}$ = 32 bar and $p_{c,out}$ = 52 bar. For the compressors, an efficiency of η_{ad} = 75 % was assumed. No other costs were included in the objective function as they would only cause an increase in the objective function value, without any real impact on the final result as, in this case, all pipeline connections are defined prior to the simulation.

Each day was separately optimized, with t = 24 h in Eq. (8). The results are illustrated by reporting the pressures at the compressors along the year and the mass flows and for three days corresponding clearly different temperatures: The first is the coldest day (–19.4 °C), the second is the warmest day (28.3 °C) and the third is one which has the median temperature (7.7 °C).

3.1 Base Case

The base case scenario includes nodes 1-11, i.e., the existing NG network in Finland. The left part of Figure 3 illustrates the resulting discharge pressures from the three compressors over the year, with the three reference days indicated by vertical lines. The corresponding total compression power requirement is depicted by a dark line in the right part of Fig. 3. The total compression requirement over a year was for the base case 69.2 GWh. The mass flow rates in the pipes during the reference days for the base case (B) are reported in the Table 1 and the pressures in Table 2. As expected, the temperature has an influence both on the demand and on the density of the gas in the pipeline, thus influences also the gas behavior in the pipe. Therefore, the largest mass flow and compression power requirement can be found during the coldest day.

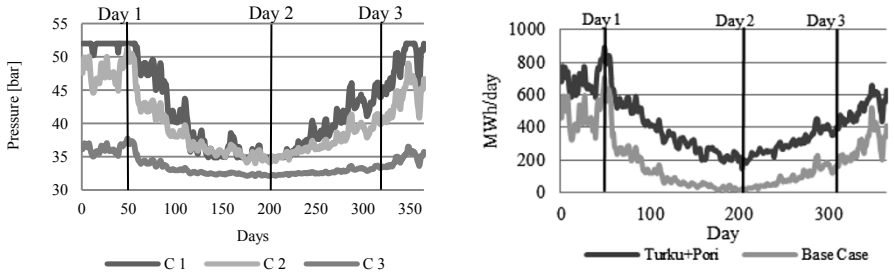

Figure 3. Left: Discharge pressures for base case. Right: Power demand of compression

3.2 Extension Scenario

In an extension scenario, nodes 12 (Pori) and 13 (Turku) are added, with maximum demands of 400 MW and 800 MW, respectively, during the coldest day. A yearly NG supply about 2 TWh from an LNG terminal in Pori into the network is assumed and the supply and demand are both distributed along the year based on the outdoor temperatures. In case the demand in Pori is less than the supply from the LNG terminal, the gas surplus can be compressed into the NG network. The compression of the gasified LNG was taken to occur in N steps with equal pressure ratios, $(p_{12}/1\ \mathrm{bar})^{1/N}$, yielding a revised objective function

$$E_2 = E_1 + N\left|m_{7,12}\right|(T_{12} - T_0)c_p t \qquad m_{7,12} \leq 0 \tag{9}$$

where T_{12} is the NG temperature after each compression step. Assuming a six-step compression (N = 6), the power demand in the optimized extension (E) scenario is illustrated by the gray line in the right panel of Figure 3. Table 1 reports the mass flow rates, where negative values indicate reversed direction of the flows in the pipe between nodes 7 and 12. The mass flow rates in the pipes during the three days are reported in Table 1 and the pressures in Table 2. The cost of the compression increases in the extension scenario, as the compression power demand increases by about 10 MW, but it should be stressed that the added demand in Turku and Pori could not be satisfied by the original network setup: Without a supply in Pori, the maximum delivery of NG to Turku and Pori (during the coldest day) would be 400 MWh and 250 MWh, respectively. The total yearly power requirement was 152.2 GWh.

4. Conclusions

The natural gas pipeline in Finland has been studied numerically by simulation and optimization. The results show a possibility to evaluate the reversion of the gas flow in the pipeline, addition of new pipeline extensions, and increase of the demand and addition of new sources to the network. The model is able to cover the nonlinearities caused by the compressibility of the gas in the pipe and also the effect of temperature and demand changes during the year. By the model, extension options of the current pipeline network can be studied. In future work, the model will be expanded to an MINLP model to optimize the network considering several potential new demand and source sites, also considering investment costs and energy efficiency aspects.

Table 1. Mass flows (kg/s) for base case (B) network and with extension (E) to Pori (node 12) and Turku (node 13), with an LNG terminal in the former.

Day	$m_{0,1}$	$m_{1,2}$	$m_{2,3}$	$m_{2,4}$	$m_{3,5}$	$m_{3,6}$	$m_{6,7}$	$m_{6,8}$	$m_{6,9}$	$m_{6,10}$	$m_{2,11}$	$m_{7,12}$	$m_{6,13}$
1B	167.6	167.6	150.9	8.4	8.4	142.5	33.5	75.4	8.4	25.1	8.4		
1E	152.6	152.6	135.9	8.4	8.4	127.5	1.7	75.4	8.4	25.1	8.4	-31.9	16.9
2B	60.8	60.8	53.2	3.8	3.8	49.4	9.1	27.4	3.8	9.1	3.8		
2E	57.5	57.5	49.9	3.8	3.8	46.1	2.1	27.4	3.8	9.1	3.8	-7.0	3.7
3B	95.8	95.8	85.7	5.0	5.0	80.7	20.2	41.6	5.0	13.9	5.0		
3E	87.5	87.5	77.4	5.0	5.0	72.4	2.5	41.6	5.0	13.9	5.0	-17.7	9.4

Table 2. Pressures (bar) for base network (B) and extended network (E) to Pori and Turku.

Day	$p_{1a}/p_{1b}/p_1$	$p_2/p_{2a}/p_{2b}$	p_3	p_4	p_5	p_{6a}/p_{6b}	p_7	p_8	p_9	p_{10}	p_{11}	p_{12}	p_{13}
1B	34.4/52.0/51.5	41.6/41.0/52.0	44.7	41.3	44.6	31.4/47.4	30.0	41.4	46.9	43.9	41.3		
1E	34.5/52.0/51.6	43.6/43.1/51.4	45.5	43.3	45.3	37.8/37.8	37.8	30.0	37.2	33.3	43.3	39.7	32.8
2B	34.9/36.2/36.1	34.1/34.0/35.9	34.4	34.0	34.4	32.3/32.3	30.4	31.0	32.1	31.5	34.0		
2E	34.9/34.9/34.8	32.9/32.8/35.1	33.8	32.8	33.7	32.3/32.3	32.3	31.0	32.1	31.5	32.8	32.4	32.0
3B	34.8/48.0/47.8	44.2/44.0/45.3	42.4	44.1	42.4	37.9/37.9	30.0	35.5	37.7	36.5	44.1		
3E	34.8/42.9/42.7	39.3/39.1/39.1	36.4	39.2	36.4	33.1/33.1	33.1	30.3	32.9	31.5	39.2	33.9	31.3

Acknowledgments

This work is part of the Efficient Energy Use (EFEU) research program under CLEEN Ltd. with funding from Tekes. Financial support of the Graduate School of Chemical Engineering is also gratefully acknowledged.

References

C. Borraz-Sánchez and D.Haugland, 2011, Minimizing fuel cost in gas transmission networks by dynamic programming and adaptive discretization, Computers & Industrial Engineering, 61(2), 364-372

A. Chebouba, F.Yalaoui, A. Smati, L.Amodeo, K.Younsi and A.Tairi, 2009, Optimization of natural gas pipeline transportation using ant colony optimization, Computers & Operations Research, 36(6), 1916-1923

D. Cobos-Zaleta and R. Z. Ríos-Mercado, 2002, A MINLP model for minimizing fuel consumption on natural gas pipeline networks, Proceedings of the XI Latin-Ibero-American Conference on Operations Research, 90-94

D. De Wolf and Y. Smeers, 2000, The gas transmission problem solved by an extension of the simplex algorithm, Management Science, 46(11), 1454-1465

Gasum Oy, 2014a, Finland´s gas transmission network, [online], [acc. 2014-09-21], Retrieved from: http://www.gasum.com/transmission-portal/Finlands-gas-network/

Gasum Oy, 2014b, Natural gas transmission and distribution. [online], [acc. 2014-09-21], Retrieved from http://www.gasum.com/Facts-about-gas-/Gas-networks/Natural-gas-transmission-and-distribution/,

Kaasuyhdistys ,2014, [online], [acc. 2014-09-21], Retrieved from: http://kaasuyhdistys.fi/sisalto/statistics

MathWorks, 2014, Documentation center: Fmincon, Retrieved from:http://www.mathworks.se/help/optim/ug/fmincon.html

P. Wong and R.Larson, 1968, Optimization of natural-gas pipeline systems via dynamic programming, Automatic Control, IEEE Transactions On, 13(5), 475-481

Krist V. Gernaey, Jakob K. Huusom and Rafiqul Gani (Eds.), 12th International Symposium on Process Systems Engineering and 25th European Symposium on Computer Aided Process Engineering.
31 May – 4 June 2015, Copenhagen, Denmark

An approach to optimize multi-enterprise biofuel supply chains including Nash equilibrium models

Ricardo A. Ortiz-Gutiérrez[a], Sara Giarola[b], Nilay Shah[b], Fabrizio Bezzo[a]

[a]*CAPE-Lab: Computer-Aided Process Engineering Laboratory, Deparment of Industrial Engineering, University of Padova, via Marzolo 9, 35131, Padova, Italy*
[b]*CPSE, Centre for Process Systems Engineering, Imperial College London, South Kensington Campus, London SW7 2AZ United Kingdom*
fabrizio.bezzo@unipd.it

Abstract

An increasing concern in the supply chain management field is the determination of policies aiming at improving the performance of the whole system while preserving an adequate reward for each partaker. The work presented here deals with this critical issue applying the Nash game theory to the development of bioenergy systems. The supply chain planning problem was formulated as a Mixed Integer Linear Programming (MILP) model using a linearized Nash-type objective function. The approach was demonstrated through a case study concerning the bioethanol production in Northern Italy. Result show significant improvements in the mechanisms of transfer price formation towards a fair profit allocation between partakers in bioenergy systems.

Keywords: Multi-enterprise supply chain, Bioethanol, Transfer pricing, Game theory.

1. Introduction

In recent years, energy production from biomass has become increasingly important, both for energy security and climate change concerns (Höök and Tang, 2013). Biofuels, corn-based ethanol in particular, have generated quite a lot of interest in the transport sector as alternative substitutes to fossils. Since the economics of first generation bioethanol strongly depends on the feedstock supply costs (Solomon and Johnson, 2009), the presence of suitable market mechanisms for a fair profit allocation among the main partakers involved, i.e. feedstock suppliers and biofuel producers, is crucial.

Game theory (GT) approaches have been widely used as mathematical and logical tools to study the interactions between the 'players' or 'agents' who are involved in a business (von Neumann and Morgenstern, 1944). However, the integration of profit allocation mechanisms with the optimization of operational decisions along a SC might require sophisticated solution algorithms (Aplak and Sogut, 2013; Zhang et al., 2013). Gjerdrum et al. (2002) proposed a mixed-integer nonlinear programming (MINLP) model based on the game-theory Nash bargaining solution approach for a two-enterprise SCs and formulated a spatial branch-and-bound solution algorithm.

There has been a general lack of focus on the multi-enterprise SC optimization for biofuel systems and only recently, Yue and You (2014) applied game-theory as a solution approach through revenue sharing policy to the arbitrary allocation of the total profit and to align the interests of individual participants in a non-cooperative biofuel SC. In this work, we aim at incorporating a game-theoretical Nash-type model approach within a Mixed Integer Linear Programming (MILP) framework in order to optimize a fair profit distribution between members of multi-enterprise SCs. The modelling framework proposed in Giarola et al. (2011) and Ortiz-Gutiérrez et al. (2013) is

extended to include GT principles and study the effects on the dynamic evolution of a bioethanol SC driven by the fulfilment of an increasing biofuel demand. Model decision variables include the biomass production per site and its supply strategy, the location and capacity of biorefineries as well as the transport logistics of the product. The transfer price policy, an efficient method to create a fair, optimized profit distribution in the biofuel SC using GT, is used as powerful tool in the decision making.

2. Problem Description

The emerging biomass-based ethanol production in Northern Italy was assessed as a real world case study to illustrate the applicability and capabilities of the proposed approach in steering the strategic design and planning of systems such as biofuels supply networks. All the assumptions concerning the case study formulation (i.e. territory discretization, logistics, biomass availability, biomass and energy market characteristics as well as technology definition) are in the work by Ortiz-Gutiérrez et al. (2013). Here, we will mainly focus on the changes applied to both the mathematical formulation and the case study in order to include a GT analysis.

The design process was conceived as an optimization problem for two-enterprise bioethanol SCs. One enterprise was devoted to growth and sale of biomass to a biorefinery (the second enterprise) in order to produce bioethanol and byproducts for their onward sale to external customers. The system is capable of meeting the bioethanol demand as defined by European Directive 2009/28 (EC, 2009). The overall timeframe of 15-years was divided into five time intervals (t) of each three-year long in order to reduce the computational burden. Northern Italy was discretized into 59 square cells, considering an additional one for biomass import. The biorefinery was described using three alternative corn-based bioethanol production technologies: (i) dry-grind process (DGP), which is the standard corn-based ethanol process; (ii) DGP-CHP plants, where the DGP byproducts are burnt to cogenerate electricity and heat; and (iii) the fermentation of the thin stillage (considering natural gas supplement for energy needs) enabling production of both electricity and DDGS (DGP-TSNG) (Ortiz-Gutiérrez et al., 2013). Three price levels have been taken into consideration for the corn purchased from the local market within a range of 100-175 €/ton, which is aligned to market price variation in the last decade. Biomass imported from foreign suppliers was supplied at a constant price of 110 €/ton. Price levels were not fixed to a certain amount of biomass supplied by farmers.

3. Mathematical Features

According to Gjerdrum et al. (2001) the Nash-type objective function, ϕ, for a two-echelon SC could be formulated as follows :

$$\varphi = \left(\Pi_{farmers} - \Pi^{L}_{farmers}\right)\left(\Pi_{biorefinery} - \Pi^{L}_{biorefinery}\right) \tag{1}$$

where Π represents the profit of each enterprise (i.e. farmer, biorefinery) which is subject to meet a minimum profit requirement (Π^{L}) as stated below.

$$\Pi_{farmers} \geq \Pi^{L}_{farmers} \;;\; \Pi_{biorefinery} \geq \Pi^{L}_{biorefinery} \tag{2}$$

Eq.(1) was linearized using a separable programming approach based on logarithmic differentiation to obtain a MILP model (Gjerdrum et al., 2001). Accordingly,

$$\hat{\phi} = \sum_{s}^{n} \lambda_{f(s)} \ln\left(\Pi_{farmers(s)} - \Pi^{L}_{farmers}\right) + \sum_{s}^{n} \lambda_{b(s)} \ln\left(\Pi_{biorefinery(s)} - \Pi^{L}_{biorefinery}\right) \quad (3)$$

$$\sum_{s}^{n} \lambda_{f(s)} \Pi_{farmers(s)} + \sum_{s}^{n} \lambda_{b(s)} \Pi_{biorefinery(s)} = \Pi_{farmers(s)} + \Pi_{biorefinery(s)} \quad (4)$$

$$\sum_{s}^{n} \lambda_{f(s)} \ , \ \sum_{s}^{n} \lambda_{b(s)} = 1 \quad (5)$$

$$\lambda_{f(s)} \ , \ \lambda_{b(s)} \geq 0 \quad (6)$$

Eq. (3) represents the new objective function ($\hat{\phi}$) where the enterprise profits were approximated as piecewise linear functions using $s \in S = [1, n]$ transfer price levels and introducing the continuous variables as the intervals $\lambda_{f(s)}$ and $\lambda_{b(s)}$ for farmers and the biorefinery, respectively. While Eq.(4)is the convexity requirement, Eq.(5) and (6) guarantee that two adjacent nodes take non zero values, using n grid points.
The overall profit of biomass growers (TFP [€]) was calculated as follows:

$$\Pi_{farmers(s)} = -TFP \quad (7)$$

$$TFP = \sum_{i} \sum_{g} \sum_{t} FR_{(i,g,t)} \varepsilon_{CF(t)} \quad (8)$$

$$FR_{(i,g,t)} = \sum_{s} Pbl_{(i,g,s,t)} Lvs_{(i,g,s)} - TOC_{(i,g,t)} \quad (9)$$

$$Pb_{(i,g,t)} \geq Pb_{(i,g,t-1)} \quad (10)$$

where $\varepsilon_{CF(t)}$ is discount factor related to time period t specific for $FR_{(i,g,t)}$ representing the incomes from biomass sale, which is evaluated by multiplying the linearized quantity, $Pbl_{(i,g,s,t)}$, of biomass i from the farmer in cell g at time t of the s available levels by the corresponding variable for biomass selling prices for each level ($Lvs_{(i,g,s)}$), $TOC_{(i,g,t)}$ stands for the farmers' total operating cost and accounts for biomass i production and transport cost at time period t. Eq. (10) constraints the farmers to long-term contracts with the biorefinery.
The mathematical model describing the biorefinery company was based on the work by Giarola et al. (2011) to which we refer for the mathematical details. The overall profit of the biorefinery represented as the NPV was calculated by summing up the discounted annual cash flows [CF_t (€/period)] for each period t minus the capital investment [TCI_t (€)] for establishing or enlarging a production facility to meet a minimum profit requirement (Π_L) as stated below.

$$\Pi_{biorefinery} = -NPV \quad (11)$$

$$NPV = \sum_{t} \left(CF_t \cdot dfCF_t - TCI_t \cdot dfTCI_t\right) \quad (12)$$

where $dfCF_t$ and $dfTCI_t$ represent the discounting factors for cash flows and capital costs, respectively. The biomass procurement costs, as part of the CF_t definition have been modified compared to the original model to include the transfer prices.

4. Results and Discussion

The optimization problem for a fair profit allocation in a 2-enterprise corn-based ethanol SC was solved by means of the CPLEX solver in the GAMS® modelling tool.
In order to apply the linearization procedure, minimum profit requirements at different transfer prices were determined solving the optimization problem described in Ortiz-Gutiérrez et al. (2013) for a single enterprise at a time (i.e. farmers and biorefinery). Table 1 reports the minimum profit values for the two enterprises at the chosen.

Table 1. Corn price levels and corresponding minimum profit for farmers and biorefinery.

Level (S)	Price (€/ton)	$\Pi_{farmers}$ (€)	$\Pi_{biorefinery}$ (€)
1	100	2.20E+08	1.00E+06
2	145	6.90E+08	3.19E+08
3	175	1.16E+09	6.37E+08

Once the minimum profit requirements were established we proceeded with the maximization of the enterprise profits ($Max\ \hat{\Phi}$). The outcome of the optimization procedure for each enterprise implementing the linearized Nash objective function, were 2.971 €/GJ_{EtOH} for the biomass growers ($\Pi_{farmers}$) and 1.034 €/GJ_{EtOH} for the biorefinery consortium. The λ multipliers used for the linear approximation took values for $\lambda_{f(1)}\lambda_{f(2)} = 0.982$, and $\lambda_{b(2)} = 1$.
Fig. (1) compares the results obtained for a two enterprise SC with and without the inclusion of a Nash GT approach. The first stacked bars were obtained when the optimized problem aimed at the maximization of an overall profit ($\Pi_G = \Pi_{biorefinery} + \Pi_{farmers}$). The second ones were obtained after the Nash optimization. As is clear in Fig. (1) the proposed approach ensures a more equal profit-split between the two enterprises involved in the SC.

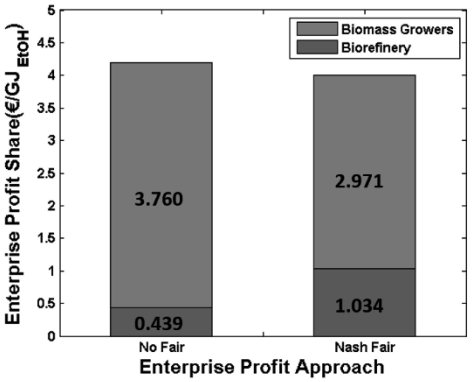

Figure 1. Profit share before and after Nash supply chain optimization and the overall improvement after fair split.

It is interesting to note that the introduction of a Nash-type approach allows the farmers to choose different price levels along the time horizon. The overall system profit embedding a Nash approach matches very close the value obtained from a pure optimization of the enterprise profit summation, which results in a better economic performance of the supply chain as a whole.
In terms of design and planning, the SC configuration at the final period is represented in Fig. (2). The optimal solution involves the establishment of four DGP bioethanol production plants operating at full capacity (over 250 kton/year). One facility is located on the coastline, although the system also relies on biomass importation. At the end of time period 5, the observed amount of imported biomass was about 42%, which reduced significantly the biomass supply costs, due to the lower price of the imported corn.

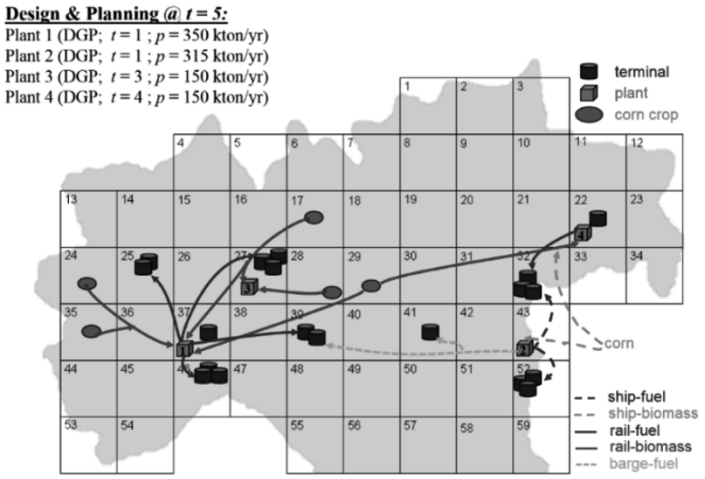

Figure 2. Design and planning strategy at time period t = 5 under Nash optimization supply chain.

Furthermore, an analysis within the Nash modelling framework was performed by fixing the price levels over the time horizon (Table (2)). It has been necessary to increase the original first corn price level (which was set to 100 €/ton) to 130 €/ton, since prices below 130 €/ton so not allow the system to reach the minimum profits established according to the Nash optimization.

Table 2. Enterprise profit under fixed price.

Fixed Price	$\Pi_{farmers}$ (€/GJ_{EtOH})	$\Pi_{biorefinery}$ (€/GJ_{EtOH})
Low (130€/ton)	2.319	1.442
Average (145 €/ton)	2.799	1.130
High (175 €/ton)	2.904	1.034

From the results, it emerges that the fairest split of the profit is obtained at the lowest corn price, where the biorefinery consortium receives about 40% of the total and the farmers' enterprise holds the 60%.

5. Final Remarks

A modelling framework which utilizes a separable programming approach to implement the game theoretical concepts developed by Nash was proposed. The purpose was to guarantee fair profit allocation in the design and planning of a two-enterprise biofuel supply chain. The proposed method guarantees fair profit levels of the separate enterprises while an optimum total profit of the entire supply chain is achieved. The transfer prices for biomass selling-acquirement which allow a fair split of the profits between the two enterprises are mostly located in the higher price level (i.e. 175 €/ton). However, when the proposed method guaranteed that even at a low corn price over the time horizon (130 €/ton) better economic performance were achieved.

The integration of GT aspects in SC optimization tools could support the decision-making among the stakeholders involved in the planning of bioenergy systems. As a matter of fact, these tools could enable the definition of planning strategies from which every single enterprise could benefit. This would facilitate the bargaining among the stakeholders as well as help the planning of bioenergy system capable achieve a better overall performance when a fair profit split is guaranteed.

6. Acknowledgement

R.A. Ortiz Gutiérrez was supported by a Ph.D. Scholarship from the Mexican National Council for Science and Technology (CONACyT).

References

H.S. Aplak, M.Z. Sogut, 2013. Game theory approach in decisional process of energy management for industrial sector. Energy Convers. Manag. 74, 70–80.

EC, 2009. European Commission (EC). Directive 2009/28/EC of the European Parliament and of the Council of 23 April 2009 on the promotion of the use of energy from renewable sources and amending and subsequently repealing Directives 2001/77/EC and 2003/30/EC. Official Journal of the European Union, Brussels.

S. Giarola, A. Zamboni, F. Bezzo, 2011. Spatially explicit multi-objective optimisation for design and planning of hybrid first and second generation biorefineries. Comput. Chem. Eng. 35, 1782–1797.

J. Gjerdrum, N. Shah, L.G. Papageorgiou, 2001. Transfer prices for multienterprise supply chain optimization. Ind. Eng. Chem. Res. 40, 1650–1660.

J. Gjerdrum, N. Shah, L.G. Papageorgiou, 2002. Fair transfer price and inventory holding policies in two-enterprise supply chains. Eur. J. Oper. Res. 143, 582–599.

M. Höök, X. Tang, 2013. Depletion of fossil fuels and anthropogenic climate changeA review. Energy Policy 52, 797–809.

R.A. Ortiz-Gutiérrez, S. Giarola, F. Bezzo, 2013. Optimal design of ethanol supply chains considering carbon trading effects and multiple technologies for side-product exploitation. Environ. Technol. 34, 2189–2199.

B.D. Solomon, N.H. Johnson, 2009. Valuing climate protection through willingness to pay for biomass ethanol. Ecol. Econ. 68, 2137–2144.

J. von Neumann, O. Morgenstern, 1944. Theory of games and economic behavior. In: Theory games Econ. Behav. Pinceton University Press.

D. Yue, F. You, 2014. Fair profit allocation in supply chain optimization with transfer price and revenue sharing: MINLP model and algorithm for cellulosic biofuel supply chains. AIChE J. 60, 3211–3229

C.-T. Zhang, L.-P. Liu, 2013. Research on coordination mechanism in three-level green supply chain under non-cooperative game. Appl. Math. Model. 37, 3369–3379.

Krist V. Gernaey, Jakob K. Huusom and Rafiqul Gani (Eds.), 12th International Symposium on Process Systems Engineering and 25th European Symposium on Computer Aided Process Engineering.
31 May – 4 June 2015, Copenhagen, Denmark

Optimal integration of the year-round operation for methane production from CO_2 and water using wind, solar and biomass

Mariano Martín, William Davis

Department of Chemical Engineering. University of Salamanca, Plz. Caídos 1-5, 37008, Salamanca, Spain

Abstract

In this paper we integrate the use of biomass, wind and solar energy for the constant production of synthetic methane over a year to determine the optimal combination of renewable energy to maintain a production level and to store it in a ready to use and practical form. Biomass is used for the production of power and/or hydrogen. Photovoltaic solar and wind energy are used to obtain power. The power is used to split water through electrolysis to generate oxygen, which is used to process the biomass and hydrogen, that is used to synthesize methane together with CO_2. The optimal operation of the facility involves the use of biomass for the production of power, while hydrogen is to be produced from water electrolysis. The investment and production costs are 175 M€ and 0.38€/Nm^3 respectively. A sensitive analysis shows that biomass is used when its price is lower than 50€/t and for investment rates below 1500€/kW. Solar energy is used for power when the price of biomass is high and only if the solar incidence is above 1200 kWh/m^2 yr. The use of wind is recommended where there is a low solar incidence and wind velocities above 9 m/s.

Keywords: Synthetic methane, CO_2, Process integration, Renewable energy

1. Introduction

Most sustainable sources of energy, namely biomass, wind and solar, present variable availability with time, seasonality and day-long variability, with the weather and the region, which results in the fact that storage systems, supplementary sources of energy or a combination of some of them (Yuand and Chen, 2012) are needed to maintain the production capacity and to meet the demand. While solar and wind energy are very volatile sources, biomass can be stored for a certain period of time and can be used to supply the need for energy during periods of lower availability of wind and solar. The availability of the different sources is also inversely correlated. For example: high intense solar areas typically have low availability of biomass and water.

In this work we evaluate the production of synthetic methane as an energy carrier to store renewable energy. The idea is to avoid idle units within the facility over a year time. The reagents used are renewable hydrogen, produced either from water electrolysis or from biomass gasification, and CO_2 from flue gases is the selected carbon source. The electricity to split the water comes from either a Brayton cycle using syngas generated out of the biomass, or from wind turbines or solar photovoltaic panels.

2. Process description

The process is divided in three zones: biomass processing for syngas production, which is further used for hydrogen or electricity production; water electrolysis that produces hydrogen and the oxygen needed in direct gasification; and methane synthesis from CO_2 and hydrogen. Water is also produced and can be recycled back to the electrolyzer.

2.1. Biomass processing

The biomass is washed and milled before the gasification, producing raw syngas. Two alternatives are considered: The Renugas gasifier operates at medium pressure using oxygen and produces a gas rich in CO_2. The light hydrocarbons generated can be further reformed to hydrogen and CO. High pressure gasification allows a large throughput per reactor volume, and reduces the need for a downstream pressurization, reducing therefore the overall power needed. However, the efficiency of the gasifier is lower, and a large amount of steam and pure oxygen are needed to avoid syngas dilution and reduce the size of the gasifier (Eggeman, 2005). The low pressure gasifier, Battelle Columbus (Ferco), is indirectly heated. The system consists of two chambers, a gasifer and a combustor. Sand, olivine, provides the energy for gasification by being heated up in the combustor with the energy released in the combustion of char. This type of gasifier produces a gas with low CO_2 content, but contains heavier hydrocarbons. The reactor is fast fluidized, allowing throughputs equal to those of the bubbling fluidized Renugas gasifier despite the nearly atmospheric operation. Working at a lower pressure decreases the operating cost (Phillips, 2007). Subsequently, the syngas is reformed to remove the hydrocarbons. Steam reforming is an endothermic reaction but provides a higher concentration of hydrogen in the syngas. Partial oxidation is exothermic but its yield to hydrogen is lower. Finally, the raw syngas is cleaned. Two steps are proposed. Cold cleaning by means of a scrubber for low pressure gasification or a ceramic filter operating at high temperature for high pressure gasification is the first one. The second step consists of a multibed PSA system, used to remove the last traces of hydrocarbons, H_2S and CO_2 in that order. Once the syngas is purified, we can use it for the production of hydrogen, via water gas shift reaction, or for the production of power using a Brayton cycle.

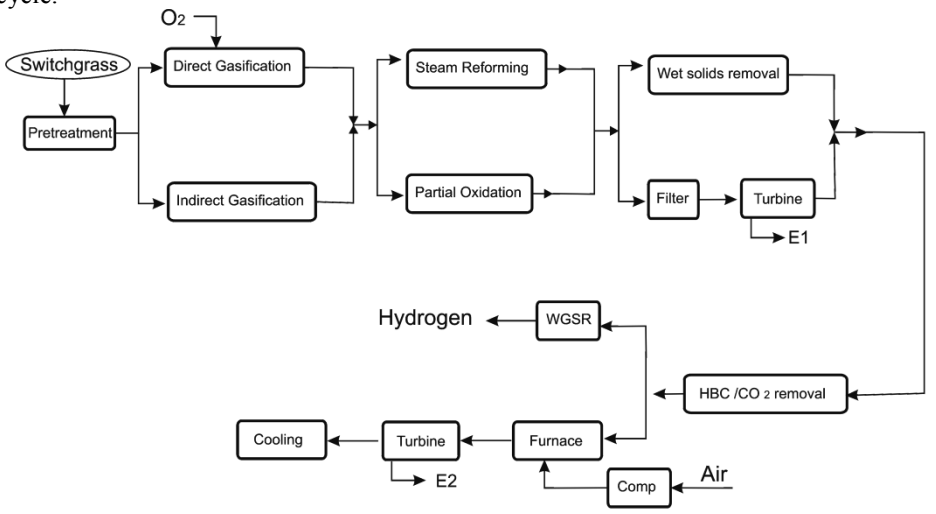

Figure 1.- Biomass processing superstructure

2.2. Water electrolysis

The second section of the facility corresponds to water electrolysis (NEL, 2012). It uses energy from the Brayton cycle, from the wind farm and/or the solar field. On the one hand, we have the line of oxygen that carries water vapor and traces of hydrogen. This water is condensed and the resulting stream is dehydrated using a zeolite adsorber, before compressing and storing the oxygen. This oxygen can be used in the direct gasifier and/or the partial oxidation section of the biomass processing process. On the other hand, we have the stream of hydrogen containing traces of oxygen and water vapor, most of which is separated by condensation. The oxygen represents a challenge for further synthetic stages, so it is eliminated by using a deoxygenation reactor where water is produced. Next, a zeolite is used to dehydrate the stream. Figure 2 shows a scheme of this section.

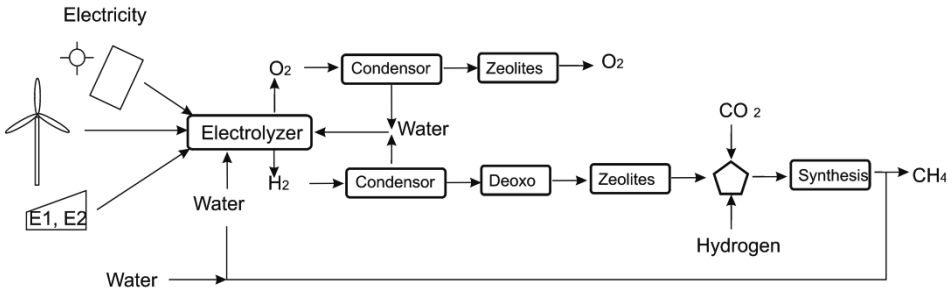

Figure 2.- Water electrolysis and methane synthesis

2.3. Methane synthesis

At this point, hydrogen is mixed with the CO_2. In order to avoid carbon deposition, the proper composition and conditions of the feed are required. Methane is produced through methanation. One important characteristic to reduce water consumption in this process consists of recycling the water produced together with the methane. Thus, the water is condensed, separated, and recycled. The gas produced, mainly methane but also containing CO, CO_2 and unreacted H_2 must meet the constraints related to composition so that the gas phase can be fed to the network that currently supplies natural gas. Figure 2also shows the scheme of this section of the flowsheet.

3. Solution procedure

3.1. Modelling approach

The different units are modelled using first principles, mass and energy balances, such as the case of heat exchangers, compressors, Brayton cycle; first principles combined with experimental data for conversions, i.e. gas reforming or species equilibrium for the WGSR and the methanation reactor (Davies & Lihou, 1971); experimental correlations define the gas composition produced form the gasifiers (Eggemann, 2005, Phillips et al., 2007); rules of thumb for the adsorbent beds or small parameter estimation problems for the performance of the wind turbines (Davis & Martín, 2014). We formulate the model for the superstructure as an MINLP problem in GAMS. The original allocation for

analysis is the Gulf of Cádiz, so that the results are comparable to previous work. (Davis & Martín, 2014).

3.2. Solution procedure

We first evaluate the operation of the facility on a monthly basis to determine the best biomass processing technology. By default, the number of wind turbines and the number of electrolyzers are considered as continuous variable. It is important to notice that their cost is given per kW of energy produced and, thus, the actual number has not a large impact on the investment cost. For each month we solve four problems, NLP's, corresponding to each of the gasifier and reforming models to determine the optimal topology. For each period, the model consists of 3000 equations and 4100 variables. The objective function is given as eqs. (1)-(4) adding a constant, 2, so that Figure 3 is more clear and easier to follow:

$$Z = 2 + F_{CH4} + C_{O2} \cdot F_{O2} - cost\_stw \cdot F_{Biomass} - wind\_t - solar\_t - bio\_t - steam\_t \quad (1)$$

$$wind\_t = \frac{1}{3} \cdot \frac{Wind_{Invest} \cdot P_{nominal} \cdot n_{wind\_turbine}}{time} + Op\_cost_{wind} \cdot P_{nominal} \cdot n_{wind\_turbine}; \quad (2)$$

$$solar\_t = \frac{1}{3 \cdot time} \cdot n_{panel} \cdot \left(P_{panel} \cdot c_{panel} + A_{pannel} \cdot c_{area} \right); \quad (3)$$

$$bio\_t = \frac{1}{3 \cdot time} \cdot cost_{bio} \cdot \left(-W(BraytonTurbine) \right); \quad (4)$$

The investment cost per kW when produced from wind is 1600 €, with an operating cost of 0.015 €/kWh. For PV panels, 2300 €/kWp for PV panels with a cost for area preparation of 5.5 €/m^2 (IRENA 2012). Finally, we use 1100 €/kW (IEA 2013) as the basic price for the energy produced from biomass using the Ferco gasifier, partial oxidation and the correction factors as function of their efficiency in producing electricity for a certain amount of fed biomass are 1.04, 1.19 and 1.24 for Ferco-Steam reforming, Renugas-Partial oxidation and Renugas-Steam Refoming, respectively.

Next, we use a multiperiod optimization formulation for the optimal operation of the selected topology over a year. Finally, we evaluate the selection of the different technologies as a function of the energy availability and cost.

4. Results

4.1. Plant topology

The optimal integration of technologies for the production of methane selects the use of the Ferco gasifier followed by steam reforming to meet the demand, fixed to be 1 kg/s of CH_4. Furthermore, solar is the preferred technology during summer time and no biomass needs to be used, see Figure 3.

4.2. Plant optimal operation

For the year long operation of the plant we assume that, if solar panels, biomass processing units or wind turbines are used at any point during the year, they need to be

bought. The excess of energy produced out of them when it is not needed for methane production can be sold to the grid. The objective function for the multiperiod optimization problem is given by eq. (5):

$$Z = 2 - \text{cost\_stw} \cdot F_{\text{Biomass}} + F_{CH4} + C_{O2} \cdot F_{O2} - \text{wind\_t} - \text{solar\_t} - \text{bio\_t} - \text{steam\_t} + \frac{C_{electro}}{12} \sum_{j \in \{months\}} Power_{generated,j} - Power_{consumed,j} \quad (5)$$

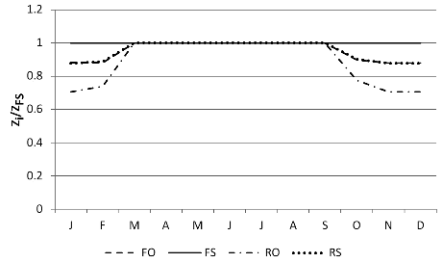

Figure 3. Biomass processing technology selection
F: Ferco; R: Renugas; S:Steam Ref.; O: Partial Oxid.

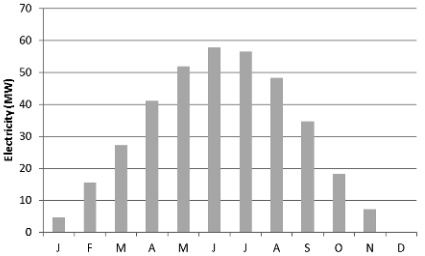

Figure 4. Excess of energy produced over a year

The biomass section operates at a constant capacity of up to 20 kg/s of biomass, resulting in the need for 42,400 panels for the operation of the plant. We produce 4.95 kg/s of oxygen as a byproduct of the electrolysis. There is a certain excess of electricity produced every month but for December, see Figure 4.

This facility requires an investment of 175 M€, 64% of which corresponds to the solar field. The production cost adds up to 46.4 M€/yr and, apart from methane, we produce oxygen and electricity. If both of them are considered as credit, at 98.8 €/t and 0.06 €/kWh respectively, the production cost of synthetic natural gas results in 0.38€/Nm^3 or 10.57€/MMBTU. Although the production cost is higher to that of the current cost of natural gas, this facility requires only one half of the investment compared to solar or wind based facilities for similar production capacity.

4.3. Sensitivity analysis

We consider an availability of up to 1700 t/d of biomass, up to 100 wind turbines, and 100,000 panels of 1kWp each with an assumed efficiency of 75% at a base cost 2300 €/kWp for solar panels and 1600€/kW for wind turbines. The biomass cost is assumed to be within 30-100€/kg, and the cost of the biomass based technology to produce electricity, 1140-2250 €/kW. Figure 5 presents a scheme of the use of the different renewable resources for meeting the methane demand as a function of the solar and wind availability and the price of the biomass.

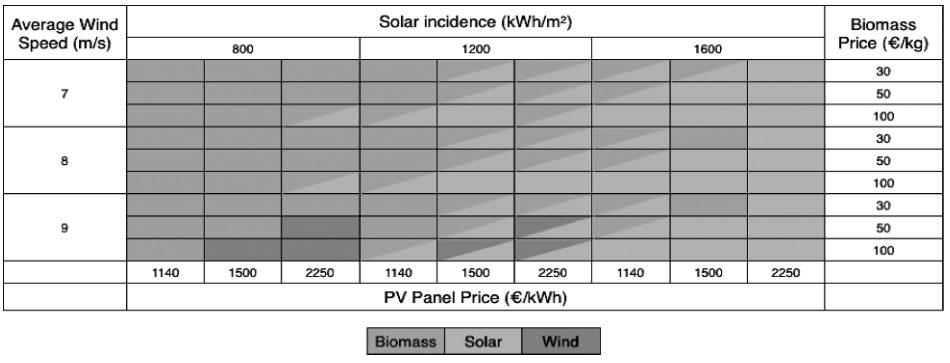

Figure 5. Selection of renewable energy source for different scenarios

Wind energy is only recommended for high wind velocities, above 9m/s, low solar irradiance, below 800 kWh/m^2 and high costs of biomass, above 50 €/t and 1500 €/kW. Solar energy is recommended above 1600 kWh/m^2 of incidence for medium to high cost of biomass. If the cost of biomass is high (above 50€/t) and the wind availability is above 9 m/s, wind turbines complement the production of energy. Otherwise, solar complements the biomass as source of energy.

5. Conclusions

In this work we have developed a mathematical formulation for the integrated use of renewable resources – biomass, wind and solar – for the constant production capacity of a chemical, based on a mathematical optimization framework.

Biomass was processed via gasification, reforming and syngas purification before it was used for either hydrogen synthesis or power production using a Brayton cycle. Wind and photovoltaic solar energies were used for power production. The power was later used in water electrolysis producing hydrogen and oxygen. While the oxygen was sold, the total amount of hydrogen, either from biomass or water electrolysis, was used together with CO_2 from flue gas for the production of methane.

The optimal operating conditions determined the use of biomass indirect gasification and steam reforming if the cost of investment and that of the biomass was low, below 1500€/kW and 50€/t respectively. Solar is the preferred complement as long as the biomass cost is high and we wish to maintain constant production capacity, while the use of wind energy is only recommended for wind velocities above 9m/s, low solar incidence and high costs of biomass. However, the large area required for the solar fields and their actual geographical allocation may favor the use of wind.

References

J. Davies, D. Lihou, 1971, Optimal design of methane steam reformer. Chem. Proc. Eng. 52,71-80

W. Davis, M. Martín, 2014, Optimal year-round operation for methane production from CO_2 and Water using wind and/or Solar energy. *J. Cleaner Prod.* 80, 252-261.

T. Eggeman , 2005, Updated Correlations for GTI Gasifier – WDYLD8. Technical memorandum for Pam Spath, National Renewable Energy Laboratory, Golden, Colorado. June 27, 2005.

IEA, 2013, Updated Capital Cost Estimates for Utility Scale Electricity Generating Plants *Independent Statistics & Analysis* U.S. Department of Energy

IRENA, 2012, Renewable Energy technologies: Cost Analysis Series. Vol. 1. Power Sector. Wind Power.

NEL Hydrogen, 2012, Technical Data. http://www.nel-hydrogen.com/home/?pid=75

S. Phillips, A. Aden, J Jechura, D Dayton, T Eggeman, 2007, Thermochemical ethanol via indirect gasification and mixed alcohol synthesis of lignocellulosic biomass. Technical Report, NREL/TP-510–41168, April 2007.

Z. Yuan, B. Chen, 2012, Process Synthesis for Addressing the Sustainable Energy Systems and Environmental Issues. AIChE J., 58 ,11, 3370-3389

Krist V. Gernaey, Jakob K. Huusom and Rafiqul Gani (Eds.), 12th International Symposium on Process Systems Engineering and 25th European Symposium on Computer Aided Process Engineering.
31 May - 4 June 2015, Copenhagen, Denmark.

Optimal Scheduling of Air Separation with Cryogenic Energy Storage

Qi Zhang[a], Clara F. Heuberger[b], Ignacio E. Grossmann[a,*], Arul Sundaramoorthy[c] and Jose M. Pinto[d]

[a]*Center for Advanced Process Decision-making, Department of Chemical Engineering, Carnegie Mellon University, Pittsburgh, USA*
[b]*Faculty of Mechanical Engineering, RWTH Aachen University, Aachen, Germany*
[c]*Praxair, Inc., Business and Supply Chain Optimization R&D, Tonawanda, USA*
[d]*Praxair, Inc., Business and Supply Chain Optimization R&D, Danbury, USA*
grossmann@cmu.edu

Abstract

The idea of cryogenic energy storage (CES), which is to store energy in the form of liquefied gas, has gained increased interest in recent years. Although CES at an industrial scale is a relatively new approach, the technology used for CES is well-known and essentially part of any cryogenic air separation unit (ASU). In this work, we assess the operational benefits of adding CES to an existing air separation plant. Three potential new opportunities are investigated: (1) increasing the plant's flexibility for load shifting, (2) storing purchased energy and selling it back to the market during higher-price periods, (3) creating additional revenue by providing operating reserve capacity. We develop a mixed-integer linear programming (MILP) scheduling model for an ASU-CES plant and apply a robust optimization approach to model the uncertainty in reserve demand. Results from an industrial case study show that the amount of wasted products can be considerably reduced and significant cost savings can be achieved by utilizing the CES.

Keywords: cryogenic energy storage, demand side management, robust optimization

1. Introduction

The concept of cryogenic energy storage (CES) is to store energy in the form of liquefied gas. When energy is needed at a later time, the liquid gas is pumped to high pressure and vaporized; the high-pressure gas can then be used to drive a turbine to generate electricity. The CES technology is being pioneered in the UK (Chen et al., 2008; Harrabin, 2012) where the company Highview Power Storage has been running a liquid air energy storage (LAES) pilot plant since 2011.

Interestingly, although CES at an industrial scale is a relatively new approach, the technology used for CES is well-known and essentially part of every air separation unit (ASU) that utilizes cryogenic separation. In cryogenic air separation, air is separated into its individual components at low temperatures, and typically, large amounts of oxygen and nitrogen are liquefied. Before being distributed to the customers, the liquid products are stored in large tanks. Hence, by adding a few pieces of equipment, namely pump, heat exchanger, and turbine, one is able to vaporize the stored liquid products and generate electricity, which by definition makes it a CES system.

This raises the following question: What are the potential benefits of an air separation plant with added CES capability? Here, we see three immediate opportunities for such an integrated ASU-CES system: (1) In general, an ASU has a limited range of oxygen to nitrogen ratio at which

it can efficiently operate. This often leads to overproduction of one product, which is typically vented and therefore wasted. With CES, instead of venting overproduced products, we can store them and recover energy from them to increase the plant's flexibility for load shifting. (2) Power generated from the CES system can be sold to the electricity market. (3) Similarly, the plant can gain additional revenue by providing operating reserve capacities which can be dispatched upon request. Operating reserves are required when the real-time electricity demand in the grid is higher than the supply, e.g. due to unexpected load increase or generator failures.

In the spirit of industrial Demand Side Management (Samad and Kiliccote, 2012; Merkert et al., 2014), we develop a scheduling model to assess the potential benefits of an integrated ASU-CES plant. In the proposed framework, robust optimization techniques are applied to model the uncertainty in operating reserve demand. This paper complements the work by Zhang et al. (2015) with a more involved industrial case study that provides additional insights into the interactions between gas and liquid production in such a plant.

2. Integrated ASU-CES Model

We consider an air separation plant that consumes air and electricity to produce gaseous oxygen (GO2), gaseous nitrogen (GN2) as well as liquid oxygen (LO2), liquid nitrogen (LN2), and liquid argon (LAr). To this existing plant, we add a CES system that can generate electricity by vaporizing LO2 or LN2. The energy drawn from the CES can be used internally to power the ASU, or we can sell it to the electricity market. Furthermore, operating reserve capacity can be provided and sold to the reserve market.

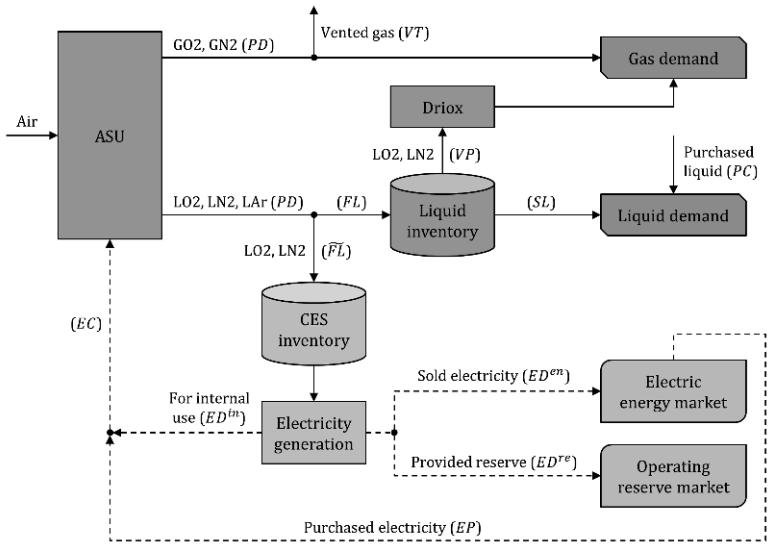

Figure 1: The flowsheet shows the integrated ASU-CES environment. The mass and power flows are depicted by solid and dashed lines, respectively. Flow variable names are shown in parentheses.

Figure 1 shows the mass and power flows in an integrated ASU-CES system. The plant has to satisfy product demand, which can be specified on an hourly basis. Gaseous product customers are connected to the plant via pipelines. We assume that there is no capacity for storing GO2 and GN2. However, there is the possibility of vaporizing LO2 and LN2 to feed the pipelines in case GO2 and GN2 production from the ASU alone is too low to satisfy the demand; in the air

separation industry, this process is referred to as *driox*. LO2 and LN2 are stored in inventory tanks and distributed to the customers when required. Alternatively, liquid products can be purchased from third-party suppliers.

The objective is to find a schedule for the integrated ASU-CES plant over a given scheduling horizon (typically a week) that minimizes the total operating cost minus the revenue from selling power and reserve capacity. This problem can be formulated as an MILP for which the complete formulation is given in Zhang et al. (2015). In the following, we highlight the main features of the proposed model:

- A common-grid discrete-time representation is applied.
- We assume that the ASU can operate in different operating modes. Each mode corresponds to a particular configuration or state of the ASU, e.g. "off", "on", or "startup". At any point in time, the ASU has to run in exactly one of the possible operating modes.
- Each operating mode is defined by a Convex Region Surrogate (CRS) model (Zhang et al., 2014), in which the feasible region is approximated by a union of convex regions in the form of polytopes. For each convex region, a linear power consumption function with respect to to the production rates is given. In this way, nonlinearities and nonconvexities are implicitly taken into account while retaining an MILP formulation.
- The formulation proposed by Mitra et al. (2013) is applied to model mode-to-mode transition constraints. These constraints include enforcing a minimum stay time in a particular mode after transitioning to it from another mode, and fixing the stay time in a mode that represents a certain process that takes a known amount of time, e.g. the startup process.

3. Robust Model with Reserve Demand Uncertainty

Selling reserve capacity is attractive because the reserve provider is rewarded even when no actual generation of power is required. In other words, the reserve provider is selling its mere capability of dispatching power upon request. However, one does not know in advance when reserve will be required. Since noncompliance would result in extremely high penalties, reserve providers have to operate in a way such that dispatch of the committed reserve capacities can be guaranteed.

We apply robust optimization techniques to account for the uncertainty in reserve demand, which is denoted ED_t^{re} for time period t. ED_t^{re} is bounded above by the reserve capacity provided in time period t, RC_t, which is a variable. The uncertainty is specified in terms of an uncertainty set from which any point is a possible realization of the uncertainty. The robust model is then formulated such that the optimal solution is feasible for all possible realizations of the uncertainty and minimizes the objective function. However, if the uncertainty is simply defined as

$$U(RC) = \left\{ \left[ED_1^{re}, \ldots, ED_{|\overline{T}|}^{re} \right]^{\mathrm{T}} : 0 \le ED_t^{re} \le RC_t \ \ \forall t \in \overline{T} \right\} \tag{1}$$

with $\overline{T}$ being the set of time periods in the scheduling horizon, the solution will have to be feasible for the maximum dispatch case in which $ED_t^{re} = RC_t \ \forall t \in \overline{T}$, which is an extremely conservative and also extremely unlikely case. Hence, in order to be able to realistically characterize the uncertainty and to adjust the level of conservatism in the model, we adopt the "budget of uncertainty" approach introduced by Bertsimas and Sim (2004). By defining the normalized reserve demand $w_t = ED_t^{re}/RC_t$, we can restrict the size of the uncertainty set by defining it as follows:

$$U(RC) = \left\{ \left[w_1, \ldots, w_{|\overline{T}|} \right]^{\mathrm{T}} : ED_t^{re} = RC_t\, w_t,\ 0 \le w_k \le 1 \ \ \forall k \le t,\ \sum_{k=1}^{t} w_k \le \Gamma_t \ \ \forall t \in \overline{T} \right\} \tag{2}$$

where the budget parameter, Γ_t, defines the maximum number of time periods in which maximum reserve dispatch can occur up to time t.

The uncertainty set given in Eq. (2) is used to formulate the robust counterpart. Here, we show the derivation for the main constraints involving reserve demand uncertainty, which are the CES inventory constraints:

$$\widetilde{IV}_t = \widetilde{IV}_0 + \sum_{k=1}^{t} u_k - \frac{1}{\eta}\sum_{k=1}^{t} RC_k w_k \qquad \forall t \in \overline{T} \tag{3a}$$

$$\widetilde{IV}^l \le \widetilde{IV}_t \le \widetilde{IV}^u \qquad \forall t \in \overline{T} \tag{3b}$$

where $\widetilde{IV}_t$ is the CES inventory level at time t, u_t is the net flow into the CES tank in time period t, and η is a conversion factor given in unit power per unit mass of liquid. Eq. (3b) sets bounds on the CES inventory levels. By substituting $\widetilde{IV}_t$ in Eq. (3b) and applying the "worst case" with respect to the given uncertainty set to each constraint, we obtain:

$$\widetilde{IV}_0 + \sum_{k=1}^{t} u_k - \frac{1}{\eta}\min_{w\in U(RC)}\left\{\sum_{k=1}^{t} RC_k w_k\right\} \le \widetilde{IV}^u \qquad \forall t \in \overline{T} \tag{4a}$$

$$-\widetilde{IV}_0 - \sum_{k=1}^{t} u_k + \frac{1}{\eta}\max_{w\in U(RC)}\left\{\sum_{k=1}^{t} RC_k w_k\right\} \le -\widetilde{IV}^l \qquad \forall t \in \overline{T} \tag{4b}$$

We can simply drop the term $\min\limits_{w\in U(RC)}\left\{\sum\limits_{k=1}^{t} RC_k w_k\right\}$ in Eq. (4a) since it always takes the value zero. To reformulate Eq. (4b), we introduce the following auxiliary problem for each $t \in \overline{T}$:

$$\max \sum_{k=1}^{t} RC_k w_k \quad \text{s.t.} \quad \sum_{k=1}^{t} w_k \le \Gamma_t, \quad 0 \le w_k \le 1 \ \ \forall k \le t \tag{5}$$

of which the dual is

$$\min \Gamma_t q_t + \sum_{k=1}^{t} s_{tk} \quad \text{s.t.} \quad q_t + s_{tk} \ge RC_k \ \ \forall k \le t, \quad q_t \ge 0, \quad s_{tk} \ge 0 \ \ \forall k \le t. \tag{6}$$

By strong duality, since Problem (5) is feasible and bounded for all $\Gamma_t \in [0,t]$, the dual problem (6) is also feasible and bounded, and moreover, (5) and (6) have the same optimal objective function value. Since Problem (6) is a minimization problem and every feasible solution will yield an objective function value equal to or greater than the minimum, we can substitute (6) for (5) in the robust counterpart formulation. The optimization will automatically drive the objective function value of (6) to its minimum, which coincides with the solution to Problem (5). Hence, we arrive at the following robust counterpart formulation for Eqs. (3):

$$\widetilde{IV}_0 + \sum_{k=1}^{t} u_k \le \widetilde{IV}^u \qquad \forall t \in \overline{T} \tag{7a}$$

$$-\widetilde{IV}_0 - \sum_{k=1}^{t} u_k + \frac{1}{\eta}\left(\Gamma_t q_t + \sum_{k=1}^{t} s_{tk}\right) \le -\widetilde{IV}^l \qquad \forall t \in \overline{T} \tag{7b}$$

$$q_t + s_{tk} \ge RC_k \qquad \forall t \in \overline{T}, k \le t \tag{7c}$$

$$q_t \ge 0,\ s_{tk} \ge 0 \qquad \forall t \in \overline{T}, k \le t \tag{7d}$$

4. Industrial Case Study

We now apply the proposed model to a real-world industrial case study for which the data are provided by Praxair. Given is an existing air separation plant that has to satisfy GO2, GN2, LO2, and LN2 demand. It is important to note that we consider an "oxygen-limited" plant, i.e. the production is driven by the oxygen demand; at such a plant, the nitrogen production often exceeds the demand, which makes venting of GN2 necessary. The scheduling horizon is one week to which we apply an hourly time discretization resulting in 168 time periods.

Assuming an overall CES efficiency of 70 %, we consider the following four cases: *Case 1* – only existing ASU; *Case 2* – existing ASU with added CES, but without reserve market participation; *Case 3* – ASU and CES with reserve market participation and budget parameter $\Gamma_t = 1 \; \forall t \in \overline{T}$; *Case 4* – ASU and CES with reserve market participation and budget parameter $\Gamma_t = 1$ for $t = [1,48]$, $\Gamma_t = 2$ for $t = [49,96]$, $\Gamma_t = 3$ for $t = [97,168]$. Case 3 and Case 4 differ in their levels of conservatism. While Case 3 represents a more realistic but maybe slightly risky uncertainty assumption, Case 4 is highly conservative and leads to very robust solutions.

Figure 2 shows the power consumption profiles for all four cases. One can observe that more power is consumed in an integrated ASU-CES plant, which indicates that the plant is utilizing more of its production capacity to benefit from the added CES capability.

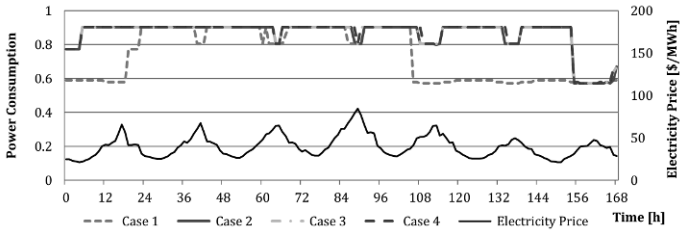

Figure 2: The power consumption profiles for the cases involving CES (Cases 2, 3, and 4) are almost identical, but differ significantly from the ASU-only Case 1.

The significant difference in the production schedules mainly stems from the handling of the produced GN2. In the ASU-only case, the GN2 production exceeds the GN2 demand by a considerable amount, of which a large portion is simply vented. As shown in Table 1, the ASU-CES plant liquefies a large amount of GN2 and uses it for energy storage instead of venting it. In this way, the amount of vented GN2 is reduced to up to 80 %.

Table 1: The normalized results from the four cases show the potential cost savings achieved by an integrated ASU-CES plant. Note that cost of purchasing products and driox cost are not listed.

	Case 1	**Case 2**	**Case 3**	**Case 4**
GN2 Vented	1	0.221	0.205	0.200
LN2 Produced	1	1.172	1.174	1.175
Electricity Cost	0.965	0.933	0.948	0.962
Revenue from Electricity Sales		0.027	0.022	0.018
Revenue from Providing Reserve			0.062	0.062
Total Net Operating Cost	1	0.935	0.894	0.911

The results given in Table 1 further show that by using power recovered from the CES to run the ASU or sell electricity to the grid, the total net operating cost can be reduced by 6.5 %. The cost

savings are even higher if we also participate in the reserve market, namely 10.6 % in Case 3 and 8.9 % in the more conservative Case 4. For Case 4, Figure 3 shows the flows into and out of the CES tank as well as the CES inventory profile resulting from the particular scenario in which no reserve power is dispatched. In each time period in which reserve capacity is provided, the CES inventory level ensures that the maximum amount of reserve can be dispatched. Since for the given budget parameter, maximum dispatch can occur up to three times, the final CES inventory level depicted here is not zero but instead three times as high as the provided reserve capacity.

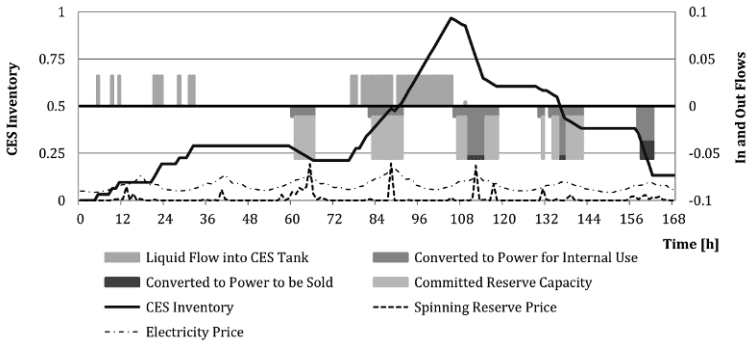

Figure 3: The CES inventory profile is shown for Case 4 for the scenario in which no reserve power is dispatched, resulting in a nonzero final CES inventory level.

5. Conclusions

This work has assessed at an operational level the economic benefits of adding a CES system to an existing cryogenic air separation plant. The proposed MILP scheduling model for an integrated ASU-CES plant incorporates the possibility of recovering energy from CES for internal use or for being sold to the electricity market. Using a robust optimization approach, this model has been further extended to consider uncertainty in operating reserve demand, which results in solutions that guarantee reserve dispatch feasibility under the committed reserve capacity. Furthermore, budget parameters are used to adjust the level of conservatism in the solution.

The proposed model has been applied to a real-world industrial case study. The results yield relative cost savings of approximately 10 % under relatively conservative uncertainty assumptions, which highlights the potential economic benefits of an integrated ASU-CES plant.

References

D. Bertsimas, M. Sim, 2004. The Price of Robustness. Operations Research 52 (1), 35–53.

H. Chen, Y. Ding, T. Peters, F. Berger, 2008. A method of storing energy and a cryogenic energy storage system.

L. Merkert, I. Harjunkoski, A. Isaksson, S. Säynevirta, A. Saarela, G. Sand, 2014. Scheduling and energy – Industrial challenges and opportunities. Computers & Chemical Engineering 72, 183–198.

Q. Zhang, C.F. Heuberger, I.E. Grossmann, A. Sundaramoorthy, J.M. Pinto, 2015. Air Separation with Cryogenic Energy Storage: Optimal Scheduling Considering Electric Energy and Reserve Markets (to appear in AIChE Journal).

Q. Zhang, I.E. Grossmann, A. Sundaramoorthy, J.M. Pinto, 2014. Data-driven construction of Convex Region Surrogate models (submitted for publication).

R. Harrabin, 2012. Liquid air 'offers energy storage hope'. URL `http://www.bbc.com/news/science-environment-19785689`

S. Mitra, L. Sun, I.E. Grossmann, 2013. Optimal scheduling of industrial combined heat and power plants under time-sensitive electricity prices. Energy 54, 194–211.

T. Samad, S. Kiliccote, 2012. Smart grid technologies and applications for the industrial sector. Computers & Chemical Engineering 47, 76–84.

Krist V. Gernaey, Jakob K. Huusom and Rafiqul Gani (Eds.), 12th International Symposium on Process Systems Engineering and 25th European Symposium on Computer Aided Process Engineering.
31 May – 4 June 2015, Copenhagen, Denmark

An Integrated Unit Commitment and Generation Expansion Planning Model

Nikolaos E. Koltsaklis[a], Michael C. Georgiadis[a,*]

[a]*Department of Chemical Engineering, Aristotle University of Thessaloniki, University Campus, Thessaloniki, 54124, Greece*
mgeorg@auth.gr

Abstract

This work presents a generic mixed integer linear programming (MILP) model that integrates the unit commitment problem (UCP) (daily energy planning) within the long-term generation expansion planning (GEP) framework. The model has been tested on an illustrative case study of the Greek power system. Our approach aims to provide useful insights into the strategic and challenging decisions to be determined by investors and/or policy makers at a national and/or regional level by providing the optimal energy roadmap according to specific assumptions and projections (e.g., electricity demand, fuel prices, and investment costs).

Keywords: Energy policy, Power sector, UCP, GEP, System marginal price.

1. Introduction

For decades, traditional long-term GEP models are based on simplifications with regard to operational costs and issues ignoring technical details such as start-up and shut-down related decisions, ramp rates and operating reserves. However, due to the intermittency and high fluctuations of rapidly penetrated renewable energy technologies (RES) (e.g., wind and solar), the net load required to be met by the hydrothermal power plants is characterized by higher uncertainty and has faster time dynamics (Palmintier and Webster, 2011). As a result, the incorporation of short-term decisions (UCP) into the long-term planning framework (GEP problem) can enhance the accuracy of the decisions to be made and guarantees power networks' stability. There are several works in the literature that have separately addressed the UCP (Simoglou et al., 2010, Marcovecchio et al., 2011) and the GEP problem (Koltsaklis et al., 2014, Cheng et al., 2015). A generic MILP model has been developed in this work integrating the UCP within the long-term GEP framework. Typical daily constraints at an hourly level such as start-up and shut-down related decisions, ramping limits, system reserves requirements are combined with representative yearly constraints such as power capacity additions, power generation bounds of each unit, peak reserve requirements, and energy policy issues (RES penetration limits, CO_2 emission cap). For modelling purposes, a representative day (24 hours) of each month over a number of years has been employed in order to determine the optimal capacity additions, system marginal prices (SMP), and daily operational planning of the studied power system.

2. Problem Statement and Mathematical Formulation

This work deals with the combined long-term GEP and UCP of a power system at a national and/or regional level. The problem under consideration is defined according to the following: The studied power system is divided into a number of sectors $s \in S$. Each

sector $s \in S$ is further divided into a set of zones $z \in Z$.The whole planning horizon is split into sets of years $y \in Y$, months $m \in M$, and hours $t \in T$. A set of power generating units $i \in I$ is available for the solution of the combined UCP and GEP problem. These units are further divided into hydrothermal $i \in I^{HT}$, thermal $i \in I^{TH}$, renewables $i \in I^{RES}$, existing $i \in I^{EX}$, and new units $i \in I^{NEW}$. A set of permissible power plants' start-up types $a \in A$ (hot, warm, and cold start-up) is taken into consideration for each hydrothermal power unit $i \in I^{HT}$. Power capacities of both hydrothermal plants and electricity imports interconnections $nc \in NC^{IMP}$, as well as exports interconnections $nc \in NC^{EXP}$, are split into a number of operational blocks $bl \in BL$ in order to represent more realistically their operational characteristics. The objective function to be optimized concerns the minimization of the total discounted cost for the development and operation of the power system, as described by Eq.(1).

$$\boldsymbol{Min\ Cost} = \overbrace{Fuel\ cost + Variable\ operating\ and\ maintenance\ cost + CO2\ emissions\ cost}^{Marginal\ cost} + \overbrace{Electricity\ imports\ cost\ - Electricity\ exports\ revenues}^{Net\ electricity\ trade\ cost} + \overbrace{Shut\ down\ cost + Start-up\ cost}^{Other\ operating\ costs} + Reserves\ provision\ cost + New\ units'\ capital\ cost + Fixed\ operating\ and\ maintenance\ cost\ of\ RES \quad (1)$$

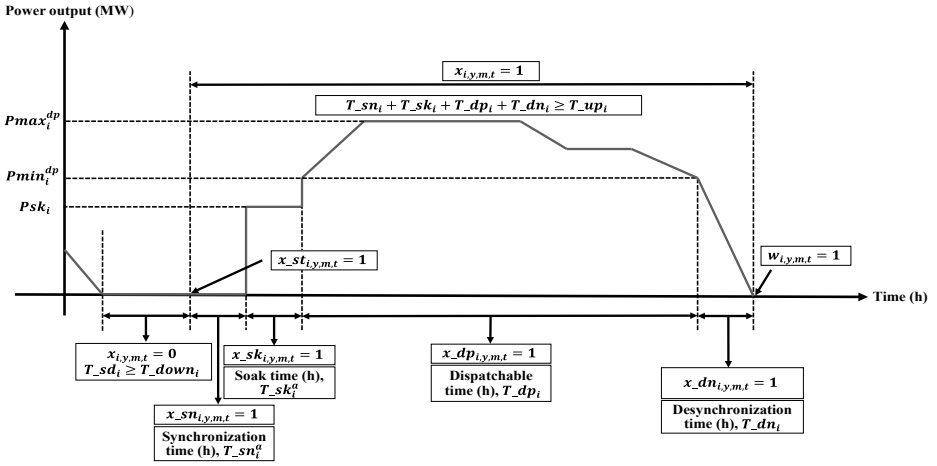

Figure 1. Operating stages of a hydrothermal unit in the UCP

All the possible operating modes of a hydrothermal unit $i \in I^{HT}$ in the UCP including start-up, synchronization, soak, desynchronization, as well as minimum up and down time constraints, are illustrated in Figure 1. More specifically: after being shut-down ($x_{i,y,m,t} = 0$) for T_sd_i hours (T_sd_i must be greater than or equal to the minimum down time of each unit $i \in I^{HT}$, T_down_i), and according to the amount of that time, T_sd_i, the unit $i \in I^{HT}$ starts-up ($x\_st_{i,y,m,t} = 1$). Note that a hydrothermal unit $i \in I^{HT}$ is able to start-up with only one start-up type $a \in A$ at each time period ($\sum_{a \in A} x\_st^a_{i,ym,t} = x\_st_{i,y,m,t} \leq 1$), depending on the value of T_sd_i. Once the appropriate start-up decision is taken ($x\_st^a_{i,ym,t} = x\_st_{i,y,m,t} = 1$ for a certain $a \in A$), the hydrothermal unit enters the synchronization operational stage ($x\_sn^a_{i,ym,t} = x\_sn_{i,y,m,t} = 1$ for a certain $a \in A$) having a duration of $T\_sn_i^a$ hours. Note that the

power output of each unit during the synchronization phase is zero. After completing the synchronization stage, the unit $i \in I^{HT}$ enters the soak operating stage ($x\_sk^{a}_{i,ym,t} = x\_sk_{i,y,m,t} = 1$ for a specific $a \in A$), having a duration of $T\_sk_i^a$ hours and during which unit's power output equals a fixed value, Psk_i. The next operational stage of each unit $i \in I^{HT}$ is that of dispatchable stage ($x\_dp_{i,y,m,t} = 1$), with a duration of T_dp_i hours and during which unit's power output is able to range from its technical minimum, $Pmin_i^{dp}$, to its maximum, $Pmax_i^{dp}$, subject to technical up and down ramp rates (RR_up_i and RR_down_i correspondingly) contributing to the power demand satisfaction, $Dem_{s,y,m,t}$, and to reserve requirements, if selected. Finally, the last possible operational stage of a unit $i \in I^{HT}$ is that of desynchronization, having a duration of T_dn_i hours. During that stage ($x\_dn_{i,y,m,t} = 1$), unit's power output decreases with a particular power sequence. Note that a shut-down decision ($w_{i,y,m,t} = 1$) cannot be taken unless $T\_sn_i + T\_sk_i + T\_dp_i + T\_dn_i \geq T\_up_i$, i.e., unit $i \in I^{HT}$ remains operational during hour $t \in T$ if it has started-up the previous ($T\_up_i - 1$) hours. Constraints (2) ensure that unit $i \in I^{HT}$ can only be at one of the possible operating states when committed. Constraints (3) and (4) model the start-up ($x\_st_{i,y,m,t}$) and shut-down ($w_{i,y,m,t}$) decision of each unit $i \in I^{HT}$ during each time period. Constraints (5) correlate design and operational decisions, i.e., a unit $i \in I^{NEW}$ is not operationally available unless the decision for its construction has been taken ($cn_{i,y} = 1$) and its installation has been completed, requiring T_con_i years. Constraints (6)-(8) specify the power output limits of each unit $i \in I^{HT}$ in each operating stage. The first three terms on the right-hand side of these constraints define unit's power output during synchronization, soak and desynchronization phases. Non-negative continuous variables $r1^{up}_{i,y,m,t}$, $r2^{up}_{i,y,m,t}$, $r2^{down}_{i,y,m,t}$, $r3^{sp}_{i,y,m,t}$ represent the contribution of each unit $i \in I^{HT}$ in primary-up, secondary-up, secondary-down, and tertiary spinning reserve type in each time period. Binary variable $x\_sc_{i,y,m,t}$ denotes if the unit $i \in I^{HT}$ contributes or not to secondary reserve in each time period. Constraints (9) and (10) describe the ramp-up and ramp-down limits of each unit $i \in I^{HT}$. Parameter RR_sec_i represents the ramp rates of each unit $i \in I^{HT}$ when providing secondary reserve ($x\_sc_{i,y,m,t} = 1$). Moreover, equations (11) describe the demand balance of the power system. More specifically, net power injection from all the installed power units ($\sum_{i \in I^s} p\_inj_{i,y,m,t}$) plus net electricity flow rates ($\sum_{s' \in S^s} cf_{s',s,y,m,t} - \sum_{s' \in S^s} cf_{s,s',y,m,t}$) and net electricity imports ($\sum_{nc \in NC^s} im\_inj_{nc,y,m,t} - \sum_{nc \in NC^s} exp_{nc,y,m,t}$) to each sector, must be equal to the sector's electricity demand $Dem_{s,y,m,t}$. Other UCP related model constraints concern: (i) reserve upper and lower bounds (primary-up, secondary-up and down, tertiary spinning and non-spinning reserves), (ii) hourly power output constraints taking into account capacity and zonal availability factors for thermal and RES units correspondingly, (iii) diversification of power output into fixed (non-priced) component including RES power injection, mandatory hydro injection and power injection from units being under commissioning status, and that of priced component based on the energy offer per power capacity block of each unit, and (iv) power system's requirements for all reserve types. An additional series of constraints concerns the GEP decisions. Constraints (12) and (13) define the additional capacity limits. Non-negative continuous variable $nc_{i,y}$ represents the newly-built capacity of unit $i \in I^{NEW}$ in year $y \in Y$ being available for the first time after T_con_i years from the decision taken for its construction ($cn_{i,y} = 1$). Parameter $IC_{i,y}$ represents the installed capacity of unit $i \in I^{EX}$ in year $y \in Y$. Other GEP related constraints of the model refer to: (i) reserve margin constraints, i.e., the

installed capacity being available in each time period plus the available imports must be adequate enough to meet the projected load plus an allowance above that level for security reasons, (ii) annual generation bounds of each unit and annual bounds on imports and exports, (iii) maximum allowable RES penetration rates, (iv) annual RES penetration targets in the power mix, and (v) maximum allowable bound of CO_2 emissions produced by all units.

$$x_{i,y,m,t} = x\_sn_{i,y,m,t} + x\_sk_{i,y,m,t} + x\_dp_{i,y,m,t} + x\_dn_{i,y,m,t} \quad \forall\, i \in I^{HT}, y \in Y, m \in M, t \in T \tag{2}$$

$$x\_st_{i,y,m,t} - w_{i,y,m,t} = x_{i,y,m,t} - x_{i,y,m,t-1} \quad \forall\, i \in I^{HT}, y \in Y, m \in M, t \in T \tag{3}$$

$$x\_st_{i,y,m,t} + w_{i,y,m,t} \leq 1 \quad \forall\, i \in I^{HT}, y \in Y, m \in M, t \in T \tag{4}$$

$$x_{i,y,m,t} \leq \sum_{y' \leq y} cn_{i,y'-T\_con_i} \quad \forall i \in I^{NEW}, y \in Y, m \in M, t \in T \tag{5}$$

$$p_{i,y,m,t} - r2^{down}_{i,y,m,t} \geq 0 \cdot x\_sn_{i,y,m,t} + p\_sk_{i,y,m,t} + p\_dn_{i,y,m,t} +$$
$$Pmin_i^{dp} \cdot (x\_dp_{i,y,m,t} - x\_sc_{i,y,m,t}) + Pmin_i^{sc} \cdot x\_sc_{i,y,m,t} \quad \forall\, i \in I^{HT}, y \in Y, m \in M, t \in T \tag{6}$$

$$p_{i,y,m,t} + r2^{up}_{i,y,m,t} \leq 0 \cdot x\_sn_{i,y,m,t} + p\_sk_{i,y,m,t} + p\_dn_{i,y,m,t} +$$
$$Pmax_i^{dp} \cdot (x\_dp_{i,y,m,t} - x\_sc_{i,y,m,t}) + Pmax_i^{sc} \cdot x\_sc_{i,y,m,t} \quad \forall\, i \in I^{HT}, y \in Y, m \in M, t \in T \tag{7}$$

$$p_{i,y,m,t} + r1^{up}_{i,y,m,t} + r2^{up}_{i,y,m,t} + r3^{sp}_{i,y,m,t} \leq 0 \cdot x\_sn_{i,y,m,t} + p\_sk_{i,y,m,t} + p\_dn_{i,y,m,t} +$$
$$Pmax_i^{dp} \cdot x\_dp_{i,y,m,t} \quad \forall\, i \in I^{HT}, y \in Y, m \in M, t \in T \tag{8}$$

$$p_{i,y,m,t} - p_{i,y,m,t-1} \leq (1 - x\_sc_{i,y,m,t}) \cdot RR\_up_i + RR\_sec_i \cdot x\_sc_{i,y,m,t} \cdot 60$$
$$\forall\, i \in I^{HT}, y \in Y, m \in M, t \in T \tag{9}$$

$$p_{i,y,m,t-1} - p_{i,y,m,t} \leq (1 - x\_sc_{i,y,m,t}) \cdot RR\_down_i + RR\_sec_i \cdot x\_sc_{i,y,m,t} \cdot 60$$
$$\forall\, i \in I^{HT}, y \in Y, m \in M, t \in T \tag{10}$$

$$\sum_{i \in I^s} p\_inj_{i,y,m,t} + \sum_{nc \in NC^s} im\_inj_{nc,y,m,t} + \sum_{s' \in S^s} cf_{s',s,y,m,t} =$$
$$\sum_{s' \in S^s} cf_{s,s',y,m,t} + \sum_{nc \in NC^s} exp_{nc,y,m,t} + Dem_{s,y,m,t} \quad \forall\, s \in S, y \in Y, m \in M, t \in T \tag{11}$$

$$nc_{i,y+T\_con_i} = Pmax_i^{dp} \cdot cn_{i,y} \quad \forall\, i \in I^{NEW}, y \in Y \tag{12}$$

$$c_{i,y} = IC_{i,y} + \sum_{y' \leq y} nc_{i,y'} \quad \forall\, i \in I, y \in Y \tag{13}$$

3. Case study description

The proposed model has been tested on the Greek power system having a total installed capacity of 16,192 MW, of which lignite accounts for 27 % of the total, natural gas makes up 26.3 %, hydro has a share of 19.8 % and followed by photovoltaics (PV) with 15 %, wind with 9.5 %, and other RES with 2.5 %. The examined period is that between

2014 and 2020. The candidate units for installation include new lignite, coal, natural gas, wind, and PV units. Typical marginal costs for lignite units range from 36 to 58 €/MWh, depending on each unit's power capacity block, time period (due to different fuel and carbon price evolution), as well as on the characteristics of each unit (e.g., age). The corresponding ones for natural gas units vary from 66 to 96 €/MWh, and for candidate coal units between 36 and 43 €/MWh. RES power generation and mandatory hydro injection (based on detailed estimations of their availability factors in each zone, month, and hour) have zero cost. Regarding electricity demand, an annual increase of 1 % is assumed, from 51.5 to 54.7 TWh. A gradual decrease in RES investment cost is also assumed, reflecting the fact that they gradually constitute mature technologies.

4. Results and Discussion

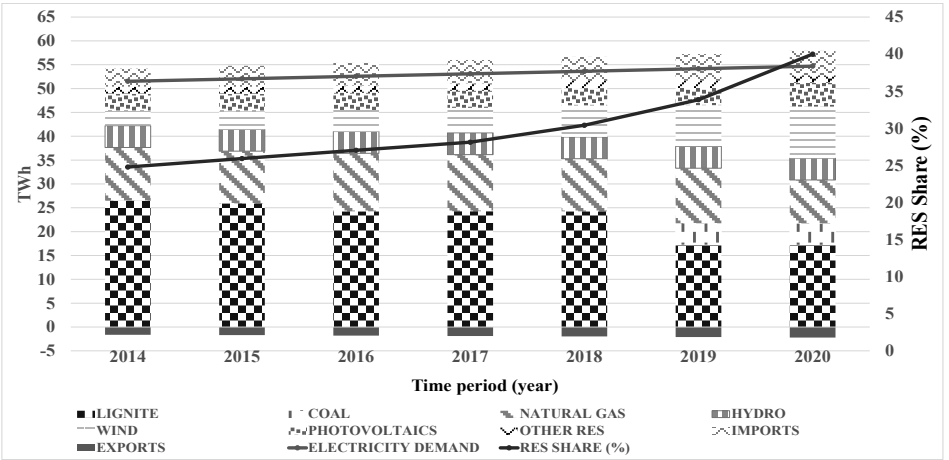

Figure 2. Power generation mix (TWh) and RES share (%) in each time period (year)

As depicted in Figure 2, the results indicate a decrease of 35 % in the projected lignite-fired power generation between 2014 and 2020. This is due to the fact that a significant proportion of them constitute old power stations and as a consequence, they have lost part of their relative competitiveness. In addition, the incorporation of energy policy measures in the mathematical model, i.e., 40 % of the electricity demand should be met by RES by 2020, and the introduction of a CO2 emission cap, contributes also to the gradual decrease of the lignite-fired electricity production. It is also worth mentioning that part of the lost thermal power generation (in favor of RES) is replaced by the installation of a new advanced coal unit, and thus, total thermal power generation (lignite and coal) decreases only by 18 % between 2014 and 2020, from 26.5 to 21.7 TWh. Natural gas production is relatively constant during the whole planning horizon with a small decrease in 2020 due to the high penetration of wind turbines to reach the 2020 RES target. The marked impact of energy policy measures is reflected in the total RES power generation, rising by 71.4 % between 2014 and 2020, from 12.7 TWh to 21.9 TWh. Wind turbines play the dominant role in that evolution accounting for 49.4 % of the total RES generation in 2020 and followed by PVs with 22.8 %, hydro with 20.8 %, and other RES (biomass, small hydro, etc.) with 6.9 %. An increasing trend is also observed in both imports and exports providing more flexibility to the power demand satisfaction. In total, 3400 MW of wind turbines and 857 MW of PV enter the system, the majority of which (1857.1 MW) in 2020 to reach the 2020 RES target, as shown in Table 1. A new coal unit is also installed in 2019 to support thermal power

generation. With regard to SMP (price to be paid to all electricity producers), the results highlight a gradual fall in its value, from 57.64 €/MWh in 2014 to 42.28 €/MWh in 2020 (a decrease of 26.7 %). This fall in SMP (annual weighted average value) can be mainly attributed to the fact that a continuously increasing share of power demand is satisfied from RES (zero marginal cost and their contribution is mandatory), and the introduction of the relatively low marginal cost coal unit into the system, since it comprises the marginal unit for several hours of its operation.

Table 1. SMP evolution (€/MWh) and capacity additions per technology, zone and year (MW)

	2014	2015	2016	2017	2018	2019	2020
New_Coal_Zone_3	-	-	-	-	-	600	-
WIND_Zone1	-	-	-	-	-	300	300
WIND_Zone2	-	-	-	-	300	300	300
WIND_Zone3	-	300	300	300	300	300	300
WIND_Zone4	-	-	-	-	-	-	100
PV_Zone3	-	-	-	-	-	-	257.1
PV_Zone4	-	-	-	-	-	-	300
PV_Zone5	-	-	-	-	-	-	300
System Marginal Price	57.64	56.75	54	51.06	48.1	45.99	42.28

5. Conclusions

An integrated GEP and UCP model has been developed in this work. The planning framework has been extended up to hourly level to better reflect the operational characteristics of thermal units along with the fluctuations arising from the intermittent nature and rapid penetration of RES into the system. The model outputs include optimal investment plan of the power sector and the SMP development. The applicability of the model has been tested on the Greek power system illustrating the impacts that energy policy measures have on the development path of the country's power system.

Acknowledgements

Financial support from the European Commission's FP7 EFENIS project (Contract No: ENER/FP7/296003) "Efficient Energy Integrated Solutions for Manufacturing Industries" is gratefully acknowledged.

References

R. Cheng, Z. Xu, P. Liu, Z. Wang, Z. Li, I. Jones, 2015, A multi-region optimization planning model for China's power sector, Applied Energy, 137, 413-426.

N. E. Koltsaklis, A. S. Dagoumas, G. M. Kopanos, E. N. Pistikopoulos, M. C. Georgiadis, 2014, A spatial multi-period long-term energy planning model: A case study of the Greek power system, Applied Energy, 115, 456-482.

M. G. Marcovecchio, A. Q. Novais, I. E. Grossmann, 2011, A deterministic optimization approach for the unit commitment problem, Computer Aided Chemical Engineering, 29, 532–536.

B. Palmintier, M. Webster, 2011, Impact of unit commitment constraints on generation expansion planning with renewables, Proceedings 2011 IEEE Power and Energy Society General Meeting, 1-7.

C. K. Simoglou, P. N. Biskas, A. G. Bakirtzis, 2010, Optimal self-scheduling of a thermal producer in short-term electricity markets by MILP, IEEE Transactions on Power Systems, 25, 4, 1965-1977.

Krist V. Gernaey, Jakob K. Huusom and Rafiqul Gani (Eds.), 12th International Symposium on Process Systems Engineering and 25th European Symposium on Computer Aided Process Engineering.
31 May - 4 June 2015, Copenhagen, Denmark.

System Design of Renewable Energy Generation and Storage Alternatives for Large Scale Continuous Processes

Oluwamayowa Amusat[a*], Paul Shearing[a] and Eric S. Fraga[a]

[a]*Centre for Process Systems Engineering, Department of Chemical Engineering, University College London, Torrington Place, London WC1E 7JE, United Kingdom*
oluwamayowa.amusat.13@ucl.ac.uk

Abstract

This work investigates the possibility of off-grid energy generation and storage for large scale continuous processes located in remote areas, such as mines. In this paper, a superstructure containing two solar energy generation alternatives (Solar panels and Central receiver system) and three energy storage alternatives is optimized to meet the hourly electrical and thermal demands of a Chile-based mine. A cost-based MINLP formulation for energy generation, storage and supply is developed from first principles and implemented in GAMS. The model determines the optimal configuration of the superstructure and design capacities of the selected alternatives. The daily and seasonal behaviour of the selected storage alternatives are also discussed.

Keywords: Energy Storage, Mining, MINLP, Systems Modelling

1. Introduction

The mining industry accounts for a significant portion of industrial energy demand. The rising demand for metals around the world, coupled with the depletion of readily accessible ore deposits, has led to mining operations moving to more remote locations. Mining operations located in remote regions face significant energy problems, since grid electricity is not usually available. Such mines typically resort to the use of diesel generators, leading to a significant increase in emissions and overall mining cost. These challenges, along with the ever-rising fossil fuel costs, have driven mining operations to seek alternative sources of energy. Renewable energy is considered to be the most promising solution to the mining industry energy problem due to the low operating cost of renewable systems and the possibility of earning tax credits (Paraszczak and Fytas, 2012). However, problems of variability and reliability have limited its use in large-scale operations.

Energy storage may enhance the viability of renewable energy generation systems. Integration of storage alternatives, such as batteries and pumped hydro systems, with renewable energy sources has been considered (Yang et al., 2009; Ma et al., 2014). However, most of the focus has been on the integration of single storage options into small-scale hybrid grid-PV-wind systems. Little consideration has been given to the integration of multiple storage systems, particularly for large-scale off-grid continuous operations. This work investigates the possibility of operating remote mines using renewable energy with a variety of energy storage schemes. A model which determines the cost-optimal energy system design for mining processes is presented. The daily and seasonal behaviours of the selected generation and storage alternatives are investigated. The novel combination of generation and storage alternatives presented in this work allows for the exploration of energy system designs best suited to large scale continuous operations.

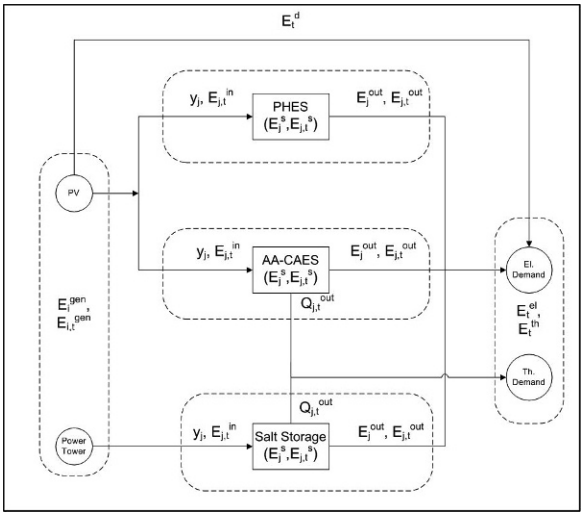

Figure 1: Superstructure for off-grid energy supply for a mine

2. Problem Statement

An off-grid plant located in a remote region with abundant solar radiation for most of the year is considered. Two solar energy collection options are available: electricity generation via photovoltaic cells and thermal energy collection in a molten salt via solar towers (concentrated solar power). Three energy storage alternatives are available. Two for electrical energy (Pumped Hydraulic Energy Storage [PHES] and Advanced Adiabatic Compressed Air Storage [AA-CAES]), while the third stores thermal energy (molten salt storage). Heated molten salt may be used for electricity generation through heating of steam for a turbine.

Figure 1 shows a schematic representation of the superstructure. In the superstructure, i represents the available energy generation options (PV =1; solar tower = 2), j the storage/delivery options (PHES =1; AA-CAES =2; salt storage = 3), while t is an index into discrete time periods of duration Δt, $t > 0$. y_j is a binary variable which determines whether a storage option within the superstructure is selected. $E_{i,t}^{gen}$ refers to the amount of energy generated by unit during time period t; E_t^d is the electrical energy generated by the panels sent directly to the process after DC/AC conversion; $E_{j,t}^{in}$ refers to the energy sent to storage option j; $E_{j,t}^s$ refers to the energy stored; $E_{j,t}^{out}$ refers to the electricity supplied delivered from a storage option; and $Q_{j,t}^{out}$ refers to the heat taken out of a storage unit to meet heat demands.

Given the hourly thermal and electrical demands of the plant (E_t^{th}, E_t^{el}), the total daily solar radiation for the plant location (H_d), and efficiencies for all mechanical units (compressors, turbines, motors, generators and pumps), we choose the optimal capacities of the energy generation units (E_i^{gen}), storage units (E_j^s) and delivery units (E_j^{out}) required to meet the given demands so as to minimize the overall capital cost, CC, of the energy system:

$$CC = \sum_{i=1}^{2} U_i^{gen} E_i^{gen} + \sum_{j=1}^{3} y_j \left(U_j^s E_j^s + U_j^{out} E_j^{out} \right) \tag{1}$$

where U_i^{gen}, U_j^s, and U_j^{out} are the unit costs of generation, storage and electricity supply respectively. The model is subject to generation, storage and process demand constraints as detailed

in the next section. The total energy supplied to the process must meet the process demands at all times. The electrical demands may be met by any storage method or directly from the solar panels, while the thermal demands are met from either the AA-CAES or molten salt systems. The capacities of the generation (delivery) units are calculated from the maximum amount of electricity generated (supplied) by the unit over the time period. The solution of the model provides energy generation ($E^{gen}_{i,t}$), storage ($E^{s}_{j,t}$) and delivery ($E^{out}_{j,t}$) profiles for all active units within the optimized superstructure.

3. Energy system models

The differential equations describing material and energy balances around the generation and storage units were discretized using Euler's method which is suitable due to the slow dynamics expected. Data from literature were used for properties which are not easily modelled, such as the mechanical efficiencies of units. The hourly global radiation (G^{tot}_t) was estimated from the total daily solar radiation using the CPRG model (Gueymard, 2000). The hourly direct normal radiation intercepted by the power tower (G^{DNI}_t) was estimated as outlined in Duffie and Beckman (2013).

3.1. Generation Models

The electricity generated in a time interval from the PV array is

$$E^{gen}_{1,t} = \eta_{1,t}\eta^{inv}G^{tot}_t A_{panel} \qquad t \geq 0 \tag{2}$$

where $\eta_{i,t}$ and η^{inv} are PV and inverter efficiencies (Evans, 1981) and A_{panel} is the total area $[m^2]$ of PV installed. Thermal energy from the power tower heats molten salt flowing through a collector:

$$E^{gen}_{2,t} = E^{in}_{3,t} = \left(\alpha\eta_{hel}A_c G^{DNI}_t\right) - Q^{conv}_t - Q^{rad}_t \qquad t \geq 0 \tag{3}$$

where Q^{conv}_t and Q^{rad}_t are the convective and radiative heat losses from the receiver [Wh]; A_c is the total collector area $[m^2]$; α is the heliostat absorptivity; and η_{hel} the heliostat efficiency.

3.2. Storage Models

For the PHES system, a material balance was carried out around the reservoir. The energy accumulated within the PHES system is given by the potential energy equation $E^{s}_{1,t} = \rho V_{1,t} g H$. Mechanical losses from the turbine and pump were incorporated as efficiencies.

The AA-CAES system stores energy in two forms: potential energy as high pressure air and thermal energy. The model incorporates two-stage compression and expansion with inter-stage cooling and heating during the charging and discharging phases and is based on a material balance around the cavern and an energy balance around the heat store. For a given stored mass of air, $m^{s}_{2,t}$, the energy accumulated within the system is estimated as:

$$E^{s}_{2,t} = m^{s}_{2,t} R_a \sum_{N} \Delta T^{tur}_t \qquad t \geq 0 \tag{4}$$

where N is the number of expansion turbines, R_a the specific gas constant for air (287 J kg^{-1} K^{-1}), and ΔT^{tur}_t is the difference in inlet and outlet operating temperatures of the turbines [K]. Expressions for the mechanical losses incurred during the air compression (compressor and motor losses) and expansion (turbine and generator losses) stages, as well as thermal losses from the thermal energy store (TES), were incorporated in the model.

In the molten salt system, energy is stored in the form of sensible heat. Enthalpy balances were carried out around the storage tanks, with the heat loss term accounting for both temperature and fill level. The minimum capacities of the storage units may be estimated from the maximum energies accumulated within them over the entire time period. The system is constrained to operate between the salt solidification and decomposition temperatures as given in Zaversky et al. (2013).

Steady state is enforced by ensuring that the initial and final states of the storage systems are the same. For PHES, the state is defined by the stored mass. For the AA-CAES and molten salt systems, the state is defined by both the mass and temperatures within the system.

4. Case Study

The case study considers the demands of Collahuasi mine, located in Chile, investigating both steady-state daily and seasonal behaviours. For the daily storage, we model two consecutive days in July. The seasonal storage considers four days, each representative of a season. Historical climate data is summarised in Table 1. The electrical data used correspond to data for power consumption for the mine in July 2013 as recorded by the Chilean electrical supply authorities (CDEC-SING, 2014). The hourly electrical demand varies between 163.9 and 177.4 MWh, with slightly higher energy demands during the day. Thermal demands are assumed to be 10 % of the electrical demands (Pellegrino et al., 2004).

For the PHES system, the reservoir height was set at 700 m (Deane et al., 2010), while the pump and turbine efficiencies are set based on Barnes and Levine (2011). The mechanical efficiencies of units within the AA-CAES system were set based on data from Hartmann et al. (2012). An insulated concrete block was selected as the TES, with thermal oil selected as the heat transfer fluid due to the operating temperature range of the TES (Laing et al., 2009). The heliostat efficiency and absorptivity were obtained from Li et al. (2010). The efficiency of the power block of the molten salt system was based on Garcia et al. (2011).

The proposed daily model, containing 5,684 variables and 8,570 equations, was implemented on GAMS 24.2 (GAMS, 2013) and solved using Baron 12.7.3 (Tawarmalani and Sahinidis, 2005). For an optimality gap of 1%, a solution was obtained after 19 minutes and is shown in Table 2. The AA-CAES system is not selected. Electricity is supplied by the PHES when solar irradiation is unavailable and the molten salt system is used for thermal demands. The unit costs for PHES and AA-CAES are similar but the latter incurs larger mechanical and thermal losses. The low efficiency of thermal-to-electrical energy conversion in the power block (approx. 40 %) makes the molten salt system less favourable for electricity generation. The comparably lower unit costs and higher storage efficiency of the molten salt system drive its choice over AA-CAES for thermal energy supply. Accounting for the turbine efficiency, the PHES system can supply almost 2500 MWh of electricity when fully charged, translating to 14 h of electricity at maximum capacity.

Figure 2 shows the behaviour of the PHES system. The plant operates in two distinct phases: charging and discharging. The charging phase lasts for 9 hours, during which direct supply of electricity from the PV system occurs. The pumping capacity is approximately three times the discharge capacity. As expected, the behaviour of the plant is cyclic (Figure 3). For the molten salt system, the partial charging phase lasts 9 h and the discharge phase for 13 h. The maximum

Table 1: Solar Availability Data (Departamento de Geofísica de la Universidad de Chile, 2012)

	Summer	Autumn	Winter	Spring
Representative day	Jan 15	April 15	July 15	October 15
H_d(MJ.m^{-2} per day)	32.40	23.04	18.36	31.32

Table 2: Optimal Solution for Daily Storage

	Unit	Description
Generation	PV System	776.74 MW_e capacity; 9,498,100 m^2 panels
	Power Tower	46.59 MW_{th} capacity; 79,457 m^2 collectors
Storage	PHES	2,729.77 MWh storage; 174.50 MW_e capacity
	Tank Storage	222.97 MWh storage,17.80 MW_{th} capacity

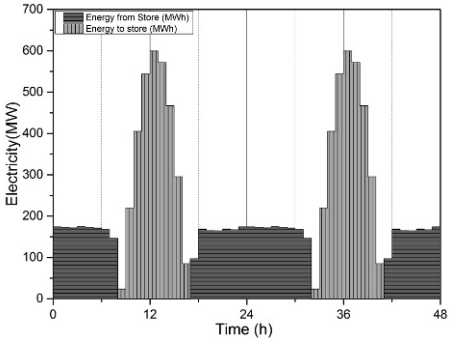

Figure 2: Daily PHES Behaviour

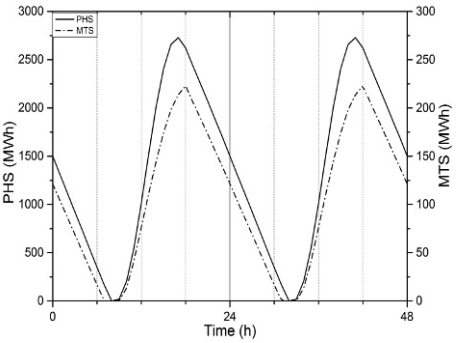

Figure 3: Energy Accumulation Profiles

heat loss from the thermal store (hot tank) is 115 kWh, representing 0.05% of the stored energy.

The seasonal model, with 17,987 equations and 10,617 variables, had a solution time of 188 minutes. Figure 5 shows the effect of seasonal solar radiation variability. The capacities of the generation and storage systems are determined by the season with the lowest solar availability (winter). The total energy generated to meet the demands for each season decreases with increasing solar radiation. Most of the process demands are met directly with PV generation for seasons with higher solar radiation (Table 3), with solar radiation available for longer periods. As a result, less electricity needs to be generated since storage losses are incurred less often. The fraction of the storage capacity required varies from 12 h during summer to 14 h during winter. The annual efficiencies of the storage systems, defined as the ratio of total output to input energy for each storage system, were estimated to be 0.764 and 0.993 for the PHES and molten salt systems respectively.

5. Conclusion

This work demonstrates the systems integration of renewable energy generation and storage techniques for off-grid continuous operations and highlights the importance of storage. The fundamental principles are applicable to other renewable energy resources. One current limitation is that daily variability, beyond the seasonal changes, of solar irradiation has not been considered.

Table 3: Analysis of Seasonal Behaviour of Electrical system

	Summer	Autumn	Winter	Spring
Total Generation (MWh)	4764.26	4832.71	4858.72	4797.05
Fraction of daily electrical demand met from Storage	0.52	0.58	0.60	0.54

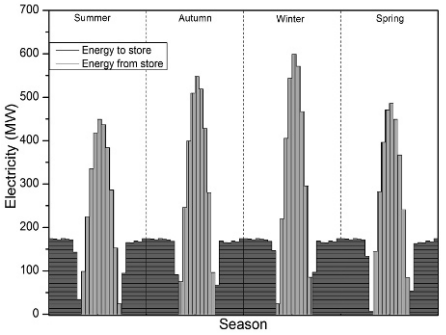

Figure 4: Seasonal PHES Behaviour

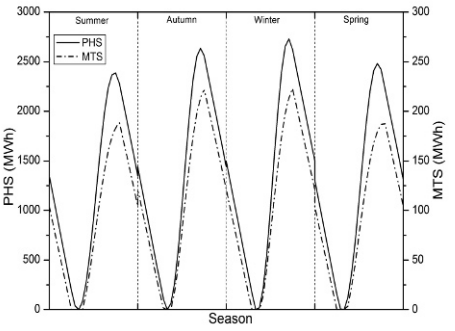

Figure 5: Seasonal Accumulation Profiles

One possible solution to the challenge which is currently being explored is the representation of renewables input with probability distribution functions generated from historical solar radiation data. A stochastic approach to renewables modelling would account for variability in the prediction of the optimal design and extend the applicability of the work, particularly to wind power.

References

Barnes, F., Levine, J., 2011. Large Energy Storage Systems Handbook. Mechanical and Aerospace Engineering Series. Taylor & Francis.

Centro de Despacho Economico de Carga del Sistema Interconectado del Norte Grande de Chile (CDEC-SING), 2014. Retiros de energía a clientes. [Online]. Available at: `http://cdec2.cdec-sing.cl/`, Accessed 04 May 2014.

Deane, J., Gallachoir, B., McKeogh, E., 2010. Techno-economic review of existing and new pumped hydro energy storage plant. Renewable and Sustainable Energy Reviews 14 (4), 1293–1302.

Departamento de Geofísica de la Universidad de Chile, 2012. Evaluación del recurso solar. [Online]. Available in Spanish at: http://walker.dgf.uchile.cl/Explorador/Solar2/, accessed 31 March 2014.

Duffie, J., Beckman, W., 2013. Solar Engineering of Thermal Processes: Fourth Edition. John Wiley & Sons, Inc., Solar Energy Laboratory, University of Wisconsin-Madison, United States.

Evans, D., 1981. Simplified method for predicting photovoltaic array output. Solar Energy 27 (6), 555–560.

GAMS Development Corporation, 2013. General Algebraic Modeling System (GAMS) Release 24.2.1. Washington, DC, USA.

Garcia, I. L., Ãlvarez, J. L., Blanco, D., 2011. Performance model for parabolic trough solar thermal power plants with thermal storage: Comparison to operating plant data. Solar Energy 85 (10), 2443 – 2460.

Gueymard, C., 2000. Prediction and performance assessment of mean hourly global radiation. Solar Energy 68 (3), 285–303.

Hartmann, N., Vahringer, O., Kruck, C., Eltrop, L., 2012. Simulation and analysis of different adiabatic compressed air energy storage plant configurations. Applied Energy 93, 541–548.

Laing, D., Lehmann, D., Fib, M., Bahl, C., 2009. Test results of concrete thermal energy storage for parabolic trough power plants. Journal of Solar Energy Engineering 131 (4), 041007.

Li, X., Kong, W., Wang, Z., Chang, C., Bai, F., 2010. Thermal model and thermodynamic performance of molten salt cavity receiver. Renewable Energy 35 (5), 981–988.

Ma, T., Yang, H., Lu, L., 2014. Feasibility study and economic analysis of pumped hydro storage and battery storage for a renewable energy powered island. Energy Conversion and Management 79, 387–397.

Paraszczak, J., Fytas, K., 2012. Renewable energy sources - A promising opportunity for remote mine sites? In: International Conference on Renewable Energies and Power Quality (ICREPQ). Article No. 288.

Pellegrino, J., Margolis, N., Justiniano, M., Miller, M., Thedki, A., 2004. Energy use, loss and opportunities analysis: US manufacturing and mining. US Department of Energy.

Tawarmalani, M., Sahinidis, N. V., 2005. A polyhedral branch-and-cut approach to global optimization. Math. Program. 103 (2), 225–249.

Yang, H., Wei, Z., Chengzhi, L., 2009. Optimal design and techno-economic analysis of a hybrid solar-wind power generation system. Applied Energy 86 (2), 163–169.

Zaversky, F., Garcia-Barberena, J., Sanchez, M., Astrain, D., 2013. Transient molten salt two-tank thermal storage modeling for CSP performance simulations. Solar Energy 93 (0), 294 – 311.

Krist V. Gernaey, Jakob K. Huusom and Rafiqul Gani (Eds.), 12th International Symposium on Process Systems Engineering and 25th European Symposium on Computer Aided Process Engineering.
31 May – 4 June 2015, Copenhagen, Denmark

Energy assessment of different configurations for the ethanol production process from lignocellulosic biomass

Cristian F. Triana, Eric S. Fraga and Eva Sorensen
Centre for Process Systems Engineering, Department of Chemical Engineering, UCL, Torrington Place, London WC1E 7JE, UK

Abstract

This work presents an evaluation of the energy requirements for the production of ethanol from corn stover for three different arrangements of the separation stage. The first configuration comprises two distillation columns and a hydrophilic membrane system. The second configuration considers a novel organophlic membrane system, one distillation column and a hydrophilic membrane system. The third approach is similar to the second, but includes a recycle of the retentate stream from the organophilic membrane system to the fermentation reactor to further the production of ethanol. For each arrangement, the overall energy demand is evaluated in order to identify the optimal heat source distribution within the process. The results show that the inclusion of the organophilic membrane system reduces the overall energy consumption significantly and also represents a reduction in the size of the plant. Recycling the retentate from the organophilic membrane increases the conversion of substrate into ethanol during the fermentation and thereby reduces the overall energy demand by reducing the energy consumption in the distillation column.

Keywords: Bioethanol, lignocellulosic, energy, membrane, distillation

1. Introduction

The production of biofuels has increased significantly in the last decades as a growing world population is demanding more energy. In countries like Brazil and the US, the production of ethanol from sugar cane bagasse and corn has been implemented into the main market of fuels resulting in an attractive option for industrial applications with low emissions of "greenhouse" gases (Karlsson et al., 2014).

However, one of the main challenges of the production of ethanol from lignocellulosic biomass is the high energy requirements leading to high operating costs. The main energy requirement is usually related to the recovery of ethanol in the separation section. Current research is focusing on the development of new technologies that allow a reduction in the energy demand in some of the separation units of the process (Triana et al., 2011; Roth et al., 2013).

Hybrid separation processes, consisting of a membrane-based system coupled with a conventional separation method, have emerged as an alternative technique to traditional separation by distillation, with high separation rates and lower energy consumption (Kreis and Górak, 2013). The separation of an ethanol/water mixture by distillation is restricted by the presence of an azeotrope. High levels of energy are required in order to achieve high concentrations of ethanol close to the azeotropic point (Fan et al., 2013).

Membrane-based operations, such as pervaporation, can dehydrate the ethanol/water mixture beyond the azeotropic concentration (Koch and Górak, 2014). This work presents three different configurations of the separation stage of the production of ethanol from corn stover. The overall energy demand for each configuration is considered, and an optimal distribution of the energy sources within the process is proposed.

2. Process description

The ethanol production process consists of four main stages:

- **Pretreatment:** The lignocellulosic material, which mainly consists of cellulose hemicellulose and lignin, is treated with dilute acid at high temperatures and pressure to degrade the lignin and to convert the hemicellulose into xylose and by-products (e.g furfural, HMF and organic acids) (Esteghlalian et al., 1997; Nigam et al., 2011).
- **Overliming:** The liquid fraction from the pretreatment stage is treated with $Ca(OH)_2$ to reduce the concentration of the by-products produced during the pretreatment that can diminish the performance of the fermenting microorganisms (Purwadi et al., 2004; Nigam et al., 2011).
- **Simultaneous saccharification and co-fermentation (SSCF):** Cellulose, which did not react in the pretreatment stage, is treated with cellulases to produce glucose and cellobiose through enzymatic hydrolysis (Moreno et al., 2013). Glucose and cellobiose, along with the xylose obtained during the pretreatment stage, are converted into ethanol and other by-products (acetic acid, CO_2, etc.). In this work, the simultaneous saccharification and co-fermentation (SSCF) using *Zymomonas mobilis ZM4(pZB5)* is considered (Morales-Rodriguez et al., 2011).
- **Separation:** Distillation is one of the most commonly used separation methods to purify ethanol produced via fermentation. The maximum concentration of ethanol achievable by this technique is 93% w/w (concentration of the minimum-boiling-point azeotrope). The separation can also be achieved using membranes, for instance, as in this work by using an novel organophilic membrane system with which ethanol is removed from the fermentation broth in the permeate (Koch and Górak, 2014), before a distillation column followed by a hydrophilic membrane system after the column which allows the dehydration of ethanol up to biofuel standard concentrations (>99% wt.) (Gaykawad et al., 2013).

3. Process alternatives

The ethanol production process considered in this work comprises two main sections, a fed-batch section and a continuous section.

3.1. Fed-Batch section

The fed-batch section consists of the pretreatment reactor, an evaporator, the overliming reactor, a mixing tank and the SSCF reactor. The pretreatment reactor is fed with the raw material until reaching the required operating volume. Once the reaction has finished, the content of the reactor is transferred to the evaporator where the concentration of reducing sugars is increased. The concentrated hydrolysates from the evaporation are treated with $Ca(OH)_2$ in the overliming reactor to degrade residual by-products from the pretreatment. The solid fraction of the pretreatment reactor, and the

detoxified hydrolysates from the overliming reactor, are mixed and sent to the SSCF stage where the reducing sugars are converted into ethanol. The output from the SSCF unit is collected in a storage tank. As soon as the material has left the pretreatment reactor, a second batch is started etc, and each batch is collected in the storage tank. The storage tank acts as the feed tank to the next main section, the separation section, which is operated continuously.

3.2. Continuous section

The continuous section comprises distillation columns and the pervaporation modules. The storage tank is the link between the fed-batch section and the continuous section as it collects the ethanol produced during the fermentation and constantly feeds the separation units. Three different configurations of the continuous section are considered in this work and are described as follows:

- **Configuration 1:** This configuration (see Figure 1) consists of two distillation columns and a pervaporation system with a hydrophilic membrane (in this work a PAN-B5 membrane) that dehydrates ethanol beyond the azeotropic point. This configuration is the most commonly used in industry (Morales-Rodriguez et al., 2011).
- **Configuration 2:** Using the same fed-batch section as Configuration 1, this arrangement introduces a new set of pervaporation modules before the distillation column. The new pervaporation system includes an organophilic membrane (in this work a PERVAP 4060 membrane). Ethanol is removed in the permeate stream and fed to the distillation column (see Figure 2).
- **Configuration 3:** The pervaporation system with the organophilic membrane becomes part of the fed-batch process as it removes the ethanol from the fermentation broth and recycles the unreacted substrate back to the SSCF reactor. This configuration increases the conversion of all the available substrate in the process and the overall amount of ethanol produced during the fermentation (see Figure 3).

4. Results

The mass and energy balances and other equations used in this work are solved using the commercial software gPROMS (PSE, 2014). As mentioned in Section 3, each configuration is divided into two main subsections: the fed-batch section and the continuous section. The batch section in every configuration runs three times in order to keep the storage tank full so it can keep on supplying the continuous section. Figures 1 to 3 show the flowsheet of each configuration and the concentration of ethanol throughout the process.

Figure 4 presents the minimum heat duty in the reboiler as a function of the number of trays. In the case of configuration 1, the energy requirement is the sum of the heat duties of both columns, assuming that both columns have the same number of trays. As shown in Figure 4, the energy requirement in the reboiler decreases with the number of trays in the column. For configuration 1, the minimum number of trays required is taken to be 10 for each column. For configurations 2 and 3 the minimum number of trays in the single column is taken to be 14 trays.

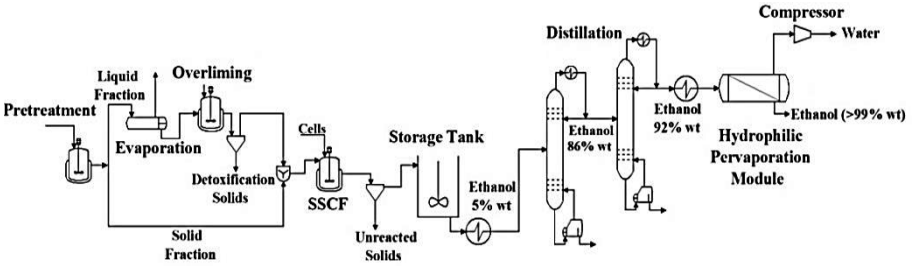

Figure 1: Configuration 1 with two distillation columns followed by a hydrophilic pervaporation system

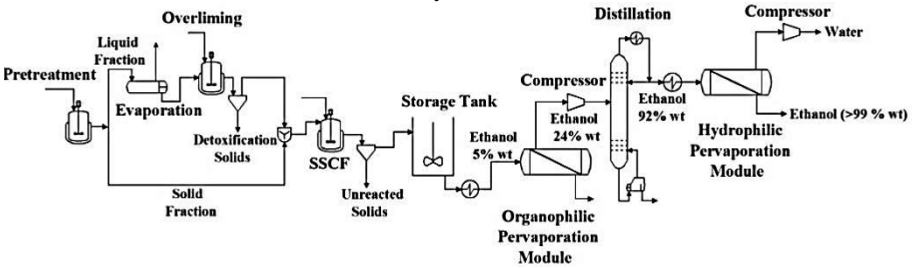

Figure 2: Configuration 2 with an organophilic system followed by one distillation column and a hydrophilic pervaporation system

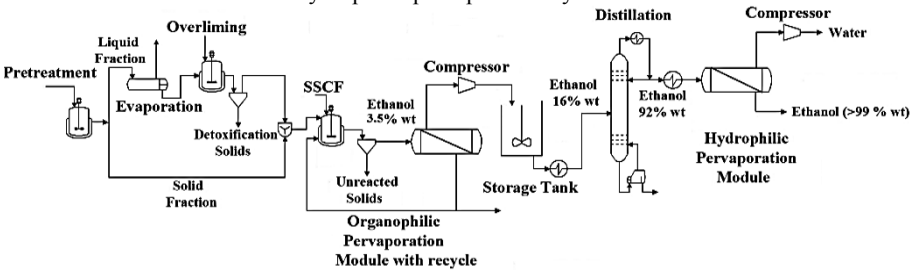

Figure 3: Configuration 3 with an organophilic system followed by one distillation column and a hydrophilic pervaporation system and with recycle of the retentate to the SSCF reactor

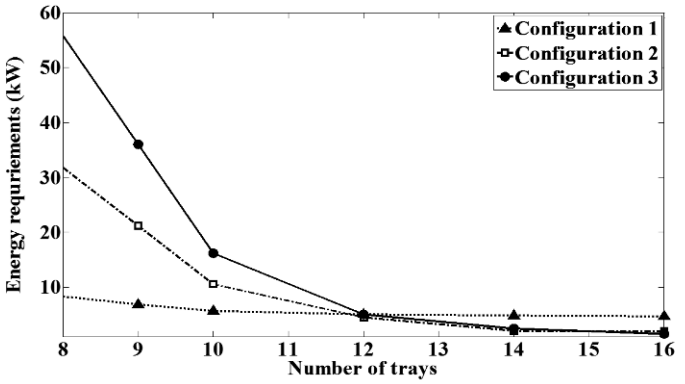

Figure 4: Minimum heat duty in the reboiler as a function of the number of trays

The area for the organophilic membrane module is determined as the area required to obtain a concentration of ethanol in the retentate $W_{Ethanol} < 0.001$. For the hydrophilic membrane system, the required area is calculated for a concentration of water in the retentate $W_{Water} < 0.001$. Table 1 summarises the parameters used in the simulation

for an annual production of 15 million litres. For the reactors, the parameters are taken from literature. For the distillation columns and the membrane systems, the parameters are obtained via optimisation using gPROMS. For the distillation columns, the optimisation consists of finding the reflux ratio that minimises the heat duty in the reboiler(s). For the membrane systems, the optimisation consists of finding the area that minimises the concentration of ethanol (in the organophilic membrane) and water (in the hydrophilic membrane) on the retentate side.

Table 1: Parameters used in the simulation of the ethanol production process from lignocellulosic biomass for three different configurations

	Configuration 1	**Configuration 2**	**Configuration 3**
Pretreatment	Acid concentration: 10% wt ; Raw material/acid solution ratio : 1:10 Temperature: 120 ^{0}C; Reaction time: 30 minutes (Esteghlalian et al., 1997; Nigam et al., 2011).		
Overliming	Acid hydrolysates are treated with $Ca(OH)_2$ for 80 minutes at 30 ^{0}C (Purwadi et al., 2004).		
SSCF	Enzymes concentration: 45 g/g of substrate; *Z. mobilis* concentration: 2.5 g/L; Temperature: 50 ^{0}C; Reaction time: 36 hours (Morales-Rodriguez et al., 2011)		
Organophilic membrane	-	Permeate pressure: 4 mbar Temperature: 50 ^{0}C Area: 3950 m^2	Permeate pressure: 4 mbar Temperature: 50 ^{0}C Area: 4100 m^2
Distillation col. 1	Reflux ratio: 3.7 Number of stages:10 Feed stage: 5	Reflux ratio: 6.3 Number of stages:14 Feed stage: 7	Reflux ratio: 8 Number of stages:14 Feed stage: 7
Distillation col. 2	Reflux ratio: 1.3 Number of stages:10 Feed stage: 5	-	-
Hydrophilic membrane	Permeate pressure: 1 mbar, Temperature: 70 ^{0}C, Area: 600 m^2		

Figure 5 shows the evaluation of the energy consumption of the whole process for each configuration. The results show a reduction of 72% on the energy consumption of the process when an organophilic membrane system is implemented. When a recycle stream, which consists mainly of unreacted reducing sugars and water, is returned to the SSCF reactor, then the operating volume increases and the concentration of ethanol decreases even if the amount of ethanol increases. Hence, the reduction in energy consumption in configuration 3 is 66%.

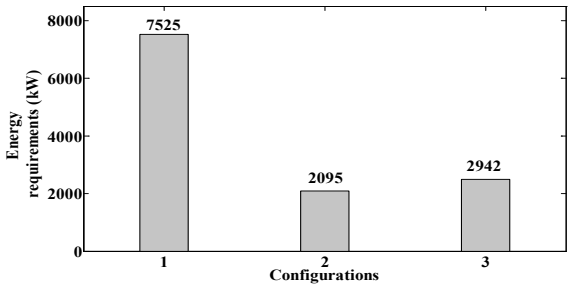

Figure 5: Overall energy consumption for each configuration

5. Conclusions

The production of biofuels from biomass aims to find new approaches and technologies with which biofuels can be obtained not only efficiently but profitably for sustainable energy generation. The results show that the implementation of an organophilic membrane contributes to the reduction of the overall energy consumption in the process by up to 72%. When the retentate stream from the organophilic membrane system is recycled to the SSCF, the amount of ethanol produced increases since all the available substrate is converted. Recycling the retentate also contributes to the reduction in the consumption of energy within the process (66%), making this configuration an attractive alternative for a successful implementation of ethanol production from biomass into industry. However, recycling streams not only increases the size of some units of the process but also presents additional operational requirements.

References

A. Esteghlalian, A. Hashimoto, J. Fenske & M. Penner, 1997, Modeling and optimization of the dilute-sulfuric-acid pretreatment of corn stover, poplar and switchgrass, Bioresource Technology, 59, 129-36

S. Fan, Z. Xiao, Y. Zhang, X. Tang, C. Chen, W. Li, Q. Deng & P. Yao, 2014, Enhanced ethanol fermentation in a pervaporation membrane bioreactor with the convenient permeate vapour recovery, Bioresource Technology, 155, 229-34

S. Gaykawad, Y. Zha, J. Punt, W. van Groenestijn, M. van der Wielen & J. Straathof, 2013, Pervaporation of ethanol from lignocellulosic fermentation broth, Bioresource Technology, 129, 469-76

H. Karlsson, P. Barjesson, P. Hansson & S. Ahlgren, 2014, Ethanol production in biorefineries using lignocellulosic feedstock-GHG performance, energy balance and implications of life cycle calculation methodology, Journal of Cleaner Production, 83, 420-27

K. Koch & A. Górak, 2014, Pervaporation of binary and ternary mixtures of acetone, isopropyl alcohol and water using polymeric membranes: Experimental characterisation and modelling, Chemical Engineering Science, 1-20

P. Kreis & A. Górak, 2013, Reactive and membrane-assisted distillation: Recent developments and perspective, Chemical Engineering Research and Design, 91, 1978-97

R. Morales-Rodriguez, A. Meyer, K. Gernaey & G. Sin, 2011, Dynamic model-based evaluation of process configurations for integrated operation of hydrolysis and co-fermentation for bioethanol production from lignocellulose, Bioresource Technology, 102, 1174-84

A. Moreno, E. Tomas-Pejo, D. Ibarra, M. Ballesteros & L. Olsson, 2013, Fed-batch SSCF using steam-exploded wheat straw at high dry matter consistencies and a xylose-fermenting *Saccharomyces cerevisiae* strain: effect of laccase supplementation, Biotechnology for Biofuels, BioMed Central, 6, 1-10

P. Nigam & A. Singh, 2011, Production of liquid biofuels from renewable resources, Progress in Energy and Combustion Science, 52-68

T. Roth, P. Kreis & A. Górak., 2013, Process analysis and optimisation of hybrid processes for the dehydration of ethanol, Chemical Engineering Research and Design, 91, 1171-85

Process Systems Enterprise, 2014, gPROMS, www.psenterprise.com/gproms

R. Purwadi, C. Niklasson & M. Taherzadeh, 2004, Kinetic study of detoxification of dilute-acid hydrolyzates by $Ca(OH)_2$, Journal of Biotechnology, 114, 187-98

C. Triana, J. Quintero, R. Agudelo, C. Cardona & J. Higuita, 2011, Analysis of coffee cut-stems (CCS) as raw material for fuel ethanol production, Energy, 36, 4182-90

Krist V. Gernaey, Jakob K. Huusom and Rafiqul Gani (Eds.), 12th International Symposium on Process Systems Engineering and 25th European Symposium on Computer Aided Process Engineering.
31 May – 4 June 2015, Copenhagen, Denmark

Integrated Solar Thermal Hydrogen and Power Coproduction Process for Continuous Power Supply and Production of Chemicals

Emre Gençer[a], Mohit Tawarmalani[b], Rakesh Agrawal[a*]

[a]*School of Chemical Engineering, Purdue University, West Lafayette, IN-47906, USA*
[b]*Krannert School of Management, Purdue University, West Lafayette, IN-47906, USA*
**agrawalr@purdue.edu*

Abstract

In this study, we introduce a novel solar thermal (ST) hydrogen and electricity coproduction process, which integrates a new solar water power (SWP) cycle and ST hydrogen production techniques. SWP cycle has a potential to generate electricity with efficiencies greater than 40 % for solar heat collection temperatures above 1250 K. Higher solar heat collection temperatures enable the integration of SWP cycle with ST hydrogen production techniques to coproduce hydrogen and oxygen. When solar energy is unavailable, we propose a turbine based hydrogen water power cycle. For a 100 MW continuous power supply plant, the overall efficiency of the proposed integrated process is estimated to be greater than 34 % in spite of the assumed 20 % solar energy loss in the solar collector system. Furthermore, the coproduced hydrogen and oxygen can be used for various applications other than energy storage to create a sustainable economy.
Keywords: solar, electricity, hydrogen, water power cycle, sustainability.

1. Introduction

Diminishing fossil fuel reserves and increasing environmental concerns urge to utilize renewable energy sources to meet energy needs. Development of renewable power production technologies is important since electric power is the largest consumer of primary energy resources and it has the highest growth rate among alternate energy use sectors. Solar energy is a prominent source due to its abundance. Yet intermittencies and land availability constraints for solar energy collection are the grand challenges for solar power generation and demand an efficient continuous solar power generation solution.

Here, we meet these challenges by introducing a novel and highly efficient solar thermal (ST) power and hydrogen coproduction process, which includes; (i) solar water power cycle, (ii) ST hydrogen production process, and (iii) turbine based hydrogen power cycle (Agrawal et al., 2014). Solar water power cycle has a potential to generate electricity with sun-to-electricity (STE) efficiencies greater than 30 % at low solar heat collection temperatures (~750 K). The cycle also promises STE efficiencies greater than 40 % for the high solar heat collection temperatures (>1250 K). For higher solar heat collection temperatures, the ST power cycle is integrated with the hydrogen production process to coproduce hydrogen and oxygen for chemical storage of solar energy. When solar energy is not available, the coproduced hydrogen is utilized to generate electricity for grid distribution around the clock. The overall STE efficiency of a 24 hour cycle is estimated to be greater than 34 %, which is comparable to batteries integrated with solar water power cycle and the storage energy density is comparable to carbon storage cycles (Gençer et al., 2014). Coproduced hydrogen can also be used as a feedstock for production of other chemicals or other applications. The process design and simulation has been

conducted using an integrated Matlab and Aspen environment. We have performed sensitivity analysis and optimization using genetic algorithm to determine key process parameters. Simulation strategy and details of an example process design are presented in the following sections.

2. Solar Thermal Hydrogen and Electricity Coproduction Strategy

Temperatures higher than ~1000 K enable water splitting reaction to form H_2, O_2 and OH. This phenomenon creates an opportunity to produce hydrogen using concentrated solar energy with high solar heat collection temperatures (Mallapragada and Agrawal, 2014). Analysis of theoretical and achievable sun-to-hydrogen efficiency for ST hydrogen production revealed that the ST hydrogen production has a grand potential to efficiently produce hydrogen (Mallapragada and Agrawal, 2014). ST hydrogen production mainly involves pressurizing, heating, vaporization and superheating of water, compression and collection of hydrogen and oxygen. The energy requirement for the water heating is likely to be supplied from solar energy and partially from the heat released due to the cooling of products prior to compression. This step is exergetically inefficient due to the use of high temperature ST energy to heat up and vaporize pumped water at low temperature. The second step of compression of products consumes electricity, which can be supplied from solar electricity produced via concentrated solar power plants or photovoltaic systems. There are mainly two routes for thermochemical hydrogen production; (i) single step membrane reactor, (ii) two step metal oxide cycle (Mallapragada and Agrawal, 2014). Two step hydrogen production involves the cyclic oxidation and reduction of a metal; for this study we considered the cyclic transformation of FeO and Fe_3O_4 that is given by Eqs. (1) and (2). Oxidation reaction (Eq. (1)) partially converts H_2O to H_2, and reduction reaction (Eq. (2)) releases O_2 using high temperature heat. FeO and Fe_3O_4 are circulated between the two reactors.

$$3FeO + H_2O \rightarrow Fe_3O_4 + H_2 \quad (1)$$

$$Fe_3O_4 \rightarrow 3FeO + 0.5O_2 \quad (2)$$

ST electricity production, involves a solar heat collection unit that contains solar concentrators, solar receiver and heat exchanger and a Rankine-type power cycle that utilizes solar heat as heat source (Siva, et al. 2013). ST hydrogen production and electricity production can be synergistically integrated to increase the overall production efficiency by minimizing the exergy losses due to utilization of high temperature heat with large temperature differences and supplying high efficiency electricity for compression of hydrogen and oxygen. An example integrated process for ST coproduction of hydrogen and electricity is depicted in Figure 1. Water is the working fluid of the ST power production unit for the integrated process. ST hydrogen and power production units are integrated, allowing mass exchange and heat exchange, *i.e.*, the entire water superheating step can be a part of the power production unit and a portion of the pressurized superheated water can be directed to hydrogen production unit. Depending on the pressure level, the unconverted water stream can be sent to power production unit to be cooled down against a process stream in the power production unit. Furthermore, depending on the utilization of coproduced hydrogen more process integration is possible.

3. Efficient Solar Thermal Hydrogen and Electricity Coproduction

Solar water hydrogen power (SWH_2P) cycle shown in Figure 1 is a novel efficient hydrogen and electricity coproduction process integrating solar water power cycle with two step ST hydrogen production process using FeO/Fe_3O_4 cycle.

3.1. Solar Water Power (SWP) Cycle

SWP is derived from a Rankine power cycle and is developed to operate at a range of solar heat collection temperatures with maximum power generation at high temperatures while minimizing exergy losses. SWP with 1-solar reheating (SWP-1) cycle, shown with solid lines in Figure 1, has eight processing steps: (i) water is pumped to a high pressure (~200 bar), (ii) pressurized water is preheated and partially vaporized against process streams, (iii) pressurized water is fully vaporized and superheated in the solar receiver, (iv) a portion of the stream is sent to high pressure turbine (HPT), (v) the expanded stream to a medium pressure is reheated to a high temperature (solar heat collection temperature for the base case), (vi) reheated stream is further expanded in a medium pressure turbine (MPT) and the discharge of the last MPT is cooled against the pressurized liquid water, (vii) the cooled stream is further expanded and partially condensed in a condensing turbine (CT), (viii) the partially condensed water is fully condensed and recycled.

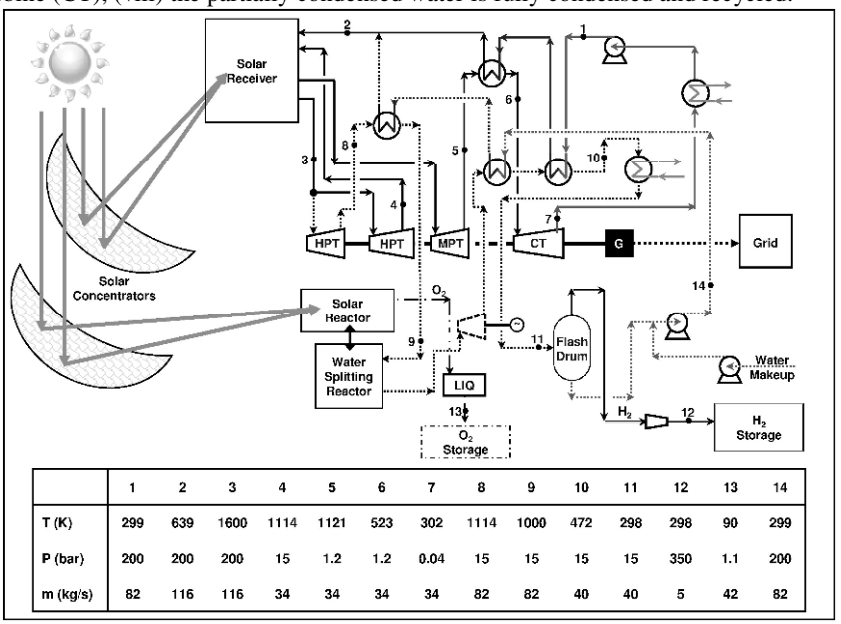

	1	2	3	4	5	6	7	8	9	10	11	12	13	14
T (K)	299	639	1600	1114	1121	523	302	1114	1000	472	298	298	90	299
P (bar)	200	200	200	15	1.2	1.2	0.04	15	15	15	15	350	1.1	200
m (kg/s)	82	116	116	34	34	34	34	82	82	40	40	5	42	82

Figure 1 Simplified process flowsheet of solar water hydrogen power cycle with two step hydrogen production. HPT, MPT, CT: high pressure, medium pressure and condensing turbine. Details of SWH_2P cycle at solar heat collection temperature of 1600 K, 200 bar operating pressure and 1 % CT condensation for 100 MW power supply with 30.9 % OSTE efficiency is given in the table.

3.2. Solar Thermal Hydrogen Production

Solar thermal hydrogen production with FeO/Fe_3O_4 cycle has nine processing steps: (i) water is pumped to a high pressure (~200 bar), (ii) pressurized water is preheated and partially vaporized against process streams, (iii) pressurized water is fully vaporized and superheated in the solar receiver, (iv) a portion of the stream is sent to HPT and expanded to the water-splitting reactor pressure, (v) the temperature of the stream is adjusted against a pressurized water stream and sent to water-splitting reactor, (vi) water is partially converted to hydrogen and hydrogen-water mixture is expanded in a turbine and cooled against pressurized water stream, (vii) the oxidized metal is fed to the solar reactor and it is reduced using ST energy and recycled to the water splitting reactor. (viii) the hydrogen-water mixture is separated, hydrogen is collected as gas and water is collected as liquid, (ix) hydrogen and oxygen are brought to their storage conditions, water is mixed with

fresh water feed and pumped to the high pressure. For continuous constant rate power supply hydrogen is stored as compressed hydrogen and oxygen is stored as liquid oxygen.

3.3. Hydrogen Water Power (H_2WP) Cycle

For continuous power supply, the electricity is produced from the stored hydrogen and oxygen when the solar energy is not available. To efficiently generate electricity and avoid shut-off of the power generation equipment (turbines, CT, etc.), we propose using a novel turbine based hydrogen power cycle, which is a modified configuration of SWP-1 cycle replacing solar thermal heating with direct hydrogen oxy-combustion.

4. Process Simulation and Determination of Operating Conditions

Detailed process simulations are performed in an integrated Aspen Plus v8.0 and Matlab environment. A Matlab script is developed to ensure the two way communication between Aspen Plus simulation files and Matlab scripts. The simplified integrated simulation flow diagram is shown in Figure 2, the dotted box is not enabled for the regular runs and sensitivity analyses but only utilized to optimize the parameters. Core Communication Script (CCS) is developed in Matlab to transfer data between different models. Transferring data between different models enables integration of various models for design and optimization of complex flowsheets (Tock and Maréchal, 2012).

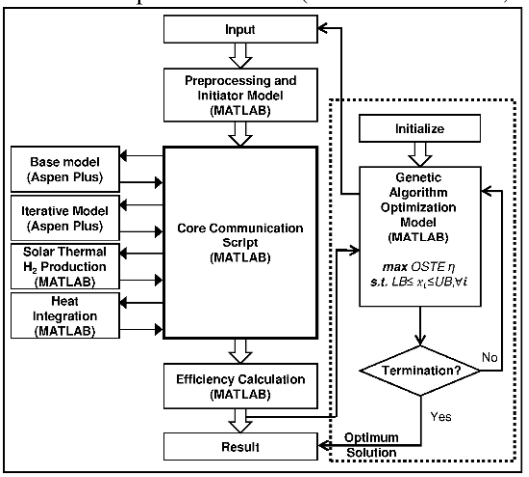

Figure 2 Integrated Aspen Plus and Matlab simulation and optimization strategy.

4.1. Process simulation models

Various Aspen and Matlab models are developed for the simulation, i.e. Preprocessing and Initiator model, Base model, Iterative model, Solar Thermal H_2 Production model and Heat Integration model, are briefly described below. The material flows for both power and hydrogen production processes are calculated via Base model, which contains all the process units, e.g. turbines, reactors, heat exchangers, etc. Detailed calculations for hydrogen production via FeO/Fe_3O_4 based thermochemical cycle are carried out in Matlab (Solar Thermal H_2 Production model) using HSC Chemistry thermodynamic data. For multiple reheating stages the Iterative model is developed and integrated with the Base model through CCS. The minimum solar heat and cooling requirement for the process is calculated from the overall process heat balance using heat cascade principle of the pinch analysis method (Duran and Grossmann, 1986), which is implemented in the Heat Integration model. The Predictive Redlich-Kwong-Soave equation of state,

NBS/NRC steam tables and HSC Chemistry database are used to retrieve the relevant thermodynamic properties for the calculations.

4.2. Process parameters and simulation initialization

Key processing parameters such as solar heat collection temperature, pressure ratio across turbines, number of reheating stages, etc. are identified and implemented as variables that can be controlled via CCS. To initiate a simulation some of the variables to be specified are solar heat collection temperature, number of reheating stages, CT allowable wetness that is a limitation for the maximum condensation in the outlet of CT. Preprocessing and Initiator model generates the initial set of specifications. For example, once the solar heat collection temperature is set the same temperature is used for all superheating and reheating heat exchangers and for the solar reactor used during hydrogen production. Similarly, the number of reheating stage determines the pressure ratio across each turbine, assuming equal pressure ratio across all turbines. The initial set of specifications is then applied to the corresponding models via CCS and the simulation starts.

4.3. Performance metrics

Two metrics of interest are sun-to-electricity (STE) efficiency given by Eq. 3 and overall sun-to-electricity (OSTE) efficiency, the former refers to the fraction of incident solar energy that is directly recovered as the net electricity output and the latter refers to the fraction of incident solar energy recovered as electricity a constant power delivery round-the-clock, i.e. over the average 24 hour production accounting for energy storage and delivery of the stored energy while solar energy is unavailable. In Eq. 3, W_{net} is the net electricity output, Q_{in} is the heat requirement of the process, Φ is the solar factor, Ω_{opt} is the optical efficiency of solar collectors, σ is the Stefan-Boltzmann constant, T is the solar heat collection temperature, I (1000 W/m^2) is the solar intensity and C is the solar concentration ratio. The expression in the denominator of Eq. 3 refers to the solar heat required for the process. Note that Eq. 3 doesn't account for the intermittency and variability associated with solar energy.

$$\text{STE efficiency} = \frac{W_{net}}{Q_{in} \cdot \Phi^{-1}} \times 100, \text{ where } \Phi = \Omega_{opt}\left(1 - \frac{\sigma T^4}{I \cdot C}\right) \tag{3}$$

4.4. Sensitivity analysis and optimization

The operating conditions of various units and topological structure are determined using sensitivity analysis and optimization. The objective function is to maximize the STE and OSTE efficiency for SWP cycle and SWH_2P cycle, respectively. The OSTE efficiency is calculated using the process information for the H_2WP cycle at the given operating temperature and pressure. The effects of solar heat collection temperature (650 K $\leq$ T $\leq$ 2300 K), operating pressure (100 bar $\leq$ P $\leq$ 1000 bar), solar energy availability (2.4 hr $\leq$ t $\leq$ 8.4 hr), etc. have been investigated by sensitivity analysis. An outer loop is introduced for the manipulated variable(s) and the simulation is performed as described in Section 4.2 for multiple initial sets. The exercised simulation strategy allows various studies, which are impractical using only a process simulation software, e.g. adding 100 reheating stages. SWH_2P cycle has been optimized using genetic algorithm to determine the process design and process parameters with maximum OSTE efficiency for a given solar heat collection temperature and water-splitting reactor temperature. Pressure ratio of turbines, CT inlet temperature and hydrogen production pressure are some of the optimized parameters. For example the optimized CT inlet temperatures are 523 K and 385 K for 1 % and 10 % CT wetness, respectively. This study revealed that the process topology is highly sensitive to the water-splitting reactor temperature and maximum OSTE efficiency may require different hydrogen production pressures for different settings.

5. Results

For all STE and OSTE estimations, efficiency of the solar concentrator system has been assumed to be 80 %. SWP-1 cycle achieves STE efficiency of greater than 30 % at relatively low solar heat collection temperature of 750 K. For solar heat collection temperature greater than 1250 K, STE efficiency of SWP-1 cycle is greater than 40 %. The maximum STE efficiency of 42.6 % is achieved at 1850 K. The sensitivity analysis on the number of solar reheating showed that the first reheating improves STE efficiency by 1 – 3 % depending on the solar heat collection temperature. Additional reheating stages have a diminishing effect on STE efficiency improvement. For uninterrupted electricity supply to the grid using an integrated process, for a scenario of 4.8 h of solar availability and 24 h of 100 MW power supply, OSTE is calculated to be greater than 34 % at 1600 K solar heat collection temperature. This efficiency compares well with best possible integrations of existing technologies for solar power generation and energy storage. For example, OSTE of an integrated molten salt solar thermal power plant with thermal storage is 20.2 %, of a single-junction PV plant integrated with Li-ion batteries is 26.7 % and of a concentrated four-junction PV integrated with Na/S batteries is 35.3 %.

6. Conclusions

In this study we have developed a solar water power cycle, a hydrogen water power cycle and an integrated solar thermal hydrogen and power coproduction process. Solar water cycles and hydrogen power cycles have potential to operate at very high efficiencies, greater than 40 % STE efficiency and greater than 64 % hydrogen-to-electricity efficiency, respectively. The integrated coproduction process provides a synergistic process that minimizes exergetic losses and increases production efficiency. Efficient coproduction of hydrogen and electricity presents a continuous power supply solution that can exceed 34 % OSTE efficiency when combined with the H_2WP cycle and also creates other opportunities because hydrogen has numerous uses in chemical industry, biofuel production, and transportation sector.

Acknowledgements

Research was supported in part by the National Science Foundation SEIGERT(0903670-DGE), EFRI(0938033-DGE), C3Bio EFRC(DE-SC0000997). Contributions of Dr. Dharik Mallapragada and Prof. François Maréchal are gratefully acknowledged.

References

R.Agrawal, E.Gençer, D.S.Mallapragada, F.Maréchal, M.Tawarmalani, 2014, US Provisional Patent Application 62/021,997.

M.A.Duran and I.E.Grossmann, 1986, Simultaneous optimization and heat integration of chemical processes, AIChE Journal, 32, 1, 123-138.

E.Gençer, E.I.Al-musleh, D. S.Mallapragada, R.Agrawal, 2014, Uninterrupted Renewable Power through Chemical Storage Cycles, Current Opinion in Chemical Engineering, 5, 29-36.

D.S.Mallapragada, R.Agrawal, 2014, Limiting and Achieveble Efficiencies for Solar Thermal Hydrogen Production, International Journal of Hydrogen Energy, 39, 1, 62-75.

R. Siva, S.C.Kaushik, K.R.Ranjan, S.K.Tyagi, 2013, State-of-the-art of solar thermal plants- a review, Renewable and Sustainable Energy Reviews, 27, 258-273.

L.Tock, F. Maréchal, 2012, Platform development for studying integrated energy conversion processes: Application to a power plant process with CO_2 capture, Proceedings of the 11th International Symposium on Process Systems Engineering, Singapore.

Krist V. Gernaey, Jakob K. Huusom and Rafiqul Gani (Eds.), 12th International Symposium on Process Systems Engineering and 25th European Symposium on Computer Aided Process Engineering.
31 May – 4 June 2015, Copenhagen, Denmark

Energy Supply Chain modeling for the optimisation of a large scale energy planning problem

Christiana Papapostolou [a], Emilia Kondili[b], Ioannis K. Kaldellis[c], Wolf Gerrit Früh [a]

[a] *Sch. of Eng. and Ph. Sciences, Heriot-Watt University, Edinburgh EH14 4AS, UK*
[b]*Optimisation of Production Systems Laboratory, TEI of Piraeus, 20 P. Ralli and Thivon St., Athens 12244, Greece*
[c]*Soft Energy Applications and Environemntal Protection Laboratory, TEI of Piraeus, 20 P. Ralli and Thivon St., Athens 12244, Greece*
ekondili@teipir.gr

Abstract

The energy planning problem becomes increasingly important during the recent years mainly due to the pressing needs that need to be taken into account in terms of economic, environmental and social aspects. At the same time, technology supports many options and alternative solutions in the design of energy and fuel supply chains (SCs), based on more holistic approaches that have their origin in the production management. Considering the introduction of an integrated framework of evaluation for alternative energy supply options, the present work applies a RTN (Resource Task Network) based representation of the Energy SCs (ESCs) along with a mathematical programming optimisation model in order to analyse and model a location specific energy planning problem. Special emphasis is given to fuel mix optimisation in terms of maximising the economic, social and environmental performance of ESCs. Furthermore, the interaction between aspects and implications under the existing limitations both in the design and technical characteristics of the system as well as in the environmental / air quality limitations, will be also revealed.
On top of the results obtained, the present work's added value relates to the development of the proposed model for the analysis of various energy planning scenarios, comprising in this way a very useful decision making tool.
Keywords: energy supply chains, energy planning, energy systems optimisation.

1. Introduction

Energy planning involves the identification of different criteria, stakeholders and goals in an interacting environment. Traditional energy planning problems which were made on the basis of single criteria approach, aiming at identifying the optimum ESC configuration under techno-economic considerations seem to be gradually abandoned, as environmental concerns and social implications need to be accounted as well. Striving for a transition towards a sustainable energy sector, policy makers must gradually balance the trade-offs between energy production and minimum environmental impacts whilst providing the opportunity at any level of production (local/regional, country/national, global (Thery and Zarate, 2009)) to mobilise the social and economic activities.

That is the reason that aided-decision making with the use of methods and tools (multicriteria decision making, modeling approaches, expert systems and multiobjective optimisation (Cai et al., 2009, Papageorgiou, 2009, Pohekar and Ramachandran, 2004)) have gained significant attention seeking to provide a supportive framework of assorted decisions under an environment of uncertainty: conflicting goals and preferences expressed by parameters and indexes, with many of them being present in an intangible basis.

To this end, modeling of ESCs and especially electricity SCs has been recently extended to include on top of economic criteria environmental and social aspects by mobilising optimisation methods and tools coupled with lifecycle considerations (Akgul et al., 2014, Papapostolou et al., 2014, Pinto et al., 2012, Vance et al., 2014, Yue and You, 2014). To this type of problems emphasis is given not only to the selection of the optimisation method and the assorted evaluation indicators but also to the representation and sustainable design: homogenous and simple framework formulations are adopted and used in order to solve large scheduling problems in the chemical process industry (State-Task Network (Kondili et al., 1993) and the Resource-Task Network (RTN) (Pantelides, 1994)).

Seeking to describe the problem of energy planning and of alternative energy and fuels SCs along the environmental and social aspects beyond the techno-economic ones, the present work will introduce the concept of energy planning optimisation under the perspective of sustainable development. To this end, based on the RTN representation of the alternative energy supply options developed in previous works of the authors, the developed MILP model will be tested for a detailed time frame of one day (24h) and one month accordingly (720h) for a wind, diesel and storage energy supply option. Model results include the adaptability of the optimisation criterion under different set of priorities considered and provide operational data for the configuration under utilisation.

2. Modeling approach

The present modeling approach is formed on the basis of maximising the total value of the optimised ESC configuration. In respect to that, all the criteria and the assorted indexes were selected and quantified appropriately. The overall value of the ESC(s) is estimated by employing three distinctive groups of criteria (on top of a set of weights applied in each value): economic, environmental and social. All parameters are expressed in €/kWh or in €/kW. More precisely, in the Economic Value the real or implied revenues minus the total costs of the electricity generation are considered i.e. investment, maintenance and operational costs. Accordingly the Environmental Value reflects the positive environmental impact of the ESCs on a Life Cycle Analysis basis compared to a– non friendly fossil based ESC (i.e. wind Vs diesel SC) in tn of CO_2 eq /kWh, all being monetised by the current price of CO_2 (in €/tn). Finally the Social Value accounts for the social benefits at the micro (employment yield €/ kWh per selected technological option) and the macro level (contribution of the selected ESC in the energy security of area investigated, with no limitations of the level being examined: local/region, country, transnational/global. With respect to that, fossil based ESCs are penalised (-1), if being selected by decision makers. Finally the weights being applied in each value (all summing up to 1, with 1 being the most important and 0 being the least important), reflect the relative importance of each criterion based on the type of initiated policy.

3. Model development

The developed mathematical model is formulated as a Mixed Integer Linear Programming (MILP) problem, seeking to combine both discrete types of decisions (to make an investment for a new energy infrastructure project or not) and continuous ones (to demonstrate the best fuel mix utilisation option under the set of existing resources). However there are no conceptual limitations to include both non-linear functions as well. In the present work a detailed operational electricity supply problem is modelled and approached as a LP mathematical model. Under the provisions of sustainable dimensions incorporation (Economic, Environmental and Social), the optimisation criterion seeks to express the maximisation of the total value of the ESCs' configuration for a preset time horizon H, for a set of resources R, storage stations S, interconnection options I and a set of users U to be satisfied::

$$Max = \sum \left\{ a_1 \times ECONV_{r,s,i} + a_2 \times ENVV_{r,s,i} + a_3 \times SOCV_{r,s,i} \right\} \quad (1)$$

Where, a_1, a_2, a_3 correspond to appropriately weighted normalisation (overall summing at 1.0) factors of the different dimensions considered. At this point one may note that the weighted factors are location-specific and case study dependent on the basis of the priorities set by the decision makers, if real energy planning problems are approached. However if future projects are considered, the weighted factors may result from a consensus / experts' based methodology i.e. a Delphi approach (Kaldellis et al., 2013).

The economic value considers the real or implied Revenues and the Total Costs of the electricity generation (Investment, Maintenance and Operational Costs) (TC) (€)

$$ECONV_{r,s,i} = REV_{r,s,i} - TC_{r,s,i} \quad \forall r,s,i \in R,S,I \quad (2)$$

In case there are no revenues, the economic value is the negative value the Total Costs.
The environmental value considers the environmental positive impact of the ESC in Life Cycle Analysis compared to an environmental – non friendly fossil based ESC with a "typical-average" impact on the environment (for example a moderate case is the Diesel SC) (€). For each time –step that we have:

$$ENVV = (ENVF_r \times EG_r + ENVF_{r,s} \times ES_{r,s} + ENVF_i \times EIN_i) \times PCO_2 \quad \forall r,s,i \in R,S,I \quad (3)$$

Where PCO_2 is the current price of CO_2 (€/kWh), $LCREF$ the reference ESC environmental value and $LCENVF_{r,s,i}$ is the environmental footprint (in LCA terms) of each ESC.
Finally the Social value of the ESC considers micro and macro – economic benefits from the implementation and operation of the different ESC configurations (€):

$$SOCV = MiSOCV + MaSOCV \quad (4)$$

$$MaSOC = (SEC_r \times EG_r + SEC_{r,s} \times ES_{r,s} + SEC_i \times EIN_i) \times PEX \quad (5)$$

Model constraints reflect the technical and physical limitations of the system. Thus for each time-step t we have:

- Energy production plants capacity limitations for each supply resource r
- Storage stations capacity limitations
- Capacity limitations of the interconnection supply sources

- Storage balance-rate of charge of the storage stations
- Land availability limitations
- Environmental impacts (in $CO2_{eq}$) from each supply resource in terms of Life Cycle Analysis.

4. Case study: Typical Greek island

Under a pre-set geographical area (typical Greek island in Cyclades complex), for a set of available energy supply options (wind, diesel, energy storage) and for a discrete time-step (hourly based load and demand profile) the present work will try to identify the optimum energy/fuel mix utilisation. Modeling is carried out under the timeframe of a single day and of a month, under different optimisation targets (economic versus social) acknowledging the differentiations that may appear in energy decision making under a cross sectional approach. Diesel and storage act as base loads with min capacities 1000 kW per hour correspondingly whilst the remaining demand has to be met a) in techno-economic terms (a_1=1, a_2=0, a_3=0) by the combination of their optimal operation for a single day (always under the very discrete time step of one hour (Figure 1) or b) just accounting for the maximum energy security (MaSOC) -(a_1=0, a_2=0, a_3=1), (Figure 2) or c) equally accounting both economic and Macro-Social implications (a_1=0.5, a_2=0, a_3=0.5) (Figure 3) in a longer time period- one month. Some preliminary parameters considered for model testing are cited in Table 1.

Table 1: Parameters considered for model optimisation

$CAP_r^{\max}$	Maximum capacity of each electricity production plant r (MW)	Wind:10, Diesel: 10
$CAP_r^{\max}$	Minimum capacity of each electricity production plant r (MW)	Diesel: 1
$ESS_s^{\max}$	Maximum capacity of the storage station (MWh)	Energy storage: 10
$ESS_s^{\min}$	Minimum capacity of the storage station (MWh)	Energy storage: 1
$OPER_{r,s,i}$	Operational cost of the selected resource, storage station or interconnection option (€/ kWh)	Wind: -0.02, Diesel: -0.03, Energy storage: -0.01
EMF_r	Direct emission factor from each energy resource r, s (in kg CO_2 eq / kWh)	Wind: 0.0, Diesel: 0.8, Energy storage: 0.0
$EMF_{ceiling}$	Emissions ceiling factor for the electricity generated (in kg CO_2 eq / kWh)	Natural gas: 0.78
PEX	Exchange losses from imported energy (and resources) (€/kWh)	0.078
PCO_2	Current commercialization price of CO_2 (€/kWh)	15

5. Results and discussion

Model simulation was undertaken with an open-source optimiser OpenSolver 2.6, 8.10.14 (Mayson, 2012) with no technical limitations in the number of variables and constraints. Results concerning the operational characteristics of an existing set of ESCs for a typical winter day and month, with low available energy production and for a corresponding winter month are illustrated as follows (Figures 1,2,3).

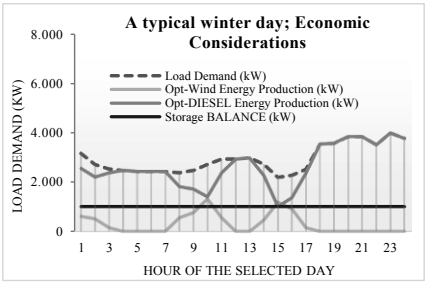

Figure 1. Optimisation results- daily load- Economic Considerations (a_1=1, a_2=0, a_3=0)

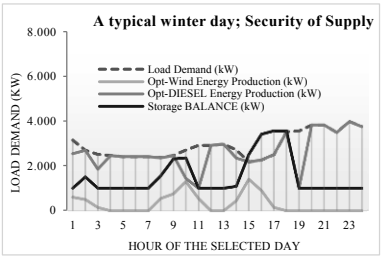

Figure 2. Optimisation results- daily load- Social/ Security of Supply Considerations (a_1=0, a_2=0, a_3=1)

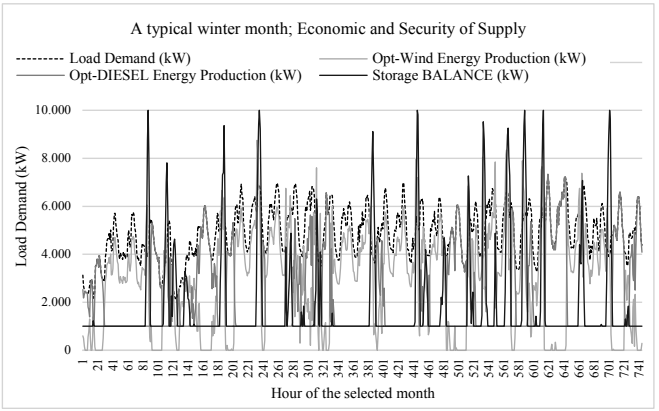

Figure 3. Optimisation results- monthly load- Economic and Macro-Social Considerations (a_1=0.5, a_2=0, a_3=0.5)

Results obtained evidence that different criteria under different set of priorities (optimisation criteria) may result to diverse ESCs configurations. One may notice that if considering the long term aspect of energy planning -especially in large scale / state level problems- the security of energy supply may be of greater importance than the minimisation of the total operational cost of the existing energy production plants. However according to the proposed modeling approach cited in the present work a temporal and local optimum may be obtained according to the location specific criteria set, in each case study under examination.

6. Conclusions

In the present work the developed mathematical model for the optimisation of alternative ESCs, formulated as a LP has been cited. Through a simple case-study the hybrid character of the model i.e. to adapt to different optimisation targets based on the policy-makers' needs was revealed. Furthermore the model also provides the possibility of being treated as a decision support tool when holistic considerations, mainly applicable at large energy planning problems occur. Decisions to be supported by model implementation include energy fuel mix diversification possibilities, local security of

energy supply, sustainability of energy supply schemes, adaptability of the energy decision making process and scheme to incorporate emerging issues and parameters in the problem under consideration. The proposed methodology due to its generic nature may equally be applied to other types of energy problems i.e. heat and water resources energy optimisation.

Acknowledgements

This work is part of the Ph.D. research thesis entitled “Social, environmental and economic impacts of alternative energy and fuel supply chains” which is financially co-supported by the “Bursary Program of individualized assessment for the academic year 2012-2013” from resources of the Operational Programme "Education and Lifelong Learning" of the European Social Fund and from the National Strategic Reference Framework (2007-2013).

References

O. Akgul, N. Mac Dowell, L.G. Papageorgiou, N. Shah, 2014, A mixed integer nonlinear programming (MINLP) supply chain optimisation framework for carbon negative electricity generation using biomass to energy with CCS (BECCS) in the UK, International Journal of Greenhouse Gas Control, 28, 189-202

Y.P. Cai, G.H. Huang, Q.G. Lin, X.H. Nie, Q.Tan, 2009, An optimization-model-based interactive decision support system for regional energy management systems planning under uncertainty, Expert Systems with Applications, 36, 3470-3482

J.K.Kaldellis, ,A. Anestis, I. Koronaki, 2013, Strategic planning in the electricity generation sector through the development of an integrated Delphi-based multi-criteria evaluation model, Fuel, 106, 212-218

E. Kondili, C.C. Pantelides, R.W.H. Sargent, 1993, A general algorithm for short-term scheduling of batch operations—I. MILP formulation, Computers & Chemical Engineering, 17,2, 211-227

A.J. Mason, 2012, OpenSolver – An Open Source Add-in to Solve Linear and Integer Progammes in Excel, Operations Research Proceedings 2011, eds. Klatte, Diethard, Lüthi, Hans-Jakob, Schmedders, Karl, Springer Berlin Heidelberg, 401-406, 2012, http://dx.doi.org/10.1007/978-3-642-29210-1_64, http://opensolver.org

C.C. Pantelides, 1994, Unified frameworks for optimal process planning and scheduling Cache Publications, New York, 253–274

L.G. Papageorgiou, 2009, Supply chain optimisation for the process industries: Advances and opportunities, Computers & Chemical Engineering, 33, 1931-1938

C. Papapostolou, E.M. Kondili, J.K. Kaldellis, 2014, Energy Supply Chain Optimisation: Special Considerations for the Solution of the Energy Planning Problem, Computer Aided Chemical Engineering, 33, 1525-1530

T. Pinto-Varela, F.Martins, A. Barbosa-Povoa, 2012, Integrating Economic and Environmental Aspects in the Design and Planning of Supply Chains: Two alternative methodologies, Computer Aided Chemical Engineering, 30, 112-116

S.D. Pohekar, M. Ramachandran, 2004, Application of multi-criteria decision making to sustainable energy planning - A review, Renewable and Sustainable Energy Reviews, 8, 365-381

R.Thery, P. Zarate, 2009, Energy planning: A multi-level and multicriteria decision making structure proposal, Central European Journal of Operations Research, 17, 265-274

L. Vance, I Heckl, B. Bertok, H. Cabezas, F. Friedler, 2014, Designing Energy Supply Chains with the P-graph Framework under Cost Constraints and Sustainability Considerations, Computer Aided Chemical Engineering, 33, 1009-1014

D. Yue, F. You, 2014, Functional-unit-based life cycle optimization of sustainable biomass-to-electricity supply chain with economic and environmental tradeoffs, Computer Aided Chemical Engineering, 34, 651-656

Krist V. Gernaey, Jakob K. Huusom and Rafiqul Gani (Eds.), 12th International Symposium on Process Systems Engineering and 25th European Symposium on Computer Aided Process Engineering.
31 May – 4 June 2015, Copenhagen, Denmark

Synthesis of Optimal Processing Pathway for Microalgae-based Biorefinery under Uncertainty

Muhammad Rizwan,[a] Jay H. Lee,[a*] Rafiqul Gani[b]

[a]*Department of Chemical and Biomolecular Engineering, Korea Advanced Institute of Science and Technology (KAIST), 291 Daehak-ro, Yuseong-gu, Daejeon 305-701, Republic of Korea*
[b]*CAPEC, Department of Chemical and Biochemical Engineering, Technical University of Denmark, DK-2800 Kgs Lyngby, Denmark*
jayhlee@kaist.ac.kr

Abstract

The research in the field of microalgae-based biofuels and chemicals is in early phase of the development, and therefore a wide range of uncertainties exist due to inconsistencies among and shortage of technical information. In order to handle and address these uncertainties to ensure robust decision making, we propose a systematic framework for the synthesis and optimal design of microalgae-based processing network under uncertainty. By incorporating major uncertainties into the biorefinery superstructure model we developed previously, a stochastic mixed integer nonlinear programming (sMINLP) problem is formulated for determining the optimal biorefinery structure under given parameter uncertainties modelled as sampled scenarios. The solution to the sMINLP problem determines the optimal decisions with respect to processing technologies, material flows, and product portfolio in the presence of uncertain parameters. The developed framework is implemented and tested on a specific case study, to identify the promising processing pathway for the production of biofuels from microalgae while accounting for modelled uncertainties.

Keywords: Uncertainty analysis, Stochastic mixed integer nonlinear programming (sMINLP), Microalgal biorefinery.

1. Introduction

Under the broad concept of microalgal biorefinery, microalgae is cultivated and processed to produce a wide range of products such as biofuels, chemicals, animal feed, pigments, power/heat, etc. (Yen et., 2013; Rawat et al., 2013). Despite the various benefits associated with the development of microalgae based biorefinery (such as potentially significant improvements in the overall economics of biofuels), there are many challenges yet to overcome and to be addressed systematically. These challenges include (1) existence of a number of potential processing pathways for biorefinery development, and (2) inconsistency and shortage in the process information available in the literature because the idea of utilizing microalgae as a renewable feedstock for the production of biofuels and chemicals is relatively new and involved processing technologies are still at a nascent stage. Potential development of additional technologies as well as the likely future improvements may further increase the uncertainty one faces at a preliminary assessment phase. Consequently, the optimal biorefinery configuration determined based on uncertain parameters can prove to be highly suboptimal later due to discrepancies among the assumed and actually realized parameter values. Stochastic programming/optimization is a widely used tool to

determine the optimal design under stochastic uncertainty, and this approach has been used in many studies (Karuppiah and Grossmann, 2008; Quaglia et al., 2013).

In this paper, we propose a systematic modelling framework to determine the promising processing pathway for the production of biofuels from microalgae by considering the effect of uncertainty present in microalgal biorefinery design. The problem of finding the promising biorefinery configuration under uncertainty is formulated as a sMINLP problem which is solved in the software package GAMS.

2. Modelling framework

In an earlier work (Rizwan et al., 2013), we addressed the problem of determining the promising pathways for the production of biodiesel from microalgal biomass by developing a superstructure based optimization model. Later the model was extended to locate the promising biorefiney configurations by coupling the utilization of microalgae residue along with the biodiesel production. In this contribution, we have incorporated the major uncertainties into the biorefinery superstructure model which results in the formulation of a stochastic optimization problem.

2.1. Problem definition

In the first step, the problem scope is defined by identifying and selecting the objective function with respect to the techno-economic constraints considering the uncertainties in the sensitive model parameters. A general problem statement is given as follows.

Given is a microalgal biorefinery superstructure (Figure 1) which consists of available potential technological alternatives/options for the various processing steps involved in the microalgal biorefinery such as cultivation of microalgae, harvesting of microalgal biomass, pre-treatment step including drying and cell disruption of harvested biomass, lipid extraction, transesterification, post-transesterfication purification, pre-treatment of microalgae residue, and conversion of residue into the useful products. The optimization problem is defined as to determine the optimal processing network(s) under uncertainty for the production of biofuels from microalgae. When the uncertainties are expressed as distributions in the parameter space or discrete scenarios sampled from it, it leads to the formulation of a sMINLP problem. The objective function chosen is to maximize the expected value of gross operating margin over the uncertain space. Use of other risk-sensitive measures is also possible but not examined in this paper.

2.2. Data collection and superstructure development

We have developed a biorefinery superstructure for the production of biodiesel from the lipid contents of microalgae and the simultaneous conversion of microalgae residue into the useful products. It includes all the major processing steps/stages for the production of biofuels from *Chlorella vulgaris*, and at each processing step various potential technological alternatives/options are considered. As shown in Figure 1, each option included in the superstructure is represented by two indices; the first index represents the option number and the subsequent second index represents the processing stage. The list of technological options included in the biorefinery superstructure model is given in Table 1. The empty boxes represent the bypassing of certain processing stages, e.g., to accommodate wet lipid extraction, in-situ transesterification, etc. The detailed description of the problem data and superstructure development can be found in our previous study (Rizwan et al., 2013).

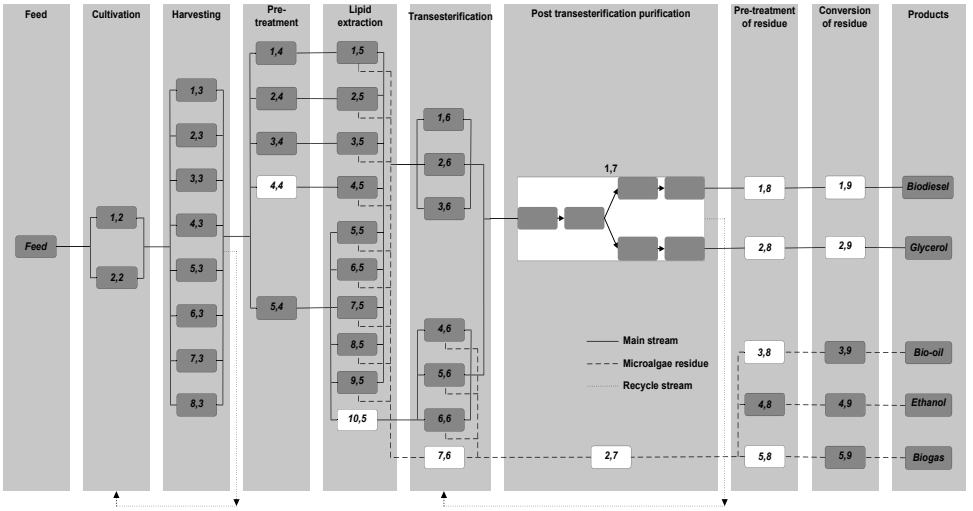

Figure 1. Biorefinery superstructure for the production of biofuels from microalgae

Table 1. Option/technological alternatives

1,1	Feed	10,5	Empty
1,2	Open pond system	1,6	Base catalyzed transesterification
2,2	Photobioreactor	2,6	Acid catalyzed transesterification
1,3	Flocculation with poly electrolyte	3,6	Enzymatic transesterification
2,3	Flocculation with NaOH	4,6	Alkaline in-situ transesterification
3,3	Flocculation with PGA	5,6	Acidic in-situ transesterification
4,3	Flocculation with chitosan acid solution	6,6	Enzymatic in-situ transesterification
5,3	Bioflocculation + Centrifugation	7,6	Empty
6,3	Centrifugation	1,7	Post transesterification purification
7,3	Auto flocculation (induced by high pH)	2,7	Empty
8,3	Microfiltration + Centrifugation	1,8	Empty
1,4	Grinding in liquid nitrogen	2,8	Empty
2,4	Drying + Ultrasound	3,8	Empty
3,4	Drying+Grinding+Microwave+Ultrasound	4,8	Enzymatic hydrolysis
4,4	Empty	5,8	Empty
5,4	Drying	1,9	Empty
1,5	Grinding assisted lipid extraction	2,9	Empty
2,5	Ultrasound assisted Extraction by [Bmim][MeSO4]	3,9	Fast pyrolysis
3,5	Ultrasound & microwave assisted lipid extraction	4,9	Fermentation
4,5	Wet lipid extraction	5,9	Anaerobic digestion
5,5	Solvent extraction (Bligh & Dyer Method)	1,10	Biodiesel
6,5	Extraction by Mod. Bligh & Dyer Method	2,10	Glycerol
7,5	Supercritical fluid extraction	3,10	Bio-oil
8,5	Extraction by ionic liquid mixture	4,10	Bioethanol
9,5	Extraction by [Bmim][MeSO4]	5,10	Biogas

2.3. Uncertainty characterization

In this step, the uncertain parameters are identified and characterized in terms of distributions. Based on the approach described in Brun et al., 2002 and Sin et al., 2009,

three classes of uncertainties such as low, medium and high are defined which correspond to 5 %, 25 % and 50 % variations around the mean value, respectively. The uncertain parameters and their class of uncertainty are given in Table 2. In this study, these classes are defined on the basis of available information or data in the literature. For example, the fractional conversion of lipids into biodiesel via base catalysed transesterification is known with good accuracy; hence, it is classified as a parameter of low uncertainty. The available information about the fractional conversion of lipids into biodiesel via in-situ transesterification, CO_2 conversion, lipid yield for wet lipid extraction method, and cost of feed are not consistent in the literature; therefore, these are classified as having medium uncertainty. The same is true for the lipid contents but with a very large range of variations; therefore, it is put in the category of high uncertainty. Even less and highly inconsistent information is available for the conversion of microalgae residue (for bioethanol and biogas production), and therefore it is also placed in the class of high uncertainty.

From the uncertain parameters space, we have generated the future scenarios with equal probability of realizations of the uncertain parameters by using Latin Hypercube Sampling (LHS) method. LHS is a well know probabilistic sampling technique for the sampling of uncertain space (Mckay et al., 1979). A good uniform coverage of the sampling space can be obtained with this technique (Sin et al., 2009). Uniform probability distribution of uncertain data is assumed in this study for scenarios generation. 200 samples are generated from the distribution to be used as scenarios.

Table 2. Uncertain parameters and their class of uncertainty

Parameters	Uncertainty class	Variations (%)
Fractional conversion of lipids (for base catalysed transesterification	Low	5
Fractional conversion of lipids (for acidic in-situ transesterification)	Medium	25
CO_2 conversion/fixation		
Lipid yield (for wet lipid extraction)		
Cost of feed		
Lipid contents	High	50
Fractional conversion of residue (for bioethanol and biogas production)		

2.4. Deterministic problem formulation

In this step, a deterministic optimization problem is formulated and solved to find the optimal processing network in the nominal conditions by disregarding the uncertainties in the model parameters. The deterministic problem results in the formulation of MINLP model. The results obtained in this step locate the deterministic optimal processing pathway for the production of biofuels from microalgae.

2.5. Decision making under uncertainty: Stochastic formulation

In this step, a stochastic optimization problem is formulated to find the optimal processing pathway under uncertainty which is solved via sample average approximation (Birge and Louveaux, 1999). The objective function is to maximize the expected value of gross operating margin over the uncertain space, which is sampled to generate 200 future scenarios. The stochastic problem is formulated and solved in the software package GAMS with DICOPT solver using a database built in Excel.

3. Case study

The developed modelling framework is implemented on a case study to determine the optimal processing pathway under uncertainty for the production of biofuels from microalgae.

The biorefinery superstructure is developed for the production of biofuels form microalgae as shown in Figure 1, and briefly described in section 2.2. The optimization problem is defined as to determine the optimal processing pathway under uncertainty. The objective function chosen is to maximize expected value of gross operating margin which is defined as the difference between total sales of products and the operating cost.

4. Results and discussion

The obtained optimization results are given in Table 3. Figure 2 represents the optimal processing pathway (for the maximization of gross operating margin) obtained by solving the stochastic programming problem, which consists of open pond cultivation, harvesting of microalgal biomass by flocculation using poly electrolyte as a flocculent, wet lipid extraction, base catalysed transesterification followed by the purification step, and anaerobic digestion for the conversion of microalgae residue into biogas.

Table 3. Optimization results obtained by solving deterministic and stochastic models

	GOM ($)	Yield biodiesel (GGEs)	Yield glycerol (GGEs)	Yield biogas (GGEs)
Nominal value for det. solution	-46.493	8.814	0.468	4.912
	Pathway: 1,1 1,2 1,3 5,4 10,5 5,6 1,7 2,7 1,8 2,8 5,8 1,9 2,9 5,9 1,10 2,10 5,10			
Exp. value for det. solution	-53.488	7.855	0.417	4.899
Exp. value for stoch. solution	-47.748	8.031	0.427	4.900
	Pathway: 1,1 1,2 1,3 4,4 4,5 1,6 7,6 1,7 2,7 1,8 2,8 5,8 1,9 2,9 5,9 1,10 2,10 5,10			

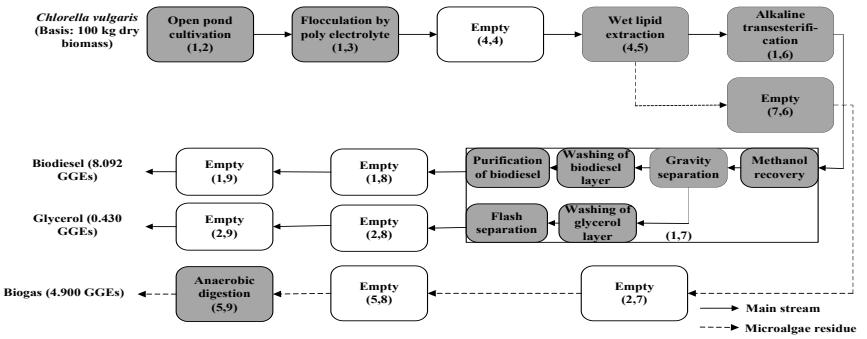

Figure 2. Optimal processing pathway obtained by solving stochastic model

By modelling the uncertainties in the parameters, the selected processing pathway by the stochastic solution maximizing the expected value of gross operating margin is different from the deterministic solution obtained in step 4. In contrast to the deterministic solution, here the biodiesel production is described by wet lipid extraction method followed by base catalyzed transesterification. The expected value of gross operating margin is found to be $-47.748, which is slightly lower than the value achieved based on the nominal parameters due to the uncertainties but higher than the expected value for the deterministic solution that did not consider them. In other words,

by solving a more elaborate stochastic program considering the uncertainties, the expected value of gross operating margin is increased by more than 10 %. These findings highlight that the uncertainties in the problem dataset have significant effect on the optimal structure of microalgal biorefinery.

5. Conclusions

In this paper, we have developed a stochastic optimization model to assess the impact of major uncertainties in the model parameters on the design of optimal processing network for the production of biofuels from microalgae. The previously developed superstructure based modelling framework was extended to formulate sMINLP problem by incorporating major uncertainties in the model parameters as a large number of sampled scenarios. The developed framework was applied to a specific case study which is based on microalgal biorefinery, to highlight the implementation and applicability of the methodology and the impact of uncertainty on the optimal design as well as on the achieved gross operating margin.

The optimization results showed that the uncertainty in the problem dataset has an impact on the optimal biorefinery configuration. As future work, the modelling framework will be extended to consider a more diverse set of objective functions that reflect risk aversion strategies.

Acknowledgement

The authors are thankful for the financial support from Advanced Biomass R&D Centre (ABC) of Global Frontier Project funded by the Ministry of Education, Science and Technology.

References

J. R. Birge, F. Louveaux, 1999, Introduction to stochastic programming (Springer Series in Operation Research), Springer, New York, U. S.

R. Brun, M. Kuhni, H. Siegrist, W. Gujer, P. Reichert, 2002, Practical identifiability of ASM2d parameters – systematic selection and tuning of parameter susets, Water Research, 36, 4113-4127.

R. Karuppiah and I. Grossmann, 2008, Global optimization of multiscenarios mixed integer nonlinear programming models arising in the synthesis of integrated water networks under uncertainty, Computers and Chemical Engineering, 32, 145-160.

M. D. Mckay, R. J. Beckam, W. J. Conover, 1979, A comparison of three methods for selecting values of input variables in the analysis of output from a computer code, Technometrics, 21, 239-245.

A. Quaglia, B. Sarup, G. Sin, R. Gani, 2013, A systematic framework for enterprise-wide optimizaion: Synthesis and design of processing networks under uncertainty, Computers and Chemical Engineering, 59, 47-62.

I. Rawat, R. R. Kumar, T. Mutanda, F. Bux, 2013, Biodiesel from microalgae: A critical evaluation from laboratory to large scale production, Applied Energy, 103, 444-467.

M. Rizwan, J. H. Lee, R. Gani, 2013, Optimal processing pathway for the production of biodiesel from microalgal biomass: A superstructure based approach, Computers and Chemical Engineering, 58, 305-314.

G. Sin, K. V. Gernaey, A. E. Lantz, 2009, Good modeling practice for PAT applications: Propgataion of input uncertainty and sensitivty analysis, AIChE Biotechnology Progress, 25 (4), 1043-1053.

H. W. Yen, I. C. Hu, C. Y. Chen, S. H. Ho, D. J. Lee, J. S. Chang, 2013, Microalgae-based biorefinery – From biofuels to natural products, Bioresource Technology, 135, 166-174.

Krist V. Gernaey, Jakob K. Huusom and Rafiqul Gani (Eds.), 12th International Symposium on Process Systems Engineering and 25th European Symposium on Computer Aided Process Engineering.
31 May – 4 June 2015, Copenhagen, Denmark

Effect of feed natural gas conditions on the performance of mixed refrigerant LNG process

Mengyu Wang, Rajab Khalilpour, Ali Abbas*

School of Chemical and Biomolecular Engineering, The University of Sydney, NSW 2006, Australia
ali.abbas@sydney.edu.au

Abstract

The natural gas wellhead conditions vary over the life of a production well. These variations affect the performance, production and product quality of liquefied natural gas (LNG) plant. This study, through a simulation-based sensitivity analysis, highlights the significance of the effects imparted by the feed natural gas conditions on process performance of a propane precooled mixed refrigerant (C3MR) LNG process. The results show that the specific shaft work and thus OPEX is sensitive to the feed composition, flowrate, and pressure. For instance, as LNG production decreases from its design capacity of 3.0 MTPA to 2.4 MTPA over time, the specific OPEX increases from $128/t-LNG to $154/t-LNG.

Keywords: LNG, modelling, C3MR, sensitivity analysis, feed gas conditions.

1. Introduction

For many countries around the world, natural gas is recognized as an important energy source from economic and environmental perspectives. Natural gas liquefaction process is a key step in the natural gas supply chain however it is an energy intensive process. The design and operation optimization of LNG plants has received significant industrial and research attention driven by the significant demand for natural gas and the sheer scale of the natural gas market. Many researchers studied optimization of LNG liquefaction process aiming at reducing energy consumption and improving energy efficiency. Lee et al. (2002) conducted a systematic method on the optimal design of a PRICO cycle seeking optimal operating conditions. Jensen et al. (2007) and Jacobsen et al. (2013) worked on operation optimization of a single mixed refrigerant (SMR) cycle. Nogal et al. (2008) presented an optimal design methodology for a SMR cycle to reduce the compression work. Aspelund et al. (2010) developed a non-deterministic search method for optimization of PRICO cycle. Khan et al. (2012) optimized a SMR process with non-linear programming along with exergy efficiency analysis. Wang et al. (2013) and Wang et al. (2014) studied the impact of numerous key variables including mixed refrigerant (MR) composition on the performance of a LNG plant. The optimization studies of natural gas liquefaction processes are reviewed by Lim et al. (2012).

In addition, efficient design and operation of LNG plants require optimal process responses to various factors including feed conditions, economics, and climate of LNG plant. These factors at a given supply source influence process performance and product quality over time. Castillo et al. (2013) evaluated performance of different LNG precooling cycles in cold and warm climates. Their results showed that a three-stage propane precooled MR cycle is more suitable for warm climates while a two-stage MR cycle is the most efficient technology for cold climates. Clementino et al. (2014) studied

sensitivity analysis of C3MR to investigate the specific shaft work required at different temperature and pressure of feed natural gas. Our literature reviews showed that less attention has been given to addressing the impact of variations in feed natural gas composition and flowrate on process performance. This study is focused on understanding, through sensitivity analysis, the effects of different feed natural gas conditions including composition, flowrate, pressure, and temperature on process performance and LNG product of a C3MR process.

2. Process description

Figure 1 shows the flow diagram of C3MR process. C3MR process consists of precooling cycle and subcooling cycle. The treated natural gas and MR is partially cooled to around -35 °C in a propane precooling cycle. The precooled MR is then separated into gaseous stream and liquid stream to provide the cooling for natural gas in main cryogenic heat exchanger (MCHE) to around -161 °C at atmospheric pressure. After that, MR is completely vaporized from the exit of MCHE and then compressed by a series of compressors to its initial inlet conditions.

3. Sensitivity analysis

The modelling package HYSYS® (Aspentech, USA) was used to model the LNG plant, shown in Figure 1, and to assess its performance under the following sensitivity analysis:

1) The effect of natural gas composition at a constant temperature of 25 °C and pressure of 5000 kPa is studied. Six different compositions of natural gas are conducted as listed in Table 1. The mole fraction of methane in natural gas is adjusted from its base value of 96.92 % to 84.55 % with 10 % decrements of component mole flow of methane while keeping the mole flow of remaining components constant.
2) The temperature of feed gas is varied within the range of 10 °C and 50 °C.
3) The pressure of feed gas is varied within the range of 3000 kPa and 5000 kPa.
4) The flowrate of feed gas is varied within the range of ±20 % of its design value.

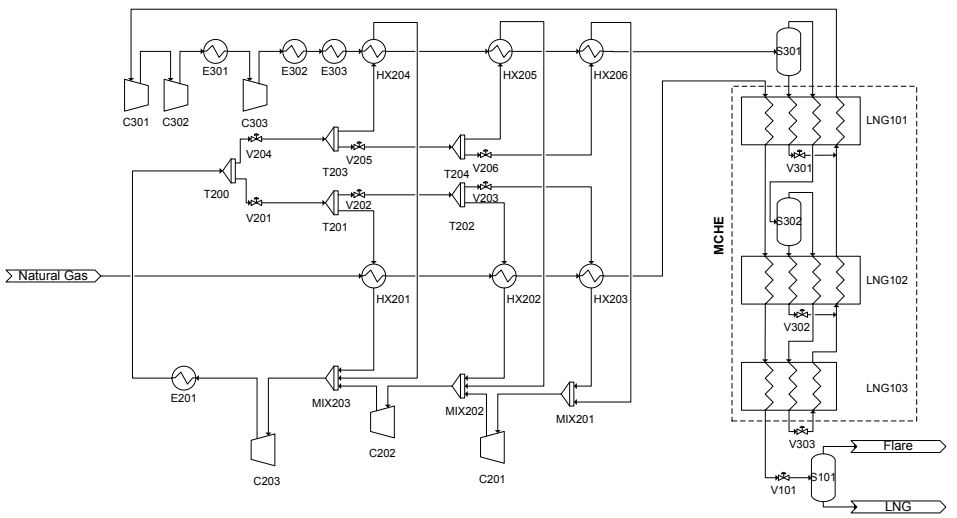

Figure 1. The flow diagram of C3MR process.

Table 1. Feed natural gas composition (in unit of mole fraction).

Feed composition case	Methane	Ethane	Propane	n-butane	Nitrogen
Base case*	96.92	2.94	0.06	0.01	0.07
NG1	96.70	3.15	0.06	0.01	0.07
NG2	96.31	3.53	0.07	0.01	0.08
NG3	94.80	4.96	0.10	0.02	0.12
NG4	91.63	7.99	0.16	0.03	0.19
NG5	84.55	14.75	0.30	0.05	0.35

*Refer to Wang et al. (2013)

3.1. Assumptions

C3MR process is modelled and simulated with the following input conditions and assumptions.

1) The feed natural gas is dry and sweet prior to entering the liquefaction process.
2) The feed gas is at T=25 °C and P=5000 kPa to produce 3.0 MTPA of LNG.
3) Natural gas is composed of 96.92 % methane, 2.94 % ethane, 0.06 % propane, 0.01 % n-butane and 0.07 % nitrogen (Wang et al., 2013).
4) The overall heat transfer coefficient and area (UA) of MCHE is fixed at design value of 16.39 MW/°C (Wang et al., 2013).
5) The prices of electricity and cooling water are $10.99/GJ and $0.40/GJ respectively (Turton et al., 2009). The price of feed natural gas is $2/mmBTU.

3.2. Performance equations

The following equations are used for calculating the total power consumption and variable operating cost of the C3MR process. Total shaft work is expressed by Eq. (1) in which W_i is the shaft work used at compressor C_i.

$$W_{Total} = \sum_{i=1}^{n} W_i \tag{1}$$

Operating expenditure (OPEX) includes electricity, water and feed natural gas. It is represented as Eq. (2).

$$OPEX = \frac{P_{Elec}\sum_{i=1}^{n} W_i + P_{Water}\sum_{j=1}^{m} Q_j + P_{NG}F_{NG}}{F_{LNG}} \tag{2}$$

where, P_{Elec} is electricity price, P_{Water} is cooling water price, P_{NG} is the price of feed natural gas.

4. Changes in natural gas conditions

The results in Figure 2 indicate that for a given amount of feed gas, the decrease of 12.37 mol% in methane concentration results in the reduction of specific shaft work by 5.17 %, while it only increases the LNG production by 0.76%. This is because methane reduction increases the molecular weight of natural gas mixture. A feed natural gas with

lower methane content which has lower dew point requires less refrigeration capacity; consequently produces more LNG products. In accordance with Clementino et al. (2014), plant operation and LNG production are also sensitive to pressure, temperature, and flowrate variation of feed natural gas. Three scenarios are carried out: change in feed flowrate, change in feed pressure, and change in feed temperature. In each scenario, feed gas composition varies is based on Table 1.

Scenario 1: Variation in natural gas composition with different feed flowrate

This scenario examined variation in natural gas composition with different feed natural gas flowrate. The specific shaft work is shown in Figure 3, along with the specific OPEX. It is obvious that decline in natural gas flowrate with a constant composition requires less cooling duty provided by C3MR process at fixed UA, which is in an agreement with Wang et al. (2013). This shows the significant impact of plant feed capacity on process operational costs.

As natural gas flowrate decreases from 4.788×10^5 kg/h to 3.129×10^5 kg/h, the base case natural gas with highest methane content shows the maximum effect on cooling duty. It results in the largest decrease of specific shaft work by 7.08% for base case and the smallest decrease by 1.34 % for NG5. However, specific OPEX increases since natural gas flowrate decreases at fixed UA. Specific OPEX for base case natural gas composition increases from \$113.3/t-LNG to \$153.6/t-LNG. Similar trend is observed for the other four feed gas compositions.

Scenario 2: Variation in natural gas composition with different feed pressure

The feed pressure of a natural gas well will decline over time. This scenario examines the effect of supplying natural gas with different composition and pressure on specific shaft work at a constant temperature of 25 °C as shown in Figure 4. The reference specific shaft work is obtained at a feed pressure of 5000 kPa. It is evident from Figure 4 that with reduction in feed gas pressure, a given amount of natural gas requires higher specific power to liquefy resulting in higher specific OPEX. This shows the influence of upstream feed pressure on the process economics, an important variable for the operator to consider as the gas well ages.

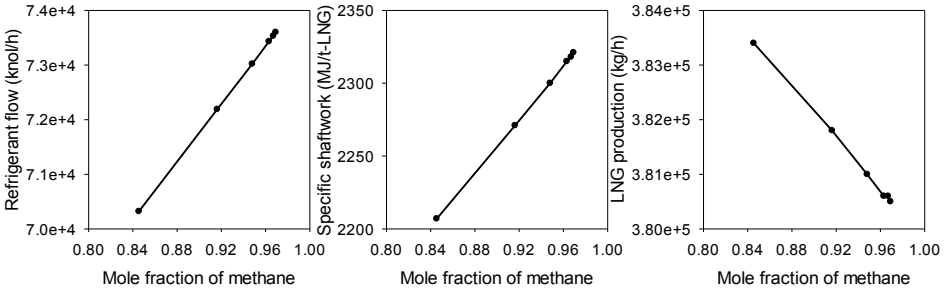

Figure 2. The effect of feed natural gas compositions change on refrigerant flow, specific shaft work and LNG production (T= 25 °C and P=5000 kPa).

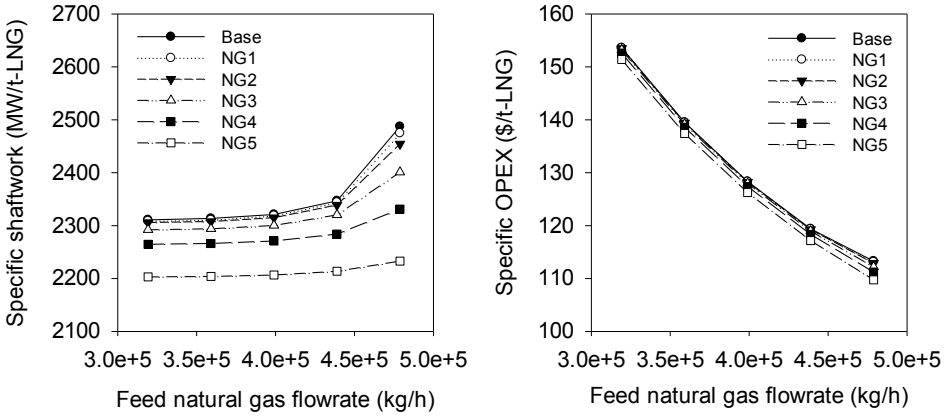

Figure 3. The effect of feed natural gas flowrate change on specific shaft work and specific OPEX (T= 25 °C and P=5000 kPa).

Scenario 3: Variation in natural gas composition with different feed temperature

Figure 5 shows the effect of natural gas temperature variation on specific shaft work at a constant feed pressure of 5000 kPa. The temperature variation of natural gas is in a range of 10 °C and 50 °C. It is evident from the figure that temperature variation of feed natural gas has a trivial effect on specific power consumption. At a constant pressure, the specific power increases by 0.73 % for base case and 0.76 % for NG5 when feed natural gas temperature increase by 40 °C increase. For the base case, natural gas containing more methane than other cases requires more compression work to produce the same amount of LNG.

5. Conclusions

This work investigated the effects of varying the inlet natural gas conditions for an existing LNG plant (i.e. with a constant UA). The findings from this study show that variations in feed natural gas composition, pressure, and flowrate have more refrigeration effect than feed temperature for given feed flowrate. With reduction in feed gas flowrate over a well's life time, the overall shaft work declines. However, the specific energy requirement per unit weight of LNG product increases translating to higher production costs.

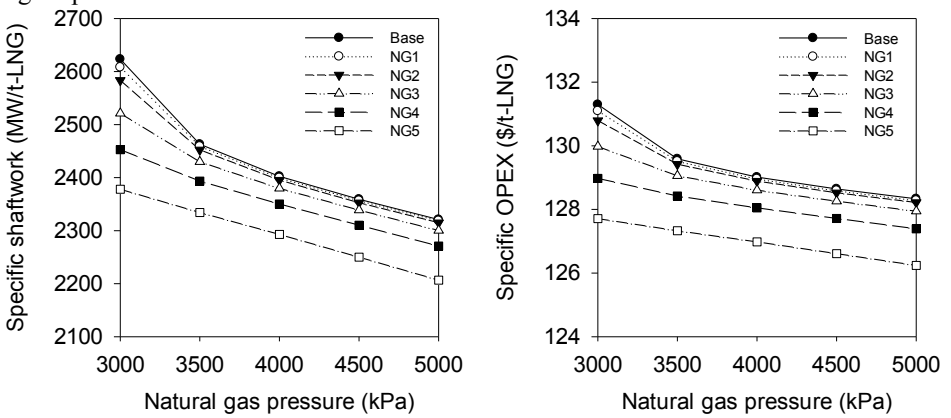

Figure 4. The effect of feed natural gas pressure change on specific shaft work and specific OPEX (T= 25 °C).

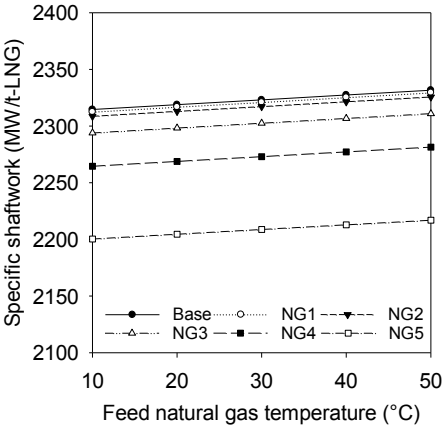

Figure 5. The effect of feed natural gas temperature change on specific shaft work (P=5000 kPa).

References

A. Aspelund, T. Gundersen, J. Myklebust, M. P. Nowak & A. Tomasgard, 2010, An optimization-simulation model for a simple LNG process, Computers & Chemical Engineering, 34**,** 1606-1617.

L. Castillo, M. Majzoub Dahouk, S. Di Scipio & C. A. Dorao, 2013, Conceptual analysis of the precooling stage for LNG processes, Energy Conversion and Management, 66**,** 41-47.

P. Clementino, S. A. Handaya & K. Sutrasno, 2014, Thermodynamic Analysis for Liquefaction of Natural Gas Using the C3-MR Refrigeration Process, International Journal of Chemical Engineering and Applications, 5.

M. G. Jacobsen & S. Skogestad, 2013, Active constraint regions for a natural gas liquefaction process, Journal of Natural Gas Science and Engineering, 10**,** 8-13.

J. B. Jensen & S. Skogestad, 2007, Optimal operation of simple refrigeration cycles: Part I: Degrees of freedom and optimality of sub-cooling, Computers & chemical engineering, 31**,** 712-721.

M. S. Khan, S. Lee & M. Lee, 2012, Optimization of single mixed refrigerant natural gas liquefaction plant with nonlinear programming, Asia-Pacific Journal of Chemical Engineering, 7**,** S62-S70.

G. C. Lee, R. Smith & X. X. Zhu, 2002, Optimal Synthesis of Mixed-Refrigerant Systems for Low-Temperature Processes, Industrial & Engineering Chemistry Research, 41**,** 5016-5028.

W. Lim, K. Choi & I. Moon, 2012, Current Status and Perspectives of Liquefied Natural Gas (LNG) Plant Design, Industrial & Engineering Chemistry Research, 52**,** 3065-3088.

F. D. Nogal, J.-K. Kim, S. Perry & R. Smith, 2008, Optimal Design of Mixed Refrigerant Cycles, Industrial & Engineering Chemistry Research, 47**,** 8724-8740.

R. Turton, R. C. Bailie & W. B. Whiting, 2009, Analysis, synthesis, and design of chemical processes, Prentice Hall.

M. Wang, R. Khalilpour & A. Abbas, 2013, Operation optimization of propane precooled mixed refrigerant processes, Journal of Natural Gas Science and Engineering, 15**,** 93-105.

M. Wang, R. Khalilpour & A. Abbas, 2014, Thermodynamic and economic optimization of LNG mixed refrigerant processes, Energy Conversion and Management, 88**,** 947-961.

Krist V. Gernaey, Jakob K. Huusom and Rafiqul Gani (Eds.), 12th International Symposium on Process Systems Engineering and 25th European Symposium on Computer Aided Process Engineering.
31 May – 4 June 2015, Copenhagen, Denmark

A Spatial Decomposition Procedure for Efficient Solution of Two-Dimensional Energy Distribution Problems

Carl Haikarainen[a], Frank Pettersson[a], Henrik Saxén[a]

[a]*Thermal and Flow Engineering Laboratory, Åbo Akademi University, Biskopsgatan 8, FI-20500 Åbo, Finland*

Abstract

As more and more technologies emerge in the energy sector, there is a possibility that structures of energy systems and networks will move towards a more distributed, decentralised structure, with multiple smaller power plants and energy supplier units providing the energy previously commonly supplied by a large centralised plant. If well planned, these distributed structures are anticipated to increase the efficiency, flexibility and security of energy systems. Many mathematical models have been formulated for aiding the design process and analysis of distributed energy systems such as district heating systems. A search for optimal structures and multi-period operational schemes of district heating networks consisting of supplier, consumer and storage nodes connected via pipelines can be formulated as a mixed-integer linear program and solved using standard algorithms, but as the problem sizes increase, the solution times become too long for practical use. For this reason, a procedure for decomposing such an optimization problem in order to reduce the required computational time is proposed. The procedure is based on dividing the geographical area of the energy system into separate sectors which are treated as nodes in a simplified network. During consecutive iterations, the number of sectors, along with the detail level of the simplified network, is increased. Each iteration reduces the search space of the original problem, thus reducing the time needed for the solution. While reaching global optima cannot be guaranteed, examples are given where the procedure finds better solutions than standard algorithms could find within any reasonable, or even relatively unreasonable, time limits.

Keywords: Distributed energy systems, Optimization, District heating

1. Introduction

One glance at a review paper by Keirstead et al. (2012) reveals the multitude of approaches taken to modelling urban energy systems. Together with the overall increase in energy use of human societies, much of this use is more and more concentrated to urban areas and other distributed energy systems. Thus, it is motivated to put more research effort into developing models that could aid in finding ways to restrain or even reduce the negative impacts of this energy use. One category of such models concerns the optimization of district heating systems providing heat from centralized plants to consumers via pipelines in the form of hot water. Some models deal with the operational optimization of the networks and the power plants, which in itself contains several problematic aspects (Vesterlund and Dahl, 2015). Then there is also the question of combining operational and structural optimization. Structural optimization has been

performed on relatively small networks (Omu et al., 2013), but some tested models come to a halt when facing larger networks, i.e. networks with more than just tens of nodes (Haikarainen et al., 2014). As a real heating network usually has hundreds or thousands of consumer nodes, it becomes necessary to develop a model that is able to handle larger networks. While Fazlollahi et al. (2014) represented urban areas as sets of "integrated zones", the method presented in this article features a sequence of similar clustered representations aimed at finding solutions for the original, non-clustered, network representation, with its complete selection of pipelines, suppliers and storages.

2. Model Description

The mathematical model which the work in this article is based on is described in detail by Haikarainen et al. (2014). In essence, it paints a picture of a network of consumer nodes with a certain demand of heat and electricity, and a set of supplier nodes which represent power plants and other energy supply units in place to satisfy the consumer demands. This is formulated as a mixed-integer linear programming (MILP) problem. The consumers may or may not be connected to the pipeline network. If not connected, consumers may also have their demands served through heat pumps or other local forms of heating. With continuous variables representing supplier capacities, enthalpy flows, water velocities, power required for pumping, etc., and binary variables representing the existence of network components and various discrete decisions, the optimization gives suggestions on which new components to build (new power plants, heat storages, or pipelines) and of which kind (fuel types, maximum capacities, pipe diameters), as well as schemes for running the entire network over multiple periods. Plausible objective functions can for instance be minimization of costs or emissions.

3. Decomposition method

The biggest issue in the original model is the large number of binary variables involved, so a decomposition procedure for reducing the number of significant binary variables, working as a pre-solver, was devised. The basic idea can be thought of as dividing the geographical area under scrutiny into separate sectors and treating the sectors as nodes in a simplified network. Starting by keeping the number of sectors small, the process is repeated increasing the number of sectors (i.e. the level of detail) with each iteration, as illustrated in Figure 1. If some network components have been deemed unfavourable in the previous iteration, they are left out in the subsequent iterations. Thus, when reaching the full level of detail of the original problem, a number of binary variables can be left out from the problem – unless every possible component is considered beneficial in the optimal solution.

Division of the geographical area into sectors is in this case essentially the same as arranging all the nodes (consumers, suppliers, storages and transition nodes) into suitable clusters. This was done using k-means clustering, which groups nodes in a way that their distances to the centres of the clusters they belong to are minimized (MacKay, 2003). Naturally, other clustering methods could be feasible as well. The decomposition was also tested as a simple division of the geographical area into equal-sized squares. This worked adequately, but a k-means clustering approach evaded any awkward situations with empty sectors.

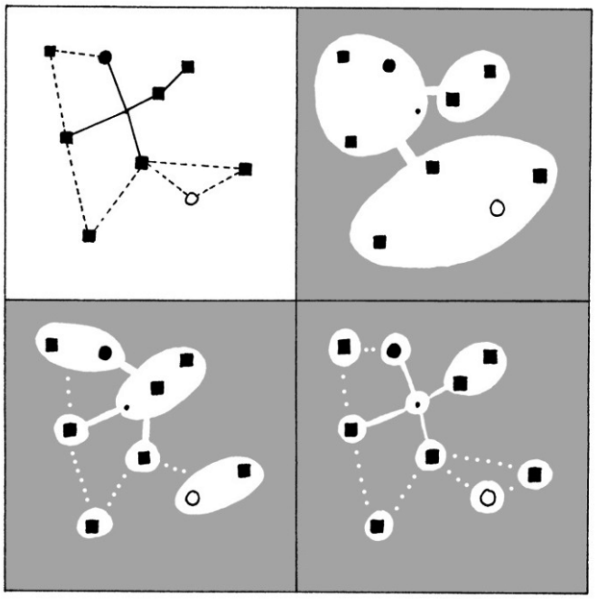

Figure 1. The network in the top-left corner is divided into 3, 6 and 9 sectors. Circles represent suppliers, squares consumers.

Each sector is treated as a node with heat and electricity demands equalling the sum of the demands of the consumer nodes it contains. Each sector can supply energy according to the supplier nodes it contains, distinguishing between known capacity from pre-existing supplier nodes and new capacity that can be built within the sector. The same goes for storage capacity. If a sector contains several possible new supplier nodes, the information of all of them is treated within the same new supplier element of the sector.

The connections between sectors accumulate information from several pipelines in the original problem. Most importantly, the 'lengths' of the connections between two sectors are calculated as the average of the length of all pipelines connecting the sectors, plus, in the case that the pipelines end at a transfer node, the average distances between the end points of the pipelines and each non-transfer node within the sectors containing said end points. To account for new pipelines within a sector, an internal cost proportional to the sector heat demand satisfied by district heating is added to the objective function:

$$C_{internal,N} = K \cdot c(l_{internal,N}) \frac{\sum_p (\dot{H}_{S,N,p} + \dot{H}_{in,N,p} - \dot{H}_{out,N,p}) t_p}{Q_{C,N}} \quad (1)$$

In Eq. (1), subscript N is the sector number and p is the period number, $C_{internal,N}$ is the approximated investment cost of pipelines within a sector, K is a model coefficient, $c(l_{internal,N})$ is the total cost of all pipelines within a sector with a total pipeline length of $l_{internal,N}$. This total pipeline length is calculated as the minimum spanning tree connecting all nodes within the sector. Furthermore, $\dot{H}_{S,N,p}$ is the enthalpy flow from supplier nodes within a sector, $\dot{H}_{in,N,p}$ and $\dot{H}_{out,N,p}$ are the enthalpy flows into and out

from a sector, t_p is the timespan of a period and $Q_{C,N}$ is the total consumer heat demand in a sector. Every optimization step solves an MILP problem, implemented in Matlab using CPLEX as a solver (IBM 2014).

4. Examples

To demonstrate the functionality of the decomposition procedure, with its strengths and weaknesses, three examples in the form of imaginary test cases will be shown. Cases of differing complexities and solution qualities were chosen, to give examples of how the method performs. The initial structures of the test cases are on display in Figure 2, with some basic data arranged in Table 1. As in Figure 1, circles represent suppliers, squares consumers, and additionally, diamonds represent storage nodes. Network components in grey are not pre-existing, but could potentially be built. All the test cases are optimized for a data set of one year divided into twelve periods, representing averages over two-month intervals with days and nights as separate periods (Haikarainen et al., 2014). Heat demands vary between seasons, and between day and night as well. Electricity demands on the other hand were chosen to be constant between seasons, for the sake of simplicity. Some characteristics of the cases are presented in Table 2.

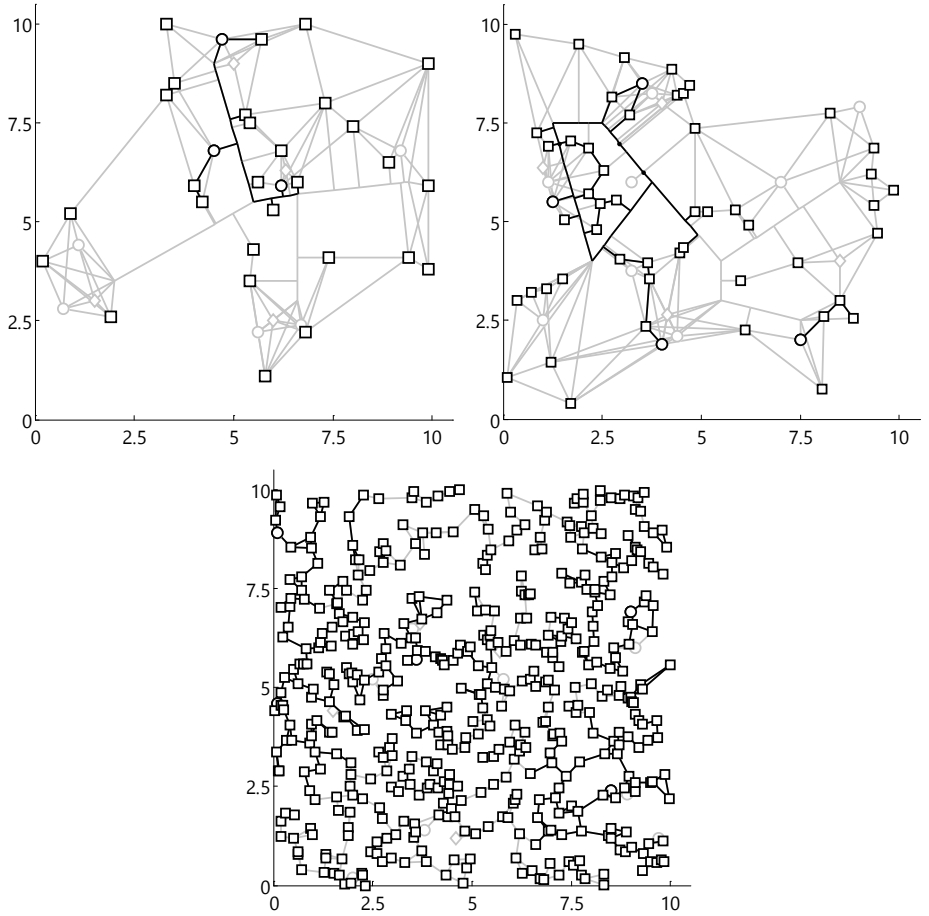

Figure 2. Three test cases are of varying complexity. Units in km.

Table 1. Basic data for the three test cases

Case	Suppliers	Consumers	Storages	Pipelines	Continuous variables	Binary variables
1	8 (3)	28	4 (0)	147 (24)	12,320	954
2	12 (4)	50	4 (0)	243 (62)	23,482	1,573
3	12 (5)	500	4 (0)	704 (332)	140,236	4,789

Numbers in brackets refer to pre-existing components.

Table 2. Variation in total consumer demands in the three test cases

Case	Max heat demand [MW]	Min heat demand [MW]	Total annual heat demand [GWh]	Electricity demand [MW]	Total annual electricity demand [GWh]
1	53	7	242	24	208
2	105	26	478	51	449
3	364	46	1,662	220	1,928

Even the simplest of the cases, despite its less than immense number of nodes, has such a structure that verifying the global optimum with the original model requires too much time, so they are all in need of some sort of alternative treatment, such as this proposed decomposition. The results of the optimization runs are assembled in Table 3. Each test case was first solved with the decomposition method with seven iterations starting with k-means clustering into 9 sectors, ending at 81 sectors, followed by a finalization run. They were then solved with the original model, limiting the solution times to the times used by the decomposition method. Each test case has quite a different behaviour with the decomposition method. In the first case, a good value is found quickly, the original model is far from securing an optimal solution, which is seen from the large optimality gap remaining, and the objective does not reach the value found by the decomposition method. This value is found after 23,679 s, but the optimality gap is still 12.56 % at that point. The same solution is still the best one after 60,000 seconds, with an optimality gap of 2.60 %, but verifying whether or not this is the global optimum would require much more time. So, in the first case, the decomposition method is very successful.

The second case is less spectacular, as it takes a much longer time to solve, and the original model finds a better solution than the decomposition method is able to find. This is a case where the structure of the network is such that the decomposition method surely cannot find the global optimum. Despite attempts with different decomposition formulations and coefficient values, better solutions were not yet found.

In the third case, the solution time is very long even with the decomposition. The solution time for the seven decomposed iterations was still a reasonable 5,419 seconds, but the finalization was slow enough to be interrupted at an, admittedly small, optimality gap of 0.46 %. Despite the generous solution time provided to the original model, CPLEX could not even get past the initial root node processing steps before hitting the time limit, at an objective value far greater than the one found by the decomposition method. This third case represents a situation where the decomposition method can at least find some solution to the problem when the original model has trouble even getting to a start due to the complexity of the problem. This is the type of problem size that the decomposition approach was developed for, so the results show promise for future implementations of the method.

Table 3. Optimized objective values and solution times of the three test cases

		Decomposition method		Original model	
Case	Solution time [s]	Objective value [M€]	Optimality gap [%]	Objective value [M€]	Optimality gap [%]
1	389	19.2	-	20.2	89.65
2	7,276	38.1	-	37.3	90.62
3	66,852	153.4	0.46	158.65	96.80

5. Conclusions

A decomposition method for solving complex distributed energy system optimization problems was developed and tested. The test cases described in this article show how the strength of the method is heavily dependent on the case being analysed. Sometimes, the method can aid in finding a near-optimal solution relatively quickly, but it is not possible to be sure of the quality of the solution. So in its current form, the method can be useful in the case that a problem is too hard to solve with the original model, as there is a possibility that the method can find a better solution within a relatively short solution time. But by itself, a good solution cannot be guaranteed. Without certainty of the solutions of either the original model or the decomposition model, there is still need for further development of reliable methods for optimizing complex distributed energy systems.

Acknowledgements

The work which this article was based upon is part of the Efficient Energy Use (EFEU) research program coordinated by CLEEN Ltd. with funding from the Finnish Funding Agency for Technology and Innovation, Tekes.

References

S. Fazlollahi, L. Girardin, F. Maréchal, 2014, Clustering Urban Areas for Optimizing the Design and the Operation of District Energy Systems, Computer Aided Chemical Engineering, Volume 33, 1291-1296

C. Haikarainen, F. Pettersson, H. Saxén, 2014, A model for structural and operational optimization of distributed energy systems, Applied Thermal Engineering, Volume 70, Issue 1, 211-218

IBM, IBM ILOG CPLEX Optimizer, 2014, www-01.ibm.com/software/commerce/optimization/cplex-optimizer (acc. 29.11.2014)

J. Keirstead, M. Jennings, A. Sivakumar, 2012, A review of urban energy system models: Approaches, challenges and opportunities, Renewable and Sustainable Energy Reviews 16, 3847-3866

D. MacKay, 2003, An Example Inference Task: Clustering, Information Theory, Inference and Learning Algorithms, Cambridge University Press, 284-292, www.inference.phy.cam.ac.uk/mackay/itprnn/ps/284.292.pdf (acc. 26.11.2014)

A. Omu, R. Choudhary, A. Boies, 2013, Distributed energy resource system optimisation using mixed integer linear programming, Energy Policy 61, 249-266

M. Vesterlund, J. Dahl, 2015, A method for the simulation and optimization of district heating systems with meshed networks, Energy Conversion and Management, Volume 89, 555-567

Krist V. Gernaey, Jakob K. Huusom and Rafiqul Gani (Eds.), 12th International Symposium on Process Systems Engineering and 25th European Symposium on Computer Aided Process Engineering.
31 May – 4 June 2015, Copenhagen, Denmark

A rolling horizon stochastic programming framework for the energy supply and demand management in microgrids

Javier Silvente[a], Georgios M. Kopanos[b,c], Antonio Espuña[a]

[a]*Universitat Politècnica de Catalunya, ETSEIB, Department of Chemical Engineering, 647 Diagonal Avenue, 08028 Barcelona, Spain.*
[b]*Imperial College London, Department of Chemical Engineering, Centre for Process Systems Engineering, London SW7 2AZ, United Kingdom.*
[c]*Cranfield University, School of Energy, Environment & Agrifood, Bedfordshire MK43 0AL, United Kingdom.*

Abstract

This work proposes a discrete-time Mixed Integer Linear Programming (MILP) formulation based on a combined rolling horizon and stochastic programming approach for the simultaneous management of energy supply and demand in microgrids, considering flexible demand profiles, which allows delays in the nominal energy demands by applying penalty costs. This mathematical formulation uses a scenario-based stochastic programming approach, which considers different scenarios associated to internal variations in the duration of the energy consumptions, to contemplate all possible scenarios related to the energy demand. However, the high complexity related the estimate the weather forecast with a high degree of precision makes unaffordable the consideration of all possible external scenarios, thereby updating input data is needed to ensure the adequate quality in the obtained results. Hence, the proactive MILP stochastic programming formulation is introduced into a rolling horizon approach.

Keywords: rolling horizon; stochastic programming; scheduling; mathematical programming; microgrid.

1. Introduction

The development of sustainable energy supply chains has led to advances in the area of Energy Systems Engineering. One example is the exploitation of renewable energy sources in microgrids, which are decentralized networks able to integrate several heat/power generation systems of low/medium capacity, with the main purpose of distributing the generated energy locally so as to reduce energy losses and improve the responsiveness to energy demand fluctuations. Several mathematical models have been developed in order to manage the energy production (Kopanos et al., 2013), energy demand (Della Vedova and Facchinetti, 2012) and the production and demand in a sequential way (Hadera et al., 2014).

One of the main drawbacks associated to managing a microgrid is the presence of uncertainty, which must be considered to ensure the operability and the reliability of the system, since the optimal solution obtained under deterministic conditions can easily be infeasible or even suboptimal in practice. The main sources of uncertainty in microgrids are associated to the external weather conditions, which affects the availability and production capacity of renewable energy generation units (i.e. wind turbines) as well as

the energy demand variations, given by the variations related to the duration of the energy consumption. Approaches under uncertainty can be classified into reactive and proactive. Typically, reactive approaches modify a nominal plan to adjust it to the updated system data. The rolling horizon approach is a reactive method that solves iteratively the deterministic problem by moving forward the optimization horizon in each iteration, assuming that the status of the system is updated as soon as the different uncertain or not accurate enough parameters became to be known. This approach considers a prediction horizon, where the uncertain parameters related to this time horizon are assumed to be known with certainty and a control horizon, where the decisions of the optimization are taken. A preliminary rolling horizon approach for the simultaneous energy production and demand management was presented by Silvente et al. (2014). Proactive approaches generate a plan that satisfies all considered scenarios. Proactive scheduling has the advantage that the solution found will be feasible for all scenarios; however it may be too conservative. Hence, a typical two-stage stochastic problem is based in first-stage variables, which does not depend on the scenario, and second-stage variables, which will be different according to each scenario. Although energy production management has been studied broadly, the scheduling of a microgrid taking into account the simultaneous management of energy production and energy demand has received limited attention, and involves a challenge in this research field. In this work, a mathematical formulation is presented to cope with the uncertainty through a rolling horizon stochastic programming approach to optimally manage a microgrid.

2. Problem statement

The problem formulation takes into account the production and storage levels to be managed by the microgrid, energy sales to the main power grid and the possibility to modify the timing of the energy consumption, in order to maximize the profit of the microgrid. The mathematical model includes the energy balance constraints required to describe the energy flows and constraints associated to the equipment and technologies involved in the microgrid. The problem under study is described in terms of these terms:

(i) A given planning horizon, which is divided into a set of equal-size time intervals $t \in T$. Also, a given Prediction Horizon (PH) and a given Control Horizon (CH).
(ii) A set of scenarios $n \in N$.
(iii) A set of energy generators $i \in I$, characterized by a minimum and maximum energy generation capacity, $P_{i,t}^{min}$ and $P_{i,t}^{max}$, and a given operational cost.
(iv) A set of energy storage systems $k \in K$, having a minimum and a maximum energy storage capacity, $SE_{k,t}^{min}$ and $SE_{k,t}^{max}$, and cost.
(v) A given energy demand, given by the amount of energy required by a set of energy consuming tasks j, f, n, where $f \in F_j$ denotes the f^h time that the consumer j is active in each scenario n. For any energy consuming task, its duration $U_{j,f,n}$ and a target starting time $Ts_{j,f}^{min}$ are established, although tasks can be delayed within certain limits $Ts_{j,f}^{max}$ generating a penalty cost. All tasks which might be active during each iteration of the rolling horizon approach are included in the dynamic set $F_j RH$.
(vi) A given set of power grids $r \in R$, which can buy the excessive energy produced, or sell additional energy if required.

The proposed rolling horizon stochastic formulation is solved iteratively, which allows to update all inputs parameters, and includes the presence of first and second stage variables through the stochastic formulation, in which different scenarios for the duration of

different consumption tasks has been considered. In this formulation, *first stage* variables are related to the decision of produce/purchase energy each energy generator i in each period of time t, whereas the main decisions associated to *second stage* variables are:

(i) The amount of power $P_{i,n,t}$ to be supplied by generator i at time interval t in each scenario n.
(ii) The energy storage $SE_{k,n,t}$ at the end of each time interval *t* in each scenario n.
(iii) The nominal time $Ts_{j,f,n}$ to execute an energy consuming task in each scenario n.

The main equations of the proposed Mixed Integer Linear Programming (MILP) are briefly described (Silvente et al., 2013). Energy production bounds for every energy generator are specified by eq 1, where $X_{i,t}$ indicates if generator i is being used or not. Eq. 2 represents the link among energy flows at a specific storage system and time in each scenario k, n, t, taking into account the storage level $SE_{k,n,t}$, the energy requirements covered by the storage $SP_{k,n,t}$, the supply flows arriving to the storage $L_{k,n,t}$ and the efficiency of the energy storage system η. The energy required by each consumption task in each scenario j, f, n is calculated with eq. 3, while eq. 4 establishes the overall energy balance of the microgrid, considering the production, the consumption, the charge and discharge of the storage unit, and the energy sales to external power grids in each scenario. Also, eq. 5 gives the bounds for the starting times $Ts_{j,f,n}$, of each energy consumption.

$$P_{i,t}{}^{min} \cdot X_{i,t} \leq P_{i,n,t} \leq P_{i,t}{}^{max} \cdot X_{i,t} \qquad \forall i, n, t \in TRH \quad (1)$$

$$SE_{k,n,t} = SE_{k,n,t-1} + \eta_k^{in} \cdot L_{k,n,t} - \frac{SP_{k,n,t}}{\eta_k^{out}} \qquad \forall k, n, t \in TRH \quad (2)$$

$$D_{n,t} = \sum_{j}^{J} \sum_{f}^{F_j} Cons_{j,f} \cdot \left[W_{j,f,n,t} \cdot DT - Z_{j,f,n,t} \cdot \left(T_{t+1} - \left(Ts_{j,f} + U_{j,f,n} \right) \right) \right] \qquad \forall n, t \in TRH \quad (3)$$

$$\sum_{i=1}^{I} P_{i,n,t} \cdot DT - D_{n,t} + \sum_{k=1}^{K} SP_{k,n,t} - \sum_{k=1}^{K} L_{k,n,t} - \sum_{r=1}^{R} S_{r,n,t} \cdot DT = 0 \qquad \forall n, t \in TRH \quad (4)$$

$$Ts_{j,f}{}^{min} \leq Ts_{j,f,n} \leq Ts_{j,f}{}^{max} \qquad \forall j, f \in F_j RH, n \quad (5)$$

The expected profit of the microgrid, which is the objective function to be maximized, is calculated considering incomes and costs for each scenario n in eq. 6, subject to the previous constraints. Each considered scenario in the proposed stochastic programming has associated a probability, Pr_n, which is taken into account to calculate the expected profit. Note that production and storage costs depend on the use of the different available energy production/storage systems, and the penalization cost is determined by the delay in satisfying each energy demand.

$$Profit = \sum_{n} Pr_n \cdot [Incomes_n - CostProduction_n - CostStock_n - CostPenalty_n] \quad (6)$$

In order to use the proposed model in a rolling horizon scheme, the following set of variables and equations are used to link past decisions with the current prediction horizon:

$$\hat{Y}_{j,f,n} + \sum_{t \in RH} Y_{j,f,n,t} = 1 \qquad \forall j, f \in F_j, n, t \quad (7)$$

$$Ts_{j,f}{}^{min} = Ts_{init}{}_{j,f}^{min} - CH \cdot it \qquad \forall j, f \in F_j, n \quad (8)$$

$$Ts_{j,f}{}^{max} = Ts_{init}{}_{j,f}^{max} - CH \cdot it \qquad \forall j, f \in F_j, n \quad (9)$$

$$Dur_{j,f,n} = Dur_{init\,j,f} - \left(CH \cdot it - Ts_{j,f,n}\right) \cdot \hat{Y}_{j,f,n} \qquad \forall j, f \in F_j, n \qquad (10)$$

$$SE_{k,n,t-1} = \widehat{SE}_{k,n,t'} \qquad \forall k, n, t, t' \in TRH, t' = T_t \cdot DT \qquad (11)$$

Binary variable $\hat{Y}_{j,f,n}$ indicates if the consumption task j, f, n has started before the beginning of the current prediction horizon, so eq. 7 establishes that all consumption tasks must start in the scheduling horizon. Minimum and maximum starting times and duration of consumptions are upload by eq. 8, 9 and 10, considering information from previous iterations. Finally, eq. 11 links the energy storage level of the previous control horizon to the initial energy storage level of the current prediction horizon. Then, the rolling horizon algorithm can be applied as follows (Kopanos and Pistikopoulos, 2014):

- Initially, set the initial conditions of the system and set the length of the scheduling, prediction and control horizons.
- Next, for the first scheduling period solve the scheduling problem.
- Update the state of the system as well as the values of the uncertain parameters and solve the scheduling problem, after moving a time step equal to the control horizon.
- Then, if this re-scheduling corresponds to the last period of time, stop. Otherwise, fix the values obtained in the optimization problem for that iteration, re-schedule and update the period of time until the last planning period is reached.

Notice that although the solution obtained in each prediction horizon is optimal for this period of time, the solution of the overall problem could be suboptimal, since future information outside the current prediction horizon is not considered. So, the length of the prediction horizon must be appropriate to guarantee the quality of the obtained results.

3. Illustrative example

The microgrid under study (Silvente et al., 2013) consists of a photovoltaic panel, a wind turbine, an energy storage system and the connection to the external power grid. The scheduling horizon considered is 24 h, and the duration of each time interval is 15 min. In order to study how the length of the PH affects the optimal solution, PHs of 5, 10, 20, and 30 time intervals have been considered. Energy consumption tasks related to two energy consumers and associated to each scenario j, f, n are considered and a limited starting time delay is allowed subject to a penalty cost. It has been considered that all input data (i.e., energy demands, weather conditions) can be updated at the beginning of every time interval. The control horizon has been established as 15 min. This allows to update uncertain parameters, what is very important in order to be able to react in front of unexpected scenario changes from the nominal plan, including for example variations in the power availability or in the duration of the consumptions. Three different durations have been assigned to five consumption tasks, which involves the presence of 3^5=243 different scenarios. Also, each scenario has an associated occurrence probability.

3.1. Results and discussion

The MILP problem has been solved in GAMS/CPLEX 12. Figure 1 displays the obtained daily schedule for energy production and consumption tasks for a PH=20 time intervals within the stochastic approach for one scenario. The energy demand has been managed by the delayed of some consumption tasks. Figure 2 shows the expected profit for the rolling horizon approach under different prediction horizons within the stochastic approach in comparison with the stochastic model (PH=96 under uncertainty) and the perfect information case (PH=96 without uncertainty). Not surprisingly, as the length of

the prediction horizon increases and the input parameters are revealed, the total objective is improved and closes the gap from the solution of perfect information.

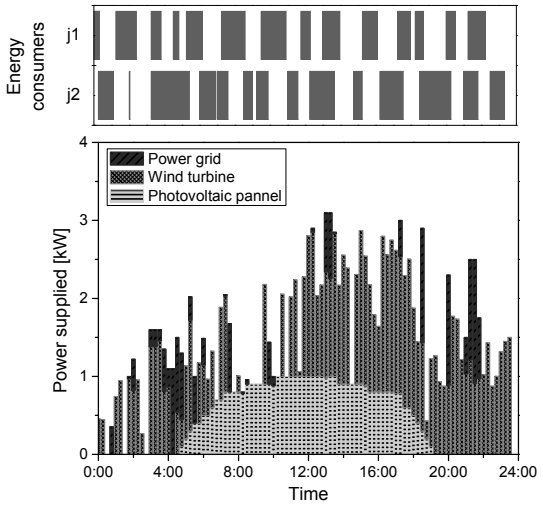

Figure 1. Daily schedule for energy production and consumption tasks (PH=20 for one of the considered scenarios).

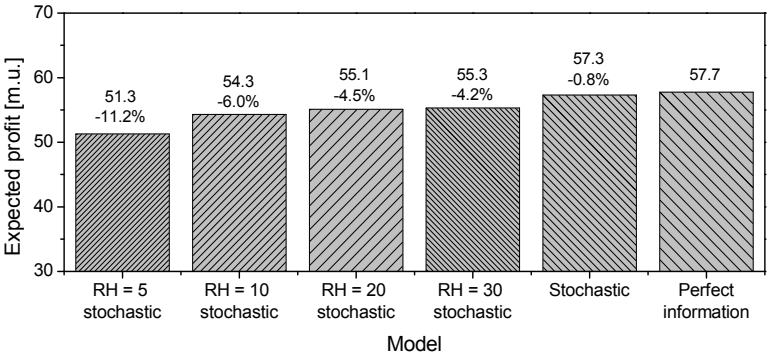

Figure 2. Expected objective value for different PHs through the rolling horizon stochastic approach and the perfect information case.

But, in spite of this obvious conclusion, what is very important is to be able to react in front of unexpected scenario changes. This reactive and proactive approach allows updating input parameters, in order to react to variations from the nominal/initial plan, including alterations in the power availability or in the duration of energy consumptions. The second situation analyses the optimization procedure if a change over the initial weather conditions (i.e. reduction in the solar and wind forecast) and in the duration of some consumptions (considered in the demand scenarios) suddenly appears.

Without the implementation of the rolling horizon approach, there is no possibility to modify the initial demand schedule, since all decisions have been taken previously. Thanks to the rolling horizon approach, it is possible to react to this alterations from the initial conditions. Figure 3 compares the obtained results for the simultaneous energy supply and demand management, for different lengths of PH and the perfect information

case. According to the results, the use of the rolling horizon approach have allows the benefit to be more than 0.9 % high compared with the perfect information case.

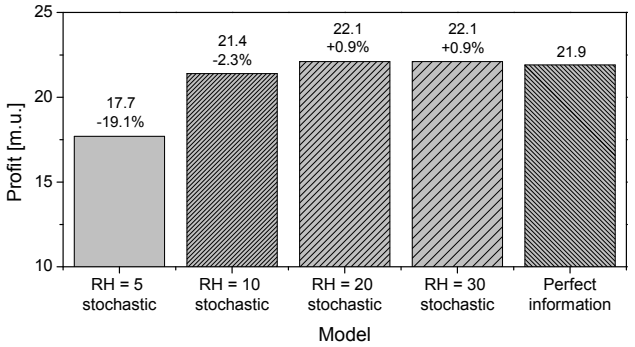

Figure 3. Objective value for different *PH*s under unexpected conditions.

4. Conclusions

A rolling horizon stochastic MILP approach has been developed for the simultaneous management of energy production and demand in microgrids, in order to optimize its profit. A combination of reactive and proactive approaches has been used to deal with the uncertainty associated to the energy production and energy demand. This approach allows updating input parameters, in order to react to variations from the nominal plan, which allows to adapt energy production and energy demand to upload parameters.

Acknowledgements

The authors would like to thank the financial support received from the Spanish "Ministerio de Economía y Competitividad" and the European Regional Development Fund (both funding the research Project SIGERA, DPI2012-37154-C02-01) and from the "Ministerio de Economía y Competitividad" (Subprograma de Formación de Personal Investigador, BES-2010-036099), and from the Generalitat de Catalunya (2014-SGR-1092-CEPEiMA).

References

M.L. Della Vedova, T. Facchinetti, 2012, Real-time scheduling for industrial load management, IEEE International Energy Conference and Exhibition, 770-776.

G.M. Kopanos, M.C. Georgiadis, E.N. Pistikopoulos, 2013, Energy production planning of a network of micro combined heat and power generators, Applied Energy, 102, 1522-1534.

G.M. Kopanos, E.N. Pistikopoulos, 2014, Reactive Scheduling by a Multiparametric Programming Rolling Horizon Framework: A Case of a Network of Combined Heat and Power Units, Industrial & Engineering Chemistry Research, 53, 4366-4386.

H. Hadera, I. Harjunkoski, I.E. Grossmann, G. Sand, S. Engell, 2014, Steel Production Scheduling Optimization under Time-sensitive Electricity Costs, Computer Aided Chemical Engineering, 33, 373-378.

J. Silvente, A. Aguirre, G. Crexells, M. Zamarripa, C. Méndez, M. Graells, A. Espuña, 2013, Hybrid time representation for the scheduling of energy supply and demand in smart grids, Computer-Aided Chemical Engineering, 32, 553-558.

J. Silvente, G.M. Kopanos, E.N. Pistikopoulos, A. Espuña, 2014, Reactive Scheduling for the Coordination of Energy Supply and Demand Management in Microgrids, Computer-Aided Chemical Engineering, 33, 493-498.

Krist V. Gernaey, Jakob K. Huusom and Rafiqul Gani (Eds.), 12th International Symposium on Process Systems Engineering and 25th European Symposium on Computer Aided Process Engineering.
31 May – 4 June 2015, Copenhagen, Denmark

Behaviour Assessment of a Fuel Cell - Battery System Using a Supervisory Control Methodology Empowered by a Hybrid Timed Automaton (HTA)

Chrysovalantou Ziogou[a,*], Damian Giaouris[a], Christos Yfoulis[b], Fotis Stergiopoulos[b], SpyrosVoutetakis[a], Simira Papadopoulou[b]

[a]*Chemical Process and Energy Resources Institute (CPERI), Centre for Research and Technology Hellas (CERTH), PO Box 60361, 57001, Thessaloniki, Greece,*
[b] *Department of Automation Engineering, Alexander Technological Educational Institute of Thessaloniki, PO Box 141, 54700, Greece,*
cziogou@cperi.certh.gr

Abstract

This work presents the design and development of a supervisory control methodology for the management of energy decisions in a hybrid powered system. More specifically the methodology implements an energy management strategy (EMS) which is applied in a fuel cell – battery system for vehicular applications and explores the behaviour of the system under a realistic operation scenario. The EMS relies on a Hybrid Timed Automaton (HTA) combined with propositional rules and formalizes the operation of the system as it thoroughly describes the dynamic transitions between each operating state. A sensitivity analysis reveals the influence of the power distribution between the two energy sources and an optimization study determines the values of the selected operating parameters. Finally the response of the Fuel Cell Electric Vehicle (FCEV) system is assessed through a combined urban and high-way driving cycle.

Keywords: hybrid systems, power management strategy, fuel cell battery vehicle

1. Introduction

Hybrid energy systems consisting of fuel cells and battery have recently emerged as a potential alternative to the conventional battery powered vehicles. A challenging issue that arises when integrating a fuel cell and a battery stack is the handling of the dynamics that arise by their use (Krewer et al., 2014). Also the management of the various decisions that are applied in order for the integrated system to operate in an optimum way, while fulfilling the frequently and rapidly changing load demand (Degliuomini et al., 2014). In that context the resulting hybrid system should be complemented by a control system that will be able to handle the complex dynamics and the discrete decisions of the overall system. At the core of the considered control system an EMS is necessary that will dictate the appropriate decisions for each subsystem at various operating conditions. The field of energy management of hybrid energy systems is of increasing importance due to the necessity for optimum operation of the various interconnected subsystems that constitute the integrated system.

2. System Description

The design and development of an efficient and modular EMS is motivated by a system that consists of a battery stack, a fuel cell system and an electric motor. The main energy provider is the fuel cell and the secondary is the battery. More specifically the subsystems of the FCEV and their specifications are:

· Polymer Electrolyte Membrane (PEM) fuel cell stack: provides the main source of power and it is rated at 85 kW nominal power and 100 kW maximum power. The nominal voltage is 288 Vdc and its average efficiency is 58 %. The fuel cell operates at 75 °C and 3 bar pressure. The nominal utilization of hydrogen and oxidant is 95 % and 50 % and the nominal consumption of fuel and air is 374 lpm and 1698 lpm.

· Hydrogen tank: The vehicle autonomy is 350 km which is equivalent to 3.5 kg of hydrogen. The consumption is considered at 100 km/kg of hydrogen.

· Lithium-ion Battery: 20 Ah, 288 Vdc, 25 kW.

· Permanent Magnet Synchronous Motor (PMSM): The output motor power is 100 kW and the maximum torque is 256 Nm.

· Power electronics: average value buck DC/DC converter with a current regulator (95% efficiency) and a 3-phase DC/AC inverter.

Figure 1 shows of three subsystems which are: the fuel cell, the electrical and the motor subsystem. The supervisory controller is responsible for the power split between the two main power sources. A set of low level controllers exist at each subsystem that translates the supervisory level actions to device specific commands. The objective of the motor subsystem is to determine the power demand of the electric motor to achieve a certain driving cycle. A dynamic mathematical model for the fuel cell (Njoya et al., 2009) and the battery (Tremblay and Dessaint, 2009) are used in order to simulate the FCEV's response and performance under the proposed supervisory EMS.

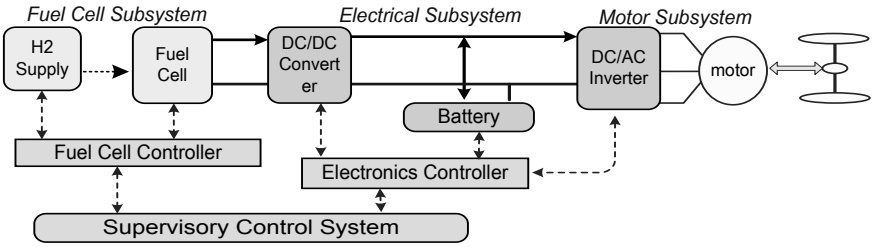

Figure 1 Topology and main components of the FCEV

3. Energy Management Framework

The exploitation of the hybrid nature of the aforementioned system requires a well-designed energy management strategy (EMS) that determines how the demanded by the load (motor) power is distributed between the two energy sources while satisfying design and operation requirements such. Thus, the purpose of the EMS is twofold, to supervise the status of each subsystem and to be able to adjust to system operational modes (Ziogou et al., 2013). During start-up, normal driving or acceleration, both the fuel cell, through the DC/DC converter and the battery deliver electrical energy to the inverter, which then drives the electric motor and subsequently the wheels via the transmission as shown at Figure 1. The PMSM can be operated in either a generator or a motor mode, determined by the mechanic torque. When the torque is positive it is the motor mode and when the torque is negative then it is the generator mode. During

deceleration, the electric motor acts as a generator which transforms the kinetic energy of the wheels into electricity which is stored at the battery. Also to avoid frequent start/stops of the fuel cell the produced power is used to charge the battery during deceleration. More specifically the State of Charge (SOC) of the battery and the available hydrogen (state of energy - SOE) at the storage tanks are the main parameters that drive the operating decisions combined with the power demand from the motor.

3.1. Hybrid Timed Automaton

The interaction between discrete and continuous operating states motivates the use of the hybrid approach and thus a Hybrid Timed Automaton or Automata (HTA) appears as a suitable formulation that includes the semantics for the realization of a generic EMS while the system requirements are translated into propositional based logic representing a set of operating rules. A hybrid automaton H is a collection $H=(Q,X,f,Init,D,E,G,R)$, where Q is a set of discrete states, X is a set of continuous states, $f:Q\times X\rightarrow X$ is a vector field, $Init\subset Q\times X$ is a set of initial states, $E\subset Q\times Q$ is a set of edges, $D:Q\rightarrow P(X)$ is a domain (invariant set), $G:E\rightarrow P(X)$ is a guard condition, $R:E\times X\rightarrow P(X)$ is a reset map. The HTA is used to define possible evolutions for their state H which is defined as $(q,x)\in Q\times X$. Starting from an initial value $(q_0,x_0)\in Init$, the continuous state x flows according to the vector field $f(q_0,\cdot)$, while the discrete state q remains constant. The continuous evolution can go on as long as x remains in $D(q_0)$. If at some point x reaches a guard $G(q_0,q_1)$, for some $(q_0,q_1)\in E$, the discrete state may change value to q_1. At the same time the continuous state gets reset to some value in $R(q_0,q_1,x)$. After this discrete transition, continuous evolution resumes and the whole process is repeated. The collection of these two maps (q, x) is denoted an execution, run or hybrid trajectory of the hybrid automaton (Lygeros, 2003). Hybrid automata are often depicted as directed graphs (Q,E) with vertices Q and edges E representing transitions between them. To each vertex $q\in Q$, a set of initial states are associated $Init_q=\{x\in X:(q,x)\in Init\}$, a vector field $f(q,\cdot)$ and a domain $D(q)$. With each edge $e\in E$ a guard $G(e)$ and a reset map $R(e,\cdot)$ is associated.

3.2. Propositional Logic used for the transition definition (guards)

The guards of the HTA are described using propositional-based logic rules which are derived by the knowledge of the operation of the system combined with information about the objectives of its operation. The status of each subsystem (BAT, FC, H2, MOT), the user requested action, pedal acceleration, which is translated to the power demand (P_{dem}) and the decision variables, SOC and SOE, define a set of Boolean variables. Each subsystem is related to one or more Boolean variables. For each guard of the HTA a logical rule is defined. More specifically the every logical function is expressed as a combination of the logical operations ($AND:\wedge, OR:\vee, NOT:!$) and the status of each subsystem or the level of stored energy is subsequently compared to the respective level or to each other using the respective operand. Furthermore a hysteresis band is used in the boundary limits of the accumulator to avoid irregular operation (reduction of frequent start-ups and shut-downs of the fuel cell). For example when only power from the battery is provided to the motor and the power demand increases beyond the predefined level (P_{dem}>50 kW) then the fuel cell is activated (P_{FC}=50 kW) and the remaining power is provided by the battery ($P_{Bat}=P_{dem}-P_{FC}$). Table 1 presents the analysis of a guard (G_{25}) that describes the use of both the fuel cell and the battery.

Table 1 Propositional rule for a Guard definition

Guard	Analysis
$G_{2,5}(q_2,q_5)=$ $(\delta_{Pow} \wedge \delta_{H2}) \vee ! \delta_{BAT}$	δ_{Pow} represents the increased power demand, P_{dem}>50 kW
	δ_{BAT} represents the status of the battery, SOC > SOC_{min}
	δ_{H2} represents the availability of hydrogen, SOE> SOE_{min}

The hybrid automaton model of the fuel cell – battery dynamical system is depicted in Figure 2. The vertices of the graph are the discrete states ($q_0,..,q_6$) representing the possible switch positions between the operation modes of the system with respect to the usage of the fuel cell and the battery for the fulfillment of the power demand.

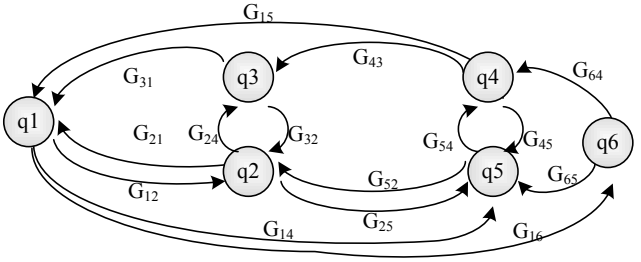

q1: Standby
q2: Battery discharge
q3: Battery charge
q4: Battery charge, FC_{on}
q5: Battery discharge, FC_{on}
q6: Start fuel cell operation (FC_{on})

Figure 2 Hybrid automaton for fuel cell – battery system

When the battery is discharged it means that the demanded power is drawn entirely from the battery (q2) or partially (q5). The battery is charged when the vehicle decelerates and part of the motor power is directed to the battery and from the fuel cell power to avoid frequent start stops.

4. System Operation

The overall objective of this study is to evaluate the effect of the hybrid storage system on the performance of the FCEV. Therefore, besides the fulfilment of the load demand, the EMS should consider the optimal use of the available hydrogen, the protection of the battery's lifetime and the preservation of the fuel cell's durability.

4.1. Parametric Sensitivity Analysis

A parametric sensitivity analysis is performed that involves mainly the battery and the fuel cell subsystem in order to determine the effect that main parameters have to the behavior and response of the integrated system.

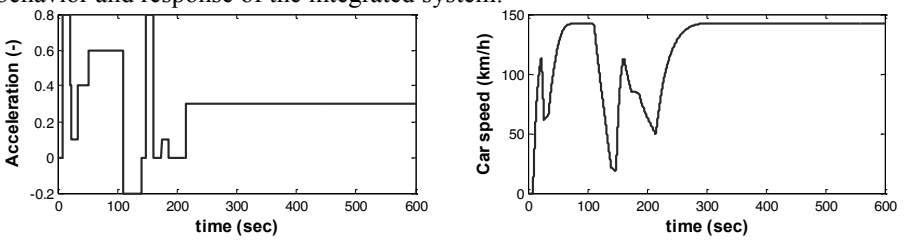

Figure 3 a) Acceleration profile, b) FCEV speed (km/h)

Figure 3 shows the acceleration profile and the resulting vehicle speed which is a combination of an urban drive cycle (first 3min) with a high-way drive cycle (next 7min). A set of simulated driving cycles where performed with different values for three main parameters related to the operation boundaries of the fuel cell ($P_{FC,min}$,$P_{FC,max}$) and

the battery ($P_{BAT,max}$) that influence the Depth of Discharge (DOD), the remaining driving distance and the overall hydrogen consumption (Table 2).

Table 2 Propositional rule for a Guard definition

Parameter	Range	DOD	Tot. H2 consumption	Driving distance (init:350km)	Power split (BAT/FC)
$P_{FC,max}$	50-100 kW	8.2 %	983-1506 lt	344-331 km	17 %/83 %
$P_{FC,min}$	2-6 kW	9.5 %	781-795 lt	345 km	19 %/81 %
$P_{BAT,max}$	21-25 kW	11.2 %	777-778 lt	344-342 km	24 %/76 %

4.2. Optimization

After the sensitivity analysis a deterministic optimization problem is formulated in order to determine the optimal values for the selected parameters. The utilization pattern of the battery and the fuel cell determines the frequency of equipment replacement and maintenance and therefore the operating costs, over the lifespan of the overall system. Thus, the optimization problem focuses on these operation parameters, the DOD for the battery and the SOE for the fuel cell. A constrained medium-scaled optimization problem is formulated, utilizing a deterministic optimization method as the subsystems are described by deterministic, non-linear models. The feasible area that the optimizer explores is determined by the variables' bounds and the operational constraints of each subsystem. The optimization was performed for a combined driving cycle, urban and high-way, and the resulting values of the decision variables are $P_{BAT,max}$*=23.7kW,* $P_{FC,min}$*=2kW,* $P_{FC,max}$*=82.5kW*.

5. Analysis Results and Behaviour Assessment

The proposed EMS is evaluated on a case study regarding the optimal operation of the system. A driving cycle (highway with traffic, 4min) was applied to explore the response of the system and the power distribution between the fuel cell and the battery. Figure 4 shows the requested acceleration and the resulted vehicle speed and the power distribution combined with the battery SOC.

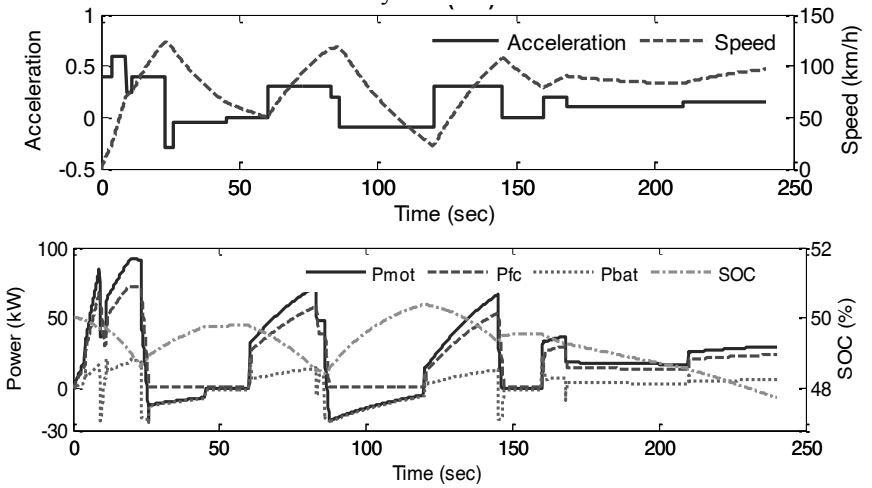

Figure 4 a) Acceleration profile & FCEV speed (km/h), b) Power distribution and SOC

The error between the requested power and the provided is <1% and the hybrid power system is able to provide the requested power. Overall the demanded power was served at a ratio of 91/9% from the fuel call and the battery, the maximum DOD was 2.65%, the fuel cell operated with an average efficiency of 43%. The fuel cell provided 96% to the motor and 4% was used to charge the battery. The power from motor (during braking) that was stored to the battery was 3.4% and the non-absorbed power was 1.8% due to the maximum charging rate of the battery. The selected case study reveals the potential of developed EMS, explores the synergy among the various subsystems and demonstrates the response of the integrated system.

6. Conclusions

An integrated model-based EMS for a FCEV was designed that implements an efficient Supervisory Algorithm based on SOC and SOE. Overall the operation results reveal the potential of the proposed EMS that explores the synergy among the various subsystems and demonstrate the response of the integrated system. The FCEV has successfully followed the driving cycle while the EMS was able to provide the requested power.
Although the methodology was developed for a FCEV vehicle it is not limited to the specific application. Since it relies on a generic formulation, due to the modular nature of the hybrid automaton and the propositional rules, the proposed approach can be used to other systems, such as hybrid renewable power generation stations, where hybrid operation is required and other applications such as stationary fuel cell systems. Also it can be parameterized to include different subsystems, such as an ultra capacitor for small-scale energy storage. Finally the proposed EMS was developed with implementation considerations in mind. Since it relies on simple propositional based logic, it is equally suitable for use at simulation environments (to study the behaviour of the system) as well as for deployment to automation systems for proof of concept (such as Supervisory Control and Data Acquisition (SCADA) systems) and embedded platforms or PLCs for validation in the relevant environment.

Acknowledgement
This work is implemented through the Op. Program "Education and Lifelong Learning", co-financed by the EU Social Fund and Greek national funds, program “Archimedes III”.

References

L. N. Degliuomini, M. Cunningham, F. Ferreyra, P. A. Luppi, M. S. Basualdo, 2014, Energy Management of a Hybrid Controlled Process with Renewable Sources, Computer Aided Chemical Engineering, 33, 2014, 1141-1146
U. Krewer, D. Schröder, C. Weinzierl, 2014, Scenario-based Analysis of Potential and Constraints of Alkaline Electrochemical Cells, Computer Aided Chemical Engineering, 33, 2014, 1237-1242.
J. Lygeros, K. H. Johansson, S. N. Simic, J. Zhang, S.S. Sastry, 2003, Dynamical properties of hybrid automata, IEEE Transactions on Automatic Control, 48(1), 2-17.
S. Njoya, O. Tremblay, L-A. Dessaint, 2009, A generic fuel cell model for the simulation of fuel cell vehicles, IEEE Vehicle Power and Propulsion Conference,
O. Tremblay, L.A. Dessaint, 2009, Experimental Validation of a Battery Dynamic Model for EV Applications, World Electric Vehicle Journal, 3, Stavanger, Norway, May 13 - 16, 2009.
C. Ziogou, D. Ipsakis, P. Seferlis, S. Bezergianni, S. Papadopoulou, S. Voutetakis, 2013, Optimal production of renewable hydrogen based on an efficient energy management strategy, Energy, 55, 58-67.

Krist V. Gernaey, Jakob K. Huusom and Rafiqul Gani (Eds.), 12th International Symposium on Process Systems Engineering and 25th European Symposium on Computer Aided Process Engineering.
31 May – 4 June 2015, Copenhagen, Denmark

Financial Considerations in Shale Gas Supply Chain Development

Andrés J. Calderón,[a] Omar J. Guerra,[b] Lazaros G. Papageorgiou,[a] Jeffrey J. Siirola,[b] Gintaras V. Reklaitis[b,*]

[a] *Department of Chemical Engineering, UCL (University College London), London WC1E 7JE, UK*
[b] *School of Chemical Engineering, Purdue University, West Lafayette IN 47907, USA*
reklaiti@purdue.edu

Abstract

In this work, an optimization framework to support the planning of the development of shale gas resources is proposed. Financial aspects are taken into account through the integration of financing options, such as own capital, and external sources, short and long term bank credit lines. The model also includes the design of well-pads in terms of total number of wells, and length and number of hydraulic fractures completed at each well. In addition, different capacities and locations are considered for compressor stations, gas separation plants, and water treatment plants. A case study involving two alternative financing strategies was conducted to demonstrate the capabilities of the model. It is found that external financing can play an important role in the development of a shale gas field, achieving an increase in net profit of almost 65 % when compared to a scenario where only own capital is considered.

Keywords: supply chain, optimization, financial aspects, shale gas.

1. Introduction

According to the BP Energy Outlook (BP, 2014), world primary energy consumption is expected to increase roughly 41 % from 2012 to 2035, with an average annual growth rate of 1.5 %. Fossil fuels will remain as the major source of energy, with a share of 81 % in 2035. Among fossil fuels, gas consumption will increase the most at 1.9 % per year. Nearly half of the growth in global gas supply will be provided by shale gas, which is projected to grow at 6.5 % per year.

The development of shale gas resources can play an important role in the expansion of chemicals production and electricity generation (Jenner and Lamadrid, 2013; Siirola, 2014). On the other hand, the production of shale gas is commonly regarded as challenging due to the petrophysical characteristics of shale formations, which have very low permeability when compared to conventional plays. These conditions require the use of advanced production technologies that can give rise to negative environmental impacts if not properly managed. All those factors are reflected in high capital investments. For example, the U.S. Energy Information Administration, in 2012 (EIA, 2012), reported that total average cost, drilling and completion expenses, per horizontal well in Bakken, Eagle Ford, and Marcellus formations varies between approximately $6.5 million and $9 million. Nonetheless because of favourable market conditions, investments in shale gas development in United States totalled $133.7 billion between 2008 and 2012. Given the high cost and volatility in market prices, careful analysis of alternative investment strategies which include choices between

using own capital or external financing such as short or long term bank credit lines is essential. In this work, we proposed an optimization approach as a decision support tool for guiding the investment in the development of shale gas resources which includes aspects such as water availability constraints, capital and operating costs and financing aspects (Laínez et. al, 2007 and Laínez et. al, 2009). The Mixed Integer Linear Programming (MILP) model presented incorporates selection of the design of well-pads in terms of total number of wells, and length and number of hydraulic fractures completed at each well. Different capacities and locations are considered for compressor stations, gas separation plants, and water treatment plants. The formulation also takes into account financial components such as short and long term bank credit lines.
Finally, the capabilities of the proposed model are shown through a case study where two scenarios are evaluated. In the first scenario, external financing is not considered and only limited amounts of own capital can be invested. In the second scenario we include financing options in order to allow more flexibility in the timing of the development plan, reflecting the most common situations in the oil and gas business.

2. Problem Statement and Mathematical Formulation

The development of shale gas resources involve many strategic and operational decisions such as selection of sources of water for fracking processes, selection of well-pad locations and designs, the design of gas and liquid pipeline networks, technology, location, and capacity for waste water treatment plants, and the location and design of gas processing plants. A general shale gas supply chain superstructure is shown in Figure 1.

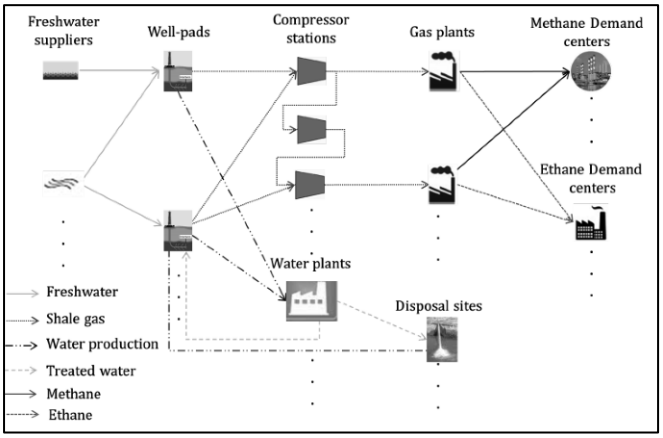

Figure 1. General superstructure for shale gas supply chain.

The features of this superstructure can be summarized as follows:

Given:

- Potential well-pad locations that allow vertical and horizontal wells to be drilled and hydraulically fractured.
- Alternative well-pad designs for each potential location and corresponding production profiles
- Water demand for drilling and fracturing according to the Well-pad designs
- Fresh water availability at potential suppliers (rivers, lakes, etc.)

- Transport and processing infrastructures for water and gas
- Gas and liquid product demands at different locations
- Investment budget and/or financing parameters

To determine:

- Drilling scheme
- Well-pad design in terms of the number of wells, length and number of stage fractures for each well
- Location, capacities, technologies, CAPEX and OPEX for water and gas treatment plants
- Total water consumption, recycled water and disposal
- Gas and water transport network

The objective function is to maximize the Net Present Value (NPV), defined as the cash flow $CashFlow(t)$ minus capital expenditures $Capex(t)$, associated with the design of the shale gas supply chain. In this work, well-pad design, location, and timing are considered the most important decisions in shale gas site development. These decisions are integrated into the binary variable $WellDes(d,w,t)$. This variable is equal to one if the well-pad design d is selected for potential well-pad w during period t, the variable is equal to zero otherwise. This variable is used to determine gas production, water consumption, water production, and capital expenses associated with the drilling operations. Salvage value SV is also included to account for the value of the assets at the end of the time horizon. In addition, the total debt due to borrowings $TotalDebt(T)$ is required to be repaid when the project finishes. Thus, the objective function used in this work is shown in Eq. (1).

$$max \quad NPV = \sum_t \frac{CashFlow(t) - Capex(t)}{(1+wacc)^{t-1}} + \frac{SV}{(1+wacc)^{T-1}} - \frac{TotalDebt(T)}{(1+wacc)^{T-1}} \tag{1}$$

where the weighted average capital cost $(wacc)$ represents the interest rate per period t and it is calculated based on the fractions of own invested capital and borrowed money from external financing sources. The total required investments $Capex(t)$ can be fulfilled with capital internal to the corporation and funds borrowed from banks $BorrowLT(t)$ through long term debt as showed in Eq. (2)

$$Capex(t) \; = \; BorrowLT(t) + \; Capital(t) \tag{2}$$

Additional equations related to long term debt are necessary to keep track of the current debt $DebLT(t)$, net transactions between borrowings and payments $NetLTC(t)$ and how much is paid in every period $RepayLT(t)$. A long term credit is subject to an interest rate $irLT(t)$ defined by an agreement stablished with the bank. This can be done by including Eq. (3)-(5).

$$DebLT(t) = (1 \; + \; irLT(t)) * DebLT(t-1) + \; BorrowLT(t) - RepayLT(t) \tag{3}$$

$$NetLTC(t) = BorrowLT(t) - RepayLT(t) \tag{4}$$

$$RepayLT(t) \geq irLT(t) * DebLT(t-1) \tag{5}$$

A similar formulation is included for short term credit lines, which are used to keep liquidity in a company in case the cash flow reaches a minimum value. A short term credit ensures there is sufficient working capital to cover short term expenditures such as transport costs, operating costs, etc. The financial model is coupled with the formulation developed for the shale gas supply chain shown in Figure 1. The integration of these models allows decision makers to establish the best options regarding strategic decisions for the shale gas supply chain development and simultaneously to optimize the financial implications of these decisions.

3. Case study

3.1. Description

A case study is implemented to demonstrate the capabilities of the optimization model for shale gas supply chain management described in the previous section of this paper. The case study has the following scope: 10 year time horizon (40 quarters), 15 potential well-pad locations, 2 freshwater suppliers , 2 compressor stations (2 sizes), 2 water treatment plants (3 sizes), 2 gas processing plants (2 sizes), 2 disposal sites, and 2 demand centers. Three different configurations for well-pads designs are included as follows: “ShortFew” with 1500 ft length for horizontal wells and 3 fracture stages, “base” with horizontal length of 3000 ft and 8 fracture stages, and “LongMany” with horizontal length of 5000 ft and 20 fracture stages, each well-pad design is composed of 5 horizontal wells. In addition, gas composition is considered to be constant. Two scenarios are studied differing in their financial aspects. In the first scenario (base case), only the use of internal capital is considered, therefore a constraint on maximum capital budget available for new investment is included. In the second scenario (financing case), in addition to own capital, long and short term credit lines are included in order to support investments and operating costs, respectively. The characteristics of the developed models are summarized in Table 1.

Table 1. Model statistics for both case studies

	Base case	Financing case
Constraints	8,777	9,141
Continuous variables	8,241	8,602
Binary variables	5,400	5,400
Non zero elements	174,065	175,306

The statistics reported in Table 1 show that the financing case contains additional equations and continuous variables which are related to the integration of the financial formulation and the shale gas supply chain optimization model. In this study, an annual interest rate of 15 % and 10 % was considered for the short and long term credit line, accordingly.

3.2. Results and discussion

The results regarding the optimal solutions for both cases are discussed in this section. The optimization problems were solved in GAMS (version 24.3.1) with CPLEX (version 12.6.0.1) as the MILP solver using an Intel i-7 @ 2.40 GHz processor with 8 GB RAM, running 64-bit Windows 8.1. The relative optimality gap was set to 3 % for both cases. For the base case, after 24.5 h the algorithm was interrupted resulting in a

candidate solution with an optimality gap of 9.2 %. The CPU time for solving the financing case was 3.1 h with a relative optimality gap of 1.04 %. These differences in CPU time and gap may be due to a tighter LP sub-problem in the financing case. The cumulative net cash flows for the two scenarios are presented in Figure 2. For the base case, the optimal net present value is determined to be around $341.3 Million and the investment for shale gas infrastructure starts in the 11th quarter when the gas price is about 5,753 US$/MMSCF. On the other hand, when external financing options are incorporated, the NPV increases up to $565.3 Million, an increment of about 65.6 % with respect to the base case. In addition, for this case it is economically feasible to invest when the gas price is around 4,143 US$/MMSCF.

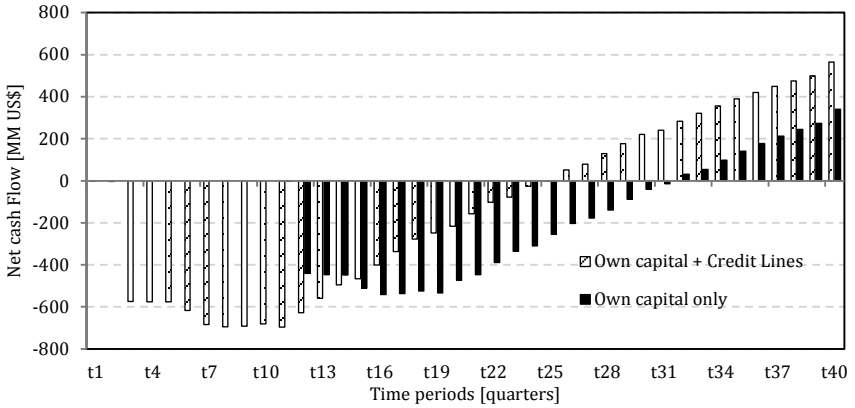

Figure 2. Accumulated net cash flow.

It is worth of mention that under capital investment restrictions (base case), the investment plan is postponed in order to take advantage of higher methane prices at the end of the time horizon, as shown in Figure 3. By contrast, when external financing resources are considered, the investment plan is selected in such a way that gas production starts earlier than in the base case, despite the relatively lower gas prices at the beginning of the time horizon. In this case, the lower gas prices are compensated by higher total gas production, which is estimated to be 281.9 billion SCF and 368.9 billion SCF for the base case and financial case models, respectively.

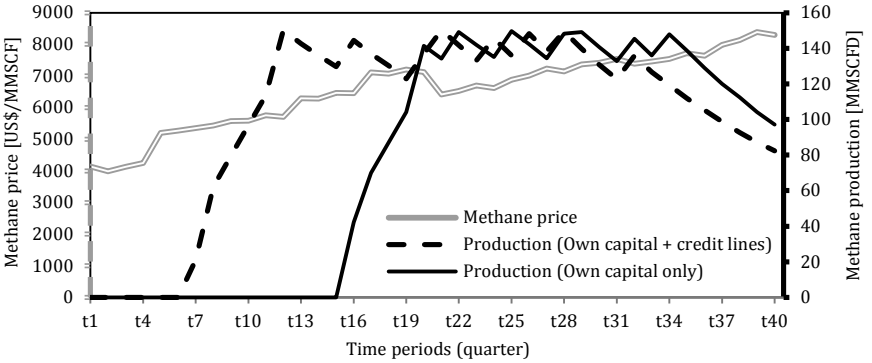

Figure 3. Methane production and gas prices.

With respect to the optimal drilling strategy, 14 well-pads (2 “base” and 12 “LongMany” designs) were chosen for the base case. Total fresh water use is about 448.7 million gallons and water reuse, defined as a % of total water production, is 60.3 %. The cumulative gas production for the 14 well-pads is approximately 281.9 billion SCF. By comparison, for the financing case, 15 well-pads with only “LongMany” designs were chosen. In this case, the total fresh water consumption for drilling and fracturing operations is about 462.7 million gallons and water reuse is 76.1 %. This increase in water reuse is due to a higher demand of water and limitations on disposal capacities, which leads to greater water treatment volumes. Finally, the cumulative gas production for the 15 well-pads is approximately 368.9 billion SCF. It is important to note that both financing and drilling strategies could be affected by the uncertainty associated to water availability, natural gas prices and production profiles.

4. Concluding Remarks and Future Work

This paper has addressed the integration of financing aspects into the optimization models for the development of shale gas resources. It was shown that the financing through external resources, such as short and long credit lines, could be appropriate for the development of shale gas resources. It was also shown that financing strategies have an important impact on the optimal drilling plan as well as the water use and management. Directions for future work include the implementation of case studies considering variations in shale gas composition over the life of the well. Additionally, since the economy of shale gas depends strongly on the market conditions, the financing strategies can be affected by this variability, therefore the development of stochastic optimization models in order to take into account the uncertainties in gas prices, water availability, and gas production profiles will be addressed.

Acknowledgements

The authors would like to acknowledge the financial support from the Colombian Science Council (COLCIENCIAS) and the Colombia-Purdue Institute for Advanced Scientific Research (CPIASR).

References

BP, 2014, BP Energy Outlook 2035, BP, London.

EIA, U.S. Energy Information Administration, 2012, [online], Available from: http://www.eia.gov/todayinenergy/detail.cfm?id=7910&src=email

S. Jenner, A.J. Lamadrid, 2013, Shale Gas vs. Coal: Policy Implications from Environmental Impact Comparisons of Shale Gas, Conventional Gas, and Coal on Air, Water, and Land in the United States, Energy Policy, 53, 442–453.

J.M. Laínez, G. Guillén-Gosálbez, M. Badell, A. Espuña, L. Puigjaner, 2007, Enhancing Corporate Value in the Optimal Design of Chemical Supply Chains, Industrial and Engineering Chemistry Research, 46, 7739–7757.

J.M. Laínez, L. Puigjaner, G.V. Reklaitis, 2009, Financial and Financial Engineering Considerations in Supply Chain and Product Development Pipeline Management, Computers and Chemical Engineering, 33, 1999–2011.

J.J. Siirola, 2014, The Impact of Shale Gas in the Chemical Industry, AIChE Journal, 60, 810–819.

Krist V. Gernaey, Jakob K. Huusom and Rafiqul Gani (Eds.), 12th International Symposium on Process Systems Engineering and 25th European Symposium on Computer Aided Process Engineering.
31 May - 4 June 2015, Copenhagen, Denmark.

Optimal Dynamic Operation of Adsorption-based Energy Systems Driven by Fluctuating Renewable Energy

Uwe Bau[a], Anna-Lena Braatz[b], Franz Lanzerath[a], Michael Herty[b] and André Bardow[a]

[a]*Chair of Technical Thermodynamics, RWTH Aachen University, Germany*
[b]*IGPM, Department of Mathematics, RWTH Aachen University, Germany*
andre.bardow@ltt.rwth-aachen.de

Abstract

Adsorption-based energy systems can provide environmentally friendly heating and cooling energy as they can be driven by low-grade heat, such as solar or waste heat. However, solar and often also waste heat are fluctuating over time. Thus, an optimal operation policy has to be identified to run adsorption-based energy systems efficiently. This work therefore presents a method to determine the optimal control for dynamic adsorption-based energy systems. To determine the optimal control, a two-step approach is used: First, the original non-linear dynamic model is approximated by a set of linear ordinary differential equations connected by Heaviside functions. In a second step, an optimal control problem is formulated and optimized for a set of control variables using a gradient method. The derived model predictive control is tested for a non-linear adsorption chiller model. The MPC shows good performance for both efficiency and specific power as objective functions.

Keywords: adsorption chiller, adsorption chiller model, adsorption heat pump, optimal control, optimal cycle time, model predictive control (MPC)

1. Introduction

Adsorption based energy systems can provide cooling or heating using heat as driving power. Heat-driven adsorption chillers or heat pumps thus enable the use of solar or waste heat (Chan et al., 2013). Adsorption-based systems operate cyclic by switching between adsorption and desorption phase. Controlling such a system means determining the duration of each phase, which has great impact on system performance. For adsorption chillers, a trade-off exists: Long cycles promote a high coefficient of performance (COP), whereas short cycles promote high specific cooling power (SCP) (Chua et al., 1999, 2004). Whether COP or SCP should be the objective function for control depends strongly on the heat source: a limited heat source requires a high COP, an unlimited heat source a high SCP (Alam et al., 2003).

Current control strategies used for adsorption-based energy systems can be clustered into three groups: (1) predefined cycle times; (2) cycle times based on physical states measured during operation; (3) model predictive control.

Predefined cycle times need knowledge of the optimal cycle times for all operating conditions, such as temperature levels, cooling and heating power, as well as system characteristics. Thus, a high amount of a priori knowledge is needed and adaption during operation is hardly possible.

Cycle times based on physical states measured during operation use, for example, the cold water temperature to determine the optimal switching point (Schicktanz, 2011). These controls are typically based on heuristics and experience. Gräber proposed a control based on the average measured cooling power for which he proved optimality regarding SCP when the heat source is unlimited (Gräber, 2013).

The third control strategy is model predictive control (MPC). MPC calculates the feedback law online, by successively solving finite–horizon optimal control (open–loop) problems, see also Morari et al. (1993). Since an accurate model of the problem is needed and an optimal control problem is solved online, MPC is the most complex control strategy described. This complexity is compensated by a high amount of flexibility regarding the optimized objective function and the adaption to changing operating conditions.

This work is structured as follows: First, a non-linear process model of an adsorption chiller is described (Section 2.1) and an MPC procedure for this class of models is derived (Section 2.2). In Section 3, the control is tested for two different objective functions (SCP and COP) using the adsorption chiller model described and a fluctuating input temperature.

2. Model predictive control

2.1. Non-linear process model

The model predictive control presented in this paper is applied to a two-bed adsorption chiller model shown in Figure 1. The chiller model is a dynamic model written in Modelica, an object-oriented, equation-based modeling language. The model is built using the adsorption energy systems library developed at RWTH Aachen University (Bau et al., 2014). The model was experimentally validated by Lanzerath et al. (2014). The chiller model consists of two adsorber beds, an evaporator and a condenser. These components are connected to heat exchangers via heat resistance models. The adsorber beds are connected to the evaporator and the condenser by valve models, describing the mass transfer. Heat losses for all components are modeled using a constant heat transfer coefficient. As model inputs, inflow temperatures and volume flow rates into the four heat exchanger are used. We define the inflow temperature levels: $T_0 < T_{\mathrm{mid}} < T_{\mathrm{high}}$.

2.1.1. Operation of adsorption chiller

The operation of each adsorber bed is divided into four phases: (1) precooling; (2) adsorption; (3) preheating and (4) desorption. During adsorption, the actual cooling power is produced by evaporating water at a low temperature level T_0. This water vapor flows to the adsorber and is adsorbed at T_{mid}. When the adsorber reaches its maximum capacity, the process is reversed by heating the adsorber to T_{high} and condensing the released water in the condenser at medium temperature T_{mid}. To close the circuit, the liquid water from the condenser returns to the evaporator. Precooling and preheating are transition phases between adsorption and desorption to change the temperatures of the adsorber beds. For the considered 2-bed system, symmetry requires equal times for precooling and preheating and for adsorption and desorption. The duration of each phase has to be determined by a controller.

2.1.2. Modeling approach

Adsorber (A), evaporator (E) and condenser (C) have the same model structure: They are modeled as dynamic lumped models with a uniform temperature T. All of them contain a media model. For evaporator and condenser, a two-phase model for saturated water is used. In the adsorber, a

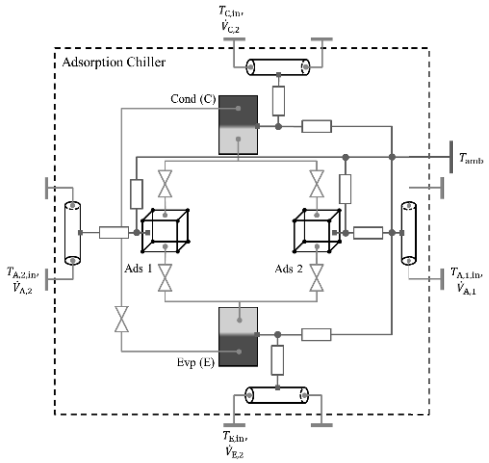

Figure 1: Structure of the adsorption chiller model: two adsorber beds (Ads 1 and Ads 2), an evaporator (E) and a condenser (C) are connected via mass transfer models (blue valve symbols). Connection to heat exchangers (tube models) via heat transfer models (red boxes). Heat losses are implemented via heat transfer resistances coupled to a heat sink at T_{amb}. (Color online)

media model describing the equilibrium data of the sorbent is used. Our adsorption energy systems library (Bau et al., 2014), contains many sorbent media models, allowing for fast changes of the sorbent material. In this work, silica gel 123 is used, described by the Dubinin model (Dubinin, 1967) with a characteristic function measured by Schawe (2001). Exemplary for all components, the mass balance of the adsorber is shown here

$$m_{\mathrm{sor}} \frac{\mathrm{d}x}{\mathrm{d}t} = \frac{\mathrm{d}m_{\mathrm{ad}}}{\mathrm{d}t} = \dot{m}_{\mathrm{E}} - \dot{m}_{\mathrm{C}} \,, \tag{1}$$

where m_{sor} is the mass of the sorbent material and m_{ad} is the mass of adsorbed water. $\dot{m}_{\mathrm{E}}$ describes the mass flow from the evaporator, $\dot{m}_{\mathrm{C}}$ the one to the condenser. The energy balance reads

$$\frac{\mathrm{d}U_{\mathrm{A}}}{\mathrm{d}t} = u_{\mathrm{ad}} \frac{\mathrm{d}m_{\mathrm{ad}}}{\mathrm{d}t} + \left(m_{\mathrm{ad}} c_{\mathrm{ad}} + m_{\mathrm{sor}} c_{\mathrm{sor}}\right) \frac{\mathrm{d}T_{\mathrm{A}}}{\mathrm{d}t} = \dot{m}_{\mathrm{E}} h_{\mathrm{E}}^{\mathrm{v}} - \dot{m}_{\mathrm{C}} h_{\mathrm{A}}^{\mathrm{v}} + \dot{Q}_{\mathrm{A}} \,. \tag{2}$$

The internal energy of the adsorber (U_{A}) is described by the specific internal energy of the adsorbed water (u_{ad}) and the temperature of the adsorber (T_{A}) multiplied by the total heat capacity ($m_{\mathrm{ad}} c_{\mathrm{ad}} + m_{\mathrm{sor}} c_{\mathrm{sor}}$). The internal energy is changed by the enthalpy flows from the evaporator and to the condenser and by a heat flow. The heat flow

$$\dot{Q}_{\mathrm{A}} = \left(\alpha A\right)_{\mathrm{A}} \left(T_{\mathrm{A}} - T_{\mathrm{A,hx}}\right) \tag{3}$$

between sorbent and the outer heat exchanger surface is described with a constant heat transfer coefficient $\left(\alpha A\right)_{\mathrm{A}}$.

Considering the mass and energy balances also for the other components (evaporator, condenser and heat exchangers), we get a coupled system of differential and algebraic equations. In general terms, the resulting system may be written as

$$\frac{\mathrm{d}}{\mathrm{d}t} x(t) = F_i(x(t)) \quad \text{for } t \in (0, t_4) \,, \tag{4}$$

where $i = 1, \ldots, 4$, denotes the current phase. The vector x contains the state variables $x \in \mathscr{C}^1([0,t_4], \mathbb{R}^{16})$ describing the physical quantities.

2.2. Controller design

To control an adsorption system, we propose a model predictive control (MPC) strategy, also called receding horizon control (Rawlings and Muske, 1993). A MPC solves an optimal control problem for a defined time horizon in the future. The obtained optimal control is then used to steer the system. After a certain time, the optimal control problem is updated by the current system state to close the feedback loop (see Figure 2).

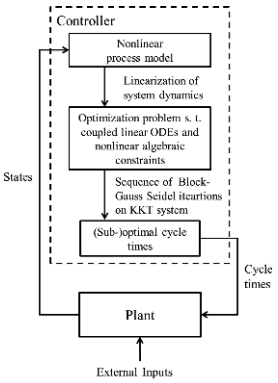

Figure 2: Scheme of the used control strategy: Controller inputs are the current system states, controller outputs are the cycle times used for the next interval. The nonlinear process model is linearized at the given states resulting in an optimization problem with linear ODEs and nonlinear algeabric constraints. This KKT system is than solved by a sequence of Block-Gauss Seidel iterations to get (sub-)optimal cycle times for the next interval.

Due to the strong nonlinearities in F_i with respect to the states x, a direct inversion for controller design is computationally expensive. Similarly, an MPC based on equation (4) leads to a large–scale nonlinear optimization problem which is again computationally challenging to solve. Therefore, we propose the design of the controller for a linearization of F_i at a given state $x(\tilde{t})$, which leads to the following system of ODEs

$$\dot{x}(t) = A_i x(t) + b_i, \quad \text{for } t \in (t_{i-1}, t_i) \tag{5}$$

with $A_i \in \mathbb{R}^{16\times 16}$, $b_i \in \mathbb{R}^{16}$ for $i = 1,\dots,4$ and where A_i and b_i, depend on $x(\tilde{t})$.

This problem is still difficult to solve due to the possible discontinuity in the right–hand side of the ODE at phase switching times between the phases. We therefore combine the ODEs (5) for all phases using a smoothed version of the indicator function.

We parameterize $[0,t_4]$ with $t = t(\tau) = t_4\tau$, $\tau \in [0,1]$ and obtain the final MPC problem for determining optimal cycle times as

$$\begin{aligned} &\min_{x,h} \int_0^1 -\dot{Q}_0(\tau,x) \quad \text{or} \quad \min_{x,h} \int_0^1 -\frac{\dot{Q}_0(\tau,x)}{\dot{Q}_{\text{in}}(\tau,x)} \\ &\text{s.t.} \quad \dot{x}(\tau) = A(\tau,h)x(\tau) + b(\tau,h), \quad \text{for } \tau \in (0,1), \\ &\qquad x(0) = x_0, \\ &\qquad h \geq 0 \end{aligned} \tag{6}$$

with

$$A(\tau,h) := \left(\sum_{k=1}^{4} h_k\right)\tilde{A}\left(\tau\sum_{k=1}^{4} h_k, h\right) \quad \text{and} \quad b(\tau,h) := \left(\sum_{k=1}^{4} h_k\right)\tilde{b}\left(\tau\sum_{k=1}^{4} h_k, h\right).$$

The first objective function in (6) maximizes the cooling power of the system, the second one maximizes the coefficient of performance (COP). The objective function should be chosen according to the available driving power: If driving power is freely available, high cooling power is desired to built compact devices; if not, a high COP is desired to use the available input power as efficient as possible.

From the Lagrange function, we derive the formal necessary optimality conditions for a cycle time h^*, a corresponding state x^* and multiplier $\lambda = \lambda(t)$ and $\mu \in \mathbb{R}^4$. The resulting system is fully coupled and linear in x and λ. We exploit the structure of the equations in the numerical method. This leads to the following iterative solution strategy for the system: Given an initial control h_{old}, we determine a new control h_{new} by first solving the system

$$\dot{x}(t) = A(t, h_{\text{old}})x(t) + b(t, h_{\text{old}}) \quad \text{for } t \in (0,1), \qquad x(0) = x_0$$

for $x(\cdot, h_{\text{old}})$, then solving the system

$$-\dot{\lambda}(t) = A(t, h_{\text{old}})^\top \lambda(t) + \nabla_x - \dot{Q}_0(\tau, x) \quad \text{for } t \in (0,1), \qquad \lambda(1) = 0$$

for $\lambda(\cdot)$. Finally, we obtain

$$h_{\text{new}} = \max\left\{ h_{\text{old}} - \sigma \left[\int_0^1 \left(\frac{\mathrm{d}}{\mathrm{d}h} \left[A(t, h_{\text{old}}) x(t) \right] \right)^\top \lambda(t) + \left(\frac{\mathrm{d}}{\mathrm{d}h} b(t, h_{\text{old}}) \right)^\top \lambda(t) \, \mathrm{d}t \right], 0 \right\} \quad (7)$$

where $\sigma > 0$ is chosen such that the integral of the chosen objective function enjoys descent. The procedure can be repeated with the new h_{old} being h_{new} until no change in the control appears; indicating optimality. A complete derivation of the control strategy including robustness tests for the different parameters of the method, such as linearization points and intervals or the smoothing parameter of the indicator function can be found in Bau et al. (2015).

3. Numerical results

In this section, the controller is applied to an adsorption chiller using different objective functions. We use the non-linear chiller model presented in Section 2.1. To represent fluctuating weather conditions, we vary the input temperature $T_{\text{high}} = 75\left(1 + 0.2 \sin {}^1\!/_{1800\,\text{s}^{-1}}\, \pi t\right)$ °C. The other temperatures are kept constant. The system is simulated with the derived MPC using both objective functions: maximum cooling power and maximum COP. The obtained solutions are compared to a controller based on the average measured cooling power (Gräber, 2013), which maximizes cooling power.

Figure 3 shows the results for the three investigated controls. The top graph shows the phase times of ad- and desorption ($h_2 = h_4$). The two bar graphs below show the obtained average cooling power and the average COP of the system. For an objective function maximizing cooling power, the derived MPC and the controller of Gräber achieve similar results, regarding cooling power and COP. This behavior is expected as Gräber's controller was derived for this case. In terms of phase times, the MPC uses slightly longer times than Gräber's control for low input temperatures (around 45, 105 and 165min), but with almost no effect on the obtained objective function. When the objective function is changed, the MPC computes significantly longer cycle times, resulting in a COP increased by 12%. Thus, the results demonstrate the flexibility of the presented MPC to adapt to the chillers' use case.

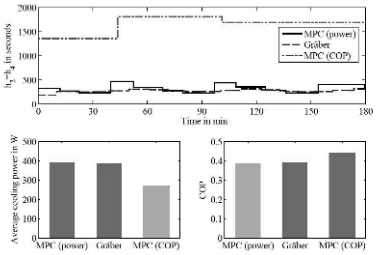

Figure 3: Comparison of the derived MPC control strategy for maximizing power and maximizing COP and a control based on measured states (Gr¨aber, 2013). Top: Phase times for adsorption and desorption (h2 = h4) of compared control strategies. Bottom: Average cooling power (left) and COP (right). (Color online)

4. Summary

This work presents a model predictive control (MPC) strategy for adsorption-based energy systems based on a non-linear process model. The derived MPC uses a two step aproach: (1) The process model is approximated using a system of linear ordinary differential equations. (2) The resulting optimization problem is solved using a sequence of Block-Gauss Seidel iterations on the Karush-Kuhn-Tucker system. Since for adsorption systems, the chosen objective function depends on the operating conditions, the derived MPC is tested with two different objective functions. The obtained results are compared to a control strategy based on measured state variables, which is only able to maximize the average cooling power. As expected, for the case of maximizing cooling power both controllers obtain similar results. For the case of maximizing COP, the MPC increases the COP by 12 %. The presented MPC proves to be a flexible method to control adsorption-based energy systems allowing for further efficiency improvements and faster adaption to changing operating conditions.

5. Acknowledgment

Funded by the Excellence Initiative of the German federal and state governments.

References

Alam, K. C. A., Kang, Y. T., Saha, B. B., Akisawa, A., Kashiwagi, T., 2003. A novel approach to determine optimum switching frequency of a conventional adsorption chiller. Energy 28 (10), 1021–1037.

Bau, U., Braatz, A.-L., Lanzerath, F., Herty, M., Bardow, A., 2015. Control of adsorption chillers by a gradient descent method for optimal cycle time allocation (submitted).

Bau, U., Lanzerath, F., Gräber, M., Schreiber, H., Thielen, N., Bardow, A., 2014. Adsorption energy systems library - modeling adsorption based chillers, heat pumps, thermal storages and desiccant systems. In: Tummescheit, H., Årzén, K.-E. (Eds.), Proceedings of the 10th International Modelica Conference. Vol. 96 of Linköping electronic conference proceedings. Modelica Association, Linköping, pp. 875–883.

Chan, C. W., Ling-Chin, J., Roskilly, A. P., 2013. A review of chemical heat pumps, thermodynamic cycles and thermal energy storage technologies for low grade heat utilisation. Applied Thermal Engineering 50 (1), 1257–1273.

Chua, H. T., Ng, K. C., Malek, A., Kashiwagi, T., Akisawa, A., Saha, B. B., 1999. Modeling the performance of two-bed, sillica gel-water adsorption chillers. International Journal of Refrigeration 22 (3), 194–204.

Chua, H. T., Ng, K. C., Wang, W., Yap, C., Wang, X. L., 2004. Transient modeling of a two-bed silica gel–water adsorption chiller. International Journal of Heat and Mass Transfer 47 (4), 659–669.

Dubinin, M. M., 1967. Adsorption in micropores. Journal of Colloid and Interface Science 23 (4), 487–499.

Gräber, M., 2013. Energieoptimale regelung von kälteprozessen. Ph.D. thesis, Technische Universität Carolo-Wilhelmina zu Braunschweig, Braunschweig, Germany.

Lanzerath, F., Bau, U., Seiler, J., Bardow, A., 2014. Optimal design of adsorption chillers based on a validated dynamic object-oriented model (accepted). HVAC&R Research.

Morari, M., Garcia, C. E., Lee, J. H., Prett, D. M., 1993. Model predictive control. Prentice Hall Englewood Cliffs, NJ.

Rawlings, J. B., Muske, K. R., 1993. The stability of constrained receding horizon control. IEEE Trans. Automat. Control 38 (10), 1512–1516.

Schawe, D., 2001. Theoretical and experimental investigations of an adsorption heat pump with heat transfer between two adsorbers. Ph.D. thesis, Universität Stuttgart, Stuttgart, Germany.

Schicktanz, M., 2011. Influence of temperature fluctuations on the operational behaviour of adsorption chillers. In: Lazzarin, R. M., Longo, G. A., Noro, M. (Eds.), International Sorption Heat Pump Conference (ISHPC 11). International Institute of Refrigeration, Paris, pp. 351–357.

Krist V. Gernaey, Jakob K. Huusom and Rafiqul Gani (Eds.), 12th International Symposium on Process Systems Engineering and 25th European Symposium on Computer Aided Process Engineering.
31 May – 4 June 2015, Copenhagen, Denmark

A Spatial Multi-Period Mixed Integer Linear Programming (MILP) Model for Optimal Power Planning: CO_2 Emissions Mitigation

Omar J. Guerra,[a] Diego A. Tejada,[b] Raúl Rodríguez,[c] Gintaras V. Reklaitis,[a]

[a] *School of Chemical Engineering, Purdue University, West Lafayette IN 47907, USA.*
[b] *XM, The Market Experts S.A., Medellín, Colombia.*
[c] *Energy and Mining Planning Unit (UPME), Bogotá, Colombia*.

Abstract

This paper presents a spatial multi-period MILP optimization model for optimal power generation expansion planning with CO_2 emission constraints. This model examines CO_2 emission and resource adequacy on a regional basis. Resource adequacy constraints, reserve margin, and spinning reserves, ensure safe and reliable operation of the grid in real time. The features of the proposed model are illustrated through case studies related to the Colombian power system, including hydroelectric, coal, and natural gas power plants.

Keywords: optimization, power planning, CO_2 emissions.

1. Introduction

According to the ExxonMobil Energy Outlook (ExxonMobil, 2014), worldwide electricity use is expected to growth by 90 % from 2010 to 2040. Developing countries account for about 85 % of that increase. Therefore, power planning is an important issue in order to provide reliable and sustainable secondary energy in timely fashion, particularly in developing countries. Consequently, energy and power planning problems have captured the attention of the academic research community (Bri-Mathias et al. (2008), Sirikitputtisak et al. (2009), Mirzaesmaeeli and Elkamel (2010), Koltsaklis et al. (2014), and Flores et al. (2014)).

Numerous publications have examined the modelling, simulation, and optimization of energy systems. Sirikitputtisak et al. (2009) and Mirzaesmaeeli and Elkamel (2010) proposed optimization models for the power generation planning of electric systems, which took into account CO_2 emissions. Koltsaklis et al. (2014) presented a spatial multi-period model for optimal long-term planning of a nationwide power generation system. This model includes CO_2 emission constraints and interregional electricity imports. Vinasco et al. (2014) suggested an optimization approach for transmission network expansion planning. The approach was applied to a case study related to the Colombian power system, which took into account various scenarios for electricity generation and demand, using the N-1 safety criterion. Sharan and Balasubramanian (2012) formulated an optimization model that integrated power generation and transmission expansion planning. This model incorporates both the first and second Kirchhoff's laws. Flores et al. (2014) developed a multi-period disjunctive optimization model for investment planning in energy sources. The model was applied to a case study related to the optimization of Argentina's energy matrix under different scenarios over a long-term horizon.

In this work we present a spatial multi-period MILP optimization model for optimal power generation expansion planning. The model includes spinning and non-spinning reserve constraints, as well as CO_2 emission constraints. Carbon Capture and Sequestration (CCS) technologies are considered for coal power plants, in order to mitigate CO_2 emissions. The model also accounts for transmission capacity and cost for power transfer between the interconnected regions. In addition, lead time is considered for construction of new power plants, since such lead times can be quite long. The novelty of the proposed model relies in the integrated assessment of the aforementioned features, which can reveal possible interactions and synergies within the power system. Particularly, the formulation enables the integration of reliability and environmental constraints into the planning of interconnected power systems.

2. Problem Formulation

The optimal design and planning of power systems (i.e. on a nationwide scale) deals with the optimization of power generation capacity expansion of each energy conversion technology for a given electricity demand over a long-term horizon. Usually, different primary energy resources are available for conversion into electricity using different existing and potential power plants that supply the electricity demand that arises in different interconnected regions during a given planning period (i.e. 15 years). Each region is characterized by a subset of existing, planned, and potential power plants, fuel availability and cost, as well as the electricity demand and interregional electricity import/export capacity. Electricity demand at each region can be met either by local power plants or by a combination of local generation and imports from other regions. Power plants (existing, planned, and potential) are characterized by their capacity, location, operating cost (fixed and variable), capital cost (planned and potential power plants only), heat rate (fossil power plants only), CO_2 emission factor, fuel cost, and availability and capacity factors. Reserve margin and spinning reserve factors are taken into account in order to ensure the safe and reliable operation of the grid in real time. Regarding CO_2 emissions mitigation, CCS technologies can be implemented in fossil power plants in order to meet CO_2 emission reduction target. The main strategic decisions related to nationwide power system planning are the timing, location, and capacity of new power plant investments. Furthermore, for each time period, there are operational decisions related to power, reserve margin and spinning reserve allocation, power plant dispatch, and power transfer between regions.

The objective function (to be minimized) is the net present value of the total cost associated with capital investment $Investment(t)$ and operational expenditures for the power system over the whole time horizon, as defined in Eq. (1), where t is the index for time periods (years). Operational expenditures include total fixed $TotFixCost(t)$ and variable $TotVarCost(t)$ cost, total fuel cost $TotFuelCost(t)$ and total transmission cost $TotTrnsCost(t)$. The electricity balance for each region is described in Eq. (2). Indices r and rr are used to denote regions. The link between power plants and regions is defined by the set lri, where i is the index for power plants. Load blocks are represented by the index b. In addition to this balance, the total power allocated for each time period should ensure enough capacity to supply electricity during peak periods while meeting the requirements on capacity reserve, as stated in Eq. (3). Moreover, capacity allocation for each power plant should not exceed its maximum capacity, as described in Eq. (4). The binary variable $Operation(i,t)$ is equal to 1 if

power plant i is operated during period t, the variable is equal to zero otherwise. Electricity output from a given power plant has to be less than or equal to the maximum energy output for that power plant, as specified in Eq. (5). Variable $Ecapture(i,b,t)$ denotes the electricity consumption associated with the operation of CO_2 capture process in power plant i during load block b in period t. A binary variable is included in the model formulation for the selection and installation of CCS facilities. This variable is used to guarantee that electricity consumption and CO_2 emission reduction associated with the operation of CO_2 capture process in power plants is set to zero if the CCS facility has not been installed yet. Spinning reserve should be greater than or equal to the spinning reserve requirements for each period, as specified in Eq. (6). CO_2 emissions are estimated using Eq. (7), where fo is the set containing all the fossil power plants. Parameter $CapPen(i)$ represents the unit electricity consumption (MWh/tonne of CO_2) for capture process in power plant i. Finally, the CO_2 emission constraint is defined in Eq. (8).

$$Min \quad TotCost = \sum_{t} \begin{pmatrix} TotFixCost(t) + TotVarCost(t) + TotFuelCost(t) + \\ TotTrnsCost(t) + Investment(t) \end{pmatrix} / (1+r)\hat{}(t-1) \tag{1}$$

$$(1-EnerLoss) * \sum_{i|(r,i)\in lri} Energy(i,b,t) + \sum_{rr} EnerFlow(rr,r,b,t) = EnergyDemand(r,b,t) + \sum_{rr} EnerFlow(r,rr,b,t) \quad \forall r,b,t \tag{2}$$

$$\sum_{i} Power(i,t) \geq (1+ResMarg) * PeakPower(t) \quad \forall t \tag{3}$$

$$Power(i,t) \leq CapFac(i) * Cap(i) * Operation(i,t) \quad \forall i,t \tag{4}$$

$$Energy(i,b,t) + Spinn(i,b,t) + Ecapture(i,b,t) \leq BlockDur(b) * AvailFac(i) * Power(i,t) \quad \forall i,b,t \tag{5}$$

$$\sum_{i} Spinn(i,b,t) \geq SpinRes * \sum_{r} EnergyDemand(r,b,t) \quad \forall b,t \tag{6}$$

$$Emission(i,t) = CO2Emi(i) * \sum_{b} \left(Energy(i,b,t) + Spinn(i,b,t) + Ecapture(i,b,t) \right) - \sum_{b} \left(\frac{Ecapture(i,b,t)}{CapPen(i)} \right) \quad \forall i | i \in fo, t \tag{7}$$

$$\sum_{i|i\in fo} Emission(i,t) \leq MaxEmi(t) \quad \forall t \tag{8}$$

3. Case Study: Colombian Power System

The proposed optimization problem formulation was applied to a case study related to the optimal planning of Colombia's electric power system which consist of 5 interconnected regions: Antioquia, Caribe, Centro, Oriente, and Valle. Colombia's electricity demand is projected to increase by about 50 % from 2013 to 2027, with different grow rates among the regions. This increase in demand will require an expansion of the power system through selective investments in new power plants in the future. Transmission line capacities are defined according to the expansion plan defined by the Mining and Energy Planning Unit (UPME in Spanish). In addition, CCS

technologies for coal power plants are consider in order meet CO_2 emission reduction targets. However, the best decisions which must be made, with regard to plant capacities, plant locations, timing, power allocation, and CO_2 mitigation strategy are not obvious. The MILP optimization model presented previously will be useful to support these decisions by taking into account economic, reliability, and environmental aspects. Colombia's electricity demand is presented in Figure **1**. In the current situation, the Colombian electric power system has a total of 40 power plants distributed between 5 interconnected regions. Existing power plants include 22 hydroelectric, 15 natural gas, and 3 coal power plants. The total installed capacity is about 13,717 MW. Power plant capacities vary from 42 MW to 1,240 MW. According to the UPME, a total of 17 power plants are already planned to start operation between 2013 and 2022. Those power plants represent a total additional capacity of about 5,139 MW, including hydroelectric, natural gas, and coal power plants. Since the total installed capacity for 2020 will not be adequate to meet electricity demand and reliability targets over the whole time horizon, new power plants, including hydroelectric, natural gas, and coal power plants, are consider in this study. Capacities for these potential power plants vary from 300 MW to 700 MW, with each power plant having a specific capacity and location. Operating parameters for power plants were taken from the Independent System Operator in Colombia (XM). Reserve margin was set to 15 % of the peak power demand. In addition, spinning reserve margin was set to 5 % of current electricity demand. Five scenarios for CO_2 emission reduction were considered, the reduction targets were set to 5 %, 10 %, 15 %, 20 %, and 25 % with respect to the base case (0 % of CO_2 emission reduction) for Scenarios I, II, III, IV, and V, respectively. The developed model has the following characteristic: Mixed Integer Linear Programming (MILP) model with 4,560 constraints (Equalities plus inequalities), 6,920 continuous variables, 1,136 binary variables, and 28,834 non zero constraint matrix elements. The optimization problems were solved in GAMS (version 24.3.1) with CPLEX (version 12.6.0.1) as the MILP solver using an Intel i-7 @ 2.40 GHz processor with 8 GB RAM, running 64-bit Windows 8.1. The relative optimality gap was set to 3 % for all of the cases.

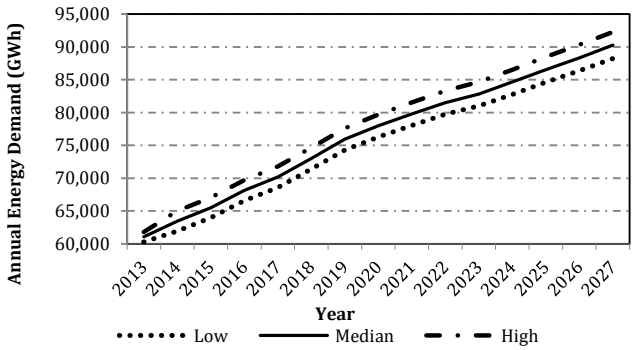

Figure 1. Colombia's forecasted annual electricity demand (GWh).

The results related to the optimal energy mix are presented in Figure 2. For the base case scenario, without constraint on CO_2 emissions, the optimal energy mix was as follows: hydropower plants supply about 75.83 %, natural gas and coal power plants supply about 18.41 % and 5.76 % of electricity requirements, respectively. As expected and confirmed by reports from XM, hydropower plants supply most of the electric

power requirements for Colombia. This is due to the fact that hydropower resources are abundant in Colombia and that hydropower generation is cheaper than other electric power generation alternatives that rely on coal or natural gas. The optimal electricity generation cost was determined to be about 50.53 $/MWh, a value which is close to the estimated generation cost of 51 $/MWh which was reported by the UPME in the power expansion plan for the same time frame.

According to the optimal power generation expansion plan, an additional capacity of around 3050 MW is required in order to meet the potential deficit in electricity supply from 2017 to 2027. To do so, the following additional power capacity should be added to the system: first, a new natural gas power plant with 500 MW of capacity needs to be built and operated from 2017 to 2027. Secondly, a new coal power plant with 300 MW of capacity should be built in 2016 and operated from 2019 to 2027. Thirdly, a new natural gas power plant with 650 MW of capacity needs to be built and operated from 2020 to 2027. Lastly, three new hydropower plants with 400 MW, 600 MW, and 600 MW of capacity should be built in 2020 and be operated from 2024 to 2027. All of the hydroelectric power plants are located in Antioquia, while the natural gas and coal power plants are located in Caribe and Centro, respectively. As regards interregional power transfer, the Caribe, Centro and Valle regions import electricity from Antioquia. Total investment in these new power plants is about $8.63 billion, about $2,829/kW. Total CO_2 emissions, over the 15 year time period considered in this study, were about 14.67 million tonnes per year. These emissions were around 0.191 tonnes of CO_2 / MWh. It was noted that a 10 % of reduction on CO_2 emissions can be achieved by increasing the generation from hydropower plants from 75.83 % to 78.09 %, without using CCS technologies for coal power plants. For a CO_2 emission reduction target of 15 %, one CCS facility should be installed in 2025. Similarly, for a 20 % reduction target, two CCS facilities need to be built in 2013 and 2018. Finally, for a 25 % reduction target, three CCS facilities should be installed in 2015, 2016, and 2025.

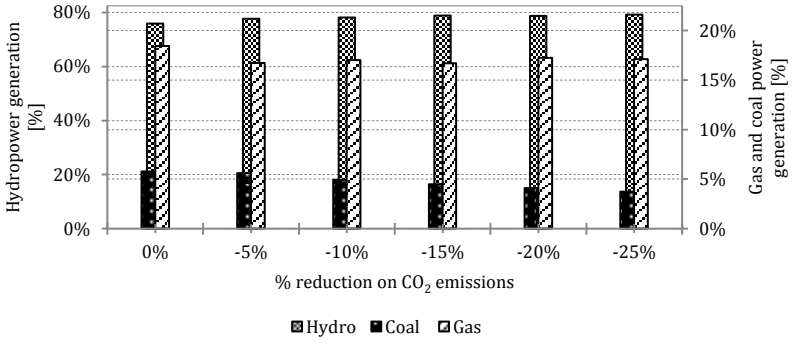

Figure 2. Optimal energy Mix.

Electricity generation and CO_2 emission reduction cost are summarized in Figure **3**. It is observed that electricity generation and CO_2 emission reduction costs increase as the CO_2 emission reduction target increases. In general, the average emission reduction cost was about $12.32/tonne of CO_2 for a reduction target equal or lower than 10 % (Scenarios I and II). Similarly, the average emission reduction cost was about $40.11/tonne of CO_2 for a reduction target equal or higher than 15 % (Scenarios III, IV, and V). The smoothness of the curve of CO_2 emission reduction costs from scenario I to II could be due to variations resulting from the choice of the optimality gap.

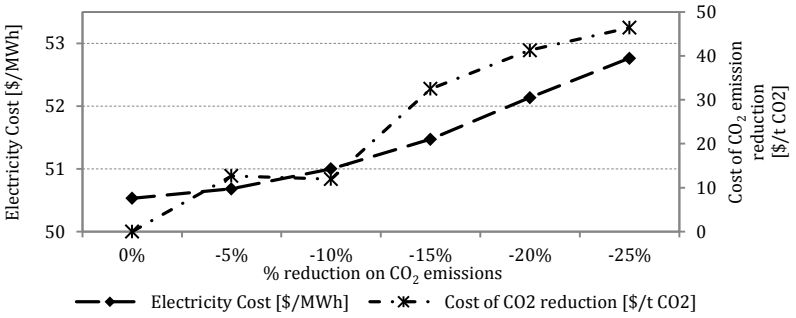

Figure 3. Electricity and CO_2 mitigation cost.

4. Conclusions

In this work, a deterministic MILP optimization model for the optimization of a distributed power systems with CO_2 emission constraints was developed. The capabilities of the proposed model were illustrated using a case study from the Colombian electric power system with different scenarios related to the CO_2 emission reduction targets. It was found that a 10 % of reduction in CO_2 emissions can be achieved by increasing the generation from hydropower plants, without using CCS technologies for coal power plants. In addition, for a CO_2 emission reduction target greater than or equal to 15 %, CCS facilities need to be installed. Future work will be focused on the extension of the deterministic model to a stochastic optimization model in order to take into account uncertainties in energy demand, availability of hydropower resources, fuel cost, as well as capital cost for power generation technologies.

Acknowledgements

The authors would like to acknowledge the financial support from the Colombian Science Council (COLCIENCIAS) and the Colombia-Purdue Institute for Advanced Scientific Research (CPIASR).

References

ExxonMobil, 2014, The Outlook for Energy: A View to 2040.

H. Bri-Mathias, S. Cremaschi, G. Blau, J. Pekny, G. Reklaitis, 2008, A Prototype Agent-Based Modeling Approach for Energy System Analysis, Comp. Aided Chem. Eng., 25, 1071–1076.

J.R. Flores, J.M. Montagna, A. Vecchietti, 2014, An Optimization Approach for Long Term Investments Planning in Energy, Appl. Energy, 122, 162–178.

N.E. Koltsaklis, A.S. Dagoumas, G.M. Kopanos, E.N. Pistikopoulos, M.C. Georgiadis, 2014, A Spatial Multi-Period Long-Term Energy Planning Model: A Case Study of the Greek Power System, Appl. Energy, 115, 456–482.

H. Mirzaesmaeeli, A. Elkamel, 2010, A Multi-Period Optimization Model for Energy Planning with CO_2 Emission Consideration, J. Environ. Manage., 91, 1063–1070.

I. Sharan, R. Balasubramanian, 2012, Integrated Generation and Transmission Expansion Planning Including Power and Fuel Transportation Constraints, Energy Policy, 43, 275–284.

T. Sirikitputtisak, H. Mirzaesmaeeli, P.L. Douglas, E. Croiset, A. Elkamel, M. Gupta, 2009, A Multi-Period Optimization Model for Energy Planning with CO_2 Emission Considerations. Energy Procedia, 1, 4339–4346.

G. Vinasco, D. Tejada, E.F. Da Silva, M.J. Rider, 2014, Transmission Network Expansion Planning for the Colombian Electrical System: Connecting the Ituango Hydroelectric Power Plant, Electr. Power Syst. Res., 110, 94–103.

Krist V. Gernaey, Jakob K. Huusom and Rafiqul Gani (Eds.), 12th International Symposium on Process Systems Engineering and 25th European Symposium on Computer Aided Process Engineering.
31 May – 4 June 2015, Copenhagen, Denmark

Bringing Non-energy Systems into a Bioenergy Value Chain Optimization Framework

Miao Guo, Nilay Shah*

Department of Chemical Engineering, Imperial College London, SW7 2AZ UK,
**n.shah@imperial.ac.uk*

Abstract

This study presents a multi-objective optimization model configured to account for a range of interrelated or conflicting issues involved in bioenergy systems. A spatial-temporal mixed integer linear programming model - ETI-BVCM (Energy Technologies Institute - Bioenergy Value Chain Model) (Samsatli et al. 2014) - was adopted and extended to incorporate resource-competing systems (bioenergy vs. non-energy) and effects on ecosystem services (ES) brought about by the land use transition in response to bioenergy penetration over five decades. The extended model functionality allows for exploring the effects of constraining ES impacts on other system-wide performance measures such as cost or greenhouse gas (GHG) emissions. The users can therefore constrain a metric which quantifies (to a certain extent) the change in ES from land use transitions. The developed model provides a decision-making tool for optimal design of bioenergy value chains supporting an economically and land-use efficient and environmentally sustainable UK energy system meanwhile delivering multiple ES. The study demonstrates the types of valuable insights the extended optimization modelling framework could provide for policy formulation to accelerate bioenergy penetration and support its sustainable development.

Keywords: optimization, bioenergy supply chain, energy system, ecosystem services

1. Introduction

Energy sectors are responsible for over 80% of the total GHG emissions in the EU-28 (EEA 2014) and approximately 83% of the UK GHG emissions in 2012 (DECC 2014). Bioenergy has been widely recognized as a strategy for mitigating climate change. This has triggered ambitious national/regional policy targets mandating the role of bioenergy within the overall energy portfolio e.g. the Renewable Energy Directive (RED) target of a 20% share of renewable energy in the EU energy mix by 2020 (EuropeanUnion 2009). However, bioenergy is a complex system, which involves many interrelated or conflicting issues e.g. economic development vs. environmental and social sustainability, interaction between energy and food sectors. Thus the large scale deployment of bioenergy requires a thorough understanding of how whole bioenergy value chains perform and the interaction of bioenergy with non-energy systems relying on the same resources and demanding the same productive lands for biomass production. The decision making should be supported by holistic and quantitative design tools considering conflicting objectives simultaneously and assessing the environmental and economic performance of bioenergy systems, considering the entire supply chain over the long-term. Mixed integer linear programming (MILP) represents an effective mathematical modelling approach to solve complex optimisation tasks and identify the potential trade-offs between conflicting objectives, which can provide a better understanding of bioenergy systems and support decision-makers elaborating the sustainable pathways towards bioenergy targets. Landscapes generate a wide range of ecosystem services but these services are often ignored in land use decisions. The land use transitions in response to the penetration of bioenergy over coming decades could affect not only supporting or regulating ES (e.g. GHG emissions, water quality and

carbon sequestration) but also various provisioning ES (e.g. biodiversity, food provisioning services). As highlighted in the Millenium Ecosystem Assessment (2005), with evidenced ongoing global degradation of ecosystem services, it is important to incorporate ES into the economic analysis underpinning real-world decision-making. Most of the optimization studies in this field focus on economic feasibility or trade-offs between economic performance and GHGs for bioenergy supply chain (SC) design but rarely consider the broader ES context. The economic performance can be investigated by conducting supply chain analysis but a full review on the supply chain models is not presented here due to space limit. To our best knowledge, no publically available study has incorporated non-energy systems and ES due to land use transitions over multiple periods into a spatially-explicit optimization model. This study aims to bring ecosystem services into the multi-objectives optimization framework supporting bioenergy SC design and optimal land use for multiple systems (energy and non-energy use).

2. Methodology

2.1 Problem statement

The underpinning concept is to bring resource-competing systems (bioenergy vs. non-energy) and the effects of bioenergy penetration on ecosystems into an optimization framework. This has been implemented by adopting and extending a spatial-temporal MILP model - ETI-BVCM (Samsatli et al. 2014). The ETI-BVCM toolkit encompasses bioenergy systems considering biomass from diverse bioresources including domestic food crops, bioenergy crops, forest, biowaste and imported biomass. It considers various pre-treatment and conversion technologies via biochemical, thermochemical and mechanical routes. It is capable of analysing UK bioenergy supply chains at a grid resolution of $50\,km \times 50\,km$ and identifying the potential trade-off between GHG targets and cost optimal solutions for bioenergy value chain design over five decades (2010s-2050s). Land types including arable lands, forestry lands, pasture lands and potential marginal lands, were considered in ETI-BVCM model and classified into four land levels according to the Corine land cover database. As reported in (Samsatli et al. 2014), level 1 represents land type 1 i.e. arable land and heterogeneous agricultural areas; level 2 is defined as level 1 plus land type 2 (shrub and herbaceous vegetation association and open spaces with little or no vegetation); level 3 is the accumulation of level 2 and land type 3 (permanent crops and pasture lands); level 4 is the accumulation of level 3 and land type 4 (forest and artificial non-agricultural vegetated areas). The non-energy systems incorporated in the extended ETI-BVCM model include food and industrial timber (e.g. roundwood) production and demand, which could compete with the bioenergy system due to their dependence on the same biomass resources and land demands (Fig 1). The economics of the system investigated focus on biomass cultivation, conversion technology, capacity assignment, logistics and transport networks. The model was configured to account for a range of ecosystem services and the ES impacts induced by the land use transition to the production of bioenergy and other products such as food and timber. A performance indicator land use intensity (LUI) was introduced into the model. The model is configured to account for annual harvested biomass extracted for socioeconomic use for multiple systems which lead to an efficient land use system supporting sustainable development of bioenergy and non-energy markets. LUI along with GHGs is evaluated using a life cycle approach to take into account the impacts of the entire bioenergy supply network on ES. Other ecosystem service impacts of land use transitions will be assessed using the matrix approach described by Holland et al. (2014). The research objective of this study is to extend the ETI-BVCM modelling framework to investigate the bioenergy system configuration to deliver optimal value chains best supporting an economically efficient, low-GHG and land-use efficient UK energy system meanwhile limiting the damages on ES and ensure UK food security and sustainable development of a lignocellulose resource market.

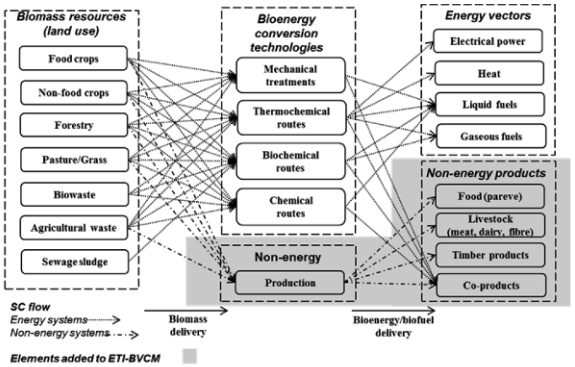

Figure 1 Bioenergy supply chains and non-energy systems

2.2 Model formulation

The multi-objective MILP model ETI-BVCM developed by Samsatli et al. (2014) was extended and formulated to account for non-energy systems, and ecosystem services (sections 2.2.1-2.2.5 & Fig 2).

2.2.1 Objective function

ETI-BVCM adopted a multi-objective optimisation approach in which the objective function was formulated as a weighted sum of costs, GHG emissions, energy production and exergy production. By giving weights, the model could either minimize the total discounted costs, minimize the total GHGs or maximize energy/exergy production or supply chain profit (Samsatli et al. 2014). In this study, the objective function is to minimize the total economic and GHG impacts of a bioenergy supply chain (Eq. (1)).

$$Obj = \sum_d \sum_{kpi} (TSCI_{kpi,d} WeightF_{kpi,d}) \quad (1)$$

2.2.2 Ecosystem services impacts

The variable $ESI_{epi,d}$ represents the change of ES brought about by land use transitions in response to bioenergy system development in each decade (*d*), which is constrained by the user-defined maximum allowed relative change to ES (Eq.(2)). As presented in Eq. (3), the decadal impacts on ES caused by the land transition to these uses can be semi-quantified by introducing land use transition factors $ESIF_{r,al,epi}$. The land transition impact matrix is being developed under this project research agenda to assess the ES impacts of land use transitions associated with a biomass production system. The principles for developing such a matrix, which identifies the direction and magnitude of the changes in ES impacts of new land use patterns have been addressed in (Holland et al. 2014) and some of the land transition matrix data will be derived from the ETI-funded ELUM project. Each land use ES change factor is divided into seven impact levels with indicator scores assigned (not spatially explicit, ESIF scores given in Fig 3). A negative score (-1,-2,-3) indicates that the land use transition would damage the ES whereas a positive (1, 2, 3) or a neutral score (0) represent beneficial effects or little/no impacts on ES. $TR_{r,c,al,d}$ denotes the transitions from areas of a reference cropping system to bioenergy feedstock (*r*) production at each land type al in cell c due to bioenergy penetration in decade d. As given by Eq. (4) decision variable $Tr_{r,c,al,d}$ is dependent on the difference in dedicated areas at each land level for bioenergy feedstock production at the end of each decade compared with the previous time period (decade d-1). A negative land use transition value indicates land use change from a bioenergy to non-energy cropping system whereas a positive value implies land transition from non-energy to bioenergy system use. Therefore, not only the land transition to bioenergy use (positive $Tr_{r,c,al,d}$) coupled with positive influences on a given epi could bring the beneficial effects (positive $ESI_{epi,d}$) but also avoidance of

negative ES impacts of bioenergy cropping system (negative $ESIF_{r,al,epi}$) by moving land use towards non-energy systems (negative $Tr_{r,c,al,d}$)could conceptually lead to an environmentally beneficial system (Fig 3). Note that (i) the key contribution here is the modelling framework and (ii) the results obtained are very sensitive to input data which suffers from paucity, hence the semi-quantitative approach.

$$ESI_{epi,\,d} \geq MinESI_{epi,\,d} \qquad \forall epi, d \tag{2}$$

$$ESI_{epi,\,d} = \sum_{r\in B}\sum_{c}\sum_{al} TR_{r,c,al,d}\, ESIF_{r,\,al,\,epi} \tag{3}$$

$$Tr_{r,c,al,d} = (A1_{r,c,al,d} - A1_{r,c,al-1,d}) - (A1_{r,c,al,d-1} - A1_{r,c,al-1,d-1})\ \forall r \in B \tag{4}$$

2.2.3 Land constraints

In addition to the constraint on land use transitions (Eq. (4)), the land areas allocated for bioenergy and non-energy resources are upper-bounded by the land availability ($MaxA_{c,al,d}$) in each cell at selected land level and the user-defined parameters for land allocation (Eq. (5), (6) and (7)).

$$\sum_{r\in B\cup FT}\sum_{c}(A1_{r,c,al,d} + A2_{r,c,al,d}) \leq \sum_{c} MaxA_{c,al,d}\gamma_{al,d} \tag{5}$$

$$\sum_{r\in B} A1_{r,c,al,d} \leq MaxA_{c,al,d}\alpha_{al,d} \tag{6}$$

$$\sum_{r\in FT} A2_{r,c,al,d} \leq MaxA_{c,al,d}\beta_{al,d} \tag{7}$$

2.2.4 Non-energy system constraints

To achieve optimal design of bioenergy value chains meanwhile limiting the damages on provisioning ES to ensure UK food security and sustainable timber supply, two constraints were introduced to limit the maximum amount of biomass resources to be used for bioenergy production. As stated in Eq. (8), UK local demand for food and timer resource r should be met by resource import and local production, which is determined by the area and annual biomass yield (Eq (9)). To further achieve the domestic food security and sustainable development of lignocellulosic provisioning services, a certain fraction of UK demand for food and timber resources r need to be met by local production(Eq. (10)).

$$\sum_{c}(Im_{r,\,c,\,d} + Pr_{r,\,c,\,d}) \geq D_{r,d} \qquad \forall r \epsilon FT \tag{8}$$

$$Pr_{r,\,c,\,d} \leq \sum_{al} A2_{r,\,c,\,al,d}\, Yield_{r,c,s,d} \qquad \forall r \epsilon FT \tag{9}$$

$$\sum_{c} Pr_{r,\,c,\,d} \geq D_{r,d} SecF_{r,d} \qquad \forall r \epsilon FT \tag{10}$$

2.2.5 Land use intensity

LUI (ton C/ha) formulated in Eq. (11) was introduced into the model - it is calculated after the model is solved. NPP is referred to as the net biomass production of an ecosystem in terms of carbon fixation rate, quantified as the net amount of carbon assimilated in a given period by vegetation (Zhuang et al. 2013). $NPPh_{r,c,s,d}$ represents the biomass extracted for further socioeconomic use and includes harvested crops, consumed crop residues, fuel wood and industrial roundwood as well as forage (including biomass directly consumed by livestock by grazing and biomass indirectly consumed through harvest for production of hay & silage). $NPPh_{r,c,s,d}$ involves above-ground harvested biomass for economic use and the used above-ground residues, which generally can be derived from Eq. (12). The parameters $Fabv_r$ HI_r $Blos_r$ Fh_r Rc_r can be obtained from publically available data sources e.g. (Zhuang et al. 2013). $NPP_{r,c,s,d}$ represents the difference between gross primary production (GPP describe the rate at which the plant produces useful chemical energy and is defined as the total amount of carbon fixed by photosynthesis) and plant respiration, and can be projected by using well-validated process-based simulation models e.g. NASA-CASA model, DeNitrification-DeComposition (DNDC).

$$LUI_d = \frac{\sum_{r\in B\cup FT}\sum_{c}\sum_{al} NPPh_{r,c,s,d}(A1_{r,\,c,\,al,d} + A2_{r,c,al,d})}{\sum_{c}\sum_{al} MaxA_{c,al,d}} \tag{11}$$

$$NPPh_{r,c,s,d} = NPP_{r,c,s,d} \cdot Fabv_r \cdot HI_r \cdot (1 - Blos_r) \cdot (1 + Fh_r \cdot Rc_r) \tag{12}$$

Sets	
$r \in R$	set of resources (biomass, non-energy resources e.g. water, sugar and energy carriers e.g. electricity, biofuel)
b	set of biomass resources used for bioenergy system $b \in B \subseteq R$
ft	set of food and timber resources used for non-energy systems ft∈FT⊆R
s	set of scenarios e.g. low/medium carbon concentration scenarios based on UK Climate Projections 2009
d	set of decades {2010s, 2020s, 2030s, 2040s, 2050s}
c	set of UK grid cells {1, 2…….157}
al	set of land levels concerning four land types {'1': "easy, established technology", '2': "pioneering plant establishment", '3': "challenging from a techno-economic and ecological aspects", '4': "last resort"}
kpi	set of key performance indicators including the cost, CO_2 and other GHGs
epi	set of ecosystem service performance indicators e.g. biodiversity, water quality and soil quality
Parameters	
$MinESI_{epi,d}$	Maximum allowed change to regulating/supporting ES or minimum food/timber/energy provisioning ES (indicator epi) in decade d
$WeightF_{kpi,d}$	Weighting factor for key performance indicator kpi in decade d; in the case of GHGs, market price for traded C emissions may be applied (£/kg CO_2 equivalence)
$ESIF_{r,al,epi}$	Impacts on ecosystem service (indicator epi) due to new land use transition patterns for cultivation of biomass resource r on land type al for bioenergy system development
$Yield_{r,c,s,d}$	Maximum yield (oven dry weight) of resource r in cell c under scenario s in decade d (odt/ha/y)
$MaxA_{c,al,d}$	Maximum available lands for crop plantation in cell c at land level al in decade d (ha)
$\alpha_{al,d}$	Fraction of area allocated for biomass cultivation for bioenergy system at land level al in decade d
$\beta_{al,d}$	Fraction of total area allocated for biomass cultivation for non-energy systems at land level al in decade d
$\gamma_{al,d}$	Fraction of total area allocated for total biomass cultivation for energy and non-energy systems at land level al in decade d
$D_{r,s,d}$	Annual demand of resource r under scenario s in decade d for non-energy system (timber, food etc.) (unit resource/y)
$SecF_{r,d}$	Security factor to ensure a certain fraction of resource r demand for provisioning ecosystem services (e.g. food, timber) to be met by local production in decade d
$NPPh_{r,c,s,d}$	Harvested net primary production (NPP) of biomass r in cell c under scenario s in decade d for socioeconomic use (t C/ha)
$Fabv_r$	Proportion of aboveground biomass for resource r
HI_r	Harvest index of biomass resource r, measuring the proportion of total aboveground biomass allocated to economic yield of crop
$Blos_r$	Proportion of biomass loss or return for resource r
Fh_r	Harvest factor for resource r representing the ratio of available above-ground residues to above-ground economic yield of harvested biomass
Rc_r	Recover rate of biomass r refers to the ratio of used above-ground residues to available above-ground residues
Continuous variables	
$TSCI_{kpi,d}$	Total impacts caused by whole bioenergy supply chain in decade d expressed as key performance indicator kpi (including cost and GHGs), consisting of the decadal impacts caused by crop production, infrastructure/capital, technology operation, resource import and storage, resource purchase, transport, carbon transport, waste disposal, credits brought by carbon capture and storage, carbon sequestration by long rotation forestry and offset by by-products
$ESI_{epi,d}$	Ecosystem services impacts of bioenergy supply chain in terms of indicator epi in decade d
$TR_{r,c,al,d}$	Area expansion/contraction of biomass r in cell c at land type al in decade d (ha) to represent the land use transition
$A1_{r,c,al,d}$	Areas dedicated for cultivation of resource r for bioenergy system in cell c at land level al in decade d (ha, non-negative)
$A2_{r,c,al,d}$	Areas dedicated for cultivation of resource r for non-energy systems in cell c at land level al in decade d (ha, non-negative)
$Im_{r,c,d}$	Import rate of resource r for non-energy systems in cell c in decade d (t/y)
$Pr_{r,c,d}$	Production rate of resource r for non-energy systems in cell c in decade d (t/y)
LUI_d	Land use intensity - harvested NPP for cultivation of a given biomass feedstock per unit available land in decade d

Figure 2 Nomenclature for extended ETI-BVCM model

ES impact level	Heavily damaged	Damaged	Slightly damaged	No impact	Slightly beneficial	Beneficial	Very beneficial
ESIF scores	-3	-2	-1	0	1	2	3
Direction of change of ecosystem services impacts brought about by land use transition towards bioenergy production system (note positive indicates an improvement)							
$ESIF_{r,al,epi}$	$TR_{r,c,al,d}$	$ESI_{epi,d}$					
+	+	+					
+	-	-					
-	+	-					
-	-	+					

Figure 3 Land transition matrix score and ecosystem services impacts

3. Illustrative example

To demonstrate the concept of extended model functionality (rather than to provide any detailed insights), the extended ETI-BVCM model has been applied to a UK case study with the EU RED target of a 10% share of renewables in the transport sector by 2020 (minimum demand of 164 PJ) where 6% share was assumed to be met by UK local production. Transport fuels including bioethanol, biodiesel, bio-butanol, biocrude oil and biomethanol derived from 1G and 2G feedstock (using the ETI-BVCM built-in database) via biochemical and thermochemical routes were modelled. The effect of constraining biodiversity ES on system-wide performance measures (cost and GHGs) for 2020 scenario were investigated. The SC cost increased by approximately 19% (increased from £11.1 bn to £13.2 bn) with shifting the lower bound for SC impacts on biodiversity (maximum allowed damage on ES ($MinESI$) moves within a range of -10,000,000 and +10,000,000). With the shift from an environmentally damaging to beneficial system, a significant reduction in land use for 1G biomass and an increase in land utilization for cultivating 2G feedstock for bioenergy demand are projected. The total UK land allocation for bioenergy system varies within the range of 12-25% whereas winter wheat food production accounts for 9.3-9.6% of total available UK lands across all configurations for 2020s. Nearly 90% of the decadal costs for transport biofuel SC are attributed to the biofuel production (operation and capital). 2G biomass cultivation contributes approximately 13% whereas the share of transport is negligible

4. Conclusion

A multi-objective bioenergy supply chain optimization model - ETI-BVCM - is extended to account for interrelated and conflicting issues in bioenergy SC design e.g. land utilization and resource potential for competing systems (bioenergy vs. non-energy) and a wider range of ecosystem services. With the proposed modelling approaches, this research highlights the valuable insights the extended optimization modelling framework could provide for strategic design of bioenergy supply chains, which best support an economically viable, land-use efficient and environmentally sustainable UK energy system meanwhile deliver multiple ecosystem services.

Acknowledgements

This study is based on the research supported by the Engineering and Physical Sciences Research Council UK through SUPERGEN Bioenergy Hub. We would like to thank all participants in consortium project Bioenergy value chains: Whole systems analysis and optimisation (EP/K036734/1). We also wish to acknowledge the Energy Technologies Institute for commissioning and funding the development of the BVCM toolkit and providing a licence for using and modifying the ETI-BVCM tool.

References

Millenium Ecosystem Assessment, 2005, Ecosystems and Human Well-being: Synthesis.

DECC, 2014, 2012 UK Greenhouse Gas Emissions, Department of Energy and Climate Change.

EEA, 2014, EEA greenhouse gas - data viewer. The European Environment Agency.

European Union, 2009, Directive 2009/28/EC of the European Parliament and of the Council on the promotion of the use of energy from renewable sources and amending and subsequently repealing Directives 2001/77/EC and 2003/30/EC.

Holland, R. A., F. Eigenbrod, A. Muggeridge, G. Brown, D. Clarke and G. Taylor, 2014, A synthesis of the ecosystem services impact of second generation bioenergy production (submitted)

Samsatli, S., N. J. Samsatli and N. Shah, 2014, BVCM: a comprehensive and flexible toolkit for whole system biomass value chain analysis and optimisation – mathematical formulation, Applied Energy (accepted).

Zhuang, Q. L., Z. C. Qin and M. Chen, 2013, Biofuel, land and water: maize, switchgrass or Miscanthus? Environmental Research Letters **8**(1): 6.

Krist V. Gernaey, Jakob K. Huusom and Rafiqul Gani (Eds.), 12th International Symposium on Process Systems Engineering and 25th European Symposium on Computer Aided Process Engineering.
31 May - 4 June 2015, Copenhagen, Denmark.

MILP Approach for the Design of Residential Microgrids with Energy Interaction Restrictions

Carmen Wouters[a], Eric S. Fraga[b,*] and Adrian M. James[a]

[a]*School of Energy and Resources, University College London, Adelaide SA 5000, Australia*
[b]*Center for Process Systems Engineering, Department of Chemical Engineering, University College London, London WC1E 7JE, UK*
e.fraga@ucl.ac.uk

Abstract

A mixed integer linear programming (MILP) approach is presented for the design of residential distributed energy systems under cost minimisation. A neighbourhood design is determined based on the selection from a pool of energy supply alternatives to meet the total annual energy demand. In addition to distributed generation units, energy integration in the form of microgrid (MG) operation and pipeline networks are considered. Location specific input data regarding cost, climate and regulations are taken into account. The effect of energy interaction restrictions, in the form of residential energy export and MG operation, on neighbourhood design is researched.

Keywords: distributed energy system, energy integration, mixed integer linear programming, trigeneration

1. Introduction

Small-scale generation units that are located close to end-consumers in the central electricity grid - so called distributed generation (DG) units - could help to address climate change issues and the finiteness of conventional energy resources (Pepermans et al., 2005). DG units are ideally combined into highly efficient microgrid (MG) environments that are able to exploit locally available renewable energy resources as well as to share locally generated energy between its participants. Distributed energy systems are therefore tailored to location specific requirements and need a cost effective and efficient design. A superstructure MILP model to achieve such design for a small residential neighbourhood is presented in this work. The decision of investing in and the choice of DG and storage units depends on the ability of the MG to export electricity to the central grid as well as on the electricity exchange allowance between households within a MG. These energy interactions are important to allow local excess generation to be exported in order to avoid MG safety issues due to local generation being higher than local demand. Furthermore, export allows houses to create an income through potential governmental support schemes in the market. Energy interaction allowances of distributed energy systems are therefore determining economic and safety factors for local energy system design and are therefore analysed in this paper.
Various papers in the field of design optimisation of distributed energy systems exist. Manfren et al. (2011) and Keirstead et al. (2012a) provided comprehensive reviews of optimal design models with specific sets of technologies and assumptions. Energy integration of distributed energy systems with regard to MG operation combined with heating is addressed in a residential setting by for example Mehleri et al. (2011, 2013), who employs a cost minimisation MILP approach. District heating and power system MILPs on 'eco-town' levels are addressed by amongst others Keirstead et al. (2012b) and Weber and Shah (2011). With regard to the focus of this work, i.e. full

energy integrated residential distributed energy systems in terms of heating, cooling as well as MG operation, and, the effect of energy interaction restrictions on design, research is limited. A deterministic MILP approach is proposed, building further on ongoing efforts in the field (Keirstead et al., 2012b; Mehleri et al., 2011, 2013; Weber and Shah, 2011). A full energy integrated approach is developed for analysis, continuing previous work of the authors (Wouters et al. (2014)).

2. Methodology

2.1. Problem description

A decision making strategy is formulated for the design of a small residential energy system while minimising the total annualised cost, C^{TOT} [AUD/year], to meet its energy demands in terms of electricity, heating and cooling. A superstructure methodology is adopted with dispatchable and intermittent DG and storage options together with non-loop pipeline and MG operation approaches. The fictive residential neighbourhood under research is framed by South Australian (SA) location specific characteristics. The potential energy supply options are an interconnection with the central distribution network, air-conditioning units, gas heaters, condensing boilers and DG units in the form of PV units (up to 10 kW), small-scale wind turbines (1.5 kW), micro combined heat and power (CHP) units with electrical capacities from 1 to 20 kW, micro absorption chillers and thermal and electrical storage units (Wouters et al., 2014). The houses can be thermally integrated through optimised pipeline networks and electricity integrated through MG operation. The model is optimised in GAMS using the CPLEX 12.4.0.1 solver to global optimum (GAMS Development Corporation, 2012). The optimisation is carried out for a typical day (24 hours) in each season over a yearly planning horizon. Several location specific inputs are required for the deterministic model: (i) climatological data; (ii) technical specifications of units; (iii) cost data with regard to investment and operation and maintenance (OM) and natural gas and electricity prices; (iv) regulations; and, (v) spatial distributions of hourly average energy demand data.

2.2. Model

The objective cost function consists of the annualised investment costs of technologies *tech*, C^{INV}_{tech}, the fixed and variable OM costs, C^{OM}_{tech}, the fuel costs associated with the consumption of natural gas for electricity and heat generation, C^{FUEL}_{tech}, the cost of purchasing electricity from the central grid by house i, $C^{GRID}_{i,BUY}$, the carbon tax imposed on each house, C^{CT}_{i}, and the potential income through governmental support schemes in the market, $C^{GRID}_{i,SELL}$.

$$minC^{TOT} = \sum_{tech}(C^{INV}_{tech} + C^{OM}_{tech} + C^{FUEL}_{tech}) + \sum_{i}(C^{GRID}_{i,BUY} + C^{CT}_{i}) - \sum_{i} C^{GRID}_{i,SELL} \tag{1}$$

The objective function is bound by energy balance equations regarding heating, cooling and electricity as well as design and operational constraints of the energy supply alternatives. The full model is omitted in this paper due to space limitations but builds further on previous work of the authors (Wouters et al., 2014). The relevant electricity interaction equations are detailed below.
Each house can only export electricity from DG units to the grid, $DG^{EXPORT}_{tech,i,s,h}$ [kW], in each hour h in each season s up to a maximum, U^{Export} [kW]. The binary decision variables $X^{snd}_{i,s,h}$ and $X^{rec}_{i,s,h}$ indicate whether a house respectively sends or receives electricity. In each hour, each house can either not interact with the grid or receive or send.

$$\sum_{tech} DG^{EXPORT}_{tech,i,s,h} \leq U^{Export} \cdot X^{snd}_{i,s,h} \qquad \forall i,s,h \tag{2}$$

$$X^{rec}_{i,s,h} + X^{snd}_{i,s,h} \leq 1 \qquad \forall i,s,h \tag{3}$$

Furthermore, each house can import electricity from the grid, $E^{GRID}_{i,s,h}$, up to a maximum U^{Import}.

$$E^{GRID}_{i,s,h} \leq U^{Import} \cdot X^{rec}_{i,s,h} \qquad \forall i,s,h \tag{4}$$

Note that if MG operation is selected, decided through binary selection variable Z, the neighbourhood as a whole can either import or export electricity in each hour. If MG operation is not selected, each house can individually interact with the central grid. MG operation refers to the sharing of locally generated electricity between households.

$$X^{snd/rec}_{i,s,h} - X^{snd/rec}_{i-1,s,h} \leq 1 - Z \qquad \forall i,s,h \text{ and } i > 1 \tag{5}$$

$$X^{snd/rec}_{i-1,s,h} - X^{snd/rec}_{i,s,h} \leq 1 - Z \qquad \forall i,s,h \text{ and } i > 1 \tag{6}$$

Electricity can be exchanged between each pair of houses i and j through MG operation determined by the uni-directional MG connection binary decision variable $MGC_{i,j,s,h}$. These connections are only possible if MG operation is installed in the neighbourhood:

$$MGC_{i,j,s,h} + MGC_{j,i,s,h} \leq Z \qquad \forall i,j,s,h \text{ and } i \neq j \tag{7}$$

The electricity send and received between each pair of households, $E^{snd/rec}_{i,j,s,h}$ [kW], is limited by an upper bound, U^{MG}, and the connection existence. Energy balances also govern this relationship.

$$E^{snd/rec}_{i,j,s,h} \leq U^{MG} \cdot MGC_{i,j,s,h} \qquad \forall i,j,s,h \text{ and } i \neq j \tag{8}$$

Note that since a deterministic approach is employed, parameter uncertainty can affect the obtained results. Further analysis would be required to assess the sensitivity of the developed model.

2.3. Case-study

A fictive neighbourhood consisting of 5 typical households in an Adelaide (SA) setting is under research (Wouters et al., 2014). Typical Adelaide based deterministic heating, cooling and electricity demand profiles are entered for a typical day in each season [kW]. The houses have in percentage varying energy demands from house 5 with the highest to house 1 with the lowest energy demands. Additionally, hourly solar irradiation [kW/m^2] and wind speeds at 15 m above ground level [m/s] are put in. Average utility energy tariffs [AUD/kWh] and the solar feed-in tariff from the SA market (0.06 AUD/kWh) are used. The lifetime of the project is taken to 20 years with an interest rate of 7.5 %. Each house can export excess self generation to the grid but can also buy electricity from the grid if local generation is not sufficient to meet the demand.
With regard to the residential export of electricity in the National Electricity Market of Australia, each state has its own requirements mainly focussing on PV units only. Within SA, a daily PV export limit per household of 45 kWh/day is in place. In Queensland, a restriction of residential PV export is proposed with currently an energy equivalent of 2 % of the installed capacity of a PV unit that can be exported at each time. The impact of this allowance is researched. For the analysis, the maximum allowed values of export and MG interaction are set to:

- the maximum electricity export of each house in each hour is set to the sum of the installed capacities of PV unit, CHP unit and small-scale wind turbine
- the maximum electricity exchange between each pair of houses in each hour through MG operation is set to the total electricity demand of the receiving household in terms of lighting and appliances, electricity for installed absorption chillers or air-conditioning units as well as potential dump loads

Three scenarios are then analysed in section 3 using the above maxima:

1. a percentage decrease of the upper limit of PV electricity export, $U^{ExportPV}$, ranging from unlimited to zero as well as the current daily limit in SA. No other DG export is allowed
2. a percentage decrease of the upper limit of total DG electricity export, $U^{ExportDG}$
3. a percentage decrease of the upper limit of MG operation, U^{MG}, for each household pair

3. Results and discussion

3.1. Scenario 1: PV export restrictions

Additional equations set either an hourly PV export limit in function of a percentage, $U^{ExportPV}$, of its installed capacity, or, a daily export limit (45 [kWh day^{-1}]). The installed capacity is determined through an optimised surface area A_i^{PV} times a rated capacity C_{prat} (Wouters et al., 2014):

$$DG_{PV,i,s,h}^{EXPORT} \leq U^{ExportPV} \cdot A_i^{PV} \cdot C_{prat} \qquad \forall i,s,h \tag{9}$$

$$\sum_s \sum_h h \cdot DG_{PV,i,s,h}^{EXPORT} \leq U_{day}^{Export} \qquad \forall i,s \tag{10}$$

The results are given in Figure 1. The neighbourhood design remains fairly constant with increasing export allowance in that it has PV units and heat storage tanks in each house, one CHP unit of 2.1 kW in house 2, one pipeline connection from the house with the CHP unit to house 4, as well as MG operation. No batteries, absorption chillers or small-scale wind turbines are installed. With increasing export allowance, the total PV capacity in the neighbourhood gradually increases from 6.3 from zero export allowance to 10.5 kW above an export allowance of 50 % of the total installed PV unit capacity. Electricity is exported up to a maximum in all cases. The total PV electricity export is mainly balanced with MG operation to take advantage of the solar feed-in tariff in the market. The design remains unchanged, i.e. constant, from an export allowance above 50 %.

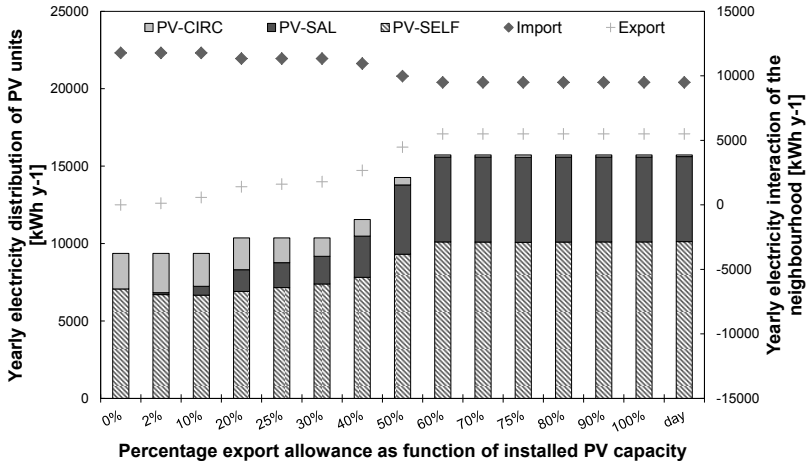

Figure 1: The share of total yearly PV electricity generation in terms of either self use by the accommodating houses, for grid export and for MG circulation [kWh y^{-1}] (see left vertical axis and bar chart) as well as the yearly electricity export and import of the neighbourhood as a whole [kWh y^{-1}] (see right vertical axis and points) in terms of percentage export allowance as function of installed capacity (horizontal axis). day=daily export allowance, CIRC=microgrid circulation, PV=photovoltaic units, SAL=export, SELF=self use.

3.2. Scenario 2: Total export restrictions

Similar constraints as presented in equations 9 and 10 are added when researching total DG electricity export restrictions from the installed PV units, CHP units and small-scale wind turbines. The results are presented in Figure 2. The neighbourhood design remains constant in the same way as in scenario 1. The installed PV unit capacity gradually increases from 6.3 kW at zero export allowance to 10.5 kW from an export allowance above 40 %. The CHP unit and corresponding uni-directional pipeline remain the same as under scenario 1 for each level of total export allowance of the neighbourhood. Additionally, with an export allowance greater than 40 %, dump loads are no longer required to absorb excess generation. The neighbourhood design and interaction behaviour becomes constant from a total DG export allowance above 50 % of the total installed DG capacity in the neighbourhood.

3.3. Scenario 3: Microgrid circulation restrictions

MG circulation restrictions are adopted by varying the percentage, U^{MGrec}, of the total load of a house, $C^{LoadTOT}_{ELEC,i,s,h}$ [kW], that can be received from another house in the neighbourhood through MG operation, $E^{rec}_{i,j,s,h}$ [kW]. The total DG export allowance is set to 45 kWh per day.

$$E^{rec}_{i,j,s,h} \leq U^{MGrec} \cdot C^{LoadTOT}_{ELEC,i,s,h} \qquad \forall i,j,s,h \text{ and } i \neq j \tag{11}$$

Figure 3 illustrates per house the installed capacities for the MG allowances that lead to the most significant neighbourhood design changes. No MG operation is adopted until an exchange allowance above 40 % and no pipeline is installed till an allowance above 60 %. The neighbourhood design becomes constant above 90 % allowance. Note that CHP units are only installed if their electricity can be used for MG circulation. The installed CHP unit changes from 1.8 kW (house 1) to 2.1 kW (house 2) from an allowance above respectively 40 % and 60 %.

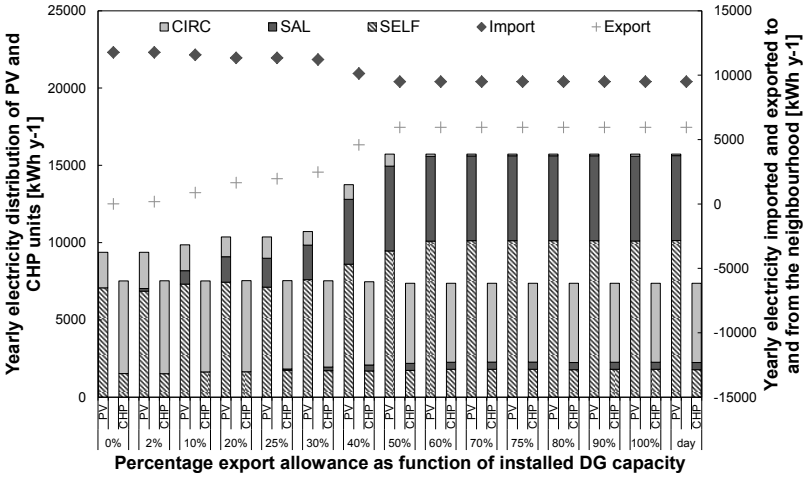

Figure 2: The share of total yearly PV and CHP electricity generation for either self use by the accommodating houses, for grid export and for MG circulation (see left vertical axis and bar charts) as well as the yearly electricity export and import of the neighbourhood as a whole [kWh y^{-1}] (see right vertical axis and points) in terms of percentage export allowance as function of total installed capacity. PV=photovoltaic units, CHP=combined heat and power units, CIRC=microgrid circulation, SAL=export, SELF=self use, day=daily export allowance. No wind turbines are installed.

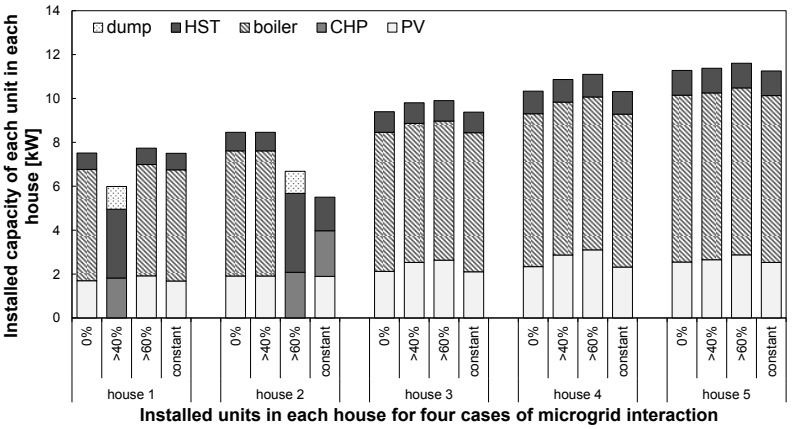

Figure 3: Installed capacities per house [kW] for MG interaction allowance of 0 %, greater than 40 % and greater than 60 % as well as constant design. CHP=combined heat and power, dump=dump load, HST=heat storage, PV=photovoltaic units.

4. Conclusion

An MILP approach has been presented for the design of residential distributed energy systems under cost minimisation. Several energy supply alternatives, such as DG units and storage, as well as energy integration in the form of MG operation and pipeline networks have been considered. The effect of energy interaction restrictions has been researched. This has shown that a total export allowance above an equivalent of 50 % of installed DG capacity leads to a constant neighbourhood design. A variation in MG interaction allowance has shown that above 40 % of the load of a house should be allowed to be supplied through MG operation to initiate the investment in a MG and CHP unit and above 60 % for pipelines in the neighbourhood.

5. Acknowledgements

The authors gratefully acknowledge BHP Billiton for providing a PhD Scholarship to C. Wouters.

References

GAMS Development Corporation, December 2012. Genetic Algebraic Modeling System. Available online: http://www.gams.com/dd/docs/bigdocs/GAMSUsersGuide.pdf (last consulted on 30 October 2013).

Keirstead, J., Jennings, M., Sivakumar, A., 2012a. A review of urban energy system models: Approaches, challenges and opportunities. Renewable and Sustainable Energy Reviews 16 (6), 3847 – 3866.

Keirstead, J., Samsatli, N., Shah, N., Weber, C., 2012b. The impact of CHP (combined heat and power) planning restrictions on the efficiency of urban energy systems. Energy 41 (1), 93–103.

Manfren, M., Caputo, P., Costa, G., 2011. Paradigm shift in urban energy systems through distributed generation: Methods and models. Applied Energy 88 (4), 1032–1048.

Mehleri, E., Sarimveis, H., Markatos, N., Papageorgiou, L., 2011. Optimal design and operation of distributed energy systems. Computer Aided Chemical Engineering 29 (21st ESCAPE), 1713–1717.

Mehleri, E., Sarimveis, H., Markatos, N., Papageorgiou, L., 2013. Optimal design and operation of distributed energy systems: Application to greek residential sector. Renewable Energy 51, 331–342.

Pepermans, G., Driesen, J., Haeseldonckx, D., Belmans, R., D'haeseleer, W., 2005. Distributed generation: definition, benefits and issues. Energy Policy 33 (6), 787 – 798.

Weber, C., Shah, N., 2011. Optimisation based design of a district energy system for an eco-town in the United Kingdom. Energy 36 (2), 1292–1308.

Wouters, C., Fraga, E. S., James, A. M., Polykarpou, E. M., 2014. Mixed-integer optimisation based approach for design and operation of distributed energy systems. In: the Australasian Universities Power Engineering Conference (AUPEC), 2014. IEEE.

Krist V. Gernaey, Jakob K. Huusom and Rafiqul Gani (Eds.), 12th International Symposium on Process Systems Engineering and 25th European Symposium on Computer Aided Process Engineering.
31 May – 4 June 2015, Copenhagen, Denmark

Engineering Design of Localised Synergistic Production Systems

Melissa Leung Pah Hang,[a] Elias Martinez-Hernandez,[b] Matthew Leach,[a] Aidong Yang[b]
[a] *University of Surrey, Guildford and GU2 7XH, United Kingdom*
[b] *University of Oxford, Oxford and OX1 2JD, United Kingdom*

Abstract

Centralised production of essential products and services based on fossil fuels and large scale distribution infrastructures have contributed to a plethora of issues such as deterioration of ecosystems, social-economic injustice and depletion of resources. The establishment of localised production systems can potentially reduce unsustainable resource consumption and bring socioeconomic and environmental benefits. The main objective of this work is to develop engineering tools for the rational design of such systems. Production of products and services is characterised as inter-linked subsystems (e.g. food, energy, water and waste). A sequential design approach is developed to design subsystems in turn, with necessary iterations. The process is illustrated through the co-design of energy, water and food production for a case study locale based on a developing eco-town in the UK. This design approach suggested an integrated system based primarily on locally available resources and allowed greater insight into the drivers and constraints on local resource use.

Keywords: local production network, mathematical programming, resource consumption

1. Introduction

With the advent of industrialisation, the supply of energy and materials to meet human needs has been driven primarily by centralised production based on fossil fuels and large scale distribution infrastructures. However, continuation of this mode of production, coupled with rising economies and growing population, has led to a range of issues such as energy supply insecurity, deterioration of ecosystems, and depletion of resources. In response to these issues, localised production networks based on locally available resources have been advocated as one possible pathway towards sustainability (Middlemiss and Parrish, 2010; The Royal Academy of Engineering, 2011). A local production system is defined in this work as a network of heterogeneous processes, integrated in a synergistic manner to achieve a high degree of resource efficiency, potentially leading to improved economic viability while preserving the ecosystem (Martinez-Hernandez et al., 2014). Such a system contributes to improved prospects for closing loops as any wastes or by-products from production processes and used products from consumption will seek to be looped within the system through symbiotic arrangements. The aim of this work is to propose a systematic design approach for a local production system given a set of local demands by finding the combination of a set of locally available sources and processes which can meet such demands by minimising total resource consumption, while observing a set of ecological and technical constraints. The design approach has so far been developed by analyzing a specific case study. The learning from this particular case study may be generalised into a general

framework for designing such localised production systems. The proposed approach is based on mathematical programming (MP) which has been widely applied in process systems engineering (Klatt and Marquardt, 2009; Klemes et al., 2013) to solve a wide range of problems such as the design of bioenergy network (Beck et al., 2008) and the synthesis of supply chains (Almansoori and Shah, 2012). The present work applies MP in a sequential and iterative approach for the integrated design of multiple production systems.

2. Methodology

Figure 1 presents the proposed framework for the co-design of food, water and energy network supported by a case study with reference to Whitehill and Bordon Eco-Town in the UK. The first step includes representing the components of the food, water and energy network and identifying the potential sources (i.e. supply of resource flow) and sinks (i.e. processes consuming the resource flows) in a superstructure. Mathematical models are then used to represent the processes (e.g. resource processing and conversion), constraints and interactions (i.e. exchange of flows). The least connected subsystem or network, i.e. the one upon which the other networks are least dependent is designed first in view of having a less constrained design problem. Food is considered the least connected network as energy and water are key resources for food production but both water and energy productions do not depend on food production in this particular case study. The water production network is assumed to be the second least connected network and is next designed while the energy production network is designed last. The objective function is to design the production network (food, water and energy) by selecting the production processes and determining the flow rates from source to sink that will minimise total resource consumption while observing a set of ecological and technical constraints for satisfying local demands. The objective function measured in terms of cumulative exergy resource consumption is calculated using the Cumulative Exergy Resource Accounting methodology (Leung Pah Hang et al., 2014).

The generic objective function for an individual production network was formulated as Eq. (1):

$$\text{Minimise } TC = \sum F_{imp} e_{imp} \quad (1)$$

where,
TC is the total resource consumption;
F_{imp} is the flow rate of imported flows to the production network (e.g. imported energy such as electricity from grid, heat from district heating, chemicals, fuels, fertilisers, imported animal feed);
e_{imp} is the cumulative exergy consumption associated with the provisioning of the imported flows.

The optimisation is to be subject to the final local need, land availability, availability of local resource, balance between sources and sinks, concentration balance for water network, nutrient balance for food network and electricity and heat balances for energy network constraints. The optimisation model for each subsystem was solved using GAMS. Both the food and energy network were solved using linear programming while the water network was solved using non-linear programming due to non-linearity in its

concentration balance. The sources and sinks considered for the three networks are shown in Table 1.

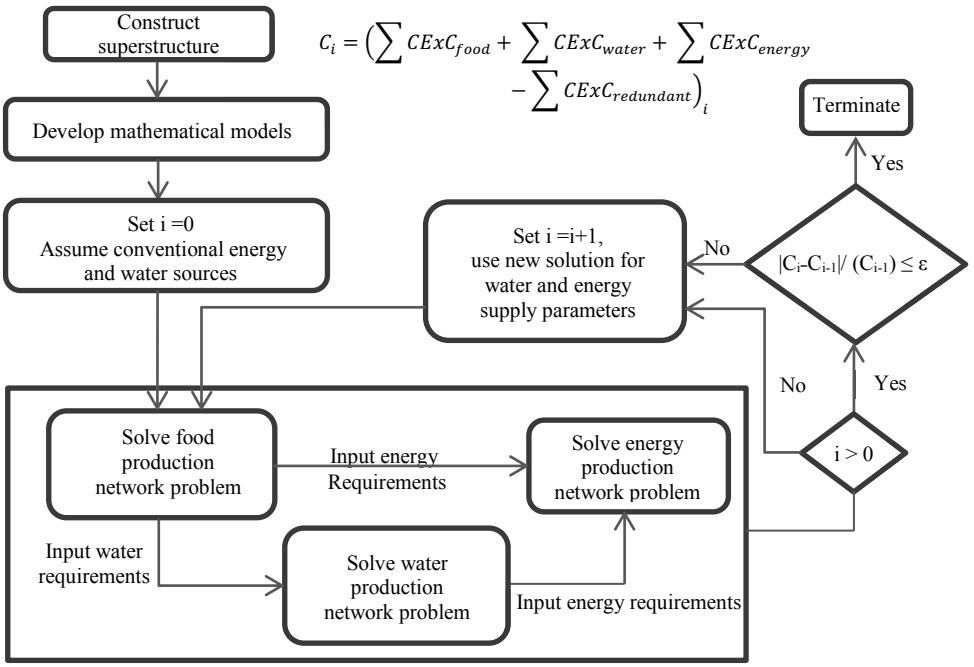

Figure 1: Methodological framework for co-design of food, water and energy network

The initial solution (i.e. i=0) is obtained by solving the three production network design problems assuming conventional energy and water sources in the sequence as illustrated in Figure 1. The conventional energy sources are assumed to be electricity supplied from the grid and heat supplied from a natural gas based district heating network while groundwater is the conventional water source. First, the food production network is designed. Second, the water production network is designed by considering the water sources and sinks in the initial solution of the food production network, which will suggest specific water streams that can be used by the food production network and other local users and the associated resource costs in terms of the cumulative exergy content. Lastly, the energy production network is designed taking into account the energy sources and sinks in the initial solutions of the food and water production networks, to determine specific energy streams that can be generated locally or obtained from centralised supply to meet various demands including those from the food production network. For the next iteration (i=i+1), the water and energy supply parameters from the solution of the previous iteration are used and the same sequence is repeated. The iteration stops when the cumulative exergy consumption to produce the streams exchanged between the three networks become stable, meaning that no further change is incurred by further iterations. This will be reflected in the overall cumulative exergy consumption for production of food, water and energy networks and can be verified using the criterion $|C_i-C_{i-1}|/ (C_{i-1}) \leq \varepsilon$ (where ε can be a small value, e.g. 0.01), as shown in Figure 1. The cumulative exergy consumption of the redundant flows refers to

the cumulative exergy consumption of the flows internal to the whole system and exchanged between the three networks.

3. Results

The initial results from the initial optimisation of the food network suggested that only bread and potatoes be produced locally. The objective function for the food production network was 1.04×10^8 MJ/y. The initial results for the water network indicated that most of the water required by the water consuming processes should be supplied by groundwater. A small portion of the wastewater generated during the bread processing is diluted by groundwater and used for both potatoes cultivation and processing. Similarly, a small amount of the wastewater produced from potatoes processing is used together with groundwater for wheat cultivation and wheat processing into bread. The objective function for the water production network was 2.05×10^6 MJ/y. The results generated from the initial optimisation of the energy production network showed that biomass CHP is the preferred option for supplying all the electricity and energy demands of both the food and water production networks. It can also satisfy all the energy demand for households. The objective function for the energy production network was determined to be 1.19×10^9 MJ/y.

Table 1: Sources and sinks in the food, water and energy production networks

Sources	Sinks	Sources	Sinks
Food production network		*Water production network*	
▪ Imported fertiliser ▪ Imported animal feed ▪ Manure from cattle ▪ Manure from pigs ▪ Wheat residues ▪ Potatoes residues	▪ Wheat cultivation and processing ▪ Potatoes cultivation and processing ▪ Cattle breeding and processing ▪ Pig breeding and processing	▪ Treated food production wastewater ▪ Wheat processing ▪ Potatoes processing ▪ Cattle breeding and processing ▪ Pig breeding and processing ▪ Treated domestic wastewater ▪ Groundwater ▪ Rainwater ▪ Treated wastewater from energy production	▪ Energy production ▪ Wheat cultivation ▪ Wheat processing ▪ Potatoes processing ▪ Cattle breeding and processing ▪ Pig breeding and processing ▪ Residential water ▪ Discharge
Energy production network			
▪ Grid ▪ Wind ▪ Solar ▪ Biomass CHP ▪ Natural gas CHP	▪ Wastewater treatment plant ▪ Food production network ▪ Residential		

The 1st iteration involves feeding back into the food production network the initial results from the optimisation of the water and energy production networks. The exergy parameter for energy used for the optimisation of the food production network now changed from 2.50 MJ/kg bread to 5.78 MJ/kg bread and for water use from 108.60

MJ/kg bread to 107.90 MJ/kg bread. The parameter for energy use for potatoes changed from 0.41 MJ/kg potatoes to 0.81 MJ/kg potatoes and for water use from 1.13 MJ/kg potatoes to 1.12 MJ/kg potatoes while the parameters used for beef and pork production remains unchanged. These changes in parameters now resulted in only potatoes and pork being produced locally; indicating that the food production network is highly sensitive to the water and energy supplies. The new objective function for the food production network after the 1st iteration (i.e. the round following the initial optimisation) was 1.05×10^8 MJ/y which is 0.18% more than the initial value of the objective function. This is because the assumed cumulative exergy consumption for conventional energy sources obtained from literature and used in the initial optimisation is much lower than the cumulative exergy consumption associated with energy supply from biomass CHP. However, there is now more potential for a locally integrated food production network based on locally available resources. The manure from pig is used to partly satisfy the nutrient requirements of potato cultivation. Also, all residues from potato cultivation are now being used as animal feed for pigs. Groundwater consumption for food production has slightly decreased with exchanged water flows from bread and potatoes manufacture being used to supply part of the network's water requirements. Moreover, the resulting integrated food production network is not dependent on imported fossil fuels for its energy requirements. The objective function for the water production network for the 1st iteration was 7.72×10^5 MJ/y; a reduction of 62% from the initial objective function of this network, primarily due to rainwater replacing about 34% of the groundwater. The objective function of the energy production network from the 1st iteration was 1.19×10^9 MJ/y; a very slight decrease of 0.10% from the initial objective function of the energy production network

A 2nd round of iteration was carried out, which led to a solution virtually identical to one obtained from a further (i.e. the 3rd) iteration. The final results are presented in Figure 2. The total potato demand and 11% of total pork demand are to be satisfied locally; water is supplied by both groundwater and rainwater while electricity and heat are supplied locally by biomass wood chip CHP. As compared to the initial solutions, the objective function of the last iteration for the food production network increased by 0.20% while the objective functions of the water and energy production networks have decreased respectively by 62% and 0.10%.

4. Concluding remarks

This work has developed a sequential and iterative approach to the co-design of the integrated production of food, water and energy to satisfy local demands by making the use of locally available resources within technical and ecological constraints while minimising aggregated resource consumption. This design approach has proved to be useful in the analysis of intermediate results contributing to better insight and understanding of the localised production system; offering an added-value to practitioners as compared to designing these three production networks simultaneously. In practice, local situations may well impede the adoption of a simultaneous approach due to the incremental nature of knowledge and data acquisition and options gathering from various stakeholders, thus there is great value in enriching the understanding of the linkages between subsystems which is enabled by the sequential approach. In particular, it was useful in gaining insight, by means of the intermediate results obtained from the iterative process, on the balance of cumulative exergy consumption between the food, energy and water networks and the trade off in using imported flows and conventional sources of energy and water and using locally available resources. As a next step, a

further comparison between this sequential approach and the simultaneous approach can be made, with the possibility of refining the current approach into a hybrid one to benefit from the advantages of both.

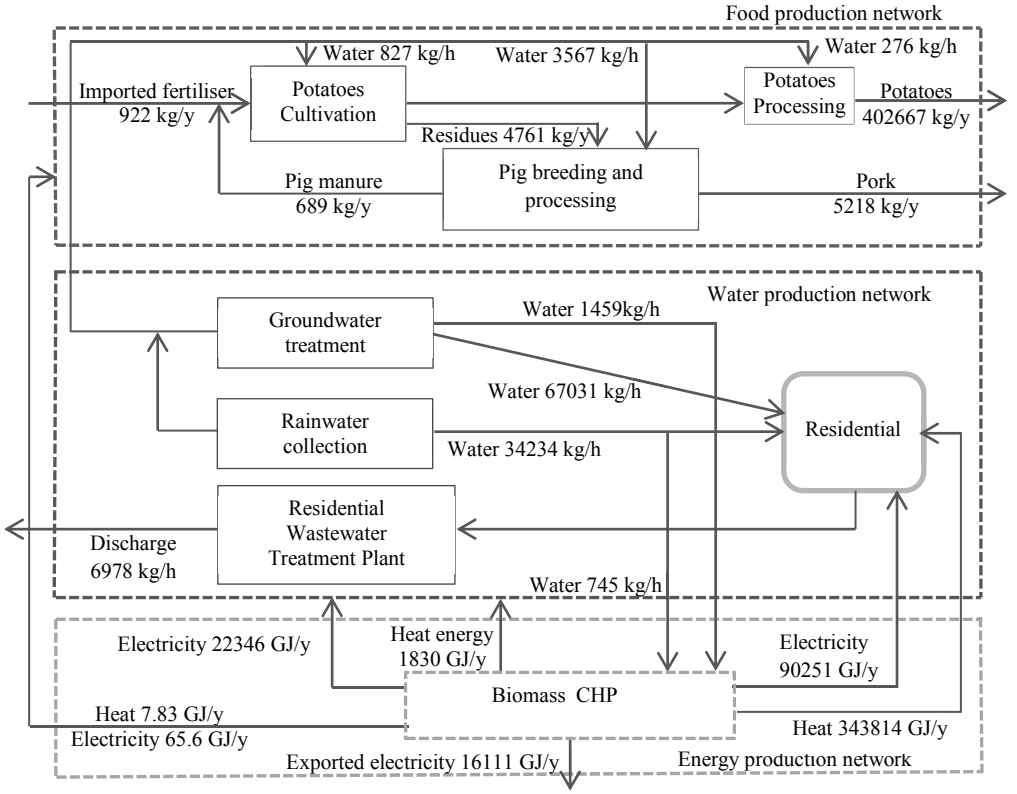

Figure 2: Detailed results from the last iteration

References

A. Almansoori and N. Shah, 2012, Design and operation of a stochastic hydrogen supply chain network under demand uncertainty, International Journal of Hydrogen Energy, 37, 3965-3977.

J. Beck, R. Kempener, B. Cohen, J. Petrie, 2008, A complex systems approach to planning, optimisation, and decision making for energy networks, Energy Policy, 36, 2795-2805.

K.U. Klatt and W. Marquardt, 2009, Perspectives for process systems engineering-Personal views from academia and industry, Computers and Chemical Engineering, 33, 536–550.

J.J. Klemes, P.S. Varbanov, Z. Kravanja, 2013, Recent developments in Process Integration, Chemical Engineering Research and Design, 91, 2037–2053.

M. Leung Pah Hang, E. Martinez-Hernandez, M. Leach, A. Yang , 2014, A multi-level framework for resource accounting. 17th European Roundtable on Sustainable Consumption and Production, 14-16 Oct 2014, Portoroz, Slovenia.

E. Martinez-Hernandez, M. Leung Pah Hang, M. Leach, A.Yang, 2014, Local Resource Calculator–a tool for assessment of local production system options. 17th European Roundtable on Sustainable Consumption and Production, 14-16 Oct 2014, Portoroz, Slovenia.

L. Middlemiss and B.D. Parrish, 2010, Building capacity for low-carbon communities: The role of grassroots initiatives, Energy Policy, 38, 7559-7566.

Royal Academy of Engineering, 2011, Infrastructure, Engineering and Climate Change Adaptation –ensuring services in an uncertain future, ISBN 1-903496-61-6.

Krist V. Gernaey, Jakob K. Huusom and Rafiqul Gani (Eds.), 12th International Symposium on Process Systems Engineering and 25th European Symposium on Computer Aided Process Engineering.
31 May – 4 June 2015, Copenhagen, Denmark

Modelling Multi Stream Heat Exchangers Using Operational Data

Harsha N. Rao,[a] Iftekhar A. Karimi[a]*

[a] *Department of Chemical & Biomolecular Engineering,4 Engineering Drive 4, National University of Singapore, Singapore-117585*
cheiak@nus.edu.sg

Abstract

Multi-stream heat exchangers (MSHE) are single process units that facilitate simultaneous exchange of heat among multiple streams and are mainly used in cryogenic processes like natural gas liquefaction, air separation, etc. Most MSHEs are proprietary and complex, and involve phase changes. MSHE models in the literature are complex MINLP models with disjunctions and are computationally expensive. Since they must be solved repeatedly inside a process optimization framework, simpler models would be highly desirable. In this work, we present a simpler superstructure of 2-stream exchangers to describe an MSHE and propose a non-linear programming (NLP) formulation to obtain a network that best fits given operational data. We demonstrate the usefulness of our work on an existing LNG plant and predict its operation successfully.

Keywords: Multi-stream heat exchangers, phase change, NLP, LNG

1. Introduction

A multi-stream heat exchanger (MSHE) is the most important heat transfer unit in many industrial and cryogenic processes such as air separation, natural gas processing, liquefied petroleum gas (LPG), petrochemicals, and refrigeration systems. (Khan et al., 2012) Some of its attractive attributes are compact design with high heat transfer area, small minimum temperature approaches (as small as 1-3℃), high heat transfer coefficients, flexibility in flow arrangement, high reliability, and ability to withstand a range of pressures. A typical MSHE has a series of sections, called bundles, with spiral wound and plate-and-fin being the most commonly used types. (Hasan et al., 2009)

Most processes employing MSHEs are energy intensive. MSHEs link their upstream and downstream sections, often involving multiple refrigeration systems. Minimizing energy consumption is critical for these processes, but system-wide optimization requires a model for MSHE. Most MSHEs are proprietary black boxes, and involve complex fluid flow patterns and phase changes which make modeling them a challenge. (Hasan et al., 2009) Furthermore, various process variations (e.g. feed conditions, ambient temperature, etc.) make their operation and control difficult. Without an accurate predictive model, the operators must rely on qualitative experience, and employ heuristic single-parameter tweaks of individual process variables. Therefore, it is beneficial to have a rigorous predictive model for an MSHE to reduce the guesswork involved in plant operation, control, and optimization.

Several approaches have been proposed for modeling an MSHE. Rigorous physiochemical models based on first principles (Goyal et al., 2014 and Skaugen et al.,

2013), which are specific to certain types MSHEs, can be developed when the internal details are known. In most cases, however, internal details are unknown, and such models are not feasible. Furthermore, such models are typically compute-intensive, and hence difficult to incorporate in process-wide optimization. Thus, simpler models that relate inputs and outputs are often desirable.

Hasan et al. (2009) proposed the idea of using a hypothetical network of 2-stream heat exchangers to model MSHE operation. They developed a novel mixed-integer nonlinear programming (MINLP) formulation for finding the best equivalent network configuration. While their formulation allowed phase changes, it assumed a single cold stream and zero pressure drops in bundles, and did not allow components such as Joule-Thompson (J-T) valves. Furthermore, their network was complex and its solution compute-intensive. In contrast, Kamath et al. (2012) presented an equation-oriented model based on the pinch concept to ensure minimum driving force and modeled MSHE as a network with no utilities. They proposed a disjunctive formulation to detect phases and perform appropriate calculations. For pressure drops, they made a simplifying assumption that pressure varies linearly with the heat load of the stream. Clearly, there is a need to develop an alternate MSHE model that addresses the aforementioned shortcomings.

In this work, we propose a nonlinear model that can be derived from the historic input-output data of any generic MSHE, and then can be used to predict its performance. Following the idea of Hasan et al. (2009), we present a much simpler superstructure of 2-stream heat exchangers based on the phases traversed by the exchanging streams. In addition, we accommodate mixing, pressure drops, and J-T expansions. Unlike the existing approaches, our approach solves an NLP rather than an MINLP to derive the best equivalent network. It also requires far fewer 2-stream exchangers than those from Hasan et al. (2009). As stated by Hasan et al. (2009), such a network can easily be simulated within a commercial process simulator.

2. Problem Statement

Consider a bundle in an existing MSHE. I hot streams (i = 1, 2. . . I) and J cold streams (j = 1, 2. . . J) pass through this bundle. Operational data for N distinct steady states (n = 1, 2. . .N) of the bundle are available. These include stream compositions, stream flows, and stream inlet/outlet temperatures and pressures. Let F_{in}^{h} be the flow into the bundle, and HIN_{in}^{h} and $HOUT_{in}^{h}$ be the inlet and outlet enthalpies, respectively, of a hot stream i in data set n. Similarly, we define F_{jn}^{c}, HIN_{jn}^{c}, and $HOUT_{jn}^{c}$ for cold stream j. Given these, we aim to derive a network of fixed-area 2-stream exchangers, which best describes the bundle operation over all N states including the streams exchanging heats in each exchanger and their flow fractions.

We assume that no heat exchange occurs between hot (cold) streams. The variations in the operational data are not drastic. Specifically, the enthalpy data for the N datasets are within some $\pm \in$ range. This is merely to ensure that the operational regimes of the exchanging streams are the same in all data sets.

3. Model Formulation

We represent MSHE by a network of simple 2-stream HEs with known heat transfer areas. Each 2-stream HE will match a portion (substream) of a hot stream with another of a cold stream.

Based on the bundle operational data, we first identify the phase regimes for each hot stream i and cold stream j. Since the data sets may vary in feed flows, compositions and ambient conditions, the bubble and dew points of exchanging streams as well as the inlet/outlet temperatures and pressures may also vary to some extents. As a result, if we wish to distinguish operational regimes sharply at the phase boundaries, they could vary between data sets. However, we desire to have a unique heat exchanger network for a particular hot stream i and the cold stream j, using all the N data sets. Therefore we introduce an offset ϵ (corresponding to a small temperature difference), based on enthalpy scale, on either sides of average dew point and bubble point for the given sets of data as shown in Figure 1.

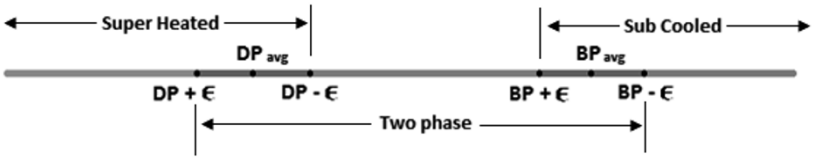

Figure 1. Enthalpy line diagram with extended superheated, two phase, and subcooled region

We include regions near the phase boundaries on either side. In other words, as depicted in figure 1, we extend superheated (SH) regime upto $DP^{avg} - \in$, two-phase (TP) region from $DP^{avg} + \in$ to $BP^{avg} - \in$, and sub-cooled (SC) regime starting from $BP^{avg} + \in$. This extension would not only solve the problem of varying datasets, but also ensures the selection of minimum number of heat exchangers when the inlet and outlet enthalpies are marginally above or below the dew point, or the bubble point.

Using the above enthalpy line, we present a novel superstructure of simple 2-stream heat exchangers between portions of hot and cold streams based on operational regimes. (Figure 2)

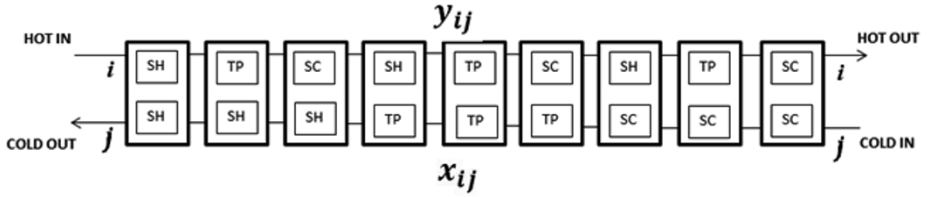

Figure 2. Superstructure for the heat exchanger network based on phase changes

It is evident that the superstructure consists of nine heat exchangers, each representing their operational regimes (Super-Heated, Sub-Cooled and Two-Phase) placed between y_{ij} portion of hot stream i and x_{ij} portion of the cold stream j in a particular bundle of which only some of them are active. This superstructure would yield a maximum of 5 heat exchangers between exchanging a hot stream and cold stream. Unlike Hasan et al., (2009) we avoid multiple heat exchange between a particular hot stream i and various portions of the cold stream j to ensure simplicity. Therefore, a hot stream i would contact only one portion of the cold stream j in a bundle.

First, we find the optimal fraction of cold stream j in contact with a portion of i hot stream which best represent the performance of the bundle. Our objective is to minimize the difference between the actual outlet temperatures and the predicted outlet temperature for hot and the cold streams. We achieve this by minimizing squares of the

differences between the observed and predicted enthalpy changes summed over the n data sets for all the streams. The constraint equations include energy balances, minimum temperature approach (MTA), merging of the substreams, summations of stream fractions. These constraints are specific to each scenario, some of which are discussed here.

3.1 No phase change within the bundle

This is a commonly observed scenario in a bundle of an MSHE. Exchanging streams may not change phase within the bundle. In such cases, only one heat exchanger would be placed between the streams. The log-mean temperature difference is calculated as shown below.Heat duty and LMTD for other heat exchangers are zero.

IF HIN_{in}^{h} & $HOUT_{in}^{h}$ both belong to *SH* or *TP* or *SC* region, according to the figure 1, and both HIN_{jn}^{c} &$HOUT_{jn}^{c}$ also belong to either *SH* or *TP* or *SC* region, we have:

$$Q1_{ijn} = F_{in}^{h} y_{ij} \left[HIN_{in}^{h} - HPOUT_{ijn}^{h}\right] = F_{jn}^{c} x_{ij} \left[HPOUT_{ijn}^{c} - HIN_{jn}^{c}\right] \quad (1)$$

$$HPOUT_{ijn}^{h} \geq HIN_{jn}^{c+\Delta T} \quad (2)$$

$$HPOUT_{ijn}^{c} \leq HIN_{in}^{h-\Delta T} \quad (3)$$

$$\Delta T1_{ijn}^{LM} = \frac{\left(TPOUT_{ijn}^{h} - TIN_{jn}^{c}\right) - \left(TIN_{in}^{h} - TPOUT_{ijn}^{c}\right)}{ln\frac{\left(TPOUT_{ijn}^{h} - TIN_{jn}^{c}\right)}{\left(TIN_{in}^{h} - TPOUT_{ijn}^{c}\right)}} \quad (4)$$

$$Q2_{ijn} = Q3_{ijn} = Q4_{ijn} = Q5_{ijn} = 0 \quad (5)$$

$$\Delta T2_{ijn}^{LM} = \Delta T3_{ijn}^{LM} = \Delta T4_{ijn}^{LM} = \Delta T5_{ijn}^{LM} = 0 \quad (6)$$

$HPOUT$ indicates predicted outlet enthalpy for exchanging streams, while eq. (2) and (3) are MTA constraints. $HIN_{jn}^{c+\Delta T}$ is the enthalpy of cold stream j corresponding to temperature $TIN_{jn}^{c} + \Delta T$ at its inlet pressure and $HIN_{in}^{h-\Delta T}$ is the enthalpy of hot stream i corresponding to temperature $TIN_{in}^{h} - \Delta T$ at the inlet pressure.

3.2 One of the two streams changes phase

This scenario is also observed in certain bundles of MSHE. Heat exchangers in series could be used to model such cases. For instance, when a cold stream does not change phase whereas a hot stream exists in both superheated (SH) phase and two-phase (TP), two heat exchangers in series between the streams, separated at the phase boundary, are obtained. Heat duty and LMTD for other three heat exchangers are zero.

$$Q1_{ijn} = F_{in}^{h} y_{ij} \left[HIN_{in}^{h} - HDP_{in}^{h}\right] = F_{jn}^{c} x_{ij} \left[HPOUT_{ijn}^{c} - HOUT1_{ijn}^{c}\right] \quad (7)$$

$$Q2_{ijn} = F_{in}^{h} y_{ij} \left[HDP_{in}^{h} - HPOUT_{ijn}^{h}\right] = F_{jn}^{c} x_{ij} \left[HOUT1_{ijn}^{c} - HIN_{jn}^{c}\right] \quad (8)$$

The same approach can be extended to the case with one stream in all three phase while the other stream is does not change phase.

Rarely, when both hot and cold streams exist in multiple regimes within a bundle, it is also necessary to know the relative lengths of the operational regimes for the exchanging streams in enthalpy scale. In such cases, it is essential to evaluate the relative positions of inlet, outlet, bubble and dew points on an enthalpy line diagram and compare the lengths of operating regimes within a bundle to write appropriate energy balance equations. We use average values of inlet and outlet enthalpies, flow rates, dew

points and bubble points to evaluate the lengths of each regime in a bundle. We calculate the following parameters to compare the lengths of regimes.

$$SH_{ij}^{h} = F_{i}^{avg} y_{ij} (HIN_{i}^{avg} - HDP_{i}^{avg}) \quad (9)$$

$$TP_{ij}^{h} = F_{i}^{avg} y_{ij} (HIN_{i}^{avg} - HBP_{i}^{avg}) \quad (10)$$

SH_{ij}^{h} and TP_{ij}^{h} indicate the average lengths of between inlet, and dew point and bubble point respectively for hot streams. Similarly, we have SH_{ij}^{c} and TP_{ij}^{c} for cold streams starting from average outlet to average dew and bubble points.

3.3 Both streams change phase

We illustrate the procedure with the scenario when both hot and cold streams exist in superheated (SH) and two-phase (TP) regime. If $SH_{ij}^{h} \geq SH_{ij}^{c}$, cold stream would first approach the phase boundary.

$$Q1_{ijn} = F_{in}^{h} y_{ij} \left[HIN_{in}^{h} - HOUT1_{ijn}^{h}\right] = F_{jn}^{c} x_{ij} \left[HPOUT_{ijn}^{c} - HDP_{jn}^{c}\right] \quad (11)$$

$$Q2_{ijn} = F_{in}^{h} y_{ij} \left[HOUT1_{ijn}^{h} - HDP_{in}^{h}\right] = F_{jn}^{c} x_{ij} \left[HDP_{jn}^{c} - HOUT1_{ijn}^{c}\right] \quad (12)$$

$$Q3_{ijn} = F_{in}^{h} y_{ij} \left[HDP_{in}^{h} - HPOUT_{ijn}^{h}\right] = F_{jn}^{c} x_{ij} \left[HOUT1_{ijn}^{c} - HIN_{jn}^{c}\right] \quad (13)$$

If$SH_{ij}^{h} \leq SH_{ij}^{c}$, hot stream would approach the dew point first.

$$Q1_{ijn} = F_{in}^{h} y_{ij} \left[HIN_{in}^{h} - HDP_{in}^{h}\right] = F_{jn}^{c} x_{ij} \left[HPOUT_{ijn}^{c} - HOUT1_{ijn}^{c}\right] \quad (14)$$

$$Q2_{ijn} = F_{in}^{h} y_{ij} \left[HDP_{in}^{h} - HOUT1_{ijn}^{h}\right] = F_{jn}^{c} x_{ij} \left[HOUT1_{ijn}^{c} - HDP_{jn}^{c}\right] \quad (15)$$

$$Q3_{ijn} = F_{in}^{h} y_{ij} \left[HOUT1_{ijn}^{h} - HPOUT_{ijn}^{h}\right] = F_{jn}^{c} x_{ij} \left[HDP_{jn}^{c} - HIN_{j,n}^{c}\right] \quad (16)$$

Similar procedure can be followed for other combinations of both streams exhibiting phase change.

Next, we obtain the heat transfer areas of the 2-stream heat exchangers by minimizing the following objective function (Eq. 17), subject to non-negative area constraint.

$$Min. \ \sum_{n} \sqrt{\sum_{j} \sum_{i} [Q1_{ijn} - U1_{ijn} A1_{ij} \Delta T1_{ijn}^{LM}]^2} \ ; A1_{ij} \geq 0 \quad (17)$$

Overall heat transfer coefficients for the heat exchangers which depend on the flow rates, fluid and exchanger properties could be found from simulators like HYSYS, appropriate correlations or experimental values available in literature. LMTD temperatures are found as described previously. Similar equations are used to find $A2_{ij}, A3_{ij}, A4_{ij}$ and $A5_{ij}$.

Overall, the working principle of this model is very simple and efficient. Based on the phases identified from the operational data, the number of active heat exchangers and energy balance is decided prior to the solution of the model, hence resulting in an NLP. The model splits the parent hot and cold streams into sub-streams, allows maximum possible heat exchange in operational regimes while ensuring negligible phase change in a heat exchanger. After having obtained the network of 2-stream heat exchangers that best mimics the operation of MSHE using historic operational data, future performance predictions of the MSHE can be made. Given the inlet conditions, this network can predict the outlet conditions satisfactorily.

4. LNG Case study

Modelling the main cryogenic heat exchanger (MCHE) used in energy intensive the natural gas liquefaction cycle is often the bottleneck in its optimization process. We applied our model on an existing MCHE of an LNG plant in Qatar, with four hot streams viz. Natural gas (NG), mixed refrigerant liquid (MRL), mixed refrigerant vapour (MRV) and liquefied petroleum gas (LPG), and mixed refrigerant (MR) as the coolant. The MCHE consists of three bundles (hot, mid and cold), with LPG being mixed with NG post its exit from the mid bundle. Due to the extreme variations of feed conditions between seasons, we used MCHE operational data over the entire year to include the effects of all possible ambient conditions. Also, we pre-processed data to remove inconsistencies, include J-T valve expansions occurring in the MCHE. Operational data from the LNG plant enables exact accounting of pressure drops and mixing. NG stream changed phase in hot bundle, hence needing two exchangers in series. Since other streams in the bundle did not change phase, a total of five exchangers were obtained. Similarly, five exchangers represented the mid bundle in which only MRV changed phase. In the cold bundle, streams showed no phase change. Overall, our model results in a far fewer 2-stream heat exchangers than Hasan et al. (2009) and successfully predicts the performance of the MCHE within allowable range of error. (Table 1)

Table 1. LNG case study results

Bundle	Hot Streams	Cold Streams	Number of 2-stream heat exchangers
Hot Bundle	NG, LPG, MRL, MRV	MR	5
Mid Bundle	NG, LPG, MRL, MRV	MR	5
Cold Bundle	NG, MRV	MRV	2

5. Conclusions

In this work, a non-linear formulation to model MSHE as a network of 2-stream heat exchangers using historic operational data is presented. The model can satisfactorily predict with the performance of any MSHE without knowing the internal details. It successfully captures phase change, results in a much simpler network of 2-stream heat exchangers, and can be easily used in the system-wide optimization framework.

References

M. M. F Hasan, I. A Karimi, H. E Alfadala and H. Grootjans, 2009, Operational Modeling of Multi-Stream Heat Exchangers with Phase Changes, AICHE Journal, 55, vol 1, 150-171.

R.S. Kamath, L.T. Biegler, and I.E. Grossmann, 2012, Modeling Multistream Heat Exchangers with and without Phase Changes for Simultaneous Optimization and Heat Integration, AICHE Journal, 58, vol 1, 190-204.

M.S. Khan , Y.A Husnil , M. Getu & M. Lee, 2012, Modeling and Simulation of Multi-stream Heat Exchanger Using Artificial Neural Network, Computer Aided Chemical Engineering, 31, 1196-1200.

M. Goyal, A. Chakravarty , M.D. Atrey, 2014, Two dimensional model for multistream plate fin heat exchangers, Cryogenics, 61, 70–78.

G. Skaugena, K. Kolsakerb, H.T Walnuma, O. Wilhelmsena, 2013, A flexible and robust modelling framework for multi-stream heat exchangers, Computers and Chemical Engineering, 49, 95– 104.

Krist V. Gernaey, Jakob K. Huusom and Rafiqul Gani (Eds.), 12th International Symposium on Process Systems Engineering and 25th European Symposium on Computer Aided Process Engineering.
31 May – 4 June 2015, Copenhagen, Denmark

Improving the Energy Efficiency of Cryogenic Air Separation Units (ASU) through Compressor Waste Heat Recovery using Direct Binary Heat Engine Cycle

Mathew Aneke, Meihong Wang*

School of Engineering, University of Hull, HU6 7RX, United Kingdom
**Corresponding author: Tel: +44 1482 466688; Fax: +44 1482 466664; Email: Meihong.Wang@hull.ac.uk*

Abstract

In this paper, the thermodynamic advantage of recovering compressor waste heat in cryogenic air separation unit (ASU) using binary cycle heat engine instead of the conventional use of cooling water is investigated through modeling and simulation using Aspen Plus® simulation software version 8.4. The simulation results based on a cryogenic ASU capable of processing 100 kg/s of atmospheric air show that the overall specific power consumption for the production of pure products of 99.90 mol. $\%O_{2\,(g)}$, 99.99 mol. % $N_{2\,(g)}$ and 97.00 mol. % $Ar_{\,(l)}$ can be reduced from 0.191 kWh/kg to 0.170 kWh/kg by converting the compressor waste heat to electricity using binary cycle heat engine which uses R134a as both the working fluid and the compressor cooling medium as against the conventional process which uses water as the cooling media. This represents an 11% reduction in the power consumed to produce the pure products. In addition, the heat engine generates about 2, 354.22 kW of power which can be sold to generate more revenue.

Keywords: Cryogenic Air Separation Unit; Organic Rankine Cycle; Binary Cycle Heat Engine; Waste Heat Recovery

1. Introduction

Air separation unit (ASU) is an integral process to many other processes mainly because of the importance of its constituent gases to many industrial processes. For example, oxygen is used in medical and other industrial processes such as metal, glass, ammonia, oxy-fuel combustion and integrated gasification combined cycle (IGCC) (Burdyny and Struchtrup, 2010, Jones et al., 2011, Liszka and Ziębik, 2010, Zhu et al., 2008), nitrogen finds use in the chemical and petroleum industries (Vinson, 2006) while argon is used as an inert shielding gas in welding and other electronics such as the light bulb.

Air in its natural form is a free commodity, however its separation into its components is both capital and energy intensive. Although there are several technologies used in the separation of air, this work will focus on cryogenic ASU.

Cryogenic ASU is mainly used for the production of high tonnage and high purity gases. This makes it the status quo in many industrial processes where oxygen and nitrogen are required in high tonnage and high purity (Fu and Truls, 2012, Yan et al., 2010).

As a result of the importance of cryogenic ASU to several industrial processes, many studies have been carried out on how to reduce the capital and energy requirement of conventional ASU. Amongst the studies are (a) the replacement of tray distillation columns with packed columns; (b) operating at higher pressure to reduce the overall column diameter; (c) improving the effectiveness of heat exchangers, the efficiency of compressors and the use of control system with real-time optimization capability (Castle, 2002, Kansha et al., 2011, Rübberdt, 2009). Others include the use of self-heat recuperation system which was found to reduce the overall energy consumption by circa 36% when compared to the conventional process (Kansha et al., 2011). For cases where the product gas (especially oxygen) is required at high pressure, Manenti et al., (2013) found that the specific power consumption of the cryogenic ASU can be reduced by pumping liquid oxygen produced instead of compressing the gaseous oxygen.

Most of the energy consumption in a cryogenic ASU occurs in the air compressor. For example, according to Fu and Gundersen (2012), about 38.4% of exergy loss in a conventional cryogenic ASU occurs in the air compressor unit. This is also confirmed by the work of Cornelissen and Hirs (1998) who found that about one-third of the exergy loss in a conventional cryogenic ASU comes from the air compressor unit. This means that the reduction in the exergy loss of the compressor will drastically improve the energy efficiency of the cryogenic ASU.

In this work, the impact of reducing the energy loss in the air compressor on the specific power consumption of a cryogenic ASU through air compressor waste heat recovery using binary heat engine cycle will be investigated through modeling and simulation using Aspen Plus® simulation software version 8.4.

2. Process Description of a Conventional Cryogenic ASU

Figure 1 shows the process flow diagram of the conventional ASU investigated in this paper. In the process, the atmospheric air is filtered, cleaned and compressed in a 3 stage compressor with intercooling to a pressure of 6.35 bar. The compressed air is split into two streams in the ratio of 5:17 and cooled against the leaving product streams (gaseous nitrogen, liquid oxygen and gaseous waste stream). The stream with the higher flowrate is sent to the high pressure distillation column (HPC) where nitrogen is separated at a pressure of about 5.7 bar. The other stream is expanded to a pressure of 1.2 bar before being sent to the low pressure distillation column (LPC). The top nitrogen product from the HPC is condensed against the boiling oxygen in the reboiler of the LPC, and depressurized before being sent to the top of the LPC. The bottom liquid product from the HPC which is rich in oxygen is also sent to the LPC after been depressurized using a JT valve. In the LPC, pure nitrogen vapour and pure liquid oxygen stream leaves from the top and bottom of the column respectively together with two vapour side streams. The side product stream towards the top of the column is regarded as a waste stream while the one towards the bottom of the column is sent to the side rectifier (ArC) where high purity argon is separated from oxygen (Kooijman et al., 2006).

The entire process is a tight integration of heat exchangers and separation columns. The HPC and LPC share the same column shell to minimize the temperature difference between the condensing nitrogen and evaporating oxygen. The condenser of the LPC exchanges heat with the reboiler of the LPC while the Joule-Thomson (JT) effect cools the rich liquid from the bottom of the HPC such that it can be used as the coolant to run

the condenser of the side rectifier (ArC) which separates argon from the oxygen. Additional cooling was provided by the JT effect of the expander which feeds compressed air directly to the LPC.

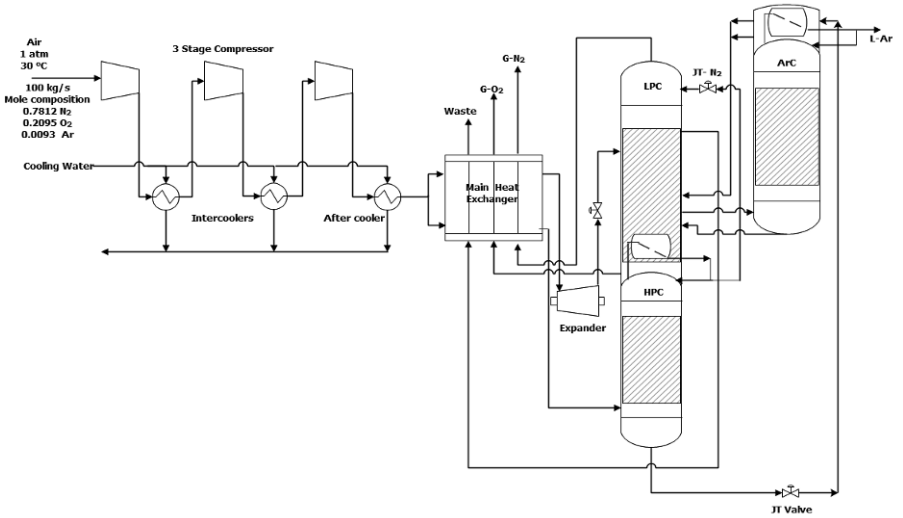

Figure 1: Conentional Cryogenic ASU with 3 Stage Compressor (Kooijman et al. 2006)

3. Cryogenic ASU Compressor Waste Heat Recovery using Binary Cycle Heat Engines

Even with the most efficient system, up to 90 % of the input power to a compressor is lost as heat (ETSU, 1998). This heat increases the temperature of the compressed gas at the compressor outlet. To maintain proper operating condition, the compressor must be cooled. In conventional systems, water is usually used as the compressor cooling medium. The use of water gives rise to a hot water stream which can only be used for heat integration application. Such application is not thermodynamically beneficial in a process such as the cryogenic ASU since there is no need for additional heat integration. Hence, recovering the compressor using a process which can convert the recovered heat to a product that is useful to the process will be of great benefit to the plant.

In a conventional cryogenic ASU described in section 2, the temperature of the air exiting the first stage compressor is 109 ^{o}C. This air is required to be cooled to 40 ^{o}C before it enters into the second stage compressor. Similarly, after the second and third stage compressor, the air temperature rises to 107 ^{o}C and 113 ^{o}C and is required to be cooled to 40 ^{o}C and 30^{o}C respectively. Using water at 20 ^{o}C and 1 bar as the cooling medium gives rise to either a hot water or steam depending on the water flowrate. Water at this condition can only be used for heat integration as explained earlier. This will not be useful in any part of the cryogenic ASU as there is no need for additional heat in the process. The conversion of the compressor waste heat to power using binary heat engines cycle technology will be of utmost benefit to the cryogenic ASU.

3.1. Simulation of Cryogenic ASU with Compressor heat recovery using Binary Heat Engine Cycle

The process flow diagram of the cryogenic ASU with compressor heat recovery using binary heat engine cycle as simulated in Aspen Plus® is shown in Figure 2. The binary heat engine cycle uses R134a as the working fluid. This working fluid also functions as the compressor cooling medium. The process parameters used to develop the Aspen model of the conventional cryogenic ASU is shown in Table 1. The performance parameter for the proposed design and the conventional process were evaluated and compared using the simulation results shown in Table 2.

The specific power consumption for producing any given pure product is defined as:

$$\alpha_{ov} = \frac{\sum(P_{in} - P_{out})}{\sum m} \quad (1)$$

where,
$\sum P_{in}$ = sum of the power inputs to the process (kW), $\sum P_{out}$ = sum of the power outputs from the process (kW), m = mass of the pure product, (kg/h)

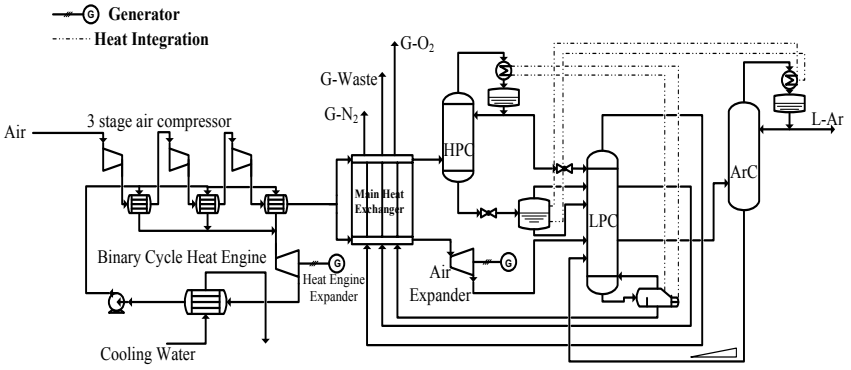

Figure 2: Cryogenic ASU with Compressor Heat Recovery using Binary Heat Engine Cycle

4. Results and Discussions

Table 2 shows the simulation results of the conventional cryogenic ASU and the proposed cryogenic ASU which uses binary heat engine cycle for compressor waste heat recovery.

The results show that the cryogenic ASU modeled in this work meets the tight heat integration required for such a process. The nitrogen produced at the top of the HPC was condensed at -177.57 ^{o}C against the boiling oxygen at -180.33 ^{o}C from the bottom of the LPC. Similarly, the argon produced in the ArC was condensed at -184.90 ^{o}C against the JT effect of the oxygen rich product from the bottom of the HPC which is at -191.10 ^{o}C.

Table 1: Process Parameters

Cryogenic ASU	
Parameter	Value
Inlet Air mass flowrate	100 kg/s
Inlet Air molar composition	
Nitrogen	0.7812
Oxygen	0.2095
Argon	0.0093
Air inlet temperature	30 ^{o}C
Low Pressure Column Pressure (LPC)	1.2 bar
Low Pressure Column no of stages	45
High Pressure Column Pressure (HPC)	6 bar
High Pressure Column no of stages	69
Argon Column Pressure	1.2 bar
Argon Column number of stages	120
Expander isentropic efficiency	80%
Binary Heat Engine Cycle	
Expander isentropic efficiency	80%
Pump efficiency	80%

Table 2: Simulation Results

Parameter	Conventional Cryogenic ASU	Conventional Cryogenic ASU with BCHE
Pure product mass flowrate (kg/h)	114,160.60	
Product purity (mole %)	99.90	
Oxygen	99.99	
Nitrogen	97.00	
Argon		
LPC Condenser duty (kW)	13405.10 @-177.57 ^{o}C	
HPC Reboiler duty (kW)	13402.20 @-180.33 ^{o}C	
ArC Column condenser duty (kW)	1493.79 @-184.90 ^{o}C	
JT Effect duty from HPC bottom (kW)	1512.75 @-191.10 ^{o}C	
LPC Feed Expander Power Output (kW)	561.60	
Compressor power consumption (kW)	22,273.54	
Cooling Water Pump Power consumption (kW)	114.25	--------
Binary Cycle Heat Engine Net Power (kW)	--------	2354.22
Process Net Power Consumption (kW)	21826.19	19357.72
α_{ov} (kWh/kg)	0.191	0.170

For the conventional process which uses water as the cooling media, the net power consumption was found to be about 21, 826.19 kW. This translates into a specific power consumption of 0.191 kWh/kg for the cumulative production of the three pure products (i.e. 99.90 mol. % oxygen, 99.99 mol. % nitrogen and 97.00 mol. % argon). Replacing the cooling water with binary cycle heat engine as proposed in this study shows that the waste heat can be converted to power. The result shows that about 2,354.22 kW of electricity can be generated by the binary heat engine cycle by using the waste heat

from the compressor. This extra power causes the net power consumption of the cryogenic ASU to drop from 21, 826.19 kW to 19, 357.72 kW which represents a reduction of circa 11% in the specific power consumption when compared with the conventional process. The power generated from the compressor waste heat is also a source of revenue for the process thus lowering the operating cost of the process.

5. Conclusions

As shown in this paper, the utilization of compressor waste heat of a cryogenic ASU for power generation is both technologically feasible and economically viable. It can significantly improve the energy efficiency of the process through reduction in the net power consumption which translates into a reduction in the specific power consumption of the process.

References

T. Burdyny and H. Struchtrup, 2010, Hybrid membrane/cryogenic separation of oxygen from air for use in the oxy-fuel process, Energy, 35, 1884 - 1897.

W. F. Castle, 2002, Air separation and liquefaction: recent developments and prospects for the beginning of the new millennium, International Journal of Refrigeration, 25, 158 - 172.

R. L. Cornelissen and G. G. Hirs, 1998, Exergy Analysis of Cryogenic Air Separation, Energy Conversion and Management, 29, 1821 - 1826.

ETSU, 1998, Energy Technology Support Unit, Heat Recovery from air compressors, Good Practice Guide, 238, 1 - 5.

C. Fu and G. Truls, 2012, Using exergy analysis to reduce power consumption in air separation units for oxy-combustion processes, Energy, 44, 60 - 68.

D. Jones, D. Bhattacharyya, R. Turton and S. E. Zitney, 2011, Optimal design and integration of an air separation unit (ASU) for an integrated gasification combined cycle (IGCC) powe plant with CO_2 capture, Fuel Processing Technology, 92, 1585 - 1595.

Y. Kansha, A. Kishimoto, T. Nakagawa and A. Tsutsumi, 2011, A novel cryogenic air separation process based on self-heat recuperation, Separation and Purification Technology, 77, 389 - 396.

H. Kooijman, R. Taylor and J. van Baten, 2006, The ChemSep/COCO Casebook: Air seperation Unit, available at chemsep.org, 1 - 5.

M. Liszka, and A. Zębik, 2010, Coal-fired oxy-fuel power unit - Process and system analysis,Energy, 35, 943 - 951.

F. Manenti, F. Rossi, G. Croce, M. G. Grottoli and M. Altavilla, 2013, Intensifying Air Separation Units, Chemical Engineering Transactions, 35, 1 - 6.

K. Rübberdt, 2009, Producing oxygen and nitrogen: Air separation techniques continue to advance. ACHEMA 2009, 29th International Exhibition Congress in Chemical Engineering, Environmental Protection and Biotechnology, Frankfurt am Main, Germany, 1 - 8.

D. Vinson, 2006, Air separation control technology,Computers & Chemical Engineering, 30, 1436 - 1446.

L. Yan, Y.Yu, , Y. Li and Z. Zhang, 2010, Energy Savings Opportunities in an Air Separation Process, International Refrigeration and Air Conditioning. Purdue.

X. Zhu, S. Sun, Y. He, Y. Cong and W. Yang, 2008, New concept on air separation, Journal of Membrane Science, 323, 221 - 224.

Krist V. Gernaey, Jakob K. Huusom and Rafiqul Gani (Eds.), 12th International Symposium on Process Systems Engineering and 25th European Symposium on Computer Aided Process Engineering.
31 May – 4 June 2015, Copenhagen, Denmark

IGCC Modelling for Simultaneous Power Generation and CO_2 Capture

Usama Ahmed [a], Umer Zahid [a], Chonghun Han [a*]

[a] *Seoul National University, Seoul, South Korea*
chhan@snu.ac.kr

Abstract

Power producing industry has largely relied on coal as a fuel source and will continue to depend on it for coming decades. However, to address the global warming problem while keeping high efficiency and economic feasibility of the processes is a key challenge. Coal-based power plants with post-combustion capture tend to have lower capital costs and cost of electricity without capture. On the other hand, pre-combustion capture plants tend to be less expensive when current CO_2 capture systems are added. This analysis suggests that pre-combustion plants can be an attractive option for the power generation if carbon capture and storage (CCS) technology is implemented on a large scale. This paper is focused on the in depth modeling and simulation of integrated gasification combined cycle (IGCC) with CO_2 capture using a physical solvent. Three case studies have been developed to analyze the overall plant output with CO_2 capture. In order to ensure a fair evaluation of analysis, a consistent and transparent methodology has been followed for all the cases. First two cases use the water gas shift reactions scheme with sour shift catalysis process. The resulted syngas free of CO_2 can either be combusted by using air or O_2. The first case uses air as an oxidant for burning H_2 and the combustor temperature is controlled by air as well. In the second case, O_2 is used as an oxidizing agent in the H_2 combustion. However, combustion temperature control is achieved by recycling the captured CO_2. In the third model, WGS reactor has been removed. The syngas composed of CO and H_2 is sent directly for combustion which makes it similar to the oxy-fuel combustion process. In this way, captured CO_2 can be recycled back to control the combustor temperature in 2nd and 3rd case. The results show that the overall plant output power for the three cases is 378 MW, 344 MW and 388 MW respectively. Case 1 and 3 are the competitive options in terms of efficiency; however the capital cost may be the deciding parameter.

Keywords: CCS, Selexol, IGCC, Pre-Combustion.

1. Introduction

With the recent studies and report published by International Energy Agency (IEA, 2014) it can be seen that with the continuous increase in electricity production, the greenhouse gas emissions have been tremendously increased during the last few decades and it will continue to increase if the emissions will not be controlled. It is expected that coal will remain the main source of power generation for the coming decades because of its abundant availability, affordability and an already existing infrastructure for power generation. Hence, there is a need to develop and improve the power generation processes that can give maximum efficiency while addressing the global warming issues at the same time.

CCS has been identified as a promising set of technologies to decrease the carbon emissions in the atmosphere. But at the same time, CCS implementation not only

increases the financial and installation cost but also put energy penalties in terms of electricity production. Most of the currently operating power plants in the world are post combustion power plants with efficiencies ranging between 25-30 % with CCS installment. On the other hand, Integrated Gasification and combined cycle (IGCC) power plants, a class of pre-combustion process have a higher efficiency (up to 38 %) when CCS is included. However, with a 90 % CO_2 capture IGCC power plant, the electricity cost is increased by 30 %, whereas the efficiency of the power plant is reduced by 8-10 % points.

Recently, a lot of research has been carried out to investigate the feasible designs for an improvement in the efficiency of IGCC plants. Cormos et al. (2014) proposed a model of IGCC based on coal and biomass co-gasification technique for simultaneous production of electricity, H_2, synthetic natural gas (SNG) and fisher-tropsch (FT) fuel. Co-gasification with multiple fuels both decreases the ash fusion temperature as well as oxygen consumption, thereby increasing efficiency of the process. Padurean et al. (2012) reported that the selexol process has least specific power and heating consumption as compared to the other physical solvents. Kawabata et al. (2013) proposed model for IGCC with exergy recuperation that gives an efficiency of 33.2 % with 90 % CO_2 capture and 43 % without capture. Ferguson et al. (2013) modified the water gas shift design in the IGCC process and showed an improved efficiency of 37.62%. Cormos et al. (2014) used co-gasification technique using different fuels and proposed a design for poly generation with the plant efficiency ranging between 27-37% with CCS technology.

Most of the previous studies were mainly focused on the design modification and optimization of the conventional IGCC process with poly generation. None of the recent studies considered design improvement in IGCC process for power generation. If the sole purpose is the power generation, the conventional design of IGCC with CO_2 capture can be modified and improved to increase the thermal efficiency of power plant compared to that of post-combustion process with CO_2 capture. This paper presents various designs for IGCC with CCS scheme that can be utilized for simultaneous power generation and CO_2 capture. All the IGCC designs are made in Aspen Plus® using Peng-Robinson equation of state and results are compared in terms of overall power generation, net power plant efficiencies and CO_2 emissions. Furthermore the sensitivity analysis has been performed to check the efficiency penalties at different percentages of CO_2 capture.

2. Process Description

IGCC process is based on five major units namely gasification unit (GU), water gas shift reactor (WGS), acid gas removal section (AGR), heat recovery steam generation (HRSG), and combined cycle (CC). Gasification unit contains the gasifier with the coal feeding system. Coal can be fed to the gasifier in two ways i.e. dry process or slurry process. Coal water slurry process has low capital cost and is more stable compared to the dry process because there are no channeling problems as it happens in the dry process. Three type of gasifiers commonly used in industry are moving bed gasifier, fluidized bed gasifier and entrained flow gasifier. Entrained flow gasifiers are best used in the coal-gasification applications as it allows all types of coals regardless of their rank and caking characteristics. It can be operated in both dry mode and slurry mode. This gasifier allows formation of syngas at a pressure and temperature up to 6.5 MPa &

1600 °C respectively with 99.5 % of carbon conversion. The water in the slurry is evaporated during gasification process producing steam that can be used in WGS reactions thus increasing overall plant efficiency. In gasification process, a part of chemical energy is converted into heat forming CO and H_2 and the rest of 65- 80 % of energy is kept into the syngas which is called as syngas efficiency. This energy can be extracted by burning syngas or by transforming syngas to other valuable products. The gasification unit is integrated with the HRSG section to maintain the temperature above the ash melting temperature to avoid any possible blockage due to agglomeration. Syngas coming from the gasification unit is allowed to pass through the water gas shift reactors which are equipped with the catalyst to convert CO in the syngas to H_2 gas as given in Eq.(1).

$$CO + H_2O \rightarrow H_2 + CO_2 \qquad \Delta H = -41 \text{ KJ/mole} \tag{1}$$

Water gas shift reactions can be carried out in two ways i.e. sweet process and sour process. If the sulfur is removed from the syngas prior to the WGS unit, it is called sweet shift conversion whereas if the sulfur is removed after the WGS unit then it is called as the sour shift. Casero et al. (2014) showed that the sour shift catalysis process is more energy efficient as compared to the sweet process because a part of syngas chemical energy is degraded due to alternative cooling and heating of syngas for H_2S removal and WGS reactions respectively. WGS reactions are generally exothermic in nature so intermediate heat exchangers are employed to generate medium pressure steam. WGS reactions lead to more than 99 % conversion of CO to H_2 gas.

3. Design options for power production

Three case studies have been developed in order to analyze the power plant output with CO_2 capture. Coal slurry with 30 % water content is fed to an entrained flow gasifier operating at a temperature and pressure of 1600°C and 32 bar respectively. The syngas produced from the gasifier is rich in CO (33 %) and H_2 (49 %) whereas the rest contains H_2O, CO_2, N_2 .Case 1 and 2 based on sour WGS reactions as shown in Figure 1 and Figure 2 respectively. In the 1st case, both the syngas combustion and burner temperature is controlled by using excess air whereas in 2nd case, the syngas combustion is done by using oxygen and the burner temperature is controlled by recycled CO_2. Figure 3 represents the 3rd case based on non-WGS reactions in which syngas is burned by using high purity oxygen and the burner temperature is controlled by recycled CO_2.To have a consistent design basis, all the case studies have been performed for 90 % CO_2 capture with the final pressure raised to a transport pressure of 80 bar.

4. Results and Discussion

The first and second cases are based on the WGS reactions with the difference in using air or oxygen as an oxidant for the syngas burning. Whereas excess air and recycled CO_2 are being used for burner temperature control in case 1 and 2 respectively. Table 1 shows the summary of all the three case studies along with their specifications, net power output and efficiencies. The net power generated in the first case comes out to be 378 MW with the overall power plant efficiency of 36.18 %. The total power generated in second case is 344 MW with the efficiency of 32.9 %. The third case used high purity oxygen gas for combustion process where the combustor temperature has been

controlled by recycled CO_2. It gave the highest power output of 388 MW with net power plant efficiency of 37.15 %.

1st Case:

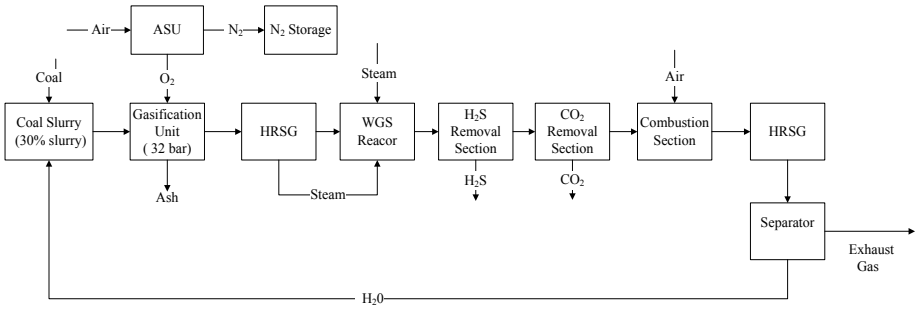

Figure 1: IGCC design with WGS reactor (Combustion oxidant: air, Combustor temp control: air)

2nd Case:

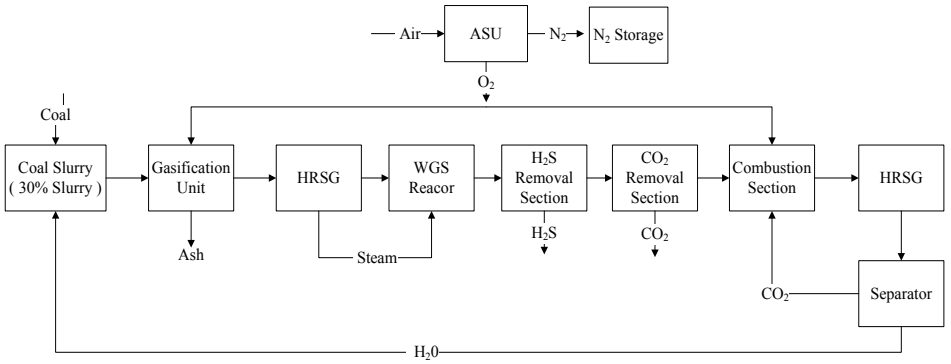

Figure 2: IGCC design with WGS reactor (Combustion oxidant: O_2, Combustor temp control: CO_2)

3rd Case:

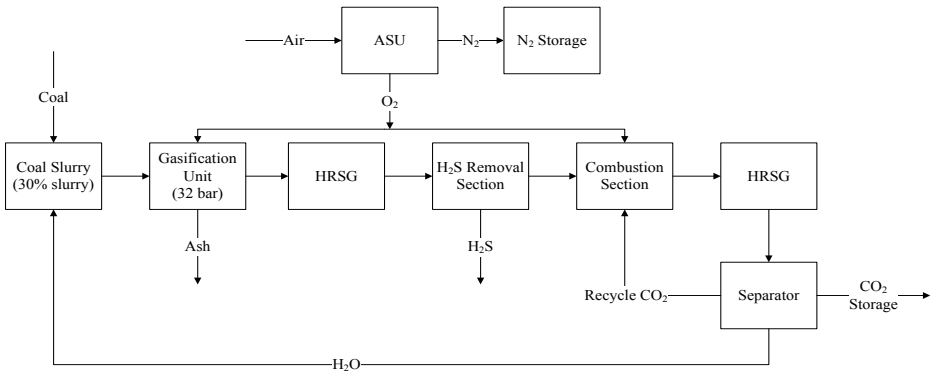

Figure 3: IGCC design without WGS reactor (Combustion oxidant: O_2, Combustor temp control: CO_2)

Case 1 and 2 consumes an intermediate pressure steam to carry out WGS reactions so the power generated from the steam cycle decreases to a great amount as compared to the 3rd case. Since oxygen is used as an oxidant for syngas combustion in the second case, it almost consumes same amount of oxygen as in the third case. However in the second case, only hydrogen is burned in the combustor with oxygen where the temperature is being controlled by using recycled CO_2. Hence, the overall low flow rate of flue gas through the gas turbine results in lesser power generation as compared to first and third case. From the results of second case it can be seen that the IGCC scheme with oxygen being used for syngas combustion along with recycled CO_2 being used for the combustor temperature control is the least efficient process. Case 1 and 3 are very competitive in terms of power production with the efficiency difference of about 0.96 %. However, as evident from the flow sheets (figure 1-3), case 1 has more unit processes along with the operating catalyst. Hence, the capital and operating cost would be much higher for case 1. Furthermore 1st case is more critical as compared to the 3rd case in terms of process control because if the temperature is not controlled precisely at inlet of WGS reactors then the activity of the catalyst will be changed that may affect the overall plant efficiency and the operating cost. On the other hand, there is no WGS and CO_2 capture unit in the third case which makes it more energy efficient process. Sensitivity analysis has been performed to analyze the impact of CO_2 capture percentage on the performance and net power plant efficiency. Figure 4 presents the variation in the net power efficiency of the power plant with the percentage change in CO_2 capture. All the three cases show the same trend of decrease in efficiency with the increase of CO_2 capture percentage.

The cost analysis has been done to estimate the CAPEX (M€) required per unit MW_{el} of electricity generation for all the three cases. The results show that the CAPEX required per unit MW_{el} for case 1, case 2 and case 3 is 2.93 M€, 3.46 M€ and 2.78 M€ respectively. The lowest CAPEX and highest energy efficiency of the 3rd case proves it to be the most economical process among all the three cases. Furthermore, the removal of WGS reactors also avoids catalyst recharging cost in the 3rd case which can save extra operating cost (OPEX).

Table 1: Case studies specification and summary

	1st Case	**2nd Case**	**3rd Case**
	WGS	**WGS**	**Non-WGS**
Gasification Agent	O_2	O_2	O_2
Syn-Gas (For	H_2	H_2	H_2+CO
Oxidant (Combustion)	Air (N_2+O_2)	O_2	O_2
Possible By-Products	H_2O, N_2	H_20	H_2O,CO_2
Burner Temp Control	Excess Air	CO_2	CO_2
Power (MW_{el})	378	344	388
Efficiency (%)	36.18	32.98	37.15

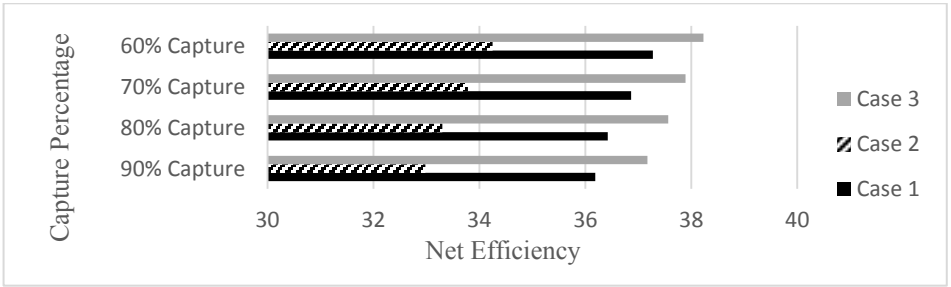

Figure 4: CO_2 capture percentage V/S Net efficiency of Power plant

5. Conclusion

Three design schemes have been developed to investigate the IGCC power plant performance with CCS technology. The 1st and 2nd case used WGS reactor scheme whereas the 3rd case didn't include any WGS reactor. The results show that the power generation from steam cycle has been decreased to a great amount if WGS reactors are used in the process. Whereas the 3rd case based on non-WGS reactors uses high purity oxygen for syngas combustion with the resulting flue gas temperature controlled by using recycled CO_2 offers the best option in terms of power generation and efficiency. Furthermore, the results show that the non-WGS scheme has the lowest cost per unit megawatt of electricity production.

Acknowledgement

This research was supported by the second phase of the Brain Korea 21 Program in 2014, by the Energy Efficiency & Resources Core Technology Program of the Korea Institute of Energy Technology Evaluation and Planning (KETEP) granted financial resource from the Ministry of Trade, Industry & Energy, Republic of Korea (No. 20132010201760) & (No. 20132010500050).

References

A.M. Cormos, C. Dinca, C.C. Cormos, 2014, Multi-fuel multi product operation of IGCC powerplants with carbon capture and storage (CCS), Applied Thermal Engineering, 1-8.

A.Padurean, C. Cormos, P. Agachi, 2012, Pre-Combustion carbon dioxide capture by gas-liquid absorption for integrated gasification combined cycle power plants, International Journal of Greenhouse Gas Control, 7, 1-11

IEA.World Energy Outlook, International Energy Agency, Paris, 2014.

M. Kawabata, O. Kurata, N. Iki, A. Tsutsumi, H. Furutani, 2013, System modeling of exergy recuperated IGCC system with pre and post combustion CO2 capture, Applied Thermal Engineering, 54, 1, 310-318

P. Casero, F.G. Pena, P. Coca, J. Trujillo, 2014, ELCOGAS 14MWth pre-combustion carbon dioxide capture pilot, Technical and economical achievements, Fuel, 116, 804-811.

S. Ferguson, G. Skinner, J. Schieke, K.C. Lee, E.V. Dorst 2013, High efficiency integrated gasification combine cycle with carbon capture via technology advancements and improved heat integration, Energy Procedia, 37, 2245-2255.

Krist V. Gernaey, Jakob K. Huusom and Rafiqul Gani (Eds.), 12th International Symposium on Process Systems Engineering and 25th European Symposium on Computer Aided Process Engineering.
31 May – 4 June 2015, Copenhagen, Denmark

Structural Similarities and Differences between Smart Grids and Process Industry Supply Chains: India Case Study

Nikita Patel, Rishabh Abhinav, Babji Srinivasan, Rajagopalan Srinivasan
Indian Institute of Technology Gandhinagar, Ahmedabad - 382424, India

Abstract

Process industry supply chains have been an active area of research for decades with advances towards decentralized management and development of closed loop resilience. Along similar lines, now electric power systems are moving towards smart grids that allow for decentralized power generation. At the surface level there are many differences between electrical grids and supply chains; for example, there is limited/no storage in case of electric power, hence supply and demand has to be matched at every time instant. However, in the recent times it has been recognized that some of the control and enterprise-wide optimization strategies that are an integral part of supply chain management have analogues in power systems as well. This article seeks to systematically identify the structural similarities and differences between these hitherto unrelated domains. We will illustrate these using a case study of Indian electrical grid.

Keywords: smart grid, supply chain management, decentralization, distributed generation

1. Introduction

The traditional approach to system management in both the supply chain and electric power domains have been (1) unidirectional flows (of material and electric power), (2) near steady supply and demand with low volatilities, (3) use of large inventories (material / spin reserves) at various stages of the system to balance supply and demand, and (4) low uncertainties. As discussed in Ritcher et al. 2012, driven by sustainability-related and other considerations, both systems are undergoing an evolution towards (1) bi-directional flows (for e.g. closed loop supply chains and distributed generation capabilities), (2) uncertain and highly variable supply and demand.

The broad strategies that the two domains have evolved to address these challenges and ensure effective system management also share broad similarities and originate from recent developments in Information & Communication Technology (ICT) and sensing. These similarities are (1) frequent, two-way information exchange between supplier & production, production & distribution, and distribution & customers; (2) shifting from centralized decision making to decentralized decision making; and (3) exploiting spatial and temporal flexibilities. The current work systematically identifies the parallels between closed-loop supply chain and smart grids. Further, implications of this analysis for smart grids in terms of utilizing the modelling and optimization strategies from their well advanced counterpart (SCN) are presented.

This paper is organized as follows: Section 2 compares the smart grid network with supply chain management. Section 3 discusses the existing approaches to model electric grid as a supply chain network. Section 4 describes the present structure of electric grid in India followed with a case study of Indian grid failure. Section 5 brings out the conclusions and future directives for smart grid in India.

2. Smart grid analogy with Supply chain

Prior to the concept of supply chain (before 1950) all the organizations worked serially to produce a single product operating as independent entity. According to M. Habib (2011) first transformation occurred around 1950 and logistics was then considered as a strategic function. The consultants in logistics first coined the concept of supply chain in 1980s. Initially supply chain considered unidirectional flow of goods and bidirectional information flow. The concept of reverse logistics made the supply chain closed loop and led to bidirectional flow of goods. The basic Supply Chain Network (SCN) involves suppliers, logistics/ transportation network, the producer and the consumer. According to Kalaitzidou et al. (2014) SCN design assumes a structure of the network with distinct and consecutive echelons, constituted of nodes with predetermined function.

Like SCN, conventional electricity grid was vertically integrated with centralized generation. Then the concept of Distributed Generation (DG) came, which helped the grid to be self-sustainable and immune to disturbances of other regions. It also helped in increasing the penetration of Renewable Energy Sources (RES). Similar to an advanced closed loop supply chain network, a smart grid comprises of centralized and distributed generation, energy storage, bi-directional electricity and information flow at all levels and an option of choosing the supplier. The smart grid has made the network of electricity complex and as shown in Figure 1 can be viewed as multi-echelon closed loop Supply Chain Network.

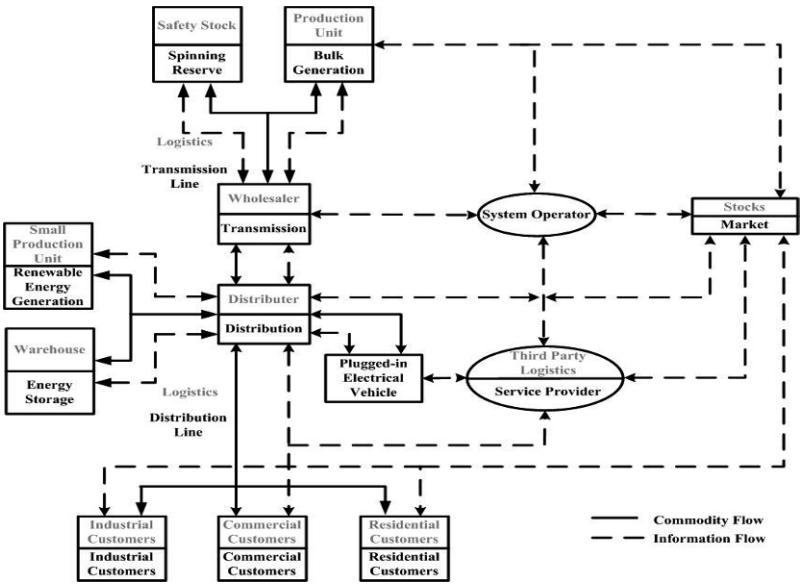

Figure 1: Structural similarities between Smart Grid (in black) and Supply chain (in grey)

2.1. Similarities between modelling approaches for smart grid & supply chain

As shown in Figure 1, smart grid can be related to closed loop supply chain at every level which calls for identifying parallels in modelling in these two domains. Traditionally, SCN is modelled to study develop a configuration to achieve optimal while a model of smart grid is developed to study the behaviour of the electric network and identify a resilient cost-effective grid under various uncertainties. Table 1 presents a comparison of smart grid & SCN in terms of modelling objectives and constraints. This helps in identifying appropriate modelling approaches in closed loop SCN that could be in development of models for smart electric grids.

Table 1: Comparison of modelling objectives and constraints

Supply Chain Modelling	**Electric Grid Modelling**
Reduction of environmental pollution	Greenhouse gas emission reduction
Improve utilization rate of resources	Optimal utilization of assets
Extend the service life of product	Reliability of electricity grid
Minimize the resource consumption	Energy conservation
Intact logistics	Reduce AT & C losses
Reverse logistics for waste management	Optimizing costumer end generation
Can keep some percentage as backup	Proper load forecasting due to storage constrain
Safety factors	
Sustainable development	

3. Modeling approaches for electric grid

As there are many structural similarities between smart grid and supply chain (table 1 & figure 1) a model of the smart grid can be developed borrowing ideas from SCN. In harmony with supply chain, the modelling approaches can be broadly classified into two categories: Top-down approach and Bottom-up approach.

3.1. Top down approach

The top-down approach treats the customer as an energy sink and does not distinguish energy consumption due to individual customer type. One of the popular top down approaches to model electric grid is real power flow method. To capture the power grid behaviour, the alternative current (AC) power flow model is the most accurate one. This model analytically determines the real and reactive flows over all the lines by using the power equations to solve the voltage magnitude and load angles at each substation (node). However, this model is very complicated due to its non-linear feature. Direct current (DC) power flow model is another type of power flow method which uses a linear equation to reflect the relationship between power flow through the lines and the power injection at the nodes. These real power flow methods are very useful in network planning and operation, determining and optimizing generation scheduling and calculating steady state conditions for stability analysis.

The other approach which aims to obtain the dynamic behaviour of the system is frequency analysis. Load Frequency Control (LFC) is the mechanism to regulate the power flow between the different regions of an interconnected system with objective to keep frequency constant. In an electrical network, different regions are interconnected to its neighbouring regions through the transmission lines, called tie-lines. Power

sharing between the two regions occurs through these tie-lines. LFC is used to regulate the flow of power among these tie-lines.

3.2. Bottom-up approach

The bottom-up approach treats all generating units as an energy source and does not distinguish between the types of primary energy used for generation. Rather than focusing on supply optimization it focuses on optimizing the costumer behaviour. In bottom up approach we start with modelling of the load profile. The factors affecting load profile can be broadly classified as technological factors and behavioural factors. Technological factors depend on the appliance type and manufacturer. Behavioural factors depend on socioeconomic and demographic characteristics, environmental conditions and the day of the year. This approach helps us to identify the customer level details of consumption and can thus be used for demand optimization to balance supply and demand. Figure 2 shows the parameters required for bottom-up approach.

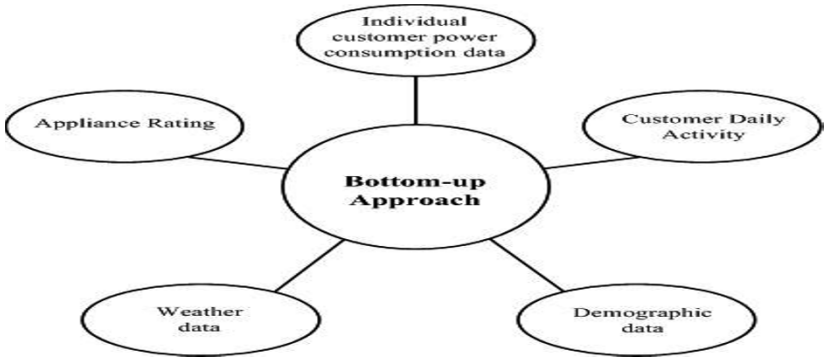

Figure 2: Factors affecting individual load profile

4. Electric Grid network in India

Indian power grid is divided into five regions namely - NR (Northern Region), WR (Western region), SR (Southern Region), ER (Eastern Region) and NER (North Eastern Region). Though these five regions are independent but electrically they are connected constituting a National Grid.

As per Indian Electricity Grid Code (2010, CERC) government organizations responsible for planning, operating and regulating the Indian electricity grid and their respective responsibilities are as follows:

- Load Dispatch Centres at National, Regional and State level (NLDC, RLDC and SLDC respectively) supervise and control the scheduling and dispatch of electricity in order to optimally utilize the available power resources at the respective levels. NLDC and RLDC keeps accounting of inter-regional and intra-regional exchange of power respectively. NLDC also coordinates for trans-nation exchange of power.
- Regional Power Committee (RPC) at regional level undertakes operational planning and analysis of the grid. It plans monthly and annual generators and transmission lines maintenance. It also works out on all issues relating to economy and efficiency in the operation of power system in that region.

- Central Electricity Authority (CEA) is responsible for coordinating activities of planning agencies (RPC) and specifying technical standards for construction, operation and management of the grid. It also collects data for generation, transmission, distribution and trading at the grid level.
- Regulatory Commissions at Central and State level (CERC and SERC respectively) are responsible for defining regulations.

The electricity flow and information flow in the present Indian electricity grid and the percentage installed capacity of generation is shown in the Figure 3.

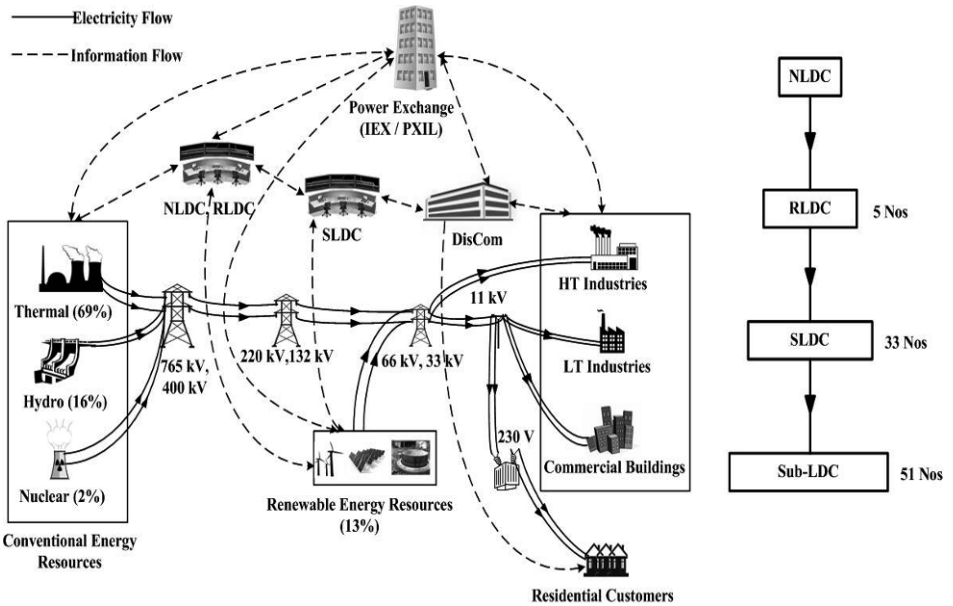

Figure 3: Structure of Present Indian Electricity Grid (Left side) & regulatory agencies (Right side)

4.1. Case Study

On 30th July 2012 and 31st July 2012, the Indian electricity grid saw two successive major blackouts which left more than 600 million people in India with no electricity. It is considered as the largest power outage in history which spread across three regional grids (NR, ER and NER) covering over 21 Indian states and 1 union territory. The main reason for this grid failure was unbalance between demand and supply in the northern region which led to the heavy loading of inter-regional links and resulted in the cascaded failure of grid.

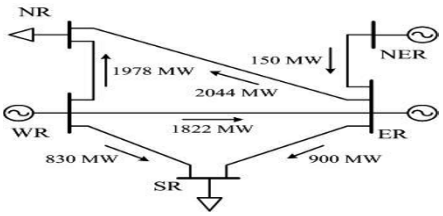

Figure 4: Antecedent conditions of Indian electricity grid on 31st July, 2014

We have studied the cascade event of 31st July and analysed the conditions prior to the event using AC power flow method. Table 2 shows that the voltage and load angle deviation at NR bus was too much which eventually resulted in the grid failure. However the exact system conditions can be obtained by analysing the frequency deviation.

Table 2: Bus voltages and load angles at each bus on 31st July, 2014

Region	Type of bus	Bus Voltage (pu)	Load Angle (deg)
Northern Region (NR)	PQ	0.84	-35.90
Eastern Region (ER)	PV	1.00	-12.92
North-Eastern Region (NER)	PV	1.00	-12.27
Western Region (WR)	Swing	1.00	0.00
Southern Region (SR)	PQ	0.99	-19.92

5. Conclusions and Future Directions

Presently, the Indian electricity system faces a number of challenges: Poor access to electricity, Shortage of power, huge losses in the grid, power theft, shortage of fuel, incompetent power consumption and poor reliability. Over 300 million people in India still have no access to electricity. A smart grid is supposed to be the solution to all these challenges and in fact essential for India's energy security in the future. Smart grid will lead to optimal utilization of resources, cost savings at the operational level and sustainable development. This caters for the need of decentralization of the electric grid with bidirectional power flow and more focus on low voltage level. The introduction of distributed generation, more emphasis on renewable resources, secure and reliable grid operation have driven the electric grid on the path of supply chain network. Due to the aforementioned similarities between closed-loop SCN & smart grids and given the fact that SCN is a well-established domain, the transformation of existing Indian electric grid to smart grids can be achieved using the lessons learnt from closed loop SCN. Acknowledging the existing similarities & differences, our future work is directed towards adapting the existing modeling, scheduling & optimization strategies for resilient supply chain networks to smart grid systems.

References

A. Richter, E. Laan, W. Ketter, K. Valogianni, 2012, Transitioning from the traditional to the smart grid: Lessons learned from closed-loop supply chains, Smart Grid Technology, Economics and Policies (SG-TEP).

M. Habib, 2011, Supply Chain Management (SCM): Theory and Evolution, Supply Chain Management – Applications and Simulations, 3-14.

M. A. Kalaitzidou, P. Longinidis, P. Tsiakis, M. C. Georgiadis, 2014, Optimal Design of Generalized Supply Chain Networks, Proceedings of the 24th European Symposium on Computer Aided Process Engineering, 385-390.

X. Han, D. Chen, D. Chen, L. Hou, 2014, Game Study of the Closed-loop Supply Chain with Random Yield and Random Demand, Journal of Information & Computational Science,Volume 11, Issue 12, 4405-4414.

L. G. Swan , V. I. Ugursal, 2009, Modeling of end-use energy consumption in the residential sector: A review of modeling techniques, Journal of Renewable and Sustainable Energy Reviews, Volume 13, 1819–1835.

Indian Electricity Grid Code, 2010, Central Electricity Regulatory Commission.

Report on the Grid Disturbances on 30th July and 31st July 2012, Central Electricity Regulation Commission.

World Energy Outlook 2014, International Energy Agency.

Krist V. Gernaey, Jakob K. Huusom and Rafiqul Gani (Eds.), 12th International Symposium on Process Systems Engineering and 25th European Symposium on Computer Aided Process Engineering.
31 May – 4 June 2015, Copenhagen, Denmark

Integrated Computational and Experimental Studies of Microalgal Production of Fuels and Chemicals

Mesut Bekirogullari[a,b], Jon Pittman[b] and Constantinos Theodoropoulos[a,*]

[a]*School of Chemical Engineering and Analytical Science,University of Manchester, M13 9PL, UK*
[b]*Faculty of Life Sciences, University of Manchester, M13 9PL, UK*

Abstract

Microalgae are sunlight-driven cell factories that carry out the same process and mechanism of photosynthesis as higher plants converting sunlight into biomass, performing more efficiently than crops (Chisti, 2007). Nevertheless, high substrate and fertilizer input requirements as well as harvesting and oil extraction costs have been found to play a significant role in both the economic viability and sustainability of microalgal biofuels production (Pittman et al., 2011). Therefore, attention has been drawn to experimental and computational studies on the microalgal oil production, aiming to increase the productivity either through the photosynthesis process or through the application of metabolic engineering (Chisti, 2007) to improve the sustainability and competitiveness of the algal-derived biofuels industry. The objective of this work is the establishment of links between algal strains grown in large raceway open ponds and innovative bioproduct generation technologies including fuels and chemicals in order to achieve positive energy balance and environmental sustainability. Multi-parameter quantification has been employed leading to a predictive model to describe algal growth and lipid accumulation in lab-scale batch systems. The model can also take into account the effects of temperature, light and pH, in order to improve the productivity of microalgae cultivation technologies. Experiments have been conducted to analyse the effect of different input parameters. The model was fitted to data from bench-scale batch experiments. The experimental setup involved tris-acetate-phosphate (TAP) media containing 1.575 g/L and 2.1 g/L acetic acid and 0.098147 g/L nitrogen under constant light illumination of 125 $\mu Em^{-2}s^{-1}$. An in-house developed optimization framework (Vlysidis et al., 2011) has been used for the estimation of the key parameters. The predictive capabilities of the model were tested on batch systems comprising TAP media containing 2.625 g/L acetic acid.

Keywords: *Chlamydomonas Reinhardtii*, Biofuels, Kinetic modelling, Microalgal oil.

1. Introduction

Microalgae are light driven cell factories which convert CO_2 to biofuels, high-value co-products, feeds, and foods (Borowitzka, 1999; Chisti, 2007). Additionally, microalgae species are useful for bioremediation processes and they can be used as nitrogen fixing fertilizers (Chisti, 2007). This work focuses on the potentials of microalgal oil production. Microalgae species produce several types of renewable biofuels such as methane through anaerobic digestion of microalgal biomass (Chisti, 2007), biodiesel from microalgal oil (Demirbas, 2011), and hydrogen through photobiology (Chisti, 2007). Although the potential of microalgae use as a source for renewable fuel

production has been known for more than 50 years (Chisti, 2007), it has just recently been increasingly taken into consideration due to the petroleum price escalation, and more importantly, due to the increasing concern about global warming associated with fossil fuel usage. Microalgal production of biofuels bears significant advantages such as rapid growth rate of microalgae, reduction of greenhouse gas (CO_2) emissions, decrease of consumption of resources (water and land), high production capacity, non-competition with agricultural land and simple growing needs (light, sugars N, P, K and CO_2) compared to other terrestrial plants (Borowitzka, 1992). Economic and scientific interest in microalgal oil production has focused on the increase of microalgal oil productivity through photosynthesis and also on the improvement of the sustainability and competitiveness of the algal-derived biofuels industry.

The main objective of this work is to establish links between algal strains grown in large raceway open ponds and innovative bioproduct generation technologies including fuels and chemicals in order to achieve positive energy balance and environmental sustainability. Therefore, multi-parameter quantification has been employed and a predictive model has been constructed to describe biomass growth, and lipid production in lab-scale batch systems. The predictive capabilities of the model have been tested for a range of growth parameters related to temperature, light and pH, in order to aid the robust design and control of microalgae cultivation technologies. Experiments have been conducted to investigate the effect of each metabolite on biomass growth and on lipid accumulation. Furthermore, an in-house developed Simulated Annealing (SA) scheme is linked to a deterministic MATLAB optimization function for the estimation of key parameters used in the bench-scale batch systems.

2. Materials and Methods

2.1. Strain and Culture Conditions

Chlamydomonas Reinhardtii (CCAP 11/32C) was obtained from the Culture Collection of Algae and Protozoa, UK. Preculture of the strain is carried out in an incubation room at 25ºC using 250 mL conical flasks, each containing 150 mL of Tris-acetate-phosphate (TAP) medium, which was placed in an orbital shaker at 120 rpm for 7-10 days. Constant illumination was used at 125 $\mu Em^{-2}s^{-1}$ intensity with white fluorescent lamps. The preculture of the strain was stopped when sufficient density was reached. An algal inoculum of 1 mL was then added to the experimental culture vessels (500 mL bottles) containing 500 mL of culture medium. The starting cell density was the same in all treatments; 0.024×10^6 cells per mL for *C. Reinhardtii*. To induce nitrogen starvation, different TAP salts solutions containing different nitrogen concentrations have been prepared and used. The samples were centrifuged for 3 min at a full speed to harvest the biomass. The obtained pellet was then washed with cold distilled water and weighed to determine the wet biomass. Subsequently, the wet biomass was dried overnight at 70 ºC to determine the dry biomass weight. The pH of the samples was analysed through the use of a bench type pH meter. The samples were stored in eppendorf tubes and placed in the refrigerator at -20ºC for further analysis of the biomass and the supernatant.

2.2. Analytical Methods

Optical Density: The biomass growth was defined through the measurement of optical density at 680 nm in a UV-VIS spectrophotometer.

HPLC Analysis of Organic Acids: The consumption and production of acids was quantified using a High Performance/Pressure Liquid Chromatographer (HPLC) equipped with a Hi- Plex 8 μm 300x7.7 mm column. Glacial acetic acid (GAA) -which

was added to the growth media as a substrate- and oxalic acid (OA), glycolic acid (GA) and formic acid (FA) -produced byproducts- (Allen, 1956) were added into standard solutions. Sulphuric Acid (SA) solution (0.05% v/v) was used as mobile phase. The flow rate of system was set to 0.6 $mLmin^{-1}$ with a pressure value around 45 bars and temperature of 50ºC while the detection wavelength was set at 210 nm. The sample preparation included filtration through 0.45 μm filter membranes

TOC/TN Analyser: Total dissolved nitrogen concentration in the growth media was quantified by the use of Total Organic Carbon / Total Nitrogen analyser (TOC/TN). Ammonium Chloride (NH_4Cl) -which was added to the growth media as a nutrient- was added into standard solutions.

Soxhlet Solvent Extraction by Using Soxtec: The freeze-dried algal biomass was homogenized with liquid nitrogen in a mortar with pestle and extracted using the Soxtec 1043 automated solvent extraction system. The following procedure was used to quantify lipid content: boiling 2 hours, rinsing 40 min and solvent recovery 20 min. Extraction temperature for the selected solvent (Hexane) was 155ºC (McNichol et al., 2012). After the oil extraction with the Soxtec 1043, extracted lipids were dried at 100ºC for 1 h, placed in vacuum applied desiccator for 1h, and weighed to define lipid yield gravimetrically.

3. Modelling

Economou et al. (2011) have described a single-cell biomass growth and oil accumulation model. Based on that study, here we have developed an improved unstructured process model to describe the microalgal growth and oil accumulation processes. Microalgae growth is given by:

$$\frac{dX}{dt} = \mu_X X \tag{1}$$

where X is the fat-free biomass concentration (g/L), and μ_X is the specific growth rate based on substrate, nitrogen and light (1/h) described by Eq.(6) later in this work.

The lipid accumulation rate can be described by:

$$\frac{dL}{dt} = q_L X \tag{2}$$

where L is the lipid concentration (g/L), and $q_L$the specific lipid accumulation rate of lipids in biomass (g lipids/ (g fat-free biomass h)) described by Eq.(7) later in this work.

The substrate consumption rate can be calculated by a simple substrate- mass balance:

$$-\frac{dS}{dt} = \left(\mu_X \frac{1}{Y_{X/S}} + q_L \frac{1}{Y_{L/S}}\right) X \tag{3}$$

where $Y_{\frac{X}{S}}$ is the yield coefficient for fat-free biomass production with respect to substrate (g fat-free biomass/ g substrate), $Y_{\frac{L}{S}}$ is the yield coefficient for lipid production with respect to substrate (g lipids /g substrate) and S is the substrate concentration (g/L). The nitrogen consumption rate is computed by:

$$-\frac{dN}{dt} = \mu_{SN} \frac{1}{Y_{X/N}} X \tag{4}$$

where $Y_{(X/N)}$ is the yield coefficient for fat-free biomass production with respect to nitrogen (g fat-free biomass/g nitrogen) and N is the nitrogen concentration (g/L).

The dependence of the pH of the microalgae cultivation system on substrate consumption is taken into account here. Thus, the pH change in the system is expressed as (Zhang et al., 1999):

$$-\frac{dH}{dt} = K_H \frac{dS}{dt} \tag{5}$$

where H is the pH of the process and K_H is a coefficient for the dimensionless pH. After the conduction of a number of experiments, we observed that high substrate concentrations lead to a significant reduction of the specific growth rate. Experiments have also shown that nitrogen deprivation triggers lipid accumulation while blocking the biomass growth. Additionally, it was found that biomass production reduces significantly at high light intensities. The Monod-Andrew double-substrate limitation model has been employed to describe both the substrate and the nitrogen effect. An additional term has been added to describe the light intensity effect. Subsequently, the specific growth rate of fat-free biomass and the specific growth rate of lipid formation depending on substrate, nitrogen and light are expressed by:

$$\mu_X(S,N,I) = \mu_{Xmax} \frac{\mathrm{S}}{K_S + \mathrm{S} + \frac{\mathrm{S}^2}{K_{i1}}} \frac{\mathrm{N}}{K_N + \mathrm{N}} \frac{I(l)}{K_I + I(l)} \tag{6}$$

$$q_L(S,N,I) = q_{Lmax} \frac{S}{K_{LS} + S + \frac{S^2}{K_{i2}}} \frac{K_2}{K_2 + N} \frac{I(l)}{K_I + I(l)} \tag{7}$$

where μ_{Xmax} is the maximum specific growth rate of biomass (1/h), q_{Lmax} is the maximum specific growth rate of lipid (g lipids /g fat-free biomass), K_S and K_{LS} are the saturation constants for substrate and lipid respectively (g/L), K_{i1} and K_{i2} are the inhibition constants (g/L) for fat-free biomass growth and lipid production respectively, K_N and K_I are the saturation constant (g/L) for nitrogen and light respectively, K_2 is a constant (g/L) that defines the inhibition of the lipid production process by nitrogen, and $I(l)$ is the local light intensity.

The light distribution during algae cultivation is expressed by the Beer-Lambert law:

$$I(l) = I_0 \exp(-\sigma X l) \tag{8}$$

where $I(l)$ is the local light intensity, l is the distance from the light source to the bottles' external surface, I_0 is the incident light intensity and σ is the extinction coefficient.

4. Results and Discussion

Estimation of the model parameter values was performed through optimisation coupling a stochastic SA algorithm, with a deterministic method, using the 'fmincon' function in MATLAB, to allow the computation of solutions around the global optimum (Vlysidis et al., 2011). The model was fitted to experimental data obtained from cultures, performed on Tris-acetate-phosphate (TAP) media containing 1.575 g/L (Figure 1) and 2.1 g/L acetic acid and 0.098147 g/L nitrogen under constant light illumination 125 $\mu Em^{-2}s^{-1}$. The parameter values obtained are shown in Table 1. The corresponding

model predictions along with the experimental observations for TAP media containing 2.625 g/L acetic acid are presented in Figure 2. As we can see in Figures 1 and 2, our model is capable of predicting the biomass growth, the substrate consumption and the lipid accumulation very accurately both qualitatively and quantitatively. Small differences are observed in the pH profiles due to the production of organic acids that are currently not taken into account in this work.

Table 1: Model Kinetic Parameters.

Parameters	Values	Parameters	Values
μ_{SNmax}	$0.0989h^{-1}$	k_2	$197.6611\frac{g}{L}$
K_S	$1.7160\ \frac{g}{L}$	$Y_{X/S}$	$0.4438\ \frac{\text{g fat} - \text{free biomass}}{\text{g substrate}}$
K_{i1}	$7.5794\ \frac{g}{L}$	$Y_{L/S}$	$0.0664\frac{\text{g Lipids}}{\text{g substrate}}$
K_N	$0.0349\ \frac{g}{L}$	$Y_{X/N}$	$5.3668\ \frac{\text{g fat} - \text{free biomass}}{\text{g nitrogen}}$
q_{Lmax}	$0.184\frac{\text{g lipids}}{\text{g fat} - \text{free biomass}}$	K_H	$0.7651\ \frac{L}{g}$
K_{LS}	$114.6521\ \frac{g}{L}$	σ	$0.0244\frac{m^3}{kg}$
K_{i2}	$6.0739\frac{g}{L}$	K_I	$6.4611\ \mu E m^{-2}s^{-1}$

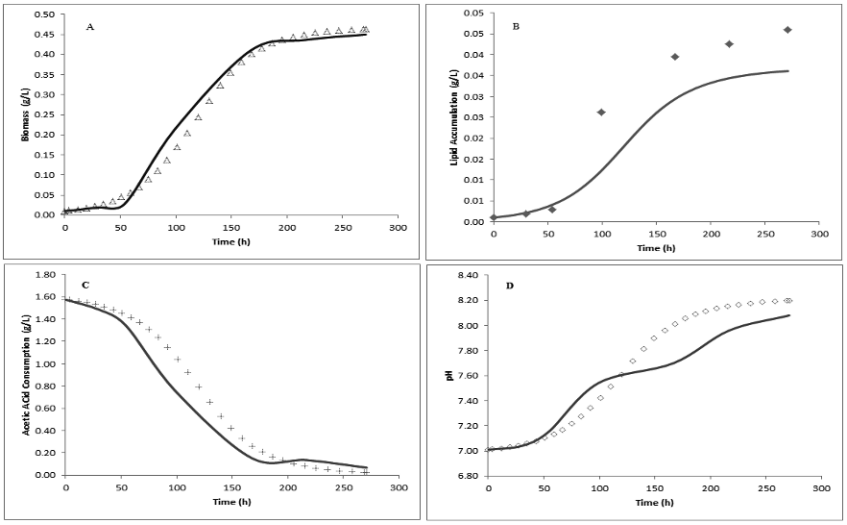

Figure 1: Profiles of experimental results (symbols) and model predictions (lines) for: (a) biomass *(C. Reinhardtii)* growth, (b) lipid accumulation, (c) substrate (acetic acid) consumption and (d) pH change, using 1.575 g/L acetic acid.

5. Conclusions

A multi-parameter model has been developed to describe the biomass growth and the lipid production in bench-scale batch systems. The formulated model also considered a

range of metabolites related to temperature, light and pH. Experiments were conducted for the investigation of the effect of each metabolite on biomass growth and on lipid accumulation. The model was validated for different sets of substrate concentrations. Such a predictive model can be exploited for the robust design and the control of microalgal oil production technologies towards an efficient system scale-up.

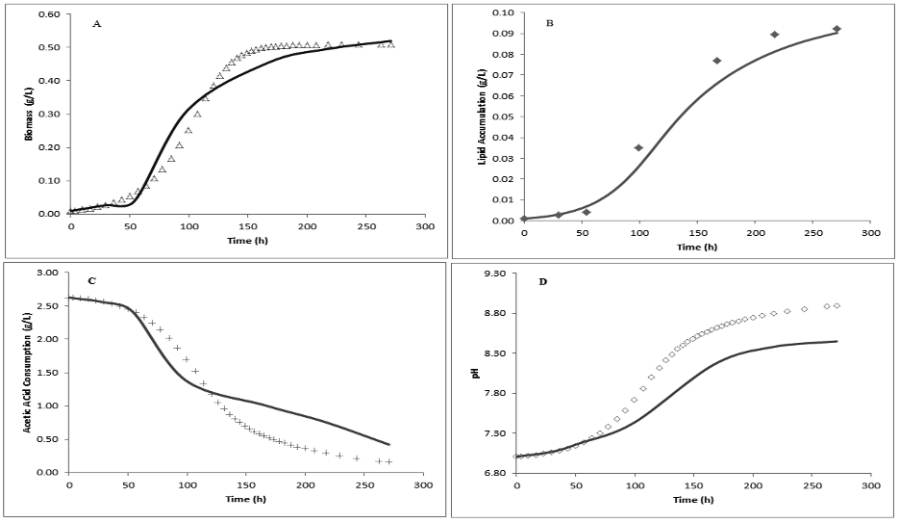

Figure 2: Profiles of experimental results (symbols) and model predictions (lines) for: (a) biomass *(C. Reinhardtii)* growth, (b) lipid accumulation, (c) substrate (acetic acid) consumption and (d) pH change, using 2.625 g/L acetic acid.

Acknowledgements

MB would like to acknowledge the financial support of Republic of Turkey Ministry of National Education.

References

M. Allen, 1956, Excretion of organic compounds by Chlamydomonas, Arch. Mikrob., 24, 163-168.

M.A. Borowitzka, 1999, Commercial production of microalgae: ponds, tanks, tubes and fermenters, J. Biotechnol., 70, 313-321.

Y. Chisti, 2007, Biodiesel from microalgae, Biotechnol. Adv., 25, 294-306.

A. Demirbas and F.M. Demirbas, 2011, Importance of algae oil as a source of biodiesel, Energy Convers. Manage., 52, 163-170.

C.N. Economou, G. Aggelis, S. Pavlou and D.V. Vayenas, 2011, Modeling of single-cell oil production under nitrogen-limited and substrate inhibition conditions, Biotechnol. Bioeng., 108, 1049-1055.

J.K. Pittman, A.P. Dean and O. Osundeko, 2011, The potential of sustainable algal biofuel production using wastewater resources, Bioresource Technol., 102, 17-25.

A. Vlysidis, M. Binns, C. Webb and C. Theodoropoulos, 2011, Glycerol utilisation for the production of chemicals: Conversion to succinic acid, a combined experimental and computational study, Biochem. Eng. J., 58–59, 1-11.

X-.W. Zhang, F. Chen and M.R. Johns, 1999, Kinetic models for heterotrophic growth of Chlamydomonas reinhardtii in batch and fed-batch cultures, Process Biochem., 35, 385-389.

Krist V. Gernaey, Jakob K. Huusom and Rafiqul Gani (Eds.), 12th International Symposium on Process Systems Engineering and 25th European Symposium on Computer Aided Process Engineering.
31 May – 4 June 2015, Copenhagen, Denmark

Process Integration and Assessment of Biogas System

Wu B., Xu Y.J., Zhang X.P.*

Beijing Key Laboratory of Ionic Liquids Clean Process, State Key Laboratory of Multiphase Complex Systems, Key Laboratory of Green Process and Engineering, Institute of Process Engineering, Chinese Academy of Sciences, Beijing 100190, China
xpzhang@ipe.ac.cn

Abstract

In this work, we established the material and energy flow charts of a base case which contains the following units: biomass collection and transportation, pretreatment, anaerobic digestion, biogas upgrading and waste management. For this biogas system, the input feedstock are fixed to human feces and corn straw, the anaerobic digestion is performed at normal temperature 25 °C, and the biogas coming from anaerobic unit is upgraded via high pressure water scrubbing method to obtain the 98 % purity biomethane. The system material and energy flows are presented to indicate that the anaerobic digestion unit generate 90 wt % of the biogas slurry and residue, and 70 % of the energy was loss with the emission of the biogas slurry and residue. As for the system energy balance, we calculate the low heating value (LHV) based system energy efficiency considering the biomass feedstocks' LHV. Furthermore, a system energy efficiency comparison between the base case and the modified case with heat exchange between biogas slurry and feedstock is made. The system energy efficiency results indicate that the heat exchange between the biogas slurry and the feedstock can enhance the system efficiency by about 0.3 %.

Keywords: biogas system, energy efficiency, green degree, system evaluation, process integration

1. Introduction

The harmful effects of the use of fossil fuels to the environment, health and society have spurred global interest in the search for cleaner sources of energy (Deng et al., 2014). As an effective method to generate renewable energy, biogas is being developed rapidly and globally, and is playing an increasingly important role in energy production and environmental protection (Wang et al., 2014).

However, biogas production is a huge system which covers different subsystems, such as the feedstock collection and transportation, pre-treatment, anaerobic digestion, digestate management and biogas utilization. All of the above mentioned subsystems contain various technologies. For feedstock transportation, the truck or tractor can be used; for pre-treatment methods both chemical methods, i.e., ionic liquids, alkali and acid are used and physical methods, i.e., steam explosion, chopping, and baling, etc. are available (Risberg et al., 2013); for anaerobic digestion technologies, according to the difference in total solid content and the temperature, methods such as mesophilic-wet, mesophilic-solid, thermophilic-wet and thermophilic-solid, etc. can be chosen. Furthermore, the variety of the anaerobic digestion reactors and one stage or two stage

anaerobic digestion processes are also alternatives for the anaerobic digestion subsystem (Schievano et al., 2014; Wan et al., 2013); for biogas utilization, the combined heat and power (CHP), fuel cell and upgrading technologies, i.e., pressure swing adsorption (PSA), membrane, high pressure water scrubbing (HPWS), etc. are common ways to utilize the biogas; for digestate management technologies, the digestate can be applied for bio-fertilizer, composted and combustion as fuel after drying. The selection or combination of the technologies presented above and the variety of the feedstock used in the process constitute a big topological network, which make the system so complex to study. Thus, giving an assessment of the whole system from energetic, environmental and economic aspects has great significance.

According to the author's knowledge, there is little literature focus on the biogas system evaluation; most of the work on biogas system evaluation was done by Börjesson and Berglund group. The published literature by them is mainly using the LCA-based environmental method to evaluate the system. For example, Börjesson and Berglund (2006) gave an analysis of fuel-cycle emissions of carbon dioxide (CO_2), carbon oxide (CO), nitrogen oxides (NO_x), sulphur dioxide (SO_2), hydrocarbons (HC), methane (CH_4), and particles from a life-cycle perspective for different biogas systems based on six different raw materials. The results indicated that biogas yields and the energy efficiency in the biogas production chain have a significant impact on the fuel-cycle emissions from biogas systems. Börjesson and Berglund (2007) indicated that the environmental impact of introducing biogas can vary significantly due to the raw materials digested, the energy service provided and the reference systems replaced, but there are also some uncertainties regarding the availability of accurate input data, assumptions about technologies and geographical conditions.

As for the energetic assessment of the biogas system, there are not more than ten references. Many studies mainly analyzed the subsystem energy balance or energy efficiency but not the whole biogas system. Chen and Chen (2014) proposed a 3-level emergetic evaluation framework to investigate the energy efficiency and sustainability of a complex biogas system (CBS) in South China. The results suggested that the metabolism of the CBS has increased over years in terms of total emergy input, among which renewable resources and non-renewable purchases contributed most. Poschl et al. (2010) gave an evaluation of the energy efficiency of different biogas systems, including single and co-digestion of multiple feedstock, different biogas utilization pathways, and waste-stream management strategies. The results demonstrated that, co-digestion is more stable process than the single digestion. Furthermore, system energy efficiency could be further enhanced through recovery of residual biogas from anaerobic digestion subsystem. Havukainen et al. (2014) investigated various system boundaries and the evaluating methods of estimating energy performance of biogas production. The results demonstrated that, the comparability of the energy performance of various biogas systems requires that the energy performance is calculated in a more consistent manner.

The aim of this study is to give the energy and material balance of the biogas system defined by ourselves, to calculate the energy efficiency of this system under fixed input feedstock type and anaerobic digestion temperature but different units technologies. Furthermore, the heat exchange between the biogas slurry and the input feedstock is considered to enhance the system energy efficiency.

2. Methodology

2.1. Biogas system description

The biogas system in this work concludes five units: 1) biomass collection and transportation. In this unit, only the corn straw is collected using a truck with 2.5 ton loading, the transport distance is 20 km; 2) biomass pretreatment. The corn straw is pretreated by physical methods, i.e., briquetting and chopping. 3) anaerobic digestion. The digestion temperature is fixed at 25 °C and the total solid content is fixed at 10 wt %, the mechanical stirring is installed to ensure the homogeneous temperature and substrate concentration in the anaerobic digester, and the volume of biogas production rate under this condition is 0.74 m^3/m^3 digester/d; 4) biogas upgrading. The high pressure water scrubbing (HPWS) method is applied with pure water as the solvent, the product CH_4 is then compressed to utilize as the vehicle fuel; 5) waste management. The digestate is handled by separating the solid and the liquid using screwing and pressing, and the solid is then dried by using the heat from outside of the system. The biogas system is presented in Figure 1. All of the data above is from the biogas demonstration project in Nanjing Tech university.

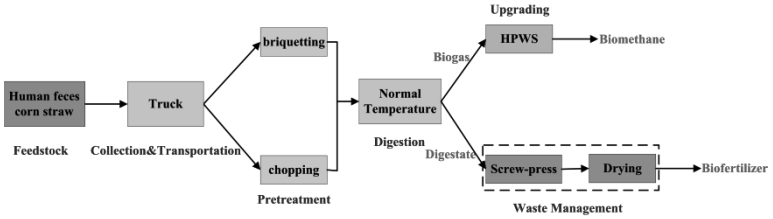

Figure 1. Biogas system boundary

2.2. Biogas system evaluation index

The energetic performance of the biogas system is evaluated by using the low heating value (LHV) based energy efficiency. The input energy into the system concludes the following parts: 1) the energy consumption in biomass collection unit is mainly due to the diesel consumption by the truck, which can be converted to the energy calculated by LHV of the diesel; 2) the energy consumption in pretreatment unit arise from briquetting and chopping the corn straw; 3) the energy consumption in anaerobic digestion unit contains the heating of the feedstock, the maintenance of the temperature of the digester and the mechanical stirring; 4) the energy consumption in biogas upgrading unit mainly contains the energy used to compress the gas mixture and the compression of the product CH_4 to a high pressure as the vehicle fuel; 5) the energy consumption in waste management unit contains separating the biogas slurry and biogas residue by screwing and pressing, and then heating the biogas residue to lower water content. The energy consumption type of the biogas system is mainly the heat and electricity. The energy consumption of electricity is calculated by the LHV of the standard coal, the standard coal consumption of power supply is 0.321 kg/kWh in China, and the LHV of the standard coal is 29.26 MJ/kg. The heat needed in the anaerobic digestion unit, the heat integration and the energy needed in the biogas upgrading unit are calculated using the Aspen plus.

3. Results and discussion

3.1. Biogas system material flow analysis

The biogas system material flow is presented in Figure 2. The material balance is calculated based on the mass of the material. The material balance in Figure 2 indicates that, the biogas and biomethane account for 3.0 wt% and 1.1 wt% of the total feedstock input in this system, respectively. Thus, the material application efficiency is low, it is imperative to develop new digestion technologies to enhance the yield of the biogas and the content of the methane. Furthermore, the process generates about 90 wt% slurry and residue, which also cause huge environment problems. How to handle these nutrient rich materials efficiently is of great importance.

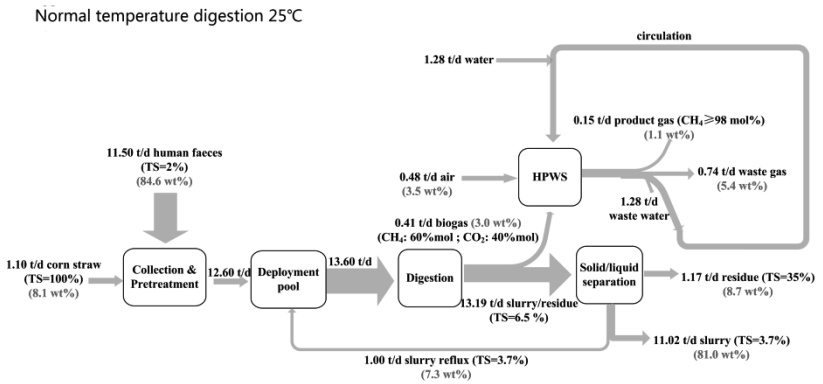

Figure 2. Biogas system material flow

3.2. Biogas system energy flow analysis

The biogas system energy flow is presented in Figure 3. The energy balance is calculated based on the LHV of the material and the standard coal. It can be seen from the Figure 3 that, the raw biogas and product gas account for 29.3% and 28.7% of the total energy input in the system, and 70% of the energy is loss with the waste gas and the slurry and residue. Thus, the heat exchange between the slurry and the feedstock should be conducted to decrease the energy loss.

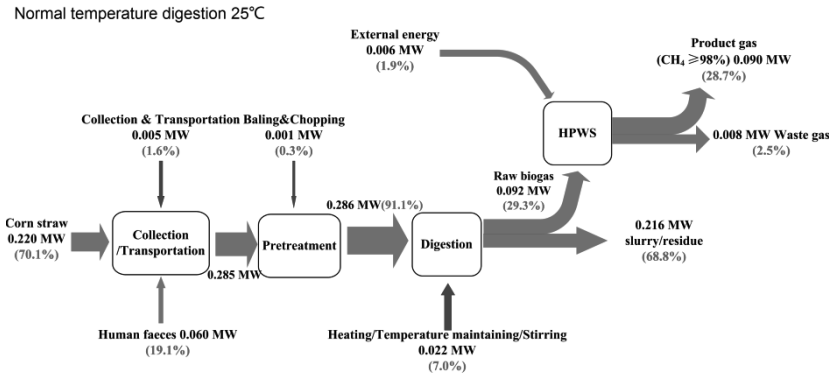

Figure 3. Biogas system energy flow

3.3. Biogas system energy efficiency comparison

To calculate the energy efficiency of the system, the energy consumption distribution should be given, the base case energy consumption distribution with no exchange of the heat between the slurry and the feedstock is presented in Figure 4. The energy efficiency of the base case is 28.7%. For the improvement of the system efficiency, the modified case with heat exchange between slurry and feedstock is calculated, the energy consumption distribution of the modified case is presented in Figure 5. In the base case, the feedstock temperature is the mean temperature of the Nanjing area, which is about 16 °C. However, the modified case assume that we use the most advanced heat exchange technologies, with the logarithmic mean temperature difference about 5 °C, lower than the general reported 10 °C. Though the heat exchange operation, the feedstock can be heated to about 20 °C. The energy efficiency of the modified case is 29.0%, which has only 0.3% enhancement compared with base case. Thus, the improvement of the energy consumption from other unit like upgrading or waste management is necessary to further enhance the energy efficiency of the system.

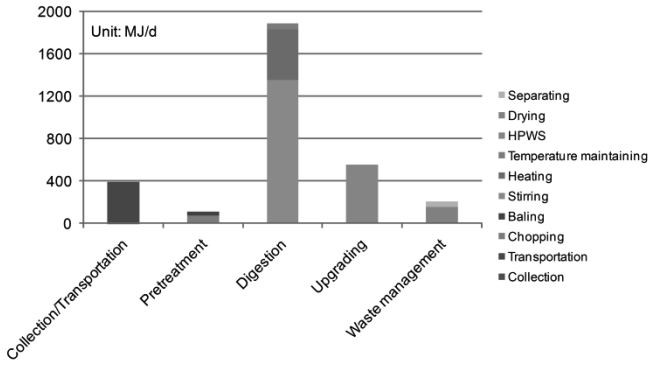

Figure 4. Biogas system energy efficiency of base case

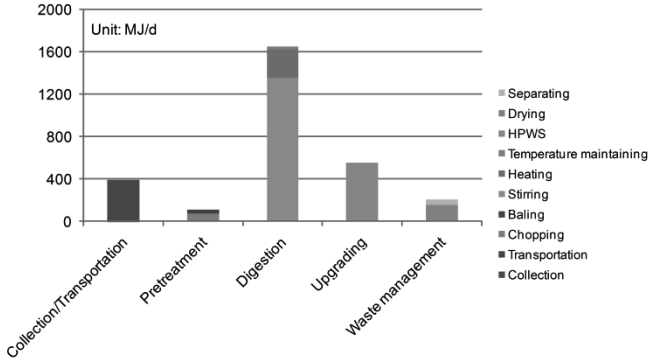

Figure 5. Biogas system energy efficiency of modified case

4. Conclusions

In this work, the biogas system is analyzed by giving the material and energy flow and the energy efficiency of the base case and modified case. First, the material flow indicate that huge amount of biogas slurry and residue (90 wt%) would cause

environment problems which should be paid more attention. Furthermore, the yield of the raw biogas (3 wt%) and biomethane (1.1%) is low, which should be enhanced by developing new anaerobic digestion technologies such as thermophilic technology and new digestion reactors. Second, the energy flow results demonstrate that, the energy loss (70%) of the system is significant due to the emission of the waste gas, biogas slurry and residue. Finally, the energy efficiency of the base case (28.7%) and modified case (29.0%) are calculated, respectively. The system energy efficiency only enhance about 0.3%, which need to improve other unit technologies like upgrading and waste management.

Acknowledgements

This work was financially supported by the National Basic Research Program of China (No. 2013CB733506, No. 2014CB744306) and the National Natural Science Foundation of China (No. 21036007, No. 51274183).

References

Börjesson, P., Berglund, M., 2006, Environmental systems analysis of biogas systems—Part I: Fuel-cycle emissions. Biomass and Bioenergy, 30, 469-485

Börjesson, P., Berglund, M., 2007, Environmental systems analysis of biogas systems—Part II: The environmental impact of replacing various reference systems. Biomass and Bioenergy, 31, 326-344

Chen, S., Chen, B., 2014, Energy efficiency and sustainability of complex biogas systems: A 3-level emergetic evaluation, Applied Energy, 115, 151-163

Deng, Y., Xu, J., Liu, Y., Mancl, K., 2014, Biogas as a sustainable energy source in China: Regional development strategy application and decision making, Renewable and Sustainable Energy Reviews, 35, 294-303

Havukainen, J., Uusitalo, V., Niskanen, A., Kapustina, V., Horttanainen, M., 2014, Evaluation of methods for estimating energy performance of biogas production, Renewable Energy, 66, 232-240

Poschl, M., Ward, S., Owende, P., 2010, Evaluation of energy efficiency of various biogas production and utilization pathways, Applied Energy, 87, 3305-3321

Risberg, K., Sun, L., Levén, L., Horn, S.J., Schnürer, A., 2013, Biogas production from wheat straw and manure – Impact of pretreatment and process operating parameters. Bioresource Technology, 149, 232-237

Schievano, A., Tenca, A., Lonati, S., Manzini, E., Adani, F., 2014, Can two-stage instead of one-stage anaerobic digestion really increase energy recovery from biomass? Applied Energy, 124, 335-342

Wan, S., Sun, L., Douieb, Y., Sun, J., Luo, W., 2013, Anaerobic digestion of municipal solid waste composed of food waste, wastepaper, and plastic in a single-stage system: Performance and microbial community structure characterization, Bioresource Technology, 146, 619-627

Wang, X., Chen, Y., Sui, P., Gao, W., Qin, F., Wu, X., Xiong, J., 2014, Efficiency and sustainability analysis of biogas and electricity production from a large-scale biogas project in China: an emergy evaluation based on LCA. Journal of Cleaner Production, 65, 234-245

Krist V. Gernaey, Jakob K. Huusom and Rafiqul Gani (Eds.), 12th International Symposium on Process Systems Engineering and 25th European Symposium on Computer Aided Process Engineering.
31 May – 4 June 2015, Copenhagen, Denmark

Development and Parameter Estimation for a Multivariate Herschel-Bulkley Rheological Model of a Nanoparticle-Based Smart Drilling Fluid

Dimitrios I. Gerogiorgis,[a] Christina Clark,[a] Zisis Vryzas,[b] Vassilios C. Kelessidis[b]

[a] *School of Engineering (IMP), University of Edinburgh, Edinburgh EH9 3JL, UK*
[b] *Petroleum Engineering Program, Texas A&M University at Qatar, Doha, Qatar*

Abstract

Smart drilling fluids containing Fe_3O_4 nanoparticles have advantages toward increasing the hydraulic efficiency of drilling operations in a variety of reservoir environments. Exploring and optimizing the rheological behavior of such new drilling fluids is critical, implying direct and significant economic savings in developing new oil and gas fields. A experimental campaign analyzing the rheology of a bentonite-based fluid produced a new multiparametric dataset, considering a wide range of realistic reservoir conditions. Non-Newtonian behaviour is confirmed by yield stress computation for all these cases. Heating and rotation induce temperature and concentration gradients at drilling depth: it is hence essential to obtain an accurate but also versatile multivariate rheological model, which will enable viscosity prediction for the analyzed and other similar drilling fluids. The enhanced Herschel-Bulkley model is developed on a multiplicative assumption, postulating and analysing candidate equations which quantify the effect of shear rate, temperature and nanoparticle concentration on drilling fluid shear stress and viscosity. Parameter estimates have been subsequently determined via systematic optimisation, using statistical metrics to quantify and compare uncertainty and predictive potential. The trivariate shear stress and viscosity models proposed are similar in form: each requires six parameters used to combine a Herschel-Bulkley yield stress expression, an Arrhenius exponential of temperature and a linear model for nanoparticle concentration.

Keywords: parameter estimation, Hershel-Bulkley model, nanoparticles, drilling fluids.

1. Introduction

Efficient drilling for oil and gas requires the pumping of fluids with specific rheology, which can in principle be achieved by understanding the effect of composition on flow behavior and developing custom-made formulations with desired flow specifications; optimal drilling is thus attainable by matching rock, fluid and equipment characteristics. Flow behavior varies widely with concentration and temperature under constant shear, and successful tuning of rheological properties is critical to efficient drilling processes which achieve high penetration rates without risks of overheating, mechanical wear or excessive cost due to high fluid injection requirements (Sheng, 2011; Dandekar, 2013).

Developing correlations which express shear stress and viscosity as explicit functions of shear rate, temperature and concentration of iron nanoparticles (Waheed et al., 2014) is critical toward modeling, designing and planning of cost-effective drilling campaigns. Because of the multi-parametric uncertainty involved in rock strata mechanical properties, it is important to develop and validate high-fidelity predictive models which can provide online reliable estimates of rheological properties as explicit functions of environmental variables (temperature, mud concentration), to use equipment efficiently.

2. Experimental methods

Bentonite (Gold Seal, Halliburton) (tan powder, mild earthy odour, pH = 8-10) which consists of 1% cristobalite, 1% tridymite, 1-5% quartz and 60-100% actual bentonite and iron oxide nanoparticles (Sigma-Aldrich) in powder form (black powder, spherical shape, diameter of <50 nm, purity of > 97%) have been used to prepare all the samples. De-ionized water (TAMUQ, pH = 6.8-7.2) is used for base bentonite fluid preparation.

2.1. Sample preparation

Samples are prepared as per American Petroleum Institute (API) 13A-13B1 standards: 7% w/v bentonite dispersions of variable concentration in de-ionized water (600 ml) are obtained using a Hamilton Beach high-speed mixer for stirring (11,000 rpm for 20 min), and samples are left to hydrate and reach equilibrium in plastic containers (16 hr). Iron oxide nanoparticles (0.5, 1, 1.5, 2, 2.5, 3% v/v) are added slowly to avoid agglomeration. Before measuring rheological properties (by Couette viscometer–Brookfield rheometer), samples are mixed again (Hamilton Beach mixer, 5 min) to have identical shear history. This procedure is uniformly followed to ensure consistency and minimize bias effects.

2.2. Measurement procedures

A Couette (Grace M3600) viscometer and a vane (Brookfield YR-1) rheometer are used to measure rheological properties at three distinct temperatures and several nanoparticle concentrations (Yan & James, 1995); the Grace viscometer is equipped with a water bath and circulator to set the cup holder at the desired temperature (Fig. 1), so as to obtain and record shear stress and viscosity data (accuracy of experiments: T= ±2 °C).

Direct yield stress measurements are obtained via the Brookfield vane rheometer using two different four-bladed vane spindles, to cover the extended yield stress range: the spindle is immersed in the test material and connected through a calibrated spiral spring to a motor drive shaft, rotating the vane at 0.1 rpm (optimal rheological analysis speed). Material resistance to movement is analysed via increasing torque values: shaft rotation is thus measured by means of calibrated spiral spring deflection via a rotary transducer.

Indirect yield stress measurements are obtained via the Grace rotational viscometer. Output parameters are shear rate (s^{-1}), shear stress (Pa), viscosity (cP), gel strength (Pa). Viscometric data are obtained at fixed speeds (3, 6, 30, 60, 100, 200, 300, 600 rpm) and Newtonian shear rates (5.11, 10.21, 51.069, 102.14, 170.23, 340.46, 510.67, 1021.38 s^{-1}) are induced at the inner fixed cylinder, respectively (Kelessidis and Maglione, 2008). Readings are recorded every 10 s for a period of 60 s periods at each setting, giving 6 measurements at each of the 8 rotational speeds above (sweeped in descending order). Yield stress is estimated in all cases from viscometer rheograms, after extrapolating the shear stress-shear rate curve to zero shear rate and fitting the selected rheological model.

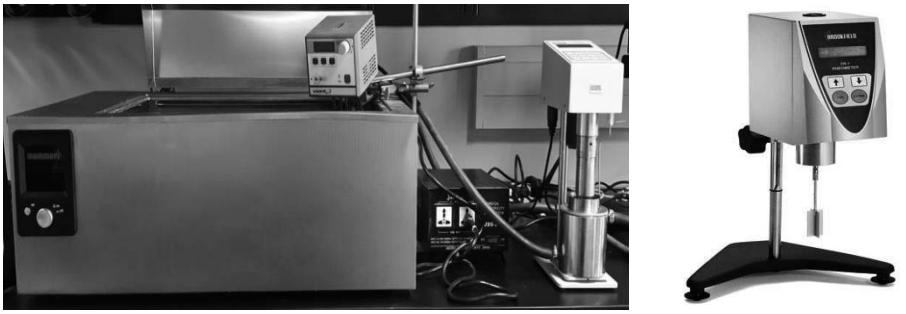

Figure 1: Grace M3600 viscometer with bath and circulator and Brookfield YR-1 rheometer.

3. Rheology modeling and parameter estimation

The prevalent correlation of shear stress and shear rate is the Herschel-Bulkley model (Kelessidis et al., 2006; Kelessidis & Maglione, 2008; Pouyafar & Sadough, 2013), a tri-parametric nonlinear correlation combining the effects of yield stress and power law behavior which outperforms the bi-parametric Bingham, power law and Casson models. The rheological parameters estimated from experimental campaigns are temperature- and concentration- dependent, and literature models are usually condition-dependent. Therefore, it is critical to first solve the optimisation problem for parameter estimation (both the univariate and the bivariate instance, for both shear stress and viscosity), and then develop a unified trivariate model, including all three independent variables (shear rate, temperature and iron nanoparticle concentration) in order to describe in detail the rheological behavior of the bentonite-based injection fluid during all drilling operations.

An extensive literature survey indicates the most widespread and suitable models of drilling fluids (Nguyen & Boger, 1992; Balmforth et al., 2014). Multivariate nonlinear least squares regression (Berge, 1993) has been employed in order to determine the most accurate model (Puxty et al., 2005) for shear stress and viscosity as functions of shear rate, temperature and additive concentration; the multi-parametric estimation problem has been subsequently solved using the novel experimental data, in order to compute the optimal set of parameters which minimise the sum of squared errors (SSE) and maximise the respective coefficient of determination, R^2 (Graybill & Iyer, 1994). Ensuring that a global optimum is achieved is of particular importance, because strongly nonlinear multivariate expressions can induce solver trapping in various local minima; the multivariate nonlinear regression has thus been performed using a systematic strategy and several starting parameter sets (a multi-start strategy) to confirm optimality. Multivariate and multi-parametric nonlinear models are plotted vs experimental data, the standard error for shear stress and viscosity at each combination of independent variables has been computed, and error bars have been obtained to illustrate uncertainty.

Explicit multiparametric rheological models have the general form given in Eqs. (1)-(2). To simplify these we invoke the multiplicative assumption, illustrated in Eqs. (3)-(4). Univariate [Eqs. (5)-(6)], bivariate [Eqs. (7)-(10)] an trivariate [Eqs. (11)-(12)] models thus imply we can consider explicit correlations which are easy to validate accordingly.

$$\tau = f(\dot{\gamma}, T, C) \quad (1) \qquad \mu = g(\dot{\gamma}, T, C) \quad (2)$$

$$\tau = f_1(\dot{\gamma}) f_2(T) f_3(C) \quad (3) \qquad \mu = g_1(\dot{\gamma}) g_2(T) g_3(C) \quad (4)$$

$$\tau = k\dot{\gamma}^n + \tau_o \quad \text{(Herschel-Bulkley model)} \quad (5) \qquad \mu = k\dot{\gamma}^n \quad \text{(Power law)} \quad (6)$$

$$\tau = (k\dot{\gamma}^n + \tau_o)(C + x) \quad (7) \qquad \mu = k\dot{\gamma}^n (C + x) \quad (8)$$

$$\tau = (k\dot{\gamma}^n + \tau_o) \exp\left(-\frac{E}{RT}\right) \quad (9) \qquad \mu = k\dot{\gamma}^n \exp\left(-\frac{E}{RT}\right) \quad (10)$$

$$\tau = (k\dot{\gamma}^n + \tau_o) \exp\left(-\frac{E}{RT}\right)(aC + b) \quad (11) \qquad \mu = k\dot{\gamma}^n \exp\left(-\frac{E}{RT}\right)(C + b) \quad (12)$$

Figure 2: Explicit univariate and multivariate shear stress (τ) and viscosity (μ) parametric models.

4. Results and discussion

Nonlinear model plots have been obtained, confirming the rheological behavior of the samples is accurately described by an enhanced multivariate Herschel-Bulkley model for shear stress and a corresponding one for viscosity (Abu-Jdayil & Ghannam, 2014).

4.1. Univariate shear stress and viscosity models

Our shear stress and viscosity correlations for all temperatures appear in Fig. 3-4.

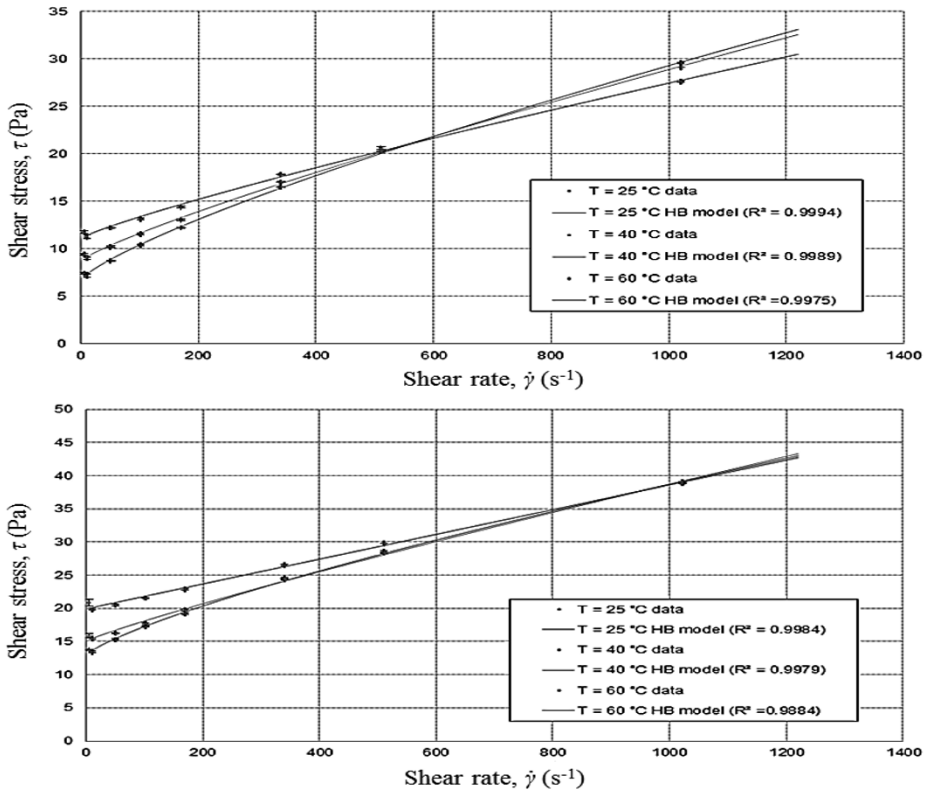

Figure 3: Shear stress vs. shear rate for all campaign temperatures (C = 0.5% up; C = 3%, down).

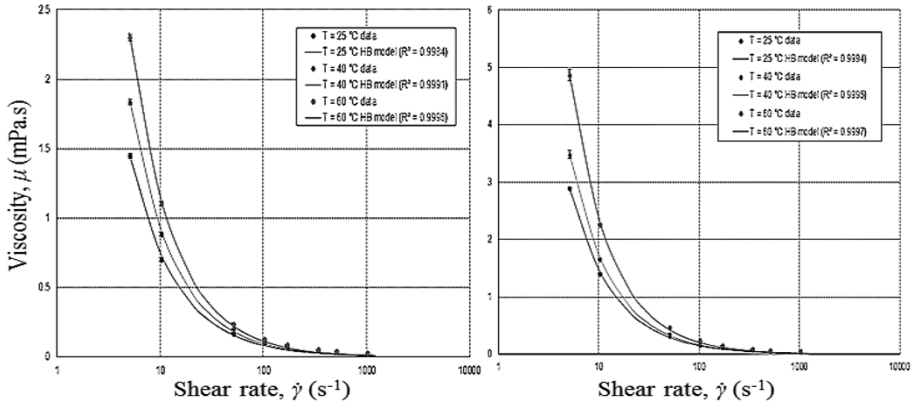

Figure 4: Viscosity vs. shear rate for all campaign temperatures (C = 0.5%, left; C = 3%, right).

4.2. Bivariate shear stress and viscosity models

Our shear stress and viscosity correlations for all three temperatures appear in Fig. 5: to enhance clarity, viscosity surfaces have been separated by displacing the origin by ±2.

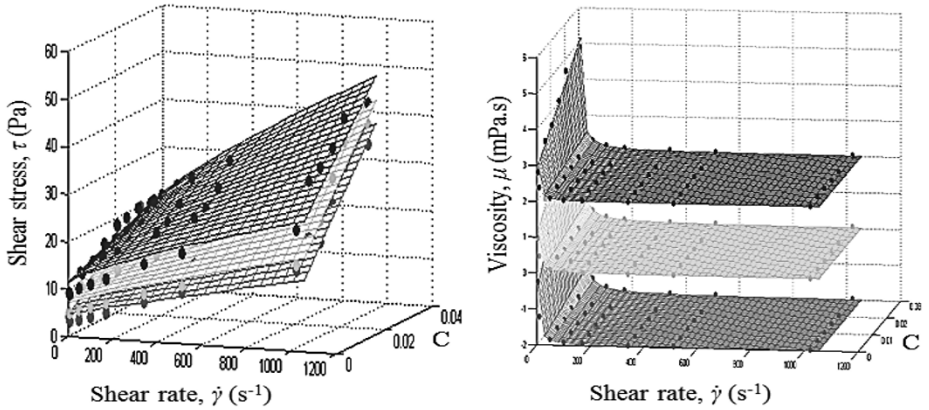

Figure 5: Shear stress (left) and viscosity (right) profiles vs. shear rate and vs. concentration.

Table 1: Parameter estimation for the univariate shear stress and viscosity parametric models.

C (%)	T (°C)	k (Pa.s^{-n})	n	τ_o(Pa)	R^2	SSE	k (kgm^{-n})	n	R^2	SSE
0	25	0.09686	0.7471	3.4915	0.9983	0.39	3.7478	-0.9486	0.9950	0.0027
	40	0.03268	0.8676	4.6598	0.9995	0.08	4.6289	-0.9647	0.9987	0.0011
	60	0.01959	0.9448	8.2149	0.9934	1.02	10.2237	-1.0810	0.9985	0.0040
0.5	25	0.10025	0.7843	6.7007	0.9994	0.25	6.84891	-0.9588	0.9984	0.0041
	40	0.05953	0.8432	8.7383	0.9989	0.38	9.23222	-0.9946	0.9991	0.0037
	60	0.04329	0.8591	11.103	0.9975	0.56	11.8929	-1.0110	0.9996	0.0030
1.0	25	0.07794	0.8216	7.9654	0.9997	0.13	7.78388	-0.9521	0.9991	0.0031
	40	0.03467	0.8886	8.6692	0.9981	0.42	9.41873	-0.8595	0.9993	0.0267
	60	0.02751	0.9011	11.2771	0.9956	0.73	12.2908	-1.0225	0.9997	0.0025
1.5	25	0.09331	0.8015	9.8931	0.9988	0.56	10.4552	-0.9895	0.9990	0.0055
	40	0.06237	0.8371	12.2577	0.9983	0.59	12.9174	-1.0002	0.9995	0.0039
	60	0.01869	0.9704	16.8437	0.9940	1.18	18.7670	-1.0383	0.9997	0.0045
2.0	25	0.12702	0.7696	12.8649	0.9991	0.50	13.1417	-0.9765	0.9994	0.0057
	40	0.05029	0.8910	15.0585	0.9977	1.10	15.8788	-1.0024	0.9997	0.0041
	60	0.01907	0.9971	19.9311	0.9957	1.29	22.1101	-1.0376	0.9997	0.0064
3.0	25	0.10828	0.7910	13.7773	0.9984	0.87	14.5247	-0.0993	0.9994	0.0064
	40	0.03905	0.9236	16.8603	0.9979	0.95	18.4641	-1.0270	0.9995	0.0075
	60	0.01182	1.0563	23.4468	0.9884	3.05	27.2611	-1.0601	0.9997	0.0102

Table 2: Parameter estimation for the bivariate shear stress and viscosity parametric models.

C (%)	k (Pa.s^{-n})	n	τ_o(Pa)	E/R(K)	R^2	SSE	k (kg.m^{-n})	n	E/R (K)	R^2	SSE
0	0.2721	0.8528	38.69	608.7	0.9296	41.22	10880	-1.035	2364	0.992	0.0334
0.5	0.1225	0.8263	16.72	198.4	0.9707	29.40	470.8	-0.995	1238	0.998	0.0130
1.0	0.2335	0.7122	16.92	214.2	0.9732	22.17	209.7	-1.003	965.1	0.997	0.0264
1.5	0.1758	0.8583	44.54	384.8	0.9436	60.05	1206	-1.017	1407	0.998	0.0221
2.0	0.1647	0.8783	50.76	361.8	0.9613	53.64	697.6	-1.013	1171	0.998	0.0360
3.0	0.2521	0.915	118.8	590	0.9411	83.29	2068	-1.037	1464	0.998	0.0567

T(°C)	k (Pa.s^{-n})	n	τ_o(Pa)	b	R^2	SSE	k (kg.m^{-n})	n	b	R^2	SSE
25	2.262	0.7882	221.1	0.02921	0.9600	1.43	346.1	-0.980	0.01408	0.9889	0.26
40	1.168	0.8823	311.4	0.02297	0.9399	1.94	429.7	-1.010	0.01421	0.9888	0.37
60	0.4955	0.9726	419.5	0.02351	0.9482	1.47	594.7	-1.044	0.01547	0.9936	0.39

5. Conclusions

Our development of an enhanced multivariate Herschel-Bulkley rheological model for a bentonite-based candidate drilling fluid with variable Fe_3O_4 nanoparticle composition is based on original data from an experimental campaign in a wide range of conditions, followed by comparative evaluation of multivariate shear stress and viscosity models. Parameter estimation via systematic optimization and comparative statistical analysis of the resulting uncertainty metrics allows the assessment of candidate expressions toward determining their suitability and quantifying their reliability for modeling and design. The shear stress and viscosity correlations describe the rheological effects of shear rate, temperature and Fe_3O_4 nanoparticle concentration: they encompass a Herschel-Bulkley model, an Arrhenius temperature exponential and a linear equation, respectively, achieving a high predictive potential in both bivariate ($R^2_{\tau(\gamma,T)} = 0.929$, $R^2_{\mu(\gamma,T)} = 0.992$) as well as in the full trivariate version of the model ($R^2_{\tau(\gamma,T,C)} = 0.987$, $R^2_{\mu(\gamma,T,C)} = 0.988$). Higher temperatures induce increased standard error for both shear stress and viscosity; heating affects fluid structure and rheology (hence prediction uncertainty) appreciably. Further investigation of concentration effects for various additives is planned, but the models already provide reliable estimates in a wide range of realistic drilling conditions.

Acknowledgement

The present publication has been made possible by NPRP Grant Number 6–127–2–050 from the Qatar National Research Fund, QNRF (a member of the Qatar Foundation). The statements which have been made herein are solely the responsibility of the authors.

References

Abu-Jdayil, B., Ghannam, M., 2014. The modification of rheological properties of sodium bentonite-water dispersions with low viscosity CMC polymer effect, *Energ. Source Part A*, **36**(10): 1037-1048.

Andertová, J., Rieger, F., 2009. Rheometry of concentrated ceramic suspensions: steps from measured to relevant data (Part 3), *Ceramics-Silikáty*, **53**(4): 283-286.

Balmforth, N.J., Frigaard, I.A., Ovarlez, G., 2014. Yielding to stress: recent developments in viscoplastic fluid mechanics, *Annu. Rev. Fluid Mech.*, **46**: 121-146.

Berge, J.M.F., 1993. *Least Squares Optimization in Multivariate Analysis*, DSWO Press.

Dandekar, A.Y., 2013. *Petroleum Reservoir Rock and Fluid Properties*, CRC Press.

Graybill, F.A., Iyer, H., 1994, *Regression Analysis: Concepts and Applications*, Duxbury Press.

Kelessidis, V.C., Maglione, R. et al., 2006. Optimal determination of rheological parameters for Herschel–Bulkley drilling fluids and impact on pressure drop, velocity profiles and penetration rates during drilling, *J. Petrol. Sci. Eng.*, **53**(3-4): 203-224.

Kelessidis, V.C., Maglione, R., 2008. Yield stress of water–bentonite dispersions, *Colloid Surface A*, **318**(1-3): 217-226.

Nguyen, Q.D., Boger, D.V., 1992. Measuring the flow properties of yield stress fluids, *Annu. Rev. Fluid Mech.*, **24**: 47-88.

Pouyafar, V., Sadough, S.A., 2013. An enhanced Herschel–Bulkley model for thixotropic flow behavior of semisolid steel alloys, *Metall. Mater. Trans. B*., **44B**(5): 1304-1310.

Puxty, G., Maeder, M., Hungerbühler, K., 2006. Tutorial on the fitting of kinetics models to multivariate spectroscopic measurements with nonlinear least squares regression, *Chemometr. Intell. Lab. Syst.*, **81**(2): 149-164.

Sheng, J.J., 2011, *Modern Chemical Enhanced Oil Recovery – Theory and Practice*, Elsevier.

Yan, J., James, A.E., 1997. The yield surface of viscoelastic and plastic fluids in a vane viscometer, *J. Non-Newton. Fluid*, **70**(3): 237-253.

Hermoso, J., Jofore, B.D. et al., 2012. High pressure mixing rheology of drilling fluids, *Ind. Eng. Chem. Res.*, **51**(4): 14399-14407.

Waheed, M., Vryzas, Z., Kelessidis, V.C., 2013, *Technical Report*, Texas A&M University, Doha.

Krist V. Gernaey, Jakob K. Huusom and Rafiqul Gani (Eds.), 12th International Symposium on Process Systems Engineering and 25th European Symposium on Computer Aided Process Engineering.
31 May – 4 June 2015, Copenhagen, Denmark

Adaptive Management of Renewable Energy Smart Grids Using a Power Grand Composite Curves Approach

Damian Giaouris[a], Athanasios I. Papadopoulos[a], Panos Seferlis[b*], Simira Papadopoulou[c], Spyros Voutetakis[a]

[a]*Chemical Process and Energy Resources Institute, Centre for Research and Technology-Hellas, 6th klm Harilaou-Thermis Rd.,57001 Thermi, Greece*
[b]*Department of Mechanical Engineering, Aristotle University of Thessaloniki, 54124 Thessaloniki, Greece*
[c]*Department of Automation Engineering, Alexander Technological Educational Institute of Thessaloniki, 57400 Thessaloniki, Greece*
spapadopoulos@cperi.certh.gr

Abstract

Hybrid energy smart grids operate based on power management strategies (PMS) addressing the time-varying reallocation of resources to meet specific targets. The identification of the PMS that best exploits the weather variability is crucial for their efficient operation. In this work, this is approached within a framework which exploits the Power Grand Composite Curves (PGCC) method to perform two functions: a) the identification of renewable energy recovery targets within a short term prediction horizon, and b) the temporal reallocation of the grid subsystems within a control horizon based on the PMS that best matches the identified targets. The PGCC is exploited within a model predictive control framework that enables the satisfaction of the system operating goals by ensuring the maintenance of a targeted minimum energy inventory. The desired energy inventory is guaranteed by selecting the appropriate PMS during the control interval that best matches the identified target. The method is presented within a formal mathematical framework and illustrated for a smart grid with power and hydrogen generation and storage features in year-round operation.

Keywords: Smart grids, power pinch, adaptive management

1. Introduction

Smart grids transform renewable energy sources (RES) into reliable power flows by adapting to unexpected external variability through the use of diverse conversion and storage equipment (e.g., fuel cells, electrolysers, accumulators and so forth). Their coordinated operation is a pre-requisite to address the underlying technical heterogeneity, while satisfying power demands with minimum participation of non-RES components. This goal is generally approached through PMS (Giaouris et al., 2013) which represent a sequence of time-varying decisions offering an efficient utilisation of resources and equipment to meet specific targets. The diverse temporal behaviour of such systems gives rise to a large number of potential PMS. Efficient operation depends on the selection of the PMS that best satisfies the system operating goals in view of RES variability. This is a non-trivial task, driven by complex interactions which are avoided in conventional systems by repeating a pre-specified PMS throughout their operation. The latter results in energy being wasted or increased non-RES power utilisation as the employed PMS is not tailored to the alternating patterns of RES.

This work proposes a more effective approach based on the iterative identification and implementation of a suitable PMS for the immediate short term time horizon, built around the PGCC method (Bandyopadhyay, 2011). Power pinch analysis exploiting power composite curves (Wan Alwi et al., 2012) or PGCC is based on the same concept as the heat pinch (Klemeš, 2013), except that instead of heat flow streams, power flow stream are plotted against time. The method has been previously formulated as the power cascade analysis (PoCA) and storage cascade table (SCT) (Rozali et al., 2013), applied in the optimal sizing of hybrid systems (Rozali et al., 2014), and modified to account for standalone hybrid systems (Ho et al., 2013). Furthermore, Chen et al. (2014) proposed an MILP transhipment model based on power pinch concepts.

2. PGCC for hybrid RES-based systems

Hybrid RES-based flowsheets may be represented through interconnected converters and accumulators that convert or store material and energy; flows and accumulation at different instants are the key features that drive their operation (Giaouris et al., 2013). The activation instance and operating period of each converter are important operating parameters as they determine their utilisation frequency. The state (level) of accumulated energy or materials in the form of diverse energy carriers is also important, prompting the activation of different converters based on their technical characteristics. The duration of activation further depends on a hysteresis based mode of operation, i.e. on whether the converter was active in the previous instant. The combination of these temporal characteristics form complex operating rule sequences called PMS which may be represented through generic models (Giaouris et al., 2013). This work proposes a mathematical framework for power pinch analysis exploiting the previous generic concepts. Let a system operating within an overall time span H divided into equal time intervals. Each interval is divided into subintervals $[t_0, T]$ of duration $\Delta T=T-t_0$ hence for the k^{th} interval $t_0=(k-1)\Delta T$ and $T=k\Delta T$. Also, let a set Q of diverse PMS that can be used in a hybrid system within each interval k, i.e. $Q=\{q_k\}$, $q\in N$. Each PMS q_k is a function of the state of accumulation ($SOAcc^l$) in accumulator l; for any $q_k\in Q$ the plot of $SOAcc^{l,qk}$ vs. time for a range of initial conditions gives the system PGCC (Figure 1a).

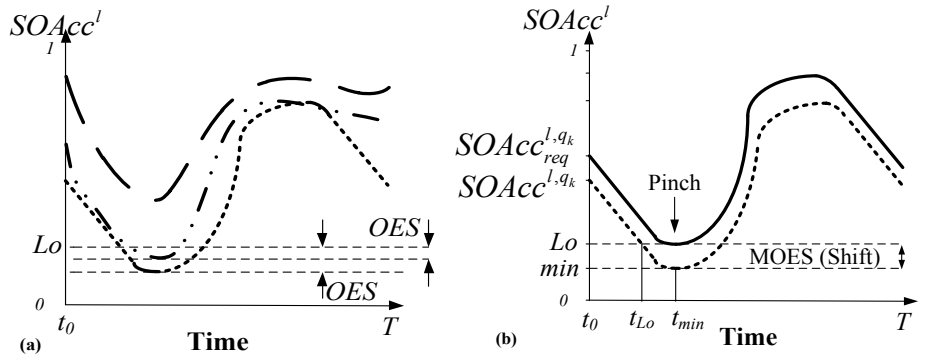

Figure 1: a) PGCCs for various initial values of $SOAcc^l$, b) Shift and Pinch of PGCC.

A major requirement in hybrid systems is to avoid the use of outsourced energy supply (OES) when $SOAcc^{l,qk}$ drops below a limit Lo (e.g., due to insufficient energy in the accumulator, an external source is required to satisfy the load demand). Starting from different $SOAcc^{l,qk}(t_0)$ at t_0 results in different OES (Figure 1a), calculated as follows:

$$OES^{l,q_k}(k) = SOAcc^{l,q_k}(t_{LO}) - SOAcc^{l,q_k}(t_{min}) \quad (1)$$

$$SOAcc^{l,q_k}(t_{\min}) = \min_{t\in[t_0,T]}\left\{SOAcc^{l,q_k}(t)\right\} \quad (2)$$

Finding the PGCC that corresponds to the maximum *OES* (called *MOES*) ensures that by covering this energy from non-RES the system will operate autonomously. Selecting and shifting the PGCC corresponding to *MOES* until it pinches the *Lo* limit at $t_{\min}$ (i.e. $SOAcc^{l,qk}(t_{\min})$) indicates the amount of energy required at t_0 (i.e. amount of $SOAcc^{l,qk}(t_0)$) to avoid the use of non-RES (Figure 1b). This is calculated as follows:

$$MOES^{l,q_k}(k) = \max_{SOAcc^{l,q_k}(t_0)}\left\{OES^{l,q_k}(k)\right\} \quad (3)$$

$$SOAcc^{l,q_k}_{req}(t_0) = SOAcc^{l,q_k}_{\min}(t_0) + MOES^{l,q_k}(k) \quad (4)$$

Note that except for a *Lo* limit several others may appear including simultaneous restrictions on multiple converters (e.g. multiple *Lo* limits or *Up* and *Lo* limits) and on multiple energy carriers. Equations (1)-(4) also apply in multiple *Lo* limits but there will be only one pinch, depending on the desired operating goals. For example, there might be a Lo_1 limit that signifies the use of external power if the energy (*SOAcc*) in the battery is low and a Lo_2 limit slightly higher in the $SOAcc^l$ axis of Figure 1b that signifies the use of a fuel cell to produce power from hydrogen as a measure to avoid external power. It might be desired to avoid the frequent activation of the fuel cell because it may result in frequent need for maintenance. This may be implemented by pinching at the Lo_2 limit. All limit combinations result in similar trade-offs, formalized as transformations of *MOES* and $SOAcc_{req}$.

3. Adaptive management using the PGCC

The described power pinch analysis may be exploited within a model-predictive control framework which is proposed in this work to support the adaptive management of smart grids. After defining the system operating goal (e.g., minimization of *OES* and/or appropriate utilisation of equipment such as fuel cells to avoid frequent maintenance), it is necessary to select a suitable time prediction horizon N_p, for which the behaviour of the system can be predicted and the PGCC estimated. The prediction horizon is an integer multiple of the time interval ΔT used for decision making. The length of the prediction horizon should be sufficient to ensure the satisfaction of the system goals for a selected PMS in view of variations. It is also necessary to select a suitable control time horizon N_c, for which decisions are taken about the sequence of equipment utilisation and operating patterns in the form of a PMS. The aim of this work is not to identify the parameter values, decision sequences or operating constraints that determine an optimum PMS. Instead, a pre-existing set of PMS is considered that enables efficient utilisation of the available resources and equipment to meet specific targets within operating constraints. We therefore propose a method to identify which of these PMS to employ in a given interval so that the system may best adapt to shorter or longer term variability. This is approached through an adaptive management procedure consisting of two successive steps:

- The *stored energy targeting step* involves the identification and shifting of the PGCC in the prediction horizon $(k+N_p-1)\Delta T$ to identify the minimum amount of stored energy (in various forms) that should be recovered from internal resources at the end of the control horizon $(k+Nc-1)\Delta T$.

- The *target matching step* requires the identification of the PMS in the control horizon $(k+N_c-1)\Delta T$ that best matches the target for stored energy identified during the prediction horizon $(k+N_p-1)\Delta T$.

To better understand the concept assume N_p=2, N_c=1 and ΔT=24h, i.e. the control horizon is the current day and the prediction horizon is stretched to the next. The *stored energy targeting step* requires the implementation of the analysis of section 2 in the prediction horizon k+1 for every PMS $q_{k+1}\in$Q, as follows:

$$SOAcc_{TAR}^{l}\left(k+1\right)=\max_{q_{k+1}\in Q} SOAcc_{req}^{l,q_{k+1}}\left(t_0\right) \tag{5}$$

$SOAcc_{TAR}^{l}\left(k+1\right)$ indicates the amount of energy that needs to become available at t=T in control horizon k in order to guarantee that regardless of the PMS that is chosen during the future prediction horizon k+1 the system will always operate above the limit *Lo*, i.e. the use of outsourced (e.g. non-RES) power will be avoided. In the *target matching step,* for control horizon k, a PMS is sought that results in a $SOAcc^{l,qk}(T)$ above and as close as possible to $SOAcc_{TAR}^{l}\left(k+1\right)$. This is expressed as follows:

$$q_k^{opt}=\left(\min_{q_k\in Q}\left(\left|SOAcc_{TAR}^{l}\left(k+1\right)-SOAcc^{l,q_k}\left(T\right)\right|\right)\right)\wedge\left(SOAcc^{l,q_k}\left(T\right)\geq SOAcc_{TAR}^{l}\left(k+1\right)\right) \tag{6}$$

Expression (6) enables the identification of the PMS that best matches the targeted, stored energy required in interval k+1, so that this energy may become available in interval k from internal system resources (Figure 2). After it ends, the time horizons shift forward in time by one decision making interval and the procedure is repeated.

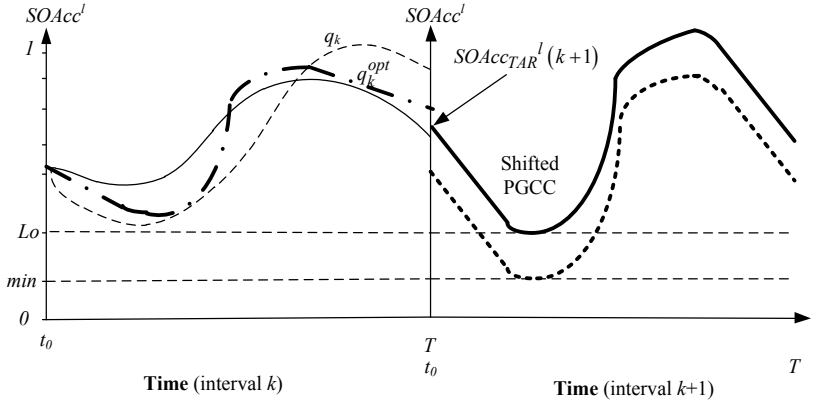

Figure 2: Illustration of the adaptive management procedure

4. Implementation

The proposed approach is illustrated in a system operating in Greece consisting of *PV* panels, wind generators (*WG*), lead-acid batteries (*BAT*), an electrolyzer (*EL*), a fuel cell (*FC*), a hydrogen compressor (*CMP*), intermediate low-pressure (*BF*) and final, high pressure hydrogen tanks (*FT*) and a diesel generator (*DSL*). We apply 9 PMS which activate the associated converters considering $SOAcc_t^{BAT}$ (denoted briefly as *S* in Table 1), the width of the hysteresis ΔH (i.e. the duration of activation or deactivation of a converter based on its previous state) and the net generated power *P*. Table 1 illustrates the combination of these parameters across different PMS (detailed in a formal mathematical framework in Giaouris et al., 2013). In PMS 1, 4 and 7 the power

produced and consumed by the *FC* and *EL* is fixed (based on some heuristic conditions), whereas in all the others the power either depends on the state of charge (PMS 3, 6 and 9) or on the net power *P* surplus/deficit. The hysteresis width is fixed throughout the year in PMS 1-3, whereas it depends on time in PMS 4-6. In PMS 7-9 the hysteresis width is zero depending on previously collected historical weather data (e.g., during summer time the hysteresis width of the *FC* is zero).

Table 1: Description of characteristics for the 9 PMS utilized

PMS	1	2	3	4	5	6	7	8	9
ΔH	Fixed	Fixed	Fixed	$\Delta H(t)$	$\Delta H(t)$	$\Delta H(t)$	0	0	0
P_{FC}	Fixed	P	$P_{FC}(S)$	Fixed	P	$P_{FC}(S)$	Fixed	P	$P_{FC}(S)$
P_{EL}		P	$P_{EL}(S)$		P	$P_{EL}(S)$		P	$P_{EL}(S)$

5. Results and discussion

Figure 3 illustrates the results obtained in several important system operating parameters when the 9 PMS are considered independently and when they are considered simultaneously in the adaptive scheme. Independently, each PMS has both merits and shortcomings. For example PMS 6 resulted in fewer *DSL* activations and minimised the operation of the *FC* but on the other hand it completely depleted the *BAT* (hence the zero $SOAcc^{BAT}$ in Figure 3a). The latter has a detrimental effect on the *BAT* life-time.

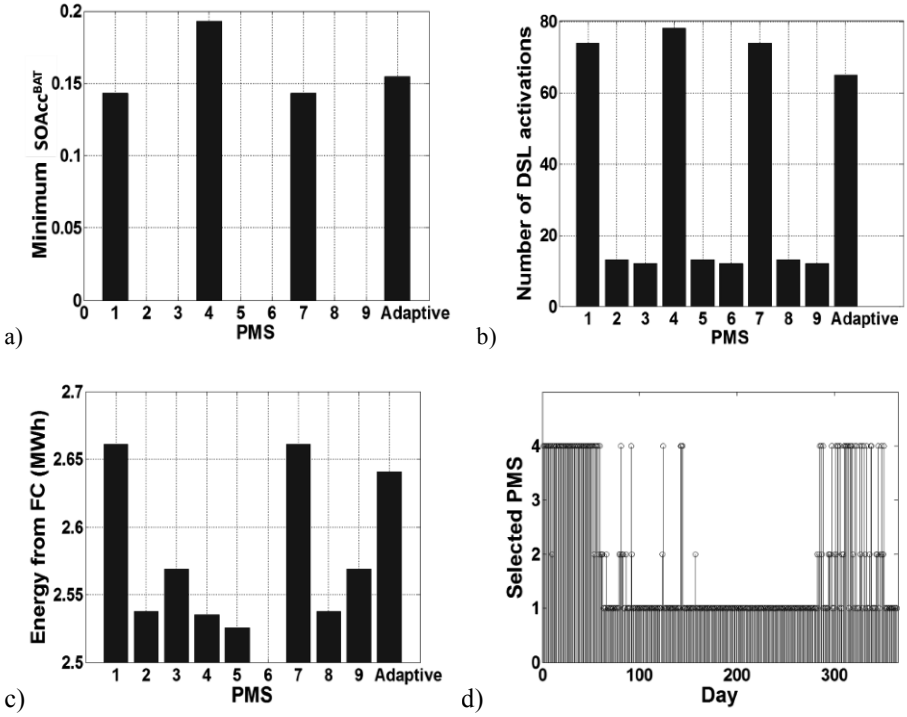

Figure 3: Results obtained from the system after the operation of 12 months under the 9 PMS and the adaptive case: (a) Minimum values reached in $SOAcc^{BAT}$, (b) Number of *DSL* activations, (c) Total energy produced by the *FC* and (d) PMS selected by the adaptive scheme for an entire year.

More specifically, while all PMS requested the same amount of energy from the *DSL* (approximately 410kWh), PMS 2, 3 5, 6, 8 and 9 resulted in fewer *DSL* activations

(around 12-13). This positive result was negated by battery depletion. The *FC* produced around 2.6MWh in all PMS, but this was achieved with approximately 80 activations in PMS 1, 4, 7 and 140 activations in the remaining PMS. The anticipated life-time of the *FC* is prolonged by fewer activations. A similar case is observed for the *EL* (approximate usage at 4.8MWh) where PMS 1, 4 and 7 resulted in 127 activations as opposed to 160 activations resulting from the other PMS. Finally, in all cases the *FT* was left empty at the end of the year, meaning that the hydrogen was depleted.
Comparing the above results with the adaptive case, a considerable improvement is observed by effectively balancing the merits and shortcomings of all PMS to avoid the *BAT* depletion and to reduce the activations of the *DSL*, *FC* and *EL*. In the adaptive case the *DSL* produced 420kWh and the *FC* approximately 2.6MWh while the *EL* consumed 4.96MWh. Although the *DSL* was activated more than it would if PMS 2,3,5,6,8,9 were used independently, the adaptive scheme used PMS 1 and 4 which enable fewer activations of the *FC* and avoid *BAT* depletion thus imposing a regular operating pattern for all units. The use of the *DSL*, *FC* and *BAT* were well balanced in terms of activations or depletion, while the system also required little power from the non-renewable *DSL*. Except for PMS 1 and 4, PMS 2 was also used in the adaptive scheme as it enables the generation of exactly as much power as necessary for the *LD* to avoid *DSL* activation. Note that in PMS where more power is produced than required by the *LD*, this is not wasted but the battery is charged faster instead.

6. Conclusions

In this work we proposed a method of exploiting power pinch analysis to best adapt the operation of a hybrid energy smart grid in view of renewable energy intermittence. The proposed adaptive management method exploits the stored energy PGCC to set energy targets in a prediction time horizon, which can then be matched by an appropriate PMS from a set of pre-selected PMS. The method was illustrated in an actual smart grid. The results showed that by continuously updating the PMS used by the system within short time intervals produces better results than when a particular PMS is employed independently of others for the system operating horizon.

References

S. Bandyopadhyay, 2011, Design and optimization of isolated energy systems through pinch analysis, Asia-Pac. J. Chem. Eng., 6, 518-526.

C.L. Chen, C.T. Lai, J.Y. Lee, 2014, Transshipment model-based MILP formulation for targeting and design of hybrid power systems, Energy, 65, 550-559.

D. Giaouris, A.I. Papadopoulos, C. Ziogou, D. Ipsakis, S. Voutetakis, S. Papadopoulou, P Seferlis, F. Stergiopoulos, C. Elmasides, 2013, Performance investigation of a hybrid renewable power generation and storage system using systemic power management models. Energy, 61, 621-635.

W.S. Ho, C.S. Khor, H. Hashim, S. Macchietto, J.J. Klemeš, 2013, SAHPPA: a novel power pinch analysis approach for the design of off-grid hybrid energy systems. Clean Technol. Envir. Policy, 16, 957-970.

J.J. Klemeš, Ed, 2013, Process integration handbook. Woodhead, Cambridge, U.K., DOI 10.1533/9780857097255.1.3, ISBN-13:978 085709 593 0

N.E.M. Rozali, S.R. Wan Alwi, Z.A. Manan, J.J. Klemeš, M.Y. Hassan, 2013, Process integration techniques for optimal design of hybrid power systems, Appl. Therm. Eng., 61, 26-35.

N.E.M. Rozali, S.R. Wan Alwi, Z.A. Manan, J.J. Klemeš, M.Y. Hassan, 2014, Optimal sizing of hybrid power systems using power pinch analysis, J. Clean. Prod., 71, 158-167.

S.R. Wan Alwi, N.E.M. Rozali, Z.A. Manan, J.J. Klemeš, 2012, A process integration targeting method for hybrid power systems, Energy, 44, 6-10.

Krist V. Gernaey, Jakob K. Huusom and Rafiqul Gani (Eds.), 12th International Symposium on Process Systems Engineering and 25th European Symposium on Computer Aided Process Engineering.
31 May – 4 June 2015, Copenhagen, Denmark

Impact of the operating conditions and position of exhaust gas recirculation on the performance of a micro gas turbine

Usman Ali*, Carolina Font Palma, Kevin J Hughes, Derek B Ingham, Lin Ma, Mohamed Pourkashanian

Energy Technology and Innovation Innitiative (ETII), Faculty of Engineering, Univeristy of Leeds, LS2 9JT, UK
pmual@leeds.ac.uk

Abstract

Gas turbines are a viable and secure option both economically and environmentally for power and heat generation. The process simulation of the micro gas turbine with exhaust gas recirculation (EGR) and its impact on performance is evaluated. This study is further extended to evaluate the effect of the operating conditions and position of the EGR on the performance of the micro gas turbine. The performance analysis for different configurations of the EGR cycle, as well as flue gas condensation temperature, results in the optimized position of EGR at the compressor inlet with partial condensation resulting in the CO_2 enhancement to 3.7 mol%.

Keywords: Micro gas turbine, Process simulation, Exhaust gas recirculation, EGR condition, EGR position.

1. Introduction

The global energy trend is changing, and this is due to the overwhelming concern regarding greenhouse gas (GHG) emissions from the power generation sector IEA (2012). Our energy supply system is under gradual transition from conventional power generation systems to more sustainable low or "zero" carbon systems. The increasing urbanization and escalating energy demand has led to a shift towards natural gas power plants around the globe in order to meet this demand with reduced emissions. Further, to minimize GHG emissions, the released CO_2 is captured through a post-combustion CO_2 capture system using the most widely adopted method of amine scrubbing. However, CO_2 concentration from the natural gas power plant is lean in comparison to those from coal fired plant, and this result in a major penalty when integrated with a CO_2 capture system. This drawback can be avoided by an exhaust gas recirculation (EGR) back to the gas turbine, which results in the enrichment of CO_2 for improved CO_2 capture efficiency.

The EGR is a novel technology in which the exhaust gas is split; one part is dried and recycled back, while the other with increased CO_2 concentration and reduced flow rate is sent to the CO_2 capture system. Despite these advantages, the maximum amount of exhaust gas to be recirculated needs to be defined, maintaining the required level of combustion stability and emissions. Ditaranto et al. (2009) experimentally reported that the minimum O_2 concentration at the combustor inlet needed for stable operation is 16 %, with CO_2 concentration of 8 % at 40 % EGR. Biliyok et al. (2013) have modelled a 440 MW natural gas combined cycle (NGCC) with EGR and performed a techno

economic analysis. An EGR of 40 % resulted in marginal power recovery with increased cooling water demand. The overnight cost increase for the EGR equipped NGCC power plant integrated with the carbon capture system was less than without EGR. In the case of the micro gas turbine (MGT), the reported literature is much limited. Cameretti et al. (2013) studied the effect of the EGR on the performance and emissions of the MGT for different kinds of fuel through CFD modelling. Majoumerd et al. (2014) studied the MGT for EGR and HAT cycles integrated with the amine capture plant. Also the effect of the ambient temperature on the performance of the MGT was reported.

Due to the limited literature found in this field, an extensive study needs to be performed on the impact of the EGR on the performance of the MGT, including the effect of the operating conditions and position of the EGR. Therefore, this study focuses on the evaluation of the impact of these parameters on the performance of the MGT.

2. MGT Cycle

In this paper, the Turbec T100 micro gas turbine is studied as the base case, which is a 100 kW_e machine capable of combined heat and power generation. The major components include the compressor, turbine, combustor, high speed generator and two heat exchangers to enhance either the electrical or overall efficiency. A recuperator to preheat the compressed air and gas-liquid heat exchanger for thermal power of ~150 kW_{th} are also part of the MGT. The combustor is a lean premixed emission type with low NO_x, CO and unburned hydrocarbons (UHC). A schematic diagram of the components of the MGT is shown in Figure 1 within the dashed rectangle.

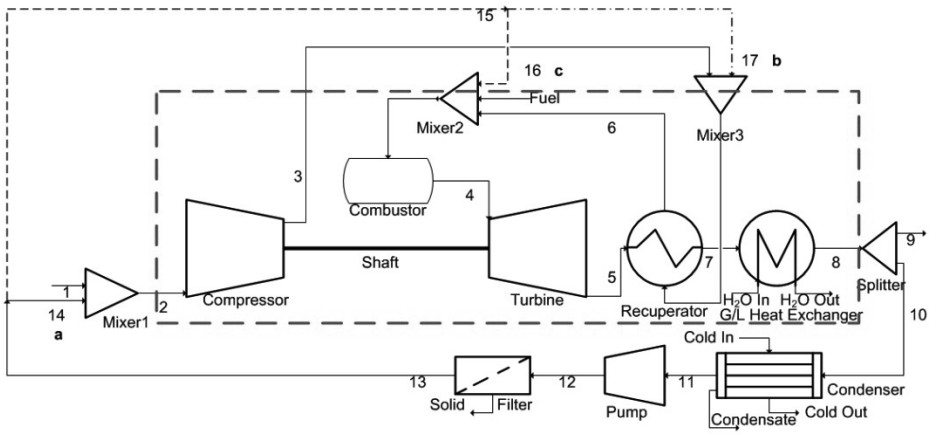

Figure 1: Schematic of the MGT with different options for the position of the EGR, stream 14: location (a), before the compressor; stream 17: location (b), after the compressor; and stream 16: location (c), in the combustor.

Air is compressed to a pressure ratio of 4.5:1 and preheated through the recuperator before the combustor. The combustion products at a turbine inlet temperature of 950 ^oC expand through the turbine to near atmospheric pressure with a turbine outlet temperature (TOT) of 650 ^oC. The exhaust heat is first utilized in the recuperator for boosting the electrical efficiency then used to generate the thermal energy by heating the water in the gas-liquid heat exchanger. The MGT in combined heat and power mode is simulated using Aspen HYSYS® V8.4. The thermodynamic property package used for the modeling is the Peng Robinson equation of state, and the minimization of the

total Gibbs free energy is used for the chemical equilibrium in the combustor. Table 1 shows the base case steady-state performance of the MGT model developed at the ISO conditions (15 ^{o}C, 1 bar and 60 % relative humidity) along with the molar composition of natural gas.

Table 1: Natural gas composition and MGT base case performance at ISO conditions.

Component	Mole fraction	Parameter	Value
CH_4	0.906	Electrical Power (kW_e)	100
C_2H_6	0.051	Thermal output (kW_{th})	153.3
C_3H_8	0.013	Electrical efficiency (%)	32.1
i-C_4H_{10}	0.002	CO_2 in flue gas (mol%)	1.6
n-C_4H_{10}	0.002	O_2 in flue gas (mol%)	17.3
N_2	0.011	Flue gas flow rate (kg/h)	0.67
CO_2	0.014	Fuel consumption (kW)	312

The steady state model is evaluated against the set of experimental data obtained through the UKCCS research centre Pilot-scale Advanced Capture Technology (PACT) facility. The simulations are performed for various power outputs (50-80 kW_e) to represent different operational modes. It was found that the simulated turbine outlet temperature and the combustion gas pollutant concentration were reasonably consistent with the experimental results as reported in (Ali et al. 2014).

The CO_2 concentration at the exhaust is very lean at 1.6 mol% and this will cause a major energy penalty when integrated with the CO_2 capture system. This drawback is avoided by the EGR back to the gas turbine, which results in the enrichment of CO_2 for improved CO_2 capture efficiency.

3. EGR Cycle

Due to the consistency and robustness of the steady state model developed, it is extended to include the exhaust gas recirculation mode to the MGT in order to study the effect of CO_2 enrichment. In the MGT model, one part of the exhaust is dried and recycled back to the MGT. The amount of the exhaust gas recirculated can be defined by the equation:

$$\text{EGR} = \frac{\text{Volume flow of recirculated exhaust gas}}{\text{Volume flow of exhuast gas}} \quad (1)$$

The additional equipment needed for EGR are: the splitter for dividing the exhaust gas into two streams, a condenser for cooling and drying of the recycle stream to the required level of moisture, and a booster fan or a compressor as illustrated in Figure 1 to recirculate the recycle stream from condensing pressure back to required pressure at the injection point. Further, the EGR ratio is varied to check its impact on the system

performance. The increase of EGR ratio results in an increase of CO_2 in the exhaust gas with a decrease in O_2 concentration both at the combustor inlet and exhaust gas, as shown in Figure 2. The decrease in O_2 concentration at the combustor inlet results in O_2 starvation which will affect the combustion stability with higher UHC and CO emissions at the outlet. The modelling suggests that EGR ratios ≤ 55 % should be maintained to stay within the oxygen levels recommended for efficient combustion, and this result in CO_2 enrichment from 1.6 mol% in the base case MGT cycle to 3.7 mol% in the EGR cycle. The enrichment in CO_2 concentration in the exhaust gas increases along with a decrease in the total mass flow, which will influence the performance of the CO_2 capture system.

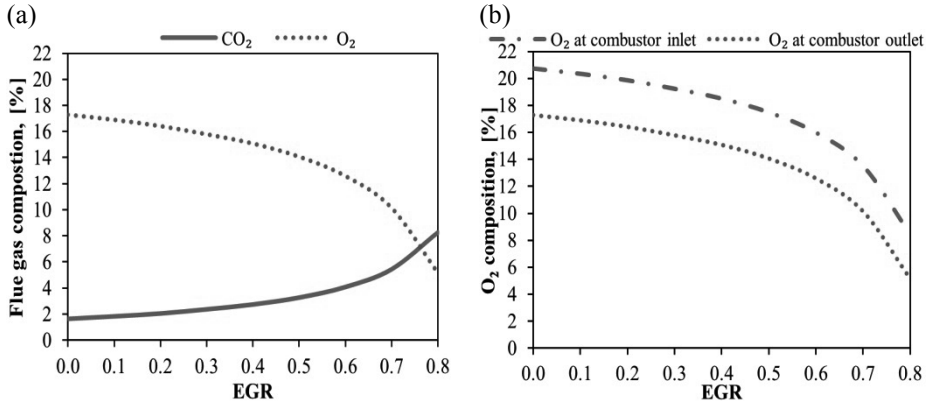

Figure 2: Impact of EGR ratio on (a) CO_2 and O_2 molar composition in flue gas; and (b) O_2 molar composition at combustor inlet and outlet.

3.1. Impact of EGR Position

Three different positions for the EGR injection into the MGT were evaluated: location (a), before the compressor; location (b), after the compressor; and location (c), in the combustor, as shown in Figure 1. These three locations have different conditions and will require varying the thermo physical nature due to the EGR inclusion. The pressure of the EGR stream should be kept the same or above the live pressure of any of the aforementioned injection locations. The process simulation indicates that the EGR injection at these different locations will have a distinctive effect on the system performance in terms of process control, operation and design. The simulations for the injection at different locations are performed at an EGR ratio of 55%. The decrease in the electrical efficiency, as shown in Figure 3(b), for location (a) recycle in comparison to other options is due to the additional work required by the inherent compressor of the MGT. In terms of the additional equipment requirements, the condenser is required for all three of the EGR locations. While the recycle back to location (a) will require a blower/fan for boosting from the condenser pressure back to the compressor inlet. However, the recycle to locations (b) or (c) will require a new compressor in the recycle loop other than the inherent compressor of the MGT, which will affect the machine default control and cause an in shaft imbalance at higher EGR ratios. In terms of CO_2 enrichment, all three cases results in an equal increase of CO_2 concentration in the flue gas, as shown in Figure 3(a). The O_2 concentration at the combustor inlet for EGR to location (c) appears to be maintained higher, however, the internal kinetics of the combustor need to be studied in detail and this may be affected due to the higher EGR

ratios. Therefore, the EGR at location (a) will result in a better performance due to the operational and control difficulties encountered in the other two options. The EGR at location (a) will be evaluated as a function of the EGR ratio and its condition to select the operating condition of the EGR for the MGT.

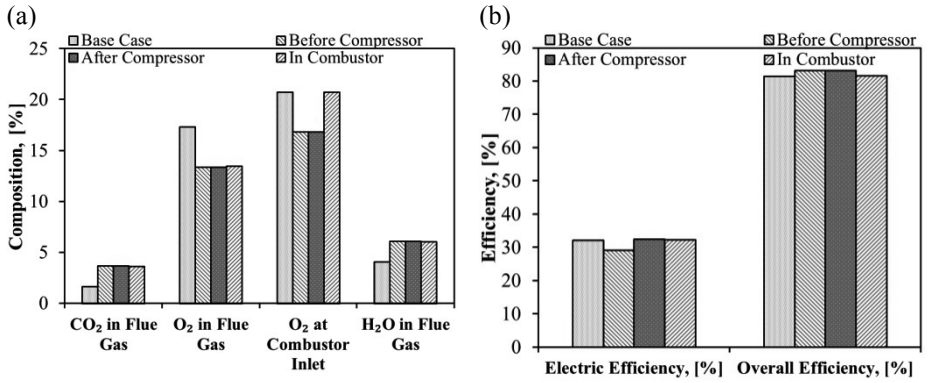

Figure 3: Impact of the EGR position on (a) flue gas, and O_2 composition at the combustor inlet and (b) the electrical and overall efficiency.

3.2. Impact of EGR Condition

The condensation temperature is an important parameter which will affect the performance of the MGT equipped with the EGR at location (a). This defines the dryness of the EGR, and the temperature and water level in the EGR will affect the power requirement for the compressor due to density effects. The three cases are defined in order to assess the impact of the EGR condition: cold EGR at ambient temperature, cold EGR with partial condensation and hot EGR without condensation. The first two cases are realized by varying the condensation temperature while for the last case there is no condenser in the recycle loop.

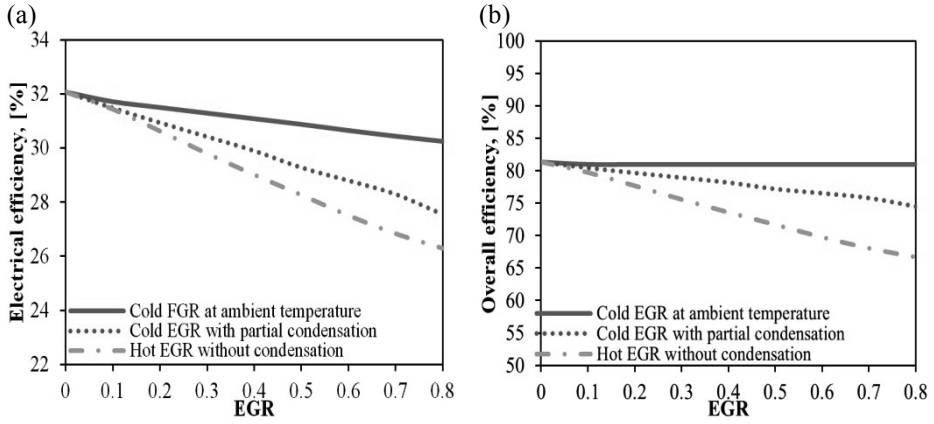

Figure 4: Impact of the EGR conditions on (a) the electrical efficiency and (b) the overall efficiency.

The cold EGR at ambient temperature is maintained at the temperature of 15 ^{o}C, the cold with partial condensation is maintained at 40 ^{o}C and the hot EGR is at 70 ^{o}C. It is observed that the electrical efficiency drop is higher as the temperature of the EGR

increases as shown in Figure 4 (a). This is due to more compressor work and higher fuel feeding requirements as the EGR temperature increases. The overall efficiency follows the same trend by keeping the thermal output of the MGT constant at the same level as in the base case as shown in Figure 4 (b). As a result, the flue gas temperature increases due to the heat capacity change of the resulting flue gas due to the increased amount of water content as the temperature and condensation rate increases. However, the decrease in the condensation temperature may lead to sulfur deposition which will affect the recirculating ducts and the blower or compressor material depending on the sulphur content in the fuel to be burnt.

4. Conclusions

This work evaluates a recuperated micro gas turbine steady state model and its modification into the EGR mode. The results indicate that different EGR cycle options have a distinctive impact on the system performance, process operation, and process design. The process system analysis assists in the selection of the best configuration, the EGR recycle back to the compressor inlet, with the partial condensation and condensation temperature at the minimum to operate. The EGR results in the CO_2 concentration enhancement to 3.7 mol% from 1.6 mol% in the base case which results in an improvement when integrated with the carbon capture system. In conclusion, the detailed analysis, modelling and simulation outcomes are an accurate demonstration for the evaluation of the optimized micro gas turbine EGR mode configuration.

Acknowledgement

The corresponding author acknowledges the grant provided by the University of Engineering and Technology, Lahore Pakistan and the partial support by the ETII, University of Leeds, UK, in support of this research.

References

Ali, U., T. Best, K. N. Finney, C. F. Palma, K. J. Hughes, D. B. Ingham and M. Pourkashanian (2014). Process Simulation and Thermodynamic Analysis of a Micro Turbine with Post-combustion CO2 Capture and Exhaust Gas Recirculation. Energy Procedia 63(0): 986-996.

Biliyok, C., R. Canepa, M. Wang and H. Yeung (2013). Techno-Economic Analysis of a Natural Gas Combined Cycle Power Plant with CO2 Capture. Computer Aided Chemical Engineering. K. Andrzej and T. Ilkka, Elsevier. 32: 187-192.

Cameretti, M. C., R. Tuccillo and R. Piazzesi (2013). Study of an EGR Equipped Micro Gas Turbine supplied with bio-fuels. Applied Thermal Engineering.

Ditaranto, M., J. Hals and T. Bjørge (2009). Investigation on the in-flame NO reburning in turbine exhaust gas. Proceedings of the Combustion Institute 32(2): 2659-2666.

IEA (2012). World Energy Outlook 2012, OECD Publishing.

Majoumerd, M. M., H. N. Somehsaraei, M. Assadi and P. Breuhaus (2014). Micro gas turbine configurations with carbon capture-Performance assessment using a validated thermodynamic model. Applied Thermal Engineering.

Krist V. Gernaey, Jakob K. Huusom and Rafiqul Gani (Eds.), 12th International Symposium on Process Systems Engineering and 25th European Symposium on Computer Aided Process Engineering.
31 May – 4 June 2015, Copenhagen, Denmark

Dynamic Response of Fuel Cell Gas Turbine Hybrid to Fuel Composition Changes using Hardware-based Simulations

Nor Farida Harun[a], David Tucker[b], Thomas A. Adams II[a]

[a]*Department of Chemical Engineering,McMaster University, 1280 Main Street West, Hamilton, Ontario L8S 4L7, Canada*
[b]*U.S. Department of Energy, National Energy Technology Laboratory, 3610 Collins Ferry Road, Morgantown, West Virginia 26507-0880, United States*

Abstract

The solid oxide fuel cell gas turbine hybrid system (SOFC/GT) is an exciting new approach to producing electricity with high efficiency and lower environmental impacts than conventional power plants. One of its key strengths is the potential for fuel flexibility, which is the ability to transition between different kinds or qualities of fuels during operation. However, there has been very little research into the dynamic performance of SOFC/GT systems in response to changes in fuel. Therefore, the open loop behaviour of SOFC/GT systems in response to fuel composition transients was experimentally investigated. In this study, hardware-based simulations were used to study transitions between using coal-derived syngas and humidified methane. A hybrid test facility at the U.S Department of Energy, National Energy Technology Laboratory, Morgantown, West Virginia, was used to adequately capture the coupling of fuel cell stacks (simulated with hardware driven by a real time dynamic model) and a gas turbine system (from actual equipment) during transient events. Given the dynamic trajectories of key process variables, the impact on the hybrid system was quantified via transfer functions. The results show that the open-loop dynamic behaviour exhibited significant inverse response which limited the range of transitions that could be achieved safely without damage to various system components such as the compressor or fuel cells. However, the results also showed that if a control system could be designed which limited the impact of the inverse response, then transitions between even very different kinds of fuels could potentially be achieved without operational problems. The resulting transient information will be used to develop a new control system for thermal management of SOFC/GT hybrid systems in future work.

Keywords: Fuel cell gas turbine hybrid, fuel flexibility, hardware-based simulations

1. Introduction

The recuperated solid oxide fuel cell gas turbine (SOFC/GT) hybrid system is an alternative power generation system that can potentially provide higher system efficiency, fuel flexibility and economic viability than traditional standalone systems. With high operating fuel cell temperatures, this configuration allows for the recovery of high quality fuel cell waste heat in the recuperated gas turbine cycle. Moreover, previous studies have shown that the overall hybrid system efficiency is not strongly affected by fuel utilization as opposed to standalone fuel cell systems (Haynes and Wepfer, 2000). As such, choosing a lower fuel utilization in a SOFC/GT hybrid would

generally reduce the risk of fuel cell starvation and also increase the fuel cell efficiency via hydrogen partial pressure and Nernst potential enhancement (Haynes and Wepfer, 2000). In that case, the fuel cell life in the hybrid configuration could be extended by ten times compared to a standalone fuel cell system operated under constant power (Tucker et al., 2014).

Integrated gasification fuel cell (IGFC) systems with a recuperated gas turbine cycle can be effectively combined with a Fischer Tropsch (FT) synthesis system in polygeneration plants (Adams et al., 2012). A portion of the coal-derived syngas from the gasification process can be used to generate electricity in the SOFC/GT system and the rest can be used for diesel and gasoline production in the FT section, depending on the desired products. Furthermore, if the downstream sections of the polygeneration system can be operated flexibly such that the amount of syngas fed to the power and fuels sections can be adjusted, it is possible to create diversity of product portfolios to match changes in market prices without having to change the gasifier throughput (Chen et al., 2011). Hence, the plant can be operated at a reduced profitability risk as compared to a 'static' plant which could not be flexibly adjusted.

Despite the aforementioned benefits, SOFC/GT hybrid systems are highly coupled. The strong interaction between the dynamics of fuel cell and gas turbine cycle results in complicated operational and control issues (McLarty et al., 2012). To ascertain that the SOFC/GT hybrid system could be operated in fuel flexible environment, its operability during fuel composition changes was experimentally investigated and presented herein. The ultimate goal for this study was to develop adequate control to support the transient operations, such that, the operability range of SOFC/GT in flexible operations can be enhanced. This provides benefits for advanced power system to maximize fuel utilization as well as to reject unfavourable impacts from fuel composition/quality changes.

2. SOFC/GT hybrid configuration

2.1. System Description

A hardware-based simulation facility of SOFC/GT hybrid system at the U.S Department of Energy, National Energy Technology Laboratory in Morgantown, West Virginia was used to execute the experimentation.

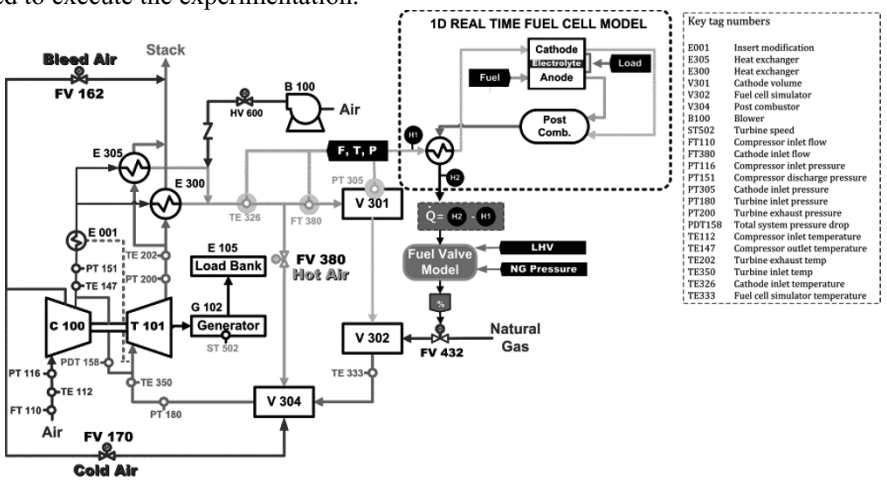

Figure 1 Schematic diagram of a recuperated SOFC/GT hybrid system at NETL (Harun et al., 2014)

This facility was uniquely designed to explore the operability and flexibility of a gasifier fuel cell gas turbine hybrid system during transient events. The complete cycle of the SOFC/GT hybrid facility is illustrated in Fig.1. Due to the prohibitive cost and maintenance of a real fuel cell, a real-time fuel cell dynamic model (as illustrated in a dashed-line box in Fig.1) is integrated to the balance of the plant hardware to represent a fuel cell system such that the exploration of fuel cell dynamics in hybrid power systems can be performed extensively without breaking any real fuel cells.

The hardware provides high reliability in measurements of the balance of the plant and maintains their real fluid dynamic behaviours. In hardware-based simulations of the hybrid power system, real-time data from three sensors that measure mass flow, temperature, and pressure of the physical cathode inlet stream (i.e. recuperated compressed air) are used as model inputs. Other model inputs, the including fuel cell configuration, can be specified by users. Detailed descriptions of this facility were published previously (Harun et al., 2014).

2.2. Test Procedures

System startup was performed using the same approaches described in previous publications (Tucker et al., 2011). Only fuel composition changes were applied in this study, while maintaining the mass flow rate of the fuel and SOFC current constant. The fuel composition changes in the SOFC/GT hybrid system involved a step transition from an initial composition of coal-derived syngas feed (CH_4 0 %, CO_2 12 %, CO 28.6 %, H_2 29.1 %, H_2O 27.1 %, N_2 3.2 %) to humidified methane composition (CH_4 13.6 %, H_2O 86.4 %) at time zero. At 145 g/s fuel mass flow rate, this represents a 20 % reduction in low heating value (LHV) of the fuel.

The turbine load command was maintained at 40 kW during all experiments. From a control perspective, operating the system with a 40 kW turbine load is required for turbine speed controllability, such that the system allows the turbine speed to change within its operational limit during open loop operations. The physical fuel valve (FV-432) corresponds to a fuel cell model output (Q) every 80 ms to simulate the fuel cell thermal effluent that eventually will be recovered in the gas turbine cycle. The interaction between the fuel cell model and the balance of the plant is in a feed forward loop. The test was run for about 5500 s to sufficiently capture the most significant transient impacts of fuel composition changes in the SOFC/GT hybrid system.

3. Open Loop Transient Trajectories

The fuel cell thermal effluent, Q, is the process variable of primary interest in controlling the hybrid system. This is because Q drives the subsequent transient impacts on the entire hybrid system performance, such as turbine speed, cathode inlet conditions (i.e. mass flow, temperature and pressure) as well as the consequent impacts in the fuel cell itself. Theoretically, Q is the total waste heat resulting from the combustion of potential chemical energy combined with thermal energy carried by cathode and anode exhaust streams before entering the gas turbine (Fig. 1).

An example of the impacts on the SOFC/GT hybrid system in response to fuel composition changes is shown in Fig. 2, which provides the trajectories of Q, turbine speed and the corresponding cathode inlet conditions in response to a switch in fuel from coal-derived syngas to humidified methane containing 13.6 % CH_4. The initial condition of each process variable shown in Fig. 2 is summarized in Table 1. As indicated in Fig. 2, without any control system in place, the system exhibited a significant inverse response in Q before slowly decreasing to the expected final transient

response. Due to the immediate overshoot in Q, fuel composition transitions could be performed safely only for a limited range of CH_4 concentrations without violating a key turbine surge margin safety constraint (Harun et al., 2014).

Table 1 Open loop initial conditions

Thermal effluent, Q	Turbine speed	Cathode inlet mass flow	Cathode inlet pressure	Cathode inlet pressure
764 kW	40,500 rpm	1.04 kg/s	973 K	246 kPag

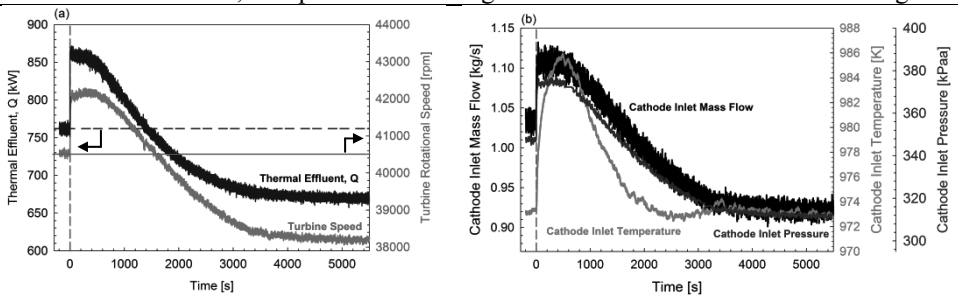

Figure 2 Open loop transient reeponse of SOFC/GT hybrid system during fuel composition changes

During the initial transient period for the example shown, Q increased by 14 %, which caused a 4 % increase in turbine speed. Accordingly, an 8 % increase in cathode inlet mass flow and cathode inlet pressure resulted due to the additional heat supplied to the gas turbine cycle. With that variation, the cathode inlet temperature only increased by 1 % from the initial value. The final reduction of Q was about 13 % below the initial condition. The decreased Q caused a 6 % decrease (from the nominal point) in turbine speed which finally reduced the cathode inlet mass flow and pressure, respectively by 12 % and 10 % (from the initial conditions). Meanwhile, the cathode inlet temperature settled approximately at the same initial temperature at 2000 s after the initiation of the step change and for the remaining course of the test.

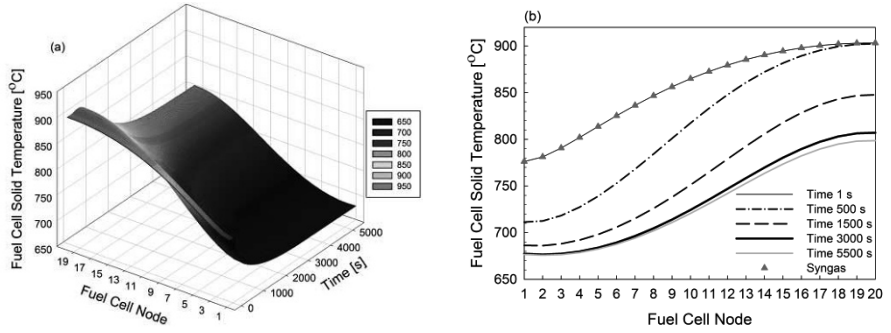

Figure 3 Fuel cell solid temperature profiles

Fig. 3 illustrates the dynamic profiles of fuel cell solid temperature over a 5500 s operation period, from the initial steady state using coal-derived syngas (before the step time) to the final state via humidified methane-feed. As depicted in Fig. 3 (b), over the first 500 s, the solid temperature at the inlet region significantly dropped, approximately by 65 °C, but gradually decreased in the following test period. Meanwhile, the profile at the cell exit clearly contrasts the inlet transient, with more apparent temperature

gradient after 500 s run. Only a slight decrease in the temperature was observed at the downstream region of the cell after time 3000 s when approaching a new steady state. Such a dynamic behaviour was dominated by the highly endothermic steam methane reforming reaction. The energy contained in the new fuel mixture was insufficient to both provide for the heat consumption of the reforming reaction and maintain the same solid temperature as using the prior fuel. Although the change in fuel composition was instantaneous in this experiment, the fuel cell temperature drops gradually because some of the heat stored in the fuel cell itself was used to power the reforming reaction until some of this heat was depleted and steady state is achieved.

On the other hand, the initial sharp rise in Q was primarily influenced by the conversion of humidified methane. This impact was indicated by the elevation in fuel heating value in the anode effluent, which eventually increased the thermal input fed into the gas turbine cycle. This led to the identical transient impacts on turbine speed, and cathode inlet conditions (Fig. 2). Due to conflicting effects between reducing cathode air mass flow and reducing thermal effluent in the SOFC/GT hybrid on temperature response in a long operation, a mitigating impact was exhibited in cathode inlet temperature. Overall, the detailed analysis has shown that Q was strongly affected by complex interactive impacts of direct electrochemical conversion of fuel, solid-gas temperature difference in the fuel cell, fuel cell thermal energy storage (due to the large fuel cell thermal capacitance), and cathode air mass flow.

4. Development of Transfer Functions

Transfer functions of turbine speed, fuel cell temperature gradient, dT/dx, total system pressure drop and cathode inlet mass flow in the SOFC/GT hybrid system in response to the change of steam/carbon ratio during fuel composition transition were developed in order to quantitatively determine the transient trajectories shown in Fig. 4.

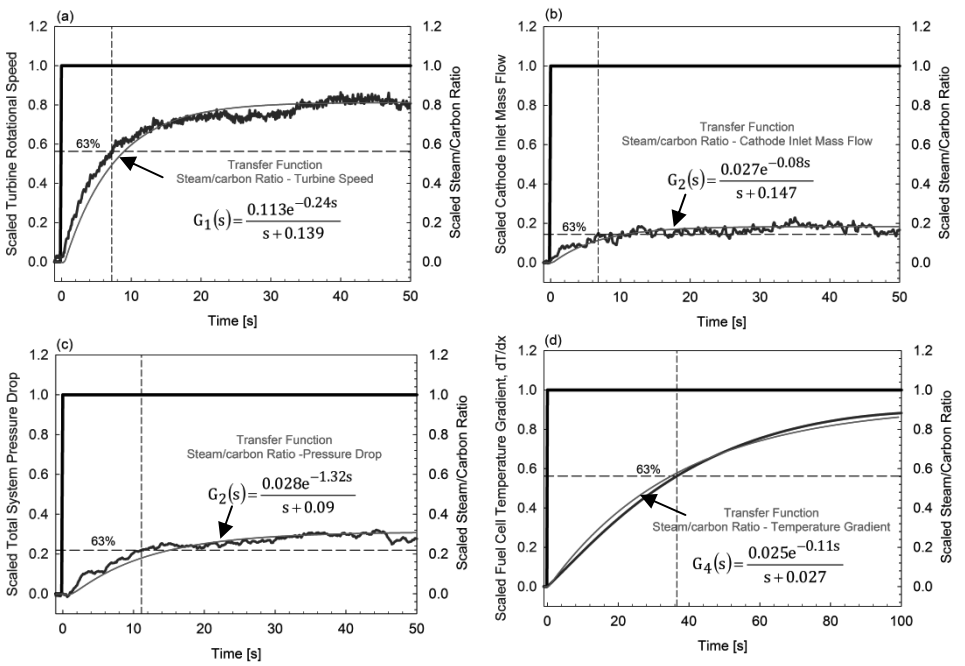

Figure 4 Transfer function shaping for, (a) turbine speed, (b) cathode inlet mass flow, (c) total system pressure drop, and (d) fuel cell temperature gradient

Although the system demonstrated higher order dynamic response in a long run as shown in Fig. 2, only initial transient trajectories (Fig. 4) were considered to mitigate the short-term unfavourable transient behaviour. Padé approximation was used to estimate the Laplace domain of the First-Order-Plus-Dead-Time (FOPDT) transfer functions. The experimental data were compared to the transfer function curves. Substantial agreement between the real behaviours and the estimated profiles was obtained in turbine speed, cathode inlet mass flow, system pressure drop, and solid temperature gradient (dT/dx) using the developed transfer functions.

5. Conclusions

Despite the lack of dynamic transient information of the coupling between the fuel cell system and the recuperated gas turbine cycle, the hybrid configuration provides more flexibility in terms of dealing with operational challenges. There are more manipulated variables that could be potentially used to mitigate the negative impacts. The hybrid system adds some degrees of freedom for control development such that the system operability can be improved. However, no control design associated with fuel flexible operations in the SOFC/GT system has yet been studied. A previous study which focused on the impacts of cathode mass flow on the SOFC/GT has shown that reducing cathode inlet mass flow resulted in a mirrored transient response in fuel cell thermal effluent, Q, as compared to the result obtained in this study (Zhou et al., 2015). The results suggested that modulating cathode air flow could be a potential mitigation strategy for the system thermal management, hence, the overshoot in the fuel cell thermal effluent during fuel composition changes could be reduced/removed to moderate the overall impacts on the hybrid performance. The time constants (i.e. time to achieve 63 % of the total output change, as indicated in Fig. 4) of the developed transfer functions in this study and for the actuator actions of cathode air mass flow were comparable. It is expected that based on these results, a new set of system identification transfer functions can be developed as the baseline for a future control design.

References

T. A. Adams II, J. Nease, D. Tucker & P. I. Barton, 2012, Energy Conversion with Solid Oxide Fuel Cell Systems: A Review of Concepts and Outlooks for the Short- and Long-Term, Ind. Eng. Chem. Res. 52, 9, 3089-3111.

Y. Chen, T. A. Adams II & P. I. Barton, 2011, Optimal Design and Operation of Flexible Energy Polygeneration Systems, Ind. Eng. Chem. Res, 50, 8, 4553-4566.

N. F. Harun, D. Tucker & T. A. Adams II, 2014, Fuel Composition Transients in Fuel Cell Turbine Hybrid for Polygeneration Applications, Journal of Fuel Cell Science and Technology, 11, 6, 1-8.

C. Haynes & W. J. Wepfer, 2000, Design for Power of a Commercial Grade Tubular Solid Oxide Fuel Cell, Energy Conversion & Management, 41, 11, 1123-1139.

D. McLarty, Y. Kuniba, J. Brouwer & S. Samuelsen, 2012, Experimental and theoretical evidence for control requirements in solid oxide fuel cell gas turbine hybrid systems, Journal of Power Sources, 209, 2012, 195-203.

D. Tucker, M. Abreu-Sepulveda & N. F. Harun, 2014, SOFC Lifetime Assessment in Gas Turbine Hybrid Power Systems, Journal of Fuel Cell Science and Technology, 11, 5, 1-7.

D. Tucker, D. Hughes & C. Haynes, 2011, IGFC Response to Initial Fuel Cell Load for Various Syngas Compositions, ASME Paper No. ESFuelCell2011-54450, 1-14.

N. Zhou, C. Yang, D. Tucker, P. Pezzini & A. Traverso, 2015, Transfer Function Development for Control of Cathode Airflow Transients in Fuel Cell Gas Turbine Hybrid Systems, International Journal of Hydrogen Energy, 40, 2015, 1967-1979.

Krist V. Gernaey, Jakob K. Huusom and Rafiqul Gani (Eds.), 12th International Symposium on Process Systems Engineering and 25th European Symposium on Computer Aided Process Engineering.
31 May - 4 June 2015, Copenhagen, Denmark.

Short-Term Planning of Cogeneration Power Plants: a Comparison Between MINLP and Piecewise-Linear MILP Formulations

Leonardo Taccari[a], Edoardo Amaldi[a], Emanuele Martelli[b] and Aldo Bischi[b]

[a]*Dipartimento di Elettronica, Informazione e Bioingegneria; Politecnico di Milano, Milano, Italy*
[b]*Dipartimento di Energia; Politecnico di Milano, Milano, Italy*
leonardo.taccari@polimi.it

Abstract

In this work we compare two optimization approaches to tackle the short-term operational planning of energy systems including power plants, boilers, heat storage, as well as cogeneration units. We first describe a mixed-integer nonlinear programming formulation for the problem and then a mixed-integer linear one, obtained using piecewise-linear approximations of the nonlinear performance functions. We report and discuss numerical results on a set of realistic test cases, comparing the quality of the solutions and the computing time of the two approaches.

Keywords: cogeneration systems, mixed integer nonlinear optimization, piecewise approximation

1. Introduction

Nowadays quite complex energy systems are used to satisfy the electricity, heat and refrigeration power demand of industrial processes as well as buildings and cities (e.g., district heating networks). Such systems generally include not only conventional power plants, boilers, and refrigeration cycles, but also heat pumps, cogeneration units and heat storage systems. Among them, cogeneration units, also called Combined Heat and Power (CHP) plants, are particularly advantageous because of their improved integration of the heat flows which leads to remarkable savings in primary energy consumption and CO_2 emissions. On the other hand, the operational planning of these units is more challenging than that of conventional power plants as the two power outputs (electricity and heat) are interrelated. In addition, the presence of a heat storage unit further complicates the planning problem as it links all the time periods making time-decomposition-based techniques unsuitable. In short-term operational planning, given a set of cogeneration units and other possible generation and heat storage units, one has to determine for each time period of a time horizon which units must be switched on/off, the value of their operating variables, and the amount of stored energy in order to minimize an objective function, while satisfying the demands of electric and thermal power over all time periods. Since the performance functions of many cogeneration units are nonlinear due to the significant efficiency decrease at partial loads, the operational planning of a cogeneration system is a nonlinear mixed integer optimization problem.

In the literature, two main approaches are adopted to model energy and cogeneration systems. In *data-driven* approaches, the behavior of the energy systems is described with approximate models obtained from experimental data. One can consider an explicit approximation of the performance functions of the units, see, e.g., Zhou et al. (2013), for linear and nonlinear models. An alternative is to project out the input variables (typically fuel), and consider a convex-hull representation in the power-heat-cost space, see, e.g., Lahdelma and Hakonen (2003) and Christidis et al. (2012). In

first-principles approaches, the system is decomposed into simpler components with well-known behavior, and thermodynamic balance equations are imposed to determine the plant operating points. This kind of approach is often necessary, for example, for complex CHP steam cycles and combined cycles with multiple operating variables, see, e.g., Dvořák and Havel (2012) and Mitra et al. (2012). Both types of approach typically lead to mixed-integer (possibly nonlinear) optimization models, that can be tackled with mathematical programming techniques.

In this article we present a Mixed-Integer Nonlinear Programming (MINLP) formulation and a Mixed-Integer Linear (MILP) one, where the nonlinear performance functions are approximated using piecewise linear functions. In the selected computational results that we report, we compare the quality of the solutions and the efficiency of the two approaches with off-the-shelf exact MINLP and MILP solvers for some realistic instances of small-to-medium size and complexity.

2. The short-term operational planning problem

We consider cogeneration energy systems involving the following types of cogeneration units:

- One-degree-of-freedom cogenerative units that simultaneously generate electric and thermal power, e.g., gas turbines, internal combustion engines, fuel cells.
- Two-degree-of-freedom cogenerative units that simultaneously generate electric and thermal power (depending on two operating variables). This class includes, e.g., gas turbines with supplementary firing and steam cycles with extraction-condensing turbine.

The system may also include conventional generation units such as boilers and compression heat pumps. In addition, storage tanks may be connected to the heat network. The electric power generated by the units can be used to fulfill the customers' demands and, at the same time, drive the compression heat pumps. Electric power can also be sold/purchased to/from the electric grid.

Given a cogeneration system, including (co)generation units and heat storage tanks, time-dependent demands of low and high-temperature thermal and electric power, and time-dependent price of electricity, the short-term operational planning problem amounts to determining the schedule that minimizes the total operating costs, while satisfying the given demands for all the time periods in a given time horizon. Adopting a data-driven approach, we consider nonlinear performance functions derived from data, either experimental or provided by the manufacturer, that well approximate the behavior of each unit. We also account for the start-up phase of units, that may incur a significant energy penalty due to their warm-up phase, and there is an upper bound on the number of start-up operations.

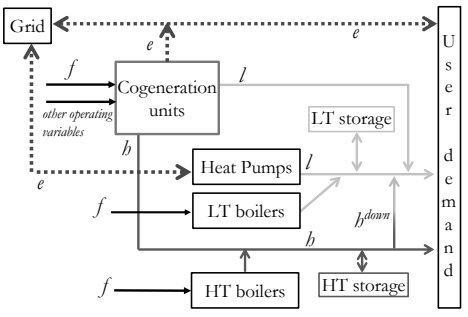

Figure 1: Schematic representation of a CHP system that cogenerates electricity and heat at two temperature levels.

3. MINLP formulation and MILP approximation

Using the sets, parameters and decision variables defined in the nomenclature, the short-term cogeneration systems planning problem can be formulated as the following MI(N)LP:

$$\min \quad \sum_{t\in\mathscr{T}}\left(\sum_{i\in\mathscr{U}} c_i^{\mathsf{OM}} z_{it} + \sum_{i\in\mathscr{U}} c_i^{\mathsf{SU}}\delta_{it} + \sum_{i\in\mathscr{F}} c_i^f f_{it} + b_t e_t^+ - p_t e_t^-\right) \tag{1}$$

$$s.t. \quad \sum_{i\in\mathscr{G}} e_{it}^{gen} - \sum_{i\in\mathscr{E}} e_{it}^{cons} + e_t^+ - e_t^- = D_t^e \qquad \forall t\in\mathscr{T} \tag{2}$$

$$\sum_{i\in\mathscr{H}} h_{it} - h_t^{down} + (u_t - \frac{u_{t+1}}{1-\alpha}) \geq D_t^{high} \qquad \forall t\in\mathscr{T}, i\in\mathscr{U} \tag{3}$$

$$\sum_{i\in\mathscr{L}} l_{it} + h_t^{down} + (v_t - \frac{v_{t+1}}{1-\beta}) \geq D_t^{low} \qquad \forall t\in\mathscr{T}, i\in\mathscr{U} \tag{4}$$

$$z_{it}F_{it}^{min} \leq f_{it} \leq z_{it}F_{it}^{max} \qquad \forall t\in\mathscr{T}, i\in\mathscr{F} \tag{5}$$

$$z_{it}E_{it}^{min} \leq e_{it}^{cons} \leq z_{it}E_{it}^{max} \qquad \forall t\in\mathscr{T}, i\in\mathscr{E} \tag{6}$$

$$\textit{performance constraints linking } z_{it}, f_{it}, e_{it}^{cons}, y_{it}, x_{it}, e_{it}^{gen}, h_{it}, l_{it} \qquad \forall t\in\mathscr{T}, i\in\mathscr{U} \tag{7}$$

$$\sum_{t\in\mathscr{T}} \delta_{it} \leq N_i \qquad \forall t\in\mathscr{T}, i\in\mathscr{U} \tag{8}$$

$$\delta_{it} \geq z_{it} - z_{it-1} \qquad \forall t\in\mathscr{T}, i\in\mathscr{U} \tag{9}$$

$$e_{it}^{gen}, h_{it}, l_{it}, h_t^{down}, e_t^+, e_t^- \geq 0 \qquad \forall t\in\mathscr{T}, i\in\mathscr{U} \tag{10}$$

$$0 \leq u_t \leq U,\ 0 \leq v_t \leq V \qquad \forall t\in\mathscr{T} \tag{11}$$

$$0 \leq \delta_{it} \leq 1,\ z_{it} \in \{0,1\} \qquad \forall t\in\mathscr{T}, i\in\mathscr{U}. \tag{12}$$

The aim is to minimize the operational costs minus the revenue obtained by selling extra electricity to the grid. In the objective function (1), the start-up penalties c_i^{SU} account for the extra cost due to the warm-up phase, while the fixed cost c_i^{OM} accounts for operation and maintenance costs proportional to the number of working hours. Constraints (2) impose that the net amount of electric power must satisfy the demand D_t^e for period t. It is necessary to distinguish between the energy that is purchased from the power grid, e_t^+, from the one that is sold, e_t^-, since their price is different. Constraints (3) and (4), balance constraints for high and low-temperature heat, ensure that the thermal requirements in period t are satisfied. High-temperature heat can be downgraded to low-temperature via h^{down}. Thermal energy can be stored in the tank for the next period, as long as the capacities U, V are not saturated, and we account for constant loss rates $\alpha, \beta \in [0,1)$. Thermal energy in excess can be dissipated with no additional costs. Constraints (5) and (6) ensure that the operating variables for a unit i (fuel, consumed electricity) are within the technical limits. Constraints (7), that model the nonlinear behavior of the generation units, are described in detail in the next two paragraphs. Constraints (8) and (9) limit the number of start-ups.

Nonlinear performance constraints: Each unit $i \in \mathscr{U}$ is described in terms of nonlinear performance functions $g_{it}(\cdot)$, that map one or more operating variables (fuel, consumed electricity, supplementary fuel) to an output variable (low or high-temperature heat, electric power). The performance functions are in general, non-convex and time-varying due to the non-negligible temperature effect. In addition, if unit $i \in \mathscr{U}$ is off, its output has to be 0. Thus, Constraints (7) can be expressed as inequalities of the form $\zeta \leq z_{it} g_{it}(\underline{\theta})$, where $\underline{\theta}$ is the vector of input variables and ζ an output variable, and the problem can be solved as a Mixed-Integer Nonlinear Program.

In the case of generation or cogeneration units with one degree of freedom (d.o.f.), each performance function g_{it} will be a function of one variable (θ is scalar). For instance, given a high-temperature auxiliary boiler, the output variable is high-temperature thermal power h_{it}, while the only operating variable is fuel f_{it}. The feasible region for h_{it} will be $\{0\} \cup [g_{it}(F_{it}^{min}), g_{it}(F_{it}^{max})]$.

In the case of cogeneration units with more degrees of freedom, the performance functions depend on two or more operating variables ($\underline{\theta}$ is a vector). Two examples are combined cycles with extraction valve regulation (left) and gas turbines with post-firing (right):

$$\begin{cases} l_{it} \leq z_{it} g^l_{it}(f_{it}, x_{it}) \\ h_{it} \leq z_{it} g^h_{it}(f_{it}, x_{it}) \\ e^{gen}_{it} \leq z_{it} g^e_{it}(f_{it}, x_{it}) \end{cases} \tag{13}$$

$$\begin{cases} l_{it} \leq z_{it} g^l_{it}(f_{it}, y_{it}) \\ h_{it} \leq z_{it} g^h_{it}(f_{it}, y_{it}) \\ e^{gen}_{it} \leq z_{it} g^e_{it}(f_{it}, y_{it}), \end{cases} \tag{14}$$

where the operating variables are the fuel quantity f_{it}, the valve opening percentage $x_{it} \in [0, 0.4]$ for the combined cycle (13) and the supplementary fuel y_{it} for the gas turbine (14).

Piecewise linear approximation: An alternative approach consists in approximating the nonlinear performance functions with piecewise linear functions, see e.g. Bischi et al. (2014), obtaining a more tractable Mixed-Integer Linear Program (MILP). The piecewise linear approximation of 1-d.o.f. performance functions is rather straightforward, as it is sufficient to select a set of discretization points on a line, and connect them via line segments. For 2-d.o.f. units the approximation involves functions of two variables. Several approaches are available for approximating 2-D functions, differing considerably in terms of accuracy of the approximation and computational cost of the resulting MILP. In our model, we consider the so-called *lambda method* described, e.g., in Lee and Wilson (2001), that is implemented by triangulating the domain of the nonlinear function. Then, the value in a point $\underline{x}$ is computed as the convex combination of the function values in the vertices of the triangle containing $\underline{x}$. This method requires the introduction of $O(n_1 \times n_2)$ binary variables, where n_1 and n_2 are the number of discretization points per dimension.

4. Computational experiments

Given the wide variety of cogeneration systems, ranging from small to large scale, we consider two scenarios from which we build several test instances.

Scenario 1: The first scenario is a micro-cogeneration system designed to provide low and high-temperature thermal power and electricity to a large building. The system consists of:

- a Solid Oxide Fuel Cell (SOFC) using natural gas to cogenerate electric and thermal power;
- a Heat Pump (HP) using electric power to generate low temperature heat;
- an Auxiliary Boiler (AB), mainly used as a backup;

and a thermal storage for high-temperature heat energy. For this scenario, we consider a single instance with 3 units that we indicate with `1-a`.

Scenario 2: The second scenario is a large scale cogeneration system providing heat to a district heating network. The system may include one or more of the following units:

- Gas Turbines (GT) with heat recovery;
- Gas Turbines (GT-2) with supplementary firing and heat recovery;
- Natural Gas Combined Cycles (NGCC) with a bottoming back-pressure steam turbine;
- Natural Gas Combined Cycles (NGCC-2) with a bottoming extraction-type steam turbine;
- Auxiliary Boilers (AB) burning natural gas to generate heat;

and a thermal storage for high-temperature heat energy. Since only thermal power is required, the whole amount of electricity cogenerated by gas turbines and combined cycles is sold to the grid. This scenario includes units with two degrees of freedom, see Eq. (13) and (14): in GT-2, supplementary fuel can be burned to increase the amount of recovered heat, and, in NGCC-2, opening the steam extraction valve reduces the electric power and increases the thermal power. Four different instances are considered (`2-a`, `2-b`, `2-c` and `2-d`), with, respectively, 5, 4, 12 and 11 (co)generation units. Instances `2-b` and `2-d` include also 2-d.o.f. cogeneration units.

Computational experiments were performed, for the MINLP formulations, with the open-source solver SCIP 3.1.0, while for the MILP formulations IBM Ilog CPLEX 12.6 was used. For the MINLP, we have also experimented with BARON, whose results are not included for sake of brevity, since its efficiency on the considered instances was slightly inferior. The tests were carried out on an Intel Xeon with E3125@3.30GHz CPUs and 16GB of RAM, with a time limit of 2 hours.

Table 1: Optimal values, computing time (seconds) and lower/upper bounds for the MINLP and the approximate MILP with an increasing number of discretization points (d.p.) per dimension.

	2 d.p.		3 d.p.		5 d.p.		9 d.p.		15 d.p.		MINLP			
	time	opt	time	opt	time	opt	time	opt	time	opt	time	LB	UB	gap
`1-a`	0.01	94.33	0.03	91.73	0.06	91.30	0.10	91.17	0.42	91.11	42.58	91.07	**91.07**	0.0
`2-a`	0.04	104.17	0.07	102.49	0.10	101.95	0.12	101.86	0.14	101.82	812.8	101.76	**101.76**	0.0
`2-b`	0.06	-80.12	0.14	-80.24	1.19	-80.33	4.53	-80.36	34.44	-80.36	7200	-94.36	-71.97	31.1
`2-c`	0.15	307.01	0.04	302.73	0.09	300.75	0.09	300.51	0.17	300.43	7200	284.83	300.19	5.4
`2-d`	0.22	121.27	0.29	119.43	0.31	118.20	0.50	118.09	3.43	118.07	7200	-83.01	140.93	∞

Table 1 summarizes the computational results. The MINLP instances turn out to be challenging. SCIP is able to certify optimality for 2 out of 5, and on `2-c` is close to the optimum, while the instances with 2-d.o.f. units are harder. In comparison, the MILP formulations can be solved to optimality by CPLEX in a few seconds. The MILP solutions are not necessarily feasible for the original formulation, since the approximate model might overestimate the amount that is generated. However, it is always possible to recover infeasibility *a posteriori* by increasing the production level. Interestingly, on our instances all the MILP optimal solutions are feasible (barring minor numerical errors), as they tend to be on the discretization points.

The results show that the approximate optimal values approach the optimal value of the original formulation as the number of discretization points is increased. The optimal values are significantly different when the approximation is less accurate – except for instance `2-b`, where the variation is small, since the solution is dominated by a large NGCC-2 unit always at full load.

The structure of the solutions can differ significantly. As an example, we report in Figure 2 two optimal schedules for a low-temperature heat pump in instance `1-a` with a 2-point MILP approximation (left) and with the MINLP model (right). Although the instance is simple, the structure of the optimal approximate solution differs from that of the optimal MINLP solution even when the number of discretization points is increased to 5. To obtain optimal solutions to these two problems that are equivalent, one needs to use at least 9 discretization points.

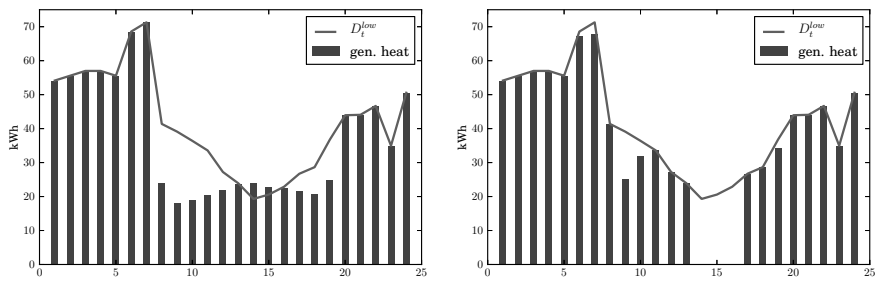

Figure 2: Optimal plan for the heat pump of instance `1-a` obtained with a 2-point piecewise approximation (left) and with the MINLP (right).

5. Concluding remarks

The summarized computational results for two relatively simple scenarios of the short-term operational planning problem indicate that even small-size instances of the MINLP can be computationally very challenging. Approximating the nonlinear performance functions with piecewise linear functions is an alternative that seems to work quite well in practice. For the considered instances, the resulting approximate MILP models can generally be solved more efficiently than their MINLP counterparts, and they appear to be already fairly accurate with a few linear pieces.

Attention must be paid to the feasibility of the solutions obtained with the approximations. Indeed, if the optimal operating point of a unit is far from the approximation discretization points, the piecewise linear function value might be quite different from the actual value. Underestimating the actual performance value may lead to suboptimal solutions with more than 3% error, while overestimating it may lead to infeasible solutions.

Nomenclature

$\mathscr{T}$: set of time periods (hours)
$\mathscr{U}$: set of all generation units
$\mathscr{F}$: set of units consuming fuel
$\mathscr{E}$: set of units consuming electricity
$\mathscr{H}$: set of units that generate high-temperature heat
$\mathscr{L}$: set of units that generate low-temperature heat
$\mathscr{G}$: set of units that generate electricity
c_i^{OM}: hourly operation and maint. cost for unit i [€]
c_i^{SU}: start-up cost for unit i [€]
c_i^f: unit cost of fuel for unit i [€/kWh]
b_t, p_t: unit price of electricity bought/sold from/to the grid at time t [€/kWh]
$F_{it}^{min}, F_{it}^{max}$: minimum and maximum fuel input for unit $i \in \mathscr{F}$ at time t [kWh]
$E_{it}^{min}, E_{it}^{max}$: minimum and maximum electricity input for unit $i \in \mathscr{E}$ [kWh]
N_i: maximum number of start-ups for unit i
U, V: capacity of low and high-temperature heat storage [kWh]
α, β: constant loss rate for thermal storage [%]
$D_t^{low}, D_t^{high}, D_t^e$: demand for low and high-temperature heat, electricity at time t [kWh]
f_{it}: fuel consumed by unit $i \in \mathscr{F}$ in period t [kWh]
y_{it}: secondary fuel consumed by unit $i \in \mathscr{F}$ with post-firing injection [kWh]
x_{it}: extraction valve opening percentage for combined cycle units [%]
e_{it}^{cons}: electricity consumed by $i \in \mathscr{E}$ in period t [kWh]
e_{it}^{gen}: electricity generated by $i \in \mathscr{G}$ in period t [kWh]
l_{it}: low-temperature heat generated by unit $i \in \mathscr{L}$ in period t [kWh]
h_{it}: high-temperature heat generated by unit $i \in \mathscr{H}$ in period t [kWh]
h_t^{down}: high-temperature heat downgraded to low-temperature in period t [kWh]
e_t^+, e_t^-: electricity bought/sold from/to the grid in period t [kWh]
u_t, v_t: high and low-temperature thermal energy stored at the beginning of period t [kWh]
z_{it}: binary variable, on/off status of unit i in period t
δ_{it}: binary start-up variable ($\delta_{it} = 1$ if unit i is switched on at beginning of period t)
$g_{it}^h, g_{it}^l, g_{it}^e$: performance functions for unit i at time t

References

A. Bischi, L. Taccari, E. Martelli, E. Amaldi, G. Manzolini, P. Silva, S. Campanari, E. Macchi, 2014, A detailed MILP optimization model for combined cooling, heat and power system operation planning, Energy 74, 12 – 26.

A. Christidis, C. Koch, L. Pottel, G. Tsatsaronis, 2012, The contribution of heat storage to the profitable operation of combined heat and power plants in liberalized electricity markets, Energy 41 (1), 75–82.

M. Dvořák, P. Havel, 2012, Combined heat and power production planning under liberalized market conditions, Applied Thermal Engineering 43, 163–173.

R. Lahdelma, H. Hakonen, 2003, An efficient linear programming algorithm for combined heat and power production, European Journal of Operational Research 148 (1), 141–151.

J. Lee, D. Wilson, 2001, Polyhedral methods for piecewise-linear functions I: the lambda method, Discrete Applied Mathematics 108 (3), 269–285.

S. Mitra, I. E. Grossmann, J. M. Pinto, N. Arora, 2012, Optimal production planning under time-sensitive electricity prices for continuous power-intensive processes, Computers & Chemical Engineering 38, 171–184.

Z. Zhou, P. Liu, Z. Li, E. N. Pistikopoulos, M. C. Georgiadis, 2013, Impacts of equipment off-design characteristics on the optimal design and operation of combined cooling, heating and power systems, Computers & Chemical Engineering 48, 40–47.

Krist V. Gernaey, Jakob K. Huusom and Rafiqul Gani (Eds.), 12th International Symposium on Process Systems Engineering and 25th European Symposium on Computer Aided Process Engineering.
31 May – 4 June 2015, Copenhagen, Denmark

Optimum Facility Location and Plant Scheduling for Biofuel Production

Chen Li, Selen Cremaschi*

Department of Chemical Engineering, The University of Tulsa, 800 South Tucker Drive, Tulsa, Oklahoma 74104, USA.
selen-cremaschi@utulsa.edu

Abstract

This paper presents a mixed integer linear program (MILP) that maximizes the net present value (NPV) of a biomass-to-biofuels supply chain (BTBSC). The BTBSC includes the biomass growth and its planting-campaign schedule, the location and the capacities of the biorefineries, and the transportation cost from the planting regions to biorefinery locations, and from biorefinery locations to demand centres. The case study considers the design and operation of a BTBSC for 18 counties of the State of Oklahoma with four different types of biomass for producing bioethanol by hydrolysis followed by fermentation route. The model recommends building a biorefinery of 100 MG/yr capacity at Tulsa County, and planting big blue stem at the same location.

Keywords: biomass-to-biofuels supply chain, biomass-planting-campaign schedule, biomass transportation cost, biofuel transportation cost, biorefinery cost

1. Introduction

Biomass is an abundant, locally available, and renewable raw material for liquid fuel production. The biomass-to-biofuels supply chain (BTBSC) contains biomass growth, biorefineries, and demand centres. The optimum design and operation of this supply chain is crucial for cost effective production of biofuels, and there are ample studies in the literature that focuses on optimizing the location and size of biorefineries for selected geographical regions. For example, Kocoloski et al. (2011) concluded that locating switchgrass-to-ethanol biorefineries optimally relative to biomass supplies and ethanol demand may reduce the cost of ethanol by 15-25% relative to uninformed biorefinery placement. Marvin et al. (2012) presented a MILP for ethanol production in a 9-state region in the Midwest and analysed the systems sensitivity to changes in parameters. Giarola et al. (2011) presented a similar model for Northern Italy, and considered a multi-objective problem also minimizing greenhouse gas emissions. However, most models assume a certain amount of biomass availability for a selected region, and hence, fail to consider the overall BTBSC. Cost of biomass growth accounts for a significant portion of the biofuel production cost, and the optimal design of BTBSC should include the batch-like characteristics of biomass growth along with biorefinery locations and capacities.

In this paper, we present a MILP for optimal design of BTBSC with biorefinery location and capacities, and campaign plan for biomass production. The objective of the model is to maximize the net present value (NPV) of the overall supply chain over the planning horizon. The NPV includes biomass growth costs, capital and operating costs for biorefineries, and transportation cost between the locations of biomass growth and

biorefineries, and between biorefineries and demand centres. The addition of biomass-growth campaign planning allows the possibility of incorporating seasonality, crop-rotation, and feedstock diversification at the BTBSC design stage. The model includes multiple potential feedstock crops, and production pathways, and determines the optimal biorefinery locations and corresponding capacities, and the biomass-growth campaign plan. The model is demonstrated with a case study considering the design of BTBSC for a region encompassing 18 counties of the State of Oklahoma.

2. Optimization Model

The biomass-to-biofuel supply chain considered in this study is shown in Figure 1. There are $a \in \mathbf{A}$ potential planting regions, which may be used for growing and supplying biomass to $b \in \mathbf{B}$ potential biorefinery locations, which in turn may supply $k \in \mathbf{K}$ demand centres. Different biomass types, $c \in \mathbf{C}$, and biofuel options, $u \in \mathbf{U}$, are considered for supplying demand. Time is discretized into $t \in \mathbf{T}$ equal time buckets, and each year in planning horizon is represented by $i \in \mathbf{I}$.

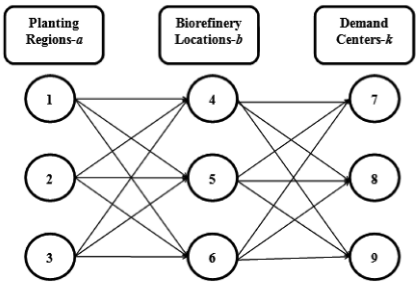

Figure 1. Biomass to biofuels supply chain

The objective is to maximize the net present value (NPV) of the BTBSC over the planning horizon, viz. Eq. (1).

$$NPV = \left[\sum_{i=1}^{|\mathbf{I}|} \frac{\sum_{u} \sum_{b} \sum_{k} BfP_u BfT_{u,b,k,i} - \left(CPL_i + CTR_i + COP_i\right)}{(1+rate)^i} \right] - CINV \tag{1}$$

Eq. (1) discounts the yearly profit using a discount rate of *rate* and subtracts the initial capital investment, *CINV*. The yearly profit is the difference between the total revenue from biofuel sales and total cost. The revenue is calculated as the sum of all biofuel types, u, transferred from biorefinery location b to demand centre k at year i, $BfT_{u,b,k,i}$, multiplied by the corresponding biofuel price, BfP_u. Total cost includes yearly planting (CPL_i), transportation (CTR_i), and biorefinery operating (COP_i) costs.

The biomass-planting-campaign schedule determines the annual planting costs. This schedule requires a finer time grid than years as biomass may be planted more than once and at any time throughout the year. The goal of the campaign schedule is to determine which biomass to plant at which time in which planting area in order to satisfy the biomass demand from the biorefineries. When a certain biomass is planted in a certain planting region, it is occupied during the cycle time (rotation period) of that biomass. The following assumptions are made to capture the dynamics of the biomass growth to an appropriate level of detail: (1) The biomass is grown in marginal farmland with a

known area for each planting region ($area_a$), (2) each area can be planted with a single age class of a biomass type at a time, (3) time is discretized using time buckets of equal size (one month), $t \in \mathbf{T}$, (4) all the properties within a time bucket is assumed to be constant, but may vary from one bucket to the next. Given these assumptions, a binary variable, $X_{a,c,t,p}$, is defined to be equal to one if a biomass type c is planted in planting region a at time bucket p and not harvested at time bucket t. Using this binary variable, the annual biomass planting cost is calculated using Eq. (2),

$$CPL_i = \sum_a \sum_c \sum_{t=12i-10}^{12i+1} \sum_{p=12i-10}^{p=12i+1} area_a PC_c X_{a,c,t,p} \tag{2}$$

where PC_c is the cost of planting biomass type c ($/(acre)(time bucket)).

The transportation costs consider the cost of transporting biomass from planting regions to biorefinery locations, and transporting biofuel from biorefinery locations to demand centres, and is calculated via Eq. (3).

$$CTR_i = \sum_a \sum_b \sum_c D_{a,b}(TCBi) BiT_{c,a,b,i} + \sum_b \sum_k \sum_u D_{b,k} TCBf_u BfT_{b,u,k,i} \tag{3}$$

Here, $D_{a,b}$ represents the distance between planting region a and biorefinery location b calculated as the shortest highway distance between the centres of each region, $TCBi$ is the unit transportation cost for transporting biomass using trucks, and $BiT_{c,a,b,i}$ is the amount of biomass type c transported from planting region a to biorefinery b at year i. By analogy, $D_{b,k}$ is the distance, and $TCBf_u$ is the unit cost for transporting biofuel u.

The annual biorefinery operating cost is assumed to change linearly with the capacity of the refinery. Given an estimate of the operating cost for a predetermined capacity from literature, unit operating cost ($UOC_{u,i}$) per year of the biorefinery configuration used for producing biofuel u is calculated by dividing this estimate with the capacity. The operating costs given in the literature includes the raw material, labour, waste disposal, utility costs, and fixed charges including depreciation, taxes and financing interest. We should note here that the cost of biomass was subtracted from the annual operating costs for calculations as this cost is considered in the biomass-growth campaigns. Hence, the annual biorefinery operating cost is calculated using Eq. (4).

$$COP_i = \sum_u \sum_b UOC_{u,i} Cap_{b,u} \tag{4}$$

The initial capital investment (CINV) is the sum of capital investments made for producing all biofuels in all biorefinery locations, i.e.,

$$CINV = \sum_u \sum_b INV_{b,u} \tag{5}$$

where $INV_{b,u}$ is the total capital investment made for producing biofuel u at biorefinery location b, and it includes the fixed and working capitals. As economies of scale dictates, the total capital investment for a plant is not a linear function of its capacity. In order to keep the model linear, we used piece-wise linear approximations to estimate how the total capital investment changes with biorefinery capacity. For the biorefinery options considered, a three piece-wise functions were deemed accurate enough for the

purposes of this model. The equation set given below summarizes the total investment cost calculation.

$$y_{1,b,u} + y_{2,b,u} \le 1 \tag{6a}$$

$$-M_1(1-y_{1,b,u}) \le INV_{b,u} - \alpha_{1,u} Cap_{b,u} \le M_2(1-y_{1,b,u}) \tag{6b}$$

$$-M_3(1-y_{2,b,u}) \le INV_{b,u} - \left(\alpha_{2,u} Cap_{b,u} + \beta_{2,u}\right) \le M_4(1-y_{2,b,u}) \tag{6c}$$

$$INV_{b,u} - \left(\alpha_{3,u} Cap_{b,u} + \beta_{3,u}\right) \le M_5(1-y_{1,b,u}-y_{2,b,u}) \tag{6d}$$

$$-M_6(1-y_{1,b,u}-y_{2,b,u}) \le INV_{b,u} - \left(\alpha_{3,u} Cap_{b,u} + \beta_{3,u}\right) \tag{6e}$$

$$Cap_{b,u} \le UC_{1,b,u} y_{1,b,u} + UC_{2,b,u} y_{2,b,u} + UC_{3,b,u}\left(1-y_{1,b,u}-y_{2,b,u}\right) \tag{6f}$$

$$Cap_{b,u} \ge UC_{1,b,u} y_{2,b,u} + UC_{2,b,u}\left(1-y_{1,b,u}-y_{2,b,u}\right) \tag{6g}$$

In Eq. (6), the binary, $y_{1,b,u}$ takes the value of one if the biorefinery capacity at location b for biofuel u falls below the upper bound of the first capacity segment ($UC_{1,b,u}$). Similarly, $y_{2,b,u}$ is set to one if the capacity falls between the upper and lower bounds of the second capacity segment ($UC_{2,b,u}$ and $UC_{1,b,u}$). If both binaries are equal to zero, then the biorefinery capacity is greater than the upper bound of the second segment ($UC_{2,b,u}$), and the third linear relationship that approximates how the total capital investment changes with the biorefinery capacity is used. The parameters of the linear total investment cost functions are represented by α's and β's in Eq. (5), and Ms are big-M constraint parameters.

The next set of constraints define the biomass planting schedule. There are six additional parameters, which are type of biomass, c, dependent: (1) $\eta_{c,u}$: biofuel u yield (gal/ton), (2) $cuttingcycle_c$: cutting cycle in units of time bucket, (3) $cycle_c$: cycle time (rotation period) in units of time buckets, (4) $cyield_c$: yield during cutting cycles (ton/acre), (5) $hyield_c$: yield at final harvest (ton/acre), (6) $mature_c$: the initial time the cutting cycles may start in units of time bucket. Using the definition of binary variable $X_{a,c,t,p}$, the constraints related to schedule of biomass planting cycles can be written as:

$$\sum_{t \ge p+cycle_c+1} X_{a,c,t,p} = 0 \qquad \text{for all } a,c,p \tag{7a}$$

$$X_{a,c,t+1,p} = X_{a,c,t,p} \qquad \text{for all } a,c,p \wedge p \le t < \left(p + cycle_c\right) \tag{7b}$$

$$\sum_{c} \sum_{p=1}^{p=t} X_{a,c,t,p} \le 1 \qquad \text{for all } a,t \wedge t < \left(p + cycle_c\right) \tag{7c}$$

Eq. (7a) ensures that a planting area a planted with biomass c at time p is harvested at time $t = p + cycle_c + 1$. Eq. (7b) makes sure that once an area is planted with a biomass type at time p, the area stays occupied until the end of biomass c's cycle time. Eq. (7c) ensures that at any given time t, there is only one biomass type planted on the planting region a.

The biomass may be produced by both interval cuttings and at full harvest. When the planted biomass becomes mature, some of it may be removed by cutting, leaving the rest of the plant intact for continued growth. The biomass related parameter $cuttingcycle_c$ describes the frequency of these cuttings for biomass type c without hindering continued growth. The yield per unit acre of land of these cuttings is defined

by the $cyield_c$ parameter. At harvest, which happens at the end of the cycle time of biomass c, all biomass is removed from the land and the yield per unit acre of land at this point is defined by $hyield_c$ parameter. With these definitions, the annual production of biomass c in area a is calculated as:

$$m_{c,a,i} = \sum_{p \le t - mature_c} \sum_{t=12i-10}^{t=12i+1} \left[\begin{array}{l} X_{a,c,t,p} area_a \left\lfloor \dfrac{t-p-mature_c}{cuttingcycle_c} + 1 \right\rfloor cyield_c \\ + X_{a,c,t,p} area_a \left\lfloor \dfrac{t-p-cycle_c}{cycle_c} + 1 \right\rfloor hyield_c \end{array} \right] \text{for all } c,a,i \qquad (8)$$

where $\lfloor z \rfloor$ is the floor function.

The model assumes yearly biomass transportation from planting regions to biorefinery locations, and ignores the possible biomass spoilage during transportation and yearly storage (Eq. (9a)). Depending on the biomass type, this amount may be significant and is left as a future extension of the model. A mass balance at each biorefinery location calculates the total biofuel production ($PBf_{b,u,i}$) at that site (Eq. (9b)), which cannot exceed the total capacity of the biorefinery at that location (Eq. (9c)). The biofuel u shipped from a biorefinery location b to all demand centres cannot exceed the production at that site (Eq. (9d)). Finally, the total amount of biofuel type u transported from all biorefinery location to demand centres are bounded by the total demand ($DM_{k,u,i}$) at those sites (Eq. (9e)).

$$\sum_b BiT_{c,a,b,i} \le m_{c,a,i} \qquad \text{for all } a,c,i \qquad (9a)$$

$$\sum_a \sum_c \eta_{c,u} BiT_{c,a,b,i} = PBf_{b,u,i} \qquad \text{for all } b,u,i \qquad (9b)$$

$$PBf_{b,u,i} \le Cap_{b,u} \qquad \text{for all } b,u,i \qquad (9c)$$

$$\sum_k BfT_{u,b,k,i} \le PBf_{b,u,i} \qquad \text{for all } b,u,i \qquad (9d)$$

$$\sum_b BfT_{u,b,k,i} \le DM_{k,u,i} \qquad \text{for all } k,u,i \qquad (9e)$$

Eqs. (1) to (9) define the overall MILP for obtaining the supply chain topology, biorefinery locations and capacities, material flows between the planting regions, biorefinery locations, and demand centres, and the biomass-planting schedule.

3. Case Study and Results

The case study considers the design of BTBSC for a region encompassing 18 counties of "Green Country" in the State of Oklahoma for 10 years. The time is discretized into equal sizes of 30 days yielding a total of 120 time buckets. The potential biomass sources include switchgrass, indiangrass, big blue stem, and poplar. The candidate planting and biorefinery regions, and the demand centres are the 18 counties. It is assumed that only marginal farmland is used for growing biomass. We considered only one technology: producing cellulosic ethanol via acid pretreatment and enzymes for the hydrolysis to simple sugars followed by fermentation. Both biomass and ethanol are assumed to be transported between counties using trucks. The distance between the

counties are calculated as the shortest highway distance provided by Google Maps when the start and end points are represented by the names of the counties. The ethanol sale price is assumed to be $2.80/gal. Demand for bioethanol is forecasted using the four-year double moving average for each counties population change over the next 10 years and multiplying this number by the 11.25% of per capita demand for transportation oil in US. All prices are at 2011 US dollars. The remaining model parameters are available from the corresponding author upon request.

The MILP is implemented in GAMS version 24.2.1, and solved using CPLEX 12.6.0.0. It had 548,688 variables of which 531,468 are discrete, and 530,526 constraints, and was solved in 537.6 CPU minutes to 1% optimality gap using an Intel Core i7-3520M CPU @ 2.90GHZ computer with 8.00 GB installed memory. The NPV is $238,390,000. Given the highest biofuel demand and its central location in the Green County, the solution recommends planting big blue stem for the whole planning horizon and building a 100,000,000 gal/yr bioethanol production plant at Tulsa County. The total capital investment is $451,150,000, and the total annual costs are dominated by the biorefinery operating costs (95%). The transportation cost only accounts for 1% of the annual cost as transportation of biomass is avoided by planting at the biorefinery location.

4. Conclusions

This paper presents a mathematical programming model to design a biomass-to-biofuels supply chain (BTBSC) by maximizing the net present value of the chain. To the best of the author's knowledge, it is the first model that integrates the biomass-growth-campaign plan with biorefinery locations and capacities for designing BTBSC. The model is demonstrated with a case study that considers the design of BTBSC for 18 counties of the State of Oklahoma. Future work will incorporate the impact of possible biomass spoilage to the model, and studying the sensitivity of the solution to model parameters. Furthermore, the resulting large-scale MILP takes considerable computational resources to solve. It may be possible to exploit its structure to develop tailored algorithms for quickly locating the optimum. It is worth noting that various model parameters, such as crop yield, demand patterns, are uncertain. Once the parameters with high impacts are identified, stochastic programming may be used to hedge against these uncertainties. However, the deterministic equivalent of this stochastic program would be difficult to solve given the size of the deterministic MILP, and its applicability would depend on the development of tailored solution algorithms.

Acknowledgements

The financial support provided by the NSF CAREER Award No 1055974 is greatly acknowledged.

References

S. Giarola, A. Zamboni, F. Bezzo, 2011, Spatially explicit multi-objective optimisation for design and planning of hybrid first and second generation biorefineries, Computers & Chemical Enginering, 35, 9, 1782-1797.

M. Kocoloski, W.G. Michael, H. M. Scott, 2011, Impacts of facility size and location decisions on ethanol production cost, Energy Policy, 39, 1, 47-56.

A.W. Marvin, L.D. Schmidt, S. Benjaafar, D.G. Tiffany, P. Daoutidis, 2012, Economic Optimization of a Lignocellulosic Biomass-to-Ethanol Supply Chain, Chemical Engineering Science, 67, 1, 68079.

Krist V. Gernaey, Jakob K. Huusom and Rafiqul Gani (Eds.), 12th International Symposium on Process Systems Engineering and 25th European Symposium on Computer Aided Process Engineering.
31 May – 4 June 2015, Copenhagen, Denmark

Energy Consumption Scheduling of Smart Homes with Microgrid under Multi-objective Optimisation

Di Zhang, Sara Evangelisti, Paola Lettieri, Lazaros G. Papageorgiou

Department of Chemical Engineering, University College London, Torrington Place, London WC1E 7JE, UK, p.lettieri@ucl.ac.uk, l.papageorgiou@ucl.ac.uk.

Abstract

Microgrid is regarded as an alternative to the current centralised energy generation systems because of its benefits from various aspects, including economic and environment. And flexible domestic electricity consumption tasks within smart homes with a common microgrid can be scheduled for better mutual benefits. This paper proposes a mixed integer linear programming (MILP) model to schedule the energy consumption within smart homes by coupling environmental and economic sustainability in a multi-objective optimisation with ε-constraint method. Electricity tariff and CO_2 intensity profiles of UK are employed and the Pareto curve for cost and CO_2 emissions present the trade-off between the two conflict objectives.

Keywords: microgrids; planning/scheduling; multi-objective optimisation; ε-constraint method, mixed integer linear programming (MILP).

1. Introduction

Energy cost and pollution reduction are two worldwide popular issues and the UK Climate Change Programming aims to cut down 80% of carbon emissions by 2050 based on Climate Change Act 2008 (Fuselli et al., 2013). Microgrid, which includes a group of distributed energy resources (DER), is regarded as an alternative to the current centralised energy generation systems to deal with these two problems. Environmental benefits can be obtained by utilising DERs with low pollutant generation. Energy management within buildings can result in both energy cost and air pollution reductions since about one third primary energy is consumed in building (Lior, 2010). Smart homes are promising in improving the indoor environmental comfort while reducing economic cost and CO_2 emissions. Customers are encouraged to participate with demand side management through economic or environmental incentive, where time varying electricity tariff or CO_2 emission intensity is available (Kin Cheong et al. 2013).

Domestic appliance scheduling problem has been addressed in several recent work (Rastegar et al. 2012 and Baraka et al. 2013), and Derin and Ferrante develop a model that considers both equipment operation and three domestic appliances order scheduling. However, only economic aspect is considered in those work while the two objectives, economic cost and CO_2 emissions, are not always positively correlated and they may conflict with each other. As an extension of our previous work (Zhang et al. 2013), which targets minimising the total energy cost, this work propose a mixed integer linear programming (MILP) model to investigate the scheduling of DER operation and the domestic energy consumption tasks by coupling environmental and economic sustainability in a multi-objective optimising model with ε-constraint method. The scheduling is based on real-time electricity pricing and CO_2 intensity.

2. Problem statement

Multiple smart homes in a smart building are considered in this work and they have a common microgrid. All the DERs within the microgrid are shared among the smart homes. The microgrid is connected for electricity importation only. The energy demand of each home depends on the household types, available electrical appliances and living habits. The operation time of domestic electricity consumption tasks can be scheduled while will influence the electrical demand. The heat demand of the whole building is provided. Electricity real time pricing and CO_2 emission intensity are forecasted and given one day in advance. The economic cost and CO_2 are desired to be reduced simultaneously although the two objectives may conflict with each other. The overall problem can be stated as follows:

Given are (a) a time horizon split into a number of equal intervals, (b) heat demand of the whole building, (c) equipment capacities, (d) efficiencies of technologies, (e) maintenance cost of all equipment, (f) heat-to-power ratio of combined heat and power (CHP) generator, (g) charge and discharge limit rates for thermal/electrical storage, (h) gas price and real-time electricity prices from grid, (i) CO_2 emission intensity, (j) earliest starting and latest finishing times, (k) task capacity profiles, (l) task duration,

Determine (a) energy production plan, (b) task starting time, (c) thermal/electrical storage plan, (d) electricity bought from grid,

So as to find the optimum energy consumption scheduling and DER operation with minimum economic cost and environmental impact.

3. Mathematical formulation

The energy consumption management problem is formed as an MILP model and the relevant constraints include equipment capacity constraints, energy demand constraints and electrical/thermal storage constraints. The main constraints involved are:

3.1. Energy balances

The electricity demand is fulfilled by the electricity generated by CHP generator, electricity received from the electrical storage and grid minus electricity sent to the electrical storage and grid.

$$\sum_{j}\sum_{i}\sum_{\theta=0}^{p_{ji}-1} C_{i\theta}E_{ji,t-\theta} = u_t + y_t - z_t + I_t \qquad \forall\, 0 \le t \le T \tag{5}$$

The heat demand is fulfilled by the heat generated from the CHP generator, boiler, heat received from the thermal storage minus heat sent to the electrical storage.

$$H_t = \alpha u_t + x_t + f_t - g_t \qquad \forall\, 1 \le t \le T \tag{6}$$

3.2. Starting time and finishing time

The operation of each task must start after the given earliest starting time and finish before the latest ending time. For each task from each home, it has to be started once.

$$\sum_{t} E_{jit} = 1 \qquad \forall j,i,T_{ji}^{S} \le t \le T_{ji}^{F} - P_{ji} \tag{7}$$

3.3. *Objectives*

The first objective is to minimise the total daily electricity cost, which includes: the operation and maintenance cost of the CHP generator, electrical storage and thermal storage; and the cost of electricity purchased from the grid.

$$\phi_1 = \sum_{t}[\delta(r/\alpha u_t + b_t I_t + r/\beta x_t + \mu^E y_t + \mu^T f_t)] \tag{8}$$

The other objective is to minimise the total CO_2 emissions, which includes: the CO_2 emissions from the CHP generator, grid electricity and boiler.

$$\phi_2 = \sum_t [\delta(\xi^{CHP} u_t + \xi_t^G I_t + \xi^B x_t)] \quad (9)$$

The above two objective functions are considered in a multi-objective formulation as

$$\underset{x \in Q}{Min}\{\phi_1(x), \phi_2(x)\} \quad (10)$$

where x is the vector of decision variables and Q is the space of feasible solutions.

3.4. The ε-constraint method with two objectives

Applying the ε-constraint to the proposed multi-objective problem $\underset{x \in Q}{Min}\{\phi_1(x), \phi_2(x)\}$ it keeps ϕ_1 as the objective function, while ϕ_2 is considered as a constraint. A single-objective function is obtained as:

$$\min_{x \in Q} \quad \phi_1(x) \quad (11)$$

s.t. $\phi_2(x) \le \varepsilon_2$

The multi-objective problem is formulated as an MILP model by the ε-constraint method.

4. Illustrative example

The energy consumption scheduling MILP model is implemented on an illustrative example with a smart building of 30 homes with same living habits as given in (Zhang et al. 2013), where 12 domestic electricity consumption tasks are provided with their flexible time-window and processing time. The installed DERs and their capacities are:

- one CHP generator with a capacity of $20kW_e$ and its electrical efficiency is 40%, heat to power ratio is 1.2, and natural gas cost is 2.7 *p/kWh*;
- one boiler with capacity of 120 kW_{th} and efficiency is 85%;
- one electrical storage unit with a capacity of 10 kW_eh; the charge/discharge efficiency is 95%, discharge limit and charge limit are both $10kW_e$, and the maintenance cost is 0.5 p/kWh_e;
- one thermal storage unit with a capacity of 20 $kW_{th}h$; the charge/discharge efficiency is 98%, discharge limit and charge limit are both 20 kW_{th}, and the maintenance cost is 0.1 p/kWh_{th};
- a grid connection for electricity importation.

CO_2 emission rates from CHP and Boiler operation are given in Table 1. They are generated as the results of the LCA, which has been performed using GaBi 6.0 sustainability software. The total heat demand profile is provided as a building with floor area of 2500m^2 on a sample summer day for UK using CHP Sizer Version 2 Software. Profiles of electricity tariff and CO_2 intensity are shown in Figure 1. The MILP model is implemented using CPLEX 12.4.0.1 in GAMS 23.9 on a PC with an Intel(R) Core(TM) i7-4770 CPU, 3.40 GHz CUP and 16.0 GB of RAM. There are 1,179 equations, 17,815 continuous variables and 17,280 discrete variables and for each run it takes about 0.15*s* CUP time.

Table 1 CO_2 emissions from CHP and Boiler for Ireland and UK

	Natural gas supply	Direct emissions	Total
CHP (*kg CO_2 eq/kwh* electrical output)	0.0396	0.5049	0.5445
Boiler (*kg CO_2 eq/kwh* thermal output)	0.0186	0.2923	0.3109

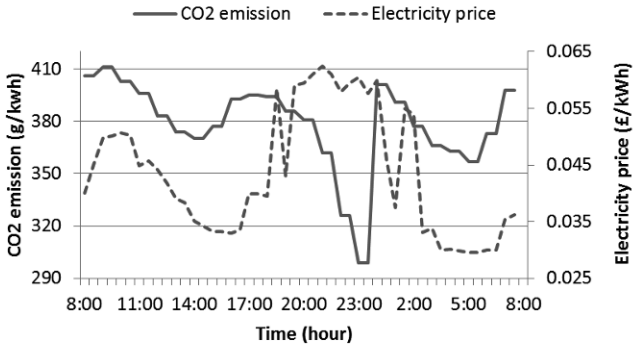

Figure 1: Electricity tariff and CO_2 intensity of UK for Aug 17th, 2013 (Balancing Mechanism Reporting system, 2014 and Earth Notes, 2014)

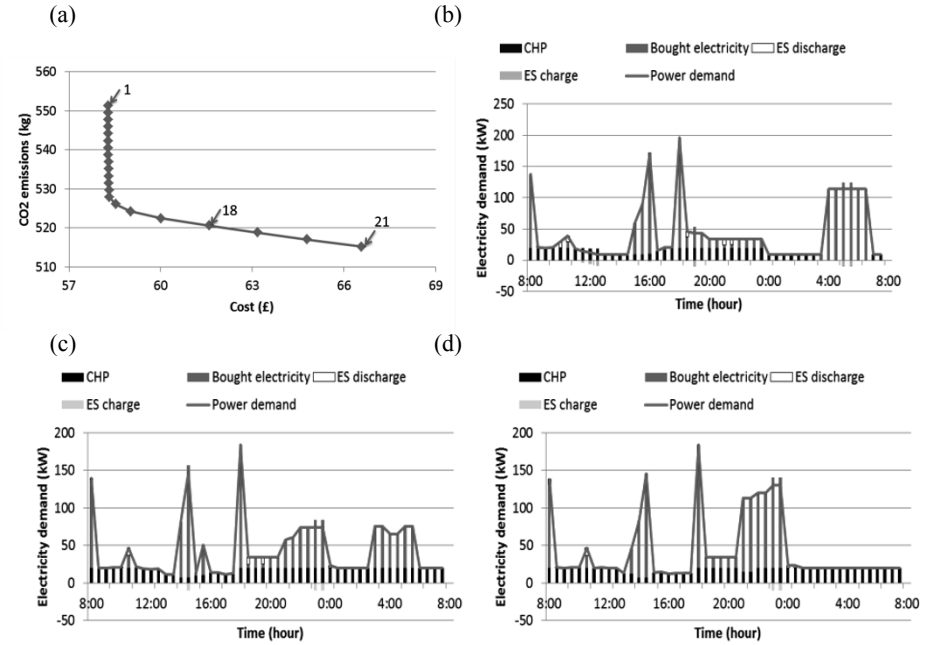

Figure 2: (a) Pareto curve for cost and CO_2 emissions and (b-d) electricity balances for points 1, 18 and 21

Figure 2 presents the optimal results and the Pareto curve for cost and CO_2 emissions is given in sub-figure (a). The differences between the maximum and minimum values for cost and CO_2 emissions are 12.5% and 7.0% individually. Since 20 intervals between the maximum and minimum values are considered in this example, there are 21 points in the curve. For the first 15 points, CO_2 emissions decrease dramatically from 552 to 525 kg while the cost difference is about £1. After point 15, it drops gradually to 515kg by point 21. Sub-figure (b)-(d) present the energy balances of the three points marked in sub-figure (a), points 1, 18 and 21. For point 1 and 21, the cost and CO_2 emissions are minimised individually without considering the other aspect, while point 18 gives the optimal scheduling based on the trade-off between the two conflicting objectives. The electricity peak hours of point 1 appear in the early morning where electricity tariff is low as shown in Figure 1. On the other hand, the electricity peak hours for point 21 are

in the night where CO_2 emission intensity is low. The peak hours move to the midnight to have a trade-off between the two objectives for point 18. CHP generator is not operated constantly mainly because of the low heat demand in summer and CHP cannot provide more electricity unless the corresponding heat generation can be consumed or stored in thermal storage. Thermal storage works here to balance the CHP generation over the day but still it cannot store heat more than its designed capacity.

5. Concluding remarks

An MILP model has been proposed to schedule the energy consumption within smart homes with microgrid on a daily basis to obtain the daily schedule. Both environmental emissions and economic cost can be minimised with trade-off between them by a multi-objective optimisation with ε-constraint method. The model has been implemented on an illustrative example for UK, where twelve domestic electrical tasks are scheduled together with DER operation in the shared microgrid. The obtained Pareto-optimal curve between cost and CO_2 emissions can provide guidelines for the customers and authorities to decide demand side energy management and DER operation. Also, scheduling of the DER operation and electrical tasks depend heavily on the energy demand patterns.

Acknowledgements

Authors gratefully acknowledge financial support from Qatar National Research Fund.

Notations

Indices

i	tasks
j	homes in the smart building
t	time interval
θ	task operation period

Parameters

b_t	electricity price at time t (£/kWh_e)
$C_{i\theta}$	power consumption capacity of task i at operation period θ (kW_e)
C	capacity of boiler (B), CHP generator (CHP), electrical storage (E) and thermal storage (T)
H_t	heat demand at time t (kW_{th})
P_{ji}	processing time of home j task i
r	price of natural gas (£/kWh)
T_{ji}^S	earliest starting time of home j task i
T_{ji}^F	latest finishing time of home j task i
α	CHP heat-to-power ratio
δ	time interval duration (*hour*)
μ	cost per unit input (maintenance) for electrical storage unit (E), thermal storage unit (T) (£/kWh)
η	efficiency of boiler (B), CHP generator (CHP), electrical storage (E) and thermal storage (T)

ξ CO_2 intensity of boiler thermal output (B), CHP electrical output (CHP) and grid electricity (*kg CO_2/kWh*)

Variables

f_t thermal storage discharge rate at time t (kW_{th})

g_t thermal storage charge rate at time t (kW_{th})

I_t electricity imported from the grid at time t (kW_e)

S^{IE} initial state of electrical storage (kWh_e)

S^{IT} initial state of thermal storage (kWh_{th})

S_t^E electricity in storage at time t (kWh_e)

S_t^T heat in storage at time t (kWh_{th})

u_t electricity output from CHP generator at time t (kW_e)

x_t heat output from boiler at time t (kW_{th})

y_t electrical storage discharge rate at time t (kW_e)

z_t electrical storage charge rate at time t (kW_e)

ϕ_1 daily electricity cost of a home (£)

ϕ_2 daily CO_2 emissions (*kg CO_2*)

Binary Variables

E_{jit} 1 if home j task i is done at time t, 0 otherwise

References

Balancing Mechnism Reporting System, 2014, http://www.bmreports.com/.

K. Baraka, M. Ghobril, S. Malek, R. Kanj, A. Kayssi, 2013, Low cost Arduino/Android-based energy-efficient home automation system with smart task scheduling, Computational Intelligence, Communication Systems and Networks (CICSyN), 296-301.

CHP Sizer Version 2, 2004, AEA Technology plc. London, UK: The Carbon Trust

O. Derin and A. Ferrante, 2010, Scheduling energy consumption with local renewable micro-generation and dynamic electricity prices, Proceedings of the First Workshop on Green and Smart Embedded System Technology: Infrastructures, Methods and Tools, 1-6.

Earth Notes, 2014, A Note On Variations in UK/GB Grid Electricity CO_2 Intensity with Time, http://www.earth.org.uk/note-on-UK-grid-CO2-intensity-variations.html.

D. Fuselli, F. De Angelis, M. Boaro, S. Squartini, Q. Wei, D. Liu, et al., 2013, Action dependent heuristic dynamic programming for home energy resource scheduling, International Journal of Electrical Power & Energy Systems, 48, 148-160.

S. Kin Cheong, M. Kordel, J. Wu, H. Sandberg, K.H. Johansson, 2013, Energy and CO_2 efficient scheduling of smart home appliances, Control Conference (ECC), 4051-4058.

N. Lior, 2010, Sustainable energy development: The present (2009) situation and possible paths to the future, Energy, 35, 3976-3994.

PE International: GaBi sustainability software, 2013, http://www.gabi-software.com/uk-ireland/software/gabi-software/.

M. Rastegar, M. Fotuhi-Firuzabad, F. Aminifar, 2012, Load commitment in a smart home. Applied Energy, 96, 45-54.

D. Zhang, N. Shah, L.G. Papageorgiou, 2013, Efficient energy consumption and operation management in a smart building with microgrid, Energy Conversion and Management, 74, 209-222.

Krist V. Gernaey, Jakob K. Huusom and Rafiqul Gani (Eds.), 12th International Symposium on Process Systems Engineering and 25th European Symposium on Computer Aided Process Engineering.
31 May – 4 June 2015, Copenhagen, Denmark

Optimization of Pressure/Vacuum Swing Adsorption with Variable Dehydration Levels for Post Combustion Carbon Capture

Karson T. Leperi, Randall Q. Snurr, Fengqi You

Northwestern University, 2145 Sheridan Road, Evanston, IL, 60208 United States

Abstract

In this paper we address the design and optimization of a pressure/vacuum swing adsorption (P/VSA) process for the post combustion capture of CO_2. HKUST-1, Ni/DOBDC, zeolite 5A and zeolite 13X are considered as potential adsorbents for the P/VSA system. A detailed simulation is set up and then optimized using a nondominant sorting genetic algorithm. This is coupled with an upstream dehydration unit to allow the impact of the presence of water to be analysed. The results show that for both the dry and wet flue gas, zeolite 13X has the lowest overall cost for capturing CO_2, with a cost of \$22.91 / ton of CO_2 captured and \$23.38 / ton of CO_2 captured, respectively.

Keywords: P/VSA, Metal-organic framework, carbon capture.

1. Introduction

In 2010, 30.6 gigatons of CO_2 were emitted into the atmosphere worldwide, with around 38% of the emissions in the US coming from the generation of electricity (IEA 2011). To reduce these emissions, there are substantial efforts to develop renewable energy technologies with minimal net carbon emissions. However, over the next few decades, fossil fuels will continue to play an important role in our energy mix (Anderson et al., 2004). There is, therefore, significant interest in reducing the CO_2 emissions from existing power plants via Carbon Capture and Storage (CCS). For post-combustion CCS, the processes most suitable are absorption (Rao et al., 2002), membranes (Ho et al., 2008), algae (Gong et al., 2014), and adsorption (Haghpanah et al., 2013). Among them, Pressure/Vacuum Swing Adsorption (P/VSA) is perhaps the most promising due to its higher performance and lower energy requirements compared to the other technologies (Zhao et al., 2013). This has led to increased interest in P/VSA cycles for carbon capture. However, in the majority of recent publications, the inlet flue gas stream is assumed to be dried before the carbon capture process. In reality, flue gas from power plants is usually saturated with water, containing around 3-5 mol%.

There are a few studies that have examined the use of P/VSA for carbon capture from wet flue gas. Li et al. (2008) experimentally demonstrated the effect of water on the performance of a VSA process for carbon capture. The VSA process used zeolite 13X as the adsorbent and consisted of three steps: pressurization, adsorption with the feed gas, and counter-current evacuation. With dry flue gas, the process achieved a recovery of 78.5% and a purity of 69%, with a column productivity of 0.287 kg/hr/kg. When wet flue gas was used, the recovery dropped to 60.4%, the productivity dropped to 0.225 kg/hr/kg, and the purity rose to 72%. This drop in performance was due to water adsorbing on the zeolite, reducing the CO_2 capacity of the adsorbent. In a follow up study, Li et al. (2014) examined the use of a layered bed using zeolite 13X along with

F200 and CDX activated alumina as the desiccant. With the layered bed, they were able to achieve a CO_2 purity of 74.8% and a recovery of 77.6%.

The effect of water on the performance of a VSA process through an optimization perspective has been studied by Krishnamurthy et al. (2014). In their work, they studied the effect water had on the performance of a 4 step VSA process with zeolite 13X. They showed that although the process was still able to achieve the overall goal of 95% purity and 90% recovery, the water increased the energy consumption to 230 kWh/ton and reduced the productivity of the bed to 1.03 ton/m^3/day. This is compared to the dry flue gas case, where the energy consumption was 154 kWh/ton and the productivity was 1.52 ton/m^3/day. They then examined a new two-bed, dual adsorbent process. The first bed contained silica gel and dehydrated the flue gas before feeding the product to the second bed containing zeolite 13X. With this configuration, they were able to achieve a minimum energy consumption of 177 kWh/ton and a productivity of 1.29 tons/m^3/day.

In all of these studies, zeolite 13X has been the adsorbent of choice. However, there exist hundreds, if not thousands, of potential of adsorbents, particularly given the recent development of metal-organic frameworks (MOFs). Recently, Liu et al. (2012) showed that the MOFs Ni/DOBDC and HKUST-1 are able to maintain their CO_2 uptake over a larger range of water loadings when compared to zeolites 13X and 5A.

In this work, we propose an integrated process for the capture of CO_2 from wet flue gas incorporating a dehydration unit, the P/VSA process, and a post-capture compression process to prepare the product for pipeline transportation. In order to overcome the limitations of the Skarstrom cycle, we use a two stage process to achieve the purity and recovery goals of CCS (see Figure 1). This process is then optimized to minimize the total cost, while maintaining the purity and recovery goals. HKUST-1, Ni/DOBDC, zeolite 13X, and zeolite 5A, are evaluated as adsorbents to determine the ideal material for obtaining the lowest overall cost of carbon capture. Three case studies are presented. The first case study determines the maximum purity each material can achieve in a single stage and is used to rank the performance of the materials. The second and third case studies use two stage processes to determine the minimum cost for dry and wet flue gas, respectively.

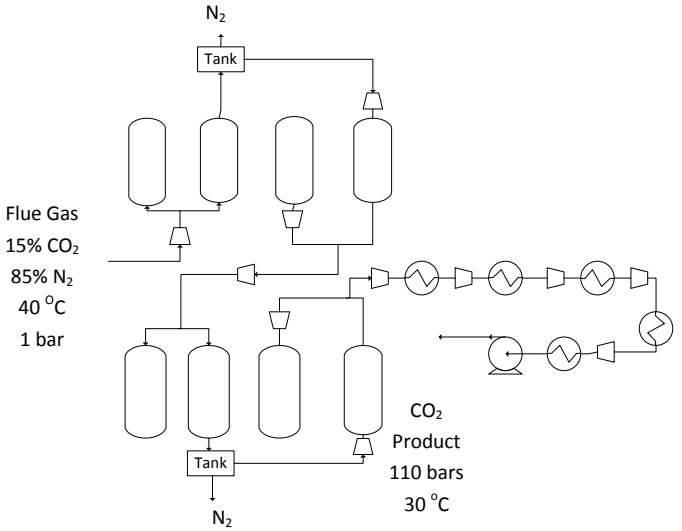

Figure 1. Two-stage P/VSA process coupled with post capture pressurization process.

2. Problem Statement

In this work, we focus on minimizing the total cost of capturing CO_2 from the flue gas of a 30 MW coal power plant. The overall process includes a dehydration unit, the P/VSA process, and a pressurization process. The feed gas is assumed to have a flow rate of 1 kmol/s and to be composed of 15% carbon dioxide, 5.5% water, and the balance nitrogen. This corresponds to the emissions from a 30 MW power plant. While minimizing the cost, the P/VSA process is required to obtain the DOE goals for carbon capture of purifying the flue gas to 90% CO_2 while recovering 90% of the CO_2 fed into the process. For the wet flue gas case study, the 90% purity is on a dry basis.

3. Process Simulation & Optimization

The model is composed of three parts: the process model for the dehydration unit and the post-capture compression, and the mathematical models for the P/VSA process. In all sections, annualized total cost for the system is defined as the sum of the operating costs and the annualized capital costs. The annualized capital cost is the sum of all bare module costs for all equipment multiplied by the capital recovery factor in addition to maintenance costs. The maintenance costs are taken to be 5% of the purchase cost of the equipment. For all equipment, the interest rate is taken as 10% and the life span is 20 years.

3.1. Dehydration Units

Two dehydration technologies were developed: Triethylene glycol (TEG) absorption and cooling and condensation (C&C). In TEG absorption, the flue gas is dehydrated by bringing it into contact with TEG. The TEG is then regenerated through distillation. In C&C, the flue gas is chilled through a refrigeration cycle incorporating Refrigerant-152a. In the cooling process, a portion of the water condenses, which is then separated from the flue gas. At lower levels of dehydration, the C&C is cheaper due to lower capital costs compared with TEG absorption. However, at higher levels of dehydration, the TEG absorption becomes the cheaper technology due to the lower operating costs. It was determined that the water level at which the two technologies are economically equivalent is 0.7 mol% water. Above this value, cooling and condensing is used, while below it TEG absorption is used.

3.2. Material Selection

For this work, four materials were initially evaluated for their potential as CO_2 adsorbents: HKUST-1, Ni/DOBDC, zeolite 5A, and zeolite 13X. For each of these materials, the CO_2 isotherm from the literature was fitted to a dual-site Langmuir model, and the N_2 isotherm was fitted to a single-site Langmuir model. For the wet flue gas case, it was also necessary to have an equation to represent the effect of water on the adsorption of CO_2 and N_2. This adsorption data was taken from the work of Liu et al. (2012). The reduction in CO_2 adsorption based on the adsorbed amount of water was fitted to an exponential function. It was assumed that the decline in performance of the material was only a function of the loading of water on the material. It was also assumed that the N_2 loading experienced a similar reduction as CO_2. For economic calculations, the life time of the adsorbent is assumed to be 5 years.

3.3. P/VSA Process

Except for the determination of the effect of water on the adsorption of CO_2, all of the governing equations, boundary conditions and bed connection equations are the same as in our previous work (Leperi et al., 2014). For determining the effect of water on the performance, both the water isotherm and the reduction in CO_2 uptake were necessary

for each material. Based on the water level in the flue gas, it was calculated how far into the column the water front would penetrate. The performance of the material behind the front was then reduced according to the concentration of water in the flue gas.
In order to solve the system of partial differential equations, they are first spatially discretized. A finite volume method is used to divide the column into 10 sections. The mid points are calculated through the Weighted Essentially Non-Oscillatory scheme (Haghpanah et al., 2013). This system of coupled ODEs is solved using solvers available in MATLAB. For the simulation of the P/VSA, it is assumed the bed is initially saturated with the flue gas. The simulation is then run, where the bed profile at the end of a cycle is the initial condition of the bed for the next cycle. This is repeated until the change in the bed profile between the beginning and the end of the cycle is less than 0.5%. At this point, the bed is assumed to be operating in a cyclic steady state, and the purity and recovery for the process are calculated.

3.4. Post_Capture Compression

For transportation through a pipeline network, it is necessary to compress the CO_2 product to 110 bar. This is accomplished through a 5-stage compressor train with intercooling to compress the stream to 90 bar. At 90 bar, the gas is then cooled and condensed at 22^{o}C. Once the CO_2 is condensed, the stream is then pressurized to 110 bar using a pump.

3.5. Solution Strategy

In order to perform multi-objective optimization on the P/VSA simulation, a nondominant sorting genetic algorithm (NDSGA-II) is employed. For the first case study, the population was set to 40, and the genetic algorithm (GA) was run for 60 generations. For the dry and wet case studies, the population was set to 50 and 55, respectively, and this was run for 100 generations.

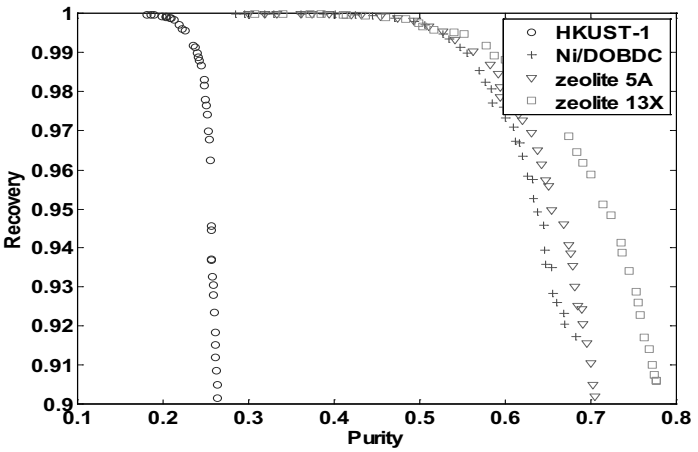

Figure 2. Pareto curves for multi-objective optimization of purity and recovery.

4. Results

4.1. Initial Material Testing

In the first case study, it was desired to determine if any of the materials were able to meet the goals in a single stage. It was also desired to determine if the material would be suitable for a two stage process. For this case study, the purity and the recovery of the

process were optimized for each material. The results from this case study are shown in figure 2.

None of the materials are able to achieve the desired goals of 90% purity and 90% recovery with a single-stage Skarstrom cycle. Thus, with the Skarstrom cycle, it is necessary to use two stages to achieve the purity and recovery goals. It is also apparent that HKUST-1 is the worst performing material of the group, being unable to purify the CO_2 above 27% while maintaining high recovery. This is probably due to its low selectivity for CO_2 over N_2 compared to the other three materials, which were able to achieve over 65% purity in a single stage while maintaining a high recovery. For the case studies below, HKUST-1 was not examined due to its poor performance in a single stage.

4.2. Dry Flue Gas

In this case study, a two stage process is used in order to obtain the desired purity and recovery for CCS. The dry flue gas was assumed to contain 15% CO_2 and the balance N_2. The results from this case study are shown in table 1. From these results, it is apparent that zeolite 13X is the best performing material. Zeolite 13X is able to achieve the desired purity and recovery goals for $3.92 million per year, which is about $ 0.2 million per year less than zeolite 5A and 1.2 million per year less than Ni/DOBDC. When comparing the breakdown of the overall cost, it is apparent that the main difference between Ni/DOBDC and the zeolites is the capital cost. The capital cost of Ni/DOBDC is approximately $600,000/ year more expensive than for the zeolites. This is due to a higher estimated cost for the large scale production of the MOF compared to the zeolites, although it must be noted that this value has a large uncertainty.

4.3. Wet Flue Gas

The results of the wet flue gas case are shown in table 2. From these results, zeolite 13X is again the optimal material, able to capture the CO_2 for $4.08 million per year. For the wet flue gas case, there was no dehydration, with the optimal water level determined to be 5.5%. The capital costs and the post-capture compression costs are roughly equivalent to the dry flue gas case, but the operating costs do increase in the presence of water. This is due to a lower vacuum pressure needed for the depressurization step and purge step to compensate for the reduced performance of the material.

Table 1. Cost break down for minimum total cost for each material for dry conditions. All costs are given in $ million per year.

Material	P/VSA Operating Cost	P/VSA Annualized Capital Cost	Post-Capture Compression Cost	Total Cost
Zeolite 13X	1.45	0.34	2.13	3.92
Zeolite 5A	1.48	0.37	2.32	4.17
Ni/DOBDC	1.95	0.95	2.34	5.24

5. Conclusion

In this paper, the capture of carbon dioxide from wet and dry flue was studied. A non-isothermal P/VSA simulation was used to conduct a GA-based optimization of the overall process. The results of the case studies revealed that the zeolite 13X was the top performing adsorbent among 4 materials studied and is able to capture CO_2 at a total cost of $22.91 / ton for the dry flue gas scenario and $24.02 / ton for the wet flue gas scenario. The results also showed that minimal dehydration occurred for the optimal results, with all three materials having dehydrated water levels above 5%.

Table 2. Cost break down for minimum total cost for each material for wet conditions. All costs are given in $ million per year.

Material	P/VSA Operating Cost	P/VSA Annualized Capital Cost	De-hydration Cost	De-hydrated Water Level	Post-Capture Compression Cost	Total Cost
Zeolite 13X	1.66	0.29	0	5.5%	2.13	4.08
Zeolite 5A	1.74	0.34	0.003	5.38%	2.34	4.42
Ni/ DOBDC	2.00	0.96	0	5.5%	2.38	5.34

Acknowledgements

This work was funded by the Global Climate and Energy Project.

References

S. Anderson, R. Newell, 2004, Prospects for carbon capture and storage technologies. Annual Review of Environment and Resources, 29, 109-142.

J. Gong, F. You, 2014, Optimal design and synthesis of algal biorefinery processes for biological carbon sequestration and utilization with zero direct greenhouse gas emissions. Industrial & Engineering Chemistry Research, 53, 1563–1579.

J. Gong, F. You, 2014, Global Optimization for Sustainable Design and Synthesis of Algae Processing Network for CO2 Mitigation and Biofuel Production Using Life Cycle Optimization. AIChE Journal, 60, 3195-3210.

R. Haghpanah, A. Majumder, R. Nilam, A. Rajendran, S. Farooq, I. Karimi, M. Amanullah, 2013, Multiobjective Optimization of a Four-Step Adsorption Process for Postcombustion CO2 Capture via Finite Volume Simulation, Industrial & Engineering Chemistry Research, 52, 4249-4265

M. Ho, G. Allison, D. Wiley, 2008, Reducing the cost of CO2 Capture from flue gases using membrane technology, Industrial & Engineering Chemistry Research, 47, 1562-1568.

IEA, 2011, Prospect of Limiting the Global Increase in Temeprature to 2oC is Getting Bleaker, <http://www.iea.org/newsroomandevents/news/2011/may/name,19839,en.html>, [20 November 2014]

S. Krishnamurthy, R. Haghpanah, A. Rajendran, S. Farooq, 2014, Simulation and Optimization of a Dual-Adsorbent, Two-Bed Vacuum Swing Adsorption Process for CO2 Capture from Wet Flue Gas, Industrial & Engineering Chemistry Research, 53, 14462-14473

K. Leperi, H. Gao, R. Snurr, F. You, 2014, Modeling and Optimization of a Two-Stage MOF-Based Pressure/Vacuum Swing Adsorption Process Coupled with Material Selection, Chemical Engineering Transactions, 39, 277-282

G. Li, P. Xiao, P. Webley, J. Zhang, R. Singh, M. Marshall, 2008, Capture of CO2 from High Humidity Flue Gas by Vacuum Swing Adsorption with Zeolite 13X, Adsorption, 14, 415-422

G. Li, P. Xiao, J. Zhang, P. Webley, D. Xu, 2014, The Role of Water on Post Combustion CO2 Capture by Vacuum Swing Adsorption: Bed Layering and Purge to Feed Ratio, AIChE, 60, 2, 673-689

J. Liu, Y. Wang, A. Beninn, P. Jakubczak, R. Willis, M. LeVan, 2012, CO2/H2O Adsorption and Equilibrium and Rates on Metal-Organic Frameworks: HKUST-1 and Ni/DOBDC, Langmuir, 26, 17, 14301-14307

A. Rao, E. Rubin, 2002, A technical, economic, and environmental assessment of amine-based CO2 capture technology for power plant greenhouse gas control, Environmental Science & Technology, 36, 4467-4475.

M. Zhao, A. Minett, A. Harris, 2013, A Review of Techno-Economic Models for the Retrofitting of Conventional Pulverised-Coal Power Plants for Post-Combustion (PCC) of CO2, Energy and Enviromental Science, 6, 25-40

Krist V. Gernaey, Jakob K. Huusom and Rafiqul Gani (Eds.), 12th International Symposium on Process Systems Engineering and 25th European Symposium on Computer Aided Process Engineering. 31 May – 4 June 2015, Copenhagen, Denmark

A Drilling Scheduling Toolbox for Oil and Gas Reservoirs

M.S. Tavallali,[a*] F. Bakhtazma,[a] A. Meymandpour,[a] F. Sadeghi,[a] M. Hamed,[a] I.A. Karimi[b**]

[a] *Department of Chemical Engineering, Islamic Azad University, Shiraz Branch, Shiraz, Iran*

[b] *Department of Chemical & Biomolecular Engineering, National University of Singapore, 4 Engineering Drive 4, Singapore 117585*

[*] Corresponding author: E-mail sadegh@u.nus.edu

[**] E-mail cheiak@nus.edu.sg, Tel +65 6516 6359; Fax +65 6779 1936;

Abstract

Drilling scheduling is a challenging task with considerable financial impacts, for which we develop a nonconvex MINLP formulation in this study. We consider the dynamics of the system and well as the economic forecasts and constrains. We develop a toolbox using genetic algorithm and an industrial reservoir simulator to address this important problem. Our method provides detailed information for both short and long-term decisions. It determines the optimal drilling order, time and location, well types and hence the number of new injector and producer wells, and finally the production and injection flow rates. Our results indicate that we can decrease the rate of return (R.O.R) of an exploitation project by optimally scheduling the drilling activities.

Keywords: Drilling schedule, optimal well placement, genetic algorithm, MINLP

1. Introduction and background

As the industrial horizons are constantly advancing, the worldwide energy demand continues to remain as the prime concern. Amongst other resources, exploitation of oil and gas fields plays the paramount role in fulfilling the energy demand (Gupta and Grossmann 2012). This expensive and complex activity requires comprehensive study of the different technical and financial aspects to determine the most efficient production and expansion plan (Tavallali and Karimi 2014). The most risky and costly step is the drilling stage, where a well of few inches diameter should be drilled in a large formation for several kilometers to produce oil and gas (Tavallali et al. 2013). The technical issues are more pronounced when a drilling company needs to drill many wells in a limited time using a few number of drilling rigs. In such cases, complex financial and technical issues related to the subsurface and surface elements and energy market arises; in the heart of them is the drilling scheduling and placement problems (Afshari et al. 2011). These problems are inherently, dynamic, multi period, highly combinatorial and complex.

Apart from the fact that multiphase flow in the porous underground reservoirs is dynamic, drilling each well takes some time and that also adds to the dynamic features of drilling problems. Firstly, wells act as energy providers (injectors) or sinks (producers) in a field under injection drive mechanisms. Hence, their production

(injection) history or future plan can alter the ultimate hydrocarbon recovery from the field. Secondly, wells are not individual entities in a field with no interactions, and in contrast, they communicate through the fluid in the subsurface formation and even the surface network. Therefore, subsurface dynamics can change drastically when a new well is drilled. Unfortunately, predicting all these changes at the initial design stage is not a simple task; there are many nonlinearities with seen and unseen uncertainties (Wang et al. 2012). Clearly scheduling the drilling activities is of utmost importance in such stage. On one hand, the delay in drilling a well can increase the rate of return (R.O.R), and on the other hand, early drilling can add to the maintenance cost without production at the nominal level. Both of which can deteriorate the financial gains.
In the current research, we follow our previous studies (Tavallali et al. 2013, Tavallali et al. 2014) on a different track. In the remaining of this article, we formulate a deterministic drilling scheduling problem, and then employ an industrial reservoir simulator in a black-box optimization structure to develop a user-friendly toolbox. Afterwards we test our approach through a comprehensive case study and analyze its outcomes. Finally, we conclude the study with a concise discussion.

1.1. Problem Definition

A drilling project over a planning horizon of H years in an oil and gas field under water injection mechanism is to be optimally scheduled. The reservoir can be of any shape, and the target wells can be of any types. Here, the problem can be summarized as:
Given:
(1) The geological and petro-physical data of the reservoir and its fluids, (2) Operational data (including the BHP, THP, and throughput limits), (3) the production horizon, as well as economic forecast and number of available drilling rigs over this horizon, (4) a list of potential drillings and their well types.
Determine:
(1) The drilling schedule (where, when and what to drill), and (2) the flow rate plan at each wellhead.
Targeting to maximize the net present value (NPV).
By assuming:
(1) All given data are deterministic. For instance, number of drilling rigs can change over time; however, they should be scheduled from the beginning. (2) Each candidate well follows only one trajectory and does not intersect with other existing or potential wells. (3) No drilling is permitted in the last period of time horizon. (4) Each drilling does not take longer than a given time period.

2. Modeling

Layers related to perforation are predetermined so our variables are just for the top side of wells at the surface. Then this can include both deviated and vertical wells.
Let the time domain be discretized into T time periods of arbitrary length of Δh_t, and the spatial domain into the cubic cells of I, J and K numbers in x, y and z directions of Cartesian system with lengths of $\Delta x_i, \Delta y_j$ and Δz_i (i =1, 2, …, I, j =1, 2, …, J and k =1, 2, …, K). We combine the spatial indices into one index $n=i + (j\text{-}1)I + (k\text{-}1)IJ$. Each well is recognized by the cell at its bottom hole and its trajectory is fixed, therefore we can refer to the well with the wellbore at n cell as well n. We define the following two subsets:
IW=[n | injector well with the bottom hole at cell n]
PW=[n | producer well with the bottom hole at cell n]

2.1. Drilling decisions

We define the following two main binary variables

$$y_n^t = \begin{cases} 1 & \text{the well at cell } n \text{ is drilled at the end of period } t \\ 0 & \text{otherwise} \end{cases}$$

$$z_n^t = \begin{cases} 1 & \text{the well at cell } n \text{ can produce or inject at period } t \\ 0 & \text{otherwise} \end{cases}$$

Logical constraint**:** The above two binaries are tightly related to each other:

$$\sum_{t=0}^{t=t'-1} y_n^t = z_n^{t'} \qquad t' > 0 \qquad (1)$$

This ensures that a well cannot simultaneously be active and be at the drilling phase. Number of drilling is bounded with drilling rigs at each time step (DR^t):

$$\sum_n y_n^t \le DR^t \qquad t < T \qquad (2)$$

Drilling budget constraint: Drilling can only be done when the drilling budget DB^t can support the costs:

$$\sum_n y_n^t C_{d,n}^t \le DB^t \qquad t < T \qquad (3)$$

Where $C_{d,n}^t$ is the drilling cost of well n and might vary over depending on the time of drilling.

2.2. Flow management and well selection

The multiphase flow inside a reservoir is represented via partial differential equations that relate the phase flow rates to the reservoir dynamic variables (saturation, pressure and gas solubility). Due to their nonlinear and complex nature, they are usually solved numerically after they are converted to a set of algebraic equations. Let us refer to them as:

$$h_n^t(q_{o,n}^t, q_{g,n}^t, q_{w,n}^t, V_n^t, r_n) = 0 \qquad t > 0 \qquad (4)$$

where $q_{o,n}^t$, $q_{g,n}^t$ and $q_{w,n}^t$ are the oil and water flow rates from well n (They are rendered as zero for cells that are not existing or potential wells), and V_n^t shows other dynamic variables, and r_n shows system parameters (geological or petro-physical).

Well selection constraint: A well is active only if it is drilled beforehand (hence $z_n^t = 1$), and once active its total (oil + water + gas) flow rate cannot exceed an upper bound (Q_n^t):

$$0 \le q_{o,n}^t + q_{g,n}^t + q_{w,n}^t \le z_n^t Q_n^t \qquad (5)$$

Field-wide flow constraints: Field oil production and water injection cannot go beyond the available surface capacities (C_O^t and C_i^t respectively) for these fluids; furthermore, oil production cannot exceed the oil demand (D_O^t):

$$\sum_{n \in IW} q_{w,n}^t \le C_i^t \qquad t > 0 \qquad (6)$$

$$\sum_{n \in PW} q_{o,n}^t \le \min(C_O^t, D_O^t) \qquad t > 0 \qquad (7)$$

Although more capacity constraints for other producing phases are possible, here we only utilized the one for oil production.

Objective Function: Our objective function comprises the oil and gas selling profits and production and injection costs, and finally the drilling costs:

$$NPV = \Sigma_{t>0} \frac{\left\{\Sigma_{n\in PW}\left(q^t_{o,n}C^t_{o,n}+q^t_{g,n}C^t_{g,n}\right)\Delta h_t - \Sigma_{n\in PW}\left(q^t_{w,n}C^t_{w,n}\Delta h_t + y^t_n C^t_{d,n}\right)\right\}}{(1+\beta)^{h^t/365}} \quad (8)$$

Where $C^t_{g,n}$ and $C^t_{o,n}$ are the oil and gas (revenue – production cost) ($ per unit flow), and $C^t_{w,n}$ is the water injection / production cost ($ per unit flow), and β is the annual discount factor. This completes our MINLP model (**G**), which is nonlinear and nonconvex.

It is necessary to mention that our model can select the most promising candidates and reject the rest. Hence, it is a well placement and scheduling model.

3. Solution strategy and the toolbox

Reservoir simulators effectively solve the governing equations represented by eqn. (4) and are industrially accepted. Having access to the underlying codes and equations of the reservoir simulators can provide much flexibility. Unfortunately, it is not always the case. These simulators serve the best option for black-box optimization approach. Furthermore, Model (**G**) is a nonconvex model and hence is a good candidate for evolutionary solution methods. Hence, in this study we utilized ECLIPSE reservoir simulator of Schlumberger and linked that with genetic algorithm (GA) of MATLAB 2014 that could handle binary variables.

Using the nature of GA, we (1) limit the optimization variables to y^t_n only, and (2) divide the constraints into two parts: drilling and flow constraints. GA uses the drilling constraints to suggests a new individual (y^t_n), and we use eqn (1) to generate z^t_n. ECLIPSE is a script-based software, therefore we translate these binaries and the flow constraints into a set of software keywords. This determines the drilling schedule and prepares required script files to communicate with ECLIPSE. Once ECLIPSE simulates the dynamic production horizon, it returns $q^t_{o,n}$, $q^t_{g,n}$ and $q^t_{w,n}$. Afterwards MATLAB can use this information to calculate NPV. Then it follows the structure of evolutionary methods to declare the termination.

The user provides the reservoir simulation file (without the well control section), list of potential wells (with their trajectory and type) as well as parameters mentioned earlier. The rest is handled automatically.

In what follows we compare the efficiency of our toolbox with a built-in key word of ECLIPSE called QDRILL. QDRILL uses a list of potential wells and activates them sequentially once the targeted production is not met.

4. Example

A 2823m × 6502.4m × 5.56m anisotropic reservoir (with *I*=30, *J*=44 and *K*=1) has been producing oil and gas for the past 380 days. These geological data are obtained from a section of upscaled SPE10 (Christie and Blunt 2001). It has three active producers (P1-P3) and five injectors (I1-I5). Three new producers (NP1-NP3) and one new injector (NI1) are suggested to be drilled for the next 2160 days. We employed 18 periods of 120 days each. All wells are vertical and the drilling cost is considered as 0.3 M$ per well. Their drilling orders and flow rates should be determined.

We define four different scenarios: (1) base case: with no new drillings, (2) QDRILL: when this keyword of ECLIPSE is used and there are no restrictions on the minimum

well flow rates, (3) QDRILL_LB_Flow: similar to scenario 2, however with imposed lower bounds on the well flow rates (at least 20 m^3/day), and (4) optimization via GA. Table 1 summarizes the results.

Table 1. Comparison of the drilling scheduling scenarios

Scenario	Base case	QDRILL	QDRILL_LB_Flow	GA
NPV (M$)	7.131	6.934	6.540	7.340
Drillings	-	NP1-NP3 and NI1 (120 days)	NP1-NP3 and NI1 (120 days)	NP1 (120 days)

This table shows that our toolbox outperforms the other scenarios. The QDRILL could not even improve the base case. This keyword does not consider the drilling (and operation) costs and is activated whenever the production falls, hence is myopic and does not predict the future efficiently. Consequently, it has opened four wells in a same time. In contrast, our toolbox learns well from different solutions. It may even tolerate deviating from the maximum possible production for a period; however, it considers the overall NPV over the entire horizon. Hence has drilled only one well.

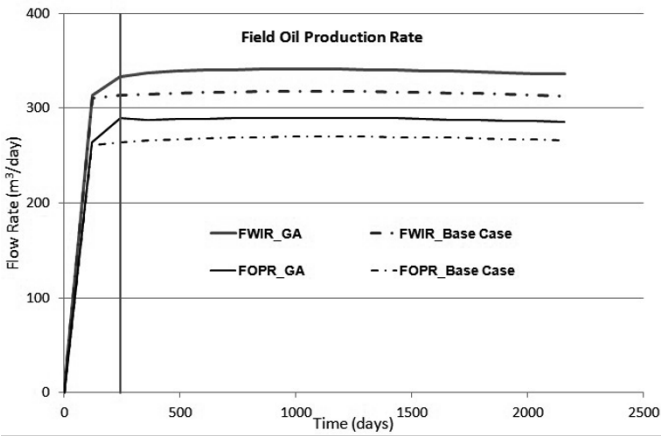

Figure 1: Field flow comparison between the base case and GA solution (FOPR: Field Oil Production Rate, and FWIR: Field Water Injection Rate), the vertical line shows the time of drilling NP1

Since the base case is in the second rank, we use that for the next detailed comparison with our solution. Figure 1 represents this comparison. Although our solution leads to higher field water injection rates, it also provides higher oil production rate. It reveals that our solution has instructed higher capital investment (a new drilling) and operation costs (higher injection cost); however, both orders have supported higher production and hence higher NPV. Clearly, this reduces the ROR of the project and motivates the drilling. This shows the utility of our toolbox.

5. Conclusion

In this study, we developed a versatile and novel toolbox based on the application of evolutionary method to help the management team with the drilling scheduling decisions. Not only it considers the subsurface dynamic, but also it analyzes the

economic concerns of the energy market. Hence, besides scheduling the drillings, it provides the throughput profiles. The case study clearly showed that our method could outperform an industrial software for the same purposes. The main reason is the differences in inspecting the time horizon. Ours considers the entire domain, and the numerical simulator packages inspects only one period at a time.

Our work tackled the large size problem of drilling scheduling by determining the time, location and type of new drillings. However, two concerns remains, one is the scalability of this approach, and the other is optimal planning of the flow rates (Bellout et al. 2012). The former is the nature of such dynamic and large size problems. We are currently addressing the latter.

Acknowledgments

Our collaborations and discussions with Mr. David Baxendale and Dr. Teo Kwong Meng have been very useful and have made indirect contributions to this article.

References

Afshari, S., B. Aminshahidy and M. R. Pishvaie (2011) "Application of an improved harmony search algorithm in well placement optimization using streamline simulation." Journal of Petroleum Science and Engineering DOI: 10.1016/j.petrol.2011.08.009.

Bellout, M. C., D. Echeverría Ciaurri, L. J. Durlofsky, B. Foss and J. Kleppe (2012). "Joint optimization of oil well placement and controls." Computational Geosciences 16(4): 1061-1079.

Christie, M. A. and M. J. Blunt (2001). Tenth SPE Comparative Solution Project: A Comparison of Upscaling Techniques. SPE Reservoir Simulation Symposium. Houston, Texas, Society of Petroleum Engineers.

Gupta, V. and I. E. Grossmann (2012). "An efficient multiperiod MINLP model for optimal planning of offshore oil and gas field infrastructure." Industrial and Engineering Chemistry Research 51(19): 6823-6840.

Tavallali, M. S. and I. Karimi (2014). Perspectives on the Design and Planning of Oil Field Infrastructure. Computer Aided Chemical Engineering. J. D. S. Mario R. Eden and P. T. Gavin, Elsevier. Volume 34: 163-172.

Tavallali, M. S., I. A. Karimi, A. Halim, D. Baxendale and K. M. Teo (2014). "Well Placement, Infrastructure Design, Facility Allocation, and Production Planning in Multireservoir Oil Fields with Surface Facility Networks." Industrial & Engineering Chemistry Research 53(27): 11033-11049.

Tavallali, M. S., I. A. Karimi, K. M. Teo, D. Baxendale and S. Ayatollahi (2013). "Optimal producer well placement and production planning in an oil reservoir." Computers & Chemical Engineering 55: 109-125.

Wang, H., D. E. Ciaurri, L. J. Durlofsky and A. Cominelli (2012). "Optimal well placement under uncertainty using a retrospective optimization framework." SPE Journal 17(1): 112-121.

Krist V. Gernaey, Jakob K. Huusom and Rafiqul Gani (Eds.), 12th International Symposium on Process Systems Engineering and 25th European Symposium on Computer Aided Process Engineering.
31 May – 4 June 2015, Copenhagen, Denmark

Preliminary analysis of systems for integrating solar thermal energy into processes with heat demand

Andreja Nemet[a], Jiří J. Klemeš[a], Zdravko Kravanja[b]

[a]*Centre for Process Integration and Intensification – CPI², Research Institute of Chemical Engineering MÜKKI, Faculty of Information Technology, University of Pannonia, 8200 Veszprém, Hungary*
[b]*Faculty of Chemistry and Chemical Engineering, University of Maribor, 2000 Maribor, Slovenia*

Abstract

The aim of this work was to develop a method for preliminary evaluation of the ratio between the investment and amount of solar thermal energy, integrated into processes with heat demands. A targeting method has been developed for maximising the amount of integrated thermal energy collected by the required size of solar collector surface area, as well as the size of heat storage. The size of the solar collector area and the heat storage is based on the number of consecutive sunny days and shady days. In the first step the data of the heat demands were collected that could be potentially satisfied from solar sources. In the second step the amount of heat per surface area unit was determined as gained during sunny days (area-specific heat). The collector system and geographical characteristics were taken into account when determining the amount of heat gained. The temperature driving forces were taken into account for heat exchanges between the solar collector medium and storage, and also between the storage and process demands. The required collector surface area has been defined as the heat demands for the sunny and shady days together divided by the product of the area-specific heat of a given collector and the number of sunny days at a given geographical location. The proposed targeting method can be applied for the pre-screening of alternatives in order to eliminate economically non-viable solutions before performing more detailed system synthesis. An illustrative case study has been performed in order to evaluate the applicability of the developed method.

Keywords: solar thermal energy, preliminary analysis, heat integration, storage capacity, solar panel, solar panel area.

1. Introduction

Compared to the annual worldwide energy consumption $5.35 \cdot 10^{11}$ GJ (BP, 2014), a vast amount of solar energy reaches the surface of the planet, $2.7 \cdot 10^{15}$ GJ (Smil, 2006). Despite the enormous differences in magnitude, and a wide-range of promising energy sectors (Lauterbach, 2014), only small amounts of energy demands are covered by solar energy, which indicates the complexity of integrating this type of renewable resource. An overview of the current state on solar collectors and thermal energy storage within solar thermal applications can be found in Tian et al. (2013). One of the major difficulties for solar integration is the fluctuations and the disparities of demand, and the solar irradiation, i.e. the available solar energy (Atkins et al., 2010). A state-of-art regarding the solar thermal technology and strategic research priorities can be found in European Technology

Platform on Renewable Heating and Cooling (2013). Nowadays numerous solar collectors with different characteristics and prices are available. Detailed analyses for all the available integration can be time and resource consuming. Therefore, a preliminary selection with preliminary assessment can decrease the resource requirements when the detailed planning of an energy system is performed only by focusing on potentially appropriate systems. Only those solar thermal integration systems that have promising ratios between the integrated amount of energy from solar source and investment should be considered for further planning.

2. Methodology

The integration system has two essential parts namely, the collector system and the storage. The aim of the first one is to produce as much heat as possible, whilst the second serves for storing heat for later usages, when there is no available energy from the solar source. The sizes of both should be planned carefully in order to allow the highest possible integration, yet still the sizes of both should be reasonable. The performance of the integration system would be affected by the days of sunny periods and days of shady periods. During the days of sunny periods the collectors' area should be large enough in order to gain the required amount of heat for both types of integrations: i) direct, during the sunny days and ii) indirect, during shady days and nights. The storage size should be high enough in order to cover the heat demand during shady day periods and for the nights, when no direct heat integration is possible due to the lack of solar irradiation.

2.1. Estimation of solar collector area

The ratio between the sunny days and consecutive shady days indicates the required speed of collecting the solar thermal energy in order to cover heat demand for this period. The solar collector area has been determined by the following steps:

Step 1. Determining the amount of heat demand within one day, which could be potentially covered by solar thermal energy. The limiting maximal temperature of capture should be taken into account in order to determine the potential heat enthalpy that can be covered by solar thermal energy $\Delta \dot{H}^{D\text{-}STE}$. The demands with higher temperature requirements will be covered by other external sources of energy. The potential amount of heat demand ΔQ_{ti}^{D-STE} that can be covered from solar thermal energy is determined by multiplying the enthalpy flow $\Delta \dot{H}_{ti}^{D-STE}$ by the time-horizon $t_{ti\text{-}1} - t_{ti}$ at each time interval separately by applying Eq. 1.

$$\Delta Q_{ti}^{D-STE} = \Delta \dot{H}_{ti}^{D-STE} \cdot \left(t_{ti\text{-}1} - t_{ti}\right) \tag{1}$$

Step 2. Determining the amount of heat potentially gained during a sunny day per unit of area. Calculating the amount of heat gained from solar source is based on average values. The data applied has been the average daily clear sky solar irradiation determined for each month separately. The sampling time of irradiation measurement has been short, usually around 15 min. The measurement of solar irradiation has been performed each day at the same time, therefore the starting and ending time boundaries of time intervals between two measurements are the same. The average of the irradiations of all of the months is determined within each time interval for obtaining the annual representative sunny day. The same procedure is applied when determining average ambient temperature within a time interval in order to obtain temperature profile of an annual representative sunny day. The amount of heat gained per unit of the solar thermal collector can be determined from the determined representative sunny day for clear sky daily irradiation. The captured amount of heat is firstly determined within each time interval separately and then summed-up over the whole day. The amount of heat from solar source within each time

interval is defined by applying Eq. 2, where ΔQ_{ti} is the amount of heat gained within time interval t_i, where A is the area of the solar collector, G_{ti} is the averaged solar irradiation of clear sky within the time interval, η_0 optical efficiency, a_1 and a_2 are thermal loss coefficients for the solar collector system, $T^{C,in}$ the inlet and $T^{C,out}$ the outlet temperatures of the media flowing through the collector system, T_{ti}^{A} is the average ambient temperature within t_i, with $t_{\text{ti-1}}$ and t_{ti} being the time boundaries of the time interval.

$$\frac{\Delta Q_{ti}^{\text{STE}}}{A} = \bar{G}_{ti} \cdot \left(\eta_o - \frac{a_1 \left(\frac{T^{C,out} + T^{C,in}}{2} - T_{ti}^{A} \right) + a_2 \left(\frac{T^{C,out} + T^{C,in}}{2} - T_{ti}^{A} \right)^2}{\bar{G}_{ti}} \right) \cdot \left(t_{\text{ti-1}} - t_{\text{ti}} \right) \tag{2}$$

Step 3. Determining the required amounts of heat that should be collected during one sunny day in order to cover all the demands set within Step 1

This calculation is based on the number of consecutive sunny and shady days. The ratio $n^{\text{all/sun}}$ between all days n^{all} (sunny and shady days together) and the number of sunny days n^{sun} is determined in order to obtain information about the number of days of heat demand for which the heat should be collected within one day. For example, if the design is made typically for two sunny days followed by three shady days, the solar thermal energy integration system should ensure enough heat for five days demand. However, as there are only two sunny days available for gaining the solar thermal energy, the solar collector system should be able to collect heat demand for $n^{\text{all/sun}}$ =5/2 = 2.5 days (Fig. 1).

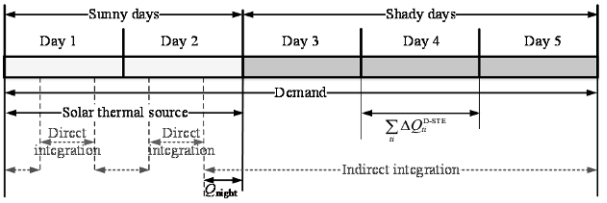

Figure 1: Basis for determining a solar thermal collector's area

Step 4. Determining the solar collection area

The solar collection area requirement can be set after the heat requirement is determined regarding the amount of heat collected during one sunny day. The area calculation is established by calculating the ratio between heat that should be collected during one sunny day and the average amount of heat potentially collected during one sunny day per unit of area (Eq. 3), multiplied by the ratio $n^{\text{all/sun}}$:

$$A^{SC} = \frac{\sum_{ti} \Delta Q_{ti}^{D-STE}}{\sum_{ti} \frac{\Delta Q_{ti}^{\text{STE}}}{A}} \cdot n^{\text{all/sun}} \tag{3}$$

2.2. Estimation of storage size requirement

Another essential part of the integration system is the storage. The estimation of the storage size is based on the previously developed approach of consecutive numbers of sunny and shady days. The storage capacity should be large enough to cover heat requirements for all of the shady days expected plus the night Q_{night} of the last sunny day, which cannot be covered by direct integration of solar thermal energy. Additionally, the heat losses should also be considered for the time period of storing the heat. Therefore, the storage size is determined from Eq. 4, where Q_{st} is the amount of heat that needs to be stored, t_{sh}^{D} is the number of consecutive shady days, t^{sun} is the number of sunny days, and $Q_{oss,day}$ is the average heat loss during one day.

$$Q_{st} = t_{sh}^{D} \cdot \Delta Q_{ti}^{D-STE} + Q_{night} + \left(t_{sh}^{D} + t^{sun}\right) \cdot Q_{loss,day} \tag{4}$$

A cascade for heat demand excluding the demand covered by direct integration of solar thermal energy has to be performed in order to determine the amount of heat required during a sunny day. Therefore, the amount of heat stored during a sunny day can also be observed. Based on this observation, the maximal heat capacity of the storage during a sunny day can be determined. This capacity has to be ensured, additionally to the capacity required for shady days. Therefore, the size of the storage should be increased by this required capacity. In addition to process demand, the preliminary calculation of storage vessel surface area is required in order to determine the heat loss during a day. The storage size depends on the amount of heat stored, the specific heat and temperature ranges of the media within the storage. The storage size is initially determined without considering heat loss. The heat losses can be determined after obtaining the initial surface area of the storage. When heat losses are available, the storage size estimation is performed again, with the amount of heat demand being increased by the amount of heat loss (Eq. 5).

$$V_{st} = \frac{t_{sh}^{D} \cdot \Delta Q_{ti}^{D-STE} + \left(t_{sh}^{D} + t^{sun}\right) \cdot Q_{loss,day} + Q_{night}}{cp \cdot \rho \cdot \left(T^{s,up} - T^{s,lo}\right)} = \frac{Q_{st}}{cp \cdot \rho \cdot \left(T^{s,up} - T^{s,lo}\right)} \tag{5}$$

3. Illustrative Case study

3.1. Estimation of solar collection area

Step 1. For calculation of potentially covered heat demand the solar collector system's upper and lower temperatures should be specified, in this case study between 80 and 120 °C.

Table 1: List of streams after heat recovery as input data (after Perry et al., 2008)

Stream	Temperature, °C		ΔH,	Type	CP,	Time interval	
	Supply	Target	kW		kW/°C	Start, h	End, h
Sanitary water 1	25	55	17.3	Cold	0.576	20	24
Laundry	55	85	18	Cold	0.600	20	24
BFW	33	60	12	Cold	0.446	0	24
Sanitary water 2	25	60	15	Cold	0.429	6	17
Sterilisation	82	121	34.1	Cold	0.874	20	24
Swimming pool water	25	28	23.1	Cold	7.700	6	15
Cooking	80	100	32	Cold	1.600	6	20
Heating	18	25	41.1	Cold	5.864	0	24
Bedpan washers	21	121	5	Cold	0.050	6	17
Space heating	15	25	88	Cold	8.800	0	24
Hot water base	15	45	25	Cold	0.833	0	24
Hot water day	15	45	65	Cold	2.167	6	20

Only one heat transfer is performed when the direct way is used, whilst for indirect heat integration the heat transfer is done twice. For targeting purposes the indirect heat transfer is considered, therefore the minimal temperature difference required for feasible heat exchange is considered twice. In this case study the required minimal temperature difference was assumed to be 10 °C for both heat transfers. Therefore, the maximal outlet temperature from the collector was 120 °C and from the storage 110 °C. Using the stream from storage a heat demand at 100 °C can be covered. Whilst the demand that could be potentially covered from the solar source of energy directly was set at 110 °C.

The heat demands below 90 °C can be covered by solar thermal energy in order to ensure the required temperature difference between the supply stream and demand. After obtaining the potential enthalpy flow-rate within each Time Slice separately, the amount of heat that can be covered from a solar source of energy can be determined by Eq. 1. Table 2 presents the solution for Time Slices separately and the sum. As can be seen in Table 2, the amount of heat that can be potentially covered from the solar source of energy is 5,765.4 kWh, and it represents 95.4 % of all demands for a day, which is 6,040.9 kWh.

Table 2: Determining the amount of heat demand that can be potentially covered by solar source

	TiSl/h				
	0-6	6-15	15-17	17-20	20-24
H^{STE} /kW	166.1	295.9	265.6	247.1	208.4
Q^{STE} /kWh	996.5	2,663.1	531.1	741.2	833.4
				Total	**5,765**

Step 2. The average potential of gaining heat within one day is determined based on an inlet temperature of the collector at 80 °C and the outlet temperature of the stream from the collector at 120 °C. The amount of heat gained during each time interval can be determined. After determining this amount of heat within each time interval separately by Eq. 2, it is summed up over a whole day. The data for solar irradiation was taken from GeoModel Solar (2014) for Veszprém, Hungary. The daily amount of heat gain during a typical sunny day is 3.12 kWh/m^2.

Step 3. When observing the data of sunny and consecutive shady days (e.g. Eumet, 2014-Siófok station) it could be seen that the more common ratio $n^{all/sun}$ is usually between 1.25 (representing four sunny days and one shady day) and 3 (which represents one sunny day followed by two shady days). Therefore, different scenarios are considered in the following analysis. It should be noted that the higher is the ratio $n^{all/sun}$ the larger is the solar collector area requirement. Therefore, for the final decision about the solar collection size (and consequently also the storage size) a trade-off between the number of shady days covered from solar source and the required investment has to be taken into account.

Step 4. The final solar collection area is determined for three different ratios $n^{all/sun}$, namely for 1, 2 and 3 (Table 3). The first results present the area requirements if no heat is stored for shady days.

Table 3: Required area of solar collectors for different time periods of storage

Ratio	1 d	2 d	3 d
A^{SC}/ m^2	1,853.8	3,707.7	5,561.5

3.2. Estimation of storage size

The storage sizes were determined for three different time periods of storing heat. The temperature range of the storage operation was assumed to be between 70 and 110 °C. The heat demand that can be covered from a solar source of energy during one day had already been determined and was 5,765.4 kWh. The amount of directly-integrated solar thermal energy should be evaluated in order to enable further steps when estimating storage size. The required enthalpy flow from storage ΔH_{STE} for covering the heat demand during sunny days was determined as the difference between the required enthalpy flow and the direct enthalpy flow from solar collectors. The required amount of heat ΔQ_{STE} could be obtained by multiplying the enthalpy flow and the time horizon of the interval. For the heat demand, which cannot be covered from solar sources of energy, a constant available utility ΔH_{HU} should be utilised. The initial volume of storage V^{init} is firstly determined where the heat losses are neglected. The surface area of storage is determined with considering a cylinder shape with radius 2.5 m and the height determined from the

initial volume. However, as the heat is stored within all sunny days and all shady days, therefore, the total heat loss for different scenarios is determined by multiplying the heat loss over one day by the number of all days. Finally, the storage volume V^{st} is determined by also considering the heat losses. A comparison between initial and final storage is made, and as can be seen the difference can be up to 5.664 m^3 (2 %).

Table 4: Determining storage size

	1 d	2 d	3 d
V^{init}/m^3	107.46	189.82	272.18
A^{st}/m^2	125.21	191.10	256.99
Q^{loss_1day}/kWh	64.384	98.2657	132.1465
Q^{loss_tot}/kWh	128,768	294,7971	528,586
V^{st}/m^3	108.374	192.625	277.844
V^{st}- V^{init}/m^3	0,914	2,805	5.664

4. Conclusions

The methodology presented in this paper can be applied for preliminary analysis of the available collector systems in order to perform the selection of potentially promising systems that should be further analysed in detail. The analysis is simple enough and can be performed quickly. The methodology has been tested on an illustrative case study. Further analysis is under way in order to evaluate the scope of validity regarding the approach.

Acknowledgement

The authors acknowledge the financial support from EC FP7 project ENER/FP7/296003/EFENIS 'Efficient Energy Integrated Solutions for Manufacturing Industries – EFENIS' and from the Slovenian Research Agency (Program No. P2-0032).

References

M. J. Atkins, M.R. Walmsley, A. S. Morrison, 2010. Integration of solar thermal for improved energy efficiency in low-temperature-pinch industrial processes, Energy, 35(5), 1867-1873.

BP, Statistical Review of World Energy June 2014. <http://www.bp.com/content/dam/bp/pdf/Energy-economics/statistical-review-2014/BP-statistical-review-of-world-energy-2014-full-report.pdf>, accessed 14.10.2014

Eumet, <eumet.hu/naprol-napra>, accessed 20.10.2014.

European Technology Platform on Renewable Heating and Cooling, Strategic Research Priorities for Solar Thermal Technology, 2013,<www.rhc-platform.org/fileadmin/Publications/Solar_thermal_SRP.pdf>, accessed 19.11.2014

GeoModel Solar, 2013, <re.jrc.ec.europa.eu/pvgis/apps4/pvest.php> accessed 10.10.2013

C. Lauterbach, Potential, system analysis and preliminary design of low-temperature solar process heat systems , 2014, <www.uni-kassel.de/upress/online/OpenAccess/978-3-86219-742-2.OpenAccess.pdf>, accessed 15.09.2014.

S. Perry, J. Klemeš, I. Bulatov, 2008, Integrating waste and renewable energy to reduce the carbon footprint of locally integrated energy sectors. Energy, 33(10), 1489-1497.

H. Schnitzer, C. Brunner, G. Gwehenberger, 2007, Minimizing greenhouse gas emissions through the application of solar thermal energy in industrial processes, Journal of Cleaner Production, 15(13-14), 1271-1286.

V. Smil, 2006. Energy: A Beginner's Guide. Oneworld Publications, 185 Banbury Road, Oxford, UK.

Y. Tian, C.Y. Zhao, 2013, A review of solar collectors and thermal energy storage in solar thermal applications, Applied Energy, 104, 538–553

Krist V. Gernaey, Jakob K. Huusom and Rafiqul Gani (Eds.), 12th International Symposium on Process Systems Engineering and 25th European Symposium on Computer Aided Process Engineering.
31 May – 4 June 2015, Copenhagen, Denmark

Process Simulation of Ammonia Recovery from Biogas Digestate by Air Stripping with Reduced Chemical Consumption.

Lene Fjerbaek Sotoft,[a*] Michael B. Pryds,[a] Anne Kjærhuus Nielsen,[b] Birgir Norddahl[a]

[a] *Institute of Chemical Engineering, Biotechnology and Environmental Technology, University of Southern Denmark, Campusvej 55, DK-5230 Odense M, Denmark*
[b] *Renew Energy, Kullinggade 31E, 5700 Svendborg*
lfj@kbm.sdu.dk

Abstract

Nitrogen can be recovered from the liquid fraction of biogas digestate by air stripping in order to make concentrated fertilizers which can be transported more efficiently from an agricultural area with manure nitrogen surplus to an area where it can replace inorganic fertilizers. The product is ammonia sulfate, as sulphuric acid absorption is used to produce the concentrate in a liquid form. Process simulations are carried out to investigate the operational and capital costs of a process treating 30,000 kg/h liquid digestate. Two designs with and without NaOH addition, respectively, are compared. Increased pH of the liquid digestate by NaOH addition favors NH_3 over NH_4^+, and hence increases process efficiency reducing capital costs, but increases the operational costs three times due to the cost of NaOH. Further, the total treatment cost is highly dependent on potential sales price of ammonia sulfate. Without NaOH, the treatment cost is 3.2-7.6 US$/m^3 and with 210kg/h NaOH the treatment cost is 5.2-9.6 US$/m^3.

Keywords: air stripping, ammonia recovery, biogas digestate, process simulation.

1. Introduction

Agriculture and the global society have a growing interest in safe and environmentally sustainable manure handling systems. Sustainable manure handling reduces local and regional pollution such as odour emissions, nutrient leaching and eutrophication as well as greenhouse gas emissions on the global scale. Biogas treatment of manure is one way to recover resources by production of renewable energy and hence reduce GHG-emissions. Furthermore, odour emissions are reduced.

Biogas digestate contains nitrogen (N) and phosphorus (P) of high fertilizer value. The N and P can be recovered and substitute inorganic fertilizers made from fossil fuels. In order to obtain a balanced fertilizer composition based on plant uptake and soil properties, separation of N and P is also of interest. P is mainly attributed to the solid fraction, where the N is mainly attributed to the liquid fraction dependent on the method of separation (Møller, 2000).

Nitrogen can be recovered from the liquid fraction by air and steam stripping followed by acid absorption. The product from the acid absorption will be $(NH_4)_2SO_4$. Air to liquid ratio, temperature and pH can be adjusted for improved mass transfer as shown for biogas digestate (Gustin & Marinsek-Logar, 2011) and swine manure waste water (Liao et al., 1995). Chemical reactions and phase transfers involved comprise both acid/base and vapour/liquid equilibria, and elevated temperature and pH can increase the amount of free ammonia in the air stripping section and hence improve nitrogen

recovery and reduce equipment size (Pryds, 2012). However, the chemical usage to raise pH increases the operational cost of the process, where lower pH increases the equipment size making the capital costs higher. The choice of the mentioned parameters can be analysed with respect to economic potential of the process, which will be done in this paper. The work simulates a plant treating 30,000 kg/hour (kg/h) liquid fraction of biogas digestate with a minimum recovery of 95% N at 90°C, which is a recovery obtained in full scale tests of an ammonia air-stripper (Hoffmann, 2011). A comparison between performance with and without addition of NaOH will be done in order to evaluate the impact of chemical dosage on operational and equipment costs. Additionally, the simulations will be optimized with respect to energy consumption as extensive heat recovery and air recycle are carried out to reduce product treatment costs.

2. Materials & Methods

The liquid biogas digestate fraction for this work is obtained after separation of biogas digestate in a decanter centrifuge. The solid fraction and components are not considered here, so the liquid fraction contains dissolved salts only. It has been defined according to chemical analysis of dissolved salts in a liquid fraction obtained from a thermophilic biogas plant from Lintrup, Denmark. The chemical analysis does not give equal molar amounts of cations and anions, which is required for charge neutrality. Hence, the chemical composition has been adjusted (+ 5.2 % for anions and – 5.2 % for cations based on charge) in order to obtain an overall electrically neutral system, see Table 1, as a requirement of thermodynamic and process simulation software.

Table 1. Liquid digestate composition before and after charge adjustment (±5.2%)

Ion	Molar mass [g/mole]	Mole concentration (before) [mole/L]	Mole conc. (after) [mole/L]	Mass conc. (after) [mg/L]
Cl^-	35.45	1.22E-02	1.29E-02	457
CH_3COO^-	60.05	3.00E-02	3.15E-02	1,895
HCO^{3-}	61.01	1.97E-01	2.07E-01	12,630
PO_4^{3-}	94.97	9.58E-03	1.01E-02	958
SO_4^{2-}	96.08	2.71E-03	2.85E-03	274
Negative ions total	-	2.51E-01	2.64E-01	-
NH_4^+	18.04	2.36E-01	2.24E-01	4,040
Ca^{2+}	40.08	2.69E-03	2.55E-03	102
Mg^{2+}	24.31	3.29E-05	3.12E-05	1
H_3O^+	19.03	1.90E-08	1.80E-08	0
Na^+	22.99	8.92E-03	8.45E-03	194
K^+	39.10	5.26E-02	4.99E-02	1,950
Positive ions total	-	3.01E-01	2.85E-01	-
H_2O	18.02	5.43E+01	5.43E+01	978,007
Total	-	5.48E+01	5.48E+01	1,000,507

Process simulations about treatment of 30,000 kg/h of liquid digestate are carried out in Aspen Plus aiming at min. 95% N recovery. The production size is estimated according to digestate treatment from a large biogas plant such as KURANA biogas in Lithuania (800 tonnes/day of stillage and organic waste).

The digestate and air enter the plant at 25°C and the digestate has a pH of 8.1. The steady-state model uses an electrolyte-NRTL thermodynamic model to calculate the properties of the system. In order to develop the model in this study, ENTRL and SRK has been used for liquid and gas calculations.

The model is an unsymmetric Electrolyte Non-Random-Two-Liquid model with Poynting correction, Redlich-Kwong cubic equation of state and a modified Henry's law. The model is useful for CO_2-NH_3-H_2O system in the range of 0-100°C, up to 16 bar and for concentrations up to 23 mole/L NH_3 and 8 mole/L CO_2 (AspenTech, 2012)

The used process simulation software is Aspen Plus 27.0 and Aspen Plus V8.0, and for economic evaluations Aspen Icarus Process Evaluator 27.0 and equipment purchase cost charts from Peters et al. (2003) are used. Equipment costs have been corrected to current costs using Chemical Engineering Plant Cost Index (2012).

The main units of the process are a stripper and an absorber with 38 wt% sulfuric acid. A flash column is included to remove CO_2 prior to the air stripper column.

The feed enters the plant and is heated to the desired temperature in two heat exchangers. A sensitivity analysis is performed to determine the temperature needed to meet the desired recovery. The first heater transfers heat from the stripped liquid to the feed in order to improve energy efficiency. The second heat exchanger raises the temperature to the desired operation temperature. The air that is used to remove the ammonia from the incoming liquid is recycled between absorber and stripper, which improves energy efficiency and reduces the overall water evaporation. However, some air must be purged to avoid accumulation of CO_2 in the air stream. The flow sheet can be seen as Figure 1. All units are assumed to be adiabatic.

A system without addition of NaOH is simulated and compared to a system with addition of 210 kg/h NaOH. The stripper column is a randomly packed column with 90mm poly propylene Flexi-rings (specific surface area 0.7218 m^2/m^3 and a void fraction of 0.95 and price according to column volume after Peters et al. (2003)). The column is designed to operate at 62% of the flooding point. Pressure drops are fixed to 0.02 atm. in the stripper column, 0.01 atm. in the absorber and 0.2 atm. in heat exchangers (Seider et al., 2004). Isentropic compressor efficiency is 72% and the efficiency for conversion of electricity and fired natural gas into heat is assumed to be 80%.

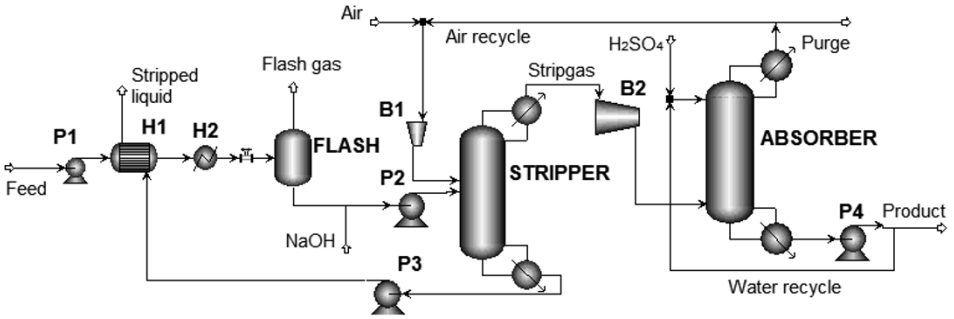

Figure 1: Flow sheet of plant recovering ammonia by air stripping and acid absorption. Prefix: P = Pump, H = Heat exchanger and B = Blower.

The process is designed to meet a minimum of 95% recovery calculated as in Eq. 1. Total ammoniacal nitrogen (TAN) includes $NH_3/NH_4^+/NH_2COO^-$.

$$\text{Recovery} = \text{stripped } NH_3 \text{ [kmole/h]} / \text{TAN in [kmole/h]} \cdot 100\% \quad (1)$$

The basis for the economical evaluation is operation in 8,000 hours/year, where operational costs include chemicals (55 US$/ton 98 wt% H_2SO_4 diluted to 38wt% onsite and 450 US$/ton 50 wt% NaOH), electricity (0.0677 US$/kWh) and natural gas (0.13 US$/$Sm^3$). Two ammonia sulfate prices are used as there is great uncertainty to the potential sales prices of the product (S), so 100 US$/ton (F.O.B China) and 423 US$/ton (USDA, 2011) are used to cover price interval of agricultural grade fertilizer. F.O.B. indicates free on board prices before delivery and installation.
The total equipment cost is calculated based on the 7 major pieces of equipment, which are two heat exchangers, two blowers, a flash drum, a stripper column and absorber column, both with random structured packings and redistributors. Finally, the total capital investment is calculated based on bare module costs (Seider et al., 2004) for installation in Western Europe, see Eq. (2)-(4).

$$\text{Total bare module cost } (C_{TBM}) = 3.291 \cdot C_{BM} \quad (2)$$

$$\text{Total capital investment } (C_{TCI}) = 2.2 \cdot C_{TBM} \quad (3)$$

$$\text{Total corrected capital investment } (C_{TCI,corrected}) = 1.2 \cdot C_{TCI} \quad (4)$$

It is assumed that chemicals and utilities comprise 60% of the total production costs (TPC) (Peters et al., 2003). See Eq. (5), where $C_{chemicals}$ is cost of chemicals and $C_{utilities}$ is cost of utilities.

$$\text{Total production costs (TPC)} = (C_{chemicals} + C_{utilities})/60\% \quad (5)$$

This enables a calculation of a minimum treatment cost [US$/$m^3$] as seen in Eq. (6).

$$\text{Treatment cost (TC)} = (\text{ROI} \cdot C_{TCI,corrected} + \text{TPC} - \text{S})/\text{production rate} \quad (6)$$

Return of investment (ROI) is fixed at 20%. Furthermore, taxes, fees, venture profit and depreciation are excluded as the economic evaluation means to estimate a minimum treatment cost of the process.

3. Results & Discussion

The simulated characteristics of the electrolyte system have been investigated to ensure the prediction of acid/base equilibrium of the species and pH. The treatment of 30,000 kg/h liquid digestate is performed to recover 95% N without addition of NaOH and is compared to addition of 210 kg/h NaOH. The overall simulation results can be seen in Table 2. The number of equilibrium stages of stripper and absorber as well as the column temperature have been determined according to the desired recovery. They are 12 stages, 5 stages and 90°C, respectively. The main difference is the consumption of NaOH and hence that two stripper and two absorber columns are needed without NaOH addition instead of one of each when NaOH is added. This is because less free ammonia is found at pH 8.1 than at higher pH, and approximately three times more air is needed to meet the specified recovery without addition of NaOH. Random-packed columns are generally not designed with a diameter above 1.5 m (Peters, 2003), so when the flow reaches a certain level two columns are needed instead of one. An optimization of purge is carried out to reduce the needed purge fraction as this reduces the overall water evaporation rate and energy consumption to heat up fresh incoming air. The purge fraction is 20%.

The ammonia sulfate is recovered as 47 wt% in water and the flow rate is comparable in the same range for the two simulations. Without addition of NaOH, the product stream has a flow 875 kg/h corresponding to 411 kg/h $(NH_4)_2SO_4$.

Table 2. Overall simulation results.

	210 kg/h NaOH	No NaOH	Unit
Digestate flow rate:	30,000	30,000	kg/h
Recovered NH_3	95.2	95.2	mole%
Air inlet flow rate	985	3,480	kg/h
Air recycled flow rate	7,417	22,162	kg/h
H_2SO_4 flow rate (as 38 wt% H_2SO_4)	925	945	kg/h
NaOH flow rate (as 50 wt% NaOH)	210	0	kg/h
Stripper column diameter	1.14	1.76	m
Stripper column packing height	9.60	9.6	m
Absorber column diameter	0.99	1.59	m
Absorber packing height	4.0	4.0	m
Purge stream flow rate	1,608	4,671	kg/h
Product stream $(NH_4)_2SO_4$ flow rate	864	875	kg/h
Heat exchanger, H1	389.3	289.8	m²
Heat duty, H2	628.8	1006	kW
Net Duty, B1	6.8	2.3	kW
Net Duty B2	14.8	39.1	kW

Table 3**.** Costs of equipment, investment, operation and production as well as sales.

Purchase of Equipment	210 kg/h NaOH	No NaOH	
Total equipment costs F.O.B.	542,000	942,000	US$
Total bare module investment	1,783,000	3,101,000	US$
Total corrected capital investment	4,708,000	8,186,000	US$
Purchase cost of chemicals and electricity			
H_2SO_4	158,000	161,000	US$/y
NaOH	756,000	0	US$/y
Total operational cost	1,007,000	314,000	US$/y
Total production cost (TPC)	1,678,000	524,000	US$/y
Sales (S) at 100 US$/ton	324,000	329,000	US$/y
Sales (S) at 423 US$/ton	1,370,000	1,392,000	US$/y
Treatment cost at 100 US$/ton	9.6	7.6	US$/$m^3$
Treatment cost at 423 US$/ton	5.2	3.2	US$/$m^3$

The total capital investment is 8,186,000 US$ and 4,708,000 US$ without and with addition of NaOH, respectively, as shown in table 3. Hence, a substantial increase in the capital cost is caused by the need of two columns for stripping and absorption when no

NaOH is added. Contrarily, the production costs are considerably decreased approximately three times from 1,867,000 to 524,000 US$/y when no NaOH is needed. The comparison shows that the use of NaOH should be kept to a minimum as it has a big influence on the operational costs, but cannot be avoided completely as it is needed to reduce the capital costs.
The treatment cost without NaOH will though be lower (3.2-7.6 US$/$m^3$) than with 210 kg/h NaOH (5.2-9.6 US$/$m^3$) highly dependent on the sales price of ammonia sulfate. The treatment costs are in the range in what has been reported in literature.
The study here however, clearly shows the importance of considering the influence of chosen process parameters on operational and capital costs. Furthermore, the uncertainty of the actual sales price of ammonia sulfate is seen and must be considered when evaluating air stripping as mean to recover nitrogen.
Additional points of the process will have an important impact on the plant viability and could be a scope for further research. They are aspects such as fouling of the stripper column, which reduces capacity when cleaning is needed, required product quality and price as well as cost of evaporation following the absorber if a solid product is necessary.

4. Conclusions

Air stripping is simulated to recover nitrogen from the liquid fraction of biogas digestate. The product is ammonia sulfate as sulfuric acid absorption is used to capture the free ammonia. The plant is designed to treat 30,000 kg/h digestate with a recovery of 95%. A design without the addition of NaOH is performed here and compared to the use of NaOH to increase the driving force. The influence of NaOH addition on total production costs and total capital costs has been investigated, where the total production costs were approximately three times higher when 210 kg/h of NaOH were used. On the contrary, the total capital were 4,708,000 US$ when using NaOH compared to 8,186,000 US$ without NaOH. The lower driving force increases the equipment size, so two columns is needed both for the stripper and absorber section to keep the individual column diameter below 1.5 m. The treatment costs are highly dependent on the potential sales price of ammonia sulfate and were 3.2-7.6 US$/$m^3$ without NaOH and 5.2-9.6 US$/m³ with NaOH.

References

AspenTech. 2012. Aspen Plus Help File.
Chemical Engineering, 2012, Chemical Engineering Plant Cost Index.
S. Gustin, R. Marinsek-Logar, 2011, Effect of pH, temperature and air flow rate on the continuous ammonia stripping of the anaerobic digestion effluent, Process Safety and Environmental Protection, 89, 1, 61-66.
A. Hoffmann, (2011), Kurana plant start-up report for ammonia air-stripper, personal comm. from company Rauschert Verfarenstechnique GmbH
P.H. Liao, A. Chen, K.V. Lo, 1995, Removal of nitrogen from swine manure wastewaters by ammonia stripping, Bioresource Technology, 54, 1, 17-20.
M.S. Peters, K.D. Timmerhaus, E.R. West, 2003, Plant Design and Economics for Chemical Engineers, 5th ed, McGraw-Hill, New York, USA.
M. B. Pryds, 2012, Theoretical Modelling of an ammonia-carbon dioxide stripper, for the recovery of ammonia in biogas digestate, master thesis, University of Southern Denmark.
W.D. Seider, J.D. Seader, D.R. Lewin, 2004, Product & Process Design Principles, 2nd ed., John Wiley & Sons Inc., New York, USA.
United States Department of Agriculture, 2011, Fertilizer Use and Price, http://www.ers.usda.gov/data-products/fertilizer-use-and-price.aspx#26727. Accessed 4/2/1.
H.B. Møller, I. Lund, S.G. Sommer, 2000, Solid–liquid separation of livestock slurry: Efficiency and cost, Bioresource Technology 74, 223–229

Krist V. Gernaey, Jakob K. Huusom and Rafiqul Gani (Eds.), 12th International Symposium on Process Systems Engineering and 25th European Symposium on Computer Aided Process Engineering.
31 May – 4 June 2015, Copenhagen, Denmark

WWSD for Distributed Treatment of Effluents

Moreira L.P.,[a] Delgado B.E.P.C., [a] Queiroz E.M.,[a] Pessoa F.L.P.[a*]

[a]*Universidade Federal do Rio de Janeiro, Centro de Tecnologia, Av Athos da Silveira Ramos,149,Bloco E, sala 209, Ilha do Fundão, Rio de Janeiro, 21941-909, Brazil*
pessoa@eq.ufrj.br

Abstract

Despite the technologies developed for water conservation inside an industrial plant some effluent streams still exist in the end of pipe. The distributed treatment of these effluent streams brings the opportunity to create wastewater treatments systems to accomplish with the environmental laws and in some cases contributes to water saving for the entire process. Wastewater Source Diagram (WWSD) is an algorithmic procedure for reducing the total wastewater treated flowrate by designing a distributed wastewater treatment system of effluents. Two criteria are taken into account for the synthesis of distributed treatment, the maximum concentration for discharge of contaminants and the treatment efficiency for contaminants. The WWSD procedure was applied to a real case to the treatment of effluents of the bioprocess laboratory with one contaminant and single treatments. The effluents streams have one contaminant and multiple treatments with different removal rates are available for the synthesis of the wastewater treatment system. Although the distributed treatment achieves the lowest treated flowrate, the centralized system uses fewer units of treatment. Multiple scenarios were studied for this minimum treated flowrate but using different units of treatment. These treatments were compared by an economic evaluation carried for the centralized treatment and the distributed treatment of effluents. The comparison with the solution by adopting the effluent centralized treatment shows that these tend to be more expensive once leading to a higher treated effluent flow rate.

Keywords: Wastewater Treatment System; process synthesis; process integration; distributed system.

1. Introduction

Environmental policies lead to the search for synthesis of wastewater treatment system respecting the maximum contaminants discharge. The end of pipe treatment of effluents in a process can have two configurations: centralized or distributed treatment. There are two ways for the distributed end of pipe treatment of effluents, with or without partial treated effluent return to the process. The distributed end of pipe treatment of effluents in a process reduces the capital and operational costs in a process. The capital cost of most treatments of effluent is proportional to the total wastewater flowrate while operational cost of most treatments increases with decreasing concentration and mass load of contaminants to be removed (Kuo and Smith, 1997). The goal is the synthesis of the effluent treatment system with a distributed wastewater treatment in order to reduce the effluent treated flowrate and reach the concentration for environmental disposal. Besides a methodology is necessary for the synthesis of the effluent treatment system with minimal cost. Hungaro (2005) developed a heuristic algorithmic procedure to target lowest flowrates of effluent to be treated. The treatment-limiting characteristics

were the maximum inlet concentrations and the limited flowrate permitted in order to meet the specified removal rate (efficiency). Removal rates were considered constant. Data of maximum concentrations for disposal were also necessary. Treatments were selected by criterion of higher removal rate (efficiency) or the number of different contaminants which could be removed. However, in order to choose treatments with similar efficiencies it would be necessary to estimate its cost as criterion, which was not considered in Hungaro´s work. Delgado (2008) also proposed an algorithmic procedure based on the Water Source Diagram (WSD) for the synthesis based on the efficiency and the minimal operational cost of the units of treatment. Kumaraprasad and Muthukumar (2009) employed the Water Source Diagram (WSD) concept (Gomes et al., 2007) coupled with water mains concept to simplify the piping network and reduce the cost. Liu *et al*. (2012) presented a simple procedure to determine the pinch concentration for the systems with one treatment process. In all situations, the discharge concentration of effluents in the end of pipe must satisfy the limits of environmental law. In this work the WWSD algorithm is been proposed for the synthesis of the distributed treatment of effluents based on some rules of Hungaro's algorithm for the synthesis of the end of pipe wastewater system. The WWSD algorithm is similar to the Water Source Diagram (WSD) to minimize the water use in industries developed by Gomes et al. (2007). The main rules of the WWSD algorithm are similar to Hungaro´s but are applied in a diagram similar to WSD algorithm. The heuristic WWSD procedure was applied in a real effluent from the laboratory of Bioprocess COPPE/UFRJ. It was observed that the WWSD obtained a lower flowrate for the distributed effluent treatment than for the centralized treatment.

2. WWSD procedure for synthesis of distributed treatment of effluent with one contaminant and a single treatment

The main objective of this work is to determine the mass exchange network with the minimum wastewater treated flowrate. The WWSD procedure for a single contaminant has five main steps, which are described in Table 1.

Table 1- WWSD procedure

Step 1: Calculate the mass load in each effluent stream (m) of the contaminant in the effluent streams using Eq.(1). $m_k = f_k (C_k - C_d)$ (1) where m is the amount of contaminant to be removed in each stream k; f_k is the flowrate of the effluent stream k; C_k is the contaminant concentration in the effluent stream k; k=1,…, $N_{streams}$ and i=1,…, N_{int} ($N_{streams}$ is the number of streams and N_{int} is the number of concentration intervals in the WWSD). C_d is the disposal concentration.
Step 2: Generation of the WWSD. Sketches the base for the WWSD, representing the concentration intervals, which are bounded by all contaminant concentrations in effluents and the limit wastewater discharge concentration. Calculate the concentration of effluents streams after treatments using Eq.(2). $C_{T,k} = C_{k,i}(1 - RR)$ (2) where RR is the treatment efficiency for contaminant removal, $C_{k,i}$ is the concentration of the contaminant in the interval i in the effluent stream k and $C_{T,k}$ is the contaminant concentration after the treatment in k.

Table 1- WWSD procedure

Step 3: Introduce the effluent streams in the WWSD diagram. Represent each effluent stream by a line from the respective inlet concentration to the disposal concentration and the limiting concentration in the diagram is the disposal concentration. The limit wastewater flowrates, f_k, are shown in a column on the left side of the diagram.

Step 4: Calculate the amount of mass to be removed by the treatment of the effluent stream in each interval by using Eq.(3).

$$\Delta m_{k,i} = f_k \left(C_{k,i} - C_{k,i-1} \right) \quad (3)$$

Where $\Delta m_{k,i}$ is the amount of contaminant removed of effluent k in interval i; f_k is the flowrate of stream k; $C_{k,i}$ is the upper limit of concentration in interval i , $C_{k,i-1}$ is the lower limit of the same interval.

Step 5: Synthesize the mass-exchange network by calculating the flowrate of the effluent stream to be treated in each interval.

Calculate the flowrate of an effluent stream sent to a treatment using Eq.(4).

$$f^{C_{T,k}}_{k,i} = \frac{\Delta m_{k,i}}{(C_{k,i} - C_{T,k})} \quad (4)$$

where $f^{CTk}_{k,i}$ is the flowrate through treatment to achieve the concentration C_{Tk} of effluent k, Δm_{ki} is the amount of contaminant in stream k removed in interval i; C_{ki} is the upper limit of the concentration interval i and C_{Tk} is the concentration of stream k for the treatment available. In the following intervals the flowrate of an effluent stream sent to a treatment is calculated by Eq.(5).

$$f^{C_{T,k}}_{k,i} = \frac{\Delta m_{k,i} - \left[f^{C_{T,k}}_{k,i-1} \left(C_{k,i} - C_{k,i-1} \right) \right]}{\left(C_{k,i} - C_{T,k} \right)} \quad (5)$$

After these five steps, sketch the mass exchange network.

3. Laboratory Case Study

The WWSD procedure was used to solve a real problem from Hungaro (2005). It deals with five effluents from a UFRJ laboratory. The activities those originate the wastewater are the following: 1.Growing of *Zymomonas mobilis* to obtain etanol; 2.Glucose tolerance test (Kit CELM); 3.Protein concentration measurement (The Bradford method); 3.1Waste from the Bradford reactant; 3.2 Waste from the analysis; 3.3Waste from the glassware cleaning. The analysis is made based on the chemical oxygen demand (COD). The COD is a parameter regulated by the Brazilian water discharge legislation, CONAMA. The limit COD condition for a discharge in saline water is 10 mg/L, therefore it is adopted as the disposal limit concentration ($\boldsymbol{C_d}$) in this case study. The data from the quantified COD from the wastewater streams is presented on the Table 2. The treatments available are activated sludge process, T1, and rotating biological contactor, T2, flocculation with ionic exchange, T3, Coagulation-floculation-sedimentation, T4. The removal rates of COD for these treatments are presented on Table 3. The removal rate of treatments in Table 3 were obtained in Quaglia et al (2013), Joyce et al. (1984), Henriksen et al. (1998) and Delgado (2008).

Table 2 – Wastewater data from Hungaro (2005).

Effluent, k	C_k (g/L)	f_k (L/month)	m_k (kg/h)
1	102.49	2.000	185.0
2	53.44	0.500	21.7
3.1	65.98	0.035	2.0
3.2	59.28	0.064	3.2
3.3	106.01	2.092	200.9

Table 3 – Removal Rate and maximum inlet concentration for the available treatments.

Treatment, T	RR_T (%)	C_{max} (g/l)
Activated Sludge (T1)	0.9	2.5
Rotating Biological Contactor (RBC)(T2)	0.8	-
Floculation and ionic exchange (T3)	0.5	-
Coagulation-Floculation-Sedimentation (T4)	0.6	-

As can be seen the wastewater streams on Table 1 are out of specification and the WWSD is going to be applied for the synthesis of a distributed treatment system for these effluents. The complete WWSD obtained using the five steps of the algorithm for this case study is shown in Figure 1. The total treated flowrate in the effluent treatment system is 7.415 L/month, as can be seen in Figure 2, where the system obtained from the WWSD is shown. In order to compare, in Figure 3 it is shown the corresponding centralized treatment system, where it can be noted a need of treating 9.382 L/month, 26.5 % larger than the amount treated in the distributed system.

The procedure was repeated using treatments T3 and T4. Data for economical evaluation of the distributed and centralized systems using the three treatments were collected from literature. The price of equipment (*Ie*) was corrected by Marshall&Stevens equipment indexes of 1061.9 as reported for the year 1998 and 1244.5 as reported for the year 2005 to calculate the capital cost (IC). Treatment (T2) RBC has an initial capacity of 79.17 m^3/h, the equipment price is 50,000 ($) (Joyce et al., 1984). Treatment (T3) Floculation and ionic exchange has an initial capacity of 0.64 m^3/h and the equipment price is 235,000 (DKK) (Henriksen et al., 1998). Treatment (T4) Coagulation+Floculation+Sedimentation has an initial capacity of 0.64 m^3/h and the equipment price is 4220 ($) (Delgado, 2008).

The treatments were compared by an economic evaluation. Fixed-capital investment was estimated by percentage of delivered equipment cost (Peters and Timmerhaus, 1991). Operational costs were not affordable because of low flowrates in the laboratory effluent streams. Note that in this study there was no need to use treatment 1, activated sludge treatment, as its maximum inlet COD concentration is higher than the disposal concentration. As the effluent is from a laboratorial scale the costs are low in Table 4. In Table 4 it can be seen that treatments costs rises with the total treated flowrate. On the contrary, the higher efficiency (RR_T) leads to the lowest cost using RBC treatment (T2). Whatever the treatment, the distributed system has lower cost than the centralized system.

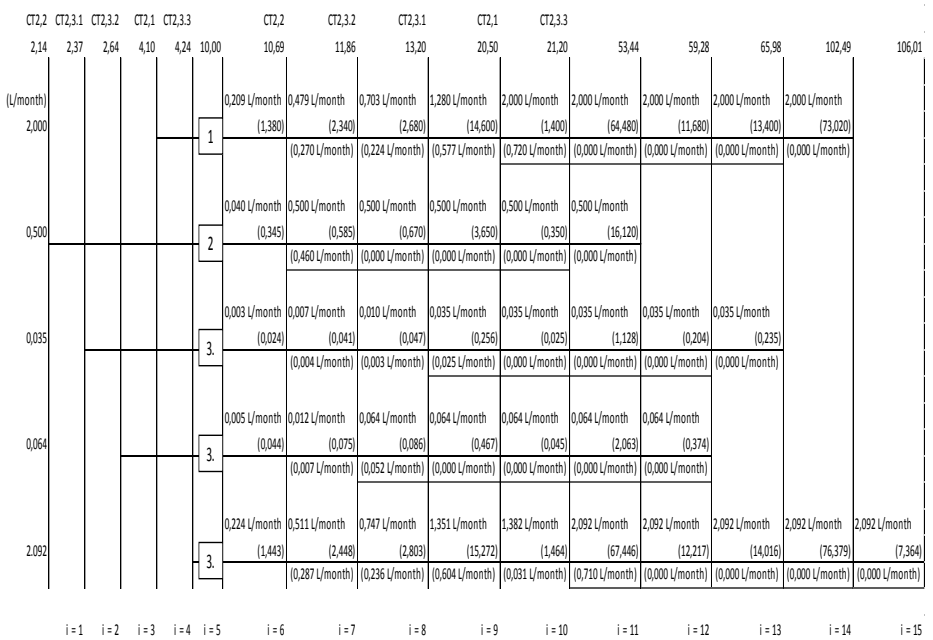

Figure 1 – WWSD for the Laboratory Case Study.

Application of WWSD reduces the treated flowrate by using by-pass of untreated effluent flowrate. The minimum total effluent flowrate found with WWSD sent to the treatment. This reduces directly the operation cost of the treatment system. The WSD (Gomes et al. 2007) provided the path for resolution and synthesis of the distributed treatment of effluent streams with few adaptations in its rules for calculation of mass balance of contaminants concentrations and the minimum treated flowrates. Similar rules of Water Source Diagram (WSD) were followed in the WWSD algorithm.

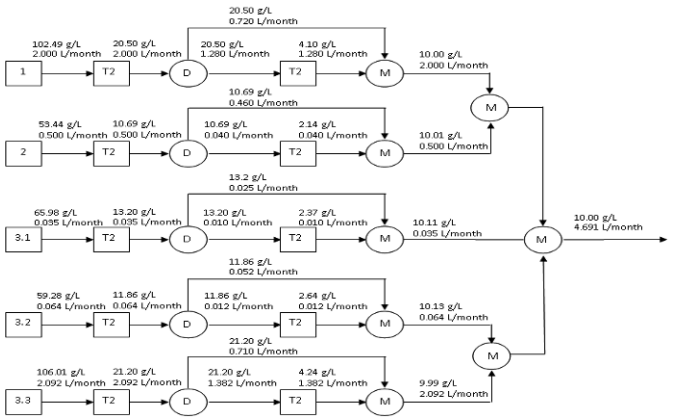

Figure 2– Distributed treatment of the Laboratory Case Study.

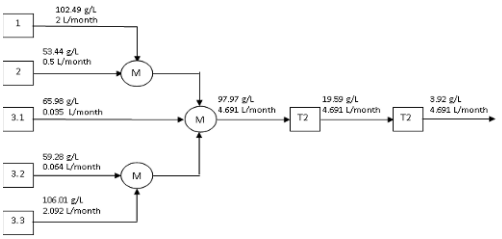

Figure 3– Centralized treatment of the Laboratory Case Study.

Table 4– Results for WWSD for one contaminant and a single treatment.

Configuration	*Flowrate (L/month)*	*Total Fixed capital and labor ($/y)*	*Treatment, T*
T2 distributed	7.42	14.10	Rotating Biological Contactor (RBC) (T2)
T2 centralized	9.38	16.65	
T3 distributed	15.70	545.40	Floculation and ionic exchange (T3)
T3 centralized	18.76	617.90	
T4 distributed	12.20	49.10	Coagulation-Floculation-Sedimentation (T4)
T4 centralized	14.10	54.40	

4. Conclusion

The Wastewater Source Diagram (WWSD) is a simple algorithm procedure for the synthesis of the distributed treatment of effluents. It reduces the total effluent flowrate sent to the treatment by searching the limit concentration for discharging of the effluent streams. The case study showed a real application of the WWSD to a laboratory, which can reduce the volume of effluents treated by applying the decentralized system and achieving the desired disposal concentration, enabling the discharge of the effluent in saline waters, by legislation.

Acknowledgments: Authors thank CAPES and CNPq for financial support.

References

Delgado, B.E.P.C. 2008. Síntese de Sistemas de Regeneração e Tratamento Final de Efluentes. Tese de Doutorado em Tecnologia de Processos Químicos e Bioquímicos, EQ/DEQ/UFRJ, Rio de Janeiro, RJ, Brazil.

Gomes, J. F., Queiroz, E. M., Pessoa, F. L, 2007. Design procedure for water/wastewater minimization: single contaminant. Journal of Cleaner Production, 15, 474-485.

Henriksen K., Berthelsen L., Matzen R., 1998. Separation of Liquid Pig Manure by Flocculation and Ion Exchange Part 2: Pilot-scale System. Journal Agric.. Eng Res., 69, 127-131.

Hungaro, L.M., 2005. Desenvolvimento de algoritmo para síntese de tratamento distribuído de efluentes líquidos, Dissertação de Mestrado, COPPE/UFRJ, Rio de Janeiro, RJ, Brazil.

Joyce T.W., Chang Hm., Campbell Jr. A.G., Gerrard E.D., Kirk T.K., 1984. A Continuous Biological Process to Decolorize Bleach Plant Effluents. Biotech Advs., 2, 301-308.

Kumaraprasad G., Muthukumar K., 2009. Design of Mass Exchange Network and Effluent Distribution System for effective water management. Journal of Cleaner Prod, 17, 1580-1593.

Kuo, W.C.J., Smith, R., 1997. Effluent Treatment System Design, Chem Eng Sci., 52, 4273-4290.

Liu Z.H., Shi J., Liu Z.Y., 2012. Design of wastewater treatment networks with single contaminant. Chemical Engineering Journal. 192, 315–325.

Peters, M.S.; Timmerhaus, K.D.; "Plant Design and Economics for Chemical Engineers", McGraw-Hill, 4.ª ed., 1991.

Quaglia A., Pennati A., Bogataj M., Kravanja Z., Sin G., Gani R., 2013. Industrial Process Water Treatment and Reuse: A Framework for Synthesis and Design. Ind. & Eng. Chem. Res., 53, 5160 -5171.

Krist V. Gernaey, Jakob K. Huusom and Rafiqul Gani (Eds.), 12th International Symposium on Process Systems Engineering and 25th European Symposium on Computer Aided Process Engineering.
31 May – 4 June 2015, Copenhagen, Denmark

Extending the benchmark simulation model n°2 with processes for nitrous oxide production and side-stream nitrogen removal

Riccardo Boiocchi[a], Krist V. Gernaey[a] and Gürkan Sin[a]

[a]*CAPEC-PROCESS, Department of Chemical Engineering, DTU, 2800-Lyngby, Denmark*

Abstract

In this work the Benchmark Simulation Model No.2 is extended with processes for nitrous oxide production and for side-stream partial nitritation/Anammox (PN/A) treatment. For these extensions the Activated Sludge Model for Greenhouse gases No.1 was used to describe the main waterline, whereas the Complete Autotrophic Nitrogen Removal (CANR) model was used to describe the side-stream (PN/A) treatment. Comprehensive simulations were performed to assess the extended model. Steady-state simulation results revealed the following: (i) the implementation of a continuous CANR side-stream reactor has increased the total nitrogen removal by 10%; (ii) reduced the aeration demand by 16% compared to the base case, and (iii) the activity of ammonia-oxidizing bacteria is most influencing nitrous oxide emissions. The extended model provides a simulation platform to generate, test and compare novel control strategies to improve operation performance and to meet the new plant performance criteria such as minimization of greenhouse gas (in particular of nitrous oxide) emissions.

Keywords: benchmark, nitrous oxide, ammonia-oxidizing bacteria, heterotrophic bacteria.

List of abbreviations:

GHG	Greenhouse Gas
PN/A	Partial Nitritation/Anammox
CANR	Complete Autotrophic Nitrogen Removal
BSM1/BSM2	Benchmark Simulation Model No.1 /No.2
ASM1/ASMG1	Activated Sludge Model No.1/ ASM1 for Greenhouse gases
ADM1	Anaerobic Digestion Model No.1
BSM2N	Benchmark Simulation Model No.2 for Nitrous oxide
BSM2NplusCANR	Benchmark Simulation Model No.2 for Nitrous oxide and Complete Autotrophic Nitrogen Removal
AOB/NOB/AnAOB	Ammonia- /Nitrite-/Anaerobic Ammonia-Oxidising Bacteria
HB	Heterotrophic Bacteria

1. Introduction

The development of novel control strategies for wastewater treatment plant (WWTP) processes is increasingly required to meet both increasingly-strict regulatory limits for effluent water quality as well as to mitigate greenhouse gas (GHG) emissions from the plant. In order to facilitate the development and the application of control strategies for WWTPs, a benchmark simulation framework was developed over the past decades to enable objective and realistic control technology testing and comparison. In particular, simulation models such as the Benchmark Simulation Model No.1 (BSM1) and Benchmark Simulation Model No.2 (BSM2) (Jeppsson et al., 2007) were developed. The main difference between the BSM1 and the BSM2 is in the plant layout. More specifically, while the BSM1 includes just the mainstream treatment unit, the BSM2 layout adds to this the side-stream treatment for wastage sludge. For this reason,

compared to the BSM1, the BSM2 can be considered allowing not only the development of a larger number of control strategies but also a more complete and thorough evaluation of control strategies. As pointed out by Jeppsson et al. (2013), the BSM2 could be further extended in order to meet newly-emerging control objectives. These extensions include the mitigation of nitrous oxide (N_2O) emissions and the enhancement of nitrogen removal through emerging technologies such as partial nitritation/Anammox (PN/A) processes. As a matter of fact, there exist a large number of evidences showing that N_2O, one of the most harmful GHGs and an ozone-depleting substance, can be produced under certain operating conditions in a significant amount during the activity of different species of bacteria typically involved in the biological nitrogen removal processes. With regard to the side-stream process, it is important to acknowledge the fact that WWT designers have been frequently upgrading their plants with PN/A processes in the side-stream in order to cope with the increasingly strict effluent regulatory limits on the reactive nitrogen species in the effluent against a reasonable cost (Lackner et al., 2014). However, in order to take advantage of these technologies, it is important to develop proper process control strategies in order to ensure optimal and stable operation against external disturbances. In this work two extensions of the BSM2 are presented. The first extension regards the mathematical model describing the processes in the mainstream with processes for nitrous oxide production. The second extension concerns the expansion of the layout of the side-stream treatment unit by including a single-stage continuous PN/A reactor. In particular, the Activated Sludge Model for Greenhouse gases No.1 (ASMG1) by Guo and Vanrolleghem (2014) is used as mathematical model instead of the Activated Sludge Model No.1 (ASM1). With regard to the layout extension, the single-stage granular reactor performing Complete Autotrophic Nitrogen Removal (CANR), whose processes were modelled by Vangsgaard et al. (2012), is included in the side-stream of the BSM2 at the bottom of the dewatering unit of the reject water from the anaerobic sludge digestion.

2. Development of the Benchmark Simulation Model for Nitrous Oxide and for side-stream Complete Autotrophic Nitrogen Removal (the BSM2NplusCANR)

The development of the new benchmark simulation model (the BSM2NplusCANR) required the following additions and modifications:

1) replacement of the ASM1 with the ASMG1,
2) extension of the ASM1-to-ADM1 and of the ADM1-to-ASM1 interfaces,
3) inclusion of new state variables in both the CANR model (CANRM) and in the ASMG1, and
4) development of interfaces mapping the state variables of ASMG1 into the ones of the CANR model and vice versa.

As an outcome from point 2), the BSM2N is obtained.

2.1. The implementation of the Activated Sludge Model for Greenhouse gases No.1

The mathematical model considered suitable for the inclusion of N_2O production into the BSM2 was the ASMG1 by Guo and Vanrolleghem (2014). This choice was taken in virtue of the fact that the model was calibrated and validated against the ASM1 which is considered to provide a realistic description of the WWT processes. Hence the effluent concentrations predicted by the model can be considered reliable. However, it should be pointed out that there are no data validating the emissions of N_2O predicted and future investigations are required to validate the model not only for the effluent concentrations

but also the nitrogen gas emissions. The mass balance equations used to model the biological reactors in the mainstream can be generically represented as:

$$\frac{dC_i}{dt} = \frac{Q}{V} \cdot (C_{in,i} - C_i) + r_i \quad (1)$$

In Equation (1) C_i is the concentration of the generic component i, Q is the volumetric flow rate (in and out the reactor), V is the reaction volume and r_i is the reaction rate. For further information, the reader is referred to Guo and Vanrolleghem (2014).

2.2. The Complete Autotrophic Nitrogen Removal model

A complete overview of the Complete Autotrophic Nitrogen Removal model used to decribe the PN/A occurring in the side-stream reactor on bottom of the dewatering unit is available in Vangsgaard et al. (2012). Here the main mass-balance equations are shown, as follows:

$$\frac{\partial S_i}{\partial t} = D_i \cdot \frac{1}{z^2} \cdot \frac{\partial}{\partial z}\left(z^2 \cdot \frac{\partial S_i}{\partial z}\right) + r_i \quad (2)$$

$$\frac{\partial X_i}{\partial t} = -\frac{\partial (X_i \cdot u_F)}{\partial z} + r_i \quad (3)$$

$$\frac{dC_i}{dt} = \frac{Q_{in} \cdot C_{i,in} - Q_{out} \cdot C_{i,bulk} - j_{bio,i} \cdot A_{bio}}{V} + r_i \quad (4)$$

In Eqs (2-4), D_i is the diffusion coefficient for soluble components S_i, z is the radial distance from the center of the granule, u_F is the biofilm net growth velocity and $j_{bio,i}$ the flux in and out the biofilm.

2.3. The ASMG1-to-ADM1 and the ADM1-to-ASMG1 interfaces

Interfaces are tools linking two mathematical models with different sets of state variables (SVs). These tools have been used in the BSM2 to map the state variables of the ASM1 into the ones of the Anaerobic Digestion Model No.1 (ADM1) and vice versa. When replacing the ASM1 with the ASMG1, the set of SVs of the mainstream model is augmented. In particular, while in the ASM1 the ammonia-oxidizing bacteria (AOB) and nitrite-oxidizing bacteria (NOB) are represented as a single variable, in the ASGM1 they appear separately. Nitrite, nitric oxide, nitrous oxide and dinitrogen represent new SVs. In order to map these new SVs, in the ASM1-to-ADM1 interface nitrite, nitric oxide and nitrous oxide were added to the pool of electron acceptors jointly with oxygen and nitrate to be consumed during the oxidation of biodegradable organic carbon by HB. AOB and NOB are used in the same way as the ASM1 variable "autotrophic bacteria", meaning that they are summed up together and assumed to decay releasing X_{ND}, X_P and X_S.

2.4. Inclusion of new state variables in the CANRM and in the ASMG1

New state variables needed to be added in both the ASMG1 and the CANRM in order to make the two models compatible with each other. These additions consisted of: anaerobic AOB (X_{AnAOB}) into the ASMG1 and soluble inerts (S_I), particulate inerts from influent (X_I) and alkalinity (S_{ALK}) into CANRM.

2.5. Development of the ASMG1-to-CANRM and of the CANRM-to-ASMG1 interfaces

Figure 1 shows schematically how each state variable of one model is mapped into those of the other model.

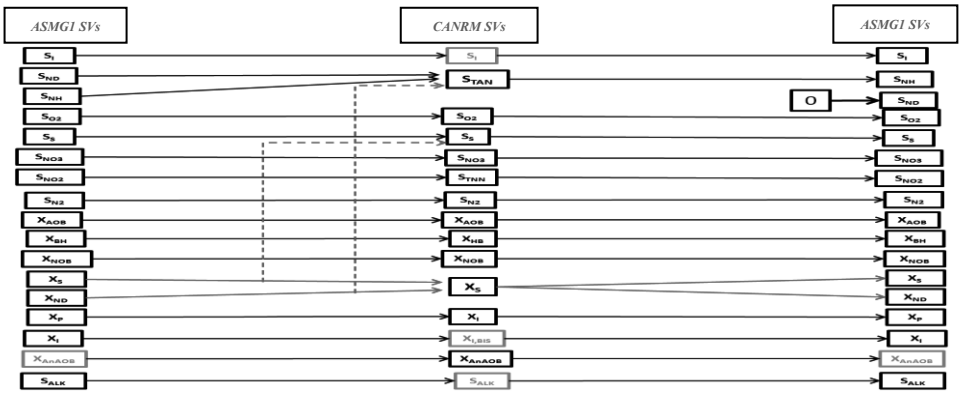

Figure 1: ASMG1-to-CANRM and CANRM-to-ASMG1 Interfaces (added SVs in green boxes, conditioned mapping in red arrows (first choice normal arrow, second choice dashed arrow)).

3. Results and discussion

In this section the impact on the model predictions of the two extensions performed is evaluated through steady-state simulation results of the BSM2N and of the BSM2NplusCANR. The results of these simulations will be used here to study:

- how the oxygen set-point in the aeration tanks affects the N_2O emissions,
- how the CANR reactor in the side-stream affects the performance of the plant,
- how the oxygen set-point in the aeration tanks affects the TN removal,
- how the oxygen demand is affected by the location of the CANR reactor.

The simulations are performed by controlling the oxygen concentration in the three mainstream aerobic tanks at 0.5 – 1 – 2 mg (-COD).L^{-1}. The reject water from the dewatering unit is recycled directly before the first mainstream anoxic tank following treatment in the CANR reactor. The water separated during the thickening of the wastage sludge is recycled before the primary clarifier (see Figure 2).

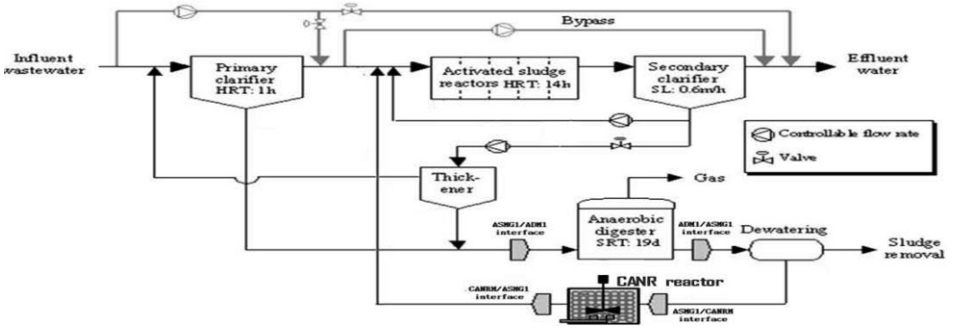

Figure 2: BSM2NplusCANR layout used for steady-state simulations.

3.1. Effect of oxygen on nitrous oxide emissions from the mainstream

The effect of the oxygen concentration in the three aerobic tanks on the emissions of N_2O from the five tanks in the mainstream of the BSM2N is here investigated. Table 1 shows: the emission factors of N_2O with respect to the N in the influent at different oxygen set points, the N_2O production and consumption rates by HB and the N_2O production by AOB.

Table 1: BSM2N N_2O emission factors and overall N_2O production and consumption rates by AOB and HB in the five biological tanks of the mainstream.

DO	N_2O emission factors	PRODUCTION RATE by HB	CONSUMPTION RATE by HB	OVERALL CONTRIBUTION by HB	PRODUCTION RATE by AOB	Liquid N_2O in the effluent
[mg(-COD).L^{-1}]	[% of g N_2O_{emit}-N.g^{-1} N_{inf}]	[g.m^{-3}.d^{-1}]	[g.m^{-3}.d^{-1}]	[g.m^{-3}.d^{-1}]	[g.m^{-3}.d^{-1}]	[g.m^{-3}]
0,5	**0,043**	412,64	-412,73	-0,09	$2{,}56 \cdot 10^{-4}$	$5{,}88 \cdot 10^{-5}$
1,0	**0,02**	402,60	-402,36	0,25	$2{,}02 \cdot 10^{-4}$	$2 \cdot 10^{-5}$
2,0	**0,022**	390,87	-390,56	0,31	$3{,}21 \cdot 10^{-4}$	$1{,}14 \cdot 10^{-5}$

First of all, it can be observed that there is no proportional correlation between the N_2O emissions and oxygen concentration. This could have been foreseen from the fact that the ASMG1 includes the N_2O production by two different types of bacteria with different kinetics. Furthermore, AOB themselves are modelled to produce N_2O through a Haldane-type function, according to which the role of oxygen switches from enhancing to inhibiting in function of the concentration of oxygen itself. Besides the mere production rates by these two species of microorganisms, also the stripping is important. Low N_2O productions occurring in a well-aerated aerobic zone can lead to significantly-high N_2O emissions due to the enhanced stripping capability. According to the model simulations, it can be observed that AOB are the driving force determining the N_2O dynamics in the system, whereas heterotrophs play a marginal role.

3.2. Effect of the inclusion of the CANR reactor on TN removal contributions

Table 2 shows the steady-state TN removal contribution by the different units respectively in the BSM2N and the BSM2NplusCANR at different operating oxygen set points. As can be noted, in the BSM2N most of the TN from the influent is removed in gaseous form (42.5 % of g N_{gas}-N.g^{-1} N_{infl}) while 13.4 % of influent TN is removed through assimilation into biomass cells through biomass growth. According to the BSM2NplusCANR approximately 17% of the influent TN is removed through the processes in the CANR reactor whereas 7% less is removed by the mainstream AS unit. The nitrogen removed through biomass growth remains unchanged. The decrease in the N removed by the processes in the AS unit is the consequence of the decrease in the nitrogen load recycled to the mainstream when the new reactor is added. As a matter of fact, this leads to a decrease in the concentration of AOB and NOB and in turn to a decreased conversion of influent nitrogen into gas in the mainstream. Summing up, when the CANR reactor is added, the total nitrogen discharged in the effluent from the plant decreases by approximately 10 %.

With regard to the effect of O_2 set-points, the main impact observed is in the decreased TN removal for increasing DO in the main activated sludge units. This is the consequence of the lower heterotrophic denitrification rate caused by oxygen inhibition.

Table 2: TN removal partitioned among the different units in function of DO set point for BSM2N and BSM2NplusCANR.

DO [mg.L^{-1}]	BSM2N		BSM2NplusCANR		
	AS N removal [%]	N storage in sludge [%]	AS N removal [%]	N storage in sludge [%]	CANR removal [%]
0,5	44,3	13,3	36,5	13,4	16,9
1	42,5	13,4	36	13,4	16,9
2	41,2	13,4	35,5	13,4	16,9

3.3. Effect the CANR reactor on total oxygen demand of the plant

Table 3 shows the different oxygen consumptions in both the BSM2N and the BSM2NplusCANR at different oxygen set points and the contributions in percentage by the three oxygen-consuming microorganisms, namely heterotrophs, ammonia-oxidizing and nitrite-oxidizing bacteria (AOB and NOB, respectively). When the CANR reactor is included, the nitrogen load recycled to the mainstream decreases considerably. At the same time the concentration of nitrifying biomass (both AOB and NOB) decreases as

well. This leads to a decrease in the total amount of oxygen consumed by AOB and NOB for nitrification. Contrarily, the heterotrophic consumption of oxygen increases. This can be explained by the fact that, as the production of nitrate by NOB is decreased, more organic biodegradable matter is available for aerobic oxidation rather than anoxic. Summing up, the savings of oxygen obtained from AOB and NOB compensate the increased oxygen consumption by HB, thus leading to an 16% overall reduction in the total plant oxygen requirements. This value may appear lower compared to the aeration requirements (i.e. 60%) reported in (Lackner et al., 2014). However it should be noted that those values reported in the literature consider local analysis of a PN/A system and not the plant-wide analysis presented here which provides a more accurate and realistic evaluation of the impact of PN/A technologies.

Table 3: Oxygen consumption by heterotrophic, ammonia-oxidizing and nitrite-oxidizing bacteria and total oxygen consumptions in both BSM2N and BSM2NplusCANR. The differences are calculated by subtracting the oxygen consumed in the BSM2N (*) and the one consumed in the BSM2NplusCANR (**).

DO_{sp} [mg/L]	OXYGEN CONSUMED [kg.d^{-1}]											
	HETEROTROPHS			AOB			NOB			TOTAL		
	(*)	(**)	Difference	(*)	(**)	Difference	(*)	(**)	Difference	(*)	(**)	Difference
0,50	1582	1734	**-153**	2959	2178	**781**	778	562	**216**	5318	4474	**844**
1	1671	1801	**-130**	2979	2195	**784**	593	419	**174**	5243	4415	**828**
2	1756	1869	**-113**	2982	2201	**782**	504	355	**149**	5241	4424	**817**

4. Conclusions

A new benchmark simulation model, the Benchmark Simulation Model No.2 for Nitrous oxide and for side-stream Complete Autotrophic Nitrogen Removal (BSM2NplusCANR), was developed. The aim of the extended model is to provide a reference simulation scenario enabling the development and the objective evaluation of novel control strategies for mitigating N_2O emissions in the mainstream and for autotrophic nitrogen removal in the side-stream. Simulation results have shown that AOB are the microorganisms with the major impact on the total N_2O emissions and that an increase of about 10% in the total nitrogen removal efficiency can be obtained when a new reactor for side-stream PN/A is implemented. At the same time, 16% savings in oxygen demand are achieved. With regard to process control options the results suggest that control strategies for N_2O emission minimization in the mainstream should focus on the AOB activity whereas in order to increase the energy savings a better PN/A performance would be needed.

References

Guo, L., Vanrolleghem, P.A., 2014. Calibration and validation of an activated sludge model for greenhouse gases no. 1 (ASMG1): prediction of temperature-dependent N2O emission dynamics. Bioprocess Biosyst. Eng. 37, 151–163. doi:10.1007/s00449-013-0978-3

Jeppsson, U., Alex, J., Batstone, D.J., Benedetti, L., Comas, J., Copp, J.B., Corominas, L., Flores-Alsina, X., Gernaey, K. V, Nopens, I., Pons, M.-N., Rodríguez-Roda, I., Rosen, C., Steyer, J.-P., Vanrolleghem, P. a, Volcke, E.I.P., Vrecko, D., 2013. Benchmark simulation models, quo vadis? Water Sci. Technol. 68, 1–15. doi:10.2166/wst.2013.246

Jeppsson, U., Pons, M.-N., Nopens, I., Alex, J., Copp, J.B., Gernaey, K. V, Rosen, C., Steyer, J.-P., Vanrolleghem, P. a, 2007. Benchmark simulation model no 2: general protocol and exploratory case studies. Water Sci. Technol. 56, 67–78. doi:10.2166/wst.2007.604

Lackner, S., Gilbert, E.M., Vlaeminck, S.E., Joss, A., Horn, H., van Loosdrecht, M.C.M., 2014. Full-scale partial nitritation/anammox experiences - An application survey. Water Res. 55, 292–303. doi:10.1016/j.watres.2014.02.032

Vangsgaard, A.K., Mauricio-Iglesias, M., Gernaey, K. V, Smets, B.F., Sin, G., 2012. Sensitivity analysis of autotrophic N removal by a granule based bioreactor: Influence of mass transfer versus microbial kinetics. Bioresour. Technol. 123, 230–241. doi:10.1016/j.biortech.2012.07.087

Krist V. Gernaey, Jakob K. Huusom and Rafiqul Gani (Eds.), 12th International Symposium on Process Systems Engineering and 25th European Symposium on Computer Aided Process Engineering.
31 May - 4 June 2015, Copenhagen, Denmark.

A Framework for the Dynamic Modelling of PI Curves in Microalgae

Andrea Bernardi[a,c], Andreas Nikolaou[b], Andrea Meneghesso[c], Benoît Chachuat[b], Tomas Morosinotto[c] and Fabrizio Bezzo[a,c]

[a]*CAPE-Lab: Computer-Aided Process Engineering Laboratory, Department of Industrial Engineering, University of Padova, via Marzolo 9, 35131 Padova, Italy*
[b]*Centre for Process Systems Engineering, Department of Chemical Engineering,, Imperial College London, South Kensington Campus, London, SW7 2AZ, UK*
[c]*PAR-Lab: Padova Algae Research Laboratory, Department of Biology and Department of Industrial Engineering, University of Padova, via Ugo Bassi 58B, 35131 Padova, Italy*

Abstract

Photosynthesis-Irradiance (PI) response curves constitute a powerful tool for characterizing the photosynthetic properties of microalgae. This paper presents a dynamic model capable of predicting the photosynthesis rate under dynamic light conditions. Fast and slow time-scale processes are coupled using fluorescence data for three different photoacclimation states. The model shows a very good agreement with the available experimental data and the values of the calibrated parameters are consistent with biological evidence. The predicted PI curves exhibit all the expected trends regarding their initial slopes, maximum photosynthesis rates, and photoinhibion effects. By analyzing the effect of different experimental protocols on the PI curve predictions, our results highlight the importance of an accurate description of the protocols used to obtain the experimental data.

Keywords: modeling, fluorescence, microalgae, PI curves

1. Introduction

Microalgae-based processes are considered one of the most promising alternative technologies for the production of liquid fuels for the transportation sector (Chisti, 2007). The main advantages of microalgae compared with other renewable feedstocks are their high potential productivity and the absence of competition with traditional crops for arable land. However, this potential is still theoretical, and algal-derived biofuel on large-scale is not profitable as of yet. Several issues need to be addressed to reach this objective, including algae cultivation, harvesting and products extraction (Williams and Laurens, 2010; Mata et al., 2010).

Reliable models of microalgae growth, able to capture the dominant physical, chemical, and biological phenomena, can expose the interactions between equipment design and product yields and eventually help to scale-up and optimize process design and operation. In practice though, and even in lab-scale conditions where certain physical phenomena can be controlled or neglected, predicting growth rates is quite complicated due to the presence of intricate mechanisms spanning multiple time-scales: *Photoproduction* encompasses all the processes from photons utilization to CO_2 fixation that occur within milliseconds (Williams and Laurens, 2010); *Photoinhibition*, the observed loss of photosynthetic production due to excess or prolonged exposure to light, acts on

a time scale of minutes to hours; *Photoregulation*, also known as non-photochemical quenching (NPQ), the set of mechanisms by which microalgae protect their photosyntheti apparatus via the dissipation of excess energy as heat, occurs within minutes; *Photoacclimation*, the ability of the cells to adjust their pigment content and composition under varying light and nutrient conditions, occurs within hours or days; finally, the mechanisms involved in *nutrient internalization* and their *metabolism* into useful products occurs within hours or days as well (Falkowski and Raven, 1997). In addition to these biological mechanisms, physical phenomena such as hydrodynamics and light attenuation also have an effect on the apparent growth rate of a microalgae culture.

Photosynthesis-Irradiance (PI) response curves constitute a powerful tool for characterizing microalgae growth rate. Accurate representation of such curves in a mechanistic manner has been an important challenge for many years, since both the effects of light and nutrients can be captured and optimal productivities of large scale production systems can be inferred this way (Bernard, 2011). The most usual approach for representing PI curves includes the use of static input-output relationships (Jassby and Platt, 1976). Despite their simple form and handiness, these models fail to explain the effects of the various biological mechanisms on the photosynthesis rate. Moreover, the experimental procedure currently in use for obtaining PI curves is not only time consuming, but a precise estimation of the growth conditions, that is, the level of photoregulation or photoinhibition, is hardly possible.

The main objective of this paper is to represent the rate of photosynthesis under varying light conditions, by accounting for the dominant regulatory and inhibitory mechanisms. More specifically, we predict PI curves using the dynamic model of chlorophyll fluorescence by Nikolaou et al. (2015), which makes use of fluorescence data to characterize the quantum yield of photosynthesis when photoproduction, photoinhibition and photoregulation are all taking place. We discuss an extension of this model for describing photoacclimation phenomena, and we calibrate the model using fluorescence data for the microalga *Nannochloropsis gaditana* acclimated at three different light intensities. Finally, we analyze the predicted PI curves and investigate the effect of different experimental protocols on these predictions.

2. Dynamic Modelling of Photosynthesis-Irradiance Curves

2.1. Fluorescence model

Fluorescence refers to the re-emission of photons by chlorophyll molecules, which can be measured by fluorometers (Papageorgiou, 2004). Modern fluorometry, such as Pulsed Amplidute Modulation (PAM), relies on complex light protocols to trigger various mechanisms in the photosynthetic response of microalgae. Specifically, under nutrient-replete conditions and at a given photoacclimation state, the fluorescence flux, F, depends on the state of the photosynthetic apparatus and the activity of photoregulation (Nikolaou et al., 2015):

$$F = \frac{S_{\mathrm{F}}\sigma}{1+\eta_{\mathrm{D}}+\overline{\eta}_{\mathrm{qE}}\,\alpha+A\,\eta_{\mathrm{P}}+C\,\eta_{\mathrm{I}}}\,, \tag{1}$$

where S_{F} is a scaling parameter proportional to the chlorophyll content, *chl*, of the sample; σ denotes the total cross section $[\mathrm{m}^2\,\mathrm{g}_{\mathrm{chl}}^{-1}]$; and $\Phi := 1/(1+\eta_{\mathrm{D}}+\overline{\eta}_{\mathrm{qE}}\,\alpha+A\,\eta_{\mathrm{P}}+C\,\eta_{\mathrm{I}})$ represents the quantum yield of fluorescence. The latter depends on: the parameters η_{P}, η_{D}, $\overline{\eta}_{\mathrm{qE}}$ and η_{I}, which stand for, respectively, the rates of photoproduction, basal thermal decay, quenching linked to photoregulation and quenching linked to photoinhibiton, all relative to the rate of fluorescence; the variable $\alpha \in [0,1]$, which represents the activity of photoregulation; and A and C are the fractions of PSUs in open and inhibited states, respectively. The flux F is minimal, denoted as F_0, when $A = 1-C$; whereas F is maximal, denoted as F_m, when $A = 0$.

The state of the photosynthetic apparatus is represented by the mechanistic model by Han (2002). According to this model the physical entity responsible for the production of one O_2 molecule,

usually refered to as Photosynthetic Unit (PSU), has three possible states: open PSUs are ready to accept photons and produce O_2; closed PSUs are occupied with already accepted photons; and damaged PSU, arise when closed PSUs receive extra photons due to excessive irradiance. The fractions of open A, closed B and damaged C PSUs, which sum to 1 at all times, are represented by the following set of differential equations:

$$\begin{aligned} \frac{dA}{dt} &= -I\,\sigma_{\mathrm{PS2}}\,A + \frac{B}{\tau} \\ \frac{dB}{dt} &= I\,\sigma_{\mathrm{PS2}}\,A - \frac{B}{\tau} + k_{\mathrm{r}}\,C - k_{\mathrm{d}}\,\sigma_{\mathrm{PS2}}\,I\,B \\ \frac{dC}{dt} &= -k_{\mathrm{r}}\,C + k_{\mathrm{d}}\,\sigma_{\mathrm{PS2}}\,I\,B\,, \end{aligned} \tag{2}$$

where I denotes the light intensity [$\mu\mathrm{E\,m^{-2}\,s^{-1}}$]; τ, the turnover time [s]; k_{d}, the damage rate constant [–]; k_{r}, the repair rate constant [$\mathrm{s^{-1}}$]; and σ_{PS2}, the effective cross section [$\mathrm{m^2\,\mu E^{-1}}$]. Following Falkowski and Raven (1997), the latter is related to the total cross section, σ, as

$$\sigma_{\mathrm{PS2}} = \Phi_{\mathrm{p}}^{A}\,\frac{\sigma}{N}\,, \tag{3}$$

where N is the number of PSUs [$\mathrm{mol\,e^-\,g_{chl}^{-1}}$], which remains constant for a given photoacclimation state; and Φ_{p}^{A} is the quantum yield of photosynthesis of an open PSU, equal to $\eta_{\mathrm{P}}/(1+\eta_{\mathrm{D}}+\overline{\eta}_{\mathrm{qE}}\alpha+\eta_{\mathrm{P}})$.

On the other hand, the activity of photoregulation, α, is described by first-order dynamics as

$$\frac{d\alpha}{dt} = \xi\,(\alpha_{\mathrm{ss}}(I)-\alpha)\,, \quad \text{with} \quad \alpha_{\mathrm{ss}}(I) := \frac{I^n}{I_{\mathrm{qE}}^n + I^n}\,, \tag{4}$$

where ξ [$\mathrm{s^{-1}}$] denotes the photoregulation time constant; and $\alpha_{\mathrm{ss}}(I)$ is the steady-state value of the photoregulation activity. Based on preliminary experimental data, the latter is modeled as a sigmoid (Hill) function of light intensity, using the parameters I_{qE} [$\mu\mathrm{E\,m^{-2}\,s^{-1}}$] and n [–].

2.2. Photoacclimation Extension

Photoacclimation refers to physiological adaptations of the photosynthetic apparatus in order for phototrophs to optimize their growth under long-term variations in the light intensity (MacIntyre et al., 2002). The most profound effect of photoacclimation is a decrease in the chlorophyll content *chl*, as the irradiance increases and vice-versa (Fisher et al., 1996). In turn, the variation in chlorophyll content affects the photosynthetic apparatus: the total cross-section σ decreases as chlorophyll increases due to shading effects (Falkowski et al., 1985), whereas the number of PSUs N can either increase or decrease as a function of chlorophyll for different species (Falkowski and Owens, 1980). Moreover, the variation in pigment composition can affect the activity of photoregulation (Anning et al., 2000). In consequence, microalgae samples that are acclimated at different light intensities will present different fluorescence responses to the same PAM protocol.

An extension of the model by Nikolaou et al. (2015) is needed in order to account for the effect of photoacclimation on the fluorescence flux. Both σ and N, which depend on the chlorophyll content, become functions the photoacclimation state, and so does the parameter S_{F}. Moreover, the photoregulation activity α can depend on the photoacclimation state via its parameters I_{qE} and η_{D}. While empirical equations could be used to describe all these dependencies, we decided not to do so in this work because the available data would not be sufficient to estimate these extra parameters confidently or discriminate between alternative modeling hypotheses. Instead, we use replicates of the fluorescence model for various photoacclimation states, whereby each replicate takes a different set of parameter values for σ, S_{F}, N, I_{qE} and η_{D}, while using the same values for all the other parameters.

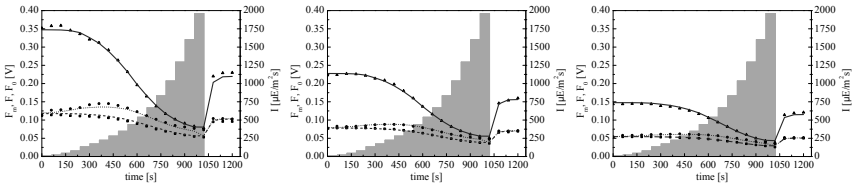

(a) $I_g = 15\mu\text{E/m}^2\text{s}$ (b) $I_g = 100\mu\text{E/m}^2\text{s}$ (c) $I_g = 625\mu\text{E/m}^2\text{s}$

Figure 1: Fitting results of the fluorescence fluxes for three different photoacclimation states.

2.3. Photosynthesis Rate

An expression of the photosynthesis rate comes forward in the form (Falkowski and Raven, 1997):

$$P = \sigma\Phi I\,, \tag{5}$$

with Φ the photosynthesis quantum yield [mol O_2 μE^{-1}]. The aforementioned units, give dimensions for P in [mol O_2 $g_{chl}{}^{-1}$ s^{-1}], which by definition is the chlorophyll specific photosynthesis rate, in terms of the oxygen production. The dynamic model of fluorescence predicts the value of the realized quantum yield of photosynthesis, Φ_{PS2} in units of [mol e^- μE^{-1}]. From the literature, it is known that Φ_{PS2} is closely related to Φ (Suggett et al., 2003). Here, we introduce a stoichiometric coefficient that aligns the electrons required for the production of each O_2 molecule. Considering the water dissociation reaction ($2H_2O + 4e^- \rightarrow O_2 + 4H^+$), we obtain a theoretical minimum value of 4 mol e^-/mol O_2.

3. Results and discussion

3.1. Model Calibration

The extended fluorescence model for PI curve prediction is calibrated using three experimental data sets of chlorophyll fluorescence for the microalga *Nannochloropsis gaditana*. Each set corresponds to a different photoacclimation light intensity, I_g, namely 15, 100 and 625 μE m^{-2} s^{-1}. Model calibration is performed in the modeling environment gPROMS (`http://www.psenterprise.com`) using maximum likelihood estimation. The model fits are presented in Fig. 1, and the values of the acclimation-dependent parameters are reported in Table 1.

Table 1: Parameter values for different photoacclimation states.

Parameter		15 μE m^{-2} s^{-1}	100 μE m^{-2} s^{-1}	625 μE m^{-2} s^{-1}
I_{qE}	[μE m^{-2} s^{-1}]	762	847	1048
σ	[m^2 g_{chl}^{-1}]	1.64	1.73	1.79
η_D	[-]	6.64	6.75	7.8
N	[mol e^- g_{chl}^{-1}]	3.5×10^{-7}	4.50×10^{-7}	6.62×10^{-7}
S_f	[g_{chl} μE^{-1} V^{-1}]	1.59	1.00	0.7

The calibration results show a good agreement between the model and the experimental data. Regarding the parameter estimates, observe that these values are consistent with the theoretical considerations discussed in Sect. 2.2. In particular, S_F, which depends linearly on the chlorophyll content shows a decreasing trend with I_g; σ is inversely related to S_F; N and η_D are both increasing with increasing I_g, an expected behavior for η_D as it linked to the accumulation of photoprotective pigments; and I_{qE} turns out to be almost linearly related to I_g, suggesting that photoregulation is activated at higher light irradiance when microalgae are also acclimated at higher light irradiance.

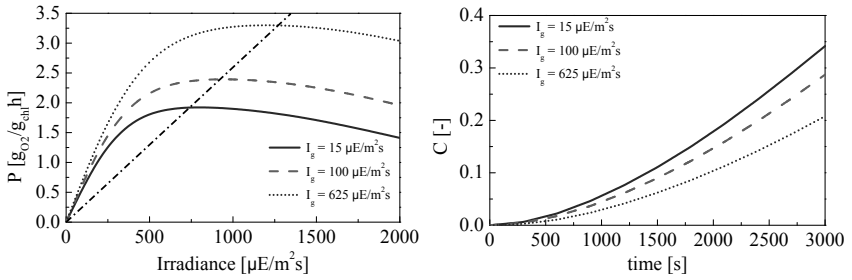

(a) PI curves (b) *C* profile

Figure 2: PI curves (left plot) and photoinhibition evolution (right plot) for three different photoacclimation states. Dotted, dashed and continuous lines correspond to 625, 100 and 15 μE m^{-2} s^{-1}.

3.2. Dynamic Simulation of PI curves

PI curves are predicted for the same three photoacclimation states as in Sect. 3.1. A fictitious experimental protocol is considered, whereby the microalgae sample is exposed to progressively increasing light intensities from 0 to 2000 μE m^{-2} s^{-1} in 10 constant light stages of 5 minutes each (increasing the irradiance by 200 μE m^{-2} s^{-1} at every stage). Then, the value of the photosynthesis rate P at the end of each stage is plotted against the corresponding light intensity. Note that during each 5-minute stage, that is between a change in the light intensity to the measurement of P, the sample does not reach static growth conditions because neither photoinhibition nor possibly some components of photoregulation have reached equilibrium yet.

The experimental protocol is simulated using the three calibrated model replicates from Sect. 3.1, which correspond to the photoacclimation states at 15, 100 and 625 μE m^{-2} s^{-1} growth irradiance. The initial fraction of inhibited PSUs is taken as $c(0) = 0$ in agreement with the experimental data used for model calibration (Nikolaou et al., 2015). It is seen on the left plot of Fig. 2 that the initial slope of the predicted PI curves is constant and that the maximum photosynthesis rate is greater for higher acclimated cells, in agreement with results from the litterature (Anning et al., 2000; MacIntyre et al., 2002). Moreover the optimum light intensities and the maxima of photosynthesis rate for different acclimation states are linearly related (Hartmann et al., 2013). Finally, the photoinhibition profiles, reported on the right plot of Fig. 2 show that cells acclimated at lower light irradiance (hence with higher chlorophyll content) are more prone to photoinhibition.

Fig. 3 compares three predicted PI curves for a sample acclimated at 100 μE m^{-2} s^{-1}. The dashed curve is identical to the profile reported in Fig. 2; the dotted line represents the profile predicted if the value of C at the beginning of the protocol is 0.1; and the continuous curve represents the predicted PI curve if a longer protocol with 20 (instead of 10) stages of 5 minutes constant light is used. We can observe that both the initial slope and the maximum photosynthesis rate decrease if the sample has a certain amount of inhibited PSUs at the beginning of the protocol. Moreover, the dynamic simulation of PI curves shows that if a longer protocol is considered, the initial slope is not affected, but a reduction of the maximum photosynthesis rate and a larger reduction of P at high irradiance are obtained.

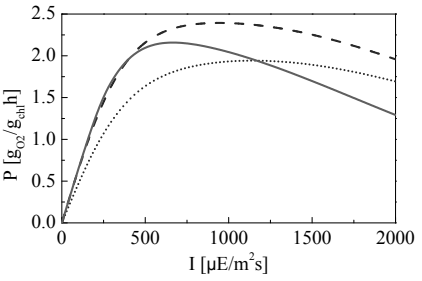

Figure 3: PI curves for a sample acclimated at 100 μE m^{-2} s^{-1}.

Note that in most of the literature, the light protocol used to derive them is not given. Our findings clearly show that the light protocol has a strong influence on the PI response curves and should always be considered to avoid drawing of misleading conclusions.

4. Conclusions

A semi-mechanistic model describing photoproduction, photoregulation and photoinhibition in microalgae has been extended to account for photoacclimation by varying a subset of the model parameters. The model predicts well experimental data of PAM fluorescence for three different acclimation states. Subsequently, a light-dependent photosynthesis rate expression has been formulated, which enables simulation of experimental protocols for the prediction of PI curves. Our results show that it is thus possible to predict PI curves using fluorescence measurements, thereby making the characterization of microalgae growth both faster and more robust. Moreover, our results underpin that the exact experimental protocol used to obtain PI curves and the initial condition of the photosynthetic apparatus are paramount and would thus need to be reported systematically. Future directions include the development of empirical relationships for photoacclimation-dependent parameters and the concurrent use of PI curve and fluorescence data for the purpose of model calibration and validation.

Acknowledgements: AN and BC gratefully acknowledge financial support by ERC career integration grant PCIG09-GA-2011-293953 (DOP-ECOS). TM gratefully acknowledges financial support by ERC starting grant 309485 (BIOLEAP). AB and FB gratefully acknowledge Fondazione Cariparo for grant Progetto Dottorati di Ricerca 2012.

References

T. Anning, H. L. MacIntyre, S. M. Pratt, P. J. Sammes, S. Gibb, R. J. Geider, 2000. Photoacclimation in the marine diatom skeletonema costatum. Limnology and Oceanography 45 (8), 1807–1817.

O. Bernard, 2011. Hurdles and challenges for modelling and control of microalgae for CO_2 mitigation and biofuel production. Journal of Process Control 21 (10), 1378–1389.

Y. Chisti, 2007. Biodiesel from microalgae. Biotechnology Advances 25 (3), 294–306.

P. G. Falkowski, Z. Dubinsky, K. Wyman, 1985. Growth-irradiance relationships in phytoplankton. Limnology and Oceanography 30 (2), 311–321.

P. G. Falkowski, T. G. Owens, 1980. Light–shade adaptation: Two strategies in marine phytoplankton. Plant Physiology 66, 592–595.

P. G. Falkowski, J. A. Raven, 1997. Aquatic photosynthesis. Vol. 256. Blackwell Science Malden, MA.

T. Fisher, J. Minnaard, Z. Dubinsky, 1996. Photoacclimation in the marine alga nannochloropsis sp.(eustigmatophyte): a kinetic study. Journal of plankton research 18 (10), 1797–1818.

B. P. Han, 2002. A mechanistic model of algal photoinhibition induced by photodamage to photosystem-II. Journal of Theoretical Biology 214 (4), 519–27.

P. Hartmann, A. Nikolaou, B. Chachuat, O. Bernard, 2013. A dynamic model coupling photoacclimation and photoinhibition in microalgae. In: Control Conference (ECC), 2013 European. IEEE, pp. 4178–4183.

A. D. Jassby, T. Platt, 1976. Mathematical formulation of the relationship between photosynthesis and light for phytoplankton.

H. L. MacIntyre, T. M. Kana, T. , R. J. Geider, 2002. Photoacclimation of photosynthesis irradiance response curves and photosynthetic pigments in microlagae and cyanobacteria. Journal of Phycology 38 (1), 17–38.

T. M. Mata, A. A. Martins, N. S. Caetano, 2010. Microalgae for biodiesel production and other applications: a review. Renewable and Sustainable Energy Reviews 14 (1), 217–232.

A. Nikolaou, A. Bernardi, A. Meneghesso, F. Bezzo, T. Morosinotto, B. Chachuat, 2015. A model of chlorophyll fluorescence in microalgae integrating photoproduction, photoinhibition and photoregulation. Journal of Biotechnology 194, 91 – 99.

G. C. Papageorgiou, 2004. Chlorophyll a fluorescence: a signature of photosynthesis. Vol. 19. Springer.

D. J. Suggett, K. Oxborough, N. R. Baker, H. L. MacIntyre, T. M. Kana, R. J. Geider, 2003. Fast repetition rate and pulse amplitude modulation chlorophyll a fluorescence measurements for assessment of photosynthetic electron transport in marine phytoplankton. European Journal of Phycology 38 (4), 371–384.

P. J. l. B. Williams, L. M. L. Laurens, 2010. Microalgae as biodiesel & biomass feedstocks: Review & analysis of the biochemistry, energetics & economics. Energy & Environmental Science 3 (5), 554–590.

Krist V. Gernaey, Jakob K. Huusom and Rafiqul Gani (Eds.), 12th International Symposium on Process Systems Engineering and 25th European Symposium on Computer Aided Process Engineering.
31 May – 4 June 2015, Copenhagen, Denmark

Progresses of PSE Studies on Water Networks and Industrial Application Practices in China

Youqi Yang,[a] Xiaoping Jia,[b] Lei Shi,[c] Qinxian Zhuang [a]

[a] *Beijing Sunbridge Softtech Ltd., Beijing 100084, China*
[b] *School of Environment and Safety Engineering, Qingdao University of Science and Technology, Qingdao 266042, China*
[c] *School of Environment, Tsinghua Univesity, Beijing100084, China*

Abstract

This work presents the overview of process systems engineering (PSE) studies on water network and the industrial applications in China. The progresses are reviewed according to three levels: (1) water network integration and optimization at a single enterprise level; (2) multiple water network integration at inter-plant level; and (3) virtual water and water footprint analysis across regions/countries. The industrial implementation approach called "three-step approach" is demonstrated in China. The three steps are: (1) enterprise-wide water balance test and measurement; (2) water system decomposition and integration; (3) wastewater regeneration and reuse. According to Chinese experience of more than 20 petrochemical and coal based chemical enterprise projects, the reduction target of 20% ~ 60% of the freshwater could be achieved with using this approach.
Keywords: water network, water footprint, process integration, three-step approach

1. Introduction

The water crisis is becoming more serious. Stricter environmental regulation, higher cost in water tariff and wastewater treatmen, and shortages of freshwater resource have encouraged efforts for water management improvement and minimization of water consumption in process industries. Research papers published on water network study have dramatically increased since about 2005 (Yang et al., 2015). This paper consisted of two parts. In the first part an overview of the progresses of PSE studies on water network is described. The industrial application approach with a case study is introduced in the second part.

2. Brief overview for water network integration

2.1. intra-plant water integration

A considerable amount of work has been reported since Wang and Smith (1994a) initiated the insight-based approach on pinch analysis for Water Using Network (WUN). In their later work, the approach was extended into Wastewater Treatment Network (WWTN) synthesis (Wang and Smith, 1994a). Kuo and Smith (1998a; 1998b) proposed an approach to optimize the water using network with regeneration unit, then to optimize Total Water Network (TWN). Bagajewicz and Faria (2009) added a water pre-treatment unit into TWN called Complete Water Network (CWN), which can further reduce freshwater consumption. Ku-Pineda and Tan (2006) considered the environment impact of the retrofitting water network with a higher environmental cost as measured using a more comprehensive metric. Recently the simultaneous integration of the water network and the surrounding watershed is presented to satisfy process and

environmental constraints (Fernando et al., 2011) . The relation of these different system boundries is shown in Figure 1.

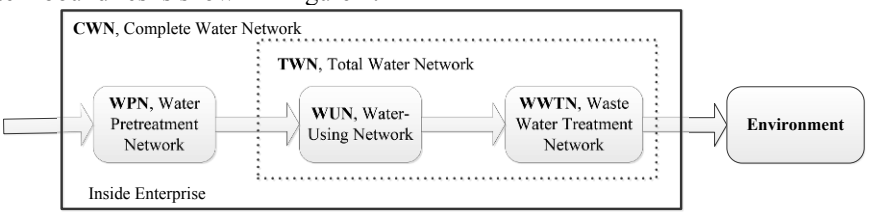

Figure 1 Different system boundaries for water network

In general, systematic design for water integration is in either of two ways: (i) targeting for the optimum profile of the process, ahead of detailed design and without commitment to the final system configuration. It is called *insight-based method;* (ii) putting the alternatives in the form of an optimization problem, using a superstructure which should be reduced to optimal solution. This method is *mathematic programming*. Various graphical techniques were proposed since the initiation of the water pinch analysis technique. Among these insight-based techniques, the three best developed techniques are limiting composite curve, material recovery pinch diagram and water cascade analysis (Foo, 2013). For the mathematic programming method, the optimization of the mathematical model associated with the superstructure is based upon non-linear programming/mixed-integer non-linear programming. An integration approach which combined the graphical approach with mathematical programming is proposed to minimize the industrial wastewater (Aiva-Argaez et al., 1998).

There are three special issues in the intra-plant water network integration, i.e. cooling water system, water-using network with internal water main and batch water network. Kim and Smith (2001) extended the water pinch analysis principle into the cooling water system. Majozi and co-workers made some extension (Majozi et al., 2006). Kim and Smith (2004) introduced the superstructure approach into the batch water network, which made the water network to be segregated by time. Since then many papers have been reported for the batch water network which have been reviewed by reference (Gouws et al., 2010).

Lots of studies have focused on the simultaneous optimization of water allocation and heat exchange network based on the mathematical programming (Klemes, 2013), which is called WAHEN (Water Allocation and Heat Exchange Network) problem. More over, in order to compare the best feedstock for gasoline schools led by Grossmann and Floudas extended into process optimization to meet the minimum freshwater, energy consumption targets (Ahmetovic et al., 2010; Baliban et al., 2011).

2.2. inter-plant water integration (IPWI)

Since the single plant can achieve the minimum freshwater consumption through direct reuse, recycle and regeneration scheme, the water minimization targeting approach for single plant is both simple to use and powerful. The system boundry is extended to two or more plants, the water saving opportunities will be improved. Indeed, in practice each water network may be grouped according to the geographical location of the water-using processes or as different plants operated by different business entities. Olesen and Polley (1996) first addressed the IPWI problem using the pinch-based load table technique. Among IPWI studies, there are two different schemes, i.e. direct and indirect integration (Chew et al., 2008). In the direct integration scheme, water sources may be integrated with sinks in different water networks directly. On the other hand, indirect integration is achieved via the centralized utility hub scheme. The implementation of

centralized utility hub improves the overall water network practicability and flexibility when serving a greater number of plants comprising the individual water network.

Recently the increase of public awareness towards eco-industrial parks (EIP) has inspired many researchers. Rubio-Castro et al. (2012) considered the optimal retrofit of water networks in the industrial zone. The freshwater cost presents a total of 75% savings with respect to the existing networks. Boix et al. (2012) formulated industrial water networks based on mixed-integer linear programming using a multi-objective optimization strategy, where fresh water, regenerated water flow rates as well as the number of network connections (integer variables) are minimized. Aviso et al. (2009) formulated a model which incorporates the benefits of networking relating to the individual goals and targets of the participants through fuzzy mathematical programming. Under the condition of freshwater price influenced by the market, Jia et al. (2010) proposed a superstructure based mathematical optimization method for total water networks with consideration of minimum cost in an industrial park.

2.3. Virtual water and water footprint studies across prefectures /countries

Virtual water refers to the water amount incorporated into the specific product such as rice and wheat, thus quantifying water consumption embodied in international trade (Allen 1997). Besides the amount, where and how water is consumed and/or discharged also affects the environmental pressure to water usages units at different scales, from process, product and company at micro level, to regional and watershed at meso-level, and to national and global scale. This consideration leads to the concept of water footprint which refers to the water amount required in the production or consumption of all goods and services at targeted scales. Three types of water footprint have been defined, including blue, green and grey water footprints, with the blue and green water footprints emphasizing the consumption of water and the grey water footprint highlighting the environmental impact of pollution (Hoekstra et al., 2012).

The water footprints concerned with industries, from the viewpoint of process systems engineering, mainly include but not limited to process, product and corporate water footprints. Process water footprint refers to the water consumption or pollution by the specific processes or plants. Product water footprint is defined as the water consumption or pollution along the product life cycle, which means the water consumed or polluted in the upper supply chains is also included. Corporate water footprint refers to the water consumption directly or indirectly to business operation.

One corporation may produce one or more products, and one product may need one or more processes to produce, thus the three kinds of water footprints are closely coupled (Sun et al., 2014). Generally, there are two methods to calculate water footprints. One is production tree method, which accounts for the water consumption of products based on the specific production cases and the utilization of water resources in different areas from the producers' point of view (Hoeksrea and Chapagain, 2007). The other is suggested by Zimmer and Renault (2003), which accounts for the water consumption by dividing products consumed into different types from the consumers' point of view.

Up to now, product water footprint has been more widely appreciated and applied. For crops, product water footprint is actually its virtual water in essence. Thus corn, wheat, rice and cotton were studied first. Later, the research extended to bread, butter, beer and other agricultural products, and then to meat, lamb, beef, chicken and other livestock products. Most of these products have high water footprints, and the livestock much higher than cropping. For example, the EU's research shows, the average water footprint of 150g beef burger is 2,350L water, nearly 15 times higher than the same amount of soy burgers (Hoekstra, 2009).

With the maturity of the water footprint concept and method, more and more industrial products such as steel, textile, paper, and even automobile complex products have been studied. Some results are shown in Figure 2. The results showed that huge structural differences between different industrial sectors and different life cycles. For example, the Volkswagen sedans have the water footprint of 52~84 m^3/car, with 95% of water consumed in the production stage, while only 1% consumed in the direct production process for papers (Manzardo et al. 2014). Unlike agriculture products, the challenges for industrial products lie in how to accurately track and quantify the complex and high-interwoven supply chains. Thus, PSE is expected to make a contribution to explore accounting, tracking and even mining policy implications to water footprints of industrial chains, industrial clusters and industrial layout on systematic level.

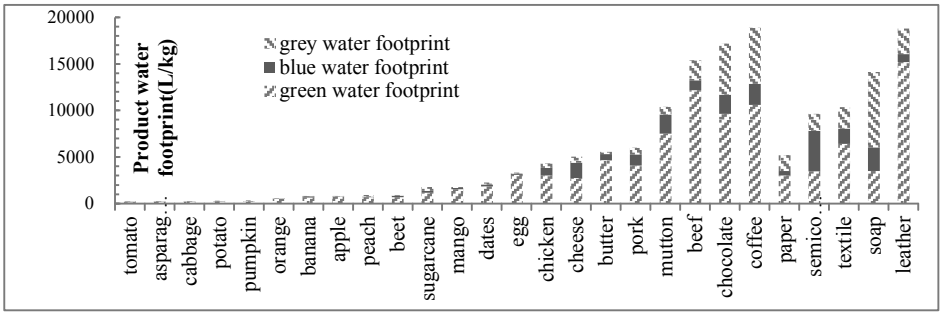

Figure 2 The water footprints of some selected agricultural and industrial products

3. Industrial application practices in China

In order to apply some developed water network integration methodologies, an approach called "three-step approach" is demonstrated in China (Yang et al., 2008; 2012). The first step is enterprise-wide water balance test and measurement. This is the most time consuming step.Water balance data are the basis of a whole project. The major results of this step are all concerned economic-technical criteria which representing the operation standard of the enterprise, such as quantity of water intake for per ton product, quantity of water intake for desalination water, steam condensate recovery ratio, quantity of wastewater for per ton product, wastewater recovery ratio, etc. The second step is water system integration and optimization in order to maximize the water reuse and minimize the wastewater discharge. The enterprise-wide water system is decomposed into seven subsystems, as shown in Figure 3. They are: freshwater treatment system, water pipeline system, process water-use system, cooling water system, condensate water system, living water system, and wastewater system. The third step is wastewater regeneration and reuse after wastewater reduction. This approach has been applied to more than 20 petrochemical and coal-based chemical enterprise projects since 2003. According to our experiences, 20% to 60% of freshwater intaken could be saved with this approach.

As a case study, this approach was applied in a coal to olefin (CTO) enterprise in Baotou, Inner Mongolia, China. According to the water balance measurement, quantity of water intake for ton olefin is 24.4 t (its designed value is 32 t); freshwater used for ton chemical water is 1.54 t (it standard value of chemical industry is 1.33 t); steam condensate recovery ratio is 85% and wastewater recovery ratio is 43.6% (its standard is ≥50%). Through improvement of the instrumentation and leakage check, about 30 t/h water could be saved. In the freshwater treatment subsystem, after optimizing the

desalination water processing and recovery of blowdown water from boilers and wash water of ultra-filter, 284 t/h of freshwater could be saved. In process water-using subsystem the water reallocation calculation was implemented with 5 impurity components, the result showed that 270 t/h freshwater could be saved. In cooling water subsystem, 1,000 t/h water is vaporized through cooling water towers. a new vapor recovery facility will recover 20% of this amount of vaporized water. The wastewater from cooling water plant is also recovered and reused as makeup water. After optimizing the whole cooling water plant, 390 t/h water could be saved. In the condensate water subsystem, recovery of vent vapor contributes 37 t/h condensate water. After above improvements of those 6 subsystems, the quantity of wastewater discharged was reduced 37%, a near zero liquid discharge technique called Non-Thermal Brine Concentrator (NTBC) is recommended. 95% inlet concentrated wastewater could be recovered for reuse; this will save 331 t/h water. Therefore, the freshwater intake is reduced from 1,796 t/h to 515 t/h. The quantity of water intake for per ton olefin from 24.4 t reduced to 7.01 t.

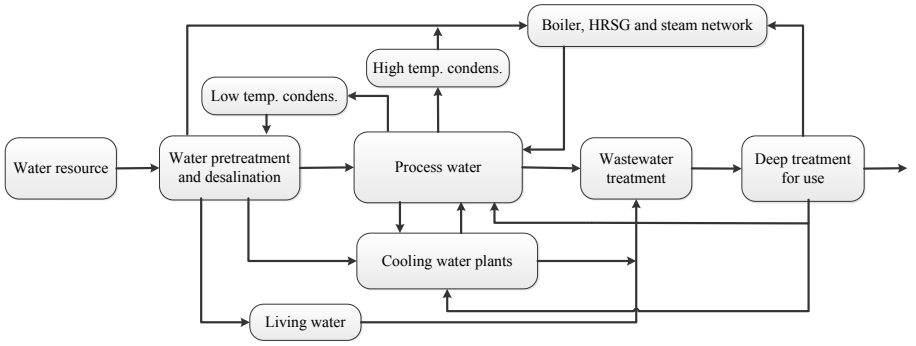

Figure 3 Seven subsystems for enterprise-wide water networks

4. Conclusions

Industrial water system optimization is a multi-scale and complex topic. Process integration and optimization methods in PSE not only play an important role in water conservation and wastewater reduction, but provide a theoretical basis for policy decisions. According to the scale boundries, this work reviewed the water network research via three levels, i.e. intra-plant, inter-plant, and regional-based. Specially, virtual water and water footprint study further broadened the field of industrial water systems. From the Chinese experiences, the industrial application of water network integration lagged far behind the theoretical studies. However, even though only few of them have been used in industries, the water saving effect is significant.

Acknowledgement

The authors acknowledge partial financial support from the National Science Foundation of China (21136003, 41101570) and the Major Science and Technology Program for Water Pollution Control and Treatment (2012ZX07203-004; 2012ZX07301-005).

References

E. Ahmetovic, M. Martın, I. E. Grossmann, 2010, Optimization of Energy and Water Consumption in Corn-Based Ethanol Plants, *Ind. Eng. Chem. Res*., 49(17): 7972-7982

T. Allan, 1997, Virtual water: a long term solution for water short Middle Eastern economies. Association Festival of Science, Roger Stevens Lecture Theatre, British: University of Leeds

A. Alva-Argaez, A. C. Kokossis, R. Smith, 1998, Wastewater Minimization of Industrial Systems Using an Integrated Approach, *Comput. Chem. Eng.,* 22:S741-S744

K. B. Aviso, R. R. Tan, A. B. Culaba, 2009, Designing eco-industrial water exchange networks using fuzzy mathematical programming. *Clean Technologies and Environmental Policy,* 12(4): 353-363

M. J. Bagajewic, D. C. Faria, 2009, On the appropriate architecture of the water/wastewater allocation problem in process plants, *Comput. Aided. Chem. Eng*., 26:1-20

R. Baliban, J. Elia, C. Floudas. 2011, Optimization framework for the simultaneous process synthesis, heat and power integration of a thermochemical hybrid biomass, coal, and natural gas facility, *Comput. Chem. Eng*., 35: 1647-1690

M. Boix, L. Montastruc, L. Pibouleau, C. Azzaro-Pantel, S. Domenech, 2012, Industrial water management by multi-objective optimization: from individual to collective solution through eco-industrial parks, *J. Clean. Prod*., 22(1): 85-97

I. M. L. Chew, R. R. Tan, D. K. S. Ng, D. C. Y. Foo, T, Majozi, J. Gouws, 2008, Synthesis of Direct and Indirect Interplant Water Network, *Ind. Eng. Chem. Res.*, 47(23): 9485–9496

L. Fernando, Lira-Barragán J., María Ponce-Ortega, El-Halwagi M M, 2011, Synthesis of water networks considering the sustainability of the surrounding watershed, *Comput. Chem. Eng.*, 35(12): 2837- 2852

D. C. Y. Foo Process Integration for Resource Conservation, NY: CRC press, 2013

J. F. Gouws, T. Majozi, D. C. Y. Foo, C. L. Chen, J.Y. Lee, 2010, Water Minimization Techniques for Batch Processes, Ind. Eng. Chem. Res. 49, 8877-8893

A. Y. Hoekstra, K. A. Chapagain, M. M. Aldaya, M. M. Mekonnen, 2012, Water Footprint Assessment Manual: Setting the Global Standard, Earthscan Ltd

A. Y. Hoekstra, K. A. Chapagain, Water footprints of nations: Water use by people as a function of their consumption pattern, *Water Resources Management*, 2007, 21(1):35-48

A. Y. Hoekstra, Human appropriation of natural capital: a comparison of ecological footprint and water footprint analysis, *Ecological Economics*, 2009, 68(7): 1963-1974

X. P. Jia, C. H. Liu, L. Shi, 2010, Synthesis of total water network based on water prices in eco-industrial parks, *Computer and Applied Chemistry*, 27(10): 1449-1452 (In Chinese)

J. Kim, R. Smith, 2004, Automated design of discontinuous water systems, *Trans. Inst. Chem. Eng*., 82(3): 238-248

J. Kim, R. Smith, 2001, Cooling water system design, *Chem. Eng. Sci.,* 56(12): 3641–3658

J. J. Klemes, Handbook of Process Integration (PI): Minimisation of Energy and Water Use, Waste and Emissions. UK: Woodhead Publishing Limited, 2013

W. J. Kuo, R. Smith, 1998a, Design of water-using systems involving regeneration, *Trans. Inst. Chem. Eng*., 76(2): 94-114

W. J. Kuo, R. Smith, 1998b, Designing for the interactions between water-use and effluent treatment, *Trans. Inst. Chem. Eng*., 76(3): 287-301

V. Ku-Pineda, R. R. Tan, 2006, Environmental performance optimization using process water integration and sustainable process index, *J. Clean. Prod.*, 14(18):1586-1592

T. B. Majozi, C. J. Rouckaert, C. A. Buckley, 2006, A graphical technique for wastewater minimization in batch processes, *Environ. Manage,* 78(4): 317-329

A. Manzardo, J. Ren, A. Piantella, A. Mazzi, A. Fedele, A. Scipioni, Integration of water footprint accounting and costs for optimal chemical pulp supply mix in paper industry, *Journal of Cleaner Production,* 2014, 72:167-173

S. G. Olesen, G. T. Polley, 1996, Dealing with Plant Geography and Piping Constraints in Water Network Design, *Process Safety and Environmental Protection*, 74(4): 273-276

E. Rubio-Castro, J. Ponce-Ortega, M. Serna-Gonzalez, M. M. El-Halwagi, 2012, Optimal reconfiguration of multi-plant water networks into an eco-industrial park, *Comput. Chem. Eng.*, 44: 58-83

Q. Sun, X. Y. Huang, L. Shi, Corporate water footprint of textile industry: methodology and case study, Research of Environmental Sciences, 2014, 27(8): 910-914

Y. P. Wang, R. Smith, 1994a, Wastewater minimization, *Chem. Eng. Sci.*, 49(7):981-1006

Y. P. Wang, R. Smith, 1994b, Design distributed effluent treatment systems, *Chem. Eng. Sci*., 49(18): 3127-3145

Y. Q. Yang, X. Q. Zhuang, 2008, Process systems engineering methods for water conservation, *Modern Chemical Industry,* 28 (1): 8-13 (In Chinese)

Y. Q. Yang, X. Q. Zhuang, 2012, Water conservation and waste water reduction of chemical and refinery enterprises, *Chemical industry and engineering progress*, 31(12):2780-2785 (In Chinese)

Y. Q. Yang, X. P. Jia, L. Shi, 2015, Progress of process systems engineering for water network and virtual water studies, *CIESC Journal*, 66(1): 32-51 (in Chinese)

D. Zimmer, D. Renault, 2003, Virtual water in food production and global trade: Review of Methodological issues and preliminary results, the Netherlands: IHE, Delft

Krist V. Gernaey, Jakob K. Huusom and Rafiqul Gani (Eds.), 12th International Symposium on Process Systems Engineering and 25th European Symposium on Computer Aided Process Engineering.
31 May – 4 June 2015, Copenhagen, Denmark

Multi-objective Optimization of Small-size Wastewater Treatment Plants Operation

Rainier Hreiz[a,b*], Nicolas Roche[b], Brahim Benyahia[c], M.A. Latifi[a]

[a]*Laboratoire Réactions et Génie des Procédés, CNRS-ENSIC, Université de Lorraine, BP-20451, 1 rue Grandville, 54001 Nancy Cedex, France*
[b]*Aix-Marseille University, CNRS - Centrale Marseille, Laboratoire de Mécanique, Modélisation et Procédés Propres - UMR7340, Europôle de l'Arbois, 13545 Aix en Provence Cedex 4, France*
[c]*Department of Chemical Engineering, Loughborough University, Loughborough, Leicestershire LE11 3TU, United Kingdom*
hreiz.rainier@gmail.com

Abstract

This paper deals with the multi-objective optimal control of a small-size wastewater treatment plant, where the excess sludge produced is incinerated for electricity production. The trade-offs between the treatment quality and operating costs are characterized. Emphasis is put on a proper formulation of the problem so as to get physically relevant solutions. Sludge incineration is shown to be quite profitable energetically, especially when a high nitrogen discharge is tolerated.

Keywords: Multi-objective optimization; Wastewater treatment; Activated sludge.

1. Introduction

The activated sludge process, ASP (Figure 1), is nowadays the most widely used process for municipal wastewater treatment. Most small-size wastewater treatment plants (WWTPs) use the alternating activated sludge (AAS) version of the ASP. It consists of: (1) a reactor operating continuously where bacteria degrade the incoming pollutants, (2) a settling tank where activated sludge (flocculated biomass) is separated from the treated wastewater, (3) a sludge recycle line allowing to keep convenient bacterial concentration in the reactor, (4) a wastage line where excess sludge is purged. The reactor is sequentially aerated to provide alternating aerobic (supplies dissolved oxygen, DO, to bacteria) and anoxic conditions (depletion of DO but presence of nitrate/nitrite, S_{NO}): this operating policy constitutes the most economical nitrogen abatement strategy. Under aerobic metabolism, ammonium is oxidized into S_{NO} (nitrification process). The aeration-off periods enable minimizing the electrical consumption, and by depriving bacteria from DO, force them to use S_{NO} as a substitute terminal electron acceptor and reduce it into nitrogen gas (denitrifcation process).

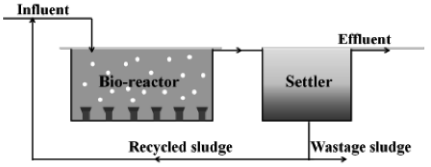

Figure 1. Schematic diagram of the activated sludge process.

Nowadays, since complying with the continuously strengthening environmental regulations involves additional costs, the wastewater industry is forced to improve the ASP functioning. In this context, dynamic optimization turns out to be a quite gainful technique since it can deal simultaneously with different objectives (minimize cost, comply with effluent limits…) and handles the high non-linearity inherent to the underlying biochemical phenomena, which is challenging even for experienced designers. Optimization has been applied to select the most lucrative operating strategy for existing ASPs, e.g. Chachuat et al. (2005), and for WWTPs to be designed (i.e. no infrastructure build yet), to simultaneously determine the units sizing and operating conditions that provide the most cost-effective treatment, e.g. Espírito-Santo et al. (2007).

However, the single-objective optimization approach hides the real nature of the problem since the conflicting aspects between the treatment quality and costs are not recognized. Therefore, in the framework of optimal control/design of ASPs, there is an increasing attention to multi-objective optimization (MOO), e.g. Hakanen et al. (2013). MOO generates a set of optimal solutions (named Pareto front, PF) expressing the minimal cost enabling to reach a given treatment efficiency. A decision maker (e.g. an expert), DM, then examines these solutions and selects which one to be implemented on the real-scale ASP. A primary advantage of MOO is that it allows benefiting from the DM experience. Indeed, given his/her expertise, he/she will avoid for example solutions that may lead to suboptimal operating conditions (e.g. poor sludge settleability).

This paper deals with the multi-objective optimal control of a small-size WWTP, where the excess sludge produced is incinerated for electricity production. Emphasis is put on a proper formulation of the MOO problem so as to get physically relevant solutions.

2. Multi-objective optimization problem statement

2.1. Process layout

The investigated ASP consists of a reactor (V=6000 m^3) equipped with a diffused aeration system, and of a cylindrical settler (height = 4 m, cross-section = 1,500 m^2). The injected air flow rate can be controlled by means of valves. During non-aeration periods, a mixer maintains the solids in suspension. The excess sludge produced is valorized in an incineration plant to produce electricity. Influent characteristics reflect typical disturbances resulting from the life patterns of households (dry-weather file by Copp (2002)). The average incoming flow rate is about 18,000 $m^3.day^{-1}$.

2.2. Process model

The bio-reactor is treated as an ideal continuous stirred-tank reactor. The occurring biochemical reactions are modelled using the well-known ASM1 model (Henze et al., 1987) which tracks the evolution of the process key variables (e.g. DO concentration). Mass balances around the reactor for each of these variables give rise to 13 highly non-linear ordinary differential equations (ODEs). Liquid-solid separation in the settler is modelled using the well-known Takács et al. (1991) model, and leads to 80 ODEs.

2.3. Optimization problem formulation

The MOO problem can be stated as follows:

$$\min_{\boldsymbol{u}} \boldsymbol{J}(\boldsymbol{x}, \boldsymbol{u}, t_f) = [\text{Operating costs}, \text{Nitrogen discharge}]^{\mathrm{T}} \quad (1)$$

Subject to:

$$\text{Process model equations: } \boldsymbol{f}(\boldsymbol{x}, \dot{\boldsymbol{x}}, \boldsymbol{u}, t) = \boldsymbol{0} \quad (2)$$

$$\text{Initial conditions: } \boldsymbol{x}(t_0) = \boldsymbol{x}_0 \quad (3)$$

$$\text{Constraints: } \boldsymbol{g}(\boldsymbol{x}, \boldsymbol{u}) \leq \boldsymbol{0} \quad (4)$$

$$\text{Decision variables bounds: } \boldsymbol{u}_L \leq \boldsymbol{u} \leq \boldsymbol{u}_U \quad (5)$$

$$\text{with } \boldsymbol{u} = [Q_{Air}(t), Q_w(t), Q_R]^{\mathrm{T}}$$

where t is the time and t_f the time horizon; $\boldsymbol{x}$ represents the set of the 13 process state variables (and $\dot{\boldsymbol{x}}$ its time derivative); $\boldsymbol{u}$ is the set of decision variables (DVs): Q_{Air} the injected air flow rate, Qw the sludge wastage flow rate and QR the external recycling flow rate. u_L and u_U are the DVs' lower and upper bounds respectively; g represents the set of inequality constraints that must be fulfilled by the optimal solution.

Nitrogen discharge is chosen as an objective function in order to characterize the trade-offs between the treatment's cost and efficiency. Indeed, it is much harder to remove nitrogenous than carbonaceous matter from municipal wastewater (Chachuat et al., 2005).

Q_{Air} and Q_w are considered as time-varying DVs. The situation can be achieved physically thanks to valves installed on the air and sludge lines. Time-varying aeration rate is necessary to allow performing nitrification and denitrification in the same tank. These variables are parameterized using the 'Control Vector Parameterization' (CVP) approach. Q_R is treated as a time-independent DV: in practice, the recycle flow is lifted by a screw pump which is generally operated at constant capacity.

The MOO problem seeks for the optimal daily operating strategies and considers a time horizon of 100 days. Such a large time frame is required so as to get solutions ensuring a sustainable plant operation: as shown by Chachuat et al. (2005), operating procedures determined from a short time operation optimization can lead to biomass washout. The operating costs objective function involves pumping, aeration and mixing power consumptions. The produced sludge is valorized through incineration to produce electricity, what reduces operating costs. The treatment quality objective function is stated as the minimization of the effluent average nitrogen concentration between the 86th and the 100th day. Such a formulation (Copp, 2002) ensures that the objective function is computed during the cyclic steady regime only, and hence, mitigates the effect of the plant's initial state with regard to the computed PF. In fact, the initial conditions should not influence the optimal solution since their effects vanish with time.

The problem is solved using an elitist genetic algorithm of which details can be found in (Benyahia et al., 2011). For all the investigated cases, a population of 400 individuals is used, and the maximum number of generations equals to 35.

2.4. Cost functions

Q_{Air} and the oxygen mass transfer coefficient (k_La) are linked through the empirical formula derived by Gillot and Héduit (2004) from on site measurements in ASPs:

$$k_L a = 1.477 h^{-0.136} S^{-1.175} S_p^{0.042} S_a^{0.145} Q_{Air}^{1.037} \quad (6)$$

where h is the water column height in m (taken as 4 m), S_a the surface covered by the diffusor modules in m^2 (taken as the surface of the reactor), S_p the total membrane surface in m^2 (taken as 7 % of the reactor surface), k_La is in h^{-1} and Q_{Air} in Nm^3.h^{-1}. To account for the detrimental effect of the concentration of suspended solids (SS) in the mixed liquor on the oxygen transfer rate, Eq.(6) is corrected using the mass transfer reduction factor α (Marrot et al. (2005); formula valid for 0 g.L^{-1}≤ SS≤ 10 g.L^{-1}):

$$\alpha = -0.072 \times SS + 1 \quad (7)$$

Thus, Eq.(6) is multiplied by (α/0.712): it is considered that the mean SS in the reactors investigated by Gillot and Héduit (2004) is 4 $g.L^{-1}$, a concentration to which corresponds an α of 0.712. Accounting for this effect is novel in the framework of the optimization of ASPs operation/design. Finally, the power delivered by the blower is calculated assuming an adiabatic compression and an efficiency of 70 %.
Recycling pumping power is calculated according to the formula:

$$Pumping\ power = \frac{\rho g Q_R \Delta H}{\eta_P} \quad (8)$$

where ρ is the fluid density, g the gravitational acceleration, ΔH the differential head (taken as 4 mWC for simplification purposes) and η_P the pump efficiency (taken as 50 %). Sludge wastage is gravity-driven and does not require pumping. Mixing is modeled according to the formulation by Alex et al. (2008): the mixer is used when $k_L a$ is lower than 20 h^{-1}, and its specific power consumption is 5 $W.m^{-3}$. The extracted sludge is thickened, dewatered and dried so it can burn. These operations are supposed to cost 1 kWh per kg of dry sludge. The dry sludge (its calorific value is taken as 15 $MJ.kg^{-1}$) is valorized in an in-site incineration plant (30 % efficiency) for electricity production.

2.5. Constraints and decision variables bounds

Effluent limits for chemical oxygen demand, biological oxygen demand and SS are handled through inequality path constraints: their instantaneous concentration must remain below the specified limits, 100, 10 and 30 $g.m^{-3}$ respectively. Compared to the literature, a more correct formulation is provided: these constraints are accounted for only after the 86th day. Indeed, activating a constraint during the transient period makes the solution depending on the arbitrarily guessed plant's initial state. Sludge age (i.e. solids retention time) is restricted between 4 and 30 days. The lower bound deals with bio-flocculation requirements, while the upper bound limits the sludge mineralization as it alters its calorific value. The screw pump is supposed to provide a maximum flow rate Q_R of 40,000 $m^3.day^{-1}$. The maximum value of Q_w is set to 1,000 $m^3.day^{-1}$. According to Grady et al. (1999), to prevent bioflocs shearing, Q_{Air} should comply with:

$$\frac{1000 Q_{air}}{Lim} \leq V \quad (9)$$

where the *Lim* factor is about 90 m^3/(min.1,000 m^3). However, in the present study, a value of *Lim* of 50 m^3/(min. 1,000m^3) is assumed so that the maximum Q_{air} matches the capacity of aerators typically used nowadays.

3. Results and discussion

3.1. Preliminary results

The MOO problem is solved for 3 situations. In the 1st problem, Q_{Air} and Q_w are allowed to change every 2 hours (12 cycles by day), which results in 25 DVs. The 2nd problem is similar, but sludge disposal and valorization are not accounted for in the exploitation costs objective function. In the 3rd problem, Q_{Air} and Q_w are taken as time-independent DVs (thus the problem involves 3 DVs) so as to characterize the benefits provided by dynamic operating conditions (sludge-related charges are taken into consideration). The PFs corresponding to the first two problems are shown in Figure 2. Each one required

about 6 days of CPU time on a 3.1 GHz personal computer. The results show that the operating costs increase with increased efficiency of nitrogen removal, and that sludge incineration is more profit-making when high nitrogen discharge limits are tolerated.

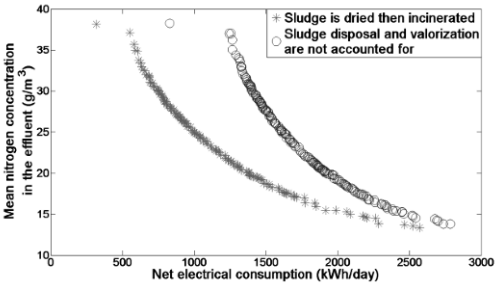

Figure 2. Effect of sludge disposal and valorization on the Pareto front.

When the 3rd problem was solved, the resulting PF (not shown here) was found to be nearly the same as for the 1st problem. At first sight, this outcome is quite surprising since a constant Q_{Air} does not allow performing both nitrification and denitrification. A closer look to the results revealed that for the 3 problems, the optimal solutions correspond to conditions of low DO in the reactor, in the range of about 0.2-0.4 $g.m^{-3}$. In fact, in the framework of ASM1, such conditions allow simultaneous nitrification and denitrification at low aeration costs, i.e. an excellent treatment with low operating charges. Although the results are mathematically correct, they are physically irrelevant since in practice, ASPs cannot achieve an efficient treatment in this range of DO concentrations. In fact, as discussed by Rigopoulos and Linke (2002), the accuracy of ASM1 in this range of DO conditions is questionable.

3.2. Results using additional constraints relative to DO concentration

To provide realistic results, supplementary constraints were used in order to restrict the solutions space to physically relevant operating conditions: at each cycle, the mean DO should be higher than 2 $g.m^{-3}$ (aerobic conditions; a similar constraint was used by Espírito-Santo et al. (2007) who focused on the static optimization of a classic ASP) or lower than 0.1 $g.m^{-3}$ (anoxic conditions). With this realistic problem formulation, MOO showed that, when using time-independent DVs (Pb. 3), the ASP could not achieve lower nitrogen discharge than 35 $g.m^{-3}$ (results not shown here). Problems 1 and 2 were also solved again, however, for computational expenses reasons, 4 h cycle lengths were used (instead of 2 h as previously). In fact, this new problem formulation results in 12 additional constraints (2 DO constraints per cycle) which dramatically increased the computational time: each PF (Fig. 3) required about 21 days of CPU time. In fact, as the feasible solution space is reduced, the genetic algorithm required more trials before it could generate a child solution that dominates its parents (Benyahia et al., 2011).

Fig. 3 shows the PFs corresponding to problems 1 and 2. Sludge incineration is shown to be quite profitable energetically, especially when a high nitrogen discharge is tolerated. Comparison with Fig. 2 reveals that the use of DO related constraints results in higher exploitation costs, and the lowest nitrogen concentration in the effluent that can be achieved increases to about 16.9 $g.m^{-3}$. However, these results are more realistic since the optimal solutions are maintained within the limits of validity of the model. For high nitrogen removal efficiencies, the optimal solutions correspond to an AAS operation: aeration is alternated so as to provide cycling anoxic and aerobic conditions.

For low treatment efficiencies, the operation strategy differs from the AAS operation since the optimizer favours non-aerated cycles in order to reduce the operating costs.

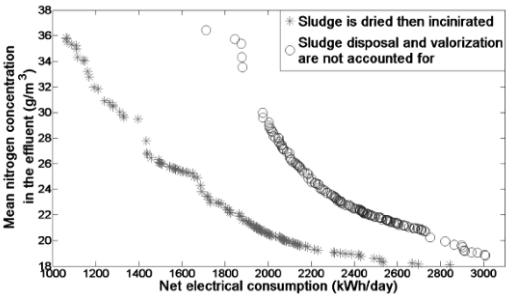

Figure 3. Pareto fronts when DO-related constraints are included in the optimization problem.

4. Conclusions

In this work, a multi-objective dynamic optimization of the operating strategy of a small-size wastewater treatment plant is carried out. The trade-offs between the treatment quality and operating costs are characterized. Compared to the literature, emphasis is put on a proper formulation of the optimization problem so as to get physically relevant solutions. Sludge incineration is shown to be quite profitable energetically, especially when a high nitrogen discharge is tolerated.

References

J. Alex, L. Benedetti, J.B. Copp, K.V. Gernaey, U. Jeppsson, I. Nopens, M.N. Pons, L. Rieger, C. Rosen, J.P. Steyer, P. Vanrolleghem, S. Winkler, 2008, Benchmark Simulation Model no.1 (BSM1), IWA taskgroup on benchmarking of control stategies for WWTPs, Technical report.

B. Benyahia, M.A. Latifi, C. Fonteix, F. Pla, 2011, Multicriteria dynamic optimization of an emulsion copolymerization reactor, Computers & Chemical Engineering, 35, 2886-2895.

B. Chachuat, N. Roche, M.A. Latifi, 2005, Long-term optimal aeration strategies for small-size alternating activated sludge treatment plants, Chemical Engineering and Processing, 44, 593-606.

J.B. Copp, 2002, The COST simulation benchmark: description and simulator manual, Office for official publications of the European communities, Luxembourg.

I.A.C.P . Espírito-Santo, E.M.G.P. Fernandes, M.M. Araújo, E.C. Ferreira, 2007, Wasted sludge treatment contributions in the WWTP total cost, WSEAS Transactions on Information Science and Applications, 4, 655-662.

S. Gillot, A. Héduit, 2004, Prédiction des capacités d'oxygénation en eau claire des systèmes d'insufflation d'air, Technical report FNDAE 31.

C.P.L. Grady, G.T. Daigger, HC. Lim, 1999, Biological wastewater treatment, Marcel Dekker Inc., New York, U.S.A.

J. Hakanen, K. Sahlstedt, K. Miettinen, 2013, Wastewater treatment plant design and operation under multiple conflicting objective functions, Environmental Modelling & Software, 46, 240-249.

B. Marrot, A. Barrios-Martinez, P. Moulin, N. Roche, 2005, Experimental study of mass transfer phenomena in a cross-flow membrane bioreactor: aeration and membrane separation, Engineering in Life Sciences, 5, 409-414.

S. Rigopoulos, P. Linke, 2002, Systematic development of optimal activated sludge process designs, Computers & Chemical Engineering, 26, 585-597.

I. Takács, G.G. Patry, D. Nolasco, 1991, A dynamic model of the clarification-thickening process, Water Research, 25, 1263-1271.

Krist V. Gernaey, Jakob K. Huusom and Rafiqul Gani (Eds.), 12th International Symposium on Process Systems Engineering and 25th European Symposium on Computer Aided Process Engineering.
31 May – 4 June 2015, Copenhagen, Denmark

Pipeline Merging Considerations for the Synthesis and Design of Interplant Water Networks with Wastewater Treatment, Regeneration and Reuse

Sabla Y. Alnouri [a,b], Patrick Linke [a,*], Mahmoud, M. El-Halwagi[b]

[a]*Department of Chemical Engineering, Texas A&M University at Qatar, P.O Box 23874, Education City, Doha, Qatar*
[b]*The Artie McFerrin Department of Chemical Engineering, Texas A&M University, College Station, Texas, USA*
patrick.linke@qatar.tamu.edu

Abstract

The development of effective wastewater regeneration and reuse networks has been a prominent research focus, in response to the growing demand for freshwater use by the industrial sector. Moreover, many industrial cities are recognizing the benefits of reducing freshwater utilization, and wastewater discharge, by promoting effective wastewater treatment. Much of the research attention so far has primarily involved identifying optimal wastewater treatment and reuse strategies, in which several wastewater-producing operations are matched with a number of water-consuming operations, and/or assigned to undergo a series of treatment steps before reuse, if necessary. Moreover, a single pipeline is designated for every viable water allocation identified. This has been consistently observed in many of the previous research contributions that involve interplant water network synthesis. In an attempt to enhance the water network design process, several representations that account for a number of pipeline merging scenarios have been investigated for wastewater reuse networks. In addition to the improved design-screening ability of less complex pipeline networks, merging together common pipe segments that carry similar water qualities have been found to allow for various cost-enhancements in the designs obtained.

Keywords: Water Networks, Industrial Cities, Pipelines, Merging

1. Introduction

Industrial water and wastewater management has become a crucial research priority in many regions, due to the immense scale of water-intensive industrial activities. Wastewater reuse certainly alleviates the depletion of available freshwater sources that are present around industrial areas. Moreover, many industrial sites that lie in proximity to coastal areas involve large volumes of unused wastewater being diverted back into the sea, which negatively impacts aquatic life (Englert, 2013). Hence, wastewater reuse also helps reduce the excessive wastewater quantities being discharged back into natural water bodies. Identifying appropriate wastewater treatment alternatives is considered of significant importance due to the stringent discharge limits being imposed on industrial wastewater, as well as the strict effluent standards that industries are expected to adhere to. Potential opportunities for industrial wastewater reuse would absolutely vary from one industry to another, depending on the quantity and quality of wastewater produced.

2. Previous Work

The design of cost-effective wastewater regeneration and reuse networks has been the primary focus of many previous studies. For instance, Chew et al. (2009) developed a centralized hub topology for collecting, treating and redistributing water amongst groups of coexisting plants. Rubio-Castro et al. (2010) devised a MINLP optimization model for interplant water networks whilst incorporating environmental regulations for wastewater discharge. A problem reformulation that handles bilinear terms was also proposed. Biox et al. (2012) also studied water network design using a multi-objective optimization strategy. Later on, a structured representation has also been proposed, so as to capture the spatial aspects of water network design (Alnouri et al., 2014a). Effective planning of wastewater reuse networks have been captured with a focus on the following elements: (1) existing processing facilities, water consumption and wastewater production capacities, (2) site locations and the spatial distribution of all site entities that entail water use or production, and (3) common infrastructure boundaries, such as the existence of industrial corridors that can be utilized for water transportation. Subsequently, the spatial aspects of wastewater regeneration and reuse networks have also been studied (Alnouri et al., 2015). Several different options for the selection of appropriate treatment technologies, as well as the efficient placement of corresponding treatment facilities, have been incorporated as follows: (1) a cluster of processing establishments sharing a common treatment facility (centralized), (2) the placement of a treatment facility as an individual entity belonging to a particular industrial site (decentralized). So far, most interplant water integration problems that have been studied associate every water allocation with a separate pipeline. In this work, a pipeline merging and assembling strategy for wastewater regeneration and reuse networks has been carried out.

3. Research Background

Exploring interplant water integration in terms of less complex and more economical options for the transmission and distribution of water in pipelines has been previously introduced for wastewater reuse networks (Alnouri et al., 2014b). In this work, efforts have been made to further improve the design process for wastewater reuse and regeneration networks. Most importantly, constructing interplant pipeline networks for water collection and transmission requires infrastructure availability, usually amongst a group of plants within geographic proximity. Moreover, the decision-making procedure involved with designing a cost-effective pipeline network for water transport can range from simple to complex. Various factors can greatly influence the design, such as the material choices available, as well as pipe construction and installation costs. Generally speaking, it is always considered more economical to employ a single-pipe transmission rather than multiple parallel pipes, especially when multiple locations are simultaneously involved. Hence, pipelines are usually constructed to accommodate a number of supply and destination points. Moreover, since pipeline systems are often made available in standard sizes, optimal diameter selection strategies for various pipe segments must also be incorporated, based on size availability.

4. Methodology

This work provides an extension to our work (Alnouri et al., 2014b) by incorporating options for the synthesis and design of merged pipeline networks involving wastewater treatment, regeneration, and reuse. In order to avoid unwanted water mixing in the merging procedure, the proposed methodology can be carried out on pipelines that carry

treated, and untreated water qualities, individually. Hence, identifying cost-effective opportunities that allow the screening of less complex pipeline networks by assembling together commonly existing pipe sections, in the course of determining optimal water networks, have been based on the following two schemes:

4.1. Forward Branching Scheme

This pipeline branching approach corresponds to the transmission of water from a common location, to multiple nearby destinations. Hence, pipelines that apply a forward branching scheme is assembled by starting with one large pipe segment that combines all water in a given location to be distributed. The segments then narrows down to smaller ones that connect to multiple destinations. Forward branching can be applied to (1) source-to-sink and (2) fresh-to-source, and (3) source-to-treatment, (4) treatment-to-sink, and (5) treatment-to-waste connectivity categories.

4.2. Backward Branching Scheme

This pipeline branching approach corresponds to the transmission of water from a number of nearby locations, to a single destination. Hence, pipelines that apply a backward branching scheme is assembled by starting with multiple small pipe segment that connect to a single location. The segments widen up and combine as the destination is approached. Backward branching can be applied to (1) source-to-sink and (2) sink-to-waste, (4) treatment-to-sink, and (5) treatment-to-waste connectivity categories.

5. Case Study

The illustrative case study described below has been utilized to demonstrate the proposed methodology. Figure 1 provides the layout of the industrial zone that has been assumed. A total of 4 co-locating plants are incorporated, 3 of which involve an on-site wastewater treatment facility. Additionally, a centralized treatment unit shared amongst all plants has also been provided, for which a specified treatment option can be selected. The total area of the region was assumed to be 64 km^2. Table 1 provides the case study flowrate and composition data for all available source and sink water streams. A total of 3 pollutant concentrations has been provided for this case study, as 3 different contaminants were assumed in all process water streams. Table 2 outlines all contaminant removal ratios, as well as the corresponding fixed and operating cost elements that are associated with the decentralized treatment units, as well as the centralized treatment option. Additional information requirements that were associated with the individual plants involve the following: (1) freshwater cost =0.13 $/t, (2) waste disposal cost =0.9 $/t, and (3) operating hours =8760 h/y. Moreover, carbon steel Schedule 80 welded pipes were assumed throughout, and the calculated pipeline diameters were rounded up in increments of 0.1, to the nearest standard size in meters. All piping costs were annualized over a 20-year lifetime. In this case study, only forward branching has been applied for the purpose of pipeline merging.

The problem described above has been formulated as a mixed integer nonlinear optimization problem (MINLP) for treatment and direct recycling. The corresponding water allocation strategy has been obtained using “what’sBest9.0.5.0” LINDO Global Solver for Microsoft Excel 2010, using a desktop PC with Intel® Core ™ i7-2620M, 2.7 GHz, 8.00 GB RAM, and a 64-bit Operating System.

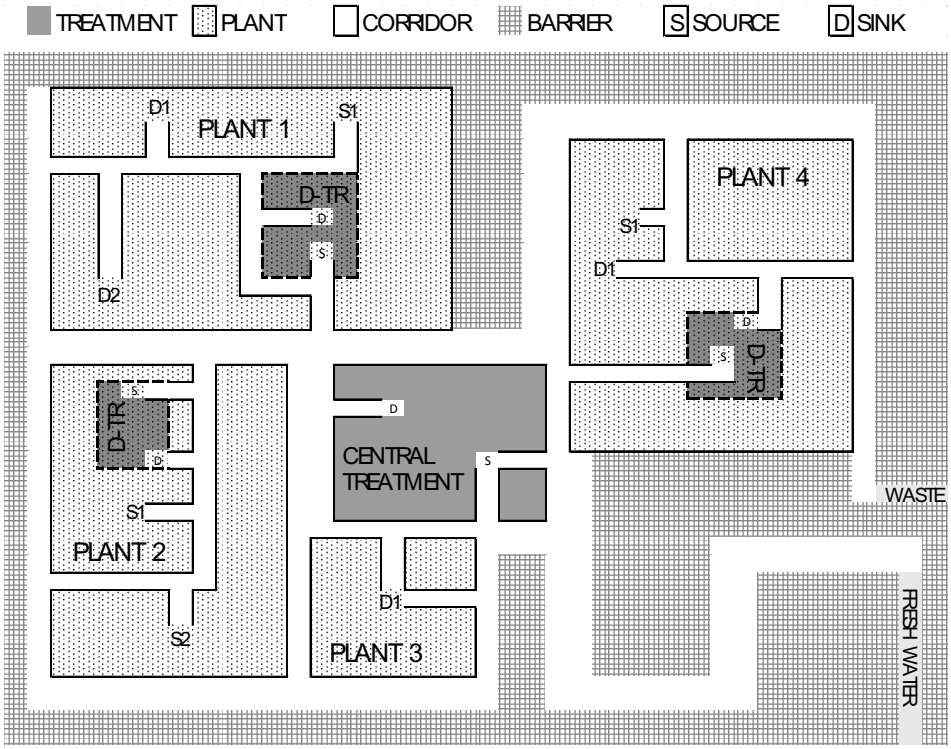

Figure 1. Case Study Layout

Table 1. Water Sink and Source Data

Sink	Flow (t/h)	Zmax 1 (ppm)	Zmax 2 (ppm)	Zmax 3 (ppm)	Source	Flow (t/h)	Y 1 (ppm)	Y2 (ppm)	Y3 (ppm)
P1D1	180	50	50	60	P1S1	100	100	80	50
P1D2	150	90	80	50	P2S1	70	120	130	110
P3D1	90	100	70	60	P2S2	160	170	130	180

Table 2. Wastewater treatment parameters in terms of pollutant removal ratios, and costs

Interceptor	Y 1	Y 2	Y 3	CAP.EX ($)	OP.EX ($-kg)
TR-P1	0.7	0.6	0	0	0.203
TR-P2	0.8	0	0.6	0	0.444
TR-P4	0	0.9	0.8	0	0.752
CTR-1	0.9	0.9	0.9	12,400	0.908

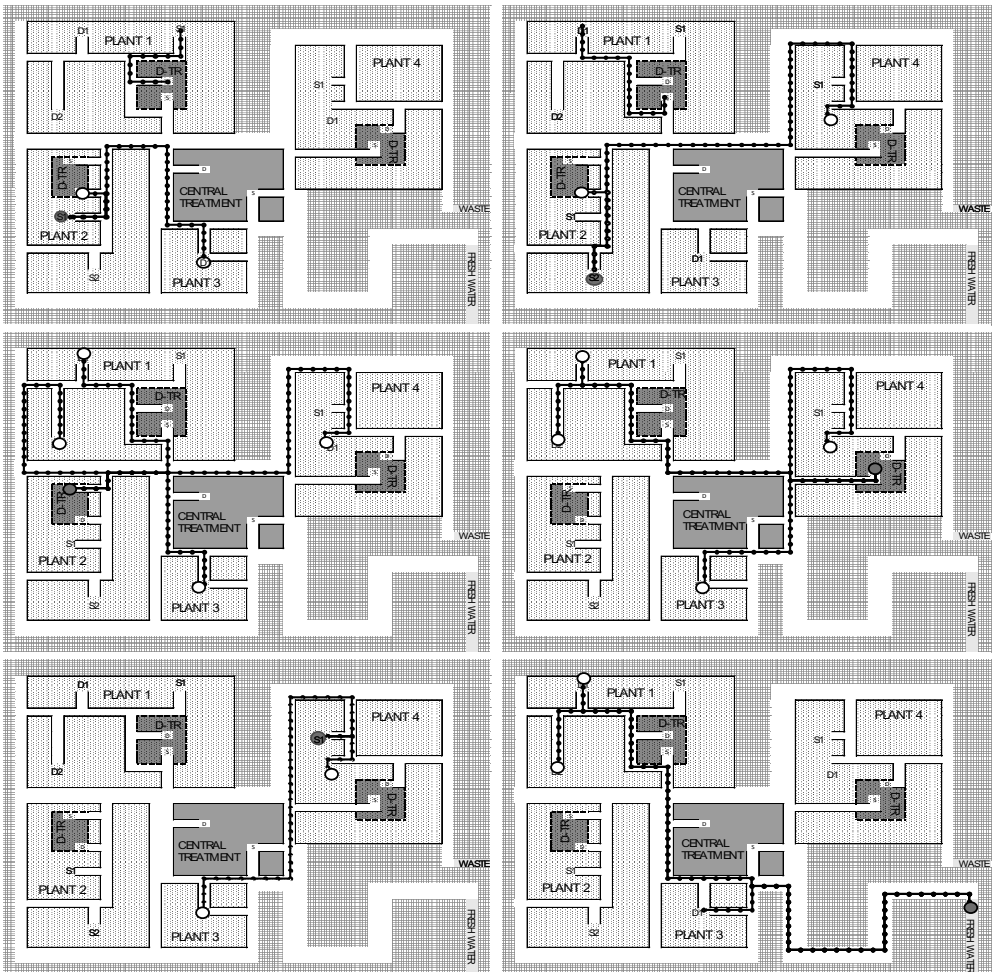

Figure 1. Forward pipeline branching illustrated

Table 3. Water flows obtained

(t/h)	P1D1	P1D2	P3D1	P4D1	TR-P1	TR-P2	TR-P4	C-TR	Waste
P1S1	0	0	0	0	100.00	0	0	0	0
P2S1	0	0	10.51	0	0	59.49	0	0	0
P2S2	0	0	0	9.69	0	150.31	0	0	0
P4S1	0	0	5.51	8.94	0	0	115.56	0	0
TR-P1	100.00	0	0	0	0	0	0	0	0
TR-P2	41.32	84.71	28.08	55.69	0	0	0	0	0
TR-P4	21.42	49.36	9.09	35.69	0	0	0	0	0
C-TR	0	0	0	0	0	0	0	0	0
Fresh	17.26	15.92	36.82	0	0	0	0	0	0

Table 3 summarizes all flowrates associated with the water allocation strategy obtained. Figure 2 illustrates the pipeline merging scenarios that have been achieved via forward branching. The total annualized cost of the water network attained was found to be $9.83x10^5$ \$/yr, after incorporating a forward branching scheme as a pipeline merging option. Freshwater consumption was found to be 70 t/h, while 0t/h of wastewater was obtained. Hence, no wastewater disposal costs were reported. The total treatment costs= $4.66x10^5$\$/yr, freshwater costs =$7.97x10^4$ \$/yr, and pipeline costs =$4.38x10^5$ \$/yr. The total annualized cost of the water network attained when no pipeline merging was involved yielded a total of $1.04x10^6$ \$/yr, with a similar treatment and freshwater performance. However, the total pipeline costs were found to increase to a total of 4.93 $x10^5$ \$/yr when no merging was implemented. Hence, the case that incorporates forward pipeline merging, allowed up to 5.64% savings on total costs (corresponding to a total of 12.7% savings on pipeline costs), when compared to the standard design.

6. Conclusions

In this work, additional considerations that account for pipeline merging scenarios has been studied for wastewater regeneration and reuse networks. The proposed framework allows cost-effective interplant water network designs to be identified, by implementing a systematic approach for interplant water network synthesis and design that incorporate for pipeline merging. An artificial case study has been implemented, involving a number of water-consuming and wastewater producing processes. Moreover, a number of centralized and decentralized wastewater treatment options were also incorporated. The results indicate very attractive wastewater treatment and reuse schemes for the water network designs extracted. Cost-efficient water networks that involve merged pipeline segments in the designs extracted, have been identified.

Acknowledgment

This publication was made possible by NPRP grant no. 4-1191-2-468 from the Qatar National Research Fund (a member of Qatar Foundation). The statements made herein are solely the responsibility of the authors.

References

E. Rubio-Castro, J.M. Ponce-Ortega, F. Napoles-Rivera, M.M El-Halwagi, M. Serna-Gonzalez, A. Jimenez-Gutierrez, 2010. Water Integration of Eco-Industrial Parks Using a Global Optimization Approach Ind. Eng. Chem. Res., 49, 9945–9960.

D. Englert, J. P. Zubrod, R. Schulz, M. Bundschuh, 2013. Effects of municipal wastewater on aquatic ecosystem structure and function in the receiving stream. Science Total Environ.454–455, 401-410.

I.M.L. Chew, D.C.Y. Foo, 2009. Automated targeting for inter-plant water integration. Chem. Eng. J., 153, 23–36.

M. Boix, L. Montastruc, L. Pibouleau, C. Azzaro-Pantel, S. Domenech, 2012 Industrial water management by multi-objective optimization: from individual to collective solution through eco-industrial parks. J.Clean. Prod. 22, 85-97.

S. Y. Alnouri, P. Linke, M.M El-Halwagi, 2014a, Water integration in industrial zones: a spatial representation with direct recycle applications. Clean. Techn Environ. Pol., 16(8), 1637-1659.

S. Y. Alnouri, P. Linke, M.M El-Halwagi, 2014b, Optimal interplant water networks for industrial zones: Addressing interconnectivity options through pipeline merging. AIChE J., 60, 2853-2874.

S. Y. Alnouri, P. Linke, M.M El-Halwagi, 2015, A synthesis approach for industrial city water reuse networks considering central and distributed treatment systems. J. Clean. Prod., 89, 231–250

Krist V. Gernaey, Jakob K. Huusom and Rafiqul Gani (Eds.), 12th International Symposium on Process Systems Engineering and 25th European Symposium on Computer Aided Process Engineering.
31 May – 4 June 2015, Copenhagen, Denmark

Simultaneous Design and Planning of CO_2 Transport Pipeline Network for Carbon Dioxide Capture and Sequestration Project

Xiong Zou,[a] Hongguang Dong,[a*] Jian Li,[a] Jinqu Wang[a]

[a]*School of Chemical Engineering, Dalian University of Technology, 2 Linggong Road, Dalian 116024, China*
hgdong@dlut.edu.cn

Abstract

Carbon dioxide Capture and Sequestration (CCS) is a major method to decrease the emissions from centralized large industrial plants. Multi-period planning and design of CCS is still a challenging problem. In this work, a superstructure-based mathematical model for the design and planning of multi-period CO_2 transport pipeline network is presented. The mapping between incidence matrix and pipeline structure is employed and the model is formulated within a mixed integer nonlinear optimization framework where the objective function is to maximize the profit of CCS while satisfying mass, pressure drop and logic constraints. A real life example is studied to demonstrate the advantages of our proposed approach.

Keywords: CCS, design, planning, supply chain, multiple-period.

1. Introduction

Carbon dioxide (CO_2) capture and sequestration (CCS) can significantly reduce emissions from large stationary sources of CO_2, which include coal- and natural-gas-fired power plants, as well as petro-chemical plants. CCS is a three-step process that includes: capture and compression, transportation (usually in pipelines), and injection and sequestration. The capital investment and operating cost of the pipeline network have a direct impact on the success or failure of a CCS project.

Considering the complexity of the scheduling of network pipeline system, several techniques are used to enhance the model performance. A hierarchical approach was developed by Beschetto and Magatão et al (2012), where the problem is decomposed into planning and assignment levels and two MILP models were solved sequentially. Fimbres Weihs and Wiley (2012) used incidence matrix to express the structure of the CCS and they obtained the design of CCS network under the assumption of fixed state flow. Recently, Zhou et al (2014) introduced a new decomposition algorithm to overcome the computational difficulty. In their work, intermediate sites were included in the network superstructure and the optimal capture amount of CO_2 was also considered.

To the best knowledge of the authors, there is no current work that considers the influence of multiple-period planning in the procedure of network and pipeline design. In this work, a superstructure-based MINLP approach for simultaneous design and planning of CO_2 transport pipeline network is presented in an attempt to maximize the

profit in a CCS project under the framework of supply chain. The advantages of this approach are summarized below:

1. The diverse CO_2 capture and sequestration capacities and costs in different sources and sinks are considered. The transporting amount of CO_2 is optimization variable rather than predefined parameter.
2. Supplier-intermediate site-customer and supplier-supplier connections are introduced in the network superstructure to achieve the sharing mechanism of pipelines in the long distance transportation, which leads to cost reduction.
3. The fluctuations of plant capacity and cost in the time horizon are also considered in the model. The planning, network structure and design specification of each pipeline in multiple periods are optimized simultaneously.

2. Problem statement

Consider a supply chain of CO_2 with all alternative sources, sinks and intermediate sites. The following information should be provided: (1) The longitude and latitude values of place nodes (2) The CO_2 capture and sequestration capacities of each source and sink in each time period (3) The seasons-dependent cost information of CCS (4) The physical property of CO_2 stream in the compressed pressure and temperature.

3. Superstructure

Our scenario of CO_2 supply chain superstructure is schematically presented in Figure 1(a), which contains 9 sources, 2 intermediate sites and 3 sinks. The circle, the triangle, and the square represent the sources, the intermediate sites, and the sinks respectively. The sources and sinks are linked by pipelines, where CO_2 is transported. Intermediate sites, where multiple streams could be mixed, also exist in the network. Each source is regarded as a supplier, which provides CO_2 raw material at its own capture cost. Each pipeline and intermediate site is treated as a factory which transports CO_2, and each sink is treated as a customer, who wants to buy CO_2 product at the price of its own unit sequestration revenue. Supplier-supplier and supplier-intermediate site-customer connections are introduced in the network superstructure. The supplier-supplier and supplier-intermediate site connections are realized by reversal pipelines. Customers are assumed to be not link to each other.

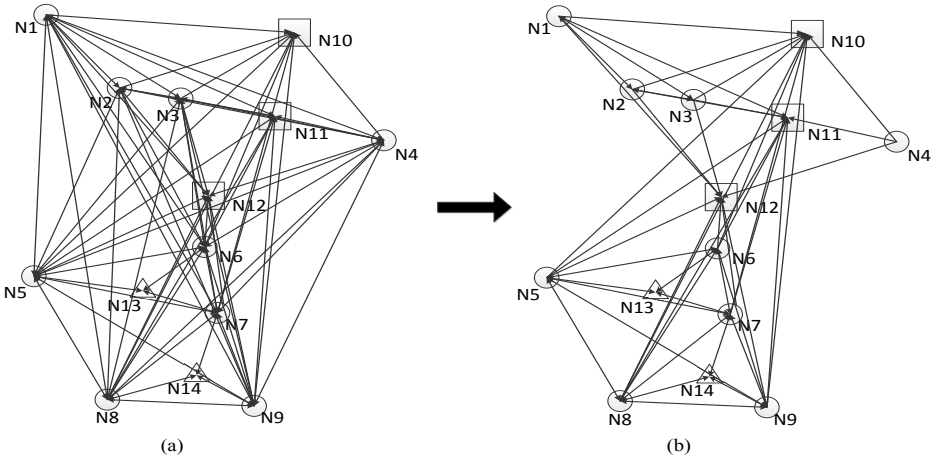

Figure 1. The superstructure of the example

To reduce the network complexity, the sources are divided into 3 parts based on cluster analysis method and only the sources in the same part are linked to each other with reversal pipeline. Each source is linked to 3 sinks respectively with directional pipeline. The first part includes N1, N2, and N3. The second part only has N4. The third part has N5-N9. The distance between sources in the different part is always overlong. So the superstructure can be simplified from Figure 1 (a) to (b) by eliminating these pipelines.

The topology relationship between the pipelines and place nodes is expressed by a node-arc incident matrix. The columns of the incident matrix represent each of the pipeline links and the rows of the matrix represent each of the place nodes. The value of element $w_{i,i}$ in the matrix is determined by the following rules: $w_{i,i}=1$ if pipeline j is the input of place node i; $w_{i,j}=-1$ if pipeline j is the output of place node i; $w_{i,j}=0$ if there isn't a connection between pipeline j and place node i. Notice that all the pipelines, between sources and intermediate sites and between sources and sources, are bidirectional and that they are represented by two single directed pipelines which cannot be activated in the same time interval.

4. Mathematical formulation

Some sets are defined for more logical and clear expression. Sinks, sources and intermediate sites are represented by set S(s_1, s_2, s_3,..), O(o_1, o_2, o_3,..), E(e_1, e_2, e_3,..), respectively, and I={S,O,E}. Pipelines are represented by set J (j_1，j_2，j_3...). Different seasons are represented by set T (t_1, t_2, t_3, t_4).

4.1. Mass balance constraints

Carbon dioxide captured from sources should be compressed and then transported to sinks. The amount of CO_2 captured is determined by the economic benefit and environmental regulation policy. $P_{s,t}$ represents the capture capacity of source *s* in the time interval *t* and PP_t represents the minimum capture quantity in the whole district based on regulation policy. $Q_{j,t}$ represents the flowrate of pipe j in time interval t. $C_{s,t}$ represents the CO_2 capture quantity of source s in time interval t. The mass balance constraints of sources are expressed as

$$\sum_j -w_{s,j} \times Q_{j,t} = C_{s,t},\ s \in S,\ t \in T \tag{1}$$

$$\sum_s \sum_j -w_{s,j} \times Q_{j,t} \geq PP_t,\ t \in T \tag{2}$$

The amount of CO_2 sequestrated should be smaller than the sequestration capacities of the sinks ($P_{o,t}$). Similarly, the mass balance equation of each sink can be expressed as follow.

$$\sum_j w_{o,j} \times Q_{j,t} = SE_{o,t},\ o \in O,\ t \in T \tag{3}$$

There are no emission and storage of CO_2 in the intermediate sites. The mass balance equation of each intermediate site can be expressed as follow.

$$\sum_j w_{e,j} \times Q_{j,t} = 0,\ e \in E,\ t \in T \tag{4}$$

4.2. Pressure drop constraints

The pressure drop ($P_{j,t}$) in the pipeline is relevant to diameter (d_j), length (L_j), and physical properties. ρ and σ are the density and viscosity of CO_2 in 9 MPa, 283K.

$$P_{j,t} = k_{drop} \times L_j \times Q_{j.t}^{2.84} \times d_j^{-4.84} \times \rho^{0.84} \times \sigma^{0.16},\ j \in J, t \in T \tag{5}$$

4.3. Logic relations

For reversal pipelines, they are represented by a couple of pipelines, which are not activated at the same time, and their diameters should be the same. Binary variable $y_{j,t}$ is used to expressed whether the pipeline j is activated in time interval t. If a pipeline j is activated in time interval t, it is equal to 1. Otherwise, it is equal to 0.

$$y_{j,t} + y_{j',t} \le 1, \text{ if j and j' are couple pipelines} \tag{6}$$

$$d_j = d_{j'}, \text{ if j and j' are couple pipelines} \tag{7}$$

When all the binary variables for the same pipeline j in different time intervals equal 0, the pipeline j does not exist. M_1 is the upper bound of the pipeline diameter.

$$d_j \le M_1 \times \sum_t y_{j,t},\ j \in J \tag{8}$$

The diameter of a pipeline should not be too small if the pipeline exists. The lower bound of the pipeline diameter M_2 is set as 0.15.

$$M_2 \times y_{j,t} \le d_j,\ j \in J, t \in T \tag{9}$$

Once the pipeline is activated in the time interval t, the flow in the pipeline should be suitable for real case, and it cannot be too small or too large. If the pipeline is not activated in the time interval t, the flow in the pipeline should be 0. The lower bound of flow M_3 equals to 0.10 and the upper bound M_4 equals to 30.

$$M_3 \times y_{j,t} \le Q_{j,t} \le M_4 \times y_{j,t}, j \in J, t \in T \tag{10}$$

4.4. Objective function

The profit is established with 5 items: government subsidy (GS), capture cost ($C_{capture}$), transportation cost ($C_{transportation}$), pipe cost (C_{pipe}) and sequestration cost ($C_{sequestration}$). The unit capture cost $U_{s,t}$, unit sequestration cost ($U_{o,t}$) and government subsidy of unit CO_2 reduction(U_{gs}) are given. Transportation cost is proportional to pressure drop. Pipe cost is related to the length and diameter of the pipe. k_{drop}, k_{pipe} and $k_{transport}$ are the coefficients of pressure drop, pipe cost, transportation cost, respectively. The sequestration revenue of each sink equals to the government subsidy of CO_2 reduction minus sequestration cost. Now the government subsidy is quite higher than the sequestration cost.

$$GS = \sum_o \sum_t (U_{gs} \times \sum_j (-w_{o,j} \times Q_{j,t})) \tag{11}$$

$$C_{pipe} = k_{pipe} \times \sum_j (L_j \times d_j^{1.5}) \tag{12}$$

$$C_{transportation} = k_{transport} \times \sum_{j} \sum_{t} P_{j,t} \tag{13}$$

$$C_{capture} = \sum_{s} \sum_{t} (U_{s,t} \times \sum_{j} (-w_{s,j} \times Q_{j,t})) \tag{14}$$

$$C_{sequestration} = \sum_{o} \sum_{t} (U_{o,t} \times \sum_{j} (-w_{o,j} \times Q_{j,t})) \tag{15}$$

$$Max \ \text{Profit} = GS - C_{pipe} - C_{transportation} - C_{capture} - C_{sequestration} \tag{16}$$

5. Example

This example is abstracted from a real-life CCS project in north China. The emission, sequestration capacity ($P_{s,t}$ $P_{o,t}$) and capture, sequestration cost ($U_{s,t}$, $U_{o,t}$) change with time periods. The computing platform is a PC with 6GB RAM memory, and Intel Core TM i7 CPU (2.67GHz). The solver DICOPT is used for solving the MINLP model to optimality in GAMS 22.5.

Case 1. The base situation of fixed planning without intermediate sites in multiple-period is solved, and the optimum results are given in Figure 2(a). Numbers around each place node represent the flowrate (kg/s) from t1 to t4 (up to down). The number in the last row represents the diameter (m) of pipelines. We have noticed that some sources are linked to the sinks directly. On the contrary, some sources prefer to link to the other sources. The total profit is 1.7427e9 $, which illustrates that the CCS project is profitable because of the government's subsidy.

Case 2. If there are intermediate sites embedded in superstructure, some new pipelines should be added into the former superstructure. The intermediate place N13 is serviced for N6, N7 and N8, and N14 is serviced for N7, N8, and N9. After optimizing the problem with intermediate sites, the results are presented in Figure 2(b) and we find that intermediate site N13 is not activated and pipeline connections between N7, N8 and N9 are different from Figure 2(a) due to the addition of intermediate site N14. The length of pipelines linking N7, N8 and N9 becomes shorter, but at the same time, a larger diameter pipeline which links N14 to N7 is used. As illustrated in Table 1, both pipe cost and transportation cost decrease. This result indicates that the added intermediate sites will provide a more completed superstructure and lead to a reduction in the total annual cost.

Case 3. In the former two situations, all CO_2 produced in the source should be captured and transported to sinks. In case 3, the minimum capture quantity in the whole district based on regulation policy is provided.

Table 1. The total annual cost, pipe cost, transportation cost of different case studies

Example	Profit ($)	Pipe cost ($)	Transportation cost ($)
Case 1	1.7427e9	7.3917e7	2.2952e7
Case 2	1.7435 e9	7.3292 e7	2.2758 e7
Case 3	2.1039 e9	6.4475 e7	2.0021 e7

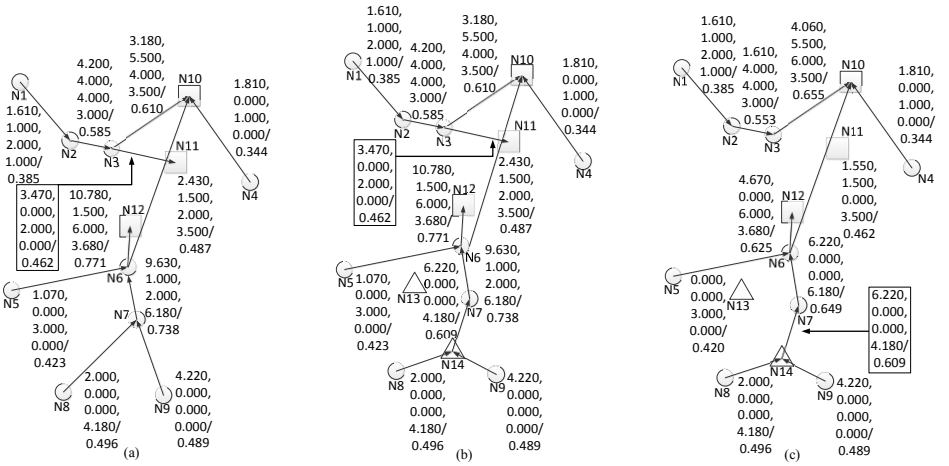

Figure 2. The results of three cases in multiple periods.

The unit capture cost is higher in some sources and the capacity of sinks with lower sequestration cost is limited, so the trade-off between different sources and sinks should be considered. In Figure 2(c), we note that in some period there are no CO_2 capture in some sources such as N2, N5, N7 and the diameters of some pipelines becomes smaller. As illustrated in Table 1, the pipe cost and transportation cost decrease substantially. If there is no restrict regulations from the government, disposing all the CO_2 is not economical and the optimal flexible arrangement is more profitable.

6. Conclusions

A superstructure-based mathematical model to simultaneously optimize the design and multiple-period planning of CO_2 transport pipeline network from the perspective of supply chain is proposed. The structure of the pipeline network is mapped to the incidence matrix and cluster analysis is applied to reduce the complexity of the superstructure. The model is formulated within a mixed integer nonlinear optimization framework where the objective function is to maximize the profit of CCS with considering government subsidy and the cost of capture, transportation, pipeline, and sequestration, while satisfying mass, pressure drop and logic constraints. The results of multiple-period real life example indicate that appropriate intermediate places and flexible arrangement have economical advantages.

Acknowledgements

This work is supported by the National Natural Science Foundation of China, under Grant No. 21276039.

References

S. N. B. Magatão, L.Magatão, H. L. Polli, F. Neves Jr., L. V. R. Arruda, S. Relvas, A. P, F. D. Barbosa-Povóa, 2012, Planning and sequencing product distribution in a real-world pipeline network: an MILP decomposition approach. Ind. Eng. Chem. Res., 51(12), 4591-4609.

G. A. Fimbres Weihs, D. E. Wiley, 2012, Steady-state design of CO_2 pipeline networks for minimal cost per tonne of CO_2 avoided. Int. J. Greenh. Gas Control. 8, 150-168.

C. Zhou, P. Liu, Z. Li, 2014, A superstructure-based mixed-integer programming approach to optimal design of pipeline network for large-scale co_2 transport. AIChE J. 60(7), 2442–2461.

Krist V. Gernaey, Jakob K. Huusom and Rafiqul Gani (Eds.), 12th International Symposium on Process Systems Engineering and 25th European Symposium on Computer Aided Process Engineering. 31 May – 4 June 2015, Copenhagen, Denmark

Environmental, Societal and Economical optimization of a bioethanol supply chain

Carlos Miret, Ludovic Montastruc, Stéphane Negny, Serge Domenech

Université de Toulouse, Laboratoire de Génie Chimique UMR CNRS/INPT/UPS 5503, BP 34038, 4 Allée Emile Monso, 31030 Toulouse Cedex 4, France

Abstract

The objective of this contribution is to present a mathematical model (Mixed Integer Linear Programming) for the facilities and biorefinery locations, and the logistic management. For the model formulation, we first need a geographical discretization of the region in which the supply chain would be implemented and the identification of the different biomass sources and their availability in this region. The technological, ecological, economic and social data are also mandatory to run the model. As in supply chain there are short-term and mid-term decisions, the time horizon must be discretised. The original contents of the model are threefold: integration of multiscale aspects, taking into account of the biomass characteristics, optimization of the supply chain with economic, environmental and social criteria. As a result the model determines the number, the location and the capacity of bio refinery and facilities.

Keywords: Biomass, Supply Chain, Multi Objective Optimization, Location problem

1. Introduction

In order to reduce greenhouse gas emissions and fossil reserve dependency, biomass has received increasing interest as a renewable source to meet the increasing demand for energy and materials substitution or complement. The two first criteria were largely discussed on the literature but on the social aspect, few studies are published in the supply chain optimization. Biomass has also an important role to play as it has the potential to promote rural development thanks to job creations for example. Consequently, we need to evaluate and to include these criteria in decision making. The sustainable utilization of biomass requires advanced approach for biomass supply chain that range from harvesting to bioproduct delivery, in order to conceive long term viable projects and to deal with biomass specificities (heterogeneity, seasonality, degradation…). This work deals with the strategic and tactical levels of the biomass supply chain by considering location problems coupled with biomass production, and biomass and bioproduct storages, transportations as they significantly influence economic, environmental and social impacts. (Kravanja and Cucek, 2013) and (Perez-Fortes et al., 2014) have presented a detail state of the art in the combination between multi objective optimization and mathematical programming. Indeed the formulation of MILP (or MINLP) allows to reach relevant data for facility and for flow. The aim of this contribution is to propose a multi objective optimization problem to fill two gaps left by previous researches. First, the social criteria were very little introduced in the objective function. To evaluate this criteria a new approach is proposed to estimate the number of jobs created by the activity generated by the implantation of a new firm in a specific area. Secondly, we propose a new mathematical approach to solve the multi objective optimization model.

2. Superstructure

The first step is to define the system boundaries, because the development of a biomass supply chain for bioethanol production considers a succession of activities from biomass harvesting to blending facilities. Once harvested the biomass is shipped to collection facilities or directly to biorefineries. In the collection facilities, the biomass is stored and then sent to processing facilities (biorefineries). The bio ethanol produced is then delivered to blending facilities. The goal of the mathematical model is to take decisions related to the supply chain and to optimize the facilities (i.e. the biorefineries and collection facilities) number, sizes and locations but also to determine the connections and the flows between collection facilities and biorefineries and between refineries and blending facilities. These decisions are based on multi criteria analysis relying on economic, environmental and social (limited to the number of jobs created) evaluations. As underlined by (Eksioglu et al., 2009) the mid and short-term decisions in a biomass supply chain relate to determine for each time period: (i) the amount of biomass harvested, (ii) the amount of biomass and bioethanol transported, (iii)) the amount of biomass processed in each biorefinerie, (v) the level of inventories of biomass in collection facilities and in biorefineries, (vi) economic, environmental and social metrics quantification…In the proposed model, the locations of the harvesting sites and blending facilities are supposed fixed and the other facilities locations are to be determined. A superstructure of complete biomass supply chain model and weekly periods are considered (Figure 1). In order to support the model formulation, we use a standardized format for the activity model.

3. Mathematical Model Description

Thanks to the activity model and a deep literature analysis, we have identified that the model proposed by (Eksioglu et al., 2009) gives an interesting base to design the supply chain and manage the logistics of biorefineries. This model relies on three types of discretization:

***Spatial discretization*:** it consists in decomposing the particular area under study into counties. For each county, we identified the harvesting sites, the blending facilities and the town where facilities can potentially be located.

Size discretization: the collection facilities and biorefineries capacities are decomposed onto a finite number of potential facilities sizes, i.e. capacity of production.

Multiperiod discretization: to take into account the dynamic nature of the decision and the biomass seasonality, the time horizon T is decomposed into a finite number of time periods. In the remainder of the paper the time horizon T is one year and the time period is fixed to one week to be coherent with the data. As the basic model was described in the paper of (Eksioglu et al., 2009), the remainder of this article presents the model evolutions and the new equations relating to the evaluation of environmental and social criteria. Our mathematical model adds two major evolutions:

-1- in the original model, there is only one type of biorefineries with different sizes. In our model we have the possibility to choose between different types of biorefineries with their specific production capacity, operating costs, investment costs… This improvement is important because it allows to compare the first and second (and later the third) generation of biorefineries. This comparison is not a posteriori but a priori as the choice of the biorefineries type is a decision variable of the model. Furthermore, with this modification the original MILP model has been transformed into a MINLP one because of new economic terms in the objective function. But a piecewise linearization of the investment costs permits to keep a MILP form to the model.

-2- probably the most important evolution is the multi criteria aspect of our objective function since it adds new constraints to the model. Indeed we found very different results according to the criterion that we wanted to favour. In addition to the economic and environmental criteria, we have included a social evaluation of a supply chain. The description of the different terms of the objective function is given.

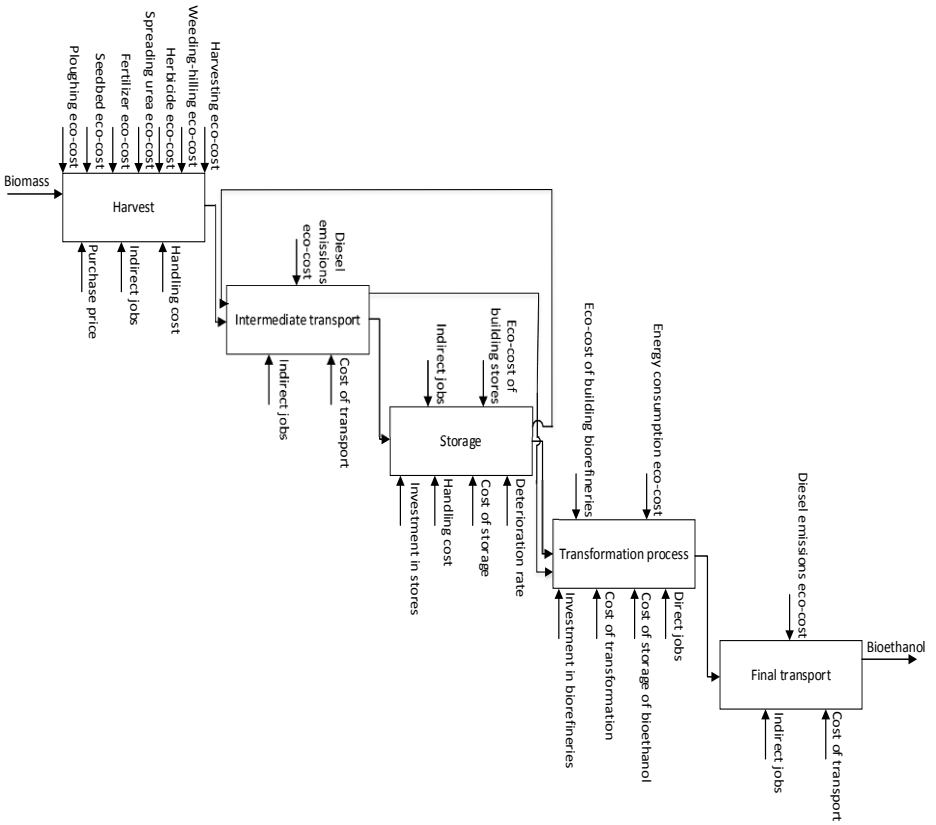

Figure 1 Superstructure of biomass supply chain model

Economic criteria: The costs of the supply chain are: the cost of raw material, transporting the raw material to the collection facility, the cost of handling and storage of biomass, the cost of transport to the biorefineries, the cost of transformation into bioethanol (discounted investment and operating costs for one year) and the cost of final transport to the blending facilities.

Environmental criteria: To evaluate the environmental impact, the Ecocosts are used. Ecocosts are a measure that expresses the environmental load of a product on the basis of prevention of that burden during the product life cycle: from the raw materials until its end of life. This indicator represents the necessary costs that should be made to counteract the negative impact of the activity made on the capacity of earth (Cucek, et al., 2012a). It quantifies the impact in terms of pollution and material depletion by allocating a cost penalizing the use of an alternative that would reduce its impact on the environment and would be called sustainable solution. The total Ecocosts are calculated with the sum of the following contributions: (i) Depletion of natural resources, (ii) Effect on ecosystems, (iii) Effects on human health, and (iv) Global warming (CO_2 and other greenhouse gases). Ecocosts allow quantifying the environmental impact as a

simple indicator easy to understand and compare with other criteria, for example economic. Furthermore, as (Cucek, et al., 2012a) have underlined, the main advantages of these Ecocosts are: (i) they are expressed as a monetary value, (ii) there is no need to compare with another product (often the case with other life cycle assessment methods), and (iii) calculations are based on European price levels and the costs are updated. In our study, Ecocosts are applied to all the activities of the supply chain. The more penalising conditions are applied in order to not underestimate this environmental impact. For calculations, the different eco-costs are divided into two groups depending on whether they are fixed or variables:

- Those that do not change whatever the solution such as cultivation of corn, denaturant added…
- Those that can have an influence on the solution and depend on decision variables of the model such as: transportation, energy consumption, creation of collection facilities or biorefineries…

Social criteria: In their review on footprint as defined indicators on order to measure impacts on sustainability (Curcek et al., 2012b) have eight social footprints: human rights, corruption, poverty, online social (online information available about a person), job, work environmental (number of lost day per unit of product or number of accidents per person), food to energy (competition between the food and energy sectors) and health. Moreover, for the design of a new system in a specific region some criteria would have no influence on the choice between some alternatives as they would not undergo large variations. As a result, for our application we only keep the employment criteria. The number of job created can be divided into three categories:

- Direct jobs: number of jobs directly created by the activity
- Indirect jobs: number of workers in subcontractors working for the new activity.
- Induced jobs: number of jobs created in the local economy. This number evaluates the employments generated by the two previous categories due to their (and their families) consumption in the local economy. It depends on the firm location because it will be more important in rural area than in densely populated area.

The difficulty of the number of jobs created calculation is that it depends on many parameters like: the size of the firm, the activity sector, the level of automation, production quantity…

Our method is based on economic data coming from the annual event and not the initial investment. Therefore, one of the advantages is the consideration of the evolution of a firm in the time that includes all the firm features. Also, job indicators are linked to the economic situation of a firm and not a supposed state estimated when it was under construction. The goal of this study is to be able to give a good estimation of employment for a new company and its impact on local employment faster and with very few data. To validate our approach, we use balance sheets published of companies in France between 2010 and 2014. We selected several companies in different sectors to compare if there is an impact on the estimation and if the proposed method can work with any kind of company. However there are some limitations as the size of samples for each sector and the validity of them. The sectors chosen are the following: Rubber and plastic, Chemical sector, Steel sector. With this way to estimate jobs we have an error of ±15%. To estimate the indirect and induced jobs we use the following equations:

$$\text{IndirectJobs} = \text{pCA} * \text{NbW}$$

Where pCA is the part of turnover coming from the activity studied on the global turnover of the contractor and NbW is the number of jobs in the subcontractor.

$$InducedJobs = JIA * PWLP * (DJ + IJ) * SF/P$$

Where DJ is the number of direct jobs, IJ number of indirect jobs, SF the average household in the place where the activity is, P the size of the population, PWLP the part of local workers supported by the local population and JIA number of jobs working in the area of the study. The parameter SF, P and PWLP are given data coming from the French statistical institute INSEE in 2012.

4. Multi Objective optimization methodology

The CPEX 12.5 algorithm implanted in ILOG is used to solve the mono objective optimization problem. The criteria are antagonistic and moreover a range of each criterion is very large. In this case, it is very important to find a good compromise between these three criteria. Several alternatives can be proposed: build the Pareto Front using an epsilon constraint method and use a Multi Criteria Decision Methodology like (Topsis) or use a goal Programming methodology. A post optimal analysis in the mono objective optimization leads to the fact that the binary variables are the most sensitive variables in the MILP optimization. Generally speaking, in the great majority of works dealing with optimization network design, the formulation of the problem only contains continuous variables what leads to continuous (or discontinuous by jumps) Pareto curves. Although not always fast enough, the research of a feasible solution in this case is consequently easy because one solution is known to exist. The great advantage of applying the methodology of goal programming to problems of supply chain network design is to avoid the generation of a complex research tree with no solutions available and thus large computational times. This method has never been applied to networks design although it is performing and particularly adapted to these problems containing binary variables and very few solutions in the research interval. The aim of the goal programming methodology is to minimize the deviation of the different objective functions. In order to do it, objective functions become constraints and deviation variables are added to them. So the value that restricts the constraint is the sum of the goal and the deviation. In this case, the goal value for each constraint is obtained when minimizing each objective function separately. Then, the objective function is the sum of all deviation variables.

5. Results and discussions

The problem is based 400 000 t per year of ethanol production in the south west of France using corn and wood as a raw material. In the table 1, the raw materials using in this biorefineries are corn and wood. Several optimizations are realized with different weights in the goal programming method to explore some points around the best compromise. The environmental impact is lower when using more wood than corn due to the storage circumstances. In addition, the best economical solution is the one that establishes a single biorefinery and uses 75% of wood. The solution that provides more employment processes more wood than corn. The investment required for the project as defined in this section ranges from € 330 million to over 420 million euros per year, depending on the number of biorefineries. This investment in biorefineries would generate between 1,500 and 3,000 jobs directly related to the biorefinery and induced jobs, for example in local trade. Either the price of bioethanol 0.73 €/ liter from the sale of 400,000 tonnes of bioethanol would be around 370 million euros.

Category / Weights	Economic: 1 Eco-cost: 1 Social: 1	Economic: 0,6 Eco-cost: 0,3 Social: 0,1	Economic: 0,5 Eco-cost: 0,25 Social: 0,25	Economic: 0,55 Eco-cost: 0,3 Social: 0,15	Economic: 0,6 Eco-cost: 0,2 Social: 0,2
Economic cost (M€)	425.8 (+31%)	329.3 (+1%)	396.3 (+22%)	428.6 (+32%)	385.8 (+19%)
Eco-cost (M€)	218.9 (+8%)	211.5 (+0.5%)	217.1 (+3%)	218.1 (+4%)	220.5 (+5%)
Total jobs created	3,043 (-2%)	1,584 (-49%)	2,829 (-9%)	3,158 (-1%)	2,871 (-8%)
Location and Capacity of biorefinery	Bordeaux (400,000) (100% wood) Toulouse (400,000) (85% corn / 15% wood)	Bordeaux (400,000) (25% corn / 75% wood)	Bordeaux (400,000) (65% corn / 35% wood) Toulouse (400,000) (70% corn / 30% wood)	Bordeaux (400,000) (55% corn / 45% wood) Toulouse (400,000) (5% corn / 95% wood)	Bordeaux (400,000) (45% corn / 55% wood) Toulouse (400,000) (80% corn / 20% wood)

Table 1 Results using corn and wood as raw material

6. Conclusions

In this study, using the goal programming methodology, the bioethanol supply chain is optimized in the case of the first and the second generation. This methodology well suited for this kind of problem in order to find the compromise point between the three objectives. Moreover, the raw material is a mix of corn and wood. Biorefineries correspond to an economic model of a mature industrial sector. The actors can then determine with very competitive prices and all parameters have been optimized (purchasing, logistics, processing, etc). However, the study will be continued using a production of biobutanol, or a third-generation bioethanol.

References

Cucek L., Drobez R., Pahor B., Kravanja Z., 2012a. Sustainable synthesis of biogas processes using a novel concept of eco-profit, Comp. Chem. Eng., 42, 87-100.

Cucek, L., Klemeš, J. J., Kravanja, Z. 2012b, A review of footprint analysis tools for monitoring impacts on sustainability. J. Clean. Prod., 34, 9–20.

Eksioglu S. D., Acharya A., Leightley L. E. & Arora S., 2009, Analyzing the design and management of biomass-to-biorefinery supply chain. Comp. Ind. Eng., 57, 1342-1352.

Kravanja Z., Cucek L., 2013, Multi-objective optimization for generating sustainable solutions considering total effects on the environment Applied Energy, 101, 67-80.

Perez-Fortes M., Lainez-Aguirre J.M., Bojarski A.D., Puigjaner L., 2014, Optimization of pre-treatment selection for the use of woody waste in co-combustion plants.Chem. Eng. Res. Res., 92, 1539-1562.

Krist V. Gernaey, Jakob K. Huusom and Rafiqul Gani (Eds.), 12th International Symposium on Process Systems Engineering and 25th European Symposium on Computer Aided Process Engineering.
31 May – 4 June 2015, Copenhagen, Denmark

Operation optimization of ammonia nitrogen removal process in coking wastewater treatment

Yuehong Zhao[a*], Mingsen Liao[a,b], Pengge Ning[a], Hongbin Cao[a], Hao Wen[a]

[a]*Institute of Process Engineering, Chinese Academy of Science, Beijing, China*
[b]*School of Chemical Engineering and Technology, Tianjin University, Tianjin, China*
yhzhao@ipe.ac.cn

Abstract

One of the key steps of coking wastewater treatment is ammonia nitrogen removal. It is normally realized by a process combining distillation operation with bio-treatment, in which the high cost distillation is designed to reduce ammonia nitrogen low enough for the following low cost bio-treatment. Many efforts have being done to optimize the structure and operating parameters of this process. However, to the authors' best knowledge, little work has been done considering the interactions between them. In this paper, a mathematical model of the overall ammonia nitrogen removal process, which combines distillation with shortcut nitrification/ANAMMOX/denitrification (short as O_1-A-O_2), is proposed for its operation and structural optimization. The proposed model is formulated as a mixed integer nonlinear programing (MINLP) problem with aim of minimizing overall operating cost. The main decisions include determining ammonia-nitrogen concentration of distillation bottom outlet, reaction recycle time and passby flowrate of O_1 reactor subject to compliance with the maximum allowable inlet ammonia nitrogen concentration limits of the bio-treatment and discharge regulations. For simplicity, we adopt shortcut models for the ammonia distillation and bio-treatment process based on rigorous model calculation data and theoretical analysis to enforce solution convergence. Computational studies are carried out via GAMS/DICOPT using industrial operating parameters of the typical coking wastewater treatment system as input. The results indicate that the minimum operating cost is obtained at ammonia-nitrogen concentration of 128 mg/L from distillation bottom outlet, 10 h reaction recycle time of O_1 and passby flowrate of 11.448 m^3/h when the ammonia-nitrogen inlet concentration of distillation column is 4,000 mg/L.
Keywords: coking wastewater, optimization, MINLP

1. Introduction

Coking wastewater discharged from coking plants contains high concentration of ammonia nitrogen and carries a lot of phenols and tars (Ren et al., 2007). For example, the concentration of ammonia nitrogen in residual ammonia water coming from coke making is 2,000-4,000 mg/L, which is much more than domestic sewage and other industrial wastewater (An and Zhang, 2004). It is needed to reduce ammonia nitrogen concentration to a very low level before discharge, i.e. 10 mg/L in China (Ministry of Environment Protection of People's Republic of China, MEPC, 2012). Currently, such treatment is difficult and expensive. Thus, how to effectively treat such coking wastewater with reasonable cost is of great importance.

To economically treat coking wastewater, it is normally realized by a process combining distillation operation with bio-treatment, in which the high cost distillation is designed to reduce ammonia nitrogen low enough for the following low cost bio-

treatment to remove residual ammonia nitrogen and other pollutants. It has been widely used in the coking wastewater treatment. Currently, high operating cost is the major obstacle for its operation. In order to reduce the treatment cost, many efforts have being done to optimize the structure and operating parameters of the energy intensive distillation unit, i.e., operating pressure, temperature and reboiler heating mode (Qiu, 2007; Guo, et al., 2009). The results show that bottom outlet ammonia nitrogen concentration of distillation has big impact on both distillation and bio-treatment, and improper operation will lead to higher total treatment cost (Liao et al., 2014). However, to the authors' best knowledge, little work has been done considering the interaction between them. For such problem, process optimization is one efficent way to solve the tradeoff given by the minimization of investment, operational and environmental costs (Martin-Sistac et al., 2008).

In this paper, a mathematical model of the overall ammonia nitrogen removal process, which combines distillation with bio-treatment of O_1-A-O_2, is proposed to study the interactions between distillation and bio-treatment and to obtain optimal operating parameters and optimal process configuration leading to minimum total operating cost. The paper is organized as following. First, models for distillation and O_1-A-O_2, and an optimization model for overall process are set up in section 2. Then, the case study is carried out in section 3. Last, conclusions are summarized in section 4.

2. Optimization Model formulation

2.1. Coking wastewater treatment process

Coking wastewater contains high concentration of ammonia nitrogen, phenols and tar, general treatment process involves pretreatment to remove oil, phenols and ammonia nitrogen, followed by bio-treatment, and optional advanced treatment to further remove residual pollutants to meet discharge requirements. In this work, our efforts is put on the ammonia nitrogen removal, a process involving the operation of a distillation tower to pre-remove the ammonia nitrogen to acceptable level (<500 mg/L) for the following bio-treatment as shown in Figure 1 is studied. For such process, if more ammonia nitrogen can be removed via ANAMMOX, lower operating cost can be obtained. Therefore, it is very important to keep the ANAMMOX reactor work at a proper operating condition. It is normally realized by keeping the ratio between nitrite nitrogen and ammonia nitrogen, R_{na}, by adjusting the concentration of nitrite nitrogen in the reactor. To realize this objective, the process configuration of O_1-A-O_2 is proposed to adjust as: if R_{na} in O_1 outlet is too low, part of O_1 outlet is directly recycled to O_1, otherwise, part of distillation outlet is directly sent to A.

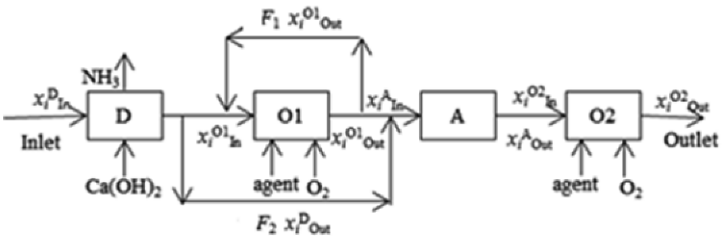

Figure 1 Ammonia nitrogen removal process

2.2. Ammonia distillation model

For ammonia distillation operation, many parameters, *i.e.*, cost of utility, reboiler heating mode, and benefit of ammonia as byproduct all can affect its operating cost. The relationship between operating cost and these parameters is very complex. According to our study on ammonia distillation operation, the concentration of ammonia nitrogen in inlet and bottom outlet of the tower is the major factor affecting its operating cost under the normal operating condition (Liao et al., 2014). In order to simplify the model, a regressed model is established based on the dataset obtained by a series of simulation of the distillation operation under the different concentration of ammonia nitrogen of inlet (x_{in}) and outlet (x_{out}) while keep other parameters constant. It is given by,

$$C^D=P_A x_1^2+P_B x_1 exp x_2+P_C x_2^2+P_D x_1 + P_E x_2 + P_F \quad (1)$$

where $x_1=x_{in}/1000$, $x_2=log(x_{out})$. The obtained parameters are listed in Table 1, which shows that model gives reasonable agreement with the error of 0.002￥/t. It should be noted that direct heat mode is adopted in our proposed model due to its better performance (Liao et al., 2014), and steam consumption is fixed as 0.084t for treating 1t wastewater. It is due to steam consumption varies in a small range (0.078-0.090 t) when x_{in} and x_{out} vary in the range of 1,000-11,000 mg/L and 10-350 mg/L for treating 1t wastewater.

Table 1 Parameters for ammonia distillation model

P_A, $\times10^{-2}$	P_B $\times10^{-4}$	P_C $\times10^{-1}$	P_D	P_E	P_F	E_{avg} $\times10^{-3}$
-5.768	4.555	1.025	-3.134	-3.028	3.274	1.889

2.3. Bio-treatment model

Conventional models for wastewater bio-treatment are based on Active Sludge Model (ASM) by assuming that overall nitrification process for ammonia nitrogen removal (Gernaey et al., 2004). In this work, O_1-A-O_2 process is adopted, which involves short nitrification process and ANAMMOX process. ASM is not the proper model for such process, the Monod equation is thus adopted for its ability to describe short nitrification process and ANAMMOX process (Monod, 1949). For simplicity, a number of assumptions are made in this model:

- All units are operated under the condition of designed pH, DO and temperature,
- O_1 reactor is an ideal tanker batched operated only for ammonia nitrogen nitrification and with stable nitrite accumulation of 95% (Xue et al., 2011),
- A is plug flow reactor and is operated only for ANAMMOX reaction,
- O_2 reactor is an ideal tanker batched operated only for overall nitrification of ammonia nitrogen and all the nitrite is removed due to enough O_2 input.

2.3.1. Ammonia nitrogen nitrification model

For ammonia nitrogen nitrification, it is realized by two steps as shown in following equations:

$$2\ NH_4^+ + 3\ O_2 \rightarrow 2\ NO_2^- + 4\ H^+ + 2\ H_2O \quad (2)$$

$$2\ NO_2^- + O_2 \rightarrow 2\ NO_3^- \quad (3)$$

To model such process, Lawrenence-McCarty equation (Christensen and McCarty, 1975) is adopted,

$$v=v_{max}\ S/(K_s+S) \quad (4)$$

Where, v is the specific degrading rate of ammonia nitrogen, d^{-1}; v_{max} is the max value of v; K_s is saturation constant, *mg/L*; S is the concentration of ammonia nitrogen, *mg/L*. The above equation can be further transformed to an equation listed as below.

$$P_G\ (exp(P_H\ t)-1)+(S-S_0)+P_1\ (lnS-lnS_0)=0 \quad (5)$$

Where, S_0 is the concentration of ammonia nitrogen in inltet, *mg/L*; PG, PH and PI are the parameters. In our work, all these parameters are obtained via regression using Li 's (Li et al., 2011) experimental data. The result is listed in Table 2.

Table 2 Parameters for ammonia nitrogen nitrification model

Parameters	P_G	P_H	P_I	E_{avg}
Value	65.560	0.124	25.889	10.646

2.3.2. ANAMMOX model

According to Jin et al. (2008), ANAMMOX reaction can be descripted by second order reaction kinetics, and the concentration of ammonia nitrogen (S_t *mg/L*) at time t (d) can be obtained using following equation using initial concentration S_0 as input,

$$S_t=S_0\ [1-\ t/\ (0.699+1.004\ t)] \quad (6)$$

In order to keep the proper R_{na} for ANAMMOX operation, it is proposed to adjust the process configuration via recycling or bypass as shown in Figure 1. The material balance equations before and after O_1 reactor are listed below.

$$F_1+F^D{}_{Out}=F_2+F^{O1}{}_{In} \quad (7)$$

$$F_2+F^{O1}{}_{Out}=F_1+F^A{}_{In} \quad (8)$$

$$F_1\,x_i^{O1}{}_{Out}+F^D{}_{Out}\,x_i^D{}_{Out}=F_2\,x_i^D{}_{Out}+F^{O1}{}_{In}\,x_i^{O1}{}_{In} \quad (9)$$

$$F_2\,x_i^D{}_{Out}+F^{O1}{}_{Out}\,x_i^{O1}{}_{Out}=F_1\,x_i^{O1}{}_{Out}+F^A{}_{In}\,x_i^A{}_{In} \quad (10)$$

To simplify the model, two constraints are incorporated into our model as followings:

- Forbid both recycling and bypass are selected

$$y_1+y_2\le 1 \quad (1)$$

- The R_{na} is kept in optimized range

$$1.2\le R_{na}\le 1.4 \quad (12)$$

2.4. Objective function

The objective function of the model involves minimizing the total operating cost as contributed by the economic and environmental sustainability drivers. It consists of costs for distillation and bio-treatment. The former can be obtained by Eq.(1). The latter consists of chemical cost C^{ag}, aeration cost C^{ae}, pollution fees C^{ch}, and sludge treatment cost C^{SS}, which is given by Eq.(13),

$$C^{BIO}=C^{ag}+C^{ch}+C^{ae}+C^{SS} \quad (13)$$

With four cost components defined as follows,

$C^{ag}=F_i p_i$ *(i=*Na_2CO_3*, F= consumption, t/h, p=price, ¥/t)*

$C^{ch}=e\,F^{O2}\,x_i^{O2}{}_{Out}$ *(i=* NH_4^+*, F=discharge, t/h, e=penalty factor)*

$C^{ae} = p_{elec} W$ *(W=power consumption, kW,* p_{elec}*=electricity price, ¥/kWh)*

$C^{SS} = F_{SS}\, p_{SS}$ *(*F_{SS}*=sludge flo, t/h,* p_{SS}*=sludge treatment cost, ¥/t)*

Combing above defined equations, the overall optimization model is thus obtained, which is a nonconvex MINLP. In our work, it is implemented on GAMS using the general MINLP solver DICOPT to obtain optimal solution.

3. Case study

We implement the proposed MINLP on an industrial-scale case study of a coking wastewater treatment process. Data on parameters for the model are provided in Table 3. The optimal configuration of the process involves the use of the bypass to adjust the R_{na} for ANAMMOX operation, which leads to minimum overall operating cost of 7.638 ¥/t, including 6.009 ¥/t for distillation, 1.592 ¥/t for O_1, 0.020 ¥/t for A and 0.017 ¥/t for O_2. It suggests further optimizing work should be put on D and O_1. In current case, the optimal operating are: bypass of 11.448 m^3/h, 128 mg/L of concentration of ammonia nitrogen in distillation bottom outlet, and 10h for O_1 recycle time.

Table 3 Parameters for operating optimization model.

parameters	Value	parameters	Value
t_{fix} /(h)	1.5	p_{elec} /(¥ kW^{-1} h^{-1})	1
t_2 /(h)	8	p_{Na2CO3}/(¥ t^{-1})	1,900
F^{D}_{In} /(m^3 h^{-1})	35	p_{ss} /(¥ t^{-1})	1,000
x^{D}_{In} /(mg L^{-1})	4,000	x^{CHG}_{Out} /(mg L^{-1})	10

To further investigate the impacts of outlet concentration of distillation on the overall operating cost, a series of calculations are carried out. As shown in Figure 2, it can be found that the cost of bio-treatment linearly increase with outlet concentration of distillation operation, while operating cost of distillation decreases correspondingly. It thus needs to keep proper balance between them. In current case, the overall cost reaches minimum at 128mg/L.

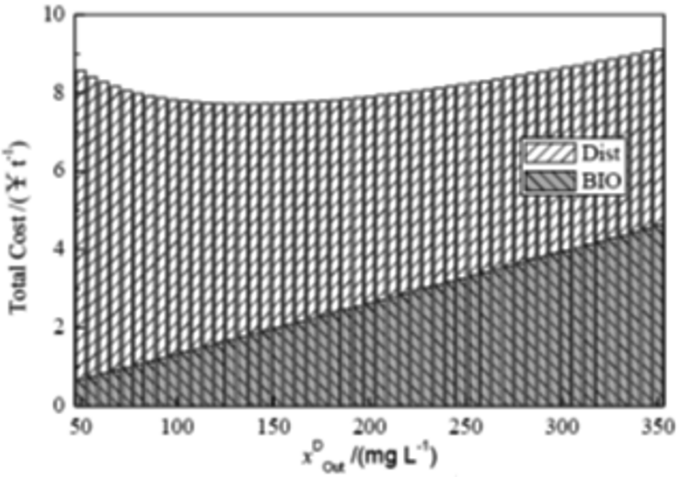

Figure 2 The relationship between operating cost and x^{D}_{Out}

4. Conclusions

This paper focuses on the optimal operation of the ammonia nitrogen removal process, D-O_1-A-O_2, for coking wastewater treatment by proposing a MINLP model. The proposed model is applied on an industrial case study with promising results.

- Bypass operation is better than recycling due to lower O_1 treatment duty leading to reducing operating cost,
- Under the operating condition of case study, optimal operating parameters are: x^D_{out}=128 mg/L, t_1=10 h, F_2=11.448 m^3/h,
- For overall process, D accounts for nearly 80% of total cost; For bio-treatment, O_1 accounts for major part of bio-treatment, while the parts of A and O_2 are negligible compared to O_1.

In our following work, we will incorporate tight bounds on the variables and more constraints that enforce certain operation and design specifications in order to more effectively solve the MINLP model to global optimality.

References

L. An, W. Zhang, 2004, Progress in denitrogenation technology of coking wastewater. Techniques and Equipment for Environmental Pollution Control, 5, 3, 23-27

D. Christensen, P. McCarty, 1975, Multi-process biological treatment model. J. Water Pollut. Contr. Fed., 47, 11, 2652-2664

K. Gernaey, M. van Loosdrecht, M. Henze, et.al., 2004, Activated sludge wastewater treatment plant modelling and simulation: state of the art. Environ Modell Softw, 19, 9, 763-783

X. Guo, H. Ma, M. Wei, et.al., 2009, Comparison between Direct Ammonia Distillation and Indirect Ammonia Distillation. Coal Chemical Industry, 1, 48-50

R. Jin, P. Zheng, C. Tang, 2008, Performance and process kinetics characteristics of ANAMMOX fixed-bed reactor, Journal of Chemical Industry and Engineering (China), 59, 10, 2518-2525

H. Li, 2011, Study on Strengthening Methods of Biological Technology for Coking Wastewater Treatment, Beijing, University of Chinese Academy of Sciences

M. Liao, Y. Zhao, P. Ning, et.al., 2014, Optimization of Distillation Operation for Coking Wastewater Treatment Based on MINLP Model, The Chinese Journal of Process Engineering, 14, 1, 86-93

C. Martin-Sistac, G. Escudero, M. Graells. General framework for solving the design and operation of wastewater treatement netwoeks, Computer Aided Chemical Engineering, 24, 1325-1330.

MEPC, 2012, Emission standard of pollutants for coking chemical industry. Beijing: China Environmental Science Press, 16171-2012

J. Monod, 1949, The growth of bacterial cultures. Annual Reviews in Microbiology, 3, 1, 371-394

Y. Qiu, 2007, Research on the Energy-saving of the Process of Steam Ammonia Distillation. Shanghai; Tongji University

Y. Ren, C. Wei, C. Wu, et.al., 2007, Environmental and biological characteristics of coking wastewater. Acta Scientiae Circumstantiae, 27, 7, 1094-1100

Z. Xue, Y. Li, H. Li, et.al., 2011, Shortcut Nitrification/Anaerobic Ammonium Oxidation/Complete Nitrification Process for Treatment of Coking Wastewater. China Water & Wastewater, 27, 1, 15-19

Krist V. Gernaey, Jakob K. Huusom and Rafiqul Gani (Eds.), 12th International Symposium on Process Systems Engineering and 25th European Symposium on Computer Aided Process Engineering.
31 May – 4 June 2015, Copenhagen, Denmark

Solubility Measurement and Process Simulation of CO_2/CH_4 Gas Mixtures Using Ionic Liquids

Jubao GAO,Yajing XU, Xin ZHANG,Xiangping ZHANG*

State Key Laboratory of Multiphase Complex Systems, Institute of Process Engineering, Chinese Academy of Sciences, Beijing, China
xpzhang@ipe.ac.cn

Abstract

Using room temperature ionic liquids (RTILs), the desirable properties of RTILs with low heat capacity, low corrosive, nonvolatile and good CO_2 solubility can be employed to separate CO_2/CH_4 gas mixture, may offer help to improve energy efficiency. Although the solubilities of CO_2/CH_4 in pure RTILs, such as 1-butyl-3-methylimidazolium tetrafluoroborate ([C4mim][BF_4]), 1-butyl-3-methylimidazolium hexafluorophosphate ([C4mim][PF_6]), 1-butyl-3-methylimidazolium acetate ([C4mim][acetate]), 1-butyl-3-methylimidazolium dicyanamide ([C4mim][DCA]) and 1-butyl-3-methylimidazolium bis(trifluoromethylsulfonyl)imide ([C4mim][Tf_2N]), have been measured in widely temperature and pressure, corresponding process simulation is scant and necessary. In this work, the solubility of CO_2/CH_4 in [C4mim][PF_6] and [C4mim][Tf_2N] is measured, and corresponding thermodynamics model is developed based on the ionic fragment method and the experimental data. An absorption and desorption flowsheet for CO_2/CH_4 separation using ionic liquids is developed and the energy consumption of CO_2 separation is evaluated. Results show that simulated solubility of CO_2/CH_4 is in good agreement with the experimental data from literature data. The total work demand for CO_2/CH_4 separation of [C4mim][PF_6] is a little smaller than that of [C4mim][Tf_2N].

Keywords: carbon dioxide, methane, solubility, simulation, ionic liquids

1. Introduction

The CO_2 capture from various mixtures of gases is of wide concern because it will contribute to global warming and climate change. The current CO_2/CH_4 separation include chemical and physical solvents, such as $Mg(OH)_2$-based sorbent, natural limestone, polyethylene glycol derivatives, refrigerated methanol, N-methyl-2-pyrolidone, zeolite and N-methyldiethanolamine (James et al., 2011; Anamaria et al., 2012). In general, carbon capture faces huge energy consumption especially for shale gas, natural gas, biogas and syngas industry. About 2% energy efficiency can be improved by saving 1 GJ/t CO_2 regeneration energy (Goto et al., 2013). To develop absorbents and optimize system process are efficient method.

Ionic Liquids (ILs), with unique feature of low heat capacity, low corrosive, nonvolatile and good CO_2 solubility (Zhang et al., 2012), are potential candidates to be applied for CO_2 separation from shale gas, natural gas, biogas and syngas with lower energy consumption on a large scale and commercialization. Pure imidazolium-based ILs, such as 1-butyl-3-methylimidazolium tetrafluoroborate[C4mim][BF_4], 1-butyl-3-methylimidazolium hexafluorophosphate [C4mim][PF_6], 1-butyl-3-methylimidazolium acetate [C4mim][acetate], 1-butyl-3-methylimidazolium dicyanamide [C4mim][DCA]

and 1-butyl-3-methylimidazolium bis(trifluoromethylsulfonyl)imide [C4mim][Tf_2N], have been studied for separation of CO_2-CH_4 gas mixture (Privalova et al., 2013; Ramdin et al., 2014a; Khonkaen et al., 2014). The real and ideal CO_2/CH_4 selectivities were provided by Ramdin, and results show that the latter decreases with temperature and ILs molecular weight increase (Ramdin et al., 2014b). However, simulation of CO_2/CH_4 separation process by pure imidazolium-based ILs is quite few, in particulate their energy consumption performance. In this work, [C4mim][PF_6] and [C4mim][Tf_2N] is employed in CO_2/CH_4 separation process to evaluate their separation performance by experiments and simulation. The solubility of CO_2/CH_4 in [C4mim][PF_6] and [C4mim][Tf_2N] is measured using a vapour-liquid equilibrium (VLE) apparatus reported by our previous work (Xu et al., 2014a; Xu et al., 2014b) to offer necessary parameters for simulation process, and evaluate selectivity coefficient, absorption rate and capacity. And then, an absorption and desorption flowsheet for CO_2/CH_4 separation is proposed and simulated to evaluate the CO_2 separation energy consumption.

2. Measurement and simulation

A schematic diagram of the VLE apparatus is shown in Figure 1. The apparatus comprises a feed tank and two equilibrium tanks which are in a temperature controlled oil bath to obtain uniform temperature of gas and liquid in the tanks.

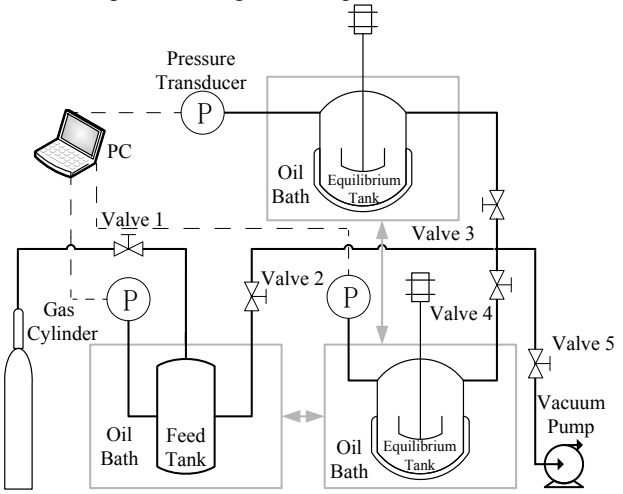

Figure.1 Flow diagram of experimental system

About 40g absorbents are weighted by an electronic analytical balance (PL4002, Sartorius Scientific Instrument Co. Ltd., China) with an accuracy of±0.01 g, and then placed in the equilibrium tank. After that, the equilibrium tank is sealed from the atmosphere environment and evacuated by vacuum pump. Meanwhile, the magnetic stirrer and oil bath is turned on to reach thermal equilibrium as soon as possible. Gas is injected to the equilibrium tank from the feed tank after achieving thermal equilibrium. All pressure is measured by Rosemount engineering pressure transducers with an

accuracy of $\pm 0.065\%$ of full scale up to 3MPa and automatically recorded per second by a program.

Experiments are carried out by pressure swing. Peng-Robinson equation is employed to calculate the number of moles of gas in absorbents as follows (Peng et al., 1976):

$$p = \frac{RT}{v-b} - \frac{a}{v^2 + 2bv - b^2} \tag{1}$$

$$a = 0.457235 \frac{R^2 T_c^2}{p_c} [1 + (0.37464 + 1.54226\omega - 0.26992\omega^2)(1 - T_r^{0.5})]^2 \tag{2}$$

$$Tr = \frac{T}{T_c} \tag{3}$$

$$b = 0.07780 \frac{R\, T_c}{p_c} \tag{4}$$

where P and T are the pressure and the temperature of gas in tank, respectively. Tc and Pc represent the critical temperature and the critical pressure, respectively. R and ω denote the universal gas constant and the acentric factor, respectively.

The thermodynamic models of VLE of separation system and the parameters are regressed based on the experimental data using Aspen plus. The physical properties of ILs, including density, viscosity, surface tension, heat capacity and critical properties, are estimated by a ionic fragment contribution-corresponding states (FCCS) method and the corresponding states principle, and the details is described in our previous work (Huang et al., 2013).

3. Results and discussion

Figure.2 showed the comparison between predicted solubility of CO_2/CH_4 with temperature ranging from 283K to 323K and pressure till to 10bar and experimental data from Anthony et al (2002).

It can be found from Figure.2 that the solubility of CO_2/CH_4 decreases with temperature but pressure increase it. The CO_2 solubility is obviously higher than CH_4 solubility. Low temperature and high pressure induce to good selectivity because of a difference of curve slope which means ILs are prefer the high CO_2 partial pressure industry process, such as biogas and syngas industry.

The predicted heat capacity using the FCCS method and the comparison with experimental result from Holbrey et al (2003) with temperature from 303K to 433K were shown in Figure.3. The heat capacity of ILs is one of the important physical properties while used to estimate the energy consumption. It is increasing with temperature as shown in Figure.3. Hence, low temperature separation is profited for energy saving.

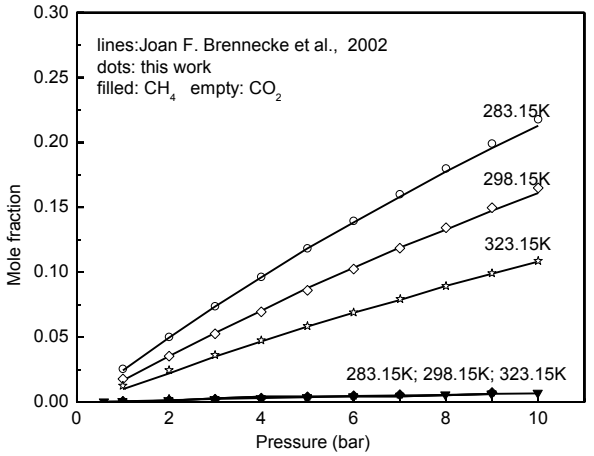

Figure.2 Predicted solubility of CO_2/CH_4

The predicted solubility of CO_2/CH_4 from the thermodynamic models and the predicted heat capacity using the FCCS method in Figure.2 and Figure.3 are in good agreement with the experimental results which implies that the models are suitable for the simulation of the whole CO_2/CH_4 separation process.

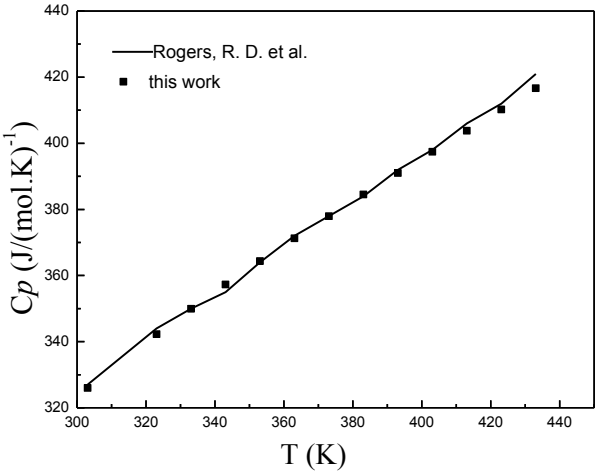

Figure.3 Predicted heat capacity using the FCCS method

In Figure.4, an absorption and desorption flowsheet for CO_2/CH_4 separation was proposed to evaluate the energy consumption of CO_2 separation with [C4mim][PF_6] and [C4mim][Tf_2N] based on the thermodynamic models using Aspen plus. The CO_2/CH_4 feed gas was first compressed to about 10bar. The CO_2 and CH_4 was separated in an absorber. The rich CH_4 as treated gas leave from the absorber top. And the rich solvent at the absorber bottom was desorbed by two stage flash. The second flash top is the rich CO_2. The CO_2 and CH_4 capture ratio are set to 97% and 95%, respectively. Total flow rate of the feed gas is 500Nm^3/h. The lower absorbent circulate rate of [C4mim][PF_6]

was found to be 57t/h, but for [C4mim][Tf_2N] it was 65t/h which results in higher pump work. It may be attributed to the good selectivity of [C4mim][PF_6] although [C4mim][Tf_2N] shows better CO_2 solubility than [C4mim][PF_6]. The compress work and vacuum work of [C4mim][PF_6] and [C4mim][Tf_2N] are almost no difference. Hence, the total work of [C4mim][PF_6] is about 0.383MJ/kgCO_2 which is a little smaller than that of [C4mim][Tf_2N] of 0.388MJ/kgCO_2.

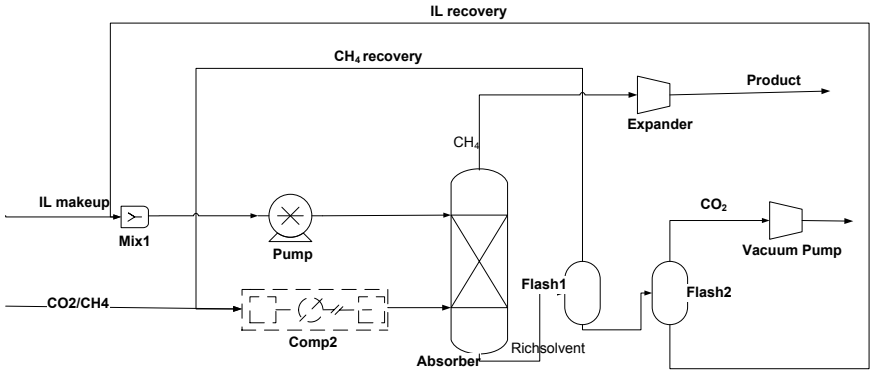

Figure.4 Flow diagram of CO_2/CH_4 separation system

4. Conclusions

The VLE apparatus was used to measure the solubility of CO_2/CH_4 in [C4mim][PF_6] and [C4mim][Tf_2N]. FCCS method based on the ionic fragment method was used to predict the physical properties of ILs. The thermodynamics model was developed based on the experimental data using Aspen plus. An absorption and desorption for CO_2/CH_4 separation was proposed to evaluate the energy consumption of CO_2 separation with [C4mim][PF_6] and [C4mim][Tf_2N] based on the thermodynamic models. The experimental and simulated results show that the FCCS method combined with the proposed thermodynamic models can be used to simulate accurately the whole CO_2/CH_4 separation process. It is suggest that the simulated method can also be used to screen ILs for CO_2/CH_4 separation. All these results in this work demonstrate that ILs is a promising solvent for CO_2/CH_4 separation technologies.

References

P. Anamaria, C.C. Calin, S.A. Paul，2012，Pre-combustion carbon dioxide capture by gas–liquid absorption for Integrated Gasification Combined Cycle power plants, Int. J. Greenhouse Gas Control, 7, 1-11.

J.L. Anthony, E.J. Maginn, J.F. Brennecke, 2002, Solubilities and thermodynamic properties of gases in the ionic liquid 1-n-butyl-3-methylimidazolium hexafluorophosphate, The Journal of Physical Chemistry B, 106(29):7315-7320.

K. Goto, K. Yogo, T. Higashii, 2013, A review of efficiency penalty in a coal-fired power plant with post-combustion CO_2 capture, Applied Energy, 111, 710-720.

Y. Huang, H.F. Dong, X.P. Zhang, C.S. Li, S.J. Zhang, 2013, A new fragment contribution-corresponding states method for physicochemical properties prediction of ionic liquids, AICHE Journal, 59, 1348-1359.

J.D. Holbrey, W.M. Reichert, R.G. Reddy, R.D. Rogers, 2003, Heat capacities of ionic liquids and their applications as thermal fluids, In: Rodgers RD, Seddon KR, eds. Ionic Liquids as Green Solvents: Progress and Prospects, 856:121-133.

C. F. James, V.S. Ranjani, W.S.Jr. Robert, 2011, Zeolite-Based Process for CO_2 Capture from High-Pressure, Moderate-Temperature Gas Streams, Ind. Eng. Chem. Res, 50, 13962-13968.

K. Khonkaen, K. Siemanond, A. Henni, 2014, Simulation of Carbon Dioxide Capture Using Ionic Liquid 1-Ethyl-3-methylimidazolium Acetate, 24th European Symposium on Computer Aided Process Engineering (ESCAPE), Computer-Aided Chemical Engineering, 33, 1045-1050.

D. Peng, D.B. Robinson, 1976, A new two-constant equation of state, Ind. Eng. Chem. Fundam,15 ,59 – 64.

E. Privalova, S. Rasi, P. Maki-Arvela, K. Eranen, J. Rintala, Y.D. Murzina, J. P. Mikkola, 2013, CO_2 capture from biogas: absorbent selection, RSC Adv, 3, 2979 – 2994.

M. Ramdin, A. Amplianitis, T.W. de Loos, T.J.H. Vlugt, 2014a, Solubility of CO_2/CH_4 gas mixtures in ionic liquids, Fluid Phase Equilibria, 375 ,134–142.

M. Ramdin, S.P. Balaji, J.M. Vicent-Luna, J.J. Gutierrez-Sevillano, S. Calero, T.W. de Loos, T.J.H. Vlugt, 2014b, Solubility of the Precombustion Gases CO_2, CH_4, CO, H_2, N_2, and H_2S in the Ionic Liquid [bmim][Tf_2N] from Monte Carlo Simulations, J. Phys. Chem. C , 118, 23599 − 23604.

Y.J. Xu, Y. Huang, B. Wu, X.P. Zhang, S.J. Zhang, 2014a, Biogas Upgrading Technologies: Energetic Analysis and Environmental Impact Assessment , CJCHE, 10.1016/j.cjche. 2014.09.048.

F. Xu, H.S. Gao, H.F. Dong, Z.L. Wang, X.P. Zhang, Z.B. Ren, S.J. Zhang, 2014b, Solubility of CO_2 in aqueous mixtures of monoethanolamine and dicyanamide-based ionic liquids, Fluid Phase Equilibria, 365, 80-87.

X.P. Zhang, X.C. Zhang, H.F. Dong, Z.J. Zhao, S.J. Zhang, Y. Huang, 2012, Carbon capture with ionic liquids: overview and progress, Energy & Environmental Science, 5, 6668-6681.

Krist V. Gernaey, Jakob K. Huusom and Rafiqul Gani (Eds.), 12th International Symposium on Process Systems Engineering and 25th European Symposium on Computer Aided Process Engineering.
31 May - 4 June 2015, Copenhagen, Denmark.

Evaluation of Qualitative Trend Analysis as a Tool for Automation

Christian M. Thürlimann[a], David J. Dürrenmatt[b] and Kris Villez[a]

[a]*Department of Process Engineering, Eawag, Swiss Federal Institute of Aquatic Science and Technology; Dübendorf, Switzerland*
[b]*Rittmeyer AG, Baar, Switzerland*
kris.villez@eawag.ch

Abstract

Ammonium (NH_4^+) load based aeration control on biological wastewater treatment plants saves costs and enhances nitrogen removal. However, the need for maintenance intensive NH_4^+ sensors hamper the controls application in practice. Alternatives, in the form of soft-sensors are broadly discussed in academia. A soft-sensor recently described in literature exploits the pH effects induced by biological NH_4^+ oxidation. This concept is now further developed by means of qualitative trend analysis (QTA). Previously, the qualitative path estimation (QPE) algorithms was proposed as a fast and reliable QTA algorithm for batch process data analysis. It does not allow online application in continuous flow systems however. In this work, a modification of QPE, call qualitative state estimation (QSE), is proposed as a suitable algorithm for continuous-flow systems. Initial tests indicate that the QSE algorithms is a robust technique for extraction of relevant information in a full-scale environment. At the WWTP Hard in Winterthur, this resulted in cost-saving automation of the aeration system. This contribution summarizes these first results.

Keywords: ammonia control, biological wastewater treatment, hidden Markov model, kernel regression, process monitoring

1. Introduction

Ammonium (NH_4^+) controlled aeration is a well known and widely applied technique (Åmand et al., 2013) for automation of biological wastewater treatment plants (WWTPs). By controlling the ammonium concentration in the effluent, energy costs can be reduced while violation of effluent concentration limits can be avoided. Furthermore, optimization of the oxidation processes ensures that denitrification capacity can be increased and enhanced biological phosphorus (bio-P) removal can take place without the need to increase reactor volumes (Rieger et al., 2014). However, economical application of such ammonium control is only feasible on larger WWTPs, where the energy and cost savings outweigh the NH_4^+ sensors installation and maintenance costs (Winkler et al., 2004; Åmand et al., 2014). Haimi et al. (2013) present numerous studies dealing with NH_4^+ soft-sensors evading the need for a physical NH_4^+ sensor. Importantly, these studies mainly investigate black-box models, which give rise to a series of challenges for widespread full-scale application such as the need to recalibrate the methods for each application, lack of transparency and trust by operators, and potentially difficult implementation and fine-tuning. A soft-sensor based on a mechanistic principle was presented by Ruano et al. (2009). This soft-sensor takes advantage of the acidifying effect of biological NH_4^+ oxidation, which is also known as nitrification. Instead of estimating the NH_4^+ concentration, the soft-sensor monitors the net effect of nitrification (acidifying) and CO_2 stripping (proton-consuming). In locations of a WWTP where nitrification

occurs, a net production of protons is typical and causes the pH to drop. Where nitrification is not occurring, a net increase of the pH results due to CO2 stripping. Ruano et al. (2012) manipulated the aeration intensity in an activated sludge system to keep the difference between two pH measurements located at the in- and outlet of an aerated tank sequence at a given setpoint. Practically, the pH difference is as a proxy for the balance between proton production due to nitrification and the proton consumption from CO_2 stripping. The combined effects of hydraulic transport, mixing conditions, oxidation, and stripping contribute to a complex relationship between the ammonia concentration and the pH. This relationship can however be understood qualitatively most of the time so that this concept is relatively easy to use for a diverse set of WWTP configuration. Under steady-state conditions, a certain pH difference corresponds to a certain NH_4^+ effluent concentration. Unfortunately, using a fixed pH difference as a control setpoint assumes perfect pH sensors. In practice, significant signal drift occurs, which can only be kept in check by a prohibitively high maintenance effort. This eliminates the advantage of pH sensors over conventional NH_4^+ sensors for ammonium control. We however claim that the pH difference signal can also be used in a less stringent fashion so that monitoring the pH difference remains useful in practice. Fig. 1 shows the recorded pH difference (top) and the measured NH_4^+ concentration measured (bottom) from the setup at the Winterthur WWTP as described in section Hardware Setup. The qualitative similarity between these two signals is obvious as the maxima in both signals are remarkably synchronous. Consequently, we present in this paper a qualitative trend analysis (QTA) method to use this qualitative similarities for an NH_4^+ load dependent aeration control. This QTA based method is used to detect peak NH_4^+ loads entering the WWTP. This detection allows to adjust the setpoints for the dissolved oxygen (DO) concentration accordingly and thereby optimise the aeration energy costs of the plant. The QTA method used here is referred to as Qualitative State Estimation (QSE) and is based on the earlier Qualitative Path Estimation (QPE) algorithm Villez (2015). The main differences are *(i)* that the Hidden Markov Model (HMM) now represents an ergodic process, as opposed to the linear Markov chain for the QPE algorithm and *(ii)* that the state estimation method is different from the Viterbi algorithm used for QPE.

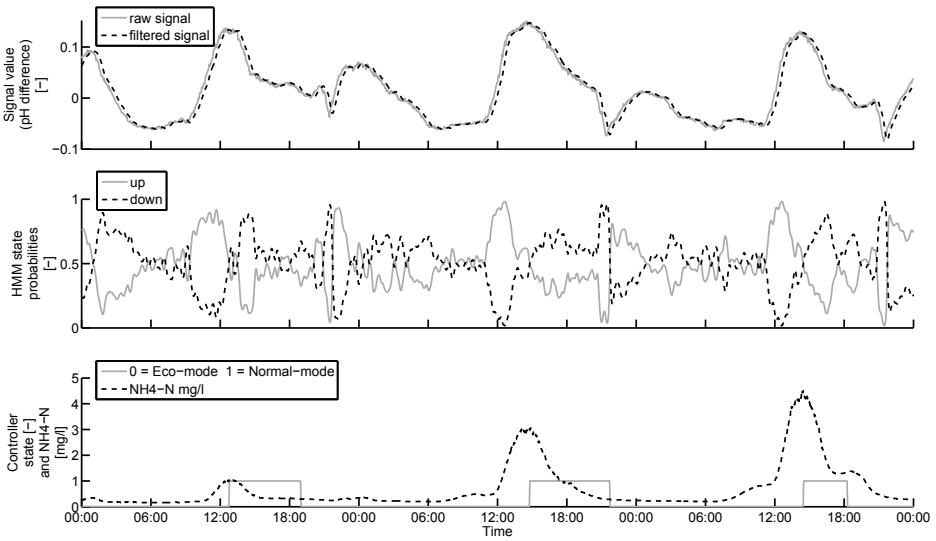

Figure 1: Demonstration of the QSE algorithm: Top – pH difference raw/filtered; Middle – Qualitative trend probabilities; Bottom – Control state and NH_4^+ measurements.

2. Methods

2.1. Hardware Setup

The studied municipal WWTP Hard, Winterthur, Switzerland exhibits one stirred and three aerated activated sludge tanks for oxidation of organic compounds as well as NH_4^+ (cfr. Fig. 2). These are located between the primary clarifier and the secondary clarifier. The signal used in the proposed control system, consists of the difference between a pH measurement in the first aerated tank (upstream, *us*) and the last aerated tank (downstream, *ds*). An ion selective electrode (ISE) measuring the NH_4^+ concentration is placed in the second aeration tank in order to validate and fine-tune the pH difference based control loop.

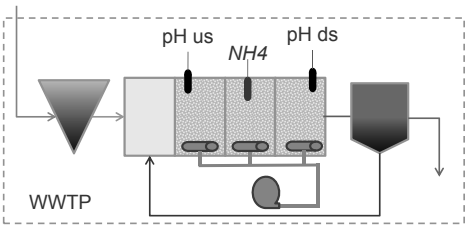

Figure 2: Location of pH sensors (pH *us* and pH *ds*) and ammonium sensor (*NH4*).

2.2. Qualitative Trend Analysis

As mentioned above, QTA comprises a set of algorithms for segmentation of time series. Each segment, referred to as an *episode*, is defined by a start and end time. Within these time points, the sign of one or more of the signal's derivatives is considered constant. In this application only the sign of the first derivative is considered as this is sufficient to define the qualitative features of interest, namely the minima and maxima. A specialised algorithm, called qualitative state estimation (QSE), is developed to enable fast and reliable identification of these extrema. It is based on the QPE algorithm, which was found to be fast and reliable for batch process diagnosis (Villez, 2015). The QSE algorithm consists of two steps.

Step 1 – Qualitative trend probabilities via kernel regression: First, the algorithm estimates the likelihood that the analysed signal is decreasing or increasing at given time points. This assessment is based on local polynomial fit to the data, which consist of pairs of an independent variable, t_j $(j = 1...m)$, which is time in our case, and the dependent variable measurement, y_j, which is a pH difference signal in this study. The polynomial coefficients, β_i, are computed for sample index i by minimising the following weighted least squares (WLS) objective function:

$$\min_{\beta_i} \sum_{j=1}^{m} K_{i,j} \cdot (y_j - \mathbf{x}_j^T \cdot \beta_i)^2 \tag{1}$$

$$\text{with } \mathbf{x}_j = \begin{bmatrix} (\mathbf{t}-t_j)^0 \\ (\mathbf{t}-t_j)^1 \\ \vdots \\ (\mathbf{t}-t_j)^p \end{bmatrix}, \quad d_{i,j} = \frac{|t_i - t_j|}{\lambda}, \quad K_{i,j} = \begin{cases} (1-d_{i,j}^3)^3, & \text{if } d \leq 1 \\ 0, & \text{otherwise} \end{cases} \tag{2}$$

The polynomial degree p is 2 or higher. Furthermore, the tri-cube kernel function is used to determine the weighting of the data points. The weights, $K_{i,j}$, are completely specified by a meta-parameter λ. Only data points within the distance of λ to the sample of interest i have a weight larger than zero and contribute to the local model. The data weights decrease as the distance from the considered sample, i, increases. Eq. 1 can be solved analytically as follows:

$$\begin{aligned} \beta_i &= \mathbf{H}_i \cdot \mathbf{y} \\ \mathbf{H}_i &= (\mathbf{X}_i^T \cdot \mathbf{W}_i \cdot \mathbf{X}_i)^{-1} \cdot \mathbf{X}_i^T \cdot \mathbf{W}_i \\ \mathbf{X}_i &= \begin{bmatrix} (\mathbf{t}-t_i)^0 & (\mathbf{t}-t_i)^1 & \cdots & (\mathbf{t}-t_i)^p \end{bmatrix} \end{aligned} \qquad \underset{m\times m}{\mathbf{W}_i} = \begin{bmatrix} K_{i,1} & \cdots & 0 & \cdots & 0 \\ \vdots & \ddots & \vdots & & \vdots \\ 0 & & K_{i,j} & & 0 \\ \vdots & & \vdots & \ddots & \vdots \\ 0 & \cdots & 0 & \cdots & K_{i,m} \end{bmatrix} \tag{3}$$

The matrix $\mathbf{X}_i$ is a polynomial basis matrix whereas $\mathbf{W}_i$ is a diagonal sample weight matrix. The polynomial fitting problem is also known as kernel regression and is equivalent to a linear projection. Theoretical point-wise covariance matrices can thus be computed when the measurement errors are assumed to be drawn independently and identically from a Gaussian distribution ($N(0;\sigma_y)$):

$$\Sigma_{\beta_i} = \mathbf{H}_i \cdot \sigma_y \cdot \mathbf{I}_n \cdot \mathbf{H}_i^T \tag{4}$$

The point-wise distribution for the coefficient of the linear term in the polynomial is then:

$$\beta_{1,i} \sim N(\beta_{1,i}(2), \Sigma_{\beta_i}(2,2)) = N(\mu_{1,i}, \sigma_{1,i}) \tag{5}$$

By integration of the probability mass under this density curve over the positive (negative) section of the real axis, one obtains the probability for a upward trend, $P_{u,i}$ (downward trend, $P_{d,i}$). More specifically, one computes these *qualitative trend probabilities* as (Fig. 1 middle):

$$P_{y,i}(1) = P_{u,i} = \int_{u=0}^{+\infty} \frac{1}{\sigma_{1,i}\sqrt{2\pi}} \cdot exp\left(-\frac{(u-\mu_{1,i})^2}{2\cdot\sigma_{1,i}^2} du\right) \qquad P_{y,i}(2) = P_{d,i} = (1-P_{u,i}) \tag{6}$$

Step 2 – Probability integration by means of a Hidden Markov Model (HMM): Discrete state estimation by means of a Hidden Markov Model is used as a filtering step to remove noisy features in the qualitative trend probabilities for the derivative signs as computed in the first step of the QSE algorithm. To this end, the monitored discrete state process is assumed to be represented by a Markov process. Mathematically, a Markov process is described by expressing the likelihood for each of the process states at time i conditionally to the likelihoods of the same states at time $i-1$:

$$\Lambda(\mathbf{s}(i) = t \mid i-1) = \sum_{p=1}^{q} \mathbf{T}_i(t,p) \cdot \Lambda(\mathbf{s}(i-1) = p \mid i-1) \tag{7}$$

The likelihoods, $\mathbf{T}_i(t,p)$, express the chance that the process state will be the target state t at time i conditional to the process being in the state p at time $i-1$. Whereas the QPE method makes use of an upper triangular matrix, $\mathbf{T}$, implying a non-ergodic Markov process, the QSE method proposed here poses no such restrictions. In addition, all transition likelihoods on the diagonal are set to one (1) and the off-diagonal elements are set to an identical and time-invariant value (γ):

$$\mathbf{T}_i(p,t) = \begin{cases} 1, & p = t \\ \gamma_i(t,p) = \gamma, & \text{otherwise} \end{cases} \tag{8}$$

The maximum likelihood (ML) state estimate at time i, $\hat{s}_i$, is now given as:

$$\hat{s} = \underset{t}{\operatorname{argmax}}\, P_{s=t}(i|i) \quad \text{with} \quad P_{s=t}(i|i) = P_{y,i}(t) \cdot \sum_p \mathbf{T}_i(t,p) \cdot P_{s=t}(i-1|i-1) \tag{9}$$

By means of the above recursive equations, one tracks the most likely state at a given time conditional to the evidence gathered until that time and represented by the qualitative trend probabilities computed by Eq. 6. It is this series of ML state estimates that are fed into the controller logic.

3. Results

3.1. Feedback Control Based on QTA

The proposed feedback control based on the QTA is a bang-bang controller. In low load situations (a.k.a. *Eco*-mode) the dissolved oxygen (DO) concentration is lowered in all tanks by reducing the DO setpoint for the corresponding slave proportional-integral (PI) control loops. This slows the nitrification process down, which in turn reduces the oxygen demand and thus the aeration energy and costs. When facing a NH_4^+ peak load (a.k.a. *Normal*-mode), one increases the DO setpoint to speed up the nitrification process so that a violation of the effluent concentration limits is prevented. Proper recognition of peak and normal loads is critical to maintain environmentally safe operation limits while minimising operational costs associated with aeration. QTA is deployed to detect the two modes (Eco and Normal) online (see Table 1). A small width for the support window (λ (cfr. Eq. 1) allows a short response time. However, small oscillations lead to the identification of irrelevant minima and maxima. The HMM-based method was therefore complemented with a number of heuristic quantitative rules, which enable the separation between these small oscillations, which are unrelated to changes in the NH_4^+ concentration, and large trends, which correlated to significant dynamics of the NH_4^+ concentration. Firstly, the recognition of the switch from Eco- to Normal-mode incorporates three rules, which are: *EN1* – At least one minimum, i.e. switch of the HMM state estimate from the downward to upward state, needs to be registered in Eco-mode; *EN2* – The difference between the current pH difference signal value and the lowest minimum registered in the Eco-mode is larger than a critical minimum level, called the *Minimal Difference*; and *EN3* – A maximum, i.e. switch of the HMM state estimate from the upward to downward state, needs to occur after both *EN1* and *EN2* are evaluated as true. These rules ensure *(i)* that the minimum NH_4^+ concentration as occurring during the Eco-mode is recognised properly and *(ii)* a recognised maximum truly corresponds to an NH_4^+ peak load. To switch back from Normal- to Eco-mode, the following heuristic rules are applied: *NE1* – The pH difference signal has to drop below the level defined by the minimum pH difference signal registered in the last Eco-mode plus a tolerance, called *Maximal Difference*. This rule ensures that the nitrification activity is at a similar (low) activity as recorded before; *NE2* – At least one minimum needs to occur after *NE1* is evaluated as true. *NE3* – The Normal-mode needs to be active for a minimal time period. These rules ensure that nitrification activity is always brought to its minimum thereby allowing for proper registration of the minimum NH_4^+ concentration. These rules govern the bang-bang controller, which switches between the Eco-mode, corresponding to low NH_4^+ loads, and the Normal-mode, which corresponds to high NH_4^+ loads.

Table 1: Control states and qualitative process properties.

Control Mode	Ammonium Load	Oxygen Setpoint	pH Difference
Eco	Low	Low	Low
Normal	High	High	High

3.2. Integration into the pre-existing control scheme.

The QTA based bang-bang controller only determines if the plant faces a high (Normal-mode) or low (Eco-mode) NH_4^+ load situation. In the Normal-mode, a high DO setpoint is set for the slave PI controllers regulating the DO concentrations. In Eco-mode, a low DO setpoint is implemented. Because the slave controllers and the aeration system exhibit their own response times, a number of safety rules are implemented to ensure the QTA-based bang-bang controller output is handled well and only when appropriate. One additional rule checks if the plant is facing a high hydraulic load. Detection of peak hydraulic loads are detected faster by means of flow measurements at the inlet of the WWTP and induce a switch to the Normal-mode without further delay. Similarly, a pH sensor at the inlet of the plant can be used as a proxy for toxic, industrial wastewater. By switching to the Normal-mode maximum survival of the sensitive bacterial community is then ensured.

3.3. Experiences and Outlook

The proposed bang-bang controller has been tested on the full-scale WWTP Hard in Winterthur. During this time, the effluent concentration of NH_4^+ did not increase significantly compared to exclusive operation in Normal-mode and remained below the legal limit. Current estimates of the aeration energy savings amount to 15%. Early development and testing was executed jointly with Rittmeyer AG, which has developed a commercially viable version as a module in the RITUNE® software for WWTP supervision and optimisation. Further work is focused on testing and evaluation of the QTA-based controller for other WWTPs. Special attention will be given to *(i)* the ease of implementation and fine-tuning and *(ii)* transparency of the controller to technical operators. QTA methods are being developed to handle *(i)* inflection points, *(ii)* discontinuities (Villez and Habermacher, 2015), as well as *(iii)* multivariate data series.

4. Conclusion

A new method for qualitative trend analysis (QTA) has been developed and tested as part of an advanced control strategy for NH_4^+ removal in biological WWTPs. By means of the QTA method, called qualitative state estimation (QSE), one can differentiate between high and low NH_4^+ load situations on the basis of cheap and reliable pH sensor signals only. Initial tests with this controller delivered reduction in aeration energy requirements of over 10%. As such, the proposed method holds great promise as a robust approach to minimise energy costs in small biological WWTPs.

5. Acknowledgement

This work was supported by the Commission for Technology and Innovation (CTI) of the Swiss Federal Department of Economic Affairs Education and Research (EAER). (CTI project no. 14351. PFIW-IW). The authors thank the staff of the WWTP Hard in Winterthur for the opportunity and assistance with this study.

References

Åmand, L., Laurell, C., Stark-Fujii, K., Thunberg, A., Carlsson, B., 2014. Lessons learnt from evaluating full-scale ammonium feedback control in three large wastewater treatment plants. Water Science & Technology 69 (7), 1573–1580.

Åmand, L., Olsson, G., Carlsson, B., 2013. Aeration control a review. Water Science & Technology 67 (11), 2374–2398.

Haimi, H., Mulas, M., Corona, F., Vahala, R., 2013. Data-derived soft-sensors for biological wastewater treatment plants: An overview. Environmental Modelling & Software 47, 88–107.

Rieger, L., Jones, R. M., Dold, P. L., Bott, C. B., 2014. Ammonia-based feedforward and feedback aeration control in activated sludge processes. Water Environment Research 86 (1), 63–73.

Ruano, M., Ribes, J., Seco, A., Ferrer, J., 2012. An advanced control strategy for biological nutrient removal in continuous systems based on pH and ORP sensors. Chemical Engineering Journal 183, 212–221.

Ruano, M. V., Ribes, J., Seco, A., Ferrer, J., 2009. Low cost-sensors as a real alternative to on-line nitrogen analysers in continuous systems. Water Science & Technology 60 (12), 3261–3268.

Villez, K., 2015. Qualitative path estimation: A fast and reliable algorithm for qualitative trend analysis. AIChE Journal Accepted, In press.

Villez, K., Habermacher, J., 2015. Shape constrained splines with discontinuities for anomaly detection in a batch process. Accepted to the 12th International Symposium on Process Systems Engineering and 25th European Symposium on Computer Aided Process Engineering (PSE2015/ESCAPE25), 31 May - 4 June 2015, Copenhagen, Denmark.

Winkler, S., Rieger, L., Saracevic, E., Pressl, A., Gruber, G., 2004. Application of ion-sensitive sensors in water quality monitoring. Water Science & Technology 50 (11), 105–114.

Krist V. Gernaey, Jakob K. Huusom and Rafiqul Gani (Eds.), 12th International Symposium on Process Systems Engineering and 25th European Symposium on Computer Aided Process Engineering.
31 May – 4 June 2015, Copenhagen, Denmark

A Detailed Mathematical Modelling Representation of Clean Water Treatment Plants

Folashade Akinmolayan[a], Nina Thornhill[b], Eva Sorensen[a]

[a]*Centre for Process Systems Engineering, Department of Chemical Engineering, University College London, London, United Kingdom. * e-mail: e.sorensen@ucl.ac.uk*
[b]*Centre for Process Systems Engineering, Department of Chemical Engineering, Imperial College London, Exhibition Road, London, United Kingdom.*

Abstract

One of the biggest operational risks to water companies arises from their ability to control the day-to-day management and optimisation of their water treatment systems. With emerging pressures to remain competitive within national and global markets, companies are looking for solutions to be able to make predictions on how their chosen treatment processes can be improved. The objective of this work is to develop a detailed mathematical modelling methodology of a conventional clean water treatment plant which includes detailed models of each of the key processing unit operations. The methodology is first validated by individual unit examples based on experimental data from literature, before the operation of a complete water treatment plant is considered.

Keywords: Clean water treatment, dynamic modelling, water purification.

1. Introduction

Supplying water of adequate quality and in sufficient quantities is one of the major challenges facing modern society. These challenges are intensified by a combination of rising populations, increased industrial and agricultural water usage, climate changes and the increased difficulty of building major new water infrastructure due to limitations in the amount of land accessible for the new developments. With growing pressures on the water treatment industry, there is now a greater need to optimise water treatment works, whether to increase throughput, reduce operational costs, or minimise capital expenditure as demonstrated by Bozkurt et al. (2014). Although clean water treatment plants have been functioning for more than a century, during the last few decades, as technology has developed, the operation has become increasingly more complex.

The operation of drinking water treatment plants are largely based on experience, but due to more stringent regulations, treatment plants have to produce water of increasingly higher quality. The European Union follows standards for potable water that has been set by a Drinking Water Directive (98/83/EC, 1998). The technologies utilised in water treatment can be energy intensive and costly, and a methodology which can predict energy usage and other key performance indicators will therefore be of great benefit to this industry. Most modelling work within clean water operations has so far been based on empirical observations or hydraulic modelling, rather than mathematically describable relationships of the process, which will be considered in this work. An accurate mathematical model can enable quick and efficient investigation and screening of different design and operating alternatives. From the concept of modelling within the process industry, it can be inferred that modelling and control is likely to lead to better water quality, cost reduction and to a more stable performance of a plant, as

well as to a better understanding of the individual treatment processes. According to Rosen (2000), by 2050 a drinking water treatment plant will be entirely controlled from a central control centre, where dedicated integral control programs, which incorporate advanced process and control models, will control the treatment processes and mitigate risk. Acquiring detailed mathematical model representations of each water treatment process is therefore essential to meet this objective.

In this work, we demonstrate the novel use of a mechanistic modelling approach to generate individual models of different types of clean water treatment process units. We then combine the models together to depict an overall process flowsheet. The main objective is the development of a complete mathematical model of an entire water treatment plant. The model is able to accurately predict the performance of the overall process, which enables a wider view on how changes in one processing unit will affect the treatment process as a whole.

2. Process description

The plant considered in this case study consists of the three main physical processes typically available on a conventional water treatment plant; a coagulation/flocculation unit, a clarification unit and a rapid gravity filtration unit. As illustrated in Figure 1, raw water, possibly from different sources, first enters the coagulation/flocculation unit, where a chemical coagulant is added. The coagulant destabilises the colloids present in the raw water by neutralising their negative charges (coagulation). The colloids will then subsequently aggregate to form flocs (flocculation). These flocs of colloidal impurities behave as suspended solids within the water as it enters the second unit, a clarification unit. Within this unit, the flocs will settle to the bottom, and this concentration of solids is then removed as a sludge flow through the bottom, thus producing an almost clear effluent at the top of the unit which flows into the final main unit to undergo filtration. During filtration, the water is passed through a bed of adsorbent material, for instance sand, which allows for the impurities to attach to the material, thus removing the impurities from the water, leaving this as clean purified water. The filtration unit will require regular back-washing. The water will then go to a final disinfection unit (this step is not considered in this work) before a holding tank.

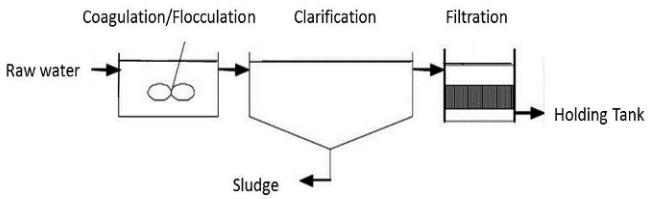

Figure 1: Flowsheet of a conventional clean water treatment work

3. Model development

The main objective of this work was to develop a mathematical model representation of clean water treatment works with sufficient accuracy to allow a detailed investigation of the behaviour, both of individual processing units, and of the overall treatment work. The individual unit models are derived based on previous work from literature and is coded within gPROMS, an equation based modelling and simulation software package (Process Systems Enterprise, 2014).

3.1. Model of the Coagulation/Flocculation unit

Argaman and Kaufman (1970) proposed a diffusion model for orthokinetic flocculation at steady state. They assumed that particles suspended in a turbulent regime experience a random motion which is similar to that of gas molecules (Equation 1):

$$\frac{\partial n}{\partial t} = K_B n G^m - K_A n_D G \tag{1}$$

where n is the number of primary particles per unit volume of water (m^{-3}), n_D is the number of floc particles formed per unit volume of water (m^{-3}) t is time (s), G is the velocity gradient (s^{-1}), m is a parameter, K_A is the floc aggregation coefficient (-), and K_B is the break up rate coefficient (s).

In developing their model, Argaman-Kaufman considered floc formation in a single continuously stirred tank reactor (CSTR) and assumed that the primary particles collide into flocs and that these flocs are removed in the following clarification unit. The model was validated experimentally by Haarhoff and Joubert (1997). The model developed in this work was validated against both the original model and the experimental data and showed good agreement (see Figure 2).

3.2. Model of the Clarification unit

The theory from secondary settling tanks in wastewater treatment works can be applied to the clarification unit in clean water treatment works (Head et al., 1997). Burger et al. (2012) proposed a non-linear partial differential equation (PDE), then used finite difference methods to derive at a one-dimensional settling-compression-dispersion model (Equations 2 and 3):

$$\frac{\partial}{\partial t}\int_{z_1}^{z_2} AC(z,t)\partial z = A\left(\emptyset|_{z=z_1} - \emptyset|_{z=z_2}\right) + \int_{z_1}^{z_2} Q_f(t)C_f(t)\,\delta(z)\partial z \tag{2}$$

where A is the cross sectional area (m^2), C is the concentration of suspended solids within the water (mg/L), Q_f is the feed volumetric flowrate (m^3/s), C_f is the feed inlet concentration, δ is the dirac delta distribution (m^{-1}), t is time (s) and the total flux, $\emptyset$ *(m^2/s)*, can be expressed as:

$$\emptyset\left(C, \frac{\partial C}{\partial z}, z, t\right) = F(C,z,t) - \left(\gamma(z) d_{comp}(C) + d_{disp}\left(z, Q_f(t)\right)\right)\frac{\partial C}{\partial z} \tag{3}$$

where F is the convective flux function ($mg/(m^2 s)$), γ is a characteristic function, d_{comp} is the compressive function and d_{disp} is the dispersion function (m^2/s).

The model describes thickening and clarification dynamically in order to predict the sludge bed height and concentration of the suspended solids in the water. In this work, the model is validated by comparing model predications using gPROMS with the batch case study presented by Burger et al. (2012), showing good agreement (see Figure 3).

3.3. Model of the Filtration unit

Han et al. (2008) developed a model for the rapid gravity filtration process, which utilised the simplified mass conservation of particles within the filter (Equation 4):

$$u\frac{\partial C}{\partial z} + \frac{\partial \sigma}{\partial t} = 0 \tag{4}$$

where C is the particle concentration (mg/L), σ is the specific deposition on the filter (mg/L), u is the superficial velocity (m/s), z is the axial position in the filter bed (m) and t is time (s).

For filtration with a clean filter, the initial and boundary conditions can be defined as:

$$C = 0, \ \sigma = 0 \quad for \quad z \geq 0, t = 0 \tag{1}$$

$$C = C_{in} \quad for \quad z = 0, t > 0 \tag{2}$$

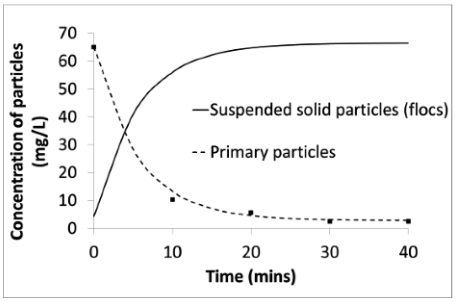

Figure 2: Model validation for the coagulation/flocculation unit. Concentration of suspended particles (flocs being formed from primary particles) as a function of time. Lines: simulation predictions from this work, Symbols: experimental results from Haarhoff and Joubert (1997).

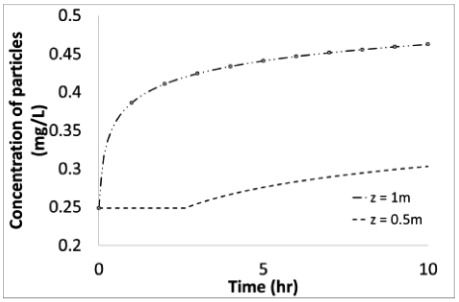

Figure 3: Model validation for the clarification unit. Concentration of setting particles in clarification unit with time from the bottom and middle of the tank. Lines: simulation predictions from this work, Symbols: simulated results from Burger et al. (2012).

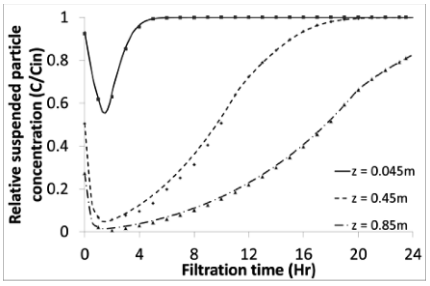

Figure 4: Model validation for the filtration unit. Relative suspended particle profiles with filtration times at varying positions within the unit. Lines: simulation predictions from this work, Symbols: experimental results from Han et al. (2008).

The authors utilise a two-stage assumption, which details that during the first stage, previously deposited particles serve as collectors to improve particle removal efficiency and the detachment of deposited particles does not occur until the specific deposit reaches a certain transient specific deposit where the second stage starts. The second stage is assumed to be a function of relative specific deposit and hydrodynamic conditions within the filter media. For validation of the filtration unit, the authors propose a ratio of suspended solid concentration remaining within the unit over the suspended solid concentration at the inlet to represent the relative suspended particles. The authors validate their model experimentally. The model developed in this work was validated against this experimental data, showing good agreement (see Figure 4).

3.4. Model of the overall plant

In a conventional water treatment plant, the main processing units are connected by pipes or troughs. In this work, these are described by simple non-reacting plug flow models. These plug flow models, combined with the individual unit models described and verified above, together constitute the overall plant model.

4. Results and Discussion

To demonstrate the applicability of the overall plant model, a sensitivity analysis was performed by considering the impact of a disturbance propagating through the process for an illustrative case study where the concentration for source of raw water inlet changes. After 2 hrs, a decrease of 40% was imposed on the inlet raw water source to test how the process would respond to a temporary change (Figure 5a). It can be seen from Figure 5 that the change in the inlet raw water concentration propagates through the whole process. There is a decrease in the concentration of flocs being formed due to the decrease of the inlet impurity concentration, which leads to a second order change in the clarification unit. As there are less flocs being formed, there is less concentration of particles settling in the clarification unit, as can also be seen from the gradual decrease in the concentration of particles settling in the clarification unit, which eventually reaches a new steady state. Within the filtration unit, there is a gradual change in concentration: this is due to the assumption that the filtration unit is used after back wash, which enables a greater deposition of particles onto the surface.

Note that a decrease in raw water inlet concentration can have a negative impact on the water purity if the number of primary particles entering is not sufficient to create flocs in the coagulation/flocculation unit, in which case these smaller particles will go through to the clarification unit. As there are more small suspended solids to floc ratio, the small particles will not settle to sludge and may pass through to the filtration unit. In theory, this can make the filtration unit saturate at a faster rate, leading to cloudy water being sent to consumer taps. The impact of the change greatly affected the first two units, as can be observed between times 2 – 6 hours, as the flocculation/coagulation unit relies on the primary concentration of particles to form flocs and the clarification unit uses the weight of the flocs as a form of separation.

5. Concluding Remarks

In this paper, a mathematical modelling representation of a conventional water treatment plant based on detailed models of individual processing units has been presented. The developed models allow a better understanding of individual unit

behaviour as well as provide a guideline of overall clean water treatment assessment. Current works involve implementing a similar methodology for alternative units of clean water treatment operation in order to develop an efficient optimisation strategy which will allow both optimal design and operation to be considered.

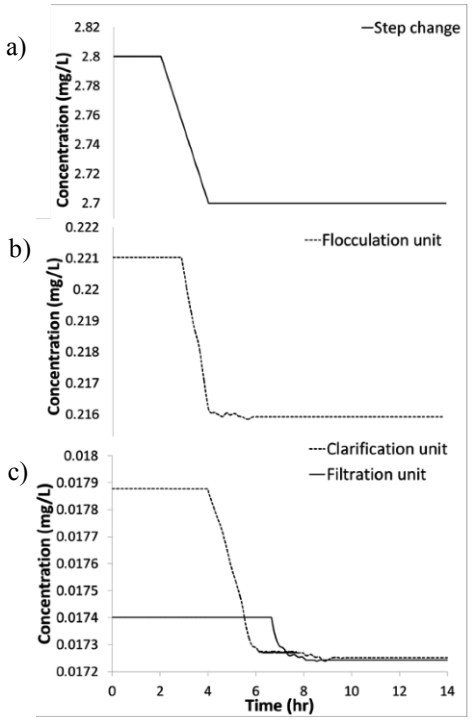

Figure 5. Sensitivity study of overall plant. a) 40% decrease in the concentration of the raw water feed at t = 2 hrs. b) Concentration of suspended solids within the flocculation unit.
c) Concentration of suspended particles settling within the clarification and filtration units.

References

Y.A. Argaman & W. J. Kaufman, 1970, Turbulence and flocculation. Journal of Sanitary engineering division, ASCE, 96, 223.

H. Bozkurt, A. Quaglia, K. V. Gernaey & G Sin, 2014, Superstructure Development and Optimization under Uncertainty for Design and Retrofit of Municipal Wastewater Treatment Plants, Computer Aided Chemical Engineering, 33, 37-42.

R. Bürger, S. Diehl, S. Farås & I. Nopens, 2012, On reliable and unreliable numerical methods for the simulation of secondary settling tanks in wastewater treatment, Computers and Chemical Engineering, 41, 93-105.

J. Haarhoff & H. Joubert, 1997, Determination of aggregation and breakup constants during flocculation, Water science and technology, 36, 4, 33-40.

R. Head, J. Hart & N. Graham , 1997, Simulating the effect of blanket characteristics on the floc blanket clarification process, Water science and technology, 36, 4, 77-84.

S. Han, C. S. Fitzpatrick & A. Wetherill, 2008, Mathematical Modelling of Particle removal and Head Loss in Rapid Gravity Filtration, Separation Science and Technology, 43, 7, 1798-1812.

Process Systems Enterprise, 2011, gPROMS, www.psenterprise.com/gproms.

J. S. Rosen, 2000, Computer-based technologies: predictions for water utilities. Journal American Water Works Association, 92, 2, 62-63.

Krist V. Gernaey, Jakob K. Huusom and Rafiqul Gani (Eds.), 12th International Symposium on Process Systems Engineering and 25th European Symposium on Computer Aided Process Engineering.
31 May – 4 June 2015, Copenhagen, Denmark

Water Resources Management with Dynamic Optimization Strategies and Integrated Models of Lakes and Artificial Wetlands

Jimena Di Maggio, Vanina Estrada, M. Soledad Diaz*

Planta Piloto de Ingeniería Química (PLAPIQUI) CONICET-Universidad Nacional del Sur, Camino La Carrindanga Km 7, Bahía Blanca 8000, Argentina
sdiaz@plapiqui.edu.ar

Abstract

In this work, we propose an integrated mechanistic model for a freshwater eutrophic reservoir and an artificial wetland and within a dynamic optimization framework. A partial differential equation system results from dynamic mass balances for the main phytoplankton groups; two zooplankton groups and two size classes of zooplanktivorous fish in the reservoir, as well as dissolved oxygen and main nutrients in both the reservoir and wetland. Algebraic equations stand for forcing functions profiles, such as temperature, solar radiation, river inflows and concentrations, etc. The model is formulated as an optimal control problem within a control vector parameterization approach in gPROMS. Optimization variables are the fraction of nutrient rich water stream that is derived through the wetland and fish removal rates from the reservoir. The objective function is the minimization of a weighted sum of integrals along the entire time horizon: the quadratic difference between phytoplankton concentration and a desired value below eutrophication limits and the quadratic difference between phosphate concentration in the wetland outflows and a desired value. Numerical results provide optimal profiles for restoration actions and their effects on the studied ecosystem.

Keywords: Optimal Control Problem, Eutrophication, Restoration, Biomanipulation

1. Introduction

Eutrophication, associated to high nutrient concentrations and recurrent algae blooms, is the most important environmental problem in many lakes and reservoirs. An issue of concern associated with algal blooms is the potential production of toxins by different phytoplankton species within the blooms, which are dangerous for human health (Paerl and Otten, 2013). The implementation of short and long term restoration strategies that contribute to health recovery of water bodies requires deep knowledge of the aquatic system, as well as detailed modelling and optimization (Estrada et al., 2011).

Water resources management must include restoration of water bodies not only affected by point sources (which has been intensively addressed by the construction of water treatment plants), but also those affected by nonpoint nutrient sources (Jeppesen *et al*., 2012). One approach applied to address the problem of nonpoint nutrient sources for water bodies is the use of artificial wetlands. They are portions of land, covered with macrophytes, through which a water stream is derived, to reduce its nutrient

concentration (nitrogen and phosphorus) before being discharged into the water body under study. Many physicochemical processes are involved in the reduction of nutrient concentration within wetlands, such as retention and assimilation by macrophytes, plankton and other microorganisms; sedimentation, adsorption from the sediments, among others (Langergraber et al., 2009). During the last decades, artificial wetlands have become an attractive alternative for water treatment since they have low maintenance cost, have a high efficiency and productivity and present ecological benefits (Reddy et al., 1999). Many lakes and water reservoirs have a positive response to reduced nutrient discharge, while others present a great resistance to improve their trophic condition due to nutrients discharge from sediments, internal recycle of nutrients and, in some cases, the presence of zooplanktivorus fish that cause a reduction on zooplankton population, which can no longer control phytoplankton growth by grazing. In this case, it may become necessary to implement inlake restoration strategies like sediment dreadging, hypolimnetic oxygenation and biomanipulation.

Experimental analysis of restoration actions is time-consuming and monitoring for long periods has large associated costs to implement. The development of ecological water models integrated to optimization strategies can help to propose and evaluate management strategies in both the short and long term (Estrada et al., 2011).

In this work, we propose an integrated mechanistic model for an eutrophic reservoir and artificial wetland within a dynamic optimization framework. Dynamic mass balances have been formulated for the main phytoplankton groups, two zooplankton groups and two size classes of zooplanktivorous fish in the reservoir, as well as dissolved oxygen and main nutrients. A simplified model has been considered for the artificial wetland. Algebraic equations stand for forcing functions profiles, such as temperature, solar radiation, river inflows and concentrations, etc. The complete model is formulated as an optimal control problem with a control vector parameterization approach (gPROMS, PSEnterprise 2014). Optimization variables characterize external reduction of nutrients (fraction of nutrient rich water stream that is derived through an artificial wetland) and biomanipulation strategies (fish removal rate). Numerical results provide optimal profiles for restoration actions. The present study has been carried out on Paso de las Piedras Reservoir, which is the drinking water source for two cities in Argentina.

2. Model description

We have formulated a water quality model as a differential algebraic system that describes temporal and spatial profiles of three phytoplankton groups (cyanobacteria, diatomea, chlorophyta), two zooplankton groups (cladocera, copepoda) and two size classes of zooplanktivorous fish (Odontesthes bonariensis), dissolved oxygen and main nutrients in the reservoir. Algebraic equations stand for forcing functions profiles, such as temperature, solar radiation, river inflows and their associated nutrient concentrations. The model takes into account concentration gradients along the water column (two horizontal layers) and horizontal averaged concentrations, constant water density and constant lake transversal area. Equations (1) to (6) correspond to main equations in the wetland and the reservoir, respectively. Equations (1) and (2) are phosphate mass balance and retention equation in the wetland:

$$V_w \frac{dC_{PO_{4,w}}}{dt} = Q_w c_{PO_{4,DIV,IN}} - kC_{PO_4,DIV,IN} Q_w - Q_w c_{PO_{4,w}} \quad (1)$$

where $\boldsymbol{C_{PO4,w}}$ is phosphate concentration at wetland output; $\boldsymbol{Q_w}$, and $\boldsymbol{V_w}$ correspond to inlet flowrate and wetland volume, respectively; $\boldsymbol{C_{PO4,DIV,IN}}$ is phosphate concentration

in wetland inlet stream and the nutrient retention rate $\boldsymbol{k}$ has been obtained from a pilot plant scale artificial wetland in the site. Equations (2) to (4) are component mass balances for the upper and lower layer in the reservoir and total mass balance, as follows:

$$\frac{dC_{Uj}}{dt} = \sum_k \frac{Q_{IN,Uk}}{V_U} c_{IN,Ujk} - \frac{Q_{OUT,U}}{V_U} c_{Uj} + r_{Uj} - \frac{k_d A}{\Delta h V_U}\left(c_{Uj} - c_{Lj}\right) - \frac{C_{Uj}}{h_U}\frac{dh_U}{dt} \quad (2)$$

$$\frac{dC_{Lj}}{dt} = -\frac{Q_{OUT,L}}{V_L} c_{Lj} + r_{Lj} - \frac{k_d A}{\Delta h V_L}\left(c_{Uj} - c_{Lj}\right) \quad (3)$$

j = NO_3,NH_4, ON, PO_4, OP, BDO, DO, Cyanobacteria, Diatomea, Chlorophyta, Cladocera, Copepoda, Odontesthes (2 size classes)

$$\frac{dh_T}{dt} = \frac{1}{A}\left[Q_{rain} - Q_{evap} + \sum_k Q_{IN,k} - \sum_m Q_{OUT,m}\right] \quad (4)$$

where $\boldsymbol{C_{IN,Ujk}}$ is component j concentration in the upper layer for tributary k (Sauce Grande River and El Divisorio Stream, in our case study); $\boldsymbol{C_{U,j}}$ and $\boldsymbol{C_{L,j}}$ are component concentrations within the water body in the upper and lower layer, respectively; $\boldsymbol{r_{U,j}}$ and $\boldsymbol{r_{L,j}}$ stand for generation/consumption terms; $\boldsymbol{Q_{IN,U}}$ refers to tributaries inputs (Sauce Grande River and El Divisorio Stream), $\boldsymbol{Q_{OUT,U}}$ is the Sauce Grande River output, $\boldsymbol{A}$ and h_T are the lake transversal area and depth, respectively, and $\boldsymbol{Q_{OUT,L}}$ refers to outputs for drinking water and industrial activities. Model parameters have been estimated based on collected data during 2004-2005 for Paso de las Piedras Reservoir (Estrada et al., 2009). For a more detailed description of the generation/consumption rate terms, see Estrada et al. (2011). The entire model has 42 differential and 110 algebraic equations.

3. Optimal Control Problem

In this work, we formulate a model including two restoration strategies: the reduction of external loading of nutrients as an optimal control problem along a long term time horizon of twelve years, and an internal lake strategy, biomanipulation, that is based on the food chain theory and is supported on top-down control on phytoplankton growth (Søndergaard *et al*., 2013). The basic idea is to perform zooplanktivorous fish removal to keep a high grazing pressure on the phytoplankton community by the herbivore zooplankton. In this work, we have considered the application of biomanipulation by fish removal, considering fish removal rate as control variable, which are included as negative terms ($S_{1.,Removal}$ and $S_{2,Removal}$) in the rate equations of fish biomass (Eqs. 5 and 6) for both size classes of *O. bonariensis* (S_1 and S_2).

$$r_{iS_1} = R_{im,pred} - R_{im,bmetab} - R_{iS_3,canib} - R_{im,recruit} + R_{im,spaw} - S_{1,Removal} \quad (5)$$

$$r_{iS_2} = R_{im,pred} - R_{im,bmetab} - R_{im,recruit} + R_{im,spaw} - S_{2,Removal} \quad (6)$$

The objective function is the minimization of a weighted sum of two integral terms. The first integral corresponds to the square difference between phytoplankton concentration in the upper layer of the lake and a tight desired value of 0.25 mg/l. The second integral is the square difference between phosphate concentration in the wetland outlet stream and a desired value of 0.02 mg/l. Both desired values are below eutrophication limits. The dynamic optimization problem is formulated as:`

$$min\ \emptyset = \left[\int_0^{tf}\left(\sum_{j=C,D,G} C_{U,j}(t) - 0.25\right)^2 dt + \int_0^{tf}\left(C_{PO_4,w}(t) - 0.02\right)^2 dt\right] \quad (7)$$

subject to

DAE Integrated Model for Wetland and Reservoir

$0 \le Q_w \le 0.5\ Q_{DIV,IN}$ (L/ day)

$LB \le C_m \le UB$ (mgC/L day) $m = S_1, S_2$

4. Results and Discussion

The optimization problem was implemented within a control vector parameterization framework in gPROMS (gPROMS, PSEnterprise, 2014), considering a time horizon of two years. Numerical results for the case study are shown in Figures 1 and 2. Optimization control variables are the fraction of tributary stream that is derived through the wetland and removal rates for the two fish size classes. Based on experimental results, obtained in a pilot scale artificial wetland, phosphorus retention of 50% and nitrogen retention of 60% are considered.

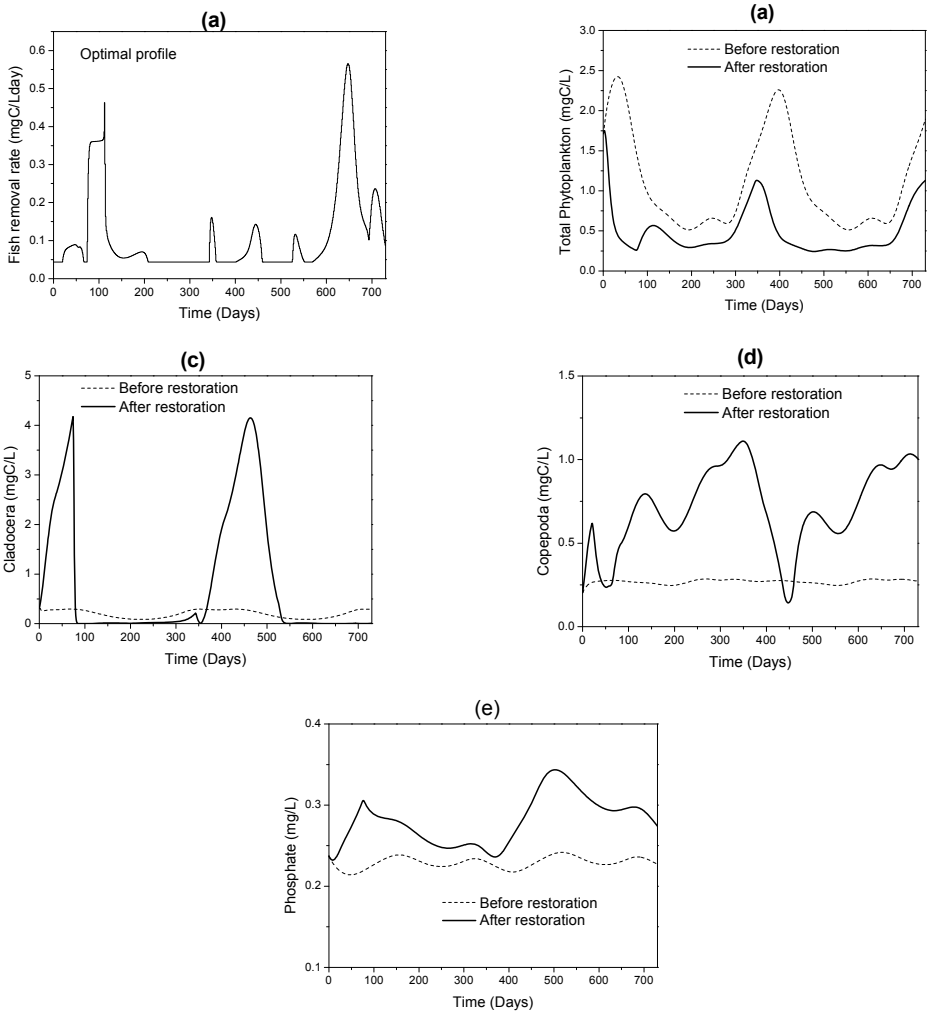

Figure 1. Optimal profiles for restoration along two years for fish removal rate (a); total phytoplankton concentration before (dashed line) and after restoration (solid line) (b), Cladocera concentration (c), Copepoda concentration (d) and phosphate concentration (e)

Figure 1(a) shows zooplanktivorous fish removal rate profile along the time horizon of two years. It can be seen that the obtained removal profile allows an important increase on

zooplankton concentration (Figs. 1(c) and 1(d)), which increases its grazing pressure on phytoplankton. Figure 1(b) shows total phytoplankton biomass profile before and after restoration, it can be seen that phytoplankton biomass peaks are reduced after restoration actions due to the increase of zooplankton biomass. Figure 1(e) shows phosphate concentration profile before and after restoration actions, it is observed that its concentration increases after fish removal, even though the fraction of tributary stream deviated through the wetland (control variable) is at its upper bound. This can be attributed to a decrease in phosphate consumption due to the decrease in phytoplankton biomass, and also to the internal recycle of nutrients within the water reservoir.

Figure 2 shows numerical results for the application of the use of wetland as a sole restoration strategy throughout a 12-year horizon (three times the residence time of Paso de las Piedras reservoir), for phosphate (a) and total phytoplankton concentration (b). Figure 2(a) shows a small reduction of phosphate concentration within the water body, from 0.237 mg/L at t=0 to 0.211 mg/L at t=4380 (days). Phytoplankton concentration presents a slow reduction along the time horizon (Fig. 2(b)). These results show that reduction on nutrients discharge is not enough to improve water quality for the short and medium term.

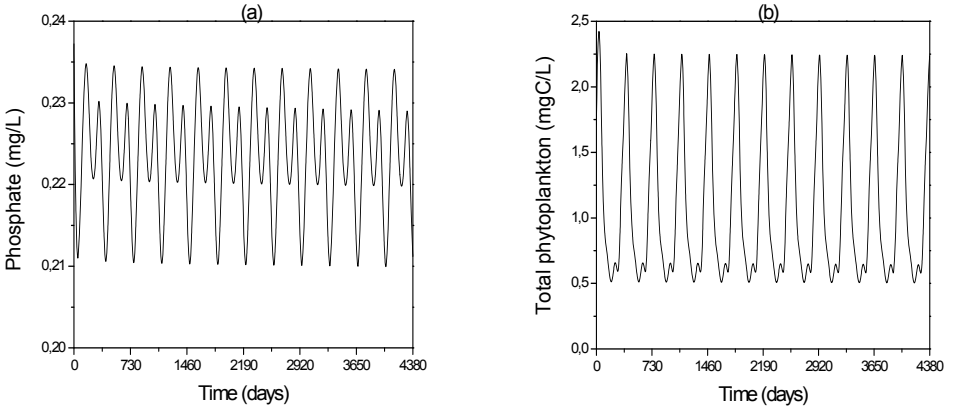

Figure 2. Temporal profiles for phosphate (a) and total phytoplankton biomass for long term restoration through an artificial wetland.

Figure 3 shows optimal profiles for total phytoplankton concentration (a) and phosphate concentration (b). Numerical results shown in Fig. 3 are obtained considering 0.21 mg/L (concentration of phosphate at t=4380 days in Fig. 2(a)) as initial concentration of phosphate within the reservoir. The comparison between Fig. 1(b) and Fig. 3(b) shows that the second peak of phytoplankton biomass can be reduced when a lower initial concentration of phosphate is considered.

Currently, the wetland model is being extended to include additional complex processes that take place within wetlands, such as nutrient (carbon, phosphorus, nitrogen) dynamics and macrophyte growth (Langergraber et al., 2009). This will allow formulating new optimal control problems to improve the wetland performance.

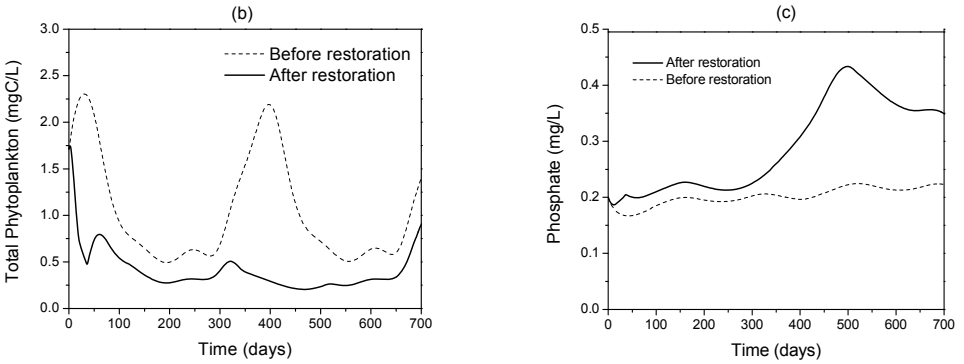

Figure 3. Optimal profile before (dashed line) and after (solid line) restoration for total phytoplankton (a) and phosphate (b), considering initial concentration of phosphate after 12 years wetland restoration

5. Conclusions

We have formulated an optimal control problem to plan short and medium time restoration in a eutrophic reservoir with a detailed ecological water model. Medium term restoration (12 years) through an artificial wetland has been explored as the sole restoration strategy. Numerical results show that both external and inlake restoration strategies must be applied simultaneously. Process systems engineering approaches have proved to be effective for the determination and planning of restoration strategies.

References

Estrada V., J. Di Maggio, M.S. Diaz, 2011. Water Sustainability: A Process Systems Engineering approach to the restoration of eutrophic lakes, COMPUT CHEM ENG 35, 1598-1613

Estrada V., E. Parodi, M.S. Diaz, 2009. Determination of biogeochemical parameters in eutrophication models as large scale dynamic parameter estimation problems, COMPUT CHEM ENG 33, 1760-1769.

Jeppesen, E., Søndergaard, M., Lauridsen, T., Davidson, T., Liu, Z., Mazzeo, N., Trochine, C., Özkan, K., Jensen, H., Tolle, D., Starling, F, Lazzaro, X., Johansson, L., Bjerring, R., Liboriussen, L., Larsen, S., Landkildehus, F., Egemose, S. & Meerhoff, M., 2012. Biomanipulation as a restoration tool to combat eutrophication: recent advances and future challenges. ADV ECOL RES, 47, 411-488.

Langergraber, G., Giraldi, D. Menac, J., Meyer, D., Peñae, M., Toscanof, A., Brovelli, A., Korkusuza, E., 2009. Recent developments in numerical modelling of subsurface flow constructed wetlands. SCI TOTAL ENVIRON 407, 3931-3943.

Paerl, H. and Otten, T., 2013. Harmful Cyanobacterial Blooms: Causes, Consequences, and Controls. ENVIRON MICROBIOLOGY 65, 995-1010.

Process Systems Enterprise, 2014. gPROMS, www.psenterprise.com/gproms

Søndergaard, M., Jeppesen, E., Lauridsen, T. L., Skov, C., van Nes, E. H., Roijackers, R., Lammens, E. & Portielje, R., 2007. Lake restoration: successes, failures and long-term effects. J APPL ECOL 44, 1095–1105.

Reddy, K. R., R. H. Kadlec , E. Flaig & P. M. Gale, 1999. Phosphorus Retention in Streams and Wetlands, A Review, CRITICAL REV ENVIRON SCI TECH 29 (1), 83-146.

Krist V. Gernaey, Jakob K. Huusom and Rafiqul Gani (Eds.), 12th International Symposium on Process Systems Engineering and 25th European Symposium on Computer Aided Process Engineering.
31 May – 4 June 2015, Copenhagen, Denmark

Life Cycle Assessment Studies of Chemical and Biochemical Processes through the new LCSoft Software-tool

Perapong Supawanich,[a] Pomthong Malakul,[a] Rafiqul Gani,[b]

[a]*The Petroleum and Petrochemical College, Chulalongkorn University, Bangkok 10330, Thailand*
[b]*CAPEC-PROCESS, Department of Chemical and Biochemical Engineering, Technical University of Denmark, DK-2800 Kgs. Lyngby, Denmark*

Abstract

Life Cycle Assessment or LCA is an effective tool for quantifying the potential environmental impacts of products, processes, or services in order to support the selection making of desired products and/or processes from different alternatives. For more sustainable process designs, technical requirements have to be evaluated together with environmental and economic aspects. The LCSoft software-tool has been developed to perform LCA as a stand-alone tool as well as integrated with other process design tools such as process simulation, economic analysis (ECON), and sustainable process design (SustainPro). An extended version of LCSoft is presented in this paper. The development work consists of four main tasks. The first task consists of the Life Cycle Inventory (LCI) calculation function. The second task deals with the extension of the Life Cycle Inventory database and improvement of the Life Cycle Impact Assessment calculation. The third task deals with analysis to investigate the contributions of processes, LCI results, and environmental impact results with respect to the production stage. Also, an uncertainty analysis is included to investigate the influence of uncertain parameters on the LCI assessment results. The fourth task has been added to validate and improve LCSoft by testing it against several case studies and compare the assessment results with other available tools.

Keywords: Life Cycle Assessment, Life Cycle Inventory, Contribution analysis, Uncertainty analysis.

1. Introduction

Environmental and sustainability awareness has lately gained much importance because of increasing depletion of natural resources, need for more efficient process-operations and product manufacturing together with sustainable waste disposal. Life Cycle Assessment is a tool for quantifying the potential environmental impact of products, processes, services and activities for the entire life cycle, of the product-process. The LCA related calculations starts from raw material extraction, raw material manufacturing, transportation, product manufacturing, product distribution, usage, and waste disposal.

According to ISO 14040 (ISO 14040 International Standard, 2006), the LCA framework are organized into four phases.

(1) Goal and scope definition: The purpose of performing LCA is clearly defined together with the system boundary.
(2) Life Cycle Inventory (LCI) analysis: LCI compiles and quantifies the amounts of all necessary input streams (natural resources, raw materials, energy types, and products) and output streams (emissions to soil, air, and water; waste; energy; products; and by-products) through relevant process within the system boundary.
(3) Life Cycle Impact Assessment (LCIA): The inventory results are classified into each impact category, such as global warming potential, natural resource depletion, human toxicity, etc., based on their effect on environment. Magnitude and potency of each substance in inventory results are characterized to impact category by using characterization factors (CFs), which represent the effect of each substance on the environment based on the reference unit.
(4) Interpretation: In order to analyze inventory results and impact assessment results, several methods are available for implementation. Sensitivity analysis, where the influence of different assumption that affects the assessment results is analyzed. Uncertainty analysis, where the influence of uncertainty in LCI data or uncertainty in calculation models on the reliability of the assessment results is analyzed. Contribution analysis that shows how processes, LCI results, environmental impacts contribute to each production stage in order to determine the significant impacts for further process improvement.

Although, several LCA software such as SimaPro (PRé Consultants, 2014), Umberto (ifu Hamburg GmbH, 2014), and Gabi (PE International, 2014) have been developed for fast and effective LCA calculations, they are not yet integrated to process synthesis-design. From a process synthesis-design point of view, there is still need for any simple software that has the ability to be integrated with other process synthesis-design tools such as process simulation, economic analysis or sustainable process design. LCSoft (Kalakul *et al.,* 2014) has been developed to fulfill this requirement under the concept of user-friendly interface such that the user can perform LCA by using LCSoft easily, effectively, and integrated with process simulation, economic analysis tool, ECON (Saengwirun, 2011); sustainable process design tool, SustainPro (Carvalho *et al.,* 2013). The objectives of this work are to develop the new version of LCSoft, which is developed with special attention to the needs of chemical and biochemical processes.

2. Development framework

The development framework of LCSoft consists of four main tasks; (1) development of LCI calculation function; (2) extension of LCI database and improvement of LCIA; (3) perform contribution analysis and uncertainty analysis; (4) validation and improvement of LCSoft.

2.1 Development of LCI calculation function

The objective of this part is to develop the LCI calculation function for compiling and quantifying input and output of given product corresponding to all relevant processes within the system boundary. The developed LCI calculation function is based on the matrix algebra approach of Heijungs and Suh (2002).

2.2 Extension of LCI database and improvement of LCIA

LCI data from US LCI (U.S. Life Cycle Inventory Database, 2014) and from other available sources are collected into LCSoft database to increase the application range of the system boundary of LCA calculations. In addition to eleven environmental impact indicators, carbon footprint calculation, and energy consumption calculation are now provided in LCSoft 2.0. Other environmental impacts added are: water resource depletion, mineral extraction, and deposited waste. Details of characterization factor for specific environmental impacts and their units are given in Table 1.

2.3 Performing contribution analysis and uncertainty analysis

Contribution analysis is divided into three parts: process contribution, LCI results contribution, and environmental impact results contribution. These results offer the user options to investigate how the results from performing LCA contribute to the production stage. Providing thereby, useful options for further process development. For investigating the influence of uncertainty in LCI data, Monte Carlo analysis is used to perform uncertainty calculations by repeating LCIA calculation with selected LCI results in various uncertainty ranges.

2.4 Validation and improvement of LCSoft

The validation of LCSoft is performed by comparing assessment results from case studies with available commercial LCA software. The results from the comparison are investigated to identify the deficiencies in LCSoft for further improvement. Within LCSoft, the calculations divided into five main steps and two optional steps: (1) check LCI data; (2) retrieve LCI data; (3) carbon footprint calculation; (4) impact assessment; (5) contribution analysis; (Optional-1) uncertainty analysis; (Optional-2) sensitivity analysis, as shown in figure 1. The details and calculation models for the five steps and two options are given in Table 2.

Table 1. Characterization factors and unit of environmental impacts

Impact Category (I^k)	Characterization factor ($CF^k{}_{t,c}$)	Unit	CF source
Acidification	$CF^{AP}{}_{t,c}$	kg H+ eq.	USEPA
Aquatic toxicity	$CF^{ATP}{}_{t,c}$	$1/LC_{50}$	
Global warming potential	$CF^{GWP}{}_{t,c}$	kg CO_2 eq.	
Photochemical oxidation	$CF^{POCP}{}_{t,c}$	kg C_2H_2 eq.	
Ozone depletion	$CF^{ODP}{}_{t,c}$	kg CFC-11 eq.	
Terrestrial toxicity	$CF^{TTP}{}_{t,c}$	$1/LD_{50}$	
Human toxicity by exposure	$CF^{HTPE}{}_{t,c}$	1/TWA	
Human toxicity by ingestion	$CF^{HTPI}{}_{t,c}$	$1/LD_{50}$	
Fresh water ecotoxicity	$CF^{ET}{}_{t,c}$	kg 2,4-D eq.	USEtox™
Human toxicity-carcinogenics	$CF^{HTC}{}_{t,c}$	kg benzene eq.	
Human toxicity-noncarcinogenics	$CF^{HTNC}{}_{t,c}$	kg toluene eq.	
Energy resource consumption	$CF^{Energy}{}_{t,c}$	MJ eq.	Cumulative Energy Demand
Mineral extraction	$CF^{Mineral}{}_{t,c}$	kg Sb eq.	CML-IA
Deposited waste	$CF^{Waste}{}_{t,c}$	UBP	Ecological scarcity 2013
Water resource consumption	$CF^{Water}{}_{t,c}$	UBP	

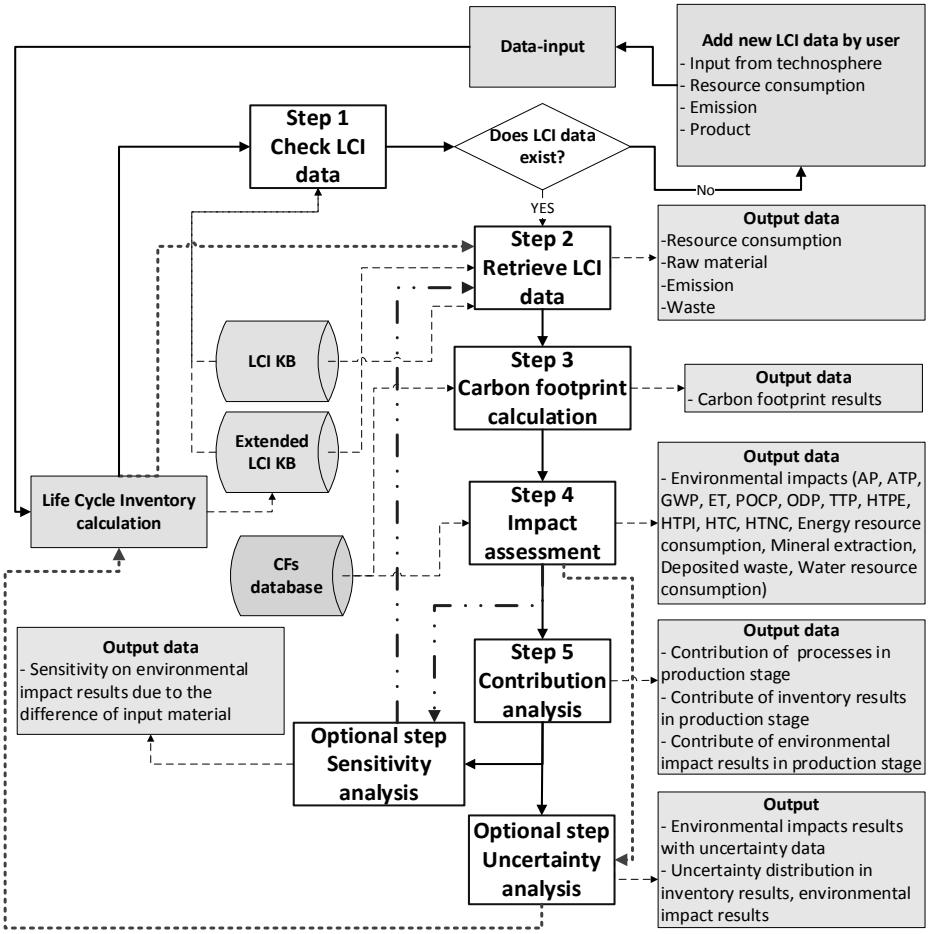

Figure 1. LCSoft framework

3. Case study

3.1 Development of LCI calculation in LCSoft

Life Cycle Inventory calculation is developed for compiling and quantifying all elementary flow through the related process based on the model given in Table 2. In Table 2, "A" represents the technology matrix that contains commodity flow of all processes. Inflow and outflow are noted by positive and negative values, respectively. "B" represents the intervention matrix that contains pollutants, natural resources, or energy emitted or consumed by processes, while, "s" is a scaling factor that is used to scale up unit processes in the technology matrix to the achieve target value defined by a functional unit. Acetic acid, 98% in H2O, at plant - RER from ecoinvent data v2.0 (Althaus *et al*., 2007) is taken to calculate LCI with LCSoft and SimaPro7.1 from cradle to gate and LCI calculation model in LCSoft is validated by comparing LCI results with SimaPro7.1. The comparison results are shown in figure 2 where the horizontal axis indicate different elementary flow (energy and substance flow) considered and the vertical axis represents the ratio of LCI results from LCSoft to SimaPro7.1. Figure 2 shows a very good match between LCSoft and SimaPro7.1.

Table 2. Calculation steps in LCSoft

Calculation step	Description	Input data/output data/calculation model
Step1: check LCI data	The LCI data of related products or processes are checked with permission to add or modify LCI data. If input from technosphere exists in added or modified data, the LCI results could be obtained by the LCI calculation function contained in software. Calculation model: Heijungs and Suh (2002).	Input data: - Mass balance (stream table) - Energy balance and duty of equipment (Equipment table) $As = f$ $g = Bs$
Step2: Retrieve LCI data	Resource consumption, raw material consumption, and emission of related products or processes are received from LCI KB for calculations in step3 and displaying of LCI results.	Output data: - Emission - Resource consumption - Energy consumption - Waste
Step3: Carbon footprint calculation	All amounts of CO2 and greenhouse gases in production process are quantified and characterized by using the Global warming potential (GWP) as an indicator. Calculation model: Guinée et al. (2002).	$CO_{2,eq} = \frac{m^{PRO}_{GHG,air} x CF^{GWP}_{GHG,air)}}{m_{product}}$ $Carbon\ footprint = \sum CO_{2,eq}$
Step4: Impact assessment	The LCI results are classified and characterized to each impact category based on their effect on environmental. Calculation model: Guinée et al. (2002).	$I^k = \sum_{t,c} EM_{t,c} x CF^k{}_{t,c}$
Step5: Contribution analysis	The process, LCI results, and impact assessment results are shown obviously in each production stage in order to investigate the contribution.	Input data: - Amount of product produced from process - LCI results - LCIA results
Optional step: Uncertainty analysis	The influence of uncertainty in LCI data to the assessment results is defined by using uncertainty analysis.	Input data: -Uncertainty range in LCI data
Optional step: Sensitivity analysis	The influence of different input material to the assessment results could be observed by using sensitivity analysis.	Input data: -Alternative input material

4. Conclusion

LCSoft, that can quantify the potential environmental impacts of products, processes, or services especially for chemical and biochemical process design in order to support the decision related to selection of a more sustainable process from different alternatives and with ability to be integrated with other process synthesis-design tools, has been

presented together with results from a case study. A new LCI calculation function has been created and to give accurate results, thus validating this new calculation option. Four impact categories have been added to software in order to increase the boundaries of the impact estimations. Future development is continuing the extension of the LCI database, creating contribution analysis functions, performing uncertainty analysis functions, validating and improving LCSoft software.

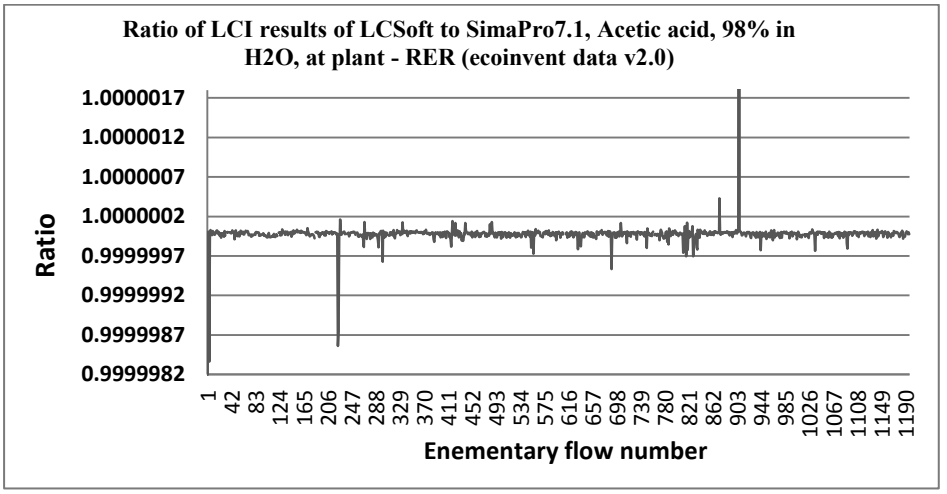

Figure 2. Ratio of LCI results of LCSoft to SimaPro7.1 (Acetic acid, 98% in H2O, at plant - RER (ecoinvent data v2.0)

References

A. Carvalho, H. Matos, R. Gani, 2013, SustainPro - a tool for systematic process analysis, generation and evaluation of sustainable design alternatives, Computers & Chemical Engineering, 50, 8-27.

H-J. Althaus, M. Chudacoff, R. Hischier, N. Jungbluth, M. Osses, A. Primas, 2007, Life Cycle Inventories of Chemicals, Final report ecoinvent data v2.0 No. 8, Swiss Centre for Life Cycle Inventories, Dübendorf, Switzerland.

Ifu Hamburg GmbH, 2014, Umberto LCA Software, www.umberto.de (accessed 1.9.14.).

ISO 14040 International Standard, 2006, Environmental management - Life cycle assessment - Principles and framework. International Organization for Standardization, Geneva, Switzerland.

J.B. Guinée, M. Gorrée, R. Heijungs, G. Huppes, R. Kleijn, A. de. Koning, L. van. Oers, A. Wegener Sleeswijk, S. Suh, H.A. Udo de Haes, H. de. Bruijn, R. van. Duin, M.A.J. Huijbregts, 2002, Handbook on Life Cycle Assessment, Kluwer Academic Publishers, Dordrecht, The Netherlands.

P. Saengwirun, 2011, Cost Calculations and Economic Analysis, The Petroleum and Petrochemical College, Chulalongkorn University, Bangkok, Thailand, MSc-thesis.

PE-International, GaBI, 2014, Software for Life Cycle Assessment, www.gabisoftware.com (accessed 1.09.14.).

PRé Consultants, 2014, SimaPro LCA Software, www.pre.nl/simapro (accessed 1.9.14.).

R. Heijungs, S. Suh, 2002, The Computational Structure of Life Cycle Assessment, Kluwer Academic Publishers, Dordrecht, The Netherlands.

S. Kalakul, P. Malakul, K. Siemanond, R. Gani, 2014, Integration of life cycle assessment software with tools for economic and sustainability analyses and process simulation for sustainable process design, Journal of Cleaner Production, 71, 98-109.

Krist V. Gernaey, Jakob K. Huusom and Rafiqul Gani (Eds.), 12th International Symposium on Process Systems Engineering and 25th European Symposium on Computer Aided Process Engineering.
31 May – 4 June 2015, Copenhagen, Denmark

Control Structure Design of an Innovative Enhanced Biological Nutrient Recovery Activated Sludge System Coupled with a Photobioreactor

Borja Valverde-Pérez[a*], José Manuel Fuentes-Martínez[a], Xavier Flores-Alsina[b], Krist V. Gernaey[b], Jakob Kjøbsted Huusom[b], Benedek Gy. Plósz[a**]
[a] *Department of Environmental Engineering, Technical University of Denmark, Miljøvej, Building 115, DK-2800, Kgs. Lyngby, Denmark (bvape@env.dtu.dk, beep@env.dtu.dk)*
[b] *Department of Chemical and Biochemical Engineering, Technical University of Denmark, Søltofts Plads, Building 229, DK-2800, Kgs. Lyngby, Denmark*

Abstract

The TRENS system is a train of biological units designed for resource recovery from wastewater. It is a sequence of a modified enhanced biological phosphorus removal and recovery system (EBP2R) coupled with a photobioreactor (PBR). The bacteria-based system constructs an optimal culture media for the downstream algae cultivation. In this work, we present a control strategy to ensure an optimal nutrient balance to feed to the PBR, so the grown algal suspension is suitable for fertigation (irrigation and fertilization of agricultural crops). The system is able to recover up to 75% of the influent load, while keeping an optimal N-to-P ratio of 16 in the influent to the PBR. The system is tested under different scenarios, where the influent quality is disturbed following a step change. The control system is able to reject most of the disturbances. However, when the P-recovery is limited by the bacteria in the reactor, the control system is not able to keep the optimal phosphorus load, but only the optimal percentage recovery from the influent phosphorus. In this scenario, the system is kept under optimal conditions – in terms of nutrient balance – because the N-to-P ratio is still at 16, so the green microalgae can take up most of the incoming nutrients into the PBR. The control system is able to keep the optimal phosphorus load during dynamic conditions. However when the influent nitrogen is limiting the process, the N-to-P ratio drops under the optimal value. Further research is needed in order to assess the controllability of the PBR and the possible impact on the upstream operation conditions.

Keywords: process control; process modelling; resource recovery; wastewater treatment

1. Introduction

Conventionally, the arrangement of biological and physical unit processes in wastewater treatment systems is chosen to remove organic carbon, nitrogen and phosphorus. This treatment approach, without focus on recycling water and nutrients (N and P), is no longer regarded as sustainable (Verstraete et al., 2009). Particular scientific interest is currently focusing on the development of cost-effective ways to recover N and P from wastewater. A complete biological process for wastewater resources recovery has been developed to recover nitrogen, phosphorus and freshwater content of used water through mixed green microalgal cultivation (Valverde-Pérez et al., 2015). This innovative system, referred to as the TRENS system, is defined as a modified enhanced biological phosphorus removal and recovery (EBP2R) system coupled with a photobioreactor

(PBR). Previous work showed that the algal growth in the PBR, as well as the effluent quality, highly depends on the nutrient content of the constructed cultivation media (Wágner et al., 2015). The outcome of our work is the development and assessment of a control structure for the EBP2R to keep the optimal cultivation conditions in the downstream PBR.

2. Material and Methods

2.1. System description

The system is defined as a sequence of tanks shown in Fig. 1. The EBP2R consists of a sequence of two anaerobic and one aerobic continuous stirred tank reactors (CSTRs). The influent composition and the consequent system design (reactor volumes) are described in Valverde-Pérez et al. (2015). The system can remove most of the bioavailable COD, either by mineralizing it (most of the soluble readily biodegradable) or conveying it to an anaerobic digester (bulk of particulate slowly biodegradable organics) for biogas production. The system promotes the growth of polyphosphate accumulating organisms (PAOs), which are used to control the phosphorus load recovered from used water. Both N and P are taken up in the downstream PBR. As a side stream process, a completely autotrophic nitrogen removal (CANR) system is used to remove the fraction of influent N which cannot be recovered by the PBR.

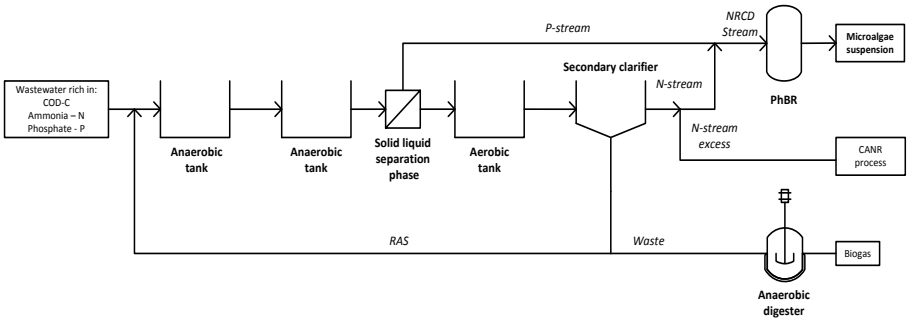

Figure 1 Flow-diagram of the TRENS system operated on discontinuous mode. CANR stands for autotrophic nitrogen removal system; NRCD stands for nutrient rich carbon depleted; RAS stands for recycling of activated sludge.

2.2. Process modeling

The EBP2R system is modelled using the activated sludge model ASM-2d from Henze et al. (1999), further adapted by Flores-Alsina et al. (2012). This model includes all the relevant bacterial groups in the EBP2R process, i.e. heterotrophs, nitrifiers and PAOs. The simulation model was implemented in Matlab-Simulink (The MathWorks, Natick, MA).

2.3. Control design procedure

The control structure was designed following a methodology adapted from plant-wide control (Larson and Skogestad, 2000). First, the goal of the system was defined. Then, the optimal operation conditions were defined through scenario simulations reported by Valverde-Pérez et al. (2015). Then, a degrees of freedom analysis was done, whereby the potential control variables as well as the available actuators in the system were

identified. The different actuators were paired with the controlled variables based on process knowledge and the resulting pairing was checked with the relative gain array (Seborg et al., 2004), thereby building the regulatory control layer. All controllers were modelled as PI controllers, unless otherwise specified, and were tuned according to Skogestad (2003). In a final step, the control structure was assessed through dynamic simulations. The dynamic influent was adapted from the benchmark simulation model 2 (BSM2, Flores-Alsina et al. 2012), including variations on the influent TCOD, TN, TP and flow rate.

3. Results and discussion

The primary objective of the control structure is to maximize the phosphorus recovered through algal cultivation, while the secondary objective is to obtain an optimal and stable nutrient balance to feed to the downstream PBR. We assume that the mixed green microalgae culture grown in the PBR is the one reported by Wágner et al. (2015), whose optimal nitrogen to phosphorus ratio in the cultivation medium is 16 mol-N/mol-P. In previous work (Valverde-Pérez et al., 2015), scenario simulations were carried out to assess the process performance in terms of both nutrient load and balance fed to the PBR (Fig. 2). According to Fig. 2a, the optimal process conditions comprise a solid retention time (SRT) of around 5 days and P-stream flow rate (Q_P) of around 30% of the influent flow, thereby recovering up to 70% of the influent phosphorus. Under other conditions, the PAOs activity may be limited by a number of factors, including SRT, availability of volatile fatty acids (VFA) and nitrate in anaerobic reactors and phosphate in the aerobic reactor, as shown in the Fig. 2a. Operating at system SRT < 3.5 days, PAOs are washed from the reactors, leading to a loss of control over the N-to-P ratio. If SRT is higher than 4.5 days, conditions support nitrifying bacteria growth, leading to nitrate production and limiting PAOs activity due to VFA starvation in the anaerobic reactors. Therefore, the maximum Q_P at high SRTs is governed by nitrate production and consequent PAOs activity limitation. When the system's SRT is lower than 4.5 days, PAOs activity is limited due to phosphorus starvation in the aerobic reactor at high Q_P. At comparably high Q_P (>45%), Fig. 2a shows a linear relation between P-load and flow rate, which implies that the system's performance is not dependent on the SRT because of the wash-out of the PAOs. Fig. 2b shows the possible effluent N-to-P ratios. At the optimal SRT (5 days), the N-to-P ratio does not accomplish with the optimal conditions, i.e. cultivation of the mixed green microalgae culture reported by Wágner et al. (2015). Therefore, it is needed to deviate 17% of the influent flow rate to the CANR system to reduce the N-to-P ratio from 19 to 16. Once the system is optimized, the oxygen set point is regulated in order to keep a stable operation. The chosen set point, based on the scenario simulations carried out in Valverde-Pérez et al. (2015), is 1.5 mg l^{-1}. The optimal operation conditions are sensitive to the influent quality, especially to the influent bio-available COD and the ammonia. In cases where there is an excess of influent COD, the inhibition by nitrate recycling is less severe than those cases that are characterized by low influent COD, thereby increasing the optimal plateau found in Fig. 2a. On the other hand, if the influent ammonia is comparably high while keeping an average influent COD, PAOs can be outcompeted in the anaerobic reactors, thereby reducing the optimal plateau in Fig. 2a.

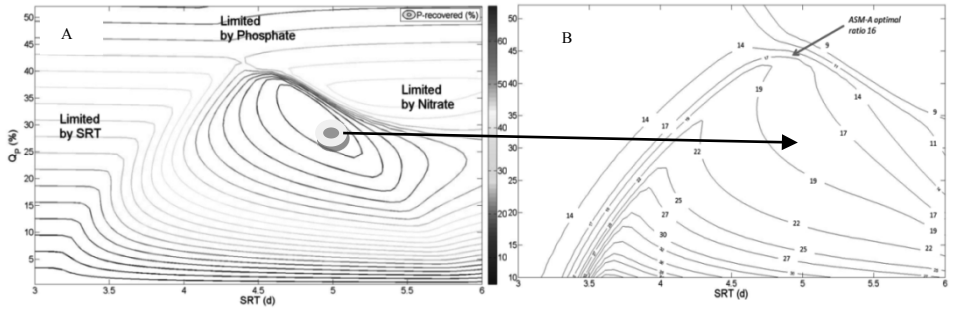

Figure 2 a) Percentage of P recovered from the influent as a function of the P-stream flow and the SRT; b) N-to-P molar ratio in the EBP2R as a function of the P-stream flow and the SRT. Adapted from Valverde-Pérez et al. (2015).

The next step is to identify the available actuators, referred to as manipulated variables (MVs), of the system: pumps, valves, mixers and air supply. The EBP2R has two different pumps. One is used to pump the Q_p while the other is placed in the recirculation line and used to waste activated sludge from the system. Both pumps are used to control the phosphorus load conveyed to the PBR and the SRT respectively. The reminder part of the influent forms the N-stream. This stream is split by a valve, so the valve controls the N-to-P ratio to the PBR by regulating the nitrogen load fed to it. The air supply is modelled as the oxygen mass-transfer coefficient (k_La). The air supply is used to keep the oxygen level at 1.5 mg l^{-1} in the aerobic tank. Since the effect of the mixing is not modelled it is not considered as a suitable actuator. The main disturbances considered in this work are the ammonia, phosphate and chemical oxygen demand (COD) influent loads. Fig. 3 shows the resulting control structure.

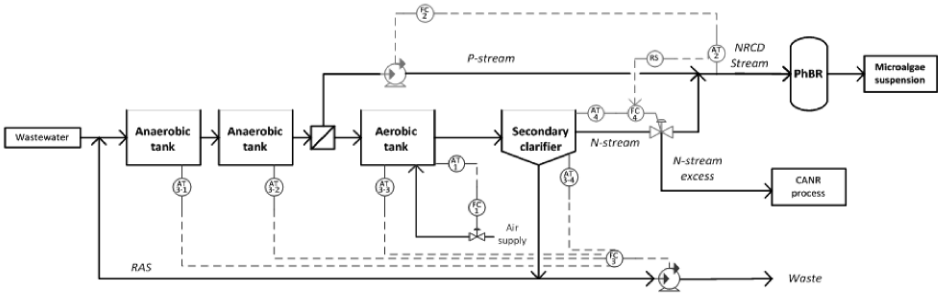

Figure 3 Layout of the control structure strategy. RAS stands for recirculation of activated sludge.

The RGA (Eq. (1)) shows that the interaction between the proposed control loops is minimal, and thus the chosen pairing is suitable for controlling the system.

$$\mathrm{RGA} = \begin{matrix} \\ \mathrm{DO} \\ \mathrm{P-load} \\ \mathrm{SRT} \\ \mathrm{N-to-P\ Ratio} \end{matrix} \begin{matrix} \begin{matrix} K_La & Q_P & Q_w & Q_n \end{matrix} \\ \begin{bmatrix} \mathbf{1.036} & 0.0027 & -0.0354 & 0.0001 \\ -0.0830 & \mathbf{0.8757} & 0.104 & 0.1032 \\ 0.0253 & 0.0058 & \mathbf{0.9189} & 0 \\ 0.0251 & 0.0658 & 0.0124 & \mathbf{0.8966} \end{bmatrix} \end{matrix} \quad (1)$$

System performance was assessed under 6 different scenarios, where the system was exposed to step disturbances on the influent TCOD (±20%), TN (±30%) and TP (± 20%). The results for the positive steps are shown in Fig. 4. Even it is not clear on the plots, due to the scale of the figure, in the moment of the step change the system barely deviates from the optimal performance. In all the three cases, the control structure is able to reject the disturbance and to keep a stable operation, thereby meeting the goals of the control system, i.e. i) stable and optimal phosphorus recovery through the P-stream; and ii) stable and balanced nutrient load conveyed to the PBR, with an N-to-P ratio of 16. Negative steps for TN and TCOD are also rejected by the control system. However, when the influent phosphorus load decreases the system is not able to keep the phosphorus load. Checking Fig. 2a again, it can be seen that by increasing Q_p the improvement on phosphorus recovery is limited by nitrifiers activity. Therefore, there is an upper boundary or maximum Q_p, beyond which PAOs are washed out from the system and the process performance cannot be recovered to the previous state. However, even the phosphorus load through the P-stream is lower than in the base case, the phosphorus recovery is still optimal in terms of percentage of influent phosphorus load, as the process operation is barely moved from the optimal conditions found through scenario simulations. In the latter scenario, emphasis should be put on controlling the N-to-P ratio, to avoid an excess of ammonia in the PBR, which would otherwise be impossible to take up by the microalgae.

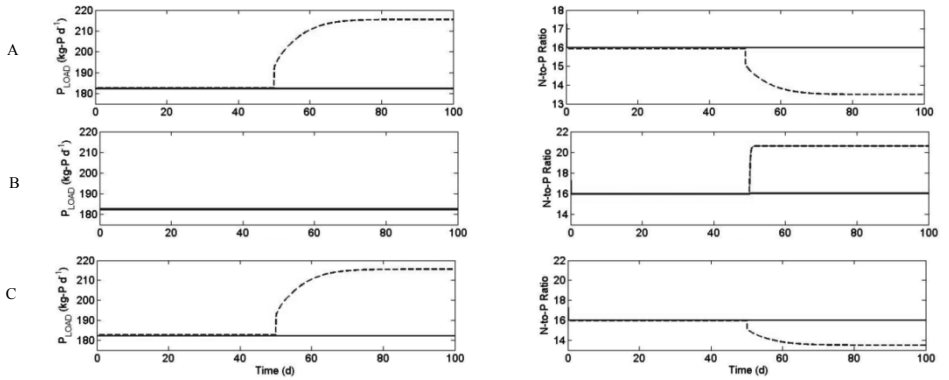

Figure 4 a) Effect of a step change of 20% on the influent phosphorus; b) effect of a step change of 30% on the influent ammonia; and c) effect of a step change on the influent TCOD of 20%. The full line represents the process response under controlled conditions, and the dashed line the process response without control.

Finally, the system is simulated under dynamic conditions. Fig. 5a shows that the control system is able to smooth the variations on the P-load, only allowing very small deviations from the set point. However, the N-to-P ratio shows some variability (Fig. 5b). When the influent nitrogen into the treatment plant is too low, the control system is not able to keep the set point and the N-to-P ratio falls under the optimal value. Nevertheless, the performance of the EBP2R is comparably better than in the case the system is not controlled. Since the algae present some flexibility due to N and P storage (Wágner et al., 2015), we expect that a comparably low deviation from the optimal N-to-P ratio does not compromise the effluent quality of the PBR.

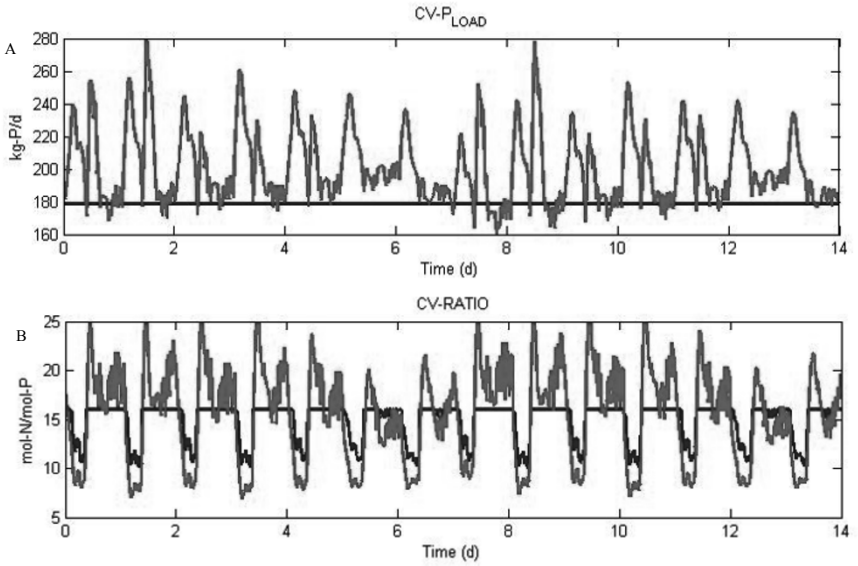

Figure 5 a) P-load fed to the PBR under dynamic conditions; b) N-to-P ratio fed to the PBR under dynamic conditions. The process response under controlled conditions (blue) and the process response without control (red) are presented.

4. Conlusion

In this work we have developed a control structure that allows a stable and optimal operation of the EBP2R. The control system is able to reject most of the disturbances. However, the process performance can be compromised when either N or P become limiting in the influent. Further research is still needed to assess the controllability of the downstream PBR and how it affects the EBP2R operation conditions.

References

X. Flores-Alsina, K.V. Gernaey K.V., U. Jeppsson U, 2012. Benchmarking biological nutrient removal in wastewater treatment plants: influence of mathematical model assumptions. Water Science and Technology, 65(8), 1496-1505.

M. Henze, W. Gujer, T. Mino, T. Matsuo, M.C. Wentzel, G.V.R. Marais, G.V.R., M.C.M. Van Loodsdtrecht, 1999. Activated sludge model nº 2d, ASM2d. Water Science and Technology, 39, 165-182.

T. Larsson, S. Skogestad 2000. Plantwide control- A review and a new design procedure. Modeling, Identification and Control, 21(4), 209-240.

D.E. Seborg, T.F. Edgar, D.A. Mellichamp, D.A., 2004. Process Dynamics and Control.

S. Skogestad 2003. Simple analytic rules for model reduction and PID controller tuning. Journal of Process Control, 13(4), 291–309.

B. Valverde-Pérez, E. Ramin, B.F. Smets, B. Gy. Plósz, 2015. An innovative enhanced biological nutrient recovery activated sludge system to develop controlled growth media for downstream algae cultivation. Water Research, 68, 821-830.

W. Verstraete , P. Van de Caveye, V. Diamantis, 2009. Maximum use of resources present in domestic ‘‘used water”. Bioresource Technology, 100(23), 5537–554.

D.S. Wágner, B. Valverde-Pérez, M. Sæbø, M. Bregua de la Sotilla, J. Van Wagenen, B.F. Smets, B. Gy. Plósz, 2015. A consensus green growth model (ASM-A) – uptake and storage of nutrients and carbon. Submitted to Environmental Science and Technology.

Krist V. Gernaey, Jakob K. Huusom and Rafiqul Gani (Eds.), 12th International Symposium on Process Systems Engineering and 25th European Symposium on Computer Aided Process Engineering.
31 May – 4 June 2015, Copenhagen, Denmark

Production of phthalic anhydride from biorenewables: process design

Sara Giarola, [a] Charles Romain, [b] Charlotte K. Williams, [b] Jason P. Hallett, [a] Nilay Shah [a]

[a]*Chemical Engineering Department, Imperial College London, London, SW7 2AZ, UK*
[b]*Chemistry Department, Imperial College London, London, SW7 2AZ, UK*

Abstract

Phthalic anhydride is widely used worldwide for an extremely broad range of applications spanning from the plastics industry to the synthesis of resins, agricultural fungicides and amines. Its production is currently based on the vapor phase oxidation of o-xylene and naphthalene. The development of an alternative production route to the petrochemical one is highly desirable to reduce the pressure on fossil use and effects of oil depletion concerns. This work proposes the process modelling of a bio-based route to phthalic anhydride. Results show how the valorization of all the carbohydrate-rich fractions present in the biomass is crucial to obtain an economically viable process.

Keywords: phthalic anhydride, process modelling, biorefinery

1. Introduction

There has been in recent years an increasing interest in the development of chemicals manufactured from renewables (i.e. bio-based chemicals) not only due to environmental policies (at both national and international levels) but also in initiatives of private companies (like Cargill and BASF) (Golden and Handfield, 2014). The emerging bioeconomy growth is currently led by the bio-plastic sector but will soon include specialty chemicals to a specific extent (OECD, 2007). The replacement of petroleum-derived products with bio-based ones is a promising answer to energy security and climate change issues. As a matter of fact, a large number of potential applications of biomass to produce bulk and niche chemicals have already been disclosed by chemistry and biotechnology researchers (EC, 2006). However, concerns regarding the technical and practical feasibility of large-scale biorefining infrastructures still hinder the expansion of these systems. The extensive research on bioethanol has revealed that process intensification is essential to cut the production costs and ensure process viability. In the biorefining context, though, only a limited number of studies have proposed rigorous techno-economic assessments of selected bio-based chemicals. The integration of lactic acid production in the sugarcane-based biorefinery was targeted by Sikder et al. (2012). Lammens et al. (2012) have developed a techno-economic feasibility analysis of bio-based products derived from glutamic acid. Cok et al. (2014) proposed an energy and greenhouse gas emission assessment of bio-based succinic acid obtained from carbohydrates.

Phthalic anhydride (PA) has a key importance in the production of plasticizers, polyesters and resins. Its production is based on fossil feedstocks and is expected to grow up to 5 Mt per year by 2018, as such its market would be affected by petroleum

depletion concerns. A renewable route to phthalic anhydride was found by Mahmoud et al. (2014) using biomass-derived furan (F) and maleic anhydride (MA).
In this work, a conceptual design of the production process of PA from corn stover is proposed to assess its actual scalability.

2. Materials and methods

A generic, simplified PA production process (displayed in Fig. (1)) using corn stover as raw material was developed and then simulated by means of a process simulator (Aspen Plus™). The composition of the feedstock was assumed to be the same as in an NREL design study (Humbird et al., 2011). The process conceptual design was developed aiming at the full exploitation of the biomass macro-components (i.e. cellulose and hemicellulose). It was based on an extensive survey of technical chemistry solutions (i.e. experimental and industrial) to screen promising process configuration alternatives. The simulation mainly uses component physical properties internal to the software as well as property data developed at NREL (Humbird et al., 2011). Vapour-liquid equilibria were described using the NRTL model, considering O_2, N_2, CO_2, CH_4 and H_2 as components following Henry's Law. Reactors have been modelled using fixed conversion units. A rigorous modelling of kinetics was outside the scope of the work.

2.1. Process description: selected reactions

The plant was designed to treat a nominal capacity of 104,167 kg/h of milled corn stover at 20 % of bulk moisture content for the production of PA. The biomass is first pretreated to extract the xylose sugars and the hydrolysate is neutralised. The C5 sugars contained in the liquid part of the hydrolysate are dehydrated to furfural (R1) which could be converted either into F (R2) or MA (R3). The C6 sugars are extracted from the cellulose through saccharification (R4). After the separation of the lignin, the glucose is isomerised to fructose (R5) which is dehydrated to HMF (hydroxymethylfurfural) (R6) and then converted into MA (R7). F and MA react on equimolar basis to produce PA (R8). A more detailed description of each single step is presented below.
PA can be produced at lab scale in two reaction steps (Mahmoud et al., 2014): a Diels-Adler cycloaddition between F and MA at room temperature and solvent free conditions (yielding 96 % of oxabornene dicarboxylic anhydride) is followed by the dehydration of the intermediate produced in the previous step at 353 K in a mixture of sulfonic carboxylic anhydrides in methanesulfonic acid. The experimental procedure was modelled in a simplified manner involving only two reactions: one between F and MA into PA which was followed by the sublimation of the anhydride from the corresponding acid (PAc). The presence of anhydrides was not modelled in the vapour-liquid equilibrium. Pure PA could be obtained via extraction and sublimation from the mixture with its own acid (7 % by weight) (Monroe, 1919). The final PA purification step was not modelled in Aspen Plus™. A side MA-rich stream (60 % by weight) is also produced. This could be additionally purified to expand the product portfolio.
F and MA are produced as proposed below.
In order to make the hemicelluloses available, the biomass must undergo pretreatment. As such, the feedstock is mixed with steam (at 7 atm and 373.15 K) before being treated at 431.15 K with dilute sulphuric acid (2.21 % of inlet solids by weight). Under these conditions, 90 % of the xylan is assumed to convert into xylose (Humbird et al., 2011). At this stage, the hydrolysate is treated in a neutralisation and a reacidification section (350 K, 3.4 atm). Ammonia is first added to convert acids into ammonium sulphate and

acetates; the excess amount of reagent reacts with sulphuric acid into ammonium sulphate (Humbird et al., 2011). Solids (i.e. unreacted hemicellulose, cellulose and lignin) are filtered and separated from the liquid hydrolysate with unitary efficiency.
C5 sugars in the liquid hydrolysate undergo a sulphuric acid-catalysed dehydration into furfural (85 % conversion) at 7.59 atm and 441.65 K (Mandalika et al., 2012).

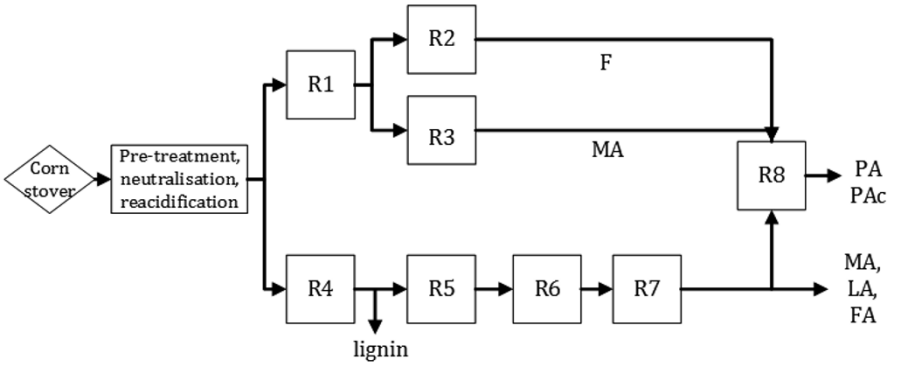

Figure 1: Phthalic anhydride proposed flowsheet. Separation steps are not shown.

Furfural in the reactor vapour outflow is immediately distilled off to avoid condensation reactions with sugars into humins. Two alternative conversions routes for furfural have been considered. In the first one, it could react with oxygen (nearly atmospheric pressure and 593 K) and be converted into maleic anhydride using VO_x/Al_2O_3 catalysts with 73 % selectivity (Alonso-Fagúndez et al., 2012). The main by-product detected after the reaction would be 2-furanone. A second avenue would be the furfural conversion into F (at 90.9 % yield) in a vapour-phase decarbonylation (atmospheric pressure and 583.15 K) in presence of a Pd-Li-alumina catalyst promoted with cesium carbonate, as described in the US patent 8710251. The main by-product reactions lead to furfuryl alcohol and THF. The optimal split ratio between the two conversion paths for furfural was found to privilege F production (60 % of the overall furfural rate).
The neutralised hydrolysate is cooled down to 321.15 K adding water, which dilutes the slurry to a 20 % solid loading before the saccharification. The enzymatic hydrolysis was modelled according to the recommendations of NREL (Humbird et al., 2011) and allowed 90 % conversion of cellulose into glucose, adding 2 % of cellulase per unit of inlet cellulose by weight. The C6 sugars (i.e. glucose) produced from the saccharification are separated from the residual solids through a centrifuge. The glucose could be dehydrated into HMF only at low yields when the reaction is carried out in an aqueous medium. Better HMF yields are achievable from fructose which could be obtained from glucose isomerisation. The isomerisation (the rate-limiting step) was modelled according to Gaily et al. (2010). The unreacted glucose was recycled to the isomerisation reactor. According to Gaily et al. (2010), a 58.9 % yield of fructose was assumed from a 10 % glucose solution at 333.15 K using immobilised isomerase enzyme (15 % by weight of the treated glucose). The obtained fructose is then dehydrated to HMF as proposed by Román-Leshkov et al. (2006), who used a biphasic system where the HMF produced in the aqueous medium (using hydrochloric acid as a catalyst) was extracted into an organic phase. Among the alternatives proposed by the authors, a good compromise between fructose conversion (91 %) and HMF selectivity (60 %) was achieved using MIBK as the extracting agent with a volumetric ratio against the liquid phase equal to 1.51. The by-products of the reaction (levulinic acid, LA, and

formic acid, FA) are recovered and sold as valuable products. The HMF is then oxidized yielding MA at 52 % over $VO(acac)_2$ catalysts according to the scheme proposed by Du et al. (2011). The system was modelled including the main reaction to MA and MA hydration to its corresponding acid. The additional by-products which lead to complete conversion of HMF (2,5 dyformylfuran, esters, humins) were modelled as side streams leaving the reactor. Acetonitrile was modelled as solvent used for the reaction.

2.2. Process description: separation system

The separation system was intended to recover the chemical intermediates at a level of purity matching as close as possible the experimental settings per each of the reactions described in section 2.1. The separation blocks are briefly explained below. Table 1 details the operating conditions for the distillation/extraction columns.

Section S1 concerns furfural purification. It is located after the xylose dehydration (R1). It is composed by a first tower (T101) which separates a bottom waste stream rich in water and salts. The distillate is then purified to extract pure furfural (T102 bottoms) via a pressure shift distillation (PSD) sequence (T102, T103).

Section S2 concerns HMF purification following R6. An extractor (E201), modelled according to the Dortmund modified UNIFAC property method, allows a preliminary separation of HMF. This is primarily concentrated in the organic phase (Román-Leshkov et al., 2006) and recovered from the solvent in T201. T202 separates an LA-rich distillate (97 % mol.) from an HMF-rich one (95 % mol.).

Section S3 concerns solvent recovery (i.e. acetonitrile). The vapour streams obtained from the oxidation reactions of furfural (R3) and HMF (R7) are cooled. The mixture is flashed and the vapour fraction treated in a water scrubber (T303). The scrubber bottoms are sent to a PSD column sequence (T300, T301, T302) to separate the water-acetonitrile azeotrope. Acetonitrile is recovered in the distillate from T302.

Section S4 concerns the purification of the intermediate of the main synthesis reaction (F, MA). The outlet stream obtained from furfural decarbonylation (R2) is cooled, flashed and the vapour sent to a water scrubber T401. The scrubber and the stabilizer bottoms (T402) are conveyed to a rectification tower T403, from which F is separated as distillate and sent to the reaction section. T402 receives the outflow of the main synthesis reactor (R8) after the solids (PA and PAc) are removed: the light compounds are separated in the overheads. T403 bottoms are sent to the MA recovery section, composed of a triple effect vacuum evaporator and a reactive distillation (T404) to remove water and promote the conversion of maleic acid to MA.

Section S5 concerns the FA recovery from E201 bottoms and evaporator condensates (S4). Residual MIBK is distilled off from T501, while T502 and T503 represent a PSD module for FA recovery (64 % mol.).

Table 1: Separation system operating specifications (pressure (atm), overheads and bottoms temperature (K)) for the separation of a) furfural and HMF, b) acetonitrile and F, c) MA and FA

Unit	T101	T102	T103	E201	T201	T202
column	distillation	distillation	distillation	extractor	distillation	distillation
pressure	1	1	0.9	1	0.013	9.2 E(-3)
o. temperature	370.78	372.86	369.15	298	289.83	393.40
b. temperature	374.55	434.5	370.19	298	408.34	409.40

a)

Unit	T300	T301	T302	T303	T401	T402
column	distillation	distillation	distillation	scrubber	scrubber	stabilizer
pressure	2.72	0.07	4	1	1	3.50
o. temperature	365.25	292.40	406.66	298.28	299.92	291.06
b. temperature	382.90	312.14	409.81	302.95	317.70	394.98

b)

Unit operation	T403	T404	T501	T502	T503
scope	distillation	distillation	distillation	distillation	distillation
pressure	1	0.026	1	2.96	0.197
o. temperature	307.46	317.76	355.35	406.68	335.27
b. temperature	373.40	370.94	373.41	437.06	423.41

c)

3. Results: overall material balance and costs

The overall mass balance with the estimation of the corresponding operating costs accounting for the inlet material flows is reported in Table 2. It was assumed that 99.5 % of the water was recovered via a sequence of anaerobic/aerobic digestion followed by reverse osmosis (Humbird et al., 2011). A 90 % recovery of oxygen and hydrogen from vents was considered obtainable through the use of advanced membrane technologies. The total cost for the input materials was 5757 £/h, which was distributed among the products i by applying a mass allocation factor $w_i = F_i / \sum_i F_i$, obtained from the ratio of the mass flow of product i F_i over the sum of all the product outputs. The unitary cost of each product was lower than the product market price and equal to 247 £/t.

4. Conclusions

This work presents a new process for the production of phthalic anhydride from corn stover. A full carbon recovery and valorisation of the carbohydrates into a broad portfolio of chemicals (PA, MA, LA, FA) is necessary in order to leverage the operating costs for the input materials among the products and improve the business viability.

Table 2: Overall material balance and cost per t of PA and PAc (a); cost allocation (b)

	biomass	water	H_2SO_4	O_2	H_2	cellulase	isomerase	MIBK	NH_3
Mass (t)	13.69	0.15	0.53	0.13	0.004	0.08	0.87	0.01	0.14
Cost (£)	0.49	0.005	0.03	0.02	0.003	0.14	NA	0.01	0.06

a)

Product	Rate (kg/h)	Cost (£/h)	Cost (£/t)
PA	7610	1881	247
MA (60 % wt.)	1377	340	247
FA (74 % wt.)	6821	1686	247
LA	7489	1851	247

b)

5. Acknowledgement

The authors would like to thank EPSRC (EP/K014676/1) who funded this work under the "Sustainable Chemical Feedstocks" programme.

References

N. Alonso-Fagúndez, M.L. Granados, R. Mariscal, M. Ojeda, 2012, Selective Conversion of Furfural to Maleic Anhydride and Furan with VO_x/Al_2O_3 Catalysts, ChemSusChem, 5, 1984 – 1990.

B. Cok, I. Tsiropoulos, A.L. Roes, M.K. Patel, 2014, Succinic acid production derived from carbohydrates: an energy and greenhouse gas assessment of a platform chemical toward a bio-based economy, Biofuels, Bioprod. Bioref. 8:16 – 29.

Z. Du, J. Ma, F. Wang, J. Liu, J. Xu, 2011, Oxidation of 5-hydromethylfurfural to maleic anhydride with molecular oxygen, Green Chem, 13, 554 – 557.

EC, 2006, The BREW Project. Final Report. Utrecht, NH.

M.H. Gaily, B.M. Elhassan, A.E. Abasaeed, M. Al-Shrhan, 2010, Isomerization and Kinetics of Glucose into Fructose, IJET-IJENS, 10, 3.

J.S. Golden, R.B. Handfield, 2014, Why biobased? Opportunities in the Emerging Bioeconomy, USDA Report, Washington, USA.

D. Humbird, R. Davis, L. Tao, C. Kinchin, D. Hsu, A. Aden, 2011, Process Design and Economics for Biochemical Conversion of lignocellulosic Biomass to Ethanol, NREL Report, Golden Colorado, USA.

T.M. Lammens, S. Gangarapu, M.C.R. Franssen, E.L. Scott, J.P.M. Sanders, 2012, Techno-economic assessment of the production of bio-based chemicals from glutamic acid, Biofuels, Bioprod. Bioref. 6,177 – 187.

E. Mahmoud, D.A.Watson, R.F. Lobo, 2014, Renewable production of phthalic anhydride from biomass-derived furan and maleic anhydride, Green Chem. 16, 167 – 175.

A. Mandalika, T. Runge, 2012, Enabling integrated biorefineries through high-yield conversion of fractionated pentosans into furfural, Green Chem., 14, 3175 – 3184.

K.P. Monroe, 1919, Phthalic anhydride. II—The melting point of pure phthalic anhydride. The system phthalic anhydride-phthalic acid, The Journal of industrial and Engineering Chemistry, 11, Issue 12.

OECD, 2009, The Bioeconomy to 2030, Designing a Policy Agenda.

O. Ronnie, 2014, Vapor phase decarbonylation process, US Patent 8710251.

Y. Román-Leshkov, J.N. Chheda, J.A. Dumesic, 2006, Phase Modifiers Promote Efficient Production of Hydromethylfurfural from Fructose, Science, 312, 1933 – 1937.

J. Sikder, M. Roy, P. Dey, P. Parimal, 2012, Techno-economic analysis of a membrane-integrated bioreactor system for the production of lactic acid from sugarcane juice, Biochemical Engineering Journal, 63, 81 – 87.

Krist V. Gernaey, Jakob K. Huusom and Rafiqul Gani (Eds.), 12th International Symposium on Process Systems Engineering and 25th European Symposium on Computer Aided Process Engineering.
31 May – 4 June 2015, Copenhagen, Denmark

Model Integration Using Ontology Input-Output Matching

Linsey Koo, Franjo Cecelja

PRISE, FEPS, University of Surrey, Guildford, Surrey. GU2 7XH, UK

Abstract

This paper introduces ontology controlled model integration framework using input-output matching in the domain of biorefining. The framework builds upon the existing framework and replaces the Common Object Request Broker Architecture (CORBA) object bus with more flexible semantic repository. Semantic Web Services Description Ontologies (OWL-S) are used to describe model inputs, outputs, preconditions, operating environment and its functionality. The OWL-S enables the automation of model integration through (i) discovery, (ii) selection, (iii) composition, and (iv) execution stages. This concept has been verified with a small scale model integration to demonstrate the flexibility of model integration through all four stages of the process.

Keywords: Model Integration, Ontology, Input-Output Matching

1. Introduction

Process System Engineering (PSE) and Computer Aided Process Engineering (CAPE) have traditionally been concerned with the development of systematic procedures and computer aided techniques for the design, control and operation of chemical process systems. Problems related to process optimisation, process integration, and process synthesis/design have been solved through the use of knowledge, and optimisation tools and methods, developed by the PSE/CAPE community. The traditional users of these tools and methods include the oil & gas industry, petrochemical industry, and the chemical industry (Alvarado-Morales et al., 2008).

Process modelling and simulation have become vital tools for process engineers, in order to plan, evaluate, assess, and develop different alternatives for the design of products and processes. In the process of developing a new model, the best suited modelling tools for different parts of the process are employed. However, to understand process design as a continuous work process from an integrated perspective requires the use of tools from diverse sources and disciplines simultaneously. The only existing model integration framework is the CAPE-OPEN, proposed by the European process industry which established a software based interface, Common Object Request Broker Architecture (CORBA). More precisely, CORBA provides a Common Interface Bus that allows individual models to reside in multiple computer systems and communicate with each other. Whilst the CAPE-OPEN standard is a widely recognised standard, a disadvantage has been identified in the lack of flexibility in input-output (I-O) architecture.

The exploitation and use of sustainable renewable resources have been recognised as an essential component in meeting future energy demand needs. Biofuels are alternative fuel sources to traditional petroleum based fuels that could be used to meet future demands. However, mainstream biofuel production faces a number of technical challenges due to the complexity of the characteristics of biomass feedstock, and associated processing technologies, which have very different characteristics when

compared to traditional petroleum processes. Gani and Grossmann (2007) addressed the importance of developing methods and tools that represent comprehensive biorefining technologies, through the adaptation of current systems and development of new systems. They can be further integrated by a single, flexible, reliable, and efficient system that has an ability to integrate methods and tools from different sources, to provide meaningful and useful simulation and optimisation tools.

In response to the challenges stated, this paper introduces the use of ontology in biorefining as a method of model integration, which has strong synthesis capabilities and functions to invite degrees of freedom. In particular, the ontology controlled model integration builds upon the existing CAPE-OPEN framework and replaces the CORBA object bus with a more flexible semantic repository, as shown in Figure 1. Models are described by Semantic Web Services (SWS) using Ontology Web Service Description (OWL-S) as an enabler of web services through service discovery, selection, composition, and execution stages. The Web Ontology Language (OWL) defines three upper ontologies, including *ServiceProfile*, *ServiceGrounding*, and *ServiceModel*. *ServiceProfile* ontology represents what a service does, and determines whether the service/model meets the requirement. *ServiceGrounding* ontology supports the details of how to access a service/model. Finally, *ServiceModel* ontology defines how the service/model works through the description of the work flow and the potential interoperation paths.

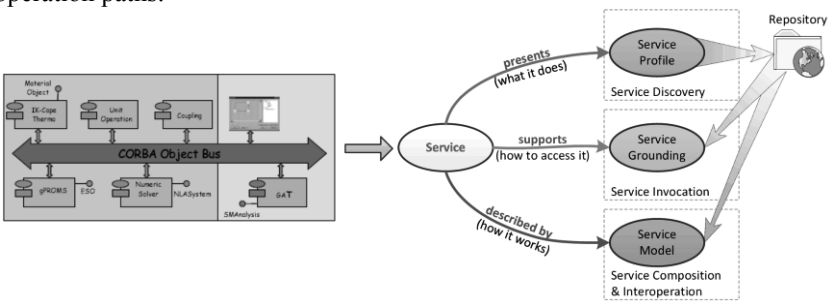

Figure 1. Introduction of repository for model integration

2. Ontological Approach to Model Integration

2.1. Basic Concept of Domain Ontology based on OWL-S Framework

Ontology is a set of interlinked common concepts and relationships between concepts, which defines the knowledge, both tacit and explicit, in a specific domain (Gruber, 1995). The synergistic relationship and interplay between tacit and explicit knowledge developed in the ontology domain, enable the generation of new knowledge. The domain ontology of biorefining, with a particular view to coordinate model integration, provides a common set of vocabulary to describe the model and data, and characterises functionality in relation to the processes of biorefining. Each model is described by the SWS to allow the models to be semantically annotated via the use of concepts from domain ontology, to form a comprehensive knowledge base which includes; model input(s), output(s), precondition(s), the environment in which it operates, as well as the functionality it performs (Raafat et. al., 2013a; Trokanas et. al., 2014). The semantically described model is then registered as an instance of the domain ontology and implemented in OWL-S framework. The respective instances are published in the purposely built public repository for I-O matching with other available models, as shown in Figure 2.

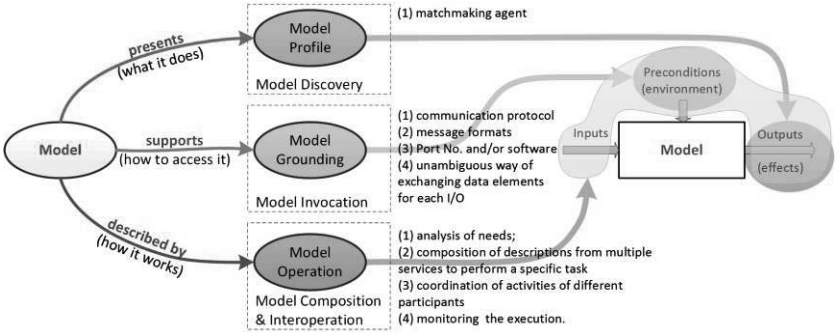

Figure 2. Semantically described model

The particular role of OWL-S ontology is to facilitate the automation of model integration through the model discovery, selection, composition, and execution stages. The discovery stage allows formation of an integrated model to organise repositories and supports the automated process of locating a model from a public repository(ies). The best option that satisfies the requestor's functionality is selected in the model selection stage. Then, the model composition stage formulates the chain of integrated models in response to the requestor's functionality. The instances of the model are created, executed and managed during the execution stage. The model selection and model composition stages are performed by semantic I-O matching (Trokanas et. al., 2014), which allows for partial matching and permits a high degree of flexibility in model integration. It is also important to mention that the proposed framework allows for integration of data residing in various forms of databases, and is concomitantly semantically described in the same way as the model with the omission of the input. The performance of the concept has been tested by large scale technology integration to satisfy requirements of industrial symbiosis, where technologies were represented by respective models (Raafat et. al., 2013b).

In a biorefining domain, a simplified model is used, which includes the conversion process itself as a black box model, desired input, targeted output streams in the form of characterisation of resources, and the environment supporting the unit operation, i.e. operating condition or software platform. To establish a common set of vocabulary and to enable the discovery of models and data that characterises functionality, a classification of biorefining is conceptualised based on two distinct concepts, which include conversion technology and resource. The term 'conversion technology' in biorefining refers to a wide array of state-of-art processes that are capable of producing value-added products, such as biofuels and biochemicals from biomass. Conversion technology has been characterised by the biorefinery platform (i.e. sugar platform, thermochemical platform), the process stage (i.e. pretreatment stage, conversion stage, separation stage), the resultant products in terms of material (i.e. biofuel, biochemical), and energy (i.e. heat, electricity). The term 'resource' in biorefining refers to both energy and material, which can be described as an input(s), output(s) and precondition(s) of the conversion process. Resources have been further characterised, by the type of material (i.e. electricity, heat, inorganic compound, organic compound) and the characteristics of property (i.e. physical property, chemical property) so that resources are processed based on the classification of the conversion process.

The relation in ontology describes the semantics of the domain between the classes and individuals. For example, the relationship *hasComposite* creates a link between type of material and characteristics of property to further describe the mereology relation. In order to encompass additional semantic information concerning the concept, the

properties that link between concepts and its data value that assist characterisation are used to define a precise characteristics, i.e. properties *hasSize* and *hasMoistureContent*. In addition, the semantic restrictions on properties provide the following: (i) the I-O matching by calculating similarity, (ii) the user navigation process through cardinality restrictions, and (iii) the inferences.

2.2. Semantic Matching

The model integration and creation of interoperability between methods and tools from different sources is referred to as the I-O matching. This allows for the automation process, and built in intelligence for automated discovery of potential and relevant models that will support model integration (Raafat et. al., 2013b).

The process of integration is performed by a purposely built matchmaker, which matches inputs and outputs of all models and data available in the public repository. There are two techniques to enable the matching, being forward and backward matching processes. The forward matching process is initialised to satisfy the requester's input parameters through an expansion, by matching inputs of the rest of the services with the outputs of the last identified service. The backward matching process is generated by identifying a suitable model, which satisfies the requested outputs. The backward matching process, compared to forward matching, avoids the processes of expansion, and can therefore be considered more efficient. After matching is completed, the respective model and data integration is reversed and perform a forward integration process. The whole process is visualised for better control and to allow intervention by the user as well as for result recording and analysis.

The semantic partial matching is considered in order to facilitate the flexibility of model integration, when the registered model is partially satisfying the input criteria. The partial matching is established through a direct matching process using semantic similarities between I-O type and property. The semantic measure for the matching by type of I-O is calculated by the distance between the respective concepts, along the class-subclass relationships in the domain ontology. The property matching is calculated from the object properties defined in respective SWS ontology. The method of measuring the similarity of the properties, which was established by industrial symbiosis case (T. Raafat et. al., 2013b), was adapted to calculate the property similarity between the property sets. Each set of property is represented as a vector:

$$p_j = \{v(d_1)\cdot w_1, v(d_2)\cdot w_2, \cdots, v(d_n)\cdot w_n\} \tag{1}$$

where p_j is set of vector properties in SWS, d_i is individual property representing concepts, $v(d_i)$ is value of the property, and w_i is weight of the property. The cosine similarity $h_k^{V,C}$ is calculated as a cosine of angle between the model vectors p_r and p_i.

$$h_k^{V,C} = \frac{p_r \cdot p_i}{\|p_r\|\|p_i\|} = \frac{\sum_{i=1}^{n} p_{r,i} \times p_{i,i}}{\sqrt{\sum_{i=1}^{n}(p_{r,i})^2} \times \sqrt{\sum_{i=1}^{n}(p_{i,i})^2}} \tag{2}$$

where n is a number of properties used for similarity calculation. To compensate in the case of the missing property value, Euclidean similarity $h_k^{V,E}$ is introduced as:

$$h_k^{V,E} = 1 - \frac{\sqrt{\sum_{i=1}^{n} w_i (p_{r,i} - p_{i,i})^2}}{max\sqrt{\sum_{i=1}^{n}(p_{r,i} - p_{i,i})^2}} \tag{3}$$

The vector similarity h_k^V is a mean average between combine cosine similarity $h_k^{V,C}$ and Euclidean similarity $h_k^{V,E}$:

$$h_k^V = \frac{h_k^{V,C} + h_k^{V,E}}{2} \tag{4}$$

The distance and property similarity, h_k^C and h_k^V respectively, are aggregate together as a fuzzy weighted average, where α and β are weighing parameters.

$$h_k = \frac{\alpha h_k^C + \beta h_k^V}{\alpha + \beta} \tag{5}$$

The above matching is comprised of three distinct stages: i) elimination, ii) semantic matching and ranking, iii) performance ranking. As a result, an optimum solution and multi-criteria analysis of model integration is established (F. Cecelja et. al., 2014).

3. Demonstration of Input-Output (I-O) Matching

A small scale model integration representing biochemical conversion technology is used to demonstrate the performance of the proposed approach. The model of co-fermentation (CF) uses the bacterium *Zymomonas Mobilis* to produce 315M litre of ethanol per year as an output from corn stover (A. Aden et. al., 2002). The operating condition of this model is temperature at 41°C with a resident time of 1.5 days and initial fermentation solids level of 20%, with an assumption that the hemicellulose sugars (arabinose, mannose, and galactose) have the same reaction and conversion as xylose, as a result, 56% of the fermentation broth is fermentable sugar.

Two models are selected as potential matches by the backward matching process. The set of respective requirements are listed in Table 1. Both of the models are pretreatment methods that break down the feedstock into fermentable sugars, dilute acid and enzymatic hydrolysis (DAEH) method and ammonia fiber expansion (AFEX) method. The DAEH process converts barley straw with composition of 38.1% glucan, 26.9% xylan, and 2.6% arabinan to monomer sugars, with yields of approximately 96% and 57% for glucose and xylose, respectively (M. Yang et. al., 2013). The AFEX process converts switchgrass with composition of 34.2% glucan, 22.1% xylan, and 3.1% arabinan to monomer sugars, with yields of approximately 93% and 70% for glucose and xylose, respectively (H. Alizadeh et. al., 2005).

Table 1. Process requirements

Process	Sugar monomer flowrate	% quantity matching	Temperature
CF (Requestor)	56 t/h	100%	41°C
DAEH	51 t/h	89%	50°C
AFEX	46 t/h	81%	37°C

In the second stage of matching, the semantic similarity by type of I-O is measured based on type of feedstock materials through class-subclass relationship. The vector similarity of the properties is then calculated related to quantity/flow rate of sugar monomers in the fermentable broth and operating temperature. As a default, the weight of the individual property and the fuzzy weight for the aggregated similarity, mentioned in Eq. 1 and Eq. 5, respectively, are equal to 1, unless user defines otherwise.

Table 2. Results from second stage matching

Resource Type	Semantic similarity	Property similarity	Aggregated results
DAEH	60%	63%	62%
AFEX	20%	50%	35%

The matching results are shown in Table 2, the DAEH and AFEX process with 62% and 35% matching similarities are found, respectively. As a result, the DAEH will be a preferable option for the requestor.
The challenges encountered while implementing the integration strategy for the models included identifying the key parameters that should be matched, and to obtain an understanding of the impact of partial matching associated with those parameters.

4. Conclusion

The wide range of models in the domain of biorefining can be described using SWS at any appropriate level of detail. A new approach was introduced to support model integration through I-O matching, which is implemented in OWL-S framework. The conversion technologies and resources in biorefining are semantically described and the relationships of SWS ontologies are established, which enables I-O matching. The backward matching process is proposed to identify a suitable model based on the input criteria. In addition, the semantic partial matching is performed to facilitate the flexibility of model integration. The proposed approach is implemented in a small scale model integration to demonstrate the flexibility, by showing model repository interaction between simulation interfaces and the data repository in the domain of biorefining.

References

A. Aden, M. Ruth, K. Ibsen, J. Jechura, K. Neeves, J. Sheehan, B. Wallace, 2002, Lignocellulosic biomass to ethanol process design and economics utilizing co-current dilute acid prehydrolysis and enzymatic hydrolysis for corn stover, NREL/TP-510-32438.

H. Alizadeh, F. Teymouri, T.I. Gilbert, B.E. Dale, 2005, Pretreatment of switchgrass by Ammonia Fiber Explosion (AFEX), Applied Biochemistry and Biotechnology, vol. 124 (1-3), pp. 1133-1141.

M. Alvarado-Morales, N. Al-Haque, K. Gernaey, J. Woodley, R. Gani, 2008, CAPE methods and tools for systematic analysis of new chemical product design and development, Computer Aided Chemical Engineering, on CD. vol. 25, pp. 997-1002.

F. Cecelja, T. Raafat, N. Trokanas, S. Innes, M. Smith, A. Yang, Y. Zorgios, A. Korkofygas, A. Kokossis, 2014, e-Symbiosis: technology-enabled support for industrial symbiosis targeting SMEs and innovation, Journal of Cleaner Production, In press.

R. Gani, I. E. Grossman, 2007, Process Systems Engineering and CAPE – What Next?, 17th ESCAPE Proceeding Book, Bucharest, Romania, vol. 24, pp. 1-5.

T. Gruber, 1995, Toward principles for the design of ontologies used for knowledge sharing, International Journal of Human-Computer Studies, vol. 43 (5-6), pp. 907-928.

R. Morales-Rodriguez, R. Gani, S. Dechelotte, A. Vacher, O. Baudouin, 2008, Use of CAPE-OPEN standards in the interoperability between modelling tools (MOT) and process simulators (Simulis Thermodynamics and ProSimPlus), Chemical Engineering Research and Design, vol. 86, pp. 823-833.

T. Raafat, F. Cecelja, N. Trokanas, B. Xrisha, 2013a, Semantic approach for pre-assessment of environmental indicator in industrial symbiosis, Computers & Chemical Engineering, vol. 59, pp. 33-46.

T. Raafat, N. Trokanas, F. Cecelja, X. Bimi, 2013b, An ontological approach towards enabling processing technologies participation in industrial symbiosis, Computers & Chemical Engineering, vol. 59, pp. 33-46.

N. Trokanas, F. Cecelja, T. Raafat, 2014, Semantic input/output matching for water processing in industrial symbiosis, Computer & Chemical Engineering, vol. 66, pp. 259-268.

M. Yang, S. Kuittinen, J. Zhang, M. Keinanen, A. Pappinen, 2013, Effect of dilute acid pretreatment on the conversion of barley straw with grains to fermentable sugars, Bioresource Technology, vol 146, pp. 444-450.

Krist V. Gernaey, Jakob K. Huusom and Rafiqul Gani (Eds.), 12th International Symposium on Process Systems Engineering and 25th European Symposium on Computer Aided Process Engineering.
31 May – 4 June 2015, Copenhagen, Denmark

Life Cycle Assessment of Biorefinery Products Based on Different Allocation Approaches

Paraskevi Karka[a*], Stavros Papadokonstantakis[b], Konrad Hungerbühler[c], Antonis Kokossis[a]

[a]*School of Chemical Engineering, National Technical University of Athens, Iroon Polytechneiou 9, 15780 Zografou, Athens, Greece*

[b]*Department of Energy and Environment, Chalmers University of Technology (CUT), Kemivägen 4, 41296 Gothenburg, Sweden*

[c]*Institute for Chemical and Bioengineering, Swiss Federal Institute of Technology (ETH) Zurich, Valdimir-Prelog-Weg 1, 8093 Zurich, Switzerland*

[*]*pkarka@chemeng.ntua.gr*

Abstract

Biorefineries constitute representative examples of multifunctional systems which are able to produce, similarly to conventional petroleum refineries, a wide range of chemicals (pharmaceutical constituents, plastics, food additives etc.), energy carriers and power through the optimal use of diverse biomass forms (wheat straw, oils, wood chips, municipal solid waste). For this purpose, biorefineries typically comprise a complicated, integrated network of physical and chemical transformation processes, such as mechanical and physical biomass pretreatment, pyrolysis, gasification, catalytic and enzymatic reactions, and downstream purification processes. For the environmental sustainability assessment of these complicated production systems, Life Cycle Analysis (LCA, ISO-Norm 14040) is considered as a widely acceptable methodology from scientists and engineers including, however, the debated aspect of partitioning the impacts among the co-products' in the biorefinery product portfolio.

The aim of this study is to present the influence of the various allocation approaches on the LCA results of biorefinery products. The framework of this analysis systematically incorporates the steps of the LCA methodology as described in the ISO norms and estimates the impacts related with the products of interest, taking into account the contribution of the co- and by-products in the overall production path. For this reason, two wider approaches were adopted, the attributional which describes the impact of the production process itself from a retrospective point of view, and the consequential which focuses on the changes in the level of the output (as well as consumption and disposal) of a product, including market effects from increasing or decreasing demand for the study product, having therefore a more prospective point of view. Several scenarios which describe the possible options for handling those products, were developed and assessed based on different allocation methodologies, namely system expansion (substitution method) and partitioning methods according to the mass, thermal and economic values of the co-products. The estimation of the life cycle impacts of the processes was performed using the Global Warming Potential (GWP), Cumulative Energy Demand (CED) and RECIPE methodologies which provide an assessment of the burdens through the associated LCA indicators.

The outcome of this approach provides a range of LCA metrics emphasizing at the variation of the results according to the followed allocation methods and to identify

those properties of products (physical, economic, thermal) and system factors (processes to be substituted from the renewable ones, degree of utilization of co- and by- products from the markets etc.) which dominate the LCA results.

Keywords: Biorefinery products, cumulative energy demand, global warming potential, allocation, system expansion

1. Introduction

Allocation is an important issue in biorefinery systems because of the multifunctionality of the processes involved along the life-cycle stages. Some well known examples are biomass fractionation processes which aim at the exploitation of the three basic components of the lignocellulosic feedstock (i.e., cellulose, xylose and lignin) and the conversion of these intermediates into a wide range of products, or the case of biodiesel plants which co-produce biodiesel and glycerol. Many studies have performed LCA on biorefinery systems as aggregated entities. These approaches have avoided to address impacts of final products and results are reported at the biorefinery level according to functional units such as 1000 kg of biomass, ha of land use, etc. (Cherubini and Jungmeier, 2010). On the other hand, other studies have focused on the investigation of all possible allocation approaches (e.g. partitioning methods, system expansion and hybrid methods) presenting the variation of results according to the followed approach, (Cherubini and Strømman, 2011).

This study highlights the variability of life cycle impact assessment indicators for biorefinery products by applying different allocation approaches (consequential and attributional) and discusses the influence of the co-producing processes and the displaced products in the results.

2. Methodology

The methodological steps followed in this study are in accordance with the ISO 14040 norms. Two approaches, the attributional and the consequential, have been applied for the Life Cycle Impact Assessment (Brander M., et al.). According to some researchers (Weidema, 2001), attributional LCA requires market allocation while consequential applications require system expansion. In this study, four different ways of handling the co-product allocation were applied:

Mass allocation: Calculations are based on the ratio of the mass of each co-product to the entire mass of co-products with the condition that they are chemical products.
Thermal allocation: It is applied in the case of different products (e.g. electricity/chemicals), the allocation factor being the Lower Heating Value (LHV) of the product streams, or of the equivalent source of the product stream (e.g natural gas for gas turbine generating electricity).
Economic allocation: It is based on market prices (Ecoinvent 3, Brew project).
Substitution by system expansion: Allocation is avoided by expanding the biorefinery system to include the alternative/conventional ways of producing the co-products. In the substitution approach, products are distinguished into: main (determining) for which the entire production process has been designed and dependent co-products which can be fully or partly utilized from the markets.

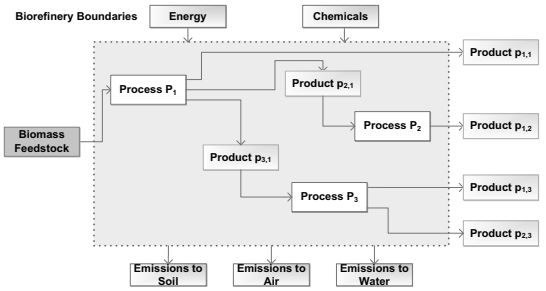

Figure 1: Example of LCA boundaries of the study system

One exemplary representation of the multiple functions of a biorefinery system is shown in Figure 1. Boundaries include a number of interacting processes, P_1, P_2...P_n, which convert biomass feedstocks into a range of products. For example, products $p_{1,1}$...$p_{m1,1}$ from process P1, (m_1 is the number of products at subdivision point 1) can be utilized either directly from the markets or they can be further converted through processes P_2...P_n into the final products $p_{1,2}$...$p_{mn,n}$,(m_n is the number of products at subdivision point n) depending on the demand for specific products each time.
The total environmental impacts EI_{total} of a specific category (e.g., acidification, global warming, water depletion etc.) can be allocated among the co-products according to the degree of the available information. In a "black box" approach no specific information is provided for the functions inside the system boundaries and allocation is applied directly among the final products. In a "detailed allocation approach" the critical subdivision points are known, followed by available information for energy and resource consumption (e.g., represented in Figure 1 by the 3 processes inside the system boundaries). The allocated environmental impact $EI_{i,j}$, for the co-product *i* produced at the subdivision point *j*, is expressed by eq.(1):

$$EI_{i,j}=\alpha_{i,j}\cdot EI_j \tag{1}$$

which finally gives the total environmental impacts

$$EI_{total}=\sum_j EI_j=\sum_j\sum_i EI_{i,j}$$

where EI_j is the environmental impact of a specific category caused at the subdivision point *j* and $\alpha_{i,j}$ is the partitioning coefficient expressed by the following equation:

$$\alpha_{i,j}=\frac{y_{i,j}\cdot c_i}{\sum_{i=1}^{mj} y_{i,j}\cdot c_i} \tag{2}$$

where $y_{i,j}$ is the flow of the co-product *i* produced by at the subdivision point *j*,(e.g., expressed in mass, energy, volume etc.), and c_i is its specific allocation factor used for partitioning related to the flow unit (e.g., MJ/unit or €/unit). It should be noted that in the "black box" approach for the system presented in Figure 1, n=1 and $m_j=m_1$=number of final products and $EI_j=EI_1=EI_{total}$.

When applying the substitution method, the first step is to define the determining (main) product based on criteria (Weidema, 2001) like mass flow, market value or other specific case rules. Then, the (dependent) co-products are investigated by defining their way of utilization (e.g treated as waste streams or by displacing other products) and the displaced equivalent products from the Ecoinvent database.

3. Impact of Allocation Scenarios

3.1. Case Study: The biodiesel platform refinery

For the selected case study, biodiesel is the main product. Glycerol is the dependent, fully utilized co-product which can be further treated through various alternative conversion processes into other co-products. Four such scenarios for the utilization of glycerol are considered in this study, namely: (S-1) biodiesel and glycerol, (S-2) biodiesel and biogas, (S-3) biodiesel and propylene glycol, (S-4) biodiesel, syngas and electricity, (Figure 2).

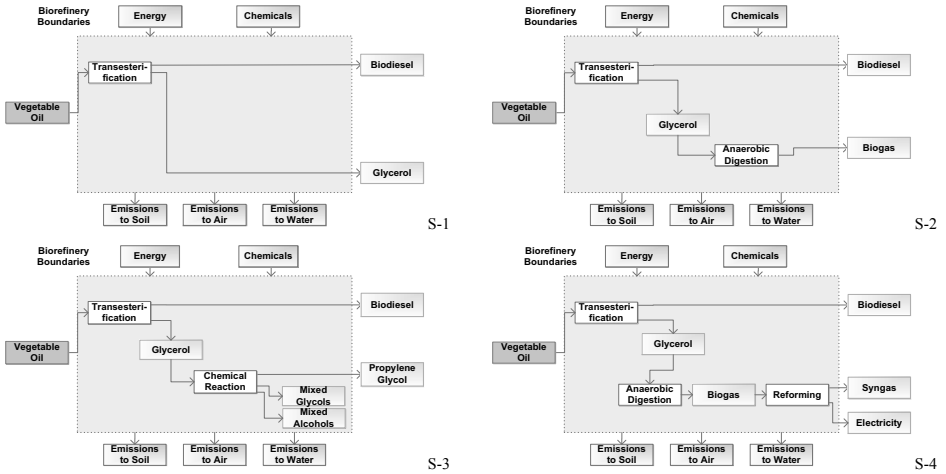

Figure 2 Configuration schemes for the scenarios included in the study

Note: S-3: mixed glycols and alcohols are assumed to be treated as waste streams due to low degree of purity, S-4: electricity is produced by heat recovery and exploitation of high pressure steam in a steam turbine)

Tables 1 and 2 show the partitioning factors and the displaced processes used in the scenarios described above for the two allocation and the substitution approaches.

Table 1 Specific values and partitioning coefficients used in the different allocation approaches

	Subdivision points (n)	Products (i)	$y_{i,n}$	c_i		Mass /Thermal Allocation	Economic Allocation
						$\alpha_{i,n}$	$\alpha_{i,n}$
S-1	n=1 transesterfication	i=1 biodiesel	$y_{1,1}$= 999.8 kg	c_1= 0.37€/kg		$\alpha_{1,1}$= 0.90	$\alpha_{1,1}$= 0.80
		i=2 glycerol	$y_{2,1}$= 113.3gk	c_2= 0.79€/kg		$\alpha_{2,1}$= 0.10	$\alpha_{2,1}$= 0.20
S-2	n=1 transesterfication	i=1 biodiesel	$y_{1,1}$= 999.8kg	c_1= 0.37€/kg		$\alpha_{1,1}$= 0.90	$\alpha_{1,1}$= 0.80
		i=2 glycerol	$y_{2,1}$= 113.3kg	c_2= 0.79€/kg		$\alpha_{2,1}$= 0.10	$\alpha_{2,1}$= 0.20
S-3	n=1 transesterfication	i=1 biodiesel	$y_{1,1}$= 999.8kg	c_1= 0.37€/kg		$\alpha_{1,1}$= 0.90	$\alpha_{1,1}$= 0.80
		i=2 glycerol	$y_{2,1}$= 113.3kg	c_2= 0.79€/kg		$\alpha_{2,1}$= 0.10	$\alpha_{2,1}$= 0.20
S-4	n=1 transesterfication	i=1 biodiesel	$y_{1,1}$= 999.8kg	c_1= 0.37€/kg		$\alpha_{1,1}$= 0.90	$\alpha_{1,1}$= 0.80
		i=2 glycerol	$y_{2,1}$= 113.3kg	c_2= 0.79€/kg		$\alpha_{2,1}$= 0.10	$\alpha_{2,1}$= 0.20
	n=2 steam reforming	i=1 syngas	$y_{1,2}$= 86.1kg	c_1= 5.2MJ/m^3, c_2= 2.75MJ/kg steam$_{eq}$	c_1= 0.14 €/m^3, c_2=0.097€/kWh$_{el}$	$\alpha_{1,2}$= 0.60	$\alpha_{1,2}$= 0.85
		i=2 electricity	$y_{2,2}$= 0.02MWh			$\alpha_{2,2}$= 0.40	$\alpha_{2,2}$= 0.15

Note:the subdivision points with one product are not included in the table

In this assessment, natural gas (gas turbine) derived electricity is assumed in the displacement procedure in order to take into account the fossil best available technologies having a GHG emission factor of 0.24 kg $CO_{2\text{-eq.}}$/kWh, while coal derived electricity has a much higher factor, i.e. 1.08 kg $CO_{2\text{-eq.}}$/kWh (average for UCTE countries, i.e. countries included in the Union for the Co-ordination of the Transmission

of Electricity). The GHG emission savings of the biorefinery systems would therefore be greater if coal electricity is displaced.

Table 2 Specific CED and GHG emissions of the displaced processes to biorefinery products

Biorefinery product	Displaced Products	LCIA values	
	Process Name (Ecoinvent V2)	GWP	CED
Glycerine	Glycerine, from epichlorohydrin, at plant/RER	4.52	74.86
Biogas	Biogas, production mix, at storage/CH S (d=1.1kg/m3)	0.53	4.1
Electricity from steam turbine	Propylene glycol, liquid, at plant/RER	4.06	78.76
Synthetic gas	Synthetic gas, production mix, at plant/CH (d=1.15kg/m3)	0.022	8.62
Electricity from steam turbine	Electricity (Natural gas, burned in gas turbine/GLO)	0.24	4.22

Table 3 shows a sample of results for the scenarios described above for the three allocation approaches and three life cycle impact assessment methods.

Table 3 Summary of selected results

Biorefinery Configurations		Mass Allocation			Economic Allocation			Substitution		
		GWP	CED	Recipe	GWP	CED	Recipe	GWP	CED	Recipe
S1	Biodiesel	2.20	17.61	0.00103	1.95	15.65	0.00092	1.93	11.09	-0.02724
	Glycerol	2.20	17.61	0.00103	4.31	34.54	0.00202	DP	DP	DP
S2	Biodiesel	2.20	17.61	0.00103	1.95	15.65	0.00092	2.44	19.78	0.00234
	Biogas	3.63	29.68	0.01252	6.83	55.35	0.01347	DP	DP	DP
S3	Biodiesel	2.20	17.61	0.00103	1.95	15.65	0.00092	2.18	14.21	-0.00382
	Propylene Glycol	3.62	36.33	0.00683	6.41	58.72	0.00814	DP	DP	DP
S4	Biodiesel	2.20	17.61	0.00103	1.95	15.65	0.00092	2.55	20.70	0.00207
	Syngas (1bara, 45ºC)	2.51	22.30	0.00753	4.20	35.80	0.00803	DP	DP	DP
	Electricity (per kWh)	7.42	65.77	0.02221	12.39	105.60	0.0236915	DP	DP	DP

Note: CED-fossil (MJeq/kg), GWP (kgCO2eq/kg) and RECIPE-Water depletion (m^3/kg) for the three allocation approaches

3.2. Correlations of allocation approaches

In order to investigate the variation of LCA metrics when applying different allocation approaches, correlations for LCA indicators were performed for a sample of 31 biomass based processes comprising (after combinations) 53 different configuration schemes. As shown in Figure 3, the correlations can be rather weak, which means that the selection of allocation approach has an important effect in the values of indicators. Some pairs were found to correlate better than others (GWP and CED for mass versus economic allocation, R^2 ranges from 0.5 to 0.8). Correlations including substitution method (Figures 3a, 3b) presented lower values. ($R^2 < 0.5$) this can be due to ambiguity in some cases in the determining of the displaced products

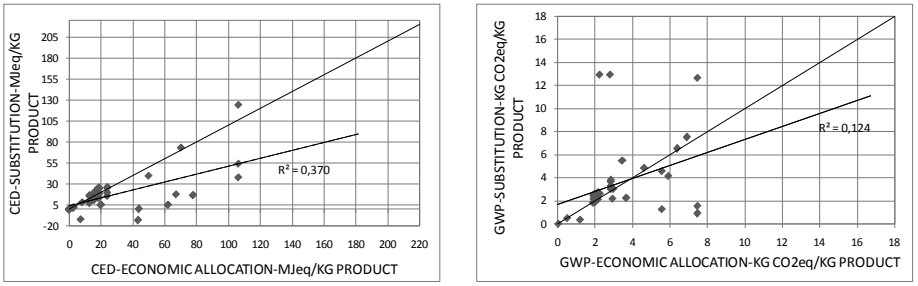

Figure 3a, 3b Cases of indicators and allocation approaches where correlation is weak

4. Conclusions and Outlook

This study investigates the effect of key parameters on the results of LCA metrics for products which are co-produced in cases of multifunctional systems. One critical parameter is the synthesis of the biorefinery configuration (i.e. the combination of the co-producing processes included in system boundaries and the type of co- and by products which attribute benefits to the main products by displacing conventional production lines). This dimension was studied in conjunction with three allocation approaches which were tested with respect to the variation of the resulting LCA metrics and the degree of subjectivity that they give to the final values.

This study is a part of an LCA database for biomass based products (chemicals, energy carriers, power) which is under development. A generic representation of the database components is shown in Figure 4.

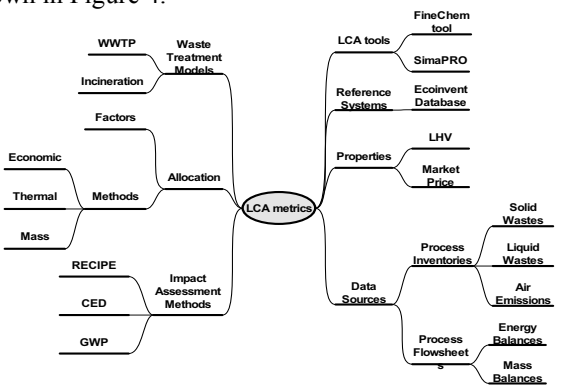

Figure 4 Components of the LCA database

LCA metrics are based on gate-to-gate inventory analysis including data from process flowsheets for mass and energy balances gathered from literature references and pilot plants. In addition, the use of existing life cycle databases (e.g., Ecoinvent database, versions 2 and 3) and tools (e.g., Simapro 8.0.2) was necessary to fill in the unavoidable data gaps. Given the variety of production paths and the number of assumptions made, LCA assessments are accompanied by the information (methodological and technical) required to provide answers on the level of individual products' scale of analysis offering the practitioners the option to select the values which fit better to the goal and scope of their study according to the adopted allocation approach.

References

F. Cherubini, G. Jungmeier., 2010, LCA of a biorefinery concept producing bioethanol, bioenergy, and chemicals from switchgrass, International Journal of Life Cycle Assessment, 15, 53–66

Weidema, 2001, Avoiding co-product allocation in life-cycle assessment, Journal of Industrial Ecology 4, 11-33

Francesco Cherubini, Anders Hammer Strømman Life cycle assessment of bioenergy systems: State of the art and future challenges, Bioresource Technology 102 (2011) 437–451

Brander, M., Tipper, R., Hutchison, C, Davis, G., Technical Paper, Consequential and Attributional Approaches to LCA: a Guide to Policy Makers with Specific Reference to Greenhouse Gas LCA of Biofuels, April 2008

Ecoinvent database, Data from V2, V3

European Commision (EC), The BREW project, In Growth Programme (DG Research), Ed. 2006

Krist V. Gernaey, Jakob K. Huusom and Rafiqul Gani (Eds.), 12th International Symposium on Process Systems Engineering and 25th European Symposium on Computer Aided Process Engineering.
31 May – 4 June 2015, Copenhagen, Denmark

Sustainable Process Design under uncertainty analysis: targeting environmental indicators

Carina L. Gargalo[a], Gürkan Sin[a*]

[a] *CAPEC-PROCESS, Department of Chemical and Biochemical Engineering, Technical University of Denmark, Building 229, DK-2800 Lyngby, Denmark*
**gsi@kt.dtu.dk*

Abstract

This study focuses on uncertainty analysis of environmental indicators used to support sustainable process design efforts. To this end, the Life Cycle Assessment methodology is extended with a comprehensive uncertainty analysis to propagate the uncertainties in input LCA data to the environmental indicators. The resulting uncertainties in the environmental indicators are then represented by empirical cumulative distribution function, which provides a probabilistic basis for the interpretation of the indicators. In order to highlight the main features of the extended LCA, the production of biodiesel from algae biomass is used as a case study. The results indicate there are considerable uncertainties in the calculated environmental indicators as revealed by CDFs. The underlying sources of these uncertainties are indeed the significant variation in the databases used for the LCA analysis. The extended LCA procedure is flexible and generic and can handle various sources of uncertainties in environmental impact analysis. This is expected to contribute to more reliable calculation of impact categories and robust sustainable process design.

Keywords: sustainable process design, LCA, uncertainty analysis, Monte Carlo, Algae biodiesel, Database.

1. Introduction

The assessment and design of sustainable chemical and biochemical processes is a complex multi-criteria and multi-objective decision-making problem, not only regarding the multi-level evaluation, but also due to the significant amount of input data required for the analysis, which may come from different sources with various degrees of uncertainties (Björklund, 2002). To support sustainability analysis, sustainability indicators (Azapagic & Perdan, 2000) have been proposed along the years as a performance measurement tool. They assist the user in two fronts, (i) analysing the performance of already built production plants, and (ii) in early stage-design, finding a solution that relatively minimizes environmental and social impact while maximizing the company's economic profit. However, the uncertainty on the input data and their impact on the decision-making procedure have not yet been entirely addressed (Björklund, 2002).

In order to characterize and quantify sources of uncertainty and their propagation to the decision-making process, a computer-aided framework for sustainable process design and assessment under economic uncertainty has been developed. It explores the economic analysis under deterministic and uncertainty conditions and proposes new design alternatives to be validated by a risk reduction strategy.

As a complementary part of the framework, the present work proposes an extended methodology for environmental life-cycle assessment (LCA) under uncertainty (Figure 1). In particular, the focus is to develop a generic and flexible methodology that systematically identifies the sources of uncertainties and quantify their impact on the environmental indicators and sustainable process analysis. Life cycle assessment (LCA) has been broadly used to (i) identify the significant environmental indicators in product systems and, (ii) to assess and compare the environmental performance of different processes (Guo & Murphy, 2012). The environmental results are often estimated based on deterministic models, where one uses a defined model (input-output mass and energy balances) and 'nominal' values for involved parameters and input data. The nominal values of parameters/data are usually taken from an LCA database. This type of analysis leads to results as point estimates conditional to the nominal set of values used in the analysis and fails to integrate the variability and uncertainty intrinsic to LCA (Lloyd & Ries, 2007). Therefore, different uncertainty categories have been identified as, (i) parameter uncertainty, (ii) scenario uncertainty and, (iii) model uncertainty (Winner, 2011). Different approaches have been proposed to quantify uncertainty in LCA (Lloyd & Ries, 2007), nonetheless, there is still a lack of a systematic approach when determining data quality, quantifying the uncertainty on the input data, and its propagation into the decision-making process (Björklund, 2002).
In this work, the life cycle principles proposed by the Environmental Protection Agency are used as a basis and extended by adding the steps for Monte Carlo based comprehensive uncertainty analysis. The extended LCA methodology aims to assist the user to identify and characterize the sources of input uncertainties and their propagation into the output environmental indicators, etc. Once the uncertainties in the output are quantified, its impact on sustainability analysis and ranking of alternatives for the decision-making is then analysed. A step-by-step explanation of the methodology is presented in the next section.

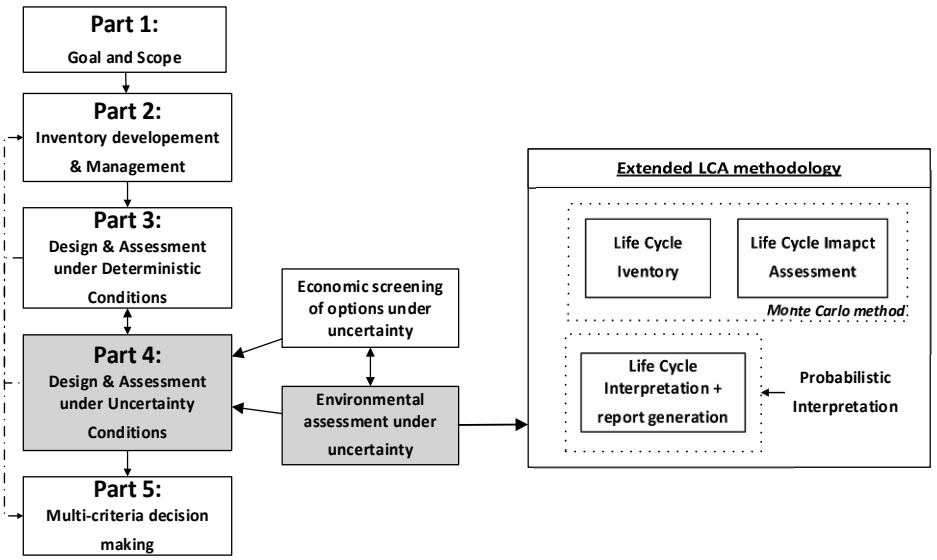

Figure 1: Framework for sustainable process design under uncertainty: focusing on the Extended LCA methodology

2. LCA extended methodology

The methodology incorporates uncertainty analysis by using the Monte Carlo technique with Latin Hypercube sampling from input uncertainty domain. A step-by-step guide through the methodology is presented as follows by applying it to two alternatives for the production of biodiesel from algae. It is noted that the alternatives being tested were identified with a first stage economic screening.

Part A: *Goal and scope*

The goal is to identify the most promising sustainable solution for the production of biodiesel from algae biomass. As mentioned, two alternatives were identified based on a first stage economic screening, they are differentiated by the transesterfication methods used, (A) H_2SO_4/Methanol and, (B) KOH/methanol (Cheali et al., 2015).

In this step, the problem statement is formulated. The following three questions were posed to of the extended LCA study: (i) which process causes the least overall environmental impact? (ii) what are the sources of uncertainty involved in the study? and, (iii) how do the uncertainties in the inputs affect the multi-criteria decision making for sustainable process design?

Part B: *Life Cycle Inventory*

This is the second stage of the extended LCA methodology and it comprised of four steps defined as follows:

Step 1: definition of the system boundaries

The boundaries were drawn around the manufacturing process including the emissions related to the utilities system.

Step 2: Database/inventory of inputs and outputs

Mass balances, energy balances and equipment duties were collected according to the system boundaries that have been defined.

Step 3: Identification and characterization of the source of uncertainty

This step is the first stage of the Monte Carlo technique and the objective is to identify the source(s) of uncertainty and characterize it through an appropriate probability distribution function. Two types of sources of uncertainty were identified: (i) process operation scenarios which refers to the different design scenarios considering the availability of fuel type for utility consumption (different energy content and composition), therefore leading to different load of gaseous emissions; and (ii) parameter uncertainty. The latter type of uncertainties is perhaps the more dominant and challenging in LCA analysis. These uncertainties refer to LCA database that compile the science-based characterization factors that are used to convert component-based inventory data into relevant categories of midpoint impact. Different databases may have different estimation/experimental values for these characterisation factors (some of them may stem from geographical/local situation, and yet some other may come from different experimental sources/measurement errors). In this study, the nominal values of the characterization factors were retrieved from an open-source database, IMPACT 2002+, which models are reported in (Humbert et al., 2002). Furthermore, due to the limited information, uniform distribution was assumed to characterize the input uncertainties. The upper and lower bound of the uniform distribution are specified by performing an analysis of data variability reported across 6 different open-source LCA databases (CML-IA-2013, *Recipe*, *IChemE*, IMPACT 2002+, IMPACT World+).

Based on the extent of variability across different databases, low (5%), medium (25%) and high (50%) level of variation around the nominal values are assigned (Sin et al., 2009).
As a motivating example, definition of the uniform distribution of the characterization factors used to estimate the photochemical oxidation potential (POP) for four of the components involved in the processes are presented in Table 1. This uncertainty definition in the input database is performed for all the relevant components in system.

Table 1: Nominal value, upper and lower bound of the uniform distribution for the characterization factors used to estimate the POP.

	Nominal/average value (IMPACT 2002+)	Lower bound	Upper bound
methanol	0.132	0.066	0.198
glycerol	0.861	0.431	1.292
ethanol	0.392	0.196	0.588
hexane	0.479	0.240	0.719
N_2O	0.700	0.350	1.050

Step 4: Latin Hypercube sampling
The output from step 3 is a definition of input uncertainty domain which is *NxN* space where N refers to total number of components (products, intermediates, raw material, etc.) in the system. In this study, *N* was 17. Latin Hypercube Sampling technique was then used to generate random samples from the input uncertainty domain. Each sample is then used to calculate the LCA model output which is the environmental impact categories. It is noted that since the correlation matrix between input sources of uncertainties is not known, instead no correlation was assumed for the sampling.
LHS technique provides a more effective coverage of uncertainty space domain with a relatively small number of sampling as compared to random sampling (the difference in the number of sampling is an order of magnitude). More information on the LHS technique and correlation control can be obtained from (Helton & Davis, 2003; Sin et al., 2009) and (Iman & Conover, 2007), respectively.
In the present case study, 200 random samples were generated by LHS for each one of the characterization factors, collected for each one of the components in the system.

Part C & Part D: *Life cycle Impact Assessment & Life Cycle Interpretation and report generation*
In the previous section the data inventory is completed, and at this stage, the user is guided towards the estimation of relevant impact categories. The potential environmental impact categories are calculated by equation (1) (EPA, 2006) as follows.

$$\text{Potential Environmental Impact}_x = \sum_i CF_i \times F_i \qquad (1)$$

where, *x* represents a certain category of impact, *i* a given component and *CF* represents the nominal value of the characterization factors that convert the component flowrates (F_i) into potential environmental impacts used to analyze the environmental performance of the processes.
For each LHS sample, eq. 1 will be calculated resulting in 200 estimates for each impact category, *x*. The distribution of impact category x, is then represented by building a cumulative distribution function (CDF). The CDF provides the basis for a probabilistic interpretation meaning that we have now a probability level for every potential environmental impact category considered relevant. To interpret the results, the impact

categories estimate that corresponds to 95% confidence level is reported and used for further analysis of process alternatives. In this way, the uncertainty analysis is complete by providing a more robust and reliable estimate of the impact category.
The cumulative distribution function of the model outputs is obtained by rewriting equation (1), where *CF* represents the sample space *N* instead of nominal values.

As illustration of the extended LCA methodology, two categories of impact (POP and GWP) were selected to evaluate and compare the environmental performance of the alternatives A and B. The y-axis in CDF reads probability of x being less than an equal to a certain value X, Pr(x < = X), while x-axis refers to the actual values of the impact categories. The range of the x-axis indicates how large the uncertainty is (the larger the range of x-axis, the larger the uncertainty). The shape of CDF function (linear, S-shape), indicates the probability of observing X. Linear CDF means that input uncertainty propagates linearly to the outputs, while S-shape CDF functions indicate input uncertainties propagate in a non-linear fashion to the output. In this CDF plot, the mean value is indicated by the probability level at 0.5 (red arrows in the figures 2 to 5 below).
As a summary of this CDF plot, we read the impact category estimates that correspond to a probability of 0.95 (black arrows in the figures 2 to 5 below). For example, for the photochemical oxidation potential (Figures 2 and 3), the upper bound (95% likelihood) is approximately 0.20 and 0.41 kg ethylene eq./ kg of biodiesel produced for alternative (A) and (B), respectively. Therefore, there is a 95% likelihood that if the plant is built the POP will potentially have values lower or equal to the upper bound identified.
Likewise, the global warming potential (Figures 4 and 5) has the upper bound equal to 4.77 and 4.93 kg CO_2 eq./ kg of biodiesel produced for alternative (A) and (B), respectively.
The decision between these two alternatives can be taken based on 0.95 probability and confidence in the estimated impact values thereby providing an improvement on the traditional LCA analysis that relies only on a single point analysis. In this case, for both impacts (POP and GWP), alternative A is a better alternative considering all the input uncertainties that went into their calculations.

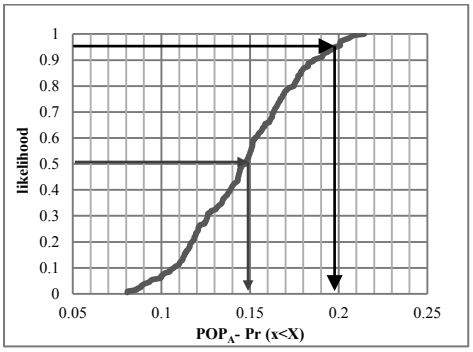

Figure 2: *Alternative A* - Cumulative distribution function for the Photochemical Oxidation Potential (POP), upper bound identification for 95% likelihood.

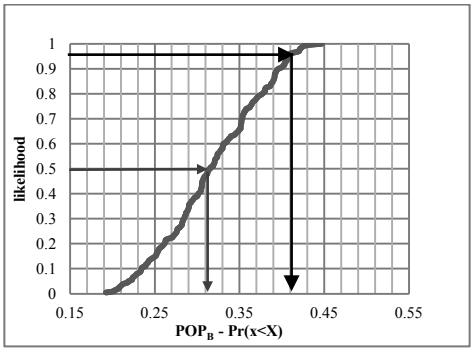

Figure 3: *Alternative B* - Cumulative distribution function for the Photochemical Oxidation Potential (POP) , upper bound identification for 95% likelihood.

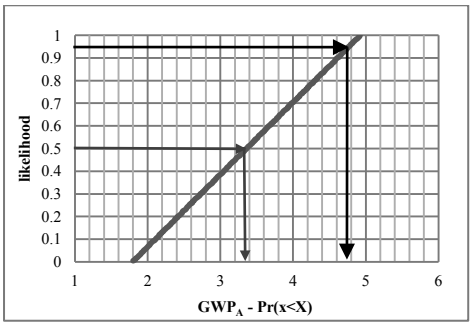

Figure 4: *Alternative A* - Cumulative distribution function for the Global Warming Potential (GWP) , upper bound identification for 95% likelihood.

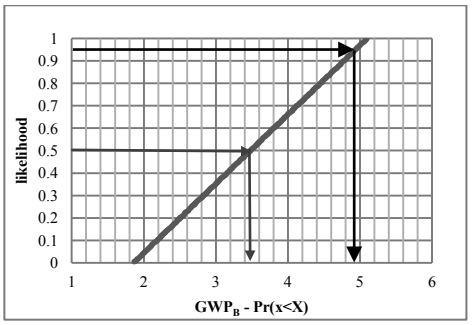

Figure 5: *Alternative B* - Cumulative distribution function for the Global Warming Potential (GWP) , upper bound identification for 95% likelihood.

3. Conclusions

In this study, the LCA methodology of EPA is extended with a comprehensive uncertainty analysis. Monte Carlo technique with Latin Hypercube sampling was used for the uncertainty analysis. To interpret the results, a probabilistic framework that uses 95% probability level of the expected value of the impact category is used.

The biodiesel production from algae biomass was used to highlight the methodology's main features. The methodology successfully quantified the uncertainties in the impact categories and is expected to contribute to performing more reliable and robust sustainability analysis of process alternatives.

References

Azapagic, A; Perdan, S (2000). Indicators of sustainable development for industry: A general framework. Process Safety And Environmental Protection; 78: 243-261.

Björklund, A. E. (2002). Survey of Approaches to Improve Reliability in LCA, *7*(2), 64–72.

Cheali, P., Vivion, A., Gernaey, K. V., & Sin, G. (2015). Algae Biorefinery Processing Networks: Optimal Design of Protein, Ethanol and Biodiesel Production. Computer aided chemical engineering, in press.

EPA (2006). *Life cycle assessment: principles and practice*, EPA/600/R-06/060. US Environmental Protection Agency/Office of research and development.

Guo, M., & Murphy, R. J. (2012). LCA data quality: sensitivity and uncertainty analysis. *The Science of the Total Environment*, *435-436*, 230–43. doi:10.1016/j.scitotenv.2012.07.006

Helton, J. C., & Davis, F. J. (2003). Latin hypercube sampling and the propagation of uncertainty in analyses of complex systems. *Reliability Engineering & System Safety*, *81*(1), 23–69. doi:10.1016/S0951-8320(03)00058-9

Humbert, S., Schryver, A. De, Margni, M., & Jolliet, O. (2002). IMPACT 2002 + : User Guide. Lausanne: Swiss Federal Institute of Technology Lausanne (EPFL). Retrieved from http://www.quantis-intl.com/pdf/IMPACT2002_UserGuide_for_vQ2.2.pdf

Iman, R. L., & Conover, W. J. (2007). A distribution-free approach to inducing rank correlation among input variables. *Communications in Statistics - Simulation and Computation*, *11*(3), 311–334. doi:10.1080/03610918208812265

Lloyd, S. M., & Ries, R. (2007). Characterizing, Propagating and Analyzing Uncertainty in Life-Cycle Assessment: A Survey of Quantitative Approaches, *11*(1).

Sin, G., Gernaey, K. V, Neumann, M. B., van Loosdrecht, M. C. M., & Gujer, W. (2009). Uncertainty analysis in WWTP model applications: a critical discussion using an example from design. *Water Research*, *43*(11), 2894–906. doi:10.1016/j.watres.2009.03.048

Winner, D. A. (2011). Exposure Factors Handbook: 2011 Edition; Release of Final Report. *Federal Register*, *76*(191).

Krist V. Gernaey, Jacob K. Huusom and Rafiqul Gani(Eds.), 12th International Symposium on Process Systems Engineering and 25th European Symposium on Computer Aided Process Engineering.
31 May – 4 June 2015, Copenhagen, Denmark

Optimization of LNG Plant Operating Conditions to Anticipate Leaner Feed Gas by Steady State Process Simulation

Ferry Adhi Perdana, Johan Anindito Indriawan

Badak LNG,Plant site, Bontang 75324, Indonesia
ferry@badaklng.co.id, indriawan@badaklng.co.id

Abstract

Badak LNG has operated for producing LNG almost 30 years, with total production capability of 22.5 million metric ton LNG per annum. Badak LNG has eight (8) LNG Trains which was designed with specific range of feed gas composition. In the future, regarding with exploration of new gas wells, it is predicted that new gas wells have leaner gas composition compared to current condition. It certainly could impact to performance of LNG plant especially in refrigeration and liquefaction system. An evaluation is required to find out the potential restrictions and new operating condition when liquefying the leaner gas. By using simulation model of LNG plant, the effect of lean gas basically could be predicted. The simulation is firstly validated by using the actual performance data and used to simulate the leaner gas with optimization methods. The optimal model simulation uses specific power as objective function, the refrigerant flow rate and composition as operating variables while the existing equipment's capacity is used as parameter constraints.

The evaluation result concludes liquefying the leaner gas will need more refrigerant flow rate to keep minimum temperature approach at Main Heat Exchanger, so the compressor duty and specific power also increases while LNG product flow rate decreases. The inlet temperature of refrigerant compresor is potentially colder than minimum specification of -50 ^{o}C, it will be a constraint when processing the leaner gas. But, optimizing the operating condition such as flow rate, pressure and composition of refrigerant, can reduce the compressor duty and specific power while temperature inlet compressor can still meet the specifiation.

Keywords: Optimization, LNG, leaner gas, Process Simulation.

1. Introduction

Natural Gas is the fossil fuel which has growing consumption fast. At present, the utilization of natural gas as fuel in power generation increases around 30 % and it is predicted growing to 37 % in 2030 (Hatcher and Khalilpour, 2012). Practically, in order to make easier in transportation and storing of the natural gas, conversion of natural gas to Liquefied Natural Gas (LNG) is one of the recommended methods.

Natural gas liquefaction is a process conversion from gas to liquid phase. In order to produce LNG, the sensible and latent heat of natural gas is removed to gain the liquid phase with cryogenic temperature of -160 ^{o}C at atmospheric pressure. This process can reduce the natural gas volume to 1/600 times. LNG plants are designed to handle a certain range of feed composition. However, during operation, feed gas composition can change due to exploration of new gas wells. Based on the feed gas predictions, CH_4 content in the feed gas tends to increase in the future (see table 1). When the feed gas becomes leaner, the specific power will be greater (Zhang et al, 2012). It could affect to performance and operating condition of process unit such as liquefaction unit, propane refrigeration units and mixed component refrigeration (MR) unit.

There are several studies about process optimization of natural gas liquefaction. Aspenlund et al., (2010) reported the optimization of a natural gas liquefaction process by using aspen Hysys with Tabu Search method and Nelder Mead Downhill Simplex (NMDS) to reduce the required number

of simulations. Hatcher and Khalilpour (2012) reported about the identification of the most appropriate objective function to increase the efficiency of the natural gas liquefaction process. Gao et al. (2009) optimized the process of liquefying of Coal Bed Methane using C3MR process by varying the nitrogen content in the feed gas. Lee et al. (2002) reported the new method for design optimization of multi-component refrigeration system which combines between mathematical and thermodynamics to obtain the optimal composition of refrigerant. These studies commonly discuss the optimization of process conditions, while only a few studies discuss the optimization of operating conditions with limits on the installed equipment capacity. Jensen and Skogestad (2009) study the optimal operation for simple LNG process, namely the PRICO process with the objective function to achieve the minimum economic cost.

Table 1. Prediction of Feed Gas Composition in mole fraction

Composition	Years	
	X(current)	Y(future)
N_2	0.001	0.001
CH_4	0.914	0.955
C_2H_6	0.041	0.023
C_3H_8	0.030	0.014
i-C_4H_{10}	0.006	0.003
n-C_4H_{10}	0.007	0.003

While, this study will discuss the optimization of operating conditions of LNG plant using C3MR process and varying the feed gas composition. For the optimization process, this study uses an objective function of minimum specific power while the installed equipments capacities are utilized as constraints.

2. Simulation Details

The simulation and optimization are performed with Hysys (Aspen Technoloy, Inc.) and uses Peng-Robinson equation of state.

2.1. Liquefaction Process

Prior to entering the main heat exchanger, the impurities (CO_2, moisture and heavier hydrocarbon) are removed from the feed gas in the upstream process. Feed gas is pre-cooled with propane refrigeration to -35 ^oC before it is liquefied in the main heat exchanger.

In propane refrigeration unit, propane is compressed to 15 kg/cm^{2}a. It is then de-superheated and condensed by using sea cooling water. Afterward, propane is expanded to high pressure level of 8 kg/cm^{2}a and used to cool the mixed component refrigerant and feed gas. Furthermore, propane is expanded to medium pressure level of 4 kg/cm^{2}a for cooling mixed component refrigerant and feed gas also. Finally, propane is expanded to low pressure level of 1.5 kg/cm^{2}a for partial condensing the mixed component refrigerant and feed gas pre-cooling. The vaporized propane is then sucked by three stages propane compressor (see figure 1).

Meanwhile, in mixed component refrigeration unit, MR refrigerant is partially condensed using propane until -35 ^oC temperature. MR vapor and MR liquid, then, goes to the main heat exchanger via different tube circuit. In the warm bundle, MR liquid is subcooled until -127 ^oC and expanded by JT valve, then it is sent back to main heat exchanger as cooling medium for feed gas, MR vapor and MR liquid. Whereas, after MR vapor is condensed in warm bundle, it will be subcooled in the cooled bundle until -147 ^oC and expanded by JT valve. It is then sent back to main heat exchanger as cooling medium for feed gas and MR vapor. After providing cooling duty, the superheated MR will flow back to suction 1st MR compressor. While, after feed gas is condensed and subcooled in the main heat exchanger, it will be expanded to 1.27 kg/cm^{2}a pressure and -158 ^oC temperature (see figure 1).

2.2. Calculation and Optimization method

This study takes an assumption the impurities (CO_2, iC_5H_{12}, nC_5H_{12} and C_6H_{14}) have been removed. Therefore, the composition of the incoming feed gas into the main heat exchanger can be

predicted as shown in Table 1. This study also doesn't consider the Benzene, Toluene and Xylene (BTX) content in feed gas. The simulation model is developed by using current feed gas composition and validated with actual operating conditions during the plant performance test as a base case.

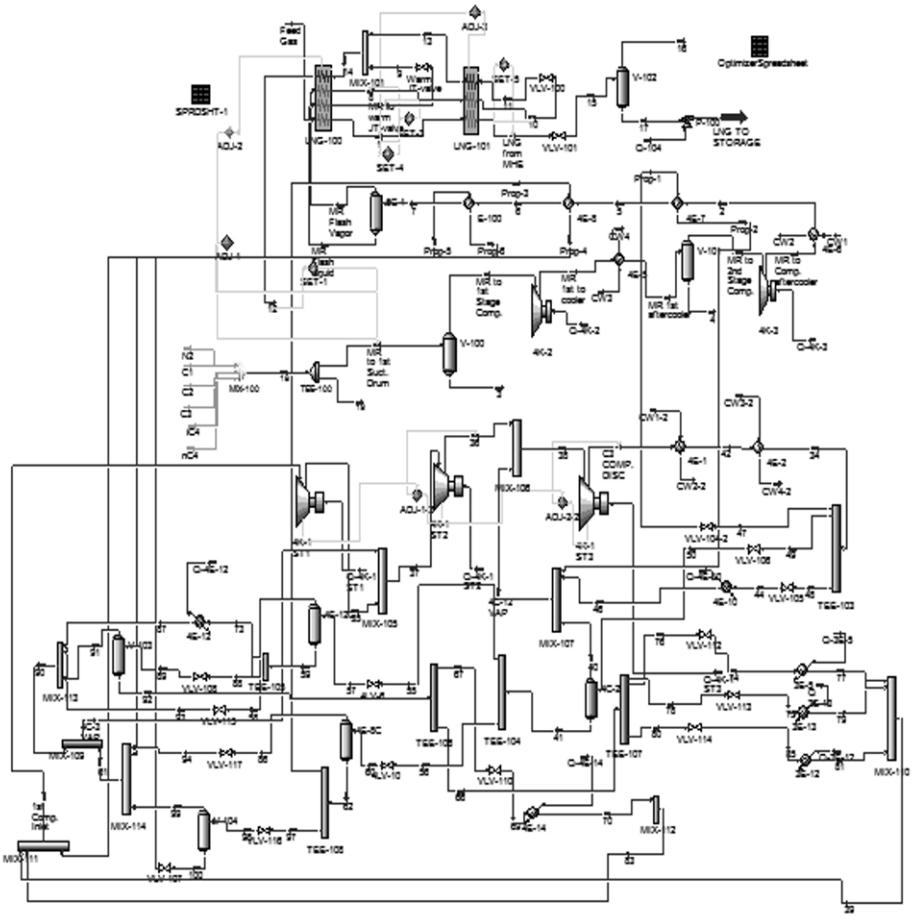

Figure 1. Simulation Model of C3MR Process

This study uses the actual capacity of existing equipment as constraint. It refers to the equipment data sheet such as compressor performance curves, sizing of sea water exchanger. Meanwhile, for the heat exchangers which are not directly related to the liquefaction are assumed have a fixed load.

2.2.1. Manipulated Inputs

There are five manipulated inputs such as MR flow rate, MR evaporating Pressure, MR composition, C3 low level Pressure, C3 medium level Pressure

2.2.2. Operational Constraints

In general, there are some constraints that must be satisfied during normal operation.

- Compressor power, capacity, surge and rotational speed: we use the actual performance curve of C3 and MR compressor
- Heat exchanger: we use overall heat transfer (UA) of sea water exchanger based on the equipment's data sheet.

- Suction temperature of MR Compressor is limited with temperature alarm low of -45 ^{o}C.
- Minimum temperature approach at main heat exchanger is 2 ^{o}C refer to the normal operation condition

It is assumed that sea water temperature steady at 30 ^{o}C, the feed gas temperature outlet of C3 pre cooler is -35 ^{o}C and feed gas has flow rate of 22,642 kmol/h,

2.2.3. Formulation of Object function

The optimization is carried through on the basis of the calculation of specific power which is one of the most important factors of liquefaction process performance. It can be calculated as Eq. (1).

$$w_s \left(\frac{HP}{mmBtu}\right) = \frac{1{,}341\ x\ w}{0.948\ x\ (HHV\ x\ q)_{LNG}} x\ 1{,}000{,}000 \quad (1)$$

Where, w is the sum of power consumption (kW) of MR compressor and C3 compressor, q is mass flow rate of LNG product (kg/h) and HHV is higher heating value (kJ/kg).

3. Result and Analysis

3.1. Effect of Feed Gas Composition to LNG Plant Performance

The simulation is an approach to know an effect of the feed gas composition to the LNG plant performance particularly propane refrigeration unit and MR unit. The simulation compares the performance of LNG plant between the two feed gas compositions as below:

- Case 1: feed gas with 90.3 % methane as base case.
- Case 2: feed gas with 95.5 % methane as the leanest feed gas.

For comparison, some parameters are kept constant for both cases such as feed gas flow rate of 22,642 kmol/h, MR composition, minimum temperature approach (MTA) in main heat exchanger. The result shows that the compressor duty at case 2 is greater than case 1, because a gap between cold composite curve and hot composite curve at case 2 is smaller than case 1 hence in order to shift the cold composite curve or keep remains MTA, it requires more MR flow rate. Since the MR flow rate is higher, the compressor duty becomes greater. In addition, suction temperature of 1st MR compressor at case 2 is also very cold, -55 ^{o}C. It is much lower than the specification of f -45 ^{o}C. Case 2 also produces LNG rate lower than case 1 because case 2 has more light component and it will flash when LNG product is expanded to 1.27 kg/cm^{2}a. Since the compressor duty increases while the LNG product rate decreases, thus the specific power of case 2 is higher than case 1.

Table 2 Comparison of Compressor Duty

Description	Duty of C3 Comp. (MW)	Duty of MR Comp. (MW)	Total duty (MW)
Case 1	42.24	77.16	119
Case 2	44.53	82.99	128

Table 3. Comparison of Specific power

Description	LNG Product rate (kg/h)	Heating value (kJ/kg)	Specific power (HP/mmBtu)
Case 1	380,729	49,289	9.00
Case 2	352,880	49,648	10.32

Based on the above evaluation, liquefying lean gas will require more refrigerant flow rate, so that the compressor duty and the specific power will also increase. The suction temperature of MR compressor is lower than specification, it will be the constraint. Therefore, the optimization of operating variable is required to achieve the minimum specific power and the suction temperature of MR compressor meet with the specification.

3.2. Optimization of Operating Variables at LNG Plant

From the evaluation, it shows that there will be any limitation for processing the leaner gas which is suction temperature of MR compressor and higher compressor's load. Therefore, in order to overcome those problems, one of the efforts is by optimizing the operating variables instead of

modifying the existing equipment. In the optimization process, there are some constraints which must be considered such as the capacity of the compressor, the heat transfer area, the minimum temperature approach of main heat exchanger and temperature low alarm of suction MR compressor.

Basically, in order to achieve the objective of optimization is to keep at distance between cold composite curve and hot composite curve to avoid a cross temperature at main heat exchanger with minimum cooling duty to obtain the lowest specific power.

Table 4. Comparison of Compressor Duty and Specific power Before and After Optimization

Description	Before	After
Suction temperature of MR Compressor (^oC)	-55.6	-42.5
MR Compressor duty (MW)	83.3	81.86
Propane Compressor duty (MW)	40.37	39.27
Total Compressor duty (MW)	124	121
LNG Production rate (kg/h)	352,880	352,880
Heating Value (kJ/kg)	49,648	49,648
Specific power (HP/mmBtu)	10.33	9.78

From the composite of curves in the warm bundle shows that after the optimization of the distance between the hot curve and cold curve become closer, it indicates that the heat transfer reaches optimum condition. By optimizing the operating variable, the compressor duty and specific power become lower and the suction temperature of MR compressor still meet the limitation. In addition, for heat exchangers area, the UA value is still lower than its design.

Table 5. Comparison UA Heat Exchanger Before and After Optimization

Description	Before	After	Design
UA MR intercooler (MW/^oC)	1.3	1.1	1.49
UA MR aftercooler (MW/^oC)	2.0	2.1	2.29
UA C_3 *desuperheater* (MW/^oC)	0.626	0.632	0.91
UA C_3 *condenser* (MW/^oC)	15.69	20.03	20.03
UA Warm Bundle (MW/^oC)	19	21	
UA Cold Bundle (MW/^oC)	2.7	2.9	

From the optimization, some of operating variables need to be re-adjusted for achieving the optimum condition when processing the leaner gas. The following is comparison of operating variable before and after optimization:

Table 6. Comparison of Operating Variable Before and After Optimization

Operating Variable	Before	After
C3 condensing Pressure (kg/cm^{2}a)	14.24	12.73
MR Flow rate (kmol/h)	33,214	33,700
Evaporating Pressure of MR (kg/cm^{2}a)	4	4
MR composition (% mol)		
Nitrogen	3.3	3.7
Methane	46	47.2
Ethane	40	39.6
Propane	10.7	9.5

The optimization indicates the existing equipment is still capable to liquefy the leaner gas with higher specific power. But, it neeed re-adjustment of the operating variables refer to the optimization result.

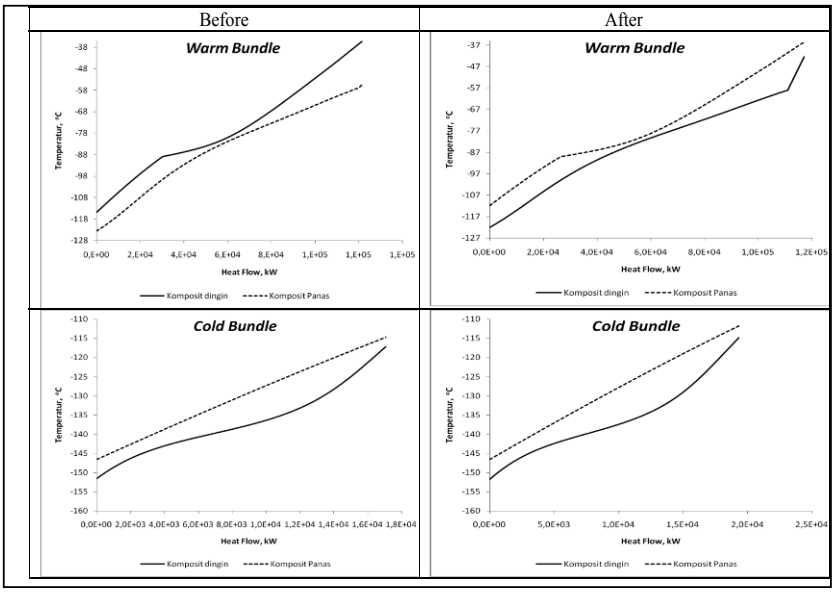

Figure 2. Comparison of Compoite Curve Before and After Optimization

4. Conclusions

The evaluation shows that leaner feed gas will results in higher compressor's load and the specific power. Meanwhile, potential obstacle will be the temperature of suction compressor. Optimizing of the operating variables can overcome the potential obstacle, and it also will reduce the compressor's load and the specific power.

References

Aspelund, A., Gundersen,T., Myklebust J., Nowak, M.P. dan Tomasgard, A. (2010). An optimization-simulation model for a simple LNG process. *Computers & Chemical Engineering* ***34***(10): 1606-1617.

Aspentech (2008), "Aspen HYSYS – Unit Operations Guide", edisi 7, Aspentech Technology, Burlington

Campbell, John M. (2004), "Gas Conditioning and Processing- Volume 2", edisi 8, Campbell Petroleum Series, Norman

Forsthoffer, W.E. (2008), "Principless of Rotating Equipment- Volume 1", edisi 3, Elsevier

Gao, T., Lin, W., GU, A., & GU, M. (2009). Optimization of coalbed methane liquefaction process adopting mixed refrigerant cycle with propane pre-cooling. *Journal of Chemical Engineering Japan*, 42, 893-901.

Hatcher, P., KhalilpourR., dan Abbas, Ali. (2012). Optimisation of LNG mixed-refrigerant processes considering operation and design objectives. *Computers & Chemical Engineering* **41**(0): 123-133.

Jenny Zhang, T. S., Tonny Tarrant dan Foster Wheeler (2012). Foster Wheeler Outlines its Latest Process for Handling Feed Gas for the Production of LNG. *LNG Journal* (May 2012): 1-11.

Jensen, J.B., & Skogestad, S, (2009a). "Single-cycle mixed fluid LNG process – Part I : Optimal design. In G. V. R. Reklaitis, H. E. Alfadala, & M.M. El-Halwagi (Eds.)", 1st Annual gas processing symposium, Qatar; Elsevier.

Jensen, J.B., & Skogestad, S, (2009a). Single-cycle mixed fluid LNG process – Part II : Optimal operation. In G. V. R. Reklaitis, H. E. Alfadala, & M.M. El-Halwagi (Eds.), *1st Annual gas processing symposium*, Qatar; Elsevier

Lee, G.C, Smith, R., dan Zhu, X, X. (2002). Optimal Synthesis of Mixed Refrigerant system for Low Temperature Processes. *Industrial & Engineering Chemistry Research,* 41, 5016-5028

Spilsbury, C., Liu,Y.N., Petrowski, J., Kennington, W., (2006), " Evolution of Liquefaction Technology for today's LNG business", 7° Jurnees Scientifiques et Techniques

Author Index

T